JANUARY 2008
Volume 19, Number 1

© *Copyright 2008 by the American Chemical Society*

Bioconjugate Chemistry

Editorial: What's New

The Chemistry of Targeting

This is the first of twelve issues of *Bioconjugate Chemistry* for 2008, a doubling of the print frequency. The change is mainly symbolic, but the underlying scientific progress is notable. One aspect of bioconjugate chemistry that has come into focus in recent years, which might be called the chemistry of targeting, has pervasively entered mainstream research in biology and medicine. Papers in this and recent issues of the journal give an idea of how it works in practice. Of course, the chemistry must come before the targeting, and there is plenty of chemistry. For example, synthetic peptides with target-binding properties, discovered by library screening, can be prepared with artificial components for conjugation to proteins (*1*). Synthetic reagents can be incorporated into natural proteins by ligation (*2*), and library-selected peptides with interesting new reactivity for conjugation to synthetic reagents can be cloned into proteins (*3*). Designing a nucleophilic affinity label to replace an electrophilic one can use an expressed protein to advantage and change the parameters of targeting (*4*), and a new fluorescent conjugate traces the intracellular targets of an electrophilic drug (*5*).

Then, the challenge of making new molecules that work *in vivo* begins. How can we add the properties of signal generation or therapeutic activity to a structure that provides affinity for particular cell types, and endow the product with the requisite biological behavior required for specific accumulation in the target? Here is an opportunity for creative thinking, especially when the goal is to deliver a payload to sites in the interior of a cell. The approach depends on the task. Cell-penetrating peptides are developing into reliable tools for intracellular targeting (*6*). Polymeric assemblies for nonviral gene delivery show promise (*7*), and quantum dots provide an interesting platform for siRNA (*8*). Delivery of proteins to cellular targets involves different strategies (*9*), as does protein-mediated delivery of small molecules (*10*).

Alongside this activity is new work related to vaccines (*11*), to highly sensitive RNA detection (*12*), and to the design of lipophilic prodrugs (*13*). And of course there are nanoparticle bioconjugates beyond those mentioned above, aimed at preparing ordered assemblies of biomolecules (*14*), liposomes guided by engineered proteins (*15*), and nanorod bioconjugates for intracellular Raman detection (*16*). Enzymatic biotinylation of DNA, followed by cross-linking with streptavidin, can lead to the stable formation of complex new synthetic nanostructures (*17*). These are only a few recent examples of bioconjugate chemistry published in the journal. Space restrictions do not allow a fuller account here; we invite you to see for yourself. As time goes forward, I believe we will see more emphasis on the construction of large, complex, multifunctional particles (*18*); clever chemistry and biology to specifically fuse biological molecules to nonbiological partners (*19*); better ways to target drugs and probes *in vivo* (*20*); and no doubt some unexpected developments in this always surprising field.

Thanks to Our Reviewers

It is a pleasure to acknowledge the contributions of the reviewers of manuscripts submitted in 2007 for publication in *Bioconjugate Chemistry*. Their unselfish service has been essential in the shaping of the 18th volume of the journal. The scientific community is fortunate that its members are willing to share their time and specialized knowledge in this way. The reviewers are listed on the following pages.

Claude F. Meares
Editor-in-Chief

10.1021/bc700467w CCC: $40.75 © 2008 American Chemical Society
Published on Web 01/16/2008

LITERATURE CITED

(1) Romanini, D., and Francis, M. B. Attachment of peptide building blocks to proteins through tyrosine bioconjugation. *Bioconjugate Chem.*,[Online early access] DOI: 10.1021/bc700231v. Published online December 11, 2007.

(2) Kalia, J., Abbott, N. L., and Raines, R. T. (2007) General method for site-specific protein immobilization by staudinger ligation. *Bioconjugate Chem. 18*, 1064–1069.

(3) Tanaka, F., Fuller, R., Asawapornmongkol, L., Warsinke, A., Gobuty, S., and Barbas, C. F. (2007) Development of a small peptide tag for covalent labeling of proteins. *Bioconjugate Chem. 18*, 1318–1324.

(4) Miao, Z., McCoy, M. R., Singh, D. D., Barrios, B., Hsu, O. L., Cheal, S. M., and Meares, C. F. Cysteinylated protein as reactive disulfide: an alternative route to affinity labeling. *Bioconjugate Chem.*,[Online early access] DOI: 10.1021/bc700330j. Published online December 7, 2007.

(5) Barnes, K. R., Blois, J., Smith, A., Yuan, H., Reynolds, F., Weissleder, R., Cantley, L. C., and Josephson, L. Fate of a bioactive fluorescent wortmannin derivative in cells. *Bioconjugate Chem.*,[Online early access] DOI: 10.1021/bc7002204. Published online November 8, 2007.

(6) Myrberg, H., Zhang, L., Mäe, M., and Langel, U. Design of a tumor-homing cell-penetrating peptide. *Bioconjugate Chem.*,[Online early access] DOI: 10.1021/bc0701139. Published online November 15, 2007.

(7) Germershaus, O., Neu, M., Behe, M., and Kissel, T. HER2 targeted polyplexes: the effect of polyplex composition and conjugation chemistry on in vitro and in vivo characteristics. *Bioconjugate Chem.*,[Online early access] DOI: 10.1021/bc700311n. Published online November 23, 2007.

(8) Derfus, A. M., Chen, A. A., Min, D. H., Ruoslahti, E., and Bhatia, S. N. (2007) Targeted quantum dot conjugates for siRNA delivery. *Bioconjugate Chem. 18*, 1391–1396.

(9) Bell, S. J., Fam, C. M., Chlipala, E. A., Carlson, S. J., Lee, J. I., Rosendahl, M. S., Doherty, D. H., and Cox, G. N. Enhanced circulating half-life and antitumor activity of a site-specific pegylated interferon-α protein therapeutic. *Bioconjugate Chem.* [Online early access] DOI: 10.1021/bc070131q. Published online November 20, 2007.

(10) Hollander, I., Kunz, A., and Hamann, P. R. Selection of reaction additives used in the preparation of monomeric antibody-calicheamicin conjugates. *Bioconjugate Chem.* [Online early access] DOI: 10.1021/bc700321z. Published online November 10, 2007.

(11) Nahas, D. D., Palladino, J. S., Joyce, J. G., and Hepler, R. W. Amino acid analysis of peptide loading ratios in conjugate vaccines: a comparison of direct electrochemical detection and 6-aminoquinolyl-*N*-hydroxysuccinimidyl carbamate pre-column derivatization methods. *Bioconjugate Chem.* [Online early access] DOI: 10.1021/bc700232z. Published online December 12, 2007.

(12) Walls, Z. F., and Gambhir, S. S. BRET-based method for detection of specific RNA species. *Bioconjugate Chem.* [Online early access] DOI: 10.1021/bc700278n. Published online December 12, 2007.

(13) Pignatello, R., Pantò, V., Salmaso, S., Bersani, S., Pistarà, V., Kepe, V., Barrio, J. R., and Puglisi, G. Flurbiprofen derivatives in Alzheimer's disease: synthesis, pharmacokinetic and biological assessment of lipoamino acid prodrugs. *Bioconjugate Chem.* [Online early access] DOI: 10.1021/bc700312y. Published online December 12, 2007.

(14) Matsuura, S. I., Itoh, T., Ishii, R., Sakaguchi, K., Tsunoda, T., Hanaoka, T., and Mizukami, F. The ensemble of heteroproteins in inorganic nanochannels. *Bioconjugate Chem.* [Online early access] DOI: 10.1021/bc700340e. Published online November 30, 2007.

(15) Messerschmidt, S. K., Kolbe, A., M∂uller, D., Knoll, M., Pleiss, J., and Kontermann, zfn > R. E. Novel single-chain Fv′ formats for the generation of immunoliposomes by site-directed coupling. *Bioconjugate Chem.* [Online early access] DOI: 10.1021/bc700349k. Published online November 8, 2007.

(16) Oyelere, A. K., Chen, P. C., Huang, X., El-Sayed, I. H., and El-Sayed, M. A. (2007) Peptide-conjugated gold nanorods for nuclear targeting. *Bioconjugate Chem. 18*, 1490–1497.

(17) Wilkinson, S., Diechtierow, M., Estabrook, R. A., Schmidt, F., Lugowski, M., Weinhold, E., and Reich, N. O. Molecular scale architecture: engineered three- and four-way junctions. *Bioconjugate Chem.*,[Online early access] DOI: 10.1021/bc700270k. Published online December 11, 2007.

(18) Oba, M., Fukushima, S., Kanayama, N., Aoyagi, K., Nishiyama, N., Koyama, H., and Kataoka, K. (2007) Cyclic RGD peptide-conjugated polyplex micelles as a targetable gene delivery system directed to cells possessing $\alpha_v\beta_3$ and $\alpha_v\beta_5$ integrins. *Bioconjugate Chem. 18*, 1415–1423.

(19) Parthasarathy, R., Subramanian, S., and Boder, E. T. (2007) Sortase A as a novel molecular "stapler" for sequence-specific protein conjugation. *Bioconjugate Chem. 18*, 469–476.

(20) Wang, D., Miller, S. C., Shlyakhtenko, L. S., Portillo, A. M., Liu, X. M., Papangkorn, K., Kopecková, P., Lyubchenko, Y., Higuchi, W. I., and Kopecek, J. (2007) Osteotropic peptide that differentiates functional domains of the skeleton. *Bioconjugate Chem. 18*, 1375–1378.

Reviewers for 2007

Seetharama Acharya
Samuel Achilefu
Toshihiro Akaike
Takeshi Akasaka
Kazunari Akiyoshi
Terry Allen
Stephen Alley
Julio Alvarez
Jane Anastassopoulou
Daniel Anderson
Carolyn Anderson
David Andreu
Peter Antal
Christophe Antczak
Ichio Aoki
Yasuhiro Aoyama
Yasushi Arano
Hidetoshi Arima
Bruce Armitage
Luis Arnaut
Ulrich Arnold
Erik Arstad
Hiroyuki Asanuma
Recep Avci
You Han Bae
Sandor Bajusz
James Baker
Milan Balaz
Suki Bansal
Giovanna Barbarella
Sailen Barik
Philippe Barthelemy
Jacqueline Barton
Serge Beaucage
Craig Beeson
Martin Behe
Jean-Paul Behr
Dennis Benjamin
David Benson
Sangeeta Bhatia
Anna Bielinska
Gary Bignami
Otto Boerman
Alexei Bogdanov
Bernard Boitrel
Ester Boix
Sylvia Bosze
Alexandre Boutorine
Luisa Bracci
Tibor Braun
David Brautigan
Martin Brechbiel
Vladimir Bregadze
Kevin Brindle
Timothy Bugg
Thomas Bugge
Kevin Burgess
Patrick Burke
Paolo Caliceti
Amin Cao
Paul Carter
Elliott Chaikof
Carole Chaix
Ken Chang
Young-Tae Chang
Dominique Charmot
A. Charrier
Arabinda Chaudhuri
Xiaoyuan Chen
Yu Chen
Jianjun Cheng
Kenneth Christensen
Bong Hyun Chung
Mary Cloninger
Wayne Cody
Seth Cohen
John Collins
George Conder
Eain Conford
Umberto Costantino
Patrick Couvreur
James Cowan
Gabriella Csik
Ekaterina Dadachova
Johanthan Dattelbaum
Mark Davis
Philip Dawson
Jean-Luc Decout
Clemens Decristoforo
Marion DeJong
Gerard Deleris
Antony D'Emanuele
Sally DeNardo
Maria Derosa
Svetlana Doronina
Trevor Douglas
Francis D'Sousa
Adriano Duatti
Stefan Dubel
Gene Dubowchik
Yves Dufrene
Pascal Dumy
Petar Dvornic
Allen Ebens
Alex Eberle
Philip Elsinga
Conan Fee
Arthur Felix
Gregg Fields
David Filpula
M. G. Finn
Valery Fokin
Andreas Frey
Wolfgang Fritzsche
Darin Furgeson
Tsutomu Furuzono
Shiroh Futaki
Xiaohu Gao
Jean Gariepy
Indraneel Ghosh
Jose Giner
Richard Goodman
Kurt Gothelf
David Grainger
Anna Grandas
Kai Griebenow
Herman Gruber
Gilles Guichard
Ajay Gupta
Michael Hamblin
Robert Haner
Atsushi Harada
Gilad Haran
Hideyoshi Harashima
Frederick Haselton
Roland Haubner
Craig Hawker
Frederic Heitz
Wim. Hennink
Greg Hermanson
Kiyotaka Hitomi
Donald Hnatowich
Mathias Hoehn
Timothy Hoffman
Daniel Horak
Jeanne Haushalter
Thomas Holstein
Fredrik Hook
Jari Hovinen
Ferenc Hudecz
Rodica-Mariana Ion
Marcos Intaglietta
T. Ishida
Yoshihiro Ito
Shinobu Itoh
Yasuhiko Iwasaki
Hiroo Iwata
Bela Ivan
Hieronim Jakubowski
Lee Josephson
Rudolph Juliano
Guenther Jung
H. Karnes
Uray Katalin
Kazunori Kataoka
Yoshiki Katayama
John Katzenellenbogen
Hiroyoshi Kawakami
Shigeru Kawakami
M. Kawashita
Christine Keating
Kimberly Kelly
David Kessel
Horst Kessler
Fabian Kiessling
Akihiko Kikuchi
SungWan Kim
William Kinney
Kent Kirshenbaum
Akio Kishida
Eva Kiss
Thomas Kissel
Alexei Kisselev
Rene Kizek
Toni Kline
Harm-Anton Klok
Hisataka Kobayashi
Kazukiyo Kobayashi
Kazuo Kobayashi
Hisashi Koga
Kentara Kogure
Laszlo Kohidal
Robert Kok
Makoto Komiyama
Akihiko Kondo
Kenji Kono
Jindrich Kopecek
Lajos Kovacs
Heinz-Bernhard Kraatz
Felix Kratz
James Kronauge
Glen Kwon
Ick Kwon
Vinod Labhasetwar
Pirjo Laakkonen
Kit Lam
Robert Langer
Jorg Langowski
Bernard Lebleu
Doo Sung Lee
Robert Lee
Sang-Bok Lee
Yan Lee
Polly Leung
Raphael Levy
Jason Lewis
Mike Lewis
Yadong Li
Karl Linden
David Link
Shuang Liu
Timothy Long
Harri Lonnberg
Zheng-Rong Lu
Robert Lyon
Robert Mach
Helmut Maecke
Hiroshi Maeda

Mizuo Maeda
Y. Magata
Michele Maggini
Yoshi Maitani
Zsuzsa Majer
Giovanna Mancini
Chengde Mao
Mauro Marastoni
Atsushi Maruyama
Kazuo Maruyama
Ralph Mason
Takehisa Matsuda
Hiroshi Matsui
William McBride
Jason McCarthy
Charlotte McDonough
Thomas Meade
Claude Meares
Igor Medintz
Morten Meldal
Oleg Melnyk
Christine Menager
Fredric Menger
Andre Merbach
Damon Meyer
Geerd Meyer
Gabor Mezo
Nils Metzler-Nolte
Tamara Minko
Anna Moore
Milan Mrksich
Tom Muir
Jogeshwar Mukherjee
Catherine Murphy
William Murphy
Igor Nabiev
Takeshi Nagasaki
Yukio Nagasaki
Shinsaku Nakagawa
Hiroyuki Nakamura
Jun Nakanishi
Mamoru Nakanishi
Arun Nandi
Dario Neri
Placido Neri
Nasri Nesnas
Martin Newcomb
Christof Niemeyer
Takuro Niidome
Yoshihior Nishida
Makiya Nishikawa
Victoria Nogues
Yuichi Ohya
Akimitsu Okamoto
Nicole Okeley
Naoto Oku
Sean O'Malley
David Oupicky
Daniel Pack
Mark Pagel
Andre Palmer
Francesco Pampaloni
Ravindra Pandey
Roberto Paolesse
Anna Papini
Wolfgang Parak
In-Kyu Park
Jong-sang Park
Kinam Park
Tae Gwan Park
David Parker
Anil Patri
Carlo Pedone
Xiaojun Peng
Andrej Petri
Lucia Pohl
Glenn Prestwich
David Putnam
Eva Rajnavolgyi
T. Ramqvist
Tariq Rana
Jianghong Rao
Ken Raymond
Francesca Reig
Raymond Reilly
Theresa Reineke
Jean-Serge Remy
Richard Renneberg
Alexander Ribbe
Kevin Rice
Steve Roffler
Anthony Romieu
Keith Rose
Vincent Rotello
Jayanta Roy
Yasuyuki Sadzuka
Ahmad Safavy
Cyrus Safinya
Hideo Saji
Kengo Sakaguchi
Shinji Sakuma
Bruno Samori
Yogesh Sanghvi
Xavier Santarelli
Angela Sastre
Toshinori Sato
A. G. Schatzlein
David Scheinberg
Cara-Lynne Schengrund
Roger Schibili
Francis Schuber
Katarina Schwarzerova
Paolo Scrimin
Frank Seela
V. Sefton
Hans Senn
Peter Senter
Takeshi Serizawa
Doron Shabat
Adam Shapiro
Frances Sharom
Wei-Chiang Shen
Dean Sherry
Kiyotaka Shiba
Injae Shin
Sepp Siefert
Daniel Silva
G. Silva
Robert Sharkey
Lonnie Shea
David Smith
Robert Spooner
Caroline Springer
Patrick Stayton
Yasuo Suda
Helga Suli-Vargha
Mike Sun
Shouheng Sun
Xue-Long Sun
Avadhesha Surolia
Ryo Suzuki
Sonke Svenson
Thomas Swihart
Frank Szoka
Yasuhiko Tabata
Maryam Tabrizian
Yoshinobu Takakura
Shinji Takeoka
Nagasaki Takeshi
Toshifumi Takeuchi
Eiichi Tamiya
Weihong Tan
Fujie Tanaka
Frederic Taran
Jack Taunton
Kai Temming
Dave Thompson
Paolo Ticilla
Louis Tiefenauer
David Tilley
Werner Tjarks
Brian Toki
Don Tomalia
Vladimir Torchilin
Alexei Touchkine
Pam Trail
Roger Tsien
Yasuo Tsutsumi
Ching Tung
Gerardo Turcatti
Karel Ulbrich
Hasan Uludag
Tadayuki Uno
Katalin Uray
Vladimir Uversky
Hiroshi Uyama
Ganesan Vaidynathan
Henry van Brocklin
Serve Van Callenbergh
Gooitzen van Dam
Johan Van Lier
Henk-Jan van Manen
Francesco Veronese
Graca Vicente
S. V. Vinogradov
Michael Vogeser
Albrecht von Arnim
Ernst Wagner
Lai-Xi Wang
Qian Wang
Colin Watts
Adam Wax
Ralph Weissleder
Michael Welch
Theodore Wensel
Sytske Welling-Wester
Hans-Juergen Wester
Shawn Wettig
Scott Wilbur
Meir Wilchek
Lon Wilson
Gayle Woloschak
Anna Wu
Hiroyasu Yamaguchi
Masayuki Yamamoto
Tetsuji Yamaoka
Ichiro Yamashita
Hao Yan
Victor Yang
Chen-Shen Yeh
Makoto Yoshimoto
Masayuki Yokoyama
Hua-Zhong Yu
Jaehoon Yu
Samuel Zalipsky
Arie Zask
Marina Zenkova
Gang Zheng
Qi-Huang Zheng
Bing Zu
Guy Zuber

BC700467W

COMMUNICATIONS

Porphyrinmaleimides: Towards Thiol Probes for Cysteine Residues in Proteins

Yihui Chen, Timothy Parr, Andrea E. Holmes,† and Koji Nakanishi*

Columbia University, Department of Chemistry, New York, New York 10027. Received July 17, 2007; Revised Manuscript Received September 21, 2007

Porphyrinmaleimides were synthesized and characterized. The thiol-containing amino acid L-cysteine reacted with 58% yield with these porphyrins to form bioconjugate adducts. The new thiol-active reagents were labeled cytoplasmic cysteine 140 and 316 in rhodopsin (Rh), a G protein coupled receptor (GPCR).

In order to gain further insight into conformational changes that occur upon light activation of the rhodopsin visual transduction cycle (*1, 2*), we needed a highly sensitive photoactive probe that absorbs in the visible light region. Thiol active–reactive dyes have been used for labeling biopolymers such as peptides, proteins, and oligonucleotides, and for demonstrating protein–nucleic acid interactions (*3–8*). Effective thiol labels include maleimides (*9*), halomethylketones, benzylic halides, and iodoacetamides (*10, 11*). Arrays of thiol-reactive agents are commercially available for studying conformational changes, topography, and interactions of proteins and membranes (*12*). Since thiol groups do not occur that frequently in proteins, these thiol-reactive agents can be introduced selectively and site-specifically.

In order to facilitate monitoring of the thiol probe reactions, sensitive assays using reagents that can be excited and absorb in the visible region are desirable. In the following, we describe the synthesis of a thiol-active porphyrin, a tetraphenylporphyrin maleimide (TPPM). Tetraarylporphyrins have high extinction coefficients, $\epsilon = 400\,000–500\,000$, and hence are highly sensitive. Their absorption in the visible region around $\lambda_{max} = 420$ nm, instead of in the UV region, results in favorable energy parameters in terms of stability of organic compounds, because visible radiation is lower in energy than UV radiation, thus expanding the scope to biological systems. Porphyrins have also been widely studied as sensitizers and are currently finding biomedical application in the treatment of malignant tumors (photodynamic therapy, PDT), plaque destruction, and psoriatic lesions, and more recently in the treatment of viral infections (*13–17*).

To our knowledge, there is no report of porphyrin containing thiol-reactive probes. Thus, we designed the porphyrin TPPM with a maleimide functional group to evaluate whether cysteine residues can be derivatized with these chromophores through thioether formation. Cysteine derivatization through thioether formation to the C-terminal can be utilized to attach fluorophores chemo- and regioselectively (*1, 2*). Of the ten Cys residues in Rh, only C140 and C316 can be derivatized, because the others are buried in the membrane, are present as disulfides, or are palmitoylated. C316 is more reactive than C140, and hence can be derivatized with high selectivity. A second porphyrin of different UV/fluorescent properties can then be linked to C140 with a large excess of the reagent. Modifications at these two positions are known not to interfere with formation of Rh photo intermediates or the interaction of Rh with the G protein.

TPPM 4 was synthesized by conventional condensation of benzaldehyde, pyrrole, and para-nitrobenzaldehyde, followed by reduction of the nitro group and subsequent derivatization of the amino moiety to the maleimide **TPPM 4** (Scheme 1). Compounds **1** and **2** were obtained according to literature procedures (*18, 19*). Porphyrin **2** was reacted with maleic anhydride to yield porphyrin **3** in 80% yield. Porphyrin **3** was converted to **TPPM 4** in 22% yield by reacting it with sodium acetate and acetic anhydride. We tested L-cysteine as an example to demonstrate that **TPPM 4** is reactive toward thiol bioconjugation. The cysteine bioconjugate **5** product was obtained by addition of L-cysteine to **TPPM 4** in DMSO (Scheme 1) at room temperature for 2 days.

TPPM 4 is soluble in nonpolar organic solvents. In order to attain water solubility under physiological conditions, we synthesized a 5,10,15,20-maleimido-tris-sulfonatophenyl porphyrin **TPPS 8** and its bioconjugate with cysteine **9** (Scheme 2).

Porphyrin **6** (Scheme 2) was obtained by treating porphyrin **2** with a large excess of concentrated sulfuric acid at 110 °C for 4 h followed by aqueous workup. The tris-sulfonated porphyrin was then converted to the ammonium salt by dissolution in excess concentrated ammonium hydroxide in 58% yield. **TPPS 8** and the L-cysteine bioconjugate **9** were obtained in 80% yield by procedures shown in Scheme 2.

Figure 1 summarizes porphyrins **4**, **8**, and **10** that were synthesized and reacted with L-cysteine. Metalloporphyrin **10** was synthesized because it is even more red-shifted than porphyrin **4** ($\lambda_{max} = 421$ nm in MeOH) and was obtained in quantitative yield by treatment of porphyrin **4** with zinc acetate. In order to determine the sensitivity of these porphyrins, we measured their extinction coefficients and fluorescence properties (Table 1). Porphyrin quantum yields are typically between 0.1% and 13% (*20, 21*). The data show that the porphyrins absorb in the visible region between 412 and 421 nm, with high extinction

* Corresponding author. Telephone 212-854-2169, fax 212-932-8273, e-mail: kn5@columbia.edu.

† Present address: Doane College, Chemistry Department, Crete, NE 68333.

10.1021/bc700267f CCC: $40.75 © 2008 American Chemical Society
Published on Web 12/08/2007

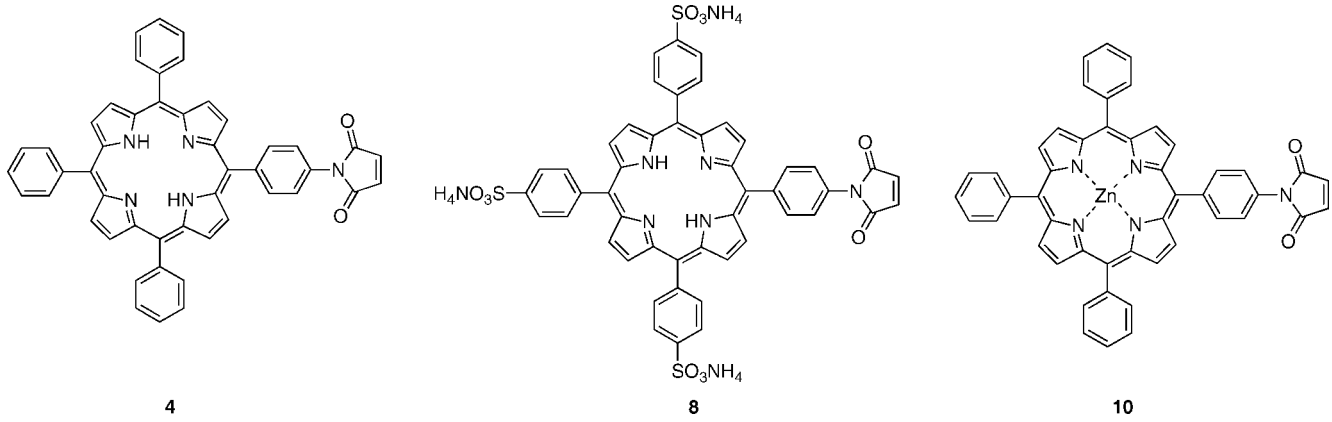

Figure 1. Porphyrins **4**, **8**, and **10** were reacted with L-cysteine and successfully formed the porphyrin cysteine conjugates via thioether formation.

Scheme 1. Synthesis of TPPM 4 and L-Cysteine Bioconjugate 5

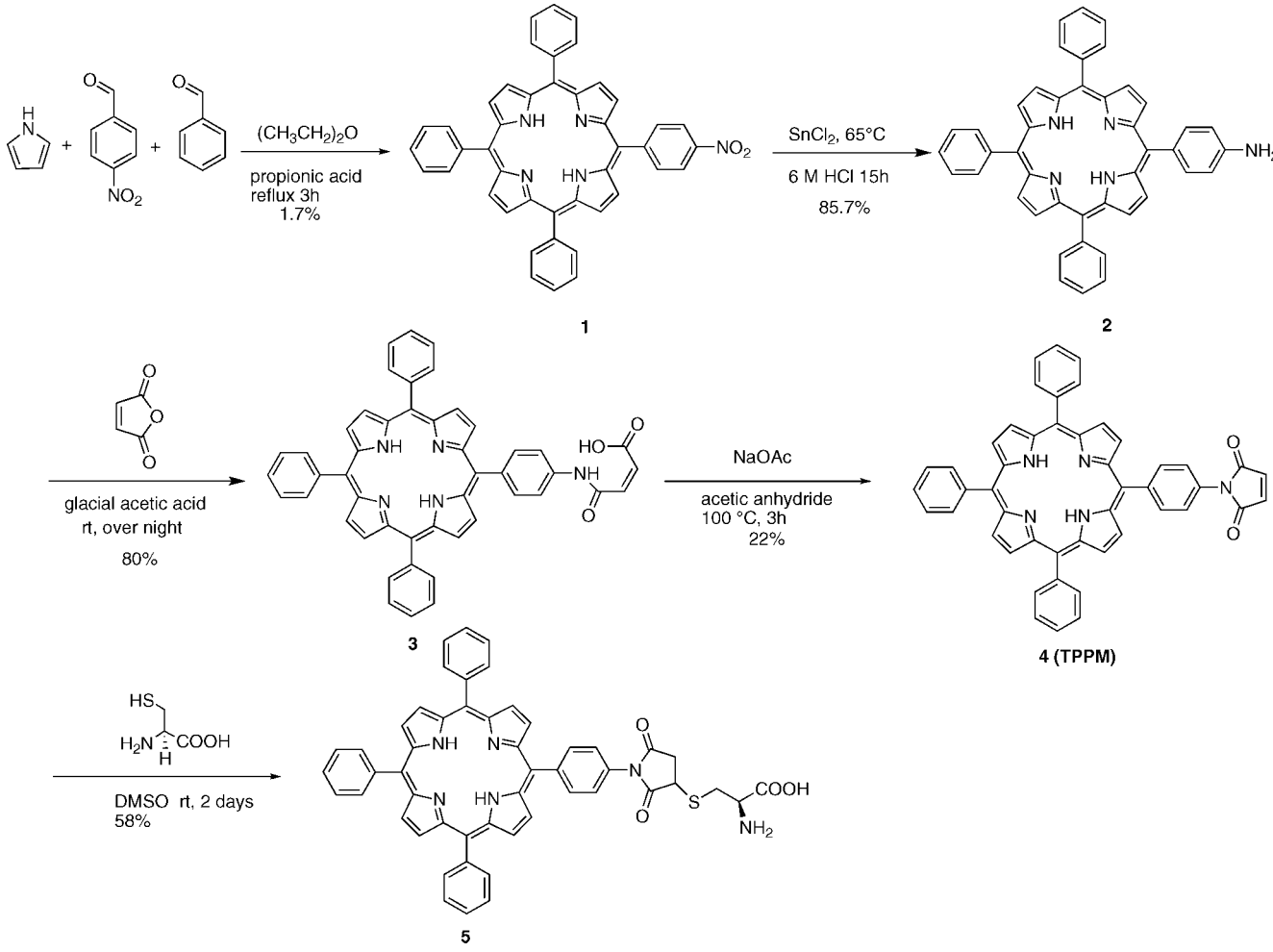

coefficients, fluorescence emissions at ≥600 nm, and reasonable quantum yields.

The UV–vis profile of **TPPM 4** is shown in Figure 2. In phosphate buffer, **TPPM 4** only shows shallow absorbance (red), which shows that TPPM had poor solubility in phosphate buffer and will only aggregate in this buffer. In contrast, in DMSO (black) and CHAPS[1] buffer [0.75% CHAPS and 10 mM Tris-HCl (pH 7.4)], the solubility of TPPM increased, and aggregation is less apparent as seen by the sharp and intense Soret bands at 420 nm (pink, blue, green, and black), $\epsilon = 180\,000$ at pH = 6.6, which is a good pH for the active state of rhodopsin-meta II. Porphyrins **8** and **10** showed similar characteristics. We also obtained UV–vis spectra of the cysteine bioconjugates **5**, its Zn(II) derivative, and the rhodopsin bioconjugate before and after bleaching. As seen in Figure 3 (left), the bioconjugation did not affect the spectroscopic properties of the porphyrins, as there were no notable absorbance changes from the precursors. Conjugation to rhodopsin in the dark shows the porphyrin peak at 420 nm and the rhodopsin

[1]Abbreviations: CHAPS, 3-[(3-cholamidopropyl)dimethylammonio]-propanesulfonic acid; MOPS, 3-(*N*-morpholino)propanesulfonic acid; ROS, rod outer segments; SDS-PAGE, sodium dodecyl sulfate polyacrylamide gel electrophoresis.

Scheme 2. Synthesis of a Water-Soluble TPPS 8 and the L-Cysteine Bioconjugate 9

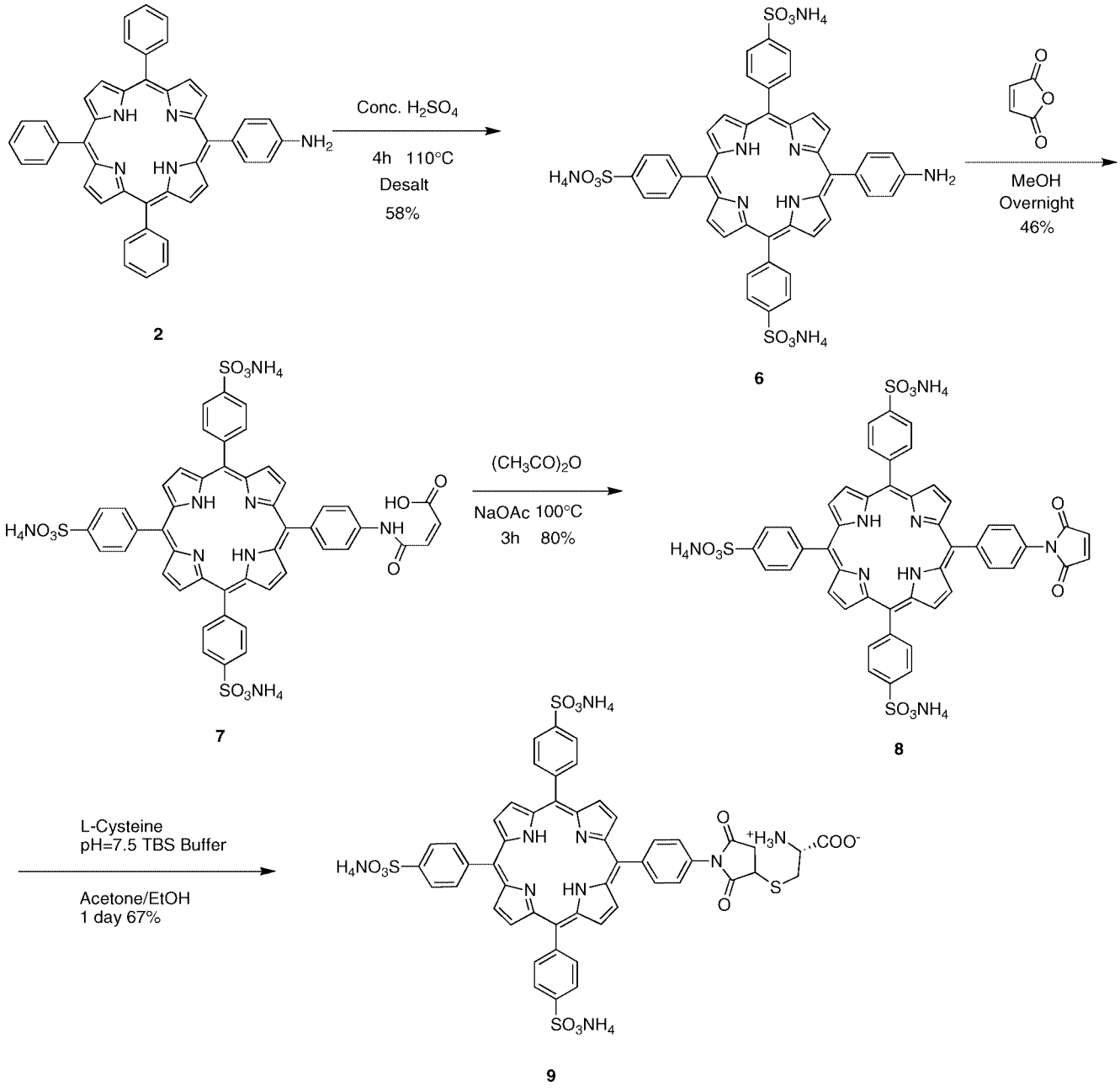

Table 1. UV Extinction Coefficient and Fluorescence Quantum Yields of the New Porphyrins

porphyrins	UV absorbance maximum (nm)	UV extinction coefficient (ϵ) cm^{-1}/M	fluorescence emission maximum (nm)	fluorescence quantum yield (φ) %
4 ($CHCl_3$)	418	532,000	647	5.8
8 (MeOH)	415	390,000	646	8.9
10 (MeOH)	421	329,000	601	6.0

peak at 495 nm. After bleaching with hydroxylamine, the rhodopsin transition disappears, and retinal oxime is produced at 365 nm. The porphyrin transition was not affected.

In order to demonstrate whether the new porphyrin probes can be used for the labeling of cysteine residues in rhodopsin, we cleaved rhodopsin after the porphyrin labeling into two fragments F1 and F2 with thermolysin. Fragment F1 contains cysteine residue 140 and F2 contains cysteine residue 316, both located on the cytoplasmic side of the protein. Using SDS-PAGE of 15% acrylamide gel, as shown in Figure 4, we monitored

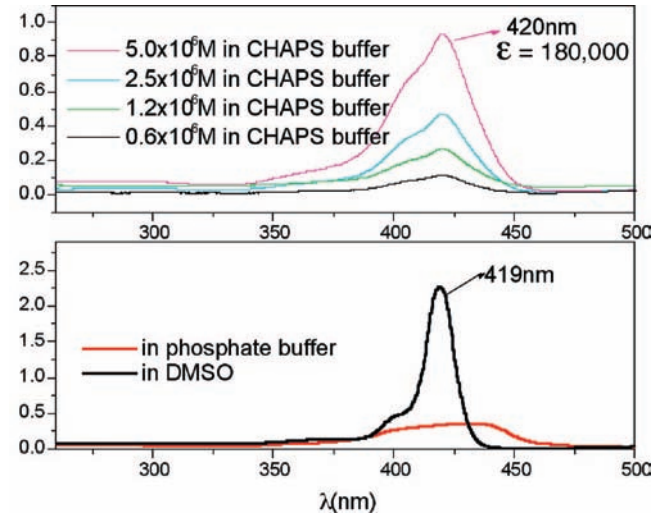

Figure 2. UV profile of **TPPM 4** in CHAPS, phosphate buffer, and DMSO.

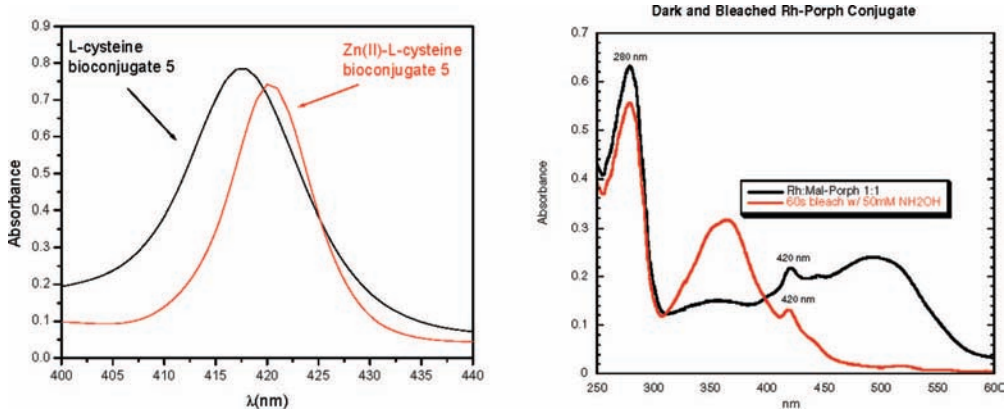

Figure 3. Left: UV–vis spectra of cysteine bioconjugate **5** and its Zn(II) derivative indicating a bathochromatic shift. Right: Dark and bleached Rh–porphyrin conjugate.

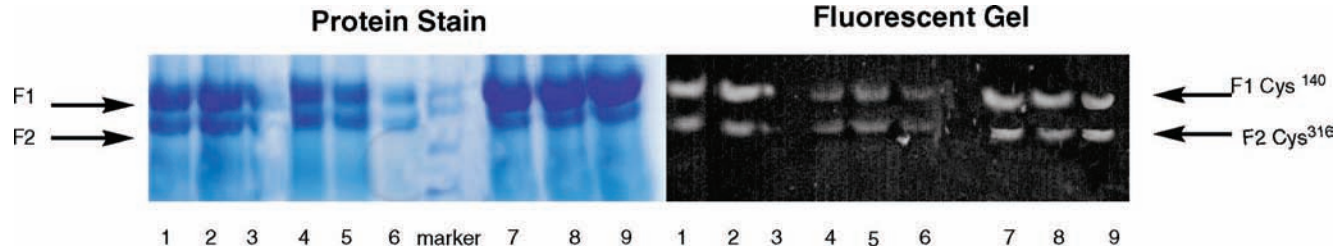

Figure 4. SDS-PAGE of the rhodopsin–porphyrin complexes with porphyrins **4**, **10**, and **8** in lanes 1–3, 4–6, and 7–10, respectively. The thermolytic F1 fragment shows labeling on Cys^{140}, whereas the F2 fragment shows labeling on Cys^{316}. The excitation wavelengths were 390–450 nm with a maximum at 435 nm. No bleaching of rhodopsin was observed in the conjugates.

the fluorescence emitted by the porphyrin-modified rhodopsin fragments. Since plain rhodopsin does not have porphyrin fluorescence, only the porphyrin-modified parts showed emission. Furthermore, SDS-PAGE determined whether both cysteine residues were labeled by the porphyrins, because both modified cysteine residue 140 and cysteine 316 will show fluorescence as labeled. Thus, rod outer segment (ROS) membranes containing about 3 mg of rhodopsin were suspended in 500 μL of 50 mM sodium phosphate buffer (pH 7.0). To the ROS suspension, 2.0 equiv of porphyrin solution (10 μM in DMSO) was added and reacted at room temperature for 2 days, then terminated with 30 μL of 55 mM glutathione. The reaction mixture was incubated in an ice bath for 30 min, then washed with 4 M urea once and twice with TRIS buffer [5 mM Tris–HCl and 0.5 mM $MgCl_2$ (pH 7.2)], and twice with ROS buffer [10 mM MOPS, 30 mM NaCl, 60 mM KCl, and 2 mM $MgCl_2$ 9 (pH 7.5)]. The porphyrin–rhodopsin complex was suspended in 10 mM Tris–HCl (pH 7.4) containing 5 mM $CaCl_2$ and 0.04 mg/mL thermolysin. The complexes were digested for 90 min at 37 °C, and then 5 μL of 50 mM EDTA was added. The SDS-PAGE in Figure 3 demonstrates successful labeling of both rhodopsin–cysteine residues with porphyrins **4**, **8**, and **10** as seen by the porphyrin fluorescence emissions of both F1 and F2.

We conclude that maleimide-containing porphryins **4**, **8**, and **10** have favorable spectroscopic parameters such as strong absorbances in the visible region, fluorescence emissions at long wavelengths, and high extinction coefficients. All the probes readily react with L-cysteine in quantitative yields. These characteristics could make these new porphyrins excellent candidates for protein labeling of specific cysteine residues, e.g., cysteines 140 and 316 on the cytoplasmic side of the visual pigment rhodopsin as seen by SDS-PAGE. Covalent attachment of prophyrins to rhodopsin would serve two purposes: 1. Porphyrins can be used as sensors to probe conformational changes of the high-energy intermediates, namely, photo, batho, lumi, meta-I, and meta-II rhodopsin by circular dichroism (CD). This technique would add an additional red-shifted spectroscopic region and could improve the sensitivity of the chiroptical signal due to the large extinction coefficients of porphyrins. 2. Rhodopsin is a prototypical example of a GPCR and has been well-characterized, especially in terms of the visual transduction pathway. Thus, rhodopsin could serve as a model for other GCPRs that yet have to be characterized and studied. Conformational studies of Rh–porphyrin conjugates are underway.

ACKNOWLEDGMENT

We acknowledge support from NIH grants GM 36564 (to K.N.) and EY 013933 (to A.E.H.). We also extend our thanks to Ms. Yimin Xu for SDS PAGE gel analysis.

Supporting Information Available: Materials and general procedures. This material is available free of charge via the Internet at http://pubs.acs.org.

LITERATURE CITED

(1) Imamoto, Y., Kataoka, M., Tokunaga, F., and Palczewski, K. (2000) Light-induced conformational changes of rhodopsin probed by fluorescent Alexa594 immobilized on the cytoplasmic surface. *Biochemistry 39*, 15225–15233.

(2) Mielke, T., Alexiev, U., Glasel, M., Otto, H., and Heyn, M. P. (2002) Light-induced changes in the structure and accessibility of the cytoplasmic loops of rhodopsin in the activated M_{II} state. *Biochemistry 41*, 7875–7884.

(3) Johnson, A. E., Adkins, H. J., Matthews, E. A., and Cantor, C. R. (1982) Distance moved by transfer RNA during translocation from the A site to the P site on the ribosome. *J. Mol. Biol. 156*, 113–40.

(4) Abrahamson, J. K., Laue, T. M., Miller, D. L., and Johnson, A. E. (1985) Direct determination of the association constant between elongation factor Tu·GTP and aminoacyl-tRNA using fluorescence. *Biochemistry 24*, 692–700.

(5) Gorman, J. J. (1987) Fluorescent labeling of cysteinyl residues to facilitate electrophoretic isolation of proteins suitable for amino-terminal sequence analysis. *Anal. Biochem. 160*, 376–387.

(6) Ansorge, W., Sproat, B., Stegemann, J., Schwager, C., and Zenke, M. (1987) Automated DNA sequencing: ultrasensitive detection of fluorescent bands during electrophoresis. *Nucleic Acids Res. 15*, 4593–4602.

(7) Ansorge, W., Rosenthal, A., Sproat, B., Schwager, C., Stegemann, J., and Voss, H. (1988) Non-radioactive automated sequencing of oligonucleotides by chemical degradation. *Nucleic Acids Res. 16*, 2203–2206.

(8) Rusinova, E., Tretyachenko-Ladokhina, V., Vele, O. E., Senear, D. F., and Alexander Ross, J. B. (2002) Alexa and OR Green dyes as fluorescence anisotropy probes for measuring protein-protein and protein-nucleic acid interactions. *Anal. Biochem. 308*, 18–25.

(9) Ishii, Y., and Lehrer, S. S. (1986) Effects of the state of the succinimido-ring on the fluorescence and structural properties of pyrene maleimide-labeled α,α-tropomyosin. *Biophys. J. 50*, 75–80.

(10) Musci, G., and Berliner, L. J. (1986) Intramolecular distance measurements in α-lactalbumin. *Biochemistry 25*, 4887–4891.

(11) Chung, D. G., and Lewis, P. N. (1986) Internal architecture of the core nucleosome: fluorescence energy transfer studies at methionine-84 of histone H4. *Biochemistry 25*, 5036–5042.

(12) Wu, P., Hogrebe, P., and Grainger, D. W. (2006) DNA and protein microarray printing on silicon nitride waveguide surfaces. *Biosens. Bioelectron. 21*, 1252–1263.

(13) Sultan, N. A. M., Maiya, B. G., and Swamy, M. J. (2004) Thermodynamic analysis of porphyrin binding to Momordica charantia (bitter gourd) lectin. *Eur. J. Biochem. 271*, 3274–3282.

(14) Hamblin, M. R., and Luke Newman, E. (1994) On the mechanism of the tumor-localizing effect in photodynamic therapy. *J. Photochem. Photobiol., B: Biol. 23*, 3–8.

(15) Fritsch, C., Lehmann, P., Stahl, W., Schulte, K. W., Blohm, E., Lang, K., Sies, H., and Ruzicka, T. (1999) Optimum porphyrin accumulation in epithelial skin tumors and psoriatic lesions after topical application of delta-aminolaevulinic acid. *Br. J. Cancer 79*, 1603–1608.

(16) Casteel, M. J., Jayaraj, K., Gold, A., Ball, L. M., and Sobsey, M. D. (2004) Photoinactivation of hepatitis A virus by synthetic porphyrins. *Photochem. Photobiol. 80*, 294–300.

(17) Sun, R. W.-Y., Yu, W.-Y., Sun, H., and Che, C.-M. (2004) In vitro inhibition of human immunodeficiency virus type-1 (HIV-1) reverse transcriptase by Gold(III) porphyrins. *ChemBioChem 5*, 1293–1298.

(18) Ding, L., Casas, C., Etemad-Moghadam, G., Meunier, B., and Cros, S. (1990) Synthesis of water-soluble, cationic functionalized metalloporphyrins having a cytotoxic activity. *New J. Chem. 14*, 421–31.

(19) Li, F., Kexin, Y., Tyhonas, J. S., MacCrum, K. A., and Lindsey, J. S. (1997) Beneficial effects of salts on an acid-catalyzed condensation leading to porphyrin formation. *Tetrahedron 53*, 12339–12360.

(20) Gottfried, V., Peled, D., Winkelman, J. W., and Kimel, S. (1988) Photosensitizers in organized media: singlet oxygen production and spectral properties. *Photochem. Photobiol. 48*, 157–63.

(21) Scalise, I., and Durantini, E. N. (2002) Synthesis and photodynamic activity of metallo 5-(4-carboxyphenyl)-10,15,20-tris(4-methylphenyl) porphyrins, *Sixth International Electronic Conference on Synthetic Organic Chemistry, C007*.

BC700267F

The Ensemble of Hetero-Proteins in Inorganic Nanochannels

Shun-ichi Matsuura,*,† Tetsuji Itoh,† Ryo Ishii,† Kengo Sakaguchi,‡ Tatsuo Tsunoda,† Takaaki Hanaoka,† and Fujio Mizukami†

Research Center for Compact Chemical Process, National Institute of Advanced Industrial Science and Technology (AIST), Nigatake 4-2-1, Miyagino-ku, Sendai 983-8551, Japan, and Department of Applied Biological Science, Tokyo University of Science, Yamazaki 2641, Noda, Chiba 278-8510, Japan. Received July 4, 2007; Revised Manuscript Received November 1, 2007

The assembly and proper alignment of two heterofluorescent proteins (sGFP and DsRed) in the mesoporous channels of ethanol-treated FSM6.2 (a folded-sheet mesoporous material with a pore diameter of 6.2 nm) was confirmed using a fluorescence resonance energy transfer (FRET) technique. The sGFP−DsRed−FSM6.2 conjugate showed a large decrease in the emission of donor (sGFP) fluorescence, indicating that the conjugate functions as an energy transfer system through the combination of the two heteroproteins, due to the successful encapsulation of the sGFP−DsRed pairs in the mesopores. Fluorescence spectral analysis demonstrated that the proteins were highly dispersed and homogeneously encapsulated in the mesopores of FSM6.2, even at high concentration, although they spontaneously aggregated and showed a red shift in solution at the concentration corresponding to that in the conjugate. Furthermore, an increase in the amount of sGFP and DsRed adsorbed to the pores of FSM6.2 led to a decrease in the distance between these proteins, resulting in enhancement of FRET efficiency.

Biomolecular assemblies such as protein subunits provide effective pathways for various chemical reactions in living bodies. Artificial assemblies of biomolecules have attracted much attention in the bioengineering field, due to potential applications to chemical processes such as catalytic reactions (*1–3*). One promising approach is the alignment of heteroproteins in the channels of mesoporous silicas. However, there have been no reports of a successful such assembly so far, the focus instead being on the incorporation of one kind of protein (*4–10*) mainly due to the difficulty in evaluating protein–protein interaction in the channels.

Here, we report the first ensemble of different proteins, which in combination function as a system for energy transfer similar to solar energy conversion (*11–16*) in the same silicate channel, i.e., the pores of folded-sheet mesoporous material (FSM) (*17, 18*). The presence of the artificial assembly of proteins in the pores was confirmed by detecting a fluorescence resonance energy transfer (FRET) between the proteins (*19, 20*). In other words, the interaction between the proteins in the pores or the assembly can be monitored by measuring FRET.

We chose sGFP and DsRed as the heteroproteins. They are fluorescent proteins having a donor–acceptor relationship in FRET, where they coexist within several nanometers (Förster radius is ∼5 nm) (*21*). The combination is also expected to be a good molecular probe to elucidate the effectiveness of mesoporous silicas as a scaffold for producing integrated proteins conjugated with FSM. In this study, two N-terminal hexa-histidine-tagged fluorescent proteins were overexpressed using BL21 Star *Escherichia coli* cells (cf. Supporting Information), after which the purified proteins were used for the FRET experiment. An engineered green fluorescent protein (GFP), sGFP (S65T) monomer, which is used for live-cell imaging in *Neurospora* (*22*) and plants (*23*), was employed as a donor. As an acceptor, a red fluorescent protein (RFP), the DsRed monomer from an IndoPacific sea anemone relative, *Discosoma* coral, was used (*24*). As the capsule for the proteins, we have developed an FSM6.2 (pore diameter of 6.2 nm) treated with hot ethanol (cf. Supporting Information) (*25*). The treatment enhances the structural stability of the framework, resulting in the successful incorporation of the proteins without damage to the framework. Thus, the heteroprotein−FSM6.2 conjugate enables us to construct an artificial biomolecular assembly. We can measure the FRET signal of the fluorescent proteins incorporated into FSM6.2 from the decrease of donor intensity (sGFP; ${\lambda_{ex}}^{max}/{\lambda_{em}}^{max}$ = 490 nm/511 nm, M_r 28 000), although the fluorescence from the acceptor (DsRed; ${\lambda_{ex}}^{max}/{\lambda_{em}}^{max}$ = 558 nm/580 nm, M_r 30 000) was very weak (*26*) compared with that of sGFP (the difference in intensity between sGFP and DsRed was a hundredfold). Donor quenching is the most convenient parameter for determining FRET efficiency, as has been reported elsewhere (*27*). The pore size of FSM6.2 is sufficient to immobilize the two fluorescent proteins, since both cylindrical proteins are 4–5 nm tall (Figures S1 and S2 in the Supporting Information). The proposed design of the FRET system in the sGFP–DsRed–FSM6.2 conjugate is shown schematically in Figure 1.

The fluorescent protein-incorporated FSM6.2 can be readily obtained (cf. Supporting Information), as shown in Figure 2. After incorporation of the proteins into FSM6.2, the conjugate was thoroughly rinsed with 20 mM Tris−HCl buffer (pH 8.0). At this point, little protein was detected in the supernatant and rinsed solution, suggesting that all proteins used for the incorporation were trapped within FSM6.2. In addition, the conjugate showed almost the same fluorescence as the original, even after several months at 4 °C. Thus, the proteins incorporated into FSM6.2 do not readily leach into the solution. On the other hand, most proteins were recovered from the supernatant when a noncalcined FSM6.2, whose mesopores were filled with surfactants, and a layered silicate, kanemite, which is the precursor before folding to give FSM (*17, 18*), were used

* Corresponding author. Tel: +81-22-237-3039. Fax: +81-22-237-3073. E-mail: matsuura-shunichi@aist.go.jp.

† National Institute of Advanced Industrial Science and Technology (AIST).

‡ Tokyo University of Science.

10.1021/bc700340e CCC: $40.75 © 2008 American Chemical Society
Published on Web 11/30/2007

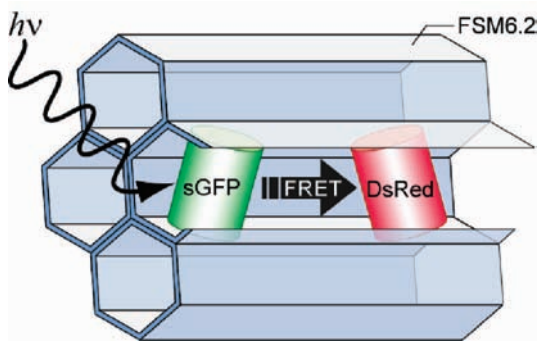

Figure 1. Schematic representation of the FRET between sGFP and DsRed in channels of FSM6.2.

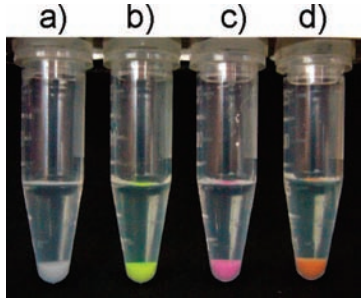

Figure 2. Picture taken without excitation of (a) FSM6.2, (b) sGFP–FSM6.2, (c) DsRed−FSM6.2, and (d) sGFP−DsRed−FSM6.2. Both sGFP and DsRed concentrations are 2 mg/mL. All samples were dispersed in 20 mM Tris−HCl buffer (pH 8.0).

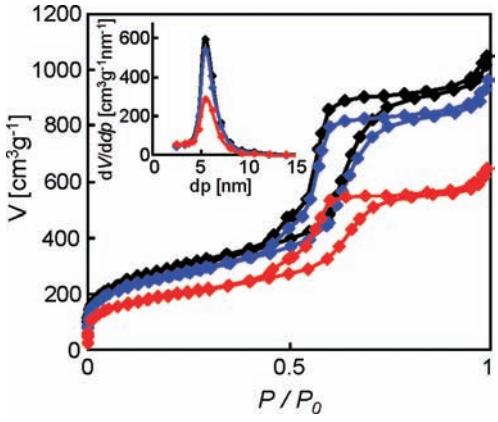

Figure 3. Changes in nitrogen adsorption–desorption isotherms and the corresponding pore size (dp) distribution curves obtained from the adsorption branch by the Barret-Joyner-Halenda (BJH) method (*28*) (inset) for sGFP−DsRed−FSM6.2 conjugates. Curves in black, blue, and red indicate the amounts of sGFP−DsRed adsorbed to the pores of FSM6.2 (50 mg): 0, 2, and 15 mg in total, respectively.

instead of FSM6.2 calcinated. This means that scarcely any proteins are adsorbed on the silica surface without mesopores.

The proportions of sGFP, DsRed, and their mixture adsorbed to the pores of FSM6.2 in 20 mM Tris−HCl buffer (pH 8.0) were approximately 40 wt % (Figure S5 in the Supporting Information). Figure 3 shows nitrogen adsorption–desorption isotherms and the corresponding pore size distribution curves for sGFP−DsRed−FSM6.2 conjugates. With an increasing amount of the proteins (0, 2, and 15 mg) confined in the pores of FSM6.2 (50 mg), the amount of nitrogen adsorbed by sGFP−DsRed−FSM6.2 progressively decreased. Simultaneously, the pore volumes decreased with an increase in the amount of the proteins (Figure 3, inset). The decline in porosity

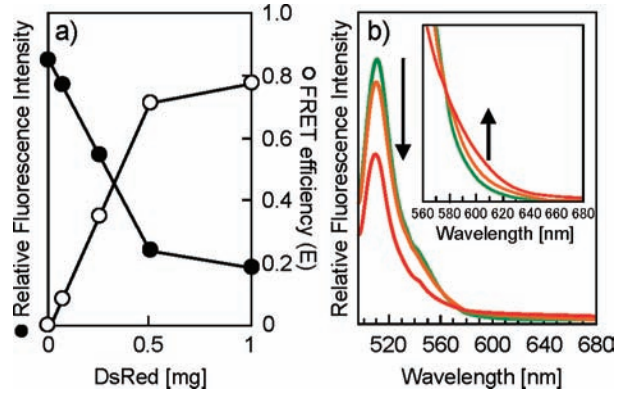

Figure 4. Effect of DsRed amount on sGFP-preimmobilized FSM6.2: (a) Fluorescence intensity of sGFP at 511 nm (filled circles) and FRET efficiency (E) (open circles). FRET efficiency; $E = 1 - (F_d'/F_d)$. Concentration of sGFP was constant (0.1 mg/mL; 50 μg sGFP/10 mg FSM6.2). (b) Fluorescence emission spectra of fluorescent proteins (λ_{ex} = 490 nm). The green, orange, and red curves indicate the fluorescence intensity in the sGFP:DsRed at quantitative ratios of 1:0, 1:1, and 1:5, respectively. Inset shows an extended figure of the emission spectra recorded at 560–680 nm. Buffer solution in all samples was 20 mM Tris−HCl (pH 8.0).

results from the incorporation of the two proteins into the mesopores of FSM6.2.

After preparing the fluorescent protein−FSM6.2 conjugate, an aliquot of 200 μL was transferred to a low-scattering microcell and the fluorescence intensity was measured using a fluorescence spectrophotometer (F-4500; HITACHI). The sample was excited at 490 nm, and the emission spectrum was recorded at 495–680 nm. To avoid any effect of the excitation light on the emission of sGFP, the slit width of the fluorescence spectrophotometer was set to 1 nm. The proteins retained their fluorescence activities after the treatment. However, the protein−FSM conjugates showed less intensity than the proteins in solution. There are two possible reasons for this. One explanation is a light-shielding effect of the silica component. The other is the low number of protein−FSM conjugates that exist within the excitation light transmissive window of the microcell in the fluorescence spectrophotometer, resulting from gravitational deposition of silica.[1]

We first examined whether energy is transferred between the proteins located in the pores of FSM6.2. Thus, we evaluated the effect of acceptor concentration on fluorescence intensity of the donor during a FRET reaction (Figure 4). Various amounts of DsRed were introduced into the mesopores after immobilization of a certain amount of sGFP (50 μg). The ratios of sGFP to DsRed in the protein−FSM6.2 conjugates obtained were 1:0, 1:1, 1:5, 1:10, and 1:20. At all ratios, proteins were completely captured into the mesopores. Figure 4a shows the fluorescence intensity of the donor at 511 nm and FRET efficiency (E). The FRET efficiency (E) from sGFP to DsRed was calculated approximately using the equation $E = 1 - (F_d'/F_d)$ (eq 1), where F_d and F_d' are the fluorescent intensities of the donor in the absence and presence of the acceptor, respectively. Fluorescence quenching of sGFP was observed when DsRed was introduced into the mesopores, with the fluorescence intensity decreasing gradually in inverse proportion to the amount of DsRed. The gradual, strong quenching indicates that energy transfer effectively occurred between sGFP and DsRed. At the same

[1] The sample was analyzed just after stirring. Although sluggish sedimentation of the conjugate started, it did not affect analysis of concentration-dependent emissions by sGFP and DsRed during measurement.

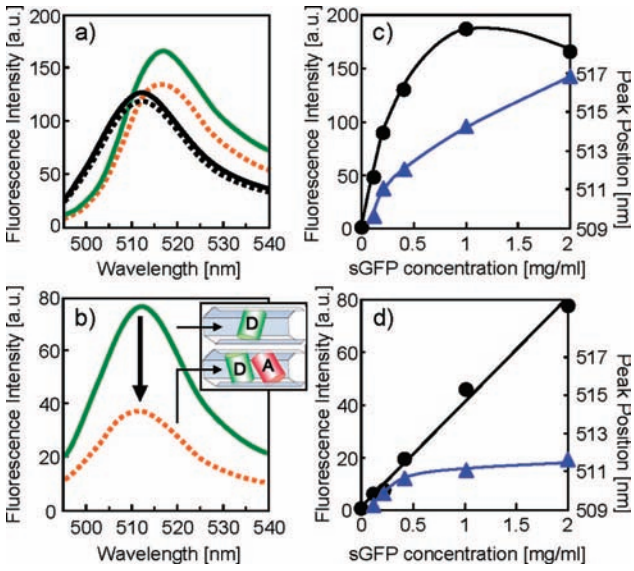

Figure 5. Fluorescence emission spectra of fluorescent proteins (λ_{ex} = 490 nm): (a) proteins only, (b) protein−FSM6.2 conjugate. Green curves and orange dashed curves indicate spectra for 2 mg/mL sGFP (D) only and the sGFP (D)−DsRed (A) mixture (2 mg/mL each), respectively. In (a), the black and black dashed curves indicate 0.4 mg/mL sGFP and the sGFP−DsRed mixture (0.4 mg/mL each). The green and orange dashed curves in (b) correspond to the samples shown in Figure 2b and d, respectively. The effect of the concentration of the sGFP solution on the maximum fluorescence intensity of sGFP (black circles) and peak position (blue triangles) is shown in (c) sGFP only and (d) sGFP−FSM6.2 conjugate. Measurement condition of fluorescence spectrophotometer slit width for both exciting light and fluorescence detection, 1 nm; voltage for photo multiplier tube, 700 V.

time, the FRET efficiency (*E*) was in proportion to the amount of DsRed. When the amount of DsRed exceeded the sGFP:DsRed quantitative ratio of 1:10, the FRET efficiency (*E*) remained at ∼0.8. This implies that DsRed cannot close with sGFP beyond a certain distance. In other words, all accessible sGFP molecules are already in contact with excess DsRed molecules. The notable FRET signal strongly indicates the possibility of high accessibility between sGFP and DsRed incorporated into the same channels of FSM6.2. Figure 4b shows the fluorescence emission spectra of the sGFP−DsRed−FSM6.2 conjugates recorded at 495–680 nm. When the fluorescence quenching of sGFP was observed with an increasing amount of DsRed, the fluorescence intensity increased in the wavelength range over the isosbestic point, resulting from the fluorescence enhancement of the acceptor. The appearance of the isosbestic point clearly indicates a transfer of energy from sGFP to DsRed, and DsRed functions effectively as a fluorescence quencher, although the acceptor emission is weak. In general, FRET can be evaluated by observing fluorescence enhancement of the acceptor, changes in the ratio of the fluorescence intensity of donor/acceptor, and fluorescence quenching of the donor (*27*). Among these indicators, the use of donor quenching is best suited to the FRET system using a sGFP−DsRed conjugate, as the FRET efficiency (*E*) from YFP (yellow fluorescent protein) to DsRed can be determined by donor quenching (*29*).

In order to demonstrate conclusively the efficacy of FSM6.2 as a capsule for energy transfer between sGFP and DsRed, we further measured the fluorescence spectra of sGFP and the same quantity of sGFP−DsRed mixture obtained at 490 nm excitation, with and without FSM6.2 (Figure 5a,b). The emission intensity of the sGFP−DsRed mixture was lower than that of sGFP, despite the concentration of sGFP being the same (Figure 5a). The lower intensity indicates a transfer of energy from sGFP to DsRed. A similar phenomenon was observed in the spectra of sGFP versus sGFP−DsRed−FSM6.2 conjugate (Figure 5b). This suggests that both proteins in the pores assume the correct conformation and interact with each other. This can be confirmed by carefully examining the intensity and peak position of the emission.

The decline in the intensity of sGFP−DsRed−FSM6.2 was considerably larger than that of the sGFP−DsRed mixture in solution. This characteristic decrease in sGFP intensity corresponds to the increase in the numbers of the FRET pair, probably due to the successful immobilization of the sGFP−DsRed pairs in the channels. Regarding the peak position of donor emission, it was found that the protein−FSM6.2 conjugate showed a distinct donor peak (511 nm, Figure 5b,d) even though 2 mg/mL of proteins without FSM6.2 showed a red shift of ∼6 nm from the peak for 0.4 mg/mL sGFP (Figure 5a,c), attributable to partial aggregation among the proteins. The retention of a suitable emission maximum can be rationalized as the uniform dispersion of monomeric proteins in channels of FSM6.2, as previously indicated by the dispersion of dye into SBA-15 (*30*) and the incorporation of chlorophyll into FSM (*31, 32*). Moreover, the intensity of the sGFP immobilized in FSM6.2 was linearly related to the sGFP concentration (Figure 5d; determination coefficient (R^2), 0.99), whereas nonimmobilized sGFP showed fluorescence quenching due to self-aggregation at a high concentration (Figure 5c). These results demonstrate that FSM6.2 provides a suitable platform for the immobilization and dispersion of proteins in mesopores with disintegration of the aggregate, even at a high concentration of proteins.

Table 1 shows the properties of the conjugates with different amounts of sGFP and DsRed adsorbed to the pores of FSM, the distance between these proteins, and FRET efficiency (*E*) from sGFP to DsRed, calculated using eq 1. As is clear from the table, the FRET efficiency (*E*) of the conjugate is considerably higher than that of the sGFP−DsRed mixture without FSM, the values for *E* in sGFP−DsRed−FSM6.2 and sGFP−DsRed (2 mg/mL each) mixture being 0.51 and 0.19, respectively. The reason for this is that the average distance between the donor and the acceptor is approximately 7 nm, which is enough for energy transfer, since the transfer of excited-state energy is inversely proportional to the sixth power of the distance between donor and acceptor dipoles, providing an effective range of no more than 10 nm (*33*). It is noteworthy that an increase in the amount of sGFP and DsRed adsorbed to the pores of FSM6.2 leads to the decrease in the distance between

Table 1. Effect of Protein Concentration with and without FSM6.2 on the Mean Distance of Proteins and FRET Efficiency

	sGFP−DsRed−FSM6.2 conjugate			sGFP−DsRed mixture	
starting concentration [mg/mL]	adsorbed amount [mg/10 mg-FSM]	mean distance[a] [nm]	FRET efficiency (E)[b] [−]	mean distance[a] [nm]	FRET efficiency (E)[b] [−]
0.4	0.4	12.0	0.23	39.6	0.06
1	1	8.9	0.33	29.2	0.16
2	2	7.0	0.51	23.2	0.19

[a] Center-to-center distance of each protein. [b] FRET efficiency; $E = 1 - (F_d'/F_d)$.

these proteins, accompanied by an enhancement of FRET efficiency (*E*).

In summary, we successfully prepared a heteroprotein−FSM conjugate and demonstrated protein–protein interaction in the mesopores of FSM by measuring intermolecular FRET. The conjugate showed a large decrease in the emission of sGFP fluorescence, which is caused by FRET, indicating that the conjugate functions as an energy transfer system through the combination of the two heteroproteins. The FRET signal indicated the possibility of high accessibility between sGFP and DsRed encapsulated in the same channels of FSM6.2. Furthermore, a fluorescence spectral analysis indicated that the proteins were highly dispersed and homogeneously encapsulated, even at high levels, in the mesoporous channels of FSM6.2, although they spontaneously aggregated with increasing content in the solution. The results reveal that mesoporous silicas are a good host for constructing protein assemblies.

ACKNOWLEDGMENT

The authors thank Res. Assoc. Yasuo Niwa (University of Shizuoka) for the gift of the *sgfp* gene, Dr. Hideaki Togashi (National Institute of Advanced Industrial Science and Technology (AIST)) for assistance in constructing an expression plasmid inserting the *sgfp* gene, and Dr. Takayuki Nara (AIST) and Ms. Chisato Sekikawa (AIST) for skilled technical assistance and valuable discussions.

Supporting Information Available: Additional experimental details. This material is available free of charge via the Internet at http://pubs.acs.org.

LITERATURE CITED

(1) Lvov, Y., Ariga, K., Ichinose, I., and Kunitake, T. (1995) Assembly of multicomponent protein films by means of electrostatic layer-by-layer adsorption. *J. Am. Chem. Soc. 117*, 6117–6123.

(2) Hartmann, M. (2005) Ordered mesoporous materials for bioadsorption and biocatalysis. *Chem. Mater. 17*, 4577–4593.

(3) Vinu, A., Miyahara, M., and Ariga, K. (2006) Assemblies of biomaterials in mesoporous media. *J. Nanosci. Nanotechnol. 6*, 1510–1532.

(4) Fan, J., Lei, J., Wang, L., Yu, C., Tu, B., and Zhao, D. (2003) Rapid and high-capacity immobilization of enzymes based on mesoporous silicas with controlled morphologies. *Chem. Commun.* 2140–2141.

(5) Katiyar, A., Ji, L., Smirniotis, P., and Pinto, N. G. (2005) Protein adsorption on the mesoporous molecular sieve silicate SBA-15: effects of pH and pore size. *J. Chromatogr., A 1069*, 119–126.

(6) Hudson, S., Magner, E., Cooney, J., and Hodnett, B. K. (2005) Methodology for the immobilization of enzymes onto mesoporous materials. *J. Phys. Chem. B 109*, 19496–19506.

(7) Oda, I., Hirata, K., Watanabe, S., Shibata, Y., Kajino, T., Fukushima, Y., Iwai, S., and Itoh, S. (2006) Function of membrane protein in silica nanopores: Incorporation of photosynthetic light-harvesting protein LH2 into FSM. *J. Phys. Chem. B 110*, 1114–1120.

(8) Itoh, T., Yano, K., Kajino, T., Inada, Y., and Fukushima, Y. (2006) Phytol-modified heme in mesoporous silica: Conjugates as models of hemoproteins. *Biotechnol. Bioeng. 93*, 476–484.

(9) Itoh, T., Ishi, R., Ebina, T., Hanaoka, T., Fukushima, Y., and Mizukami, F. (2006) Encapsulation of myoglobin with a mesoporous silicate results in new capabilities. *Bioconjugate Chem. 17*, 236–240.

(10) Urabe, Y., Shiomi, T., Itoh, T., Kawai, A., Tsunoda, T., Mizukami, F., and Sakaguchi, K. (2007) Encapsulation of hemoglobin in mesoporous silica FSM)-enhanced thermal stability and resistance to denaturants. *ChemBioChem 8*, 668–674.

(11) Furukawa, H., Watanabe, T., and Kuroda, K. (2001) Immobilization of chlorophyll derivatives into mesoporous silica and energy transfer between the chromophores in mesopores. *Chem. Commun.* 2002–2003.

(12) Murata, S., Furukawa, H., and Kuroda, K. (2001) Effective inclusion of chlorophyllous pigments into mesoporous silica modified with alpha,omega-diols. *Chem. Mater. 13*, 2722–2729.

(13) Calzaferri, G., Huber, S., Maas, H., and Minkowski, C. (2003) Host-guest antenna materials. *Angew. Chem., Int. Ed. 42*, 3732–3758.

(14) Minkowski, C., Pansu, R., Takano, M., and Calzaferri, G. (2006) Energy collection, transport, and trapping by a supramolecular organization of dyes in hexagonal zeolite nanocrystals. *Adv. Funct. Mater. 16*, 273–285.

(15) Ruiz, A. Z., Li, H., and Calzaferri, G. (2006) Organizing supramolecular functional dye-zeolite crystals. *Angew. Chem., Int. Ed. 45*, 5282–5287.

(16) Ganschow, M., Hellriegel, C., Kneuper, E., Wark, M., Thiel, C., Schulz-Ekloff, G., Bräuchle, C., and Wöhrle, D. (2004) Panchromatic chromophore mixtures in an AlPO4–5 molecular sieve: Spatial separation effects and energy transfer cascades. *Funct. Mater. 14*, 269–276.

(17) Yanagisawa, T., Shimizu, T., Kuroda, K., and Kato, C. (1990) The preparation of alkyltriinethylaininonium–kaneinite complexes and their conversion to microporous materials. *Bull. Chem. Soc. Jpn. 63*, 988–992.

(18) Inagaki, S., Fukushima, Y., and Kuroda, K. (1993) Synthesis of highly ordered mesoporous material from a layered polysilicate. *J. Chem. Soc.: Chem. Commun.* 680–682.

(19) Selvin, P. R. (1995) *Methods in Enzymology: Fluorescence resonance energy-transfer*, Volume *246*, pp 300–334, Academic Press, San Diego,

(20) Ha, T., Enderle, T., Ogletree, D. F., Chemla, D. S., Selvin, P. R., and Weiss, S. (1996) Probing the interaction between two single molecules: Fluorescence resonance energy transfer between a single donor and a single acceptor. *Proc. Natl. Acad. Sci. U.S.A. 93*, 6264–6268.

(21) Erickson, M. G., Moon, D. L., and Yue, D. T. (2003) DsRed as a potential FRET partner with CFP and GFP. *Biophys. J. 85*, 599–611.

(22) Freitag, M., Hickey, P. C., Raju, N. B., Selker, E. U., and Read, N. D. (2004) GFP as a tool to analyze the organization, dynamics and function of nuclei and microtubules in Neurospora crassa. *Fungal Genet. Biol. 41*, 897–910.

(23) Niwa, Y., Hirano, T., Yoshimoto, K., Shimizu, M., and Kobayashi, H. (1999) Non-invasive quantitative detection and applications of non-toxic, S65T-type green fluorescent protein in living plants. *Plant J. 18*, 455–463.

(24) Campbell, R. E., Tour, O., Palmer, A. E., Steinbach, P. A., Baird, G. S, Zacharias, D. A, and Tsien, R. Y. (2002) A monomeric red fluorescent protein. *Proc. Natl. Acad. Sci. U.S.A. 99*, 7877–7882.

(25) Itoh, T., Ishii, R., Ebina, T., Hanaoka, T., Ikeda, T., Urabe, Y., Fukushima, Y., and Mizukami, F. (2007) Effective immobilization of subunit protein in mesoporous silica modified with ethanol. *Biotechnol. Bioeng. 97*, 200–205.

(26) Shaner, N. C., Steinbach, P. A., and Tsien, R. Y. (2005) A guide to choosing fluorescent proteins. *Nat. Methods 2*, 905–909.

(27) He, L., Olson, D. P., Wu, X., Karpova, T. S., McNally, J. G., and Lipsky, P. E. (2003) A flow cytometric method to detect protein-protein interaction in living cells by directly visualizing donor fluorophore quenching during CFP→YFP fluorescence resonance energy transfer FRET). *Cytom. Part A 55A*, 71–85.

(28) Barret, E. P., Joyner, L. G., and Halenda, P. P. (1951) The determination of pore volume and area distributions in porous substances. I. computations from nitrogen isotherms. *J. Am. Chem. Soc. 73*, 373–380.

(29) He, L., Wu, X., Simone, J., Hewgill, D., and Lipsky, P. E. (2005) Determination of tumor necrosis factor receptor-associated factor trimerization in living cells by CFP→YFP→mRFP FRET detected by flow cytometry. *Nucleic Acids Res.* 33–61.

(30) Wang, L., Shao, Y., Zhang, J., and Anpo, M. (2006) Study on the fluorescence properties of fluorescein dye incorporated into SBA-15. *Opt. Mater. 28*, 1232–1234.

(31) Itoh, T., Yano, K., Inada, Y., and Fukushima, Y. (2002) Photostabilized chlorophyll a in mesoporous silica: Adsorption properties and photoreduction activity of chlorophyll a. *J. Am. Chem. Soc. 124*, 13437–13441.

(32) Itoh, T., Yano, K., Inada, Y., and Fukushima, Y. (2002) Stabilization of chlorophyll a in mesoporous silica and its pore size dependence. *J. Mater. Chem. 12*, 3275–3277.

(33) Wu, P. G., and Brand, L. (1994) Resonance energy transfer: methods and applications. *Anal. Biochem. 218*, 1–13.

BC700340E

Cysteinylated Protein as Reactive Disulfide: An Alternative Route to Affinity Labeling

Zheng Miao, Mark R. McCoy, Diment D. Singh, Brianda Barrios, Oliver L. Hsu, Sarah M. Cheal, and Claude F. Meares*

Department of Chemistry, University of California, Davis, California 95616. Received August 28, 2007; Revised Manuscript Received November 8, 2007

Engineering the permanent formation of a receptor−ligand complex has a number of promising applications in chemistry, biology, and medicine. Antibodies and other proteins can be excellent receptors for synthetic ligands such as probes or drugs. Because proteins possess an array of nucleophilic sites, the placement of an electrophile on the synthetic ligand to react with a nucleophile on the macromolecule is a standard practice. Previously, we have used the site-directed incorporation of cysteine nucleophiles at the periphery of an antibody's binding site, paired with the chemical design of weakly electrophilic ligands, to produce receptor–ligand pairs that conjugate specifically and permanently (Corneillie et al. (2004) *Bioconjugate Chem. 15,* 1392–1402 and references therein). After protein expression in Drosophila S2 cells, we found, as is frequently observed, that the engineered cysteine was reversibly blocked by disulfide linkage to a cysteine monomer (cysteinylated). Removal of the cysteine monomer requires some care because of the need to preserve other disulfide linkages in the protein. Here, we report that cysteinylation can be used to advantage by treating the cysteine monomer as a leaving group and the protein disulfide as an electrophile with special affinity for thiols. Two ligands bearing thiol side chains were synthesized and incubated with the cysteinylated antibody Fab fragment 2D12.5 G54C, with the finding that both ligands become covalently attached within a few minutes under physiological conditions. The attachment is robust even in the presence of excess thiol reagents. This rapid, specific conjugation is particularly interesting for biomedical applications.

According to Means and Feeney (*1*), site-specific derivatization of proteins (affinity labeling) began with the attachment of haloacetyl reagents to enzyme active sites, resulting in irreversible inhibition (e.g., *2, 3*) and the diazonium coupling of a hapten to an antibody's binding site (*4*). The derivatizing reagents were prepared by synthesizing a substrate or ligand for the macromolecular target and incorporating an electrophilic reactive group. The ligand's strong affinity for a particular site concentrates the reactive group there, where its reaction with a nearby amino acid side chain is promoted by mutual proximity. This approach has been widely employed in biomedical research, from protein structural studies to the development of new pharmaceuticals (e.g., (*5*)). Notably, even the antibiotic penicillin may be regarded as an affinity label (*6*).

Recently, an enhanced form of affinity labeling has been introduced which is aimed at the development of macromolecules that permanently capture small probe molecules (*7–12*). Here, the macromolecular target site is genetically modified to make a reactive partner for the affinity label, thus permitting rapid attachment by modestly reactive synthetic ligands that bind near the mutated residue. A related strategy, used for drug discovery screening, is tethering library ligands to a cysteine mutant receptor by disulfide formation (*13–15*). Here, the small molecules are in disulfide form, to react with free cysteine on the protein; a reducing buffer containing a thiol provides selective pressure so that only the ligands with highest affinity remain bound *in vitro*.

* Address correspondence to Claude F. Meares, Department of Chemistry, University of California, One Shields Avenue, Davis, California 95616, Phone (530) 752-0936, Fax (530) 752-8938, E-mail cfmeares@ucdavis.edu, http://www-chem.ucdavis.edu/people/meares.shtml.

Because proteins and other biological molecules commonly possess an array of nucleophilic sites but rarely contain electrophilic groups, the placement of an electrophile on the synthetic ligand to react with a nucleophile on the macromolecule seems to be a universal practice (e.g., *13–20*). A potential weakness of this strategy is that the electrophilic reagent may react with nucleophiles other than the target because there are so many. This is manifested by the occasional development of allergic reactions to drugs such as penicillin (*21*).

For the capture of probe molecules, it is attractive to use an antibody's binding site and engineer the antibody to display an appropriately located cysteine thiol side chain because of its distinctive nucleophilicity (*12*). However, in practice it is frequently observed that such Cys mutant proteins have their solvent-accessible cysteines reversibly blocked by disulfide linkage to a cysteine monomer, or sometimes another natural thiol such as glutathione or coenzyme A (*22, 23*).

Reductive removal of this naturally occurring protecting group without reducing the natural disulfide bonds of an antibody is difficult to achieve quantitatively (*10, 24*). While seeking improved strategies for this step, we conjectured that, rather than removing the cysteine monomer during purification of the protein, it might be possible to use protein cysteinylation as an advantage by thinking of the disulfide as a specialized electrophile and the cysteine monomer as a leaving group. An affinity label bearing a nucleophilic thiol group might bind and displace the cysteine, forming a new disulfide bond as illustrated in Figure 1. This hypothesis was plausible because we had engineered the antibody such that this cysteine would lie to the side of the antibody's binding site, not likely to interfere with normal binding of the synthetic ligand. Here, we describe experimental proof that this reaction does indeed take place, with a rate and efficiency that point to further development.

10.1021/bc700330j CCC: $40.75 © 2008 American Chemical Society
Published on Web 12/07/2007

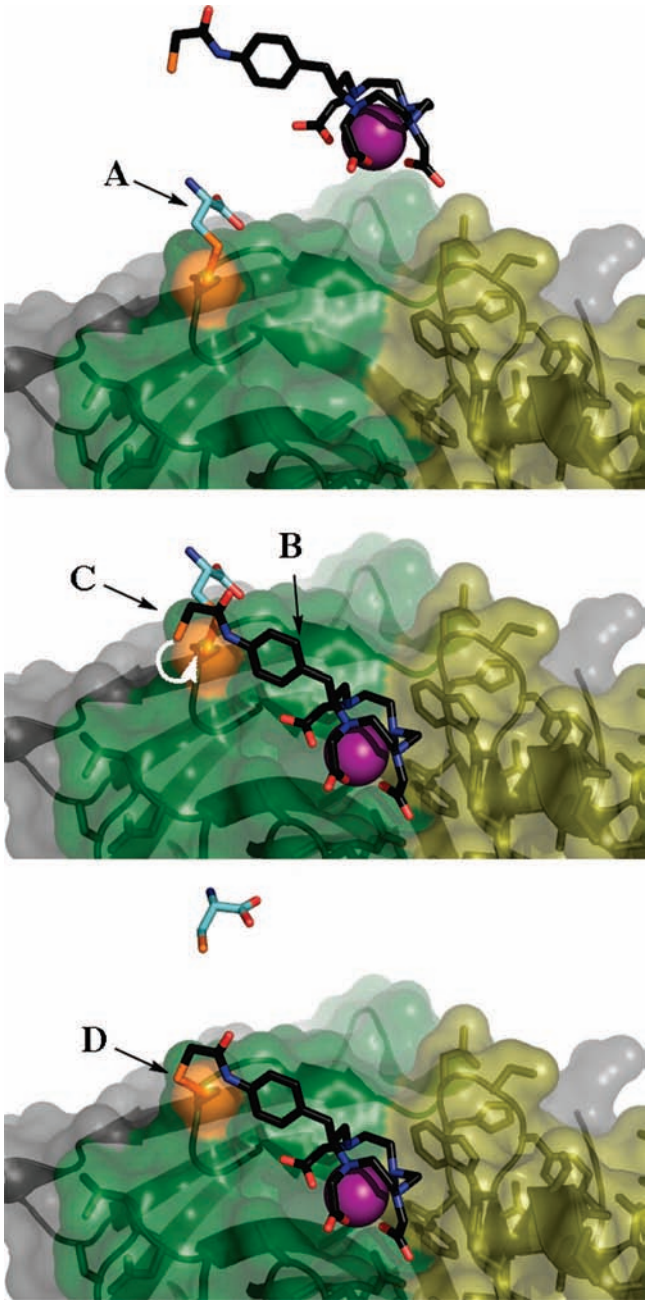

Figure 1. Infinite affinity binding of ligand **1** with cysteinylated 2D12.5 G54C Fab. Top: A cysteine monomer (A) is in disulfide linkage with the G54C when the protein is first expressed. The binding pocket of the 2D12.5 G54C Fab is pictured with CDR heavy chain regions shown in green, CDR light chain regions shown in yellow, and constant regions shown in gray. Ligand **1** is rendered in cpk colors, with the metal in purple. All sulfur atoms involved in the bond formation are colored orange. Middle: Association of chelate **1** with the binding pocket of the Fab (B) allows the free thiol group on the ligand to displace the cysteine monomer (C). Bottom: The disulfide bond (D) between the 2D12.5 G54C Fab and chelate **1** prevents dissociation of the ligand from the binding pocket.

We expressed the cysteinylated anti-DOTA[1] antibody Fab fragment 2D12.5 G54C in Drosophila S2 cells as described (*10*). After DTT reduction, we used amino acid analysis to confirm the release of cysteine monomer from the Fab.[2] As test affinity

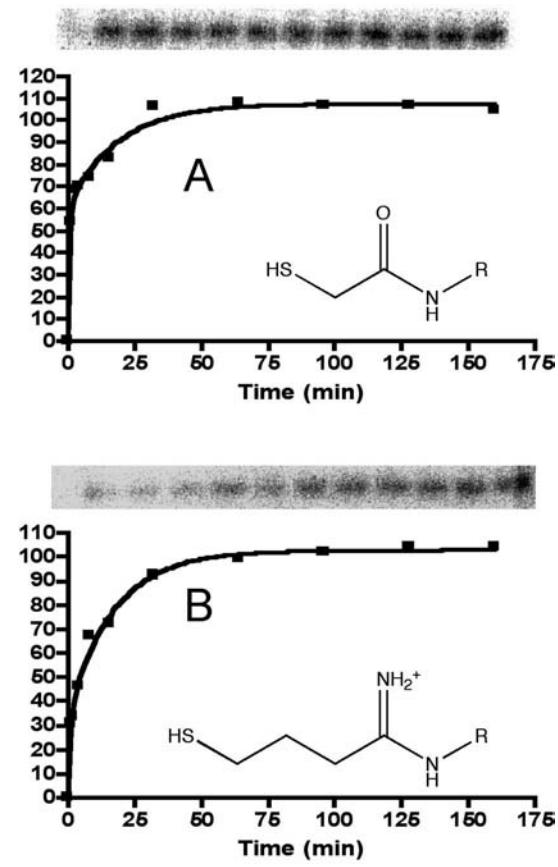

Figure 2. Panel A: covalent attachment of ^{90}Y-**1** to 2D12.5 G54C Fab as a function of time at 37 °C, pH 7.4, showing gel phosphorimages and plot of density. Panel B: covalent attachment of ^{90}Y-**2** to 2D12.5 G54C Fab.

Table 1. Covalent Attachment, As a Percentage of Total Bound Ligand, of ^{90}Y-1and ^{90}Y-3 to 2D12.5 G54C Fab with and without DTT Treatment[2]

	2D12.5 G54C	2D12.5 G54C w/DTT
^{90}Y-**1**[a]	83 ± 4%	77 ± 5%
^{90}Y-**3**	7.6 ± 0.1%	47 ± 1%

[a] ^{90}Y-**1** had a notably high efficiency of binding to DTT-treated G54C, which is only partially reduced to the sulfhydryl form, because the ^{90}Y-**1** sample contained both the free sulfhydryl (71%) and disulfide form (29%) of ^{90}Y-**1**.

labels, we synthesized nucleophilic compounds **1** and **2** to compare with previously reported electrophiles **3** and **4** (Chart 1). The method of Weiss (*25*) was used to prepare **1** from thiocyanate, bromoacetate, and aminobenzyl-DOTA; Traut's reagent was used to prepare **2**.[2]

Determination of Covalent Bond Formation between the Cysteinylated 2D12.5 G54C Fab Protein and ^{90}Y-1 or ^{90}Y-2. As suggested by Figure 1, each chelate was added to cysteinylated Fab to allow the formation of a new disulfide linkage. To ensure that the measured rates of covalent attachment would reflect the reaction in the binding site rather than the rate of association, the final concentration of the ^{90}Y-chelate was 10 μM and that of the protein was 1 μM in PBS buffer, pH 7.4. This solution was allowed to incubate at 37 °C for periods up to 160 min.[2]

In each case, the half-lives for covalent attachment were a few minutes at 37 °C, pH 7.4, and the attached ligands migrated with the protein during denaturing (nonreducing) gel electrophoresis. The results for ligands **1** and **2**, shown in Figure 2, are similar to the previous results for electrophiles **3** and **4** reacting with the free sulfhydryl form of this antibody (*10*).

[1] Abbreviations: BME, β-mercaptoethanol; DOTA, 1,4,7,10-tetraazacyclododecane-*N*,*N*′,*N*″,*N*‴-tetraacetic acid; DTT, dithiothreitol; Fab, antigen-binding fragment of an antibody.

[2] Experimental details are provided in Supporting Information.

Chart 1. M = yttrium(III)

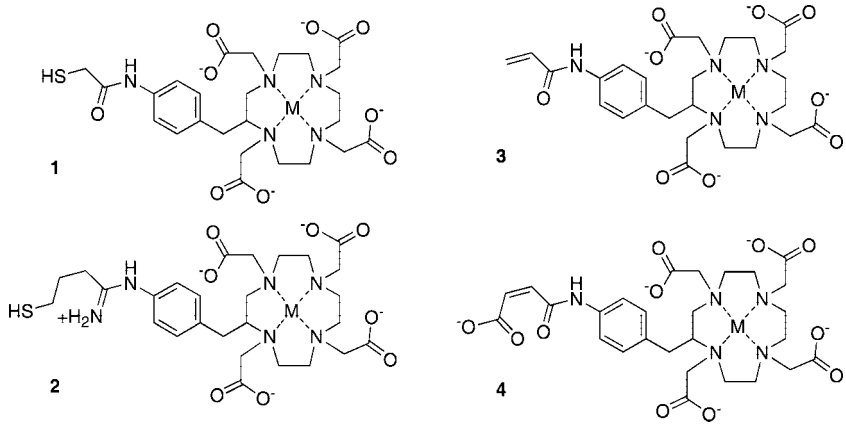

Quantitation of Covalent Bond Formation between the Cysteinylated 2D12.5 G54C Fab and ^{90}Y-1 or ^{90}Y-3 Before and After Mild Reduction. As will be shown below, the protein as expressed contains a small fraction of heavy chain cysteine-54 with a free thiol side chain (~7%), and a larger fraction of cysteinylated cysteine-54. Normally, before the 2D12.5 G54C Fab protein can react to a satisfactory degree with either **3** or **4** it must be reduced in order to increase the proportion of free thiol side chain at Cys-54, because the disulfide is nonreactive with electrophiles. This must be a mild treatment in order to avoid reduction of the structurally important disulfides, such as the interchain disulfide between the light and heavy chains of the Fab protein.

A sample of 2D12.5 G54C was treated with 25 μM DTT[1] followed by overnight incubation at 4 °C (*10*). Samples of 2D12.5 Fab G54C with or without DTT treatment were incubated with excess ^{90}Y-**1** or ^{90}Y-**3**, followed by gel filtration to remove excess chelate not associated with the Fab. The resulting samples of Fab contained both reversibly bound ligand and covalently bound ligand. To determine the percentage of chelate covalently bound to the protein, reversibly bound chelate was separated from the protein on a denaturing (nonreducing) polyacrylamide gel.[2]

The results for the four samples, reduced or nonreduced 2D12.5 G54C Fab reacting with either ^{90}Y-**1** or ^{90}Y-**3**, are shown in Table 1. For the naturally expressed protein without

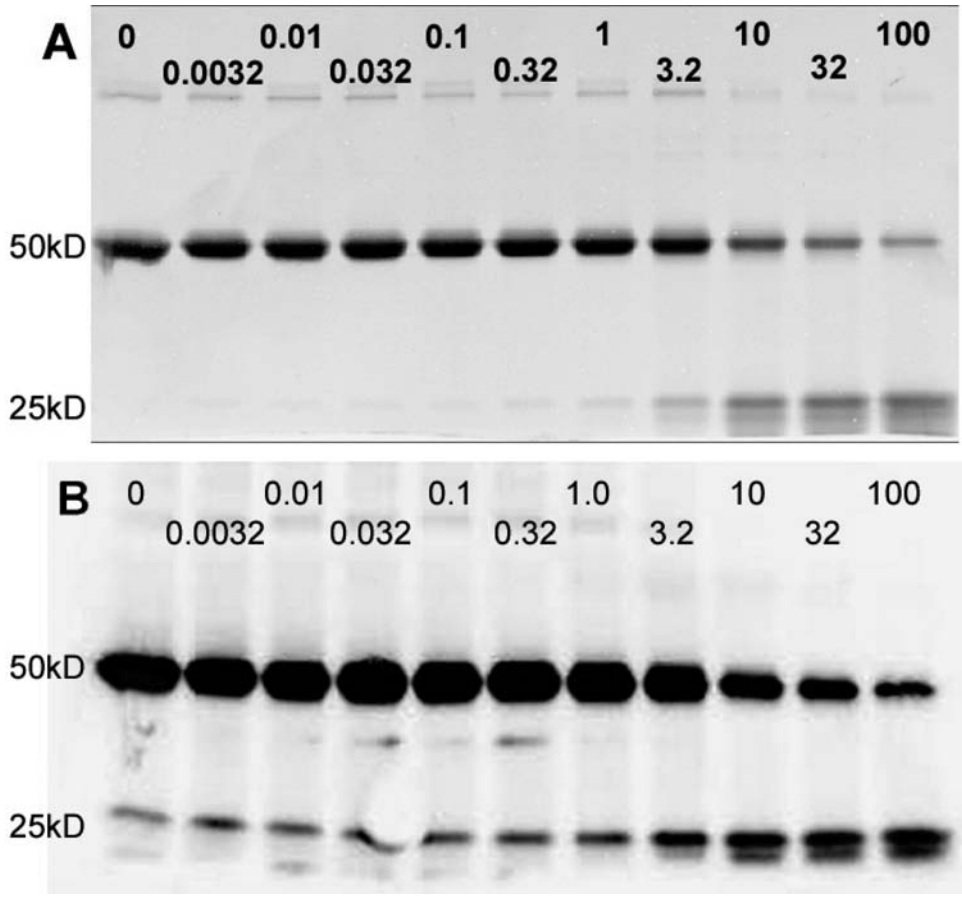

Figure 3. Sypro total protein stained gel (A) and anti-DOTA Western blot (B) analysis of samples of 2D12.5 G54C Fab conjugated to Y-**2** by disulfide bond formation. From left to right in each panel, the samples were treated with increasing concentrations of β-mercaptoethanol; numbers shown are BME concentration, mM.

DTT treatment, covalent bond formation with thiol ^{90}Y-**1** was approximately 11× more likely than reaction with acrylamide ^{90}Y-**3**. Mild reduction of the cysteinylated Fab increased covalent attachment of electrophile ^{90}Y-**3** approximately 6×, but had little effect on the covalent attachment of ^{90}Y-**1**. The reason for ^{90}Y-**1** having such a high efficiency here is that it becomes partially oxidized during metalation: for this experiment, 29% was in the disulfide form,[2] which can react with the reduced Cys-54.

Having formed the disulfide, we sought an indication of how stable the bond is. Because the binding site has high affinity for the DOTA chelate, the loss of the chelate after disulfide reduction should be disfavored. This may be envisioned as similar to the situation of the light and heavy chains of the Fab, which are held together by strong van der Waals interactions in addition to the interchain disulfide bond. We treated samples of the Y-**2**-Fab disulfide with increasing amounts of BME.[1] We analyzed the samples by denaturing, nonreducing gel electrophoresis immediately after removing the BME by a desalting column (Figure 3), finding that there is neither significant reduction of the Fab interchain disulfide nor loss of Y-**2** until the concentration of free BME exceeds 1 mM, where a small amount of interchain disulfide reduction becomes detectable. At 10 mM BME, the interchain disulfide is half-reduced, whereas the Y-**2**-Fab disulfide is only approximately 20% reduced.[2] It is also notable that a significant portion of the 25 kD disulfide-linked Y-**2**-heavy chain is produced at higher BME concentrations, confirming that the interchain disulfide is reduced while the Y-**2** disulfide remains intact. Since the Y-**2**-Fab disulfide bond is more stable than the interchain disulfide, Y-**2**-Fab should remain intact under physiological conditions.

While all four ligands in Chart 1 were designed to be unreactive in ordinary circumstances but to react quickly upon binding to the specific antibody, the thiol−disulfide reaction is particularly mild. The properties of the disulfide bond are of special interest for probe capture applications, because under physiological conditions, the only likely reaction is thiol−disulfide interchange. In the human circulatory system, thiol−disulfide interchange reactions are possible since both thiols and disulfides are present. Normally, there are micromolar concentrations of small thiol-containing molecules in human plasma. However, studies of the relative concentrations of cysteine (∼9 μM) and its oxidation partner cystine (∼47 μM), compared to glutathione (∼2 μM) and oxidized glutathione (∼0.05 μM), show that the partners are not in equilibrium (*26*). Thus, interchange reactions do not occur efficiently in the absence of a special circumstance such as proximity in a binding site.

Another interesting feature of this system is that it may be possible to displace the cysteine monomer *in vitro* with other thiols, either natural or synthetic, before use with the affinity label. In this way, we might adjust the reactivity of the disulfide, or perhaps attach a drug or probe molecule to be released upon ligand binding.

ACKNOWLEDGMENT

We thank other members of the Meares lab for their contributions and helpful discussions, and NIH Research Grants CA016861 and CA098207 (C.F.M.) for support.

Supporting Information Available: Experimental details and spectra for chelate synthesis, determination of the Cys-blocking residue, proof of the specificity of the disulfide that is formed, and comparison of disulfide stability. This material is available free of charge via the Internet at http://pubs.acs.org.

LITERATURE CITED

(1) Means, G. E., and Feeney, R. E. (1990) Chemical modifications of proteins: history and applications. *Bioconjugate Chem. 1*, 2–12.

(2) Baker, B. R., Lee, W. W., Tong, E., and Ross, L. O. (1961) Potential anticancer agents. LXVI. Non-classical antimetabolites. III. 4-(Iodoacetamido)-salicylic acid, an exo alkylating irreversible inhibitor of glutamic dehydrogenase. *J. Am. Chem. Soc. 83*, 3713–3714.

(3) Schoellmann, G., and Shaw, E. (1963) Direct evidence for the presence of histidine in the active center of chymotrypsin. *Biochemistry 2*, 252–255.

(4) Wofsy, L., Metzger, H., and Singer, S. J. (1962) Affinity labeling-A general method for labeling the active sites of antibody and enzyme molecules. *Biochemistry 1*, 1031–1039.

(5) Fry, D. W., Bridges, A. J., Denny, W. A., Doherty, A., Greis, K. D., Hicks, J. L., Hook, K. E., Keller, P. R., Leopold, W. R., Loo, J. A., McNamara, D. J., Nelson, J. M., Sherwood, V., Smaill, J. B., Trumpp-Kallmeyer, S., and Dobrusin, E. M. (1998) Specific, irreversible inactivation of the epidermal growth factor receptor and erbB2, by a new class of tyrosine kinase inhibitor. *Proc. Natl. Acad. Sci. U.S.A. 95*, 12022–12027.

(6) Yocum, R. R., Waxman, D. J., Rasmussen, J. R., and Strominger, J. L. (1979) Mechanism of penicillin action: penicillin and substrate bind covalently to the same active site serine in two bacterial D-alanine carboxypeptidases. *Proc. Natl. Acad. Sci. U.S.A. 76*, 2730–2734.

(7) Chmura, A. J., Orton, M. S., and Meares, C. F. (2001) Antibodies with infinite affinity. *Proc. Natl. Acad. Sci. U.S.A. 98*, 8480–8484.

(8) Chmura, A. J., Schmidt, B. D., Corson, D. T., Traviglia, S. T., and Meares, C. F. (2002) Electrophilic chelating agents for binding of metal chelates to engineered antibodies. *J. Controlled Release 78*, 249–258.

(9) Corneillie, T. M., Whetstone, P. A., Lee, K. C., Wong, J. P., and Meares, C. F. (2004) Converting weak binders into infinite binders. *Bioconjugate Chem. 15*, 1389–1391.

(10) Corneillie, T. M., Lee, K. C., Whetstone, P. A., Wong, J. P., and Meares, C. F. (2004) Irreversible engineering of the multielement-binding antibody 2D12. 5 and its complementary ligands. *Bioconjugate Chem. 15*, 1392–1402.

(11) Corneillie, T. M., Whetstone, P. A., and Meares, C. F. (2006) Irreversibly binding anti-metal chelate antibodies: Artificial receptors for pretargeting. *J. Inorg. Biochem. 100*, 882–890.

(12) Butlin, N. G., and Meares, C. F. (2006) Antibodies with infinite affinity: origins and applications. *Acc. Chem. Res. 39*, 780–787.

(13) Erlanson, D. A., Braisted, A. C., Raphael, D. R., Randal, M., Stroud, R. M., Gordon, E. M., and Wells, J. A. (2000) Site-directed ligand discovery. *Proc. Natl. Acad. Sci. U.S.A. 97*, 9367–9372.

(14) Arkin, M. R., Randal, M., DeLano, W. L., Hyde, J., Luong, T. N., Oslob, J. D., Raphael, D. R., Taylor, L., Wang, J., McDowell, R. S., Wells, J. A., and Braisted, A. C. (2003) Binding of small molecules to an adaptive protein-protein interface. *Proc. Natl. Acad. Sci. U.S.A. 100*, 1603–1608.

(15) Buck, E., and Wells, J. A. (2005) Disulfide trapping to localize small-molecule agonists and antagonists for a G protein-coupled receptor. *Proc. Natl. Acad. Sci. U.S.A. 102*, 2719–2724.

(16) Pollack, S. J., Nakayama, G. R., and Schultz, P. G. (1988) Introduction of nucleophiles and spectroscopic probes into antibody combining sites. *Science (Washington, DC) 242*, 1038–1040.

(17) Salerno, A., and Lawrence, D. S. (1993) Covalent modification with concomitant inactivation of the cAMP-dependent protein kinase by affinity labels containing only L-amino acids. *J. Biol. Chem. 268*, 13043–13049.

(18) Yan, X. W., Corbin, J. D., Francis, S. H., and Lawrence, D. S. (1996) Precision targeting of protein kinases - An affinity label that inactivates the cGMP- but not the cAMP-dependent protein

kinase. *J. Biol. Chem. 271*, 1845–1848.

(19) Levitsky, K., Ciolli, C. J., and Belshaw, P. J. (2003) Selective inhibition of engineered receptors via proximity-accelerated alkylation. *Org. Lett. 5*, 693–696.

(20) Chen, G., Heim, A., Riether, D., Yee, D., Milgrom, Y., Gawinowicz, M. A., and Sames, D. (2003) Reactivity of functional groups on the protein surface: development of epoxide probes for protein labeling. *J. Am. Chem. Soc. 125*, 8130–8133.

(21) Blanca, M., Cornejo-Garcia, J. A., Torres, M. J., and Mayorga, C. (2005) Specificities of B cell reactions to drugs. The penicillin model. *Toxicology 209*, 181–184.

(22) Gadgil, H. S., Bondarenko, P. V., Pipes, G. D., Dillon, T. M., Banks, D., Abel, J., Kleemann, G. R., and Treuheit, M. J. (2006) Identification of cysteinylation of a free cysteine in the Fab region of a recombinant monoclonal IgG1 antibody using Lys-C limited proteolysis coupled with LC/MS analysis. *Anal. Biochem. 355*, 165–174.

(23) Odaka, M., Kiribuchi, K., Allison, W. S., and Yoshida, M. (1993) In vivo affinity label of a protein expressed in Escherichia coli. Coenzyme A occupied the AT(D)P binding site of the mutant F1-ATPase beta subunit (Y307C) through a disulfide bond. *FEBS Lett. 336*, 231–235.

(24) Stimmel, J. B., Merrill, B. M., Kuyper, L. F., Moxham, C. P., Hutchins, J. T., Fling, M. E., and Kull, F. C., Jr. (2000) Site-specific conjugation on serine right-arrow cysteine variant monoclonal antibodies. *J. Biol. Chem. 275*, 30445–30450.

(25) Weiss, U. (1947) N-Arylamides of mercaptoacetic acid. I. Analogs of a carbamylmercaptoacetanilide. *J. Am. Chem. Soc. 69*, 2682–2684.

(26) Jones, D. P., Mody, V. C., Jr., Carlson, J. L., Lynn, M. J., and Sternberg, P., Jr. (2002) Redox analysis of human plasma allows separation of pro-oxidant events of aging from decline in antioxidant defenses. *Free Rad. Biol. Med. 33*, 1290–1300.

BC700330J

Fluorometric Identification of 5-Methylcytosine Modification in DNA: Combination of Photosensitized Oxidation and Invasive Cleavage

Hisatsugu Yamada, Kazuhito Tanabe,* and Sei-ichi Nishimoto*

Department of Energy and Hydrocarbon Chemistry, Graduate School of Engineering, Kyoto University, Katsura Campus, Kyoto 615-8510, Japan. Received August 29, 2007; Revised Manuscript Received November 7, 2007

An efficient fluorometric detection system of DNA methylation has been developed by a combination of a photooxidative DNA cleavage reaction with 2-methyl-1,4-naphthoquinone (NQ) chromophore and an invasive cleavage reaction with human Flap endonuclease-1. Enzymatic treatment of a mixture of photochemically fragmented target oligodeoxynucleotides (ODNs) at 5-methylcytosine (^{m}C) and hairpin-like probe oligomer possessing a fluorophore (F) and a quencher (D) resulted in a dramatic enhancement of fluorescence. In contrast, fluorescence emission for the ODN containing cytosine but not ^{m}C at the target sequence was extremely weak. In addition, by monitoring the fluorescence change, this system allows for the detection of ^{m}C in DNA at subfemtomole amounts. This system would provide a highly sensitive protocol for determining the methylation status in DNA by fluorescence emission.

Fluorescence technology provides considerable potential for obtaining sequence information of genes in a fast and simple manner. Various fluorescence-labeled DNAs that give signals in a sequence-specific fashion have found wide-ranging applications to gene analysis (*1–3*); e.g., TaqMan probe, molecular beacon probe, base-discriminating fluorescent probe, and invader assays.

Methylated cytosine (^{m}C) at the 5-position is a physiologically modified nucleobase involved in the epigenetic repression of genetic information that can cause various human diseases including cancer (*4–6*). Establishment of a means of assessing the methylation status of specific cytosine (C) residues in DNA is important for elucidating the biological effects of C methylation. Several protocols have been developed to identify the methylation status of a gene, representative examples of which are the methylation-insensitive restriction enzyme assay, sequencing with a bisulfite modification, Maxam−Gilbert modification, and labeling of ^{m}C with an osmium complex (*7–15*). While individual methods have their own advantages, most of the conventional methods present practical drawbacks to some extent, such as complicated procedures, long reaction periods for chemical modification, limitations in the detectable base sequences, and low sensitivity. Therefore, much recent effort has been made to explore more simple and efficient detection methods with easy procedures, short reaction times, and sequence-independent reactions in association with an epigenetic analysis of human genome.

We present herein a fluorometric method by which the normal C and its modified ^{m}C in DNA can be sensitively discriminated. The proposed system consists of the 2-methyl-1,4-naphthoquinone (NQ)-photosensitized strand cleavage at ^{m}C of DNA and the subsequent invasive cleavage reaction that is one of the most successful methods for fluorometric detection of single-nucleotide polymorphisms (SNPs) without PCR amplification (*16–18*). In the previous study, we displayed an exclusive strand cleavage at ^{m}C in the partial sequence of the human p53 gene, which occurred in a sequence-specific manner by photosensitization of NQ-tethered complementary oligodeoxynucleotide (ODN) (*19, 20*). Although the present NQ-sensitized site-selective strand cleavage at ^{m}C is a promising detection system for cytosine methylation with high sequence selectivity (*20*), sensitivity and convenience of the system are limited because of the low yield of photochemical cleavage at ^{m}C and the requirement of time-consuming gel electrophoresis to determine the methylation status. To overcome these problems, we attemptted to incorporate the Invader assay (*16–18*) with a highly sensitive fluorometry into the ^{m}C-selective photochemical fragmentation of the target strand. We observed intense fluorescence emission from the sample solution containing ODN with the target ^{m}C upon photooxidation followed by the invasive cleavage, whereas only weak fluorescence was detected from a control solution containing the reference ODN with C at the corresponding target. In addition, we confirmed that the present system is capable of detecting ^{m}C in DNA at the subfemtomole level, presumably because of the large turnover number in the efficient enzymatic cleavage of the invasive substrate.

The protocol for fluorometric discrimination between C and ^{m}C by a combination of the NQ-photosensitized strand cleavage and the invasive cleavage assay is shown in Figure 1a. We designed a modified ODN containing an NQ chromophore in the interior of the strand so as to hybridize to target ODNs containing C or ^{m}C. Photooxidation and subsequent alkali treatment of the duplex with ^{m}C induced exclusive strand cleavage at ^{m}C to generate the characteristic ODN fragments. To the resulting solution was added a fluorescent hairpin oligomer probe (Probe ODN) containing fluorescein at the 5′-end and a dabcyl quencher in the interior of the strand to be hybridized with the photolyzed ODN fragment into a complex that could form an overlap structure as a recognition domain of human Flap endonuclease-1 (FEN-1) (*21, 22*). Thus, treatment of the complex by FEN-1 led to the strand cleavage of Probe ODN at the invasive site, releasing the fluorophore that showed intense fluorescence emission as a result of separation from the intramolecular quencher. In contrast to the intense emission observed for the DNA with target ^{m}C site, faint fluorescence emission was observed when the DNA sequence contained the normal C instead of the target ^{m}C, which was stable to

* To whom correspondence should be addressed. Phone: +81-75-383-2500. FAX: +81-75-383-2501. E-mail: tanabeka@scl.kyoto-u.ac.jp, nishimot@scl.kyoto-u.ac.jp.

10.1021/bc7003318 CCC: $40.75 © 2008 American Chemical Society
Published on Web 11/27/2007

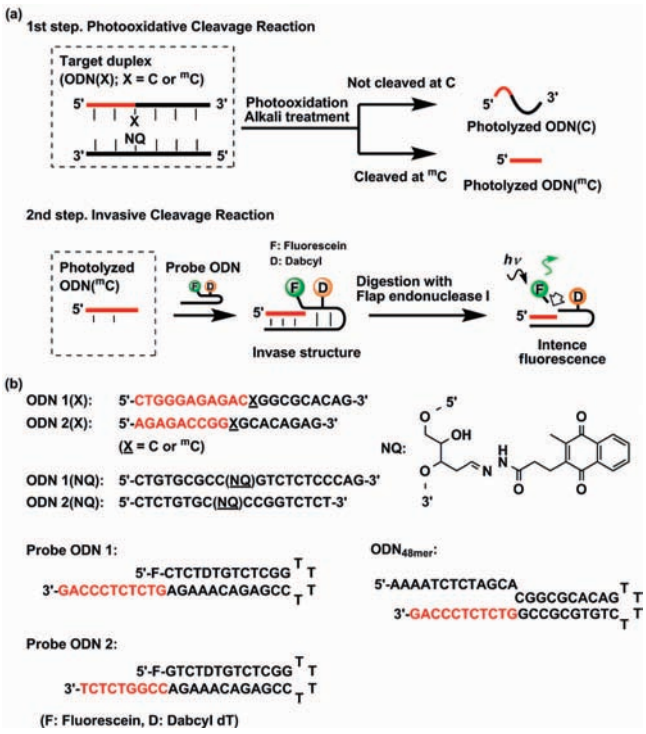

Figure 1. (a) Protocol for fluorometric discrimination between C and ^{m}C in DNA using the photooxidative-invasive dual cleavage system. "F" and "D" of Probe ODNs denote fluorescein and dabcyl groups, respectively. (b) Sequences and structures of ODNs used in this study.

photosensitized oxidation and alkali treatment, so that hybridization with the Probe ODN could not occur.

We performed discrimination analysis between C (ODN 1(C)) and ^{m}C (ODN 1(^{m}C)) in a partial sequence of the human p53 gene corresponding to codons 278–284 of exon 8, which has been identified as a methylation hot spot (*23*). The sequences of ODNs used in this study are summarized in Figure 1b. Duplex of ODN 1(NQ) with 500 fmol ODN 1(C) or ODN 1(^{m}C) was photoirradiated with 312 nm UV light at 0 °C in 2 mM sodium cacodylate buffer (pH 7.0) containing 20 mM NaCl and treated with hot piperidine to produce fragments with a specified base sequence. We estimated the cleavage efficiency of ODN 1(^{m}C) at ^{m}C to be 5.1% yield by densitometric anaylsis of the gel image (See Supporting Information Figure S1).[1] Probe ODN and FEN-1 were then added to the photolyzed ODNs and incubated at 30 °C. As shown in Figure 2a, intense fluorescence emission was observed for the sample derived from enzymatic digestion by FEN-1 of the photolyzed ODN 1(^{m}C), whereas fluorescence intensity for the similarly photolyzed and digested ODN 1(C) was at background level as in the digestion of Probe ODN 1 alone.[2] Fluorescent microscopic analysis of the digested mixture was also carried out in agarose gel. The highly viscous medium of agarose gel can effectively suppress dynamic fluorescence quenching by molecular oxygen, resulting in an enhanced visualization of the fluorescence emission (*24, 25*).[3] Intense green fluorescence was thus observed in the gel containing the photolyzed ODN 1(^{m}C), whereas only faint

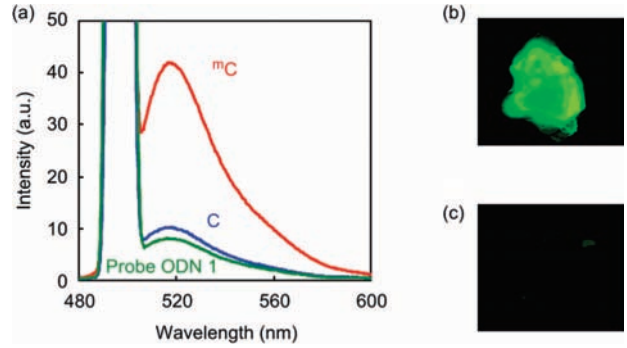

Figure 2. Fluorometric discrimination between C and ^{m}C in a partial sequence of the p53 gene using a combination of photosensitized oxidation and invasive cleavage. (a) Fluorescence spectra (excitation at 495 nm) of the reaction mixture after photoirradiation of the 500 fmol ODN 1(NQ)/ODN 1(X) duplexes, piperidine treatment, and enzymatic digestion by FEN-1: photolyzed ODN 1(^{m}C)/Probe ODN 1, red line; photolyzed ODN 1(C)/Probe ODN 1, blue line; Probe ODN 1 alone, green line. Fluorescence micrograph of the gel containing (b) photolyzed ODN 1(^{m}C) or (c) photolyzed ODN 1(C).

fluorescence could be detected in the gel containing the photolyzed reference ODN 1(C) (Figure 2b,c). Similar fluorometric identification of ^{m}C in a different site of exon 8 in the p53 gene (ODN 2(X)) was conducted, using the corresponding ODN 2(NQ) and Probe ODN 2. Consequently, we also confirmed intense fluorescence emission for the ODN containing ^{m}C at the target site (See Supporting Information Figure S3). These results strongly suggest that the methylation status of DNA can be quantified as a positive signal by fluorometry of the photolyzed target ODN(^{m}C) after hybridization with appropriate Probe ODNs and treatment with FEN-1.

An attempt was also made to determine the concentration limit of modified ^{m}C for discrimination from normal C in the same DNA with a partial sequence of the p53 gene, using the present combination protocol of NQ-sensitized photoreaction and invasive cleavage reaction. We evaluated the photoreaction of ODN 1(NQ) in the presence of 500 to 0.5 fmol ODN 1(C) or ODN 1(^{m}C), followed by the enzymatic digestion of an excess amount of Probe ODN 1 using FEN-1. As shown in Figure 3, the fluorescence intensity for photolyzed ODN 1(^{m}C)/Probe ODN 1 decreased with decreasing concentration of target ODN 1(^{m}C), in which we could detect a distinct emission even at 0.5 fmol target DNA. Thus, the present protocol provides a simple visualization procedure that is capable of detecting ^{m}C in target DNA at the subfemtomole level.

It is noteworthy that the fluorescence emission from the FEN-1-digested sample containing 0.5 fmol ODN 1(^{m}C) was similar to that from 5 fmol Probe ODN digested completely by calf intestinal alkaline phosphatase, nuclease P1, and phosphodiesterase I. This result indicates occurrence of a turnover process, in which a net amount of ca. 5 fmol free fluorescein was released from Probe ODN 1 by the proposed mechanism during the FEN-1 digestion for 5 min in the presence of only 0.5 fmol ODN 1(^{m}C). Since the enzymatic digestion reaction was performed near the melting temperature (T_m = ca. 33 °C) of the hybrid of Probe ODN 1 with a fragment derived from the target photolyzed ODN 1(^{m}C),[4] the Probe ODN 1 digested to release fluorescein could be readily replaced by an undigested probe into a fresh hybrid. This strand exchange may occur consecutively during the enzymatic reaction at around the T_m, resulting in significant enhancement of fluorescence due to the

[1] To characterize a photolyzed product, we performed MALDI-TOF mass analysis of photoirradiated and alkali-treated ODN 1(NQ)/ODN 1(^{m}C), which indicated the 5′-fragment of ODN 1(^{m}C) as a photolyzed ODN 1(^{m}C): 5′-d(CTGGGAGAGAC)-3′ *m/z* 3405.75 (calcd. for $[M - H]^{-}$ = 3405.24).

[2] We also confirmed that photoirradiation and alkali treatment are responsible for the fluorometric detection of ^{m}C (See Supporting Information Figure S2).

[3] The dynamic fluorescence quenching rate constant (k_q) of fluorescein with molecular oxygen decreases with increasing medium viscosity, thus resulting in the increased fluorescence quantum yields; see ref (*25*).

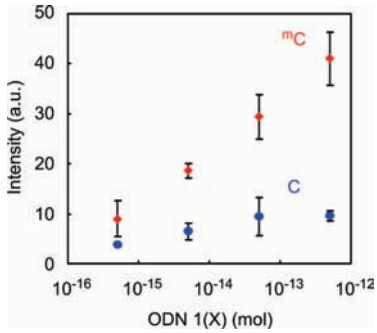

Figure 3. The detection limit of the present protocol for fluorometric identification of ^{m}C modification in a partial sequence of the p53 gene using the present combination protocol. The fluorescence intensity at 518 nm (excitation at 495 nm) of the reaction mixture upon varying the concentration of ODN 1(X): for photolyzed ODN 1(^{m}C)/Probe ODN 1, ♦ (red); photolyzed ODN 1(C)/Probe ODN 1, (blue).

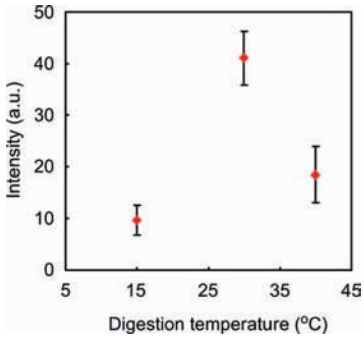

Figure 4. The influences of temperature on the FEN-1 digestion and the fluorescence intensity of the photolyzed ODN 1(^{m}C)/Probe ODN 1. Fluorescence intensity at 518 nm (excitation at 495 nm) of the reaction mixture was monitored after photoirradiation of 500 fmol ODN 1(NQ)/ODN 1(^{m}C) duplex, piperidine treatment, and enzymatic digestion by FEN-1 at given temperatures of 15, 30, and 40 °C.

accumulation of released fluorescein. Therefore, highly sensitive discrimination between C and ^{m}C in a subfemtomolar amount of DNA is accessible by the rational use of photochemical site-selective cleavage at ^{m}C in the target sequence and subsequent enzymatic digestion.

To confirm the influence of temperature on the enzymatic digestion with turnover process, we carried out the enzymatic reaction of Probe ODN 1 in the presence of photolyzed ODN 1(^{m}C) at various temperatures. As shown in Figure 4, the fluorescence intensity values for photolyzed ODN 1(^{m}C)/Probe ODN 1 digested at both 15 and 40 °C were much smaller than the corresponding intensities upon similar digestion at 30 °C. In view of the characteristic melting temperature of $T_m = 33.8$ °C corresponding to the dissociation of photolyzed ODN 1(^{m}C)/Probe ODN 1,[4] the apparent activity of the enzyme decreases due to dissociation of duplex DNA at the higher temperature of 40 °C, while the enzymatic digestion reaction is more accelerated with increasing temperature. At present, however, another possibility cannot be ruled out: FEN-1 may be less active for strand cleavage at 40 °C. In any event, there should be an appropriate temperature below T_m for the enzymatic digestion in order to obtain the maximum intensity of fluorescence emission.

To gain insight into a reaction mechanism by which Probe ODNs form hybrids with fragments derived from photolysis of ODNs to undergo enzymatic digestion, we performed a control enzymatic reaction by FEN-1, using ^{32}P-labeled ODN$_{48mer}$ instead of fluorescein-bearing Probe ODNs. To a solution of ODN 1(^{m}C) and ODN 1(NQ) after photosensitized oxidation and alkali treatment were added ^{32}P-labeled ODN$_{48mer}$ and FEN-1, and the resulting reaction mixture was analyzed by PAGE. As shown in Figure 5, the major cleavage band observed is consistent with a 13-mer ODN marker, demonstrating that enzymatic strand cleavage could occur at the invasive site of ODN$_{48mer}$. It is also evident that the strand cleavage releasing similar 13-mer ODN occurs in negligible amount comparable to the background level, when the hybrid of ^{32}P-labeled ODN$_{48mer}$ with photolyzed ODN 1(C) was digested by FEN-1. These results are a strong indication that the intense fluorescence emission is attributable to the efficient occurrence of the prescribed cleavage at the invasive site.

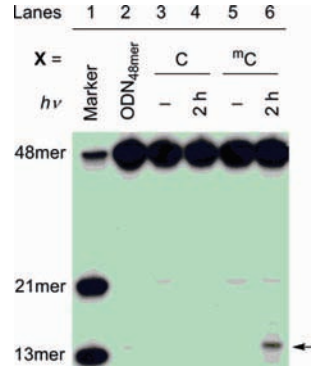

Figure 5. A representative autoradiogram of denaturing gel electrophoresis for ^{32}P-labeled ODN$_{48mer}$. Photoreaction of the duplexes containing NQ chromophore was carried out for 0 h (lanes 3 and 5) or 2 h (lanes 4 and 6), followed by a hot piperidine treatment. ^{32}P-labeled ODN$_{48mer}$ was added to the solution and incubated with FEN-1 at 30 °C for 7 h: lane 1, marker lane; lane 2, ODN$_{48mer}$; lanes 3 and 4, photolyzed ODN 1(C)/ODN$_{48mer}$; lanes 5 and 6, photolyzed ODN 1(^{m}C)/ODN$_{48mer}$.

It has been reported that the Invader assay requires absolute complementarity between the probe and the target sequence at the position of overlap for efficient enzymatic cleavage, by which a cleavage rate at least 300 times higher than that for a noncomplementary substrate can be achieved (*17*, *18*). In a control experiment, we also examined the enzymatic digestion of a mixture containing photolyzed ODN 1(^{m}C) and fluorescein-bearing ODN with a noncomplementary base sequence. As predicted, no fluorescence emission was observed using such a noncomplement Probe ODN, indicating that the present detection system requires accurate complementation as in the Invader assay to detect SNPs. It is also noted that this procedure allows site-specific discrimination of modified ^{m}C and normal C in a given DNA (See Supporting Information Figure S5).

In summary, we developed a simple and sensitive method for fluorometric discrimination between C and ^{m}C in DNA using the dual action of photosensitized oxidative cleavage and a modified Invader method. Distinct fluorescence emission was detected upon invasive digestion reaction of the hybrid of fluorescein-bearing Probe ODNs with the sequences-specific fragment released photochemically from the target DNA containing the ^{m}C site, by which the discrimination between ^{m}C and C in the target DNA is feasible even at the subfemtomole level. Because of such a high sensitivity, the present fluorometric system may be a promising protocol to determine the methylation status of DNA.

ACKNOWLEDGMENT

The authors wish to thank Dr. Takeo Ito for providing helpful discussions. H.Y. acknowledges fellowship from Japan Society for the Promotion of Science (JSPS).

Supporting Information Available: Experimental details, autoradiograms of a denaturing gel, UV spectra of the related

DNA samples, and spectral data on the photoreaction and enzymatic reaction. This material is available free of charge via the Internet at http://pub.acs.org.

LITERATURE CITED

(1) Strerath, M., and Marx, A. (2005) Genotyping–From genomic DNA to genotype in a single tube. *Angew. Chem., Int. Ed. 44*, 7842–7849.
(2) Ranasinghe, R. T., and Brown, T. (2005) Fluorescence based strategies for genetic analysis. *Chem. Commun.* 5487–5502.
(3) Okamoto, A., Saito, Y., and Saito, I. (2005) Design of base-discriminating fluorescent nucleosides. *J. Photochem. Photobiol., C 6*, 108–122.
(4) Robertson, K. D., and Wolffe, A. P. (2000) DNA methylation in health and disease. *Nat. Rev. Genet. 1*, 11–19.
(5) Ehrlich, M. (2002) DNA methylation in cancer: too much, but also too little. *Oncogene 21*, 5400–5413.
(6) Bird, A. (2002) DNA methylation patterns and epigenetic memory. *Gene. Dev. 16*, 6–21.
(7) Shiraishi, M., Oates, A. J., and Sekiya, T. (2002) An overview of the analysis of DNA methylation in mammalian genomes. *Biol. Chem. 383*, 893–906.
(8) Ohmori, H., Tomizawa, J., and Maxam, A. M. (1978) Detection of 5-methylcytosine in DNA sequences. *Nucleic Acids Res. 5*, 1479–1485.
(9) Church, G. M., and Gilbert, W. (1984) Genomic sequencing. *Proc. Natl. Acad. Sci. U.S.A. 81*, 1991–1995.
(10) Frommer, M., McDonald, L. E., Millar, D. S., Collis, C. M., Watt, F., Grigg, G. W., Molloy, P. L., and Paul, C. L. (1992) A genomic sequencing protocol that yields a positive display of 5-methylcytosine residues in individual DNA strands. *Proc. Natl. Acad. Sci. U.S.A. 89*, 1827–1831.
(11) Clark, S. J., Harrison, J., Paul, C. L., and Frommer, M. (1994) High-sensitivity mapping of methylated cytosines. *Nucleic Acids Res. 22*, 2990–2997.
(12) Herman, J. G., Graff, J. R., Myöhänen, S., Nelkin, B. D., and Baylin, S. B. (1996) Methylation-specific PCR: A novel PCR assay for methylation status of CpG islands. *Proc. Natl. Acad. Sci. U.S.A. 93*, 9821–9826.
(13) Okamoto, A., Tanabe, K., and Saito, I. (2002) Site-specific discrimination of cytosine and 5-methylcytosine in duplex DNA by peptide nucleic acids. *J. Am. Chem. Soc. 124*, 10262–10263.
(14) Stains, C. I., Furman, J. L., Segal, D. J., and Ghosh, I. (2006) Site-specific detection of DNA methylation utilizing mCpG-SEER. *J. Am. Chem. Soc. 128*, 9761–9765.
(15) Tanaka, K., Tainaka, K., Kamei, T., and Okamoto, A. (2007) Direct labeling of 5-methylcytosine and its applications. *J. Am. Chem. Soc. 129*, 5612–5620.
(16) Lyamichev, V., Mast, A. L., Hall, J. G., Prudent, J. R., Kaiser, M. W., Takova, T., Kwiatkowski, R. W., Sander, T. J., de Arruda, M., Arco, D. A., Neri, B. P., and Brow, M. A. D. (1999) Polymorphysm identification and quantitative detection of genomic DNA by invasive cleavage of oligonucleotide probes. *Nat. Biotechnol. 17*, 292–296.
(17) Lyamichev, V. I., Kaiser, M. W., Lyamicheva, N. E., Vologodskii, A. V., Hall, J. G., Ma, W.-P., Allawi, H. T., and Neri, B. P. (2000) Experimental and theoretical analysis of the invasive signal amplification reaction. *Biochemistry 39*, 9523–9532.
(18) Hall, J. G., Eis, P. S., Law, S. M., Reynaldo, L. P., Prudent, J. R., Marshall, D. J., Allawi, H. T., Mast, A. L., Darhlberg, J. E., Kwiatkowski, R. W., de Arruda, M., Neri, B. P., and Lyamichev, V. I. (2000) Sensitive detection of DNA polymorphisms by the serial invasive signal amplification reaction. *Proc. Natl. Acad. Sci. U.S.A. 97*, 8272–8277.
(19) Yamada, H., Tanabe, K., and Nishimoto, S. (2005) Cleavage at 5-methylcytosine in DNA by photosensitized oxidation with 2-methyl-1,4-naphthoquinone tethered oligodeoxynucleotides. *Bioorg. Med. Chem. Lett. 15*, 665–668.
(20) Tanabe, K., Yamada, H., and Nishimoto, S. (2007) One-electron photooxidation and site-selective strand cleavage at 5-methylcytosine in DNA by sensitization with 2-methyl-1,4-naphthoquinone-tethered oligonucleotides. *J. Am. Chem. Soc. 129*, 8034–8040.
(21) Nolan, J. P., Shen, B., Park, M. S., and Sklar, L. A. (1996) Kinetic analysis of human flap endonuclease-1 by flow cytometry. *Biochemistry 35*, 11668–11676.
(22) Bornarth, C. J., Ranalli, T. A., Henricksen, L. A., Wahl, A. F., and Bambara, R. A. (1999) Effect of flap modifications on human FEN1 cleavage. *Biochemistry 38*, 13347–13354.
(23) Tornaletti, S., and Pfeifer, G. P. (1995) Complete and tissue-independent methylation of CpG sites in the p53 gene: Implications for mutations in human cancers. *Oncogene 10*, 1493–1499.
(24) Hashimoto, S. E., Wang, B., and Hecht, S. M. (2001) Kinetics of DNA cleavage by Fe(II)-bleomycins. *J. Am. Chem. Soc. 123*, 7437–7438.
(25) Arık, M., Çelebi, N., and Onganer, Y. (2005) Fluorescence quenching of fluorescein with molecular oxygen in solution. *J. Photochem. Photobiol., A: Chem. 170*, 105–111.

BC7003318

Comparison of a Tartaric Acid Derived Polymeric MRI Contrast Agent to a Small Molecule Model Chelate

Robie L. Lucas, Michael Benjamin, and Theresa M. Reineke*

Department of Chemistry, University of Cincinnati, Cincinnati, Ohio 45221-0172. Received October 6, 2007

Contrast agents with high relaxivity are needed to increase the sensitivity of magnetic resonance imaging (MRI) for novel clinical and research applications. For this reason, polymeric structures containing multiple Gd(III) chelates are of current interest. Described in this communication are the syntheses and characterization of a glycopolymer derived from L-tartaric acid, Gd**4**(H_2O), as well as a low molecular weight compound, Gd**10**(H_2O), that models the Gd(III) chelate structure in the repeat unit of polymer Gd**4**(H_2O). Luminescence lifetime measurements in H_2O and D_2O for Eu(III) analogues of Gd**4**(H_2O) and Gd**10**(H_2O) [named Eu**4**(H_2O) and Eu**10**(H_2O)] reveal that the lanthanide in both structures likely has one water ligand in the primary coordination sphere. The relaxivity of the model chelate Gd**10**(H_2O) at 400 MHz and 310 K was determined to be 4.7 $mmol^{-1}\cdot s^{-1}$, representing a nearly 50% increase over Magnevist (3.2 $mmol^{-1}\cdot s^{-1}$). Relaxivity values on a per Gd basis for the polymeric structure Gd**4**(H_2O) prepared at two degrees of polymerization, $n = 12$ and 19, are similar, but slightly lower than Gd**10**(H_2O) (4.4 $mmol^{-1}\cdot s^{-1}$ and 4.5 $mmol^{-1}\cdot s^{-1}$, respectively). However, their molecular relaxivities of 51 $mmol^{-1}\cdot s^{-1}$ and 80 $mmol^{-1}\cdot s^{-1}$, respectively, provide a substantial increase over that of Magnevist.

The utility of magnetic resonance imaging (MRI) is currently being expanded beyond its role as the leading imaging modality in diagnostic medicine (*1*). MRI is noninvasive and provides real-time images, which make it an ideal research tool for visualizing drug delivery (*2*, *3*), monitoring biological processes, and following functional changes in vivo (*4*). To reach the full potential of MRI for such advanced imaging applications requires that the inherently low sensitivity of MRI be modulated with contrast agents containing paramagnetic metal ions, such as Gd(III) (*5*, *6*). However, current clinically used contrast agents based on low molecular weight Gd(III) chelates, such as Magnevist, do not sufficiently enhance water proton relaxation rates enough to function for these purposes (*7*), and their image-enhancing properties dramatically diminish at the increasingly higher magnetic fields of modern MRI instruments (*8*). In fact, the advanced applications described above will likely require macromolecular systems with multiple Gd(III) centers (*6*), which may retain their high relaxivities at high magnetic field strengths. Several design strategies have been used to incorporate multiple Gd(III) chelates within macromolecular structures, including linear polymers (*9*–*12*), dendritic systems (*13*–*16*), carbon nanotubes (*17*), and self-assembled bimetallic complexes (*18, 19*). For example, Kiessling and co-workers recently reported a linear polymer prepared via ring-opening metathesis polymerization that contained hydroxypyridonate (HOPO)-based Gd(III) chelates (*12*). Incorporating the high relaxivity HOPO-Gd(III) chelates (*20*) into a polymeric structure provided a contrast agent with per Gd and molecular relaxivities substantially higher than those of clinical contrast agents at 60 MHz. This example clearly demonstrates the ability of multivalent systems to significantly enhance relaxation properties. However, the influence of specific features of molecular structure in polymeric systems on relaxation properties has not been clearly established, particularly at higher magnetic field strengths (*21*).

Our previous work has demonstrated that incorporating carbohydrate residues along a polymer backbone decreases the toxicity of gene delivery vectors (*22*). Here, we extend this strategy to create a system that contains repeated carbohydrates with Gd(III) chelates along the polymer backbone. Incorporating carbohydrate-based components within the repeat unit increases hydrophilicity and may serve to enhance biocompatibility. Herein, a linear polymer, Gd**4**(H_2O), has been prepared that contains a repeat unit consisting of a tartaric acid diamide moiety, an ethylenediamine-derived linker, and a Gd(III)-DTPA(bisamide) chelate (Figures 1 and 2). In addition, to assist our understanding of the coordination environment of this polymer, a low molecular weight chelate, Gd**10**(H_2O), intended to model the Gd(III) chelate within the polymer repeat unit has been synthesized. These structures are allowing us to investigate the influence of polymer and repeat unit structure on the relaxivity properties of glycopolymer contrast agents. The syntheses, characterization, relaxivities, and water coordination properties of these macromolecular systems are presented.

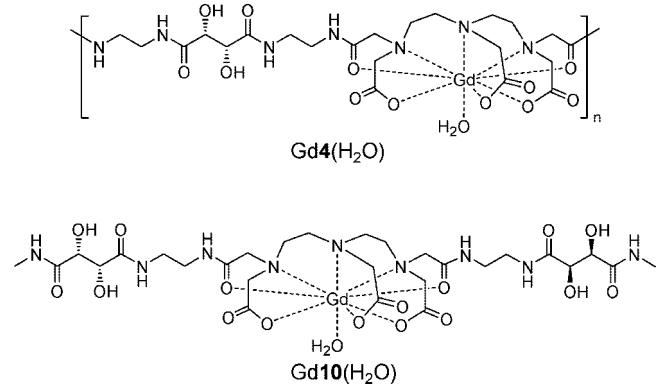

Figure 1. Target structures of the tartaramide-based polymer Gd**4**(H_2O) and model chelate Gd**10**(H_2O).

We have developed a methodology to prepare carbohydrate−diamine monomers that undergo step-growth polymerization with diethylenetriaminepentaacetic acid-bisanhydride (DTPA-BA) to yield novel glycopolymers that chelate Gd(III). To

* Corresponding author E-mail: theresa.reineke@uc.edu

10.1021/bc700375m CCC: $40.75 © 2008 American Chemical Society
Published on Web 12/20/2007

Scheme 1. Synthetic Protocol for the Polymer Gd4(H_2O)[a]

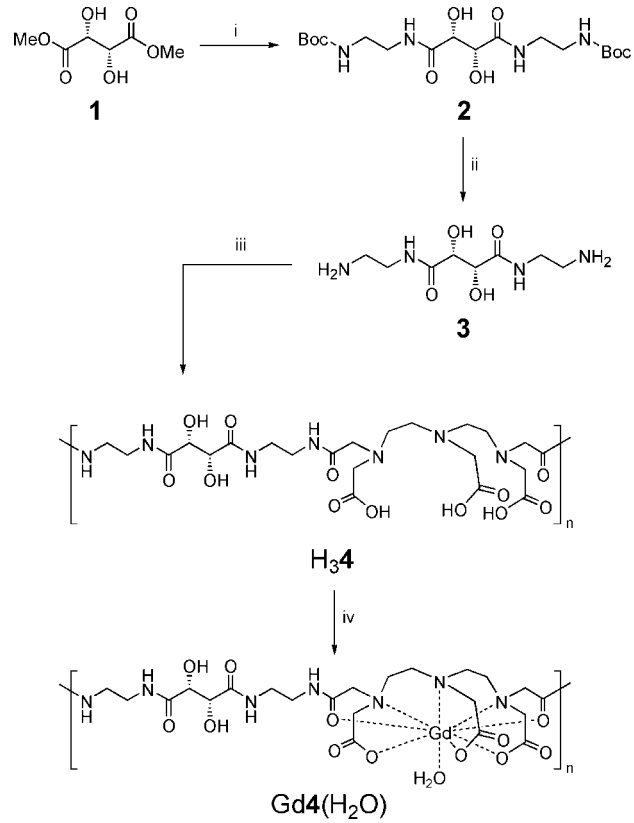

[a] (i) Mono-*N*-Boc-ethylenediamine, MeOH, Δ; (ii) 4.0 M HCl in 1,4-dioxane; (iii) DTPA-BA, DMSO, 24 or 72 h; (iv) $GdCl_3 \cdot 6H_2O$, NaOH, H_2O, pH 6−7.

prepare the carbohydrate−diamine monomer **3**, dimethyl L-tartrate **1** was refluxed with 2 equiv of mono-*N*-Boc-ethylenediamine in MeOH, which provided the Boc-protected tartaric acid diamide **2** in 67% yield (Scheme 1). Treatment of the diamide **2** with a solution of HCl in 1,4-dioxane to remove the Boc groups, followed by purification of the resulting diamine hydrochloride salt via ion exchange chromatography, yielded the pure monomer **3** in quantitative yield. The polymer precursors H_3**4** were synthesized by condensing **3** with DTPA-BA in DMSO at room temperature, and the molecular weight was varied by increasing the polymerization time. After the polymerizations were complete, the polymers were purified by exhaustive dialysis against ultrapure water using 3500 MWCO membranes and were then lyophilized to dryness. Formation of Gd**4**(H_2O) occurred by treatment of the polymers H_3**4** with $GdCl_3$ in aqueous solution, while maintaining a pH of 6–7 with aqueous NaOH. Following Gd(III) chelation, the polymers were again purified by exhaustive dialysis in 1000 MWCO membranes against ultrapure water to remove any unchelated Gd(III) ions and other salts. Characterization of Gd**4**(H_2O) was accomplished by gel permeation chromatography (GPC) using a triple detection system of refractive index, viscometry, and static light scattering. Two polymers were synthesized with weight-averaged molecular weights (M_w) of 8.9 kDa and 14.0 kDa, which correspond to degrees of polymerization of $n = 12$ and $n = 19$, respectively. The polymers revealed relatively low polydispersity indices for a step-growth mechanism (1.4 and 1.6, respectively), which is likely an artifact of the dialysis step. The Mark–Houwink−Sakurada α values (0.6–0.7) obtained from viscometry data demonstrated the formation of linear, randomly coiled polymers.

Synthesis of the small molecule chelate to model the polymer repeat unit required the preparation of an unsymmetrical tartaric acid diamide with only a single primary amine (compound **9** in Scheme 2). To prepare this compound, we made use of the known di-*O*-acetyl protected tartaric anhydride **6**, which was prepared from L-tartaric acid **5** in 81% yield by refluxing in acetic anhydride in the presence of sulfuric acid (*23*). The anhydride **6** was subsequently converted to the *N*-methyltartaramic acid **7** in 75% yield by treatment of the anhydride with a solution of methylamine in THF. This sequence was deemed more practical than attempting a selective monoamidation of L-tartaric acid directly. Standard coupling conditions using *N*,*N*′-dicyclohexylcarbodiimde (DCC) were used for amide bond formation between tartaramic acid **7** and mono-*N*-Boc-ethylenediamine to provide the diamide **8** in 47% yield. Simultaneous removal of the Boc (*24*) and acetyl (*25*) protecting groups was then achieved with 3 equiv of *p*-toluenesulfonic acid monohydrate in a CH_2Cl_2−MeOH solvent system. The crude product resulting from this reaction was purified and neutralized by ion exchange chromatography, giving the unsymmetrical tartaric acid diamide **9** in 91% yield. The ligand of the model chelate H_3**10** was then obtained in 65% yield by reacting 2 equiv of **9** with DTPA−BA in DMF at 65 °C. The ESI mass spectrum of H_3**10** showed only two significant peaks at $m/z = 768$ and $m/z = 385$, corresponding to the proton adduct $[H_3\mathbf{10} + H]^+$ of the desired product and its doubly charged derivative $[H_3\mathbf{10} + 2H]^{2+}$, respectively. The model chelate Gd**10**(H_2O) was prepared by treating an aqueous solution of the ligand H_3**10** with $GdCl_3$ at a pH of 6–7 and purifying by exhaustive dialysis in a 1000 MWCO membrane against ultrapure water. The major peak in the ESI mass spectrum corresponded to the proton adduct of the anhydrous chelated product {$[Gd\mathbf{10} + H]^+$, $m/z = 923$}. Complete loading of Gd(III) was also evidenced by the absence of a peak at $m/z = 768$ (the proton adduct of the unchelated ligand H_3**10**).

Knowledge of the structure of a Gd(III) chelate in aqueous solution is important for understanding the factors that dictate its capacity to enhance proton relaxation. Of particular importance is knowing the number of water molecules bound in the primary coordination sphere, *q*, of the Gd(III) center. The isostructural nature of Ln(III) complexes with a common chelating ligand is useful for probing the solution structure of Gd(III) chelates (*7*). Replacement of Gd(III) with Eu(III) makes it possible to determine *q* by using the proportionality of their corresponding luminescence decay rates in H_2O and D_2O (*26*). With this in mind, the Eu(III) analogues of the model chelate and the polymer were synthesized in a fashion similar to the related Gd(III) structures. Analysis of Eu**4**(H_2O) via GPC indicated a polymer with a M_w value of 18.6 kDa (25 repeat units). Luminescence lifetimes were measured for both Eu(III) structures in H_2O and D_2O, and *q* values were calculated using an equation developed by Horrocks et al., [$q = 1.11(k_{H_2O} - k_{D_2O} - 0.31 + 0.075n_{O=CNH})$] (*27*). These experiments revealed the same *q* values of 1.2 for both the Eu(III) model chelate, Eu**10**(H_2O), and for the Eu(III) polymer, Eu**4**(H_2O). It should be noted that these results (Table 1) are in good agreement with other Ln(III)-DTPA derivatives with a single water molecule in the primary coordination sphere (*27*).

Relaxivity values for the model chelate Gd**10**(H_2O) and the polymers Gd**4**(H_2O) were determined at 400 MHz (9.4 T) and 310 K. For comparison to a clinical contrast agent at this magnetic field, we measured the relaxivity, r_1, of Magnevist and obtained a value of 3.2 $mmol^{-1} \cdot s^{-1}$. The relaxivity value of the model chelate Gd**10**(H_2O) was found to be 4.7 $mmol^{-1} \cdot s^{-1}$, which represents an approximately 50% increase over Magnevist. The relaxivity values for the polymeric chelates Gd**4**(H_2O) on a per Gd basis are slightly lower than that obtained for the small molecule model chelate, with values of 4.4 $mmol^{-1} \cdot s^{-1}$ (for $n = 12$) and 4.5 $mmol^{-1} \cdot s^{-1}$ (for $n = 19$).

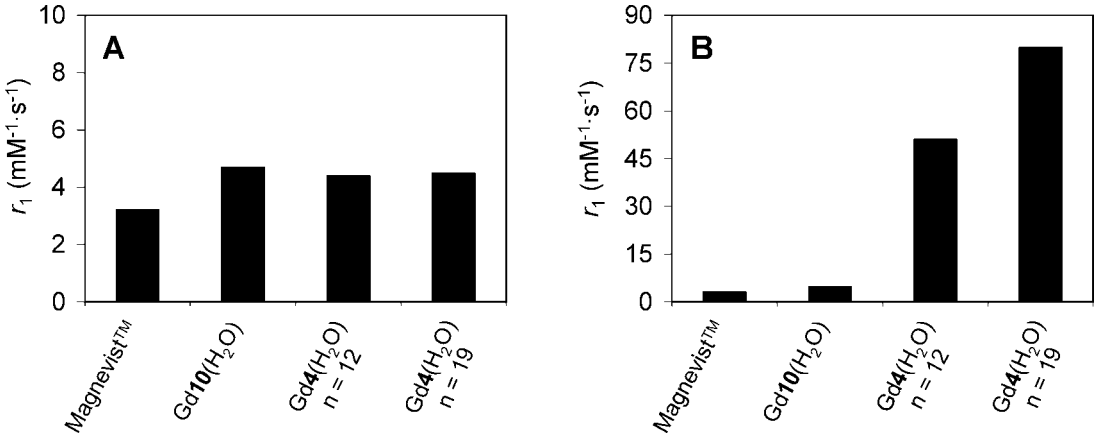

Figure 2. Per Gd(III) ion (A) and per molecule (B) relaxivities of Magnevist, the small molecule model chelate Gd**10**(H_2O), and the polymeric system Gd**4**(H_2O) with 12 and 19 repeat units.

Scheme 2. Synthesis of the Model Chelate Gd10(H_2O)[a]

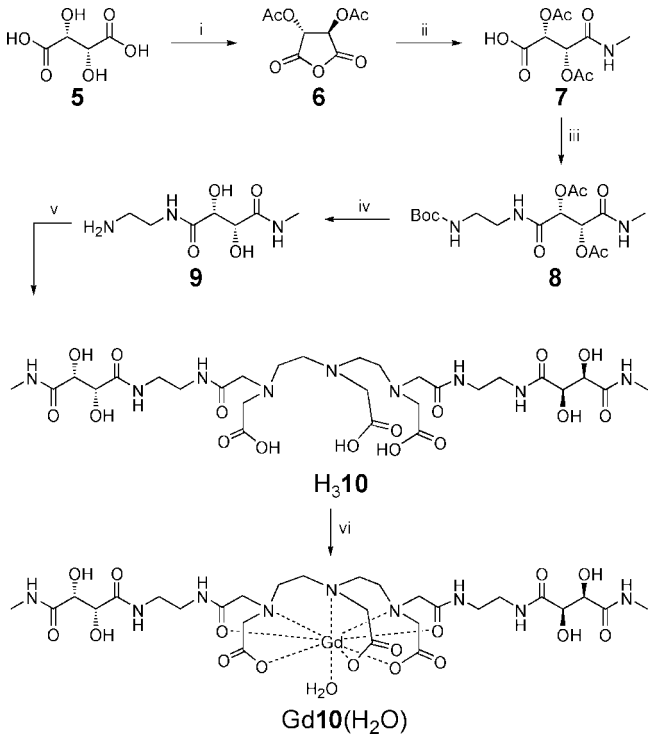

[a] (i) Acetic anhydride, H_2SO_4, Δ; (ii) 2.0 M methylamine in THF; (iii) *N,N′*-dicyclohexylcarbodiimide, CH_2Cl_2, 0 °C to rt; (iv) *p*-toluenesulfonic acid monohydrate, MeOH−CH_2Cl_2 (1:9); (v) DTPA−BA, DMF, 65 °C; (vi) $GdCl_3·6H_2O$, NaOH, H_2O, pH 6−7.

Table 1. Luminescence Lifetime Data for the Polymer Eu4(H_2O) and Model Chelate Eu10(H_2O)[a]

compound	τH_2O (ms)	τD_2O (ms)	q^a
Eu**4**(H_2O)	0.60	2.3	1.2
Eu**10**(H_2O)	0.62	2.5	1.2

[a] The polymer Eu**4**(H_2O) consists of 25 repeat units based on M_w from GPC analysis. Values of q were determined using the equation developed by Horrocks et al. (*27*).

These relaxivity values suggest that the relatively short polymers have considerable internal flexibility, despite incorporating the DTPA-based Gd(III) chelates directly into the polymer backbone. In addition, the lack of rigidity may facilitate electronic relaxation via Gd−Gd interactions and decrease relaxivity (*28*). Merbach et al. previously synthesized a series of related linear polymers prepared by polymerizing DTPA−BA with simple straight-chain alkyldiamines, where the number of methylenes between the amino groups was 4, 6, 10, or 12 (*9*). The high relaxivities exhibited by the polymers formed from diamines with 10 and 12 methylene groups was attributed to the formation of micelle structures with strong hydrophobic interactions, a consequence of using lipophilic alkyldiamine monomers. The polar diamine monomer **3** used in the present study is hydrophilic and would not form micelle-like structures in aqueous solution. Besides the influence of rotational properties, the limited relaxivity gains for Gd**4**(H_2O) and Gd**10**(H_2O) versus Magnevist may also be due to the well-established slow water exchange rate of Gd(III)-DTPA(bisamides) (*29*). Despite the fact that the per Gd relaxivity does not increase for the polymers of the present study versus the model chelate, the molecular relaxivities are very high for the polymers of $n = 12$ and $n = 19$, with values of 51 mmol^{-1}·s^{-1} and 80 mmol^{-1}·s^{-1}, which represent 16- and 25-fold increases, respectively, over the molecular relaxivity of Magnevist. Molecular relaxivities for polymeric systems are substantial, as they demonstrate the potential for higher Gd concentration to increase local proton relaxation in the vicinity of the contrast agent.

Advanced biomedical and molecular imaging applications using MRI contrast agents will likely require incorporating multiple Gd(III) chelates into macromolecular structures (*6, 21, 30*). We have presented the synthesis, characterization, and properties of two novel contrast agents, a small molecule model chelate, Gd**10**(H_2O), and a polymeric structure, Gd**4**(H_2O), which were formed by coupling tartaric acid derived amines with DTPA−BA. The relaxivity properties of the Gd(III) chelates within the polymeric structures are similar to that of their low molecular weight analogue Gd**10**(H_2O) on a per Gd basis; however on a molecular basis, the polymers clearly yielded substantially higher relaxivities. The generality of the synthetic protocol for these polymers is currently being utilized to generate a series of related polymeric materials using different carbohydrate-based monomers. The influence of carbohydrate structural variation within this series is currently under investigation.

ACKNOWLEDGMENT

The authors thank Drs. Jing-Huei Lee, Wen-Jang Chu, and Elwood Brooks for assistance with inversion–recovery experiments. This work was supported by the National Institutes of Health (1-R21-EB007244-01), the University of Cincinnati Department of Chemistry, and University of Cincinnati Chemical Sensors Group.

Supporting Information Available: Synthetic procedures and analytical data for **2**–**9**, Gd**4**(H_2O), Eu**4**(H_2O), H$_3$**10**,

Gd**10**(H_2O), and Eu**10**(H_2O). Experimental procedures for relaxivity and luminescence lifetime measurements. This material is available free of charge via the Internet at http://pubs.acs.org.

LITERATURE CITED

(1) Rudin, M., and Weissleder, R. (2003) Molecular imaging in drug discovery and development. *Nat. Rev. 2*, 123–131.

(2) Richardson, J. C., Bowtell, R. W., Mäder, K., and Melia, C. D. (2005) Pharmaceutical applications of magnetic resonance imaging (MRI). *Adv. Drug Delivery Rev. 57*, 1191–1209.

(3) Ye, F., Ke, T., Jeong, E.-K., Wang, X., Sun, Y., Johnson, M., and Lu, Z.-R. (2006) Noninvasive visualization of poly(L-glutamic acid) using contrast-enhanced MRI. *Mol. Pharm. 3*, 507–515.

(4) Louie, A. Y., Hüber, M. M., Ahrens, E. T., Rothbächer, U., Moats, R., Jacobs, R. E., Fraser, S. E., and Meade, T. J. (2000) In vivo visualization of gene expression using magnetic resonance imaging. *Nat. Biotechnol. 18*, 321–325.

(5) Aime, S., Barge, A., Cabella, C., Crich, S. G., and Gianolio, E. (2004) Targeting cells with MR imaging probes based on paramagnetic Gd(III) chelates. *Curr. Pharm. Biotechnol. 5*, 509–518.

(6) Caravan, P. (2006) Strategies for increasing the sensitivity of gadolinium based MRI contrast agents. *Chem. Soc. Rev. 35*, 512–523.

(7) Caravan, P., Ellison, J. J., McMurry, T. J., and Lauffer, R. B. (1999) Gadolinium(III) chelates as MRI contrast agents: structure, dynamics, and applications. *Chem. Rev. 99*, 2293–2352.

(8) Tóth, É., Helm, L., and Merbach, A. E. (2002) Relaxivity of MRI contrast agents. *Top. Curr. Chem. 221*, 61–101.

(9) Tóth, É., Helm, L., Kellar, K. E., and Merbach, A. E. (1999) Gd(DTPA-bisamide)alkyl copolymers: a hint for the formation of MRI contrast agents with very high relaxivity. *Chem. Eur. J. 5*, 1202–1211.

(10) Ladd, D. L., Hollister, R., Peng, X., Wei, D., Wu, G., Delecki, D., Snow, R. A., Toner, J. L., Kellar, K., Eck, J., Desai, V. C., Raymond, G., Kinter, L. B., Desser, T. S., and Rubin, D. L. (1999) Polymeric gadolinium chelate magnetic resonance imaging contrast agents: design, synthesis, and properties. *Bioconjugate Chem. 10*, 361–370.

(11) Duarte, M. G., Gil, M. H., Peters, J. A., Colet, J. M., Vander Elst, L., Muller, R. N., and Geraldes, C. F. G. C. (2001) Synthesis, characterization, and relaxivity of two linear Gd-(DTPA)-polymer conjugates. *Bioconjugate Chem. 12*, 170–177.

(12) Allen, M. J., Raines, R. T., and Kiessling, L. L. (2006) Contrast agents for magnetic resonance imaging synthesized with ring-opening metathesis polymerization. *J. Am. Chem. Soc. 128*, 6534–6535.

(13) Wiener, E. C., Brechbiel, M. W., Brothers, H., Magin, R. L., Gansow, O. A., Tomalia, D. A., and Lauterbaur, P. A. (1994) Dendrimer-based metal chelates: a new class of magnetic resonance imaging contrast agents. *Magn. Reson. Med. 31*, 1–8.

(14) Bryant, L. H., Jr, Brechbiel, M. W., Wu, C., Bulte, J. W. M., Herynek, V., and Frank, J. A. (1999) Synthesis and relaxometry of high-generation ($G = 5$, 7, 9, and 10) PAMAM dendrimer-DOTA-gadolinium chelates. *J. Magn. Reson. Imaging 9*, 348–352.

(15) Fulton, D. A., Elemento, E. M., Aime, S., Chaabane, L., Botta, M., and Parker, D. (2006) Glycoconjugates of gadolinium complexes for MRI applications. *Chem. Commun.* 1064–1066.

(16) Jászberényi, Z., Moriggi, L., Schmidt, P., Weidensteiner, C., Kneuer, R., Merbach, A. E., Helm, L., and Tóth, É. (2007) Physicochemical and MRI characterization of Gd^{3+}-loaded polyamidoamine and hyperbranched dendrimers. *J. Biol. Inorg. Chem. 12*, 406–420.

(17) Sitharaman, B., Kissell, K. R., Hartman, K. B., Tran, L. A., Baikalov, A., Rusakova, I., Sun, Y., Khant, H. A., Ludtke, S. J., Chiu, W., Laus, S., Tóth, É., Helm, L., Merbach, A. E., and Wilson, L. J. (2005) Superparamagnetic gadonanotubes are high-performance MRI contrast agents. *Chem. Commun.* 3915–3917.

(18) Livramento, J. B., Tóth, É., Sour, A., Borel, A., Merbach, A. E., and Ruloff, R. (2005) High relaxivity confined to a small molecular space: a metallostar-based, potential MRI contrast agent. *Angew. Chem., Int. Ed. 44*, 1480–1484.

(19) Pierre, V. C., Botta, M., Aime, S., and Raymond, K. N. (2006) Fe(III)-templated Gd(III) self-assemblies—a new route toward macromolecular MRI contrast agents. *J. Am. Chem. Soc. 128*, 9272–9273.

(20) Raymond, K. N., and Pierre, V. C. (2005) Next generation, high relaxivity gadolinium MRI contrast agents. *Bioconjugate Chem. 16*, 3–8.

(21) Bottrill, M., Kwok, L., and Long, N. (2006) Lanthanides in magnetic resonance imaging. *Chem. Soc. Rev. 35*, 557–571.

(22) Liu, Y., and Reineke, T. M. (2005) Hydroxyl stereochemistry and amine number within poly(glycoamidoamine)s affect intracellular DNA delivery. *J. Am. Chem. Soc. 127*, 3004–3015.

(23) Dobashi, Y., and Hara, S. (1987) A chiral stationary phase derived from (*R*,*R*)-tartramide with broadened scope of application to the liquid chromatographic resolution of enantiomers. *J. Org. Chem. 52*, 2490–2496.

(24) Goodacre, J., Ponsford, R. J., and Stirling, I. (1975) Selective removal of the *t*-butyloxycarbonyl protecting group in the presence of *t*-butyl and *p*-methoxybenzyl esters. *Tetrahedron Lett.* 3609–3612.

(25) González, A. G., Brouard, I., León, F., Padrón, J. I., and Bermejo, J. (2001) A facile chemoselective deacetylation in the presence of benzoyl and *p*-bromobenzoyl groups using *p*-toluenesulfonic acid. *Tetrahedron Lett. 42*, 3187–3188.

(26) Horrocks, W. D., Jr., and Sudnick, D. R. (1979) Lanthanide ion probes of structure in biology. Laser-induced luminescence decay constants provide a direct measure of the number of metal-coordinated water molecules. *J. Am. Chem. Soc. 101*, 334–340.

(27) Supkowski, R. M., and Horrocks, W. D., Jr. (2002) On the determination of the number of water molecules, *q*, coordinated to europium(III) ions in solution from luminescence decay lifetimes. *Inorg. Chim. Acta 340*, 44–48.

(28) Tóth, É., Helm, L., Merbach, A. E., Hedinger, R., Hegetschweiler, K., and Jánossy, A. (1998) Structure and dynamics of a trinuclear gadolinium(III) complex: the effect of intramolecular electron spin relaxation on its proton relaxivity. *Inorg. Chem. 37*, 4104–4113.

(29) Aime, S., Botta, M., Fasano, M., Paoletti, S., Anelli, P. L., Uggeri, F., and Virtuani, M. (1994) NMR evidence of a long exchange lifetime for the coordinated water in Ln(III)-bis(methyl amide)-DTPA complexes (Ln = Gd, Dy). *Inorg. Chem. 33*, 4707–4711.

(30) Jacques, V., and Desreux, J. F. (2002) New classes of MRI contrast agents. *Top. Curr. Chem. 221*, 123–164.

BC700375M

ARTICLES

Optimizing Size and Copy Number For PEG-fMLF (*N*-Formyl-methionyl-leucyl-phenylalanine) Nanocarrier Uptake by Macrophages

Li Wan,[†] Xiaoping Zhang,[†] Shahriar Pooyan,[†] Matthew S. Palombo,[†] Michael J. Leibowitz,[‡,§] Stanley Stein,[†] and Patrick J. Sinko*[,†,§,△]

Department of Pharmaceutics, Ernest Mario School of Pharmacy, Rutgers, The State University of New Jersey, 160 Frelinghuysen Road, Piscataway, New Jersey 08854, Department of Molecular Genetics, Microbiology & Immunology, University of Medicine and Dentistry of New Jersey-Robert Wood Johnson Medical School, 675 Hoes Lane, Piscataway, New Jersey 08854, Cancer Institute of New Jersey, 195 Little Albany Street, New Brunswick, New Jersey 08903-2681, and Environmental and Occupational Health Science Institute, 170 Frelinghuysen Road, Piscataway, New Jersey 08854. Received February 26, 2007; Revised Manuscript Received October 31, 2007

Curing HIV-1 infection has remained elusive because of low and fluctuating drug levels arising from poor absorption, the development of viral reservoirs and sanctuary sites, toxicity, and patient nonadherence. The present study addresses the issue of insufficient drug exposure in macrophages. Viral reservoir sites such as macrophages are believed to be responsible for the viral rebound effect observed upon the discontinuation of anti-HIV drug therapy. In our proposed model, a drug can be covalently attached to a nanocarrier in order to facilitate the delivery of therapeutic agents to the site(s) of infection. As an initial step, we propose the covalent attachment of several copies of *N*-formyl-Met-Leu-Phe (fMLF), a known chemo-attractant for macrophages. In this article, one or more copies of fMLF were conjugated to multifunctional commercially available or novel, peptide-based PEG nanocarriers in which the structure was varied by appending PEGs with average molecular weights of 5, 20, and 40 kDa. U937 cell-specific binding and cellular uptake were analyzed. The results of uptake studies indicate that (i) uptake is energy dependent and mediated by a fMLF receptor, (ii) appending only 2 copies of the targeting ligand to the multifunctional nanocarrier appears sufficient for binding *in vitro*, and (iii) of the three configurations studied, the nanocarrier with a molecular weight of about 20 kDa, corresponding to a size of 20–60 nm, demonstrated the highest uptake. The results of the current studies demonstrate the feasibility of targeting macrophages and the suitability of using these synthetically versatile peptide−backbone PEG nanocarriers. The convenience, flexibility and possible limitations of this nanocarrier approach are discussed.

INTRODUCTION

Infection by human immunodeficiency virus type 1 (HIV-1) is the cause of acquired immunodeficiency syndrome (AIDS). AIDS is characterized by the severe impairment of immune system functions resulting in a profound decrease in the number of CD4+ T cells. The advent of highly active antiretroviral therapy (HAART), a multiple drug treatment regimen, has led to a dramatic decrease in both the morbidity and mortality of HIV patients (*1*). Despite this success, curing HIV infection has remained an elusive goal because of many challenges, including low and fluctuating drug concentrations due to poor drug absorption or patient nonadherence (*2*), the presence of viral reservoirs and sanctuary sites (*3*), and drug toxicity due to chronic therapy (*4*).

* Corresponding author. Phone: (732) 445-3831, ext. 213. Fax: (732) 445-4271. eFAX: (732) 875-1090. E-mail: sinko@rci.rutgers.edu.
[†] Rutgers, the State University of New Jersey.
[‡] University of Medicine and Dentistry of New Jersey-Robert Wood Johnson Medical School.
[§] Cancer Institute of New Jersey.
[△] Environmental and Occupational Health Science Institute.

Macrophages are infected early during HIV infection and play an important role throughout the course of infection (*5*). Viral strains that establish infection in the new host are macrophage-tropic in over 95% of early asymptomatic individuals (*5*, *6*). HIV enters macrophages via interactions with surface receptor CD4 (cluster designation 4) and coreceptor CCR5 (chemokine C-C motif receptor 5). Individuals bearing a homozygous deletion of CCR5 (CCR5 △ 32) are highly resistant to HIV-1 infection despite multiple sexual exposures (*7*, *8*). HIV-1 infection of macrophages is productive but noncytopathic, permitting them to serve as a long-lived source of HIV production. Infected macrophages are found in all tissues including the brain, gut, liver, lungs, lymphoid tissues, and spleen. More significantly, they represent major viral reservoirs and are responsible for the relapse of infection and development of resistance upon the discontinuation of treatment. Taken together, macrophages represent a key target and an important HIV cellular reservoir for therapeutic approaches aimed at decreasing the replication of the residual virus that survives HAART (*9*).

Among the major causes of HIV treatment failure, insufficient drug exposure due to poor penetration into viral reservoirs is

10.1021/bc070066k CCC: $40.75 © 2008 American Chemical Society
Published on Web 12/20/2007

one of the areas where little progress has been made, and efforts are generally lacking. Macrophage-specific drug delivery could significantly improve current anti-HIV therapy by improving therapeutic efficacy, minimizing systemic toxicity, and simplifying administration regimens. Targeting may possibly be achieved by covalently attaching a drug to a macrophage-specific ligand via a polymeric nanocarrier. A number of natural ligands for macrophage targeting have been explored. An example of such a ligand is IgG-derived immunomodulating peptide tuftsin (Thr-Lys-Pro-Arg), which has been conjugated to the HIV reverse transcriptase inhibitor 3′-azido-3′-deoxythymidine (AZT) (*10*). The AZT−tuftsin chimera possessed characteristics of both components, including inhibition of reverse transcriptase and HIV−antigen expression, stimulation of IL-1 release from mouse macrophages, and augmentation of the immunogenic function of the cell. Similarly, acetylated low-density lipoprotein (AcLDL), a ligand for macrophage scavenger receptors, has been conjugated to AZT (*11*). A 10-fold increase in the uptake of AcLDL−AZT was observed as compared to AZT in murine (J774) and human (U937) macrophage cell lines.

N-formyl peptides are cleavage products of bacterial and mitochondrial proteins and serve as potent chemoattractants for mammalian phagocytic leukocytes. The synthetic peptide *N*-formyl-methionyl-leucyl-phenylalanine (fMLF) is the first identified and most potent chemoattractant for human macrophages (*12*). fMLF binds to the formyl peptide receptor (FPR) with high affinity (10–30 nM) and to its variant FPRL1 with low affinity (*12*). When the free fMLF chemotactic peptide binds to a phagocytic cell, rapid receptor-mediated internalization takes place (*13*). After binding to the receptors, fMLF activates phagocytic leukocytes through a G-protein-mediated signaling cascade resulting in increased cell migration, calcium mobilization, and the heterologous down-regulation of the expression and function of the two chemokine receptors CCR5 and CXCR4, which are the key fusion coreceptors for HIV-1 (*12*). fMLF has been used for imaging of infection and inflammation (*14*).

Previous work by our group showed that increasing the number of fMLF residues (up to eight) attached to a single PEG polymer resulted in enhanced avidity (K_d = 0.18 nM) for neutrophil-like differentiated HL-60 cells relative to free fMLF (K_d = 28 nM) (*15*). A PEG polymer bearing four fMLF and four digoxigenin residues showed specific enhancement in binding to differentiated HL-60 cells and mouse peritoneal macrophages *in situ* relative to a polymeric carrier lacking fMLF. Furthermore, increasing copy numbers of fMLF increased avidity more potently than it increased cell activation, suggesting that toxicity due to excessive phagocyte activation might not be a problem. These early results provided conceptual feasibility. However, further studies are required in order to evaluate if biologically compatible polymer conjugates bearing multiple fMLF residues can be used as effective targeted drug delivery systems for phagocytic cells. In general, the successful development of a nanocarrier delivery system requires an understanding of (1) the relationship between cell uptake and the copy number, size, and shape of the constituent PEG chains, (2) the avidity and specificity of the interactions between the ligands appended to the nanocarriers and the cognate receptors on the target cell, and (3) the chemical reactions required for the synthesis of such macromolecules, including the stability of the conjugates prior to administration and disassembly and release of the active drug after reaching the target site.

In the present study, a series of PEG nanocarriers with different numbers of fMLF and various PEG structures were designed, synthesized, and evaluated *in vitro* for targeting to human U937 cells induced to differentiate into a macrophage phenotype. The relationship between the molecular features of PEG-fMLF nanocarriers (i.e., number of targeting peptide and PEG sizes) and cell uptake was elucidated. The current studies further demonstrate the feasibility of using macrophage-targeted nanocarriers, while also introducing a new nanocarrier that allows for the attachment of multiple drugs and targeting moieties resolving a potentially major limitation of commercially available PEGs.

MATERIALS AND METHODS

Materials. *N*-formyl-Met-Leu-Phe-Lys-Cys-amide and the backbone peptides acetyl-Cys(thiopyridine)-(β-Ala-β-Ala-Lys)$_n$-amide (n = 2, 4) were synthesized via Fmoc Chemistry by the W.M. Keck Facility (New Haven, CT). *N*-hydroxysuccinimide (NHS)-PEG-vinyl sulfone (VS; NHS-PEG-VS) (MW ∼5 kDa), mPEG-MAL (MW ∼5.5 kDa), mPEG-(MAL)$_2$ (MW ∼5.5 kDa, 20 kDa, and 40 kDa), mPEG-NH$_2$ (MW ∼5 kDa), and 4-arm PEG-(NH$_2$)$_4$ (MW ∼10 kDa) were obtained from Nektar Therapeutics (Huntsville, AL). *N*-maleimidobutyryloxysuccinimide ester (GMBS) was obtained from Pierce Biotechnology (Rockford, IL). NHS-carboxyfluorescein was obtained from Sigma-Aldrich (St. Louis, MO). Fluo-4 AM (acetoxymethyl ester) was obtained from Molecular Probes (Eugene, OR). DMF **(**dimethylformamide), DIEA (diisopropylethylamine), acetonitrile (ACN), trifluoroacetic acid (TFA), ether, and other chemical reagents were purchased from Sigma-Aldrich (St. Louis, MO).

Synthesis and Characterization of PEG-fMLF Nanocarriers. *PEG$_{5k}$-fMLF(fMLFK(FLUORESCEIN)C-mPEG$_{5K}$) and PEG$_{5K,20K,40K}$-(fMLF)$_2$ ([fMLFK(FLUORESCEIN)C]$_2$-mPEG$_{5K,20K,40K}$).* mPEG$_{5K}$-maleimide (11.2 mg, 2 mmol) was dissolved in 1 mL of phosphate-buffered saline (PBS, pH 7.4) at room temperature. To this were added 3 equivalents of fMLFKC (4 mg, 6 mmol). The reaction was stirred overnight at room temperature. For the 2-copy forked conjugates (PEG$_{5K,20K,40K}$-(fMLF)$_2$ ([fMLFK(FLUORESCEIN)C]$_2$-mPEG$_{5K,\ 20K,\ 40K}$) a similar protocol was used (e.g., 3 equiv 8 mg, 12 mmol fMLFKC was utilized for PEG$_{5K}$-(fMLF)$_2$ ([fMLFK(FLUORESCEIN)C]$_2$-mPEG$_{5K}$)). The excess solvent was removed under reduced pressure. The solid PEGylated product was further reacted with 3 equiv of NHS−carboxyfluorescein (3 mg, 6 mmol) and 1% DIEA (5 μL) in 500 μL of DMF. The reaction was stirred for 3 h at room temperature. The final product was recrystallized from cold ether, washed three times to remove impurities, and lyophilized. The dried product was then dissolved in ∼5 mL of ddH_2O and subjected to dialysis against ddH_2O for 2 days in the dark in order to remove the excess unreacted reagents (NHS−carboxyfluorescein, fMLFKC) and salts, which might have not been removed during the ether precipitation step. The solution was then lyophilized to yield the purified product. [fMLFK(fluorescein)C]$_2$-mPEG$_{20K,40K}$ was synthesized using a similar approach (Scheme 1).

PEG$_{10k}$-(fMLF)$_4$ [fMLFK(FLUORESCEIN)C]$_4$. PEG$_{10K}$-(NH$_2$)$_4$ (20 mg, 2 mmol) was first activated with a 3-fold molar excess of the heterobifunctional cross-linker GMBS in DMF to form a maleimide-activated PEG. The reaction was stirred overnight at room temperature. The product was precipitated with cold ether and dried under vacuum to yield the solid PEGylated product. The GMBS linker essentially converts a primary amino group to a maleimide group that can react with a thiol group to form a stable thioether bond. This activated intermediate was reacted with 3 equiv of fMLFKC (16 mg, 24 mmol) in 1 mL of phosphate-buffered saline (PBS, pH 7.4) at room temperature. The reaction was stirred overnight at room temperature. The excess solvent was removed under reduced pressure. The reaction product was further reacted with 3 equiv of NHS−carboxyfluorescein (12 mg, 24 mmol) and 1% DIEA (5 μL) in 500 μL of DMF. The reaction was stirred for 3 h at room temperature. The final product was recrystallized from cold ether and washed three times to remove impurities. Then

Scheme 1. Synthesis of PEG-fMLF Nanocarriers with 1 Copy (PEG_{5k}-fMLF, Scheme A), 2 Copies (PEG_{5k}-$(fMLF)_2$,Scheme B), and 4 Copies (PEG_{10k}-$(fMLF)_4$, Scheme C) of fMLF, and the Fluorescein-Labeled Control PEG_{5k} without fMLF Peptides (Scheme D)[a]

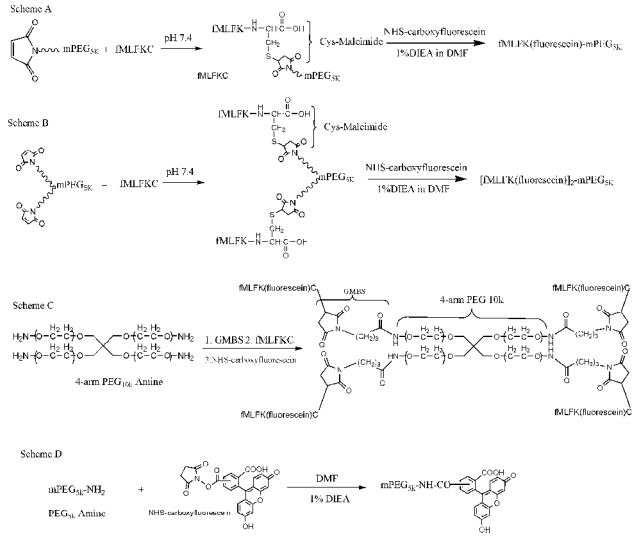

[a] Note that PEG does not have any charge. It tends to give a weak signal in MALDI-TOF.

Scheme 2. Design of Peptide-Based PEG Nanocarriers with 2 and 4 Copies of fMLF Peptides[a]

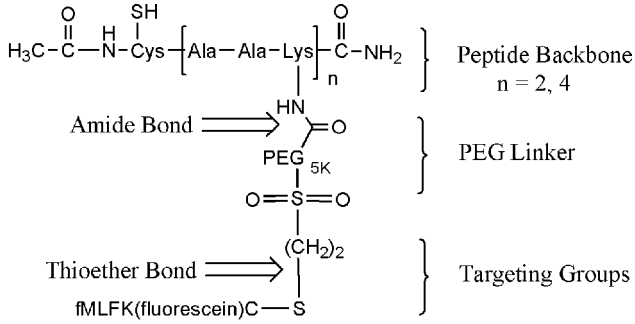

[a] The peptide acetyl-Cys-(β-Ala-β-Ala-Lys)*n*-amide (n = 2, 4) is the backbone. NHS-PEG_{5k}-VS is the linker between the peptide backbone and targeting groups fMLFKC, which form an amide bond with amine group on acetyl-Cys-(β-Ala-β-Ala-Lys)*n*-amide and a thioether bond with the thiol group on fMLFKC.

the dried product was dissolved in ~5 mL of ddH_2O and was subject to dialysis against ddH_2O for 2 days in the dark. The solution was lypholyzed to yield the purified product.

PEG_{5k} ($mPEG_{5K}$-FLUORESCEIN). The amino groups of $mPEG_{5k}$-NH_2 (5 mg, 1 mmol) were reacted with 3 equiv of NHS−carboxyfluorescein (1.5 mg, 3 mmol) and 1% DIEA (5 μL) in 500 μL of DMF to yield $mPEG_{5k}$-fluorescein. The reaction was stirred for 3 h at room temperature. The final product was recrystallized from cold ether, washed three times to remove impurities, and dried under vacuum. Then the dried product was dissolved in ~5 mL of ddH_2O and was subject to dialysis against ddH_2O for 2 days in the dark. The solution was lyophilized to give the purified product.

Peptide−Backbone PEG-fMLF Nanocarriers. To achieve a branch shape and multiple coupling sites, peptide−backbone PEG nanocarriers were designed (Scheme 2). In order to synthesize fMLF PEG nanocarriers with two copies of fMLF (Scheme 2), the backbone peptide acetyl-Cys(thiopyridine)-β-Ala-β-Ala-Lys-β-Ala-β-Ala-Lys-amide (1.4 mg, 2 mmol) was reacted with 2 equiv of NHS-PEG_{5k}-VS (40 mg, 8 mmol) and 1% DIEA (5 μL) in 500 μL of DMF. The reaction was carried out at room temperature for 3 h. The PEGylated intermediate acetyl-Cys(thiopyridine)-[β-Ala-β-Ala-Lys(PEG_{5k}-VS)]$_2$-amide was purified by size-exclusion chromatography on a TSK Gel-3000pw column. The size of the product in eluted fraction volume was confirmed by MALDI-TOF mass spectrometry, and peak fractions were pooled and dried under vacuum. The PEGylated intermediate was dissolved in 1 mL of phosphate-buffered saline (PBS, pH 7.4) at room temperature. To this, 3 equiv of fMLFKC (8 mg, 12 mmol) was added. The reaction was stirred overnight at room temperature. The product was then treated with a 5 M excess of dithiothreitol (DTT) for another 2 h. The product was dialyzed against ddH_2O for 2 days. Then the excess solvent was removed under reduced pressure. The solid PEGylated product was further reacted with 3 equiv of NHS−carboxyfluorescein (6 mg, 12 mmol) and 1% DIEA (5 μL) in 500 μL of DMF. The reaction was stirred for 3 h at room temperature. The final product was recrystallized from cold ether, washed three times to remove impurities, and dried under vacuum. Then the dried product was dissolved in ~5 mL of ddH_2O and was subject to dialysis against ddH_2O for 2 days in the dark. The solution was dried under vacuum to give the purified product. The PEG nanocarrier with four copies of fMLF and fluorescein was synthesized by a similar scheme (Scheme 2).

Size-Exclusion Chromatography (SEC). Purified nanocarriers were dissolved in ddH_2O at a final concentration of ~1 mg/mL. The solution was loaded into a Waters HPLC equipped with a SEC TSK-GEL G3000PW HPLC column (Tosoh Corp., Japan). The mobile phase was 100% ddH_2O, and the flow rate was 1 mL/min. Eluents were monitored for absorbance at 220 nm with a Waters UV detector.

MALDI-TOF Mass Spectrometry. Mass spectrometry was performed using an Applied Biosystems Voyager DE Pro matrix-assisted laser desorption time-of-flight mass spectrometer (MALDI-TOF). The instrument was operated in the linear positive ion mode at 25.0 kV utilizing delayed extraction (100 ns). Data were collected over a mass range of 2000–10,000 M/z with 100 shots per spectrum. Samples were dissolved in 50:50 H_2O/ACN with 0.1% TFA at ~10 mg/mL. The matrix solution was (10 mg/mL) α-cyano-4-hydrocinnamic acid (10 mg/mL) in 50:50 H_2O/ACN with 0.1% TFA. A sample (4 μL) was combined with 1 μL of matrix solution. This mixture was then spotted onto the sample plate and allowed to dry. The instrument was externally calibrated by analysis of a three-component peptide mixture over a mass range of ~1000–10000 *m/z*. Data analysis consisted of baseline correction and noise reduction utilizing Data Explorer software, version 5.1 (Applied Biosystems). The difference in molecular weight between the final nanocarrier and the unreacted PEG corresponds to the molecular weight additions on the PEG skeleton. The relative intensity for unconjugated PEG is much lower than that of its peptidic core conjugated counterpart since the unconjugated PEG cannot be ionized to the same extent. (Figure 1).

Amino Acid Analysis. Amino acid analysis of the free fMLF, PEG_{5k}-fMLF, PEG_{5K}-$(fMLF)_2$, PEG_{10k}-$(fMLF)_4$, and peptide-based PEG_{10k}-$(fMLF)_2$ and PEG_{20k}-$(fMLF)_4$ nanocarriers was performed at the Protein Facility of the Iowa State University Office of Biotechnology (Ames, Iowa) to confirm the presence and concentration of fMLF on PEG nanocarriers. The sample was transferred to a hydrolysis tube and dried under vacuum. The tube was placed in a vial containing 6 N HCl and a small amount of phenol, and the samples were hydrolyzed by the HCl vapors under vacuum for 65 min at 150 °C. Following hydrolysis, each sample was dissolved in distilled water containing EDTA. An aliquot containing ~1 nmol of each amino acid was placed on a sample slide, and derivatization was done under basic conditions for 30 min with phenyliso-

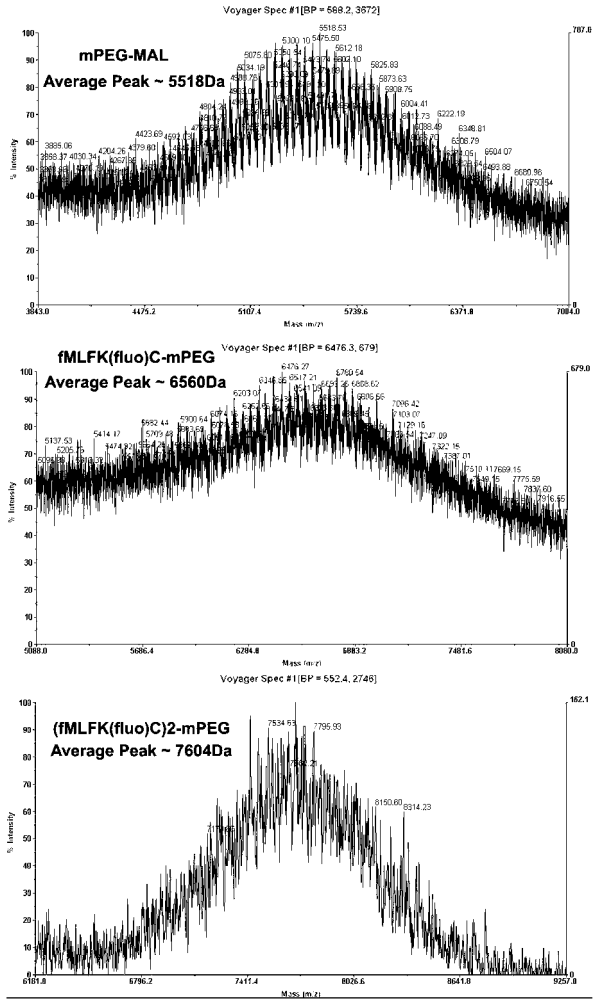

Figure 1. MALDI-TOF spectra of PEG-fMLF nanocarriers. The starting material mPEG-MAL showed the polydisperse peaks with average molecular weight at about 5518 Da. fMLFK(fluorescein)C-mPEG showed an average peak at 6560 Da, and [fMLFK(fluorescein)C]$_2$-mPEG showed an average peak at 7604 Da.

thocyanate (PITC). The resulting phenylthiocarbamyl (PTC) derivatives were separated by reverse-phase chromatography and quantitated by absorbance at 254 nm.

Stability in PBS and Rabbit Plasma. The stability of the fluorescein-labeled PEG-fMLF nanocarriers was tested in 10 mM PBS (pH 7.4) and rabbit plasma at 37 °C for 24 h. The nanocarrier solutions were incubated separately in 10 mM PBS (pH 7.4) or in spiked rabbit plasma at 37 °C. Aliquots were withdrawn at different time points and centrifuged at 14,000*g* for 90 min with a Microcon filter (molecular weight cutoff = 3,000 Da) (Amicon Inc., Beverly, MA). The free fMLF cleaved from the PEG nanocarrier during the incubation passes through the filter, whereas the fMLF that remains linked is retained. The eluents and retentates resulting from the different incubation time points were withdrawn and subjected to fluorescence detection. Each measurement was done in triplicate.

Cell Lines. The U937 cell line, which had been isolated from a patient suffering from histiocytic lymphoma, was later found capable of terminal differentiation upon induction into a macrophage phenotype. U937 cells were grown in RPMI 1640 DM medium supplemented with 10% FBS (fetal bovine serum) as suspended cells. They differentiated into macrophage-like cells after treatment with 1 mM dibutyryl-cAMP for 48 h, remaining suspended. The U937 cell line is potentially an excellent model system to study formyl peptide receptors because, in the undifferentiated state, these cells express low

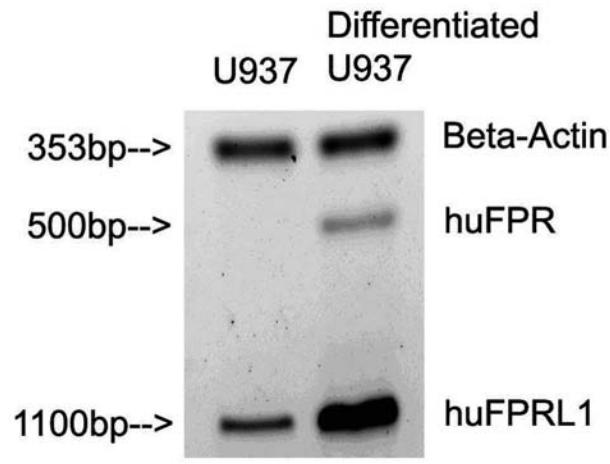

Figure 2. mRNA expression of formyl peptide receptor (FPR) and formyl peptide receptor-like 1 (FPRL1) in undifferentiated and differentiated U937 by RT-PCR determined using semiquantitative RT-PCR. Differentiated U937 cells expressed high levels of FPR mRNA (500 bp product) and FPRL1 mRNA (1100 bp product), while undifferentiated U937 cells only expressed a low level of FPRL1 mRNA and no FPR mRNA.

levels of formyl peptide receptors and showed no movement toward any stimuli (*16, 17*). A variety of differentiating agents induce U937 cells toward a more mature phenotype in which they express formyl peptide receptors and display migratory properties similar to those of peripheral blood monocytes or neutrophils.

Expression of Formyl Peptide Receptors. The expression of the two relevant human receptors for fMLF, FPR and FPRL1, was evaluated using semiquantitative RT-PCR. Total RNA was extracted from U937 and differentiated U937 cells. RNA (2 μg) was used as a template for RT-PCR. The sense oligonucleotide primer 52-CTGCTGGTGCTGCTGGCAAG-32 and antisense primer 52-AATATCCCTGACCCCATCCTCA-32 based on the sequences flanking the human FPRL1 coding region (1.1 kb) were designed to amplify FPRL1. The sense primer 52-CTCCAGTTGGACTAGCCACA-32 (nucleotide 1639–1658 in exon 2) and antisense primer 52-CCATCACCCAGGGC-CCAATG –32 (nucleotide 5341–5359 in the coding region of exon 3) were designed to amplify human FPR. The sense primer 5′-GCTCG TCGTC GACAA CGGCT C-3′ and the antisense primer 5′-CAAAC ATGAT CTGGG TCATC TTCTC-3′ for beta-Actin were used as controls.

A commercially available rabbit polyclonal antibody was used in a Western Blot analysis without success. The antibody should have been able to detect both receptors but produced bands that were not always reproducible or consistent with the expected sizes.

Time-Dependent Cellular Association of PEG-fMLF Nanocarriers in Differentiated U937 Cells. U937 cells in suspension were differentiated into macrophage-like cells after treatment with 1 mM dibutyryl-cAMP for 48 h. The suspended differentiated cells were washed by centrifugation twice with uptake buffer (Hanks Balanced Salt Solutions (HBSS) with 20 mM HEPES to adjust pH to neutral). The washed cells were added to wells of 24-well polycarbonate plates at a density of 1×10^5 cells/well in the presence of 50 nM fluorescein-labeled PEG-fMLF nanocarriers for 1, 2, 4, or 8 h at 37 °C. The concentrations of all fMLF-bearing nanocarriers were normalized based on the fMLF moiety concentration. That is, a nanocarrier bearing one copy of fMLF was used at 50 nM fMLF and 50 nM whole-molecule concentration, a nanocarrier bearing two copies of fMLF was used at 50 nM fMLF and 25 nM whole-molecule concentration, and so forth. At the end of an

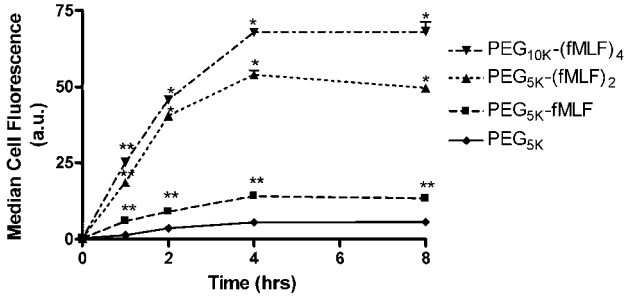

Figure 3. Time course of total cell-associated fluorescein-labeled PEG-fMLF nanocarriers in differentiated U937 cells at 37 °C. Differentiated U937 cells were incubated for the indicated time periods and plotted against the cell-associated nanocarrier amounts. The cell-associated fluorescence was measured by cell flowcytometry and reported as the medium value of intensity distribution. The means ± SD for three independent experiments are shown for each nanocarriers. PEG_{5K}-fMLF enhanced macrophage association about 15-fold ($p < 0.05$) after 4 h of incubation at 37 °C compared to the control PEG_{5k}. The values were about 45- and 60-fold higher for PEG_{5k}-$(fMLF)_2$ and PEG_{10k}-$(fMLF)_4$, respectively, than for the control PEG_{5k} ($p < 0.01$). (Statistically significant differences were observed between the PEG-fMLF nanocarriers and the control PEG_{5k}, * $p < 0.01$, ** $p < 0.05$.)

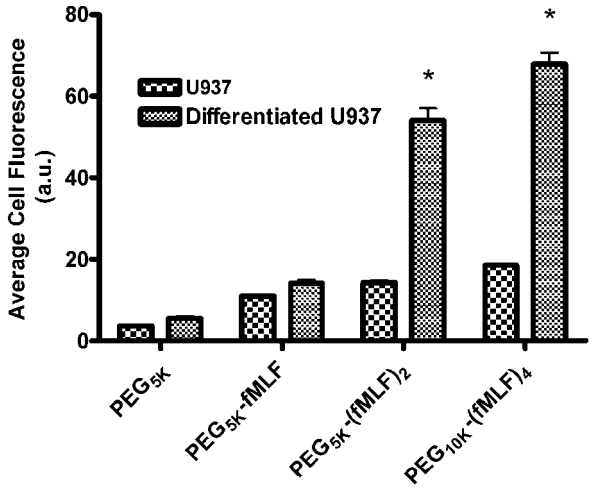

Figure 4. Total cellular association (uptake from now on) of fluorescein-labeled PEG-fMLF nanocarriers in the undifferentiated and the differentiated U937 cells at 37 °C after 4 h of incubation. The means ± SD for three independent experiments are shown for each value. (*, statistically significant difference between undifferentiated and differentiated U937 cells, $p < 0.01$.)

incubation period, washing the cells twice with ice-cold uptake buffer stopped the uptake. The cells were subsequently resuspended in uptake buffer. Cell-associated fluorescence was analyzed by flow cytometry using a Coulter EPICS PROFILE (Fullerton, CA) equipped with a 25 mW argon laser. For each analysis, 10,000 to 20,000 events were accumulated. The results are shown in Figure 3.

U937 Cell Uptake by Undifferentiated and Differentiated U937 Cells. To show that the cellular association of 50 nM PEG-fMLF nanocarriers was based on uptake, the uptake experiments were performed with both undifferentiated and differentiated U937 cells as described above for the time-dependent cellular association. The results are shown in Figure 4.

Temperature-Dependent Uptake of PEG-fMLF Nanocarriers. To further demonstrate that the cellular association of 50 nM PEG-fMLF nanocarriers was based on uptake, differentiated U937 cells were incubated with fluorescein-labeled PEG-fMLF nanocarriers for 4 h at 37 or 4 °C. At the end of an incubation period, the cells were washed, and resuspended, and cell-

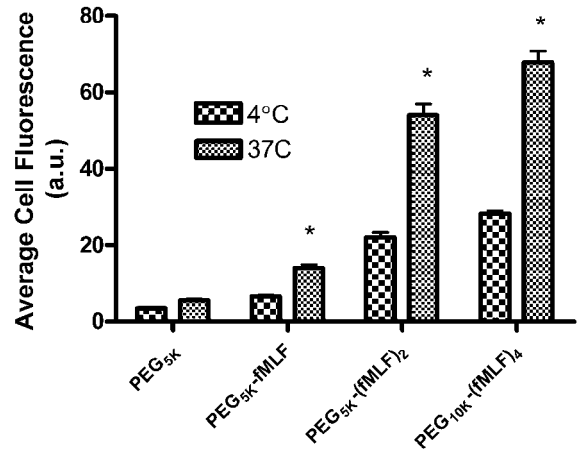

Figure 5. Uptake of fluorescein-labeled PEG-fMLF nanocarriers in differentiated U937 cells at 4 and 37 °C after 4 h of incubation. The means ± SD for three independent experiments are shown for each value. (*, statistically significant difference between 4 and 37 °C treatments, $p < 0.01$.)

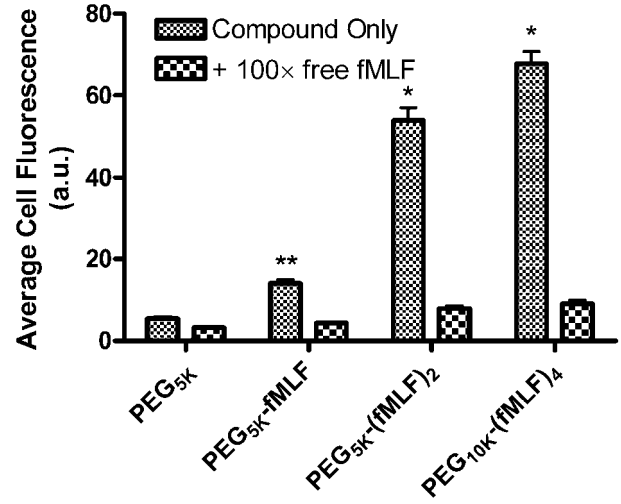

Figure 6. Uptake of fluorescein-labeled PEG-fMLF nanocarriers in differentiated U937 cells at 37 °C after 4 h of incubation in the absence and presence of 5 μM free fMLF (100× in excess to the concentration of the labeled nanocarriers). The means ± SD for three independent experiments are shown for each value. (Statistically significant difference between the differentiated U937 cells incubated with and without free fMLF * $p < 0.01$, ** $p < 0.05$.)

associated fluorescence was analyzed by flow cytometry as described above. The results are shown in Figure 5.

Uptake Inhibition by Free fMLF Peptide. The involvement of formyl peptide receptors in differentiated U937 cell uptake of PEG-fMLF nanocarriers was also investigated using inhibition studies. Free fMLF peptide (5 μM), a competitive substrate of formyl peptide receptor, was coincubated with 50 nM fluorescein-labeled PEG, mPEG-fMLF, mPEG-$(fMLF)_2$, or PEG-$(fMLF)_4$ nanocarriers. Uptake assays were performed as described above for the temperature-dependent uptake. The results are shown in Figure 6.

Uptake by Fluorescence Microscopy. Differentiated U937 cells were incubated in 24-well microplates with 50 nM fluorescein-labeled PEG, mPEG-fMLF, mPEG-$(fMLF)_2$, or PEG-$(fMLF)_4$ nanocarriers for 4 h. After incubation, the cells were washed twice using centrifugation and resuspended in Hanks Balanced Salt Solutions (HBSS). The stained cell suspension was placed on slides, covered, and observed under a Zeiss Axiostar Plus fluorescence microscope (Thornwood, NY) with an objective magnification of 63× and an Insight digital

Table 1. Results of Amino Acid Analysis of PEG-fMLF Nanocarriers[a]

sample name	amino acid ratio (normalized by phenylalanine) Met	Leu	Phe	Lys	concentration (nM) (expected 50 nM)
fMLF	0.90	1.20	1.00	1.00	36.00
PEG-(fMLF)	0.95	1.20	1.00	1.00	37.10
PEG-$(fMLF)_2$	0.97	1.23	1.00	0.95	37.87
PEG-$(fMLF)_4$	0.91	1.19	1.00	1.01	42.00
PB-PEG-$(fMLF)_2$	0.91	1.17	1.00	2.08	40.00
PB-PEG-$(fMLF)_4$	0.96	1.19	1.00	1.87	37.90

[a] The amino acids were normalized relative to phenylalanine. PB: peptide-based.

camera (Sterling, MI) with proper filter sets. Digital images were taken with the Insight digital camera and its companion Spot software.

Calcium Mobilization. Differentiated U937 cells were loaded with 4 μmol/L fluo-4 AM in HBSS for 30 min at 37 °C in the dark. The cells were washed and incubated for 30 min at room temperature to allow the Fluo-4 AM dye to completely de-esterify. The cells were washed, resuspended in HBSS, and treated with 1 μM PEG-fMLF nanocarriers at 37 °C. Fluorescence readings were obtained using a Tecan fluorescence plate reader for 400 at 2 s intervals.

Statistical Analysis. All statistical tests were performed using GraphPad Instat (GraphPad Software, Inc., San Diego, CA). A minimal *p*-value of 0.05 was used as the significance level for all tests. One-way analysis of variance and the Tukey test were performed on the uptake data. All data are reported as means ± SD of three observations, unless otherwise noted. The graphs were plotted using GraphPad Prism 4.01 (GraphPad Software, Inc., San Diego, CA).

RESULTS

Synthesis and Characterization of PEG-fMLF Nanocarriers. The PEG-fMLF nanocarriers $mPEG_{5K}$-fMLF, $mPEG_{5K}$-$(fMLF)_2$, and PEG_{10K}-$(fMLF)_4$ were prepared by coupling the fMLFKC to mPEG-MAL, mPEG-(MAL)2, and PEG-$(NH_2)_4$ according to the procedures described in Scheme 1. All nanocarriers were purified by the removal of low molecular weight contaminants using 3 kDa dialysis bags in ddH_2O for 2 days. The structures of purified products were confirmed by a combination of SEC, MALDI-TOF, and amino acid analysis. Amino acid analysis of the final nanocarrier showed the presence of methionine, leucine, phenylalanine, lysine, and cysteine in the proper ratios (Table 1). Matrix-assisted laser desorption/ionization time-of-flight (MALDI-TOF) mass spectrometry was used to accurately determine the molecular masses of polydisperse polymeric nanocarriers (Figure 1). A comparison of the MALDI-TOF spectra of unreacted mPEG-MAL (MW ~5518 Da) with that of the fMLFK(fluorescein)C-mPEG (~6560 Da) and $[fMLFK(fluorescein)C]_2$-mPEG (~7604 Da) revealed average mass peak shifts of ~1040 Da and ~2080 Da, respectively, confirming that the polymeric nanocarriers created were derivatized with either fMLFK(fluorescein)C (1042 Da) or $[fMLFK(fluorescein)C]_2$ (2084 Da). Thus, although the polymer is polydisperse because of variations in the number of ethylene glycol repeats, the fMLFK(fluorescein) content of each preparation is monodisperse.

Novel peptide−backbone nanocarriers were prepared by coupling the peptide backbone, acetyl-Cys(TP)-(β-Ala-β-Ala-Lys-)$_n$-amide (n = 2, 4) to a heterobifunctional PEG, NHS-PEG-VS (Scheme 2). The NHS moiety reacts specifically with the ε-amine group of the backbone peptide, and the VS group is used for the attachment of PEG to the sulfhydryl (SH) moiety of the fMLFKC peptide. The linkages formed amide (for NHS) and thioether (for VS) bonds between PEG and the fMLFKC and the peptide backbone, respectively. Both bonds are highly stable under physiological conditions. The thiol group of the cysteine moiety in the peptide backbone provides a suitable site for the attachment of a drug moiety. This moiety is protected by thiopyridine, which is an excellent leaving group that can be readily reacted with sulfhydryl-containing drugs or peptides. TP is replaced by fMLFKC during synthesis via a reversible thiol linkage. The product was further reacted with DTT in order to remove the reversibly linked fMLFKC peptide. Thus, the targeting moiety fMLFKC in the nanocarrier is attached via stable and nonreversible thioether linkage. The β-alanine moiety in the scaffold serves as a spacer, reducing steric hindrance during the PEGylation reaction. Scaffold (peptide-based PEG carrier) size was varied by using peptide backbones of different lengths, which could be conjugated with different (2 or 4) numbers of copies of NHS-PEG-VS in reactions proceeding to complete peptide derivatization. In Scheme 2, the Cys residue in the backbone peptide is shown with an −SH group. However, during the synthesis reactions, the thiol must be protected such as with a thiopyridine group, which may later be removed for other conjugation reactions, as shown in Scheme 2.

Stability in PBS and Plasma. The stability of the fluorescein-labeled PEG-fMLF nanocarriers was tested in 10 mM PBS (pH 7.4) and rabbit plasma at 37 °C for 24 h. For nonpeptide PEG-fMLF nanocarriers, the linkages formed a thioether bond between fMLFKC and PEG, and a urethane bond between the fMLFKC and the fluorescein. For peptide−backbone PEG nanocarriers, the linkages formed urethane (from NHS) bonds between PEG and the peptide backbone or a thioether (from VS) bond between PEG and fMLFKC. All bonds were highly stable under physiological conditions. Stability was analyzed by the release of the fluorescence tag. The released fluorescence tag was monitored after 24 h of incubation in PBS or plasma at 37 °C. The degraded product was quantitatively detected in the filtrate using ultrafiltration (5 kDa MWCO). The nanocarriers were found to be stable with less than 3% degradation in PBS or plasma during a 24 h incubation at 37 °C.

Expression of Formyl Peptide Receptors. The expression of the two relevant fMLF receptors, FPR and FPRL1, in the undifferentiated and differentiated U937 cells was confirmed using semiquantitative RT-PCR. Differentiated U937 cells expressed high levels of the formyl peptide receptor (FPR, 500 bp RT-PCR product) and formyl peptide receptor-like 1 (FPRL1, 1100 bp RT-PCR product) transcripts, while undifferentiated U937 cells only expressed low levels of FRPL1 and no detectable FPR (Figure 2). Even though an FPRL-1 antibody was available, we had limited success using it because of inconsistency in size and reproducibility. The RT-PCR result is in agreement with known U937 cell phenotype in the literature.

Time-Dependent Total Cellular Association of PEG-fMLF Nanocarriers in Differentiated U937 Cells. To understand how differentiated U937 cells would interact with PEG-fMLF nanocarriers, we first investigated the time course of total cellular association of 50 nM nanocarriers using flow cytometry. The association of PEG-fMLF nanocarriers with macrophage-like differentiated U937 cells at 37 °C showed a progressive increase from 0 h through 4 h, with steady-state apparently being reached at 4 h (Figure 3). The results are the average of three independent experiments performed on three separate days, and they showed that PEG_{5k} lacking fMLF had very low uptake at all time points during the incubation. In general, the attachment of 1, 2, or 4 copies of fMLF to PEG significantly increased the cellular association at all time points. Specifically, PEG_{5K}-fMLF enhanced macrophage cellular association about 15-fold (p < 0.05) after 4 h of incubation at 37 °C compared to the control

PEG_{5k}. PEG_{5k}-$(fMLF)_2$ and PEG_{10k}-$(fMLF)_4$ further increased uptake about 45- and 60-fold ($p < 0.01$), respectively, compared to the control PEG_{5k}. The correlation between fMLF copy numbers per nanocarrier with the amount of association suggests that the association is mainly mediated by fMLF receptors. Since data below further suggests fMLF receptor-mediated active uptake, from now on we will replace the term total cellular association with the term uptake.

U937 Cell Uptake by Undifferentiated and Differentiated U937 Cells. To show that the uptake of 50 nM PEG-fMLF nanocarriers was mediated by fMLF receptors, a comparison was made between the uptake in undifferentiated U937 cells expressing low levels of FPRL1/no FPR and differentiated U937 cells expressing high levels of FPR and FPRL1 (Figure 4). The results represent the average of three independent experiments performed on three separate days. The uptake of the control PEG_{5k} was low and showed no significant difference between undifferentiated and differentiated U937 cells. In contrast, the uptake of PEG-fMLF nanocarriers with 1, 2, or 4 copies of fMLF was significantly higher in differentiated as compared to undifferentiated U937 cells ($p < 0.01$). PEG_{5k}-fMLF uptake in differentiated U937 cells increased 1.52-fold as compared to undifferentiated U937 cells. Similarly, PEG_{5k}-$(fMLF)_2$ and PEG_{10k}-$(fMLF)_4$ increased 3.76-fold and 3.65-fold, respectively. Significantly higher uptake in differentiated U937 cells expressing FPR and FPRL1 is consistent with uptake being specifically mediated by formyl peptide receptors.

Temperature-Dependent Uptake of PEG-fMLF Nanocarriers. To confirm the expectation that uptake occurred mainly by an active cellular process, temperature-dependent uptake was investigated. The uptake of PEG-fMLF nanocarriers in differentiated U937 cells after 4 h of incubation at 4 °C showed significantly lower cell uptake than at 37 °C in three separate experiments (Figure 5). Nonderivatized PEG_{5k} showed similar low uptake levels at both temperatures. PEG_{5k}-fMLF uptake at 4 °C was only 46.2% of that at 37 °C, while the ratio of 4:37 °C for PEG_{5k}-$(fMLF)_2$ and PEG_{10k}-$(fMLF)_4$ was 40% and 41.6%, respectively. A substantial portion of cell-associated nanocarriers at low temperature are bound to the cell surface but are not internalized, representing both specific receptor binding as well as binding to other cell-surface components. Thus, the temperature-dependent portion at 37 °C is consistent with a receptor-mediated active uptake mechanism.

Uptake Inhibition by Free fMLF Peptide. The specificity of uptake was further investigated using differentiated U937cells incubated with 50 nM PEG-fMLF nanocarriers at 37 °C in the presence of 5 μM free fMLF, which was 100-fold greater than the 50 nM fMLF moiety nanocarrier concentration (Figure 6; the results are the average of three independent experiments performed on three separate days). The presence of 100-fold excess fMLF significantly inhibited the average uptake of PEG-fMLF nanocarriers in differentiated U937 cells. The inhibition led to a relative decrease in the uptake of PEG-fMLF nanocarriers with 1, 2, and 4 copies of fMLF to 31.5%, 14.8%, and 13.5%, respectively. Excess fMLF did not significantly affect the amount of cell-associated PEG_{5k}. Complete inhibition of uptake may not occur because of the fact that there is always some nonspecific binding that occurs, regardless of the concentration of free fMLF that is used (*15*). Taken together, these results further suggest that PEG-fMLF nanocarrier uptake was mediated by formyl peptide receptors.

In the presence of free f-MLF, all three f-MLF-bearing PEG nanocarriers still show statistically higher uptake into U937 cells than PEG_{5k} ($p < 0.05$). PEG-fMLF is higher than PEG_{5k} ($p = 0.011$), and PEG-(fMLF)2 and PEG-(fMLF)4 are higher than PEG-fMLF ($p = 0.018$), whereas there is no difference between PEG-(fMLF)2 and PEG-(fMLF)4 ($p = 0.254$). We roughly estimate that the receptors on the cells are saturated with the 5 μM free fMLF and largely occupied by the 50 nM fMLF-equivalents of fMLF-bearing PEG nanocarriers. Despite receptor saturation by free fMLF and high occupancy by all fMLF-bearing PEG nanocarriers, there is still some correlation between fMLF copy number and the amount of uptake. The reason for this is not clear but could have something to do with the PEG moiety of the fMLF-bearing nanocarriers.

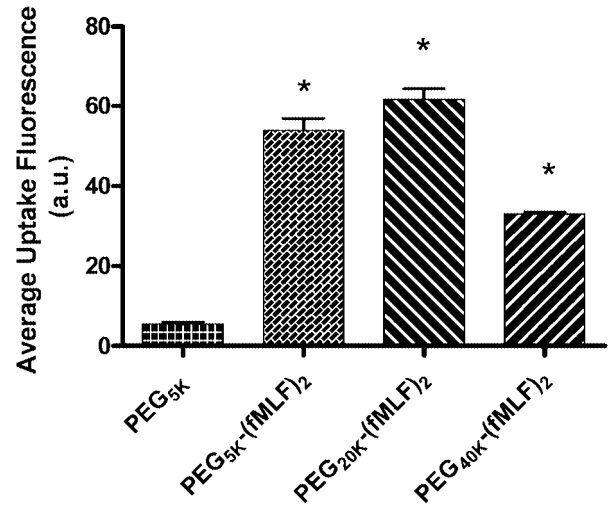

Figure 7. Uptake of fluorescein-labeled PEG-fMLF nanocarriers of different sizes in differentiated U937 cells after 4 h of incubation at 37 °C. The means ± SD for three independent experiments are shown for each value. (*, statistically significant difference between the PEG_{5k} and the derivatized nanocarriers, $p < 0.01$.)

Effect of PEG Sizes on PEG-fMLF Nanocarrier Uptake. To evaluate the effect of PEG size on macrophage uptake, PEG-$(fMLF)_2$ prepared using 5 K, 20 K, or 40 K PEGs were incubated with differentiated U937 cells for 4 h at 37 °C (Figure 7). Increasing PEG size from 5 kDa to 20 kDa slightly enhanced the uptake of PEG-$(fMLF)_2$ by about 14.4% ($p < 0.05$). However, when PEG size increased to 40 kDa, the uptake of PEG-$(fMLF)_2$ decreased by 38.6% ($p < 0.05$), suggesting that 20 kDa was the optimal size in this group and that 20–40 kDa should be further explored.

Peptide-Based PEG Nanocarriers. The PEG-fMLF nanocarriers synthesized from commercially available multifunctional PEGs showed enhanced macrophage uptake. However, the limited ability to produce PEGs with a defined number of cargo moieties, especially in high numbers, limits their use as nanocarriers when multiple targeting or therapeutic moieties are necessary. Thus, a novel peptide−backbone PEG nanocarrier was designed and synthesized to overcome this limitation. The peptide-PEG scaffold comprises the peptide backbone, acetyl-Cys(TP)-[β-Ala-β-Ala-Lys]$_{2,4}$-amide. PEG is attached to the scaffold via the ε-amine group of lysine. The heterobifunctional PEG (NHS-PEG-VS) is linked to the scaffold by a stable urethane linkage that is the result of the succinimidyl reaction with the ε-amino group of lysine. The targeting moieties are appended to the other end of the PEG. The peptide−backbone acetyl-C-[AAK(PEG_{5K}-(fMLFK(fluorescein)C]$_2$-amide and acetyl-C-[AAK(PEG_{5K}-(fMLFK(fluorescein)C]$_4$-amide demonstrated increased macrophage uptake after 4 h of incubation at 37 °C, about 4.2- and 5.7-fold more than PEG-fMLF (Figure 8), respectively. This is similar to but slightly higher than PEG-$(fMLF)_2$ and PEG-$(fMLF)_4$ derived from the commercially available PEGs. The results indicate that the number of attached targeting groups has much greater impact on the extent of macrophage uptake than other factors such as nanocarrier shape or the geometric distribution of attached groups. Previously, we

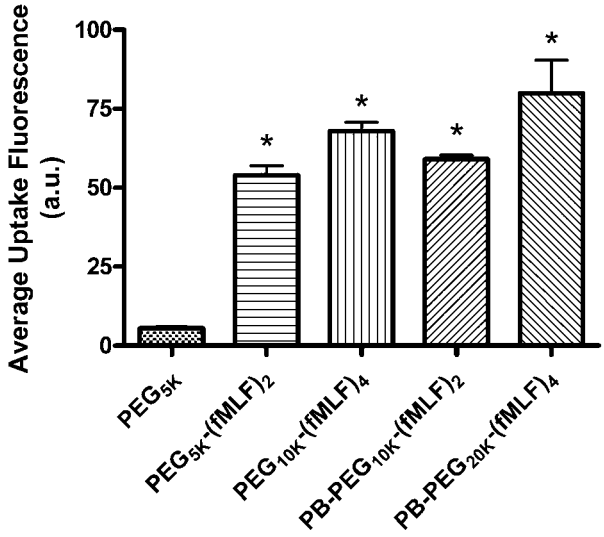

Figure 8. Uptake of fluorescein-labeled PEG-fMLF nanocarriers derived from Nektar PEGs or peptide−backbone (PB-)PEGs in differentiated U937 cells after 4 h of incubation at 37 °C. The means ± SD for three independent experiments are shown for each value. (*, statistically significant difference between the control PEG_{5k} and PEG-fMLF nanocarriers, $p < 0.01$.)

showed that a linear 30 kDa PEG with 4 conjugated fMLF moieties has a FPR binding constant that is practically indistinguishable from an 8-arm 20 kDa PEG with 4 appended fMLF.

Fluorescence Microscopy. Cells incubated with the control, fluorescein-labeled PEG_{5k}, lacking fMLF, showed no signal by fluorescence microscopy (Figure 9A). PEG_{5k}-fMLF showed faint fluorescence in cells, suggesting weak uptake (Figure 9B). The presence of punctate fluorescence suggested that the nanocarriers were internalized via endocytosis, which is typical of macromolecular uptake. PEG_{5k}-$(fMLF)_2$ and PEG_{10k}-$(fMLF)_4$ exhibited strong fluorescence throughout the cell, suggesting significantly higher binding/uptake to cells. A representative histogram of flow cytometry results for PEG_{5k} (PEG), PEG_{5k}-fMLF, PEG_{5k}-$(fMLF)_2$, and PEG_{10k}-$(fMLF)_4$ (Figure 9E) confirmed the microscopic observations. Since the same ratio of fluorescein moiety to fMLF moiety was maintained in each nanocarrier particle, and the local fluorescein environment in different particles were similar, the fluorescence intensity per nanocarrier particle was expected to be similar. Therefore, the binding/uptake results could be reasonably compared.

Calcium Mobilization. All PEG-fMLF nanocarriers showed decreased ability to activate macrophages cells, relative to free fMLF, as measured by transient stimulation of the release of calcium ions from intracellular stores into the cytoplasm. The change of cytoplasmic calcium concentration was monitored by the fluorescent calcium indicator Fluo-4 AM preloaded in the cell cytoplasm. The linkage to PEG decreased calcium release by about 40% in all PEG-fMLF nanocarriers compared to that in the free fMLF peptide (Figure 10). Interestingly, the linkage to PEG not only decreased macrophage activation of fMLF but also delayed the starting time of activation. This time delay and reduced activation by fMLF linked to PEG versus free fMLF was observed in our previous study in differentiated HL-60 cells (*15*) and may reflect a difference in the molecular pathways for macrophage activation and ligand internalization mediated by the same formyl peptide receptors.

DISCUSSION

The clinical potential of anti-HIV agents has been limited by a variety of factors, such as drug toxicity in uninfected cells, and the development of drug resistance, which leads to

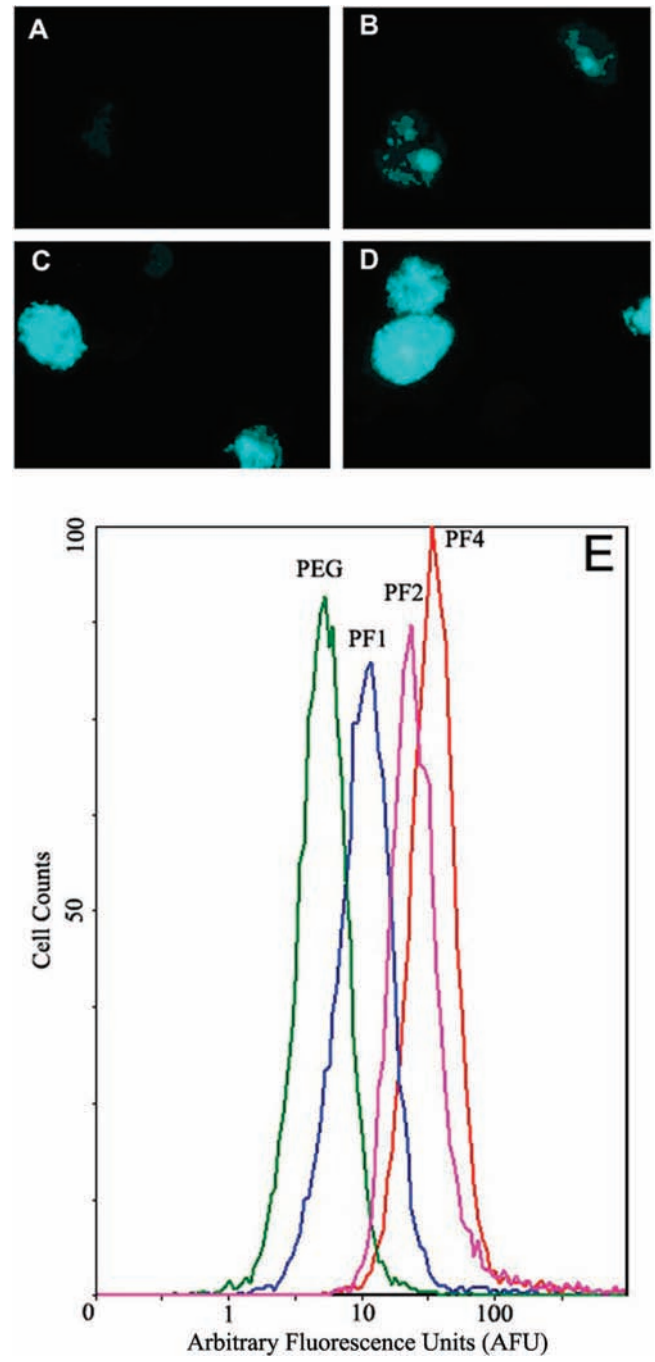

Figure 9. Fluorescence images of differentiated U937 cells incubated with fluorescein-labeled (A) PEG_{5k}, (B) PEG_{5k}-fMLF, (C) PEG_{5k}-$(fMLF)_2$, and (D) PEG_{10k}-$(fMLF)_4$, all at 50 nM concentrations. (E) Representative histogram of flow cytometry results for PEG_{5k} (PEG), PEG_{5k}-fMLF (PF1), PEG_{5k}-$(fMLF)_2$ (PF2), and PEG_{10k}-$(fMLF)_4$ (PF4).

subtherapeutic drug levels and the formation of viral reservoirs. Better drug delivery and targeting technologies are required to specifically increase target-cell exposure. Therefore, drug-delivery nanocarriers specifically targeted to macrophage cell-surface receptors could potentially improve therapeutic efficacy and minimize the systemic toxicity of anti-HIV drugs.

fMLF was chosen as the targeting moiety for the formyl peptide receptor on macrophages. fMLF resembles the amino terminus of unprocessed eubacterial proteins and binds avidly to the formyl peptide receptors on the surface of macrophages, where it serves as a chemoattractant, triggers cellular activation, and enters the cells to which it binds (*18*). The potential of using

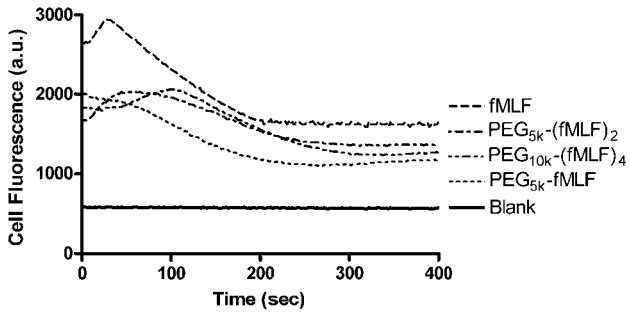

Figure 10. Calcium mobilization of U937 cells after exposure to fMLF and PEG-fMLF nanocarriers. One hundred nanomolars of each compound was tested in differentiated U937 cells preloaded with the calcium indicator Fluo-4 AM, and the calcium flux was monitored in cellular fluorescence at Ex485 nm and Em530 nm for up to 400 s.

fMLF as a targeting peptide to deliver PEG nanocarriers into macrophages was investigated in this study. The fMLF peptide was chosen as the targeting agent for several reasons. First, formyl peptide receptors are specifically expressed on phagocytic cells, such as macrophages, dendritic cells, and neutrophils. Second, fMLF specifically binds to formyl peptide receptors on macrophages with high affinity. Third, fMLF activates macrophages and down-regulates the coreceptors of HIV entry, CCR5 and CXCR4. The down-regulation of CCR5 coreceptor by fMLF could potentially inhibit viral entry in macrophages, which might potentiate the therapeutic effects of such targeted nanoparticles.

In the current study, multiple copies of fMLF were conjugated to various PEG nanocarriers and evaluated for targeting to human macrophage-like differentiated U937 cells. Since the formyl peptide retains its binding constant for FPR even with the covalent addition of several amino acids to its C-terminus, we were not concerned with a possible reduction in binding activity due to conjugation of the peptide (*15, 18*). The formyl, methionine and phenylalanine moieties are most crucial for receptor binding (*18*). Those moieties were specifically left unmodified, but we added a lysine (for fluorescence tagging) and a cysteine for PEG attachment to the C-terminus of the formyl peptide. The number of copies (1, 2, and 4) of fMLFKC conjugated to a single PEG nanocarrier was evaluated in order to determine the effects on avidity and macrophage uptake. Our previous work has shown that increasing the number of fMLF residues (up to eight) attached to a single PEG polymer results in enhanced avidity (K_d = 0.18 nM) for neutrophil-like differentiated HL-60 cells relative to free fMLF (K_d = 28 nM), with less enhancement of activation than of binding by increasing fMLF number (*15*). In the current study, we show that increasing the number of fMLF residues attached to a single PEG polymer from one to two resulted in significantly enhanced uptake (~4-fold, $p < 0.05$) in macrophage-like differentiated U937 cells, while further increasing this number from two to four only resulted in a modest increase in uptake. While the molecular basis of enhanced avidity by multivalency (i.e., multiple ligands attached to a single polymeric carrier molecule) is not proven, it is likely due to multimeric ligands interacting with multiple cellular receptors.

PEG was chosen as the pharmaceutical nanocarrier for the macrophage-targeted drug delivery system because of our long experience with this polymer class. PEGylation, the process of attaching polyethylene glycol (PEG) to drug molecules, has been a highly successful strategy for improving the pharmacokinetics and pharmacodynamics of pharmaceuticals, especially for protein and peptide therapeutics (*19–25*). In previous reports from our laboratory, we have shown that multicomponent macromolecular conjugates consisting of PEG, saquinavir, and R.I.CK-Tat retained antiviral activity *in vitro* and showed favorable therapeutic indices (*26, 27*). Studies of PEG in solution showed that each ethylene glycol subunit is tightly associated with two or three water molecules. The binding of water to PEG makes PEGylated compounds physically behave as though they are 3 to 9 times larger than a corresponding soluble protein of similar molecular weight (*28, 29*). In drug conjugates, PEG polymers with associated water molecules act like a shield to protect the attached drug from enzymatic degradation, inhibit interactions with cell-surface proteins, and provide increased size to prevent rapid renal filtration and clearance. These stealth properties of PEG have proven to be very valuable in prolonging drug persistence in the systemic circulation. However, the inability of PEG to interact with cell surfaces theoretically limits its use as a biomaterial for cell-surface or intracellular drug delivery and targeting. Therefore, the very property of PEGylation that has made it clinically useful and commercially successful is exactly the opposite of what is needed for promoting effective targeted drug therapy in diseases such as AIDS. In other words, currently used PEGylation approaches that have been enormously successful for treating certain diseases such as cancer may not be appropriate for treating HIV infection in viral reservoirs or sanctuary sites, such as macrophages, the central nervous system, and the testis. Our approach to functionalize PEG in order to shift the site of drug delivery from the blood to target cells is novel and counterintuitive given the current use of PEG. However, the general stealth properties of the PEG moiety may reduce toxicity by reducing nanocarrier binding to cells not expressing FPR and FPRL1.

Experimental studies on targeted drug delivery into cells have identified size as an important factor in the cellular uptake of nanomaterials. It has been shown that particles with radii <50 nm exhibit significantly greater uptake compared with particles >50 nm (*30, 31*). Aoyama and co-workers (*32, 33*) reported on the effect of size on receptor-mediated endocytosis in glycoviral gene delivery by excluding potential complications arising from charge effects. They concluded that receptor-mediated endocytosis is strongly size-dependent and that the optimal size is around 25 nm. In our study, increasing PEG size from 5 K to 20 K slightly enhanced nanocarrier uptake, but uptake decreased when the size was further increased to 40 K. The estimated molecular size of a 5 kDa PEG molecule is ~2 nm, while that of a 20 kDa PEG is 7 nm and 10 nm for 40 kDa (*34*). The effective or apparent size of PEG nanocarriers is significantly increased by the binding of water to PEG; the hydrodynamic radius of the hydrated PEG nanocarrier is 3 to 9 times higher than that predicted by their molecular weight (*34*). Therefore, a 20 kDa PEG-$(fMLF)_2$ has an effective molecular size of 20–60 nm. The optimal uptake of this nanocarrier and its size are consistent with the suggestions of Aoyama et al. However, 5 kDa and 40 kDa PEG-$(fMLF)_2$ showed less uptake because their effective sizes are either <25nm or >50 nm. Effective targeting to macrophages residing in tissues depends on multiple factors, including plasma clearance, tissue distribution, receptor binding, and cell uptake. The pharmacokinetics and biodistribution of nanocarriers relate to their size, charge, shape, and rigidity and are primarily controlled by renal glomerular filtration (*35*). The current results suggest that a delicate balance must be struck between maximizing the circulation half-life of nanocarriers in blood and their penetration into macrophage tissue compartments.

PEGylated systems made from commercially available multifunctional PEGs have a linear or forked shape. However, they have limited capacity to conjugate mulutiple copies of functional groups or drugs. These limitations have affected their potential as pharmaceutical drug carriers. Therefore, we designed and

synthesized a prototypical novel peptide-based PEG nanocarrier. The central component of the proposed nanocarriers is the peptide-based PEG scaffold that comprised the peptide backbone, Cys-(β-Ala-β-Ala-Lys-)$_n$-amide ($n = 2$, 4, or more), with 1 thiol group on the cysteine side chain and amino groups on lysine side chains. The flexibility of this peptide-based PEG nanocarrier is evident. For example, if a higher number of targeting agents is needed, a larger scaffold with more lysine moieties for PEG attachment can be utilized. Drugs can be attached by a disulfide (reversible) or thiosulfonyl (nonreversible) via a vinyl sulfone bond. The disulfide linkage can possibly be cleaved after the entry of the nanocarrier into the cell because of the high concentration of reduced glutathione within the cell. In this scenario, the drug is released from the nanocarrier. The scaffold consisting of a peptide backbone and PEG are the critical central feature of the nanocarrier drug conjugates since (1) it controls body and cellular disposition, and uptake/retention, (2) it allows us to add functional groups (i.e., effectors) to target specific cell types and cause surface binding or uptake, and (3) it allows us to attach exact numbers of multiple drugs or multiple targeting moieties using releasable or nonreleasable bonds. Furthermore, the molecular population of nanocarriers is monodisperse in its derivatization, a distinct advantage over other PEGylation carriers. Using these features, we could potentially precisely control how, when, and where anti-HIV drugs are able to exert their therapeutic effect.

CONCLUSIONS

The current results demonstrate that PEG nanocarriers with multiple copies of fMLF can specifically target human macrophage-like cells *in vitro* and that the number of fMLF copies attached determines the extent of uptake. The results suggest that two fMLF residues are sufficient for achieving targeting and improving uptake *in vitro*. We also demonstrated that 20 kDa (corresponding to 20–60 nm) may be the optimal PEG nanocarrier size for improved macrophage uptake. Since typical commercially available multifunctional PEGs limit the numbers of copies of drugs and targeting groups that may be attached to a nanocarrier, we designed an alternate carrier that retained the targeting and uptake properties of nonpeptide-based PEGs. However, the new nanocarrier allows for far greater flexibility in attaching multiple drugs, copies of drugs, and/or targeting moieties. These results indicate great promise for improving targeted drug delivery to HIV-infected macrophages, which may eventually allow for better therapeutic regimens by reducing dose and improving tolerability and patient compliance with complicated regimens.

ACKNOWLEDGMENT

This work was supported by National Institutes of Health Grants AI 33789 and AI 51214.

LITERATURE CITED

(1) Vandamme, A. M., Van Vaerenbergh, K., and De Clercq, E. (1998) Anti-human immunodeficiency virus drug combination strategies. *Antiviral Chem. Chemother. 9*, 187–203.

(2) Bangsberg, D. R., Hecht, F. M., Charlebois, E. D., Zolopa, A. R., Holodniy, M., Sheiner, L., Bamberger, J. D., Chesney, M. A., and Moss, A. (2000) Adherence to protease inhibitors, HIV-1 viral load, and development of drug resistance in an indigent population. *AIDS 14*, 357–66.

(3) Schrager, L. K., and D'Souza, M. P.,1998) Cellular and anatomical reservoirs of HIV-1 in patients receiving potent antiretroviral combination therapy *JAMA 280*, 67–71.

(4) Richman, D. D. (2001) HIV chemotherapy. *Nature 410*, 995–1001.

(5) Schuitemaker, H., Kootstra, N. A., de Goede, R. E., de Wolf, F., Miedema, F., and Tersmette, M. (1991) Monocytotropic human immunodeficiency virus type 1 (HIV-1) variants detectable in all stages of HIV-1 infection lack T-cell line tropism and syncytium-inducing ability in primary T-cell culture. *J. Virol. 65*, 356–363.

(6) Roos, M. T., Lange, J. M., de Goede, R. E., Coutinho, R. A., Schellekens, P. T., Miedema, F., and Tersmette, M. (1992) Viral phenotype and immune response in primary human immunodeficiency virus type 1 infection. *J. Infect. Dis. 165*, 427–432.

(7) Connor, R. I., Paxton, W. A., Sheridan, K. E., and Koup, R. A. (1996) Macrophages and CD4+ T lymphocytes from two multiply exposed, uninfected individuals resist infection with primary non-syncytium-inducing isolates of human immunodeficiency virus type 1. *J. Virol. 70*, 8758–8764.

(8) Liu, R., Paxton, W. A., Choe, S., Ceradini, D., Martin, S. R., Horuk, R., MacDonald, M. E., Stuhlmann, H., Koup, R. A., and Landau, N. R. (1996) Homozygous defect in HIV-1 coreceptor accounts for resistance of some multiply-exposed individuals to HIV-1 infection. *Cell 86*, 367–377.

(9) Aquaro, S., Calio, R., Balzarini, J., Bellocchi, M. C., Garaci, E., and Perno, C. F. (2002) Macrophages and HIV infection: therapeutical approaches toward this strategic virus reservoir. *Antiviral Res. 55*, 209.

(10) Fridkin, M., Tsubery, H., Tzehoval, E., Vonsover, A., Biondi, L., Filira, F., and Rocchi, R. (2005) Tuftsin-AZT conjugate: potential macrophage targeting for AIDS therapy. *J Pept Sci 11*, 37–44.

(11) Hu, J., Liu, H., and Wang, L. (2000) Enhanced delivery of AZT to macrophages via acetylated LDL. *J. Controlled Release 69*, 327–335.

(12) Le, Y., Yang, Y., Cui, Y., Yazawa, H., Gong, W., Qiu, C., and Wang, J. M. (2002) Receptors for chemotactic formyl peptides as pharmacological targets. *Int. Immunopharmacol. 2*, 1–13.

(13) Niedel, J. E., Kahane, I., and Cuatrecasas, P. (1979) Receptor-mediated internalization of fluorescent chemotactic peptide by human neutrophils. *Science 205*, 1412–1414.

(14) van Eerd, J. E., Boerman, O. C., Corstens, F. H., and Oyen, W. J. (2003) Radiolabeled chemotactic cytokines: new agents for scintigraphic imaging of infection and inflammation. *Q. J. Nucl. Med. 47*, 246–255.

(15) Pooyan, S., Qiu, B., Chan, M. M., Fong, D., Sinko, P. J., Leibowitz, M. J., and Stein, S. (2002) Conjugates bearing multiple formyl-methionyl peptides display enhanced binding to but not activation of phagocytic cells. *Bioconjugate Chem, 13*, 216–223.

(16) Fischer, D. G., Pike, M. C., Koren, H. S., and Snyderman, R. (1980) Chemotactically responsive and nonresponsive forms of a continuous human monocyte cell line. *J. Immunol. 125*, 463–465.

(17) Pike, M. C., Fischer, D. G., Koren, H. S., and Snyderman, R. (1980) Development of specific receptors for N-formylated chemotactic peptides in a human monocyte cell line stimulated with lymphokines. *J. Exp. Med. 152*, 31–40.

(18) Prossnitz, E. R., and Ye, R. D. (1997) The N-formyl peptide receptor: a model for the study of chemoattractant receptor structure and function. *Pharmacol. Ther. 74*, 73–102.

(19) Kozlowski, A., and Harris, J. M. (2001) Improvements in protein PEGylation: pegylated interferons for treatment of hepatitis C. *J. Controlled Release 72*, 217–224.

(20) Harris, J. M., Martin, N. E., and Modi, M. (2001) Pegylation: a novel process for modifying pharmacokinetics. *Clin. Pharmacokinet. 40*, 539–551.

(21) Kozlowski, A., Charles, S. A., and Harris, J. M. (2001) Development of pegylated interferons for the treatment of chronic hepatitis C. *BioDrugs 15*, 419–429.

(22) Conover, C. D., Greenwald, R. B., Pendri, A., Gilbert, C. W., and Shum, K. L. (1998) Camptothecin delivery systems:

enhanced efficacy and tumor accumulation of camptothecin following its conjugation to polyethylene glycol via a glycine linker. *Cancer Chemother. Pharmacol. 42*, 407–414.
(23) Greenwald, R. B. (2001) PEG drugs: an overview. *J. Controlled Release 74*, 159–71.
(24) Greenwald, R. B., Choe, Y. H., McGuire, J., and Conover, C. D. (2003) Effective drug delivery by PEGylated drug conjugates. *Adv. Drug Delivery Rev. 55*, 217–250.
(25) Roberts, M. J., Bentley, M. D., and Harris, J. M. (2002) Chemistry for peptide and protein PEGylation. *Adv. Drug Delivery Rev. 54*, 459–476.
(26) Gunaseelan, S., Debrah, O., Wan, L., Leibowitz, M. J., Rabson, A. B., Stein, S., and Sinko, P. J. (2004) Synthesis of poly(ethylene glycol)-based saquinavir prodrug conjugates and assessment of release and anti-HIV-1 bioactivity using a novel protease inhibition assay. *Bioconjugate Chem. 15*, 1322–1333.
(27) Wan, L., Zhang, X., Gunaseelan, S., Pooyan, S., Debrah, O., Leibowitz, M. J., Rabson, A. B., Stein, S., and Sinko, P. J. (2006) Novel multi-component nanopharmaceuticals derived from poly-(ethylene) glycol, retro-inverso-Tat nonapeptide and saquinavir demonstrate combined anti-HIV effects. *AIDS Res. Ther. 3*, 12.
(28) Harris, J. M. (1991) *Poly(Ethylene Glycol) Chemistry: Biotechnical and Biomedical Applications*, Plenum Press, New York.
(29) Sherman, M. R., Williams, L. D., Saifer, M. C. P., French, J. A., Kwak, L. W., and Oppenheim, J. J. (1997) *Conjugation of High, Molecular Weight Poly(ethylene glycol) to Cytokines: Granulocyte-Macrophage Colony Stimulating Factors As Model Substrates.*, ACS, Washington, DC.
(30) Desai, M. P., Labhasetwar, V., Walter, E., Levy, R. J., and Amidon, G. L. (1997) The mechanism of uptake of biodegradable microparticles in Caco-2 cells is size dependent. *Pharm. Res. 14*, 1568–1573.
(31) Prabha, S., Zhou, W. Z., Panyam, J., and Labhasetwar, V. (2002) Size-dependency of nanoparticle-mediated gene transfection: studies with fractionated nanoparticles. *Int. J. Pharm. 244*, 105–115.
(32) Nakai, T., Kanamori, T., Sando, S., and Aoyama, Y. (2003) Remarkably size-regulated cell invasion by artificial viruses. Saccharide-dependent self-aggregation of glycoviruses and its consequences in glycoviral gene delivery. *J. Am. Chem. Soc. 125*, 8465–8475.
(33) Osaki, F., Kanamori, T., Sando, S., Sera, T., and Aoyama, Y. (2004) A quantum dot conjugated sugar ball and its cellular uptake. On the size effects of endocytosis in the subviral region. *J. Am. Chem. Soc. 126*, 6520–6521.
(34) Caliceti, P., and Veronese, F. M. (2003) Pharmacokinetic and biodistribution properties of poly(ethylene glycol)-protein conjugates. *Adv. Drug Delivery Rev. 55*, 1261–1277.
(35) Arendshorst, W. J., and Navar, L. G. (1988) *Renal Circulation and Glomerular Hemodynamics*, Brown, Boston, MA.

BC070066K

Conjugated Platinum(IV)−Peptide Complexes for Targeting Angiogenic Tumor Vasculature

Sumitra Mukhopadhyay,[†,§] Carmen M. Barnés,*[,‡,§] Ariel Haskel,[†] Sarah M. Short,[‡] Katie R. Barnes,[†] and Stephen J. Lippard*[,†]

Department of Chemistry, Massachusetts Institute of Technology, Cambridge, Massachusetts 02139, and Vascular Biology Program, Children's Hospital and Harvard Medical School, Boston, Massachusetts 02115. Received January 29, 2007; Revised Manuscript Received June 14, 2007

The integrins $\alpha_v\beta_3$ and $\alpha_v\beta_5$ and the membrane-spanning surface protein aminopeptidase N (APN) are highly expressed in tumor-induced angiogenesis, making them attractive targets for therapeutic intervention. Both integrins and APN recognize a broad range of peptides containing RGD (Arg-Gly-Asp) and NGR (Asn-Gly-Arg) motifs, respectively. Here, we describe the design, synthesis, and characterization of a series of mono- and difunctionalized platinum(IV) complexes in which a conjugated peptide motif, containing RGD, (CRGDC)c, (RGDfK)c, or NGR, is appended as a "tumor-homing device" to target tumor endothelial cells selectively over healthy cells. Platinum(IV)−peptide complexes with nonspecific amino acids or peptide moieties were prepared as controls. Concentration–response curves of these compounds were evaluated against primary proliferating endothelial cells and tumor cell lines and compared to those of cisplatin, a well-described platinum-based chemotherapeutic agent. The Pt(IV)−RGD conjugates were highly and specifically cytotoxic to cell lines containing $\alpha_v\beta_3$ and $\alpha_v\beta_5$, approaching the activity of cisplatin. The Pt(IV)−NGR complexes were less active than Pt(IV)−RGD-containing compounds but more active than nonspecific Pt−peptide controls. Integrin $\alpha_v\beta_3$ mediated, at least in part, the anti-proliferative effect of a Pt(IV)−RGD conjugate, as demonstrated by a decreased inhibitory response when endothelial cells were either (1) incubated with an excess of $\alpha_v\beta_3/\alpha_v\beta_5$-specific RGD pentapeptides or (2) transfected with RNAi for β_3, but not β_1, integrins. These results suggest a rational approach to improved chemotherapy with Pt(IV)−peptide conjugates by selective drug delivery to the tumor compartment.

INTRODUCTION

Cisplatin, *cis*-diamminedichloroplatinum(II), is standard chemotherapy for testicular, ovarian, cervical, head, neck, esophageal, and non-small-cell lung cancer (*1–6*). Cisplatin displays limited activity toward the more common colon and breast cancers, however, and toxic side effects are associated with its intake (*1*). A key objective of our current research program is to synthesize novel Pt-based drugs with equal potency but reduced toxicity derived from their ability to target tumor tissue. Targeted platinum therapy has the potential to increase the net amount of platinum that reaches the tumor environment, thereby decreasing the amount of platinum required and consequently reducing side effects on healthy, noncancerous tissues.

Tumor cell survival, growth, and metastasis are driven by angiogenesis, the process by which new blood vessels are formed (*7–9*). Tumor blood vessels are permeable and morphologically distinct from normal blood vessels. Because the tumor endothelial cell can be selectively recognized, it has become a major target for treating cancer (*10*).

Among the cell surface proteins upregulated in endothelial cells and on certain tumor cells during tumor growth and metastasis are the $\alpha_v\beta_3$ and $\alpha_v\beta_5$ integrins (*11–13*) and aminopeptidase N (APN or CD13) (*14*), which are absent or barely detectable in resting endothelial cells. Integrins are transmembrane-spanning receptors that participate in cell−cell and cell−matrix interactions in all normal and malignant cell types (*15, 16*). The integrin $\alpha_v\beta_3$ plays a critical role in the adhesion and migration of endothelial cells to extracellular matrix components. Integrins $\alpha_v\beta_3$ and $\alpha_v\beta_5$ and APN recognize the peptide motifs RGD (Arg-Gly-Asp) (*17, 18*) and NGR (Asn-Gly-Arg) (*14*), respectively, with high affinity. The $\alpha_v\beta_3$ integrin can also bind NGR but with lower affinity (*19*). RGD- and NGR-containing peptide motifs and peptidomimetics specifically target the tumor vasculature (*10, 14, 20*) and have been evaluated as antagonists of $\alpha_v\beta_3$ and APN. RGD-containing peptides compete in the binding of ECM proteins to cell surface $\alpha_v\beta_3$ and $\alpha_v\beta_5$, preventing cellular adhesion to the extracellular matrix, thwarting cell metastasis, and inducing apoptosis (*21, 22*). Linear and cyclic RGD peptide motifs have been employed as delivery agents for small molecular weight drugs, peptides, and proteins to the tumor endothelial cells, as recently reviewed (*23*).

On the basis of these findings, we have developed a strategy to prepare new platinum(IV) anticancer drug candidates in which the conjugated peptide motif, containing either RGD or NGR, would serve as a "tumor-targeting device"and selectively kill angiogenic tumor endothelial cells. Here, we describe the design, synthesis, and characterization of the first such conjugates, mono- and difunctionalized Pt(IV)−peptide complexes. As previously reported for platinum(IV) analogues containing a tethered steroid hormone moiety, reduction in the cell releases the axially appended ligand to unmask cisplatin (*24*).

As targeting moieties, we have used the RGD and NGR linear tripeptides; an RGD-containing disulfide-bridged cyclic pentapeptide, (CRGDC)c; and the cyclic pentapeptide, (RGDfK)c. (CRGDC)c and (RGDfK)c were chosen because cyclic peptides target angiogenic endothelial cells more efficiently compared to their linear counterparts (*12, 21, 25, 26*). The two cysteine

* Corresponding authors. Email: carmen.barnes@childrens.harvard.edu, lippard@mit.edu.
[†] Massachusetts Institute of Technology.
[‡] Harvard Medical School.
[§] These authors contributed equally to the work.

10.1021/bc070031k CCC: $40.75 © 2008 American Chemical Society
Published on Web 09/11/2007

Chart 1. Designations, Abbreviations, and Charges on Complexes

No.	Complex	Charge at pH 7.0
	Cisplatin	0
1	[Pt-$(NH_3)_2Cl_2$(succinate)$_2$]	-2
2a	Pt-RGD-mono	-1
2b	Pt-RGD-bis	0
3a	Pt-NGR-mono	0
3b	Pt-NGR-bis	+2
4a	Pt-AGR-mono	0
4b	Pt-AGR-bis	+2
5a	Pt-Gly-mono	-1
5b	Pt-Gly –bis	0
6	Pt-(CRGDC)c-mono	-1
7a	Pt-(RGDfK)c-mono	-1
7b	Pt-(RGDfK)c-bis	0

residues in CRGDC form a disulfide bond which gives the RGD portion a constrained bent structure that facilitates specific recognition by the integrins on the cell surface (*20*, *21*, *25*, *26*). (RGDfK)c is an antiangiogenic peptide derived from the $\alpha_v\beta_3$ and $\alpha_v\beta_5$ inhibitor (RGDfV)c. (RGDfK)c preserves the biological activity of its parent compound (*27*) but can be readily attached to different moieties through the lysine ϵ-amino group without losing its selectivity properties (*28*). In addition, several other Pt(IV) compounds linked to a nonspecific amino acid or a tripeptide have been prepared as controls.

All peptides or amino acid residues were attached by means of an amide bond to the terminal carboxylate group of the axially coordinated succinato ligands in *cis*,*cis*,*trans*-diamminedichlorodisuccinatoplatinum(IV) complex, *cis*,*cis*,*trans*-[$Pt(NH_3)_2Cl_2$(succinate)$_2$] (**1**) (*24*). Numerical designations and abbreviations of these complexes and their charges at pH 7 are given in Chart 1 (*29*). Concentration−response curves of these Pt(IV)−peptide complexes along with that of cisplatin and **1** were assessed against different primary endothelial cells and tumor cell lines, which include bovine capillary endothelial (BCE) cells, human umbilical vein endothelial cells (HUVEC), human dermal microvascular endothelial cells (HMVEC), human glioblastoma (U87), human pancreatic carcinoma (ASPC1), human uterine sarcoma (MES-SA), and human cervical carcinoma (HeLa) cells. We found that both endothelial cells and the tumor lines tested were positive either for both $\alpha_v\beta_3$ and $\alpha_v\beta_5$ or for $\alpha_v\beta_5$ integrins. The activity profiles of all the platinum complexes against these cells are described herein.

EXPERIMENTAL PROCEDURES

Materials. Potassium tetrachloroplatinate(II) was a gift from Englehard. Cisplatin, *cis*,*cis*,*trans*-diamminedichlorodihydroxyplatinum(IV), and *cis*,*cis*,*trans*-diamminedichlorodisuccinatoplatinum(IV) were synthesized according to literature procedures (*24*, *30*, *31*). (RGDfK)c was prepared as reported (*32*, *33*). Chemicals and solvents were of reagent-grade quality and used as received from commercial suppliers. Abbreviations are listed in reference 29.

Instrumentation and Analytical Measurements. An Advanced ChemTech automated instrument (model ACT 348Ω) was used for peptide synthesis. HPLC purifications using C18 analytical (VYDAC, 4 mm × 250 mm) and C18 semipreparative (VYDAC, 40 mm × 250 mm) columns were performed with Waters instrumentation comprising a 600S system controller coupled with an absorption detector (Waters 2487) and pump (Waters 616). Purifications with a C18 preparative (VYDAC, 100 mm × 250 mm) column used a Waters 600E system controller coupled with an absorption detector (Waters 486) and pump (Waters 600). LC-MS analyses were performed on an Agilent 1100 series instrument using a ZORBAX extended SB-C18 column of dimensions 4.6 mm × 150 mm and a ZORBAX 80A extended C18 column of dimensions 2.1 mm × 100 mm. High-resolution mass spectral analyses were performed at the MIT Department of Chemistry Instrument Facility (DCIF).

Synthesis of Peptides and Platinum Complexes RGD, NGR, AGR, (CRGDC)c. The linear peptides were prepared by using the standard Fmoc protocol on an automated peptide synthesizer. The rink amide resin with a loading capacity of 0.61 mmol/g was used as the solid support. In a typical 16-well synthesis, a total of 1.2 g (0.74 mmol) of the resin and a 10-fold excess of each amino acid (7.36 mmol) in 24 mL of *N*-methyl-2-pyrrolidinone (NMP) solution were used in the presence of 1,3-diisopropylcarbodiimide (DIC), acetic anhydride, 1-hydroxybenzotriazole (HOBt), and diisopropylethylamine (DIPEA) (0.5 M solution of each in DMF). Fmoc-Asn(Trt)-OH, Fmoc-Asp(OtBu)-OH, Fmoc-Arg(Pbf)-OH, and Fmoc-Cys(Trt)-OH provided sources of Asn, Asp, Arg, and Cys, respectively. The Fmoc protecting group was removed with a 20% piperidine solution in DMF. After the synthesis, the peptides were cleaved from the resin with a solution of 95% TFA, 2.5% triisopropylsilane (TIPS), and 2.5% water to obtain amide functionalization at the C-terminus. The resulting peptides were precipitated by cold ether. The aqueous solution of linear CRGDC was air-oxidized overnight to form the S−S bridged (CRGDC)c. The purification of these peptides was carried out by reverse-phase HPLC by using a C18 preparative column (VYDAC, 100 mm × 250 mm) in greater than 90% yield. Their purity was verified by LC-MS and mass spectrometry. ESI-MS: for RGD: calcd $[M + H]^+$ 346.36 amu; found 346.3 amu; for NGR: calcd $[M + H]^+$ 345.38 amu, found 345.51 amu; for AGR: calcd $[M + H]^+$ 302.35 amu, found 302.29 amu; and for (CRGDC)c: calcd $[M + H]^+$ 550.2 amu, found 550.4 amu.

RGD-Conjugated Diamminedichloroplatinum(IV) Complexes (2a and 2b). To a solution of **1** (0.025 g, 0.043 mmol) in 200 μL of water was added a 100 μL solution of EDC (0.082 g, 0.43 mmol), followed by a 100 μL solution of NHS (0.050 g, 0.43 mmol) with vigorous stirring. This solution was then added to an aqueous solution (200 μL) of RGD tripeptide (0.075 g, 0.22 mmol) in a dropwise manner. The reaction mixture was stirred for ∼24 h in the dark. The products were purified by reverse-phase HPLC (C18 semipreparative column, 40 mm × 250 mm, linear gradient from 100% H_2O to 15% acetonitrile over 30 min). The mono- (**2a**) and diconjugated (**2b**) products were collected separately and lyophilized to yield ∼4.3 mg of **2a** (11.6% with respect to the starting complex, **1**) and ∼2.4 mg of **2b** (5% with respect to **1**). The purity of these complexes was confirmed by LC-MS and mass spectrometry. ESI-MS: for **2a**, calcd $[M + H]^+$ 861.1665 amu, found 861.1646; for **2b**, calcd $[M + H]^+$ 1188.332 amu, found 1188.3235 amu; and calcd $[(M + 2H)/2]^{2+}$ 594.6699 amu, found 594.6680 amu.

NGR-Conjugated Diamminedichloroplatinum(IV) Complexes (3a and 3b). These complexes were prepared and purified following the same procedure described above for **2a** and **2b** except that the linear NGR tripeptide was used instead of RGD, and a shorter linear gradient was used in the HPLC purification (25 min). The mono- (**3a**) and diconjugated (**3b**) products were collected separately and lyophilized to afford 14% of **3a** and 8% of **3b**. The purity of these complexes was confirmed by LC-MS and mass spectrometry. ESI-MS: for **3a**, calcd $[M + H]^+$ 860.1825 amu, found 860.1618; for **3b**, calcd $[M + H]^+$ 1186.3639 amu, found 1186.3735 amu; and calcd $[(M + 2H)/2]^{2+}$ 593.6859 amu, found 593.6715 amu.

AGR-Conjugated Diamminedichloroplatinum(IV) Complexes (4a and 4b). These complexes were prepared and purified by following the same procedure as described above for **2a** and **2b** but with the linear AGR tripeptide instead of RGD. The mono- (**4a**) and diconjugated (**4b**) products were collected separately and lyophilized to afford 16% of **4a** and 7% of **4b**. The purity of these complexes was confirmed by LC-MS and mass spectrometry. ESI-MS: for **4a**, calcd $[M + H]^+$ 817.1766 amu, found 817.1735 amu; for **4b**, calcd $[M + H]^+$ 1100.3523 amu, found 1100.372 amu; and calcd $[(M + 2H)/2]^{2+}$ 550.68 amu, found 550.50 amu.

Glycinamide-Conjugated Diamminedichloroplatinum (IV) Complexes (5a and 5b). These complexes were prepared by following a procedure similar to that for the other platinum(IV)−peptide conjugates except that glycinamide was used instead of a tripeptide. The complexes were purified as described for **3a** and **3b**. The mono (**5a**) and diconjugated (**5b**) products were collected separately and lyophilized to afford ∼50% of **5a** and ∼44% of **5b**. The purity of these complexes was confirmed by LC-MS and mass spectrometry. ESI-MS: for **5a**, calcd $[M + H]^+$ 590.0384 amu, found 590.0389 amu; for **5b**, calcd $[M + H]^+$ 646.0759 amu, found 646.0757 amu.

(CRGDC)c-Conjugated Diamminedichloroplatinum(IV) Complex (6). This complex was prepared by following the same procedure as described above for the Pt(IV)−RGD complexes using (CRGDC)c peptide. A white precipitate, observed in the reaction mixture upon stirring overnight, was discarded by filtration. In this case, however, the diconjugated complex was not detected by LC-MS or HPLC. The monoconjugated product, **6**, was purified by reverse-phase HPLC as described above for **2a** and lyophilized to afford the product in ∼10% yield. The purity of this complex was confirmed by LC-MS and mass spectrometry. ESI-MS: for **6**, calcd $[M + H]^+$ 1066.17 amu, found 1066.2 amu.

(RGDfK)c-Conjugated Diamminedichloroplatinum(IV) Complexes (7a and 7b). These complexes were prepared by following a procedure similar to that described for the other platinum(IV)−peptide conjugates except that the cyclic pentapeptide, (RGDfK)c, was used instead of a tripeptide, and the lysine ϵ-amino group of (RGDfK)c was activated with DIPEA prior to reaction with **1**. The products were purified by reverse-phase HPLC as described above for **3a** and **3b**. The mono- (**7a**) and diconjugated (**7b**) products were collected separately and lyophilized to afford ∼12% of **7a** and ∼8% of **7b**. The purity of these complexes was confirmed by LC-MS and mass spectrometry. ESI-MS: for **7a** calcd $[M + H]^+$ 1120.30 amu, found 1120.20 amu; for **7b** calcd $[M + H]^+$ 1705.61 amu, found 1705.3 amu; and calcd $[(M + 2H)/2]^{2+}$ 853.81 amu, found 853.80 amu.

Cell Culture. Endothelial and tumor cells were all grown at 37 °C under a 5% CO_2 atmosphere, except for bovine capillary endothelial (BCE) cells, which were grown at 10% CO_2. BCEs were isolated from bovine adrenal cortex and cultured in pregelatinized tissue culture plates in Dulbecco's modified Eagle's medium (DMEM; Invitrogen/GIBCO) containing 10% bovine calf serum (Hyclone Laboratories, Logan, UT) and 3 ng/mL basic fibroblast growth factor (bFGF), and 1% GPS, as previously described (*34*). Human dermal microvascular endothelial cells (HMVEC-d; Lonza Inc. and Cascade Biologics, Portland, OR) and human umbilical vein endothelial cells (HUVEC; Lonza Inc.) were maintained according to supplier's directions. HMVEC-d were cultured in microvascular endothelial growth medium (EGM-MV; Cambrex Bio Science); human umbilical vein endothelial cells (HUVEC; Cambrex Bio Science) were cultured in endothelial growth medium-2 (EGM-2; Cambrex Bio Science). All endothelial cells were plated on pre-gelatinized tissue culture plates (1.5% gelatin in PBS). Human glioblastoma cell line U87, purchased from the American type Culture Collection (ATCC, Rockville, MD), and HeLa cells were grown in DMEM supplemented with 10% heat-inactivated (56 °C for 40 min) fetal calf serum (hi-FCS) (Invitrogen/GIBCO, Grand Island, NY), 2 mM L-glutamine, and 1% penicillin−streptomycin (GPS, glutamine/penicillin/streptomycin; Invitrogen/GIBCO). Human uterine sarcoma MES-SA cells (ATCC) were cultured in modified McCoy's 5a medium (ATCC) supplemented with 10% hi-FCS and 1% GPS. Human pancreatic adenocarcinoma cell line ASPC-1 (ATCC) was cultured in RPMI 1640 (ATCC) containing 10% hi-FBS and 1% GPS.

Concentration−Response Curves of Platinum Complexes. BCE cells were plated at 7.5×10^3 cells per well in DMEM containing 10% bovine calf serum. After overnight incubation at 37 °C (in 10% CO_2), the medium was replaced with DMEM containing 5% BCS, 2.0 ng/mL, and various concentrations of the Pt compound (stock solutions prepared in PBS) to a final concentration range of 10 nM to 1 mM. Wells with and without bFGF in the absence of platinum complex were kept as positive and negative controls, respectively. All concentrations were tested in triplicate. After 72 h, viable cells were trypsinized (Trypsin-EDTA; Invitrogen/GIBCO BRL), resuspended in isotonic diluent (Fisher Scientific, Pittsburgh, PA), and counted using a particle counter. Data were analyzed as described below.

HMVEC-d (passages 2–5) were seeded at 7.5×10^3 cells per well in pre-gelatinized 48-well plates in endothelial basal medium (EBM-2; Cambrex Bio Science) supplemented with 5% FBS and incubated at 37 °C (in 5% CO_2). After 24 h, the medium was replaced with microvascular endothelial growth medium (EGM-MV) and the Pt compound dissolved in PBS (10% volume) or PBS alone (positive control). For the negative control, the medium was replaced with EBM-2 supplemented with 5% FBS instead. Cells were incubated for 72 h, trypsinized, and counted on a particle counter. HUVEC were performed as described for HMVEC-d with the following changes. Cells were plated in EBM-2 supplemented with 2% FBS, challenged with EGM-2, and EBM-2 containing 2% FBS was used as a negative control.

To investigate the effect of Pt(IV) complexes in tumor lines, tumor cells were seeded at a density of 5.0×10^3 cells per well. For plating and challenging, the corresponding cultivation medium supplemented with 5% hi-FBS and 1% GPS were used (DMEM in the case of U87 and HeLa cells; modified McCoy's 5a medium was employed in the case of MES-SA and MES-SA/Dx; RPMI-1640 for ASPC-1). After 24 h, the medium was replaced with fresh medium containing 5% FCS and the Pt compound dissolved in PBS (10% volume). Cells were incubated for 72 h, trypsinized, counted on a particle counter, and analyzed as described below.

Analysis of Concentration−Response Curves and Determination of IC_{50} Values. Cell numbers determined from the concentration−response curves were converted to percent cell number. For each cell line and each compound tested, the data for all independent experiments (*2–9*) were combined and analyzed by nonlinear regression to a hyperbolic decay equation. The data were fit by using *SigmaPlot 8.0* to a two-parameter hyperbolic decay model $y = a \times b/(b + x)$, where $y =$ % cell number and $x =$ concentration of platinum compound. A three-parameter hyperbolic decay model ($y = y_0 + a \times b/(b + x)$, tested both in the absence and presence of constraints ($a = 95$, $y_0 = 5$), yielded larger P values and was therefore not used. The IC_{50} values were determined on the basis of the fitted data, and standard error and P values were derived from the b parameter.

Competition Studies in BCE with Free Peptides. BCE cells were plated as described for the concentration-dependent curves. After 24 h, the medium was replaced with DMEM containing 5% BCS, 2.0 ng/mL basic fibroblast growth factor, with or without **2a** (2 μM), and with or without various concentrations of RGD peptides (0.1–1 mM). The effects of the RGD tripeptide and the cyclic pentapeptides, (CRGDC)c and (RGDfK)c, in **2a**-treated cell proliferation were assessed. Wells with and without bFGF in the absence of platinum complex were kept as positive and negative controls, respectively. All concentrations were tested in triplicate. After 72 h, viable cells were trypsinized and counted using a particle counter. Data were analyzed as described above.

siRNA Transfection. The β_1, β_3, and α_v integrins and control siRNAs were purchased as four oligonucleotide SmartPools (Dharmacon Research, Inc.), containing an approximate 50% guanidine−cytosine content (Dharmacon Research, Inc.). Subconfluent HMVEC-d were washed with HBSS and transfected with 10 nM siRNAs using SiLentFect (Biorad) following the manufacturer's protocol. The medium was changed after a 4 h transfection period. Cells were trypsinized 24 h post-transfection and plated onto gelatin-coated 48-well plates at a density of 7500 cells/well, in EBM-2 supplemented with 5% FBS. After overnight incubation at 37 °C, cells were challenged with either **2a** or cisplatin. Cells were counted after 72 h, and results were analyzed as described above.

Western Analysis. Downregulation of protein expression following RNAi interference was confirmed by Western analysis of cell lysates harvested 120 h post-transfection, at the same time that proliferation plates were counted. Lysate preparation and Western analysis were performed as described previously (*35*). mAbs against integrin subunits included: anti-β_1 (clone B3B11, Chemicon International), anti-β_3 (R&D Systems), anti-α_v (Chemicon). mAb against α-actin (Abcam) was used as a control for equal protein loading. Immunoreactivity was detected on Hyperfilm using ECL (Amersham Biosciences). Films were scanned and band intensities were quantitated with *Image J 1.37* software. Band intensities were normalized to actin and shown as percent protein levels.

Fluorescence-Activated Cell Sorting. The expression of integrins $\alpha_v\beta_3$ and $\alpha_v\beta_5$ was detected by immunofluorescence in unfixed cells. Cells were briefly trypsinized, washed in PBS containing 2% FBS, and incubated on ice for 1 h with Cy5-conjugated anti-human $\alpha_v\beta_3$ (MAB1976S) or $\alpha_v\beta_5$ (MAB1961S) monoclonal antibodies in PBS containing 2% FBS (10 μg/mL; Chemicon, Temecula, CA). Unlabeled cells were used as negative controls. BCE and HMVEC cells were analyzed for APN expression using mouse anti-human CD13 IgG (10 μg/mL; BD Biosciences Pharmingen, San Jose, CA). Mouse IgG was used as a negative control. After incubation on ice for 1 h, the cells were washed three times in PBS containing 2% FBS, incubated with FITC-labeled horse anti-mouse IgG (1:100) (Vector Laboratories, Burlingame, CA) for an additional hour, and then washed again. Cells were analyzed on a fluorescence-activated cell sorting (FACS) VantageSE flow cytometer using the *Cell Quest* software (Beckton Dickinson, San Jose, CA). For each cell type, the fluorescence emitted by negative control cells was used to set a threshold gate. FITC or Cy5-labeled cells emitting higher fluorescence than the threshold value were considered positive and were used to determine the percentage of positively labeled cells. Each experiment was performed twice. FACS images were overlaid in *Adobe Photoshop 7.0*.

RESULTS AND DISCUSSION

Synthesis and Characterization of Pt(IV)−Peptide Conjugates. Cisplatin and other platinum(II) drugs are generally administered to patients intravenously, whereas platinum(IV) agents can be taken orally because of their greater stability in the gastrointestinal (G.I.) tract (*31, 36*). One such compound, *cis,trans,cis*-amine(cyclohexylamine)diacetatodichloroplatinum(IV), or satraplatin, is currently in a phase III clinical trial for hormone-refractory prostate cancer (*37*). Whereas the half-life of satraplatin in tissue culture medium and human plasma is long (22 and 5.3 h, respectively), the Pt(IV) compound undergoes rapid biotransformation in blood to a Pt(II) species, with a half-life of only 6.3 min (*38*). The Pt(II) metabolite of satraplatin, *cis*-amine(cyclohexylamine)dichloroplatinum(II), forms DNA cross-links that are structurally very similar to those of cisplatin (*39*).

A targeting Pt(IV) complex requires a sufficiently long half-life to reach the tumor environment. Because the average cardiac output in an adult resting human is 5 L per minute, and the average total circulating volume in an adult male is 5 L, it takes approximately 1 min for the blood to circulate once through the body. On the basis of the satraplatin half-life in blood, we estimate that an intravenous administration of a targeting Pt(IV) compound should have sufficient time to reach the tumor site before its conversion to Pt(II).

By exploiting integrin- and APN-specific peptide recognition as the guiding strategy, we have designed new Pt(IV) anticancer drug candidates for targeting angiogenic tumor endothelial cells and tumor cells expressing such integrins. The RGD and NGR containing tri- and pentapeptide sequences in these molecules are tethered as axial ligands to the Pt(IV) center. Following selective binding to the tumor cell surfaces, these Pt(IV) species have the potential to enter the cells where they will be readily reduced by glutathione or other intracellular reductants to afford cisplatin (*40–42*). If successful, the level of toxicity of these complexes toward normal cells should be greatly diminished.

cis,trans,cis-Diamminedisuccinatodichloroplatinum(IV), *cis-cis-trans*-[Pt-$(NH_3)_2$(succinate)$_2Cl_2$] (**1**), was employed as the precursor in the synthesis of all Pt−peptide conjugates. Compound **1**, prepared as reported elsewhere (*24*), is suitable for additional derivatization at its axial positions by appropriate coupling with the terminal carboxylate groups of the succinato moieties. A similar strategy was employed successfully in our laboratory to obtain a series of estrogen-tethered platinum(IV) compounds, which are capable of inducing the overexpression of HMGB1 (high mobility group binding protein 1) in MCF-7 cells and thus sensitizing them to the conjugates (*24*).

Three different tripeptide sequences, RGD, NGR, and AGR, and the disulfide-bridged pentapeptide, (CRGDC)c, were prepared by solid-phase synthesis. The –SH groups of cysteine residues in linear CRGDC peptide were oxidized in air to form intrapeptide S−S bridged (CRGDC)c. The peptides were purified by reverse-phase HPLC on a C18 column and characterized by LC-MS, MALDI, and ESI-MS. The cyclopentapeptide, (RGDfK)c, was prepared by following the literature procedure (*32, 33*).

Five monofunctionalized $Pt^{IV}(NH_3)_2Cl_2$−peptide conjugates, denoted as Pt-RGD-mono (**2a**), Pt-NGR-mono (**3a**), Pt-AGR-mono (**4a**), Pt-(CRGDC)c-mono (**6**), and Pt-(RGDfK)c-mono (**7a**), and four difunctionalized analogues designated Pt-RGD-bis (**2b**), Pt-NGR-bis (**3b**), Pt-AGR-bis (**4b**), and Pt-(RGDfK)c-bis (**7b**), were synthesized (Scheme 1). These complexes form upon treatment of **1** with peptide molecules in aqueous solution in the presence of 1-[3-(dimethylamino)propyl]-3-ethylcarbodiimide (EDC) and *N*-hydroxysuccinimide (NHS) as activators and coupling reagents. In the case of (RGDfK)c, the ϵ-amino group of the lysine side chain was activated with a base, DIPEA, before it was allowed to react with **1**. Except for the (CRGDC)c peptide, these reactions afforded both mono- and diconjugated Pt−peptide species, which were separated and purified by reverse-phase HPLC. An HPLC chromatogram for the purifica-

Scheme 1. Synthesis and Labeling of Complexes[a,b]

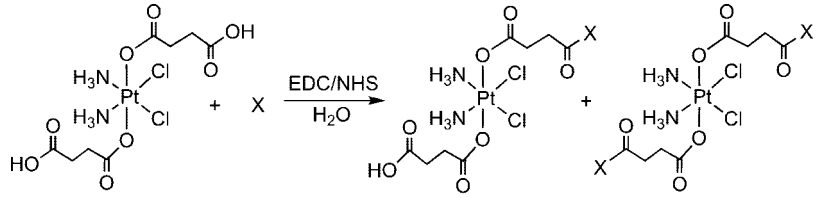

[a] n.o. = not observed. [b] ϵ-amino group of the lysine side chain was activated by using a base, DIPEA, before reacting it with **1**.

tion of linear RGD conjugated Pt(IV) complexes, **2a** and **2b**, is shown in Figure S1 (Supporting Information). For the (CRGDC)c peptide, no difunctionalized complex was detected in the reaction mixture. In addition to the aforementioned complexes, a single amino acid residue, glycinamide, was tethered to the succinato group(s) in a similar fashion to obtain mono- and difunctionalized Pt(IV) conjugates, **5a** and **5b**. These complexes were characterized by LC-MS and high-resolution ESI-MS. The experimental mass spectral data are in excellent agreement with the calculated values and display the proper isotopic mass distribution patterns (see Figure S2, Supporting Information, for representative mass spectra). Lower yields were obtained for the platinum−peptide conjugates in comparison to the glycinamide−platinum conjugates. The decreased yield is most likely the consequence of steric effects generated by the longer amino acid side chains of tri- and pentapeptides. In contrast, glycinamide is a single amino acid containing hydrogen as a side chain; therefore, the coupling reaction is facilitated.

Concentration−Response Curves of the Pt(IV)−Peptide Conjugates on Proliferating Cells. In vitro activity studies of the monofunctionalized (**2a**−**5a**, **6**, and **7a**) and difunctionalized (**2b**−**5b** and **7b**) platinum(IV) complexes, as well as cisplatin and **1**, were performed on proliferating endothelial and tumor cells that express APN and/or the integrins $\alpha_v\beta_3/\alpha_v\beta_5$, discussed above. Cisplatin was used as positive control; compounds **4a**, **4b**, **5a**, and **5b**, and complex **1** were investigated as negative controls. We used primary cultures of endothelial cells, including bovine capillary endothelial (BCE) cells, human microvascular endothelial cells (HMVEC), and human umbilical vein endothelial cells (HUVEC). The tumor cell lines glioblastoma (U87), pancreatic carcinoma (ASPC1), uterine sarcoma (MES-SA and MES-SA/Dx-5), and cervical (HeLa) were also tested on the basis of their expression of at least one of the two $\alpha_v\beta_3$ or $\alpha_v\beta_5$ integrins (*43–47*), which we determined by fluorescence-activated cell sorting (Supporting Information, Figure S3). The expression of aminopeptidase N (CD13) was also confirmed in BCE and HMVEC cells. As shown in Table 1. and Figure S3, only endothelial cells and the tumor lines U87 and ASPC1 expressed $\alpha_v\beta_3$; all cells expressed $\alpha_v\beta_5$.

Cell growth was evaluated in subconfluent, serum- and growth factor-stimulated endothelial cells or serum-stimulated tumor cells in the presence or absence of Pt compounds. BCE cells were stimulated with basic fibroblast growth factor (bFGF); HMVEC and HUVEC were stimulated with endothelial growth media containing bFGF, insulin-like growth factor 1 (IGF-1), hepatocyte growth factor (HGF), and vascular endothelial growth factor (VEGF). The activities of the platinum complexes were determined after 72 h by comparing the number of viable cells as a function of platinum concentration in treated versus untreated cells. Short preincubation times (2 or 6 h) of cisplatin and **1** with BCE and HMVEC cells afforded limited decrease in cell viability, indicating the rates of internalization or activation of platinum complexes to be relatively slow. The activities of these complexes were independent of serum concentration, tested at 5% and 10% (data not shown).

Table 1. Expression Level of $\alpha_v\beta_3$ and $\alpha_v\beta_5$ Integrins in Different Cell Lines

	% labeling		
cell line	$\alpha_v\beta_3$	$\alpha_v\beta_5$	APN
BCE	77 ± 12	44 ± 23	25 ± 5
HMVEC	45 ± 3	98 ± 5	96 ± 1
HUVEC	90 ± 5	96 ± 5	n. d.
U87	82 ± 7	94± 7	n. d.
ASPC1	12 ± 6	46 ± 5	n. d.
MES-SA	1 ± 1	59 ± 26	n. d.
HeLa	1 ± 0.02	83 ± 13	n. d.

Concentration−response curves of the platinum−peptide complexes in all the cells were compared to those with cisplatin and **1**. To ensure unbiased data, two additional independent double-blinded experiments with all the complexes were performed in BCE cells, with reproducible results.

Inhibition of BCE and HMVEC Proliferation by Pt(IV) Conjugates. The IC_{50} values of these complexes, defined as the concentration at which 50% of the cells are viable, were determined for BCE and HMVEC and are summarized in Table 2.

The concentration−response curves of the monoconjugated and diconjugated platinum(IV) complexes, together with that of cisplatin and **1**, toward the BCE cells are plotted in Figure 1A,B, respectively. Among all these complexes, cisplatin was most efficient at inhibiting cell growth ($IC_{50} \approx 1.1$ μM). All Pt(IV) compounds containing conjugated targeting moieties were significantly more inhibitory than **1**, with difunctionalized and monofunctionalized compounds being equally effective. Targeted complexes **2a**, **2b**, containing the linear RGD tripeptide, and **7a**, **7b**, containing the (RGDfK)c pentapeptide, were the

Table 2. IC_{50} (μM) Values of Platinum Complexes for BCE and HMVEC Cells[a]

complex	BCE IC_{50}	*P*-value	HMVEC IC_{50}	*P*-value
Cisplatin	1.1 ± 0.11	****	1.2 ±0.22	****
1	21 ± 3.0	****	33 ± 3.7	****
2a	3.1 ± 0.33	****	5.5 ±0.74	****
2b	2.1 ± 0.31	****	4.5 ± 1.4	**
3a	5.1 ± 0.61	****	5.9 ±0.66	****
3b	7.1 ± 0.86	****	5.1 ±0.45	****
4a	18 ± 2.2	****	n.d.	
4b	28 ± 3.9	****	n.d.	
5a	19 ± 2.6	****	55 ± 11	***
5b	30 ± 3.4	****	55 ± 6.0	****
6	n.d		2.7 ±0.60	**
7a	2.8 ± 0.43	****	3.4 ±0.67	***
7b	3.4 ± 0.55	****	3.3 ±0.85	**
2a/cisplatin	2.8		4.5	
7a/cisplatin	2.5		2.8	
5a/cisplatin	17		45	

[a] *P*-value = $P < 0.01$ (**), $P < 0.001$ (***), and $P < 0.0001$ (****); n.d. = not determined.

most active ($IC_{50} \approx 2.1$–3.4 μM), followed by **3a** and **3b** consisting of NGR tripeptide. In contrast, all platinum(IV) conjugates containing nontargeting peptides or amino acid residues were equal to or less active than **1**. The monofunctionalized compounds **4a** and **5a** are comparable in activity to **1** ($IC_{50} \approx 18.5$ μM), whereas their difunctionalized counterparts are less active (**4b**, **5b**) ($IC_{50} \approx 29$ μM).

A similar inhibitory trend was observed when the complexes were tested on HMVEC (Figure 2). The Pt(IV)−RGD conjugates, mainly **6**, **7a**, and **7b**, were most potent at inhibiting proliferation ($IC_{50} \approx 2.7$–3.4 μM) and comparable to cisplatin ($IC_{50} \approx 1.2$ μM), followed by **2a**, **2b**, and the Pt−NGR conjugates, **3a** and **3b** ($IC_{50} \approx 4.5$–5.9 μM). Nontargeting platinum(IV) complexes, **1**, **4a**, **4b**, **5a**, and **5b** were approximately an order of magnitude less potent ($IC_{50} \approx 33$–55 μM) (see Table 2).

The enhanced activity of RGD-containing Pt(IV) compounds was not caused by the targeting peptide moiety, as shown in Figure 1C. None of the free peptides, RGD, (CRGDC)c, or (RGDfK)c, inhibited BCE growth, even at very high concentrations. In addition, nonconjugated 1:1 and 2:1 mixtures of free RGD and **1** did not improve the concentration−response of **1** ($IC_{50} \approx 36$ μM) (data not shown). These results are consistent with the inhibitory properties of RGD peptides in vitro. RGD peptides interfere with cellular adhesion and migration by antagonizing the interaction between integrins and the extracellular matrix, but do not affect cellular proliferation when administered to subconfluent preadherent cells, as is the case in our study.

Competition Studies of 2a with Free RGD-Containing Peptides in BCE Cells. To determine whether the increased inhibitory response of RGD-containing platinum compounds could be blocked with an excess of RGD-containing peptides, we performed competition studies in BCE cells using **2a** as the RGD−platinum compound, and RGD, (RGDfK)c, and (CRGDC)c as the free peptides. As shown in Figure 3, the more constrained cyclic pentapeptides (CRGDC)c (purple) and (RGDfK)c (light green) could partially decrease the inhibitory effect of **2a** in BCE cells treated with 2 μM of the Pt−RGD compound, and this effect was statistically significant. In contrast, the RGD tripeptide had no effect, even at millimolar concentrations (light blue). By themselves, none of the free peptides affected BCE proliferation ((CRGDC)c in gray, (RGDfK)c in dark green, and RGD in dark blue), consistent with our previous findings (Figure 1C). The fact that the integrin-specific $\alpha_v\beta_3$ and $\alpha_v\beta_5$ ligand (RGDfK)c could reduce the inhibitory effect of the monofunctionalized RGD−Pt(IV) compound suggests that these integrins are playing a role in the recognition of RGD-containing Pt(IV) compounds.

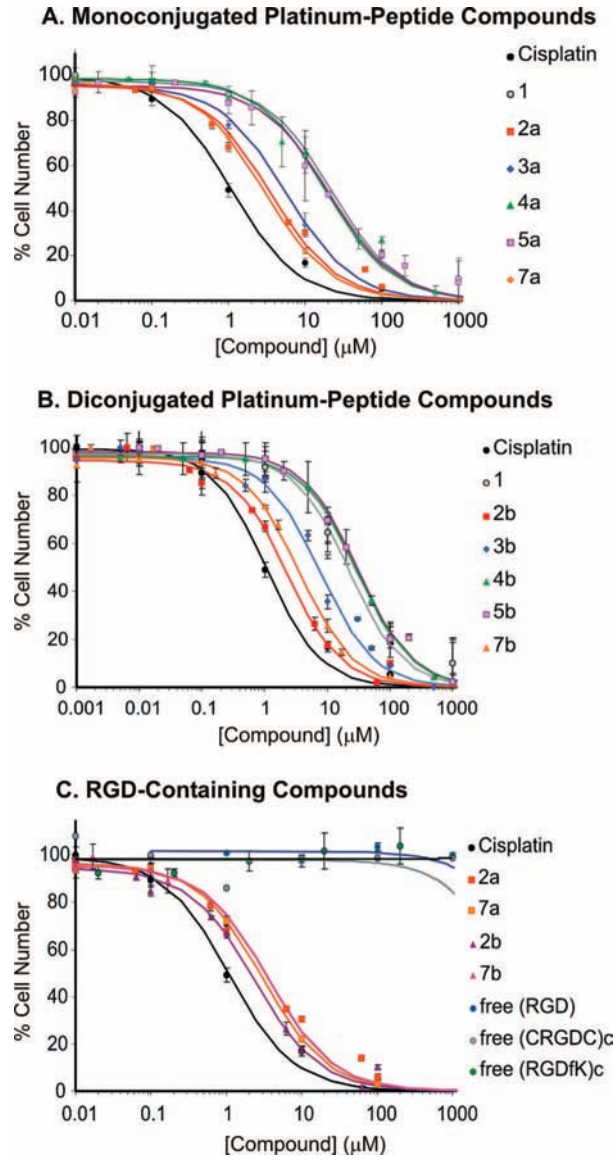

Figure 1. Concentration−response curves of the platinum complexes on BCE cells. (A) Monofunctionalized platinum(IV) complexes along with cisplatin and **1**. (B) Difunctionalized platinum(IV) complexes along with cisplatin and **1**. (C) Pt-RGD complexes and the RGD-containing tri- and pentapeptides. The cells were treated for 72 h with each complex and counted by using a Coulter Counter.

Concentration−Response Curves in HMVEC-d Lacking α_v, β_1, and β_3 integrins. Although the RGD tripeptide can bind to 8 of the 24 known integrin heterodimers of the integrin family, only 3 of these, $\alpha_5\beta_1$, $\alpha_v\beta_3$, and $\alpha_v\beta_5$, have been reported to be expressed in endothelial cells (reviewed in ref *48*). Integrin levels $\alpha_5\beta_1$, $\alpha_V\beta_5$, and $\alpha_V\beta_3$ are increased, mobilized, or induced during angiogenesis, and they can promote apoptosis of angiogenic endothelial cells in vitro and in vivo (*48*). To determine whether some or all of these integrins are responsible for the increased sensitivity of cells toward RGD-containing platinum compounds, we performed RNAi interference studies on HMVEC-d cells. HMVEC-d cells were transfected with β_1, β_3, α_v, or control RNAi, and loss of the integrins was confirmed by Western analysis at the end of the experiment (120 h post-transfection). Complete knockdown of the integrins was obtained for β_1 and β_3 but not for α_v, for which a significant

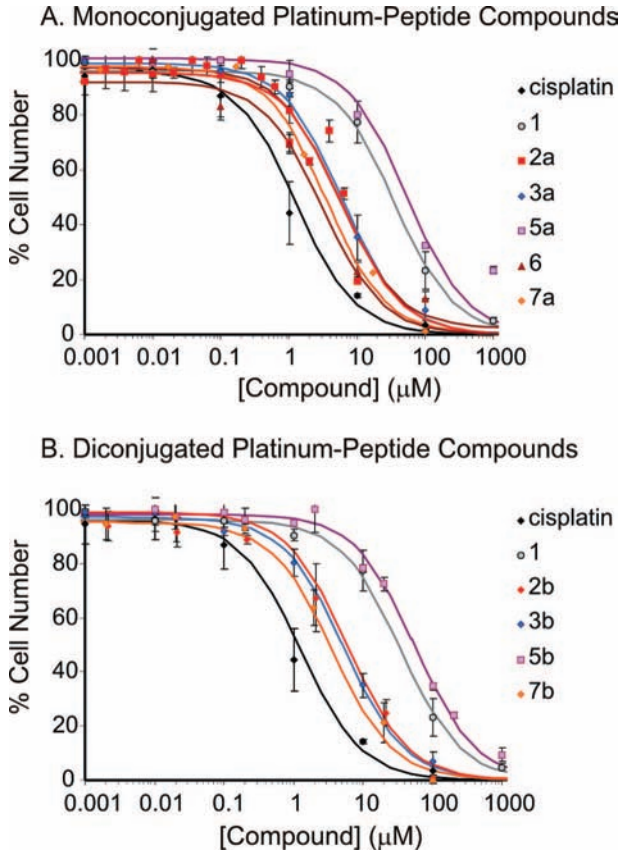

Figure 2. Concentration−response curves of platinum complexes on HMVEC cells. (A) Monofunctionalized platinum(IV) complexes along with cisplatin and **1**. (B) Difunctionalized platinum(IV) complexes along with cisplatin and **1**. The cells were treated for 72 h with each complex and counted using Coulter counter.

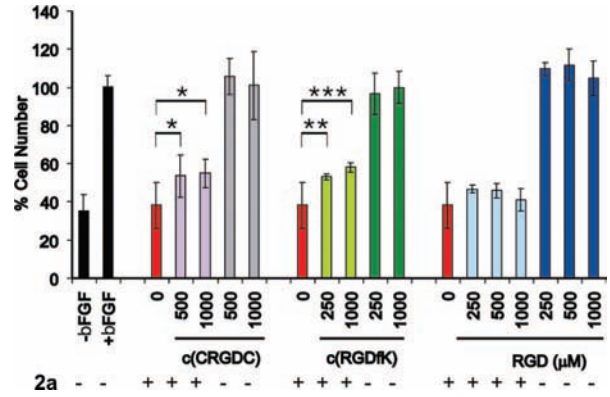

Figure 3. Competition of **2a** with RGD peptides in BCE cells. bFGF-stimulated BCE cells treated with **2a** (2 μM) either alone (red) or in the presence of a large excess of RGD-containing peptides: (CRGDC)c (purple), (RGDfK)c (light green), RGD (light blue). Controls: BCE proliferation with and without bFGF (black), and with bFGF and free RGD-peptides ((CRGDC)c in gray, (RGDfK)c in dark green, and RGD in dark blue). Asterisks indicate statistical significance, as measured with one-way analysis of variance (ANOVA), using the Tukey-Kramer multiple comparison test ($P < 0.05$ (*); $P < 0.01$ (**); $P < 0.001$ (***)). Samples run in triplicate; experiments performed in duplicate.

decrease in protein expression was achieved (Figure 4E,F). An increase in β_3 and β_1 protein expression was observed in cells transfected with β_1 and α_v, respectively, suggesting compensation by other integrin pairs. This was not the case of β_3-transfected cells, for which a decrease in α_v integrin was also observed.

Cells were plated 24 h after RNAi transfection, treated with either cisplatin or **2a**, and counted 3 days after treatment. We found poor cell growth in HMVEC-d transfected with β_3 RNAi. The cell numbers in β_3 knockdown cells 72 h post-treatment were nearly identical to the number of plated cells, demonstrating the critical role of β_3 integrin in endothelial cell proliferation (see Figure 4A,B). In contrast, HMVEC-d transfected with control RNAi, α_v, and β_1 integrins proliferated and had comparable cell numbers at the end of the experiment.

Despite differences in cell growth between the integrin knockdown HMVEC cells, cisplatin treatment afforded identical concentration−response curves (Figure 4C). In contrast, a shift in IC-50 was obtained with **2a** (Figure 4D), particularly with β_3 knockdown (5 to 13 μM), demonstrating that this integrin is involved in **2a**-mediated inhibition of cell growth (see also Table 3). Integrin β_5 could be compensating for the remaining targeting in the β_3 knockdown cells. Although α_v RNAi transfections were intended to remove the contribution from $\alpha_v\beta_3$ and $\alpha_v\beta_5$ integrins, it was not possible to knock down α_v entirely (Figure 4E,F), possibly due to the importance of integrin $\alpha_v\beta_3$ in endothelial cell proliferation. The low levels of α_v found in α_v-transfected HMVEC-d may be sufficient to mediate an inhibitory effect by RGD−Pt(IV). Given the differences in β_1 expression in β_1 and α_v-transfected cells (Figure 4E,F) and their similarities in IC_{50} values (Table 3), β_1 is most likely not involved in the inhibition of cell proliferation by **2a**.

Because the (RGDfK)c pentapeptide specifically binds to $\alpha_v\beta_3$ and $\alpha_v\beta_5$, and our results with RGD− and (RGDfK)c−Pt(IV) conjugates are comparable, recognition of the Pt(IV) complex by the cells most likely occurs, at least in part, through either the $\alpha_v\beta_3$ or $\alpha_v\beta_5$ integrin. This conclusion is supported by our RNAi knockdown studies. Incorporation of NGR-containing Pt(IV) conjugates **3a/3b** may also be mediated in part by integrin $\alpha_v\beta_3$, because this integrin binds NGR peptides, albeit with lower affinity than their RGD analogues (*19*). APN does not appear to be solely responsible for recognition of **3a/3b** given that the IC_{50} values were comparable in BCE and HMVEC despite differences in their APN/CD13 expression levels (Table 1).

Inhibition of Cell Proliferation by RGD-Containing Pt(IV) Conjugates in $\alpha_v\beta_3$ Positive and $\alpha_v\beta_3$ Negative Cells. To determine whether $\alpha_v\beta_5$ could mediate delivery of the RGD-containing complexes in the absence of $\alpha_v\beta_3$, we compared the inhibition of Pt(IV) conjugates in endothelial cells or tumor lines that were positive (HUVEC, U87) and negative (MES-SA, MES-SA/DX-5, HeLa) for $\alpha_v\beta_3$. The concentration−response curves of the Pt−RGD conjugates were comparable on HUVEC, U87, ASPC1, MES-SA, and HeLa cell lines. The IC_{50} values of these complexes and cisplatin are summarized in Table 4 (See Figure S4, Supporting Information, for U87). Because each cell type had a different sensitivity to cisplatin, the IC_{50} ratio between **2a**/cisplatin and **7a**/cisplatin was used to compare the RGD and (RGDfK)c conjugates (see Tables 2 and 4). The best inhibitory effect was obtained in BCE, U87, ASPC1, and HeLa; because the last two cell lines are negative for $\alpha_v\beta_3$, our results suggest that $\alpha_v\beta_5$ is equally efficient at delivering Pt(IV) into the cell.

Targeting Efficiency: Linear vs Cyclic Peptides. According to literature reports, the cyclic RGD and NGR peptides containing cysteine residues that form disulfide bonds mark angiogenic endothelial cells with more efficiency compared to their linear counterparts (*20*, *21*, *25*, *26*). It is believed that the presence of disulfide linkage in the cyclic peptides provides the RGD and NGR motifs a constrained conformational arrangement resulting in stronger interactions with the integrins expressed on the cell surfaces. In some cases, the cyclic peptides

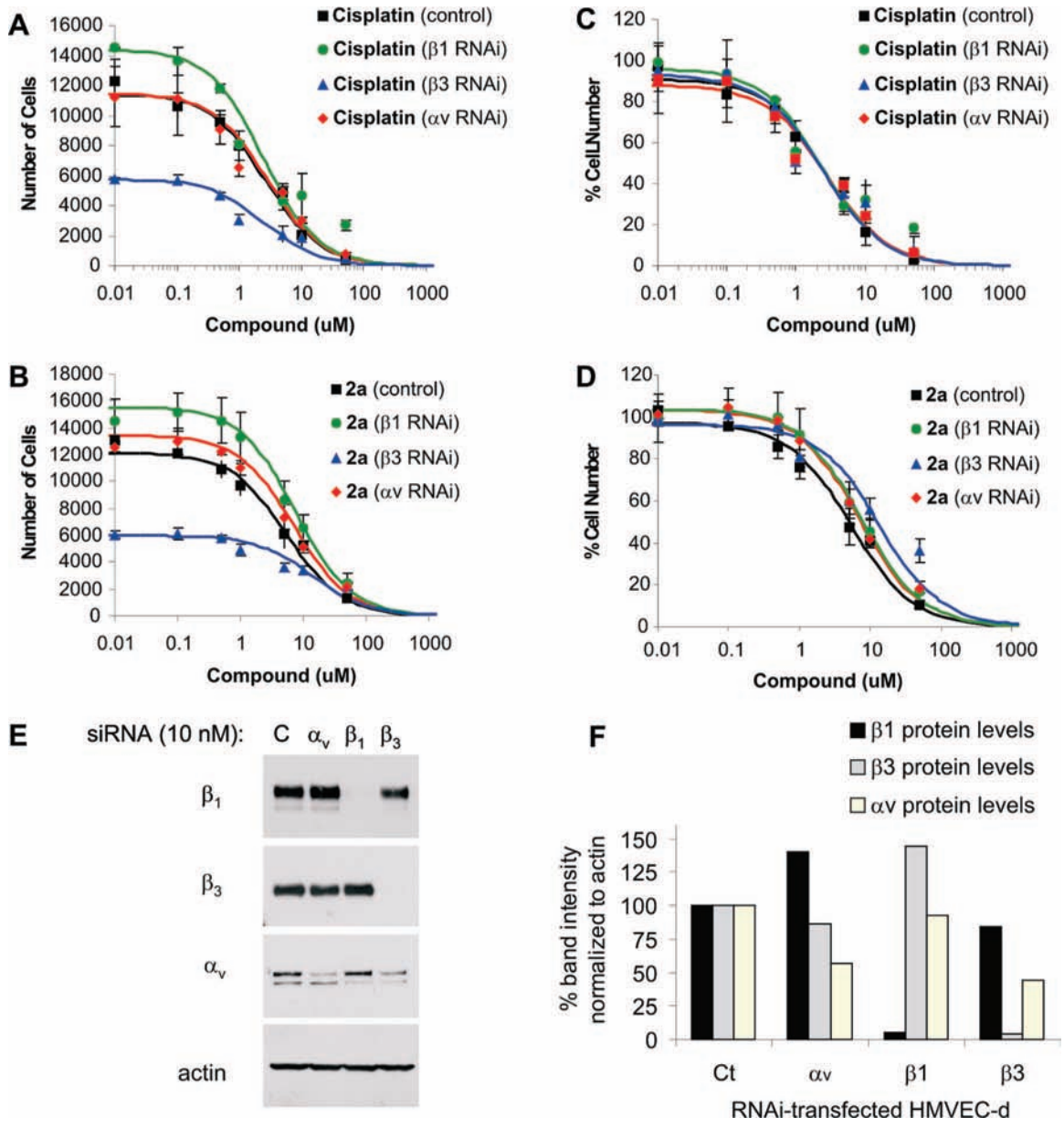

Figure 4. Integrin $\beta 3$ partially mediates Pt(IV)−RGD inhibition of proliferation in HMVEC-d cells. Concentration−response curves in HMVEC-d cells after RNAi knockdown of integrins β_1, β_3, or α_v displayed as total cell number (A,B) or percent cell number (C,D) 72 h after treatment. Poor cell growth was observed in HMVEC-d cells lacking integrin β_3, but not α_v or β_1 (A,B). Despite differences in cell growth between control, β_1 and β_3 knockdown cells, identical concentration–response curves were obtained with cisplatin (C). In contrast, a shift in IC-50 was obtained with **2a** (D), particularly with β_3 knockdown. (E) Western Blot of lysates from transfected HMVEC 120 h post-transfection. In lanes: control, α_v, β_1, and β_3 RNAi transfected HMVEC; in rows: lysates probed with mAb against integrins β_1, β_3, α_v, and Actin. (F) Gel quantitation and normalization to Actin, demonstrating nearly complete knockdown of β_1 and β_3, increased β_1 levels in α_v-transfected cells, and increased β_3 levels in β_1-transfected cells. Integrin α_v was significantly decreased (>45%) in both α_v- and β_3-transfected cells.

Table 3[a]

IC_{50} on HMVEC-d	Cisplatin (μM)	*P*-value	**2a** (μM)	*P*-value
control RNAi	2.2 ± 0.4	**	5.1 ± 0.8	**
α-v RNAi	2.2 ± 0.6	*	7.5 ± 0.7	****
β-1 RNAi	2.2 ± 0.8	*	8.0 ± 0.7	***
β-3 RNAi	2.2 ± 0.7	*	13 ± 4.3	*

[a] *P*-value = $P < 0.05$ (*), $P < 0.01$ (**), $P < 0.001$ (***), and $P < 0.0001$ (****); n.d. = not determined.

containing the RGD and NGR motifs were 10- to 200-fold more effective over the corresponding linear peptides in recognizing the receptors (*21*, *25*, *26*). In the present study, we examined both linear RGD and cyclic (CRGDC)c peptides to serve as the marker to transport the attached platinum complexes to the tumor cells. We also included the cyclic pentapeptide, (RGDfK)c, which is a potent inhibitor of $\alpha_v\beta_3/\alpha_v\beta_5$ (*27*, *49*).

The differential recognition of linear vs cyclic RGD peptides to integrins was indirectly confirmed in our competition studies, because both cyclic pentapeptides, (CRGDC)c and (RGDfK)c, could partially compete the inhibitory effect of **2a** in BCE cells, whereas the linear tripeptide RGD was ineffective. Although we have not yet determined the binding affinities of the linear RGD-containing Pt(IV) compounds and the cyclic RGD-containing Pt(IV) complexes, our results indicate that the linear RGD tripeptide containing Pt(IV) complexes are equally effective in inhibiting cell proliferation and cell killing, Only for about half of the cells tested did we find that the mono- and diconjugated (RGDfK)c compounds were slightly superior to

Table 4. Inhibition by Cisplatin and RGD-Targeted Pt(IV) Compounds in Endothelial and Non-Endothelial Cells[a]

	cell				
IC_{50}	HUVEC	U87	ASPC1	MES-SA	HeLa
Cisplatin	0.52 ± 0.08 ****	0.38 ± 0.09 ***	0.24 ± 0.08 **	0.15 ± 0.03 ****	1.3 ± 0.22 ****
2a	2.6 ± 0.31 ****	1.6 ± 0.61 *	0.79 ± 0.19 **	1.7 ± 0.33 ***	4.6 ± 0.79 ****
2b	11 ± 2.8 **	3.6 ± 0.66 ***	1.5 ± 0.38 **	1.3 ± 0.19 ****	3.5 ± 0.96 **
6	4.2 ± 0.6 ****	1.5 ± 0.58 *	n. d.	3.9 ± 1.1 **	n. d.
7a	3.5 ± 0.51 ****	0.99 ± 0.10 ****	1.6 ± 0.51 *	0.59 ± 0.12 ****	3.9 ± 0.81 **
7b	5.9 ± 1.2 ***	0.66 ± 0.15 **	2.1 ± 0.62 *	0.41 ± 0.05 ****	4.9 ± 0.85 *
5a	110 ± 29 **	20 ± 7 *	n.d.	13 ± 3.2 **	n.d.
5b	45 ± 14 **	50 ± 9.7 ****	n.d.	6.8 ± 1.3 ***	n.d.
2a/cisplatin	5.0	4.2	3.3	11	3.5
7a/cisplatin	6.7	2.6	6.6	3.9	3.0
5a/cisplatin	211	52	n.d.	87	n.d.

[a] *P*-value = $P < 0.05$ (*), $P < 0.01$ (**), $P < 0.001$ (***), and $P < 0.0001$ (****); n.d. = not determined.

the mono- and bis-conjugated RGD compounds (HMVEC, U87, MES-SA). As supported by the values listed in Table 4, the IC_{50} ratios of the monoconjugated RGD containing Pt(IV) complexes, **2a** and **7a**, with respect to cisplatin are quite comparable for a given cell type. We have also demonstrated that at least some of the antiproliferative effect of **2a** is mediated by the $\alpha_v\beta_3/\alpha_v\beta_5$ integrins, because (1) the $\alpha_v\beta_3/\alpha_v\beta_5$ integrin-specific ligand, (RGDfK)c, and (CRGDC)c could partially compete off **2a** in BCE cells, and (2) loss of β_3 in HMVEC increased the IC_{50} of **2a** but not of cisplatin. It is possible that, upon conjugation to the succinate group in Pt(IV), the RGD linear tripeptide and the cyclic RGD pentapeptide targeting moieties become comparable at recognizing $\alpha_v\beta_3/\alpha_v\beta_5$ integrins. The Pt(IV) center could sterically hinder binding of the cyclic pentapeptides, decreasing their enhanced binding, or the Pt(IV) center may impose a more rigid conformation to the RGD linear targeting moiety enhancing its binding potential to the $\alpha_v\beta_3/\alpha_v\beta_5$ integrins. A high degree of targeting ability with a linear RGD tripeptide attached to glycosylated porphyrins was also observed in photodynamic cancer therapy against K562 leukemia cell lines (*50*).

Cell Internalization of Pt−Peptide Conjugates. The platinum complexes can enter the cells selectively, through internalization by a surface marker such as $\alpha_v\beta_3$ integrin, or nonselectively, by diffusion across the cell membrane or via other transporters or carriers. Cisplatin, a small neutral molecule, enters cells by passive diffusion (*4*) and, to a degree not yet quantified, by other transporters (*51, 52*). Differences in the size and overall charge on the complex will affect passive diffusion of the complexes through the cell membrane, with smaller, planar, and neutral complexes being more readily incorporated than large, nonplanar, and charged ones. Some of our platinum–peptide complexes are neutral at pH 7 in aqueous solution, whereas a few of the complexes are positively charged and several of them are negative (Chart 1). All of the Pt(IV) complexes have an octahedral geometry which, together with their variable overall charges, makes it unlikely that they would be internalized by passive diffusion. Except for cisplatin, the nontargeted Pt complexes should therefore enter cells by selective uptake. The toxicity profiles of the negatively charged monoglycinamide-tethered complex (**5a**), the neutral mono-AGR (**4a**) and bis-glycinamide complexes (**5b**), and the positively charged bis-AGR complexes (**4b**) are quite similar to that of **1**, which is smaller and negatively charged in aqueous solution. Although the monoconjugated RGD complexes are negatively charged, and the diconjugated complexes are neutral in water, they have a very similar inhibitory effect and are significantly more potent than the nontargeting Pt(IV) complexes. No significant differences in antiproliferative effect were observed between the targeting mono- and diconjugated complexes, suggesting that only one ligand is sufficient for cell surface recognition. These results indicate that the cellular uptake of the targeting platinum(IV) complexes is most likely mediated by internalization by surface markers, $\alpha_v\beta_3$ and $\alpha_v\beta_5$ integrins, which would account for their greater potency compared to the nontargeting analogues.

From the perspective of evaluating compounds for further study in animal models and, eventually, human cancer treatment, it would have been valuable to test them against cells that were $\alpha_v\beta_5$ negative. The cell lines that we tested were all positive for this integrin (Table 1), however. Nevertheless, the significantly improved effectiveness of the targeting RGD, (RGDfK)c, and (CRGDC)c conjugates compared to the nontargeting AGR, Gly, and disuccinate precursor clearly establishes the value of targeting receptors involved in tumor vasculature as a strategy for improving the efficacy and selectivity of platinum-based drugs.

CONCLUSION

Targeted drug delivery is currently an active area of research in cancer therapy. It offers two major advantages over traditional chemotherapy: (1) it avoids damage to the normal tissue, and (2) it can limit drug resistance, which is a real concern for the current palette of platinum anticancer drugs. In the present investigation, several Pt(IV)−peptide conjugates were designed and synthesized for the purpose of targeted drug delivery to tumor endothelial cells and tumor cells expressing $\alpha_v\beta_3/\alpha_v\beta_5$ integrins. The tri- and pentapeptides, containing either an RGD or an NGR motif, attached by an amide linkage to the platinum(IV) center through a succinato group, serve as tumor-targeting units. The concentration–response curves of these complexes were examined against different endothelial and human cancer cells *in vitro*. RGD-tethered Pt(IV) complexes are potent inhibitors of cellular proliferation when compared to both nontargeting platinum(IV) compounds and to the unconjugated targeting RGD tri- and pentapeptide moieties. NGR conjugates were less inhibitory than RGD counterparts but were still more active than nonspecific Pt(IV)−peptide analogues, suggesting greater affinity of RGD units to the transmembrane receptors over NGR-containing peptides. These results introduce the possibility of selective transport of platinum anticancer agents into tumor endothelial cells.

ACKNOWLEDGMENT

This research was supported by grant CA34992 from the National Cancer Institute. CMB was supported by Postdoctoral Fellowship Grant #PF-03-111-01-CSM from the American Cancer Society and by the Eleanor and Miles Shore Faculty Career Development Award from Children's Hospital, Boston, MA. AH thanks the Pew Latin American Fellows Program in the Biomedical Sciences sponsored by the Pew Charitable Trusts. The MIT Department of Chemistry Instrument Facility is funded by the National Science Foundation (CHE-9808061, CHE-9808063, and DBI-9729592). We thank Prof. Judah Folkman and Catherine Butterfield at the Vascular Biology Program, Children's Hospital for helpful suggestions and for generously providing BCE cells used in this study. We thank Dr. Deborah Freedman, Children's Hospital, Boston, for providing the basic fibroblast growth factor, and Ryan Todd (Massachusetts Institute of Technology), and Arshiya Ahuja (Children's Hospital) for their experimental assistance.

Supporting Information Available: HPLC trace showing the separation of the Pt−RGD conjugates (**2a** and **2b**), ESI-MS results for these compounds, fluoresecence-activated cell sorting of primary endothelial cells and tumor cell lines labeled with mAb against $\alpha_v\beta_3$, $\alpha_v\beta_5$, and APN, and concentration−response assay of platinum compounds on U87 cells. This material is available free of charge via the Internet at http://pubs.acs.org.

LITERATURE CITED

(1) Wong, E., and Giandomenico, C. M. (1999) Current status of platinum-based antitumor drugs. *Chem. Rev. 99*, 2451–2466.

(2) Jamieson, E. R., and Lippard, S. J. (1999) Structure, recognition, and processing of cisplatin-DNA adducts. *Chem. Rev. 99*, 2467–2498.

(3) Trimmer, E. E., and Essigmann, J. M. (1999) Cisplatin. *Essays Biochem. 34*, 191–211.

(4) Cohen, S. M., and Lippard, S. J. (2001) Cisplatin: From DNA damage to cancer chemotherapy. *Prog. Nucleic Acid Res. Mol. Biol. 67*, 93–130.

(5) Barnes, K. R., and Lippard, S. J. (2004) Cisplatin and related anticancer drugs: Recent advances and insights. *Met. Ions Biol. Syst. 42*, 143–177.

(6) Wang, D., and Lippard, S. J. (2005) Cellular processing of platinum anticancer drugs. *Nat. Rev. Drug Discovery 4*, 307–320.

(7) Folkman, J. (1995) Angiogenesis in cancer, vascular, rheumatoid and other disease. *Nat. Med. 1*, 27–31.

(8) Hanahan, D., and Folkman, J. (1996) Patterns and emerging mechanisms of the angiogenic switch during tumorigenesis. *Cell 86*, 353–364.

(9) Kerbel, R., and Folkman, J. (2002) Clinical translation of angiogenesis inhibitors. *Nat. Rev. Cancer 2*, 727–739.

(10) Ruoslahti, E. (1996) RGD and other recognition sequences for integrins. *Annu. Rev. Cell Dev. Biol. 12*, 697–715.

(11) Brooks, P. C., Clark, R. A. F., and Cheresh, D. A. (1994) Requirement of vascular integrin $\alpha_v\beta_3$ for angiogenesis. *Science 264*, 569–571.

(12) Friedlander, M., Brooks, P. C., Shaffer, R. W., Kincaid, C. M., Varner, J. A., and Cheresh, D. A. (1995) Definition of two angiogenic pathways by distinct α_v integrins. *Science 270*, 1500–1502.

(13) Erdreich-Epstein, A., Shimada, H., Groshen, S., Liu, M., Metelitsa, L. S., Kim, K. S., Stins, M. F., Seeger, R. C., and Durden, D. L. (2000) Integrins $\alpha_v\beta_3$ and $\alpha_v\beta_5$ are expressed by endothelium of high-risk neuroblastoma and their inhibition is associated with increased endogenous ceramide. *Cancer Res. 60*, 712–721.

(14) Pasqualini, R., Koivunen, E., Kain, R., Lahdenranta, J., Sakamoto, M., Stryhn, A., Ashmun, R. A., Shapiro, L. H., Arap, W., and Ruoslahti, E. (2000) Aminopeptidase N is a receptor for tumor-homing peptides and a target for inhibiting angiogenesis. *Cancer Res. 60*, 722–727.

(15) Hood, J. D., and Cheresh, D. A. (2002) Role of integrins in cell invasion and migration. *Nat. Rev. Cancer 2*, 91–100.

(16) Hynes, R. O. (2002) Integrins: bidirectional, allosteric signaling machines. *Cell 110*, 673–687.

(17) Ruoslahti, E. (2002) Specialization of tumour vasculature. *Nat. Rev. Cancer 2*, 83–90.

(18) Arap, W., Pasqualini, R., and Ruoslahti, E. (1998) Cancer treatment by targeted drug delivery to tumor vasculature in a mouse model. *Science 279*, 377–380.

(19) Healy, J. M., Murayama, O., Maeda, T., Yoshino, K., Sekiguchi, K., and Kikuchi, M. (1995) Peptide ligands for integrin $\alpha_v\beta_3$ selected from random phage display libraries. *Biochemistry 34*, 3948–3955.

(20) Hart, S. L., Knight, A. M., Harbottle, R. P., Mistry, A., Hunger, H.-D., Cutler, D. F., Williamson, R., and Coutelle, C. (1994) Cell binding and internalization by filamentous phage displaying a cyclic Arg-Gly-Asp-containing peptide. *J. Biol. Chem. 269*, 12468–12474.

(21) Aumailley, M., Gurrath, M., Müller, G., Calvete, J., Timpl, R., and Kessler, H. (1991) Arg-Gly-Asp constrained within cyclic pentapeptides. Strong and selective inhibitors of cell adhesion to vitronectin and laminin fragment P1. *FEBS Lett. 291*, 50–54.

(22) Frisch, S. M., and Francis, H. (1994) Disruption of epithelial cell-matrix interactions induces apoptosis. *J. Cell Biol. 124*, 619–626.

(23) Temming, K., Schiffelers, R. M., Molema, G., and Kok, R. J. (2005) RGD-based strategies for selective delivery of therapeutics and imaging agents to the tumour vasculature. *Drug Resist. Update 8*, 381–402.

(24) Barnes, K. R., Kutikov, A., and Lippard, S. J. (2004) Synthesis, characterization, and cytotoxicity of a series of estrogen-tethered platinum(IV) complexes. *Chem. Biol. 11*, 557–564.

(25) Colombo, G., Curnis, F.De, Mori, G. M. S., Gasparri, A., Longoni, C., Sacchi, A., Longhi, R., and Corti, A. (2002) Structure-activity relationships of linear and cyclic peptides containing the NGR tumor-homing motif. *J. Biol. Chem. 277*, 47891–47897.

(26) Koivunen, E., Wang, B., and Ruoslahti, E. (1995) Phage libraries displaying cyclic peptides with different ring sizes: ligand specificities of the RGD-directed integrins. *Bio/Technology 13*, 265–270.

(27) Haubner, R., Gratias, R., Diefenbach, B., Goodman, S. L., Jonczyk, A., and Kessler, H. (1996) Structural and functional aspects of RGD-containing cyclic pentapeptides as highly potent and selective integrin $\alpha_v\beta_3$ antagonists. *J. Am. Chem. Soc. 118*, 7461–7472.

(28) Boturyn, D., Coll, J.-L., Garanger, E., Favrot, M.-C., and Dumy, P. (2004) Template assembled cyclopeptides as multimeric system for integrin targeting and endocytosis. *J. Am. Chem. Soc. 126*, 5730–5739.

(29) Abbreviations: A (Ala), a. A., aminopeptidase N; BCE, bovine capillary endothelial; bFGF, basic fibroblast growth factor; C (Cys), cysteine; D (Asp), aspartic acid; DIC, 1,3-diisopropylcarbodiimide; DIPEA, diisopropylethylamine; DMEM, Dulbecco's modified Eagle's medium; EDC, 1-[3-(dimethylamino)propyl]-3-ethylcarbodiimide; f, D-phenylalanine; FCS, fetal calf serum; G (Gly), glycine; HMVEC, human microvascular endothelial cell; HOBt, 1-hydroxybenzotraizole ($C_6H_5N_3O$); IC_{50}, the concentration at which 50% of cell death occurs; L (Leu), leucine; N (Asn), asparagine; NHS, *N*-hydroxysuccinimide; NMP, *N*-methyl-2-pyrrolidinone; S (Ser), serine; R (Arg), arginine; TFA, trifluoroacetic acid; TIPS, triisopropylsilane.

(30) Dhara, S. C. (1970) A rapid method for the synthesis of *cis*-$[Pt(NH_3)_2Cl_2]$. *Indian J. Chem. 8*, 193–194.

(31) Giandomenico, C. M., Abrams, M. J., Murrer, B. A., Vollano, J. F., Rheinheimer, M. I., Wyer, S. B., Bossard, G. E., and Higgins, J. D. (1995) Carboxylation of kinetically inert platinum(IV) hydroxy complexes. An entrée into orally active platinum(IV) antitumor agents. *Inorg. Chem. 34*, 1015–1021.

(32) Dai, X., Su, Z., and Liu, J. O. (2000) An improved synthesis of a selective $\alpha_v\beta_3$-integrin antagonist cyclo(-RGDfK-). *Tetrahedron Lett. 41*, 6295–6298.

(33) McCusker, C. F., Kocienski, P. J., Boyle, F. T., and Schätzlein, A. G. (2002) Solid-phase synthesis of c(RGDfK) derivatives: on-resin cyclization and lysine functionalization. *Bioorg. Med. Chem. Lett. 12*, 547–549.

(34) O'Reilly, M. S., Holmgren, L., Shing, Y., Chen, C., Rosenthal, R. A., Moses, M., Lane, W. S., Cao, Y., Sage, E. H., and Folkman, J. (1994) Angiostatin: a novel angiogenesis inhibitor that mediates the suppression of metastases by a Lewis lung carcinoma. *Cell 79*, 315–328.

(35) Short, S. M., Talbott, G. A., and Juliano, R. L. (1998) Integrin-mediated signaling events in human endothelial cells. *Mol. Biol. Cell 9*, 1969–1980.

(36) Hambley, T. W., Battle, A. R., Deacon, G. B., Lawrenz, E. T., Fallon, G. D., Gatehouse, B. M., Webster, L. K., and Rainone, S. (1999) Modifying the properties of platinum(IV) complexes

in order to increase biological effectiveness. *J. Inorg. Biochem. 77*, 3–12.

(37) Oh, W. K., Tay, M.-H., and Huang, J. (2007) Is there a role for platinum chemotherapy in the treatment of patients with hormone-refractory prostate cancer? *Cancer 109*, 477–486.

(38) Carr, J. L., Tingle, M. D., and McKeage, M. J. (2002) Rapid biotransformation of satraplatin by human red blood cells in vitro. *Cancer Chemother. Pharmacol. 50*, 9–15.

(39) Silverman, A. P., Bu, W., Cohen, S. M., and Lippard, S. J. (2002) 2.4-Å Crystal structure of the asymmetric platinum complex{Pt(ammine)(cyclohexylamine)}$^{2+}$ bound to a dodecamer DNA duplex. *J. Biol. Chem. 277*, 49743–49749.

(40) Choi, S., Filotto, C., Bisanzo, M., Delaney, S., Lagasee, D., Whitworth, J. L., Jusko, A., Li, C., Wood, N. A., Willingham, J., Schwenker, A., and Spaulding, K. (1998) Reduction and anticancer activity of platinum(IV) complexes. *Inorg. Chem. 37*, 2500–2504.

(41) Lemma, K., Sargeson, A. M., and Elding, L. I. (2000) Kinetics and mechanism for reduction of oral anticancer platinum(IV) dicarboxylate compounds by L-ascorbate ions. *J. Chem. Soc., Dalton Trans.* 1167–1172.

(42) Lemma, K., Shi, T., and Elding, L. I. (2000) Kinetics and mechanism for reduction of the anticancer prodrug *trans*, *trans*,*trans*-[$PtCl_2(OH)_2$(c-$C_6H_{11}NH_2$)(NH_3)] (JM335) by thiols. *Inorg. Chem. 39*, 1728–1734.

(43) Aida, K., Onda, M., Asano, G., and Nakazawa, N. (1997) Predisposition of subclones of pancreatic carcinoma cells, AsPC-1, to changes in functional and histopathological features of xenograft tumors with response to extracellular matrix. *Nippon Ika Daigaku Zasshi 64*, 163–171.

(44) Arao, S., Masumoto, A., and Otsuki, M. (2000) β1 integrins play an essential role in adhesion and invasion of pancreatic carcinoma cells. *Pancreas 20*, 129–137.

(45) Hong, S.-Y., Lee, H., You, W.-K., Chung, K.-H., Kim, D.-S., and Song, K. (2003) The snake venom disintegrin salmosin induces apoptosis by disassembly of focal adhesions in bovine capillary endothelial cells. *Biochem. Biophys. Res. Commun. 302*, 502–508.

(46) Liu, Z.-J., Snyder, R., Soma, A., Shirakawa, T., Ziober, B. L., Fairman, R. M., Herlyn, M., and Velazquez, O. C. (2003) VEGF-A and $\alpha_v\beta_3$ integrin synergistically rescue angiogenesis via N-Ras and PI3-K signaling in human microvascular endothelial cells. *FASEB J. 17*, 1931–1933.

(47) Yokoyama, Y., and Ramakrishnan, S. (2005) Addition of an aminopeptidase N-binding sequence to human endostatin improves inhibition of ovarian carcinoma growth. *Cancer 104*, 321–331.

(48) Stupack, D. G., and Cheresh, D. A. (2004) Integrins and angiogenesis. *Curr. Top. Dev. Biol. 64*, 207–238.

(49) Haubner, R., Finsinger, D., and Kessler, H. (1997) Stereoisomeric peptide libraries and peptidomimetics for designing selective inhibitors of the $\alpha_v\beta_3$ integrin for a new cancer therapy. *Angew. Chem., Int. Ed. Engl. 36*, 1374–1389.

(50) Chaleix, V., Sol, V., Huang, Y.-M., Guilloton, M., Granet, R., Blais, J. C., and Krausz, P. (2003) RGD-porphyrin conjugates: Synthesis and potential application in photodynamic therapy. *Eur. J. Org. Chem.* 1486–1493.

(51) Safaei, R. (2006) Role of copper transporters in the uptake and efflux of platinum containing drugs. *Cancer Lett. 234*, 34–39.

(52) Zhang, S., Lovejoy, K. S., Shima, J. E., Lagpacan, L. L., Shu, Y., Lapuk, A., Chen, Y., Komori, T., Gray, J. W., Chen, X., Lippard, S. J., and Giacomini, K. M. (2006) Organic cation transporters are determinants of oxaliplatin cytotoxicity. *Cancer Res. 66*, 8847–8857.

BC070031K

Use of Multiple Carboxylates to Increase Intracellular Retention of Fluorescent Probes Following Release From Cell Penetrating Fluorogenic Conjugates

Xiaoxu Li,[†,§] Ryuji Higashikubo,[‡] and John-Stephen Taylor*[,†]

Chemistry Department, Washington University, St. Louis, Missouri 63130, and Department of Radiation Oncology, Washington University School of Medicine, St. Louis, Missouri 63108. Received March 8, 2007; Revised Manuscript Received September 18, 2007

Fluorogenic reporter systems for use inside cells require that the fluorophore be retained inside the cell following activation to ensure accumulation of an observable signal. In the process of developing ester-based nucleic acid-triggered probe activation systems for use in cells, we found that simple O-alkylated fluorescein esters coupled to cell-penetrating peptides led to very poor signals, presumably because the released fluorophore was too membrane permeable and rapidly exited the cell. To circumvent this problem, we have examined the effect of adding one or two carboxylates to the fluorescein to reduce its membrane permeability. *N*-maleimido D-valine and α-methyl-*β*-L-alanine esters of fluorescein, in which the second phenolic hydroxyl group was derivatized with a carboxymethyl group and then further conjugated with glutamate, were linked to the cell-penetrating peptide Arg_9Cys through conjugate addition of the thiol group to the maleimido group. HeLa cells were incubated with these conjugates, washed, and then further incubated for various times prior to analysis by flow cytometry. Quantitative analysis of the data by a simplified kinetic scheme showed that the fluorescein with two appended carboxylic acid groups effluxed with a rate constant of about 0.00113 min^{-1}, corresponding to a half-life of 8.8 h. The dicarboxylated fluorescein effluxed about 6.1 times more slowly than the fluorescein with a single carboxylic acid group and led to a fairly stable signal. The analysis also showed that the D-Val ester was hydrolyzed about 4.6 times more slowly than the *β*-alanine ester and had a half-life of about 31 min. These data indicate that the fluorescein with two appended carboxylates may be a useful membrane-impermeant fluorophore for fluorogenic probe applications inside living cells.

INTRODUCTION

Fluorogenic compounds have found extensive use as probes for a wide range of intracellular biomolecules and processes by becoming fluorescent only after activation by a specific chemical or enzymatic event (*1–7*). Fluorogenic compounds can also be used to assist the development and optimization of prodrugs by enabling the lability of the prodrug-activating reaction to be monitored in target and nontarget cells (*8–10*). Recently, we have proposed a new approach to chemotherapy and diagnostics called NATPA for nucleic acid-triggered prodrug and probe release (*11–15*). This new approach depends on a disease-specific mRNA sequence to template the association of a complementary prodrug or probe with a catalytic component that then catalyzes the release of the prodrug or probe. For this system to work efficiently, the prodrug or probe must be both stable to the diverse biological environments it will encounter and labile to the catalyst.

Selecting an optimal prodrug or probe for NATPA requires screening a large number of candidates in serum and inside cells. An ideal fluorogenic probe would be one that enters the cell faster than it is activated and one for which the fluorescent product effluxes from the cell more slowly than it is produced (Figure 1). Recently, we developed a general fluorogenic system **1** (Figure 2) that could be used for monitoring the stability of ester-based prodrugs and probes inside cells that consists of a fluorogenic ester of a monoalkylated fluorescein attached to a cell-penetrating Arg_9 peptide (*16*).

The advantage of using the cell-penetrating peptide, Arg_9, to deliver a fluorogenic substrate is that this short peptide has been shown to rapidly deliver attached cargo into cells, irrespective of their inherent membrane permeability or size. The Arg_9 peptide, which has charge and amino acid composition similar to that of HIV Tat peptide 46–57, promotes rapid cellular uptake of diverse types of molecules, such as drugs, peptides, and enzymes into cells, in many different cell lines (*17–20*). A strategy based on using a cell-penetrating peptide for delivering fluorogenic substrates is therefore much more flexible and general than one that requires that the fluorogenic agent itself be membrane permeable and that relies on the activation reaction to render the fluorophore less membrane permeable (*21*). This latter strategy is severely limited by how permeable the fluorogenic substrate can be made as well as how much less permeable the fluorescent probe can be made by the activating reaction. However, attachment of a cell-penetrating carrier such as Arg_9 makes it possible to transport a variety of different fluorogenic probes into cells rapidly so that the activation rates of various probes can be easily compared and quantified. This method of cellular delivery has recently been applied to the design of a number of fluorogenic reagents (*22*).

Esters of mono-O-alkylated fluoresceins were chosen as the fluorogenic ester component because monoalkylated fluoresceins have fluorescence properties similar to those of fluorescein and are easy to prepare, thereby making it easy to tailor the efflux properties of the fluorescein (*16*). When the remaining phenolic oxygen of a monoalkylated fluorescein is esterified, the fluorescein derivative becomes trapped in its nonfluorescent lactone

* To whom correspondence should be addressed. Department of Chemistry, Campus Box 1134, Washington University, One Brookings Drive, St. Louis, MO 63130. E-mail: taylor@wustl.edu.

[†] Washington University.

[‡] Washington University School of Medicine.

[§] Present address: Department of Chemical Engineering and Columbia Genome Center, Columbia University, New York, NY 10032.

10.1021/bc070079y CCC: $40.75 © 2008 American Chemical Society
Published on Web 11/20/2007

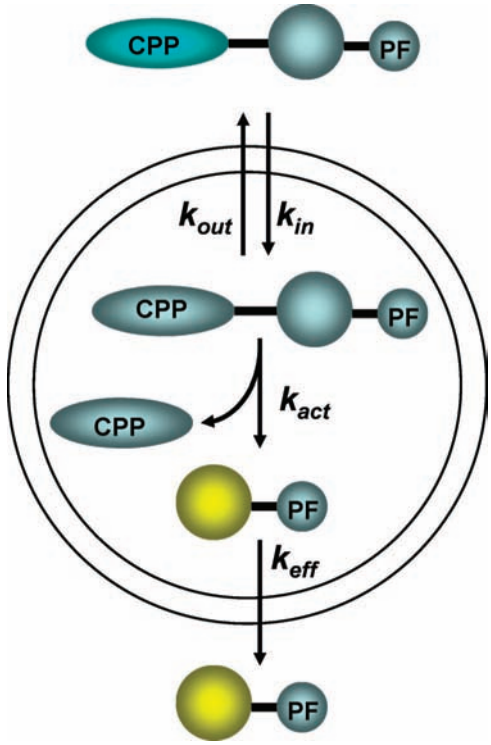

Figure 1. General mechanistic scheme for the entry and activation of a fluorogenic ester conjugate of a cell-penetrating peptide. In the first step, the conjugate enters the cell with rate constant k_{in}, presumably by an endocytotic mechanism mediated by the cell-penetrating peptide (CPP), and exits by a slower, more complex mechanism. In the second step, the ester linkage is cleaved by endogenous enzymes, thereby activating the fluorophore with rate constant k_{act}. Depending on the nature of the permeability factor (PF), the fluorophore will efflux the cell with rate constant k_{eff}.

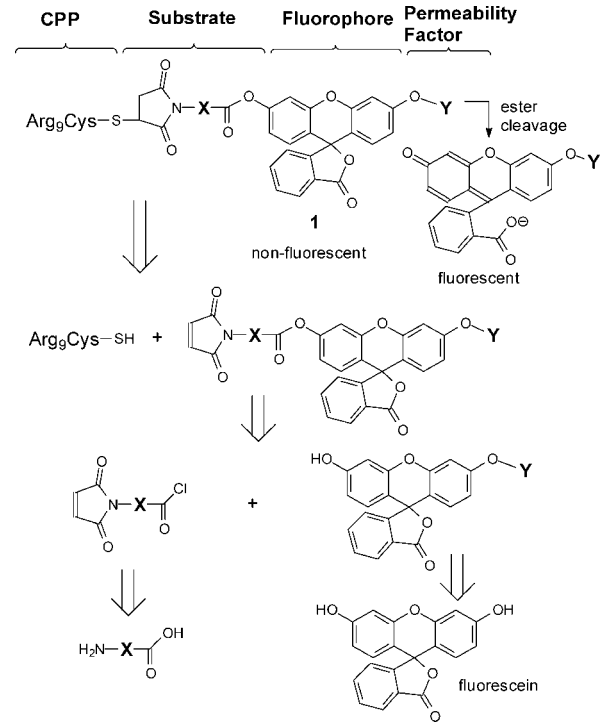

Figure 2. Design and retrosynthesis of the fluorogenic ester conjugate **1**. Cleavage of the ester linkage results in the formation of a fluorescent monoalkylated fluorescein derivative whose efflux rate depends on the properties of the attached permeability factor. Linkage of the cell-penetrating peptide Arg_9Cys is carried out through conjugate addition of the thiol group on the peptide to the maleimido group on the fluorogenic ester. The fluorogenic ester is prepared by reacting the acid chloride of an *N*-maleoyl amino acid with a monoalkylated fluorescein that is prepared from fluorescein.

form. As a result, di-O-substituted fluoresceins have been widely used as fluorogenic substrates for *in vitro* enzyme activity studies. For example, mono-O-alkylated fluorescein phosphate has been used as a fluorogenic substrate for the continuous assay of phosphoinositide-specific phospholipase C, (*23, 24*) and *N*-acetyl-β-D-glucosaminides of 6-O′-alkylated fluorescein derivatives have been used as substrates for a kinetic assay of *N*-acetyl-β-D-glucosaminidase (*25*). In these studies, enzyme activities were quantified by analysis of the fluorescence resulting from enzymatic formation of the fluorescent monoalkylated fluorescein.

As part of our program to develop fluorogenic probes for *in vivo* gene expression, we wanted to examine fluorescent activation of the *N*-maleimido α-D,L-methyl-β-alanine and D-valine esters of monoalkylated fluoresceins. We have previously shown that nitrophenyl and fluorescein esters tethered to an oligodeoxynucleotide (ODN) or peptide nucleic acid (PNA) that is complementary to a target nucleic acid sequence can be hydrolyzed by imidazole tethered to another ODN or PNA that is complementary to the adjacent site on that sequence (*11–13, 15*). For our system to work *in vivo*, however, requires that the background spontaneous or enzyme-catalyzed hydrolysis of the fluorescein esters occurs much more slowly than the mRNA templated hydrolysis of the esters by imidazole. We had already shown that increasing substitution of the ester slows down the background hydrolysis in human serum (*12*) but did not know what the effect would be inside human cells.

In our previous study, we synthesized conjugates of *N*-maleimido β-L-alanine and D-valine esters of a series of monoalkylated fluoresceins with Arg_9Cys for the purpose of studying the stability of these ester linkages in cells (*16*). To render the monoalkylated fluorescein component more water soluble and less membrane permeable, we had replaced the hydrophobic butyl substituent of a reported fluorescein derivative with methoxyethoxymethyl (MEM) and ethylmethylethene (EME) groups. Unfortunately, in subsequent studies, we found that these conjugates showed very little fluorescence inside cells in spite of other data indicating that these esters should have hydrolyzed rapidly. This suggested to us that the released fluorescein derivatives were effluxing faster than they were being produced. This is consistent with previous findings that fluorescein and some of its derivatives quickly exit numerous types of cell lines either via passive cell membrane permeation or via multidrug resistance protein 1(MRP1)-mediated transport (*26–28*). However, carboxylate-derivatized forms of fluorescein are not substrates for export by MRP1, and the presence of additional charges lowers their membrane permeability (*28–30*).

In this article, we report the synthesis of Arg_9 conjugates of fluorogenic esters of monoalkylated fluoresceins bearing one or two carboxylic groups. We also show that the fluorescein with two carboxylates effluxes much more slowly than the one with one carboxylate and that both lead to intracellular fluorescence signals in HeLa cells that can be quantified by flow cytometry. By using these conjugates, we were able to estimate the rates of background hydrolysis of the *N*-maleimido α-D,L-methyl-β-alanine and D-valine ester linkages and the efflux rates of the two fluorophore derivatives.

EXPERIMENTAL PROCEDURES

General Procedures. Dichloromethane (DCM) and triethylamine (TEA) were dried by refluxing with CaH_2 overnight followed by distillation. Fluorescein, *t*-butyl-bromoacetate, ethyl-bromoacetate, thionyl chloride, D-valine, D,L-3-amino-2-methylpropionic acid, DCC, DIPEA, and TFA were purchased from

Aldrich. Fmoc amino acids, *t*-butyl glutamic acid diester, resin, and ByPOP for solid phase peptide synthesis were purchased from NovaBiochem. *N*-maleoyl-D,L-α-methyl-*β*-alanine and *N*-maleoyl-D-valine were prepared as previously described (*12*). ^{1}H NMR spectra were obtained on a 300 MHz Varian UnityPlus-300 or Varian Mercury-300 spectrometer. Proton chemical shifts are expressed in ppm from tetramethylsilane. Flash chromatography was performed on Selecto Scientific silica gel. TLC and preparative TLC were run on precoated 254-nm fluorescent silica gel sheets manufactured by Alltech Associates. Fluorescence spectra were recorded on a SPEX Fluoromax instrument. UV spectral data were acquired on a Bausch and Lomb Spectronic 1001 spectrophotometer or Varian Cary 100 Bio UV–visible Spectrophotometer. Matrix-assisted laser desorption–ionization (MALDI) mass spectra of peptide conjugates were measured on a PerSeptive Voyager RP MALDI-time of flight (TOF) mass spectrometer. HR-FAB mass spectra were obtained on a MS-50TA (Ion Spec B126). HPLC purifications were carried out on Beckman Coulter System Gold 126 with RP C18 semi preparative columns.

Compound 3a. *t*-Butyl-bromoacetate (1.07 g, 1.57 mL, 10.6 mmol) was added dropwise with stirring to a suspension of the disodium salt of fluorescein **2** (*12*) (1 g, 2.65 mmol) in DMF (30 mL) containing catalytic NaI at RT and then heated to 90 °C with stirring for 5 h. The DMF was removed from the mixture by evaporation under reduced pressure. The residue was redissolved in 50 mL of CH_2Cl_2 and washed with H_2O (2 × 40 mL), then dried over Na_2SO_4, and evaporated to give the crude product. Further purification by chromatography on silica gel using hexane/ethyl acetate (2:1) gave 0.325 g (27.5% yield) of **3a** as a yellow powder. ^{1}H NMR (CD_3COCD_3): δ 1.47 (s, 9H), 4.71 (s, 2H), 6.64–6.66 (m, 2H), 6.69–6.77 (m, 3H), 6.84 (d, *J*=2.1 Hz 1H), 7.30 (d, $J = 7.5$ Hz, 1H), 7.74 (td, $J = 7.2$, 1.2 Hz, 1H), 7.81 (td, $J = 7.5$, 1.2 Hz, 1H), 7.98 (d, $J = 7.5$ Hz, 1H), 9.02 (s, 1H); HR FAB MS (*m/z*), calculated for $C_{26}H_{23}O_7$ ($M + H^+$) 447.1444; found, 447.1442.

Compound 3b. Compound **5** (50 mg, 0.128 mmol) and *t*-butyl glutamic acid diester (free base) (35 mg, 0.134 mmol) were dissolved in 10 mL of DCM/DMF (50/50), and DCC (52 mg, 0.252 mmol) was added. The reaction mixture was stirred at RT for 1 h, after which 20 mL of DCM was added. After removal of the precipitate, the organic phase was washed with 1% $KHSO_4$ aqueous solution (2 × 20 mL) and H_2O (1 × 20 mL), dried over Na_2SO_4, and evaporated. The residue was purified by Flash silica gel chromatography using ethyl acetate/hexane (1:1.3) to give 70 mg of compound **3b** as a yellow syrup (87% yield). ^{1}H NMR (CD_3COCD_3): δ 1.41 (s, 9H), 1.44 (s, 9H), 1.69–1.79 (m, 2H), 2.32 (t, $J = 7.5$ Hz, 2H), 4.44–4.49 (m, 1H), 4.65 (d, $J = 2.7$ Hz, 2H), 6.61–6.67 (m, 2H), 6.69–6.83 (m, 3H), 6.95 (d, $J = 2.1$ Hz, 1H), 7.29 (d, $J = 7.5$ Hz, 1H), 7.74 (t, $J = 7.2$ Hz, 1H), 7.82 (t, $J = 7.2$ Hz, 1H), 7.98 (d, $J = 7.5$ Hz, 1H); HR FAB MS (*m/z*), calculated for $C_{35}H_{38}O_{10}N$ ($M + H^+$) 632.2496; found, 632.2500.

Compound 5. Ethyl-bromoacetate (1.18 mL, 1.77 g, 10.6 mmol) was added dropwise with stirring to a suspension of the disodium salt of fluorescein **2** (1.00 g, 2.65 mmol) in DMF (30 mL) at RT and then heated at 90–100 °C with stirring for 5 h. The DMF was removed from the mixture by evaporation under reduced pressure and the residue treated with 25 mL of 4% NaOH in MeOH/water (3:1, v/v) and stirred for 2 h. After the removal of MeOH in vacuum with a rotatory evaporator, the solution was then acidified by the dropwise addition of 1 M aqueous HCl until a pH of about 2.0. The aqueous solution was extracted with ethyl acetate (3 × 20 mL), and the combined ethyl acetate fractions were dried over Na_2SO_4, and evaporated to give the crude product. Further purification by flash chromatography on silica gel using ethyl acetate/hexane (3:1) then ethyl acetate/methanol (10:1) gave 0.53 g (51% yield) of **5** as a yellow powder. ^{1}H NMR (CD_3OD): δ 4.73 (s, 2H), 6.55–6.58 (m, 2H), 6.68–6.73 (m, 3H), 6.85–6.86 (m, 1H), 7.20 (d, $J = 7.2$ Hz, 1H), 7.70 (td, $J = 7.5$ Hz, 1.2 Hz, 1H), 7.78 (td, $J = 7.2$, 1.2 Hz, 1H), 8.01 (d, $J = 7.5$ Hz, 1H); HR FAB MS (*m/z*), calculated for $C_{22}H_{15}O_7$ ($M + H^+$) 391.0818; found, 391.0818.

Compound 8a. This compound was prepared as described for compound **9a**. *N*-maleoyl-D,L-3-amino-2-methylpropionic acid (36 mg, 0.18 mmol) was treated with 5 mL of thionyl chloride, and the resulting mixture was slowly added to a stirred mixture of **3a** (40 mg, 0.090 mmol) and triethylamine (TEA) (25 μL, 18 mg, 0.18 mmol) in 10 mL of CH_2Cl_2 at 0 °C and allowed to warm to room temperature for 3 h. Following workup, the residue was purified by preparative silica gel TLC (1:2 ethyl acetate–hexane) to give 42 mg (77% yield) of compound **8a** as a white powder. ^{1}H NMR (CD_3OCD_3): δ 1.26 (d, $J = 7.2$ Hz, 3H), 1.47 (s, 9H), 3.08–3.16 (m, 1H), 3.76 (dd, $J = 14.1$, 6 Hz, 1H), 3.92 (dd, $J = 14.1$, 7.5 Hz, 1H), 4.73 (s, 2H), 6.74–6.83 (m, 2H), 6.88–6.97 (m, 5H), 7.23–7.25 (m, 1H), 7.36 (d, $J = 7.2$ Hz, 1H), 7.77 (td, $J = 7.5$ Hz, 1.2 Hz, 1H), 7.84 (td, $J = 7.5$, 1.2 Hz, 1H), 8.03 (d, $J = 7.2$ Hz, 1H); HR FAB MS (*m/z*), calculated for $C_{34}H_{30}NO_{10}$ ($M + H^+$) 612.1869; found, 612.1871.

Compound 8b. Compound **8b** was prepared from *N*-maleoyl-D,L-α-methyl-*β*-alanine (22 mg, 0.11 mmol) and **3b** (34 mg, 0.054 mmol) following the same procedure described for the preparation of **8a**. Preparative silica gel TLC (1:2 ethyl acetate–hexane) gave 24 mg (56% yield) of **8b** as a white powder. ^{1}H NMR (CD_3COCD_3): δ 1.26 (d, $J = 7.2$ Hz, 3H), 1.41 (s, 9H), 1.44 (s, 9H), 1.70–1.80 (m, 2H), 2.32 (t, $J = 7.5$ Hz, 2H), 3.08–3.17(m, 1H), 3.76 (dd, $J = 14.1$, 6 Hz, 1H), 3.92 (dd, $J = 13.5$, 7.5 Hz, 1H), 4.43–4.51 (m, 1H), 4.67 (d, $J = 2.1$ Hz, 2H), 6.72–6.86 (m, 2H), 6.87–7.02 (m, 5H), 7.23–7.25 (m, 1H), 7.35 (d, $J = 7.2$ Hz, 1H), 7.77 (t, $J = 7.5$ Hz, 1H), 7.84 (t, $J = 7.5$, 1H), 8.03 (d, $J = 7.5$ Hz, 1H); HR FAB MS (*m/z*), calculated for $C_{43}H_{45}O_{13}N_2$ ($M + H^+$) 797.2921; found, 797.2922.

Compound 9a. *N*-Maleoyl-D-valine (29 mg, 0.14 mmol) (*11*) was dissolved in 5 mL of thionyl chloride and heated at reflux until gas evolution had ceased; at which point, the excess thionyl chloride was removed under reduced pressure. The residual thionyl chloride was removed by dissolving the residue in carbon tetrachloride and then removing the solvent under reduced pressure. The crude acid chloride **7** was dissolved in 5 mL of CH_2Cl_2 and was slowly added to a stirred mixture of 3′-*O*-butyloxycarbonylmethyl-fluorescein (**3a**) (30 mg, 0.067 mmol) and triethylamine (19 μL, 14 mg, 0.14 mmol) in 10 mL of CH_2Cl_2 at 0 °C. The reaction mixture was allowed to warm to RT. After stirring for 3 h, the reaction mixture was diluted with 20 mL of CH_2Cl_2, washed with brine and water (2 × 25 mL), dried over Na_2SO_4, and concentrated in vacuo. The residue was purified by silica gel TLC (1:2 ethyl acetate–hexane) to afford 22.3 mg (53% yield) of **9a** as a white powder. ^{1}H NMR (CD_3OCD_3): δ 0.94 (d, $J = 6.9$ Hz, 3H), 1.14 (d, $J = 6.9$ Hz, 3H), 1.47 (s, 9H), 2.58–2.70 (m, 1H), 4.73 (s, 2H), 4.83 (d, $J = 7.2$ Hz, 1H), 6.74–6.83 (m, 2H), 6.87–6.95 (m, 3H), 7.05–7.14 (m, 1H), 7.34 (d, $J = 7.2$ Hz, 1H), 7.76 (t, $J = 7.2$ Hz, 1H), 7.83 (t, $J = 7.5$, 1H), 8.02 (d, $J = 7.2$ Hz, 1H); HR FAB MS (*m/z*), calculated for $C_{35}H_{32}NO_{10}$ ($M + H^+$) 626.2026; found, 626.2010.

Compound 9b. Compound **9b** was prepared from *N*-maleoyl-D-valine (23 mg, 0.11 mmol) and **3b** (34 mg, 0.054 mmol) following the same procedure described for the preparation of **9a**. Preparative silica gel TLC (1:2 ethyl acetate–hexane) gave 15 mg (34% yield) of **9b** as a white powder. ^{1}H NMR (CD_3COCD_3): δ 0.94 (d, $J = 6.9$ Hz, 3H), 1.12 (d, $J = 6.9$ Hz,

3H), 1.41 (s, 9H), 1.44 (s, 9H), 1.69–1.79 (m, 2H), 2.32 (t, J = 7.5 Hz, 2H), 2.58–2.69 (m, 1H), 4.43–4.49 (m, 1H), 4.67 (d, J = 2.1 Hz, 2H), 4.78 (d, J = 7.2 Hz, 1H), 6.71–7.00 (m, 5H), 7.04–7.14 (m, 3H), 7.34 (d, J = 7.5 Hz, 1H), 7.76 (t, d, J = 7.5, 1.2 Hz, 1H), 7.83 (t, d, J = 7.2, 1.2 Hz, 1H), 8.02(d, J = 7.2 Hz, 1H). HR FAB MS (*m/z*), calculated for $C_{44}H_{47}O_{13}N_2$ ($M + H^+$) 811.3078; found, 811.3072.

General Procedure for the Preparation of Compounds 10a,b and 11a,b. Compounds **8a**,**b** and **9a**,**b** were dissolved in TFA-DCM (50/50, v/v) and stirred under N_2 at RT for 4 h. Complete removal of TFA and DCM under reduced pressure afforded the corresponding deprotected compounds **10a**,**b** and **11a**,**b** as white solids.

Compound 10a. ^{1}H NMR (CD_3OCD_3): δ 1.25 (d, J = 7.2 Hz, 3H), 3.06–3.17 (m, 1H), 3.76 (dd, J = 14.1, 5.7 Hz, 1H), 3.92 (dd, J = 14.1 Hz, 7.8 Hz, 1H), 4.83 (s, 2H), 6.76–6.82 (m, 2H), 6.89–6.96 (m, 5H), 7.23–7.25 (m, 1H), 7.35 (d, J = 7.5 Hz, 1H), 7.76 (t, J = 7.5 Hz, 1H), 7.83 (t, J = 7.2 Hz, 1H), 8.02 (d, J = 7.2 Hz, 1H); HR FAB MS (*m/z*), calculated for $C_{30}H_{22}NO_{10}$ ($M + H^+$) 556.1243; found, 556.1223.

Compound 10b. ^{1}H NMR (CD_3COCD_3): δ 1.26 (d, J = 7.2 Hz, 3H), 1.70–1.80 (m, 2H), 2.45 (t, J = 7.5 Hz, 2H), 3.08–3.18 (m, 1H), 3.76 (dd, J = 14.1, 6 Hz, 1H), 3.92 (dd, J = 13.8, 7.5 Hz, 1H), 4.58–4.65 (m, 1H), 4.67 (s, 1H), 4.91 (s, 1H), 6.72–6.85 (m, 2H), 6.87–7.02 (m, 5H), 7.23–7.25 (m, 1H), 7.35 (d, J = 7.2 Hz, 1H), 7.77 (t, J = 7.2 Hz, 1H), 7.84 (t, J = 7.5, 1H), 8.03 (d, J = 7.2 Hz, 1H); HR ESI MS (*m/z*), calculated for $C_{35}H_{28}O_{13}N_2Na$ ($M+Na^+$) 707.1513; found, 707.1498.

Compound 11a. ^{1}H NMR (CD_3OCD_3): δ 0.89 (d, J = 7.2 Hz, 3H), 1.10 (d, J=7.2 Hz, 3H), 2.54–2.66 (m, 1H), 4.58 (s, 2H), 4.81 (d, J = 6.9 Hz, 1H), 6.55–7.06 (m, 6H), 7.34 (m, 1H), 7.59–7.75 (m, 2H), 7.95 (d, J = 6.9 Hz, 1H); HR FAB MS (*m/z*), calculated for $C_{31}H_{24}NO_{10}$ ($M + H^+$) 570.1400; found, 570.1404.

Compound 11b. ^{1}H NMR (CD_3COCD_3): δ 0.93 (d, J = 6.9 Hz, 3H), 1.12 (d, J = 6.9 Hz, 3H), 1.69–1.81 (m, 2H), 2.42 (t, J = 7.5 Hz, 2H), 2.58–2.69 (m, 1H), 4.47–4.54 (m, 1H), 4.65 (s, 1H), 4.78 (d, J = 7.2 Hz, 1H), 4.91 (s, 1H), 6.71–7.00 (m, 5H), 7.04–7.14 (m, 3H), 7.34 (d, J = 7.2 Hz, 1H), 7.76 (t,d J = 7.5, 1.2 Hz, 1H), 7.83 (t,d J = 7.5, 1.2 Hz, 1H), 8.02 (d, J = 7.5 Hz, 1H). HR FAB MS (*m/z*), calculated for $C_{36}H_{31}O_{13}N_2$ ($M + H^+$) 699.1826; found, 699.1829.

Synthesis of TyrArg$_9$Cys. The oligopeptide H_2N-Tyr-(Arg)$_9$-Cys-$CONH_2$ was synthesized by standard solid phase Fmoc peptide synthesis methodology as described previously (*16*). The oligopeptide was purified by semipreparative RP-HPLC with a 30 min 0–40% gradient of A (acetonitrile containing 0.1% TFA) in B (water containing 0.1% TFA) at a flow rate of 1.0 mL/min and detection at 270 nm. MALDI-TOF MS (*m/z*), calculated ($M + 1$) 1689; found, ($M + 1$): 1689.8.

General Method for the Preparation of Arg$_9$Cys Fluorogenic Ester Conjugates. Compounds **10a**,**b** and **11a**,**b** (4 equiv) were each dissolved in 50 μL of acetonitrile, added separately to TyrArg$_9$Cys in 0.5 mL of deoxygenated MeOH, and then shaken under N_2 for 2–4 h at RT. Ethyl ether (10-fold excess) was then added to precipitate the products. Purification was carried out by semipreparative RP-HPLC with a 1.0 mL/min 30 min 0–40% gradient of B (acetonitrile containing 0.1% TFA) in A (water containing 0.1% TFA) with detection at 270 nm. MALDI-TOF MS (*m/z*), calculated ($M + 1$); observed, **12a**, 2244, 2245.73; **12b**, 2373, 2374.37; **13a**, 2258, 2259.51; **13b**, 2387, 2389.41.

Flow Cytometry. Exponentially growing HeLa cells were subcultured 48 h before the studies at a concentration that would ensure the exponential growth of cells at the time of experimentation. The cells were monodispersed by trypsinization and washed twice with 5 mL of Hanks' balanced salt solution containing 10 mM Hepes (pH 7.3), 1 mM MgCl, 1 mM CaCl, and 0.1% bovine serum albumin (HBSS buffer). An aliquant of the samples were examined by flow cytometry to establish the background fluorescence intensity level. To 1 mL of cell suspension containing approximately 0.75×10^6 cells, an appropriate volume of a probe was added, and flow cytometric observation was conducted at 1 min after the addition. Cells were incubated for 5 min with 40 μM probe, washed twice with 5 mL of HBSS, and resuspended in 1 mL of HBSS. Cells were kept at room temperature in the dark and analyzed by flow cytometry at the times indicated. Flow cytometry was carried out on a Becton Dickinson FACS 440 (San Jose, CA). The cells were excited with 300 mW of 488 nm argon ion laser, and fluorescence was detected through a 525 nm band-pass filter. A minimum of 20,000 events, gated by forward and side-scatter intensities, were recorded for each time point in list mode in a CYTOMATION CICERO/CYCLOPS data acquisition/analysis system (Ft. Collins, CO). The mean intensity of green fluorescence for intact cells was calculated and normalized to the background fluorescence intensity of unlabeled cells. Three independent experiments were conducted for each of the probes, and their means are presented in the data (except for **12a**, for which only two of the data sets were used because of a data collection problem). Following flow cytometric examination, samples containing fluorescent cells were examined by fluorescence microscopy (Olympus BX40, Olympus, Center Valley, PA).

RESULTS AND DISCUSSION

Design. The fluorogenic esters were designed so that it would be easy to systematically vary the cell-penetrating peptide, ester substrate, and the permeability and other properties of the fluorophore (Figure 2). The peptide component can be synthesized by solid phase Fmoc synthesis, while ester linkage can be made directly from a variety of natural and unnatural amino acids through a simple two-step procedure. The permeability properties of fluorescein can be tailored through a side chain attached to one of the phenolic oxygens. Though the fluorogenic esters prepared in this article were made by solution-phase synthesis, it would be quite easy to adapt the synthetic scheme to a solid supported route, as we have previously found that the phenyl esters are stable to the deprotection conditions for the peptide and carboxylate groups.

Synthesis of the Monoalkylated Fluoresceins. Fluorescein was monoalkylated as illustrated in Scheme 1 by a method we previously reported for the synthesis of other monoalkylated derivatives (*16*). The disodium salt of fluorescein **2** was prepared by treatment of fluorescein **1** with 2 equiv of NaOH and then alkylated with *t*-butyl α-bromoacetate to afford *t*-butylcarboxymethyl fluorescein (**3a**) and dialkylated product **4.** The dialkylated product could be converted back to **3a** by hydrolysis with NaOH followed by acidification but was never carried out in practice. Removal of the *t*-butyl group with TFA then provided carboxylic acid **5**, which is a more versatile intermediate than fluorescein for adding functionality, as it can be easily coupled to a wide variety of functionalized amines and amino acids by amide bond formation. Compound **5** could be obtained in a better overall yield of 52%, however, by basic hydrolysis of the mixture of monoalkylated and dialkylated fluoresceins that is produced by treatment of the disodium salt of fluorescein **2** with ethylbromoacetate instead of *t*-butylbromoacetate. To prepare an acid labile precursor to a dicarboxylate, compound **5** was coupled to the amino group of the di-*t*-butyl ester of L-glutamic acid with DCC to produce compound **3b** in 53% yield.

Synthesis of *N*-Maleoyl Amino Acid Esters of the Monoalkylated Fluoresceins. The monoalkylated fluoresceins **3a** and **3b** were then converted to the *N*-maleoyl-α-methyl-β-

Scheme 1. Synthesis of the Monoalkylated Fluorescein Building Blocks 3a and 3b

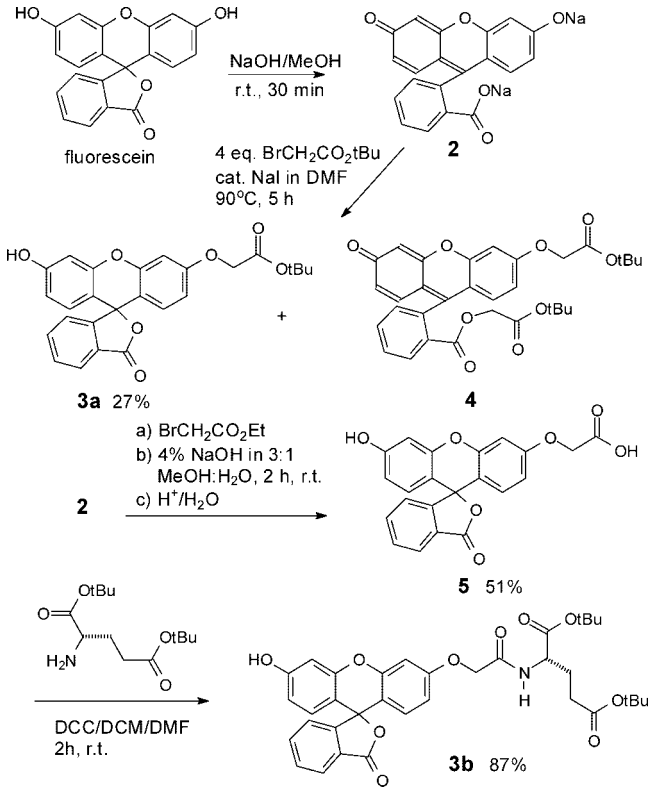

Scheme 2. Synthesis of the *N*-Maleoyl Amino Acid Esters of the Monoalkylated Fluoresceins, 10a,b and 11a,b

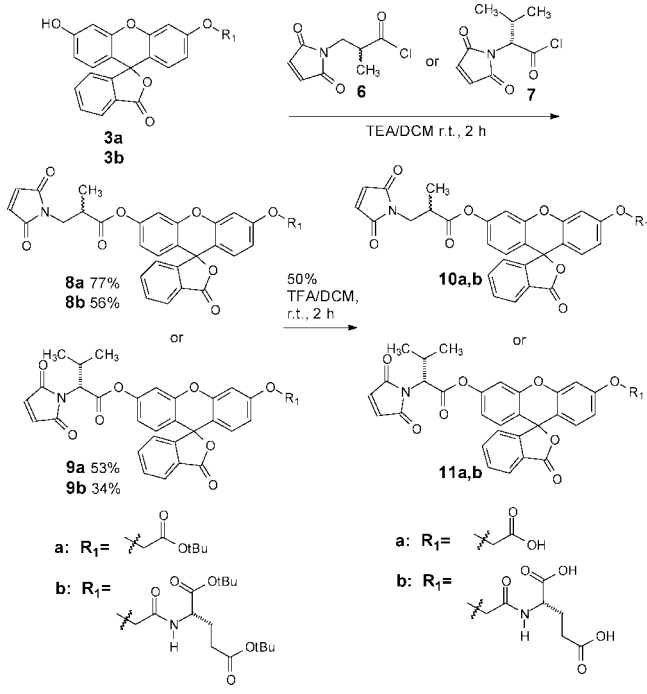

amino butyric acid and *N*-maleoyl-D-Val esters **8a**,**b** and **9a**,**b** via acid chlorides **6** and **7** in the presence of triethylamine (Scheme 2). These acids chlorides are readily prepared in two steps from the corresponding amino acids (*11*). The *t*-butyl groups were then removed by TFA to afford the maleimido fluorogenic esters **10a**,**b** and **11a**,**b** bearing one and two carboxylates.

Scheme 3. Synthesis of the Arg_9Cys Conjugates of the Fluorogenic Esters, 12a,b and 13a,b

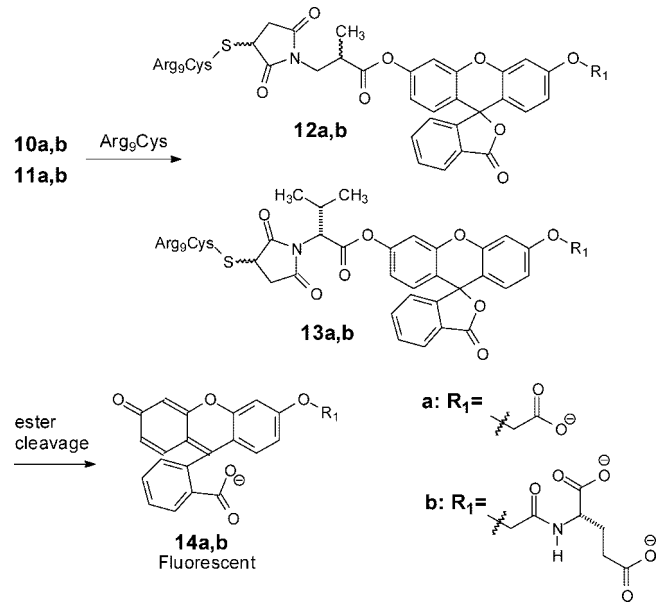

Conjugation of the *N*-Maleimido Amino Acid Esters of the Monoalkylated Fluoresceins to Arg_9Cys. The cell-penetrating peptide Arg_9 with a cysteine at the carboxy terminus was synthesized by standard Fmoc solid phase synthesis. The cysteine was introduced to provide a thiol group at the carboxy terminus of the peptide for conjugating to the maleimide group of the *N*-maleoyl amino acid esters **10a**,**b**, and **11a**,**b**. The resulting fluorogenic ester conjugates **12a**,**b** and **13a**,**b** were obtained by incubating the peptide with the maleimido esters in a 1:4 ratio for 2 h (Scheme 3). Methanol was preferred as a solvent because of its ability to dissolve both reactants and from which the conjugated products could be easily isolated by ether precipitation. All of the conjugates were purified by RP-HPLC and characterized by MALDI-TOF MS.

Flow Cytometry. To determine the stability of the esters inside living cells, the Arg_9 peptide fluorescein ester conjugates **12a**,**b** and **13a**,**b** were incubated with Hela cells (one million/mL) in media for 5 min at a concentration of 40 μM, after which

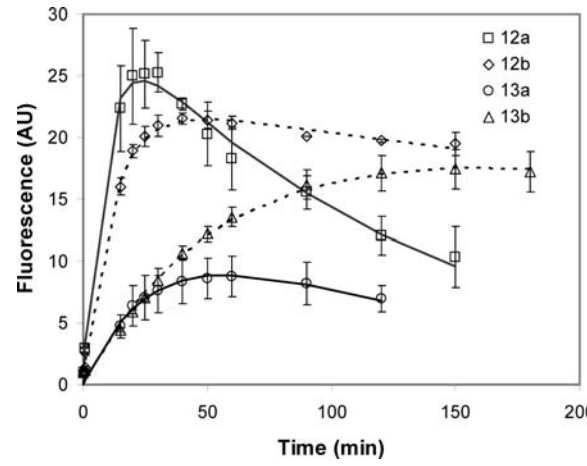

Figure 3. Fluorescence activation of the fluorogenic ester conjugates **12a**,**b** and **13a**,**b** in HeLa cells. A plot of the average fluorescence observed in HeLa cells as a function of time and fitted to an analytical expression for two sequential irreversible first order steps is shown. The error bars represent the standard deviation for three separate experiments (except for **12b**, which is for two experiments). All values for the plot are given in Table 1.

Table 1. Kinetic Parameters for the Fluorescence Activation of the Ar_9 Fluorogenic Ester Conjugates 12a,b and 13a,b by Fitting Each Curve Individually To an Expression for Two Sequential Irreversible Steps

cmpd	amino acid	no. of carboxylates	Ao	k_{act} (min^{-1})	k_{eff} (min^{-1})
12a	α-methyl-β-Ala	1	29.7 ± 1.0	0.12 ± 0.016	0.008 ± 0.0006
12b	α-methyl-β-Ala	2	22.9 ± 0.6	0.087 ± 0.007	0.0013 ± 0.0003
13a	D-Val	1	14.1 ± 0.9[a]	0.032 ± 0.005[a]	0.008[a]
13b	D-Val	2	21.7 ± 0.5[b]	0.017 ± 0.0008[b]	0.0013[b]

[a] Values from fitting when k_{eff} is fixed at 0.008 min^{-1}. [b] Values from fitting when k_{eff} is fixed at 0.0013 min^{-1}.

the cells were washed twice to remove agents that had not penetrated the cells. The cells were then incubated under standard conditions (37 °C, 5% CO_2), for various times, after which the average fluorescence intensity of the cells was determined by flow cytometry for three separate experiments and then averaged except for **12b** for which two data sets were averaged (Figure 3). Fluorescence from the α-methyl-β-alanine ester conjugate bearing a single carboxylate, **12a**, increased more rapidly than that from D-valine conjugate **13a**, but both lost fluorescence at longer incubation times. This behavior is what would be expected for a fluorescent probe that is able to escape from the cell. Fluorescence from the α-methyl-β-alanine ester conjugate bearing two carboxylates, **12b**, also increased more rapidly than for D-valine conjugate **13b**, but unlike the conjugates bearing a single carboxylate, **12a** and **13a**, the fluorescence did not appreciably decrease at longer incubation times. Thus, it would appear that having two additional negative charges on the fluorophore was sufficient to render it practically membrane impermeable. Attempts to visualize the location of the released probes by fluorescence microscopy 30 and 120 min after treatment revealed only faint images, possibly due to low concentration and diffuse, nonlocalized distribution of the probes.

Semi-Quantitative Analysis of the Flow Cytometry Data. Because of the limited data, it was not possible to reliably fit all the rate constants in Scheme 1 for the four different probes. Therefore, we decided to carry out a semiquantitative assessment of the rates of fluorescent probe activation and efflux from the cells by fitting the fluorescence data to an analytical expression (*31*) for two sequential irreversible first order steps, $A_{in} \rightarrow B_{in} \rightarrow B_{out}$, with rate constants k_{act} and k_{eff} as follows: $[B_{in}] = [A_{in}]_o * (\tau^{\kappa} - \tau)/(1 - \kappa)$, where $\tau = \exp(-k_{act}t)$ and $\kappa = k_{eff}/k_{act}$.

In this expression, k_{act} corresponds to the rate constant for activating the fluorogenic probe A inside the cell, and k_{eff} corresponds to the rate constant for efflux of the resulting fluorophore B from inside the cell as diagrammed in Figure 1. This simplified analysis is based on the assumption that there is no external fluorogenic probe that can enter the cell (k_{in}) following washing of the cells and that efflux of the fluorogenic probe from the cell (k_{out}) is negligible compared to k_{act}. This would appear to be a reasonable set of assumptions given the results of many studies indicating that cationically charged cell-penetrating peptides enter cells rapidly through macropinocytosis and become trapped in endosomes (*32–34*). Furthermore, any activation of the fluorogenic probe bound to the surface would not contribute to the signal observed by flow cytometry, as it would be released into the medium.

Fits of the fluorescence data for the two α-methyl-β-alanine conjugates to the two-step model gave a rate constant of 0.12 min^{-1} for fluorescence activation of the conjugate with one negative charge (**12a**), which was very similar to that of 0.087 min^{-1} for the conjugate with two negative charges (**12b**). The average half-life for the activation of these two conjugates was about 6.8 min. The efflux rates of the released fluoresceins, however, differ by a factor of about 6.1, with the fluorescein bearing two carboxylates (**14b**, Scheme 3) effluxing with a rate constant of about 0.0013 min^{-1}, corresponding to a half-life of 8.8 h. The fluorescein bearing one carboxylate (**14a**), however, effluxes much more rapidly with a rate constant of 0.008 min^{-1} corresponding to a half-life of 87 min. The amplitudes, $[A_{in}]_o$ for the fits to **12a** and **12b** differed slightly (29.7 vs 22.9) and might have been due to differing amounts of material absorbed by the cells and/or to differing experimental conditions.

Attempts to fit the data for the two D-valine ester conjugates **13a** and **13b** in a similar fashion resulted in rate constants and amplitudes with large standard deviations, indicating that the fit for these curves was underdetermined. To reduce the number of variables to be fit, we fixed the efflux rate constants for the activated probes **14a** and **14b** to be the same as those obtained from fitting the data for **12a** and **12b**, which release the same probes. Fixing the efflux rates in this manner led to good fits with small standard deviations. The activation rate constants and amplitudes differed by almost a factor of two, however, suggesting that the kinetic scheme may be more complicated for this set of probes and warrants further study. The average of the activation rate constants for the D-valine ester (0.025 min^{-1}) determined in this fashion is about 4.6 times less than the average for the alanine esters of 0.11 min^{-1}, indicating that the D-valine ester is more stable than the alanine ester inside HeLa cells. This is consistent with previous studies on the stability of D-valine esters compared to glycine esters in human serum (*12*). The calculated half-life of about 31 min for the D-valine ester, though much longer than that of about 7 min for the alanine ester, is probably too short to be useful for NATPA *in vivo*. We propose, however, to use this assay system to screen for a more stable ester.

CONCLUSIONS

In our studies, we found that the Arg_9 peptide can rapidly transport a sufficient amount of fluorogenic ester into cells to lead to quantifiable signals in flow cytometry that can be analyzed by a simple two-step kinetic scheme involving fluorescence activation followed by efflux. These conjugates would therefore appear to be useful for evaluating libraries of fluorogenic esters in which the structure and properties of the ester and the permeability factor are systematically varied. In this way, we should be able to identify fluorogenic esters suitable for NATPA and possibly fluorogenic esters capable of distinguishing between various cell types and conditions. The ability to tune the hydrolysis and efflux rates could be very useful for optimizing fluorogenic compounds for particular assays.

ACKNOWLEDGMENT

This work was financially supported by an NIH grant (RO1-CA92477). Mass spectrometry was provided by the Washington University Mass Spectrometry Resource (Grant No. P41RR0954).

LITERATURE CITED

(1) Boonacker, E., and Van Noorden, C. J. (2001) Enzyme cytochemical techniques for metabolic mapping in living cells, with special reference to proteolysis. *J. Histochem. Cytochem. 49*, 1473–1486.

(2) Wahler, D., and Reymond, J. L. (2001) High-throughput screening for biocatalysts. *Curr. Opin. Biotechnol. 12*, 535–544.

(3) Fang, X., Mi, Y., Li, J. J., Beck, T., Schuster, S., and Tan, W. (2002) Molecular beacons: fluorogenic probes for living cell study. *Cell Biochem. Biophys. 37*, 71–81.
(4) Becker, S., Schmoldt, H. U., Adams, T. M., Wilhelm, S., and Kolmar, H. (2004) Ultra-high-throughput screening based on cell-surface display and fluorescence-activated cell sorting for the identification of novel biocatalysts. *Curr. Opin. Biotechnol. 15*, 323–329.
(5) Martinez-Manez, R., and Sancenon, F. (2005) New advances in fluorogenic anion chemosensors. *J. Fluoresc. 15*, 267–285.
(6) Mohr, G. J. (2006) New chromogenic and fluorogenic reagents and sensors for neutral and ionic analytes based on covalent bond formation: a review of recent developments. *Anal. Bioanal. Chem. 386*, 1201–1214.
(7) Lavis, L. D., Chao, T. Y., and Raines, R. T. (2006) Fluorogenic label for biomolecular imaging. *ACS Chem. Biol. 1*, 252–260.
(8) Stoeckel, K., Hofheinz, W., Laneury, J. P., Duchene, P., Shedlofsky, S., and Blouin, R. A. (1998) Stability of cephalosporin prodrug esters in human intestinal juice: implications for oral bioavailability. *Antimicrob. Agents Chemother. 42*, 2602–2606.
(9) Oliyai, R., Shaw, J. P., Sueoka-Lennen, C. M., Cundy, K. C., Arimilli, M. N., Jones, R. J., and Lee, W. A. (1999) Aryl ester prodrugs of cyclic HPMPC. I: Physicochemical characterization and in vitro biological stability. *Pharm. Res. 16*, 1687–1693.
(10) Yang, C., Gao, H., and Mitra, A. K. (2001) Chemical stability, enzymatic hydrolysis, and nasal uptake of amino acid ester prodrugs of acyclovir. *J. Pharm. Sci. 90*, 617–624.
(11) Ma, Z., and Taylor, J.-S. (2000) Nucleic acid triggered catalytic drug release. *Proc. Natl. Acad. Sci. U.S.A. 97*, 11159–11163.
(12) Ma, Z., and Taylor, J. S. (2001) Nucleic acid triggered catalytic drug and probe release: a new concept for the design of chemotherapeutic and diagnostic agents. *Bioorg. Med. Chem. 9*, 2501–2510.
(13) Ma, Z., and Taylor, J. S. (2003) PNA-based RNA-triggered drug-releasing system. *Bioconjugate Chem. 14*, 679–683.
(14) Cai, J., Li, X., Yue, X., and Taylor, J. S. (2004) Nucleic acid-triggered fluorescent probe activation by the Staudinger reaction. *J. Am. Chem. Soc. 126*, 16324–16325.
(15) Cai, J., Li, X., and Taylor, J. S. (2005) Improved nucleic acid triggered probe activation through the use of a 5-thiomethyluracil peptide nucleic acid building block. *Org. Lett. 7*, 751–754.
(16) Li, X., and Taylor, J. S. (2004) General strategy for the preparation of membrane permeable fluorogenic peptide ester conjugates for in vivo studies of ester prodrug stability. *Bioorg. Med. Chem. 12*, 545–552.
(17) Rothbard, J. B., Garlington, S., Lin, Q., Kirschberg, T., Kreider, E., McGrane, P. L., Wender, P. A., and Khavari, P. A. (2000) Conjugation of arginine oligomers to cyclosporin A facilitates topical delivery and inhibition of inflammation. *Nat. Med. 6*, 1253–1257.
(18) Chen, L., Wright, L. R., Chen, C. H., Oliver, S. F., Wender, P. A., and Mochly-Rosen, D. (2001) Molecular transporters for peptides: delivery of a cardioprotective epsilonPKC agonist peptide into cells and intact ischemic heart using a transport system, R(7). *Chem. Biol. 8*, 1123–1129.
(19) Jin, L. H., Bahn, J. H., Eum, W. S., Kwon, H. Y., Jang, S. H., Han, K. H., Kang, T. C., Won, M. H., Kang, J. H., Cho, S. W., Park, J., and Choi, S. Y. (2001) Transduction of human catalase mediated by an HIV-1 TAT protein basic domain and arginine-rich peptides into mammalian cells. *Free Radical Biol. Med. 31*, 1509–1519.
(20) Futaki, S. (2006) Oligoarginine vectors for intracellular delivery: design and cellular-uptake mechanisms. *Biopolymers 84*, 241–249.
(21) Haugland, R. P. (1999) *Handbook of Fluorescent Probes and Research Chemicals*, Molecular Probes, Eugene, OR.
(22) Bullok, K. E., Gammon, S. T., Violini, S., Prantner, A. M., Villalobos, V. M., Sharma, V., and Piwnica-Worms, D. (2006) Permeation peptide conjugates for in vivo molecular imaging applications. *Mol. Imaging 5*, 1–15.
(23) Rukavishnikov, A. V., Smith, M. P., Birrell, G. B., Keana, J. F., and Griffith, O. H. (1998) Synthesis of a new fluorogenic substrate for the assay of phosphoinositide-specific phospholipase. *Tetrahedron Lett. 39*, 6637–6640.
(24) Zaikova, T. O., Rukavishnikov, A. V., Birrell, G. B., Griffith, O. H., and Keana, J.F.W. (2001) Synthesis of fluorogenic substrates for continuous assay of phosphatidylinositol-specific phospholipase C. *Bioconjugate Chem. 12*, 307–313.
(25) Kasai, K., Okada, K., and Yamaji, N. (1993) Glycosides having chromophores as substrates for sensitive enzyme analysis. V. Synthesis of 6′-O-substituted 2′,7′-dichlorofluorescein N-acetyl-b-D-glucosaminides as substrates for the rate-assay of N-acetyl-b-D-glucosaminidase. *Chem. Pharm. Bull. 41*, 1513–1520.
(26) Rotman, B., and Papermaster, B. W. (1966) Membrane properties of living mammalian cells as studied by enzymatic hydrolysis of fluorogenic esters. *Proc. Natl. Acad. Sci. U.S.A. 55*, 134–141.
(27) Prosperi, E., Croce, A. C., Bottiroli, G., and Supino, R. (1986) Flow cytometric analysis of membrane permeability properties influencing intracellular accumulation and efflux of fluorescein. *Cytometry 7*, 70–75.
(28) Rychlik, B., Balcerczyk, A., Klimczak, A., and Bartosz, G. (2003) The role of multidrug resistance protein 1 (MRP1) in transport of fluorescent anions across the human erythrocyte membrane. *J. Membr. Biol. 193*, 79–90.
(29) Dive, C., Cox, H., Watson, J. V., and Workman, P. (1988) Polar fluorescein derivatives as improved substrate probes for flow cytoenzymological assay of cellular esterases. *Mol. Cell. Probes 2*, 131–145.
(30) Homolya, L., Hollo, Z., Germann, U. A., Pastan, I., Gottesman, M. M., and Sarkadi, B. (1993) Fluorescent cellular indicators are extruded by the multidrug resistance protein. *J. Biol. Chem. 268*, 21493–21496.
(31) Chien, J.-Y. (1948) Kinetic analysis of irreversible consecutive reactions. *J. Am. Chem. Soc. 70*, 2256–22561.
(32) Potocky, T. B., Menon, A. K., and Gellman, S. H. (2003) Cytoplasmic and nuclear delivery of a TAT-derived peptide and a beta-peptide after endocytic uptake into HeLa cells. *J. Biol. Chem. 278*, 50188–50194.
(33) Kaplan, I. M., Wadia, J. S., and Dowdy, S. F. (2005) Cationic TAT peptide transduction domain enters cells by macropinocytosis. *J. Controlled Release 102*, 247–253.
(34) Fotin-Mleczek, M., Fischer, R., and Brock, R. (2005) Endocytosis and cationic cell-penetrating peptides: a merger of concepts and methods. *Curr. Pharm. Des. 11*, 3613–3628.

BC070079Y

Matrix Metalloproteinase-Assisted Triggered Release of Liposomal Contents

Nihar Sarkar,[†] Jayati Banerjee,[†] Andrea J. Hanson,[†] Adekunle I. Elegbede,[†] Theresa Rosendahl,[†] Aaron B. Krueger,[‡] Abir L. Banerjee,[‡] Shakila Tobwala,[‡] Rongying Wang,[§] Xiaoning Lu,[§] Sanku Mallik,*[,†] and D. K. Srivastava*[,‡]

Department of Pharmaceutical Sciences and Department of Chemistry, Biochemistry, and Molecular Biology, North Dakota State University, Fargo, North Dakota 58105, and Proteomics Core Facility, School of Medicine and Health Sciences, University of North Dakota, Grand Forks, North Dakota 58202. Received March 8, 2007; Revised Manuscript Received September 25, 2007

We offer a novel methodology for formulating liposomes by incorporating sequence-specific collagen-mimetic peptides such that they are specifically "uncorked" by a matrix metalloproteinase, MMP-9. By encapsulating carboxyfluorescein (as a self-quenching fluorescent dye), we demonstrate that the time-dependent release of the dye from liposomes is due to the specific enzymatic cleavage of the surface-exposed collagen-mimetic peptides. The specificity of such cleavage is attested by the fact that the liposomal "uncorking" and their content release occur only by MMP-9 and not by a general proteolytic enzyme, trypsin, despite the fact that the collagen mimetic peptides contain the trypsin cleavage site. The mechanistic details underlying the formulations of liposomes and their enzyme-selective "uncorking" and content release are discussed. Arguments are presented that such liposomes can be fine-tuned to serve as the drug delivery vehicles for the detection and treatment of various human diseases, which occur due to the overexpression of a variety of pathogenic matrix metalloproteinases.

INTRODUCTION

Of the four major classes of extracellular matrix degrading enzymes (viz., cysteine proteases, aspartic proteases, serine proteases, and metalloproteases,), matrix metalloproteases (MMPs) have been implicated in several diseases (*1, 2*). On the basis of the structural features (including the amino acid sequences, domain organizations, etc.), 26 different types of MMPs have been recognized in human tissues, which fall into six major classes: (i) collagenases, (ii) gelatinases, (iii) stromelysins and stromelysin-like MMPs, (iv) matrilysins, (v) membrane-type MMPs, and (vi) other MMPs (viz., MMP-20, MMP-23, and MMP-28) (*3*). Although many of these MMPs have been implicated in different types of human diseases, MMP-2 and MMP-9 have been widely recognized to be involved in the progression and metastasis of most of the human tumors. They have been found to be overexpressed in breast tumors (*4*), colorectal tumors (*5*), lung tumors (*6*), prostate tumors (*7*), pancreatic tumors (*8*), and ovarian tumors (*9*). In view of their involvement in different human diseases, there have been major efforts to design MMP-selective inhibitors as therapeutic agents and develop strategies for delivering them to their target sites (*10*).

Of the different approaches of delivering drugs (e.g., via liposomes, polymers, microspheres, antibody−drug conjugates etc.), the liposome-assisted drug delivery systems offer several advantages. Presently, there are about 13 liposome-mediated drug delivery systems approved for treating a variety of human diseases (e.g., breast cancer, ovarian cancer, meningitis, fungal infections, leukemia, etc.), and about 30 additional systems for delivering small molecule drugs, DNA fragments, diagnostic compounds, and so forth, are currently at different stages of clinical trials (*11, 12*). Hence, the selective targeting of liposomes is of significant importance to ensure the delivery of therapeutic "loads" to the diseased tissue sites. This feature has been considerably optimized by attaching cell surface-specific antibodies (*13*), peptides (*14*), and small molecule agonists/antagonists of the cell surface receptors (*15*) to differently formulated liposomes.

Usually, liposomes slowly deliver their contents via fusion with the cell membranes, micropinocytosis, endocytosis, or simply by slow dissociation and passive diffusion of drugs from the liposomal lumen to the interior of the affected cells (*11, 12*). In order to accelerate the drug delivery process, liposomes are often "armed" with triggering devices. Some of the "triggering" agents include change in pH (*16*), mechanical stress (*17*), metal ions (*18*), temperature (*19*), light (*20*), enzymes (*21*), and so forth. Hence, both recognition of the diseased tissues and triggered release of the contents are the desirable features of the liposome-assisted drug delivery system. As will be noted in the following sections, both of these features are intrinsically built in our uniquely formulated liposomes. In addition, these liposomes can be "uncorked" in the vicinity of the cancerous tissues, which express high amounts of MMP-9.

Out of about 25 000 papers (listed in PubMed) and 600 patents (listed at the USPTO site) on liposomes, there are only a handful of papers (less than 15) on the triggered release of liposomal contents by enzymes. Some of the enzymes utilized for cleaving liposomes and releasing their contents include elastase, alkaline phosphatase, trypsin, and phospholipase A_2 (*21*). Herein, we report the design of triple helical peptides and their lipopeptide derivatives, incorporation of those lipopeptides into liposomes (such that the triple helical peptides protrude from the surface of the liposomes for facile cleavage), and MMP-9-assisted "uncorking" of the liposomes and release of their contents. We believe the overall strategy can be fine-tuned to diagnose and treat human diseases which occur due to overexpression of pathogenic matrix metalloproteinases, such as MMP-9 (*22*).

EXPERIMENTAL PROCEDURES

Synthesis of the Peptides. The peptides were synthesized on a Rainin Symphony Quartet automatic peptide synthesizer,

* Sanku.Mallik@ndsu.edu; DK.Srivastava@ndsu.edu, Tel: 701-231-7888; Fax: 701-231-8333.

[†] Department of Pharmaceutical Sciences.

[‡] Department of Chemistry, Biochemistry, and Molecular Biology.

[§] Proteomics Core Facility.

10.1021/bc070081p CCC: $40.75 © 2008 American Chemical Society
Published on Web 12/14/2007

using standard Fmoc-protected amino acids and HBTU−HOBT as the coupling reagents. The commercially available CLEAR acid resin was used as the solid support. Each coupling step took 3 h and was repeated twice with 5-fold excess of reagents. Cleavage was performed for 3 h using a cocktail of CF_3CO_2H, anisole, and water (95%/2.5%/2.5%). The crude peptides were precipitated in ice-cold ether and purified by a semipreparatory RP-HPLC, using a linear gradient of 0–70% acetonitrile in water over 40 min. Each solvent contained 0.1% trifluoroacetic acid. The purified peptides were characterized by the CD and mass spectroscopy (MALDI-TOF).

Conditions for Analytical HPLC. Vydac C_{18} analytical HPLC column (238TP5415); eluant, linear gradient of 0–70% acetonitrile in water over 40 min; both solvents contained 0.1% CF_3CO_2H; flow rate, 1.5 mL/min.

Conditions for Semipreparatory HPLC. Vydac C_{18} HPLC column (238TP152022); eluant, linear gradient of 0–70% acetonitrile in water over 40 min; both solvents contained 0.1% CF_3CO_2H; flow rate, 5 mL/min.

Synthesis of the Lipopeptides. After the completion of the peptide synthesis, the N-terminal Fmoc group was removed from the peptide. Conjugation with stearic acid was performed using the same procedure as the amino acid coupling with 5-fold excess of reagents. A shaker was used for better mixing of reagents. Cleavage conditions were the same as that for the peptides. The crude lipopeptides were purified by RP-HPLC, employing a Vydac semipreparatory diphenyl column (RP 219TP510).

Analytical HPLC Conditions. Vydac analytical HPLC column (219TP5415); eluant, linear gradient of 0–70% acetonitrile in water over 40 min; both solvents contained 0.1% CF_3CO_2H; flow rate, 1.5 mL/min.

Semipreparatory HPLC Conditions. Vydac HPLC column (219TP510); eluant, linear gradient of 0–70% acetonitrile in water over 40 min; both solvents contained 0.1% CF_3CO_2H; flow rate, 5 mL/min.

The mass spectral data for the reported peptides and the lipopeptides are provided in Supporting Information.

Circular Dichroism Spectroscopy. CD spectra were recorded on a Jasco J-815 instrument using a cell of 0.2 mm path length. The concentration of the peptides or lipopeptides was 1 mg/mL in 10 mM phosphate buffer, pH = 4.0. The solutions were stored for 12 h at 4 °C before recording the spectra. For temperature-dependent CD spectra, the sample was equilibrated for 15 min at each temperature before recording the spectra.

Cloning, Expression, and Purification of MMP-9. The catalytic and fibronectin domains (truncating the hemopexin domains from the full-length enzymes) of human MMP-9 were cloned in pET20b vector (Novagen), and the enzyme was overexpressed in BL21(DE3) *Escherichia coli* cells. The expressed proteins were primarily recovered from the inclusion bodies. The purified MMP-9 showed a single band on SDS gel electrophoresis. The yield from 1 L of bacterial culture was in the range 30–80 mg. The experimental details of the cloning, expression, and purification of MMP-9 will be published elsewhere.

Peptide and Lipopeptide Cleavage Studies with MMP-9 and Trypsin. For the cleavage studies, the conditions are: [peptide] or [lipopeptide] = 1 mg/mL in 25 mM HEPES buffer, pH = 8.0, containing 10 mM $CaCl_2$; [MMP-9] = 5 nM, 25 °C. At different time intervals, 50 μL samples were withdrawn and 2 μL of CF_3COOH was added to stop the reaction. The products were analyzed by RP-HPLC, using the same elution condition as employed for the analysis of the peptides and lipopeptides.

Liposomal Formulation. MMPP_4HFA (30 mol %) and POPC (1-palmitoyl-2-oleoyl-*sn*-glycero-3 phosphocholime, 70 mol %, total lipid concentration of 1 mg/mL) were dissolved in $CHCl_3$. A thin film was prepared by evaporating the solvent using a rotary evaporator. The film was placed under high vacuum for 12 h. The film was then hydrated with 100 mM 5-carboxyfluorescein solution (prepared in 25 mM in HEPES buffer, 10 mM $CaCl_2$ at pH = 8.0) for 1 h at 60 °C followed by sonication for another hour at 60 °C. Nonencapsulated dye was separated from liposomes via gel filtration chromatography with a Sephadex G75 column. Before loading the crude liposomal preparation on the column, the osmolarity of the elution buffer (with same composition) was adjusted by the addition of solid NaCl.

Kinetics of Release of Carboxyfluorescein from Liposomes. MMP-9 (10 μL of 200 μM solution) was added to a 2 mL solution of liposome in 25 mM HEPES buffer, pH 8.0, containing 10 mM $CaCl_2$ at 25 °C. The emission spectra of the control and liposomes with MMP-9 were measured. The emission intensity at 518 nm (excitation: 480 nm) was monitored as a function of time for 5 h. The experimental condition for the leakage studies with trypsin was the same as that for MMP-9.

RESULTS

It is known that incorporation of Gly Pro-Hyp repeats in polypeptide chains tend to form the triple-helical collagen-mimetic peptides (*23*). The magnitude of such helicity increases with either attachment of alkyl groups at the N-terminus (*24*) or introduction of cysteine knots (*25*), or metal ions (*26*). To incorporate collagen-mimetic triple helical peptides on the surface of liposomes for their recognition by MMP-9 and subsequent cleavage, we synthesized a few such peptides and conjugated them with stearic acid via their N-terminal NH_2 groups. Four criteria were taken into consideration for syntheses of such lipopeptides: (i) the peptides should exhibit the triple helical conformations, (ii) the peptides should contain the cleavage site for MMP-9, (iii) the peptides should be resistant to the cleavage by general proteases, (iv) the triple helical peptides must exhibit propensity to undergo facile unwinding to be effectively cleaved by MMP-9. With these criteria in mind, we synthesized a series of lipopeptide conjugates and investigated their physicochemical properties.

Although the natural substrate for MMP-9 is the type IV collagen (which is cleaved between Gly^{439}−Val^{440} bond), the enzyme exhibits overlapping substrate specificity for a variety of synthetic (collagen mimetic) peptide substrates (*27, 28*). Usually, the enzyme cleaves between **G** and **X** (where **X** = Leu, Ile, or Val) of a peptide sequence GPQ**GX**AGQR. In view of the amino acid sequence around Gly^{904} of type I collagen, as well as GPO or GPP repeats (responsible for forming the triple helical units), we synthesized the following peptides:

MMPP3_H: H_2N-G^{904}PQ**GL**A**GQ**RGIVGLOG^{919}-COOH
MMPP4_H: H_2N-G^{904}PQ**GI**A**GQ**R$(GPO)_4$GG-COOH
MMPP4_GPP: H_2N-G^{904}PQ**GL**A**GQ**R$(GPP)_4$GG-COOH
MMPP5_H: H_2N-G^{904}PQ**GL**A**GQ**R$(GPO)_4$GG-COOH
MMPP7_H: H_2N-G$(GPO)_4$**GL**A**GQ**R$(GPO)_4$GG-COOH
MMPP8 (control): H_2N-G^{904}PQ**GA**A**GQ**RGIVGLOG^{919}-COOH.

Whereas these peptides are known to be efficiently cleaved by collagenases (MMP-1, -8, and -13), they are also cleaved (albeit somewhat sluggishly) by gelatinases (MMP-2 and -9) (*28, 29*), and thus they are ideally suited for investigating the MMP-9-assisted cleavage reaction on longer time scales. We undertook the standard Fmoc-based, solid-phase synthetic protocol for synthesizing the above peptides, and subsequently purified those by the HPLC method. Of these, **MMPP8** was neither expected to be cleaved by MMP-9 (due to the lack of the cleavage site) nor had the potential to form the triple helix (due to the lack of the GPO or GPP repeats). On the other hand, although **MMPP3_H** could not form the triple helical structure (due to the lack of the GPO or GPP repeats), it contained the

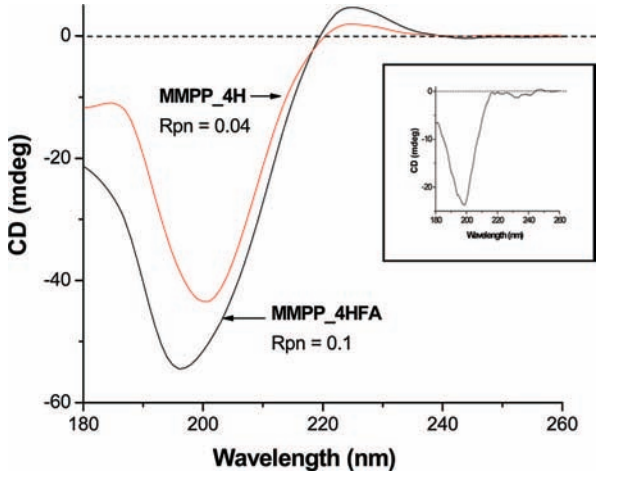

Figure 1. Circular dichroic spectra of **MMPP3_H** (inset), **MMPP4_H** and **MMPP4_HFA** in 10 mM phosphate buffer, pH = 4.0 at 4 °C. The concentration of each peptide/lipopeptide was 1 mg/mL. The solutions were stored at 4 °C for 12 h before recording the spectra.

cleavage site for MMP-9. The GPP repeats in **MMPP4_GPP** and the presence of the GPO repeats on both sides of the cleavable sequence in **MMPP7_H** were utilized to ascertain their potentials to form the triple helices, as well as the feasibility of unwinding during the MMP-9-dependent cleavage reaction. The N-termini of all these peptides were conjugated with stearic acids using the HBTU/HOBt coupling agents. The corresponding lipopeptides (identified by the suffix "**FA**", to denote the fatty acid conjugation, after the name of the parent peptides) were subjected to final purification by HPLC, followed by their characterizations by CD and mass spectroscopy.

Figure 1 shows the representative CD spectra of **MMPP3_H, MMPP4_H** and its fatty acid conjugate **MMPP4_HFA**. Note that all these peptides are characterized by negative elliptical bands at 196–200 nm and positive elliptical bands at 220–223 nm regions. However, the latter band is miniscule (or nonexistent) in the case of **MMPP3_H** (Figure 1, inset), suggesting the lack of the triple helical structure in its sequence. This was not unexpected, since it contained neither the GPO nor GPP repeat units. In contrast, both **MMPP4_H** and **MMPP4_HFA** exhibited pronounced ellipticities in the 220–223 nm regions, suggesting their ordered helical structures (Figure 1). The ratio of θ_{198} to θ_{225} (referred to as the Rpn value) (*29*) for **MMPP4_H** and **MMPP4_HFA** was found to be equal to 0.04 and 0.1, respectively. Given that the Rpn value of naturally occurring "collagen" is equal to 0.13 (*30*), it appears evident that the addition of a fatty acid chain to **MMPP4_H** (forming **MMPP4_HFA**) considerably enhances the magnitude of the triple helicity in the above peptide.

We recorded the spectra of all the synthetic peptides and their fatty acid conjugates (Supporting Information) and calculated their Rpn values (Table 1). The data of Table 1 reveal that the magnitude of the triple helicity of all peptides containing GPO (and to a lesser extent containing GPP) repeats increases upon converting them to their fatty acid derivatives. As expected, the control peptide **MMPP8** did not show any evidence of the triple helical structure. These data are consistent with the previous studies of Fields and his collaborators on the alkyl group assisted formation of the triple helical structures in collagen-mimetic peptides (*24*).

To determine the stability of our synthetic collagen-mimetic peptides, we subjected them to thermal denaturation. We incubated each peptide at different temperatures for 15 min and then recorded their CD spectra. Figure 2 shows a representative set of CD spectra of **MMPP4_H** (Figure 2A) and **MMPP4_HFA** (Figure 2B) as a function of temperature. The

Table 1. Rpn Values and Melting Temperatures (T_m) of Synthetic Peptides and Lipopeptides

peptides/ lipopeptides	Rpn	T_m (°C)
MMPP3_H	-	-
MMPP3_HFA	-	-
MMPP4_H	0.04	-
MMPP4_HFA	0.1	57
MMPP4_GPP	-	-
MMPP4_GPPFA	0.04	34
MMPP5_H	0.05	37
MMPP5_HFA	0.099	75
MMPP7_H	0.06	42
MMPP7_HFA	0.08	55
MMPP8	-	-
MMPP8_FA	-	-

temperature-dependent spectral data of both these peptides exhibit a decrease in the magnitude of the negative and positive elliptical peaks, with isosbestic points at 210 and 213 nm, respectively. This feature is consistent with a one-step transition between triple helices and their monomeric forms. The insets of Figure 2 show the positive elliptical peaks at 225 nm as a function of temperature.

The solid lines are the best fits of the data according to the conventional equation (*24*) for determining the T_m value from the temperature-dependent spectral changes. As apparent from the data of Figure 2A (inset), the T_m value of **MMPP4_H** is not easily resolvable, and its magnitude appears to be smaller than 57 °C for **MMPP4_HFA** peptide (Figure 2B, inset). Hence, besides enhancing the extent of triple helicity, the fatty acid conjugation with **MMPP4_H** increases its stability. Identical experiments were performed with other synthetic collagen-mimetic peptides and their fatty acid conjugates (Supporting Information). It should be mentioned that, although the thermal transition of most of the peptides/lipopeptides conformed to the single isosbestic point, **MMPP4_GPPFA** exhibited at least two isosbestic points (Supporting Information). The origin of the latter features is not clear at this point. A cumulative account of the spectral and thermal transition data of Figures 1 and 2 for all peptides and lipopeptides is presented in Table 1. An inspection of spectral and thermodynamic parameters of different peptides/lipopeptides revealed that **MMPP4_HFA** would be the best-suited lipopeptide for formulating liposomes and investigating their uncorking by MMP-9. Hence, all subsequent experiments were performed with **MMPP4_H** and **MMPP4_HFA** pair. Since the cleavage and the liposomal leakage studies are performed at pH = 8.0, we recorded the CD spectrum of the lipopeptide **MMPP4_HFA** at that pH. The CD spectrum indicated that **MMPP4_HFA** retains its triple helical conformation at pH = 8.0 (Rpn = 0.12) with a melting temperature of 42 °C (Figure S3, Supporting Information).

To determine whether or not **MMPP4_H** and **MMPP4_HFA** would be efficiently cleaved by MMP-9, we incubated individual peptides (5 μM) with 5 nM MMP-9 in 25 mM HEPES buffer, pH = 8.0. At different time intervals, 50 μL aliquots were withdrawn and transferred to a vial containing 2 μL of trifluoroacetic acid (TFA). The latter was used to denature the enzyme and stop further cleavage of the peptides. The aliquots collected at different time intervals were subjected to the HPLC analysis using a C_{18} Vydac analytical column and monitoring the elution profile at 214 nm. Figure 3A,B shows the time course of the HPLC profiles for the cleavage of **MMPP4_H** and **MMPP4_HFA**, respectively, by MMP-9. From the HPLC profiles of Figure 3A, it is evident that, at zero time, **MMPP4_H** elutes as a single (nearly symmetrical) peak at 15 min. Upon cleavage for 5 min, the above peak diminishes, and a new peak emerges (due to the formation of one of the cleaved products exhibiting high absorption at 214 nm) at 13 min. The absence

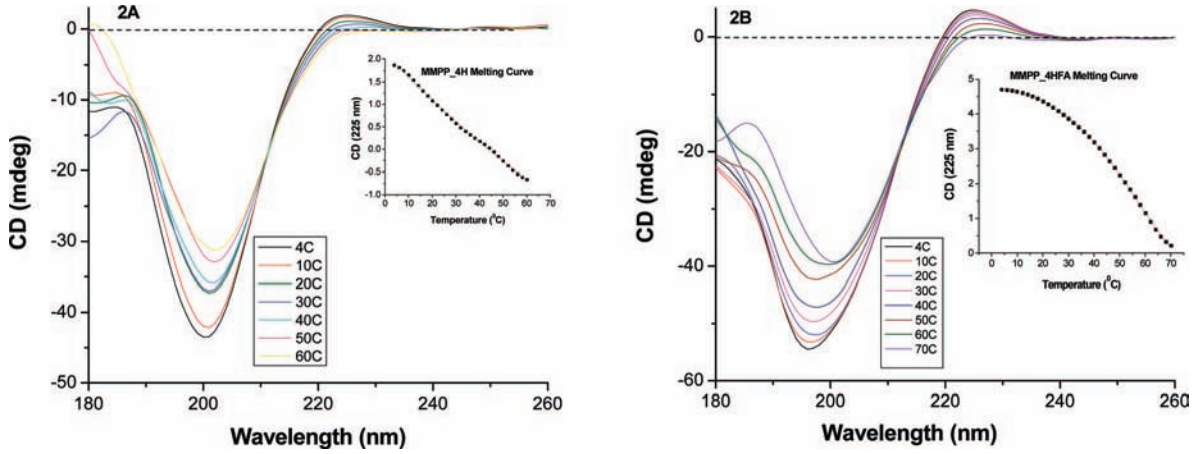

Figure 2. Temperature-dependent CD spectra for **MMPP4_H** (A) and **MMPP4_HFA** (B) are shown. The insets show the melting curves obtained by plotting the peak intensities at 225 nm as a function of temperature. The solid lines in the insets are the fitted curves. The experimental conditions are the same as those of Figure 1.

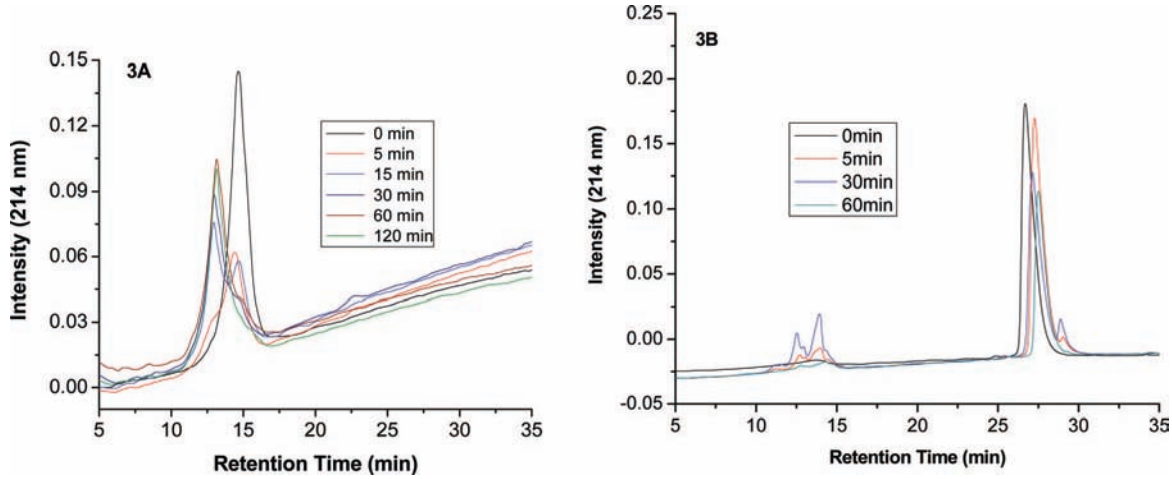

Figure 3. HPLC elution profiles for the cleavage of **MMPP4_H** (A) and **MMPP4_HFA** (B). The cleavage reactions were performed using 5 μM peptide/lipopeptide and 5 nM MMP-9 in 25 mM HEPES buffer, pH = 8.0, 25 °C.

of the second peak (expected to be formed upon treatment with MMP-9) on the HPLC profile is presumably due to its shorter chain length, showing low absorption at 214 nm. As the time of cleavage reaction progresses, the peak at 15 min decreases in magnitude and the peak at 13 min increases. This pattern is suggestive of the MMP-9-assisted cleavage of the peptides. Due to the presence of fatty acid chain in **MMPP4_HFA**, the HPLC cleavage peaks were significantly separated, with reactant and products eluting at 27 and 14 min, respectively.

As observed for the cleavage of **MMPP4_H**, the diminution of the reactant HPLC peak at 27 min proceeded concomitant with the increase in the product peak at 14 min. Qualitatively, it appeared that the **MMPP4_H** was being cleaved about 4-fold more efficiently than its fatty acid conjugate, **MMPP4_HFA**, by the same amount of MMP-9. Given that the magnitude of triple helicity is more pronounced with **MMPP4_HFA** (Rpn = 0.1) compared to **MMPP4_H** (0.04), it is tempting to speculate that the MMP-9-assisted cleavage of the collagen-mimetic peptide requires unwinding of the triple helix. Such a mechanistic feature was also envisaged by Fields (*31*).

As a hindsight control, we probed whether or not a general proteolytic enzyme, such as trypsin, can cleave either **MMPP4_H** or **MMPP4_HFA** or both. Trypsin was chosen because the above peptides contained the Arg-Gly peptide bond, which is recognized and cleaved by the enzyme. We observed that, whereas trypsin could efficiently cleave the above bond in the case of **MMPP4_H** peptide, it failed to cleave the same bond in **MMPP4_HFA** lipopeptide (at least up to 2 h of incubation; data not shown). Clearly, the trypsin cleavable bond is not accessible to the enzyme in the triple helical conformation of the lipopeptide.

Having established the cleavage of the collagen-mimetic triple helical **MMPP4_HFA** by MMP-9, we proceeded to formulate liposomes using the above lipopeptide as minor components (30 mol %) and 1-palmotoyl-2-oleoyl-*sn*-glycero-3-phosphocholine (POPC) as the major component (70 mol %). While preparing liposomes, a self-quenching fluorescent dye (carboxyfluorescein) was encapsulated (*32*). The free dye was separated from the liposome-encapsulated by the Sephadex G-75 gel filtration column chromatography. The dye-encapsulated liposomes thus prepared showed a fairly uniform distribution of their size on TEM, and their average diameter can be determined as being equal to 50 nm (Supporting Information).

The fluorescence emission intensity of liposome encapsulated carboxyfluorescein (λ_{ex} = 480 nm, λ_{em} = 518 nm) remains quenched (due to the local concentration effect) until it is released to the surrounding medium (*32*). This feature serves as a prototype for monitoring the release of the liposomal content under different experimental conditions. We determined the influence of MMP-9 on cleavage of the **MMPP4_HFA** lipopeptide incorporated in the liposomes, and their subsequent destabilization and release of the entrapped carboxyfluorescein. During these experiments, we incubated 2 mL solution of liposomes (100 μg lipids) with 1 μM MMP-9 in 25 mM HEPES

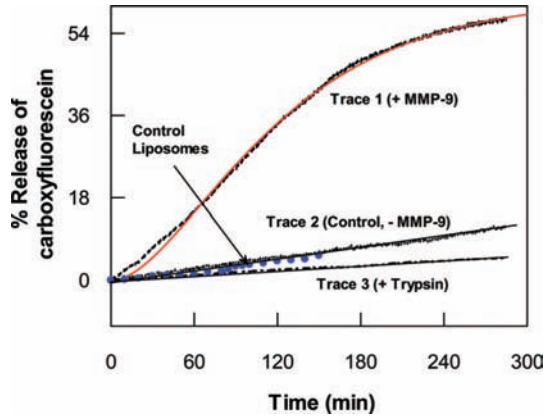

Figure 4. Time courses of release of carboxyfluorescein from liposomes under different conditions. Trace 1: in the presence of 1 μM MMP-9; the solid smooth red line is the best fit of the data according to eq 2 with k_1 and k_2 values of 0.018 and 0.014 min^{-1}, respectively. Trace 2: in the absence of MMP-9 (control). Trace 3: in the presence of 1 μM trypsin. The blue circles indicate the release profile from control liposomes (formulated without **MMPP4_HFA**) in the presence of 1 μM MMP-9. The solid lines of traces 2 and 3 are linear regression analyses of the data.

buffer, pH = 8.0, containing 10 mM $CaCl_2$, and monitored the time course of the increase in the fluorescence emission intensity at 518 nm (λ_{ex} = 480). Figure 4, trace 1, shows the time-dependent profile for the release of carboxyfluorescein under the above experimental condition. To ensure that the release of carboxyfluorescein from liposome was due to the cleavage of the collagen-mimetic lipopeptide, we performed a control experiment exactly under the above condition, but without MMP-9 (Figure 4, trace 2). Note that the time-dependent release of the dye in the absence of MMP-9 (trace 2) is far less pronounced than that observed in the presence of the enzyme (trace 1). To calculate the percent release of the dye during the above experiments, the liposomes were completely disrupted with a 5% aqueous solution of a detergent, Triton-X, and the total increase in fluorescence was determined (taken as a measure of 100% release of the dye from the liposomes). Given these data, we propose that, due to cleavage of the surface-exposed collagen-mimetic triple helical peptide by MMP-9, the lipid domains of the liposomes are destabilized, resulting in the release of the encapsulated fluorescent dye. The overall process is cumulatively referred to as the liposomal "uncorking". If the liposomes do not contain any **MMPP4_HFA**, the enzyme MMP-9 does not release the dye to any significant extent (Figure 4, blue circles).

We already demonstrated that, despite the presence of the trypsin cleavage site in **MMPP4_HFA**, the enzyme does not cleave the latter lipopeptide. If this property remained unchanged upon incorporation of **MMPP4_HFA** into liposomes, trypsin would not be able to "uncork" the liposomes. This expectation was clearly substantiated when we incubated the **MMPP4_HFA**-containing liposomes with 1 μM trypsin, precisely under the experimental conditions of trace 1 of Figure 4. As shown by trace 3 of Figure 4, the time course of leakage of the fluorescent dye matches that of the control experiment (performed in the absence of any enzyme), and it is significantly slower than that observed in the presence of MMP-9 (trace 1, Figure 4). As an additional control, we prepared the liposomes incorporating the stearic acid conjugate of the peptide **MMPP8** (i.e., **MMPP8_FA**) encapsulating carboxyfluorescein. In the presence of MMP-9 (1 μM), these liposomes showed a release profile very similar to trace 3 in Figure 4 (data not shown). The lipopeptide **MMPP8_FA** does not contain the cleavage site for the enzyme MMP-9; hence, it is not surprising that MMP-9 does not release the encapsulated dye from the liposomes incorporating the lipopeptide **MMPP8_FA**.

One apparent feature of the MMP-9-assisted uncorking of liposomes is the presence of a lag phase. A simple mechanistic explanation for the prevalence of such a lag phase is the involvement of at least one intermediary step during the overall uncorking process. However, even if one or multiple intermediary steps predominate during the course of liposome uncorking, the observed signal is given only by the carboxyfluorescein release step. For example, if the above liposome is cleaved by MMP-9, but its content is not released until the lipid domains are reorganized, the overall kinetic profile would involve a finite lag phase similar to that observed in Figure 4. Assuming that the MMP-9-assisted uncorking adhered to a two-step process, we analyzed the kinetic profile of Figure 4 (trace 1) by a two-step mechanism (see Discussion). The solid smooth (red) line is the best fit of the data for the k_1 and k_2 values of 0.018 $\pm$ 0.0034 and 0.014 $\pm$ 0.0016 min^{-1}, respectively. However, it should be noted that the fitted line does not precisely correspond to the experimental data (broken black line, trace 1). Clearly, the overall uncorking process is more complex than that explainable in light of the two-step mechanism (see Discussion).

DISCUSSION

The formulation of MMP-9-cleavable liposomes required synthesis of collagen-mimetic peptides, which could provide the cleavage sites for the enzyme. Of the different lipopeptides (synthesized on the basis of the amino acid sequences present around the cleavable site of type I collagen), **MMPP4_HFA** was found to be the best-suited for formulating such liposomes. The other lipopeptides either did not form adequate triple helical structures, comparable to those found in the natural collagen (e.g., **MMPP3_HFA**, **MMPP4_GPPFA**, **MMPP8_HFA**), or they formed triple helices that were too compact as evidenced by their high T_m values (e.g., **MMPP5_HFA)**, cleaved somewhat sluggishly by MMP-9 (**MMPP7_HFA)**, or cleaved non-specifically, such as by trypsin (**MMPP7_HFA**). It should be mentioned that, although **MMPP4_H** contained the trypsin-cleavage site (and it was cleaved by the enzyme in its native/unconjugated state), its stearic acid derivative (i.e., **MMPP4_HFA**) was not cleaved by trypsin. Clearly, the trypsin cleavage site of the original (monomeric) peptide (**MMPP4_H**) is masked upon formation of the triple helical structure in **MMPP4_HFA**. Whether or not the oligomerization of polypeptide units in triple helical peptides incorporates selectivity for matrix metalloproteinases, and obviates their cleavage by general proteases (e.g., trypsin, chymotrypsin, etc.), remains to be investigated. However, our experimental data provide clues as to why cellular matrices are constituted of fibrillar proteins, and they are specifically cleaved by matrix metalloproteinases.

The fact that a small segment of collagen-mimetic peptide (e.g., **MMPP3_H**) is devoid of the triple helical structure, whereas the native collagen is predominantly triple helical in nature, implies that the origin of the triple helicity lies in the cooperative interaction among the extended polypeptide chains. The latter feature is augmented by the presence of the GPO and GPP repeats in the polypeptide chains. The cooperative interaction among "shorter" chain containing peptides appears to be significantly enhanced upon attachment of C_{18} hydrophobic tail at the N-terminal end (*24*). This is apparent from the data of Figure 1; the Rpn value of **MMPP4_H** is increased from 0.04 to 0.1 upon conjugation with stearic acid. The question arises whether the Rpn value of 0.04 in **MMPP4_H** is simply due to its preponderance in the form of polyproline II helix (*33*) or its ability to form a partial triple helical structure. In attempting to answer this question, we realized that the peptide containing the GPP (instead of GPO) repeats (viz.,

Scheme 1. Proposed Thermodynamic Model of the Monomer−Trimer Equilibria of MMPP4_HFA Lipopeptide

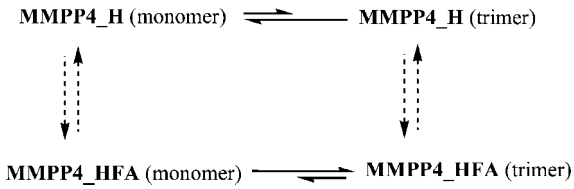

MMPP4_HGPP) does not contain any discernible positive elliptical peak at 225 nm. Since the presence of the GPO repeats in the peptide sequence facilitates the formation of the triple helical structure, it follows that **MMPP4_H** exists in an equilibrium mixture of the monomeric and trimeric (i.e., triple helical) forms. This equilibrium is favored toward the trimeric form upon conjugation with the stearic acid as depicted by the model of Scheme 1.

Consistent with the model of Scheme 1, the temperature-dependent CD spectra of **MMPP4_H** and **MMPP4_HFA** (Figure 2) conform to single isosbestic points. As the temperature increases, the magnitude of elipticity at both 195 and 225 nm decreases, albeit by different amounts. This feature results in a continuous diminution in the Rpn value as a function of increasing temperature, presumably because of the conversion of the triple helical form (trimer) form of **MMPP4_HFA** to the monomeric form.

The observation that **MMPP4_H** appears to be more efficiently cleaved by MMP-9 than **MMPP4_HFA** implies that the conjugation of stearic acid impairs the catalytic activity of the enzyme. We believe the origin of the above disparity lies in the preference of MMP-9 to cleave the monomeric rather than triple helical peptides. This is consistent with the postulate that MMP-9 unwinds the triple helical peptides prior to cleaving them (*31*). Given this, we surmise that the sluggish rate of cleavage of **MMPP4_HFA** (*vis a vis* **MMPP4_H**) by MMP-9 is due to the rate-limiting unwinding of the triple helical peptide to its monomeric form. The question arises as to why the triple helical form of the peptide is not unwound to produce the monomeric unit prior to their cleavage by trypsin. The most plausible answer to this question is that the unwinding of the triple helix requires assistance from specialized proteases, such as MMP-9 (which contain noncatalytic fibronectin domain), and such functions are not accomplished by general proteases such as trypsin.

A marked success in our overall endeavor has been the demonstration that the lipopeptide, **MMPP4_HFA**, could be easily incorporated in the liposomes, and the latter are selectively "uncorked" by MMP-9 but not by trypsin. On the basis of the literature (*32*), it is expected that the C_{16}-hydrocarbon moiety of the lipopeptide **MMPP4_HFA** will be embedded in the lipid bilayer of the liposomes. The triple helical peptide portion of the molecules will protrude outside the lipid bilayer. The amino acids GPQ may act as a spacer, making the MMP-9 cleavage site of the peptide accessible to the enzyme. Since the cleavage of the triple helical peptides destabilizes the lipid domains, their contents are released.

Due to ease in performing the liposomal uncorking experiments, we chose a self-quenching fluorescent dye, carboxyfluorescein. As long as the dye remains confined inside the liposomal lumen, its fluorescence remains quenched (*33*). As soon as the dye leaks out from the liposomes, its fluorescence starts increasing. The time course of the increase in fluorescence emission intensity at 518 (Figure 4) is the sum of a sequence of microscopic events associated with the overall uncorking process. Hence, it is not surprising that the overall kinetic profile is complex (Figure 4, trace 1). However, since the kinetics of increase in the fluorescence intensity involved a finite lag phase, and the signal of measurement came from the release of carboxyfluorescein to the exterior environment, a minimal two-step model of uncorking was envisaged (eq 1).

$$\mathrm{L-F} \xrightarrow{k_1} \mathrm{L*F} \xrightarrow{k_2} \mathrm{L*} + \mathrm{F} \qquad (1)$$

Where L and F represent liposomes and carboxyfluorescein, respectively. The first step involves the cleavage and destabilization of the liposomes. The intermediary species L*−F is representative of the cleaved liposomes, but fluorescence dye still remains confined in the liposomal lumen. The second step is release of the fluorescence dye with concomitant increase in the fluorescence emission intensity at 518 nm. For this two irreversible step model, the time course of formation of F can be given by eq 2 (*34*).

$$\mathrm{F} = [\mathrm{L-F}]\left[1 + \left(\frac{1}{k_1 - k_2}\right)\left(k_2 e^{-kt} - k_2 e^{-kt}\right)\right] \qquad (2)$$

The solid, smooth line of trace 1 (Figure 4) is the best fit of the data according to eq 2, with k_1 and k_2 being equal to 0.018 ± 0.0034 min^{-1} and 0.014 ± 0.0016 min^{-1}, respectively. However, since the fitted line (red) somewhat deviates from the experimental data (broken black lines), it appears that the sequence of events of the MMP-9-assisted uncorking is more complex than that conceivable in light of the two-step model. This is not unexpected, since even after the cleavage of the triple helical peptides, a series of microscopic steps may intervene prior to the onset of the final step of the dye release. The lipopeptide **MMPP4_HFA** contains one fatty acid, and this may not form tight domain boundaries with the major lipid of the liposomes, POPC (*35*). The 10% release of the dye in the absence of MMP-9 (Figure 4, trace 2) may arise from these domain boundaries.

We have observed that, in buffer solutions (pH = 8.0), the recombinant MMP-9 self-hydrolyzes and inactivates itself within 3 h. This self-hydrolysis is one of the possible reasons for not releasing all of the liposomal contents. In order to test this hypothesis, we repeated the liposomal release experiments under the conditions as described previously. We observed that the rate of release of the encapsulated carboxyfluorescein decreases considerably after 130 min (54% release, as indicated in Figure 4). However, the addition of a second aliquot of MMP-9 (10 μL of 200 μM solution) restarted the release of carboxyfluorescein from the liposomes. Cumulatively, 94% of the encapsulated dye was released in 6 h (Figure 5). We are currently in the process of fine-tuning the molecular mechanism of liposomal uncorking and its content release, and we will report on these findings subsequently.

In conclusion, we have provided the first detailed studies on the formulation of liposomes, which harbor the MMP-9-cleavable collagen-mimetic peptides on their surface. The cleavage of the above peptides by MMP-9 results in destabilization of the lipid domains of the liposomes, leading to the release of their encapsulated contents (referred to as "uncorking"). Since MMP-9 is invariably expressed in most of the cancerous tissues, our liposomal formulation will find unique application as a drug delivery vehicle not only for inhibiting MMP-9, but for all other pathogenic enzymes/proteins which are expressed at the target sites. When liposomes will be encapsulated with an MMP-9-specific inhibitor, the triple helical peptides will serve as the "bait" for the enzyme, and the enzyme will essentially "commit suicide" once it "uncorks" the liposomes and releases its own inhibitor. Once the enzyme is inhibited, it will lose its potency to further uncork the liposomes. In this way, our overall approach has the potential to serve as a "self-adjusting" drug delivery system, where the amount of drug released will be

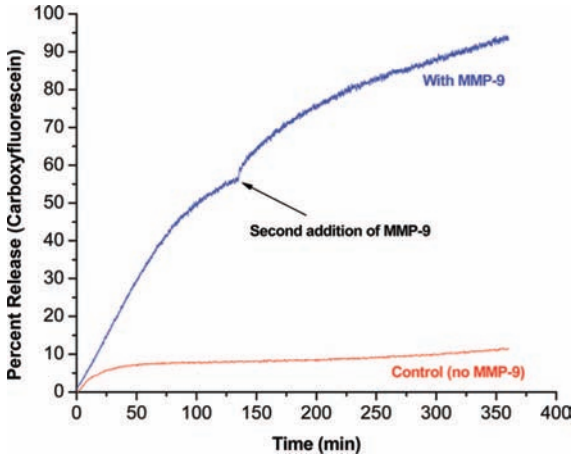

Figure 5. The increase in the fluorescence intensity due to the release of the liposome-encapsulated dye (carboxyfluorescein) is shown (λ_{ex} = 480 nm, λ_{em} = 518 nm) in the presence of the recombinant human MMP-9 (blue trace, 1 μM enzyme, 25 mM HEPES buffer, pH = 8.0, 20 °C) and in the absence of the enzyme (red trace). A second aliquot of MMP-9 was added after 150 min. In the presence of MMP-9, 94% encapsulated carboxyfluorescein was released in 6 h.

dictated by the amount of the catalytically active enzyme present in its resident environment. On the other hand, if the liposomes are encapsulated with fluorescent or magnetic resonance contrast agents, the triggered release of their contents will find usage in imaging the diseased tissues (expressing MMP-9). Both these features of our uniquely designed liposomes are of prime importance in diagnosis and treatment of a wide variety of cancers in human patients.

ACKNOWLEDGMENT

This research was supported by the NIH grant 1R01 CA113746 and NSF DMR-0705767 to S.M. and D.K.S. A.J.H. was supported by the NSF-EPSCoR award EPS-0447679. X.L. thanks the support of the proteomics core facility by NIH Grant P20 RR016741 from the INBRE Program of the NCRR.

Supporting Information Available: Mass spectral data and CD spectra for the synthesized peptides and lipopeptides and TEM picture of the liposomes incorporating **MMPP4_HFA**. This material is available free of charge via the Internet at http://pubs.acs.org/BC.

LITERATURE CITED

(1) Malemud, C. J. (2006) Matrix metalloproteinases (MMPs) in health and disease: an overview. *Front. Biosci. 11*, 1696–1701.
(2) Deryugina, E. I., and Quigley, J. P. (2006) Matrix metalloproteinases and tumor metastasis. *Cancer Metastasis Rev. 25*, 9–34.
(3) Verma, R. P., and Hansch, C. (2007) Matrix metalloproteinases (MMPs): chemical-biological functions and (Q)SARs. *Bioorg. Med. Chem. 15*, 2223–2268.
(4) La Rocca, G., Pucci-Minafra, I., Marrazzo, A., Taormina, P., and Minafra, S. (2004) Zymographic detection and clinical correlations of MMP-2 and MMP-9 in breast cancer sera. *Br. J. Cancer 90*, 1414–1421.
(5) Mook, O. R. F., Frederiks, W. M., and Van Noorden, C. J. F. (2004) The role of gelatinases in colorectal cancer progression and metastasis. *Biochim. Biophys. Acta 1705*, 69–89.
(6) Osinsky, S. P., Ganusevich, I. I., Bubnovskaya, L. N., Valkovskaya, N. V., Kovelskaya, A. V., Sergienko, T. K., and Zimina, S. V. (2005) Hypoxia level and matrix metalloproteinases-2 and -9 activity in Lewis lung carcinoma: Correlation with metastasis. *Exp. Oncol. 27*, 202–205.
(7) Dong, Z., Bonfil, R. D., Chinni, S., Deng, X., Trindade Filho, J. C., Bernardo, M., Vaishampayan, U., Che, M., Sloane, B. F., Sheng, S., Fridman, R., and, and Cher, M. L. (2005) Matrix metalloproteinase activity and osteoclasts in experimental prostate cancer bone metastasis tissue. *Am. J. Pathol. 166*, 1173–1186.
(8) Keleg, S., Büchler, P., Ludwig, R., Büchler, M. W., and Friess, H. (2003) Invasion and metastasis in pancreatic cancer. *Mol. Cancer 2*, 14–20.
(9) Roomi, M. W., Ivanov, V., Kalinovsky, T., Niedzwiecki, A., and Rath, M. (2006) Inhibition of matrix metalloproteinase-2 secretion and invasion by human ovarian cancer cell line SK-OV-3 with lysine, proline, arginine, ascorbic acid and green tea extract. *J. Obstet. Gynaecol. Res. 32*, 148–157.
(10) Fisher, J. F., and Mobashery, S. (2006) Recent advances in MMP inhibitor design. *Cancer Metastasis Rev. 25*, 115–136.
(11) Cuenca, A. G., Jiang, H., Hochwald, S. N., Delano, M., Cance, W. G., and Grobmyer, S. R. (2006) Emerging implications of nanotechnology on cancer diagnosis and therapeutics. *Cancer 107*, 459–466.
(12) Torchilin, V. P. (2005) Recent advances with liposomes as pharmaceutical carriers. *Nat. Rev. Drug Discovery 4*, 145–160.
(13) Anderson, T. L., Jensen, S. S., and Jorgensen, K. (2005) Advanced strategies in liposomal cancer therapy: problems and prospects of active and tumor specific drug release. *Prog. Lipid Res. 44*, 68–97.
(14) Torchilin, V. P. (2006) Recent approaches to intracellular delivery of drugs and DNA and organelle targeting. *Ann. Rev. Biomed. Eng. 8*, 343–375.
(15) Gabizon, A. A., Shmeeda, H., and Zalipsky, S. (2006) Pros and cons of the liposome platform in cancer drug targeting. *J. Liposome Res. 16*, 175–183.
(16) Karanth, H., and Murthy, R. S. R. (2007) pH-sensitive liposomes-principle and application in cancer therapy. *J. Pharm. Pharmacol. 59*, 469–483.
(17) Karoonuthaisiri, N., Titiyevskiy, K., and Thomas, J. L. (2003) Destabilization of fatty acid-containing liposomes by polyamidoamine dendrimers. *Colloids Surf., B: Biointerfaces 27*, 365–375.
(18) Davis, S. C., and Szoka, F. C. (1998) Cholesterol phosphate derivatives: synthesis and incorporation into a phosphate and calcium sensitive triggered release liposome. *Bioconjugate Chem. 9*, 783–792.
(19) Hauck, M. L., LaRue, S. M., Petros, W. P., Poulson, J. M., Yu, D., Spasojevic, I., Pruitt, A. F., Klein, A., Case, B., Thrall, D. E., Needham, D., and Dewhirst, M. W. (2006) Phase I trial of doxorubicin-containing low temperature sensitive liposomes in spontaneous canine tumors. *Clin. Cancer Res. 12*, 4004–4010.
(20) Liu, X. M., Yang, B., Wang, Y. L., and Wang, J. Y. (2005) Photoisomerisable cholesterol derivatives as photo-trigger of liposomes: effect of lipid polarity, temperature, incorporation ratio, and cholesterol. *Biochim. Biophys. Acta 1720*, 28–34.
(21) Andresen, T. L., Jensen, S. S., Kaasgaard, T., and Jørgensen, K. (2005) Triggered activation and release of liposomal prodrugs and drugs in cancer tissue by secretory phospholipase A2. *Curr. Drug Delivery 2*, 353–362.
(22) Sarkar, N. R., Rosendahl, T., Krueger, A. B., Banerjee, A. L., Benton, K. A., Mallik, S., and Srivastava, D. K. (2005) "Uncorking" of liposomes by matrix metalloproteinase-9. *J. Chem. Soc.: Chem. Commun.* 999–1001.
(23) Lauer-Fields, J. L., Sritharan, T., Stack, M. S., Nagase, H., and Fields, G. B. (2003) Selective hydrolysis of triple-helical substrates by matrix metalloproteinase-2 and -9. *J. Biol. Chem. 278*, 18140–18145.
(24) Gore, T., Dori, Y., Talmon, Y., Tirrell, M., and Bianco-Peled, H. (2001) Self-assembly of model collagen amphiphiles. *Langmuir 17*, 5352–5260.
(25) Barth, D., Kyrieleis, O., Frank, S., Renner, C., and Moroder, L. (2003) The role of cystine knots in collagen folding and

stability, part II. Conformational properties of (Pro-Hyp-Gly)n model trimers with N- and C-terminal collagen type III cystine knots. *Chem.—Eur. J. 9*, 3703–3714.

(26) Koide, T., Yuguchi, M., Kawakita, M., and Kono H. (2002) Metal assisted stabilization and probing of collagenous triple helices. *J. Am. Chem. Soc. 124*, 9388–9389.

(27) Minod, D., Lauer-Fields, J. L., Nagase, H., and Fields, G. B. (2004) Matrix metalloproteinase triple-helical peptidase activities are differentially regulated by substrate stability. *Biochemistry 43*, 11474–11481.

(28) Lauer-Fields, J. L., Broder, T., Sritharan, T., Chung, L., Nagase, H., and Fields, G. B. (2001) Kinetic analysis of MMP activity using fluorogenic triple-helical substrates. *Biochemistry 40*, 5795–5803.

(29) Lauer-Fields, J. L., and Fields, G. B. (2002) Triple helical peptide analysis of collagenolytic protease activity. *Biol. Chem. 383*, 1095–1105.

(30) Fiori, S., Sacca, B., and Moroder, L. (2002) Structural properties of collagenenous heterotrimer that mimics the collagenase cleavage site of collagen type I. *J. Biol. Chem. 319*, 1235–1242.

(31) Minond, D., Lauer-Fields, J. L., Cudic, M., Overall, C. M., Pei, D., Brew, K., Moss, M. L., and Fields, G. B. (2007) Differentiation of secreted and membrane-type metrix metalloproteinase activities based on substitutions and interruptions of triple-helical sequences. *Biochemistry 46*, 3724–3733.

(32) Rezler, E. M., Khan, D. R., Lauer-Fields, J., Cudic, M., Baronas-Lowell, D., and Fields, G. B. (2007) Targeted drug delivery utilizing protein-like molecular architecture. *J. Am. Chem. Soc. 129*, 4961–4972.

(33) Pokorny, A., Birkbeck, T. H., and Almeida, P. F. F. (2002) Mechanism and kinetics of δ-lysin interaction with phospholipid vesicles. *Biochemistry 41*, 11044–11056.

(34) Kakinoki, S., Hirano, Y., and Oka, M. (2005) On the stability of polyproline-I and II structures of proline oligopeptides. *Polym. Bull. 53*, 109–115.

(35) Potma, E. O., and Xie, X. S. (2005) Direct visualization of lipid phase segregation in single lipid bilayers with coherent anti-stokes Raman scattering microscopy. *ChemPhysChem 6*, 77–79.

BC070081P

2′-Anthraquinone-Conjugated Oligonucleotide as an Electrochemical Probe for DNA Mismatch

Satoshi Kumamoto, Mariko Watanabe, Naoko Kawakami, Mitsunobu Nakamura, and Kazushige Yamana*

Department of Materials Science and Chemistry, Graduate School of Engineering, University of Hyogo, 2167 Shosha, Himeji, Hyogo 671-2201, Japan. Received March 19, 2007; Revised Manuscript Received September 26, 2007

We previously prepared the oligonucleotides (ODNs) conjugated to an anthraquinone (AQ) group via one carbon linker at the 2′-sugar position. When these modified ODNs bind to cDNA sequences, the AQ moiety can be intercalated into the predetermined base-pair pocket of a duplex DNA. In this paper, 2′-AQ-modified ODNs are shown to be an excellent electrochemical probe to clarify the effect of a mismatch base on the charge transfer (CT) though DNA. Two types of DNA-modified electrodes were constructed by assembly of disulfide-terminated 2′-AQ-ODN duplexes onto gold electrodes. One type of electrodes (system I) contains fully matched base pairs or a single-base mismatch in duplex DNA between the redox center and the electrode. The other (system II) consists of the mismatch but at the outside of the redox center. The modified electrodes were analyzed by cyclic voltammetry to estimate the CT rate through duplex DNA. In system I, the CT rate was found to be $\sim 50\ s^{-1}$ for the fully matched AQ-ODN duplexes, while the CT rates of the mismatched DNA were considerably slower than that of the fully matched DNA. In system II, the AQ-ODN duplexes showed almost similar CT rates ($\sim 50\ s^{-1}$) for the fully matched DNA and for the mismatched DNAs. The detection of a single-base mismatch was then performed by chronocoulometry (CC). All the DNA duplexes containing a mismatch base in system I gave the reduced electrochemical responses when compared to the fully matched DNA. In particular, the mismatched DNAs including G−A mismatch can be differentiated from fully matched DNA without using any electrochemical catalyst. We further tested the usefulness of single-stranded (ss) AQ-ODN immobilized on a gold electrode in the electrochemical detection of a single-base mismatch through hybridization assay. The ss-AQ-ODN electrodes were immersed in target-containing buffer at room temperature, and the CC measurements were carried out to see the changes in the integrated charge. Within 60 min, the mismatched DNA was clearly distinguishable by the CC differences from the fully matched target. Thus, the electrochemical hybridization assay provides an easy and convenient detection for DNA mutation that does not require any extra reagents, catalyst, target labeling, and washing steps.

INTRODUCTION

The DNA sequence variation among individuals is of interest because it provides the basis of heritable variation in disease susceptibility (*1*). The most common type of human genetic variation is the single-nucleotide polymorphisms (SNPs), which can serve as genetic markers for identification of disease genes. Ongoing challenges are being directed toward the discovery of functional SNPs that are associated with susceptibility of certain disease (*2–4*). SNP genotyping will thus play an important role in future diagnostics. The development of simple and accurate methods for SNP assay is the current subject of intense research.

Electrochemical methods for SNP genotyping are attractive because of their rapid electrochemical transduction, sensitive detection, and ease of fabrication of microdevices. Several methods for electrochemical detection of DNA mutation have been reported, each of which has specific advantages. One approach is based on the electrochemical transduction of the hybridization event using exogenous redox-active reporters having preferential affinity for duplex DNA (*5*). The other approach is the so-called sandwich assay by the use of redox-labeled oligonucleotide probes that bind to target DNA sequence (*6–8*). Although these approaches are straightforward, they usually suffers from several problems such as background signal due to nonspecific binding of redox reporters, hybridization error, and difficulties in the design of probe sequences. Another possible approach, first reported by Barton et al., is the method that relied on long-range charge transport (CT) though DNA (*9–14*). The efficiency of CT though DNA is significantly decreased when any perturbation of base-pair stacking such as due to a mismatched base occurs within DNA. The presence of a single-base mismatch in DNA can be determined from the reduced charge transferability compared with fully matched DNA. While the CT-based assays do not require any stringent washing steps, they need a densely packed DNA array, a specific redox-active intercalator, and an electrocatalyst.

The design of oligonucleotide probes covalently attached to a redox reporter has been an important subject to develop a practical electrochemical method for mutation detection based on a CT-based approach (*12–14*). As a part of our research efforts to develop an electrochemical assay of SNPs, we focused on an anthraquinone derivative that is site-specifically incorporated into DNA oligonucleotides. We previously prepared the oligonucleotides conjugated to an anthraquinone group via one carbon linker at the 2′-sugar position (*15, 16*). When these modified oligonucleotides bind to cDNA sequences, the anthraquinone moiety can be intercalated into the predetermined base-pair pocket of a duplex DNA (*16–20*). In this paper, we demonstrate that 2′-anthraquinone-modified oligonucleotides are indeed an excellent probe to measure long-range charge transfer through duplex DNA. With this measurement, mismatch-containing DNA can be distinguished by the reduced charge transferability from fully matched DNA. Unlike other mismatch

* Corresponding Author. E-mail: yamana@eng.u-hyogo.ac.jp, Tel.: +81-79-267-4895, Fax: +81-79-267-4895.

10.1021/bc070097f CCC: $40.75 © 2008 American Chemical Society
Published on Web 11/08/2007

detections based on CT through DNA (*9–11*), our method does not require any exogeneous reagents and catalyst. When compared to the method using ferrocene-modified oligonucleotide probes (*13*), the design and fabrication of our anthraquinone-modified DNA bound electrodes are relatively simple and easy. The assay format solely involves conventional electrochemical measurements, which is in contrast to the photoelectrochemical assay (*14*). Our approach therefore provides easy and convenient detection of DNA mutation.

EXPERIMENTAL PROCEDURES

Materials. Deoxyribonucleoside phosphoramidites and 1-*O*-dimethoxytritylpropyl disulfide-modified CPG were purchased from Transgenomics and Glen Research Inc., respectively. 2′-Anthraquinone-modified uridine phopshoramidite was prepared according to a reported procedure (*16*). 2′-Anthraquinone-modified oligonucleotides containing a disulfide anchor at the 3′-teminus and other oligonucleotides were synthesized on an ABI 394 DNA/RNA synthesizer, purified using reversed-phase HPLC, and characterized as described (*16*). Au[111] surfaces on glass slides were prepared by Osaka Vacuum Chemical (Osaka, Japan) by the vapor deposition method.

Double-Stranded DNA Bound Electrodes. Before DNA modification, the Au surface was soaked at room temperature in piranha solution (H_2O_2/H_2SO_4 = 1:3, v/v) for 15 min × 2, washed with deionized water, and dried with a blow of nitrogen gas. The clean Au−glass was attached to a window (geometrical area: 0.36 cm^2) of a glassware cell that is designed for electrochemical measurements. 2′-Anthraquinone-modified oligonucleotide containing a disulfide anchor at the 3′-teminus was mixed with cDNA to form a duplex and then used for DNA modification. The modification was performed by immersion of the Au electrode (0.36 cm^2) in 0.1 mM DNA (50 μL) in 0.1 M NaCl, 0.01 M sodium phosphate, and 0.01 M $MgCl_2$ (pH 7) at room temperature for 12 h. The modified surface was then exposed to 100 μL of 2.5 mM mercaptopropanol in the same buffer for 2 h.

Electrochemical Measurements. Electrochemical measurements were carried out in the cell consisting of the modified Au electrode (0.36 cm^2), a Pt wire auxiliary electrode, and a Ag/AgCl reference electrode, using an electrochemical analyzer (ALS/H CHI model 612B or 630C). All cyclic voltammetry and chronocoulometry measurements were performed at room temperature in a pH 7 buffer (2 mL) containing 0.1 M NaCl and 0.01 M sodium phosphate. The buffer was thoroughly degassed with nitrogen before measurements.

Mismatch Detection via Hybridization Assays. The single-stranded (ss) 2′-anthraquinone-modified oligonucleotide containing a disulfide anchor at the 3′-teminus was assembled on the Au electrode, and the remaining Au surface was covered with mercaptopropanol in a similar way as described for double-stranded DNA modification. The charge (I_{ss}) required for the reduction of the ss anthraquinone−DNA probe during the integration time (5 s) was first recorded in the phosphate buffer by chronocoulometry (CC). Target DNA (4 nM) was then poured into the buffer, and the same CC measurements were performed at the defined time intervals to obtain the charge after hybridization (I_{hb}). The % changes in charge responses are defined as $[(I_{hb} - I_{ss})/I_{ss}] \times 100$. All CC measurements started at an applied voltage of −100 mV vs Ag/AgCl, and then the potential was changed to −600 mV vs Ag/AgCl and held at the defined time period.

RESULTS AND DISCUSSION

Double-Stranded 2′-Anthraquinone-Modified DNA Bound Electrodes. In our electrochemical study of charge transfer (CT) through DNA, 2′-anthraquinone-modified oligonucleotides containing a disulfide anchor at the 3′-teminus were prepared using an anthraquinone-modified nucleoside phosphoramidite (*16*) and a solid support linked to a hydroxypropyl disulfide. The duplexes of disulfide-containing anthraquinone−oligomers with appropriate DNA sequences were assembled on gold electrode surfaces by a usual method (*20*). To clarify the effect of a mismatch base on the CT through DNA, two types of DNA-modified electrodes were constructed as shown in Figure 1. One type of electrode contains fully matched base pairs or a single-base mismatch in duplex DNA between the redox center and the electrode (system I, AQ-ODN Duplex 1–3). The other consists of the mismatch but at the outside of the redox center (system II, AQ-ODN Duplex 4).

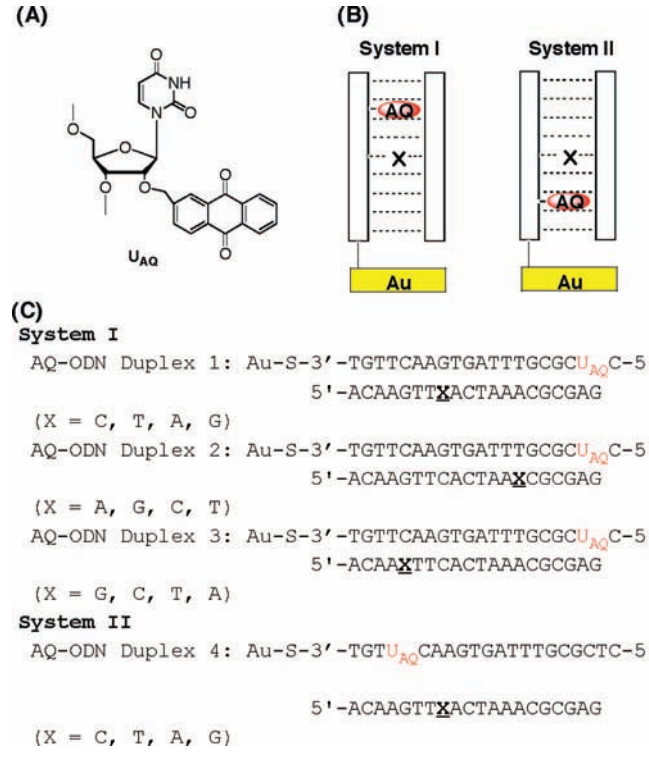

Figure 1. (A) 2′-Anthraquinone-modified uridine (U_{AQ}). (B) Double-stranded anthraquinone-modified oligonucleotide bound electrodes. Electrodes of system I contain fully matched base pairs or a single-base mismatch in duplex DNA between the redox center and the electrode. The others (system II) consist of the same mismatch but at the outside of the redox center. (C) Sequences of anthraquinone-modified oligonucleotides and their target DNAs in systems I and II.

Electrochemical Characterization of DNA-Modified Electrodes. The modified electrodes were characterized by cyclic voltammetry (CV). The typical CV curves (AQ-ODN Duplex 1; X = C; and AQ-ODN Duplex 4; X = C) are shown in Figure 2. Reversible waves associated with the reduction and oxidation of the pendant anthraquinone group were obtained with $E_{1/2}$ of −0.44 ∼ −0.42 V vs Ag/AgCl and are very similar to that of an unmodified anthraquinone molecule in the shape of the CV responses. As the CV scan rates were increased, both the anodic and cathodic peak currents were intensified. The plots of the peak current vs CV scan rate (Figure 2, inset) are linear, confirming that the observed CVs are derived from the surface-confined redox molecule. Similarly, the mismatch-containing DNAs showed the scan rate dependence of the CV peak current (Supporting Information). The CV responses of the DNA-modified electrodes against $Fe(CN)_6^{3-}$ were decreased when compared with the bare Au electrode, being consistent with the DNA monolayer on the gold surface. The surface coverage of the anthraquinone−DNA duplexes were determined by the

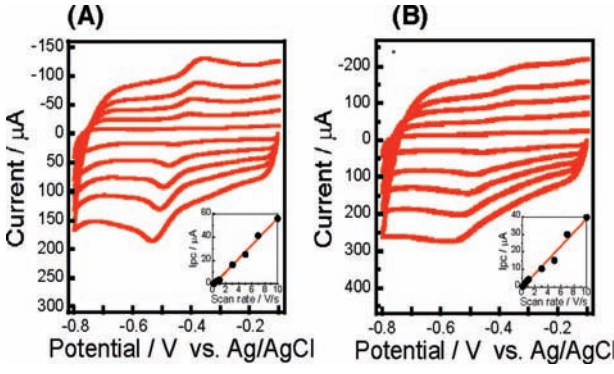

Figure 2. (A) Cyclic voltammograms of anthraquinone-modified oligonucleotide (AQ-ODN Duplex 1; X = C of system I) bound electrode at various scan rates of 0.5, 1, 3, 5, 7, and 10 V/s. (B) Cyclic voltammogram of anthraquinone-modified oligonucleotide (AQ-ODN Duplex 4; X = C of system II) bound electrode at various scan rates of 0.5, 1, 3, 5, 7, and 10 V/s. Insets show the plot of anodic peak current vs scan rate.

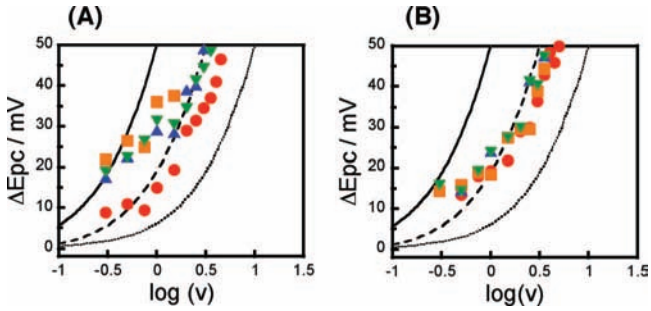

Figure 3. Plots of the peak splitting ΔE_{pc} ($=E_{pc} - E^0$) vs log(υ), where υ = scan rate. Panel A: red, AQ-ODN Duplex 1, X = C; green, AQ-ODN Duplex 1, X = T; blue, AQ-ODN Duplex 1, X = A; orange, AQ-ODN Duplex 1, X = G. Panel B: red, AQ-ODN Duplex 4, X = G; green, AQ-ODN Duplex 4, X = C; blue, AQ-ODN Duplex 4, X = T; orange, AQ-ODN Duplex 4, X = A. Simulation curves for electron transfer rates of 10 s^{-1} (solid lines), 50 s^{-1} (broken line), and 100 s^{-1} (dotted line) are indicated for comparison.

ruthenium hexamine assay (*21*) to be 2 ∼ 3 pmol/cm^2, which indicates that the duplex DNAs were not densely packed. It is noted that the DNA duplexes should adopt upright orientation along the electrode surface at the applied CV potentials (−100 ∼ −800 mV vs Ag/AgCl) because of the electrostatic repulsion of the DNA polyanion (*22*).

Effect of Mismatch Bases on Charge-Transfer Rate through DNA. The CV data were analyzed to estimate the electron transfer (CT) rate through DNA (*9, 23*). Figure 3 shows the plots of the peak splitting ΔE_{pc} ($=E_{pc} - E^0$) versus log(υ) (where υ = scan rate). Comparison of the experimental data with the simulated curves gave a CT rate that is estimated to be ∼50 s^{-1} for the fully matched AQ-ODN Duplex 1 of system I. The ΔE_{pc} for the mismatched DNA duplexes (AQ-ODN Duplex 1; X = T, A, G) became wider at the CV scan rates <1 V/s than those for the fully matched DNA and significantly deviated from the simulated curves. These observations indicate that the CT rates of the mismatched DNA are considerably slower than that of the fully matched DNA. In contrast, the AQ-ODN duplexes (AQ-ODN Duplex 4 of system II) containing a mismatched base at the site out of the redox center showed almost similar CT rates (∼50 s^{-1}) for the fully matched DNA and for the mismatched DNAs. It is thus clearly shown that the anthraquinone intercalator appended onto the 2′-sugar residue of DNA can be used for probing the slower CT rates through mismatch-containing DNA than fully matched DNA. Interestingly, the CT rates through the perfectly matched DNA

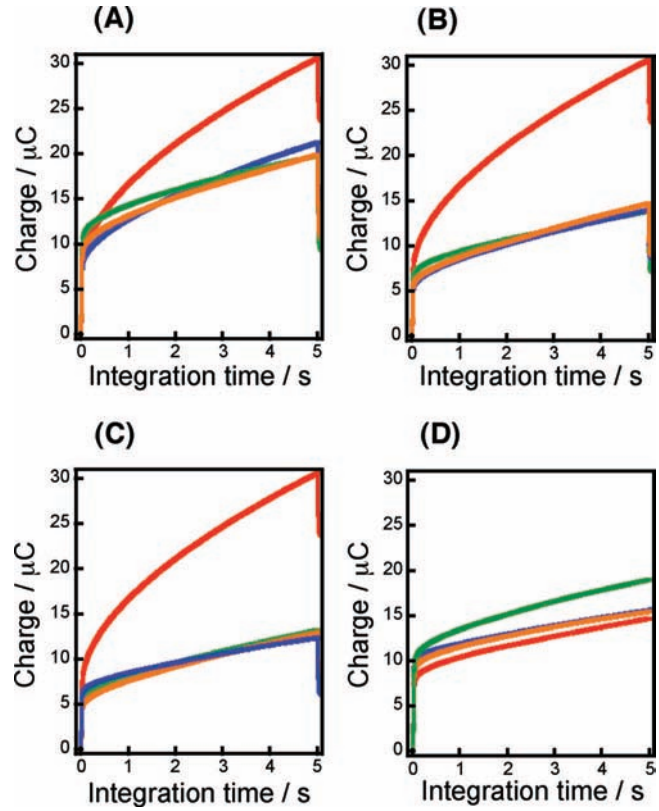

Figure 4. Charge responses for double-stranded anthraquinone-modified oligonucleoitde bound electrodes obtained from chronocoulometry. Panel A: red line, AQ-ODN Duplex 1, X = C; green line, AQ-ODN Duplex 1, X = T; blue line, AQ-ODN Duplex 1, X = A; orange line, AQ-ODN Duplex 1, X = G. Panel B: red line, AQ-ODN Duplex 2, X = A; green line, AQ-ODN Duplex 2, X = G; blue line, AQ-ODN Duplex 2, X = C; orange line, AQ-ODN Duplex 2, X = T. Panel C: red line, AQ-ODN Duplex 3, X = G; green line, AQ-ODN Duplex 3, X = C; blue line, AQ-ODN Duplex 3, X = T; orange line, AQ-ODN Duplex 3, X = A. Panel D: red line, AQ-ODN Duplex 4, X = C; green line, AQ-ODN Duplex 4, X = T; blue line, AQ-ODN Duplex 4, X = A; orange line, AQ-ODN Duplex 4, X = G. The measurements started at the initial potential of −100 mV vs Ag/AgCl. The applied potential was then changed to −600 mV vs Ag/AgCl and held at that potential for the defined time period.

duplexes (AQ-ODN Duplex 1 and AQ-ODN Duplex 4) are not dependent on the intervening DNA length between the redox center and the electrode, which is in agreement with the earlier study (*24, 25*).

DNA Mutation Detection by Chronocoulometry. The detection of a single-base mismatch was performed by chronocoulometry involving the measurements of charge as a function of time. The measurements started at the initial potential of −100 mV vs Ag/AgCl at which there is no electrolysis. The applied potential was then changed to −600 mV vs Ag/AgCl that leads to reduction of the pendant anthraquinone group and was held at that potential for the defined time period. The results are shown in Figure 4. In system I, regardless of the kinds and positions of the base mismatches, all the DNA duplexes containing a base mismatch in studies here gave reduced electrochemical responses when compared to the fully matched DNA. In particular, the mismatched DNAs including a G−A mismatch can be differentiated from fully matched DNA without using an electrochemical catalyst. As expected, in system II, the DNA with the same mismatch that is placed out of the site from the redox center did not show any significant differences in the electrochemical response from the fully matched DNA.

DNA Mutation Detection via Hybridization Assay. As outlined in Figure 5, the usefulness of single-stranded (ss) AQ-

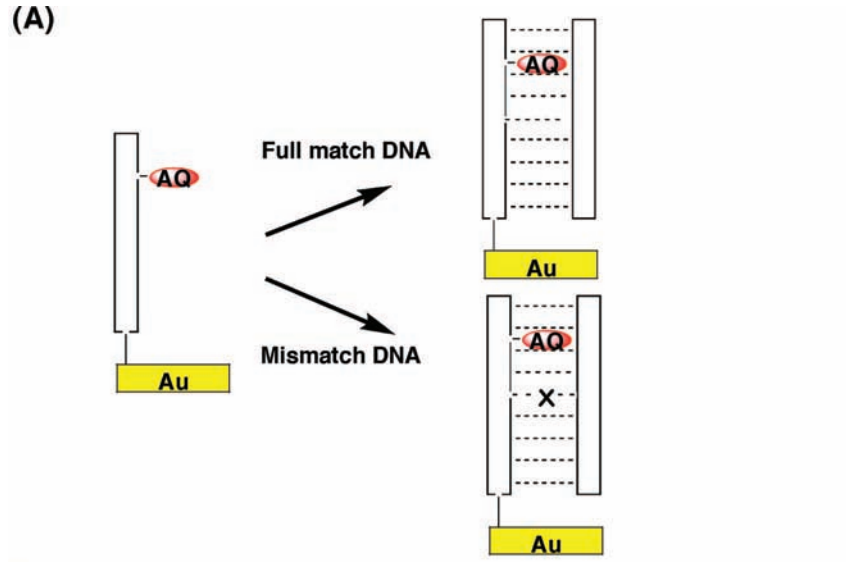

Figure 5. (A) Systematic representation of DNA mutation detection using anthraquinone-modified oligonucleotide bound electrodes via hybridization assay. (B) Sequences of anthraquinone-modified oligonucleotide probes and their target DNA used for an electrochemical detection of a single-base mismatch in DNA.

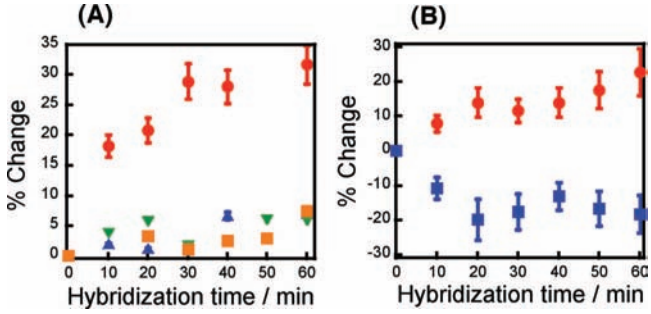

Figure 6. (A) % changes in charge responses of AQ-ODN Chip 1 when hybridized with DNA. Red line, target DNA 1, X = C; green line, target DNA 1, X = T; blue line, Target DNA 1, X = A; orange line, target DNA 1, X = G. (B) % changes in charge responses of AQ-ODN Chip 2 upon hybridization with DNA. Red line, target DNA 2, X = G; blue line, target DNA 2, X = A.

ODN (2 pmol/cm^2) immobilized on a gold electrode was tested in the electrochemical detection of a single-base mismatch through hybridization assay. The charge required for the reduction of the anthraquinone moiety of ss-AQ-ODN Chips (AQ-ODN Chip 1 and 2) was first recorded in the absence of target DNA using chronocoulometry (CC). Then, the chips were immersed in target-containing buffer (4 nM target DNA) at room temperature, and the CC measurements were carried out at an appropriate time interval to measure the changes in the integrated charge. The results are shown in Figure 6. It should be noted that the present assay for DNA mutation does not involve any washing steps. We confirmed by the ruthenium hexamine assay (*20*) that, after 1 h of the assay conditions, ca. 65% of ss-AQ-ODNs on the chip were hybridized with both fully matched and mismatch-containing DNAs. AQ-ODN Chip 1 showed the relatively large chronocoulometrical response after hybridization with fully matched DNA, while the hybrids with oligonucleotides containing a single-base mismatch did not show significant changes in the charge responses. We also investigated the performance of AQ-ODN Chip 2 that was designed for the detection of SNP associated with susceptibility to myocardial infarction (*4*). In this case, the mismatched DNA gave the reduced charge responses compared to ss-AQ-ODN Chip 2, which is clearly distinguishable from the fully matched target that yield larger charges than ss-AQ-ODN.

CONCLUSION

In summary, we have demonstrated that an anthraquinone-modified oligonucleotide is a useful probe to measure the charge transfer (CT) through a π-stack of DNA at the metal surface. The significant differences between mismatch-containing DNA and fully matched DNA were observed in electrochemical responses due to the reduced CT from a single-base mismatch. Owing to the simplicity of the analysis format and ease of making the redox-DNA bound chip, our method provides a promising way for sensitive detection of single-base mismatches in DNA.

ACKNOWLEDGMENT

This paper is dedicated to Prof. Dr. Isao Saito on the occasion of his 65th birthday. This research was supported by a Grant-in-Aid for Scientific Research from JSPS (K.Y.) and in part by SORST of JST. We would like to express sincere gratitude to Prof. Dr. Isao Saito for his encouragements.

Supporting Information Available: CV data for the electrodes bound to mismatch-containing DNA. This material is available free of charge via the Internet at http://pubs.acs.org.

LITERATURE CITED

(1) Wang, D. G., Fan, J-B, Siao, C-J, Berno, A., Young, P., Sapolsky, R., Ghandour, G., Perkins, N., Winchester, E., Spencer, J., Kruglyak, L., Stein, L., Hsie, L., Topaloglou, T., Hubbell, E., Robinson, E., Mittmann, M., Morris, M. S., Shen, N., Kilburn, D., Rioux, J., Nusbaum, C., Rozen, S., Hudson, T. J., Lipshutz, R., Chee, M., and Lander, E. S. (1998) Large-scale identification, mapping, and genotyping of single-nucleotide polymorphisms in the human genome. *Science 280*, 1077–1082.

(2) Gubbi, M. D., Viprakasit, V., Hughes, J. R., Fisher, C., Buckie, V., Ayyub, H., Gibbons, R. J., Vernimmen, D., Yoshinaga, Y., Jong, P. D., Cheng, J.-F., Rubin, E. M., Wood, W. G., Bowden, D., and Higgs, D. R. (2006) A regulatory SNP causes a human genetic disease by creating a new transcriptional promoter. *Science 312*, 1215–1217.

(3) Seki, S., Kawaguchi, Y., Chiba, K., Mikami, Y., Kizawa, H., Oya, T., Mio, F., Mori, M., Miyamoto, Y., Masuda, I., Tsunoda, T., Kamata, M., Kubo, T., Toyama, Y., Kimura, T., Nakamura, Y., and Ikegawa, S. (2005) A functional SNP in CILP, encoding cartilage intermediate layer protein, is associated with susceptibility to lumber disc disease. *Nat. Genet. 37*, 607–612.

(4) Ozaki, K., Ohnishi, Y., Iida, A., Sekine, A., Yamada, R., Tsunoda, T., Sato, H., Hori, M., Nakamura, Y., and Tanaka, T. (2002) Functional SNPs in the lymphotoxin-α gene that are associated with susceptibility to myocardial infarction. *Nat. Genet. 32*, 650–654.

(5) Wakai, J., Takagi, A., Nakayama, M., Miya, T., Miyahara, T., Iwanaga, T., Takenaka, S., Ikeda, Y., and Amano, A. (2004) A novel method of identifying genetic mutations using an electrochemical DNA array. *Nucleic Acids Res. 32*, e141.

(6) Yu, C. J., Wan, Y., Yowanto, H., Chunlin, J. L., Tao, C., James, M. D., Tan, C. L., Blackburn, C. F., and Meade, T. J. (2001) Electronic detection of single-base mismatches in DNA with ferrocene-modified probes. *J. Am. Chem. Soc. 123*, 11155–11161.

(7) Fan, C. H., Plaxco, K. W., and Heeger, A. (2003) Electrochemical interrogation of conformational changes as a reagentless method for the sequence-specific detection of DNA. *Proc. Natl. Acad. Sci. U.S.A. 100*, 9134–9137.

(8) Xiao, Y., Lubin, A. A., Baker, B. R., Plaxco, K. W., and Heeger, A. J. (2006) Single-step electronic detection of femtomolar DNA by target-induced strand displacement in an electrode-bound duplex. *Proc. Natl. Acad. Sci. U.S.A. 103*, 16677–16680.

(9) Kelly, S. O., Boon, E. M., Barton, J. K., Jackson, N. M., and Hill, M. G. (1999) Single-base mismatch detection based on charge transduction though DNA. *Nucleic Acids Res. 27*, 4830–4837.

(10) Boon, E. M., Ceres, D. M., Drummond, T. G., Hill, M. G., and Barton, J. K. (2000) Mutation detection by electrocatalysis at DNA-modified electrodes. *Nat. Biotechnol. 18*, 1096–1100.

(11) Wong, E. L. S., and Gooding, J. J. (2006) Charge transfer though DNA: a selective electrochemical DNA biosensor. *Anal. Chem. 78*, 2138–2144.

(12) Liu, T., and Barton, J. K. (2005) DNA electrochemistry though base pairs not the sugar-phosphate backbone. *J. Am. Chem. Soc. 127*, 10160–10161.

(13) Inoue, M., Ikeda, R., Takase, M., Tsuri, T., and Chiba, J. (2005) Single-nucleotide polymorphism detection with "wire-like" DNA probes that display quasi "on-off" digital action. *Proc. Natl. Acad. Sci. U.S.A. 102*, 11606–11610.

(14) Okamoto, A., Kamei, T., and Saito, I. (2006) DNA hole transport on an electrode: application to effective photoelectrochemical SNP typing. *J. Am. Chem. Soc. 128*, 658–662.

(15) Yamana, K., Nishijima, Y., Ikeda, T., Gokota, T., Ozaki, H., Nkano, H., Sangen, O., and Shimidzu, T. (1990) Synthesis and interactive properties of an oligonucleotide with anthraquinone at the sugar fragment. *Bioconjugate Chem. 1*, 319–324.

(16) Yamana, K., Mitsui, T., Yoshioka, J., Isuno, T., and Nakano, H. (1996) Incoporation of two anthraquinonylmethyl groups into the 2′-O-positions of oligonucleotides: Increased affinity and sequence specificity of anthraquinone-modified oligonucleotides in hybrid formation with DNA and RNA. *Bioconjugate Chem. 7*, 715–720.

(17) Deshmukh, H. M., Joglekar, S. P., and Broom, A. D. (1995) Self-complementary oligodeoxyribonucleotides containing 2′-O-(anthraquinone-2-methyl)adenosine. *Bioconjugate Chem. 6*, 578–586.

(18) Ly, D., Sanii, L., and Schuster, G. B. (1999) Mechanism of charge transport in DNA: Internally-linked anthraquinone conjugates support phonon-assisted polaron hopping. *J. Am. Chem. Soc. 121*, 9400–9410.

(19) Yamana, K., Kumamoto, S., Nakano, H., Matsuo, Y., and Sugie, Y. (2001) Cyclic voltammetric responses in hybrid formation of 2′-anthraquinone-modified oligonucleotide. *Chem. Lett.* 1132–1133.

(20) Yamana, K., Kumamoto, S., Hasegawa, T., Nakano, H., and Sugie, Y. (2002) Electrochemistry of 2′-anthraquinone-modified oligonucleotide immobilized on gold surface: Differential electron transfer efficiency between single and double helical forms. *Chem. Lett.* 506–507.

(21) Steel, A. B., Herne, T. M., and Tarlov, M. J. (1998) Electrochemical quantitation of DNA immobilized on gold. *Anal. Chem. 70*, 4670–4677.

(22) Sam, M., Boon, E. M., Barton, J. K., Hill, M. G., and Spain, E. M. (2001) Morphology of 15-mer duplexes tethered to Au(111) probed using scanning probe microscopy. *Langmuir 17*, 5727–5730.

(23) Tender, L., Carter, M. T., and Murray, R. W. (1994) Cyclic voltammetric analysis of ferrocene alkanethiol monolayer electrode kinetics based on Marcus theory. *Anal. Chem. 66*, 3173–3181.

(24) Drummond, T. G., Hill, M. G., and Barton, J. K. (2004) Electron transfer rates in DNA films as a function of tether length. *J. Am. Chem. Soc. 126*, 15010–15011.

(25) Nakamura, M., Ueda, M., Watanabe, S., Kumamoto, S., and Yamana, K. (2007) Synthesis of anthraquinone-capped DNA hairpins and electrochemical redox-responses from their self-assembled monolayers on gold electrode. *Teterahedron Lett. 48*, 6159–6162.

BC070097F

Design of a Tumor-Homing Cell-Penetrating Peptide

Helena Myrberg,*,† Lianglin Zhang,‡ Maarja Mäe,† and Ülo Langel†

Department of Neurochemistry, Stockholm University, Svante Arrhenius väg 21A, SE-106 91 Stockholm, Sweden, Burnham Institute for Medical Research, 10901 North Torrey Pines Road, La Jolla, California 92037, and NanoTUMOR Center, Moores Cancer Center, University of California San Diego. 3855 Health Sciences Drive, La Jolla, California 92093. Received April 3, 2007; Revised Manuscript Received October 9, 2007

Chemotherapy is often limited by toxicity to normal cells. Therefore, an ideal anticancer drug should discriminate between normal tissue and tumors. This would require a target receptor molecule mostly present in tumors. The cyclic peptide cCPGPEGAGC (PEGA) is a homing peptide that has previously been shown to accumulate in breast tumor tissue in mice. PEGA peptide does not cross the plasma membrane *per se*; however, when attached to the cell-penetrating peptide *p*VEC, the conjugate is taken up by different breast cancer cells *in vitro*. Additionally, the homing capacity of the PEGA-*p*VEC is conserved *in vivo*, where the conjugate mainly accumulates in blood vessels in breast tumor tissue and, consequently is taken up. Furthermore, we show that the efficacy of the anticancer drug, chlorambucil, is increased more than 4 times when the drug is conjugated to the PEGA-*p*VEC chimeric peptide. These data demonstrate that combining a homing sequence with a cell-penetrating sequence yields a peptide that combines the desirable properties of the parent peptides. Such peptides may be useful in diagnostics and delivery of therapeutic agents to an intracellular location in a specific tumor target tissue.

INTRODUCTION

Breast cancer is one of the major causes of death in developed countries, and there is a 1 in 7 risk of developing cancer during a woman's lifetime. Today, there are several choices available for treating breast cancer, including hormone therapy, aromatase inhibitors, and cytotoxins (for review, see ref (*1*)). Still, there is a need for improvement, i.e., to target the cytotoxic agents to the cancer cells in order to reduce side effects and toxicity in noncancer cells.

Blood vessels in normal individual tissues and different tumor tissues express different molecular markers (*2, 3*). In tumors, both blood and lymphatic vessels differ from their normal counterparts (*4*). Furthermore, lymphatic and blood vessels are distinguishable in different tumor types and various stages of tumor development (*5*). Numerous peptides that detect such differences have been isolated by combining *ex vivo* and *in vivo* screening of phage display libraries for tumor homing (*6–9*). One of these vascular homing peptides is a cyclic nonapeptide, cCPGPEGAGC, henceforth referred to as PEGA peptide, with a disulfide bridge between the two cysteines in the sequence (*8*). The PEGA peptide accumulates in breast vasculature as well as in premalignant breast tissue and primary breast tumors, and is thought to bind to the membrane-bound aminopeptidase P which is expressed at high levels in mouse breast tissue (*8, 10*).

Cell-penetrating peptides (CPPs)[1] are peptides which translocate the cell membrane and have the ability to transport different cargos such as oligonucleotides (*11*), plasmids (*12*), and proteins (*13*) across the cell membrane. CPPs can be divided into different classes depending on their origin (for review, see ref (*14*)); a common trait is that the CPPs are rich in basic amino acid residues. The translocation mechanism for CPPs is still not clear and might vary between the different classes of CPPs, as well as depending on cargo, and so forth; however, there is increasing evidence that endocytosis plays a significant role in the CPP uptake at least in cases where cargo molecules are attached (*15, 16*). A major drawback with most CPPs is that they are not cell-type specific.

The nitrogen mustard, chlorambucil (Cbl), is a well-known cytotoxic agent, which acts by alkylating and cross-linking the DNA, concomitantly inhibiting further cell proliferation. The effect is mediated through alkylation of guanine N7 in the major groove of DNA and subsequent interstrand cross-linking (*17, 18*). Moreover, this interstrand cross-link may induce apoptosis (*18, 19*). Cancer chemotherapy is often limited by toxicity to normal cells and tissues (for review, see ref (*20*)). Whether a drug such as chlorambucil can be administered at a dose that eliminates a tumor generally depends on the toxicity of the same dose to normal cells. An ideal anticancer drug is targeted toward cancer cells that are subsequently killed, but it has little or no effect on normal cells.

In the present study, we have designed and synthesized a breast tumor homing cell-penetrating peptide in order to provide a more effective and specific vector for anticancer drug delivery. We combined a tumor-specific vascular homing peptide cCPGPEGAGC (PEGA) sequence (*8*) with a well-studied CPP, *p*VEC (*21*), and demonstrated that the resultant PEGA-*p*VEC peptide colocalizes with the tumor vasculature marker and furthermore accumulates in tumor cells *in vivo*. We also showed *in vitro* that the efficacy of chlorambucil toward breast cancer cells is several fold higher when conjugated to PEGA-*p*VEC as compared to treatment with chlorambucil alone.

EXPERIMENTAL PROCEDURES

Peptide Synthesis. Peptides (Table 1) were synthesized on an Applied Biosystems model 433A by solid-phase method using a small-scale (0.1 mmol) *t*-Boc strategy on *p*-methylbenzhydrylamine resin (Neosystem) generating C-terminally ami-

* To whom correspondence should be addressed. Department of Neurochemistry, Stockholm University, Svante Arrhenius väg 21A, 106 91 Stockholm, Sweden. Tel (+46-8-164196), Fax (+46-8-161371), e-mail: helenam@neurochem.su.se.

† Stockholm University.

‡ Burnham Institute for Medical Research and Moores Cancer Center.

[1]Abbreviations: c, cyclic; CPP, cell-penetrating peptide; DAPI, 4′,6-diamidino-2-phenylindole; Cbl, chlorambucil; FBS, fetal bovine serum; Fluo, fluoresceinyl-; PBS, phosphate buffered saline; PEGA, cCPGPEGAGC; RT, room temperature.

10.1021/bc0701139 CCC: $40.75 © 2008 American Chemical Society
Published on Web 11/15/2007

Table 1. Sequences of the Studied Peptides

name	sequence
PEGA	cCPGPEGAGC-NH_2[a,b]
PEGA-*p*VEC	cCPGPEGAGC-LLIILRRRIRKQAHAHSK-NH_2[a,b,c]
*p*VEC	LLIILRRRIRKQAHAHSK-NH_2[b,c]
TP10	AGYLLGKINLKALAALAKKIL-NH_2

[a] PEGA, PEGA-*p*VEC are cyclic peptides, cyclized between the two cysteins. [b] For uptake studies, PEGA, PEGA-*p*VEC, and *p*VEC were fluoresceinyl-labeled at the N-terminus of the peptide. [c] For toxicity studies, PEGA-*p*VEC and *p*VEC were conjugated to chlorambucil at the N-terminus of the peptide.

dated peptides as reported previously (*22*). Stepwise coupling reactions were performed with *t*-Boc-protected amino acids (Neosystem), 1-hydroxybenzotriazole, *N,N′*-dicyclohexylcarbodiimide (4:4:4 equiv, 35 min, RT), followed by N-terminal deprotection of the *t*-Boc group with TFA/dichloromethane (1:1) (14 min, RT). For fluorophore labeling, the peptides were coupled N-terminally with 5(6)-carboxyfluorescein succinimidyl ester (Molecular Probes) (2 equiv) and diisopropylethylamine (2 equiv) in dimethyl sulfoxide/dimethylformamide (1:1) in the dark overnight. For chlorambucil coupling, chlorambucil (4 equiv) was coupled to the N-terminal amino group of the peptide with activation by 1-hydroxybenzotriazole and diisopropylethylamine (4:4 equiv, 30 min, RT) in dimethyl sulfoxide/dimethylformamide (1:1). After deprotection and cleavage of peptides, the disulfide bond formation between the two cysteines in the PEGA and PEGA-*p*VEC sequences was carried out by oxidation in excess of dimethyl sulfoxide overnight (*23*). Deprotection of the dinitrophenyl group was performed by treating the peptide (*p*VEC and PEGA-*p*VEC) with thiophenol:dimethylformamide (1:5) (1 h, RT), and the formyl group was removed by treating the peptide (TP10) with piperidin/dimethylformamide (1:5) (30 min, RT). Final cleavage of the peptides from the resin was performed in liquid hydrofluoric acid (1 h, 0 °C) in the presence of *p*-cresol and *p*-thiocresol. All peptides were purified by RP-HPLC (Discovery C-18 HPLC column, 25 cm, 21.2 mm, 5 μM) using a gradient of acetonitrile/water containing 0.1% TFA (50 min, 8 mL/min). The identity of the purified products was verified by matrix-assisted laser desorption–ionization time-of-flight mass spectrometer (Voyager-DE STR, Applied Biosystems). The mass spectra were acquired in positive ion reflector mode using α-cyano-4-hydroxycinnamic acid as a matrix (Sigma-Aldrich) (10 mg/ml, 7:3 acetonitrile/water, 0.1% TFA).

Cell Culture. The human breast cancer cell lines MDA-MB-231 and MCF-7 (ATCC) were cultured in RPMI-1640 supplemented with 10% fetal bovine serum (FBS), sodium pyruvate (1 mM), penicillin (100 U/mL), streptomycin (100 μg/mL), and 1% nonessential amino acids (further denoted as complete medium) (Invitrogen). The human breast cancer cell line MDA-MB-435 was maintained in DMEM supplemented with 10% fetal calf serum, penicillin (100 U/mL), and streptomycin (100 μg/mL). All cells were incubated at 37 °C in 5% CO_2.

Quantitative Cellular Uptake Studies. 150 000 cells/well were seeded two days before the experiment on a 12 well plate to get cells at 80% confluence. On the day of the experiment, the cells were washed with phosphate buffered saline (PBS) (1000 μL) and incubated with fluoresceinyl peptides (500 μL, 5 μM) in complete medium for 30 min at 37 °C. Cells were washed with PBS (2 × 1000 μL), whereafter trypsin (200 μL) was added and incubated for 5 min at 37 °C. PBS was added (1000 μL), and cells were transferred to Eppendorf tubes and centrifuged (10 min, 1000 *g*). Cells were lysed in sodium hydroxide solution (0.1 M, 300 μL) for 1 h and centrifuged (10 min, 10 000 *g*). The fluorescence (494/518 nm) was measured with SPECTRAmax GEMINI XS spectrofluorometric plate reader (Molecular Devices). The amount of internalized peptide was normalized against the amount of protein (Lowry, BioRad).

Microscopic Analysis of Cellular Peptide Uptake. MCF-7, MDA-MB-231, and MDA-MB-435 cells (20 000 cells/well) were seeded two days before the experiment on a Laboratory-Tek 8-well chamber slide (NUNC). The cells were washed with PBS (400 μL) and exposed to fluoresceinyl peptides (400 μL, 5 μM) in complete medium for 30 min at 37 °C. The cells were washed with PBS (3 × 400 μL) and visualized with an UltraView ERS Confocal Live Cell Imager microscope (Perkin-Elmer).

Toxicity Studies. Cell viability was measured using the Promega CellTiter-Glo assay according to the manufacturer's instructions. MCF-7 and MDA-MB-231 cells (20 000 cells/well) were seeded in a 48 well plate two days before the experiment. The cells were exposed to chlorambucil-conjugated peptide solution or free chlorambucil solution at different concentrations in complete media containing 1% FBS. After 3 h, complete media containing 10% FBS was added to achieve 5% FBS and then incubated for another 45 h at 37 °C. After reaching RT, CellTiter-Glo Reagent was added, the plate was incubated for 10 min at RT, and then the luminescence was measured. In the CellTiter-Glo assay, luciferin and luciferase are used to measure ATP content in the cells after incubation with peptides in different concentrations for 48 h. The ATP content is proportional to the amount of viable, metabolically active cells.

***In Vivo* Tumor Homing Analysis of Chimeric Peptides.** To produce tumors, nude BALB/c mice were orthotopically injected with 1 × 10^6 MDA-MB-435 tumor cells into the mammary fat pad. The tumor-bearing mice were used for homing analysis of peptides when the tumor diameter reached about 10 mm. Tissue distribution of fluoresceinyl-labeled peptides was studied by intravenously injecting the peptides (100 μM in 200 μL PBS) into tumor-bearing mice. The injected peptides were allowed to circulate 2 h, and the mice were perfused with 4% paraformaldehyde through the left ventricle of the heart. Tumors and various control tissues were dissected and frozen in OCT embedding medium (Tissue-Tek, Elkhart, IN). Frozen sections were prepared for immunohistological analysis and were observed under a Radiance MP confocal microscope to determine the internalization of peptides into cells *in vivo*. The immunohistochemical staining of tumor blood vessels was performed as previously described (*5, 9*). Briefly, frozen tissue sections were air-dried, fixed with cold acetone for 1 min, and washed with PBS three times. The slides were incubated with blocking buffers (PBS with 5% normal goat serum and 1% BSA) for 30 min at RT and then incubated with rat antimouse MECA-32 antibody (BD PharMingen) (1:50) overnight at 4 °C. After washing, the corresponding secondary antibody AlexaFluor-594 goat antirat or rabbit IgG (1:1000; Molecular Probes) was added and incubated for 1 h at RT. The slides were washed three times with PBS and mounted in Vectashield mounting medium with 4′,6-diamidino-2-phenylindole (DAPI; Vector Laboratories).

RESULTS

Selection of CPP. We tested the toxicity of two well-known CPPs, *p*VEC (*21*) and TP10 (*24*), in MCF-7 cells using a luciferase-based assay (Figure 1). TP10 shows considerable toxicity already at a concentration of 10 μM resulting in 48% of viable cells. *p*VEC exhibited toxicity first at 50 μM, where the amount of viable cells was reduced to 60%. Since *p*VEC was less toxic among the two studied CPPs, it was selected for coupling to a homing peptide sequence.

Cellular Uptake of Homing CPP *in Vitro*. The uptake of fluoresceinyl-labeled PEGA, PEGA-*p*VEC, and *p*VEC was studied by fluorescence microscopy in MDA-MB-231, MCF-7, and MDA-MB-435 cells. As expected, fluoresceinyl-*p*VEC was internalized into the tested cells. The homing peptide,

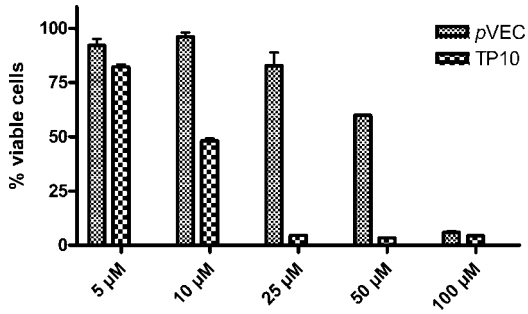

Figure 1. Effects of CPPs *p*VEC and TP10 on MCF-7 cell viability. The cells were exposed to different concentrations of peptides in media for 48 h followed by measurement of the amount of ATP (i.e., viable cells). Cells in untreated cultures were set to 100% viable. Mean ± SEM is presented.

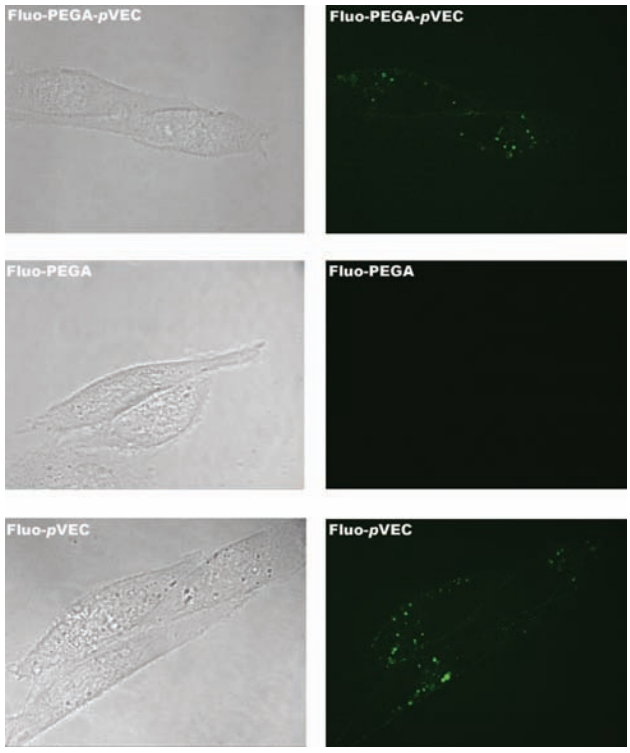

Figure 2. Detection of fluoresceinyl peptides in MDA-MB-231 cells by confocal laser scanning microscopy. Cells were incubated with 5 μM fluoresceinyl peptide, as indicated in the figure, for 30 min followed by imaging in bright field (left column) and corresponding image in fluorescence mode (green; right column).

fluoresceinyl-PEGA, alone did not enter the cells, while the conjugate, fluoresceinyl-PEGA-*p*VEC, was internalized in MDA-MB-231 (Figure 2), MCF-7, and MDA-MB-435 cells (data not shown).

Cellular uptake of the peptides was quantified by the detection of the intracellular amount of fluoresceinyl-labeled PEGA, PEGA-*p*VEC, and *p*VEC in MCF-7 and MDA-MB-231 cells. The results are presented in Figure 3 where the amount of the internalized peptide is normalized against the amount of total cellular protein in the culture well. The pattern of uptake was similar in both MDA-MB-231 cells and MCF-7 cells but slightly higher in MDA-MB-231 cells. As shown in Figure 3 for MDA-MB-231 cells, we confirmed that the homing peptide fluoresceinyl-PEGA alone did not display cell-penetrating properties; its uptake was 1 pmol/mg protein, whereas when conjugated to *p*VEC, the uptake increased to 630 pmol/mg protein. Fluoresceinyl-*p*VEC showed the highest uptake at 2400 pmol/mg protein.

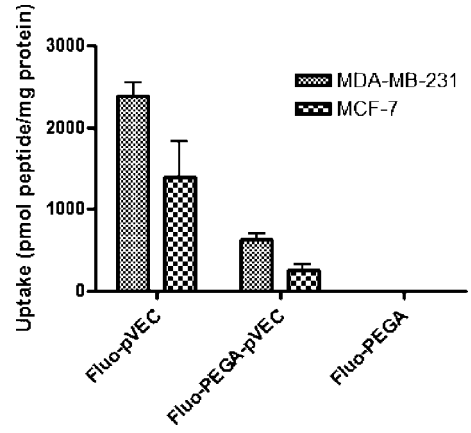

Figure 3. Uptake of fluoresceinyl peptides into MDA-MB-231 and MCF-7 cells. Cells were exposed to 5 μM fluoresceinyl peptide solution for 30 min, followed by removal of extracellular peptide by washing and trypsination of the cells. The cells were lysed in 0.1 M sodium hydroxide, and fluorescence at 494/518 nm was measured. The amount of internalized peptide was calculated on the basis of linear relation between fluorescence and concentration and normalized to the amount of protein. Mean ± SEM is presented.

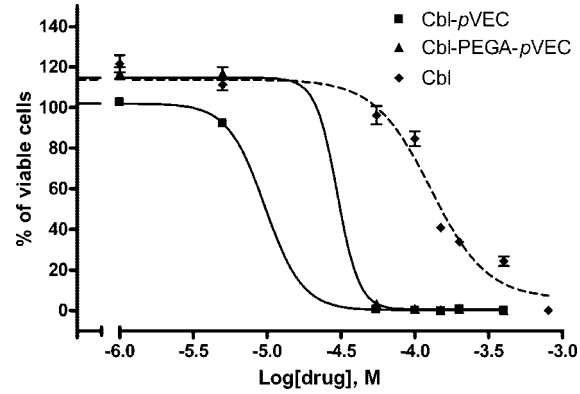

Figure 4. Cytotoxicity of chlorambucil (Cbl), Cbl-*p*VEC, and Cbl-PEGA-*p*VEC to MCF-7 cells. Cells were exposed to different concentrations of the chlorambucil-conjugated peptide solution or free chlorambucil in media for 48 h. Cells in untreated cultures were set to 100% viable. The results are presented as mean ± SEM. Data are analyzed using nonlinear regressions, *GraphPad Prism* software.

***In Vitro* Drug Activity.** In order to evaluate whether the activity of chlorambucil is improved when conjugated to PEGA-*p*VEC, we exposed chlorambucil or chlorambucil-conjugated peptides at different concentrations to MCF-7 and MDA-MB-231 breast cancer cells for 48 h. After incubation, the ATP content was measured. The IC_{50} was similar in both MCF-7 (Figure 4) and MDA-MB-231 cells (data not shown). The calculated IC_{50} for chlorambucil alone in MCF-7 cells was 128 μM, while the IC_{50} for chlorambucil conjugated to *p*VEC was 9.6 μM. When chlorambucil was conjugated to the PEGA-*p*VEC, the IC_{50} value was 30 μM. The toxicity appears to be due to the chlorambucil moiety of the conjugate, since *p*VEC alone displayed little toxicity at concentrations below 50 μM (Figure 1).

Homing Specificity of PEGA-pVEC Peptide *in Vivo*. To evaluate the homing specificity of the PEGA-*p*VEC, MDA-MB-435 tumor-bearing mice were intravenously injected with 100 μM of fluoresceinyl-PEGA-*p*VEC chimeric peptide or fluoresceinyl-PEGA or fluoresceinyl-*p*VEC as controls in 200 μL PBS. Each of the peptides was detected in tumor tissue (Figure 5), where they partially colocalized with a blood vessel specific marker MECA-32 that stained with anti-MECA-32 antibody; the colocalization was particularly prominent with fluoresceinyl-

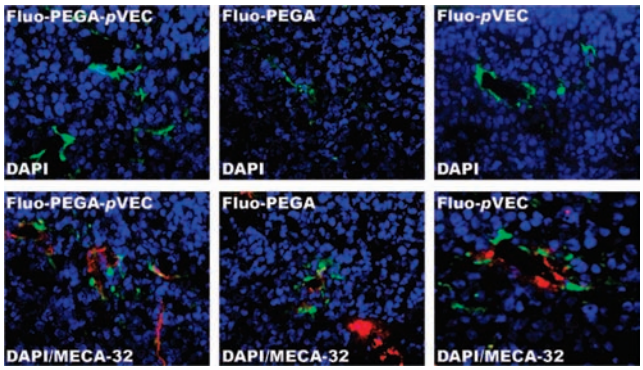

Figure 5. Localization of fluoresceinyl peptides in MDA-MB-435 tumors. The mice were injected i.v. with fluoresceinyl peptides as indicated in the figure, and tissue sections were examined for fluorescence. Fluoresceinyl peptides (green) and blood vessels stained with anti-MECA-32 antibody (red; bottom row) in tumor tissue. Anti-MECA-32 antibody is specific for vascular endothelial cells. Nuclei were detected by DAPI staining (blue).

PEGA-*p*VEC (Figure 5). At some parts, fluoresceinyl-PEGA-*p*VEC and fluoresceinyl-*p*VEC appeared to be in nuclei in the tumor cells. Apparently, the amount of fluoresceinyl-PEGA-*p*VEC in nontumor tissues was much lower than that of fluoresceinyl-*p*VEC (Figure 6). These data show that the peptide chimera combines the main desirable properties of the component peptides, specific homing to tumors and internalization into target cells.

DISCUSSION

In this report, we show, for the first time, that by combining homing and cell-penetrating peptide sequences a new effective tumor-specific peptide with the capability to translocate cargo inside target cells is obtained. Moreover, this new peptide shows considerable improvement in anticancer drug cytotoxicity.

Here, we used a cyclic homing peptide cCPGPEGAGC (PEGA) that has been previously isolated by *in vivo* phage display library screening (*8*). The PEGA peptide is not cell-penetrating *per se*; however, by conjugation it to the well-studied CPP, *p*VEC (*21*), both the cell-penetrating property of *p*VEC and the homing property of PEGA are achieved in a chimeric peptide. The quantitative and qualitative *in vitro* uptake studies in MCF-7, MDA-MB-231, and MDA-MB-435 cells (data not shown) confirmed that PEGA-*p*VEC is a CPP. There are studies of homing peptides with cell-penetrating abilities (*7, 9, 25*), but they are not extensively characterized so far.

There are different classes of CPPs depending on their origin (for review, see ref (*14*)); common for all classes is that CPPs are rich in basic amino acids. The PEGA peptide withholds no basic amino acids but a negatively charged glutamic acid, and as expected, the PEGA peptide has no CPP properties (Figures 2 and 3). However, when conjugated to the well-characterized CPP, *p*VEC, the lack of basic amino acids in the PEGA sequence is compensated with the basic residues in *p*VEC. The reduced uptake of the PEGA-*p*VEC peptide compared to *p*VEC might be a result of the reduced net positive charge of the PEGA-*p*VEC peptide in relation to *p*VEC. These results are in accordance to a CPP prediction method outlined by Hällbrink et al. (*26*) suggesting differential cell-penetrating properties of these two peptides.

The PEGA-peptide has previously been shown to accumulate in breast vasculature as well as in premalignant breast tissue and to primary breast tumors *in vivo* (*8*). We confirmed with our study that the fluoresceinyl-PEGA-*p*VEC translocates breast cancer cells and also human aortic endothelial cells *in vitro* (unpublished data).

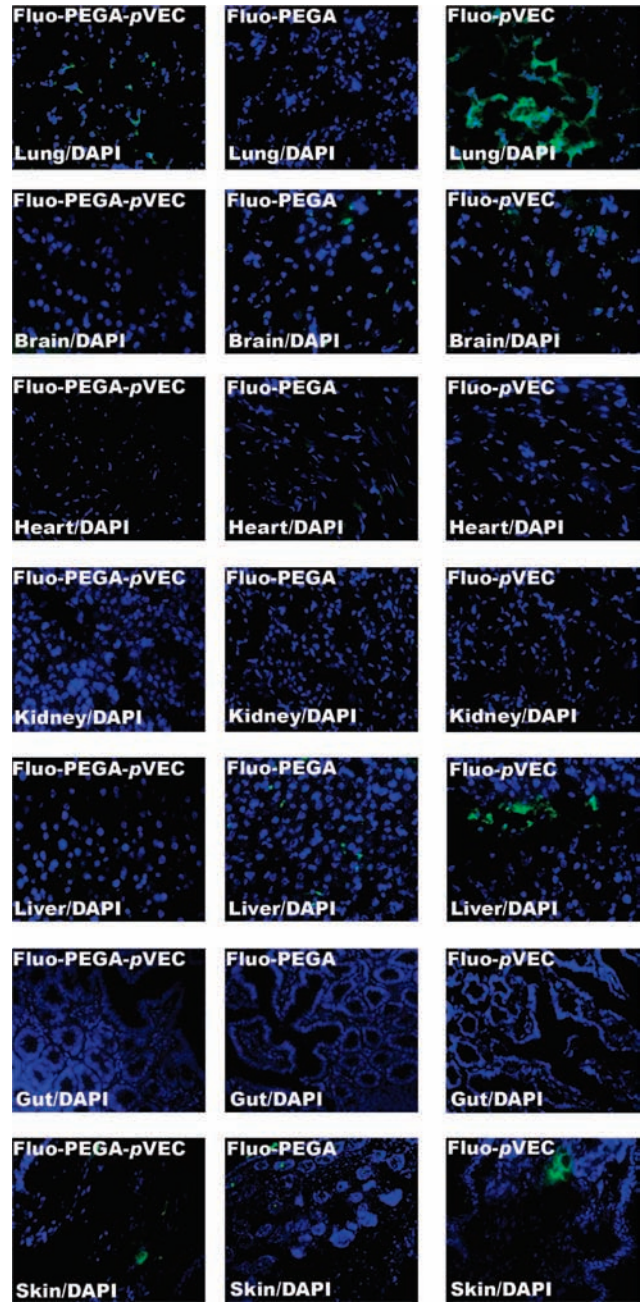

Figure 6. Distribution of fluoresceinyl peptides (green) in nontumor tissues of mice bearing MDA-MB-435 tumors. The mice were injected i.v. with fluoresceinyl-PEGA-*p*VEC (left column), fluoresceinyl-PEGA (middle column), and fluoresceinyl-*p*VEC (right column).The tissue sections, as indicated in the figure, were examined for fluorescence. Nuclei were detected by DAPI staining (blue).

The major obstacle in cancer treatment is the lack of specificity of therapeutic agents to cancer cells. It has been shown that drug therapy can be improved if the drug is targeted to tumor cells (*27, 28*). *In vivo* accumulation of fluoresceinyl-labeled PEGA-*p*VEC into the MDA-MB-435 tumor vasculature as well as tumor cells and not into control tissues suggested that our chimeric peptide could also be used for this purpose. In order to test this idea, we conjugated the DNA alkylating anticancer drug chlorambucil (*17, 18*) to PEGA-*p*VEC and studied the cytotoxicity of the conjugate in breast cancer cells. The efficacy of cytotoxicity measured as IC_{50} value of chlorambucil is lowered by more than 4-fold when the drug is conjugated to PEGA-*p*VEC (Figure 4). Chlorambucil is believed to be taken up by passive diffusion (*29*); however, that mechanism is less

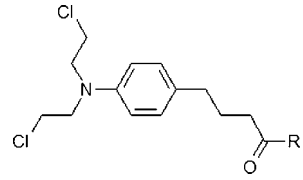

Figure 7. Chlorambucil coupled to the N-terminus of the *p*VEC and PEGA-*p*VEC (R), via an amide bond.

efficient as compared to conjugation to a CPP. *p*VEC contributes to transport of chlorambucil over the cell membrane, enhancing the efficiency of the drug. Chlorambucil is conjugated to the N-terminus of the peptides via an amide bond (Figure 7) leaving the alkylating moiety of chlorambucil available for the reaction to be able to exert its effect.

The uptake mechanism of CPPs is not yet clear and might vary among different CPPs; endocytosis seems to be one route for cellular import of CPPs (for review, see ref (*30*)). The uptake mechanism for PEGA-*p*VEC will be a subject for further studies. Preliminary experiments show that the fluoresceinyl-PEGA-*p*VEC is not colocalized with lysosomal marker (LysoTracker Red DND-99, Molecular Probes) (data not shown). In the *in vivo* studies, the fluoresceinyl peptides are injected intravenously in the mice; already after 2 h, it is possible to detect the accumulation of the peptides in the tumor cells (Figure 5). The colocalization of fluoresceinyl-PEGA-*p*VEC with the blood vessel marker, MECA-32, and the translocation of the fluoresceinyl-PEGA-*p*VEC in the breast cancer cells in the tumor, indicates that chlorambucil-PEGA-*p*VEC could be used for *in vivo* targeting of breast cancer cells as well as tumor microvascular endothelial cells.

Another possible approach for fluoresceinyl-labeled PEGA-*p*VEC is to use the peptide for imaging of tumors. This application could be useful in detection of tumors in early as well as progressed stages and for studying the response to therapy, i.e., imaging of tumor growth. Imaging of tumors and cancer cells has successfully been carried out by other homing peptides, i.e., fluoresceinyl-labeled Lyp-1 peptide *in vivo* in mice (*31*).

In summary, we have characterized a breast tumor-homing peptide, PEGA-*p*VEC, which translocates the cell membrane *in vitro* and homes to breast tumor tissue *in vivo*. We have also shown that by conjugating chlorambucil to PEGA-*p*VEC the efficacy of chlorambucil to tumor cells was increased more than 4-fold *in vitro*.

ACKNOWLEDGMENT

This work was funded by European Community (QLK3-CT-2002-01989), Swedish Research Council (VR-NT and VR-Med), CBR at Stockholm University, Cepep III, and supported by Cancer Center Support Grant CA 30199 from the U.S. National Cancer Institute to Burnham Institute for Medical Research and fellowship DAMD17-02-0309 from the Department of Defense (L. Zhang). We thank Professor Erkki Ruoslahti for fruitful discussions and help with the manuscript.

LITERATURE CITED

(1) Marsh, S., and McLeod, H. L. (2007) Pharmacogenetics and oncology treatment for breast cancer. *Exp. Opin. Pharmacother. 8*, 119–127.

(2) Ruoslahti, E. (2002) Drug targeting to specific vascular sites. *Drug Discovery Today 7*, 1138–1143.

(3) Ruoslahti, E. (2002) Specialization of tumour vasculature. *Nat. Rev. Cancer. 2*, 83–90.

(4) Ruoslahti, E. (2004) Vascular zip codes in angiogenesis and metastasis. *Biochem. Soc. Trans. 32*, 397–402.

(5) Zhang, L., Giraudo, E., Hoffman, J. A., Hanahan, D., and Ruoslahti, E. (2006) Lymphatic zip codes in premalignant lesions and tumors. *Cancer Res. 66*, 5696–5706.

(6) Arap, W., Pasqualini, R., and Ruoslahti, E. (1998) Cancer treatment by targeted drug delivery to tumor vasculature in a mouse model. *Science 279*, 377–380.

(7) Hoffman, J. A., Giraudo, E., Singh, M., Zhang, L., Inoue, M., Porkka, K., Hanahan, D., and Ruoslahti, E. (2003) Progressive vascular changes in a transgenic mouse model of squamous cell carcinoma. *Cancer Cell 4*, 383–391.

(8) Essler, M., and Ruoslahti, E. (2002) Molecular specialization of breast vasculature: a breast-homing phage-displayed peptide binds to aminopeptidase P in breast vasculature. *Proc. Natl. Acad. Sci. U.S.A. 99*, 2252–7.

(9) Laakkonen, P., Porkka, K., Hoffman, J. A., and Ruoslahti, E. (2002) A tumor-homing peptide with a targeting specificity related to lymphatic vessels. *Nat. Med. 8*, 751–755.

(10) Lasch, J., Moschner, S., Sann, H., Zellmer, S., and Koelsch, R. (1998) Aminopeptidase P--a cell-surface antigen of endothelial and lymphoid cells: catalytic and immuno-histotopical evidences. *Biol. Chem. 379*, 705–709.

(11) Gait, M. J. (2003) Peptide-mediated cellular delivery of antisense oligonucleotides and their analogues. *Cell. Mol. Life. Sci. 60*, 844–853.

(12) Rittner, K., Benavente, A., Bompard-Sorlet, A., Heitz, F., Divita, G., Brasseur, R., and Jacobs, E. (2002) New basic membrane-destabilizing peptides for plasmid-based gene delivery in vitro and in vivo. *Mol. Ther. 5*, 104–114.

(13) Wadia, J. S., Stan, R. V., and Dowdy, S. F. (2004) Transducible TAT-HA fusogenic peptide enhances escape of TAT-fusion proteins after lipid raft macropinocytosis. *Nat. Med. 10*, 310–315.

(14) Järver, P., and Langel, , Ü. (2006) Cell-penetrating peptides--a brief introduction. *Biochim. Biophys. Acta 1758*, 260–263.

(15) Richard, J. P., Melikov, K., Vivés, E., Ramos, C., Verbeure, B., Gait, M. J., Chernomordik, L. V., and Lebleu, B. (2003) Cell-penetrating peptides. A reevaluation of the mechanism of cellular uptake. *J. Biol. Chem. 278*, 585–590.

(16) Thorén, P. E., Persson, D., Isakson, P., Goksor, M., Önfelt, A., and Norden, B. (2003) Uptake of analogs of penetratin, Tat(48–60) and oligoarginine in live cells. *Biochem. Biophys. Res. Commun. 307*, 100–107.

(17) Faguet, G. B. (1994) Chronic lymphocytic leukemia: an updated review. *J. Clin. Oncol. 12*, 1974–1990.

(18) Mattes, W. B., Hartley, J. A., and Kohn, K. W. (1986) DNA sequence selectivity of guanine-N7 alkylation by nitrogen mustards. *Nucleic Acids Res. 14*, 2971–2987.

(19) Whiteside, G., Ferguson, L. R., Denny, W. A., and Weir, I. E. (2003) Mode of cell death induced in Chinese hamster cells by sequence-selective DNA minor groove binding nitrogen mustards: comparison with untargeted mustards and with Hoechst 33342. *Oncol. Res. 13*, 491–502.

(20) Szakacs, G., Paterson, J. K., Ludwig, J. A., Booth-Genthe, C., and Gottesman, M. M. (2006) Targeting multidrug resistance in cancer. *Nat. Rev. Drug Discovery 5*, 219–234.

(21) Elmquist, A., Lindgren, M., Bartfai, T., and Langel, , Ü. (2001) VE-cadherin-derived cell-penetrating peptide, pVEC, with carrier functions. *Exp. Cell. Res. 269*, 237–244.

(22) Langel, , Ü., Land, T., and Bartfai, T. (1992) Design of chimeric peptide ligands to galanin receptors and substance P receptors. *Int. J. Pept. Protein Res. 39*, 516–522.

(23) Tam, J. P., Wu, C., Liu, W., and Zhang, J. (1991) Disulfide bond formation in peptides by dimethyl sulfoxide. Scope and applications. *J. Am. Chem. Soc. 113*, 6657–6662.

(24) Soomets, U., Lindgren, M., Gallet, X., Hällbrink, M., Elmquist, A., Balaspiri, L., Zorko, M., Pooga, M., Brasseur, R., and Langel, , Ü. (2000) Deletion analogues of transportan. *Biochim. Biophys. Acta 1467*, 165–176.

(25) Porkka, K., Laakkonen, P., Hoffman, J. A., Bernasconi, M., and Ruoslahti, E. (2002) A fragment of the HMGN2 protein homes to the nuclei of tumor cells and tumor endothelial cells in vivo. *Proc. Natl. Acad. Sci. U.S.A. 99*, 7444–9.

(26) Hällbrink, M., Kilk, K., Elmquist, A., Lundberg, P., Lindgren, M., Jiang, Y., Pooga, M., Soomets, U., and Langel, , Ü. (2005) Prediction of cell-penetrating peptides. *Int. J. Peptide Res. Ther. 11*, 249–259.

(27) Ellerby, H. M., Arap, W., Ellerby, L. M., Kain, R., Andrusiak, R., Rio, G. D., Krajewski, S., Lombardo, C. R., Rao, R., Ruoslahti, E., Bredesen, D. E., and Pasqualini, R. (1999) Anti-cancer activity of targeted pro-apoptotic peptides. *Nat. Med. 5*, 1032–1038.

(28) Chen, Y., Xu, X., Hong, S., Chen, J., Liu, N., Underhill, C. B., Creswell, K., and Zhang, L. (2001) RGD-Tachyplesin inhibits tumor growth. *Cancer Res. 61*, 2434–2438.

(29) Eisenhut, M., Hull, W. E., Mohammed, A., Mier, W., Lay, D., Just, W., Gorgas, K., Lehmann, W. D., and Haberkorn, U. (2000) Radioiodinated N-(2-diethylaminoethyl)benzamide derivatives with high melanoma uptake: structure-affinity relationships, metabolic fate, and intracellular localization. *J. Med. Chem. 43*, 3913–22.

(30) Fotin-Mleczek, M., Fischer, R., and Brock, R. (2005) Endocytosis and cationic cell-penetrating peptides-a merger of concepts and methods. *Curr. Pharm. Des. 11*, 3613–3628.

(31) Laakkonen, P., Akerman, M. E., Biliran, H., Yang, M., Ferrer, F., Karpanen, T., Hoffman, R. M., and Ruoslahti, E. (2004) Antitumor activity of a homing peptide that targets tumor lymphatics and tumor cells. *Proc. Natl. Acad. Sci. U.S.A. 101*, 9381–9386.

BC0701139

Peptide-Functionalized Poly(ethylene glycol) Star Polymers: DNA Delivery Vehicles with Multivalent Molecular Architecture

Katye M. Fichter,[†] Le Zhang,[‡] Kristi L. Kiick,*[,‡] and Theresa M. Reineke*[,†]

Department of Chemistry, University of Cincinnati, Cincinnati, Ohio 45221-0172, and Department of Materials Science and Engineering, University of Delaware, and Delaware Biotechnology Institute, Newark, Delaware 19716-3106. Received April 4, 2007; Revised Manuscript Received July 3, 2007

Exploring the development of nonviral nucleic acid delivery vectors with progressive, specific, and novel designs in molecular architecture is a fundamental way to investigate how aspects of chemical and physical structure impact the transfection process. In this study, macromolecules comprised of a four-arm star poly(ethylene glycol) and termini modified with one of five different heparin binding peptides have been investigated for their ability to bind, compact, and deliver DNA to mammalian cells *in vitro*. These new delivery vectors combine a PEG-derived stabilizing moiety with peptides that exhibit unique cell-surface binding ability in a molecular architecture that permits multivalent presentation of the cationic peptides. Five peptide sequences of varying heparin binding affinity were studied; each was found to sufficiently bind heparin for biological application. Additionally, the macromolecules were able to bind and compact DNA into particles of proper size for endocytosis. In biological studies, the PEG-star peptides displayed a range of toxicity and transfection efficiency dependent on the peptide identity. The vectors equipped with peptides of highest heparin binding affinity were found to bind DNA tightly, increase levels of cellular internalization, and display the most promising transfection qualities. Our results suggest heparin binding peptides with specific sequences hold more potential than nonspecific cationic polymers to optimize transfection efficiency while maintaining cell viability. Furthermore, the built-in multivalency of these macromolecules may allow simultaneous binding of both DNA at the core of the polyplex and heparan sulfate on the surface of the cell. This scheme may facilitate a bridging transport mechanism, tethering DNA to the surface of the cell and subsequently ushering therapeutic nucleic acids into the cell. This multivalent star shape is therefore a promising architectural feature that may be exploited in the design of future polycationic gene delivery vectors.

INTRODUCTION

The delivery of nucleic acids by nonviral vectors is an intense area of research due to the promise of synthetic materials to be tailored for specific drug targets (*1, 2*). It has been found that even moderate chemical modifications of the vector architecture may significantly affect the ability of the molecule to transfect cells efficiently (*3–8*). Under many conditions of polycation—DNA complex (polyplex) formation, the surface charge on positively charged polyplexes is neutralized, which allows polyplex—polyplex aggregation to occur, and even in the absence of complete charge neutralization, cationic polyplexes can bind and flocculate with oppositely charged serum proteins. By preventing this aggregation, polyplexes can remain in circulation for extended time periods, avoid clearance by macrophages, and maintain a small, uniform size for vascular penetration and cellular endocytosis under *in vivo* conditions (*9–12*). The addition of poly(ethylene glycol) chains to polycationic vectors has previously been shown to favorably stabilize polycation/DNA complexes, known as polyplexes, against flocculation in conditions containing salt and serum, which has improved their potential for *in vivo* gene delivery (*13*).

Nitrogen-dense polycations such as Poly(ethyleneimine) (PEI) have been shown to have high transfection efficiency; however, the cytotoxicity of this and many similar vectors are high in many cell lines (*14*). To retain high transfection efficiency and minimize toxicity, modified polycationic systems have been created. For instance, the modification of PEI with PEG has been developed either as a copolymer or with a grafted architecture (*15–17*). In addition, PEGylated poly(L-lysine) vectors have recently been shown to have very low cytotoxicity as well as notable stability *in vivo*, although increasing the transfection efficiency of these vectors is still a current research goal (*18–20*). To understand the architectural impact of these vectors, a wide variety of novel methods for the incorporation of hydrophilic moieties are being examined. For example, supramolecular vectors utilizing a PEG moiety grafted onto preformed DNA/polycationic vectors (*21*) or even rotaxane-type vectors utilizing cyclodextrin molecules threaded around hydrophilic polymers (*22–24*) have been developed. Additionally, low molecular weight branched PEI conjugated onto the end of star-shaped PEG molecules has been found to have promising transfection potential (*25*). In our work reported here, we have incorporated cationic peptide chains derived from the binding portion of heparin binding proteins (HBPs) onto the termini of star-shaped PEG macromolecules to create multivalent DNA vectors that can both efficiently complex DNA and target heparan sulfate-containing endocytic receptors.

There have been numerous reports implicating the role of proteoglycans in the uptake of polyplexes into cells (*26, 27*). We hypothesize that polyplexes containing heparin binding peptides may increase cell-surface adhesion and subsequent uptake, more so than classical nonspecific polycationic vectors. This may occur through specific interaction with ubiquitous heparan sulfate moieties on cell surfaces, which are similar to heparin in structure. Specific HBP−proteoglycan binding may enhance cellular uptake via sequence-specific association. This could eliminate the need to design highly charge-dense vectors

* E-mail addresses: Theresa.Reineke@uc.edu (T.M.R.); kiick@udel.edu (K.L.K.).
[†] University of Cincinnati.
[‡] University of Delaware.

10.1021/bc0701141 CCC: $40.75 © 2008 American Chemical Society
Published on Web 10/04/2007

Table 1. Peptides Incorporated into the PEG-Star Peptide Vectors

peptide	sequence	source
$PF4_{ZIP}$	CGGRMKQLEDKVKKLLKKNYHLENEVARLKKLVG	platelet factor 4 (*39, 40*)
RRP	CGGRRRRRRRGG	arginine-rich peptide (*31*)
HIP	CRPKAKAKAKAKDQTK	heparin-interacting protein (*35, 36, 38*)
sHIP	CKAAKRPKAAKDKQTK	scrambled HIP sequence
ATIII	CK(βA)FAKLAARLYRKA	antithrombin III (*35, 37*)

that nonspecifically bind heparan sulfate (*5, 28*), and negatively impact cell viability (*14*). Such approaches employing PEG-HBPs for complexation of nucleic acids therefore offer unique opportunities for controlling and improving DNA delivery.

The specificity and affinity of protein interactions with heparin are governed by the specific placement of cationic amino acid residues relative to the sulfation pattern of heparin. This pattern may provide a strategy for manipulating heparin binding affinity and DNA delivery. Literature. reports suggest that heparin-interacting protein (HIP) and antithrombin III (ATIII) bind to similar pentasaccharide sequences found in heparin (*29*). Four tetrasaccharides are thought to be required for efficient heparin binding of human platelet factor 4 (PF4) (*30*), thus providing higher affinity binding for PF4 over that of HIP and ATIII. Furthermore, peptides that contain multiple arginine residues have been suggested to have high heparin binding affinity, since similar structures are found in heparin binding proteins (*31, 32*).

The reported PEG-star peptide bioconjugates have been previously exploited to assemble noncovalently cross-linked hydrogels (*33–37*) via the interactions of the heparin binding termini (peptide mimics of the heparin binding domains of ATIII (*38*), HIP (*39*), PF4 *30, 40*)) with PEG-star molecules modified with heparin. The mechanical and biological properties of such hydrogels can be engineered on the basis of the heparin−BP interactions and applied in the controlled delivery of proteins *35, 40*). Electrostatic interactions are a key component in HBP−heparin associations (*41*); therefore, it is likely that these PEG star HBP conjugates will also be capable of mediating the binding, condensation, and delivery of other polyanions such as DNA. Furthermore, the multivalent nature of these molecular stars may permit the simultaneous interaction of the bioconjugate with both DNA at the core of the polyplex and glycosaminoglycan at the cell surface through the interaction of both DNA-bound peptide arms and unbound arms on the surface of the nanoparticle. This simultaneous interaction may tether the DNA complexes to the cell surface, which may subsequently act to usher nucleic acid–based therapeutics into cells.

To this end, we have measured the heparin binding affinities and kinetics for the HBPs, examined their complexation with DNA, and correlated this information with the transfection efficiencies of the resulting polyplexes. Polyplexes formed with two of the structures described here, PEG-star $PF4_{ZIP}$ and PEG-star RRP, inhibit serum-mediated aggregation and exhibit promising transfection in the presence of serum. In addition, physical characterization of polyplexes created with these novel vectors as well *in vitro* biological activity profiles are presented. Figure 1and Table 1 show details of the PEG-star peptide structure, the proposed transfection scheme, and the amino acid sequences used to create these unique bioconjugates.

EXPERIMENTAL PROCEDURES

I. Materials. For the synthesis of the PEG-HBPs, low molecular weight heparin sodium salt (LMWH) from porcine intestinal mucosa (average molecular weight 3000 g/mol) was obtained from Sigma (St. Louis, MO), and heparin from porcine intestinal mucosa (average molecular weight 6000 g/mol) was purchased from Celsus Laboratory., Inc. (Cincinnati, OH). Hydroxy-terminated four-arm PEG (M_n = 10 300; M_w = 11 300 g/mol; M_w/M_n = 1.1) and thiol-terminated, four-arm PEGs (M_n = 10 000; M_w = 10 800 g/mol; M_w/M_n = 1.1) were purchased from Polymer Source (Dorval, Quebec, Canada). Deionized water (18 MΩ) was applied in all the experiments (Barnstead NANOpure Diamond Ultrapure water Systems, Barnstead Inc., Dubuque, IA). Amino acids, rink amide MBHA (4-methylbenzhydrylamine) resin, and HBTU were purchased from Novabiochem Corp. (San Diego, CA). DMF and acetonitrile (HPLC grade) were obtained from Fisher Scientific (Fairlawn, NJ). General chemicals were all purchased from Sigma-Aldrich unless otherwise specified. Triethylamine (TEA) was distilled from CaH_2. All other reagents were used as received.

Branched polyethylenimine (PEI), a positive control used in some experiments, was obtained from Aldrich. For the execution of biological studies, pCMVβ plasmid DNA and gWiz-Luc were acquired from PlasmidFactory (Bielefeld, Germany) and Aldevron (Fargo, ND), respectively. Nuclease-free water, Opti-MEM, and DMEM (supplemented with 10% fetal bovine serum (FBS), 100 units/mL penicillin, 100 μg/mL streptomycin, 0.25 μg/mL amphortericin), and PBS were all purchased from Invitrogen (Carlsbad, CA). For the luciferase assay, cell culture lysis buffer and the luciferase substrate assay reagent were purchased from Promega (Madison, WI). For the viability assay, a Bio-RAD DC protein assay kit was purchased from Bio-Rad (Hercules, CA), and bovine albumin (98%) was purchased from Sigma (St. Louis, MO).

II. Synthesis and Characterization of the PEG-HBPs. The synthesis of the PEG-star HBP conjugates was conducted via addition reactions between vinyl sulfone-terminated four-arm star-PEG and cysteine-terminated HBPs. The synthetic protocols for preparing the peptides and bioconjugates for the PEG-ATIII, PEG-HIP, and PEG-$PF4_{ZIP}$ have been described previously (*35, 36, 40*).

Synthesis of RRP and sHIP. The RRP peptide RRRRRRRGGG and the sHIP peptide CKAAKRPKAAKDKQTK were prepared on Rink Amide MBHA resin via solid-phase peptide synthesis with Fmoc protection using a PTI PS3 peptide synthesizer (Protein Technologies, Inc., AZ). A preparative-scale Delta 600 HPLC (Waters) equipped with a Waters Symmetry 300 C18 column (5 μm particle size, 19 × 150 mm) was applied for the crude RRP peptide purification. Solvent A (water/0.1% TFA) and solvent B (acetonitrile/0.1% TFA) were employed as HPLC solvents in programmed gradients. Peptides isolated as single fractions via HPLC were characterized via ESI mass spectrometry. The mass of the purified RRP was confirmed via ESI mass spectrometry, m/z = 641.9[$(M^+2H)^{2+}$, calcd 642.2] and m/z = 428.0[$(M^+3H)^{3+}$, calcd 428.5]. The mass of the purified sHIP was similarly confirmed, m/z = 886.2[$(M^+2H)^{2+}$, calcd 887.5], m/z = 591.3[$(M^+3H)^{3+}$, calcd 591.7], and m/z = 443.8[$(M^+4H)^{3+}$, calcd 444.0] (see Supporting Information). These peptides were used in heparin affinity measurements and circular dichroic spectroscopy, while peptides with an N-terminal cysteine were used in the synthesis of the PEG conjugates. Because of the virtually identical synthesis and purification, it is assumed that this slight modification in sequence does not significantly alter the peptide for our purposes.

Synthesis of PEG-RRP and PEG-sHIP Conjugates. The synthesis of PEG-RRP and PEG-sHIP conjugates was accomplished using a similar method applied previously for the synthesis of other PEG-HBP conjugates (*36*). Characterization

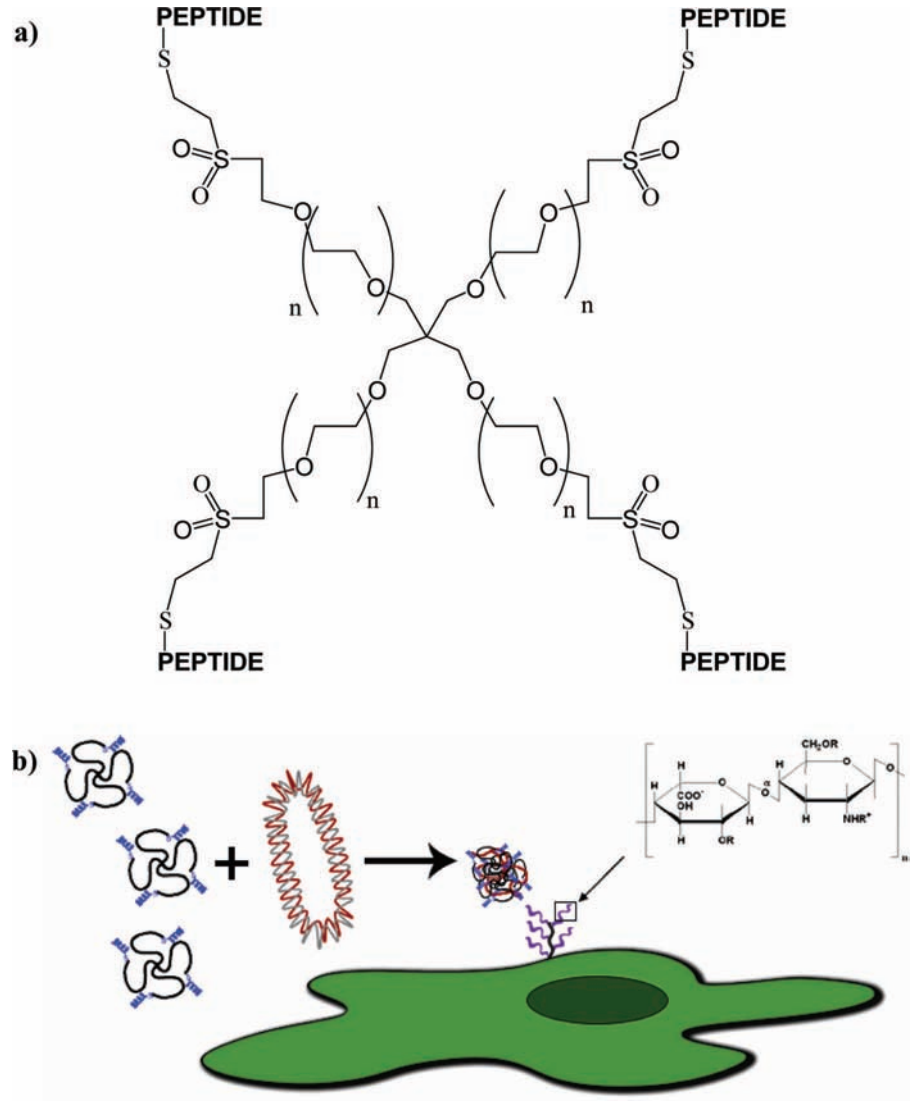

Figure 1. (a) Chemical structure of PEG-star peptides depicting their molecular architecture. "PEPTIDE"refers to one of 5 different peptides listed in Table 1. $n = 60$. (b) Proposed scheme for the transfection of mammalian cells with pDNA using PEG-star HBP vectors. The star polymers are multivalent and peptides functionalized on the termini of the PEG-star should be competent to bind both DNA in the core of the polyplex and heparan sulfate on the surface of cells simultaneously.

data for these macromolecules via size exclusion chromatography and NMR are given in the Supporting Information.

III. Heparin Affinity Measurements. *Affinity Liquid Chromatography.* The heparin affinities of the HBPs and PEG-HBPs were first determined via heparin-sepharose affinity liquid chromatography on an ÄKTA Explorer FPLC equipped with a HiTrap Heparin HP column (5 mL, ~10 mg heparin/mL gel, Amersham Biosciences Corp, Piscataway, NJ), using previously described procedures in which peptides bound to a heparin-modified affinity column are eluted with buffer of varying concentrations of sodium chloride (*35*).

Surface Plasmon Resonance (SPR). SPR characterization of the binding of HBPs to LMWH was performed on a Biacore 3000 instrument (Biacore Inc., Piscataway, NJ), employing a high-capacity LMWH surface created on a commercially available streptavidin-coated SA chip via treatment with biotinylated LMWH, as previously described (*35*). Equilibrium dissociation constants (K_D) were calculated from experimentally determined association and dissociation rate constants, via standard fitting protocols previously described (*35*) and described in the Supporting Information.

IV. DNA Binding Assay. To determine whether these materials bind and complex pDNA, a series of gel shift assays were performed with polyplexes formulated at a range of charge ratios. This charge ratio represents the number of positive charges on the peptide side chain to the number of phosphate groups along the DNA backbone. A more thorough treatment of this calculation for the PEG-star peptides can be found in the Supporting Information.

Polyplexes were formed by adding a solution of the PEG-HBP (150 μL) dissolved in nuclease-free water to an equal volume of solution of plasmid DNA (15 μg) at various charge ratios. After a 30 min incubation period, 1 μL of running buffer (Blue Juice, Invitrogen, Carlsbad, CA) was added to each sample. Ten microliters of each polyplex sample was then loaded into the wells of a 0.6% agarose gel prepared in TAE buffer containing 0.06 μg/mL ethidium bromide. The samples were subsequently electrophoresed in an electric field of 60 V.

V. Circular Dichroic Spectroscopy (CD). Circular dichroic spectroscopy was used to characterize the structures of select peptides while bound to pDNA. Characterization was conducted on $PF4_{ZIP}$ and HIP peptides in solution with pDNA (rather than on PEG-HBPs) in order to preserve the optical clarity of the solutions for CD measurements. CD spectra were acquired at 25 °C on a Jasco J-810 spectropolarimeter (Jasco Inc., Easton, MD) equipped with a Jasco PTC-424S temperature controller.

Polyplexes consisting of heparin binding peptides and pDNA were formulated at a charge ratio of 5, and the final DNA concentration of the polyplex formulation was chosen to be 1 μg/100 μL in PBS to match that used in DNA transfection experiments. To form the polyplexes, either $PF4_{ZIP}$ or HIP was added to the pDNA solution to reach a final peptide concentration of 15.2 μM or 21.6 μM, respectively. Polyplexes at a charge ratio of 1 were formed at the same concentration (21.6 μM) of HIP, but with 1 μg/20 μL pDNA.

Samples were equilibrated at 25 °C for 30 min prior to data collection. The equilibration of the samples was indicated by the absence of further changes in the CD signal at longer equilibration times. All CD spectra were taken in a 1 mm path length quartz cuvette, at wavelengths from 200 to 250 nm. Data points were recorded at every nanometer with a 4.0 s response time. (Refer to Supporting Information for spectra.)

VI. Polyplex Size and Zeta Potential Measurements. In order to characterize polyplex stability, the size and zeta potential of polyplexes formulated by complexing pDNA with the PEG-HBPs were measured via dynamic light scattering using a Zetasizer Nano ZS[Malvern Instruments (Malvern, UK) equipped with a 633 nm laser]. Ultrapure water, Opti-MEM, and DMEM were filtered with a 0.2 μm filter before any polyplexes were formed to remove particulates and dust from the initial solutions. The solutions were not filtered after polyplex formation. Polyplexes were formed in a similar manner as described above for the gel shift assays, except 3 μg pDNA was used and the polyplexes were created at a charge ratio of 5. Measurements were performed at 25 °C. After initial incubation for 1 h, the polyplex solutions were diluted to 900 μL with Millipore water, Opti-MEM (serum-free media), or DMEM containing 10% fetal bovine serum. Solutions were then immediately transferred to a cuvette and measured. Polyplex size measurements were taken consecutively at 0, 20, 40, 60, and 120 min. Zeta potential measurements were taken consecutively at 0 and 20 min.

VII. Cell Viability and Transfection Efficiency. BHK-21 cells were cultured under the conditions recommended by the ATCC. Twenty-four hours before transfection, cells were seeded in 24 well plates at 50000 cells per well and incubated in supplemented DMEM at 37 °C and 5% CO_2. Immediately before transfection, the polyplexes were created with pDNA (gWiz-Luc) as described above for the previous experiments (gel-shift and particle size assays). For the delivery experiments, the polyplexes were created at a range of charge ratios as well as a charge ratio of 0, which represents the delivery of naked pDNA. One hour after polyplex formation, 600 μL of Opti-MEM or DMEM was added to each polyplex solution. Prior to the transfections, the media in each well was aspirated off, the cells were washed with PBS, and 300 μL of the polyplex solution was added. This volume was used to normalize the delivery of DNA to each well to 1 μg. Controls of both untransfected cells and cells transfected with pDNA only were also performed. Transfections at all charge ratios and the controls were performed in triplicate. Four hours after transfection, 800 μL of DMEM supplemented with 10% FBS was added to each well. Twenty-four hours after transfection, the media was removed from each well, and 1000 μL of fresh DMEM was added. Forty-eight hours after transfection, the media was removed from each well, the cells were washed with PBS, and 100 μL of lysis buffer was added to each well. The cell lysates were then assayed for luciferase expression using the protocol provided by Promega and protein content using the protocol provided with the Bio-Rad DC protein assay kit. The results of the protein assay were analyzed using a standard curve of bovine serum albumin and normalized against the untransfected control to obtain the fraction of cell survival.

VIII. Cellular Internalization. BHK-21 cells were cultured under conditions recommended by the ATCC. Twenty-four hours before transfection, cells were seeded in 6 well plates at 250 000 cells/well and incubated in DMEM supplemented with 10% FBS at 37 °C and 5% CO_2. Formulation of polyplexes proceeded in the manner described above except 250 μL of each PEG-Star HBP was added to 5 μg Cy5-labeled DNA (250 μL total DNA solution volume) to formulate polyplexes at an N/P ratio of 5. After incubation for 1 h, 1 mL of Opti-MEM was added to each polyplex solution. The cells were washed with PBS and each well was transfected with a corresponding polyplex solution in Opti-MEM and subsequently incubated for 4 h. Afterward, the transfection media was aspirated and each well was washed twice, with 2 mL and then 1 mL PBS, to remove bound polyplexes from the cell surface. The cells were subsequently incubated for two more hours in DMEM with 10% FBS to allow further trafficking of DNA. After this final incubation period, the media was removed and cells were again washed with 1 mL PBS and subsequently trypsinized at 37 °C for 10–15 min. Next, 1 mL DMEM was added to each well and the cells were transferred to Falcon tubes and spun at 1000 rpm for 10 min. The supernatant was then removed, 1 mL PBS was used to wash the pellet, and the cells were spun again in the same conditions. Again, the supernatant was removed and the pellet was resuspended in PBS supplemented with 2% FBS. The cell suspensions were analyzed with a FACS Calibur flow cytometer, using appropriate forward and side scatter gates, and the Cy5 fluorescence intensity of 50 000 cells in each sample was measured. A control of untransfected cells was used to create a gate less than 1% of cells exhibiting Cy5 fluorescence. This gate was used for subsequent samples transfected with the PEG-HBPs to determine the percent of cells transfected.

RESULTS AND DISCUSSION

I. PEG-HBP Synthesis and Characterization. Polysaccharides, such as heparan sulfate, are widely distributed on a broad range of cell types. Many cell-surface receptors involve the binding of an external molecule to heparan sulfate to initiate internalization via receptor-mediated endocytosis. By improving the polyplex-cell surface interaction involving these anionic polysaccharides, the cellular internalization, and thus transfection efficiency, may also be improved. For example, adeno and adeno-associated viral vectors with heparan sulfate and heparin binding domains have been previously constructed as gene delivery vectors (*42*, *43*), to enhance cellular internalization via heparan-sulfate-associated receptors. Additionally, adenoviral vectors with modified fiber coat proteins containing cationic poly(lysine) have been shown to increase the transduction of macrophages, as well as endothelial, smooth muscle, glioblastoma, and T cells (*44*). However, to the best of our knowledge, polymeric DNA delivery agents comprising heparin binding domains attached to star-shaped PEG molecules have not yet been applied for pDNA delivery and may offer advantages in both reduced aggregation and improved transfection efficiency.

In this study, we chose to examine the PEG-HBP macromolecules for their ability to complex pDNA and deliver it into a mammalian cell line. As displayed in Figure 1, five different heparin binding peptides (HIP, sHIP, ATIII, $PF4_{ZIP}$, and RRP) were selected for attachment to the PEG-star macromolecules. All five peptides are positively charged at physiological pH and should therefore be capable of electrostatically complexing DNA. The peptide sequences were each selected for their high affinity for heparin. The HIP and ATIII peptides are derived from the heparin binding domains of heparin-interacting protein and antithrombin III, respectively (*38, 39*). The peptide denoted sHIP represents a motif generated by scrambling the HIP sequence, which was synthesized to confirm the role of sequence

Table 2. Heparin Binding Affinity Data (at 25 °C) for Heparin Binding Peptides Determined via Affinity Chromatography and SPR at pH = 7.4

HBP	salt required for elution from heparin column (mM)	k_a ($M^{-1}s^{-1}$)	k_d (s^{-1})	K_D (M)	PEG-HBP	salt required for elution from heparin column (mM)
$PF4_{ZIP}$[a]	882 ± 3	$2.24 \pm 0.05 \times 10^5$	$2.56 \pm 0.10 \times 10^{-3}$	$1.14 \pm 0.03 \times 10^{-8}$	PEG-$PF4_{ZIP}$	798 ± 13
RRP	1160 ± 10	$2.64 \pm 0.08 \times 10^5$	$1.18 \pm 0.12 \times 10^{-3}$	$4.47 \pm 0.34 \times 10^{-9}$	PEG-RRP	1271 ± 1
HIP[b]	695 ± 14	$1.10 \pm 0.08 \times 10^3$	$4.64 \pm 0.02 \times 10^{-3}$	$4.21 \pm 0.3 \times 10^{-6}$	PEG-HIP	628 ± 7
sHIP	929 ± 4	$9.29 \pm 0.17 \times 10^4$	$5.62 \pm 0.13 \times 10^{-3}$	$6.05 \pm 0.03 \times 10^{-8}$	PEG-sHIP	763 ± 4
ATIII[b]	594 ± 2	$1.56 \pm 0.06 \times 10^2$	$2.00 \pm 0.3 \times 10^{-3}$	$1.28 \pm 0.13 \times 10^{-5}$	PEG-ATIII	558 ± 1

[a] SPR data for $PF4_{ZIP}$ peptide previously reported (*37*). [b] SPR data for HIP and ATIII peptides previously reported (*35*).

specificity in heparin binding (*45*) and to test the hypothesis that heparin binding alone, outside of changes in peptide composition and charge density, plays a role in controlling DNA delivery. The $PF4_{ZIP}$ sequence is a dimeric coiled-coil, heparin binding peptide modeled after the heparin binding domain of human platelet factor 4 (*40*). The RRP sequence (Table 1) was chosen on the basis of the fact that arginine is a commonly identified residue in randomly synthesized 7-mer peptides that have been shown to efficiently bind to and immobilize heparin (*31, 32*). Additionally, polyarginine peptides have been shown to have promising transfection properties (*46*). The glycine residues were included in the RRP sequence to provide flexible linkers between the short oligo-arginine sequence and the PEG backbone.

The previously unreported PEG-RRP and PEG-sHIP conjugates have been successfully synthesized via Michael addition reactions between vinyl sulfone-terminated four-arm PEG (*47*) and cysteine-terminated HBPs, using a similar method applied previously for the synthesis of other PEG-HBP conjugates (*36*). Functionalization of the PEG-star termini with the HBPs has yielded values of 77% (*35*), 63% (*36*), and 59% (*37*) for the PEG-HBP modified with the heparin binding proteins HIP, ATIII, and $PF4_{ZIP}$, respectively. Similarly, in these investigations, the compositions of the PEG-RRP and the PEG-sHIP were determined from their ^1H NMR spectrum (see Supporting Information). Functionalization of the PEG-RRP was found to be 119%. This may result from association of the RRP peptides during synthesis and purification. Significant aggregation is not suggested to occur between the PEG-RRP conjugates, as solutions of the PEG-RRP remain clear and nonviscous. Functionalization of the PEG-sHIP was found to be 100%. It has been previously demonstrated that the PEG-HBPs readily associate with multivalent heparin moieties to form noncovalently associated hydrogels (*35–37*). Therefore, although the precise number of termini modified with RRP cannot be determined, we anticipated that a sufficient number of PEG termini were modified with the RRP to support network, and therefore polyplex, formation (functionalization ≥2). The functionalization values of 77% (PEG-HIP), 100% (PEG-sHIP), 63% (PEG-ATIII), 59% (PEG-$PF4_{ZIP}$), and 119% (PEG-RRP) were used in all charge ratio calculations for PEG-HBP/pDNA polyplexes.

II. Heparin Binding Affinity of HBPs. Previous reports have demonstrated that targeting ligands, such as monoclonal antibodies, peptides, and sugars, can be conjugated to DNA carriers to promote receptor-mediated endocytosis (*48, 49*). Additionally, a limited number of reports suggest that modification of viral vectors via the use of heparin and heparan-binding peptides enhance binding with heparan sulfate-associated endocytic receptors on a broad range of cell types, thus increasing internalization (*42, 43*). Heparin-sepharose affinity chromatography and surface plasmon resonance (SPR) experiments were therefore performed to compare the heparin binding affinity of different HBPs to confirm the potential difference in cellular uptake between PEG-HBP/pDNA complexes. Results of these experiments are summarized in Table 2. For heparin affinity chromatography experiments, the concentration of NaCl required for HBP elution from a heparin-sepharose column is used as an indication of the affinity of the peptide for heparin. Elution from the heparin-sepharose column required a salt concentration of 1160 ± 10 mM for RRP and 929 ± 4 mM for sHIP (Table 2). Comparison of these values to those obtained with the previously synthesized peptides (HIP: 695 ± 14 mM, ATIII: 594 ± 2 mM, $PF4_{ZIP}$: 882 ± 3 mM) indicates that RRP has the highest heparin binding affinity. The enhanced heparin binding of the nonspecific RRP sequence is likely due to the high cationic charge density of this peptide and suggests the potential for the PEG-RRP to elicit the highest cellular uptake of the PEG-HBPs.

The sHIP peptide, which is composed of a scrambled HIP sequence, was actually found to have higher binding affinity for heparin than the natural HIP sequence. Although this result was not anticipated, the sHIP sequence serves as an excellent comparison for assessing the role of heparin binding affinity in DNA transfection efficiency because it removes the complications of differences in composition and charge density. In order to support this initial finding, further SPR binding experiments were conducted.

The interaction of the five HBPs with a low molecular weight heparin-modified SA chip surface was investigated and results are reported in Table 2. No mass transport limitations, linked reactions, or nonspecific binding of HBP to SA chips were observed in any of the SPR measurements, as assessed via manufacturer-recommended standard control experiments (see Supporting Information). Analysis of the association and dissociation regions of the binding curves provided relative association and dissociation rates for comparison to previous studies conducted on the same chip surface (*35, 37*). The measured association of the RRP with LMWH proceeds with a rate constant of $2.64 \pm 0.08 \times 10^5$ M^{-1} s^{-1} based on the analysis of the association regions of the binding curves, while the dissociation proceeds with a rate constant of $1.18 \pm 0.12 \times 10^{-3}$ s^{-1}, yielding a K_D of $4.47 \pm 0.34 \times 10^{-9}$ M. Similar calculations resulted in a K_D value of $6.05 \pm 0.03 \times 10^{-8}$ M for the sHIP peptide (Table 2). Comparison of these results to our previous studies indicates that faster association kinetics for RRP, sHIP, and $PF4_{ZIP}$, relative to those reported for the ATIII and HIP (*35*), are the primary cause of the lower calculated K_D values, and the trend of the dissociation constants is consistent with the chromatography results. Furthermore, relative to the reported value for HIP, the K_D value of the sHIP peptide is lower and agrees with our chromatography results. This confirms the higher heparin affinity of the sHIP sequence versus the natural HIP sequence. Overall, the more rapid association rate, coupled with the similar dissociation rate of RRP, sHIP, and $PF4_{ZIP}$ versus the other HBPs, suggest the strong binding of anionic heparin by these peptides, which suggests their strong interaction with cell surfaces.

Heparin affinity of the PEG-HBP conjugates was also investigated using column chromatography. As shown in Table 2, the trend in heparin binding affinity of the PEG conjugates correlate well with the free peptides, with PEG-RRP, $PF4_{ZIP}$,

Table 3. Heparin Binding Affinity Data (at 25 °C) for $PF4_{ZIP}$ (peptide) at Various pH Values, as Determined via SPR

pH	k_a (M^{-1} s^{-1})	k_d (s^{-1})	K_D (M)
6	$1.11 \pm 0.03 \times 10^4$	$7.05 \pm 0.03 \times 10^{-4}$	$6.35 \pm 0.20 \times 10^{-8}$
7.4	$2.24 \pm 0.05 \times 10^5$	$2.56 \pm 0.10 \times 10^{-3}$	$1.14 \pm 0.03 \times 10^{-8}$
8	$1.97 \pm 0.08 \times 10^4$	$8.70 \pm 0.49 \times 10^{-3}$	$4.42 \pm 0.63 \times 10^{-7}$

Table 4. Heparin Binding Affinity Data (at 25 °C) for RRP (peptide) at Different pH Values, as Determined via SPR

pH	k_a (M^{-1} s^{-1})	k_d (s^{-1})	K_D (M)
6	$1.35 \pm 0.13 \times 10^4$	$1.00 \pm 0.01 \times 10^{-3}$	$7.41 \pm 0.82 \times 10^{-8}$
7.4	$2.64 \pm 0.08 \times 10^5$	$1.18 \pm 0.12 \times 10^{-3}$	$4.47 \pm 0.34 \times 10^{-9}$
8	$9.94 \pm 0.26 \times 10^3$	$5.33 \pm 0.15 \times 10^{-3}$	$5.36 \pm 0.01 \times 10^{-7}$

Table 5. Heparin Binding Affinity Data (at 25 °C) for sHIP (peptide) at Various pH Values, as Determined via SPR

pH	k_a (M^{-1} s^{-1})	k_d (s^{-1})	K_D (M)
6	$2.73 \pm 0.08 \times 10^4$	$1.36 \pm 0.01 \times 10^{-2}$	$4.98 \pm 0.12 \times 10^{-7}$
7.4	$9.29 \pm 0.17 \times 10^4$	$5.62 \pm 0.13 \times 10^{-3}$	$6.05 \pm 0.03 \times 10^{-8}$
8	$2.26 \pm 0.22 \times 10^4$	$1.82 \pm 0.04 \times 10^{-2}$	$8.05 \pm 0.86 \times 10^{-7}$

and sHIP displaying highest binding affinity. In general, the PEG-HBP conjugates required slightly lower salt concentration for elution from the heparin-modified column. This seemed surprising, since multivalent presentation of binding epitopes often results in binding enhancements due to statistical and multivalent effects. However, the PEG-HBP conjugates are of low molecular weight and low valency (3–4 peptides per conjugate), and such polymers often do not show significant multivalent enhancement (*50*). In any case, the focus of these studies was to determine the heparin binding affinity of the PEG-HBPs for correlation to DNA delivery efficiency, and our results demonstrate that the heparin binding affinities of the HBPs have similar trends regardless of their conjugation to PEG.

As a control, we performed chromatography experiments on PEI, which is a commonly used transfection reagent. It was found that PEI eluted at 1980 ± 0.002 mM NaCl, which indicates that this incredibly charge-dense polycation binds heparin with very high affinity. However, the PEI−heparin binding mechanism likely involves a great deal of cooperativity, which may cause the dissociation of pDNA at the cell surface and decreased cellular uptake. We propose that the multivalent cationic nature of the PEG-HBPs holds the most promise for simultaneous binding of DNA and cell-surface heparan via electrostatic interactions.

Cellular uptake and release of PEG-HBP/pDNA complexes via endocytosis may be directly affected by the progressive acidification from the physiological pH (7.4) of the extracellular medium to pH 6.5–6.0 in endosomes (*51*). The heparin binding kinetics between low molecular weight heparin and the peptides of highest heparin affinity (RRP, sHIP, and $PF4_{ZIP}$) were monitored via SPR at pH values between 6 and 8, to determine potential changes in binding kinetics that might alter the process of cellular uptake or release of pDNA from the PEG-HBP/pDNA complex. An increase in the K_D value signifies a decrease in the affinity of the peptide for heparin. As shown in Tables 3, 4, and 5, K_D values for PEG-RRP, sHIP, and $PF4_{ZIP}$ generally increase slightly as the pH is lowered below 7.4, which suggests that the PEG-HBP/pDNA bound to the cell-surface heparan sulfates will likely remain associated with these proteoglycans during internalization, but may begin to dissociate from heparan sulfate as the polyplex/heparan sulfate complexes begin to traffic through the progressively acidifying vesicles of the endocytic pathway. Such dissociation of the vectors from internalized heparan sulfate in the endosomes may enhance the intracellular motility of the complexes out of these vesicles.

III. DNA Binding. For use as potential nucleic acid delivery vectors, the conjugates must be able to package DNA into small particles capable of being endocytosed. The PEG-HBP/pDNA complexes are described by their charge ratio, which is a ratio that indicates the number of positively charged residues in the peptide sequence to the number of anionic phosphate residues in the DNA backbone. The amount of material needed to completely complex the DNA is established by this assay, with results shown in Figure 2. The lane in which pDNA no longer migrates through the gel is regarded as the charge ratio at which the PEG-HBPs completely complex pDNA (see Figure 2a, lanes 2–50). This assay indicates that the PEG-HBPs are able to complex pDNA at a charge ratio of 2 or lower. Similar values have been reported for PEGylated poly(L-lysine) vectors which have previously shown promising transfection characteristics (*19, 20, 52*).

At higher charge ratios, the bands produced by polyplexes created with PEG-RRP and PEG-ATIII appeared to fade and disappear (*i.e.*, Figure 2b,e, lanes 5–50), which may indicate that these star polymers were able to bind pDNA sufficiently tightly to exclude the intercalating agent ethidium bromide used to visualize the bands. Moreover, the ATIII peptide has two aromatic residues that may be capable of intercalating pDNA; this may displace ethidium bromide as well and contribute to the low charge ratio needed to complex pDNA. It is worth noting that both PEG-RRP and PEG-ATIII demonstrate similar qualitative pDNA binding in these gel experiments, despite the significant differences in their heparin binding affinity, suggesting that the strength of heparin binding does not correlate to the ability of the polymer to complex pDNA, as might be expected since the associations involve different binding motifs.

CD characterization of peptide conformation at charge ratios of 5 (sufficient to completely complex DNA in all cases) and 1 (to increase the relative amount of bound peptide in the sample) indicated that the HBPs showed no significant change in conformation upon binding DNA (see Supporting Information), although changes in peptide conformation upon the binding of DNA have been previously observed for select peptides (*53*). Therefore, it is expected that observed differences in DNA binding and transfection efficiency result from the physicochemical properties of the peptide and not from additional conformational changes upon complexation.

IV. Polyplex Size. The salt and serum stability of polyplexes is critical for their application *in vivo*; if the particles are unstable at high ionic strength and in the presence of serum proteins, they may aggregate to form large particles which would be detrimental to their efficacy. Dynamic light scattering was therefore employed to measure the size of the PEG-HBP/pDNA polyplexes in various dispersants over time.

The size of the polyplexes formed between the star macromolecules and pDNA, shown in Figure 3, again displayed a dependence on the cationic peptide moiety of the vector. The polyplex solutions created with PEG-HIP in Opti-MEM and PEG-ATIII created in DMEM revealed bimodal peaks in size measurements. The large difference in size between the two populations likely indicates that the shapes of the polyplexes created with these vectors are too complex to fit to the simple algorithm supplied by the manufacturer, which assumes spherical particles. Furthermore, inspection of the size distribution fit depicts three slopes, which likely indicate more than one mode of motion over time and also suggest the lack of spherical shape of the particles. Previous work has shown that the morphology of DNA/polycation complexes varies with the chemical structure of the cationic vector (*54*). Particularly, AFM microscopy studies have shown that polyplexes created with PEGylated poly(amidoamines) exhibit both torodial and rodlike morphologies (*55*). These studies also have reported the visualization of a dynamic

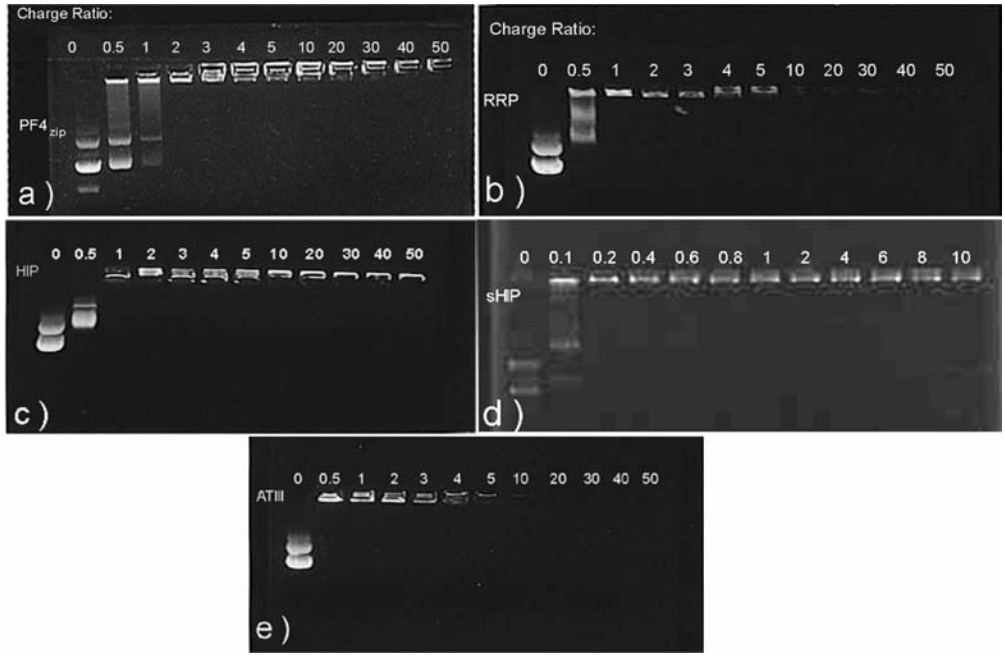

Figure 2. Results of the gel shift assays. (a) PEG-$PF4_{ZIP}$. (b) PEG-RRP. (c) PEG-HIP. (d) PEG-sHIP. (e) PEG-ATIII. Polyplexes were created at the indicated charge ratios in water. Samples were electrophoresed in an agarose gel under a 60 V electric field.

equilibrium in the spatial conformations of the polyplexes (*55*). Our experiments are consistent with the potential existence of varied structures in polyplexes created with PEG-HIP in Opti-MEM and PEG-ATIII in DMEM, so an accurate assessment of particle size under these conditions cannot be made. No other polyplex/condition exhibited such bimodality. Further investigations of the size and morphology of these polyplexes via TEM studies are in progress.

In water, the polyplex size varies between about 90 and 200 nm, which is consistent with the sizes of polyplexes created with un-PEGylated polycations (*54*, *56–58*). Upon the addition of Opti-MEM, PEG-$PF4_{ZIP}$ and PEG-ATIII polyplexes did not aggregate and showed a small and uniform polyplex size over 120 min. In the presence of DMEM (containing 10% serum), all of the PEG-HBP polyplexes showed some increase in size. PEG-HIP polyplexes rapidly aggregated to almost 5 μm after 20 min. In contrast, PEG-$PF4_{ZIP}$, PEG-sHIP, and PEG-RRP polyplexes yielded particles of roughly 500 nm upon initial DMEM addition that did not change significantly in size (relative to the other systems) over the course of 120 min. PEG-sHIP appears to be particularly stable in serum-containing media relative to the other PEG-HBP vectors. The utility of particles in this size range is suggested by previous studies. For example, particles as large as 200 nm can enter the endocytic pathway through clathrin- and caveolae-mediated endocytosis, and particles as large as 2 μm can enter the cell through macropinocytosis (*59*, *60*). Additionally, it has been shown that polyplexes can enter the cell through multiple uptake pathways (*61*). The ability of the polyplexes to be trafficked in the nucleus may be less clear, as recent research has shown that the nuclear pore complex is capable of importing particles up to 39 nm in size (*62*). While this topic is still being actively investigated in *in vivo* systems utilizing slowly dividing cells, the scope of our current research focuses on *in vitro* procedures that likely allow polyplex diffusion into the nucleus during the rapid mitosis of cell lines in culture. Although the sizes of PEG-$PF4_{ZIP}$, PEG-sHIP, and PEG-RRP polyplexes are somewhat larger than ideal, the size stability of these vectors over the course of 2 h evidence their promise for future studies, particularly given the low molecular weight of the PEG employed (~2700 Da per arm). The use of PEG star polymers of higher molecular weight may result in particles that are completely stable from aggregation in the presence of serum; previous studies have shown that PEG_{5000} is typically required to stabilize the size of polyplexes formed from PEG-PEI polymers (*63*).

V. Cell Viability Studies. To examine how well the PEG-HBPs perform under biological conditions, *in vitro* transfection studies were conducted with BHK-21 (golden Syrian hamster kidney) cells. A commonly used transfection polymer, PEI, was used as a positive control to compare the relative toxicity of the novel experimental vectors. The toxicity of polyplexes was measured via a protein assay of the cell lysates, normalized against a nontransfected control, to obtain the fraction of cell survival. This assay was performed on cells transfected both without serum (Opti-MEM) and in culture media containing 10% FBS (DMEM) to help draw conclusions about the serum stability of the complexes and their efficacy.

Figure 4a reveals the viability of BHK-21 cells transfected in Opti-MEM over a variety of charge ratios. The results show that the cell survival in the presence of PEG-$PF4_{ZIP}$, PEG-HIP, and PEG-sHIP polyplexes remains high (>90%) up to a charge ratio of 15, and greater than 50% survival was found at a charge ratio of 30. PEG-sHIP shows particularly low toxicity, even at high charge ratio doses. In contrast, the polyplexes formed with PEI, PEG-RRP, and PEG-ATIII were found to be quite toxic. Notably, PEG-ATIII is extremely toxic—even more toxic than PEI, which is well-known to exhibit high cytotoxicity in many cell lines. PEG-RRP appears to have low cytotoxicity at a low charge ratio of 5, but the toxicity rapidly increases at higher doses. All three of these vectors, PEG-ATIII, PEG-RRP, and PEI, show less than 50% viability at an N/P ratio of 15 or above. Figure 4b depicts the viability of BHK-21 cells transfected in the presence of 10% serum; the data indicate the reduced toxicity of all of the vectors under these experimental conditions, which is likely to result from a simple reduction in cellular uptake of the polyplexes as a result of their larger size in serum, consistent with previous reports of decreasing cellular uptake of polycationic vectors in the presence of serum (*6*).

The trend of toxicity among PEG-HBPs generally correlates with the cationic charge density of the peptide, with the PEG-RRP displaying greater cytotoxicity than the PEG-$PF4_{ZIP}$ or PEG-HIP. Other studies have also shown that the cytotoxicity

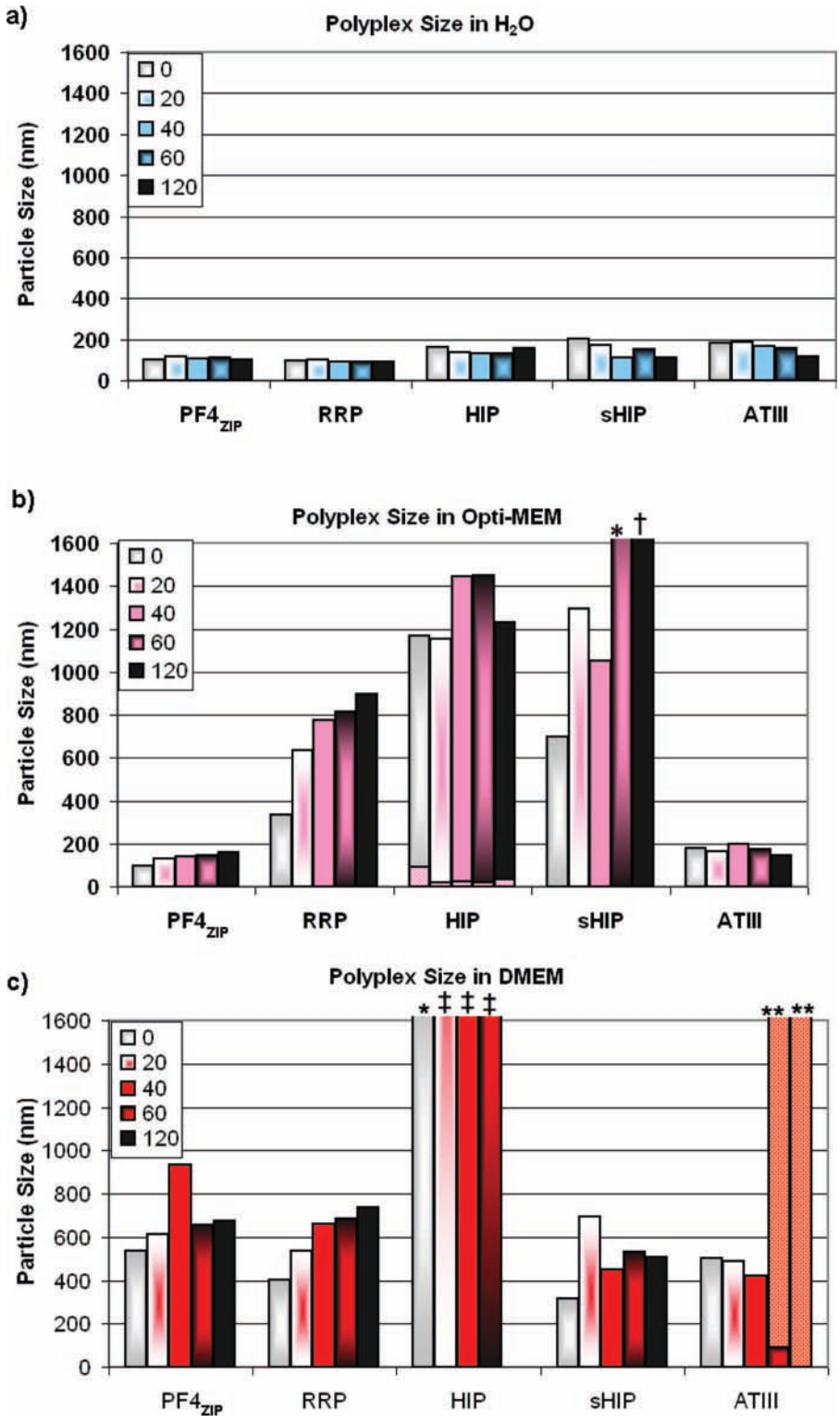

Figure 3. Particle sizes of PEG-HBP/pDNA polyplexes in various dispersants. Polyplexes were formed by adding an equal volume of PEG-HBP solution to pDNA at a charge ratio of 5 in water. Dynamic light scattering was used to measure the hydrodynamic diameter of the polyplexes at time 0 (immediately after addition of dispersant) and thereafter consecutively at 20, 40, 60, and 120 min. (a) Sizes of the polyplexes dispersed in water. (b) Sizes of the polyplexes dispersed in serum-free Opti-MEM. (c) Sizes of the polyplexes dispersed in DMEM containing 10% FBS. Overlaid bars are indicative of bimodal data. * denotes ~2 μm, ** denotes ~3 μm, † denotes ~4 μm, ‡ denotes 4.5–5 μm.

of PEG-RRP is high even compared with other cationic peptides, such as antennapedia, TAT, and transportan (*64*), likely as a result of this high charge density (*14*). The RRP peptide employed in these studies has a charge density of 0.58 (7 arginines out of 12 total amino acids), while the ATIII, HIP, and $PF4_{ZIP}$ peptides have charge densities of 0.33, 0.31, and 0.18, respectively. The PEG-sHIP vector deviates slightly from this trend. However, the toxicity is very low and similar to PEG-HIP, which is expected given their identical composition. The unusually high toxicity of the PEG-ATIII polyplexes, despite the lower cationic charge density, most likely results from the higher hydrophobicity of the peptide (which contains two aromatic residues). This is consistent with the previously reported toxicity of positively charged and hydrophobic peptides

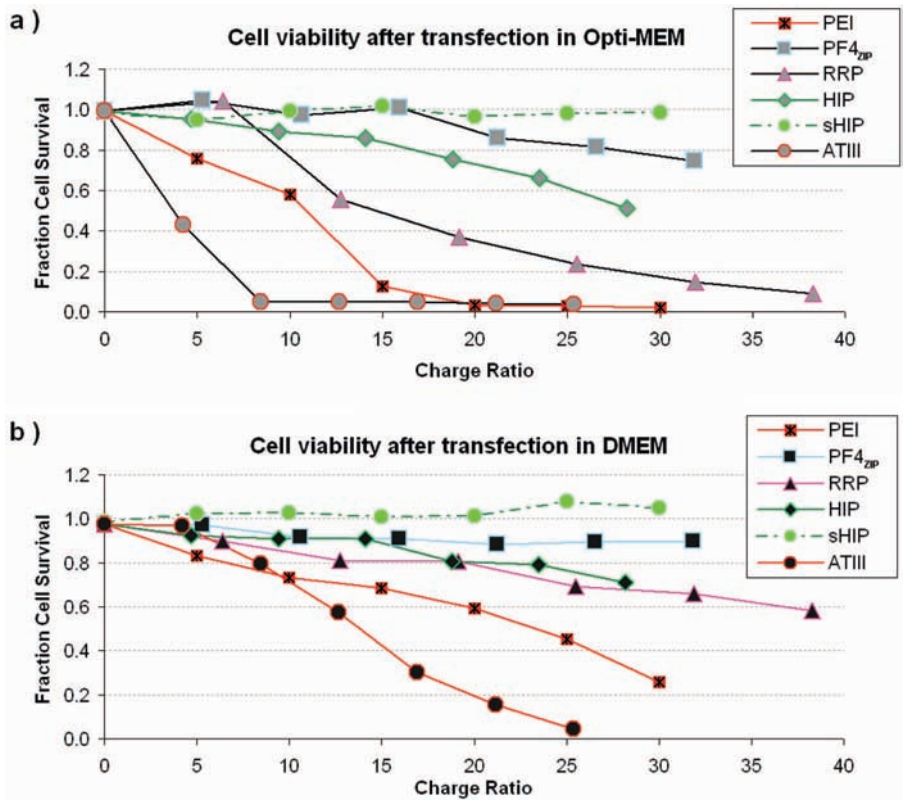

Figure 4. Viability of BHK-21 cells after transfection with polyplexes created with PEG-HBPs in both (a) nonserum and (b) 10% serum conditions at the indicated charge ratios for 48 h. Cells were lysed after 48 h, and protein content was assayed and normalized against a nontransfected control to obtain the fraction of cell survival. Data are reported as a mean ± standard of deviation of three replicates.

of similar cationic charge (of about 5–7 positive charges per peptide) (*65*, *66*). Importantly, the cell viability profiles of transfections performed with PEG-sHIP, PEG-$PF4_{ZIP}$, and PEG-HIP are very promising in comparison to the unmodified PEI control and are also significantly improved relative to that reported for PEGylated PEI polymers (in which cells reveal less than 50% cell viability in transfection experiments performed above a charge ratio of 20) (*17*). PEG-$PF4_{ZIP}$ and PEG-sHIP, in particular, show extremely promising cell viability data, with at least 80% cell viability at a high charge ratio of 30, even under serum-free conditions.

VI. Transfection Efficiency Studies. To determine the overall transfection efficiency of the vectors, the PEG-HBPs were complexed with plasmids encoding the luciferase reporter gene for transfection of BHK-21 cells. A luciferase reporter gene assay was performed in both serum-free conditions (Opti-MEM) and conditions containing serum (DMEM with 10% FBS) to study the transfection efficiency of these vectors. Again, the widely used polymer, PEI, was included as a positive control, as this vector has shown high transfection efficiency despite its increased toxicity. Figure 5 depicts the results of these reporter gene assays.

The results of transfection efficiency in Opti-MEM shows that PEG-$PF4_{ZIP}$, PEG-sHIP, and PEG-RRP polyplexes demonstrated significantly higher transfection efficiencies ($\sim 1 \times 10^8$ RLU/mg protein) than PEG-HIP and PEG-ATIII polyplexes ($<1 \times 10^7$ RLU/mg protein), as shown in Figure 5a. Although transfection efficiency for the PEI positive control is initially high, it was only measurable up to an N/P ratio of 10 in Opti-MEM due to the high toxicity of this vector at elevated doses, which detracts from its utility as a delivery vector. Similarly, delivery data for PEG-ATIII polyplexes in Opti-MEM and DMEM could only be obtained at maximum charge ratios of 5 and 25, respectively. Despite the apparent high transfection efficiency of PEG-ATIII, the toxicity profile is unsuitable for delivery applications, and this vector will not be discussed further.

The data in Figure 5a also indicate the similar transfection efficiencies of PEG-$PF4_{ZIP}$, PEG-sHIP, and PEG-RRP polyplexes, despite the large difference in their aggregation behavior (Figure 3b), indicating that other steps in the transfection pathway such as endosomal escape and subsequent intracellular mobility play a large role in the overall transfection efficiency. It is well-documented that the intracellular travel of polyplexes likely involves acidic vesicles of the endosomal trafficking pathway (*61*). The K_D of the HBPs with heparin measured at acidic pH values (Tables 3–5) suggests the potential for increased dissociation of the peptides from heparan sulfate (bound to the internal membrane of endosomal vesicles) during intracellular travel. A positive effect on the transfection efficiency pathway could result and may be due to the increase in the mobility of the pDNA once inside the cell.

In addition, these vectors showed maximum transfection efficiencies at a charge ratio of 5, suggesting the utility of these and similar vectors owing to the low toxicity (Figure 4a) and vector concentration needed to promote efficient delivery. The transfection efficiencies of PEG-RRP and PEG-$PF4_{ZIP}$ are nearly identical up to a charge ratio of 25, although the PEG-RRP vectors were highly toxic, and the $PF4_{ZIP}$ vectors showed little toxicity at the same transfection level. The PEG-sHIP exhibits similar transfection efficiency as that of PEG-$PF4_{ZIP}$, with no toxicity, and a greater efficiency than PEG-HIP, consistent with the heparin binding data. Overall, the transfection assays in Opti-MEM strongly indicate the potential and enhanced utility of HBPs of specific sequences, relative to other nonspecific, high charge density polymers such as polyarginine and PEI, via the optimization of transfection efficiency per unit of cationic charge.

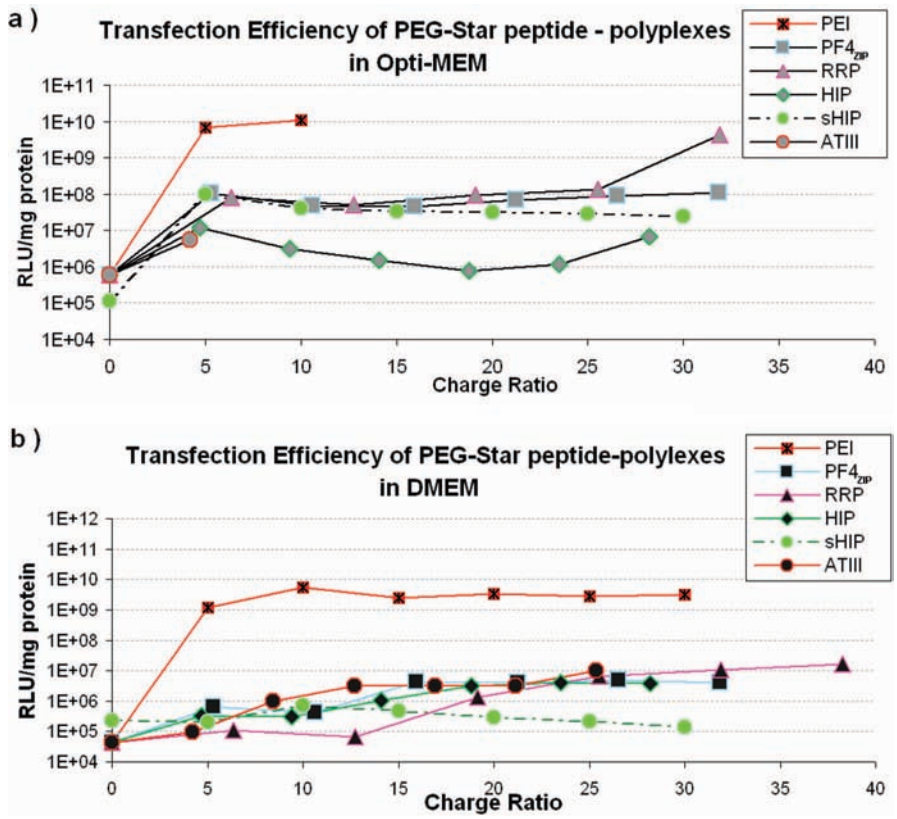

Figure 5. The transfection efficiency of PEG-HBP/pDNA polyplexes in (a) nonserum- and (b) serum-containing conditions. BHK-21 cells were transfected with polyplexes containing the reporter gene for luciferase and incubated for 48 h. A luciferase assay was performed on the cell lysates and data is displayed as RLU/mg protein. Data are reported as a mean ± standard of deviation of three replicates.

Comparison of the data in Figure 5a and b reveals that transfections with most of the PEG-HBPs in DMEM (Figure 5b) displayed a 10- to 100-fold reduction in efficiency when compared to transfections performed in Opti-MEM (Figure 5a). Such a decrease was not observed for PEI in these experiments. When coupled with the decrease in viability of cells transfected with PEI at increasing N/P ratios (80% at N/P 5, 40% at N/P 25), these results may suggest differences in endosomal escape, DNA protection from nucleases, and nuclear trafficking for the PEI relative to the PEG-HBPs. Engineering such responses in the PEG-HBPs could significantly improve their transfection performance in serum-containing media. In addition, the plateau in transfection efficiency of the polyplexes in DMEM did not occur until a charge ratio of approximately 20–25, which may reflect the increased amount of polymer required to sufficiently stabilize the pDNA polyplexes in medium containing serum. Indeed, the transfection efficiency of the PEG-sHIP vector, which appears to be more serum stable than the rest of the PEG-HBP vectors, plateaus at a lower charge ratio of 10, in agreement with this observation.

Taken altogether, the data from these investigations show a general correlation between the heparin binding affinity of the peptide and the transfection efficiency of the PEG-HBP conjugate. The heparin affinity chromatography and SPR experiments (Table 2) indicated heparin binding affinity in the order RRP > $PF4_{ZIP}$ ≈ sHIP > HIP > ATIII, which is very similar to the trend in transfection efficiency in Opti-MEM. That is, PEG-RRP, PEG-sHIP, and PEG-$PF4_{ZIP}$ show significantly increased transfection efficiencies over the PEG-HIP and PEG-ATIII vectors. This correlation suggests the importance of cell-surface association with glycosaminoglycans in the trafficking of these vectors, promoting enhanced cellular uptake by increasing polyplex—glycosaminoglycan affinity. To further examine specific events involving cellular binding and internalization, we investigated the cellular uptake of DNA via flow cytometry.

VII. Cellular Internalization Studies. To more specifically concentrate on the effect of cell-surface binding and internalization of the PEG-HBPs, flow cytometry was used to measure the amount of DNA internalized by transfected cells. BHK-21 cells were transfected with Cy5-labeled pDNA and subjected to analysis via flow cytometry. An N/P ratio of 5 was chosen, as it showed maximum transfection efficiency for the vectors in serum-free media. In all samples, greater than 80% of cells exhibited Cy5 fluorescence (data not shown). Figure 6 depicts the results of these internalization studies.

The trend in cellular internalization of Cy5-labeled pDNA among PEG-HBPs (PEG-RRP > PEG-$PF4_{ZIP}$ >PEG-sHIP > PEG-HIP ≈ PEG-ATIII) is almost identical to the observed trend in heparin affinity (RRP > $PF4_{ZIP}$ ≈ sHIP > HIP > ATIII). Furthermore, the increased heparin binding affinity of sHIP versus HIP is reflected in the internalization experiments. Interestingly, PEG-ATIII, which has been shown to give stable polyplexes in nonserum-containing media (Figure 3b), shows very low cellular uptake. This result is likely due to the lowered affinity of this peptide for heparin (Table 2) and further illustrates the utility of cell-surface binding peptides for controlling internalization.

These cellular uptake results also corroborate the trend in luciferase gene expression and further substantiate our hypothesis that enhanced cell binding increases cellular delivery. Furthermore, the trend in the magnitude of internalization generally correlates with gene expression; for example, the internalization and transfection efficiency of PEG-RRP and PEG-$PF4_{ZIP}$ are about 1 order of magnitude higher than those of PEG-HIP. This may be due to the combined effect of the

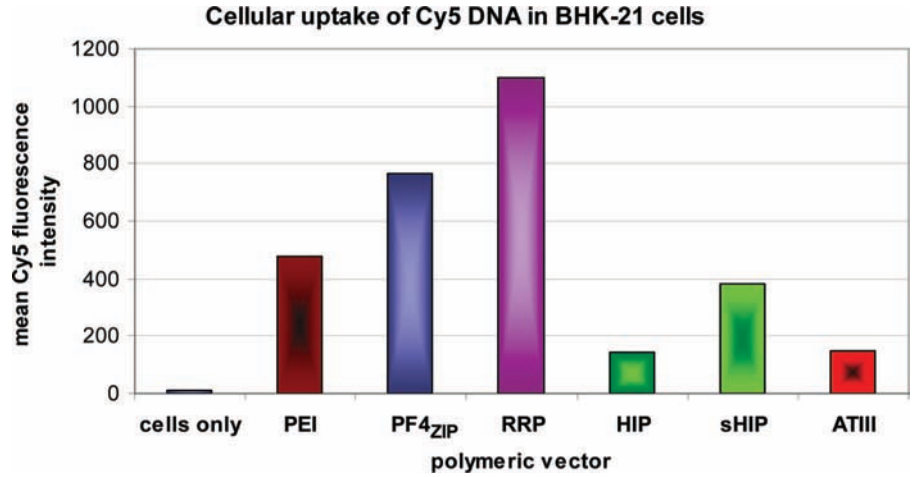

Figure 6. The cellular uptake of Cy5-labeled DNA via polyplexes in nonserum-containing media. BHK-21 cells were transfected with polyplexes formulated with Cy5-labled DNA. Four hours after transfection, the cells were washed well with PBS and allowed to traffic for 2 more hours. The cells were then trypsinzed and analyzed via flow cytometry. Each sample represents the mean fluorescence in 50 000 cells.

decreased polyplex stability (Figure 3b) and heparin binding affinity (Table 2) of the HIP peptide.

The two strongest binding PEG-HBPs, PF_{4ZIP} and RRP, were internalized to a larger degree than the positive control, PEI, despite the higher heparin binding affinity of PEI. These data lend further confidence to our proposal that the multivalent star architecture of the PEG-star HBPs allows simultaneous binding of DNA at the core of the polyplex and heparan sulfate at the surface of the cell. Conversely, the PEI-DNA polyplex, dependent on cooperative interactions between the polymers to remain intact, may be more susceptible to competition with extracellular polyanions such as heparan sulfate. PEI from the surface of the polyplex may bind with heparan sulfate at the surface of the cell in a cooperative manner, leading to extracellular unpackaging of DNA. Clearly, the molecular architecture of the polymeric ligand, as well as the heparin binding affinity of the cationic moiety plays a large role in the cell-surface kinetics and internalization pathways of the polyplexes. It should be noted that although the cellular uptake of PEG-RRP and PEG-$PF4_{ZIP}$ was higher than that of PEI (Figure 6) their gene expression profiles were still lower than observed with PEI (Figure 5). This suggests that endosomal escape could be a barrier for the PEG-HBP vectors.

CONCLUSIONS

Five PEG-HBPs, capable of multivalent interactions with polyanionic biological molecules, have been shown to bind both heparin and plasmid DNA sufficiently well to make them useful for a variety of applications. Examination of dynamic light scattering data revealed that three polyplexes, produced with PEG-RRP, PEG-sHIP, and PEG-$PF4_{ZIP}$, had notable stability against aggregation in cell culture media containing 10% serum. Transfection studies complemented these results and showed that these vectors also appear to have significant transfection efficiency in BHK-21 cells under both conditions. With the exception of the PEG-ATIII polyplex (which is very cytotoxic), increased heparin affinity correlated with increased transfection efficiency. This correlation was further indicated in the relationship between heparin affinity and cellular uptake. Most clearly, this is evidenced by the increased cellular uptake of PEG-sHIP polyplexes relative to those prepared with PEG-HIP; these are compositionally identical peptides which differ only in that the sHIP sequence demonstrated higher heparin affinity than the nonscrambled HIP sequence. These results suggest that cell-surface binding and uptake, mediated by heparan sulfate, play a large role in the overall transfection pathway of these vectors.

Comparison of polyplexes created with PEG-$PF4_{ZIP}$ and charge-dense polyplexes (PEG-RRP and PEI) demonstrates that an increase in heparin affinity alone can confer improved transfection efficiency without requiring an increase in the charge density and resulting toxicity. Furthermore, the PEG-HBPs which bind heparin mostly strongly, PEG-RRP and PEG-$PF4_{ZIP}$, have enhanced cellular uptake compared to PEI, whose charge density is much higher than any of the PEG conjugates. These data corroborate our proposal that the multivalent presentation of peptides permit simultaneous interaction between DNA at the core of the polyplex and heparan sulfate at the surface of the cell without disruption of the polyplex, enhancing cellular uptake. Given the flexibility of synthetic strategies for producing PEG-HBPs with varying architectures and peptide identity, these results suggest that the star PEG-HBPs are promising and versatile candidates as gene delivery vectors.

ACKNOWLEDGMENT

We gratefully acknowledge the National Institutes of Health (1-R01-EB003172-1) and the Arnold and Mabel Beckman Foundation for partial funding of the synthetic aspects of this project (KLK and LZ). TMR and KMF thank the Arnold and Mabel Beckman Foundation and the Department of Chemistry at the University of Cincinnati for partial funding of the biological studies performed herein. Additionally, we recognize and thank Nori Yamaguchi for assistance with the synthesis of some PEG−peptide conjugates and Yemin Liu for performing some of the gel-shift assays.

Supporting Information Available: Experimental details of the synthesis and characterization of PEG-RRP, heparin affinity studies, DNA binding assays, and CD spectra peptide−DNA complexes. This material is available free of charge via the Internet at http://pubs.acs.org.

LITERATURE CITED

(1) Akhtar, S. (2006) Non-viral cancer gene therapy: Beyond delivery. *Gene Ther. 13*, 739–740.
(2) Reineke, T. M., and Grinstaff, M. W. (2005) Designer materials for nucleic acid delivery. *MRS Bull. 30*, 635–638.
(3) Deshpande, M. C., Davies, M. C., Garnett, M. C., Williams, P. M., Armitage, D., Bailey, L., Vamvakaki, M., Armes, S. P., and Stolnik, S. (2004) The effect of poly(ethylene glycol molecular architecture on cellular interaction and uptake of DNA complexes. *J. Controlled Release 97*, 143–156.

(4) Liu, Y., Wenning, L., Lynch, M., and Reineke, T. M. (2004) New poly(D-glucaramidoamine)s induce DNA nanoparticle formation and efficient gene delivery into mammalian cells. *J. Am. Chem. Soc. 126*, 7422–7423.

(5) Liu, Y. M., and Reineke, T. M. (2005) Hydroxyl stereochemistry and amine number within poly(glycoamidoamine)s affect intracellular DNA delivery. *J. Am. Chem. Soc. 127*, 3004–3015.

(6) Liu, Y., and Reineke, T. M. (2006) Poly(glycoamidoamine)s for gene delivery. Stability of polyplexes and efficacy with cardiomyoblast cells. *Bioconjugate Chem. 17*, 101–108.

(7) Liu, Y., Wenning, L., Lynch, M., and Reineke, T. M. (2006) Gene delivery with novel poly(L-tartaramidoamine)s. In *Polymeric Drug Delivery Volume I-Particulate Drug Carriers* (Svenson, S., Ed.)American Chemical Society, Washington, DC.

(8) van de Wetering, P., Moret, E. E., Schuurmans-Nieuwenbroek, N. M. E., van Steenbergen, M. J., and Hennink, W. E. (1999) Structure-activity relationships of water-soluble cationic methacrylate/methacrylamide polymers for nonviral gene delivery. *Bioconjugate Chem. 10*, 589–597.

(9) Davis, M. E. (2002) Non-viral gene delivery systems. *Curr. Opin. Biotechnol. 13*, 128–131.

(10) Pouton, C. W., and Seymour, L. W. (1998) Key issues in nonviral gene delivery. *Adv. Drug Delivery Rev. 34*, 3–19.

(11) Collard, W. T., Yang, Y., Kwok, K. Y., Park, Y., and Rice, K. G. (2000) Biodistribution, metabolism, and *in vivo* gene expression of low molecular weight glycopeptide polyethylene glycol peptide DNA co-condensates. *J. Pharm. Sci. 89*, 499–512.

(12) Dash, P. R., Read, M. L., Barrett, L. B., Wolfert, M. A., and Seymour, L. W. (1999) Factors affecting blood clearance and *in vivo* distribution of polyelectrolyte complexes for gene delivery. *Gene Ther. 6*, 643–650.

(13) Verbaan, F. J., Oussoren, C., van Dam, I. M., Takakura, Y., Hashida, M., Crommelin, D. J., Hennink, W. E., and Storm, G. (2001) The fate of poly (2-dimethyl amino ethyl)methacrylate-based polyplexes after intravenous administration. *Int. J. Pharm. 214*, 99–101.

(14) Fischer, D., Li, Y., Ahlemeyer, B., Krieglstein, J., and Kissel, T. (2003) *In vitro* cytotoxicity testing of polycations: influence of polymer structure on cell viability and hemolysis. *Biomaterials 24*, 1121–1131.

(15) Kabanov, A. V., Vinogradov, S. V., Suzdaltseva, Y. G., and Alakhov, V. Y. (1995) Water-soluble block polycations as carriers for oligonucleotide delivery. *Bioconjugate Chem. 6*, 639–643.

(16) Vinogradov, S. V., Bronich, T. K., and Kabanov, A. V. (1998) Self-assembly of polyamine-poly(ethylene glycol) copolymers with phosphorothioate oligonucleotides. *Bioconjugate Chem. 9*, 805–812.

(17) Sung, S., Min, S. H., Cho, K. Y., Lee, S., Min, Y., Yeom, Y. I., and Park, J. (2003) Effect of polyethylene glycol on gene delivery of polyethylenimine. *Biol. Pharm. Bull. 26*, 492–500.

(18) Ahn, C., Chae, S. Y., Bae, Y. H., and Kim, S. W. (2004) Synthesis of biodegradable multi-block copolymers of poly(L-lysine) and poly(ethylene glycol) as non-viral gene carrier. *J. Controlled Release 97*, 567–574.

(19) Toncheva, V., Wolfert, M. A., Dash, P. R., Oupicky, D., Ulbrich, K., Seymour, L. W., and Schacht, E. H. (1998) Novel vectors for gene delivery formed by self-assembly of DNA with poly(L-lysine) grafted with hydrophilic polymers. *Biochim. Biophys. Acta 1380*, 354–368.

(20) Männistö, M., Vanderkerken, S., Toncheva, V., Elomaa, M., Ruponen, M., Schacht, E., and Urtti, A. (2002) Structure-activity relationships of poly(L-lysines): effects of pegylation and molecular shape on physicochemical and biological properties in gene delivery. *J. Controlled Release 83*, 169–182.

(21) Erbacher, P., Bettinger, T., Brion, E., Coll, J., Plank, C., Behr, J., and Remy, J. (2004) Genuine DNA/polyethylenimine (PEI) complexes improve transfection properties and cell survival. *J. Drug Targeting 12*, 223–236.

(22) Shuai, X., Merdan, T., Unger, F., and Kissel, T. (2005) Supramolecular gene delivery vectors showing enhanced transgene expression and good biocompatibility. *Bioconjugate Chem. 16*, 322–329.

(23) Wang, L., Wang, J., and Dong, C. (2005) Supramolecular inclusion complexes of star-shaped poly(ϵ-caprolactone) with α-cyclodextrin. *J. Polym. Sci., Part A: Polym. Chem. 43*, 4721–4730.

(24) Ooya, T., Choi, H. S., Yamashita, A., Yui, N., Sugaya, Y., Kano, A., Maruyama, A., Akita, H., Ito, R., Kogure, K., and Harashima, H. (2006) Biocleavable polyrotaxane-plasmid DNA polyplex for enhanced gene delivery. *J. Am. Chem. Soc. 128*, 3852–3853.

(25) Petersen, H., Kunath, K., Martin, A. L., Stolnik, S., Roberts, C. J., Davies, M. C., and Kissel, T. (2002) Star-shaped poly(ethylene glycol)-*block*-polyethylene copolymers enhance DNA condensation of low moleular weight polyethylenimines. *Biomacromolecules 3*, 926–936.

(26) Mislick, K. A., and Baldeschwieler, J. D. (1996) Evidence for the role of proteoglycans in cation-mediated gene transfer. *Proc. Natl. Acad. Sci. U.S.A. 93*, 12349–12354.

(27) Kopatz, I., Remy, J. S., and Behr, J. P. (2004) A model for non-viral gene delivery: through syndecan adhesion molecules and powered by Actin. *J. Gene Med. 6*, 769–776.

(28) Koping-Hoggard, M., Varum, K. M., Issa, M., Danielsen, S., Christensen, B. E., Stokke, B. T., and Artursson, P. (2004) Improved chitosan-mediated gene delivery based on easily dissociated chitosan polyplexes of highly defined chitosan oligomers. *Gene Ther. 11*, 1441–1452.

(29) Liu, S., Zhou, F., Hook, M., and Carson, D. D. (1997) A heparin-binding synthetic peptide of heparin/heparan sulfate-interacting protein modulates blood coagulation activities. *Proc. Natl. Acad. Sci. U.S.A. 94*, 1739–1744.

(30) Ibel, K., Poland, G. A., Baldwin, J. P., Pepper, D. S., Luscombe, M., and Holbrook, J. J. (1986) Low-resolution structure of the complex of human blood platelet factor 4 with heparin determined by small-angle neutron scattering. *Biochim. Biophys. Acta 870*, 58–63.

(31) Fromm, J. R., Hileman, R. E., Caldwell, E. E. O., Weiler, J. M., and Linhardt, R. J. (1995) Differences in the interaction of heparin with arginine and lysine and the importance of these basic amino acids in the binding of heparin to acidic fibroblast growth factor. *Arch. Biochem. Biophys. 323*, 279–287.

(32) Caldwell, E. E. O., Nadkarni, V. D., Fromm, J. R., Linhardt, R. J., and Weiler, J. M. (1996) Importance of specific amino acids in protein binding sites for heparin and heparan sulfate. *Int. J. Biochem. Cell Biol. 28*, 203–216.

(33) Seal, B. L., and Panitch, A. (2006) Viscoelastic behavior of environmentally sensitive biomimetic polymer matrices. *Macromolecules 39*, 2268–2274.

(34) Seal, B. L., and Panitch, A. (2003) Physical polymer matrices based on affinity interactions between peptides and polysaccharides. *Biomacromolecules 4*, 1572–1582.

(35) Yamaguchi, N., Chae, B. S., Zhang, L., Kiick, K. L., and Furst, E. M. (2005) Rheological characterization of polysaccharide-poly(ethylene glycol) star copolymer hydrogels. *Biomacromolecules 6*, 1931–1940.

(36) Yamaguchi, N., and Kiick, K. L. (2005) Polysaccharide-poly(ethylene glycol) star copolymer as a scaffold for the production of bioactive hydrogels. *Biomacromolecules 6*, 1921–1930.

(37) Zhang, L., Furst, E. M., and Kiick, K. L. (2006) Manipulation of hydrogel assembly and growth factor delivery via the use of peptide-polysaccharide interactions. *J. Controlled Release 114*, 130–142.

(38) Tyler-Cross, R., Sobel, M., McAdory, L. E., and Harris, R. B. (1996) Structure-function relations of antithrombin III-heparin interactions as assessed by biophysical and biological assays and molecular modeling of peptide-pentasaccharide-docked complexes. *Arch. Biochem. Biophys. 334*, 206–213.

(39) Liu, S., Smith, S. E., Julian, J., Rohde, L. H., Karin, N. J., and Carson, D. D. (1996) cDNA cloning and expression of HIP, a novel cell surface heparan sulfate/heparin-binding protein of human uterine epithelial cells and cell lines. *J. Biol. Chem. 271*, 11817–11823.

(40) Butcher, D. J., Kowalska, M. A., Li, S., Luo, Z. W., Shan, S. M., Lu, Z. X., Niewiarowski, S., and Huang, Z. W. (1997) A natural motif approach to protein design: A synthetic leucine zipper peptide mimics the biological function of the platelet factor 4 protein. *FEBS Lett. 409*, 183–187.

(41) Spillmann, D., and Lindahl, U. (1994) Glycosaminoglycan protein interactions-a question of specificity. *Curr. Opin. Struct. Biol. 4*, 677–682.

(42) Grifman, M., Trepel, M., Speece, P., Gilbert, L. B., Arap, W., Pasqualini, R., and Weitzman, M. D. (2001) Incorporation of tumor-targeting peptides into recombinant adeno-associated virus capsids. *Mol. Ther. 3*, 964–975.

(43) Wickham, T. J., Roelvink, P. W., Brough, D. E., and Kovesdi, I. (1996) Adenovirus targeted to heparan-containing receptors increases its gene delivery efficiency to multiple cell types. *Nat. Biotechnol. 14*, 1570–1573.

(44) Wickham, T. J., Tzeng, E., Shears, L. L., Roelvink, P. W., Li, Y., Lee, G. M., Brough, D. E., Lizonova, A., and Kovesdi, I. (1997) Increased *in vitro* and *in vivo* gene transfer by adenovirus vectors containing chimeric fiber proteins. *J. Virol. 71*, 8221–8229.

(45) Capila, I., and Linhardt, R. J. (2002) Heparin-protein interactions. *Angew. Chem., Int. Ed. 41*, 390–412.

(46) Plank, C., Tang, M. X., Wolfe, A. R., and Szoka, F. C. (1999) Branched cationic peptides for gene delivery: Role of type and number of cationic residues in formation and *in vitro* activity of DNA polyplexes. *Hum. Gene Ther. 10*, 319–332.

(47) Lutolf, M. P., Tirelli, N., Cerritelli, S., Cavelli, L, and Hubbel, J. A. (2001) Systematic modulation of Michael-type reactivity of thiols through the use of charged amino acids. *Bioconjugate Chem. 12*, 1051–1056.

(48) Bartsch, M., Weeke-Klimp, A. H., Meijer, D. K. F., Scherphof, G. L., and Kamps, J. (2005) Cell-specific targeting of lipid-based carriers for ODN and DNA. *J. Liposome Res. 15*, 59–92.

(49) Nishikawa, M. (2005) Development of cell-specific targeting systems for drugs and genes. *Biol. Pharm. Bull. 28*, 195–200.

(50) Lundquist, J. J., and Toone, E. J. (2002) The cluster glycoside effect. *Chem. Rev. 102*, 555–578.

(51) Mukherjee, S., Ghosh, R. N., and Maxfield, F. R. (1997) Endocytosis. *Phys. Rev. 77*, 759–803.

(52) Lee, M., Han, S., Ko, K. S., Koh, J. J., Park, J. S., Yoon, J. W., and Kim, S. W. (2001) Repression of GAD autoantigen expression in pancreas β-cells by delivery of antisense plasmid/PEG-g-PLL complex. *Mol. Ther. 4*, 339–346.

(53) Gonçalves, E., Kitas, E., and Seelig, J. (2006) Structural and thermodynamic aspects of the interaction between heparan sulfate and analogues of melittin. *Biochemistry 45*, 3086–3094.

(54) Vijayanathan, V., Thomas, T., Antony, T., Shirahata, A., and Thomas, T. J. (2004) Formation of DNA nanoparticles in the presence of novel polyamine analogues: a laser light scattering and atomic force microscopic study. *Nucleic Acids Res. 32*, 127–134.

(55) Martin, A. L., Davies, M. C., Rackstraw, B. J., Roberts, C. J., Stolnik, S., Tendler, S. J. B., and Williams, P. M. (2000) Observation of DNA-polymer condensate formation in real time at a molecular level. *FEBS Lett. 480*, 106–112.

(56) Bötcher, C., Endisch, C., Fuhrhop, J., Catterall, C., and Eaton, M. (1998) High yield preparation of oligomeric C-type DNA toroids and their characterization by cryoelectron microscopy. *J. Am. Chem. Soc. 120*, 12–17.

(57) Arscott, P., Li, A., and Bloomfield, V. (1990) Condensation of DNA by trivalent cations. 1. effects of DNA length and topology on the size and shape of condensed particles. *Biopolymers 30*, 619–630.

(58) Lin, Z., Wang, C., Feng, X., Liu, M., Li, J., and Bai, C. (1998) The observation of the local ordering characteristics of spermidine-condensed DNA: atomic force microscopy and polarizing microscopy studies. *Nucleic Acids Res. 26*, 3228–3234.

(59) Johannes, L., and Lamaze, C. (2002) Clathrin-dependent or not: is it still the question? *Traffic 3*, 443–451.

(60) Rejman, J., Oberle, V., Zuhorn, I. S., and Hoekstra, D. (2004) Size dependent internalization of particles via the pathways of clathrin- and caveolae-mediated endocytosis. *Biochem. J. 377*, 159–169.

(61) Medina-Kauwe, L. K., Xie, J., and Hamm-Alvarez, S. (2005) Intracellular trafficking of nonviral vectors. *Gene Ther. 12*, 1734–1751.

(62) Pante, N., and Kann, M. (2002) Nuclear pore complex is able to transport macromolecules with diameters of about 39 mm. *Mol. Biol. Cell 13*, 425–434.

(63) Glodde, M., Sirsi, S. R., and Lutz, G. J. (2006) Physiochemical properties of low and high molecular weight poly(ethylene glycol)-grafted poly(ethylene imine) copolymers and their complexes with oligonucleotides. *Biomacromolecules 7*, 347–356.

(64) Jones, S. W., Christison, R., Bundell, K., Voyce, C. J., Brockbank, S. M. V., Newham, P., and Lindsay, M. A. (2005) Characterization of cell-penetrating peptide mediated peptide delivery. *Br. J. Pharmacol. 145*, 1093–1102.

(65) Yang, N., Strom, M. B., Mekonnen, S. M., Svendsen, J. S., and Oystein, R. (2004) The effects of shortening lactoferrin derived peptides against tumour cells, bacteria, and normal human cells. *J. Pept. Sci. 10*, 37–46.

(66) Zhang, S., Xu, Y., Wang, B., Qiao, W., Liu, D., and Li, Z. (2004) Cationic compounds used in lipoplexes and polyplexes for gene delivery. *J. Controlled Release 100*, 165–180.

BC0701141

A Versatile Bifunctional Chelate for Radiolabeling Humanized Anti-CEA Antibody with In-111 and Cu-64 at Either Thiol or Amino Groups: PET Imaging Of CEA-Positive Tumors with Whole Antibodies

Lin Li,[†] James Bading,[‡] Paul J. Yazaki,[‡] Amitkumar H. Ahuja,[‡] Desiree Crow,[‡] David Colcher,[‡] Lawrence E. Williams,[§] Jeffrey Y. C. Wong,[||] Andrew Raubitschek,[‡] and John E. Shively*[,†]

Division of Immunology, Beckman Research Institute of the City of Hope, Duarte, California 91010, Division of Cancer Immunotherapeutics and Tumor Immunology, Division of Diagnostic Radiology, and Division of Radiation Oncology, City of Hope National Medical Center, Duarte, California 91010. Received May 3, 2007; Revised Manuscript Received September 3, 2007

Radiolabeled anti-carcinoembryonic antigen (CEA) antibodies have the potential to give excellent images of a wide variety of human tumors, including tumors of the colon, breast, lung, and medullar thyroid. In order to realize the goals of routine and repetitive clinical imaging with anti-CEA antibodies, it is necessary that the antibodies have a high affinity for CEA, low cross reactivity and uptake in normal tissues, and low immunogenicity. The humanized anti-CEA antibody hT84.66-M5A (M5A) fulfills these criteria with an affinity constant of $>10^{10}$ M^{-1}, no reactivity with CEA cross-reacting antigens found in normal tissues, and >90% human protein sequence. A further requirement for routine clinical use of radiolabeled antibodies is a versatile method of radiolabeling that allows the use of multiple radionuclides that differ in their radioemissions and half-lives. We describe a versatile bifunctional chelator, DO3A-VS (1,4,7-tris(carboxymethyl)-10-(vinylsulfone)-1,4,7,10-tetraazacyclododecane) that binds a range of radiometals including ^{111}In for gamma-ray imaging and ^{64}Cu for positron emission tomography (PET), and which can be conjugated with negligible loss of immunoreactivity either to sulfhydryls (SH) in the hinge region of lightly reduced immunoglobulins or surface lysines (NH) of immunoglobulins. Based on our correlative studies comparing the kinetics of radiolabeled anti-CEA antibodies in murine models with those in man, we predict that ^{64}Cu-labeled intact, humanized antibodies can be used to image CEA positive tumors in the clinic.

INTRODUCTION

In order to be effective tumor imaging agents, radiolabeled antitumor antibodies must demonstrate both high tumor uptake and high tumor to normal tissue ratios (*1*). Monoclonal antibodies (150 kDa) have a relatively slow blood clearance (second phase half-life $t_{1/2\,\beta} = 48$–72 h), allowing ample time for high accumulation in tumor, but suffer from low tumor to normal tissue contrast due to slow clearance from the vasculature. In order to improve the dynamic biodistribution, researchers have focused their attention on engineering recombinant antibody fragments. For example, single-chain (sc) Fv recombinant antibodies (25 kDa) are rapidly cleared from the blood ($t_{1/2\,\beta} = 0.5$–2.0 h), resulting in very high tumor to blood ratios, but suffer from low accumulation of radioactivity in tumor. For this reason, intermediate-sized antibody fragments have been engineered and studied intensively (*2*). We have shown that, in order to predict optimal tumor imaging, one must account for both tumor uptake and tumor to normal tissue contrast using pharmacokinetic analytic indicators such as the Imaging Figure of Merit (*1*). In spite of the advancement of engineered antibody fragments, the fact remains that most new antibodies with clinical potential originate as intact immunoglobulins. Conversion of IgGs to optimized recombinant fragments is time-consuming and fraught with many problems, including the potential loss of immunoreactivity, loss of the original high affinity for target antigen, and difficulty in obtaining high production yields in culture. Therefore, we have investigated the development of methods that allow the direct imaging of tumors using intact immunoglobulins.

Another major consideration in developing a versatile radioimmunoimaging agent is the choice of radionuclide. While most intact antibodies can be easily and inexpensively radioiodinated, a potential drawback to radioiodinated antibodies is that they may be rapidly metabolized and dehalogenated in tissues, including the tumor, especially if the antigen undergoes internalization after binding to cells. Even in the case of anti-CEA antibodies that undergo negligible internalization, we and others have observed higher tumor uptake and persistence at the tumor site for radiometal, compared to radioiodine-labeled antibodies (*3*). For this reason, we have favored the use of radiometals for labeling antibodies, but there are still drawbacks including high normal tissue accumulation in the kidney and liver (*4*). Furthermore, to take advantage of the wide range of radiometals available, the antibody must be conjugated to a bifunctional chelator. Although much progress has been made in this area (*5*–*8*), the search for a truly versatile bifunctional chelator continues. In this report, we describe such a bifunctional chelator (DO3A-VS), based on the stable metal ion binding properties of the tetraazamacrocyle ring with pendent carboxymethy groups and the chemically reactive linker (vinylsulfone, VS) that can be conjugated to either the easily reduced disulfides in the immunoglobulin hinge region or surface lysines of intact antibodies. We demonstrate the versatility of DO3A-

* To whom correspondence should be addressed. J. E. Shively, Tel: 626-359-8111ext 62601, E-mail: jshively@coh.org.

[†] Division of Immunology, Beckman Research Institute of the City of Hope.

[‡] Division of Cancer Immunotherapeutics and Tumor Immunology, City of Hope National Medical Center.

[§] Division of Diagnostic Radiology, City of Hope National Medical Center.

[||] Division of Radiation Oncology, City of Hope National Medical Center.

10.1021/bc700161p CCC: $40.75 © 2008 American Chemical Society
Published on Web 11/08/2007

VS in labeling a humanized anti-CEA antibody hT84.66-M5A and imaging tumors in a murine xenograft model using both ^{111}In for gamma-ray imaging and ^{64}Cu for PET imaging. The PET images obtained for ^{64}Cu-labeled M5A show excellent tumor to normal tissue ratios as early as 24 h postinjection, suggesting that intact antibodies radiolabeled with ^{64}Cu can be useful for imaging CEA-positive tumors in man.

PET imaging with the glucose analogue [^{18}F]fluorodeoxyglucose (FDG) has, in recent years, become the modality of choice for assessing extent of disease in many types of cancer, including those in which CEA expression is common. PET/FDG is also increasingly used for assessment of residual tumor viability and recurrence following treatment. Nonetheless, there remains a potential role for tumor-targeted PET imaging agents (immuno-PET, (*9*)) such as ^{64}Cu anti-CEA MAbs both due to the limitations of FDG (including uptake in regions of inflammation, high accumulation in bladder, and a tendency for low to moderate uptake in less aggressive tumors) and the need to assess tumor targeting and biodistribution in radioimmunotherapy with these antibodies. The use of radiometal positron emitters for immuno-PET is especially attractive, since they can be chelated to antibody–chelate conjugates in a kit form. Among the current choices are ^{86}Y with a half-life of 14.7 h (*10*), ^{89}Zr with a 3.3 d half-life (*11*), and ^{64}Cu with a 12.7 h half-life (*12*). Although ^{86}Y has the potential advantage of being coupled to ^{90}Y β particle therapy, its availability and prompt γ-emissions make its use limited. ^{86}Zr is attractive in terms of its long half-life and good spatial imaging, but has a potential problem with a 909 keV γ-emission. Appropriate BFCs for this metal ion have only recently been described (*11*). ^{64}Cu was chosen for the studies reported here based on its wide availability, good spatial resolution, and relatively short half-life, limiting its potential imaging dose to patients.

MATERIALS AND METHODS

Materials, Cell Culture, Antibody, Immunoreactivity, and Mass Spectrometry. DO3A tri-*t*-butyl ester and NHS-DOTA were obtained from Macrocyclics, Inc. (Dallas TX) The synthesis of DO3A-VS was previously described (*13*). SATA (*N*-succinimidyl-*S*-acetylthioacetate) was purchased from Pierce Biotechnology (Rockford, IL). All other reagents were obtained from Aldrich-Sigma (St. Louis, MO). LS-174T cells were purchased from ATCC and maintained in sterile growth media consisting of Eagle's Minimal Essential Media 1X (EMEM) (Cellgro, Herndon, VA) supplemented with 10% heat inactivated fetal bovine serum (FBS) (Omega Scientific, Tarzana, CA), and 1% L-glutamine, 10 mM sodium pyruvate, 0.1 mM non-essential AA. The production and purification of anti-CEA hT84.66-M5A has been previously described (*14*). Chelate conjugated antibodies were radiolabeled either with ^{111}In (Mallinckrodt, St. Louis. MO, 74–259 MBq/mg of protein) or with ^{64}Cu (Washington University, St. Louis, MO, 148–351 MBq/mg of protein). Percent labeling was measured by ITLC or by size exclusion chromatography (SEC) on a TSK column (1 × 30 cm, 1 mL/min, TOSOH Bioscience) or a Superdex 75 column (1 × 30 cm, 0.5 mL/min, Pharmacia Biotech). Radiolabeled antibody was purified by SEC on the same columns (in saline, fraction sizes of 1.0 and 0.5 mL, respectively). Immunoreactivity was determined by incubating the purified radiolabeled sample with a 20-fold excess by mass of CEA or a two-domain recombinant version of CEA, NA3 (*15*), at 37 °C for 15 min and then running the sample over a Superose 6HR10/30 column (GE Healthcare). Immunoreactivity was calculated as percentage total radioactivity that shifted to complexes of higher molecular weight. MALDI-MS was performed on a Perkin-Elmer-Sciex prOTOF 2000 using sinapinic acid [10 mg/mL in TFA/water/acetonitrile (0.1/50/50 v/v/v)] as a matrix. Prior to mixing with matrix, the sample was desalted on a Sephadex G25 spin column (100–200 mg in a 250 μL pipet tip) that was equilibrated in water.

Conjugation and Radiolabeling.*SH-DO3A-VS-M5A.* For conjugation of DO3A-VS to reduced cysteine hinge residues, M5A antibody (2 mg of 6.5 mg/mL, 13 nmol in PBS pH 7.5) was mixed with 144 μL of PBS and 2 μL of TCEP (tris-carboxyethyl phosphine, 200 mM, 400 nmol) and reduced for 2 h at 37 °C under argon on a rotator. Excess TCEP was removed on a Sephadex G25 spin column (1 mL, in PBS, 1200 rpm, 2 min), reacted with 3.6 μL of DO3A-VS (100 mg/mL in water, 774 nmol) under argon for 2 h at RT on a rotator, and dialyzed vs pH 7.0 0.25 M ammonium acetate containing 1 g/L Chelex for 5 d with five changes of buffer. Aliquots were removed to confirm (a) complete reduction by SDS gel electrophoresis and (b) reaction with DO3A-VS by MALDI-TOF-MS and IEF gel electrophoresis.

NH-DO3A-VS-M5A. For conjugation of DO3A-VS to surface lysine residues, 2 mg (13 nmol) of M5A (6.5 mg/mL in PBS) was mixed with 100 μL of PBS plus 6.2 μL of DO3A-VS (100 mg/mL in water, 1.3 μmol), the pH was adjusted to 9.0 with 0.1 NaOH, and the mixture was reacted for 18 h at RT on a rotator. The sample was dialyzed vs 0.25 M ammonium acetate as described above.

SATA-DO3A-VS-M5A. For conjugation of DO3A-VS to SATA generated surface sulfhydryls, 2 mg (13 nmol) of M5A (6.5 mg/mL in PBS) was mixed with 100 μL of PBS plus 2 μL of SATA (0.2 M in DMF, 400 nmol), reacted for 2 h at RT on a rotator, and then treated with 6 μL of hydroxylamine hydrochloride (0.2 M, 1200 nmol) to remove the acetyl protecting groups. The product was purified on a Superdex 200 column (Amersham, 1 × 30 cm, in PBS, 0.5 mL/min) and the antibody peak fraction (at 25 min) collected, concentrated to 0.4 mL on a Amicon Ultra-4, and reacted with 3.6 μL of DO3A-VS (100 mg/mL, 0.77 μmol) for 2 h at RT on a rotator. The sample was dialyzed vs 0.25 M ammonium actetate as above.

NHS-DOTA-M5A. For conjugation of DOTA to surface lysine residues, M5A was conjugated at a molar ratio of 20:1 chelate/antibody with DOTA-NHS-ester. Briefly, 10.5 mg (70 nmol) of M5A (7 mg/mL) was dialyzed against PBS + chelex, pH 7.2, and 0.1 M $NaHCO_3$ + chelex, pH 8.5, in a Slide-A-Lyzer cassette (Pierce, Rockford, IL). 150 μL of DOTA-NHS-ester (7.6 mg/mL in water, 1.4 μmol) was added and reacted for 2 h at RT on a rotator. The sample was dialyzed vs 0.25 M ammonium acetate as described above.

Conjugates were concentrated to 3–5 mg/mL in a Amicon Ultra-4 10 000 cutoff (Millipore, Billerica, MA) and sterile-filtered. Conjugates were characterized by both SDS and IEF gel electrophoresis (see Results section). The antibody conjugates were buffered with 0.25 M ammonium acetate, pH 7, except for M5A-NHS-DOTA that was buffered with 0.25 M sodium acetate, pH 7.2. Also, M5A-NHS-DOTA was more concentrated (7.7 mg/mL) than the other conjugates (3–5 mg/mL).

For labeling with ^{111}In no additional buffer was added to the reaction mixture except for NHS-DOTA-M5A, where 0.25 M sodium acetate, pH 6.5, was added. This mixture was incubated for 45–60 min at 43 °C, and the reaction was terminated by the addition of one-ninth the reaction volume of 10 mM DTPA to achieve a final concentration of 1 mM. The radiolabeled product was then purified on a size exclusion column. For labeling with ^{64}Cu, 0.1 M ammonium citrate, pH 5.5, was added to the reaction mixture. This mixture was incubated for 45 min at 43 °C, and the reaction was terminated by the addition of one-ninth the reaction volume of 10 mM DTPA to achieve a final concentration of 1 mM. The radiolabeled product was then purified on a size exclusion column.

Serum Stability Studies. The DO3A-VS NH and SH M5A antibody conjugates were radiolabeled with ^{64}Cu at a specific activity of 11 μC/μg (80 μg of antibody) using 0.87 mC of $^{64}CuCl_2$ for 45 min at 43 °C in ammonium citrate (0.1 M, pH 5.5). The radiolabeled samples were purified on a TSK G2000 SW size exclusion column (7.5 mm × 30 cm) and the peak IgG fractions pooled and counted. One aliquot (ca. 10 000 000 cpm) was incubated with human serum (15 μL sample plus 150 μL human serum) at 37 °C and aliquots (200 000 cpm uncorrected for decay) removed at various times for analysis by SEC (Pharmacia Superose 6, 1 × 30 cm). A second aliquot (10 μC, 1–2 μg) was injected into a nude mouse, blood removed at various times, and the serum fraction analyzed by SEC as above.

Xenograft Model, Biodistributions, and PET imaging. Female, athymic nu/nu mice (Charles River), 10–12 weeks old, were injected with LS-174T human colon cancer cells (5×10^6) s.c. in the flank. Tumors were established within 7–10 days postinjection. Athymic mice bearing LS-174T xenografts were injected via a tail vein with 200 μL of 133–148 kBq/1.7–2.2 μg ^{111}In or 333–370 kBq/2–2.4 μg of ^{64}Cu labeled DO3AVS-conjugates. Five mice were sacrificed at various time points (see Results section) and dissected for biodistribution measurements. Samples (blood, liver, spleen, kidneys, lungs, tumor, and carcass) were weighed with an analytical balance and assayed for radioactivity using a calibrated gamma counter. Measured activities were corrected for radiodecay after injection, and percentage of injected activity dose per gram of tissue (%ID/g) was calculated for each specimen.

Tumor-bearing mice (22–26 g) were injected i.v. with ^{64}Cu-labeled antibody and imaged beginning at 1.0–1.7 h, 4.5–5.5 h, 21–26 h, and 45–48 h with a small-animal PET scanner (microPET model R4; Siemens/CTIMI, Knoxvillle, TN). Injected activity and protein load ranged from 42 to 127 kBq/g and from 0.3 to 0.6 μg/g, respectively. Shortly before scanning, mice were anesthetized with isoflurane, secured in a prone position on a thin cardboard platform attached across the scanner bed, and centered in the instrument's field of view. Scan duration was 20 min for the two earliest time points and 60 min for the two later time points. The microPET's laser alignment tool was used to position the base of the tail approximately 4.0 cm from the axial center of the 8.0-cm-long field of view in each scan; mice were placed in approximately the same orientation for each scan by aligning them with body outlines traced on the cardboard platforms prior to the scans at 1 h.

Immediately after completion of the final scan, a blood sample (0.2 cc) was obtained by cardiac puncture, the mouse was sacrificed, and the tumor and various major organs were excised, weighed, and counted. Measured activities were corrected for radiodecay after injection, and percentage of injected activity dose per gram of tissue (%ID/g) was calculated for each specimen. Tumor weights at time of sacrifice ranged from 126 to 227 mg.

Image processing and analysis were performed with the standard microPET software. Scan data were sorted into two-dimensional sinograms using the Fourier rebinning method and corrected for intrascan radiodecay, detector nonuniformity, and random coincidence noise. Images were reconstructed by the iterative ordered subsets expectation maximization (OSEM) method (4 iterations, 16 subsets). Volumetric regions of interest (VOIs) were defined to include the hottest 10–15% of voxels in the images of heart and the hottest 40–50% of voxels in the images of tumor. For liver, VOIs were drawn to lie well within the organ boundaries while excluding the region containing the large central blood vessels. Image activity densities were decay-corrected to time of injection to obtain relative time–activity curves (TACs). Absolute TACs for tumor, liver, and blood (in units of %ID/g) were obtained by normalizing the final time points of the PET-derived TACs to the direct tissue assays. Blood TACs were equated with heart TACs normalized to the blood samples taken just before sacrifice.

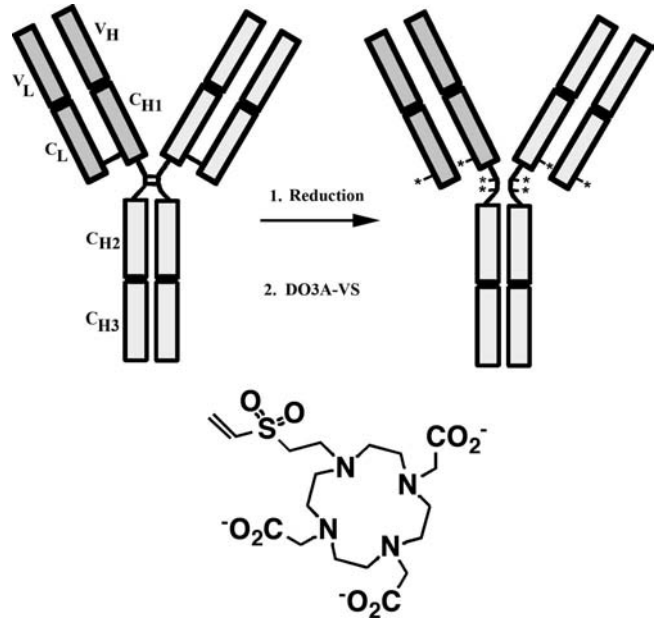

Figure 1. Schematic model of an immunoglobulin (IgG1) showing reduction of hinge sulfhydryls (*). In the second step, the sulfhydryls are reacted with DO3A-VS.

RESULTS AND DISCUSSION

DO3AVS-M5A Conjugates. In developing a bifunctional chelator for conjugation to intact immunoglobulins, our criteria were rapid synthesis, high and stable metal ion binding to a variety of radiometals, and an ability to conjugate to either sulfhydryl or amino groups present on the immunoglobulin molecule. Indeed, we had such a bifunctional chelator (DO3A-VS) in hand that previously had been shown to have high metal binding stability when conjugated to an antibody (*13*). Our interest in the use of vinyl sulfone as a bifunctional linker stems from its ability to react with primary surface amines at pH 9, as well as with thiols at acidic to neutral pH (*13*). In addition, we found that the thiol conjugates were chemically more stable than the often-used maleimide–thiol conjugates (*8*). The most accessible and/or reactive disulfides of immunoglobulins are located in the hinge region away from the antigen combining sites, and require only mild reduction of the antibody for generation of free sulfhydryls, and they can be targeted by DO3A-VS under very specific reaction conditions (pH 5.0–7.0 after mild reduction). Many studies have shown that modification of the hinge sulfhydryl groups has little or no effect on the antigen binding properties of an antibody (*16–19*), making this an ideal approach for site-specific conjugation (Figure 1). Nonetheless, the insertion of any derivative into the hinge region requires careful documentation of retention of antigen-binding activity. In addition, we have shown that vinyl sulfone-Cys-DOTA conjugates can react with surface lysine residues on antibodies at pH 9.0 (*13*). Thus, by control of pH and/or prior reduction of the antibody, one can conjugate DO3A-VS either to hinge region sulfhydryls or surface lysine residues.

Based on the concepts outlined above, the bifunctional reagent DO3A-VS was reacted either with the hinge region sulfhydryls (SH) or the surface lysines (NH) of hT84.66-M5A (M5A), and immunoreactivity and specific isotope incorporation were measured (Table 1). From these studies, we determined that both SH- and NH-DO3A-VS-M5A retained high immunoreac-

Table 1. Radiolabeling of DO3AVS-M5A Conjugates.[a]

conjugate	labeling buffer	ratio (μCi/ug)	% labeling	S.A. (μCi/ug)	% IR
SH-DO3AVS, In-111	none	2.1	99.8	2.1	100
SH-DO3AVS, Cu-64	0.1 M ammonium citrate, pH 5.55	4.2	100	4.2	100
NH-DO3AVS, In-111	none	2.2	83.8	1.8	100
NH-DO3AVS, Cu-64	0.1 M ammonium citrate, pH 5.5	9.5	50	4.8	100
SATA-DO3AVS, In-111	none	2.9	97	2.8	100
NH-NHS-DOTA, In-111	0.25 M sodium acetate, pH 6.5	7.1	99.3	7.1	100
NH-NHS-DOTA, Cu-64	0.1 M ammonium citrate, pH 5.5	8.3	99	8.2	100

[a] Reaction conditions include radiolabeling buffer with pH. Ratio refers to the μCi of isotope to μg of protein. Percent labeling efficiency was determined by HPLC purification. Specific activity (S.A.) was calculated by multiplying the labeling ratio with percent labeling. Percent immunoreactivity (%IR) was determined by in vitro incubation with 20 times mass excess of CEA (except for SH-DO3AVS, In-111, which was tested against 20× mass excess of NA3).

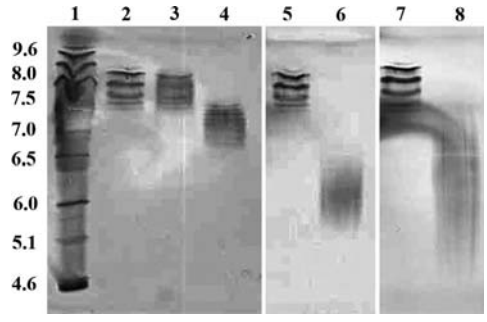

Figure 2. Characterization of DO3A-VS-M5A conjugates by IEF gel electrophoresis. 1. IEF standards (see pI values to the left). 2, 5, and 7. Unconjugated M5A. 3. M5A after reduction with TCEP. 4. SH-DO3A-VS-M5A. 6. NH-DO3A-VS-M5A. 8. SATA-DO3A-VS-M5A.

tivity and had isotope incorporation activities comparable to those published for other DOTA–antibody conjugates (*13*). We determined the relative degree of conjugation of DO3A-VS to M5A by IEF (Figure 2), an analysis that showed a shift to more acidic pI (pH) with increasing amounts of chelate substitution. Based on this analysis, conjugation of DO3A-VS to surface lysines was more extensive than to reduced sulfhydryls in the hinge region. To further characterize the degree of modification of the antibody with DO3A-VS, MALDI-TOF analysis was performed on the SH-modified sample. The results shown in Figure 3 reveal that both the light chain and heavy chain have been extensively modified (0.7 DO3A-VS per light chain and 3.3 DO3A-VS per heavy chain). Thus, the total number of chelates per 150 kDa immunoglobulin was 8.

In order to compare these conjugates to a more traditional DOTA conjugate, M5A was also reacted with a commercially available bifunctional chelator, DOTA-NHS. This DOTA conjugate could also be labeled well with ^{111}In and ^{64}Cu and retained high immunoreactivity (Table 1). MALDI-TOF analysis of this conjugate also revealed an average of eight chelates/immunoglobulin (data not shown). Other methods for conjugating DOTA to antibodies include that developed by Meares and co-workers, where lysines on the antibody were first reacted with iminothiolane and then conjugated to the bifunctional chelator BAT (*20*). To approximate this approach, we first reacted surface lysines with SATA, then with hydroxylamine to deprotect the lysine-coupled protected thiol groups, followed with DO3A-VS. This conjugate also gave high levels of isotope

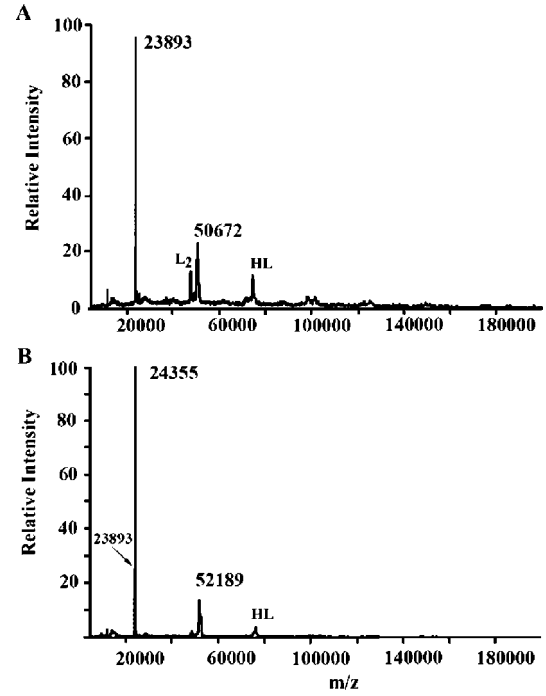

Figure 3. MALDI-TOF-MS analysis of SH-DO3A-VS-M5A. (A) Reduced M5A. The peak at 23 893 is the light chain, the peak at 50 672 is the heavy chain, and the peaks labeled L2 and HL are light chain and heavy–light chain dimers, respectively. (B) SH-DO3A-VS-M5A. The light chain has two peaks, one unmodified at *m*/*z* 23 893, and one increased by 462 mass units corresponding to the addition of one DO3A-VS. Based on peak heights, the degree of modification for the light chain is 0.67. The heavy chain has increased by 1517 mass units corresponding to the addition of an average 3.3 DO3A-VS. Note: The light chain has one "hinge" cysteine and the heavy chain three hinge cysteine residues in an IgG1 molecule.

incorporation and retained its high immunoreactivity (Table 1), but contained up to 10% dimers due to sulfhydryl cross-linking (Figure 4).

Prior to proceeding to biodistibution studies, we analyzed each of the radiolabeled conjugates by SEC before and after the addition of CEA to determine if the sample was homogeneous (single peak of the correct size) and if it was fully immunoreactive (shifted to higher molecular weight by the addition of a two-domain recombinant form of CEA, NA3, or human CEA). The results shown in Figure 4 demonstrate that the SH- and NH-DO3A-VS-M5A as well as the DOTA-NHS-M5A conjugates were free of aggregates, while the SATA-DO3A-VS-M5A conjugate contained up to 10% aggregates, but importantly, all four conjugates were 100% immunoreactive. For three of the conjugates tested, the results were equivalent whether labeled with ^{111}In or ^{64}Cu.

Since the serum stability of ^{64}Cu-labeled DOTA-based BFCs has been questioned (*21*, *22*), it was necessary to test both their in vitro and in vivo serum stabilities. When either SH or NH conjugated ^{64}Cu-labeled DO3A-VS-M5A was incubated with human serum at 37 °C and analyzed by SEC, 100% of the radioactivity remained in the IgG peak over a time course of 70 h, after which too few remaining counts remained for analysis (Figure 5A,B). In addition, when both radiolabeled conjugates were injected into mice, blood removed, and the serum fractions analyzed by SEC, 100% of the radioactivity was found in the IgG fraction over the time course of the analysis (Figure 5C,D). These analyses demonstrate that no significant transchelation of ^{64}Cu occurs in serum either in vitro or in vivo for both conjugates. These data are similar to that reported by Lewis et al. (*23*) who showed that both ^{64}Cu-labeled biotin DOTA and a ^{64}Cu-labeled DOTA–antibody conjugate were 100% stable

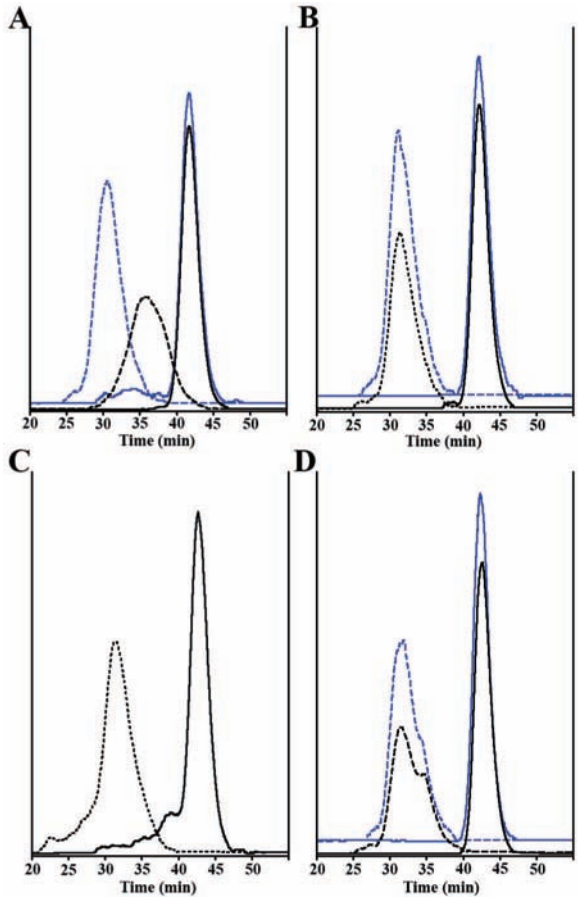

Figure 4. SEC analysis of radiolabeled M5A conjugates. (A) SH-DO3A-VS-M5A radiolabeled with ^{111}In (black) or ^{64}Cu (blue) before and after the addition of NA3 (black dotted) or CEA (blue dotted). (B) NH-DO3A-VS-M5A radiolabeled with ^{111}In (black) or ^{64}Cu (blue) before and after the addition of CEA (black or blue dotted). (C) SATA-DO3A-VS-M5A radiolabeled with ^{111}In (black) before and after the addition of CEA (black dotted). (D) DOTA-NHS-M5A radiolabeled with ^{111}In (black) or ^{64}Cu (blue) before and after the addition of CEA (back or blue dotted). Radioactivity (arbitrary units) shown on the *y*-axis.

in serum for up to 48 h. We conclude that the so-called instability of ^{64}Cu DOTA or TETA based conjugates refers to metabolism of the radiolabeled chelates or their conjugates in the liver where uptake of the radiolabel into SOD has been documented (*24*, *25*). The redistribution of radiolabels into other proteins after metabolism is a well-recognized phenomenon as illustrated by the metabolic redistribution of radioiodine from radioiodinated proteins into thyroglobulin.

Biodistributions of Radiolabeled M5A Conjugates. SH- and NH-conjugated DO3A-VS-M5A were radiolabeled with ^{111}In or ^{64}Cu, and biodistibutions were performed in nude mice bearing CEA positive LS-174T xenografts. The results shown in Figure 6 demonstrate high tumor uptake, reaching a maximum of 40–50% ID/g at 48–96 h. It is noteworthy that, overall, the dynamic biodistributions are similar between SH and NH conjugates whether radiolabeled with ^{111}In or ^{64}Cu in terms of both kinetics of tumor and normal tissue uptake and the ratios of tumor to normal tissue uptake. The one exception may be higher tumor uptake for ^{64}Cu-labeled NH-DO3A-VS-M5A, but in this experiment, higher blood levels track with the higher tumor uptake, leading to similar tumor to blood ratios compared to the other radiolabeled conjugates. We conclude from this study that SH- and NH-DO3A-VS conjugates give equivalent biodistributions whether radiolabeled with ^{111}In or ^{64}Cu.

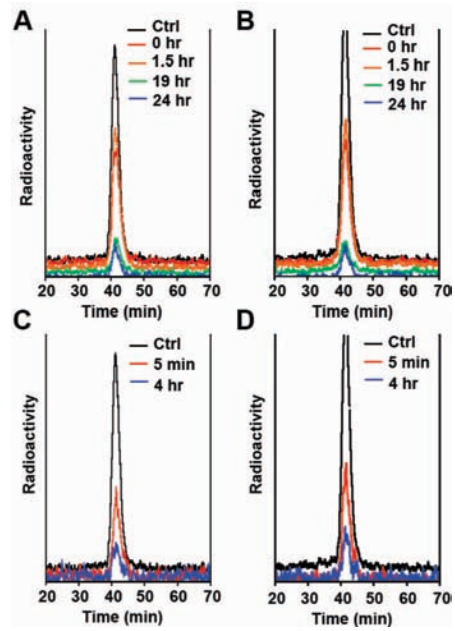

Figure 5. Serum stability analysis of ^{64}Cu-labeled M5A conjugates. ^{64}Cu labeled DO3A-VS-M5A was incubated with human serum and analyzed over time by SEC. The major peak at 42 min corresponds to the elution time for IgG. (A) SH-DO3A-VS-M5A. (B) NH-DO3A-VS-M5A. The sample was also injected into nude mice, blood removed over time, and the serum fraction analyzed by SEC. (C) SH-DO3A-VS-M5A. (D) NH-DO3A-VS-M5A.

As mentioned above, we were interested in comparing the SH- and NH-DO3A-VS-M5A conjugates with (a) DO3A-VS conjugated to surface sulfhydryls introduced into M5A by reaction of surface lysines with SATA and (b) the more conventional DOTA-NHS conjugated antibody. The results shown in Figure 7 demonstrate roughly equivalent tumor uptakes for both conjugates compared to each other and to those shown in Figure 6, but have interesting differences in the liver clearances. Over the period 0–96 h, the SATA conjugate had almost twice the liver uptake of the SH- and NH-DO3A-VS-M5A conjugates, while the DOTA-NHS conjugate had about a 25–50% increase in liver uptake compared to SH- and NH-DO3A-VS-M5A. The higher liver uptake for the SATA conjugate is likely due to the presence of aggregates that are absent in the other three conjugates (see Figure 4). However, the increase in liver uptake observed for the DOTA-NHS conjugate is harder to explain and implies that the SH- and NH-DO3A-VS conjugates may have improved imaging properties over those of the conventional DOTA-NHS conjugate.

^{64}Cu PET Imaging of SH- and NH-DO3A-VS-M5A. Based on the above biodistribution results, we predicted that tumors would be visualized as early as 24 h with ^{64}Cu-labeled conjugates for whole antibody, since tumor to blood ratios were >1.0 by that time. [Due to the constraint on injected activity because of radiation dose considerations, 24 h is a practical upper time limit on ^{64}Cu ($t_{½} = 13$ h) imaging in humans.] The dynamic biodistributions of radiolabel in the LS174T tumor/nude mouse model following injection of ^{64}Cu SH- and NH-DO3A-VS-M5A are illustrated via serial microPET images in Figure 8. The kinetics of the radiolabel were very similar for both forms of ^{64}Cu M5A antibody. At 1 and 5 h, the activity remained primarily intravascular, with tumor beginning to appear at the second time point. Tumor was the primary site of localization by 22 h, and tumor to normal tissue contrast was further increased by 45 h. Time–activity curves (TACs) derived from the microPET experiments (Figure 9) are quantitatively

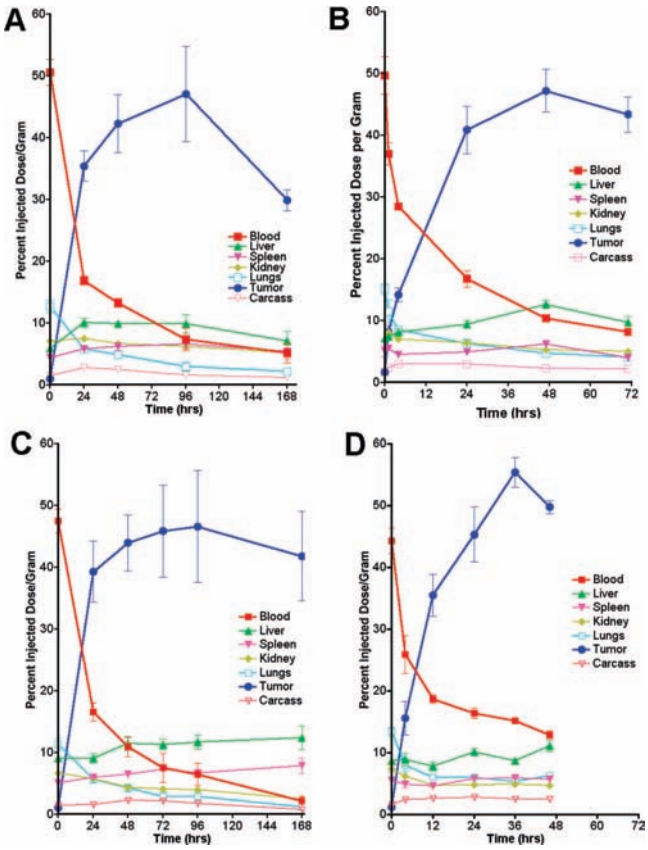

Figure 6. Biodistributions of ^{111}In- and ^{64}Cu-SH- and NH-DO3A-VS-M5A in nude mice bearing LS174T xenografts. The average %ID/g (±sem.) of five animals per time point is shown. (A) ^{111}In-labeled SH-DO3A-VS-M5A. (B) ^{64}Cu-labeled SH-DO3A-VS-M5A. (C) ^{111}In-labeled NH-DO3A-VS-M5A. (D) ^{64}Cu-labeled NH-DO3A-VS-M5A.

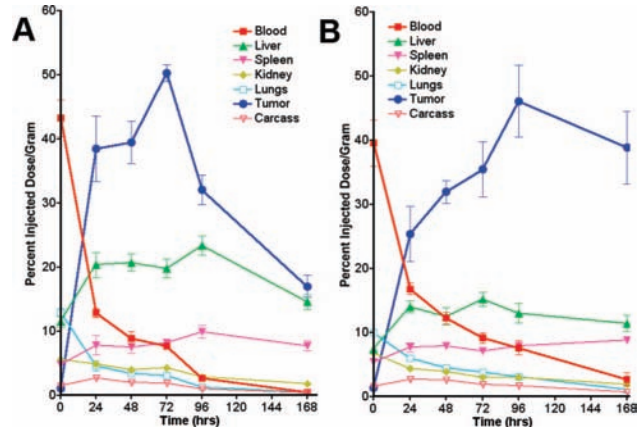

Figure 7. Biodistributions of ^{111}In- SATA-DO3A-VS-M5A and DOTA-NHS-M5A in nude mice bearing LS174T xenografts. The average %ID/g (±sem) of five animals per time point is shown. (A) ^{111}In-labeled SATA-DO3A-VS-M5A. (B) ^{111}In-labeled DOTA-NHS-M5A.

similar to those obtained in the direct-assay biodistribution experiments for ^{64}Cu SH- and NH-DO3A-VS-M5A (Figure 6C,D).

Note that, in spite of the very small sample sizes ($n = 2$ or 3 per data point), the standard deviations of the microPET time–activity curves (Figure 9) are similar to those of the standard biodistribution experiments, where $n = 5$ per data point (Figure 6). This illustrates a major advantage of serial quantitative imaging over the standard biodistribution approach, since it allows the determination of an entire TAC for a single mouse.

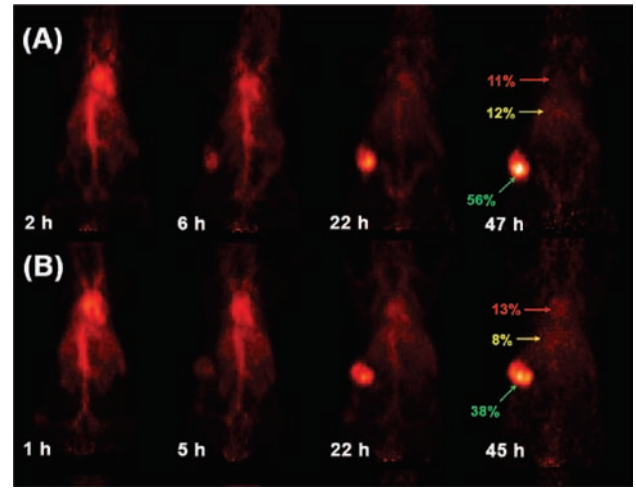

Figure 8. Dynamic biodistribution of ^{64}Cu-labeled hT84.66-M5A MAbs in athymic mice peripherally xenografted with CEA-positive LS-174T colon tumors. (A) SH-DO3A-VS-M5A; (B) NH-DO3A-VS-M5A. Images are PET anterior-view maximum intensity projections (MIPs) normalized to reflect radiodecay-corrected relative image intensity per unit injected activity. Labels in red, yellow, and green show directly measured %ID/g in blood (heart), liver, and tumor, respectively. Tumor weights at time of sacrifice were 126 and 155 mg in (A) and (B), respectively.

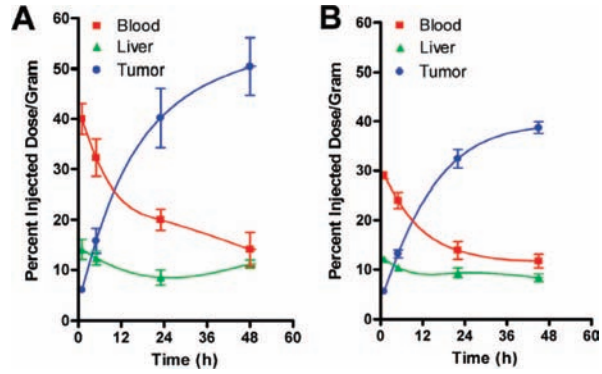

Figure 9. Time–activity curves derived from serial microPET studies. Data are average %ID/g (±sem.) for three (first three time points for SH-DO3A-VS-M5A) or two (NH-DO3A-VS-M5A and final time point for SH-DO3A-VS-M5A) mice.

CONCLUSIONS

Although much progress has been made in engineering radiolabeled antibodies for tumor imaging, many challenges still exist. In this study, we have returned to the use of intact antibodies because they arise at the earliest stage of clinical antibody development and can be produced in large quantities. Since recombinant engineering of antibodies is a time-consuming process and fraught with many obstacles, it is important to determine at the earliest point possible if the antibody of interest can indeed provide high targeting of tumor relative to normal tissue. If it can, then one could potentially use it at this stage of development as an in vivo diagnostic agent.

Until recently, radioimaging with antibodies was limited to the use of planar or SPECT imaging modalities, which have relatively poor spatial resolution and are not quantitative. Although PET has the potential to solve this problem, the need to match the isotope half-life with the blood clearance time of the antibody has limited most immuno-PET studies to antibody fragments labeled with short half-life radionuclides such as ^{18}F.

The newly available, 12.7 h half-life positron emitter ^{64}Cu offers a potential solution to this problem because it can be used to radiolabel whole antibody–chelate conjugates in a kit format. Based on the animal studies shown here, intact anti-CEA MAbs may deliver sufficient radiolabel to tumor to allow PET imaging as early as 22 h after injection. The improvement in PET images over those obtained with planar or SPECT imaging of ^{123}I- or ^{111}In-labeled antibodies is obvious; however, the ability to image tumors with low normal tissue background with whole ^{64}Cu-labeled antibodies in the mouse model came as a surprise, because most of our experience has been with planar gamma images. We attribute the majority of this improvement not only to the 3D nature and relatively high resolution of the microPET images, but also to the change in chelates, where DO3A-VS conjugates show less liver uptake that the more conventional DOTA-NHS conjugates. The ability to measure dynamic biodistributions in individual mice with micro-PET/^{64}Cu-labeled-mAb, as illustrated here, confers greater precision for a given sample size or, alternatively, permits substantial reduction in the number of mice required.

The practical advantages of using DO3A-VS-whole antibody conjugates include a versatile chemistry allowing conjugation at thiols in the mildly reduced hinge region or to surface amino groups in immunoglobulins, as well as maintaining the inherent metal ion binding and stability of the macrocyclic ring. Although reaction of DO3A-VS at the hinge region requires mild reduction of the antibody and removal of excess reducing agent, this is easily accomplished by the use of a spin column, and the resulting hinge thiols remain in the reduced state for up to 72 h before reoxidation occurs. Reaction of DO3A-VS at lysine residues requires brief exposure of the antibody to pH 9, conditions which, in our hands, have not compromised antigen-binding activity of several antibodies. Thus, DO3A-VS may be conjugated to antibodies under several conditions offering the researcher alternatives to the conventional NHS-active ester derivatives of DOTA that are inherently unstable and therefore less predictable in batch-to-batch conjugations. In addition, the quality of the PET images obtained within 24 h after injection indicates that PET/^{64}Cu-DO3A-VS-M5A should be evaluated for clinical use.

ACKNOWLEDGMENT

This research was supported by NCI grant CA43904.

LITERATURE CITED

(1) Williams, L. E., Wu, A. M., Yazaki, P. J., Liu, A., Raubitschek, A. A., Shively, J. E., and Wong, J. Y. (2001) Numerical selection of optimal tumor imaging agents with application to engineered antibodies. *Cancer Biother. Radiopharm. 16*, 25–35.

(2) Kenanova, V., and Wu, A. M. (2006) Tailoring antibodies for radionuclide delivery. *Expert Opin. Drug Delivery 3*, 53–70.

(3) Yazaki, P. J., Wu, A. M., Tsai, S. W., Williams, L. E., Ikler, D. N., Wong, J. Y., Shively, J. E., and Raubitschek, A. A. (2001) Tumor targeting of radiometal labeled anti-CEA recombinant T84.66 diabody and T84.66 minibody: comparison to radioiodinated fragments. *Bioconjugate Chem. 12*, 220–8.

(4) Li, L., Yazaki, P. J., Anderson, A. L., Crow, D., Colcher, D., Wu, A. M., Williams, L. E., Wong, J. Y., Raubitschek, A., and Shively, J. E. (2006) Improved biodistribution and radioimmunoimaging with poly(ethylene glycol)-DOTA-conjugated anti-CEA diabody. *Bioconjugate Chem. 17*, 68–76.

(5) Milenic, D. E., Garmestani, K., Chappell, L. L., Dadachova, E., Yordanov, A., Ma, D., Schlom, J., and Brechbiel, M. W. (2002) In vivo comparison of macrocyclic and acyclic ligands for radiolabeling of monoclonal antibodies with 177Lu for radioimmunotherapeutic applications. *Nucl. Med. Biol. 29*, 431–42.

(6) Gansow, O. A. (1991) Newer approaches to the radiolabeling of monoclonal antibodies by use of metal chelates. *Int. J. Radiat. Appl. Instrum., Part B 18*, 369–81.

(7) Lewis, M. R., Raubitschek, A., and Shively, J. E. (1994) A facile, water-soluble method for modification of proteins with DOTA. Use of elevated temperature and optimized pH to achieve high specific activity and high chelate stability in radiolabeled immunoconjugates. *Bioconjugate Chem. 5*, 565–576.

(8) Lewis, M. R., and Shively, J. E. (1998) Maleimidocysteineamido-DOTA derivatives: new reagents for radiometal chelate conjugation to antibody sulfhydryl groups undergo pH-dependent cleavage reactions. *Bioconjugate Chem. 9*, 72–86.

(9) Verel, I., Visser, G. W., and van Dongen, G. A. (2005) The promise of immuno-PET in radioimmunotherapy. *J. Nucl. Med. 46 Suppl 1*, 164S–71S.

(10) Garmestani, K., Milenic, D. E., Plascjak, P. S., and Brechbiel, M. W. (2002) A new and convenient method for purification of 86Y using a Sr(II) selective resin and comparison of biodistribution of 86Y and 111In labeled Herceptin. *Nucl. Med. Biol. 29*, 599–606.

(11) Borjesson, P. K., Jauw, Y. W., Boellaard, R., de Bree, R., Comans, E. F., Roos, J. C., Castelijns, J. A., Vosjan, M. J., Kummer, J. A., Leemans, C. R., Lammertsma, A. A., and van Dongen, G. A. (2006) Performance of immuno-positron emission tomography with zirconium-89-labeled chimeric monoclonal antibody U36 in the detection of lymph node metastases in head and neck cancer patients. *Clin. Cancer Res. 12*, 2133–40.

(12) Wu, A. M., Yazaki, P. J., Tsai, S., Nguyen, K., Anderson, A. L., McCarthy, D. W., Welch, M. J., Shively, J. E., Williams, L. E., Raubitschek, A. A., Wong, J. Y., Toyokuni, T., Phelps, M. E., and Gambhir, S. S. (2000) High-resolution microPET imaging of carcinoembryonic antigen-positive xenografts by using a copper-64-labeled engineered antibody fragment. *Proc. Natl. Acad. Sci. U.S.A. 97*, 8495–500.

(13) Li, L., Tsai, S. W., Anderson, A. L., Keire, D. A., Raubitschek, A. A., and Shively, J. E. (2002) Vinyl sulfone bifunctional derivatives of DOTA allow sulfhydryl- or amino-directed coupling to antibodies. Conjugates retain immunoreactivity and have similar biodistributions. *Bioconjugate Chem. 13*, 110–5.

(14) Yazaki, P. J., Sherman, M. A., Shively, J. E., Ikle, D., Williams, L. E., Wong, J. Y., Colcher, D., Wu, A. M., and Raubitschek, A. A. (2004) Humanization of the anti-CEA T84.66 antibody based on crystal structure data. *Protein Eng. Des. Sel. 17*, 481–9.

(15) You, Y. H., Hefta, L. J., Yazaki, P. J., Wu, A. M., and Shively, J. E. (1998) Expression, purification, and characterization of a two domain carcinoembryonic antigen minigene (N-A3) in pichia pastoris. The essential role of the N-domain. *Anticancer Res. 18*, 3193–201.

(16) Feehally, J., and Allen, A. C. (1999) Pathogenesis of IgA nephropathy. *Ann. Med. Interne (Paris) 150*, 91–8.

(17) Baranowska-Kortylewicz, J., and Kassis, A. I. (1993) Labeling of immunoglobulins with bifunctional, sulfhydryl-selective, and photoreactive coumarins. *Bioconjugate Chem. 4*, 300–4.

(18) Wright, J. K., Engel, J., and Jaton, J. C. (1978) Selective reduction and proteolysis in the hinge region of liganded and unliganded antibodies: identical kinetics suggest lack of major conformational change in the hinge region. *Eur. J. Immunol. 8*, 309–14.

(19) Sanderson, R. J., Hering, M. A., James, S. F., Sun, M. M., Doronina, S. O., Siadak, A. W., Senter, P. D., and Wahl, A. F. (2005) In vivo drug-linker stability of an anti-CD30 dipeptide-linked auristatin immunoconjugate. *Clin. Cancer Res. 11*, 843–52.

(20) Kukis, D. L., Diril, H., Greiner, D. P., DeNardo, S. J., DeNardo, G. L., Salako, Q. A., and Meares, C. F. (1994) A comparative study of copper-67 radiolabeling and kinetic stabilities of antibody-macrocycle chelate conjugates. *Cancer 73*, 779–86.

(21) Boswell, C. A., McQuade, P., Weisman, G. R., Wong, E. H., and Anderson, C. J. (2005) Optimization of labeling and metabolite analysis of copper-64-labeled azamacrocyclic chelators by radio-LC-MS. *Nucl. Med. Biol. 32*, 29–38.

(22) Boswell, C. A., Sun, X., Niu, W., Weisman, G. R., Wong, E. H., Rheingold, A. L., and Anderson, C. J. (2004) Comparative in vivo stability of copper-64-labeled cross-bridged and conventional tetraazamacrocyclic complexes. *J. Med. Chem. 47*, 1465–74.

(23) Lewis, M. R., Wang, M., Axworthy, D. B., Theodore, L. J., Mallet, R. W., Fritzberg, A. R., Welch, M. J., and Anderson, C. J. (2003) In vivo evaluation of pretargeted 64Cu for tumor imaging and therapy. *J. Nucl. Med. 44*, 1284–92.

(24) Bryan, J. N., Jia, F., Mohsin, H., Sivaguru, G., Miller, W. H., Anderson, C. J., Henry, C. J., and Lewis, M. R. (2005) Comparative uptakes and biodistributions of internalizing vs. noninternalizing copper-64 radioimmunoconjugates in cell and animal models of colon cancer. *Nucl. Med. Biol. 32*, 851–8.

(25) Bass, L. A., Wang, M., Welch, M. J., and Anderson, C. J. (2000) In vivo transchelation of copper-64 from TETA-octreotide to superoxide dismutase in rat liver. *Bioconjugate Chem. 11*, 527–32.

BC700161P

Modified "4 + 1" Mixed Ligand Technetium-Labeled Fatty Acids for Myocardial Imaging: Evaluation of Myocardial Uptake and Biodistribution

Peter Mirtschink,*,† Sebastian N. Stehr,§ Hans J. Pietzsch,‡ Ralf Bergmann,‡ Jens Pietzsch,‡ Gerd Wunderlich,|| Anke C. Heintz,§ Joachim Kropp,⊥ Hartmut Spies,+ Werner Kraus,# Andreas Deussen,† and Martin Walther‡

Institute of Physiology, Department of Anesthesiology, and Department of Nuclear Medicine, Technical University Dresden, D-01307 Dresden, Institute of Radiopharmacy, Forschungszentrum Dresden-Rossendorf, D-01314 Dresden, Department of Nuclear Medicine Carl Thiem-Hospital Cottbus, D-03048 Cottbus, and Federal Institute for Materials Research and Testing (BAM), D-12205 Berlin, Germany. Received May 7, 2007; Revised Manuscript Received September 3, 2007

Our group previously synthesized ^{99m}Tc-labeled fatty acids suitable for myocardial metabolism and flow imaging. In this set of experiments, 29 new analogues were synthesized according to the "4 + 1" mixed ligand approach with some specific differences. Conventional "4 + 1" ^{99m}Tc-fatty acids are built in the sequence: Tc-chelate, alkyl chain, and carboxylic group. We developed compounds following a new design with the sequence: carboxylic group, alkyl chain, Tc-chelate, and lipophilic tail. Therefore, the ^{99m}Tc-chelate was transferred to a more central position of the compound, aiming toward an improved myocardial profile and an accelerated liver clearance. In this context, several functional groups incorporated in the lipophilic tail section were tested to evaluate their influence on the compound's character. In addition to biodistribution studies *in vivo*, the myocardial first-pass extraction of the compounds was tested in an isolated Langendorff rat heart model. A satisfactory myocardial uptake of up to 20% of the injected dose (% ID) in the perfused heart and a fast liver clearance *in vivo* with only 0.29% ID/g at 60 min postinjection demonstrate that the induced molecular modifications affect the kinetics of ^{99m}Tc-radiolabeled fatty acid compounds favorably. From the data set, rules for estimating the biodistribution of fatty acids tracers are deduced.

INTRODUCTION

The development of ^{99m}Tc-labeled fatty acids (FA) suitable for evaluation of myocardial function and metabolism has been studied by various research groups since 1975 (*1*). The greatest challenge has been proven to be the design of ligands, which offer a stable binding between the FA and the metal core. Simultaneously, these ligands should not interfere with the biological properties of the FA, allowing an unimpeded recognition by membranous and intracellular proteins. Of the broad variety of neutral and small-sized mixed ligand chelate types, square-pyramidal Tc(V) oxocomplexes of tetradentate ligands are most commonly used (*2–9*). Because of disappointing results in biodistribution studies, a strong interference with the metal oxo-unit was assumed, influencing the molecular properties and the *in vivo* behavior of FA. Besides these types, lipophilic Tc(I) species were evaluated (*10, 11*).

After gaining experiences in FA labeling with oxotechnetium(V) complexes (*12, 13*), we focused on the development of "4 + 1" mixed ligand Tc(III) FA derivatives (*13, 14*). The presently available evidence suggests that in the "4 + 1" donor atom arrangement the radiometal is well-shielded by both a tripodal tetradentate ligand and a monodentate ligand bearing the FA moiety (*15*).

* Corresponding author: Peter Mirtschink, Institute of Physiology, Medical Faculty Carl Gustav Carus Technical University of Dresden, Fetscherstr. 74 01307, Dresden, Germany. Tel.: +49 351 458 6014. Fax: +49 351 458 6301. E-mail: peter_mirtschink@web.de.

† Institute of Physiology, Technical University Dresden.

§ Department of Anesthesiology, Technical University Dresden.

‡ Institute of Radiopharmacy.

|| Department of Nuclear Medicine, Technical University Dresden.

⊥ Department of Nuclear Medicine Carl Thiem-Hospital Cottbus.

BAM.

+ Deceased on March 25, 2007.

In experiments using the isolated guinea pig heart, the evaluated compounds clearly outmatched the extraction results of the "3 + 1" oxotechnetium(V) FA analogues. Furthermore, no *in vitro* transchelation reaction with glutathione was observed, indicating a high stability toward those challenging agents (*15*).

Although promising uptake results were achieved with the isolated heart model, no "4 + 1" FA compound synthesized so far had similarly advantageous biodistribution parameters to those of established iodinated FA tracers (e.g., iodine-labeled 15-(*p*-iodophenyl)pentadecanoic acid, ^{123}I-IPPA, and 15-(*p*-iodophenyl)-3-(*R,S*)-methylpentadecanoic acid, ^{123}I-BMIPP). Therefore, the main problems, namely, the high liver uptake, as observed for many other ^{99m}Tc-labeled FA compounds, and a decelerated liver clearance, remained.

In an attempt to synthesize ^{99m}Tc-labeled FA based on the promising "4 + 1" mixed ligand approach with an improved myocardial profile and a faster liver washout, some innovative structural modifications were introduced. While the conventional "4 + 1" ^{99m}Tc-FA are built in the sequence Tc-chelate, alkyl chain, and carboxylic group, modified compounds were designed according to the sequence carboxylic group, alkyl chain, Tc-chelate, and lipophilic tail. Therefore, the ^{99m}Tc-chelate was transferred to a more central position, to avoid nonrecognition by membranous and intracellular enzymes because of a terminally positioned artificial ^{99m}Tc-chelate.

In the following, we describe the chemistry of modified "4 + 1" ^{99m}Tc-FA as well as some improvements and adaptation of the recently published labeling procedure (*14*). Moreover, we correlate changes in molecular structure of the synthesized ^{99m}Tc compounds with biological behavior, namely, uptake and biodistribution. For better clarity, Tc complexes and their corresponding Re compounds were organized into groups (denoted by **I-VII** and **ReI-ReVII** or rather **ReMeI-ReMeVII**

10.1021/bc700164c CCC: $40.75 © 2008 American Chemical Society
Published on Web 12/04/2007

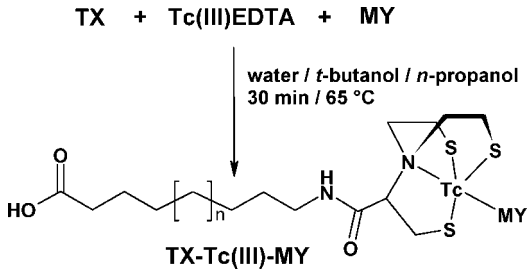

Figure 1. The compound groups **I**–**VII** of the recent "4 + 1"-^{99m}Tc/Re FA complexes with different metabolic stability depending on the chemical properties of the monodentate ligand. All compounds are shown in Table 1. Unfunctionalized isocyanides in **Ia**–**Ie**. Unfunctionalized phosphines in **IIa**–**IId**. Phosphines or phospinites in **IIIa**–**IIIb**. Isocyano alkylamides in **IVa**–**VIe**. Alkyl isocyano alkanoates in **Va**–**Vh**. Carboxyl group containing phosphines or isocyanides in **VIa**–**VIc**. Unsubstituted tetradentate ligand fatty acid containing phosphine in **VII**.

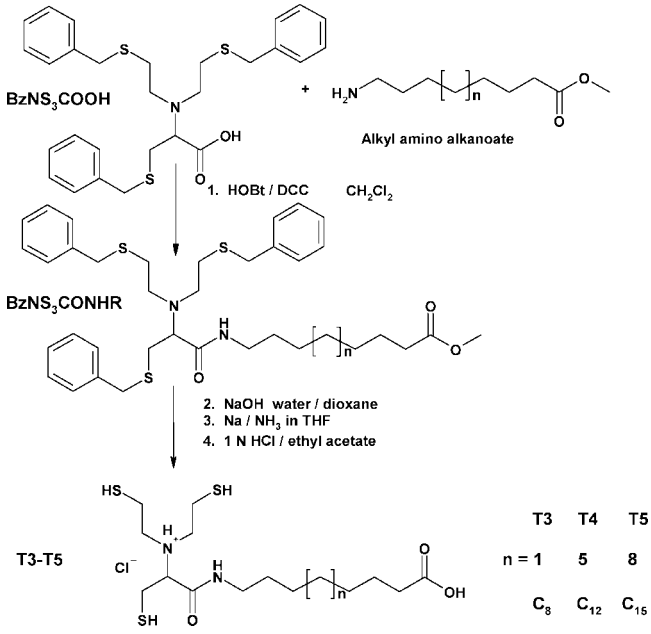

Figure 2. Synthesis of the FA substituted tristhiolate ligand.

for the corresponding Re(methyl) derivatives) according to their physicochemical properties determined by the monodentate ligands (Figure 1).

EXPERIMENTAL PROCEDURES

Materials and Instrumental Techniques. EDTA was purchased from Riedel-deHaen. $PhPMe_2$ (M0), PPh_3 (M1), Ph_2P-*p*-C_6H_4COOH (M2), $P(PropCN)_3$ (M3), P(*o*-Tol)$_3$ (M4), Ph_2POEt (M5), and trifluoroacetic acid (TFA) were purchased from Aldrich. 2-Isocyano-2-methylpropane (or TBI *t*-butyl isonitril) (M7) were purchased from Alfa products and a commercial Cardiolite kit with 1-isocyano-2-methoxy-2-methylpropane (or MIBI 2-methoxyisobutyl isonitril) (M8) from Bristol-Myers-Squibb. All commercial reagents were used without further purification. 2,3,5,6-Tetrafluorophenyl 4-isocyanobutanoate and 2,3,5,6-tetrafluorophenyl 4-(isocyanomethyl) benzoate, serving as precursors for the monodentate isocyano ligand, and 3-(benzylthio)-2-{bis-[2-(benzylthio)ethyl]amino} propanoic acid ($BzNS_3COOH$) were prepared as described (*16*). The alkyl (isocyano) alkanoates ethyl 8-isocyanooctanoate (M12), ethyl 4-isocyanobutyrate (M13), ethyl 2-isocyanoacetate (M14), methyl 15-isocyanopentadecanoate (M15-Me), methyl 5-[(7-isocyanoheptyl)thio]pentanoate (M16-Me) and methyl 12-isocyanododecanoate (M19-Me) were prepared according the procedure that was used before (*14*) (see Figure 1 in Supporting Information for detail).

Proton nuclear resonance (^{1}H NMR) spectra were recorded on a 400 MHz Varian Inova 400 spectrometer (^{1}H 400 MHz, ^{13}C 100 MHz, ^{31}P 162 MHz). The ^{1}H and ^{13}C chemical shifts are reported in parts per million (ppm) relative to residual solvent signals or TMS as reference. ^{31}P chemical shifts are reported relative to H_3PO_4 as an external reference. Mass spectrometric measurements were performed with a Micromass Tandem Quadropole Mass Spectrometer (Quadro LC) operating in the MS mode. Mass spectral data were recorded in the positive or negative ESI mode. About 10^{-4} M of the sample dissolved in 1.0 mL of methanol or acetonitrile was injected at a flow rate of 5 mL/min. Elemental analyses were performed on a LECO Elemental Analyzer CHNS-932. UV/vis spectra were recorded on a Varian Cary 50 Bio spectrometer. HPLC analysis and purification of ^{99m}Tc-complexes were performed using a Perkin-Elmer instrument consisting of a Turbo LC System with a quaternary pump (series 200 LC pump) and a programmable absorbance detector model 785A. Infrared spectra were recorded on a FTIR-Spectrophotometer Spectrum 2000 (Perkin-Elmer). Determination of melting points was carried out with the help of a BÜCHI Melting Point B-540 machine. Analytical thin layer chromatography was performed on POLYGRAM SIL G/UV_{254} foils (Machery-Nagel). Nonradioactive rhenium complexes were monitored by their UV absorption at 254 nm, and ^{99m}Tc-complexes by gamma-ray detection (Bohrloch, NaI(Tl) crystal).

Synthesis of Tetradentate NS_3-Ligands (T3-T5). *General Coupling to FA.* DCC (433 mg, 2.1 mM), dissolved in 5 mL dichloromethane, was added dropwise at 0 °C to a solution of 3-(benzylthio)-2-{bis-[2-(benzylthio)-ethyl]-amino}-propanoic acid [($BzNS_3COOH$) 1074 mg, 2.1 mM] in 10 mL dichloromethane. After stirring for 15 min, 1-hydroxybenzotriazole (284 mg, 2.1 mM) was added. Subsequently, the alkyl-ω-aminoalkanoate (2.5 mM) dissolved in 10 mL dichloromethane was added, after the deliverance of the amine in the organic phase via extraction with a saturated solution of potassium carbonate from the corresponding hydrochloride. The reaction mixture was stirred first for 2 h at 0 °C, then 12 h at room temperature. After filtering off the precipitated byproduct, *N*,*N*′-dicyclohexylurea, the solvent was removed in vacuo. The purification of the yellow, oily crude product was performed chromatographically (*n*-hexane/ethyl acetate = 1/1, R_f = 0.6–0.85 depending on chain length) and yielded a slightly yellow, viscous oil (selected NMR data are shown in Supporting Information). To the alkyl ($BzNS_3CONH$-) alkanoate (0.25 mM) dissolved in 10 mL dioxane was added 4 mL 1 N aqueous sodium hydroxide for the saponification of the ester function. After stirring overnight, the reaction mixture was acidified with 1 N aqueous hydrochloric acid. This step was necessary, because the reducing conditions in the following deprotection step led to alkanoles in the case of esters. After acidification with TFA to pH 3–4 and evaporation of the solvent, a 3-fold extraction with chloroform/water followed. The united organic phases were dried with $MgSO_4$, and the solvent was evaporated under reduced pressure. The residue was purified by column chromatography (*n*-hexane/ethyl acetate = 1/1, R_f = 0.55–0.65) (selected NMR data are shown in Supporting Information).

Deprotection of the Tris-Thiolate Ligand. The FA containing $BzNS_3CONH$R-ligand (0.49 mM) was dissolved in 3 mL waterfree THF and added dropwise to liquid ammonia at −50 °C. Under gentle stirring, pieces of sodium were added. The termination of the reaction was seen in the excess of sodium, giving the reaction mixture a deep blue color. Subsequently, the evaporation of the solvent followed in a nitrogen gas stream. The remaining solid was carefully dissolved in 10 mL water,

acidified with 1 N hydrochloric acid (to pH 3–4), and extracted 5 times, each with 7 mL ethyl acetate. The product was obtained by concentration of the organic phases in vacuo and precipitation of the product with hexane. Because of the product instability, no more purification steps were performed.

The syntheses of the unsubstituted tetradentate ligands (TX), the oxalic acid salt of tris(2-mercaptoethyl)amine (T1), and 1-carboxy-3-mercapto-*N*,*N*-bis(2-mercaptoethyl)-1-oxopropan-2-aminium chloride (T2) have been described recently (*16*, *17*).

1-[(7-carboxyheptyl)amino]-3-mercapto-*N*,*N*-bis(2-mercaptoethyl)-1-oxopropan-2-aminium chloride (T3). ^{1}H NMR (CD_3CN): 1.31 (m, 6H, CH_2), 1.46–1.57 (m, 4H, CH_2), 2.28 (t, 2H, CH_2COO, ^3J = 8.0 Hz), 2.63 (t, 2H, CONHCH_2, ^3J = 8.0 Hz), 3.14–3.21 (m, 10H, 2 × NCH_2CH_2SH, NCH_2), 3.35–3.37 (m, 1H, C*H*CONH). ^{13}C NMR (CD_3CN): 22.1, 23.0, 23.5, 24.8, 26.7, 28.9, 29.4 (2C), 33.5, 39.0, 54.2, 54.8, 72.3, 169.2, 175.1. IR (KBr): 3410 (COOH, CONH), 2928, 2853 (CH_2), 1715 (COOH), 1648 (CONH). ESI-MS (MeOH): *m*/*z* (%) = 383 (90) for $[C_{15}H_{31}N_2O_3S_3]^+$.

1-[(11-carboxyundecyl)amino]-3-mercapto-*N*,*N*-bis(2-mercaptoethyl)-1-oxopropan-2-aminium chloride (T4). ^{1}H NMR ($CDCl_3$): 1.21–1.27 (m, 14H, CH_2), 1.49–1.54 (m, 4H, CH_2), 2.28 (t, 2H, CH_2COO, ^3J = 7.8 Hz), 2.60 (t, 2H, CONHCH_2, ^3J = 7.9 Hz), 3.00–3.28 (m, 10H, 2 × NCH_2CH_2SH, NCH_2). 3.33–3.36 (m, 1H, C*H*CON). ^{13}C NMR ($CDCl_3$): 22.3, 23.9, 25.9, 27.2, 29.2, 29.3, 29.4 (2C), 29.5 (2C), 29.6, 29.7 (2C), 32.9, 39.9, 54.5, 67.1, 72.9, 169.5, 176.8. IR (KBr): 3426 (COOH, CONH), 2926, 2853 (CH_2), 1710 (COOH), 1645 (CONH). ESI-MS (MeOH): *m*/*z* (%) = 439 (35) for $[C_{19}H_{39}N_2O_3S_3]^+$.

1-[(14-carboxytetradecyl)amino]-3-mercapto-*N*,*N*-bis(2-mercaptoethyl)-1-oxopropan-2-aminium chloride (T5). ^{1}H NMR ($CDCl_3$): 1.20–1.27 (m, 20H, CH_2), 1.50 (m, 4H, CH_2), 2.28 (t, 2H, CH_2COO, ^3J = 8.0 Hz), 2.62 (t, 2H, CONHCH_2, ^3J = 7.9 Hz), 3.00–3.30 (m, 10H, 2 × NCH_2CH_2SH, NCH_2). 3.36 (m, 1H, C*H*CON). ^{13}C NMR ($CDCl_3$): 22.0, 22.9, 25.5, 26.0, 26.9, 28.9, 29.2, 29.4 (2C), 29.5 (4C), 29.6, 29.7 (2C), 33.5, 39.9, 54.5, 54.6, 72.7, 169.5, 177.2. ESI-MS (MeOH): *m*/*z* (%) = 481 (90) for $[C_{22}H_{45}N_2O_3S_3]^+$.

Syntheses of Monodentate Ligands MY (M6, M9–M11, and M17–M18).*Phosphorus(III) Ligands*. The phosphorus(III) ligands M0–M5 were commercial reagents and were used without further purification.

12-{[(Diphenylphosphino)acetyl]amino}dodecanoic acid (M6). The coupling of 12-aminododecanoic acid with diphenyl phosphine acetate was carried out with DCC as described above for $BzNS_3CONHR$, the precursors for T3–T5. DCC (43 mg, 0.21 mM), dissolved in 1 mL dichloromethane, was added dropwise at 0 °C to a solution of diphenyl phosphine acetate (49 mg, 0.2 mM) in 2 mL dichloromethane. After stirring for 15 min, 1-hydroxybenzotriazole (27 mg, 0.2 mM) was added first, followed by the 12-amino-dodecanoic acid (43 mg, 0.2 mM) suspended in 5 mL dichloromethane. The reaction mixture was stirred for 2 h at 0 °C, then for 12 h at room temperature. After filtering off the precipitated byproduct *N*,*N*′-dicyclohexylurea and unreacted amino acid, the solvent was removed in vacuo. Because of the product instability toward oxygen, no more purification steps were performed. Yield: 67 mg (76%); colorless waxy solid. ^{1}H NMR ($CDCl_3$): broad signals, because of an equilibrium of tautomeric species, 1.12–1.37 (m, 14H), 1.56 (m, 2H), 1.60 (m, 2H), 2.18 (m, 2H), 3.10 (m, 2H), 3.53 (m, 2H, PC H_2CONH), 6.6 (s, 1H, N*H*), 7.30 (m, 2H, phenyl), 7.38 (m, 4H, phenyl), 7.80 (m, 4H, phenyl). ^{13}C NMR ($CDCl_3$): 25.2, 25.9, 26.3, 26.9, 29.5 (3C), 34.2, 39.9, 49.1, 63.5, 129.0 (4C), 130.9 (2C), 132.6 (2C), 169.3 (*C*ONH), 179.8 (*C*OO). ^{31}P NMR ($CDCl_3$): −16.3. ESI-MS (MeOH): *m*/*z* (%) = 465 (100) for $[C_{26}H_{36}NNaO_3P]^+$.

Isocyano Ligands M9–M11 and M17–M18.*Isocyano Alkylamide Ligands M9–M11.General Procedures.* 0.10 mM of the amine, dissolved in 1 mL THF, was added dropwise to 2,3,5,6-tetrafluorophenyl 4-isocyanobutanoate (0.10 mM) and 2,3,5,6-tetrafluorophenyl 4-(isocyanomethyl)-benzoate (0.10 mM) dissolved in 1 mL THF. The reaction mixture was stirred for 2.5 h at room temperature. Then, separation of the solvent in vacuo and purification by column chromatography followed.

4-Isocyano-*N*-octylbutanamide (M9). After removal of the solvent, the crude product was purified by column chromatography (silica gel 60, *tert*-butyl methyl ether/*n*-hexane = 2/1, R_f = 0.10). Yield from 12.9 mg (0.10 mM) 1-aminooctane: 14.5 mg (65%) colorless oil. ^{1}H NMR ($CDCl_3$): 0.86 (t, 3H, CH_3, ^3J = 7.0 Hz), 1.25–1.28 (m, 10H, CH_2), 1.48 (m, 2H, CH_2), 1.95–2.03 (m, 2H, CH_2), 2.33 (t, 2H, CH_2CONH, ^3J = 7.0 Hz), 3.22 (m, 2H, NHCH_2), 3.47 (tt, 2H, CNCH_2, $^3J_{HH}$ = 6.2 Hz, $^2J_{HN}$ = 1.7 Hz), 5.56 (s, 1H, CON*H*). ^{13}C NMR ($CDCl_3$): 14.3, 22.8, 24.9, 27.1, 29.4, 29.5, 29.8, 32.0, 32.5, 39.8 (NH*C*H_2), 41.2 (t, CN*C*H_2, $^2J_{CN}$ = 6.5 Hz), 156.5 (t, *C*N, $^1J_{CN}$ = 5.8 Hz), 171.0. IR (KBr): 3313, 2957, 2927, 2856 (CH_2, CH_3), 2148 (CN), 1642, 1554. ESI-MS (MeOH): *m*/*z* (%) = 225 (100) for $[C_{13}H_{25}N_2O]^+$.

***N*-butyl-4-isocyano-*N*-methylbutanamide (M10).** Column chromatography (silica gel 60; *tert*-butyl methyl ether/*n*-hexane = 4/1, R_f = 0.40. Yield: (70%) colorless oil. ^{1}H NMR ($CDCl_3$): particular doubling of signals because of the mixture of cis/trans isomers, 0.90 (t, 3H, CH_3, ^3J = 7.2 Hz), 0.93 (t, 3H, CH_3, ^3J = 7.0 Hz), 1.21–1.36 (m, 4H, CH_2), 1.42–1.57 (m, 4H, 2 × CH_2), 1.92–2.03 (m, 4H, CH_2), 2.44 (t, 2H, CH_2CONH, ^3J = 6.8 Hz), 2.47 (t, 2H, CH_2CONH, ^3J = 6.8 Hz), 2.89 (s, 3H, NCH_3), 2.96 (s, 3H, NCH_3), 3.25 (t, 2H, NCH_2, ^3J = 7.6 Hz), 3.33 (t, 2H, NCH_2, ^3J = 7.6 Hz), 3.50 (tt, 4H, CNCH_2, $^3J_{HH}$ = 6.2 Hz, $^2J_{NH}$ = 1.9 Hz). ^{13}C NMR ($CDCl_3$): 14.0, 14.1, 20.2, 20.3, 24.5, 24.7, 28.7, 29.4, 29.6, 30.7, 33.6 (N *C*H_3), 35.3 (N *C*H_3), 41.4 (t, CN*C*H_2, $^2J_{CN}$ = 6.2 Hz), 41.5 (t, CN*C*H_2, $^2J_{CN}$ = 6.1 Hz), 47.8, 49.8, 156.2 (broad, *C*N), 170.8. ESI-MS (MeOH): *m*/*z* (%) = 183 (95) for $[C_{10}H_{19}N_2O]^+$.

4-(Isocyanomethyl)-*N*-octylbenzamide (M11). Column chromatography (silica gel 60, *tert*-butyl methyl ether/*n*-hexane = 2/1, R_f = 0.34). Yield: (91%) colorless solid. Mp 82 °C. ^{1}H NMR ($CDCl_3$): 0.86 (t, 3H, CH_3, ^3J = 6.6 Hz), 1.24–1.37 (m, 10H, CH_2), 1.60 (m, 2H, CH_2), 3.43 (t, 2H, NHCH_2, ^3J = 7.1 Hz), 4.68 (s, 2H, CNCH_2Ph), 6.23 (s, 1H, CON*H*), 7.38 (d, 2H, phenyl, ^3J = 8.4 Hz), 7.78 (d, 2H, phenyl, ^3J = 6.4 Hz). ^{13}C NMR ($CDCl_3$): 14.3, 22.9, 29.4, 29.5, 29.9, 31.8, 32.0, 40.4, 45.5 (t, CN*C*H_2Ph, $^2J_{CN}$ = 6.9 Hz), 126.9 (2C), 127.8 (2C), 135.3, 135.6, 156.8 (t, *C*N, $^1J_{CN}$ = 5.6 Hz), 166.9. IR (KBr): 3348, 3063 (CH-phenyl), 2954, 2921, 2851 (CH_2, CH_3), 2158 (CN), 1632. ESI-MS (MeOH): *m*/*z* (%) = 273 (100) for $[C_{17}H_{25}N_2O]^+$.

Alkyl isocyanoalkanoate. Preparation according the other described alkyl-(isocyano)alkanoates (*14*).

Octyl isocyanoacetate (M17). Yield: (86%) viscous colorless oil. ^{1}H NMR ($CDCl_3$): 0.86 (t, 3H, CH_3, ^3J = 6.0 Hz), 1.25–1.35 (m, 10H, CH_2), 1.61–1.69 (m, 2H, CH_2), 4.18–4.20 (m, 4H, CNCH_2+ OCH_2). ^{13}C NMR ($CDCl_3$): 14.3, 22.8, 25.9, 26.0, 28.6, 29.3, 31.9, 43.7, 67.1, 157.4 (broad), 164.2. ESI-MS (MeOH): *m*/*z* (%) = 198 (100) for $[C_{11}H_{20}NO_2]^+$.

Dodecyl Isocyanoacetate (M18). Yield: (89%) viscous colorless oil. ^{1}H NMR ($CDCl_3$): 0.84 (t, 3H, CH_3, ^3J = 6.2 Hz), 1.20–1.36 (m, 18H, CH_2), 1.60–1.68 (m, 2H, CH_2), 4.16–4.19 (m, 4H, CNCH_2+ OCH_2).^{13}C NMR ($CDCl_3$): 14.2, 22.6, 25.8, 26.1, 28.5, 29.1 (2C), 29.3 (2C), 29.6, 31.8, 43.5, 67.0, 156.8 (broad), 166.4. ESI-MS (MeOH): *m*/*z* (%) = 254 (100) for $[C_{15}H_{28}NO_2]^+$.

Preparation of Selected $^{185/187}$Rhenium and ^{99g}Technetium Complexes as Reference Compounds. "4 + 1" FA-NS_3 Re-dimethylphenylphosphine derivatives (TX-Re-M0) were used in ligand exchange reactions as ideal FA precursor complexes for the preparation of the corresponding isocyano-substituted compounds.

[Methyl 12-({*N*,*N*-bis[2-(mercapto-κS)ethyl]cysteinyl-κ^2N^2,S^3}amino)dodecanoate](dimethylphenylphosphine)rhenium (III) (MeT4-Re-M0). The tripodal ligand 1-[(11-carboxyundecyl)amino]-3-mercapto-*N*,*N*-bis(2-mercaptoethyl)-1-oxopropan-2-aminium chloride (T4) (100 mg, 0.21 mM) and the monodentate ligand dimethyl phenyl phosphine (M0) (58 mg, 0.42 mM) were refluxed for 3 h in methanol with the hexathiourea Re(III) complex $\{Re[SC(NH_2)_2]_6\}Cl_3 \times 1H_2O$ (161.5 mg, 0.21 mM) as an appropriate Re(III) precursor. The hydrochloric acid formed during the reaction in the methanol leads to esterification of the carboxyl group (MeT4). (This esterification does not happen with the no carrier added (nca) preparation of the appropriate ^{99m}Tc compounds in predominantly aqueous medium.) After removal of the solvent, the crude product was purified by column chromatography (silica gel 60, chloroform/ethyl acetate, 4/1, $R_f = 0.50$). Yield: 75 mg (46%) green solid. ^{1}H NMR ($CDCl_3$): 1.22–1.31 (m, 14H, CH_2), 1.50 (m, 2H, CH_2), 1.59 (m, 2H, CH_2), 2.07 (d, 6H, PCH_3, $^3J = 3.2$ Hz), 2.28 (t, 2H, CH_2COO, $^3J = 7.4$ Hz), 2.33–2.41 (m, 1H, NCH_2), 2.68–2.83 (m, 6H), 3.03–3.30 (m, 7H), 3.35–3.38 (m, 1H, NCH_2), 3.63 (s, 3H, OCH_3), 3.65–3.73 (m, 1H, C*H*CONH), 5.98 (t, 1H, CON*H*, $^3J = 5.6$ Hz), 7.25–7.29 (m, 1H, phenyl), 7.37–7.41 (m, 2H, phenyl), 7.70–7.75 (m, 2H, phenyl). ^{13}C NMR ($CDCl_3$): 25.1, 27.1, 28.9, 29.1 (2C), 29.3, 29.4 (2C), 29.5, 29.6 (2C), 34.3 (*C*H_2COO), 40.1 (CONH*C*H_2), 47.3, 47.4, 50.1, 51.4, 51.7 (O *C*H_3), 73.0 (*C*HCONH), 128.2 (2C), 128.9, 130.5 (2C), 130.6, 169.1 (*C*ONH), 174.7 (CH_2*C*OOR). ^{31}P NMR ($CDCl_3$): –13.4. IR (KBr): 3070, 3052 (phenyl), 2925, 2853 (CH_2, CH_3), 1737 (COOR), 1676 (CO). UV/vis ($CHCl_3$): λ_{max} (nm): 335.6, 465.4.

[12-({*N*,*N*-Bis[2-(mercapto-κS)ethyl]cysteinyl-κ^2N^2,S^3}amino) dodecanoato][2-(isocyano-κC)-2-methylpropane]rhenium(III) (ReIb). The Re-dimethylphenylphosphino precursor complex (MeT4-Re-M0) (10 mg, 0.0129 mM) was stirred with 2-isocyano-2-methylpropane (M7) (2 mg, 0.026 mM) for 2 h at room temperature in 2 mL chloroform. After an additional step for ester saponification and removal of the solvent, the crude product was purified by column chromatography (silica gel 60; chloroform/ethyl acetate = 4/1, $R_f = 0.65$). Yield: 8.6 mg (95%) green solid. ^{1}H NMR ($CDCl_3$): 1.21–1.36 (m, 14H, CH_2), 1.44 (s, 9H, CCH_3), 1.48–1.80 (m, 4H, CH_2), 3.44 (m, 1H, CH_2), 3.64 (m, 1H, CH_2), 3.78 (m, 1H), 3.94 (m, 1H, C*H*CON), 6.82 (s, broad, 1H, CON*H*). ^{13}C NMR ($CDCl_3$): 24.8, 25.5, 25.7, 26.6, 26.9, 28.4, 29.3, 29.4 (2C), 29.7, 31.0, 31.5, 32.9, 36.2, 40.1, 47.1, 49.7, 56.2, 71.2, (N*C*HCO), 164.9 (*C*NC(CH)$_3$), 169.5 (*C*ONH), 179.2 (*C*OOH). ESI-MS (MeOH): *m*/*z* (%) = 705 (100) for $[C_{24}H_{45}N_3O_3ReS_3]^+$.

[8-({*N*,*N*-Bis[2-(mercapto-κS)ethyl]cysteinyl-κ^2N^2,S^3}amino)-octanoic acid](triphenylphosphine)rhenium(III) (ReIIa). Prepared according the procedure for MeT4-Re-M0 under the use of T3 (19 mg, 0.05 mM), the hexathiourea Re(III) complex (38 mg, 0.05 mM) and M1 (26 mg, 0.1 mM) and an additional step for ester saponification. Column chromatography (silica gel 60, chloroform/ethyl acetate = 2/1, $R_f = 0.3$). Yield: 28 mg (69%) green solid. ^{1}H NMR (CD_3CN): 1.27–1.37 (m, 6H, CH_2), 1.55 (m, 4H, CH_2), 2.27 (t, 2H, CH_2CO, $^3J = 8.0$ Hz), 2.60–2.72 (m, 3H, CH_2), 2.96–3.11 (m, 3H, CONHCH_2 and CH_2), 3.14–3.28 (m, 2H), 3.37 (m, 1H, CH_2), 3.75 (m, 2H, C*H*CON), 6.84 (s, broad, 1H, CON*H*), 7.35 (m, 9H, phenyl), 7.46 (m, 6H, phenyl). ^{13}C NMR (CD_3CN): 24.7, 26.6, 28.7, 28.9, 29.1, 31.3, 33.4, 35.7, 39.2, 46.4, 49.8, 50.7, 56.3, 56.8, 72.4 (N*C*H), 127.8 (d, $^2J_{CP} = 8.0$ Hz), 129.2, 134.1 (d, $^3J_{CP} = 10.0$ Hz), 144.6 (d, $^1J_{CP} = 45.0$ Hz), 168.3 (*C*ONH), 174.4 (*C*OOH). ^{31}P NMR ($CDCl_3$): 28.5 (Re*P*Ph$_3$). ESI-MS (MeOH): *m*/*z* (%) = 827 (100) for $[C_{33}H_{42}N_2O_3PReS_3]^+$.

[12-({*N*,*N*-Bis[2-(mercapto-κS)ethyl]cysteinyl-κ^2N^2,S^3}amino) dodecanoato](triphenylphosphine)rhenium(III) (ReIIb). Prepared according to the procedure for MeT4-Re-M0 under the use of T4 (48 mg, 0.1 mM), the hexathiourea Re(III) complex (77 mg, 0.1 mM) and M1 (52 mg, 0.2 mM) and an additional step for ester saponification. Column chromatography (silica gel 60, chloroform/ethyl acetate = 2/1, $R_f = 0.45$). Yield: 53 mg (60%) green solid. ^{1}H NMR ($CDCl_3$): 1.23–1.36 (m, 14H, CH_2), 1.52–1.82 (m, 4H, CH_2), 1.91 (m, 2H), 2.38 (t, 2H, CH_2COOH, $^3J = 6.0$ Hz), 2.50 (m, 1H, CH_2), 2.75–2.89 (m, 4H, CH_2), 3.06–3.32 (m, 4H, CONHCH_2 and CH_2), 3.42 (m, 1H, CH_2), 3.64 (m, 1H, CH_2), 3.75 (m, 1H), 3.88 (m, 1H, C*H*CON), 5.89 (s, broad, 1H, CON*H*), 7.26–7.32 (m, 9H, phenyl), 7.47 (m, 6H, phenyl). ^{13}C NMR ($CDCl_3$): 25.0, 25.6, 25.7, 26.6, 27.0, 29.3, 29.4, 29.5, 29.7, 31.2, 32.9, 36.1, 40.1, 46.9, 49.7, 50.0, 51.0, 56.3, 73.1 (N*C*HCO), 127.9 (d, $^2J_{CP} = 9.0$ Hz), 129.1, 134.3 (d, $^3J_{CP} = 11.0$ Hz), 143.7 (d, $^1J_{CP} = 46.0$ Hz), 168.9 (*C*ONH), 179.8 (*C*OOH). ^{31}P NMR ($CDCl_3$): 28.1 (Re*P*Ph$_3$). ESI-MS (MeOH): *m*/*z* (%) = 883 (95) for $[C_{37}H_{50}N_2O_3PReS_3]^+$.

[Methyl15-({*N*,*N*-Bis[2-(mercapto-κS)ethyl]cysteinyl-κ^2N^2,S^3}-amino)pentadecanoate](triphenylphosphine)rhenium(III) (ReMeIIc). Prepared according to the procedure for MeT4-Re-M0 under the use of T5 (26 mg, 0.05 mM), the hexathiourea Re(III) complex (38 mg, 0.05 mM) and M1 (26 mg, 0.1 mM). Column chromatography (silica gel 60, chloroform/ethyl acetate = 5/4, $R_f = 0.45$). Yield: 30 mg (65%) green solid. Crystals are available from acetonitrile solution at 4 °C. ^{1}H NMR ($CDCl_3$): 1.20–1.29 (m, 20H, CH_2), 1.49–1.61 (m, 4H, CH_2), 2.28 (t, 2H, CH_2CO, $^3J = 8.0$ Hz), 2.49 (m, 1H, CH_2), 2.76–2.91 (m, 4H, CH_2), 3.08–3.31 (m, 4H, CONHCH_2 and CH_2), 3.41 (m, 1H, CH_2), 3.64 (s, 3H, OCH_3), 3.75 (m, 1H, C*H*CON), 5.83 (s, broad, 1H, CON*H*), 7.27–7.34 (m, 9H, phenyl), 7.47 (m, 6H, phenyl). ^{13}C NMR ($CDCl_3$): 25.2, 27.7, 29.3, 29.4 (2C), 29.6, 29.7 (5C), 29.9, 34.5, 40.0, 46.9, 47.0, 49.8, 50.9, 51.7, 56.3, 73.1 (N*C*H), 127.9 (d, $^2J_{CP} = 10.1$ Hz), 129.8, 134.4 (d, $^3J_{CP} = 11.1$ Hz), 143.7 (d, $^1J_{CP} = 46.3$ Hz), 168.9 (*C*ONH), 174.7 (*C*OOMe). ^{31}P NMR ($CDCl_3$): 28.2 (Re*P*Ph$_3$). ESI-MS (MeOH): *m*/*z* (%) = 940 (90) for $[C_{41}H_{59}N_2O_3PReS_3]^+$.

[15-({*N*,*N*-Bis[2-(mercapto-κS)ethyl]cysteinyl-κ^2N^2,S^3}amino)pentadecanoic acid](triphenylphosphine)rhenium(III) (ReIIc). The ester function was saponified by addition of 0.5 mL 1 N sodium hydroxide to a solution of 1 mg of (**ReMeIIc**) in 2 mL dioxane kept at 75 °C for 10 min After acidification with 1 N hydrochloric acid to pH 3–4, the FA complex (**ReIIc**) was purified by semipreparative HPLC (Hypersil RP-18; eluent, acetonitrile/water/0.1% TFA; gradient, in 10 min from 50 → 100% acetonitrile; flow rate, 2 mL/min; retention time, 16.2 min ESI-MS (MeOH), *m*/*z* (%) = 926 (80) for $[C_{40}H_{57}N_2O_3PReS_3]^+$.

[12-({*N*,*N*-Bis[2-(mercapto-κS)ethyl]cysteinyl-κ^2N^2,S^3}amino)dodecanoic acid](ethyldiphenylphosphinite-κP)rhenium (III) (ReIIIb). Prepared according to the procedure for MeT4-Re-M0 by use of T4 (24 mg, 0.05 mM), the hexathiourea Re(III) complex (38 mg, 0.05 mM) and M5 (23 mg, 0.1 mM). Column chromatography (silica gel 60, *tert*-butyl methyl ether/hexane = 3/1, $R_f = 0.75$). Yield: 8 mg 19% of a dark green solid. ^{31}P NMR ($CDCl_3$): 16.5 (Re*P*Ph$_2$OEt). UV/vis ($CHCl_3$): λ_{max} (nm) 444.5. ESI-MS (MeOH): *m*/*z* (%) = 875 (100) for $[C_{33}H_{50}NaN_2O_4PReS_3]^+$. ESI-MS negative mode (MeOH): *m*/*z* (%) = 851 (100) for $[C_{33}H_{50}N_2O_4PReS_3]^-$.

[12-({*N*,*N*-Bis[2-(mercapto-κ*S*)ethyl]cysteinyl-κ^2*N*^{2},*S*^{3}}amino)-dodecanoic acid][4-(isocyano-κ*C*)-*N*-octylbutanamide]rhenium(III) (ReIVa). The precursor Re-dimethylphenylphosphine complex (MeT4-Re-M0) (12 mg, 0.0155 mM) was stirred with 4-isocyano -*N*-octylbutanamide (M9) (7 mg, 0.031 mM) for 2 h at room temperature in chloroform. After an additional step for ester saponification and removal of the solvent, the crude product was purified by column chromatography (silica gel 60, chloroform/ethyl acetate = 5/4, +0.1% TFA, $R_f = 0.35$). Yield: 12 mg (93%) green solid. ^{1}H NMR ($CDCl_3$): 0.85 (t, 3H, C*H*$_3$, ^3J = 6.8 Hz), 1.19–1.35 (m, 24H, C*H*$_2$), 1.46 (m, 2H, C*H*$_2$), 1.55 (m, 4H, C*H*$_2$), 2.09 (m, 2H, C*H*$_2$), 2.27 (t, 2H, C*H*$_2$CO, ^3J = 7.4 Hz), 2.39–2.45 (m, 1H, C*H*$_2$), 2.51 (t, 2H, C*H*$_2$CO, ^3J = 7.0 Hz), 2.78–2.91 (m, 2H, C*H*$_2$), 2.98 (m, 1H, C*H*$_2$), 3.09–3.42 (m, 9H), 3.49 (m, 1H, C*H*$_2$), 3.88 (m, 1H, NC*H*), 4.70 (t, 2H, CNC*H*$_2$, ^3J = 5.8 Hz), 6.02 (t, 1H, CONH, ^3J = 5.6 Hz), 6.41 (t, 1H, CONH, ^3J = 5.3 Hz). ^{13}C NMR ($CDCl_3$): 14.3, 22.9, 24.9, 27.1, 27.2, 29.0, 29.2, 29.3, 29.4 (2C), 29.5 (3C), 29.6, 29.7, 32.0, 32.1, 33.8, 34.1, 39.9, 40.2, 44.2, 44.8, 46.7, 48.0, 55.4, 71.7 (N*C*H), 166.4 (*C*N), 168.5 (CONH), 172.6 (*C*ONH), 178.3 (*C*OOH). ESI-MS (MeOH): *m*/*z* (%) = 868 (80) for $[C_{32}H_{59}N_4NaO_4ReS_3]^+$.

^{99g}Tc [12-({*N*,*N*-bis[2-(mercapto-κ*S*)ethyl]cysteinyl-κ^2*N*^{2},*S*^{3}}amino)-dodecanoato][octyl(isocyano-κ*C*)acetate]technetium(III) (Vc). The "carrier added" ^{99g}Tc reference complex was prepared according to the ^{99m}Tc complex synthesis by addition of 20 μL of a 10^{-6} M $Na^{99g}TcO_4$ solution to the 0.5 mL generator eluate. The complex was purified via semipreparative HPLC (Hypersil RP-18; eluent, acetonitrile/water/0.1% TFA; gradient, in 10 min from 50 → 100% acetonitrile; flow rate, 2 mL/min; retention time, 15.4 min). ESI-MS (MeOH): *m*/*z* (%) = 732 (100) for $[C_{30}H_{55}N_3O_5S_3Tc]^+$.

{*N*,*N*-Bis[2-(mercapto-κ*S*)ethyl]cysteinato(3-)-κ^2*N*,*S*^{3}}[methyl 15-(isocyano-κ*C*)pentadecanoate]rhenium(III) (ReMeVIb). A further "4 + 1" NS_3-Re-triphenylphosphine derivative (T2-Re-M1) described in ref (*18*) (13 mg, 0.019 mM) was used as precursor in ligand exchange reactions with methyl 5-{[6-(isocyano-κ*C*)hexyl]thio} pentanoate (M16-Me) (8 mg, 0.03 mM). Column chromatography (silica gel 60, chloroform/ethyl acetate = 1/1, $R_f = 0.65$). Yield: 6.7 mg (59%) green solid. ^{1}H NMR ($CDCl_3$): 1.20–1.35 (m, 20H, C*H*$_2$), 1.51–1.61 (m, 2H, C*H*$_2$), 1.73–1.80 (m, 2H, C*H*$_2$), 2.28 (t, 2H, C*H*$_2$COO, ^3J = 7.6 Hz), 2.41–2.48 (m, 1H, C*H*$_2$), 2.63–2.70 (m, 1H, C*H*$_2$), 2.84–2.98 (m, 3H, CONHC*H*$_2$ and C*H*$_2$), 3.14–3.20 (m, 1H), 3.25–3.29 (m, 1H), 3.35–3.40 (m, 1H), 3.45–3.49 (m, 1H, C*H*$_2$), 3.53–5.58 (m, 1H), 3.66 (s, 3H, OC*H*$_3$), 3.73–3.77 (m, 1H, NC*H*CON), 4.75 (t, 2H, ^3J = 6.4 Hz, CNC*H*$_2$). ^{13}C NMR ($CDCl_3$): 25.1, 26.9, 29.2, 29.4, 29.5, 29.7 (2C), 29.8 (2C), 29.9, 33.3, 34.4, 44.4, 45.3, 46.6, 48.2, 51.9, 55.1, 56.4, 69.3 (N*C*H), 163.8 (*C*NCH$_2$), 175.2 (*C*OOMe). ESI-MS (MeOH): *m*/*z* (%) = 705 (90) for $[C_{24}H_{43}N_2O_4ReS_3]^+$.

{*N*,*N*-bis[2-(mercapto-κ*S*)ethyl]cysteinato(3-)-κ^2*N*,*S*^{3}}[15-(isocyanoκ*C*)pentadecanoic acid] rhenium(III) (ReVIb). The ester function was saponified by the addition of 0.5 mL 1 N sodium hydroxide to a solution of 1 mg of **ReMeVIb** in 2 mL dioxane kept at 75 °C for 10 min After acidification with 1 N hydrochloric acid to pH 3–4, the FA was purified by semipreparative HPLC (Hypersil RP-18; eluent, acetonitrile/water/0.1% TFA; gradient, in 10 min from 50 → 100% acetonitrile; flow rate, 2 mL/min; retention time, 13.0 min). ESI-MS (MeOH): *m*/*z* (%) = 691 (90) for $[C_{23}H_{41}N_2O_4ReS_3]^+$.

{*N*,*N*-Bis[2-(mercapto-κ*S*)ethyl]cysteinato(3-)-κ^2*N*,*S*^{3}}[methyl 5-{[6-(isocyano-κ*C*)hexyl]thio} pentanoate]rhenium(III) (ReMeVIc). The "4 + 1" NS_3-Re-triphenylphosphine derivative (T2-Re-M1) described in ref (*18*) (15 mg, 0.022 mM) was used as the precursor in a ligand exchange reactions with methyl 15-isocyanopentadecanoate (M16-Me) (11 mg, 0.04 mM). Column chromatography (silica gel 60, chloroform/ethyl acetate = 1/1, $R_f = 0.55$). Yield: 10 mg (65%) green solid. ^{1}H NMR ($CDCl_3$): 1.18–1.27 (m, 2H, C*H*$_2$), 1.41–1.47 (m, 2H, C*H*$_2$), 1.57–1.81 (m, 8H, C*H*$_2$), 2.32 (t, 2H, C*H*$_2$COO, ^3J = 7.6 Hz), 2.45 (m, 1H, C*H*$_2$), 2.48–2.52 (m, 4H, C*H*$_2$SC*H*$_2$), 2.63–2.70 (m, 1H, C*H*$_2$), 2.82–2.98 (m, 2H), 3.14–3.20 (m, 1H), 3.25–3.29 (m, 1H), 3.35–3.42 (m, 1H), 3.45–3.49 (m, 1H, C*H*$_2$), 3.54–5.57 (m, 1H), 3.65 (s, 3H, OC*H*$_3$), 3.73–3.77 (m, 2H, NC*H*CON + C*H*$_2$), 4.76 (t, 2H, CNC*H*$_2$, ^3J = 8.0 Hz). ^{13}C NMR ($CDCl_3$): 24.4, 26.5, 28.5, 29.3, 29.8, 29.9, 31.9, 32.3, 33.1, 33.9, 44.4, 45.2, 46.5, 48.2, 51.8, 55.1, 56.4, 69.6 (N*C*H), 161.6 (*C*NCH$_2$), 174.3 (*C*OOMe). ESI-MS (MeOH): *m*/*z* (%) = 594 (90) for $[C_{20}H_{35}N_2O_4ReS_4]^+$.

{*N*,*N*-Bis[2-(mercapto-κ*S*)ethyl]cysteinato(3-)-κ^2*N*,*S*^{3}}[5-{[6-(isocyano-κ*C*)hexyl]thio}pentanoic acid]rhenium(III) (ReVIc). The ester function was saponified by addition of 0.5 mL 1 N sodium hydroxide to a solution of 1 mg of (**ReMeVIc**) in 2 mL dioxane kept at 75 °C for 10 min After acidification with 1 N hydrochloric acid to pH 3–4, the FA was purified per semipreparative HPLC (Hypersil RP-18; eluent, acetonitrile/water/0.1% TFA; gradient, in 10 min from 50 → 100% acetonitrile; flow rate, 2 mL/min; retention time, 11.8 min). ESI-MS (MeOH): *m*/*z* (%) = 580 (90) for $[C_{19}H_{33}N_2O_4ReS_4]^+$.

(12-{[(Diphenylphosphino-κ*P*)acetyl]amino}dodecanoic acid)[2,2′,2″-(nitrilo-κ*N*)triethane thiolato-(3-)-κ*S*]rhenium(III) (T1-Re-M6 = ReVIIa). 28 mg (0.97 mM) of the oxalic acid salt of tris(2-mercaptoethyl)amine (T1) and 100 mg (1.9 mM) of the crude monodentate 12-{[(diphenylphosphino)acetyl]-amino}dodecanoic acid (**M6**) were refluxed for 3 h in methanol with 35 mg (0.046 mM) hexathiourea Re(III) complex $\{Re[SC(NH_2)_2]_6\}Cl_3 \times 1H_2O$ as an appropriate Re(III) precursor. After removal of the solvent, the crude product was purified by column chromatography (silica gel 60, chloroform/ethyl acetate = 4/1, $R_f = 0.50$). The acidic reaction conditions in methanol lead to the corresponding methyl dodecanoato FA complex. (NMR data of the methyl ester Re complex are shown in Supporting Information.) For the saponification of the ester function, 1 mL 1 N aqueous sodium hydroxide was added to the dissolved methyl ester complex in 5 mL dioxane and stirred for 24 h. After acidification with TFA to pH 3–4 and evaporation of the solvent, a 3-fold extraction with chloroform/water followed. The united organic phases were dried with $MgSO_4$, and the solvent was evaporated under reduced pressure. The residue was purified by column chromatography (silica gel 60, chloroform/ethyl acetate = 9/1, $R_f = 0.5$). Yield: 23 mg (58%). Mp > 220 °C (decomp.). ^{1}H NMR ($CDCl_3$): 1.05–1.30 (m, 16H), 1.58–1.63 (m, 2H), 2.33 (t, 2H, ^3J = 7.4 Hz), 2.60–3.20 (m, 12H), 3.0 (q, 2H, ^3J = 6.5 Hz), 3.75 (d, 2H, PC*H*$_2$CONH, $^2J_{HP}$ = 3.4 Hz), 6.2 (s, broad, 1H, CONH), 7.28 (t, 2H, phenyl, ^3J = 7.1 Hz), 7.36 (t, 4H, phenyl, ^3J = 7.4 Hz), 7.67 (dd, 4H, $^3J_{HH}$ = 7.6 Hz, $^3J_{HP}$ = 9.0 Hz). ^{13}C NMR ($CDCl_3$): 24.9, 27.0, 29.0, 29.1, 29.2, 29.4, 29.4, 29.4, 29.5, 33.9, 40.1 (*C*H$_2$NHCO), 47.0, 48.0 (d, P*C*H$_2$CONH, $^1J_{CP}$ = 19.7 Hz), 60.4, 128.1 (d, $^3J_{CP}$ = 9.5 Hz), 129.4, 133.0 (d, $^2J_{CP}$ = 11.4 Hz), 144.4 (d, $^1J_{CP}$ = 44.8 Hz), 168.5 (*C*ONH), 177.2 (*C*OO). ^{31}P NMR ($CDCl_3$): 17.0. ESI-MS (MeOH): *m*/*z* (%) = 845 (70) $[C_{32}H_{48}N_2NaO_3PReS_3]^+$.

X-ray Data Collection and Processing. The X-ray data were collected at room temperature (293 or 273 K) on a SMART-CCD diffractometer (Siemens), using graphite monochromatized Mo Kα radiation (λ = 0.710 73 Å). A summary of the crystallographic data of **ReMeIIc** is given in Table 2. The structures were solved by direct methods. After anisotropic refinement of the nonhydrogen atoms, the hydrogen positions were calculated according to ideal geometries. Empirical absorption corrections were made. Most of the calculations were carried out in the SHELXTL system with some local modifications. Selected bond lengths and angles are reported in figure

Table 1. Composition and Structures of Investigated Tc Compounds I–VII

Nr	TX-Tc-MY	Structure
Ia	T3-Tc-M7	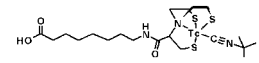
Ib	T4-Tc-M7	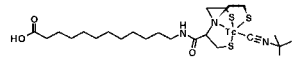
Ic	T5-Tc-M7	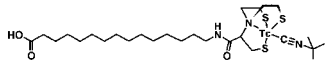
Id	T3-Tc-M8	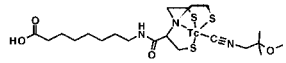
Ie	T4-Tc-M8	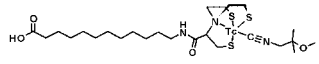
IIa	T3-Tc-M1	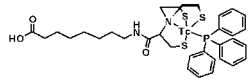
IIb	T4-Tc-M1	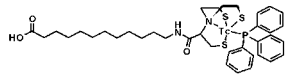
IIc	T5-Tc-M1	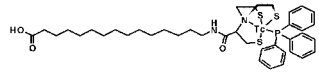
IId	T4-Tc-M3	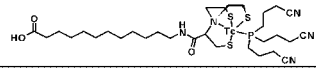
IIIa	T5-Tc-M4	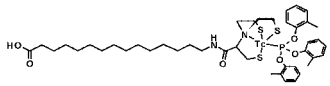
IIIb	T4-Tc-M5	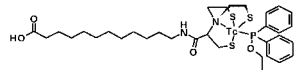
IVa	T4-Tc-M9	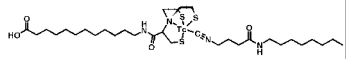
IVb	T5-Tc-M9	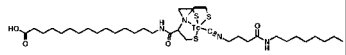
IVc	T4-Tc-M11	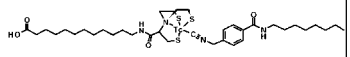
IVd	T5-Tc-M11	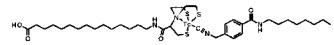
IVe	T4-Tc-M10	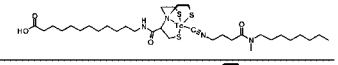
Va	T4-Tc-M14	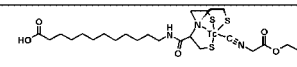
Vb	T4-Tc-M13	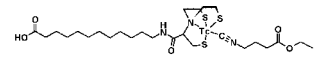
Vc	T4-Tc-M17	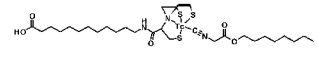
Vd	T3-Tc-M12	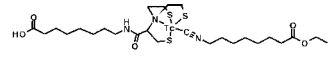
Ve	T3-Tc M17	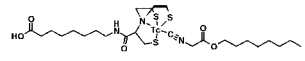
Vf	T5-Tc-M17	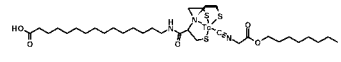
Vg	T2-Tc-M17	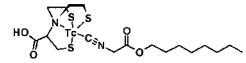
Vh	T2-Tc-M18	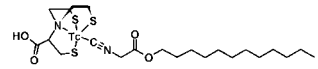
VIa	T3-Tc-M2	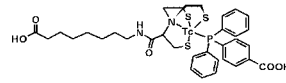
VIb	T2-Tc-M16	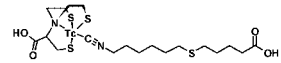
VIc	T2-Tc-M19	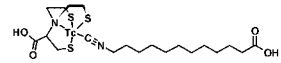
VId	T2-Tc-M15	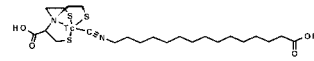
VII	T1-Tc-M6	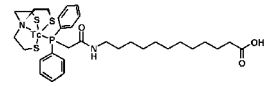

legends of the crystal structures. CCDC 638660 (**ReMeIIc**) contains the supplementary crystallographic data for this paper. These files can be obtained free of charge via http://www.ccdc.cam.ac.uk/data_request/cif, by e-mailing data_request@ccdc.cam.ac.uk, or by contacting The Cambridge Crystallographic Data Centre, 12, Union Road, Cambridge CB2 1EZ, UK; fax +44 1223 336033.

Synthesis Procedure for the Modified "4 + 1" ^{99m}Tc Complexes. ^{99m}Tc-[12-({*N*,*N*-bis[2-(mercapto-κS)ethyl]cysteinyl-κ^2N^2,S^3}amino)dodecanoic Acid][4-(isocyano-κC)-*N*-octylbutanamide]technetium(III) (IVa). Before usage, all isocyano ligands were transferred to their corresponding Cu(I) complexes by addition of 0.25 equiv of Cu(I) chloride. 0.5 mL pertechnetate solution (100–500 MBq generator eluate) were added to a prepared EDTA kit containing EDTA (1 mg) and stannous (II) chloride (0.08 mg), as well as mannitol (5 mg). After 20 min tempering at 37 °C, a purity control was followed by radio TLC (silicagel/acetone). The ^{99m}Tc(III)–EDTA complex resulted with over 99% radiochemical purity.

The aqueous EDTA-complex solution was added to a solution of the tetradentate ligand TX (0.5 mg) in 0.1 mL *t*-butyl alcohol {exemplary: 1-[(11-carboxyundecyl)amino]-3-mercapto-*N*,*N*-bis(2-mercaptoethyl)-1-oxopropan-2-aminium chloride (T4)}, and the monodentate phosphine or isocyano ligand MY (0.05 mg) in 0.2 mL *n*-propyl alcohol (exemplary: Cu(I) complex of 4-isocyano-*N*-octylbutanamide M9), and heated 30 min at 65 °C. After cooling to room temperature, the ^{99m}Tc–FA complex was purified via semipreparative HPLC (Hypersil RP-18; eluent, acetonitrile/water/0.1% TFA; gradient, in 10 min from 50 → 100% acetonitrile; flow rate, 2 mL/min (retention time for **IVa**, 14.6 min). For each compound group, at least one representative was identified as the expected ^{99m}Tc-FA by comparison of retention times with the nonradioactive Re reference FA complex. After the removal of acetonitrile by vacuum evaporation, 200 μL propylene glycol was added. The radiochemical yield of **I**–**VII** was 50–80%.

Animals. All experiments were carried out on Wistar rats of both gender (body weight 200–250 g) purchased by Charles River (Sulzfeld, Germany). The investigations conformed to the Guide for the Care and Use of Laboratory Animals issued by the U.S. National Institutes of Health and were approved by the local government authority (AZ 24-9168.24-1-2002-14, AZ 24-9168.21-4/2004-1). Animals were kept under a 12 h light–dark cycle and fed with commercial animal diet and water ad libitum.

Table 2. Crystallographic Data for the X-ray Diffraction Study of Rhenium FA Complexes ReMeIIc

	ReMeIIc
formula	$C_{41}H_{58}N_2O_3PReS_3$
formula weight	940.24
crystal system	monoclinic
space group	*P*2(1)/*n*
a [Å]	19.80 (3)
b [Å]	9.719 (14)
c [Å]	23.21 (3)
α [°]	90
β [°]	109.46 (3)
γ [°]	90
volume [Å ^{3}]	4212 (11)
Z	4
T [K]	273 (2)
ρ [g/cm^3]	1.483
absorption coeff. [mm^{-1}]	4.838
F(000)	1920
λ (Mo Kα) [Å]	0.71073
crystal size [mm^3]	0.3 × 0.25 × 0.2
θ-range from data collection	1.65–25.00
index ranges	$-23 \le h \le 12$ $-11 \le k \le 10$ $-27 \le l \le 27$
reflections collected	21769
independent reflections	7402
goodness-of-fit on F^2	1.097
R [$I > 2\sigma(I)$]	R1 = 0.1363 wR2 = 0.2208
R (all data)	R1 = 0.2328 wR2 = 0.2552

Isolated Heart Preparation. Anesthesia was performed in two steps: After resting in a diethyl ether chamber for a short time, deep anesthesia was achieved by an intraperitoneal (i.p.) injection of 2–3 mL urethane (15%). In addition, 1000 U/kg i.p. heparin was injected. Hearts were rapidly removed during continuous cooling (Krebs-Henseleit buffer (KHB) 4 °C) and mounted within 1 min via the aorta vertically on a perfusion cannula. Perfusion was immediately started according to the Langendorff technique with a modified KHB containing (mM/L): NaCl 116, KCl 4.6, $MgSO_4$ 1.2, KH_2PO_4 1.2, $NaHCO_3$ 25, $CaCl_2$ 2.5, glucose 11, and pyruvate 2. The buffer was equilibrated with a 95% O_2/5% CO_2 gas mixture (resulting pH 7.38), FA free bovine albumin (BSA) (0.1%/14.9 μM/L), and maintained at 37 °C. The pulmonary artery was catheterized to permit anaerobic collection of the coronary venous effluent perfusate. Total coronary flow was measured using an ultrasonic transit-time flowmeter (T206 Transonic Systems Inc., Ithaca, NY) inserted in the arterial perfusion line and kept constant at 10 mL/min. Coronary perfusion pressure (CPP) was measured through a pressure transducer (Gould Statham, USA) connected to the perfusion cannula. Heart rate was calculated manually from a CPP printout. "Arterial" and "venous" perfusate samples collected anaerobically were analyzed for pO_2, pCO_2, pH, HCO_3^- × (AVL 990S, AVL Scientific Corporation, Roswell, GA) before each intervention.

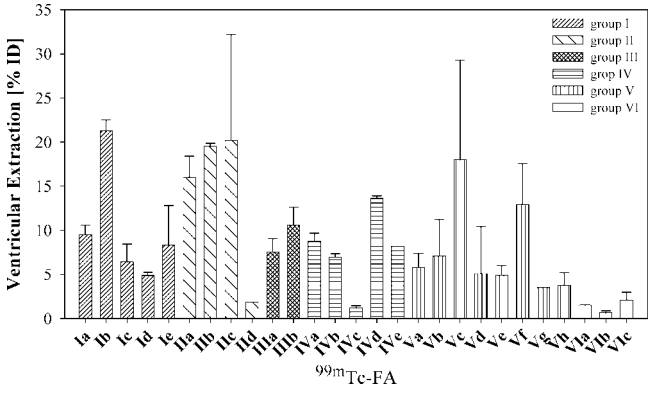

Figure 3. Ventricular extraction (in % of infused activity) of modified ^{99m}Tc-labeled FA evaluated with the Langendorff model.

Experimental Procedure. ^{99m}Tc-labeled FA were diluted in a ratio of 1:2 with KHB enriched with 6% BSA and left to equilibrate at room temperature for 30 min. After a period of 30 min to achieve hemodynamic stabilization of the beating heart, the ^{99m}Tc-labeled FA were infused proximal to the perfusion cannula in a ratio of 1:1000.

Starting with the FA infusion, the complete venous effluent perfusate was collected in 12 consecutive samples of 15 s each (samples 1–12). Following the stop of radioactivity infusion, another four samples during sole KHB perfusion were collected (rinse out of possible coronary radiolabeled substances; samples 13–16). Released radioactivity (A_{eff}) was taken to equal the sum of the radioactivity recovered from these 16 effluent perfusate samples corrected for background activity. Then, perfusion was stopped, and hearts were quickly removed and separated into atria and right and left ventricles. For input calculation (A_{in}), 5 15 s perfusate samples were collected under identical radioactivity infusion and flow settings directly from the perfusion cannula in the absence of a heart. All perfusate and heart samples were measured with a gamma counter (Wallac 1470 Wizard, PerkinElmer Freiburg, Germany).

Only experiments were used in which the calculated input (A_{in}) was in a range of ±20% of the measured total radioactivity of perfusate plus heart tissue samples ($A_{eff} + A_{tiss}$). Ventricular extraction (E_v) was calculated by dividing ventricular tissue radioactivity by the summed radioactivity of perfusate samples (A_{eff}) plus heart tissue samples (A_{tiss}).

Biodistribution Studies in Rats. Anesthesia was performed with an intraperitoneal injection (i.p.) of urethane (1.5 g/kg). A tail vein was surgically exposed, and a 200 μL (0.5 MBq) bolus of a solution containing the "4 + 1" ^{99m}Tc-FA compound and HSA (6%) in a 1:2 ratio were injected. The animals were sacrified by decapitation at 60 min after injection. The blood was immediately withdrawn by cardiac puncture with a heparinized syringe and the activity was counted. Organs were excised and weighed, and the radioactivity was determined (Wallac 1480 WizardTM gamma counter, PerkinElmer, Shelton, CT). The accumulated ^{99m}Tc activity in organs and tissues was calculated as percentage of the injected dose per organ (% ID/organ) or per gram tissue (% ID/g tissue). Data are given as mean ± standard deviation (SD) of four animals each.

RESULTS

Syntheses of FA Derivatives. With respect to the synthesis procedures, three important aspects deserve particular attention. First, the possibility to introduce the FA moiety to the tetradentate NS_3 ligand results in more influentual capabilities for the Tc–FA complex properties by variation of the monodentate ligand. Functionalized isocyano ligands can be used as well as different commercially available phosphines or phosphites with varying chemical and sterical characteristics. Second, the design of isocyano-substituted active esters provides easy access to various isocyano compounds by multifarious functionalization reactions at the active ester group. Third, the application of the isocyanide compounds as Cu(I) complexes is a very important fact regarding enhancement of reactivity toward ligand exchange at the [Tc(FA-NS_3)] core and concurrent stability of the isocyano group in the reaction medium. The advantages of this method are most obvious in all preparations in which the free FA appeared. As a consequence, the last saponification step, necessary when the isocyano FA is applied in the form of its ester, is redundant now, and thus, the synthesis proceeds more rapidly [50 min instead of 60 min; when

Table 3. Biodistribution of Modified ^{99m}Tc "4 + 1" FA Derivatives in Rats[a]

	Ia		**IIa**		**IIb**	
time p.i.	5 min	60 min	5 min	60 min	5 min	60 min
heart	0.78 ± 0.08	0.33 ± 0.02	2.88 ± 0.19	1.12 ± 0.22	0.96 ± 0.14	0.87 ± 0.07
liver	11.83 ± 0.78	5.51 ± 0.99	14.14 ± 0.52	17.14 ± 0.59	9.71 ± 1.39	7.62 ± 0.55
blood	1.57 ± 0.02	0.62 ± 0.01	0.51 ± 0.08	0.24 ± 0.01	2.53 ± 0.52	0.43 ± 0.07
lungs	1.21 ± 0.06	0.47 ± 0.02	1.04 ± 0.14	0.39 ± 0.03	2.96 ± 0.31	2.00 ± 0.33
kidneys	6.95 ± 0.51	2.59 ± 0.36	3.65 ± 0.22	1.57 ± 0.13	0.91 ± 0.06	0.91 ± 0.07
heart/liver	0.07	0.06	0.20	0.07	0.10	0.11
heart/blood	0.50	0.53	5.65	4.67	0.38	2.02
heart/lungs	0.64	0.70	2.77	2.87	0.32	0.49
	Vc		**Vd**		**IVa**	
time p.i.	5 min	60 min	5 min	60 min	5 min	60 min
heart	0.34 ± 0.04	0.04 ± 0.02	0.30 ± 0.03	0.05 ± 0.01	0.58 ± 0.18	0.38 ± 0.02
liver	4.96 ± 0.31	0.29 ± 0.08	12.45 ± 0.92	2.47 ± 1.10	5.10 ± 0.77	5.13 ± 0.30
blood	0.43 ± 0.05	0.10 ± 0.04	0.56 ± 0.17	0.13 ± 0.03	0.27 ± 0.02	0.09 ± 0.00
lungs	0.59 ± 0.09	0.14 ± 0.04	0.85 ± 0.19	0.38 ± 0.21	0.66 ± 0.26	0.36 ± 0.05
kidneys	1.38 ± 0.18	0.30 ± 0.13	2.27 ± 0.42	0.68 ± 0.23	0.98 ± 0.25	0.91 ± 0.11
heart/liver	0.07	0.14	0.02	0.02	0.11	0.07
heart/blood	0.79	0.40	0.54	0.38	2.15	4.22
heart/lungs	0.58	0.29	0.35	0.13	0.88	1.06
	VIc		**VId**		**VII**	
time p.i.	5 min	60 min	5 min	60 min	5 min	60 min
heart	1.46 ± 0.70	0.29 ± 0.09	1.15 ± 0.30	0.17 ± 0.03	1.04 ± 0.17	0.27 ± 0.03
liver	13.38 ± 1.45	0.88 ± 0.39	8.31 ± 0.78	0.60 ± 0.07	7.39 ± 0.56	5.94 ± 0.61
blood	3.36 ± 1.10	0.40 ± 0.06	3.36 ± 1.10	0.40 ± 0.06	0.66 ± 0.11	0.22 ± 0.03
lungs	2.00 ± 0.57	0.83 ± 0.54	2.11 ± 1.21	0.39 ± 0.11	1.87 ± 0.37	0.54 ± 0.02
kidneys	5.60 ± 0.88	1.06 ± 0.18	6.79 ± 1.63	0.71 ± 0.16	3.04 ± 0.48	0.84 ± 0.07
heart/liver	0.11	0.33	0.14	0.28	0.14	0.05
heart/blood	0.40	0.45	0.34	0.43	1.58	1.23
heart/lungs	0.73	0.35	0.55	0.44	0.56	0.50

[a] MW ± SD expressed as % ID/g organ, $n = 4$ per time point.

comparing the reaction conditions for the nca procedure given in ref (*14*)]. A further positive aspect is the decreased reaction temperature (from 90 to 65 °C), which causes no drop in the yields (in some cases, the yields are even higher) and diminishes the risk of forming the corresponding Tc(I) hexaisocyanide derivatives as byproducts.

The reaction route for the synthesis of "4 + 1" ^{99m}Tc/Re FA complexes with monodentate ligands bearing different metabolically stable functional groups is demonstrated in Figure 1.

Experiments on the Isolated Perfused Rat Heart. Figure 3 shows the extraction results of all synthesized and investigated compounds (the complex composition of each FA derivative in addition to uptake values is presented in Table 2 in the Supporting Information). The length of the FA chain in the tetradentate ligand varied among 1, 8, 12, and 15 carbon atoms. The highest value of ventricular extraction in the isolated perfused Langendorff rat heart was achieved with the dodecanoic FA derivative **Ib** with 21.25 ± 1.28% ID. Four other compounds (**IIa**, **IIb**, **IIc**, and **Vc**) also exceeded the extraction value of ^{123}I-IPPA, for which a ventricular extraction of 15.51% ID was measured (*14*). The lowest extraction (0.6–2.09% ID) showed the "4 + 1" ^{99m}Tc-FA with a tetradentate ligand bearing only a carboxylic group (**VIa–c**).

Biodistribution Studies in Rats. Table 3 shows the biodistribution of modified ^{99m}Tc "4 + 1" labeled FA in Wistar rats. Rapid clearance from blood was observed for all investigated compounds. The highest uptake in heart was achieved for **IIa** (2.88 ± 0.19% ID/g) with a remarkably high heart/blood ratio of 5.65 at 5 min postinjection (p.i.). **Vc** showed the most rapid washout from liver. Here, the initial liver uptake of 4.96 ± 0.31% ID/g was reduced down to 0.29 ± 0.08% ID/g at 60 min p.i.

The elimination of compounds from group **I–V** proceeded predominantly via the hepatobiliary system, whereas **VIc** and **VId** were excreted via the kidneys into the urine. The brain and the thyroid gland were almost free from radioactive species.

DISCUSSION

The development of ^{99m}Tc-labeled FA, suitable for myocardial metabolism imaging is a challenging task. In an effort to synthesize ^{99m}Tc-"4 + 1" FA compounds with an improved liver clearance and high myocardial uptake rate, the concept of simple linear molecules with an end-positioned chelate was abandoned for more complex molecules with the chelate unit within the chain. This structure modification is enabled by a carboxylic group at the chelate backbone that allows binding of the FA moiety by an ω-amino group via the carboxylic acid amide bound.

Thus, the remaining free coordination site on the tripodal metal core can additionally be functionalized by isocyanides or phosphorus(III) donors. The molecular structure of the triphenylphosphine complex **ReMeIIc**, the corresponding methyl ester of **ReIIc**, is presented as an example for the modified "4 + 1" FA species, bearing the FA unit bound to the tetradentate NS_3 ligand. The compound crystallizes as a racemic structure in the monoclinic spacegroup $P2(1)/n$ (see crystallographic data in Table 2). The centrosymmetry of the structure converts the 24(R) configuration into a 24(S) configuration. The structure of the chelate unit shows a large agreement with the basic structure of the unsubstituted "4 + 1" NS_3-triphenylphosphine complex (*19*). The complex unit adopted a trigonal bipyramidal geometry where the three NS_3 thiolate sulfurs form the trigonal plane and the amine nitrogen of the tetradentate FA ligand and the phosphorus atom of PPh_3 occupy the apical positions (Figure 4). Figure 5 shows the linkage of the molecules via hydrogen bonds between the nitrogen of the amide and one oxygen of the carboxyl group, resulting in a head-to-tail arrangement. This interaction leads to the formation of chains running parallel to the *b*-axis.

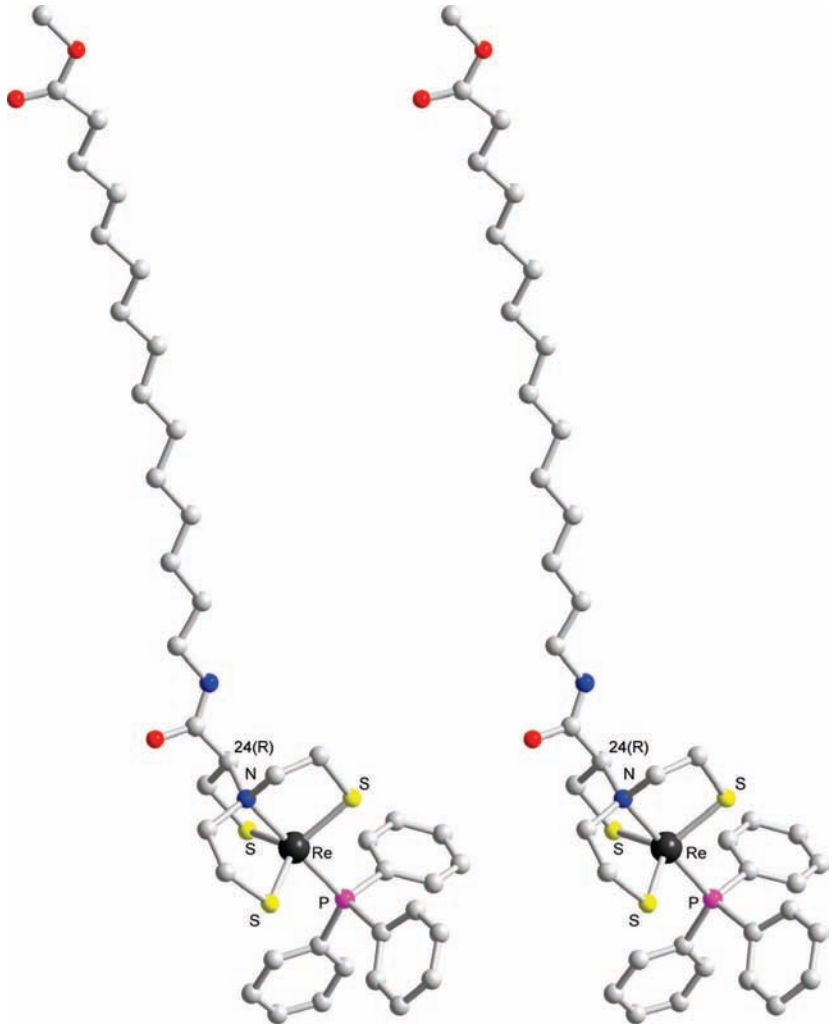

Figure 4. Stereo drawing of the "4 + 1" FA-Re-triphenylphosphine complex with selected bond lengths (pm) and angels (deg) Re-P 230.0(5), Re-N1 221.7(17), Re-S1 222.5(6), Re-S2 222.2(6), Re-S3 221.9(6), and N1-Re-P 178.0(5).

These structures allow variations on both parts of the chain by introducing metabolically active groups (e.g., ester or amide) and, thus, the tuning of the breakdown properties to vary the clearance characteristics, especially from the liver. The potentially improved recognition by membranous and cellular FA transport and degradation enzymes would be an additional advantage of the modified "4 + 1" compounds. The chelate is positioned relatively far away from both the lipophilic tail section and the polar acid section, and on both endings of the FA compound, only inartificial groups were found.

The configuration of natural FA was approximated by transferring the chelate from the end into the interior of the compound combined with a structural variation of the lipophilic tail composition. With the end-positioned carboxyl group, the synthesized derivates have a polar head serving as an important recognition feature. This polar section is so firmly connected with the chelate unit that decomposition is exclusively possible via β-oxidation. A lipophilic tail was constructed at the monodentate ligand, which represents a crucial characteristic of FA. Due to the included functional groups being cleaved in liver with a rate sequence of ester > ether > amide, the rapid formation of polar metabolites allows a fast washout from the liver (Figure 7).

Within this structure, the position of the chelate was varied and moved from the carboxyl group to the lipophilic tail. Therefore, the influence on heart uptake and biodistribution of the total length of the resulting molecule and the relation of the polar section to the lipophilic section were studied.

Regarding the results obtained from the isolated heart model, some of the newly synthesized compounds achieved extraction results of about 20% ID. The common characteristics of these well-extracted compounds are the high level of lipophilicity and a FA chain length between 12 and 15 carbon atoms. Thus, functional groups with particular lipophilic properties incorporated in the tail section are an important feature to increase the myocardial uptake. However, the length of the tail section and the chelate position have a minor influence. In contrast, a shortening of the alkyl chain down to the carboxylic group as done in **Vg** or **Vh** clearly decreases the myocardial uptake in the Langendorff heart model from 18.01% ID as achieved with **Vc** down to 3.51% and 3.77% ID, respectively. The room-filling "4 + 1" ^{99m}Tc-chelate reflecting a dodecanoic FA derivative with respect to elongation, comparable with palmitic acid, may explain the preference for the mentioned FA chain length.

Regarding the monodentate ligands used, isocyanides are preferred in consideration of the structural simplicity. However, one should keep in mind that the encumbering phosphine moiety is a part of many myocardium affine Tc tracers such as ^{99m}Tc-tetrofosmin or ^{99m}Tc-bis(diphosphines). Thus, it is not only permissive to involve phosphorus donor ligands in the intended tracer design, but rather reasonable profit may result from the binding properties of the phosphorus to technetium and the structural variability given by the three substituents. It involves the chance to locate positions at the phosphorus ligand that can be metabolized (as the phosphinite in complex **Vb**). Also worth mentioning is the prolonged myocardial retention time as

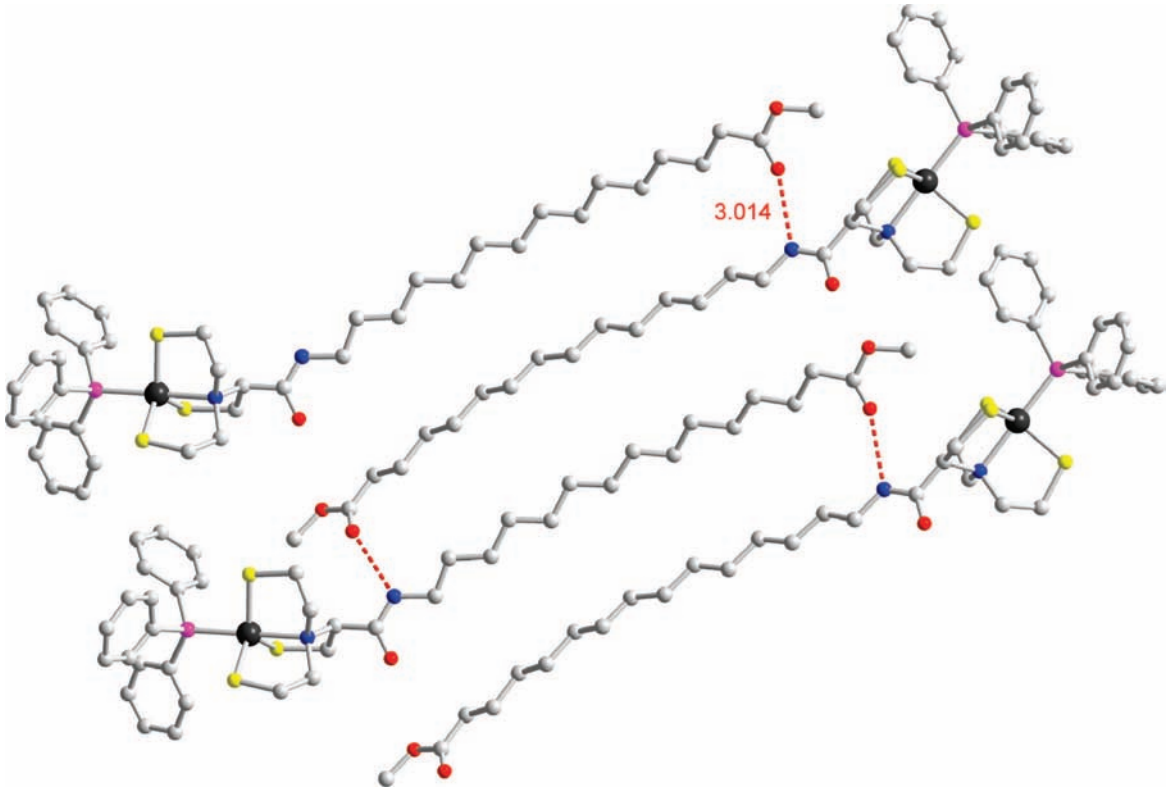

Figure 5. Molecules of the "4 + 1" FA-Re-triphenylphosphine complex building chains in the crystal structure. Dotted red lines indicate hydrogen bonds.

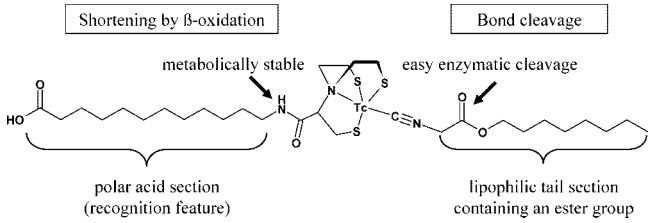

Figure 6. Lead structure (**V**) of the modified "4 + 1" ^{99m}Tc-FA concept for combining high myocardial uptake and fast liver clearance.

observed in biodistribution studies of **VII**, a "conventional" "4 + 1" FA derivative with an FA-bearing phosphine, and the triphenylphosphine containing compounds **IIa** and **IIb.** This fact is particularly obvious in comparison with "conventional" "4 + 1" FA with isocyano ligands (*14*). Initially, concerning in vivo stability of the presented ^{99m}Tc-FA compounds, metabolically stable ("inert") monodentate ligands (e.g., phosphines and amides [groups **II**–**IV**]) were synthesized. In further course, better metabolizable ligands (e.g., ester [group **V**]) were developed. In this context, group **IV** compounds with an NH-amide group incorporated into the tail can be regarded as precursors for derivatives developed later. At those compounds, the lipophilic tail is easily enzymatically cleaved by the introduction of an ester group (group **V**) (Figure 6).

A good example of how structural changes in the monodentate ligand are reflected in biodistribution patterns is given by comparison of FA derivatives with the phosphino monodentate (group **II**) vs isocyanide/ester compounds (group **V**) (Figure 7). **IIa** fulfills the demand for high lipophilicity resulting in promising uptake values in the isolated perfused rat heart and in biodistribution (Table 2 and Figure 7). Furthermore, convenient heart/blood and heart/lung ratios at 5 min p.i. were found. Unfortunately, data on liver clearance were disappointing. Compared with the value after 5 min p.i., the measured concentration of radioactive species in the liver at 60 min p.i.

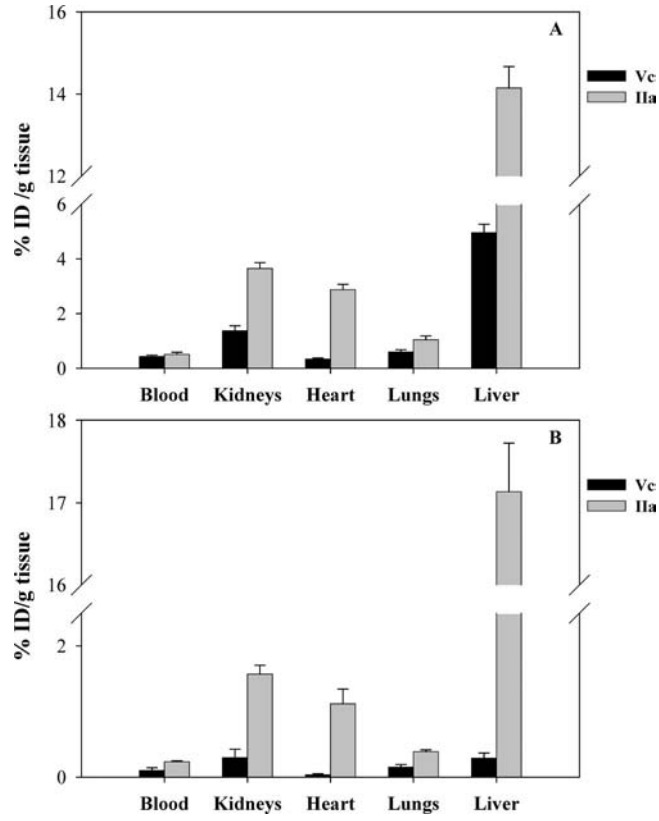

Figure 7. Biodistribution of ^{99m}Tc radioactivity concentration (% ID/g tissue) in male Wistar rats ($n = 4$) at 5 min (A) and 60 min (B) after intravenous injection of ^{99m}Tc-labeled FA.

was even higher, indicating the formation of lipophilic metabolites. A similar high accumulation in the liver is described for unsubstituted "4 + 1" $TcNS_3$–phosphine complexes (*16*).

In contrast, **Vc** exhibited accelerated liver clearance. Unfortunately, the myocardial uptake in biodistribution studies was rather low (Table 3). A possible reason for this shortcoming could be the untimely hydrolysis by plasma esterases. This is confirmed by the finding that the biodistribution of the dicarboxylic acid complexes **VIb** and **VId** shows a similar characteristic (low heart uptake and fast liver clearance). However, it should be considered that a more rapid rate of enzymatic hydrolysis in blood of rats (and mouse) is well-known. In addition, in case of the cationic technetium(I) hexakis (2-carbomethoxy-2-isocyano propane)$_6^+$ (^{99m}Tc-CPI), metabolic products are less lipophilic and of negative charge, leading to a disabled myocardial uptake. In contrast, in species with decreased plasma hydrolysis activity such as guinea pigs, rabbits, and chickens, myocardial accumulation was clearly increased (*20*). Therefore, it is likely that ester hydrolysis in **Vc** by blood plasma enzymes may be slow enough for a high initial heart uptake in other animal species and in humans. In addition, evidence for a satisfactory heart uptake of **Vc** in the absence of rat plasma esterases is given in experiments with the isolated perfused rat heart model, where a ventricular extraction of 18.01% ID was obtained. For a better evaluation of this result, one should bear in mind that the myocardial extraction of ^{123}I-IPPA in the same experimental setup was 15.51% ID (*14*).

A further attempt in the case of compounds **VIa–VId** was the combination of a tetradentate ligand containing the carboxyl group with a monodentate ligand bearing a free carboxyl group. It is well-known that the introduction of a carboxyl group in the NS_3 ligand results in a distinct decrease of lipophilicity (*16*). Therefore, the extraction obtained in the isolated heart was low, no matter whether a carboxyl group containing isocyano ligand as in **VIb** or a phosphine as in **VIa** was used as a monodentate ligand. However, the renal excretion of the dicarboxylic acid derivatives **VIb** and **VId** was increased and the clearance from liver was accelerated. These results are in good agreement with the fast liver clearance of the ester containing compound **Vc**, which was metabolized by esterases to the corresponding dicarboxylic acid. As expected, the heart uptake obviously decreased in the isolated heart and to a lesser extent in biodistribution studies compared to the more promising results of the recently presented "conventional" "4 + 1" ^{99m}Tc-FA with unsubstituted tetradentate NS_3 and isocyano FA ligands (*14*).

In comparison with the recently presented ^{99m}Tc-cyclopentadienyltricarbonyltechnetium-pentadecanoic acid, [^{99m}Tc] CpTT-PA (*21*), only **IIa** showed a similar myocardial uptake (2.88% ID/g). However, the heart/blood ratio at 5 min p.i. was clearly more promising for **IIa** (5.65 vs 2.93). Advantageous for the [^{99m}Tc] CpTT-PA is the combination of a satisfying uptake in heart and a rather low liver uptake.

In conclusion, 29 modified ^{99m}Tc-"4 + 1" FA dedicated in groups **I–VII** according to their physicochemical properties were synthesized and evaluated using the isolated heart model and in vivo biodistributution studies. Differences in heart uptake and biodistribution were induced by varying the position of the Tc chelate, the FA chain length, the incorporation of various functional groups (amide, ether, ester) into the lipophilic tail, the insertion of blocking groups (thiol, phenylene, and alkine) in both the alkyl chain and the tail section, and the usage of two different kinds of monodentate ligands (isocyanides vs phosphines). Whereas some compounds show a high myocardial uptake, others are characterized by an accelerated washout from the liver. However, to date no compound has been found in which both properties are combined properly. Thus, the heart/liver ratio could not be improved by the accomplished alterations of the binding mode between the "4 + 1" ^{99m}Tc chelate and the FA and the variations of the chelate position within the FA chain. Although a clear structure/biobehavior relationship is still missing, nevertheless some important rules were objectified.

ACKNOWLEDGMENT

This study was supported by an intramural grant (MedDrive programme 2003) funded by the Medical Faculty Carl Gustav Carus, by the DFG (Deutsche Forschungsgemeinschaft) grant SP 401, and by Nihon Medi-Physics Co., Inc., 9-8 Rokutanjicho, Nishinomiya-shi, Hyogo, 662-0918, Japan. The authors would like to thank Bianca Müller, Birgit Zatschler, and Regina Herrlich for excellent technical assistance.

Supporting Information Available: Figure with used monodentate ligands, analytical data of benzyl-protected FA tristhiolate ligands, analytical data of precursors for isocyano ligands, analytical data of selected precursors of "4 + 1" Re reference compounds, and data for crystal structure. This material is available free of charge via the Internet at http://pubs.acs.org/BC.

LITERATURE CITED

(1) Eckelman, W. C., Karesh, S. M., and Reba, R. C. (1975) New compounds: fatty acid and long chain hydrocarbon derivatives containing a strong chelating agent. *J. Pharm. Sci. 64*, 704–706.

(2) Mach, R. H., Kung, H. F., Jungwiwattanaporn, P., and Guo, Y. Z. (1991) Synthesis and biodistribution of a new class of ^{99m}Tc-labeled fatty acid analogs for myocardial imaging. *Int. J. Rad. Appl. Instrum. B 18*, 215–226.

(3) Jones, G. S., Jr., Elmaleh, D. R., Strauss, H. W., and Fischman, A. J. (1994) Synthesis and biodistribution of a new ^{99m}technetium fatty acid. *Nucl. Med. Biol. 21*, 117–123.

(4) Maresca, K. P. (2002) Synthesis, characterization, and biodistribution of a technetium-99m '3+1′ fatty acid derivative. The crystal and molecular structures of a series of oxorhenium model complexes. *Inorg. Chim. Acta 338*, 149–156.

(5) Kung, H. F., Guo, Y. Z., Yu, C. C., Billings, J., Subramanyam, V., and Calabrese, J. C. (1989) New brain perfusion imaging agents based on ^{99m}Tc-bis(aminoethanethiol) complexes: stereoisomers and biodistribution. *J. Med. Chem. 32*, 433–437.

(6) Efange, S. M., Kung, H. F., Billings, J., Guo, Y. Z., and Blau, M. (1987) Technetium-99m bis (aminoethanethiol) complexes with amine sidechains--potential brain perfusion imaging agents for SPECT. *J. Nucl. Med. 28*, 1012–1019.

(7) Efange, S. M., Kung, H. F., Billings, J. J., and Blau, M. (1988) Synthesis and biodistribution of ^{99m}Tc-labeled piperidinyl bis(aminoethanethiol) complexes: potential brain perfusion imaging agents for single photon emission computed tomography. *J. Med. Chem. 31*, 1043–1047.

(8) Magata, Y., Kawaguchi, T., Ukon, M., Yamamura, N., Uehara, T., Ogawa, K., Arano, Y., Temma, T., Mukai, T., Tadamura, E., and Saji, H. (2004) A Tc-99m-labeled long chain fatty acid derivative for myocardial imaging. *Bioconjugate Chem. 15*, 389–393.

(9) Yamamura, N., Magata, Y., Arano, Y., Kawaguchi, T., Ogawa, K., Konishi, J., and Saji, H. (1999) Technetium-99m-labeled medium-chain fatty acid analogues metabolized by beta-oxidation: radiopharmaceutical for assessing liver function. *Bioconjugate Chem. 10*, 489–495.

(10) Chu, T., Zhang, Y., Liu, X., Wang, Y., Hu, S., and Wang, X. (2004) Synthesis and biodistribution of (99m)Tc-carbonyltechnetium-labeled fatty acids. *Appl. Radiat. Isot. 60*, 845–850.

(11) Lee, B. C., Choe, Y. S., Chi, D. Y., Paik, J. Y., Lee, K. H., Choi, Y., and Kim, B. T. (2004) 8-cyclopentadienyltricarbonyl ^{99m}Tc 8-oxooctanoic acid: a novel radiotracer for evaluation of medium chain fatty acid metabolism in the liver. *Bioconjugate Chem. 15*, 121–127.

(12) Jung, C. M., Kraus, W., Leibnitz, P., Pietzsch, H. J., Kropp, J, and Spies, H. (2002) Syntheses and First Crystal Structures

of Rhenium Complexes Derived from ω- Functionalized Fatty Acids as Model Compounds of Technetium Tracers for Myocardial Metabolism Imaging. *Eur. J. Inorg. Chem. 2002*, 1219–1225.

(13) Heintz, A. C., Jung, C. M., Stehr, S. N., Mirtschink, P, Walther, M., Pietzsch, J., Bergmann, R., Pietzsch, H. J., Spies, H., Wunderlich, G., Kropp, J., and Deussen, A. (2007) Myocardial uptake and biodistribution of newly designed technetium labeled fatty acid analogues. *Nucl. Med. Commun. 28*, 637–645.

(14) Walther, M., Jung, C. M., Bergmann, R., Pietzsch, J., Rode, K., Fahmy, K., Mirtschink, P., Stehr, S., Heintz, A., Wunderlich, G., Kraus, W., Pietzsch, H. J., Kropp, J., Deussen, A., and Spies, H. (2007) Synthesis and biological evaluation of a new type of (99m)technetium-labeled fatty acid for myocardial metabolism imaging. *Bioconjugate Chem. 18*, 216–230.

(15) Pietzsch, H. J., Gupta, A., Syhre, R., Leibnitz, P., and Spies, H. (2001) Mixed-ligand technetium(III) complexes with tetradendate/monodendate NS(3)/isocyanide coordination: a new nonpolar technetium chelate system for the design of neutral and lipophilic complexes stable in vivo. *Bioconjugate Chem. 12*, 538–544.

(16) Seifert, S., Kunstler, J. U., Schiller, E., Pietzsch, H. J., Pawelke, B., Bergmann, R., and Spies, H. (2004) Novel procedures for preparing ^{99m}Tc(III) complexes with tetradentate/monodentate coordination of varying lipophilicity and adaptation to ^{188}Re analogues. *Bioconjugate Chem. 15*, 856–863.

(17) Spies, H., Glaser, M., Pietzsch, H.-J., Hahn, F. E., Kintzel, O., and Lügger, T. (1994) Trigonal-bipyramidale Rhenium-Komplexe mit vierzähnigen tripodalen NS_3Liganden. *Angew. Chem., Int. Ed. Engl.* 1354–1356.

(18) Schiller, E., Kraus, W., Reck, G., Spies, H., and Pietzsch, H.-J. (2005) [2-Carboxy-2,2′,2″nitrilotris(ethanethiolato)κ^4*N*,*S*,*S*′, *S*″](triphenylphosphine-κP)rhenium(III) acetone solvate. *Acta Crystallogr., Sect. E 61*, m1373–m1375.

(19) Schiller, E., Seifert, S., Tisato, F., Refosco, F., Kraus, W., Spies, H., and Pietzsch, H. J. (2005) Mixed-ligand rhenium-188 complexes with tetradentate/monodentate NS3/P ('4 + 1′) coordination: relation of structure with antioxidation stability. *Bioconjugate Chem. 16*, 634–643.

(20) Kronauge, J. F., Noska, M. A., Davison, A., Holman, B. L., and Jones, A. G. (1992) Interspecies variation in biodistribution of technetium (2-carbomethoxy-2-isocyanopropane)6+. *J. Nucl. Med. 33*, 1357–1365.

(21) Uehara, T., Uemura, T., Hirabayashi, S., Adachi, S., Odaka, K., Akizawa, H., Magata, Y., Irie, T., and Arano, Y. (2007) Technetium-99m-labeled long chain fatty acid analogues metabolized by beta-oxidation in the heart. *J. Med. Chem. 50*, 543–549.

BC700164C

Near-Infrared Fluorescent Labeled Peptosome for Application to Cancer Imaging

Hiroki Tanisaka,[†] Shinae Kizaka-Kondoh,[‡] Akira Makino,[†] Shotaro Tanaka,[‡] Masahiro Hiraoka,[‡] and Shunsaku Kimura*[,†]

Department of Material Chemistry, Graduate School of Engineering, Kyoto University, Kyoto-Daigaku-Katsura, Nishikyo-ku, Kyoto 615-8510, Japan, and Department of Radiation Oncology and Image-Applied Therapy, Graduate School of Medicine, Kyoto University, 54 Kawahara-cho, Shogoin, Sakyo-ku, Kyoto 606-8507, Japan. Received May 8, 2007; Revised Manuscript Received November 12, 2007

Nonionic amphiphilic copolypeptides, which were composed of hydrophilic poly(sarcosine) and hydrophobic poly(γ-methyl L-glutamate) blocks, were synthesized with varying chain lengths of the blocks. The polypeptides having a suitable hydrophilic and hydrophobic balance were found to form vesicular assemblies of 100 nm size in buffer, which was evidenced by the TEM observation, the DLS analysis, and the encapsulation experiment. The genuine peptide vesicles, peptosomes, were labeled with a near-infrared fluorescence (NIRF) probe. *In vivo* retention in blood experiment showed long circulation of the peptosome in rat blood as stable as the PEGylated liposome. NIRF imaging of a small cancer on mouse by using the peptosome as a nanocarrier was successful due to the EPR effect of the peptosome. Peptosome is shown here as a novel excellent nanocarrier for molecular imaging.

INTRODUCITON

Molecular imaging has attracted more and more attention in the past decades (*1–3*) to target biological molecules (*4, 5*) and tumor tissues (*6, 7*) and so on. To image the biological objects, various modalities using positron-emission tomography (PET), magnetic resonance (MR), and fluorescence have been popular. Fluorescence imaging, particularly near-infrared fluorescence (NIRF) imaging (*8*), has an advantage for living body imaging, because the near-infrared and far-red light (650–900 nm) can avoid strong absorption by red blood cells and water to allow the light to permeate a biological body in the depth of several centimeters (optical window). The NIRF imaging has several benefits: cost efficiency in preparation of the probes and hardware for detection, high sensitivity, and low risk for the living body (*9, 10*). However, NIRF probes should be carried on a vehicle for selective accumulation of the imaging probes into the tumor tissue on a minute scale for early therapy.

There have been several targeting techniques using vehicles as the imaging probes (*11–14*). Using polymers or nanocarriers to support the probes is one of the most popular techniques to provide probes with targeting functionality (*15, 16*). In tumor tissues, submicron-sized defects exist on the vascular wall because of the rapid angiogenesis, enabling permeation of macromolecules through the wall. Further, the lymph system around tumor tissue grows too slowly to exclude foreign compounds from the tumor tissue (the enhanced permeability and retention (EPR) effect) (*17, 18*). Nanocarriers the size of 100 nm are considered to target passively and therefore to accumulate into tumor tissue by the EPR effect (*19, 20*).

Nanocarriers the size of 100 nm, which will exert the EPR effect, can be constructed via self-assembly of the amphiphilic molecules. Recently, spherical molecular assemblies of micelles (*21–23*) or vesicles (*24–26*) have been reported for applications to the drug delivery system (DDS) because of their capability to carry hydrophilic, lipophilic, or conjugated drugs (*27–30*). When molecular assembly is employed as a nanocarrier for *in vivo* use, such as molecular imaging and DDS, it is required to be biocompatible and/or biodegradable. The liposome, which is a vesicular assembly of lipids and therefore is considered to be excellent in terms of biocompatibility and biodegradability, has attracted continuous attention as the nanocarrier in DDS. For *in vivo* use, the liposomes have been PEGylated (modified with poly(ethylene glycol) (PEG) on their surfaces) in order to improve their retention in blood and to suppress the clearance by the reticuloendothelial system (RES) of the liver and spleen (*31, 32*). The PEGylated liposome containing anticancer drug has already been allowed for clinical application in Europe and the United States (*33, 34*). However, several risks of the PEGylated liposome in clinical use have been also reported: the conjugated PEG chains are artificial and nondegradable, and the PEGylated liposome has several side effects on the human body, including complement activation (*35, 36*). An alternative hydrophilic nonionic polymer for the nanocarrier is therefore expected to be developed.

Polypeptides are considered to be excellent in terms of biocompatibility and biodegradability (*37*). In addition, functionalization of polypeptides is rather facile by using their side chains (*38*). Our group has already reported that amphiphilic polypeptides formed vesicular assemblies in the sizes of ca. 100 nm in the aqueous medium, and named them "peptosome" (*39–41*). As in the case of liposome, peptosome can encapsulate water-soluble compounds suitably to DDS. Further, peptosome is a polymer vesicle, which has a more robust membrane via hydrophobic interaction among hydrophobic polymer chains than a liposome of small lipids (*24*).

In the present study, we designed and synthesized AB-type amphiphilic block copolypeptides composed of poly(sarcosine) (PSar) and poly(γ-methyl-L-glutamate) (PMLG) as a hydrophilic and hydrophobic block, respectively (Figure 1). The PSar block

* Corresponding author. Shunsaku Kimura. E-mail: shun@scl.kyoto-u.ac.jp, Department of Material Chemistry, Graduate School of Engineering, Kyoto University, Kyoto-Daigaku-Katsura, Nishikyo-ku, Kyoto 615-8510, Japan. Phone +81-75-383-2400. Fax +81-75-383-2401.

[†] Graduate School of Engineering.

[‡] Graduate School of Medicine.

10.1021/bc7001665 CCC: $40.75 © 2008 American Chemical Society
Published on Web 12/29/2007

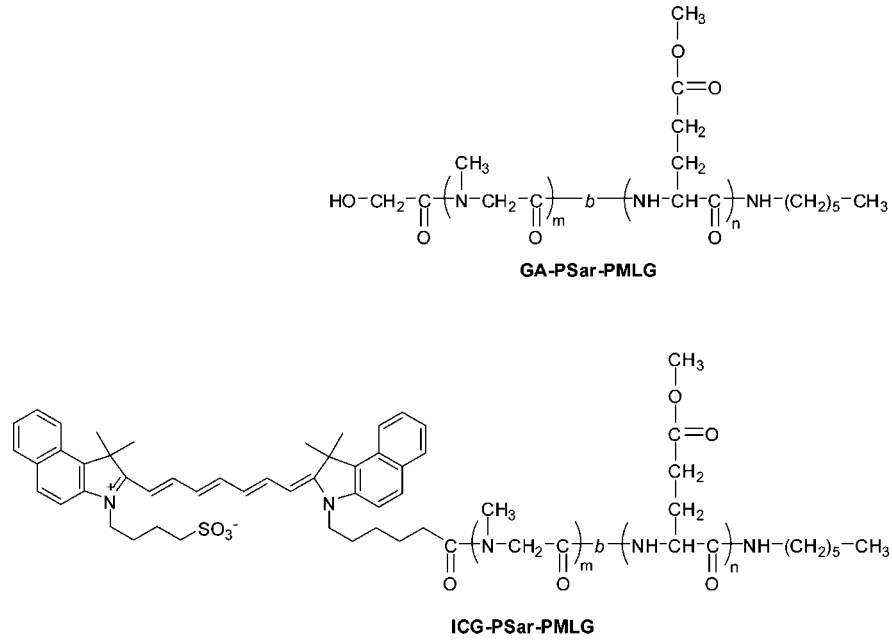

Figure 1. Chemical structures of amphiphilic block polypeptides, PSar-PMLGs. GA-PSar-PMLGs were used to prepare peptide assemblies, whereas ICG-PSar-PMLG was used for NIRF-labeling of peptosome.

is nonionic and hydrophilic like PEG, which will suppress the capture of the peptide assemblies by the RES due to the formation of a hydration layer on their surface (*42*, *43*). Further, sarcosine is a naturally occurring amino acid, and the structure is a part of creatine which helps to supply energy to muscle cells. Sarcosine is degraded endogenously by sarcosine dehydrogenase. No side effect of sarcosine was reported except the cases of sarcosinaemia, and so forth (*44*). PSar is therefore expected to be biocompatible. PSar-PMLGs of a variety of compositions were synthesized via a sequential *N*-carboxyanhydride (NCA) polymerization method (*45*). NIRF-labeled peptosomes were successfully prepared with using PSar-PMLGs. *In vivo* experiments about retention in rat blood and NIRF imaging of cancer on mouse by using the peptosomes as nanocarrier are discussed.

EXPERIMENTAL PROCEDURES

Materials. All reagents and solvents were purchased commercially and were used as received unless otherwise noted. Solvents used for NCA preparation and polymerization and *n*-hexylamine used as an initiator were purified just before usage according to the ordinary procedures. ICG (indocyanine green)-Sulfo-OSu, DY-675, and m-dPEG12 amine were purchased from Dojin Laboratory Ltd., Dyomics GmbH, and Quanta BioDesign, Ltd., respectively, and was used as received.

Synthesis. Amphiphilic block polypeptides, PSar-PMLGs, were synthesized by the NCA polymerization method. PMLG block was obtained from γ-methyl-L-glutamate-*N*-carboxyanhydride (Glu(OMe)-NCA) using *n*-hexylamine as an initiator, followed by polymerization of sarcosine-*N*-carboxyanhydride (Sar-NCA). The number-average molecular weight of the polymers prepared in the present study was in the range 2800−8300. The *N*-terminal of the polypeptides was successively capped by glycolic acid using HATU as a coupling reagent to afford GA-PSar-PMLG, or by ICG-Sulfo-OSu to afford ICG-PSar-PMLG (Figure 1). Crude polypeptides were purified by a Sephadex LH20 column with *N*,*N*-dimethylformamide (DMF) as eluent. The compositions of the polypeptides were determined by ^{1}H NMR spectrum analysis using trifluoroacetic acid-*d* as deuterated solvent. Degrees of polymerization (DP) of PMLG and PSar blocks were determined from methyl ester protons and *N*-methyl protons, respectively, in comparison with signals from the initiator. The capping reaction of the *N*-terminal was also confirmed by ^{1}H NMR. The detail of the synthesis is as follows.

Sar-NCA. Benzyloxycarbonyl sarcosine (10.0 g, 44.8 mmol) was dissolved in $SOCl_2$ (10 mL), and the solution was shaken vigorously for 8 min at 50 °C. The solution was poured into petroleum ether (200 mL) to afford Sar-NCA as a white solid. The crude Sar-NCA was purified three times by recrystallization from ethyl acetate/petroleum ether. FT-IR: 1850, 1780 cm^{-1}. Melting point: 95–96 °C.

Glu(OMe)-NCA. To a suspension of H-Glu(OMe)-OH (7.11 g, 44.1 mmol) in tetrahydrofuran (THF, 70 mL) at 50 °C was added triphosgene (4.36 g, 14.7 mmol). After 1 h stirring, another triphosgene (0.86 g, 2.91 mmol) was added, and the mixture was stirred for 2 h. The reaction mixture was poured into hexane (210 mL), and the suspension was cooled at −20 °C to complete crystallization. The crude Glu(OMe)-NCA was purified two times by recrystallization from THF/hexane. FT-IR: 1850, 1780, 1710 cm^{-1}. Melting point: 95–97 °C.

GA-PSar-PMLG. To a solution of Glu(OMe)-NCA (0.1 M) in dry DMF under Ar atmosphere was added *n*-hexylamine with the amount of the specified monomer/initiator ratio in feed, and the solution was stirred for 3 h at room temperature. After confirmation of the disappearance of NCA signals from the solution by FT-IR measurement, Sar-NCA in DMF was added with the amount of the specified ratio of Sar block (PSar) and Glu(OMe) (PMLG) block in the copolymer. The solution was kept stirring until the NCA was fully consumed. To the solution were added glycolic acid (5 equiv), *O*-(7-azabenzotriazol-1-yl)-1,1,3,3-tetramethyluronium hexafluorophosphate (HATU) (5 equiv), and *N*,*N*-diisopropylethylamine (DIEA) (7.5 equiv) at 0 °C, and the solution was stirred at room temperature for 12 h under N_2 atmosphere. Additional portions of HATU (3 equiv) and DIEA (4 equiv) were added further to the solution at 0 °C, and the solution was kept stirring at room temperature for another 12 h under N_2 atmosphere. The solution was concentrated and purified by a Sephadex LH 20 column with DMF as eluent. The fraction of the copolymer was collected, and the product was precipitated from DMF/diethyl ether, followed by washing with acetone. The composition of PSar/PMLG in the

product was determined by ^{1}H NMR (trifluoroacetic acid (TFA)-*d*) with comparing the signal strengths of *N*-CH_3 of PSar, methyl ester of PMLG, and the terminal methyl of the initiator.

ICG-PSar-PMLG. Instead of glycol acid at the capping reaction in the preparation of GA-PSar-PMLG, ICG-sulfo-OSu (5 equiv of the terminal amino group) was added to the polymerization solution. The product was purified similarly to the case of GA-PSar-PMLG. The capping with ICG at the *N*-terminal of the copolymer was confirmed by ^{1}H NMR using 2,2,2-trifluoroethanol-d_3 as solvent.

DY-PEG. To a solution of DY-675 (5.0 mg, 7.1 μmol) and CH_3O-PEG_{12}-NH_2 (4.3 mg, 7.8 μmol, m-dPEG12 amine) in DMF were added HATU (3.0 mg, 7.8 μmol) and DIEA (2.0 μL, 12 μmol) at 0 °C, and the solution was stirred at room temperature for 6 h under N_2 atmosphere. HATU (0.55 mg, 1.4 μmol) and DIEA (0.37 μL, 2.6 μmol) were added further to the solution, and the solution was kept stirring at room temperature for another 16 h under N_2 atmosphere. The solution was concentrated under reduced pressure, and the residue was purified by a Sephadex LH 20 column with using DMF as eluent to afford the product. Mass analysis (FAB, matrix; nitrobenzylalcohol): *m*/*z* 1248.6 (calcd for $C_{67}H_{98}N_3O_{17}S$ [$(M + H)^+$] *m*/*z* 1248.66).

Preparation of Aqueous Dispersion. Polypeptides were dispersed in a Tris-buffered saline (TBS) (10 mM Tris−HCl, 100 mM NaCl, pH 7.4) by the injection method using 2,2,2-trifluoroethanol (TFE) as solvent. GA-PSar-PMLG (4.5 mg) was dissolved in 75 μL of TFE, and the solution was rapidly injected into 1.5 mL of TBS, which was stirred and cooled on ice. The aqueous dispersion was applied on a Sephacryl S-100 column (1.5 × 30 cm, GE healthcare Bio-Sciences) using TBS as eluent to remove TFE and others. The peptide concentration was in the range 0.5–0.8 mg/mL. Labeling of the polypeptide assembly with NIRF was achieved by adding a few wt % of ICG-PSar-PMLG to GA-PSar-PMLG in a TFE solution before injection.

Dynamic Light Scattering Analysis. The size of the molecular assemblies formed in aqueous dispersion was analyzed by dynamic light scattering (DLS) on a Photal DLS-8000 (Otsuka Electronics Co., Japan) using a cylindrical optical cell of 1 cm diameter. Vertically polarized light of either wavelength 632.8 nm from a He−Ne laser or 488 nm from an Ar laser was used as the incident beam from a scattering angle of 90°. All measurements were performed at 25 °C. In order to avoid contamination of dust, all aqueous dispersions were prepared in a clean room and filtered through a 0.80 μm cellulose acetate membrane filter. The autocorrelation function was analyzed by the time interval method of photon correlation. The light scattering data were analyzed by the program of Contin (*46, 47*).

TEM Observation. TEM images were taken using a JEOL JEM-2000EXII at an accelerating voltage of 100 kV. For the observation of molecular assembly, a dispersion of GA-PSar56-PMLG12 in 10 mM Tris−HCl buffer (pH 7.4) was applied on a carbon-coated Cu grid, and the sample was stained negatively with 2% uranyl acetate, followed by suction of the excess fluid with a filter paper.

Encapsulation of Water-Soluble Drug Model. A solution of a mixture of GA-PSar43-PMLG18 and GA-PSar65-PMLG18 (3:1) and 1 wt % ICG-PSar63-PMLG20 in TFE was injected rapidly into 1.5 mL TBS containing 4 mg/mL FITC−dextran (MW: 4000). The mixture of ICG-labeled molecular assembly and FITC−dextran was applied on a Sephacryl S-100 column (1.5 × 30 cm) with using TBS as eluent, and the elution profile was monitored by absorbance at 780 and 490 nm of ICG and FITC, respectively. Encapsulation of DY-PEG was also done similarly to the method of encapsulation of FITC−dextran.

Circular Dichroism. To analyze the conformation of polypeptides in their aqueous dispersion, circular dichroism (CD) spectroscopy was carried out on a JASCO J600 spectropolarimeter with an optical cell of 0.1 cm optical path length at room temperature.

***In Vivo* Retention in Blood Measurement.** *In vivo* retention in blood of peptosome was evaluated by using rats as the experimental animals. Seven-week-old Crl:CD(SD) male rats were used. Peptosomes prepared from GA-PSar56-PMLG12 ($n = 2$) and a mixture of GA-PSar43-PMLG18 and GA-PSar65-PMLG18 (1:1) ($n = 3$) were NIRF-labeled with the addition of 5 wt % ICG-PSar63-PMLG20. The dispersions were administered at 0.8 mg/mL/kg to rats via tail vein. After administration of the peptosome, blood samples of 0.5 mL were taken temporally from rats and were centrifuged to collect the blood plasma samples. The amount of the ICG-labeled peptosome in the sample was estimated by fluorescence assay (Ex, 768 nm; Em, 807 nm). *In vivo* retention in the blood of the peptide micelle from GA-PSar93-PMLG12 and 5 wt % ICG-PSar63-PMLG20 was also evaluated by the same procedure ($n = 2$).

Cell Culture and Hypoxic Treatment *in Vitro*. SUIT-2 human pancreatic cancer cell line was purchased from the American type Culture Collection. SUIT-2/EF-Luc cells that carry the luciferase reporter gene under control of pEF constitutive promoter were isolated by the same method as described elsewhere. SUIT2/EF-Luc cells were maintained at 37 °C with 5% FBS-Dulbecco's modified Eagle medium (Nacalai Tesque, Kyoto, Japan).

Tumor Model. SUIT-2/pEF-luciferase cells were subcutaneously inoculated at 1×10^6 cells/mL of phosphate-buffered saline (PBS) into front legs, hind legs, or back of 8-week-old female nude mice (BALB/c nu/nu; Japan SLC Inc., Hamamatsu, Japan).

***In Vivo* Cancer Imaging.** For taking images of bioluminescence from the SUIT2/EF-luc xenografts, tumor-bearing mice were intraperitoneally injected with 100 μL D-luciferin solution (10 mg/mL in PBS; Promega Corp., Madison, WI). In 20 min, the mice were set in an IVIS-200 *in vivo* photon-counting device (Xenogen Corp., Alameda, CA). For taking fluorescence images from the NIRF-labeled peptosome, tumor-bearing mice were set in the IVIS-200 at the indicated time following intravenous injection of the peptosome dispersion (ca. 0.5 mg/mL, 200 μL). During imaging process, the mice were kept on the imaging stage under anesthetized condition with 2.5% of isoflurane gas in oxygen flow (1.5 L/min).

The fluorescence images from ICG were taken with the accessory ICG filter set, and those from DY-675 were taken with the Cy5.5/Cy5.5 Bkg filter sets. The pseudo images from the photon counts were constructed by *Living Image 2.50 - Igor Pro 4.09A* software (Xenogen Corp.).

RESULTS AND DISCUSSION

Synthesis of Polypeptides and Their Dispersibility in TBS. Amphiphilic block copolypeptides, GA-PSar-PMLGs and ICG-PSar-PMLG (Figure 1), were newly designed and synthesized by the conventional NCA method with the capping reaction using HATU as a coupling reagent or using active ester. Compositions of PSar-PMLGs were estimated by ^{1}H NMR analysis and found to be close to the monomer/initiator ratios in the feed (Table 1). GA-PSar-PMLGs having more than 43 sarcosine residues (entries 3–8) were dispersed stably in TBS by the TFE injection method (*48*), whereas those with shorter PSar chains yielded precipitates (entries 1, 2). Moderately long PSar chains are therefore necessary for PMLG chains of 12–18 residues to be dispersed stably in buffer.

Morphology of Molecular Assembly. Size and shape of molecular assembly of GA-PSar-PMLGs formed in buffer were analyzed by the DLS measurement and the TEM observation. Size distribution analysis by the DLS measurements suggested

Table 1. Compositions of PSar-PMLGs and Properties in Aqueous Dispersion

entry	monomer ratio in feed [Sar]/[Glu(OMe)]	composition of polypeptide [Sar]/[Glu(OMe)]	abbreviation[a]	molecular assembly[b]	size (nm)
1	15/15	15/12	GA-PSar15-PMLG12	precipitate (group PRE)	
2	25/15	25/12	GA-PSar25-PMLG12	precipitate (group PRE)	
3	40/20[e]	43/18	GA-PSar43-PMLG18	P (group PEP)	150
4	60/20	56/12	GA-PSar56-PMLG12	M, P (group MIC)	40, 150
5	60/20[e]	65/18	GA-PSar65-PMLG18	M, P (group MIC)	30, 90
6	80/20	93/12	GA-PSar93-PMLG12	M (group MIC)	40
7		entry 3/5=1/1[c]	mixture of GA-PSar43-PMLG18 and GA-PSar65-PMLG18 (1:1)	P, M (group PEP)	100, 30
8		entry 3/5=3/1[d]	mixture of GA-PSar43-PMLG18 and GA-PSar65-PMLG18 (3:1)	P, M (group PEP)	100, 30
9	60/20	63/20	ICG-PSar63-PMLG20		

[a] GA, capped *N*-terminal with glycolic acid, ICG, capped *N*-terminal with ICG-Sulfo-OSu. [b] P, peptosome, M, micelle, the former capital letter of P, M or M, P represents the predominant morphology of the mixed molecular assemblies. The block polypeptides are categorized into three groups, group PRE (precipitate), group PEP (peptosome), and group MIC (micelle), according to the predominant morphology in buffer (shown in the parentheses). [c] A mixture of GA-PSar43-PMLG18 and GA-PSar65-PMLG18 at the molar ratio of 1:1. [d] A mixture of GA-PSar43-PMLG18 and GA-PSar65-PMLG18 at the molar ratio of 3:1. [e] A solution of DMF and chloroform (3/1 v/v) was used for polymerization of entries 3 and 5. In other cases, DMF was used.

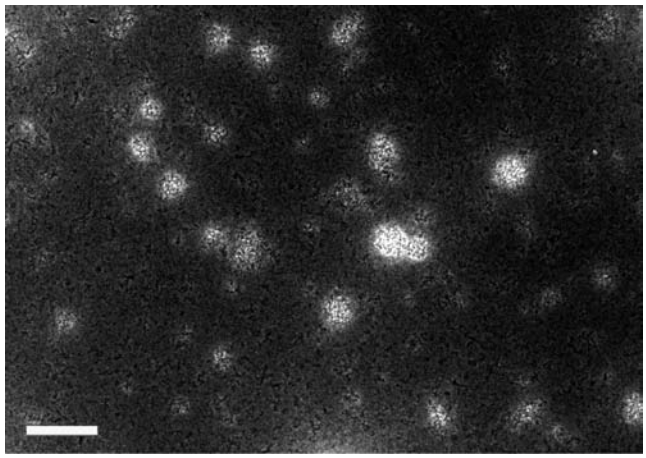

Figure 2. TEM image of peptosome in the aqueous dispersion of GA-PSar56-PMLG12. The sample was stained negatively with uranyl acetate. Scale bar represents 0.5 μm.

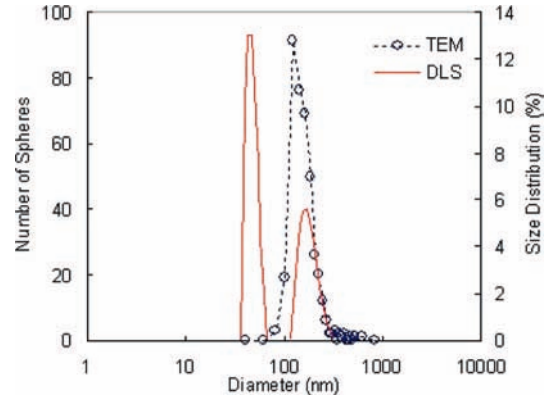

Figure 3. Comparison of size distributions determined by DLS measurement and TEM image (histogram). In both measurements, GA-PSar56-PMLG12 was used for preparation of the peptide assembly.

a bimodal distribution for some polypeptides (Table 1, entries 4, 5, 7, 8) due to formation of two types of molecular assemblies. However, the regularization procedure such as Contin used here may overfit the data to produce apparently two peaks. Indeed, upon changing the scattering angles in the DLS measurements, the bimodal distribution could become a smooth monomodal distribution in some cases. Table 1 shows two values as the molecular assembly size in some cases, but the sizes of the minor components are not thus fully convincing. In addition to the DLS measurements, we therefore analyzed the elution profiles of the molecular assemblies through gel permeation chromatography using Sephacryl S-100 or Sephadex 4B. The elution profiles were agreeable with the results of the DLS measurements summarized in Table 1. So, the sizes of the minor components of the molecular assemblies are shown in Table 1 despite their inaccuracy.

The fraction ratio of the two assemblies differs depending on the length of the PSar block in the copolypeptides. Diameter of the smaller assembly is in the range from 30 to 40 nm, and that of the larger one from 100 to 200 nm. Since the molecular length of GA-PSar-PMLGs is estimated to be about 20 nm with an extended form of the PSar block and α-helical conformation of the PMLG block, the smaller molecular assembly is assigned to a spherical micelle having a hydrophobic core and a hydrophilic shell.

An aqueous dispersion of GA-PSar56-PMLG12 was observed by TEM with negative staining (Figure 2). Spheres in the size range from 100 to 200 nm were present in the TEM image, and the size distribution of these large spheres is in agreement with that of the larger assemblies detected by DLS (Figure 3). Even though the detail analysis of the smaller assemblies detected by DLS was not possible by TEM due to the poor resolution, the peptide micelle should be formed with GA-PSar56-PMLG12 from the elution profile through gel permeation chromatography. On the other hand, GA-PSar43-PMLG18, a block polypeptide with a shorter PSar segment and a longer PMLG segment, formed the large spheres of ca. 150 nm from the DLS analysis (Table 1). These observations of amphiphilic polypeptides are consistent with previous reports that the morphology of molecular assemblies is related generally with the hydrophilic and hydrophobic balance of amphiphiles (*49*, *50*); with increasing the hydrophobic property of amphiphiles, the major morphology shifts from a small micelle to cylinder and a large vesicle in water. When this relationship is applied to the present polypeptides, the large assembly of GA-PSar43-PMLG18 in buffer should be a vesicle. This structural point is discussed later with the encapsulation experiment.

Adjustment of the assembly size by mixing two kinds of polypeptides was examined (Table 1, entries 7, 8). Interestingly, the size of molecular assembly of GA-PSar43-PMLG18 was reduced from 150 to 100 nm by incorporation of GA-PSar65-PMLG18 at the molar ratios of 1:1 and 3:1 (GA-PSar43-PMLG18: GA-PSar65-PMLG18). The longer PSar block of GA-PSar65-PMLG18 in the mixture should favor staying at the outer surface of the spherical assembly to reduce the steric congestion compared with staying at the inner surface, resulting in a large curvature of the smaller spherical assembly. GA-PSar65-PMLG18 is thus considered to be inserted into the outer surface to increase the curvature of the vesicle due to the bulky PSar

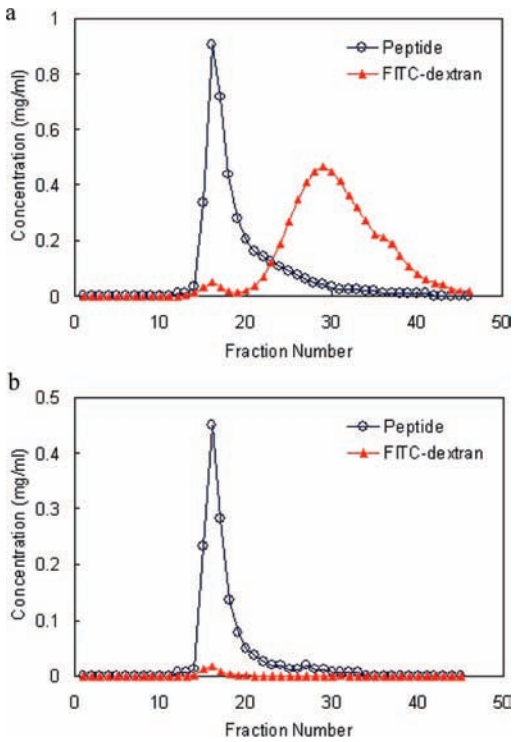

Figure 4. Encapsulation experiment of FITC−dextran in ICG-labeled molecular assembly prepared from a mixture of GA-PSar43-PMLG18 and GA-PSar65-PMLG18 (3:1). Elution profiles of size exclusion chromatography by a Sephacryl S-100 column were monitored by absorption of ICG (○) and fluorescein (▲). (a) First elution of the peptide dispersion prepared in a buffer containing FITC-dextran. (b) The repeated elution of the peptide fraction of the first elution.

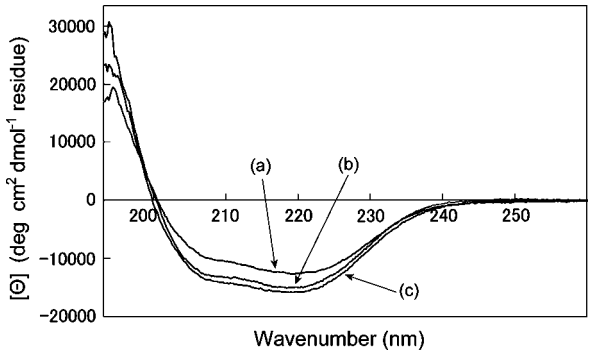

Figure 5. CD spectra of (a) GA-PSar43-PMLG18, (b) GA-PSar65-PMLG18, and (c) a mixture of GA-PSar43-PMLG18 and GAPSar65-PMLG18 (1:1) in 10 mM Tris buffer containing 0.1 M NaCl and 5% TFE. The residue concentration of Glu(OMe) was set at 5×10^{-4} M for all the samples.

block at the outer surface. The mixing effect on the assembly size, however, was not so sensitive in the mixing ratios of 1:1 and 3:1.

To obtain information on the molecular assembly of 100 nm, the encapsulation experiment was carried out with using the peptide assembly of a mixture of GA-PSar43-PMLG18 and GA-PSar65-PMLG18 (3:1) labeled with 1 wt % ICG-PSar63-PMLG20. The elution profile through a SEC column of the peptide assembly prepared in the presence of FITC-dextran (Mw: 4000) in buffer shows coelution of FITC−dextran with the peptide assembly (Figure 4a). The amount of the encapsulated dextran in the peptide assembly looks small, but the ratio of the encapsulated dextran against the total amount of dextran in buffer is consistent with the ratio of the total inner volume of the vesicles against the total solution

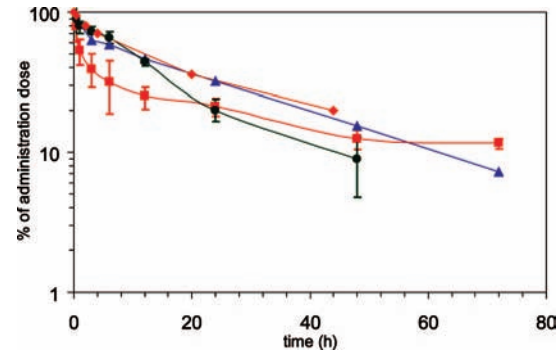

Figure 6. *In vivo* blood clearance curves of ICG-labeled peptosome (blue ▲, GA-PSar56-PMLG12; red ■, a mixture of GA-PSar43-PMLG18 and GA-PSar65-PMLG18 (1:1)) and ICG-labeled peptide micelle (green ●, GA-PSar93-PMLG12), in comparison with that of PEGylated liposomal doxorubicin, Doxil, in the literature (*53*) (orange ♦).

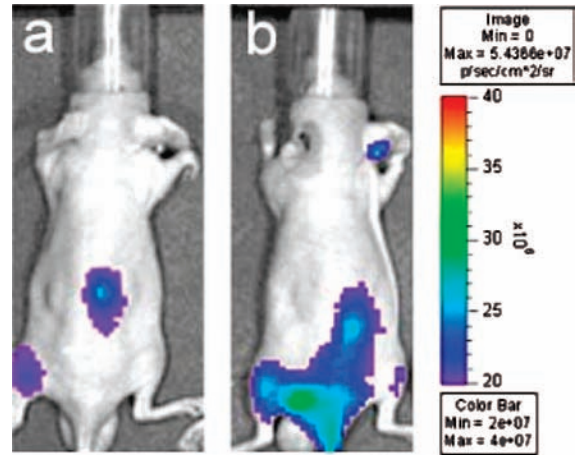

Figure 7. *In vivo* cancer imaging using NIRF-labeled peptosome. ICG-labeled peptosome prepared from a mixture of GA-PSar43-PMLG18 and GA-PSar65-PMLG18 (1:1) labeled with 3 wt % ICG-PSar63-PMLG20 was used. (a) Bioluminescence image of SUIT2/EF-luc xenografts on the tumor-bearing mouse after administration of D-luciferin. (b) Image of fluorescence from ICG, 1 day after the administration of ICG-labeled peptosome.

volume at the preparation, which was calculated under the following assumptions: the vesicular assembly of 100 nm diameter, the diameter of 2 nm for one peptide molecule occupying at the membrane, and interdigitation structure of the membrane. Further, the repeated column chromatography of the peptide fraction did not reduce the relative intensity of FITC−dextran, suggesting that FITC−dextran was encapsulated firmly in the vesicle (Figure 4b). Consequently, the peptide assembly of 100 nm has an inner aqueous phase to encapsulate a water-soluble compound, indicating the peptide assembly of vesicle, so-called “peptosome”.

After our previous reports on preparation of peptosome in the size range of 100 nm (*39–41*), Deming et al. have also reported preparation of micrometer-sized vesicular assembly from ionic polypeptides (*51*). They reduced the size of assembly into about 100 nm by using the extruder method. In our case, a 100 nm sized peptosome was spontaneously formed only by injection of the peptide solution into buffer, and the size remained stable for weeks.

Conformation of polypeptides in the molecular assemblies was studied by CD spectroscopy. The aqueous dispersion of GA-PSar43-PMLG18 (group PEP; Table 1) showed negative Cotton effects at 222 and 208 nm (Figure 5), indicating α-helical conformation of the hydrophobic PMLG block (*52*). Since the signal at 222 nm was more intensive than that at 208 nm, α

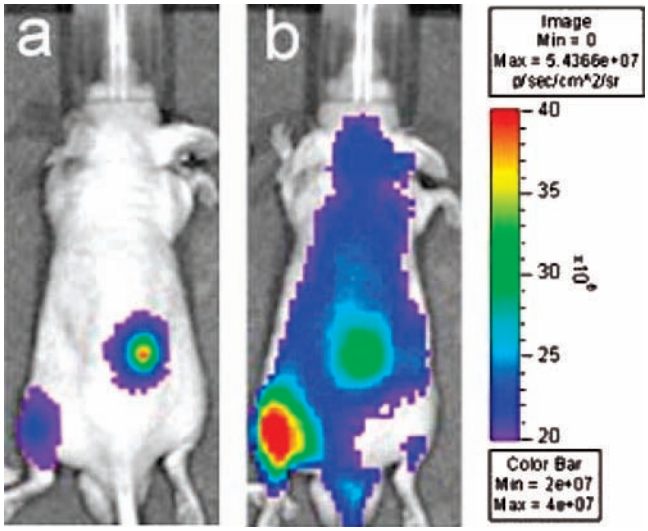

Figure 8. *In vivo* cancer imaging using NIRF-labeled peptide micelle. ICG-labeled peptide micelle prepared from GA-PSar93-PMLG12 labeled with 3 wt % ICG-PSar63-PMLG20 was used. (a) Bioluminescence image of SUIT2/EF-luc xenografts on the tumor-bearing mouse after administration of D-luciferin. (b) Image of fluorescence from ICG, 1 day after the administration of ICG-labeled peptide micelle.

helices should form a bundle structure in the peptide membrane. Similar results were obtained with GA-PSar65-PMLG18 (group MIC; Table 1) and a mixture of GA-PSar43-PMLG18 and GA-PSar65-PMLG18 (1:1) (group PEP). The α-helical structure in the peptide assembly makes a contrast to our previous report on amphiphilic poly(sarcosine)-*b*-poly(alanine), in which the hydrophobic poly(alanine) block took β-sheet structure in peptide micelle or aggregates (*27*). The conformation difference between these two types of block polypeptides in the molecular assemblies may be attributed to the difference of the side chains between alanine and Glu(OMe). The large hydrophobic side chain of Glu(OMe) may prevent the PMLG block from taking β-sheet structure of the tight molecular packing.

***In Vivo* Retention in Blood Measurement.** GA-PSar56-PMLG12 (group PEP) and a mixture of GA-PSar43-PMLG18 and GA-PSar65-PMLG18 (1:1) (group PEP) were chosen for preparation of about 100 nm sized peptosomes, and were subjected to *in vivo* retention in blood assay. The ICG-labeled peptosomes were administered to rats via a tail vein. Residual amounts of ICG-labeled peptosomes in blood plasma at different times were determined by fluorescence photometry (Figure 6). A small fraction of the peptosomes was cleared at the beginning stage, but the greatest part showed long retention circulating in the rat blood. When the two-compartment model was applied to the clearance curve, the half-lives at the β phase of the clearance curves were estimated to be about 20–40 h for these peptosomes. The relatively long half-life of the peptosomes is comparable to PEGylated liposome under the same experimental conditions (*54*).

ICG-labeled peptide micelle prepared from GA-PSar93-PMLG12 (group MIC) also showed a long retention circulation (Figure 6). However, the peptide micelle disappeared completely in 48 h, whereas a part of peptosome remained in blood even after 72 h from the injection. This result may be ascribed to the smaller size of the peptide micelle, which should promote its accumulation in liver (*55, 56*).

***In Vivo* Cancer Imaging.** *In vivo* NIRF imaging of cancer on mouse was carried out with using ICG-labeled peptosome prepared from a mixture of GA-PSar43-PMLG18 and GA-PSar65-PMLG18 (1:1) (group PEP). At 1 day after the administration, intensive fluorescence from ICG was observed at the two transplanted cancer sites (Figure 7b), which was confirmed by the bioluminescence from luciferin (Figure 7a). The peptosome is therefore considered to accumulate in the tumor tissue by the EPR effect.

ICG-labeled peptide micelle prepared from GA-PSar93-PMLG12 (group MIC) was also administered to the tumor-bearing mouse, and NIRF imaging was carried out. The intensive fluorescence from ICG was observed similarly at the tumor tissue (Figure 8). However, the fluorescence level at the background was moderately high. The peptide micelle may be

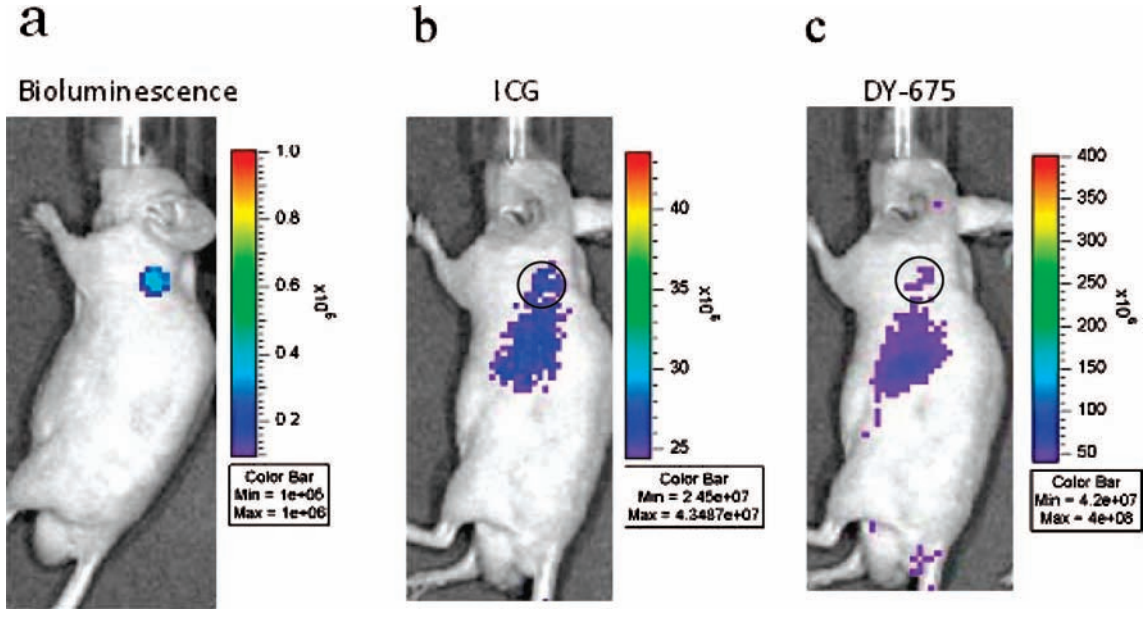

Figure 9. *In vivo* cancer imaging using NIRF-labeled peptosome encapsulating water-soluble far-red fluorophore. ICG-labeled peptosome prepared from a mixture of GA-PSar43-PMLG18 and GA-PSar65-PMLG18 (3:1) labeled with 3 wt % ICG-PSar63-PMLG20 and encapsulating DY-PEG in the inner aqueous phase (the concentration of DY-PEG was set at 4 mg/mL at the preparation). (a) Bioluminescence image of SUIT2/EF-luc xenografts on the tumor-bearing mouse after administration of D-luciferin. (b) Image of fluorescence from ICG, 2 days after the administration of peptosome. (c) Image of fluorescence from DY-675, 2 days after the administration of peptosome. Black circles in b and c represent the tumor site.

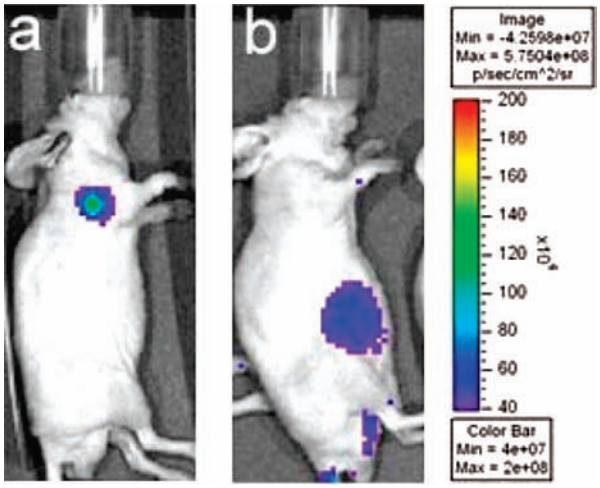

Figure 10. Control imaging experiment using water-soluble far-red fluorophore, DY-PEG. The amount of DY-PEG was adjusted to that used in the doubly labeled peptosome shown in Figure 9. (a) Bioluminescence image of SUIT2/EF-luc xenografts on the tumor-bearing mouse after administration of D-luciferin. (b) Image of fluorescence from DY-675, 2 days after the administration of DY-PEG.

partly incorporated into normal tissues probably due to the small size or physical instability.

Doubly labeled peptosome, in which the peptide membrane was labeled with ICG peptide and the inner aqueous phase encapsulated DY-675 labeled PEG (DY-PEG), was prepared and administered to the tumor-bearing mouse. These two kinds of fluorophores can be detected separately by choosing proper optical filters of the imaging apparatus, because ICG and DY-675 fluoresce at far-red and near-infrared region, respectively. ICG-labeled peptosome was prepared from a mixture of GA-PSar43-PMLG18 and GA-PSar65-PMLG18 (3:1) (group PEP) in a buffer containing DY-PEG. At 2 days after the intravenous administration to the tumor-bearing mouse, fluorescence from ICG was detected at the cancer site (Figure 9b), and at the same site, fluorescence from DY-675 was also observed (Figure 9c). In these images, accumulation of the peptosome in liver was also detected by both probes. On the other hand, when DY-PEG alone was administered to the tumor-bearing mouse, fluorescence at the cancer site was not observed at all even though accumulation in bladder was detected (Figure 10). Taken together, the peptosome was confirmed to be accumulated in the tumor tissue while maintaining its vesicular structure and preserving the water-soluble compound inside. The selective accumulation is therefore due to the EPR effect.

PSar chains around the peptosome are expected to take a role of suppressing the capture of peptosome by the RES, and *in vivo* retention in blood of peptosome was actually proven to be extremely long. In the case of PEGylated liposomes, the retention time in blood was improved by optimization of the mixing ratio of long and short PEG chains (*51*). Therefore, peptosome coated by optimized PSar layer may show further retention in blood, which is currently under investigation. Further, poly(ethylene glycol) (PEG), which is a common artificial water-soluble polymer and is used frequently for biocompatible materials, may be replaced with PSar in many cases.

In conclusion, we have succeeded in preparation of 100 nm sized peptosome, which is a vesicular assembly of genuine amphiphilic polypeptide, using PSar as a hydrophilic block and PMLG as a hydrophobic block. NIRF-labeled peptosome was prepared by adding ICG-conjugated polypeptide. Diameter of the peptosome prepared from GA-PSar-PMLGs was in the range from 100 to 200 nm, which is the appropriate size for the passive targeting into the solid tumor by the EPR effect. *In vivo* retention in blood of ICG-labeled peptosome was assayed by using rats as experimental animals, and the retention time was proven to be as long as the PEGylated liposome. ICG-labeled peptosome was also administered to the tumor-bearing mouse and successfully detected the tumor tissue due to the EPR effect.

ACKNOWLEDGMENT

This study is a part of joint research, which is focusing on the development of the basis of technology for establishing COE for nanomedicine, carried out through Kyoto City Collaboration of Regional Entities for Advancing Technology Excellence (CREATE) assigned by Japan Science and Technology Agency (JST). *In vivo* retention in blood studies were carried out with help of Termo Co. Japan.

LITERATURE CITED

(1) Weissleder, R., and Mahmood, U. (2001) Molecular imaging. *Radiology 219*, 316–333.
(2) Herschman, H. R. (2003) Molecular imaging: looking at problems, seeing solutions. *Science 302*, 605–608.
(3) Sharma, P., Brown, S., Walter, G., Santra, S., and Moudgil, B. (2006) Nanoparticles for bioimaging. *Adv. Colloid Interface Sci. 123*, 471–485.
(4) Tada, H., Higuchi, H., Watanabe, T. M., and Ohuchi, N. (2007) In vivo real-time tracking of single quantum dots conjugated with monoclonal anti-HER2 antibody in tumors of mice. *Cancer Res. 67*, 1138–1144.
(5) Josephson, L., Kircher, M. F., Mahmood, U., Tang, Y., and Weissleder, R. (2002) Near-infrared fluorescent nanoparticles as combines MR/optical imaginprobes. *Bioconjugate Chem. 13*, 554–560.
(6) Gao, X., Cui, Y., Levenson, R. M., Chung, L. W. K., and Nie, S. (2004) *In vivo* cancer targeting and imaging with semiconductor quantum dots. *Nat. Biotechnol. 22*, 969–976.
(7) Lyons, S. K. (2005) Advances in imaging mouse tumour models *in vivo. J. Pathol. 205*, 194–205.
(8) Ntziachristos, V., Bremer, C., and Weissleder, R. (2003) Fluorescence imaging with near-infrared light: new technological advances that enable in vivo molecular imaging. *Eur. Radiol. 13*, 195–208.
(9) HSu, A. R., Hou, L. C., Veeravau, A., Greve, J. M., Vogel, H., Tse, V., and Chen, X. (2006) *In vivo* near-infrared fluorescence imaging of integrin $\alpha_v\beta_3$ in an orthotopic glioblastoma model. *Mol. Imaging Biol. 8*, 315–323.
(10) Christian, N. A., Milone, M. C., Ranka, S. S., Li, G., Frail, P. R., Davis, K. P., Bates, F. S., Therien, M. J., Ghoroghchian, P. P., June, C. H., and Hammer, D. A. (2007) Tat-Functionalized near-infrared emissive polymersomes for dendritic cell labeling. *Bioconjugate Chem. 18*, 31–40.
(11) Cai, W., Shin, D.-W., Chen, K., Gheysens, O., Cao, Q., Wang, S. X., Gambhir, S. S., and Chen, X. (2006) Peptide-labeled near-infrared quantum dots for imaging tumor vasculature in living subjects. *Nano Lett. 6*, 669–676.
(12) Otsuji, E., Kuriu, Y., Okamoto, K., Ichikawa, D., Hagiwara, A., Ito, H., Nishimura, T., and Amagishi, H. (2006) Monoclonal antibody A7 coupled to magnetic particles as a contrast enhancing agent for magnetic resonance imaging of human colorectal carcinoma. *Cancer Immunol. Immunother. 55*, 728–733.
(13) Huh, Y.-M., Jun, Y.-W., Song, H.-T., Kim, S., Choi, J.-S., Lee, J.-H., Yoon, S., Kim, K.-S., Shin, J.-S., Suh, J.-S., and Cheon, J. (2005) *In vivo* magnetic resonance detection of cancer by using multifunctional magnetic nanocrystals. *J. Am. Chem. Soc. 127*, 12387–12391.

(14) Manchester, M., and Singh, P. (2006) Virus-based nanoparticles (VNPs): Platform technologies for diagnostic imaging. *Adv. Drug Delivery Rev. 58*, 1505–1522.
(15) Torchilin, V. P. (2007) Micellar nanocarriers: pharmaceutical perspectives. *Pharm. Res. 24*, 1–16.
(16) Lee, B.-S., Fujita, M., Khazenzon, N. M., Wawrowsky, K. A., Wachsmann-Hogiu, S., Farkas, D. L., Black, K. L., Ljubimova, J. Y., and Holler, E. (2006) Polycefin, a new prototype of a multifunctional nanoconjugate based on poly(L-malic acid) for drug delivery. *Bioconjugate Chem. 17*, 317–326.
(17) Matthews, S. E., Pouton, C. W., and Threadgill, M. D. (1996) Increased accumulation of PEG—PE micelles in the area of experimental myocardial infarction in rabbits. *Adv. Drug Delivery Rev. 18*, 219–267.
(18) Lukyanov, A. N., Hartner, W. C., and Torchilin, V. P. (2004) Increased accumulation of PEG—PE micelles in the area of experimental myocardial infarction in rabbits. *J. Controlled Release 94*, 187–193.
(19) Hashizume, H., Baluk, P., Morikawa, S., McLean, J. W., Thurston, G., Roberge, S., Jain, R. K., and McDonald, D. M. (2000) Openings between defective endothelial cells explain tumor vessel leakiness. *Am. J. Pathol. 156*, 1363–1380.
(20) Monsky, W. L., Fukumura, D., Gohongi, T., Ancukiewcz, M., Weich, H. A., Torchilin, V. P., Yuan, F., and Jain, R. K. (1999) Augmentation of transvascular transport of macromolecules and nanoparticles in tumors using vascular endothelial growth factor. *Cancer Res. 59*, 4129–4135.
(21) Turner, J. L., and Wooley, K. L. (2004) Nanoscale cage-like structures derived from polyisoprene-containing shell cross-linked nanoparticle templates. *Nano Lett. 4*, 683–688.
(22) Qi, K., Ma, Q., Remsen, E. E., Clark, C. G., Jr., and Wooley, K. L. (2004) Determination of the bioavailability of biotin conjugated onto shell cross-linked (SCK) nanoparticles. *J. Am. Chem. Soc. 126*, 6599–6607.
(23) Wang, F., Bronich, T. K., Kabanov, A. V., Rauh, R. D., and Roovers, J. (2005) Synthesis and evaluation of a star amphiphilic block copolymer from poly(ϵ-caprolactone) and poly(ethylene glycol) as a potential drug delivery carrier. *Bioconjugate Chem. 16*, 397–405.
(24) Discher, D. E., and Eisenberg, A. (2002) Polymer vesicles. *Science 297*, 967–973.
(25) Choucair, A., Lavigueur, C., and Eisenberg, A. (2004) Polystyrene-*b*-poly(acrylic acid) vesicle size control using solution properties and hydrophilic block length. *Langmuir 20*, 3894–3900.
(26) Schreief, H., and Bouwstrab, J. (1994) Liposomes and niosomes as topical drug carriers: dermal and transdermal drug delivery. *J. Controlled Release 30*, 1–15.
(27) Kidchob, T., Kimura, S., and Imanishi, Y. (1998) Amphiphilic poly(Ala)-b-poly(Sar) microspheres loaded with hydrophobic drug. *J. Controlled Release 51*, 241–248.
(28) Sengupta, S., Eavarone, D., Capila, I., Zhao, G., Watson, N., Kiziltepe, T., and Sasisekharan, R. (2005) Temporal targeting of tumour cells and neovasculature with a nanoscale delivery system. *Nature (London) 436*, 568–572.
(29) Koide, A., Kishimura, A., Osada, K., Jang, W.-D., Yamasaki, Y., and Kataoka, K. (2006) Semipermeable polymer vesicle (PICsome) self-assembled in aqueous medium from a pair of oppositely charged block. *J. Am. Chem. Soc. 128*, 5988–5989.
(30) Jaturanpinyo, M., Harada, A., Yuan, X., and Kataoka, K. (2004) Preparation of bionanoreactor based on core-shell structured polyion complex micelles entrappingtrypsin in the core cross-linked with glutaraldehyde. *Bioconjugate Chem. 15*, 344–348.
(31) Klibanov, A. L., Maruyama, K., Torchilin, V. P., and Huang, L. (1990) Amphipathic polyethyleneglycols effectively prolong the circulation time of liposomes. *FEBS Lett. 268*, 235–237.
(32) Papahadjopoulos, D., Allen, T. M., Gabizon, A., Mayhew, E., Matthay, K., Huang, S. K., Lee, K. D., Woodle, M. C., Lasic, D. D., Redemann, C., and Martin, F. J. (1991) Sterically stabilized liposomes: improvements in pharmacokinetics and antitumor therapeutic efficacy. *Proc. Natl. Acad. Sci. U.S.A. 88*, 11460–11464.
(33) Lyass, O., Uziely, B., Ben-Yosef, R., Tzemach, D., Heshing, N. I., Lotem, M., Brufman, G., and Gabizon, A. (2000) Correlation of toxicity with pharmacokinetics of pegylated liposomal doxorubicin (Doxil) in metastatic breast carcinoma. *Cancer 89*, 1037–1047.
(34) Muggia, F. M., Hainsworth, J. D., Jeffers, S., Miller, P., Groshen, S., Tan, M., Roman, L., Uziely, B., Muderspach, L., Garcia, A., Burnett, A., Greco, F. A., Morrow, C. P., Paradiso, L. J., and Liang, L. J. (1997) Phase II study of liposomal doxorubicin in refractory ovarian cancer: antitumor activity and toxicity modification by liposomal encapsulation. *J. Clin. Oncol. 15*, 987–993.
(35) Koukourakis, M. I., Koukouraki, S., Giatromanolaki, A., Archimandritis, S. C., Skarlatos, J., Beroukas, K., Bizakis, J. G., Retalis, G., Karkavitsas, N., and Helidonis, E. S. (1999) Liposomal doxorubicin and conventionally fractionated radiotherapy in the treatment of locally advanced non—small-cell Lung cancer and head and neck cancer. *J. Clin. Oncol. 17*, 3512–3521.
(36) Uziely, B., Jeffers, S., Isacson, R., Kutsch, K., Weitsao, D., Yehoshua, Z., Libson, E., Muggia, F. M., and Gabizon, A. (1995) Liposomal doxorubicin: antitumor activity and unique toxicities during two complementary phase I studies. *J. Clin. Oncol. 13*, 1777–1785.
(37) Obst, M., and Steinbüchel, A. (2004) Microbial degradation of poly(amino acid)s. *Biomacromolecules 5*, 1166–1176.
(38) Kidchob, T., Kimura, S., and Imanishi, Y. (1998) Thermoresponsive release from poly(Glu(OMe))-block-poly(Sar) microcapsules with surface-grafting of poly(N-isopropylacrylamide). *J. Controlled Release 50*, 205–214.
(39) Fujita, K., Kimura, S., and Imanishi, Y. (1999) Spherical self-assembly of a synthetic α-helical peptide in water. *Langmuir 15*, 4377–4379.
(40) Kimura, S., Kim, D. H., Sugiyama, J., and Imanishi, Y. (1999) Vesicular self-assembly of a helical peptide in water. *Langmuir 15*, 4461–4463.
(41) Kimura, S., Muraji, Y., Sugiyama, J., Fujita, K., and Imanishi, Y. (2000) Spontaneous vesicle formation by helical glycopeptides in water. *J. Colloid Interface Sci. 222*, 265–267.
(42) Osada, K., and Kataoka, K. (2006) Drug and gene delivery based on supramolecular assembly of PEG-Polypeptide hybrid block copolymers. *Adv. Polym. Sci. 202*, 113–153.
(43) Otsuka, H., Nagasaki, Y., and Kataoka, K. (2001) Self-assembly of poly(ethylene glycol)-based block copolymers for biomedical applications. *Curr. Opin. Colloid Interface Sci. 6*, 3–10.
(44) Tsai, G., Lane, H.-Y., Yang, P., Chong, M.-Y., and Lange, N. (2004) Glycine transporter I inhibitor, N-mehylglycine (sarcosine), added to antipsychotics for the treatment of Schizophernia. *Biol. Psychiatry 55*, 452–456.
(45) Kidchob, T., Kimura, S., and Imanishi, Y. (1996) Preparation, structure and release profile of polypeptide microcapsules. *J. Controlled Release 40*, 285–291.
(46) Provencher, S. W. (1988) A constrained regularization method for inverting data represented by linear algeraic or integral equations. *Comput. Phys. Commun. 27*, 213–227.
(47) Provencher, S. W. (1988) Contin: General purpose constrained regularization program for inverting noisy linear algeraic or integral equations. *Comput. Phys. Commun. 27*, 229–242.
(48) Pons, M., Foradada, M., and Estelrich, J. (1993) Liposomes obtained by the ethanol injection method. *Int. J. Pharm. 95*, 51–56.
(49) Cullis, P. R., and De Kruijiff, G. (1979) Lipid polymorphism and the functional roles of lipids in biological-membranes. *Biochim. Biophys. Acta 559*, 399–420.
(50) Van Hest, J. C. M., Delnoye, D. A. P., Baars, M. W. P. L., van Genderen, M. H. P., and Meijer, E. W. (1995) Polystyrene-

dendrimer apmphilic block-copolymers with a generation-dependent aggregation. *Science 268*, 1592–1595.

(51) Holowka, E. P., Pochan, D. J., and Deming, T. J. (2005) Charged polypeptide vesicles with controllable diameter. *J. Am. Chem. Soc. 127*, 12423–12428.

(52) Holzwarth, G., and Doty, P. (1965) The ultraviolet circular dichroism of polypeptides. *J. Am. Chem. Soc. 87*, 218–228.

(53) Bao, A. D., Goins, B., Klipper, R., Negrete, G., and Phillips, W. T. (2004) Direct ^{99m}Tc labeling of pegylated liposomal doxorubicin (Doxil) for pharmacokinetic and non-invasive imaging studies. *J. Pharmacol. Exp. Ther. 308*, 419–425.

(54) Klibanov, A. L., Maruyama, K., Beckerleg, A. M., Torchilin, V. P., and Huang, L. (1991) Activity of amphipathic poly(ethylene glycol) 5000 to prolong the circulation time of liposomes depends on the liposome size and is unfavorable for immunoliposome binding to target. *Biochim. Biophys. Acta 1062*, 142–148.

(55) Litzinger, D. C., Buiting, A. M. J., Vanrooijen, N., and Huang, L. (1994) Effect of liposome size on the circulation time and intraorgan distribution of amphipathic poly(ethylene glycol)-containing liposomes. *Biochim. Biophys. Acta 1190*, 99–107.

(56) Sadzuka, Y., Nakade, A., Tsuruda, T., and Sonobe, T. (2003) Study on the characterization of mixed polyethyleneglycol modified liposomes containing doxorubicin. *J. Controlled Release 91*, 271–280.

BC7001665

Bimodal Paramagnetic and Fluorescent Liposomes for Cellular and Tumor Magnetic Resonance Imaging

Nazila Kamaly,[†] Tammy Kalber,[‡] Ayesha Ahmad,[†] Morag H. Oliver,[†] Po-Wah So,[‡] Amy H. Herlihy,[‡] Jimmy D. Bell,[‡] Michael R. Jorgensen,[†] and Andrew D. Miller*[,†,§]

Imperial College Genetic Therapies Centre, Department of Chemistry, Flowers Building, Armstrong Road, Imperial College London, London, SW7 2AZ, Molecular Imaging Group and Biological Imaging Centre, Imaging Sciences Department, MRC Clinical Sciences Centre, Imperial College London, Hammersmith Hospital, London, W12 0HS, ImuThes Ltd, Flowers Building, Armstrong Road, London SW7 2AZ, United Kingdom. Received May 12, 2007; Revised Manuscript Received September 14, 2007

A novel bimodal fluorescent and paramagnetic liposome is described for cellular labeling. In this study, we show the synthesis of a novel gadolinium lipid, Gd.DOTA.DSA, designed for liposomal cell labeling and tumor imaging. Liposome formulations consisting of this lipid were optimized in order to allow for maximum cellular entry, and the optimized formulation was used to label HeLa cells *in vitro*. The efficiency of this novel bimodal Gd-liposome formulation for cell labeling was demonstrated using both fluorescence microscopy and magnetic resonance imaging (MRI). The uptake of Gd-liposomes into cells induced a marked reduction in their MRI T_1 relaxation times. Fluorescence microscopy provided concomitant proof of uptake and revealed liposome internalization into the cell cytosol. The optimized formulation was also found to exhibit minimal cytotoxicity and was shown to have capacity for plasmid DNA (pDNA) transfection. A further second novel neutral bimodal Gd-liposome is described for the labeling of xenograft tumors *in vivo* utilizing the enhanced permeation and retention effect (EPR). Balb/c nude mice were inoculated with IGROV-1 cells, and the resulting tumor was imaged by MRI using these *in vivo* Gd-liposomes formulated with low charge and a poly(ethylene glycol) (PEG) calyx for long systemic circulation. These Gd-liposomes which were less than 100 nm in size were shown to accumulate in tumor tissue by MRI, and this was also verified by fluorescence microscopy of histology samples. Our *in vivo* tumor imaging results demonstrate the effectiveness of MRI to observe passive targeting of long-term circulating liposomes to tumors in real time, and allow for MRI directed therapy, wherein the delivery of therapeutic genes and drugs to tumor sites can be monitored while therapeutic effects on tumor mass and/or size may be simultaneously observed, quantitated, and correlated.

INTRODUCTION

As an established noninvasive clinical imaging modality, magnetic resonance imaging (MRI) has recently received much interest within the field of molecular imaging (*1, 2*). MRI is capable of producing three-dimensional images of tissues containing water with a high degree of spatial resolution. In MRI, contrast agents are used to further improve the quality of an image. These agents consist of molecules which incorporate a paramagnetic metal ion, most commonly gadolinium (Gd) or iron (Fe). Image improvement arises due to the effect of the enhancement of longitudinal (T_1) or transverse (T_2) relaxation rates of the surrounding bulk water protons by the coordinated metal ion under an applied magnetic field. Contrast agents incorporating Gd increase both $1/T_1$ and $1/T_2$ but are generally used in T_1-weighted imaging where their $1/T_1$ effect is greater in tissue than their $1/T_2$ enhancement. In contrast, Fe containing agents lead to more substantial increases in $1/T_2$ and are therefore visualized with T_2-weighted images (*3*).

As a result of the successful coupling of the main Gd-chelating ligands 1,4,7,10-tetraazacyclododecane-1,4,7,10-tetraacetic acid (DOTA) and diethylenetriamine pentaacetic acid (DTPA), which are also clinical contrast agents, to various biologically relevant molecules, a large number of specific second generation contrast agents have been developed to further enhance the clinical potential of MRI. Specific Gd-chelating contrast agents have been designed for a whole host of biological MRI applications; ranging among gene expression (*4*), tumor imaging (*5*), angiogenesis (*6*), atherosclerosis (*7*), and neurological diseases (*8*), However, a limitation encountered when using Gd-based agents is local concentration; the tissue concentration necessary to image with T_1 contrast agents is often high, and therefore method development is needed to increase the number of Gd moieties bound per contrast agent molecule. As such, there have been a number of reports concerning the conjugation of Gd chelates to macromolecules such as dendrimers, linear polymers, and proteins, as well as the use of liposomes as Gd-chelate carriers (*9–11*).

Liposomes are versatile tools used traditionally in drug and gene delivery and are easily adapted for use *in vitro*, *ex vivo*, or *in vivo*. The overall liposome property can be adjusted using parameters such as lipid composition, head group charge, and lipid tail size. It is known that cationic liposomes are effective at mediating cell entry *in vitro* and that their circulation time *in vivo* is greatly enhanced with the use of neutral PEG polymers (*12–14*). Here, we report the utility of liposomes as bimodal paramagnetic and fluorescent imaging systems both for *in vitro* cell labeling and *in vivo* tumor imaging. In addition, the synthesis of the novel Gd-lipid Gd.DOTA.DSA **1** is shown. Based on the structural paradigm described by Miller et al. (*15*), *in vitro* Gd-**B** liposomes and *in vivo* stealth Gd-**BC** liposomes were prepared, whereby **B** represents the lipidic layer and **C** represents the PEG polymer masking layer designed to allow

* Author e-mail address: a.miller@imperial.ac.uk; fax: +44 (0)20 7594 5803; tel: +44 (0)20 7594 5869.
[†] Imperial College Genetic Therapies Centre.
[‡] Molecular Imaging Group and Biological Imaging Centre.
[§] Hammersmith Hospital.

10.1021/bc7001715 CCC: $40.75 © 2008 American Chemical Society
Published on Web 11/07/2007

for tumor Gd and fluorescence labeling. The cell labeling efficiency *in vitro* was achieved by the inclusion of a cationic lipid in the formulation and tumor imaging was made possible *in vivo* by formulating neutral Gd-liposomes for prolonged blood circulation and consequent extravasations through leaky tumor vasculature due to angiogenic blood vessels (*16*). This study demonstrates that Gd-liposomal systems are useful multifunctional platforms or tools for understanding the underlying problems associated with drug or nucleic acid delivery and for elucidating potential solutions. Further modification of these Gd-**BC** liposomes would involve the condensation of nucleic acids (**A** layer) within their aqueous core producing Gd-**ABC** liposomal therapeutic nanoparticles which can also be bestowed with specificity by adding a targeting **D** layer in the form of a suitable ligand (hence Gd-**ABCD** liposomal nanoparticles).

EXPERIMENTAL PROCEDURES

Materials. N^1-cholesteryloxycarbonyl-3,7-diaza-1,9-diaminonane (CDAN), 1,2-dioleoyl-*sn*-glycero-3-phosphoethanolamine (DOPE), phosphatidylethaolamine Lissamine rhodamine B (DOPE-Rhodamine), cholesterol, 1,2-dioleoyl-*sn*-glycero-3-phosphocholine (DOPC), and 1,2-distearoyl-*sn*-glycero-3-phosphoethanolamine-*n*-methoxy(poly(ethylene glycol))-2000 (DSPE-PEG_{2000}) were purchased from Avanti Polar Lipids Inc. (Alabaster, AL). Organic compounds were purchased from Sigma-Aldrich, Lancaster, or Merck Biosciences. ^{1}H and ^{13}C NMR spectra were recorded on a 400 MHz Bruker Advance 400 spectrometer. Infrared (IR) spectra were recorded on a JASCO FT/IR-620 infrared spectrophotometer. Analytical HPLC was conducted on a Hitachi-LaChrom L-7150 pump system equipped with a Polymer laboratories PL-ELS 1000 evaporative light-scattering detector. Flash column chromatography was performed using Merck 0.040 to 0.063 mm, 230 to 400 mesh silica gel. MRI experiments were conducted on a 4.7 T Magnex magnet (Oxford, UK) Varian Unity Inova console (Palo Alto, CA). All procedures on animals were conducted in accordance with UK Home Office regulations and the Guidance for the Operation of Animals (Scientific Procedures) Act (1986).

2-(4,7,10-Tris(2-*tert*-butyloxycarbonylmethyl)-1,4,7,10-tetraazacyclododecan-1yl)acetic Acid (2). 2-Chlorotrityl chloride resin (916.7 mg, 1.265 mmol) was added to a solid-phase synthesis vessel and swelled by the addition of CH_2Cl_2 (40 mL) and the vessel agitated for 30 min (0.8 mmol.g^{-1} loading). Bromoacetic acid (1.758 g, 12.65 mmol, 10 equiv) and *i*Pr_2NEt (1.107 mL, 6.325 mmol, 5 equiv) were added to the resin, and the vessel was agitated on a motor shaker overnight at room temperature. MeOH (1000 equiv) was added as a capping reagent and the reaction agitated for a further 10 min; the solution was filtered, and the resin was washed by alternating between CH_2Cl_2 and *i*PrOH (3×) and MeOH (2×) and finally dried. Cyclen (2.179 g, 12.65 mmol, 10 equiv) was dissolved in CH_2Cl_2 (40 mL) and added to the vessel containing the bromoacetyl resin; the reaction mixture was agitated for 4 h at room temperature. The solvent was filtered and the resin washed alternating among CH_2Cl_2 and *i*PrOH (3×), CH_2Cl_2 and MeOH (3×), distilled H_2O (2×), and finally CH_2Cl_2 and *i*PrOH (3×). The chloroanil test was positive. The resin was then washed with DMF (2×) and dried. *tert*-Butyl bromoacetate (3.064 mL, 18.975 mmol, 5 equiv per free amine), NEt_3 (1.587 mL, 11.389 mmol, 3 equiv per free amine) were dissolved in DMF (40 mL) and added to the cyclen-functionalized resin. The reaction was left shaking for a further 12 h at room temperature. The solvent was removed by filtration, and the resin was washed with *i*PrOH and distilled H_2O (3×), CH_2Cl_2 and *i*PrOH (3×), MeOH (2×), toluene (2×), and finally diethyl ether (2×). The chloroanil test was negative. The resin was transferred to a round-bottomed flask, stirred into a solution of CH_2Cl_2/trifluroethanol 2:1 (v/v) for a further 2 h at room temperature, and subsequently filtered and washed with CH_2Cl_2 (3×), and the filtrate was collected and reduced *in vacuo* to give a yellow oil. The compound was purified by flash column chromatography ((eluted with CH_2Cl_2/MeOH/H_2O 34.5:9:1): CH_2Cl_2 3:7 v/v) to yield a crystalline pale yellow solid (361.79 mg, 51%, mp = 88–93 °C), R_f [CH_2Cl_2/MeOH/H_2O 34.5:9:1 v/v] 0.48. ^{1}H NMR (400 MHz, d_6-DMSO, 400 K): δ (ppm) 3.14 (s, br, 8H, 4× $CH_2COOC(CH_3)_3$), 2.58 (s, br, 16H, 4× NCH_2CH_2N), 1.46 (s, 27H, $C(CH_3)_3$ 3×). ^{13}C NMR (400 MHz, $CDCl_3$): δ (ppm) 174.9 (*C*OOH), 172.3 (*C*OO*t*-Bu), 82.3 ($C(CH_3)_3$ 2×), 82.0 ($C(CH_3)_3$), 56.7 (CH_2COOH), 56.1 (CH_2COO*t*-Bu), 55.7 (CH_2COO*t*-Bu), 50.9 (CH_2 2×), 50.2 (CH_2 2×), 28.1 ($C(CH_3)_3$). FTIR: (cm^{-1}) 3735, 3397, 2925, 2853, 2726, 2366, 1731, 1458, 1377, 1310, 1262, 1227, 1160. HPLC t_R = 16.0 min, column C-4 peptide: gradient mix A = MeCN/0.1% TFA; mix B = H_2O/TFA; mix C = MeOH/$CHCl_3$ mix D = MeOH, 0.0 min [100% B], 15–25.0 min [100% A], 25.1–45.0 min [100% D], 45.1–55.0 min [100% C]; flow 1 mL/min. HRMS (FAB^+) calcd for $C_{28}H_{52}N_4O_8$ *m/z* 573.3785, found 573.386 (M–H).

***N,N*-Distearylamidomethylcarbamic Acid *tert*-Butyl Ester (8).** Boc-glycine (310 mg, 1.77 mmol) and dioctadecylamine (923.96 mg, 1.77 mmol) were dissolved in dry chloroform (30 mL). HBTU (804.12 mg, 2.12 mmol) and DMAP (648.72 mg, 5.31 mmol) were added to the solution, and the reaction was stirred at room temperature under N_2 for 12 h. The solvents were removed *in vacuo*. The mixture was dissolved in CH_2Cl_2 (50 mL) and extracted with H_2O (3 × 50 mL). The combined aqueous extracts were back-extracted with CH_2Cl_2/MeOH (2 × 50 mL), the solvents reduced and redissolved in diethyl ether, and a subsequent extraction with 7% citric acid and H_2O was performed; the organic layer was washed with brine, collected, and filtered through celite and finally dried over $MgSO_4$. The diethyl ether was evaporated *in vacuo* to yield a pure white solid (1.164 g, 97% yield, mp = 82–85 °C). R_f [CH_2Cl_2/MeOH/H_2O, 34.5:9:1 v/v] 0.56. ^{1}H NMR (400 MHz, $CDCl_3$): δ (ppm) 5.50 (br, s, 1H, amide N*H*), 3.99 (s, br, 2H, $NHCH_2$), 3.35–3.25 (d, br, 2H, $OCNCH_2$), 3.17–3.07 (d, br, 2H, $OCNCH_2$), 1.44 (s, 9H, $C(CH_3)_3$), 1.61–1.44 (m, 13H, $C(CH_3)_3$ and $OCN(CH_2CH_2)$), 1.25 (s, 60H, CH_2's alkyl chain), 0.872 (s, br, 6H, CH_3 2×). ^{13}C NMR (400 MHz, $CDCl_3$): δ (ppm) 167.6 ($CON(CH_2)_{17}$), 156.0 ($C(CH_3)_3COCO$), 79.0 ($C(CH_3)_3$), 46.9 ($N(CH_2CH_2)_9$), 46.1 ($N(CH_2CH_2)_9$), 42.2 ($NHCH_2CO$), 31.9–26.9 (CH_2 30×), 22.7 ($N(CH_2CH_2)_9$), 14.1 ($C(CH_3)_3$). FTIR: (cm^{-1}) 2953, 2923, 2853, 2360, 1723, 1650, 1610, 1460, 1160, 1580, 1377, 837, 721. HPLC: t_R= 36.08 min, column C-4 peptide: gradient mix A = MeCN/0.1% TFA; mix B = H_2O/TFA; mix C = MeOH/$CHCl_3$; mix D = MeOH, 0.0 min [100% B], 15–25.0 min [100% A], 25.1–45.0 min [100% D], 45.1–55.0 min [100% C]; flow 1 mL/min. HRMS: (FAB+) calcd for $C_{43}H_{86}N_2O_3$ *m/z* 678.660, found 679.6953 $(M + H)^+$.

***N,N*-Distearylamidomethylamine (DSA) (3).** The protected amine was dissolved in anhydrous CH_2Cl_2 (5 mL), to which was added trifluoroacetic acid (3 mL). The reaction was stirred under an atmosphere of N_2 for 2 h. The solvents were removed *in vacuo* and the product dried under vacuum to obtain a white powder (158 m, 94% yield, mp = 59–64 °C). R_f [hexane/ethyl acetate 9:1 v/v] 0.44.^{1}H NMR (400 MHz, $CDCl_3$): δ (ppm) 3.85 (s, 2H, $OCCH_2NH_2$), 3.32 (t, J = 7.2 Hz, 2H, $OCNCH_2CH_2$), 3.13 (t, J = 7.2 Hz, 2H, $OCNCH_2CH_2$), 2.39 (s, very br, 2H, NH_2), 1.61–1.55 (m, 4H, $OCNCH_2CH_2$), 1.26 (s, 60H, chain CH_2's), 0.86 (t, 6H, J = 6.8, CH_3 2×). ^{13}C NMR (400 MHz, $CDCl_3$): δ (ppm) 168.8 (*C*O), 43.7 ($OCNCH_2$), 41.9 ($OCNCH_2$), 35.6 ($CH_3CH_2CH_2$), 33.4 (alkyl chain CH_2's), 32.3, 31.1 ($NCH_2CH_2CH_2$), 22.7–14.1 (alkyl chain CH_2's). FTIR: (cm^{-1}) 2953, 2922, 2852, 1681, 1534, 1464, 1377, 1313, 1206, 1174, 1132, 915, 834, 722. HPLC: t_R = 31.46 min, column C-4

peptide: gradient mix A = MeCN/0.1% TFA; mix B = H_2O/TFA; mix C = MeOH/$CHCl_3$; mix D = MeOH, 0.0 min [100% B], 15–25.0 min [100% A], 25.1–45.0 min [100% D], 45.1–55.0 min [100% C]; flow 1 mL/min. HRMS: (FAB+) calcd for $C_{38}H_{78}N_2O$ *m/z* 578.6114, found 579.6199 $(M+H)^+$.

2-{4,7-Bis-*tert*-butyloxycarbonylmethyl-10-[(*N*,*N*-distearylamidomethyl-*N*′-amidomethyl]-1,4,7,10-tetraazacyclododec-1-yl}acetic Acid *tert*-Butyl Ester (4). Bis(steroyl amide) (4.837 mg, 0.0084 mmol) and *tert*-butyloxycarbonyl DOTA acid (*2*) (4.35 mg, 0.0076 mmol) were added to a dry round-bottomed flask followed by the addition of dry $CHCl_3$ (8 mL). HBTU (3.46 mg, 0.0091 mmol) and DMAP (2.785 mg, 0.022 mmol) were also added, and the reaction was stirred at 40 °C for 6 h until TLC indicated completion. The solvents were removed *in vacuo*, and the crude mixture was purified by flash column chromatography (eluted with (CH_2Cl_2/MeOH/NH_3 34.5:9:1): CH_2Cl_2 1:9 → 1:1, v/v) to yield a yellowish oil (7.58 mg, 88% yield). R_f [CH_2Cl_2/MeOH/H_2O 34.5:9:1 v/v] 0.84. ^{1}H NMR (400 MHz, $CDCl_3$, 318 K): δ (ppm) 3.98 (s, 2H, OCCH_2NCH_2), 3.31 (t, 2H, J = 7.6 Hz, OCNCH_2CH_2), 3.15 (s, br, 8H, 4× CH_2COOC$(CH_3)_3$), 3.13 (t, 2H, J = 7.6 Hz, OCNCH_2CH_2), 2.58 (s, br, 16H, 4× NCH_2CH_2N), 2.35 (s, very br, 2H, CH_2N*H*), 1.67–1.59 (m, 4H, OCNCH_2CH_2), 1.46−1.44 (d of s, 27H, J = 6.0, C(CH_3)$_3$ 3×),1.25 (s, 60H, chain CH_2′s), 0.90 (t, 6H, J = 6.8, CH_3 2×). ^{13}C NMR (400 MHz, $CDCl_3$): δ 172.9 (C$(CH_3)_3$OCO), 171.3 (NCH_2CONH), 166.8 (*C*ONC$H_2$$(CH_2)_{16}$), 81.7 (*C*$(CH_3)_3$), 81.5 (*C*$(CH_3)_3$), 55.8 (C$(CH_3)_3$OCOC$H_2$N), 53.4 (NC$H_2CH_2$N), 47.1 (NC$H_2$), 41.1 (NH*C*$H_2$CON), 32.0 (NC$H_2CH_2CH_2$*C*$H_2$), 29.7–27.1 (C(*C*$H_3$)$_3$ and chain *C*H_2's), 22.7 (*C*H_2CH_3), 14.6 (CH_2*C*H_3). FTIR: (cm^{-1}) 3054, 2923, 2853, 2306, 1456, 1377, 1265, 896. HPLC: t_R = 27.71 min, column C-4 peptide: gradient mix A = MeCN/0.1% TFA; mix B = H_2O/TFA; mix C = MeOH/$CHCl_3$; mix D = MeOH, 0.0 min [100% B], 15–25.0 min [100% A], 25.1–45.0 min [100% D], 45.1–55.0 min [100% C]; flow 1 mL/min. HRMS: (FAB+) calcd for $C_{66}H_{128}N_6O_8$ *m/z* 1132.9794, found 1155.9669 $(M + Na)^+$.

2-{4,7-Bis-carboxymethyl-10-[(*N*,*N*-distearylamidomethyl-*N*′-amidomethyl]-1,4,7,10-tetraazacyclododec-1-yl}acetic Acid (DOTA.DSA) (5). *tert*-Butyl-protected DOTA.DSA was dissolved in a 1:1 mixture of c.HCl/1,4-dioxane and the reaction stirred for 2 h. The solvents were removed *in vacuo*, the mixture suspended in water and freeze-dried to yield a white powder of DOTA.DSA (5 mg, 68% yield). R_f [CH_2Cl_2/MeOH/H_2O 34.5:9:1 v/v] 0.61. ^{1}H NMR (400 MHz, $CDCl_3$, 300 K): δ (ppm) 10.55 (s, br, 3H, 3× COO*H*), 5.30 (s, br, 1H, CH_2N*H*COO), 3.65 (m, 6H, 3× NCH_2COOH), 3.22 (m, 6H, 2× NCH_2CH_2, 1× NCH_2CONH), 2.58 (s, br, 16H, 4× NCH_2CH_2N), 2.29 (s, br, 2H, CH_2NH), 1.67–1.59 (m, 4H, OCNCH_2CH_2), 1.46−1.44 (d of s, 27H, J = 6.0, C(CH_3)$_3$ 3×), 1.25 (s, 60H, chain CH_2's), 0.90 (t, 6H, J = 6.8, CH_3 2×). FTIR: (cm^{-1}) 3948, 3853, 3750, 3689, 3567, 3364, 2947, 2922, 2852, 2726, 2234, 1991, 1889, 1793, 1681, 1534, 1497, 1464, 1388, 1377, 1207, 1318, 1132, 688. HPLC: t_R= 34.16 min, column C-4 peptide: gradient mix A = MeCN/0.1% TFA; mix B = H_2O/TFA; mix C = MeOH/$CHCl_3$; mix D = MeOH, 0.0 min [100% B], 15–25.0 min [100% A], 25.1–45.0 min [100% D], 45.1–55.0 min [100% C]; flow 1 mL/min. HRMS: (FAB+) calcd for $C_{54}H_{104}N_6O_8$ *m/z* 964.7916, found 987.7833 $(M + Na)^+$.

Gadolinium(III) 2-{4,7-Bis-carboxymethyl-10-[(*N*,*N*-distearylamidomethyl-*N*′-amidomethyl]-1,4,7,10-tetraazacyclododec-1-yl}acetic Acid (Gd.DOTA.DSA) (1). A stoichiometric amount of $Gd.Cl_3.6H_2O$ (28.118 mg, 0.075 mmol) was added to DOTA.DSA (5) (73 mg, 0.0757 mmol), and the reaction was stirred in distilled H_2O (20 mL) at 90 °C overnight (pH dropped to 3.5 upon Gd addition). The water was freeze-dried to yield a white powder (83.9 mg, 99% yield, decomp 348 °C). R_f [CH_2Cl_2/MeOH/H_2O 34.5:9:1 v/v] 0.55. The Xylenol orange test indicated no detectable free Gd^{3+} ions. FTIR: (cm^{-1}) 3948, 3853, 3750, 3689, 3567, 3364, 2947, 2922, 2852, 2726, 2234, 1991, 1889, 1793, 1681, 1534, 1498, 1464, 1388, 1377, 1206, 1318, 1132, 1068, 1044, 668. HPLC: t_R= 36.22 min, column C-4 peptide: gradient mix A = MeCN/0.1% TFA; mix B = H_2O/TFA; mix C = MeOH/$CHCl_3$; mix D = MeOH, 0.0 min [100% B], 15–25.0 min [100% A], 25.1–45.0 min [100% D], 45.1–55.0 min [100% C]; flow 1 mL/min. HRMS: (FAB+) calcd for $C_{54}H_{101}GdN_6O_8$ *m/z* 1119.6654, found 1120.10 $(M + H)^+$.

[*N*,*N*-Bis-stearylamidomethyl-*N*′-amidomethyl]diethylenetriamine Tetraacetic Acid (DTPA.BSA). A solution of octadecylamine (301.86 mg, 1.2 mmol) dissolved in chloroform (30 mL) was added to a solution of DTPA bisanhydride (200 mg, 0.560 mmol) previously dissolved in DMF (40 mL). The reaction was stirred at 40 °C for 2 h. The white precipitate formed was collected by filtration and washed with acetone and dried under vacuum overnight. The white solid was stirred in water at 80 °C for 3 h to dissolve any excess DTPA. The insoluble residue was filtered and dried under vacuum overnight. The white solid was then washed with boiling chloroform and stirred in chloroform for 2 h, and then filtered and dried (198 mg, 40% yield, mp = 168–173 °C). R_f [CH_2Cl_2/MeOH/H_2O 34.5:9:1 v/v] 0.55. ^{1}H NMR (400 MHz, CF_3-COOD at δ = 11.30 ppm): δ (ppm) 4.55 (d, 8H, J = 5.2, HOOCCH_2N), 4.09 (t, 6H, NCH_2CH_2N 2× and HOOCCH_2N), 3.69 (t, 4H, J = 4.8 and J = 19.6, NCH_2CH_2N 2×), 3.34 (t, 4H, J = 7.2, NHCH_2 2×), 1.57 (d, 4H, J = 6.0, NHCH_2CH_2 2×), 1.27 (d, 60H, 30× CH_2 alkyl chain), 0.83 (t, 6H, J = 7.2, CH_2CH_3 2×). ^{13}C NMR (400 MHz, CF_3-COOD at δ = 116.6 and 164.2 ppm): δ (ppm) 170.2 (*C*H_2COOH), 166.1 (NCH_2CONHCH_2CH_2), 58.5 (HOOC*C*H_2), 57.2–55.0 (NCH_2CONH), 51.8 (NCH_2*C*H_2N-(CH_2COOH)CH_2CH_2N), 42.5 (NH*C*H_2CH_2), 32.8 (NH*C*H_2-CH_2), 30.530.2 (chain *C*H_2's), 27.4 (NHCH_2CH_2*C*H_2), 23.1, 14.1 (*C*H_3). FTIR: (cm^{-1}) 3948, 3883, 3780, 3675, 3596, 3482, 3358, 2922, 2272, 1991, 1869, 1771, 1684, 1653, 1576, 1497, 1396, 1069, 1044. HPLC: t_R = 34.23 min, column C-4 peptide: gradient mix A = MeCN/0.1% TFA; mix B = H_2O/TFA; mix C = MeOH/$CHCl_3$; mix D = MeOH, 0.0 min [100% B], 15–25.0 min [100% A], 25.1–45.0 min [100% D], 45.1–55.0 min [100% C]; flow 1 mL/min. HRMS: (FAB^+) calcd for $C_{50}H_{97}GdN_5O_8$ *m/z* 895.73, found 896.7423 $(M + H)^+$.

Gd(III) [*N*,*N*-Bis-stearylamidomethyl-*N*′-amidomethyl]diethylenetriamine Tetraacetic Acid (Gd.DTPA.BSA). A stoichiometric amount of $Gd.Cl_3.6H_2O$ (45 mg, 0.0502 mmol) was added to BSA.DTPA (18.67 mg, 0.0502 mmol), and the reaction was stirred in distilled H_2O (20 mL) at 90 °C for 3 h (pH dropped to 3.5). The water was freeze-dried to yield a white powder (48 mg, 91% yield, decomp 350 °C). R_f [CH_2Cl_2/MeOH/H_2O 34.5:9:1 v/v]. The Xylenol orange test indicated no detectable free Gd^{3+} ions. FTIR: (cm^{-1}) 3947.57, 3882.97, 3779.8, 3674.69, 3595.63, 3481.85, 3357.46, 2921.63, 2271.73, 1991.14, 1868.68, 1771.3, 1683.55, 1652.7, 1575.56, 1497, 1396.21, 1317.14, 1068.37, 1044.26, 668.214. HPLC: t_R= 34.60 min, column C-4 peptide: gradient mix A = MeCN/0.1% TFA; mix B = H_2O/TFA; mix C = MeOH/$CHCl_3$; mix D = MeOH, 0.0 min [100% B], 15–25.0 min [100% A], 25.1–45.0 min [100% D], 45.1–55.0 min [100% C]; flow 1 mL/min. HRMS: (FAB+) calcd. for $C_{50}H_{94}GdN_5O_8$ *m/z* 1050.56, found 1051.10 $(M + H)^+$.

Xylenol Orange Test. The presence of free gadolinium ions in Gd-incorporated compounds was determined by measuring the absorbance at 573 nm of a mixture of Xylenol orange solution (990 μL, 0.5 mM in sodium acetate buffer (0.1 M, pH 5.2) and test solution (in an appropriate solvent) containing the

Gd compound (10 μL). Extinction coefficient ε = 20, 700 L mol^{-1} cm^{-1}, whereby [Free Gd] = A573/ε.

Chloroanil Test. To 1–5 mg of resin was added one drop of 2% acetaldehyde in DMF (v/v) followed by one drop of 2% *p*-chloranil in DMF (w/v). The sample was allowed to stand at room temperature for 5 min. Blue-stained beads indicate the presence of secondary amines.

Liposome Preparations. All lipids were stored as stock solutions in anhydrous organic solvents ($CHCl_3$, MeOH, or a mixture of both), at −20 °C under argon. Liposomes were made with a range of defined molar ratios of individual lipids to give a predetermined total lipid concentration of 1.2 mg mL^{-1} in water for *in vitro* and 30 mg mL^{-1} in HEPES (20 mM, NaCl 135 mM, pH 6.5) for *in vivo* experiments. Fluorescent liposomes always contained 0.5 mol % and 1 mol % DOPE–Rhodamine (Avanti Polar Lipids Inc., USA) for *in vitro* and *in vivo* experiments, respectively. Appropriate volumes of each lipid stock were placed in a round-bottom flask (typically 5 mL) containing distilled CH_2Cl_2 (500 μL) and stirred to ensure thorough mixing of the lipids. The solvent was slowly removed *in vacuo* to ensure production of an even lipid film. The film was rehydrated with water or buffer at a defined volume. The resulting solution was sonicated for 5–8 min for *in vitro* formulations and 30 min (at 30 °C) for *in vivo* formulations in order to form liposomes of appropriate size. The pH of the liposomal suspension was checked by pH Boy (Camlab Ltd., Over, Cambridgeshire, UK) and if appropriate adjusted to neutral by addition of aqueous solutions of NaOH (0.99 M) and HCl (0.99 M). For each preparation, the size of the liposomes was measured by photon correlation spectroscopy (PCS) to ensure a size distribution of below 250 nm for *in vitro* experiments and 100 nm for *in vivo* experiments.

MRI Analysis of Gd.DOTA.DSA and Gd.DTPA.BSA. For T_1 analysis, Gd.DOTA.DSA **1**, Gd.DTPA.BSA, and controls of the metal-free compounds and Magnevist (Schering AG, Germany) were added to water to give a final concentration of 0.5 mM. The solutions (200 μL) were placed in Eppendorf tubes and T_1 relaxation values measured on a 4.7T Varian MR scanner at ambient temperature. For relaxivity measurements; Gd liposome formulations were prepared in order to obtain five different Gd concentrations between 0.55 and 1.85 mM in 200 μL of distilled water, and the molar relaxivity r_1 (m M^{-1} s^{-1}) determined. T_1 values were obtained using saturation recovery experiments performed with a standard spin–echo sequence and a 2 mm single slice acquisition (TR = 50, 100, 200, 300, 500, 700, 1200, 3000, 5000, 7000 ms; TE = 15 ms), the number of signal averages was 2, FOV; 70 × 70 mm^2, collected into a matrix of 256 × 128.

***In Vitro* Fluorescent Cell Uptake Assay.** At 24 h prior to Gd-liposome uptake experiments, adherent HeLa cells were grown in Dulbecco's Modified Eagle culture medium (DMEM) with 10% fetal calf serum and 1% penicillin–streptomycin (Sigma), in a 48-well plate (80 000 cells per well, 250 μL of complete medium) and in a wet (37 °C) 10% CO_2/90% air atmosphere. The cells were grown until 80% confluence was reached. The media was then removed and replaced with fresh media (same volume as previous). Bimodal Gd liposomes (see Table 2) containing 0.5 mol % DOPE–Rhodamine were then added at three different doses to the wells, swirled to ensure even dispersion, and then incubated in a wet (37 °C) 10% CO_2/90% air atmosphere for 4, 6, 8, or 10 h. The amount of Gd per liposome sample added to each well was as follows: For the 6 μg Gd liposome dose, liposomes 1 and 2 contained 0.358 μg; liposomes 3 and 4, 0.449 μg; liposomes 5 and 6, 0.554 μg; and liposomes 7 and 8 contained 610.32 μg of Gd. For the 12 μg Gd liposome dose, liposomes 1 and 2 contained 0.716 μg; liposomes 3 and 4, 0.898 μg; liposomes 5 and 6, 1.108 mg; liposomes 7 and 8, 1.220 mg of Gd. Finally, for the 18 μg Gd liposome dose, liposomes 1 and 2 contained 1.074 mg; liposomes 3 and 4, 1.347 mg; liposomes 5 and 6, 1.662 mg; and liposomes 7 and 8, 1.831 mg of Gd. After liposome uptake, the cells were washed with PBS (2 × 200 μL) and then treated with lysis buffer (100 μL per well). Cell lysate (80 μL) was diluted with MeOH (50 μL) and $CHCl_3$ (300 μL). The resulting solution was vigorously vortexed and then allowed to separate into two phases (organic and aqueous). The organic layer was isolated, and its fluorescence was recorded on a RF-5301PC Shimadzu spectrofluorophotometer (λ_{ex} 545 nm, λ_{em} 585 nm). As a positive control, control Gd liposomes (6, 12, or 18 μg) were added to the lysate of untreated cells, to provide a 100% liposome uptake result. The amount of cellular protein was quantified with a BCA assay (Pierce, Rockford, IL).

Lactate Dehydrogenase Toxicity Assay. Twenty-four hours prior to the assay, adherent HeLa cells were grown in Dulbecco's Modified Eagle culture medium (DMEM) with 10% fetal calf serum and 1% penicillin–streptomycin (Sigma), in 48-well (4×10^4 cells per well, 250 μL of complete medium) plates and in a wet (37 °C) 10% CO_2/90% air atmosphere. The cells were grown until 80% confluent, and the media was then removed and replaced with fresh media (same volume as previous). The same Gd liposomes used in the *in vitro* fluorescence cell uptake assay (see Table 2) were added to each well at the previously stated three doses and the cells incubated in a wet (37 °C) 10% CO_2/90% air atmosphere for 4, 6, 8, or 10 h. In addition, this experiment was repeated; however, at the end of each incubation period the cells were washed and then incubated for a further 24 h period. The LDH assay was carried out using the CytoTox 96 non-radioactive cytotoxicity assay (Promega, USA).

MRI Analysis of Cells. Twenty-four hours prior to liposome uptake, adherent HeLa cells were grown in Dulbecco's Modified Eagle culture medium (DMEM) with 10% fetal calf serum and 1% penicillin–streptomycin (Sigma), in a 25 cm^3 culture flask (5×10^5 cells per well, 5 mL of growth medium) and in a wet (37 °C) 10% CO_2/90% air atmosphere. The cells were grown until 80% confluent, and the media was then removed and replaced with fresh media. Gd liposomes (144 μL of 1.2 mg mL^{-1} liposome solution containing 4.49 μg Gd (the optimal dose was scaled up from the *in vitro* fluorescence assay to label 5×10^5 cells) were then added to each flask, swirled to ensure even dispersion, and then incubated in a wet (37 °C) 10% CO_2/90% air atmosphere for 8 h. After liposome uptake, the cells were washed with PBS (2 × 2 mL) and then treated with trypsin–EDTA (500 μL trypsin, 1 mM EDTA) for 2 min at 37 °C. DMEM (complete, 3 mL) was added to neutralize the trypsin. The cells were washed with PBS and then centrifuged in PBS buffer (1 mL), the solution was decanted, and the cells reconstituted in PBS by vortexing and spun (1500 rpm for 5 min) into pellets in Eppendorf tubes filled with 200 μL PBS. The tubes were imaged and T_1 values were measured on a 4.7T Varian MR Scanner. T_1 values were obtained from saturation recovery experiments performed with a standard spin–echo sequence and a 10 mm single slice acquisition (TR = 50, 100, 200, 300, 500, 700, 1200, 3000, 5000, 7000 ms; TE = 15 ms), four signal averages, FOV; 100 × 100 mm^2, collected into a matrix of 256 × 128. As negative controls; cells treated with liposomes containing no Gd lipid (substituted for by using the Gd free lipid DOTA.DSA); untreated cells and an Eppendorf containing PBS buffer were also imaged.

Fluorescence Microscopy. Twenty-four hours prior to Gd liposome uptake, adherent HeLa cells were grown in Dulbecco's Modified Eagle culture medium (DMEM) with 10% fetal calf serum (FCS, sigma) and 1% penicillin–streptomycin (Sigma), in a 6-well (1.25×10^5 cells per well, 3 mL of complete

medium) plate fitted with plastic microscopy slides, in a wet (37 °C) 10% CO_2/90% air atmosphere. The cells were grown until 80% confluent, and the media was then removed and replaced with fresh media (same volume as previous). Fluorescent Gd liposomes, 37.5 μg per well (31.25 μL of 1.2 mg mL^{-1} liposomes containing 5.26 μg of Gd, based on scaling up of optimal dose from *in vitro* fluorescence assay) were then added to appropriate wells, swirled to ensure even dispersion, and then incubated in a wet (37 °C) 10% CO_2/90% air atmosphere for 8 h. After liposome uptake, the media was removed, and the cells were washed with PBS (2×), heparin (1× (20 mg mL) in order to remove unbound liposomes from cell surface), PBS (2×), paraformaldehyde (PFA) (1× (20 min at 37 °C)), PBS (2×), glycine (1× (20 mM, 20 min at 37 °C)), PBS (2×). The slides were removed from the wells and fixed. Microscopy images were obtained on an Olympus 251 scope.

Gd-AB Liposomes (Gd-Lipoplexes) for Transfection. Gd-lipoplexes (Gd-LD's) were prepared as per the Trojene transfection protocol (Avanti Polar Lipids Inc., USA). At 24 h prior to transfection, adherent HeLa cells were grown in OptiMEM media with 10% fetal calf serum (FCS, Sigma) and 1% penicillin–streptomycin (Sigma), in 24-well (6×10^4 cells per well, 300 μL of complete medium) plates and in a wet (37 °C) 10% CO_2/90% air atmosphere. The cells were grown until 80% confluence was reached. The media was then removed and replaced with fresh media. Gd-LD mixtures were added to each well, swirled to ensure even distribution, and then incubated in a wet (37 °C) 10% CO_2/90% air atmosphere for 4 h. The media was removed, and the cells washed with PBS and then replaced with fresh media (300 μL). The cells were then incubated for a further 24 h. Before the luciferase assay was carried out, the cells were washed with PBS and harvested with lysis buffer (100 μL).

Luciferase Reporter Assay. Luciferase gene expression was measured with the Luciferase Assay System purchased from Promega. Light output readings were done on a Berthold Lumal LB 9507 luminometer. Transfection efficiency, measured in relative light units (RLU), was normalized to the total mass of cellular protein using the Bio-Rad Protein Assay Dye Reagent (Bio-Rad).

ICP–AES Analysis. 150 μL of sample was pipetted and diluted to 3.75 mL with 2% nitric acid to give a total dilution of 1 in 25. All data were corrected for these dilutions, and the values from a blank 2% nitric acid sample were also analyzed. Samples were run on a Varian VISTA PRO instrument.

Tumor Model. 5×10^6 IGROV-1 cells were implanted into the flanks of 6–8 week old Balb/c nude mice for generation of subcutaneous tumors. After ~2 weeks (estimated tumor weights 40–50 mg), the mice were anaesthetized with an isoflurane/O_2 mix and placed into a quadrature ^{1}H volume coil and positioned into the magnet. Baseline scans were obtained, and then the mice were injected intravenously via lateral tail vein with a 200 μL liposome solution (HEPES (20 mM, NaCl 135 mM, pH 6.5)) and imaged at 3, 16, and 24 h postinjection at 4.7T (spin–echo sequence, TR = 400–2800 ms, TE = 10 ms, FOV = 45 × 45 cm^2; averages, 1; matrix size, 256 × 128 thickness; 2.0 mm, and 20 slices). The injected volume contained 9.87 μmol of Gd.

Histology Experiments. Following MRI, the animals were sacrificed and tumors excised, frozen in liquid nitrogen, embedded in OCT (VWR) embedding fluid, and 10 μm thick sections cut, mounted on slides, and studied by fluorescence microscopy.

RESULTS

Our previous work has shown the novel Gd-lipid Gd.DOTA-.Chol to be an effective MR signal enhancer and MAGfect, a liposome formulation containing this Gd-lipid, an efficient cellular dual labeling and transfection vehicle (*17*). The need to provide a more robust membrane anchor designed ultimately for *in vivo* applications led us to investigate an alternative saturated long-chain alkyl moiety in place of the cholesteryl functionality. For this purpose, a novel paramagnetic lipid Gd.DOTA.DSA **1** was synthesized using a combination of solution- and solid-phase chemistries. The DOTA chelate was conjugated to the lipid via a stable yet biodegradable amide functional group. Gd-lipid **1** was also designed with a five-atom spacer between the Gd chelator and lipidic alkyl chain moieties. This spacing between the Gd chelator and lipidic alkyl chain moieties was selected to be optimal to ensure maximum exposure of the Gd-chelate to water on the hydrophilic surface of a liposome particle. Furthermore, Gd-lipid **1** was also designed with the DOTA chelate rather than DTPA, since the former macrocyclic ligand is considered to be a more effective chelator of Gd, able to retain the metal ion even in the acidic environment of the endosome (*18*).

The synthetic approach toward the protected precursor DOTA macrocycle **2** utilized a similar route as carried out by Peterson et al. (*19*). Solid-phase synthesis offers a cleaner and more selective option for the synthesis of compounds such as **2**, allowing for the functionalization of three sites on the azamacrocycle while the fourth position is attached to the resin and hence temporarily protected (Scheme 1). Initially, MeOH partial capping was used to prevent molecular overcrowding in the chlorotrityl resin (Scheme 1). Thereafter, the resin was then functionalized with bromoacetic acid to yield an acyl bromide. An excess of cyclen was then added, leading to resin-bound cyclen wherein each cyclen was associated with resin via combination with a single acyl bromide site, leaving three uncombined secondary amine sites per bound cyclen. These remaining free amine sites were then further modified with the introduction of three *tert*-butyloxycarbonyl (Boc) protecting groups, and the reaction was then judged to have reached completion using the chloroanil test. A facile resin cleavage in mildly acidic conditions yielded macrocycle **2**, in reasonable purity (60–70% yield depending upon the freshness of resin used). Macrocycle **2** was then reacted with lipid amine **3** under typical peptide bond synthesis conditions to yield **4**, employing 2-(1*H*-benzotriazol-1-yl)-1,1,3,3-tetramethyluronium hexafluorophosphate (HBTU) and dimethylamino pyridine (DMAP) as carboxylic acid activators. Initially, amide bond formation appeared to be hindered significantly by steric crowding imposed by the bulky Boc groups on DOTA, leading to poor yields of coupled product **4**. However, this problem was overcome by making use of highly pure reagents, dry chloroform, and elevated reaction temperatures, leading to improved yields (ranging from 60% to 88%) and product quality. The DOTA cyclic ring is a highly conformationally strained system and can therefore adopt a more flexible conformation upon heating, rendering better access to the preactivated carboxylate site for conjugation with lipid amine **3**.

A simple deprotection of **4** using HCl/dioxane 1:1 v/v ratio gave DOTA.DSA **5** in good yield and purity. With **5** in hand, Gd complexation was carried out by simple stoichiometric addition of $GdCl_3.6H_2O$ to **5** in water at 90 °C for optimum solubility of the starting materials, thereby generating Gd-DOTA.DSA **1**. No significant free Gd^{3+} ions were detectable post-complexation according to the xylenol orange assay, and the pH was observed to have dropped to 3.5 (Scheme 1). Potentiometric studies of Moreau et al. have shown that the complexation of lanthanide cations to DOTA involves the instantaneous formation of metal ion complexes as soon as metal ions are combined with ligand, leading to proton expulsion and

Scheme 1[a]

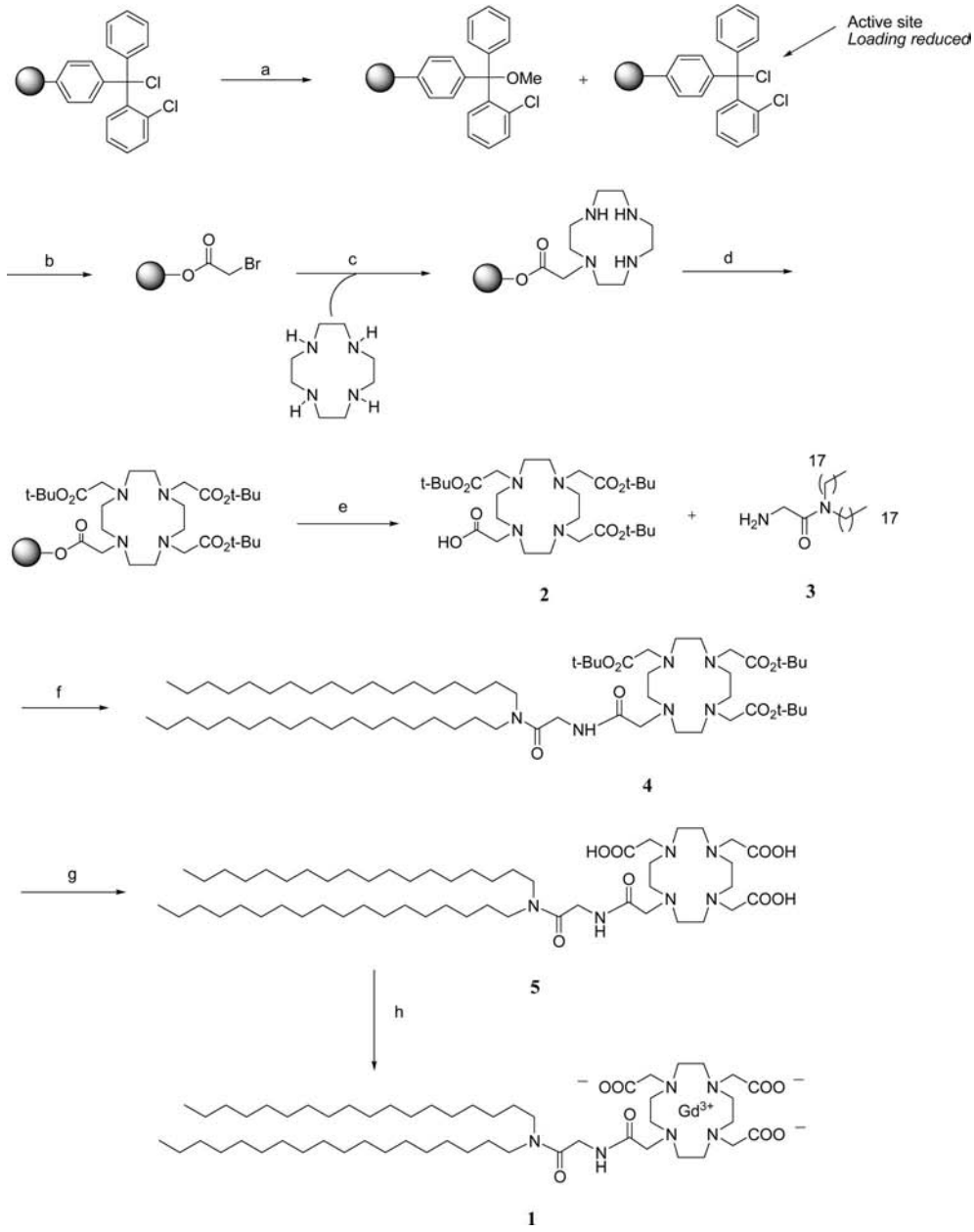

[a] (a) MeOH, DIEA, CH_2Cl_2, rt, 4 h; (b) $BrCH_2COOH$, DIEA, CH_2Cl_2, rt, 12 h; (c) Cyclen, rt, 4 h; (d) $BrCH_2CO_2C(CH_3)_3$, Et_3N, DMF, rt, 12 h; (e) TFEtOH/CH_2Cl_2, rt, 2 h, 69%; (f) HBTU, DMAP, dry $CHCl_3$, 40 °C, 12 h, 88%; (g) c.HCl/dioxane, rt, 2 h, 68%; (h) $GdCl_3$, H_2O, 90 °C, 12 h, 99%.

Scheme 2[a]

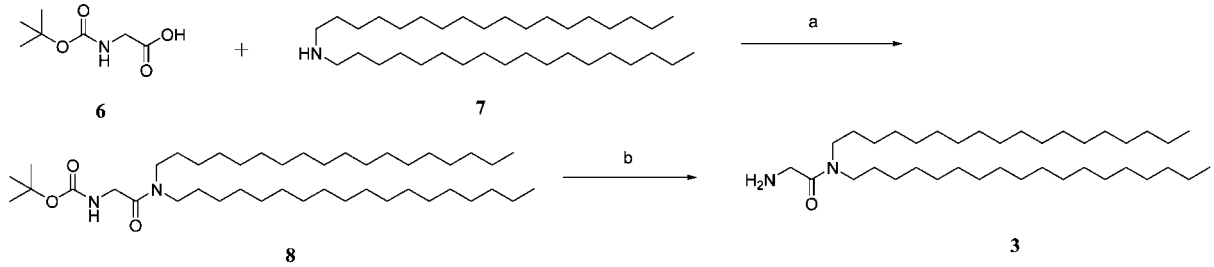

[a] (a) HBTU, DMAP, rt, 12 h, 38%; (b) TFA:CH_2Cl_2, rt, 3 h, 94%.

a dramatic reduction in reaction pH (*20*). Synthesis of precursor lipid amine **3** was accomplished in two steps as shown (Scheme 2). Amide coupling of Boc–glycine **6** with distearylamine **7** resulted in protected lipid amine **8**. A facile deprotection afforded lipid amine **3** [*N*,*N*-distearylamidomethylamine (DSA)] in good yield and purity.

Gd-DTPA-bis(stearylamide) (Gd.DTPA.BSA) was also synthesized for control MRI relaxivity studies. Since the use of

Table 1. T_1 Values and Images of Gd.DOTA.DSA 1 and Gd.DTPA.BSA with Relative Controls

Sample		T_1 (ms)
1	0.5 mM Gd.DOTA.DSA	400.1 ± 15.92
2	0.5 mM DOTA.DSA	2356 ± 112.588
3	Magnevist® *	371.0 ± 4.321
4	H_2O	2750 ± 121.8
5	0.5 mM Gd.DTPA.BSA	687.5 ± 26.03
6	0.5 mM DTPA.BSA	3760 ± 211.7

* Dose calculated to ensure an equivalent Gd atom content relative to sample **1**. The T_1 values for controls of the compound without Gd complexed are also shown for completeness.

this compound in liposome formulations has had precedence in recent literature, the method of Nepveu et al. was adapted for the synthesis of this molecule (*21*).

MRI Studies of Aqueous Solutions of Gd.DOTA.DSA 1. In order to establish the relaxation properties of Gd.DOTA.DSA **1**, MRI studies of the lipid in aqueous solution were performed and T_1 values and relaxivity parameters generated in milliseconds. The efficacy of Gd-lipid **1** was compared to the clinical contrast agent Magnevist (Schering AG) and Gd.DTPA.BSA (see Table 1), and was found to compare favorably at the clinically relevant dose. These data also showed **1** to have a comparable, if slightly better, T_1 relaxation than the widely used Gd.DTPA.BSA lipid. A standard T_1 saturation recovery method was used to determine T_1 values (according to eq 1), where x is TR (time to repeat), and S_i is the measured signal for a given TR.

$$S_i = S_0(1 - e^{(-x/T_1)}) \quad (1)$$

Liposomes were also formulated with Gd.DOTA.DSA **1** and relaxivities measured. Relaxivity can be defined as the capability of a contrast agent to increase the relaxation rate ($mM^{-1}\ s^{-1}$) of surrounding water proton spins. The relaxivity for Gd.DOTA.DSA **1** in liposome formations was found to be 4.10 ± 0.34 $mM^{-1}\ s^{-1}$ according to calculations made using eq 2 where R_1 is the relaxivity and $1/T_1[C]$ is the measured solvent relaxation rate in the presence of Gd.DOTA.DSA **1** liposomes, with α_1 and [C] being the T_1 relaxation and Gd concentration values, respectively.

$$R_1[C] = 1/T_1[C] + \alpha_1 \times C \quad (2)$$

Optimization of Liposome Formulations. In order to establish the cellular labeling efficiency of liposomes prepared with Gd.DOTA.DSA **1**, a series of eight liposome formulations were tested on HeLa cells so that an ideal nontoxic cell labeling liposome formulation could be determined able to deliver a maximal amount of Gd to the cells. HeLa (human ovarian carcinoma) cells were chosen, since they require minimum handling, are a robust cell line, and are therefore adequate for our proof of concept study of cellular labeling prior to progressing to more challenging and specialized cells. A simple method to quantify the uptake of liposomes into cells is the inclusion of a small mole percent of a fluorescent component in the liposome formulation, in this case, the fluorescent lipid DOPE–Rhodamine. Here, the measured fluorescence intensity of the cell lysate can be used to estimate the amount of liposome and hence Gd-lipid that is internalized by the cells. Additionally, incorporation of a fluorescent lipid can be used to examine the process of cellular uptake by means of fluorescence microscopy studies. The liposome formulations studied were prepared using Gd.DOTA.DSA **1**, N^1-cholesteryloxycarbonyl-3,7-diazanonane-1,9-diamine (CDAN), dioleoyl-L-α-phosphatidylethanolamine (DOPE), and DOPE-Rhodamine lipids in various mole percentages relative to each other. Other parameters investigated were incubation time and dose. Our objective was to determine a formulation, dose, and incubation period that resulted in the most ample liposome uptake into cells without the appearance of cellular toxicity. Gd-liposomes **1**–**4** (Table 2) displayed a high percentage uptake consistent with the presence of both CDAN and DOPE at high mole percentages. Gd-liposomes **5** and **6** were less effective, consistent with the absence of either DOPE or CDAN, supporting the hypothesis that both the cationic charge and fusogenic properties of CDAN and DOPE lipids, respectively, are necessary for effective cellular entry and cytosolic delivery. Gd-liposomes **8** were similarly less effective owing to formulation toxicity and lack of effective cationic charge for cell surface adhesion. Given the superior performances of Gd-liposomes **1**–**4** and **7**, cell toxicity studies were then performed with Gd-liposomes **1**, **2**, and **7**. Gd-liposome **4** showed the highest fluorescence uptake; however, it was not carried forward for toxicity studies due to the presence of an excess of cationic charge.

Table 2. Gd-Liposome Formulations Assessed for Their Cell Labeling Efficiency with Their Associated Mean Sizes[a]

liposome	Gd.DOTA.DSA (%)	CDAN (%)	DOPE (%)	DOPE–Rhoda (%)	liposome size (nm)	fluorescence uptake (%)
1	30	40	29.5	0.5	263.6	31
2	30	30	39.5	0.5	275.1	23
3	40	30	29.5	0.5	206.5	22
4	40	40	19.5	0.5	209.6	35
5	50	49.5	-	0.5	242.5	13
6	50	-	50	0.5	261.6	2
7	60	29.5	10	0.5	228.2	22
8	60	19.5	20	0.5	297.0	14

[a] Stock solutions of lipids were mixed in relevant mol % ratios.

Lactate Dehydrogenase Cytotoxicity Assay. In order to assess the toxic effects of the three selected Gd-liposome formulations (**1**, **2**, and **7**) chosen from the fluorescence uptake studies on cells, a lactate dehydrogenase assay (LDH) assay was carried out. The toxic effects of the liposomes were all found to be minimal over a 24 h period (Figure 1). Indeed, there was little difference in toxicity between all Gd-liposome formulations studied (Table 2) irrespective of incubation times (4, 6, 8, 10, and 24 h) and total lipid doses (6, 12, and 18 μg/well.). After initial incubation periods (4, 6, 8, and 10 h), the cells were allowed to grow for 24 h; LDH release from these cells was minimal in all cases, suggesting that normal cell growth and proliferation were taking place in spite of the presence of Gd-liposomes. From the liposome fluorescence uptake assay and LDH toxicity assay data, it was concluded that the optimal formulation for cellular uptake and Gd cell labeling could be Gd-liposome formulation **1**, administered at a total lipid dose of 12 μg/well (48-well, containing 0.716 μg/well of Gd) and incubated for 8 h.

ICP–AES and MRI of Cells Labeled with Gd-Liposomes. Once favorable *in vitro* conditions for Gd-liposome cellular uptake were determined, inductively coupled plasma atomic emission spectroscopy (ICP–AES) studies were carried out using cell lyzate postincubation with Gd-liposome formulation **1** to assess the amount of Gd internalized into the cells more precisely. From this, we determined that 21% of the

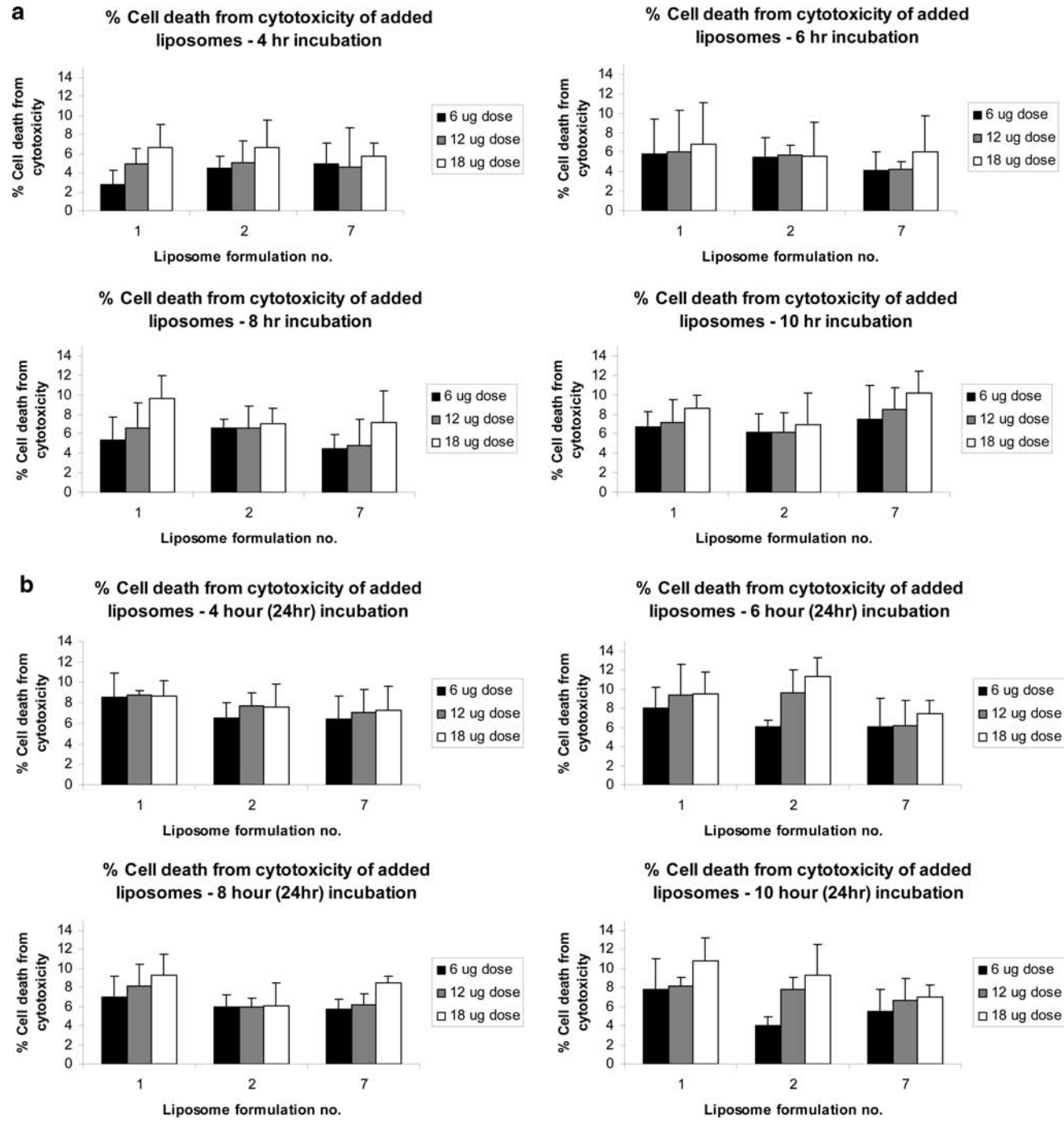

Figure 1. (a) Lactate dehydrogenase (LDH) assay results calculated to show % cytotoxicity as a result of added Gd-liposome formulations **1**, **2**, and **7** at three liposome doses (6, 12, and 18 μg) and 4 incubation periods (4, 6, 8, and 10 h). (b) LDH assay calculated to show % cytotoxicity as a result of added Gd-liposomes as per (a); in addition, cells being washed after the initial incubation periods and then allowed to grow for up to 24 h. These results show cytotoxicity induced by the added Gd-liposomes to be in general <10% of total cell death.

administered Gd was retained within the cells. This result is within 10% error in comparison to the fluorescence uptake assay (see Table 2), and validates this fluorescence method as a quick and simple method for screening large numbers of differing formulations prior to more accurate ICP-MS analysis of Gd content. The ability of Gd-liposome formulation **1** to produce *in vitro* contrast enhancement postadministration to cells was assessed with the labeling of approximately 1×10^6 HeLa cells. After 8 h incubation with Gd-liposome formulation **1**, cells were spun into pellets and imaged by MRI at 4.7 T using a spin–echo T_1 weighted sequence. The results of cell labeling are described in terms of T_1-weighted images and resulting T_1 values, relative to controls (Table 3). The MRI analysis of HeLa cell pellets labeled with Gd-liposome **1** produced a brightly visible mass of cells, and the T_1 value in cells was measured at 65% the level measured in control cells (Table 3). This promising result demonstrated the cell labeling efficiency of the novel Gd-liposome formulation **1** *in vitro*.

Cellular Uptake of Gd-Liposomes and Transfection. In order to examine the intracellular uptake of Gd-liposome formulation **1** into HeLa cells, we chose to take advantage of the imaging bimodality of this liposome, in that a fluorescent lipid was included with the paramagnetic liposome (DOPE-Rhodamine, Avanti Polar Inc.). In this instance, the cell labeling conditions were set up for the labeling of 1.25×10^5 HeLa cells/well, and any noninternalized Gd-liposomes not taken up

Table 3. T_1 Weighted Images and Resulting T_1 Values, Relative To Controls[a]

		Sample	T_1 (ms)
	1	Gd-liposome **1** solution	311.4 ± 40.10
	2	Gd-liposome **1** incubated with HeLa cells	688.6 ± 53.60
	3	Control liposome incubated with HeLa cells	1940 ± 65.95
	4	HeLa cells alone	2149 ± 92.70
	5	PBS	1750 ± 47.80

[a] T_1 values for Gd-liposome formulation **1** incubated with HeLa cells (control liposome: CDAN/DOPE/DOTA.DSA: 40/30/30 mol %).

were washed away after the conclusion of the uptake period of 8 h. Fluorescence microscopy revealed that the cellular uptake of these bimodal Gd-liposomes led to intracellular, cytosolic accumulation of the fluorescent label, which is in accordance with endocytosis-mediated uptake followed by endosomolysis (Figure 2). This result is consistent with successful Gd-labeling implied by reduction of T_1 values, relative to controls (Table 3).

Gd-liposome formulation **1** mediated transfection of HeLa cells was investigated with plasmid DNA (pDNA) expressing the luciferase gene. Here, the level of luciferase enzyme activity in cells post pDNA delivery represents a quantitative measure of transfection efficiency. Gd-liposome formulation **1** was combined with pDNA (12:1 w/w) to form Gd-liposome-plasmid DNA complex (Gd-lipoplex: Gd-LD) particles. Gd-LD transfection data are shown (Figure 3). Gd-liposome formulation **1** mediated transfection appears to be equivalent to CDAN/DOPE (50:50 mol %) (Trojene) mediated transfection, demonstrating that the Gd incorporation does not interfere with liposome-mediated transfection of HeLa cells to any perceptible degree. Furthermore, successful Gd-liposome mediated transfection of HeLa cells provides functional proof for Gd-liposome cellular entry by endocytosis followed by endosomolysis and cytosolic accumulation, as observed by fluorescence microscopy, since transfection is contingent on successful endocytosis and endosomolysis. Gd-LD particles prepared with Gd-liposome formulation **1** were also shown not to be toxic according to LDH assay data as well (data not shown).

***In Vivo* Tumor MRI.** Having demonstrated successful bimodal cellular MRI and fluorescence imaging of HeLa cells by means of Gd-liposome formulation **1**, as well as bifunctional labeling and transfection, we wanted to demonstrate the efficacy of our Gd-lipid, Gd.DOTA.DSA, toward imaging of xenograft tumors *in vivo*. Tumors were established by induction of IGROV-1 (human ovarian cancer cells) xenografts in nude mice. In this instance, we replaced the *in vitro* suited Gd-liposome formulation **1** with charge-neutral Gd-liposome formulation **9**, Gd.DOTA.DSA/DOPC/Cholesterol/DSPE-PEG_{2000}: 30/32/30/7 mol % (also containing 1 mol % DOPE-Rhodamine). This formulation was rendered stable to biological fluids by the incorporation of a stealth/biocompatibility polymer outer-coat calyx comprising poly(ethylene glycol) (PEG). In terms of our synthetic self-assembly **ABCD** nanoparticle concept, this can be described as a Gd-**BC** liposome nanoparticle system (*15*). Post i.v. injection of Gd-liposome **9**, xenograft tumors ($n = 3$) were monitored by MRI over a 24 h period. Over this period, we observed a substantial 60% reduction in tumor T_1 values compared to the situation with control liposomes (without Gd) and visibly enhanced tumor image brightness (Figure 4). This outcome suggested that the neutral Gd-liposome **9** was in fact a liposome system with a substantial systemic half-life ($t_{1/2} >$ 4 h) capable of long-term circulation in the blood and passive targeting to the xenograft tumor by an enhanced permeation and retention (EPR) mechanism due to the porous nature of the endothelial cell layer (*22*). This finding was supported by fluorescence imaging of tumor tissue slices (postmortem) taking advantage of the bimodal imaging capacity of our Gd-liposome **9** for MRI and fluorescence microscopy. The fluorescence images obtained demonstrate liposome accumulation in intravascular spaces and in surrounding viable tumor tissue (Figure 5).

DISCUSSION

The synthesis of a new Gd-lipid contrast agent (Gd.DOTA.DSA **1**) was carried out, and this lipid was shown to have similar T_1 relaxation behavior to the common clinical contrast agent Magnevist at the clinically relevant dose of 0.5 mM (see Table 1). This can be attributed to the mixed micellar structures of the Gd.DOTA.DSA lipid in water whereby the rotational tumbling rate is reduced as a result. Also, Gd.DOTA.DSA was shown to be 10% more effective than the commonly used Gd.DTPA.BSA lipid at reducing bulk water T_1. The relaxivity for Gd.DOTA.DSA in liposome form was established, and further liposomes were formulated (Table 2). The *in vitro* Gd-liposome formulation **1** was shown to effect bimodal labeling of HeLa cells for MRI and fluorescent imaging (Figure 2; Table 3) which was made possible by mediating the delivery of chelated Gd to cells and subsequent shortening of T_1 relaxation times. This formulation was found to be nontoxic to HeLa cells by the LDH assay (Figure 1) and to be capable of bifunctional labeling with transfection (Figure 3) consistent with a cell labeling mechanism in which Gd liposomes enter by endocytosis followed by endosomolysis leading to cytoplasmic accumulation of the label (Figure 2). The neutral Gd-liposome **9** was shown to assist the visualization of xenograft tumors *in vivo* by means of MRI (Figure 4), apparently by concentrating Gd in viable tumor tissue by the widely reported passive targeting and EPR effect originally described by Maeda et al., whereby as a result of slow venous return and poor lymphatic clearance in tumor tissue liposomal particles can become trapped, leading to their accumulated concentration in solid tumors (*23*). It also appears that the colloidal Gd liposomes extravasate in areas of vascular hyperpermeability within the tumor mass, which can shed light on the more intense and heterogeneous fluorescence pattern observed throughout the tumor tissue (Figure 5). Here, the potential extent of Gd labeling is demonstrated by making use of the bimodal imaging capacity of our neutral Gd-liposome **9** for MRI and fluorescence imaging.

The traditional method of encapsulating contrast agents, mainly clinically used Gd chelates, has the disadvantage of entrapped agents easily "leaking" out of liposome cavities prior to reaching the target site. This can be avoided by chelation of Gd with lipid-chelate molecules such as **5** (Scheme 1) that readily insert their dialkyl chains into the bilayer of a liposome, thereby anchoring Gd to a liposome surface instead. Also, the potential downfall of an encapsulation approach is reduced water flux in the vicinity of Gd, leading to reduced paramagnetic relaxation of water and weaker T_1 reductions in contrast to the situation observed with free Gd-chelates. However, our data suggest that liposome presented lipidic Gd-chelates remain useful paramagnetic relaxation agents both *in vitro* and *in vivo*. The bifunctional capacity of Gd-liposome formulation **1** to simultaneously label and transfect HeLa cells relies on the dual capacities of CDAN and DOPE which are known to be

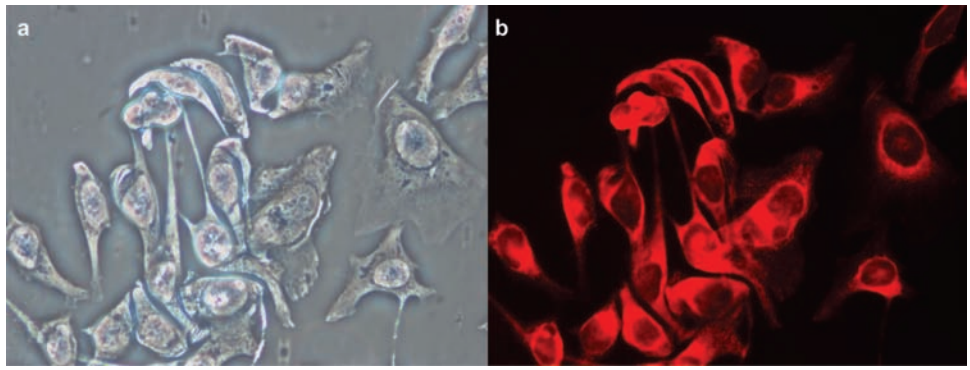

Figure 2. (a) Bright field image of HeLa cells labeled with Gd-liposome formulation **1**. (b) Red fluorescence image of HeLa cells labeled with Gd-liposome formulation **1**, at 40× magnification.

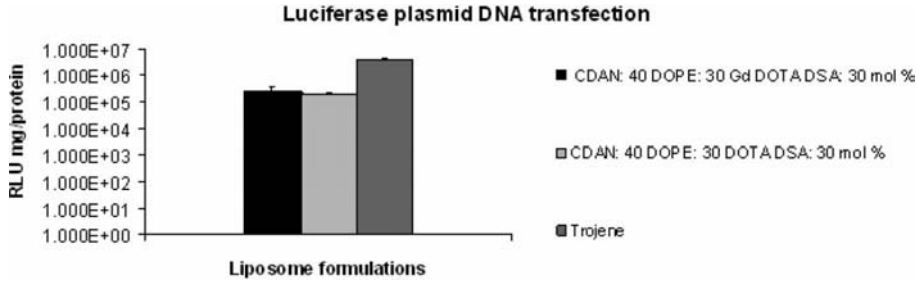

Figure 3. Gd-lipoplex (Gd-liposome **1** plus DNA) transfection of HeLa cells compared with control Gd-free lipoplex transfection and CDAN/DOPE (50:50 mol %) (Trojene mediated transfection). Transfection is comparable in both DMEM and OptiMEM media in the presence of 10% fetal calf serum (data not shown.).

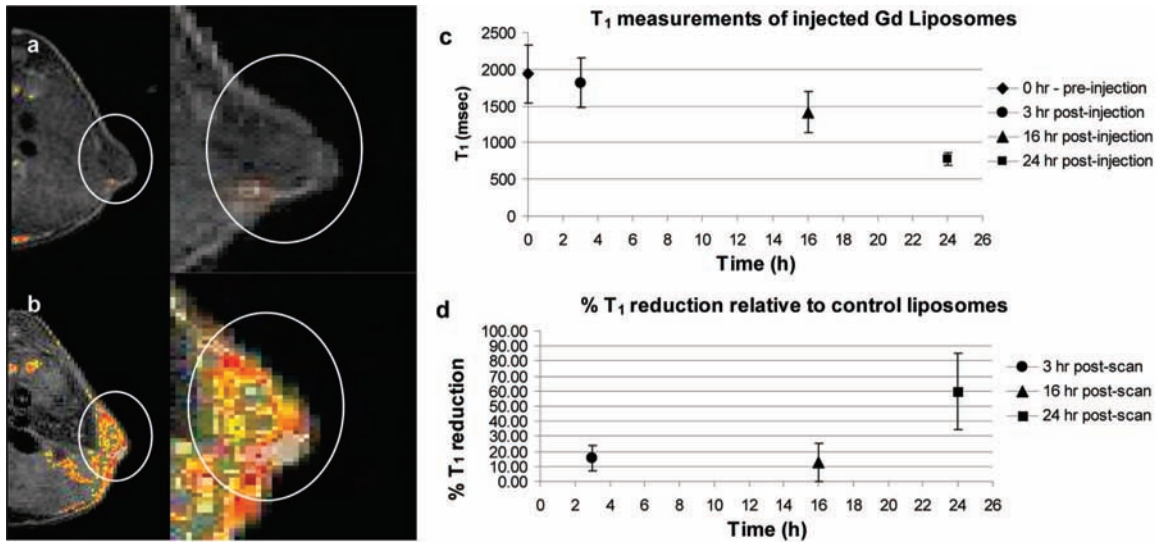

Figure 4. (a) Preinjection MR images of induced IGROV-1 tumors under the right flanks of nude Balb/c mice: large white circle represents zoomed image of tumor area marked with small circle. (b) MR images 24 h post i.v. injection of Gd-liposomes **9**; the color map shows enhancement of tumor area: large white circle is zoomed image of tumor area marked with small circle. (c) T_1 measurements were obtained from tumor slices. (d) Image enhancement is supported by a 60% measured reduction in tumor T_1 values 24 h post i.v. injection relative to control liposomes (no Gd complexed; Gd.DOTA.DSA replaced with DOTA.DSA).

nontoxic (*24, 25*). In addition, CDAN comprises a head-group that possesses amine functional groups with notably perturbed pK_a values. It is known that higher pK_a amine groups function to neutralize, condense, and assist nucleic acid encapsulation, not to mention assist cell binding and endocytosis, while lower pK_a amine functional groups provide the means for endosome buffering post cell entry leading to potential endosomolysis by osmotic shock (*12*). The inclusion of DOPE is widely believed to assist endosomolysis owing to the fusogenic character of DOPE *in vitro* (*26*). These characteristics are most likely helpful to ensure Gd access to the cellular cytosol for optimal cellular Gd labeling at a level appropriate for cellular MRI.

The success of the neutral Gd-liposome **9** with respect to tumor Gd and fluorescence labeling almost certainly relies on a different assembly of liposomal properties. Excessive cationic charge and size are a detriment to effective long-term circulation *in vivo*, and therefore the control of both is essential (*15*). Minimal charge tending to neutrality and sizes of 100 nm and below are clear requirements here. Alternatively, elements of stability can be introduced into the **B**-layer lipid structure (*27*)

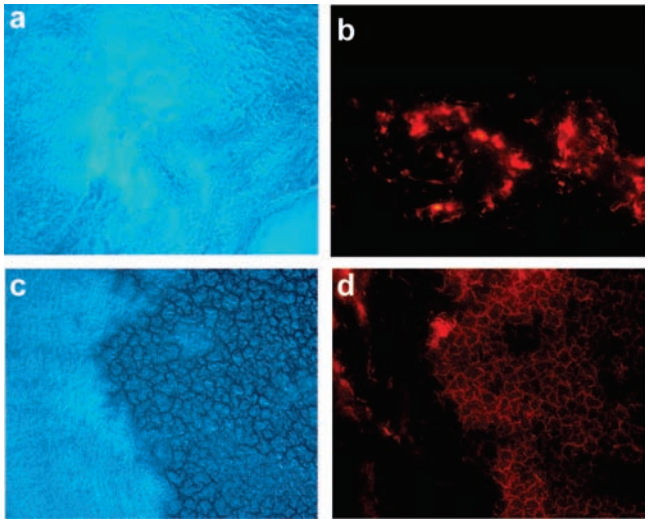

Figure 5. Histology images of the tumor in Figure 4 are shown: (a) and c) are bright field images of sectioned IGROV-1 tumors 24 h postadministration of Gd-liposome formulation **9**, where **a** represents a middle and **b** a surface slice of the excised tumor. (b) and (d) are corresponding fluorescent images at 20× magnification.

such that lipids used tend to favor the presence of lamellar phases over inverted hexagonal lyotropic mesophases under physiologically relevant conditions of temperature and pH (*28*). The neutral Gd-liposome **9** was designed to comply with all these requirements. Furthermore, a PEG stealth/biocompatibility outer layer was introduced. This is essential to reduce the uptake of liposomes in general by the reticulo-endothelial system (RES) in the spleen and liver (*29*). PEG also renders a liposome surface substantially hydrophilic in character, thereby decreasing the adsorption of serum proteins and opsonins to the surface of the liposome bilayer, and in this manner, the nonspecific recognition of liposomes by macrophages is also curtailed (*16*). Overall, our combined imaging data appear to suggest that the neutral Gd-liposome formulation **9** is a useful indication of formulations appropriate for long-term circulation and tumor delivery of an associated payload.

CONCLUSION

We have demonstrated the utility of novel bimodal fluorescent and paramagnetic liposomes for *in vitro* cellular labeling and *in vivo* tumor imaging, and covalidated our observed results by both MR and fluorescence imaging. The ability of liposomes to become "trapped" both inside and in vicinal tumor areas can be exploited further for drug and nucleic acid delivery. There is ample evidence of the effectiveness of actively targeted liposomes functionalized with targeting agents such as antibodies and ligands (*30–37*); however, we have demonstrated both *in vitro* and *in vivo* the effectiveness of the more facile passive targeting of Gd liposomes for the labeling of cancer cells and the detection of solid tumors by MRI and fluorescence microscopy.

ACKNOWLEDGMENT

We thank Dr. Ian McNeish (CRUK) for the kind gift of IGROV-1 cells, the Natural History Museum (London) for ICP-AES analysis, and Ms. Lorraine Lawrence (Imperial College London) for assistance with histology experiments. Funding for Nazila Kamaly was provided by the GTC and MRC.

LITERATURE CITED

(1) Shah, K., Jacobs, A., Breakefield, X. O., and Weissleder, R. (2004) Molecular imaging of gene therapy for cancer. *Gene Ther. 11*, 1175–1187.

(2) Massoud, T. F., and Gambhir, S. S. (2003) Molecular imaging in living subjects: seeing fundamental biological processes in a new light. *Gene Dev. 17*, 545–580.

(3) Caravan, P., Ellison, J. J., McMurry, T. J., and Lauffer, R. B. (1999) Gadolinium(III) chelates as MRI contrast agents: Structure, dynamics, and applications. *Chem. Rev. 99*, 2293–2352.

(4) Louie, A. Y., Huber, M. M., Ahrens, E. T., Rothbacher, U., Moats, R., Jacobs, R. E., Fraser, S. E., and Meade, T. J. (2000) In vivo visualization of gene expression using magnetic resonance imaging. *Nat. Biotechnol. 18*, 321–325.

(5) Raatschen, H. J., Swain, R., Shames, D. M., Fu, Y. J., Boyd, Z., Zierhut, M. L., Wendland, M. F., Misselwitz, B., Weinmann, H. J., Wolf, K. J., and Brasch, R. C. (2006) MRI tumor characterization using Gd-GlyMe-DOTA-perfluorooctyl-mannose-conjugate (Gadofluorine M (TM)), a protein-avid contrast agent. *Contrast Media Mol. Imaging 1*, 113–120.

(6) Winter, P. M., Lanza, G. M., Caruthers, S. D., Schmieder, A., Harris, T. D., Billerica, N., Chinen, L., Williams, T., Watkins, M. P., Allen, J. S., and Wickline, S. A. (2002) Molecular imaging of angiogenesis in atherosclerosclerotic rabbits by MRI at 1.5 T with alpha(v)beta(3)-targeted nanoparticles. *Circulation 106*, 151–151.

(7) Chen, J. W., Pham, W., Weissleder, R., and Bogdanov, A. (2004) Human myeloperoxidase: a potential target for molecular MR imaging in atherosclerosis. *Magn. Reson. Med. 52*, 1021–1028.

(8) Poduslo, J. F., Curran, G. L., Peterson, J. A., McCormick, D. J., Fauq, A. H., Khan, M. A., and Wengenack, T. M. (2004) Design and chemical synthesis of a magnetic resonance contrast agent with enhanced in vitro binding, high blood-brain barrier permeability, and in vivo targeting to Alzheimer's disease amyloid plaques. *Biochemistry 43*, 6064–6075.

(9) Kobayashi, H., Sato, N., Kawamoto, S., Saga, T., Hiraga, A., Haque, T. L., Ishimori, T., Konishi, J., Togashi, K., and Brechbiel, M. W. (2001) Comparison of the macromolecular MR contrast agents with ethylenediamine-core versus ammonia-core generation-6 polyamidoamine dendrimer. *Bioconjugate Chem. 12*, 100–107.

(10) Hueber, M. M., Staubli, A. B., Kustedjo, K., Gray, M. H. B., Shih, J., Fraser, S. E., Jacobs, R. E., and Meade, T. J. (1998) Fluorescently detectable magnetic resonance imaging agents. *Bioconjugate Chem. 9*, 242–249.

(11) Langereis, S., Kooistra, H. A. T., van Genderen, M. H. P., and Meijer, E. W. (2004) Probing the interaction of the biotin-avidin complex with the relaxivity of biotinylated Gd-DTPA. *Org. Biomol. Chem. 2*, 1271–1273.

(12) Keller, M., Jorgensen, M. R., Perouzel, E., and Miller, A. D. (2003) Thermodynamic aspects and biological profile of CDAN/DOPE and DC-Cho1/DOPE lipoplexes. *Biochemistry 42*, 6067–6077.

(13) Lian, T., and Ho, R. J. Y. (2001) Trends and developments in liposome drug delivery systems. *J. Pharm. Sci. 90*, 667–680.

(14) Le, U. M., and Cui, Z. (2006) Long-circulating gadolinium-encapsulated liposomes for potential application in tumor neutron capture therapy. *Int. J. Pharm. 312*, 105–112.

(15) Kostarelos, K., and Miller, A. D. (2005) Synthetic, self-assembly ABCD nanoparticles; a structural paradigm for viable synthetic non-viral vectors. *Chem. Soc. Rev. 34*, 970–994.

(16) Ayyagari, A. L., Zhang, X., Ghaghada, K. B., Annapragada, A., Hu, X., and Bellamkonda, R. V. (2006) Long-circulating liposomal contrast agents for magnetic resonance imaging. *Mag. Reson. Med. 55*, 1023–1029.

(17) Oliver, M., Ahmad, A., Kamaly, N., Perouzel, E., Caussin, A., Keller, M., Herlihy, A., Bell, J., Miller, A. D., and Jorgensen, M. R. (2006) MAGfect: a novel liposome formulation for MRI labelling and visualization of cells. *Org. Biomol. Chem. 4*, 3489–3497.

(18) Unger, E. C., Fritz, T. A., Tilcock, C., and New, T. E. (1991) Clearance of liposomal gadolinium: in vivo decomplexation. *J. Mag. Reson. Imaging. 6*, 689–693.

(19) Peterson, J. J., Pak, R. H., and Meares, C. F. (1999) Total solid-phase synthesis of 1,4,7,10-tetraazacyclododecane-N,N′,N",N-tetraacetic Acid-functionalized peptides for radioimmunotherapy. *Bioconjugate Chem. 10*, 316–320.

(20) Moreau, J., Guillon, E., Pierrard, J. C., Rimbault, J., Port, M., and Aplincourt, M. (2004) Complexing mechanism of the lanthanide cations Eu^{3+}, Gd^{3+}, and Tb^{3+} with 1,4,7,10-tetrakis-(carboxymethyl)-1,4,7,10-tetraazacyclododecane (dota)-characterization of three successive complexing phases: study of the thermodynamic and structural properties of the complexes by potentiometry, luminescence-spectroscopy, and EXAFS. *Chemistry 10*, 5218–5232.

(21) Jasanada, F., and Nepveu, F. (1992) Synthesis of amphiphilic chelating-agents - bis(hexadecylamide) and bis(octadecylamide) of diethylenetriaminepentaacetic acid. *Tetrahedron Lett. 33*, 5745–5748.

(22) Mulder, W. J. M., Strijkers, G. J., Habets, J. W., Bleeker, E. J. W., van der Schaft, D. W. J., Storm, G., Koning, G. A., Griffioen, A. W., and Nicolay, K. (2005) MR molecular imaging and fluorescence microscopy for identification of activated tumor endothelium using a bimodal lipidic nanoparticle. *FASEB J. 19*, 2008–2010.

(23) Iyer, A. K., Khaled, G., Fang, J., and Maeda, H. (2006) Exploiting the enhanced permeability and retention effect for tumor targeting. *Drug Discovery Today 11*, 812–818.

(24) Spagnou, S., Miller, A. D., and Keller, M. (2004) Lipidic carriers of siRNA: differences in the formulation, cellular uptake, and delivery with plasmid DNA. *Biochemistry 43*, 13348–13356.

(25) Takahashi, T., Kono, K., Itoh, T., Emi, N., and Takagishi, T. (2003) Synthesis of novel cationic lipids having polyamidoamine dendrons and their transfection activity. *Bioconjugate Chem. 14*, 764–773.

(26) Stewart, L., Manvell, M., Hillery, E., Etheridge, C. J., Cooper, R. G., Stark, H., van-Heel, M., Preuss, M., Alton, E. W. F. W., and Miller, A. D. (2001) Physico-chemical analysis of cationic liposome-DNA complexes (lipoplexes) with respect to in vitro and in vivo gene delivery efficiency. *J. Chem. Soc., Perkin Trans. 2*, 624–632.

(27) Fletcher, S., Ahmad, A., Perouzel, E., Jorgensen, M. R., and Miller, A. D. (2006) A dialkynoyl analogue of DOPE improves gene transfer of lower-charged, cationic lipoplexes. *Org. Biomol. Chem. 4*, 196–199.

(28) Fletcher, S., Ahmad, A., Perouzel, E., Heron, A., Miller, A. D., and Jorgensen, M. R. (2006) In vivo studies of dialkynoyl analogues of DOTAP demonstrate improved gene transfer efficiency of cationic liposomes in mouse lung. *J. Med. Chem. 49*, 349–357.

(29) Moghimi, S. M., and Szebeni, J. (2003) Stealth liposomes and long circulating nanoparticles: critical issues in pharmacokinetics, opsonization and protein-binding properties. *Prog. Lipid Res. 42*, 463–478.

(30) Brandwijk, R. J. M. G. E., Mulder, W. J. M., Nicolay, K., Mayo, K. H., Thijssen, V. L. J. L., and Griffioen, A. W. (2007) Anginex-conjugated liposomes for targeting of angiogenic endothelial cells. *Bioconjugate Chem. 18*, 785–790.

(31) Mulder, W. J. M., Strijkers, G. J., Griffioen, A. W., van Bloois, L., Molema, G., Storm, G., Koning, G. A., and Nicolay, K. (2004) A liposomal system for contrast-enhanced magnetic resonance imaging of molecular targets. *Bioconjugate Chem. 15*, 799–806.

(32) Bertini, I., Bianchini, F., Calorini, L., Colagrande, S., Fragai, M., Franchi, A., Gallo, O., Gavazzi, C., and Luchinat, C. (2004) Persistent contrast enhancement by sterically stabilized paramagnetic liposomes in murine melanoma. *Mag. Reson. Med. 52*, 669–672.

(33) Hassane, F. S., Frisch, B., and Schuber, F. (2006) Targeted liposomes: convenient coupling of ligands to preformed vesicles using "click chemistry". *Bioconjugate Chem. 17*, 849–854.

(34) Elbayoumi, T. A., and Torchilin, V. P. (2006) Tumor-targeted immuno-liposomes for delivery of therapeutics and diagnostics. *Pharm. Eng. 26*, 96–105.

(35) Erdogan, S., Roby, A., Sawant, R., Hurley, J., and Torchilin, V. P. (2006) Gadolinium-loaded polychelating polymer-containing cancer cell-specific immunoliposomes. *J. Lipid Res. 16*, 45–55.

(36) Maruyama, K., Ishida, O., Takizawa, T., and Moribe, K. (1999) Possibility of active targeting to tumor tissues with liposomes. *Adv. Drug Delivery Rev. 40*, 89–102.

(37) Mastrobattista, E., Koning, G. A., and Storm, G. (1999) Immunoliposomes for the targeted delivery of antitumor drugs. *Adv. Drug Delivery Rev. 40*, 103–127.

BC7001715

Fate of a Bioactive Fluorescent Wortmannin Derivative in Cells

Katie R. Barnes,[†,§] Joseph Blois,[†,§] Adam Smith,[†] Hushan Yuan,[†] Fred Reynolds,[†] Ralph Weissleder,[†] Lewis C. Cantley,[‡] and Lee Josephson*[,†]

Center for Molecular Imaging Research, Massachusetts General Hospital and Harvard Medical School, 149, 13th Street, Charlestown, Massachusetts 02129, and Department of Systems Biology, Harvard Medical School and Division of Signal Transduction, Beth Israel Deaconess Medical Center, 77 Avenue, Louis Pasteur, Boston, Massachusetts 02115. Received June 19, 2007; Revised Manuscript Received September 13, 2007

Here, we report on NBD-Wm, a fluorescent wortmannin (Wm) probe that maintains the bioactivity of Wm as an inhibitor of PI3 kinase and as an antiproliferative agent. The attachment of the NBD fluorochrome permits NBD-Wm in cells to be monitored by NBD fluorescence-based methods such as FACS or fluorescence microscopy or with an anti-NBD antibody. The fluorescence of NBD-Wm treated cells reached a peak at 1.5 h and then decreased because of the extrusion of a fluorescent compound into the culture media. Cells accumulated NBD-Wm to levels about 30-fold higher than those in the media. NBD-Wm modified five major proteins, with the modification of the catalytic subunit of PI3 kinase being a minor band. The bioactivity of NBD-Wm, coupled with a variety of techniques available for determining its disposition, suggest that NBD-Wm can be a useful tool in understanding the mechanism of action of viridins.

INTRODUCTION

Wm is a fungal product that covalently reacts with a lysine residue in the active site of the p110 catalytic subunit of PI3K and is a nonisotype specific inhibitor of these enzymes, which are important regulators of a wide variety of biological processes. Wm has been widely used to define the PI3 kinase dependence of biological phenomena, with some 4700 Medline citations (1995–2007) after the 1994 observation (*1*) that it was an inhibitor of this enzyme. The central role played by PI3 kinase suggests that compounds inhibiting its activity might be useful in diverse conditions including the treatment of cancer (*2, 3*) or as anti-inflammatory/immune suppressive agents (*4–6*). Efforts to develop Wm derivatives as drugs involve the antiproliferative and anticancer activities (*7, 8*) of these compounds.

However, using Wm to define the PI3 kinase dependence of biological processes, or as a scaffold for drug development, is complicated since both the fate of Wm in biological systems and mechanism of interaction with molecular targets are so unlike those of man-made kinase inhibitors. Wm has a short half-life in various culture media (*9*) and reacts with amino acids such as lysine or proline in PBS (*10*). These observations, as well as others, led us to propose that Wm's instability in culture media was due to its reaction with amino acids at the C20 position but that the resulting WmC20 amino acid derivatives maintain biological activity because of their ability to regenerate Wm (*11*). The unusual properties of Wm suggest that understanding its fate in biological systems will be essential to understanding its mechanism of action.

Our objectives were to demonstrate the antiproliferative bioactivity of a fluorescent wortmannin conjugate (NBD-Wm) and to describe the fate of NBD-Wm in cultured cells at the micromolar concentrations needed for the antiproliferative effects of Wm or Wm derivatives (see below). By fate we mean both the chemical reactions Wm undergoes when added to a biological fluid and its disposition, which includes its time course, concentration, and intracellular location. Our studies employed 10 μM NBD-Wm, a concentration that is modest in relation to its antiproliferative effects but which is several orders of magnitude higher than the concentrations needed for many actions of Wm. The IC50 values for the inhibition of cell proliferation by Wm or Wm derivatives are in the micromolar range with all cell lines (see Table 1 or refs *7*, *12*, and *13*. At concentrations below 100 nM, Wm antagonizes insulin-stimulated glucose transport (*14–16*), histamine release (*17, 18*), or respiratory burst (*19–21*). Earlier studies examining Wm-modified proteins using fluorescent (*22, 23*) and radioactive (*24*) forms of Wm employed lower concentrations than that employed here. In addition, others have employed low concentrations of Wm to demonstrate its reaction with a lysine in the ATP site of PI3 kinase (*25*), with polo-like kinase (*23*) and DNA-PK (*22, 23*). The antiproliferative actions of Wm are typically measured by exposing cells to relatively high micromolar concentrations and for long

Table 1. Biological Activity of Wm and NBD-Wm[a]

Inhibition of PI3 Kinase (IC50 in nM)			
compound	Wm	NBD-Wm	
IC50	17	24	
Antiproliferative Activity of Wm and NBD-Wm (IC50 in μM)			
compound cell line	Wm	NBD-Wm	*p* value
A549	11.4 ± 0.5 $n = 4$	12.2 ± 0.8 $n = 5$	$p > 0.05$
MCF-7	5.3 ± 0.4 $n = 3$	4.1 ± 0.4 $n = 4$	$p > 0.05$
BT-20	29.7 ± 1.0 $n = 4$	13.1 ± 0.4 $n = 4$	$p < 0.001$
HeLa	32.4 ± 1.0 $n = 4$	15.8 ± 1.0 $n = 4$	$p < 0.001$
HT29	24.0 ± 0.6 $n = 4$	19.2 ± 0.8 $n = 4$	$p < 0.001$
SKOV3	14.1 ± 1.2 $n = 3$	10.5 ± 1.9 $n = 2$	$p < 0.01$

[a] 95% confidence limits.

* To whom correspondence should be addressed. Tel: (617) 726-6478. Fax: (617) 726-5708 . E-mail: ljosephson@partners.org.

[†] Massachusetts General Hospital and Harvard Medical School.

[‡] Beth Israel Deaconess Medical Center.

[§] These authors contributed equally to this work.

10.1021/bc7002204 CCC: $40.75 © 2008 American Chemical Society
Published on Web 11/08/2007

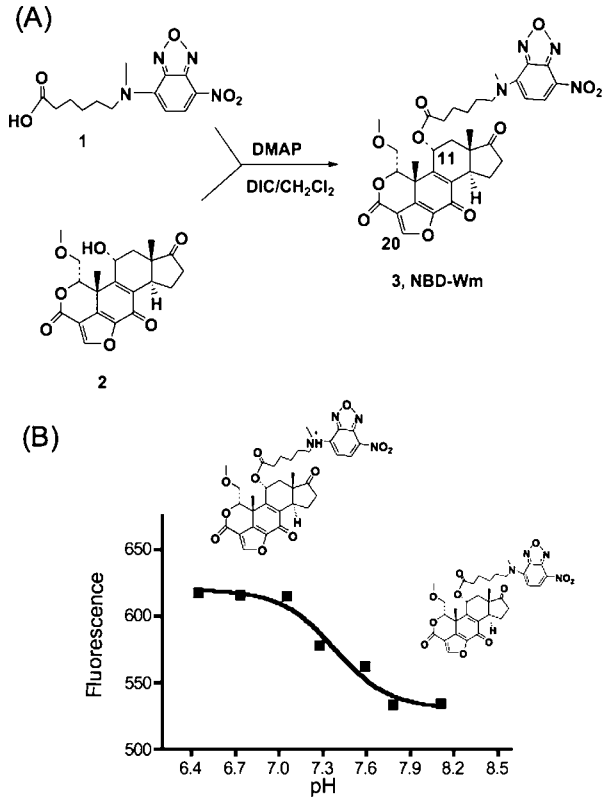

Figure 1. Synthesis and ionic forms of NBD-Wm. (A) Synthesis of NBD-Wm. (B) Fluorescence of compound 1 as a function of pH. An apparent pK_a of 7.5 was obtained. NBD-Wm exists as a neutral (pH >> 7.5) or positively charged species (pH << 7.5).

periods of time, 24–72 h; such long exposure times are necessary to allow cell proliferation and measure its inhibition. The antiproliferative effects of Wm and Wm derivatives are of interest because of recent efforts to develop anticancer drugs using these materials (*7*, *8*, *26*, *27*).

Using the fluorescence of NBD-Wm, we determined the time course of the compound's uptake by cells (by FACS), its intracellular distribution (by fluorescence microscopy), and its cellular concentration (by lysate fluorescence). Using an antibody to NBD, we determined the time course and molecular weights of Wm-modified proteins with the usual Western blot method. NBD-Wm can be a useful compound to further our understanding of the mechanism of action of the viridin class of antibiotics of which Wm is the best studied member.

MATERIALS AND METHODS

The scheme and nomenclature for the synthesis of molecules used in this study are shown in Figure 1. Wortmannin was a gift of the natural products branch of the NCI. All reagents and solvents were of standard quality. Compound 1 was prepared by reacting *N*-methyl-6-aminohexanoicacid and 4-chloro-7-nitrobenz-2-oxa-1,3-diazole (NBD-Cl) as previously described (*28*), while compound 2 was prepared according to earlier procedures (*29*, *30*). NMR was performed on a Varian 400 MHz instrument (Varian Instruments, Palo, Alto, CA) with $CDCl_3$ as the solvent, while mass spectra were obtained on a Micromass LCT instrument with a time-of-flight ESI technique (Waters, Milford, MA). HPLC (Varian Prostar 210 with a variable wavelength PDA 330 detector) employed reverse phase C18 columns (VYDAC, Cat.#: 218TP1022) with water containing 0.1% trifloroacetic acid (buffer A) and acetonitrile (containing 20% buffer A) (buffer B) as elution buffer.

Preparation of NBD-Wm, 3. To a mixture of compound **1** (19.3 mg, 0.05mmol) and compound **2** (37 mg, 0.12mmol) in anhydrous dichloromethane (4 mL) were added DIC (diisopropylcarbodiimide) (40 μL) and DMAP (2 mg). The color of the reaction turned from red to blue. The reaction could be completed in a few minutes. Water (5 mL) was added, and the aqueous layer was extracted with dichloromethane (3 × 5 mL). After drying over Na_2SO_4, the organic layers were concentrated, and the residue was further purified by preparative TLC with dichloromethane and methanol. A red powder **3** was obtained. Yield, 91%. MS: calcd $C_{34}H_{36}N_4O_{11}$, 677.2459 ($M + H^+$), found 677.2455; ^{1}H NMR: 0.97 (3H, s, CH_3-13), 1.23 (2H, b), 1.42–1.52 (2H, m), 1.52–1.60 (1H, m), 1.73 (3H, s, CH_3-10), 1.76–1.86 (2H, m), 1.99–2.16 (1H, m), 2.20–2.32 (1H, m), 2.34–2.50 (2H, m), 2.54–2.64 (2H, m), 2.84–2.92 (1H, m), 2.92–3.00(1H, m), 3.12–3.22 (4H, m), 3.40–3.56 (4H, m, CH_3N, CH_3OCH_2), 4.06–4.16 (2H, b, CH_2N), 4.69–4.74 (1H, m, H-1), 6.11 (1H, d, $J = 9$ Hz, Ar-H), 6.14–6.22 (1H, m, H-11), 8.25 (1H, s, H-20), 8.45 (1H, d, $J = 9$ Hz, Ar-H). ^{13}C NMR: 14.75, 23.16, 24.43, 26.25, 26.69, 27.67, 34.02, 35.91, 36.38, 40.93, 41.52, 44.33, 49.39, 55.89, 59.68, 70.36, 73.09, 88.77, 101.31, 114.39, 122.64, 135.63, 140.60, 142.92, 144.72, 145.04, 145.09, 145.50, 149.59, 150.29, 157.68, 172.21, 172.76, 216.42. Proton and 13C NMR spectra are provided in Supporting Information.

Cell Culture. Human cervical cancer HeLa, lung cancer A549, breast cancer MCF-7 and BT20, colon cancer HT29, and ovarian cancer SKOV3 cells were purchased from the American Type Culture Collection (Manassas, VA). HeLa, BT20, and MCF-7 cells were grown in MEM supplemented with 10% FBS, 1 mM sodium pyruvate, 0.1 mM nonessential amino acids, 2 mM L-glutamine, 100 units/mL penicillin, and 100 μg/mL streptomycin. A549 cells were grown in RPMI supplemented with 10% FBS, 2 mM L-glutamine, 100 units/mL penicillin, and 100 μg/mL streptomycin. HT29 and SKOV3 cells were grown in McCoy's medium supplemented with 10% FBS, 2 mM L-glutamine, 100 units/mL penicillin, and 100 μg/mL streptomycin. All cells were incubated at 37 °C under a 5% CO_2 atmosphere. A549 cells were used for all experiments, with additional cell lines used in Table 1.

PI3 Kinase and Antiproliferative Assays. The PI3 kinase assay was the fluorescent energy transfer method (*31*). The assay has higher IC50 values for Wm (12 nM) than the radioactive lipid phosphorylation assays (1–4 nM) because it uses a higher ATP concentration (100 μM). IC50 values for both assays were determined by curve fitting performed using Prism 4.0a software. The antiproliferative activity was evaluated by the sulforhodamine-B (SRB) method (*32*). Briefly, cells were seeded in 96-well plates at a density of 5000 cells/well in 100 μL media and allowed to incubate overnight at 37 °C. Cells were incubated with 0–100 μM Wm or Wm derivative added once, at the start of the 48 h incubation at 37 °C. Following incubation with Wm or NBD-Wm, cells were fixed by the addition of 50% cold TCA and subsequent incubation at 4 °C for 1 h. The cells were then washed with tap water, allowed to air-dry O/N, and stained with 100 μL of 0.4% SRB in 1% acetic acid for 10 min at RT. Unbound SRB was removed by washing plates with 1% acetic acid. Bound SRB was solubilized in 200 μL of 10 mM Tris buffer, after which the absorbance of each well was measured at 490 nm using an E_{max} precision microplate reader (Molecular Devices, Sunnyvale, CA). Percent cell survival was calculated using Prism 4 software (GraphPad Software, San Diego, CA) for each concentration as the ratio of the measured absorbance to that of the untreated wells. Statistical tests were done using Graph Prism and analyzed by two-way ANOVA.

NBD-Wm Uptake. A549 cells were incubated with 10 μM NBD-Wm for the indicated time, washed three times with HBSS, and detached with trypsin. Cell fluorescence was measured using a FACS Calibur flow cytometer (Becton-Dickinson, Franklin Lakes, NJ) of the live cell population

identified using forward and side light scattering measurements. Cell-associated NBD was measured in the FL1 channel. Fluorescence was calculated as the geometric mean of labeled cells divided by the geometric mean of unlabeled cells, termed relative cell fluorescence or RCF.

Cell-Associated NBD-Wm Concentration. A549 cells were seeded in 96-well plates at a density of 10^4 cells/well in 100 μL media. Cells were treated with 10 μM NBD-Wm at 37 °C for varying times. After treatment, the media was removed from each well, and the cells were washed 3 times with 300 μL of HBSS. Cells were then lysed in 100 μL of lysis buffer (150 mM NaCl, 1% NP-40, and 50 mM Tris at pH 8.0) for 1 h at RT and the fluorescence measured (ex 485 nm, em 535 nm) by a SpectraMax Gemini XS plate reader (Molecular Devices, Sunnyvale, CA). Protein content was determined using the BCA assay (Pierce, Rockford, IL) and used to determine the number of cells, where the amount of protein per cell was determined for cells counted by a hemocytometer. Cell volume was then the number of cells times 2.4 pL/cell for A549 cells from (*33*).

Visualizing Wortmannylated Proteins by Western Blots and in Immunoprecipitates. A549 cells were seeded in 12-well plates and grown to 70–80% confluence. Cells were treated with 10 μM NBD-Wm continuously for the times indicated. After treatment, the culture medium was removed, and the cells were washed 2× in ice-cold PBS. Whole-cell protein extracts were prepared from adherent cells by adding 250 μL of ice-cold radioimmune precipitation assay (RIPA) buffer (20 mM Tris at pH 7.4, 100 mM NaCl, 1% sodium deoxycholate, 1% Nonidet NP-40, and 1% SDS). On the day of use, the lysis buffer was supplemented with the following: 1 mM Na_3VO_4, 1 mM NaF, 1 mM PMSF, 50 mM β-glycerophospate, and 50 μL/mL protease inhibitor cocktail (Sigma-Aldrich, St. Louis, MO) to each well of the 12-well tissue culture plate. The cells were lysed for 15 min on ice and the lysate cleared by centrifugation at 16,000 rpm at 4 °C for 15 min.

Alternatively, for the immunoprecipitation of PI3 kinase, cells were grown to confluence in 10 cm plates ($\sim 10^6$ cells/well). Cell were treated with 2 mL of culture medium or 2 mL of medium with NBD-Wm (10 μM) and incubated for 2 h. Cultures were then washed twice with ice-cold HBSS and incubated with 1 mL of NP40 lysis buffer (1% Nonidet NP-40, 100 mM NaCl, and 20 mM Tris at pH 7.4), which was supplemented with the inhibitors used in RIPA the day of use, for 15 min at 4 °C with rocking. Plates were scraped and debris and lysate collected and cleared as described before. Lysates were pooled and 750 μL aliquoted for immediate use or brief storage at −20 °C. Lysates were then incubated with 5 μg of either anti-NBD, anti-p85α, anti-p110α, or an equivalent nonimmune isotype control overnight with rotation at 4 °C. Protein A/G agarose beads (Santa Cruz Biotechnology, Santa Cruz, CA) were slurried and washed five times with lysis buffer. Washed beads were then aliquoted, combined with lysates, and incubated for 4 h at 4 °C with rotation. Immune complexed beads were pelleted for 1 min at 1500 rpm at 4 °C. Supernatants were transferred to new tubes, and immune complexed beads were washed five times with cold lysis buffer.

Cell lysates were analyzed for total protein concentrations as determined by BCA protein assay (Pierce, Rockland, IL). Typically, 10 μg of total protein was added to 2× SDS sample buffer (100 mM Tris at pH 6.8, 20% glycerol, 4% SDS, and 0.15 mM bromophenol blue) made by 1% β-mercaptoethanol and boiled for 5 min. Immune complexes were eluted from agarose beads with 35 μL of 2× SDS sample buffer, boiled for 5 min, and cleared by centrifugation at 16K rpm for 10 min. Samples were then resolved by SDS–PAGE on a 7.5% Tris·HCl Ready Gel (BioRad, Hercules, CA) run at 50 V for 3 h and then transferred to a PVDF membrane (BioRad) overnight at 35 V. Membranes were blocked for 1 h at room temperature in 5% nonfat milk in Tris buffered saline with Tween (TBST) and probed with a 1:3000 dilution of anti-NBD rabbit polyclonal antibody (Biogenesis, Munich, Germany), anti-p85α mouse monoclonal (Upstate, Temecula, CA), anti-p110α rabbit polyclonal (Cell Signaling, Danvers, MA), or anti-HSP90 mouse monoclonal (Stressgen, Ann Arbor, MI) in TBST for 3 h at RT or overnight at 4 °C. The PVDF membrane was washed 3× at RT with TBST and subsequently incubated with a 1:5000 dilution of goat antirabbit-HRP or goat antimouse-HRP secondary antibody (Chemicon, Temecula, CA and Santa Cruz, respectively) for 1 h at RT. The PVDF membrane was washed 3× with TBST and incubated with ECL detection reagent (Amersham Biosciences, Piscataway, NJ) for 90 s. Proteins were detected by exposing the PVDF membrane to BioMax MR autoradiography film (Eastman Kodak, Rochester, NY). Immunoblots were stripped with restore buffer (Pierce) and reprobed with anti-HSP90 to visualize equal loading of protein. Films, where indicated, were evaluated for relative band intensity using ImageJ version 1.38n software. Total protein was also evaluated by Imperial protein stain (Pierce) according to the manufacturer's protocol.

Fluorescent Microscopy. A549 cells were seeded in 24-well plates and grown to 60–70% confluence, and treated with 10 μM NBD-Wm at 37 °C. For nuclear staining, cells were incubated with 1 μg/mL Hoechst 33342 (Molecular Probes, Eugene, OR) for 30 min at 37 °C. For plasma membrane staining, cells were incubated with 5 μg/mL of FM 4-64 (Molecular Probes, Eugene, OR) for 1 min at RT. Images were acquired on either a Nikon Eclipse TE2000S fluorescent microscope equipped with a Spot Insight QE CCD camera (Diagnostic Instruments, Sterling Heights, MI) or a Nikon Eclipse 80i fluorescent microscope equipped with a Photometrics (Tucson, AZ) Cascade 512B CCD camera. Images obtained on the Nikon Eclipse TE2000S microscope were processed using Spot Software (Diagnostic Instruments). Images obtained on the Nikon Eclispe 80i microscope were processed using IPLab (Scanalytics, Inc., Rockville, MD) software.

Fluorescence Titration of Compound 1. The pH of a solution of sodium citrate (0.1 M) and sodium phosphate (0.1 M) was adjusted with 6 M HCl to give a series of buffers whose pH values differed by 0.25 pH units. Compound 1, dissolved in DMSO, was added to 200 μL of buffer to give a final concentration of 10 μM and a fluorescence read (466 nm excitation, 536 nm emission) using a Spectromax gemini XS plate reader (Molecular Devices, Sunnyvale, CA).

RESULTS

The synthesis of NBD-Wm was accomplished by reacting compound 1 with compound 2 as shown in Figure 1A. The ester bond of NBD-Wm was highly stable in PBS, pH 6.8, with a half-life of greater than 700 h when assessed by the times dependence of HPLC peak area (*10*). To assess the ionic forms of NBD-Wm, which might contribute to an understanding of its membrane permeability, compound 1 was titrated by fluorescence (Figure 1B). The titration of NBD-Wm was not attempted because the lactone group of Wm hydrolyzes above pH 8, complicating titration data (Yuan and Josephson, unpublished observations). At physiological pH values close to the pK_a of 7.5, NBD-Wm exists both as a singly protonated and neutral species. Implications of the charged species of NBD-Wm are discussed below.

We first compared Wm and NBD-Wm for their ability to inhibit PI3 kinase activity as shown in Table 1. The IC50 of NBD-Wm was 1.84-fold higher than Wm, consistent with other studies that lipophilic modifications of Wm at C11 can have little effect on the ability of Wm derivatives to inhibit PI3

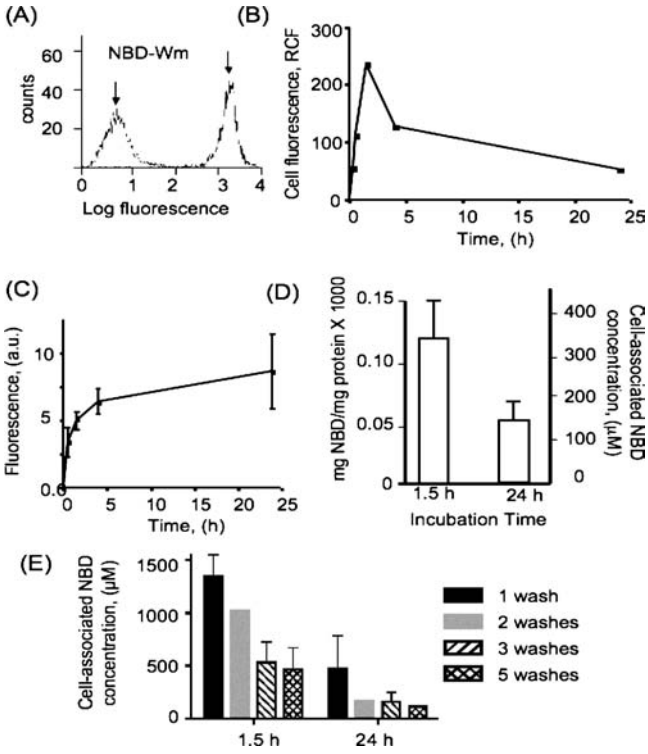

Figure 2. Cellular fate of NBD-Wm in A549 cells. The uptake (B), extrusion(C), and cellular concentrations of NBD-Wm (D) are shown. (A) Cell fluorescence by FACS after exposure to NBD-Wm is also shown (1.5 h, 10 μM). The arrows indicate the median fluorescences of NBD-Wm exposed or unexposed cells that were used to calculate relative cell fluorescence (RCF). Cells were uniformly labeled by NBD-Wm. (B) Time course as the RCF for cells exposed to 10 μM NBD-Wm. RCF is the median fluorescence of labeled cells divided by the median of cells not exposed to NBD-Wm. Even though NBD-Wm is present in the media for 24 h, a peak of fluorescence at 1.5 h is obtained. (C) Time course of culture media fluorescence for cells exposed to NBD-Wm (10 μM, 1.5 h). NBD-Wm-containing media were replaced at 1.5 h with fresh media at $t = 0$. (D) Cellular concentrations of NBD-Wm. Cells were exposed to 10 μM NBD-Wm for 1.5 or 24 h, washed, lysed, and cell-associated NBD determined. (E) Effect of wash number on the concentration of cell-associated NBD-Wm. A549 cells were incubated with 10 μM NBD-Wm for 1.5 or 24 h, washed 1–6 times with HBSS, and lysed. The concentration of cell-associated NBD-Wm was determined as described in 2D.

kinase (*29*, *34*). We next compared the antiproliferative effect of NBD-Wm and Wm on various cell lines as shown in Table 1. The IC50 of NBD-Wm was the same as that of Wm in two cell lines (A549, MCF-7) or lower than that of Wm in four others (SKOV-3 HeLa, HT-29, and BT-20). Therefore, the addition of the NBD-NMeHA adduct to the C11 of Wm did not impair the ability of Wm to enter cells with the six cell lines tested. NBD-Wm is therefore a Wm probe with a bioactivity similar to or better than that of Wm in both the cell-free PI3 kinase assay and cell-based antiproliferative activity and was therefore used to obtain data on the kinetics of Wm uptake, the target proteins it modified, and its intracellular concentration and disposition.

We examined the uptake of NBD-Wm by exposing cells to 10 μM NBD-Wm, detaching cells with trypsin, and analyzing cell fluorescence by FACS. As shown in Figure 2A, cells were uniformly labeled, with arrows showing the geometric means of labeled or unlabeled cell populations. These geometric means were used to obtain the relative cellular fluorescence or RCF (geometric mean labeled cells/geometric mean unlabeled cells), which was used to quantify the amount of fluorescence of a labeled cell population.

We next determined the time course of cellular uptake as the RCF versus incubation time with a 10 μM NBD-Wm; see Figure 2B. Cell fluorescence reached a peak at 1.5 h and then fell precipitously, even though NBD-Wm had not been removed from the media. To determine whether the decrease in cellular fluorescence between 1.5 and 24 h of exposure to NBD-Wm was due to cells transporting a fluorescent material to the media, cells were incubated with NBD-Wm (10 μM, 1.5 h), and the media containing NBD-Wm was removed and replaced with fresh, non NBD-Wm-containing media. As shown in Figure 2C, media fluorescence rapidly increased during the first 5 h, corresponding to the rapid decrease in cell fluorescence seen with FACS during this time period.

To obtain values for the amounts NBD-Wm cells internalized and to further verify the unusual drop in fluorescence between 1.5 and 24 h (Figure 2C), cells were incubated with 10 μM NBD-Wm for 1.5 or 24 h and the amount of cell-associated NBD-Wm determined from lysate fluorescence and NBD-Wm standards. Cell-associated NBD was significantly higher at 1.5 than 24 h ($p < 0.001$; see Figure 2D) and paralleled the time dependence of cell fluorescence seen with FACS (Figure 2B). The amount of cell-associated NBD was expressed as both per mg of cell protein in the lysate, a value that does not reflect cell volume, and as the average cellular concentration using literature values for the volume of an A549 cell. The fluorescence-based average cellular concentrations were 360 $\pm$ 20 μM and 110 $\pm$ 20 μM at 1.5 and 24 h, respectively, compared to the media concentration of 10 μM. (The means have at least four data points.) Thus, exposure of A549 cells to NBD-Wm had two unusual features: a transient peak at 1.5 h and an accumulation to cellular concentrations at least 10-fold higher than that of the media. These observations with NBD-Wm were not unique to A549 cells but were also seen with HeLa cells (data not shown) and are further discussed below. The concentration of cell-associated NBD obtained was independent of the number of cell washes once three washes were employed ($p > 0.05$ for 3 or 5 washes; see Figure 2E).

We next examined the time course with which NBD-Wm modified cellular protein as shown in Figure 3A. Cells were incubated with 10 μM NBD-Wm for the indicated times and lysed, and the cell protein was analyzed by the Western blot method using anti-NBD. Six bands at 35, 50, 75 85, 95, and 130 kDa were seen. The time course of the six wortmannylated species was determined by quantitative analysis of band intensity as shown in Figure 3B, with the total amount of wortmannylated protein (sum of the intensities of six bands) shown in Figure 3C. Total wortmannylated protein reached a peak at 1.5 h and declined slowly thereafter.

Proteins modified by reaction with NBD-Wm were next examined in greater detail as shown Figure 4. Wortmannylated proteins, visualized by reaction with anti-NBD, and total cell protein were compared as shown in Figure 4A. Wortmannylated proteins occurred with molecular weights and with band intensities that differed markedly from the pattern seen with the total protein, indicating that NBD-Wm-modified proteins were a distinct subset of total cell proteins. To demonstrate that the catalytic subunit of PI3 kinase, p110, was modified by NBD-Wm, we employed an immunoprecipitation (IP) with anti-p85, the regulatory subunit of the enzyme. As shown in Figure 4B, the clarified lysate (CL) from the anti-p85 IP did not appear to be missing a band in the vicinity of 110 kDa. However, when the IP pellet was then electrophoresed and stained with anti-NBD (Figure 4C), a wortmannylated band at 110 kDa was present in NBD-Wm-treated cells and not in control cells. However, the amount of total cellular p110 was sufficient to enable visualization by anti-p110 without IP purification (Figure 4D). We conclude that NBD-Wm reacts with the catalytic subunit of PI3

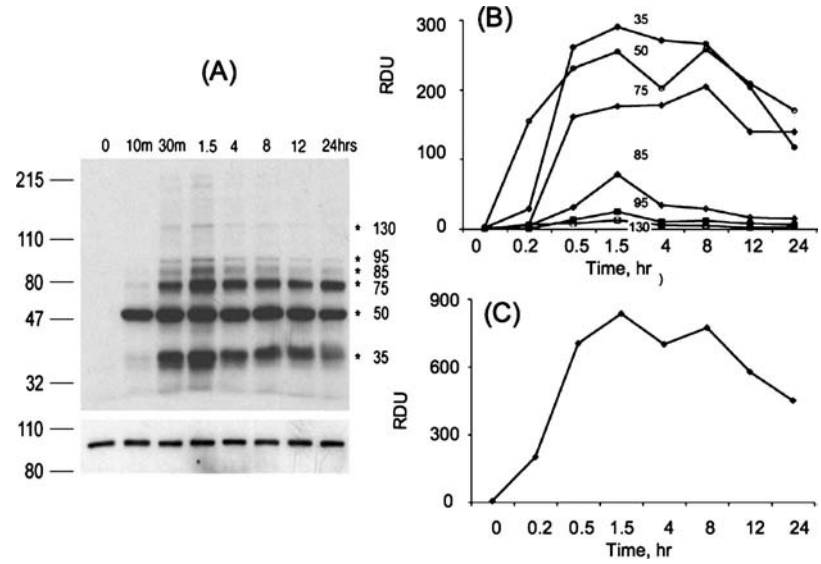

Figure 3. Time course for the wortmanylation of proteins by NBD-Wm. (A) Cells were exposed NBD-Wm (10 μM) for the indicated time, lysed, and stained for modification by NBD-Wm with anti-NBD. Molecular weights of prominent wortmanylated proteins (asterisks) are given on the right. (B) Densitometric scan for the time course wortmannylated protein from A. The numbers refer to the molecular weights from A. RDU = relative density units. (C) Time course for the total amount of wortmannylated protein. The values are the sum of the six wortmannylated proteins shown in B.

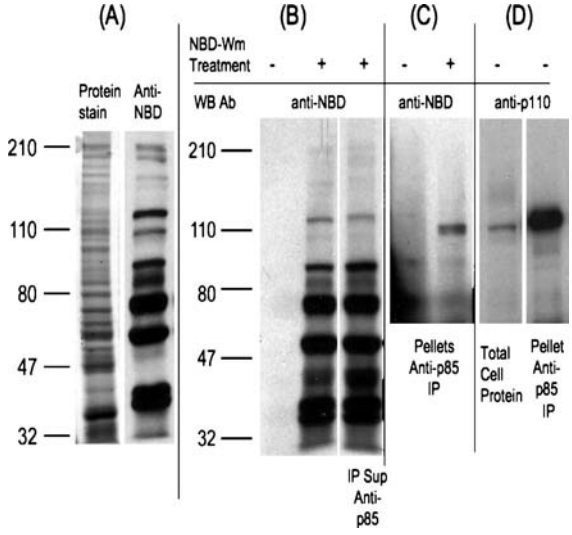

Figure 4. Comparison of total cell protein, wortmannylated protein, and wortmannylated p110 from cells. (A) Cells were exposed to NBD-Wm (4 h, 10 μM) and then stained for total protein. Wortmannylated proteins were visualized by Western blot (WB) with anti-NBD. Wortmannylated proteins were a distinct subset of total cell proteins. (B) Cells were treated with NBD-Wm as indicated and immunoprecipated (IP'ed) with anti-p85 to remove p110 from cell lysates. The IP supernatant (IP Sup, Anti-p85) was not missing a band at 110 kDa. WB Ab indicates the use of the Western blot method with the indicated antibody. (C) IP pellets from NBD-Wm were treated and control cells reacted with anti-NBD. A band at 110 kDa was visible. (D) WB with anti-p110 for total cell protein or the IP Pellet. p110 was visible in total cell protein and prominent in IP Pellet.

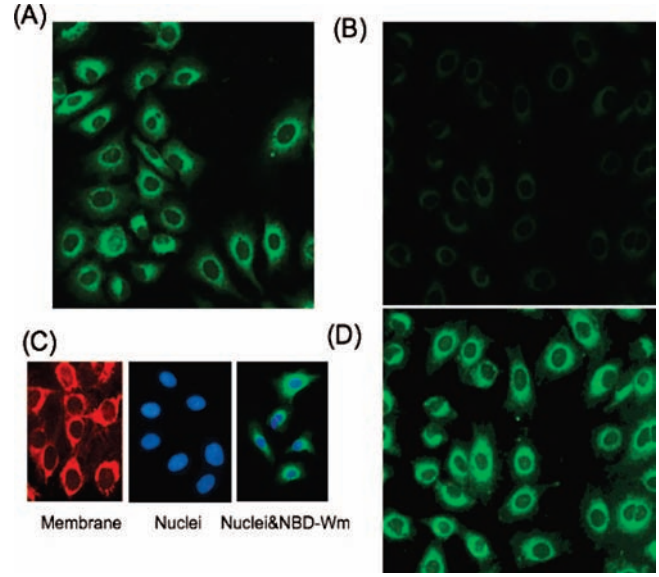

Figure 5. Fluorescent microscopy with NBD-Wm. Cells were incubated with 10 μM NBD-Wm for 1.5 (A) or 24 h (B). Cells incubated for 24 h have far less fluorescence. (C) Cells stained for membranes, nuclei, or nuclei and NBD-Wm. (D) The intensity of the cells shown in (B) was increased to permit the comparison of intracellular distribution of cells shown in A and B.

kinase (p110), but the amount of NBD-Wm-modified p110 is extremely small compared to the other proteins it modifies.

The intracellular distribution of NBD-Wm was monitored by fluorescence microscopy as shown in Figure 5. Fluorescence at 1.5 h (Figure 5A) was distinctly higher than that at 24 h (Figure 5B), paralleling cell fluorescence data obtained from FACS analysis (Figure 3B). The fluorescence intensity from Figure 5B was increased through image processing (Figure 5D) to permit comparison of the intracellular fluorescence (Figure 5A and B). Fluorescence intensity by microscopy (compare Figure 5A at 1.5 h to Figure 5B at 24 h) closely paralleled the time course of fluorescence seen with FACS (Figure 2B). To shed light on the subcellular localization of NBD fluorescence, cells were stained for nuclei and membranes and NBD fluorescence viewed against those stains (Figure 5C). At both 1.5 h (Figure 5A) and 24 h (Figure 5D), cells treated with NBD-Wm showed a distinct pattern of perinuclear fluorescence that colocalized with a membrane stain (red stain, Figure 5C). The colocalization of NBD fluorescence with membrane structures, high cellular concentrations of NBD-Wm (Figure 2D), and the hydrophobic nature of NBD-Wm suggest that a large pool of NBD-Wm is solubilized in membranes.

Our results on the fate of NBD-Wm in A549 cells are summarized in Figure 6. The model describes the major

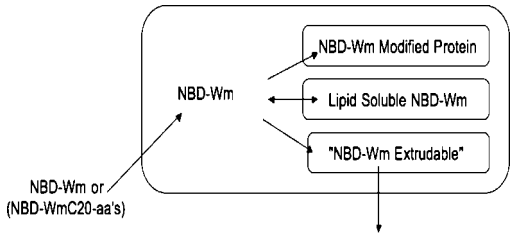

Figure 6. Pools of NBD-Wm in cells. NBD-Wm (or NBD-WmC20 amino acid derivatives) enters cells. NBD-Wm is found in two pools, an intramembrane pool and as modified proteins. Once in cells, NBD-Wm is converted to a second chemical entity termed NBD-Wm extrudable, whose efflux from cells causes the drop in cell fluorescence (1.5–24 h; see Figure 2B).

intracellular pools of NBD, the form that enters cells, and the formation of a fluorescent form that is extruded by cells.

Form of NBD-Wm Entering Cells. The model proposes that either NBD-Wm or NBD-WmC20 amino acid derivatives enter the cells. The possibility that NBD-WmC20 derivatives may enter cells is based on (i) the fact that C20 of Wm reacts rapidly with amino acids (half-life of 0.99 min in culture media (*11*)) and (ii) the fact that with antiproliferation assays many Wm amino derivatives, which bear negative, positive, or zwitter ion charges, are more active than Wm (*7, 11, 35*). Since NBD-Wm reacts with amino acids under physiological conditions, it is difficult to determine which species enters the cells.

Major Intracellular Pools of NBD-Wm. Two major pools of NBD-Wm proposed by the model are a membrane-localized pool, based on the colocalization of NBD fluorescence and a stain for membranes shown in Figure 5, and as covalently reacted with protein, based on the NBDylated protein (see in Figure 3). Other minor pools or forms of NBD-Wm may exist, and the model does not propose that any specific form gives rise to biological or pharmacological effects of Wm. For example, a minor cytoplasmic form of NBD-Wm might not appear on fluorescence microscopy and yet react with kinases and cause important physiological effects. Using an HPLC method (*11*), the ester bond in NBD-Wm was found to be highly stable in PBS, with a half-life longer than 700 h at 37 °C in PBS (data not shown). Nonenzymatic hydrolyzis of the ester bond of NBD-Wm is therefore unlikely. As mentioned with respect to Figure 2D, NBD-Wm was added to cell culture media, lysis buffer, or lysis buffer with cell protein, and each time yielded a time independent, stable fluorescence. For these reasons, the fluorescence from NBD is assumed to be from NBD-Wm in Figure 6, a simplifying assumption.

Formation of an Extrudable Form of NBD. The characteristic peak accumulation of cell fluorescence at 1.5 h and the decrease thereafter was seen when A549 cells were incubated with NBD-Wm with multiple techniques. These included (i) FACS (Figure 2B), (ii) lysate fluorescence (Figure 2D), and (iii) fluorescence microscopy (compare Figure 5A at 1.5 h vs Figure 5B at 24 h)). This transient peak of cell-associated NBD was inconsistent with a model where a single fluorescent entity (or single class of fluorescent molecules) equilibrated between two compartments (media and cells), a mechanism through which the cell-associated NBD-Wm would asymptotically approach a maximum value. Since cells extrude fluorescence into the culture media (Figure 2C), we propose that NBD-Wm must be converted to a second form, which undergoes rapid cell extrusion.

DISCUSSION

Here, we describe the bioactivity of a fluorescent Wm probe, NBD-Wm, and its fate in a cell-based system. Our experiments differ from those of others who have used Bodipy or tetramethylrhodamine-based Wm probes to label cell protein (*22, 23*). First, we have demonstrated that NBD-Wm is similar to or better than Wm in a quantitative bioassay using intact cells, the antiproliferation assay. The physical basis of the similar bioactivity of NBD-Wm and Wm is further discussed below. Second, we employed the fluorescence of NBD-Wm to determine its uptake and visualize its intracellular disposition in cells by FACS and fluorescence microscopy. Third, we employed NBD-Wm to determine the average cellular concentrations of NBD, demonstrating the ability of cells to concentrate this compound above the concentrations found in media. Using a linker different from our own linker, Giner et al. conjugated NBD to Wm and showed that the conjugate was an effective inhibitor of PI3 kinase (*34*).

The similar or superior bioactivity of NBD-Wm relative to Wm may reflect the relatively small increase in size that results from NBD attachment. The nominal molecular weights of Wm and NBD-Wm were 428 and 677 Da, respectively. Support for the view that the size of the fluorochrome attached at the C11 of Wm can be an important determinant of the bioactivity of the resulting conjugate can be obtained from our earlier studies. Attachment of fluorescein to Wm, a fluorochrome far larger than NBD, resulted in a conjugate that was a poor inhibitor of PI3 kinase. (See compound 7c of Table 1 from ref *30*.) The charge of NBD-Wm may also contribute to its bioactivity since it exists with a single positively charged species below pH 7.5 and as a neutral species above pH 7.5 (Figure 1B). Although our biotinylated-Wm inhibited PI3 kinase (compound 7a of Table 1 from *30*), its antiproliferative IC50 (A549 cells) was 63.0 $\pm$ 2.2 μM, compared to the IC50 of 11.4 $\pm$ 0.5 μM for Wm and 12.2 $\pm$ 0.8 μM for NBD-Wm (see Table 1). Similar poor results with the biotinylated-Wm were obtained in other cell lines examined (HeLa, MCF-7, and HT-29; data not shown). For these reasons, NBD-Wm was superior to the fluorescent and biotinylated Wm probes we have synthesized earlier.

At a concentration of 10 μM, NBD-Wm initially labeled a 50 kDa protein (10 min exposure) followed by a labeling of four additional proteins, a distinct subset of the total cell protein. The p110 catalytic subunit of PI3 kinase was a minor band; however, when p110 was concentrated by immunoprecipitation, labeling of this band was apparent. The time course for the formation of wortmannylated protein exhibited a broad plateau between 1 and 24 h, with substantial levels present 24 h after NBD-Wm was added to cells (Figure 3). Using 20 nM tritiated Wm, Thelen et al. showed that a single protein (110 kDa) was labeled in human neutrophils (*24*). However, when Bodipy-Wm was used to label YZ5 cells, multiple labeled bands were obtained (see Figure 6 of ref *22*), as was the case with a tetramethyrhodamine-Wm (50 nM) and Jurkat T cell lysates (see Figure 2 of ref *23*). In both studies, the reaction of fluorescent Wm probes was specific for proteins of certain molecular weights (Wm displaceable) and nonspecific for others (non-Wm displaceable). Given the very high levels of NBD-Wm achieved in cells (Figure 2D) and the ability of Wm to react with the epsilon amino groups of lysine in PBS (*11*), NBD-Wm may react with the epsilon amino groups of a select subset of cellular proteins (Figure 4A), whose function remains unknown, in addition to labeling the lysines in the ATP sites of kinases.

Though we considered it surprising that A549 cells accumulated NBD-Wm at far higher concentrations than those of the culture media of 10 μM (see Figure 2D), a variety of factors indicate that this observation is correct. First, our method of determining the concentration of cell-associated NBD-Wm employed a high detergent lysis buffer, one containing 1% w/v of the nonionic detergent NP-40, which disrupts cell structure

and completely solubilizes cell membranes and organelles. To obtain cell-associated NBD concentrations, fluorescent standards were employed; these standards were obtained by diluting known amounts of NBD-Wm into lysate buffer containing protein from lysed cells. Our method of determining cell-associated NBD concentrations destroyed cell structure and read the fluorescence of standards and unknowns in precisely the same media so that possible environmental effects on NBD fluorescence would not yield incorrect values. Second, the fluorescence of NBD-Wm when added to culture media, lysis buffer, or lysis buffer plus cell protein was stable for at least 24 h, indicating a lack of enzymatic or nonenzymatic mechanisms for altering fluorescence (data not shown). Third, the use of our standard three wash protocol reduced cell-associated fluorescence to a value that was independent of the number of washes employed. At both 1.5 and 24 h of incubation, cell-associated fluorescence reached a plateau after three washes that was not affected by additional washes (Figure 2E). Fourth, we considered that the high cellular concentrations of NBD-Wm that we obtained might be secondary to toxic effects of the NBD-Wm. However, cells exposed to the nonfluorescent Wm (10 μM, 23 h) then internalized 10 μM NBD-Wm in a manner identical to that of non-Wm exposed cells. Finally, key observations made with A549 cells (Figure 2B, time course of cell fluorescence, and Figure 2D, average cellular concentration) were also made with HeLa cells as well, indicating that our observations were not cell line specific. On the basis of these experiments, A549 cells apparently accumulate NBD-Wm to far higher levels than that present in the media, reaching average cell-associated concentrations as high as 300 μM when incubated with 10 μM NBD-Wm (1.5 h exposure).

An interesting issue is the implication of these findings for the molecular targets of Wm and Wm derivatives. Literature values for the IC50 values of Wm for kinases are 1–4 nM (PI3 kinase *1, 29*), 24 nM (polo-like kinase (*23*)), 200 nM (mTOR (*36*)), and 200 nM (DNA-dependent protein kinase (*37*)). The micromolar concentrations of NBD-Wm needed to inhibit cell proliferation, coupled to the observation that cells concentrate NBD-Wm to values far above that in culture media (Figure 2D), means that the average cellular concentrations of NBD-Wm far exceeds the IC50 values of all known kinases for Wm. For example, if a selective PI3 kinase inhibition were the basis of NBD-Wm's antiproliferative effects, on the basis of known IC50 values, a cytoplasmic concentration on the order of 10 nM NBD-Wm would be required. This concentration is some 30,000-fold lower than the 300 μM concentration of cell-associated NBD-Wm we obtained. While it is technically difficult to determine the concentration of NBD-Wm in the environment of an enzyme, we regard such a massive reduction in concentration unlikely and instead propose that the antiproliferative effects of NBD-Wm result from the inhibition of a variety of targets, one of which is PI3 kinase. Consistent with the proposed lack of selectivity of NBD-Wm as a specific PI3 kinase inhibitor in vivo was its ability to modify many proteins, of which the p110 catalytic subunit of PI3 kinase was an extremely minor band.

Others have determined Wm-modified proteins using radioactive (*24*) or fluorescent Wm probes at lower concentrations than those employed here (*22, 23*). A different pattern of Wm-modified proteins maybe obtained at these low Wm concentrations, which are adequate to produce many important effects on cells. Our goal, however, was to describe the fate of NBD-Wm in cells at concentrations associated with its antiproliferative effects.

Our objectives were to demonstrate that the bioactivity of NBD-Wm was similar to (or better than) Wm and to describe the fate of NBD-Wm in cultured cells associated with its antiproliferative effects using a variety of techniques (microscopy, FACS, and Western blot). Immunochemical methods of detecting of NBD can in principle be extended from Wm to other NBD-based probes or drugs that covalently modify proteins in cell-based systems. Antibody-based methods are not subject to interference from background fluorescence and amenable to enzyme amplification to increase sensitivity. On the basis of the variety of fluorescence-based and immunochemical methods for detecting NBD, we envision NBD-Wm as a powerful tool for future investigations concerning the mechanism of action of viridins.

ACKNOWLEDGMENT

This work was supported in part by NIH Grants R01EB00662 (to L.J.), R01 EB004472(to L.J.), and 2P50CA86355 (to R.W.).

Supporting Information Available: Proton NMR spectra of NBD-Wm and 13C NMR spectra of NBD-Wm. This material is available free of charge via the Internet at http://pubs.acs.org.

LITERATURE CITED

(1) Powis, G., Bonjouklian, R., Berggren, M. M., Gallegos, A., Abraham, R., Ashendel, C., Zalkow, L., Matter, W. F., Dodge, J., and Grindey, G., et al. (1994) Wortmannin, a potent and selective inhibitor of phosphatidylinositol-3-kinase. *Cancer Res. 54*, 2419–2423.

(2) Workman, P. (2004) Inhibiting the phosphoinositide 3-kinase pathway for cancer treatment. *Biochem. Soc. Trans. 32*, 393–396.

(3) Luo, J., Manning, B. D., and Cantley, L. C. (2003) Targeting the PI3K-Akt pathway in human cancer: Rationale and promise. *Cancer Cell 4*, 257–262.

(4) Wymann, M. P., Bjorklof, K., Calvez, R., Finan, P., Thomast, M., Trifilieff, A., Barbier, M., Altruda, F., Hirsch, E., and Laffargue, M. (2003) Phosphoinositide 3-kinase gamma: a key modulator in inflammation and allergy. *Biochem. Soc. Trans. 31*, 275–280.

(5) Laffargue, M., Calvez, R., Finan, P., Trifilieff, A., Barbier, M., Altruda, F., Hirsch, E., and Wymann, M. P. (2002) Phosphoinositide 3-kinase gamma is an essential amplifier of mast cell function. *Immunity 16*, 441–451.

(6) Finan, P. M., and Thomas, M. J. (2004) PI 3-kinase inhibition: a therapeutic target for respiratory disease. *Biochem. Soc. Trans. 32*, 378–382.

(7) Ihle, N. T., Williams, R., Chow, S., Chew, W., Berggren, M. I., Paine-Murrieta, G., Minion, D. J., Halter, R. J., Wipf, P., Abraham, R., Kirkpatrick, L., and Powis, G. (2004) Molecular pharmacology and antitumor activity of PX-866, a novel inhibitor of phosphoinositide-3-kinase signaling. *Mol. Cancer Ther. 3*, 763–372.

(8) Zhu, T., Gu, J., Yu, K., Lucas, J., Cai, P., Tsao, R., Gong, Y., Li, F., Chaudhary, I., Desai, P., Ruppen, M., Fawzi, M., Gibbons, J., Ayral-Kaloustian, S., Skotnicki, J., Mansour, T., and Zask, A. (2006) Pegylated wortmannin and 17-hydroxywortmannin conjugates as phosphoinositide 3-kinase inhibitors active in human tumor xenograft models. *J. Med. Chem. 49*, 1373–1378.

(9) Holleran, J. L., Egorin, M. J., Zuhowski, E. G., Parise, R. A., Musser, S. M., and Pan, S. S. (2003) Use of high-performance liquid chromatography to characterize the rapid decomposition of wortmannin in tissue culture media. *Anal. Biochem. 323*, 19–25.

(10) Yuan, H., Luo, J., Weissleder, R., Cantley, L., and Josephson, L. (2006) Wortmannin-C20 conjugates generate wortmannin. *J. Med. Chem. 49*, 740–747.

(11) Yuan, H., Barnes, K. R., Weissleder, R., Cantley, L., and Josephson, L. (2007) Covalent reactions of wortmannin under physiological conditions. *Chem. Biol. 14*, 321–328.

(12) Schultz, R. M., Merriman, R. L., Andis, S. L., Bonjouklian, R., Grindey, G. B., Rutherford, P. G., Gallegos, A., Massey, K., and Powis, G. (1995) In vitro and in vivo antitumor activity of

the phosphatidylinositol-3-kinase inhibitor, wortmannin. *Anticancer Res. 15*, 1135–1139.
(13) Lemke, L. E., Paine-Murrieta, G. D., Taylor, C. W., and Powis, G. (1999) Wortmannin inhibits the growth of mammary tumors despite the existence of a novel wortmannin-insensitive phosphatidylinositol-3-kinase. *Cancer Chemother. Pharmacol. 44*, 491–497.
(14) Okada, T., Kawano, Y., Sakakibara, T., Hazeki, O., and Ui, M. (1994) Essential role of phosphatidylinositol 3-kinase in insulin-induced glucose transport and antilipolysis in rat adipocytes. Studies with a selective inhibitor wortmannin. *J. Biol. Chem. 269*, 3568–3573.
(15) Clarke, J. F., Young, P. W., Yonezawa, K., Kasuga, M., and Holman, G. D. (1994) Inhibition of the translocation of GLUT1 and GLUT4 in 3T3-L1 cells by the phosphatidylinositol 3-kinase inhibitor, wortmannin. *Biochem. J. 300*, 631–635.
(16) Evans, J. L., Honer, C. M., Womelsdorf, B. E., Kaplan, E. L., and Bell, P. A. (1995) The effects of wortmannin, a potent inhibitor of phosphatidylinositol 3-kinase, on insulin-stimulated glucose transport, GLUT4 translocation, antilipolysis, and DNA synthesis. *Cell Signalling 7*, 365–376.
(17) Yano, H., Nakanishi, S., Kimura, K., Hanai, N., Saitoh, Y., Fukui, Y., Nonomura, Y., and Matsuda, Y. (1993) Inhibition of histamine secretion by wortmannin through the blockade of phosphatidylinositol 3-kinase in RBL-2H3 cells. *J. Biol. Chem. 268*, 25846–25856.
(18) Kitani, S., Teshima, R., Morita, Y., Ito, K., Matsuda, Y., and Nonomura, Y. (1992) Inhibition of IgE-mediated histamine release by myosin light chain kinase inhibitors. *Biochem. Biophys. Res. Commun. 183*, 48–54.
(19) Baggiolini, M., Dewald, B., Schnyder, J., Ruch, W., Cooper, P. H., and Payne, T. G. (1987) Inhibition of the phagocytosis-induced respiratory burst by the fungal metabolite wortmannin and some analogues. *Exp. Cell Res. 169*, 408–418.
(20) Arcaro, A., and Wymann, M. P. (1993) Wortmannin is a potent phosphatidylinositol 3-kinase inhibitor: The role of phosphatidylinositol 3,4,5-triphosphate in neutrophil responses. *Biochem. J. 296*, 297–301.
(21) Jackson, J. K., Lauener, R., Duronio, V., and Burt, H. M. (1997) The involvement of phosphatidylinositol 3-kinase in crystal induced human neutrophil activation. *J. Rheumatol. 24*, 341–348.
(22) Yee, M. C., Fas, S. C., Stohlmeyer, M. M., Wandless, T. J., and Cimprich, K. A. (2005) A cell-permeable, activity-based probe for protein and lipid kinases. *J. Biol. Chem. 280*, 29053–29059.
(23) Liu, Y., Shreder, K. R., Gai, W., Corral, S., Ferris, D. K., and Rosenblum, J. S. (2005) Wortmannin, a widely used phosphoinositide 3-kinase inhibitor, also potently inhibits mammalian polo-like kinase. *Chem. Biol. 12*, 99–107.
(24) Thelen, M., Wymann, M. P., and Langen, H. (1994) Wortmannin binds specifically to 1-phosphatidylinositol 3-kinase while inhibiting guanine nucleotide-binding protein-coupled receptor signaling in neutrophil leukocytes. *Proc. Natl. Acad. Sci. U.S.A. 91*, 4960–4964.
(25) Walker, E. H., Pacold, M. E., Perisic, O., Stephens, L., Hawkins, P. T., Wymann, M. P., and Williams, R. L. (2000) Structural determinants of phosphoinositide 3-kinase inhibition by wortmannin, LY294002, quercetin, myricetin, and staurosporine. *Mol. Cell 6*, 909–919.
(26) Yu, K., Lucas, J., Zhu, T., Zask, A., Gaydos, C., Toral-Barza, L., Gu, J., Li, F., Chaudhary, I., Cai, P., Lotvin, J., Petersen, R., Ruppen, M., Fawzi, M., Ayral-Kaloustian, S., Skotnicki, J., Mansour, T., Frost, P., and Gibbons, J. (2005) PWT-458, a novel pegylated-17-hydroxywortmannin, inhibits phosphatidylinositol 3-kinase signaling and suppresses growth of solid tumors. *Cancer Biol. Ther. 4*, 538–545.
(27) Ihle, N. T., Paine-Murrieta, G., Berggren, M. I., Baker, A., Tate, W. R., Wipf, P., Abraham, R. T., Kirkpatrick, D. L., and Powis, G. (2005) The phosphatidylinositol-3-kinase inhibitor PX-866 overcomes resistance to the epidermal growth factor receptor inhibitor gefitinib in A-549 human non-small cell lung cancer xenografts. *Mol. Cancer Ther. 4*, 1349–1357.
(28) Petersen, N. O. (1983) A new fluorescent derivative of amphotericin B: synthesis, characterization and application in fluorescence photobleaching. *Spectroscopy (Amsterdam) 2*, 408–414.
(29) Creemer, L. C., Kirst, H. A., Vlahos, C. J., and Schultz, R. M. (1996) Synthesis and in vitro evaluation of new wortmannin esters: potent inhibitors of phosphatidylinositol 3-kinase. *J. Med. Chem. 39*, 5021–5024.
(30) Yuan, H., Luo, J., Field, S., Weissleder, R., Cantley, L., and Josephson, L. (2005) Synthesis and activity of C11-modified wortmannin probes for PI3 kinase. *Bioconjugate Chem. 16*, 669–675.
(31) Gray, A., Olsson, H., Batty, I. H., Priganica, L., and Peter Downes, C. (2003) Nonradioactive methods for the assay of phosphoinositide 3-kinases and phosphoinositide phosphatases and selective detection of signaling lipids in cell and tissue extracts. *Anal. Biochem. 313*, 234–245.
(32) Papazisis, K. T., Geromichalos, G. D., Dimitriadis, K. A., and Kortsaris, A. H. (1997) Optimization of the sulforhodamine B colorimetric assay. *J. Immunol. Methods 208*, 151–158.
(33) Ngan, V. K., Bellman, K., Hill, B. T., Wilson, L., and Jordan, M. A. (2001) Mechanism of mitotic block and inhibition of cell proliferation by the semisynthetic Vinca alkaloids vinorelbine and its newer derivative vinflunine. *Mol. Pharmacol. 60*, 225–232.
(34) Giner, J. L., Kehbein, K. A., Cook, J. A., Smith, M. C., Vlahos, C. J., and Badwey, J. A. (2006) Synthesis of fluorescent derivatives of wortmannin and demethoxyviridin as probes for phosphatidylinositol 3-kinase. *Bioorg. Med. Chem. Lett. 16*, 2518–2521.
(35) Wipf, P., Minion, D. J., Halter, R. J., Berggren, M. I., Ho, C. B., Chiang, G. G., Kirkpatrick, L., Abraham, R., and Powis, G. (2004) Synthesis and biological evaluation of synthetic viridins derived from C(20)-heteroalkylation of the steroidal PI-3-kinase inhibitor wortmannin. *Org. Biomol. Chem. 2*, 1911–1920.
(36) Brunn, G. J., Williams, J., Sabers, C., Wiederrecht, G., Lawrence, J. C., Jr., and Abraham, R. T. (1996) Direct inhibition of the signaling functions of the mammalian target of rapamycin by the phosphoinositide 3-kinase inhibitors, wortmannin and LY294002. *EMBO J. 15*, 5256–5267.
(37) Hartley, K. O., Gell, D., Smith, G. C., Zhang, H., Divecha, N., Connelly, M. A., Admon, A., Lees-Miller, S. P., Anderson, C. W., and Jackson, S. P. (1995) DNA-dependent protein kinase catalytic subunit: a relative of phosphatidylinositol 3-kinase and the ataxia telangiectasia gene product. *Cell 82*, 849–856.

BC7002204

Layered Inorganic/Enzyme Nanohybrids with Selectivity and Structural Stability upon Interacting with Biomolecules

Guo-Jing Chen, Ming-Cheng Yen, Jen-Ming Wang, Jiang-Jen Lin,† and Hsin-Cheng Chiu*

Department of Chemical Engineering, National Chung Hsing University, Taichung 402, Taiwan. Received June 20, 2007; Revised Manuscript Received November 1, 2007

Effective intercalation of protein molecules within the galleries of montmorillonites can be achieved via simple space enlarging and exchange processes while retaining the native conformation of the guest protein and the multilayered structure of the bioinert host plates. The capacity of accommodating protein molecules in the galleries can be markedly larger than that governed by the Langmuir-type adsorption of protein molecules on the external surfaces of particles. The basal spacing in the multilayered structure of clay is abruptly enlarged when the extent of protein intercalation increases to a critical point. Beyond this critical point, the nanohybrids show well-preserved catalytic activity in hydrolyzing small substrates while establishing a barrier to interactions with large biomacromolecules. Furthermore, the structural stability of the inorganic/organic nanohybrids is enhanced such that neither exchange of biomolecules nor exfoliation of layered clay particles occurs when exposed to other proteins. The results indicate that, through the benign accommodation of protein species between the inorganic platelets, this nanoscaled manipulation of protein functions can be highly useful in developing new inorganic/enzyme nanohybrids for protein therapeutics and tissue engineering.

INTRODUCTION

Inorganic/organic nanohybrids formed via accommodating bioactive macromolecules inside the galleries of inorganic materials with layered structure have found a variety of potential applications in biomedical and biochemical fields. For example, inorganic layered double hydroxide (LDH)/DNA hybrids can facilitate the endocytic uptake of DNA fragments and their intracellular release from the hybrids by complete dissolution of LDH in the acidic environment of endosomes (*1, 2*). Biologically active proteins such as enzymes incorporated in synthetic layered α-zirconium phosphate, while retaining their conformation and activity, have been found capable of acting as nanoscale biocatalytic systems (*3–9*). Mutual interactions between guest biomolecules and inorganic host plates occur mainly by electrostatic attraction (*10, 11*). Small DNA fragments and antisense oligonucleotides can be readily embedded within the galleries of cationic LDH layered structures by either direct anionic exchange or coprecipitation in the in situ formation of LDH layers (*1, 2*). The hybrids prepared from the latter approach can accommodate double-stranded DNAs over a wide range of molecular sizes (*2*). Similarly, owing to the three-dimensional size, large globular proteins can be successfully embedded within inorganic layered hosts only by self-assembly with synthetic exfoliated plates in aqueous phase into hybrids of double- or triple-layered structure (*3–8*). Hybrids with elevated stacking in the layered structure that act as highly efficient bioreactors have not been attainable due to the instability problem encountered. On the other hand, montmorillonite (MMT), one of the most abundant smectite clays, consists of aluminosilicate plates with dimensions of ca. $100 \times 100 \times 1$ nm^3 in each plate piling in a primary stack of ca. 8−10 layers through intensive charge attraction (*12*). Therefore, it is easily realized that, by taking the advantage of the high aspect ratio surface area of each layer within a multilayered structure, MMT may serve as a benign host to provide spacious sites for protein accommodation. Unfortunately, the basal spacing in multilayers of MMT homoionic, for example, to Na^+ (Na^+-MMT) is 1.2 nm. With the thickness of each layer equal to 1 nm, the interlayer free space is 0.2 nm. Interactions of the multilayered particles with such narrow galleries and most large globular proteins are inevitably restricted to their external bulk surfaces. The incorporation of guest biomolecules in the clay galleries is therefore severely limited in variety and adsorption/intercalation capacity.

In this study, inorganic/enzyme hybrids were obtained by a simple exchange process of the protein molecules with an originally intercalated linear synthetic polymer within the spatially enlarged galleries of MMT. Taking advantages of its globular structure and catalytic activity in hydrolyzing both low molecular weight and macromolecular substrates, α-chymotrypsin (CHT) was employed as a model protein intercalant. In addition to detailed characterization of morphology and structure of the hybrids, the selectivity and stability of the hybrids regarding interactions with biomolecules of varying sizes was studied.

EXPERIMENTAL SECTION

Materials. CHT (EC 3.4.21.2, type II, from bovine pancreas), bovine serum albumin (BSA), catalase (from bovine liver), *N*-benzoyl-L-tyrosine *p*-nitroanilide (Bz-Tyr-NAp), and *N*-succinyl-L-phenylalanine *p*-nitroanilide (Su-Phe-NAp) were purchased from Sigma. α,ω-Diaminopoly(oxypropylene) (POP, Mw 2000 g/mol) was obtained from Aldrich. Na^+-MMT with a cationic exchange capacity (CEC) of 1.15 mequiv/g was obtained from Kunimine. Deionized water used in the protein intercalation, and buffer preparation was prepared from Milli-Q Synthesis (Millipore). All other chemicals were reagent grade and used as received.

Inorganic/Enzyme Hybrid Preparation. Preparation of the inorganic/enzyme hybrids was carried out first by spatial enlargement of the galleries of MMT via cationic exchange of

* To whom correspondence should be addressed. E-mail: hcchiu@dragon.nchu.edu.tw (H.-C. Chiu).

† Current address of J. J. Lin: Institute of Polymer Science and Engineering, National Taiwan University, Taipei, Taiwan 106.

10.1021/bc700224q CCC: $40.75 © 2008 American Chemical Society
Published on Web 12/11/2007

POP with sodium counterions within the galleries of MMT, followed by exchange of POP with the CHT molecules. The POP intercalation was performed as described previously (*13*). In brief, to a Na^+-MMT slurry in deionized water was added the aqueous solution of POP/HCl (1:1 in mole ratio) to a stoichimetric ratio of POP/CEC at 1.0 with stirring at 80 °C for 24 h. The inorganic/organic weight ratio of the MMT/POP hybrids was determined to be 31/69 by thermal gravimetric analysis. The mechanism of the POP intercalation and structure of MMT/POP hybrids have been studied in detail previously (*13–15*). The intercalation/adsorption of CHT on MMT/POP and Na^+-MMT particles, respectively, was performed by the addition of a prescribed amount of CHT in the aqueous clay suspension solutions (4.7 mg of Na^+-MMT in 15 mL phosphate buffer (pH 7.0, I 0.01 M) or 15.0 mg/15 mL of MMT/POP, equivalent to 4.7 mg of clay in 15 mL of the aqueous solution) at 4 °C for 12 h with stirring. The inorganic/enzyme composite particles were subjected repeatedly to centrifugation (10 000 g at 4 °C for 30 min) and resuspension with phosphate buffer and deionized water until protein in the supernatant was no longer detected. The products were then collected by lyophilization and stored at −20 °C for further characterization of their structure and enzymatic activity. The extent of the protein intercalation/adsorption was determined by measuring the protein concentration in the combined supernatants via the Bradford protein assay (Bio-Rad protein assay reagent) at 596 nm. The intercalation/adsorption isotherms were established by plotting the amount of CHT intercalated/adsorbed per gram of clay (μmol/g clay) versus the equilibrium CHT concentration (μM) in aqueous solution, i.e., the protein concentration in the supernatant after the equilibrium adsorption. The released amount of POP from the MMT/POP composite particles in protein intercalation was estimated by gel permeation chromatography (GPC) measurements (Superose 12, FPLC, GE-Pharmacia, the eluent: Tris buffer, 0.4 mL/min, RI detection) of the POP concentration in the supernatant of the first centrifugation.

Structural and Morphologic Characterization. The X-ray powder diffraction measurements of the MMT/CHT hybrids were performed using a powder diffractometer (Mac Science MXP-18) with a Cu target at 30 kV and 20 mA. The basal spacing was determined from their reflections (00l, $l = 1, 2, 3$, etc.) using the Bragg's law ($l\lambda = 2d \sin\theta$). For the atomic force microscopic (AFM) image analyses, the sample was suspended in deionized water (10^{-6} mg/mL) and spin-coated on the surfaces of glass substrate. The measurement was performed with scanning probe microscopy (SPM, dynamic force mode, Seiko, SPI 3800N) using rectangular Si cantilevers with 129 kHz resonant frequency and 12 N/m spring constant (Seiko, SI-DF20).

Enzymatic Activity Characterization. The hybrids were first tested for activity in catalytic hydrolysis of two small substrates, namely, Bz-Tyr-NAp and Su-Phe-NAp. The substrate stock solutions were prepared in DMSO at a concentration of 5.0×10^{-3} M. The reaction was performed in Tris buffer (0.08 M Tris + 0.01 M $CaCl_2$, pH 8.0) at 37 °C with a DMSO content less than 5.0% (v/v) of the incubation mixtures. The enzyme concentration in the reaction solution was 2.0×10^{-7} M, unless stated otherwise. The release of *p*-nitroaniline was monitored at 410 nm, and its molar absorptivity of 8800 M^{-1} cm^{-1} at this wavelength was employed to calculate its concentration over time (*16*). The kinetic parameters were obtained according to the Michaelis–Menten kinetic model, and each set of kinetic measurements was performed in duplicate with eight different substrate concentrations.

For the activity of the hybrids toward biomacromolecules, reactions were carried out with the concentrations of substrates (BSA and catalase, respectively) of 5 mg/mL and of CHT 2×10^{-5} M in Tris buffer at 37 °C. The MMT/CHT hybrids with a degree of CHT intercalation of 176 μmol/g clay were used. The extents of cleavage at different time intervals were evaluated in terms of the reduction (%) of the molecular peak of the substrates with respect to that at $t = 0$ in the GPC measurements under UV detection at 280 nm (*16*).

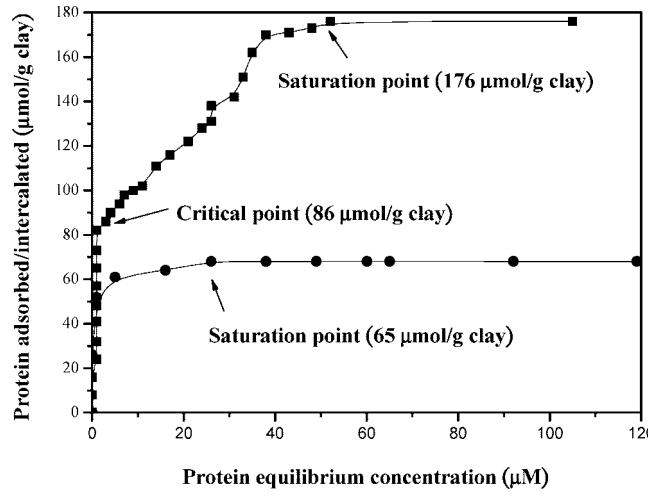

Figure 1. Adsorption/intercalation isotherms of CHT on the native Na^+-MMT particles (●) and MMT/POP hybrids (■) at 4 °C.

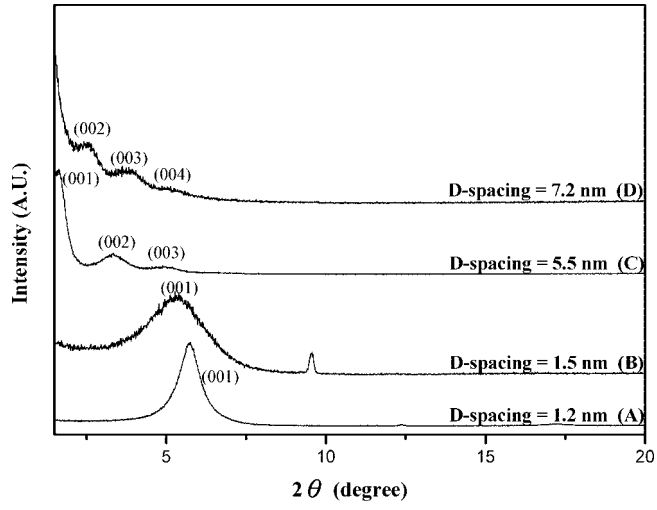

Figure 2. Powder XRD patterns of the native Na^+-MMT particles before (A) and after (B) CHT adsorption (65 μmol/g clay) and of the MMT/POP hybrids before (C) and after (D) the CHT intercalation/adsorption (MMT/CHT; 176 μmol/g clay).

RESULTS AND DISCUSSION

The intercalation/adsorption of CHT on MMT/POP particles significantly enhances the amount of CHT incorporated into the particles to 176 μmol/g clay (the saturation point) in comparison with that of only 65 μmol/g clay on native Na^+-MMT particles, as evidenced by two different adsorption isotherms in Figure 1. The adsorption behavior of CHT on Na^+-MMT particles is described well by the ideal Langmuir adsorption model as shown in the Supporting Information. In addition, after the CHT adsorption, the basal spacing of the clay particles was only slightly enlarged from 1.2 to ca. 1.5−2.2 nm by X-ray diffraction characterization (Figure 2). Apparently, the narrow interlayer space of Na^+-MMT particles (0.2 nm) fails to accommodate the globular CHT molecules with an original dimension of ca. $5 \times 6 \times 6$ nm^3, and the adsorption of protein species occurs to

a significant extent through the electrostatic interactions with the external particle surfaces (*10, 11, 17*). On the other hand, owing to the enlarged basal spacing of the clay layered particles by POP intercalation from 1.2 to ca. 5.5 nm (Figure 2), the complex isotherm of interacting CHT with the MMT/POP nanohybrids exhibits two different phases with respect to the simple Langmuir-type adsorption of CHT on Na^+-MMT. In the first phase, where the adsorption/intercalation amount is less than 86 μmol/g, the protein molecules are significantly adsorbed on the external surfaces of the multilayered particles. With only few CHT molecules being intercalated into each interlayer gallery, the basal spacing originally expanded by POP was slightly reduced (Supporting Information) due to the significant release of POP without sufficient incorporation of CHT. At an adsorption/intercalation extent of 80 μmol/g clay, it was observed that more than 40% of the POP molecules originally intercalated were released and the basal spacing was decreased from the initial 5.5 to 5.2 nm. Further expansion of the basal spacing to 7.2 nm was accomplished (Figure 2) by the enzyme entrapment amounting to 86 μmol/g (referred to as the critical point signifying the onset of the second phase) with the initial enzyme concentration in slurry at 440 μM. The basal spacing thereafter remained at ca. 7.2 nm, while the protein intercalation continued to proceed until equilibrium saturation was reached (Supporting Information). The expanded interlayer space of MMT/CHT at 6.2 nm is consistent with the molecular dimension of CHT, but significantly larger than those (with the basal spacing enlarged to a range of only 1.5−3.0 nm) by external surface adsorption and partial intercalation of various large protein molecules in previous reports (*18–21*). Herein, the extents of CHT (65 μmol/g clay at the saturation point) adsorbed on the surfaces of external plates of the Na^+-MMT particles and partially intercalated within their galleries were estimated based upon the saturation adsorption/intercalation of CHT at 176 μmol/g clay via MMT/POP. Assuming that each clay particle consists of 10 aluminosilicate plates and the CHT molecules are adsorbed/intercalated evenly on each of the external plate surfaces (×2) and within each of galleries (×9) of individual particles via MMT/POP, the enzyme adsorption on the external plate surfaces of particles amounts to ca. 32 μmol/g clay. With the same amount (32 μmol/g) of CHT adsorbed on the external plate surfaces, the extent of the protein intercalation within the Na^+-MMT galleries is only 33 μmol/g with respect to that of 144 μmol/g via MMT/POP. It has been reported that partial intercalation of large protein molecules takes place primarily in the outer regions of the interlayer spaces of native MMT particles, which, in agreement with our findings, results in only a small shift to higher basal spacing and a broadening of the d_{001} peak in the XRD measurements (*21*). Since the protein intercalation within Na^+-MMT occurs only in the outer regions of the galleries, herein it is referred to as a portion of the external particle surface adsorption for convenience. It is noteworthy that the MMT/POP particles originally in an extensively aggregated state at ambient temperature due to the inherent lower critical solution temperature (ca. 16−19 °C) of POP in water became well-dispersed at 4 °C, at which the clay structure became accessible to the protein intercalation and the biological functions of the protein were well-preserved. After the intercalation of the protein and release of POP, the new nanohybrids became easily dispersed in aqueous phase at ambient temperature. The SPM characterization of the MMT/CHT nanohybrids beyond the critical point shows that the hybrids were expanded to ca. 62−68 nm in height (Figure 3), as compared to only ca. 15−22 nm of Na^+-MMT particles with the maximum external surface adsorption of CHT (Supporting Information). With the basal spacing of 7.2 nm and the protein adsorption on the particle external surfaces taken into account,

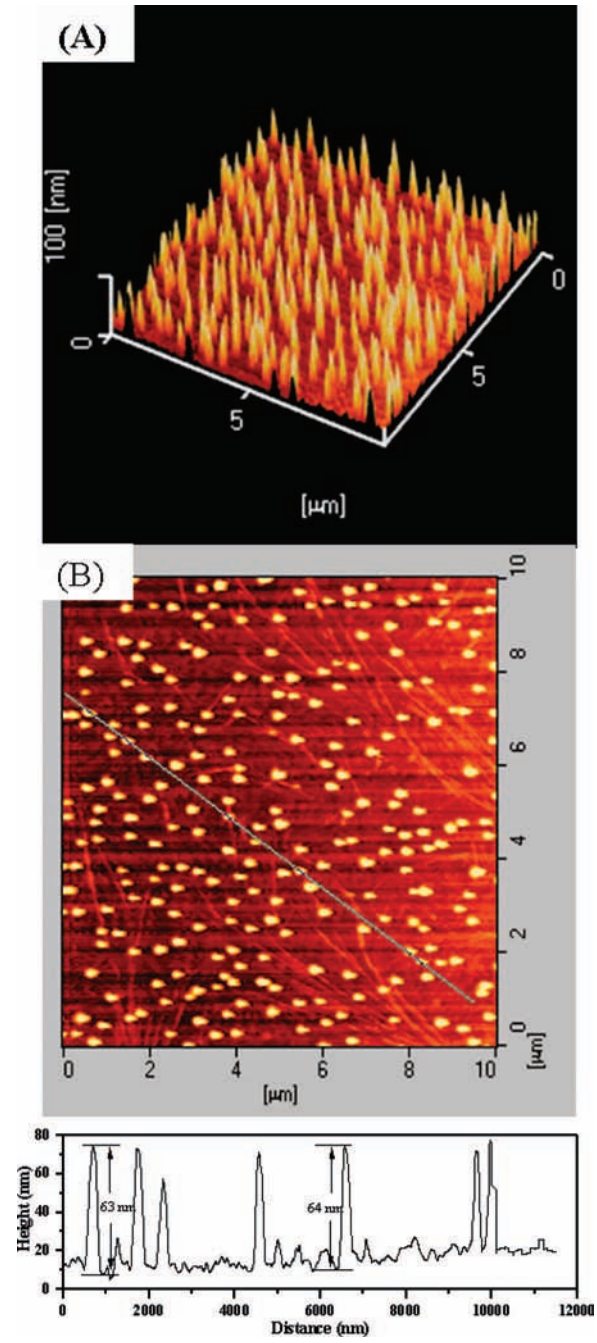

Figure 3. (A) Three dimensional AFM image and (B) the SPM topographical image of the MMT/CHT hybrids (176 μmol CHT/g clay) with lateral heights of ca. 62−68 nm.

the MMT/CHT nanohybrids are piling into ca. 8–10 platelets in a stack per particle. With further examination of the native Na^+-MMT and composite MMT/POP particles by SPM, the observations of the particle heights (ca. 11−13 and 40−45 nm, respectively, as shown in the Supporting Information) is in good agreement with the structure of 8−10 layers in a stack. Obviously, neither the intercalation of POP in Na^+-MMT nor exchange of the enzyme from the MMT/POP complexes leads to exfoliation of the clay multilayered structure.

Figure 4 illustrates the dependence of the enzyme activity in cleaving a small substrate, Bz-Tyr-NAp, on the extents of CHT intercalated and adsorbed on MMT particles (via MMT/POP and Na^+-MMT), respectively, at constant enzyme (2×10^{-7} M) and substrate (1.67×10^{-4} M) concentrations at 37 °C for 1 h. For comparison, free CHT has shown the capability of catalyzing the hydrolysis of the substrate to 78% under identical

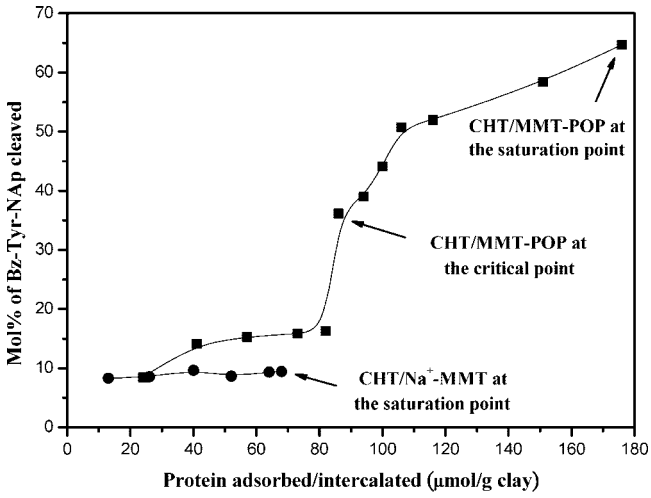

Figure 4. Dependence of the catalytic activity of CHT in hydrolyzing Bz-Tyr-NAp (mol %) on the extents of CHT adsorbed on Na^+-MMT particles (●) and intercalated within MMT/CHT hybrids (■). The reactions were carried out with a substrate concentration of 1.67×10^{-4} M at 37 °C for 1 h.

Table 1. Kinetic Parameters of the Cleavage of Two Small Substrates by Free CHT and MMT/CHT Hybrids[a]

Bz-Tyr-NAp	k_{cat} (s^{-1})	K_M (M) × 10^4	k_{cat}/K_M (s^{-1} M^{-1})
free CHT	0.437 ± 5.3%	1.60 ± 11.0%	2731 ± 10.0%
CHT/MMT-POP	0.422 ± 4.9%	3.15 ± 4.5%	1340 ± 2.3%
CHT/Na^+-MMT	0.288 ± 6.9%	3.70 ± 5.0%	778 ± 7.7%
Su-Phe-NAp	k_{cat} (s^{-1})	K_M (M) × 10^4	k_{cat}/K_M (s^{-1} M^{-1})
free CHT	0.182 ± 1.1%	7.00 ± 2.9%	257 ± 1.0%
CHT/MMT-POP	0.185 ± 3.2%	15.20 ± 5.8%	120 ± 4.3%
CHT/Na^+-MMT	0.084 ± 6.3%	17.20 ± 8.0%	49 ± 7.2%

[a] The extents of CHT intercalated in the MMT/CHT hybrids were 176 μmol/g clay and of adsorbed on external Na^+-MMT surfaces 65 μmol/g clay.

conditions. Independent of the extent of CHT adsorbed on the Na^+-MMT external particle surfaces, the enzyme shows reduced but constant activity. On the other hand, the MMT/CHT hybrids first show relatively low activity at the extents of the CHT intercalation below the critical point (86 μmol/g clay), where most CHT molecules reside on the external particle surfaces, and then abruptly enhanced activity beyond the critical point. Apparently, the spatially enlarged host galleries are essential for the enzyme to preserve its conformation and activity. The enzymatic activity continued to increase thereafter with increasing ratio of CHT embedded in the galleries to that adsorbed on the external particle surfaces until saturation of the CHT intercalation was achieved. Based upon the Michaelis–Menten kinetic theory, the kinetic parameters of the MMT/CHT hybrids in hydrolyzing two small substrates are listed in Table 1. The intercalated enzyme exhibits essentially identical catalytic activity (k_{cat}) to its free counterpart. However, the Michaelis constants (K_M) in interaction of both substrates increase significantly compared to the free enzyme. This can be ascribed to the reduced rate constant (k_1) in forming the enzyme/substrate complexes due to more retarded diffusion of the nonpolar substrates within the hybrids than that in bulk aqueous phase. In contrast, the enzyme suffers a dramatic reduction in activity (as signified by both the decreased k_{cat} and the increased K_M) when they are immobilized on the external particle surfaces of Na^+-MMT. The fully preserved activity of the intercalated CHT molecules within the clay galleries can be accounted for by the salt-bridge effect resulting from the electrostatic interactions of the enzyme molecules with negatively charged platelets of both top and bottom sides on stabilizing the native conformation of the protein in a manner similar to that of the engineered proteins (*4, 22*). Confinement of the enzyme molecules within the rigid clay galleries may additionally protect the protein from unfolding by steric hindrance (*23*). The protein conformation can also be partially stabilized by reducing the activity of water molecules in the galleries and therefore reducing the extents of hydration of the nonpolar groups of the intercalated proteins and of dehydration of their polar groups, which is suggested to be essential for protein unfolding (*4, 24*). On the other hand, owing to the absence of the electrostatic interactions with both the top and bottom platelet surfaces, the enzyme molecules, when being adsorbed on the Na^+-MMT external plate surfaces, can be more easily denatured. In addition, it is expected that the conformation of the CHT molecules intercalated in the outer regions of the Na^+-MMT galleries be largely perturbed due to the compressive effects of the inorganic platelets with the narrow basal spacing of 1.5−2.2 nm. Similar results on the reduction of catalytic activity of the enzymes upon immobilization on MMT surfaces have been observed and ascribed to the perturbation of protein conformation and modification of their active centers, mostly using the FTIR measurements (*10, 19–21, 25, 26*).

Taking advantage of CHT as a protease, the clay/enzyme nanohybrids were tested for their residual activity toward Bz-Tyr-NAp after preincubating the clay/enzyme suspensions alone for 1 h at varying temperatures. Figure 5A shows the relative activity of CHT in varying forms (the free, externally adsorbed, and intercalated, respectively) after preincubation at different temperatures to that preincubated at 5 °C as a function of the extent of intercalation (via MMT/POP) or external particle surface adsorption (via Na^+-MMT) at a constant enzyme concentration (2.0×10^{-7} M) in solutions. Figure 5B emphasizes the effects of the enzyme concentrations (1.0×10^{-6} and 2.0×10^{-7} M) in solutions, while the extent of CHT intercalated (100 μmol/g) or adsorbed (41 μmol/g) was kept unchanged. With increasing enzyme concentration and preincubation temperature (up to 55 °C, the temperature for the optimal activity of CHT, both the free and intercalated), the degree of reduction in the relative activity of the free CHT increases primarily as a result of the proteolytic action on CHT molecules themselves (self-digestion). In contrast, for the CHT adsorbed on the external surfaces of Na^+-MMT particles, the activity profile upon preincubation was independent of both the enzyme concentration and the adsorption extent, strongly indicative of the lack of significant self-interactions and -digestion of the enzyme molecules. The observed temperature effect on the reduction in the activity of CHT adsorbed on the external particle surfaces is attributed to thermally facilitated protein denaturation on the external surfaces of inorganic particles. On the other hand, the residual activity of the intercalated CHT is influenced markedly by both the preincubation temperature and the intercalation extent at a constant enzyme concentration, but is insensitive to change in the enzyme concentration in solutions for the MMT/CHT nanohybrids of a certain extent of enzyme intercalation. Similar to free CHT, the change of the relative activity is caused significantly by self-digestion, but occurs within the nanohybrids exclusively. Strong dependence of self-cleavage on the intrinsic concentration of enzyme within the nanohybrids was hence observed. However, one of the prerequisites for the protease molecules to self-digest so extensively in their medium relies more likely on their ability to migrate freely to interact with each other. Owing to negative charges evenly distributed throughout the plate interior surfaces, enzyme molecules residing in the galleries retain not only the native structure but also the mobility in sliding in a two-dimensional manner within the confinement without deterioration of the electrostatic attractions. The difference in the concentrations between the intercalated CHT within the nanohybrids and the

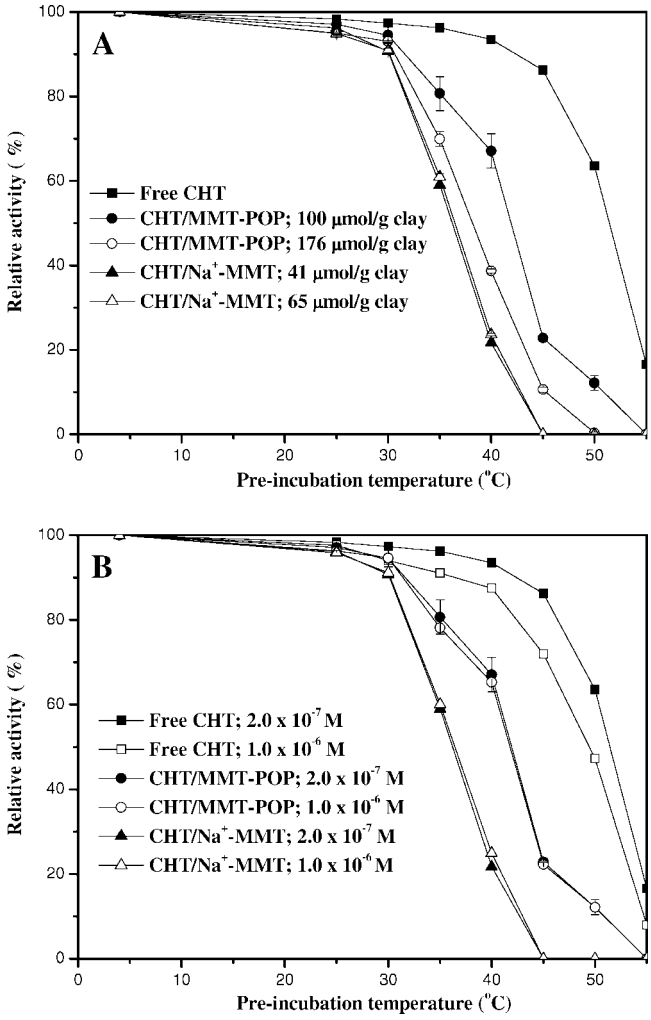

Figure 5. Effects of the preincubation of the aqueous solution of CHT in the free, intercalated (via MMT/POP hybrids), and adsorbed (on Na^+-MMT particles) forms at varying temperatures on relative residual activity in hydrolyzing Bz-Tyr-NAp to that of the preincubation at 5 °C as functions of (A) the extents of CHT intercalated and adsorbed at a constant enzyme concentration (2.0×10^{-7} M) and (B) of the enzyme concentration with the constant extents of intercalation at 100 μmol/g clay (via MMT/POP) and of external adsorption at 41 μmol/g clay (Na^+-MMT), respectively.

free counterpart in aqueous solution also leads to varying degrees of self-digestion and therefore the residual activity. It should be noted that the self-digestion occurs usually by proteases only and is not observed from nonproteolytic enzymes, including those employed for protein therapeutics and biomedical applications.

The interaction of CHT within the hybrids with biomacromolecules was characterized in terms of the extent of proteolytic cleavage of protein–substrates (BSA and catalase, respectively) by incubating with the MMT/CHT particles in aqueous solutions. The degradation was evaluated by monitoring the change in the molecular peaks of protein–substrates from the GPC measurements with time. Figure 6 shows that catalase was only degraded slightly (<18% in the molecular cleavage) by the MMT/CHT nanohybrids within an incubation time interval of 72 h while extensive proteolysis (>92%) occurred by the free CHT. Similarly, BSA, being employed as the other macromolecular substrate, was severely restricted to interacting with the CHT molecules embedded within the galleries of the MMT particles in comparison with its rapid digestion by the free enzyme (Supporting Information). The restriction of interacting the intercalated CHT molecules with biomacromolecular substrates is caused primarily by both the steric hindrance of the inorganic host plates in the layered structure and the limited free space remaining within the host galleries in addition to the CHT occupation. The observed proteolytic action of the MMT/CHT hybrids on both catalase and BSA is most probably due to the accessibility of the CHT molecules that reside on the external particle surfaces (including the outer regions of the clay galleries) to interaction with the substrates. Morphologic examination of the MMT/CHT nanohybrids after incubating with catalase by SPM demonstrates that the lateral heights of

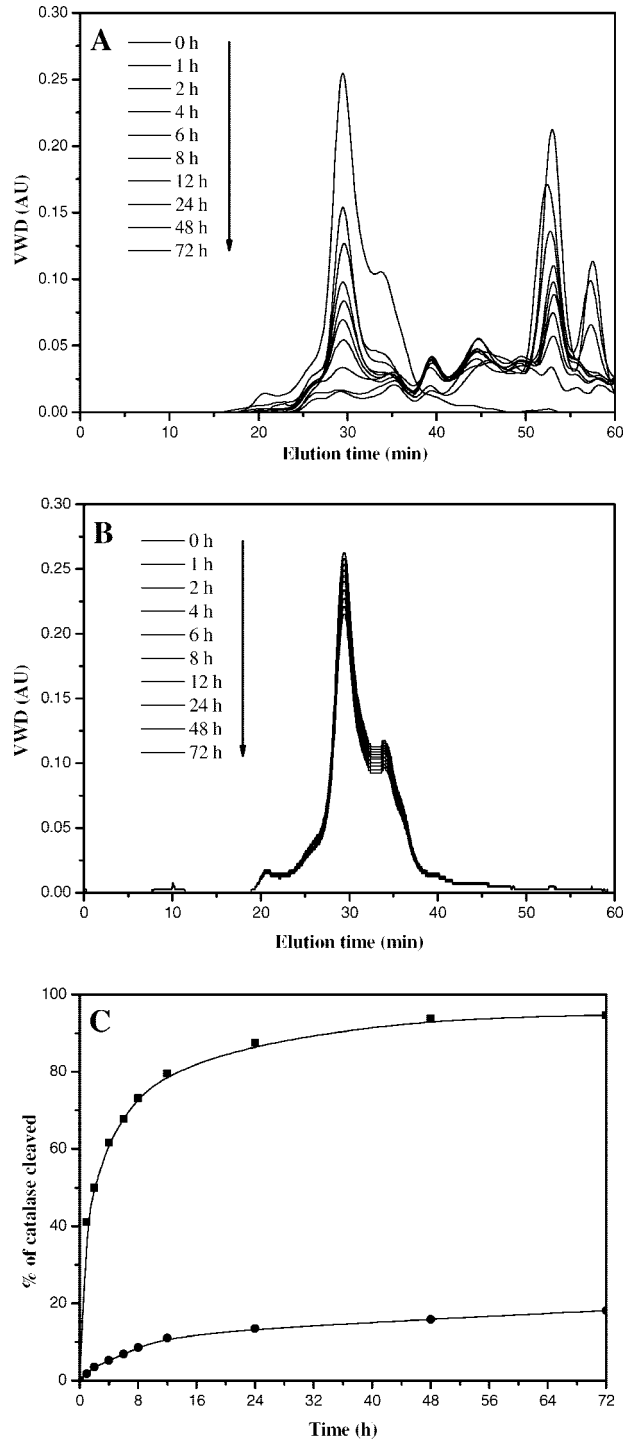

Figure 6. GPC spectra of catalase as a function of the incubation time with (A) the free CHT and (B) MMT/CHT hybrids (176 μmol/g clay), respectively. (C) Cleavage extents of catalase in terms of the decreases (%) of the molecular peak height of catalase by proteolytic action of the free CHT (■) and MMT/CHT hybrids (●) with time.

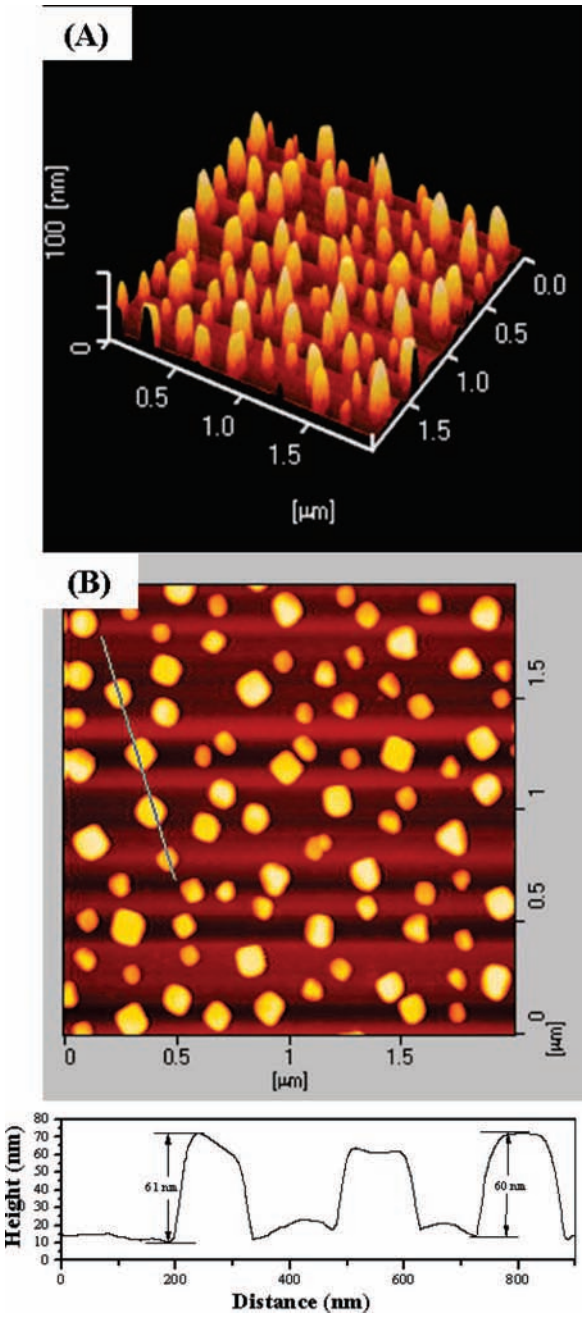

Figure 7. (A) Three-dimensional AFM image and (B) the SPM topographical image of the MMT/CHT hybrids (176 μmol/g clay) with lateral heights of ca. 60∼70 nm after incubation with catalase for 72 h.

the nanohybrids in the range 60−70 nm were essentially the same as those prior to the incubation reactions (Figure 7). Similar observation was obtained from the incubation of the hybrids with BSA (Supporting Information). The results further suggest that neither exfoliation of the clay multilayered structure nor exchange with the originally intercalated CHT occur by catalase and BSA in approaching the MMT/CHT hybrids, although the latter has been found capable of being intercalated in the galleries of MMT/POP via cationic exchange with POP (*27*). It has been confirmed that the expansion of the basal spacing from 1.2 to 5.5 nm with the POP intercalation to a critical extent is supported mainly by significant hydrophobic segregation of the polymer strains in aqueous medium within the gallery (*15*). The different fates of BSA while in contact with MMT/POP and MMT/CHT hybrids suggest that the stability of the inorganic layered structure becomes enhanced by accommodating protein molecules within the galleries due to the more extensive electrostatic attractions with negatively charged platelets on both top and bottom sides and the more compact hydrophobic association of the protein globular structure in nature. Therefore, it is not surprising that the CHT molecules originally intercalated within the clay multilayered structure underwent conformational change by placing the lyophilized hybrids in organic solvents, such as DMSO, leading to inactivation of the enzyme molecules and exfoliation of the clay layered structure (data not shown).

The MMT/CHT nanohybrids reported herein have shown similarity in several aspects to PEG−enzyme adducts. The enzyme molecules residing within the galleries of the MMT particles most likely retain their structure in the native conformation. However, the enzyme functions are tailored such that the enzymatic activity toward small substrates can be fully preserved and interactions with the approaching biomacromolecules effectively inhibited. On the other hand, the hybrids in nanoscale render themselves particularly useful when fixation or immobilization is strongly preferred. This nanoscaled manipulation of enzyme functions through a clay accommodation and immobilization can be a valuable approach whereby hybrids of therapeutically active enzymes with preference for activity only in small substrates can possibly be developed as new therapeutics or bioreactors in tissue engineering, taking advantage of their easy fixation and reduced interactions with biomacromolecules, including those responsible for proteolytic action and immune response.

CONCLUSIONS

The MMT/enzyme nanohybrids obtained by a facile exchange process of the enzyme molecules with POP in space-enlarged galleries of MMT/POP have shown the capability of retaining the layered structure of the inorganic host and enzymatic activity of the guest molecules in hydrolyzing small substrates while rejecting interactions with large biomacromolecules. The capacity in accommodating protein within clay galleries is much larger than that by only adsorption on the external surfaces of Na^+-MMT particles. In addition, the stability of the layered structure of MMT/CHT nanohybrids can be further enhanced as compared to MMT/POP, leading to the observation that neither exchange nor exfoliation occurred when the hybrids were in contact with other proteins. This study indicates that, through the accommodation capability of clay, the simple nanoscaled manipulation of protein functions can be highly useful in developing new clay/enzyme nanohybrids for protein therapeutics and tissue engineering.

ACKNOWLEDGMENT

This work is supported in part by the National Science Council and the Ministry of Education of Taiwan under the ATU plan.

Supporting Information Available: The Langmuir-type adsorption isotherm of CHT on Na^+-MMT, the XRD diffraction patterns of MMT/CHT nanohybrids with varying extents of intercalation, the three-dimensional AFM images and the SPM topographical images of Na^+-MMT, CHT-adsorbed Na^+-MMT, MMT/POP, and MMT/CHT hybrids after incubating with BSA and the enzymatic degradation of BSA by free CHT and MMT/CHT nanohybrids. This material is available free of charge via the Internet at http://pubs.acs.org.

LITERATURE CITED

(1) Choy, J.-H., Kwak, S.-Y., Jeong, Y.-J., and Park, J.-S. (2000) Inorganic layered double hydroxides as nonviral vectors. *Angew. Chem. Int. Ed. 39*, 4041–4045.

(2) Desigaux, L., Belkacem, M. B., Richard, P., Cellier, J., Léone, P., Cario, L, Leroux, F, Taviot-Gueho, C., and Pitard, B. (2006) Self-assembly and characterization of layered double hydroxide/DNA hybrids. *Nano Lett. 6*, 199–204.

(3) Kumar, C. V., and Chaudhari, A. (2000) Protein immobilized at the galleries of layered α-zirconium phosphate: Structure and activity studies. *J. Am. Chem. Soc. 122*, 830–837.

(4) Kumar, C. V., and Chaudhari, A. (2002) High temperature peroxidase activities of HRP and hemoglobin in the galleries of layered Zr(IV) phosphate. *Chem. Commun.* 2382–2383.

(5) Kumar, C. V., and Chaudhari, A. (2003) Unusual thermal stabilities of some proteins and enzymes bound in the galleries of layered α-Zr(IV)phosphate/phosphonates. *Microporous Mesoporous Mater. 57*, 181–190.

(6) Bellezza, F., Cipiciani, A., Costantino, U., Negozio, and M, E. (2002) Zirconium phosphate and modified zirconium phosphates as supports of Lipase. Preparation of the composites and activity of the supported enzyme. *Langmuir 18*, 8737–8742.

(7) Bellezza, F., Cipiciani, A., Costantino, U., and Nicolis, S. (2004) Catalytic activity of myoglobin immobilized on zirconium phosphonates. *Langmuir 20*, 5019–5025.

(8) Bellezza, F., Cipiciani, A., Costantino, U., and Marmottini, F. (2006) Adsorption of myoglobin onto porous zirconium phosphate and zirconium benzenephosphonate obtained with template synthesis. *Langmuir 22*, 5064–5069.

(9) Kumar, C. V., and Chaudhari, A. (2001) Efficient renaturation of immobilized Met-hemoglobin at the galleries of α-zirconium phosphate. *Chem. Mater. 13*, 238–240.

(10) Baron, M. H., Revault, M., Servagent-Noinville, S., Abadie, J., and Quiquampoix, H. (1999) Chymotrypsin adsorption on montmorillonite: Enzymatic activity and kinetic FTIR structure analysis. *J. Colloid Interface Sci. 214*, 319–332.

(11) Ding, X., and Henrichs, S. M. (2002) Adsorption and desorption of proteins and polyamino acids by clay minerals and marine sediments. *Mar. Chem. 77*, 225–237.

(12) Usuki, A., Hasegawa, N., Kadoura, H., and Okamoto, T. (2001) Three-dimensional observation of structure and morphology in Nylon-6/clay nanocomposite. *Nano Lett. 5*, 271–272.

(13) Lin, J.-J., Cheng, I.-J., Wang, R., and Lee, R.-J. (2001) Tailoring basal spacings of montmorillonite by poly(oxyalkylene)diamine intercalation. *Macromolecules 34*, 8832–8834.

(14) Chou, C.-C., Shieu, F.-S., and Lin, J.-J. (2003) Preparation, organophilicity, and self-assembly of poly(oxypropylene)amine-clay hybrids. *Macromolecules 36*, 2187–2189.

(15) Lin, J.-J., Chen, I.-J., and Chou, C.-C. (2003) Critical conformational change of poly(oxypropylene)diamines in layered aluminosilicate confinement. *Macromol. Rapid Commun. 24*, 492–495.

(16) Chiu, H.-C., Zalipsky, S., Kopečková, P., and Kopeček, J. (1993) Enzymatic activity of chymotrypsin and its poly(ethylene glycol) conjugates toward low and high molecular weight substrates. *Bioconjugate Chem. 4*, 290–295.

(17) Mattews, B. W., Sigler, P. B., Henderson, R., and Blow, D. M. (1967) Three-dimensional structure of tosyl-α-chymotrypsin. *Nature (London) 214*, 652–656.

(18) Cristofaro, A. D., and Violante, A. (2001) Effect of hydroxy-aluminum species on the sorption and interlayering of albumin onto montmorillonite. *Appl. Clay Sci. 19*, 59–67.

(19) Calamai, L., Lossi, I., Stotzky, G., Fusi, P., and Ristori, G. G. (2000) Interaction of catalase with montmorillonite homoionic to cations with different hydrophobicity: Effect on enzymatic activity and microbial utilization. *Soil Biol. Biochem. 32*, 815–823.

(20) Naidja, A., and Huang, P. M. (1996) Deamination of aspartic acid by aspartase-Ca-montmorillonite complex. *J. Mol. Catal., A: Chem. 106*, 255–265.

(21) Fusi, P., Ristori, G. G., Calamai, L., and Stotzky, G. (1989) Adsorption and binding of protein on "clean" (homoionic) and "dirty" (coated with Fe oxyhydroxides) montmorillonite, Illite and kaolinite. *Soil Biol. Biochem. 21*, 911–920.

(22) Spek, E. J., Bui, A. H., Lu, M., and Kallenbach, N. R. (1998) Surface salt bridges stabilize the GCN4 leucine zipper. *Protein Sci. 7*, 2431–2437.

(23) Zhou, H.-X., and Dill, K. A. (2001) Stabilization of proteins in confined spaces. *Biochemistry 40*, 11289–11293.

(24) Khechinashvili, N. (1990) Thermodynamic properties of globular proteins and the principle of stabilization of their native structure. *Biochim. Biophys. Acta, Protein Struct. Molec. Enzym. 1040*, 346–354.

(25) Naidja, A., Huang, P. M., and Bollag, J.-M. (1997) Activity of tyrosinase immobilized on hydroxylaluminum-montmorillonite complex. *J. Mol. Catal., A: Chem. 115*, 305–316.

(26) Asthagiri, D., and Lenhoff, A. M. (1997) Influence of structure details in modeling electrostatically driven protein adsorption. *Langmuir 13*, 6761–6768.

(27) Lin, J.-J., Wei, J.-C., Juang, T.-Y., and Tsai, W.-C. (2007) Preparation of protein-silicate hybrids from polyamine intercalation of layered montmorillonite. *Langmuir 23*, 1995–1999.

BC700224Q

PLGA Nanoparticle−Peptide Conjugate Effectively Targets Intercellular Cell-Adhesion Molecule-1

Na Zhang,[†,§] Chuda Chittasupho,[†] Chadarat Duangrat,[†,||] Teruna J. Siahaan,[†] and Cory Berkland*[,†,‡]

Departments of Pharmaceutical Chemistry, and Chemical and Petroleum Engineering, University of Kansas, Lawrence, Kansas 66047. Received June 20, 2007; Revised Manuscript Received July 23, 2007

Targeted delivery of therapeutics possesses the potential to localize therapeutic agents to a specific tissue as a mechanism to enhance treatment efficacy and abrogate side effects. Antibodies have been used clinically as therapeutic agents and are currently being explored for targeting drug-loaded nanoparticles. Peptides such as RGD peptides are also being developed as an inexpensive and stable alternative to antibodies. In this study, cyclo(1,12)PenITDGEATDSGC (cLABL) peptide was used to target nanoparticles to human umbilical cord vascular endothelial cell (HUVEC) monolayers that have upregulated intercellular cell-adhesion molecule-1 (ICAM-1) expression. The cLABL peptide has been previously demonstrated to possess high avidity for ICAM-1 receptors on the cell surface. Poly(DL-lactic-coglycolic acid) nanoparticles conjugated with polyethylene glycol and cLABL demonstrated rapid binding to HUVEC with upregulated ICAM-1, which was induced by treating cells with the proinflammatory cytokine, interferon-γ. Binding of the nanoparticles could be efficiently blocked by preincubating cells with free peptide suggesting that the binding of the nanoparticles is specifically mediated by surface peptide binding to ICAM-1 on HUVEC. The targeted nanoparticles were rapidly endocytosed and trafficked to lysosomes to a greater extent than the untargeted PLGA-PEG nanoparticles. Verification of peptide-mediated nanoparticle targeting to ICAM-1 may ultimately lead to targeting therapeutic agents to inflammatory sites expressing upregulated ICAM-1.

INTRODUCTION

A variety of drug treatments have been investigated in recent decades outlining the potential of targeting specific cytokines or cell adhesion molecules that facilitate leukocyte recruitment in inflammatory diseases (*1–4*). In particular, monoclonal antibodies (mAbs) have been developed to target and bind molecules to disrupt the inflammatory pathway. However, the application of mAbs may be limited by immunogenicity, production cost, low physicochemical stability, and short *in vivo* half-life. As an alternative, nanoparticles may be targeted to a specific tissue with up-regulated cell adhesion molecules such as intercellular cell-adhesion molecule-1 (ICAM-1), which is dramatically up-regulated (~10-fold or more) on the vascular endothelium in response to the increased production of proinflammatory cytokines, such as interleukin-1-β, interferon-γ, and tumor necrosis factor-α (*5*). Recent studies have indicated that coupling anti-ICAM-1 mAbs to the surface of nanoparticles facilitated binding and internalization on the vascular endothelium (*6, 7*). In light of these findings, drugs encapsulated into nanoparticles and targeted to ICAM-1 may have the potential to pool to sites of ICAM-1 upregulation for a localized therapeutic effect (*7*).

Inhibition of ICAM-1 binding to leukocytes using mAbs has been shown to suppress T-cell activation (*8, 9*). In addition, therapies combining drugs such as methotrexate with mAbs against proinflammatory cytokines (e.g., TNF-α) have shown great promise in halting the progression of joint deterioration (*10, 11*). A variety of therapeutic strategies utilizing mAbs against CD4, CD5, CD7, CD25, and CD52 have also been investigated in an effort to interfere with the activation of CD4+T cells, thus, blocking inflammation (*1, 12, 13*). Previously, Siahaan and others found linear and cyclic peptides derived from the α- and β-subunits of LFA-1 that can inhibit homotypic and heterotypic T-cell adhesion as well as mixed lymphocyte reaction (*14*). The peptide cyclo(1,12)PenITDGEATDSGC (cLABL) demonstrated the highest avidity for domain-1 (D1) of ICAM-1 and could block ICAM-1-mediated T-cell adhesion. In addition, this peptide was internalized by ICAM-1 and entered into the cytoplasmic domain of activated T cells and endothelial cells (*14*). cLABL, has also been shown to provide therapeutic benefit by mitigating T-cell adhesion in the pancreatic microvasculature (*15*). Further enhancement of the demonstrated therapeutic efficacy may be afforded by multivalent peptide/receptor interactions (e.g., on a nanoparticle surface) coupled with sustained, localized release of appropriate therapeutics.

Nanoparticles have garnered attention for use as delivery vehicles for therapeutic drugs since they can be designed to slip between intercellular spaces, enter cells, or transport directly through biological barriers to access disease sites (*16–18*). Nanoparticles also encapsulate therapeutic agents offering potential protection from enzymatic degradation, metabolism, and filtration. Choosing the proper particle-forming materials allows the controlled release of drug over time or in response to a biological cue (*19, 20*). Delivering drugs in this manner also allows functionalization of the nanoparticle surface without compromising the activity of the drug itself, often a problem when covalently bonding targeting ligands to therapeutics as a prodrug strategy.

Surface modification of nanoparticles is a key requisite for extending circulation half-life and promoting localization. For example, nanoparticles coated with a highly cationic

* To whom correspondence should be addressed. Phone: (785) 864-1455. Fax: (785) 864-1454. E-mail: berkland@ku.edu.

[†] Department of Pharmaceutical Chemistry.

[§] Current address: The School of Pharmaceutical Science, Shandong University, 44 Wen Hua Xi Lu, Ji'nan, Shandong Province, China.

[||] Current address: Department of Pharmaceutical Sciences, Faculty of Pharmacy, Chiang Mai University, Chiang Mai, Thailand.

[‡] Department of Chemical and Petroleum Engineering.

10.1021/bc700227z CCC: $40.75 © 2008 American Chemical Society
Published on Web 11/13/2007

Table 1. Nanoparticle Properties at Specified Reaction Points

	PLGA[a]	PLGA-PEG	PLGA-PEG-Alexa 488	PLGA-PEG-cLABL	PLGA-PEG-cLABL-Alexa 488
size (nm)	177 ± 11	202 ± 11	224 ± 14	244 ± 15	268 ± 19
polydispersity	0.052	0.080	0.116	0.215	0.181
zeta potential (mV)	−40.2 ± 3.7	−31.4 ± 4.0	−15.4 ± 1.2	−23.3 ± 1.0	−8.3 ± 0.9

[a] PLGA nanoparticles fabricated using PEMA surfactant.

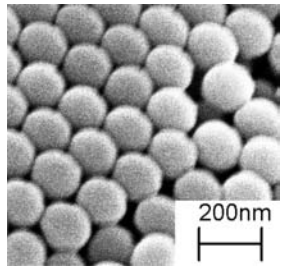

Figure 1. Scanning electron micrograph of PEMA-coated PLGA nanoparticles.

polymer have been used to enhance cellular uptake or open intercellular tight junctions (*16*, *21*). Recently, folate receptors overexpressed on the surface of malignant human cells were targeted by grafting folate on the surface of nanoparticles (*22*). Studies revealed that the nanoparticles attained a 10-fold higher affinity for the surface folate binding protein than free folate (*23*). Researchers reasoned that the multivalent form of folate on the nanoparticle surface interacted strongly with folate receptors, which often cluster on the surface of cancer cells, similar to the clustering of ICAM-1 during T-cell adhesion. Finally, research efforts are ongoing to improve nanoparticle performance *in vivo* by extending nanoparticle circulation and limiting interaction with blood constituents (*17*, *24*–*26*).

In this article, cLABL was conjugated to the surface of biodegradable PLGA nanoparticles to target ICAM-1 on the surface of human umbilical cord vascular endothelial cells (HUVEC). The amino terminus of modified polyethylene glycol was conjugated to carboxylic acid groups on PLGA nanoparticles via a peptide bond. The density of carboxyl groups on the nanoparticle surface was augmented using poly(ethylene-maleic acid) (PEMA) as a surfactant on the basis of methods recently described by Saltzman and others (*27*). Particles were further modified by conjugating the N-terminus of cLABL to the carboxylic acid group of PEG on the nanoparticle surface. The cLABL nanoparticles demonstrated rapid binding to HUVEC in comparison to PLGA-PEG particles. The binding of cLABL nanoparticles was enhanced upon upregulation of ICAM-1 receptors by interferon-γ and was interrupted by incubating HUVEC with free cLABL peptide prior to nanoparticle introduction. Labeling lysosomes revealed that cLABL nanoparticles trafficked to lysosomes and accumulated to a much greater extent than PLGA-PEG nanoparticles. This research provides evidence that cLABL nanoparticles can rapidly and specifically targeted to cells with upregulated ICAM-1, thus offering the potential for site-specific drug delivery.

EXPERIMENTAL PROCEDURES

Materials. Poly(DL-lactic-coglycolic acid) (50:50) (PLGA, inherent viscosity 0.89, Mw ∼150 kDa) was purchased from Absorbable Polymers. Poly(ethylene-maleic anhydride) (PEMA), was purchased from Polysciences, Inc. Fmoc-PEG_{3400}-COOH was purchased from Nektar. Alexa Fluor 488, LysoTracker Red, and Texas Red (10,000 kDa, lysine fixable) were purchased from Molecular Probes. Human interferon-γ (hIFN-γ, 100,000 U) was purchased from Roche Applied Science. Six-well glass bottom microwell dishes were purchased from MatTek corporation and 8-well BD Falcon* Culture Slides and 4% paraformaldehyde were purchased from Fisher Scientific. Acrodisc Syringe Filters with Supor PES Membrane were acquired from VWR international, Inc. Dulbecco's modified Eagle's medium and Triton X-100 were purchased from Sigma Aldrich. Penicillin−streptomycin, nonessential amino acids, and fetal bovine serum (FBS) were purchased from Invitrogen. Float-A-Lyzers (MWCO 500) were purchased from Spectrum laboratories. Micro BCA protein assay kit was purchased from Pierce Chemical Company.

Preparation of PLGA Nanoparticles. PLGA nanoparticles were prepared by a solvent diffusion method. Briefly, 50 mg of PLGA was dissolved in 3.0 mL of acetone, and the PLGA solution was added to 0.2% PEMA (30 mL) through a syringe pump (20 mL/h) under stirring at 200 rpm in a hood to evaporate acetone. PEMA was utilized as a surfactant to increase the number of carboxyl groups on the particle surface. Saltzman and others have previously reported this method to form stable antibody conjugates on PLGA particles (*27*). The nanoparticles produced were collected by centrifugation (15,000 rpm, 45 min). The nanoparticles were washed three times using double-distilled water. The sizes and zeta potentials of the PLGA nanoparticles were determined using a ZetaPALS dynamic light scattering system (Brookhaven, ZetaPALS).

Synthesis of PEGylated-PLGA Nanoparticles and cLABL Conjugation. Deprotection of the amine of Fmoc-PEG_{3400}-COOH was accomplished by stirring Fmoc-PEG_{3400}-COOH in 1.5 mL of 20% piperidine in DMF for 2 h at room temperature. The solution was transferred to polypropylene centrifuge tubes, and water was added. Centrifugation and filtration (MWCO 5,000) essentially resulted in the complete removal of Fmoc. The solution was further subjected to extensive dialysis in 500 MWCO Float-A-Lyzers before being lyophilized to dryness.

Five milligrams of PLGA nanoparticles in suspension (∼0.2 mg/mL in double-distilled water) were incubated with 23 mg of *N*-hydroxysuccinimide (NHS, 0.2 mmol), the pH was adjusted to 5.80, and then 153 mg of 1-(3-dimethylaminopropyl)-3-ethylcarbodimide hydrochloride (EDC, 0.8 mmol) was added and incubated for 2 h at room temperature with gentle stirring. The resulting NHS-activated particles were covalently linked to 10 mg of NH_2-PEG-COOH. The resulting PLGA-PEG-COOH nanoparticles were again washed, resuspended, and preserved in suspension form in double-distilled water. PLGA-PEG-COOH nanoparticles were activated by NHS as described above. The resulting NHS-activated particles were covalently linked to 5 mg of cLABL peptide or 0.2 mg of Alexa 488. PLGA-PEG-Alexa 488 particles served as control particles for all studies. The resulting PLGA-PEG-peptide-COOH nanoparticles were again activated by NHS as described above. The resulting NHS-activated particles were covalently linked to 0.2 mg of Alexa 488.

Quantification of PEG and cLABL Peptide on the Surface of Nanoparticles. The unreacted PEG or the unreacted cLABL peptide was separated from nanoparticles after the corresponding reaction step by centrifugation at 15,000 rpm for 45 min The amount of free PEG or cLABL peptide in the supernatant was determined using 2,4,6-trinitro-benzenesulphonic acid (TNBS) as a colorimetric assay (*28*). Seven hundred microliters of aqueous solution containing free PEG or cLABL peptide was added to 700 μL of 0.1 M sodium borate buffer (pH 9.2). Three hundred and fifty microliters of TNBS aqueous

Table 2. Density of Conjugated Molecules

	size (nm)	total surface area (m^2/mg)	surface PEG (pmol/cm^2)	surface peptide (pmol/cm^2)	surface Alexa 488 (pmol/cm^2)
PLGA-PEG	202	22.14	4.0 ± 0.8		
PLGA-PEG-Alexa 488	224	20.05			0.011 ± 0.002
PLGA-PEG-cLABL	244	18.36		2.3 ± 0.9	
PLGA-PEG-cLABL-Alexa 488	269	16.7			0.012 ± 0.002

solution (1.65 mg/mL) was added, and the solution was rapidly mixed. After incubation at 40 °C for 45 min, the reaction was stopped by adding 350 μL of 0.1 M NaH_2PO_4 containing 1.5 mM Na_2SO_3, and absorption at 420 nm was determined on a UV/vis spectrometer (Agilent 8453). The amounts of PEG and cLABL peptide on the surface of nanoparticles were calculated by subtracting the free amount from the total amount added into the reaction system.

The amount of Alexa 488 on the surface of nanoparticles was analyzed by the fluorescence intensity of nanoparticles using a fluorescence plate reader (SpectraMax M5; Ex., 490 nm; Em., 520 nm). Standard curves were obtained by diluting the free Alexa 488 with blank PLGA-PEMA nanoparticles (size = 266 nm) over a concentration range from 0.01 to 0.1 μg/mL (r = 0.9991).

Binding and Uptake of Nanoparticles in HUVEC Culture. Pooled HUVEC were grown in DMEM medium supplemented with 10% FBS, 0.1% nonessential amino acids, and 0.1% penicillin−streptomycin and were maintained at a density of 1×10^5 to 1×10^6 cells/mL at 37 °C in a humidified 5% CO_2 atmosphere. HUVEC were plated in 8-well BD Falcon* Culture Slides at a density of 1.0×10^5 cells/mL and used for uptake studies on day 2. Freshly prepared nanoparticles were diluted with serum-free medium to give a concentration of 0.3 mg/mL. Two hundred microliters of the nanoparticle suspension was added to each well. The cells were incubated with nanoparticles for different time periods to allow surface binding, washed three times with serum-free medium, incubated at 37 or 4 °C for different time periods, washed three times with ice-cold PBS, and fixed with 3.7% paraformaldehyde at room temperature.

For studies using free peptide as an inhibitor, HUVEC monolayers were preincubated for 30 min at 37 °C in the presence of different concentrations of free cLABL peptide, washed three times with serum-free media, and incubated with nanoparticles as described above. At varying periods of time, the cell monolayers were fixed, lysed, and the fluorescence determined. For ICAM-1 upregulation studies, HUVEC were activated with hIFNγ for 16–18 h, then washed three times with serum-free media, and incubated with nanoparticles as described above for uptake studies.

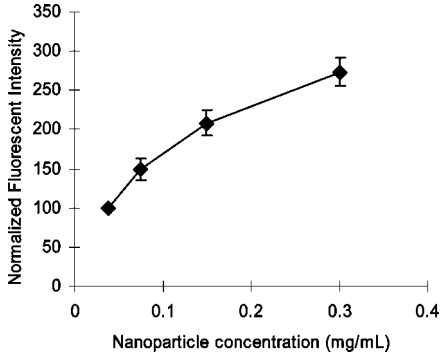

Figure 2. Fluorescent intensity increased in HUVEC as nanoparticle concentration increased. cLABL peptide-modified PLGA nanoparticle binding time was 1 h, followed by washing and incubation for 2 h prior to cell lysis.

Quantification of Nanoparticle Interaction with HUVEC. The experiments above were terminated by washing the cells three times with ice-cold phosphate-buffered saline (PBS; 8 g/L NaCl, 0.2 g/L KCl, 1.44 g/L Na_2HPO_4, and 0.24 g/L KH_2PO_4 in water at pH 7.4) and solubilizing the cells with 1 mL of 0.5% Triton X-100 in 0.2 M NaOH. Nanoparticle content was quantified by analyzing the cell lysate using a fluorescence plate reader (SpectraMax M5; Ex., 490 nm; Em., 520 nm). Uptake was normalized to the amount of cellular protein. The protein content of the cell lysate was determined using the Micro BCA protein assay kit. The plate reader was calibrated with standard preparations of nanoparticles, which were diluted with a cell lysate solution prepared by solubilizing 2×10^5 HUVEC in 1 mL of 0.5% Triton X-100/0.2 N NaOH solution. Linear calibration curves (r = 0.9991) over the nanoparticle concentration range of 6 to 48 μg/mL were obtained.

Intracellular Trafficking of Nanoparticles. To follow intracellular trafficking of nanoparticles, HUVEC were incubated for 2 h at 37 °C with Lysotracker to label lysosomes, washed three times with serum-free medium, and incubated with nanoparticles as described above for uptake studies. Briefly, freshly prepared nanoparticles were diluted to 0.3 mg/mL with serum-free medium. Two hundred microliters of the nanoparticle suspension was added into each well. The cells were incubated with nanoparticles for 10 min to allow surface binding, washed three times with serum-free medium, and incubated at 37 °C. At varying periods of time after internalization, the cells were washed three times with ice-cold PBS, and fixed with 3.7% paraformaldehyde at room temperature. Then, the colocalization of nanoparticles within Lysotracker-labeled cellular compartments was determined. The results were confirmed by labeling lysosomes with Texas Red dextran (10,000 kDa) following a similar protocol (*7*, *29*).

RESULTS

Preparation of Nanoparticles. As previously described by Saltzman and others (*27*), multiple molecules were conjugated to PLGA nanoparticles in the presence of PEMA surfactant by

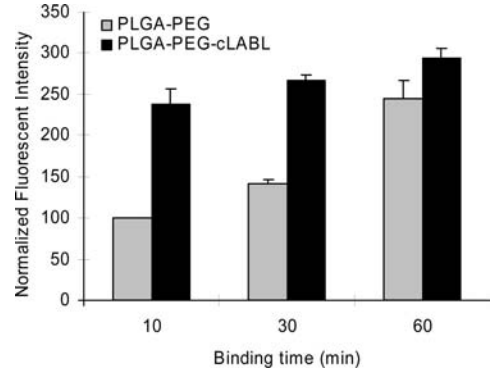

Figure 3. Fluorescent intensity of nanoparticles associated with HUVEC was significantly higher for targeted cLABL nanoparticles for short binding times ($p < 0.001$ for 10 and 30 min). Nanoparticle binding time was followed by washing and incubation for 2 h prior to cell lysis.

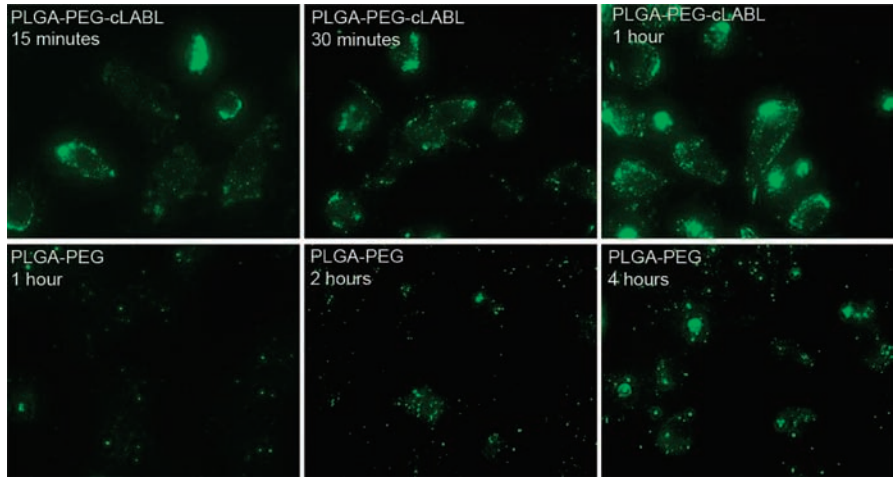

Figure 4. Fluorescent micrographs demonstrate that the binding of PLGA nanoparticles mediated by cLABL occurred rapidly. Significant localized fluorescence was noted at 15 min for cLABL nanoparticles; however, PLGA-PEG nanoparticles required >2 h to demonstrate similar localization to cells. No significant differences in fluorescence were observable after 4 h. Nanoparticle binding time was 10 min, followed by washing and incubation for 2 h prior to cell lysis or imaging.

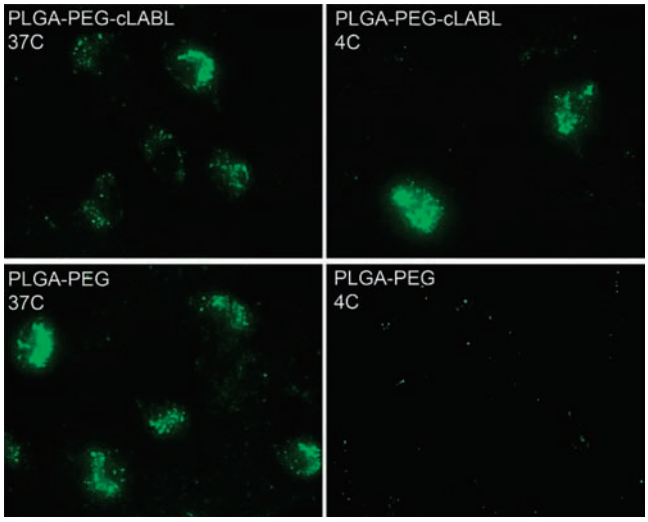

Figure 5. Nanoparticle binding was studied at 4 °C to mitigate energy dependent endocytic pathways. Binding of cLABL nanoparticles was still apparent at low temperature. Nanoparticle binding time was 1 h, followed by washing and incubation for 2 h prior to cell imaging.

sequentially activating and conjugating the available terminal carboxyl groups. Original PLGA particles coated with PEMA were ~175 nm in size with a relatively low polydispersity (Table 1). Dynamic light scattering results were confirmed by scanning electron microscopy, which verified the narrow particle size distribution and revealed a relatively smooth surface morphology (Figure 1). Reacting the terminal amine of PEG to PEMA carboxyl groups resulted in a slight increase in the average particle size and polydispersity. Further addition of the fluorescent dye, Alexa 488, or cLABL produced a further increase in average particle size and polydispersity. This trend continued when linking Alexa 488 to free carboxyl terminus of cLABL. Increasing particle size, presumably due to particle agglomeration, was suspected to result from the addition of NHS when conjugating molecules since NHS presents a relatively hydrophobic intermediate on the particle surface. Sequential conjugations also demonstrated a systematic increase in nanoparticle zeta potential, presumably a result of the occupation of carboxyl sites and increasing particle size.

The density of molecules on the nanoparticle surface was estimated after each reaction step. The total particle surface area was calculated assuming a normal Gaussian particle size distribution. The concentration of molecules was determined indirectly by quantifying the amount of molecules left in solution. Appropriate controls were utilized to ensure that this method was accurate (i.e., no loss of molecules through nonspecific adsorption to the vial, etc.) The density of PEG on the surface of PLGA particles corresponded well with other reports (Table 2) (*30, 31*). In addition, the density of peptide was sufficient to facilitate particle interactions *in vitro*. Alexa 488 surface concentration provided a significant signal for detection by fluorescent microscopy and spectroscopy.

To effectively determine nanoparticle interactions with cells, colloidal stability is a key requisite. PEGylated nanoparticles with and without peptide possessed good colloidal stability in both water and serum-free cell culture media. A slight increase in particle size, polydispersity, and zeta potential was evident in media. Large precipitates were not obvious in either water or media, although larger, ~1 μm, agglomerates were visible by fluorescence microscopy on rare occasions. Preincubation of nanoparticles with cell culture media in an ultrasound bath prior to dispersing into wells helped to mitigate the agglomeration of nanoparticles.

The cLABL peptide has been previously shown to bind to the D1 domain of ICAM-1 (*32*). ICAM-1 is expressed at a basal concentration of 5–10 $\times$ 10^4 sites/cell, although the expression may be increased to 3.5 $\times$ 10^6 sites/cell upon treatment of HUVEC with TNF-α (*33*). To determine the binding avidity to HUVEC expressing basal levels of ICAM-1, nanoparticles were incubated with HUVEC for 1 h and washed, and fluorescence was quantified after 2 h. Increasing the concentration of peptide-labeled nanoparticles resulted in a corresponding increase in the fluorescence intensity (Figure 2). The decreasing effect of increasing particle concentration may be indicative of the saturation of ICAM-1 receptors or the removal of ICAM-1 from the surface via endocytosis at high nanoparticle concentrations.

HUVEC were incubated with PLGA nanoparticles grafted with PEG or PEG-cLABL at 300 μg/mL to assess the specificity of binding mediated by cLABL. The presence of cLABL on nanoparticles resulted in an ~2.5-fold enhancement of the fluorescent intensity in HUVEC (Figure 3). Increasing the binding time decreased the differential between cLABL and nonspecific nanoparticle interactions with HUVEC. Fluorescent micrographs were also collected over time to observe the kinetic interaction of nanoparticles with HUVEC. Rapid localization of cLABL nanoparticles to the cell periphery was observed (Figure 4). This observation was consistent with the short

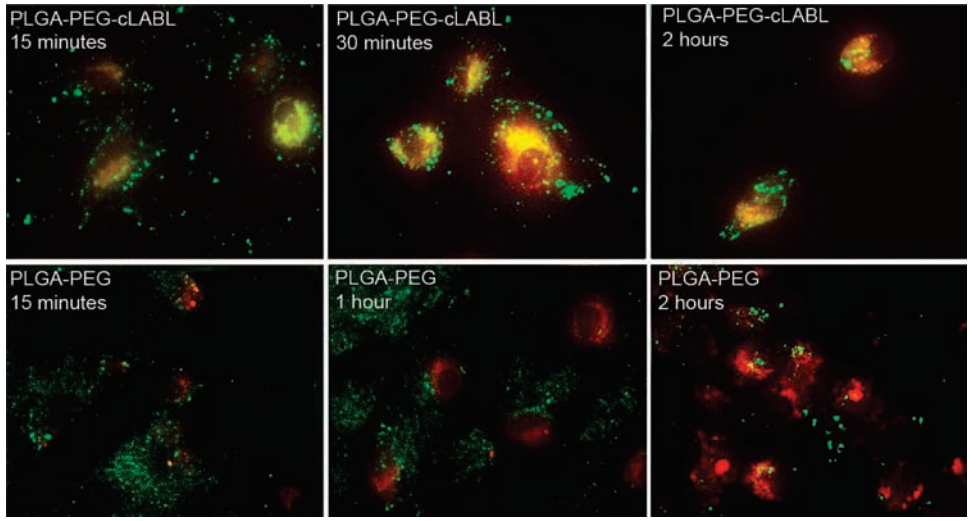

Figure 6. Fluorescent microscopy was utilized to assess the colocalization of nanoparticles (green) with lysosomes using Lysotracker (red). Images confirm the rapid binding of cLABL nanoparticles. In addition, cLABL nanoparticles rapidly trafficked to the lysosome with colocalization visible within 15 min. PLGA-PEG nanoparticles began to appear in lysosomes after 2 h. Nanoparticle binding time was 10 min, followed by washing and incubation for different times prior to cell imaging.

nanoparticle binding times determined spectroscopically. Punctate fluorescent patterns developed very quickly (∼15 min), which suggested rapid internalization of cLABL nanoparticles as well. Focusing on the cell midline and deconvoluting these images, that is, removing of out of focus fluoresent light, provided additional evidence that fluorescent foci were indeed inside the cells. In contrast, fluorescence in PLGA-PEG nanoparticle incubations remained relatively disperse over more than 2 h, and a similar localization of fluorescence was not noted until later times, providing circumstantial evidence that these particles did not enter cells to as great an extent.

Since studies revealed that the binding of cLABL nanoparticles occurred rapidly, experiments were designed to further determine if nanoparticles were indeed entering cells. Reports from Muro and others have verified that ICAM-1 mediates endocytosis along a novel pathway (*34*) and prior work by Labhasetwar and others demonstrated the endocytosis and exocytosis of PLGA nanoparticles in multiple cell lines (*35*, *36*). HUVEC were incubated at 4 °C to minimize energy dependent endocytic pathways. Uptake of nanoparticles was effectively mitigated at low temperature. For cLABL nanoparticles, association with cells was still apparent at 4 °C, confirming that the binding of these nanoparticles was not substantially reduced at low temperature (Figure 5).

Lysotracker was utilized to determine the rate at which nanoparticles were transported to lysosomes in HUVEC. This dye accumulates in lysosomes, staining them with red fluorescence; therefore, nanoparticles (green) accumulating in these organelles produced a yellow color. Some punctate yellow color was noted after only 15 min of incubation with cLABL nanoparticles subsequent to the 10 min binding time (Figure 6). PLGA-PEG nanoparticles remained dispersed for longer periods and did not appear in lysosomes until a minimum of 2 h had passed. Also, PLGA-PEG nanoparticles were much more dispersed in the cell culture. These studies were confirmed using a pulse−chase approach to label lysosomes with texas red dextran as reported by colleagues (*7, 29*). This method provided additional evidence of the rapid binding and internalization of cLABL nanoparticles. In addition, the green fluorescence of nanoparticles separated from lysosomes at later time points (Figure 7; ∼6 h.) Colocalization of nanoparticles with lysosomes was assessed semiquantitatively by summing the number of yellow pixels from images and dividing by the number of cells in a particular field of view at selected time

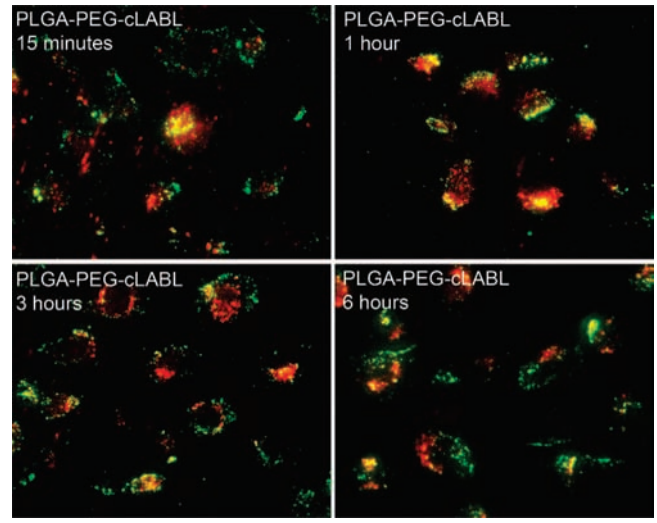

Figure 7. Lysosomes were labeled with fluorescent dextran (red) to confirm results obtained with Lysotracker using cLABL nanoparticles. Again, nanoparticles (green) rapidly colocalized with lysosomes and remained for about 4–6 h. For times >4–6 h, colocalization was no longer as apparent. Nanoparticle binding time was 10 min, followed by washing and incubation for different times prior to cell imaging.

points. Kinetic data derived from images showed that cLABL nanoparticles appeared in lysosomes to a much greater extent than PLGA-PEG nanoparticles (Figure 8). In addition, cLABL nanoparticles steadily disappeared from lysosomes after 4 h, while PLGA-PEG nanoparticle accumulation continued to steadily increase. This result suggested that cLABL nanoparticles, cleaved peptide with dye, or cleaved dye may have entered a recycling endosome, a process that is known to return ICAM-1 to the cell surface (*7*). Alternatively, cLABL nanoparticles, cleaved peptide with dye, or cleaved dye may have escaped the endolysosomal pathway and entered the cytosol; however, this hypothesis was not confirmed.

HUVEC were grown as monolayers to determine the effect of receptor upregulation on nanoparticle binding. For this study, the surface of HUVEC was incubated for ∼16–18 h with different concentrations of human IFN-γ. The relative ICAM-1 concentration on the surface of HUVEC was determined using fluorescent anti-ICAM-1 mAbs and normalized to basal concentrations of ICAM-1 on control cells (Figure 9A). ICAM-1

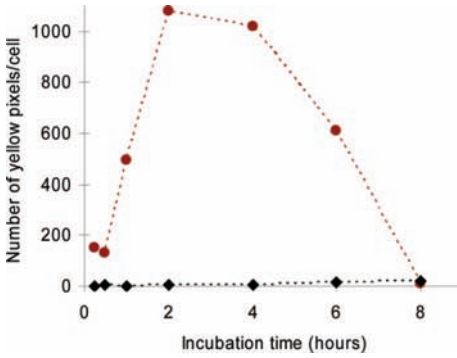

Figure 8. Yellow pixels signifying colocalization of nanoparticles (green) with lysosomes (red) were quantified over time demonstrating the rapid and transient localization of cLABL nanoparticles (circles) with lysosomes. Relatively fewer PLGA-PEG nanoparticles transitioned to lysosomes at later times (>2–4 h).

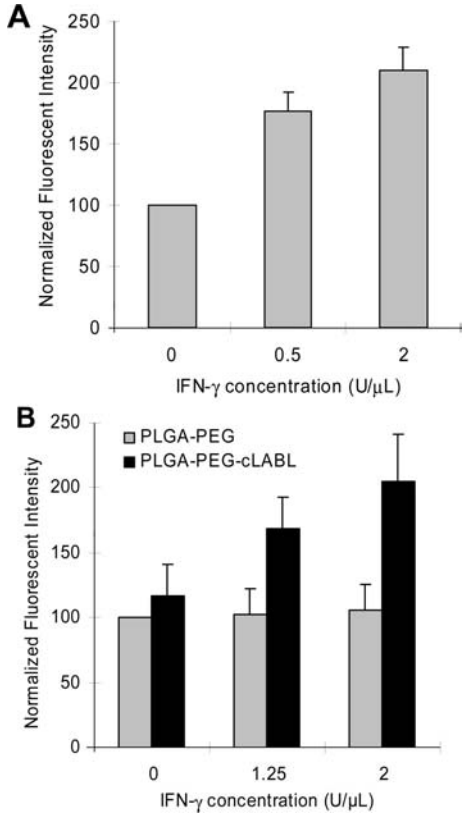

Figure 9. (A) Fluorescence spectrophotometry was used to quantify ICAM-1 expression in response to IFN-γ and normalized to basal ICAM-1 expression (blank). (B) Fluorescent spectrophotometry demonstrated that fluorescent intensity increased in HUVEC as IFN-γ concentration increased ($p < 0.001$ for 1.25 U/μL and 2 U/μL). Nanoparticle binding time was 1 h, followed by washing and incubation for 2 h prior to cell lysis or imaging.

concentration on the surface of HUVEC could be enhanced more than 2-fold. Upregulated ICAM-1 significantly enhanced the binding of cLABL nanoparticles (Figure 9B). The level of enhancement of nanoparticle interaction with HUVEC corresponded well to the relative enhancement of ICAM-1 expression induced by INF-γ. In contrast, PLGA-PEG nanoparticles showed no sensitivity to ICAM-1 expression levels. Studies were conducted using a long nanoparticle binding time (~1 h) to achieve similar fluorescence levels of targeted and untargeted nanoparticles at basal ICAM-1 expression levels (see Figure 2). Binding studies using upregulated ICAM-1 receptors were also verified by fluorescence microscopy; in this case, the overall

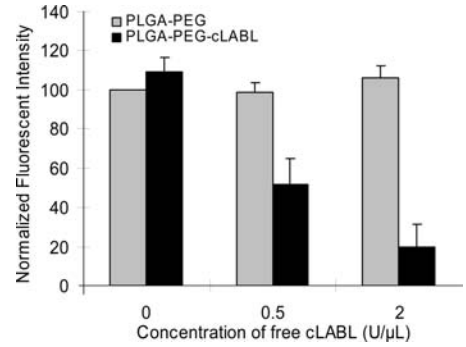

Figure 10. Fluorescent spectrophotometry demonstrates that binding of cLABL nanoparticles was inhibited by preincubating HUVEC with free peptide ($p < 0.001$ for 0.5 U/μL and 2 U/μL). PLGA-PEG nanoparticle binding was unaffected. Nanoparticle binding time was 1 h, followed by washing and incubation for 2 h prior to cell lysis or imaging.

fluorescence for cLABL formulations was enhanced as ICAM-1 expression increased on the cell surface (data not shown).

Free cLABL peptide was utilized as a competitive inhibitor of cLABL-modifed nanoparticle binding to HUVEC. The free peptide was incubated at various concentrations with cells prior to the introduction of nanoparticles to the media. The extended nanoparticle binding time (1 h) was again selected to minimize differentials between particle types attributable to binding kinetics (see Figure 3). Increasing free peptide concentration resulted in a corresponding decrease in fluoresence intensity; thus, even for long binding times, inhibition of nanoparticle-cell interactions was evident (Figure 10). The dramatic inhibition of the uptake of cLABL nanoparticles suggests a reduced role for other endocytic pathways in the uptake of these drug delivery vehicles. In a separate experiment, fluorescent micrographs confirmed the trend of free peptide inhibition of cLABL nanoparticle binding (data not shown). No inhibition was evident in PLGA-PEG nanoparticles via spectroscopic measurement of cell lysate fluorescence or in fluorescent micrographs.

DISCUSSION

Therapeutic interventions stand to benefit greatly from site-specific drug targeting. Substantial research efforts have focused on targeting molecular markers in cancer, infectious disease, and other diseases. The vascular endothelium remains a prime target for localizing drug delivery, and ICAM-1 is an attractive receptor for therapeutic interventions (*37*) and for targeting therapeutic drug carriers to vascular endothelium because it has shown to be upregulated during a variety of disease states, including infections, injuries, ischemia, autoimmune diseases, and certain cancers (*38–40*). In addition, localized upregulation of ICAM-1 facilitates the recruitment of leukocytes, suggesting that circulating drug carriers may selectively pool at these regions.

The cLABL peptide was derived from the I-domain of the α-subunit of LFA-1. This peptide has been shown to inhibit ICAM-1/LFA-1-mediated homotypic (*41*) and heterotypic (*42*) T-cell adhesion. Interestingly, the peptide blocked adhesion of T cells but not monocytes to pancreatic islet microvascular endothelium, thus demonstrating specificity (*43*). Recently, the cLABL peptide was shown to block the formation of microtubule-organizing center at the cell−cell contact region of human T-lyphotropic virus (HTLV-1)-infected T cells, suggesting that cLABL can be used to inhibit the spread of HLTV-1 from infected to noninfected human T cells (*44*). The mechanism of activity of this peptide is partly due to its binding to ICAM-1 at the LFA-1 binding site. Using monoclonal antibodies, it has been shown that the cLABL peptide binds to the D1 domain of

Table 3. Nanoparticle Colloidal Stability

	sizes (nm)	polydispersity	zeta potential (mV)
PLGA-PEG-cLABL- Alexa 488 in water	269 ± 19	0.181	−8.3 ± 0.9
PLGA-PEG-Alexa 488 in water	224 ± 14	0.116	−15.4 ± 1.2
PLGA-PEG-cLABL- Alexa 488 in media	292 ± 8.9	0.219	−13.4 ± 1.7
PLGA-PEG-Alexa 488 in media	272 ± 13	0.141	−21.3 ± 2.2

ICAM-1 (*32*). The peptide has been specifically designed with a stable conformation including a β-II′ turn at Asp4-Gly5-Glu6-Ala7 and a β-I turn at Pen1-Ile2-Thr3-Asp4 as determined by NMR spectroscopy (*45*). Molecular docking experiments suggest that this peptide binds to ICAM-1 at the F and C strands of D1 domain (*45*). By itself, the fluorescent-labeled cLABL peptide was internalized into activated Molt-3 T cells, presumably by ICAM-1 receptors (*32*). Recently, we have shown that the Ile2, Asp4, and Glu6 residues in cLABL and the β-turn structure at Asp4-Gly5-Glu6-Ala7 are important for peptide activity. In addition, a cyclic hexapeptide, cyclo(1,6)ITDGEA, derived from cLABL has been shown to have activity comparable with that of the parent cLABL; this cyclic peptide is currently being optimized by mutating some of its residues. In the future, this smaller cyclic peptide may also be used to target drugs or nanoparticles to cells with high expression of ICAM-1 as shown here.

Multiple groups have validated the potential of utilizing ICAM-1 as a molecular marker for targeting therapeutic particles. Eniola and others have reported the importance of multiple ligand–receptor interactions in achieving firm adhesion of particles in flow fields (*3, 46*). Elegant work by Muro and others has also established ICAM-1 as a valid target for delivering therapeutic nanoparticles. They demonstrated that nanoparticles conjugated with anti-ICAM-1 mAbs were rapidly bound and endocytosed by HUVEC via a novel endocytic pathway (*6*). Targeting the same receptor, cLABL nanoparticles reported here were also observed to bind rapidly and traffic to lysosomes in ∼1–2 h. Any minor differences in the trafficking kinetics of these two nanoparticle types may be due to the surface concentration of ligand on nanoparticles and/or the relative avidity of targeting molecules (mAbs vs peptides). Perhaps, the lower density and lower binding strength of cLABL to ICAM-1 may lead to easier disruption of binding events and a slightly more rapid transit to lysosomal compartments. It is also possible that cluster formation of ICAM-1 receptors on the cell surface during binding to cLABL-modified nanoparticles is different from that of anti-ICAM-1-modified particles.

In this work, we have successfully modified the surface of nanoparticles with cLABL peptide to target the vascular endothelium with upregulated ICAM-1. The cLABL peptide effectively mediated rapid nanoparticle binding and internalization. Binding was enhanced upon upregulation of ICAM-1 on HUVEC, and this binding could be specifically inhibited by blocking ICAM-1 receptor sites with free cLABL peptide. These results suggest that the cLABL-nanoparticle conjugates may have dual therapeutic applications, namely, inhibition of the infiltration of immune cells via blockage or internalization of ICAM-1 receptors coupled with the ability to localize drug delivery to regions of ICAM-1 upregulation.

ACKNOWLEDGMENT

These studies were funded by grants from the Juvenile Diabetes Research Foundation, the American Heart Association, and the NIH (1R03 AR054035-01A1, P20 RR016443, and P20 RR015563). We are sincerely grateful to the China Scholarship Council in the People's Republic of China for the partial support of Na Zhang as a postdoctoral researcher. Special thanks to Russ Middaugh and to Jeff Krise for the use of laboratory equipment.

LITERATURE CITED

(1) Schulze-Koops, H., Burkhardt, H., and Kalden, J. R. (1999) What we have learned from trials of immunomodulatory agents in rheumatoid arthritis: Future directions. *Drugs Today 35*, 327–351.

(2) Schulze-Koops, H., and Kalden, J. R. (2000) Where is biological therapy going? *Arthritis Res. Ther. 2*, 337–341.

(3) Eniola, A. O., and Hammer, D. A. (2005) Characterization of biodegradable drug delivery vehicles with the adhesive properties of leukocytes II: effect of degradation on targeting activity. *Biomaterials 26*, 661–670.

(4) Omolola Eniola, A., and Hammer, D. A. (2005) In vitro characterization of leukocyte mimetic for targeting therapeutics to the endothelium using two receptors. *Biomaterials 26*, 7136–7144.

(5) Furuzawa-Carballeda, J., Rodriquez-Calderon, R., Diaz de Leon, L., and Alcocer-Varela, J. (2002) Mediators of inflammation are down-regulated while apoptosis is up-regulated in rheumatoid arthritis synovial tissue by polymerized collagen. *Clin. Exp. Immunol. 130*, 140–149.

(6) Muro, S., Cui, X., Gajewski, C., Murciano, J. C., Muzykantov, V. R., and Koval, M. (2003) Slow intracellular trafficking of catalase nanoparticles targeted to ICAM-1 protects endothelial cells from oxidative stress. *Am. J. Physiol.: Cell Physiol. 285*, C1339–C1347.

(7) Muro, S., Gajewski, C., Koval, M., and Muzykantov, V. R. (2005) ICAM-1 recycling in endothelial cells: a novel pathway for sustained intracellular delivery and prolonged effects of drugs. *Blood 105*, 650–658.

(8) Jois, S. D. S., and Siahaan, T. J. (2003) A peptide derived from LFA-1 that modulates T-cell adhesion binds to soluble ICAM-1 protein. *J. Biomol. Struct. Dyn. 20*, 635–644.

(9) Anderson, M. E., and Siahaan, T. J. (2003) Targeting ICAM-1/LFA-1 interaction for controlling autoimmune diseases: Designing peptide and small molecule inhibitors. *Peptides 24*, 487–501.

(10) Breedveld, F. C., Emery, P., Keystone, E., Patel, K., Furst, D. E., Kalden, J. R., St Clair, E. W., Weisman, M., Smolen, J., Lipsky, P. E., and Maini, R. N. (2004) Infliximab in active early rheumatoid arthritis. *Ann. Rheum. Dis. 63*, 149–155.

(11) Lipsky, P. E., van der Heijde, D. M., St Clair, E. W., Furst, D. E., Breedveld, F. C., Kalden, J. R., Smolen, J. S., Weisman, M., Emery, P., Feldmann, M., Harriman, G. R., and Maini, R. N. (2000) Infliximab and methotrexate in the treatment of rheumatoid arthritis. Anti-tumor necrosis factor trial in rheumatoid arthritis with concomitant therapy study group. *N. Engl. J. Med. 343*, 1594–1602.

(12) Burmester, G. R., and Emmrich, F. (1993) Anti-CD4 therapy in rheumatoid arthritis. *Clin. Exp. Rheumatol. 11*, S139–S145.

(13) Kalden, J. R., Breedveld, F. C., Burkhardt, H., and Burmester, G. R. (1998) Immunological treatment of autoimmune diseases. *Adv. Immunol. 68*, 333–418.

(14) Yusuf-Makagiansar, H., Anderson, M. E., Song, X., Murray, J., and Siahaan, T. J. (2000) Modulation of adhesion molecules in lymphocyte activation and cell-cell interaction. *Curr. Top. Biochem. Res. 2*, 33–49.

(15) Huang, M., Matthews, K., Siahaan, T. J., and Kevil, C. G. (2005) Alpha L-integrin I domain cyclic peptide antagonist selectively inhibits T cell adhesion to pancreatic islet microvascular endothelium. *Am. J. Physiol.: Gastrointest. Liver Physiol. 288*, G67–G73.

(16) Yamamoto, H., Kuno, Y., Sugimoto, S., Takeuchi, H., and Kawashima, Y. (2005) Surface-modified PLGA nanosphere with chitosan improved pulmonary delivery of calcitonin by mucoadhesion and opening of the intercellular tight junctions. *J. Controlled Release 102*, 373–381.

(17) Moghimi, S. M., Hunter, A. C., and Murray, J. C. (2001) Long-circulating and target-specific nanoparticles: theory to practice. *Pharmacol. Rev. 53*, 283–318.
(18) Moghimi, S. M., Illum, L., and Davis, S. S. (1990) Physiopathological and physicochemical considerations in targeting of colloids and drug carriers to the bone marrow. *Crit. Rev. Ther. Drug Carrier Syst. 7*, 187–209.
(19) Na, K., Lee, K. H., and Bae, Y. H. (2004) pH-sensitivity and pH-dependent interior structural change of self-assembled hydrogel nanoparticles of pullulan acetate/oligo-sulfonamide conjugate. *J. Controlled Release 97*, 513–525.
(20) Chaw, C. S., Chooi, K. W., Liu, X. M., Tan, C. W., Wang, L., and Yang, Y. Y. (2004) Thermally responsive core-shell nanoparticles self-assembled from cholesteryl end-capped and grafted polyacrylamides: drug incorporation and in vitro release. *Biomaterials 25*, 4297–4308.
(21) Prego, C., Garcia, M., Torres, D., and Alonso, M. J. (2005) Transmucosal macromolecular drug delivery. *J. Controlled Release 101*, 151–162.
(22) Brigger, I., Dubernet, C., and Couvreur, P. (2002) Nanoparticles in cancer therapy and diagnosis. *Adv. Drug Delivery Rev. 54*, 631–651.
(23) Stella, B., Arpicco, S., Peracchia, M. T., Desmaele, D., Hoebeke, J., Renoir, M., D'Angelo, J., Cattel, L., and Couvreur, P. (2000) Design of folic acid-conjugated nanoparticles for drug targeting. *J. Pharm. Sci. 89*, 1452–1464.
(24) Gref, R., Minamitake, Y., Peracchia, M. T., Domb, A., Trubetskoy, V., Torchilin, V., and Langer, R. (1997) Poly(ethylene glycol)-coated nanospheres: potential carriers for intravenous drug administration. *Pharm. Biotechnol. 10*, 167–198.
(25) Gref, R., Minamitake, Y., Peracchia, M. T., Trubetskoy, V., Torchilin, V., and Langer, R. (1994) Biodegradable long-circulating polymeric nanospheres. *Science 263*, 1600–1603.
(26) Kim, D., El-Shall, H., Dennis, D., and Morey, T. (2005) Interaction of PLGA nanoparticles with human blood constituents. *Colloids Surf., B 40*, 83–91.
(27) Keegan, M. E., Falcone, J. L., Leung, T. C., and Saltzman, W. M. (2004) Biodegradable microspheres with enhanced capacity for covalently bound surface ligands. *Macromolecules 37*, 9779–9784.
(28) Zhang, N., Ping, Q. N., Huang, G. H., and Xu, W. F. (2005) Investigation of lectin-modified insulin liposomes as carriers for oral administration. *Int. J. Pharm. 294*, 247–259.
(29) Duvvuri, M., and Krise, J. P. (2005) A novel assay reveals that weakly basic model compounds concentrate in lysosomes to an extent greater than pH-partitioning theory would predict. *Mol. Pharmaceutics 2*, 440–448.
(30) Vila, A., Gill, H., McCallion, O., and Alonso, M. J. (2004) Transport of PLA-PEG particles across the nasal mucosa: effect of particle size and PEG coating density. *J. Controlled Release 98*, 231–244.
(31) Popielarski, S. R., Pun, S. H., and Davis, M. E. (2005) A nanoparticle-based model delivery system to guide the rational design of gene delivery to the liver. 1. Synthesis and characterization. *Bioconjugate Chem. 16*, 1063–1070.
(32) Yusuf-Makagiansar, H., and Siahaan, T. J. (2001) Binding and internalization of an LFA-1-derived cyclic peptide by ICAM receptors on activated lymphocyte: a potential ligand for drug targeting to ICAM-1-expressing cells. *Pharm. Res. 18*, 329–335.
(33) Dustin, M. L., and Springer, T. A. (1988) Lymphocyte function-associated antigen-1 (LFA-1) interaction with intercellular adhesion molecule-1 (ICAM-1) is one of at least three mechanisms for lymphocyte adhesion to cultured endothelial cells. *J. Cell Biol. 107*, 321–331.
(34) Muro, S., Schuchman, E. H., and Muzykantov, V. R. (2006) Lysosomal enzyme delivery by ICAM-1-targeted nanocarriers bypassing glycosylation- and clathrin-dependent endocytosis. *Mol. Ther. 13*, 135–141.
(35) Panyam, J., and Labhasetwar, V. (2003) Dynamics of endocytosis and exocytosis of poly(D,L-lactide-co-glycolide) nanoparticles in vascular smooth muscle cells. *Pharm. Res. 20*, 212–220.
(36) Qaddoumi, M. G., Ueda, H., Yang, J., Davda, J., Labhasetwar, V., and Lee, V. H. (2004) The characteristics and mechanisms of uptake of PLGA nanoparticles in rabbit conjunctival epithelial cell layers. *Pharm. Res. 21*, 641–648.
(37) Arnold, R., Neumann, M., and Konig, W. (2007) Peroxisome proliferator-activated receptor-gamma agonists inhibit respiratory syncytial virus-induced expression of intercellular adhesion molecule-1 in human lung epithelial cells. *Immunology 121*, 71–81.
(38) Weishaupt, C., Munoz, K. N., Buzney, E., Kupper, T. S., and Fuhlbrigge, R. C. (2007) T-cell distribution and adhesion receptor expression in metastatic melanoma. *Clin. Cancer Res. 13*, 2549–2556.
(39) Ramudo, L., De Dios, I., Yubero, S., Vicente, S., and Manso, M. A. (2007) ICAM-1 and CD11b/CD18 expression during acute pancreatitis induced by bile-pancreatic duct obstruction: effect of N-acetylcysteine. *Exp. Biol. Med. (Maywood) 232*, 737–743.
(40) Eniola, A. O., and Hammer, D. A. (2003) Artificial polymeric cells for targeted drug delivery. *J. Controlled Release 87*, 15–22.
(41) Tibbetts, S. A., Jois, S. D. S., Siahaan, T. J., Benedict, S. H., and Chan, M. A. (2000) Linear and cyclic LFA-1 and ICAM-1 peptides inhibit T-cell adhesion and function. *Peptides 21*, 1161–1167.
(42) Yusuf-Makagiansar, H., Makagiansar, I. T., and Siahaan, T. J. (2001) Inhibition of the adherence of T-lymphocyte to epithelial cells by a cyclic peptide derived from inserted domain of lymphocyte function-associated antigen-1. *Inflammation 25*, 203–214.
(43) Huang, M., Matthews, K., Siahaan, T. J., and Kevil, C. G. (2005) Alpha L-integrin I domain cyclic peptide antagonist selectively inhibits T cell adhesion to pancreatic islet microvascular endothelium. *Am. J. Physiol.: Gastrointest. Liver Physiol. 288*, G67–G73.
(44) Barnard, A. L., Igakura, T., Tanaka, Y., Taylor, G. P., and Bangham, C. R. (2005) Engagement of specific T-cell surface molecules regulates cytoskeletal polarization in HTLV-1-infected lymphocytes. *Blood 106*, 988–95.
(45) Xu, C. R., Yusuf-Makagiansar, H., Hu, Y., Jois, S. D., and Siahaan, T. J. (2002) Structural and ICAM-1-docking properties of a cyclic peptide from the I-domain of LFA-1: an inhibitor of ICAM-1/LFA-1-mediated T-cell adhesion. *J. Biomol. Struct. Dyn. 19*, 789–799.
(46) Eniola, A. O., Krasik, E. F., Smith, L. A., Song, G., and Hammer, D. A. (2005) I-domain of lymphocyte function-associated antigen-1 mediates rolling of polystyrene particles on ICAM-1 under flow. *Biophys. J. 89*, 3577–3588.

BC700227Z

Attachment of Peptide Building Blocks to Proteins Through Tyrosine Bioconjugation

Dante W. Romanini[†] and Matthew B. Francis*[,‡]

Department of Chemistry, University of California, Berkeley, California 94720-1460, and Materials Sciences Division, Lawrence Berkeley National Labs, Berkeley, California 94720-1460. Received June 21, 2007; Revised Manuscript Received October 4, 2007

Recent efforts have yielded a number of short peptide sequences with useful binding, sensing, and cellular uptake properties. In order to attach these sequences to tyrosine residues on intact proteins, a three-component Mannich-type strategy is reported. Two solid phase synthetic routes were developed to access peptides up to 20 residues in length with anilines at either the N- or C-termini. In the presence of 20 mM formaldehyde, these functional groups were coupled to tyrosine residues on proteins under mild reaction conditions. The identities of the resulting bioconjugates were confirmed using mass spectrometry and immunoblot analysis. Screening experiments have demonstrated that the method is compatible with substrates containing all of the amino acids, including lysine and cysteine residues. Importantly, tyrosine residues on proteins exhibit much faster reaction rates, allowing short peptides containing this residue to be coupled without cross reactions.

INTRODUCTION

Structural studies on naturally occurring proteins have identified a number of short peptide sequences with functions ranging from ion sensing to cellular uptake enhancement (*1–4*). In terms of *de novo* strategies, techniques such as phage display (*5*) and combinatorial synthesis (*6*) have yielded numerous peptides with specific target binding capabilities. These building blocks allow new functions to be added to virtually any protein of interest, provided that a convenient strategy is available for their incorporation into the full sequence. While genetic methods often suffice for the introduction of desired sequences at the N- and C-termini or in flexible loops, such additions are limited to proteins that are expressed in exogenous hosts and are difficult to use for the introduction of peptides containing unnatural amino acids.

To expand the available options, several chemical strategies have been developed to incorporate synthetic peptides into full-sized proteins. In particular, the native chemical ligation has emerged as a powerful tool for the total or semisynthesis of proteins through the coupling of C-terminal thioesters to N-terminal cysteine residues (*7, 8*). To introduce peptides at locations other than the termini, a chemoselective Staudinger ligation has been used to attach peptide−phosphine conjugates to azides displayed on carbohydrate moieties (*9, 10*) and unnatural amino acids (*11–13*). More recently, a Cu(I)-catalyzed cycloaddition reaction has been reported for the attachment of peptides to azides and alkynes previously introduced using NHS−ester coupling reactions (*14*).

To add to these methods, we have applied a one-step Mannich-type coupling reaction for the conjugation of synthetic aniline-containing peptides (**1**) to native tyrosine residues on proteins (eq 1) (*15*). We have performed this reaction with peptides containing all the amino acids without cross reactivity, including the target side chain of tyrosine, in contrast to methods such as cysteine alkylation or lysine acylation. Furthermore, we have devised a simple synthetic route toward the reagents to allow the attachment of peptides via their N- or C-termini.

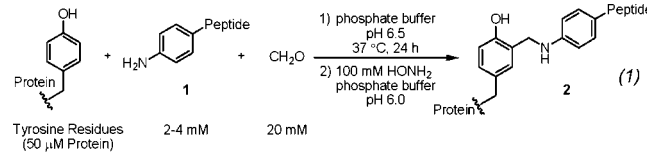

EXPERIMENTAL PROCEDURES

General Procedures and Materials. Unless otherwise noted, all chemicals and reagents were obtained from commercial sources and used without further purification. Protected amino acids were obtained from Novabiochem (San Diego, CA, USA). Water used in biological procedures or as a reaction or chromatography solvent was deionized using a NANOpure purification system (Barnstead, USA). Acetonitrile was HPLC-grade and was used without purification. Dry dimethylformamide was obtained from Acros Organics (USA). Chymotrypsinogen A, Hen Egg White Lysozyme, and RNase A were obtained from Sigma (USA) and used without purification. Enhanced Green Fluorescent Protein was obtained from Aaron Esser-Kahn (*16*).

Instrumentation and Sample Analysis Preparations. UV–vis spectroscopic measurements were conducted on a Tidas-II benchtop spectrophotometer (J & M, Germany). Centrifugations were conducted with the following: (1) Allegra 64R Tabletop Centrifuge (Beckman Coulter, Inc., USA); (2) Sorvall RC5C refrigerated high-speed centrifuge (Sorvall, USA); or (3) 5415D Benchtop Centrifuge (Eppendorf, Germany).

Desalting and removal of other small molecules of protein samples was achieved using Microcon YM-10 (10,000 MWCO) centrifugal concentrators (Millipore, USA).

^{1}H and ^{13}C spectra were measured with either a Bruker AVB-400 (400 MHz) or DRX-500 (500 MHz) spectrometer, as indicated. Proton chemical shifts are reported as δ in units of parts per million (ppm) relative to chloroform-*d* (δ 7.26, s) or deuterium oxide (δ 4.79, s). Multiplicities are reported as follows: s (singlet), d (doublet), t (triplet), q (quartet), dd (doublet of doublets), m (multiplet), and br (broadened). Coupling constants are reported as a *J* value in Hertz (Hz). The number

* Corresponding author. Phone: 510-643-9915. Fax: 510-643-3079. E-mail: francis@cchem.berkeley.edu.
[†] University of California.
[‡] Lawrence Berkeley National Labs.

10.1021/bc700231v CCC: $40.75 © 2008 American Chemical Society
Published on Web 12/11/2007

of protons (*n*) for a given resonance is indicated as nH and is based on spectral integration values. ^{13}C NMR spectra are reported as δ in units of parts per million (ppm) relative to chloroform-*d* (δ 77.23, t).

HPLC was performed on an Agilent 1100 series HPLC system (Agilent Technologies, USA). The mobile phases used were (A) ddH_2O + 0.1% TFA; (B) MeCN + 0.1% TFA. Sample analysis for all HPLC experiments was achieved with an inline diode array detector (DAD) and an inline fluorescence detector (FLD). Analytical chromatography was performed using a Jupiter 5 μm C18 300 Å reversed phase column (2.0 mm × 150 mm) (Phenomenex, USA). Preparative HPLC was performed on a Zorbax 300SB-C18 300 Å reversed phase column (9.4 mm × 250 mm) (Agilent).

Fast atom bombardment (FAB) mass spectra were obtained at the UC Berkeley Mass Spectrometry facility. Matrix assisted laser desoprtion-ionization time of flight (MALDI-TOF) mass spectra were obtained on Voyager DE-PRO (Applied Biosystems, USA). MALDI matrices were prepared daily as solutions (generally 10 mg/mL). For protein and peptide analysis, α-cyano-4-hydroxycinnamic acid (CHCA) or sinapinic acid in 3:2 MeCN/H_2O (0.1% TFA) were used. Electrospray ionization (ESI) mass spectra were obtained on a Bruker Apex II FT-ICR mass spectrometer (Bruker, Germany) or an API 150EX system (Applied Biosystems, USA) equipped with a Turbospray ion source and an Agilent 1100 series LC pump. Peptide chromatography was performed using a Jupiter 5 μm C18 300 Å reversed phase column (2.0 mm × 150 mm) (Phenomenex, USA). Protein chromatography was performed using a Jupiter 5 μm C5 300 Å reversed phase column (2.0 mm × 150 mm) (Phenomenex). A MeCN/ddH_2O gradient mobile phase containing 0.1% formic acid (250 μL/min) was used for all LC/MS. Protein mass reconstruction was performed on the charge ladder with Analyst software (version 1.3.1, Applied Biosystems).

For protein analysis, sodium dodecyl sulfate−polyacrylamide gel electrophoresis (SDS−PAGE) was accomplished on a Mini-Protean apparatus (Bio-Rad, USA). Commercially available markers (Bio-Rad, USA) were applied to one lane of each gel for the calculation of apparent molecular weights. Visualization of protein bands was accomplished by staining with Coomassie Brilliant Blue R-250 (Fisher, USA). Gel imaging was performed on an EpiChem3 Darkroom system (UVP, USA). Relative protein amounts were determined from densitometry of gel bands with ImageJ software (NIH, USA).

3-(4-Azidophenyl)propionic Acid (9). To a solution of 3-(4-aminophenyl)propionic acid (200 mg, 1.21 mmol) in 20% sulfuric acid (20 mL) at 0 °C was added sodium nitrite (92 mg, 1.3 mmol) dissolved in ddH_2O (3 mL). After stirring for 15 min, a solution of sodium azide (157 mg, 2.42 mmol) in ddH_2O (3 mL) was added. Following continued stirring at 0 °C for 1 h, a white precipitate formed. The precipitate was collected by filtration, and the filtrate was placed at 4 °C for 2 h. Following this, a new crop of precipitate was collected. The combined white solids, 146 mg (64%), were used without further purification. ^1H NMR (500 MHz, $CDCl_3$): δ 7.20 (d, 2H, J = 8.5 Hz), 6.96 (d, 2H, J = 8 Hz), 2.94 (t, 2H, J = 7.5 Hz), 2.67 (t, 2H, J = 7.5 Hz). ^{13}C NMR (125 MHz, $CDCl_3$): δ 178.1, 138.1, 136.8, 129.6, 119.1, 35.4, 29.9. HRMS (FAB) calcd for $C_9H_9N_3O_2$ (M^+) 191.0695, found 191.0692.

2-(4-Azidophenyl)ethylamine, Tosylate Salt (10). To a stirring solution of 2-(4-aminophenyl)ethylamine (800 mg, 5.87 mmol) and *p*-toluenesulfonic acid monohydrate (3.91 g, 20.5 mmol) in ddH_2O (60 mL) at 0 °C was added sodium nitrite (425 mg, 6.16 mmol) dissolved in ddH_2O (3 mL). Upon the addition of sodium nitrite, the solution turned a slight orange−brown color. After stirring for 15 min, a solution of sodium azide (954 mg, 14.7 mmol) in ddH_2O (3 mL) was added. A thick white precipitate immediately formed. The precipitate was collected by filtration, and the filtrate was placed at 4 °C for 2 h. Following this, a new crop of precipitate was collected. The combined off-white solids, 1453 mg (74%), were used without further purification. ^1H NMR (500 MHz, D_2O): δ 7.64 (d, 2H, J = 8), 7.23 (d, 2H, J = 8 Hz), 7.28 (d, 2H, J = 8 Hz), 7.06 (d, 2H, J = 8 Hz), 3.21 (t, 2H, J = 7.5 Hz), 2.93 (t, 2H, J = 7.5 Hz), 2.35 (s, 3H). ^{13}C NMR (125 MHz, D_2O): δ 142.3, 139.2, 138.6, 133.1, 130.2, 129.3, 125.2, 119.2, 40.4, 32.1, 20.3. HRMS (FAB) calcd for $C_8H_{11}N_4$ (M^+) 163.0984, found 163.0982.

General Procedures for Peptide Synthesis. Peptides were synthesized using standard Fmoc-based chemistry. The side chain protecting groups used were as follows: Asn(Trt), Asp(tBu), Arg(Pbf), Cys(Trt), Gln(Trt), Glu(tBu), His(Trt), Lys(Boc), Ser(tBu), Thr(tBu), Trp(Boc), and Tyr(tBu). Synthesis was accomplished through one of the following methods: (1) manually, using 5 equiv of amino acid in dimethylformamide with *O*-(benzotriazol-1-yl)-*N*,*N*,*N*′,*N*′-tetramethyluronium hexafluorophosphate (HBTU) (5 equiv) as the coupling reagent with 1-hydroxybenzotriazole (HOBT) (5 equiv) and *N*,*N*-diisopropylethylamine (DIPEA) (10 equiv) as additives; (2) on an Apex 396 Peptide Synthesizer (AAPPTech, USA) using 10 equiv of amino acid in *N*-methylpyrrolidone with diisopropylcarbodiimide (10 equiv) as the coupling reagent with HOBT (10 equiv) as an additive; and (3) by the Howard Hughes Mass Spectrometry and Peptide Synthesis facility at the University of California, Berkeley, on a model 433 peptide synthesizer (Applied Biosystems, USA).

All peptides were cleaved from resin using a cocktail of 94% trifluoroacetic acid, 5% H_2O, and 1% triisopropylsilane and precipitated in cold *tert*-butylmethylether. In the cases of peptides containing cysteine, ethanedithiol was added at 1% v/v to the cleavage cocktail. Crude peptides were purified using preparative reversed-phase HPLC and subsequently lyophilized before use.

Synthesis of C-terminal Anilines though Backbone Amide Linker: Reductive Amination to Form 7. To a 50 mL round-bottom flask equipped with a Teflon stirbar was added (4-formyl-3-methoxyphenoxy)butyryl AM resin (200 mg, 0.18 mmol aldehyde) (Novabiochem, USA) and dimethylformamide (5 mL). The resin was stirred and allowed to swell for 30 min. *N*,*N*-Diisopropylethylamine (219 mg, 1.69 mmol) was added, followed by a solution of **10** (595 mg, 1.78 mmol) in 99:1 DMF/AcOH (5 mL). Sodium cyanoborohydride (112 mg, 1.78 mmol) was added as a solid, and any residual solids were washed into the suspension with DMF. The mixture was stirred at room temperature overnight. The resin was then transferred to a fritted peptide synthesis tube (Econopak tubes, BioRad, USA) and washed with CH_2Cl_2 (5 mL), DMF (5 mL), 9:1 DMF/DIPEA (5 mL), DMF (2 × 5 mL), and CH_2Cl_2 (3 × 5 mL).

Acylation of 7. The resin was swelled in dry DMF (3 mL) for 15 min with gentle end-over-end agitation and then filtered. In a separate vessel were combined *N*-Fmoc-glycine (265 mg, 0.89 mmol), *O*-(7-azabenzotriazol-1-yl)-*N*,*N*,*N*′,*N*′-tetramethyluronium hexafluorophosphate (HATU, 312 mg, 0.89 mmol), and dry DMF (3 mL). After the addition of DIPEA (230 mg, 1.78 mmol), this solution was immediately added to the resin, and agitation was continued at room temperature for 6 h. The resin was then filtered and washed with DMF (3 × 5 mL), CH_2Cl_2 (3 × 5 mL), and MeOH (1 × 5 mL). UV quantitation of dibenzofulvene released during Fmoc removal generally showed between 60 and 90% yield over two steps. Following these steps, peptides were synthesized according to standard methods.

Scheme 1. Synthesis of Peptides with N- and C-Terminal Anilines[a]

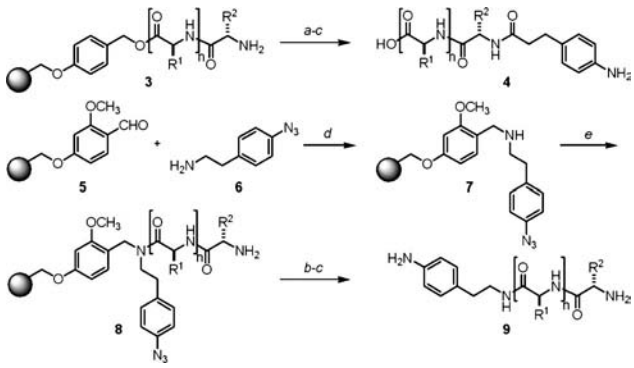

[a] Reagents: (a) 3-(4-Azidophenyl)propionic acid, HBTU, HOBT, DIPEA, and DMF. (b) $(NH_4)_2S$, H_2O/DMF. (c) TFA, H_2O, TIPS. (d) $NaCNBH_3$, DMF. (e) *N*-Fmoc-AA, HATU, DIPEA, DMF, then Fmoc SPPS.

General Procedure for the Reduction of Aryl Azides on Solid Support. Dry resin containing the protected peptide was placed in a disposable peptide synthesis tube. Dimethylformamide (1800 uL) was added, and the resin was incubated with gentle end-over-end agitation for 15 min. Ammonium sulfide (aqueous solution, 21.2% w/v, 200 μL) was added to the resin suspension, which immediately turned green. Agitation was continued for 2 h at room temperature. The resin was then filtered and washed with DMF (4 × 5 mL), CH_2Cl_2 (3 × 5 mL), MeOH (5 mL), CH_2Cl_2 (5 mL), and MeOH (2 × 5 mL), and dried.

General Procedure for Protein Labeling Reactions. In a 0.6 mL conical centrifuge tube were combined solutions of protein (1 μL of 1 mM in pH 6.5 phosphate buffer), peptide (8 μL of 10 mM in pH 6.5 phosphate buffer), formaldehyde (3.3 μL of 150 mM in pH 6.5 phosphate buffer), and 100 mM phosphate buffer (pH 6.5) to a final volume of 20 μL. Final concentrations were 50 μM in protein, 4 mM in peptide, and 25 mM in formaldehyde. For peptides with reduced cysteines, tris(carboxyethyl)phosphine (TCEP) was added to a final concentration of 10 mM. Reactions were incubated at 37 °C in a heated incubator for 20–24 h. This procedure was preferable to incubation in a water bath, which led to solvent evaporation and condensation on the caps of the tubes and concomitant precipitation of protein. Reactions were quenched with the addition of a 1 M solution of hydroxylamine HCl (pH adjusted to 6 with 5 N NaOH) to a final concentration of 100 mM. Samples were purified using centrifugal dialysis or size-exclusion chromatography.

General Procedure for Immunoblots. Protein samples were separated by SDS−PAGE according to the procedure developed by Laemmli. Proteins were then transferred to nitrocellulose using a Mini Trans-Blot assembly (BioRad) in 13 mM $NaHCO_3$ buffer at pH 9.9 (with 20% MeOH) at 350 mA for 1 h. The nitrocellulose membrane was blocked with 5% dry milk in TBS-Tween20 at room temperature overnight. Primary antibody (mouse α-FLAG conjugated to horseradish peroxidase, Sigma, USA) was added at 1:1000 to 1:5000 dilution in 5% milk/TBS-T and was incubated at RT for 1–2 h. Membrane was washed 4 × 5 min in TBS-T and visualized by treatment with an ECL detection kit (Amersham Biosciences, UK) and exposing BioMax MR Film (Kodak, USA).

RESULTS AND DISCUSSION

To access aniline-bearing peptides, two similar solid-phase strategies were developed (Scheme 1). In the first, a peptide containing the Myc epitope (*17*) (EQKLISEEDL) was synthesized on acid-cleavable Wang resin (*18*) to yield **3**. The terminal amino group was then acylated with 3-(4-azidophenyl)propionic acid using HBTU as a coupling agent. Reduction of the aryl azide with ammonium sulfide in DMF/H_2O proved to be the most effective method for unmasking the aniline group, affording quantitative conversion in less than 2 h. Peptide−aniline **4** was obtained following resin cleavage and protecting group removal using trifluoroacetic acid (TFA).

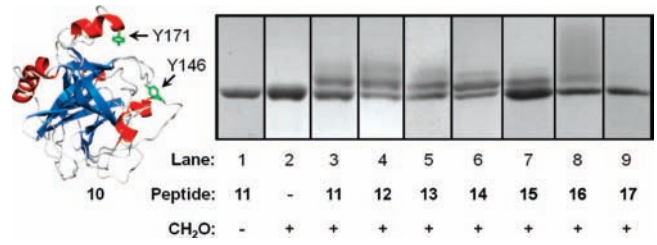

Figure 1. Chymotrypsinogen A (**10**) after incubation with 4 mM peptide aniline and 20 mM formaldehyde at 37 °C for 20 h. Higher molecular-weight bands indicate Mannich products. In the absence of formaldehyde (lane 1) or peptide (lane 2), no addition was observed.

A second synthetic route was developed to prepare peptides bearing an aniline at the C-terminus. Following the attachment of amine **6** to 4-formyl-3-methoxyphenoxybutyryl AM resin (*19*) (**5**) via reductive amination with $NaCNBH_3$, the resulting secondary amine (**7**) was acylated with N-Fmoc-glycine and HATU. Standard Fmoc solid-phase peptide synthesis was then carried out to produce a resin-bound protected peptide of the desired sequence (**8**). After the reduction of the azide with ammonium sulfide, peptide **9** was cleaved from the resin and deprotected using TFA. The peptides prepared using both methods were purified using HPLC and characterized via ESI-MS (Table 1).

Following the synthesis and purification of the peptides, tyrosine modification was achieved by exposing a 50 μM solution of α-chymotrypsinogen A (**10**) to 2–4 mM peptide−aniline and 20 mM formaldehyde in phosphate buffer (pH 6.5) at 37 °C for 24 h. The reactions were then treated with a solution of hydroxylamine (previously adjusted to pH 6.0), a step we have found to be necessary to cleave any remaining formaldehyde imines. This quenching step was found to be less effective at pH values below 6. Following the removal of the small molecules using ultrafiltration, protein modification could be observed through the appearance of a new higher molecular weight band in a Coomassie-stained SDS−PAGE gel (Figure 1, Lanes 3–8). Mass spectral analysis of these samples indicated an increase in mass corresponding to the peptide plus 1 equiv of formaldehyde (Figure 2a). No new bands were observed when either formaldehyde (lane 1) or the peptide (lane 2) was withheld from the reaction mixture. We have found that this amount of formaldehyde does not lead to protein cross-linking (protocols for this purpose typically use concentrations at least 10 times higher). It is notable that these concentrations of reactants are lower than our previously reported amounts necessary for adequate labeling using this method (*15*). In the case of these anilines, we have successfully performed the reaction with concentrations up to an order of magnitude lower.

In addition to the Myc tag, several other useful peptide anilines were synthesized and coupled to **10** (Table 1). This set included the FLAG epitope (**13**) (*20*), an HIV-Tat derived peptide (**14**) (*2*), a sequence that nucleates gallium arsenide nanocrystals (**15**) (*21*), and a sequence that binds terbium(III) ions (**16**) (*22*). In each case, 34% to 84% conversion was achieved, as determined using densitometry measurements after Coomassie staining (Table 1). In general, an increase in the number of flexible glycine residues between the aniline and the α-branched amino acids led to an increase in reactivity,

Table 1. Peptide Anilines Screened in the Mannich Reaction[a]

peptide	sequence	function	mass[b]	MW (calcd)	MW (found)	+0	+1	+2	ref
11	AnEQKLISEEDL	Myc	$(M+H)^+$	1350.7	1351.3	47	42	11	*17*
12	AnGGGEQKLISEEDL	Myc	$(M+H)^+$	1521.7	1522.4	26	49	25	*17*
13	DYKDDDDKGGGGGAn	FLAG	M^+	1415.6	1415.6	35	45	21	*20*
14	AnGGGRKKRRQRRR	Tat	$(M+H)^+$	1658.0	1658.7	17	64	20	*2*
15	AQNPSDNNTHTHGGGAn	GaAs	$(M+H)^+$	1624.7	1625.3	66	34	0	*21*
16	ACADYNKDGWYEELECAGGGAn	LBT	M^+	2267.9	2267.9	66	34	0	*22*
17[c]	ACADYNKDGWYEELECAGGGAn	LBT	M^+	2266.0	2266.0	100	0	0	*22*

[a] An indicates the site of the aniline, either 3-(4-aminophenyl)propionic acid (N-terminal anilines, i.e., 4) or 2-(4-aminophenyl)ethylamine (C-terminal anilines, i.e., 9). Coupling yields (expressed as percents, $+n$ where n is the number of modifications) were determined through densitometry analysis of the Coomassie-stained gel in Figure 1. [b] Calculated peptide masses are monoisotopic. Spectra for multiply charged species were deconvoluted to the parent mass. [c] Peptide 17 was oxidized to form a cyclic disulfide.

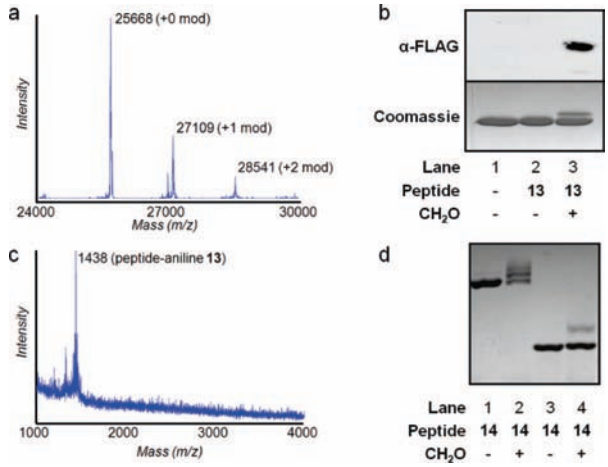

Figure 2. (a) Typical ESI-MS spectrum of chymotrypsinogen (**10**) modified with peptide-aniline **13**. (b) Immunoblot and Coomassie stained gel of **10** modified with **13**. Antibody binding was observed only when both peptide-aniline and formaldehyde are present. (c) MALDI-TOF MS of **13** after incubation with formaldehyde for 20 h at 37 °C. (d) Coomassie-stained gels of proteins following reaction with **11**. Proteins are eGFP (Lanes 1 and 2) and Myoglobin (Lanes 3 and 4).

suggesting that the steric environment around the aniline was crucial to its ability to undergo the Mannich reaction. Both N- and C-terminal peptide−anilines provided similar coupling results. Notably, a peptide containing free cysteine residues (**16**) participated in the reaction, but upon oxidation to form disulfide **17**, reactivity was abrogated.

To confirm that the new species observed in the gels contained desired peptide, a sample of chymotrypsinogen A modified with FLAG sequence **13** was transferred to nitrocellulose and probed with HRP-conjugated anti-FLAG antibodies. The presence of the FLAG epitope was only detected in reactions containing both peptide−aniline and formaldehyde (Figure 2b).

Trypsin digests of Chymotrypsinogen labeled with **14** indicated the modification of a peptide fragment containing Y171. The small amount of double labeling is presumed to occur at Y146, which has been observed to participate in other coupling reactions (*15*, *23*); however, neither this nor other modified fragments could be identified in the digested samples.

In previous studies (*15*), we have observed that this coupling reaction proceeds much more rapidly on proteins than on peptide and small molecule substrates. Presumably, this is due to hydrophobic interactions between the reactive partners that serve to increase the effective concentration. This reactivity difference suggested that tyrosine-containing peptides could also be used as substrates in the reaction. To examine this possiblity, peptides **13**, **16**, and **17** were incubated with formaldehyde under reaction conditions in the presence and absence of protein. No peptide cross-linking was observed with MALDI-TOF mass spectrometry (Figure 2c). These experiments demonstrate the compatibility of tyrosine-containing peptides with the Mannich-type reaction, which is a potential advantage of this method compared to lysine- and cysteine-targeting strategies. While it is likely that cross-reactivity could occur in some situations, these results suggest that a wide range of sequences may be compatible with the Mannich-type coupling. Consistent with previous observations of this reaction, eGFP (*24*) (which has several exposed tyrosines on its surface when viewed as a crystal structure) participates readily, while myoglobin demonstrates poor levels of reactivity (Figure 2d). Clearly, the local environments of tyrosine residues have a significant impact on their reactivity, a feature that is anticipated to yield significant advantages for site selectivity as these effects are elucidated.

CONCLUSIONS

We have demonstrated the utility of a previously reported three-component tyrosine bioconjugation reaction for the coupling of peptides to preexisting proteins. Such ligations are challenging propositions for which few methods exist. This method should find use in cellular uptake and trafficking studies, protein purification, and materials applications. It also provides a simple way to add peptides containing unnatural amino acids to full-size proteins. We are currently investigating these peptides for use in other bioconjugation reactions involving anilines (*25*), and we are continuing to examine the mechanisms of bioconjugation reactions to improve and expand the options available to protein chemists and biochemists.

ACKNOWLEDGMENT

We gratefully acknowledge the NIH (GM072700-01) and the DOE Nanoscale Science, Engineering, and Technology Program (NSET) for funding. We also thank David King and Jason Rush for lending their peptide synthesis knowledge and Arnold Falick for his mass spectrometry expertise.

Supporting Information Available: Procedures and spectra for protein digests and specific control experiments. This material is available free of charge via the Internet at http://pubs.acs.org.

LITERATURE CITED

(1) Adermann, K., John, H., Standker, L., and Forssmann, W. G. (2004) Exploiting natural peptide diversity: novel research tools and drug leads. *Curr. Opin. Biotechnol. 15*, 599–606.

(2) Anderson, D. C., Nichols, E., Manger, R., Woodle, D., Barry, M., and Fritzberg, A. R. (1993) Tumor cell retention of antibody fab fragments is enhanced by an attached HIV TAT protein-derived peptide. *Biochem. Biophys. Res. Commun. 194*, 876–884.

(3) Vives, E., Granier, C., Prevot, P., and Lebleu, B. (1997) Structure-activity relationship study of the plasma membrane translocating potential of a short peptide from HIV-1 Tat protein. *Lett. Pept. Sci. 4*, 429–436.

(4) Wender, P. A., Mitchell, D. J., Pattabiraman, K., Pelkey, E. T., Steinman, L., and Rothbard, J. B. (2000) The design, synthesis, and evaluation of molecules that enable or enhance cellular uptake: Peptoid molecular transporters. *Proc. Natl. Acad. Sci. U.S.A. 97*, 13003–13008.

(5) Azzazy, H. M. E., and Highsmith, W. E. (2002) Phage display technology: clinical applications and recent innovations. *Clin. Biochem. 35*, 425–445.

(6) Falciani, C., Lozzi, L., Pini, A., and Bracci, L. (2005) Bioactive peptides from libraries. *Chem. Biol. 12*, 417–426.

(7) Dawson, P. E., Muir, T. W., Clarklewis, I., and Kent, S. B. H. (1994) Synthesis of proteins by native chemical ligation. *Science 266*, 776–779.

(8) Cotton, G. J., and Muir, T. W. (1999) Peptide ligation and its application to protein engineering. *Chem. Biol. 6*, R247–R256.

(9) Saxon, E., and Bertozzi, C. R. (2000) Cell surface engineering by a modified Staudinger reaction. *Science 287*, 2007–2010.

(10) Prescher, J. A., Dube, D. H., and Bertozzi, C. R. (2004) Chemical remodelling of cell surfaces in living animals. *Nature 430*, 873–877.

(11) Kiick, K. L., Saxon, E., Tirrell, D. A., and Bertozzi, C. R. (2002) Incorporation of azides into recombinant proteins for chemoselective modification by the Staudinger ligation. *Proc. Natl. Acad. Sci. U.S.A. 99*, 19–24.

(12) Nilsson, B. L., Kiessling, L. L., and Raines, R. T. (2000) Staudinger ligation: A peptide from a thioester and azide. *Org. Lett. 2*, 1939–1941.

(13) Nilsson, B. L., Soellner, M. B., and Raines, R. T. (2003) Protein assembly using the staudinger ligation. *Biopolymers 71*, 306–306.

(14) Sen Gupta, S., Kuzelka, J., Singh, P., Lewis, W. G., Manchester, M., and Finn, M. G. (2005) Accelerated bioorthogonal conjugation: A practical method for the Ligation of diverse functional molecules to a polyvalent virus scaffold. *Bioconjugate Chem. 16*, 1572–1579.

(15) Joshi, N. S., Whitaker, L. R., and Francis, M. B. (2004) A three-component Mannich-type reaction for selective tyrosine bioconjugation. *J. Am. Chem. Soc. 126*, 15942–15943.

(16) Gilmore, J. M., Scheck, R. A., Esser-Kahn, A. P., Joshi, N. S., and Francis, M. B. (2006) N-terminal protein modification through a biomimetic transamination reaction. *Angew. Chem., Int. Ed. 45*, 5307–5311.

(17) Kari, B., Lussenhop, N., Goertz, R., Wabukebunoti, M., Radeke, R., and Gehrz, R. (1986) Characterization of monoclonal-antibodies reactive to several biochemically distinct human cytomegalovirus glycoprotein complexes. *J. Virol. 60*, 345–352.

(18) Wang, S. S. (1973) Para-alkoxybenzyl alcohol resin and para-alkoxybenzyloxycarbonylhydrazide resin for solid-phase synthesis of protected peptide fragments. *J. Am. Chem. Soc. 95*, 1328–1333.

(19) Jensen, K. J., Alsina, J., Songster, M. F., Vagner, J., Albericio, F., and Barany, G. (1998) Backbone Amide Linker BAL) strategy for solid-phase synthesis of C-terminal-modified and cyclic peptides. *J. Am. Chem. Soc. 120*, 5441–5452.

(20) Einhauer, A., and Jungbauer, A. (2001) The FLAG (TM) peptide, a versatile fusion tag for the purification of recombinant proteins. *J. Biochem. Biophys. Methods 49*, 455–465.

(21) Whaley, S. R., English, D. S., Hu, E. L., Barbara, P. F., and Belcher, A. M. (2000) Selection of peptides with semiconductor binding specificity for directed nanocrystal assembly. *Nature 405*, 665–668.

(22) Franz, K. J., Nitz, M., and Imperiali, B. (2003) Lanthanide-binding tags as versatile protein coexpression probes. *ChemBioChem 4*, 265–271.

(23) Tilley, S. D., and Francis, M. B. (2006) Tyrosine-selective protein alkylation using pi-allylpalladium complexes. *J. Am. Chem. Soc. 128*, 1080–1081.

(24) Tsien, R. Y. (1998) The green fluorescent protein. *Annu. Rev. Biochem. 67*, 509–544.

(25) Hooker, J. M., Esser-Kahn, A. P., and Francis, M. B. (2006) Modification of aniline containing proteins using an oxidative coupling strategy. *J. Am. Chem. Soc. 128*, 15558–15559.

BC700231V

Streptavidin in Antibody Pretargeting. 5. Chemical Modification of Recombinant Streptavidin for Labeling with the α-Particle-Emitting Radionuclides ^{213}Bi and ^{211}At

D. Scott Wilbur,*,† Donald K. Hamlin,† Ming-Kuan Chyan,† and Martin W. Brechbiel‡

Department of Radiation Oncology, University of Washington, Seattle, Washington, and National Cancer Institute, National Institutes of Health, Bethesda, Maryland. Received June 30, 2007; Revised Manuscript Received September 29, 2007

We are investigating the use of recombinant streptavidin (rSAv) as a carrier molecule for the short-lived α-particle-emitting radionuclides ^{213}Bi ($t_{1/2}$ = 45.6 min) and ^{211}At ($t_{1/2}$ = 7.21 h) in cancer therapy. To utilize rSAv as a carrier, it must be modified in a manner that permits rapid chelation or bonding with these short-lived radionuclides and also modified in a manner that diminishes its natural propensity for localization in the kidney. Modification for labeling with ^{213}Bi was accomplished by conjugation of rSAv with the DTPA derivative *p*-isothiocyanatobenzyl-CHX-A″ (CHX-A″), **3a**. Modification for *direct labeling* with ^{211}At was accomplished by conjugation of rSAv with an isothiocyanatophenyl derivative of a *nido*-carborane (nCB), **3b**, or an isothiocyanatophenyl-dPEG/decaborate(2-) derivative, **3c**. After conjugation of the chelating or bonding moiety, rSAv was further modified by reaction with an excess (50–100 equivalents) of succinic anhydride. Succinylation of the lysine amines has previously been shown to greatly diminish kidney localization. rSAv modified by conjugation with **3a** and succinylated rapidly radiolabeled with ^{213}Bi (<5 min), providing a 72% isolated yield. ^{211}At labeling of modified rSAv was accomplished in aqueous solution using chloramine-T as the oxidant. Astatination of rSAv conjugated with **3b** and succinylated occurred very rapidly (<1 min), providing a 50% isolated radiochemical yield. Astatination of rSAv conjugated with **3c** and succinylated was also very rapid (<1 min) providing 66–71% isolated radiochemical yields. Astatination of succinylated rSAv, **2a**, which did not have conjugated borane cage moieties, resulted in a much lower radiolabeling yield (18%). The ^{213}Bi or ^{211}At-labeled modified rSAv preparations were mixed with the corresponding ^{125}I-labeled rSAv, and dual-label in vivo distributions were obtained in athymic mice. The in vivo data show that ^{213}Bi-labeled succinylated rSAv [^{213}Bi]**6a** has tissue concentrations similar to those of ^{125}I-labeled modified rSAv [^{125}I]**6b**, suggesting that ^{213}Bi is quite stable toward release from the chelate in vivo. In vivo data also indicate that the ^{211}At-labeled rSAv conjugated with **3b** or **3c** and succinylated are stable to in vivo deastatination, whereas succinylated rSAv lacking a boron cage moiety is subject to some deastatination. The modified rSAv conjugated with *nido*-carborane derivative **3b** has a higher retention in many tissues than rSAv without the carborane conjugated. Interestingly, the rSAv conjugated with **3c**, which also contains an m-dPEG$_{12}$ moiety, has significantly decreased concentrations in blood and other tissues when compared with those of direct-labeled rSAv, suggesting that it may be a good candidate for further study. In conclusion, rSAv that has been modified with CHX-A″ and succinylated (i.e., **5a**) may be useful as a carrier of ^{213}Bi. The encouraging results obtained with the PEGylated decaborate(2-) derivative **3c** and succinylated (i.e., **5c**) suggests that its further study as a carrier of ^{211}At in pretargeting protocols is warranted.

INTRODUCTION

α-Emitting radionuclides are of high interest for targeted radionuclide therapy (TRT[1]) of disseminated (micro)metastatic cancer (*1–4*). The short path length of the α-particle results in the deposition of a large amount of energy in a few cell diameters, providing very effective cell killing for single cells or small clumps of cells without affecting the surrounding normal tissues. Two of the most promising α-particle-emitting radionuclides for use in TRT are ^{213}Bi and ^{211}At (*5*). Unfortunately, both of these radionuclides have relatively short half-lives (45.6 min and 7.21 h, respectively), making it imperative that rapid and efficient radiolabeling chemistry be available or developed. The short half-lives of these radionuclides also makes it imperative that the cancer-targeting carrier molecule be able to localize rapidly to the cancer cells in the body. Furthermore, the high cytotoxicity of these radionuclides requires that they remain attached to the carrier molecule during the period they are present in the body.

The cancer-targeting agent is a critical component in TRT. While there are a large number of biological agents to choose from, making the choice of an appropriate cancer-targeting agent to carry highly cytotoxic, short half-lived, α-emitting radionuclides is not easy. For systemic delivery, intact monoclonal antibodies (mAbs) and their F(ab′)$_2$ fragments are questionable for carrying ^{213}Bi or ^{211}At because of their inherent properties (*6–8*) and unfavorable tumor-targeting pharmacokinetics. Smaller mAb fragments, engineered proteins, and peptides are also unfavorable because of their propensity to localize in the kidney, although a number

* To whom correspondence should be addressed. Department of Radiation Oncology, University of Washington, Box 355016, 616 N. E. Northlake Place, Seattle, WA 98105. Phone: 206-616-9246. Fax: 206-616-8798. E-mail: dswilbur@u.washington.edu.

† University of Washington.

‡ National Institutes of Health.

[1]Abbreviations: Av, avidin; BM, binding moiety or bonding moiety; ChT, chloramine-T; cpm, counts per minute; decaborate(2-), undecahydrodecaborate, $[B_{10}H_9]^{2-}$-R; DTPA, diethylenetetraaminepentaacetic acid; EDTA, ethylenediaminetetraacetic acid; IEF, isoelectric focusing; iv,intravenous; mAb, monoclonal antibody; %ID/g, percent injected dose/gram; nCB, *nido*-carborane; PBS, phosphate-buffered saline; pi, post injection; rSAv, recombinant streptavidin; rt, room temperature, SAv, streptavidin.

10.1021/bc7002428 CCC: $40.75 © 2008 American Chemical Society
Published on Web 12/12/2007

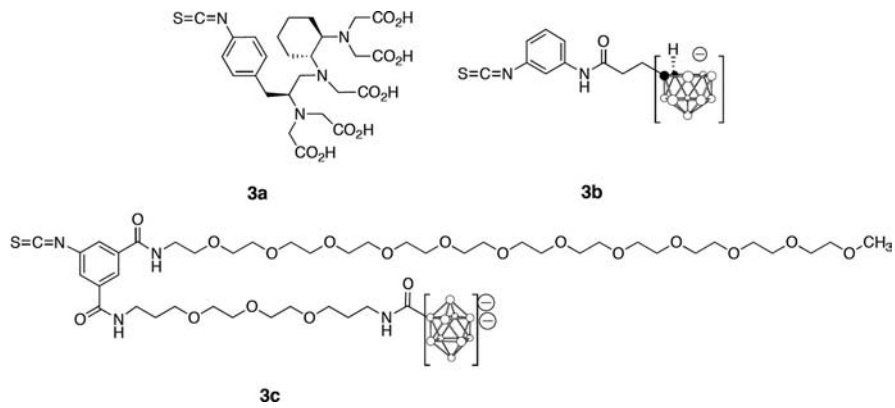

Figure 1. Structures of protein-reactive (phenylisothiocyanate) compounds used to modify recombinant streptavidin for the chelation of ^{213}Bi (**3a**) or bonding with ^{211}At (**3b**, **3c**). In the structures of the borane cage moieties, the open circles represent boron or B-H atoms and solid (black) circles represent carbon atoms.

of studies to decrease localization have been published (*9–13*). As an alternative, we have been investigating the use of two different two-step approaches[2] for targeting ^{213}Bi and ^{211}At to cancer cells in vivo termed pretargeting. In one form of the two-step pretargeting approach (*14, 15*), monoclonal antibodies (mAbs) are conjugated with a biotin derivative, and that conjugate is injected to target the cancer cells. At some time later (i.e., 24 h post injection of the mAb-biotin), a radiolabeled recombinant streptavidin (rSAv) is injected to bind with the tumor cell-surface-associated mAb-biotin.

Proteins, such as rSAv, cannot be labeled with ^{213}Bi or ^{211}At without conjugation of a binding or bonding moiety (BM) first. Furthermore, proteins such as rSAv, which have molecular weights of ~50 kDa, can localize rapidly to the kidney (*16*), posing the same serious limitations of mAb fragments and peptides. Fortunately, prior studies have reported several methods to decrease the kidney localization of rSAv without significantly affecting the biotin-binding affinity (*17–19*). Of these options, succinylation of the amines on rSAv is perhaps the most readily achieved and provides low kidney concentrations. Thus, the use of rSAv as a carrier of radionuclides requires two modification steps: the first is to conjugate a binding or bonding moiety, and the second is to react all (or most) of the remaining surface lysine amines with a molecule that neutralizes the lysine's positive charge, such as a succinic anhydride moiety.

A cyclohexyl-DTPA derivative, isothiocyanato-benzyl-CHX-A″, was chosen for conjugation with rSAv for ^{213}Bi labeling. This choice was based on our prior studies (*20, 21*) and those of other investigators (*22–26*) that have demonstrated that proteins conjugated with the CHX-A″ moiety are rapidly labeled with ^{213}Bi in high radiochemical yields. The choice for the modification of rSAv to attain efficient ^{211}At labeling was not as readily apparent. Unlike radioiodination, direct astatination of proteins can result in an unstable label when injected in vivo (*27, 28*). The application of *p*- or *m*-astatobenzoate NHS esters often used in protein astatinations (*29, 30*) was considered for labeling rSAv. However, the use of such astatinated benzoate derivatives appeared problematic because of the requirement of modification of rSAv to eliminate kidney localization following the radiolabeling step. Additionally, it was desirable to obtain a simpler and perhaps higher yielding approach for astatination of rSAv. In other studies, we have shown that astatination of a mAb Fab′ can be accomplished rapidly in high yield using borane cage moieties (*31*). Because of the differences noted previously for *nido*-carborane conjugates and decaborate(2-) conjugates, we felt that it was important to evaluate both options in this investigation. The protein-reactive α-emitting radionuclide's binding (chelating) or bonding moieties used to modify rSAv are shown in Figure 1.

The primary goals of this investigation were to determine whether modifications made to rSAv for ^{213}Bi and ^{211}At labeling altered its in vivo properties and whether the rSAv conjugates prepared for study were stable to in vivo release of the radionuclides. A secondary goal was to evaluate the efficiency of radiolabeling with these expensive radionuclides, as that may impact on whether these radionuclides can be successfully applied to cancer therapy. The results obtained in the investigation are reported herein.

EXPERIMENTAL PROCEDURES

General Procedures. All chemicals purchased from commercial sources were of analytical grade or better and were used without further purification. Succinic anhydride and most other chemicals were obtained from Aldrich (Sigma-Aldrich Corp., Milwaukee, WI). The m-dPEG$^{TM}_{12}$ amine was obtained from Quanta BioDesign, Ltd. (Powell, OH). Chloramine-T (ChT) and phosphate-buffered saline (PBS) were obtained from Sigma (St. Louis, MO). Avidin was obtained from Pierce (Rockford, IL). Bismuth metal used as the target for the preparation of ^{211}At was obtained from Alpha Aesar (Ward Hill, MA) as Puratronic 99.999%. Solvents for HPLC analysis were obtained as HPLC grade and were filtered (0.2 μm) prior to use. Recombinant streptavidin (rSAv) was obtained from Boehringer Mannheim (Indianapolis, IN). Silica gel chromatography was conducted with 70–230 mesh 60 Å silica gel (Aldrich Chemical Co.). Sephadex G-25 desalting columns (PD-10 and NAP-10) were obtained from Amersham Biosciences (Piscataway, NJ). Centricon-30 centrifugation concentrators were obtained from Amicon (Beverly, MA).

Radioactivity. All radioactive materials were handled according to approved protocols at the University of Washington. Na[^{125}I]I was purchased from Perkin-Elmer Life and Analytical Services as high concentration/high specific activity radioiodide in 0.1 N NaOH. [^{225}Ac]Actinium nitrate was purchased from the Department of Energy (Oak Ridge, TN) on a column (actinide resin, 100–200 mesh, EiChrom Technology Inc., Darien, IL) ready for elution of ^{213}Bi in the radiolabeling experiments. ^{211}At was produced by an α-particle irradiation (28 MeV) of natural bismuth, ^{209}Bi(α, 2n)^{211}At, on a Scandatronix MC-50 cyclotron. The ^{211}At activity was distilled from the bismuth target at 650–700 °C into a cooled trap as previously described (*32*). The dry distillation of ^{211}At was conducted in a charcoal filtered glovebox (Innovative Technologies, radioisotope glovebox). The distilled ^{211}At was trapped in a cooled

[2]The term two-step is often not accurate because a clearing step may be used to rid the blood of remaining mAb-biotin or mAb-SAv conjugates, in effect making it a three-step approach.

(−78 °C) vial or peek tubing (1 mm ID × 35 cm length) (*33*) and was rinsed from the vial with $CHCl_3$ or 0.05 N NaOH for use in the labeling experiments.

Radiohalogenation reactions were conducted in a charcoal-filtered Plexiglas enclosure (Biodex Medical Systems Inc., Shirley, NY) housed within a radiochemical fume hood. The radiohalogenation reactions (^{125}I or ^{211}At) were conducted in vials capped with Teflon-coated septa. Reaction vials were vented through a 10 mL charcoal-filled syringe. Additions of reagents and radionuclides to, or removal of materials from, radiohalogenation vials were conducted by passing a syringe needle through the septa.

Measurement of ^{213}Bi, ^{211}At, and ^{125}I was accomplished on a Capintec CRC-15R. The calibration numbers provided by Capintec Technical Services were used for measurement of ^{213}Bi and ^{211}At on these instruments. Tissue samples containing these radionuclides were counted in a Wallac Wizard gamma counter (PerkinElmer Life and Analytical Sciences, Wellesley, MA). The tissue samples had either ^{213}Bi or ^{211}At, along with ^{125}I. Total radioactivity counts (cpm) for the samples were obtained by counting in all channels of the detector. To determine the counts from each radionuclide in tissues, the tissue samples were allowed to decay for 1–2 days, resulting in <0.01% ^{213}Bi being present (<0.01%) or 3–5 days resulting in <0.1% ^{211}At being present. Re-counting tissue samples after the decay period provided the ^{125}I counts. The total counts and ^{125}I counts for tissues were transferred to an Excel (Microsoft Corp., Redmond, WA) spreadsheet. The counts for ^{213}Bi or ^{211}At radioactivity were calculated by subtracting the ^{125}I counts from the total cpm for each tissue sample, and the ^{213}Bi and ^{211}At counts were corrected for the decay of each sample during the counting process.

Spectral Analyses. ^1H and ^{11}B NMR spectra for compounds were obtained on either a Bruker AV 300 (300 MHz) or Bruker AV 500 (500 MHz) instrument. ^1H chemical shifts are expressed as ppm using tetramethylsilane as an internal standard (δ = 0.0 ppm). ^{11}B chemical shifts were referenced to BF_3OEt_2 as an external standard. High-resolution mass spectra (HRMS) and low-resolution mass spectra (LRMS) were obtained on a Bruker APEX III 47e Fourier Transform Mass Spectrometer using electrospray ionization. For analysis, the samples were dissolved in 50/50 MeOH/H_2O and were introduced by an integral syringe infusion pump (Cole Parmer Series 74900).

Analytical Chromatography. All synthetic reactions were monitored by HPLC. Samples were assessed on a system that contained a Hewlett-Packard quaternary 1050 gradient pump, a variable wavelength UV detector (254 nm), and a Varex ELSD MKIII evaporative light-scattering detector. Analyses of HPLC data were conducted using Hewlett-Packard HPLC ChemStation software. Reversed-phase HPLC chromatography was carried out on an Alltech Altima C-18 column (5 μm, 250 × 4.5 mm) using a gradient solvent system at a flow rate of 1 mL/min. A gradient of MeOH and H_2O/0.1% HOAc was used. Starting with 40% MeOH, the initial solvent mixture was held for 2 min, then the gradient was increased to 100% MeOH over the next 10 min, then held at 100% MeOH for 8 min. Retention times (t_R) under these conditions for new compounds are provided with the compound experimental data.

HPLC separations of the (nonradioactive) modified rSAv were conducted on a Hewlett-Packard isocratic system consisting of a Model 1050 pumping system and a Model 1050 Multiple Wavelength Detector (280 nm). The proteins were evaluated on a Protein Pak 300 SW glass size-exclusion column (10 μm, 8 mm × 30 cm, Waters Corporation, Milford, MA) run at 1.0 mL/min, eluting with 50 mM sodium phosphate buffer (pH 6.8), which contained 300 mM NaCl, 1 mM EDTA, and 1 mM sodium azide. Analyses of the HPLC data were conducted on Hewlett-Packard HPLC ChemStation software. Retention time (t_R) for the succinylated r-SAv was 9.8 min and that for boron cage-modified rSAv was ~10.5 min using these conditions.

Radiolabeled rSAv. Size-exclusion chromatography was also used to evaluate radiolabeled modified rSAv. HPLC separations of radioiodinated proteins were conducted on a system consisting of a Model 1050 pumping system, a Waters Lambda-Max 481 UV detector, and a Beckman model 170 radioisotope detector. The detectors were connected to a computer through a Hewlett-Packard Model 35900 interface, and data from the chromatograms was obtained on a computer running Hewlett-Packard ChemStation Software. The same size-exclusion column and elution conditions were used for the radiolabeled proteins as unlabeled proteins.

Isoelectric Focusing. IEF was obtained on a Novex PowerEase 500 instrument with the XCell II chamber using Invitrogen (Novex) precast gels, pH 3–10 (1.0 mm, 12 well), running under the standard IEF Program. The protein was stained with GelCode Blue Stain (Pierce). IEF standards were from Serva Electrophoresis GmbH: (pI) 10.7, cytochrome C; 9.5, ribonuclease A; 8.3, 8.0, 7.8, lectin; 7.4, 6.9, myoglobin; 6.0, carbonic anhydrase; 5.3, 5.2, δ-lactoglobulin; 4.5, trypsin inhibitor; 4.2, glucose oxidase; 3.5, amyloglucosidase.

Syntheses. The following compounds were prepared as previously described: isothiocyanatobenzyl-CHX-A″ DTPA[3], **3a** (*34*) ; 3-(3′-(*nido*-carboranyl)propionyl)amino-1-isothiocyanatobenzene, **3b** (*35*); 5-*N*-(*tert*-butyloxycarbonyl)-aminoisophthalate bis-tetrafluorophenyl ester, **7** (*36*); $[Et_3NH]B_{10}H_9$-CO-trioxatridecanediamine, **10** (*31*).

5-(*N*-*tert*-Butyloxycarbonylamido)-3-(m-dPEG$_{12}$-amido)-isophthalamic Acid 2,3,5,6-Tetra-fluorophenyl Ester, 9. A solution of m-dPEG$_{12}$-amine, **8**, (100 mg, 0.18 mmol) in anhydrous DMF (2 mL) was added dropwise over 30 min to a solution of **7** (207 mg, 0.36 mmol) and Et_3N (30 μL, 0.36 mmol) in anhydrous DMF (5 mL) at room temperature. After the addition was complete, the reaction mixture was stirred at room temperature for an additional 10 min, then the volatile materials were removed under vacuum. The crude residue was purified by silica gel chromatography, eluting with 10% MeOH/EtOAc to give 138 mg (80%) of **9** as a colorless oil. ^1H NMR (CD_3OD, 300 MHz): δ 1.59 (s, 9H), 3.35 (s, 3H), 3.51–3.71 (m, 48H), 7.46–7.58 (m, 1H), 8.23 (t, J = 2.0 Hz, 1H), 8.28 (t, J = 1.6 Hz, 1H), 8.51 (t, J = 1.9 Hz, 1H), 8.72 (t, J = 5.2 Hz, 1H). HRMS (ES+) $C_{44}H_{66}N_2O_{17}F_4Na$ $(M + Na)^+$; calcd, 993.4195; found, 993.4193. HPLC: t_R = 14.2 min.

5-(*N*-*tert*-Butyloxycarbonylamido)-3-(m-dPEG$_{12}$-amido)-1-((13′-nonahydro-*closo*-decaborate(2-))-4,7,10-trioxatridecanediamine)-aminoisophthalate, 11. A solution containing $[Et_3NH]$**10** (53 mg, 0.113 mmol), **9** (110 mg, 113 μmol), Et_3N (32 μL, 0.227 mmol), and anhydrous DMF (5 mL) was stirred at room temperature for 2 h. EtOAc (20 mL) was added, and the mixture was stirred for an additional 10 min. The liquid was decanted from the residue. The crude product was redissolved in MeOH/water (1/1) and purified by flash chromatography (Biotage C18 FLASH 25+M column), eluting with a gradient mixture composed of MeOH and 0.1% aqueous HOAc (pH 3.25). The starting gradient mixture of 25% MeOH was held for 2 min, increased to 100% MeOH over the next 10 min, then held at 100% MeOH for 8 min. Isolation yielded 112 mg (78%) of **11** as a light-brown tacky solid. ^1H NMR (DMSO-d_6, 500 MHz): δ 1.17 (t, J = 7.3 Hz, 9H), 1.46 (s, 9H), 1.71–1.81 (m, 4H), 3.04–3.09 (m, 6H), 3.21 (s, 3H), 3.29 (dd, J = 6.6, 12.4 Hz, 2H), 3.39–3.72 (m, 71H), 7.72 (bs, 1H), 7.82 (s, 1H), 7.98 (d, J = 8.0 Hz, 2H), 8.43 (t, J = 5.5 Hz, 1H), 8.47 (t, J =

[3]This reagent is available commercially from Macrocyclics, Dallas, TX (www.macrocyclics.com).

5.5 Hz, 1H), 9.28 (bs, 1H), 9.58 (s, 1H). ^{11}B NMR (DMSO-d_6, 96.29 MHz): δ −5.03 (2B), −15.90 (2B), −24.66 (6B). LRMS (MALDI$^-$) $C_{49}H_{95}B_{10}N_4O_{20}K$ $(M + K)^-$; calcd, 1208.7; found, 1208.8. HPLC: t_R = 11.0 min.

5-(Isothiocyanato)-3-(m-dPEG$_{12}$-amido)-1-((13′-nonahydro-*closo*-decaborate(2-))-4,7,10-trioxatridecanediamine)-aminoisophthalate, 3c. A quantity of **11** (100 mg, 0.079 mmol) was dissolved in neat TFA (1 mL), and that solution was stirred at room temperature for 10 min. The excess TFA was removed under a stream of Argon, then the residue was dissolved in a solution of MeOH (3 mL) and Et_3N (0.2 mL). After solvents were evaporated on a rotoevaporator, the deprotected compound was dried under vacuum for 2 h, then dissolved in anhydrous DMF (1 mL).

To the DMF solution was added thiocarbonyldiimidazole (28 mg, 0.157 mmol). That solution was stirred at room temperature for 1 h. Et_2O was added, and the solution was stirred for an additional 30 min. The solvents were decanted, and the residue was washed with EtOAc (3 × 15 mL) to afford 91 mg (95%) of **3c**. ^{1}H NMR (DMSO-d_6, 500 MHz): δ 1.16 (t, J = 7.2 Hz, 9H), 1.71–1.77 (m, 4H), 3.06 (q, J = 7.3 Hz, 6H), 3.16 (s, 1H), 3.21 (s, 2H), 3.30 (dd, J = 6.6, 12.3 Hz, 2H), 3.39–3.74 (m, 71H), 7.40 (s, 2H), 7.93 (d, J = 8.1 Hz, 2H), 8.24 (s, 1H), 8.51 (s, 1H), 8.66 (t, J = 5.2 Hz, 1H), 8.75 (t, J = 5.1 Hz, 1H). ^{11}B NMR (DMSO-d_6, 96.29 MHz): δ −5.25 (2B), −16.67 (2B), −25.99 (6B). HPLC: t_R = 13.1 min.

Succinylation of rSAv, 2a. Succinylation of rSAv was accomplished as previously described (*17*). Briefly, a 200 μL aliquot of a 5 mg/mL solution of rSAv (1 mg, 1.9×10^{-2} μmol) was added to 370 μL of 50 mM $NaHCO_3$ buffer (pH 8.5). To this solution was added 100 equivalents (188 μg; 1.88 μmol) of succinic anhydride in 20 μL of DMSO. After 30 min at room temperature, the contents were transferred to a Centricon-10 and concentrated to approximately 50 μL. PBS (500 μL) was added, and the solution was again concentrated to 50 μL. This wash step was repeated 5 times.

Preparation of Succinylated rSAv-CHX-A″, 5a. Three steps were taken to prepare the rSAv conjugate, **5a**, such that it could be radiolabeled with ^{213}Bi. The first step involved demetalation of rSAv. The second step involved conjugation of the CHX-A″ chelate, **3a**, then succinylation of that conjugate. The third step was purification of the modified rSAv under demetalation conditions. The conditions used in each step are described below.

Demetalation of rSAv. The rSAv (5 mg) was dialyzed against 2 L of metal-free HEPES buffer with a minimum of 5 buffer changes over 3 days at 4 °C using a Slide-A-Lyzer 10K cassette (Pierce, Rockford, IL). All buffers used were prepared with metal-free (18 mega-ohm) water passed over a column of Chelex-100 resin (250 g/12 L). Chelex-100 resin (10 g) was added to each buffer change. The demetallated mAbs were removed from dialysis and placed in acid-washed 15 mL conical vials, and care was taken to ensure that no metals were introduced.

Conjugation of 3a and Succinylation. To the demetallated rSAv (4.5 mg, 85 nmol) in 1 mL of demetallated HEPES buffer at pH 8.5 at room temperature was added 44 μL (1.7 μM) of an isothiocyanatobenzyl-CHX-A″, **3a**, solution (22.4 mg/mL in DMSO). The reaction mixture was stirred at room temperature for 18 h to yield **4a**. After that time, 0.43 mg (4.24 μmol) of succinic anhydride was added, and the mixture was stirred for another 1 h at room temperature to give **5a** (80%, 4.5 mg/mL, 0.8 mL).

Purification and Second Dialysis. After the conjugation reaction was complete, the reaction mixture was placed in a dialysis cassette and dialyzed against 3 × 2 L of metal-free citrate buffer (50 mM sodium citrate, 150 mM NaCl, 0.05% NaN_3 adjusted to pH 5.5) over 2 days and against 4 × 2 L of 150 mM NaCl for 2 days. The number of CHX-A″ chelates per rSAv molecule in **5a** was assessed using the yttrium−arsenazo III complex spectrophotometric assay (*37*). The modified rSAv was stored at 4 °C until used.

Preparation of Succinylated rSAv-nCB, 5b. To 2.5 mg (500 μL at 5 mg/mL in PBS at pH 7.2) of rSAv was added 1 mL of 50 mM sodium bicarbonate buffer at pH 8.5, followed by 40 μL of a solution of **3b** (4.85 mg/mL in DMSO). This was allowed to react overnight at room temperature. The solution was then passed over a PD-10 column (Pharmacia, Uppsala, Sweden) eluting 1 mL fractions with 0.9% saline. The protein fractions were combined and concentrated using Centricon-30 (Millipore, Bedford, MA) to give 2.4 mg (400 μL of 6 mg/mL; 96%) of rSAv-nCB, **4b**.

To 1.0 mg of rSAv-nCB (167 μL of 6 mg/mL in 0.9% saline solution) was added 334 μL of 50 mM sodium bicarbonate buffer at pH 8.5, followed by 20 μL of a solution of 4.7 mg/mL succinic anhydride in DMSO. After 30 min at room temperature, the solution was passed over a PD-10 column and collected in 0.9% saline. The protein fractions were combined and concentrated in a Centricon-30 to give 0.94 mg (260 μL of 3.6 mg/mL solution; 94%) of succinylated rSAv-*nido*-carborane, **5b**.

Preparation of Succinylated rSAv-B$_{10}$H$_9$-m-dPEG$_{12}$, 5c. To 11 mg (207 nmol) of rSAv in 1 mL of 500 mM sodium borate buffer at pH 8.0 was added 137 μL (2.08 μmol) of a solution of **3c** (20 mg/mL in DMF). This was allowed to react overnight at room temperature. The solution was then passed over a PD-10 column and collected in PBS at pH 7.2. The protein-containing fractions were combined and concentrated in Centricon-30 to give 790 μL of a 12.7 mg/mL solution (91%). To 700 μL of this solution (8.9 mg) was added 700 μL of 100 mM sodium bicarbonate at pH 8.5, followed by 1.68 mg of succinic anhydride in 30 μL of DMF. After 30 min at room temperature, the solution was concentrated in Centricon-30 and washed with 4 × 1 mL of PBS at pH 7.2. This yielded 7.9 mg (1.1 mL at 7.2 mg/mL; 88%) of succinylated rSAv-B10/dPEG, **5c**.

Preparation of [^{213}Bi]6a. ^{213}Bi was obtained from ^{225}Ac ($t_{1/2}$ = 10 days) by elution of the generator column with 1 M HCl using a dual syringe pump (*38*). As the elution proceeded, the ^{213}Bi/HCl solution was mixed with water (in a plastic chamber) and run across an MP-50 cation-exchange column. ^{213}Bi was trapped on the ion-exchange column, and the column was removed from the generator system. The column was then eluted with freshly prepared 0.1 N HI, then the pH of the eluant was adjusted to 4.2–4.5 using 3 M NH_3OAc (Ultrex grade).

A 200 μg quantity of demetallated and succinylated rSAv with approximately 1.5 CHX-A″ chelates/molecule in 120 μL of PBS was diluted with 100 μL of 1 M NaOAc (pH 4), then 300 μL of ^{213}Bi eluant (95 MBq; 2.56 mCi) was added. After 5 min at room temperature, the reaction mixture was passed over a PD-10 column, and 68 MBq (72%) of [^{213}Bi]**6a** was obtained. The radiochemical purity of the [^{213}Bi]**6a** was analyzed using instant thin-layer chromatography (ITLC) on an ITLC-SG strip (Gelman, Ann Arbor, MI). After spotting, the ITLC strips were allowed to air-dry, then were placed in a development chamber containing 80% methanol/20% 10 mM DTPA in water as eluant. When the solvent had nearly reached the top of the strip, it was air-dried, cut in sections, and counted in a gamma counter. The percent bound activity was obtained by dividing the activity in the first half of the strip (from point of spotting) divided by the total activity on the ITLC strip (×100).

^{211}At/^{125}I Labeling and Preparation of [^{211}At]2b, [^{125}I]2b, [^{125}I]6b, [^{211}At]6c, [^{125}I]6c, [^{211}At]6d, and [^{125}I]6d. The following general procedures were used to obtain the ^{211}At- and ^{125}I-labeled rSAv conjugates.

[^{125}I]6b. To a solution of **5a** (100 μL of 4.5 mg/mL in PBS) was added 25 μL of sodium phosphate (500 mM, pH 7.4), then 1 μL of Na[^{125}I]I (195 μCi in 0.1 N NaOH). That addition was followed by 12 μL of a 1 mg/mL solution of ChT in water. After 5 min at room temperature, the reaction was quenched with 1.2 μL of a 10 mg/mL solution of sodium metabisulfite in water. The reaction mixture was then placed on a NAP-10 column (Amersham Pharmacia Biotech) and eluted with PBS. The protein fractions were combined to yield 166 μCi (85%) of [^{125}I]**6b**.

[^{125}I]2b and [^{125}I]6c. To 600 μg of succinylated rSAv-nCB, **5b** (1.7 mg/mL in PBS), or succinylated rSAv, **2a** (12.6 mg/mL in PBS), was added 25 μL of sodium phosphate 500 mM at pH 7.4. This was followed by 1.5 μL (310 μCi) of Na[^{125}I]I in 0.1 N NaOH and 38 μL of a solution of 1 mg/mL ChT in water. After 30 s at room temperature, 3.8 μL of a solution of 10 mg/mL sodium metabisulfite in water was added to quench the reaction. The mixture was then passed over a NAP-10 column and collected in 0.9% saline. The protein fractions were combined. This procedure gave radiochemical yields of 54% for [^{125}I]**2b** and 68% for [^{125}I]**6c**.

[^{211}At]2b and [^{211}At]6c. To 600 μg of succinylated rSAv-*nido*-carborane, **5b** (1.7 mg/mL in PBS) or succinylated rSAv, **2a** (12.6 mg/mL in PBS) was added 100 μL of 500 mM sodium phosphate at pH 7.4. This was followed by 40 μL (360–410 μCi) of Na[^{211}At]At solution at pH 7 and 38 μL of a solution of 1 mg/mL ChT in water. After 30 s at room temperature, 3.8 μL of a solution of 10 mg/mL sodium metabisulfite in water was added to quench the reaction. The mixture was then passed over a NAP-10 column (Pharmacia, Uppsala, Sweden) and collected in 0.9% saline. The protein fractions were combined. This procedure gave radiochemical yields of 18% for [^{211}At]**2b** and 50% for [^{211}At]**6c**.

[^{211}At]rSAv-B$_{10}$, [^{211}At]6d. To 750 μg of **5c** (2.9–7.2 mg/mL in PBS) was added 100 μL of 500 mM sodium phosphate at pH 7.4. This was followed by the addition of 400–500 μL (600–660 μCi) of Na[^{211}At]At solution in 0.05 N NaOH. To this solution was added 75 μL of a solution of 1 mg/mL ChT in water. After 1 min at room temperature, the reaction was quenched with 75 μL of 1 mg/mL sodium metabisulfite in water. The mixture was then passed over a NAP-10 column and collected in 0.9% saline. The protein fractions were combined to give radiochemical yields of 66 and 71% (2 radiolabeling reactions) for [^{211}At]**6d**.

[^{125}I]rSAv-B$_{10}$, [^{125}I]6d. To 750 μg of **5c**, (7.2 mg/mL in PBS) was added 25 μL 500 mM sodium phosphate at pH 7.4. This was followed by the addition of 2 μL (800–980 μCi) of Na[^{125}I]I solution in 0.1 N NaOH. To this solution was added 20 μL of a solution of 1 mg/mL ChT in water. After 30 s at room temperature, the reaction was quenched with 20 μL of 1 mg/mL sodium metabisulfite in water. The mixture was then passed over a NAP-10 column and collected in 0.9% saline. The protein fractions were combined to give radiochemical yields of 81 and 86% (two radiolabeling reactions) for [^{125}I]**6d**.

Biodistribution Studies. The animal studies were approved by the University of Washington's Institutional Animal Care and Use Committee prior to being conducted. Male athymic mice (BALB/c *nu/nu*), 4–5 weeks of age, were obtained from Simonsen Laboratories (Gilroy, CA). The mice were housed for a minimum of 1 week in the animal facility prior to the study. In dual-label experiments, the ^{213}Bi or ^{211}At-labeled modified rSAv was mixed with the appropriate (matched) ^{125}I-labeled modified rSAv. That mixture was diluted in phosphate-buffered saline (PBS) to prepare quantities of ~100 μL for administration. In each set of experiments, the dual-labeled succinylated rSAv was injected into 15 athymic mice via the lateral tail vein. The actual amount of injectant each animal received was determined by weighing the administering syringe before and after injection. Groups of five mice were sacrificed by cervical dislocation at 45, 90, and 180 min for samples containing ^{213}Bi, or 1, 4, and 24 h post injection for samples containing ^{211}At. Blood samples were obtained by cardiac puncture immediately before sacrifice. Urine samples were obtained by syringe bladder tap at the time the tissues were excised. The tissues were excised, blotted free of blood, weighed, and counted. Excised tissues are listed in Tables S1−S4 (Supporting Information). The amount of radioactivity and quantity of rSAv, as well as the average animal weights in the biodistributions, are provided in the legends for Tables S1−S4. Calculation of the percent injected dose (%ID) and percent injected dose per gram (%ID/g) in the tissues was obtained by measuring standards containing 10 μL of the injected dose. The ^{213}Bi and ^{211}At counts were adjusted for decay from the time of counting standards. Total blood volume was estimated to be 6.0% of body weight (*39*) for the calculations. Statistical analysis of the data was conducted using the paired Student's *t*-test. Differences were considered statistically significant when $p < 0.05$.

RESULTS

Reagents for Conjugation. Reagents containing bonding or chelating moieties that were used for the modification of rSAv were synthesized. The protein-reactive isothiocyanatobenzyl-CHX-A″ DTPA derivative, **3a**, was obtained in a multistep synthesis as previously reported (*34*). The isothiocyanatophenyl-*nido*-carborane derivative, **3b**, was also obtained in a multistep synthesis as previously described (*31*). The protein-reactive decaborate(2-) derivative, **3c**, was obtained as shown in Scheme 1. In that synthesis, the reaction of an excess of 5-*N*-(t-Boc)-aminoisophthalate-bis-tetrafluorophenyl (TFP) ester, **7**, (*36*) with m-dPEG$_{12}$ amine, **8**, and Et$_3$N in DMF for 40 min at room temperature provided 5-*N*-(t-Boc)-1-(m-dPEG^{12} amino)-aminoisophthalate TFP ester, **9**, in 80% yield after purification. Reaction of **9** with 2-(4,7,10-trioxatridecane-13-amine-1-amido)-undecahydro-*closo*-decaborate (2-), **10**, and Et$_3$N in DMF for 2 h at room temperature gave a 78% yield of **11**. Deprotection of the aniline in neat TFA for 10 min at room temperature yielded the free amine, which was converted to the isothiocyanate derivative **3c** in 95% yield by reaction with thiocarbonyldiimidazole in DMF for 1 h at room temperature.

Modification of rSAv. The reactions used to modify rSAv are shown in Scheme 2. In all examples studied, rSAv was modified by succinylation of surface amines to decrease kidney localization. For comparison, succinylated rSAv, **2a**, was prepared without a binding or bonding moiety (BM). That preparation was accomplished by reaction of rSAv with 50–100[4] molar equivalents of succinic anhydride in $NaHCO_3$ buffer at pH 8.5 at room temperature for 30 min. Good protein recovery yields (e.g., 85–95%) are generally obtained in this reaction. In the preparation of the other modified rSAv, succinylation was conducted after conjugation of **3a**, **3b**, or **3c**.

Modification of rSAv for binding (chelating) ^{213}Bi or bonding ^{211}At was conducted by reaction with 10 mol equiv of the protein-reactive reagents **3a**, **3b**, and **3c** (Figure 2) in HEPES buffer at pH 8.5, at room temperature for 18 h to provide **4a**, **4b**, and **4c**. After that time, the modified rSAv species were

[4]The initial studies were conducted with 50 equivalents of succinic anhydride, but later studies used 100 equivalents to be certain that as many amines are capped as possible.

Scheme 1. Synthetic Pathway for the Preparation of Protein-Reactive Phenylisothiocyanato-undecahydro-decaborate(2-) Derivative, 3c[a]

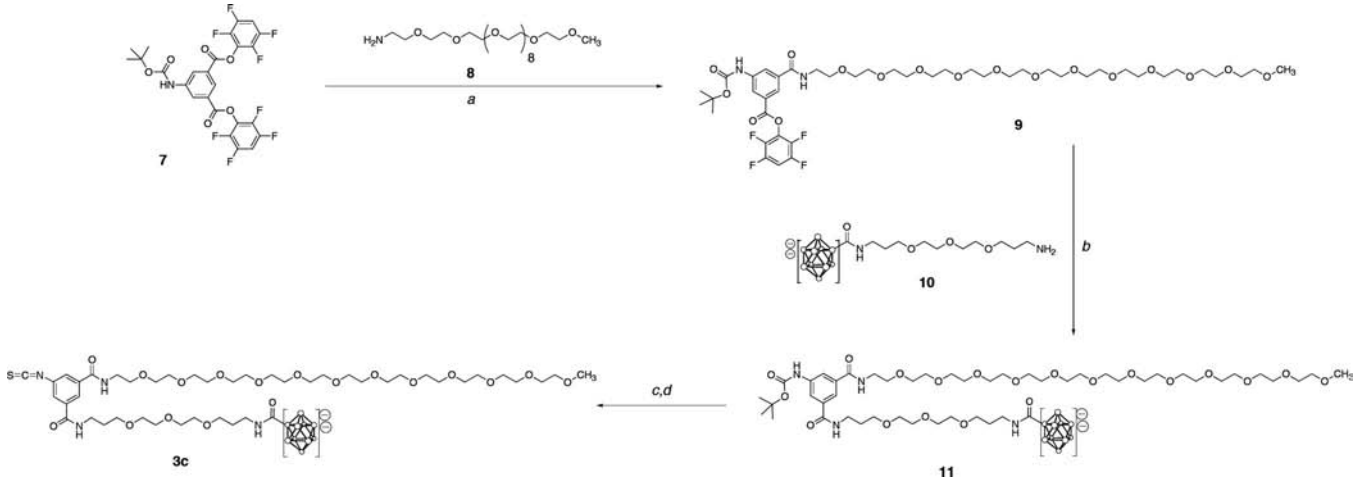

[a] In the structures of the decaborate(2-) moiety, the open circles represent boron or B-H atoms. (a) **8**, DMF, Et_3N, rt, 40 min, 80%; (b) **10**, Et_3N, rt, 2 h, 78%; (c) TFA, rt, 10 min; (d) TCDI, rt, 1 h, 95%.

Scheme 2. Chemical Steps for the Modification of rSAv and Radiolabeling with ^{213}Bi, ^{211}At, or ^{125}I[a]

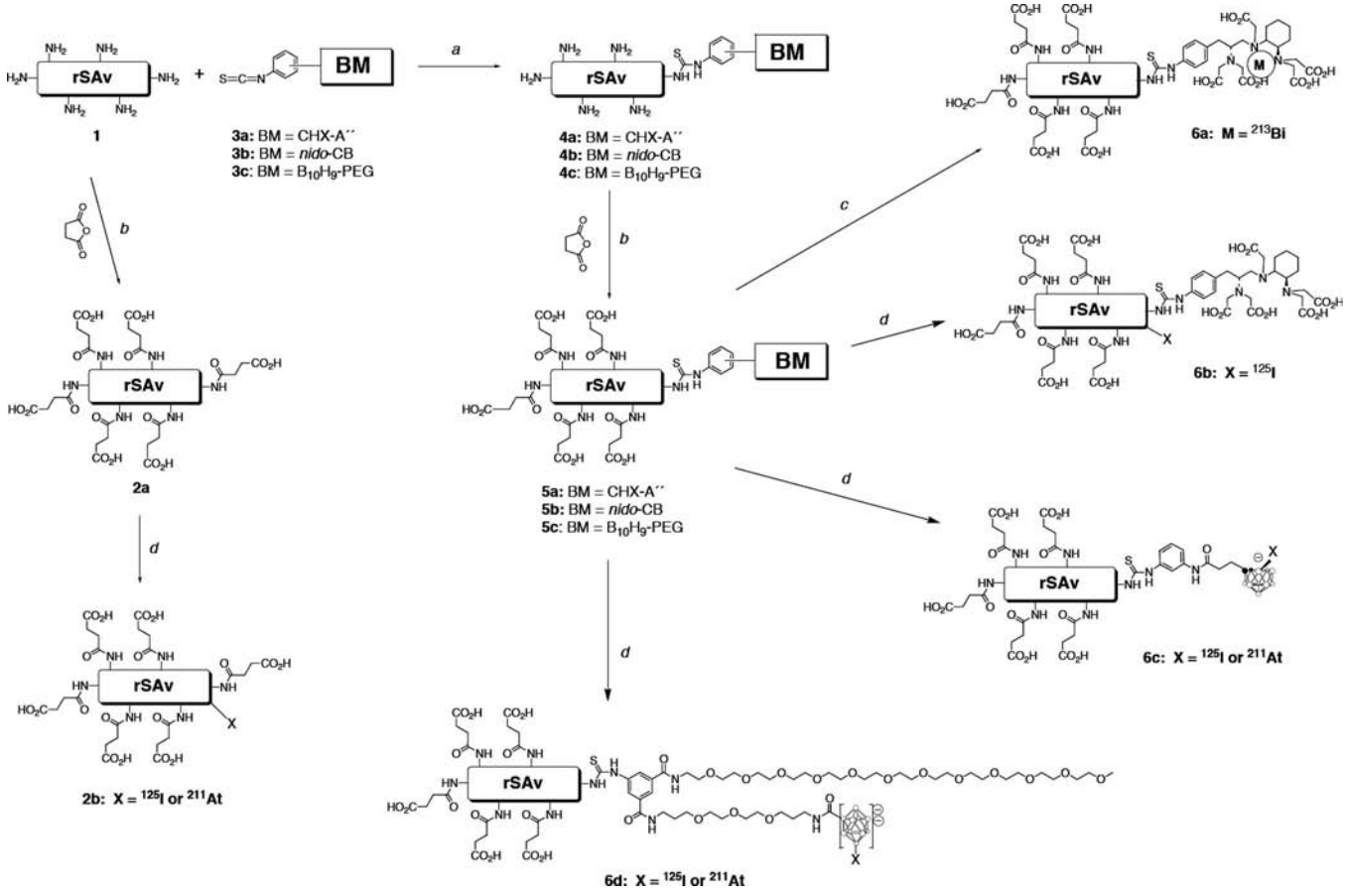

[a] (a) **3a**, **3b** or **3c**, HEPES, pH 8.6, rt, 18 h; (b) succinic anhydride, DMSO, $NaHCO_3$, pH 8.5, 30 min, rt; (c) $BiCl_3$, pH 4–5, NaOAc, HOAc; (d) Na[^{211}At]At or Na[^{125}I]I, ChT, H_2O, HOAc, rt, 30 s.

not isolated, but rather 50–100[4] equivalents of succinic anhydride were added, and the reaction was allowed to proceed for an additional 30 min. Prior to and after conjugation of the modified DTPA derivative, **3a**, the rSAv was demetallated using Chelex-100 resin. The recovery of modified rSAv species, **5a**, **5b**, and **5c** varied with the protein-reactive reagent used. Size-exclusion HPLC of the modified rSAv showed very little change from unmodified rSAv. For rSAv modified with **3a** (CHX-A″), the number of CHX-A″ moieties conjugated was determined by the spectrophotometric assay using the yttrium−arsenazo III complex (*37*). Using this method, it was determined that there were ~1.5 chelates/rSAv in the preparation used for the animal study (i.e., Table S1, Supporting Information). Quantification of the number of **3b** (*nido*-CB moieties) and **3c** (dPEG[a]/B_{10} moieties) conjugated with rSAv was not readily accomplished. However, changes in isoelectric points (pI) brought about by conjugation were evaluated by IEF analyses. An example of an IEF gel is shown in Figure 2. IEF gels showed that rSAv had protein bands in the range of pH 7.4–7.8. The protein bands (pI) shifted to pH 7.0–5.2 when conjugated with monoanion

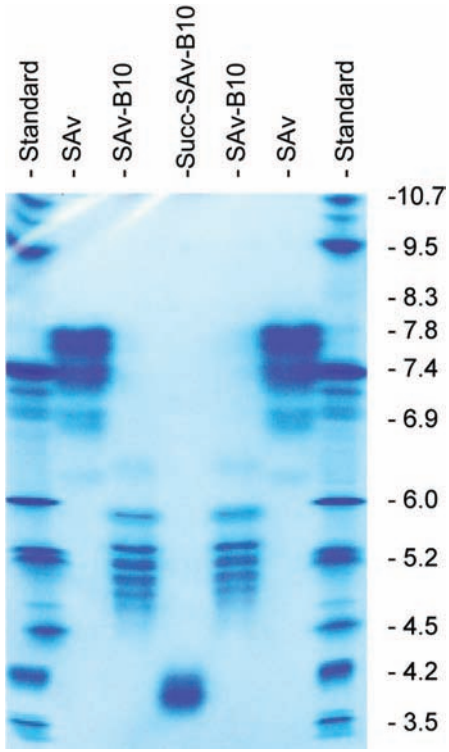

Figure 2. Digitized image of an IEF gel showing changes in pI when rSAv is modified with the decaborate(2-) derivative **3c** to prepare conjugate **4c** and after further modification with succinic anhydride to give **5c**. Lanes 1 and 7: IEF standards (Serva electrophoresis GmbH, broad pI; 3–10) run in the direction of application (bottom to top) and in the direction opposite to the application of sample (e.g., top to bottom). Lanes 2 and 6: unmodified rSAv. Lane 3 and 5: r-SAv conjugated with **3c**. Lane 4: r-SAv conjugated with **3c** and further modified by reaction with an excess succinic anhydride.

3b. The protein bands (pI) shifted further to pH 5.2–4.3 when rSAv-**3b** (**4b**) was succinylated. Greater shifts in the pI were noted (5.9–4.7) when rSAv was conjugated with dianionic **3c**. Succinylation of rSAv-**3c** (**4c**) shifted the pI even further (4.1–3.7). The fact that none of the unmodified rSAv is present after conjugation of **3b** or **3c** indicates that all rSAv tetramers have at least one of these moieties conjugated. In fact, it is likely that each tetramer has more than two conjugates, or some of the unmodified rSAv would be present.

Radiolabeled Modified rSAv: Preparation of 2b, 6a, 6b, 6c. The modified rSAv was radiolabeled with either ^{213}Bi or ^{211}At to assess radiochemical yields and in vivo stability. rSAv conjugates **2a**, **5a**, **5b**, and **5c** were also radioiodinated with ^{125}I. Radioiodination of rSAv was conducted to provide a comparison with the astatination yields and to provide an internal control for comparisons in vivo. The ^{225}Ac/^{213}Bi generator system previously described (*38*) was used to obtain ^{213}Bi for labeling. The succinylated rSAv-CHX-A″, **5a**, was reacted in 1 M NaOAc buffer at pH 4 for 5 min. Purification was accomplished by size-exclusion chromatography (NAP-10 column) to give a 72% isolated yield of [^{213}Bi]**6a**. Dry distillation of an irradiated bismuth target provided ^{211}At for labeling. Astatination was very rapid (<1 min) using chloramine-T in phosphate-buffered saline (PBS) at pH 7.4. After purification by size-exclusion chromatography (NAP-10), isolated yields of 18% for [^{211}At] **2b** and 50%–88% for [^{211}At]**6c** and [^{211}At]**6d** were obtained.

Biodistribution Studies. Four biodistribution studies were conducted in athymic mice. In each study, the ^{213}Bi- or ^{211}At-labeled rSAv was mixed with a radioiodinated version of the same modified rSAv and injected into three sets of 5 mice each. Because rSAv is very resistant to protease degradation, direct radioiodination can be used to provide a standard that closely reflects the distribution of the modified rSAv (*16*). In the first biodistribution study, [^{213}Bi]**6a** and [^{125}I]**6b** were coinjected, and tissue samples were obtained at 45 min and 90 and 180 min (~1, 2, and 4 half-lives) post injection (pi). The data obtained at 90 and 180 min are plotted in Figure 3, panel A, and the data obtained at all three time points are provide in Table S1 (Supporting Information). The plotted data show that the tissue concentrations of the two radionuclides are very similar at the two time points. Analysis of the concentrations of radionuclides in mice by the paired Student's *t*-test indicated that the only tissue with a significant difference in concentrations of ^{213}Bi and ^{125}I was kidney at the 180 min time point.

In a second biodistribution, ^{211}At-labeled succinylated rSAv, [^{211}At]**2b**, and ^{125}I-labeled succinylated rSAv, [^{125}I]**2b**, were coinjected, and tissue samples were obtained at 1, 4, and 24 h (~0.14, 0.6, and 3.3 half-lives) pi. The data obtained at 4 and 24 are plotted in Figure 3, panel B, and the data obtained at all three time points are provided in Table S2 (Supporting Information). The plotted data show differences in concentrations of radionuclides in blood, kidney, spleen, neck, and stomach. When analyzed by the Student's *t*-test, several differences were found to be significant. At the 1 and 4 h time points, the concentration of radionuclides in blood, spleen, neck, and stomach were significantly different. The differences in concentrations of ^{211}At and radioiodine in lung, spleen, neck, and stomach are an indication that there was free [^{211}At]astatide in vivo (*40*). It is interesting to note that at 24 h pi, there is no difference between the radionuclide concentrations in any tissue except muscle (Table S2, Supporting Information).

In the third biodistribution, [^{211}At]**6c** and [^{125}I]**6c** were coinjected, and tissue samples were obtained at 1, 4, and 24 h pi. The data obtained at 4 and 24 are plotted in Figure 3, panel C, and the data obtained at all three time points are provided in Table S3 (Supporting Information). By inspection of Figure 3C, it can be seen that with the exception of concentrations of radionuclides in blood at the 1 h time point, the concentrations of the two radionuclides in tissues are quite similar at the two time points plotted. A small but significant difference in the radionuclide concentrations was found in the stomach at 1 h pi, but the lack of significant differences in concentrations in other tissues makes it likely that very little free [^{211}At]astatide was present. At the 4 h time point, significant differences in radionuclide concentrations were seen in the blood, muscle, kidney, and spleen. Again, lack of significant differences in the lung, stomach, and neck makes it unlikely that the differences were reflective of astatide release from the rSAv conjugates.

In a fourth biodistribution, [^{211}At]**6d** and [^{125}I]**6d** were coinjected, and tissue samples were obtained at 1, 4, and 24 h pi. The data obtained at 4 and 24 are plotted in Figure 3, panel D, and the data obtained at all three time points are provided in Table S4 (Supporting Information). From the plotted data, it is apparent that concentrations of ^{211}At and ^{125}I are essentially the same in all tissues, indicating a high degree of stability toward deastatination. When subjected to the paired Student's *t*-test, a small but significant difference was noted for the radionuclide concentration in only one tissue (spleen) examined and that only at 4 h pi. Because there were no differences observed in the lung, stomach, or neck, it seems unlikely that the observed difference was due to free astatide. Interestingly, the concentration of both radionuclides (^{125}I and ^{211}At) was considerably lower in the blood and other tissues than that observed with the other radiolabeled rSAv conjugates. Indeed, the blood and tissue concentrations of [^{125}I]**6d** are less than half-that obtained with the other labeling methods. While that is the case, the liver concentrations were found to be similar to that

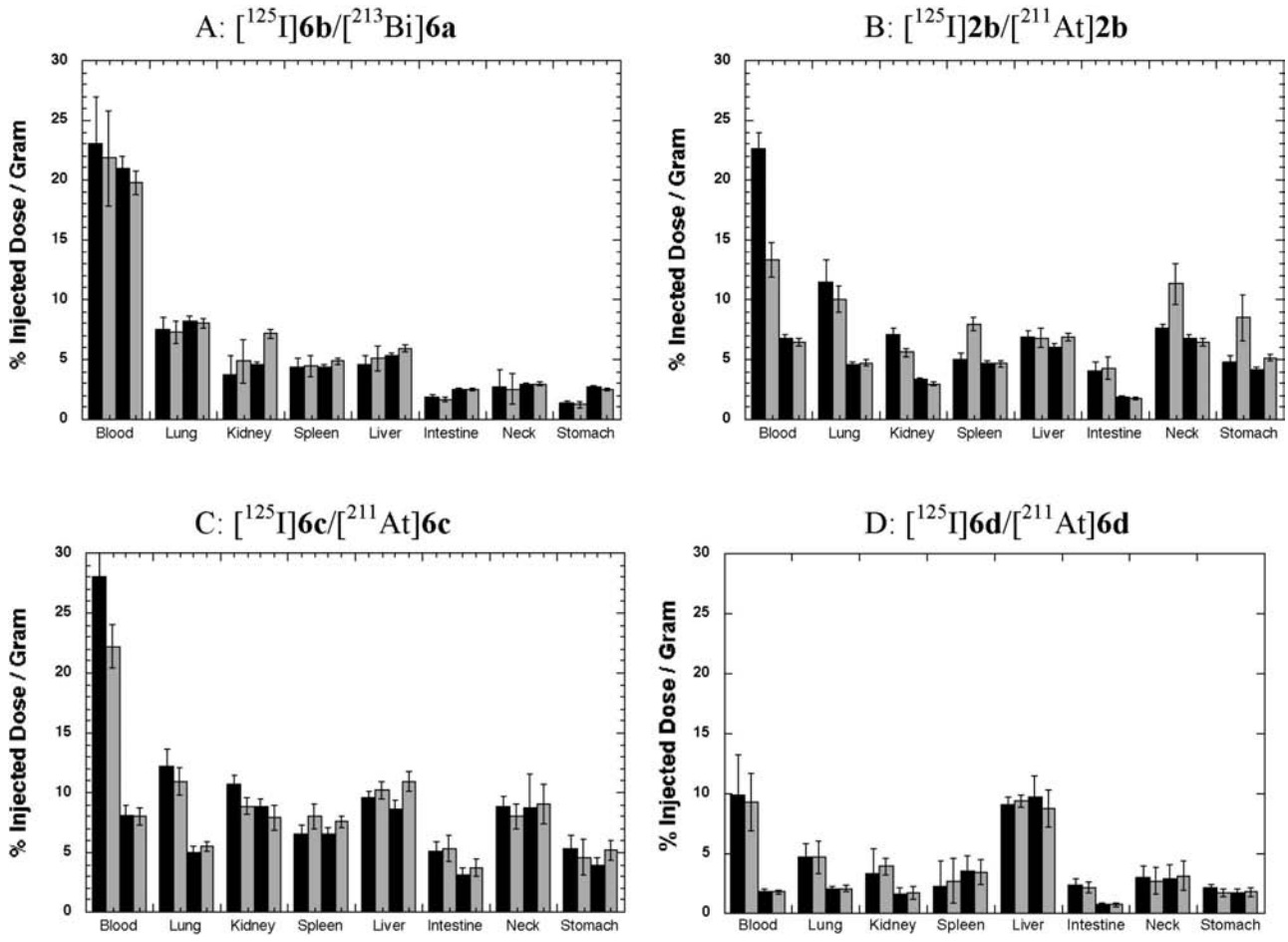

Figure 3. Bar graphs of selected biodistribution data obtained from coinjections (^{125}I- and α-emitter ^{213}Bi or ^{211}At-labeled) modified rSAv. ^{125}I-labeled modified rSAv data are plotted as black bars in each panel. ^{213}Bi or ^{211}At biodistribution data are plotted as gray bars. Panel A shows tissue distributions of ^{213}Bi-labeled succinylated rSAv-CHX-A″, [^{213}Bi]**6a**, in comparison with ^{125}I-labeled succinylated rSAv-CHX-A″, [^{125}I]**6b**, at 1.5 h (1st pair of bars) and 3 h (2nd pair of bars) pi. Panel B shows tissue distributions of ^{211}At- and ^{125}I-labeled succinylated rSAv that had no boron cage conjugated, [^{211}At]**2b** and [^{125}I]**2b**, at 4 (1st pair of bars) and 24 h (2nd pair of bars) pi. Panel C shows tissue distributions of ^{211}At- and ^{125}I-labeled succinylated rSAv that had *nido*-carborane cages conjugated, [^{211}At]**6c** and [^{125}I]**6c**, at 4 and 24 h pi. Panel D shows tissue distributions of ^{211}At- and ^{125}I-labeled succinylated rSAv that had decaborate(2-) cages conjugated, [^{211}At]**6d** and [^{125}I]**6d**, at 4 and 24 h post injection. Tables (S1−S4) of biodistribution data are provided in Supporting Information.

observed for the *nido*-carborane conjugate, [^{125}I]**6c**. Those concentrations were 3–5%ID/g higher than that found for the rSAv conjugated with CHX-A″, [^{125}I]**6b**, or when there was no bonding/binding moiety conjugated, [^{125}I]**2b**.

DISCUSSION

There are only a few α-emitting radionuclides that are considered reasonable candidates for TRT applications. Of those, ^{213}Bi and ^{211}At are particularly attractive because of the fact that they do not decay to α-particle-emitting daughter radionuclides. While they are very different in many aspects, choosing between ^{213}Bi and ^{211}At for TRT is difficult because each radionuclide has its own strengths and weaknesses. For example, ^{213}Bi is available from a generator system, ^{225}Ac/^{213}Bi (*41*), which could potentially allow widespread use in clinics and treatment centers. Furthermore, the short half-life of ^{213}Bi may allow repeated (fractionated) treatments in an outpatient setting while posing minimal danger to the patients' family and health care providers. However, the half-life of ^{213}Bi may be problematic, as targeting approaches may not be rapid enough in some tissues to adequately target cancer cells before decay occurs. The longer half-life of ^{211}At (∼9.4×) may circumvent this shortcoming of ^{213}Bi. Additionally, at present, it is difficult to obtain clinical quantities of ^{225}Ac (for ^{213}Bi production), whereas ^{211}At can be prepared in quantities sufficient for clinical studies (*42*). However, treatment with an ^{211}At-labeled molecule may require being within a short distance from the cyclotron used for its production. Rather than argue the merits of either ^{213}Bi or ^{211}At, our approach has been to investigate both. The strengths and weaknesses of each radionuclide will likely dictate usefulness for a specific therapeutic application.

A key issue with the use of the short half-lived α-emitting radionuclides ^{213}Bi and ^{211}At is employing an appropriate cancer-targeting approach. Several preclinical therapy studies using intact monoclonal antibodies or their fragments have shown promising results with ^{213}Bi (*43–46*) and ^{211}At (*47*, *48*). However, we believe that another antibody-based approach, termed pretargeting (*49*), may be the most promising for the short half-lived α-emitting radionuclides. That belief is based primarily on results from studies using antibody−rSAv chemical conjugates or fusion proteins in conjunction with biotin labeled with β-emitting radionuclides (*50–53*). The belief is also supported by results obtained in a study using ^{213}Bi in a pretargeting protocol for the therapy of adult T-cell leukemia in a murine model (*54*). In that study, pretargeted ^{213}Bi provided effective therapy, whereas ^{90}Y did not.

In the majority of pretargeting studies, including those cited above, the radionuclide is carried by biotin. But there is an alternative approach where a biotinylated mAb is administered first (pretargeted), and radiolabeled rSAv is administered

later (*49, 55–58*). In this investigation, initial steps of rSAv toward evaluating the potential for this alternate pretargeting approach to target short half-lived α-emitting radionuclides have been taken. We hypothesize that using streptavidin as a carrier for treating minimal residual disease with α-emitting radionuclides may have advantages. Its longer serum half-life should allow higher concentrations in blood and tissues, perhaps allowing a lower quantity of expensive radionuclides to be administered. While recombinant streptavidin, a ∼53 kDa protein, will not penetrate solid tumors as rapidly as radiolabeled biotin, with minimal residual disease such as micrometastatic lesions, tissue penetration may not be a problem. Furthermore, in contrast to significant normal tissue irradiation from β-emitting radionuclides such as ^{90}Y, the short path length of the α-particle should cause minimal normal tissue damage and toxicity when decaying in blood. Data from bone marrow conditioning studies have provided some evidence that supports this hypothesis (*20*). Although the use of succinylated rSAv as a carrier of radionuclide in pretargeting protocols may limit the second administration of the radioactive material because of its immunogenicity, we believe that the potential for efficient targeting of α-emitting radionuclides to metastatic disease warrants investigation.

The primary goals of this investigation were to evaluate methods for modifying radiolabeling rSAv with ^{213}Bi and ^{211}At and determine the effect that modification had on tissue distribution and pharmacokinetics in the mouse model. An important factor in the studies was normal tissue localization of the radiolabeled rSAv. Fortunately, prior investigations (*17, 18*) had shown that the natural propensity for kidney localization of rSAv (i.e., 20+ % ID/g (*16*)) could be dramatically decreased by succinylation. The results of these studies demonstrate that even in the case where succinylation of rSAv is conducted after modifying with binding or bonding moieties, this modification greatly diminishes sequestration in the kidney.

Another important aspect of the studies was to determine whether the α-emitting radionuclides remained stably attached to the rSAv in vivo. While quantification of released bismuth is not readily achieved, a reasonable assessment of the stability of ^{213}Bi-labeled rSAv can be obtained by comparing coinjected ^{213}Bi- and ^{125}I-labeled succinylated rSAv localized in the kidney. Free bismuth localizes to kidney (*59, 60*), thus, if *excess* ^{213}Bi activity is found in the kidney, it is a good indicator that ^{213}Bi has been released from the labeled rSAv. The DTPA derivative isothiocyanatobenzyl-CHX-A″, **3a**, was chosen for conjugation with rSAv for the chelation of ^{213}Bi. Studies have shown that ^{111}In and ^{90}Y can be chelated rapidly on bioconjugates containing this group, and the resultant labeled molecules have been shown to be stable to in vivo demetalation (*61–63*). In our prior studies, **3a** was conjugated with mAbs against antigens on canine hematopoietic cells, then radiolabeled with ^{213}Bi, and evaluated in dogs (*20, 21, 38*). In these studies, kidney enzymes were monitored for several months, and no damage to that tissue was noted, likely indicating that ^{213}Bi was not released in vivo.

In this investigation, rSAv was modified with CHX-A″, succinylated and radiolabeled with ^{213}Bi. The data plotted in Figure 3, panel A (Table S1 in Supporting Information) show that the distributions of the radionuclides are very similar. Indeed, the only significant difference between the ^{213}Bi and ^{125}I concentrations (by Student's *t*-test) is in the kidney at 3 h pi. From the data, it appears that there is a small amount of ^{213}Bi released in vivo. However, the important consideration is that release is relatively slow, and the magnitude of difference is quite small. At the 3 h time point, 4 half-lives of ^{213}Bi have passed; therefore, ∼94% of the radioactivity has decayed. An alternative labeling method is to conjugate the DOTA-chelation group to rSAv for binding ^{213}Bi (*64*). This may result in essentially no release of ^{213}Bi in vivo, but it is much more difficult to obtain the radiolabeled rSAv, as elevated temperatures (e.g., 37–45 °C) are required for up to an hour to achieve reasonable labeling yields. Thus, it appears that the CHX-A″ is the appropriate chelation group for executing ^{213}Bi-labeled rSAv studies.

Instability of ^{211}At-labeled proteins and small molecules has presented a serious problem with its application to cancer therapy. We considered using *m*-[^{211}At]astatobenzoate NHS ester (*29*) and *p*-[^{211}At]astatobenzoate NHS ester (*32*) for labeling rSAv with ^{211}At. Either of these derivatives would be expected to be stable to in vivo deastatination because rSAv is very resistant to protease degradation. However, in our experience, 40–60% labeling yields in the two-step labeling procedure are the best that can be (consistently) obtained with those reagents. Obtaining a high efficiency of radionuclide labeling is very important with ^{211}At as well. Rather than use the benzoate-labeling reagents, we chose to evaluate anionic borane cage pendent groups already under investigation in this laboratory (*31*). With conjugates of boron cage moieties, *direct astatination* yields of up to 81% had been obtained. Unfortunately, studies of ^{211}At-labeled benzoate and *nido*-carborane derivatives (*35*) did not provide encouraging results regarding in vivo stability. However, because of the protease resistance of rSAv, we chose to investigate a *nido*-carborane conjugate **3b** as a pendent group for direct astatination. The *nido*-carborane derivative **3b** had been previously evaluated in conjugates of a mAb Fab′ fragment. We chose to investigate a decaborate(2-) derivative as well since its use with Fab′ gave higher ^{211}At-labeling yields and appeared to impart less perturbation of the in vivo properties of the protein.

For this investigation, we could not readily adapt either of the two decaborate (2-) derivatives previously prepared for use with ^{211}At (*31*). One decaborate (2-) derivative was conjugated by reaction with sulfhydryl groups, while the other contained a biotin moiety. Since rSAv does not have disulfide bonds to reduce for reaction with maleimide derivatives (and we did not want to use reagents to produce sulfhydryl groups on rSAv), the sulfhydryl-reactive reagent did not appear to be a good candidate. Similarly, the use of a biotin-containing decaborate (2-) was not appropriate for conjugation with rSAv. Therefore, a new reagent containing a decaborate (2-) moiety and a methoxyl-terminated discrete-length (dPEG) polyethylene glycol moiety was prepared. The rationale for the use of dPEG moiety was that such a group might keep the dianionic decaborate moiety from interacting with serum proteins. Furthermore, other investigators have shown that PEGylation of avidin (Av) (albeit with larger PEG moieties) can improve their in vivo properties for pretargeting applications (*65, 66*).

Before labeling the rSAv conjugated with **3b** or **3c**, direct labeling of succinylated rSAv, **2a**, was evaluated. Astatination studies of an mAb Fab′ fragment resulted in none (<1%) of the astatinated protein being recovered after labeling using ChT and reducing with sodium metabisulfite (*31*). Other investigators obtained similar results (e.g., <5% bound) when ChT was used as oxidant (*67–69*). Therefore, it was interesting that an 18% isolated radiochemical yield was obtained with directly labeled succinylated rSAv in this investigation. The reason for the difference in radiolabeling yields is not known. However, it may be due to the presence of disulfides in the Fab′ molecule or a lack of them in the rSAv molecule. Investigators have shown that electrochemical oxidation and oxidation with H_2O_2 can provide higher yields of astatinated proteins (*68*); however, studies indicate that ^{211}At is bound with sulfhydryl groups rather than tyrosine moieties (*69, 70*). An important point is that rSAv has no disulfides or cysteine or methionine residues (*71*); therefore, the labeling can not be associated with sulfhydryl or

thioether groups. Streptavidin has six tyrosine residues per subunit. Although one tyrosine residue is buried in the biotin-binding pocket, five are on each subunit, giving a total of 20 tyrosine residues per molecule that might be astatinated. In related studies, ^{211}At-labeling of succinylated avidin, which has only one tyrosine per subunit (in biotin binding pocket), gave low radiochemical yields (unreported results)[5]. The combined results are suggestive that electrophilic ^{211}At can react with tyrosine residues in proteins when no disulfides are present. Early astatine-labeling studies demonstrated that direct labeling of tyrosine was possible (*72*).

The three ^{211}At-labeled rSAv preparations ([^{211}At]**2b**, [^{211}At]**6c**, [^{211}At]**6d**) have noticeably different distributions. The tissue distribution of radioiodinated succinylated rSAv, [^{125}I]**2b**, correlates well with data obtained in a previous study (*16*). If that iodinated derivative is compared with directly labeled [^{211}At]**2b**, it is apparent that there is some instability of the astatinated rSAv. However, when the boron cage moieties **3b** and **3c** are conjugated to rSAv, in vivo deastatination is not detected. A noticeable difference in tissue (e.g., kidney, spleen, and liver) accumulation and retention is observed for the *nido*-carborane conjugated rSAv relative to succinylated [^{125}I]rSAv. In contrast to this, the astatinated decaborate(2-)−rSAv conjugate [^{211}At]**6d** appears to be cleared from the blood much more rapidly than the succinylated native protein. It is not known why this conjugate has such a rapid blood clearance. Clearance is more rapid from all tissues except the liver, which has concentrations similar to that of native protein at the times studied. One possible explanation for the rapid clearance is that the m-dPEG$_{12}$ moiety destabilizes the rSAv tetramer by inserting between the rSAv monomers. Higher molecular weight fusion proteins made of antibody single chain constructs and rSAv have also been noted to have much more rapid clearance than rSAv or chemical conjugates of rSAv and antibodies (*51*). A plausible explanation for the observed fast clearance in that case is that the fused four scFv destabilize the rSAv tetramer.

Summary. This investigation has demonstrated that after appropriate modification, rSAv can be labeled with either ^{213}Bi or ^{211}At in good radiochemical yield. Most importantly, the data obtained from biodistributions conducted in athymic mice have shown that the ^{213}Bi-labeled succinylated rSAv has nearly the same distribution and pharmacokinetics as the nonmetallated rSAv conjugate. While there is slight (but significant) difference in the distributions after 4 half-lives (3 h) of ^{213}Bi, at that time there is less than 10% of the activity remaining, and the magnitude of specific kidney localization appears small. From the data, we conclude that the ^{213}Bi-labeled succinylated CHX-A″-rSAv has adequate stability to be used in pretargeting protocols. The biodistribution data obtained for succinylated rSAv directly labeled with ^{211}At, that is, [^{211}At]**2b**, indicate that this labeling approach is not adequate for pretargeting studies because of low radiochemical yields and low in vivo stability. Higher in vivo stability was obtained with the *nido*-carborane conjugated rSAv, [^{211}At]**6c**, but that functional moiety appears to increase blood and tissue retention such that it is not an ideal conjugate either. The data obtained from the in vivo studies with the PEGylated decaborate(2-)-conjugated rSAv, [^{211}At]**6d**, suggests that this method of labeling not only provides a stable label but also provides very good radiochemical yields and modifies the in vivo pharmacokinetics in what appears to be a favorable manner. Therefore, additional studies with the PEGylated decaborate(2-) conjugate are planned to evaluate its use in pretargeting protocols.

[5]Astatination of succinylated avidin and succinylated avidin conjugated with the *nido*-carborane moiety, **3b**, was also conducted to show the difference in yields. Avidin has only 1 tyrosine residue per subunit, making it less likely to be astatinated. Astatination of succinylated avidin gave a radiochemical yield of 5%, whereas astatination of succinylated avidin conjugated with **3b** gave a 52% radiochemical yield.

ACKNOWLEDGMENT

We thank Kent Buhler, Janna Quinn, Nicole Lavoie, Holly Nguyen, and Dr. Robert Vessella for assistance with the animal studies conducted in this investigation, and Dr. Ruedi Risler for assistance with the production of ^{211}At. We are particularly grateful to the Department of Defense (DAMD 17-98-1-8258) and National Cancer Institute, NIH (5 RO1 CA113431) for financial support of the studies. This research was supported in part by the Intramural Research Program of the NIH, National Cancer Institute, Center for Cancer Research. We thank Quanta BioDesign (http://www.quantabiodesign.com) for the gift of m-dPEG$^{TM}_{12}$ amine used in the studies.

Supporting Information Available: Numerical data for the four biodistributions conducted in this investigation. This information is available free of charge via the Internet at http://pubs.acs.org.

LITERATURE CITED

(1) Mulford, D. A., Scheinberg, D. A., and Jurcic, J. G. (2005) The promise of targeted α-particle therapy. *J. Nucl. Med. 46*, 199S–204S.

(2) Couturier, O., Supiot, S., Degraef-Mougin, M., Faivre-Chauvet, A., Carlier, T., Chatal, J. F., Davodeau, F., and Cherel, M. (2005) Cancer radioimmunotherapy with alpha-emitting nuclides. *Eur. J. Nucl. Med. Mol. Imaging 32*, 601–614.

(3) Imam, S. K. (2001) Advancements in cancer therapy with alpha-emitters: a review. *Int. J. Radiat. Oncol. Biol. Phys. 51*, 271–278.

(4) Zalutsky, M. R., and Vaidyanathan, G. (2000) Astatine-211-labeled radiotherapeutics: an emerging approach to targeted alpha-particle radiotherapy. *Curr. Pharm. Des. 6*, 1433–1455.

(5) Feinendegen, L. E., and McClure, J. J. (1997) Alpha-emitters for medical therapy: workshop of the United States Department of Energy. *Radiat. Res. 148*, 195–201.

(6) Goldenberg, D. M. (2002) Targeted therapy of cancer with radiolabeled antibodies. *J. Nucl. Med. 43*, 693–713.

(7) Melo e Silva, M. C., Patricio, L., Gano, L., Sa e Melo, M. L., Inohae, E., Mataka, S., and Thiemann, T. (2001) Synthesis and biological evaluation of two new radiolabelled estrogens: [^{125}I](E)-3-methoxy-17α-iodovinylestra-1,3,5(10),6-tetraen-17β-ol and [^{125}I](Z)-3-methoxy-17α-iodovinylestra-1,3,5(10),6-tetraen-17β-ol. *Appl. Radiat. Isot. 54*, 227–239.

(8) Stinchcomb, T. G., and Roeske, J. C. (1992) Analytic microdosimetry for radioimmunotherapeutic alpha emitters. *Med. Phys. 19*, 1385–1393.

(9) Li, L., Yazaki, P. J., Anderson, A. L., Crow, D., Colcher, D., Wu, A. M., Williams, L. E., Wong, J. Y., Raubitschek, A., and Shively, J. E. (2006) Improved biodistribution and radioimmunoimaging with poly(ethylene glycol)-DOTA-conjugated anti-CEA diabody. *Bioconjugate Chem. 17*, 68–76.

(10) Kobayashi, H., Le, N., Kim, I. S., Kim, M. K., Pie, J. E., Drumm, D., Paik, D. S., Waldmann, T. A., Paik, C. H., and Carrasquillo, J. A. (1999) The pharmacokinetic characteristics of glycolated humanized anti-Tac Fabs are determined by their isoelectric points. *Cancer Res. 59*, 422–430.

(11) Fu, P. P., Unruh, L. E., Miller, D. W., Huang, L. W., and Yang, D. T. C. (1985) Synthesis of 3-Aryl-3,4-dihydroisocoumarins. *J. Org. Chem. 50*, 1259–1261.

(12) Fujioka, Y., Satake, S., Uehara, T., Mukai, T., Akizawa, H., Ogawa, K., Saji, H., Endo, K., and Arano, Y. (2005) In vitro system to estimate renal brush border enzyme-mediated cleavage of peptide linkages for designing radiolabeled antibody fragments of low renal radioactivity levels. *Bioconjugate Chem. 16*, 1610–1616.

(13) Behe, M., Becker, W., Gotthardt, M., Angerstein, C., and Behr, T. M. (2003) Improved kinetic stability of DTPA-dGlu as compared with conventional monofunctional DTPA in chelating indium and yttrium: preclinical and initial clinical evaluation of radiometal labelled minigastrin derivatives. *Eur. J. Nucl. Med. Mol. Imaging 30*, 1140–1146.

(14) Goodwin, D. A., and Meares, C. F. (1997) Pretargeting: general principles. *Cancer 80*, 2675–2680.

(15) Zhu, H., Jain, R. K., and Baxter, L. T. (1998) Tumor Pretargeting for radioimmunodetection and radioimmunotherapy. *J. Nucl. Med. 39*, 65–76.

(16) Wilbur, D. S., Stayton, P. S., To, R., Buhler, K. R., Klumb, L. A., Hamlin, D. K., Stray, J. E., and Vessella, R. L. (1998) Streptavidin in antibody pretargeting. Comparison of a recombinant streptavidin with two streptavidin mutant proteins and two commercially available streptavidin proteins. *Bioconjugate Chem. 9*, 100–107.

(17) Wilbur, D. S., Hamlin, D. K., Buhler, K. R., Pathare, P. M., Vessella, R. L., Stayton, P. S., and To, R. (1998) Streptavidin in antibody pretargeting. 2. Evaluation of methods for decreasing localization of streptavidin to kidney while retaining its tumor binding capacity. *Bioconjugate Chem. 9*, 322–330.

(18) Wilbur, D. S., Hamlin, D. K., Meyer, D. L., Mallett, R. W., Quinn, J., Vessella, R. L., and Press, O. W. (2002) Streptavidin in antibody pretargeting. 3. Comparison of biotin binding and tissue localization of 1,2-cyclohexanedione and succinic anhydride modified recombinant streptavidin. *Bioconjugate Chem. 13*, 611–620.

(19) Wilbur, D. S., Hamlin, D. K., Sanderson, J., and Lin, Y. (2004) Streptavidin in antibody pretargeting. 4. Site-directed mutation provides evidence that both arginine and lysine residues are involved in kidney localization. *Bioconjugate Chem. 15*, 1454–1463.

(20) Sandmaier, B. M., Bethge, W. A., Wilbur, D. S., Hamlin, D. K., Santos, E. B., Brechbiel, M. W., Fisher, D. R., and Storb, R. (2002) Bismuth 213-labeled anti-CD45 radioimmunoconjugate to condition dogs for nonmyeloablative allogeneic marrow grafts. *Blood 100*, 318–326.

(21) Bethge, W. A., Wilbur, D. S., Storb, R., Hamlin, D. K., Santos, E. B., Brechbiel, M. W., Fisher, D. R., and Sandmaier, B. M. (2003) Selective T-cell ablation with bismuth-213-labeled anti-TCR$\alpha\beta$ as nonmyeloablative conditioning for allogeneic canine marrow transplantation. *Blood 101*, 5068–5075.

(22) Camera, L., Kinuya, S., Garmestani, K., Wu, C., Brechbiel, M. W., Pai, L. H., McMurry, T. J., Gansow, O. A., Pastan, I., Paik, C. H., and Carrasquillo, J. A. (1994) Evaluation of the serum stability and in vivo biodistribution of CHX-DTPA and other ligands for yttrium labeling of monoclonal antibodies. *J. Nucl. Med. 35*, 882–889.

(23) Milenic, D. E., Roselli, M., Mirzadeh, S., Pippin, C. G., Gansow, O. A., Colcher, D., Brechbiel, M. W., and Schlom, J. (2001) In vivo evaluation of bismuth-labeled monoclonal antibody comparing DTPA-derived bifunctional chelates. *Cancer Biother. Radiopharm. 16*, 133–146.

(24) Adams, G. P., Shaller, C. C., Chappell, L. L., Wu, C., Horak, E. M., Simmons, H. H., Litwin, S., Marks, J. D., Weiner, L. M., and Brechbiel, M. W. (2000) Delivery of the α-emitting radioisotope bismuth-213 to solid tumors via single-chain Fv and diabody molecules. *Nucl. Med. Biol. 27*, 339–346.

(25) Nikula, T. K., McDevitt, M. R., Finn, R. D., Wu, C., Kozak, R. W., Garmestani, K., Brechbiel, M. W., Curcio, M. J., Pippin, C. G., Tiffany-Jones, L., Geerlings, M. W., Sr., Apostolidis, C., Molinet, R., Geerlings, M. W., Jr., Gansow, O. A., and Scheinberg, D. A. (1999) Alpha-emitting bismuth cyclohexylbenzyl DTPA constructs of recombinant humanized anti-CD33 antibodies: pharmacokinetics, bioactivity, toxicity and chemistry. *J. Nucl. Med. 40*, 166–176.

(26) McDevitt, M. R., Finn, R. D., Ma, D., Larson, S. M., and Scheinberg, D. A. (1999) Preparation of alpha-emitting 213 Bi-labeled antibody constructs for clinical use. *J. Nucl. Med. 40*, 1722–1727.

(27) Vaughan, A. T. M., and Fremlin, J. H. (1978) The preparation of astatine labelled proteins using an electrophilic reaction. *Int. J. Nucl. Med. Biol. 5*, 229–230.

(28) Vaughan, A. T. M., Bateman, W. J., and Fisher, D. R. (1982) The In vivo fate of a ^{211}At labelled monoclonal antibody with known specificity in a murine system. *Int. J. Radiat. Oncol. Biol. Phys. 8*, 1943–1946.

(29) Zalutsky, M. R., and Narula, A. S. (1988) Astatination of proteins using an N-succinimidyl tri-n-butylstannyl benzoate intermediate. *Appl. Radiat. Isot. 39*, 227–232.

(30) Hadley, S. W., Wilbur, D. S., Gray, M. A., and Atcher, R. W. (1991) Astatine-211 labeling of an antimelanoma antibody and its Fab fragment using N-succinimidyl *p*-[^{211}At]astatobenzoate: comparisons in vivo with the *p*-[^{125}I]iodobenzoyl conjugate. *Bioconjugate Chem. 2*, 171–179.

(31) Wilbur, D. S., Chyan, M.-K., Hamlin, D. K., Vessella, R. L., Wedge, T. J., and Hawthorne, M. F. (2007) Reagents for astatination of biomolecules. 2. Conjugation of anionic boron cage pendant groups to a protein provides a method for direct labeling that is stable to in vivo deastatination. *Bioconjugate Chem. 18*, 1226–1240.

(32) Wilbur, D. S., Vessella, R. L., Stray, J. E., Goffe, D. K., Blouke, K. A., and Atcher, R. W. (1993) Preparation and evaluation of *para*-[^{211}At]astatobenzoyl labeled anti-renal cell carcinoma antibody A6H F(ab′)$_2$. In vivo distribution comparison with *para*-[^{125}I]iodobenzoyl labeled A6H F(ab′)$_2$. *Nucl. Med. Biol. 20*, 917–927.

(33) Lindegren, S., Back, T., and Jensen, H. J. (2001) Dry-distillation of astatine-211 from irradiated bismuth targets: a time-saving procedure with high recovery yields. *Appl. Radiat. Isot. 55*, 157–160.

(34) Brechbiel, M. W., and Gansow, O. A. (1992) Synthesis of C-functionalized trans-cyclohexyldiethylenetriaminepenta-acetic acids for labelling of monoclonal antibodies with the bismuth-212 α-particle emitter. *J. Chem. Soc., Perkin Trans. 1*, 1173–1178.

(35) Wilbur, D. S., Chyan, M. K., Hamlin, D. K., Kegley, B. B., Risler, R., Pathare, P. M., Quinn, J., Vessella, R. L., Foulon, C., Zalutsky, M., Wedge, T. J., and Hawthorne, M. F. (2004) Reagents for astatination of biomolecules: comparison of the in vivo distribution and stability of some radioiodinated/astatinated benzamidyl and *nido*-carboranyl compounds. *Bioconjugate Chem. 15*, 203–223.

(36) Hamblett, K. J., Kegley, B. B., Hamlin, D. K., Chyan, M. K., Hyre, D. E., Press, O. W., Wilbur, D. S., and Stayton, P. S. (2002) A streptavidin-biotin binding system that minimizes blocking by endogenous biotin. *Bioconjugate Chem. 13*, 588–98.

(37) Pippin, C. G., Parker, T. A., McMurry, T. J., and Brechbiel, M. W. (1992) Spectrophotometric method for the determination of a bifunctional DTPA ligand in DTPA-monoclonal antibody conjugates. *Bioconjugate Chem. 3*, 342–345.

(38) Bethge, W. A., Wilbur, D. S., Storb, R., Hamlin, D. K., Santos, E. B., Brechbiel, M. W., and Sandmaier, B. M. (2004) Radioimmunotherapy with bismuth-213 as conditioning for nonmyeloablative allogeneic hematopoietic cell transplantation in dogs: a dose deescalation study. *Transplantation 78*, 352–359.

(39) Kaplan, H. M., Brewer, N. R., and Blair, W. H. (1983) The Mouse in Biomedical Research, in *The Mouse in Biomedical Research* (Foster, H. L., Small, J. D., and Fox, J. G., Eds.) pp 248–292, Academic Press, New York.

(40) Hamilton, J. G., Asling, C. W., Garrison, W. M., and Scott, K. G. (1953) The accumulation, metabolism and biological effects of astatine in rats and monkeys. *Univ. Calif. Publ. Pharmacol. 2*, 283–343.

(41) Bray, L. A., Tingey, J. M., DesChane, J. R., Egorov, O. B., Tenforde, T. S., Wilbur, D. S., Hamlin, D. K., and Pathare, P. M. (2000) Development of a unique bismuth (Bi-213) automated generator for use in cancer therapy. *Ind. Eng. Chem. Res. 39*, 3189–3194.

(42) Zalutsky, M. R., Zhao, X.-G., Alston, K. L., and Bigner, D. (2001) High-level production of α-particle-emitting ^{211}At and preparation of ^{211}At-labeled antibodies for clinical use. *J. Nucl. Med. 42*, 1508–1515.

(43) Qu, C. F., Song, E. Y., Li, Y., Rizvi, S. M., Raja, C., Smith, R., Morgenstern, A., Apostolidis, C., and Allen, B. J. (2005) Pre-clinical study of ^{213}Bi labeled PAI2 for the control of micrometastatic pancreatic cancer. *Clin. Exp. Metastasis 22*, 575–586.

(44) Milenic, D., Garmestani, K., Dadachova, E., Chappell, L., Albert, P., Hill, D., Schlom, J., and Brechbiel, M. (2004) Radioimmunotherapy of human colon carcinoma xenografts using a ^{213}Bi-labeled domain-deleted humanized monoclonal antibody. *Cancer Biother. Radiopharm. 19*, 135–147.

(45) McDevitt, M. R., Barendswaard, E., Ma, D., Lai, L., Curcio, M. J., Sgouros, G., Ballangrud, A. M., Yang, W.-H., Finn, R. D., Pellegrini, V., Geerlings, M. W., Jr., Lee, M., Brechbiel, M. W., Bander, N. H., Cordon-Cardo, C., and Scheinberg, D. A. (2000) An α-particle emitting antibody ([^{213}Bi]J591) for radioimmunotherapy of prostate cancer. *Cancer Res. 60*, 6095–6100.

(46) Behr, T. M., Behe, M., Stabin, M. G., Wehrmann, E., Apostolidis, C., Molinet, R., Strutz, F., Fayyazi, A., Wieland, E., Gratz, S., Koch, L., Goldenberg, D. M., and Becker, W. (1999) High-linear energy transfer (LET) alpha versus low-LET beta emitters in radioimmunotherapy of solid tumors: therapeutic efficacy and dose-limiting toxicity of ^{213}Bi- versus ^{90}Y-labeled CO17–1A Fab′ fragments in a human colonic cancer model. *Cancer Res. 59*, 2635–2643.

(47) Zhang, M., Yao, Z., Zhang, Z., Garmestani, K., Talanov, V. S., Plascjak, P. S., Yu, S., Kim, H. S., Goldman, C. K., Paik, C. H., Brechbiel, M. W., Carrasquillo, J. A., and Waldmann, T. A. (2006) The anti-CD25 monoclonal antibody 7G7/B6, armed with the α-emitter ^{211}At, provides effective radioimmunotherapy for a murine model of leukemia. *Cancer Res. 66*, 8227–8232.

(48) Elgqvist, J., Andersson, H., Back, T., Hultborn, R., Jensen, H., Karlsson, B., Lindegren, S., Palm, S., Warnhammar, E., and Jacobsson, L. (2005) Therapeutic efficacy and tumor dose estimations in radioimmunotherapy of intraperitoneally growing OVCAR-3 cells in nude mice with (211)At-labeled monoclonal antibody MX35. *J. Nucl. Med. 46*, 1907–1915.

(49) Paganelli, G., Malcovati, M., and Fazio, F. (1991) Monoclonal Antibody pretargetting techniques for tumour localization: the avidin-biotin system. *Nucl. Med. Commun. 12*, 211–234.

(50) Pagel, J. M., Hedin, N., Subbiah, K., Meyer, D., Mallet, R., Axworthy, D., Theodore, L. J., Wilbur, D. S., Matthews, D. C., and Press, O. W. (2003) Comparison of anti-CD20 and anti-CD45 antibodies for conventional and pretargeted radioimmunotherapy of B-cell lymphomas. *Blood 101*, 2340–2348.

(51) Pagel, J. M., Lin, Y., Hedin, N., Pantelias, A., Axworthy, D., Stone, D., Hamlin, D. K., Wilbur, D. S., and Press, O. W. (2006) Comparison of a tetravalent single-chain antibody-streptavidin fusion protein and an antibody-streptavidin chemical conjugate for pretargeted anti-CD20 radioimmunotherapy of B-cell lymphomas. *Blood 108*, 328–336.

(52) Press, O. W., Corcoran, M., Subbiah, K., Hamlin, D. K., Wilbur, D. S., Johnson, T., Theodore, L., Yau, E., Mallett, R., Meyer, D. L., and Axworthy, D. (2001) A comparative evaluation of conventional and pretargeted radioimmunotherapy of CD20-expressing lymphoma xenografts. *Blood 98*, 2535–2543.

(53) Axworthy, D. B., Reno, J. M., Hylarides, M. D., Mallett, R. W., Theodore, L. J., Gustavson, L. M., Su, F., Hobson, L. J., Beaumier, P. L., and Fritzberg, A. R. (2000) Cure of human carcinoma xenografts by a single dose of pretargeted yttrium-90 with negligible toxicity. *Proc. Natl. Acad. Sci. U.S.A. 97* 1802–1807.

(54) Zhang, M., Yao, Z., Garmestani, K., Axworthy, D. B., Zhang, Z., Mallett, R. W., Theodore, L. J., Goldman, C. K., Brechbiel, M. W., Carrasquillo, J. A., and Waldmann, T. A. (2002) Pretargeting radioimmunotherapy of a murine model of adult T-cell leukemia with the α-emitting radionuclide, bismuth 213. *Blood 100*, 208–216.

(55) Zhang, M., Yao, Z., Saga, T., Sakahara, H., Nakamoto, Y., Sato, N., Nakada, H., Yamshina, I., and Konishi, J. (1998) Improved intratumoral penetration of radiolabeled streptavidin in intraperitoneal tumors pretargeted with biotinylated antibody. *J. Nucl. Med. 39*, 30–33.

(56) Maraveyas, A., RowlinsonBusza, G., Murray, S., and Epenetos, A. A. (1998) Improving tumour targeting and decreasing normal tissue uptake by optimizing the stoichiometry of a two-step biotinylated-antibody/streptavidin-based targeting strategy: Studies in a nude mouse xenograft model. *Int. J. Cancer 78*, 610–617.

(57) Saga, T., Weinstein, J. N., Jeong, J. M., Heya, T., Lee, J. T., Le, N., Paik, C. H., Sung, C., and Neumann, R. D. (1994) Two-step targeting of experimental lung metastases with biotinylated antibody and radiolabeled streptavidin. *Cancer Res. 54*, 2160–2165.

(58) Paganelli, G., Pervez, S., Siccardi, A. G., Rowlinson, G., Deleide, G., Chiolerio, F., Malcovati, M., Scassellati, G. A., and Epenetos, A. A. (1990) Intraperitoneal radio-localization of tumors pre-targeted by biotinylated monoclonal antibodies. *Int. J. Cancer 45*, 1184–1189.

(59) Hassfjell, S., and Brechbiel, M. W. (2001) The development of the alpha-particle emitting radionuclides ^{212}Bi and ^{213}Bi, and their decay chain related radionuclides, for therapeutic applications. *Chem. Rev. 101*, 2019–2036.

(60) Zidenberg-Cherr, S., Parks, N. J., and Keen, C. L. (1987) Tissue and subcellular distribution of bismuth radiotracer in the rat: considerations of cytotoxicity and microdosimetry for bismuth radiopharmaceuticals. *Radiat. Res. 111*, 119–129.

(61) Kobayashi, H., Wu, C. C., Yoo, T. M., Sun, B. F., Drumm, D., Pastan, I., Paik, C. H., Gansow, O. A., Carrasquillo, J. A., and Brechbiel, M. W. (1998) Evaluation of the in vivo biodistribution of yttrium-labeled isomers of CHX-DTPA-conjugated monoclonal antibodies. *J. Nucl. Med. 39*, 829–836.

(62) Roselli, M., Milenic, D. E., Brechbiel, M. W., Mirzadeh, S., Pippin, C. G., Gansow, O. A., Colcher, D., and Schlom, J. (1999) In vivo comparison of CHX-DTPA ligand isomers in athymic mice bearing carcinoma xenografts. *Cancer Biother. Radiopharm. 14*, 209–220.

(63) Chen, J. Q., Strand, S. E., Brechbiel, M. W., Gansow, O. A., and Sjoegren, H. O. (1996) Combination of biotinylation and indium-111 labeling with chelate SCN-Bz-CHX-A-DTPA for chimeric BR96: Biodistribution and pharmacokinetic studies in colon carcinoma isografted rats. *Tumor Targeting 2*, 66–75.

(64) Junghans, R. P., Dobbs, D., Brechbiel, M. W., Mirzadeh, S., Raubitschek, A. A., Gansow, O. A., and Waldmann, T. A. (1993) Pharmacokinetics and bioactivity of 1,4,7,10-tetra-azacylododecane N,N′,N″N‴-tetraacetic acid (DOTA)-bismuth-conjugated anti-Tac antibody for α-emitter (^{212}Bi) therapy. *Cancer Res. 53*, 5683–5689.

(65) Caliceti, P., Chinol, M., Roldo, M., Veronese, F. M., Semenzato, A., Salmaso, S., and Paganelli, G. (2002) Poly(ethylene glycol)-avidin bioconjugates: suitable candidates for tumor pretargeting. *J. Controlled Release 83*, 97–108.

(66) Salmaso, S., Semenzato, A., Bersania, S., Chinol, M., Paganelli, G., and Caliceti, P. (2005) Preparation and characterization of active site protected poly(ethyleneglycol)-avidin bioconjugates. *Biochim. Biophys. Acta 1726*, 57–66.

(67) Smit, J. A., Myburgh, J. A., and Neirinckx, R. D. (1973) Specific inactivation of sensitized lymphocytes in vitro using antigens labelled with astatine-211. *Clin. Exp. Immunol. 14*, 107–116.

(68) Aaij, C., Tschroots, W. R. J. M., Lindner, L., and Feltkamp, T. E. W. (1975) The preparation of astatine labelled proteins. *Int. J. Appl. Radiat. Isot. 26*, 25–30.

(69) Visser, G. W. M., Diemer, E. L., and Kaspersen, F. M. (1981) The nature of the astatine-protein bond. *Int. J. Appl. Radiat. Isot. 32*, 905–912.

(70) Visser, G. W. M., Diemer, E. L., and Kaspersen, F. M. (1979) The preparation and stability of astatotyrosine and astato-iodotyrosine. *Int. J. Appl. Radiat. Isot. 30*, 749–752.
(71) Savage, M. D., Mattson, G., Desai, S., Nielander, G. W., Morgensen, S., and Conklin, E. J. (1992) *Avidin-Biotin Chemistry: A Handbook*, Pierce Chemical Company, Rockford, IL.
(72) Vaughan, A. T. M., and Fremlin, J. H. (1977) The preparation of astatotyrosine. *Int. J. Appl. Radiat. Isot. 28*, 595–598.

BC7002428

Oligothiophene-5-Labeled Deoxyuridines for the Detection of Single Nucleotide Polymorphisms

Massimo L. Capobianco,* Antonella Cazzato,† Silvia Alesi, and Giovanna Barbarella

Istituto per la Sintesi Organica e la Fotoreattività del Consiglio Nazionale delle Ricerche (ISOF-CNR).
Via P. Gobetti 101, 40129 Bologna, Italy. Received July 10, 2007; Revised Manuscript Received September 13, 2007

We report the synthesis of four oligothiophene-5-labeled deoxyuridines. These modified fluorescent nucleosides have been incorporated into oligodeoxynucleotides designed to be used as probes to discriminate, through changes in fluorescence emission, between hybridization with a perfectly complementary strand and that with a single nucleotide mismatch facing the modified uridines. Upon hybridization, remarkable differences (up to 47%) of the emitted light, depending on the uridine facing base, were observed.

INTRODUCTION

Single mutations of nucleosides inside DNA, even in the absence of mutagens, can be randomly produced during DNA replication with an esteemed frequency in the range 10^{-7}–10^{-11} per replication. Such mutations can be inherited and are known as single nucleotide polymorphism (SNP) (*1*). Most of the time, SNPs occur in untranscribed DNA or into introns, but occasionally, they can affect an exon and alter the gene translation, leading to a truncated or a mutated protein. Detection of SNPs is thus of great importance in medicine and biology, and a great effort has been devoted to finding suitable methods of analysis. Among a plethora of methodologies (*2*–*6*), based on sequencing, selective hybridization (*7*), amplification (*8*, *9*), colorimetric methods (*10*), mass spectrometry, (*2*–*4*) and so forth, those based on variation of the emitted light of modified nucleosides, inserted into a probe in front of the mutation spot of the oligonucleotide to be analyzed, are perhaps the most straightforward (*11*, *12*). The methods rely on the fact that the electronic distribution of a nucleobase is modified by the presence (or absence) of the Watson–Crick hydrogen bonds formed with the facing nucleoside in a duplex. If a suitable fluorophore is conjugated on the nucleobase opposite the presumed mutated base, it can be affected from that variation, and fluoresce in a different way whether correctly paired or mispaired.

Our group is studying the fluorescence properties of oligothiophenes as markers for proteins and oligonucleotides (*13*, *14*) and exploring their use as diagnostic tools in biotechnologies (*15*). As part of this study, we have synthesized four deoxyuridine derivatives (Figure 1) in which bi- or terthiophene moieties have been conjugated to the 5-position of a 2′-deoxyuridine with or without an ethynyl spacer. We have used phosporamidite chemistry to insert each of these labeled compounds at the center of an oligonucleotide, designed to hybridize with model oligonucleotides corresponding to a region known to contain an SNP (A to G transition), that occurs in some patients that present a mutated form of hemoglobin. For this work, the probes

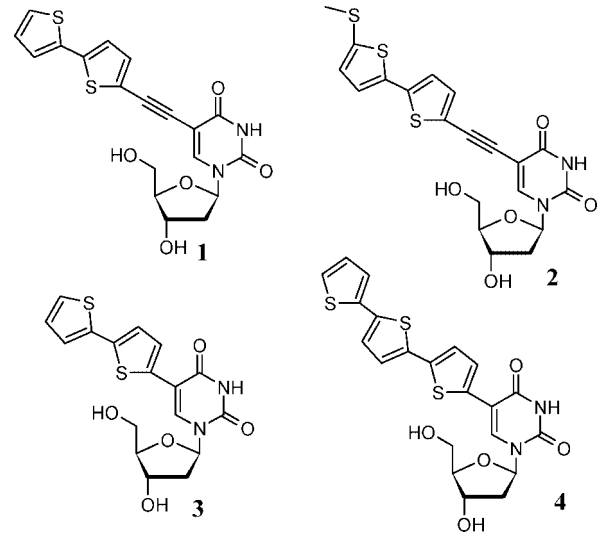

Figure 1. The 5-labelled uridines used in the work.

(**P1**–**4**), the normal (**A**), and the three mutated targets (**G**, **C**, and **T**) containing mismatches (Table 1) were prepared and purified.

MATERIALS AND METHODS

Materials and Instrumentation. All chemicals were of commercial grade unless otherwise stated. Microwave reactions were performed with a Prolabo synthwave 402 oven. The synthesis of the oligonucleotides was achieved with a Pharmacia Gene Assembler 2. NMR analysis were carried out with a Varian VXR-200 or a Varian Mercury 400 spectrophotometer. UV–vis and melting temperature were recorded with a Perkin Elmer lambda 20 spectrophotometer. Fluorescence measurements were performed with a Perkin Elmer LS-50B spectrofluorimeter. Mass analysis were performed with a Finningan Mat GCQ or in ESI[1] mode with a Bruker Esquire 3000+. HPLC analysis and purifications were done with a Waters 600 E, using a Waters UV detector and a Varian Pro Star 363 spectrofluorimeter.

* E-mail capobianco@isof.cnr.it
† Mediteknology s.r.l. Via P. Gobetti 101, 40129 Bologna, Italy.

[1]Abbreviations: aq, aqueous; equiv, equivalents; ESI, electron spray ionization; GC, gas chromatography; NBS, *N*-bromosuccinimide; NIS, *N*-iodosuccinimide; TLC, thin layer chromatography; R_H–R_L, higher running–lower running isomer; rt, room temperature; sat, saturated; TEA, triethylamine.

10.1021/bc7002555 CCC: $40.75 © 2008 American Chemical Society
Published on Web 11/13/2007

Table 1. Oligonucleotides Used in This Work[a]

P1–4	3′ AC TGA GGA *U*TC CTC TTC A 5′
Target-A	5′ TG ACT CCT *A*AG GAG AAG T 3′
Target-G	5′ TG ACT CCT *G*AG GAG AAG T 3′
Target-C	5′ TG ACT CCT *C*AG GAG AAG T 3′
Target-T	5′ TG ACT CCT *T*AG GAG AAG T 3′

[a] ***U*** = modified uridine (compounds **1**–**4** as in Figure 1). Triplets correspond to reading codons.

5-Iodo-[2,2′]bithiophene (5). The synthesis and characterization of this compound have already been reported (*16*, *17*).

[2,2′]Bithiophenyl-5-ethynyltrimethylsilane (6). The microwave oven reactor was charged with 5-iodo-[2,2′]bithiophene (**5**) (500 mg, 1.7 mmol), ethynyltrimethylsilane (380 μL, 2.7 mmol), tetrakis(triphenylphosphine)palladium (100 mg, 0.085 mmol), CuI (98 mg 0.51 mmol), and TEA (10 mL). After 20 min of irradiation at 150 °C, TLC on silica gel with *n*-hexane as eluent showed the absence of **5**. The mixture was diluted with Et_2O (20 mL) and washed with 4 M aq HCl (15 mL) and water (15 mL), and then the organic phase was dried over Na_2SO_4 and the solvent removed. After chromatography, a brown solid was isolated (355 mg, 79% yield).

MS (*m/z*): 262 [$M^{\cdot+}$] (calcd for $C_{13}H_{14}S_2Si$ 262), 247 [M – CH_3]$^+$. ^{1}H NMR ($CDCl_3$ 200 MHz) δ 7.24 (d, 2.7 Hz, 1H), 7.18 (d, 1.8 Hz, 1H), 7.14 (d, 1.8 Hz 1H), 7.03–7.01 (dd, 2 Hz, 2H), 0.29 (s, 9H). ^{13}C NMR ($CDCl_3$ 50 MHz) δ 138.84, 136.65, 133.42, 127.9, 125.03, 124.23, 123.24, 121.73, 99.90, 97.36, −0.164.

5-Ethynyl-[2,2′]bithiophene (7). The 5-trimethylsilyl protecting group was removed from [2,2′]bithiophenyl-5-ethynyltrimethylsilane (**6**) (355 mg, 1.35 mmol) by reacting it with K_2CO_3 (560 mg 4.05 mmol, 3 equiv) in of *n*-hexane/MeOH (8:2) (15 mL) at rt for 2 h. The reaction was quenched by adding water (1 mL), diluted with Et_2O (20 mL), and washed with water (2 × 15 mL). The organic layer was dried over Na_2SO_4 and evaporated. The desilylated compound was isolated as a yellow oil (190 mg, 74% yield) and used in the following step without further purification.

MS (*m/z*): 190 [$M^{\cdot+}$] (calcd for $C_{10}H_6S_2$ 190). ^{1}H NMR ($CDCl_3$ 400 MHz) δ 7.25 (d, 5.2 Hz, 1H), 7.19 (d, 3.6 Hz, 1H), 7.17 (d, 3.6 Hz, 1H), 7.03–7.01 (m, 2H), 3.4 (s, 1H).

5-(5-Ethynyl-[2,2′]bithiophenyl)-2′-deoxy-5′-*O*-(4,4′-dimethoxytrityl)uridine (8). 5-Ethynyl-[2,2′]bithiophene (**7**) (200 mg, 2 equiv, 1.05 mmol), 5′-*O*-(4,4′)-dimethoxytrityl)-5-iodo-2′-deoxyuridine (*1819*) (346 mg, 1 equiv, 0.527 mmol), $Pd(PPh_3)_4$ (30 mg, 0.026 mmol, 0.05 equiv), CuI (7 mg, 0.037 mmol, 0.07 equiv), and TEA (368 μL, 2.635 mmol, 5 equiv) were dissolved in DMF (7 mL). The solution was stirred under nitrogen for 3 h at 25 °C. The reaction mixture was concentrated in vacuo, then diluted with CH_2Cl_2 (15 mL), washed with water (2 × 10 mL), and purified by flash chromatography eluting with CH_2Cl_2/MeOH (95:5) to achieve the desired product (227 mg, 60% yield) as a yellow solid.

ESI-MS (*m/z*): 740.8 [M + Na]$^+$ (calcd for $C_{40}H_{34}N_2O_7S_2$ + Na 741), 303 [DMT]$^+$. ^{1}H NMR ($CDCl_3$, 400 MHz) δ 9.60 (bs, 1H), 8.11 (s, 1H), 7.36–7.08 (m, 11H), 7.01 (d, 3.2 Hz, 1H), 6.895 (dd, 3.6 Hz, 1H), 6.808 (d, 4 Hz, 1H), 6.77–6.66 (m, 4H), 6.28 (t, 6.6 Hz, 1H), 4.51 (t, 2.4 Hz, 1H), 4.09 (d, 2.4 Hz 1H), 3.61 (s, 6H), 3.34–3.24 (m, 2H), 2.54–2.50 (m, 1H), 2.28–2.23 (m, 1H). ^{13}C NMR ($CDCl_3$, 100 MHz): δ 161.42, 158.5, 149.37, 144.26, 142.38, 138.99, 136.61, 135.50, 135.31, 133.35,129.94, 129.84, 127.98, 127.86, 126.96, 124.87, 124.06, 123.09, 120.96, 113.27, 100. 20, 87.01, 86.84, 86.07, 84.59, 72.42, 55.15, 63.53, 35.4.

5-(5-Ethynyl-[2,2′]bithiophenyl]-2′-deoxy-5′-*O*-(4,4′-dimethoxytrityl)uridine-3′-*O*-(2-cyanoethyl-*N*,*N*-diisopropyl)phosphoramidite (9). 5-(5-Ethynyl-[2,2′]bithiophenyl)-2′-deoxy-5′-*O*-(4,4′-dimethoxytrityl)uridine (**8**) (200 mg, 0.279 mmol, 1 equiv) and ethyl-*N*,*N*-diisopropylamine (238 μL, 1.4 mmol, 5 equiv) were stirred in dichloromethane (2 mL) and treated with 2-cyanoethyl-*N*,*N*-diisopropylchlorophosphoramidite (93 μL, 0.42 mmol, 1.5 equiv) under nitrogen. After 30 min at rt, the reaction mixture was diluted with dichloromethane (5 mL) and washed with sat aq $NaHCO_3$ (5 mL). The aqueous phase was re-extracted twice with dichloromethane (2 × 5 mL), and the combined organic phases were dried over Na_2SO_4. After solvent evaporation, the crude residue was purified by flash chromatography (silica gel, column prepared with CH_2Cl_2/TEA 9:1 and eluted with CH_2Cl_2/TEA/MeOH 98:1:1) to yield **9** (191 mg, 76% yield) as a yellow solid mixture of diasteroisomers.

^{31}P NMR (80 MHz, $CDCl_3$): δ 149.07 R_L, 148.65 R_{Hr}. ^{1}H NMR ($CDCl_3$, 400 MHz): δ 9.60 (bs, 2H, R_H + R_L), 8.22 (s, 1H, R_H), 8.17 (s, 1H, R_L), 7.44–7.15 (m, 22H, R_H + R_L), 7.10 (d, 4 Hz, 1H, R_L), 7.09 (d, 3.6 Hz, 1H, R_H), 6.99 (dd, 4 Hz, 3.6 Hz, 2H, R_H + R_L), 6.90 (d, 4 Hz, 1H, R_L), 6.88 (d, 4 Hz, 1H, R_H), 6.817–6.775 (m, 6H, R_H + R_L), 6.72 (d, 3.6 Hz, 1H, R_L), 6.68 (d, 3.6 Hz, 1H, R_H), 6.34 (t, 6 Hz, 1H, R_L), 6.32 (t, 6 Hz, 1H, R_H), 4.6 (m, 2H, R_H + R_L), 4.2 (m, 4H, R_H + R_L), 3.88–3.80 (m, 2H, R_H + R_L), 3.72 (s, 6H, R_L), 3.71 (s, 6H, R_H), 3.67–3.50 (m, 4H, R_H + R_L), 3.50–3.26 (m, 4H, R_H + R_L), 2.63 (m, 4H, R_H + R_L), 2.44 (t, 6.4 Hz, 2H, R_H + R_L), 2.35 (m, 2H, R_H + R_L), 1.18 (d, 6.5 Hz, 12H, R_L), 1.16 (d, 6.0 Hz, 12H, R_H).

2-Bromo-5-thiomethylthiophene (10). To a solution of 2-thiomethylthiophene (500 mg, 3.8 mmol, 1 equiv) in CH_2Cl_2/CH_3COOH (1:1) (33 mL) under nitrogen was added NBS (547 mg, 3.07 mmol, 0.8 equiv) at −15 °C in 30 min. After 2 h, the reaction mixture was diluted with CH_2Cl_2 (20 mL) and washed with 10% aq KOH (40 mL), sat aq $NaHCO_3$ (40 mL), and water (40 mL). The organic layer was dried over Na_2SO_4 and evaporated. The crude product was isolated as a colorless oil (583 mg, 73% yield) and used in the following step without further purification.

MS (*m/z*): 208, 210 [$M^{\cdot+}$] (calcd for $C_5H_5BrS_2$ 208, 210), 193, 195, [M – Me]$^+$. ^{1}H NMR ($CDCl_3$, 400 MHz) δ 6.90 (d, 4.0 Hz, 1H), 6.87 (d, 4.0 Hz, 1H), 2.46 (s, 3H).

5-Thiomethyl-[2,2′]bithiophene (11). The microwave oven reactor was charged with 2-bromo-5-thiomethylthiophene (**10**) (583 mg, 2.79 mmol, 1 equiv), 2-(tributylstannyl)thiophene (886 μL 2.8 mmol, 1 equiv), $Pd(PPh_3)_4$ (322 mg, 0.28 mmol, 0.1 equiv) in toluene (10 mL). After 45 min of irradiation at 120 °C, TLC on silica gel with *n*-hexane as eluent showed the absence of **10**. The solvent was removed in vacuo, and the crude mixture was directly charged on a chromatography column. After chromatography eluting with *n*-hexane, the title compound was isolated (414 mg 70% yield).

MS (*m/z*): 212 [$M^{\cdot+}$] (calcd for $C_9H_8S_3$ 212), 197 [M – Me]$^+$. ^{1}H NMR ($CDCl_3$, 200 MHz) δ 7.21 (d, 4.2 Hz, 1H), 7.13 (d, 3.4 Hz, 1H), 7.03–6.97 (m, 3H), 2.5 (s, 3H). ^{13}C NMR ($CDCl_3$, 50 MHz) δ 139.95, 137.10, 136.70, 131.79, 127.79, 124.53, 123.82, 123.76, 22.11.

5-Iodo-5′-thiomethyl-[2,2′]bithiophene (12). To a solution of 5-thiomethyl-[2,2′]bithiophene (414 mg, 1.95 mmol, 1 equiv) in CH_2Cl_2/CH_3COOH (1:1) (33 mL) under nitrogen was added NIS (395 mg, 1.76 mmol, 0.9 equiv) at –15 °C over 30 min After 2 h, the reaction mixture was diluted with CH_2Cl_2 (30 mL) and washed with 10% aq KOH (40 mL), sat aq $NaHCO_3$ (40 mL), and distilled water (40 mL). The organic layer was dried over Na_2SO_4 and evaporated. After chromatography eluting with *n*-hexane, the target product (488 mg, 74% yield) was isolated as a colorless oil.

MS (*m/z*): 338 [$M^{\cdot+}$] (calcd for $C_9H_{12}IS_3$ 338), 323 [M – Me]$^+$, 196 [M – Me – I]$^+$. ^{1}H NMR ($CDCl_3$, 400 MHz) δ 7.14 (d, 4.0 Hz, 1H), 6.96 (d, 3.6 Hz, 1H), 6.95 (d, 3.6 Hz, 1H),

6.79 (d, 4.0 Hz, 1H), 2.5 (s, 3H). ^{13}C NMR ($CDCl_3$, 100 MHz) δ 142.87, 138.08, 137.62, 137.12, 131.48, 124.98, 124.20, 22.92.

5-(Ethynyl)-2′-deoxy-5′-*O*-(4,4′-dimethoxytrityl)uridine (13). The synthesis and characterization of 5-(ethynyl)-2′-deoxy-5′-*O*-(4,4′-dimethoxytrityl)uridine (**13**) have been reported elsewere (*20*).

5-(5-Ethynyl-5′-tiomethyl-[2,2′]bithiophenyl)-2′-deoxy-5′-*O*-(4,4′-dimethoxytrityl)uridine (14). To a solution of 5-iodo-5′-thiomethyl-[2,2′]bithiophene (68 mg, 0.2 mmol) in anhydrous DMF (2 mL) under nitrogen was added CuI (8 mg, 0.04 mmol, 0.2 equiv), TEA (140 μl, 5 equiv), 5-(ethynyl)-2′-deoxy-5′-*O*-(4,4′-dimethoxytrityl)uridine (**13**) (111 mg, 0.2 mmol) and $Pd(PPh_3)_4$ (23 mg, 0.1 equiv, 0.02 mmol). The mixture was stirred 3 h at rt. The reaction mixture was concentrated in vacuo, then diluted with CH_2Cl_2 (20 mL), and washed with sat aq citric acid (15 mL), sat aq $NaHCO_3$ (15 mL), and water (15 mL). The organic phase was dried over Na_2SO_4, the solvent removed, and the crude mixture purified by flash chromatography eluting with 5% MeOH in CH_2Cl_2. The desired product was obtained as brown oil (110 mg, 66% yield).

ESI-MS (*m/z*): 786.9 $[M + Na]^+$ (calcd for $C_{41}H_{36}N_2O_7S_3$ + Na 787). ^{1}H NMR ($CDCl_3$, 200 MHz) δ 8.11 (s, 1H), 7.80 (bs, 1H), 7.90 (dd, 3.6 Hz, 1H), 7.58–7.50 (m, 1H), 7.44–7.38 (m, 2H), 7.36–7.14 (m, 9H), 6.84–6.70 (m, 4H), 6.33 (t, 6.6 Hz, 1H), 4.60 (m, 1H), 4.08 (d, 2.4 Hz 1H), 3.65 (s, 6H), 3.40–3.20 (m, 2H), 2.54–2.50 (m, 1H), 2.50 (s, 3H), 2.28–2.23 (m, 1H).

5-(5-Ethynyl-5′-tiomethyl-[2,2′]bithiophene)-2′-deoxy-5′-*O*-(4,4′-dimethoxytrityl)uridine-3′-*O*-(2-cyanoethyl-*N*,*N*-diisopropyl)phosphoramidite (15). A 0.45 M solution of tetrazole (0.104 mmol, 0.232 mL, 1 equiv) in anhydrous CH_3CN was added, with stirring under a flow of nitrogen, to a solution of 5-(5-ethynyl-5′-thiomethyl-[2,2′]bithiophenyl)-2′-deoxy-5′-*O*-(4,4′-dimethoxytrityl)uridine (**14**) (80 mg, 0.104 mmol, 1 equiv) in anhydrous CH_3CN (222 μL), followed by a solution of 2-cyanoethyl *N*,*N*,*N*′,*N*′-tetraisopropylphosphorodiamidite (32 μL, 0.0708 mmol, in 40 μL of anhydrous CH_3CN). TLC analysis showed that the reaction was completed within 45 min with the formation of two diastereoisomers. The precipitated diisopropylammonium tetrazolide was removed by filtration and the solution diluted with anhydrous CH_3CN (1 mL) to give a 0.1 M solution of **15**. The solution was immediately used in the phosphitlylation step on the automated synthesizer, without further purification or analysis except for a check of the presence of the correct phosphoroamidite specie by phosphorous NMR analysis, on a small aliquot of the solution.

^{31}P NMR($CDCl_3$, 80 MHz) δ 149.46, 149.75.

5-(5-[2,2′]Bithiophenyl)-2′-deoxy-5′-*O*-(4,4′-dimethoxytrityl)uridine (17a). A mixture of 5′-*O*-(4,4'dimethoxytrityl)-5-iodo-2′-deoxyuridine (100 mg, 0.152 mmol 1 equiv), 5-tributylstannyl-[2,2′]-bithiophene (**16a**) (*21*) (277 mg, 0.610 mmol 4 eq) and $Pd(PPh_3)_2Cl_2$ (11 mg, 0.0152 mmol, 0.1 equiv) in dioxane (5 mL) was heated at 95 °C for 4 h. The solution was cooled and evaporated, and the mixture was purified by flash chromatography eluting with CH_3CN:H_2O (80:20). **17a** was obtained as a yellow solid (102 mg, 97% yield).

ESI-MS (*m/z*): 716.8 $[M + Na^+]$ (calcd for $C_{38}H_{34}N_2O_7S_2$ + Na 717). ^{1}H NMR (400 MHz, DMSO-d_6) δ 9.5 (brs, 1H), 7.92 (s,1H), 7.38 (d, 7.2 Hz, 2H), 7.30–7.10 (m, 9H), 6.99 (d, 3.6 Hz, 1H), 6.94 (dd, 3.6 Hz, 1H), 6.76–6.71 (m, 5H), 6.19 (t, 6.5 Hz, 1H), 4.49–4.47 (m, 1H), 4.15–4.12 (m, 1H), 3.65 (s, 6H), 3.45–3.41 (m, 1H), 3.35–3.31 (m, 1H), 2.05–1.95 (m, 1H), 2.35–2.25 (m, 1H).

5-(5-[2,2′]Bithiophenyl)-2′-deoxy-5′-*O*-(4,4′-dimethoxytrityl)uridine-3′-*O*-(2-cyanoethyl-*N*,*N*-diisopropyl)phosphoramidite (18a). 5-(5-[2,2′]Bithiophenyl)-2′-deoxy-5′-*O*-(4,4′-dimethoxytrityl)uridine (**17a**) (100 mg, 0.144 mmol, 1 equiv) and ethyl-*N*,*N*-diisopropylamine (123 μL, 0.72 mmol, 5 equiv) were stirred in THF (1 mL) and treated with 2-cyanoethyl-*N*,*N*-diisopropylchlorophosporamidite (48 μL, 0.216 mmol, 1.5 equiv) under nitrogen. After 30 min at rt, the reaction mixture was diluted with dichloromethane (5 mL) and washed with sat $NaHCO_3$ (5 mL). The aqueous phase was re-extracted twice with CH_2Cl_2 (2 × 5 mL), and the combined organic phases were dried over Na_2SO_4. After solvent evaporation, the crude residue was purified by flash chromatography (silica gel, column eluted with EtOAc/TEA/*n*-hexane 80:1:19) to give **18a** (102 mg, 80% yield) as a yellow solid mixture of diasteroisomers.

^{31}P NMR (80 MHz, $CDCl_3$) δ 150.27, 149.77 (R_L + R_H). ^{1}H NMR ($CDCl_3$, 400 MHz) δ 9.60 (bs, 2H, R_H + R_L), 7.98 (s, 1H, R_H), 7.93 (s, 1H, R_L), 7.69–7.63 (m, 2H, R_H + R_L), 7.57–7.51 (m, 2H, R_H + R_L), 7.48–7.15 (m, 20H, R_H + R_L), 6.98–6.93 (m, 4H, R_H + R_L), 6.76–6.67 (m, 10H, R_H + R_L), 6.38 (t, 7.2 Hz, 1H, R_L), 6.37 (t, 7.2 Hz, 1H, R_H), 4.65 (m, 2H, R_H + R_L), 4.40 (m, 4H, R_H + R_L), 3.71 (s, 12H, R_L + R_H), 3.64–3.45 (m, 8H, R_H + R_L), 2.63–2.15 (m, 4H, R_H + R_L), 2.42–2.38 (m, 4H, R_H + R_L), 2.35–2.20 (m, 4H, R_H + R_L), 1.18 (d, 6.5 Hz, 12H, R_L), 1.16 (d, 6.0 Hz, 12H, R_H).

5-(5-[2,2′],[5′,2″]Terthiophene)-2′-deoxy-5′-*O*-(4,4′-dimethoxytrityl)uridine (17b). A mixture of 5′-*O*-(4,4′-dimethoxytrityl)-5-iodo-2′-deoxyuridine (230 mg, 0.35 mmol, 1 equiv), 5-(tributylstannyl)-[2,2′],[5′,2″]terthiophene (**16b**) (*22*) (750 mg, 1.4 mmol, 4 equiv), and $Pd(PPh_3)_2Cl_2$ (25 mg, 0.035 mmol, 0.1 equiv) in dioxane (10 mL) was heated at 95 °C for 4 h. The solution was cooled and evaporated, and the mixture was purified by chromatography on reversed-phase C-18 silica gel, eluting with CH_3CN/H_2O (80:20). **17b** was obtained as a yellow solid (109 mg, 40% yield).

ESI-MS (*m/z*): 774.7 $[M - H]^+$ (calcd for $C_{42}H_{35}N_2O_7S_3$ 775). ^{1}H NMR (400 MHz, DMSO-d_6) δ 11.8 (s, 1H), 7.97 (s, 1H), 7.4–7.3 (m, 4H), 7.30–7.14 (m, 9H), 7.09 (dd, 3.6 Hz, 1H), 7.03 (d, 4.0 Hz, 1H), 6.99 (d, 4.0 Hz, 1H), 6.80 (dd, 5.6 Hz, 4H), 6.19 (t, 6.5 Hz, 1H), 4.45 (brs, 1H), 3.95–3.90 (m, 1H), 3.65 (s, 6H), 3.40 (m, 1H), 2.70–2.90 (m, 1H), 2.25–2.35 (m, 1H), 1.60 (m, 2H).

5-(5-[2,2′],[5′,2″]Terthiophenyl)-2′-deoxy-5′-*O*-(4,4′-dimethoxytrityl)uridine-3′-*O*-(2-cyanoethyl-*N*,*N*′-diisopropyl)phosphoramidite (18b). A 0.45 M solution of tetrazole (0.07 mmol, 0.157 mL, 1 equiv) in anhhydrous CH_3CN was added at rt, stirring under N_2 atmosphere, to a solution of 2′-deoxy-5′-*O*-(4,4′-dimethoxytrityl)-5-[-[2,2′],[5′,2″]terthiophene]uridine (**17b**) (55 mg, 0.07 mmol, 1 equiv) in 350 μL of anhydrous CH_3CN followed by 2-cyanoethyl *N*,*N*,*N*′,*N*′-tetraisopropylphosphorodiamidite (0.0708 mmol, 22.5 μL, 1 equiv). TLC analysis showed that the reaction was completed within 45 min with formation of two diastereoisomers. The precipitated diisopropylammonium tetrazolide was removed by filtration and the solution diluted with CH_3CN (350 μL) to give a 0.1 M solution of **14**, which was immediately used in the following step without further purification.

RESULTS AND DISCUSSION

Synthesis. The 5′-dimethoxytrityl derivatives of compounds **1**–**4** were prepared from the corresponding 5′-dimethoxytrityl of 5-iodouridine (*18*, *19*) applying Sonogashira's or Stille's coupling. The compounds were then converted to phosphoramidites using the 2-cyanoethyl-*N*,*N*-diisopropylchlorophosphoramidite or the 2-cyanoethy *N*,*N*,*N*′,*N*′-tetraisopropylphosphorodiamidite. The synthetic pathways are showed in Schemes 1 and 2.

Compound **8** was obtained via Sonogashira's coupling of the ethynyl bithiophene **7** with the dimethoxytritylated iodouridine (*18, 19*); the S-Me analogue **14** was prepared with the same methodology but a reverse strategy, in which the ethynyl moiety

Scheme 1. Synthesis of 5-Alkinyl-Oligothiophene-Deoxyuridine Phosphoramidites[a]

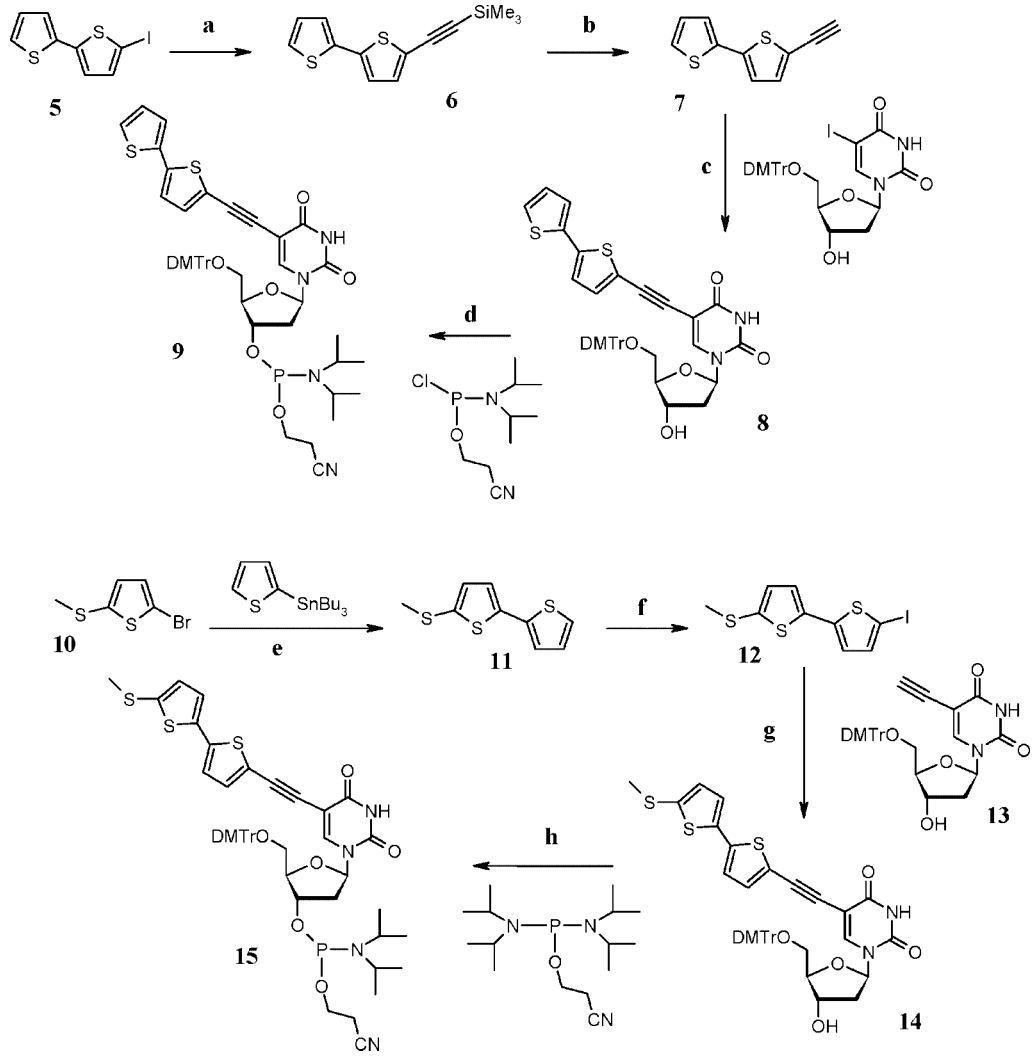

[a] **a.** trimethylsilyl acetylene, $Pd(PPh_3)_4$, CuI, TEA in DMF, 20 min microwave irradiation, (79% yield); **b.** K_2CO_3 in 8/2 hexane/MeOH, 2 h rt, (74% yield); **c.** $Pd(PPh_3)_4$, CuI, TEA in DMF, 3 h rt, (60% yield), **d.** DIPEA in CH_2Cl_2, 30 min rt (76% yield); **e.** $Pd(PPh_3)_4$ in toluene, 45 min microwave irradiation, (70% yield), **f.** NIS dropwise in 1:1 CH_2Cl_2/AcOH at −15 °C then 2 h at rt (74% yield); **g.** $Pd(PPh_3)_4$,CuI, TEA in DMF, 3 h rt, (66% yield); **h.** 1/1 CH_2Cl_2/CH_3CN, tetrazole, 45 min rt, (yield >90% on TLC, compound not isolated).

Scheme 2. Synthesis of 5-Oligothiophene-Deoxyuridine Phosphoramidites[a]

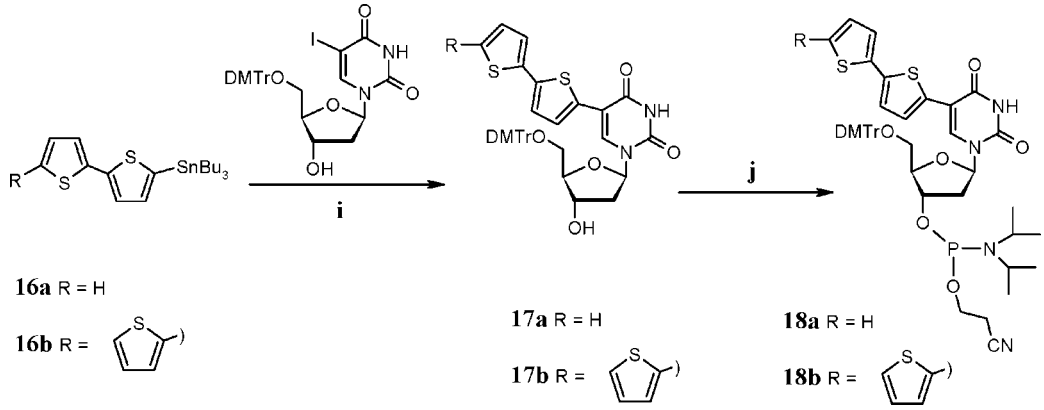

[a] **i.** $Pd(PPh_3)_2Cl_2$ in dioxane, 4 h 95°C, (yields: **17a** 97%, **17b** 40%); **j.** [(**a** 2-cyanoethyl-chloro-diisopropylaminophosphoramidite, DIPEA in THF, 30 min rt, 80% yield). (**b.** 2-cyanoethyl *N,N,N′,N′*-tetraisopropylphosphorodiamidite, tetrazole in 1/1 CH_2Cl_2/CH_3CN, 45 min rt, yield >90% on TLC, compound not isolated)].

was previously linked to the uridine nucleoside, since this allowed an easier purification step. Furthermore, compound **14**, available in a limited amount (80 mg left after analysis) was phosphitylated by using 1 equiv of 2-cyanoethyl *N,N,N′,N′*-tetraisopropylphosphorodiamidite and 1 equiv of tetrazole. This gave, after the filtration of the diisopropylammonium tetrazolide, a concentrated solution that was diluted with CH_3CN to a formal concentration of 0.1 M and immediately used for the automated

Table 2. T_m (in °C) at 1 μM Concentration in Aqueous Buffer Containing 100 mM NaCl, 10 mM Sodium Cacodylate at pH 7.0[a]

	P1 (ethynyl-t_2)	**P2** (ethynyl-t_2-SMe)	**P3** (t_2)	**P4** (t_3)
A	50	50	52	48
C	49	49	49	47
G	47	49	49	46
T	46	48	49	47

[a] Precision ± 1 °C. t_2 and t_3 refer to the number of thiophene rings.

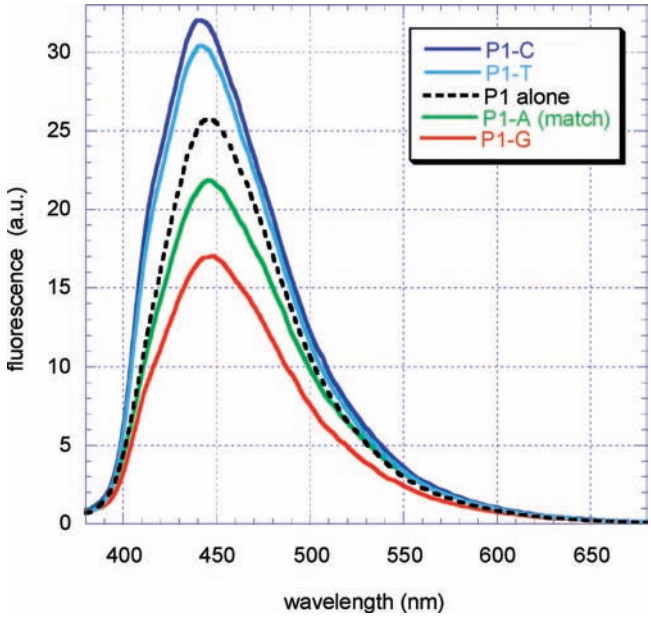

Figure 2. Fluorescence emission of **P1** alone and hybridized with the four targets after irradiation at 360 nm.

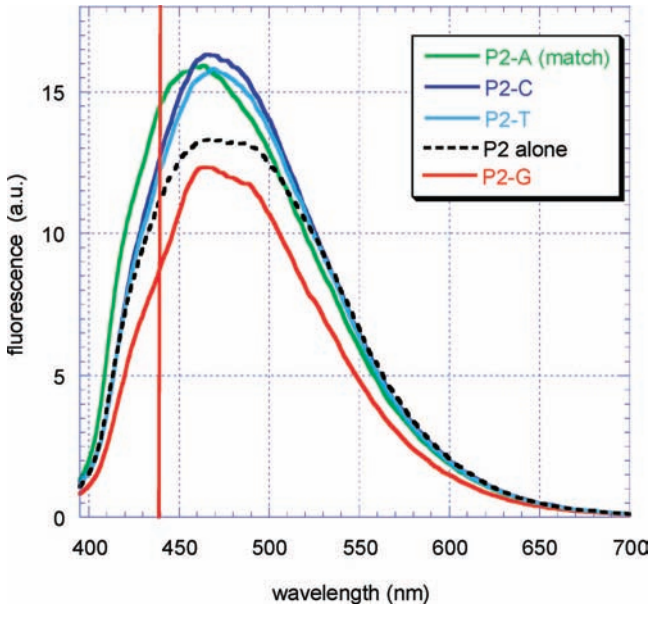

Figure 3. Fluorescence emission of **P2** alone and hybridized with the four targets after irradiation at 375 nm.

synthesis of the probe **P2**. This procedure (*23*) allowed us to carry out the synthesis of the probe without risking any loss of the amidite **15** (due to hydrolysis or manipulation) in the purification steps.

Compounds **17**(**a** and **b**) were obtained using the Stille's coupling of dimethoxytrityliodouridine with the tributhylstannyl derivative of the bi- or terthiophene **16**. The coupling gave an almost quantitative yield in the case of the bithiophene derivative **17a**, but a moderate yield in the case of the compound **17b** probably due to a lower reactivity of the larger oligothiophene and to severe product loss during the chromatographic purification step. Phosporoamidite **18b** was obtained by use of 2-cyanoethyl *N*,*N*,*N*′,*N*′-tetraisopropylphosphorodiamidite without isolation step.

All the probes were synthesized on a Pharmacia Gene Assembler 2, repeating two times the coupling step for the modified uridine, without the intervening capping, with a 2 min longer coupling time, on a 1.3 μmol scale. With these precautions, we did not notice any lowering of efficiency in the coupling steps.

The oligonucleotide targets (**A**, **C**, **G**, **T**) were prepared on the same synthesis scale using commercial reagents. All the oligonucleotides were deblocked by treatment with 30% aqueous ammonia at 50 °C for 16 h, then lyophilized. The targets were purified by precipitation with *n*-BuOH and judged sufficiently pure by reversed-phase HPLC analysis at 260 nm (80–85%). The probes were purified by reversed-phase HPLC using double detection: UV at 260 nm and fluorescence at the maximum of emission of every derivative. Final compounds were judged more than 90% pure by UV and more than 95% pure by fluorescence. The identity of the probes was determined by a careful analysis of the UV–vis spectra (giving the expected ratio UV/vis) and from ESI-MS analysis: **P1** calcd *m*/*z* for $C_{184}H_{225}N_{62}O_{108}P_{17}S_2$ 5623.88, found 5624.02; **P2** calcd *m*/*z* for $C_{185}H_{227}N_{62}O_{108}P_{17}S_3$ 5669.97, found 5669.17; **P3** calcd *m*/*z* for $C_{182}H_{225}N_{62}O_{108}P_{17}S_2$ 5599.86, found 5599.64; **P4** calcd *m*/*z* for $C_{186}H_{227}N_{62}O_{108}P_{17}S_3$ 5681.98, found 5682.00.

UV and Fluorescence Experiments. The UV–vis and the fluorescence emission spectra of the each probe were registered at 25 and at 70 °C at 1 μM concentration in an aqueous buffer containing 100 mM NaCl and 10 mM sodium cacodylate at pH 7.0. They did not reveal any significative changes but a 10–15% loss of fluorescence emission at the higher temperature. This behavior was already observed in our previous work (*15*) with this class of fluorophores and was attributed to a slight loss of coplanarity of the thiophene rings and increasing collisional quenching due to the heating.

Three more cuvettes were prepared for each probe at 1 μM concentration in the same buffer and checked against the first sample, UV and fluorescence intensity were found in a range of less than 0.5–1% difference. To each cuvette of 3000 μL was then added 1.2 equiv (10–20 μL from concentrated aqueous solution) of the four complementary strands. The samples were heated to 90 °C and left to cool in a beaker (in about 3 h) to favor the annealing. The UV-melting profile was then recorded at 260 nm during both heating and cooling, in the range 10–75 °C, at a rate of 0.5 °C/min. The found melting temperatures are reported on Table 2.

After the melting experiments, the very same samples were used to measure the variation of fluorescence of the four hybrids of the **P1**–**P4** probes. These measurements are the core of this research and show interesting features that will be presented on the same scale and discussed in detail. All the probes were excited at the maximum of their visible absorption. To ensure that the measurements of the mixtures were not affected by the presence of accidental quenchers in the target solutions, we recorded the fluorescence of every mixture at 70 °C and found them equal to those obtained with the corresponding isolated probe at the same temperature.

Fluorescence of **P1** *(ethynyl-t_2) and Its Hybrids.* Fluorescence emissions of **P1** alone and hybridized with the four targets are shown in Figure 2.

The graph shows that **P1** is able to discriminate between the perfect match with **target-A** (−20% in the emitted intensity

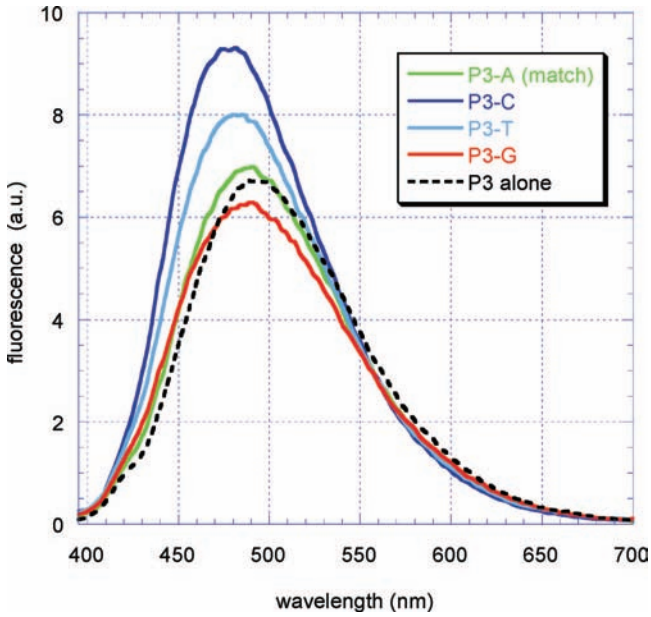

Figure 4. Fluorescence emission of **P3** alone and hybridized with the four targets after irradiation at 360 nm.

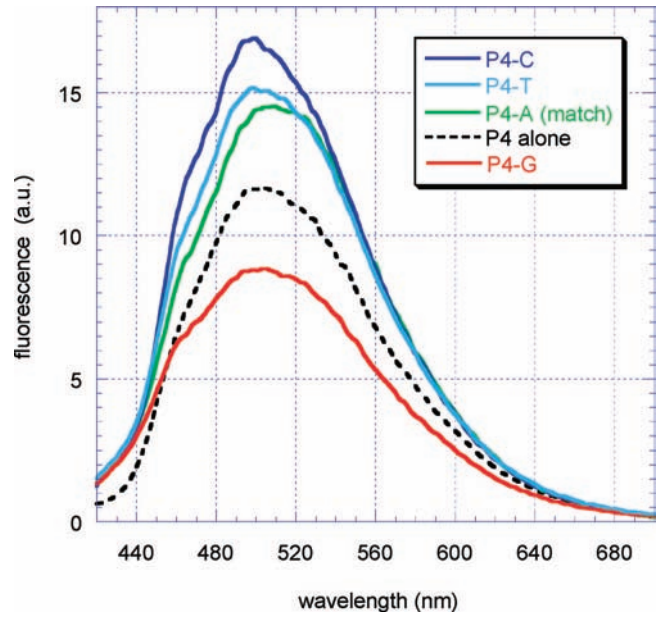

Figure 5. Fluorescence emission of **P4** alone and hybridized with the four targets after irradiation at 400 nm.

respect to unhybridized **P1**), **target-G** (−35%), and the pair of **targets C** and **T** (+15, +18%).

Fluorescence of **P2** *(ethynyl-t_2-SMe) and Its Hybrids.* The fluorescence characteristics of **P2** and its hybrids are reported in Figure 3.

Compared to the previous probe, **P2** shows lower and broader signals, reflecting the increased dimension of the molecular orbital, now including an S-Me substituent. Here, we can see that hybrids formed with **probes C** and **T** show very similar signals; the hybrid with **probe A** has a similar intensity to the previous two, but its maximum is blue-shifted by about 10 nm. The three signals are about 18% more intense than the isolated probe. The hybrid with **probe G** shows a signal 10% weaker than that showed by the single-strand probe. If we look at the value of the emitted light at 440 nm, we can easily observe that the emission of the probe alone is halfway between that of the mismatch with **probe G** (−20%) and that of the match with **probe A** (+36%). Again, the mismatches with **probes C** and **T** (+18%) are too close to be distinguished. This can be considered an ideal probe to look for a G to A transition: it is sufficient to record the emission of the probe alone and hybridize it with the unknown target; then, if the emission is higher than before, this reveals a match, and if it is lower, it is a G mismatch (besides, C and T mismatch can also be detected with a careful measurement).

Fluorescence of **P3** *(t_2) and Its Hybrids.* The graphics of the fluorescence emission of **P3** and its hybrids are reported in Figure 4.

There is no clear difference in intensity between the signal of the single strand and those of the hybrids with **A** and **G targets**; instead, the intensities of the maxima of the hybrids with **targets T** (+18%) and **C** (+44%) can clearly be distinguished. Small differences perhaps exploitable for the recognition of the formed hybrids can be seen in the positions of the maxima: they move from 492 (**P3** alone), to 488 (**P3-G**, **P3-A**), to 482 (**P3-T**), to 478 (**P3-C**).

By comparing the emission of this probe with those of **P1**, it can be seen that the intensity of the emission is between three and four times lower in the absence of the ethynyl linker.

Fluorescence of **P4** *(t_3) and Its Hybrids.* The graphics of the fluorescence emissions of **P4** hybrids and isolated **P4** are reported in Figure 5.

These emissions are the widest and the most structured among the four probes. Compared to the signal of the **P4** probe alone, hybrids with **targets C** (+47%), **T** (+30%), and **A** (+26%) are clearly distinguishable even if the last two are closely grouped; the hybrid with **target G** can also be neatly recognized (−22%). Furthermore, all compounds have an emission maximum centered at 500 nm except for the hybrid with **target-A** that is shifted to 510 nm.

Only a few methods of mismatch detection based on fluorescence of the facing base have been reported in the literature. Among the most recent ones, Tor reports the use of 1,10-phenantroline-ethynyl-5-uridine (*11*) and demonstrates a fair sensitivity in recognizing the pairing nucleosides comparing the emission ratio at two different wavelengths in a range from 0.95 for the match with adenosine to 1.2 for the worst tolerated mismatch with cytidine; Kim shows the ablility to appreciate with the naked eye the correct pairing of a 5-(1-ethynylpyrenyl)-2′-deoxyuridine incorporated into an oligonucleotide with respect to the three possible mismatches (*12*); however, all of them are not very fluorescent and their emissions quite similar.

With the aim to explore the potentialities of oligothiophenes as markers for biomolecules, we have developed the synthesis of oligothiophene-5-labeled deoxyuridines. (Compound **3** was previously obtained, by a different strategy, by Van Aerschot's group (*24*), and studied for its antiviral properties.) Our results demonstrate that the new uridines, integrated into an oligonucleotide, are apt to discriminate between the correct pairing and mispairings.

Despite the steric hindrance of the labels, uridines did not interfere significantly with the hybridization process (differences between the match and mismatches are less than 3 °C); neither showed any tendency to intercalate between base pairs, as demonstrated by lack of variance of absorbance in the visible part of the spectra and by structures obtained by the modeling of **P3** with all the probes (not shown). Akin to the case of molecular beacons (*15*), the emissions of oligothiophene derivatives are exquisitely sensitive to the local environment, and this characteristic is potentially exploitable for the analysis of SNPs. Usually, the mutation to be analyzed is well-known and consists of a single nucleoside exchange: A to G (as in our case), but if different exchanges are possible, probes like **P3** and **P4** can be used to reveal each of them.

In our case, we observed the lowest emission when any of the probes was facing G, a feature common to several fluorophores (*15*, *25*, *26*). The behavior of the single probes with **C**, **T**, and **A** is still unclear and might be the object of a future communication. At this stage, the prevision of a higher or lower fluorescence emission, in case of a match or a mismatch, cannot easily be made, and more experimental studies are required. In particular, it could be interesting to see what kind of results are obtained by tagging nucleosides other than dU.

CONCLUSION

We have synthesized four different probes containing a deoxyuridine modified with oligothiophene derivatives at the 5-position. All the probes fluoresce at different wavelengths, and all show variations of emission intensity (from 10% to 47% higher or lower than those of the isolated probes), upon hybridization with targets containing all four bases opposite the uridine. These variations are comparable or even superior to those reported in similar studies and could be potentially exploited for an easy SNP recognition in biological laboratories equipped with a bench spectrofluorimeter or automatic high-throughput devices.

ACKNOWLEDGMENT

We thank Giorgia Brancolini (ISOF-CNR) for modeling studies performed on hybrids of **P3**. This work was partially funded by FIRB RBNE03S7XZ_005 (SYNERGY) project.

LITERATURE CITED

(1) http://nci.nih.gov/cancertopics/understandingcancer/geneticvariation

(2) Jurinke, C., Oeth, P., and van den Boom, D. (2004) MALDI-TOF mass spectrometry - A versatile tool for high-performance DNA analysis. *Mol. Biotechnol. 26*, 147–163.

(3) Petkovski, E., Keyser-Tracqui, C., Hienne, R., and Ludes, B. (2005) SNPs and MALDI-TOF MS: Tools for DNA typing in forensic paternity testing and anthropology. *J. Forensic Sci. 50*, 535–541.

(4) Sauer, S. (2006) Typing of single nucleotide polymorphisms by MALDI mass spectrometry: Principles and diagnostic applications. *Clin. Chim. Acta 363*, 95–105.

(5) Wang, L., Luhm, R., and Lei, M. (2007) SNP and mutation analysis. *Adv. Exp. Med. Biol. 593*, 105–116.

(6) Cottingham, K. (2004) Multiple choices for SNPs - Researchers face a myriad of SNP genotyping choices. *Anal. Chem. 76*, 179a–181a.

(7) Salimullah, M., Hamano, K., Tachibana, M., Inoue, K., and Nishigaki, K. (2005) Efficient SNP analysis enabled by joint application of the mu TGGE and heteroduplex methods. *Cell. Mol. Biol. Lett. 10*, 237–245.

(8) Solinas, A., Brown, L. J., McKeen, C., Mellor, J. M., Nicol, J. T. G., Thelwell, N., and Brown, T. (2001) Duplex Scorpion primers in SNP analysis and FRET applications. *Nucleic Acids Res. 29*, e96.

(9) Gibson, N. J. (2006) The use of real-time PCR methods in DNA sequence variation analysis. *Clin. Chim. Acta 363*, 32–47.

(10) Ihara, T., Chikaura, Y., Tanaka, S., and Jyo, A. (2002) Colorimetric SNP analysis using oligonucleotide-modified nanoparticles. *Chem. Commun.* 2152–2153.

(11) Hurley, D. J., Seaman, S. E., Mazura, J. C., and Tor, Y. (2002) Fluorescent 1,10-phenanthroline-containing oligonucleotides distinguish between perfect and mismatched base pairing. *Org. Lett. 4*, 2305–8.

(12) Hwang, G. T., Seo, Y. J., and Kim, B. H. (2004) A highly discriminating quencher-free molecular beacon for probing DNA. *J. Am. Chem. Soc. 126*, 6528–9.

(13) Barbarella, G. (2002) Oligothiophene isothiocyanates as fluorescent markers. *Chem. Eur. J. 8*, 5072–5077.

(14) Barbarella, G., Zambianchi, M., Ventola, A., Fabiano, E., DellaSala, F., Gigli, G., Anni, M., Bolognesi, A., Polito, L., Naldi, M., and Capobianco, M. (2006) Bright oligothiophene N-succinimidyl esters for efficient fluorescent labeling of proteins and oligonucleotides. *Bioconjugate Chem. 17*, 58–67.

(15) Cazzato, A., Capobianco, M. L., Zambianchi, M., Favaretto, L., Bettini, C., and Barbarella, G. (2007) Oligothiophene molecular beacons. *Bioconjugate Chem. 18*, 318–322.

(16) Field, J. S., Haines, R. J., Lakoba, E. I., and Sosabowski, M. H. (2001) Novel diphenylphosphine derivatives of 2,2′-bithiophene, 2,2′: 5′,2″-terthiophene, 2-(2′-thienyl)pyridine and 2,6-di-2′-thienylpyridine. Crystal structures of 5,5′-bis(diphenylphosphino)-2,2′-bithiophene, diphenyl{5-[6′-(diphenylphosphino)-2′-pyridyl]-2-thienyl}phosphine and 2,6-bis[5′-(diphenylphosphino)-2′-thienyl]pyridine. *J. Chem. Soc., Perkin Trans. 1*, 3352–3360.

(17) Pappenfus, T. M., and Mann, K. R. (2002) Synthesis and characterization of radical oligothiophenes: A new class of thiophene-based conjugated homologues. *Org. Lett. 4*, 3043–3046.

(18) Sheardy, R. D., and Seeman, N. C. (1986) The synthesis of a deoxyoligonucleotide incorporating 5-iododeoxyuridine. *J. Org. Chem. 51*, 4301–4303.

(19) Ahmadian, M., Zhang, P. M., and Bergstrom, D. E. (1998) A comparative study of the thermal-stability of oligodeoxyribonucleotides containing 5-substituted 2'deoxyuridines. *Nucleic Acids Res. 26*, 3127–3135.

(20) Hurley, D. J., and Tor, Y. (1998) Metal-containing oligonucleotides - solid-phase synthesis and luminescence properties. *J. Am. Chem. Soc. 120*, 2194–2195.

(21) Barbarella, G., Favaretto, L., Sotgiu, G., Zambianchi, M., Arbizzani, C., Bongini, A., and Mastragostino, M. (1999) Controlling the electronic properties of polythiophene through the insertion of nonaromatic thienyl S,S-dioxide units. *Chem. Mater. 11*, 2533–2541.

(22) Bilge, A., Zen, A., Forster, M., Li, H. B., Galbrecht, F., Nehls, B. S., Farrell, T., Neher, D., and Scherf, U. (2006) Swivel-cruciform oligothiophene dimers. *J. Mater. Chem. 16*, 3177–3182.

(23) Thuong, N. T., and Chassignol, M. (1988) Solid phase synthesis of oligo-alpha- and oligo-beta-deoxynucleotides covalently linked to an acridine. *Tetrhaedron Lett. 29*, 5905–5908.

(24) Liu, J., Van Aerschot, A., Luyten, I., Wigerinck, P., Pannecouque, C., Balzarini, J., Declercq, E., and Herdewijn, P. (1995) Synthesis and antiviral activities of some new 5-heteroaromatic substituted derivatives of 2′-deoxyuridine. *Nucleosides Nucleotides 14*, 525–528.

(25) Crockett, A. O., and Wittwer, C. T. (2001) Fluorescein-labeled oligonucleotides for real-time PCR: Using the inherent quenching of deoxyguanosine nucleotides. *Anal. Biochem. 290*, 89–97.

(26) Nazarenko, I., Pires, R., Lowe, B., Obaidy, M., and Rashtchian, A. (2002) Effect of primary and secondary structure of oligodeoxyribonucleotides on the fluorescent properties of conjugated dyes. *Nucleic Acids Res. 30*, 2089–2095.

BC7002555

BRET-Based Method For Detection of Specific RNA Species

Zachary F. Walls[†] and Sanjiv S. Gambhir*[,‡]

Department of Molecular and Medical Pharmacology, Geffen School of Medicine at UCLA, Los Angeles, California, and Molecular Imaging Program at Stanford, Departments of Radiology and Bioengineering, Bio-X Program, Stanford University, Stanford, California. Received July 23, 2007; Revised Manuscript Received September 24, 2007

RNA detection and quantitation is a common necessity in modern molecular biology research. Most methods, however, are complex and/or time-intensive. Presented here is a BRET (bioluminescene resonance energy transfer)-based method that can accomplish the task of RNA identification quickly and easily. By conjugating BRET enzymes to two different oligonucleotides that are complementary to the same target sequence, probes were developed that could detect RNA using a solution-based assay. This assay was optimized for spacer length between the binding sites (found to be 10 nucleotides), and sensitivity was determined to be 1 μg for a specific species of RNA within a mixed population. Specificity of the assay was assessed using *in vitro* transcribed cRNA and found to be statistically siginificant ($p = 3.11 \times 10^{-6}$, ANOVA, multiple range test). This assay represents a possibility for a less technically demanding, streamlined alternative to canonical RNA assays.

INTRODUCTION

Seqeunce-specific RNA detection and quantitation have become increasingly critical components of biological research since the completion of the human genome sequencing project. Recently, a number of efforts have been made to look at global levels of gene transcripts, while many other investigators have looked specifically at transcription levels of a few key genes under different conditions. Several methods currently exist to accomplish this task with varying levels of complexity. The Northern blot was developed several decades ago and represents one of the first efforts to detect specific RNA sequences using isotopic DNA probes (*1*). Since then, many other methods have been developed to accomplish essentially the same task including, but not limited to, RNase-protection assays, RT-PCR, and multiwell plate-based sandwich assays (*2–4*). All of these assays require time and effort to optimize and can often frustrate and sometimes deter inexperienced researchers. In an attempt to simplify the process of RNA detection, a BRET (bioluminescence resonance energy transfer)-based method for RNA detection in solution has been developed.

BRET is a phenomenon originally described in several marine organisms and developed as a technique to monitor protein–protein interactions, among other molecular events (*5*). In its classical form, a bioluminescent enzyme is fused to one protein and a fluorescent protein to another. If and when the two proteins interact, the BRET proteins become colocalized. Then, if the bioluminescent enzyme's emission spectrum overlaps with the excitation spectrum of the fluorescent protein, an energy transfer reaction occurs producing emission of photons at the fluorescent protein's emission wavelength. The advantage of using BRET over the more traditional fluorescence resonance energy transfer is that the bioluminescent enzyme catalyzes the energy needed for the reaction by oxidizing its substrate, hence obviating the need for input photons and eliminating the risk of photobleaching. The necessity of a laser to produce excitation photons increases costs and limits generalizability. Additionally, the omission of input photons makes BRET-based technologies more amenable to imaging of living subjects, due to the absorptive properties of tissue for lower wavelengths of light (*6–8*).

In order to apply BRET technology to RNA detection, a pair of BRET proteins (RL8 and GFP^2) were produced in bacteria and purified using several rounds of chromatography. RL8 is a thermostable variant of *Renilla* luciferase, and GFP^2 is a spectral variant of green fluorescent protein (*7*, *9*). These proteins were then chemically conjugated to two different functionally derivatized antisense oligonucleotides, each complementary to a different portion of the same target RNA. The target then served as a scaffold upon which the bioconjugates could bind. Thus, in the presence of the target RNA, the enzymes were able to colocalize and carry out the BRET reaction (Figure 1). However, in the absence of the target, only light from the BRET donor (RL8) was seen. A solution-based assay was developed to demonstrate specificity and sensitivity, as well as determine the optimal spacing between binding sites.

METHODS

Protein Production. RL8, a thermostable mutant of *Renilla* luciferase, containing an N-terminal pelB signal sequence and a C-terminal 6×His tag was periplasmically expressed in bacteria as previously described (*7*). Briefly, bacteria transformed with the expression plasmid were grown at 32 °C until an OD_{600} of 0.7 was reached. The cells were induced with 0.2% arabinose and harvested 12–14 h later. The periplasmic fraction was isolated by osmotic shock and then purified by affinity chromatography using Ni-NTA agarose resin. Further purification was unnecessary due to the initial purity of the elution fraction. GFP^2, a spectral mutant of GFP, was cloned into the pBAD/myc-HisA vector (Invitrogen) using PCR to append an NcoI site to the 5′ end and a *Hin*dIII site onto the 3′ end. LMG-bacteria transformed with the expression plasmid were grown at 37 °C until an OD_{600} of 0.6 was reached. The cells were induced with 0.2% arabinose, and the cultures were incubated at 30 °C with shaking (200 rpm) for 24 h. Cells were pelleted by centrifugation at 6000 × *g* for 15 min at 4 °C. The

* To whom correspondence should be addressed. Molecular Imaging Program at Stanford (MIPS), Departments of Radiology and Bioengineering, Bio-X Program, Stanford University James H. Clark Center, 150 East Wing, 1st Floor, 318 Campus Drive, Stanford, CA 94305-5427, E-mail: sgambhir@stanford.edu.

[†] Geffen School of Medicine at UCLA.

[‡] Stanford University.

10.1021/bc700278n CCC: $40.75 © 2008 American Chemical Society
Published on Web 12/12/2007

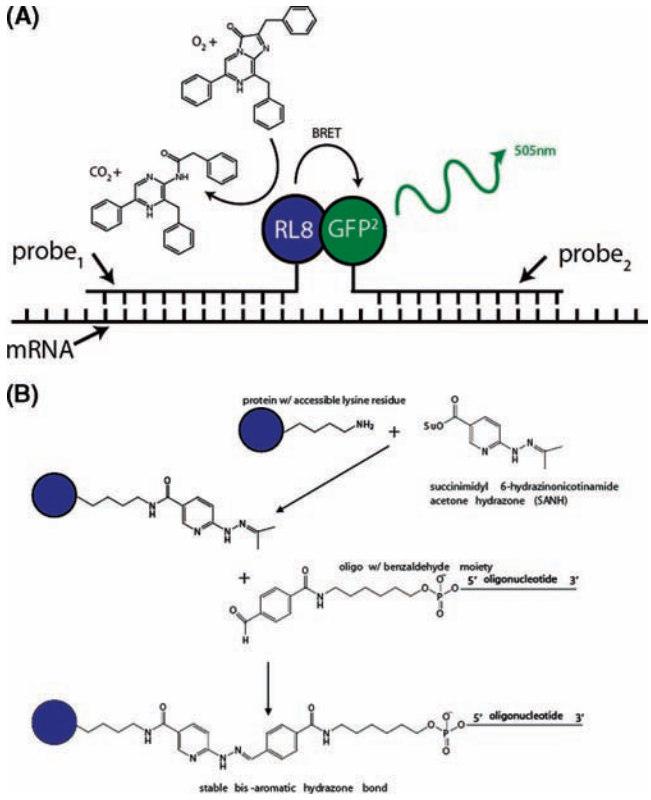

Figure 1. (a) General strategy for BRET-based RNA detection. Probe$_1$ consists of a 20-mer oligonucleotide conjugated at the 5′ end to the thermostable bioluminescent protein (RL8). Probe$_2$ consists of a 20-mer oligonucleotide conjugated at the 3′ end to the fluorescent protein GFP^2. Both probes are complementary to different portions of the same mRNA target gene. Thus, the target mRNA serves as a scaffold upon which the probes can bind, bringing the proteins into proximity with one another. When RL8 oxidizes its substrate, the energy produced is nonradiatively transferred to GFP^2, which then emits photons at a characteristic wavelength as its chromophore returns to the ground state. (b) Chemical scheme for conjugation. SANH is used to modify endogenous lysines on the protein to contain hydrazone moieties. The modified proteins are then reacted with benzaldehyde-modified oligonucleotides to produce bioconjugates joined by a stable bis-aromatic hydrazone bond.

supernatant was decanted and the pellets stored at −20 °C overnight. Pellets were resuspended 1:20 (volume depended on original culture volume) in lysis buffer (50 mM NaH_2PO_4, 300 mM NaCl, 10 mM imidazole, pH 8.0) plus 1 mg/mL lysozyme and allowed to incubate at RT for 1 h. The resuspended cells were then sonicated with six 10 s bursts, with 10 s intervals on ice. Insoluble material was then pelleted by centrifugation at 10 000 × *g* for 30 min, 4 °C. The soluble fraction was incubated with a Ni-NTA agarose (Qiagen) slurry for 1 h with rotation at 4 °C and then poured into an empty column and allowed to flow through the settled resin. The resin was then washed with wash buffer (50 mM NaH_2PO_4, 300 mM NaCl, 20 mM imidazole, pH 8.0) and the protein eluted with elution buffer (50 mM NaH_2PO_4, 300 mM NaCl, 250 mM imidazole, pH 8.0). The elution fraction was buffer-exchanged into 20 mM Tris, pH 8.0, using PD-10 columns and then purified using Source 15Q media and an AKTA basic (GE Healthcare). Fractions containing GFP^2 were pooled and concentrated.

Chemical Conjugation of Proteins to Oligonucleotides. Proteins (<200 μg) were reacted with 60 mol equiv of succinimidyl 6-hydrazinonicotinate acetone hydrazone (SANH, SoluLink) at RT with rotation in 130 μL total volume, made up with PBS for >2 h. The modified proteins were then desalted into conjugation buffer (100 mM MES, 150 mM NaCl, pH 4.7) using Zeba desalt spin columns, 0.5 mL (Pierce), according to the manufacturer's protocol. Protein concentration was remeasured following desalting using BioRad protein assay reagent. 20-mer oligonucleotides with a phosphodiester backbone and containing either a 5′ or 3′ aldehyde moiety were synthesized by TriLink. The sequences of the oligos used in this study are as follows: AS-1a, 5′*Ald*TGCATACGACGATTCTGTGA3′ (sequence graciously provided by Dr. Tracie Pierce, University of Melbourne); AS-1b, 5′*Ald*TCACAGAATCGTCGTATGCA3′; AS-2a, 5′AGAAGTTAAGAAATACGGCC *Ald*3′; AS-3, 5′CCGGCATAAAGAATTGAAGA *Ald*3′. These sequences are either complementary (AS-1a:585-604, AS-3:615-634) or homologous (AS-1b:585-604) to the firefly luciferase gene sequence (M15077). AS-2a is the reverse sequence of AS-3. Modified proteins were reacted with 1.5 mol equiv of oligonucleotide at RT with rotation in conjugation buffer for >2 h. These reaction conditions are in general agreement with a previously described report using this conjugation method to link proteins with oligonucleotides (*8*). The degree and efficiency of conjugation were assessed by reducing SDS-PAGE and stained using Imperial protein stain (Pierce) according to the manufacturer's protocol.

Luciferase Assay. Purified RL8 and oligonucleotide-conjugated RL8 were subjected to a luciferase assay using a Turner 20/20n luminometer. Equal mass amounts of the conjugated and unconjugated protein were combined with 100 μL of assay buffer (5 mM Tris, 0.5 mM EDTA, 0.6 M NaCl, 50 mM KPO_4, 0.1 g/L BSA, 0.03 mM NaN_3). 1 μL of coelenterazine (0.5 μg/μL in 50:50 methanol/propylene glycol) was added to the solution, vortexed briefly, and then placed inside the luminometer. Photon flux was collected over 10 s.

Assay Development for Probe Validation. Two separate assays were used to determine the properties of the oligo−protein conjugates described above. For the single probe experiments, target DNA oligonucleotides were 5′-end-labeled with biotin by the PAN facility at Stanford University. These target oligonucleotides (<125 pmol/well) were bound to 96-well, black, streptavidin-coated plates (Pierce). The wells were first washed 3 times with 200 μL PBST (phosphate buffered saline, pH 7.4, plus 0.05% Tween 20), and then the oligonucleotides, diluted in a total of 100 μL PBST/well, were dispensed into each well and incubated at RT for 1 h. The wells were then washed 3 times with 200 μL PBST. RL8-conjugated probes (to either AS-1a or AS-1b) were diluted in PBST and then aliquoted into the appropriate wells (3.38 μM, 100 μL/well). The plates were sealed with tape to prevent evaporation and allowed to hybridize at 45 °C for 30 min. Wells were washed 3 times with 200 μL PBST. Prior to imaging, wells were kept in 50 μL assay buffer (5 mM Tris, 0.5 mM EDTA, 0.6 M NaCl, 50 mM KPO_4, 0.1 g/L BSA, 0.03 mM NaN_3). Immediately prior to imaging, 50 μL of assay buffer plus 2 μL/mL of coelenterazine (0.5 μg/μL in 50:50 methanol/propylene glycol, 10 μM final concentration) was added to each well. The plate was imaged in an IVIS-50 (Caliper Life Sciences Inc., Alameda, CA) for 15 s using the highest binning. For assays involving dual probes, experiments were carried out using regular 96-well, black plates. Target oligonucleotides or *in vitro* transcribed cRNA were diluted in 50 μL PBST and aliquoted into each well. Target oligonucleotides for the dual probe assay were 5′-end-labeled with biotin and synthesized by the PAN facility at Stanford University. Their sequences are as follows: 1b/2a, 5′TCACAGAATCGTCGTATGCA(N)$_n$AGAAGTTAAGAAATACGGCC3′; 1b/2b, 5′TCACAGAATCGTCGTATGCA(N)$_n$GGCCGTATTTCTTAACTTCT3′, where N is a random base and *n* is 10, 20, 30, or 40. Probes were diluted in PBST to 50 μL/well and added to the appropriate wells (2.54 μM final concentration). The plate was sealed and incubated at 40 °C for 30 min. Immediately prior to imaging, 50 μL of assay buffer

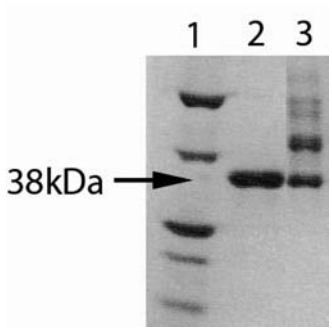

Figure 2. Results of conjugation reaction between SANH-modified RL8 and 20-mer aldehyde-functionalized oligo visualized by reducing SDS-PAGE using bis-tris 4–15% polyacrylamide gels and stained with Imperial Stain. Lane 1: ladder. Lane 2: unconjugated RL8 protein at 38 kDa. Lane 3: conjugation reaction products showing unconjugated RL8, monoconjugates at 45 kDa, and polyconjugates at 7 kDa intervals. This reaction condition produced a majority of monoconjugates.

plus 2 μL/mL of bisdeoxycoelenterazine (DBC, 0.5 μg/μL in 50:50 methanol/propylene glycol, 1.28 μM final concentration) was added to each well. DBC is a coelenterazine analogue, which, when oxidized by RL8, produces photons with a peak at 395 nm, compared to the 480 nm emission peak produced by the oxidation of native coelenterazine (*7*). The plate was imaged in an IVIS-200 (Caliper Life Sciences Inc.) for 15 s using the highest binning and a GFP^2-specific filter (500–570 nm), and then for 15 s using the highest binning and an RL8/DBC-specific filter (370–450 nm). Both the IVIS-50 and IVIS-200 use a cooled CCD (charge-coupled device) camera to detect photons of light. The IVIS-200 is additionally equipped with BRET-specific filters.

***In Vitro* Transcription.** Firefly luciferase (Fluc) cRNA was transcribed *in vitro* by linearizing a plasmid containing the gene downstream of the prokaryotic T7 promotor. Promega's T7 RiboMAX express kit was used according to the manufacturer's protocol to produce Fluc cRNA as well as RNA from the pGEM linear control DNA supplied with the kit. Following DNase treatment, the *in vitro* transcription reactions were purified using Qiagen's RNeasy mini kit for enzymatic cleanup according to the manufacturer's protocol. Quality and quantity of RNA was assessed spectrophotometrically using 10 mM Tris, pH 7.5, as the dilution buffer.

Data Analysis and BRET Calculations. Images using both the IVIS-50 and IVIS-200 were analyzed using *LivingImage 2.50* software. Absolute values were reported in photons/seconds/square centimeters/steradian (p/s/cm^2/sr). Regions of interest (ROIs) of equal size were drawn over each well and then measured for average radiance. To calculate BRET signal from samples that contained both RL8 and GFP^2, the following formula was used:

$$\mathrm{BRET}_{\mathrm{signal}} = \frac{\mathrm{Em}_{\mathrm{GFP2}} - \mathrm{Cf} \times \mathrm{Em}_{\mathrm{RL8}}}{\mathrm{Em}_{\mathrm{RL8}}}$$

where $\mathrm{Cf} = \mathrm{Em}_{\mathrm{GFP}}{}^2/\mathrm{Em}_{\mathrm{RL8}}$ for a control sample which has the same conditions, but in which RL8 cannot transfer energy to GFP^2 (*10*).

RESULTS

Chemical Conjugation of Proteins to Oligonucleotides. RL8 and GFP^2 were expressed and purified such that no other proteins could be visualized by Imperial protein staining (Figure 2). Yields for RL8 were typically >100 mg/L and >10 mg/L for GFP^2. To determine the appropriate molar ratios of protein, succinimidyl 6-hydrazinonicotinate acetone hydrazone (SANH), and oligonucleotide necessary for efficient conjugation, a series of experiments were performed varying the concentration of SANH and oligo while keeping the mass amount of RL8 constant. SANH was reacted with RL8 at 20-, 40-, 60-, 80-, and 100-fold molar excess, and then each condition was buffer-exchanged and reacted with either 1- or 10-fold molar excess of AS-1a. No change was seen between the 1× and 10× oligonucleotide conditions. The 60× SANH condition produced the greatest fraction of monoconjugated species while also limiting the number of polyconjugated species as determined by visual inspection following reducing SDS-PAGE (Figure 2). The time of the SANH-modification reaction was also varied to determine its effect on conjugation efficiency. Reactions were allowed to progress 2, 4, 6, or 8 h, desalted, and then conjugated to oligonucleotides. Extending the reaction time beyond 2 h had no significant effect on the conjugation reaction.

Using the 60 × SANH/1 × oligonucleotide condition with a 2 h conjugation reaction time, conjugates were produced to assess the loss of luminescence as a result of the conjugation reaction. The luciferase assay revealed that the conjugation reaction was able to retain ~20% of the bioluminescence compared to unconjugated RL8 subjected to identical reaction conditions.

Assay Development for Probe Validation. To assess the retention of both luciferase activity and nucleic acid binding potential following conjugation, the RL8/AS-1a probe was first tested by itself. An assay was developed to determine the bifunctionality of the bioconjugate. Single-stranded biotinylated DNA target oligos were bound to the wells of streptavidin-coated plates, then RL8-conjugated probes were hybridized to the targets and the excess probe was washed away. Coelenterazine was added to the wells and the plate was imaged briefly in the IVIS-50 (Figure 3). Target oligos were hybridized with probe sequences that were either exactly homologous or exactly complementary. Significant signal was seen only from wells in which complementary oligos had been hybridized ($p < 0.04$, Kruskal–Wallis test).

After demonstrating that the bioconjugate probes retained dual functionality, the assay was modified to test the potential of the two-probe approach. For this purpose, target oligos were constructed that contained either one or both binding sites for the probes, separated by *n* random nucleotides. Target oligos and probe conjugates (sequences AS-1a and AS-2a) were combined in solution and allowed to hybridize as before. Without washing, DBC was added to the wells and imaged briefly in the IVIS-200 using BRET-specific filters. BRET signal was observed only in wells for which both binding sites were present (Figure 4). For each spacer length, the experimental group was statistically different from its control ($p < 0.004$, paired, two-tailed *t* test). The BRET signals for each spacer length were also statistically different ($p = 1.15 \times 10^{-6}$, ANOVA) and the groups signified by different letters in Figure 4 were statistically different from each other (multiple range test).

To show that this assay was compatible with RNA detection, two species of cRNA were transcribed *in vitro*. As before, the cRNA was hybridized with dual BRET probes and imaged using BRET-specific filters (Figure 5). Only when the correct probes were combined with the target RNA (Fluc) was a significant BRET signal observed ($p = 3.11 \times 10^{-6}$, ANOVA, multiple range test). To investigate the sensitivity of the assay, different amounts of target and control RNA were combined (keeping the total amount of RNA constant) and probed as previously described (Figure 6). It was found that as little as 5.5 pmol (1

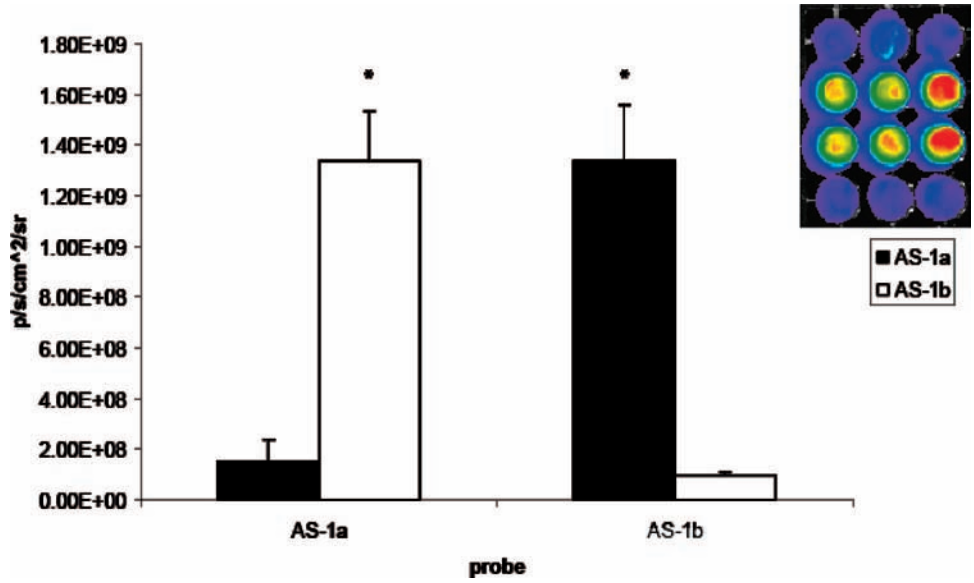

Figure 3. Single probe assay demonstrating retention of both antisense binding and RL8 activity of probes (avg ± s.d.). RL8 was conjugated with one of two different oligonucleotides (AS-1a and AS-1b, complementary to one another), and then used to probe either homologous or complementary sequences using a multiwell plate-based assay. Only when complementary probes were mixed with one another was significant signal observed. Inset: raw image obtained by the IVIS-50. Rows top to bottom match columns left to right of figure. *$p < 0.04$, Kruskal–Wallis, multiple comparison test.

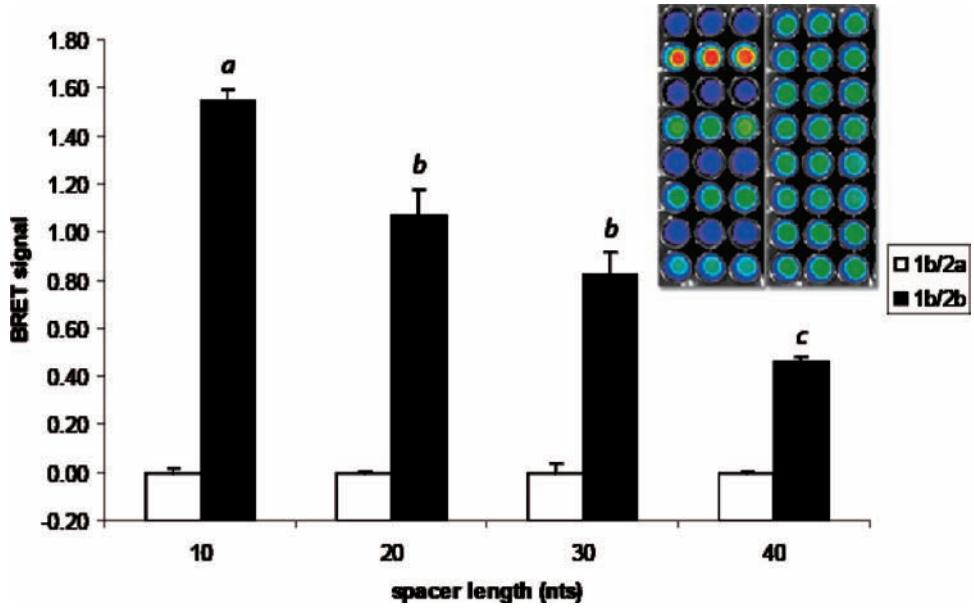

Figure 4. Dual probe assay using DNA oligos as targets to optimize spacer length between binding sites (avg ± s.d.). RL8 was conjugated with AS-1a (complementary to AS-1b) while GFP^2 was conjugated with AS-3 (complimentary to AS-2b). Both bioconjugates were combined with either a target that contained one binding site (1b/2a) or a target with both binding sites (1b/2b), separated by *n* random nucleotides (where $n = 10$, 20, 30, or 40). Significant BRET signal was seen for all targets that contained both binding sites, and statistical differences were seen between groups using different spacer lengths. Inset: raw image obtained in IVIS-200. Rows top to bottom match columns left to right of figure; image on left shows GFP^2 filter, image on right shows RL8 filter. Letters *a*, *b*, and *c* denote groups with statistical difference from one another ($p = 1.15 \times 10^{-6}$, ANOVA).

μg) of RNA in a mixed population could be statistically detected ($p < 0.05$, *t* test against "0 μg target RNA" group).

DISCUSSION

A multiprobe, BRET-based solution assay for the detection of specific RNA has been developed. The strategy detailed in this study required the successful optimization of several different variables (Figure 1). The conjugation of enzymes and oligonucleotides was accomplished using a bis-aromatic hydrazone chemistry scheme. This method was able to preserve the bioluminescent and fluorescent activity of the proteins used, as well as the nucleotide-binding properties of the oligos. Due to its generalizability, both the sequence of the oligos and the identity of the enzymes could be changed without altering the efficiency of the reaction. Thus, this method could be applied to detect any mRNA of interest, simply by changing the sequence of the oligos, and could even be used to simultaneously detect several different species of mRNA by using multiple BRET pairs (*11*). In addition to the conjugation chemistry, the optimal spacing between the probes was assessed. If the binding sites of the two probes are too near one another, steric hindrance prevents both probes from binding at the same time. However,

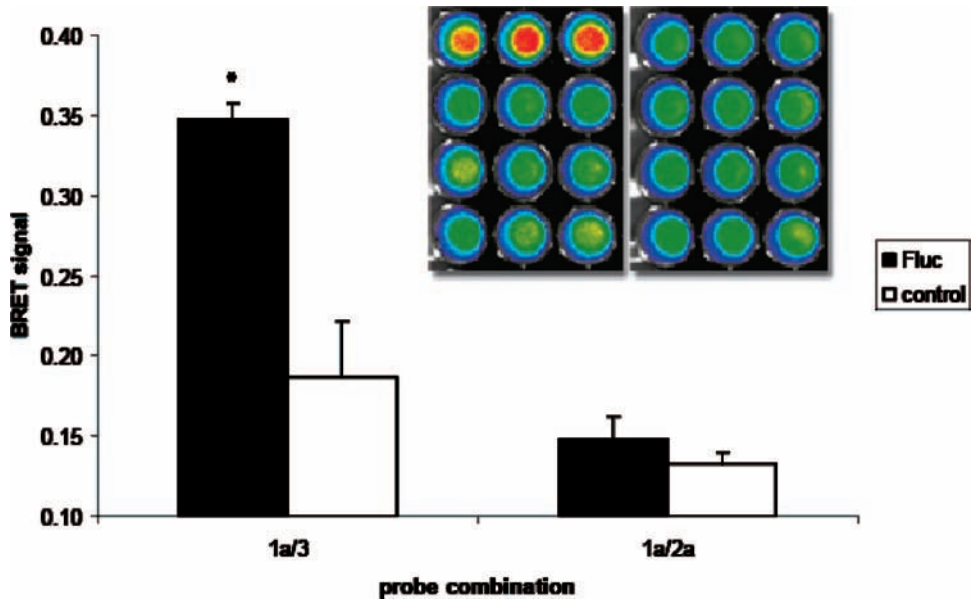

Figure 5. Dual probe assay using *in vitro* transcribed cRNA as targets (avg ± s.d.). RL8 was conjugated with AS-1a (complementary to Fluc cRNA) and GFP^2 was conjugated to either AS-3 (complementary to a different portion of Fluc cRNA) or AS-2a (reverse sequence of AS-3). RL8-1a was combined with either GFP^2-2a or GFP^2-3 and hybridized to either Fluc cRNA or nontarget cRNA. Only in wells containing Fluc target cRNA, RL8-1a, and GFP^2-3 was significant signal observed. Inset: raw image obtained in IVIS-200. Rows top to bottom match columns left to right of figure; image on left shows GFP^2 filter; image on right shows RL8 filter. $*p = 3.11 \times 10^{-6}$, ANOVA, multiple range test.

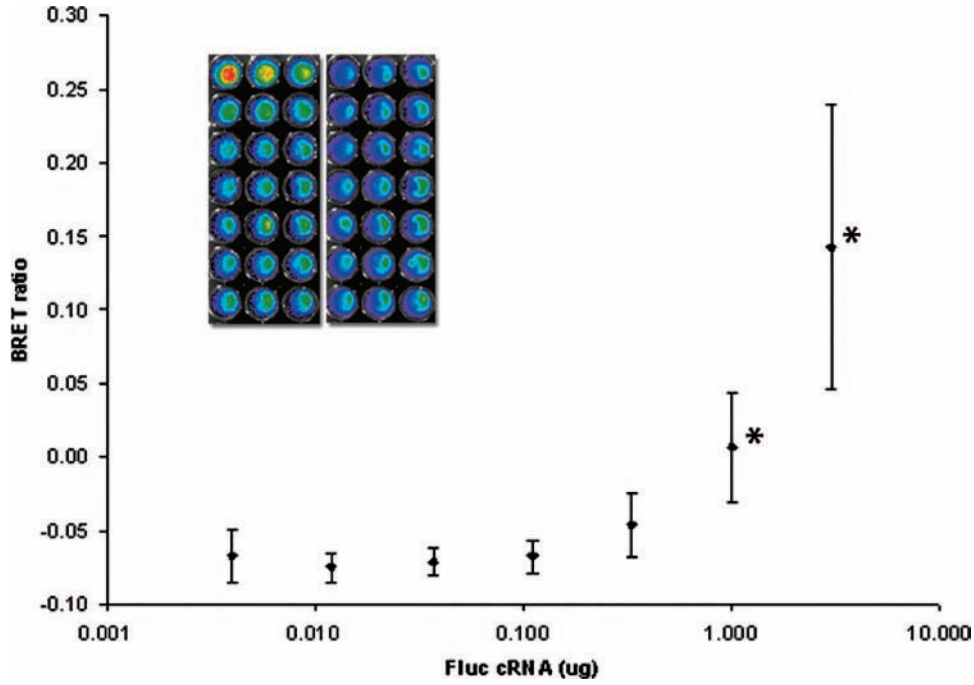

Figure 6. Dual probe assay testing sensitivity with mixed populations of *in vitro* transcribed cRNA as targets (avg ± s.d.). RL8-1a and GFP^2-3 were combined with various amounts of Fluc cRNA, while keeping the level of total cRNA constant by supplementing with nontarget cRNA. Statistically significant BRET signal was seen for as little as 1 μg Fluc cRNA. Inset: raw image obtained in IVIS-200. Rows top to bottom match columns left to right of figure; image on left shows GFP^2 filter; image on right shows RL8 filter. $*p < 0.05$, *t* test against "0 μg Fluc cRNA" group.

if the binding sites are two far apart, the BRET enzymes cannot undergo energy transfer. This variable was optimized for the firefly luciferase mRNA, and the result (10 nucleotides) can be reasonably extrapolated to other targets.

The concept of using multiple probes to increase the specificity of nucleic acid detection has been demonstrated previously, although typically with FRET (*12–19*). FRET has particular advantages for high-magnification imaging, given that its resolution is theoretically limited by the emission wavelength of the acceptor fluorophore. However, its utility is limited for many applications due to the required input of excitation photons. As with any fluorescence-based technique, FRET is incompatible with photoresponsive cells and is restricted in many cases by autofluorescence and photobleaching. In addition, the simultaneous excitation of the donor and acceptor fluorophores can add noise to the system. FRET is especially ill-suited for imaging in small animals due to the light-absorbing properties of living tissue. BRET, on the other hand, does not require input photons, thus eliminating many of the issues delineated above, and has been demonstrated

to be a powerful research tool for investigating molecular events in living animals (*20*).

In order to apply this methodology to RNA imaging, several challenges had to be overcome. The first challenge was the production of bioconjugates that retained the functionality of both the enzyme (luciferase) and antisense components. These types of conjugates have been described before, specifically for the detection of nucleic acids and with varying levels of success (*21–26*). The method of conjugation presented here is not regioselective with respect to the enzyme, nor is the degree of conjugation easily controlled. However, it is relatively rapid, and the reaction conditions are amenable to the retention of enzymatic activity. Monoconjugates were not purified away from unconjugated enzyme or polyconjugated probes, as the design of the assays did not require such purification and each additional step of purification could potentially diminish enzymatic activity. Future studies may explore different methods of conjugation, including those that are regioselective. The advantage of such a method would be the increased generalizability of the overall method. Since the chemistry displayed here capitalizes on the manipulation of exposed lysine residues of the enzyme being conjugated, it was fortunate that both RL8 and GFP^2 did not require these residues to carry out their functions. However, it is possible that other proteins may not have available lysines for conjugation, limiting the utility of the method.

After constructing the bioconjugate probes, the appropriate distance between binding sites had to be established. Since the BRET phenomenon is distance-dependent, we used estimates to determine the physical space occupied by both the oligos and proteins, hypothesizing that 32nts would be the most optimal spacer to produce an efficient BRET signal. This estimate was made using approximations of protein space based on crystal structures (2.48 $Å^3$/Da, personal communication with Duilio Cascio, University of California at Los Angeles). Then, assuming that the proper spacing would be achieved by spacing the enzymes apart such that there was no overlap, and using the 3.4 Å base pair spacing for double-stranded DNA (*27*), the estimate of 32 nucleotides between binding sites was calculated. This estimate assumed that the proteins would take a spherical shape, the optimal configuration for resonance energy transfer was nonoverlapping, and that the nucleotide spacer would remain somewhat linear. By experimentation, however, we found that a much smaller spacer (10nts) produced the greatest signal. The discrepancy between our predictions and observations can most likely be explained by the lack of rigidity not taken into account when we performed our calculations. Due to the floppy nature of the tripartite signal generator (RNA target plus two probes), our calculations of distance and space were rendered suboptimal. It was found that the lack of a spacer between binding sites, however, did not produce a BRET signal (data not shown). This is most likely due to steric hindrance of two bioconjugate probes attempting to bind immediately adjacent to one other. As with any method predicated on antisense binding, the binding sequence must be determined largely empirically. However, as the RNA used in this protocol was heated prior to hybridization to relax the secondary structure, these concerns were rendered moot. Thus, as long as the protocol includes a step that linearizes the target RNA, the identity of the binding sequence should remain largely inconsequential.

A surprising result from the spacer optimization experiment was the linear relationship between distance and BRET signal. Since the Förster equation states that the degree of resonance energy transfer is inversely proportional to the sixth power of the distance between the proteins, it is unclear exactly why the results shown here do not mirror the expectations of the formula (*28*). Our observations might be explained by the floppy nature of the target oligos. Although the number of nucleotides between the binding sites changes, it does not necessarily relate to the distance between the binding sites given that the oligonucleotides can fold into various conformations in space, bringing the binding sites closer together than their spacer length might predict. Another possible explanation is the presence of polyconjugated probes. Since a small fraction of the conjugation reaction products contained multiple oligonucleotides per protein, it is possible that these polyconjugates could bind to multiple target oligos, effectively altering the ratio of RL8 to GFP^2 from 1:1 and altering the efficiency at which the energy is transferred.

Currently, this approach is limited as a reliable *in vitro* method by sensitivity. Despite its ability to image as little as 1 μg of Fluc cRNA ($\sim$5.5 pmol), this quantity is far less than the level of gene expression in a transiently transfected population of mammalian cells. Real-time RT-PCR analysis (data not shown) demonstrated that a 100 ng sample of total RNA purified from cells transfected with the Fluc gene contained 7.42 pg of Fluc RNA. Therefore, in order to obtain even 100 ng of Fluc RNA (one-tenth of the current detection limit) in a transiently transfected sample, more than 1 mg of total RNA would have to be harvested, much more than the typical 30 μg usually obtained from 5×10^6 cells.

Several factors may be contributing to the sensitivity limits. One of the central problems is the inefficiency with which RL8 oxidizes DBC. According to published reports, the quantum yield of RL8 with native coelenterazine is approximately 60 times greater than that of RL8 with DBC (*7*). The reasons the RL8/DBC-GFP^2 BRET system was used in this study were the availability of appropriate filters and the known stability of RL8 compared to other bioluminescent proteins. It is quite possible that using a different BRET system, newer substrates, or even a split-reporter system (*29*) could improve the sensitivity of the assay. However, there are no guarantees that the same methods of protein purification and/or bioconjugation would be compatible with any other pair of proteins.

If the sensitivity of this assay is improved, these probes could also be applied to imaging mRNA in living subjects. BRET has proven its value as a molecular imaging tool in small animal imaging. By using an amino acid based delivery method, these bioconjugates could be engineered to cross biological membranes and colocalize with target mRNA. Cell-penetrating peptides have been shown to be able to deliver a variety of biological cargos (*30, 31*), and membrane translocating antibodies have also been applied for similar purposes (*32*). This method is particularly appealing because the amino acid sequence coding for the delivery agent could be fused directly to the reporter enzyme and expressed as a single protein. Alternatively, it has been shown that large macromolecules can be delivered via hydrodynamic injection, and this may prove to be a reliable substitute (*33*).

This assay represents a new possibility for the detection of RNA. In contrast with other widely used methods, it does not require any washing steps or RNA manipulation postpurification. Given its ease of use and amenability to automation, this technique could fulfill all the requisites of a routine diagnostic assay. The material costs of the probes are negligible, and although a dedicated small animal imaging system was used in this study for the spectral detection of photons, there is every reason to anticipate the evolution of stand-alone gene chips or multiwell plates that are capable of spectral detection (*34*), thus obviating the need for a separate detection device and making the technique more cost-effective. Unlike fluorescent methods, the BRET-based technique does not require the presence of a laser to excite the donor probe. This alone has the potential to

reduce costs and increase the ease of manipulation. And unlike isotopic methods, this assay does not have the potential hazards associated with radioactivity or the instability of an isotopic probe. Overall, the BRET-based detection of RNA described here is more rapid than most methods of RNA detection and involves significantly fewer steps. With improvements to its sensitivity, it could easily become a part of the molecular biology canon and possibly much more.

ACKNOWLEDGMENT

We would like to acknowledge funding support from NIC ICMIC P50 CA114747 (SSG), and NCI 5R01 CA82214 (SSG).

LITERATURE CITED

(1) Alwine, J. C., Kemp, D. J., and Stark, G. R. (1977) Method for detection of specific RNAs in agarose gels by transfer to diazobenzyloxymethyl-paper and hybridization with DNA probes. *Proc. Natl. Acad. Sci. U.S.A. 74*, 5350–4.

(2) Wong, M. L., and Medrano, J. F. (2005) Real-time PCR for mRNA quantitation. *BioTechniques 39*, 75–85.

(3) Prediger, E. A. (2001) Detection and quantitation of mRNAs using ribonuclease protection assays. *Methods Mol. Biol. (Totowa, NJ, U. S.) 160*, 495–505.

(4) Nicholls, P. J., and Malcolm, A. D. (1989) Nucleic acid analysis by sandwich hybridization. *J. Clin. Lab. Anal. 3*, 122–35.

(5) Xu, Y., Piston, D. W., and Johnson, C. H. (1999) A bioluminescence resonance energy transfer (BRET) system: application to interacting circadian clock proteins. *Proc. Natl. Acad. Sci. U.S.A. 96*, 151–6.

(6) De, A., Loening, A. M., & Gambhir, S. S. (2007) An improved bioluminescence resonance energy transfer strategy for imaging intracellular events in single cells and living subjects, *Cancer Res. 67*.

(7) Loening, A. M., Fenn, T. D., Wu, A. M., and Gambhir, S. S. (2006) Consensus guided mutagenesis of Renilla luciferase yields enhanced stability and light output. *Protein Eng. Des. Sel. 19*, 391–400.

(8) Kozlov, I. A., Melnyk, P. C., Stromsborg, K. E., Chee, M. S., Barker, D. L., and Zhao, C. (2004) Efficient strategies for the conjugation of oligonucleotides to antibodies enabling highly sensitive protein detection. *Biopolymers 73*, 621–30.

(9) Jensen, A. A., Hansen, J. L., Sheikh, S. P., and Brauner-Osborne, H. (2002) Probing intermolecular protein-protein interactions in the calcium-sensing receptor homodimer using bioluminescence resonance energy transfer (BRET). *Eur. J. Biochem. 269*, 5076–87.

(10) Angers, S., Salahpour, A., Joly, E., Hilairet, S., Chelsky, D., Dennis, M., and Bouvier, M. (2000) Detection of beta 2-adrenergic receptor dimerization in living cells using bioluminescence resonance energy transfer (BRET). *Proc. Natl. Acad. Sci. U.S.A. 97*, 3684–9.

(11) Arai, R., Nakagawa, H., Kitayama, A., Ueda, H., and Nagamune, T. (2002) Detection of protein-protein interaction by bioluminescence resonance energy transfer from firefly luciferase to red fluorescent protein. *J. Biosci. Bioeng. 94*, 362–4.

(12) Tsuji, A., Koshimoto, H., Sato, Y., Hirano, M., Sei-Iida, Y., Kondo, S., and Ishibashi, K. (2000) Direct observation of specific messenger RNA in a single living cell under a fluorescence microscope. *Biophys. J. 78*, 3260–74.

(13) Lobashevsky, A. L., Jiang, X. L., and Thomas, J. M. (2002) Allele-specific in situ analysis of microchimerism by fluorescence resonance energy transfer (FRET) in nonhuman primate tissues. *Hum. Immunol. 63*, 108–20.

(14) Dirks, R. W., Molenaar, C., and Tanke, H. J. (2003) Visualizing RNA molecules inside the nucleus of living cells. *Methods (San Diego, CA, U. S.) 29*, 51–7.

(15) Okabe, K., Ikeda, H., Harada, Y., and Funatsu, T. (2005) Development of real time imaging of specific messenger RNA in a living cell using artificial antisense nucleic acids. *Nucleic Acids Symp. Ser. 2004*, 207–8.

(16) Santangelo, P. J., Nix, B., Tsourkas, A., and Bao, G. (2004) Dual FRET molecular beacons for mRNA detection in living cells. *Nucleic Acids Res. 32*, e57.

(17) Tsourkas, A., Behlke, M. A., Xu, Y., and Bao, G. (2003) Spectroscopic features of dual fluorescence/luminescence resonance energy-transfer molecular beacons. *Anal. Chem. 75*, 3697–703.

(18) Okamura, Y., Kondo, S., Sase, I., Suga, T., Mise, K., Furusawa, I., Kawakami, S., and Watanabe, Y. (2000) Double-labeled donor probe can enhance the signal of fluorescence resonance energy transfer (FRET) in detection of nucleic acid hybridization. *Nucleic Acids Res. 28*, E107.

(19) Cardullo, R. A., Agrawal, S., Flores, C., Zamecnik, P. C., and Wolf, D. E. (1988) Detection of nucleic acid hybridization by nonradiative fluorescence resonance energy transfer. *Proc. Natl. Acad. Sci. U.S.A. 85*, 8790–4.

(20) De, A., and Gambhir, S. S. (2005) Noninvasive imaging of protein-protein interactions from live cells and living subjects using bioluminescence resonance energy transfer. *FASEB J. 19*, 2017–9.

(21) Renz, M., and Kurz, C. (1984) A colorimetric method for DNA hybridization. *Nucleic Acids Res. 12*, 3435–44.

(22) Salisch, H., Ryll, M., Leise, R., and Neumann, U. (2000) Use of an alkaline phosphatase-labelled probe for the detection of Mycoplasma synoviae in chickens. *J. Vet. Med. 47*, 27–35.

(23) Jablonski, E., Moomaw, E. W., Tullis, R. H., and Ruth, J. L. (1986) Preparation of oligodeoxynucleotide-alkaline phosphatase conjugates and their use as hybridization probes. *Nucleic Acids Res. 14*, 6115–28.

(24) Guerasimova, A., Ivanov, I., and Lehrach, H. (1999) A method of one-step enzyme labelling of short oligonucleotide probes for filter hybridisation. *Nucleic Acids Res. 27*, 703–5.

(25) Ruth, J. L. (1996) Oligozymes. Oligonucleotide-enzyme conjugates. *Mol. Biotechnol. 6*, 163–78.

(26) Matsuhisa, A., Kishi, Y., and Shiba, K. (1994) A simple staining method for dna and rna blotted on a membrane using a polyethyleneimine-enzyme conjugate. *J. Biochem. 116*, 478–81.

(27) Watson, J. D., and Crick, F. H. (1953) Molecular structure of nucleic acids; a structure for deoxyribose nucleic acid. *Nature (London) 171*, 737–8.

(28) Stryer, L. (1978) Fluorescence energy transfer as a spectroscopic ruler. *Annu. Rev. Biochem. 47*, 819–46.

(29) Paulmurugan, R., Umezawa, Y., and Gambhir, S. S. (2002) Noninvasive imaging of protein-protein interactions in living subjects by using reporter protein complementation and reconstitution strategies. *Proc. Natl. Acad. Sci. U.S.A. 99*, 15608–13.

(30) Jones, S. W., Christison, R., Bundell, K., Voyce, C. J., Brockbank, S. M., Newham, P., and Lindsay, M. A. (2005) Characterisation of cell-penetrating peptide-mediated peptide delivery. *Br. J. Pharmacol. 145*, 1093–102.

(31) Al-Taei, S., Penning, N. A., Simpson, J. C., Futaki, S., Takeuchi, T., Nakase, I., and Jones, A. T. (2006) Intracellular traffic and fate of protein transduction domains HIV-1 TAT peptide and octaarginine. Implications for their utilization as drug delivery vectors. *Bioconjugate Chem. 17*, 90–100.

(32) Shi, N., Boado, R. J., and Pardridge, W. M. (2000) Antisense imaging of gene expression in the brain in vivo. *Proc. Natl. Acad. Sci. U.S.A. 97*, 14709–14.

(33) Kobayashi, N., Kuramoto, T., Yamaoka, K., Hashida, M., and Takakura, Y. (2001) Hepatic uptake and gene expression mechanisms following intravenous administration of plasmid DNA by conventional and hydrodynamics-based procedures. *J. Pharmacol. Exp. Ther. 297*, 853–60.

(34) Thrush, E., Levi, O., Ha, W., Wang, K., Smith, S. J., Jr., and Harris, J. S. (2003) Integrated bio-fluorescence sensor. *J. Chromatogr. 1013*, 103–10.

BC700278N

Novel FRET-Based Assay to Detect Reverse Transcriptase Activity Using Modified dUTP Analogues

Joseph F. Krebs* and Anilkumar R. Kore

Ambion/Applied Biosystems, Research and Development Department, 2130 Woodward Austin, Texas 78744. Received July 27, 2007; Revised Manuscript Received December 11, 2007

We have developed a novel continuous assay to measure reverse transcriptase (RT) polymerase activity. The assay uses fluorescence energy transfer measurements to detect the incorporation of complementary pairs of fluorescently labeled deoxyuridine into cDNA product. The fluorescently labeled dUTP substrates were prepared using commercially available reagents with a simple coupling reaction. The fluorescent dye pairs have significant spectral overlap which allows FRET interaction between dyes incorporated into the cDNA. Using a polyA/oligo dT primer/template, the assay can readily detect DNA polymerase activity from any viral reverse transcriptase enzyme. The reaction proceeds linearly over time, and the rate is proportional to the enzyme concentration. We used the assay to compare the thermostability of a number of wild-type and mutant viral RT enzymes. Our results indicate that the wild-type AMV (avian myeloblastosis virus) enzyme is slightly more stable at 43 °C than the HIV-1 (human immunodeficiency virus) or MMLV (Moloney murine leukemia virus) enzymes. The thermostability of the RT enzyme was dramatically increased by the presence of primer/template with the enzyme. We also used the assay to study the effects of inhibitors on HIV-1 RT polymerase activity. This assay may be highly useful for the identification and characterization of potent RT inhibitors which could be candidates for development as therapeutic antiviral agents.

INTRODUCTION

Reverse transcriptases (RT) are RNA-directed DNA polymerases that synthesize DNA complementary to RNA sequences. These enzymes are essential for retroviral replication in infected cells and are important targets for the development of new drugs to fight retroviruses such as HIV-1, the human immunodeficiency virus (*1*). Drugs which target RT enzymes usually function by inhibiting the polymerase activity of the enzyme. Some RT inhibitors are nucleotide analogues which directly compete with dNTP monomers to block extension of the cDNA, while others are structurally unrelated to nucleotides and noncompetitively bind to a regulatory site on the enzyme (*2*). While both of these inhibitor classes can provide substantial benefit in slowing the progression of viral replication, over time all drugs targeting RT enzymes lose therapeutic efficacy due to the high rates of retroviral mutation which produces resistant strains of virus. The inevitable loss of drug efficacy necessitates the continual development of new RT inhibitor drugs to block replication of drug resistant viruses (*3*, *4*).

Currently, RT enzymatic activity is typically measured using discontinuous multistep assays which are cumbersome, expensive, and difficult to scale up. These assays generally involve the use of radioactive isotopes and usually require extensive sample handling to remove aliquots at various time points to study the time course of the reaction (*5*). These issues make detailed kinetic and mechanistic characterization of large numbers of drug candidates difficult. While a few continuous assays have been developed (*6*, *7*), they generally have relatively high background signal, which can limit their sensitivity. Also, some RT assays require the use of DNA templates which can mask potential effects of RNase H activity and other contaminating nucleases on polymerase activity. The development of direct, continuous-format enzyme activity assays will enhance identification and characterization of new RT inhibitors.

Fluorescence resonance energy transfer (FRET) is a phenomenon that can be used to measure the physical proximity of chemical moieties in solution. This method relies on the observation that excited fluorophores (donors) can transfer energy to neighboring ($<$100 Å) complementary chromophores or fluorophores (acceptors) (*8*). If the acceptor is itself fluorescent, energy transferred from the donor is emitted from the acceptor as light (*9*). This method allows identification of binding or proximity events in complex mixtures, since the spectral properties of the FRET enabled complexes are fundamentally different than those of the uncomplexed free fluorophores. FRET methods have been used to characterize many complex biochemical processes such as protein–protein association, nucleic acid hybridization, and ligand binding. An analogous method has been used to measure the ligation of labeled DNA molecules by DNA ligase (*10*). Since fluorescently modified nucleotides can be incorporated into nucleic acids by polymerases, it is possible that FRET-based detection methods could be adapted to study DNA polymerases.

We have developed a novel FRET-based method for the continuous real-time measurement of reverse transcriptase activity. This method utilizes dUTP analogues modified with complementary fluorescent groups and works for all RT enzymes tested. We have used this method to measure the thermostability of several RT enzymes and characterize the inhibition of RT by the inhibitor 3′-AZT triphosphate.

EXPERIMENTAL PROCEDURES

Biochemicals and Enzymes. Reverse transcriptase (RT) enzymes: HIV RT (10 U/μL), AMV RT (10 U/μL) and ArrayScript (200 U/μL), MMLV-RT (100 U/μL), *Tth* polymerase (10 U/μL), and 10X RT reaction buffer were obtained from Applied Biosystems (Foster City, CA). Sodium pyrophosphate was obtained from Invitrogen (Carlsbad, CA). With the exception of the reagents listed below, all other reagents are from Sigma-Aldrich.

* Address correspondence to jkrebs@ambion.com; (512) 721-3702.

10.1021/bc700284y CCC: $40.75 © 2008 American Chemical Society
Published on Web 12/29/2007

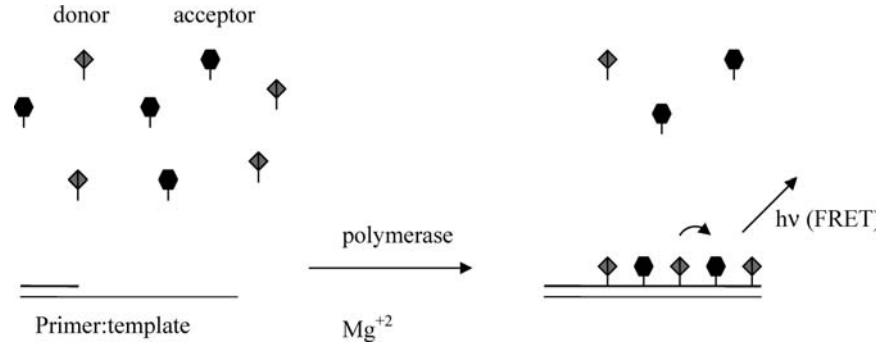

Figure 1. Continuous FRET-based assay to measure DNA polymerase activity. Dye-conjugated nucleotide pairs in solution do not interact to produce a FRET signal. Addition of polymerase to the reaction causes incorporation of the dye−nucleotides into the cDNA. The close proximity of the two dyes in the polymer allows interaction between the dyes causing the generation of a FRET signal proportional to the amount of cDNA produced in the sample.

General Procedure for Conjugation of AA-dUTP with PyMPO, SE, and 7-MCC, SE. In a typical reaction, aminoallyl-dUTP (**1**) (Ambion, Inc.) (4.7 mg, 0.0079 mmol) in 2 mL of 0.1 M sodium borate buffer (pH 8.0) was treated with (5 mg, 0.0089 mmol) of the 1-(3-(succinimidyloxycarbonyl)benzyl)-4-(5-(4-methoxyphenyl)oxazol-2-yl)pyridinium bromide (**2**), i.e., PyMPO, SE (Invitrogen Inc.) in 2 mL of DMSO. While for 7-MCC, SE, AA-dUTP (**1**) (42 mg, 0.071 mmol) in 4 mL of 0.1 M sodium borate buffer (pH 8.0) was treated with (25 mg, 0.0788 mmol) of 7-methoxycoumarin-3-carboxylic acid, succinimidyl ester (**4**) (Invitrogen, Inc.) in 4 mL of DMSO. The reaction mixture was stirred at room temperature for 4 h in the dark. The pH of the crude reaction was adjusted to 5.0 and purified using a Strata column (Phenomenox) as per the manufacturer's protocol. Both products **3** and **5** were analyzed by LC/MS: For compounds (**3**), MS (*m*/*z*) 891.4 $[M]^+$; and for compound (**5**) MS (*m*/*z*) 724 $[M]^+$. The purity of the final products was determined using anion-exchange HPLC analysis with a 250 × 4.6 mm Hypersil SAX (5 um) column using a using linear gradient system from 0% to 100% of buffer B over a period of 35 min. Buffer A was 5 mM $(NH_4)H_2PO4$, pH 2.8, and buffer B was 750 mM $(NH_4)H_2PO4$, pH 3.7. Using this method, compounds **3** and **5** were determined to be greater than 98% pure.

Polymerase Activity Measurements. All experiments using reverse transcriptase were performed using oligo dT_{18} primer (IDT) and poly A template (GE Healthcare) at final concentrations of 2 ng/μL and 17 ng/μL, respectively. The primer and template were annealed in RT reaction buffer and heated to 65 °C for 3 min. The mixture was cooled to 42 °C and mixed with 0.5 volume 3X master mix (150 mM Tris Cl, pH 8.3, 225 mM KCl, 9 mM $MgCl_2$, 3 mM DTT, and the two fluorescent dUTP substrates, **3** and **5**, were at concentrations of 22.5 μM and 90 μM, respectively in the 3X mix). 56−59 μL of this reaction mix was mixed with 40–200 units of reverse transcriptase (1−4 μL) in 96 well plates. The polymerase reaction was monitored for 20 min via the fluorescence increase (ex 348 nm, em 560 nm) in each well at 26 °C using a SpectraMax Gemini fluorescence plate reader (Molecular Devices).

RT Thermostability Measurements. RT enzymes were diluted 1:12−1:25 into 400 μL RT reaction buffer and incubated at 43 °C. At various time points (0–135 min), 40 μL sample aliquots were removed from the incubator and stored on ice. After the last time point was collected, a 30 μL aliquot from each time point was transferred to a 96 well round-bottom polypropylene plate. 30 μL of a 2X master mix (4 ng/μL oligo dT, 34 ng/uL polyA, 60 μM 7-MCC dUTP (compound **5**), 15 μM pyMPO dUTP (compound **3**), 100 mM TrisCl pH 8.3, 150 mM KCl, 6 mM $MgCl_2$, 2 mM DTT). The fluorescence increase (ex 348 nm, em 560 nm) in each well was measured for 20 min at 26 °C as described above. Control experiments indicated that no detectable loss of enzymatic activity occurs during incubation on ice.

AZT Inhibition Measurements. AZT triphosphate (100 mM stock, Calbiochem) was diluted to 4 μM in 1X RT buffer and then serially diluted to 40 nM in the same buffer. The diluted AZT solutions were mixed with an identical volume of pyMPO dUTP (**5**) and 7-MCC dUTP (**3**) (at concentrations of 2 and 8 μM, respectively). 30 μL of the AZT/dUTP mixtures were then mixed in duplicate with 30 μL of 1X RT reaction buffer containing oligo dT/polyA and HIV RT (200 nM final concentration). The fluorescence increase was measured for 20 min at 26 °C. The plotted data of the enzyme inhibition as a function of AZT-triphosphate concentration was fit to a quadratic equation (eq 1) to determine the inhibition constant (K_i) and the enzyme concentration (*11*).

Equation 1: FRET increase $= A \times ([E] - ((([E] + [AZT] + K_i) - (([E] + [AZT] + K_i)^2 - (4 \times [E]) \times [AZT]))^{0.5})/2))$ where A is a scalar constant, [E] is the concentration of enzyme, K_i is the inhibition constant for the inhibitor (15 nM) (*12*), and [AZT] is the concentration of AZT-triphosphate in the reaction.

Protein concentrations were determined in duplicate using the BCA kit from Pierce (Rockford, IL) per the manufacturer's instructions using BSA as a calibration standard.

RESULTS

Measurement of Reverse Transcriptase Polymerase Activity Using Complementary Fluorescent dUTP Analogues. FRET (fluorescence resonance energy transfer)-based fluorescence techniques measure a fluorescence signal generated from the specific interaction between physically associated donor and acceptor fluorophores. They are often used to study the physical proximity of fluorescently labeled groups even in the presence of free, unincorporated fluorophores. Potentially, this process could be used to measure nucleic acid synthesis, since a number of polymerases can incorporate dye-modified nucleotide analogues into nucleic acid products (*13*, *14*). If two spectrally overlapping pairs of dye-modified nucleotides (donor and acceptor) could be incorporated into nucleic acids by a polymerase, it might be possible to monitor nucleic acid synthesis using FRET-based fluorescence signals (Figure 1).

Therefore, we sought to examine whether polymerases such as reverse transcriptase could incorporate FRET-compatible pairs of dye-modified deoxynucleotides into cDNA products. Specifically, we examined whether pyMPO- and 7-MCC-modified dUTP (compounds **3** and **5**) could be synergistically used by RT to make cDNA. These compounds are derived from aminoallyl dUTP, a parent compound which has been previously used to create functional nucleotide substrates for polymerase enzymes (*15*). The emission wavelength of the 7-MCC fluorophore (415 nm) overlaps the excitation wavelength of the

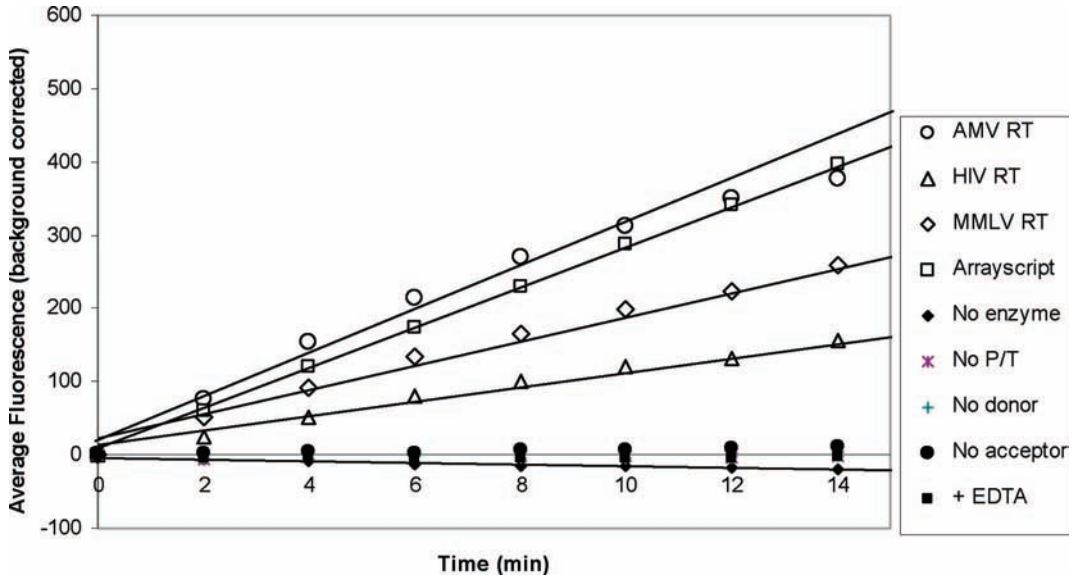

Figure 2. Reaction time course for polymerase activity measured using the FRET assay for four reverse transcriptase enzymes. 1–4 μL of enzyme was added in duplicate to 56–59 μL of reaction mix of RT buffer containing 3 mM $MgCl_2$, 2 ng/uL oligo dT, 17 ng/ μL polyA, 7.5 uM pyMPO dUTP, and 30 uM 7-MCC-dUTP in 96 well plates. After addition of the enzyme, the fluorescence increase (ex = 348 nm, em = 560 nm) was continually measured every two minutes at 26 °C. A lack of activity is observed in control reactions which contain either 7.5 uM pyMPO dUTP or 30 uM 7-MCC-dUTP.

pyMPO group (420 nm). When pure retroviral RT enzyme, from HIV-1, AMV, or MMLV or ArrayScript (an MMLV variant), was added to a reaction buffer containing these nucleotides, $MgCl_2$, and primer/template (oligo-dT/polyA RNA), a time-dependent increase in fluorescence was observed (Figure 2). The fluorescence is derived from a FRET interaction, since the time-dependent increase in fluorescence is greatest at the excitation wavelength of 348 nm and an emission wavelength of 560 nm, which correspond to the excitation and emission wavelengths of the 7-MCC and pyMPO fluorophores, respectively. Although a slight increase in fluorescence is observed in reactions containing the donor (7-MCC dUTP) alone, both nucleotides are required for robust activity (Figure 2). Omission of the RT enzyme completely eliminates the fluorescence increase (Figure 2). Addition of EDTA completely abolishes the fluorescence increase (Figure 2), indicating that, as expected, the reaction is Mg ion dependent. Likewise, template (polyA) and primer (oligo-dT) are absolutely required for the FRET activity (Figure 2). Although the progress curve for the AMV RT enzyme is somewhat nonlinear after 10 min (Figure 2), the curvature is not due to pyrophosphate product inhibition, since the RT enzymes are not inhibited by pyrophosphate in the concentration range ($<$100 μM) used for the nucleotide substrates in the reaction ((*16*) and Supporting Information). Dramatically decreased signal was observed when heteropolymeric templates were used in the reaction. Little activity was observed in the assay for the thermophilic enzyme *Tth* DNA polymerase at 30 °C (see Supporting Information).

We next varied the fluorescent nucleotide concentrations (1–50 μM) to achieve optimal enzymatic activity, maximal FRET signal, and minimal background fluorescence. During these optimization studies, we noticed that increased FRET signals were generally obtained when using pyMPO-dUTP:7-MCC-dUTP ratios of $<$1 in the reaction (Figure 3). This effect was especially prominent for the AMV reverse transcriptase enzyme where low pyMPO:7-MCC ratios produce much higher FRET increases compared to reactions using equimolar levels of the nucleotides (Figure 3). This phenomenon could be caused by several different reasons (*17*) including inner-filter effects, self-quenching of the fluorophores after incorporation, or preferential interactions of RT enzymes between the two

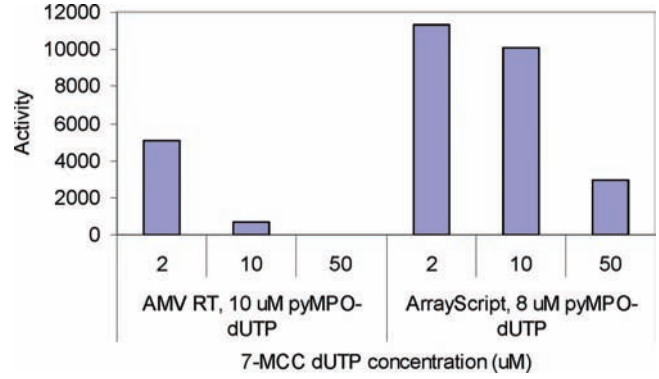

Figure 3. Effect of varying the ratio of 7-MCC-dUTP to pyMPO-dUTP nucleotides on the FRET signal from the MMLV-RT and AMV-RT polymerases. The concentration of the acceptor (pyMPO-dUTP) nucleotide was varied in the range 2–50 μM, while the concentrations of the donor nucleotide (7-MCC dUTP) were held constant at 8 μM (ArrayScript) or 10 μM (AMV RT).

nucleotide conjugates. We subsequently analyzed this phenomenon to determine its source. These studies indicate that, for the reasons described below, the decreased FRET emissions observed for reactions utilizing increased levels of pyMPO-dUTP arise from differential binding interactions between the two different dUTP conjugates and the enzyme rather than from inner filter or self-quenching effects. First, the effect cannot likely be attributed to an inner filter effect (*17*), since the pyMPO fluorophore does not absorb light at the emission wavelength (560 nm) and significant decreasing FRET signal is observed even at pyMPO-dUTP concentrations below 10 μM (Supporting Information). Second, the effect does not appear to be caused by self-quenching because spiking nonfluorescent nucleotides (dTTP, aminoallyl dUTP, and biotin in the range 0.2$-$100 μM) into the reaction to decrease the density of fluorescent nucleotides along the length of the cDNA did not increase the fluorescence signal (Supporting Information). Finally, it should be noted that the severity of the effect is enzyme-dependent: The AMV RT catalyzed reactions are strongly affected by increasing the pyMPO concentration above 10 μM, while the assay signals observed using ArrayScript (MMLV variant) are

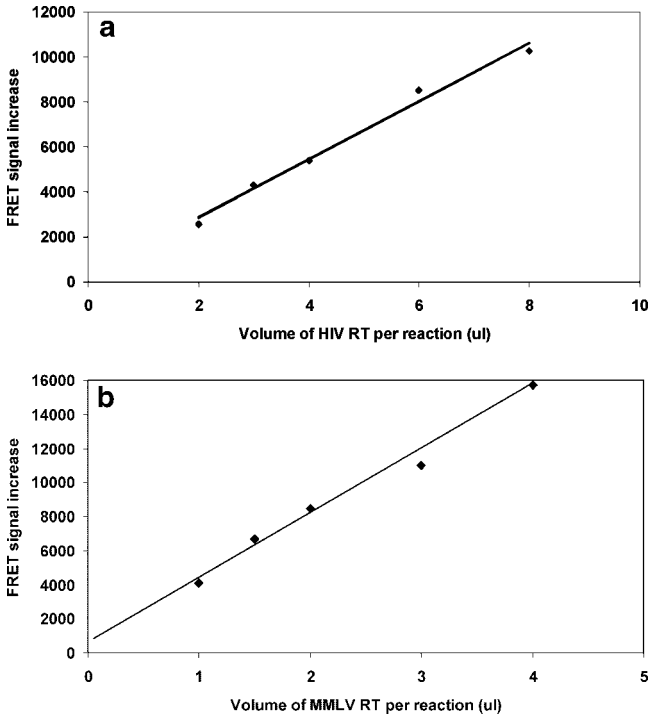

Figure 4. FRET signal increase of the FRET RT assay is linearly dependent on the enzyme concentration. HIV RT (panel A) or MMLV RT (panel B) enzymes were serially diluted into RT buffer, and then duplicate aliquots were mixed with an equal volume (30 uL) of 2X master mix (6 mM $MgCl_2$, 4 ng/uL oligo dT, 34 ng/μL polyA, 15 uM 7-methoxycoumarin AA dUTP, and 60 uM pyMPO AA dUTP). The fluorescence increase in 15 min for each of the dilutions is plotted as a function of the volume of enzyme stock added to each reaction.

only modestly affected (Figure 3 and Supporting Information). These results strongly suggest that the RT enzymes interact differentially with the two fluorescent nucleotides. In addition to improving the FRET signal generated by the enzyme, reducing the pyMPO-dUTP nucleotide also dramatically lowers the background fluorescence (time zero) for the reaction. Therefore, in most subsequent experiments, we employed final concentrations of 30 uM and 7.5 uM for the 7-MCC and pyMPO-labeled nucleotides to obtain near-maximum assay signal and sensitivity for the retroviral enzymes tested.

Characterization of RT DNA Polymerase Activity Using the FRET-Based Assay. To investigate the versatility of the FRET method to detect RT polymerase activity, we tested a range of RT enzymes. The FRET-based signal can be used to measure the polymerase activity of any RT enzymes tested: MMLV RT, AMV RT, and HIV RT. The progress curves for the reaction are fairly linear for all enzymes tested over a 15 min time interval (Figure 2). Under our assay conditions, the fluorescence increase is linearly proportional to the amount of enzyme added to the reaction (Figure 4). The linearity of the reaction with respect to time and enzyme concentration suggests that the assay should be highly useful for quantitative measurements such as enzyme inhibition by small molecules.

Characterization of RT Thermostability Using the FRET Assay. Since the reaction rate is linearly proportional to the enzyme concentration (Figure 4), we realized that the FRET assay could be used to measure and compare the thermostability of RT enzymes. RT enzyme was diluted into reaction buffer and incubated at elevated temperature. At various time points, aliquots were removed and placed on ice. After collection of the last time point, the polymerase activity of each of the samples was measured using the assay (Figure 5). The activity of the aliquots was stable on ice, since under these

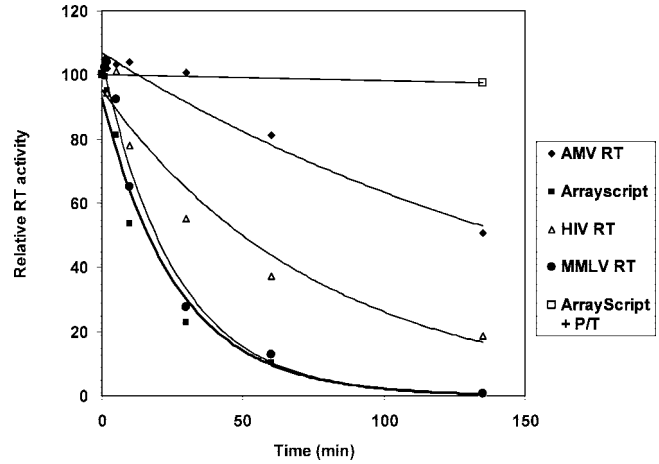

Figure 5. Measurement of thermal inactivation of pure RT enzymes using the continuous FRET assay. Diluted RT enzymes were incubated for various times at 43 °C, and the remaining enzymatic activity in each aliquot was determined by mixing with an equal volume of 2X reaction mix containing RT buffer primer/template and dye-modified nucleotides. For each enzyme, the time-dependent loss of enzymatic activity was plotted using a single exponential decay function (line fits shown). The half-lives of each enzyme at 43 °C determined from these fits are as follows: AMV RT, 133 min; HIV RT, 54 min; ArrayScript, 21 min; and MMLV RT, 18 min. Addition of primer/template to the ArrayScript enzyme before heating at 43 °C completely prevents the loss of activity (open squares).

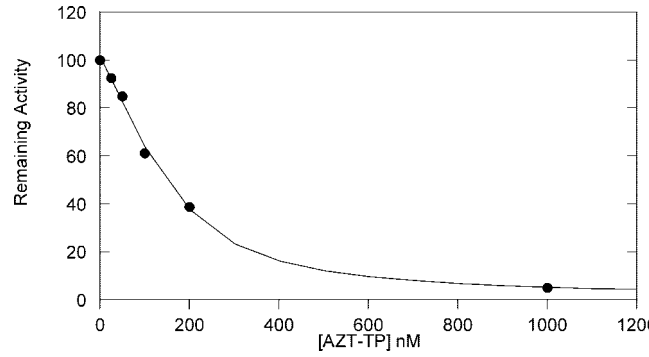

Figure 6. Detection of HIV RT inhibition by AZT triphosphate using the FRET assay. AZT triphosphate was serially diluted to 40−4000 nM in RT buffer and mixed with an identical volume of dye-labeled AA nucleotides. 30 μL of the AZT/dUTP mixtures were then mixed in duplicate with 30 μL of 1X RT reaction master mix containing HIV RT (196 nM final concentration by BCA protein assay). Enzyme activity was measured for 15 min at 26 °C. The titration data, when fit to a quadratic binding model (*12*) is consistent with an enzyme concentration of 202 nM.

conditions, no detectable loss of enzyme activity was observed for enzyme aliquots incubated on ice for 2 h (data not shown). A range of half-lives was observed for the various enzymes tested: the half-life of the wild-type MMLV RT at 43 °C was near 18 min, while the half-life of AMV RT enzyme was >2 h (Figure 5). Including polyA/dT (primer/template) during the incubation at elevated temperatures prevents the thermal inactivation of the RT enzymes (Figure 5, open squares).

Inhibition of RT Polymerase by 3′ AZT Triphosphate. We next used the FRET assay to analyze the inhibition of RT by inhibitors. As a model system, we chose to measure the inhibition of HIV-1 RT by AZT triphosphate. The inhibitor was serially diluted and added to the reaction master mix (10–1000 nM concentration range). A dose-dependent decrease in enzymatic activity was observed (Figure 6). The linear characteristics of the inhibition curve reflect the high affinity of the inhibitor for the enzyme ($K_i \approx 15$ nM (*12*)). We used these inhibition

Scheme 1. Conjugation of AA-dUTP with PyMPO, SE[a]

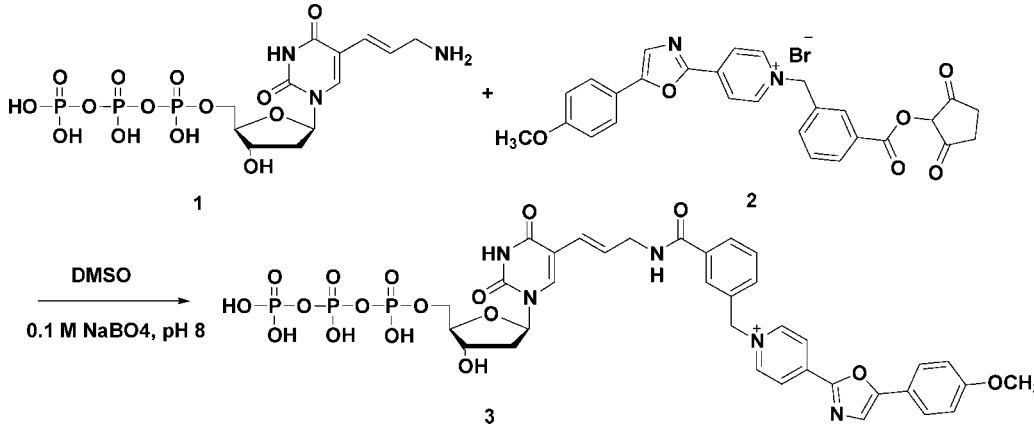

[a] Conditions: 5-Aminoallyl dUTP, PyMPO SE, 0.1 M sodium borate buffer (pH 8.0), DMSO, 4 h, at RT.

Scheme 2. Conjugation of AA-dUTP with 7-Methoxycoumarin-3-Carboxylinc Acid SE[a]

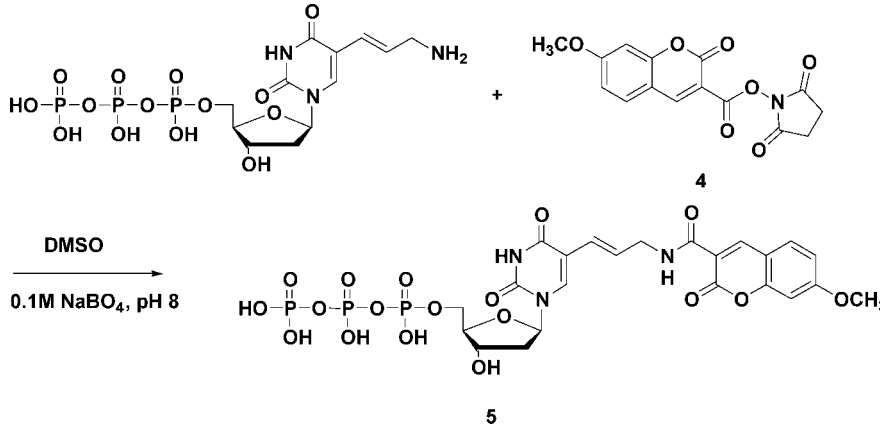

[a] Conditions: 5-Aminoallyl dUTP, 7-methoxycoumarin-3-carboxylinc acid SE, 0.1 M sodium borate buffer (pH 8.0), DMSO, 4 h, at RT.

data to measure (titrate) the concentration of functional HIV RT enzyme in the sample; we determined that the concentration of active enzyme in the reaction is 202 nM (*11*). This value is in good agreement with the enzyme concentration determined using the BCA protein concentration assay (194 nM). These results suggest that the commercial enzyme preparation is highly active and contains little or no inactive protein.

DISCUSSION

We have developed a novel FRET-based enzymatic assay to measure the polymerase activity of RT enzymes using an RNA-based template (polyA). Unlike other assays which measure the incorporation of dNTPs into the cDNA, our assay has a continuous format which allows real-time monitoring of the polymerization reaction. Our assay uses complementary pairs of fluorescently labeled dUTP analogues. The fluorescent groups have overlapping spectra in which the emission wavelength of donor overlaps the excitation wavelength of the acceptor fluorophore.

The fluorescently labeled dUTP analogues are readily synthesized from commercially available precursors using a facile conjugation procedure (Schemes 1 and 2). The aminoallyl dUTP precursor is a versatile synthetic reagent capable of producing a wide variety of other fluorescently modified nucleotides. In this study, we used 7-MCC and pyMPO-conjugated dUTP analogues to generate a FRET emission derived from the cDNA product. We selected these fluorophores for our study for three reasons: (1) their spectral overlap, (2) the commercial availability of amine-reactive forms of the dyes, and (3) their large cumulative Stoke's shift (>200 nm). By selecting fluorophores which possess these properties, we were able to rapidly develop a highly sensitive assay with low background signal. While we have not tested other pairs of fluorescent nucleotides, we are confident that this methodology could be adapted using other pairs of fluorophores to develop other assays for RT enzymes, since aminoallyl-dUTP has been shown to be an excellent backbone for the synthesis of conjugates which are efficiently incorporated by reverse transcriptase enzymes into cDNA (*15, 18–20*). Since a number of other polymerases can utilize dye-modified dUTP and dCTP substrates (*15*), it is possible that our FRET-based approach could be used to develop similar assays for non-RT enzymes using poly(dA) templates.

Our assay has improved performance characteristics compared to previously developed methods to detect reverse transcriptase activity (*5, 6*). Many existing methods are discontinuous and require extensive sample manipulation, which is time-intensive and error-prone. Some of these methods also use undesirable radioactive substrates (*5*). Our simple one-pot method allows accurate, scaleable measurement of RT activity in a matter of minutes in an ordinary fluorescence plate reader. Many existing methods suffer from high background signal in the absence of enzyme. Because of the very large Stoke's shift associated with our FRET based method, at lower nucleotide concentrations, the background fluorescence is very low and highly consistent between days. This characteristic is a significant benefit of FRET-based assay methods which provides high signal to background ratios and increasing the accuracy of the activity measurement.

Maximal assay signal is generally observed by lowering the concentration of the FRET acceptor (pyMPO-dUTP) below 10 μM in the reaction, while higher concentrations of the FRET donor permit higher activity (Figure 3 and Supporting Information). Subsequent analysis of this phenomenon revealed that it arises from the differential interactions of the two labeled nucleotides with RT enzymes. At low nucleotide concentrations, the pyMPO-dUTP is a better substrate than the 7-MCC-dUTP substrate for RT enzymes. At higher concentrations (>10 μM), the high binding affinity of the pyMPO-dUTP nucleotide substantially hinders the FRET signal from AMV RT (Supporting Information). We were somewhat surprised by this binding preference, since the size of the pyMPO moiety is significantly larger than the methoxycoumarin group of the 7-MCC-nucleotide (Schemes 1 and 2). Perhaps the positively charged pyMPO group is better able to interact with polar solvent molecules at the surface of the active site. Alternatively, the preferential incorporation of the pyMPO nucleotide may result from the increased flexibility of the extended pyMPO moiety compared to the aromatic napthyl structure of the coumarin-based fluorophore. Elucidation of the basis of the substrate preference will likely require detailed molecular modeling studies or additional structural modifications of the nucleotide conjugates and/or the enzymes.

We have used this assay to measure and compare the thermostability of RT enzymes. Our results indicate that, of the wild-type RT enzymes, AMV-RT has the longest half-life, followed by HIV-RT and then by MMLV RT (Figure 5). These results are in good agreement with those from other published studies (*21*). Interestingly, the addition of primer/template to the enzyme dramatically enhanced the half-life of the MMLV RT enzyme at 43 °C (Figure 5, square symbols). In contrast, addition of dNTP to the enzyme did not enhance thermostability, even at high concentrations of nucleotide (data not shown). These results are consistent with those of Gerard et al. which suggest that binding interactions between the enzyme and the primer/template (but not dNTPs) confer structural stability on the RT (*21*). The results of our thermostability measurements can best be interpreted in the context of the accepted kinetic mechanism of RT enzymes (*22*). The free RT binds the substrates in a specific order: first, the enzyme binds the primer/template and then the dNTP substrate to form the ternary catalytic complex. Given this mechanism, it is likely that the primer/template could bind to the RT to form and stable, extended complex while dNTP substrates are incapable of forming stable interactions with the enzyme, even at high temperature.

We also used the FRET assay to measure the inhibition of the HIV-1 RT enzyme by AZT triphosphate. The convenient real-time format of the assay allows rapid and sensitive detection of enzyme–inhibitors. The binding curve for the titration is consistent with the high binding affinity of the AZT triphosphate to the enzyme. Titration of enzymatic activity with the AZT inhibitor indicated that the concentration of active enzyme was nearly identical to the concentration as measured using a protein assay (Figure 6). RT enzyme preparations have been shown to sometimes contain significant levels of inactive or suboptimally active protein (*23, 24*). Our real-time titration method may prove to be a convenient, economical means to measure the amount of active enzyme in RT samples as well as the shelf life of RT enzymes over time.

Supporting Information Available: Additional related figures and tables. This material is available free of charge via the Internet at http://pubs.acs.org/BC.

LITERATURE CITED

(1) Barber, A. M., Hizi, A., Jr, and Hughes, S. H. (1990) HIV-1 reverse transcriptase: structure predictions for the polymerase domain. *AIDS Res. Hum. Retroviruses 6*, 1061–72.

(2) Althaus, I. W., Chou, J. J., Gonzales, A. J., Deibel, M. R., Chou, K. C., Kezdy, F. J., Romero, D. L., Aristoff, P. A., Tarpley, W. G., and Reusser, F. (1993) Steady-state kinetic studies with the non-nucleoside HIV-1 reverse transcriptase inhibitor U-87201E. *J. Biol. Chem. 268*, 6119–24.

(3) Domaoal, R. A., and Demeter, L. M. (2004) Structural and biochemical effects of human immunodeficiency virus mutants resistant to non-nucleoside reverse transcriptase inhibitors. *Int. J. Biochem. Cell Biol. 36*, 1735–51.

(4) Sarafianos, S. G., Das, K., Hughes, S. H., and Arnold, E. (2004) Taking aim at a moving target: designing drugs to inhibit drug-resistant HIV-1 reverse transcriptases. *Curr. Opin. Struct. Biol. 14*, 716–30.

(5) Goulian, M., Lucas, Z. A., and Kornberg, A. (1968) Enzymatic synthesis of deoxyribonucleic acid. XXV. Purification and properties of deoxyribonucleic acid polymerase induced by infection with phage T4. *J. Biol. Chem. 243*, 627–38.

(6) Seville, M., West, A. B., Cull, M. G., and McHenry, C. S. (1996) Fluorometric assay for DNA polymerases and reverse transcriptase. *BioTechniques 21*, 664–672.

(7) Baillon, J. G., Nashed, N. T., Sayer, J. M., and Jerina, D. M. (1991) Continuous microspectrophotometric measurement of DNA polymerase activity: application to the Klenow fragment of *Escherichia coli* DNA polymerase I and human immunodeficiency virus type 1 reverse transcriptase. *Proc. Natl. Acad. Sci. U.S.A. 88*, 1014–8.

(8) Lorenz, M., and Diekmann, S. (2006) Distance determination in protein-DNA complexes using fluorescence resonance energy transfer. *Methods Mol. Biol. 335*, 243–55.

(9) Okamura, Y., and Watanabe, Y. (2006) Detecting RNA/DNA hybridization using double-labeled donor probes with enhanced fluorescence resonance energy transfer signals. *Methods Mol. Biol. 335*, 43–56.

(10) Chen, X. C., Hentz, N. G., Hubbard, F., Meier, T. I., Sittampalam, and S., and Zhao, G. (2002) Development of a fluorescence resonance energy transfer assay for measuring the activity of *Streptococcus pneumoniae* DNA ligase, an enzyme essential for DNA replication, repair, and recombination. *Anal. Biochem. 309*, 232–40.

(11) Pingoud, A., Urbanke, C., Hoggett, J., and Jeltsch, A. (2002) *Biochemical Methods, A Concise Guide for Students and Researchers*, Wiley VCH, Weinheim.

(12) Baba, M., Clercq, E. D., Tanaka, H., Ubasawa, M., Takashima, H., Sekiya, K., Nitta, I., Umezu, K., Nakashima, H., Mori, S., Shigeta, S., Walker, R. T., and Miyasaka, T. (1991) Potent and selective inhibition of human immunodeficiency virus type 1 (HIV-1) by 5-ethyl-6-phenylthiouracil derivatives through their interaction with the HIV-1 reverse transcriptase. *Proc. Natl. Acad. Sci. U.S.A. 88*, 2356–2360.

(13) Cruickshank, K. A. (1999) Quantitation of fluorescent nucleotide incorporation by capillary gel electrophoresis and laser-induced fluorescence detection. *Anal. Biochem. 269*, 21–31.

(14) Tasara, T., Bernhard Angerer, B., Damond, M., Winter, H., Dörhöfer, S., Hübscher, U., and Amacker, M. (2003) Incorporation of reporter molecule-labeled nucleotides by DNA polymerases.II High-density labeling of natural DNA. *Nucleic Acids Res. 31*, 2636–46.

(15) Anderson, J. P., Angererer, B., and Loeb, L. A. (2005) Incorporation of reporter-labeled nucleotides by DNA polymerases. *Biotechniques 38*, 257–64.

(16) Sarafianos, S. G., Pandey, V. N., Kaushik, N., and Modak, M. J. (1995) Site-directed mutagenesis of arginine 72 of HIV-1 reverse transcriptase. Catalytic role and inhibitor sensitivity. *J. Biol. Chem. 270*, 19729–35.

(17) Lakowicz, J. R. (1999) *Principles of fluorescence spectroscopy*. pp 5354, Kluwer/Plenum, New York.

(18) Muller, B., Restle, T., Reinstein, J., and Goody, R. S. (1991) Interaction of fluorescently labeled dideoxynucleotides with HIV-1 reverse transcriptase. *Biochemistry 30*, 3709–15.

(19) Schena, M., Shalon, D., Heller, R., Chai, A., Brown, P. O., and Davis, R. W. (1996) Parallel human genome analysis: microarray-based expression monitoring of 1000 genes. *Proc. Natl. Acad. Sci. U.S.A. 93*, 10614–9.

(20) D'iachenko, L. B., Chenchik, A. A., Lukin, M. A., Aleksandrova, L. A., Kraevskii, A. A., and Bibilashvili, R. S. (1994) Derivatives of ddUTP, modified at the 5-position of uridine, as substrate terminators of reverse transcriptase. Hydrolysis of oligonucleotides, terminated by these analogs, by phosphodiesterase I. *Mol. Biol. (Mosk) 28*, 102–12.

(21) Gerard, G. F., Potter, R. J., Smith, M. D., Rosenthal, K., Dhariwal, G., Lee, J., and Chatterjee, D. K. (2002) The role of template-primer in protection of reverse transcriptase from thermalinactivation. *Nucleic Acids Res. 30*, 3118–29.

(22) Hsieh, J.-C., Zinnen, S., and Modrich, P. (1993) Kinetic mechanism of the DNA-dependent DNA polymerase activity of human immunodeficiency virus reverse transcriptase. *J. Biol. Chem. 268*, 24607–13.

(23) Basu, A., Basu, S., and Modak, M. J. (1992) Structure-activity analyses of HIV-1 reverse transcriptase. *Biochem. Biophys. Res. Commun. 183*, 1131–8.

(24) Grandgenett, D. P. (1976) Dissociation of DNA polymerase of avian myeloblastosis virus by dimethyl sulfoxide. *J. Virol. 17*, 950–61.

BC700284Y

Agonist−Antagonist Dilemma in Molecular Imaging: Evaluation of a Monomolecular Multimodal Imaging Agent for the Somatostatin Receptor

W. Barry Edwards, Baogang Xu, Walter Akers, Philip P. Cheney, Kexian Liang, Buck E. Rogers, Carolyn J. Anderson, and Samuel Achilefu*

Department of Radiology, Washington University School of Medicine, St. Louis, Missouri 63110. Received August 1, 2007; Revised Manuscript Received October 4, 2007

The combination of different imaging modalities, each providing information according to its strengths, can be a powerful method for diagnosing diseases. We have synthesized a monomolecular multimodal imaging agent (MOMIA), LS172, containing a subtype-2 somatostatin receptor (SSTr2)-avid peptide (Y3-octreotate or Y3-TATE), a radiometal chelating group (DOTA) and a near-infrared (NIR) fluorescent dye (cypate). In addition to optical methods, radiolabeling LS172 with ^{64}Cu and ^{177}Lu provides a strategy for in vitro evaluation or in vivo multimodal imaging by positron emission tomography (PET) and single photon emission computed tomography (SPECT), respectively. Determination of the binding affinity of LS172, ^{nat}Cu- and ^{nat}Lu-LS172 in SSTr2-transfected A427 cells (A427-7) showed that they all displayed high binding affinity toward SSTr2 with K_i values of 0.234 nM, 11.5 nM, and 2.15 nM respectively. In contrast to cypate-labeled Y3-TATE (cytate), fluorescence microscopy showed that LS172 and ^{nat}Cu-LS172 accumulate modestly in A427–7 cells by SSTr2-mediated endocytosis, in spite of their relatively high binding affinity. In vivo, the biodistribution of the SSTr2 receptor specific ^{64}Cu- and ^{177}Lu-LS172 in AR42J tumor-bearing rats exhibited low (≤1% ID/g) accumulation in tumor tissue. Clearance from circulation was predominantly hepatobiliary (>90% ID/liver). Both optical and radionuclear biodistribution studies showed a similar in vivo distribution profile. Surprisingly, the strong binding of LS172 to SSTr2 did not translate into high SSTr2-mediated endocytosis in cells or uptake in tumor in vivo. Considering that LS172 is a putative antagonist, the poor accumulation of the labeled MOMIAs in SSTr2 positive tumor tissue supports the paradigm that agonists with their concomitant internalization favors appreciable target tissue accumulation of receptor-specific ligands.

INTRODUCTION

Accurate diagnosis and treatment of diseases may be achieved by integrating a multimodal imaging strategy as part of the therapeutic regimen. With the aid of fast computational methods and algorithms for image reconstruction, coregistration of diseased tissue images can yield complimentary information, thus enhancing diagnosis. For example, computed tomographic images (CT) can be coregistered with positron emission tomographic images (PET) or single photon emission computed tomography (SPECT) (*1, 2*). In this way, the combination of anatomical information from CT with functional information from PET or SPECT allows cancers to be staged and precisely localized.

Optical imaging is an emerging method that could act synergistically with another imaging modality. Optical imaging itself is a highly sensitive technique that can detect, in vitro as well as in vivo, minute quantities of light-emitting materials. Additionally, it uses low energy radiation in the visible or near-infrared (NIR) regions of light to assess biological processes. As the light penetrates deeper in tissues, tissue chromophores, cellular organelles, and the matrix mediate scattering and absorption of emitted light. While algorithms can deconvolute light propagation through tissues, accurate models of the complex photon migration in heterogeneous biological systems are not available. This limitation would benefit from pairing optical with another imaging modality such as PET. By coupling together an optical and a radionuclear method, the location of a target tissue could first be confirmed by PET then monitored longitudinally by optical imaging for such changes as tumor response to therapy.

Previously, we and others have developed near-infrared fluorescent and radiolabeled monomolecular multimodal imaging agents (MOMIAs) for combined optical radionuclear small animal imaging (*3–5*). Typically, these MOMIAs were labeled with gamma-emitting ^{111}In for scintigraphy or SPECT. These studies demonstrated the capability of obtaining coregistered images of the distribution of the MOMIAs in small animals by both fluorescence and gamma imaging methods. However, previous studies focused on using the MOMIA strategy for multimodal imaging. Interestingly, the ability of some radionuclides to emit photons for imaging and therapeutic applications provides a strategy to incorporate therapeutic radionuclides into the MOMIA concept. This can be accomplished by using ^{177}Lu or ^{64}Cu radiometals in MOMIA constructs.

^{177}Lu ($t_{½}$ = 6.65 days) has gamma emissions (208 keV; 11%) for SPECT imaging and therapeutic properties (β^-, 497 keV; 78%). A peptide conjugate of this radiometal, ^{177}Lu-DOTA-Y3-TATE, has demonstrated excellent tumor localization and good clearance properties as well as significant tumor regression in an animal model (*6, 7*). SPECT has many advantages as an imaging method, but PET is the current method of choice for both human and small animal molecular imaging because of its exceptionally high sensitivity and in vivo quantitative measurements of the early kinetics of drug distribution. A widely used radiometal for PET is ^{64}Cu because of it is convenient half-life ($t_{½}$ = 12.7 h) and decay properties (β^+ (19%); β^- (39%)) that are suitable for PET as well as radiotherapy. Both radiometals form stable complexes with tetraazamacrocycle

* Corresponding author. 4525 Scott Avenue, St. Louis, MO, 63110. Phone: 314-362-8599. Fax: 314-747-5191. E-mail: achilefus@mir.wustl.edu.

10.1021/bc700291m CCC: $40.75 © 2008 American Chemical Society
Published on Web 11/20/2007

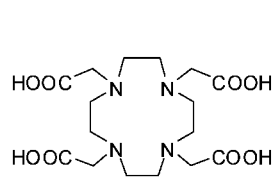

DOTA

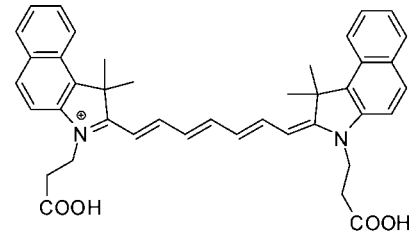

cypate

DOTA-f-cyclo-(CYwKTC)-TK (cypate)-NH_2

LS172

cypate-f-cyclo-(CYwKTC)-T -OH

cytate

Figure 1. Structures of compounds used for this study. Lower case letters denote non-natural D configuration of the amino acid. DOTA and cypate are conjugated to amino groups via the carboxylic acid.

DOTA, which can be conjugated to bioactive molecules such as peptides and proteins for specific delivery to target tissue (*7–10*).

To take advantage of the multimodal approach, we have developed a single imaging agent that contains reporters for both optical and SPECT or PET imaging modalities as well as radiotherapeutic properties. These MOMIAs offer minimization of data analysis errors due to differences in the pharmacokinetics of two different imaging agents used for each modality, sources of error resulting from the interaction of the two imaging probes in vivo, and patient toxicity from repeated administration of multiple probes.

Toward this goal, we chose the well characterized somatostatin receptor subtype-2 (SSTr2) as a target and an oactapeptide Y3-TATE as the targeting ligand (*11, 12*). Y3-TATE has been labeled with a variety of radiometals for diagnostic imaging and radiotherapy, utilizing macrocyclic chelators usually conjugated to the *N*-terminal amine (*6, 7*). For optical imaging, we used the near-infrared fluorescent dye cypate (*13*). Cypate, when conjugated to the *N*-terminus of Y3-TATE (cytate, Figure 1), was shown by optical imaging to be localized in subcutaneous SSTr2-positive tumors in rat with high selectivity (*14*). The NIR spectral properties of cypate match the low absorption of intrinsic naturally occurring molecules, resulting in an overall enhancement of the signal.

The three-component molecular design (receptor-avid peptide, radiometal chelate, and NIR fluorescent dye) was synthesized on solid support, where DOTA was conjugated to the *N*-terminal amine of D-Phe and cypate was conjugated to the ε-amino group of a *C*-terminal lysine. The resultant MOMIA, LS172 (Figure 1), was evaluated for its ability to displace ^{111}In-DTPA-Y3-TATE in an in vitro binding assay. After radiolabeling with either ^{64}Cu- or ^{177}Lu-, LS172 was evaluated in a well characterized tumor model (AR42J) for in vivo tumor localization and clearance properties (*9, 10, 15, 16*). Finally, the cellular internalization of LS172 and ^{nat}Cu-LS172 was determined by fluorescence microscopy. Together, the results demonstrate that the measured high receptor binding affinity of LS172 did not translate into high cellular internalization or in vivo tumor uptake mediated by somatostatin receptor, suggesting that LS172 is an antagonist.

EXPERIMENTAL PROCEDURES

Materials. Chemicals were obtained from Sigma-Aldrich (St. Louis, MO) unless noted differently. Amino acids were purchased from Novabiochem (San Diego, CA). Cypate and cytate were synthesized as previously described (*14, 17*). ^{64}Cu was produced on a CS-15 biomedical cyclotron at the Washington University School of Medicine. ^{177}Lu was obtained from Missouri Resource Reactor (Colombia, MO). The SSTr2-positive A427-7 cells were supplied by B.E. Rogers (*18*). ^{125}I-SS-14 (^{125}I-iodotyrosil-11-somatostatin-14) was purchased from GE Healthcare (Piscataway, NJ). Protein assays were performed using the BCA assay (Pierce, Rockford, IL). Peptides were analyzed by reversed-phase HPLC (RP-HPLC) on a system consisting of a binary pumping system (Shimadzu LC-10AD, solvent A = H_2O and 0.1% TFA, and solvent B = acetonitrile and 0.1% TFA), UV/vis (Shimadzu SPD-20AV), and fluorescence (Shimadzu RF-10AXL) detectors, and electrospray ionization mass spectrometer (Shimadzu LCMS-2010A).

Peptide Synthesis. LS172 was synthesized entirely on resin with an ACT APEX 396 peptide synthesizer by standard Fmoc protocols as previously described (*14, 19*). Briefly, starting with Rink Amide resin (30 μmol), the Fmoc-protected *C*-terminal amino acid (lysine; 75 μmol) was activated with a mixture of the coupling reagents HOBt (75 μmol) and HBTU (75μmol) in the presence of DIEA (150 μmol). Deprotection of the Fmoc protecting group was accomplished with 20% piperidine in DMF. The free carboxylic acid of tri-*t*-butyl-DOTA was coupled to the *N*-terminal amine. The orthogonal 4,4-dimethyl-2,6-dioxocyclohex-1-ylidene (Dde) protecting group, which was used to protect the ε-amino group of the *C*-terminal lysine, was removed selectively with 2% hydrazine in dimethylformamide (DMF) before coupling cypate to the resultant free ε-amino group via a carboxylic acid of cypate. Simultaneous removal of side-chain protecting groups and cleavage of the product from solid support was accomplished with a mixture of 95% TFA and 5% water. After lyophilization, the crude product was obtained as a green powder and purified by semipreparative HPLC. The purity of LS172 was greater than or equal to 96% after RP-HPLC purification (based on UV peak areas of 217 and 280 nm); calculated, M = 2169; observed, $[M]^{2+}$, 1085; $[M]^{3+}$, 724. LS172 was quantified on the basis of the extinction coefficient of cypate in 20% DMSO (224, 000 M^{-1} cm^{-1}) (*17*).

Preparation of ^{nat}Cu- and ^{nat}Lu-LS172. LS172 (26 μg, 12 nmol, 0.91 μg/μL, 20% DMSO) was added to reaction buffer (278 μL, 100 mM NH4OAc, pH 4.0) containing DMSO (80 μL). $LuCl_3$ (14 nmol, 0.4 mg $LuCl_3-6H_2O$/mL, 100 mM HCl) was added to prepare ^{nat}Lu-LS172 (*20*). ^{nat}Cu-LS172 was prepared similarly with $CuCl_2$ (14 nmol, 0.2 mg $CuCl_2-2H_2O$/mL, 100 mM HCl) in a more alkaline reaction buffer (279 μL, 100 mM NH_4OAc, pH 5.5) (*21*). The reactions were monitored by RP-HPLC (Supelco ABZ plus, C-18, 3 μm, 4.6 × 150 mm, linear gradient of 35–55%B, 20 min). ^{nat}Lu-LS172 was formed in >99% conversion and identified by LCMS, but the formation of ^{nat}Cu-LS172 was incomplete (80% conversion), as determined

by UV/vis (780 nm). Therefore, an aliquot of the reaction mixture (325 μL) was treated with additional $CuCl_2$ (65 nmol, 56.9 μL, 0.2 mg $CuCl_2-2H_2O$/mL, 100 mM HCl) and heated (50 °C, 1 h), but no additional conversion was observed. ^{nat}Cu-LS172 was purified by RP-HPLC (3 × ~4 μg portions, Supelco ABZ plus, C-18, 3 μm, 4.6 × 150 mm, linear gradient of 35–55% B, 20 min). The purity of ^{nat}Cu-LS172 was 95% after HPLC purification (based on UV peak area, 780 nm). ^{nat}Lu-LS172 was used without purification because of the complete conversion of LS172 to the metal complex. ^{nat}Cu-BS29, calculated, [M] = 2232; observed, $[M]^{3+}$, 744; $[M]^{2+}$, 1115; ^{nat}Lu-LS172, calculated [M] = 2169, observed, $[M]^{3+}$, 781; $[M]^{2+}$, 1170.

Radiochemistry. LS172 was radiolabeled with ^{64}Cu as previously described (*21*). Radiochemical purity of ^{64}Cu-LS172 was ≥95% after heating (95 °C, 60 min), and final specific activities were 153 μCi/ug (332 μCi/nmol). ^{177}Lu (100 μCi) was added to labeling buffer (ammonium acetate, 100 mM, pH 5.5) along with LS172 (8 μg, 3.7 nmol) and DMSO (final concentration of 20% by volume). Purity was determined by radio-RP-HPLC (A = water, 0.1%TFA; B = acetonitrile 0.1% TFA; Vydac 201HS5415, 4.6 × 150 mm, linear gradient 30% to 70% B in 10 min, 1 mL/min). Radiochemical purity of ^{177}Lu-LS172 was ≥99% after heating (80 °C, 80 min), and final specific activity was 12.5 μCi/μg (27 μCi/nmol). For receptor-binding assays, DTPA-Y3-TATE was radiolabeled with ^{111}In (100 mM NH4OAc, pH 5.5) at a specific acitivity of 700 μCi/μg. Purity was >99% (10% to 75% B, 10 min, linear gradient). Gentisic acid (2,5-dihydroxy-benzoic acid) was added at a final concentration of 1 mM to prevent radiolysis (*22*).

Spectral Properties of LS172. Excitation and emission spectra were performed on a Jobin-Yvon Flurolog 3 and absorption measurements were performed in Beckman DU-145. Stock solutions (~1 mM) of indocyanine green (ICG) and LS172 were prepared in DMSO, and serial dilutions were made to obtain an absorbance level of ~0.02 (720 nm). The quantum yield of LS172 (Φ_{LS172}) relative to ICG was determined by the equation $\Phi_{LS172} = \Phi_{ICG}$ (slope$_{LS172}$/slope$_{ICG}$), where the slope is determined from a linear regression of integrated fluorescence intensity (735 to 830 nm) versus the absorbance (720 nm) of serially diluted LS172 in DMSO (*23, 24*).

Cell Culture. The A427-7 cell line expressing the human SSTr2 receptor was maintained at 37 °C in a humidified atmosphere containing 5% CO_2 in Eagle's minimal essential medium (EMEM) containing 4 mmol/L L-glutamine, 0.1 mM NEAA, 1.0 mM sodium pyruvate, 500 μg/mL G418, 100 U/mL penicillin, and 10% fetal bovine serum. HEK293 cells were grown in Dulbecco's modified Eagle's medium (DMEM) containing 100 U/mL penicillin, 4 mmol/L L-glutamine, and 10% fetal bovine serum at 37 °C in a humidified atmosphere containing 5% CO_2.

Fluorescence Microscopy and Internalization Assays. A427-7 and HEK293 cells were grown in 8-well chambers and incubated in EMEM and DMEM culture media (0.2 mL/well) overnight at 37 °C in a humidified atmosphere containing 5% CO_2. Cytate, LS172, and ^{nat}Cu-LS172 were incubated with A427-7 cells at 25 or 50 nM in the presence or absence of 5 μM Y3-TATE as a competitor. After 0, 15, 30, 60, and 90 min of incubation (37 °C), the slides containing the cells were placed on ice to stop the internalization process, washed (3×) with PBS (4 °C, 1 mM Ca^{2+}), fixed (4% paraformaldehyde), and air-dried. The fixed cells were then imaged with a confocal microscope (Olympus FV1000) equipped with excitation (775nm/50nm) and emission filters (845nm/55nm) for fluorescence detection in the NIR region. To generate values of relative fluorescence units (rfu) for internalized dye-conjugated peptides, a region of interest was generated by drawing a line (that excluded the cell membrane) spanning the cytoplasm and transversing the region of greatest fluorescence intensity (Olympus FV10-ASW 1.4 software). The rfu are reported as an average of intensity of the drawn line. A cell was arbitrarily chosen from each corner as well as the center of the field as a representative sample (n = 5). Because the background fluorescence was negligible, it was not subtracted from the total fluorescence.

In Vitro Binding Assay. The receptor binding assays were carried out as previously described (*14*). For the inhibition assays, varying concentrations of the competitor were incubated with ^{111}In-DTPA-Y3-TATE and membranes enriched in SSTr2 receptor (A427-7, 2 h, ambient temperature). Membrane levels were adjusted so that no more than 10% of the added radioactivity was bound (2.5 μg protein/well). To determine B_{max}, increasing concentrations of ^{125}I-SS-14 were incubated with A427-7 membranes from either cultured cells or from xenografted tumors. Bound radiotracers were separated from unbound radiotracers by filtration through fiberglass filter pads (Millipore Multiscreen system). After rinsing, radioactivity in the pads was assessed by gamma counting. The data were fit by nonlinear regression to the following equation: Y = bottom + (top-bottom)/(1+ 10 exp(X log IC$_{50}$)), where Y is cpm bound and X is log concentration. K_i values were obtained with the Cheng−Prussof equation. To determine K_D and B_{max} values, data were fit by nonlinear regression to total saturation binding with ligand depletion, where X is the amount of ^{125}I-SS-14 (cpm) added, and Y is the total amount (cpm) of radiotracer bound. Nonlinear regression calculations were determined with GraphPad Prism (version 4.00 for Windows, GraphPad Software, San Diego, CA).

Radiochemical Biodistribution of MOMIAs. AR42J tumors were implanted bilaterally in the legs of male Lewis rats from donor rats (*9*). After 10–14 days, the tumors had grown ~1.5 to 2.0 g. ^{64}Cu-LS172 was formulated in 20% DMSO in PBS by volume to prevent the adherence of the radioligand to the vessel. ^{64}Cu-LS172 (4 μCi/27 ng/12 pmol/rat, n = 5) was administered via the tail vein. Y3-TATE (100 μg/95 nmol/rat, n = 4) was included as a competitive dose. ^{177}Lu-LS172 (6.2 μCi/500 ng/230 pmol/rat) was formulated in 20% DMSO in PBS by volume with 10 μg/μL gentisic acid to prevent radiolysis. Y3-TATE (100 μg/95 nmol/rat, n = 5) was included as a competitive dose.

Optical Imaging and Biodistribution. Six 4-week-old male NCR nu/nu mice were anesthetized with ketamine (87 mg/kg) and xylazine (13 mg/kg) via intraperitoneal injection. About 5 × 10^5 A427-7 cells were injected subcutaneously in the right and left flanks of each mouse. Tumors were allowed to grow to 5–10 mm maximum diameter before treatment. For in vivo imaging, mice were anesthetized with a ketamine/xylazine cocktail as described above. LS172 (2 nmol in 100 μL of 20% DMSO) was injected intravenously via the lateral tail vein, alone (n = 3) and with a competitive dose of Y3-TATE (100 μg/95 nmol/mouse) (n = 2). In vivo imaging of the treated mice was performed with a multimodal planar imaging system (IS4000MM Eastman Kodak Company, New Haven, CT). Broadband illumination from a 150 W halogen lamp was filtered by a 755/35 nm optical bandpass filter (Eastman Kodak Company, New Haven, CT), and the emitted light captured via cooled CCD camera after 830 wide-angle long-pass filter (e830WA, Eastman Kodak Company, New Haven, CT). Brightfield and NIR fluorescence images were collected at 1, 4, 8, and 24 h postinjection. Regions of interest (ROIs) were drawn within the areas related to the liver, kidneys, tumor, and a control region on the opposite flank for comparison of relative in vivo fluorescence distribution at each time point. After 24 h, the mice were euthanized by cervical dislocation under anesthesia. Tissue

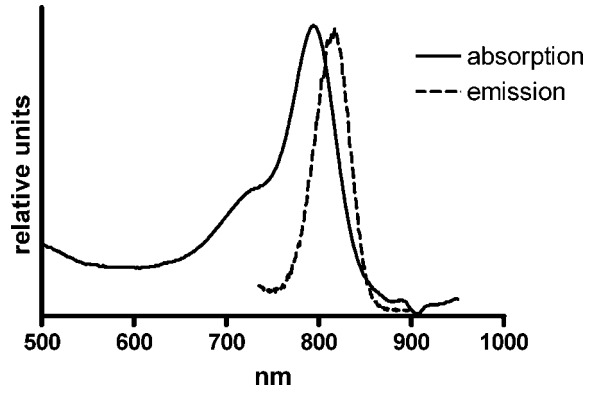

Figure 2. Absorption and emission spectra of LS172 (100% DMSO). $\lambda_{max,abs} = 793$ nm, $\lambda_{max,em} = 816$ nm, and $\Phi_F = 0.12$.

samples from muscle, liver, kidney, adrenal gland, pancreas, spleen, brain, skin, and tumor were harvested for ex-vivo fluorescence biodistribution imaging using the same settings as those described above.

Statistical Methods. Mean fluorescence intensities for the two experimental and control groups were compared with unpaired *t*-tests performed using GraphPad Prism version 4.00 for Windows (GraphPad Software, San Diego, CA).

RESULTS

Synthesis and Spectral Properties. Y3-TATE is widely used to target somatostatin receptors that are up-regulated in cancer and other pathologic conditions (*6, 10, 19, 20*). This peptide is typically labeled with radiometal chelators or fluorescent probes for imaging applications. To design radionuclear optical MOMIA, it would be easier to incorporate a lysine residue at the *N*-terminus of the peptide to provide two amino groups for conjugating DOTA and cypate. However, in a previous study, we showed that this molecular construct can compromise the peptide's binding affinity for SSTr2 (*14*). In developing a macrocyclic scaffold for molecular optical imaging, we found that adding lysine to the *C*-terminus of Y3-TATE (Y3-K9-TATE) retained the binding affinity of Y3-TATE (*17*) and provided a second reactive group for coupling cypate at a distal position to DOTA. Thus, LS172 was prepared by conjugating DOTA and cypate at the *N*- and *C*-terminal positions of Y3-K9-TATE, respectively. To construct the entire molecule on solid support, we had to use the orthogonal Dde protecting group for lysine. This allowed us to complete the peptide synthesis and DOTA coupling before Dde removal and subsequent conjugation of cypate. The procedure is advantageous because cypate, which is unstable under basic conditions, was added toward the end of MOMIA synthesis. Thus, exposure of cypate to basic conditions was minimized, and the subsequent cleavage of the product from solid support was carried out under acidic conditions, where the NIR fluorescent dye is very stable. The structures of LS172 and other compounds used in this study are shown in Figure 1.

LS172 exhibited excellent spectral properties, including similar absorption and emission spectra to the precursor dye cypate (Figure 2). Typical of many heptamethine dyes, LS172 has a narrow Stokes shift (23 nm), but the broad excitation and emission bands allow for a wide range of wavelength choices for excitation or fluorescent detection in biological assays or in vivo imaging (*25*). The relative quantum yield of LS172 ($\Phi_F = 0.12$) was the same as the reported quantum yield of ICG, indicating that conjugation of cypate to MOMIA did not compromise detection sensitivity. ^{nat}Cu-LS172 was highly fluorescent and maintained the same fluorescent properties of the parent analogue LS172 with minimal Cu-mediated quenching. Both natural and radioactive Cu and Lu were incorporated into LS172 with high radiochemical purity and specific activities for the radiometals.

Table 1. Heterologous Competitive Binding of ^{111}In-DTPA-Y3-TATE to A427-7 Cell Membranes ($n = 3$ for Each Data Point)[a]

competitor	IC_{50} (nM)	95% CI (nM)	K_i (nM)	95% CI (nM)
cytate	1.32	0.953 to 1.83	0.234	0.169 to 0.324
Y3-TATE	2.42	1.80 to 3.25	0.427	0.318 to 0.575
SS-14	0.375	0.265 to 0.531	0.0660	0.0469 to 0.0939
LS172	8.13	5.62 to 11.7	2.03	1.14 to 2.94
^{nat}Cu-LS172	45.9	33.7 to 62.4	11.5	8.40 to 15.6
^{nat}Lu-LS172	8.60	4.36 to 17.0	2.15	1.09 to 4.24

[a] K_i values were calculated from the Cheng−Prussof equation.

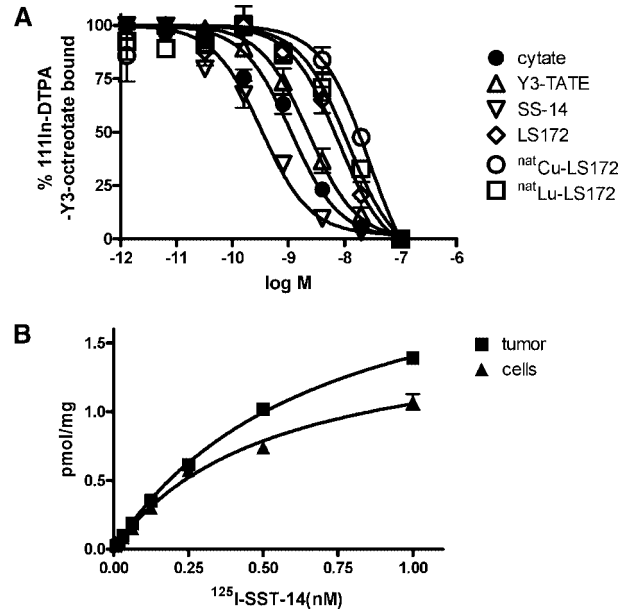

Figure 3. (A) Heterologous competitive inhibition assays with ^{111}In-DTPA-Y3-TATE on A427-7 cell membranes. (B) Saturation binding assays of 125I-SS-14 on membranes from A427-7 cells harvested from xenografts (tumor) or from cultured cells (cells).

In Vitro Receptor Binding Assays. A heterologous receptor binding assay was performed with A427-7 cell membranes, where ^{111}In-DTPA-Y3-TATE was displaced by various competitors (Table 1, and Figure 3A). Utilizing a value of $K_D = 0.13$ nM and a concentration of 0.39 nM, the Cheng−Prussof equation was used to calculate the K_i values for all of the competitors. Cytate, SS-14 and Y3-TATE display affinity for SStr2 in the subnanomolar region. The K_i values indicate that LS172 has strong affinity for SSTr2 ($K_i = 2.03$ nM), and the complexation with lutetium had very little effect on the affinity ($K_i = 2.15$ nM). However, the addition of copper to the chelator decreased affinity by approximately 5-fold ($K_i = 11.5$ nM).

^{125}I-SS-14 was used to assess the receptor densities of SSTr2 on xenografted and cultured A427-7 cells (Figure 3B). The xenografted cells expressed 2.3 pmol/mg (0.5 to 4.0 pmol/mg 95%CI), while the cultured cells expressed 1.0 pmol/mg (0.3 to 1.7 pmol/mg 95% CI). The K_D of ^{125}I-SS-14 was essentially the same ($p < 0.05$, F-test) for both membrane preparations (0.3 nM, 0.03 to 0.5 nM, 95% CI, cultured A427-7 cells). The nonspecific binding was ~2%.

Internalization by Fluorescence Microscopy. The internalization of the MOMIAs LS172 and ^{nat}Cu-LS172 was evaluated by fluorescence microscopy in the near-infrared region in A427-7 and negative control HEK293 (SSTr2 negative) cells and compared with cytate. Cytate was strongly internalized in a time-dependent manner (Figures 4 and 5), and the internaliza-

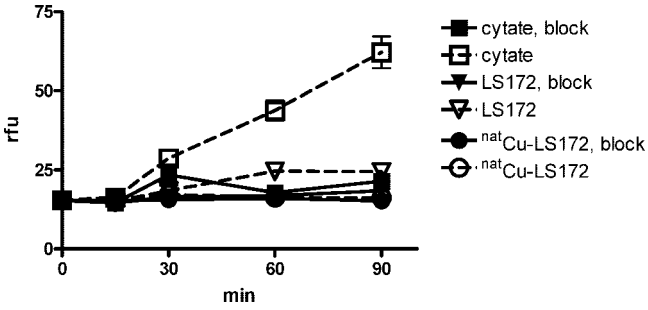

Figure 4. Uptake of cypate-conjugated Y3-TATE analogues determined by confocal fluorescence microscopy. Cypate-conjugated Y3-TATE analogues (25 nM) incubated (37 °C) with A427-7 cells with and without a competitive concentration of Y3-TATE (5 μM).

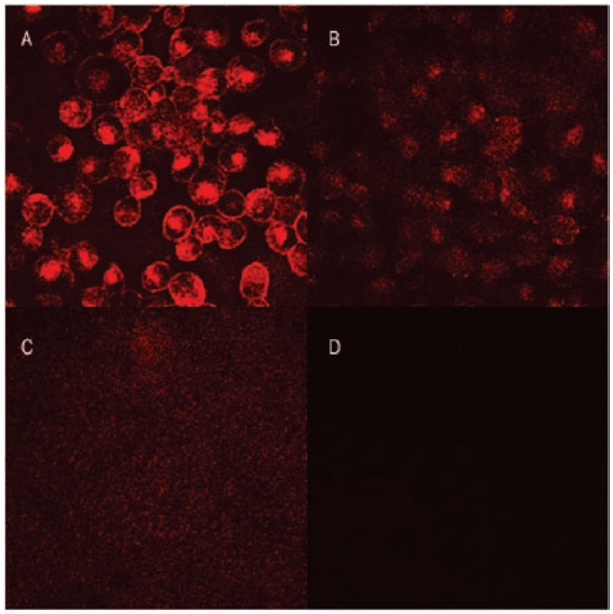

Figure 5. Cellular uptake of NIR dye-labeled peptides in either SSTr2-positive A427-7 cells (A and B) or SSTr2-negative HEK cells (C and D) incubated with 50 nM cytate (A and C) or LS172 (B and D) for 90 min. All of the images were normalized to the highest fluorescent intensity from the image in panel A.

tion was successfully blocked with a competitive dose of Y3-TATE. In contrast, LS172 was weakly internalized at 25 nM. A competing dose of Y3-TATE inhibited its accumulation until later time points (Figure 5). Surprisingly, ^{nat}Cu-LS172 was not internalized to any significant extent in the cells (Figure 5). The apparent externalization of some of the ligands at 30 min could be attributed to an error arising from the inherently low fluorescence intensities at this early time point.

Radiochemical Biodistribution. Both ^{64}Cu- and ^{177}Lu-LS172 displayed relatively similar pharmacokinetic profiles with a rapid blood clearance of 0.151 ± 0.027 and 0.228 ± 0.047% ID/g, respectively, at 1 h postinjection (Table 2). Clearance was predominately hepatic for both ^{64}Cu-LS172 (16.824 ± 1.520% ID/g, 95.8 ± 7.12% ID/liver, 1 h) and ^{177}Lu-LS172 (17.862 ± 3.286% ID/g, 89.6 ± 3.16% ID/live, 1 h) with relatively low kidney accumulation (~1 to 2% ID/g). Accumulation of activity for both radiolabeled MOMIAs in the SSTr2-positive tissues of adrenal, pituitary, pancreas, and tumor (average of left and right) were relatively low (≤1% ID/g) in all cases. ^{64}Cu-LS172 accumulation in tumor decreased with the coadministration of a competitive dose of Y3-TATE in the tumor ($P < 0.05$), but the observed decrease in other SSTr2-positive organs was not significant. The decreases in the accumulation of ^{177}Lu-LS172 in SSTr2-positive tissues with the coadministration of a competitive dose of Y3-TATE were significant ($P < 0.05$) in all target tissues except the bone.

Table 2. Biodistribution of ^{64}Cu-LS172 and ^{177}Lu-LS172 in AR42J Tumor Bearing Rats at 1 h, with and without the Coadministration of a Competing Dose of Y3-TATE[a]

tissue	^{64}Cu, 1 h	^{64}Cu, 1 h block	^{177}Lu, 1 h	^{177}Lu, 1 h block
blood	0.151 ± 0.027	0.146 ± 0.019	0.228 ± 0.047	0.225 ± 0.034
lung	1.428 ± 0.738	1.081 ± 0.311	2.249 ± 0.348	1.549 ± 0.342
liver	16.824 ± 1.520	14.547 ± 5.227	17.862 ± 3.286	15.478 ± 2.829
spleen	8.069 ± 1.808	8.013 ± 2.997	5.371 ± 1.516	6.413 ± 1.734
kidney	1.138 ± 0.352	1.256 ± 0.101	1.626 ± 0.184	1.600 ± 0.202
pituitary	0.483 ± 0.538	0.085 ± 0.720	0.747 ± 0.144[b]	0.417 ± 0.232
bone	nd[c]	nd[c]	0.225 ± 0.086	0.138 ± 0.016
adrenals	0.258 ± 0.087	0.156 ± 0.060	1.037 ± 0.128[b]	0.337 ± 0.041
pancreas	0.148 ± 0.027	0.114 ± 0.022	0.307 ± 0.054[b]	0.138 ± 0.015
tumor	0.287 ± 0.046[b]	0.220 ± 0.042	0.319 ± 0.049[b]	0.139 ± 0.025

[a] Data are presented as %ID/g ± standard deviation. [b] $P < 0.05$ vs blocked (two-tailed unpaired *t*-test). [c] Not determined.

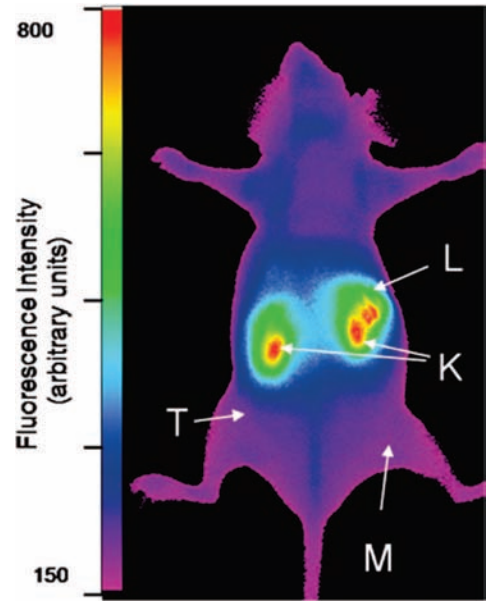

Figure 6. Optical Biodistribution of LS172 in nude mice xenografted with A427-7 cells (24 h). Representative fluorescence intensity image of a living mouse bearing a subcutaneous A427-7 xenograft 24 h after an injection of LS172. Liver (L), kidney (K), muscle (M), and tumor (T) regions of interest are indicated by arrows. The tumor is indistinguishable from surrounding muscle tissue by fluorescence intensity. Illumination light was selected with optical bandpass filter centered at 755 nm, and emission was captured with a cooled CCD camera after the 830 nm long-pass filter.

Optical Imaging. The receptor-binding assay suggests that Cu chelation reduces the affinity of LS172. Because cypate in this MOMIA provides the NIR fluorescence signal, we were able to assess its relative biodistribution in vivo and ex vivo without metal chelation to delineate the effect of radiolabeling on LS172. Thus, we noninvasively evaluated the biodistribution of LS172 in A427-7 tumor-bearing mice at 1, 4, 8, and 24 h. LS172 rapidly accumulated in the liver and kidneys, with low concentrations detected in the tumor and muscle tissues (Figures 6−8). At 24 h, representative tissues and organs were harvested and imaged ex-vivo to determine the relative tissue uptake of LS172 (Figure 9). In addition to the liver and kidneys, LS172 accumulated in the spleen and accounted for 35% of the fluorescence intensity relative to the liver (Figure 9). LS172 accumulation in mouse kidney was somewhat higher than that of the radiolabeled analogues in rat kidney, possibly indicating

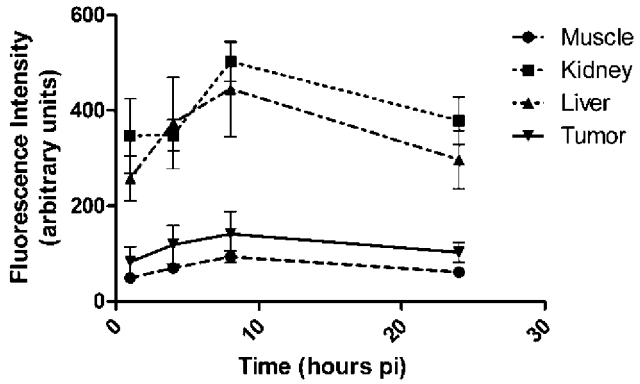

Figure 7. Measured fluorescence intensity of selected regions of interest that indicate the accumulation of LS172 in normal muscle, kidney, liver, and tumor tissues at specified time after an injection of contrast agent ($n = 3$). Fluorescence detected in the regions of the liver and kidney was significantly higher than muscle or tumor intensity for all time points. Accumulation of contrast agent in tumor tissue paralleled that of normal tissues as determined by NIR fluorescence imaging in living mice. Error bars represent SEM.

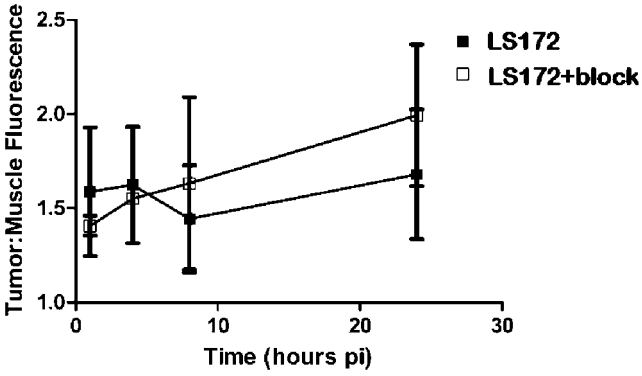

Figure 8. Ratios of tumor to muscle fluorescence intensities measured in living mice at given time points after an injection of LS172 ($n = 3$) or LS172 with Y3-TATE as blocking agent ($n = 2$). Linear regression of each data set showed that the slopes were not significantly nonzero, indicating that tumor accumulation of LS172 was not different from that of normal muscle tissue. Error bars represent SEM.

the reduction of overall charge on the DOTA upon chelation with a metal.

In spite of the high SSTr2, in vivo imaging did not show significant tumor accumulation of LS172 relative to normal tissue at different time points (Figure 7), and competitive inhibition with Y3-TATE did not significantly alter the tumor-to-muscle uptake ratio (Figure 8). The uptake and blood clearance profiles of LS172 in tumor-bearing A427-7 mice were similar to that of ^{177}Lu-LS172 and ^{64}Cu-LS172 in tumor-bearing AR42J rats. Inhibition studies with a competitive dose of Y3-octreotate showed that the observed uptake of LS172 in all tissues examined is attributable to nonspecific accumulation, including SSTr2-positive adrenal, pancreas, and tumor tissues (Figure 9).

DISCUSSION

Somatostatin peptide analogues are well characterized as radioimaging and therapeutic agents for the somatostatin receptor (*6, 7, 10, 15*). Previous studies have shown that labeling these peptides with fluorescent dyes provides a method to image SSTr2-positive tumors in mice (*14, 19, 26*). The goal of this work was to determine whether a somatostatin peptide analogue, labeled with a radiometal and a NIR fluorescent dye, would localize in a receptor-specific manner to a target tissue, such as a xenografted tumor. The somatostatin analogue was chosen on the basis of the structure of Y3-TATE, where the tetraazamacrocycle, DOTA, was conjugated to the *N*-terminal D-phenylalanine residue, and the near-infrared dye, cypate, was conjugated to the ε-amino group of lysine at the *C*-terminus. This compound, LS172, was used for NIR fluorescence imaging or labeled with ^{64}Cu and ^{177}Lu and evaluated in tumor-bearing rats by nuclear methods. In addition, LS172 was also metallated with the natural Cu and Lu for receptor-binding studies as well as cell-uptake experiments.

In the receptor-binding studies, ^{nat}Cu-LS172 and ^{nat}Lu-LS172 were used to displace ^{111}In-DTPA-Y3-TATE (Table 1 and Figure 3A). The IC_{50} values were converted to K_i values and compared to those of Y3-TATE, cytate, and SS14. The addition of cypate to the *N*-terminus of Y3-TATE (cytate) did not significantly change the binding affinity. However, modifications of both the *N*- and *C*-termini decreased the binding affinity of LS172 by about 10- and 5-fold relative to cytate and Y3-TATE, respectively. Moreover, while the complexation of ^{nat}Lu with DOTA had little effect on affinity, complexation of ^{nat}Cu reduced the affinity of LS172 by approximately 5-fold. In spite of the fact that the SSTr2-binding amino acid sequence of the peptide, the Phe (or Tyr)-D-Trp-Lys-, is relatively isolated from the termini, modifications at these sites still can affect binding. Previous studies have shown that the addition of the peptide PKKKRKV(OH) via an aminohexanoic acid linker to the *C*-terminal threonine residue of DOTA-Y3-TATE resulted in a relatively weak binding peptide when labeled with ^{111}In (K_D ~280 nM) (*27*). Furthermore, DOTA-Y3-octreotide was a weaker competitor ($IC_{50} = 14 \pm 2.6$, SEM) toward radioiodinated SS-14 than DOTA-Y3-TATE ($IC_{50} = 1.5 \pm 0.4$ nM, SEM), indicating that the relatively small change from the *C*-terminal alcohol to that of the carboxylic acid can result in a nearly 10-fold increase in affinity (*28*). Changing the radiometal in the chelator can also affect affinity. ^{nat}Ga-DOTA-Y3-octreotide bound the SSTr2 subtype with 5-fold higher affinity than the corresponding Y^{3+} derivative. This difference was ultimately attributed to a conformational change in the *N*-terminal D-Phe residue of the Y^{3+} analogue as a result of the binding of the amide D-Phe carbonyl oxygen in the metal-coordination sphere (*29*). Nevertheless, the observed affinities of ^{nat}Cu-LS172 and ^{nat}Lu-LS172 are sufficiently strong for receptor imaging, and therefore, they were radiolabeled with the corresponding radioisotopes and investigated in animal cancer models.

A well characterized tumor model, AR42J rat pancreatic xenografts, was chosen for evaluating the radiolabeled MOMIA. This model has been successful and reliable in the evaluation of a variety of radiolabeled somatostatin analogues targeted to the SSTr2 with the added benefit of confirming receptor-specific uptake in SSTr2-rich organs of the adrenal, pituitary, and pancreas (*9, 10, 15, 16*). Previous investigations of radiolabeled somatostatin analogues showed uptakes in AR42J xenografts that ranged from low ~1% ID/g up to ~6% ID/g. For example, the accumulation of ^{64}Cu-DOTA-D-Y1-octreotate ($K_D = 0.2$ nM) at 1 h was 1.52% ID/g and decreased to 0.468% ID/g with a competing dose of D-Y1-TATE (*9*). However, SSTr2-positive tissue uptake in pituitary, adrenal, and pancreas was 1.99, 1.37, and 1.49% ID/g, respectively, with concomitant decreases upon coadministration of a competing dose of unlabeled Y1-TATE. In another study, ^{64}Cu-TETA-Y3-TATE accumulation in AR42J xenografts at 1 h was ~1.7% ID/g with observed accumulation in pancreas and adrenals ~3.0 and 2.5% ID/g, respectively. A competing dose of Y3-TATE resulted in >90% inhibition of accumulation in these tissues (*16*). The observed accumulation of ^{64}Cu-LS172 in AR42J xenografts was lower, uniformly less than 1% (Table 2). Furthermore, while coadministration of a

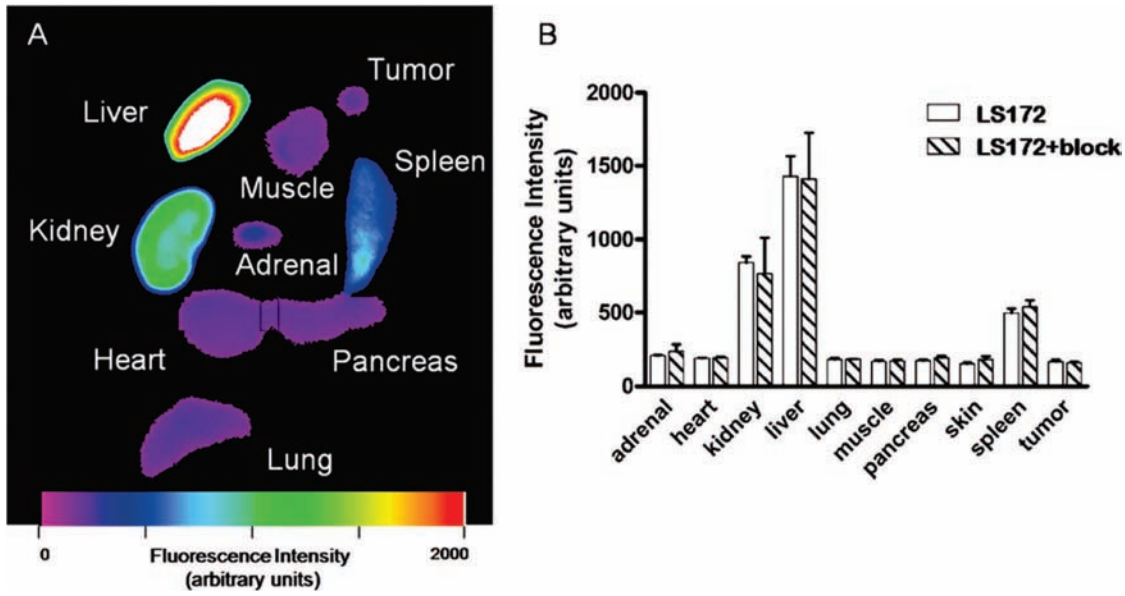

Figure 9. (A) Fluorescence intensity image of ex vivo organ tissues 24 h after an injection of LS172 representative of molecular probe biodistribution in mice. Liver, kidney, and spleen tissues showed high fluorescence intensity relative to that of other organs. (B) Optical biodistribution of LS172 in nude mice xenografted with A427-7 cells (24 h).

competing dose of Y3-TATE resulted in decreased uptake in all SSTr2-positive tissues, the results were significant only for the xenografted AR42J tumors ($P < 0.05$, two-tailed unpaired *t*-test). Other features of the ^{64}Cu-LS172 biodistribution included relatively rapid blood clearance (1 h), predominantly hepatobiliary clearance, and relatively high spleen uptake.

The biodistribution of ^{177}Lu-LS172 bore many similarities to that of ^{64}Cu-LS172, including clearance pathways and rates, high spleen uptake, and lower SSTr2-positive tissue uptake (≤1%; Table 2). The exception was that SSTr2-positive tissue uptake of ^{177}Lu, except for bone, was inhibited by a competitive competing dose of Y3-TATE ($P < 0.05$, two-tailed unpaired *t*-test). For comparison, the accumulation of ^{177}Lu-DOTA-Y3-TATE in pancreas, adrenals, and bone (femur) at 1 and 4 h was ≥10% (*6, 7*). Competing doses of octreotide at later time points confirmed that the accumulation was receptor-specific (*6*). Specific activity is not considered a likely confounding factor in this study because the specific activity was 3.5-fold less (27 μCi/nmol) than the reported specific activity (94 μCi/nmol) where high accumulation in bone and pancreas were observed (*7*). While saturation assays on dissected AR42J xenografts were not performed to verify that they retained expression of SSTr2, the low accumulation of both ^{64}Cu- and ^{177}Lu-LS172 in other SSTr2-positive tissues demonstrates the poor specific uptake of LS172 in vivo. For these reasons, biodistribution of the radiolabeled LS172 at later time points was not performed in this study.

Surprised by the in vivo outcome using AR42J cells, we explored the use of an alternative cell line rich in SSTr2. We recently developed a new cell line, A427-7 (A427 clone 7) that meets our need (*18*). SSTr2 was transfected into A427 cells with relatively large receptor numbers (~7.0 pmol/mg protein). The transfected receptor appeared to function in identically to the wild type receptor because recent studies with SSTr2-avid ^{64}Cu-TETA-octreotide showed it was internalized by A427-7 cells and had relatively high SSTr2 specific accumulation in vivo (*18*). Therefore, this cell line provides a method to evaluate the MOMIAs in another cell line.

Considering that the SSTr2 binding assay demonstrated that radiolabeling of LS172 with Cu reduced the affinity, we imaged the distribution and uptake of the NIR fluorescent LS172 in A427-7 tumor-bearing nude mice by fluorescence imaging. LS172 was administered to the mice with and without a competing dose of Y3-TATE. This allowed us to determine whether the radiometal played a role in the relatively low tumor accumulations in AR 42J cells in rat.

Longitudinal, noninvasive optical imaging provided relative biodistribution data at multiple times during the 24 h after injection (Figure 7). Despite these changes, in vivo optical imaging showed that LS172 accumulation paralleled that of the radiochemical biodistribution with relatively rapid blood clearance and predominant hepatobiliary clearance with no apparent receptor-specific accumulation in the A427-7 tumor or other SSTr2-positive tissues. In vivo and ex vivo fluorescence imaging did not show significantly higher LS172 accumulation in tumor tissue relative to healthy tissues (Figures 6−9). The observed increase in kidney retention relative to radionuclear biodistribution could be attributed to species differences. Alternatively, the absence of metals in LS172 increases the net negative charge on DOTA, thereby favoring kidney uptake.

To determine whether the low accumulation of LS172 in the A427-7 cells was due to receptor downregulation, saturation assays with ^{125}I-SS-14 were performed on homogenized A427-7 tumors dissected from mice. The results showed robust expression of SSTr2 (2.3 pmol/mg), indicating that receptor loss in the xenografts was not the cause of the low observed tumor accumulation (Figure 3B). Our observed values of SSTr2 receptor densities in the xenografted tumors were lower than the reported values (*18*). The difference could be attributed to differences in the method used for these measurements. Whereas we determined receptor expression level with ^{125}I-SS-14, the reported values were determined with ^{64}Cu-TETA-octreotide.

Recently, saturation assays with radiolabeled SSTr2 agonists and antagonists identified differing receptor densities, raising the intriguing possibility that there are differing active receptor conformations that are dependent on the radioligand (*27*). These observations may further explain the differing levels of receptor identified in this work relative to that previously determined (*18*).

Because it was unusual that ligands with such high affinity failed to localize to receptor-rich tissues in vivo, we investigated the uptake of LS172 and ^{nat}Cu-LS172 relative to cytate in A427-7 cells in vitro. Cytate was included as a reference because of its high SSTr2-specific accumulation in a xenografted tumor

(CA20948) in as little as 90 min (*14*, *19*). The internalization of LS172 and ^{nat}Cu-LS172 by A427-7 cells was directly observed by NIR fluorescence microscopy because they are both conjugated to cypate (Figures 4 and 5). Expectedly, cytate was rapidly internalized in A427-7 cells. While LS172 also internalized, it did so at a far slower rate and to a much lower extent than cytate. Internalization of cytate and LS172 was inhibited with a competitive dose of Y3-TATE, thus demonstrating that endocytosis was mediated by the SSTr2 receptor. Lack of observed internalization of either cytate or LS172 in the SSTr2-negative HEK293 cells further confirmed the involvement of SSTr2-specific uptake in A427-7 cells. However, it should be noted that HEK293 cells express low levels of SSTr2 (*30*).

The hallmark of agonism is the internalization of the receptor–ligand complex (*12*, *15*). Antagonists do not stimulate internalization. LS172, with its extremely weak internalization properties, and Cu-LS172 appear to be antagonists and cytate an agonist. Recently, the correlation between agonism, defined as the ability of a putative agonist to inhibit forskolin-stimulated cAMP production, and internalization was investigated (*31*). The concentration required to stimulate internalization was determined by ELISA. Both methods linked these abilities to the concentration required to obtain 50% effect (EC_{50}). The EC_{50} ratio of internalization to cAMP inhibition of SS-28 and SS-14 was ∼1. However, for other ligands, such as octreotide, the ratio rose to ∼10, indicating that octreotide is 10-fold better at stimulating adenylate cyclase than at stimulating receptor internalization. These results show that inhibition of cAMP production may not be the best approach to determine the ability of an agonist to stimulate receptor internalization.

Internalization is considered a key feature for successful in vivo accumulation of the radiotracer at the target site (*15*). The rationale is that after binding of the radiotracer, the receptor–ligand complex internalizes into an endocytotic pathway while the unbound ligand clears from blood and nontarget tissues. Recently, a high degree of correlation between the rate of internalization of SSTr2-avid ligands in vitro and accumulation in SSTr2-enriched xenograft (AR42J) and natural organ (pancreas) in vivo was observed (*10*). Moreover, successful imaging and therapy with radiolabeled somatostatin analogues in humans have utilized tracers that were internalized in vitro (*32*, *33*). Therefore, the low accumulation of LS172 and ^{64}Cu-LS172 in xenografted tumors in vivo appeared to be due to a lack of internalization of these apparent antagonists, while the high receptor-specific accumulation of cytate is due to its ability to internalize.

This result stands in sharp contrast to a recent observation that an antagonist (^{111}In-DOTA-SSTr2-ANT) accumulated to a high level (∼29% ID/g, 4 h) in SSTr2-positive tumor xenografts (HEK-SSTr2 transfected tumors in nude mice) (*34*). The accumulation exceeded that of ^{111}In-DOTA-Y3-TATE (∼16% ID/g, 4 h). The authors determined that ^{nat}In-DOTA-SSTr2-ANT was an antagonist by its inability to inhibit forskolin-stimulated cAMP production as well as by its inability to stimulate SSTr2 internalization (immunofluorescence microscopy). Part of the explanation was that the higher number of receptors identified by the antagonist (15-fold more than the agonist) offset the internalization effect. Unfortunately, the receptor concentrations were not normalized to protein weight, which makes a comparison with our current results difficult. The A427-7 cell line maintained robust expression of the SSTr2 as a xenograft, and this high expression level (2.3 pmol/mg) did not offset the lack of internalization of LS172.

In conclusion, LS172, a monomolecular multimodal imaging agent, was radiolabeled with both ^{64}Cu and ^{177}Lu and evaluated as an SSTr2 receptor-imaging agent by both optical and radionuclear methods in vitro and in vivo. All of the compounds have high SSTr2 binding affinity and retained their fluorescence properties before and after labeling with metal. In spite of the high expression level of the target, LS172 along with its radiolabeled analogues, ^{64}Cu- and ^{177}Lu-LS172, did not accumulate in levels commensurate with their high affinity and high target expression in tumor xenografts. Moreover, accumulation in tissues endogenously expressing SSTr2 was also very low. We attribute the low accumulation to a lack of internalization of the labeled ligands in a receptor–ligand complex characteristic of successful SSTr2 imaging agents. Although the anticipated receptor-mediated accumulation in target tissues was not observed, the excellent agreement between the optical and radiochemical biodistributions demonstrates the utility of multimodal monomolecular imaging agents (MOMIAs). In addition, the quantitative radionuclear method is useful for validating data from the high throughput qualitative planar optical imaging method. Overall, high receptor binding affinity in vitro is a necessary but not sufficient criterion for selecting ligands for in vivo imaging application. The use of dual radioimaging and therapeutic radiometals provides a strategy for monitoring treatment response, initially by either PET or SPECT, followed by optical imaging at later time points.

ACKNOWLEDGMENT

We thank Dr. Yunpeng Ye for preparing cypate and Mr. Christopher Sherman for performing the radio-biodistribution study. This study was supported in part by the NIH (grants R33 CA100972, R01 EB1430, R21 CA123537, and R01 CA64475).

Supporting Information Available: Chromatograms, radiochromatograms, and mass spectral data for LS172. This material is available free of charge via the Internet at http://pubs.acs.org.

LITERATURE CITED

(1) Gayed, I. W., Kim, E. E., Broussard, W. F., Evans, D., Lee, J., Broemeling, L. D., Ochoa, B. B., Moxley, D. M., Erwin, W. D., and Podoloff, D. A. (2005) The value of 99mTc-sestamibi SPECT/CT over conventional SPECT in the evaluation of parathyroid adenomas or hyperplasia. *J. Nucl. Med. 46*, 248–252.

(2) Jaffer, F. A., and Weissleder, R. (2005) Molecular imaging in the clinical arena. *J. Am. Med. Assoc. 293*, 855–862.

(3) Zhang, Z., and Achilefu, S. (2005) Spectral properties of promultimodal imaging agents derived from a NIR dye and a metal chelator. *Photochem. Photobiol. 81*, 1499–1504.

(4) Zhang, Z., Liang, K., Bloch, S., Berezin, M., and Achilefu, S. (2005) Monomolecular multimodal fluorescence-radioisotope imaging agents. *Bioconjugate Chem. 16*, 1232–1239.

(5) Houston, J. P., Ke, S., Wang, W., Li, C., and Sevick-Muraca, E. M. (2005) Quality analysis of in vivo near-infrared fluorescence and conventional gamma images acquired using a dual-labeled tumor-targeting probe. *J. Biomed. Opt. 10*, 054010.

(6) de Jong, M., Breeman, W. A., Bernard, B. F., Bakker, W. H., Schaar, M., van Gameren, A., Bugaj, J. E., Erion, J., Schmidt, M., Srinivasan, A., and Krenning, E. P. (2001) [177Lu-DOTA(0),Tyr3] octreotate for somatostatin receptor-targeted radionuclide therapy. *Int. J. Cancer 92*, 628–633.

(7) Lewis, J. S., Wang, M., Laforest, R., Wang, F., Erion, J. L., Bugaj, J. E., Srinivasan, A., and Anderson, C. J. (2001) Toxicity and dosimetry of (177)Lu-DOTA-Y3-octreotate in a rat model. *Int. J. Cancer 94*, 873–877.

(8) Breeman, W. A., de Jong, M., de Blois, E., Bernard, B. F., Konijnenberg, M., and Krenning, E. P. (2005) Radiolabelling DOTA-peptides with 68Ga. *Eur. J. Nucl. Med. Mol. Imaging 32*, 478–485.

(9) Li, W. P., Lewis, J. S., Kim, J., Bugaj, J. E., Johnson, M. A., Erion, J. L., and Anderson, C. J. (2002) DOTA-D-Tyr(1)-octreotate: a somatostatin analogue for labeling with metal and

halogen radionuclides for cancer imaging and therapy. *Bioconjugate Chem. 13*, 721–728.
(10) Storch, D., Behe, M., Walter, M. A., Chen, J., Powell, P., Mikolajczak, R., and Macke, H. R. (2005) Evaluation of [99mTc/EDDA/HYNIC0]octreotide derivatives compared with [111In-DOTA0,Tyr3, Thr8]octreotide and [111In-DTPA0]octreotide: does tumor or pancreas uptake correlate with the rate of internalization? *J. Nucl. Med. 46*, 1561–1569.
(11) Forrer, F., Waldherr, C., Maecke, H. R., and Mueller-Brand, J. (2006) Targeted radionuclide therapy with 90Y-DOTATOC in patients with neuroendocrine tumors. *Anticancer Res. 26*, 703–707.
(12) Hofland, L. J., and Lamberts, S. W. (2003) The pathophysiological consequences of somatostatin receptor internalization and resistance. *Endocr. Rev. 24*, 28–47.
(13) Bugaj, J. E., Achilefu, S., Dorshow, R. B., and Rajagopalan, R. (2001) Novel fluorescent contrast agents for optical imaging of in vivo tumors based on a receptor-targeted dye-peptide conjugate platform. *J. Biomed. Opt. 6*, 122–133.
(14) Achilefu, S., Jimenez, H. N., Dorshow, R. B., Bugaj, J. E., Webb, E. G., Wilhelm, R. R., Rajagopalan, R., Johler, J., and Erion, J. L. (2002) Synthesis, in vitro receptor binding, and in vivo evaluation of fluorescein and carbocyanine peptide-based optical contrast agents. *J. Med. Chem. 45*, 2003–2015.
(15) Hofland, L. J., Lamberts, S. W., van Hagen, P. M., Reubi, J. C., Schaeffer, J., Waaijers, M., van Koetsveld, P. M., Srinivasan, A., Krenning, E. P., and Breeman, W. A. (2003) Crucial role for somatostatin receptor subtype 2 in determining the uptake of [111In-DTPA-D-Phe1]octreotide in somatostatin receptor-positive organs. *J. Nucl. Med. 44*, 1315–1321.
(16) Sprague, J. E., Peng, Y., Sun, X., Weisman, G. R., Wong, E. H., Achilefu, S., and Anderson, C. J. (2004) Preparation and biological evaluation of copper-64-labeled tyr3-octreotate using a cross-bridged macrocyclic chelator. *Clin. Cancer. Res. 10*, 8674–8682.
(17) Ye, Y., Li, W. P., Anderson, C. J., Kao, J., Nikiforovich, G. V., and Achilefu, S. (2003) Synthesis and characterization of a macrocyclic near-infrared optical scaffold. *J. Am. Chem. Soc. 125*, 7766–7767.
(18) Parry, J. J., Eiblmaier, M., Andrews, R., Meyer, L. A., Higashikubo, R., Anderson, C. J., and Rogers, B. E. (2007) Characterization of somatostatin receptor subtype 2 expression in stably transfected a-427 human cancer cells. *Mol. Imaging 6*, 56–67.
(19) Achilefu, S., Dorshow, R. B., Bugaj, J. E., and Rajagopalan, R. (2000) Novel receptor-targeted fluorescent contrast agents for in vivo tumor imaging. *Invest. Radiol. 35*, 479–485.
(20) Breeman, W. A., De Jong, M., Visser, T. J., Erion, J. L., and Krenning, E. P. (2003) Optimising conditions for radiolabelling of DOTA-peptides with 90Y, 111In and 177Lu at high specific activities. *Eur. J. Nucl. Med. Mol. Imaging 30*, 917–920.
(21) Rogers, B. E., Bigott, H. M., McCarthy, D. W., Della Manna, D., Kim, J., Sharp, T. L., and Welch, M. J. (2003) MicroPET imaging of a gastrin-releasing peptide receptor-positive tumor in a mouse model of human prostate cancer using a 64Cu-labeled bombesin analogue. *Bioconjugate Chem. 14*, 756–763.
(22) Edwards, W. B., Liang, K., Xu, B., Anderson, C. J., and Achilefu, S. (2006) Synthesis and radiolabeling of a somatostatin analog for multimodal imaging. *Proc. SPIE 6097*, 609701–609708.
(23) Demas, J. N., and Crosby, G. A. (1971) Measurement of photoluminescence quantum yields. *J. Phys. Chem. 75*, 991–1023.
(24) Philip, R., Penzkofer, A., Baumler, W., Szeimies, R. M., and Abels, C. (1996) Absortion and fluorescence spectroscopic investigation of indocyanine green. *J. Photochem. Photobiol. A 96*, 137–148.
(25) Ye, Y., Bloch, S., Kao, J., and Achilefu, S. (2005) Multivalent carbocyanine molecular probes: synthesis and applications. *Bioconjugate Chem. 16*, 51–61.
(26) Becker, A., Hessenius, C., Licha, K., Ebert, B., Sukowski, U., Semmler, W., Wiedenmann, B., and Grotzinger, C. (2001) Receptor-targeted optical imaging of tumors with near-infrared fluorescent ligands. *Nat. Biotechnol. 19*, 327–331.
(27) Cescato, R., Schulz, S., Waser, B., Eltschinger, V., Rivier, J. E., Wester, H. J., Culler, M., Ginj, M., Liu, Q., Schonbrunn, A., and Reubi, J. C. (2006) Internalization of sst2, sst3, and sst5 receptors: effects of somatostatin agonists and antagonists. *J. Nucl. Med. 47*, 502–511.
(28) Reubi, J. C., Schar, J. C., Waser, B., Wenger, S., Heppeler, A., Schmitt, J. S., and Macke, H. R. (2000) Affinity profiles for human somatostatin receptor subtypes SST1-SST5 of somatostatin radiotracers selected for scintigraphic and radiotherapeutic use. *Eur. J. Nucl. Med. 27*, 273–282.
(29) Deshmukh, M. V., Voll, G., Kuhlewein, A., Macke, H., Schmitt, J., Kessler, H., and Gemmecker, G. (2005) NMR studies reveal structural differences between the gallium and yttrium complexes of DOTA-D-Phe1-Tyr3-octreotide. *J. Med. Chem. 48*, 1506–1514.
(30) Law, S. F., Yasuda, K., Bell, G. I., and Reisine, T. (1993) Gi alpha 3 and G(o) alpha selectively associate with the cloned somatostatin receptor subtype SSTR2. *J. Biol. Chem. 268*, 10721–10727.
(31) Liu, Q., Cescato, R., Dewi, D. A., Rivier, J., Reubi, J. C., and Schonbrunn, A. (2005) Receptor signaling and endocytosis are differentially regulated by somatostatin analogs. *Mol. Pharmacol. 68*, 90–101.
(32) Beutler, D., Avoledo, P., Reubi, J. C., Macke, H. R., Muller-Brand, J., Merlo, A., and Kuhne, T. (2005) Three-year recurrence-free survival in a patient with recurrent medulloblastoma after resection, high-dose chemotherapy, and intrathecal Yttrium-90-labeled DOTA0-D-Phe1-Tyr3-octreotide radiopeptide brachytherapy. *Cancer 103*, 869–873.
(33) Bodei, L., Paganelli, G., and Mariani, G. (2006) Receptor radionuclide therapy of tumors: a road from basic research to clinical applications. *J. Nucl. Med. 47*, 375–377.
(34) Ginj, M., Zhang, H., Waser, B., Cescato, R., Wild, D., Wang, X., Erchegyi, J., Rivier, J., Macke, H. R., and Reubi, J. C. (2006) Radiolabeled somatostatin receptor antagonists are preferable to agonists for in vivo peptide receptor targeting of tumors. *Proc. Natl. Acad. Sci. U.S.A. 103*, 16436–16441.

BC700291M

Linker Effects on Biological Properties of ^{111}In-Labeled DTPA Conjugates of a Cyclic RGDfK Dimer

Bing Jia,[†,‡] Zhaofei Liu,[†] Jiyun Shi,[†,‡] Zilin Yu,[†] Zhi Yang,[§] Huiyun Zhao,[†] Zhengjie He,[△] Shuang Liu,*[,△] and Fan Wang*[,†]

Medical Isotopes Research Center, Peking University, Beijing 100083, Department of Isotopes, China Institute of Atomic Energy, Beijing 102413, Department of Nuclear Medicine, Peking University Oncology School, Beijing 100036, China, and School of Health Sciences, Purdue University, Indiana 47907. Received August 8, 2007; Revised Manuscript Received October 7, 2007

In this report, we present *in vitro* and *in vivo* evaluation of three ^{111}In-labeled DTPA conjugates of a cyclic RGDfK dimer: DTPA-Bn-SU016 (SU016 = E[c(RGDfK)]$_2$; DTPA-Bn = 2-(*p*-isothioureidobenzyl)diethylenetriaminepentaacetic acid), DTPA-Bn-E-SU016 (*E* = glutamic acid) and DTPA-Bn-Cys-SU016 (Cys = cysteic acid). The integrin $\alpha_v\beta_3$ binding affinities of SU016, DTPA-Bn-SU016, DTPA-Bn-E-SU016, and DTPA-Bn-Cys-SU016 were determined to be 5.0 ± 0.7 nM, 7.9 ± 0.6 nM, 5.8 ± 0.6 nM, and 6.9 ± 0.9 nM, respectively, against ^{125}I-c(RGDyK) in binding to integrin $\alpha_v\beta_3$, suggesting that E or Cys residue has little effect on the integrin $\alpha_v\beta_3$ affinity of E[c(RGDfK)]$_2$. It was also found that the ^{111}In-labeling efficiency of DTPA-Bn-SU016 and DTPA-Bn-E-SU016 is 3–5 times better than that of DOTA analogues due to fast chelation kinetics and high-yield ^{111}In-labeling under mild conditions (e.g., room temperature). Biodistribution studies were performed using BALB/c nude mice bearing U87MG human glioma xenografts. ^{111}In-DTPA-Bn-SU016, ^{111}In-DTPA-Bn-E-SU016, and ^{111}In-DTPA-Bn-Cys-SU016 all displayed rapid blood clearance. Their tumor uptake was comparable between 0.5 and 4 h postinjection (p.i.) within experimental error. ^{111}In-DTPA-Bn-E-SU016 had a significantly lower ($p < 0.01$) kidney uptake than ^{111}In-DTPA-Bn-SU016 and ^{111}In-DTPA-Bn-Cys-SU016. The liver uptake of ^{111}In-DTPA-Bn-SU016 was 1.69 ± 0.18% ID/g at 24 h p.i., while the liver uptake values of ^{111}In-DTPA-Bn-E-SU016 and ^{111}In-DTPA-Bn-Cys-SU016 were 0.55 ± 0.11% ID/g and 0.79 ± 0.15% ID/g at 24 h p.i., respectively. Among the three ^{111}In radiotracers evaluated in this study, ^{111}In-DTPA-Bn-E-SU016 has the lowest liver and kidney uptake and the best tumor/liver and tumor/kidney ratios. Results from metabolism studies indicated that there is little metabolism (<10%) for three ^{111}In radiotracers at 1 h p.i. Imaging data showed that tumors can be clearly visualized at 4 h p.i. with good contrast in the tumor-bearing mice administered with ^{111}In-DTPA-Bn-E-SU016. It is concluded that using a glutamic acid linker can significantly improve excretion kinetics of the ^{111}In-labeled E[c(RGDfK)]$_2$ from liver and kidneys.

INTRODUCTION

Integrin $\alpha_v\beta_3$ plays a critical role in tumor angiogenesis and metastasis (*1–5*). The highly restricted expression of integrin $\alpha_v\beta_3$ during tumor growth, invasion, and metastasis makes it an interesting molecular target for development of the integrin $\alpha_v\beta_3$-targeted radiotracers (*6–9*). In the past decade, many radiolabeled cyclic RGD peptides have been evaluated as potential radiotracers for early detection of the integrin $\alpha_v\beta_3$-positive tumors by single photon emission computed tomography (SPECT) or positron emission tomography (PET). [^{18}F]Galacto-RGD has become the first PET radiotracer under clinical investigation for noninvasive visualization of integrin $\alpha_v\beta_3$ expression in cancer patients (*10–12*). The integrin $\alpha_v\beta_3$-targeted radiotracers have been reviewed extensively (*13–18*).

We and others have been using cyclic RGD dimers, such as E[c(RGDfK)]$_2$ (SU016), to develop integrin $\alpha_v\beta_3$-targeted diagnostic (^{64}Cu, ^{99m}Tc, and ^{111}In) and therapeutic (^{90}Y and ^{177}Lu) radiotracers (*19–36*). It has been found that the radiolabeled cyclic RGD dimers have much better tumor uptake than monomeric analogues due to their higher integrin $\alpha_v\beta_3$ binding affinity. Recently, we reported the impact of pharmacokinetic modifying (PKM) linkers on biological properties of the ^{99m}Tc-labeled HYNIC-PKM-SU016 (HYNIC= 6-hydrazinonicotinamide; PKM = glutamic acid (E), lysine (K), or PEG$_4$ (15-amino-4,7,10,13-tetraoxa-pentadecanoic acid)) (*23*). Even though they have minimal impact on the integrin $\alpha_v\beta_3$ affinity of SU016, all three PKM linkers are able to reduce the radiotracer uptake in blood, kidneys, liver, and lungs, and increase target-to-background (T/B) ratios. E and K have advantages over PEG$_4$ due to lower liver uptake and higher tumor/liver ratios of the ^{99m}Tc-labeled E[c(RGDfK)]$_2$ (*23*). For ^{111}In-labeled DOTA-PKM-E[c(RGDfK)]$_2$ (DOTA = 1,4,7,10-tetraazacyclododecane-1,4,7,10-tetraacetic acid), however, PEG$_4$ appears to be a better linker than E and K, since ^{111}In-DOTA-PEG$_4$-E[c(RGDfK)]$_2$ has the highest tumor-to-blood ratio and lowest uptake in liver and kidneys (*33*).

The disadvantage of using DOTA as the bifunctional chelator (BFC) for ^{111}In-labeling of small biomolecules is its slow chelation kinetics and low radiolabeling efficiency (*33, 37, 38*). In contrast, DTPA has higher radiolabeling efficiency (*37–39*),

* Correspondence should be addressed to Dr. Shuang Liu, School of Health Sciences, Purdue University, 550 Stadium Mall Drive, West Lafayette, IN 47907. Phone: 765-494-0236, Fax: 765-496-3367, E-mail: lius@pharmacy.purdue.edu; or Dr. Fan Wang, Medical Isotopes Research Center, Peking University, 38# Xueyuan Road Beijing 100083, China. Phone and Fax: 86-10-82801145, E-mail: wangfan@bjmu.edu.cn.

† Peking University.

‡ China Institute of Atomic Energy.

§ Peking University Oncology School.

△ Purdue University.

10.1021/bc7002988 CCC: $40.75 © 2008 American Chemical Society
Published on Web 12/11/2007

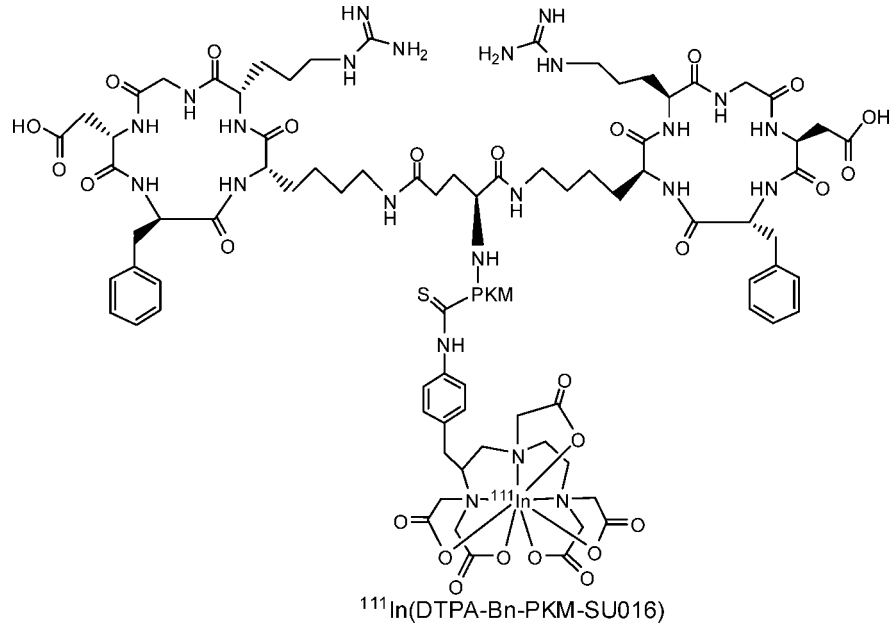

Figure 1. Schematic presentation of ^{111}In-labeled cyclic RGDfK dimer DTPA conjugates: ^{111}In(DTPA-Bn-PKM-SU016) (PKM = direct bond, glutamic acid (E) and cysteic acid (Cys); SU016 = E[c(EGDfK)]$_2$).

and has been successfully used for ^{90}Y, ^{177}Lu, and ^{111}In-labeling of biomolecules, including antibodies (*40–44*) and small peptides (*39, 40, 45, 46*). In this study, we report three new cyclic RGDfK dimer DTPA conjugates (Figure 1), DTPA-Bn-SU016(DTPA-Bn=2-(*p*-isothiocyanobenzyl)diethylenetriaminepentaacetic acid), DTPA-Bn-E-SU016, and DTPA-Bn-Cys-SU016 (Cys = cysteic acid), and the evaluation of their ^{111}In complexes (Figure 1) as the integrin $\alpha_v\beta_3$-targeted radiotracers in the BALB/c nude mice bearing U87MG human glioma xenografts. ^{111}In is of particular interest to us, since it has been widely (second only to ^{99m}Tc) used for SPECT imaging, and the ^{111}In-labeled E[c(RGDfK)]$_2$ can be used as the imaging surrogate to evaluate the potential of the ^{90}Y-labeled E[c(RGDfK)]$_2$ as the integrin $\alpha_v\beta_3$-targeted radiotracer for tumor radiotherapy. The main objective of this study is to explore the effect of linkers (E and Cys) on biodistribution characteristics of the ^{111}In-labeled E[c(RGDfK)]$_2$. The ultimate goal of using different linkers is to increase T/B ratios by minimizing radiotracer uptake in non-cancerous organs while maintaining high tumor uptake.

EXPERIMENTAL SECTION

Materials. All chemicals were purchased from Sigma/Aldrich, unless specified otherwise. The cyclic pentapeptide, c(RGDfK), was obtained from Peptides International, Inc. (Louisville, KY). 2-(*p*-Isothiocyanobenzyl)diethylenetriaminepentaacetic acid (*p*-SCN-Bn-DTPA) was purchased from Macrocyclics (Dallas, TX). $^{111}InCl_3$ was obtained from Perkin-Elmer Life and Analytical Sciences (North Billarica, MA). E[c(RGDfK)]$_2$ and E-E[c(RGDfK)]$_2$ were prepared according to the procedure described in our previous communications (*21, 23*). The reversed-phase C-18 SepPak cartridges were obtained from Waters (Milford, MA). The ammonium acetate buffer for ^{111}In-labeling studies was passed over a Chelex-100 column (1 × 15 cm) to minimize the trace metal contaminants.

HPLC and ITLC Methods. HPLC method 1 used a LabAlliance semiprep HPLC system equipped with a UV/vis detector (λ = 254 nm) and a reverse-phase Zorbax C_{18} column (9.4 mm × 250 mm, 100 Å pore size). The flow rate was 2.5 mL/min. The mobile phase was isocratic with 90% solvent A (0.1% acetic acid in water) and 10% solvent B (0.1% acetic acid in acetonitrile) at 0–5 min, followed by a gradient mobile phase going from 90% solvent A and 10% solvent B at 5 min to 60% solvent A and 40% solvent B at 20 min. The radio-HPLC method (method 2) used a HP Hewlett Packard series 1100 HPLC system equipped with Radioflow Detector LB509 and Agilent Zorbax SB-C18 column (4.6 mm × 250 mm, 5 μm). The flow rate was 1.0 mL/min. The mobile phase was isocratic with 90% solvent A (25 mM NaOAc buffer, pH = 5.0) and 10% solvent B (acetonitrile) at 0–2 min, followed by a gradient mobile phase going from 10% solvent B at 2 min to 15% solvent B at 5 min and to 20% solvent B at 20 min, then to 10% solvent B at 25 min. The radio-ITLC method used GelmanSciences silica-gel paper strips and a 1:1 mixture of acetone and saline as the eluant. Using this method, the ^{111}In-labeled cyclic RGDfK peptide dimer migrates to the solvent front, while the "free" or "unchelated" ^{111}In remains at the origin.

DTPA-Bn-SU016. DTPA-Bn-SCN (2.7 mg, 4 μmol) and SU016 (3.0 mg, 2 μmol) were dissolved in 1 mL of anhydrous dimethylformamide (DMF). The pH in the reaction mixture was adjusted to 8.5–9.0 with DIEA. The reaction mixture was stirred at room temperature for ~6 h. After addition of 3 mL of 100 mM NH_4OAc buffer (pH = 7.0), the resulting solution was filtered, and the filtrate was subjected to HPLC purification (method 1). The fraction at ~15 min was collected. Lyophilization of the collected fractions afforded the expected product as a white power. The yield was 1.8 mg (48%). ESI-MS (positive mode) for DTPA-Bn-SU016: m/z = 1859.62 for $[M + H]^+$ (M = 1858.82 calcd for $C_{81}H_{116}N_{23}O_{26}S$).

DTPA-Bn-E-SU016. DTPA-Bn-SCN (2.7 mg, 4 μmol) and E-E[c(RGDfK)]$_2$ (3.0 mg, 2 μmol) were dissolved with anhydrous DMF (1 mL). The mixture was stirred at room temperature for 10 min. DIEA was added to adjust pH to ~8.0. The reaction mixture was stirred at room temperature for 6 h. After addition of 100 mM NH_4OAc buffer (3 mL, pH = 7.0), the resulting solution was subjected to semiprep HPLC purification (method 1). The fractions at ~17.5 min were collected. Lyophilization of collected fractions gave the desired product as a white powder. The yield was 1.5 mg (38%). ESI-MS (positive mode) for DTPA-Bn-E-SU016: m/z = 1989.68 for $[M + H]^+$ (M = 1988.87 calcd for $C_{86}H_{124}N_{24}O_{29}S$).

BOC-Protected Cysteic acid (Boc-Cys-OH). To a solution of cysteic acid hydrate (0.56 g, 3 mmol) and triethylamine (0.61 g, 6 mmol) in anhydrous DMF (10 mL) was added a solution of di-*tert*-butyl dicarbonate (0.78 g, 3.6 mmol) in 5 mL of DMF. The mixture was stirred at room temperature for 48 h. Evaporation of the solvent under vacuum gave a colorless oil. The residue was dissolved in methylene chloride (10 mL). Upon addition of diethyl ether (30 mL) with vigorous stirring, a white precipitate was formed. Solvents were decanted and discarded. The solid residue was washed with anhydrous diethyl ether (10 mL) and dried under vacuum to give a foamlike white solid. The yield was 0.89 g (80%). ^{1}H NMR (δ in ppm, $CDCl_3$): 6.60 (d, NH, J = 5.4 Hz), 3.78 (m, 1H, CH), 2.45 (m, 2H, CH_2), 1.15 (s, 9H, t-Bu).

BOC-Protected Cysteic Acid Succinimidyl Ester (Boc-Cys-OSu). To a solution of Boc-Cys-OH (as its triethylamine salt) (0.89 g, 2.4 mmol) and NHS (0.345 g, 3 mmol) in anhydrous DMF (20 mL) was added DCC (0.618 g, 3 mmol). The resulting mixture was stirred at room temperature for 24 h. Acetic acid (1.0 mL) was added into the mixture above, and the stirring was continued for 3 h. The precipitate DCU was filtered off. The filtrate was evaporated to dryness. The residue was dissolved in methylene chloride (15 mL). Upon removal of a small amount of DCU precipitate, the expected product was precipitated out by adding the filtrate into anhydrous diethyl ether (30 mL). The solid was washed with diethyl ether (20 mL) and dried under vacuum to give a white solid. The yield was 1.20 g (100%). ^{1}H NMR (δ in ppm, $CDCl_3$): 6.46 (s, 1H, NH), 4.88 (m, 1H, CH), 3.40 (m, 2H, CH_2), 2.80 (s, 4H, CH_2CH_2), 1.42 (s, 9H, t-Bu).

Boc-Cys-SU016. To a solution of Boc-Cys-OSu (7.2 mg, 0.015 mmol) in DMF (1 mL) was added SU016 (13.2 mg, 0.01 mmol). DIEA was added to adjust pH in the reaction mixture to 8.5–9.0. The resulting mixture was stirred at room temperature for 30 min, and the pH was adjusted to ~8.5, if necessary. The reaction was stirred at room temperature overnight. The desired product was isolated from the reaction mixture by HPLC purification (method 1). The collected fractions at ~15 min were combined. Lyophilization of the combined fractions afforded the expected product as a white powder. The yield was 6.4 mg (41%). ESI-MS (positive mode) for Boc-Cys-SU016: m/z = 1570.75 for $[M + H]^+$ (M = 1569.71 calcd for $C_{67}H_{101}N_{20}O_{22}S$).

Cys-SU016. Boc-Cys-SU016 (5 mg, 0.003 mmol) was treated with 2 mL of anhydrous trifluoroacetate (TFA) at room temperature for 30 min. Volatiles were completely removed under vacuum. The residue was dissolved in 100 mM NH_4OAc buffer (3 mL). The resulting solution was filtered, and the filtrate was purified by HPLC (method 1). The fractions at ~15.5 min were collected. Lyophilization of collected fractions gave the desired product as a white powder (3.5 mg). ESI-MS (positive mode) for Cys-SU016: m/z = 1469.57 for $[M + H]^+$ (M = 1468.65 calcd for $C_{62}H_{92}N_{20}O_{20}S$).

DTPA-Bn-Cys-SU016. DTPA-Bn-SCN (2.7 mg, 4 μmol) and Cys-SU016 (3.0 mg, 2 μmol) were dissolved in anhydrous DMF (1 mL). The mixture was stirred at room temperature for 10 min. DIEA was used to adjust pH in the mixture to 8.5–9.0. The reaction mixture was stirred at room temperature for another 6 h while maintaining pH at 8.5–9.0. Upon addition of 100 mM NH_4OAc (3 mL, pH = 7.0), the resulting solution was filtered. The filtrate was subjected to HPLC purification (method 1). The fractions at ~15.5 min were collected. Lyophilization of collected fractions gave the desired product as a white powder. The yield was 1.5 mg (35%). ESI-MS (positive mode) for DTPA-Bn-Cys-SU016: m/z = 2012.08 for $[M + H]^+$ (M = 2010.81 calcd for $C_{84}H_{122}N_{24}O_{30}S_2$).

^{111}In-Labeling and Solution Stability. To a clean Eppendorf tube were added 200 μL of DTPA-Bn-SU016 or DTPA-Bn-E-SU016 or DTPA-Bn-Cys-SU016 solution (0.2–0.5 mg/mL in 0.2 M NaOAc buffer, pH = 5.5), and 15 μL of $^{111}InCl_3$ solution (1–5 mCi, in 0.05 M HCl). The reaction mixture was kept at room temperature for 20 min. A sample of the resulting solution was analyzed by radio-HPLC and ITLC. The solution stability of all three radiotracers was determined in saline and 6 mM EDTA solution (pH = 5.0). Samples were analyzed by radio-HPLC at 2, 8, 12, and 24 h after Sep-Pak C-18 purification.

Doses Preparation. All ^{111}In radiotracers for animal studies were purified with a Sep-Pak C-18 cartridge. To chelate free ^{111}In, 30 μL of EDTA (6 mM, pH = 5.5) was added to the reaction mixture 5 min before purification. The cartridge was activated with ethanol (10 mL), followed by H_2O (10 mL). After the radiotracer was loaded, the cartridge was washed with saline (10 mL). The radiotracer was eluted with 80% ethanol (0.4 mL). Volatiles were completely removed under vacuum. Doses for animal studies were made by dissolving the purified radiotracer in saline to 80 μCi/mL for biodistribution studies and 2.0 mCi/mL for metabolism or imaging studies. For the blocking experiment, E[c(RGDfK)]$_2$ was used as the blocking agent. Doses were prepared by dissolving E[c(RGDfK)]$_2$ in saline to give a final concentration of 3.0 mg/mL. Each tumor-bearing mouse was injected with 0.1 mL of solution (~15 mg/kg).

Water−Octanol Partition Coefficient. All three ^{111}In radiotracers were purified with a Sep-Pak C-18 cartridge to avoid interference from radioimpurities. The purified radiotracer was dissolved in an equal volume mixture of 25 mM phosphate buffer (3 mL, pH = 7.4) and *n*-octanol (3 mL). After stirring for ~20 min at room temperature, the mixture was centrifuged at a speed of 8000 rpm for 5 min. Samples (in triplicate) from aqueous and *n*-octanol layers were counted in a γ-counter (Wallac 1470–002, Perkin-Elmer, Finland). Partition coefficients were calculated. The log P value was measured three times and reported as an average of three independent measurements plus the standard deviation.

Integrin $\alpha_v\beta_3$ Receptor Binding Assay. The in vitro integrin-binding affinities and specificities of cyclic RGD peptides were determined in a whole-cell displacement assay using ^{125}I-c(RGDyK) as the integrin-specific radioligand. ^{125}I-c(RGDyK) was prepared in high specific activity (~1200 Ci/mmol) according to the literature method (*55*). The receptor binding experiments were performed using U87MG human glioma cells. In short, the U87MG glioma cells were seeded in 24-well plates (2×10^5 cells/well) and incubated overnight at 37 °C and 5% CO_2 in Dulbecco's modified Eagle's medium (DMEM) containing 10% fetal bovine serum (FBS) to allow adherence. During the cell-binding experiments, the plates were rinsed twice with binding buffer (20 mM Tris, pH 7.4, 150 mM NaCl, 2 mM $CaCl_2$, 1 mM $MgCl_2$, 1 mM $MnCl_2$, 0.1% BSA). The glioma cells were incubated with ^{125}I-c(RGDyK) in the presence of a cyclic RGD peptide (0–1000 nM). The total incubation volume was then adjusted to 300 μL. After the glioma cells were incubated at 4 °C for 2 h, the supernatant was removed. The glioma cells were washed three times with cold binding buffer, were then dissolved with 2 M NaOH at 37 °C. The cell-associated radioactivity was collected and determined using a γ-counter (Wallac 1470–002, Perkin-Elmer, Finland). The same experiments were carried out twice with quadruple samples for each. The IC_{50} values were calculated by fitting the data by nonlinear regression using *GraphPad Prism 4.0*, San Diego, CA). The IC_{50} values are reported as an average of samples plus the standard deviation.

Animal Model. The human U87MG human glioma cells from Professor Jingde Zhu (Shanghai Cancer Research Institute) were maintained at 37 °C and 5% CO_2 in Dulbecco's modified

Eagle's medium (DMEM) containing 10% fetal bovine serum (FBS). Female BALB/c nude mice (4–5 weeks of age) were purchased from Department of Animal Experiment, Peking University Health Center. The U87MG cells (5×10^6) were implanted subcutaneously into the right upper flanks of mice. When tumors reached ~0.8 cm in mean diameter, the tumor-bearing mice were used to biodistribution and imaging studies.

Biodistribution. Biodistribution studies were performed by Dr. Wang's group in accordance with guidelines of Peking University Health Science Center Animal Care Committee. Sixteen tumor-bearing mice were randomly divided into four groups. Each animal was administered intravenously with ~8 μCi of ^{111}In radiotracer via tail-vein. Four animals were anesthetized with intraperitoneal injection of sodium pentobarbital (45.0 mg/kg), and sacrificed by cervical dislocation at 0.5, 1, 4, and 24 h p.i. Blood, heart, liver, spleen, kidney, stomach, intestine, muscle, bone, and tumor were harvested, weighed, and measured for radioactivity in a γ-counter (Wallac 1470–002, Perkin-Elmer, Finland). Organ uptake was calculated as a percentage of injected dose per gram of tissue (%ID/g). In the blocking experiment, each animal was administered with excess E[c(RGDfK)]$_2$ 30 min prior to injection of ^{111}In-DTPA-Bn-E-SU016. Four animals were sacrificed at 4 h p.i. for biodistribution using the same procedure.

Gamma Imaging. The imaging study was performed by administering with 200 μCi of ^{111}In-DTPA-Bz-E-SU016 in 0.1 mL saline into each animal via tail vein. Animals were anesthetized with intraperitoneal injection of sodium pentobarbital at a dose of 45.0 mg/kg, then were placed supine on a two-head γ-camera (SIEMENS, E. CAM) equipped with a parallel-hole, middle-energy, and high-resolution collimator. Anterior images were acquired at 4 and 24 h p.i. and stored digitally in a 128 × 128 matrix. The acquisition count limits were set at 200 K. After completion of imaging, animals were sacrificed by cervical dislocation.

Metabolism. The metabolic stability of all three ^{111}In radiotracers was evaluated in normal BALB/c mice. Each mouse was administered with 200 μCi of the radiotracer in 0.1 mL saline via intravenous injection. Urine samples were collected at 1 h postinjection, and were mixed with 100 μL of 6 mM EDTA (pH = 5.0). The mixtures were centrifuged at a speed of 1500 rpm for 15 min. The supernatants were collected and filtered through a 0.22 μm Millex-LG syringe-driven filter unit. The filtrates were analyzed by radio-HPLC (method 2).

Statistical Analysis. Biodistribution data and target-to-background ratios are reported as an average plus the standard variation. Comparison between two different radiotracers was also made using the two-way ANOVA test (*GraphPad Prism 4.0*, GraphPad Software, San Diego, CA). The level of significance was set at $p < 0.05$.

RESULTS

DTPA Conjugates. DTPA-Bn-SU016 was prepared by reacting E[c(RGDfK)]$_2$ with excess *p*-SCN-Bn-DTPA in DMF under slightly basic conditions (pH = 8.0–9.0). The same procedure was used for preparation of DTPA-Bn-E-SU016 and DTPA-Bn-Cys-SU016. All three conjugates were purified by HPLC with the purity >98% before being used for radiolabeling and animal studies. The ESI-MS data were completely consistent with the proposed formula for DTPA-Bn-SU016, DTPA-Bn-E-SU016, and DTPA-Bn-Cys-SU016.

Integrin $\alpha_v\beta_3$ Binding Affinity. The integrin $\alpha_v\beta_3$ binding affinities of DTPA-Bn-SU016, DTPA-Bn-E-SU016, and DTPA-Bn-Cys-SU016 were determined using the integrin $\alpha_v\beta_3$-positive U87MG human glioma cells. For comparison purposes, c(RGDyK) and SU016 were also evaluated in the same assay. Figure 2 shows the displacement curves of c(RGDyK), SU016, DTPA-Bn-SU016, DTPA-Bn-E-SU016, and DTPA-Bn-Cys-SU016 against the binding of ^{125}I-c(RGDyK) to integrin $\alpha_v\beta_3$ on U87MG glioma cells. The IC_{50} values were calculated to be 31.9 ± 4.0 nM for c(RGDyK, 5.0 ± 0.7 nM for SU016, 7.9 ± 0.6 nM for DTPA-Bn-SU016, 5.8 ± 0.6 nM for DTPA-Bn-E-SU016, and 6.9 ± 0.9 nM for DTPA-Bn-Cys-SU016.

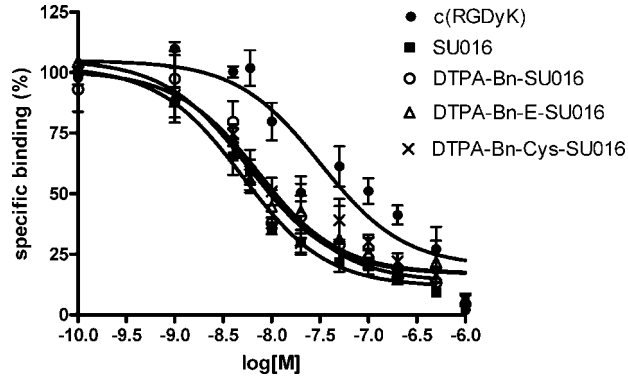

Figure 2. Inhibition of ^{125}I-c(RGDyK) binding to $\alpha_v\beta_3$ integrin on U87MG human glioma cells by c(RGDyK) (●), SU016 (■), DTPA-Bn-SU016 (○), DTPA-Bn-E-SU016 (Δ), and DTPA-Bn-Cys-SU016 (×). IC_{50} values were calculated to be 31.9 ± 4.0 nM for c(RGDyK), 5.0 ± 0.7 nM for SU016, 7.9 ± 0.6 nM for DTPA-Bn-SU016, 5.8 ± 0.6 nM for DTPA-Bn-E-SU016, and 6.9 ± 0.9 nM for DTPA-Bn-Cys-SU016, respectively.

Radiochemistry. ^{111}In-DTPA-Bn-SU016, ^{111}In-DTPA-Bn-E-SU016, and ^{111}In-DTPA-Bn-Cys-SU016 were prepared by reacting $^{111}InCl_3$ with the DTPA conjugate in NH_4OAc buffer (200 mM, pH = 5.5). Radiolabeling was almost instantaneous at room temperature, particularly at higher concentrations of the DTPA conjugate. Their radiochemical purity (RCP) was >99% after Sep-Pak purification. The specific activity was in the range 100–150 mCi/μmol, which is consistent with that obtained for the ^{111}In-labeled DTPA conjugate of a cyclic RGDfK monomer (*40*). The specific activity obtained at room temperature for all three ^{111}In radiotracers in this study was 3–5 times better than that of the ^{111}In-labeled DOTA conjugates (~30 mCi/μmol obtained at 100 °C) (*33*). It should be noted that the radiolabeling conditions used in this study are not optimized. The specific activity of ^{111}In-DTPA-Bn-SU016, ^{111}In-DTPA-Bn-E-SU016, and ^{111}In-DTPA-Bn-Cys-SU016 could be further improved at elevated temperatures. All three ^{111}In radiotracers were analyzed using the same HPLC method (method 2). Their HPLC retention times were 18.2, 11.3, and 11.7 min, respectively. Their log *P* values were determined in an equal volume mixture of *n*-octanol and 25 mM phosphate buffer (pH = 7.4), and were calculated to be −2.7 ± 0.1 (n = 3), −3.4 ± 0.1 (n = 3), and −3.3 ± 0.2 (n = 3), respectively. Both HPLC retention time and log *P* values suggest that incorporation of E and Cys amino acid linkers increases hydrophilicity of the ^{111}In-labeled cyclic RGDfK dimer.

Solution Stability. High solution stability is a requirement for both diagnostic and therapeutic radiotracers. In this study, we studied solution stability of ^{111}In-DTPA-Bn-SU016, ^{111}In-DTPA-Bn-E-SU016, and ^{111}In-DTPA-Bn-Cys-SU016 both in saline and in the presence of EDTA challenge. Figure 3 shows their solution stability data in saline (a) and 6 mM EDTA solution (b). It was clear that all three ^{111}In radiotracers remained stable for >24 h in saline and in aqueous solution of 6 mM EDTA.

Biodistribution Characteristics. Biodistribution properties of ^{111}In-DTPA-Bn-SU016, ^{111}In-DTPA-Bn-E-SU016, and ^{111}In-DTPA-Bn-Cys-SU016 were evaluated using the BALB/c nude mice bearing the U87MG human glioma xenografts. Selected biodistribution data are listed in Tables 1, 2, and 3. Figure 4

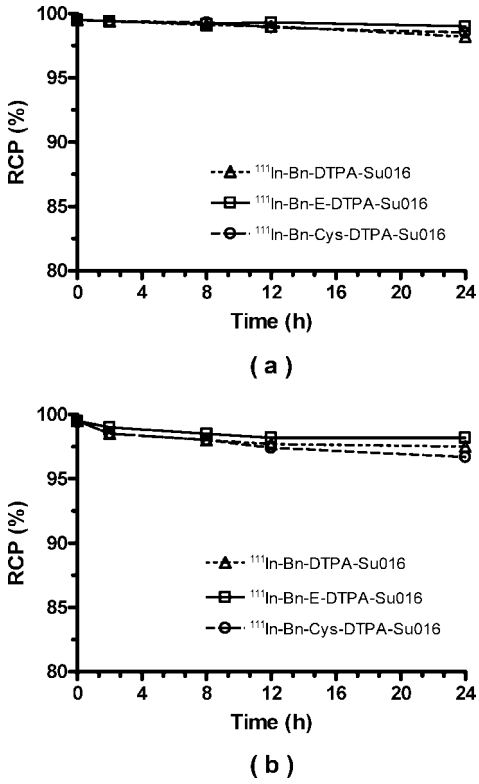

Figure 3. Solution stability data of ^{111}In-DTPA-Bn-SU016, ^{111}In-DTPA-Bn-E-SU016, and ^{111}In-DTPA-Bn-Cys-SU016 in saline (a) and 6 mM EDTA solution (b).

Table 1. Selected Biodistribution Data of ^{111}In-DTPA-Bn-SU016 in BALB/c Nude Mice Bearing U87MG Human Glioma Xenografts[a]

organ	0.5 h	1 h	4 h	24 h
tumor	2.53 ± 0.63	2.21 ± 0.65	1.86 ± 0.34	1.69 ± 0.18
blood	0.69 ± 0.02	0.22 ± 0.04	0.09 ± 0.06	0.05 ± 0.02
heart	1.07 ± 0.09	0.95 ± 0.40	0.49 ± 0.05	0.43 ± 0.09
liver	2.48 ± 0.22	2.49 ± 0.38	2.86 ± 0.53	1.93 ± 0.28
spleen	2.04 ± 0.13	2.56 ± 1.11	1.83 ± 0.37	1.94 ± 0.41
kidney	9.07 ± 1.29	7.34 ± 0.70	7.05 ± 1.49	6.14 ± 1.34
muscle	0.49 ± 0.10	0.35 ± 0.04	0.24 ± 0.06	0.21 ± 0.04
gut	6.46 ± 0.25	5.08 ± 0.92	3.18 ± 0.19	4.16 ± 0.77
stomach	3.88 ± 0.39	2.86 ± 0.15	1.78 ± 0.15	1.55 ± 0.24
bone	0.93 ± 0.07	0.76 ± 0.14	0.52 ± 0.23	0.51 ± 0.11

[a] The organ uptake is expressed as %ID/g. Each data point represents an average of biodistribution data in four animals.

Table 2. Selected Biodistribution Data of ^{111}In-DTPA-Bn-E-SU016 in BALB/c Nude Mice Bearing U87MG Human Glioma Xenografts[a]

organ	0.5 h	1 h	4 h	24 h	4.0 h/block
tumor	2.45 ± 0.43	2.33 ± 0.55	1.86 ± 0.15	0.89 ± 0.17	0.25 ± 0.06
blood	0.71 ± 0.10	0.21 ± 0.07	0.06 ± 0.01	0.03 ± 0.01	0.04 ± 0.01
heart	1.06 ± 0.14	0.72 ± 0.10	0.47 ± 0.05	0.20 ± 0.04	0.06 ± 0.00
liver	2.94 ± 0.38	3.12 ± 0.38	2.15 ± 0.09	0.55 ± 0.11	0.29 ± 0.04
spleen	2.13 ± 0.26	2.01 ± 0.43	1.60 ± 0.22	0.79 ± 0.25	0.18 ± 0.03
kidney	6.04 ± 1.40	5.29 ± 0.51	3.80 ± 0.33	1.37 ± 0.16	2.58 ± 0.42
muscle	0.52 ± 0.06	0.37 ± 0.06	0.22 ± 0.03	0.12 ± 0.02	0.04 ± 0.00
gut	5.36 ± 1.98	5.36 ± 0.49	4.31 ± 0.52	1.73 ± 0.22	0.40 ± 0.09
stomach	3.92 ± 0.28	3.00 ± 0.30	1.64 ± 0.11	0.70 ± 0.06	0.22 ± 0.07
bone	0.97 ± 0.20	0.77 ± 0.23	0.40 ± 0.08	0.34 ± 0.04	0.08 ± 0.02

[a] The organ uptake is expressed %ID/g. Each data point represents an average of biodistribution data in four animals.

shows the comparison of excretion kinetics and T/B ratios among ^{111}In-DTPA-Bn-SU016, ^{111}In-DTPA-Bn-E-SU016, and ^{111}In-DTPA-Bn-Cys-SU016. Since they share the same cyclic RGDfK dimer (SU016) and ^{111}In-DTPA chelate, the differences

Table 3. Selected Biodistribution Data of ^{111}In-DTPA-Bn-Cys-SU016 in BALB/c Nude Mice Bearing U87MG Human Glioma Xenografts[a]

organ	0.5 h	1 h	4 h	24 h
tumor	2.72 ± 0.28	1.78 ± 0.09	1.53 ± 0.64	0.98 ± 0.29
blood	0.83 ± 0.16	0.24 ± 0.06	0.06 ± 0.01	0.03 ± 0.01
heart	1.19 ± 0.16	0.72 ± 0.18	0.46 ± 0.03	0.29 ± 0.02
liver	3.08 ± 0.60	2.41 ± 0.15	2.32 ± 0.38	0.79 ± 0.15
spleen	2.08 ± 0.19	1.74 ± 0.62	1.58 ± 0.11	1.08 ± 0.24
kidney	14.78 ± 2.31	12.20 ± 1.76	10.70 ± 1.19	4.96 ± 0.62
muscle	0.57 ± 0.04	0.37 ± 0.05	0.23 ± 0.03	0.14 ± 0.02
gut	7.09 ± 0.86	5.03 ± 0.81	3.48 ± 0.44	3.41 ± 0.82
stomach	4.12 ± 0.25	2.77 ± 0.44	1.61 ± 0.16	1.10 ± 0.07
bone	1.01 ± 0.26	0.54 ± 0.12	0.53 ± 0.23	0.35 ± 0.03

[a] The organ uptake is expressed %ID/g. Each data point represents an average of biodistribution data in four animals.

in their biodistribution and excretion characteristics is caused by the linker (E and Cys).

In general, all three ^{111}In radiotracers displayed a rapid blood clearance predominantly via the renal route. Their blood clearance curves were almost identical (Figure 4), and their bone uptake was relatively low (Tables 1,, and 3). The tumor uptake of ^{111}In-DTPA-Bn-SU016, ^{111}In-DTPA-Bn-E-SU016, and ^{111}In-DTPA-Bn-Cys-SU016 was comparable between 0.5 and 4 h p.i. within the experimental error. At 24 h p.i., however, ^{111}In-DTPA-Bn-SU016 had the tumor uptake (1.69 ± 0.18% ID/g) that was significantly higher ($p < 0.05$) than that of ^{111}In-DTPA-Bn-E-SU016 (0.89 ± 0.17% ID/g) and ^{111}In-DTPA-Bn-Cys-SU016 (0.98 ± 0.29% ID/g). The kidney uptake of ^{111}In-DTPA-Bn-E-SU016 was much lower ($p < 0.001$) than that of ^{111}In-DTPA-Bn-SU016 and ^{111}In-DTPA-Bn-Cys-SU016 over the 24 h study period. The liver uptake of ^{111}In-DTPA-Bn-SU016, ^{111}In-DTPA-Bn-E-SU016, and ^{111}In-DTPA-Bn-Cys-SU016 was comparable between 0.5 and 1 h p.i. (Figure 4), but it was significantly higher ($p < 0.001$) for ^{111}In-DTPA-Bn-SU016 than that for ^{111}In-DTPA-Bn-E-SU016 and ^{111}In-DTPA-Bn-Cys-SU016 at 24 h p.i. For example, the liver uptake of ^{111}In-DTPA-Bn-SU016 was 1.69 ± 0.18% ID/g at 24 h p.i., and the liver uptake of ^{111}In-DTPA-Bn-E-SU016 and ^{111}In-DTPA-Bn-Cys-SU016 was only 0.55 ± 0.11% ID/g and 0.79 ± 0.15% ID/g at 24 h p.i., respectively. Among the three ^{111}In radiotracers evaluated in this animal model, ^{111}In-DTPA-Bn-E-SU016 has the lowest uptake in liver and kidneys, and the best tumor/liver and tumor/kidney ratios (Figure 4) at 24 h p.i.

The blocking experiment was used to demonstrate tumor specificity of the radiotracer. In this experiment, E[c(RGDfK)]$_2$ (15 mg/kg or ~300 μg/mouse) was used as the blocking agent. Such a high dose was used to make sure that the integrin $\alpha_v\beta_3$ is almost completely blocked. Figure 5 illustrates biodistribution data of ^{111}In-DTPA-Bn-E-SU016 at 4 h p.i. in the presence of E[c(RGDfK)]$_2$. Apparently, pre-injection of excess E[c(RGDfK)]$_2$ significantly reduced the tumor uptake of ^{111}In-DTPA-Bn-E-SU016, suggesting that its tumor uptake is indeed integrin $\alpha_v\beta_3$-mediated. However, its uptake in liver, spleen, stomach, gut, and kidneys was also reduced significantly, most likely due to the blockage of integrin $\alpha_v\beta_3$ in these organs.

Metabolism. Metabolism studies on ^{111}In-DTPA-Bn-SU016, ^{111}In-DTPA-Bn-E-SU016, and ^{111}In-DTPA-Bn-Cys-SU016 were performed using normal BALB/c nude mice. Urine samples were analyzed to determine whether they are able to retain their chemical integrity at 1 h p.i. We also tried to analyze feces samples at 1 h p.i., but the radioactivity level was too low to be detected. Figure 6 shows HPLC chromatograms of ^{111}In-DTPA-Bn-SU016, ^{111}In-DTPA-Bn-E-SU016, and ^{111}In-DTPA-Bn-Cys-SU016 in the urine at 1 h p.i. It is quite clear that there is little metabolite (<10%) in urine during the 1 h study period.

Imaging Study. A planar image study was performed on ^{111}In-DTPA-Bn-E-SU016 using the BALB/c nude mice bearing

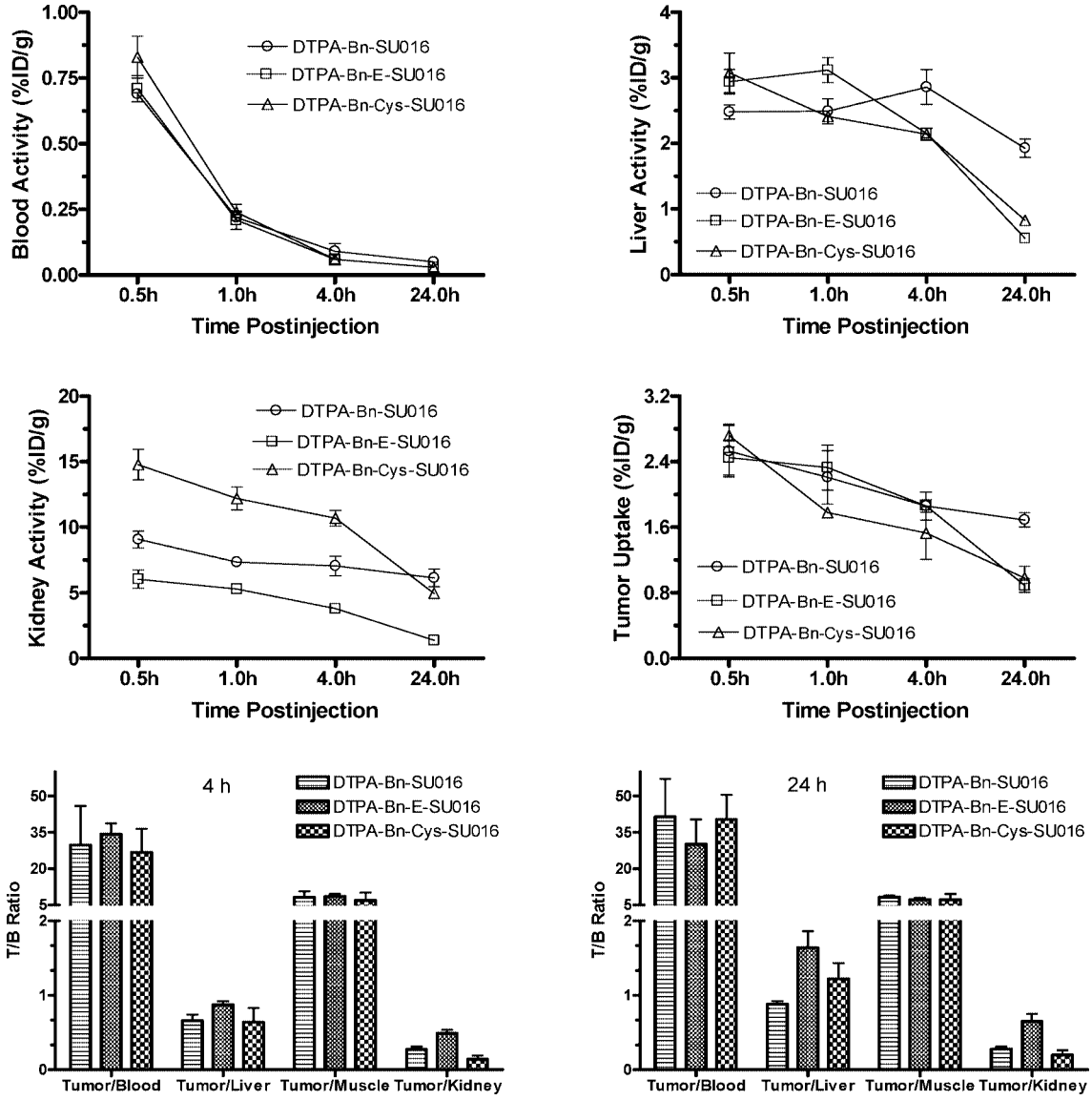

Figure 4. Direct comparison of the excretion kinetics and tumor-to-background ratios between ^{111}In-DTPA-Bn-SU016, ^{111}In-DTPA-Bn-E-SU016, and ^{111}In-DTPA-Bn-Cys-SU016 in selected organs of the BALB/c nude mice bearing the U87MG human glioma xenografts.

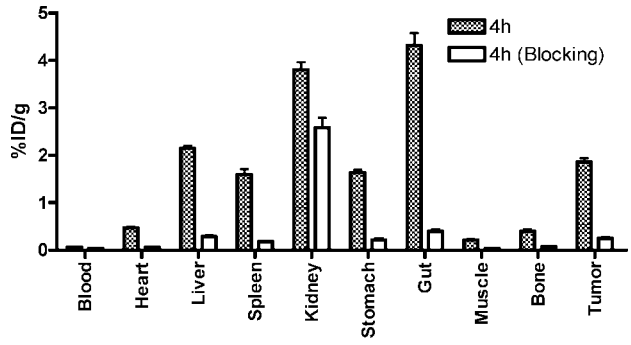

Figure 5. Biodistribution data of ^{111}In-DTPA-Bn-E-SU016 at 4 h p.i. with/without the presence of excess E[c(EGDfK)]$_2$ in BALB/c nude mice bearing the U87MG human glioma xenografts.

U87MG human glioma xenografts. Figure 7 illustrates representative scintigraphic images of the tumor-bearing mouse administered with ~200 μCi ^{111}In-DTPA-Bn-E-SU016 at 4 and 24 h p.i. The tumor was visualized as early as 1 h p.i. (data not shown). The tumor/muscle ratio was 5.6 ± 1.2 (n = 3) at 4 h p.i. and 6.1 ± 1.1 (n = 3) at 24 h p.i., which were in good agreement with that obtained from direct tissue sampling (Tables 1 and 3). Because of high kidney and liver activity, the tumor/kidney and tumor/liver ratios were relatively low (0.4 ± 0.1 and 1.0 ± 0.1 at 4 h, 1.9 ± 0.4 and 2.3 ± 0.3 at 24 h, respectively).

DISCUSSION

Many factors may influence the tumor uptake and tumor retention of a radiotracer (*13–15*). These include binding affinity, receptor population, protein binding, and pharmacokinetics. The fact that [^{18}F]Galacto-RGD has been successfully used as the first PET radiotracer for noninvasive visualization of integrin $\alpha_v\beta_3$ in cancer patients strongly suggests that there is sufficient integrin $\alpha_v\beta_3$ expressed in tumor for PET or SPECT imaging. While the radiolabeled cyclic RGD peptide monomers, such as c(RGDfK), are useful for imaging the integrin $\alpha_v\beta_3$ expression in tumors, they will have limited clinical utility in visualizing tumors in the lower abdomenal region due to their relatively low tumor uptake and partial hepatobiliary excretion. Therefore, there is a continuing need to further improve the tumor targeting capability and excretion kinetics of radiotracers.

To improve integrin $\alpha_v\beta_3$ binding affinity, the multivalent concept has been successfully used to prepare multimeric cyclic RGD peptides, such as E[c(RGDfK)]$_2$ and E{E[c(RGDfK)]$_2$}$_2$,

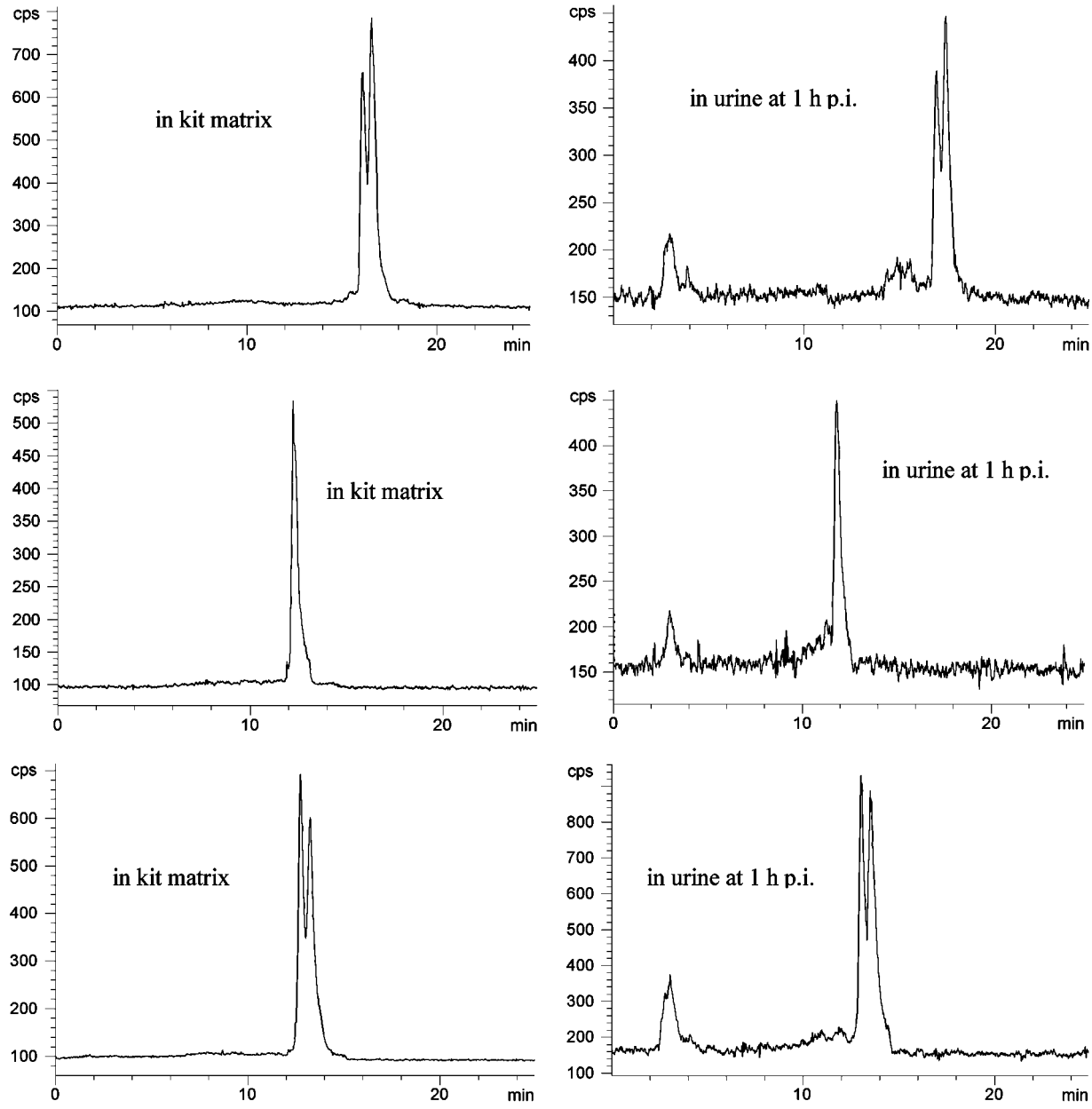

Figure 6. Radio-HPLC chromatograms of ^{111}In-DTPA-Bn-SU016 (top), ^{111}In-DTPA-Bn-E-SU016 (middle), and ^{111}In-DTPA-Bn-Cys-SU016 (bottom) in the kit matrix and urine at 1 h p.i. Each normal BALB/c mouse was administered with 200 μCi of radiotracer. Two mice were used for each radiotracer.

for development of the integrin $\alpha_v\beta_3$-targeted diagnostic (^{64}Cu, ^{99m}Tc, and ^{111}In) and therapeutic (^{90}Y and ^{177}Lu) radiotracers (*19–36*). Different PKM linkers have been used to improve excretion kinetics of the radiolabeled peptides. For example, a sugar moiety was used to increase T/B ratios of ^{125}I- and ^{18}F-labeled cyclic RGD peptides (*47–50*). The sugar moiety has also been used to improve tumor uptake and TB ratios of the ^{111}In-labeled DOTA-somatostatin peptide conjugates (*51*). Small peptides, such as di(cysteic acid), have been used to improve blood clearance and to minimize liver accumulation of radiolabeled peptides and nonpeptide integrin $\alpha_v\beta_3$ antagonists (*38, 52–54*). It has been reported that introduction of the poly(ethylene glycol) (PEG) linker can improve not only tumor uptake but also excretion kinetics of ^{125}I- and ^{18}F-labeled c(RGDyK) and ^{64}Cu-labeled E[c(RGDyK)]$_2$ (*55, 56*). PEG$_4$ and amino acid linkers, such as E and K, have also been used to improve excretion kinetics of ^{111}In- and ^{99m}Tc-labeled E[c(RGDfK)]$_2$ (*23, 33*). PKM linkers and their applications to improve excretion kinetics of radiolabeled small biomolecules have been reviewed recently (*15, 16, 37*).

In this study, we prepare ^{111}In-DTPA-Bn-SU016, ^{111}In-DTPA-Bn-E-SU016, and ^{111}In-DTPA-Bn-Cys-SU016 with high specific activity (100–150 mCi/μmol). We are particularly interested in DTPA as the BFC because of its high ^{111}In-labeling efficiency. The specific activity obtained for these three ^{111}In radiotracers was 3–5× better than that of the ^{111}In-labeled DOTA-PKM-E[c(RGDfK)]$_2$ (PKM = E, K, and PEG$_4$) conjugates (*33*). We also examined the effect of E and Cys linkers on integrin $\alpha_v\beta_3$ binding affinity of the cyclic RGDfK dimer DTPA conjugate, and found that the integrin $\alpha_v\beta_3$ binding affinity of DTPA-Bn-SU016, DTPA-Bn-E-SU016, and DTPA-Bn-Cys-SU016 was almost identical (Figure 2). This suggests that introduction of the E and Cys linker does not affect the integrin $\alpha_v\beta_3$ binding affinity of E[c(RGDfK)]$_2$. A similar conclusion has been made for the HYNIC and DOTA conjugates of E[c(RGDfK)]$_2$ (*23*).

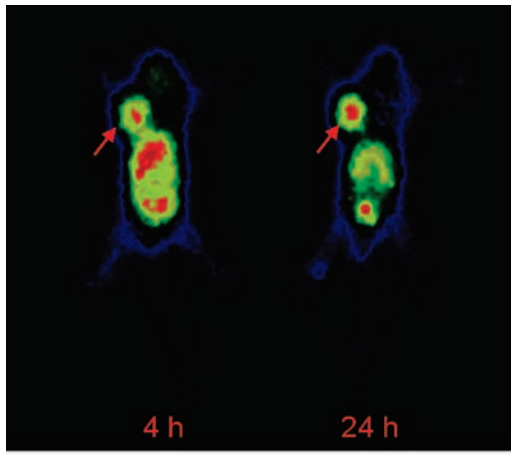

Figure 7. A representative scintigraphic image of the tumor-bearing mouse administered with ~200 μCi of ^{111}In-DTPA-Bn-E-SU016. The arrow indicates presence of tumor.

The main difference among ^{111}In-DTPA-Bn-SU016, ^{111}In-DTPA-Bn-E-SU016, and ^{111}In-DTPA-Bn-Cys-SU016 is the linker group. Data from both HPLC and log *P* suggest that the use of E and Cys linker groups increases hydrophilicity of the ^{111}In radiotracer. The tumor-targeting capability of ^{111}In-DTPA-Bn-SU016, ^{111}In-DTPA-Bn-E-SU016, and ^{111}In-DTPA-Bn-Cys-SU016 has been evaluated by direct tissue sampling and gamma imaging in BALB/c nude mice bearing U87MG human glioma xenografts. Results from biodistribution studies show that there is no significant difference in their tumor uptake during the first 4 h p.i. (Figure 4), suggesting that E and Cys linkers have little impact on targeting capability of the ^{111}In-labeled E[c(RGDfK)]$_2$. This conclusion is supported by similar integrin $\alpha_v\beta_3$ binding affinity of SU016, DTPA-Bn-SU016, DTPA-Bn-E-SU016, and DTPA-Bn-Cys-SU016 (Figure 2). The blood clearance patterns of ^{111}In-DTPA-Bn-SU016, ^{111}In-DTPA-Bn-E-SU016, and ^{111}In-DTPA-Bn-Cys-SU016 are almost identical over the 24 h study period, indicating that introduction of E and Cys linkers did not significantly affect their protein binding. In addition, ^{111}In-DTPA-Bn-SU016, ^{111}In-DTPA-Bn-E-SU016, and ^{111}In-DTPA-Bn-Cys-SU016 are also able to retain their chemical integrity with <10% metabolism detected in the urine samples at 1 h p.i. The fact that very little radioactivity was detected in feces samples from the mice administered with ^{111}In-DTPA-Bn-SU016, ^{111}In-DTPA-Bn-E-SU016, and ^{111}In-DTPA-Bn-Cys-SU016 suggests that they are excreted mainly via the renal route.

Despite their similarities, E and Cys linkers have a significant impact on organ uptake and excretion kinetics of the ^{111}In-labeled cyclic RGDfK dimer. For example, the kidney uptake follows the order of ^{111}In-DTPA-Bn-E-SU016 < ^{111}In-DTPA-Bn-SU016 < ^{111}In-DTPA-Bn-Cys-SU016 (Figure 4). The tumor/kidney ratios of ^{111}In-DTPA-Bn-E-SU016 and ^{111}In-DTPA-Bn-Cys-SU016 are significantly lower ($p < 0.05$) than that of ^{111}In-DTPA-Bn-SU016 at 24 h p.i. In general, small biomolecules in the blood plasma are filtered through glomerular capillaries in kidneys and may be subsequently reabsorbed by the proximal tubular cells (*33*). Membranes of renal tubular cells contain negatively charged sites to which the positively charged groups (such as guanidine in the RGD sequence) are expected to bind. The carboxylic group of the glutamic acid residue is deprotonated under physiological conditions. Therefore, it is not surprising that the use of E linker in ^{111}In-DTPA-Bn-E-SU016 results in the reduced kidney uptake (Figure 4). However, it is not clear why ^{111}In-DTPA-Bn-Cys-SU016 has higher kidney uptake than ^{111}In-DTPA-Bn-E-SU016 even though their log *P* values and HPLC retention times (Figure 6) are very similar.

Another significant difference is the liver uptake. Both ^{111}In-DTPA-Bn-E-SU016 and ^{111}In-DTPA-Bn-Cys-SU016 have lower liver uptake and better tumor/liver ratios ($p < 0.05$) than ^{111}In-DTPA-Bn-SU016 at 24 h p.i. These data strongly suggest that the liver uptake could be reduced by introducing the negatively charged amino acid residues due to increased hydrophilicity of the radiotracer. A similar conclusion has been made for the ^{99m}Tc-labeled HYNIC-PKM-SU016 (PKM = E, K, or PEG$_4$) conjugates (*23*). However, this conclusion seems to contradict to that made by Dijkgraaf and co-workers (*33*) for the ^{111}In-labeled DOTA-PKM-E[c(RGDfK)]$_2$ (PKM = E, K, and PEG$_4$) conjugates. Apparently, the impact of PKM linkers on both liver uptake and liver clearance kinetics of the radiotracer may vary with the change of bifunctional chelator and its radiometal chelate.

CONCLUSION

In this study, we evaluated the integrin $\alpha_v\beta_3$ binding affinities of SU016, DTPA-Bn-SU016, DTPA-Bn-E-SU016, and DTPA-Bn-Cys-SU016. It was found that introduction of the glutamic acid and cysteic acid linkers did not affect the integrin $\alpha_v\beta_3$ binding affinity of the cyclic RGDfK dimer DTPA conjugate. Another important finding of this study is that the ^{111}In-labeling efficiency of all three DTPA conjugates (DTPA-Bn-SU016, DTPA-Bn-E-SU016, and DTPA-Bn-Cys-SU016) is significantly better than that of DOTA analogues. In this regard, DTPA has the advantage over DOTA due to its fast chelation kinetics and high-yield ^{111}In-labeling under mild conditions (e.g., room temperature). All three radiotracers (^{111}In-DTPA-Bn-SU016, ^{111}In-DTPA-Bn-E-SU016, and ^{111}In-DTPA-Bn-Cys-SU016) have high in vitro and in vivo solution stability. Results from biodistribution studies show that incorporation of the glutamic acid linker between DTPA and E[c(RGDfK)]$_2$ increases the clearance of ^{111}In-labeled E[c(RGDfK)]$_2$ from the liver and kidneys. Among the three radiotracers evaluated in this study, ^{111}In-DTPA-Bn-E-SU016 has the best tumor/liver and tumor/kidney ratios.

ACKNOWLEDGMENT

Authors would thank Professor Jingde Zhu, Shanghai Cancer Research Institute, for providing the U87MG human glioma cells. This work is supported, in part, by Peking University Health Science Center (F.W.) and research grants: 30640067 (F.W.) from NSF (China), 1R01 CA115883-01A2 (S.L.) from National Cancer Institute (NCI), BCTR0503947 (S.L.) from Susan G. Komen Breast Cancer Foundation, AHA0555659Z (S.L.) from the Greater Midwest Affiliate of American Heart Association, R21 EB003419-02 (S.L.) from National Institute of Biomedical Imaging and Bioengineering (NIBIB) and R21 HL083961-01 (S.L.) from National Heart, Lung, and Blood Institute (NHLBI).

LITERATURE CITED

(1) Folkman, J. (2003) Fundamental concepts of the angiogenic process. *Curr. Mol. Med. 3*, 643–651.
(2) Jin, H., and Varner, J. (2004) Integrins: roles in cancer development and as treatment targets. *Br. J. Cancer 90*, 561–565.
(3) Howe, A., Aplin, A. E., Alahari, S. K., and Juliano, R. L. (1998) Integrin signaling and cell growth control. *Curr. Opin. Cell Biol. 10*, 220–231.
(4) Longhurst, C. M., and Jennings, L. K. (1998) Integrin-mediated signal transduction. *Cell. Mol. Life Sci. 54*, 514–526.
(5) Zitzmann, S., Ehemann, V., and Schwab, M. (2002) Arginine-glycine-aspartic acid (RGD)-peptide binds to both tumor and tumor endothelial cells in vivo. *Cancer Res. 62*, 5139–5143.

(6) Weber, W. A., Haubner, R., Vabuliene, E., Kuhnast, B., Webster, H. J., and Schwaiger, M. (2001) Tumor angiogenesis targeting using imaging agents. *Q. J. Nucl. Med. 45*, 179–182.

(7) Van de Wiele, C., Oltenfreiter, R., De Winter, O., Signore, A., Slegers, G., and Dierckx, R. A. (2002) Tumor angiogenesis pathways: related clinical issues and implications for nuclear medicine imaging. *Eur. J. Nucl. Med. 29*, 699–709.

(8) McQuade, P., and Knight, L. C. (2003) Radiopharmaceuticals for targeting the angiogenesis marker $\alpha_v\beta_3$. *Q. J. Nucl. Med. 47*, 209–220.

(9) Haubner, R. H., Wester, H. J., Weber, W. A., and Schwaiger, M. (2003) Radiotracer-based strategies to image angiogenesis. *Q. J. Nucl. Med. 47*, 189–199.

(10) Haubner, R., Kuhnast, B., Mang, C., Weber, W. A., Kessler, H., Wester, H. J., and Schwaiger, M. (2004) [^{18}F]Galacto-RGD: synthesis, radiolabeling, metabolic stability, and radiation dose estimates. *Bioconjugate Chem. 15*, 61–69.

(11) Beer, A. J., Haubner, R., Goebel, M., Luderschmidt, S., Spilker, M. E., Webster, H. J., Weber, W. A., and Schwaiger, M. (2005) Biodistribution and pharmacokinetics of the $\alpha_v\beta_3$-selective tracer ^{18}F-galacto-RGD in cancer patients. *J. Nucl. Med. 46*, 1333–1341.

(12) Haubner, R., Weber, W. A., Beer, A. J., Vabuliene, E., Reim, D., Sarbia, M., Becker, K. F., Goebel, M., Hein, R., Wester, H. J., Kessler, H., and Schwaiger, M. (2005) Noninvasive visuallization of the activiated $\alpha_v\beta_3$ integrin in cancer patients by positron emission tomography and [^{18}F]Galacto-RGD. *PLOS Med. 2 e70*, 244–252.

(13) Liu, S., Robinson, S. P., and Edwards, D. S. (2003) Integrin $\alpha_v\beta_3$ directed radiopharmaceuticals for tumor imaging. *Drugs of the Future 28*, 551–564.

(14) Liu, S., Robinson, S. P., and Edwards, D. S. (2005) Radiolabeled integrin $\alpha_v\beta_3$ antagonists as radiopharmaceuticals for tumor radiotherapy. *Top. Curr. Chem. 252*, 193–216.

(15) Liu, S. (2006) Radiolabeled multimeric cyclic RGD peptides as integrin $\alpha_v\beta_3$-targeted radiotracers for tumor imaging. *Mol. Pharm. 3*, 472–487.

(16) Haubner, R., and Wester, H. J. (2004) Radiolabeled tracers for imaging of tumor angiogenesis and evaluation of anti-angiogenic therapies. *Curr. Pharm. Des. 10*, 1439–1455.

(17) Wester, H. J., and Kessler, H. (2005) Molecular targeting with peptides or peptide-polymer conjugates: just a question of size. *J. Nucl. Med. 46*, 1940–1945.

(18) Chen, X. (2006) Multimodality imaging of tumor integrin $\alpha_v\beta_3$ expression. *Mini Rev. Med. Chem. 6*, 227–234.

(19) Liu, S., Edwards, D. S., Ziegler, M. C., Harris, A. R., Hemingway, S. J., and Barrett, J. A. (2001) ^{99m}Tc-Labeling of a hydrazinonicotinamide-conjugated vitronectin receptor antagonist useful for imaging tumors. *Bioconjugate Chem. 12*, 624–629.

(20) Liu, S., Cheung, E., Rajopadhye, M., Ziegler, M. C., and Edwards, D. S. (2001) ^{90}Y- and ^{177}Lu-labeling of a DOTA-conjugated vitronectin receptor antagonist useful for tumor therapy. *Bioconjugate Chem. 12*, 559–568.

(21) Liu, S., Hsieh, W. Y., Kim, Y. S., and Mohammed, S. I. (2005) Effect of coligands on biodistribution characteristics of ternary ligand ^{99m}Tc complexes of a HYNIC-conjugated cyclic RGDfK dimer. *Bioconjugate Chem. 16*, 1580–1588.

(22) Jia, B., Shi, J., Yang, Z., Xu, B., Liu, Z., Zhao, H., Liu, S., and Wang, F. (2006) ^{99m}Tc-labeled cyclic RGDfK dimer: initial evaluation for SPECT imaging of glioma integrin $\alpha_v\beta_3$ expression. *Bioconjugate Chem. 17*, 1069–1076.

(23) Liu, S., He, Z. J., Hsieh, W. Y., Kim, Y. S., and Jiang, Y. (2006) Impact of PKM linkers on biodistribution characteristics of the ^{99m}Tc-labeled cyclic RGDfK dimer. *Bioconjugate Chem. 17*, 1499–1507.

(24) Liu, S., Hsieh, W. Y., Jiang, Y., Kim, Y. S., Sreerama, S. G., Chen, X., Jia, B., and Wang, F. (2007) Evaluation of a ^{99m}Tc-labeled cyclic RGD tetramer for noninvasive imaging integrin $\alpha_v\beta_3$-positive breast cancer. *Bioconjugate Chem. 18*, 438–446.

(25) Liu, S., Kim, Y. S., Hsieh, W. Y., and Sreerama, S. G. Coligand effects on solution stability, biodistribution and metabolism of ^{99m}Tc-labeled cyclic RGDfK tetramer. *Nucl. Med. Biol.* ASAP.

(26) Chen, X., Liu, S., Hou, Y., Tohme, M., Park, R., Bading, J. R, and Conti, P. S. (2004) MicroPET imaging of breast cancer α_v-integrin expression with ^{64}Cu-labeled dimeric RGD peptides. *Mol. Imag. Biol. 6*, 350–359.

(27) Chen, X., Park, R., Tohme, M., Shahinian, A. H., Bading, J. R., and Conti, P. S. (2004) MicroPET and autoradiographic imaging of breast cancer α_v-integrin expression using ^{18}F- and ^{64}Cu-labeled RGD peptide. *Bioconjugate Chem. 15*, 41–49.

(28) Chen, X., Park, R., Hou, Y., Khankaldyyan, V., Gonzales-Gomez, I., Tohme, M., Bading, J. R., Laug, W. E., and Conti, P. S. (2004) MicroPET imaging of brain tumor angiogenesis with ^{18}F-labeled PEGylated RGD peptide. *Eur. J. Nucl. Med. Mol. Imaging 31*, 1081–1089.

(29) Wu, Y., Zhang, X., Xiong, Z., Cheng, Z., Fisher, D. R., Liu, S., Gambhir, S. S., and Chen, X. (2005) MicroPET imaging of glioma $\alpha_v\beta_3$ integrin expression using ^{64}Cu-labeled tetrameric RGD peptide. *J. Nucl. Med. 46*, 1707–1718.

(30) Zhang, X., Xiong, Z., Wu, Y., Cai, W., Tseng, J. R., Gambhir, S. S., and Chen, X. (2006) Quantitative PET imaging of tumor integrin $\alpha_v\beta_3$ expression with ^{18}F-FRGD2. *J. Nucl. Med. 47*, 113–121.

(31) Janssen, M. L., Oyen, W. J. G., Dijkgraaf, I., Massuger, L. F. A. G., Frielink, C., Edwards, D. S., Rajopadyhe, M., Boonstra, H., Corsten, F. H., and Boerman, O. C. (2002) Tumor targeting with radiolabeled $\alpha_v\beta_3$ integrin binding peptides in a nude mouse model. *Cancer Res. 62*, 6146–6151.

(32) Janssen, M. L., Frielink, C., Dijkgraaf, I., Oyen, W. J., Edwards, D. S., Liu, S., Rajopadhye, M., Massuger, L. F., Corstens, F. H., and Boerman, O. C. (2004) Improved tumor targeting of radiolabeled RGD-peptides using rapid dose fractionation. *Cancer Biother. Radiopharm. 19*, 399–404.

(33) Dijkgraaf, I., Liu, S., Kruijtzer, J. A. W., Soede, A. C., Oyen, W. J. G., Liskamp, R. M. J., Corstens, F. H. M., and Boerman, O. C. (2007) Effect of linker variation on the in vitro and in vivo characteristics of an ^{111}In-labeled RGD Peptide. *Nucl. Med. Biol. 34*, 29–35.

(34) Dijkgraaf, I., John, A. W., Kruijtzer, J. A. W., Liu, S., Soede, A., Oyen, W. J. G., Corstens, F. H. M., Liskamp, R. M. J., and Boerman, O. C. (2007) Improved targeting of the $\alpha_v\beta_3$ integrin by multimerization of RGD peptides. *Eur. J. Nucl. Med. Mol. Imaging 34*, 267–273.

(35) Poethko, T., Schottelius, M., Thumshirn, G., Herz, M., Haubner, R., Henriksen, G., Kessler, H., Schwaiger, M., and Wester, H.-J. (2004) Chemoselective pre-conjugate radiohalogenation of unprotected mono- and multimeric peptides via oxime formation. *Radiochim. Acta 92*, 317–327.

(36) Thumshirn, G., Hersel, U., Goodman, S. L., and Kessler, H. (2003) Multimeric cyclic RGD peptides as potential tools for tumor targeting: solid-phase peptide synthesis and chemoselective oxime ligation. *Chem.—Eur. J. 9*, 2717–2725.

(37) Liu, S., and Edwards, D. S. (2001) Bifunctional chelators for therapeutic lanthanide radiopharmaceuticals. *Bioconjugate Chem. 12*, 7–34.

(38) Onthank, D. C., Liu, S., Silva, P. J., Barrett, J. A., Harris, T. D., Robinson, S. P., and Edwards, D. S. (2004) ^{90}Y and ^{111}In complexes of A DOTA-conjugated integrin $\alpha_v\beta_3$ receptor antagonist: different but biologically equivalent. *Bioconjugate Chem. 15*, 235–241.

(39) Liu, S., Cheung, E., Rajopadhye, M., Williams, N. E., Overoye, K. L., and Edwards, D. S. (2001) Isomerism and solution dynamics of ^{90}Y-labeled DTPA-biomolecule conjugates. *Bioconjugate Chem. 12*, 84–91.

(40) Liu, S, and Edwards, D. S. (2001) Synthesis and characterization of two ^{111}In-labeled DTPA-peptide conjugates. *Bioconjugate Chem. 12*, 630–634.

(41) Camera, L., Kinuya, S., Garmestani, K., Wu, C., Brechbiel, M. W., Pai, L. H., McMurry, T. J., Gansow, O. A., Pastan, I.,

Paik, C. H., and Carrasquillo, J. A. (1994) Evaluation of the serum stability and in vivo biodistribution of CHX-DTPA and other ligands for yttrium labeling of monoclonal antibodies. *J. Nucl. Med. 35*, 882–889.

(42) McMurray, T. J., Pippin, C. G., Wu, C., Deal, K. A., Brechbiel, M. W., Mirzadeh, S., and Gansow, O. A. (1998) Physical parameters and biological stability of yttrium(III) diethylenetriaminepentaacetic acid derivative conjugates. *J. Med. Chem. 41*, 3546–3549.

(43) Carrasquillo, J. A., White, J. D., Paik, C. H., Raubitschek, A., Le, N., Rotman, M., Brechbiel, M. W., Gansow, O. A., Top, L. E., Perentesis, P., Reynolds, J. C., Nelson, D. L., and Waldmann, T. A. (1999) Similarities and differences in ^{111}In- and ^{90}Y-labeled 1B4M-DTPA antiTac monoclonal antibody distribution. *J. Nucl. Med. 40*, 268–276.

(44) Camera, L., Kinuya, S., Garmestani, K., Brechbiel, M. W., Wu, C., Pai, L. H., McMurry, T. J., Gansow, O. A., Pastan, I., Paik, C. H., and Carrasquillo, J. A. (1994) Comparative biodistribution of indium- and yttrium-labeled B3 monoalonal antibody conjugated to either 2-(p-SCN-Bz)-6-methyl-DTPA (1B4M-DTPA) or 2-(p-SCN-Bz-)-1,4,7,10-tetraazacyclododecane tetraacetic acid (2B-DOTA). *Eur. J. Nucl. Med. 21*, 640–646.

(45) Smith-Jones, P. M., Stolz, B., Albert, R., Ruser, G., Briner, U., Mäcke, H. R., and Bruns, C. (1998) Synthesis and characterization of [^{90}Y]-Bz-DTPA-oct: a yttrium-90-labelled octreotide analogue for radiotherapy of somatostatin receptor-positive tumors. *Nucl. Med. Biol. 25*, 181–188.

(46) De Jong, M., Bernard, B. F., De Bruin, E., Van Gameren, A., Bakker, W. H., Visser, T. J., Mäcke, H. R., and Krenning, E. P. (1998) Internalization of radiolabelled [DTPA^{o}]octreotide and [DOTA^{o}, Tyr^{3}]octreotide: peptides for somatostatin receptor-targeted scintigraphy and radionuclide therapy. *Nucl. Med. Commun. 19*, 283–288.

(47) Haubner, R., Wester, H. J., Senekowitsch-Schmidtke, R., Diefenbach, B., Kessler, H., Stöcklin, G., and Schwaiger, M. (1997) RGD-peptides for tumor targeting: biological evaluation of radioiodinated analogs and introduction of a novel glycosylated peptide with improved biokinetics. *J. Labelled Compd. Radiopharm. 40*, 383–385.

(48) Haubner, R., Wester, H. J., Reuning, U., Senekowisch-Schmidtke, R., Diefenbach, B., Kessler, H., Stöcklin, G., and Schwaiger, M. (1999) Radiolabeled $\alpha_v\beta_3$ integrin antagonists: a new class of tracers for tumor imaging. *J. Nucl. Med. 40*, 1061–1071.

(49) Haubner, R., Wester, H. J., Burkhart, F., Senekowisch-Schmidtke, R., Weber, W., Goodman, S. L., Kessler, H., and Schwaiger, M. (2001) Glycolated RGD-containing peptides: tracer for tumor targeting and angiogenesis imaging with improved biokinetics. *J. Nucl. Med. 42*, 326–336.

(50) Haubner, R., Wester, H. J., Weber, W. A., Mang, C., Ziegler, S. I., Goodman, S. L., Senekowisch-Schmidtke, R., Kessler, H., and Schwaiger, M. (2001) Noninvasive imaging of $\alpha_v\beta_3$ integrin expression using ^{18}F-labeled RGD-containing glycopeptide and positron emission tomography. *Cancer Res. 61*, 1781–1785.

(51) Antunes, P., Ginj, M., Walter, M. A., Chen, J., Reubi, J. C., and Maecke, H. R. (2007) Influence of different spacers on biological profile of a DOTA-Somatostatin Analogue. *Bioconugate. Chem. 18*, 84–92.

(52) Harris, T. D., Kalogeropoulos, S., Nguyen, T., Liu, S., Bartis, J., Ellars, C. E., Edwards, D. S., Onthanks, D., Yalamanchili, P., Robinson, S. P., Lazewatsky, J., and Barrett, J. A. (2003) Design, synthesis and evaluation of radiolabeled integrin $\alpha_v\beta_3$ antagonists for tumor imaging and radiotherapy. *Cancer Biother. Radiopharm. 18*, 627–641.

(53) Harris, T. D., Kalogeropoulos, S., Nguyen, T., Dwyer, G., Edwards, D. S., Liu, S., Bartis, J., Ellars, C., Onthank, D., Yalamanchili, P., Heminway, S., Robinson, S., Lazewatsky, J., and Barrett, J. A. (2006) Structure-activity relationships of ^{111}In- and ^{99m}Tc-labeled quinolin-4-one peptidomimetics as ligands for the vitronectin receptor: potential tumor imaging agents. *Bioconjugate Chem. 17*, 1294–1313.

(54) Harris, T. D., Cheesman, E., Harris, A. R., Sachleben, R., Edwards, D. S., Liu, S., Bartis, J., Ellars, C., Onthank, D., Yalamanchili, P., Heminway, S., Silva, P., Robinson, S., Lazewatsky, J., Rajopadhye, M., and Barrett, J. A. (2007) Radiolabeled divalent peptidomimetic vitronectin receptor antagonists as potential tumor radiotherapeutic and imaging Agents. *Bioconjugate Chem. 18*, 1266–1279.

(55) Chen, X., Park, R., Shahinian, A. H., Bading, J. R., and Conti, P. S. (2004) Pharmacokinetics and tumor retention of ^{125}I-labeled RGD peptide are improved by PEGylation. *Nucl. Med. Biol. 31*, 11–19.

(56) Chen, X., Sievers, E., Hou, Y., Park, R., Tohme, M., Bart, R., Bremner, R., Bading, J. R., and Conti, P. S. (2005) Integrin $\alpha_v\beta_3$-targeted imaging of lung cancer. *Neoplasia 7*, 271–279.

BC7002988

Modification of DNA with Octadiynyl Side Chains: Synthesis, Base Pairing, and Formation of Fluorescent Coumarin Dye Conjugates of Four Nucleobases by the Alkyne−Azide "Click" Reaction

Frank Seela,* Venkata Ramana Sirivolu, and Padmaja Chittepu

Laboratory for Bioorganic Chemistry and Chemical Biology, Center for Nanotechnology, Heisenbergstrasse 11, 48149 Münster, Germany, and Laboratorium für Organische and Bioorganische Chemie, Institut für Chemie, Universität Osnabrück, Barbarastrasse 7, 49069 Osnabrück, Germany. Received August 9, 2007; Revised Manuscript Received October 1, 2007

Oligonucleotides incorporating 5-(octa-1,7-diynyl)-2′-deoxycytidine **1a**, 5-(octa-1,7-diynyl)-2′-deoxyuridine **2a** and 7-deaza-7-(octa-1,7-diynyl)-2′-deoxyguanosine **3a**, 7-deaza-7-(octa-1,7-diynyl)-2′-deoxyadenosine **4a** were prepared. For this, the phosphoramidites **7**, **10**, and **13** were synthesized and employed in solid-phase oligonucleotide synthesis. The octa-1,7-diynyl nucleosides **1a**−**4a** were obtained from their corresponding iodo derivatives using the palladium-assisted Sonogashira cross-coupling reaction. The T_m values demonstrated that DNA duplexes containing octa-1,7-diynyl nucleosides show a positive influence on the DNA duplex stability when they are introduced at the 5-position of pyrimidines or at the 7-position of 7-deazapurines. The terminal alkyne residue of oligonucleotides were selectively conjugated to the azide residue of the nonfluorescent 3-azido-7-hydroxycoumarin (**38**) using the protocol of copper(I)-catalyzed [3 + 2] Huisgen−Sharpless−Meldal cycloaddition "click chemistry" resulting in the formation of strongly fluorescent 1,2,3-triazole conjugates. The fluorescence properties of oligonucleotides with covalently linked coumarin−nucleobase assemblies were investigated. Among the four modified bases, the 7-deazapurines show stronger fluorescence quenching than that of pyrimidines.

INTRODUCTION

The chemical modification of DNA of defined sequence is an invaluable tool to study DNA structure and recognition. Modified DNAs find applications as therapeutic and diagnostic agents. Areas of antisense and antigene therapy (*1–3*) or DNA detection and sequencing (*4, 5*) are studied intensively; new fields such as DNA-based nanotechnology are emerging (*6–9*). The most common DNA modification sites are the sugar moieties, the phosphodiester backbone, and the nucleobases. Minimal changes of the DNA-duplex structure by nucleoside-shaped mimics (*10–13*) are the prerequisites for a modified DNA to behave as the parent molecule. However, in a number of cases, larger residues, e.g., dye reporters, have to be introduced that can alter the structure of DNA. The 5-position of the pyrimidine bases (*14–17*) and 7-position of 7-deazapurines (*18, 19*) are "ideal" sites for DNA modifications (purine numbering is used throughout the discussion). Such groups are well-accommodated in the DNA major groove of the B-DNA duplex not disturbing the DNA helical structure. The introduction of substituents of moderate size–7-substituents into 7-deazapurines or 5-substituents into pyrimidines–can even cause duplex stabilization when compared to the canonical DNA constituents. These residues strengthen the base pairs as was shown for halogeno or alkynyl groups (*20–25*). A series of such modified nucleosides containing propynyl groups (**1b**−**4b**) have been synthesized and incorporated into DNA (*26–32*).

Recently, the copper(I)-catalyzed Huisgen−Sharpless−Meldal alkyne−azide 1,3-dipolar cycloaddition reaction has gained significant importance because of its applications in organic synthesis, molecular biology, and materials science (*33, 34*). The high potential energy of the azide and alkyne components make this a thermodynamically favored reaction ($\Delta H^\circ = -45$ to -55 kcal/mol). Although both azides and alkynes are highly reactive, they are orthogonal to a broad range of reagents, solvents, and other functional groups. Copper(I) dramatically enhances the reaction rate of azides with terminal alkynes leading to the formation of stable regiospecific 1,4-disubstituted-[1,2,3]-triazoles. To apply this chemistry to the four building blocks of DNA, nucleosides bearing the octa-(1,7-diynyl) group at the 5-position of pyrimidine bases (**1a**, **2a**) or at the 7-position of 7-deazapurines (**3a**, **4a**) were synthesized (Scheme 1).

In a recent Communication, we reported on the synthesis and properties of 5-(octa-1,7-diynyl)-2′-deoxyuridines and performed the "click" reaction with AZT or aromatic azides (*35*); we outlined the principle for dG, dC, and dT modification (*36*). Now, we present the syntheses of the three building blocks related to dC, dG, and dA in order to complete a set of canonical DNA building blocks bearing octadiynyl side chains and report on their duplex stability. They all contain the same Watson–Crick recognition sites as those of canonical DNA. For dye labeling, we introduce a nonfluorescent coumarin reporter molecule for the above-mentioned octadiynyl derivatives, which becomes fluorescent after the "click" reaction (Scheme 2). These reporter groups occupy well-defined positions within the DNA helix, without disturbing the native DNA structure (*35–38*). On the basis of this principle of the 1,3-dipolar cycloaddition, we performed the "click" reaction on oligonucleotides containing nucleoside residues bearing side chains with terminal triple bonds (**1a**−**4a**) with the nonfluorescent coumarin azide **38** to generate strongly fluorescent 1,2,3-triazole coumarin conjugates. The dye conjugates containing the 7-deazapurines show a strong photoinduced intramolecular electron transfer between the coumarin dye and the 7-deazapurine system, which is almost negligible in the case of pyrimidines. A general outcome of the work is the design of the four DNA building blocks **1a**−**4a** showing the same recognition pattern as the canonical DNA constituents; they can be labeled with almost any reporter group

* Tel. +49(251)53406500; Fax +49(251)53406857; E-mail: Frank.Seela@uni-osnabrueck.de. URL:http://www.seela.net.

10.1021/bc700300f CCC: $40.75 © 2008 American Chemical Society
Published on Web 11/20/2007

Scheme 1

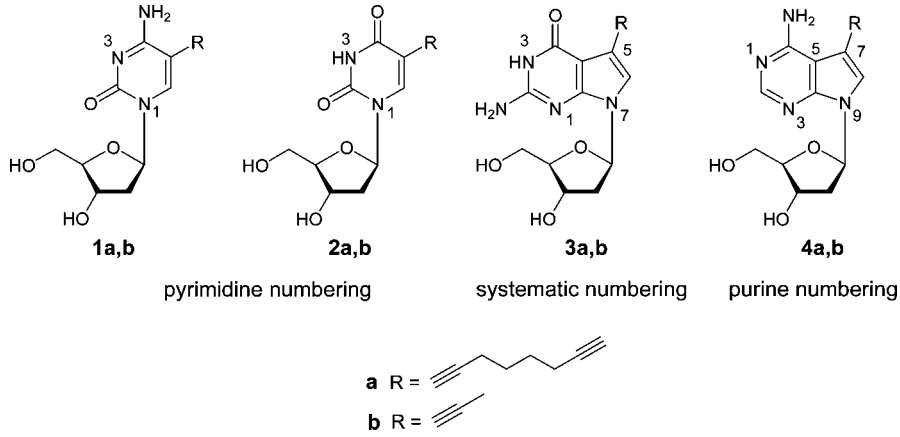

Scheme 2. Huisgen−Sharpless−Meldal Cycloaddition of Terminal Alkyne with Azide Generating a Fluorescent 1,4-Disubstituted 1,2,3-Triazole Product

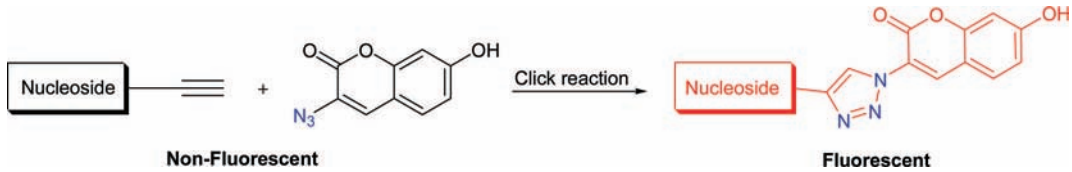

or an otherwise active moiety leading to the structurally "undisturbed" DNA duplexes.

EXPERIMENTAL SECTION

General. All chemicals were purchased from Acros, Sigma-Aldrich (Sigma-Aldrich Chemie GmbH, Deisenhofen, Germany). Solvents were of technical grade and freshly distilled before use. Thin layer chromatography (TLC): aluminum sheets, silica gel 60 F_{254}, 0.2 mm layer (VWR, Germany). Column flash chromatography (FC): silica gel 60 (VWR, Germany) at 0.4 bar; sample collection with an UltroRac-II fraction collector (LKB Instruments, Sweden). UV spectra: U-3200 spectrometer (Hitachi, Tokyo, Japan); λ_{max} (ϵ) in nm. NMR spectra: Avance-DPX-250 or AMX-500 spectrometers (Bruker, Karlsruhe, Germany) at 250.13 MHz for ^{1}H and ^{13}C; chemical shifts (δ) are in ppm relative to Me_4Si as internal standard or external 85% H_3PO_4 for ^{31}P; *J* values in Hz. Elemental analyses were performed by Mikroanalytisches Laboratorium Beller (Göttingen, Germany). Electron spray ionization (ESI) MS for the nucleosides: Bruker-Daltonics-MicroTOF spectrometer with loop injection (Bremen, Germany). The molecular masses of the oligonucleotides were determined by MALDI-TOF-MS with a Biflex-III mass spectrometer (Bruker Saxonia, Leipzig, Germany) and Applied Biosystems Voyager DE PRO with 3-hydroxypicolinic acid (3-HPA) as a matrix. The detected masses were identical to the calculated values. The fluorescence measurements were performed in bidistilled water at 20 °C. Fluorescence spectra were recorded in the wavelength range between 320 and 600 nm using the fluorescence spectrophotometer F-2500 (Hitachi, Tokyo, Japan).

Synthesis, Purification, and Characterization of the Oligonucleotides. The oligonucleotide synthesis was performed on a DNA synthesizer, model 392–08 (Applied Biosystems, Weiterstadt, Germany) at 1 μmol scale using the phosphoramidites **7**, **10**, and **13** following the synthesis protocol for 3′-(2-cyanoethyl phosphoramidites) (user's manual for the 392 DNA synthesizer, Applied Biosystems, Weiterstadt, Germany). The coupling efficiency was always higher than 95%. After cleavage from the solid support, the oligonucleotides were deprotected in 25% aqueous NH_3 solution for 14–16 h at 60 °C; during this process, the amine protecting groups of the nucleobases—adenine, cytosine with tBPA (4-tert-butylphenoxy)acetyl) protecting group, and guanine, **4a** with iB (isobutyryl)—were removed. The purification of 5′-dimethoxytrityl oligomers was carried out on reversed-phase HPLC (Merck-Hitachi-HPLC; RP-18 column; gradient system (A = 0.1 M (Et_3NH)OAc (pH 7.0)/MeCN 95:5, B = MeCN): 3 min 20% B in A, 12 min 20–50% B in A, and 25 min 20% B in A; flow rate 1.0 mL/min. The purified "trityl-on" oligonucleotides were treated with 2.5% $CHCl_2COOH/CH_2Cl_2$ for 5 min at 0 °C to remove the 4,4′-dimethoxytrityl residues. The detritylated oligomers were purified again by reversed-phase HPLC (gradient: 0–20 min 0–20% B in A; flow rate 1 mL/min). The oligomers were desalted on a short column (RP-18, silica gel) and lyophilized on a Speed-Vac evaporator to yield colorless solids which were frozen at −24 °C.

Melting curves were measured with a Cary-1/3 UV/vis spectrophotometer (Varian, Australia) equipped with a Cary thermoelectrical controller. The temperature was measured continuously in the reference cell with a Pt-100 resistor, and the thermodynamic data of duplex formation were calculated by the *Meltwin 3.0* program. The Cary 100 Bio UV–vis spectrophotometer was used for the UV-melting curves of oligonucleotides containing **4a** with a heating rate of 1 °C.

The enzymatic hydrolysis of the oligonucleotides containing **1a** and **3a** was performed as described (*9*) with snake venom phosphodiesterase (EC 3.1.15.1, *Crotallus adamanteus*) and alkaline phosphatase (EC 3.1.3.1, *Escherichia coli* from Roche Diagnostics GmbH, Germany) in 0.1 M Tris−HCl buffer (pH 8.3) at 37 °C, which was analyzed by reversed-phase HPLC (RP-18, at 260 nm) showing the peaks of the modified and unmodified nucleosides (Figure 1a,b). Quantification of the constituents was made on the basis of the peak areas, which were divided by the extinction coefficients ϵ_{260} of the nucleosides: dA 15 400 (H_2O), dC 7300 (H_2O), dG 11 700 (H_2O), dT 8800 (H_2O), **1a** 4900 (MeOH), **3a** 7300 (MeOH). For the fluorescence quenching experiments, the enzymatic hydrolysis was performed using 1.7 μM single-stranded oligonucleotide dissolved in 1 mL of 0.1 M Tris−HCl buffer (pH 8.3). To this solution, 3–10 μL of snake venom phosphodiesterase and 3–10

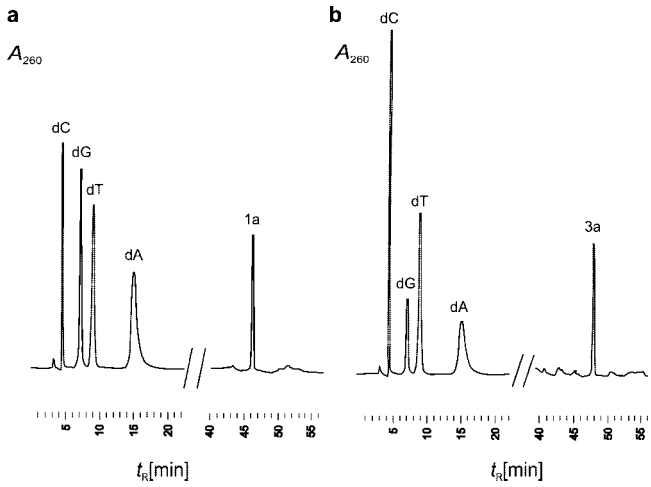

Figure 1. HPLC profiles of the enzymatic hydrolysis products (a) of the oligonucleotide 5′-d(TAG GT**1a** AAT ACT); (b) of oligonucleotide 5′-d(A**3a**T ATT GAC CTA) obtained by digestion with snake venom phosphodiesterase and alkaline phosphatase in 0.1 M Tris−HCl buffer (pH 8.3) at 37 °C. Gradient for (a) 25 min 100% A, 25–60 min 0–50% B in A; (b) 25 min 100% A, 25–60 min 0–60% B in A; flow rate 0.7 mL/min (A = 0.1 M (Et_3NH)OAc (pH 7.0)/MeCN 95:5, B = MeCN).

μL alkaline phosphatase were added and the fluorescence spectra measured at different time intervals with an emission 479 nm.

1-(2-Deoxy-β-D-*erythro*-pentofuranosyl)-5-(octa-1,7-diynyl)-cytosine (1a). To a suspension of 5-iodo-2′-deoxycytidine (0.6 g, 1.7 mmol) and CuI (65.5 mg, 0.34 mmol) in anhydrous DMF (9 mL) was added successively [$Pd(PPh_3)_4$] (196 mg, 0.17 mmol), anhydrous Et_3N (344 mg, 3.4 mmol), and octa-1,7-diyne (1.8 g, 17.0 mmol). The mixture was stirred at room temperature under argon atmosphere and allowed to proceed until the starting material was consumed (TLC monitoring). The reaction mixture was diluted with MeOH/CH_2Cl_2 1:1 (20 mL), and Dowex 1 × 8 (100–200 mesh; 0.6 g, hydrogen carbonate form) was introduced. After additional stirring for 1 h, the mixture was filtered and the resin washed with MeOH/CH_2Cl_2 1:1 (30 mL). The combined filtrate was concentrated and the residue purified by FC (silica gel, column 15 × 3 cm, CH_2Cl_2/MeOH 96:4): **1a** (0.42 g, 75%). Colorless amorphous solid. TLC (CH_2Cl_2/MeOH 9:1): R_f 0.40. UV λ_{max} (MeOH)/nm (ϵ/dm^3 mol^{-1} cm^{-1}) 236 (15900), 299 (7200). ^{1}H NMR ((D$_6$) DMSO): 1.54–1.62 (m, 4 H, 2CH_2), 2.0–2.15 (m, 3 H, H$_\alpha$-C(2′), CH_2), 2.22–2.44 (m, 3 H, H$_\beta$-C(2′), CH_2), 2.76 (s, 1 H, C≡CH), 3.54–3.62 (m, 2 H-C(5′)), 3.79 (m, H-C(4′)), 4.20 (m, H-C(3′)), 5.04 (t, J = 4.96, OH-C(5′)), 5.20 (d, J = 4.1, OH-C(3′)), 6.12 (t, J = 6.5, H-C(1′)), 6.71 (s, NH_a), 7.67 (s, NH_b), 8.07 (s, H-C(6)). Anal. Calcd for $C_{17}H_{21}N_3O_4$ (331.15): C 61.62, H 6.39, N 12.68. Found: C 61.44, H 6.77, N 12.45.

2-Amino-7-(2-deoxy-β-D-*erythro*-pentofuranosyl)-5-(octa-1,7-diynyl)-3,7-dihydro-4-*H*-pyrrolo[2,3-*d*]pyrimidin-4-one (3a). As described for **1a**, with 7-deaza-7-iodo-2′-deoxyguanosine (0.7 g, 1.78 mmol) and CuI (68 mg, 0.36 mmol) in anhydrous DMF (10 mL) were added successively [$Pd(PPh_3)_4$] (208 mg, 0.18 mmol), anhydrous Et_3N (360 mg, 3.56 mmol), and octa-1,7-diyne (1.89 g, 17.8 mmol). FC (silica gel, column 15 × 3 cm, CH_2Cl_2/MeOH 94:6), afforded **3a** (0.47 g, 71%) as a colorless amorphous solid. TLC (CH_2Cl_2/MeOH 9:1): R_f 0.19. UV λ_{max} (MeOH)/nm (ϵ/dm^3 mol^{-1} cm^{-1}) 238 (22600), 273 (10600), 290 (8800). ^{1}H NMR ((D$_6$) DMSO): 1.46 (m, 4 H, 2 CH_2), 1.95–2.18 (m, 3 H, H$_\alpha$-C(2′), CH_2), 2.25–2.38 (m, 3 H, H$_\beta$-C(2′), CH_2), 2.64 (s, 1 H, C≡CH), 3.28 (m, 2 H-C(5′)), 3.62 (m, H-C(4′)), 4.14 (m, H-C(3′)), 4.81 (t, OH-C(5′)), 5.11 (d, OH-C(3′)), 6.14 (t, J = 6.3 Hz, H-C(1′)), 6.20 (s, NH_2), 7.01 (s, H-C(8)), 10.31 (s, NH). ESI-HR-MS: 393.15 ([M + Na])$^+$, $C_{19}H_{22}N_4O_4^+$; calcd 370.16.

1-[2-Deoxy-5-*O*-(4,4′-dimethoxytrityl)-β-D-*erythro*-pentofuranosyl]-5-(octa-1,7-diynyl)cytosine (5). Compound **1a** (0.5 g 1.5 mmol) was dried by repeated coevaporation with anhydrous pyridine (2 × 5 mL) before dissolving in anhydrous pyridine (10 mL). Then, 4,4′-dimethoxytrityl chloride (0.61 g, 1.80 mmol) was added in three portions to the remaining solution at room temperature under stirring for 6 h. Thereupon, MeOH (2 mL) was added, and the mixture was stirred for another 30 min. The reaction mixture was dissolved in CH_2Cl_2 (2 × 50 mL) and extracted with 5% aqueous $NaHCO_3$ solution (100 mL) followed by H_2O (80 mL), dried over Na_2SO_4, and then concentrated. Purification by FC (silica gel, column 15 × 3 cm, CH_2Cl_2/acetone 70:30) gave a colorless foam of **5** (0.82 g, 86%). TLC (CH_2Cl_2/MeOH 95:5): R_f 0.25. UV λ_{max} (MeOH)/nm (ϵ/dm^3 mol^{-1} cm^{-1}) 235 (32000), 83 (6500), 299 (6600). ^{1}H NMR ((D$_6$) DMSO): 1.39 (m, 2 CH_2), 2.06–2.26 (m, 6 H, H-C(2′)), 2 CH_2), 2.74 (s, 1 H, C≡CH), 3.10–3.23 (m, 2 H-C(5′)), 3.73 (s, 6 H, 2 MeO), 3.92 (m, H-C(4′)), 4.27 (m, H-C(3′)), 5.33 (d, J = 3.9, OH-C(3′)), 6.12 (t, J = 6.5, H-C(1′)), 6.76 (s, NH_a), 6.86–7.42 (m, H-arom), 7.71 (s, NH_b), 7.89 (s, H-C(6)). Anal. Calcd for $C_{38}H_{39}N_3O_6$ (633.28): C 72.02, H 6.20, N 6.63. Found: C 71.86, H 6.20, N 6.58.

N^4-Acetyl-1-[2-deoxy-5-*O*-(4,4′-dimethoxytrityl)-β-D-*erythro*-pentofuranosyl]-5-(octa-1,7-diynyl)cytosine (6). To a suspension of compound **5** (200 mg, 0.32 mmol) in *N*,*N*-dimethylformamide (2 mL) was added acetic anhydride (36 μL, 0.38 mmol) and the reaction mixture stirred at room temperature for 20 h. After evaporation of DMF under reduced pressure, the residue was applied to FC (silica gel, column 15 × 3 cm, CH_2Cl_2/acetone 80:20). Compound **6** was isolated as colorless foam (0.18 g, 84%). TLC (CH_2Cl_2/MeOH 95:5): R_f 0.73. UV λ_{max} (MeOH)/nm (ϵ/dm^3 mol^{-1} cm^{-1}) 236 (40000), 282 (4200), 317 (5300). ^{1}H NMR ((D$_6$) DMSO): 1.42 (m, 2 CH_2), 2.10–2.17 (m, 2 H-C(2′)), 2.22 (s, 3 H, COMe), 2.36 (m, 2 CH_2), 2.77 (s, 1 H, C≡CH), 3.20 (m, 2 H-C(5′)), 3.75 (s, 6 H, 2-MeO), 4.0 (m, H-C(4′)), 4.3 (m, H-C(3′)), 5.39 (d, J = 4.0, OH-C(3′)), 6.10 (t, J = 6.2, H-C(1′)), 6.89–7.44 (m, H-arom), 8.24 (s, H-C(6)), 9.24 (s, NH). Anal. Calcd for $C_{40}H_{41}N_3O_7$ (675.29): C 71.09, H 6.12, N 6.22. Found: C 71.15, H 6.20, N 6.35.

N^4-Acetyl-1-[2-deoxy-5-*O*-(4,4′-dimethoxytrityl)-β-D-*erythro*-pentofuranosyl]-5-(octa-1,7-diynyl)cytosine 3′-(2-Cyanoethyl)-*N*,*N*-diisopropylphosphoramidite (7). A stirred solution of **6** (250 mg, 0.37 mmol) in anhydrous CH_2Cl_2 (5 mL) was preflushed with argon and treated with (i-Pr)$_2$EtN (100 μL, 0.58 mmol) followed by 2-cyanoethyl-*N*,*N*-diisopropylphosphoramidochloridite (130 μL, 0.60 mmol). After stirring for 45 min at room temperature, the solution was diluted with CH_2Cl_2 (30 mL) and extracted with 5% aqueous $NaHCO_3$ solution (20 mL). The organic layer was dried over Na_2SO_4 and concentrated. FC (silica gel, column 10 × 2 cm, CH_2Cl_2/acetone 95:5) gave **7** (260 mg, 80%). Colorless foam. TLC (CH_2Cl_2/acetone 95:5): R_f 0.74. ^{31}P NMR ($CDCl_3$): 150.25, 149.6.

7-(2-Deoxy-β-D-*erythro*-pentofuranosyl)-5-(octa-1,7-diynyl)-3,7-dihydro-2-[(*N*,*N*-dimethylamino)methylidene]amino-4*H*-pyrrolo[2,3-*d*]pyrimidin-4-one (8). To a solution of **3a** (400 mg, 1.08 mmol) in MeOH (12 mL) was added *N*,*N*-dimethylformamide dimethylacetal (425 μL, 3.2 mmol). The reaction mixture was stirred at 40 °C for 1 h, and the solvent was evaporated to dryness. The resulting residue was applied to FC (silica gel, column 15 × 3 cm, CH_2Cl_2/MeOH 95:5). Compound **8** was isolated as a colorless solid (335 mg, 73%). TLC (CH_2Cl_2/MeOH, 9:1): R_f 0.31. UV λ_{max} (MeOH)/nm (ϵ/dm^3 mol^{-1} cm^{-1}) 232 (17000), 253 (24000), 316 (18000). ^{1}H NMR ((D$_6$) DMSO): 1.60 (m, 2 CH_2), 2.20 (m, 3 H, H$_\alpha$-C(2′), CH_2), 2.39 (m, 3 H, H$_\beta$-C(2′), CH_2), 2.77 (s, 1 H, C≡CH), 3.01 (s, 3 H, NCH_3),

3.14 (s, 3 H, NCH_3), 3.50 (m, 2 H-C(5′)), 3.76 (m, H-C(4′)), 4.30 (m, H-C(3′)), 4.91 (t, OH-C(5′)), 5.25 (d, OH-C(3′)), 6.41 (t, J = 6.3, H-C(1′)), 7.27 (s, H-C(8)), 8.54 (s, H, N=CH), 11.05 (s, NH). Anal. Calcd for $C_{22}H_{27}N_5O_4$ (425.21): C 62.10, H 6.40, N 16.46. Found: C 62.14, H 6.50, N 16.34.

7-(2-Deoxy-5-*O*-(4,4′-dimethoxytrityl)-*β*-D-*erythro*-pentofuranosyl)-5-(octa-1,7-diynyl)-3,7-dihydro-2-[(*N*,*N*-dimethylamino)methylidene]amino-4 *H*-pyrrolo-[2,3-*d*]pyrimidin-4-one (9). As described for **5**, compound **8** (0.35 g 0.82 mmol) in anhydrous pyridine (6 mL) was treated with 4,4′-dimethoxytrityl chloride (370 mg, 1.09 mmol). Purification by FC (silica gel, column 15 × 3 cm, CH_2Cl_2/acetone, 1:1) gave a colorless foam of **9** (0.45 g, 75%). TLC (CH_2Cl_2/MeOH 97:3): (B): R_f 0.25: UV λ_{max} (MeOH)/nm (ϵ/dm^3 mol^{-1} cm^{-1}) 232 (45000), 279 (16000), 296 (15000). ^{1}H NMR ((D$_6$) DMSO): 1.61 (m, 2 CH_2), 2.09–2.19 (m, 3 H, H$_\alpha$-C(2′), CH_2), 2.40 (m, 3 H, H$_\beta$-C(2′), CH_2), 2.77 (s, 1 H, C≡CH), 3.02 (s, 3 H, NCH_3), 3.15 (s, 3 H, NCH_3), 3.74 (s, 6 H, 2-MeO), 3.90 (m, H-C(4′)), 4.31 (m, H-C(3′)), 5.33 (d, OH-C(3′)), 6.46 (t, J = 6.52, H-C(1′)), 6.85–7.32 (m, H-arom), 7.4 (s, H-C(8)), 8.57 (s, H, N=CH), 11.09 (s, NH). Anal. Calcd for $C_{43}H_{45}N_5O_6$ (727.34): C 70.96, H 6.23, N 9.62. Found: C 71.08, H 6.26, N 9.70.

7-(2-Deoxy-5-*O*-(4,4′-dimethoxytrityl)-*β*-D-*erythro*-pentofuranosyl)-5-(octa-1,7-diynyl)-3,7-dihydro-2-[(*N*,*N*-dimethylamino)methylidene]amino-4-*H*-pyrrolo-[2,3-*d*]pyrimidin-4-one 3′-(2-Cyanoethyl)-*N*,*N*-diisopropylphosphoramidite (10). As described for **7**, with **9** (200 mg, 0.27 mmol), (i-Pr)$_2$EtN (72 μL, 0.42 mmol), and 2-cyanoethyl-*N*,*N*-diisopropylphosphoramidochloridite (103 μL, 0.47 mmol). FC (silica gel, 10 × 2 cm, solvent system, CH_2Cl_2/acetone 93:7) gave a colorless foam of **10** (160 mg, 62%). TLC (CH_2Cl_2/acetone 90:10): R_f 0.68. ^{31}P NMR ($CDCl_3$): 149.95, 149.65.

7-(2-Deoxy-*β*-D-*erythro*-pentofuranosyl)-4-(iso-butyrylamino)-5-(octa-1,7-diynyl)-7-*H*-pyrrolo[2,3-*d*]pyrimidine (11). To a solution of compound **4a** (*19*) (248 mg, 0.7 mmol) in anhydrous pyridine (4 mL) was added Me_3SiCl (910 μL, 7.14 mmol) and stirred at room temperature. After 45 min, the isobutyric anhydride (770 mg, 4.9 mmol) was introduced, and the solution stirred for another 2 h. The mixture was cooled to 0 °C, diluted with H_2O (3 mL), and stirred for 10 min. After the addition of 12% aq NH_3 (3 mL), stirring was continued for 1 h at room temperature. The solution was evaporated, and the residue was applied to FC (silica gel, column 10 × 3 cm, CH_2Cl_2/MeOH 95:5). Compound **11** was isolated as a colorless solid (210 mg, 71%). TLC (CH_2Cl_2/MeOH, 90:10): R_f 0.64. UV λ_{max} (MeOH)/nm (ϵ/dm^3 mol^{-1} cm^{-1}) 213 (19000), 241 (26000), 305 (7000). ^{1}H NMR ((D$_6$) DMSO): 1.17 (s, 2 CH_3), 1.60 (m, 2 CH_2), 2.20 (m, 3 H, H$_\alpha$-C(2′), CH_2), 2.38–2.58 (m, 3 H, H$_\beta$-C(2′), CH_2), 2.77 (s, 1 H, C≡CH), 2.88 (m, 1 H, CH), 3.50 (m, 2 H-C(5′)), 3.83 (m, H-C(4′)), 4.35 (m, H-C(3′)), 4.99 (t, J = 4.87, OH-C(5′)), 5.30 (d, OH-C(3′)), 6.61 (t, J = 6.7, H-C(1′)), 7.98 (s, H-C(6)), 8.59 (s, 1 H, H-C(2)), 9.96 (s, 1H, NH). Anal. Calcd for $C_{23}H_{28}N_4O_4$ (424.21): C 65.08, H 6.65, N 13.20. Found: C 65.22, H 6.70, N 13.11.

7-(2-Deoxy-5-*O*-(4,4′-dimethoxytrityl)-*β*-D-*erythro*-pentofuranosyl)-4-(isobutyrylamino)-5-(octa-1,7-diynyl)-7-*H*-pyrrolo-[2,3-*d*]pyrimidine (12). As described for **5**, compound **11** (250 mg 0.59 mmol) in anhydrous pyridine (5 mL) was treated with 4,4′-dimethoxytrityl chloride (275 mg, 0.81 mmol). Purification by FC (silica gel, column 12 × 3 cm, CH_2Cl_2/acetone, 7:3) gave a colorless foam of **12** (365 mg, 85%). TLC (CH_2Cl_2/MeOH 95:5) R_f 0.33. UV λ_{max} (MeOH)/nm (ϵ/dm^3 mol^{-1} cm^{-1}) 214 (36400), 237 (42000), 275 (9400). ^{1}H NMR ((D$_6$) DMSO): 1.17 (s, 2 CH_3), 1.58 (m, 2 CH_2), 2.14–2.41 (m, 6 H, H-C(2′), 2 CH_2), 2.77 (s, 1 H, C≡CH), 2.88 (m, 1 H, CH), 3.2 (m, 2 H-C(5′)), 3.72 (s, 6 H, 2-MeO), 3.96 (m, 1 H-C(4′)), 4.39 (m, H-C(3′)), 5.37 (d, J = 4.20, OH-C(3′)), 6.62 (t, J = 6.7, H-C(1′)), 6.82 (m, 4 H, H-arom), 7.20–7.38 (m, 9 H, H-arom), 7.86 (s, 1 H, H-C(6)), 8.57 (s, 1 H, H-C(2)), 9.96 (s, 1 H, NH). Anal. Calcd for $C_{44}H_{46}N_4O_6$ (726.34): C 72.71, H 6.38, N 7.71. Found: C 72.82, H 6.48, N 7.70.

Scheme 3[a]

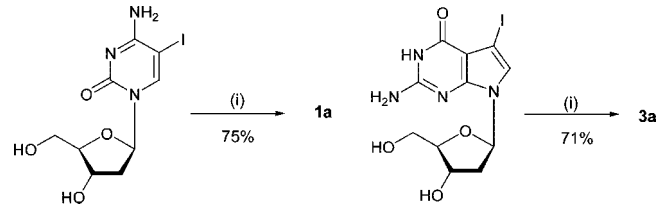

[a] (i) [Pd^0(PPh$_3$)$_4$], CuI, Et$_3$N, DMF, octa-1,7-diyne, rt.

7-(2-Deoxy-5-*O*-(4,4′-dimethoxytrityl)-*β*-D-*erythro*-pentofuranosyl)-4-(isobutyrylamino)-5-(octa-1,7-diynyl)-7-*H*-pyrrolo-[2,3-*d*]pyrimidine-3′-(2-cyanoethyl)-*N*,*N*-diisopropylphosphoramidite (13). As described for **7**, with **12** (300 mg, 0.41 mmol), (i-Pr)$_2$EtN (150 μL, 0.87 mmol), and 2-cyanoethyl-*N*,*N*-diisopropylphosphoramidochloridite (210 μL, 0.96 mmol). FC (silica gel, 10 × 2 cm, solvent system, CH_2Cl_2/acetone 94:6) gave colorless foam of **13** (230 mg, 60%). TLC (CH_2Cl_2/acetone 90:10): R_f 0.70. ^{31}P NMR ($CDCl_3$): 149.97, 149.81.

Huisgen−Sharpless−Meldal [3 + 2] Cycloaddition Performed in Aqueous Solution for Oligonucleotides 23, 30, 34, and 42 with the Nonfluorescent Coumarin Azide 38. To the single-stranded oligonucleotide (5 A_{260} units), $CuSO_4$−TBTA ligand complex (35 μL of a 20 mM stock solution in *t*-BuOH/H_2O 1: 9), tris(carboxyethyl)phosphine (TCEP) (35 μL of a 20 mM stock solution in water), 3-azido-7-hydroxycoumarin (**38**; 50 μL of a 20 mM stock solution in dioxane/H_2O 1: 1), and 35 μL of DMSO were added, and the reaction was run at room temperature for 15–20 h. The "click" products **39**, **40**, **41**, and **43** were further purified by reversed-phase HPLC in the trityl-off modus (see above). The molecular masses of the oligonucleotides were determined by MALDI-TOF spectroscopy.

RESULTS AND DISCUSSION

Synthesis and Physical Properties of Monomers. The nucleosides **1a** and **3a** were synthesized from the corresponding 5-iodo 2′-deoxycytidine or 7-deaza-7-iodo-2′-deoxyguanosine (*23*) employing the Sonogashira cross-coupling reaction. The reaction was carried out in dry DMF in the presence of triethylamine using the palladium catalyst Pd^0(PPh$_3$)$_4$ and CuI. An excess amount of octa-1,7-diyne was used for the efficient cross-coupling reaction (*20*), leading to the exclusive formation of the monofunctionalized octa-1,7-diynyl nucleosides **1a** and **3a** in 75% and 71% yield, respectively (Scheme 3). The synthesis of the corresponding c^{7}dA$_d$ (**4a**) and 2′-deoxyuridine (**2a**) nucleosides were already reported (*20*, *35*). Reaction at the second terminal C≡C bond can be accomplished when compounds **1a**−**4a** are isolated and employed as intermediates in a second cross-coupling reaction to form bis-nucleosides (*7*). The structure of the isolated nucleosides was confirmed on the basis of ^{1}H and ^{13}C NMR spectroscopy as well as by elemental analysis or mass spectra. The characteristic signal for the terminal C≡C proton at δ(H) 2.76 (for **1a**) and 2.64 (for **3a**) reveals the formation of 5- or 7-octa-1,7-diynylated nucleosides. The chemical shifts and the terminal triple bonds of the nucleosides can be clearly identified on the basis of coupling pattern taken from the gated-decoupled ^{1}H/^{13}C NMR spectra. The side chain carbon atom of terminal C≡C of **1a** showed a C, H coupling (^1J(C,H) = 250 Hz).

The physical and biological properties of oligonucleotides can be influenced by introducing various alkyne or diyne

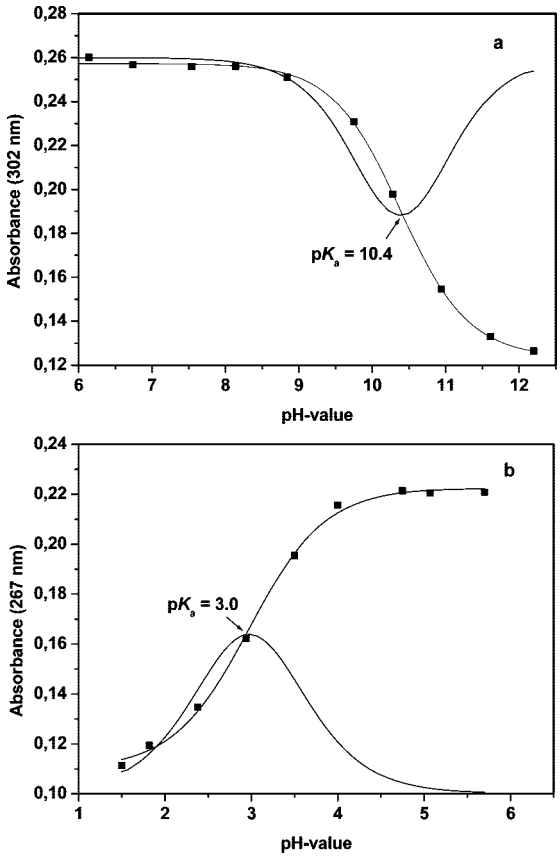

Figure 2. UV spectra of compounds **3a** and **1a** measured in phosphate buffer (7.8 g $NaH_2PO_4 \cdot H_2O$ in 500 mL H_2O). Absorbance (a) of compound **3a** as a function of pH values measured at 302 nm from pH 1.5 to 12.5 and (b) of compound **1a** at 267 nm.

substituents at the 5-position of pyrimidine or at the 7-position of 7-deazapurine nucleosides. To evaluate the impact of these side chain units on the hydrophobicity, the log *P* values are calculated and compared for the heterocyclic bases with the help of *ACD/log P 1.0* program. For the natural bases, the log *P* values are negative, which reflects the hydrophilicity of these compounds. The maximum log *P* value is observed for the octa-1,7-diynyl nucleosides (1.23 ± 0.75 for **1a**, 1.51 ± 1.30 for **3a**, 2.69 ± 1.43 for **4a**) when compared with the propynylated nucleosides (−0.24 ± 0.75 for **1b**, 0.03 ± 1.29 for **3b**, 1.22 ± 1.42 for **4b**). Moreover, the presence of long-chain hydrophobic substituents enhances the polarizability, $\alpha_m/10^{-24}$ cm^3; the calculated data (*ACD/ChemSketch 2.51*) are of the nucleobases (25.36 for **1a**, 29.22 for **3a**, and 27.87 for **4a**). These values are higher when compared with the propynylated nucleobases (16.23 for **1b**, 20.08 for **3b**, and 19.56 for **4b**).

In order to understand the relative base-pairing strength of DNA duplexes, it is necessary to know the pK_a values of the monomeric donor and acceptor residues involved in hydrogen bonding (*39*). The effect of octa-1,7-diynyl residue on the pyrrolo[2,3-*d*]pyrimidine as well as on the pyrimidine system was studied. The pK_a values were determined by spectrophotometric titration (*40*) (pH 1.5 to 11.50) at 220–350 nm (see Figure 2). The octa-1,7-diynyl group of **1a** (pK_a = 3.0), **2a** (pK_a = 8.7), **3a** (pK_a = 10.4), and **4a** (pK_a = 4.4) does not change the pK_a value significantly when compared with the propynylated nucleosides (3.3 for **1b**, 8.7 for **2b**, 10.2 for **3b**, and 4.3 for **4b**). The pK_a values of the natural pyrimidine 2′-deoxyribonucleosides dC (pK_a = 4.2) and dT (pK_a = 9.3) and purine 2′-deoxyribonucleosides dG (pK_a = 9.2) and dA (pK_a = 3.8) (*41*) are significantly different when compared to the octadiynylated nucleosides. The octa-1,7-diynyl side chains of pyrimidine 2′-deoxyribonucleosides make them more acidic than the parent compounds and have an impact on the base pair stability and base discrimination. Moreover, the octadiynyl side-chain containing nucleosides show rather different UV spectra and extinction coefficients than those of natural nucleosides (Figure 3a−d and Table 1).

Phosphoramidite Synthesis. In order to investigate the properties of oligonucleotides containing the octa-1,7-diynyl nucleosides, a series of phosphoramidites **7**, **10**, and **13** were prepared. The synthesis of 5-octadiynyl 2′-deoxyuridine phosphoramidite has already been reported (*35*). Various protecting groups were studied for the protection of the amino group of different monomers. First, we used the transient protection protocol to protect the amino group of **1a** with a benzoyl residue at the nucleoside level but obtained a rather low yield. Next, isobutyric anhydride was employed for protection and was also discarded for poor reactivity and hygroscopic nature. Thus, it became clear that the presence of a bulky alkynyl side chain influences protection. To avoid this, nucleoside **1a** was first converted into the 4,4′-dimethoxytrityl derivative **5**, which increased the solubility, and then the amino group was protected with the less bulky acetyl group using acetic anhydride in DMF. This results in the formation of the derivative **6** in 84% yield, which was subsequently converted into the phosphoramidite buiding block **7** (Scheme 4).

In the case of 7-deaza-2′-deoxyguanosine **3a**, the amino group was protected with the formamidine residue furnishing compound **8**, which is subsequently converted into the DMT derivative **9**. Phosphitylation of the DMT derivative results in the formation of phosphoramidite building block **10** (Scheme 5). We have already reported on the use of different protecting groups for the amino group of 7-alkynylated 7-deaza 2′-deoxyadenosines (*21*). In the case of **4a**, formamidine and acetamidine protection was not successful due to the unstable products which turned brown when exposed to the light. On the basis of these observations, the isobutyric residue was chosen. The nucleoside **4a** was treated with trimethylsilyl chloride in pyridine followed by isobutyric anhydride (transient protection) (*42*), yielding the derivative **11**. The protected nucleoside was obtained in 71% yield, which was further converted into phosphoramidite building block **13** via the DMT derivative **12** (Scheme 6).

All the compounds were characterized by ^1H, ^{13}C, and ^{31}P NMR spectra and by elemental analysis (Table 2 and Experimental Section). The δ(C) of the C≡C bonds were in good agreement with the literature data of the related compounds (*20, 35*). Moreover, the nucleobase as well as the protecting group carbon atom signals of 7-deazapurines and pyrimidines were assigned on the basis of literature data (*31*). The above synthesized phosphoramidites were further employed in solid-phase oligonucleotide synthesis.

Duplex Stability of Tridentate "dG−dC" Base Pair Modified by 5-Octadiynyl-2′-deoxycytdine (1a) and 7-Deaza-7-octadiynyl-2′-deoxyguanosine (3a). To evaluate the influence of base-modified nucleosides on the duplex stability, hybridization experiments were performed by using the oligonucleotide duplex 5′-d(TAGGTCAATACT)-3′ (**14**) 3′-d(ATCCAGTTATGA)-5′ (**15**) as a reference. Earlier, it was reported from our laboratory that the pyrimidine nucleoside **1b** increase the thermal stability of duplexes by 2–3 °C per modification (*32*) when incorporated in the place of dC (motif I, Figure 4). Herein, we studied the role of octa-1,7-diyne in the duplexes **14** and **15** by incorporating compound **1a** instead of 2′-deoxycytidine. The 5-(octa-1,7-diynyl) nucleoside **1a** enhances the stability of a dG−dC base pair by 2–3 °C per modification (Table 3).

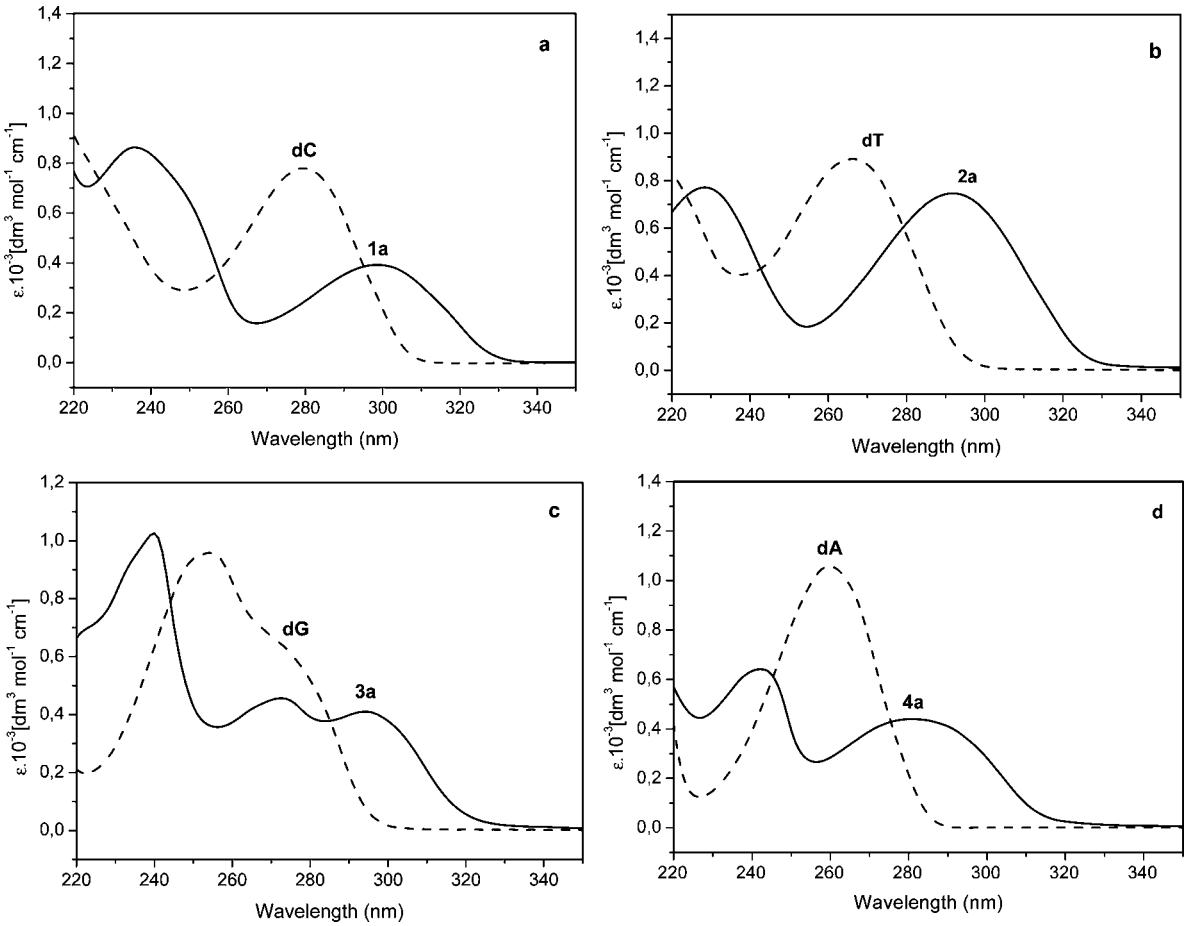

Figure 3. UV/vis spectra of (a) compounds dC and **1a**; (b) dT, **2a**; (c) dG, **3a**; (d) dA, **4a** measured in MeOH.

Table 1. Extinction Coefficients of Octadiynylated 2′-Deoxyribonucleosides[a]

compd	wavelength (λ_{max}) [nm]	extinction coefficient (ϵ)
1a	236	15900
	260	4900
	299	7200
2a	228	12800
	260	3800
	292	12400
3a	240	20200
	260	7300
	273	9000
	294	8100
4a	239	15700
	260	5300
	281	10600

[a] Measured in MeOH.

The oligonucleotides with longer alkynyl chains linked to the 7-position of 7-deaza-2′-deoxyguanosine show an unfavorable influence on the DNA duplex stability (*24*). Moreover, it was found that introduction of the propynyl group at this position enhances the DNA duplex stability significantly (*31*). Recently, we reported the single-crystal X-ray analysis of the 7-propynylated nucleoside **3b** (*43*) which shows an anti [$\chi = -117.2$ (5)°] orientation of the nucleobase related to the sugar moiety with pseudorotational parameters $P = 152.5°$ and $\tau_m = 41.9°$. The linear 7-propynyl residue is placed almost in-plane with the base moiety and protruding into the major groove with steric freedom. From these findings, it was concluded that the duplex stability can be tuned by an appropriate selection of a 7-substituent. To evaluate this, nucleoside **3a** was incorporated in the standard duplex 5′-d(TAGGTCAATACT)-3′ (**14**) 3′-d(ATCCAGTTATGA)-5′ (**15**) in place of dG. The incorporation of the **3a** residue results in a T_m increase of 2–3 °C per modification (Table 3). These values are more or almost similar when compared with the oligonucleotides containing the 7-propynyl derivative **3b** (Table 1 in Supporting Information). Thus, it is shown that the octa-1,7-diynyl group is a more effective substituent for duplex stabilization. These results led us to study the influence of the octa-1,7-diynyl group at the 7-position of 7-deazaadenine.

Duplex Stability of the Bidentate dA−dT Base Pair Modified by 7-Deaza-7-octadiynyl-2′-deoxyadenosine (4a) and 5-Octadiynyl-2′-deoxyuridine (2a). The 7-deaza-7-(octa-1,7-diynyl)-2′-deoxyadenosine **4a** was introduced into the duplex 5′-d(TAGGTCAATACT)-3′ (**14**) 3′-d(ATCCAGTTATGA)-5′ (**15**) replacing dA. From Table 4, it is concluded that single or double incorporation of **4a** (motif VI, Figure 4) does not show much influence on the stability, whereas three incorporations enhances the T_m value by 3 °C (**30•31**) when compared to the standard sequence in high-salt buffer (Table 4). In the low-salt buffer, there is no significant influence of this side chain on the duplex stability when compared to **4b** (data not shown). In the case of 5-octadiynyl 2′-deoxyuridine (**2a**), a T_m increase of 1–2 °C per modification was observed, similar to that of **2b** (motif VIII, Figure 4).

The above results clearly demonstrate that the octa-1,7-diynyl nucleosides with side chains located at the 7-position of 7-deazapurine nucleosides or at the 5-position of pyrimidine nucleosides show a very similar behavior to that of four canonical DNA constituents with a tendency of duplex stabilization. From the above data, it can be concluded that bidentate base pair reacts more sensitively to this change than the

Scheme 4[a]

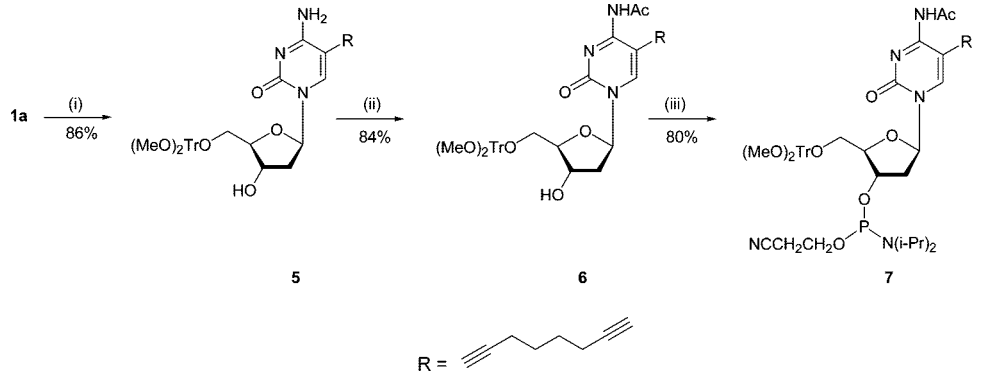

[a] (i) 4,4′-Dimethoxytriphenylmethyl chloride, anhydrous pyridine, rt, 6 h; (ii) acetic anhydride, DMF, rt, 20 h; (iii) 2-cyanoethyl-*N*,*N*-diisopropylchlorophosphoramidite, *N*,*N*-diisopropylethylamine, CH_2Cl_2, rt, 45 min.

Scheme 5[a]

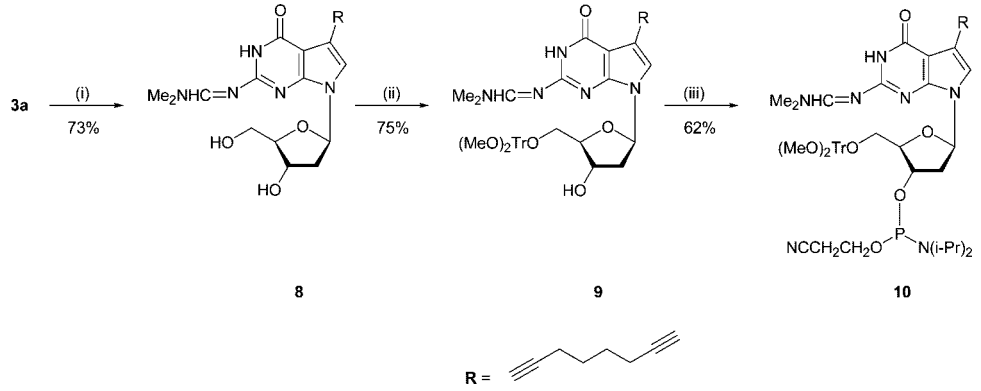

[a] (i) *N*,*N*-Dimethylformamide dimethylacetal, MeOH, 40 °C, 1 h; (ii) 4,4′-dimethoxytriphenylmethyl chloride, anhydrous pyridine, rt, 6 h; (iii) 2-cyanoethyl-*N*,*N*-diisopropylchlorophosphoramidite, *N*,*N*-diisopropylethylamine, CH_2Cl_2, rt, 45 min.

Scheme 6[a]

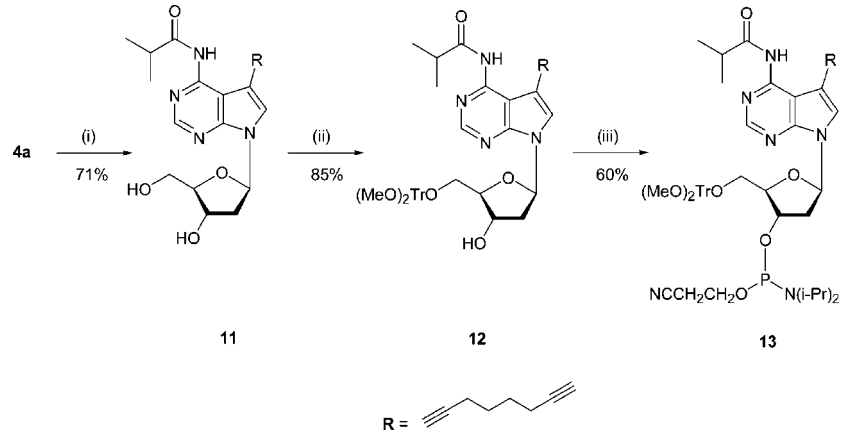

[a] (i) Me_3SiCl, isobutyric anhydride, anhydrous pyridine, rt; (ii) 4,4′-dimethoxytriphenylmethyl chloride, anhydrous pyridine, rt, 6 h; (iii) 2-cyanoethyl-*N*,*N*-diisopropylchlorophosphoramidite, *N*,*N*-diisopropylethylamine, CH_2Cl_2, rt, 45 min.

tridentate pair. The octa-1,7-diynyl groups are protruding into the major groove, which does not distort the base pairs significantly. The higher stability for such a long chain is due to the presence of terminal triple bonds.

Functionalization of Terminal C≡C Bonded Oligonucleotides in Solution with the Coumarin Azide 38 Employing the Huisgen−Sharpless−Meldal [3 + 2] Cycloaddition ("Click" Chemistry). The Huisgen−Sharpless−Meldal "click" chemistry is defined as a selective chemical reaction between alkynes and organic azides (*44*). The reaction is tolerant of a variety of solvents and functional groups to form stable 1,2,3-triazoles. Independently, the Sharpless (*45*) and Meldal (*46*) groups reported the copper(I)-catalyzed coupling protocol which enhances the reaction rate significantly and leads to regioselective ring closure. Previous work includes the demonstration of this chemistry in nucleic acids (*36, 47–49*) for the construction of fluorescent oligonucleotides for DNA sequencing (*50*), for the intramolecular circularization and catenation of DNA (*51*), and also to attach oligonucleotide probes on monolayers (*52*). Recently, we reported on the functionalization of alkynyl-modified 2′-deoxyuridines using "click" chemistry at the nucleoside as well as at the oligonucleotide levels (*35*).

Table 2. ^{13}C NMR Chemical Shifts (δ) of 5-Substituted Pyrimidine 2′-Deoxyribonucleosides and 7-Substituted 7-Deazapurines[a]

compd	C(2)[b]C(2)[c]	C(4)[b]C(6)[c]	C(4a)[b]C(5)[c]	C(5)[b]C(7)[c]	C(6)[b]C(8)[c]	C(7a)[b]C(4)[c]	C(1′)	C(2′)	C(3′)	C(4′)	C(5′)	C=O/C=N	C≡C	CH_2
1	153.9	164.3		95.4	143.5		84.6	[e]	70.2	87.5	60.9		90.3, 84.2	17.2, 18.5
													72.1, 71.2	27.1, 27.2
3a	153.1	157.9	99.5[d]	89.6	121.0	150.2	82.2	[e]	71.0	87.1	61.9		99.4[d], 84.4	17.3, 18.5
													74.7, 71.3[d]	27.2, 27.5
3b (*31*)	152.9[d]	157.8	99.3	85.4	120.9	150.0[d]	82.1	[e]	70.8	87.0	61.8		99.3, 73.7	
4a (*20*)	152.5	157.4	102.3	95.4	125.4	149.0	83.0	[e]	70.9	87.4	61.8		95.4, 71.3	
4b	152.5[d]	157.5	102.3	95.6	125.4	148.9[d]	83.1	[e]	70.9	87.4	61.9		88.4, 72.6	
5	153.5	164.4		95.3	143.0		85.7[d]	[e]	70.3	85.4[d]	63.6		90.7, 84.2	17.2, 18.5
													71.6, 71.3	26.9, 27.2
6	152.4	161.0		96.8	145.6		86.3[d]	[e]	70.1	85.9[d]	63.3		93.6, 84.1	17.1, 18.3
													71.3, 70.8	26.8, 27.1
8	157.4	158.7	102.5	89.6	122.4	156.5	82.2	[e]	71.0	87.2	61.9	148.9	99.4, 84.3	17.8, 18.5
													74.6, 71.3	27.1, 27.5
9	158.0	158.8	102.5	89.6	122.1	157.5[d]	82.0	[e]	70.8	85.4	64.3	148.9	99.7, 84.3	17.3, 18.5
													74.5, 71.3	27.0, 27.5
11	150.9	151.3	110.4	97.0	129.8	151.0[d]	83.0	[e]	70.9	87.5	61.8	175.7	91.2, 84.2	17.3, 18.7
													73.8, 71.4	27.3, 27.4
12	150.9	151.3	110.4	97.1	129.8	151.0[d]	83.0	[e]	70.8	85.5	64.2	175.7	38.4, 37.8	17.3, 18.7
														27.3, 27.4

[a] Measured in DMSO-d_6. [b] Systematic numbering. [c] Purine numbering. [d] Tentative. [e] Superimposed by DMSO.

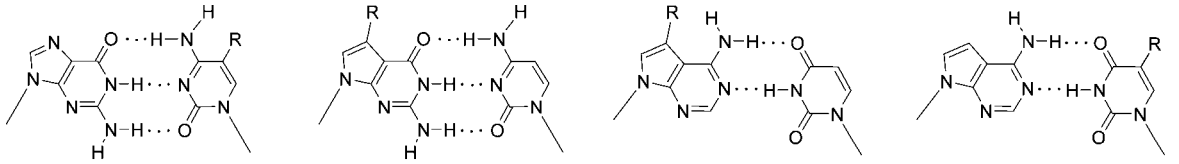

Figure 4. Base Pair Motifs in Duplexes Containing Octadiynyl and Propynyl Nucleosides.

Table 3. T_m Values and Thermodynamic Data of Oligonucleotide Duplexes Containing 5-Octadiynyl-2′-deoxycytidine 1a and 7-Deaza-7-octadiynyl-2′-deoxyguanosine 3a[a]

duplex	T_m [°C]	$\Delta G\,°_{310}$ [kcal/mol]
5′-d(TAG GTC AAT ACT) (**14**)	50	−11.8
3′-d(ATC CAG TTA TGA) (**15**)		
5′-d(TAG GT **1a** AAT ACT) (**16**)	53	−12.1
3′-d(ATC CAG TTA TGA) (**15**)		
5′-d(TAG GT **1a** AAT A **1a**T) (**17**)	54	−12.0
3′-d(ATC CAG TTA TGA) (**15**)		
5′-d(TAG GTC AAT ACT) (**14**)	55	−12.9
3′-d(AT **1a** **1a**AG TTA TGA) (**18**)		
5′-d(TAG GT **1a** AAT ACT) (**16**)	57	−12.6
3′-d(AT **1a** **1a**AG TTA TGA) (**18**)		
5′-d(TA **3a** GTC AAT ACT) (**22**)	52	−11.8
3′-d(ATC CAG TTA TGA) (**15**)		
5′-d(TAG GTC AAT ACT) (**14**)	52	−11.8
3′-d(ATC CAG TTA T **3a**A) (**23**)		
5′-d(TA **3a** **3a**TC AAT ACT) (**24**)	53	−12.3
3′-d(ATC CAG TTA TGA) (**15**)		
5′-d(TA **3a** **3a**TC AAT ACT) (**24**)	55	−12.7
3′-d(ATC CAG TTA T **3a**A) (**23**)		
5′-d(TA **3a** **3a**TC AAT ACT) (**24**)	58	−14.0
3′-d(ATC CA **3a** TTA T **3a**A) (**25**)		

[a] Measured at 260 nm in 1 M NaCl, 100 mM $MgCl_2$ and 60 mM Na cacodylate (pH 7.0) with 5 μM + 5 μM single-strand concentration.

Table 4. T_m Values and Thermodynamic Data of Oligonucleotide Duplexes Containing 7-Deaza-7-octadiynyl-2′-deoxyadenosine 4a, 5-Octadiynyl-2′-deoxyuridine 2a[a]

duplex	T_m [°C]	$\Delta G\,°_{310}$ [kcal/mol]
5′-d(TAG GTC AAT ACT) (**14**)	51	−12.2
3′-d(ATC CAG TTA TGA) (**15**)		
5′-d(TAG GTC **4a**AT ACT) (**30**)	51	−12.2
3′-d(ATC CAG TTA TGA) (**15**)		
5′-d(TAG GTC AAT ACT) (**14**)	51	−12.1
3′-d(ATC C **4a**G TT **4a** TGA) (**31**)		
5′-d(TAG GTC **4a**AT ACT) (**30**)	54	−12.8
3′-d(ATC C **4a**G TT **4a** TGA) (**31**)		
5′-d(TAG G **2a**C AAT ACT) (**34**)	52	−11.9
3′-d(ATC CAG TTA TGA) (**15**)		
5′-d(TAG GTC AAT ACT) (**14**)	53	−12.4
3′-d(ATC CAG **2a2a**A TGA) (**35**)		
5′-d(TAG G **2a**C AAT ACT) (**34**)	55	−12.3
3′-d(ATC CAG **2a2a**A TGA) (**35**)		

[a] Measured at 260 nm in 1 M NaCl, 100 mM $MgCl_2$, and 60 mM Na cacodylate (pH 7.0) with 5 μM + 5 μM single-strand concentration.

Here, we report on the use of oligonucleotides containing octa-1,7-diynyl nucleosides **1a**−**4a** with terminal C≡C bonds for further functionalization using the protocol of [3 + 2] cycloaddition with a nonfluorescent coumarin azide to produce highly fluorescent 1,2,3-triazolyl oligonucleotides. Coumarin is a compound found in many plants, notably as the sweet scent of newly mown hay. It has clinical value as the precursor for several anticoagulants and is used as a gain medium in some dye lasers. Among many fluorophores, coumarin derivatives have been extensively studied because of their special photophysical properties with no low-lying electronic states that interact with their first excited states (*53*). Moreover, the fluorescence properties of coumarin derivatives depend on the nature of the substituents present at the 6- or 7-position of the coumarin ring (*54*–*56*) and can be explained in terms of the intramolecular charge transfer (ICT) mechanism (*57*). Coumarins were used as potential fluorescent probes to study the structural dynamics of DNA (*58*), for the specific labeling of nucleic acids (*59*) and mainly as nucleobase-specific quenchers (*60, 61*).

At first, the "click" reaction was performed using the purified oligonucleotide **30** containing one 7-deaza-7-(octa-1,7-diynyl)-2′-deoxyadenynyl residue and the nonfluorescent coumarin azide **38**. The reaction was carried out in aqueous solution (H_2O/*t*-BuOH/DMSO) in the presence of a 1:1 complex of $CuSO_4$−TBTA (tris(benzyltriazoylmethyl)amine) (*62*) and TCEP (tris(carboxyethyl)phosphine), a water-soluble reducing agent, to give the strongly fluorescent functionalized

Scheme 7

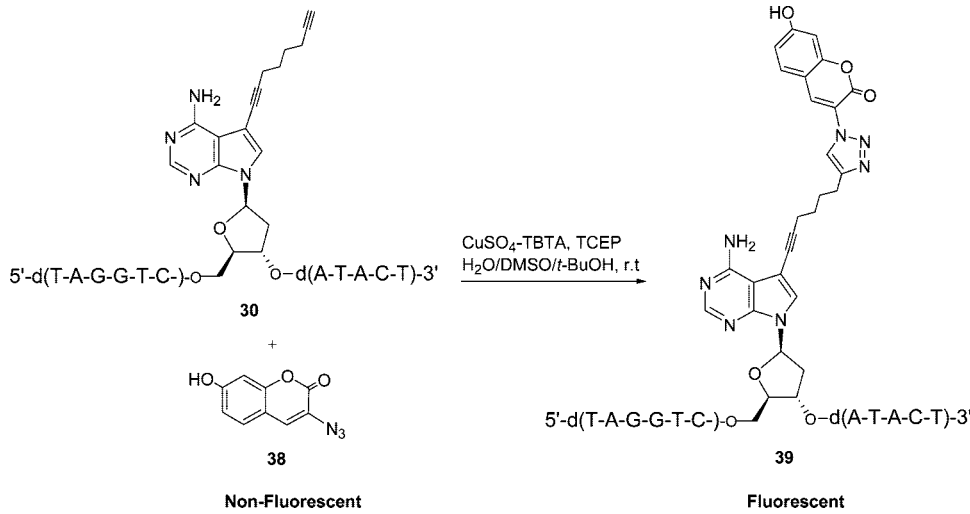

Scheme 8

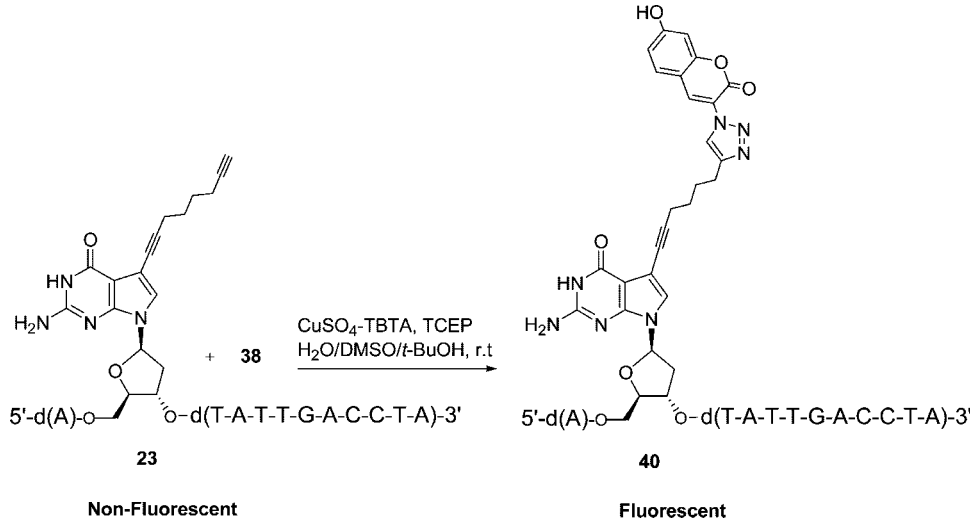

oligonucleotide **39**. The reaction was complete in 15 h at room temperature when an excess molar ratio of coumarin azide was used. The reaction mixture was purified by reversed-phase HPLC, and the strongly fluorescent oligonucleotide **39** was isolated (Scheme 7). The 1,2,3-triazole ring formed by the 1,3-dipolar cycloaddition of the alkyne and azido derivatives of coumarin was found to be strongly fluorescent (*63*). Such reactions are already used for the preparation of fluorogenic probes (*64*) and also for the fluorescence visualization of synthesized mammalian proteins (*65*).

Next, a similar reaction was performed on the oligonucleotide 5′-d(A**3a**T ATT GAC CTA)-3′ (**23**) containing one 7-deazaguanine residue **3a** resulting in the formation of the highly flourescent 7-deazaguanine coumarin conjugate **40** (Scheme 8). The same reaction conditions were used for the click reaction as mentioned above. After the reaction was performed on the 7-deazapurine derivatives, the corresponding pyrimidines were investigated. For this, the oligonucleotide **34** containing **2a** was used, which was conjugated with the coumarin azide **38** to give the click product **41** (Scheme 9). In a similar fashion, 5′-d(AGT ATT GA**1a** CTA)-3′ (**42**) containing 5-(octa-1,7-diynyl)-2′-deoxycytidine was functionalized with the coumarin azide **38** to give **43** (Scheme 10). The ligated 1,2,3-triazolyl "click" oligonucleotides were identified by MALDI-TOF mass spectrometry (Table 3, Supporting Information).

Fluorescence Properties of Oligonucleotides Containing 1,2,3-Triazole Coumarin Derivatives. The fluorescence spectra of the single-stranded oligonucleotide **39** show a strong fluorescence with an emission at 479 nm and an excitation at 400 nm. In the case of the DNA duplex **15•39**, the fluorescence was strongly decreased, a quenching of 85% is observed (Figure 5). This arises from the stacking of dye with the neighboring bases, which is significantly higher in duplex DNA when compared to the single-stranded DNA. In the case of single strands, the dye has a higher degree of steric freedom with negligible stacking with the nucleobases, leading to a higher fluorescence.

It has been reported that the fluorescence of some fluorescent dyes is quenched by the interaction between the dyes and the nucleobases. This quenching is useful to monitor the conformational dynamics of oligonucleotides in solution. However, the dependency of fluorescence quenching is mainly based on the distance between a dye and a nucleobase; in this perspective, several fluorescent dyes like acridine, stilbene, and pyrene were studied (*66*, *67*). Moreover, the quenching of coumarin dyes by nucleobase derivatives in aqueous solution is caused by the photoinduced electron transfer, which is dependent on the oxidation and reduction potential values of the nucleobases (*60*) and the dye. In order to understand the quenching behavior of coumarin dye attached to the modified canonical nucleosides **1a**−**4a** on single-stranded DNA, a series of the above-prepared

Scheme 9

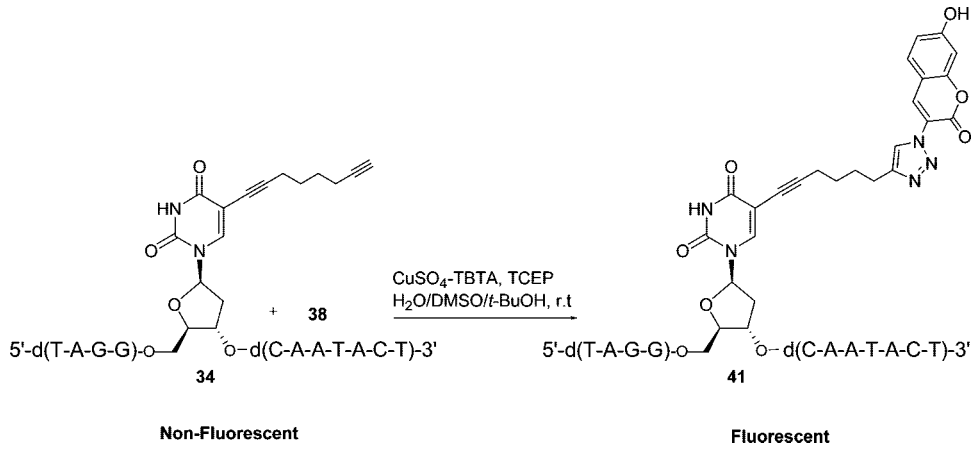

Scheme 10

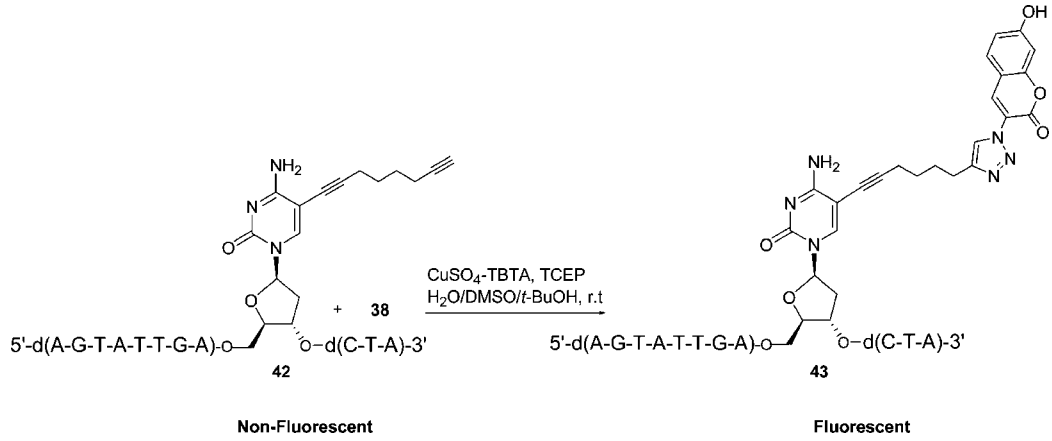

click-functionalized oligonucleotides were used, and the fluorescence quenching properties of such covalently linked coumarin-nucleobase assemblies were investigated by performing enzymatic hydrolysis. The oligomer **39** containing 7-deazaadenine conjugate was digested with snake venom phosphodiesterase and alkaline phosphatase, and fluorescence spectra were measured before and after 3–10 h of cleavage (Figure 6) with an emission observed at 479 nm. Surprisingly, we observed a decrease in fluorescence intensity after addition of enzyme from 3 to 10 h; even after the addition of excess enzyme, the fluorescence was further decreased by 10% and remained constant afterward.

Then, the oligonucleotide **40** containing the 7-deazaguanine conjugate was subjected to enzymatic hydrolysis, and fluorescence emission was recorded at different time intervals (Figure 7) with an emission observed at 479 nm, when excited at 400 nm. From Figure 7, it is clear that the 7-deazaguanine moiety strongly quenches the fluorescence of the coumarin dye attached to it, similar to that of the 7-deazaadenine moiety. Apparently, an intramolecular photoinduced electron transfer plays a role in fluorescence quenching. The 7-deazapurines can act as electron donors, and the 7-deazapurine nucleobase quenches the triazolyl coumarin dye attached to it. The purine bases quench

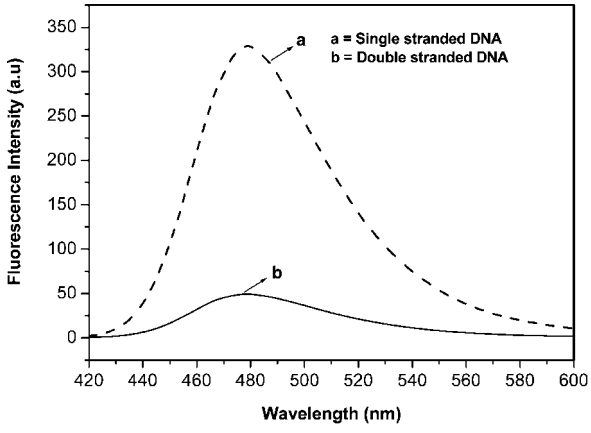

Figure 5. Fluoresence emission spectra of **39** (2 μM single strand) and duplex DNA **15•39** (2 μM of each strand) in bidistilled water at 25 °C when excited at 400 nm.

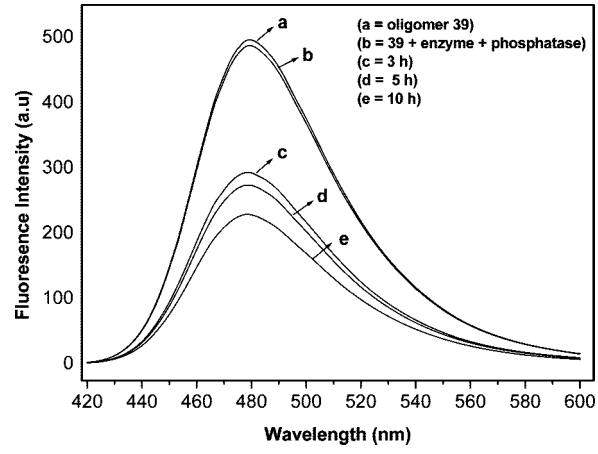

Figure 6. Enzymatic digestion of 1.7 μM single-stranded oligonucleotide **39** with snake venom phosphodiesterase followed by alkaline phosphatase in 0.1 M Tris−HCl buffer (pH 8.3) at 37 °C.

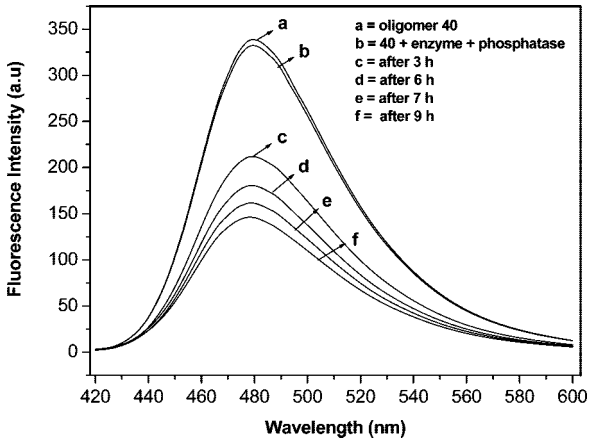

Figure 7. Enzymatic digestion of 1.7 μM single-stranded oligonucleotide **40** with snake venom phosphodiesterase followed by alkaline phosphatase in 0.1 M Tris−HCl buffer (pH 8.3) at 37 °C.

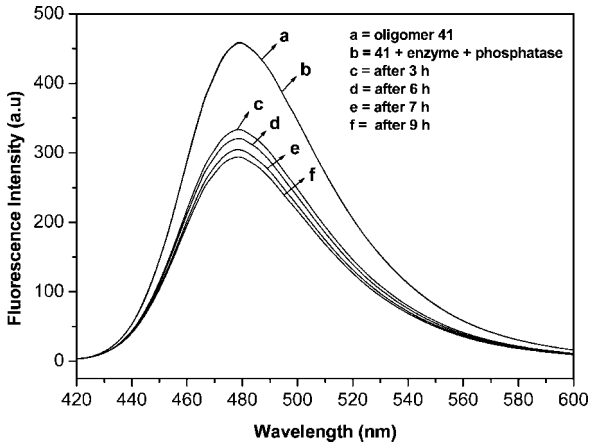

Figure 8. Enzymatic digestion of 1.7 μM single-stranded oligonucleotide **41** with snake venom phosphodiesterase followed by alkaline phosphatase in 0.1 M Tris−HCl buffer (pH 8.3) at 37 °C.

the excited singlet state of coumarins more effectively than pyrimidine bases (*68*). The above results prompted us to study the quenching properties of pyrimidine nucleoside dye conjugates. For that purpose, the enzymatic hydrolysis of the single-stranded oligonucleotide **41** containing the uracil moiety was performed under conditions as described earlier. When oligonucleotide **41** was cleaved, an unexpected fluorescence quenching was observed (Figure 8). However, this quenching was less effective than that observed for the oligonucleotides containing the 7-deazapurine nucleosides **3a** and **4a**. From the HPLC profile of the enzymatic digest of oligomer **41** which contains additional unidentified peaks, it can be concluded that side reactions occurred during irradiation. Such side reactions could be caused by the photoinduced cycloaddition involving the dT−coumarin conjugate within the oligonucleotide chain (*69*). The monomeric click product of octadiynyl 2′-deoxyuridine with azidocoumarin did not form side products under those conditions (data not shown).

In contrary to the above results, a rather different result was observed for oligonucleotide **43** (Figure 9), after the enzymatic digestion for 12 h. There is very little quenching for the 5-(octa-1,7-diynyl)-2′-deoxycytidine dye conjugate when compared with 7-(octa-1,7-diynyl) 7-deazapurines. This shows that the 7-deazapurine bases are strong quenchers of fluorescence when compared to pyrimidines. By changing the oligonucleotide concentration of **40** and **43** from 1.7 μM to 4 μM without changing the enzyme concentration, similar results were obtained in both series of experiments (Figures 7, 9, 10, and 11).

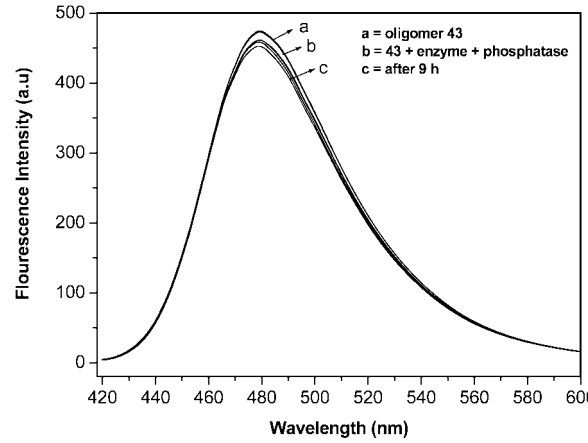

Figure 9. Enzymatic digestion of 1.7 μM single-stranded oligonucleotide **43** with snake venom phosphodiesterase followed by alkaline phosphatase in 0.1 M Tris−HCl buffer (pH 8.3) at 37 °C.

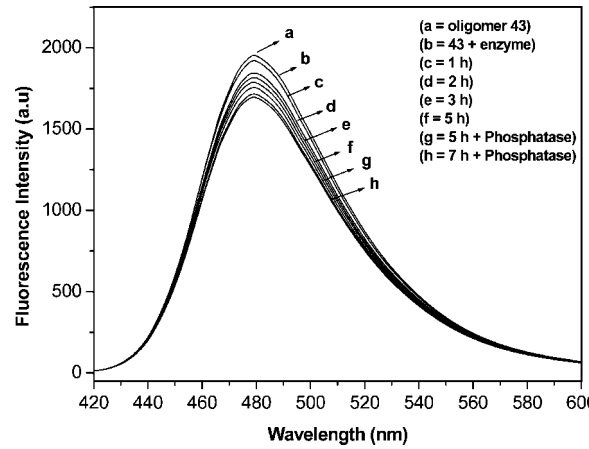

Figure 10. Enzymatic digestion of 4 μM single-stranded oligonucleotide **43** with snake venom phosphodiesterase followed by alkaline phosphatase in 0.1 M Tris−HCl buffer (pH 8.3) at 37 °C.

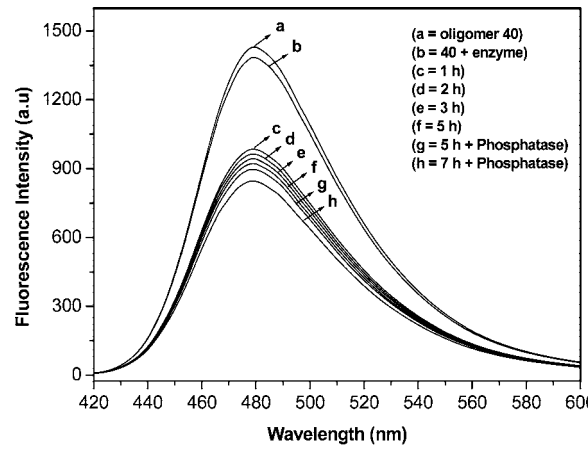

Figure 11. Enzymatic digestion of 4 μM single-stranded oligonucleotide **40** with snake venom phosphodiesterase followed by alkaline phosphatase in 0.1 M Tris−HCl buffer (pH 8.3) at 37 °C.

The HPLC profile of the enzymatically digested oligonucleotide **43** clearly indicates the formation of free nucleosides, and the complete digestion pattern was observed after 7 h.

The most probable reason for this behavior can be explained in terms of intramolecular photoinduced electron transfer from the nucleobase to the coumarin dye attached to it, which strongly quenches the fluorescence when they are in close proximity (Figure

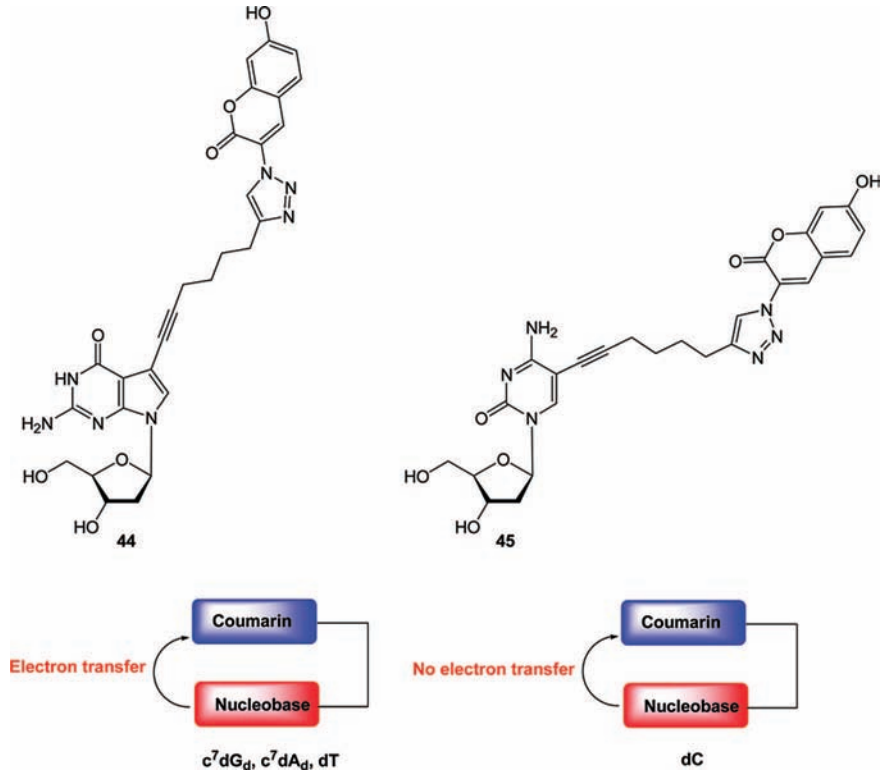

Figure 12. Electron transfer between the nucleobases and coumarin dye attached to it when they are in close proximity.

12). This is evidenced from the fluorescence quantum yield measurements of the monomeric nucleoside−coumarin conjugates in bidistilled water. The 7-deaza-2′-deoxyguanosine−coumarin conjugate **44** shows a quantum yield (Φ) of only 0.11 when compared to that of 2′-deoxycytidine−coumarin conjugate **45** (Φ = 0.22). The quantum yield of fluorescence for nucleoside−dye conjugates was determined relative to quinine sulfate in 0.1 N H_2SO_4 as the standard with Φ = 0.53. The excited coumarins serve as an electron acceptor and the nucleobase as a ground-state donor. A stacked arrangement of the nucleobase and the coumarin dye appears to be a prerequisite for fluorescence quenching. This quenching occurs much more efficiently in the monomeric nucleosides dye conjugates than within a single-stranded oligonucleotide. The latter already shows a preformed helical structure with weakly stacked nucleobases. In this form, the bases are positioned in a way that they are apparently not able to interact with the coumarin dye, while in the duplex structure, the dye molecule interacts with the stacked base pair. Consequently, quenching occurs either in the form of a duplex or within the coumarin−nucleobase assembly, which is generated after the enzymatic digestion of the oligonucleotide. The intramolecular quenching is highly efficient only at short distances; collisional quenching is expected to be comparably inefficient. One should note that the octadiynyl groups might have an influence on the redox potentials of the nucleobases.

CONCLUSION

Nucleosides containing the octa-1,7-diynyl residue at the 5-position of 2′-deoxycytidine or at the 7-position of 7-deazapurines were synthesized by the palladium-assisted Sonogashira cross-coupling reaction resulting in a selective monoderivatization of the diyne starting material. The oligonucleotides incorporating the octa-1,7-diynyl derivatives of 2′-deoxycytidine and 7-deazapurines stabilize the DNA duplexes significantly when compared with the alkynyl counterparts. This group enhances the stability more or equal to that of propynyl residue. Such oligonucleotides containing octa-1,7-diynyl derivatives **1a**−**4a** were further annelated with the nonfluorescent coumarin azide **38** by Huisgen−Sharpless−Meldal "click" chemistry to generate a set of highly fluorescent oligomers **39**, **40**, **41**, and **43**. The enzymatic hydrolysis of such 1,2,3-triazolyl oligonucleotide conjugates revealed that strong fluorescence quenching was observed for 7-deazapurines compared to pyrimidines. The quenching efficiency is in the order $c^7dA_d \approx c^7dG_d > dU > dC$. So, the nucleobase specific quenching of base-modified nucleosides is useful to monitor conformational dynamics of oligonucleotides in solution. The click methodology allows the introduction of various reporter groups like dyes or other functionalized residues, which do not change the water shells of a DNA molecule by retaining stable duplexes. The generation of fluorescence by the "click" reaction can be used for the footprinting of DNA accessible in solution or buried in DNA–protein complexes. The reaction kinetics of this bioorthogonal chemical reporter strategy (nonfluorescent dye becomes fluorescent) can be used for the labeling and visualization of biomolecules in vivo.

ACKNOWLEDGMENT

We thank Dr. H. Rosemeyer and S. Budow for measuring the NMR spectra and Dr. P. Leonard for providing nucleobase precursors. We also thank Mr. K. I. Shaikh and Dr. T. Koch from Roche Diagnostics GmbH, Penzberg, Germany, for the measurement of the MALDI spectra and Mrs. E. Michalek for the oligonucleotide syntheses. Financial support by ChemBiotech, Muenster, Germany, is gratefully acknowledged.

Supporting Information Available: T_m values and thermodynamic data of oligonucleotide duplexes containing propynyl nucleosides **1b**−**4b** (Tables 1 and 2); molecular masses ($[M + H]^+$) of oligonucleotides measured by MALDI-TOF mass spectrometry (Table 3). This material is available free of charge via the Internet at http://pubs.acs.org.

LITERATURE CITED

(1) Uhlmann, E., and Peyman, A. (1990) Antisense oligonucleotides: A new therapeutic principle. *Chem. Rev. 90*, 543–584.

(2) Praseuth, D., Guieysse, A. L., and Helene, C. (1999) Triple helix formation and the antigene strategy for sequence-specific control of gene expression. *Biochim. Biophys. Acta 1489*, 181–206.

(3) Beaucage, S. L., and Iyer, R. P. (1993) The synthesis of modified oligonucleotides by the phosphoramidite approach and their applications. *Tetrahedron 49*, 6123–6194.

(4) Erlich, H. A., Gelfand, D., and Sninsky, J. J. (1991) Recent advances in the polymerase chain reaction. *Science 252*, 1643–1651.

(5) Jain, K. K. (2001) Biochips for gene spotting. *Science 294*, 621–623.

(6) Summerer, D., and Marx, A. (2002) A molecular beacon for quantitative monitoring of the DNA polymerase reaction in real-time. *Angew. Chem., Int. Ed. 41*, 3620–3622.

(7) Seela, F., Jawalekar, A. M., Sirivolu, V. R., Rosemeyer, H., He, Y., and Leonard, P. (2005) Novel DNA nanoparticles and networks. *Nucleosides, Nucleotides, Nucleic Acids 24*, 855–858.

(8) Seela, F., Budow, S., and Leonard, P. (2007) Oligonucleotides forming an i-motif: The pH-dependent assembly of individual strands and branched structures containing 2′-deoxy-5-propynylcytidine. *Org. Biomol. Chem. 5*, 1858–1872.

(9) Seela, F., and Becher, G. (2001) Pyrazolo[3,4-*d*]pyrimidine nucleic acids: Adjustment of dA-dT to dG-dC base pair stability. *Nucleic Acids Res. 29*, 2069–2078.

(10) Seela, F., Peng, X., and Li, H. (2005) Base-pairing, tautomerism, and mismatch discrimination of 7-halogenated 7-deaza-2′-deoxyisoguanosine: Oligonucleotide duplexes with parallel and antiparallel chain orientation. *J. Am. Chem. Soc. 127*, 7739–7751.

(11) Seela, F., and Zulauf, M. (1998) Synthesis of 7-alkynylated 8-aza-7-deaza-2′-deoxyadenosines via the Pd-catalysed cross-coupling reaction. *J. Chem. Soc., Perkin Trans. 1* 3233–3239.

(12) He, J., Mikhailopulo, I., and Seela, F. (2003) 3-Bromopyrazolo[3,4-d]pyrimidine 2′-deoxy-2′-fluoro-β-D-arabinonucleosides: Modified DNA constituents with an unusually rigid sugar N-conformation. *J. Org. Chem. 68*, 5519–5524.

(13) Gao, J., Liu, H., and Kool, E. T. (2004) Expanded-size bases in naturally sized DNA: Evaluation of steric effects in watson-crick pairing. *J. Am. Chem. Soc. 126*, 11826–11831.

(14) Froehler, B. C., Wadwani, S., Terhorst, T. J., and Gerrard, S. R. (1992) Oligodeoxynucleotides containing C-5 propyne analogs of 2′-deoxyuridine and 2′-deoxycytidine. *Tetrahedron Lett. 33*, 5307–5310.

(15) Graham, D., Parkinson, J. A., and Brown, T. (1998) DNA duplexes stabilized by modified monomer residues: Synthesis and stability. *J. Chem. Soc., Perkin Trans. 1* 1131–1138.

(16) Sági, J., Szemzö, A., Ébinger, K., Szabolcs, A., Sági, G., Ruff, É., and Ötvös, L. (1993) Base-modified oligodeoxynucleotides. I: Effect of 5-alkyl, 5-(1-alkenyl) and 5-(1-alkynyl) substitution of the pyrimidines on duplex stability and hydrophobicity. *Tetrahedron Lett. 34*, 2191–2194.

(17) Kottysch, T., Ahlborn, C., Brotzel, F., and Richert, C. (2004) Stabilizing or destabilizing oligodeoxynucleotide duplexes containing single 2′-deoxyuridine residues with 5-alkynyl substituents. *Chem. Eur. J. 10*, 4017–4028.

(18) Seela, F., and Peng, X. (2005) Base-modified oligodeoxyribonucleotides: Pyrrolo[2,3-*d*]pyrimidines replacing purines. *Current Protocols in Nucleic Acid Chemistry* (Beaucage, S. L., Bergstrom, D. E., Glick, G. D., and Jones, R. A., Eds.) John Wiley & Sons.

(19) Seela, F., Peng, X., and Budow, S. (2007) Advances in the synthesis of 7-deazapurine-pyrrolo[2,3-*d*]pyrimidine-2′-deoxyribonucleosides including D-and L-enantiomers, fluoro derivatives and 2′,3′-dideoxyribonucleosides. *Curr. Org. Chem. 11*, 427–462.

(20) Seela, F., and Zulauf, M. (1996) Palladium-catalyzed cross coupling of 7-iodo-2′-deoxytubercidin with terminal alkynes. *Synthesis* 726–730.

(21) Seela, F., and Zulauf, M. (1998) 7-Deazaadenine-DNA: Bulky 7-iodo substituents or hydrophobic 7-hexynyl chains are well accommodated in the major groove of oligonucleotide duplexes. *Chem. Eur. J. 4*, 1781–1790.

(22) Seela, F., and Zulauf, M. (1999) Oligonucleotides containing 7-deazaadenines: The influence of the 7-substituent chain length and charge on the duplex stability. *Helv. Chim. Acta 82*, 1878–1898.

(23) Seela, F., and Ramzaeva, N. (1996) Duplex stability of 7-deazapurine DNA: Oligonucleotides containing 7-bromo or 7-iodo-7-deazaguanine. *Helv. Chim. Acta 79*, 1549–1558.

(24) Ramzaeva, N., Mittelbach, C., and Seela, F. (1997) 7-Deazaguanine DNA: Oligonucleotides with hydrophobic or cationic side chains. *Helv. Chim. Acta 80* 1809–1822.

(25) Rosemeyer, H., Ramzaeva, N., Becker, E.-M., Feiling, E., and Seela, F. (2003) Oligonucleotides incorporating 7-(aminoalkynyl-1-yl)-7-deaza-2′-deoxyguanosines: Duplex stability and phosphodiester hydrolysis by exonucleases. *Nucleosides, Nucleotides, Nucleic Acids 22*, 1231–1234.

(26) Barnes, T. W., III, and Turner, D. H. (2001) Long-range cooperativity in molecular recognition of RNA by oligodeoxynucleotides with multiple C5-(1-propynyl) pyrimidines. *J. Am. Chem. Soc. 123*, 4107–4118.

(27) Wagner, R. W., Matteucci, M. D., Lewis, J. G., Gutierrez, A. J., Moulds, C., and Froehler, B. C. (1993) Antisense gene inhibition by oligonucleotides containing C-5 propyne pyrimidines. *Science 260*, 1510–1513.

(28) Gutierrez, A. J., Matteucci, M. D., Grant, D., Matsumura, S., Wagner, R. W., and Froehler, B. C. (1997) Antisense gene inhibition by C-5-substituted deoxyuridine-containing oligodeoxynucleotides. *Biochemistry 36*, 743–748.

(29) Ahmadian, M., Zhang, P., and Bergstrom, D. E. (1998) A comparative study of the thermal stability of oligodeoxyribonucleotides containing 5-substituted 2′-deoxyuridines. *Nucleic Acids Res. 26*, 3127–3135.

(30) Buhr, C. A., Wagner, R. W., Grant, D., and Froehler, B. C. (1996) Oligodeoxynucleotides containing C-7 propyne analogs of 7-deaza-2′-deoxyguanosine and 7-deaza-2′-deoxyadenosine. *Nucleic Acids Res. 24*, 2974–2980.

(31) Seela, F., and Shaikh, K. I. (2005) Oligonucleotides containing 7-propynyl-7-deazaguanine: Synthesis and base pair stability. *Tetrahedron 61*, 2675–2681.

(32) He, J., and Seela, F. (2002) Propynyl groups in duplex DNA: Stability of base pairs incorporating 7-substituted 8-aza-7-deazapurines or 5-substituted pyrimidines. *Nucleic Acids Res. 30*, 5485–5496.

(33) Bock, V. D., Hiemstra, H., and van Maarseveen, J. H. (2006) Cu^{I}-catalyzed alkyne-azide "click" cycloadditions from a mechanistic and synthetic perspective. *Eur. J. Org. Chem.* 51–68.

(34) Binder, W. H., and Kluger, C. (2006) Azide/alkyne-"click" reactions: Applications in material science and organic synthesis. *Curr. Org. Chem. 10*, 1791–1815.

(35) Seela, F., and Sirivolu, V. R. (2007) Nucleosides and oligonucleotides with diynyl side chains: Base pairing and functionalization of 2′-deoxyuridine derivatives by the copper(I)-catalyzed alkyne-azide "click" cycloaddition. *Helv. Chim. Acta 90*, 535–552.

(36) Seela, F., and Sirivolu, V. R. (2006) DNA containing side chains with terminal triple bonds: Base-pair stability and functionalization of alkynylated pyrimidines and 7-deazapurines. *Chem. Biodiv. 3*, 509–514.

(37) Ramzaeva, N., Rosemeyer, H., Leonard, P., Mühlegger, K., Bergmann, F., von der Eltz, H., and Seela, F. (2000) Oligonucleotides functionalized by fluorescein and rhodamine dyes: Michael addition of methyl acrylate to 2′-deoxypseudouridine. *Helv. Chim. Acta 83*, 1108–1126.

(38) Seela, F., Ramzaeva, N., Leonard, P., Chen, Y., Debelak, H., Feiling, E., Kröschel, R., Zulauf, M., Wenzel, T., Fröhlich, T., and Kostrzewa, M. (2001) Phosphoramidites and oligonucleotides containing 7-deazapurines and pyrimidines carrying aminopro-

pargyl side chains. *Nucleosides, Nucleotides, Nucleic Acids 20*, 1421–1424.
(39) Acharya, P., Cheruku, P., Chatterjee, S., Acharya, S., and Chattopadhyaya, J. (2004) Measurement of nucleobase p K_a values in model mononucleotides shows RNA-RNA duplexes to be more stable than DNA-DNA duplexes. *J. Am. Chem. Soc. 126*, 2862–2869.
(40) Albert, A., and Serjeant, E. P. (1971) *The Determination of Ionization Constants*, pp 44−64, Chapman and Hall Ltd., London.
(41) Theruvathu, J. A., Flyunt, R., Aravindakumar, C. T., and von Sonntag, C. (2001) Rate constants of ozone reactions with DNA, its constituents and related compounds. *J. Chem. Soc., Perkin Trans. 2*, 269–274.
(42) Ti, G. S., Gaffney, B. L., and Jones, R. A. (1982) Transient protection: Efficient one-flask syntheses of protected deoxynucleosides. *J. Am. Chem. Soc. 104*, 1316–1319.
(43) Seela, F., Shaikh, K., and Eickmeier, H. (2004) 7-deaza-2′-deoxy-7-propynylguanosine. *Acta Crystallogr. C60*, o489–o491.
(44) Huisgen, R. (1989) Kinetics and reaction mechanisms: Selected examples from the experience of forty years. *Pure Appl. Chem. 61*, 613–628.
(45) Rostovtsev, V. V., Green, L. G., Fokin, V. V., and Sharpless, K. B. (2002) A stepwise huisgen cycloaddition process: Copper(I)-catalyzed regioselective "ligation" of azides and terminal alkynes. *Angew. Chem., Int. Ed. 41*, 2596–2599.
(46) Tornøe, C. W., Christensen, C., and Meldal, M. (2002) Peptidotriazoles on solid phase: [1,2,3]-Triazoles by regiospecific copper(I)-catalyzed 1,3-dipolar cycloadditions of terminal alkynes to azides. *J. Org. Chem. 67*, 3057–3064.
(47) Weller, R. L., and Rajski, S. R. (2005) DNA methyltransferase-moderated click chemistry. *Org. Lett. 7*, 2141–2144.
(48) Burley, G. A., Gierlich, J., Mofid, M. R., Nir, H., Tal, S., Eichen, Y., and Carell, T. (2006) Directed DNA metallization. *J. Am. Chem. Soc. 128*, 1398–1399.
(49) Gierlich, J., Burley, G. A., Gramlich, P. M. E., Hammond, D. M., and Carell, T. (2006) Click chemistry as a reliable method for the high-density postsynthetic functionalization of alkyne-modified DNA. *Org. Lett. 8*, 3639–3642.
(50) Seo, T. S., Li, Z., Ruparel, H., and Ju, J. (2003) Click chemistry to construct fluorescent oligonucleotides for DNA sequencing. *J. Org. Chem. 68*, 609–612.
(51) Kumar, R., EI-Sagheer, A., Tumpane, J., Lincoln, P., Wilhelmsson, L. M., and Brown, T. (2007) Template-directed oligonucleotide strand ligation, covalent intramolecular DNA circularization and catenation using click chemistry. *J. Am. Chem. Soc. 129*, 6859–6864.
(52) Devaraj, N. K., Miller, G. P., Ebina, W., Kakaradov, B., Collman, J. P., Kool, E. T., and Chidsey, C. E. D. (2005) Chemoselective covalent coupling of oligonucleotide probes to self-assembled monolayers. *J. Am. Chem. Soc. 127*, 8600–8601.
(53) Lewis, J. E., and Maroncelli, M. (1998) On the (uninteresting) dependence of the absorption and emission transition moments of coumarin 153 on solvent. *Chem. Phys. Lett. 282*, 197–203.
(54) Takadate, A., Masuda, T., Murata, C., Isobe, A., Shinohara, T., Irikura, M., and Goya, S. (1997) A derivatizing reagent-kit using a single coumarin fluorophore. *Anal. Sci. 13*, 753–756.
(55) Murata, C., Masuda, T., Kamochi, Y., Todoroki, K., Yoshida, H., Nohta, H., Yamaguchi, M., and Takadate, A. (2005) Improvement of fluorescence characteristics of coumarins: Syntheses and fluorescence properties of 6-methoxycoumarin and benzocoumarin derivatives as novel fluorophores emitting in the longer wavelength region and their application to analytical reagents. *Chem. Pharm. Bull. 53* (7), 750–758.
(56) Atkins, R. L., and Bliss, D. E. (1978) Substituted coumarins and aza coumarins: Synthesis and fluorescent properties. *J. Org. Chem. 43*, 1975–1980.
(57) de Silva, A. P., Gunaratne, H. Q. N., Gunnlaugsson, T., Huxley, A. J. M., McCoy, C. P., Rademacher, J. T., and Rice, T. E. (1997) Signaling recognition events with fluorescent sensors and switches. *Chem. Rev. 97*, 1515–1566.
(58) Coleman, R. S., Berg, M. A., and Murphy, C. J. (2007) Coumarin base-pair replacement as a fluorescent probe of ultrafast DNA dynamics. *Tetrahedron 63*, 3450–3456.
(59) Kosiova, I., Janicova, A., and Kois, P. (2006) Synthesis of coumarin or ferrocene labeled nucleosides via staudinger ligation. *Beilstein J. Org. Chem. 2*, 23.
(60) Seidel, C. A. M., Schulz, A., and Sauer, M. H. M. (1996) Nucleobase-specific quenching of fluorescent dyes. 1. Nucleobase one-electron redox potentials and their correlation with static and dynamic quenching efficiencies. *J. Phys. Chem. 100*, 5541–5553.
(61) Seidel, C. A. M. (1991) Nucleic acid base specific quenching of a coumarin-120-derivative in nucleotide-conjugates-photoinduced electron transfer. *Proc. SPIE-Int. Soc. Opt. Eng. (Biomolecular Spectroscopy II) 1432*, 91–104.
(62) Chan, T. R., Hilgraf, R., Sharpless, K. B., and Fokin, V. V. (2004) Polytriazoles as copper(I)- stabilizing ligands in catalysis. *Org. Lett. 6*, 2853–2855.
(63) Sivakumar, K., Xie, F., Cash, B. M., Long, S., Barnhill, H. N., and Wang, Q. (2004) A fluorogenic 1,3-dipolar cycloaddition reaction of 3-azidocoumarins and acetylenes. *Org. Lett. 6*, 4603–4606.
(64) Zhou, Z., and Fahrni, C. J. (2004) A fluorogenic probe for the copper(I)-catalyzed azide-alkyne ligation reaction: Modulation of the fluorescence emission via ^{3}. (n,π^*)-^{1}(π,π^*) inversion. *J. Am. Chem. Soc. 126*, 8862–8863.
(65) Beatty, K. E., Liu, J. C., Xie, F., Dieterich, D. C., Schuman, E. M., Wang, Q., and Tirrell, D. A. (2006) Fluorescence visualization of newly synthesized proteins in mammalian cells. *Angew. Chem., Int. Ed. 45*, 7364–7367.
(66) Zahavy, E., and Fox, M. A. (1999) Photophysical quenching mediated by guanine groups in pyrenyl-*N*-alkylbutanoamide end-labeled oligonucleotides. *J. Phys. Chem. B 103*, 9321–9327.
(67) Fukui, K., and Tanaka, K. (1998) Distance dependence of photoinduced electron transfer in DNA. *Angew. Chem., Int. Ed. 37*, 158–161.
(68) Kang, H. K., Shin, E. J., and Shim, S. C. (1992) Transient absorption spectra and quenching of coumarin excited states by nucleic acid bases. *J. Photochem. Photobiol., B: Biol. 13*, 19–28.
(69) Straub, K., Kanne, D., Hearst, J. E., and Rapoport, H. (1981) Isolation and characterization of pyrimidine-psoralen photoadducts from DNA. *J. Am. Chem. Soc. 103*, 2347–2355.

BC700300F

SUPPORTING INFORMATION

The Modification of DNA with Octadiynyl Side Chains: Synthesis, Base Pairing and Formation of Fluorescent Coumarin Dye Conjugates of Four Nucleobases by the Alkyne–Azide "Click" Reaction

Frank Seela*, Venkata Ramana Sirivolu and Padmaja Chittepu

Laboratory for Bioorganic Chemistry and Chemical Biology, Center for Nanotechnology, Heisenbergstrasse 11, 48149 Münster, Germany, and Laboratorium für Organische und Bioorganische Chemie, Institut für Chemie, Universität Osnabrück, Barbarastrasse 7, 49069 Osnabrück, Germany

Tel. +49(251)53406500; Fax +49(251)53406857;

E-mail: Frank.Seela@uni-osnabrueck.de. URL:http://www.seela.net

Table of Contents

Table 1: T_m Data of Oligonucleotide Duplexes **S2**

Table 2: T_m Data of Oligonucleotide Duplexes **S3**

Table 3: Molecular Masses of Oligonucleotides **S4**

Table 1. T_m Values and Thermodynamic Data of Oligonucleotide Duplexes Containing 5-Propynyl-2′-deoxycytidine 1b, 7-Deaza-7-propynyl-2′-deoxyguanosine 3b[a]

Duplex	T_m [°C]	$\Delta G°_{310}$ [kcal/mol]	Duplex	T_m [°C]	$\Delta G°_{310}$ [kcal/mol]
5′-d(TAG GTC AAT ACT) (**14**) 3′-d(ATC CAG TTA TGA) (**15**)	50	-11.8	5′-d(TA**3b** GTC AAT ACT) (**26**) 3′-d(ATC CAG TTA TGA) (**15**)	50	-11.3
5′-d(TAG GT**1b**AAT ACT) (**19**) 3′-d(ATC CAG TTA TGA) (**15**)	53	-12.4	5′-d(TAG GTC AAT ACT) (**14**) 3′-d(ATC CAG TTA T**3b**A) (**27**)	51	-11.6
5′-d(TAG GT**1b** AAT A**1b**T) (**20**) 3′-d(ATC CAG TTA TGA) (**15**)	54	-12.8	5′-d(TA**3b 3b**TC AAT ACT) (**28**) 3′-d(ATC CAG TTA TGA) (**15**)	53	-12.5
5′-d(TAG GTC AAT ACT) (**14**) 3′-d(AT**1b 1b**AG TTA TGA) (**21**)	55	-12.8	5′-d(TA**3b 3b**TC AAT ACT) (**28**) 3′-d(ATC CAG TTA T**3b**A) (**27**)	54	-13.0
5′-d(TAG GT**1b** AAT ACT) (**19**) 3′-d(AT**1b 1b**AG TTA TGA) (**21**)	58	-13.4	5′-d(TA**3b 3b**TC AAT ACT) (**28**) 3′-d(ATC CA**3b** TTA T**3b**A) (**29**)	55	-12.8

[a] Measured at 260 nm in 1 M NaCl, 100 mM $MgCl_2$ and 60 mM Na-cacodylate (pH 7.0) with 5 µM + 5
5 µM single-strand concentration.

Table 2. T_m Values and Thermodynamic Data of Oligonucleotide Duplexes Containing 7-Deaza-7-propynyl-2′-deoxyadenosine 4b, 5-Propynyl-2′-deoxyuridine 2b[a]

Duplex	T_m [°C]	$\Delta G°_{310}$ [kcal/mol]	Duplex	T_m [°C]	$\Delta G°_{310}$ [kcal/mol]
5′-d(TAG GTC AAT ACT) (**14**) 3′-d(ATC CAG TTA TGA) (**15**)	47[b]	-10.9	5′-d(TAG G**2b**C AAT ACT) (**36**) 3′-d(ATC CAG TTA TGA) (**15**)	52	-11.9
5′-d(TAG GTC **4b**AT ACT) (**32**) 3′-d(ATC CAG TTA TGA) (**15**)	49[b]	-11.3	5′-d(TAG GTC AAT ACT) (**14**) 3′-d(ATC CAG **2b2b**A TGA) (**37**)	52	-12.2
5′-d(TAG GTC AAT ACT) (**14**) 3′-d(ATC C**4b**G TT**4b** TGA) (**33**)	51[b]	-11.8	5′-d(TAG G**2b**C AAT ACT) (**36**) 3′-d(ATC CAG **2b2b**A TGA) (**37**)	53	-12.5
5′-d(TAG GTC **4b**AT ACT) (**32**) 3′-d(ATC C**4b**G TT**4b** TGA) (**33**)	53[b]	-11.8			

[a] Measured at 260 nm in 1 M NaCl, 100 mM $MgCl_2$ and 60 mM Na-cacodylate (pH 7.0) with 5 µM + 5 µM single-strand concentration. [b] Measured at 260 nm in 0.1 M NaCl, 10 mM $MgCl_2$ and 10 mM Na-cacodylate (pH 7.0) with 5 µM + 5 µM single-strand concentration.

Table 3. Molecular Masses ([M+H]$^+$) of Oligonucleotides Measured by MALDI-TOF Mass Spectrometry[a]

Duplex	[M+H]$^+$ (calc)	[M+H]$^+$ (found)
5′-d(TAG GTC AAT ACT)-3′ (**14**)	3645.4	3645.0
5′-d(AGT ATT GAC CTA)-3′ (**15**)	3645.4	3645.1
5′-d(TAG GT**1a** AAT ACT)-3′ (**16**)	3747.7	3747.8
5′-d(TAG GT**1a** AAT A**1a**T)-3′ (**17**)	3851.8	3852.6
5′-d(AGT ATT GA**1a 1a**TA)-3′ (**18**)	3851.8	3852.3
5′-d(TAG **3a**TC AAT ACT)-3′ (**22**)	3747.6	3746.4
5′-d(A**3a**T ATT GAC CTA)-3′ (**23**)	3747.6	3747.6
5′-d(TA**3a 3a**TC AAT ACT)-3′ (**24**)	3850.7	3850.6
5′-d(A**3a**T ATT **3a**AC CTA)-3′ (**25**)	3850.7	3850.4
5′-d(TAG GTC **4a**AT ACT)-3′ (**30**)	3749.1	3748.0
5′-d(AGT **4a**TT G**4a**C CTA)-3′ (**31**)	3851.2	3851.2
5′-d(TAG GTC **4a**[a]AT ACT)-3′ (**39**)	3952.0	3951.2
5′-d(A**3a**[a]T ATT GAC CTA)-3′ (**40**)	3950.2	3950.3
5′-d(TAG G**2a**[a]C AAT ACT)-3′ (**41**)	3938.2	3938.5
5′-d(AGT ATT GA**1a** CTA)-3′ (**42)**)	3748.0	3748.5
5′-d(AGT ATT GA**1a**[a] CTA)-3′ (**43**)	3951.1	3951.0

[a] Functionalized with coumarin azide **38**

Novel Near-Infrared Fluorescent Integrin-Targeted DFO Analogue

Yunpeng Ye, Sharon Bloch, Baogang Xu, and Samuel Achilefu*

Department of Radiology, Washington University, 4525 Scott Avenue, St. Louis, Missouri 63110. Received August 9, 2007

Desferrioxamine (DFO), a siderophore initially isolated from *Streptomyces pilosus*, possesses extraordinary metal binding properties with wide biomedical applications that include chelation therapy, nuclear imaging, and antiproliferation. In this work, we prepared a novel multifunctional agent consisting of (i) a near-infrared (NIR) fluorescent probe-cypate; (ii) an integrin $\alpha_v\beta_3$ receptor (ABIR)-avid cyclic RGD peptide, and (iii) a DFO moiety, DFO-cypate-cyclo[RGDfK(∼)] (**1**, with ∼ representing the cypate conjugation site at the side chain of lysine; f is D-phenylalanine). Compound **1** and two control compounds, cypate-cyclo[RGDfK(∼)] (**2**) and cypate-DFO (**3**), were synthesized by modular assembly of the corresponding protected RGD peptide cyclo[R(Pbf)GD(OBut)fK] and DFO on the dicarboxylic acid-containing cypate scaffold in solution. The three compounds exhibited similar UV–vis and emission spectral properties. Metal binding analysis shows that DFO as well as **1** and **3** exhibited relatively high binding affinity with Fe(III), Al(III), and Ga(III). In contrast to Ga(III), the binding of Fe to **1** and **3** quenched the fluorescence emission of cypate significantly, suggesting an efficient metal-mediated approach to perturb the spectral properties of NIR fluorescent carbocyanine probes. In vitro, **1** showed a high ABIR binding affinity (10^{-7} M) comparable to that of **2** and the reference peptide cyclo(RGDfV), indicating that both DFO and cypate motifs did not interfere significantly with the molecular recognition of the cyclic RGD motif with ABIR. Fluorescence microscopy showed that internalization of **1** and **2** in ABIR-positive A549 cells at 1 h postincubation was higher than **3** and cypate alone, demonstrating that incorporating ABIR-targeting RGD motif could improve cellular internalization of DFO analogues. The ensemble of these findings demonstrate the use of multifunctional NIR fluorescent ABIR-targeting DFO analogues to modulate the spectral properties of the NIR fluorescent probe by the chelating properties of DFO and visualize intracellular delivery of DFO by receptor-specific peptides. These features provide a strategy to explore the potential of **1** in tumor imaging and treatment as well as some molecular recognition processes mediated by metal ions.

INTRODUCTION

Recent research efforts have demonstrated that molecular imaging is a powerful tool for localizing, identifying, and characterizing a host of disease-specific targets. Examples include imaging molecular interactions, cell trafficking, tumor vitality, cell proliferation, apoptosis, angiogenesis, and response to treatment. In particular, optical molecular imaging holds great promise to accelerate drug discovery and development, including compound screening, lead discovery, optimization, pharmacokinetic studies, and clinical trials (*1–3*).

An attractive feature of optical imaging is its ability to unravel the molecular basis of cancers and other diseases, thereby providing vital information for diagnosing, staging, and monitoring therapeutic response (*4–6*). These applications emanate from numerous advantages of optical methods, including high detection sensitivity, real-time monitoring, convenience, and accessibility. In contrast to other established imaging methods such as radionuclear and X-ray-computed tomography, the use of low-energy (nonionizing) radiation for optical imaging provides additional benefit, especially in longitudinal studies. Over the past few years, tremendous progress has been made in the development of optical contrast agents for in vivo tumor optical imaging. For instance, we and others have developed NIR fluorescent probes such as cyanine dyes and their bioconjugates, including somatostatin and RGD peptide analogues, as optical contrast agents for in vitro and in vivo tumor optical imaging (*7–13*). These results have inspired us to further apply optical imaging and related optical contrast agents in the discovery and development of novel, multifunctional, and targeted oncologic drugs. For example, the biological properties of therapeutic agents such as desferrioxamine (DFO) can be altered by linkage to a target-specific NIR fluorescent probe and the intracellular transport visualized by optical methods.

DFO, a siderophore initially isolated from *Streptomyces pilosus*, is a selective iron chelator (*14*). This siderphore and some analogues have been used in chelation therapy to treat iron-overload diseases, such as thalassemia, sickle-cell anemia, and hemochromatosis (*15–17*). DFO has also been shown to possess antiproliferative activities, and clinical studies have demonstrated its potential as an adjunct to chemotherapy regimens (*18–21*). Its radiosensitizing activities have been utilized in radiation oncology (*22*). DFO has also served as a good chelator for radioactive metals in cancer nuclear imaging as demonstrated by the use of radioactive ^{67}Ga/^{68}Ga-[DFO]-octreotide to image somatostatin receptor-positive tumors by positron emission tomography (*23*). Despite its lack of oral bioavailability and difficulties in patient compliance, the continued use of DFO in clinical settings strongly attests to its great potential in biomedical applications. It further suggests the potential use of DFO as a lead compound for discovering and developing novel DFO analogues and synthetic mimetics with improved biological properties and activities (*24–27*). However, the biological activity of DFO is not targeted to a specific molecular process and its hydrophilic nature limits its internalization in cells. For these reasons, conjugation of DFO with a receptor-specific ligand such as $\alpha_V\beta_3$ integrin receptor (ABIR)-avid RGD peptide could overcome these problems.

Integrins are heterodimeric cell-surface receptors that mediate cell−cell and cell−matrix adhesion, metastasis, and angiogenesis processes (*28–31*). In particular, the overexpression of ABIR

* Corresponding author. Phone: 314-362-8599. Fax: 314-747-5191. achilefus@mir.wustl.edu.

10.1021/bc7003022 CCC: $40.75 © 2008 American Chemical Society
Published on Web 11/27/2007

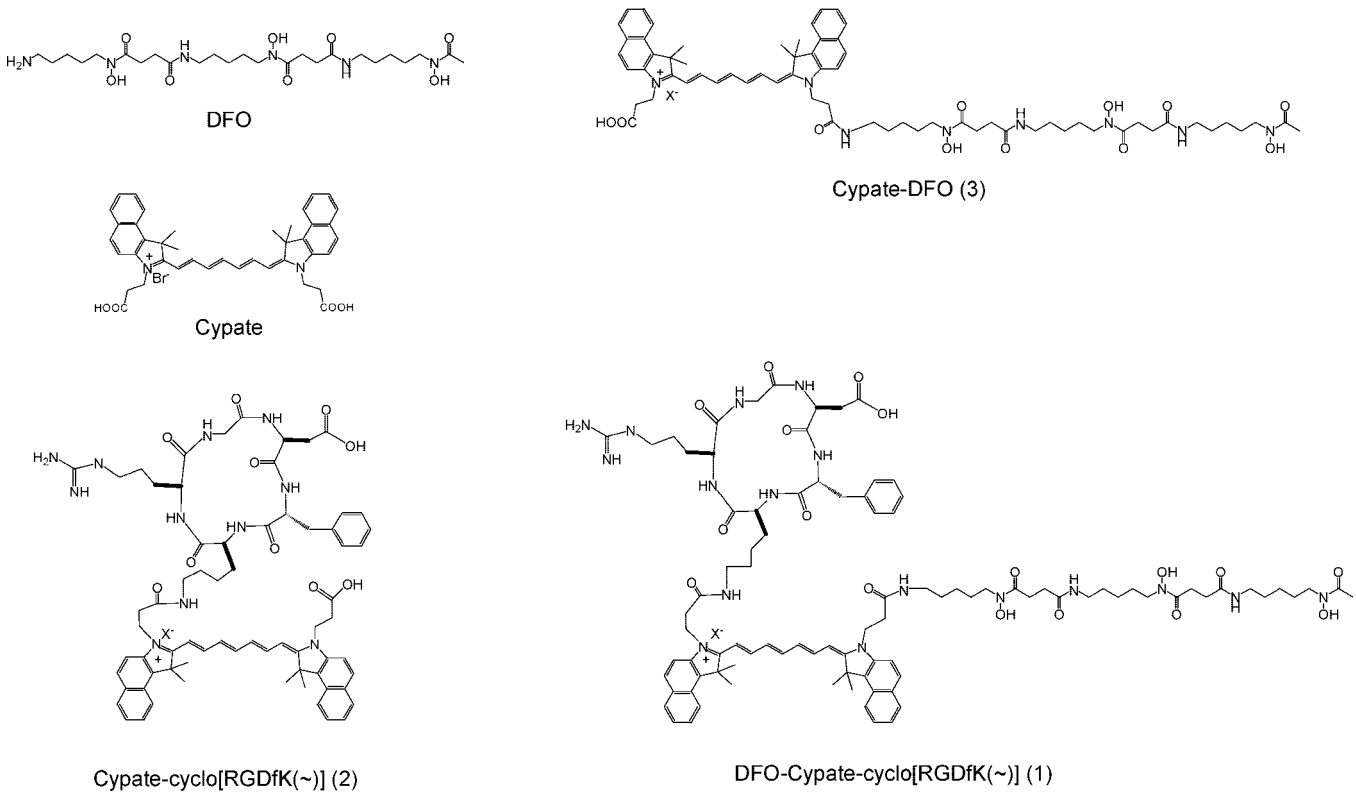

Figure 1. Structures of DFO-cypate-[RGDfK(∼)] (**1**) and the related compounds.

on activated endothelial cells in the neovasculature of tumors such as breast cancer, lung carcinomas, melanomas, and glioblastomas has been correlated with tumor growth, invasion, and metastasis. Therefore, ABIR is an attractive molecular target for tumor imaging, early diagnosis, and therapy (*32*–*37*). Diverse ligands, including peptides and peptidomimetics have been found to interact with ABIR. Some of the high ABIR-binding peptides have been successfully used to elucidate the structure and mechanisms as well as targeted delivery of NIR fluorescent probes, radionuclides, and anticancer agents (*38*–*44*).

In this study, we report the synthesis and in vitro evaluation of **1** and its two analogues, that is, cypate-[RGDfK(∼)] (**2**) and cypate-DFO (**3**) for targeting ABIR (Figure 1). The RGD peptide in the novel multifunctional NIR fluorescent RGD-bearing DFO (**1**) enhanced the cellular uptake of DFO. We also found that the metal-chelating properties of DFO can modulate the NIR fluorescence emission of cypate.

EXPERIMENTAL PROCEDURES

General. All reagents and solvents were purchased from commercial sources. Solvents and chemicals were reagent grade and used without further purification. Cypate was prepared as previously reported (*45*). Analytical (Vydac C-18 column; 250 × 4.6 mm) and semipreparative (Vydac C-18 column; 25 × 2.2 cm) HPLC were performed at a flow rate of 1.0 mL/min and 9.5 mL/min, respectively. HPLC solvents consisted of solvent A (water containing 0.05% trifluoroacetic acid (TFA)) and solvent B (acetonitrile (ACN) containing 0.05% TFA). Linear gradient elution protocol for analytical HPLC started from 90% A to 30% A in B for 20 min. The gradient for semipreparative HPLC ranged from 90% A to 30% A over 15 min and was held at 30% for 30 min. The elution profile was monitored by UV/vis at 214 and 254 nm. Mass spectra (ES-MS) were obtained using a Shimadzu mass spectrometer (LCMS-2010A) in the positive electrospray mode.

Solid Phase Peptide Synthesis. All the peptides were assembled manually on resin using conventional Fmoc chemistry (*46*). The coupling reactions were carried out by adding a preactivated solution of N-α-Fmoc-protected amino acid (3 equiv), 1-hydroxybenzotriazole (HOBt, 3 equiv), 2-(1*H*-benzotriazole-1-yl)-1,1,3,3-tetramethyluronium hexafluorophosphate (HBTU, 3 equiv), and *N*,*N*-diisopropylethylamine (DIEA, 6 equiv) in anhydrous *N*,*N*-dimethylformamide (DMF, 3–5 mL/g resin) to the resin (1 equiv) and mixing for 2 h. The progress of the coupling was monitored by the Kaiser test. The Fmoc-protecting group was removed by treating the product with a solution of 20% piperidine in DMF for 10 min (2×). The resin was washed with methanol (1 min, 3 mL, 2×) and DMF (1 min, 3 mL, 6×) and used in subsequent reactions.

Cyclo[Asp(OBut)-phe-Lys-Arg(Pbf)-Gly]. The resin-bound protected peptide (H-Asp(OBut)-phe-Lys-Arg(Pbf)-Gly resin) was assembled manually from H-Gly-2-chlorotrityl resin (1.0 g, 0.54 mmol/g) as described above. The side-chain-protected peptide was cleaved by mixing the resin with 1% TFA in dichloromethane (DCM) for 5 min. The filtrate was added to a solution of pyridine (5 mL)/methanol (10 mL). and the resin was washed with methanol and dichloromethane. The cleavage procedure was repeated 5 times. The combined filtrates were concentrated and washed with water to afford the desired protected RGD pentapeptide H-Asp(OBut)-phe-Lys-(Dde)-Arg-(Pbf)-Gly-OH; 561 mg, 95% yield; ES-MS: $[MH]^+/[MH]^{2+}$ 1094.5/547.8).

The linear peptide obtained was dissolved in DMF (10 mL) and added dropwise into a solution of benzotriazole-1-yl-oxy-tris-pyrrolidino-phosphonium hexafluorophosphate (PyBOP, 520 mg, 1.0 mmol), HOBT (135 mg, 1.0 mmol), and DIEA (207 mg, 1.6 mmol) in DMF (80 mL)/DCM (720 mL). The mixture was stirred overnight, concentrated, and washed with water to give the crude product cyclo[Asp(OBut)-phe-Lys(Dde)-Arg-(Pbf)-Gly] (ES-MS: $[MH]^+$ 1076.3). The solid was dissolved in ACN (47.5 mL)/water (2.5 mL), followed by the addition of hydrazine (2.5 mL). The mixture was stirred for 15 min, concentrated, washed with water, and dried. The product, cyclo[Asp(OBut)-phe-Lys-Arg(Pbf)-Gly], was further purified

by column chromatography (silica gel, methanol/dichloromethane) to afford the desired compound (295 mg, 60% yield; ES-MS: $[MH]^+$ 912.3).

Cypate-cyclo[phe-Lys(~)-Arg(Pbf)-Gly-Asp(OBut)] and Cypate-cyclo[phe-Lys(~)-Arg-Gly-Asp] (2). The protected cyclic peptide obtained above (50 mg, 0.05 mmol) was swirled with a mixture of cypate (141 mg, 0.2 mmol), HOBT (13 mg, 0.1 mmol), and *N*-(3-dimethylaminopropyl)-*N*′-ethylcarbodiimide hydrochloride (EDCI, 29 mg, 0.15 mmol) in DMF (2.0 mL) overnight. The mixture was concentrated to afford the crude product (ES-MS: $[MH_2]^{2+}$ 759.8) and split into two portions, one of which was dissolved in a mixture of TFA/water (95:5) and deblocked for 4 h. The TFA mixture was added to cold methyl *tert*-butyl ether (MTBE, 10 mL). Finally, the solid precipitate was collected by filtration and purified by HPLC to afford the desired product cypate-cyclo[phe-Lys(~)-Arg-Gly Asp] (9.0 mg, 13% yield; ES-MS: $[MH]^+/[MH_2]^{2+}$ 1210.3/606.0).

DFO-cypate-cyclo[phe-Lys(~)-Arg(Pbf)-Gly-Asp(OBut)] and DFO-cypate-cyclo[phe-Lys(~)-Arg-Gly-Asp] (1). A mixture of DFO (106 mg, 0.15 mmol) and DIEA (19.4 mg, 0.15 mmol) in DMSO (3 mL) was sonicated to obtain a clear solution. The solution was added to cypate-cyclo[phe-Lys(~)-Arg(Pbf)-Gly-Asp(OBut)] (80 mg, 0.05 mmol) in DMF (3 mL), followed by the addition of EDCI (29 mg, 0.15 mmol) and HOBT (21 mg, 0.15 mmol). The mixture was stirred for 3 h and concentrated under high vacuum. Addition of the residue to water (5 mL) precipitated the product, which was collected and purified by HPLC to obtain DFO-cypate-cyclo[phe-Lys(~)-Arg(Pbf)-Gly-Asp(OBut)] (27 mg, 25% yield; ES-MS: $[MH]^{2+}$ 1031.6). The resultant solid (20 mg) was dissolved in TFA (1 mL) and kept at room temperature for 2 h. The TFA solution was concentrated and purified by HPLC to afford DFO-cypate-cyclo[phe-Lys(~)-Arg-Gly-Asp] (7 mg, 40% yield; ES-MS: $[MH]^{2+}/[MH_2]^{3+}$ 877.2/585.1).

Cypate-DFO (3). Deferoxamine mesylate salt (131 mg, 0.2 mmol) was dissolved in DMSO (3 mL) in the presence of DIEA (26 mg, 0.2 mmol) by sonication, followed by the addition of HOBT (27 mg, 0.2 mmol), cypate (141 mg, 0.2 mmol), and EDCI (38 mg, 0.2 mmol). The mixture was stirred at room temperature for 2 h and added with stirring to ether. The precipitate was collected by filtration, one-third of which was purified by HPLC to afford cypate-DFO (25 mg, 30%; ES-MS: $[MH]^+/[MH]^{2+}$ 1167.1/584.4).

Absorption and Emission Spectral Analysis. Absorption and fluorescence spectra were recorded on a DU 640 UV–visible spectrophotometer and Fluorolog-3 fluorometer, respectively. Stock solutions (1.0 mM) were prepared by dissolving each sample in 80% aq DMSO, unless otherwise stated. UV–vis and fluorescence measurements were carried out by sequentially adding 5.0 μL aliquots of the stock solutions via a micropipette into 3 mL of 20% aq DMSO solution in a quartz cuvette. The fluorescence quantum yields of **1**, **2**, **3**, cypate, and ICG in DMSO were determined according to an established protocol and referenced to ICG in DMSO (Q.Y. = 0.13). The absorbance of five serial dilutions of each compound was measured in the concentration range between 0.1 and 1.0 μM. The quantum yield (Φ) was determined according to the following equation (*47*):

$$\Phi_s = \Phi_r(\mathrm{Grad}_s)/(\mathrm{Grad}_r)(\eta_s^2/\eta_r^2)(q_s/q_r)$$

where the subscripts s and r refer to sample and reference ICG (obtained by HPLC purification of commercially available ICG from Aldrich), respectively. η represents the refractive index of the solvent, and q represents a correction factor for the excitation wavelength used. q_s/q_r was assumed to be 1 under similar excitation conditions.

Metal Binding Studies. Stock solutions (1 mM) of compounds **1**, **3**, and DFO were first prepared with 50% aq ACN. We also prepared stock solutions (1 mM) of the following metal salts in distilled water: $Fe(NO_3)_3$, $FeSO_4$, $Al_2(SO_4)_3$, $Ga_2(SO_4)_3$, $InCl_3$, $GdCl_3$, $CuSO_4$, $ZnSO_4$, $Co(NO_3)_2$, $NiCl_2$, $MnCl_2$, $CaCl_2$, $MgCl_2$, and $MgSO_4$. All test solutions (100 μL each) containing 100 μM ligand and 200 μM metal ion were prepared by mixing compounds **1**, **3**, or DFO (10 μL, 1.0 mM) and a metal ion (20 μL, 1.0 mM) in 70 μL of 50% aq ACN. After the solutions were stirred for 2 h, 20 μL of the resulting solutions were subjected to ESI-MS analysis. Each solution (30.0 μL) was added to 2970.0 μL of 20% aq DMSO for UV–vis and fluorescence emission analysis.

ABIR Binding Affinity. Receptor binding assays were performed by using human-purified ABIR protein from Chemicon International, Inc. (Temecula, CA) using the method reported previously (*48*). Briefly, assays were carried out in the Millipore Duropore membrane 96-well plates and the Millipore MultiScreen system (Bedfore, MA). ^{125}I-echistatin was purchased from Amersham Biosciences (Piscataway, NJ). The specific activity of the radiolabeled peptide was ~2000 Ci/mmol. Radiochemical purity (90%) was determined by reverse-phase HPLC. The 96-well membrane plate was blocked with 0.1% polyethylenimine blocking solution overnight at 4 °C. ^{125}I-echistatin (50 nmol/L) was added to the binding buffer (50 mM Tris-HCl, pH 7.4, 100 mM NaCl, 2 mM $CaCl_2$, 1 mM $MgCl_2$, 1 mM $MnCl_2$, and 1% BSA) containing integrin ABIR protein (50 ng per well in 96-well membrane plate) and ligands in a total volume of 200 μL per well. The concentration range of ligand was between 0.01 μM and 100 μM. The mixtures were incubated for 2 h at room temperature, filtered by centrifugation at 1500*g*, and washed with 0.20 mL of ice-cold binding buffer (3×). The filters containing radioactivity-bound ABIR were removed using a punch apparatus and counted using a Packard Cobra II Autogamma counter (Meriden, CT). Nonspecific binding of ^{125}I-echistatin was between 5 to 10% of the total binding. The 50% inhibitory concentrations (IC_{50}) were calculated by nonlinear regression analysis using GraphPad Prism 4 data fitting software (GraphPad Software, Inc., San Diego, CA). Three independent binding assays were performed in triplicate per sample.

Cell Culture. The human nonsmall cell carcinoma cell line A549 is widely used to study the role of integrins in normal and pathophysiological processes. These cells were purchased from ATCC and grown in 75 cm tissue culture flasks or on Laboratory-Tek chambered slides in Ham's F12K medium with 2 mM L-glutamine supplemented with 1.5 g/L sodium bicarbonate, 10% fetal calf serum, 100 units/mL penicillin, and 100 units/mL streptomycin under humidified atmosphere containing 5% CO_2 at 37 °C.

Internalization and Fluorescence Microscopy. A549 cells were grown on Laboratory-Tek slides. The culture medium was replaced, and the cells were incubated for different times up to 24 h at 37 °C in the presence of the cypate-labeled DFO probes (1 μM in 0.02% DMSO). After treatment, cells were washed (3×) with PBS containing 1 mM $CaCl_2$ and mounted with Prolong Gold containing DAPI mounting medium and coverslipped (Invitrogen). For fluorescence microscopy, cells were visualized with an Olympus FV1000 microscope using a 60X/1.20M, 0.13–0.21 NA water immersion objective. Fluorescence emission was detected from 805–830 nm using a 780 nm laser at 100% transmission for excitation. Images of each group of slides were acquired with the same microscope settings during a single imaging session, allowing for qualitative comparison of the relative fluorescence. The relative fluorescence intensity of five regions of interest for each image was determined with Slidebook software from Olympus and the results averaged. The

Scheme 1. Synthesis of DFO-cypate-[RGDfK(∼)] (1)

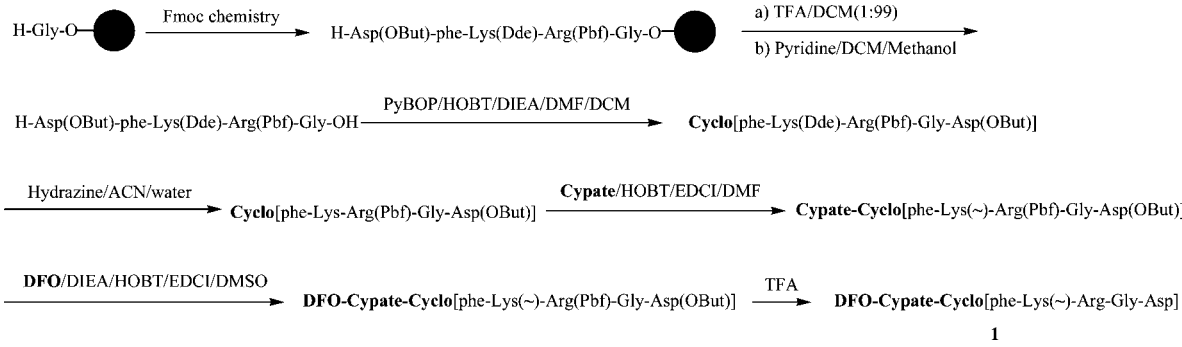

results were normalized to the average relative fluorescence of DFO-cypate treated cells.

For mitochondrial staining, 5 nm Mitotracker Green (Invitrogen) was added during the last 15 min of incubation. For lysosomal staining, cells were stained with anti-LAMP1 antibody as described in the literature (*49*). Briefly, cells were fixed for 15 min with 4% paraformaldehyde for 15 min, after which they were washed 3× with PBS containing 1 mM $CaCl_2$. Slides were incubated for 1 h at room temperature with 10% rabbit serum to block nonspecific binding after which they were incubated overnight at 4 °C with 2 μg/mL anti-LAMP1 goat polyclonal IgG (Santa Cruz). After washing 3× with PBS, slides were incubated for 1 h at room temperature with 10 μg/mL Cy3 conjugated rabbit antigoat IgG (Zymed). After washing 3× with PBS, slides were mounted with Prolong Gold and coverslipped. Cells were visualized with an Olympus FV1000 microscope using a 60X/1.20M, 0.13–0.21 NA water immersion objective. Fluorescence emission was detected by using a 488 nm laser at 5% transmission and 500–600 nm emission (Mitotracker green) or by using a 543 nm laser at 15% transmission and 555–655 nm emission (LAMP-1).

RESULTS AND DISCUSSION

Molecular Design. Previously, we reported the synthesis and applications of a dicarboxylic acid-containing carbocyanine fluorophore (cypate) (*10, 45*). The facile synthesis of cypate and its excellent NIR spectral properties have allowed us to conveniently label diverse peptides and other bioactive molecules with cypate in solution and on solid support. Particularly, the two carboxylic acid groups of cypate have facilitated its use as an optical scaffold to construct diverse bioactive NIR fluorescent molecular probes, such as monomeric, dimeric, macrocyclic, and multivalent analogues (*8,45,50,51*). Conjugation of cypate with small peptides that target specific cell-surface receptors, such as ABIR and the somatostatin receptor, allows site-specific targeting of diseased tissues for optical imaging (*9, 10, 51*). In particular, previous reports have shown that cyclic RGD pentapeptide cyclo(RGDfV) and some of its analogues bind to ABIR with high affinity and selectivity. Further modification of the biological properties of cypate-labeled RGD peptides could be obtained by incorporating another bioactive molecule such as DFO.

The metal-binding properties and the related biological activities of DFO have been ascribed to its three hydroxamate groups (*26, 52*). Therefore, the amino group of DFO provides a desirable site for its structural modification. In this work, we used cypate to construct a three-pronged architecture bearing both the DFO motif and ABIR-targeting RGD peptide (cyclo[RGDfK(∼)] (Figure 1). We anticipated that the new NIR fluorescent RGD-bearing DFO compound (**1**) would serve as a multifunctional platform for biomedical applications. For example, the RGD peptide motif could be used for the targeted delivery of DFO to ABIR positive tumors, while cypate serves as the optical antenna to track, visualize, and quantify the fate of **1** in cells and in vivo by NIR fluorescence imaging. In addition, the integration of DFO and RGD peptide into cypate could cooperatively enhance the related biological activities. Finally, the metal-binding DFO could modify the structure, function, and regulation of divalent, cation-dependent ABIR (*28, 38*). Together, these potential applications of NIR fluorescent DFO compounds motivated the design, synthesis, and evaluation of the compounds described in this article.

Synthesis. As shown in Scheme 1, synthesis of the multifunctional compound **1** consists of three major steps: (i) synthesis of the protecting RGD peptide, (ii) cypate conjugation, and (iii) DFO conjugation. The resin-bound protected RGD penta-peptide, H-Asp(OBut)-phe-Lys(Dde)-Arg(Pbf)-Gly-O-Resin (**1**), was first assembled on a H-Gly-loaded 2-chlorotrityl resin using conventional Fmoc chemistry. Cleavage of the protected peptide with 1% TFA in DCM afforded the desired protected RGD pentapeptide, H-Asp(OBut)-phe-Lys(Dde)-Arg-(Pbf)-Gly-OH. This linear peptide was cyclized to form cyclo-[phe-Lys(Dde)-Arg(Pbf)-Gly-Asp(OBut)] in the presence of PyBOP, HOBT, and DIEA in solution. Removal of the ε-amino lysine-protecting Dde group with hydrazine in aqueous acetonitrile afforded cyclo[phe-Lys-Arg(Pbf)-Gly-Asp(OBu^t)], which was further purified by flash column chromatography. The conjugation of the cyclic peptide (1 equiv) and cypate (3 equiv) was achieved in the presence of EDCI and HOBT in anhydrous DMF. Similarly the crude product, cypate-[Arg(Pbf)-Gly-Asp(OBut)-phe-Lys(∼)], was coupled with DFO, as reported previously (*53*). Aqueous TFA was used to deblock the resultant product, DFO-cypate-[Arg(Pbf)-Gly-Asp(OBut)-phe-Lys(∼)], which was then purified by HPLC to give the desired compound **1**, DFO-cypate-cyclo[Arg-Gly-Asp-phe-Lys]. The identity and purity of the compound were confirmed by both HPLC and ES-MS. A combination of solution and solid-phase reactions facilitated the preparation of all compounds used in this study.

Spectral Properties. Stock solutions (1 mM) of the DFO-containing compounds were prepared in DMSO, and spectral measurements were carried out by adding 5 μL aliquots of the stock solutions via a micropipette into 3 mL of DMSO solution in a quartz cuvette. All of the compounds showed similar spectral features, with minor spectral shifts in the absorption and emission maxima (Figure 2). The attachment of cyclo-[RGDfK(∼)] to cypate increased the molar absorptivity (ε) while the DFO attachment decreased ε (Table 1). Compound **1** containing both DFO and cyclo[RGDfK(∼)] showed similar ε with cypate. Overall, conjugation of the highly hydrophilic DFO to cypate improved the water solubility of the dye without effect on its spectral properties.

Metal Binding Studies. Siderophores such as DFO are good ligands for Fe(III), and the biological activities of DFO are

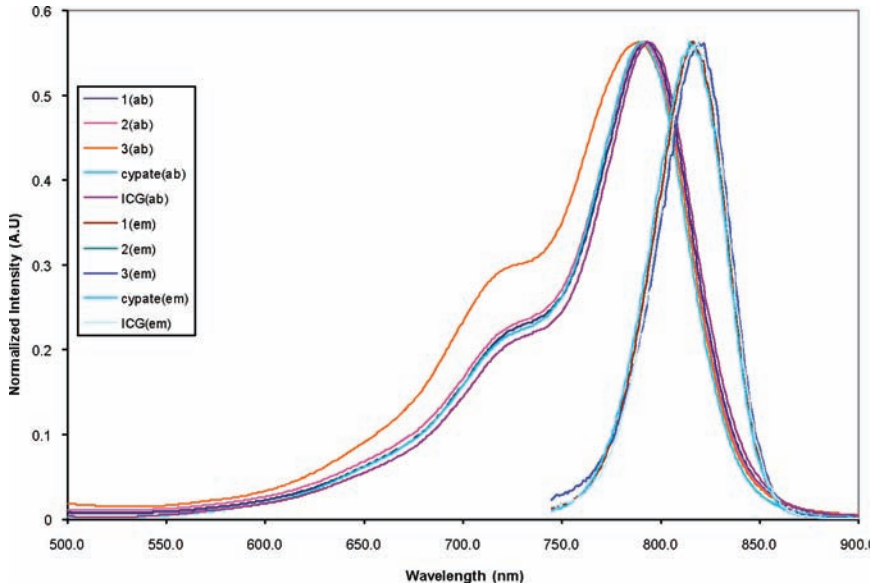

Figure 2. Normalized UV–vis and emission spectra of DFO-cypate-[RGDfK(∼)] (**1**), cypate-[RGDfK(∼)] (**2**), and cypate-DFO (**3**) in DMSO.

Table 1. Optical Properties of the Compounds in DMSO

compds	$\lambda_{max(ab)}$	$\lambda_{max(em)}$	ε (cm^{-1} M^{-1})	Φ (excited at 730 nm)
1	793	816	2.0×10^5	0.10
2	792	817	2.3×10^5	0.10
3	788	815	1.4×10^5	0.17
cypate	791	814	2.1×10^5	0.12
ICG	794	820	1.9×10^5	0.13

related to its metal-binding properties (*20*, *54–56*). Previous studies have shown that DFO and the related hydroxamate compounds also possess high binding affinities with Al(III) and Ga(III) (*26*, *53*). Therefore, we evaluated the metal-binding properties of **1** and the related effects on the corresponding optical properties of DFO-bearing fluorescent compounds. Because of its high sensitivity, we used ES-MS to study metal coordination with DFO, as described previously (*26*, *57*). This method is suitable for screening the relative metal-binding selectivity and affinity of some compounds, especially those in limited supply.

Compounds **1**, **3**, and DFO (100 μM in 50% aq acetonitrile) were screened for their binding with 13 different metal ions, Fe(III), Al(III), Ga(III), In(III), Gd(III), Cu(II), Zn(II), Co(II), Ni(II), Mn(II), Fe(II), Ca(II), and Mg(II), at 200 μM in water. All the three DFO-bearing compounds exhibited high binding affinity and selectivity for Ga(III), Al(III), and Fe(III) compared to the other metal ions. The ES-MS spectra of **1** and the metal chelates shown in Figure 3 are representative of the trend observed for these compounds. Compound **1** showed two typical doubly and triply charged peaks at 876.7 and 584.9 in its ES-MS spectrum. Upon metal binding, these peaks were replaced by the corresponding doubly charged (903.5, 889.0, and 910.1) and triply charged (602.2, 592.8, and 607.5) peaks of the resulting Ga(III), Al(III), and Fe(III) complexes, respectively. These peaks were correlated with the theoretical masses based on $[(L\text{-}3H)MH_n]^{n+}$, where L and M represent the molecular weight of a ligand and a metal, respectively. The high abundance of the desired metal chelate peaks with negligible residue from the starting DFO ligands strongly suggests the complete formation of 1:1 metal complexes in aq ACN.

We further calculated the relative metal-binding affinity (%) of each ligand as a percentage of the relative abundance of the metal-binding ligand peaks with the total ligand-related peaks in a positive ES-MS spectrum according to the following equation, as reported previously (*26*, *58*):

$$[LFe^2 + LFe^3]/[L^2 + L^3 + LFe^2 + LFe^3 + L]\times 100\%$$

where L^2 and LFe^2 are the doubly charged peak abundance of a ligand and its complex, while L^3 and LFe^3 are the triply charged peak abundance of a ligand and its complex. The related peaks associated with the addition of sodium ions were also calculated. As shown in Figure 4, the ES-MS analysis clearly demonstrated the relative metal binding selectivity and affinity with Fe(III), Fe(II), Ga(III), Al(III), and In(III). Despite their structural differences, the metal binding selectivity of **1**, **3**, and DFO was similar, indicating that the chelating property of DFO was maintained, independent of the molecular design.

In contrast to the ES-MS spectra of Ga(III) and Al(III), the addition of Fe(III) and Cu(II) resulted in complicated ES-MS spectra with multiple peaks around the doubly and triply charged peaks. This observation suggests that Cu(II) had weaker binding with **1**, but might greatly impact the ionization of **1** and the stability of the resulting ions in gas phase. In addition, the low abundance of the related 1:1 ligand/metal complex indicates that Cu(II) binding might occur between two or more ligands of **1** with two or more Cu(II).

The relatively high binding affinity of DFO-bearing compounds with Fe(III), Al(III), and Ga(III) makes it possible to further functionalize **1** via metal binding. Therefore, we prepared and isolated the Ga(III) complex of **1** to demonstrate the feasibility of obtaining fluorescent DFO chelates. By mixing **1** with excess Ga(III) in aq ACN, the Ga(III) complex was obtained by HPLC purification and further characterized by ES-MS. The metal complex has a longer retention time than **1**, suggesting that the coordination of Ga(III) by the three DFO hydroxamates reduces the hydrophilicity of **1** (Figure 5). The successful preparation and characterization of the Ga(III) complex provide an exciting dimension for exploring additional applications of this compound in biomedicine.

Spectrally, there was no significant change in the green color of **1** upon the additions of the metals, with the exception of Fe(III), Fe(II), and Cu(II), where a change was observed (Figure 6). Clearly, the addition of Cu(II) and Fe(III) markedly decreased the UV–vis absorption and quenched the fluorescence emission of **1** as shown in Figure 6. On the basis of the ES-MS analysis discussed above, it is likely that spectral changes by these metals occurred by different

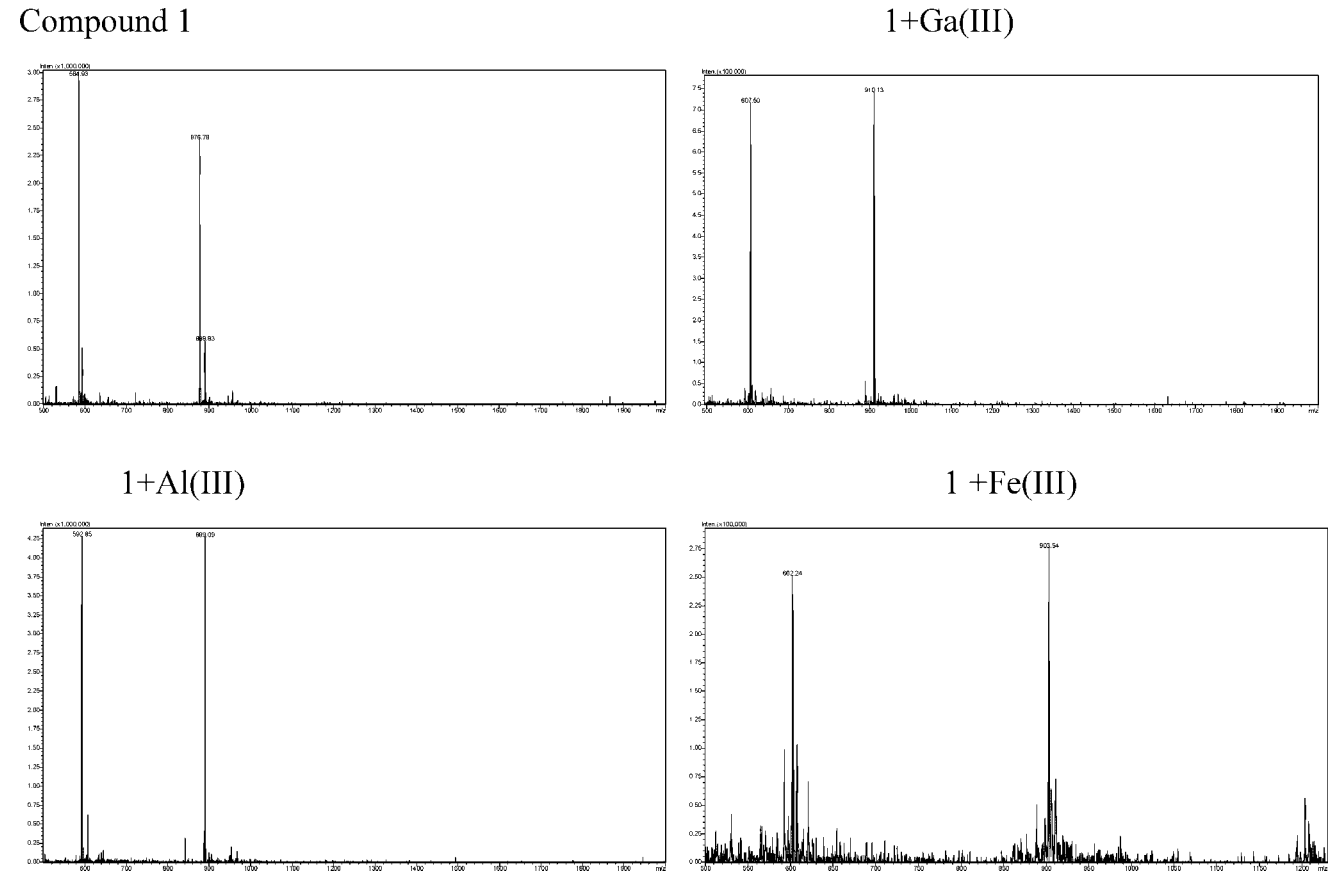

Figure 3. ES-M spectra of **1** and its Ga(III), Al(III), and Fe(III) complexes (100 μM) in 50% aq ACN.

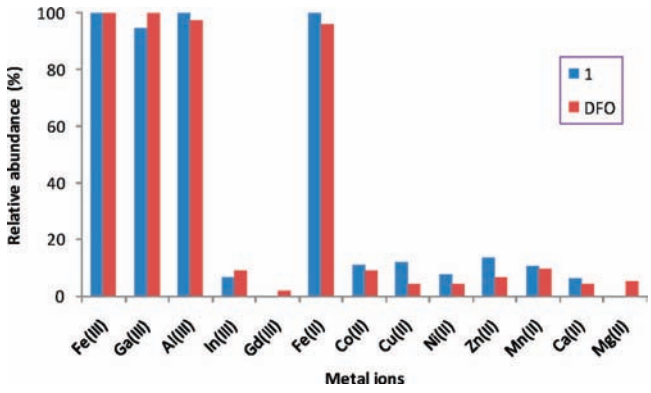

Figure 4. Relative binding affinities of **1**and DFO with different metal ions at a molar ratio of 1:2 as determined by ES-MS.

mechanisms. While Cu (II) appears to quench fluorescence by interacting directly with the cypate motif, the stable Fe complex may quench fluorescence by the photoinduced electron transfer mechanism. In contrast to Fe(III) and Cu(II), Ga(III) binding did not significantly alter the UV–vis absorbance of **1**. Interestingly, Ga(III) seemed to enhance light emission to some extent. This finding is in agreement with a previous study with **3**, where a similar enhancement was observed (*53*). Considering that a DFO chelate of radioactive Ga(III) has been used previously for nuclear imaging, the Ga(III)-mediated fluorescence enhancement favors the use of the Ga(III) complex of compounds **1** and **3** to develop a dual optical-nuclear imaging agent. In addition, the contrasting effects of Fe(III) and Ga(III) on the optical properties of cypate provide an efficient approach to perturb the spectral properties of NIR fluorescent carbocyanine probes via metal binding.

Receptor Binding Assays. Among the diverse RGD peptides that have been developed for targeting ABIR, the lactam-based cyclic penta-peptide cyclo(RGDfV) and its analogues are well known for their high binding affinity and selectivity with ABIR. In this study, commercially available ABIR-avid peptide cyclo(RGDfV) was used as a reference compound to study the effect of DFO on the ABIR binding affinity of **1** and **2**. The IC_{50} values of these compounds were determined by competitive inhibition of Echistatin binding to purified ABIR, as described previously (*48, 59*). Echistatin is a polypeptide that binds irreversibly with high affinity and specificity to the ABIR and the radiolabeled analogue. ^{125}I-echistatin was used as a tracer in the binding assay. Compounds **1**, **2**, and cyclo(RGDfV) were found to have IC_{50} values of 1.8×10^{-7} M, 7.7×10^{-8} M, and 4.1×10^{-7} M, respectively. Under similar conditions, the presence of the DFO motif in **1** decreased the ABIR affinity of **2** by a factor of about 2, but the resulting affinity was comparable to that of the reference cyclic RGD compound. These findings indicate that the RGD peptide can modulate the biological activities of DFO through receptor-mediated delivery of this otherwise nonspecific drug to target tissue and cells.

Cell Internalization. Uptake and distribution of drugs and contrast agents in cells provide a key index for understanding the functions and predicting the in vivo behavior of fluorescent compounds. Therefore, labeling DFO with fluorescent dye allows the use of the resultant molecule as molecular probe for imaging DFO distribution in cells. Considering that the ABIR binding assay revealed the retention of RGD peptide binding affinity by **1**, we assessed the internalization and subcellular distribution of **1**, **2**, and **3** in an ABIR-positive cell line, A549. The incubation of A549 cells with **3** (1 μM) in medium containing 0.02% DMSO showed minimal uptake of the compound, with normalized fluorescence similar to the back-

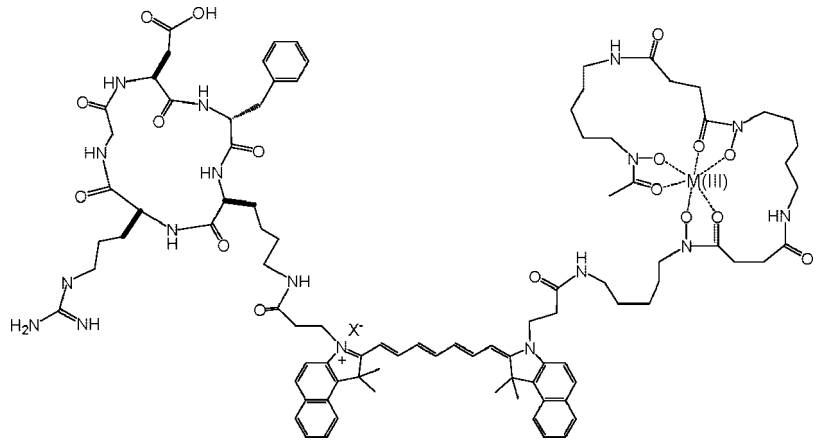

Figure 5. Proposed metal complex structure of **1**.

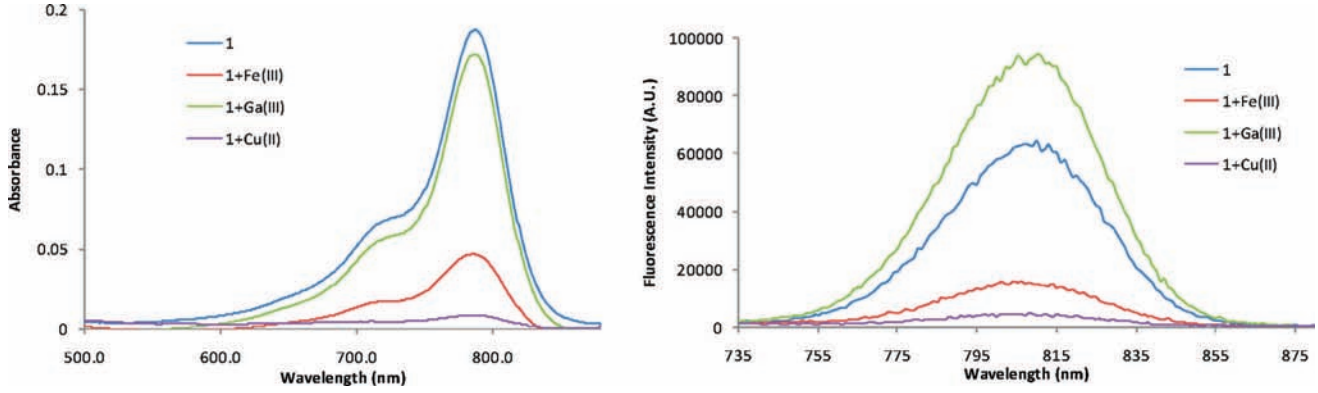

Figure 6. Effects of Ga(III), Fe(III), and Cu(II) ions on UV–vis and emission spectra of 1 in 20% aq DMSO.

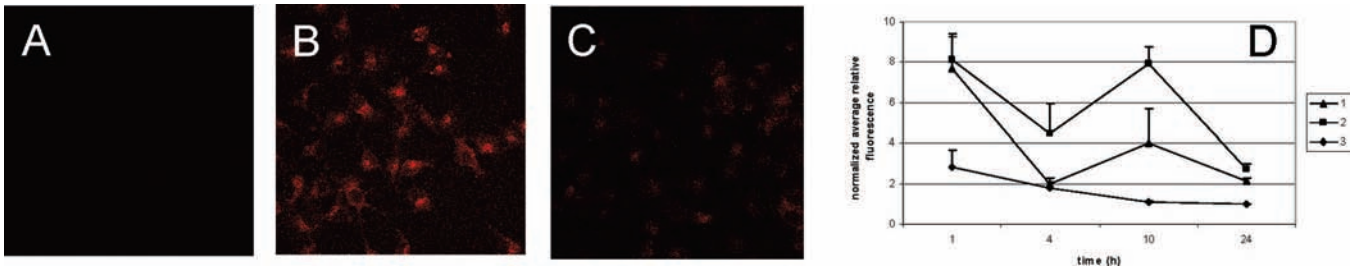

Figure 7. Internalization in A549 cells treated for 10 h with 1 μM of compounds **3** (A), **2** (B), or **1** (C) and quantitation of the internalization of each compound as a function of time (D).

ground signal (Figure 7). Expectedly, hydrophilic molecules such as DFO have difficulty crossing the plasma membranes of cells without an active transport mechanism. In contrast, both **1** and **2** internalized rapidly within 1 h post incubation and remained in the intracellular space up to 10 h. The enhanced internalizations of **1** and **2** could be ascribed to the interaction of the RGD peptide with ABIR in the cell membranes. Thus, the RGD peptide provided an endocytotic pathway for DFO. At 1 h postincubation, the internalization of **1** and **2** in A549 cells was similar to each other, but the retention of **1** in the cells was lower at longer incubation times than that of **2** (Figure 7D). The differences in the internalization rate appear to correlate with their ABIR binding affinity, with **2** having higher affinity than **1**. Once internalized, however, the rates of subsequent efflux of the two compounds from the cell were similar, with the intracellular fluorescence intensity for both compounds approaching background at 24 h post incubation. The fluctuations in fluorescence shown in Figure 7D could be attributed to changes in receptor density as a function of time.

On the basis of the dissimilarity in structural features, ABIR binding affinity, and internalization rates, we expected differences in the intracellular distribution of compounds **1**, **2**, and **3**. Interestingly, once inside the cell, all three compounds appeared to localize in the mitochondria, the lysosomes, and the cytosol (Figures 8 and 9). The absence of identifiable uptake in the cell nuclei favors using the fluorescent DFO compounds as imaging agents because of the need to minimize nuclear translocation of imaging agents, thereby preventing the potential mutagenic effect on the cells.

CONCLUSIONS

We have developed a novel multifunctional molecular probe consisting of a metal-chelating DFO, a NIR fluorescent cypate, and an ABIR-avid cyclic RGD peptide. Each component synergistically contributes to the overall properties of new compound **1**. Cypate provides a detectable signal for imaging purposes; the RGD peptide effectively delivers both cypate and DFO into cells; and metal-binding DFO efficiently

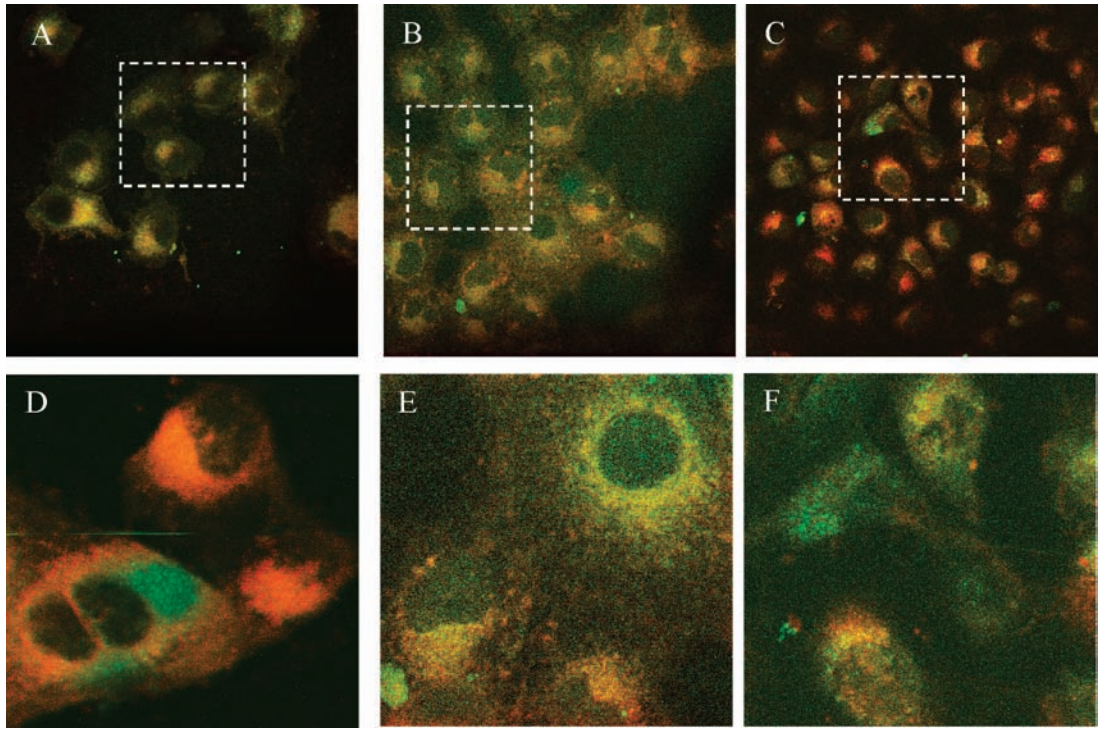

Figure 8. Subcellular distribution of cells treated for 10 h with 1 μM **3** (A), **2** (B), or **1** (C) in medium containing 0.02% DMSO costained with Mitotracker green. (D−F) Inserts at 3× magnification corresponding to A, B, and C, respectively.

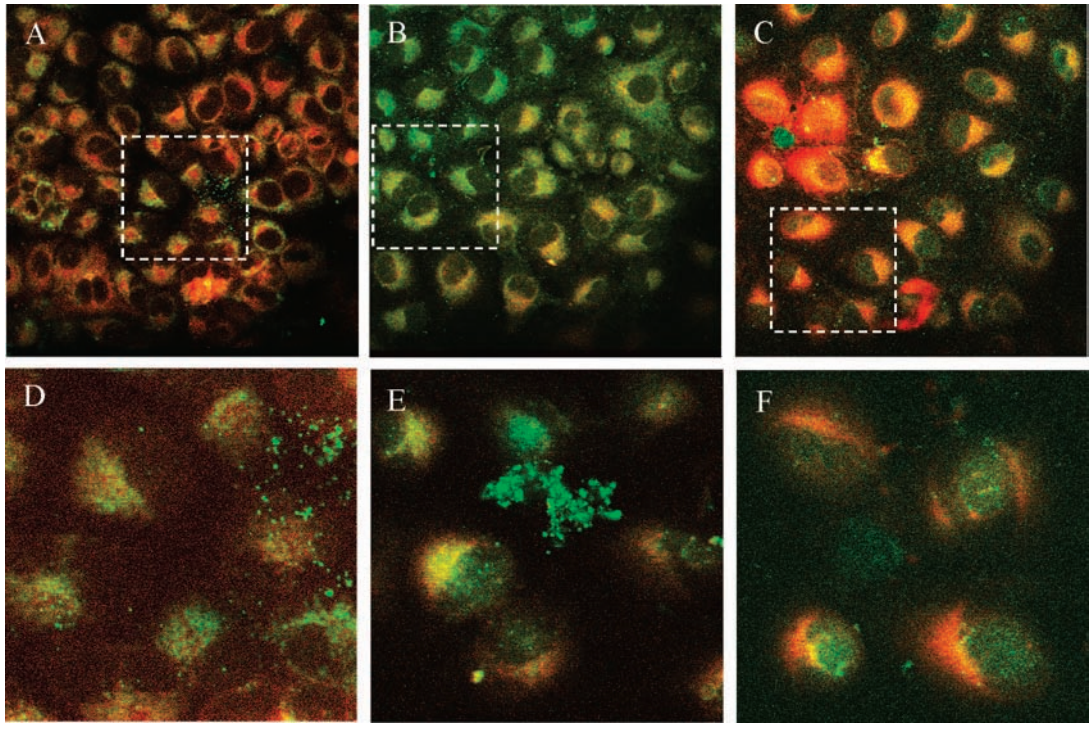

Figure 9. Subcellular distribution of cells treated for 10 h with **3** (A), **2** (B), or **1** (C) costained with anti-LAMP1 antibody. (D−F) Inserts at 3× magnification corresponding to A, B, and C, respectively.

modulates the optical properties of cypate. The impressive ABIR-mediated internalization of **1** in cells without permeating the cell nucleus is advantageous for imaging applications, where nuclear uptake can be detrimental to the cells and living organisms. This work represents our initial effort toward the discovery and development of novel ABIR-targeting DFO compounds for optical imaging. Specifically, **1** provides a multifunctional molecular platform for optimizing the structure, improving biological activities, exploring new applications, and understanding the mechanisms of action. The synthetic approach we used is amenable to combinatorial chemistry and the parallel synthesis of diverse NIR fluorescent DFO analogues.

ACKNOWLEDGMENT

This study was supported in part by the NIH (R01 CA109754, R33 CA100972, and R21 CA123537).

LITERATURE CITED

(1) Kelloff, G. J., Krohn, K. A., Larson, S. M., Weissleder, R., Mankoff, D. A., Hoffman, J. M., Link, J. M., Guyton, K. Z., Eckelman, W. C., Scher, H. I., O'Shaughnessy, J., Cheson, B. D., Sigman, C. C., Tatum, J. L., Mills, G. Q., Sullivan, D. C., and Woodcock, J. (2005) The progress and promise of molecular imaging probes in oncologic drug development. *Clin. Cancer Res. 11*, 7967–7985.

(2) El-Deiry, W. S., Sigman, C. C., and Kelloff, G. J. (2006) Imaging and oncologic drug development. *J. Clin. Oncol. 24*, 3261–3273.

(3) Apisarnthanarax, S., and Chao, K. S. (2005) Current imaging paradigms in radiation oncology. *Radiat. Res. 163*, 1–25.

(4) Toms, S. A., Konrad, P. E., Lin, W. C., and Weil, R. J. (2006) Neuro-oncological applications of optical spectroscopy. *Technol. Cancer Res. Treat. 5*, 231–238.

(5) Harada, H., Kizaka-Kondoh, S., and Hiraoka, M. (2005) Optical imaging of tumor hypoxia and evaluation of efficacy of a hypoxia-targeting drug in living animals. *Mol. Imaging 4*, 182–193.

(6) Schellenberger, E. A., Bogdanov, A., Jr., Petrovsky, A., Ntziachristos, V., Weissleder, R., and Josephson, L. (2003) Optical imaging of apoptosis as a biomarker of tumor response to chemotherapy. *Neoplasia 5*, 187–192.

(7) Perlitz, C., Licha, K., Scholle, F. D., Ebert, B., Bahner, M., Hauff, P., Moesta, K. T., and Schirner, M. (2005) Comparison of two tricarbocyanine-based dyes for fluorescence optical imaging. *J. Fluoresc. 15*, 443–454.

(8) Achilefu, S., Jimenez, H. N., Dorshow, R. B., Bugaj, J. E., Webb, E. G., Wilhelm, R. R., Rajagopalan, R., Johler, J., and Erion, J. L. (2002) Synthesis, in vitro receptor binding, and in vivo evaluation of fluorescein and carbocyanine peptide-based optical contrast agents. *J. Med. Chem. 45*, 2003–2015.

(9) Achilefu, S. (2004) Lighting up tumors with receptor-specific optical molecular probes. *Technol. Cancer Res. Treat. 3*, 393–409.

(10) Achilefu, S., Dorshow, R. B., Bugaj, J. E., and Rajagopalan, R. (2000) Novel receptor-targeted fluorescent contrast agents for in vivo tumor imaging. *Invest. Radiol. 35*, 479–485.

(11) Chen, X., Conti, P. S., and Moats, R. A. (2004) In vivo near-infrared fluorescence imaging of integrin alphavbeta3 in brain tumor xenografts. *Cancer Res. 64*, 8009–8014.

(12) Licha, K., Riefke, B., Ebert, B., and Grotzinger, C. (2002) Cyanine dyes as contrast agents in biomedical optical imaging. *Acad. Radiol. 9*, S320–S322.

(13) Licha, K., Hessenius, C., Becker, A., Henklein, P., Bauer, M., Wisniewski, S., Wiedenmann, B., and Semmler, W. (2001) Synthesis, characterization, and biological properties of cyanine-labeled somatostatin analogues as receptor-targeted fluorescent probes. *Bioconjugate Chem. 12*, 44–50.

(14) Richardson, D., Ponka, P., and Baker, E. (1994) The effect of the iron(III) chelator, desferrioxamine, on iron and transferrin uptake by the human malignant melanoma cell. *Cancer Res. 54*, 685–689.

(15) Singer, S. T., and Vichinsky, E. P. (1999) Deferoxamine treatment during pregnancy: is it harmful? *Am. J. Hematol. 60*, 24–26.

(16) Hershko, C. M., Link, G. M., Konijn, A. M., and Cabantchik, Z. I. (2005) Iron chelation therapy. *Curr. Hematol. Rep. 4*, 110–116.

(17) Hershko, C., Link, G., Konijn, A. M., and Cabantchik, Z. I. (2005) Objectives and mechanism of iron chelation therapy. *Ann. N.Y. Acad. Sci. 1054*, 124–135.

(18) Dayani, P. N., Bishop, M. C., Black, K., and Zeltzer, P. M. (2004) Desferoxamine (DFO)-mediated iron chelation: rationale for a novel approach to therapy for brain cancer. *J. Neurooncol. 67*, 367–377.

(19) Gao, J., and Richardson, D. R. (2001) The potential of iron chelators of the pyridoxal isonicotinoyl hydrazone class as effective antiproliferative agents, IV: The mechanisms involved in inhibiting cell-cycle progression. *Blood 98*, 842–850.

(20) Kicic, A., Chua, A. C., and Baker, E. (2001) Effect of iron chelators on proliferation and iron uptake in hepatoma cells. *Cancer 92*, 3093–3110.

(21) Tam, T. F., Leung-Toung, R., Li, W., Wang, Y., Karimian, K., and Spino, M. (2003) Iron chelator research: past, present, and future. *Curr. Med. Chem. 10*, 983–995.

(22) Cook, J. (2001) Radiation sensitization of mammalian cells by metal chelators. *Radiat. Res. 155*, 304–310.

(23) Smith-Jones, P. M., Stolz, B., Bruns, C., Albert, R., Reist, H. W., Fridrich, R., and Macke, H. R. (1994) Gallium-67/gallium-68-[DFO]-octreotide--a potential radiopharmaceutical for PET imaging of somatostatin receptor-positive tumors: synthesis and radiolabeling in vitro and preliminary in vivo studies. *J. Nucl. Med. 35*, 317–325.

(24) Chaston, T. B., and Richardson, D. R. (2003) Iron chelators for the treatment of iron overload disease: relationship between structure, redox activity, and toxicity. *Am. J. Hematol. 73*, 200–210.

(25) Lovejoy, D. B., and Richardson, D. R. (2003) Iron chelators as anti-neoplastic agents: current developments and promise of the PIH class of chelators. *Curr. Med. Chem. 10*, 1035–1049.

(26) Ye, Y., Liu, M., Kao, J. L., and Marshall, G. R. (2006) Novel trihydroxamate-containing peptides: design, synthesis, and metal coordination. *Biopolymers 84*, 472–489.

(27) Ouchetto, H., Dias, M., Mornet, R., Lesuisse, E., and Camadro, J. M. (2005) A new route to trihydroxamate-containing artificial siderophores and synthesis of a new fluorescent probe. *Bioorg. Med. Chem. 13*, 1799–1803.

(28) Xiong, J. P., Stehle, T., Diefenbach, B., Zhang, R., Dunker, R., Scott, D. L., Joachimiak, A., Goodman, S. L., and Arnaout, M. A. (2001) Crystal structure of the extracellular segment of integrin alpha Vbeta3. *Science 294*, 339–345.

(29) Liu, W., Reinmuth, N., Stoeltzing, O., Parikh, A. A., Fan, F., Ahmad, S. A., Jung, Y. D., and Ellis, L. M. (2002) Antiangiogenic therapy targeting factors that enhance endothelial cell survival. *Semin. Oncol. 29*, 96–103.

(30) Kumar, C. C. (1998) Signaling by integrin receptors. *Oncogene 17*, 1365–1373.

(31) Choe, Y. S., and Lee, K. H. (2007) Targeted in vivo imaging of angiogenesis: present status and perspectives. *Curr. Pharm. Des. 13*, 17–31.

(32) Vellon, L., Menendez, J. A., and Lupu, R. (2005) AlphaVbeta3 integrin regulates heregulin (HRG)-induced cell proliferation and survival in breast cancer. *Oncogene 24*, 3759–3773.

(33) Trikha, M., Zhou, Z., Timar, J., Raso, E., Kennel, M., Emmell, E., and Nakada, M. T. (2002) Multiple roles for platelet GPIIb/IIIa and alphavbeta3 integrins in tumor growth, angiogenesis, and metastasis. *Cancer Res. 62*, 2824–2833.

(34) Lamfers, M. L., Grill, J., Dirven, C. M., Van Beusechem, V. W., Geoerger, B., Van Den Berg, J., Alemany, R., Fueyo, J., Curiel, D. T., Vassal, G., Pinedo, H. M., Vandertop, W. P., and Gerritsen, W. R. (2002) Potential of the conditionally replicative adenovirus Ad5-Delta24RGD in the treatment of malignant gliomas and its enhanced effect with radiotherapy. *Cancer Res. 62*, 5736–5742.

(35) Chen, X., Plasencia, C., Hou, Y., and Neamati, N. (2005) Synthesis and biological evaluation of dimeric RGD peptide-paclitaxel conjugate as a model for integrin-targeted drug delivery. *J. Med. Chem. 48*, 1098–106.

(36) Shen, S. I., Kotamraj, P. R., Bhattacharya, S., Li, X., and Jasti, B. R. (2007) Synthesis and characterization of RGD-fatty acid amphiphilic micelles as targeted delivery carriers for anticancer agents. *J. Drug Target 15*, 51–58.

(37) Arap, W., Pasqualini, R., and Ruoslahti, E. (1998) Cancer treatment by targeted drug delivery to tumor vasculature in a mouse model. *Science 279*, 377–380.

(38) Xiong, J. P., Stehle, T., Zhang, R., Joachimiak, A., Frech, M., Goodman, S. L., and Arnaout, M. A. (2002) Crystal structure of the extracellular segment of integrin alpha Vbeta3 in complex with an Arg-Gly-Asp ligand. *Science 296*, 151–155.

(39) Lin, H. Y., Lansing, L., Merillon, J. M., Davis, F. B., Tang, H. Y., Shih, A., Vitrac, X., Krisa, S., Keating, T., Cao, H. J., Bergh, J., Quackenbush, S., and Davis, P. J. (2006) Integrin alphaVbeta3 contains a receptor site for resveratrol. *FASEB J. 20*, 1742–1744.

(40) Chen, X., Sievers, E., Hou, Y., Park, R., Tohme, M., Bart, R., Bremner, R., Bading, J. R., and Conti, P. S. (2005) Integrin alpha v beta 3-targeted imaging of lung cancer. *Neoplasia 7*, 271–279.

(41) Chen, X., Hou, Y., Tohme, M., Park, R., Khankaldyyan, V., Gonzales-Gomez, I., Bading, J. R., Laug, W. E., and Conti, P. S. (2004) Pegylated Arg-Gly-Asp peptide: 64Cu labeling and PET imaging of brain tumor alphavbeta3-integrin expression. *J. Nucl. Med. 45*, 1776–1783.

(42) Cheng, Z., Wu, Y., Xiong, Z., Gambhir, S. S., and Chen, X. (2005) Near-infrared fluorescent RGD peptides for optical imaging of integrin alphavbeta3 expression in living mice. *Bioconjugate Chem. 16*, 1433–1441.

(43) Li, Z. B., Cai, W., Cao, Q., Chen, K., Wu, Z., He, L., and Chen, X. (2007) 64Cu-Labeled Tetrameric and Octameric RGD Peptides for Small-Animal PET of Tumor {alpha}v{beta}3 Integrin Expression. *J. Nucl. Med. 48*, 1162–1171.

(44) Wu, Z., Li, Z. B., Cai, W., He, L., Chin, F. T., Li, F., and Chen, X. (2007) (18)F-labeled mini-PEG spacered RGD dimer ((18)F-FPRGD2): synthesis and microPET imaging of alpha (v)beta (3) integrin expression. *Eur. J. Nucl. Med. Mol. Imaging*, *34*, 1823–1831

(45) Ye, Y., Bloch, S., Kao, J., and Achilefu, S. (2005) Multivalent carbocyanine molecular probes: synthesis and applications. *Bioconjugate Chem. 16*, 51–61.

(46) Chan, W. C., and White, P. D., Eds. (2000) *Fmoc Solid Phase Peptide Synthesis: A Practical Approach*, Oxford University Press, New York.

(47) Li, C., Greenwood, T. R., Bhujwalla, Z. M., and Glunde, K. (2006) Synthesis and characterization of glucosamine-bound near-infrared probes for optical imaging. *Org. Lett. 8*, 3623–3626.

(48) Ye, Y., Bloch, S., Xu, B., and Achilefu, S. (2006) Design, synthesis, and evaluation of near infrared fluorescent multimeric RGD peptides for targeting tumors. *J. Med. Chem. 49*, 2268–2275.

(49) Wasylnka, J. A., and Moore, M. M. (2003) Aspergillus fumigatus conidia survive and germinate in acidic organelles of A549 epithelial cells. *J. Cell Sci. 116*, 1579–1587.

(50) Ye, Y., Li, W. P., Anderson, C. J., Kao, J., Nikiforovich, G. V., and Achilefu, S. (2003) Synthesis and characterization of a macrocyclic near-infrared optical scaffold. *J. Am. Chem. Soc. 125*, 7766–7767.

(51) Achilefu, S., Bloch, S., Markiewicz, M. A., Zhong, T., Ye, Y., Dorshow, R. B., Chance, B., and Liang, K. (2005) Synergistic effects of light-emitting probes and peptides for targeting and monitoring integrin expression. *Proc. Natl. Acad. Sci. U.S.A. 102*, 7976–7981.

(52) Bergeron, R. J., Wiegand, J., McManis, J. S., and Perumal, P. T. (1991) Synthesis and biological evaluation of hydroxamate-based iron chelators. *J. Med. Chem. 34*, 3182–3187.

(53) Ye, Y., X, B., Bloch, S., and Achilefu, S. (2006) Synthesis, Metal Coordination, and Cellular Internalization of a Siderophore-bearing NIR Fluorescent Carbocyanine Probe. In *Proceedings of SPIE-The International Society for Optical Engineering*, Vol. 6097 60970G-(1-5); Optical Molecular Probes for Biomedical Applications II (Achilefu, S., Bornhop, D. J., and Raghavachari, R., Eds.).

(54) Jeremy, J. Y., Kontoghiorghes, G. J., Hoffbrand, A. V., and Dandona, P. (1988) The iron chelators desferrioxamine and 1-alkyl-2-methyl-3-hydroxypyrid-4-ones inhibit vascular prostacyclin synthesis in vitro. *Biochem. J. 254*, 239–244.

(55) Glickstein, H., Breuer, W., Loyevsky, M., Konijn, A. M., Shanzer, A., and Cabantchik, Z. I. (1996) Differential cytotoxicity of iron chelators on malaria-infected cells versus mammalian cells. *Blood 87*, 4871–4878.

(56) Kontoghiorghes, G. J. (2006) Iron mobilization from transferrin and non-transferrin-bound-iron by deferiprone. Implications in the treatment of thalassemia, anemia of chronic disease, cancer and other conditions. *Hemoglobin 30*, 183–200.

(57) Tubaro, M., Marotta, E., Tisato, F., Bolzati, C., Porchia, M., Refosco, F., Tomasin, P., Cavazza-Ceccato, M., and Traldi, P. (2004) Electrospray mass spectrometry of a series of mixed nitrido 99gTc- heterocomplexes conjugated with bioactive molecules. *Eur. J. Mass. Spectrom. 10*, 605–611.

(58) Ye, Y., Liu, M., Kao, J. L., and Marshall, G. R. (2003) Peptide-bond modification for metal coordination: peptides containing two hydroxamate groups. *Biopolymers 71*, 489–515.

(59) Kumar, C. C., Nie, H., Rogers, C. P., Malkowski, M., Maxwell, E., Catino, J. J., and Armstrong, L. (1997) Biochemical characterization of the binding of echistatin to integrin alphavbeta3 receptor. *J. Pharmacol. Exp. Ther. 283*, 843–853.

BC7003022

Evaluation of Maleimide Derivative of DOTA for Site-Specific Labeling of Recombinant Affibody Molecules

Sara Ahlgren,[†] Anna Orlova,[‡,§] Daniel Rosik,[‡] Mattias Sandström,[||] Anna Sjöberg,[‡] Barbro Baastrup,[‡] Olof Widmark,[‡] Gunilla Fant,[‡] Joachim Feldwisch,[‡,§] and Vladimir Tolmachev*[,†,‡,§]

Division of Nuclear Medicine, Department of Medical Sciences, Uppsala University, Uppsala, Sweden, Affibody AB, Bromma, Sweden, Division of Biomedical Radiation Sciences, Rudbeck Laboratory, Uppsala University, Uppsala, Sweden, Hospital Physics, Department of Oncology, Uppsala University Hospital, Uppsala, Sweden. Received August 15, 2007; Revised Manuscript Received October 4, 2007

Affibody molecules are a new class of small (7 kDa) scaffold affinity proteins, which demonstrate promising properties as agents for *in vivo* radionuclide targeting. The Affibody scaffold is cysteine-free and therefore independent of disulfide bonds. Thus, a single thiol group can be engineered into the protein by introduction of one cysteine. Coupling of thiol-reactive bifunctional chelators can enable site-specific labeling of recombinantly produced Affibody molecules. In this study, the use of 1,4,7,10-tetraazacyclododecane-1,4,7-tris-acetic acid-10-maleimidoethylacetamide (MMA-DOTA) for ^{111}In-labeling of anti-HER2 Affibody molecules His_6-$Z_{HER2:342}$-Cys and $Z_{HER2:2395}$-Cys has been evaluated. The introduction of a cysteine residue did not affect the affinity of the proteins, which was 29 pM for His_6-$Z_{HER2:342}$-Cys and 27 pM for $Z_{HER2:2395}$-Cys, comparable with 22 pM for the parental $Z_{HER2:342}$. MMA-DOTA was conjugated to DTT-reduced Affibody molecules with a coupling efficiency of 93% using a 1:1 molar ratio of chelator to protein. The conjugates were labeled with ^{111}In to a specific radioactivity of up to 7 GBq/mmol, with preserved binding for the target HER2. In vivo, the non-His-tagged variant ^{111}In-[MMA-DOTA-Cys^{61}]-$Z_{HER2:2395}$-Cys demonstrated appreciably lower liver uptake than its His-tag-containing counterpart. In mice bearing HER2-expressing LS174T xenografts, ^{111}In-[MMA-DOTA-Cys^{61}]-$Z_{HER2:2395}$-Cys showed specific and rapid tumor localization, and rapid clearance from blood and nonspecific compartments, leading to a tumor-to-blood-ratio of 18 ± 8 already 1 h p.i. Four hours p.i., the tumor-to-blood ratio was 138 ± 8. Xenografts were clearly visualized already 1 h p.i.

INTRODUCTION

A growing number of cellular genotype and phenotype changes associated with the malignant transformation of cells have been identified. This knowledge is utilized for development of drugs that target particular alterations in gene expression. Due to the diversity of cancer phenotypes, only a fraction of all patients may benefit from a given targeted therapeutic drug. Therefore, targeting medicines need to be personalized, i.e., adapted to the cancer phenotype of the individual patient. For example, the HER2 tyrosine kinase receptor is the target for the humanized monoclonal antibody trastuzumab (Herceptin), which is approved for the clinical treatment of breast cancer. However, only 25–30% of all breast cancer patients display tumor disease overexpressing HER2, and *in vivo* detection of HER2 overexpression is therefore necessary (*1*, *2*). Radionuclide molecular imaging of HER2 expression in tumors may help to avoid problems associated with biopsies, such as sampling errors and discordance of HER2 expression in primary tumors and metastases. Initial attempts for radionuclide imaging were done using ^{111}In-labeled trastuzumab to identify potential responders to trastuzumab therapy (*3*). However, the sensitivity of detection was low (*4*). Generally speaking, low sensitivity is a problem when using full-size IgG antibodies as targeting agents for imaging, since their long residence time in blood causes high background and reduces contrast of imaging. The use of smaller targeting proteins, e.g., $(Fab')_2$, Fab, and scFv antibody fragments, with more rapid tumor localization and more rapid clearance is considered a promising way to increase the radionuclide imaging contrast.

One class of promising candidates for *in vivo* targeting agents are Affibody molecules, small (7 kDa) proteins based on a modified scaffold of the B-domain of protein A (*5*). Affibody molecule libraries are constructed by randomization of 13 amino acids in helix 1 and 2 of the modified domain B. Selection is performed, e.g., by phage display and enables development of high-affinity binders to protein targets. The selection of the Affibody molecule $Z_{HER2:342}$, binding the extracellular domain of HER2 with an affinity of 22 pM, was described earlier (*6*), and high-contrast imaging of HER2-expressing xenografts after indirect radioiodination was demonstrated. However, indirect radioiodination is a two-step labeling procedure followed by purification, which might complicate its translation into hospital radiopharmacy and delay introduction into routine clinical use. A coupling of suitable chelators and the use of radioactive metals, such as, e.g., ^{111}In ($T_{1/2}$ = 2.8 days), as labels enables kit formulation and simplifies logistics of radiopharmaceutical distribution and preparation. The use of benzyl isothiocyanate derivatives of DTPA (*7*) and DOTA (*8*) has been evaluated for labeling of recombinant $Z_{HER2:342}$ with ^{111}In. Both types of chelator could be used to make conjugates capable of specific imaging of HER2 *in vivo*, but ^{111}In-benzyl-DTPA-$Z_{HER2:342}$ (further referred to as ^{111}In-Bz-DTPA-Z_{342}) provided better tumor-to-blood ratio (50 ± 14 vs 23 ± 5) and tumor-to-liver

* Communicating author. Vladimir Tolmachev, Biomedical Radiation Sciences, Rudbeck Laboratory, Uppsala University, S-751 81 Uppsala, Sweden. Phone: +46 18 471 3414, Fax: + 46 18 471 3432, Vladimir.tolmachev@bms.uu.se.

[†] Department of Medical Sciences, Uppsala University.

[‡] Affibody AB.

[§] Rudbeck Laboratory, Uppsala University.

[||] Department of Oncology, Uppsala University Hospital.

10.1021/bc700307y CCC: $40.75 © 2008 American Chemical Society
Published on Web 12/29/2007

ratio (3.2 ± 0.6 vs 1.5 ± 0.1) than ^{111}In-Bz-DOTA-Z_{342} in a direct head-to-head comparison 4 h p.i. in mice bearing HER2-expressing xenografts (*8*). Isothiocyanate reacts to amino groups. The $Z_{HER2:342}$ Affibody molecule contains 7 amino groups, 1 at the N-terminus and 6 on lysine residue side chains. As expected, coupling with isothiocyanate produced a heterogeneous mixture of conjugates, containing different numbers of chelators, attached randomly at different positions. Clearly, a controlled site-specific attachment of chelator is more desirable, since it provides a homogeneous product with high batch-to-batch reproducibility. The spontaneously folding cysteine-independent structure of Affibody molecules enables a complete peptide synthesis of this protein and site-specific incorporation of different functional groups (*9*). Synthetic Affibody molecules $Z_{HER2:342}$ with chelators incorporated at the N-terminus have been prepared and characterized *in vivo* (*10*−*12*). DOTA has been used for labeling with ^{111}In (*10*) and mercaptoacetyl-containing peptide-based chelators maGGG and maSSS for labeling with ^{99m}Tc (*11, 12*). *In vivo* molecular imaging using synthetic ^{111}In-DOTA-$Z_{HER2:342}$ (further referred to as ^{111}In-DOTA-Z_{342}) resulted in specific and high-contrast targeting of HER2-expressing xenografts in mice (tumor-to-blood ratio of 7 already 1 h p.i.). Moreover, the clinical utility of this tracer in SPECT and PET has been confirmed, following labeling with ^{111}In or ^{68}Ga, respectively (*13, 14*).

Chemical production is only suitable for production of small proteinaceous agents such as monovalent Affibody molecules. Larger molecules, including dimeric or bispecific Affibody molecules, have to be produced recombinantly. Also, in this case, site-specific labeling is desirable. The absence of cysteines in the Affibody molecule provides the possibility to obtain a unique attachment site by introduction of a single cysteine, e.g., as a C-terminal residue. The use of a bifunctional chelator, linker molecule, or other reporter with a thiol-reactive moiety, e.g., maleimide or iodoacetamide, enables directed conjugation with this particular cysteine. This has been used previously for coupling of, e.g., Oregon Green 488 or horseradish peroxidase (HRP) to the dimeric Affibody molecule $(Z_{HER2:477})_2$-Cys (*15*) for *in vitro* detection of HER2. The use of the ((4-hydroxyphenyl)ethyl)maleimide (HPEM) linker molecule enabled site-specific labeling of a dimeric form of a previous generation of the HER2-binding Affibody molecule with radiobromine (*16*) and radioiodine (*17*).

The goal of the present study was to evaluate site-specific labeling of cysteine-containing Affibody molecules with ^{111}In using the chelator maleimide-monoamide-DOTA (MMA-DOTA; 1,4,7,10-tetraazacyclododecane-1,4,7-tris-acetic acid-10-maleimidoethylacetamide). For this purpose, several cysteine-containing variants of Affibody molecules were produced, conjugated with MMA-DOTA, and labeled with ^{111}In. In a comparative biodistribution, a His-tag containing variant, ^{111}In-[MMA-DOTA-Cys^{61}]-His_6-$Z_{HER2:342}$-Cys (further referred to as ^{111}In-DOTA-H_6-Z_{342}-C), was compared with non-His-tagged ^{111}In-[MMA-DOTA-Cys^{61}]-$Z_{HER2:2395}$-Cys (further referred to as ^{111}In-DOTA-Z_{2395}-C) and synthetic ^{111}In-DOTA-Z_{342} variants. The tumor-targeting properties of the best recombinant cysteine-containing site-specifically labeled variant, ^{111}In-DOTA-Z_{2395}-C, were compared in tumor-bearing mice with the synthetic ^{111}In-DOTA-Z_{342} and the best previous recombinantly produced conjugate with non-site-specific coupling of the chelator, ^{111}In-Bz-DTPA-Z_{342}.

MATERIALS AND METHODS

Materials. MMA-DOTA was purchased from Macrocyclics (Dallas, TX, USA). A synthetic DOTA-$Z_{HER2:342}$ was made by standard Fmoc peptide synthesis in a single chemical process by Bachem (Bubendorf, Switzerland) and labeled as described by Orlova et al. (*10*). A recombinant ^{111}In-Bz-DTPA-Z_{342} was produced and labeled according to Tolmachev et al. (*6*). Buffers, such as 0.1 M phosphate buffered saline (PBS), pH 7.5, and 0.2 M ammonium acetate, pH 5.5, were prepared using common methods from chemicals supplied by Merck (Darmstadt, Germany). High-quality Milli-Q water (resistance higher than 18 MΩ/cm) was used for preparing solutions. Buffers, which were used for conjugation and labeling, were purified from metal contamination using Chelex 100 resin (Bio-Rad Laboratories, Richmond, CA, USA). PD-10 and NAP-5 size exclusion columns were from Amersham Biosciences, Uppsala, Sweden. [^{111}In]indium chloride was purchased from Tyco. Silica gel impregnated glass fiber sheets for instant thin-layer chromatography (ITLC SG) were from Gelman Sciences Inc. Cells in the *in vitro* experiments were detached using trypsin-EDTA solution (0.25% trypsin, 0.02% EDTA in buffer, Biochrom AG, Berlin, Germany). Ketalar (50 mg/mL, Pfizer, NY, USA), Rompun (20 mg/mL, Bayer, Leverkusen, Germany), and Heparin (5000 IE/mL, Leo Pharma, Köpenhamn, Danmark) were obtained commercially. Data on cellular uptake, biodistribution, and gamma camera images were analyzed by unpaired, two-tailed *t*-test using *GraphPad Prism* (version 4.00 for Windows GraphPad Software, San Diego, California, USA) in order to determine any significant differences ($P < 0.05$).

Instrumentation. The radioactivity was measured using an automated gamma counter with 3 in. NaI(Tl) detector (1480 WIZARD, Wallac Oy, Turku, Finland). ^{111}In was measured with the use of both photopeaks and summation peak (energy setting from 140 to 507 keV). Distribution of radioactivity along the ITLC strips and SDS-PAGE gels was measured on a Cyclone Storage Phosphor System (further referred to as PhosphorImager) and analyzed using the *OptiQuant* image analysis software. Cells were counted using electronic cell counter (Beckman Coulter). The Affibody molecule were analyzed by high-performance liquid chromatography and online mass spectrometry (HPLC-MS) using an Agilent 1100 HPLC/MSD. The mass spectrometer was equipped with electrospray ionization (ESI) and single quadropol. The software used for analysis and evaluation was *Chemstation Rev. B.02.01*. (Agilent). For HPLC-MS analysis, 60 μL of diluted sample (1:1 dilution with solution A: 0.1% TFA in MQ-water) was loaded onto a Zorbax 300SB-C18 (4.6 × 150, 3.5 μm) RPC column equilibrated with solution A with 15% solution B (0.1% TFA in acetonitrile) at a flow rate of 1 mL/min. After 2 min with 15% B solution, the proteins were eluted using a linear gradient, 15–65% solution B in 22 min. The mass spectrometer was run according to the manufacturer's recommendations. SDS-PAGE analysis was performed using NuPAGE 4–12% Bis-Tris Gel (Invitrogen) in MES buffer (200 V constant). Affinity of Affibody molecules to HER2 was analyzed using a Biacore 2000 instrument (Biacore, Uppsala, Sweden) according to the method described earlier (*10*). Melting point analysis was performed using a JASCO J-810 spectropolarimeter (JASCO, Tokyo, Japan) as described earlier (*11*).

Protein Expression and Purification. A C-terminal cysteine was introduced into Affibody molecules according to a method described earlier (*16*). *Escherichia coli* BL21(DE3)/pAY01662 was run in an 800 mL batch fermentor cultivation (System Greta, Belach Bioteknik AB, Sweden) at 37 °C using TSB+YE-medium (30 g/L Tryptic Soy Broth (Merck), 5 g/L Yeast Extract (Merck)) supplemented with 50 mg/mL Kanamycin. The culture was automatically induced at an OD (600 nm) of 1 by the addition of IPTG to a concentration of 0.5 mM. Five hours after induction, the culture was automatically cooled to <10 °C and harvested by centrifugation (20 min at 15 900*g*).

His_6-tagged proteins were IMAC purified under denaturing conditions using QIAfilter 96 Plates Ni-NTA Superflow kit and

Scheme 1. Conjugation of the MMA-DOTA to Cysteine-Containing Affibody Molecules and Labeling of the Conjugate[a]

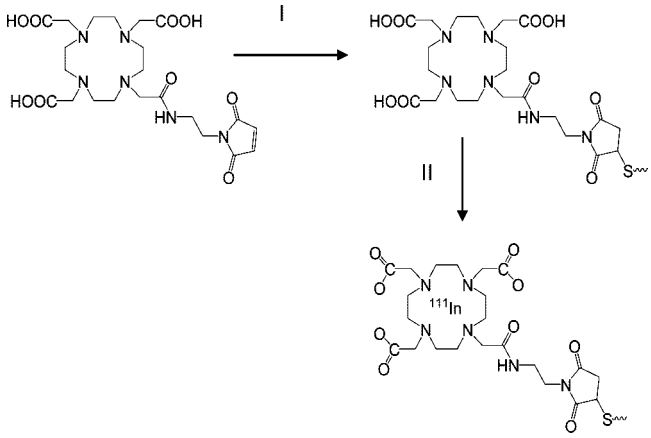

[a] Reagents and conditions: (I) Affibody molecule reduced by DTT, in 0.02 M ascorbic acid; acetate buffer, pH 5.5; 37 °C; overnight; purification on NAP-5, elution in 0.2 M ammonium acetate, pH 5.5. (II) ^{111}In-$InCl_3$, 0.2 M ammonium acetate buffer, pH 5.5, 60 °C, 30 min.

QIAsoft 4.1, medium-scale protein/Ni-NTA Superflow 96 Denat program on a Biorobot 3000 (Qiagen). The protein samples refolded when dialyzed in PBS using Slide-A-Lyzer (Pierce) according to the manufacturer's recommendations.

For purification of $Z_{HER2:2395}$-Cys without His_6-tag, the bacterial pellet was first resuspended in 20 mL 20 mM Tris pH 7.5 and then incubated at 90 °C for 3 min. After centrifugation (25 000*g*, 20 min, 4 °C), the supernatant was loaded onto a 20 mL Q Sepharose FF packed in a XK16 column, at a flow rate of 2 mL/min. The flowthrough was collected and DTT added to a final concentration of 20 mM. After incubation for 30 min at room temperature, acetonitrile (ACN) was added to a final concentration of 10%, and the solution was loaded onto a 1 mL Resource 15RPC column. The Affibody molecule was eluted using a linear gradient of 0–50% B in 15 min (A, 0.1% TFA/H_2O, 10% ACN/H_2O; B, 0.1% TFA, 80% ACN in H_2O). The buffer of the eluate was changed to PBS on a PD-10 column, and the protein concentration was calculated from the measured absorption values at 280 nm. Extinction coefficients were theoretically calculated from the primary amino acid sequence. A non-HER2-specific Z_{Taq}-Cys Affibody molecule was produced similarly to $Z_{HER2:2395}$-Cys. All proteins were analyzed by HPLC-MS and SDS-PAGE, as described in the Instrumentation section.

Conjugation and Labeling Chemistry. The conjugation of MMA-DOTA to the Affibody molecules was performed according to Scheme 1.

Before labeling, a solution of Affibody molecules (2 mg/mL in PBS) was treated with dithiothreitol (DTT, E. Merck, Darmstadt, Germany) in order to reduce spontaneously formed intermolecular disulfide bonds. Typically, 0.5 mL of stock Affibody solution (2 mg/mL in PBS) was mixed with 15 μL of DTT (1 M solution in water, freshly prepared) and incubated for 120 min at 37 °C. Thereafter, the mixture was applied to NAP-5 size-exclusion columns, pre-equilibrated and eluted with well-degassed 0.02 M ascorbic acid in MilliQ water, and the first 900 μL of the high-molecular-weight (HMW) fraction were used for coupling. For the coupling with a calculated chelator-to-Affibody molecule ratio of 1:1, 300 μL of the solution of reduced $Z_{HER2:2395}$ was mixed with 34 μL MMA-DOTA solution in MilliQ water (1 mg/mL), and 100 μL 1 M ammonium acetate buffer, pH 5.5 was added. The vial was filled with argon gas and incubated at 37 °C overnight. Purification from nonconjugated chelators and the change to a 0.2 M ammonium acetate buffer, pH 5.5, was made on a disposable NAP-5 size exclusion column. The conjugate solution was frozen and stored at −18 °C before labeling. The coupling efficiency was analyzed by HPLC-MS.

To evaluate kinetics of labeling, experiments were performed at 60 °C at least in duplicates. Conjugate (25 μg in 0.2 M ammonium acetate) was mixed with 7.5 MBq ^{111}In in 0.05 M HCl and incubated for 60 min. At predesignated time points (15, 30, and 60 min), a sample of 0.5 μL was taken and analyzed using ITLC SG with 0.2 M citric acid as the mobile phase. Additionally, radiolabeled Affibody molecules were analyzed using SDS-PAGE.

In further experiments, specific radioactivity was increased up to 1 MBq/μg (7 GBq/μmol).

For biodistribution experiments and cell studies, 60 min incubation was used for the labeling. For cell studies and biodistribution experiments, the sample was diluted with PBS.

Affibody molecules used in comparison experiments, i.e., [MMA-DOTA]-Z_{Taq}-Cys, and DOTA-H_6-Z_{342}-C, were conjugated and labeled in the same way as DOTA-Z_{2395}-C. Labeling yield after 60 min was analyzed using ITLC.

As a label stability test, two samples of ^{111}In-DOTA-Z_{2395}-C were mixed with a 1000-fold molar excess of EDTA in PBS. The samples were incubated at room temperature. After 3 h, the samples were analyzed using ITLC.

***In Vitro* Cell Binding and Retention.** Binding specificity of ^{111}In-DOTA-Z_{2395}-C and ^{111}In-DOTA-H_6-Z_{342}-C were tested on HER2-expressing SKOV-3 ovarian cancer cells. For each conjugate, two groups of Petri dishes (3 dishes/group; diameter, 3.5 cm; $\sim 3 \times 10^5$ cells/dish) were incubated using a 1:1 molar ratio of the radiolabeled Affibody molecule to HER2 receptors (1.2×10^6 receptors per cell (*18*)). The cells in one group were presaturated with 1000-fold excess of nonlabeled $Z_{HER2:342}$ for 5 min before the radiolabeled conjugate was added. Cells were incubated with labeled conjugate for 1 h at 37 °C before incubation medium was collected. The cells were washed once with cold serum-free medium followed by treatment with 0.5 mL trypsin-EDTA solution for 10 min at 37 °C. When cells were detached, 0.5 mL complete media was added to each dish, and the cells were resuspended and collected. The radioactivity associated with the cells and medium, respectively, was measured in an automatic gamma counter.

To study cellular retention and internalization of radioactivity, cultured SKOV-3 cells were incubated for 3 h at 4 °C using a 5:1 molar ration of ^{111}In-DOTA-Z_{2395}-C to HER2 receptors. All procedures were performed on ice. Thereafter, the incubation media was discarded, and the cells were washed three times using ice-cold serum-free medium. After addition of 1 mL complete medium, the cells were incubated further at 37 °C. At designated time points, up to 24 h, one group of three dishes was analyzed for cell-associated radioactivity. Medium was collected; cells were washed three times with ice-cold serum-free medium (these two steps were omitted for time point 0 h) and treated with 0.5 mL 4 M urea solution in 0.2 M glycine buffer, pH 2.5, for 5 min on ice. The acid fraction was collected, and cells were washed with additional 0.5 mL acid solution. The radioactivity in the acid wash fraction was considered membrane-bound radioactivity. After addition of 0.5 mL 1 M NaOH, the cells were incubated at 37 °C for at least 0.5 h, and basic solution was collected. Dishes were washed with additional 0.5 mL basic solution. The radioactivity in the alkaline fractions was considered internalized radioactivity. The radioactivity content of the samples was measured as mentioned above. To evaluate if the radioactivity in the media presented intact dissociated ^{111}In-DOTA-Z_{2395}-C or externalized radiocatabolites, the media, taken at 4, 8, and 24 h after start of incubation, was

Table 1. Characterization of Recombinant Cysteine-Containing Affibody Molecules

peptide	molecular weight[a] (Da)	k_a[b] (1/Ms)	k_d[b] (1/s)	K_D[b] (M)	T_m (°C)
His_6-$Z_{HER2:342}$-Cys	8317	4.72×10^6	1.38×10^{-4}	2.92×10^{-11}	65
$Z_{HER2:2395}$-Cys	6994.6	1.35×10^7	3.63×10^{-4}	2.68×10^{-11}	70

[a] Molecular weight was determined after reduction with DTT. [b] For Biacore measurement of affinity to HER2-Fc, Affibody molecules were reduced with DTT, and cysteine was capped with *N*-ethylmaleimide.

analyzed using NAP-5 disposable size-exclusion columns (cutoff for globular proteins 5 kDa), pre-equilibrated with 2% albumin in PBS.

Animal Studies. The animal experiment were planned and performed in accordance with national legislation on laboratory animals' protection. The animal study plans have been approved by the local Ethics Committee for Animal Research in Uppsala. Biodistribution studies in non-tumor-bearing mice were performed in female immunocompetent Naval Medical Research Institute (NMRI) mice. In all experiments on tumor-bearing mice, female outbreed BALB/c nu/nu mice were used. The mice were kept using standard diet, bedding, and environment with free access to food and water. All mice were acclimatized for one week at the Rudbeck Laboratory animal facility before any experimental procedures. Xenografts of HER2-expressing LS174T colon adenocarcinoma cell line were subcutaneously implanted in the right hind leg. For xenografting, 7×10^5 LS174T cell were used. At the time of experiment, the average tumor size was 0.26 ± 0.08 g.

In each experiment, mice were randomized into groups of four. Animals were injected intravenously with 1 μg conjugate (50 kBq) in 100 μL PBS. In all biodistributions, the mice were sacrificed at the predetermined time point, 4 h postinjection (p.i.) (except one group of animals, bearing LS174T xenografts, which was sacrificed 1 h p.i.). After an intraperitoneal injection of Ketalar-Rompun solution (20 μL of solution per gram body weight; Ketalar [ketamine]: 10 mg/mL; Rompun [xylazin]: 1 mg/mL), the mice were euthanized with heart puncture using a 1 mL syringe, prewashed with diluted heparin (5000 IE/mL). Blood was collected in preweighed vials. Lung, liver, spleen, colon, kidneys, tumor (from xenografted mice), muscle, bone, gastrointestinal tract (with its content), and remaining carcass were excised and collected in preweighed plastic vials. Organs and tissue samples were weighed and measured for radioactivity using an automatic gamma counter. The tissue uptake values were calculated as percent injected activity per gram tissue (% IA/g) except for the gastrointestinal tract and the carcass, which were calculated as % IA per whole sample. The radioactivity in the gastrointestinal tract with its content was used as a measure of hepatobiliary excretion, while the small (about 100 mg) part of the colon provided information concerning radioactivity accumulation in the intestine wall.

The biodistributions on NMRI mice were performed as a comparison of three different labeled constructs, two recombinant, ^{111}In-DOTA-H_6-Z_{342}-C and non-His-tagged ^{111}In-DOTA-Z_{2395}-C, along with one synthetic ^{111}In-DOTA-Z_{342} for one time point, 4 h p.i.

In the study on animals bearing LS174T xenografts, tumor targeting and biodistribution of ^{111}In-DOTA-Z_{2395}-C at 1 and 4 h p.i. was performed. Animals in the blocking experiments were subcutaneously injected with 600 μg of unlabeled His_6-$Z_{HER2:342}$ 45 min before injection of radiolabeled Affibody molecule. Mice in the blocking group were killed 4 h after injection. As another specificity test, the biodistribution of non-HER2-specific ^{111}In-[MMA-DOTA-Cys^{61}]-Z_{Taq}-Cys (further referred to as ^{111}In-DOTA-Z_{Taq}-C) was studied 4 h p.i. in mice bearing LS174T xenografts. For comparison, biodistributions of synthetic ^{111}In-DOTA-Z_{342} and recombinant ^{111}In-Bz-DTPA-Z_{342} were studied in the same batch of LS174T-grafted mice, 4 h p.i.

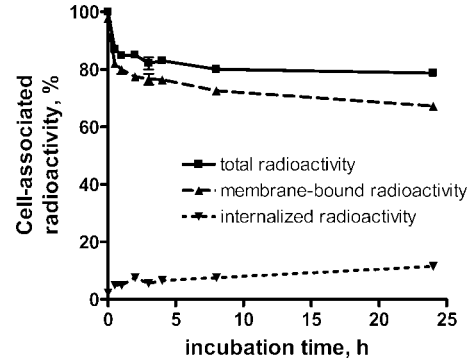

Figure 1. Cell-associated radioactivity as a function of time after interrupted incubation of SKOV-3 cells with ^{111}In-[MMA-DOTA-Cys^{61}]-$Z_{HER2:2395}$-Cys. The cell-associated radioactivity at time zero after the interrupted incubation was considered to be 100%. The radioactivity, which was removed from cells by treatment with 4 M urea solution in 0.2 M glycine buffer, pH 2.5, was considered membrane-bound, and the rest, internalized. Data are presented as mean $\pm$ SD ($n = 3$). Error bars might not be seen because they are smaller that point symbols.

For gamma camera imaging, four LS174T xenograft-bearing mice were injected with 4.5 MBq ^{111}In-DOTA-Z_{2395}-C (amount of protein 3 μg). Two of the animals, used as a blocking group, were preinjected with unlabeled Affibody molecules as described above. Immediately before imaging, 1 h postinjection, the animals were sacrificed by overdosing Ketalar/Rompun. After euthanasia, the urine bladders were dissected. Imaging was performed at the department of Nuclear Medicine at Uppsala University Hospital using a Millenium GE gamma camera equipped with a medium-energy general purpose (MEGP) collimator. Static images (10 min), obtained with a zoom factor of 3, were digitally stored in a 256×256 matrix. The evaluation of the images was performed using a Hermes system (Nuclear Diagnostics, Stockholm). In each animal, a region of interest (ROI) was drawn around the tumor. The same region was copied to a contralateral thigh. Tumor-to-contralateral thigh ratios were calculated on the basis of total counts in the ROIs.

RESULTS

Analysis of Peptides. Data concerning characterization of Affibody molecules are presented in Table 1. All purified proteins demonstrated a single peak on LC-MS with a mass, coinciding with the theoretically calculated accuracy of ± 1.5 Da, which is within the accuracy of the instrument. All proteins also demonstrated one single band on SDS-PAGE gel. Apparently, an introduction of a cysteine at the C-terminus did not have any effect on the binding to HER2, since the dissociation constant of both cysteine-containing derivatives did not deviate from the dissociation constant (K_D) of the parental $Z_{HER2:342}$ Affibody molecule, within the accuracy of the measurement method.

Conjugation and Labeling Chemistry. The LC-MS analysis showed that a coupling efficiency of 93% was obtained using a 1:1 molar ratio of chelator to Affibody molecule, and that a single chelator was attached per protein. In the case of chelators-to-protein molar ration 3:1, no unconjugated Affibody molecules were detected in the product. The ^{111}In labeling kinetics of DOTA-Z_{2395}-C was monitored by ITLC, and yields of 95 $\pm$

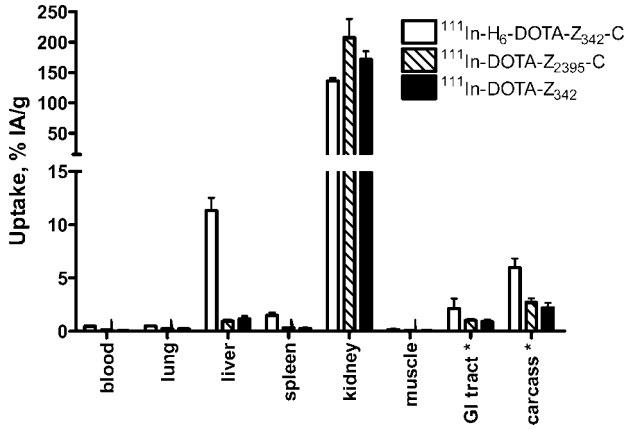

Figure 2. Biodistribution of radiolabeled recombinant ^{111}In-[MMA-DOTA-Cys^{61}]-His$_6$-Z$_{HER2:342}$-Cys (^{111}In-DOTA-H$_6$-Z$_{342}$-C), a non-His-tagged ^{111}In-[MMA-DOTA-Cys^{61}]-Z$_{HER2:2395}$-Cys (^{111}In-DOTA-Z$_{2395}$-C), and a synthetic ^{111}In-DOTA-Z$_{HER2:342}$ (^{111}In-DOTA-Z$_{342}$) Affibody molecules in NMRI normal mice 4 p.i. Data are expressed as % IA/g (percent of injected radioactivity per gram tissue) and presented as an average from four animals ± SD *Data for the gastrointestinal tract (with its content) and for carcass are presented as % IA per whole sample.

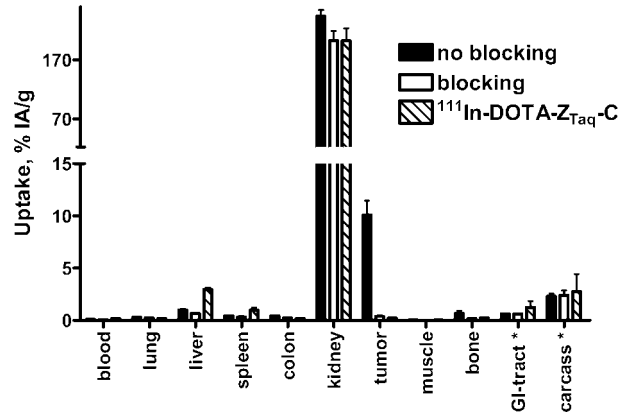

Figure 3. Specificity of ^{111}In-[MMA-DOTA-Cys^{61}]-Z$_{HER2:2395}$-Cys tumor uptake in LS174T xenografts, 4 h p.i. In order to saturate HER2 receptors in tumors, one group of animals was preinjected with 600 μg nonlabeled Z$_{HER2:342}$ 45 min before injection of radiolabeled conjugate (designated as blocking). As another negative control, one group was injected with non-HER2-specific ^{111}In-[MMA-DOTA-Cys^{61}]-Z$_{Taq}$-Cys (designated as ^{111}In-DOTA-Z$_{Taq}$-C). All animals were injected with 1 μg of labeled Affibody molecules. Data are expressed as % IA/g (percent of injected radioactivity per gram tissue) and presented as an average from four animals ± SD. *Data for the gastrointestinal tract (with its content) and for carcass are presented as % IA per whole sample.

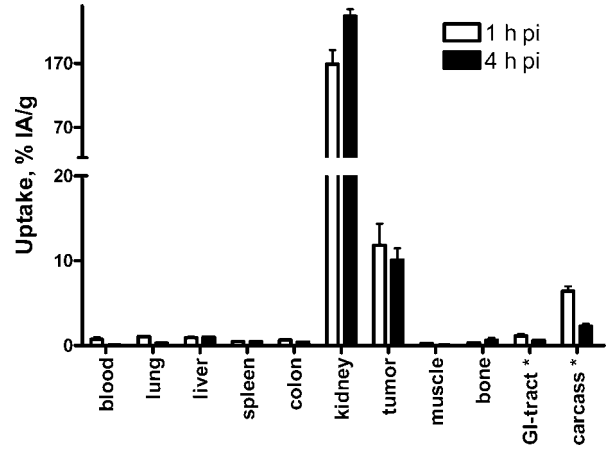

Figure 4. Biodistribution of ^{111}In-[MMA-DOTA-Cys^{61}]-Z$_{HER2:2395}$-Cys (^{111}In-DOTA-Z$_{2395}$-C) in BALB/C nu/nu mice bearing LS174T xenografts 1 and 4 p.i. Data are expressed as % IA/g (percent of injected radioactivity per gram tissue) and presented as an average from four animals ± SD. *Data for the gastrointestinal tract (with its content) and for carcass are presented as % IA per whole sample.

6%, 97 ± 1%, and 100% ^{111}In-DOTA-Z$_{2395}$-C were obtained after 15, 30, and 60 min, respectively. A specific radioactivity of 7 GBq/μmol was obtained. A PhosphorImager analysis of radioactivity distribution on an SDS-PAGE gel demonstrated a single radioactivity peak at a position of DOTA-Z$_{2395}$-C. The conjugate was stable. After 3 h challenge with 1000-fold molar excess of EDTA, 97.1 ± 0.6% of the radioactivity was still associated with ^{111}In-DOTA-Z$_{2395}$-C. Labeling of other MMA-DOTA-conjugated Affibody molecules, such as DOTA-H$_6$-Z$_{342}$-C or nonspecific control Affibody molecule DOTA-Z$_{Taq}$-C, provided radiochemical purity of more than 95% after 60 min labeling at 60 °C. For biological experiments, all conjugates were used without additional purification.

***In Vitro* Binding and Retention.** In the specificity test, 42 ± 1% of the added radioactivity was cell-bound to the nonblocked HER2-expressing SKOV-3 cells after 1 h of incubation at 37 °C. In the group where the HER2 receptors were saturated with nonlabeled Affibody molecules, the cell-bound radioactivity was significantly reduced to 1.3 ± 0.3% ($p < 1 \times 10^{-5}$). This demonstrated that binding of ^{111}In-DOTA-Z$_{2395}$-C to HER2-expressing cells was specific. Similarly, the binding of ^{111}In-DOTA-H$_6$-Z$_{342}$-C to SKOV-3 cells was also found to be specific.

The result of the cellular retention and internalization test of ^{111}In-DOTA-Z$_{2395}$-C is presented in Figure 1. The conjugate was efficiently retained by HER2-expressing cells. The internalization was, however, slow and inefficient. The percentages of nondegraded Affibody molecules in the incubation media were 77.3 ± 1.0%, 69.2 ± 0.8%, and 54.9 ± 0.6%, after 4, 8, and 24 h, respectively.

Apparently, cellular retention of the total radioactivity was quite good, with 78.7 ± 0.6% of cell-associated radioactivity after 24 h of incubation at 37 °C. On the other hand, the internalization of ^{111}In-DOTA-Z$_{2395}$-C was relatively slow, with less than 12% of internalized radioactivity after 24 h. An increasing fraction of low-molecular-weight radioactivity indicates, however, that at least a part of the conjugate was intracellularly degraded and radiocatabolites were externalized. Still, this fraction accounts even after 24 h for only about 10% of the radioactivity, initially bound to the cells.

Animal Studies. A comparison of the biodistributions of three different labeled constructs, two recombinant, ^{111}In -DOTA-H$_6$-Z$_{342}$-C and non-His-tagged ^{111}In-DOTA-Z$_{2395}$-C, as well as one synthetic ^{111}In-DOTA-Z$_{342}$ in NMRI mice at 4 h after i.v. injection is presented in Figure 2.

The biodistribution data of ^{111}In-DOTA-Z$_{342}$ were in very good agreement with the previously published data (*10*). The general pattern of all three conjugates is characterized by quick clearance of radioactivity from blood as well as the majority of organs and tissues, but accumulation in kidneys due to predominantly renal excretion and reabsorption in the proximal tubulae. The biodistributions of the recombinant ^{111}In-DOTA-Z$_{2395}$-C and the synthetic ^{111}In-DOTA-Z$_{342}$ were nearly identical. The only significant difference between these two conjugates was a lower level of blood radioactivity of ^{111}In-DOTA-Z$_{342}$, 0.06 ± 0.02 vs 0.10 ± 0.01 ($p < 0.05$) at 4 h p.i. The biodistribution of ^{111}In-DOTA-H$_6$-Z$_{342}$-C differed appreciably from the biodistributions of the two other conjugates. Although radioactivity accumulation in muscle and gastrointestinal tract did not differ significantly, the blood levels were 5−8-fold higher. The level of radioactivity in the organs, which are in

Table 2. Tumor-to-Organ Ratios in BALB/C nu/nu Mice Bearing LS174T Xenografts[a]

	^{111}In-DOTA- Z_{2395}-C		^{111}In-DOTA-Z_{342}	^{111}In-Bz-DTPA-Z_{342}
	1 h	4 h	4 h	4 h
blood	18 ± 8^b	116 ± 36	138 ± 8	88 ± 9
lung	11 ± 3^b	35 ± 5	23 ± 8	26 ± 10
liver	13 ± 2	11 ± 2	7 ± 6	5 ± 2^d
spleen	25 ± 5	24 ± 4	7 ± 2^c	18 ± 6
colon	18 ± 5	24 ± 2	53 ± 11^c	20 ± 8
kidney	$0.07^b \pm 0.01$	0.044 ± 0.005	0.069 ± 0.005^c	0.030 ± 0.009^d
muscle	59 ± 24^b	201 ± 97	220 ± 14	103 ± 36
bone	37 ± 15^b	14 ± 1	69 ± 11^c	20 ± 4

[a] Data are presented as an average from four animals ± SD. [b] Significant difference ($p < 0.05$) between tumor-to-organ ratios at 1 and 4 h p.i. for ^{111}In-[MMA-DOTA-Cys^{61}]-His$_6$-$Z_{HER2:342}$-Cys (^{111}In-DOTA-Z_{2395}-C). [c] Significant difference ($p < 0.05$) between tumor-to-organ ratios 4 h p.i. for ^{111}In-DOTA-Z_{2395}-C and synthetic ^{111}In-DOTA-$Z_{HER2:342}$ (^{111}In-DOTA-Z_{342}). [d] Significant difference ($p < 0.05$) between tumor-to-organ ratios 4 h p.i. for ^{111}In-DOTA-Z_{2395}-C and ^{111}In-benzyl-DTPA-$Z_{HER2:342}$ (^{111}In-Bz-DTPA-Z_{342}).

equilibrium with blood, such as lung and spleen, was higher accordingly. Furthermore, the clearance from the rest of the body was slower. However, the largest difference was seen in the liver uptake, which was about 10-fold higher for His-tagged ^{111}In-DOTA-H_6-Z_{342}-C than for the other two conjugates. Most likely, an arrest of radioactivity in the liver was the reason for reduced renal uptake of ^{111}In-DOTA-H_6-Z_{342}-C (136 ± 4% IA/g) in comparison with ^{111}In-DOTA-Z_{2395}-C and ^{111}In-DOTA-Z_{342} (194 ± 17% IA/g and 172 ± 13% IA/g, respectively). Overall, the biodistributions indicated that ^{111}In-DOTA-H_6-Z_{342}-C was considerably less suitable for future imaging applications compared to ^{111}In-DOTA-Z_{2395}-C, wherefore the His-tagged conjugate was excluded from further evaluation.

To investigate whether the tumor uptake *in vivo* was receptor-mediated, a biodistribution of ^{111}In-DOTA-Z_{2395}-C in nude mice bearing LS174T xenografts was compared with biodistribution of non-HER2-specific Affibody molecule ^{111}In-DOTA-Z_{Taq}-C, which was labeled in the same way and had the same structure, but 12 amino acids in the binding site were different. In addition, another group of mice was preinjected with a large amount of nonlabeled His6-$Z_{HER2:342}$ in order to saturate HER2 receptors in the xenografts. The results of *in vivo* specificity tests are presented in Figure 3. Presaturation of receptors led to more than a 26-fold decrease in tumor uptake of radioactivity, from 10.7 ± 0.6% IA/g to 0.4 ± 0.1% IA/g ($p < 0.0001$). Somewhat lower uptake in other organs after blocking indicates, probably, saturation of murine counterpart of HER2. In the mice injected with ^{111}In-DOTA-Z_{Taq}-C, the tumor uptake was also much lower, 0.21 ± 0.05% IA/g ($p < 0.0001$). The results of these two independent tests demonstrate specific uptake of ^{111}In-DOTA-Z_{2395}-C in tumor xenografts.

A comparison of the biodistribution of ^{111}In-DOTA-Z_{2395}-C in nude mice bearing LS174T xenografts 1 and 4 h p.i. is presented in Figure 4. The conjugate was characterized by quick blood clearance, with 0.73 ± 0.24% IA/g remaining in the blood 1 h p.i. and only 0.10 ± 0.03% IA/g 4 h p.i. High renal uptake indicates that the substance was cleared almost exclusively through the kidneys. The radioactivity in the gastrointestinal tract (with its content) was low at both time points, showing the minor role of the hepatobiliary clearance. The radioactivity in the kidneys increased between 1 and 4 h p.i., along with clearance from carcass and nonspecific tissues, such as blood, lung, colon, and muscle. Besides kidneys, the only site of high uptake was the tumor. A high tumor uptake (11.8 ± 2.6% IA/g) was already detected 1 h after injection and did not change significantly during the experiment, showing rapid tumor localization of the tracer. At this time point, the radioactivity concentrated in the tumor significantly exceeded the concentration in all organs and tissues, including blood (see tumor-to-blood ratios, Table 2). The only exception from this was the kidneys. Generally, tumor-to-organ ratios increased between 1 and 4 h p.i. due to decrease of the radioactivity in nonspecific organs.

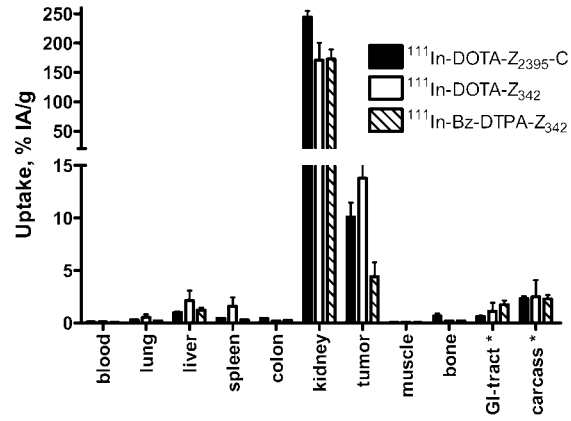

Figure 5. Biodistribution of a radiolabeled ^{111}In-[MMA-DOTA-Cys^{61}]-$Z_{HER2:2395}$-Cys (^{111}In-DOTA-Z_{2395}-C), synthetic ^{111}In-DOTA-$Z_{HER2:342}$ (^{111}In-DOTA-Z_{342}), and randomly coupled ^{111}In-benzyl-DTPA-$Z_{HER2:342}$ (^{111}In-Bz-DTPA-Z_{342}) Affibody molecules in BALB/C nu/nu mice bearing LS174T xenografts 4 p.i. Data are expressed as % IA/g (percent of injected radioactivity per gram tissue) and presented as an average from four animals ± SD. *Data for the gastrointestinal tract (with its content) and for carcass are presented as % IA per whole sample.

The comparison of biodistribution of ^{111}In-DOTA-Z_{2395}-C with biodistribution of the recombinant ^{111}In-Bz-DTPA-Z_{342} and the synthetic ^{111}In-DOTA-Z_{342} in nude mice bearing LS174T xenografts (4 h p.i.) are shown in Figures 5, 6 and Table 2. The radioactivity uptake of ^{111}In-Bz-DTPA-Z_{342} and ^{111}In-DOTA-Z_{342} in normal tissues was in good agreement with the data on these conjugates published earlier (*5, 8, 10*). Generally, the overall pattern of biodistribution of all three conjugates was similar. All conjugates were cleared rapidly from blood and normal tissues. The clearance was predominantly renal, with a high degree of reabsorption in kidneys. The degree of hepatobiliary clearance, as indicated by radioactivity in gastrointestinal tract, was low. Still, there were some distinct features of the conjugates. For example, tumor uptake of ^{111}In-Bz-DTPA-Z_{342} (with a randomly coupled chelator) was significantly ($p < 0.01$) lower than uptake of both conjugates with a site-specific attachment of DOTA. On the other hand, this conjugate provided significantly lower radioactivity content in blood, lung, spleen, colon, and kidneys in comparison to the ^{111}In-DOTA-Z_{2395}-C. Recombinant ^{111}In-DOTA-Z_{2395}-C had significantly lower accumulation in liver, spleen, and colon in comparison to synthetic ^{111}In-DOTA-Z_{342}, but higher in kidneys and bones. The tumor uptake of both conjugates did not differ significantly.

Gamma Camera Imaging. Images acquired 1 h after the i.v. injection of the ^{111}In-DOTA-Z_{2395}-C into immunodeficient

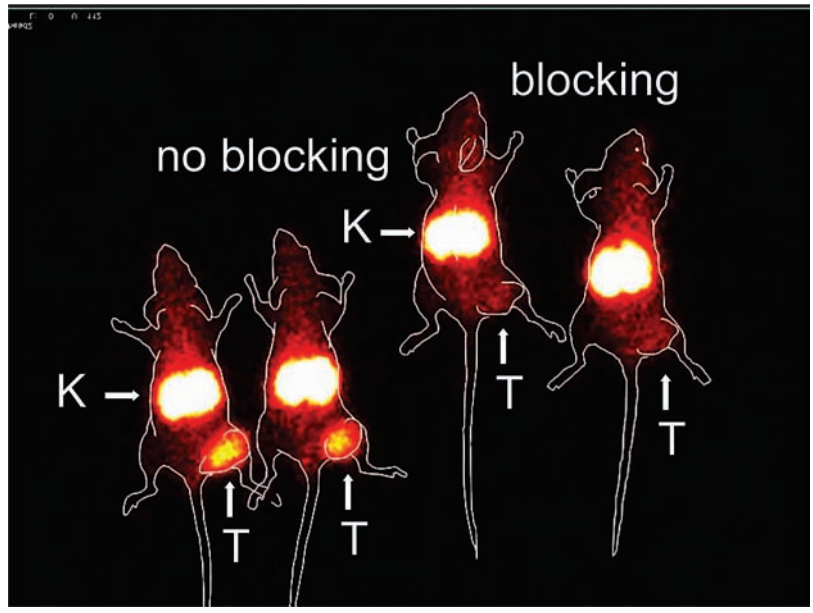

Figure 6. Imaging of HER2 expression in LS174T xenografts in BALB/c nu/nu mice using ^{111}In-[MMA-DOTA-Cys^{61}]-$Z_{HER2:2395}$-Cys (^{111}In-DOTA-Z_{2395}-C). In the blocking experiment, the HER2 receptors were saturated through a preinjection of 600 μg nonlabeled Affibody molecules. Planar gamma images were collected 1 h after administration of ^{111}In-DOTA-Z_{2395}-C. Tumors (right hind leg) were clearly visualized without blocking but were not seen in the blocking experiment, indicating specific HER2 binding of ^{111}In-DOTA-Z_{2395}-C. Animal contours were derived from a digital photograph and superimposed over γ-camera image to facilitate interpretation. Arrows point at tumors (T) and kidneys (K).

mice bearing subcutaneous LS174T xenografts confirmed feasibility of tumor visualization already at this time point (Figure 6). As predicted from the biodistribution studies, described above, the renal route of elimination of the conjugates also led to substantial kidney retention. Other organs and tissues were not visualized, and the contrast was high. Tumor-to-contralateral thigh ratio was 11.8 $\pm$ 1.2 (average $\pm$ max error). Specificity of HER2 imaging using ^{111}In-DOTA-Z_{2395}-C was also confirmed in this experiment, since LS174T xenografts on mice preinjected with nonlabeled Affibody molecule to saturate HER2 receptors were not visualized. Tumor-to-contralateral thigh ratio was 2.9 $\pm$ 0.3 in the case of receptor saturation.

DISCUSSION

Earlier, several commercially available chelators, such as isothiocyanatobenzyl-DTPA (*7*), isothiocyanatobenzyl-DOTA (*8*), and CHX-A″-DTPA (*19*) have been coupled to amino groups of recombinantly produced anti-HER2 Affibody molecules. This resulted in ^{111}In-labeled conjugates with good imaging properties, although some important differences have been observed. For example, at the same degree of coupling, the use of acyclic chelators provided lower liver uptake and higher tumor-to-liver ratios in comparison with DOTA. This is important, since the liver is a common site for metastases from many different malignancies, and high tumor-to-liver contrast is desirable. Although successful with the HER2-binding Affibody molecule, other Affibody molecules and targeting agents might contain lysines in the binding site, which due to conformational features could be more prone to coupling to isothiocyanate, resulting in conjugates with reduced targeting capacity. To obtain a pure homogeneous product becomes a challenge as soon as there is more than one amine group available for coupling, unless the protein is made by peptide synthesis.

Although site-specific labeling at the N-terminal amine of Affibody molecules has been obtained by peptide synthesis, site-specific coupling of a chelator to a C-terminal cysteine may be a more generally applicable method than N-terminal modification of Affibody molecules, because the C-terminus is located further away from the binding site.

The use of commercially available MMA-DOTA enabled a straightforward coupling of the chelator to Affibody molecules with a high yield. The use of slightly acidic conditions enabled a high degree of coupling specificity due to protonation of the amino groups (a maleimide might couple to deprotonated amines). By the use of chelator-to-protein ratio of 3 in the reaction mixture, a uniform conjugate was obtained.

A labeling of the conjugate with ^{111}In was rapid and efficient at the modestly elevated temperature, 60 °C. Earlier, we showed that even warming up to 90 °C did not decrease binding capacity of parental Affibody molecule $Z_{HER2:342}$ (*10*). The results of the EDTA challenge indicate that, after labeling during 30 min at 60 °C, ^{111}In is stably bound to the Affibody ligand *via* the chelator and not by occasional binding sites on the protein backbone or by unstable off-cage binding to DOTA. The results of the *in vitro* studies on HER2-expressing SKOV-3 carcinoma cells indicated that both ^{111}In-DOTA-H_6-Z_{342}-C and ^{111}In-DOTA-Z_{2395}-C preserved their binding specificity after labeling. The cellular retention of ^{111}In-DOTA-Z_{2395}-C by SKOV-3 was good during the whole experiment (24 h) and was mainly due to a high-strength membrane binding, not due to intracellular trapping. Although an internalization of a targeting peptide with an residualizing label was generally considered a prerequisite for successful retention (*20*), the recent finding with somatostatin analogues suggest that noninternalizing antagonists may enable sufficient targeting provided that affinity is high enough (*21*).

Although the *in vitro* experiments demonstrated high stability of the conjugate and its firm binding, a biodistribution characterization is an important step. It is known that changes of chelator or a few amino acids in somatostatin analogues may change the biodistribution of the tracer (*22*). Moreover, conformation changes due to change of nuclide affect both their affinity and biodistribution (*23*). Although Affibody molecules are substantially bigger, we have observed that a change of chelator may affect the biodistribution. For example, appreciable shifts in excretion pathways have been observed in the case of the change of a single amino acid in ^{99m}Tc-labeled Affibody molecules (*11, 12, 24*).

One aspect of the current study was to obtain a straight comparison between two alternative methods of site-specific

labeling *in vivo*. The biodistribution of ^{111}In-DOTA-Z_{2395}-C was very similar to the biodistribution of the synthetic ^{111}In-DOTA-Z_{342}, but the liver uptake of the recombinant protein was lower. With lower background levels, the tumor-to-background situation is more favorable. Another aspect of the current study was to evaluate if a His tag may be added onto the N-terminus, something which is attractive if several candidate proteins are to be produced and compared. Unfortunately, the addition of a His tag on the N-terminus had a dramatic negative effect on the biodistribution properties, leading to appreciable uptake in the liver. The mechanism of an elevated liver uptake is not known but might be associated with lipophilicity of histidines, which would create a local lipophilic "patch" at the N-terminus. Interestingly, we have previously observed high liver uptake in murine models of His-tag-containing Affibody molecules, which were labeled using $[^{99m}Tc(CO)_3]^+$ to the His tag (*25*). For this reason, only a variant ^{111}In-DOTA-Z_{2395}-C, which does not contain the His tag, was evaluated in tumor-bearing mice.

The specificity of ^{111}In-DOTA-Z_{2395}-C tumor uptake *in vivo* was confirmed by two independent methods, by the presaturation of receptors and by the use of non-HER2-specific structural analogue Z_{Taq}, labeled with the same methods as ^{111}In-DOTA-Z_{2395}-C. ^{111}In-DOTA-Z_{2395}-C displayed rapid tumor targeting and rapid clearance from nonspecific tissues, which enabled high-contrast imaging already 1 h p.i. (Figure 6). The tumor-to-organ ratios were increasing up to 4 h p.i., enabling further increase of the contrast during the day of injection. The only organ with the higher radioactivity accumulation than tumor was kidneys. A high kidney accumulation is a general feature of small targeting proteins (<60 kDa) labeled with residualizing radiometals (*26*). Two problems associated with high renal uptake are high renal radiation dose and difficulty of visualizing targets localized close to kidneys due to reconstruction artifacts. The first is important in radionuclide therapy using high-energy beta emitters but only a minor concern in radionuclide imaging using low levels of ^{111}In radioactivity, since Auger and conversion electrons, emitted by ^{111}In, are less damaging for the kidneys than beta particles (*27*). In clinical trials on the use of ^{111}In octreotide for therapy, renal doses as high as 45 Gy (after more than 90 GBq injected radioactivity) did not cause negative kidney side effects (*27, 28*). For imaging, only 100–200 MBq would be injected, resulting in several orders of magnitude lower renal doses. The problem of reconstruction artifacts in visualization of metastases in the vicinity of the kidney may be reduced with the use of new iterative SPECT reconstruction algorithms. In addition, several substances have been proposed, e.g., cationic amino acids (*29*), polyglutamic acid (*30*), or gelofusine (*31*), which are efficient in blocking of renal uptake of radiopeptides.

In the mice bearing LS174T xenografts, ^{111}In-DOTA-Z_{2395}-C provided as good tumor-to-blood ratios as synthetic ^{111}In-DOTA-Z_{342}. It provided better tumor-to-spleen ratios, even though the tumor-to-bone ratio was lower. Tumor-to-organ ratios for ^{111}In-DOTA-Z_{2395}-C appreciably exceeded values reported for this early time point after administration of radiometal-labeled HER2-targeting antibody fragments (*32, 33*). The nonspecifically labeled ^{111}In-Bz-DTPA-Z_{342} displayed lower blood concentration and lower tumor uptake than ^{111}In-DOTA-Z_{2395}-C. As a result, the tumor-to-blood ratio of ^{111}In-DOTA-Z_{2395}-C was not significantly better than that of the best recombinant protein with lysine-attached chelator. However, the important tumor-to-liver ratio was appreciably better for the site-specific conjugate. The significantly better tumor uptake of ^{111}In-DOTA-Z_{2395}-C can be also important, since it would provide a better signal in the SPECT camera. Another advantage of a DOTA-containing conjugate is the potential for labeling with positron-emitting generator-produced ^{68}Ga ($T_{1/2}$ = 68 min), which creates a precondition for the use of PET imaging with its advantages. The conjugates with acyclic chelators do not allow stable gallium labeling due to lower stability against transchelation of gallium to transferrin (*34*).

In conclusion, coupling of MMA−DOTA to an Affibody molecule with a single C-terminal cysteine provides a homogeneous conjugate which can be labeled with ^{111}In with preserved binding activity and specificity to HER2 and reduced liver uptake compared to with the corresponding construct containing a DOTA moiety attached at the N-terminus. The conjugate provides efficient targeting of HER2-expressing xenografts, while it is cleared rapidly from all normal tissues, except kidneys. The presence of an N-terminal His tag is not advisable, because this causes elevated liver uptake. The biodistribution and targeting properties of ^{111}In-DOTA-Z_{2395}-C are similar to properties of synthetic ^{111}In-DOTA-Z_{342}. In comparison to non-site-specifically labeled ^{111}In-Bz-DTPA-Z_{342}, ^{111}In-DOTA-Z_{2395}-C provides better tumor-to-liver ratio and higher tumor uptake. The method has a potential for site-specific labeling of Affibody molecules, which cannot be made by peptide synthesis, e.g., multimeric constructs, and for labeling of other proteinaceous tracers.

ACKNOWLEDGMENT

This research was financially supported by a grant from Swedish Cancer Society (Cancerfonden). Sara Ahlgren expresses her gratitude to Schuberts fond for a research scholarship. The authors expressed their genuine gratitude to staff of the animal department of the Rudbeck Laboratory for excellent care about the animals.

LITERATURE CITED

(1) Bast, R. C., Jr., Ravdin, P., Hayes, D. F., Bates, S., Fritsche, H., Jr., Jessup, J. M., Kemeny, N., Locker, G. Y., Mennel, R. G., and Somerfield, M. R. (2001) American Society of Clinical Oncology Tumor Markers Expert Panel. 2000 update of recommendations for the use of tumor markers in breast and colorectal cancer: clinical practice guidelines of the American Society of Clinical Oncology. *J. Clin. Oncol. 19*, 1865–1878.

(2) Molina, R., Barak, V., van Dalen, A., Duffy, M. J., Einarsson, R., Gion, M., Goike, H., Lamerz, R., Nap, M., Sölétormos, G., and Stieber, P. (2005) Tumor markers in breast cancer- European Group on Tumor Markers recommendations. *Tumour Biol. 26*, 281–293.

(3) Behr, T. M., Behe, M., and Wormann, B. (2001) Trastuzumab and breast cancer. *N. Engl. J. Med. 345*, 995–996.

(4) Perik, P. J., Lub-De Hooge, M. N., Gietema, J. A., van der Graaf, W. T., de Korte, M. A., Jonkman, S., Kosterink, J. G., van Veldhuisen, D. J., Sleijfer, D. T., Jager, P. L., and de Vries, E. G. (2006) Indium-111-labeled trastuzumab scintigraphy in patients with human epidermal growth factor receptor 2-positive metastatic breast cancer. *J. Clin. Oncol. 24*, 2276–2282.

(5) Tolmachev, V., Orlova, A., Nilsson, F. Y., Feldwisch, J., Wennborg, A., and Abrahmsen, L. (2007) Affibody molecules: potential for in vivo imaging of molecular targets for cancer therapy. *Exp. Opin. Biol. Ther. 7*, 555–568.

(6) Orlova, A., Magnusson, M., Eriksson, T., Nilsson, M., Larsson, B., Höiden-Guthenberg, I., Widström, C., Carlsson, J., Tolmachev, V., Ståhl, S., and Nilsson, F. Y. (2006) Tumor imaging using a picomolar affinity HER2 binding Affibody molecule. *Cancer Res. 66*, 4339–4348.

(7) Tolmachev, V., Nilsson, F. Y., Widstï, om, C., Andersson, K., Gedda, L., Wennborg, A., and Orlova, A. (2006) ^{111}In-benzyl-DTPA-$Z_{HER2:342}$, an Affibody-based conjugate for in vivo imaging of HER2 expression in malignant tumors. *J. Nucl. Med. 47*, 846–853.

(8) Orlova, A., Tran, T., Widström, C., Engfeldt, T., Karlström, A. E., and Tolmachev, V. (2007) Pre-clinical evaluation of [^{111}In]-benzyl-DOTA-Z342, a potential agent for imaging of HER2-expression in malignant tumors. *Int. J. Mol. Med. 20*, 397–404.

(9) Engfeldt, T., Renberg, B., Brumer, H., Nygren, P. Å., and Karlström, A. E. (2005) Chemical synthesis of triple-labelled three-helix bundle binding proteins for specific fluorescent detection of unlabelled protein. *ChemBioChem 6*, 1043–1050.

(10) Orlova, A., Tolmachev, V., Pehrson, R., Lindborg, M., Tran, T., Sandström, M., Nilsson, F. Y., Wennborg, A., Abrahmsén, L., and Feldwisch, J. (2007) Synthetic Affibody molecules: A novel class of affinity ligands for molecular imaging of HER2 expressing malignant tumors. *Cancer Res. 67*, 2178–2189.

(11) Engfeldt, T., Orlova, A., Tran, T., Bruskin, A., Widström, C., Karlström, A. E., and Tolmachev, V. (2007) Imaging of HER2-expressing tumours using a synthetic Affibody molecule containing the ^{99m}Tc-chelating mercaptoacetyl-glycyl-glycyl-glycyl (MAG3) sequence. *Eur. J. Nucl. Med. Mol. Imaging 34*, 722–733.

(12) Engfeldt, T., Tran, T., Orlova, A., Widström, C., Karlström, A. E., and Tolmachev, V. (2007) ^{99m}Tc-chelator engineering to improve tumour targeting properties of a HER2-specific Affibody molecule. *Eur. J. Nucl. Med. Mol. Imaging 34*, 1843–1853.

(13) Baum, R. P., Orlova, A., Tolmachev, V., and Feldwisch, J. (2006) A novel molecular imaging agent for diagnosis of recurrent HER2 positive breast cancer. First time in human study using an Indium-111- or Gallium-68-labeled Affibody molecule. *Eur. J. Nucl. Med. Mol. Imaging 33*, 591.

(14) Feldwisch, J., Orlova, A., Tolmachev, V., and Baum, R. (2006) Clinical and pre-clinical application of HER2-specific affibody molecules for diagnosis of recurrent HER2 positive breast cancer by SPECT or PET/CT. *Mol. Imaging 5*, 215.

(15) Lundberg, E., Höidén-Guthenberg, I., Larsson, B., Uhlén, M., and Gräslund, T. (2007) Site-specifically conjugated anti-HER2 Affibody molecules as one-step reagents for target expression analyses on cells and xenograft samples. *J. Immunol. Methods 319*, 53–63.

(16) Mume, E., Orlova, A., Nilsson, F., Larsson, B., Nilsson, A. S., Sjöberg, S., and Tolmachev, V. (2005) Evaluation of (4-hydroxyphenyl)ethyl)maleimide for site-specific radiobromination of anti-HER2 affibody. *Bioconjugate Chem. 16*, 1547–1555.

(17) Tolmachev, V., Orlova, A., Mume, E., Nilsson, A., Sjöberg, S., and Nilsson, F. Y. (2005) Improving tumor targeting by the use of ((4-hydroxyphenyl)ethyl)maleimide (I-HPEM) for radioiodination of anti-HER2 Affibody molecules. *Eur. J. Nucl. Med. Mol. Imaging 32*, 79.

(18) Persson, M., Tolmachev, V., Andersson, K., Gedda, L., Sandström, M., and Carlsson, J. (2005) [^{177}Lu]pertuzumab: experimental studies on targeting of HER-2 positive tumour cells. *Eur. J. Nucl. Med. Mol. Imaging 32*, 1457–1462.

(19) Orlova, A., Rosik, D., Sandström, M., Lundqvist, H., Einarsson, L. and Tolmachev, V. (2007) Evaluation of [$^{111/114m}$In]CHX-A″-DTPA-Z(HER2:342), an Affibody ligand conjugate for targeting of HER2-expressing malignant tumors. *Q. J. Nucl. Med. Mol. Imaging 51*, 314–323.

(20) Bodei, L., Paganelli, G., and Mariani, G. (2006) Receptor radionuclide therapy of tumors: a road from basic research to clinical applications. *J. Nucl. Med. 47*, 375–377.

(21) Ginj, M., Zhang, H., Waser, B., Cescato, R., Wild, D., Wang, X., Erchegyi, J., Rivier, J., Mäcke, H. R., and Reubi, J. C. (2006) Radiolabeled somatostatin receptor antagonists are preferable to agonists for *in vivo* peptide receptor targeting of tumors. *Proc. Natl. Acad. Sci. U.S.A. 103*, 16436–16441.

(22) Froidevaux, S., Heppeler, A., Eberle, A. N., Meier, A. M., Häusler, M., Beglinger, C., Béhé, M., Powell, P., and Mäcke, H. R. (2000) Preclinical comparison in AR4–2J tumor-bearing mice of four radiolabeled 1,4,7,10-tetraazacyclododecane-1,4,7,10-tetraacetic acid-somatostatin analogs for tumor diagnosis and internal radiotherapy. *Endocrinology 141*, 3304–3312.

(23) Antunes, P., Ginj, M., Zhang, H., Waser, B., Baum, R. P., Reubi, J. C., and Maecke, H. (2007) Are radiogallium-labelled DOTA-conjugated somatostatin analogues superior to those labelled with other radiometals? *Eur. J. Nucl. Med. Mol. Imaging 34*, 982–993.

(24) Tran, T., Engfeldt, T., Orlova, A., Widström, C., Bruskin, A., Tolmachev, V., and Karlström, A. E. (2007) In vivo evaluation of cysteine-based chelators for attachment of ^{99m}Tc to tumor-targeting Affibody molecules. *Bioconjugate Chem. 18*, 549–558.

(25) Orlova, A., Nilsson, F. Y., Wikman, M., Widström, C., Ståhl, S., Carlsson, J., and Tolmachev, V. (2006) Comparative in vivo evaluation of technetium and iodine labels on an anti-HER2 affibody for single-photon imaging of HER2 expression in tumors. *J. Nucl. Med. 47*, 512–519.

(26) Behr, T. M., Goldenberg, D. M., and Becker, W. (1998) Reducing the renal uptake of radiolabeled antibody fragments and peptides for diagnosis and therapy: present status, future prospects and limitations. *Eur. J. Nucl. Med. 25*, 201–212.

(27) Valkema, R., De Jong, M., Bakker, W. H., Breeman, W. A., Kooij, P. P., Lugtenburg, P. J., De Jong, F. H., Christiansen, A., Kam, B. L., De Herder, W. W., Stridsberg, M., Lindemans, J., Ensing, G., and Krenning, E. P. (2002) Phase I study of peptide receptor radionuclide therapy with [In-DTPA]octreotide: the Rotterdam experience. *Sem. Nucl. Med. 32*, 110–122.

(28) Kwekkeboom, D. J., Mueller-Brand, J., Paganelli, G., Anthony, L. B., Pauwels, S., Kvols, L. K., O'dorisio, T. M., Valkema, R., Bodei, L., Chinol, M., Maecke, H. R., and Krenning, E. P. (2005) Overview of results of peptide receptor radionuclide therapy with 3 radiolabeled somatostatin analogs. *J. Nucl. Med. 46*, 62S–66S.

(29) Rolleman, E. J., Valkema, R., de Jong, M., Kooij, P. P., and Krenning, E. P. (2003) Safe and effective inhibition of renal uptake of radiolabelled octreotide by a combination of lysine and arginine. *Eur. J. Nucl. Med. Mol. Imaging 30*, 9–15.

(30) Béhé, M., Kluge, G., Becker, W., Gotthardt, M., and Behr, T. M. (2005) Use of polyglutamic acids to reduce uptake of radiometal-labeled minigastrin in the kidneys. *J. Nucl. Med. 46*, 1012–1015.

(31) Vegt, E., Wetzels, J. F., Russel, F. G., Masereeuw, R., Boerman, O. C., van Eerd, J. E., Corstens, F. H., and Oyen, W. J. (2006) Renal uptake of radiolabeled octreotide in human subjects is efficiently inhibited by succinylated gelatin. *J. Nucl. Med. 47*, 432–436.

(32) Smith-Jones, P. M., Solit, D. B., Akhurst, T., Afroze, F., Rosen, N., and Larson, S. M. (2004) Imaging the pharmacodynamics of HER2 degradation in response to Hsp90 inhibitors. *Nat. Biotechnol. 22*, 701–706.

(33) Adams, G. P., Shaller, C. C., Dadachova, E., Simmons, H. H., Horak, E. M., Tesfaye, A., Klein-Szanto, A. J., Marks, J. D., Brechbiel, M. W., and Weiner, L. M. (2004) A single treatment of yttrium-90-labeled CHX-A″-C6.5 diabody inhibits the growth of established human tumor xenografts in immunodeficient mice. *Cancer Res. 64*, 6200–6206.

(34) Weiner, R. E., and Thakur, M. L. (2003) Chemistry of gallium and indium radiopharmaceuticals. *Handbook of radiopharmaceuticals* (Welch, M. J., and Redvanly, C. S., Eds.) pp 363–399, Chapter 11, John Wiley and Sons, Chichester, UK.

BC700307Y

HER2 Targeted Polyplexes: The Effect of Polyplex Composition and Conjugation Chemistry on in Vitro and in Vivo Characteristics

Oliver Germershaus,[†] Michael Neu,[†] Martin Behe,[‡] and Thomas Kissel*[,†]

Department of Pharmaceutics and Biopharmacy, Philipps Universität Marburg, Ketzerbach 63, 35032 Marburg, Germany, and Department of Nuclear Medicine, Philipps Universität Marburg, Baldingerstrasse, 35043 Marburg, Germany. Received August 17, 2007; Revised Manuscript Received October 10, 2007

Knowledge of the influence of targeting ligands on pharmacokinetics and biodistribution of polymeric nonviral vectors is presently limited. We investigated the properties of three structurally different conjugates of polyethylenglycol-modified polyethylenimine coupled to the HER2 specific antibody Trastuzumab. Unlike polyethylenimine, conjugates formed small (100–230 nm) DNA polyplexes with zeta-potentials of ± 2 mV at a broad range of N/P ratios. Stability as assessed by heparin displacement was slightly improved compared to unmodified copolymers. Erythrocyte aggregation and hemolysis were strongly reduced with conjugates. Conjugate polyplexes showed significant differences in specificity and transfection efficiency in vitro. These could be attributed to differences in cell binding and uptake assessed by flow cytometry. Pharmacokinetics of conjugates in mice revealed significant improvements over free plasmid DNA and polyethylenimine. Area under the plasma level−time curve of conjugates was increased up to 48% or 114% compared to that of polyethylenimine or free plasmid DNA, respectively. Deposition of conjugate polyplexes in lung and spleen was significantly reduced compared to that of polyethylenimine. Differences could be attributed to antibody conjugation since no significant differences in pharmacokinetics and biodistribution were found between conjugates. These findings demonstrate that conjugated antibodies not only confer active targeting but also significantly improve in vivo properties of polyplexes.

INTRODUCTION

Therapeutic nonviral gene delivery holds great potential for the treatment of many acquired and inherited diseases, such as viral infections and cancer (*1*). To efficiently achieve in vivo cancer gene therapy, especially to distant tumors or disseminated metastases, systemic administration of such vector systems is indispensable. For this purpose, the vector system should be efficient, nontoxic, and specific to its target cells. The vector should also be easily producible in a tailor-made fashion in large quantities. Cationic polymers, namely, poly(ethylene imine) (PEI), are exceptionally suitable for this purpose. PEI is known to exhibit superior transfection properties in vivo because of its ability to efficiently package, protect, and deliver DNA (*2, 3*). Unfortunately, the cationic nature of polymer/DNA complexes (polyplexes) causes aggregation with blood components and opsonization in vivo (*4*). Unmodified polyplexes are quickly cleared by first pass organs of the reticuloendothelial system such as liver and spleen or are trapped in lung capillaries (*5–8*). To achieve a stealth effect similar to that of polyethylenglycol (PEG)-modified liposomes (*9*), hydrophilic polymers such as PEG or poly(*N*-(2-hydroxypropyl)methacrylamide) (pHPMA) were attached before or after complex formation with DNA (*4, 10–12*). This strategy led to a reduction of surface charge, increased circulation times (*4, 10*), decreased unspecific transfection (*11, 13*), and improved biocompatibility, solubility, and stability for freeze-drying (*14*). Such stealth vectors are able to passively target tumor tissues because of the enhanced penetration and retention effect (*7*). To facilitate active tumor targeting in vivo, gene delivery vectors need to be recognized and taken up by the target cells. This can be achieved by the coupling of cell-binding ligands, such as antibodies or peptides (*15–17*).

Several studies using cationic polymers for in vivo gene delivery have been published (*2, 4, 6, 18–20*). The in vivo pharmacokinetics and/or biodistribution of these vectors was less often addressed (*4, 6–8, 10, 12, 21–23*). Only a minority of the studies dealt with the influence of hydrophilic polymers on polyplex disposition and kinetics (*4, 8, 10, 12, 21, 22*). The results of these studies were controversial. While Mullen et al. (*8*), Oupicky et al. (*12*), and Merdan et al. (*21*) found decreased polyplex stability in circulation after modification with hydrophilic polymers, Ogris et al. (*4*), Kunath et al. (*10*), and Hildebrandt et al. (*22*) reported increased tumor association and/or prolonged kinetics. Because of significant differences in study design, direct comparison of these results proved to be difficult.

Further modification of relatively small cationic polymers or copolymers (typically about 25–75 kDa) with large targeting molecules such as transferrin (∼80 kDa) or IgG (∼150 kDa) caused significant changes of polyplex properties. We hypothesized that targeting ligands not only mediate active targeting of tumor cells but also affect in vivo disposition and pharmacokinetics of the vector system. These changes may in effect be as important for efficient transfection of tumors in vivo as efficient binding to the target cells. A literature search on the contribution of targeting antibodies on pharmacokinetics and biodistribution of nonviral vector systems in vivo showed that this question was not systemically addressed so far.

We synthesized three structurally different conjugates consisting of branched PEI, PEG, and an antibody, Trastuzumab, directed against HER2. We determined sizes, zeta-potentials, and stability parameters of the resulting complexes with DNA at different charge ratios (N/P: polymer nitrogen/DNA phosphate). HER2-positive and -negative cell lines were used to evaluate transfection efficiencies and specificities of conjugates in vitro. Cell binding and uptake was studied by flow cytometry.

* To whom correspondence should be addressed. Tel: +49 6421 28 25881. Fax: +49-6421-282-7016. E-mail: kissel@staff.uni-marburg.de.
[†] Department of Pharmaceutics and Biopharmacy.
[‡] Department of Nuclear Medicine.

10.1021/bc700311n CCC: $40.75 © 2008 American Chemical Society
Published on Web 11/23/2007

In vivo pharmacokinetics and biodistribution were determined following tail vein injection of polyplexes in BALB/c mice in a 120 min time frame.

MATERIALS AND METHODS

Materials. Branched Polyethylenimine (Polymin, 25 kDa) was a gift from BASF (Ludwigshafen, Germany). Luciferase plasmid pCMV-Luc was purchased from Plasmid Factory (Bielefeld, Germany). *N*-succinimidyl-3-(2-pyridyldithio)propionate (SPDP) was obtained from Sigma-Aldrich (Taufkirchen, Germany). *N*-hydroxysuccinimidyl ester of 2 kDa orthopyridyl-disulfide polyethylenglycol (SPA-PEG(2 kDa)-OPSS) was purchased from Nektar Therapeutics (San Carlos, CA, USA). YOYO-1 iodide was obtained from Invitrogen (Karlsruhe, Germany). Trastuzumab (Herceptin) was purchased from Roche (Basel, Switzerland). All other chemicals used were of analytical grade.

Cell Culture. SK-BR-3 and OVCAR-3 cells were purchased from ATCC, Teddington, U.K. and maintained in RPMI 1640 (PAA Laboratories, Cölbe, Germany) supplemented with 10% and 20% fetal calf serum (Cytogen, Sinn, Germany), respectively, in humidified atmosphere with 5% CO_2 at 37 °C.

Synthesis of Conjugates. Polyethylenglycol (2 kDa)$_{10}$-graft-polyethylenimine (25 kDa) (abbreviated as PEG(2)-PEI) and polyethylenglycol (30 kDa)$_{1.1}$-graft-polyethylenimine (25 kDa) (abbreviated as PEG(30)-PEI) copolymers were synthesized and characterized as described previously (*24*). For the synthesis of conjugates based on PEG-PEI copolymers, the method described was refined (*16*). PEG(2 kDa)$_{10}$-PEI or PEG(30 kDa)$_1$-PEI (0.11 μmol) was dissolved in 0.5 mL reaction buffer consisting of 150 mM sodium chloride and 20 mM 4-(2-hydroxyethyl)-1-piperazine ethane sulfonic acid (HEPES) at pH 7.5. SPDP (0.2 μmol) in 20 μL of 100% ethanol was added while stirring and allowed to react for 60 min at RT. Purification of the product was performed by gel chromatography on a PD-10 column (Amersham Pharmacia Biotech, Freiburg, Germany) in reaction buffer. SPDP-activated PEG-PEI was reduced for 1 h at 37 °C using an excess of dithiothreitol (DTT) to yield PEG-PEI-SH. The degree of substitution with SH-reactive ortho-pyridyl groups was determined by pyridine-2-thione release upon addition of an excess of DTT (*25*).

In a second synthesis route, we used unmodified PEI (25 kDa) and covalently coupled Trastuzumab via a heterobifunctional PEG linker (SPA-PEG(2 kDa)-OPSS). Reactivity of SPA-PEG-OPSS was determined by pyridine-2-thione release and base-catalyzed NHS-ester hydrolysis. PEI (0.12 μmol) was dissolved in 1 mL of reaction buffer, and 1.2 μmol SPA-PEG-OPSS was added in 100 μL of 100% ethanol while stirring. The mixture was allowed to react for 1 h at room temperature, and the product was purified by gel chromatography and reduced as described above to yield PEI-PEG-SH. The degree of substitution was determined by pyridine-2-thione release as described above.

Trastuzumab (0.15 μmol) in reaction buffer was allowed to react with 0.24 μmol of SPDP (10 mM in pure ethanol) under stirring at room temperature and was purified as described above. SPDP-activated Trastuzumab was added to purified, activated PEG-PEI and allowed to react for 24 h at room temperature.

Purification of the conjugates was performed by a modified ion-exchange chromatography method first described by Kircheis et al. (*16, 26*). PEI concentration was quantified by copper complexation (*27*). The concentration of Trastuzumab was determined by UV-spectrometry at 280 nm with background correction using a solution of PEG-PEI or PEI of equal concentration.

Formation of Polyplexes. Polyplex formation was performed as described earlier (*16*). Briefly, pDNA was diluted with 150 mM sodium chloride, 10 mM HEPES at pH 7.4 to 0.04 g/L and mixed in equal parts with the appropriate amount of polymer in the same buffer. All experiments were performed at a N/P ratio of 6 and a final pDNA concentration of 0.02 g/L unless stated otherwise.

Size and ζ-Potential. Hydrodynamic diameters and ζ-potentials of freshly prepared polyplexes were determined using a Zetasizer Nano ZS (Malvern Instruments, Herrenberg, Germany) equipped with a 4 mW He-Ne laser at a wavelength of 633 nm at 25 °C. Scattered light was detected at a 173° backward scattering angle. The viscosity and refractive index of water at 25 °C was used for data analysis. Five hundred microliters of polyplex solution was prepared and incubated for 10 min at RT. Measurements were performed in a folded capillary cell in triplicate. DTS software 4.10 was used for data acquisition and analysis. The accuracy of the instrument was maintained using reference polymer particles (nanosphere size standards of 50, 100, and 200 nm, Duke Scientific Corp., Palo Alto, CA, USA) and with the zeta potential transfer standard (Malvern Instruments, Herrenberg, Germany).

Agarose Gel Electrophoresis. For heparin displacement, 50 μL of polyplex solutions were prepared at N/P 6 and incubated for 10 min at RT. Then, polyplexes were challenged with 0.05 to 0.35 U heparin for 30 min at RT. Glycerol (10% v/v) was added, and 10 μL of the solution was carefully applied to a 1% agarose gel in TAE (40 mM Tris/HCl, 1% acetic acid, and 1 mM EDTA at pH 7.4) containing 0.6 μg/mL of ethidium bromide. Electrophoresis (Electro-4, Thermo Electron, Waltham, MA, USA) was carried out at a constant voltage of 80 V for 1 h in TAE buffer. Ethidium bromide fluorescence was detected using a gel documentation system (BioDocAnalyze, Biometra, Göttingen, Germany) and images were processed with ImageJ 1.37v (http://rsb.info.nih.gov/ij/) (*28*).

Erythrocyte Aggregation and Hemolysis. The hemolytic activity and erythrocyte aggregation of polyplexes were investigated as reported earlier (*29*). Briefly, human erythrocytes were isolated from fresh citrated blood from healthy volunteers by centrifugation at 850 $\times$ *g*. Red blood cells were washed in HEPES-buffered saline (HBS) until the supernatant was clear and colorless. Erythrocytes were diluted with HBS to 5×10^8 cells/mL. Polyplexes were prepared at N/P 6 in a total volume of 125 μL (DNA concentration 0.1 μg/μL). Triton X-100 (1%) in HBS (100% lysis) and pure HBS (0% lysis) were used as control. Aliquots (40 μL) of polyplex solutions were mixed with 40 μL of erythrocyte suspension. Samples were incubated for 30 min at 37 °C under constant shaking. After centrifugation at 850 $\times$ *g*, the supernatant was analyzed for hemoglobin release at 415 nm (Ultrospec 3000, GE Healthcare, Munich, Germany). The Pellet was resuspended with 500 μL of HBS and used for microscopic evaluation of erythrocyte aggregation.

Transfection Experiments. For transfection experiments SK-BR-3 and OVCAR-3 cells were plated at a density of 1×10^4 cells per well in a 96-well plate. After 24 h of growth, the medium was replaced with 0.2 mL of fresh, complete cell culture medium containing 0, 10, 50, or 250 μg of free Trastuzumab. Cells were incubated for 15 min at 37 °C. Polyplexes were prepared in a final volume of 30 μL (containing 0.63 μg pDNA) per well, incubated for 10 min at RT, and subsequently added to the wells. The medium was exchanged again after 4 h, and cells were incubated for an additional 44 h.

Luciferase gene expression was quantified using a commercial kit (Promega, Mannheim, Germany) and photon counting on a luminometer (Sirius, Berthold, Pforzheim, Germany). Results were measured in relative light units per second (RLU/s) and converted to nanograms of luciferase using a standard curve of recombinant luciferase (Promega, Mannheim, Germany). Protein concentration was determined using a modified BCA assay

(Perbio Science, Bonn, Germany) with bovine serum albumin as a standard (*30*). All experiments were performed in quadruplicate, and results were normalized to the transfection efficiency of unmodified PEG-PEI copolymers.

Flow Cytometry. For flow cytometry experiments, cells were seeded in 24-well plates at a density of 6×10^4 cells per well. After 24 h of growth, the cell culture medium was exchanged with 0.5 mL of fresh medium. Polyplexes were prepared in a final volume of 150 μL (containing 2.5 μg YOYO-1 labeled pDNA (*31*)) at N/P 6, incubated for 10 min at room temperature, and then added to the wells. In the case of polyplex binding experiments, cells were incubated at 4 °C for 15 min before and after the addition of polyplexes. Subsequently, cells were washed 2 times with ice cold PBS. For the uptake experiments, cells were incubated with the polyplexes for 3 h at 37 °C. Cells were then washed 4 times for 3 min with 0.5 mg/mL heparin in PBS to remove surface-bound polyplexes. Cells were detached with trypsin and suspended in an ice-cold 1:1 mixture of FACS-Flow (BD Biosciences, San Jose, USA) and 4% paraformaldehyde in PBS.

Flow cytometry was performed using FACScan (BD Biosciences, San Jose, USA) equipped with a 488 nm argon-ion laser. The emission filter setting was 530/30 bandpass. Viable cells were gated according to forward and sideward scatter of untreated cell samples. At least 5000 gated events were collected and subjected to further analysis. All experiments were performed in triplicate. Results were normalized to binding or uptake efficiency of the respective unmodified PEG-PEI copolymers. CellQuest 3.3 software (BD Biosciences, San Jose, USA) was used for data acquisition. Analysis was performed with FCS Express V3 (De Novo Software, Thornhill, Canada).

In Vivo Experiments. All animal experiments were carried out according to the German law of protection of animal life and approved by an external review committee for laboratory animal care.

Pharmacokinetic and Biodistribution Studies. 100 ng pCMV-Luc were labeled with 32-P-α-CTP (Hartmann, Germany) using a Nick translation kit N5000 (GE Healthcare, Germany) according to the manufacturer's protocol. The reaction mixture was purified using microspin columns (Wizard SV Gel and PCR Clean-Up System, Promega, Germany) and the labeled plasmid was used immediately after synthesis.

Polyplexes were prepared using 25 μg of the pCMV-Luc plasmid spiked with the ^{32}P-labeled plasmid as described earlier (*21*). A volume equal to a dose of 1 μg of pCMV-Luc per gram of mouse of the polyplex solution was injected in anesthetized male balb/c mice via the tail vein. Blood samples of 25 μL were drawn from the retrobulbar plexus 1, 3, 5, 15, 30, 60, and 120 min postinjection. After 120 min, mice were sacrificed by cervical dislocation, and organs were excised. Organ samples were dissolved in Soluene 350 (PerkinElmer, Germany), and blood samples were dissolved overnight in a 1:1 mixture of isopropanol/Soluene 350 at 55 °C and subsequently bleached with 200 μL of hydrogen peroxide. After the addition of 15 mL of scintillation cocktail (Hionic Fluor, PerkinElmer, Germany), the activity of ^{32}P in each sample was determined using a TriCarb 2900 liquid scintillation counter (PerkinElmer, Germany) with a counting time of 10 min, active static controller, and half-life correction. Disintegrations per minute (DPM) were calculated with a ^{32}P quench curve using tSIE/AEC as the quench indicator. The injected dose was calculated on the basis of activity measurements of the injected solution. All experiments were performed at least in triplicate, and the AUC was determined using a noncompartmental mixed logarithmic linear algorithm. Concentration−time data were fitted to a biexponential disposition function ($C(t) = A\ e^{-\alpha t} + B\ e^{-\beta t}$, iterative reweighing with $1/C_{obs}$) using the software Kinetica 1.1. from Simed (Créteil Cedex, France). Plasmid concentrations in the samples were calculated as the percent of the injected dose per organ or as percent injected dose per milliliter of blood.

RESULTS

Synthesis of Conjugates. Conjugates were prepared using two different polyethylenglycol−polyethylenimine copolymers (*24*). To study the influence of PEGylation, these copolymers represent two extremes concerning the degree of PEGylation and PEG chain length while keeping the weight ratio of PEG to PEI approximately constant. In both cases, the targeting moiety was coupled to PEI via the heterobifunctional linker *N*-succinimidyl-3-(2-pyridyldithio)propionate (SPDP). The degree of substitution with SPDP, determined by pyridine-2-thion release, was 1.5 and 1.7 mol of 2-pyridyl disulphide per mole of PEI for PEG(2)-PEI and PEG(30)-PEI, respectively. A third conjugate was prepared by modifying PEI with a heterobifunctional PEG linker. This synthesis resulted in a degree of substitution of ∼10 mol of PEG per mole of PEI. The degree of substitution with 2-pyridyl disulphide was determined to be 5 moles per mole of PEI. The reaction of SPDP with Trastuzumab resulted in a degree of substitution of 1.3 mol of 2-pyridyl disulphide per mole of antibody. Finally, the degree of substitution of conjugates with Trastuzumab was determined to be 0.74, 1.5, and 0.38 mol/mol Trastuzumab/PEI for PEG(2)-PEI-Trastuzumab, PEG(30)-PEI-Trastuzumab, and PEI-PEG(2)-Trastuzumab, respectively (Figure 1). The overall polymer yield after purification varied between 50 and 70% as determined by copper complexation.

Size and ζ-Potential. Hydrodynamic diameters decreased with increasing N/P ratio for all complexes (Figure 2a). At N/P 6 and 12, all complexes revealed a similar size of 100−230 nm, facilitating efficient uptake by absorptive endocytosis (*32*). At N/P 3, PEI formed large complexes of about 1200 nm. Because of efficient shielding, PEG-PEI and conjugate polyplexes were significantly smaller than PEI complexes with sizes of only 100−300 nm.

In contrast to PEI polyplexes, which showed high ζ-potentials of about +27 mV at N/P 6 and 12, the surface charge of PEG-PEI polyplexes was significantly reduced (Figure 2b). Modification of PEG-PEIs with Trastuzumab further decreased ζ-potentials. These polyplexes were near neutral at all N/P ratios tested.

Stability against Heparin Displacement. To evaluate polyplex stability against displacement of pDNA by competing polyanions, the polyplexes were challenged with free heparin (Figure 3). Heparin amounts as low as 0.1 U displaced DNA from the complex in the case of PEI and PEG-PEI copolymers. Trastuzumab conjugate complexes showed a slightly improved stability against heparin displacement. With these polyplexes, free plasmid DNA was observed at heparin concentrations of 0.20 U and above.

Erythrocyte Hemolysis and Aggregation. Interactions with blood components, namely, erythrocytes, are likely to occur after injection of polyplexes into the bloodstream (*4, 33*). The hemolytic activity of polyplexes and the tendency to form aggregates with erythrocytes was studied in an in vitro assay using freshly purified human red blood cells.

For polyplexes prepared with unmodified PEI at N/P 6, hemolysis of 16% of the erythrocytes was found, which is in good correlation with earlier reports (Figure 4) (*34*). PEGylation of PEI significantly reduced hemolysis both in the case of short (PEG(2)-PEI) and long (PEG(30)-PEI) PEG chains. Modification of PEG-PEI copolymers with Trastuzumab significantly decreased erythrocyte lysis compared to the unmodified PEG-

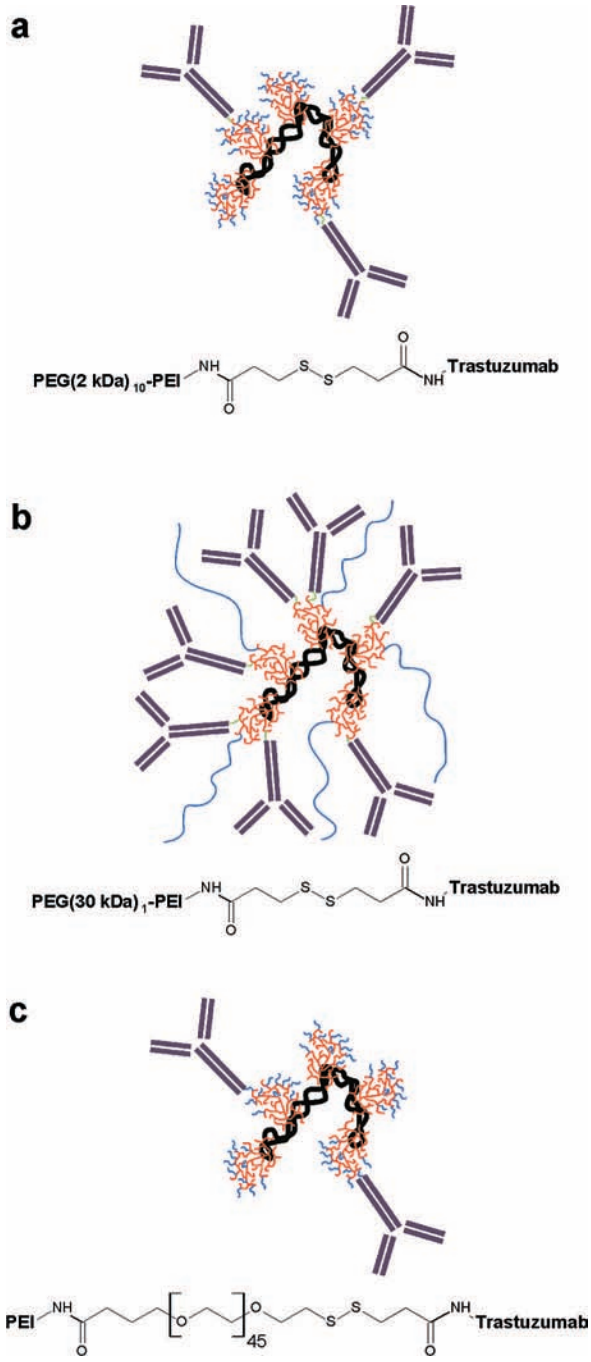

Figure 1. Chemical structure of conjugates and illustration of hypothetical complexes with plasmid DNA (black). Branched PEI (25 kDa) (red) was substituted with PEG (light blue) of different molecular weights to different degrees, and Trastuzumab (dark blue) was coupled directly to PEI via SPDP (green) in the case of (PEG(2)-PEI-Trastuzumab (a) and PEG(30)-PEI-Trastuzumab (b). PEI-PEG(2)-Trastuzumab (c) was prepared by the modification of branched 25 kDa PEI with a heterobifunctional PEG linker, and Trastuzumab was coupled to the distal end of the PEG chains.

PEI copolymers. Only 1.0 to 2.4% hemolysis was observed with Trastuzumab conjugates.

Erythrocyte suspensions were then microscopically examined for aggregate formation (Figure 4). The addition of PEI polyplexes resulted in rapid and extensive erythrocyte aggregation. Interaction with erythrocytes was decreased using PEG-PEI polyplexes but still moderate to severe aggregate formation was found. Using Trastuzumab-modified copolymers, no erythrocyte aggregation was seen.

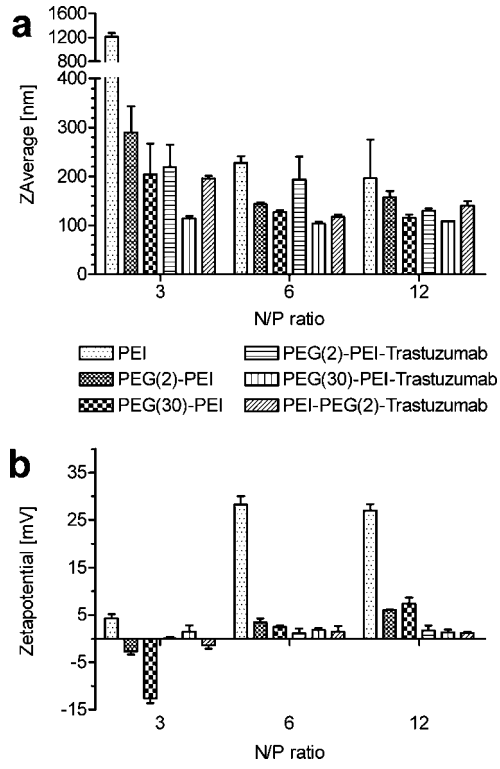

Figure 2. Hydrodynamic diameters (a) and zeta-potentials (b) of polyplexes prepared with pDNA and unmodified polymers or Trastuzumab conjugates at the indicated N/P ratios. Polyplexes were prepared as described in the Materials and Methods section and were measured in a folded capillary cell in quintuplicate (a) or triplicate (b). Values are given as the means + SD.

Transfection Experiments. For transfections in vitro, two different cell lines with different HER2 expression levels were used. OVCAR-3 cells were shown to express only low amounts of HER2 and therefore served as a negative control (*16*). In contrast, SK-BR-3 cells are known to overexpress HER2 (*16, 35*). Specificity of transfection was evaluated by competitive inhibition with free Trastuzumab during incubation with polyplexes.

In SK-BR-3 cells, PEG(2)-PEI-Trastuzumab showed a significant ($p < 0.01$) 6.6-fold increase in reporter gene expression compared to PEG(2)-PEI. Significant inhibition ($p < 0.05$) was seen with at least 1.69 μmol/L free Trastuzumab (Figure 5a). By contrast, transfection efficiency of PEG(30)-PEI-Trastuzumab was not significantly increased compared to PEG(30)-PEI, and no significant inhibition was seen with free Trastuzumab in cell culture media (Figure 5c). PEI-PEG(2)-Trastuzumab had a reporter gene expression 34-fold higher compared to that of PEG(2)-PEI. Significant inhibition ($p < 0.001$) was achieved with Trastuzumab concentrations as low as 0.34 μmol/L (Figure 5e). None of the conjugates showed a specific reporter gene expression in HER2-negative OVCAR-3 cells (Figures 5b, d, and f).

Flow Cytometry. Binding efficiencies of Trastuzumab conjugates relative to those of unmodified PEG-PEI copolymers at 4 °C are depicted in Figure 6a. Increased binding to SK-BR-3 cells was observed for all conjugates. Compared to the respective untargeted copolymer, PEI-PEG(2)-Trastuzumab showed the most efficient binding, followed by PEG(2)-PEI-Trastuzumab and PEG(30)-PEI-Trastuzumab. A smaller increase of the binding of conjugates was also found for OVCAR-3 cells. HER2 expression of OVCAR-3 cell was found to be very low but still detectable by flow cytometry (*16*), which may explain the slightly increased binding efficiencies.

To evaluate the uptake of particles, OVCAR-3 and SK-BR-3 cells were incubated with polyplexes for 3 h at 37 °C. Cell-

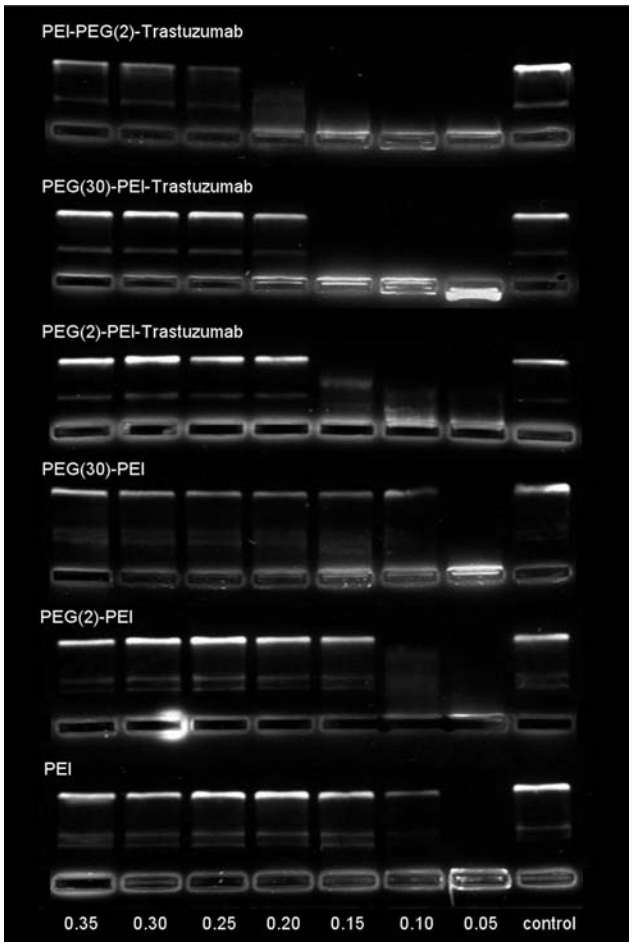

Figure 3. Heparin displacement assay using PEI, copolymer, and conjugate polyplexes. Polyplexes were formed at N/P 6 and incubated for 30 min with increasing heparin concentrations. Free plasmid DNA is shown to the right.

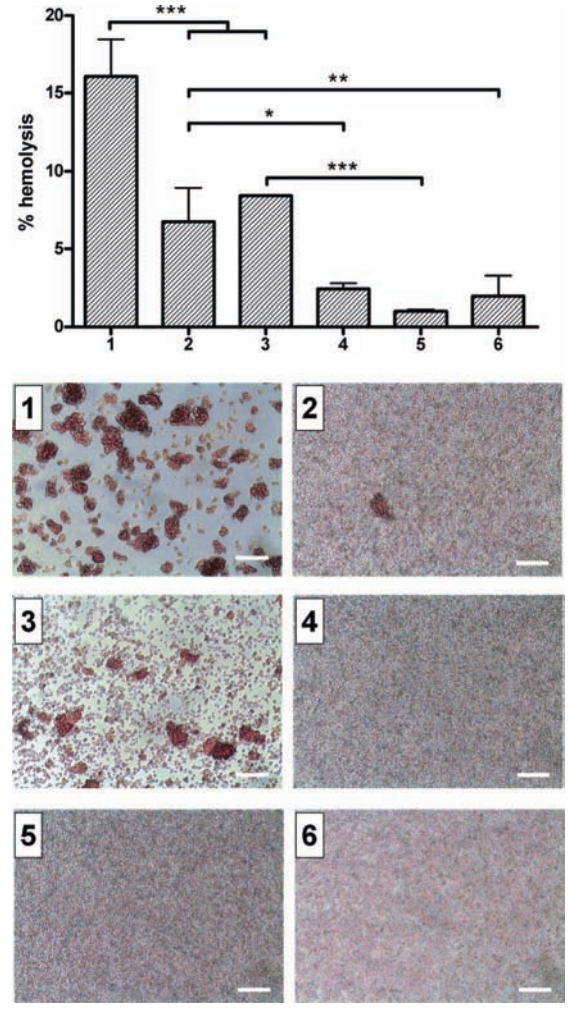

Figure 4. Lysis and aggregation of human erythrocytes induced by polyplexes prepared at N/P 6 with PEI (1), PEG(2)-PEI (2), PEG(30)-PEI (3), PEG(2)-PEI-Trastuzumab (4), PEG(30)-PEI-Trastuzumab (5), and PEI-PEG(2)-Trastuzumab (6). Values are given as the means + SD of triplicates. Significance was tested using one-way ANOVA with Bonferroni's multiple comparison test (* $p < 0.05$; ** $p < 0.01$; *** $p < 0.001$). Scale bars represent 100 μm.

surface-bound polyplexes were then removed, and intracellular fluorescence was determined by flow cytometry as well. Figure 6b shows the uptake efficiencies of conjugates relative to unmodified PEG-PEI copolymers. A very efficient and specific uptake can be observed for PEI-PEG(2)-Trastuzumab with a 4.3-fold increased uptake compared to that of the Trastuzumab-free copolymer. PEG(2)-PEI-Trastuzumab also showed a modest increase in uptake efficiency (2.8-fold). PEG(30)-PEI-Trastuzumab showed only a 1.9-fold increase in uptake.

Pharmacokinetics and Biodistribution in Mice. For in vivo experiments, polyplexes were injected into the tail vein of male BALB/c mice at a dose of 1 μg/g of radiolabeled DNA per mouse. To ensure the integrity of labeled plasmid, DNA was used immediately after performing the labeling reaction and subsequent purification procedures.

Free pDNA was removed quickly and efficiently from the blood stream. After 60 min, only about 1% of the injected dose per mL (ID/mL) was found in the blood (Figure 7a), which is in good agreement with earlier reports (*36*). If pDNA was complexed with unmodified PEI, a biphasic disposition with a very rapid decay in the alpha phase was observed. With PEI, the onset of the β phase was earlier, and the *B* value was significantly increased compared to that of pDNA alone (Table 1). The area under the curve (AUC) was thereby increased from 532.16 to 770.10% ID min^{-1} mL^{-1}, which again is in excellent agreement with earlier findings (*21*).

All Trastuzumab conjugates were found to improve pharmacokinetics of pDNA with minor differences between conjugates. Complexes composed of PEG(2)-PEI-Trastuzumab showed a significant increase in the *B* value and AUC compared to those of PEI polyplexes. Pharmacokinetics of the block-copolymer like PEG(30)-PEI based conjugate were slightly improved compared to PEI. The *B* value was increased to 7.71% ID mL^{-1}, and AUC was significantly increased over PEI. PEI-PEG(2)-Trastuzumab showed similar kinetics, but differences compared to PEI were less pronounced. An increase in *B* value and AUC compared to those of PEI was seen, but differences were not statistically significant in this case.

The biodistribution of labeled plasmid DNA was assessed 120 min postinjection (Figure 7b). The uptake of uncomplexed DNA was negligible in most organs. PEI polyplexes accumulated mainly in the liver, lung, kidneys, and spleen. When conjugates were used to prepare polyplexes, the main uptake occurred in the liver as well. However, the uptake into the lung and spleen was significantly decreased for all Trastuzumab conjugates compared to that of PEI.

DISCUSSION

Several studies on the pharmacokinetics and biodistribution of PEI- (*37, 38*) as well as PEG-PEI/DNA (*4, 10, 21*) polyplexes have been undertaken. Until now, the influence of targeting

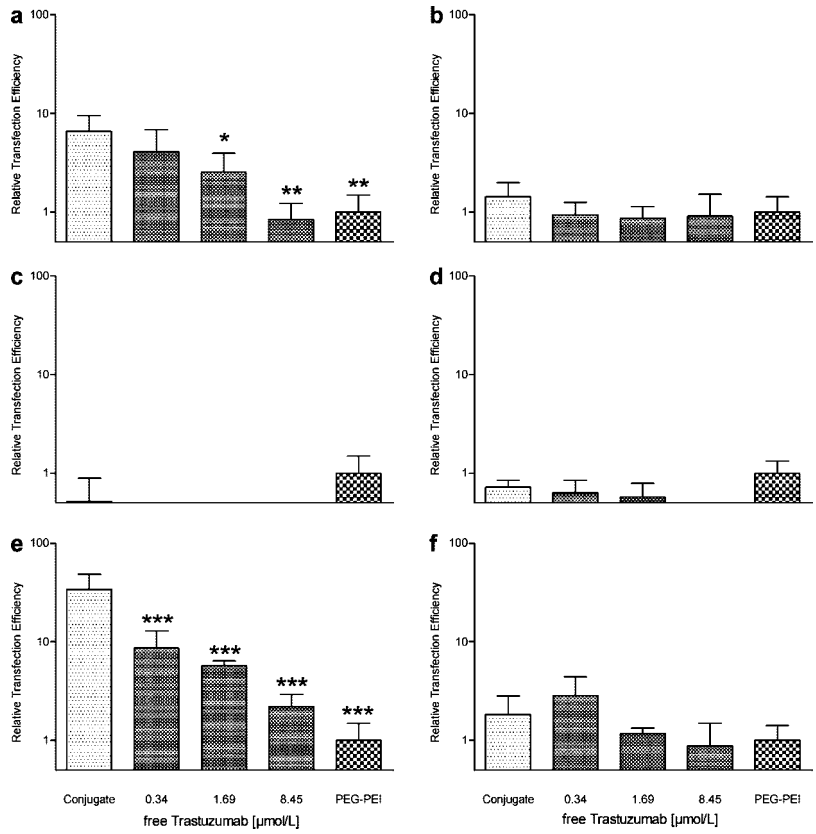

Figure 5. Transfection efficiencies and specificity of conjugates compared to the respective unmodified copolymer in HER2-positive SKBR-3 cells (b, c, and e) and HER2 negative OVCAR-3 cells (b, d, and f). Polyplexes were formed with pDNA and PEG(2)-PEI-Trastuzumab (a and b), PEG(30)-PEI-Trastuzumab (c and d), and PEI-PEG(2)-Trastuzumab (e and f) at N/P 6. To test the specificity of transfection, cells were incubated with indicated concentrations of free Trastuzumab for 15 min before the addition of the polyplexes. Values are given as the means + SD of quadruplicates. Significance was tested using one-way ANOVA with Dunnett's multiple comparison test with transfection efficiency of conjugate set as control (* $p < 0.05$; ** $p < 0.01$; *** $p < 0.001$).

ligands such as antibodies, antibody fragments, or peptides on the pharmacokinetics and biodistribution of the resulting vector system was not systemically evaluated. Achievement of high and long lasting blood levels is considered to be a prerequisite for the efficient use of nonviral vectors under in vivo conditions. The final goal for the gene delivery system presented in this study was the targeting of tumor tissues, which will be the subject of a separate investigation. Before addressing this goal, the effects of targeting ligands and PEGylation on in vivo pharmacokinetics and distribution needed to be clarified. To elucidate the effects of PEG and antibody, three conjugates were synthesized. These were composed of branched PEI (25 kDa) as the condensing agent, PEG as the nonspecific interaction reducing agent, and Trastuzumab as a targeting ligand. Variations included linker chemistry, PEG chain length, and substitution degree (Figure 1).

The efficacy of nonviral gene delivery systems administered via the intravenous route depends on several crucial parameters: polyplex size, surface charge, stability in the bloodstream, and interaction with blood components. One impediment for successful transfection of tumor tissue in vivo is early entrapment of the polyplexes after intravenous injection. Ogris et al., Merdan et al., and Hildebrandt et al. stressed the importance of polyplex size and aggregation behavior in terms of organ distribution (*4, 21, 22*). These investigations showed that deposition in the lung, which is the first capillary bed reached after i.v. injection, as well as lethality after treatment depends on polyplex size and aggregation behavior. It was shown by Petersen et al. that PEI does not produce stable polyplexes especially at low N/P ratios, and an increase in complex size over time was observed. In contrast, PEG-PEI copolymers with PEG chains longer than 550 kDa formed stable complexes under these conditions, and no aggregation over time occurred (*24*). In our study, unmodified PEI polyplexes formed large particles in micrometer range at N/P 3 in vitro. In contrast, all PEG-PEI copolymers and Trastuzumab conjugates produced small complexes with DNA with sizes not exceeding 300 nm in a wide range of N/P ratios. After i.v. injection, PEI is known to form aggregates with blood components, such as erythrocytes or albumin (*39*). Erythrocyte aggregation and hemolysis studied using human red blood cells showed severe aggregation of erythrocytes with PEI polyplexes. In contrast, PEGylated PEIs showed reduced erythrocyte aggregation and hemolysis, which is in accordance with the findings of Petersen et al. (*24*). Most importantly, Trastuzumab-modified PEG-PEI copolymers even surpassed PEG-PEI in these experiments and showed virtually no aggregation or hemolysis of erythrocytes.

The surface charge of polyplexes is an important parameter closely related to the above-mentioned characteristics. ζ-potentials of polyplexes prepared with Trastuzumab conjugates were lower than those of polyplexes prepared with unmodified PEI or with the respective PEG-PEI copolymers. Actually, conjugate polyplexes remained close to neutral in a wide range of N/P ratios because of the additional steric shielding by the coupled antibody. Similar shielding effects were observed with transferrin-PEI polyplexes subsequently modified with PEG (*4*) and with PEG-PEI covalently modified with anti-OA3 Fab′ (*25*). Ward et al. and Ogris et al. showed that shielded complexes decreased nonspecific interactions with blood components and nontargeted cells (*4, 40*). Plank et al. found that positively charged DNA complexes can activate the alternative complement system (*41*). The authors also showed that modification

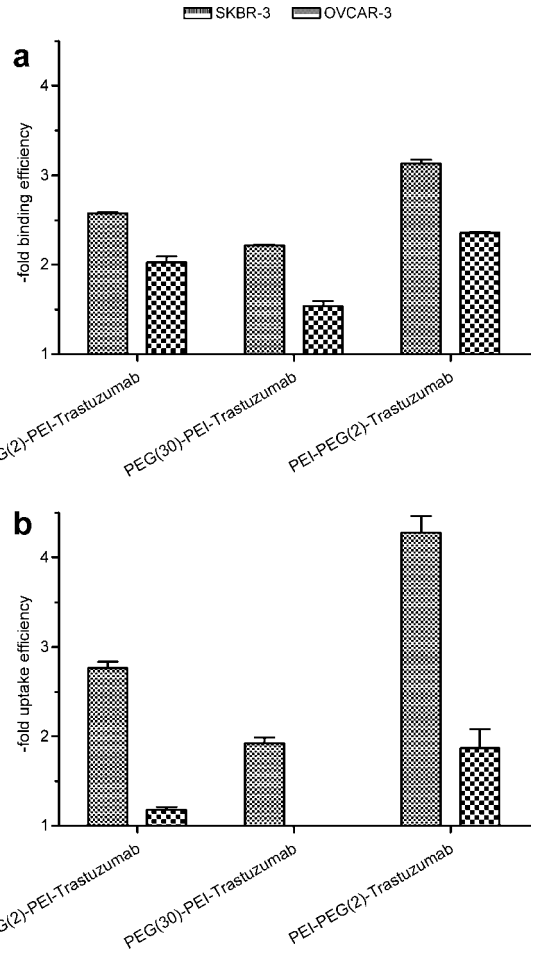

Figure 6. Binding (a) and uptake efficiencies (b) of polyplexes prepared at N/P 6. Conjugate uptake or binding is shown relative to the corresponding unmodified PEG-PEI copolymer. Polyplexes were incubated with the cells for 15 min at 4 °C (a) or 3 h at 37 °C (b). In the case of the uptake experiment (b), cells were washed 4 times with heparin in PBS to dissociate and remove surface bound polyplexes. Cells were then analyzed for mean fluorescence intensity by flow cytometry. Values are given as the means + SD of triplicates.

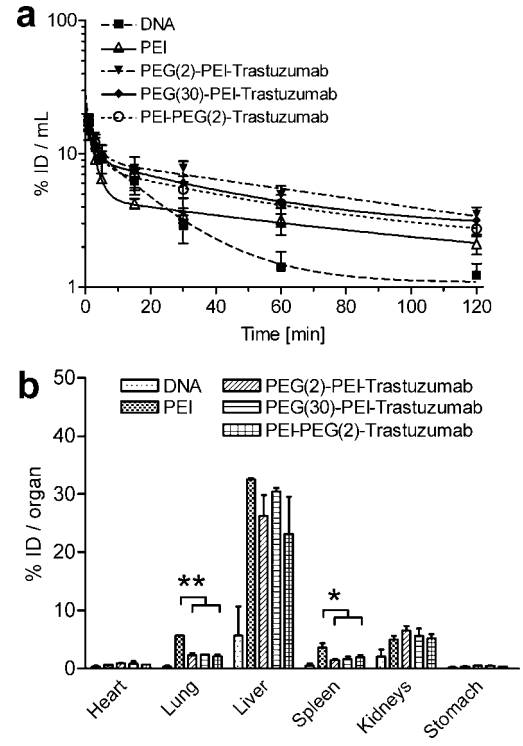

Figure 7. Pharmacokinetic profiles (a) and biodistribution (b) of PEI (open triangle, solid line), PEG(2)-PEI-Trastuzumab (filled triangle, dashed-dotted line), PEG(30)-PEI-Trastuzumab (filled square, solid line), and PEI-PEG(2)-Trastuzumab (open circle, dotted line) polyplexes compared to those of free plasmid DNA (filled square, dashed line) in male BALB/c mice. Polyplexes were prepared at N/P 6 with 1 μg/g pDNA per mouse and injected via the tail vein in a volume of about 200 μL. Blood samples were taken at indicated time points from the retrobulbar plexus. Organs were withdrawn after 120 min, and the amount of radiolabeled plasmid was determined by liquid scintillation counting. Significance was tested using one-way ANOVA and Dunnett's multiple comparison test with PEI polyplexes set as control (* $p < 0.05$; ** $p < 0.01$).

of polylysine/DNA complexes with PEG can considerably reduce complement activation. We speculated that further reduction of surface charge in the case of Trastuzumab-modified PEG-PEI polyplexes could result in reduced complement activation.

Polyplexes injected into circulation encounter relatively harsh conditions, such as shear stress during injection and circulation, lytic enzymes, and a multitude of salts and proteins, that may negatively influence complex integrity and DNA stability (*42, 43*). To investigate complex stability, we tested the susceptibility of polyplexes to heparin displacement. The polyanion heparin releases DNA from polyplexes and is a good measure for complex stability against competing anions. All Trastuzumab conjugates were slightly less susceptible to heparin displacement compared to PEI and their respective unmodified copolymers. We hypothesize that the dense shell formed by PEG and Trastuzumab may prevent heparin from entering the complex as easily as in the case of unmodified PEI polyplexes.

Therefore, all Trastuzumab conjugate complexes appear sufficiently stable to remain intact during circulation and are at the same time less susceptible to aggregation and nonspecific interaction than unmodified PEI.

Apart from size and stability, tumor specificity of polyplexes is crucial. The target tissue should ideally be transfected with high efficiency while leaving nontargeted tissues unaffected. Strehblow et al. showed that conjugation chemistry may have a significant effect on transfection efficiency and specificity in vitro (*44*). In this study, three different linkers were used to prepare HER2 or CD90 targeted conjugates. Using these linkers, major differences in the degrees of conjugation and in target cell specificity of the resulting conjugates were found. Interestingly, none of the conjugates prepared with SPDP as a linker showed target cell specificity. In contrast, SPDP was successfully used as a linker by Merdan et al. and Kircheis et al. under comparable conditions (*25, 26*). Kunath et al. showed that if RGD peptide was used as a targeting moiety, only direct coupling of the peptide to PEI via SPDP mediated efficient and specific transfection, while a RGD-PEG-PEI conjugate was inefficient (*45*). In contrast, Moffatt et al. successfully utilized a PEG linker for coupling anti-PSMA antibody to PEI/DNA polyplexes (*17*).

In this study, we used three structurally different conjugates which were comparable in physicochemical properties but different in transfection, binding, and uptake efficiencies. Two conjugates were based on presynthesized PEG-PEI copolymers. Trastuzumab was in these cases coupled to the PEI core via SPDP. The PEG(2)-PEI copolymer was well established for conjugation purposes in our laboratory (*16, 25*). To study the influence of PEGylation, PEG(30)-PEI with fewer but longer PEG chains was used as a second copolymer. The PEG content of both copolymers was comparable (45% vs 56%). PEG-PEI with a lower substitution degree was used to promote substitution with antibody and possibly increase specificity. It was found

Table 1. Pharmacokinetic Properties of Trastuzumab Conjugate, PEI Polyplexes, and Free Plasmid DNA[a,b]

	Cmax[c] [% ID]	A[c] [% ID mL^{-1}]	$T_{1/2\alpha}$[c] [min]	B[c] [% ID mL^{-1}]	$T_{1/2\beta}$[c] [min]	AUC[d] [% ID mL^{-1} min^{-1}]
PEI	16.11 ± 1.38	17.94 ± 2.87	1.60 ± 0.04 (***/-)	4.45 ± 0.26 (*/-)	108.92 ± 5.10	770.10 ± 169.57 (ns/-)
PEG(2)-PEI-Trastuzumab	17.06 ± 1.13	12.80 ± 2.90	1.57 ± 0.58 (***/ns)	9.54 ± 1.45 (**/*)	85.65 ± 12.34	1139.40 ± 58.55 (***/**)
PEG(30)-PEI-Trastuzumab	14.58 ± 1.94	9.58 ± 5.34	1.95 ± 0.75 (***/ns)	7.71 ± 2.99 (*/ns)	89.23 ± 11.42	1088.12 ± 114.12 (***/*)
PEI-PEG(2)-Trastuzumab	17.65 ± 1.50	14.86 ± 0.68	1.97 ± 0.10 (***/ns)	7.23 ± 1.25 (*/ns)	85.95 ± 26.11	905.79 ± 18.21 (**/ns)
pDNA (pCMV-Luc)	17.35 ± 2.40	14.36 ± 3.05	8.54 ± 0.66 (-/***)	2.18 ± 0.78 (-/*)	205.34 ± 113.24	532.16 ± 20.08 (-/ns)

[a] All values given as the means + SD. [b] Significance was tested using 1way ANOVA with Bonferroni's multiple comparison test with DNA or PEI (vs DNA/vs PEI) set as control (ns: not significant; * $p < 0.05$; ** $p < 0.01$; *** $p < 0.001$). [c] Concentration−time data was fitted to a biexponential disposition function. [d] AUC was determined using a noncompartmental mixed logarithmic linear algorithm.

that the substitution degree could be increased 2-fold by using PEG(30)-PEI rather than PEG(2)-PEI. This in turn decreased reporter gene expression compared to that of PEG(2)-PEI-Trastuzumab, and transfection was nonspecific. This result can be explained by a comparably lower binding to target cells and most importantly by lower uptake efficiency as shown by flow cytometry. It was hypothesized that longer PEG chains may hinder target recognition by partial masking of antigen binding domains. The decrease in uptake efficiency may be attributed to the cross-linking of several receptors on the cell surface or intercellular cross-linking due to the comparably high antibody substitution degree of this conjugate. For the third conjugate, a PEG linker was used. This enhanced the presentation of the targeting moiety and increased the specificity and efficiency of the resulting Trastuzumab conjugate. We herein showed by flow cytometry analysis that this conjugate was the most efficient in binding and uptake.

As a result, the efficiency of PEG-PEI-antibody conjugates strongly depends on copolymer composition and conjugation chemistry. In our study, the presentation of antibody at the distal end of a PEG spacer was most efficient. Our second approach of using presynthesized PEG-PEI copolymers showed that long PEG chains may hinder the proper presentation of the antibody. In contrast, good results were obtained with a PEG-PEI copolymer consisting of shorter PEG blocks with a higher PEG grafting ratio.

In vivo behavior of conjugate polyplexes was compared with unmodified PEI polyplexes as well as with uncomplexed plasmid. Blood levels followed a biexponential disposition curve with a rapid distribution phase and a subsequent prolonged elimination phase. PEI polyplexes showed a pronounced distribution phase with a comparably low remaining DNA concentration in blood after distribution. In contrast, Trastuzumab conjugates were more rapidly distributed and higher concentrations remained in circulation after distribution. Elimination half-lives of PEI and Trastuzumab conjugate complexes were comparable. Consequently, the AUC of Trastuzumab conjugate polyplexes were 18 to 48% higher than the AUC of PEI polyplexes and 70 to 114% higher than that of free DNA.

In a previous study, Merdan et al. determined the pharmacokinetic profiles of PEI and PEG(2)-PEI complexes under similar conditions. At a DNA dose of 25 μg/mouse, no significant differences in pharmacokinetics were found between PEI and PEG(2)-PEI polyplexes. Furthermore, the pharmacokinetic profiles showed that DNA is associated with both PEI and PEG(2)-PEI at least until 60 min postinjection under these conditions (*21*). At a lower DNA dose of 1.5 μg/mouse, significantly increased blood levels were found for pDNA complexed with PEG(2)-PEI compared to that of PEI. However, at this low dose, complex dissociation indicated by differing pharmacokinetic profiles of radioactively labeled polymer and DNA was observed.

PEI polyplexes are known to rapidly distribute to and remain in highly perfused organs, such as the liver, lung, and spleen. (*20*) These phenomena seem to be in part due to the aggregation of polyplexes, interaction with blood components such as erythrocytes, and recognition by the reticulo-endothelial system (*4, 24, 39, 43*). By using stealth polyplexes, in vivo toxicity, aggregation, and complement activation can be reduced (*4, 10*). However, studies on PEG-PEI copolymers have shown that PEGylation alone does not significantly improve pharmacokinetics compared to that of unmodified PEI (*21, 46*). De Wolf et al. recently hypothesized that polyplexes prepared using PEG-grafted PEI (pre-PEGylation approach) are still prone to opsonization and therefore are relatively rapidly eliminated (*46*). Interestingly, post-PEGylated polyplexes, where DNA is first condensed with the unmodified polycation and polyplexes are subsequently PEGylated, seem to be more efficient in improving pharmacokinetics (*7, 40*). However, from our point of view, this approach has serious drawbacks regarding polyplex preparation and characterization, especially in a clinical setting.

In our study, Trastuzumab modified PEG(2)-PEI at the same dose used by Merdan et al. significantly improved pharmacokinetics compared to that of PEI polyplexes (*21*). Comparable pharmacokinetics were observed for all Trastuzumab conjugates despite their different structure. Trastuzumab modification decreased the surface charge and increased polyplex stability in the case of all three conjugates. Most importantly, aggregation with erythrocytes was strongly decreased with all conjugates. Thereby, entrapment of polyplexes in small capillaries and recognition by the reticulo-endothelial system is reduced, and AUC increases. We hypothesized that in the case of the PEG-PEI copolymer used in the study of Merdan et al., PEGylation alone could not sufficiently inhibit erythrocyte aggregation. This might be one of the major reasons that no significant difference between PEI and PEG-PEI was found in this study. This suggests that the additional steric shielding introduced by antibody modification has a stronger effect on pharmacokinetics than the structure of PEG-PEI copolymers or linker chemistry.

The biodistribution of polyplexes was assessed 120 min after injection. Using a free, uncomplexed plasmid, only minor amounts of radioactivity were found in the liver and in the kidneys, which both are involved in plasmid excretion (*47*). Polyplexes prepared with PEI were taken up mainly by the liver and to a minor extent by the lung, spleen, and kidneys. The accumulation of polyplexes tended to be increased in highly perfused organs, such as the liver and kidneys (*47*). Furthermore, the liver and spleen possess discontinuous or fenestrated endothelia, which may facilitate the accumulation of polyplexes (*48*). Finally, positively charged polyplexes can activate the alternative complement system, which will result in the enhanced uptake in the liver and spleen (*41, 49*). Lung deposition is most likely due to the aggregation of polyplexes themselves, with erythrocytes, or both (*4, 21*). With all Trastuzumab conjugates, lung and spleen deposition was significantly reduced compared to that of PEI. We assume that the nearly neutral ζ-potential and the decreased erythrocyte aggregation mainly accounted for these changes in organ distribution as well.

In summary, the composition of polyplexes affected both in vitro specificity and in vivo pharmacokinetics. Concerning in vitro transfection efficiency and target cell specificity, PEGylation and linker chemistry were of major importance. Long PEG chains, as used in PEG(30)-PEI-Trastuzumab, hindered proper antigen recognition. The uptake of these polyplexes was

decreased potentially due to the high degree of substitution. In contrast, conjugates composed of PEG-PEI with shorter PEG chains or synthesized using a PEG linker successfully transfected the target cells with high specificity. Concerning the situation in vivo, it was found that antibody modification, irrespective of the linker chemistry or the PEG-PEI copolymer used, governed pharmacokinetics and biodistribution. Antibody modification in all cases resulted in higher AUC and lower disposition in lung and spleen compared to that of PEI polyplexes, which is potentially due to decreased ζ-potentials, improved polyplex stability, and decreased interaction with blood components.

ACKNOWLEDGMENT

We are grateful to Cornelia Brendel (FACS laboratory, Department of Hematology, Oncology and Immunology, University Hospital Marburg) for the generous use of equipment. We are indebted to Eva Mohr (Department of Pharmaceutics and Biopharmacy, Philipps Universität Marburg) for her technical support concerning cell culture. We are grateful to Terry Steele and Olivia Merkel (Department of Pharmaceutics and Biopharmacy, Philipps Universität Marburg) for the critical review of this manuscript.

LITERATURE CITED

(1) Merdan, T., Kopecek, J., and Kissel, T. (2002) Prospects for cationic polymers in gene and oligonucleotide therapy against cancer. *Adv. Drug Delivery Rev. 54*, 715–758.

(2) Goula, D., Benoist, C., Mantero, S., Merlo, G., Levi, G., and Demeneix, B. A. (1998) Polyethylenimine-based intravenous delivery of transgenes to mouse lung. *Gene Ther. 5*, 1291–1295.

(3) Boussif, O., Lezoualc'h, F., Zanta, M. A., Mergny, M. D., Scherman, D., Demeneix, B., and Behr, J. P. (1995) A versatile vector for gene and oligonucleotide transfer into cells in culture and in vivo: polyethylenimine. *Proc. Natl. Acad. Sci. U.S.A. 92*, 7297–7301.

(4) Ogris, M., Brunner, S., Schuller, S., Kircheis, R., and Wagner, E. (1999) PEGylated DNA/transferrin-PEI complexes: reduced interaction with blood components, extended circulation in blood and potential for systemic gene delivery. *Gene Ther. 6*, 595–605.

(5) Fenske, D. B., MacLachlan, I., and Cullis, P. R. (2001) Long-circulating vectors for the systemic delivery of genes. *Curr. Opin. Mol. Ther. 3*, 153–158.

(6) Ward, C. M., Read, M. L., and Seymour, L. W. (2001) Systemic circulation of poly(L-lysine)/DNA vectors is influenced by polycation molecular weight and type of DNA: differential circulation in mice and rats and the implications for human gene therapy. *Blood 97*, 2221–2229.

(7) Verbaan, F. J., Oussoren, C., Snel, C. J., Crommelin, D. J., Hennink, W. E., and Storm, G. (2004) Steric stabilization of poly(2-(dimethylamino)ethyl methacrylate)-based polyplexes mediates prolonged circulation and tumor targeting in mice. *J. Gene Med. 6*, 64–75.

(8) Mullen, P. M., Lollo, C. P., Phan, Q. C., Amini, A., Banaszczyk, M. G., Fabrycki, J. M., Wu, D., Carlo, A. T., Pezzoli, P., Coffin, C. C., and Carlo, D. J. (2000) Strength of conjugate binding to plasmid DNA affects degradation rate and expression level in vivo. *Biochim. Biophys. Acta 1523*, 103–110.

(9) Woodle, M. C. (1998) Controlling liposome blood clearance by surface-grafted polymers. *Adv. Drug Delivery Rev. 32*, 139–152.

(10) Kunath, K., von Harpe, A., Petersen, H., Fischer, D., Voigt, K., Kissel, T., and Bickel, U. (2002) The structure of PEG-modified poly(ethylene imines) influences biodistribution and pharmacokinetics of their complexes with NF-kappaB decoy in mice. *Pharm. Res. 19*, 810–817.

(11) Nguyen, H.-K., Lemieux, P., Vinogradov, S. V., Gebhart, C. L., Guérin, N., Paradis, G., Bronich, T. K., Alakhov, V. Y., and Kabanov, A. V. (2000) Evaluation of polyether-polyethyleneimine graft copolymers as gene transfer agents. *Gene Ther. 7*, 126–138.

(12) Oupicky, D., Howard, K. A., Konak, C., Dash, P. R., Ulbrich, K., and Seymour, L. W. (2000) Steric stabilization of poly-L-Lysine/DNA complexes by the covalent attachment of semitelechelic poly[N-(2-hydroxypropyl)methacrylamide]. *Bioconjugate Chem. 11*, 492–501.

(13) Deshpande, M. C., Davies, M. C., Garnett, M. C., Williams, P. M., Armitage, D., Bailey, L., Vamvakaki, M., Armes, S. P., and Stolnik, S. (2004) The effect of poly(ethylene glycol) molecular architecture on cellular interaction and uptake of DNA complexes. *J. Controlled Release 97*, 143–156.

(14) Wagner, E. (2004) Strategies to improve DNA polyplexes for in vivo gene transfer: will "artificial viruses" be the answer? *Pharm. Res. 21*, 8–14.

(15) Furgeson, D. Y., Yockman, J. W., Janat, M. M., and Kim, S. W. (2004) Tumor efficacy and biodistribution of linear polyethylenimine-cholesterol/DNA complexes. *Mol. Ther. 9*, 837–845.

(16) Germershaus, O., Merdan, T., Bakowsky, U., Behe, M., and Kissel, T. (2006) Trastuzumab-polyethylenimine-polyethylene glycol conjugates for targeting Her2-expressing tumors. *Bioconjugate Chem. 17*, 1190–1199.

(17) Moffatt, S., Papasakelariou, C., Wiehle, S., and Cristiano, R. (2006) Successful in vivo tumor targeting of prostate-specific membrane antigen with a highly efficient J591/PEI/DNA molecular conjugate. *Gene Ther. 13*, 761–772.

(18) Boeckle, S., von Gersdorff, K., van der Peipen, S., Culmsee, C., Wagner, E., and Ogris, M. (2004) Purification of polyethylenimine polyplexes highlights the role of free polycations in gene transfer. *J. Gene Med. 6*, 1102–1111.

(19) Magin-Lachmann, C., Kotzamanis, G., D'Aiuto, L., Cooke, H., Huxley, C., and Wagner, E. (2004) In vitro and in vivo delivery of intact BAC DNA -- comparison of different methods. *J. Gene Med. 6*, 195–209.

(20) Wightman, L., Kircheis, R., Rossler, V., Carotta, S., Ruzicka, R., Kursa, M., and Wagner, E. (2001) Different behavior of branched and linear polyethylenimine for gene delivery in vitro and in vivo. *J. Gene Med. 3*, 362–372.

(21) Merdan, T., Kunath, K., Petersen, H., Bakowsky, U., Voigt, K. H., Kopecek, J., and Kissel, T. (2005) PEGylation of poly(ethylene imine) affects stability of complexes with plasmid DNA under in vivo conditions in a dose-dependent manner after intravenous injection into mice. *Bioconjugate Chem. 16*, 785–792.

(22) Hildebrandt, I. J., Iyer, M., Wagner, E., and Gambhir, S. S. (2003) Optical imaging of transferrin targeted PEI/DNA complexes in living subjects. *Gene Ther. 10*, 758–764.

(23) Neu, M., Germershaus, O., Mao, S., Voigt, K. H., Behe, M., and Kissel, T. (2007) Crosslinked nanocarriers based upon poly(ethylene imine) for systemic plasmid delivery: In vitro characterization and in vivo studies in mice. *J. Controlled Release 118*, 370–380.

(24) Petersen, H., Fechner, P. M., Martin, A. L., Kunath, K., Stolnik, S., Roberts, C. J., Fischer, D., Davies, M. C., and Kissel, T. (2002) Polyethylenimine-graft-poly(ethylene glycol) copolymers: influence of copolymer block structure on DNA complexation and biological activities as gene delivery system. *Bioconjugate Chem. 13*, 845–854.

(25) Merdan, T., Callahan, J., Petersen, H., Kunath, K., Bakowsky, U., Kopeckova, P., Kissel, T., and Kopecek, J. (2003) Pegylated polyethylenimine-Fab′ antibody fragment conjugates for targeted gene delivery to human ovarian carcinoma cells. *Bioconjugate Chem. 14*, 989–996.

(26) Kircheis, R., Kichler, A., Wallner, G., Kursa, M., Ogris, M., Felzmann, T., Buchberger, M., and Wagner, E. (1997) Coupling of cell-binding ligands to polyethylenimine for targeted gene delivery. *Gene Ther. 4*, 409–418.

(27) von Harpe, A. (2000) Thesis, Department of Pharmaceutics and Biopharmacy, Philipps University, Marburg, Germany.

(28) Abramoff M. D., Magelhaes P. J., Ram S. J., 2004 Image Processing with ImageJ. *Biophotonics International*, Volume 11, Issue 7, 36–42.

(29) Kloeckner, J., Wagner, E., and Ogris, M. (2006) Degradable gene carriers based on oligomerized polyamines. *Eur. J. Pharm. Sci. 29*, 414–425.

(30) Hill, H. D., and Straka, J. G. (1988) Protein determination using bicinchonic acid in the presence of sulfhydryl reagents. *Anal. Biochem. 170*, 203–208.

(31) Ogris, M., Steinlein, P., Carotta, S., Brunner, S., and Wagner, E. (2001) DNA/polyethylenimine transfection particles: influence of ligands, polymer size, and PEGylation on internalization and gene expression. *AAPS Pharm. Sci. 3*, E21.

(32) Mellman, I. (1996) Endocytosis and molecular sorting. *Annu. Rev. Cell Dev. Biol. 12*, 575–625.

(33) Dash, P. R., Read, M. L., Barrett, L. B., Wolfert, M. A., and Seymour, L. W. (1999) Factors affecting blood clearance and in vivo distribution of polyelectrolyte complexes for gene delivery. *Gene Ther. 6*, 643–650.

(34) Neu, T., Sitterberg, J., Bakowsky, U., and Kissel, T. (2006) Stabilized nanocarriers for plasmids based upon cross-linked poly(ethylene imine). *Biomacromolecules 7*, 3428–3438.

(35) Lewis, G. D., Figari, I., Fendly, B., Wong, W. L., Carter, P., Gorman, C., and Shepard, H. M. (1993) Differential responses of human tumor cell lines to anti-p185HER2 monoclonal antibodies. *Cancer Immunol. Immunother. 37*, 255–263.

(36) Kawabata, K., Takakura, Y., and Hashida, M. (1995) The fate of plasmid DNA after intravenous injection in mice: involvement of scavenger receptors in its hepatic uptake. *Pharm. Res. 12*, 825–830.

(37) Koshkina, N. V., Agoulnik, I. Y., Melton, S. L., Densmore, C. L., and Knight, V. (2003) Biodistribution and pharmacokinetics of aerosol and intravenously administered DNA-polyethyleneimine complexes: optimization of pulmonary delivery and retention. *Mol. Ther. 8*, 249–254.

(38) Kunath, K., von Harpe, A., Fischer, D., Petersen, H., Bickel, U., Voigt, K., and Kissel, T. (2003) Low-molecular-weight polyethylenimine as a non-viral vector for DNA delivery: comparison of physicochemical properties, transfection efficiency and in vivo distribution with high-molecular-weight polyethylenimine. *J. Controlled Release 89*, 113–125.

(39) Kircheis, R., Wightman, L., Schreiber, A., Robitza, B., Rossler, V., Kursa, M., and Wagner, E. (2001) Polyethylenimine/DNA complexes shielded by transferrin target gene expression to tumors after systemic application. *Gene Ther. 8*, 28–40.

(40) Ward, C. M., Pechar, M., Oupicky, D., Ulbrich, K., and Seymour, L. W. (2002) Modification of pLL/DNA complexes with a multivalent hydrophilic polymer permits folate-mediated targeting in vitro and prolonged plasma circulation in vivo. *J. Gene Med. 4*, 536–47.

(41) Plank, C., Mechtler, K., Szoka, F. C., Jr., and Wagner, E. (1996) Activation of the complement system by synthetic DNA complexes: a potential barrier for intravenous gene delivery. *Hum. Gene Ther. 7*, 1437–1446.

(42) Fischer, D. (2005) In vivo fate of polymeric gene carriers, in *Biomaterials for Delivery and Targeting of Proteins and Nucleic Acids* (Mahato, R. I., Ed.) pp 295−321, CRC Press, Boca Raton, FL.

(43) Sharma, V. K., Thomas, M., and Klibanov, A. M. (2005) Mechanistic studies on aggregation of polyethylenimine-DNA complexes and its prevention. *Biotechnol. Bioeng. 90*, 614–620.

(44) Strehblow, C., Schuster, M., Moritz, T., Kirch, H. C., Opalka, B., and Petri, J. B. (2005) Monoclonal antibody-polyethyleneimine conjugates targeting Her-2/neu or CD90 allow cell type-specific nonviral gene delivery. *J. Controlled Release 102*, 737–747.

(45) Kunath, K., Merdan, T., Hegener, O., Haberlein, H., and Kissel, T. (2003) Integrin targeting using RGD-PEI conjugates for in vitro gene transfer. *J. Gene Med. 5*, 588–599.

(46) de Wolf, H. K., Snel, C. J., Verbaan, F. J., Schiffelers, R. M., Hennink, W. E., and Storm, G. (2007) Effect of cationic carriers on the pharmacokinetics and tumor localization of nucleic acids after intravenous administration. *Int. J. Pharm. 331*, 167–175.

(47) Nishikawa, M., Takakura, Y., and Hashida, M. (2005) Theoretical considerations involving the pharmacokinetics of plasmid DNA. *Adv. Drug Delivery Rev. 57*, 675–688.

(48) de Wolf, H. K., Luten, J., Snel, C. J., Oussoren, C., Hennink, W. E., and Storm, G. (2005) In vivo tumor transfection mediated by polyplexes based on biodegradable poly(DMAEA)-phosphazene. *J. Controlled Release 109*, 275–287.

(49) Fischer, D., Osburg, B., Petersen, H., Kissel, T., and Bickel, U. (2004) Effect of poly(ethylene imine) molecular weight and pegylation on organ distribution and pharmacokinetics of polyplexes with oligodeoxynucleotides in mice. *Drug Metab. Dispos. 32*, 983–992.

BC700311N

In Vivo Production of scFv-Displaying Biopolymer Beads Using a Self-Assembly-Promoting Fusion Partner

Katrin Grage and Bernd H. A. Rehm*

Institute of Molecular Biosciences, Massey University, Private Bag 11222, Palmerston North 4442, New Zealand. Received September 10, 2007; Revised Manuscript Received October 29, 2007

Recombinant production and, in particular, immobilization of antibody fragments onto carrier materials are of high interest with regard to diagnostic and therapeutic applications. In this study, the recombinant production of scFv-displaying biopolymer beads intracellularly in *Escherichia coli* was investigated. An anti-β-galactosidase scFv (single chain variable fragment of an antibody) was C-terminally tagged with the polymer-synthesizing enzyme PhaC from *Cupriavidus necator* by generating the respective hybrid gene. The functionality of the anti-β-galactosidase scFv-PhaC fusion protein was assessed by producing the respective soluble fusion protein in an *Escherichia coli* AMEF mutant strain. AMEF (antibody-mediated enzyme formation) strains contain an inactive mutant β-galactosidase, which can be activated by binding of an anti-β-galactosidase antibody. *In vivo* activation of AMEF β-galactosidase indicated that the scFv is functional with the C-terminal fusion partner PhaC. It was further demonstrated that polymer biosynthesis and bead formation were mediated by the scFv-PhaC fusion protein in the cytoplasm of recombinant *E. coli* when the polymer precursor was metabolically provided. This suggested that the C-terminal fusion partner PhaC acts as a functional insolubility partner, providing a natural cross-link to the bead and leading to *in vivo* immobilization of the scFv. Overproduction of the fusion protein at the polymer bead surface was confirmed by SDS−PAGE and MALDI-TOF/MS analysis of purified beads. Antigen binding functionality and specificity of the beads was assessed by analyzing the binding of β-galactosidase to scFv-displaying beads and subsequently eluting the bound protein at pH 2.7. A strong enrichment of β-galactosidase suggested the functional display of scFv at the bead surface as well as the applicability of these beads for antigen purification. Binding of β-galactosidase to the scFv-displaying beads was quantitatively analyzed by enzyme-linked assays measuring β-galactosidase activity. These indicated that the anti-β-galactosidase scFv-displaying beads bound a maximum of 38 ng of β-galactosidase per 1 μg of bead protein, showing an apparent equilibrium dissociation constant (K_D) of 12×10^{-7} M. This study clearly demonstrated that anti-β-galactosidase scFv-displaying polymer beads can be produced in engineered *E. coli* in a one-step process by using PhaC as a self-assembly-promoting fusion partner.

INTRODUCTION

Recombinant production and engineering of antibodies enable a variety of new diagnostic and therapeutic applications. Most research now focuses on recombinant antibody fragments, which retain full antigen binding capacity and are easier to produce than the structurally more complex complete immunoglobulins (Igs). Some examples are scFv (single-chain variable fragment), Fab (antigen-binding fragment of antibodies) and V_{HH} (variable domain of heavy chain antibodies), with the scFv now being the most widely used fragment in bioengineering applications. Antibody fragments can be produced in a variety of hosts, including mammalian cells, yeast, and bacteria. Particular attention has been paid to production in the bacterial cytoplasm for several reasons. On the one hand, this is an attractive system because it is comparatively inexpensive and can give high yields for recombinant proteins. On the other hand, there is a definite need for further improvement because the bacterial cytoplasm has the disadvantage of providing a reducing environment, which does impair antibody disulfide bond formation. Approaches to overcome this problem have included refolding from inclusion bodies (*1, 2*), mutagenesis of antibody fragment-encoding genes (*3–5*), use of *E. coli* host strains with a more oxidizing cytoplasm (*trxB gor* mutant strains), coproduction of molecular chaperones, and fusion of antibody fragments to solubility-enhancing tags (*6–11*). Apart from further improving recombinant production systems for antibody fragments, a lot of research is currently focusing more directly on applications, one important tool being the immobilization of antibody fragments onto surfaces or carriers for use as, for example, biosensors or in immunotargeting (*12–16*).

There have been a few recent examples of proteins that could be overproduced at the surface of intracellular reserve polymer inclusions in bacteria by fusing the protein of interest to the polymer-generating enzyme PhaC (*17, 18*). PhaC is the key enzyme of this bacterial reserve polymer biosynthesis pathway, and it catalyzes the polymerization of (*R*)-3-hydroxyacyl-CoA to the respective polyester (polyhydroxyalkanoate) (*19*). The enzyme remains covalently attached to the growing polymer chain. Eventually, the self-assembly of several polyester chains leads to the formation of a spherical polymer bead with a hydrophobic polyester core and PhaC covalently attached to its surface (*20, 21*). Various protein engineering approaches have demonstrated that it is possible to (a) produce these polymer inclusions recombinantly in *E. coli* and (b) fuse other proteins to the N-terminus of PhaC without impairing PhaC activity and polymer bead assembly. The fusion partners, that is, proteins of interest, have been found to be displayed at the bead surface (*22, 23*). The beads that have a diameter of between 100 and 500 nm can be isolated from the production host and retain their integrity outside of the cell. In all examples reported

* Corresponding author. E-mail: b.rehm@massey.ac.nz. Phone: +64 6 350 5515 ext. 7890. Fax: +64 6 350 5688.

10.1021/bc7003473 CCC: $40.75 © 2008 American Chemical Society
Published on Web 12/19/2007

Scheme 1. The scFv Fusion Partner, The Polymer Forming Enzyme PhaC, Provides a Natural Cross-Link to the Polymer Bead[a]

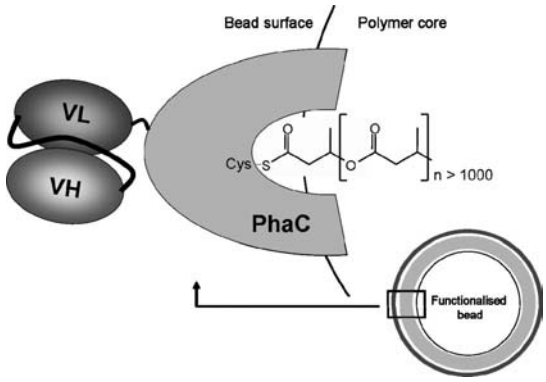

[a] V_H and V_L: variable domain of the heavy and light chains of the scFv, respectively.

so far, the fusion partners retained their function, and some data suggested an even improved stability (*17, 18, 24*).

In this study, the natural cross-linking ability of the polymer-synthesizing enzyme PhaC was harnessed to generate polymer beads that display a functional scFv, an anti-β-galactosidase scFv, covalently bound to the bead surface (Scheme 1). This was achieved by constructing a hybrid gene of the scFv gene and *phaC* from *C. necator* and expressing it in a suitable, that is, polymer-accumulating metabolic background of *E. coli*. The used antibody fragment, scFv13R4, originates from a mutagenesis approach screening for improved expression (*5*). Anti-β-galactosidase scFv-displaying beads were isolated and successfully used for specific and reversible binding of their antigen β-galactosidase, enabling, for example, antigen purification or removal as well as assessment of the binding affinity by an enzyme-linked assay. To our knowledge, this is not only the first example of *in vivo* assembly of antibody fragment displaying polymer beads but also the first example of covalent and oriented scFv immobilization on beads in a one-step procedure.

EXPERIMENTAL PROCEDURES

Bacterial Strains and Growth Conditions. The bacterial strains used in this study are listed in Table 1. All *E. coli* strains were grown at 37 °C unless other conditions are specifically described. When required, antibiotics were used at the following concentrations: ampicillin, 75 μg/mL; chloramphenicol, 30 μg/mL; and tetracycline, 12.5 μg/mL.

Induction of gene expression was achieved by the addition of 1 mM IPTG (isopropyl β-D-thiogalactopyranoside) to the culture medium in the case of the *lac* and T7 promoters or by the addition of 20 μg/mL IAA (3 β-indoleacrylic acid) in the case of the *trp* promoter. For scFv13R4-PhaC overproduction and PHA granule formation, *E. coli* BL21(DE3) bearing the respective plasmids was grown in LB medium containing 1% (w/v) glucose. After induction at an OD_{600} (optical density at 600 nm) of 0.4–0.5, cultures were shifted from 37 to 30 °C and incubated for approximately 48 h.

MacConkey agar (Merck) was prepared according to the manufacturer's instructions. M9 lactose minimal medium was prepared as described elsewhere (*25*). X-gal agar contained 0.004% (w/v) x-gal (5-bromo-4-chloro-3-indolyl-β-D-galactopyranoside) and 1 mM IPTG.

Plasmids, DNA Constructs, And Oligonucleotides. All plasmids and oligonucleotides used in this study are listed in Table 1. General cloning procedures were performed as described elsewhere (*26*). DNA primers, deoxynucleoside triphosphate, and *Taq* and Platinum *Pfx* polymerases were purchased from Invitrogen (CA). The DNA sequences of new plasmid constructs were confirmed by DNA sequencing according to the chain termination method using an ABI310 automatic sequencer.

The gene encoding scFv13R4 was amplified from plasmid pPM163R4 using primers scFv13R4-fwd and scFv13R4-rev. The PCR product was ligated into the cloning vector pGEM-T Easy (Promega, WI), and a spacer consisting of two 5′-phosphorylated oligonucleotides was inserted using restriction sites *Cla*I and *Hind*III. The scFv13R4-spacer fragment was then subcloned into the *Spe*I restriction site of $pCWE_{Spe}$ to generate $pCWE_{Spe}$-scFv13R4. This plasmid encodes a translational fusion of scFv13R4 and PhaC in which the fusion partners are connected by a $SerGly_4SerGly_4SerGly_4Ser$ linker. Plasmid pHAS-scFv13R4 was constructed by subcloning an *Xba*I/*Bam*HI fragment containing the scFv13R4-*phaC* gene from $pCWE_{Spe}$-scFv13R4 into pET-14b.

Isolation of Polymer Beads. Polymer bead isolation was carried out as described previously (*18*). Briefly, cells were harvested by centrifugation, resuspended in 50 mM potassium phosphate buffer at pH 7.2, and disrupted by passage through a cell disrupter Z Plus (Constant Systems, UK). The whole-cell lysate was subjected to centrifugation at 4000*g* for 15 min at 4 °C to sediment polymer beads. To enhance purity, the sediment was again resuspended in potassium phosphate buffer and loaded onto a glycerol gradient (88% and 44% (v/v) glycerol in potassium phosphate buffer). After ultracentrifugation for 2.5 h at 100,000*g* and 10 °C, beads could be isolated from a layer at the boundary between 88% and 44% glycerol. The polymer beads were washed once more with potassium phosphate buffer (50 mM, pH 7.2) and centrifuged at 100,000*g* for 1 h at 10 °C. The sediment containing the beads was suspended in potassium phosphate buffer containing 20% (v/v) glycerol and stored at 4 °C. For storage over longer time periods, protease inhibitor (EDTA-free protease inhibitor cocktail (Roche, Germany)) was added to the bead suspension.

***In Vivo* Functionality of the Polymer-Synthesizing Enzyme PhaC.** *In vivo* PhaC activity was obtained by analyzing the polyester content of the respective bacterial cells. The amount of accumulated polyester corresponds to the relative *in vivo* PhaC activity. Polyester contents were qualitatively and quantitatively determined by gas chromatography/mass spectrometry (GC/MS) after the conversion of the polyester into 3-hydroxymethylester by acid-catalyzed methanolysis (*27*).

Transmission Electron Microscopy (TEM) Analysis. Cells or beads were prepared for electron microscopy as follows: samples were fixed in primary fixative (3% glutaraldehyde and 2% formaldehyde in 0.1 M phosphate buffer) for 1 h, sedimented, and resuspended in 20% (w/v) BSA. Cells or beads were incubated again for 1 h in the primary fixative. After incubation, excess fixative was removed by washing three times with 0.1 M phosphate buffer. Osmium tetroxide (1% (w/v)) was applied as secondary fixative for 30 min. Excess fixative was removed as described above. Samples were then dehydrated in serially increased acetone concentrations and embedded in Procure 812 epoxy resin. Resin blocks were cured for 48 h at 60 °C. Light microscope sections (1 μm thick) were cut and stained with 0.5% (w/v) toluidine blue to locate concentrated areas of cells in the pellet, and the corresponding blocks were trimmed and TEM sections cut using a diamond knife and a Leica Ultracut R Ultramicrotome. Sections were stained with uranyl acetate and lead citrate, and studied using a Philips CM10 TEM.

Protein Analysis. Protein samples were routinely analyzed by SDS−PAGE (sodium dodecyl sulfate−polyacrylamide gel electrophoresis) as described elsewhere (*28*). The gels were

Table 1. Bacterial Strains, Plasmids, and Oligonucleotides Used in This Study

strains	genotype	source or reference
E. coli XL1-Blue	*recA1 endA1 gyrA96 thi-1 hsdR17 supE44 relA1 lac [F′ proAB lacI^{q}lacZ ΔM15 Tn10 (Tet^r)]*	Stratagene
E. coli BL21(DE3)	F$^-$ *ompT hsdS$_B$(r_B^- m_B^-) gal dcm* (DE3)	Novagen
E. coli AMEF 959	*lac*$^-_{aba}$	(*30, 31*)
E. coli AMEF 6101	*lac*$^-_{aba}$	(*30, 31*)

plasmids	characteristics	source or reference
pCWE	pBluescriptSK$^-$ derivative containing the *Nde*I/*Bam*HI inserted *phaC* gene from *C. necator*	(*22*)
pCWE$_{Spe}$	pCWE with an additional *Spe*I site for 5′-end fusions to PhaC	(*23*)
pHAS	pET-14b derivative containing the *Nde*I/*Bam*HI inserted *phaC* gene from *C. necator*	(*39*)
pET-14b	Ap^r, T7 promoter	Novagen
pMCS69	pBBR1MCS derivative containing genes *phaA* and *phaB* from *C. necator*	(*40*)
pPM163R4	pPM160 containing the anti-β-galactosidase scFv13R4 gene	(*5*)
pCWE$_{Spe}$-scFv13R4	pCWE$_{Spe}$ containing *Spe*I inserted anti-β-galactosidase scFv13R4 gene with the 3′-end spacer	this study
pHAS-scFv13R4	pET-14b containing *Xba*I/*Bam*HI fragment from pCWE$_{Spe}$-scFv13R4, comprising the gene scFv13R4-*phaC*	this study

oligonucleotides	sequence in 5′-3′ direction[a]	source or reference
scFv13R4-fwd	AGAACTAGTATGGCCGAGGTGCAGCTGGTGG	this study
scFv13R4-rev	TTATCGATTTGAAGCTTTGCTGCCGCACCTAGGACGGCC	this study
spacer-fwd	Phos-AGCTCAGCGGCGGTGGCGGTAG CGGTGGCGGTGGCAGCGGCGGTGGCGGTAGCACTAGTGGC	this study
spacer-rev	Phos-CGGCCACTAGTGCTACCGCCACC GCCGCTGCCACCGCCACCGCTACCGCCACCGCCGCTG	this study

[a] The restriction enzyme recognition sites are underlined.

stained with Coomassie brilliant blue G250. Protein bands of interest were cut out off the gel and analyzed by matrix assisted laser desorption/ionization time-of-flight mass spectrometry (MALDI-TOF MS). Protein concentrations were determined using the Bio-Rad Protein Assay.

MALDI-TOF Mass Spectrometry. Mass spectrometric analyses of tryptic peptides were carried out on a MALDI VOYAGER DE-PRO time-of-flight mass spectrometer from PerSeptive BioSystems (Framingham, MA), utilizing a nitrogen laser, emitting at 337 nm, and an accelerating voltage of 25 kV. Measurements were performed in the delayed extraction mode using a low mass gate of 2000. The mass spectrometer was used in the positive ion detection and linear modes. Samples of the digestion mixture were placed directly on a 100-position sample plate and allowed to air-dry after the addition of an equal volume of a saturated solution of 3,5-dimethoxy-4-hydroxycinnaminic acid (sinapinic acid) in 50% (v/v) acetonitrile and 0.3% (v/v) TFA.

Acidic pH Treatment of scFv-Displaying Beads. In order to remove any β-galactosidase of the *E. coli* production host that may have remained bound to the anti-β-galactosidase-scFv during the bead isolation process, scFv-displaying and control beads were treated with low pH. A volume of beads corresponding to 3 mg of bead protein was sedimented by centrifugation and resuspended in 1 mL of 50 mM glycine at pH 2.7. After another centrifugation, beads were washed once in 1 mL of 50 mM potassium phosphate buffer at pH 7.2 and once in 1 mL of PBS/Tween (phosphate buffered saline (10 mM potassium phosphate buffer at pH 7.2 and 0.5% (w/v) NaCl) and 0.05% (v/v) Tween 20) before being resuspended in the original volume of potassium phosphate buffer containing 20% (v/v) glycerol.

Reversible Binding of β-Galactosidase to Anti-β-galactosidase-scFv-Displaying Beads. scFv-displaying and control beads displaying only PhaC were sedimented by centrifugation, resuspended in PBS/Tween, and then mixed with β-galactosidase (27 μg) and BSA (50 μg) in a total volume of 600 μL. In each case 660 μg of bead protein was used in each case. Samples were incubated for 3 h at room temperature while slight rocking kept the beads in suspension. Beads were sedimented by centrifugation and subjected to a series of washes, either once in PBS/Tween, twice in high salt buffer (50 mM Tris at pH 7.4 and 500 mM NaCl), once in low salt buffer (10 mM Tris at pH 7.4 and 37.5 mM NaCl), and once in PBS/Tween or simply five times in PBS/Tween. Elution of β-galactosidase from the beads was achieved by resuspension in 80 μL of 50 mM glycine at pH 2.7. The eluate was centrifuged once more to ensure the removal of any residual beads and only 70 μL kept as the final eluate. The same beads were then subjected to a second elution step with 50 mM glycine at pH 1.9.

β-Galactosidase Activity Assay to Assess scFv Functionality. ScFv-displaying beads and control beads displaying only PhaC were diluted to the desired concentration in potassium phosphate buffer. *E. coli* β-galactosidase (Calbiochem) was diluted in blocking buffer (2% (w/v) skim milk powder in PBS/Tween). For a standard assay, 100 μL of beads (100 μg of protein) and 100 μL of β-galactosidase (1 μg) were added to 300 μL of blocking buffer in a microtube. All assays were carried out in triplicate. Samples were incubated for 1 h or 90 min at room temperature while slight rocking kept the beads in suspension. Beads were then sedimented by centrifugation, washed three times in PBS/Tween, and resuspended in 700 μL of Z-buffer (60 mM Na_2HPO_4, 40 mM NaH_2PO_4, 10 mM KCl, 1 mM $MgCl_2$, and 50 mM β-mercaptoethanol). Upon the addition of 100 μL of ONPG (2-nitrophenyl β-D-galactopyranoside; stock solution of 8 mg/mL in Z-buffer), samples were incubated at 37 °C for 5−15 min and the reaction stopped by addition of 400 μL of a 1 M Na_2CO_3 solution. Samples were clarified by centrifugation and absorbance of the supernatant measured at 420 nm (Libra S5 spectrophotometer, Biochrom). If beads had been pretreated at pH 2.7, the same volume as

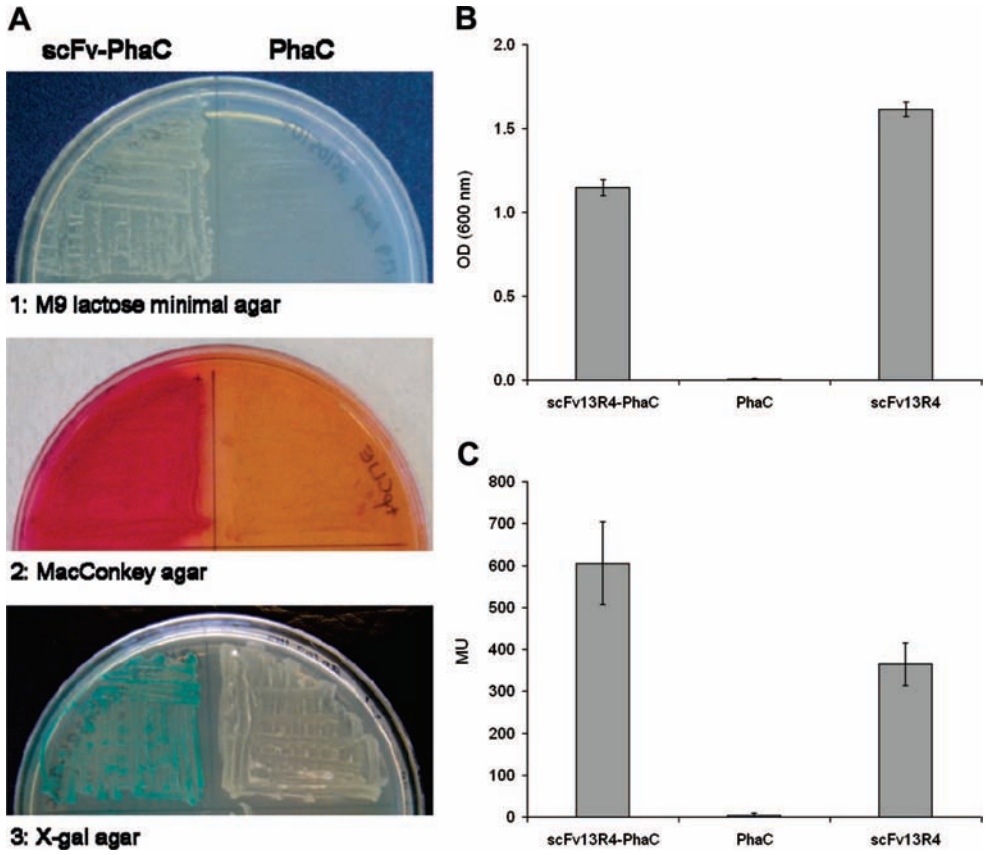

Figure 1. (A) Growth phenotyes of *E. coli* AMEF on different media, demonstrating *in vivo* activation of AMEF β-galactosidase by recombinantly produced anti-β-galactosidase scFv-PhaC fusion protein. *E. coli* AMEF 6101 harboring pCWE-scFv13R4 or pCWE (negative control) was streaked out on M9 lactose minimal, MacConkey, and X-gal agar plates. Growth on lactose as sole carbon source as well as color changes on MacConkey and X-gal agar require an activated AMEF β-galactosidase and thus a functional scFv-PhaC fusion protein. (B) *In vivo* rescue of *E. coli* AMEF in M9 lactose minimal medium by recombinantly produced anti-β-galactosidase scFv-PhaC fusion protein. Displayed is the final OD_{600} after 24 h of growth. Strains used were AMEF 959 harboring pCWE-scFv13R4, AMEF 959 harboring pCWE (negative control), and AMEF 959 harboring pPM163R4 (positive control). (C) Quantification of β-galactosidase activity after *in vivo* activation of AMEF β-galactosidase by recombinantly produced anti-β-galactosidase scFv-PhaC fusion protein. *E. coli* AMEF 959 harboring pPM163R4 (positive control), pCWE-scFv13R4, and pCWE (negative control), respectively, was cultivated, and cells were used to determine β-galactosidase activity by measuring conversion of ONPG into nitrophenol at 420 nm, enabling the calculation of MU (Miller units).

that of the original beads was used regardless of the protein concentration.

For the determination of the binding capacity of the scFv-displaying beads and the apparent equilibrium dissociation constant (K_D), the assay was performed with different β-galactosidase concentrations ranging from 0.067 to 10.65 μg, while the bead concentration remained unchanged (70 μg of protein). Control beads were only incubated with the highest β-galactosidase concentration. In order to test the temperature stability of the beads, they were incubated at increasing temperatures for 15 min, and scFv functionality was then assessed by measuring the binding of β-galactosidase as described above. All assays were carried out in triplicate.

***In Vivo* Activation of AMEF Proteins.** For qualitative assessment of *in vivo* AMEF activation, *E. coli* AMEF 959 or *E. coli* AMEF 6101 harboring plasmids $pCWE_{Spe}$-scFv13R4, pPM163R4, or pCWE was streaked out on MacConkey agar, M9 lactose minimal agar, and X-gal agar or incubated in liquid M9 lactose minimal medium. For a more quantitative assessment, essentially the same β-galactosidase activity assay as that for isolated beads was used. Tests were done in triplicate. *E. coli* AMEF 959 bearing the different plasmids was grown in LB medium overnight and the final OD_{600} of each culture recorded. An aliquot of each culture was harvested by centrifugation. Cells were resuspended in Z-buffer and permeabilized by adding CTAB (hexadecyltrimethylammonium bromide) and sodium deoxycholate. After the addition of ONPG, samples were incubated at 37 °C until sufficient yellow color had developed, and Na_2CO_3 was added to stop the reaction. The reaction time was recorded. After centrifugation, absorbance of the supernatant at 420 nm and at 550 nm was measured. MU (Miller units) were calculated as described elsewhere (*29*).

RESULTS

***In Vivo* Activation of AMEF β-Galactosidase by Soluble Anti-β-galactosidase scFv-PhaC Fusion Protein.** The plasmid $pCWE_{Spe}$-scFv13R4 was generated by inserting the anti-β-galactosidase scFv (scFv13R4) encoding gene into $pCWE_{Spe}$ immediately upstream of *phaC*, generating a hybrid gene under *lac* promoter control. Expression of this hybrid gene should enable the production of an anti-β-galactosidase scFv-PhaC fusion protein in which the fusion partners are connected by a 16 amino acid linker ($SerGly_4SerGly_4SerGly_4Ser$). In order to investigate whether the anti-β-galactosidase scFv retains its functionality when C-terminally fused to another protein, $pCWE_{Spe}$-scFv13R4 was tested for *in vivo* activation of AMEF β-galactosidase. AMEF (antibody-mediated enzyme formation) β-galactosidases are mutant β-galactosidases, which are inactive but can be activated by the binding of an anti-β-galactosidase antibody (*30*, *31*). Two different *E. coli* AMEF strains were used: AMEF 959 and AMEF 6101. Plasmids $pCWE_{Spe}$-scFv13R4 and pCWE were introduced into *E. coli* AMEF 6101 and the strains streaked out on MacConkey, M9 lactose minimal,

and X-gal agar (Figure 1A). Similarly, AMEF 959 harboring $pCWE_{Spe}$-scFv13R4, pCWE, or pPM163R4 was inoculated in liquid M9 lactose minimal medium (Figure 1B). Plasmid pCWE encodes only PhaC and served as a vector control, and pPM163R4 encodes the original unfused scFv13R4 and was used as a positive control.

Growth on lactose as the sole carbon source as well as color changes on MacConkey and X-gal agar require an activated AMEF β-galactosidase and thus a functional anti-β-galactosidase scFv. Here, both proteins, the scFv13R4 and the scFv13R4-PhaC, mediated growth on M9 lactose minimal medium (Figure 1A and 1B), whereas only PhaC did not. The observed color change of AMEF 6101 harboring $pCWE_{Spe}$-scFv13R4 on MacConkey agar indicated a pH drop caused by lactose fermentation and thus also confirmed that the scFv13R4-PhaC fusion protein bound and activated AMEF β-galactosidase (Figure 1A). Similarly, the cleavage of X-gal by β-galactosidase was observed only in the presence of scFv13R4-PhaC, as indicated by the blue color (Figure 1A). All these results demonstrated that the anti-β- galactosidase scFv as part of a scFv-PhaC fusion protein retained its antigen-binding functionality.

For a more quantitative assessment of the performance of scFv13R4-PhaC, β-galactosidase activity of overnight cultures of *E. coli* AMEF 959 harboring $pCWE_{Spe}$-scFv13R4, pCWE, or pPM163R4 was measured by monitoring the conversion of ONPG into nitrophenol. Both scFv13R4-PhaC and scFv13R4 clearly activated AMEF β-galactosidase. β-Galactosidase activity of AMEF 959 producing scFv13R4-PhaC reached on average 606 MU (Miller units), and on average 365 MU were obtained with AMEF 959 producing unfused scFv13R4 (Figure 1C). Almost no background β-galactosidase activity (4 MU) was detected for AMEF 959 bearing only the control plasmid pCWE. The relatively high difference between the *in vivo* AMEF activation achieved with scFv13R4-PhaC and scFv13R4 can probably be at least partly attributed to the different plasmids from which the respective genes were expressed. Plasmid pPM163R4 has a *trp* promoter, while in plasmid pCWE and its derivatives, genes are under the control of the *lac* promoter. Previous promoter strength analyses indicated that the strength of the *trp* promoter is about 30–40% of the strength of the *lac* promoter (*32*).

Overproduction of scFv13R4-PhaC at the Surface of Polymer Beads. To enable overproduction of the fusion protein under T7 promoter control, the scFv13R4-*phaC* hybrid gene from $pCWE_{Spe}$-scFv13R4 was inserted into pET-14b. In the activation experiments described above, no polymer beads were formed because of the absence of plasmid pMCS69. Plasmid pMCS69 carries the genes encoding two proteins, PhaA and PhaB, which mediate the provision of the polymer precursors and are thus required for polymer biosynthesis. In order to enable bead production and overproduction of the fusion protein at the bead surface, plasmid pHAS-scFv13R4 was introduced into *E. coli* BL21(DE3) harboring pMCS69. This recombinant strain mediated the production of anti-β-galactosidase scFv-displaying beads, which were isolated for further analysis. Control beads were isolated from *E. coli* BL21(DE3) (pMCS69 and pHAS). GC/MS analysis confirmed that the scFv-PhaC fusion protein mediates polymer production (data not shown). Polymer-accumulating cells as well as isolated beads were subjected to TEM in order to confirm the presence and shape of the beads (data not shown). Beads were found to be within the size range as previously described (*19–21*). On average, between 1.2 and 1.5 g (wet weight) of beads were obtained per 1 L of culture, corresponding to 92–108 mg of total bead protein.

Proteins attached to the beads were separated by SDS−PAGE (Figure 2). Plasmid pHAS-scFv13R4 mediated the production of beads showing an overproduced prominent protein with an apparent molecular weight of about 92 kDa. This corresponded to the predicted molecular weight of the fusion protein. The protein was identified as scFv13R4-PhaC by MALDI-TOF/MS analysis of tryptic peptide fragments (Table 2). In addition, the prominent protein found on the control beads, which corresponds to unfused PhaC, is absent from the scFv-displaying beads.

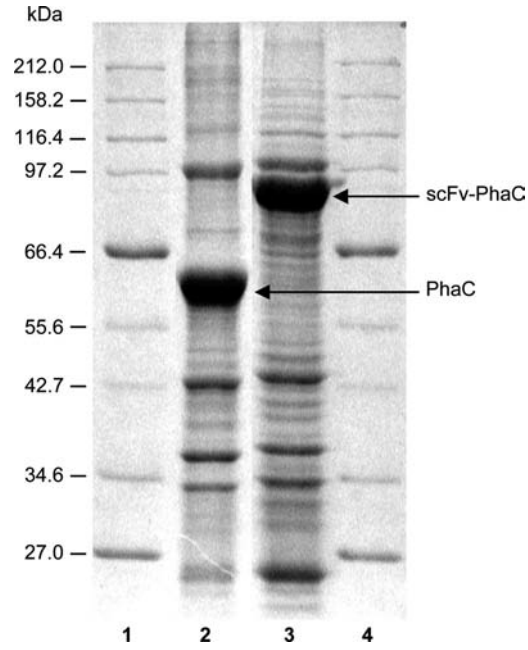

Figure 2. SDS−PAGE analysis of polymer beads produced in *E. coli* BL21(DE3). Lanes 1 and 4, molecular weight standard; lane 2, beads isolated from *E. coli* BL21(DE3) harboring pHAS (only PhaC); lane 3, beads isolated from *E. coli* BL21(DE3) harboring pHAS-scFv13R4 (scFv13R4-PhaC). The arrows indicate PhaC and the anti-β-galactosidase scFv-PhaC fusion protein, which was confirmed by peptide mass fingerprinting using MALDI-TOF MS.

Reversible Binding of β-Galactosidase to Anti-β-galactosidase scFv-Displaying Beads. In order to demonstrate that immobilized anti-β-galactosidase scFv is functional and retains its antigen-binding properties, beads were used to purify β-galactosidase from a mixture of β-galactosidase and bovine serum albumin (BSA). Beads were incubated with the protein mixture, washed several times, and bound proteins eluted with glycine at pH 2.7 and glycine at pH 1.9. Only a protein corresponding in size to β-galactosidase was eluted from scFv-displaying beads, the majority of it during the pH 2.7 elution step (Figure 3). The protein was identified as β-galactosidase by MALDI-TOF/MS analysis of tryptic peptide fragments (Table 2). No β-galactosidase was eluted from control beads not displaying the scFv (Figure 3). This indicates that β-galactosidase was specifically and reversibly bound to the scFv displayed as scFv-PhaC fusion protein on the bead surface and that no unspecific binding to the remaining bead surface occurred.

Enzyme-Linked Assays Using Anti-β-galactosidase scFv-Displaying Beads.*In Vitro Detection of β-Galactosidase Activity.* One of the main objectives of this study was to test the performance of scFv-displaying beads in enzyme-linked assays, similar to ELISA but taking advantage of the bead as a carrier material. In all assays, β-galactosidase activity was measured to assess the binding of β-galactosidase to the scFv. In order to establish a standard assay, beads were incubated with β-galactosidase for 1 h or 90 min, washed several times, and incubated with the β-galactosidase substrate ONPG. Conversion of ONPG into nitrophenol was determined by measuring the absorption at 420 nm (Abs_{420}). This assay showed that β-galactosidase bound to the scFv on the bead surface and converted ONPG

Table 2. Identified Peptide Fragments of Proteins Analyzed by MALDI-TOF/MS

protein	peptide fragments
scFv13R4-PhaC	Q41-R58, G46-R58 or R194-K206, Y59-R69, D75-R89, L186-R201, L245-K276, S287-R307, V292-R307, Q308-K333, I334-R345, Y346-K361, A362-R371, A362-R372, R372-R379, F373-R379, T380-R396, F386-R396, A397-K410, A397-R412, I415-R440, F417-R440, L441-R451, N456-R463, G464-R478, I466-R478, Y521-R534, H535-R549, N550-R570, A571-K583, F772-K789, R834-R844, A835-R844, Y845-R854, A847-R854, A847-K857
β-galactosidase	R15-R27, D16-R27, L28-R38, S54-R60, W159-R167, L168-R179, A180-R191, L185-R191, W192-R205, D212-R231, F232-R238, V257-R283, L294-K300, L301-R311, I338-R353, Q382-R389, Y406-R426, W433-R440, D448-R474, N450-R474, V507-K518, Y553-R558, L563-K578, Y579-R600, H623-R631, L632-R646, Q679-R700, V701-R722, K775-R782, Q776-R782, Q776-R787, A788-R801, A788-R810, I802-R810, I859-R882, V896-R910, W919-R939, E944-R953, G954-R962, Y963-R974

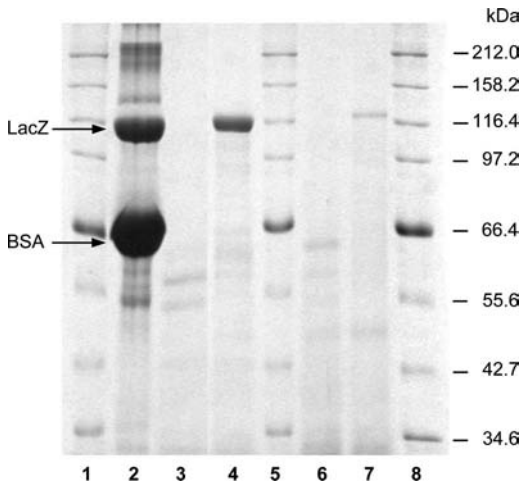

Figure 3. SDS−PAGE analysis of *in vitro* binding of β-galactosidase to anti-β-galactosidase scFv-displaying beads and release of β-galactosidase after elution. Lanes 1, 5, and 8, molecular weight standard; lane 2, mixture of BSA and β-galactosidase, prior to incubation with beads; lane 3, proteins eluted at pH 2.7 from control beads (PhaC); lane 4, β-galactosidase eluted at pH 2.7 from anti-β-galactosidase scFv-displaying beads; lane 6, proteins eluted at pH 1.9 from control beads; lane 7, β-galactosidase eluted at pH 1.9 from anti-β-galactosidase scFv-displaying beads. Eluted β-galactosidase was confirmed by peptide mass fingerprinting using MALDI-TOF MS.

into nitrophenol (Figure 4). Control beads not displaying the scFv did not convert ONPG.

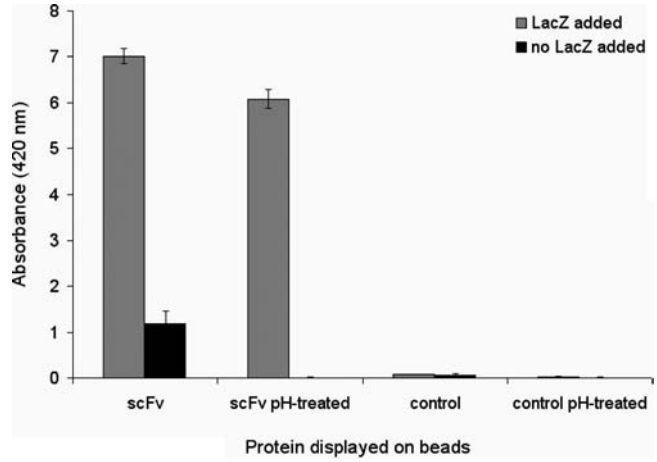

Figure 4. Enzyme-linked assay using β-galactosidase-mediated conversion of ONPG to detect specific binding of β-galactosidase by scFv13R4 displayed on the bead surface. Anti-β-galactosidase scFv-displaying and control beads were either used without prior acidic pH treatment or washed with glycine buffer at pH 2.7. Beads were then incubated with β-galactosidase (light gray), or no β-galactosidase was added (dark gray), and absorption at 420 nm was measured to determine the conversion of ONPG into nitrophenol.

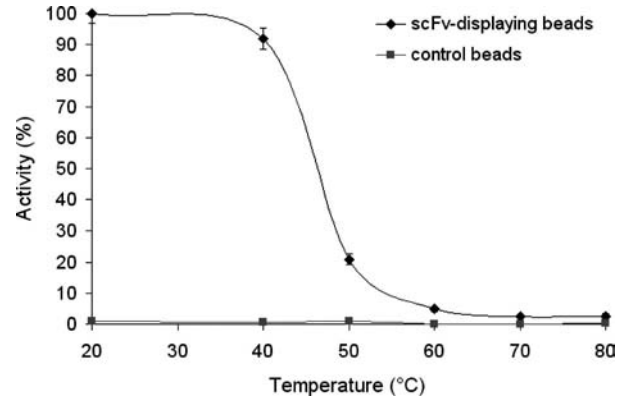

Figure 5. Temperature stability of anti-β-galactosidase scFv-displaying beads. Beads were incubated at increasing temperatures for 15 min, and β-galactosidase activity was subsequently measured to assess the remaining anti-β-galactosidase scFv functionality.

Acidic pH Treatment for Additional Purification of Anti-β-galactosidase scFv-Displaying Beads. Since the beads were produced in a commercially available *E. coli* BL21(DE3), which possesses a *lacZ* gene, it was investigated whether any β-galactosidase derived from the host strain binds to the scFv on the bead surface inside the cell and also remains bound after bead isolation. In order to address this question, β-galactosidase activity assays of scFv-displaying and control beads were carried out with and without the addition of β-galactosidase. Control beads showed no significant β-galactosidase binding. Anti-β-galactosidase scFv-displaying beads showed a weak background β-galactosidase activity corresponding to $Abs_{420} = 1.2$, whereas the same beads incubated with β-galactosidase showed a maximum $Abs_{420} = 7.0$ (Figure 4). In order to remove the residual β-galactosidase, beads were washed with glycine buffer at pH 2.7, which successfully eliminated any background β-galactosidase activity. Upon addition of β-galactosidase, these pretreated beads again showed a high absorbance at 420 nm, indicating that the β-galactosidase binding ability of the scFv was not impaired by exposure to acidic pH (Figure 4).

Antigen-Binding Characteristics. In order to assess the stability, that is, antibody functionality, of the scFv-displaying beads, β-galactosidase binding assays were repeatedly conducted

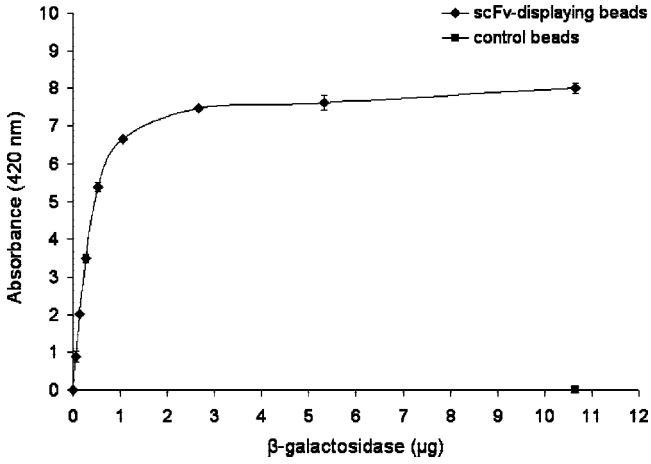

Figure 6. Determination of the binding capacity of anti-β-galactosidase scFv-displaying beads. Beads were incubated with increasing concentrations of β-galactosidase, and the conversion of ONPG was measured to detect β-galactosidase activity. Control beads were only incubated with the highest β-galactosidase concentration. An absorption maximum was observed for $\geq$2.66 μg of β-galactosidase.

(data not shown). After three months of storage at 4 °C, no decrease in antigen (β-galactosidase)-binding ability was detectable.

Temperature stability was tested by subjecting anti-β-galactosidase scFv-displaying beads to increasing temperatures and then assessing scFv functionality by standard β-galactosidase activity assays (Figure 5). The beads retained almost full binding capacity (92%) up to 40 °C. It then dropped quickly to about 21% at 50 °C, and no more binding was detectable at 70 °C.

The binding capacity of anti-β-galactosidase scFv-displaying beads and the apparent equilibrium dissociation constant (K_D) were determined by β-galactosidase activity assays using varying concentrations of β-galactosidase. Beads corresponding to 70 μg of protein and 0.067–10.65 μg of β-galactosidase were used. Beads were incubated with β-galactosidase for 1 h, washed, and incubated with the β-galactosidase substrate ONPG. The mean absorption at 420 nm was measured. An absorption maximum of 7.5 was observed for amounts $\geq$2.66 μg of β-galactosidase, which is approximately the amount of β-galactosidase that can be bound by 70 μg of bead protein (Figure 6). The half-maximum binding capacity can thus be determined at an absorption of 3.75, which corresponds to 300 ng of β-galactosidase (Figure 6). Taking into account the molecular weight of β-galactosidase (465.396 g/mol) and the assay volume (525 μL), an apparent equilibrium dissociation constant (K_D) of 12×10^{-7} M could be deduced.

DISCUSSION

In this study, the display of a functional scFv at the surface of biopolymer beads intracellularly assembled in *E. coli* by a protein engineering approach using a favorable insolubility fusion partner was investigated. The fusion partner mediated the *in vivo* self-assembly of polymer beads with a hydrophobic polymer core surrounded by the fusion partner, enabling surface display of the scFv (Figure 7). Here, an anti-β-galactosidase scFv was C-terminally fused to the polymer bead forming enzyme PhaC from *C. necator* by constructing the respective hybrid gene. Production of this fusion protein in *E. coli* led to the formation of the desired scFv-displaying beads, which can then be isolated by a simple centrifugation step and are ready to use straight after isolation (Figure 7).

Assessment of the *in vivo* functionality of the anti-β-galactosidase scFv-PhaC fusion protein using *in vivo* activation of the AMEF β-galactosidase clearly suggested that the fusion protein binds to the AMEF β-galactosidase (Figure 1). Activation of the AMEF β-galactosidase by the anti-β-galactosidase scFv-PhaC fusion protein enabled growth of the respective recombinant AMEF strain on lactose as the sole carbon source (Figure 1A and 1B) and the detection of AMEF β-galactosidase activity (Figure 1C). When polymer precursors were metabolically provided, polymer bead formation was mediated by the anti-β-galactosidase scFv-PhaC fusion protein as assessed by TEM and GC/MS. Protein analysis of isolated beads demonstrated a strong overproduction of anti-β-galactosidase scFv-PhaC fusion protein at the bead surface (Figure 2). The functionality of the bead-bound fusion protein was clearly confirmed by applying the beads for batch purification of β-galactosidase to electrophoretic homogeneity from a protein mixture (Figure 3). Specific β-galactosidase binding was further

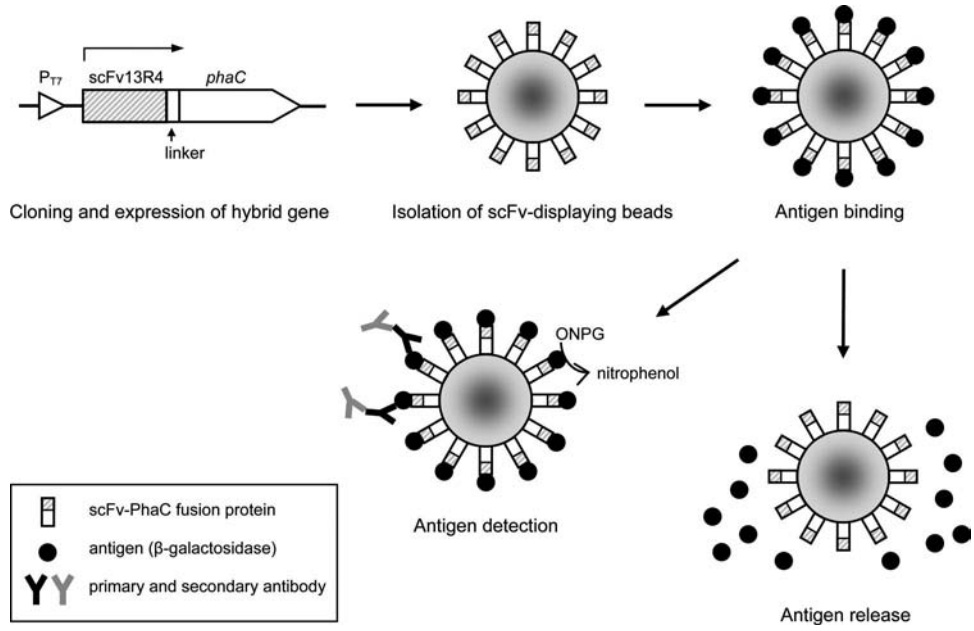

Figure 7. Schematic overview of the *in vivo* self-assembly of scFv-displaying polymer beads as well as possible applications of the respective isolated beads.

confirmed by assessment of the β-galactosidase activity of β-galactosidase bound to the beads (Figure 4). The beads themselves did not show unspecific binding of β-galactosidase (Figures 3 and 4). However, analysis of scFv-displaying beads isolated from recombinant *E. coli* BL21(DE3) showed that some β-galactosidase molecules were already bound (Figure 4). Acidic pH 2.7 treatment completely removed bound β-galactosidase, while maintaining bead and scFv functionality for the subsequent binding of β-galactosidase. The anti-β-galactosidase scFv-displaying beads showed a strong decline in β-galactosidase binding capacity when incubated at temperatures above 40 °C (Figure 5). This rather low thermal stability is presumably due to the lack of one set of disulphide bonds in this particular scFv (*5*). Similar observations were made in a previous study analyzing the thermal stability of the respective soluble scFv13R4. An apparent equilibrium dissociation constant (K_D) of 1.2 μM suggested an ~75-fold increase in binding affinity, when compared to that of the soluble scFv13R4 (*33*). Consistently, it was previously demonstrated in binding assays that nanoparticles diplaying an antibody at high-density show a higher binding affinity than the antibody itself, enhancing the sensitivity of a diagnostic assay (*34*).

This study demonstrated the feasibility of a novel approach for one-step *in vivo* scFv immobilization. Emerging key requirements for the immobilization of antibody fragments include stable, that is, covalent, attachment and directed versus random orientation to minimize loss of functionality as well as preservation of native state (*35*). Several sophisticated approaches have been reported, for example, the fusion of different antibody fragments to cutinase followed by the binding of these fusion proteins to phosphonate capture ligands presented on self-assembled monolayers; fusion of a scFv to a C_L domain with a C-terminal cysteine residue and cross-linking to a gold surface by a maleimide linker; recrystallization of a bacterial S-layer protein fused to a V_{HH} on a gold surface precoated with thiolated SCWP (secondary cell wall polymer); and cross-linking of a cysteine-tagged scFv to immunoliposomes by a maleimide linker (*12–15*). However, all these examples require separate tagging and coating or cross-linking steps. In addition, apart from the immunoliposomes, they all result in planar functionalized surfaces. A nonplanar organization, for example, spherical beads, can have significant advantages such as an increased binding surface, leading to a wide range of applications in laboratory methods. Another example for scFv-coated beads is the immobilization of scFv-CBD fusion proteins to chitin beads for immunoaffinity chromatography, but this again is not a covalent interaction (*36*). The scFv-displaying polymer beads described here meet the criteria of covalent and oriented binding of the immobilized antibody fragment. Furthermore, they can be generated by a simple one-step process without the need for additional coating or cross-linking of a preformed bead, suggesting a novel and economic production strategy (Figure 7). Further investigations will be required to elaborate the simultaneous display of different functionalities on the bead surface, analogous to fusions of soluble antibody fragments to other molecules such as drugs or toxins for immunotargeting (*37, 38*). In addition, the hydrophobic bead core could provide a significant payload for water-insoluble drugs, the targeted delivery of which could be mediated by display of the desired binding affinity.

ACKNOWLEDGMENT

We thank Pierre Martineau for providing the plasmid pPM163R4 and the *E. coli* AMEF strains, the latter with the kind permission of Franco Celada. This study was supported by research funding from Institute of Molecular Biosciences at Massey University as well as Massey University.

LITERATURE CITED

(1) Lee, M. H., Park, T. I., Park, Y. B., and Kwak, J. W. (2002) Bacterial expression and *in vitro* refolding of a single-chain Fv antibody specific for human plasma apolipoprotein B-100. *Protein Expression Purif. 25*, 166–173.

(2) Guo, J. Q., You, S. Y., Li, L., Zhang, Y. Z., Huang, J. N., and Zhang, C. Y. (2003) Construction and high-level expression of a single-chain Fv antibody fragment specific for acidic isoferritin in *Escherichia coli*. *J. Biotechnol. 102*, 177–189.

(3) Worn, A., and Pluckthun, A. (1998) An intrinsically stable antibody scFv fragment can tolerate the loss of both disulfide beads and fold correctly. *FEBS Lett. 427*, 357–361.

(4) Rungpragayphan, S., Kawarasaki, Y., Imaeda, T., Kohda, K., Nakano, H., and Yamane, T. (2002) High-throughput, cloning-independent protein library construction by combining single-molecule DNA amplification with in vitro expression. *J. Mol. Biol. 318*, 395–405.

(5) Martineau, P., Jones, P., and Winter, G. (1998) Expression of an antibody fragment at high levels in the bacterial cytoplasm. *J. Mol. Biol. 280*, 117–127.

(6) Levy, R., Weiss, R., Chen, G., Iverson, B. L., and Georgiou, G. (2001) Production of correctly folded Fab antibody fragment in the cytoplasm of *Escherichia coli trxB gor* mutants via the coexpression of molecular chaperones. *Protein Expression Purif. 23*, 338–347.

(7) Jurado, P., Ritz, D., Beckwith, J., de Lorenzo, V., and Fernandez, L. A. (2002) Production of functional single-chain Fv antibodies in the cytoplasm of *Escherichia coli*. *J. Mol. Biol. 320*, 1–10.

(8) Venturi, M., Seifert, C., and Hunte, C. (2002) High level production of functional antibody Fab fragments in an oxidizing bacterial cytoplasm. *J. Mol. Biol. 315*, 1–8.

(9) Bach, H., Mazor, Y., Shaky, S., Shoham-Lev, A., Berdichevsky, Y., Gutnick, D. L., and Benhar, I. (2001) *Escherichia coli* maltose-binding protein as a molecular chaperone for recombinant intracellular cytoplasmic single-chain antibodies. *J. Mol. Biol. 312*, 79–93.

(10) Jurado, P., de Lorenzo, V., and Fernandez, L. A. (2006) Thioredoxin fusions increase folding of single chain Fv antibodies in the cytoplasm of *Escherichia coli*: Evidence that chaperone activity is the prime effect of thioredoxin. *J. Mol. Biol. 357*, 49–61.

(11) Zheng, L., Baumann, U., and Reymond, J. L. (2003) Production of a functional catalytic antibody ScFv-NusA fusion protein in bacterial cytoplasm. *J. Biochem. (Tokyo) 133*, 577–581.

(12) Pleschberger, M., Saerens, D., Weigert, S., Sleytr, U. B., Muyldermans, S., Sara, M., and Egelseer, E. M. (2004) An S-layer heavy chain camel antibody fusion protein for generation of a nanopatterned sensing layer to detect the prostate-specific antigen by surface plasmon resonance technology. *Bioconjugate Chem. 15*, 664–671.

(13) Xu, L., Huang, C. C., Huang, W. Q., Tang, W. H., Rait, A., Yin, Y. Z., Cruz, I., Xiang, L. M., Pirollo, K. F., and Chang, E. H. (2002) Systemic tumor-targeted gene delivery by anti-transferrin receptor scFv-immunoliposomes. *Mol. Cancer Ther. 1*, 337–346.

(14) Torrance, L., Ziegler, A., Pittman, H., Paterson, M., Toth, R., and Eggleston, I. (2006) Oriented immobilisation of engineered single-chain antibodies to develop biosensors for virus detection. *J. Virol. Methods 134*, 164–170.

(15) Kwon, Y., Han, Z., Karatan, E., Mrksich, M., and Kay, B. K. (2004) Antibody arrays prepared by cutinase-mediated immobilization on self-assembled monolayers. *Anal. Chem. 76*, 5713–5720.

(16) Sugimura, Y., Ueda, H., Maki, M., and Hitomi, K. (2007) Novel site-specific immobilization of a functional protein using a preferred substrate sequence for transglutaminase 2. *J. Biotechnol. 131*, 121–127.

(17) Brockelbank, J. A., Peters, V., and Rehm, B. H. A. (2006) Recombinant *Escherichia coli* strain produces a ZZ domain displaying biopolyester granules suitable for immunoglobulin G purification. *Appl. Environ. Microbiol. 72*, 7394–7397.
(18) Peters, V., and Rehm, B. H. A. (2006) *In vivo* enzyme immobilization by use of engineered polyhydroxyalkanoate synthase. *Appl. Environ. Microbiol. 72*, 1777–1783.
(19) Rehm, B. H. A. (2007) Biogenesis of microbial polyhydroxyalkanoate granules: a platform technology for the production of tailor-made bioparticles. *Curr. Issues Mol. Biol. 9*, 41–62.
(20) Rehm, B. H. A. (2003) Polyester synthases: natural catalysts for plastics. *Biochem. J. 376*, 15–33.
(21) Rehm, B. H. A. (2006) Genetics and biochemistry of polyhydroxyalkanoate granule self-assembly: The key role of polyester synthases. *Biotechnol. Lett. 28*, 207–213.
(22) Peters, V., and Rehm, B. H. A. (2005) *In vivo* monitoring of PHA granule formation using GFP-labeled PHA synthases. *FEMS Microbiol. Lett. 248*, 93–100.
(23) Peters, V., Becher, D., and Rehm, B. H. (2007) The inherent property of polyhydroxyalkanoate synthase to form spherical PHA granules at the cell poles: The core region is required for polar localization. *J. Biotechnol. 132*, 238–245.
(24) Backstrom, B. T., Brockelbank, J. A., and Rehm, B. H. A. (2007) Recombinant *Escherichia coli* produces tailor-made biopolyester granules for applications in fluorescence activated cell sorting: functional display of the mouse interleukin-2 and myelin oligodendrocyte glycoprotein. *BMC Biotechnol. 7*.
(25) Miller, J. H. (1992) *A Short Course in Bacterial Genetics: A Laboratory Manual and Handbook for Escherichia coli and Related Bacteria* Cold Spring Harbor Laboratory Press, Plainview, NY.
(26) Sambrook, J., Fritsch, E. F., and Maniatis, T. (1988) *Molecular Cloning: A Laboratory Manual*, Cold Spring Harbor Laboratory Press, Cold Spring Harbor, NY.
(27) Brandl, H., Gross, R. A., Lenz, R. W., and Fuller, R. C. (1988) Pseudomonas oleovorans as a source of poly(β-hydroxyalkanoates) for potential applications as biodegradable polyesters. *Appl. Environ. Microbiol. 54*, 1977–1982.
(28) Laemmli, U. K. (1970) Cleavage of structural proteins during assembly of head of bacteriophage-T4. *Nature 227*, 680–685.
(29) Miller, J. H. (1972) *Experiments in Molecular Genetics*, Cold Spring Harbor Laboratory Press, Cold Spring Harbor, NY.
(30) Rotman, M. B., and Celada, F. (1968) Antibody-mediated activation of a defective β-D-galactosidase extracted from an *Escherichia coli* mutant. *Proc. Natl. Acad. Sci. U.S.A. 60*, 660–667.
(31) Messer, W., and Melchers, F. (1970) Genetic analysis of mutants producing defective β-galactosidase which can be activated by specific antibodies. *Mol. Gen. Genet. 109*, 152–161.
(32) Kajitani, M., and Ishihama, A. (1983) Determination of the promoter strength in the mixed transcription system: promoters of lactose, tryptophan and ribosomal protein L10 operon from *Escherichia coli*. *Nucleic Acids Res. 11*, 671–686.
(33) Laden, J. C., Philibert, P., Torreilles, F., Pugniere, M., and Martineau, P. (2002) Expression and folding of an antibody fragment selected *in vivo* for high expression levels in *Escherichia coli* cytoplasm. *Res. Microbiol. 153*, 469–474.
(34) Soukka, T., Harma, H., Paukkunen, J., and Lovgren, T. (2001) Utilization of kinetically enhanced monovalent binding affinity by immunoassays based on multivalent nanoparticle-antibody bioconjugates. *Anal. Chem. 73*, 2254–2260.
(35) Cretich, M., Damin, F., Pirri, G., and Chiari, M. (2006) Protein and peptide arrays: Recent trends and new directions. *Biomol. Eng. 23*, 77–88.
(36) Blank, K., Lindner, P., Diefenbach, B., and Pluckthun, A. (2002) Self-immobilizing recombinant antibody fragments for immunoaffinity chromatography: generic, parallel, and scalable protein purification. *Protein Expression Purif. 24*, 313–322.
(37) Huston, J. S., McCartney, J., Tai, M. S., Mottola-Hartshorn, C., Jin, D., Warren, F., Keck, P., and Oppermann, H. (1993) Medical applications of single-chain antibodies. *Int. Rev. Immunol. 10*, 195–217.
(38) Verma, R., Boleti, E., and George, A. J. T. (1998) Antibody engineering: Comparison of bacterial, yeast, insect and mammalian expression systems. *J. Immunol. Methods 216*, 165–181.
(39) Yuan, W., Jia, Y., Tian, J. M., Snell, K. D., Muh, U., Sinskey, A. J., Lambalot, R. H., Walsh, C. T., and Stubbe, J. (2001) Class I and III polyhydroxyalkanoate synthases from *Ralstonia eutropha* and *Allochromatium vinosum*: Characterization and substrate specificity studies. *Arch. Biochem. Biophys. 394*, 87–98.
(40) Amara, A. A., and Rehm, B. H. A. (2003) Replacement of the catalytic nucleophile cysteine-296 by serine in class II polyhydroxyalkanoate synthase from *Pseudomonas aeruginosa*-mediated synthesis of a new polyester: identification of catalytic residues. *Biochem. J. 374*, 413–421.

BC7003473

Preparation of Ribonuclease S Domain-Swapped Dimers Conjugated with DNA and PNA: Modulating the Activity of Ribonucleases

Daniel Pulido,[†,§] Jorge Pedro López-Alonso,[‡,§] Vicente Marchán,[†] Carlos González,[‡] Anna Grandas,[†] and Douglas V. Laurents*[,‡]

Department de Química Orgànica, Institut de Biomedicina de la Universitat de Barcelona (IBUB), Facultat de Química, Universitat de Barcelona, Martí i Franquès 1-11, E-08028 Barcelona, Spain, and Instituto de Química Física "Rocasolano" (C.S.I.C.), Serrano 119, E-28006, Madrid, Spain. Received March 22, 2007; Revised Manuscript Received October 9, 2007

Obtaining highly specific and active ribonuclease activities is an important goal with numerous medical and biochemical applications. As a step toward more active and specific ribonucleases, we describe the preparation and the enzymatic and structural properties of RNase S monomers and dimers conjugated to DNA and PNA molecules. Poly(dT)$_n$ (2′-oligodeoxyribonucleotides, $n = 8$, 15) and t_8 peptide nucleic acid (PNA) chains have been conjugated to the S-peptide of ribonuclease S. Monomers and dimers of the conjugated enzyme have been obtained and characterized by ^{1}H NMR spectroscopy, showing that DNA or PNA conjugation does not alter the native structure of ribonuclease S. The oligonucleotide-conjugated RNase S monomer and dimer show significant activity against single-stranded RNA and very low/negligible hydrolysis of double-stranded poly(A)·poly(U). In contrast, the t_8-conjugated RNase S monomer and dimer show substantial activity against both ssRNA and dsRNA. These results highlight the importance of positive charges near but not in the active site in enhancing activity against dsRNA and reveal the promise of PNA−RNase conjugates for modulating RNase activity.

INTRODUCTION

Many natural ribonucleases (RNases[1]) play key roles in RNA processing (*1*), splicing (*2*), and, as more recently discovered, in gene silencing (*3*). In the latter case, formation of an RNA-induced silencing complex (*4*) that incorporates an RNA chain allows the recognition and specific cleavage of RNA molecules whose sequence is complementary to that of the nucleic acid component. This natural example suggests that catalytically active and specifically targetable RNases can be generated by linking a complementary oligonucleotide to a ribonuclease. Such active and targetable RNases are expected to have many uses in medicine and biotechnology. Alternatively, specific RNA cleavage has been achieved by coupling DNA strands to groups with ribonucleolytic activity, such as imidazole groups (*5*), or coordinated copper (*6*) or lanthanide ions (*7*). However, the reaction times of these artifical RNases is slow (hours time scale), and their *in vivo* effectiveness has not been established yet.

Among the many ribonucleases that can be conjugated to a nucleic acid chain, bovine pancreatic ribonuclease A exhibits several interesting advantages (*8*). First, this protein is a highly active monomeric enzyme, whose domain-swapped oligomers have a potent cytotoxic activity against human tumors transplanted onto nude mice (*9*). The basis of the selective cytotoxicity of RNase oligomers is not completely understood yet, but one contributing factor seems to be their enhanced activity against duplex RNA. This augmented activity is due to a higher density of positive charges on the surface of the oligomers relative to the monomer, rather than a cooperativity or synergy between the active sites in the oligomer (*10*). Second, bovine pancreatic RNase A can be specifically cleaved by subtilisin between residues 20 and 21. The two fragments, called S-peptide (residues 1–20) and S-protein (residues 21–124) remain noncovalently bound together, and their complex (RNase S) retains the same enzymatic activity of uncleaved RNase A (*11*). This property of RNase S has been used in many studies on protein stability, folding and enzyme catalysis (*12–14*). Both RNase A and RNase S monomers have a very strong specificity for pyrimidines at the position 5′ to the scissile bond, prefer A at the position 3′ to the scissile bond, and prefer purines at the following position (*15, 16*) and possess low activity against dsRNA (*17*). Recently, we have shown that RNase S can also form domain-swapped dimers with the same enhanced activity against dsRNA as does the corresponding "C-dimer" of RNase A (dimeric form of RNase A in which the C-terminal residues (115–124) are swapped between two monomers) (*18*).

These peculiar features of RNase S are very attractive for protein−nucleic acid conjugation, since the short length of the S-peptide facilitates the synthesis of variants of S-peptide that recombine with S-protein to produce semisynthetic RNase S. Previous work has shown that conjugating oligonucleotides to monomeric Ribonuclease S can endow the enzyme with a greatly enhanced, restriction enzyme-like specificity against the complementary RNA (*19*). In the same way, the covalent linkage of an oligonucleotide or a nucleic acid recognizing component

* Address correspondence to D. V. Laurents, Instituto de Química Física "Rocasolano" (C.S.I.C.), Serrano 119, E-28006, Madrid Spain. Tel: + 34 91 561 9400; Tel: + 34 91 564 2431; E-mail: dlaurents@iqfr.csic.es.

† Universitat de Barcelona.

‡ Instituto de Química Física "Rocasolano" (C.S.I.C.).

§ These authors contributed equally.

[1]Abbreviations used: C-dimer, the dimeric form of RNase A in which the C-terminal residues (115-124) are swapped between two monomers; MALDI-TOF MS, matrix-assisted laser desorption ionization time of flight mass spectroscopy; MOPS 3-(*N*-morpholine) propanosulfonic acid; RNase A, bovine pancreatic ribonuclease A; RNase S, bovine pancreatic RNase A containing a proteolytic cleavage between residues 20 and 21; S-peptide, the small fragment of RNase S, residues 1−20; S-protein, the large fragment of RNase S, residues 21−124; ssDNA, single-stranded DNA; ssRNA, single-stranded RNA; dsRNA, double-stranded RNA; poly(dT)$_n$ (2′- deoxyribonucleotides, $n = 8$, 15); t_8, peptide nucleic acid (PNA) chains; Fmoc, fluorenylmethoxycarbonyl group; DMF, *N*,*N*-dimethylformamide; HATU, *O*-(7-azabenzotriazol-1-yl)-1,1,3,3-tetramethyluronium hexafluorophosphate; ACN, acetonitrile.

10.1021/bc700374q CCC: $40.75 © 2008 American Chemical Society
Published on Web 12/29/2007

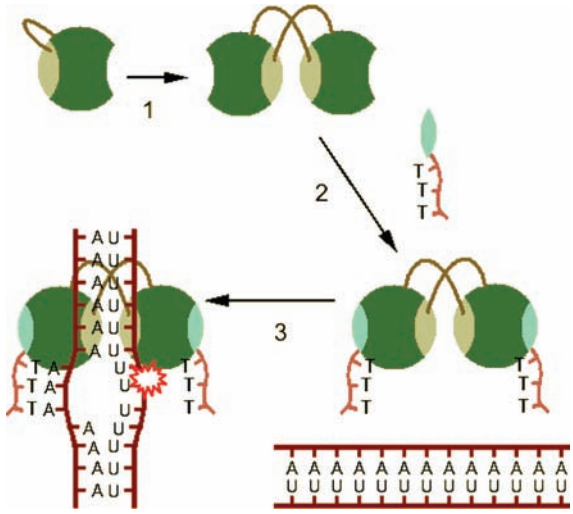

Figure 1. Strategy followed to modulate RNase activity by conjugation to oligothymines. Step 1, S-protein is dimerized by lyophilization from 40% aq acetic acid. During this process, the protein cores (dark green) are linked to form a metastable dimer by swapping of the C-terminal β-strand (light green). Step 2, the dimeric RNase S is reconstituted by addition of S-peptide conjugated to polythymine, whose backbone can be negatively charged (2′-oligodeoxyribonucleotides) or neutral (peptide nucleic acid). Step 3, interaction of polythymine component with a complementary region in dsRNA promotes degradation by the RNase.

to RNase oligomers should increase their specificity and improve their chemotherapeutic properties. In addition, this conjugated, complementary sequence could help disrupt double-helical regions of cellular RNA, leading to enhanced cleavage by RNase (Figure 1).

The main purpose of this work is to take a first step toward developing highly selective RNase S conjugates with the enhanced dsRNase activity of RNase A oligomers. We have prepared RNase S monomers and dimers from S-peptide molecules conjugated to nucleic acid recognizing molecules to assess the effect of the appending chain on RNase activity. Positive charges on the surface of the RNase, which are near the active site but not part of it, are thought to stabilize transient open regions of duplex RNA, that are subsequently cleaved by the enzyme (*10*, *17*, *20*, *21*). Since the negative charges on the phosphodiester backbone might interact with the positively charged groups of the enzyme and interfere with its activity, we have conjugated RNase S to both a polyanionic and a neutral chain, namely, 2′-oligodeoxyribonucleotides and a peptide nucleic acid (PNA). The latter offers the additional advantage that peptide nucleic acids are known to form very stable complexes with complementary sequences of RNA or DNA (*22*). Although PNA conjugation has been extensively employed to enhance PNA activities or for delivery in biological systems (see, for instance, refs *23*−*27*), the present work is, to our knowledge, the first report of an RNase conjugated to PNA.

EXPERIMENTAL PROCEDURE

DNA−S-Peptide Conjugate Preparation. The DNA−S-peptide conjugates, dT_8-KETAAAKFERQHMDSSTSAA and dT_{15}-KETAAAKFERQHMDSSTSAA, were prepared following the recently reported Diels–Alder approach (*28*). Briefly, the oligonucleotide chains were synthesized on controlled-pore glass using the standard phosphite triester methodology, which was also used to incorporate the phosphoramidite derivative of the diene. After deprotection with concentrated aqueous ammonia (4 h, room temperature), the target products were purified by reversed-phase medium-pressure liquid chromatography. MALDI-TOF mass spectrometric characterization (trihydroxyacetophenone/ammonium citrate, negative mode, linear) gave the following values: diene-$^{5'}$dTTTTTTTT, *m*/*z* 2530.56 $[M - H]^-$ (calc mass: 2530.44); diene-$^{5'}$dTTTTTTTTTTTTTTT, *m*/*z* 4652.88 $[M - H]^-$ (calc mass: 4658.76).

Solid-phase synthesis on a 2-chlorotrityl chloride polystyrene−1% divinylbenzene resin (Novabiochem, loading: 1.49 mmol Cl/g) was used to prepare the maleimide−peptide. The peptide chain was elongated using N^{α}-Fmoc derivatives [Arg(Pbf), Asp(O*t*Bu), Gln(Trt), Glu(O*t*Bu), His(Trt), Lys(Boc), Ser(*t*Bu), and Thr(*t*Bu)] and *N*,*N*′-diisopropylcarbodiimide/1-hydroxybenzotriazole activation, which was followed by incorporation of 3-maleimidepropionic acid. The desired product was obtained after cleavage with a 1:1:98 mixture of trifluoroacetic acid, 1,2-ethanedithiol, and dichloromethane (5 × 30 s, room temperature), deprotection with 2.5:2.5:2.5:1:91.5 thioanisole/H_2O/1,2-ethanedithiol/triisopropylsylane/trifluoroacetic acid mixture (4.5 h, room temperature), and purification by reversed-phase medium-pressure liquid chromatography. MALDI-TOF mass spectrometric characterization (2,5-dihydroxybenzoic acid, positive mode, reflector) gave a *m*/*z* ratio for the product of 2316.98 $[M + H]^+$ (calc mass: 2316.04).

The products were conjugated by reacting equimolar amounts of maleimide−peptide and diene−oligonucleotide in water, at 37 °C. After 20 h, an aliquot was removed from the reaction mixture and analyzed by reversed-phase HPLC. If the conversion of diene−oligonucleotide to peptide–oligonucleotide conjugate after that time was not quantitative, an amount of maleimide−peptide equimolar to the amount of unreacted diene−oligonucleotide was added, and the mixture was left to react for an additional period of 4 to 8 h. The target conjugates were isolated after gel filtration (Sephadex G-25) or HPLC. MALDI-TOF mass spectrometric characterization (trihydroxyacetophenone/ammonium citrate, negative mode, linear): dT_8-KETAAAKFERQHMDSSTSAA, *m*/*z* 4842.21 $[M - H]^-$ (calc mass: 4847.89); dT_{15}-KETAAAKFERQHMDSSTSAA, *m*/*z* 6968.32 $[M - H]^-$ (calc mass: 6974.80).

Synthesis of Diene-t_8. The peptide nucleic acid was assembled on 100 mg of 2-chlorotrityl chloride resin (see above). For the incorporation of the first monomer, 0.6 equiv of Fmoc-*t*-OH (Applied Biosystems), 5 equiv of *N*,*N*-diisopropylethylamine and anhydrous dichloromethane were added to the solid matrix, and the mixture was stirred for 45 min. After filtration and washings, the remaining reactive sites were capped by reaction with 100 μL of methanol. Removal of the Fmoc group from an aliquot of Fmoc-T-resin (20% piperidine in DMF, 2 × 10 min) and spectrophotometric quantification of the *N*-(9-fluorenylmethyl)piperidine formed indicated that the loading of Fmoc-T-resin was 0.21 mmol Fmoc/g. Subsequent t monomers were incorporated following standard PNA synthesis procedures. The Fmoc group was removed as indicated above. Two solutions were prepared before each coupling. Solution A was obtained by dissolving 5 equiv of Fmoc-*t*-OH in the minimum amount of *N*-methylpyrrolidone; solution B was prepared by adding 5.5 equiv of *N*,*N*-diisopropylethylamine and 5.5 equiv of 2,6-lutidine to a solution of 4.5 equiv of HATU in the minimum amount of anhydrous DMF. Immediately prior to coupling, the two solutions (A and B) were mixed and stirred at room temperature for 2 min, and the resulting mixture added to the solid matrix. After 45 min, the resin was washed (dichloromethane, DMF, and methanol), and an aliquot of support was withdrawn to determine the loading (see above). The coupling yield of the second Fmoc-*t*-OH monomer was about 40%, but a second coupling did not improve the yield. The coupling yield for the incorporation of the subsequent monomers ranged between 92% and 98%. A capping step was performed after each coupling by reaction with a 5:6:89 mixture of Ac_2O/2,6-lutidine/DMF (5 min).

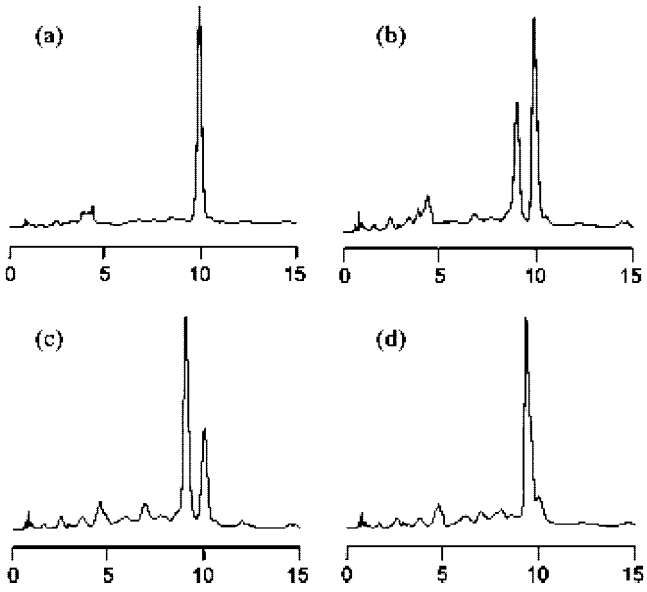

Figure 2. Reversed-phase HPLC traces of crude diene-t_8 (a), and conjugation reaction between diene-t_8 and maleimide-Lys-Glu-Thr-Ala-Ala-Ala-Lys-Phe-Glu-Arg-Gln-His-Met-Asp-Ser-Ser-Thr-Ser-Ala-Ala-OH after 24 h (b), 3 days (c), and 4 days (d).

(4*E*)-Hepta-4,6-dienoic acid was prepared following the described procedures (*29*)with minor modifications. Purification of ethyl (4*E*)-hepta-4,6-dienoate was carried out by silica gel column chromatography eluting with hexanes and increasing amounts of dichloromethane (5% to 40%). Ester hydrolysis was accomplished by treatment with 5 equiv of LiOH in a 3:1 (v/v) ethanol/water mixture for 2 h at 50 °C. Ethanol was removed in vacuo, and the resulting aqueous solution was extracted with dichloromethane, acidified with 10% aq HCl to pH 2–3, and reextracted with dichloromethane. The organic solution was dried over $MgSO_4$, filtered, and evaporated to dryness, which afforded the target acid in 84% yield.

Incorporation of (4*E*)-hepta-4,6-dienoic acid onto t_8-resin (85 mg, loading 0.06 mmol Fmoc/g): 10 equiv of the acid was coevaporated from anhydrous ACN (3×) and dissolved in the minimum amount of *N*-methylpyrrolidone (solution A). HATU (9 equiv) was dissolved in the minimum amount of anhydrous DMF, followed by addition of *N*,*N*-diisopropylethylamine (11 equiv) and 2,6-lutidine (11 equiv) (solution B). The two solutions were mixed and stirred at room temperature for 2 min, added to t_8-resin, and the mixture stirred for 45 min. Filtration and washings were followed by the capping step.

Cleavage from the solid support was carried out by reaction with a 1:99 trifluoroacetic acid/dichloromethane mixture (5 × 30 s treatment). Trifluoroacetic acid and most of the dichloromethane were removed by bubbling N_2 into the solution, and the resulting residue was poured onto cold ether to precipitate the target diene-t_8. The resulting pellet was insoluble in water and in most organic solvents (acetonitrile, tetrahydrofurane, dioxane) but completely soluble in hexafluoroisopropanol. Reverse-phase HPLC analysis and MALDI-TOF MS confirmed high homogeneity (92%) and the identity of the target diene-t_8, respectively. Due to insolubility problems, diene-t_8 was used in the Diels–Alder conjugation without further purification.

Diene-t_8: anal. HPLC (A: 0.045% trifluoroacetic acid in water, B: 0.036% trifluoroacetic acid in acetonitrile, linear gradient from 10% to 40% of B in 15 min, X-terra C18 column, 2.5 μm, 1 mL/min): t_R 10.0 min (Figure 2a); MALDI-TOF MS (synapinic acid, positive mode, reflector): *m*/*z* 2278.10 $[M + Na]^+$, 2294.04 $[M + K]^+$ (calc mass: 2254.88).

Diels–Alder Conjugation between Maleimide-Lys-Glu-Thr-Ala-Ala-Ala-Lys-Phe-Glu-Arg-Gln-His-Met-Asp-Ser-Ser-Thr-Ser-Ala-Ala-OH and Diene-t_8. 643.2 nmol of maleimide−peptide and 214.4 nmol of crude diene-t_8 (3:1 ratio) were dissolved in a 1:1 (v/v) water/hexafluoroisopropanol mixture and reacted at 40 °C (diene-t_8 concentration in the reaction medium: 0.21 mM). The progress of the reaction was monitored by reversed-phase HPLC, showing a 36% conjugation yield after 24 h (Figure 2b). An additional 4 equiv of S-peptide was added, and the HPLC traces showed that the yield increased to 66% after 3 days and 89% after 4 days (Figure 2c,d, respectively). The t_8−S-peptide conjugate was purified by reversed-phase HPLC (same solvents as analysis conditions, 30 min gradient, Hamilton PRP-1 polystyrene−divinylbenzene column, 10 μm, 2 mL/min).

t_8−S-peptide: anal. HPLC (A: 0.045% trifluoroacetic acid in water, B: 0.036% trifluoroacetic acid in acetonitrile, linear gradient from 10% to 40% of B in 15 min, X-terra C18 column, 2.5 μm, 1 mL/min): t_R 9.2 min; MALDI-TOF MS (synapinic acid, positive mode, reflector): *m*/*z* 4571.30 $[M + H]^+$ (calc mass: 4570.92).

Formation of DNA−RNase and PNA−RNase Dimers and Monomers. The formation of DNA−RNase S dimers followed the procedures used previously to obtain RNase S dimers containing unmodified S-peptide (Figure 1) (*18*). S-protein, obtained from Sigma, was incubated in 40% (v/v) acetic acid/water at a concentration of 15 mg/mL for 1 h, and then the solution was lyophilized. The resulting dry powder was redissolved in a solution containing an excess of the $(dT)_n$−S-peptide conjugate or t_8−S-peptide conjugate and 0.20 M sodium phosphate buffer (pH 6.7). The mixture of $(dT)_n$−RNase S dimers, $(dT)_n$−RNase S monomers, and the excess $(dT)_n$−S-peptide conjugate (or t_8−RNase S dimer, monomer, and excess t_8−S-peptide conjugate) were separated by gel filtration chromatography using a Superdex 75 column on an Amersham Biosystems ÄKTA FPLC system.

Assays for Enzymatic Activity. To assess the sequence specificity of cleavage, RNAs were purchased from Dharmacon RNA Technologies (2′OH form, purified and desalted). The names and sequences of the RNAs are

Substrate 1: 5′-GGCGGCGGAAAAAAAAGGCGGCGG-3′
Substrate 2: 5′-CCGCCGCCUUUUUUUUCCGCCGCC-3′
Control 1: 5′-GGCGGCGGAUAUAUAUGGCGGCGG-3′
Control 2: 5′-CCGCCGCCUAUAUAUACCGCCGCC-3′

These sequences were chosen so that the "substrate RNAs" would contain a segment (eight consecutive As) that is complementary to the stretch of eight Ts in the conjugate. Whereas the "control dsRNAs" have the same overall G + C: A + U ratio as the "substrate dsRNAs", the As and Us alternate so that it is not expected that this RNA will be recognized by the conjugate. The sequences were designed to avoid hairpin or homoduplex formation. GC-rich segments are placed at termini to minimize fraying when substrate 1 and substrate 2 or control 1 and control 2 are combined to form double-stranded RNA. To test the importance of a single stranded region within a dsRNA for efficient cleavage by RNase A species, the central region of substrate dsRNA is complementary, whereas that of control dsRNA is not.

RNase activity against single-stranded RNAs was measured using the Kunitz assay (*30*). The Kunitz spectroscopic assay is based on the blue shift in the ultraviolet spectrum of single-stranded RNA upon hydrolysis at pH 5, which produces a decreased absorbance at 300 nm. This assay was also used to monitor the hydrolysis of *Saccharomyces cerevisiae* RNA, product no. R6750 from Sigma, which is a purification of all RNA species in yeast. It contains mainly rRNA and tRNA species, which are rich in single-stranded regions, but also possess some double-stranded regions.

The hydrolysis of the double-stranded, sequence-specific substrate and control RNAs, and of synthetic, double-stranded

Table 1. Activity of RNase A Monomer and C-Dimer against Specific Target RNAs[a]

enzyme species	substrate	specific activity
RNase A	substrate 1	110
RNase A	substrate 2	940
RNase A	control 1	250
RNase A	control 2	4600
RNase A	substrate dsRNA[b]	0.058
RNase A C-dimer	substrate dsRNA	0.46
RNase A	control dsRNA	110
RNase A C-dimer	control dsRNA	540

[a] RNA sequences:

```
Substrate 1: 5′-GGCGGCGGAAAAAAAAGGCGGCGG-3′
Substrate 2: 5′-CCGCCGCCUUUUUUUUCCGCCGCC-3′
  Control 1: 5′-GGCGGCGGAUAUAUAUGGCGGCGG-3′
  Control 2: 5′-CCGCCGCCUAUAUAUACCGCCGCC-3′
```

[b] Whereas double-stranded substrate RNA is fully complementary, control double-stranded RNA contains a central single-stranded "bubble" region:

```
Substrate dsRNA:  5′-GGCGGCGGAAAAAAAAGGCGGCGG-3′
                  3′-CCGCCGCCUUUUUUUUCCGCCGCC-5′

                                AUAUAUAU
Control dsRNA:    5′-GGCGGCGG         GGCGGCGG-3′
                  3′-CCGCCGCC         CCGCCGCC-5′
                                AUAUAUAU
```

Table 2. Activity of RNase and Conjugated RNase Species against Yeast ssRNA and ds poly(A)·poly(U)[a]

enzyme species	specific activity on yeast ssRNA	specific activity on dsRNA poly(A)·poly(U)
RNase A	100	1.4
RNase S	115	1.4
RNase A C-dimer	79	7.6[b]
$(dT)_8$-RNase S	92	0.06
$(dT)_{15}$-RNase S	93	0.23
$[(dT)_8$-RNase S$]_2$	82	0.10
S-protein	<0.02	<0.02
t_8 - S-peptide	<0.02	0[c]
t_8-RNase S	111	1.6
$[t_8$-RNase S$]_2$	185	10.5

[a] The assays were conducted at 28 °C using 5 μg of RNase moiety per mL of enzyme species. The experimental uncertainties are ±10% (ssRNA) and ±15% (dsRNA). [b] The RNase A C-dimer and RNase S dimer have highly similar activities against poly(A)·poly(U). [c] The t_8−S-peptide induces spectral changes in poly(A)·poly(U), which appears to reflect the formation of a complex, but does not seem to be due to cleavage. See text for more details.

RNA substrate poly(A)·poly(U) was assessed using the method of Libonati and Sorrentino at neutral pH (*31*). In this assay, ribonucleolytic activity is detected as an increased absorbance at 260 nm, due to the reduced hypochromism of cleaved dsRNA. Typically, reactions were initiated by adding RNase species (1 μg of ribonuclease moiety) to a buffered RNA solution (200 μL), mixing, and then recording the absorbance change at 300 or 260 nm. The summarized results presented in Tables 1 and 2 represent the average of at least two independent experiments. Both RNA substrates were obtained from Sigma, and the data were acquired on a temperature-regulated Shimadzu UV-2100 UV/vis spectrometer interfaced to a PC. Additional assays were performed and monitored using denaturing (8 M urea) 20% polyacrylamide gel electrophoresis. Gels were stained with toluidine blue to detect nucleic acids. After mixing RNase species (0.10 to 0.30 fmol) and target RNA (10 to 200 pmol), aliquots were withdrawn after certain times and the reaction was stopped by adding SDS (final concentration = 2.5%). The size of the RNA fragments generated by cleavage was gauged using standard-length single-stranded DNA oligos containing 4, 8, 12, 16, 20, and 24 bases. RNA fragments smaller than 4 bases are undetectable. These DNA oligos were ordered from Isogen and have base composition of G = A = T = C = 25% and sequences which were designed to avoid stem loop formation.

Nuclear Magnetic Resonance Spectroscopy. NMR spectra were acquired on a Bruker Advance spectrometer operating at 800 MHz and equipped with a quadruple resonance probe, at 25 °C in neutral pH buffer (100 mM MOPS, 200 mM NaCl) containing 90% H_2O and 10% D_2O. The spectra were transformed, analyzed, and integrated using the Bruker TOPSPIN software.

RESULTS AND DISCUSSION

Formation of DNA− and PNA−RNase Conjugates. S-peptide was conjugated to $(dT)_8$ or $(dT)_{15}$ 2′-oligodeoxyribonucleotides (Figure 3a) or t_8 PNA (Figure 3b) using the Diels–Alder cycloaddition reaction in aqueous solution (*28*). This reaction, unlike conjugates of DNA and S-peptide prepared using disulfide bond formation (*19*), has the advantage of producing a link that is stable in reducing environments such as the interior of living cells. Although a t_8−S-peptide conjugate could have been prepared by stepwise solid-phase assembly, the Diels–Alder methodology was always used to obtain conjugates with the same linkage between the two moieties, in order to avoid possible activity differences which might arise from a different linkage. The overall synthesis yields were: diene−dT_8 39%; diene−dT_{15} 21%; dT_8−S-peptide 60%; dT_{15}−S-peptide 62%, diene−t_8 29%; t_8−S-peptide 18%. DNA- or PNA-conjugated RNase S dimers were formed by adding the $(dT)_n$−S-peptide conjugate or t_8−S-peptide conjugate in 0.20 M sodium phosphate buffer (pH 6.7) to S-protein that had been dimerized by lyophilization from 40% aq acetic acid. DNA conjugated RNase S monomers and dimers were separated from the free DNA−S-conjugate by gel filtration chromatography (Figure 3c). The yield of RNase S dimer to monomer (1.0:3.0) was similar to that obtained when native S-peptide is used (*18*). A similar chromatogram was observed for the isolation of PNA conjugates of dimeric and monomeric RNase S, though a lower dimer/monomer ratio was obtained (Figure 3d). An excess of S-peptide was previously observed to decrease RNase S dimer disassociation (*18*). The lower yield of t_8−RNase S dimer relative to its monomer (1.0:9.0) is likely due to greater dissociation of the dimer during purification, due to a smaller excess of t_8−S-peptide conjugate.

NMR Characterization of $(dT)_n$−RNase Conjugates. NMR spectroscopy was used to gain insight into how the conjugation of a DNA strand affected the structural properties of the RNase S. ^{1}H NMR spectra of the monomer of RNase S and its $(dT)_8$ conjugate were recorded and analyzed. The polypeptide resonances, as revealed by 1D ^{1}H and 2D ^{1}H NOESY spectra, are essentially equivalent in RNase S as compared to $(dT)_8$-conjugated RNase S (data not shown). This indicates that the tertiary structure of the RNase S moiety is practically identical to that of the unmodified protein. The thymidine resonances in the complex are very poorly dispersed. As can be seen in Figure 4a, all H6 protons are clustered close together around 7.7 ppm and the H1′ around 6.3 ppm. All the thymidine methyls and H2′/H2″ protons lie at virtually identical chemical shifts. No ^{1}H NOE signals between the thymidine and the polypeptide moieties of RNase S were observed. This suggests that the thymidine bases of the DNA moiety are mainly disordered and do not adopt a particular conformation on the surface of the protein. This is an interesting result, since thymine bases might enter into the active site and inhibit the enzyme, as occurs in many ribonuclease complexes with mono- and dinucleotides (*32,33*).

Although ^{1}H NMR spectra indicate that oligonucleotide conjugation does not affect appreciably the structure of the

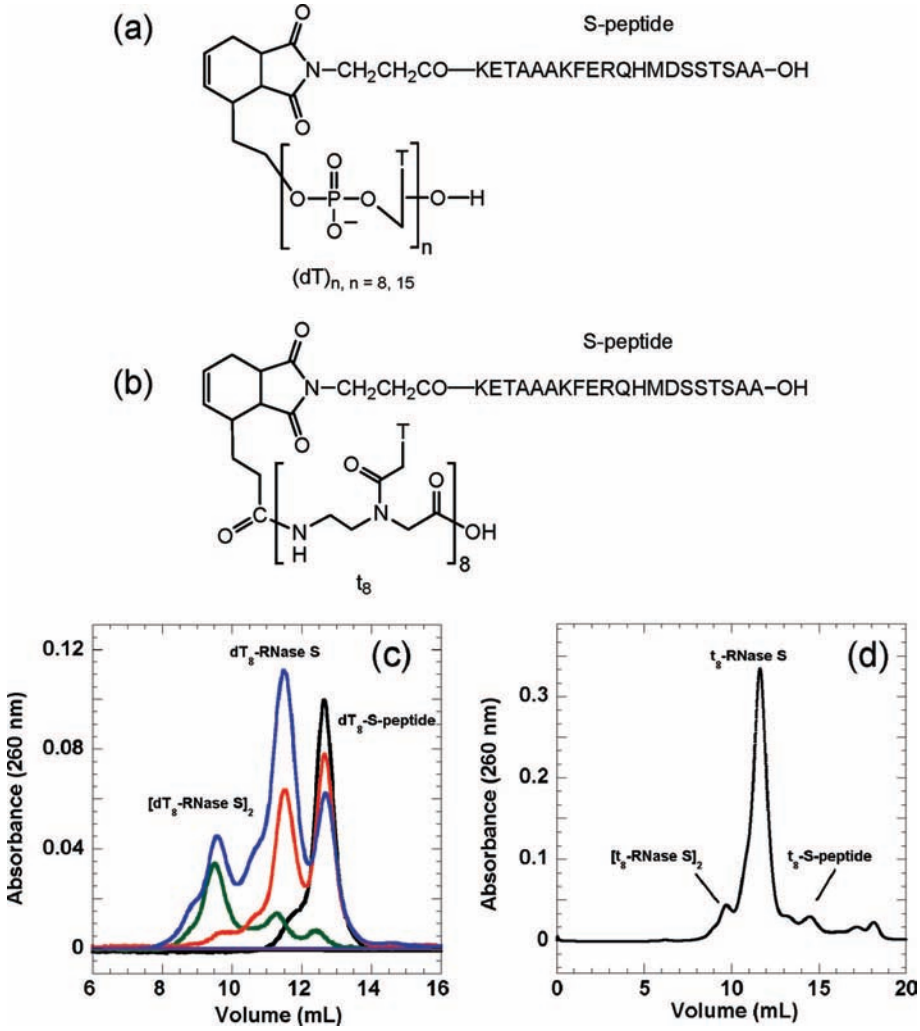

Figure 3. Structures of the oligothymine−S-peptide conjugates, showing the linkage between the S-peptide and the oligonucleotide (a) and the PNA (b) chains. c. Gel filtration chromatograms of $(dT)_8$−S-peptide conjugate (black curve), $(dT)_8$−RNase monomer (red curve), $(dT)_8$−RNase S dimer (blue curve), and reinjection of the purified $(dT)_8$−RNase S dimer (green curve). d. Gel filtration chromatogram revealing the separation of t_8−RNase S dimers, t_8−RNase S monomers, and free t_8−S-peptide conjugate, as indicated.

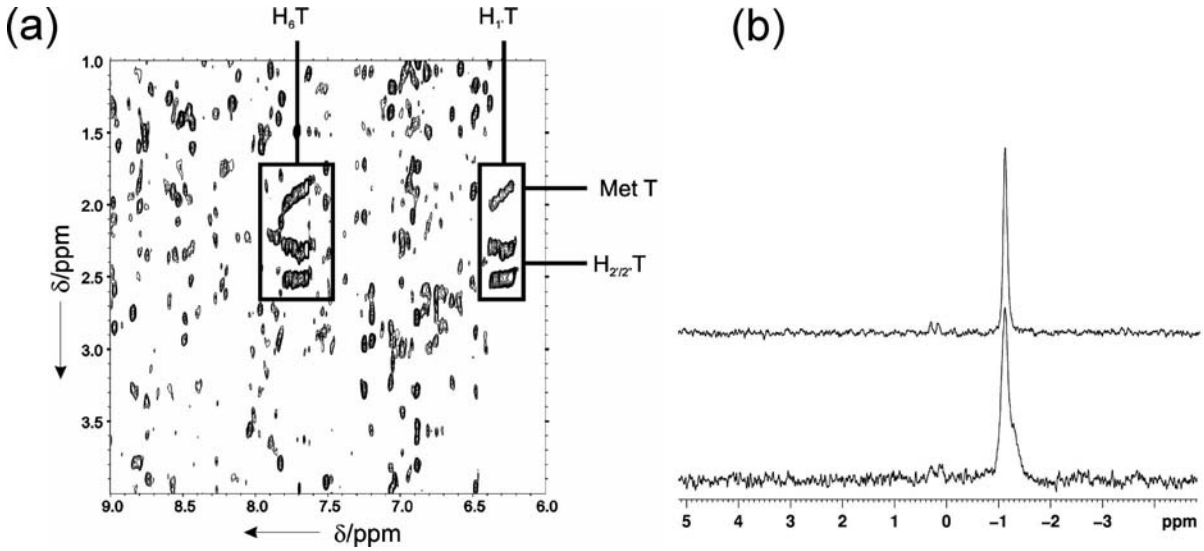

Figure 4. NMR characterization of the $(dT)_8$−RNase S conjugate. a. 2D ^{1}H NOESY NMR spectrum (180 ms mixing time) of the DNA−RNase S conjugate. Met T refers to the thymidine methyl groups. b. 1D ^{31}P NMR spectra of $(dT)_{15}$−S-peptide conjugate, alone (top) and bound to S-protein to form DNA RNase S conjugate (bottom).

enzyme, some evidence of interaction between the oligonucleotide and S-protein moieties of the complex could be detected by ^{31}P NMR (Figure 4b). The $(dT)_{15}$−S-peptide spectrum shows one major peak, arising from phosphorus nuclei in phosphodi-

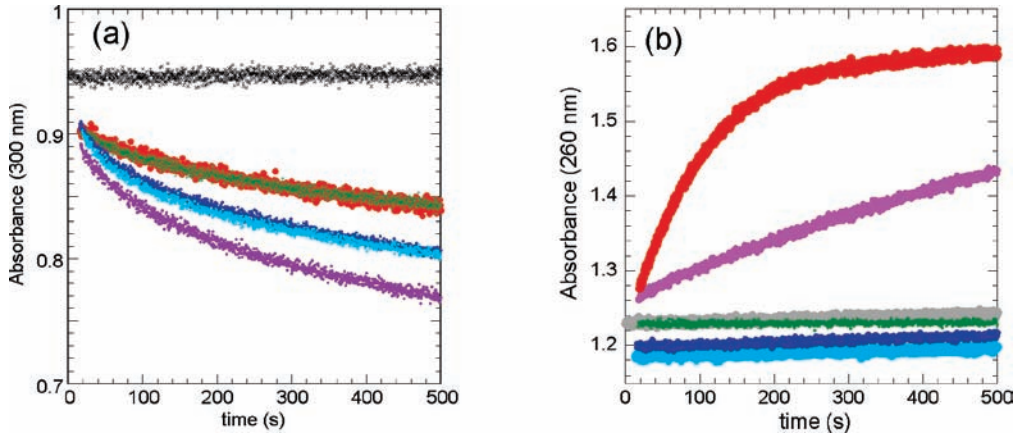

Figure 5. Activity of $(dT)_n$−RNase conjugates. a. Representative assays for ribonucleolytic activity against ssRNA at 28 °C. Data were offset vertically for ease of comparison. "x" ssRNA alone, red RNase A C-dimer, green $(dT)_{15}$−RNase S monomer, dark blue $(dT)_8$−RNase S dimer, light blue $(dT)_8$−RNase S monomer, purple RNase A monomer. b. Typical assay results for hydrolysis of poly(A)·poly(U) RNA at 28 °C. gray poly(A)·poly(U) alone, red RNase A C-dimer, green $(dT)_{15}$−RNase S monomer, dark blue $(dT)_8$−RNase S dimer, light blue $(dT)_8$−RNase S monomer, purple RNase A monomer.

ester bonds, and two small signals which could arise from the 5′- and 3′-terminal phosphorus nuclei. Upon binding to S-protein, the ^{31}P resonances of the $(dT)_{15}$−S-peptide conjugate broaden. This likely reflects a slower tumbling time for the bound conjugate. In addition, the major peak acquires a shoulder that contains five to six phosphate groups, as estimated by peak integration. This shoulder could arise from the interaction of phosphate groups with positively charged residues in the protein moiety. The charged residues involved are probably a subset of the residues; namely, K7, K31, K33, K39, K41, K66, R85, K91, and K98, in monomeric RNase A, which were observed to interact with polydeoxyadenosine by X-ray crystallography (*20*). The ^{1}H and ^{31}P NMR data suggest that the DNA chain does not bind at the active site but does affect the electrostatic environment around the protein, possibly screening the positive charges necessary for efficient cleavage of dsRNA.

Activity of RNase Species Against Sequence-Specific RNAs. Using the Kunitz assay, the activity of monomeric RNase A toward the sequence-specific substrates was found to vary in the order (from highest to lowest activity) control 2> sustrate 2> control 1> substrate 1 (Table 1). The lower activity of monomeric RNase A for substrate 1 is consistent with the fact that the enzyme is specific for a pyrimidine base 5′ to the scissile bond; therefore, the stretch of 8 consecutive As in the center of the sequence should be relatively resistant to hydrolysis catalyzed by RNase A. To investigate this point in more detail, we also monitored the activity of monomeric RNase A against the specific target RNAs using denaturing polyacrylamide gel electrophoresis. Substrate 2 and control 2 RNAs were degraded within 30 s and control 1 RNA was hydrolyzed within several minutes, whereas substrate 1 RNA was slowly cleaved over 15–25 min time, producing fragments containing 14 to 20 bases (Supporting Information Figure 1). These 14 to 20 base fragments could well contain the poly(A) stretch of substrate 1. Additional gel-monitored assays of the activity of the monomeric t_8−RNase S conjugate on single-stranded substrate 1, substrate 2, and control 2 RNAs were performed and revealed relative activities of control 2> substrate 2 ≈ substrate 1.

Next, equimolar amounts of substrate 1 and substrate 2 RNAs were combined to form a double-stranded RNA. Likewise, equimolar amounts of control 1 and control 2 were combined to form a dsRNA containing an internal single-stranded region. The activity of RNase A and the RNase A C-dimer on the sequence-specific substrate and control dsRNAs was determined (Table 1). The RNase A C-dimer was 8.0 and 4.8 times more active than monomeric RNase A on substrate and control dsRNAs, respectively. Both enzymes are more than a thousand times more active on control RNA than on the substrate RNA, which strikingly illustrates the importance of small single-stranded regions for efficient cleavage of a dsRNA by RNase A. This validates our approach (Figure 1) to increase dsRNA cleavage by designing a RNase conjugate that can recognize and stabilize transient ssRNA regions within dsRNA.

Activity of $(dT)_n$−RNase Conjugates Against ssRNA. The ribonucleolytic activity of the $(dT)_n$-RNase conjugates was tested against yeast ssRNA; some typical data are shown in Figure 5a. The $(dT)_8$−RNase S dimer and monomer conjugates were slightly less active against yeast ssRNA (Table 2) than the unmodified dimer and monomer, as determined using the Kunitz assay (*30*). The substantial catalytic activity of $(dT)_n$−RNase conjugates against ssRNA indicates that the DNA moiety neither blocks the active site nor inhibits the ribonucleolytic action of the enzyme. The lower activity of unconjugated dimers relative to monomers toward ssRNA has been described previously (*10*). Neither the S-protein nor the $(dT)_8$−S-peptide conjugate exhibited any significant activity against ssRNA.

Activity of $(dT)_n$−RNase Conjugates Against dsRNA. The cleavage of the double-stranded RNA poly(A)·poly(U) was gauged following the protocol of Libonati and Sorrentino (*31*). In a control experiment, the RNase A C-dimer activity was first tested against the poly(A)·poly(U), and the results were in agreement with those reported previously (Figure 5b). In contrast, the activity of the DNA−RNase S dimer conjugate against poly(A)·poly(U) was reduced to background levels. One hypothesis that can account for these results is that the negative charges in the DNA moiety could be interacting with the positive charges on the surface of RNase S that are required for efficient cleavage of dsRNA, as suggested by the NMR results (see above).

Activity of the t_8−RNase Conjugates Against ssRNA. The enzymatic activity of t_8−RNase conjugates against ssRNA was evaluated using the Kunitz assay. Some representative data are shown in Figure 6a, and the average results are given alongside those of the $(dT)_n$−RNase conjugates in Table 2. The S-protein alone and the t_8−S-peptide conjugate alone show negligible activity. As seen previously, both monomeric RNase A (100) and RNase S (115) are highly active against ssRNA, while the RNase A C-dimer (79) is somewhat less active. The activity of the t_8−RNase S monomer (111) is similar to that of the RNases A and S and higher than that of the $(dT)_n$−RNase S conjugates.

Interestingly, the t_8−RNase S dimer shows a remarkably high activity (185). Natural RNase A cleaves polypyrimidine chains

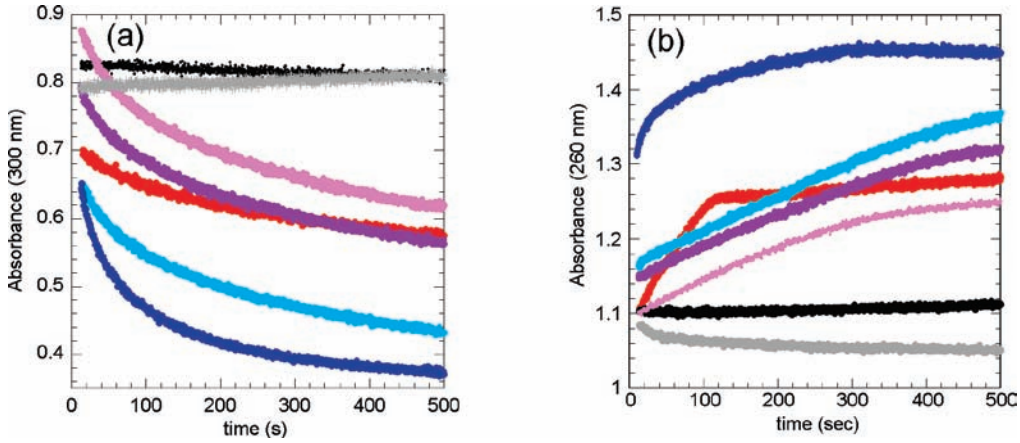

Figure 6. Activity of t_8−RNase Conjugates. a. Typical assay results for hydrolysis of yeast ssRNA at 28 °C by t_8−RNase conjugates and control species: black S-protein alone, gray t_8−S-peptide, fuschia RNase S monomer, magenta RNase A monomer, red RNase A C-dimer, light blue t_8−RNase monomer, dark blue t_8−RNase dimer. b. Libonati−Sorrentino assay for hydrolysis of poly(A)·poly(U) at 28 °C by t_8−RNase conjugates and control species. black S-protein alone, gray t_8−S-peptide, fuschia RNase S monomer, magenta RNase A monomer, red RNase A C-dimer, light blue t_8−RNase monomer, dark blue t_8−RNase dimer.

in a distributive manner; that is, it binds RNA, cleaves RNA, and then releases RNA before rebinding and recleaving the resulting fragments (*34*). In contrast, progressive enzymes, such as DNA polymerase, bind a polymeric substrate and catalyze multiple reactions before releasing it. The increased ssRNase activity shown by the t_8−RNase S dimer could possibly arise from an increased progressivity due to binding of the t_8 moiety to short complementary sequences within the ssRNA, which acts to maintain the hydrolyzed fragments near the active site.

Activity of the t_8−RNase Conjugates Against dsRNA. Some representative assays of t_8−RNase activity against poly(A)·poly(U) are depicted in Figure 6b, and the mean specific activity values are summarized in Table 2. As expected, the S-protein fragment alone shows little or no activity. A curious decrease in the absorbance reading at 260 nm occurs when the t_8−S-peptide molecule is added to the dsRNA substrate. This decrease might arise from a stabilization of the double-stranded structure of poly(A)·poly(U) by positive charges in the S-peptide moiety or from the formation of a complex between the dsRNA and the t_8 moiety, or both. Unconjugated and monomeric RNase S and RNase A show modest activity when assayed against dsRNA; the calculated specific activity value is 1.4. The t_8−RNase S monomer, in contrast to the corresponding DNA conjugate which is essentially inactive (see above), shows a specific activity value of 1.6 toward dsRNA, which is similar to the activity of monomeric RNase A or RNase S.

As observed previously, the RNase A C-dimer shows a much higher activity against dsRNA (specific activity = 7.6) as compared to monomeric RNase A or S. Interestingly, the t_8−RNase S conjugate dimer shows a specific activity of 10.5, which is marginally higher than the activity shown by the RNase A C-dimer. To test if the enhanced activity of the t_8−RNase S conjugate dimer against poly(A)·poly(U) is due to its dimeric state, an aliquot was heated to 53 °C for 15 min, then allowed to cool to room temperature. This heat treatment, which is known to completely monomerize RNase S dimers (*18*), reduced the dsRNase activity to levels typical of monomeric species. As noted in the Experimental Procedures section, aliquots of t_8−RNase S conjugate dimer always contained an excess of free t_8−S-peptide to maintain the stability of the quaternary complex. If this excess free conjugate were to form a complex with the poly(A)·poly(U) substrate, it might displace a single-stranded segment of the poly(U) substrate. As single-stranded poly(U) is a good substrate for RNase A, it is possible that the enhanced activity of the t_8−RNase S dimer conjugate might be due to the presence of the excess free t_8−S-peptide conjugate, rather than the complex. To check this possibility, assays were performed with monomeric RNase A and C-dimer in the presence of excess free t_8−S-peptide. For monomeric RNase A and the C-dimer, the presence of excess free t_8−S-peptide increased the activity against dsRNA by about 35% and 10%, respectively, with the latter value being within the threshold of the experimental uncertainty. Taken together, these results suggest that the increased dsRNase activity of t_8−RNase S conjugate dimer is not due the excess t_8−S-peptide but arises from the combination of the dimeric state of the RNase with conjugation to t_8.

The observation of hydrolysis of poly(A)·poly(U) in the t_8−RNase S conjugate monomer and dimer supports the idea that negative charges in the DNA conjugate do indeed screen the positive charges in RNase that are essential for cleavage of dsRNA.

CONCLUSIONS

Some novel conclusions can be drawn from the results reported here. Ribonuclease S monomers and dimers conjugated to $(dT)_{8 \text{ or } 15}$ (DNA) or t_8 (PNA) have been prepared, and their ability to cleave ssRNA and dsRNA has been determined. Conjugation to DNA essentially completely impedes the cleavage of dsRNA. However, conjugation to PNA endows dimeric RNase with enhanced activity against both ssRNA and dsRNA, although the increase is marginal in the latter case. Since conjugation does not affect the structure of the protein moiety, as shown by NMR spectroscopy and the observation of activity against ssRNA, we conclude that the inhibition of dsRNA hydrolysis provoked by the DNA conjugation is due to interactions between the negative charges on the DNA moiety and positive charges on the surface of RNase, which have previously been implicated in efficient hydrolysis of dsRNA. Therefore, our results show that PNA conjugation to RNase offers clear advantages over DNA conjugation as an approach to modulating ribonucleolytic activity.

ACKNOWLEDGMENT

This work was supported by grants CTQ2004-08275 and 2005SGR-693, and the Centre de Referència de Biotecnologia. We thank Profs. M. Rico and J. Santoro Said for additional support (MEyC GEN2003-20642-C09-03 and BIO2002-00720, respectively) and the latter for implementation of NMR pulse sequences. D.P. thanks a fellowship from the Spanish Ministry

of Education. J.P.L.A. gratefully acknowledges a fellowship from the Consejería de Educación de la Comunidad de Madrid y el Fondo Social Europeo. D.V.L. was a "Ramón y Cajal" Fellow. We are deeply indebted to Dr. M. Menéndez for lending equipment, to Dr. José Manuel Pérez Cañadillas for his expert advice on RNA electrophoresis and to Prof. M. Libonati for critically reading the manuscript.

Supporting Information Available: One figure showing representative gels of RNase catalyzed hydrolysis of sequence-specific RNAs. This material is available free of charge via the Internet at http://pubs.acs.org.

LITERATURE CITED

(1) Guerrier-Takada, C., Gardiner, K., Marsh, T., Pace, N., and Altman, S. (1983) The RNA moiety of RNase P is the catalytic subunit of the enzyme. *Cell 35*, 849–857.

(2) Zaug, A. J., and Cech, T. R. (1986) The intervening sequence RNA of tetrahymena is an enzyme. *Science 231*, 470–475.

(3) Fire, A., Xu, S., Montgomery, M. K., Kostas, S. A., Driver, S. E., and Mello, C. C. (1998) Potent and specific genetic interference by double-stranded RNA in *Caenorhabditis elegans*. *Nature 391*, 806–811.

(4) Filipowicz, W. (2005) RNAi: the nuts and bolts of the RISC machine. *Cell 122*, 17–20.

(5) Beloglazova, N. G., Fabani, M., Bichenkova, E. V., Polushin, N. N., Sil'nikov, V. V., Douglas, K. T., and Vlassov, V. V. (2004) Sequence-specific artificial ribonucleases. I. Bis-imidazole-containing oligonucleotide conjugates prepared using precursor-based strategy. *Nucleic Acids Res. 32*, 3887–3897.

(6) Bashkin, J. K., Frolova, E. I., and Sampath, U. S. (1994) Sequence-specific cleavage of HIV mRNA by a ribozyme mimic. *J. Am. Chem. Soc. 116*, 5981–5982.

(7) Hall, J., Hüsken, D., and Häner, R. (1996) Towards artificial ribonucleases: the sequence-specific cleavage of RNA in a duplex. *Nucleic Acids Res. 24*, 3522–3526.

(8) Leland, P. A., and Raines, R. T. (2001) Cancer chemotherapy-ribonucleases to the rescue. *Chem. Biol. 8*, 405–413.

(9) Matousek, J., Gotte, G., Pouckova, P., Soucek, J., Slavik, T., Vottariello, F., and Libonati, M. (2003) Antitumor and other biological actions of oligomers of ribonuclease A. *J. Biol. Chem. 278*, 23817–23822.

(10) Libonati, M., and Gotte, G. (2004) Oligomerization of bovine ribonuclease A: Structural and functional features of its multimers. *Biochem. J. 380*, 311–327.

(11) Richards, F. M., and Vithayathil, P. J. (1959) The preparation of subtilisin-modified ribonuclease and the separation of the peptide and protein components. *J. Biol. Chem. 234*, 1459–1465.

(12) Varadarajan, R., and Richards, F. M. (1992) Crystallographic structures of Ribonuclease S variants with nonpolar substitution at position 13: packing and cavities. *Biochemistry 31*, 12315–12327.

(13) Thomson, J., Ratnaparkhi, G. S., Varadarajan, R., Sturtevant, J. M., and Richards, F. M. (1994) Thermodynamic and structural consequences of changing a sulfur atom to a methylene group in the M13Nle mutation in Ribonuclease S. *Biochemistry 33*, 8587–8593.

(14) Goldberg, J. M., and Baldwin, R. L. (1998) Kinetic mechanism of a partial folding reaction: 1. Properties of the reaction and effects of denaturants. *Biochemistry 37*, 2546–2555.

(15) Nogués, M. V., Vilanova, M., and Cuchillo, C. M. (1995) Bovine pancreatic ribonuclease A as a model of an enzyme with multiple substrate binding sites. *Biochim. Biophys. Acta 1253*, 16–24.

(16) Raines, R. T. (1998) Ribonuclease A. *Chem. Rev. 98*, 1045–1065.

(17) Libonati, M, and Sorrentino, S. (1992) Revisiting the action of bovine ribonuclease A and pancreatic-type ribonucleases on double-stranded RNA. *Mol. Cell. Biochem. 117*, 139–151.

(18) López-Alonso, J. P., Bruix, M., Ribó, M., Vilanova, M., Rico, M., Gotte, G., Libonati, M., González, C., and Laurents, D. V. (2006) Formation, structure and dissociation of the RNase S three-dimensional domain-swapped dimer. *J. Biol. Chem. 281*, 9400–9406.

(19) Zuckermann, R. N., and Schultz, P. G. (1988) A hybrid sequence-selective ribonuclease S. *J. Am. Chem. Soc. 110*, 6592–6594.

(20) McPherson, A., Brayer, G., Cascio, D., and Williams, R. (1986) The mechanism of binding of a polynucleotide chain to pancreatic ribonuclease. *Science 232*, 765–768.

(21) Sorrentino, S., Naddeo, M., Russo, A., and D'Alessio, G. (2003) Degradation of double-stranded RNA by human pancreatic ribonuclease: crucial role of noncatalytic basic amino acid residues. *Biochemistry 42*, 10182–10190.

(22) Uhlmann, E., Peyman, A., Breipohl, G., and Will, D. W. (1998) PNA: Synthetic polyamide nucleic acids with unusual binding properties. *Angew. Chem., Int. Ed. 37*, 2796–2823.

(23) Lohse, J., Nielsen, P. E., Harrit, N., and Dahl, O. (1997) Fluorescein-conjugated lysine monomers for solid phase synthesis of fluorescent peptides and PNA oligomers. *Bioconjugate Chem. 8*, 503–509.

(24) Kozlov, I. A., Nielsen, P. E., and Orgel, L. E. (1998) A method for the ^{32}P labeling of peptides or peptide nucleic acid oligomers. *Bioconjugate Chem. 9*, 415–417.

(25) Mokhir, A. A., and Kraemer, R. (2003) Conjugates of PNA with naphthalene diimide derivatives having a broad range of DNA affinities. *Bioconjugate Chem. 14*, 877–883.

(26) Muratovska, A., Lightowers, R. N., Taylor, R. W., Turnbull, D. M., Smith, R. A., Wilce, J. A., Martin, S. W, and Murphy, M. P. (2001) Targeting peptide nucleic acid (PNA) oligomers to mitochondria within cells by conjugation to lipophilic cations: implications for mitochondrial DNA replication, expression and disease. *Nucleic Acids Res. 29*, 1852–1863.

(27) Hamzavi, R., Dolle, F., Tavitian, B., Dahl, O., and Nielsen, P. E. (2003) Modulation of the pharmacokinetic properties of PNA: Preparation of galactosyl, mannosyl, fucosyl, N-acetylgalactosaminyl, and N-acetylglucosaminyl derivatives of aminoethylglycine peptide nucleic acid monomers and their incorporation into PNA oligomers. *Bioconjugate Chem. 14*, 941–954.

(28) Marchán, V., Ortega, S., Pulido, D., Pedroso, E., and Grandas, A. (2006) Diels-Alder cycloadditions in water for the straightforward preparation of peptide-oligonucleotide conjugates. *Nucleic Acids Res. 34*, e24.

(29) Baillie, L. C., Batsanov, A., Bearder, J. R., and Whiting, D. A. (1998) Synthesis of the A/E/F sections of conaconitine, napelline and related diterpenoid alkaloids of the aconitine group. *J. Chem. Soc., Perkin Trans. 1*, 3471–3478.

(30) Kunitz, M. (1946) A spectrophotometric method for the measurement of ribonuclease activity. *J. Biol. Chem. 164*, 563–568.

(31) Libonati, M., and Sorrentino, S. (2001) Degradation of double-stranded RNA by mammalian pancreatic-type ribonucleases. *Methods Enzymol. 341*, 234–248.

(32) Toiron, C., González, C., Bruix, M., and Rico, M. (1996) Three-dimensional structure of the complexes of ribonuclease A with 2′,5′-CpA and 3′,5′-d(CpA) in aqueous solution, as obtained by NMR and restrained molecular dynamics. *Protein Sci. 5*, 1633–1647.

(33) Leonidas, D. D., Chavali, G. B., Oikonomakos, N. G., Chrysina, E. D., Kosmopoulou, M. N., Vlassi, M., Frankling, C., and Acharya, K. R. (2003) High-resolution crystal structures of ribonuclease A complexed with adenylic and uridylic nucleotide inhibitors. Implications for structure-based design of ribonucleolytic inhibitors. *Protein Sci. 12*, 2559–2574.

(34) delCardayré, S. B., and Raines, R. T. (1994) Structural determinants of enzymatic processivity. *Biochemistry 33*, 6031–6037.

BC700374Q

Modification of Different IgG1 Antibodies via Glutamine and Lysine using Bacterial and Human Tissue Transglutaminase

Thomas L. Mindt,[†] Vera Jungi,[†] Sara Wyss,[†] Alexandra Friedli,[‡] Gloria Pla,[§] Ilse Novak-Hofer,[‡] Jürgen Grünberg,[‡] and Roger Schibli*[,†,‡]

Department of Chemistry and Applied Biosciences of the ETH Zurich, 8093 Zurich, Switzerland, Center for Radiopharmaceutical Science ETH-PSI-USZ, Paul Scherrer Institute, 5232 Villigen, Switzerland, and Facultat de Farmàcia, Universitat de Barcelona, 08028 Barcelona, Spain. Received August 15, 2007; Revised Manuscript Received September 18, 2007

The modification of proteins by chemical methods is well-established, however usually difficult to control. In this paper, we describe the posttranslational modification of different IgGs via the Lys or Gln side chains catalyzed by bacterial and human tissue transglutaminase (BTGase and TG2). For proof of concept, different IgG1s (commercial bovine IgG1, and L1CAM targeting chCE7 and $chCE7_{aglycosylated}$) were enzymatically functionalization with different fluorescent TGase substrates based on the CY3 analogue Dy547. The optimal reaction conditions were determined in order to assess the two enzymes. The efficiency of the enzymatic method was also compared with a standard chemical method employing a reactive NHS ester of Dy547. Three new TGase substrates were synthesized for this study including Lys–substrate **1** useful for BTGase and TG2 and two Gln–substrates tailor-made for BTGase (substrate **2**) and TG2 (substrate **3**). Of the two TGases tested, BTGase incorporated Lys–substrate **1** more efficiently than TG2. On the other hand, both enzymes reacted equally efficiently with the corresponding Gln–substrates **2** and **3**. Reproducible labeling could be achieved in a broad concentration "window" of the substrates (up to 400 μM) without the risk of overlabeling of chCE7 or $chCE7_{aglycosylated}$. The biological activities of the functionalized antibodies were unaltered as shown by in vitro antigen affinity measurements and cell internalization experiments using confocal laser scanning microscopy. A maximum label-to-protein ratio of approximately 1 was achieved with $chCE7_{aglycosylated}$ and substrate **1** using BTGase. It is important to recognize that the enzymatic activity of TGases enables the stable functionalization of proteins via the side chains of Gln, which is not possible by any chemical method available today. In addition, we could prove that the enzymatic modification of all antibodies occurred selectively at the heavy chain whereas the chemical method led to labeling of both the heavy and the light chains.

INTRODUCTION

The functionalization of antibodies for the imaging of molecular processes as well as for diagnostic and therapeutic applications is an integral part of biochemical and biomedical research. Today, the decoration of proteins with various probes of interest is predominantly achieved by applying chemical functionalization strategies (*1*–*3*). However, the modification of proteins by chemical methods is often difficult to control, and laborious optimizations are necessary to achieve reproducible results. Chemically reactive probes usually display a limited selectivity with respect to the different functional parts of an antibody (Fc, Fv region) and can attack at different amino acid side chains. Thus, the risk of heterogeneous modification and overlabeling is inherent. This can have deleterious effects on the biological activity of the protein (*4*, *5*).

Part of our research efforts focus on the development of radiometal-labeled antibodies for use in radio immunodiagnosis and therapy (RID/RIT). We are particularly interested in the antibody chCE7, a high-affinity, chimeric, and internalizing monoclonal antibody (IgG1) directed against the cell adhesion molecule L1 (L1-CAM), which is overexpressed by a number of cancer cells (*6*). Radiolabeled chCE7 and an aglycosylated form $chCE7_{agl}$ (as the result of the single-site mutation Asn297Gln) have shown promising characteristics for application in RIT. In radiolabeled form, optimal pharmacokinetics and high tumor accumulation were achieved with a moderate degree of functionalization of the antibodies with metal chelates (*7*, *8*). We have experienced that the modification of such proteins with a defined number of metal chelators is difficult to reproduce by conventional chemical labeling protocols (e.g., with NHS esters or isothiocyanates). Therefore, the development of alternative approaches for the controlled functionalization of proteins is of significant interest.

Enzymes of the family of transglutaminases (TGase, EC 2.3.2.13) catalyze the formation of stable isopeptidic bonds between the side chains of glutamine (Gln) and lysine (Lys), with the loss of ammonia (*9*). TGases have emerged as a powerful biotechnological tool for the modification of proteins. For example, TGases have been used for the attachment of small-molecule probes to proteins (*9*) and cell surfaces (*10*), and two examples of the enzymatic modification of antibodies have been reported (*11*, *12*). To date, most TGase applications have been carried out with bioengineered proteins presenting an accessible, TGase-recognizable peptide sequence at the N- or C-terminus which contains Lys-(K-tag) or Gln-(Q-tag) residues (see, e.g., ref (*13*)). Yet, a systematic investigation of TGase-mediated labeling of whole antibodies using both Lys- and Gln-substrates and different TGases has not been described.

The mild reaction conditions for protein modification are attractive features of TGases. In addition, employment of TGases is the only method, which allows the functionalization of

* Roger Schibli, Center for Radiopharmaceutical Science ETH-PSI-USZ, Telephone: +41-56-310-2837. Fax: +41-56-310-2849, E-mail address: roger.schibli@pharma.ethz.ch.

[†] ETH Zurich.

[‡] Paul Scherrer Institute.

[§] Universitat de Barcelona.

10.1021/bc700306n CCC: $40.75 © 2008 American Chemical Society
Published on Web 11/08/2007

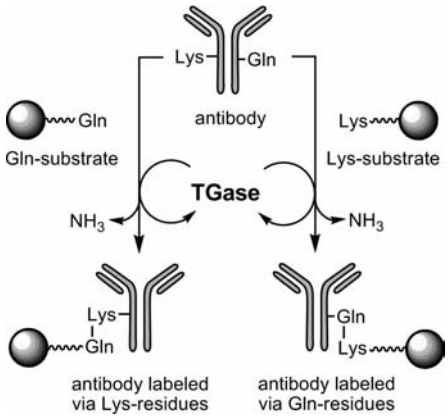

Figure 1. Schematic drawing of the TGase-mediated protein (antibody) modification via the side chains of Gln or Lys. Spheres represent various probes (e.g., fluorophores) to be attached to the protein, and squiggled lines symbolize different spacers.

proteins via the side chain of Gln, an amino acid not available for chemical modification. For proof of concept, we set out to investigate the utility of two different TGases to covalently attach a fluorescent probe (CY3 analogue) to antibodies in general and our chCE7 antibody formats in particular (Figure 1).

EXPERIMENTAL PROCEDURES

General Methods. Infrared spectra were recorded on a Jasco FT/IR-6200 ATR-IR and UV spectra on a Cary 300 (Varian). NMR spectra were recorded with a Bruker 400 MHz spectrometer with the corresponding solvent signals as an internal standard. Chemical shifts are reported in parts per million (ppm) relative to tetramethylsilane (0.00 ppm). Values of the coupling constant, *J*, are given in hertz (Hz). Low-resolution mass spectra (LR-MS) were recorded with a Micromass Quattro micro API LC-ESI and high-resolution mass spectra (HR-MS) with a Bruker FTMS 4.7T BioAPEXII (ESI). HPLC was performed on a Merck-Hitachi L-7000 system equipped with an L-7400 tunable absorption detector and an XTerra column (MSC18, 5μm, 4.6 × 150 mm, Waters). All HPLC were performed with the following solvent system: 0.1% TFA_{aq} (solvent A), acetonitrile (solvent B), 1 mL/min; 0–5 min, 95% A; 5–20 min, 95% → 40% A; 20–22 min, 40% → 10% A; 22–24 min, 10% A; 24–25 min, 10% → 95% A. Gel electrophoresis was performed with a mini-PROTEAN 3 Electrophoresis System (Bio-Rad) and EPS 600 power supply (Pharmacia Biotech). The gels (12% acrylamide) were analyzed with a Diana III Camera System (Ray test) using CY3 optical filters followed by computational analysis of the obtained pictures with the freeware SCION. Size exclusion chromatography was performed with the above-described HPLC system and a Superdex 200 10/300 GL column (cross-linked agarose und dextran, 13 μm, 1 × 30 cm, Amersham Biosciences) with PBS (0.15 M, pH 7.4, 0.44 mL/min, 45 min/run). Confocal data sets were sampled on a Zeiss LSM 510 META inverted microscope. Image processing was done with the *IMARIS* software (Bitplane AG, Zurich, Switzerland).

Recombinant bacterial transglutaminase (BTGase), recombinant His-tagged human transglutaminase 2 (TG2), ZGlnGly OPF **7**, and ZGlnGlnProLeu-Cadavarine **10** were purchased from N-Zyme BioTec GmbH and Dy547-NHS **4** from Dyomics. Antibodies chCE7 and $chCE7_{agl}$ were provided by the group of Dr. Ilse Novak-Hofer at the Paul Scherrer Institute, Villigen, Switzerland. HEK293 cells were obtained from the German Collection of Microorganisms and SKOV3ip human ovarian carcinoma cells were a gift from Prof. P. Altevogt (German Cancer Center, Heidelberg, Germany). Cell media and additives were obtained from BioConcept, goat antihuman IgG-FITC from LabForce, Moviol from Hoechst Pharmaceuticals, and pcDNA3.1+ and G418 from Invitrogen. All other chemicals and reagents were purchased from Sigma-Aldrich or Hänseler AG and used as supplied. Generation of transfected HEK293 cells with human L1-CAM antigen was performed according to the literature (*7*).

Chemical Syntheses.*Synthesis of Lys–Substrate, Cadavarine-DY547 (***1***).* To DY547-NHS **4** (1 mg, 1.35 μmol) were added at rt stock solutions of DIPEA (5.7 μmol in 20 μL DMF) and mono-Boc-protected cadaverine **5** (1.35 μmol in 82 μL DMF). The resulting solution was kept in the dark at rt overnight. The product was purified by HPLC, and the collected fractions containing the coupling product **6** were treated with TFA (10%) overnight at rt. Quantitative conversion of intermediate **6** to Lys–substrate **1**, cadavarine-DY547, was confirmed by HPLC. The solution was evaporated and the obtained red solid dissolved in a defined volume of buffer yielding a stock solution of Lys–substrate, cadavarine-DY547 (1) (52% yield by UV spectroscopy: $\lambda = 557$ nm, $d = 1$ cm, $\varepsilon = 150\,000\ M^{-1}\ cm^{-1}$): purity according to HPLC >96%; LR-MS $[M + H]^+ = 701.39$ (calcd for $C_{35}H_{49}N_4O_7S_2$: 701.30).

Synthesis of Compound **8.** Mono-Boc-protected cadaverine **5** (50 mg, 0.25 mmol) and ZGlnGly OPF **7** (126 mg, 0.25 mmol) were dissolved in dry DMF (3 mL) and DIPEA (215 μL, 1.24 mmol) was added at 0 °C. After 30 min, the reaction mixture was warmed to rt, stirred for additional 4 h, and evaporated under reduced pressure. Flash chromatography on silica gel with CH_2Cl_2/MeOH (9:1) yielded product **8** as a white powder (107 mg, 84%): mp 166–168 °C; IR (neat) υ 3302, 2934, 1681, 1637, 1531, 1240, 1169, 1047 cm^{-1}; ^1H NMR (DMSO-d_6) δ 8.17 (t, 1H, $J = 5.6$ Hz), 7.65 (t, 1H, $J = 5.3$ Hz), 7.57 (d, 1H, $J = 7.2$ Hz), 7.40–7.22 (m, 6H), 6.80–6.69 (m, 2H), 5.05 (d, 1H, $J = 12.7$ Hz), 5.01 (d, 1H, $J = 12.7$ Hz), 3.95 (dd, 1H, $J = 13.6$ und 7.3 Hz), 3.65 (d, 2H, $J = 5.48$ Hz), 3.10–2.94 (m, 2H), 2.95–2.80 (m, 2H), 2.17–2.04 (m, 2H), 1.95–1.83 (m, 1H), 1.80–1.64 (m, 1H), 1.44–1.27 (m, 4H), 1.36 (s, 9H), 1.27–1.10 (m, 2H) ppm; ^{13}C NMR (DMSO-d_6) δ 173.7, 171.9, 168.4, 156.1, 155.6, 136.9, 128.3, 127.8, 127.6, 77.3, 65.5, 54.6, 42.1, 39.7, 38.5, 31.4, 29.1, 28.7, 28.2, 27.3, 23.6 ppm; HR-MS $[M + Na]^+ = 544.2748$ (calcd for $C_{25}H_{39}N_5O_7Na$: 544.2742).

Synthesis of Compound **9.** Intermediate **8** (53 mg, 0.10 mmol) was dissolved in TFA/CH_2Cl_2 (1:3, 4 mL) and stirred at rt overnight. Evaporation under reduced pressure yielded the TFA salt of product **9** as a colorless oil (61 mg, 98%): IR (neat) υ 3288, 3198, 3073, 2940, 1667, 1541, 1456, 1258, 1205, 1133 cm^{-1}; ^1H NMR (MeOH-d_4) δ 7.40–7.25 (m, 5H), 5.13 (d, 1H, $J = 12.3$ Hz), 5.09 (d, 1H, $J = 12.7$ Hz), 4.06 (dd, 1H, $J = 8.2$ und 5.9 Hz), 3.85 (d, 1H, $J = 17.09$ Hz), 3.79 (d, 1H, $J = 16.6$ Hz), 3.28–3.10 (m, 2H), 2.90 (t, 2H, $J = 7.52$ Hz), 2.34 (t, 2H, $J = 7.5$ Hz), 2.14–2.03 (m, 1H), 2.03–1.90 (m, 1H), 1.70–1.58 (m, 2H), 1.58–1.48 (m, 2H), 1.43–1.31 (m, 2H) ppm; ^{13}C NMR (MeOH-d_4) δ 177.9, 175.29, 171.7, 158.96, 138.2, 129.7, 129.2, 128.9, 68.0, 56.8, 43.9, 40.7, 40.0, 32.6, 29.7, 28.5, 28.2, 24.6 ppm; HR-MS $[M]^+ = 422.2400$ (calcd for $C_{20}H_{32}N_5O_5$: 422.2398).

*Synthesis of BTGase Gln–Substrate, ZGlnGly Cadavarine-DY547 (***2***).* Stock solutions of intermediate **9** (1.35 μmol in 82 μL DMF) and DIPEA (5.7 μmol in 20 μL DMF) were added to Dy547-NHS **4** (1 mg, 1.35 μmol) at rt. The resulting red solution was kept in the dark at rt overnight. The mixture was purified by HPLC, and collected fractions containing product **2** were evaporated under reduced pressure. The obtained red solid was dissolved in a defined volume of buffer yielding a stock solution of BTGase Gln–substrate, ZGlnGly cadavarine-DY547 (**2**) (40% yield by UV spectroscopy: $\lambda = 557$ nm, $d = 1$ cm, ε

$= 150\,000\ M^{-1}\ cm^{-1}$): purity according to HPLC >96%; LR-MS $[M]^+ = 1020.17$ (calcd for $C_{50}H_{65}N_7O_{12}S_2$: 1020.22).

*Synthesis of TG2 Gln–Substrate, Z-GlnGlnProLeu-Cadavarine-DY547 (**3**).* Stock solutions of the TFA salt of ZGlnGlnProLeucadavarine **10** (1.3 μmol in 82 μL DMSO) and DIPEA (5.7 μmol in 20 μL DMSO) were added to DY547-NHS **4** (1 mg, 1.35 μmol) at rt. The resulting red solution was kept in the dark at rt overnight. The mixture was purified by HPLC, and collected fractions containing product **3** were evaporated under reduced pressure. The obtained red solid was dissolved in a defined volume of Tris buffer (0.15 M, pH 8) yielding a stock solution of TG2 Gln–substrate, ZGlnGlnProLeu-cadavarine-DY547 (**3**) (40% yield by UV spectroscopy: $\lambda =$ 557 nm, $d = 1$ cm, $\varepsilon = 150\,000\ M^{-1}\ cm^{-1}$): purity according to HPLC > 94%; HR-MS $[M+H]^+ = 1301.5939$ (calcd for $C_{64}H_{89}N_{10}O_{15}S_2$: 1301.5945).

Enzymatic Antibody Labeling. Unless stated otherwise, reactions with BTGase were conducted in PBS (0.15 M) at pH 8 and 37 °C. Due to the solubility of the required cofactor Ca^{2+}, experiments with TG2 were conducted in Tris (0.15 M containing 10 mM $CaCl_2$ and 15 mM glutathione) at pH 8 and 37 °C. For all experiments, an antibody concentration of 0.5–1.0 mg/mL was used. To ensure that >90% of the maximal labeling degree was achieved by the time samples were taken for analysis, experiments with bovine IgG and chCE7 were run for at least 20 min in the case of TG2 and 2 h for BTGase. The reaction time for experiments conducted with BTGase and $chCE7_{agl}$ was set to 5 h even though a slightly higher labeling degree was achieved after 7 h (see kinetics in Figure 5). Optimized reaction conditions refer to the following: (i) For BTGase: 10 μM BTGase, 100 μM Lys–substrate **1**, or 400 μM Gln–substrate **2**. (ii) For TG2: 80 nM TG2, 400 μM Lys–substrate **1**, or 100 μM Gln–substrate **3**.

In a typical enzymatic labeling experiment, defined amounts of TGases (reconstituted in water and stored at −20 °C) and the corresponding substrates (stock solutions in buffer, stored at 4 °C) were added to solutions of antibodies in buffer. The pH was adjusted by addition of buffer of pH 12, in amounts determined previously by titration. The reaction mixtures were incubated at 37 °C while being gently shaken. To obtain kinetic data, samples were taken after the indicated time periods and denatured for 10 min at 95 °C in the presence of mercaptoethanol. All experiments were monitored by SDS-PAGE and fluorescence imaging followed by Coomassie staining of the gels. Data was analyzed with the freeware SCION and the *GraphPad Prism* program.

For determination of the labeling degree and for use of labeled antibodies in in vitro experiments, labeled antibodies were purified by size exclusion chromatography. Retention times were as follows: 15–20 min (minor peaks of antibody aggregates formed upon storage and not due to TGase-mediated cross-linking); 24 min (antibodies), 28 min (TG2) or 32 min (BTGase), respectively; 41 min (unreacted substrates). Determination of labeling degrees of purified fluorescent conjugates was performed by UV/vis spectroscopy, measuring the concentration of both the fluorophore DY547 ($\lambda = 557$ nm, $d = 1$ cm, $\varepsilon = 150\,000\ M^{-1}\ cm^{-1}$) and the protein ($\lambda = 280$ nm, $d =$ 1 cm, $\varepsilon = 210\,000\ M^{-1}\ cm^{-1}$), the latter of which was corrected according to literature by the fraction of the absorbance attributed to the fluorophore (*24*). Obtained solutions of labeled antibodies (ca. 0.1 mg/mL) were stored at 4 °C and used for in vitro experiments the following day. For longer storage (−20 °C), 0.1% BSA was added to prevent aggregation.

Chemical Antibody Labeling. The chemical labeling of antibodies (1 mg/mL) was performed in PBS buffer at pH 8 and 37 °C by adding freshly prepared solutions of DY537-NHS **4** in buffer. Comparison of the achieved labeling degrees with those of the enzymatic labeling method was done by SDS-PAGE and fluorescence imaging of the gels.

In Vitro Binding Affinity Experiments. Competition binding assays were performed with $chCE7_{agl}$ and $chCE7_{agl}$-(**1**) (1 DY547/antibody) on SKOV3ip cells. Triplicate samples of fixed concentration of ^{125}I-labeled chCE7 (50 ng) and increasing concentrations of $chCE7_{agl}$ and $chCE7_{agl}$-(**1**) (1 ng to 3000 ng) with 0.5×10^6 SKOV3ip were suspended in 500 μL PBS containing 0.5% bovine serum albumin (BSA) on a shaking platform for 2 h at 37 °C. Nonspecific binding was determined by parallel incubations in the presence of 10 μg $chCE7_{agl}$ and $chCE7_{agl}$-(**1**). After incubation, 2 mL of PBS containing 0.5% BSA was added, and the suspension was centrifuged for 5 min at 2000 rpm and the supernatant was aspirated from the cells. Two milliliters of PBS containing 0.5% BSA was added, and the suspension was again centrifuged to remove unbound immunoconjugates. Displacement was measured with a gamma counter. Nonspecific binding was subtracted, and data were analyzed with the *GraphPad Prism* program using nonlinear regression with one site competition.

In Vitro Cell Uptake and Fluorescence Microscopy. HEK293 cells or stably transfected HEK293 cells expressing the human full-length L1-CAM were grown on poly(L-lysine) (100 μg/mL) coated 12 mm glass coverslips. Cells were incubated with DMEM (0.5% FCS, 15 mM HEPES) containing either 10 μg/mL chCE7 or $chCE7_{agl}$ in its labeled or unlabeled form for 2 h at 4 °C. Unbound antibody was then washed off with PBS and incubation continued for 3 h at 37 °C to allow for L1 endocytosis. After 2 washes with PBS, cells were fixed with 4% paraformaldehyde in PBS for 20 min, quenched with 50 mM NH_4Cl for 10 min, and permeabilized with 0.5% Triton-X100 in PBS for 10 min at rt. After washes, cells were blocked with 1% BSA–PBS for 1 h at rt, followed by incubation with goat antihuman-IgG-FITC (1:100) for 1 h in the dark. Cells were washed twice with PBS and then incubated with 1 μg/mL Hoechst33258 for 10 min for nuclear staining. Cells were finally washed once more, embedded in MOVIOL, viewed, and photographed through a confocal microscope.

RESULTS

Syntheses. The synthesis of the fluorescent TGase substrates is outlined in Scheme 1. In brief, mono-Boc-protected cadaverine **5** was coupled with DY547-*N*-hydroxysuccinimide ester (DY547-NHS) **4** to afford, after deprotection of intermediate **6**, Lys–substrate cadavarine-DY547 (**1**). Coupling of substrate **5** with the reactive intermediate **7** afforded intermediate **8**. After deprotection, the resulting amine **9** was reacted in an equimolar ratio with **4** to yield the BTGase Gln–substrate ZGlnGly cadavarine-DY547 (**2**). Similarly, coupling of ZGlnGlnProLeu-cadaverine **10** with DY547-NHS **4** gave TG2 Gln–substrate ZGlnGlnProLeu-cadavarine-DY547 (**3**). Intermediates **8** and **9** were fully characterized by spectroscopic methods (NMR, IR, MS), and the identity of final products (purity >90% according to HPLC) was confirmed by mass spectroscopy.

Optimization of the pH, the Enzyme, and the Substrate Concentrations. All reactions were monitored by SDS-PAGE. Samples for analysis were taken after time periods that ensured that >90% of the maximal labeling degree was achieved (see Experimental Procedures section). Protein concentrations were set to 0.5–1 mg/mL for all experiments. In the following, only representative examples of conducted experiments are illustrated.

First, we investigated the effect of the pH of the reaction media on the enzymatic labeling. Figure 2 shows the labeling degrees achieved at different pH values by the BTGase-mediated modification of chCE7 and $chCE7_{agl}$ with Gln–substrate **2**. The most efficient labeling was detected at slightly basic reaction conditions (pH 8). The labeling of antibodies with Lys–substrate

Scheme 1. Structure of DY547-NHS 4, and Synthesis of Fluorescent TGase Substrates[a]

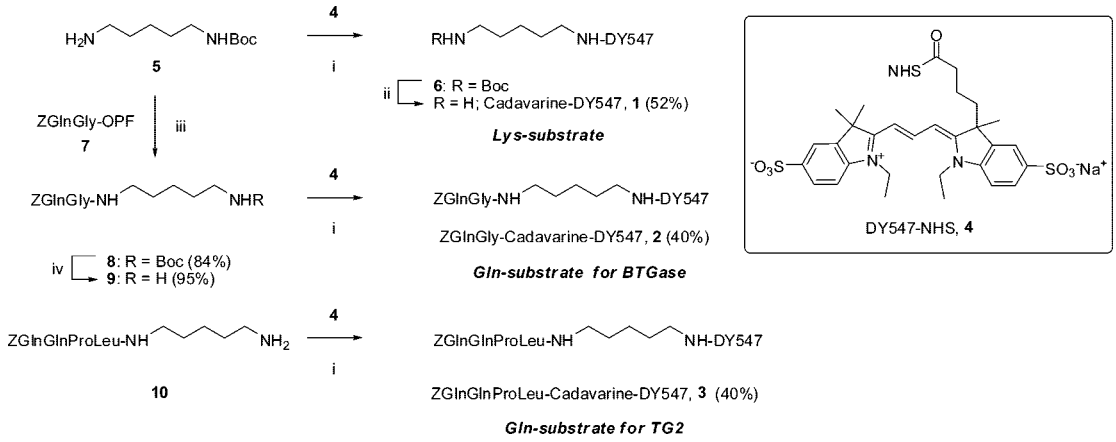

[a] (i) DIPEA, DMF, rt; (ii) H_2O/TFA (10%), rt; (iii) DIPEA, DMF, 0 °C to rt; (iv) CH_2Cl_2/TFA (20%), rt.

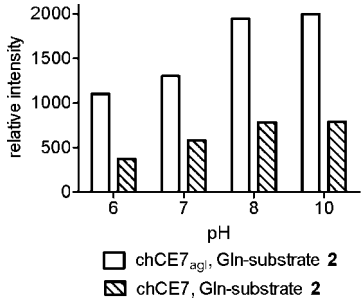

Figure 2. Labeling of chCE7 and chCE7$_{agl}$ (0.8 mg/mL) with BTGase (10 μM) and Gln–substrate **2** (100 μM) at different pH values.

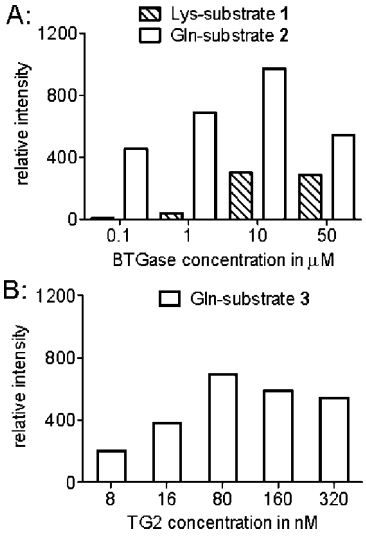

Figure 3. Labeling of bovine IgG (1 mg/mL) with Lys–substrate **1** and Gln–substrates **2** or **3** (100 μM) at pH 8 and different concentrations of BTGase (A) and TG2 (B).

1 was less influenced by the pH, and similar labeling degrees were achieved at pH 6–10. Similar observations were made with bovine IgG as well as for the labeling of antibodies with TG2 (data not shown).

Next, the effect of enzyme concentrations was investigated. Figure 3A shows the labeling of bovine IgG with Lys–substrate **1** and Gln–substrate **2** employing different concentrations of BTGase. Figure 3B depicts the labeling of bovine IgG with Gln–substrate **3** at different concentrations of TG2; the combination TG2/Lys–substrate **1** resulted in a very weak labeling of the antibody at all enzyme concentrations and is thus not

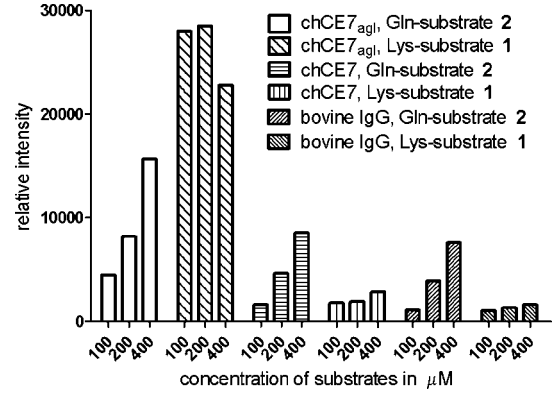

Figure 4. Labeling of bovine IgG, chCE7, and chCE7$_{agl}$ (0.8 mg/mL) with BTGase (10 μM) at pH 8 and different concentrations of Lys–substrate **1** and Gln–substrate **2**.

displayed. Higher labeling yields were achieved with increasing enzyme concentrations for both BTGase (0.1–10 μM) and TG2 (8–80 nM). At concentrations above 10 μM (BTGase) and 80 nM (TG2), respectively, the labeling yields decreased for yet unknown reasons. Labeling experiments of tumor-targeting chCE7 and chCE7$_{agl}$ with Lys– and Gln–substrates at varying concentrations of BTGase or TG2 gave similar results (data not shown).

As a further parameter for optimization, we examined the effect of the substrate concentration. Figure 4 shows the labeling of bovine IgG, chCE7, and chCE7$_{agl}$ with BTGase employing varying concentrations of Lys–substrate **1** and Gln–substrate **2**. Increasing concentrations of the substrates resulted in a higher labeling yield for all substrates, proteins, and enzymes examined with the exception of the combination chCE7$_{agl}$ and substrate **1**. The best labeling of the antibodies was achieved with Gln–substrate **2** at the highest concentration applied (400 μM) and with Lys–substrate **1** at a concentration of 100–200 μM. Because of the limited solubility of the TGase substrates in aqueous buffer (containing a maximum of 10% DMSO), higher concentrations could not be investigated. With TG2, a maximum labeling of antibodies was achieved with Gln–substrate **3** at a concentration of 50–100 μM, whereas only weak labeling was observed with Lys–substrate **1** for all antibodies even at the highest possible substrate concentration (data not shown).

Time Dependence of the Enzymatic Labeling and Determination of the Average Labeling Degrees. Bovine IgG, chCE7, and chCE7$_{agl}$ were labeled with BTGase or TG2 and the corresponding substrates under optimized reaction conditions as determined above. The reaction profiles were monitored by

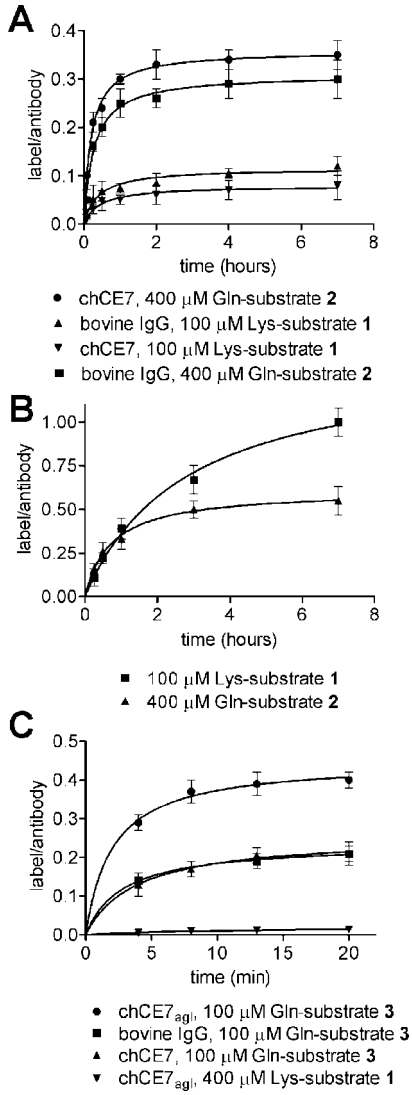

Figure 5. Comparison of kinetics and labeling efficiencies of the enzymatic antibody modification under optimized reaction conditions. (A) Labeling of bovine IgG and chCE7 (each 1 mg/mL) with BTGase (10 μM). (B) Labeling of chCE7$_{agl}$ (0.85 mg/mL) with BTGase (10 μM). (C) Labeling of bovine IgG, chcE7, and chCE7$_{agl}$ (each 0.9 mg/mL) with TG2 (80 nM); number of experiments $n = 2$–3. Because the TG2-mediated labeling of antibodies with Lys–substrate **1** resulted in a weak labeling with all three antibodies, only one example is shown in part C. Note the different time scale.

SDS-PAGE of samples taken at indicated time points. For determination of the average labeling degrees, reactions were stopped after 20 min for TG2 experiments, after 2 h for BTGase experiments with bovine IgG and chCE7, and after 5 h for BTGase experiments with chCE7$_{agl}$. Labeled antibodies were separated from the enzymes and unreacted substrates by size exclusion chromatography, and the average labeling degrees of purified conjugates were determined by UV/vis spectroscopy. Figure 5 shows the kinetics of the enzymatic modification of antibodies as well as the average labeling degrees achieved.

The labeling of bovine IgG, chCE7, and chCE7$_{agl}$ with BTGase reached a plateau after 2 h, culminating in an average label/antibody ratio of approx 0.3–0.5 for Gln–substrate **2** (Figure 5A and B). Employment of BTGase with Lys–substrate **1** resulted in an average label/antibody ratio of 0.1 for bovine IgG and chCE7 within 2 h (Figure 5A), whereas with chCE7$_{agl}$, the highest labeling degree of 1 label/antibody was obtained after a prolonged reaction time of approximately 5 h (Figure 5B). For all antibodies, a maximum labeling degree of 0.2–0.4 label/antibody was achieved with TG2 and Gln–substrate **3** after 20 min, while only low labeling was observed with Lys–substrate **1** (Figure 5C).

Comparison of the Enzymatic Labeling versus Chemical Modification. Bovine IgG, chCE7, and chCE7$_{agl}$ were labeled using the chemically reactive probe DY547-NHS **4** (see Scheme 1) at varying concentrations. Samples were taken after 10 min, a time after which no further increase of the labeling degree was observed. A comparison of the labeling degrees achieved by the chemical modification of chCE7$_{agl}$ with **4** and the enzymatic labeling method performed with BTGase under optimized reaction conditions is shown in Figure 6 A. A concentration of approximately 2–5 μM of **4** was required to obtain a labeling degree in the range of those achieved by the enzymatic method. Similar results were obtained from experiments with bovine IgG and chCE7 (data not shown).

Data obtained by SDS-PAGE analysis of the experiments described above also allowed a comparison of the selectivity of two methods with regard to the labeling of the antibodies' heavy and light chains (Figure 6B). For example, the chemical modification of chCE7$_{agl}$ resulted in a labeling ratio of heavy-to-light chain of approximately 7:3. The same ratio was found for all concentrations of **4** examined (1–100 μM; data not shown). On the other hand, the enzymatic labeling of chCE7$_{agl}$ with BTGase or TG2 and Gln– or Lys–substrates resulted in an almost exclusive labeling of the antibodies' heavy chains (>90%) in all cases. Similar results were obtained with bovine IgG and chCE7 (data not shown).

Affinity Measurements and Cell Internalization Experiments. chCE7 and chCE7$_{agl}$ were labeled with BTGase under optimized reaction conditions, purified by size exclusion chromatography, and the average labeling degree of the conjugates determined by UV/vis spectroscopy. The solutions of fluorescent conjugates chCE7-(**2**), chCE7$_{agl}$-(**1**), or chCE7$_{agl}$-(**2**) (as a mixture with unlabeled antibodies) were further examined for their biological activity in vitro. For affinity measurements, increasing concentrations of unmodified chCE7$_{agl}$ and labeled chCE7$_{agl}$-(**1**) (1 label/antibody) were used to displace ^{125}I-labeled intact chCE7 bound to SKOV3ip cells. The results showed a typical sigmoid curve when the log of the concentration of competitors is plotted versus % displaced activity on the cells (data not shown). Complete displacements were achieved with 3000 ng of the competitor. 50% displacement (IC_{50}) occurred with 22 ng of unmodified chCE7$_{agl}$ and 28 ng of chCE7$_{agl}$-(**1**). Cell internalization studies were performed using L1-CAM expressing HEK-293 cells. Antigen binding and cell internalization of chCE7$_{agl}$-(**1**) (1 label/antibody), chCE7$_{agl}$-(**2**) (0.4 label/antibody), and chCE7-(**2**) (0.3 label/antibody) were compared with those of unlabeled chCE7 and chCE7$_{agl}$ (detected with a secondary, FITC-labeled, antihuman antibody) (*14*) Analysis of cell samples by confocal laser scanning microscopy revealed similar cell surface binding and internalization of all antibodies and antibody conjugates tested (Figure 7).

DISCUSSION

Commercial recombinant bacterial TGase (BTGase, from *Streptomyces mobaraensis*) and human tissue transglutaminase 2 (TG2, from *E. coli*) were selected for the enzymatic modification of antibodies as two representative examples of enzymes of the family of TGases. As TGase substrates, we used known Lys(mimicking) (*15*) and Gln–derivatives (*16, 17*) to which the fluorophore DY547 (CY3 analogue) was conjugated (*25*). Lys–substrate cadaverine-DY547 (**1**) and Gln–substrates (ZGlnGly cadaverine-DY547 (**2**) and ZGlnGlnProLeu-cadavarine-DY547 (**3**), respectively) were synthesized by standard peptide coupling reactions as outlined in Scheme 1. TGase substrates **1**–**3** were obtained in 1–3 synthetic steps in good overall yields after HPLC purification.

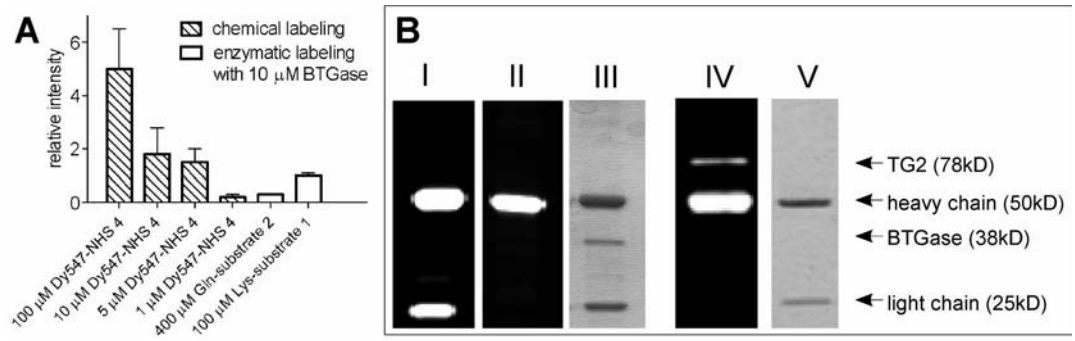

Figure 6. (A) Chemical modification of chCE7$_{agl}$ (0.75 mg/mL) with varying concentrations of DY547-NHS **4** (1–100 μM) and comparison of the labeling degrees with the one achieved by the BTGase-mediated labeling under optimized conditions (number of experiments $n = 2$). (B) Comparison of the labeling of the heavy and light chains of chCE7$_{agl}$ by chemical modification and the enzymatic method using TGases. I. Chemical labeling with 5 μM DY547-NHS **4**. II. Enzymatic labeling with 10 μM BTGase and 100 μM Lys–substrate **1**. III. Coomassie staining of gel B. IV. Enzymatic labeling with 80 nM TG2 and 400 μM Gln–substrate **3**. V. Coomassie staining of gel IV. Fluorescence images were obtained with a CY3 optical filter.

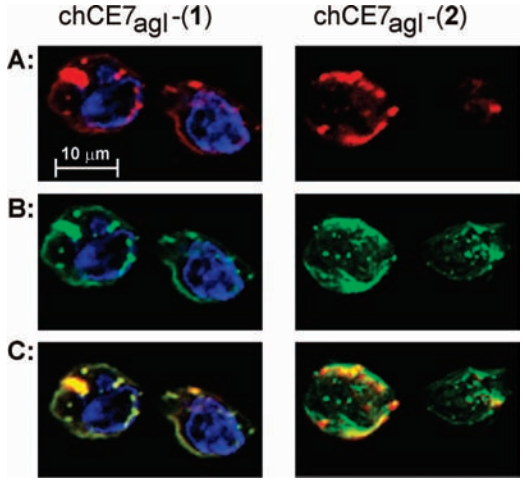

Figure 7. Confocal laser scanning microscopic analysis of the internalization of labeled antibodies chCE7$_{agl}$-(**1**) and chCE7$_{agl}$-(**2**) into L1-CAM HEK-293 cells. (A) Detection of DY547 fluorophore using a rhodamine optical filter (red). (B) Detection via secondary FITC-labeled antihuman antibody using a FITC optical filter (green). (C) Overlay (yellow). Cell nuclei (blue) were additionally stained with a DAPI analogue in the case of chCE7$_{agl}$-(**1**).

With fluorescent TGase substrates in hand, we studied and optimized the labeling of model antibody bovine IgG as well as the tumor-targeting antibodies chCE7 and chCE7$_{agl}$ by enzymatic modification of the proteins via their Lys and Gln side chains, respectively. The influence of several reaction parameters such as pH, substrate and enzyme concentration, and time was carefully investigated for both enzymes. We observed that slightly basic reaction conditions (pH 8) gave the best results for the antibody labeling with Gln–substrates with both TGases (Figure 2) while modifications with Lys–substrate **1** were less influenced by the pH. Optimal enzyme concentrations were found to be 10 μM for BTGase and, considerably lower, 80 nM for TG2 (Figure 3). Under all conditions examined, no high molecular weight aggregates as the result of cross-linking of proteins were detected by SDS-PAGE analyses. Self-labeling of the enzymes with fluorescent substrates was only observed in the case of TG2 (Figure 6). Such self-labeling of mammalian TGase is known (*18*). For BTGase, the most efficient labeling was achieved with Gln–substrate **2** at the highest concentration applicable (400 μM). The effect of substrate concentration on the labeling degree was less pronounced with Lys–substrate **1**, and a maximal labeling of antibodies was achieved at a concentration of 100–200 μM (Figure 4). In comparison, labeling of antibodies with TG2 and Gln–substrate **3** peaked at a substrate concentration of 50–100 μM, while only a negligible labeling of antibodies was obtained with Lys–substrate **1** even at the highest possible concentration (Figure 5C).

For both bovine IgG and chCE7, employment of TGases together with their corresponding Gln–substrates **2** and **3** resulted in an up to 6-fold higher labeling degree compared to Lys–substrate **1** (Figure 5). (*26*, *27*).These results may reflect the more abundant Lys residues exposed on the surface of antibodies (*11*) or, alternatively, the known specificity of TGases toward certain amino acid sequences neighboring the Gln residues (*19*). A maximum labeling degree of 0.2–0.3 fluorescent label per antibody was achieved with Gln–substrates in less than 2 h in the case of BTGase and after approximately 20 min with TG2. Even though TG2 was very efficient, we experienced that this enzyme is more delicate to handle than BTGase, which led to variable results (*20*, *28*).

To our surprise, the antibody chCE7$_{agl}$ exhibited a quite different labeling behavior (Figure 5B). We found that employment of BTGase and Lys–substrate **1** gave rise to a label/protein ratio of approximately 1:1. On the other hand, antibody modification with TG2 and Lys–substrate **1** resulted in a very low labeling degree (Figure 5C). These findings may illustrate the higher Gln–substrate specificity of TG2 compared to that of BTGase. While the labeling with BTGase and Gln–substrate **3** still gave reasonable results, no attachment of fluorophores to antibodies was observed when the combination TG2/Gln–substrate **2** was employed. The use of Gln–substrates **2** and **3** with TG2 and BTGase, respectively, culminated in a labeling degree of 0.4–0.5 label per chCE7$_{agl}$ (Figure 5C). We attribute the higher labeling degrees achieved with chCE7$_{agl}$ to the single-site mutation (Asn297Gln) which potentially introduces an additional Gln coupling site or may result in subtle structural changes of the protein, which make other Gln residues more accessible. Similar effects of single-site mutations introducing Gln residues on TGase-mediated protein modification have been reported (*21*).

Next, we compared the enzymatic labeling of antibodies with chemical modifications using the NHS–ester **4**. Clearly, more Lys residues are prone to be labeled by the chemical modification than by the enzymatic labeling using TGases. Thus, in order to achieve the same labeling degree as observed for the enzymatic method (100–400 μM substrate), a concentration of only 2–5 μM of the chemically reactive probe DY547-NHS **4** was required (Figure 6A). While the labeling with DY547-NHS **4** proceeded very efficiently, SDS-PAGE analysis of the conjugates revealed that the chemical modification led to attachment of fluorescent probes to the antibodies at the heavy (70%) and light (30%) chain, a ratio which corresponds to their

size (~80 kDa and ~25 kDa, respectively). The enzymatic reaction, on the other hand, resulted in an almost exclusive labeling of the heavy chain (>90% for model bovine IgG and chCE7, and >95% for $chCE7_{agl}$) with either combination of TGase and substrate. Such selectivity could not be achieved by the chemical labeling protocol using the NHS ester. Site-specific modification of monoclonal antibodies at the heavy chain via a chemical method is reported in the literature and uses the oligosaccharide attached to the hinge region of the antibody (*22*). However, this chemical protocol is quiet laborious, requiring delicate periodate oxidation of carbohydrate 1,2-diols to aldehydes (*23*) and two or more purification steps.

Binding assays performed with ^{125}I-labeled $chCE7_{agl}$ on SKOV3ip cells showed that $chCE7_{agl}$-(**1**) (revealing the highest labeling degree) competed almost equally effectively for the antigen than did unmodified $chCE7_{agl}$, indicating unaltered affinity (*29*).

Analysis of cell samples by confocal laser scanning microscopy revealed that the enzymatic modification of chCE7 and $chCE7_{agl}$ with fluorescent substrates had no influence on their cell binding and internalization. Figure 7 shows the characteristic formation of endosomes as the result of internalization of fluorescent antibodies by endocytosis. $chCE7_{agl}$-(**1**) and $chCE7_{agl}$-(**2**) (and unlabeled chCE7/ $chCE7_{agl}$) were codetected with the FITC-labeled, secondary antibody as a control. Overlay of the pictures obtained with a rhodamine (detection of DY547, Figure 7A) and FITC optical filter (detection of secondary antibody, Figure 7B) shows the correlation of DY547-labeled and unlabeled antibodies bound and internalized into HEK-293 cells (Figure 7A). Good overlap of the fluorescence was observed for $chCE7_{agl}$-(**1**) indicating that the majority of bound and internalized antibodies were indeed labeled with the DY547 fluorophore (~1 DY547 per antibody). As expected, some mismatch of the fluorescence was observed for the in vitro experiment with $chCE7_{agl}$-(**2**) due to the lower labeling degree (~0.3 DY547 per antibody) which translates into the presence of approximately 60% of unmodified $chCE7_{agl}$ in the protein fraction isolated from size exclusion chromatography.

CONCLUSION

In conclusion, we have shown that the TGase-mediated labeling of different IgG1 antibodies proceeds under mild reaction conditions with different TGases and both fluorescent Lys– and Gln–substrates. The enzymatic modification of model bovine IgG and tumor-targeting antibodies chCE7 and $chCE7_{agl}$ occurred selectively at the heavy chain of the antibodies, seemingly without influencing their biological activities as shown by in vitro cell experiments. Reproducible labeling can be achieved in a broad concentration "window" of the substrates and enzymes without the risk of overlabeling the antibodies. Of the two TGases tested, BTGase incorporated the Lys–substrate **1** more efficiently than did TG2. On the other hand, both enzymes were equally efficient with the corresponding Gln–substrate (**2** or **3**, respectively). Because TG2 is more delicate to handle, employment of BTGase is preferred for our purposes. The labeling degrees of antibodies achieved so far by the enzymatic method were moderate, but sufficient for optical imaging of cell samples and are also likely to be adequate for other applications. Further investigations of the enzymatic labeling of proteins aimed toward application of TGase substrates attached to probes other than fluorophores, including metal chelating moieties for SPECT, PET, and MRI, are currently ongoing.

ACKNOWLEDGMENT

The authors thank the Swiss National Science Foundation for financial support (SNF-112437), Dr. Kai Oertel and Dr. Ralph Pasternack (N-Zyme Biotec GmbH) for helpful discussions and assistance, Maja Günthert (ETH Zurich) for conducting confocal laser scanning microscopy, and Susan Cohrs (PSI) for carrying out the in vitro binding experiments.

LITERATURE CITED

(1) Tirat, A., Freuler, F., Stetter, T., Mayr, L. M., and Leder, L. (2006) Evaluation of two novel tag-based labelling technologies for site-specific modification of proteins. *Int. J. Biol. Macromol. 39*, S66–S76.

(2) Barat, B., and Wu, A. M. (2007) Metabolic biotinylation of recombinant antibody by biotin ligase retained in the endoplasmic reticulum. *Biomol. Eng.* In press.

(3) Hermanson, G. T. (1996) *Bioconjugate Techniques*, Academic Press, San Diego.

(4) Pitt, J. C., Lindemeier, J., Habbes, H. W., and Veh, R. W. (1998) Haptenylation of antibodies during affinity purification: a novel and convenient procedure to obtain labeled antibodies for quantification and double labeling. *Histochem. Cell Biol. 110*, 311–322.

(5) Saviranta, P., Haavisto, T., Rappu, P., Karp, M., and Lovgren, T. (1998) In vitro enzymatic biotinylation of recombinant fab fragments through a peptide acceptor tail. *Bioconjugate Chem. 9*, 725–735.

(6) Arlt, M. J. E., Novak-Hofer, I., Gast, D., Gschwend, V., Moldenhauer, G., Grunberg, J., Honer, M., Schubiger, P. A., Altevogt, P., and Kruger, A. (2006) Efficient inhibition of intraperitoneal tumor growth and dissemination of human ovarian carcinoma cells in nude mice by anti-L1-cell adhesion molecule monoclonal antibody treatment. *Cancer Res. 66*, 936–943.

(7) Knogler, K., Grunberg, J., Novak-Hofer, I., Zimmermann, K., and Schubiger, P. A. (2006) Evaluation of ^{177}Lu-DOTA-labeled aglycosylated monoclonal anti-L1-CAM antibody chCE7: influence of the number of chelators on the in vitro and in vivo properties. *Nucl. Med. Biol. 33*, 883–889.

(8) Zimmermann, K., Grunberg, J., Honer, M., Ametamey, S., Schubiger, P. A., and Novak-Hofer, I. (2003) Targeting of renal carcinoma with $^{67/64}$Cu-labeled anti-L1-CAM antibody chCE7: selection of copper ligands and PET imaging. *Nucl. Med. Biol. 30*, 417–427.

(9) Mehta, K., and Eckert, R. (2005) Transglutaminases: family of enzymes with diverse functions, *Progress in Experimental Tumor Research* (Bertino, J. R., Ed.), Karger AG, Basel, Switzerland.

(10) Lin, C. W., and Ting, A. Y. (2006) Transglutaminase-catalyzed site-specific conjugation of small-molecule probes to proteins in vitro and on the surface of living cells. *J. Am. Chem. Soc. 128*, 4542–4543.

(11) Josten, A. E., Haalck, L., Spener, F., and Meusel, M. (2000) Use of microbial transglutaminase for the enzymatic biotinylation of antibodies. *J. Immunol. Methods 240*, 47–54.

(12) Takazawa, T., Kamiya, N., Ueda, H., and Nagamune, T. (2004) Enzymatic labeling of a single chain variable fragment of an antibody with alkaline phosphatase by mircobial transglutaminase. *Biotechnol. Bioeng. 86*, 399–404.

(13) Kamiya, N., Takazawa, T., Tanaka, T., Ueda, H., and Nagamune, T. (2003) Site-specific cross-linking of functional proteins by transglutamination. *Enzyme Microb. Technol. 33*, 492–496.

(14) Novak-Hofer, I., Amstutz, H. P., Morgenthaler, J. J., and Schubiger, P. A. (1994) Internalization and degradation of monoclonal-antibody chCE7 by human neuroblastoma-cells. *Int. J. Cancer 57*, 427–432.

(15) Lajemi, M., Demignot, S., Borge, L., ThenetGauci, S., and Adolphe, M. (1997) The use of Fluoresceincadaverine for detecting amine acceptor protein substrates accessible to active transglutaminase in living cells. *Histochem. J. 29*, 593–606.

(16) Pasternack, R., Laurent, H. P., Ruth, T., Kaiser, A., Schon, N., and Fuchsbauer, H. L. (1997) A fluorescent substrate of transglutaminase for detection and characterization of glutamine acceptor compounds. *Anal. Biochem. 249*, 54–60.

(17) Sugimura, Y., Hosono, M., Wada, F., Yoshimura, T., Maki, M., and Hitomi, K. (2006) Screening for the preferred substrate sequence of transglutaminase using a phage-displayed peptide library - Identification of peptide substrates for TGase 2 and Factor XIIIA. *J. Biol. Chem. 281*, 17699–17706.

(18) Fleckenstein, B., Qiao, S.-W., Larsen, M. R., Jung, G., Roepstorff, P., and Sollid, L. M. (2004) Molecular characterization of covalent complexes between tissue transglutaminase and gliadin peptides. *J. Biol. Chem. 279*, 17607–17616.

(19) Jager, M., Nir, E., and Weiss, S. (2006) Site-specific labeling of proteins for single-molecule FRET by combining chemical and enzymatic modification. *Protein Sci. 15*, 640–646.

(20) Jeitner, T. M., Fuchsbauer, H.-L., Blass, J. P., and Cooper, A. J. L. (2001) A sensitive fluorometric assay for tissue transglutaminase. *Anal. Biochem. 292*, 198–206.

(21) Coussons, P. J., Kelly, S. M., Price, N. C., Johnson, C. M., Smith, B., and Sawyer, L. (1991) Selective modification by transglutaminase of a glutamine side-chain in the hinge region of the histidine-388-]glutamine mutant of yeast phosphoglycerate kinase. *Biochem. J. 273*, 73–78.

(22) Rodwell, J. D., Alvarez, V. L., Lee, C., Lopes, A. D., Goers, J. W. F., King, H. D., Powsner, H. J., and McKearn, T. J. (1986) Site-specific covalent modification of monoclonal antibodies: in vitro and in vivo evaluations. *Proc. Natl. Acad. Sci. U.S.A. 83*, 2632–2636.

(23) Hage, D. S., Wolfe, C. A. C., and Oates, M. R. (1997) Development of a kinetic model to describe the effective rate of antibody oxidation by periodate. *Bioconjugate Chem. 8*, 914–920.

(24) See, e.g., the online technical handbook Amersham CyDye™ mono-reactive NHS Ester, http://www.gelifesciences.com.

(25) Initially, the antibody labeling experiments were conducted with similar results using BTGase and commercial cadavarine-dansyl and ZGlnGly cadavarine-dansyl substrates. However, the dansyl fluorophore proved to be unsuitable for fluorescence microscopy of cell samples.

(26) Similar results were obtained with commercial human and chicken IgG.

(27) Interestingly, Josten et al. have reported a labeling degree of 1.1 to 1.4 labels per antibody for the BTGase-mediated biotinylation of a monoclonal IgG using a Lys–substrate (*11*).

(28) For example, storage of solutions of TG2 on ice for 1 h resulted in a decrease of the enzyme's activity by 50% (data not shown, loss of activity of mammalian TGases has previously been reported by Jeitner et al. (*20*)). No loss of activity was observed for BTGase even after storage of solutions at rt for several hours.

(29) Josten et al. (*11*) and Takazawa et al. (*12*) also report unaltered antigen binding of antibodies and antibody fragments that were modified by TGases.

BC700306N

Postsynthetic Derivatization of Fluorophores with α-Sulfo-β-alanine Dipeptide Linker. Application to the Preparation of Water-Soluble Cyanine and Rhodamine Dyes

Anthony Romieu,*,† Dominique Brossard,† Maxime Hamon,† Hakim Outaabout,† Christophe Portal,‡ and Pierre-Yves Renard*,†

Equipe de Chimie Bio-Organique, Université de Rouen, INSA de Rouen, CNRS UMR 6014, COBRA, IRCOF, 1, rue Lucien Tesnière, 76131 Mont-Saint-Aignan Cedex, France, and QUIDD, Technopôle du Madrillet, 50, rue Ettore Bugatti, 76800 Saint-Etienne du Rouvray, France. Received August 27, 2007; Revised Manuscript Received October 23, 2007

A straightforward method to enhance water solubility of fluorescent organic dyes (cyanines and rhodamines) by a postsynthetic chemical derivatization of their carboxylic acid functionality with an original disulfonated heterobifunctional linker is described. Significant water solubility enhancement is achieved without compromising either the photophysical properties (especially large molar extinction coefficients and high quantum yields) or bioconjugation efficiency of the parent non-water-soluble fluorophores. The results both demonstrate the strong potential of these new compounds as fluorescent labels for a broad range of biotechnology and biomedical applications and illustrate the utility of such an easy-to-handle water-solubizing group.

INTRODUCTION

Fluorescent organic dyes are the central focus of numerous chemical, analytical, biological, and spectroscopic studies, since their use as powerful detection tools for life science applications is now well-established (*1*). Among the multitude of available fluorophores, those absorbing and emitting in the relatively long wavelength range (i.e., around or beyond 600 nm) are more desirable; especially as probes for emerging and more challenging biotechnology and biomedical applications such as DNA sequencing (*2*), diagnostic imaging (*3*), and photodynamic therapy (*4*). Indeed, the advantages of a fluorescence occurring in the low-energy region of the electromagnetic spectrum are numerous and have been extensively discussed (*2, 5*). Prominent among these advantages is the absence or the significant reduction of background absorption, fluorescence, and light scattering, along with the availability of low-cost sources of irradiation. To obtain new analogues of longer-wavelength absorption and emission, the most popular synthetic strategy consists in the extension of the π-conjugation system of some widely used fluorophore precursors, such as fluorescein, rhodamine, BODIPY, and so forth. However, the attachment of one or more aromatic poly(hetero)cycles to these latter fluorescent cores often leads to molecules poorly or not soluble in aqueous media and therefore not suitable for biolabeling applications. Consequently, recent efforts have been devoted to the development of water-soluble analogues of some long-wavelength fluorophores belonging to the BODIPY (*6, 7*), cyanine (*3, 8, 9*), oxazine (*10*), and rhodamine (*11–13*) families. A modification in the molecular structure by adding ionizable hydrophilic groups such as carboxylic acid, phosphonic acid, sulfonic acid, hydroxyl, and ammonium groups to the dye improves the water solubility but diversely affects the quantum yield and photostability. Moreover, for the majority of fluorophores, modulation of such physicochemical properties requires restarting the synthesis of the fluorescent core from the beginning with building blocks bearing the water-solubilizing groups (for a recent example, see (*14*)). Such a *de novo* approach has three main drawbacks which dramatically affect the overall yield of the synthetic process: (1) the laborious and time-consuming handling and purification of highly polar synthetic intermediates, (2) the extent of byproducts resulting from undesirable side reactions of some free reactive groups (i.e., carboxylic acid, phosphonic acid, and hydroxyl groups), and thus (3) in most cases, the requirement of additional protection/deprotection steps. To overcome these limitations and to speed up the development of new beneficial water-soluble fluorophores, an alternative synthetic approach is preferred, based on the postsynthetic functionalization of hydrophobic fluorescent precursors ("convertible organic dyes") readily available through convenient and high-yield synthetic protocols. Indeed, after completion of the fluorescent core synthesis, the specific chemical derivatization of the reactive group (typically a carboxylic acid group) of this convertible organic dye with a hydrophilic heterobifunctional linker enables the introduction of both water-solubilizing moieties and a terminal reactive group for bioconjugation. Thus, the laborious workup and purification steps of polar fluorescent materials are limited to the isolation of the final water-soluble fluorophore. Recently, we have used this "post-synthetic derivatization" approach for the synthesis of a novel analogue (Figure 1, dye **1**) of commercially available cyanine dye Cy 5.5 (*8, 15, 16*). Acylation of the amino group of a cyanine-based amino acid with *N*-hydroxysuccinimidyl ester of trisulfonated linker **2** derived from 3,5-diaminobenzoic acid (Figure 1), afforded **1** in good yield. However, linker **2** is not easily accessible in high yields, and its aromatic core negatively affects the fluorescence properties (i.e., quantum yield) of the resulting water-soluble fluorophore. To circumvent these problems, the use of a hydrophilic alkyl linker derived from a peptidic architecture is an interesting alternative to explore and can rely on the numerous and efficient methods described for the peptide coupling reactions. To our knowledge, only one publication from Meltola et al. describes the postsynthetic derivatization of fluorophores with a hydrophilic peptide linker

* pierre-yves.renard@univ-rouen.fr or anthony.romieu@univ-rouen.fr. Phone: +33-2-35-52-24-14 or (24-15). Fax: +33-2-35-52-29-59.

† IRCOF, Equipe de Chimie Bio-Organique.

‡ QUIDD.

10.1021/bc7003268 CCC: $40.75 © 2008 American Chemical Society
Published on Web 12/15/2007

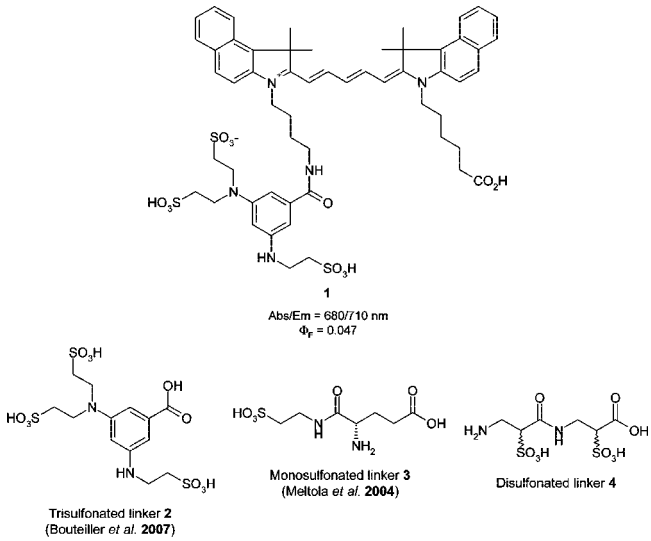

Figure 1. Structures of Cy 5.5 analogue **1** and of the hydrophilic linkers.

(*6*). Monosulfonated linker **3** derived from L-glutamic acid (Figure 1) has been synthesized and attached to the carboxylic acid side chain of some BODIPY dyes to get fluorescent labels for two-photon excited fluorometry. However, this strategy limits the number of additional sulfonic acid moieties to one, which is insufficient for an efficient enhancement of the water solubility of fluorescent cores bearing four or more aromatic rings.

In this article, we wish to report the synthesis and use of an original disulfonated linker **4** resulting from the coupling between two α-sulfo-β-alanine units and its use in the preparation of novel water-soluble analogues of cyanine dye Cy 5.5, rhodamine 6G, and sulforhodamine 101 (i.e., Texas Red). This strategy results in an unchanged carboxylic group available for bioconjugation reactions, and allows grafting of additional sulfonic acid moieties.

EXPERIMENTAL PROCEDURES

Chemicals and Reagents. Reversed-phase column flash chromatographies were performed on octadecyl-functionalized silica gel (mean pore size 60 Å) from Aldrich. DMF was dried by distillation over BaO. DIEA and TEA were distilled from CaH_2 and stored over BaO. Cyanine dye **7** was prepared in four steps from 1,1,2-trimethyl-1*H*-benz[*e*]indole by using the convergent synthetic scheme recently reported by us (*8*). Rhodamine carboxylic acid derivative **10** was prepared from rhodamine 6G (Aldrich, dye content ~95%) by using the three-step synthetic procedure developed by Afonso et al. (i.e., pyrolysis, alkylation with benzyl bromoacetate, and hydrogenolysis of benzyl ester) (*17*). Alexa Fluor 594 carboxylic acid was synthesized by using a multistep synthetic procedure described in a PCT International Application from Invitrogen (formerly Molecular Probes, Inc.) and entitled "Sulfonated xanthene derivatives synthesis and applications as fluorescent stains" (*18*). The two isomers of this water-soluble rhodamine derivative were resolved by flash chromatography on a RP-C_{18} silica gel column. The first eluted isomer (i.e., the most polar) was named isomer I and the second one isomer II. Structural assignment of each isomer was achieved by ^{1}H NMR spectroscopy: isomer I corresponds to the 1,4-dicarboxylic acid derivative, whereas isomer II is the 1,3-dicarboxylic acid derivative. Sulforhodamine 101 (free acid, 99%, laser grade) was purchased from Acros. Glycine *tert*-butyl ester hydrochloride (H-Gly-OtBu·HCl) was from Alfa Aesar. Recombinant human caspase-3 enzyme (5.52 U/mg) was purchased from Sigma. The HPLC-gradient-grade CH_3CN was obtained from Panreac. Buffers (bicarbonate, borate, caspase-3, and phosphate buffer saline (PBS)) and aq mobile phases for HPLC were prepared using water purified with a Milli-Q system (purified to 18.2 MΩ.cm). Triethylammonium acetate (TEAA, 1.0 M) and triethylammonium bicarbonate (TEAB, 1.0 M) buffers were prepared from distilled triethylamine and glacial acetic acid or CO_2 gas.

Instruments. ^{1}H and ^{13}C NMR spectra were recorded on a Bruker DPX 300 (Bruker, Wissembourg, France). Chemical shifts are expressed in parts per million (ppm) from D_2O (δ_H = 4.79) or DMSO-d_6 (δ_H = 2.50, δ_C = 39.52) (*19*). *J* values are expressed in Hz. Analytical HPLC was performed on a Thermo Electron Surveyor instrument equipped with a PDA detector. Semipreparative HPLC was performed on a Finnigan SpectraSYSTEM liquid chromatography system equipped with UV–vis 2000 detector. UV–vis spectra were obtained on a Varian Cary 50 scan spectrophotometer. Fluorescence spectroscopic studies were performed either in a semimicrofluorescence cell (Hellma, 104F-QS, 10 × 4 mm, 1400 μL) or in an ultramicrofluorescence cell (Hellma, 105.51-QS, 3 × 3 mm, 45 μL) with a Varian Cary Eclipse spectrophotometer. Mass spectra were obtained with a Finnigan LCQ Advantage MAX (ion trap) apparatus equipped with an electrospray source.

HPLC Separations. Several chromatographic systems were used for the analytical experiments and the purification steps. Each one of these systems was optimized in order to improve separation conditions.

System A: RP-HPLC (Thermo Hypersil GOLD C_{18} column, 5 μm, 4.6 × 150 mm) with CH_3CN and 0.1% aq trifluoroacetic acid (aq TFA, 0.1%, v/v, pH 2.0) as eluents [100% TFA (5 min), linear gradient from 0% to 80% (40 min) of CH_3CN] at a flow rate of 1 mL/min. UV detection was achieved at 260 nm.

System B: System A with the following gradient [80% TFA (5 min), linear gradient from 20% to 40% (5 min) and 40% to 64% (20 min) of CH_3CN]. Triple UV–vis detection was achieved at 530, 595, and 675 nm.

System C: RP-HPLC (Thermo Hypersil GOLD C_{18} column, 5 μm, 4.6 × 150 mm) with CH_3CN and TEAA buffer (100 mM, pH 7.0) as eluents [80% TEAA (5 min), linear gradient from 20% to 40% (5 min) and 40% to 64% (20 min) of CH_3CN] at a flow rate of 1 mL/min. Triple UV–vis detection was achieved at 260, 595, and 675 nm.

System D: RP-HPLC (Varian Kromasil C_{18} column, 10 μm, 21.2 × 250 mm) with CH_3CN and 0.1% aq TFA as eluents [90% TFA (5 min), linear gradient from 10% to 30% (10 min) and 30% to 80% (50 min) of CH_3CN] at a flow rate of 20 mL/min. UV detection was achieved at 260 nm.

System E: RP-HPLC (Varian Kromasil C_{18} column, 10 μm, 21.2 × 250 mm) with CH_3CN and TEAB buffer (50 mM, pH 7.5) as eluents [90% TFA (5 min), linear gradient from 10% to 80% (70 min) of CH_3CN] at a flow rate of 20 mL/min. UV detection was achieved at 300 nm.

System F: RP-HPLC (Waters XTerra MS C_{18} column, 5 μm, 7.8 × 100 mm) with CH_3CN and TEAB buffer (50 mM, pH 7.5) as eluents [75% TEAB (2 min), linear gradient from 25% to 30% (3 min) and 30% to 75% (60 min) of CH_3CN] at a flow rate of 1.5 mL/min. UV detection was achieved at 260 nm.

α-Sulfo-β-alanine. Oleum (25% SO_3) (40 mL) was added to β-alanine (2.7 g, 30.30 mmol) with cooling in an ice−salt bath. The resulting reaction mixture was left at room temperature for 4 days, and then diluted cautiously with cold water (80 mL). The solution was left overnight at 4 °C to crystallize. The white solid was isolated by filtration, washed with cold deionized water. After drying by lyophilization, racemic α-sulfo-β-alanine was obtained as a white powder (2.77 g, 16.4 mmol, yield 54%). mp >260 °C. IR (KBr) 3190 (broad), 1727, 1613, 1589, 1504,

1459, 1303, 1204 (broad), 1111, 1043. ^{1}H NMR (300 MHz, D_2O): δ 3.56 (m, 2H, H-3 and H-3′), 4.16 (t, $J = 6.4$ Hz, 1H, H-2). ^{13}C NMR (75.5 MHz, D_2O): δ 37.8 (1C, C-3), 61.9 (1C, C-2), 169.0 (1C, C-1). MS (ESI, positive mode) *m/z*: 169.93 $[M + H]^+$. MS (ESI, negative mode) *m/z*: 168.06 $[M - H]^-$, calcd mass for $C_3H_7NO_5S$ 169.16. Anal. Calcd for $C_3H_7NO_5S$: C 21.30, H 4.17, N 8.28, S 18.96. Found: C 20.06, H 4.04, N 7.78, S 19.76 ($C_3H_7NO_5S \cdot H_2SO_4$, 94/6).

***N*-(9-Fluorenylmethyloxycarbonyl)-α-sulfo-*β*-alanine (5).** Racemic α-sulfo-*β*-alanine (0.5 g, 1.87 mmol) was dissolved in 8.5% sodium carbonate solution (aq) (7 mL) and cooled to 4 °C. A solution of Fmoc-OSu (0.5 g, 1.49 mmol) in 1,4-dioxane (5 mL) was added in one portion to the stirred solution, and the mixture was left at room temperature overnight. The reaction was checked for completion by RP-HPLC (system A) and the mixture was acidified to pH ∼2 with 10% HCl (aq). After partial removal of 1,4-dioxane under reduced pressure, the reaction mixture was lyophilized. The resulting residue was purified by flash chromatography on an RP-C_{18} silica gel column (20 g) with a stepwise gradient of CH_3CN (0–30%) in aq TFA as the mobile phase. The product-containing fractions were lyophilized to give protected amino acid **5** as a white amorphous powder (0.69 g, yield 95%). IR (KBr) 3372 (broad), 1723, 1538, 1449, 1236 (broad), 1048. ^{1}H NMR (300 MHz, DMSO-d_6): δ 3.39–3.60 (m, 3H), 4.20 (bs, 3H), 7.02 (bs, 1H, N*H*), 7.29–7.89 (m, 8H, *H*-Fmoc). ^{13}C NMR (75.5 MHz, DMSO-d_6): δ 38.3 (masked by DMSO peak), 46.7, 65.0, 65.6, 120.1 (2C), 125.4, 127.1 (2C), 127.7 (2C), 140.7 (2C), 143.9 (2C), 156.0, 169.5 (2C). HPLC (system A): $t_R = 25.17$ min, purity >95%. MS (ESI, negative mode) *m/z*: 390.00 $[M - H]^-$, calcd mass for $C_{18}H_{17}NO_7S$ 391.40. Compound **5** proved to be too hygroscopic for a suitable elemental analysis.

***N*-(9-Fluorenylmethyloxycarbonyl)-α-sulfo-*β*-alaninyl-α-sulfo-*β*-alanine (6).** (a) Preparation of *N*-hydroxysuccinimidyl ester. A mixture of **5** (368 mg, 0.94 mmol) and *N*-hydroxysuccinimide (108 mg, 0.94 mmol) was dissolved in dry DMF (5 mL). DCC (194 mg, 0.94 mmol) was added, and the resulting reaction mixture was stirred at room temperature for 24 h. The reaction was checked for completion by RP-HPLC (system A), DMF (0.5 mL) was added and the solution was transferred in 1.5 mL Eppendorf tubes and centrifuged to remove the major amount of DCU. The clear liquid phase containing the active ester was used in the coupling reaction without further purification. Yield was assumed to be quantitative. HPLC (system A): $t_R = 27.5$ min (compared to $t_R = 25.2$ min for the free acid **5**).

(b) Coupling reaction. α-Sulfo-*β*-alanine (191 mg, 1.13 mmol) was dissolved in 6.8% sodium bicarbonate solution (aq) (4.2 mL) and cooled to 4 °C. The crude solution of *N*-hydroxysuccinimidyl ester in DMF was added dropwise to the stirred solution, and the mixture was left at room temperature for 1 h. The reaction was checked for completion by RP-HPLC (system A), and the mixture was acidified to pH ∼2 with 10% HCl (aq). The reaction mixture was evaporated under reduced pressure. The resulting residue was purified by flash chromatography on an RP-C_{18} silica gel column (30 g) with a stepwise gradient of CH_3CN (0–30%) in aq TFA as the mobile phase. The product-containing fractions were lyophilized to give the dipeptide **6** as a white amorphous powder (435 mg, yield 85%, mixture of two racemic diastereomers). IR (KBr) 3396 (broad), 1711, 1544, 1534, 1247 (broad), 1042. ^{1}H NMR (300 MHz, DMSO-d_6): δ 3.12 (m, 1H), 3.35–3.70 (m, 5H), 4.20 (bs, 3H), 6.98 (bd, 1H, N*H*), 7.01, 7.30–7.89 (m, 8H, *H*-Fmoc). ^{13}C NMR (75.5 MHz, DMSO-d_6): δ 38.3 (1C, *β*-CH_2, two diastereomers), 38.4 (1C, *β*-CH_2, two diastereomers), 46.7 (1C, CH-Fmoc, two diastereomers), 64.7 (1C, α′-CH, two diastereomers), 64.9 (1C, α-CH, one diastereomer), 65.0 (1C, α′-CH, one diastereomer), 65.8 (1C, CH_2-Fmoc, two diastereomers), 120.2 (2C, Fmoc, two diastereomers), 125.5 (1C, Fmoc, two diastereomers), 127.3 (2C, Fmoc, two diastereomers), 127.7 (2C, Fmoc, two diastereomers), 140.7 (2C, Fmoc, two diastereomers), 144.0 (2C, Fmoc, two diastereomers), 155.8 (1C, Fmoc, two diastereomers), 167.1 (1C, two diastereomers), 169.2 (1C, two diastereomers), 169.3 (1C, two diastereomers). HPLC (system A): $t_R = 21.7$ and 22.0 min (two diastereomers), purity >95%. MS (ESI, negative mode) *m/z*: 269.93 $[M - 2H]^{2-}$, 541.00 $[M - H]^-$, calcd mass for $C_{21}H_{22}N_2O_{11}S_2$ 542.54. Anal. Calcd for $C_{21}H_{22}N_2O_{11}S_2$: C 46.49, H 4.09, N 5.16, S 11.82. Protected dipeptide **6** proved to be too hygroscopic for a suitable elemental analysis.

α-Sulfo-*β*alaninyl-α-sulfo-*β*-alanine (4). *N*-Fmoc α-sulfo-*β*-alanine dipeptide **6** (88 mg, 0.16 mmol) was dissolved in DMF (1 mL) and cooled to 4 °C. Et_2NH (0.1 mL, 0.96 mmol) was added and the resulting reaction mixture was stirred at room temperature for 1 h. The reaction was checked for completion by RP-HPLC (system A), and the mixture was evaporated under reduced pressure. The resulting residue was taken up in deionized water (10 mL) and washed with CH_2Cl_2 (2 × 5 mL). Finally, the aq solution was lyophilized to give the α-sulfo-*β*-alanine dipeptide linker **4** as a white amorphous powder (66 mg, yield 87%, mixture of two racemic diastereomers). ^{1}H NMR (300 MHz, D_2O): δ 1.23 (t, $J = 7.5$ Hz, 12H, N-CH_2-C*H*$_3$), 3.03 (q, $J = 7.5$ Hz, $J = 14.7$ Hz, 8H, N-C*H*$_2$-CH_3), 3.45–3.63 (m, 3H), 3.78–3.97 (m, 2H), 4.06 (t, $J = 6.4$ Hz, 1H). ^{13}C NMR (75.5 MHz, D_2O): δ 10.9 (4C, N-CH_2-C*H*$_3$), 37.9 (1C, *β*-CH_2, two diastereomers), 39.6 (1C, *β*′-CH_2, two diastereomers), 42.6 (4C, N-C*H*$_2$-CH_3), 61.8 (1C, α-CH, two diastereomers), 61.9 (1C, α′-CH, two diastereomers), 166.5 (1C, two diastereomers), 166.7 (1C, two diastereomers). HPLC (system A): $t_R = 4.8$ min (broad peak, two diastereomers), purity >95%. MS (ESI, negative mode) *m/z*: 159.00 $[M - 2H]^{2-}$, 319.00 $[M - H]^-$, calcd mass for $C_6H_{12}N_2O_9S_2$ 320.30. Dipeptide **4** proved to be too hygroscopic for suitable IR and elemental analyses.

NIR5.5-WS. (a) Preparation of *N*-hydroxysuccinimidyl ester **8**. Cyanine dye **7** (71.2 mg, 0.10 mmol) was dissolved in dry DMF (1.7 mL). TSTU reagent (31.0 mg, 0.10 mmol) and DIEA were added (0.31 mmol). The resulting reaction mixture was protected from light and stirred at room temperature for 30 min. The reaction was checked for completion by RP-HPLC (system B), and the resulting *N*-hydroxysuccinimidyl ester was used without further purification. HPLC (system B): $t_R = 20.5$ min (compared to $t_R = 19.5$ min for cyanine dye carboxylic acid **7**).

(b) Coupling reaction. α-Sulfo-*β*-alanine-α-sulfo-*β*-alanine **4** (52 mg, 0.11 mmol) was dissolved in borate buffer (50 mM, pH 8.2, 1.5 mL) and cooled to 4 °C. The crude solution of *N*-hydroxysuccinimidyl ester in DMF was added dropwise to the stirred solution, and the mixture was left at room temperature overnight. The reaction was checked for completion by RP-HPLC (system C). Finally, the reaction mixture was quenched by dilution with aq TEAB (50 mM, pH 7.5) and purified by flash chromatography on a RP-C_{18} silica gel column (20 g) with a step gradient of CH_3CN (0–60%) in aq TEAB as the mobile phase. The product-containing fractions were lyophilized twice to give the TEA salt of **NIR5.5-WS** as a blue amorphous powder (133 mg, yield 65%, mixture of two racemic diastereomers). ^{1}H NMR (300 MHz, DMSO-d_6): δ 1.13 (t, $J = 7.1$ Hz, 27H, N-CH_2-C*H*$_3$), 1.40 (m, 2H), 1.52 (m, 2H), 1.73 (m, 2H), 1.94 (s, 6H, C*H*$_3$), 1.97 (s, 6H, C*H*$_3$), 2.01–2.06 (m, 4H), 2.63 (t, $J = 6.8$ Hz, 2H), 2.99 (q, $J = 6.8$ Hz, $J = 13.9$ Hz, 18H, N-C*H*$_2$-CH_3), 3.33–3.73 (m, 6H, C*H*$_2$-C*H*(SO_3^-)-CO-), 4.23 (m, 2H), 4.42 (m, 2H), 6.41–6.54 (m, 2H), 6.67 (t, $J = 12.9$ Hz, 1H), 7.47–8.25 (m, 12H), 8.46 (t, $J = 13.2$ Hz, 2H). HPLC (system C): $t_R = 14.5$ min, purity >95%. UV–vis (PBS, pH 7.4, 25 °C): $\lambda_{max} = 679$ nm (197 000 M^{-1} cm^{-1}). UV–vis (DMSO, 25 °C): $\lambda_{max} = 688$ nm (147 000 M^{-1} cm^{-1}). UV–vis (EtOH, 25

°C): λ_{max} = 685 nm (138 000 M^{-1} cm^{-1}). Φ_F (PBS, pH 7.4, 25 °C): 0.066. Φ_F (DMSO, 25 °C): 0.26. Φ_F (EtOH, 25 °C): 0.16. MS (ESI, positive mode): *m/z* 1094.33 $[M + TEA + H]^+$, 1195.13 $[M + 2TEA + H]^+$, 1295.93 $[M + 3TEA + H]^+$. (ESI, negative mode): *m/z* 495.20 $[M - 2H]^{2-}$, 991.27 $[M - H]^-$, calcd for $C_{48}H_{56}N_4O_{13}S_3$ (**NIR5.5-WS**, acid form) 993.19.

R6G-WS. (a) Preparation of *N*-hydroxysuccinimidyl ester. A mixture of **10** (60.9 mg, 0.11 mmol) and *N*-hydroxysuccinimide (13.8 mg, 0.12 mmol) was dissolved in dry DMF (2.5 mL). DCC (24.8 mg, 0.12 mmol) was added, and the resulting reaction mixture was protected from light and stirred at room temperature overnight. The reaction was checked for completion by ESI-MS, and the resulting *N*-hydroxysuccinimidyl ester was used without further purification. MS (ESI, positive mode) *m/z*: 570.33 $[M + H]^+$, calcd for $C_{32}H_{32}N_3O_7^+$ 570.63.

(b) Coupling reaction. α-Sulfo-β-alanine-α-sulfo-β-alanine **4** (56 mg, 0.12 mmol) was dissolved in borate buffer (50 mM, pH 8.2, 1.9 mL) and cooled to 4 °C. The crude solution of *N*-hydroxysuccinimidyl ester in DMF was added dropwise to the stirred solution, a further amount of DMF (0.5 mL) was added, and the mixture was left at room temperature overnight. The reaction was checked for completion by RP-HPLC (system B). Finally, the reaction mixture was quenched by dilution with aq TFA and purified by RP-HPLC (system D, three injections, t_R = 18.5–20.0 min). The product-containing fractions were lyophilized to give **R6G-WS** as a red amorphous powder (yield 38%, mixture of two racemic diastereomers). ^{1}H NMR (300 MHz, DMSO-d_6): δ 1.25 (t, *J* = 7.0 Hz, 6H, N-CH_2-CH_3), 2.09 (s, 6H, CH_3), 3.23 (m, 1H), 3.45–3.62 (m, 9H, N-CH_2-CH_3 and CH_2-$CH(SO_3^-)$-CO-), 4.39 (s, 2H, O-CH_2-CO-), 6.79 (s, 2H), 6.91 (s, 2H), 7.44 (d, *J* = 7.2 Hz, 1H), 7.67–7.93 (m, 6H, 4 × NH and 2 × ArH), 8.47 (m, 1H). HPLC (system B): t_R = 12.8 min, purity >95%. UV–vis (PBS, pH 7.4, 25 °C): λ_{max} = 528 nm (65 000 M^{-1} cm^{-1}). UV–vis (DMSO, 25 °C): λ_{max} = 539 nm (79 000 M^{-1} cm^{-1}). Φ_F (PBS, pH 7.4, 25 °C): 1.02. MS (ESI, positive mode): *m/z* 775.20 $[M + H]^+$. (ESI, negative mode): *m/z* 773.20 $[M - H]^-$, calcd for $C_{34}H_{38}N_4O_{13}S_2$ (**R6G-WS**, acid form) 774.83.

***N*-(Sulforhodamine 101)-L-glycine (12).** (a) Preparation of *N*-(sulforhodamine 101)-L-glycine *tert*-butyl ester **11**. Sulforhodamine 101 (50 mg, 0.08 mmol) was dried under high vacuum for 2 h. The resulting dried powder was mixed with 310 μL of phosphorus oxychloride (3.38 mmol). The mixture was stirred at room temperature under an argon atmosphere for 19 h. Thereafter, $POCl_3$ was removed under vacuum, and the resulting residue was dried under high vacuum at room temperature for 1 h. A 25 mL round-bottom flask containing a solution of H-Gly-OtBu (HCl salt, 31.5 mg, 0.19 mmol) and TEA (58 μL, 0.42 mmol) in dry DMF (0.6 mL) was cooled to 4 °C, and a DMF solution of the crude Texas Red sulfonyl chloride (1.4 mL) was dropwise added over 10 min. The resulting reaction mixture was protected from light and stirred overnight at room temperature under an argon atmosphere. The reaction was checked for completion by TLC (CH_2Cl_2/CH_3OH 9:1, v/v, R_f 0.53). The reaction mixture was evaporated under reduced pressure. The resulting residue was dissolved in CH_2Cl_2 (20 mL) and washed with deionized water (20 mL). The organic layer was dried over Na_2SO_4 and purified by flash chromatography on a silica gel column (silica gel 60A CC, 70–200 μm, Chromagel, SdS, 15 g) with 10% methanol in CH_2Cl_2 as eluant to give 37 mg of *tert*-butyl ester derivative **11**.

(b) Removal of *tert*-butyl ester. The above *tert*-butyl ester **11** was dissolved in CH_2Cl_2 (2 mL) and cooled to 4 °C. TFA (382 μL) and deionized water (10 μL) were added, and the resulting reaction mixture was warmed to room temperature and stirred for 4 h. The reaction was checked for completion by RP-HPLC (system B), and the mixture was evaporated to dryness. TFA was removed by azeotropic distillation with chloroform (2 × 10 mL). The resulting residue was partially dissolved in deionized water and lyophilized, giving the TFA salt of **12** as a bluish red amorphous powder (46 mg, overall yield 62%, mixture of the two regioisomers in a ratio 8:2). The analytical sample of the dye (TEA salt) was obtained by RP-HPLC purification (system E, t_R = 22.5–24.0 min). ^{1}H NMR (300 MHz, DMSO-d_6): δ 1.11 (t, *J* = 7.1 Hz, 9H, N-CH_2-CH_3), 1.84–2.01 (bm, 8H, 4 × CH_2), 2.50–2.97 (m, 14H, 4 × CH_2 and N-CH_2-CH_3), 3.49 (bm, 10H, 4 × CH_2 and CH_2-Gly), 6.53 (s, 1.55H, major regioisomer), 6.58 (s, 0.45H, minor regioisomer), 7.32 (bd, *J* = 7.9 Hz, 1H, ArH), 7.88–7.98 (m, 1H, ArH), 8.24 (s, 0.22H, ArH, minor regioisomer), 8.37 (s, 0.78H, ArH, major regioisomer). HPLC (system B): t_R = 14.3 and 15.6 min (two regioisomers), purity >90%. MS (ESI, positive mode): *m/z* 664.33 $[M + H]^+$. MS (ESI, negative mode): *m/z* 662.07 $[M - H]^-$, calcd for $C_{33}H_{33}N_3O_8S_2$ 663.77.

TR-WS. (a) Preparation of *N*-hydroxysuccinimidyl ester. Texas Red carboxylic acid (14.2 mg, 16 μmol) was dissolved in dry DMF (300 μL). TSTU reagent (4.80 mg, 16 μmol) and DIEA were added (11 μL, 63.7 μmol). The resulting reaction mixture was protected from light and stirred at room temperature for 90 min. The reaction was checked for completion by RP-HPLC (system B) and ESI-MS. The resulting *N*-hydroxysuccinimidyl ester was used without further purification. HPLC (system B): t_R = 22.0 min. MS (ESI, positive mode), *m/z*: 761.20 $[M + H]^+$, calcd for $C_{37}H_{36}N_4O_{10}S_2$ 760.85.

(b) Coupling reaction. α-Sulfo-β-alanine-α-sulfo-β-alanine **4** (12 mg, 25.6 μmol) was dissolved in bicarbonate buffer (0.1 M, pH 8.2, 0.5 mL) and cooled to 4 °C. The crude solution of *N*-hydroxysuccinimidyl ester in DMF was added dropwise to the stirred solution, a further amount of bicarbonate buffer (0.3 mL) was added, and the mixture was left at room temperature overnight. The reaction was checked for completion by RP-HPLC (system C). Finally, the reaction mixture was quenched by dilution with aq TEAB (50 mM, pH 7.5) and purified by RP-HPLC (system E, two injections, t_R = 19.5–21.0 min). The product-containing fractions were lyophilized thrice to give the TEA salt of **TR-WS** as a bluish red amorphous powder (7.1 mg, yield 34%, mixture of two regioisomers, each consisting of two racemic diastereomers). ^{1}H NMR (300 MHz, D_2O): δ 1.23 (t, *J* = 7.3 Hz, 27H, N-CH_2-CH_3), 1.86 (bm, 8H, 4 × CH_2), 2.56–3.07 (m, 8H, 4 × CH_2), 3.16 (q, *J* = 7.3 Hz, *J* = 14.6 Hz, 18H, N-CH_2-CH_3), 3.27–3.95 (m, 16H, 4 × CH_2, 2 × CH_2-$CH(SO_3^-)$-CO- and CH_2-Gly), 6.47 (s, 1.25H, major regioisomer), 6.51 (s, 0.75H, minor regioisomer), 7.19 (bd, *J* = 8.2 Hz, 0.37H, ArH, minor regioisomer), 7.26 (bd, *J* = 7.3 Hz, 0.63H, ArH, major regioisomer), 8.07 (bd, *J* = 8.4 Hz, 0.63H, ArH, major regioisomer), 8.13 (bd, *J* = 7.5 Hz, 0.37H, ArH, minor regioisomer), 8.48 (s, 0.63H, ArH, major regioisomer), 8.55 (s, 0.37H, ArH, minor regioisomer). HPLC (system C): t_R = 12.4 and 12.5 min (two regioisomers, each consisting of two racemic diastereomers), purity >98%. UV–vis (PBS, pH 7.4, 25 °C): λ_{max} = 590 nm (85 000 M^{-1} cm^{-1}). Φ_F (PBS, pH 7.4, 25 °C): 0.52. MS (ESI, negative mode): *m/z* 964.00 $[M - H]^-$, calcd for $C_{39}H_{43}N_5O_{16}S_4$ (**TR-WS**, acid form) 966.06.

General Procedure for the Conversion of Water-Soluble Fluorophores into Amine-Reactive Derivatives. Water-soluble dye carboxylic acid (1.72 μmol, weighed in a 1.5 mL Eppendorf tube) was dissolved in 50 μL of dry NMP (or DMF). 25 μL of a solution of TSTU reagent in dry NMP (or DMF) (0.51 mg, 1.72 μmol) and 1.2 μL of DIEA (6.88 μmol) were added, and the resulting reaction mixture was protected from light and periodically vortexed for 30 min. The reaction was checked for completion by ESI-MS, and the amine-reactive derivatives (mixture of NHS ester and oxazinone intermediate) were used in the next step without further purification.

Scheme 1. Preparation of Disulfonated Peptide Linker 4

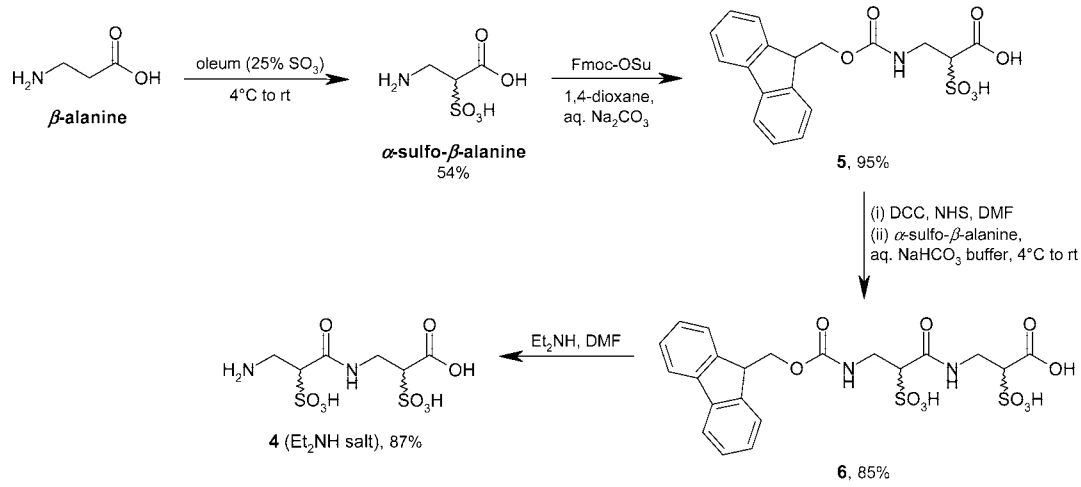

Optical Properties of Water-Soluble Fluorophores. The absorption spectrum of the novel water-soluble cyanine and rhodamine dyes were recorded (220–900 nm) in DMSO, EtOH, and PBS (0.1 M phosphate, 0.15 M NaCl, pH 7.4) (concentration: 1.0–5.0 μM) at 25 °C. Emission spectra were recorded under the same conditions after excitation at the following wavelengths: 488 nm (for **R6G-WS**), 550 nm (for **TR-WS**), and 600 nm (for **NIR5.5-WS**) (excitation and emission slit = 5 nm). Relative quantum yields were measured in DMSO, EtOH, and PBS at 25 °C by a relative method using sulfocyanine dye Cy 5.0 (for **NIR5.5–3**, $\Phi_F = 0.20$ in PBS), rhodamine 6G (for **R6G-WS**, $\Phi_F = 0.90$ in water), or sulforhodamine 101 (for **TR-WS**, $\Phi_F = 0.90$ in EtOH). The following equation was used to determine the relative fluorescence quantum yield:

$$\Phi_F(X) = (A_S/A_X)(F_X/F_S)(n_X/n_S)^2\ \Phi_F(S)$$

Where A is the absorbance (in the range 0.01–0.1 A.U.), F is the area under the emission curve, n is the refractive index of the solvents (at 25 °C) used in measurements ($n = 1.337$ for PBS, 1.361 for EtOH, and 1.479 for DMSO), and the subscripts s and x represent standard and unknown, respectively.

Synthesis of Ac-Lys(NIR5.5-WS)-Asp-Glu-Val-Asp-Lys-(NIR5.5-WS)-NH_2 (15). Hexapeptide Ac-Lys-Asp-Glu-Val-Asp-Lys-NH_2 **14** (0.24 μmol, weighed in a 1.5 mL Eppendorf tube) was dissolved in 0.1 M sodium bicarbonate buffer (pH 8.5, 200 μL) and cooled to 4 °C. A crude solution of the amine-reactive derivatives of NIR5.5-WS **13** (0.50 μmol) was added. The reaction mixture was protected from light and stirred at room temperature for 2 h. Thereafter, 0.1 M borate buffer (pH 8.75, 200 μL) and DMF (200 μL) were added and the reaction mixture was stirred at room temperature overnight. The progress of the reaction was checked by RP-HPLC (system C). Finally, the reaction mixture was quenched by dilution with aq TEAB (50 mM, pH 7.5, 1 mL) and purified by RP-HPLC (system F, 1 injection). The product-containing fractions were lyophilized to give the peptide Ac-Lys(**NIR5.5-WS**)-Asp-Glu-Val-Asp-Lys(**NIR5.5-WS**)-NH_2 **15** as a blue amorphous powder. Stock solution of fluorogenic caspase-3 substrate **15** was prepared in Milli-Q grade water and quantification was achieved by UV–vis measurements in DMSO (to prevent the formation of the intramolecular homodimer between the two **NIR5.5-WS** units) at λ_{max} = 689 nm of **NIR5.5-WS** by using the ϵ value 147 000 M^{-1} cm^{-1} (yield after RP-HPLC purification: 25%). UV–vis (PBS, 25 °C): λ_{max} = 627 nm. UV–vis (DMSO, 25 °C): λ_{max} = 689 nm (147 000 M^{-1} cm^{-1}). HPLC (system C): t_R = 18.4, 18.8, 19.1, and 19.4 min (16 diastereomers), purity >95%. MS (ESI, negative mode): m/z 1361.00 $[M - 2H]^{2-}$, calcd mass for $C_{128}H_{163}N_{17}O_{37}S_6$ 2724.20.

***in Vitro* Peptide Cleavage by Recombinant Human Caspase-3.** A 1.0 μM solution of peptide **15** was prepared in 50 μL of caspase-3 buffer (100 mM NaCl, 40 mM HEPES, 10 mM DTT, 1 mM EDTA, 10% (w/v) sucrose, and 0.1% (w/v) CHAPS, pH 7.4) and transferred into an ultramicrofluorescence cell. 2 μL of human recombinant caspase-3 (3.2 10^{-3} U) was added, and the resulting mixture was incubated at 37 °C. After excitation at 679 (excitation slit = 5 nm), fluorescence emission at 705 nm (emission slit = 5 nm) was monitored over time with measurements recorded every 5 s.

RESULTS AND DISCUSSION

Synthesis. α-Sulfo-β-alanine was chosen as the monomer for the targeted disulfonated peptide linker **4** for the following reasons: (1) the presence of a sulfonic acid moiety which is probably the most popular fluorophore water-solubilizing functionality, (2) chemical reactivity similar to that of natural amino acids especially in the context of peptide synthesis (i.e., protection/deprotection and peptide coupling reactions), and (3) commercial availablility or easy synthesis on a large scale from cheap starting materials (i.e., β-alanine and oleum). Surprisingly, few synthetic applications of this non-natural amino acid have been reported to date in the literature. In the field of nucleic acid chemistry, it has only been successfully used to modify the electrophoretic mobility of fluorescent nucleotides to simplify the implementation of dye-terminator DNA sequencing (*20*).

The target disulfonated linker **4** was prepared as depicted in Scheme 1. A sulfonic acid group was first introduced on β-alanine using fuming sulfuric acid (i.e., oleum) (*21*). Racemic α-sulfo-β-alanine was then converted to the *N*-Fmoc-protected derivative **5** by reaction with *N*-hydroxysuccinimidyl 9-fluorenylmethyl carbonate (Fmoc-OSu) under standard conditions (*22*). Purification by flash chromatography on a RP-C_{18} silica gel column provided **5** in almost quantitative yield. Thereafter, peptide coupling reaction of **5** with a second unit of α-sulfo-β-alanine was achieved by using the DCC/*N*-hydroxysuccinimide (NHS) method (for a recent review on peptide coupling reagents, see (*23*)). To avoid two additional steps (i.e., protection/deprotection of the carboxylic acid function of α-sulfo-β-alanine), **5** carboxylic acid moiety was converted to the NHS active ester and then coupled onto the unprotected α-sulfo-β-alanine under Schotten−Baumann conditions (*22*), providing the *N*-Fmoc-protected dipeptide **6** in 85% yield (mixture of two racemic diastereomers). Removal of the Fmoc protective group by treatment with a six-fold excess of diethylamine in DMF afforded the bis(diethylammonium) salt of α-sulfo-β-alaninyl-

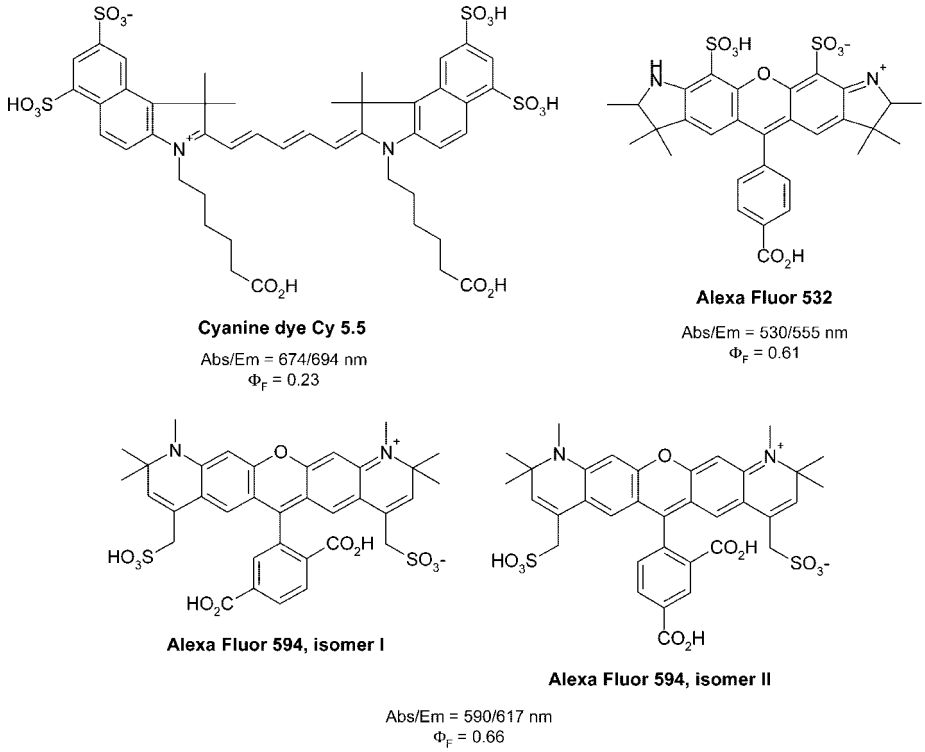

Figure 2. Structures and spectral properties in PBS of commercially available cyanine dye Cy 5.5 and Alexa Fluor 532 and 594 dyes.

Scheme 2. Synthesis of Cy 5.5 Analogue NIR5.5-WS

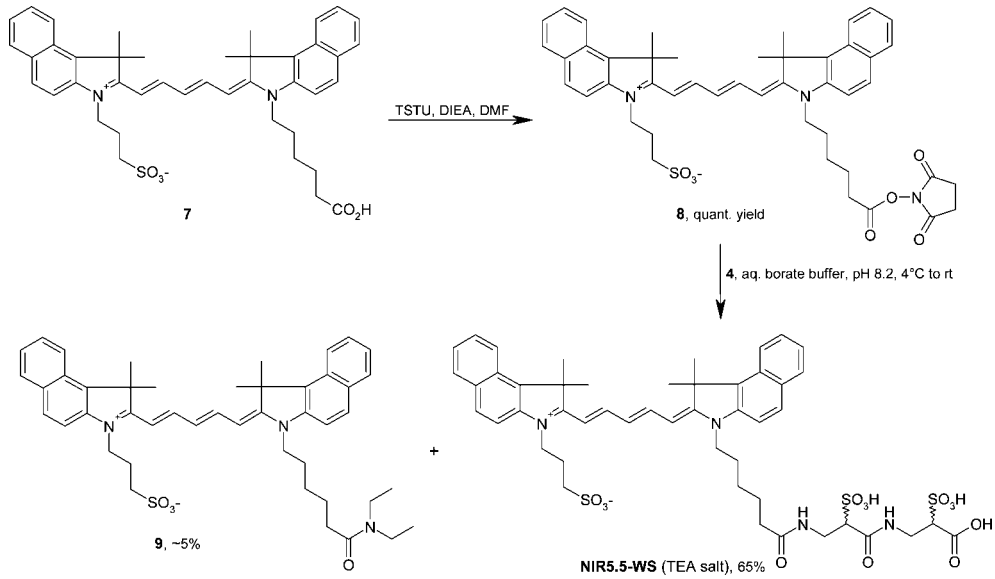

α-sulfo-*β*-alanine **4** as an inseparable mixture of two racemic diastereomers (yield 87%).

To demonstrate the utility of this dipeptide linker as both a highly effective water-solubilizing agent and a reactive spacer for biolabeling applications, we explored the postsynthetic derivatization of three different long-wavelength highly hydrophobic fluorophores. First, the linker was grafted on cyanine dye **7** through a peptide coupling reaction. This near-infrared (NIR) organic dye exhibits the same spectral properties as the widely used sulfobenzoindocyanine dye Cy 5.5 (commercially available from GE Healthcare; Figure 2). It was conveniently prepared using a four-step reaction (overall yield 70%) and could be purified by flash chromatography on a silica gel column at gram quantities, contrary to its parent tetrasulfonated dye Cy 5.5 (*8*). As expected, dye **7** was found to be poorly soluble in water and related aqueous buffers (pH range 2–9). In order to increase its solubility in aqueous solutions, hydrophilic linker **4** was attached to the carboxylic acid side chain in a two-step procedure as described in Scheme 2. Dye **7** was quantitatively converted into the corresponding *N*-hydroxysuccinimidyl ester **8** by treatment with the peptide coupling uronium reagent TSTU and DIEA in dry DMF (*24*). Thereafter, acylation of the primary amino group of **4** with the crude active ester **8** in borate buffer (pH 8.2) containing DMF (to avoid precipitation of **8**) with a controlled slow warming from 4 °C to room temperature, yielded almost exclusively the targeted water-soluble analogue **NIR5.5-WS**. A small amount of (*N*,*N*-diethyl)carboxamide derivative **9** (∼5%) resulting from the acylation reaction of the counterion of disulfonated linker **4**, was also detected in the crude reaction mixture. **NIR5.5-WS** was readily purified by flash chromatog-

Scheme 3. Synthesis of Rhodamine 6G Analogue R6G-WS

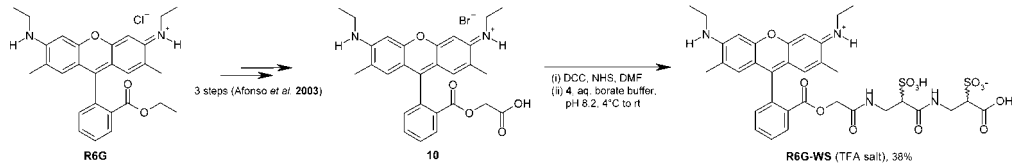

Scheme 4. Synthesis of Texas Red Analogue TR-WS

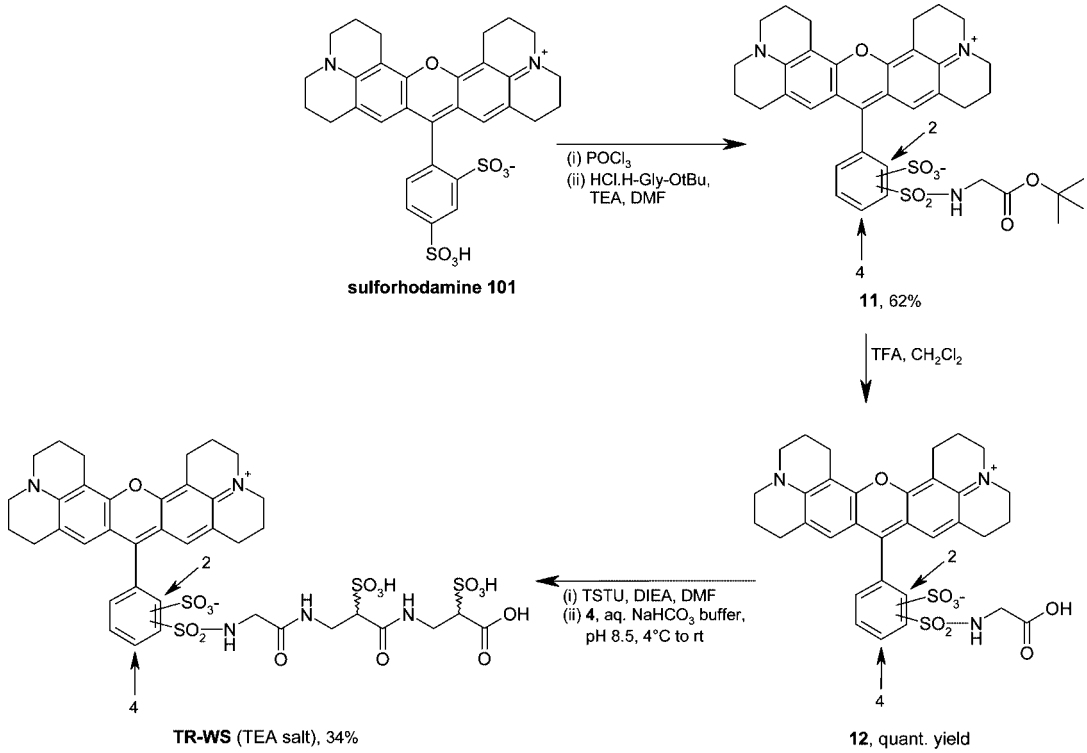

raphy on an RP-C_{18} silica gel column (mixture of two racemic diastereomers, isolated yield 65%) using triethylammonium bicarbonate buffer (TEAB, 50 mM, pH 7.5) and acetonitrile as eluents. The covalent attachment of disulfonated linker **4** to the γ-carboxypentyl arm of cyanine dye **7** was confirmed by detailed measurements, including ESI mass spectrometry and NMR analyses. As expected, **NIR5.5-WS** was found to be perfectly soluble in water and related aqueous buffers in the concentration range (1 μM to 10 mM) suitable for biomolecular labeling applications.

To extend the scope of reagent **4** to the water solubilization of rhodamine derivatives, the efficient postsynthetic sulfonation procedure (described above) was applied to rhodamine 6G (R6G) and sulforhodamine 101 (i.e., Texas Red, TR).

As R6G dye does not contain any free carboxylate functionality, it was first converted to the rhodamine carboxylic acid **10** using a three-step procedure reported by Afonso et al. (*17*). This reactive R6G analogue was coupled to the disulfonated linker **4** in the same manner as described for dye **7** (Scheme 3), to give the desired water-soluble rhodamine **R6G-WS** in a moderate yield (isolated yield 38%). Indeed, a significant amount of starting material **10** was detected in the crude reaction mixture and recovered after RP-HPLC purification. The NHS ester of **10** seems to be more prone to hydrolysis than the NHS ester of **7**. Purification of **R6G-WS** was achieved by semipreparative RP-HPLC using 0.1% aqueous trifluoroacetic acid (TFA, pH 2.0) and acetonitrile as eluents. Contrary to the purification of cyanine dye **NIR5.5-WS**, aqueous TFA afforded better peak resolution than TEAB buffer for the purification of **R6G-WS**.

Conjugation of sulforhodamine 101 to disulfonated dipeptide **4** also required prior functionalization of one of the two sulfonate groups of its lower ring component. The most popular fluorescent labeling reagents derived from this disulfonated rhodamine, Texas Red sulfonyl chloride (TR-SC) (*25*) and Texas Red-X succinimidyl ester (TR-X-SE) (*26*), are of delicate use for bioconjugation. TR-SC is known to be unstable to moisture during storage and prone to hydrolysis in the conjugation reactions, especially those performed in aqueous buffers. TR-X-SE exhibits improved labeling properties, but this compound contains a six-atom-long hydrophobic spacer (i.e., HN-$(CH_2)_5$-) between the fluorescent label and the reactive carboxylic acid group. In order to get a water-soluble Texas Red analogue with a shorter heterobifunctional linker, we envisaged the introduction of a glycine residue (Scheme 4). Sulforhodamine 101 was first converted to TR-SC by treatment with a large excess of phosphorus oxychloride. After removal of $POCl_3$, the crude sulfonyl chloride derivative was directly reacted with glycine *tert*-butyl ester and TEA in dry DMF to give ester **11** in 62% yield. This product was obtained as a 8:2 mixture of two regioisomers (i.e., ortho and para monosulfonamides) which was used in the next steps without chromatographic resolution. Quantitative removal of *t*Bu ester by treatment with TFA (100 equiv) in CH_2Cl_2 provided the sulforhodamine 101 carboxylic acid **12**. Despite the presence of two hydrophilic groups within its rhodamine core, **12** was found to be poorly soluble in aqueous solutions even after conversion to its bis(triethylammonium) salt. Preactivation of **12** with TSTU/DIEA afforded amide bond formation between **12** and linker **4** to give the target water-

Table 1. Optical Properties of Water-Soluble Cyanine and Rhodamine Dyes

compound	solvent	$\lambda_{max,abs}$ (nm)	$\lambda_{max,em}$ (nm)	Stokes shift (nm)	ϵ (M^{-1} cm^{-1})	Φ_F[c]
Cy 5.5[a]	PBS	674	694	20	195 000	0.23
Cy 5.5 analogue 7[b]	DMSO	688	711	23	147 000	0.27
Cy 5.5 analogue 1	PBS	680	710	30	197 000	0.047
NIR5.5-WS	PBS	679	700	21	197 000	0.066
R6G-WS	PBS	528	553	25	65 000	1.00
TR-WS	PBS	590	609	19	85 000	0.52
Alexa Fluor 594, isomer I	PBS	584	608	24	73 000	0.61[d]
Alexa Fluor 594, isomer II	PBS	585	612	27	73 000	0.56[d]

[a] Values reported by Mujumdar et al. (*37*). [b] Determination of QY in PBS was not possible due to the nonsolubility of this Cy 5.5 analogue in aq buffers even at low concentrations. [c] Determined at 25 °C by using sulfocyanine dye Cy 5.0 (for **NIR5.5-WS**, $\Phi_F = 0.20$ in PBS (*38*)), rhodamine 6G (for **R6G-WS**, $\Phi_F = 0.90$ in water (*39*)), or sulforhodamine 101 (for **TR-WS**, $\Phi_F = 0.90$ in EtOH according to PhotochemCAD database available free of charge at http://omlc.ogi.edu/spectra/PhotochemCAD/html/Sulforhodamine101.html) as a standard. [d] Determined in our conditions but slightly different from the QY value reported by Invitrogen ($\Phi_F = 0.66$ for Alexa Fluor 594 carboxylic acid, succinimidyl ester in 50 mM potassium phosphate, 150 mM NaCl pH 7.2 at 22 °C).

Scheme 5. Fluorescent Labeling of Caspase-3 Cleavable Hexapeptide Ac-Lys-Asp-Glu-Val-Asp-Lys-NH_2 14 with NIR5.5-WS

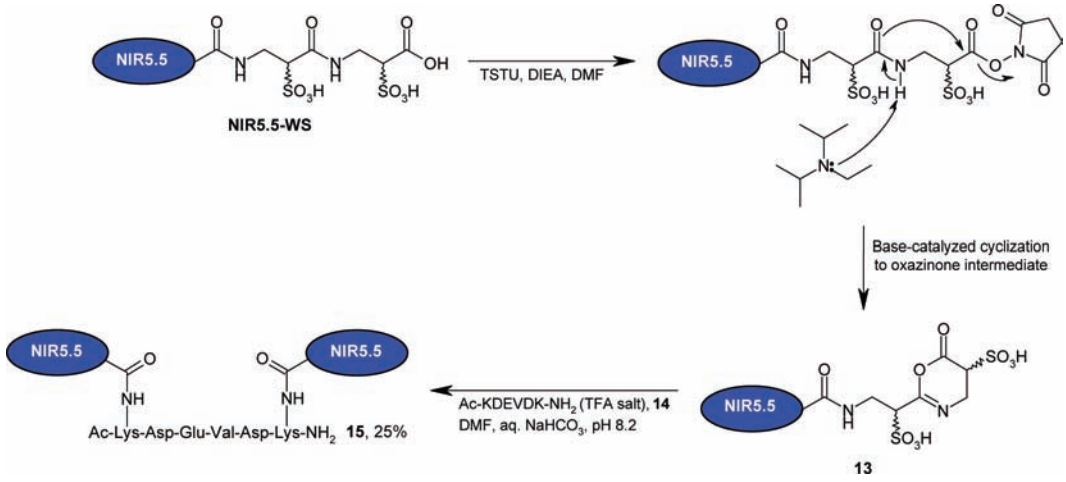

soluble rhodamine **TR-WS**. RP-HPLC purification using TEAB buffer and acetonitrile as eluents provided **TR-WS** in a pure form (mixture of two regioisomers, each consisting of two racemic diastereomers, isolated yield 34%), together with the recovery of 50% of the sulforhodamine 101 carboxylic acid derivative **12** resulting from the partial early hydrolysis of NHS ester. The structures of **R6G-WS** and **TR-WS** were unambiguously confirmed by ESI mass and NMR analyses. As expected, these rhodamine derivatives show perfect water solubility in the same concentration range as that determined for **NIR5.5-WS**.

Photophysical Properties. The photophysical properties of the three novel water-soluble fluorophores available were evaluated and collected in Table 1 (for their normalized absorption and emission spectra, see Supporting Information). In order to know whether the presence of the hydrophilic dipeptide linker affected the spectral properties of the fluorophore core, fluorescence data were compared with those of the original water-insoluble analogues. **NIR5.5-WS**, **R6G-WS**, and **TR-WS** have absorption and emission bands that match closely those of **7**, R6G, and TR, respectively, in both phosphate-buffered saline (PBS) and DMSO. Furthermore, molar absorption coefficients (ϵ) are comparable to these latter starting materials, and quantum yields (Φ) are good to excellent for the rhodamine derivatives. Interestingly, brightness ($\Phi\epsilon$) of **TR-WS** was found to be similar to that of Alexa Fluor 594 dye (isomer I or II), a water-soluble analogue of Texas Red commercially available from Invitrogen (Figure 2) (*11*). However, the structure of Alexa dye is not directly accessible through the chemical derivatization of sulforhodamine 101. Its synthesis using an original five-step sequence as described (*18*) is more difficult and tedious than that of **TR-WS**, and consequently, the corresponding fluorescent labeling reagent (i.e., NHS ester, two mixed regioisomers) is very expensive. The relative fluorescence quantum yield of cyanine dye **NIR5.5-WS** measured in PBS is slightly higher than the one we obtained for the Cy 5.5 analogue bearing the trisulfonated aryl linker **1** (0.066 compared to 0.047) but significantly lower than the one reported for Cy 5.5 dye (0.066 compared to 0.23). This severe quenching of fluorescence cannot be explained by a photoinduced electron transfer (PET) process or by the self-aggregation of cyanine dye molecules. Indeed, **NIR5.5-WS** does not contain amino-aromatic ring moieties, and its UV–vis absorption maximum is not blue-shifted by about 50 nm as expected when dye-dye aggregation occurs (see Supporting Information) At this stage of the study, we do not have relevant explanation(s) for the fluorescence intensity decrease of **NIR5.5-WS** observed in aqueous solutions.

Labeling Properties. To demonstrate the general applicability of these novel water-soluble organic dyes as biocompatible fluorescent labeling reagents, **NIR5.5-3**, **R6G-WS**, and **TR-WS** were converted into amine-reactive derivatives and subsequently coupled to peptides and proteins. As an illustrative example, caspase-3 cleavable hexapeptide Ac-Lys-Asp-Glu-Val-Asp-Lys-NH_2 **14** (cleavage site after the aspartic acid residue at the C-terminal side) was fluorescently labeled with **NIR5.5-WS** on each side of the cleavage site (Scheme 5) in order to get a novel fluorogenic substrate useful for imaging apoptosis (for other examples of FRET-based probes used for caspase-3 detection, see *27–31*). Indeed, cyanine dyes such as Cy 5.5 (or these analogues) are known to form dimers (i.e., H-aggregates) when two fluorophores are closely associated within a peptide architecture, the spectral characteristics of these H-type dimers are a blue shift in absorption spectrum and the loss of

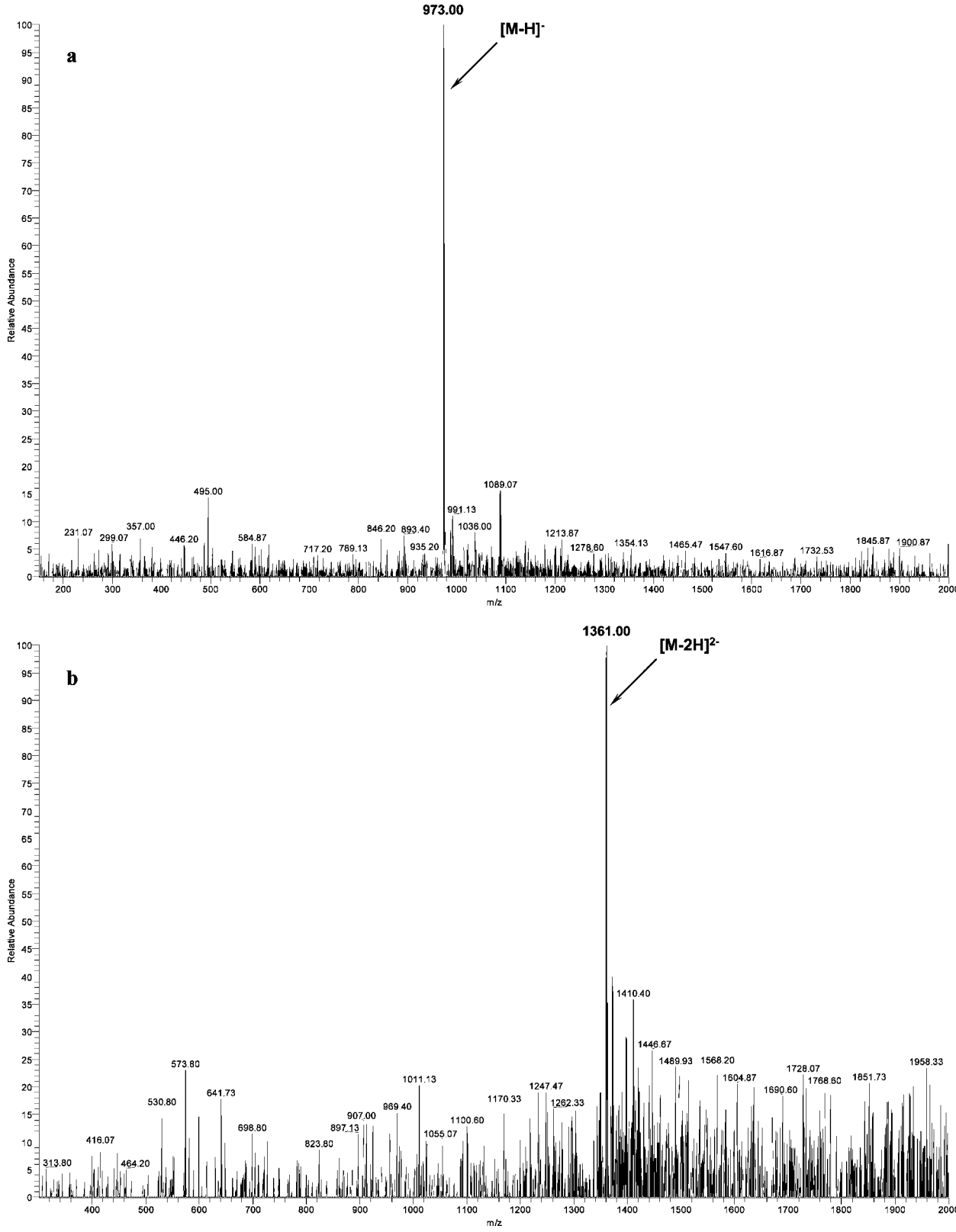

Figure 3. ESI mass spectra of oxazinone intermediate **13** (a) and fluorogenic substrate of caspase-3 **15** (b), in the negative mode. For compound **13** $[M - H]^-$: *m*/*z* calcd mass 973.28, found 973.00. For peptide **15** $[M - 2H]^{2-}$: *m*/*z* calcd mass 1359.98, found 1361.00.

fluorescence (*32*, *33*). Cleavage of such a dual-fluorescent-labeled peptide by the suitable protease results in disruption of the H-type dimer and appearance of fluorescence. The hydrophilic dye **NIR5.5-WS** was converted into an amine-reactive derivative by treatment with TSTU/DIEA in dry DMF. Interestingly, this reaction mainly led to a dehydration product (the molecular ion $[M - 18 - H]^-$ was observed in the ESI mass spectrum of each crude active ester mixture, Figure 3a), probably the oxazinone intermediate **13** (i.e., sulfonated 4,5-dihydro-6*H*-1,3-oxazin-6-one) resulting from base-catalyzed intramolecular cyclization of the generated NHS ester. This side reaction is of no consequence, since the reactivity of **13** toward amine-containing compounds is similar to the NHS ester initially targeted. Acylation of both lysine residues of hexapeptide **14**

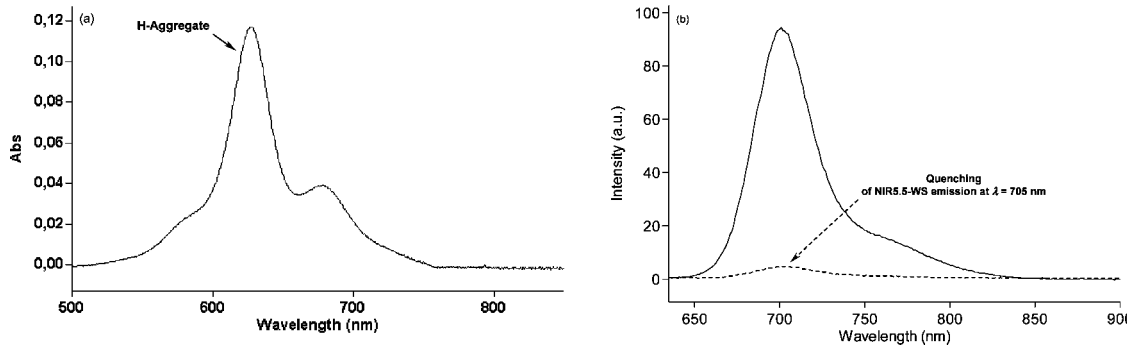

Figure 4. (a) Absorption spectrum of probe **15** at 25 °C in PBS. (b) Emission spectra (Ex. $\lambda = 625$ nm) of **NIR5.5-WS** (—) and probe **15** (---) at 25 °C in PBS (concentration 3.3 μM).

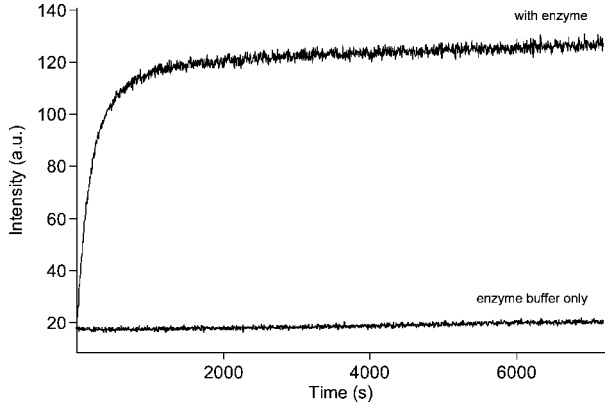

Figure 5. Fluorescence emission time course of probe **15** (concentration 1.0 μM) with recombinant human caspase-3 (3.2 10^{-3} U, incubation time 120 min) in caspase assay buffer (100 mM NaCl, 40 mM HEPES, 10 mM DTT, 1 mM EDTA, 10% (w/v) sucrose and 0.1% (w/v) CHAPS, pH 7.2, 37 °C) at 705 nm (Ex. $\lambda = 679$ nm).

with this reactive oxazinone derivative in a mixture of DMF and bicarbonate buffer (pH 8.5) provided, after RP-HPLC purification, the NIR dye−peptide conjugate **15** (yield 25%, purity >95%). Its structure was confirmed by ESI mass spectrometry (Figure 3b), a single peak at *m*/*z* 1361.00 corresponding to the doubly charged negative ion $[M - 2H]^{2-}$ of **15** was observed. The formation of a H-dimeric complex between the two **NIR5.5-WS** units was inferred from absorption and emission spectra of the probe recorded in PBS (Figure 4). Indeed, a new peak, which is blue-shifted by about 50 nm from the absorption peak of the free **NIR5.5-WS** dye, was observed, and no significant emission at 700 nm corresponding to the **NIR5.5-WS** fluorescence was detected (diminished by 20 fold compared to the fluorescence of free **NIR5.5-WS** dye at the same concentration). Finally, this fluorogenic probe was tested against human recombinant caspase-3. Within 120 min, the fluorescence emission of **15** at 705 nm has increased about 7-fold, while no activation was observed when peptide **15** was incubated only with the caspase-3 buffer (Figure 5). This observation confirms that this fluorogenic peptide-based probe is a substrate for recombinant caspase-3 protease.

CONCLUSION

In conclusion, we have described the synthesis and photophysical properties of three novel water-soluble long-wavelength fluorophores **NIR5.5-WS**, **R6G-WS**, and **TR-WS** which are potential substitutes of commercially available Cy 5.5, Alexa Fluor 532, and Alexa Fluor 594 labels, respectively. The developed "postsynthetic derivatization" approach, involving the selective introduction of a hydrophilic dipeptide linker on the carboxylic acid functionality of fluorescent scaffold, enables straightforward synthetic access to the targeted water-soluble analogues. With this method, it will also be possible to enhance the water solubility of a wide range of highly hydrophobic dyes for which there are no hydrophilic analogues (e.g., boron-stabilized cyanine dyes (*34*), perylene-3,4:9,10-tetracarboxydiimide (PTCDI) chromophores (*35*), etc.), by increasing the number of α-sulfo-β-alanine residues in the linker arm. Furthermore, preliminary experiments have clearly shown that the C-terminal side chain of the disulfonated linker found in **NIR5.5-WS**, **R6G-WS**, and **TR-WS** can be easily converted into an amine-reactive group (i.e., active ester or oxazinone intermediate), a thiol-reactive group (i.e., iodoacetyl derivative), or a terminal alkyne (by coupling with a propargylamine moiety) bioconjugatable through the Huisgen reaction (*36*). Thus, these novel water-soluble bright dyes possess strong potential for a broad range of biolabeling applications. Furthermore, such a poly(α-sulfo-β-alanine) linker can be used as an inert and biocompatible spacer in surface engineering (to make biopolymer microarrays) and in the modification of proteins and peptides for drug delivery.

ACKNOWLEDGMENT

The contribution of Dr. Evelyne Muller (Manteia Predictive Medicine SA) to the total synthesis of Alexa Fluor 594 dye is greatly acknowledged. We thank Annick Leboisselier (CNRS UMR 6014) for the determination of elemental analyses, Dr. Jérôme Leprince (U 413 INSERM/IFRMP 23) for the solid-phase synthesis of hexapeptide **14**, and Dr. Céline Pérollier (University of Geneva) for NMR characterization of both isomers of Alexa Fluor 594 dye. Financial support for this work was provided by "Région Haute Normandie" and by "Fondation pour la Recherche Médicale."

Supporting Information Available: Characterization data for compounds **4-12**, **NIR5.5-WS**, **R6G-WS**, and **TR-WS**. RP-HPLC elution profile of fluorogenic probe **15**. This material is available free of charge via the Internet at http://pubs.acs.org/BC.

LITERATURE CITED

(1) Haugland, R. P. (2006) *The Handbook. A Guide to Fluorescent Probes and Labeling Technologies*, 11th ed., Invitrogen, Oregon.

(2) Gómez-Hens, A., and Aguilar-Caballos, M. P. (2004) Long-wavelength fluorophores: new trends in their analytical use. *Trends Anal. Chem. 23*, 127–136.

(3) Tung, C.-H. (2004) Fluorescent peptide probes for in vivo diagnostic imaging. *Biopolymers 76*, 391–403, and references cited therein.

(4) Taquet, J.-P., Frochot, C., Manneville, V., and Barberi-Heyob, M. (2007) Phthalocyanines covalently bound to biomolecules

for a targeted photodynamic therapy. *Curr. Med. Chem. 14*, 1673–1687.
(5) Buschmann, V., Weston, K. D., and Sauer, M. (2003) Spectroscopic study and evaluation of red-absorbing fluorescent dyes. *Bioconjugate Chem. 14*, 195–204, and references cited therein.
(6) Meltola, N. J., Wahlroos, R., and Soini, A. E. (2004) Hydrophilic labeling reagents of dipyrrylmethene-BF2 dyes for two-photon excited fluorometry: syntheses and photophysical characterization. *J. Fluorescence 14*, 635–647.
(7) Thivierge, C., Bandichhor, R., and Burgess, K. (2007) Spectral dispersion and water solubilization of BODIPY dyes via palladium-catalyzed C-H functionalization. *Org. Lett. 9*, 2135–2138, and references cited therein.
(8) Bouteiller, C., Clavé, G., Bernardin, A., Chipon, B., Massonneau, M., Renard, P.-Y., and Romieu, A. (2007) Novel water-soluble near-infrared cyanine dyes: synthesis, spectral properties, and use in the preparation of internally quenched fluorescent probes. *Bioconjugate Chem. 18*, 1303–1317, and references cited therein.
(9) Toutchkine, A., Nguyen, D.-V., and Hahn, K. M. (2007) Simple one-pot preparation of water-soluble, cysteine-reactive cyanine and merocyanine dyes for biological imaging. *Bioconjugate Chem. 18*, 1344–1348.
(10) Jose, J., and Burgess, K. (2006) Benzophenoxazine-based fluorescent dyes for labeling biomolecules. *Tetrahedron 62*, 11021–11037.
(11) Panchuk-Voloshina, N., Haugland, R. P., Bishop-Stewart, J., Bhalgat, M. K., Millard, P. J., Mao, F., Leung, W.-Y., and Haugland, R. P. (1999) Alexa dyes, a series of new fluorescent dyes that yield exceptionally bright, photostable conjugates. *J. Histochem. Cytochem. 47*, 1179–1188.
(12) Bandichhor, R., Petrescu, A. D., Vespa, A., Kier, A. B., Schroeder, F., and Burgess, K. (2006) Synthesis of a new water-soluble rhodamine derivative and application to protein labeling and intracellular imaging. *Bioconjugate Chem. 17*, 1219–1225.
(13) Bandichhor, R., Petrescu, A. D., Vespa, A., Kier, A. B., Schroeder, F., and Burgess, K. (2006) Water-soluble through-bond energy transfer cassettes for intracellular imaging. *J. Am. Chem. Soc. 128*, 10688–10689.
(14) Wang, H., Lu, Z., Lord, S. J., Moerner, W. E., and Twieg, R. J. (2007) Modifications of DCDHF single molecule fluorophores to impart water solubility. *Tetrahedron Lett. 48*, 3471–3474.
(15) Chipon, B., Clavé, G., Bouteiller, C., Massonneau, M., Renard, P.-Y., and Romieu, A. (2006) Synthesis and post-synthetic derivatization of a cyanine-based amino acid. Application to the preparation of a novel water-soluble NIR dye. *Tetrahedron Lett. 47*, 8279–8284.
(16) Chipon, B., Clavé, G., Bouteiller, C., Massonneau, M., Renard, P.-Y., and Romieu, A. (2007) Corrigendum to "Synthesis and post-synthetic derivatization of a cyanine-based amino acid. Application to the preparation of a novel water-soluble NIR dye". *Tetrahedron Lett. 48*, 501.
(17) Afonso, C. A. M., Santhakumar, V., Lough, A., and Batey, R. A. (2003) An expedient synthesis of cationic rhodamine fluorescent probes suitable for conjugation to amino acids and peptides. *Synthesis* 2647–2654.
(18) Mao, F., Leung, W.-Y., and Haugland, R. P. PCT Int. Appl. 9915517, 1999.
(19) Gottlieb, H. E., Kotlyar, V., and Nudelman, A. (1997) NMR chemical shifts of common laboratory solvents as trace impurities. *J. Org. Chem. 62*, 7512–7515.
(20) Finn, P. J., Sun, L., Nampalli, S., Xiao, H., Nelson, J. R., Mamone, J. A., Grossmann, G., Flick, P. K., Fuller, C. W., and Kumar, S. (2002) Synthesis and application of charge-modified dye-labeled dideoxynucleoside-5′-triphosphates to 'direct-load' DNA sequencing. *Nucleic Acids Res. 30*, 2877–2885.
(21) Wagner, D., Gertner, D., and Zilkha, A. (1968) One-step synthesis of α-sulfo-*β*-alanine. *Tetrahedron Lett.* 4479–4480.
(22) Lapatsanis, L., Milias, G., Froussios, K., and Kolovos, M. (1983) Synthesis of N-(2,2,2-trichloroethoxycarbonyl) L-amino acids and N-(9-fluorenylmethoxycarbonyl) L-amino acids involving succinimidoxy anion as a leaving group in amino acid protection. *Synthesis*, 671–673.
(23) Han, S.-Y., and Kim, Y.-A. (2004) Recent development of peptide coupling reagents in organic synthesis. *Tetrahedron 60*, 2447–2467.
(24) Bannwarth, W., and Knorr, R. (1991) Formation of carboxamides with N,N,N',N'-tetramethyl(succinimido)uronium tetrafluoroborate in aqueous organic solvent systems. *Tetrahedron Lett. 32*, 1157–1160.
(25) Titus, J. A., Haugland, R., Sharrow, S. O., and Segal, D. M. (1982) TX Red, a hydrophilic, red-emitting fluorophore for use with fluorescein in dual parameter flow microfluorometric and fluorescence microscopic studies. *J. Immunol. Methods 50*, 193–204.
(26) Lefevre, C., Kang, H. C., Haugland, R. P., Malekzadeh, N., Arttamangkul, S., and Haugland, R. P. (1996) TX Red-X and Rhodamine Red-X, new derivatives of sulforhodamine 101 and lissamine rhodamine b with improved labeling and fluorescence properties. *Bioconjugate Chem. 7*, 482–489.
(27) Mizukami, S., Kikuchi, K., Higuchi, T., Urano, Y., Mashima, T., Tsuruo, T., and Nagano, T. (1999) Imaging of caspase-3 activation in HeLa cells stimulated with etoposide using a novel fluorescent probe. *FEBS Lett. 453*, 356–360.
(28) Komoriya, A., Packard, B. Z., Brown, M. J., Wu, M. L., and Henkart, P. A. (2000) Assessment of caspase activities in intact apoptotic thymocytes using cell-permeable fluorogenic caspase substrates. *J. Exp. Med. 191*, 1819–1828.
(29) Pham, W., Weissleder, R., and Tung, C.-H. (2002) An azulene dimer as a near-infrared quencher. *Angew. Chem., Int. Ed. 41*, 3659–3662.
(30) Bullok, K., and Piwnica-Worms, D. (2005) Synthesis and characterization of a small, membrane-permeant, caspase-activatable far-red fluorescent peptide for imaging apoptosis. *J. Med. Chem. 48*, 5404–5407.
(31) Bullok, K. E., Maxwell, D., Kesarwala, A. H., Gammon, S., Prior, J. L., Snow, M., Stanley, S., and Piwnica-Worms, D. (2007) Biochemical and *in vivo* characterization of a small, membrane-permeant, caspase-activatable far-red fluorescent peptide for imaging apoptosis. *Biochemistry 46*, 4055–4065.
(32) Weissleder, R., Tung, C. H., Mahmood, U., and Bogdanov, A., Jr. (1999) In vivo imaging of tumors with protease-activated near-infrared fluorescent probes. *Nat. Biotechnol. 17*, 375–378.
(33) Galande, A. K., Hilderbrand, S. A., Weissleder, R., and Tung, C.-H. (2006) Enzyme-targeted fluorescent imaging probes on a multiple antigenic peptide core. *J. Med. Chem. 49*, 4715–4720.
(34) Ziessel, R., Ulrich, G., and Harriman, A. (2007) The chemistry of bodipy: a new el dorado for fluorescence tools. *New J. Chem. 31*, 496–501.
(35) Zhao, C., Zhang, Y., Li, R., Li, X., and Jiang, J. (2007) Di(alkoxy)- and Di(alkylthio)-substituted perylene-3,4;9,10-tetracarboxy diimides with tunable electrochemical and photophysical properties. *J. Org. Chem. 72*, 2402–2410.
(36) Bräse, S., Gil, C., Knepper, K., and Zimmermann, V. (2005) Organic azides. An exploding diversity of a unique class of compounds. *Angew. Chem., Int. Ed. 44*, 5188–5240.
(37) Mujumdar, S. R., Mujumdar, R. B., Grant, C. M., and Waggoner, A. S. (1996) Cyanine-labeling reagents: sulfobenzindocyanine succinimidyl esters. *Bioconjugate Chem. 7*, 356–362.
(38) Mujumdar, R. B., Ernst, L. A., Mujumdar, S. R., Lewis, C. J., and Waggoner, A. S. (1993) Cyanine dye labeling reagents: sulfoindocyanine succinimidyl esters. *Bioconjugate Chem. 4*, 105–111.
(39) Magde, D., Wong, R., and Seybold, P. G. (2002) Fluorescence quantum yields and their relation to lifetimes of rhodamine 6g and fluorescein in nine solvents: improved absolute standards for quantum yields. *Photochem. Photobiol. 75*, 327–334.

BC7003268

Site-Specific Delivery of Oligonucleotides to Hepatocytes after Systemic Administration

Lin Zhu, Zhaoyang Ye, Kun Cheng, Duane D. Miller, and Ram I. Mahato*

Department of Pharmaceutical Sciences, University of Tennessee Health Science Center, Memphis, Tennessee 38163. Received April 13, 2007; Revised Manuscript Received July 2, 2007

We previously complexed ODN with galactosylated poly(L-lysine) (Gal-PLL) to enhance its site-specific delivery to hepatocytes. To avoid the use of polycations, in this study we conjugated galactosylated poly(ethylene glycol) (Gal-PEG (MW of PEG: 3486 ± 500 Da)) to ODN via an acid-labile ester linkage of β-thiopropionate. Following tail vein injection into rats, Gal-PEG-^{33}P-ODN rapidly cleared from the circulation and 60.2% of the injected dose accumulated in the liver at 30 min postinjection, which was significantly higher than that deposited after injection of ^{33}P-ODNs. The plasma concentration versus time profile of Gal-PEG-^{33}P-ODN was biphasic, with 4.38 ± 0.36 min as $t_{1/2}$ of distribution and 118.61 ± 22.06 min as $t_{1/2}$ of elimination. Prior administration of excess Gal-BSA decreased the hepatic uptake of Gal-PEG-^{33}P-ODN from 60.2% to 35.9%, suggesting galactose triggers the asialoglycoprotein receptor-mediated endocytosis of Gal-PEG-^{33}P-ODN by hepatocytes. A large proportion of the injected Gal-PEG-^{33}P-ODN was taken up by the hepatocytes as evidenced by determination of radioactivity in the digested liver cells upon liver perfusion and separation by centrifugation on a Nycodenz gradient. In conclusion, Gal-PEG-ODN conjugate may be used for treating a variety of liver diseases.

INTRODUCTION

Oligonucleotides (ODNs) have attracted much attention as a new class of therapeutic agents that can be used for gene modulation. However, in vivo gene silencing by ODNs has not yet been successful because of several obstacles, including the nonspecific interaction with plasma proteins, wide distribution, and poor stability against enzymatic degradation. Since phosphodiester ODNs have extremely short half-lives due to degradation by nucleases, phosphorothioate (PS) ODNs are commonly used. PS ODNs are fairly stable in vivo, but readily bind to serum proteins, leading to undesirable biological events. To address these problems, a variety of delivery systems composed of cationic lipids (*1–3*) and cationic polymers (*4–6*) have been developed. Some of these delivery systems substantially enhanced the enzymatic stability and uptake into the target cells in vitro (*7*). However, most of these cationic carriers are inefficient in vivo because of their nonspecific biodistribution in the body.

We and others have shown that ODNs are cleared rapidly from the circulation and accumulated in most of the peripheral tissues, with the highest accumulation in the liver and kidney (*8–12*). The asialoglycoprotein receptor is located on parenchymal liver cells (e.g., hepatocytes) and recognizes terminal galactose (*13*) or lactose residues (*14, 15*). Therefore, we previously used galactosylated poly(L-lysine) (Gal-PLL) for complex formation with ODNs and demonstrated enhanced hepatic uptake of ODNs, which was influenced by the particle size, zeta potential, sugar substitution, and molecular weight of both polycations and ODNs (*16*). Although the uptake of Gal-PLL/ODN complexes by hepatocytes was significantly higher than that of naked ODNs, the difference of their distribution to different liver cells was only moderate. To avoid the use of polycations, Rajur et al. (1997) covalently conjugated ODNs to asialoorosomucoid via a disulfide bond using sulfosuccinimidyl 6-[3′-(2-pyridyldithio) propionamido] hexanoate (sulfo-LC-SPDP), but the authors did not test the conjugate in vivo (*17*).

PEGylation is known to significantly enhance the ODN stability against exonucleases and reduce renal clearance compared to unmodified ODNs (*18*). The in vivo activity of a drug depends in part on its rate of excretion and degradation. PEGylation should promote the bioactivity of an ODN by increasing plasma residence time and decreasing nuclease degradation. PEGylation also shields the inherent negative charge of the ODN, thereby possibly facilitating cellular uptake of the conjugated drug. Additionally, PEGylation could potentially diminish the immunostimulatory effects of the ODNs (*19, 20*). Keeping these benefits in mind, Bonora et al. (1997) conjugated ODNs to poly(ethylene glycol) (PEG) through a covalent linkage (*21*). However, these PEG-ODN conjugates were less effective, since PEG could not be cleaved early from the ODNs in the cytoplasm. Therefore, Oishi et al. conjugated ODN to acrylated or lactosylated PEG through a pH-responsive ester (*22, 23*). However, these authors did not determine the biodistribution of Lac-PEG-ODN and used in conjunction with a cationic polymer like linear polyethyleneimine (PEI), which is likely to promote nonspecific interaction with plasma proteins and uptake by phagocytic cells.

In this study, we used fully phosphorothioate G-rich ODN, which is fairly stable, but binds to serum proteins (*24*). To minimize binding to plasma proteins, enhance stability, and prolong circulation time, we conjugated Gal-PEG to ODN using an acid-labile linker. Gal-PEG is expected to enhance ODN delivery to the hepatocytes whose inflammation and injury lead to progression of liver fibrosis (*25*). In this study, we conjugated ODN to Gal-PEG via an acid-labile ester linkage and used it without any cationic polymers or lipids to avoid cytotoxicity and nonspecific interaction. Following conjugation and in vitro characterization, we determined the biodistribution of Gal-PEG-^{33}P-ODN at whole body, organ (liver), and cellular (liver cells) levels after tail vein injection into rats.

* Corresponding author. Ram I. Mahato, Ph.D., 19 Manassas, Room 224, Memphis, TN 38163, USA, Tel: (901) 448-6929, Fax: (901) 448-6092, E-mail: rmahato@utmem.edu, http://cop.utmem.edu/rmahato.

10.1021/bc070126m CCC: $40.75 © 2008 American Chemical Society
Published on Web 09/13/2007

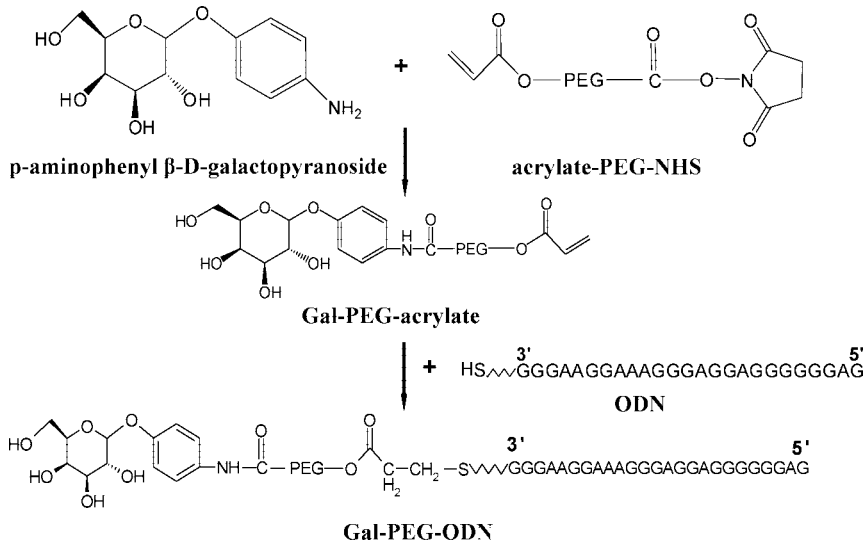

Figure 1. Synthesis scheme of Gal-PEG-ODN. *p*-Nitrophenyl *β*-D-galactopyranoside was reduced to *p*-aminophenyl *β*-D-galactopyranoside and then conjugated to 3′-thiol ODN by Michael addition.

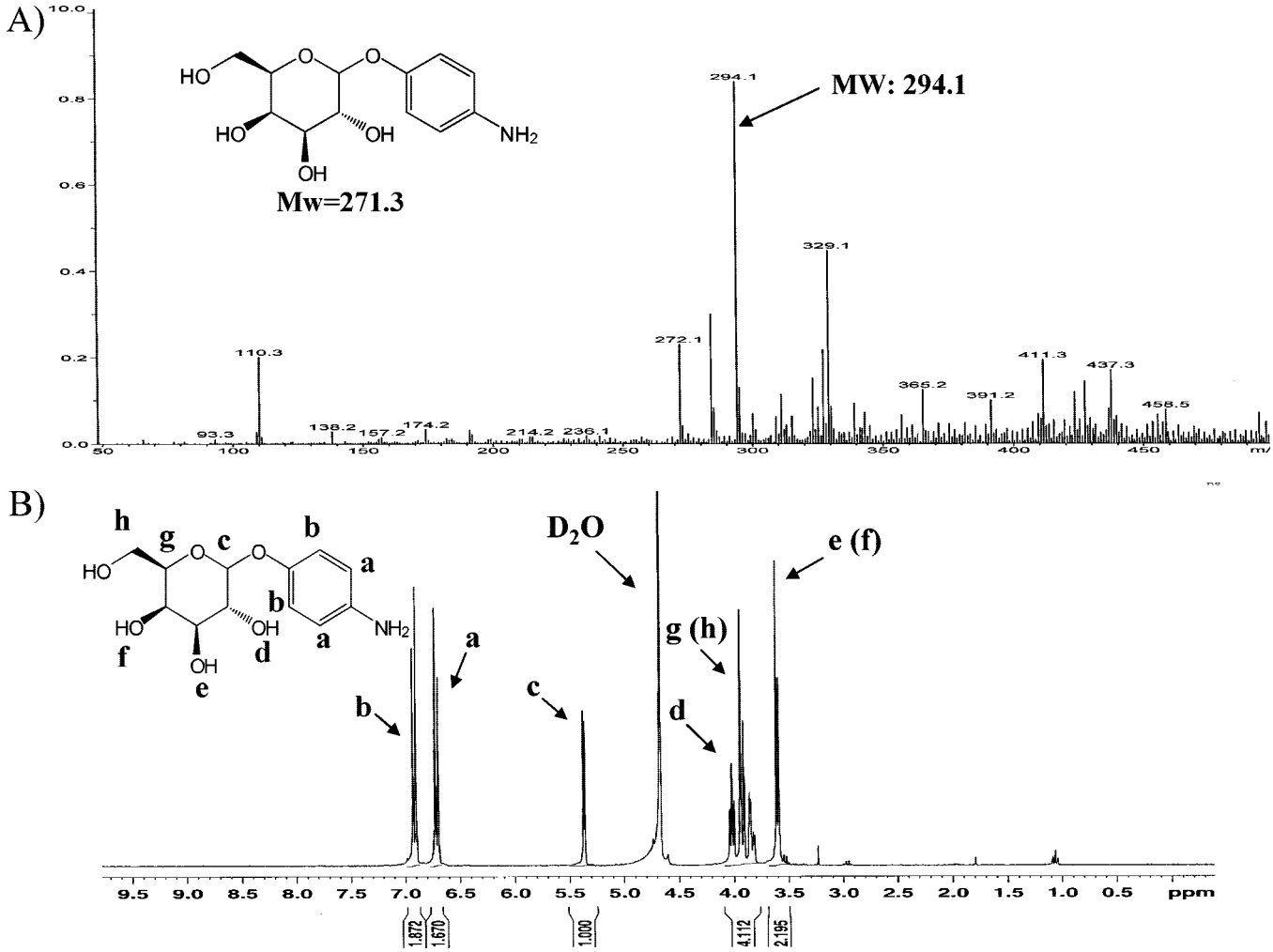

Figure 2. Characterization of *p*-aminophenyl *β*-D-galactopyranoside with electron spray ionization mass spectrometry (ESI-MS) and ^{1}H NMR. (A) Electron spray ionization mass spectra were obtained after dissolving the product in methanol on an ESQUIRE-LC Ion Trap LC/MS system. (B) For ^{1}H NMR, samples were dissolved in D_2O and the spectra were recorded on a Bruker ARX-300 MHz NMR spectrometer at 25 °C.

MATERIALS AND METHODS

Materials. 25-mer ODN (5′ GAG GGG GGA GGA GGG AAA GGA AGG G 3′) modified with a sulfhydryl group at the 3′ end was purchased from Invitrogen Corporation (Carlsbad, CA).[γ-^{33}P]ATP was obtained from MP Biomedicals (Irvine, CA) and T4 polynucleotide kinase (T4-PNK) from New England Biolabs (Beverly, MA). Bio-Gel P-6DG gel was obtained from Bio-Rad Laboratories (Hercules, CA). PD-10 desalting columns

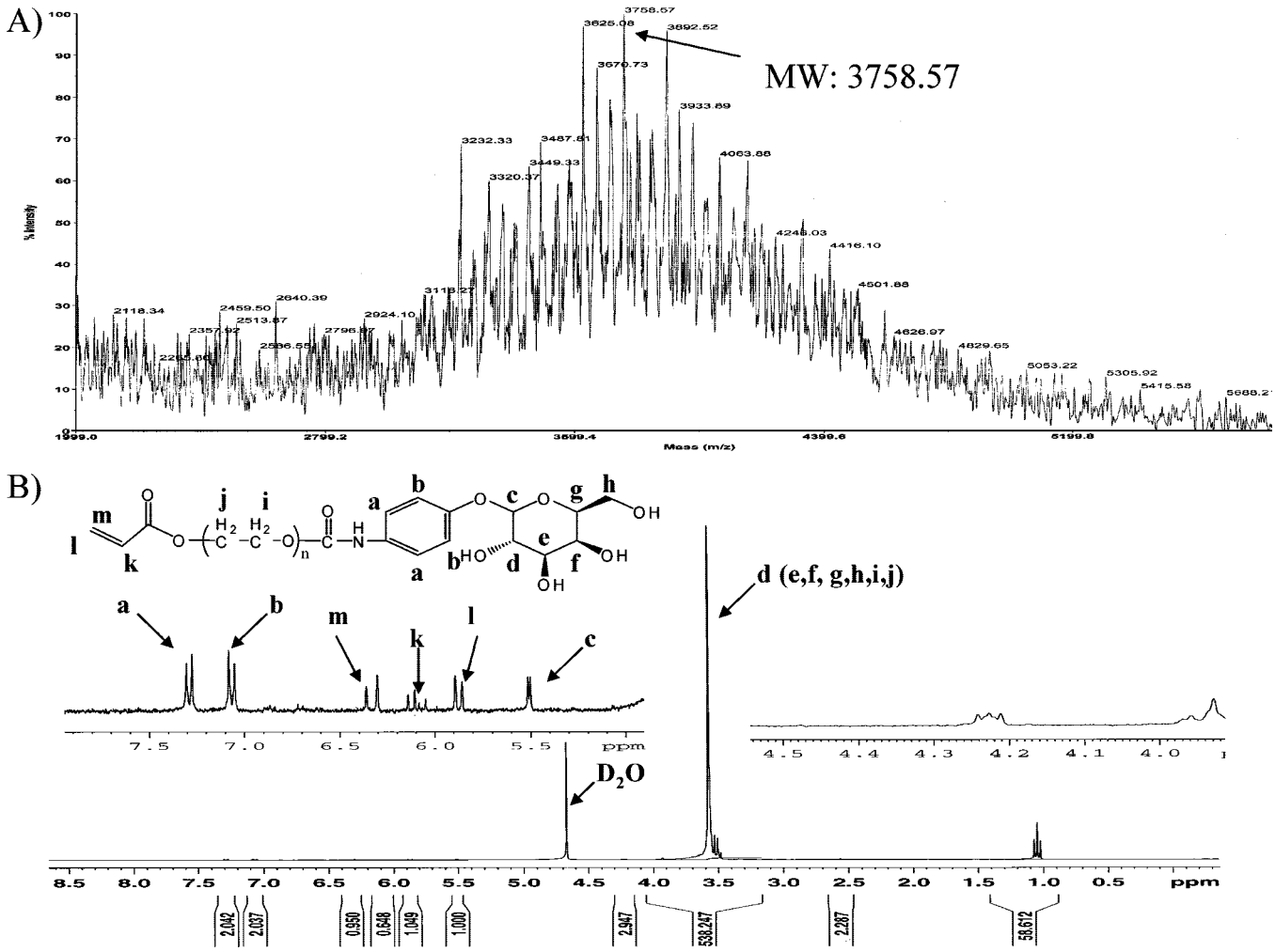

Figure 3. Characterization of Gal-PEG-acrylate with MALDI-TOF—MS and ^{1}H NMR. (A) In MALDI-TOF—MS the ratio between Gal-PEG-acrylate and DHB was 1:2. The spectrum was recorded on Voyager-DE RP (PerSeptive Biosystems Inc., MA). (B) For ^{1}H NMR, samples were dissolved in D_2O, and the spectra were recorded on a Bruker ARX-300 MHz NMR spectrophotometer at 25 °C.

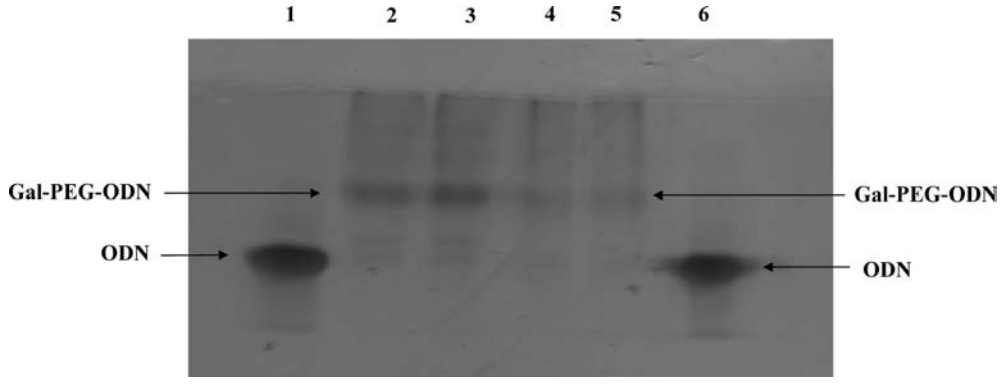

Figure 4. Identification of Gal-PEG-ODN by polyacrylamide gel electrophoresis (PAGE) at 80 V for 100 min, followed by staining with methylene blue for one night. Lanes 1 and 6: ODN 2 μg. Lanes 2 and 3: Gal-PEG-ODN 2 μg. Lanes 4 and 5: Gal-PEG-ODN 1 μg.

were obtained from Pharmacia Fine Chemicals AB (Uppsala, Sweden). Soluene-350 (tissue solubilizer) and Hionic-Fluor (scintillation fluid) were purchased from Perkin-Elmer (Boston, MA). Isoflurane was obtained from Baxter Health Corporation (Deerfield, IL). Type IV collagenase was purchased from Worthington Biochemical Corporation (Lakewood, NJ). Nycodenz AG was obtained from Greiner Bio-One Inc. (Longwood, FL). PE-60 polyethylene tubing was purchased from Becton Dickinson and Company (Sparks, MD) and heparin solution was procured from American Pharmaceutical Partners, Inc. (Los Angeles, CA). Acrylate-PEG-NHS (MW: 3486 ± 500 Da) was purchased from Nektar Therapeutics (Huntsville, AL). Bovine serum albumin (BSA) (fraction V, purity >98%) was purchased from USB Corporation (Cleveland, OH). Palladium (10 wt% on activated carbon), thiophosgene, Brilliant Blue R Staining Solution, dithiothreitol (DTT), *p*-nitrophenyl β-D-galactopyranoside, dimethylformamide (DMF), 2,5- dihydroxy benzoic acid (DHB), methylene blue, deuterium oxide (D_2O), triethylamine (TEA, HPLC grade), and Pronase were purchased from Sigma-Aldrich Chemicals Limited (St. Louis, MO). Dialysis tubing

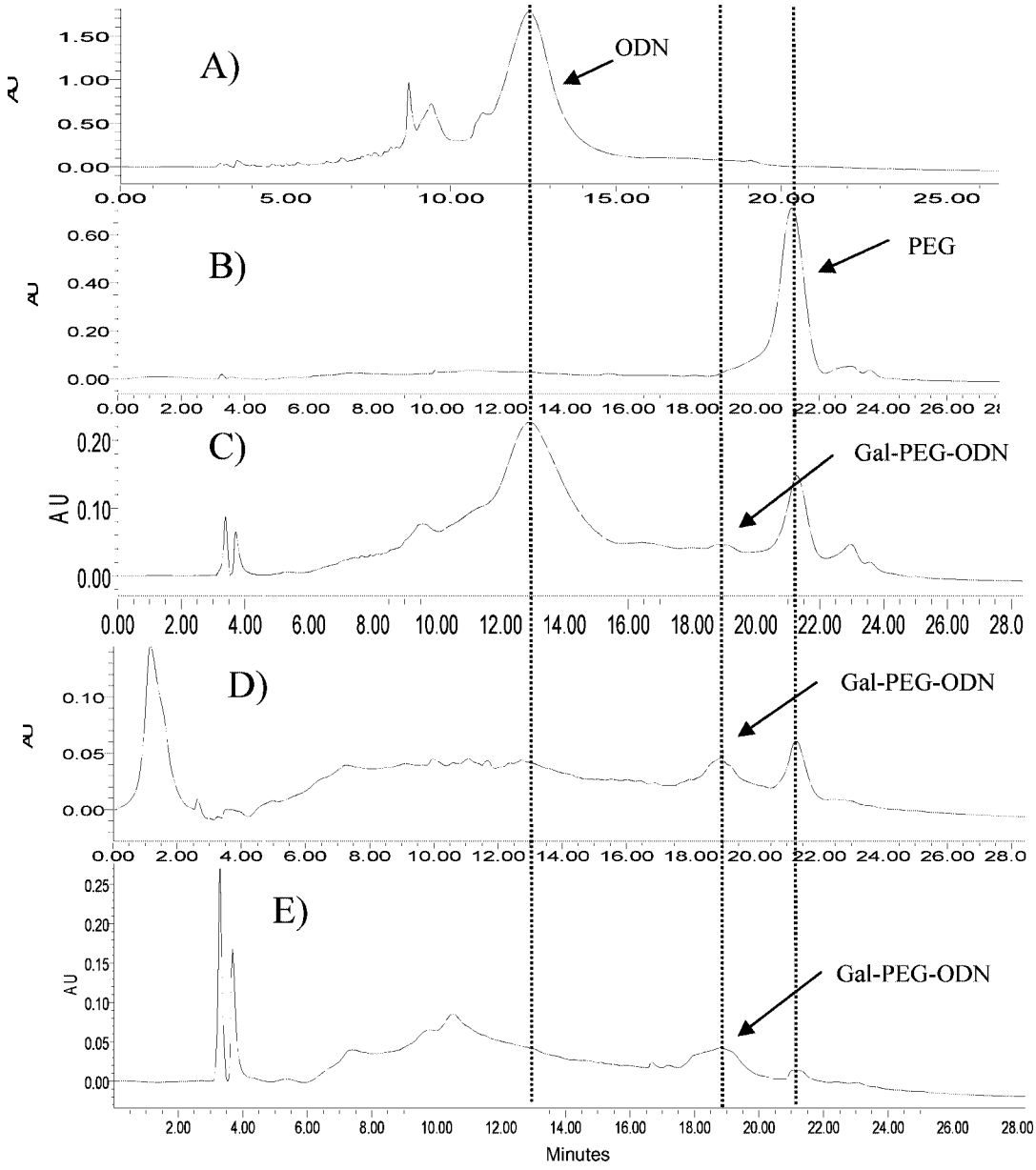

Figure 5. HPLC chromatograms of (A) ODN, (B) PEG, (C) reaction mixture, (D) during purification, and (E) after purification of Gal-PEG-ODN.

(MWCO 1000 Da) was purchased from Spectrum Laboratories, Inc. (Houston, TX). Amicon Centricon filter devices (MWCO 10 000 Da) were purchased from Millipore Corporation (Billerica, MA). Hydrogen peroxide (H_2O_2), acetic acid, acetonitrile (ACN, HPLC grade), and water (HPLC grade) were purchased from Fisher Chemical (Fair Lawn, NJ). Ca^{2+}/Mg^{2+}-free Hank's balanced salt solution (Cellgro) was purchased from Media Tech (Washington, DC).

Animals. Male Sprague−Dawley rats weighing 140–160 g were purchased from Harlan Co. (San Diego, CA) and were housed individually under the controlled light (12/12 h) and temperature conditions and had free access to food and water.

Synthesis of Gal-PEG-ODN Conjugate. *p*-Nitrophenyl β-D-galactopyranoside (200 mg) was reduced with 200 mg of 10% palladium on activated carbon under hydrogen (1 atm) in 30 mL of a 1:1 (v/v) ethanol−water mixture for 2 h, as described by Monsigny et al. (*26*). The product, *p*-aminophenyl β-D-galactopyranoside, was concentrated by solvent removal under vacuum and characterized using ^{1}H NMR and mass spectrometry after dissolving in D_2O, and the NMR spectra were recorded on a Bruker ARX-300 MHz spectrometer at 25 °C. Chemical shifts were recorded in ppm relative to D_2O (δ 4.79, 1H). Electron spray ionization (ESI) mass spectra were obtained after dissolving the product in methanol on an ESQUIRE-LC Ion Trap LC/MS system. Acrylate poly(ethylene glycol) *N*-hydroxysuccinimidyl (NHS) ester (acrylate-PEG-NHS) (58 mg) and *p*-aminophenyl β-D-galactopyranoside (43.4 mg) were dissolved separately in 0.4 mL of DMF, mixed together, and dialyzed in 500 mL water for 48 h with MWCO 1000. The product, galactose (Gal)-PEG-acrylate was characterized by ^{1}H NMR after dissolving the product in D_2O. The molecular weight of Gal-PEG-ODN was determined using matrix assisted laser desorption/ionization time-of-flight (MALDI-TOF) mass spectrometry with DHB as a matrix.

Modified ODNs were treated with 0.2 M DTT in 0.1 M, pH 9.0 glycine buffer containing 0.1 M NaCl for 3 h at room temperature to generate a 3′-thiol functional group. Excess DTT was removed by extraction with ethyl acetate, and ODN was precipitated by adding 2.6 volume of ethanol after addition of sodium acetate (NaOAc) to 0.3M. The mixture was kept at −30 °C overnight and centrifuged at 13 000 *g* for 30 min. The ODN with 3′-thiol functional group and Gal-PEG-acrylate were

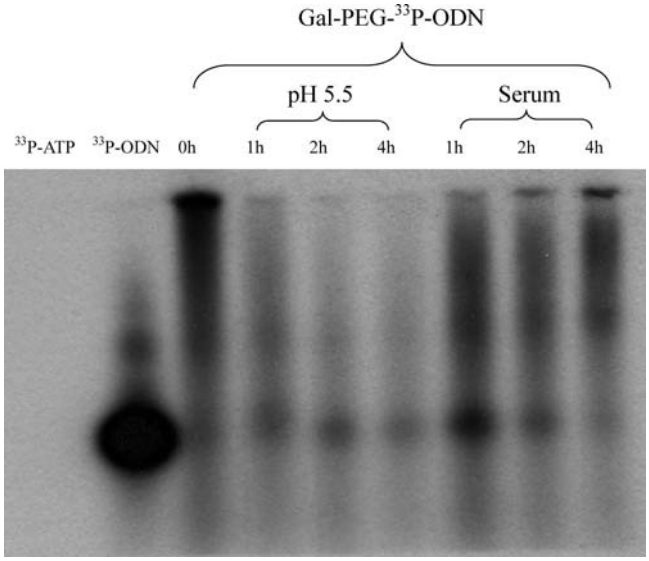

Figure 6. Dissociation and stability study of Gal-PEG-^{33}P-ODN. Dissociation of ^{33}P-ODN from Gal-PEG-^{33}P-ODN was determined by incubating the conjugate at 37 °C in pH 5.5 buffer, while its stability was determined by incubating the conjugate at 37 °C in rat serum. The band for Gal-PEG-^{33}P-ODN decreases with time when incubated at acidic pH.

dissolved in 0.4 mL water at a molar ratio of 1:100, stirred under nitrogen protection at room temperature for 6 h, and the mixture centrifuged by Amicon Centricon filter device (MWCO 10 000 Da) at 2500 *g* for 30 min. The upper solution of the filter device was collected and lyophilized. The formation of Gal-PEG-ODN was verified on 20% native polyacrylamide gel electrophoresis at 8 V/cm for 100 min at room temperature, followed by gel staining with methylene blue. The reaction mixtures and the purity of intermediate and final products were monitored by reverse phase-high performance liquid chromatography (RP-HPLC), which was carried on a reverse phase C18 column (250 mm 4.6 mm, Alltech, Deerfield, IL) by an HPLC system (Waters, Milford, MA) with detection at 260 nm using a gradient of 5% to 80% ACN in 0.1 M triethylammonium acetate at a flow rate of 1.0 mL/min at 56 °C.

Synthesis of Galactosylated Albumin. Gal-BSA was synthesized from *p*-aminophenyl β-D-galactopyranoside and BSA (MW 66 000 Da) using a modified method described by Sando and Karson (*27*). After conjugation, Gal-BSA was purified by PD-10 column and identified by sodium dodecyl sulfate polyacrylamide gel electrophoresis (SDS-PAGE) followed by staining with Brilliant Blue R Staining Solution. The molar ratio of galactose and BSA was about 15. Sugar (galactose) content was determined by the resorcinol−sulfuric acid method as described by Monsigny et al. (*28*).

Radiolabeling of Oligonucleotides. The 25-mer ODN or Gal-PEG-ODN was labeled by adding γ-^{33}P to the 5′ end using [γ-^{33}P] ATP and T4-PNK, using the manufacturer's protocol. Briefly, 1 μg of ODN or Gal-PEG-ODN was mixed with 5 μL of T4-PNK buffer, 2 μL of T4-PNK, and 4 μL of [γ-^{33}P] ATP. The reaction mixture was incubated at 37 °C for 60 min, followed by incubation at 70 °C for 10 min to stop the reaction. Unincorporated [γ-^{33}P] ATP was removed from radiolabeled ODN or Gal-PEG-ODN by size exclusion chromatography with Bio-Gel P-6DG gel. Radioactivity was measured on a TRI-CARB2000 liquid scintillation analyzer (Packard Instrument Company, Meridon, CT). The incorporation efficiency of the purified ^{33}P-ODN was determined by trichloroacetic acid (TCA) precipitation method and the value was more than 95%. The specific activity of ^{33}P-ODN was about 5×10^5 to 10×10^5 cpm/μg.

Dissociation and Stability. To determine whether ODNs can dissociate from Gal-PEG-ODN conjugate after endocytosis, this conjugate was incubated at 37 °C in Tris−HCl buffer of pH 5.5 for 1, 2, and 4 h. In addition, we also incubated this conjugate in the rat serum at 37 °C to determine its stability. These samples were then detected by 20% polyacrylamide gel electrophoresis and autoradiography.

Biodistribution of Gal-PEG-ODN. The animal protocol was approved by the Animal Care and Use Committee (ACUC), Department of Comparative Medicine, University of Tennessee Health Science Center, Memphis, TN 38163. Male Sprague−Dawley rats weighing 140–160 g were used in this study and four rats were used for each time point. Unlabeled and Gal-PEG-^{33}P-ODN were mixed in saline to give a final concentration of 1 mg/mL and specific activity of 1×10^6 cpm/mL. Rats were anesthetized by inhalation of isoflurane, and Gal-PEG-^{33}P-ODN or ^{33}P-ODN was injected via tail vein at a dose of 0.2 mg/kg body weight. At 2.5, 5, 15, 30, 90, 240, and 1440 min postinjection, 0.5 mL blood was collected by cardiac puncture in heparinized tubes, and urine was collected directly from the bladder using a 0.26 gauge needle syringe. The animals were then sacrificed and major tissues (liver, kidney, spleen, heart, lung, and muscle) were collected, washed, blotted dry, weighed, and stored at −80 °C. The radioactivity of the urine sample was counted directly after adding 10 mL of scintillation fluid. Two hundred microliters of plasma and 200 mg of each tissue were incubated with 2 mL tissue solubilizer for 3 h at 55 °C and overnight at 37 °C in a shaker. Four hundred microliters of H_2O_2 was added and incubated at 55 °C for another 30 min. Ten milliliters of scintillation fluid was added to each sample and the radioactivity was counted using a liquid scintillation counter.

Determination of Pharmacokinetic Profiles. Plasma data were analyzed using *WinNonlin Professional* (version 5.0.1, Pharsight Corporation, Mountainview, CA). The Gal-PEG-^{33}P-ODN plasma concentration data versus time were fitted using one- and two-compartment models, and pharmacokinetic parameters were calculated as area under the curve (AUC), C_{max}, T_{max}, and clearance (CL). The data were best fitted to a two-compartment model where

$$C_t = Ae^{-\alpha t} + Be^{-\beta t} \quad (1)$$

and C_t equals concentration at time t, A and B are the y-axis intercepts, and α and β are the hybrid constants for distribution and elimination, respectively. Tissue distribution data of Gal-PEG-^{33}P-ODN were analyzed in terms of clearance and tissue uptake rate index using biexponential equations as described previously (*8*). The change in the amount of radioactivity in a tissue with time can be described as follows:

$$dT(t)/t = CL_{in}C(t) - K_{out}T(t) \quad (2)$$

where $T(t)$ (% of dose/g) represents the amount of radioactivity in 1 g of the tissue, $C(t)$ (% of dose/mL) is the plasma concentration of radioactivity, CL_{in} (mL h^{-1} g^{-1}) is the tissue uptake rate index from the plasma to the tissue, and K_{out} (h^{-1}) is the rate constant for efflux from the tissue. In the present study, the efflux process can be considered negligible during the initial time points up to 90 min. Hence, eq 1 integrates to

$$CL_{in} = T(t_1)\int_0^{t_1} C(t_1)dt = T(t_1)/AUC_{0-t_1} \quad (3)$$

where t_1 (h) is the sampling time. According to eq 1, the tissue uptake rate index is calculated using the amount of radioactivity in the tissue and the area under the plasma concentration−time curve (AUC). Then, the organ clearance (CL_{org}) is expressed as follows:

$$CL_{org} = CL_{in}W \quad (4)$$

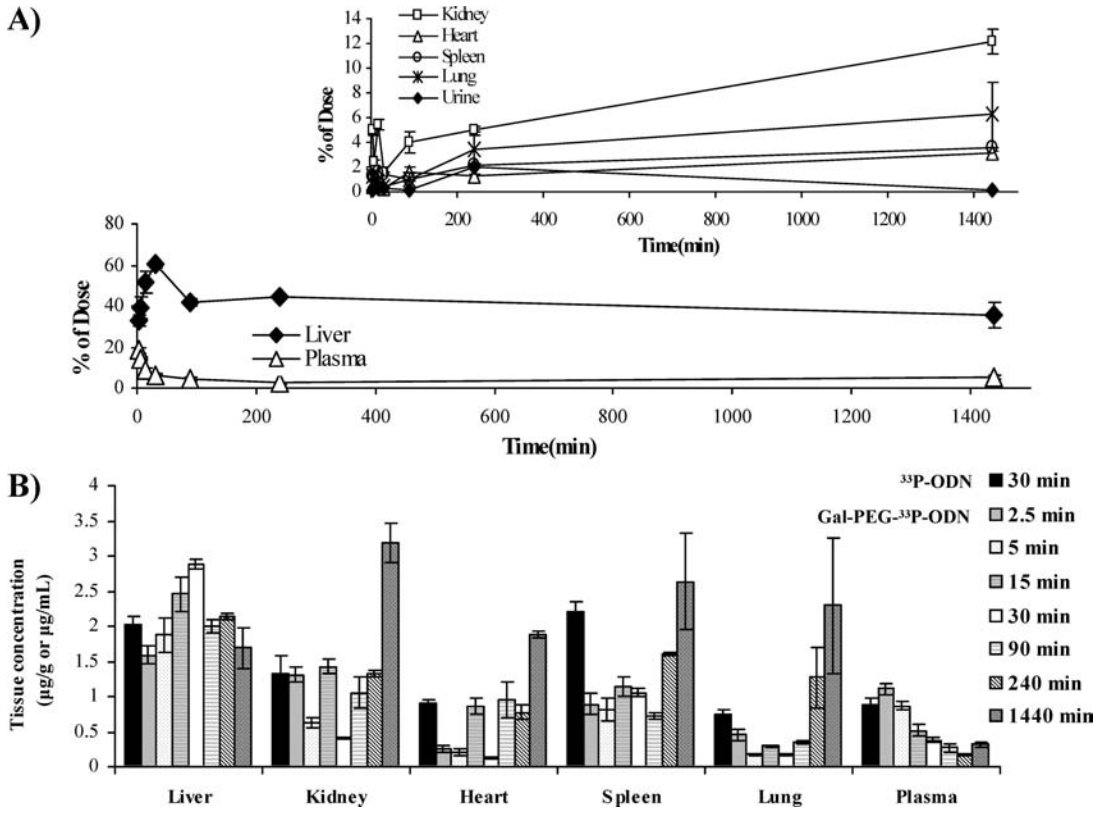

Figure 7. Accumulation (A) and concentration (B) of Gal-PEG-^{33}P-ODN after tail vein injection into rats at a dose of 0.2 mg ODN/kg of body weight. To compare the biodistribution profiles of Gal-PEG-^{33}P-ODN, ^{33}P-ODN was also injected, and ODN accumulation and concentration in different tissues were determined at 30 min postinjection. Following blood collection by cardiac puncture and urine collection from the bladder, the tissues were isolated, digested, and subjected to radioactivity measurement. Results are presented as the mean ± SD ($n = 4$).

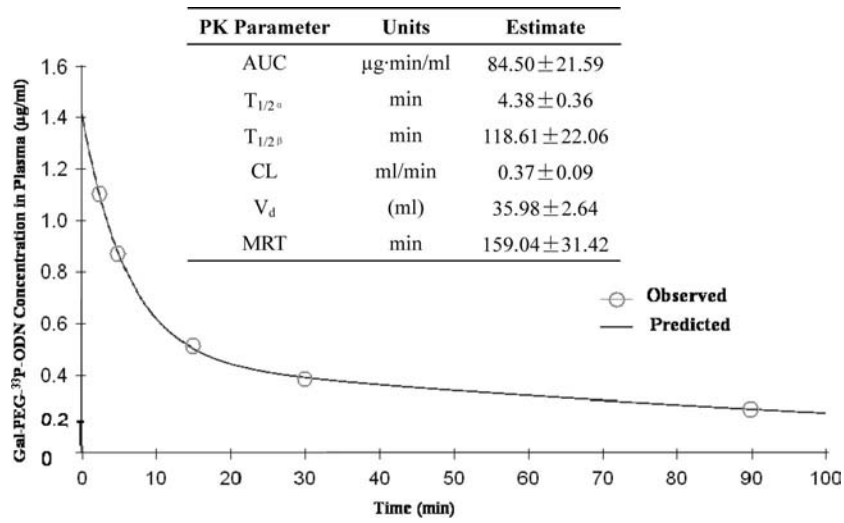

PK Parameter	Units	Estimate
AUC	μg·min/ml	84.50±21.59
$T_{1/2\alpha}$	min	4.38±0.36
$T_{1/2\beta}$	min	118.61±22.06
CL	ml/min	0.37±0.09
V_d	(ml)	35.98±2.64
MRT	min	159.04±31.42

Figure 8. Plasma data was analyzed using a two-compartment model with *WinNonlin Professional* (version 5.0.1) software. Data are represented as the mean ± SD ($n = 4$).

where W (g) is the total weight of the organ. When the tissue uptake process followed nonlinear kinetics, CL_{in} values would represent an average value for the overall experimental period. Total body clearance (CL_{total}) was calculated from AUC for infinite time (AUC_∞) by the following equation:

$$CL_{total} = \text{dose}/AUC_\infty \quad (5)$$

The tissue uptake clearance and index were calculated using the values up to 30 min after injection, assuming that ODNs were fairly stable within this period.

Competition in Hepatic Uptake of Gal-PEG-ODN. Two minutes before the injection of Gal-PEG-^{33}P-ODN at a dose of 0.2 mg/kg (specific activity: 1×10^6 cpm/mL), rats received 10 mg/kg of Gal-BSA via tail vein injection. At 30 min postinjection, blood and urine were collected; other major organs were harvested as described above for radioactive measurement.

Hepatic Cellular Distribution of Gal-PEG-ODN. To determine the effect of conjugation with Gal-PEG on the hepatic uptake of ODNs, the liver was isolated and perfused in situ with Ca^{2+}/Mg^{2+}-free Hank's balanced salt solution containing 0.1% Pronase and 0.05% collagenase at 30 min postintravenous injection of ^{33}P-ODN or Gal-PEG-^{33}P-ODN into rats as described previously (*24*). Briefly, rats (200–250 g) were anesthetized by inhalation of isoflurane, and 100 IU of heparin

Table 1. Tissue Uptake Rate Index and Clearance of ^{33}P-ODN and Gal-PEG-^{33}P-ODN after Systemic Administration into Rats

sample	AUC (μg·min/mL)	tissue uptake rate index (μL·h^{-1}·g^{-1})					organ clearance (μL·h^{-1})				
		liver	kidney	heart	spleen	lung	liver	kidney	heart	spleen	lung
^{33}P−ODN	95.15 ± 5.11	376.15 ± 38.34	235.23 ± 29.39	48.76 ± 3.42	204.73 ± 9.64	55.28 ± 8.90	2218.09 ± 205.68	241.00 ± 41.08	22.96 ± 1.94	82.85 ± 7.32	42.21 ± 8.44
Gal-PEG-^{33}P−ODN	84.50 ± 21.59	2663.27 ± 56.63	376.52 ± 11.16	119.24 ± 10.81	969.26 ± 51.79	161.16 ± 7.00	16674.22 ± 354.55	428.81 ± 12.71	59.67 ± 5.41	395.84 ± 21.15	131.22 ± 5.70

was injected via tail vein, the abdomen was opened, and the portal vein was cannulated with PE-60 polyethylene tubing. The liver was preperfused with 2 mL diluted heparin solution, then with 200 mL Ca^{2+}/Mg^{2+}-free Hank's balanced salt solution and finally with Hank's balanced salt solution containing 0.05% type IV collagenase and 0.1% Pronase for additional 250 mL. All the perfusion solutions were incubated at 37 °C. After perfusion, different liver cell types were separated by Nycodenz gradient (*29*) and radioactivity was measured. The contributions of various cell types to the total liver uptake were calculated as percentage of total hepatic uptake.

Statistical Analysis. Data were expressed as the mean ± standard deviation (SD). The difference between any two groups was determined by ANOVA. $P < 0.05$ was considered statistically significant.

RESULTS

Chronic injury and inflammation of hepatocytes often lead to liver fibrosis and loss of sinusoidal fenestrae, suggesting that liposomal and nanoparticulate delivery systems may not be good for ODN delivery to the hepatocytes. Therefore, we synthesized Gal-PEG and conjugated to ODN by β-thiopropionate, an acid-labile linkage which is easily cleaved at acidic pH, leading to endosomal release of ODNs after endocytosis (*23*). Following synthesis and characterization, we determined the biodistribution at whole body, organ (liver), and cellular (liver cells) levels after systemic administration of Gal-PEG-^{33}P-ODN in rats.

Synthesis and Characterization of Gal-PEG-Acrylate and Gal-PEG-ODN. The synthesis scheme of Gal-PEG-ODN conjugate is shown in Figure 1. *p*-Nitrophenyl β-D-galactopyranoside was reduced to *p*-aminophenyl β-D-galactopyranoside. ESI-MS and ^{1}H NMR results of this intermediate product are shown in Figure 2. ESI-MS (positive ion mode): 294.1 ([M + Na]$^+$) (Figure 2A). ^{1}H NMR (D_2O): δ 6.73 (d, 1H), 6.90 (d, 1H), 5.35 (s, 1H), 3.76–4.09 (m, 4H), 3.61 (m, 2H) (Figure 2B). Gal-PEG-acrylate was synthesized from acrylate-PEG-NHS and identified by MALDI-TOF MS and ^{1}H NMR. For MALDI-TOF MS, DHB was used as a matrix at the weight ratio of 1:2 (Gal-PEG-acrylate/DHB). Molecular weight of Gal-PEG-acrylate was 3758 Da after conjugation between acrylate-PEG-NHS (MW 3486 Da) and *p*-aminophenyl β-D-galactopyranoside (MW 271 Da) (Figure 3A). ^{1}H NMR (D_2O): δ 7.35 (d, 2H), 7.12 (d, 2H), 5.54 (s, 1H), 3.48–3.92 (m, 538H), 5.93 (d, 2H), 6.17(t, 1H), 6.40 (d, 1H) (Figure 3B). Gal-PEG was then conjugated to ODN by Michael addition from *p*-aminophenyl β-D-galactopyranoside and Gal-PEG-acrylate. Gal-PEG-ODN was also identified by native polyacrylamide gel electrophoresis and staining with methylene blue (Figure 4). For the purification process, the RP-HPLC was used to monitor the mixtures and the purity of the intermediate and final products. From the HPLC chromatograms of ODNs, PEG, and Gal-PEG-ODN conjugate shown in Figure 5, almost all PEG and ODNs were removed from the conjugate after purification. G-rich ODNs used in this study has the tendency to form G-quartets, which may decrease the recovery of the conjugate.

Dissociation and Stability. To determine the dissociation and stability of Gal-PEG-^{33}P-ODN, the radioactivity of the samples was measured after gel electrophoresis and autoradiography at 0, 1, 2, and 4 h postincubation of the conjugate in Tris−HCl buffer of pH 5.5 and rat serum, respectively. In the pH 5.5 buffer, the band of Gal-PEG-^{33}P-ODN gradually disappeared along the incubation time, while the band of the ^{33}P-ODN was still there even up to 4 h (Figure 6). In contrast, this conjugate was fairly stable in rat serum for at least 4 h. The result suggests that the conjugate was fairly stable in serum, but its acid-labile ester linkage can be cleaved at acidic pH. Our study also confirmed the previous report about this kind of conjugate by Oishi et al. (*23*).

Biodistribution of Gal-PEG-ODN Conjugate. Following synthesis and purification of Gal-PEG and then conjugation to ^{33}P-ODN, we determined the biodistribution of Gal-PEG-^{33}P-ODN at 2.5, 5, 15, 30, 90, 240, and 1440 min postinjection into the tail vein of rats. Figure 7A shows the time course of radioactivity in the plasma, urine, liver, kidney, lung, heart, and spleen (radioactivity in muscle was too low, not shown here). Gal-PEG-^{33}P-ODN was rapidly cleared from the circulation with less than 10% of radioactivity detected in the plasma at 30 min postinjection. Correspondingly, hepatic uptake of Gal-PEG-^{33}P-ODN increased with time and reached its peak at 30 min postadministration and then decreased with time. To compare the biodistribution profiles of Gal-PEG-^{33}P-ODN, ^{33}P-ODN was also injected into rats, and ODN accumulation and concentration in different organs were determined at 30 min postinjection. Figure 7B shows the tissue concentration of Gal-PEG-^{33}P-ODN in the plasma (μg/mL) and tissues (μg/g) after tail vein injection into rats, while the conjugation of ODN with Gal-PEG significantly increased the accumulation of radioactivity (% of dose) in the liver, as compared to that of ^{33}P-ODN. Gal-PEG-^{33}P-ODN concentration was high not only in the liver, but also in the spleen and kidney (Figure 7). Almost 60.2% (about 2.88 μg ODN/g liver tissue) of the conjugate accumulated in the liver compared to about 40% (data not shown) (about 2.01 μg ODN/g liver tissue) accumulation by free ODNs at 30 min postadministration.

Plasma elimination of Gal-PEG-^{33}P-ODN was biphasic with a distribution half-life ($t_{1/2\alpha}$) of 4.38 ± 0.36 min and elimination half-life ($t_{1/2\beta}$) of 118.61 ± 22.06 min. Figure 8summarizes the pharmacokinetic parameters such as AUC, V_d, CL, and MRT. Consistent with rapid clearance (0.37 ± 0.09 mL/min), Gal-PEG-^{33}P-ODN had a large V_d of 35.98 ± 2.64 mL. Table 1 summarizes the AUC, tissue uptake rate index, and organ clearance for representative organs after systemic administration of ^{33}P-ODN and Gal-PEG-^{33}P-ODN in rats. The liver uptake rate index and clearance of Gal-PEG-^{33}P-ODN were significantly higher than those of ^{33}P-ODN: 2663.27 ± 56.63 versus 376.15 ± 38.34 μL·h^{-1}·g^{-1} and 16674.22 ± 354.55 versus 2218.09 ± 205.68 μL·h^{-1}·g^{-1}, respectively. The spleen was in the second place with the tissue uptake rate index of 969.26 ± 51.79 versus 204.73 ± 9.64 μL·h^{-1}·g^{-1} and CL_{org} of 395.84 ± 21.15 versus 82.85 ± 7.32 μL·h^{-1}. The tissue uptake rate indices and organ clearances of heart, kidney, and lung were significantly higher than those of ^{33}P-ODN, possibly due to increased in vivo stability of ODN upon conjugation with Gal-PEG.

Competition in Hepatic Uptake of Gal-PEG-^{33}P-ODN. The role of asialoglycoprotein receptor on biodistribution of Gal-PEG-^{33}P-ODN in rats was assessed by determining the effect of excess Gal-BSA on the accumulation of Gal-PEG-^{33}P-ODN

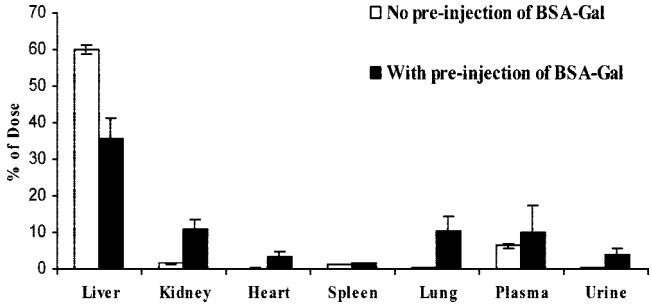

Figure 9. Effect of Gal-BSA on biodistribution of Gal-PEG-^{33}P-ODN after systemic administration into rats. Gal-BSA (10 mg/kg) was injected intravenously into rats 2 min before the injection of Gal-PEG-^{33}P-ODN at a dose of 0.2 mg/kg. At 30 min postinjection, rats were sacrificed, major organs were isolated, and radioactivity was determined. Values are the mean ± SD of 4 rats.

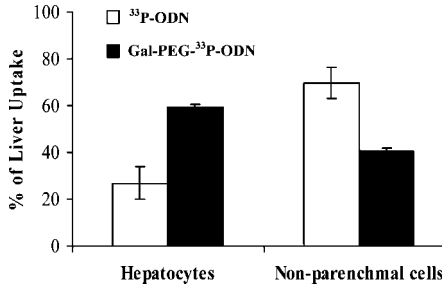

Figure 10. Hepatic cellular localization of ^{33}P-ODN and Gal-PEG-^{33}P-ODNs. The liver was perfused by collagenase/Pronase digestion at 30 min postinjection of ^{33}P-ODN or Gal-PEG-^{33}P-ODN at a dose of 0.2 mg/kg. Parenchymal and nonparenchymal cells were separated and the associated radioactivity was measured. Values are the mean ± SD of 4 rats.

in the liver. Galactosylated proteins or polymeric systems are known to be taken up by asialoglycoprotein receptor-mediated endocytosis. We have previously demonstrated that 1 min preinjection of excess Gal-BSA can saturate asialoglycoprotein receptors present on the surface of hepatocytes, resulting in decreased hepatic uptake of Gal-PLL/ODN complexes. Staud et al. (1999) also injected galactosylated superoxide dismutase (Gal-SOD) 2 min postinjection of excess Gal-BSA and demonstrated significant decrease in the hepatic uptake of Gal-SOD (*13*). Therefore, a 2 min interval between the intravenous injections of Gal-BSA and Gal-PEG-ODN is reasonable for the competition study. Systemic administration of excess Gal-BSA is known to saturate the asialoglycoprotein receptor of the hepatocytes (*30*). Prior administration of Gal-BSA at a dose of 10 mg/kg caused a significant decrease in the hepatic uptake of Gal-PEG-^{33}P-ODN, but increase in the radioactivity in plasma and other organs at 30 min postinjection. The hepatic uptake of Gal-PEG-^{33}P-ODN decreased from 60.2% to 35.9% (Figure 9). This suggests the involvement of asialoglycoprotein receptor in their hepatic uptake.

Hepatic Cellular Localization. To determine the intrahepatic localization of Gal-PEG-^{33}P-ODN and to determine whether the uptake of this conjugate by hepatocytes is mediated by asialoglycoprotein receptors, the liver was perfused at 30 min post tail vein injection of ^{33}P-ODN or Gal-PEG-^{33}P-ODN, and different types of liver cells were isolated for determining the amount of radioactivity in these cells. As shown in Figure 10, the hepatocytes were the major site for the uptake of Gal-PEG-^{33}P-ODN. At 30 min about 58% of the total liver recovery was in the hepatocytes compared to only 30% for the ^{33}P-ODNs (Figure 10). Accordingly, the uptake of Gal-PEG-^{33}P-ODN in the liver nonparenchymal cells (NPC) was 42% compared to 70% for ^{33}P-ODN. This suggests that a large percentage of the injected Gal- PEG-^{33}P-ODN was taken up by the liver via asialoglycoprotein receptor-mediated endocytosis.

DISCUSSION

Systemic delivery of ODNs is promising for treating both genetic and acquired diseases. Phosphorothioate (PS) ODNs are by far the most extensively studied, and significant progress has been made which resulted in one commercial product (Vitravene) as well as several promising clinical trials (*31*). To enhance the cellular uptake of ODNs by HepG2.2.15 cells, which are stably transfected with hepatitis B virus (HBV), Wu and Wu conjugated asialoorosomucoid to poly(L-lysine) and then formed complex with 21-mer ODN complementary to a portion of human HBV. There was significant increase in ODN uptake by HepG 2.2.15 cells, and the concentration of Hepatitis B surface antigen (HBsAg) was 80% lower than controls after 24 h (*32*). However, these authors did not determine the biodistribution of asialooromucoid-PLL/ODN complexes after systemic administration in rodents.

We have previously shown that, although complex formation with Gal-PLL enhances ODN uptake by hepatocytes after systemic administration in mice, the difference in the intracellular distribution of Gal-PLL/ODN and ODN was only moderate, possibly because of the nonspecific ionic interaction due to polycations (*8*). Therefore, in this study, we conjugated ODN to Gal-PEG via an acid-labile ester linkage of β-thiopropionate, which will be cleaved in response to a pH decrease in the endosome. Oishi et al. (2003) demonstrated the hydrolysis of β-thiopropionate linkage (easter linkage) of the PEG-ODN conjugate at pH 5.5, but not at pH 7.4 even after incubation at 37 °C for 24 h (*23*).

Consistent with our results on Gal-PLL/ODN complexes (*8*), the plasma kinetic disposition of Gal-PEG-^{33}P-ODN was characterized by rapid distribution to most peripheral tissues, with the highest disposition in the liver (Figure 7A,B). Bioconjugation with Gal-PEG decreased the urinary clearance of ODNs to a great extent (*8*). The liver accumulation of Gal-PEG-^{33}P-ODN, including radioactivity and ODN concentration, significantly increased within a short time and reached its peak at 30 min postadministration. Generally, after the peak time point the accumulation of the radioactivity and the concentration should decrease along the time. However, in the present study both of them showed a slight increase in the hepatic uptake at 240 min and then decreased, while in other organs, the accumulation and concentration of ODNs increased significantly until 24 h. The possible reason for this phenomenon is that after endocytosis of Gal-PEG-ODN by the liver cells the β-thiopropionate linkage becomes unstable and ODN will be released from conjugate gradually. The degradation reaction makes the cell an ODN depot. Then, some of ODNs can be distributed all over the body.

We determined the role of the asialoglycoprotein receptors on biodistribution of Gal-PEG-^{33}P-ODN in rats by the competition effect of excess Gal-BSA on the hepatic uptake of ODNs. There was significant decrease in ODN deposition to the liver, but an increase in its accumulation to other organs and tissues, suggesting that Gal-PEG-ODN was taken up by hepatocytes via the galactose-specific asialoglycoprotein receptor-mediated endocytosis (Figure 9). The higher uptake of ODNs in hepatocytes compared with nonparenchymal cells in the cellular distribution (Figure 10) and the highest accumulation of ODNs in liver compared with other organs in whole body level biodistribution after ODN conjugated with Gal-PEG (Figure 7) further confirmed this result.

In conclusion, in this study we synthesized a Gal-PEG-ODN conjugate for site-specific delivery to hepatocytes. In contrast to ^{33}P-ODN, Gal-PEG-^{33}P-ODN was efficiently taken up by hepatocytes and less efficiently by nonparenchymal cells (Figure

10). Thus, nonionic Gal-PEG-ODN is a promising delivery system which can be used for targeted delivery of ODN or siRNA into hepatocytes to treat various liver diseases associated with hepatocyte injury and inflammation.

ACKNOWLEDGMENT

This work was supported by a grant EB003922 from the NIH. The authors thank Dr. Ying Tu for her help with optimization of HPLC condition.

LITERATURE CITED

(1) Felgner, J. H., Kumar, R., Sridhar, C. N., Wheeler, C. J., Tsai, Y. J., Border, R., Ramsey, P., Martin, M., and Felgner, P. L. (1994) Enhanced gene delivery and mechanism studies with a novel series of cationic lipid formulations. *J. Biol. Chem. 269*, 2550–61.

(2) Liu, F., Yang, J., Huang, L., and Liu, D. (1996) New cationic lipid formulations for gene transfer. *Pharm. Res. 13*, 1856–60.

(3) Mahato, R. I., Rolland, A., and Tomlinson, E. (1997) Cationic lipid-based gene delivery systems: pharmaceutical perspectives. *Pharm. Res. 14*, 853–9.

(4) Goula, D., Remy, J. S., Erbacher, P., Wasowicz, M., Levi, G., Abdallah, B., and Demeneix, B. A. (1998) Size, diffusibility and transfection performance of linear PEI/DNA complexes in the mouse central nervous system. *Gene Ther. 5*, 712–7.

(5) Benns, J. M., Choi, J. S., Mahato, R. I., Park, J. S., and Kim, S. W. (2000) pH-sensitive cationic polymer gene delivery vehicle: N-Ac-poly(L-histidine)-graft-poly(L-lysine) comb shaped polymer. *Bioconjugate Chem. 11*, 637–45.

(6) De Smedt, S. C., Demeester, J., and Hennink, W. E. (2000) Cationic polymer based gene delivery systems. *Pharm. Res. 17*, 113–26.

(7) Mahato, R. I., Cheng, K., and Guntaka, R. V. (2005) Modulation of gene expression by antisense and antigene oligodeoxynucleotides and small interfering RNA. *Exp. Opin. Drug Delivery 2*, 3–28.

(8) Mahato, R. I., Takemura, S., Akamatsu, K., Nishikawa, M., Takakura, Y., and Hashida, M. (1997) Physicochemical and disposition characteristics of antisense oligonucleotides complexed with glycosylated poly(L-lysine). *Biochem. Pharmacol. 53*, 887–95.

(9) Temsamani, J., Roskey, A., Chaix, C., and Agrawal, S. (1997) In vivo metabolic profile of a phosphorothioate oligodeoxyribonucleotide. *Antisense Nucleic Acid Drug Devel. 7*, 159–65.

(10) Graham, M. J., Crooke, S. T., Monteith, D. K., Cooper, S. R., Lemonidis, K. M., Stecker, K. K., Martin, M. J., and Crooke, R. M. (1998) In vivo distribution and metabolism of a phosphorothioate oligonucleotide within rat liver after intravenous administration. *J. Pharmacol. Exp. Ther. 286*, 447–58.

(11) Rusckowski, M., Qu, T., Roskey, A., and Agrawal, S. (2000) Biodistribution and metabolism of a mixed backbone oligonucleotide (GEM 231) following single and multiple dose administration in mice. *Antisense Nucleic Acid Drug Devel. 10*, 333–45.

(12) Graham, M. J., Crooke, S. T., Lemonidis, K. M., Gaus, H. J., Templin, M. V., and Crooke, R. M. (2001) Hepatic distribution of a phosphorothioate oligodeoxynucleotide within rodents following intravenous administration. *Biochem. Pharmacol. 62*, 297–306.

(13) Staud, F., Nishikawa, M., Takakura, Y., and Hashida, M. (1999) Liver uptake and hepato-biliary transfer of galactosylated proteins in rats are determined by the extent of galactosylation. *Biochim. Biophys. Acta 1427*, 183–92.

(14) Attie, A. D., Pittman, R. C., and Steinberg, D. (1980) Metabolism of native and of lactosylated human low density lipoprotein: evidence for two pathways for catabolism of exogenous proteins in rat hepatocytes. *Proc. Natl. Acad. Sci. U.S.A. 77*, 5923–7.

(15) Biessen, E. A., Beuting, D. M., Vietsch, H., Bijsterbosch, M. K., and Van, Berkel, T. J. (1994) Specific targeting of the antiviral drug 5-iodo 2′-deoxyuridine to the parenchymal liver cell using lactosylated poly-L-lysine. *J. Hepatol. 21*, 806–15.

(16) Ye, Z., Cheng, K., Guntaka, R. V., and Mahato, R. I. (2006) Receptor-mediated hepatic uptake of M6P-BSA-conjugated triplex-forming oligonucleotides in rats. *Bioconjugate Chem. 17*, 823–30.

(17) Rajur, S. B., Roth, C. M., Morgan, J. R., and Yarmush, M. L. (1997) Covalent protein-oligonucleotide conjugates for efficient delivery of antisense molecules. *Bioconjugate Chem. 8*, 935–40.

(18) Healy, J. M., Lewis, S. D., Kurz, M., Boomer, R. M., Thompson, K. M., Wilson, C., and McCauley, T. G. (2004) Pharmacokinetics and biodistribution of novel aptamer compositions. *Pharm. Res. 21*, 2234–46.

(19) Zhao, H., Greenwald, R. B., Reddy, P., Xia, J., and Peng, P. (2005) A new platform for oligonucleotide delivery utilizing the PEG prodrug approach. *Bioconjugate Chem. 16*, 758–66.

(20) Zhao, H., Peng, P., Longley, C., Zhang, Y., Borowski, V., Mehlig, M., Reddy, P., Xia, J., Borchard, G., Lipman, J., Benimetskaya, L., and Stein, C. A. (2007) Delivery of G3139 using releasable PEG-linkers: impact on pharmacokinetic profile and anti-tumor efficacy. *J. Controlled Release 119*, 143–52.

(21) Bonora, G. M., Ivanova, E., Zarytova, V., Burcovich, B., and Veronese, F. M. (1997) Synthesis and characterization of high-molecular mass polyethylene glycol-conjugated oligonucleotides. *Bioconjugate Chem. 8*, 793–7.

(22) Oishi, M., Nagasaki, Y., Itaka, K., Nishiyama, N., and Kataoka, K. (2005) Lactosylated poly(ethylene glycol)-siRNA conjugate through acid-labile beta-thiopropionate linkage to construct pH-sensitive polyion complex micelles achieving enhanced gene silencing in hepatoma cells. *J. Am. Chem. Soc. 127*, 1624–5.

(23) Oishi, M., Sasaki, S., Nagasaki, Y., and Kataoka, K. (2003) pH-responsive oligodeoxynucleotide (ODN)-poly(ethylene glycol) conjugate through acid-labile beta-thiopropionate linkage: preparation and polyion complex micelle formation. *Biomacromolecules 4*, 1426–32.

(24) Cheng, K., Ye, Z., Guntaka, R. V., and Mahato, R. I. (2005) Biodistribution and hepatic uptake of triplex-forming oligonucleotides against type alpha1(I) collagen gene promoter in normal and fibrotic rats. *Mol. Pharm. 2*, 206–17.

(25) Guicciardi, M. E., and Gores, G. J. (2005) Apoptosis: a mechanism of acute and chronic liver injury. *Gut 54*, 1024–33.

(26) Monsigny, M., Roche, A. C., and Midoux, P. (1984) Uptake of neoglycoproteins via membrane lectin(s) of L1210 cells evidenced by quantitative flow cytofluorometry and drug targeting. *Biol. Cell 51*, 187–96.

(27) Sando, G. N., and Karson, E. M. (1980) p-Isothiocyanatophenyl 6-phospho-alpha-D-mannopyranoside coupled to albumin. A model compound recognized by the fibroblast lysosomal enzyme uptake system. 1. Chemical synthesis and characterization. *Biochemistry 19*, 3850–5.

(28) Monsigny, M., Petit, C., and Roche, A. C. (1988) Colorimetric determination of neutral sugars by a resorcinol sulfuric acid micromethod. *Anal. Biochem. 175*, 525–30.

(29) Hendriks, H. F., Brouwer, A., and Knook, D. L. (1990) Isolation, purification, and characterization of liver cell types. *Methods Enzymol. 190*, 49–58.

(30) Terada, T., Nishikawa, M., Yamashita, F., and Hashida, M. (2006) Analysis of the molecular interaction of glycosylated proteins with rabbit liver asialoglycoprotein receptors using surface plasmon resonance spectroscopy. *J. Pharm. Biomed. Anal. 41*, 966–72.

(31) Orr, R. M., and Dorr, F. A. (2005) Clinical studies of antisense oligonucleotides for cancer therapy. *Methods Mol. Med. 106*, 85–111.

(32) Wu, G. Y., and Wu, C. H. (1992) Specific inhibition of hepatitis B viral gene expression in vitro by targeted antisense oligonucleotides. *J. Biol. Chem. 267*, 12436–9.

BC070126M

Enhanced Circulating Half-Life and Antitumor Activity of a Site-Specific Pegylated Interferon-α Protein Therapeutic

Stacie J. Bell,[†] Christine M. Fam,[†] Elizabeth A. Chlipala,[‡] Sharon J. Carlson,[†] Ji I. Lee,[†] Mary S. Rosendahl,[†] Daniel H. Doherty,[†] and George N. Cox*[,†]

Bolder BioTechnology, Inc., 2945 Wilderness Place, Boulder, Colorado 80301, and BolderPATH, Inc., Campus Box 347, University of Colorado, Boulder, Colorado 80309. Received April 18, 2007; Revised Manuscript Received October 2, 2007

Recombinant interferon alpha-2 (IFN-α2) has proven useful for treating a variety of human cancers and viral diseases. IFN-α2 has a short circulating half-life *in vivo*, which necessitates daily or thrice weekly administration to patients. It is possible to extend the circulating half-life of IFN-α2 by random modification of lysine residues in the protein with polyethylene glycol (PEG); however, such preparations have heterogeneous structures and low specific activities, and may not provide optimal therapeutic benefits to patients. A long-acting, site-specific, monoPEGylated IFN-α2 protein has now been created by targeted attachment of a 20 kDa or a 40 kDa maleimide-PEG to a cysteine analogue of IFN-α2, M111C. *In vitro* bioactivities of the purified 20 kDa and 40 kDa PEG-M111C proteins were within 2- to 3-fold of those of wild type IFN-α2 and 7- to 10-fold better than that of a 40 kDa PEG IFN-α2 protein created using nontargeted, amine-PEGylation methodology. The 20 kDa and 40 kDa PEG-M111C proteins demonstrated 26- to 38-fold longer half-lives, respectively, than IFN-α2 following subcutaneous administration to rats. The 20 kDa PEG M111C protein inhibited growth of human NIH:OVCAR-3 cells transplanted into nude mice by >90%, as measured by tumor size, tumor weight, and number of animals with detectable tumors at necropsy, and was significantly more effective than a comparable dose of IFN-α2. These data extend our previous findings that bioactivity of IFN-α2 can be largely preserved by targeted attachment of PEG moieties to nonessential sites in the protein and provide evidence that site-specific PEGylated IFN-α2 proteins possess enhanced tumoricidal properties *in vivo*.

INTRODUCTION

Interferon alpha 2 (IFN-α2) is a 20 kDa cytokine that is a potent inhibitor of viral replication and tumor cell growth (*1–3*). Recombinant human IFN-α2 proteins have proven useful for treating viral diseases, such as hepatitis B, hepatitis C, and genital warts, and for treating cancers, such as hairy cell leukemia, lymphoma, melanoma, renal carcinoma, and Kaposi's sarcoma. Because of the short circulating half-life of recombinant IFN-α2, frequent administration (daily or thrice weekly) at high concentrations is required to achieve desired outcomes. Therefore, patient discomfort is higher, as are the side effects experienced. Several modified forms of IFN-α2 with improved pharmacokinetic properties have been developed recently (*4–7*). Animal and human studies suggest that the increased half-lives and consequent greater systemic exposure of these longer-acting IFN-α2 proteins enhance their ability to protect against viral infections (*8–12*). These proteins are being tested in animal cancer models and human clinical trials to determine if they possess enhanced tumoricidal properties as well (*4, 12–16*).

Increasing the circulating half-life of IFN-α2 was approached initially by modification of the protein with amine-reactive polyethylene glycol (PEG) reagents and by fusion of IFN-α2 to human albumin (*4–7*). However, these products have heterogeneous structures and/or low specific activities, which increases the cost of the drug and may not maximize the potential therapeutic benefits of the protein to patients. PEG-Intron (Schering Corporation) is modified with a relatively small 12 kDa PEG, which allows the protein to retain significant activity (3- to 4-fold reduction from that of wild type IFN-α2), but confers only a moderate improvement in half-life as compared to that of the unmodified protein (*7, 17–19*). Approximately 47% of the PEG molecules in PEG-Intron are attached to histidine-34 (H34), but the remaining 53% of the PEG molecules are attached to other amino acids, principally lysine residues (K31, K83, K121, K131, and K134) and the N-terminal cysteine residue (*7, 17, 19*). The PEG-H34 bond is unstable and undergoes hydrolysis in aqueous solution, resulting in the dissociation of PEG from the protein. The instability of the PEG-H34 bond limits potential formulations for the protein and contributes to the relatively short half-life of the protein (*7, 18*). A second PEG-IFN-α2 protein, PEGASYS (Roche), is modified with a larger 40 kDa PEG and comprises a complex mixture of four major (K31, K121, K131, and K134) and several minor PEG−protein isoforms, each of which differs in bioactivity (*4, 19, 20*). PEGASYS has a long half-life but possesses only 1–7% of wild type IFN-α2 *in vitro* bioactivity (*4, 19*). The albumin- IFN-α2 fusion protein (Albuferon, Human Genome Sciences) has a long half-life, but possesses only about 1% of the *in vitro* bioactivity of wild type IFN-α2 (*6*).

Recently, it was shown that introducing a cysteine residue into the IFN-α2 protein and using a cysteine-specific PEG reagent (site-specific PEGylation) provided an alternative method for PEGylating IFN-α2 that resulted in a homogeneously modified, monoPEGylated protein (*21*). Three regions of IFN-α2 were identified where a cysteine residue could be introduced and PEGylated without appreciably altering *in vitro* bioactivity of the protein. The cysteine mutein characterized in most detail was Q5C (substitution of cysteine for glutamine at amino acid position 5). In this article, a second site-specific, monoPEGylated IFN-α2 analogue, M111C, that retains near complete *in vitro* bioactivity, even when modified with a large 40 kDa PEG, is

* Corresponding author. Tel: (303) 420-4420. Fax: 303-420-4426. E-mail: jcox@bolderbio.com.

[†] Bolder BioTechnology, Inc.

[‡] BolderPATH, Inc.

10.1021/bc070131q CCC: $40.75 © 2008 American Chemical Society
Published on Web 11/20/2007

characterized. The M111C protein was modified with PEG moieties of various molecular weights and the PEG-proteins purified to homogeneity. The PEG-M111C proteins possessed significantly longer half-lives than IFN-α2 in rats. One of the PEG-M111C proteins was evaluated for efficacy in an athymic mouse tumor model and shown to be significantly more effective than IFN-α2 at inhibiting the growth of human tumor cells in mice. This study is the first demonstration of *in vivo* efficacy of a site-specific PEGylated IFN-α2 protein therapeutic.

EXPERIMENTAL PROCEDURES

Construction, Expression and Purification of Recombinant IFN-α2-M111C. The IFN-α2b-M111C analogue was constructed by site-directed mutagenesis and expressed in *Escherichia coli* essentially as described (*21*). Induced *E. coli* cells were harvested by centrifugation and the cell pellets stored at −80 °C. Frozen cells from 400 mL cultures were thawed and resuspended in 10 mL of 8 M guanidine, 20 mM cysteine, 2% (v/v) Tween 20, and 20 mM MES at pH 3. After mixing for 3 h, the solution was diluted 20-fold, the guanidine concentration was adjusted to 0.6 M, urea and copper sulfate were added to final concentrations of 1 M and 40 μM, respectively, and the solution was adjusted to pH 6. The refold mixture was incubated for 1–2 d at 4 °C, adjusted to pH 3, and clarified by centrifugation. The supernatant was diluted 4-fold with H_2O and loaded onto a 5 mL HiTrap S-Sepharose column (GE Healthcare, Piscataway, NJ) equilibrated in 20 mM MES at pH 5.0. The bound proteins were eluted with a linear salt gradient from 0 to 100% buffer B (500 mM NaCl, 20 mM MES, and 10% ethylene glycol at pH 5.0). Column fractions enriched for the M111C protein were identified by nonreducing SDS−PAGE. These fractions were pooled and loaded onto a 1 mL Cu^{2+} IMAC Hi Trap column (GE Healthcare) equilibrated in 40 mM sodium phosphate at pH 6.0, 1 M NaCl, and 0.1% (v/v) Tween 20. The M111C protein was eluted with a reverse pH gradient from 5.5 to 4.1 in 40 mM sodium phosphate, 1 M NaCl, and 0.1% Tween 20. Column fractions were analyzed by nonreducing SDS−PAGE ,and fractions containing properly folded M111C protein and no visible contaminants were pooled. The IMAC column pool was equilibrated to room temperature, diluted 1:4 with 20 mM Tris at pH 8.0, and solid ammonium sulfate added to a final concentration of 10% (w/v). The protein was loaded onto a 1 mL Phenyl Sepharose column (GE Healthcare) equilibrated in 20 mM Tris-HCl at pH 8.0 and 10% (w/v) ammonium sulfate. The protein was eluted using a linear reverse salt gradient from 0 to 100% Buffer B (20 mM Tris-HCl and 30% ethylene glycol at pH 8.0). Column fractions were analyzed by nonreducing SDS−PAGE, and fractions containing properly folded M111C protein were pooled, quantitated, and stored at −80 °C.

Site-Specific PEGylation of IFN-α2-M111C. Small scale (microgram quantities) PEGylation reactions were performed essentially as described (*21*) using TCEP (Tris [2-carboxyethylphosphine] hydrochloride, Pierce Chemical Company, Rockford, IL) to partially reduce the purified M111C protein. To prepare larger quantities (milligrams) of the PEG-M111C protein for animal studies, the purified M111C protein was diluted to a final concentration of 6.6 μM in 25 mM Tris-HCl at pH 8.0 and partially reduced by incubation with a 25-fold molar excess of dithiothreitol (DTT) for 20 min at room temperature. The mixture was then dialyzed against 20 mM MES at pH 5 to remove the DTT. The PEGylation reaction mixtures contained 2.6 μM M111C, a 10-fold molar excess of maleimide PEG reagent, 100 mM Tris at pH 7.5, and 0.5 mM EDTA. After 1 h at room temperature, the PEGylation reaction was stopped by diluting the mixture 1:4 with 20 mM MES at pH 5 and adjusting the pH to ≤4. PEGylated M111C protein was separated from unPEGylated protein by S-Sepharose chromatography using the column chromatography conditions described above, except that 10% glycerol was substituted for 10% ethylene glycol. This method was used to prepare the M111C protein modified with a 20 kDa maleimide PEG and a branched 40 kDa maleimide PEG (Nektar, Inc., Huntsville, AL).

Pharmacokinetic Evaluation of PEG-IFN-α2-M111C in Rats. All animal experiments were performed with the approval of BolderPATH's Institutional Animal Care and Use Committee. The rat pharmacokinetic studies were performed following previously described procedures (*21*), except that plasma levels of the test proteins were quantitated using human IFN-α2 ELISA kits obtained from Research Diagnostics, Inc. (Flanders, NJ, catalog number 41100-1; sensitivity range of 12.5 to 500 pg/mL). Standard curves were prepared for each protein and conjugate in the ELISA and used to adjust the final plasma values. Three male Sprague–Dawley rats were used per test protein. Rats were obtained from Harlan Sprague–Dawley, Inc. (Indianapolis, IN) and weighed ∼350 g each. Pharmacokinetic parameters of the test proteins were determined from plasma concentrations using WinNonlin (Pharsight, Inc., Mountain View, CA, version 4.0.1), using noncompartmental methods following subcutaneous administration.

Mouse Tumor Xenograft Study. The human ovarian carcinoma cell line NIH:OVCAR-3 was obtained from the American Type Culture Collection (Manassas, VA, catalog number HTB-161). Cells were grown *in vitro* in MEM media containing 10% fetal bovine serum, 2 mM glutamine, 50 units/mL penicillin, and 50 μg/mL streptomycin. Female athymic nude (nu/nu) mice, 5 to 6 weeks of age and weighing approximately 23 g at study initiation, were obtained from Charles River (Wilmington, MA). The NIH:OVCAR-3 cells were harvested by trypsinization, washed, and resuspended at a concentration of 25×10^6 cells per mL in a 50:50 mixture of MEM media/Matrigel. Matrigel was purchased from BD Biosciences (Bedford, MA). Animals were randomized to different test groups according to body weight on day 0. Mice received subcutaneous injections of 0.2 mL of the MEM media/Matrigel mixture containing 5×10^6 cells in the axillary area on day 0. One group of 5 mice received no further injections (referred to as untreated controls). The remaining mice (9–11 animals/group) received subcutaneous injections (0.2 mL/animal) of the test compounds beginning on day 1 and continuing through day 69 using a 3×/week dosing schedule (Monday, Wednesday, Friday). Mice were weighed on day 0, prior to the injection of cells, and on the days of tumor measurements. Tumors were measured using calipers at 3–4 day intervals for 10 weeks post injection. Tumor volume was determined using a formula of (width × width) × length)/2. The different treatment groups received injections of vehicle solution [phosphate buffered saline containing 0.1 mg/mL of mouse albumin (Sigma-Aldrich, Inc., St. Louis, MO)], wild type IFN-α2b in vehicle solution (5 μg/injection/mouse), or 20 kDa PEG-M111C in vehicle solution (5 μg/injection/mouse). Wild type IFN-α2b was prepared as described (*21*). Differences between groups were compared using Mann–Whitney statistical methods.

Miscellaneous Methods. Protein samples were analyzed by SDS−PAGE on precast Tris-glycine polyacrylamide gels (Invitrogen Corporation, Carlsbad, CA) and stained with Coomassie Blue or Silver. 2-Mercaptoethanol was added to a final concentration of 1–5% (v/v) in sample buffer to reduce the proteins. Protein concentrations were determined using a Bradford protein assay kit (Bio-Rad Laboratories, Richmond, CA), using bovine serum albumin as the protein standard. *In vitro* bioactivities of the proteins were measured using a Daudi cell growth inhibition assay, essentially as described (*21*). Roferon (Roche, Inc.), PEGASYS (Roche, Inc.), and PEG-Intron (Scher-

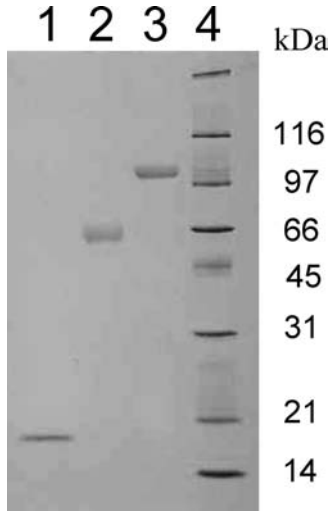

Figure 1. Nonreducing SDS−PAGE analysis of purified IFN-α2-M111C and PEG-M111C proteins. Lane 1, M111C; lane 2, 20 kDa PEG-M111C; lane 3, 40 kDa PEG-M111C; lane 4, molecular weight markers. Gels were stained with Coomassie blue.

ing Corporation) were analyzed in the Daudi assay using similar methods. Roferon was concentrated by S-Sepharose column chromatography as described above, except that 10% glycerol rather than 10% ethylene glycol was used in buffer B. The concentrated protein was stored in aliquots at −80 °C. N-terminal protein sequencing was performed by Macromolecular Resources (Fort Collins, CO) using an Edman degradation procedure.

RESULTS

Expression, Purification and Analysis of IFN-α2-M111C. IFN-α2 has a globular structure comprising 5 α helices joined by nonhelical loops (*22*). The helices are named A−E starting from the N-terminus of the protein, and the loops are named for the helices they join, for example, the C−D loop joins helices C and D. Previously, several IFN-α2 cysteine muteins that retained high *in vitro* bioactivity when modified with a small 5 kDa PEG were reported (*21*). These cysteine analogues were substitutions for amino acids located in the region preceding helix A, the C−D loop, and the region following helix E in IFN-α2. On the basis of these initial findings, a larger set of cysteine analogues constructed in these regions of IFN-α2 were screened. From this screen, the M111C analogue, which is located in the C−D loop, was identified as a promising candidate for further development. The M111C protein was expressed recombinantly in *E. coli* using the STII signal sequence to direct secretion of the protein to the *E. coli* periplasm (*21*). The signal sequence is efficiently cleaved from the protein when the induced *E. coli* cultures are grown at pH 5.5 (*21*). The properly processed M111C protein was present in both the soluble and insoluble fractions of cell lysates. To optimize recovery of the protein, a procedure for refolding the protein from whole cell lysates was developed. The refolded M111C protein was purified by sequential S-Sepharose, Cu^{2+} IMAC, and hydrophobic interaction column chromatography steps, as described in Experimental Procedures. The purified M111C protein migrated as a single band by reducing and nonreducing SDS−PAGE (Figure 1) and comigrated with wild type IFN-α2 under these conditions (data not shown). The identity and purity of the M111C mutein was verified by N-terminal sequencing, reversed-phase high pressure liquid chromatography and silver staining (data not shown). The protein purity was estimated to be >90%, as judged by densometric scanning of SDS−PAGE gels. The protein structural integrity was evaluated by circular dichroism

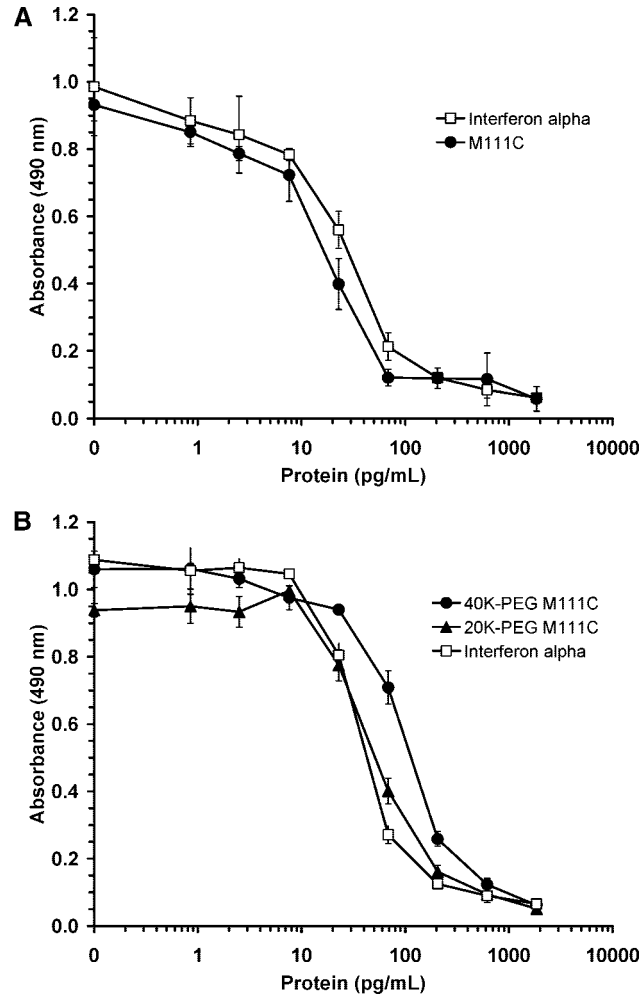

Figure 2. *In vitro* bioactivities of IFN-α2-M111C and PEG-M111C proteins. Serial dilutions of the indicated proteins were incubated with human Daudi cells for 4 days at 37 °C in 96 well tissue culture plates. At this time, an indicator dye was added to the wells and plates incubated for an additional 1–4 h. Absorbance values on the y-axis are proportional to cell number. Data are means ± SD for triplicate wells for each protein dilution. Experiments were repeated at least 3 times for each protein. Panel A compares M111C and IFN-α2 (Roferon). Panel B compares PEG-M111C proteins and IFN-α2 (Roferon).

Table 1. *In vitro* Bioactivities of PEG-M111C Proteins and IFN-α2 for Inhibiting Growth of Human Daudi Cells

protein	IC_{50} (pg/mL)[a]
IFN-α2[b]	31 ± 8
M111C	20 ± 4
20 kDa PEG-M111C	48 ± 18
40 kDa PEG-M111C	91 ± 37

[a] Means ± SD for at least 3 assays for each protein. The IC_{50} is the concentration of protein required for half-maximal inhibition of cell proliferation. [b] Roferon.

spectroscopy and was essentially identical to that of the wild type protein (data not shown). *In vitro* bioactivity of the M111C protein was compared to that of IFN-α2 (Roferon) in a cell growth inhibition assay using human Daudi cells. The M111C protein inhibited growth of Daudi cells with the same potency as that of IFN-α2 (Figure 2A and Table 1).

Site-Specific PEGylation of M111C. The purified M111C protein contains a mixed disulfide formed between M111C and cysteine added during the refold procedure. The mixed disulfide stabilizes the protein during purification, but must be disrupted for efficient modification of the protein with maleimide-PEG reagents. The purified M111C protein was partially reduced with

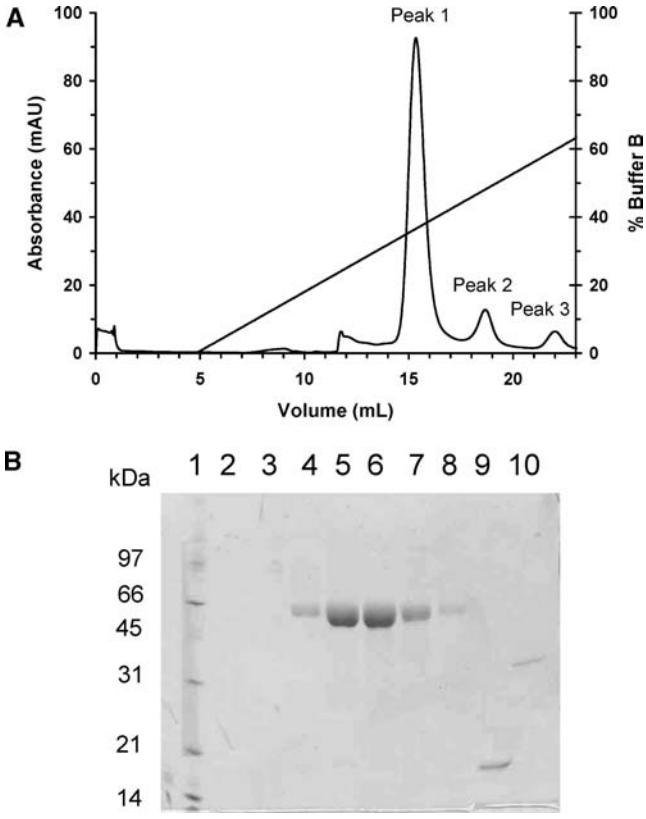

Figure 3. Column fractionation of PEG-M111C from unPEGylated protein. Panel A shows an S-Sepharose column chromatogram of the PEGylation reaction mixture. The large early-eluting peak (Peak 1) is PEG-M111C protein. The smaller trailing peaks represent unmodified M111C protein (Peak 2) and M111C protein dimers (Peak 3). Panel B shows nonreducing SDS−PAGE analysis of fractions from the various column peaks. Lane 1, molecular weight markers; lanes 2–8, fractions across Peak 1, which is monoPEGylated-M111C protein; lane 9, Peak 2, which is unmodified M111C protein; and lane 10, which is Peak 3 and corresponds to M111C protein dimers.

DTT to disrupt the mixed disulfide and allow the protein/maleimide-PEG reaction. The M111C protein PEGylated efficiently with 20 kDa and 40 kDa maleimide PEGs, with typical PEGylation efficiencies of 80% or greater (Figure 3). The PEGylated M111C protein was separated from unmodified protein by S-Sepharose column chromatography. An S-Sepharose column chromatogram of a typical PEGylation reaction with the M111C protein using a 20 kDa maleimide PEG is shown in Figure 3A. The PEG−protein is the large peak (Peak 1) that elutes earlier from the column than the unmodified protein (Peak 2) and disulfide-linked protein dimers (Peak 3) that form during the PEGylation reaction. SDS−PAGE analysis indicated that the PEG−protein peak was monoPEGylated protein (Figure 3B). Fractions consisting predominantly of the monoPEGylated-M111C protein were pooled. Nonreducing SDS−PAGE analysis of the purified M111C protein modified with 20 kDa and 40 kDa PEGs is shown in Figure 1.

Analysis of *in Vitro* Bioactivity of PEG-M111C. *In vitro* potency of the 20 kDa PEG-M111C protein in the Daudi cell growth inhibition assay was reduced less than 2-fold as compared to that of IFN-α2, whereas potency of the 40 kDa PEG-M111C protein was reduced about 3-fold relative to that of IFN-α2 (Figure 2B and Table 1). When potencies of the 20 kDA and 40 kDa PEG-M111C proteins were compared directly to PEG-Intron and PEGASYS in the Daudi cell assay, the PEG-M111C proteins exhibited *in vitro* potencies comparable to that of PEG-Intron and 7- to 10-fold greater than

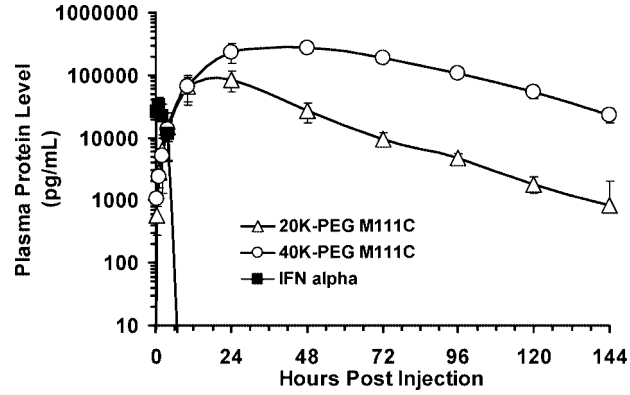

Figure 4. Plasma concentrations of PEG-M111C proteins and IFN-α2 (Roferon) following subcutaneous administration to rats. Data are means ± SD for three rats per group. Each rat received a 100 μg protein/kg subcutaneous dose. Plasma levels of the proteins were measured by ELISA.

that of PEGASYS (data not shown). Similar relative potencies of PEG-Intron, PEGASYS and IFN-α2 were reported previously (*19*).

Analysis of Pharmacokinetic Parameters of PEG-M111C Proteins in Rats. Circulating half-lives of the 20 kDa and 40 kDa PEG-M111C proteins were compared to that of wild type IFN-α2 (Roferon, Roche) following subcutaneous injection in rats (Figure 4). Circulating levels of the proteins were measured using human IFN-α2 ELISA kits. Plasma concentrations of wild type IFN-α2 peaked 1 h postadministration, then decreased rapidly, and were undetectable 10 h postadministration. The terminal half-life of IFN-α2 was 0.7 h, similar to the 1.2 h half-life for IFN-α2 reported previously (*21*). In contrast, maximum plasma levels of the PEG-M111C proteins were not attained until 24 h (20 kDa PEG-M111C) and 48 h (40 kDa PEG-M111C) postinjection (Figure 4). The maximum plasma level of the 40 kDa PEG-M111C protein (275 ng/mL) was higher than that of the 20 kDa PEG-M111C protein (84 ng/mL), both of which were higher than that of IFN-α2 (33 ng/mL). Similarly, the level of systemic exposure ($AUC_{0\rightarrow\infty}$) also was increased from 0.11 μg h/mL for IFN-α2 to 3.4 μg h/mL and 21 μg h/mL for the 20 kDa PEG and 40 kDa PEG-M111C proteins, respectively. Terminal half-lives for the 20 kDa PEG and 40 kDa PEG-M111C proteins were 18 h and 27 h, respectively.

Efficacy of 20 kDa PEG-M111C for Inhibiting Growth of Human Cancer Cells in Athymic Nude Mice. IFN-α2 inhibits the growth of a number of human tumor cell lines such as NIH:OVCAR-3 cells *in vitro* and *in vivo* in athymic mice (*23*). We compared the ability of IFN-α2 and the 20 kDa PEG-M111C protein to inhibit the growth of human NIH:OVCAR-3 tumor cells transplanted into athymic nude mice. The mice received an injection of 5×10^6 NIH:OVCAR-3 cells in Matrigel on day 0. Beginning on day 1, different groups of mice received 3×/week subcutaneous administration of vehicle solution (phosphate buffered saline containing 0.1 mg/mL of mouse serum albumin), wild type IFN-α2 prepared by us (5 μg/injection/mouse), or 20 kDa PEG-M111C (5 μg/injection/mouse). The mice received injections for 10 weeks, and tumor volumes were measured twice per week during this time. One group of control mice received no treatment injections (referred to as untreated controls).

Figure 5 shows the mean tumor volumes for the different test groups over time. Final tumor volumes, weights, and number of viable tumors at necropsy are summarized in Table 2. All of the test groups showed an initial decline in tumor volume through about day 13, which is likely due to absorption of the MEM media/Matrigel scaffold. From about day 13 until the end

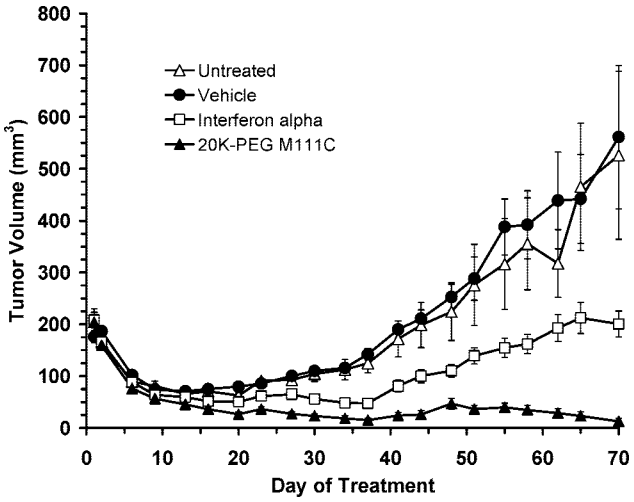

Figure 5. Inhibition of human tumor xenograft growth in athymic mice by PEG-M111C. Tumor volume (mm^3) is plotted vs day of treatment. Data are means ± SE for 9–11 mice per group, except for the untreated control group, which contained 5 mice. Athymic mice received an injection of 5×10^6 NIH:OVCAR-3 cells on day 0. The untreated control group received no further treatments. Mice in the other groups received 3×/week subcutaneous administrations of vehicle solution, wild type IFN-α2 prepared by us (5 μg/injection) or 20 kDa-PEG-M111C (5 μg/injection).

Table 2. Effects of 20 kDa PEG-M111C and IFN-α2 on Human Tumor Xenograft Volume and Weight in Mice after 70 Days of Treatment

treatment group[a]	tumor volume (mm^3)[b]	tumor weight (mg)[b]	animals with visible tumors at necropsy
untreated (5)	526 ± 162	346 ± 123	5/5
vehicle (9)	561 ± 139	354 ± 93	9/9
IFN-α2 (11)	201 ± 25[c]	94 ± 19[c]	11/11
PEG-M111C (11)	13 ± 7[c,d]	9 ± 5[c,d]	1/11

[a] The number of animals in each group is in parentheses. [b] The means ± SE for each group. [c] Significantly different from vehicle using the Mann–Whitney U test. [d] Significantly different from IFN-α2 using the Mann–Whitney U test.

of the study (day 70), mean tumor volumes increased in the untreated control animals and in animals receiving vehicle solution. At the termination of the study, mean tumor volumes and weights in animals receiving vehicle injections were comparable to those of the untreated control animals, indicating that the subcutaneous treatments and vehicle solution did not influence tumor growth in the animals. Mean tumor volumes in animals treated with PEG-M111C and IFN-α2 were significantly smaller (98% and 64%, respectively) than mean tumor volumes in animals treated with vehicle solution. Mean tumor volumes in animals treated with PEG-M111C were significantly smaller (94%) than mean tumor volumes in animals treated with IFN-α2. Tumor volumes in animals receiving 20 kDa PEG-M111C or IFN-α2 were significantly smaller than tumor volumes in animals receiving vehicle solution at all times from about day 16 to day 70. Mean tumor weights at necropsy (day 70) also were significantly reduced in animals receiving 20 kDa PEG-M111C (98% decrease) and IFN-α2 (73% decrease) compared to mean tumor weights in animals receiving injections of vehicle solution. Tumor weights were significantly smaller (90%) in animals treated with 20 kDa PEG-M111C compared to those of animals treated with IFN-α2. Only 1/11 animals in the group receiving 20 kDa PEG-M111C possessed a visible tumor mass at necropsy; the remaining animals showed an area of brown discoloration where the cells had been implanted. In contrast, all untreated control animals (5/5) and all animals receiving injections of vehicle solution (9/9) or IFN-α2 (11/11) had visible tumors at necropsy.

DISCUSSION

An earlier report (*21*) identified several regions in IFN-α2 where a cysteine residue can be introduced and modified with a 5 kDa PEG without appreciably reducing the bioactivity of the protein. One of these regions was the C−D loop, where M111 is located. Following analysis of several cysteine analogues in this region, the M111C protein was chosen for further analysis because it expressed well, displayed wild type *in vitro* biological activity, and PEGylated efficiently. The PEG-M111C protein retains high *in vitro* bioactivity in the Daudi cell growth inhibition assay even when modified with large 20 kDa and 40 kDa PEG moieties (within 2- to 4-fold of wild type IFN-α2). Similar results were reported with the PEG-Q5C protein in which PEG is attached to an amino acid located close to the amino-terminus of IFN-α2 (*21*). Preliminary studies indicate that the 20 kDa and 40 kDa PEG-M111C proteins also possess bioactivities comparable to that of wild type IFN-α2 in an *in vitro* antiviral assay using herpes simplex virus and human lung fibroblast cells (unpublished results). The high *in vitro* potencies of the 40 kDa PEG-M111C and 40 kDa PEG-Q5C (*21*) proteins stand in contrast to the results reported for amine-PEGylated IFN-α2, which shows at least a 14-fold loss of *in vitro* bioactivity (using either the Daudi cell assay or an antiviral assay) when modified with a 40 kDa PEG (*4, 19, 20*). These data and those of others (*4, 17, 19, 20*) indicate that loss of *in vitro* bioactivity upon PEGylation is not an inherent feature of IFN-α2, but is critically dependent upon the site at which the PEG is attached to the protein. The key receptor-binding contacts in IFN-α2 have been localized to the N-terminal end of the A−B loop, helices C and D, and the D−E loop of the protein (*19, 20, 22, 24–26*). The major sites for attachment of PEG in PEG-Intron and PEGASYS are located in these regions of the protein (K31 and H34 in the A−B loop; K83 in helix C; K121 and K131 in helix D; and K134 in the D−E loop). Although H34 retains acceptable activity when modified with a 12 kDa PEG, its activity decreases significantly when modified with a larger 30 kDa PEG (*19*). The low specific activities of these PEG-IFN-α2 isoforms probably results from the large PEG inhibiting proper receptor contacts. M111 and Q5C are located in regions of IFN-α2 that are distant from the identified receptor-binding domains of the protein, and modification of these residues with large PEG molecules seems to have little effect on *in vitro* bioactivity. PEGylation efficiency of M111C appears to be superior to that of the Q5C (*21*). According to details provided by the crystal structure of the protein, Q5 is partially buried in IFN-α2 (*22*), which may account for the lower PEGylation efficiency of Q5C. M111 is located in a surface-exposed, highly flexible region of IFN-α2 (*22, 25*), which may be more amenable to high PEGylation efficiency. Although we have not shown directly that the PEG is attached to the added cysteine in M111C (rather than to a native cysteine), several lines of evidence suggests that this is the case. First, the native C29−C138 disulfide is absolutely required for IFN-α2 bioactivity (*27*). Given the high specific activity of the PEG-M111C protein, it is unlikely that the C29−C138 disulfide is disrupted in the PEG-M111C protein. The C1−C98 native disulfide is not required for IFN-α2 bioactivity (*27, 28*), but PEG-IFN-α2 proteins in which C1 is PEGylated display greater than 10-fold loss of *in vitro* bioactivity (*19*), which is a much greater loss of activity than what we see with PEG-M111C. Random PEGylation of the native cysteines in IFN-α2 reduces *in vitro* bioactivity of the protein by 10- to 38-fold, depending upon whether the modified protein contains one or two PEGs and whether one or both of the native disulfides are disrupted (*29*). Again, this loss of activity is much greater than what we observe

with the PEG-M111C protein. The PEGylation reactions for the M111C protein also yielded predominantly monoPEGylated protein (Figure 3B). We would have expected to see significant amounts of multiply PEGylated species if we were reducing the native disulfides and PEGylating all of the cysteines in the protein. While these data strongly suggest that the PEG is attached to the added cysteine in M111C, detailed peptide mapping studies will be required to prove that this is the case.

The circulating half-life of the PEG-M111C protein varied depending upon the size of the attached PEG moiety, with 40 kDa PEG extending the half-life more than 20 kDa PEG. The 40 kDa PEG-M111C protein also took longer to reach peak plasma levels than the 20 kDa PEG protein, indicating that PEG size influences systemic absorption characteristics of the proteins. Peak plasma concentrations and overall systemic exposure of the proteins also were proportional to PEG size. Similar results were reported for the PEG-Q5C IFN-α2 analogue (*21*). The subcutaneous half-lives of the 20 kDa and 40 kDa PEG-M111C proteins in rats (18 and 27 h, respectively) were shorter than those reported for the 20 kDa and 40 kDa PEG-Q5C protein [27 and 48 h, (*21*)] and 40 kDa amine-PEG IFN-α2 [51 h, (*4*)]. Since half-lives of the proteins have not been compared in the same experiment or over the same time intervals, this result must be considered accordingly. Little is known about how PEG attachment sites influence the shape, hydrodynamic properties, and pharmacokinetic behavior of proteins.

The 20 kDa PEG-M111C protein strongly inhibited the growth of human NIH:OVCAR-3 tumor xenografts in mice when administered 3×/week and was significantly more effective than a comparable dose of IFN-α2, as measured by tumor volume, tumor weight, and the presence of detectable tumors at the termination of the study. Only 1/11 animals treated with PEG-M111C possessed a viable tumor at necropsy, as compared to 11/11 animals treated with IFN-α2 or 9/9 animals treated with vehicle solution. Lindner and Borden (*23*) reported that a daily injection of 5 μg of IFN-α2 inhibited the growth of NIH:OVCAR-3 cells transplanted into athymic mice by about 80% after 10 weeks of treatment. We found that administration of the same dose of IFN-α2 using a less frequent dosing schedule (3×/week) inhibited NIH:OVCAR-3 cell growth in mice by about 50%. Lindner and Borden (*23*) also reported that all of the mice treated with daily injections of IFN-α2 had viable tumors at necropsy, indicating a failure of IFN-α2 to completely suppress tumor growth *in vivo*. They were able to completely suppress tumor growth in the majority of mice by combining IFN-α2 treatment with the antiestrogen drug tamoxifen. Our data suggest that failure of IFN-α2 to completely suppress NIH:OVCAR-3 cell growth in athymic mice is not due to the inability of IFN-α2 to completely suppress tumor growth as a monotherapy, but rather is due to the short half-life of the protein, which results in suboptimal circulating levels of the protein in mice over time. Increasing the half-life of IFN-α2 by PEGylation or other means permits circulating IFN-α2 levels to remain at efficacious levels for longer periods of time, resulting in greater tumor cell death and fewer animals with viable tumors. The 20 kDa PEG-M111C protein, rather than the 40 kDa PEG-M111C protein, was used in the tumor xenograft study because the 20 kDa PEG protein may distribute more effectively from the blood stream into tissues, which is required to inhibit tumor growth in this model. (Human IFN-α2 is inactive in mice and exerts its antitumor effects by directly inhibiting the growth and/or viability of the human tumor cells.) Future tumor xenograft studies will compare the efficacy of the M111C protein modified with PEG molecules of different size.

This study and that of Bailon et al. (*4*) provide evidence that PEG-IFN-α2 proteins possess enhanced tumoricidal properties compared to IFN-α2 and complement studies indicating that PEG-IFN-α2 proteins possess enhanced antiviral properties (*8–12*). The enhanced therapeutic properties of PEG- IFN-α2 proteins likely are due to their longer half-lives and greater systemic exposure compared to those of IFN-α2. The long half-lives and superior efficacy of site-specifically PEGylated IFN-α2 proteins in animal tumor xenograft models support further evaluation of their potential as cancer therapeutics.

ACKNOWLEDGMENT

The publication's contents are solely the responsibility of the authors and do not necessarily represent the official views of the National Cancer Institute. We thank Rebecca Vanderslice, Stephen Eisenberg, and Jennifer Hughes for their contributions to this work. This work was supported by grants 1R43 CA079361 and 2R44 CA079361 to G.C. from the National Cancer Institute of the National Institutes of Health.

LITERATURE CITED

(1) Pestka, S., and Langer, J. A. (1987) Interferons and their actions. *Annu. Rev. Biochem. 56*, 727–777.

(2) Gutterman, J. U. (1994) Cytokine therapeutics: Lessons from interferon α. *Proc. Natl. Acad. Sci. U.S.A. 91*, 1198–1205.

(3) Lindner, D. J., Kalvakolanu, D. V., and Borden, E. C. (1997) Increasing effectiveness of interferon -α for malignancies. *Semin. Oncol. 24*, S99–104.

(4) Bailon, P., Palleroni, A., Schaffer, C. A., Spence, C. L., Fung, W. -J., Porter, J. E., Ehrlich, G. K., Pan, W., Xu, Z. -X., Modi, M. W., Farid, A., Berthold, W., and Graves, M. (2001) Rational design of a potent, long-acting form of interferon: a 40 kDa branched polyethylene glycol-conjugated interferon α2a for the treatment of hepatitis C. *Bioconjugate Chem. 12*, 195–202.

(5) Monkarsh, S. P., Ma, Y., Aglione, A., Bailon, P., Ciolek, D., DeBarbieri, B., Graves, M. C., Hollfelder, K., Michel, H., Palleroni, A., Porter, J. E., Russoman, E., Roy, S., and Pan Y.-C. (1997) Positional isomers of monopegylated interferon α-2a: isolation, characterization and biological activity. *Anal. Biochem. 247*, 434–440.

(6) Osborn, B. L., Olsen, H. S., Nardelli, B., Murray, J. H., Zhou, J. X., Garcia, A., Moody, G., Zaritskaya, L. S., and Sung, C. (2002) Pharmacokinetic and pharmacodynamic studies of a human serum albumin-interferon -α fusion protein in cynomolgus monkeys. *JPET 303*, 540–548.

(7) Wang, Y. -S., Youngster, S., Bausch, J., Zhang, R., McNemar, C., and Wyss, D. F. (2004) Identification of the major positional isomer of PEGylated interferon alpha-2b. *Biochemistry 39*, 10634–10640.

(8) Zeuzem, S., Feinman, S. V., Rasenack, J., Heathcote, E. J., Lai, M. Y., Gane, E., O'Grady, J., Reichen, J., Diago, M., Lin, A., Hoffman, J., and Brunda, M. J. (2000) Peginterferon alpha-2a in patients with chronic hepatitis C. *N. Engl. J. Med. 343*, 1666–1672.

(9) Craxi, A., and Cooksley, W. G. (2003) Pegylated interferons for chronic hepatitis B. *Antiviral Res. 60*, 87–89.

(10) Craxi, A., and Licata, A. (2003) Clinical trial results of peginterferons in combination with ribavirin. *Semin. Liver Dis. 23*, 35–46.

(11) Foster, G. R. (2003) Pegylated interferon with ribavirin therapy for chronic infection with hepatitis C virus. *Expert Opin. Pharmacother. 4*, 685–691.

(12) Matthews, S. J., and McCoy, C. (2004) Peginterferon alfa-2a: a review of approved and investigational uses. *Clin. Ther. 26*, 991–1025.

(13) Huang, S. F., Kim, S. -J., Lee, A. T., Karashima, T., Bucana, C., Kedar, D., Sweeney, P., Mian, B., Fan, D., Shepherd, D., Fidler, I. J., Dinney, C. P., and Killion, J. J. (2002) Inhibition of growth and metastasis of orthotopic human prostate cancer in athymic mice by combination therapy with PEGylated interferon-α−2b and docetaxel. *Cancer Res. 62*, 5720–5726.

(14) Choueiri, T. K., Hutson, T. E., and Bukowski, R. M. (2003) Evolving role of pegylated interferons in metastatic renal cell carcinoma. *Expert Rev. Anticancer Ther. 3*, 823–829.
(15) Krepler, C., Certa, U., Wacheck, V., Jansen, B., Wolff, K., and Pehamber, H. (2004) PEGylated and conventional interferon-α induce comparable transcriptional responses and inhibition of tumor growth in a human melanoma SCID mouse xenotransplantation model. *J. Invest. Dermatol. 123*, 664–669.
(16) Talpaz, M., Rakhit, A., Rittweger, K., O'Brien, S., Cortes, J., Fettner, S., Hooftman, L., and Kantarjian, H. (2005) Phase I evaluation of a 40-kDa branched-chain long-acting PEGylated IFN-α2a with and without cytarabine in patients with chronic myelogenous leukemia. *Clin. Cancer Res. 11*, 6247–6255.
(17) Gilbert, C. W., and Park-Cho, M. (1999) Interferon Polymer Conjugates, U.S. Patent 5,951,974.
(18) Pedder, S. C. J. (2003) Pegylation of interferon alpha: structural and pharmacokinetic properties. *Semin. Liver Dis. 23*, 19–22.
(19) Grace, M. J., Lee, S., Bradshaw, S., Chapman, J., Spond, J., Cox, S., Delorenzo, M., Brassard, D., Wylie, D., Cannon-Carlson, S., Cullen, C., Indelicato, S., Voloch, M., and Bordens, R. (2005) Site of PEGylation and polyethylene glycol molecule size attenuate interferon-α antiviral and antiproliferative activities through the JAK/STAT signaling pathway. *J. Biol. Chem. 280*, 6327–6336.
(20) Dhalluin, C., Ross, A., Leuthold, L. -A., Foser, S., Gsell, B., Muller, F., and Seen, H. (2005) Structural and biophysical characterization of the 40 kDa PEG-interferon-alpha 2a and its individual positional isomers. *Bioconjugate Chem. 16*, 504–517.
(21) Rosendahl, M. S., Doherty, D. H., Smith, D. J., Carlson, S. J., Chlipala, E. A., and Cox, G. N. (2005) A long-acting, highly potent interferon α-2 conjugate created using site-specific PEGylation. *Bioconjugate Chem. 16*, 200–207.
(22) Radhakrishnan, R., Walter, L. J., Hruka, A., Reichert, P., Trotta, P. P., Nagabhushan, T. L., and Walter, M. R. (1996) Zinc mediated dimer of human interferon-alpha 2b revealed by X-ray crystallography. *Structure 4*, 1453–1463.
(23) Lindner, D. J., and Borden, E. C. (1997) Synergistic antitumor effects of a combination of interferon and tamoxifen on estrogen receptor-positive and receptor-negative human tumor cell lines in vivo and in vitro. *J. Interferon Cytokine Res. 17*, 681–693.
(24) Uze, G., Lutfalla, G., and Mogensen, K. E. (1995) Alpha and beta interferons and their receptor and their friends and relations. *J. Interferon Cytokine Res. 15*, 3–26.
(25) Klaus, W., Gsell, B., Labhardt, A. M., Wipf, B., and Senn, H. (1997) The three-dimensional high resolution structure of human interferon α-2a determined by heteronuclear NMR spectroscopy in solution. *J. Mol. Biol. 274*, 661–675.
(26) Roisman, L. C., Piehler, J., Trosset, J. -Y., Scheraga, H. A., and Schreiber, G. (2001) Structure of the interferon-receptor complex determined by distance constraints from double mutant cycles and flexible docking. *Proc. Natl. Acad. Sci. U.S.A. 98*, 13231–13236.
(27) Morehead, H., Johnson, P. D., and Wetzel, R. (1984) Roles of the 29–138 disulfide bond of subtype A of human α interferon in its antiviral activity and conformational stability. *Biochemistry 23*, 2500–2507.
(28) DeChiara, T. M., Erlitz, F., and Tarnowski, S. J. (1986) Procedures for *in vitro* mutagenesis of human leukocyte interferon sequences. *Methods Enzymol. 119*, 403–15.
(29) Balan, S., Choi, J. W., Godwin, A., Teo, I., Laborde, C. M., Heidelberger, S., Zloh, M., Shaunak, S., and Brocchini, S. (2007) Site-specific PEGylation of protein disulfide bonds using a three-carbon bridge. *Bioconjugate Chem. 18*, 61–76.

BC070131Q

Lipopolythiourea Transfecting Agents: Lysine Thiourea Derivatives

Jeanne Leblond, Nathalie Mignet,* Céline Largeau, Johanne Seguin, Daniel Scherman, and Jean Herscovici*

Inserm, U640, Paris F-75006, France, CNRS, UMR8151, Paris F-75006, France, Ecole Nationale Supérieure de Chimie de Paris, Paris F-75005, France, Unité de Pharmacologie Chimique et Génétique, France, Université Paris-Descartes, Faculté de Pharmacie, Paris F-75270, France, and Chimie Moléculaire de Paris Centre, CNRS, FR 2769, Paris F-75005, France. Received May 28, 2007; Revised Manuscript Received September 14, 2007

Synthetic vectors represent an alternative to recombinant viruses for gene transfer. We have recently explored the transfection potential of a class of noncationic lipids bearing thiourea moieties as DNA-associating headgroups. The encouraging results obtained with lipopolythioureas derived from serinol prompted us to further investigate this family of vectors. In the present study, we considered the transfection properties of a series of derivatives based on a different thiourea polar headgroup bearing a lysine scaffold. The synthesis of these compounds could be readily achieved in three steps with good yields. We found that these lipopolythioureas (LPT) might be considered as alternative systems for gene transfection since their activity reached the same magnitude range as that of cationic vectors in the presence of serum. LPT with 14-carbon length chains appeared to be more efficient as a transfecting agent than the ones with shorter chains. Toxicity studies proved that the hydration film method led to particles well tolerated both by the cells *in vitro* and by the mice *in vivo*. The ability to induce gene expression *in vivo* was demonstrated by intratumoral injection. Finally, biodistribution studies showed that the quantity recovered in blood circulation, 2 h after systemic injection, was improved as compared to that in cationic lipids.

INTRODUCTION

Gene delivery requires, in most cases, a vector to protect DNA from enzymatic degradation and to allow DNA cellular uptake. Synthetic (*1*) and viral vectors (*2*) are currently being developed as gene delivery systems. Among artificial vectors, cationic lipids (*3*) and polymers (*4*) are particularly attractive as they can be easily prepared and have been extensively characterized (*5*). However, their cationic charges lead to nonspecific interaction with anionic serum components, strongly decreasing their transfection efficiency (*6, 7*) and inducing unspecific delivery *in vivo* (*8*). Numerous studies have been undertaken to improve serum resistance by hiding the cationic charges (*9–11*). Alternative delivery systems have been introduced, using nonelectrostatic interaction with DNA. For instance, Aoyama et al. succeeded in trapping DNA in virus-like saccharidic clusters (*12*), and Barthelemy et al. developed nucleoside-based amphiphile-associating plasmids (*13*). However, with the exception of artificial glycovirus (*14*), these systems required a cationic charge to show some transfection activity *in vitro* (*15*). Strictly neutral systems, such as liposomes (*16*) or spherulites (*17*), have been worked out for gene delivery, but, to the best of our knowledge, they have not shown any transfection properties.

Recent studies from our laboratory (*18, 19*) demonstrated the feasibility of using bis-thiourea as a noncationic lipid headgroup for gene transfer both *in vitro* and *in vivo* (*20*). Thiourea moieties are strong hydrogen bond donors and are able to interact with a wide range of derivatives, including carbohydrates, carboxylates (*21*), and nitrate (*22*) and phosphate groups (*23*). This last acid derivative is known to lead to the strongest interactions (*24*). These properties, together with their structural potential variety, make them good candidates to develop alternative vectors for gene transfer based on nonelectrostatic interaction. In our growing interest in noncationic delivery systems based on thiourea interacting groups, we developed a new family of lipopolythiourea (LPT) lipids designed around a 2,6-bis(thiocarbamoyl-amino)hexanoic acid scaffold. The new transfecting agents, described here, are readily available from lysine. In this article, we describe the synthesis of these compounds, and present their transfection efficiency data, cytotoxicity studies, and *in vivo* behavior.

* To whom correspondence should be addressed. E-mail: Nathalie.Mignet@univ-paris5.fr (N.M.). E-mail: jean-herscovici@enscp.fr (J.H.).

EXPERIMENTAL PROCEDURES

Materials and Methods. All solvents were purchased from Carlo Erba-SDS (Peypin, France). Dichloromethane was distilled from P_2O_5. DMF was dried over 3 Å molecular sieves and pyridine over KOH. All chemicals were purchased from Sigma-Aldrich-Fluka or Lancaster. Tosyl chloride (petroleum ether) and cholesteryl chloroformate (acetone) were recrystallized, and diglycolic anhydride was dehydrated (P_2O_5) prior to use. Other solvents and products were used without further purification. Reactions were monitored by thin-layer chromatography using Merck precoated 60 F254 silica gel plates. Column chromatography was performed over SDS (Peypin France) 35–70 m silicagel according to the method of Still, Khan, and Mitra (*25*) or by using small column flash chromatography (SFC) according to the following procedure: a plastic syringe was filled with silicagel (product/silicagel, 1/5) and connected to a vacuum pump. The column was equilibrated with heptane, then the sample, dissolved in a minimum of dichloromethane, was added to the top. The column was eluted by 10 fractions (volume equal to the silicagel volume) of a heptane/ethyl acetate mixture. For each fraction, the amount of ethyl acetate was increased (10% to 100% (v/v) heptane in ethyl acetate). Inverse phase SPE was performed on a Supelco Superclean C8 cartridge using an H_2O/CH_3CN/CH_3OH mixture. ^1H and ^{13}C NMR spectra were recorded on a BRUKER Avance DRX-300 spectrometer at 300.13 MHz for the proton and 75.47 MHz for the carbon. NMR spectra were processed using Xwinnmr (Bruker) or SwaN-MR (*26*). MS were carried out on a Shimazu 2010A LC-MS on ESI mode. High resolution MS and elemental analysis were carried out by the Service Central de Micro-analyse du CNRS, Vernaison, France. Dipalmytoylphosphatidylcholine (DPPC),

10.1021/bc7001924 CCC: $40.75 © 2008 American Chemical Society
Published on Web 12/07/2007

Dioleylphosphatidylethanolamine (DOPE), and phosphatidylethanolamine–lissamine rhodamine were purchased from Aventi Polar Lipids (Alabaster Alabama). Polyethyleneimine (PEI) was purchased from Sigma-Aldrich-Fluka. The lipopolyamine 2-{3-[bis-(3-amino-propyl)-amino]-propylamino}-*N*-ditetradecylcarbamoyl methyl-acetamide (RPR209120) was previously prepared in our laboratory, the synthesis is described in the supplementary information of ref *9*. The plasmid pVax1 was provided by Invitrogen.

Synthesis of Lipolythioureas.*(S)-tert-Butyl [1-(didecylcarbamoyl)-6-tert-butoxycarbonylamino-hexyl]aminoformate (***3a***).* *N*-hydroxysuccinimide (0.093 g, 0.81 mmol) and *N,N′*-dicyclohexylcarbodiimide (DCC) (0.42 g, 2.03 mmol) were added to a solution of acid **2** (0.28 g, 0.81 mmol) in dry THF (30 mL). The solution was stirred for 1 h before the addition of didecylamine **1a** (0.20 g, 0.68 mmol). The stirring was continued for 17 h, and then the reaction mixture was diluted with dichloromethane and washed twice with water. The organic layer was dried ($MgSO_4$) and evaporated under reduced pressure. The resulting oil was purified first by SFC and then by flash chromatography (heptane/ethyl acetate, 9/1) to yield **3a** as an oil (0.32 g, 63%). ^{1}H NMR ($CDCl_3$) δ 0.88 (t, 6H, J = 6.0 Hz, CH_3), 1.26 (m, 30H, $-CH_2-$), 1.43 (s, 9H, $(CH_3)_3$), 1.45 (m, 2H, $-CH_2-$), 1.55 (m, 4H, $-CH_2-$), 1.80 (m, 2H, CH_2), 3.11 (m, 2H, $-CH_2N$), 3.25 (m, 2H, $-CH_2N$), 3.47 (m, 2H, $-CH_2N$), 4.52 (m, 1H, CH), 4.54 (m, 1H, NH), 5.35 (d, 1H, J = 7.5 Hz, NH). ^{13}C NMR ($CDCl_3$) δ 14.11 (s, CH_3), 22.73 (m, $-CH_2-$), 27.05 (s, $-CH_2-$), 27.67 (s, $-CH_2-$), 28.45 (s, $(CH_3)_3$), 29.62 (m, $-CH_2-$), 31.95 (s, $-CH_2-$), 33.09 (s, CH_2), 40.51 (s, CH_2N), 46.10 (s, CH_2N), 47.86 (s, CH_2N), 49.92 (s, CH), 79.18 (s, $C(CH_3)_3$), 79.80 (s, $C(CH_3)_3$), 155.94 (s, OC=O), 156.31 (s, OC=O), 171.52 (s, NC=O).

*(S)-tert-Butyl [1-(didodecylcarbamoyl)-6-tert-butoxycarbonylamino-hexyl]aminoformate (***3b***).* *N*-hydroxysuccinimide (0.24 g, 2.05 mmol) and DCC (1.06 g, 5.1 mmol) were added to a solution of acid **2** (0.71 g, 2.05 mmol) in dry THF (60 mL). The solution was stirred for 2 h before the addition of didodecylamine **1b** (0.61 g, 1.72 mmol). Stirring was continued for 20 h, and then the reaction mixture was diluted with dichloromethane and washed twice with water. The organic layer was dried ($MgSO_4$) and evaporated under reduced pressure. The resulting oil was purified by flash chromatography (heptane/ethyl acetate, 95/5) to yield **3b** as an oil (0.65 g, 46%). ^{1}H NMR ($CDCl_3$) δ 0.84 (t, 6H, J = 6.0 Hz, CH_3), 1.22 (m, 38H, $-CH_2-$), 1.39 (s, 9H, $(CH_3)_3$), 1.49 (m, 2H, CH_2), 1.54 (m, 6H, $-CH_2-$), 3.06 (m, 2H, $-CH_2N$), 3.22 (m, 2H, $-CH_2N$), 3.45 (m, 2H, $-CH_2N$), 4.49 (m, 1H, CH), 4.68 (m, 1H, NH), 5.36 (d, 1H, J = 8.7 Hz, NH). ^{13}C NMR ($CDCl_3$) δ 14.09 (s, CH_3), 22.65 (m, $-CH_2-$), 26.99 (s, $-CH_2-$), 27.63 (s, $-CH_2-$), 28.42 (s, $(CH_3)_3$), 29.38 (s, $-CH_2-$), 29.62 (m, $-CH_2-$), 31.93 (s, $-CH_2-$), 33.81 (s, CH_2), 40.43 (s, $-CH_2N$), 46.07 (s, $-CH_2N$), 47.83 (s, $-CH_2N$), 49.89 (s, CH), 78.95 (s, $C(CH_3)_3$), 79.39 (s, $C(CH_3)_3$), 155.56 (s, OC=O), 156.03 (s, OC=O), 171.92 (s, C=O). MS (ESI, *m/z*) 682 $(M + H)^+$, 704 $(M + Na)^+$.

*(S)-tert-Butyl [1-(ditetradecylcarbamoyl)-6-tert-butoxycarbonylamino-hexyl]aminoformate (***3c***).* *N*-hydroxysuccinimide (0.17 g, 1.44 mmol) and DCC (0.74 g, 3.60 mmol) were added to a solution of acid **2** in dry THF (50 mL). The solution was stirred for 1 h before the addition of ditetradecylamine **1c** (0.50 g, 1.21 mmol). Stirring was continued for 20 h, and then the reaction mixture was diluted with dichloromethane and washed twice with water. The organic layer was dried ($MgSO_4$) and evaporated under reduced pressure. The resulting oil was purified by flash chromatography (heptane/ethyl acetate, 95/5) to yield **3c** as an oil (0.73 g, 67%). ^{1}H NMR ($CDCl_3$) δ 0.88 (t, 6H, J = 6.0 Hz, CH_3), 1.26 (m, 30H, $-CH_2-$), 1.44 (s, 9H, $(CH_3)_3$), 1.45 (m, 2H, CH_2), 1.58 (m, 6H, $-CH_2-$), 3.11 (m, 2H, $-CH_2N$), 3.25 (m, 2H, CH_2N), 3.49 (m, 2H, $-CH_2N$), 4.52 (m, 1H, CH), 4.54 (m, 1H, NH), 5.39 (d, 1H, J = 7.5 Hz, NH). ^{13}C NMR ($CDCl_3$) δ 14.17 (s, CH_3), 22.76 (m, $-CH_2-$), 27.05 (s, $-CH_2-$), 27.67 (s, $-CH_2-$), 28.45 (s, $(CH_3)_3$), 29.62 (m, $-CH_2-$), 31.94 (s, $-CH_2-$), 33.74 (s, CH_2), 40.40 (s, CH_2N), 46.10 (s, CH_2N), 47.85 (s, CH_2N), 49.90 (s, CH), 79.38 (s, $C(CH_3)_3$), 155.94 (m, OC=O), 171.85 (s, C=O). MS (ESI, *m/z*) 760 $(M + Na)^+$.

*(S)- 2,7-Diamino-N,N-didecyl-heptanamide (***4a***).* A solution of amide **3a** (1.31 g, 2.1 mmol) in dichloromethane (2 mL) was treated with a TFA/CH_2Cl_2 mixture (3:1, 8 mL). The reaction mixture was stirred for 24 h, then treated with solid $NaHCO_3$, filtered, and washed with water, and then 2 N NaOH was added to the aqueous phase until it reached a pH of 9. The water layer was extracted three times with dichloromethane. The organic layers were dried ($MgSO_4$) and evaporated under reduced pressure to yield **4a** (0.9 g, 100%) as a yellow oil, which was used without further purification. ^{1}H NMR ($CDCl_3$) δ 0.87 (t, 6H, J = 6.0 Hz, CH_3), 1.26 (m, 30H, $-CH_2-$), 1.55 (m, 6H, $-CH_2-$), 1.65 (m, 2H, CH_2), 2.03 (m, 4H, NH), 2.72 (m, 2H, CH_2NH_2), 3.11 (m, 2H, $-CH_2N$), 3.24 (m, 2H, CH_2N), 3.52 (m, 2H, CH), 5.40 (m, 1H, NH). δ 14.13 (s, CH_3), 22.74 (s, $-CH_2-$), 23.22 (s, $-CH_2-$), 27.08 (s, $-CH_2-$), 27.78 (s, $-CH_2-$), 29.62 (m, -CH2-), 31.94 (s, $-CH_2-$), 33.06 (s, CH_2), 41.74 (s, CH_2NH_2), 46.28 (s, CH_2N), 47.55 (s, CH_2N), 51.17 (s, CH), 173.05 (s, C=O).

*(S)- 2,7-Diamino-N,N-didodecyl-heptanamide (***4b***).* A solution of amide **3b** (0.65 g, 0.95 mmol) in dichloromethane (2 mL) was treated with a TFA/CH_2Cl_2 mixture (3:1, 5 mL). The reaction mixture was stirred for 3 h, and then it was treated with solid $NaHCO_3$, filtered, and washed with water. NaOH (2 N) was added to the aqueous phase until it reached a pH of 9. The water layer was extracted three times with dichloromethane. The organic layers were dried ($MgSO_4$) and evaporated under reduced pressure to yield **4b** (0.5 g, 100%) as a yellow oil, which was used without further purification. ^{1}H NMR ($CDCl_3$) δ 0.86 (t, 6H, J = 6.0 Hz, CH_3), 1.23 (m, 38H, $-CH_2-$), 1.49 (m, 6H, $-CH_2-$), 2.94 (m, 2H, CH_2NH_2), 3.11 (m, 4H, CH_2N), 3.80 (m, 2H, CH), 6.24 (m, 4H, NH). ^{13}C NMR ($CDCl_3$) δ 14.09 (s, CH_3), 21.89 (s, $-CH_2-$), 22.71 (s, $-CH_2-$), 27.12 (s, $-CH_2-$), 27.51 (s, $-CH_2-$), 29.70 (m,–CH2–), 31.96 (s, $-CH_2-$), 33.94 (s, CH_2), 39.16 (s, CH_2NH_2), 46.50 (s, CH_2N), 47.72 (s, CH_2N), 50.73 (s, CH), 173.10 (s, C=O). MS (ESI, *m/z*) 483 $(M + H)^+$, 262 $((M + 2H + 2Na)/2)^+$.

*(S)-2,7-Diamino-N,N-ditetradecyl-heptanamide (***4c***).* A solution of amide **3c** (0.73 g, 1 mmol) in a TFA/CH_2Cl_2 mixture (4:1, 5 mL) was stirred for 3 h. Then the reaction mixture was treated with solid $NaHCO_3$, filtered, and washed with water. NaOH (2 N) was added to the aqueous phase until it reached a pH of 9. The water layer was extracted three times with dichloromethane. The organic layers were dried ($MgSO_4$) and evaporated under reduced pressure to yield **4c** (0.36 g, 68%) as a yellow oil, which was used without further purification. ^{1}H NMR ($CDCl_3$) δ 0.86 (t, 6H, J = 6.0 Hz, CH_3), 1.23 (m, 30H, $-CH_2-$), 1.47 (m, 6H, $-CH_2-$), 1.88 (m, 2H, CH_2), 2.81 (m, 2H, CH_2NH_2), 3.10 (m, 2H, CH_2N), 3.24 (m, 2H, CH_2N), 3.47 (m, 2H, CH), 5.40 (m, 1H, NH). ^{13}C NMR ($CDCl_3$) δ 14.12 (s, CH_3), 22.72 (m, $-CH_2-$), 27.10 (s, $-CH_2-$), 27.70 (s, $-CH_2-$), 29.70 (m, $-CH_2-$), 31.97 (s, $-CH_2-$), 34.00 (s, $-CH_2-$), 40.91 (s, CH_2NH_2), 46.33 (s, CH_2N), 47.58 (s, CH_2N), 51.48 (s, CH), 171.85 (s, C=O). MS (ESI, *m/z*) 539 $(M + H)^+$.

*(S)-2,7-Bis[(2,2-dimethyl-1,3-dioxolan-4-yl)methylthiocarbamoylamino]-N,N-didecyl-heptanamide (***6a***).* A solution of amine **4a** (0.21 g, 0.5 mmol) and *N,N*-diisopropylethylamine (0.87 mL, 5 mmol) in dichloromethane (5 mL) was stirred for 10 mn before the addition of isothiocyanate **5** (0.22 g, 1.3 mmol). The reaction mixture was stirred overnight and evaporated under reduced pressure. Purification of the crude by SFC

afforded **5a** (0.32 mg, 83%) as a colorless oil. ^{1}H NMR ($CDCl_3$) δ 0.86 (t, 6H, J = 6.0 Hz, CH_3), 1.24 (m, 32H, –CH_2–), 1.31 (s, 6H, $(CH_3)_2$), 1.33 (s, 6H, $(CH_3)_2$), 1.43 (m, 4H, –CH_2–), 1.66 (m, 2H, –CH_2–), 3.20 (m, 4H, CH_2NCO), 3.45 (m, 2H, CH_2NCS) 3.68 (m, 4H, CH_2NCS), 4.01 (m, 4H, CH_2O), 4.27 (m, 4H, CHO), 5.55 (m, 1H, CH), 6.85 (m, 2H, NH), 7.85 (m, 2H, NH). ^{13}C NMR (CDCl3) δ 13.98 (s, CH_3), 22.72 (s, –CH_2–), 23.40 (s, –CH_2–), 25.30 (s, $(CH_3)_2$), 27.05 (s, $(CH_3)_2$), 27.71 (s, –CH_2–), 28.76 (s, –CH_2–), 29.38 (s, –CH_2–), 29.66 (m, –CH_2–), 31.95 (s, –CH_2–), 33.70 (s, CH_2), 44.58 (s, CH_2NCS), 46.78 (m, CH_2NCS, CH_2N), 48.70 (s, CH_2N), 53.77 (s, CH), 68.67 (s, CH_2O), 75.05 (s, CHO), 109.50 (s, $CO_2(CH_3)_2$), 172.91 (s, C=O), 183.26 (s, C=S). Anal. Calcd for $C_{40}H_{77}N_5O_5S_2$: C, 62.22; H, 10.05; N, 9.07; S, 6.30. Found: C, 62.17; H, 10.17; N, 8.94; S, 7.07. MS (ESI, *m/z*) = 794 $(M + Na)^+$, 770 $(M - H)^-$, 808 $(M + Cl)^+$.

*(S)-2,7-Bis[(2,2-dimethyl-1,3-dioxolan-4-yl)methylthiocarbamoylamino]-N,N-didodecyl-heptanamide (***6b***).* A solution of amine **4b** (0.24 g, 0.5 mmol) and *N,N*-diisopropylethylamine (0.44 mL, 2.5 mmol) in dichloromethane (2 mL) was stirred for 10 min before the addition of isothiocyanate **5** (0.095 g, 0.55 mmol). The reaction mixture was stirred overnight and evaporated under reduced pressure. Purification of the crude by SFC afforded **6b** (0.23 g, 55%) as a colorless oil. ^{1}H NMR ($CDCl_3$) δ 0.87 (t, 6H, J = 6.0 Hz, CH_3), 1.25 (m, 40H, –CH_2–), 1.32 (s, 6H, $(CH_3)_2$), 1.34 (s, 6H, $(CH_3)_2$), 1.44 (m, 4H, –CH_2–), 1.68 (m, 2H, –CH_2–), 3.21 (m, 4H, CH_2NCO), 3.47 (m, 2H, CH_2NCS) 3.70 (m, 4H, CH_2NCS), 4.05 (m, 4H, CH_2O), 4.29 (m, 4H, CHO), 5.59 (m, 1H, CH), (m, 2H, NH), 7.86 (m, 2H, NH). ^{13}C NMR (CDCl3) δ 14.13 (s, CH_3), 22.73 (s, –CH_2–), 25.27 (s, $(CH_3)_2$), 26.87 (s, $(CH_3)_2$), 27.71 (s, –CH_2–), 28.71 (s, –CH_2–), 29.07 (s, –CH_2–), 29.68 (m, –CH_2–), 31.98 (s, –CH_2–), 33.68 (s, CH_2), 44.58 (s, CH_2NCS), 46.76 (m, CH_2NCO, CH_2NCS), 48.63 (s, CH_2NCO), 53.77 (s, CH), 66.63 (s, CH_2O), 75.01 (s, CHO), 109.62 (s, $CO_2(CH_3)_2$), 172.76 (s, C=O), 183.23 (s, C=S). Anal. Calcd for $C_{44}H_{85}N_5O_5S_2$: C, 63.80; H, 10.34; N, 8.45; S, 7.74. Found: C, 63.94; H, 10.51; N, 7.80; S, 7.46. MS (ESI, *m/z*) = 850 $(M + Na)^+$, 828 $(M + Cl)^-$.

*(S)-2,7-Bis[(2,2-dimethyl-1,3-dioxolan-4-yl)methylthiocarbamoylamino]-N,N-ditetradecyl-heptanamide (***6c***).* A solution of amine **4c** (0.12 g, 0.22 mmol) and *N,N*-diisopropylethylamine (0.3 mL, 2.2 mmol) in dichloromethane (1.5 mL) was stirred for 10 min before the addition of isothiocyanate **5** (0.1 g, 0.55 mmol). The reaction mixture was stirred overnight and evaporated under reduced pressure. Purification of the crude by SFC afforded **6c** (75 mg, 38%) as a colorless oil. ^{1}H NMR ($CDCl_3$) δ 0.87 (t, 6H, J = 6.0 Hz, CH_3), 1.25 (m, 44H, –CH_2–), 1.33 (s, 6H, $(CH_3)_2$), 1.37 (s, 6H, $(CH_3)_2$), 1.44 (m, 4H, –CH_2–), 1.67 (m, 2H, CH_2), 3.20 (m, 4H, CH_2NCO), 3.45 (m, 2H, CH_2NCS), 3.69 (m, 4H, CH_2NCS), 4.05 (m, 4H, CH_2O), 4.29 (m, 4H, CHO), 5.59 (m, 1H, CH), 6.85 (m, 2H, NH), 7.80 (m, 2H, NH). ^{13}C NMR ($CDCl_3$) δ 14.15 (s, CH_3), 22.74 (m, –CH_2–), 25.26 (s, $(CH_3)_2$), 27.06 (s, $(CH_3)_2$), 27.15 (s, –CH_2–), 28.69 (s, –CH_2–), 29.07 (s, –CH_2–), 29.68 (m, –CH_2–), 31.97 (s, –CH_2–), 33.69 (s, CH_2), 44.54 (s, CH_2NCS), 46.74 (m, CH_2NCO, CH_2NCS), 46.63 (s, CH_2NCO), 53.74 (s, CH), 66.61 (s, CH_2O), 75.01 (s, CHO), 109.60 (s, $CO_2(CH_3)_2$), 172.79 (s, C=O), 183.19 (s, C=S). MS (ESI, *m/z*) 907 $(M + Na)^+$, 931 $(M + HCOO)^-$. Anal. Calcd for $C_{48}H_{93}N_5O_5S_2$: C, 65.19; H, 10.60; N, 7.92; S, 7.25. Found: C, 65.18; H, 10.66; N, 7.21; S, 6.58. HR-ESMS Calcd for $C_{48}H_{93}N_5O_5NaS_2$: 906.6516. Found: 906.6498.

Liposome Preparation.*Ethanolic Injection Method.* Lipopolythiourea and DPPC were dissolved in ethanol and were added dropwise to 10 volumes of water under vigorous agitation. The mixture was stirred overnight and then evaporated under reduced pressure at room temperature to obtain a solution of liposomes.

For example, compound **6c** (1.77 mg, 2 μmol) and DPPC (1.47 mg, 2 μmol) were dissolved in 300 μL of ethanol. This solution was added dropwise into 3 mL of stirred, filtered water. The mixture was stirred overnight then evaporated under reduced pressure at RT to obtain a clear suspension of **6c/DPPC** (0.380 mL, 10.5 mM total lipids).

Film Hydration Method. Lipopolythiourea and DPPC were dissolved in chloroform. The solvent was evaporated slowly under vacuum to obtain a thin film on the glass. Water was then added to hydrate the lipids and obtain a solution of liposomes.

For example, compound **6c** (4.0 mg, 4.5 μmol) and DPPC (3.2 mg, 4.3 μmol) were dissolved in chloroform (500 μL). The solvent was evaporated slowly under vacuum to obtain a thin film on the glass. Water (430 μL) was then added to hydrate the lipids and obtain a solution of liposomes (20 mM total lipids).

Size Measurement. Particle diameter was determined by dynamic light scattering on Zeta Sizer NanoSeries Malvern (Malvern Instruments, France). Concentration of the lipids = 0.1 mM in H_2O, and the mean value of 3 runs is given (1 min equilibration, 3 min run).

Preparation of Plasmid DNA. pVax2 is a derivative of the commercial plasmid pVax1 (InVitrogen). pVax1 was digested with the restriction enzymes HincII and *Bam*HI to excise the promoter. The plasmid was then blunted with the Klenow fragment and dephosphorylated with alkaline phosphatase. pCMVbeta (Clontech) was digested with EcoR1 and *Bam*HI to excise the CMV promoter. The CMV promoter was blunted with the Klenow enzyme and ligated into the blunted pVax1 to give pVax2. The plasmid pXL3031 was digested with *Eco*RI and *Bam*HI, and then treated with the Klenow fragment to produce a blunted fragment containing luciferase cDNA. This fragment was ligated into pVax2 after EcoRV digestion and phosphatase alkaline dephosphorylation to give pVax2-Luc.

Preparation of LPT/DNA Complexes. Plasmid DNA (pVax2-luc, 100 μL, 0.02 g/L in H_2O), prepared using the procedure described above, was added dropwise with constant vortexing to various amounts of LPT/DPPC liposomes (in 100 μL of H_2O) at RT. TU/P indicates the ratio in nmol of thiourea function (2 per lipid) versus DNA phosphates. Cationic lipoplexes were formed in the same way from RPR209120/DOPE liposomes (1/1, hydration film method, 4 nmol in 100 μL of 150 mM NaCl) mixed with plasmid DNA at a ratio of N/P = 8 (0.5 μg in 100 μL 150 mM NaCl). PEI/DNA polyplexes were prepared from PEI (1 μg in 100 μL of 5% glucose) mixed with plasmid DNA (0.5 μg in 100 μL 5% glucose) at an N/P ratio = 15.

Gel Retardation Experiments. Complexes were prepared as described above with liposomes made by ethanolic injection (20 μL), and 5 μL of bromophenol blue were added. The mixture was loaded onto a 0.8% agarose gel in TBE buffer (1 M Tris, 0.9 M boric acid, 0.01 M EDTA) at 80 V/cm. DNA was revealed with ethidium bromide and visualized under UV light.

DNA Protection. Twenty microliters of culture medium (MEM with 10% or 50% murine fresh serum) were added to 20 μL of LPT/DPPC/DNA complexes (0.1 g/L DNA, prepared by ethanolic injection) or to cationic lipoplexes made of RPR209120 (0.1 g/L DNA). Samples were incubated at 37 °C. After 6 h, 10 μL of samples were frozen at −20 °C. After 24 h, all the samples were replaced at RT. SDS 2% (5 μL), EDTA (2 μL, 0.5 M), and bromophenol blue (3 μL) were added to each sample (10 μL). The mixture was loaded onto 1% agarose gel containing 0.05% SDS at 80 V/cm. After 24 h of washing in

water, DNA was revealed with ethidium bromide and visualized under UV light.

Transfection Method. B16 murine cells were grown into DMEM supplemented with L-glutamin (29.2 mg/mL), penicillin (50 units/mL), streptomycin (50 units/mL), and 10% fetal bovine serum. One day before transfection, cells were treated with trypsin and deposited into 24-well plates (45,000 cells/well) and incubated for 24 h at 37 °C. Then, 100 μL of LPT/DNA complexes (prepared by ethanolic injection), 100 μL of RPR209120/DOPE/DNA (prepared as above, ratio N/P = 8), and PEI/DNA polyplexes (prepared as above, ratio N/P = 15), all formulations corresponding to 0.5 μg DNA, were loaded onto each well, and the plates were incubated at 37 °C for 48 h. Then the cells were washed twice with PBS and treated with 200 μL of a passive lysis buffer (Promega). After 15 min, the cells were centrifuged for 5 min at 12,000 r/min. Supernatant (10 μL) and iodoacetamide (10 μL) were added to a 96-well plate, which was incubated at 37 °C for 1 h. Protein quantification was performed with the BCA protein assay KIT (PIERCE) and reported to BSA taken as a reference curve. Luciferase activity was quantified using a commercial kit Luciferase assay system (PROMEGA). On 10 μL of the lysed cells, 50 μL of the luciferase substrate was injected via an injector, and the absorbance was read immediately at 563 nm on a Wallac Victor2 1420 Multilabel Counter (Perkin Elmer).

Cytotoxicity on B16 Murine Cells. Murine B16 melanoma cells were grown in DMEM containing 2 mM L-glutamine, 10% fetal bovine serum, 100 U/mL penicillin, and 100 μg/mL streptomycin (37 °C, 5% CO_2). Exponentially growing B16 cells were plated onto 96-well plates at 5000 cells per well in 100 μL of culture medium. Twenty-four hours after plating, 100 μL of medium containing the compound of interest (final concentrations ranging from 1.56 μg/mL to 100 μg/mL, in 2-fold dilutions) was added to the wells (in triplicate) containing the cells and incubated for 48 h at 37 °C and 5% CO_2. After the 48 h exposure period to the test compounds, cell viability was assayed using the MTT test (*27*), and absorbance was read at 562 nm in a microplate reader (BioKinetics Reader, EL340). Appropriate controls with DMEM only and MTT were run to substract background absorbance. Results are presented as percent of controls cells. The concentration of compound that inhibited cell viability by 50% (inhibitory concentration for 50% of cells, or IC_{50}) was determined using the GraphPad Prism software. Results are presented as means ± SEM of 6 independent experiments, each run in triplicate.

***In Vivo* Acute Toxicity Test. 6c**/DPPC particles (0.75 μmol, 200 μL) were injected into Swiss mice tail veins (3 mice for the sample, 3 mice control). The weight, behavior pattern, skin and fur modifications, and somatomotor activity of the animals were observed daily over 16 days (*28*). The dose was considered as toxic if the weight was lower than 80% of that of the controlled mice.

Intratumoral Injection. 6c/DPPC/DNA (40 μL, 10 μg DNA, 40 TU/P, TU/P = mol thiourea functions/mol DNA phosphate group) and RPR209120/DOPE/DNA (prepared as described above; ratio N/P = 6) were injected into 3LL tumors of 3 mice C57BL\6 bearing 3LL tumors. Mice were sacrificed 24 h after injection, then tumors were removed, weighed, crushed in 1 mL of lysis buffer, and centrifuged for 10 min (12,000 rpm, 4 °C). The supernatant (50 μL) was loaded onto a 96-well plates, and luciferase activity was quantified using a commercial kit (Protein Assay). The absorbance was read at 563 nm on a Wallac Victor2 1420 Multilabel Counter (Perkin Elmer).

Biodistribution Study. Experiments were conducted following NIH recommendation for animal experimentation. Rhodamine-labeled **6c**/DPPC/DNA complexes (200 μL, 11 μg DNA, 40 TU/P) were injected into the tail veins of five mice C57BL\6 bearing 3LL tumors. Blood was collected by cardiac puncture after 2 h, and mice were euthanized after samples were obtained. In the distribution study, liver, lungs, spleen, and tumors were removed, weighed, and homogenized in phosphate-buffered saline (PBS, 5 mL/g tissue) at pH 7.4 . Rhodamine-labeled lipids were extracted as previously described (*29*) from 100 μL of blood or tissue homogenates with 3 mL of $CHCl_3$-CH_3OH (1:1, v/v) by vigorous mixing for 30 min for blood and 45 min for tissue homogenates followed by centrifugation (1000 rpm, 10 min). The fluorescence intensity corresponding to rhodamine was assayed on the supernatant with a fluorospectrophotometer (Victor, Perkin Elmer_Wallac multiplate reader; λ_{exc}, 530 nm; λ_{em}, 570 nm). The amount of complexes in the blood or tissue homogenates was evaluated with a calibration curve of the initial **6c**/DPPC/DNA complexes containing 0.5% LPT-rhodamine and expressed as the remaining percentage of injected dose.

Scheme 1. Preparation of Lipopolythiourea[a]

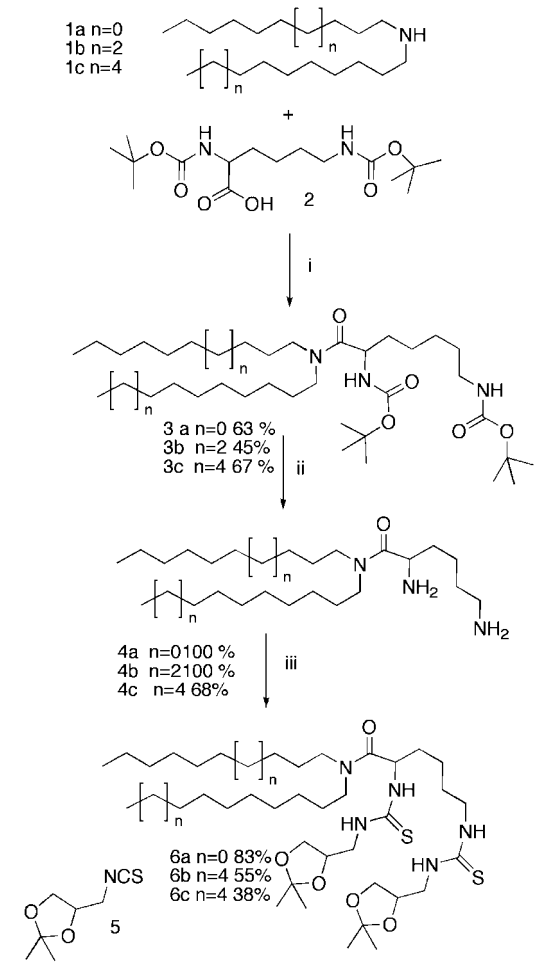

[a] (i) NHS, DCC, THF, RT. (ii) TFA, CH_2Cl_2, RT. (iii) DIPEA, **5**, CH_2Cl_2, RT.

RESULTS

Chemistry. The lipopolythioureas were prepared as shown in Scheme 1. The synthesis started from boc lysine **2** that reacted with dialkylamine **1a**, **1b**, and **1c** to yield dialkylamide **3a–c** (45 to 67%). Boc removal using TFA in dichloromethane led to diamines **4a–c** in good yields (100, 100, and 68%, respectively). Treatment of the diamine with isothiocyanate **5** afforded the protected thioureas (**6a**, 83%; **6b**, 55%; **6c**, 38%). Attempts to remove the acetal group failed, giving only the starting alkylamine **1**. This result suggests a rearrangement leading to a

Table 1. Formulation and DNA association with lipopolythiourea 6a, 6b, and 6c[a]

LPT	chain length	formulation (ethanolic injection)	diameter (nm)	PDI	TU/P for DNA association	LPT/DNA diameter (nm)	PDI
6a	10 C	**6a**/DPPC 1/1	76.5 ± 11	0.337	40	96 ± 2	0.253
6b	12 C	**6b**/DPPC 1/1	102 ± 8	0.329	20	122 ± 6	0.165
6c	14 C	**6c**/DPPC 1/1	141 ± 50	0.239	10	164 ± 3	0.115

[a] The diameter is given as the mean of 3 values. PDI: polydispersity index. TU/P for DNA association is the number of thiourea/DNA phosphate ratio needed to retain DNA in the wells of an agarose gel. The diameters of LPT/DNA complexes are given as the ratio needed for the association.

cyclic thiourea under protic catalysis since such cyclic compounds have been described in literature (*30*). However, despite our efforts, we were unable to identify such a compound.

Formulation Study and DNA Association. The three compounds prepared **6a**, **6b**, and **6c** exhibit the same thiourea headgroup and differentiate themselves by their lipidic length, varying from 10 to 12 to 14 carbons, respectively. First, we tried to evaluate if their hydrophilic/lipophilic balance would allow the formation of homogeneous particles. This was achieved thanks to the adjunction of dipalmytoyl-phosphatidylcholine (DPPC) at a ratio 1 to 1 with the polythiourea lipid. Particle diameter is given in Table 1. The diameter was slightly higher for **6c** as compared to those of **6b** and **6a.** Also, the suspension formed was more homogeneous with compound **6c**, as shown by the polydispersity index. This might suggest a better interaction of compound **6c** with DPPC due to its longer chain length.

Addition of DNA to these particles induced a slight increase in particle diameter. LPT/DNA interaction was evidenced by this size increase along with gel electrophoresis. We relate in Table 1 the ratio between the thiourea and the phosphate functions (TU/P) needed to fully retain DNA on the wells of an agarose gel. As can be seen, all LPT were able to complex the plasmid. Moreover, the longer the lipid chain, the less the amount of LPT needed to obtain a full interaction with DNA, reaching a minimum for **6c** (10 TU/P). This could be linked to the homogeneity of the suspension obtained when DPPC was mixed with lipid **6c**.

Lipoplex Sensitivity to Serum. The complexes formed between LPT and DNA have been submitted to a treatment in fresh mice serum at 37 °C for 6 h and 24 h, and then loaded on a denaturing agarose gel. As observed in Figure 1, free plasmid DNA was partially degraded after 6 h and fully degraded after 24 h under these conditions, whereas complexed DNA was still intact. With regard to the sensitivity of the technique, no difference between the three lipids could be detected. These results confirm that the interaction occurring between LPT and DNA is strong enough to protect plasmid DNA from degradation in the presence of serum.

Transfection Efficiency *in Vitro.* Compounds **6a**, **6b**, and **6c** were further evaluated for their transfection activity. Since the aim of these nonelectrostatic systems is to improve *in vivo* gene delivery, we carried out *in vitro* studies as preliminary tests for *in vivo* experiments. Thus, we performed the experiments in the presence of serum with particles of nanometric size. Two different TU/P ratios were evaluated for the three different formulations and compared to the cationic lipid (RPR209120) (*31*) and the cationic polymer PEI (*32*) (Figure 2) mixed with DNA.

As can be seen in Figure 3, transfection efficiency was dependent on the LPT used. Hence, higher transfection activity was obtained when increasing the lipid length from 10 to 14 carbons, from **6a** to **6c**, respectively. Moreover, increasing the amount of LPT, from TU/P = 20 to 40, also led to improved

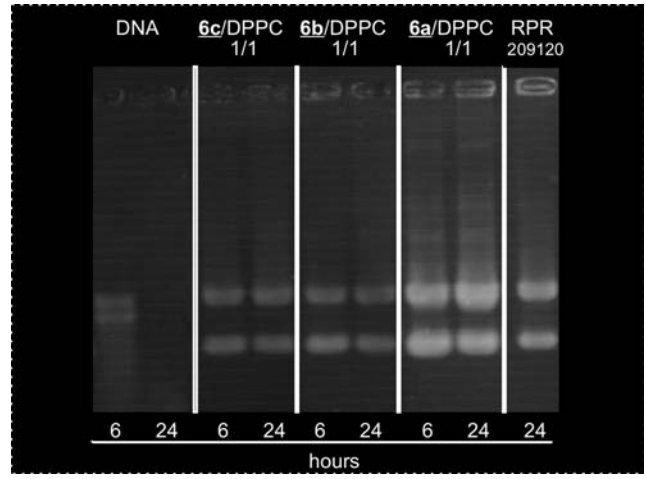

Figure 1. Lipoplex sensitivity to serum. Complexes LPT/DNA (20 LPT/P, prepared by ethanolic injection) as well as the cationic lipoplexes RPR209120/DOPE/DNA were incubated for 6 and 24 h in 10% serum at 37 °C, then treated with 2% SDS and 0.5 M EDTA, and loaded onto a 1% agarose gel containing 0.05% of SDS (80V/cm) in TBE (1×) . Complexes were revealed by ethidium bromide staining.

transfection. However, for higher LPT amounts, we observed a decrease of the protein amount, suggesting some cytotoxicity.

Cytotoxicity. In order to reduce cytotoxicity, we have studied the effect of different formulation protocols. Particles mentioned in the previous experiments were formulated via an ethanolic injection protocol (*33*). We also prepared LPT particles via the film hydration method (*34*). After preparation, we submitted the cells to an MTT test and compared the IC_{50} values of the two different formulations. As can be seen in Figure 4, the cytotoxicity IC_{50} obtained for compound **6a** formulated via an injection method was 15 μM, while no toxicity could be measured when the same compound was formulated via the hydration method. This significant reduction of toxicity might be due to the reduction of the number of thiourea presented at the surface of the liposome since multilamellar vesicles (MLV) are formed by the hydration method, whereas unilamellar vesicles (SUV) are obtained by ethanolic injection (*35*). The *in vitro* efficiency of theses complexes was also evaluated and showed slightly the same level of transfection as compared to the previous one (9900 RLU/μg protein for a ratio TU/P = 20). This good tolerance prompted us to use the hydration method for the following *in vivo* studies.

According to the *in vitro* cytotoxicity results, we evaluated the *in vivo* toxicity of the least toxic and most efficient formulation: **6c**/DPPC, prepared by the hydration film method. The formulation was injected once at $t = 0$, then the weight of the mice as well as different toxicity signs, such as locomotion, behavior, and changes in skin and fur, were followed over a period of 2 weeks. The formulations were considered as nontoxic if weight loss was lower than 20% as compared to that of control mice. The formulation **6c**/DPPC prepared via the hydration method displayed an excellent tolerance since the somatomotor activity, the behavior pattern, and skin and fur characteristics were unchanged as assayed over a period of 16 days. The weight also remained stable from 98.6% at day 2, to 97.6% at day 5, to 98.65% of the controls at day 16.

***In Vivo* Properties.** The absence of toxicity for the formulation **6c**/DPPC prompted us to further investigate the *in vivo* behavior of these particles.

First, we evaluated the transfection activity of the formulation **6c**/DPPC after intratumoral injection and compared it (*36*) to the lipoplexes composed of the lipopolyamine RPR209120. We did not observe a significant difference between the two

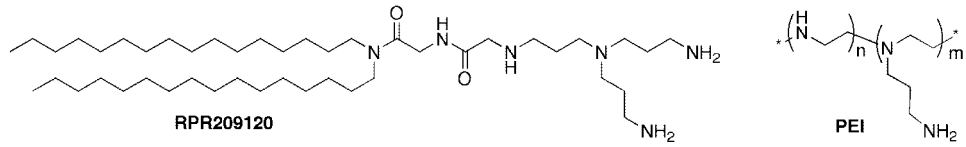

Figure 2. 2-{3-[Bis-(3-amino-propyl)-amino]-propylamino}-*N*-ditetradecylcarbamoyl methyl-acetamide (RPR209120) and polyethyleneimine (PEI) used as reference transfecting agents.

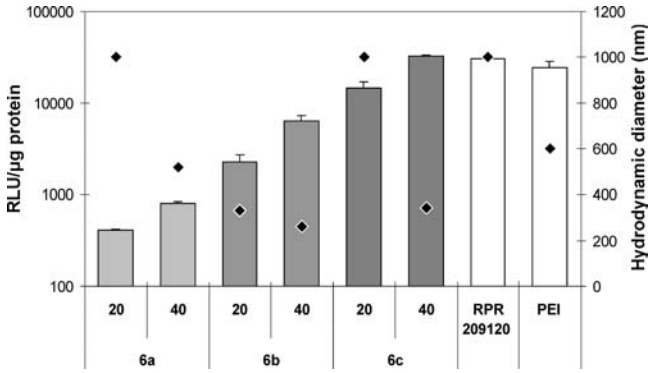

Figure 3. *In vitro* transfection results. Hydrodynamic diameter (lozenge symbols, right scale) and gene transfection (bars, left scale), measured by luciferase activity of LPT/DNA complexes at 20 and 40 TU/P ratios after 48 h of incubation on B16 cells in the presence of serum. LPT/DNA complexes were prepared by ethanolic injection at 20 and 40 TU/P in H_2O. RPR209120/DOPE/DNA lipoplexes was prepared at an N/P ratio = 8 in 150 mM NaCl. PEI/DNA polyplexes were prepared at N/P = 15 in 5% glucose. The complexes were then added to the cells in DMEM + 10% FBS at 37 °C. Results are expressed as the mean of an experiment performed in triplicate, with the error bars indicating the standard error of the mean.

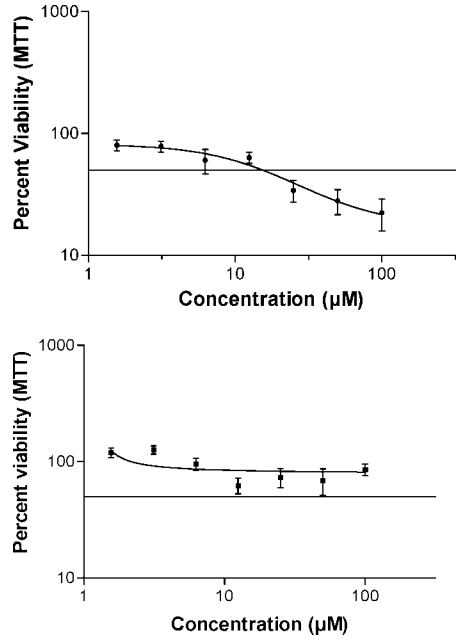

Figure 4. Cytotoxicity *in vitro*. IC_{50} of **6c**/DPPC formulated by (left) ethanolic injection (IC_{50} = 14.96 μM) and (right) hydration method, determined by a MTT test on B16 cells *in vitro*.

formulations; both were able to induce luciferase activity 24 h postinjection.

Biodistribution of **6c**/DPPC was evaluated by the introduction of a fluorescent lipid marker and compared to a cationic formulation of the lipopolyamine RPR209120/DOPE prepared via an identical hydration film procedure. Two hours after injection, different organs were removed and assessed for their fluorescence content. As shown in Figure 5a, significative gain of a factor of 4 to 5 ($p < 0.01$) was obtained in the blood circulation particles using the neutral **6c**/DPPC formulation as compared to the cationic one. Despite this higher circulation time in blood, no significant difference was found in tumor localization. Furthermore, an important difference was observed in the lung ($p < 0.01$). Nonspecific accumulation of the particles in the lung, which has often been reported for cationic particles (*37*), did not occur in the case of the LPT formulation. A similar amount was found in the liver for the two formulations, which was expected because elimination by Kupffer cells is mostly related to particle size (*38*).

DISCUSSION

The above data show that the described lysine-derived polythiourea mixed with DPPC are able to associate to plasmid DNA, to protect it from degradation in the presence of serum and to induce gene expression in cultured cells. Transfection efficiency was shown to be chain-length dependent, the lipid **6c** bearing the longer chain exhibiting the highest transfection activity. Some results have shown that a shorter chain was more appropriate for optimized transfection (*39*). We had also observed that with a lipopolythiourea bearing a serinol headgroup (*20*). Figure 6 represents the comparison of the *in vitro* results mediated by the two lipopolythiourea families. It shows that indeed the transfection level is reversed between the two LPT families: the shorter chain is preferable for the serinol thiourea lipids (compounds **Ia**–**Ic**, Figure 7), while the longer chain is preferable for the lysine thiourea lipids. That could be related to the improved hydrophilic/lipophilic balance in the lipid. In this work, the hydrophobic nature of the LPT required the use of a colipid, and obviously, the colipid effect is of great importance, as was previously reported (*40*). Mixing LPT with DPPC (bearing 16 carbons in the alkyl chain) might be more appropriate for the LPT **6c**, inducing improved lipid packing as the chain length of the LPT increases from 10 to 14 carbons. Indeed, suspension polydispersity decreased from the formulation **6a**/DPPC to **6c**/DPPC. The shorter chain LPT might create disorder in the lipid bilayer, eventually leading to unstable particles (*41*). Alternatively, we can hypothesize that the bulky and unsymmetrical LPT headgroup might also interfere with lipid packing and that a stronger hydrophobic interaction between LPT and the colipid might counterbalance headgroup interference.

Despite its structure, this lysine-based uncharged headgroup allowed for efficient interaction with DNA at an LPT/DNA ratio similar to the one previously obtained for LPT bearing a serinol headgroup (TU/P = 15). This ratio was the lowest for the formulation **6c**/DPPC, as compared to that for **6b** and **6a**, which is probably related to the more homogeneous structure formed between lipid **6c** and DPPC.

The most efficient transfection obtained with lipid **6c** was higher than the previously reported serinol LPT at the ratio used (*20*) (Figure 6) and comparable to that of cationic formulations in the presence of serum. This is of particular interest considering that LPT formulations exhibit no positive charges and might interact less favorably with the anionic cell membranes. The absence of cationic charges was also confirmed by the *in vivo* improved kinetic properties of LPT/DNA complexes, which avoided nonspecific accumulation in the lung and blood

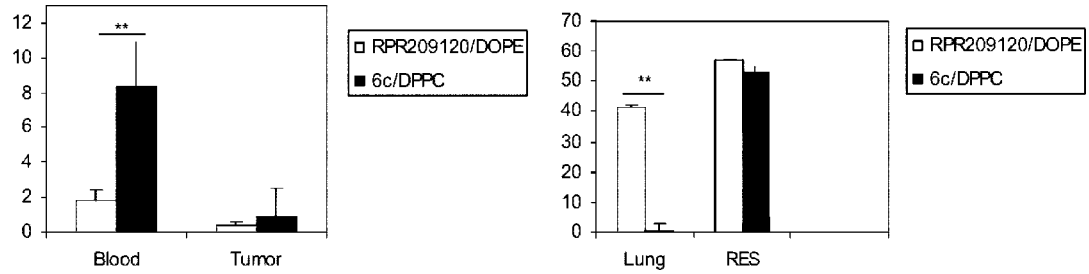

Figure 5. Biodistribution of rhodamine-labeled particles 2 h after intravenous injection in mice bearing 3LL subcutaneous tumors. RPR209120/DOPE and **6c**/DPPC were prepared by the hydration film method. Results are expressed as the percentage of the injected dose. (**$p < 0.01$ by the Mann–Whitney U-test, significant in blood and lung, not in the tumor and RES.)

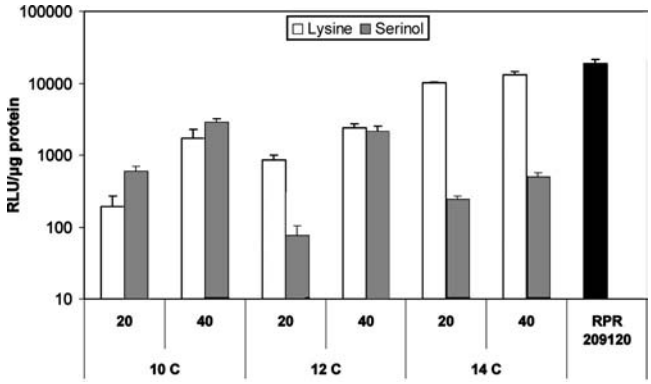

Figure 6. Comparison of gene transfection levels of lysine derivatives LPT (white bars) and previously published LPT (*20*) (gray bars) according to their ratio TU/P and chain length. Lysine LPT structures 10C, 12C, and 14C correspond to **6a**, **6b**, and **6c**, respectively. Previously published LPT structures 10C, 12C, and 14C correspond to compounds Ic, Ib, and Ia, respectively, represented in Figure 7. Luciferase activity of LPT/DNA complexes at 20 and 40 TU/P ratios was measured after 48 h of incubation in B16 cells in the presence of serum. RPR209120/DOPE/DNA lipoplexes were prepared at an N/P ratio = 6 in 150 mM NaCl. Results are expressed as the mean of an experiment performed in triplicate, with the error bars indicating the standard error of the mean.

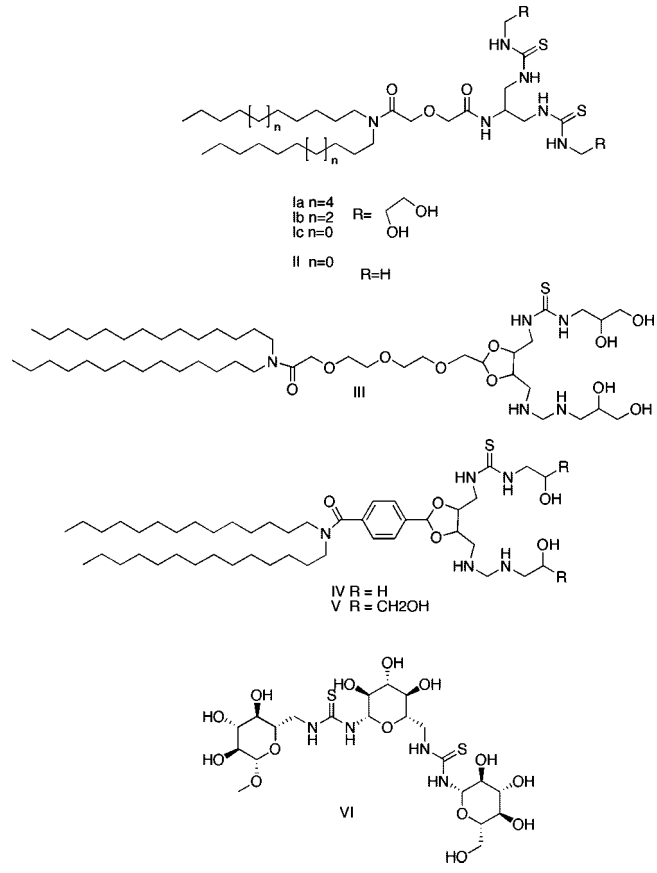

Figure 7. Previously published lipopolythiourea and thiourea compounds: I-II (*20*), III-V (*19*), and VI (*43*).

circulation. However, this stealth advantage did not enhance passive accumulation in our tumor model in opposition to the proposed enhanced permeability and retention effect (*42*). We have already observed this lack of passive accumulation in 3LL tumors after chemical passivation of the cationic charges of lipoplexes (*9*). This points to the use of a targeting ligand at the surface of these DNA/lipid particles in order to deliver DNA at a proper site, especially as this strategy has already been validated in the case of lipopolythiourea (*19*).

In conclusion, we described here new noncationic transfecting agents bearing a polythiourea moiety. From this and previous results, we can deduce that a wide range of geometry and termini allowed LPT/DNA interaction. With the present compound **6c**, this association was found to be strong enough to protect the plasmid in the presence of serum and to obtain *in vitro* efficient cell transfection, comparative to that obtained with cationic lipids. Moreover, we could find a nontoxic window for the *in vivo* use of these complexes. Intratumoral injection of LPT/DNA complexes showed that *in vivo* transfection ability and biodistribution were favorably improved as compared to that of cationic complexes. Finally, we have found in our previous studies that the size of the hydrophobic anchor seemed to be one of the factors controlling the physico-chemical and the transfecting properties of the LPTU. Structural comparison between **6a**–**6c** and **Ia**–**Ic** (Figure 7) shows two main differences between them. First, the lack of a linker and second, the presence of a 1,5-diamine instead of a 1,3-diamine for the headgroups. This suggests that a larger diamino chain would lead to better phosphate/thiourea interactions. This hypothesis is supported by the study of Bianco et al. (*43*) that demonstrate strong thiourea/phosphate interaction for thiourea-linked glycooligomers (Figure 7, compound **VI**). In these molecules, the two thioureas are in a 1,4 relationship favoring their participation in bidentate hydrogen bond interactions with oxoanions. Compounds **III**, **IV**, and **V** (Figure 7) also possess a 1,5 relationship between the two thioureas (*19*). However, their lack of transfecting properties is probably due to their hydrophobicity. In addition, the presence of the acetal ring adds a constraint that could diminish the strength of hydrogen bonds. New models have been synthesized and are now under investigation to verify these hypotheses.

ACKNOWLEDGMENT

This work was financially supported by INSERM, CNRS, MNERT, and the Région Ile de France (SESAME, CPER). J.L. thanks MNERT for a doctoral fellowship.

LITERATURE CITED

(1) Miller, A. D. (1998) Cationic liposomes for gene therapy. *Angew. Chem., Int. Ed. 37*, 1768–1785.

(2) Verma, I. M., and Weitzman, M. D. (2005) Gene therapy: twenty-first century medicine. *Annu. Rev. Biochem. 74*, 711–738.

(3) Simberg, D., Weisman, S., Talmon, Y., and Barenholz, Y. (2004) DOTAP (and other cationic lipids): chemistry, biophysics, and transfection. *Crit. Rev. Ther. Drug Carrier Syst. 21*, 257–317.

(4) Pack, D. W., Hoffman, A. S., Pun, S., and Stayton, P. S. (2005) Design and development of polymers for gene delivery. *Nature Rev. Drug Discovery 4*, 581–593.

(5) Ewert, K., Slack, N. L., Ahmad, A., Evans, H. M., Lin, A. J., Samuel, C. E., and Safinya, C. R. (2004) Cationic lipid-DNA complexes for gene therapy: understanding the relationship between complex structure and gene delivery pathways at the molecular level. *Curr. Med. Chem. 11*, 133–149.

(6) Tandia, B. M., Vandenbranden, M., Wattiez, R., Lakhdar, Z., Ruysschaert, J. M., and Elouahabi, A. (2003) Identification of human plasma proteins that bind to cationic lipid/DNA complex and analysis of their effects on transfection efficiency: implications for intravenous gene transfer. *Mol. Ther. 8*, 264–273.

(7) Escriou, V., Ciolina, C., Lacroix, F., Byk, G., Scherman, D., and Wils, P. (1998) Cationic lipid-mediated gene transfer: effect of serum on cellular uptake and intracellular fate of lipopolyamine/DNA complexes. *Biochim. Biophys. Acta 1368*, 276–288.

(8) Eliyahu, H., Servel, N., Domb, A., and Barenholz, Y. (2002) Lipoplex-induced hemagglutination: potential involvement in intravenous gene delivery. *Gene Ther. 9*, 850–858.

(9) Thompson, B., Mignet, N., Hofland, H., Lamons, D., Seguin, J., Nicolazzi, C., de la Figuera, N., Kuen, R. L., Meng, X. Y., Scherman, D., and Bessodes, M. (2005) Neutral postgrafted collloidal particles for gene delivery. *Bioconjugate Chem. 16*, 608–614.

(10) Mignet, N., and Gregoriadis, G. (2006) *Liposome Technology* (Gregoriadis, G., Ed.) 3rd ed., Vol. 2, Chapter 16, Informa Healthcare, London.

(11) Faneca, H., Simoes, S., and Pedroso de Lima, M. C. (2004) Association of albumin or protamine to lipoplexes: enhancement of transfection and resistance to serum. *J. Med. Chem. 6*, 681–692.

(12) Aoyama, Y., Kanamori, T., Nakai, T., Sasaki, T., Horiuchi, S., Sando, S., and Niidome, T. (2003) Artificial viruses and their application to gene delivery. Size-controlled gene coating with glycocluster nanoparticles. *J. Am. Chem. Soc. 125*, 3455–3457.

(13) Arignon, J., Prata, C. A., Grinstaff, M. W., and Barthelemy, P. (2005) Nucleic acid complexing glycosyl nucleoside-based amphiphiles. *Bioconjugate Chem. 16*, 864–872.

(14) Nakai, T., Kanamori, T., Sando, S, and Aoyama, Y. (2003) Remarkably size-regulated cell invasion by artificial viruses. Saccharide-dependent self-aggregation of glycoviruses and its consequences in glycoviral gene delivery. *J. Am. Chem. Soc. 125*, 8465–8475.

(15) Chabaud, P., Camblo, M., Payet, D., Serin, G., Moreau, L., Barthelemy, P., and Grinstaff, M. W. (2006) Cationic nucleoside lipids for gene delivery. *Bioconjugate Chem. 17*, 466–472.

(16) Bailey, A., and Sullivan, S. M. (2000) Efficient encapsulation of DNA plasmids in small neutral liposomes induced by ethanol and calcium. *Biochim. Biophys. Acta 1468*, 239–252.

(17) Roux, D., Chenevier, D., Pott, T., Navailles, L., Regev, O., and Mondain Monval, O. (2004) Conception and realization of a non-viral and non-cationic DNA vector. *Curr. Med. Chem. 11*, 169–177.

(18) Tranchant, I., Mignet, N., Crozat, E., Leblond, J., Girard, C., Scherman, D., and Herscovici, J. (2004) DNA complexing lipopolythiourea. *Bioconjugate Chem. 15*, 1342–1348.

(19) Leblond, J., Mignet, N., Leseurre, L., Largeau, C., Bessodes, M., Scherman, D., and Herscovici, J. (2006) Design, synthesis, and evaluation of enhanced DNA binding new lipopolythioureas. *Bioconjugate Chem. 17*, 1200–1208.

(20) Leblond, J., Mignet, N., Largeau, C., Spanedda, M-V., Seguin, J., Scherman, D., and Herscovici, J. (2007) Lipopolythioureas: a new non-cationic system for gene transfer. *Bioconjugate Chem. 18*, 484–493.

(21) Benito, J. M., Gomez-Marcia, M., Jimenez Blanco, J. L., Ortiz Mellet, C., and Garcia Fernandez, J. M. (2001) Carbohydrate-based receptors with multiple thiourea binding sites. Multipoint hydrogen bond recognition of dicarboxylates and monosaccharides. *J. Org. Chem. 66*, 1366–1372.

(22) Takemoto, Y. (2005) Recognition and activation by ureas and thioureas: stereoselective reactions using ureas and thioureas as hydrogen-bonding donors. *Org. Biomol. Chem. 3*, 4299–4306.

(23) Gómez, D. E., Fabbrizzi, L., Licchelli, M., and Monzani, E. (2005) Urea vs. thiourea in anion recognition. *Org. Biomol. Chem. 3*, 1495–1500.

(24) Bühlmann, P., Nishizawa, S., Xiao, K. P., and Umezawa, Y. (1997) Strong hydrogen-bond mediated complexation of $H_2PO_4^-$ by neutral bis-thiourea hosts. *Tetrahedron 53*, 1647–1654.

(25) Still, W. C., Kahn, M., and Mitra, A. (1978) *J. Org. Chem. 43*, 2923–2926.

(26) Balacco, G. (1994) SwaN-MR: A complete and expansible NMR software for the Macintosh. *J. Chem. Inf. Comput. Sci. 34*, 1235–1241.

(27) Scudiero, D. A., Shoemaker, R, H., Paull, K. D., Monks, A., Tierney, S., Nofziger, T. H., Currens, M. J., Seniff, D., and Boyd, M. R. (1988) Evaluation of a soluble tetrazolium/formazan assay for cell growth and drug sensitivity in culture using human and other tumor cell lines. *Cancer Res. 48*, 4827–4833.

(28) Guidance Document on the Recognition Assessment and Use of Clinical Signs as Human Endpoints for Experimental Animals Used in Safety Evaluation. (2000) OECD Environmental Health and Safety Monograph Series on Testing and Assessment, No. 19.

(29) Nicolazzi, C., Mignet, N., de la Figuera, N., Cadet, M., Ibad, R. T., Seguin, J., Scherman, D., and Bessodes, M. (2003) Anionic polyethyleneglycol lipids added to cationic lipoplexes increase their plasmatic circulation time. *J. Controlled Release 88*, 429–443.

(30) Mac Kay, A. F., Tarlton, E. J., Petri, S. I., Steyermark, P. R., and Mosley, M. A. (1958) Amino Acids. V. 1,3-di-(ω-carboxyalkyl)-thioureas and their chemistry. *Can. J. Chem. 80*, 1510–1517.

(31) Byk, G., Dubertret, C., Escriou, V., Jaslin, G., Rangara, R., Pitard, B., Crouzet, J., Wils, P., Schwartz, B., and Scherman, D. (1998) Synthesis, activity, and structure-activity relationship studies of novel cationic lipids for DNA transfer. *J. Med. Chem. 41*, 224–235.

(32) Boussif, O., Lezoualc'h, F., Zanta, M. A., Mergny, M. D., Scherman, D., Demeneix, B., and Behr, J. P. (1995) A versatile vector for gene and oligonucleotide transfer into cells in culture and in vivo: polyethylenimine. *Proc. Natl. Acad. Sci. U.S.A. 92*, 7297–7301.

(33) Campbell, M. J. (1995) Lipofection reagents prepared by a simple ethanol injection technique. *Biotechniques 18*, 1027–1032.

(34) Bangham, A. D., Standish, M. M., and Waltkins, J. C. (1965) Diffusion of univalent ions across the lamellae of swollen phospholipids. *J. Mol. Biol. 13*, 238–252.

(35) Delattre, J., Couvreur, P., Puisieux, F., Philippot, J. R., and Schuber, F. (1993) Les liposomes, Aspects technologiques, biologiques et pharmacologiques. *Ed. Inserm* 54–62.

(36) Tranchant, I., Thompson, B., Nicolazzi, C., Mignet, N., and Scherman, D. (2004) Physicochemical optimisation of plasmid delivery by cationic lipids. *J. Gene Med.* S24–S35.

(37) Simberg, D., Weisman, S., Talmon, Y., Faerman, A., Shoshani, T., and Barenholz, Y. (2003) The role of organ vascularization and lipoplex-serum initial contact in intravenous murine lipofection. *J. Biol. Chem. 278*, 39858–39865.

(38) Takakura, Y., Mahato, R. I., and Hashida, M. (1998) Extravasation of macromolecules. *Adv. Drug Delivery Rev. 34*, 93–108.

(39) Gilot, D., Miramon, M. L., Benvegnu, T., Ferrieres, V., Loreal, O., Guguen-Guillouzo, C., Plusquellec, D., and Loyer, P. (2002) Cationic lipids derived from glycine betaine promote efficient and nontoxic gene transfection in cultured hepatocytes. *J. Gene Med. 4*, 415–427.

(40) Ferrari, E., Rusalov, D., Enas, J., and Wheeler, C. (2002) Synergy between cationic lipid and co-lipid determines the macroscopic structure and transfection activity of lipoplexes. *Nucleic Acids Res. 30* 1808–1816.

(41) Sijbren, O., Janout, V., DiGiorgio, A., Young, M. C., and Regen, S. L. (2000) Detection of nonideal mixing of phospholipids in fluid bilayers *J. Am. Chem. Soc. 122* 1200–1204.

(42) Gabizon, A., Shmeeda, H., and Zalipsky, S. (2006) Pros and cons of the liposome platform in cancer drug targeting. *J. Controlled Release 16*, 175–183.

(43) Blanco, J. L., Bootello, P., Benito, J. M., Mellet, O., and Fernandez, G. (2006) Urea-, thiourea-, and guanidine- as phosphate binders in water. *J. Org. Chem. 71*, 5136–5143.

BC7001924

Ligand-Modified Aminobisphosphonate for Linking Proteins to Hydroxyapatite and Bone Surface

Robin S. Ehrick,[†] Marcello Capaccio,[†] David A. Puleo,[‡] and Leonidas G. Bachas*[,†]

Department of Chemistry, University of Kentucky, Lexington, Kentucky 40506-0055, and Center for Biomedical Engineering, University of Kentucky, Lexington, Kentucky 40506-0070. Received May 30, 2007; Revised Manuscript Received September 14, 2007

An increase in bone resorption is one of the main symptoms of osteoporosis, a disease that affects more and more individuals every day. Bisphosphonates are known to inhibit bone resorption and thus are being used as a treatment for osteoporosis. Aminobisphosphonates present a functionality that can be easily used for conjugation to other molecules, such as peptides, proteins, and ligands for protein recognition. In this study, an aminobisphosphonate conjugated with biotin was used as a model linker for protein attachment to bone. With this system, the interaction of biotinylated aminobisphosphonate with hydroxyapatite, a major mineral component of bone, was investigated. Quantification of the binding of aminobisphosphonate to hydroxyapatite was performed using a fluorescently labeled antibody for biotin. Additionally, the interaction of the biotinylated aminobisphosphonate with multiple treatments of cortical bone from the midshaft of a cow femur was studied. It was demonstrated that modified aminobisphosphonate reagents can bind hydroxyapatite and bone at high levels, while the biotin functionality is free to be recognized by the fluorescently labeled antibiotin antibody, suggesting that modified aminobisphosphonates could be used to link other peptides or proteins to the bone surface.

INTRODUCTION

In 2000, over 10 million people in the United States had been diagnosed with osteoporosis (*1*), a disease characterized by a reduction in bone mass caused by an increase in bone resorption with minimal regeneration. Another 34 million were affected by low bone mineral density. Two types of bone cells, osteoblasts and osteoclasts, constantly work together to remodel bone. Osteoblasts, or bone-forming cells, regenerate bone tissue, while bone is resorbed by the osteoclast cells (*2*). In healthy individuals, the rate of bone resorption is similar to the rate of bone regeneration. In a patient diagnosed with osteoporosis, the balance of osteoblastic and osteoclastic activity is disrupted in such a way that the rate of bone resorption is higher than the rate of bone regeneration (*3*).

Popular treatments for osteoporosis include calcium and vitamin D supplementation, hormone replacement therapy, and use of bisphosphonates, among others (*4*). Calcium and vitamin D supplementation and hormone replacement therapy have been criticized recently over their inability to prevent fractures (*5, 6*) and the increased side effects with treatment (*7–9*), respectively. It has also been suggested that calcium and vitamin D supplements may result in only minimal increase in bone mineral density (*10, 11*). While this may be beneficial overall, it was found recently that supplementation has little to no effect at preventing fractures and can increase the occurrence of kidney stones (*6*). A high rate of fracture with minimal injury is one of the main symptoms of osteoporosis. Hormone replacement therapy, involving the administration of a combination of estrogen and progestin, had been widely prescribed as a treatment for osteoporosis in postmenopausal women (*7*) because of the effect that estrogen has at inhibiting the action of osteoclast cells (*12, 13*). Unfortunately, the long-term effects of estrogen therapy were found to include an increased risk of breast cancer, heart attack, stroke, blood clots, and Alzheimer's disease and other dementias (*8, 9*). Because of these risks, hormone replacement therapy is now only prescribed for postmenopausal women with extreme osteoporosis, where the benefits outweigh the risks associated with treatment.

A treatment for osteoporosis that is gaining popularity is bisphosphonate therapy. Bisphosphonates are antiresorptive medications that bind to the mineral phase of bone and inhibit the activity of osteoclasts (*14*). Bisphosphonates have a long history with many applications including use as detergent additives in hard water treatment, in toothpaste to prevent tartar buildup, as treatment for Paget's disease, and as a diagnostic tool for bone tumor treatment (*14, 15*). In recent years, they have been mainly studied as an osteoporosis therapy because of their ability to inhibit bone resorption. The complex mechanism of action of bisphosphonates has only recently been understood (*16–18*), but in general, bisphosphonate binds to hydroxyapatite, the main mineral component of bone. When osteoclasts begin to resorb the bone, bisphosphonate is taken up by the cell, which then loses its resorptive function and undergoes apoptosis. The loss in the ability of the osteoclast to resorb bone following the administration of bisphosphonates causes an increase in bone mineral density.

While both osteoblasts and osteoclasts are essential to bone remodeling, a majority of osteoporosis research focuses on inhibiting the osteoclast (*3, 4, 14, 16, 17, 19–24*). The innate structure of bisphosphonates allows for numerous analogues to be produced that can have a wide scale of activities. Nitrogen-containing bisphosphonates, or aminobisphosphonates, have already been shown to have higher antiresorptive effects than bisphosphonates that do not contain a nitrogen atom (*16*). The conjugation of a peptide or protein that can stimulate bone formation to an aminobisphosphonate could produce an agent that would not only slow resorption, but would also help to increase bone mineral density.

Aminomethylene bisphosphonic acid (aminobisphosphonate) presents an amine functionality that can be easily attached to a

* To whom correspondence should be addressed. 125 Chemistry-Physics Building, University of Kentucky, Lexington, KY 40506-0055. Tel: 859-257-6350. Fax: 859-323-1069. E-mail: bachas@uky.edu.

[†] Department of Chemistry.

[‡] Center for Biomedical Engineering.

10.1021/bc700196q CCC: $40.75 © 2008 American Chemical Society
Published on Web 11/15/2007

biomolecule. Conjugation of aminobisphosphonate to proteins has previously been explored in the literature (*25–29*), demonstrating that various proteins conjugated with bisphosphonate have a high affinity for both hydroxyapatite and bone. In these studies, aminobisphosphonate was conjugated at multiple sites on the proteins leading to more than one bisphosphonate per protein. This results in various binding orientations of the protein on the bone surface. We propose to conjugate aminobisphosphonate with a protein-binding ligand that subsequently can be used to recruit proteins to the bone surface. The linked protein could be presented in a rationally oriented manner based on the attachment site of the ligand. Toward this goal, a novel aminobisphosphonate was synthesized that contains a conjugated biotin moiety. This molecule was explored as a model system for the delivery of a linker for protein attachment to bone. The biotinylated aminobisphosphonate was incubated with both hydroxyapatite and bone. The attachment to the mineral surfaces was quantified using a fluorescently labeled antibiotin antibody. We have demonstrated that a conjugated aminobisphosphonate could be bound to the bone surface and subsequently recognized by a biomolecule.

EXPERIMENTAL PROCEDURES

Materials. Dibenzyl amine, triethyl orthoformate, silica gel, palladium on carbon, active carbon, dimethylformamide, reagent-grade hydroxyapatite (HA) powder (catalog number 289396), D-biotin, bovine serum albumin (BSA), casein from bovine milk, and monoclonal antibiotin−FITC antibody were purchased from Sigma-Aldrich (St. Louis, MO). Hexane, methanol, sodium hydroxide, and sodium phosphate dibasic heptahydrate were purchased from Mallinckrodt (Hazelwood, MO). Sodium chloride, sodium sulfate, hydrochloric acid, and triethylamine were obtained from EMD Chemicals (Gibbstown, NJ). Avidin from egg white was purchased from EMD Biosciences (San Diego, CA). Diethyl phosphite and cyclohexene were received from Fluka (Milwaukee, WI). Deuterium oxide NMR solvent was purchased from Cambridge Isotope Laboratories (Andover, MA). Argon gas was supplied through Scott-Gross Company (Lexington, KY). Ethyl acetate and ether were obtained from VWR (Westchester, PA). Fetal bovine serum (FBS) was obtained from Invitrogen (Carlsbad, CA). Tetraethyl(aminomethylene) bisphosphonate was purchased from Epsilon Chimie (Brest, France). 2-Anilinonaphthalene-6-sulfonic acid was obtained from Molecular Probes (Eugene, OR).

Apparatus. ^{1}H NMR spectra were obtained on a Varian INOVA 400 MHz spectrometer (Palo Alto, CA). Electrospray ionization mass spectrometry was performed on a ThermoFinnigan LCQ mass spectrometer (Waltham, MA). Lyophilization was performed using a Christ Alpha 2–4 freeze-dryer (Martin Christ, Osterode am Harz, Germany) equipped with a Pfeiffer Vacuum Pump (Asslar, Germany). Fluorescence readings were performed on a Cary Eclipse fluorescence spectrophotometer (Varian, Walnut Creek, CA). Deionized water was produced using a Milli-Q water purification system (Millipore, Bedford, MA).

Synthesis of Biotinyl-Aminomethylenediphosphonic Acid Triethylammonium Salt (AMB-Biotin). Aminomethylene bisphosphonic acid (aminobisphosphonate) **3** was synthesized following the procedure published by Kantoci et al. (*30*) and outlined in Scheme 1. *N,N*-Dibenzylamine-bisphosphonate tetraethyl ester **1** was synthesized from dibenzylamine, diethyl phosphite, and triethyl orthoformate. The amine was deprotected using Pd/C and hexene to form tetraethyl(aminomethylene) bisphosphonate **2**. Hydrogenation of the ester groups using aqueous hydrochloric acid produced **3**. Biotin *N*-hydroxysuccinimide ester (biotin NHS ester) was conjugated with **3** in a one-step synthesis. Triethylamine (600 μL) was added to a

Scheme 1. Synthesis of Biotinyl-Aminomethylenediphosphonic Acid Triethylammonium Salt (AMB-Biotin)

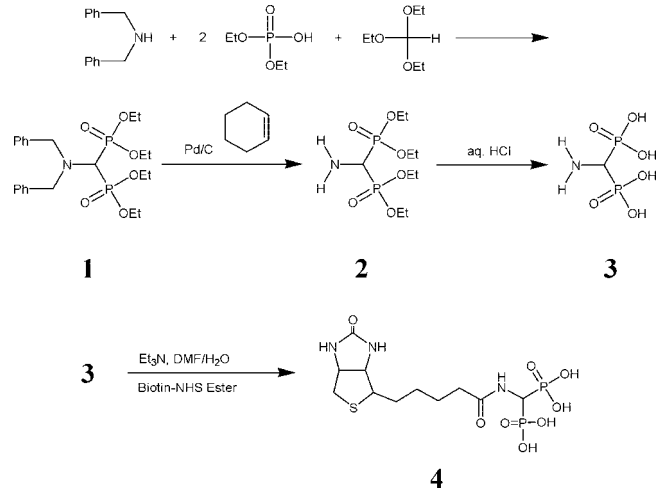

1 **2** **3** **4**

solution of **3** (100 mg, 0.52 mmol) in deionized water (3 mL). A solution of biotin NHS ester (179 mg, 0.52 mmol) in dimethylformamide (DMF, 6 mL) was added dropwise at 0 °C. The solution was stirred for 30 min at this temperature and then overnight at room temperature. The reaction mixture was evaporated to a minimal volume, and the final product was precipitated with diethyl ether. The solid was collected using a Buchner funnel and washed first with a few drops of DMF, then a few drops of ether, and finally with a few drops of methanol. Biotinyl-aminomethylenediphosphonic acid triethylammonium salt (AMB-Biotin) **4** was obtained as a white solid in 80% yield. Intermediate compound **2** was also purchased from Epsilon Chimie (Brest, France) and used in the synthesis of **4**. ^{1}H NMR (400 MHz, D_2O): δ 1.55 (triplet, S*CH*CH of biotin ring, 1H), δ 1.63 (triplet, S*CH*$_2$CH of biotin ring, 2H), δ 2.58 (triplet, 2H), δ 2.79 (singlet, 6H), δ 3.02 (singlet, PO(OH)$_2$*CH*PO(OH)$_2$ of bisphosphonate, 1H), δ 4.46, 4.63 (multiplets, NH*CHCH*NH of bridge of biotin ring, 2H). Mass spectral data were obtained at the University of Kentucky Mass Spectrometry Facility. *m/z* (ESI-MS) 416 ([M − H]$^-$, 100%).

Preparation of Bone Samples. Bone samples were taken from the midshaft of a cow femur. Cortical bone was cut into a rod approximately 7 mm × 7 mm square. The rod was then sliced into 500 μm thick pieces. Of the bone slices, one-half of the samples were left untreated, while the remaining samples were demineralized by soaking them in 0.6 M hydrochloric acid for 48 h. After 24 h, fresh acid solution was exchanged. After acid treatment, the bone was rinsed thoroughly with deionized water. Additional samples of untreated bone, approximately 7 mm × 7 mm × 1 cm in size, were ashed by heating the bone to 800 °C for 24 h. Subsequently, the ashed bone was crushed into a powder using a mortar and pestle.

Binding Studies of AMB-Biotin on Hydroxyapatite. A 3 mg sample of AMB-Biotin was dissolved in 1 mL of 0.5 M phosphate buffer, pH 7.4. HA, in the amount of 6 mg, was added to this solution, and the sample was incubated overnight at room temperature on a rotator (Glas-Col mini-rotator, Terre Haute, IN). The suspension was centrifuged for 15 min at 13 000 rpm (Eppendorf Centrifuge 5417R, Brinkmann Instruments, Westbury, NY) to collect the insoluble HA, and the pellet was washed twice with buffer and three times with deionized water. The sample was then lyophilized overnight and resuspended in 1 mL of FITC-labeled antibiotin antibody in phosphate buffer at a concentration of 29 μg/mL. The suspension was incubated on a rotator for 3 h at 4 °C. After incubation, the sample was centrifuged again to collect the solid, and the fluorescence of the supernatant was measured. As controls, a 3 mg sample of

aminobisphosphonate (AMB) and a 1 mL sample of 29 μg/mL FITC-labeled antibiotin antibody in phosphate buffer were subjected to the same conditions for incubation with HA as above. All samples were prepared in triplicate.

AMB-Biotin Binding on Hydroxyapatite in the Presence of Free Biotin. Three samples were prepared to study the interactions with HA in the presence of free biotin. These samples were examined to determine whether AMB-Biotin could interact with HA through the bisphosphonate or the biotin moieties. First, a 3 mg sample of AMB-Biotin was prepared in 1 mL phosphate buffer. The second sample contained 3 mg of free biotin in 1 mL phosphate buffer. Finally, a sample was prepared that contained 3 mg each of both AMB-Biotin and free biotin dissolved together in 1 mL phosphate buffer to determine what effect, if any, free biotin had on the interactions between AMB-Biotin and HA. An amount of 6 mg of HA was added to all three samples. Samples were prepared in triplicate and treated as described for AMB-Biotin on HA.

AMB-Biotin Binding on Hydroxyapatite in the presence of BSA or Serum. Because bisphosphonates are administered either orally or intravenously, the ability of the modified bisphosphonate to interact with HA in the presence of biological molecules was examined. For the BSA studies, a total of five samples were prepared to study the effect of BSA on AMB-Biotin binding to HA. The first sample was prepared by dissolving 3 mg of AMB-Biotin in 1 mL phosphate buffer. For the second sample, 0.3 mg of BSA was dissolved in 1 mL phosphate buffer. The third sample contained both 3 mg of AMB-Biotin and 0.3 mg BSA in 1 mL phosphate buffer to determine how the presence of BSA affects the interaction with HA. To each of these three samples, 6 mg of HA was added. These first three samples were treated as described previously for AMB-Biotin.

The final two samples were prepared differently. For these two samples, 3 mg of AMB-Biotin and 0.3 mg of BSA were each preincubated with 6 mg HA. These samples were washed and lyophilized as before. However, after lyophilization, the AMB-Biotin sample was resuspended in a 0.3 mg/mL BSA solution in phosphate buffer, and the BSA sample was resuspended in a 3 mg/mL solution of AMB-Biotin in phosphate buffer. These two samples were incubated for 3 h at room temperature on the rotator before centrifuging to remove the insoluble HA. The sample of (AMB-Biotin + HA) + BSA examined the strength of the interaction of the preincubated AMB-Biotin sample, while the (BSA + HA) + AMB-Biotin sample helped to determine the specificity of the AMB-Biotin interaction with the HA surface.

All five samples were then resuspended in 1 mL of 29 μg/mL FITC-labeled antibiotin antibody in phosphate buffer and incubated on a rotator for 3 h at 4 °C. HA was collected by centrifugation, and the fluorescence of the supernatants was measured and compared to a standard of FITC-labeled antibiotin antibody.

While the BSA studies looked at the effect of a low concentration of albumin (0.3 mg/mL) on AMB-Biotin binding to HA, additional studies were performed to study binding at higher concentrations of protein using fetal bovine serum (FBS). Three milligram samples of AMB-Biotin were prepared in 1 mL solutions of 25%, 50%, and 75% FBS in phosphate buffer along with solutions of 100% buffer and 100% FBS. Six milligrams of HA were added to each of the samples at the various levels of serum. The samples were treated following the procedure for AMB-Biotin.

Binding Studies of AMB-Biotin on Bone. A 3 mg sample of AMB-Biotin was dissolved in 1 mL of 0.5 M phosphate buffer, pH 7.4. To this solution, either a slab of untreated or demineralized bone or 6 mg of crushed ashed bone was added. The sample was incubated overnight at room temperature on a rotator. The sample was centrifuged for 15 min at 13 000 rpm to collect the bone, which was washed twice with buffer and three times with deionized water. The sample was then lyophilized overnight and resuspended in 1 mL of FITC-labeled antibiotin antibody in phosphate buffer at a concentration of 5.8 μg/mL. The suspension was incubated on a rotator for 3 h at room temperature. After the incubation, the sample was centrifuged again to collect the solid, and the fluorescence of the supernatant was measured. As controls, a 3 mg sample of free biotin and a 1 mL sample of FITC-labeled antibiotin antibody in phosphate buffer were subjected to the same conditions as listed for the AMB-Biotin sample.

AMB-Biotin Binding on Ashed Bone in the Presence of Casein. Samples were again prepared to examine the binding of AMB-Biotin in the presence of a biological molecule, this time using casein. Four total samples were prepared to study the interactions of AMB-Biotin and casein with ashed bone. The first sample was prepared by dissolving 3 mg AMB-Biotin in 1 mL phosphate buffer. For the second sample, 5 mg of casein was dissolved in 1 mL of phosphate buffer. The third sample contained both 3 mg of AMB-Biotin and 5 mg of casein in 1 mL phosphate buffer. Ashed bone in the amount of 6 mg was added to all three of these samples, which were treated as previously described for the AMB-Biotin samples on HA.

The final sample was prepared by preincubating 3 mg of AMB-Biotin with 6 mg of ashed bone in 1 mL phosphate buffer. The washes and lyophilization were performed along with the other samples. However, after lyophilization, this sample was resuspended in a 1 mL solution of 5 mg/mL casein in phosphate buffer. The sample was incubated on a rotator at room temperature for 3 h. After incubation, the sample was centrifuged to collect the solid and the supernatant was removed.

All four of the samples were then resuspended in 1 mL each of 5.8 μg/mL FITC-labeled antibiotin antibody, placed on a rotator and incubated for 3 h at room temperature. Subsequently, the samples were centrifuged to collect the bone, and the fluorescence of the supernatant was measured and compared to a standard of FITC-labeled antibiotin antibody.

Kinetics of AMB-Biotin Binding to Ashed Bone. The kinetics of AMB-Biotin binding to bone were established by using a fluorescence assay based on avidin and 2-anilinonaphthalene-6-sulfonic acid (2,6-ANS), where 2,6-ANS occupies the biotin binding sites of avidin (*31*). 2,6-ANS has two different emission wavelengths, depending on whether it is in the bound or unbound state. In the presence of biotin, or in this case AMB-Biotin, the fluorescent probe is released from avidin. The amount of AMB-Biotin remaining unbound in solution can be determined using a calibration plot of increasing concentrations of AMB-Biotin in the presence of the avidin-2,6-ANS complex.

Three milligram samples of AMB-Biotin were incubated with 6 mg each of ashed bone for 0, 15, 30, 60, and 120 min in 1 mL of phosphate buffer. After the designated time period, the samples were centrifuged at 13 000 rpm for 15 min. Aliquots of 12.5 μL of each of the supernatants were incubated with 800 μL of the avidin-2,6-ANS complex that was prepared at 8 μM avidin and 50 μM 2,6-ANS. Samples for the calibration plot were prepared using a solution of 3 mg/mL AMB-Biotin. AMB-Biotin was added to 800 μL of avidin-2,6-ANS in 12.5 μL increments. Ten total samples were prepared ranging from 0.09 mg/mL AMB-Biotin to 0.7 mg/mL. The excitation wavelength was set at 328 nm, while the fluorescence emission was

measured from 400 to 500 nm. 2,6-ANS has an emission maximum at 438 nm when bound to avidin and 462 nm when unbound.

RESULTS AND DISCUSSION

To synthesize AMB-Biotin, aminobisphosphonate was prepared first by following a published procedure (*30*). This compound was subsequently functionalized with biotin. For this, biotin *N*-hydroxysuccinimide ester was used because of its reactivity toward aliphatic amines. AMB-Biotin was produced in high yield, and the NMR and MS data confirmed the production of a ligand-modified aminobisphosphonate.

AMB-Biotin binds to HA through its bisphosphonate portion. This binding can be followed by using a fluorescently labeled antibiotin antibody that recognizes the biotin functionality on AMB-Biotin. Because of the difficulty in measuring fluorescence on the solid microparticles, the extent of binding was determined by measuring the fluorescence remaining in solution after the antibody reaction with the immobilized AMB-Biotin. Excitation of the fluorescent antibody was performed at 490 nm, while the emission was scanned from 500 to 600 nm. Figure 1A shows a representative set of spectra of AMB-Biotin binding on HA and the corresponding controls. The emission spectra have a maximum at 523 nm, which is characteristic of FITC-labeled proteins. The fluorescence intensity at 523 nm was used to calculate relative binding using the following equation:

$$\text{relative binding} = (F_0 - F_{\text{sample}})/(F_0 - F_{\text{highest}})$$

where F_0 is the fluorescence of the solution of antibiotin antibody prior to addition of HA, F_{sample} is the fluorescence remaining in the solution following the binding event, and F_{highest} is the fluorescence of the sample exhibiting the highest binding. Figure 1B shows data for the relative binding calculations for all samples of AMB-Biotin on HA and the controls.

As can be seen in the spectra in Figure 1A, a considerable loss in the solution fluorescence is observed when hydroxyapatite was treated with AMB-Biotin. This suggests that AMB-Biotin is bound to the insoluble hydroxyapatite; antibiotin antibody binds to the immobilized biotin and is removed from solution following centrifugation. When the relative binding is calculated, the AMB-Biotin-treated hydroxyapatite exhibited the highest extent of binding (Figure 1B). This binding is more than twice the binding seen for the nonspecific interaction of the antibody with untreated HA and HA treated with an aminobisphosphonate lacking the biotin moiety. Analysis of variance (ANOVA) and post hoc tests were performed to determine the statistical similarity or difference between the samples. In Figure 1B, the symbol * denotes that there is no statistical difference between the sample of HA treated with AMB and the untreated HA. However, both of these samples are statistically different from the AMB-Biotin + HA sample at a probability (p) of greater than 0.01.

Strong binding of AMB-Biotin is also observed in the presence of free biotin, as can be seen in Figure 2. In this figure, the symbols * and † denote statistically similar samples. There is no statistical difference among the Untreated HA, Free Biotin + HA, and AMB-Biotin + Free Biotin + HA samples, as denoted by the symbol *. There is also no statistical difference between the AMB-Biotin + HA sample and the AMB-Biotin + Free Biotin + HA sample, denoted by the symbol †. There is, however, a statistically significant difference ($p > 0.01$) between the Untreated HA and AMB-Biotin + HA samples. There is also a significant difference between the Free Biotin + HA and AMB-Biotin + HA samples ($p > 0.01$). The difference observed between the free biotin and AMB-Biotin samples demonstrates that the binding of the biotinylated bisphosphonate is indeed through the bisphosphonate moiety and not through the biotin functionality. Binding does not occur through the biotin group, since no statistical difference was found between the Free Biotin + HA and the Untreated HA samples.

The results observed for the binding of AMB-Biotin in the presence of BSA are summarized in Figure 3. The highest

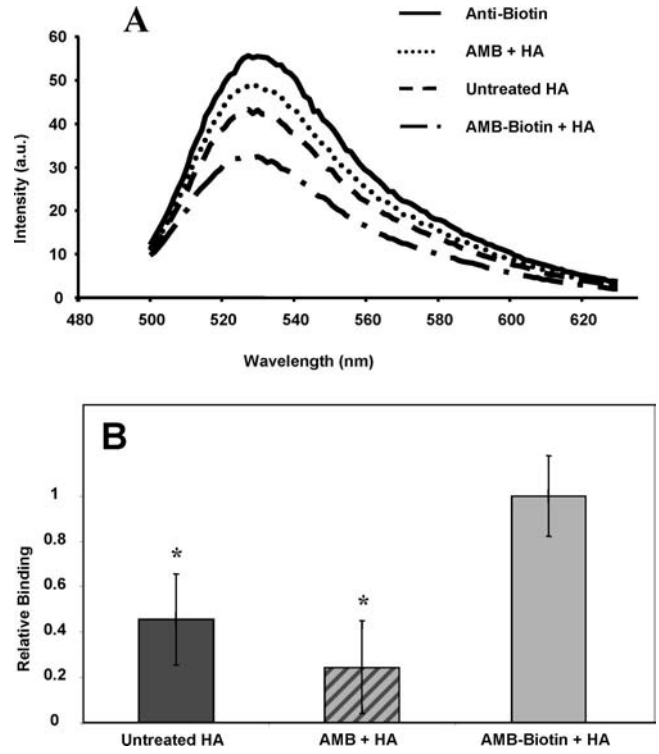

Figure 1. Binding of FITC-labeled monoclonal antibiotin antibody to hydroxyapatite treated with AMB-Biotin and various controls. (A) Fluorescence signal of the supernatants (λ_{ex} 490 nm) after removal of insoluble HA treated with AMB (•••) and AMB-Biotin (— • —), and untreated HA (— — —) compared to the spectrum of the FITC-labeled antibiotin antibody solution used in the experiments (solid line). (B) Relative binding for untreated HA ($n = 5$), AMB treated HA ($n = 6$), and AMB-Biotin treated HA ($n = 6$). The * denotes statistically similar results. AMB-Biotin is statistically different from the AMB-treated and untreated HA samples at $p > 0.01$.

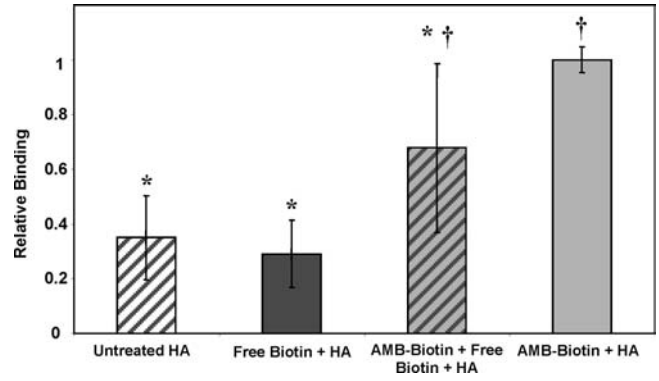

Figure 2. Binding measurements in the presence of free biotin quantified using a fluorescently labeled antibiotin antibody. Relative binding for untreated HA, free biotin treated HA, AMB-Biotin and free biotin incubated together with HA, and HA treated with AMB-Biotin. For all samples, $n = 3$. The symbols * and † denote statistically similar results. There is no statistical difference among the Untreated HA, Free Biotin, and AMB-Biotin + Free Biotin + HA samples, nor is there a difference between the AMB-Biotin + Free Biotin + HA and AMB-Biotin samples. However, there is a statistical difference ($p > 0.01$ for each sample) among the Untreated HA, Free Biotin + HA, and the AMB-Biotin +HA samples.

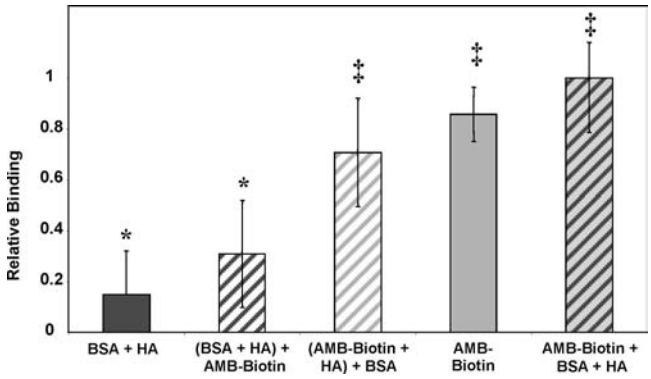

Figure 3. Binding measurements of AMB-Biotin in the presence of BSA based on the loss in fluorescence of the supernatants after incubation with a FITC-labeled antibiotin antibody. Relative binding for BSA, BSA preincubated with HA, AMB-Biotin preincubated with HA, AMB-Biotin alone on HA, and AMB-Biotin and BSA incubated together with HA. All samples were prepared in triplicate. The symbols * and ‡ denote statistically similar samples. The statistically significant difference between the samples denoted with the symbol * and those with the symbol ‡ was at least $p > 0.05$.

relative binding observed was from the sample treated simultaneously with both AMB-Biotin and BSA. High relative binding was also observed for the AMB-Biotin + HA sample at almost 90% and for the sample of HA pretreated with AMB-Biotin and subsequently incubated with BSA at over 70%. In the ANOVA and post hoc calculations, these three samples were found to be statistically similar, as denoted by the symbol ‡. These three samples are statistically different ($p > 0.05$) from the two samples where HA was treated with BSA alone or pretreated with BSA and then exposed to AMB-Biotin, which are statistically similar as denoted by the symbol *. These results emphasize the specific binding ability of AMB-Biotin on HA, even when BSA is present in the sample.

While the BSA studies were performed at a low protein concentration (0.3 g/L), additional studies were carried out at higher levels of protein using FBS. Binding of AMB-Biotin to HA was performed in solutions of FBS in phosphate buffer at concentrations of 0%, 25%, 50%, 75%, and 100% (v/v) FBS. The highest binding was seen for 0% FBS. The sample showing the least amount of binding was the 75% serum sample, which showed binding of only 40% relative to the 0% FBS sample (data not shown). These levels of binding indicate that, even at high concentrations of protein, AMB-Biotin still binds to HA. This leads one to believe that, in the complexity of a living system, where there is a high level of protein and other biomolecules present, there will still be specific interaction of a conjugated aminobisphosphonate with the natural bone matrix.

The initial characterization of the biotinylated aminobisphosphonate was performed under the conditions of a model system, specifically using hydroxyapatite to simulate bone and BSA as a general blocking protein. While this model system is beneficial initially, additional studies were performed to better understand how this bisphosphonate would behave with real bone. Three different treatments were used to prepare the bone samples. Samples of untreated, demineralized, and ashed bone were incubated with AMB-Biotin. Data from the bone samples can be seen in Figure 4. Figure 4A contains the data from the untreated bone samples, Figure 4B summarizes the data for the demineralized bone samples, and Figure 4C displays the results for the ashed bone samples. The symbol * denotes statistically similar binding between samples. Although a positive trend was observed for binding of AMB-Biotin to the untreated bone samples versus free biotin, there was no statistical difference between the samples. Additionally, there is no statistical

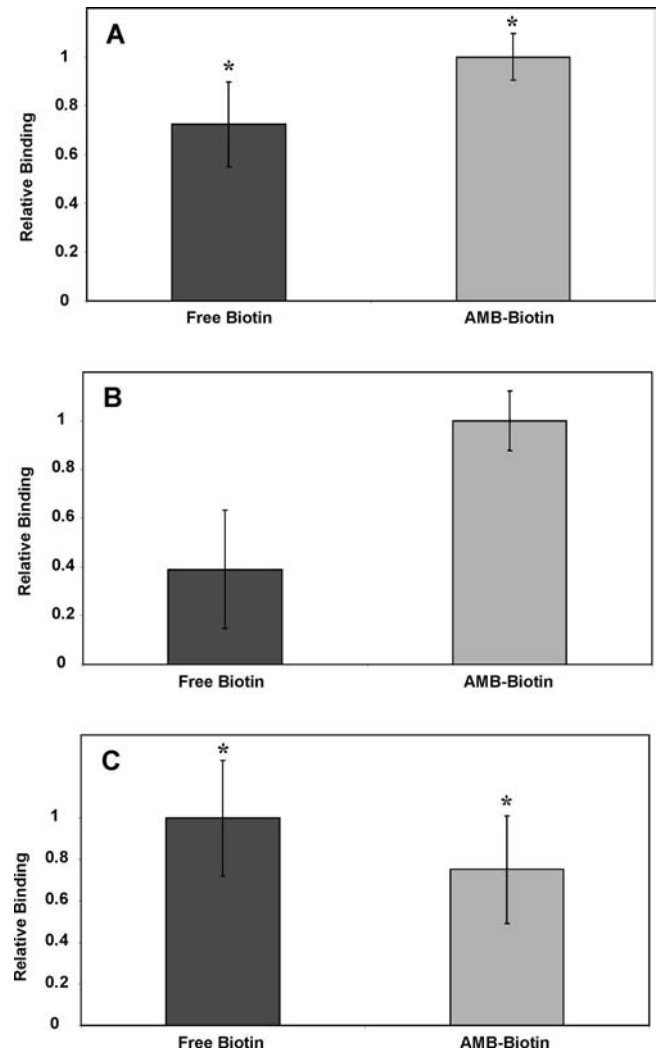

Figure 4. Binding measurements of AMB-Biotin and free biotin on multiple treatments of bone. The three treatments studied were untreated bone (A), demineralized bone (B), and ashed bone (C). Binding was quantified on the basis of the binding of a fluorescently labeled antibiotin antibody. For all samples, $n = 3$. The symbol * denotes statistically similar results. There is no statistical difference between the free biotin and AMB-Biotin samples on untreated and ashed bone. There is only a statistically significant ($p > 0.025$) difference between the AMB-Biotin and free biotin samples on demineralized bone.

difference observed between the samples of ashed bone. The only bone treatment that showed a statistical difference between the free biotin sample and AMB-Biotin sample was the demineralized bone. This difference is observed at $p > 0.025$. It is unclear why there was no difference between biotin and AMB-biotin binding in the case of untreated and ashed bone. The data suggest that biotin is likely attached to the surface of these two samples through ion exchange because of residual positive charges on the surface of the bone samples. Ashing the bone samples removes organic bone matrix that blocks access to the mineral phase (*26*). More binding sites on the mineral surface are exposed, thus increasing the probability of binding through electrostatic interactions.

The binding of AMB-Biotin to bone was further investigated in the presence of protein. In four different sets of experiments, ashed bone was treated with (a) casein, (b) AMB-Biotin, (c) AMB-Biotin followed by exposure to casein, and (d) simultaneous exposure to AMB-Biotin and casein. The results of this study can be seen in Figure 5. Casein proves to be a good blocking protein, allowing 15% of the binding of the antibiotin

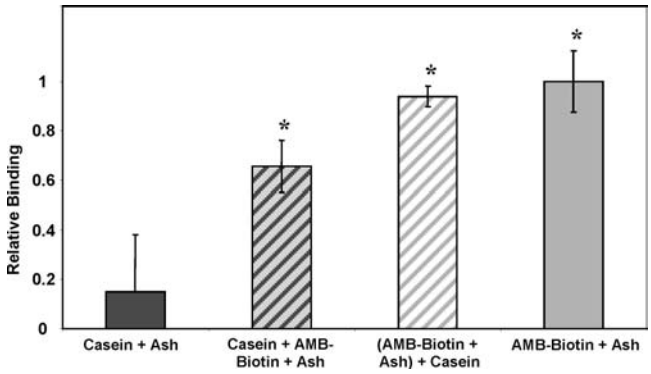

Figure 5. Binding measurements of AMB-Biotin in the presence of casein. Binding was measured using FITC-labeled antibiotin antibody. Relative binding on ashed bone of casein, casein and AMB-Biotin, AMB-Biotin preincubated with bone, and AMB-Biotin. Samples were prepared in triplicate. The symbol * denotes statistically similar samples. There is no statistical difference among the Casein + AMB-Biotin + Ash, (AMB-Biotin + Ash) + Casein, and AMB-Biotin + Ash samples. All are statistically different from the Casein + Ash sample by at least $p > 0.05$.

antibody on the ashed bone relative to the ashed bone treated with AMB-Biotin. The extent of binding of AMB-Biotin on ashed bone was the highest for this sample set. On the basis of the ANOVA and post hoc tests, it was found that there was no statistical difference among the Casein + AMB-Biotin + Ash, (AMB-Biotin + Ash) + Casein, and AMB-Biotin + Ash samples. This similarity is denoted in Figure 5 by the symbol *. All three of these samples were found to be statistically different from the Casein + Ash sample by a probability of at least >0.05. Again, this suggests that the binding of AMB-Biotin has the greater impact on the system, because there is still strong binding of the biotinylated aminobisphosphonate in the presence of protein.

It is generally accepted that conjugation of a therapeutic agent to bisphosphonate affects the properties of the bisphosphonate in terms of kinetics, affinity, and its ability to function as a drug (*32, 33*). Therefore, the kinetics of AMB-Biotin association to bone were determined. To evaluate the kinetics of the interaction between AMB-Biotin and ashed bone, a study was performed under pseudo first-order conditions, where the ashed bone was present in excess over the AMB-Biotin. A calibration plot was used to determine the concentration of AMB-Biotin remaining in solution after incubation with ashed bone at various time intervals. The rate constant of the reaction was calculated to be 5.7 ($\pm$1.7) $\times$ 10^{-4} min^{-1}, where the error is the standard deviation of the data set. After 2 h of incubation with ashed bone, the amount of AMB-Biotin remaining in solution was negligible. Since in all experiments described the bisphosphonate samples were incubated with either HA or bone overnight, there was sufficient time allowed to ensure binding of the bisphosphonate to the matrix material.

This work shows that a ligand-modified aminobisphosphonate can bind bone successfully. While this is a model system used to explore the conjugation of a protein-linking molecule to an aminobisphosphonate, it may also help deliver peptides and proteins to the bone surface by linking them with a biotin-binding protein, such as an antibiotin antibody. The availability of "humanized" antibodies overcomes the immunogenic challenges of avidin and streptavidin. A humanized antibody or antibody fragment could be conjugated to a therapeutic agent for delivery to the bone surface. Antibodies can also be used to introduce sites for the delivery of small molecules, such as drug carriers and anticancer, antibacterial, and antiresorptive agents (*34*).

Overall, the applications for bisphosphonates in the field of osteoporosis research are endless. The novel biotinylated aminobisphosphonate prepared herein retains its ability to bind to both hydroxyapatite and bone. The binding is specific enough that competing reagents, such as free biotin, or protein blocking agents, such as BSA, FBS, or casein, do not inhibit the affinity of the biotinylated bisphosphonate for bone. Aminomethylene bisphosphonic acid was chosen because it has a simple structure and fairly straightforward synthesis. The conjugation with biotin was performed using NHS ester chemistry. This technique could be performed on a variety of other bisphosphonates that are currently prescribed for osteoporosis treatment, such as pamidronate, alendronate, olpadronate, and ibandronate (*34*). Any of these molecules could be functionalized with biotin in the manner described and could therefore also be used to target proteins to the bone surface. While currently prescribed bisphosphonates function mainly to inhibit further bone resorption by the osteoclast, linking a molecule with osteogenic properties to a bisphosphonate would not only inhibit resorption but also stimulate regeneration.

ACKNOWLEDGMENT

The authors acknowledge financial support from the National Institutes of Health (AR048700). Also acknowledged are Dr. Bert Lynn and Dr. Jack Goodman of the University of Kentucky Mass Spectrometry Facility, Lexington, KY. Mr. Don Cho and Mr. Jivan Yewle (University of Kentucky, Lexington, KY) are thanked for assistance in acquiring NMR spectra.

LITERATURE CITED

(1) Kiberstis, P., Smith, O., and Norman, C. (2000) Bone health in the balance. *Science 289*, 1497.
(2) Ducy, P., Schinke, T., and Karsenty, G. (2000) The osteoblast: A sophisticated fibroblast under central surveillance. *Science 289*, 1501–1504.
(3) Teitelbaum, S. L. (2000) Bone resorption by osteoclasts. *Science 289*, 1504–1508.
(4) Rodan, G. A., and Martin, T. J. (2000) Therapeutic approaches to bone diseases. *Science 289*, 1508–1514.
(5) Finkelstein, J. S. (2006) Calcium plus vitamin D for postmenopausal women - bone appetit? *N. Engl. J. Med. 354*, 750–751.
(6) Jackson, R. D., LaCroix, A. Z., Gass, M., Wallace, R. B., Robbins, J., Lewis, C. E., Bassford, T., Beresford, S. A. A., Black, H. R., Blanchette, P., Bonds, D. E., Brunner, R. L., Brzyski, R. G., Caan, B., Cauley, J. A., Chlebowski, R. T., Cummings, S. R., Granek, I., Hays, J., Heiss, G., Hendrix, S. L., Howard, B. V., Hsia, J., Hubbel, F. A., Johnson, K. C., Judd, H., Kotchen, J. M., Kuller, L. H., Langer, R. D., Lasser, N. L., Limacher, M. C., Ludlam, S., Mason, J. E., Margolis, K. L., McGowan, J., Ockene, J. K., O'Sullivan, M. J., Phillips, L., Prentice, R. L., Sarto, G. E., Stefanick, M. L., Van Horn, L., Wactawski-Wende, J., Whitlock, E., Anderson, G. L., Assaf, A. R., and Barad, D. (2006) Calcium plus vitamin D supplementation and the risk of fractures. *N. Engl. J. Med. 354*, 669–683.
(7) Fletcher, S. W., and Colditz, G. A. (2002) Failure of estrogen plus progestin therapy for prevention. *J. Am. Med. Assoc. 288*, 366–368.
(8) Rossouw, J. E., Anderson, G. L., Prentice, R. L., LaCroix, A. Z., Kooperberg, C., Stefanick, M. L., Jackson, R. D., Beresford, S. A. A., Howard, B. V., Johnson, K. C., Kotchen, J. M., and Ockene, J. (2002) Risks and benefits of estrogen plus progestin in healthy postmenopausal women. *J. Am. Med. Assoc. 288*, 321–333.
(9) Shumaker, S. A., Legault, C., Rapp, S. R., Thal, L., Wallace, R. B., Ockene, J. K., Hendrix, S. L., III, B. N. J., Assaf, A. R.,

Jackson, R. D., Kotchen, J. M., Wassertheil-Smoller, S., and Wactawski-Wende, J. (2003) Estrogen plus progestin and the incidence of dementia and mild cognitive impairment in postmenopausal women. *J. Am. Med. Assoc. 289*, 2651–2662.
(10) Cumming, R. G. (1990) Calcium intake and bone mass: A quantitative review of the evidence. *Calcif. Tissue Int. 47*, 194–201.
(11) Shea, B., Wells, G., Cranney, A., Zytaruk, N., Robinson, V., Griffith, L., Ortiz, Z., Peterson, J., Adachi, J., Tugwell, P., and Guyatt, G. (2002) Meta-analyses of therapies for postmenopausal osteoporosis. VII. Meta-analysis of calcium supplementation for the prevention of postmenopausal osteoporosis. *Endocr. Rev. 23*, 552–559.
(12) Horowitz, M. C. (1993) Cytokines and estrogen in bone: Anti-osteoporotic effects. *Science 260*, 626–627.
(13) Sunyer, T., Lewis, J., Collin-Osdoby, P., and Osdoby, P. (1999) Estrogen's bone-protective effects may involve differential IL-1 receptor regulation in human osteoclast-like cells. *J. Clin. Invest. 103*, 1409–1418.
(14) Lin, J. H. (1996) Bisphosphonates: A review of their pharmacokinetic properties. *Bone 18*, 75–85.
(15) Williams, K. R. (2004) The bisphosphonate story: From detergents to bone disease. *J. Chem. Educ. 81*, 1406–1407.
(16) Reszka, A. A., and Rodan, G. A. (2003) Mechanism of action of bisphosphonates. *Curr. Osteoporosis Rep. 1*, 45–52.
(17) Rodan, G. A., and Reszka, A. A. (2002) Bisphosphonate mechanism of action. *Curr. Mol. Med. 2*, 571–577.
(18) Reszka, A. A., Halasy-Nagy, J. M., Masarachia, P. J., and Rodan, G. A. (1999) Bisphosphonates act directly on the osteoclast to induce caspase cleavage of Mst1 kinase during apoptosis. *J. Biol. Chem. 274*, 34967–34973.
(19) Bagi, C. M. (2005) Targeting of therapeutic agents to bone to treat metastatic cancer. *Adv. Drug Delivery Rev. 57*, 995–1010.
(20) Bansal, G., Gittens, S. A., and Uludağ, H. (2004) A di(bisphosphonic acid) for protein coupling and targeting to bone. *J. Pharm. Sci. 93*, 2788–2799.
(21) Frith, J. C., Monkkonen, J., Blackburn, G. M., Russell, R. G. G., and Rogers, M. J. (1997) Clodronate and liposome-encapsulated clodronate are metabolized to a toxic ATP analog, adenosine 5′-(β,γ-dichloromethylene) triphosphate, by mammalian cells in vitro. *J. Bone Miner. Res. 12*, 1358–1367.
(22) Green, J. R. (2004) Zoledronic acid: pharmacologic profile of a potent bisphosphonate. *J. Organomet. Chem. 690*, 2439–2448.
(23) Halasy-Nagy, J. M., Rodan, G. A., and Reszka, A. A. (2001) Inhibition of bone resorption by alendronate and risedronate does not require osteoclast apoptosis. *Bone 29*, 553–559.
(24) Lipton, A. (2004) Toward new horizons: The future of bisphosphonate therapy. *The Oncologist 9*, 38–47.
(25) Gittens, S. A., Matyas, J. R., Zernicke, R. F., and Uludağ, H. (2003) Imparting bone affinity to glycoproteins through the conjugation of bisphosphonates. *Pharm. Res. 20*, 978–987.
(26) Uludağ, H., Kousinioris, N., Gao, T., and Kantoci, D. (2000) Bisphosphonate conjugation to proteins as a means to impart bone affinity. *Biotechnol. Prog. 16*, 258–267.
(27) Gittens, S. A., Bagnall, K., Matyas, J. R., Löbenberg, R., Uludağ, and H. (2004) Imparting bone mineral affinity to osteogenic proteins through heparin-bisphosphonate conjugates. *J. Controlled Release 98*, 255–268.
(28) Uludağ, H., Gao, T., Wohl, G. R., Kantoci, D., and Zernicke, R. F. (2000) Bone affinity of a bisphosphonate-conjugated protein in vivo. *Biotechnol. Prog. 16*, 1115–1118.
(29) Uludağ, H., and Yang, J. (2002) Targeting systemically administered proteins to bone by bisphosphonate conjugation. *Biotechnol. Prog. 18*, 604–611.
(30) Kantoci, D., Denike, J. K., and Wechter, W. J. (1996) Synthesis of aminobisphosphonate. *Synth. Commun. 26*, 2037–2043.
(31) Przyjazny, A., and Bachas, L. G. (1991) Competitive-binding approach to liquid chromatographic postcolumn reactions with fluorimetric detection. *Anal. Chim. Acta 246*, 103–112.
(32) Nancollas, G. H., Tang, R., Phipps, R. J., Henneman, Z., Gulde, S., Wu, W., Mangood, A., Russell, R. G. G., and Ebetino, F. H. (2006) Novel insights into actions of bisphosphonates on bone: Differences in interactions with hydroxyapatite. *Bone 38*, 617–627.
(33) Uludağ, H. (2002) Bisphosphonates as a foundation of drug delivery to bone. *Curr. Pharm. Des. 8*, 1929–1944.
(34) Zhang, S., Gangal, G., and Uludağ, H. (2007) "Magic bullets" for bone diseases: Progress in rational design of bone-seeking medicinal agents. *Chem. Soc. Rev. 36*, 507–531.

BC700196Q

Amino Acid Analysis of Peptide Loading Ratios in Conjugate Vaccines: A Comparison of Direct Electrochemical Detection and 6-Aminoquinolyl-*N*-Hydroxysuccinimidyl Carbamate Pre-Column Derivatization Methods

Deborah D. Nahas,* Jennifer S. Palladino, Joseph G. Joyce, and Robert W. Hepler

Merck Research Laboratories, 770 Sumneytown Pike, P.O. Box 4, WP16-107, West Point, Pennsylvania 19486. Received June 22, 2007; Revised Manuscript Received September 24, 2007

Amino acid analysis using direct electrochemical detection was compared with precolumn fluorescent derivatization using 6-aminoquinolyl-*N*-hydroxysuccinimidyl carbamate (AQC) for evaluation of the degree of covalent coupling of peptides to a carrier–protein complex derived from the bacteria *Neisseria meningitidis*. AQC derivatization was found to give superior sensitivity compared to electrochemical detection, with less interference from sample components such as carbohydrates or buffer salts. Hydrolysis time and temperature were optimized for maximal recoveries of the marker amino acid 6-aminohexanoic acid (ε-Ahx) and the unique amino acids *S*-dicarboxyethyl cysteine (SDCEC) and *S*-carboxymethyl homocysteine (SCHMC), which are generated upon the hydrolysis of the covalent linkage between the peptide and the carrier protein. Quantitation of these amino acids enabled the determination of the ratio of peptide to protein in the conjugate samples.

INTRODUCTION

Certain classes of antigens, including peptides, carbohydrates, or polysaccharides, are often covalently coupled to carrier proteins in order to enhance their poor native immunogenicity. Such bioconjugates can be used as potential vaccine candidates or, in the cases of small peptides, as immunogens to generate antibodies against a particular target protein (*1–3*). The conjugation of poorly immunogenic molecules to carrier proteins, such as keyhole limpet hemocyanin (KLH), diphtheria toxoid, and *Neisseria meningitidis* outer membrane protein complex (OMPC), has been demonstrated to facilitate the induction of T-cell-dependent immune responses (*4–6*).

OMPC is a multiprotein complex with associated lipids that has proven to be an excellent carrier in several licensed and experimental conjugate vaccines because of its unique immunostimulatory properties (*7–9*). Studies have shown that OMPC also possesses adjuvant-like properties based on its ability to activate B-cells through its lipopolysaccharide and protein components (*4, 10*). Additionally, neisserial porins are capable of activating B-cells by mediating toll-like receptor (TLR) signaling through the effector molecule MyD88 (*11*).

Our group has prepared a number of covalent OMPC–peptide conjugates employing two different thiol-based coupling strategies. In the first strategy, OMPC was thiolated on surface-exposed lysines with *N*-acetyl homocysteine thiolactone (NAHT) and then reacted with a bromoacetylated peptide. In the second strategy, lysine residues in OMPC were derivatized using the heterobifunctional cross-linker sulfosuccinimidyl 4-(*N*-maleimidomethyl) cyclohexane-1-carboxylate (sSMCC) in order to introduce a maleimide group for reaction with a cysteine-containing peptide. These thiol-based conjugation chemistries allow directional coupling due to the fact that the reactive thiol or haloacetyl functionality can be added at either the N-terminus or at the C-terminus of the peptide of interest. Another advantage is that the levels of activation can be monitored and controlled, which is often critical to maintaining the solubility and stability of peptide–carrier conjugates.

In the current study, the OMPC–peptide conjugates were analyzed by amino acid analysis, which is the technique most commonly employed to quantitate the molar ratio of peptide to protein in a conjugate (*12, 13*). This ratio is critical for calculating doses to be administered in immunization studies and assessing the comparability of different vaccine preparations. Amino acid analysis is also useful for monitoring the level of incorporation of the activating functionality on the protein carrier. In the case of sSMCC-mediated maleimidation, this is equivalent to the amount of tranexamic acid (Txa) generated upon acid hydrolysis of the conjugate. In this way, activation levels can be controlled, which is often critical to maintaining the solubility and stability of peptide–carrier conjugates.

RP-HPLC with precolumn derivatization using 6-aminoquinolyl-*N*-hydroxysuccinimidyl carbamate (AQC) is compared with direct electrochemical detection of amino acids by high pH anion exchange chromatography with pulsed amperometric detection (HPAE-PAD) for the analysis of OMPC–peptide conjugates. The gradient separations were optimized for both HPLC methods in order to resolve all 17 common amino acids: the peptide-derived spacer amino acid, 6-aminohexanoic acid (ε-Ahx); the activation reporter residue, tranexamic acid (Txa); and the coupling chemistry-specific amino acids *S*-dicarboxyethyl cysteine (SDCEC) and *S*-carboxymethyl homocysteine (SCMHC) generated by hydrolysis of the peptide–protein conjugate bond. The effects of hydrolysis time and temperature on the recovery of all relevant amino acids are also reported.

EXPERIMENTAL PROCEDURES

Preparation of Peptide–OMPC Conjugates. Synthetic peptides were prepared by standard *t*-Boc or Fmoc solid phase synthesis. The spacer ε-Ahx was incorporated in the peptide between the primary sequence and the amino terminal cysteine or between the primary sequence and bromoacetyl group on the carboxy terminus. The thiol-based conjugation chemistries

* Corresponding author. Phone: 215-652-2198. Fax: 215-652-7320. E-mail: debbie_nahas@merck.com.

10.1021/bc700232z CCC: $40.75 © 2008 American Chemical Society
Published on Web 12/12/2007

Scheme 1[a]

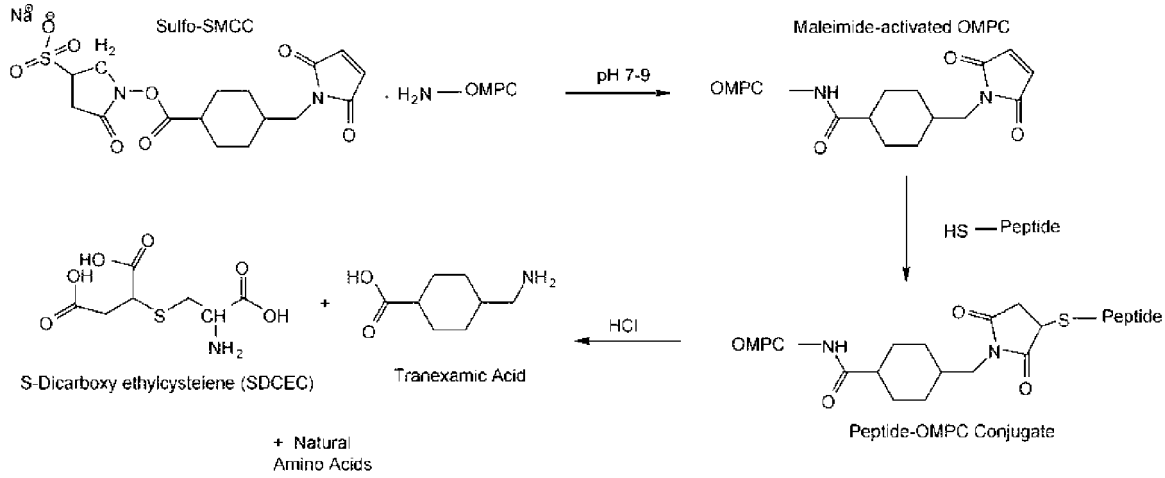

[a] A carrier protein is maleimide-activated with sSMCC, which reacts with primary amines (Lys residues and N-terminus). Then a cysteine-containing peptide reacts with the maleimide-activated carrier protein to form a peptide–protein conjugate. Acid hydrolysis of the resulting conjugate liberates SDCEC and tranexamic acid in addition to the constituent amino acids of the peptide and the carrier protein. Quantitation of SDCEC by amino acid analysis can be used to determine the ratio of peptide to carrier protein.

used to couple the synthetic peptides to OMPC have been previously described in detail. Cysteinylated peptide Ac-EKTNE-KFHQIEKEFSEVEGRIQDLEKYVENTKINLWSYNAEL-Ahx-C-NH_2 was conjugated to OMPC that had been maleimidated with sSMCC according to the method of Fan, et al. (*1*), and the peptide bromoacetyl-Ahx-(Peg)AEDVGSNK-(Peg)-DAEFRHDS-NH2 was conjugated to OMPC that had been thiolated using NAHT (*14*). For each conjugation protocol, a sample of activated OMPC without added peptide was carried through the reaction and desalting steps as a control.

Amino Acid Analysis. Vapor phase hydrolysis of the OMPC peptide conjugates was performed with constant-boiling 6N HCl, 1% phenol at 110 °C for 20–70 h using an ELDEX (Napa, CA) H/D workstation. Protein hydrolysates and amino acid standards were derivatized with AQC using the Waters AccQ Tag Chemistry Package according to the manufacturer's directions (*15*). AQC reacts with primary and secondary amines to form stable, fluorescent derivatives that can be separated by RP-HPLC (*16–19*). The fluorescent AQC derivatives were separated on an AccQ Tag Nova-Pak C18, 4 μM, 3.9 × 150 mm column using a modified gradient program (Modified Chromatography for Cell Culture Analysis; http://www.waters.com). Alternatively, protein hydrolysates and amino acid standards were dissolved in high purity deionized water and directly injected onto an AminoPac PA10 2 × 250 mm analytical column with a 2 × 50 mm AminoPac PA10 guard column (*20, 21*).

Calculation of Peptide to OMPC Ratio. The amino acid composition of OMPC was empirically determined as the micromoles of each amino acid detected in a known amount of OMPC total protein (as determined independently by modified Lowry protein assay (*23*)). The following 11 hydrolysis-stable residues were used for routine quantitation: Ala, Arg, Asp, Glu, Gly, His, Ile, Leu, Lys, Phe, and Val. The amount of OMPC in the OMPC–peptide conjugate sample was calculated from the empirically determined amino acid composition using those acid-stable residues not present within the sequence of the peptide.

The two thiol-based conjugation chemistries employed in this study result in conjugates that liberate unique, non-natural amino acids upon acid hydrolysis, in addition to the constituent amino acids of the peptide and the carrier protein (*23*). Conjugates prepared with a cysteinylated peptide and maleimide activated OMPC liberate SDCEC and tranexamic acid (Scheme 1), and conjugates prepared from NAHT-activated OMPC and a bromoactelyated peptide liberate SCMHC (Scheme 2) (*14*). Quantitation of these unique residues by amino acid analysis was used to determine the ratio of peptide to carrier protein. Also, since each mole of peptide contained a fixed and known amount of ε-Ahx (typically 1 or 2 mol ε-Ahx/ mol peptide), the molar amount of peptide in the conjugate was equivalent to the molar concentration of ε-Ahx, assuming complete removal of free peptide. Finally, the molar ratio of peptide to protein was calculated by quantitative comparison of conjugate and OMPC-only compositions using the modified least-squares algorithm described by Shuler, et al. (*12*).

RESULTS

The modified elution conditions developed for amino acid analysis of cell culture supernatants by RP-HPLC proved suitable for resolving the unique conjugate-specific amino acids SDCEC, SCMHC, ε-Ahx and Txa from the 17 common peptide- and protein-derived amino acids within a single 60 min run. RP-HPLC analysis of the AQC derivatives provided a linear response for all components between 1.5 pmol and 50 pmol injected on the column.

AAA Direct amino acid analysis by HPAE-PAD did not prove useful for the analysis of OMPC–peptide conjugates because of peaks that interfered with the detection of Arg and His, and the fact that HEPES buffer, which was used for conjugate preparation, interfered with the detection of leucine and caused excessive fouling of the gold electrode surface. Also, the method was considerably less sensitive than fluorescent detection of AQC-derivatized amino acids. The limit of detection for all amino acids using the AAA Direct method was 50 pmol, compared with 1.5 pmol for the AccQTag method.

Comparison of Amino Acid Analysis by Direct Detection versus Precolumn Derivatization. The amino acid composition of a single lot of OMPC was determined following acid hydrolysis by an independent contract laboratory, using cation exchange chromatography with postcolumn ninhydrin derivatization (AAASL, Boring, OR). The results were compared with those obtained from the RP-HPLC method with precolumn AQC derivatization and direct analysis of hydrolyzed samples by HPAE-PAD (Table 1). In general, the differences between our AccQTag results and those of the contract laboratory were within experimental error (3–12% RSD). However, significant differences were observed between the

Scheme 2[a]

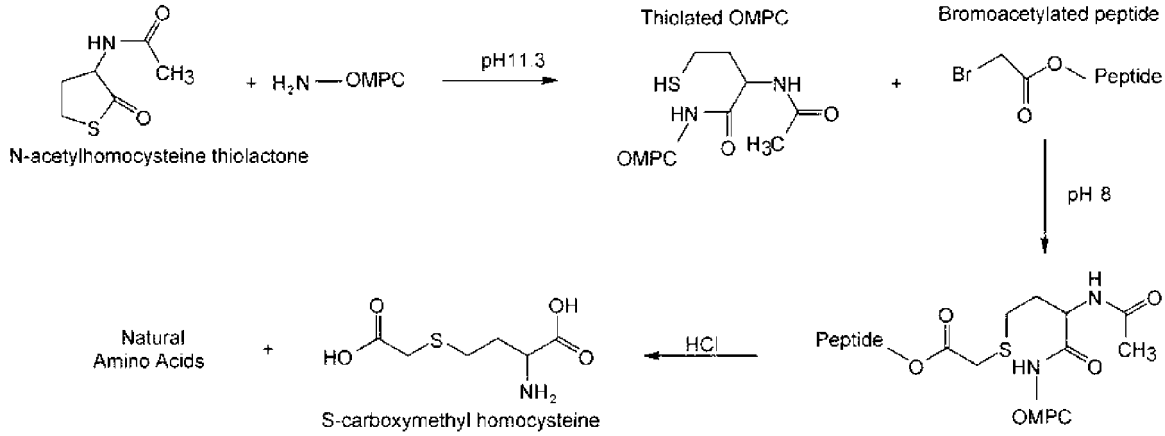

[a] A carrier protein, such as OMPC, is activated with *N*-acetylhomocysteine thiolactone \(NAHT\), which reacts with primary amines \(Lys residues and N-terminus\). Then a bromoacetylated peptide can react with the NAHT-activated carrier protein to form a peptide–protein conjugate. Acid hydrolysis of the resulting conjugate liberates SCMHC in addition to the constituent amino acids of the peptide and the carrier protein. Quantitation of SCMHC by amino acid analysis can be used to determine the ratio of peptide to carrier protein.

Table 1. Amino Acid Composition of OMPC from *Neisseria meningitidis*

	contract laboratory[b]			AAA direct (HPAE-PAD)[c]			AccQTag(RP-HPLC FLD)[c]		
amino acid[a]	average	standard deviation	% CV	average	standard deviation	% CV	average	standard deviation	% CV
arginine	0.3547	0.0130	4%	0.7503[d]	0.0465	6%	0.3550	0.0084	2%
lysine	0.5211	0.0197	4%	0.5523	0.0489	9%	0.5029	0.0195	4%
alanine	0.8405	0.0502	6%	0.7346	0.0318	4%	0.7805	0.0332	4%
glycine	0.6979	0.0297	4%	0.6195	0.0201	3%	0.7307	0.0112	2%
valine	0.6104	0.0231	4%	0.5373	0.0073	1%	0.5733	0.0244	4%
isoleucine	0.2846	0.0121	4%	0.1999	0.0244	12%	0.2300	0.0088	4%
leucine	0.4274	0.0198	5%	0.3699	0.0160	4%	0.4173	0.0147	4%
histidine	0.1454	0.0054	4%	0.1291	0.0216	17%	0.1212	0.0056	5%
phenylalanine	0.2675	0.0112	4%	0.2431	0.0204	8%	0.2470	0.0103	4%
glutamate	0.6493	0.0623	10%	0.6948	0.0725	10%	0.7178	0.0248	3%
aspartate	0.6878	0.0279	4%	0.7020	0.0740	11%	0.7688	0.0281	4%

[a] Quantitation of acid-stable residues reported as the average μmol residue/mg OMPC $\pm$ standard deviation. [b] Nine replicates were analyzed in a single run, using postcolumn ninhydrin detection. [c] Three replicates were analyzed on three separate days. [d] An unresolved peak that is also present in the buffer blank interferes with the detection of arginine.

AAA Direct method and the other methods. The AAA Direct method resulted in significantly lower values for alanine, glycine, valine, isoleucine, and leucine, and 2-fold higher concentrations for arginine (because of an interfering peak). The average variability observed with the AAA Direct method (8% RSD) was also twice as high as the average variability of the AccQTag method (4% RSD).

Optimization of Hydrolysis Conditions for Peptide/Carrier Conjugates. Because the AAA Direct analysis was less sensitive and was affected by interferences from buffer components, we focused hydrolysis optimization efforts solely on the AccQTag method. Hydrolysis time and temperature were evaluated in order to maximize the recoveries of the conjugate-specific unique amino acids. Acid hydrolysis of amino acid standards with 6 N HCl and 1% phenol revealed a 24% reduction in peak area for SCMHC and a 13% reduction in peak area for SDCEHC within 20 h at 110 °C. However, peak areas for SCMC, SDCEC, ε-Ahx, and Txa remain stable even after 70 h of hydrolysis.

Peptide–carrier conjugates prepared from both thiolated and maleimide-activated OMPC were also analyzed with hydrolysis times ranging from 20 to 70 h at 110 °C. The average results for the ε-Ahx/OMPC ratio, SDCEC/OMPC ratio, and SCMHC/OMPC ratio were then calculated for the various different hydrolysis conditions, along with the peptide loading determined by the LSA spreadsheet method. For both conjugates, the total protein concentrations did not vary significantly with increasing

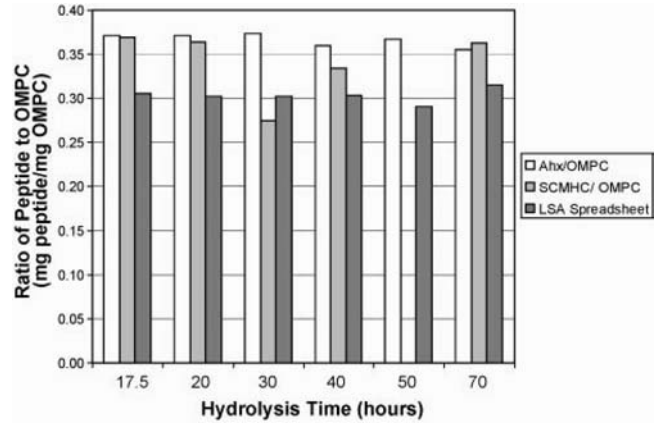

Figure 1. A conjugate prepared from a bromoacetylated peptide and thiolated OMPC was hydrolyzed at 110 °C for 17.5–70 h. The hydrolyzates were derivatized with AQC and analyzed by RP-HPLC. The ratio of peptide to OMPC was then calculated from either (a) the amount of ε-Ahx linker, (b) the amount of SCMHC, or (c) using the least-squares regression method of Shuler, et al.

hydrolysis time (data not shown). The ratio of peptide to OMPC calculated from the concentration of SCMHC was essentially constant with hydrolysis time, as was the ratio of ε-Ahx to OMPC (Figure 1), even though a standard of SCMHC was shown to degrade at hydrolysis times longer than 20 h. Interestingly, for the conjugate sample that was prepared from

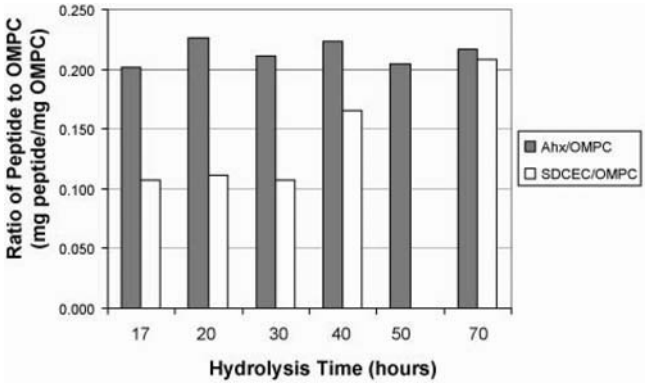

Figure 2. A conjugate prepared from a cysteine containing peptide and maleimide-activated OMPC was hydrolyzed at 110 °C for between 17.5 and 70 h. The hydrolyzates were derivatized with AQC and analyzed by RP-HPLC. The ratio of peptide to OMPC was then calculated from either the amount of ε-Ahx linker or the amount of SDCEC.

maleimide-activated OMPC, 70 h of hydrolysis at 110 °C was required to obtain maximal recovery of SDCEC (Figure 2). The need for extended hydrolysis times in order to quantitatively recover SDCEC from thiol–maleimide adducts has been previously demonstrated (*23*).

DISCUSSION

Amino acid analysis provided a reliable means for assessing the covalent attachment of peptide to carrier protein because acid hydrolysis of the nascent conjugate bonds generates novel amino acids such as SDCEC or SCMHC, depending on the choice of chemistry used. The total amount of peptide in the complex can also be quantified by monitoring the concentration of a unique peptide-specific component, such as the ε-Ahx linker described here. In the current report, ratios of peptide to OMPC carrier protein were calculated using both methods, with equivalent results. Of the methods for calculating the peptide content of the conjugate, only measurement of the unique amino acid formed upon hydrolysis of the conjugate bond provides conclusive evidence of the covalent attachment of the peptide to the protein. Incomplete removal of aggregated peptide from OMPC conjugate samples during dialysis can lead to overestimation of the amount of peptide incorporated into the carrier when this ratio is calculated using either the LSA approach or the quantitation of ε-Ahx.

Importantly, our results clearly demonstrate that optimization of the hydrolysis conditions used for amino acid analysis is critical to obtaining consistent and accurate results when utilizing unique amino acid residues. In our hands, ε-Ahx was quantitatively recovered following the hydrolysis of peptide–OMPC conjugates under relatively standard conditions (15–20 h), whereas a more extensive hydrolysis time of 70 h was required for SDCEC. In contrast, SCMHC was recovered quantitatively in hydrolysates prepared at 20 h, and the ratio of SCMHC to OMPC did not change significantly with longer hydrolysis times. Our observations, to a large degree, are likely related to the complex nature of a multicomponent lipoprotein carrier such as OMPC, and the results of a similar comparison may be quite different for peptides coupled to a soluble monomeric protein carrier such as bovine serum albumin, even when employing the same conjugation chemistries. These differences exemplify the requirement for rigorous optimization of experimental parameters when seeking to employ these quantitative methods in a reliable and reproducible manner.

ACKNOWLEDGMENT

We thank Jay Gambee at AAA Service Laboratory, Inc. for performing amino acid analysis, Chengwei Wu for peptide synthesis, and Dr. Craig Przysiecki for providing unique amino acid standards.

Supporting Information Available: Hydrolysis time course of amino acid standards, RP-HPLC chromatogram of amino acid standards, and HPAE-PAD chromatogram of amino acid standards. This information is available free of charge via the Internet at http://pubs.acs.org.

LITERATURE CITED

(1) Fan, J., Liang, X., Horton, M. S., Perry, H. C., Citron, M. P., Heidecker, G. J., Fu, T.-M., Joyce, J., Przysiecki, C. T., Keller, P. M., Garsky, V. M., Ionescu, R., Rippeon, Y., Shi, L., Chastain, M. A., Condra, J. H., Davies, M.-E., Liao, J., Emini, E. A., and Shiver, J. W. (2004) Preclinical study of influenza virus A M2 peptide conjugate vaccines in mice, ferrets, and rhesus monkeys. *Vaccine 22*, 2993–3003.

(2) Girard, M. P., Preziosi, M. P., Aguado, M. T., and Kieny, M. P. (2006) A review of vaccine research and development: meningococcal disease. *Vaccine 24*, 4692–4700.

(3) Hatsukami, D. K., Rennard, S., Jorenby, D., Fiore, M., Koopmeiners, J., de Vos, A., Horwith, G., and Pentel, P. R. (2005) Safety and immunogenicity of a nicotine conjugate vaccine in current smokers. *Clin. Pharmacol. Ther. 78*, 456–467.

(4) Pérez-Melgosa, M., Ochs, H. D., Linsley, P. S., Laman, J. D., van Meurs, M., Flavell, R. A., Ernst, R. K., Miller, S. I., and Wilson, C. B. (2001) Carrier-mediated enhancement of cognate T cell help: the basis for enhanced immunogenicity of meningococcal outer membrane protein polysaccharide conjugate vaccine. *Eur. J. Immunol. 31*, 2373–2381.

(5) El Bashir, H., Heath, P. T., Papa, T., Ruggeberg, J. U., Johnson, N., Sinha, R., Balfour, G., and Booy, R. (2006) Antibody responses to meningococcal (groups A, C, Y and W135) polysaccharide diphtheria toxoid conjugate vaccine in children who previously received meningococcal C conjugate vaccine. *Vaccine 24*, 2544–2549.

(6) Donnelly, J. J., Deck, R. R., and Liu, M. A. (1990) Immunogenicity of a *Haemophilus influenzae* polysaccharide-*Neisseria meningitidis* outer membrane protein complex conjugate vaccine. *J. Immunol. 145*, 3071–3079.

(7) Bianchi, E., Liang, X., Ingallinella, P., Finotto, M., Chastain, M. A., Fan, J., Fu, T. M., Song, H. C., Horton, M. S., Freed, D. C., Manger, W., Wen, E., Shi, L., Ionescu, R., Price, C., Wenger, M., Emini, E. A., Cortese, R., Ciliberto, G., Shiver, J. W., and Pessi, A. (2005) Universal influenza B vaccine based on the maturational cleavage site of the hemagglutinin precursor. *J. Virol. 79*, 7380–7388.

(8) Joyce, J., Cook, J., Chabot, D., Hepler, R., Shoop, W., Xu, Q., Stambaugh, T., Aste-Amezaga, M., Wang, S., Indrawati, L., Bruner, M., Friedlander, A., Keller, P., and Caulfield, M. (2006) Immunogenicity and protective efficacy of *Bacillus anthracis* poly-gamma-D-glutamic acid capsule covalently coupled to a protein carrier using a novel triazine-based conjugation strategy. *J. Biol. Chem. 281*, 4831–4843.

(9) Lindberg, A. A. (1999) Glycoprotein conjugate vaccines. *Vaccine 17*, S28–S36.

(10) Liu, M. A., Friedman, A., Oliff, A. I., Tai, J., Martinez, D., Deck, R. R., Shieh, J. T., Jenkins, T. D., Donnelly, J. J., and Hawe, L. A. (1992) A vaccine carrier derived from + with mitogenic activity for lymphocytes. *Proc. Natl. Acad. Sci. U.S.A. 89*, 4633–4637.

(11) Massari, P., Henneke, P., Ho, Y., Latz, E., Golenbock, D. T., and Wetzler, L. M. (2002) Cutting edge: immune stimulation by neisserial porins is toll-like receptor 2 and MyD88 dependent. *J. Immunol. 168*, 1533–1537.

(12) Shuler, K. R., Dunham, R. G., and Kanda, P. (1992) A simplified method for determination of peptide-protein molar ratios using amino acid analysis. *J. Immunol. Methods 156*, 137–149.

(13) Tsao, J. L., Lin, X., Lackland, H., Tous, G., Wu, Y. L., and Stein, S. (1991) Internally standardized amino acid analysis for determining peptide/carrier protein coupling ratio. *Anal. Biochem. 197*, 137–142.

(14) Marburg, S., Jorn, D., Tolman, R. L., Arison, B., McCauley, J., Kniskern, P. J., Hagopian, A., and Vella, P. P. (1986) Bimolecular chemistry of macromolecules: synthesis of bacterial polysaccharide conjugates with *Neisseria meningitidis* membrane protein. *J. Am. Chem. Soc. 108*, 5282–5287.

(15) Millipore Corporation (1993) *Waters AccQTag Chemistry Package Instruction Manual*, Manual Number WAT052874, Millipore Corporation, Milford, PA.

(16) Cohen, S. A. (2003) Amino acid analysis using pre-column derivatization with 6-aminoquinolyl-N-hydroxysuccinimidyl carbamate. Analysis of hydrolyzed proteins and electroblotted samples. *Methods Mol. Biol. 211*, 143–154.

(17) Cohen, S. A. (2000) Amino acid analysis using precolumn derivatization with 6-aminoquinolyl-N-hydroxysuccinimidyl carbamate. *Methods Mol. Biol. 159*, 39–47.

(18) De Antonis, K. M., Brown, P. R., and Cohen, S. A. (1994) High-performance liquid chromatographic analysis of synthetic peptides using derivatization with 6-aminoquinolyl-*N*-hydroxysuccinimidyl carbamate. *Anal. Biochem. 223*, 191–197.

(19) Strydom, D. J., and Cohen, S. A. (1994) Comparison of amino acid analyses by phenylisothiocyanate and 6-aminoquinolyl-n-hydroxysuccinimidyl carbamate precolumn derivatization. *Anal. Biochem. 222*, 19–28.

(20) Clarke, A. P., Jandik, P., Rocklin, R. D., Liu, Y., and Avdalovic, N. (1999) An integrated amperometry waveform for the direct, sensitive detection of amino acids and amino sugars following anion-exchange chromatography. *Anal. Chem. 71*, 2774–2781.

(21) Yu, H., Ding, Y.-S., and Mou, S.-F. (2003) Some factors affecting separation and detection of amino acids by high-performance anion-exchange chromatography with integrated pulsed amperometric detection. *J. Chromatogr. A 997*, 145–153.

(22) Lowry, O. H., Rosebrough, N. J., Farr, A. L., and Randall, R. J. (1951) Protein measurement with the folin phenol reagent. *J. Biol. Chem. 193*, 265–275.

(23) Smyth, D. J., Blumenfield, O. O., and Konigsberg, W. (1964) Reactions of N-ethylmaleimide with peptides and amino acids. *Biochem. J. 91*, 589–595.

BC700232Z

Rapid DNA Chemical Ligation for Amplification of RNA and DNA Signal

Hiroshi Abe,*,† Yuko Kondo,†,‡ Hiroshi Jinmei,† Naoko Abe,† Kazuhiro Furukawa,†,§ Atsushi Uchiyama,†,§ Satoshi Tsuneda,§ Kyoko Aikawa,‡ Isamu Matsumoto,‡ and Yoshihiro Ito*,†

Nano Medical Engineering Laboratory, Discovery Research Institute, RIKEN, 2-1, Hirosawa, Wako-Shi, Saitama, 351-0198 Japan, Department of Chemistry, Faculty of Science, Ochanomizu University, 2-1-1 Otsuka, Bunkyo-ku, Tokyo 112-8610, Japan, and Department of Life Science and Medical Bio-Science, Waseda University, 3-4-1 Ohkubo, Shinjuku-ku, Tokyo 169-8555, Japan. Received July 3, 2007; Revised Manuscript Received September 17, 2007

Enzymatic ligation methods are useful in the diagnostic detection of DNA sequences. Here, we describe the investigation of nonenzymatic phosphorothioate−iodoacetyl DNA chemical ligation as a method for the detection and identification of RNA and DNA. The specificity of ligation on the DNA target is shown to allow the discrimination of a single point mutation with a drop in the ligation yield of up to 16.1-fold. Although enzymatic ligation has very low activity for RNA targets, this reaction is very efficient for RNA targets. The speed of the chemical ligation with an RNA target achieves a 70% yield in 5 s, which is equal to or better than that of ligase-enzyme-mediated ligation with a DNA target. The reaction also exhibits a significant level of signal amplification under thermal cycling in periods as short as 100–120 min, with the RNA or DNA target acting in a catalytic way to ligate multiple pairs of probes.

INTRODUCTION

Much work has been carried out recently to develop molecular strategies for sensing nucleic acid sequences and distinguishing single nucleotide differences (*1–3*). Enzymatic methods are one of the most common strategies in current use (*4–6*). cDNAs treated with PCR-based amplification are analyzed with these methods. Of the enzymes used, DNA ligases such as T4 and T*th* are quite sensitive to base mismatches and can amplify DNA signals under thermal cycling conditions, in the ligase chain reaction (LCR) (*7, 8*). Although they are quite useful, enzymatic ligation methods for sequence detection also have some limitations. For example, ligases have low activities for RNAs (*9*). Furthermore, although very short probes have the highest sequence specificity, ligase enzymes are inefficient with short oligonucleotides (*10*).

As a result, the consideration of alternatives to enzymatic methods, such as those involving ligases, seems justified for some applications. DNA template chemical ligation might be one candidate for a general approach to the detection of oligonucleotides (*11, 12*). Removing the need for an enzyme can lower the cost, and RNA samples can be targeted directly without reverse transcription to the corresponding cDNA. A number of ligation chemistries have been developed (*13–16*). Some methods require the addition of ligating reagents to the oligonucleotide probes. Autoligation chemistries that do not require added reagent are even simpler for these applications. Photochemical ligation (*17, 18*) or 1,3-dipolor cycloaddition (*19*) on a DNA template, and also ligation based on the nucleophilic displacement of the sulfur on the bromoacetyl (*20, 21*), maleimide (*22*), tosyl (*23, 24*), or iodo nucleoside groups (*25, 26*). have been reported. Among these strategies, the chemical reaction between the phosphorothioate and the bromoacetyl group offers the fastest ligation, within 20 min (*27*). However, it is still slower than the ligase enzymatic reaction, which is completed within 2 min in the LCR method. A faster chemical ligation reaction must be developed to achieve thermal cycling amplification.

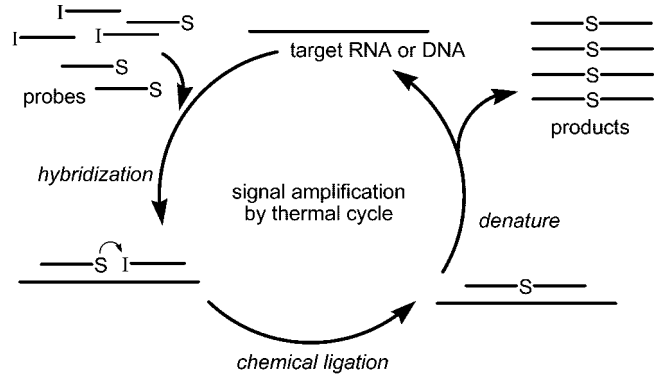

Figure 1. Signal amplification by multiple chemical ligations. The reaction is carried out in a thermal cycler instrument designed for PCR. DNA probes bind to the DNA or RNA target, and ligate together. After this step, the reaction mixture is heated to promote the dissociation of the ligated products from the target. The reaction then proceeds to the second round.

Here, we describe a chemical ligation using a pair of phosphorothioate and iodoacetyl groups. The reaction is almost complete within 60 s and achieves a turnover under thermal cycling conditions (Figure 1). The chemistry was applied to single-base discrimination and direct RNA sensing with signal amplification.

EXPERIMENTAL PROCEDURES

Preparation of Probes and Target. DNA and RNA oligonucleotides were synthesized on a 0.2 μmol scale on a Gene World (Tokyo, Japan) H-8 DNA synthesizer using standard β-cyanoethylphosphoramidite coupling chemistry. Phosphorylation was carried out using Phosphate-ON reagent from Glen Research (Sterling, VA). For the 3′-phosphorothioate sequence,

* H.A. e-mail h-abe@riken.jp. Y.I. e-mail y-ito@riken.jp. Nano Medical Engineering Laboratory, Discovery Research Institute, RIKEN, 2-1, Hirosawa, Wako-Shi, Saitama, 351-0198 Japan; TEL +81-(0)48-467-9303; FAX +81-(0)48-467-9300.

† RIKEN.

‡ Ochanomizu University.

§ Waseda University.

10.1021/bc700244s CCC: $40.75 © 2008 American Chemical Society
Published on Web 11/09/2007

the first nucleotide added on 3′-phosphate CPG column (Glen Research) was sulfurized with a sulfurizing reagent (Glen Research), and further synthesis was carried out according to normal protocol. For the 5′-amino-dT sequence, after normal DNA synthesis, 5′-amino-dT phosphoroamidite (Glen Research) was attached on the oligonucleotides at the last step. The oligonucleotides were treated with concentrated ammonia for 4 h at 55 °C and purified on a Sep-Pak column and then by reversed-phase high-performance liquid chromatography (HPLC; 0−30% acetonitrile/50 mM triethylammonium acetate buffer). To incorporate the iodoacetyl group, 100 nmol of the 5′-amino-dT sequence in 500 μL of 0.075 M sodium tetraborate (pH 8.5) was incubated for 10 m at room temperature with 4 μmol of *N*-succinimidyl iodoacetate (Sigma-Aldrich) in 375 μL of DMF. The probes were purified by reversed-phase HPLC (0−30% acetonitrile/50 mM TEAA buffer). The probe structures were analyzed by MALDI-TOF mass spectrometry. Iodoacetyl probe (8-mer): Calcd mass $C_{80}H_{101}IN_{31}O_{47}P_7$, 2591.37(MH+); found 2592.38.

Ligation Reaction. To trace the reaction, the phosphorothioate probe was labeled with ^{32}P isotope at the 5′ terminus using T4 polynucleotide kinase (Roche) and γ-^{32}P-ATP. The reaction was carried out with 1 μM probe and target concentrations in Tris−borate buffer (pH 8.0) containing 10 mM $MgCl_2$ and 10 mM DTT at 25 °C. To stop the reaction, 90% formamide loading buffer was added to the reaction mixture. The reactions were analyzed by 20% denaturing polyacrylamide gel electrophoresis using a 0.35 mm thick gel (length 40 cm), in Tris−borate−EDTA buffer, with electrophoresis at 30 W for 1.5 h. The radioactive ligation bands were visualized and quantitated with a BAS-2000 image analyzer (Fuji Film, Japan). The templated ligation signal was calculated with the subtraction of the background signal without target.

Turnover Experiments. Experiments were carried out on the com-DNA target or com-RNA target using a ^{32}P-labeled 6-mer phosphorothioate probe and an 8-mer iodoacetyl probe. For each equivalent of target strand, 1–1000 equiv of probe were present, with a target concentration of 1–1000 nM. Reactions were performed under the following cycling conditions using a thermal cycler designed for PCR: DNA target (55 cycles for 2 h), chemical ligation step at 25 °C for 120 s and denaturation step at 55 °C for 15 s; RNA target (99 cycles for 100 min), chemical ligation step at 30 °C for 10 s and denaturation step at 60 °C for 10 s. The reactions were then analyzed by denaturing gel electrophoresis. Turnover number is given as equivalents of radioactive signal per mole of target strand.

Thermal Denaturation. Solutions of 2.0 μM DNA were prepared as 600 μL samples in melt buffer (10 mM $MgCl_2$ in 70 mM Tris−borate buffer, pH = 7.0). The melting studies were carried out in Teflon-stoppered 1 cm path length quartz cells under nitrogen atmosphere on a JASCO V-550 UV–vis spectrophotometer equipped with a Peltier temperature controller. Absorbance was monitored at 260 nm, while temperature was increased from 10 to 90 °C at a rate of 1.0 °C/min. In all cases, the complexes displayed sharp, apparently two-state transitions.

RESULTS

Design and Synthesis of Chemical Ligation Probes. We chose the iodoacetyl group and the phosphorothioate group for ligation probes, because these functional groups are most reactive and seem to offer the best ligation rate (Figure 2). *N*-Succinimidyl iodoacetate was reacted with the 5′-amino group of the DNA probe to prepare an electrophilic iodoacetyl probe (*21*). The 3′-phosphorothioate probe was prepared according to the procedure reported previously (*25*). The ligated product has an extra linker consisting of acetamide, compared with the native

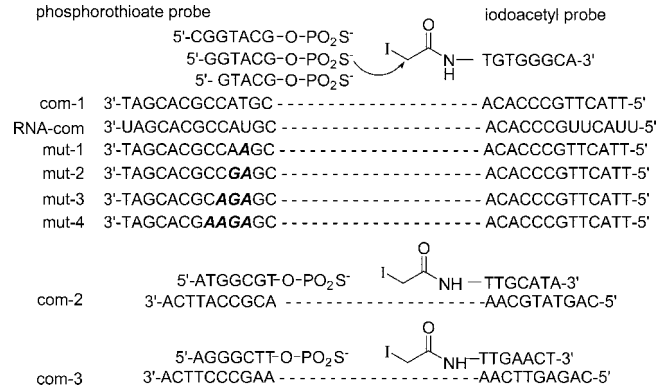

Figure 2. Structures and sequences of the DNA probes and targets. Chemical ligation proceeds, involving the S_N2 reaction between the phosphorothioate probe and iodoacetyl probe, on a DNA or RNA template. The phosphorothioate probe was designed to be a 5-mer, 6-mer, or 7-mer, and the iodoacetyl probe to be an 8-mer; these are complementary to the com-1 or RNA−com target. A series of mutant targets was also designed, such that mut-1−mut-4 had mismatches of 1–4 bases, respectively. The phosphorothioate probes and iodoacetyl probes were also designed to be 7-mers and are complementary to the com-2 or com-3 target.

DNA strand. Letsinger reported that the linker does not destabilize the resulting double strand (*20*), so thermal cycling to dissociate the ligated products from the target strand is required to achieve multiple turnovers (Figure 1). Relatively short probes were designed for high sequence selectivity and to minimize product inhibition. For the com-1 target, the iodoacetyl probe was designed as an 8-mer and the length of the phosphorothioate probe varied from a 5-mer to a 7-mer. Com-1 and RNA−com-1 were fully complementary to the probes, and the mutated DNAs, mut-1−mut-4, had a mismatch of from one to four bases, respectively, relative to the phosphorothioate probe. The iodoacetyl probe and phosphorothioate probe for the com-2 target were also designed as 7-mers. The com-3 target sequence is a junction site of the *bcr*/*abl* gene translocation between chromosomes 9 and 22, which is seen in about 20% of patients with acute lymphoblastic leukemia (*28*). Thus, detection of the *bcr*/*abl* gene is very important for clinical applications. Probes for the com-3 target were designed as 7-mers.

Ligation to DNA and RNA Templates. To optimize the ligation rate, we tested a series of phosphorothioate probes: 5-mer, 6-mer, or 7-mer. A synthetic 26-mer DNA (com-1) was used as the target sequence. Ligations were carried out at 25 °C with 1.5 μM iodoacetyl probe, 1.0 μM phosphorothioate, and 1.0 μM com-1, in a Tris−borate buffer (pH 8.0) containing 10 mM Mg^{2+}. The phosphorothioate probe was labeled at the 5′ terminus with ^{31}P for the trace. The reactions were stopped by the addition of 80% formamide solution, followed by 20% polyacrylamide gel electrophoretic analysis.

The initial slopes of the product yields were measured as a function of time. The 6-mer phosphorothioate probe produced the fastest ligation rate of 24% yield per 15 s compared with that of the 7-mer (20% per 15 s) and the 5-mer (2% per 15 s) (Figure 3A). The temperature of the ligation reaction was varied from 15 to 55 °C to determine the optimal temperature (Figure 3B). In the temperature range 15−35 °C, the 6-mer probe showed a better yield than did the 5-mer or 7-mer probes. Ligation of the 6-mer probe produced its best yield at 25 °C. Therefore, we considered the best temperature for the ligation reaction to be 25 °C and used the 6-mer probe for further experiments, because the shorter 6-mer probe offers higher selectivity in mismatch discrimination than the 7-mer probe.

To investigate the differences in ligation between an RNA target and a DNA target, we prepared a synthetic 26-mer RNA

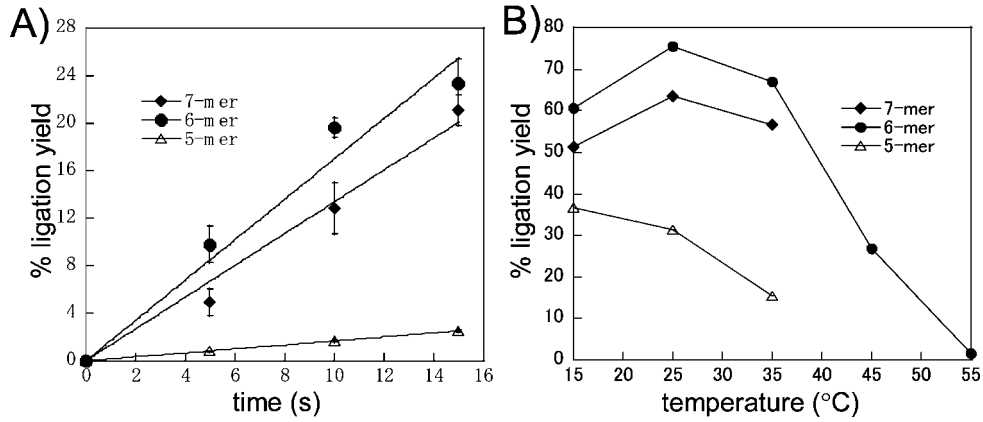

Figure 3. Effects of probe length and temperature on the ligation reaction. (A) Comparison of the initial ligation rates of the 5-mer, 6-mer, and 7-mer phosphorothioate probes for 15 s. (B) Comparison of the effects of temperature on ligation yield for 5 min with the 5-mer, 6-mer, and 7-mer phosphorothioate probes. The reaction was performed under the following conditions: iodoacetyl probe (1.5 μM), phosphorothioate probe (1.0 μM), com−DNA (1.0 μM) in 70 mM Tris−borate buffer (pH 7.0) containing $MgCl_2$ (10 mM) and DTT (1 mM).

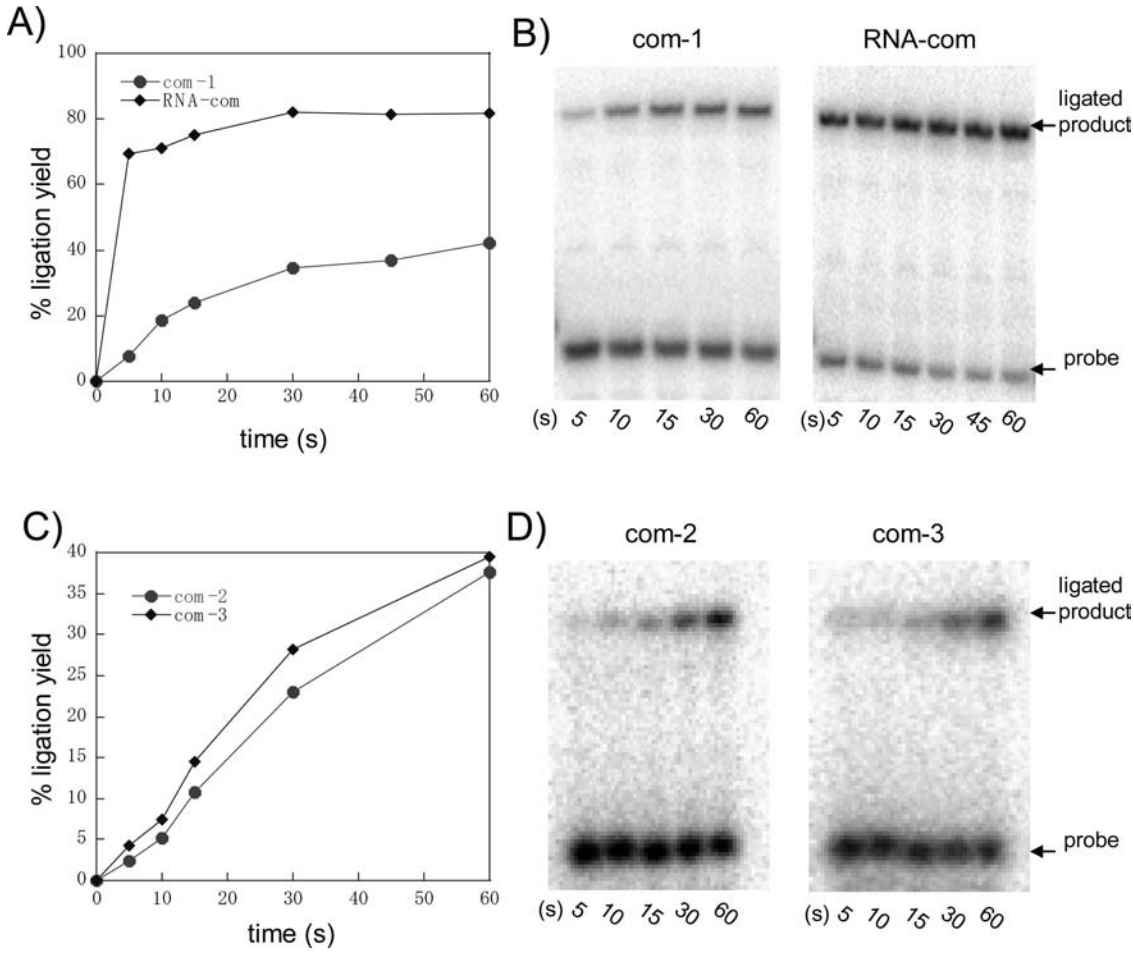

Figure 4. Comparison of the ligation reactions using RNA target or DNA targets. The reaction was performed under the same conditions described for Figure 3, with RNA−com or com-1 as the target. The reactions for the com-2 and com-3 targets were also performed. (A) Time course of the ligation reaction for 60 s with com-1 (circle) and RNA−com (diamond). (B) 20% gel electrophoretic analysis of the ligation reactions in the com-1 or RNA−com target. Phosphorothioate probe was labeled with ^{32}P for the trace. (C) Time course of the ligation reaction for 60 s with com-2 (circle) and com-3 (diamond). (D) 20% gel electrophoretic analysis of the ligation reaction of the com-2 or com-3 target.

target (RNA−com) corresponding to DNA com-1, and performed the ligation reaction (Figure 4A). The reaction took place over a period of 60 s on com-1, reaching a 40% yield. Significantly, the reaction on RNA−com occurred roughly seven times faster in the initial stage than that on com-1, reaching a 70% yield in 5 s, and plateauing at an 80% yield after 30 s. Com-2 DNA and com-3 DNA showed moderate reaction rates with a 37% yield in 60 s and a 40% yield in 60 s, respectively (Figure 4C,D).

Thermal Stability of Probes and Ligated Products. It is important to know the melting temperatures (T_m) between probes and the target DNA or between the corresponding ligated product and the target DNA to optimize the ligation reactions and thermal cycling conditions, because the ligation reaction

Table 1. Melting Temperatures of Probes and Ligation Products[a]

	com-1	com-2	com-3
probe	37.2	38.4	34.8
ligation product	67.8	61.6	61.9

[a] Probes or ligated products were tested for their binding to the target DNAs com-1, com-2, and com-3. Conditions: 5.0 μM oligonucleotide, 10 mM $MgCl_2$ in 70 mM Tris−borate buffer (pH 7.0).

proceeds well at temperatures below the T_m of the probe, whereas thermal cycling conditions require temperatures higher than the T_m of the ligated product in the denaturing step to overcome product inhibition. To evaluate the T_m, we synthesized a series of DNA sequences corresponding to the probes and ligated products. Native DNA structures were used for T_m measurements instead of the iodoacetyl probe or ligated product with a thio-acetamide linkage. The resulting melting curves and T_m values are shown in Supporting Information Figure S1 and Table 1, respectively. In the case of probes, both the phosphorothioate probe and DNA probe which corresponds to the iodoacetyl probe were mixed together before the measurement of the T_m. The T_m values of the probes for com-1, com-2, and com-3 were 37.2, 38.4, and 34.8 °C, respectively. The T_m of the ligated products was higher for com-1 (67.8 °C) than for com-2 (61.6 °C) or com-3 (61.9 °C).

Discrimination of Mismatches. To investigate the ability of the process in sequence discrimination, we tested the ligation reaction with a series of mutant targets, mut-1−mut-4. At first, the reaction was performed at 25 °C for 5 min (Figure 5A). Mut-1, with a single base difference, gave a 37% product yield, equivalent to one-half the yield achieved with the com-1 target. Very small amounts of product were observed after the ligation reactions with mut-2 and mut-3, which have two and three base mutations, respectively. The mut-4 target showed the same level of signal as the reaction without target DNA. To achieve higher selectivity in single-base discrimination, the ligation reaction was tested at various temperatures (Figure 5B). The results show the ratio of ligation yield achieved with com-1 to that with mut-1. The lowest selectivity of 1.41 was observed at 15 °C. The selectivity increased with increasing temperature, reaching a maximum of 16.3 at 45 °C, and dropping off to 9.0 at 55 °C. Thus, we conclude that high sequence selectivity can be achieved by controlling the reaction temperature.

Signal Amplification under Thermal Cycling Conditions. DNA templates have been observed in some cases to facilitate the ligation of multiple equivalents of ligating strands, by dissociation of the ligated product followed by the binding and ligation of a new pair of ligating strands (Figure 1). This turnover is commonly inhibited when the binding of the product to the template is favored over the binding of the unligated strands to the template. To overcome this product inhibition, thermal cycling conditions were used for the ligase-enzyme-mediated ligation to achieve multiple turnovers. (*7*) This should be valuable in possible diagnostic applications, because one target would produce more than one ligated signal. Iodoacetyl−phosphorothioate probe pairs offer very rapid ligation, equal to the ligation achieved with ligase enzyme, and the reaction also accepts an RNA template, which the ligase enzyme cannot. This suggests the possibility of turnover under thermal cycling conditions.

Turnover, and the associated signal amplification, is useful when target concentrations are low. Under these conditions, one would typically use a large excess of probes relative to the number of targets. To measure turnover with the current probes, we compared the number of equivalents of signal to moles of target. This required the development of a method of carefully quantitating the signal, and confirming that the signal arises from true template-dependent intermolecular ligation reactions rather than from background sources, such as intermolecular ligation independent of the target strand. To evaluate this, we performed ligations using a radiolabeled phosphorothioate probe at various target concentrations, and we separated the products from excess unreacted probes by gel electrophoresis. The radioactivity in the ligated product bands was quantitated by digital phosphorimaging. We first prepared a standard dilution curve to make a ^{32}P-labeled phosphorothioate oligonucleotides in a gel lane. This plot showed good linearity and allowed us to take a given signal and, from the plot, determine the number of moles of radioactive oligonucleotide product in a given band on the gel (*29*).

We carried out a ligation reaction using 1–1000 equiv of probe per equivalent of DNA or RNA target strand, and investigated the yields of ligated product as a function of target concentrations in the range 1–1000 nM. This was performed with the same synthetic DNAs: the com-1, com-2, com-3, and RNA−com targets. To determine the optimal cycling conditions, ligation reactions on the DNA target (com-1) were performed in the temperature range from 15 to 55 °C with the 6-mer phosphorothioate probe (Figure 3B). Efficient ligation occurred at 25 °C and less efficient ligation at temperatures higher than 45 °C, because the probes dissociated from the target at temperatures higher than the T_m (37.2 °C). The double strand between the ligated product and com-1 had a T_m of 67.8 °C

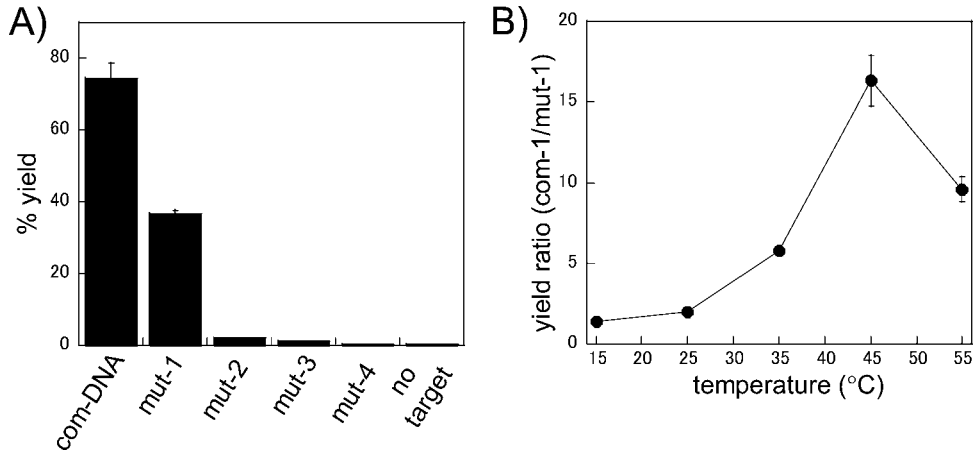

Figure 5. Effect of mutant target and temperature on the ligation reaction. (A) Comparison of ligation yield with various mutant targets. Ligations were performed with mutant targets mut-1−mut-4 or with no target, under the following conditions: iodoacetyl probe, 1.5 μM; 6-mer phosphorothioate probe 1.0 μM; target DNA, 1.0 μM at 25 °C for 5 min. (B) Effects of temperature on the discrimination of a single base difference. The ratio of com−DNA yield to mut-1 yield was calculated for each temperature.

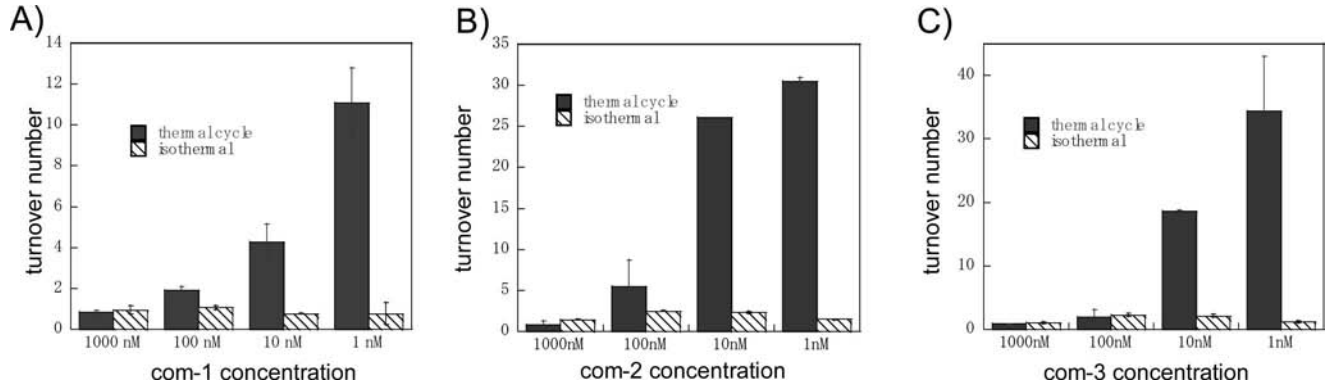

Figure 6. Effects of target DNA concentration and temperature on turnover. Turnover number is given in equivalents of radioactive signal per mole of target DNA. The concentration of the target DNA was varied from 1000, 100, 10, to 1 nM in 70 mM Tris−borate buffer (pH 7.0) containing 1.5 μM iodoacetyl probe, 1.0 μM phosphorothioate probe, 10 mM $MgCl_2$, and 1 mM DTT. Thermal cycling conditions were as follows: ligation at 25 °C for 120 s and denaturation 55 °C for 15 s (55 cycles for 120 min). Isothermal conditions were 25 °C for 120 min. The reactions were analyzed by 20% polyacrylamide gel electrophoresis. (A) com-1 target. (B) com-2 target. (C) com-3 target. The reactions were repeated at least twice, and the data were averaged. Error bars show standard deviations.

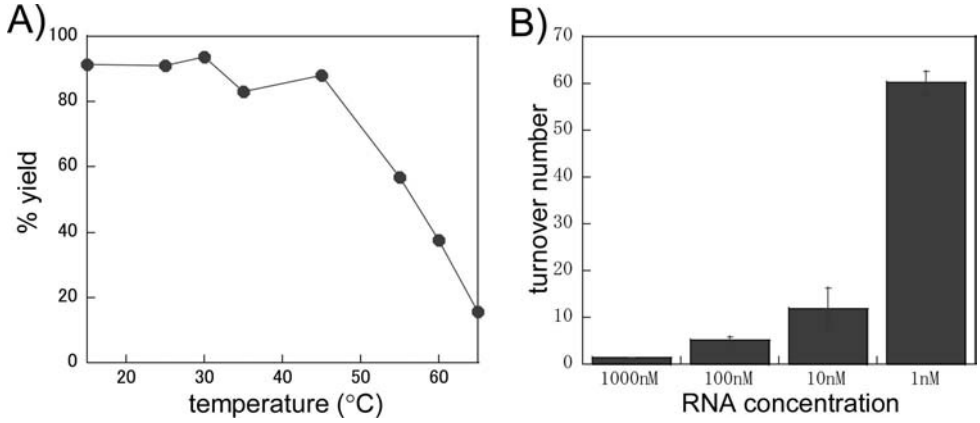

Figure 7. Effects of temperature and target RNA concentration on turnover. Turnover number is given as equivalents of radioactive signal per mole of target RNA. The concentration of the RNA−com was varied from 1000, 100, 10, to 1 nM in 70 mM Tris−borate buffer (pH 7.0) containing 1.5 μM iodoacetyl probe, 1.0 μM phosphorothioate probe, 10 mM $MgCl_2$, and 1 mM DTT. Thermal cycling conditions were ligation at 30 °C for 10 s and denaturation at 60 °C for 10 s (100 cycles for 100 min).

when the concentration of the DNA double strand was 5 μM. Although it is important to know the T_m of the ligated product to determine the temperature of the denaturation step in the thermal cycle, the target concentration is different from that under the actual experimental conditions, which achieve the best turnover number, when 1 nM target DNA is used against excess probe (1 μM). The actual T_m value must be lower than 67.8 °C. Moreover, the iodoacetyl probe is unstable at higher temperatures because of hydrolysis. Therefore, we used a temperature of 55 °C for the denaturation step, which is slightly lower than the experimental T_m. The thermal cycling conditions for the com-1 target were as follows: chemical ligation step at 25 °C for 120 s, denaturation step at 55 °C for 15 s (55 cycles for 120 min). There was significant turnover at the lower target concentrations (Figure 6A). The turnover number increased at the lower target concentrations. We observed eleven turnovers at the lowest concentration of the com-1 target (1 nM) under thermal cycling conditions for 120 min. In contrast, there was no significant turnover without thermal cycling (isothermal at 25 °C), even at the lowest concentration. Other DNA sequences were also tested under these thermal cycling conditions. The same thermal cycling conditions as those used for com-1 were used for the com-2 and com-3 targets. The results are shown in Figure 6B, C. Again, a significant turnover number was observed under these thermal cycling conditions and a low turnover number under isothermal conditions. Higher turnover numbers were observed at lower target concentrations. The high turnover numbers were 30 for the com-2 target and 35 for the com-3 target, when the target concentration was 1 nM.

Next, we performed ligation reactions with the RNA−com target, which corresponds to the DNA com-1 target. To determine the optimal cycling conditions for the RNA target, the ligation reactions were tested in the temperature range 15−65 °C for 5 min (Figure 7A). No significant change was seen in the conversion yield from 15 to 45 °C. However, the conversion yield decreased at temperatures higher than 55 °C, because of the dissociation of the probes. Furthermore, ligation with the RNA target was 70% complete within 5 s (Figure 4A). Thus, the following thermal cycling conditions were used to amplify the com−RNA target: chemical ligation step at 30 °C for 10 s, denaturation step at 60 °C for 10 s (99 cycles for 100 min). The turnover was more efficient than that achieved with the DNA target. Similarly, as with the DNA target, the turnover number increased at the lower target concentrations. The maximum turnover number of 60.1 was observed at the lowest target concentration under thermal cycling for 100 min (Figure 7).

DISCUSSION

The iodoacetyl-phosphorothioate probes described here allow very rapid reactions. Ligation with the DNA target proceeded to a 10% yield in 5 s. Notably, the RNA target allows a substantial increase in the ligation rate over that of the DNA

target, reaching a 70% yield in 5 s. One reason for the rate enhancement on the RNA target is presumably the thermal stability of the RNA−DNA double strand, which is more stable than the DNA−DNA double strand. This tendency is shown in Figure 3B and Figure 7A, in which the ligation reaction with the RNA target gives a better yield, even at higher temperatures (>45 °C), than the reaction with the DNA target with the 6-mer phosphorothioate probe. The surprising reaction speed can be explained because the iodoacetyl group is the most reactive electrophile and the thioxide anion of the phosphorothioate group is the most reactive nucleophile. We are unaware of any other chemical ligation method with such a rapid reaction rate. This reaction rate is equal to or better than that of ligase-enzyme-mediated ligation, although the DNA ligase enzyme shows very low activity for RNA targets (*9*).

The present probe shows moderate mismatch selectivity, which is similar or a little worse than that of other chemical ligation methods (*11, 25*). The discrimination of a single base difference was achieved by controlling the reaction temperature. In the case of a T→A point mutation, maximum selectivity was achieved at 45 °C, with a 16-fold drop in ligation yield. This probe could potentially be used to identify DNA or RNA sequences, although further optimization is required.

The amplification of nucleic acid signals should clearly be helpful in detecting RNAs or DNAs at low concentrations or at low copy numbers. Several laboratories have recently investigated strategies for using pairs of modified oligonucleotides to generate amplified products or signals under isothermal conditions. Kool has reported a ligation chemistry with significant amplification using the iodo or dabsyl group as the leaving group (*25, 29*). Seitz has developed peptide nucleic acid (PNA) probes that ligate by native chemical ligation (*30*). Other ligation approaches have been investigated by von Kiedrowski (*31*) and by Lynn (*16*). These approaches use denaturation cycles (unlike thermal cycling) and a separate reagent for turnover, respectively. In another novel approach that does not require ligation, Taylor and Kramer have described the combination of hydrolysis catalysis on one oligonucleotide with a leaving group on the other, resulting in the release of multiple leaving groups for each targeted DNA (*32–34*). Seitz has recently described the transfer of a reporter group from one probe to another probe on the DNA target, resulting in multiple products (*35*). Although all these methods succeed in isothermal amplification, they take a long time (∼24 h) to achieve turnovers, because the reaction rates are relatively slow. In contrast, the current strategy is based on thermal cycling and achieves significant turnovers in a short time (100–120 min) by using a thermal cycler instrument designed for PCR. When RNA is targeted, 60.1 turnovers were achieved in 100 min. The very rapid chemical reaction, similar to the enzymatic reaction, makes this strategy possible.

There are numerous enzymatic amplification strategies, such as PCR and RT-PCR, for genetic detection. In the PCR methods, the signal is amplified exponentially. Conversely, the current method amplifies the signal linearly. Therefore, our method is inferior to PCR in terms of turnover and sensitivity. However, PCR cannot directly detect target RNA. Although the RNA signal can be amplified and detected by RT-PCR, this method is time-consuming (RT-PCR usually requires 3–4 h) and consists of several amplification steps that require cumbersome procedures to prevent carryover contamination. Therefore, the chemical ligation method has some advantages in genetic detection compared with PCR-based detection. Furthermore, the chemical ligation probes can be readily modified with fluorescent dyes to make the signal detectable.

CONCLUSION

The present study demonstrates a very rapid chemical ligation method that amplifies a DNA or RNA signal. The method uses commercially available thermal cyclers designed for PCR for amplification and uses cycling condition similar to those used in the LCR method. A few femtomoles of RNA were detected using a radioisotope-labeled probe under thermal cycling conditions. Discrimination of a single base difference was achieved with a 16.1-fold drop in the ligation yield, although this technique still requires optimization. Ongoing work will be aimed at developing a dye-labeled probe for detecting RNA in real time.

ACKNOWLEDGMENT

H.A. was financially supported by the Riken Directors' Fund, MEXT (Ministry of Education, Culture, Sports, Science, and Technology), and NEDO (New Energy and Industrial Technology Development Organization). Y.I. was supported by Grant-in-Aid for Scientific Research on Priority Areas "Lifesurveyor" from MEXT.

Supporting Information Available: Melting curves of probes and ligation products. This material is available free of charge via the internet at http://pubs.acs.org.

LITERATURE CITED

(1) Kwok, P. Y. (2001) Methods for genotyping single nucleotide polymorphisms. *Annu. Rev. Genomics Hum. Genet. 2*, 235–258.
(2) Shi, M. M. (2001) Enabling large-scale pharmacogenetic studies by high-throughput mutation detection and genotyping technologies. *Clin. Chem. 47*, 164–172.
(3) Chen, X., and Sullivan, P. F. (2003) Single nucleotide polymorphism genotyping: biochemistry, protocol, cost and throughput. *Pharmacogenomics J. 3*, 77–96.
(4) Whitcombe, D., Theaker, J., Guy, S. P., Brown, T., and Little, S. (1999) Detection of PCR products using self-probing amplicons and fluorescence. *Nat. Biotechnol. 17*, 804–807.
(5) Whitcombe, D., Newton, C. R., and Little, S. (1998) Advances in approaches to DNA-based diagnostics. *Curr. Opin. Biotechnol. 9*, 602–608.
(6) Guo, Z., Liu, Q., and Smith, L. M. (1997) Enhanced discrimination of single nucleotide polymorphisms by artificial mismatch hybridization. *Nat. Biotechnol. 15*, 331–335.
(7) Barany, F. (1991) Genetic disease detection and DNA amplification using cloned thermostable ligase. *Proc. Natl. Acad. Sci. U.S.A. 88*, 189–193.
(8) Wu, D. Y., and Wallace, R. B. (1989) Specificity of the nick-closing activity of bacteriophage T4 DNA ligase. *Gene 76*, 245–54.
(9) Nilsson, M., Barbany, G., Antson, D.-O., Gertow, K., and Landegren, U. (2000) Enhanced detection and distinction of RNA by enzymatic probe ligation. *Nat. Biotechnol. 18*, 791–793.
(10) Favis, R., Day, J. P., Gerry, N. P., Phelan, C., Narod, S., and Barany, F. (2000) Universal DNA array detection of small insertions and deletions in BRCA1 and BRCA2. *Nat. Biotechnol. 18*, 561–564.
(11) Silverman, A. P., and Kool, E. T. (2006) Detecting RNA and DNA with templated chemical reactions. *Chem. Rev. 106*, 3775–3789.
(12) Li, X., and Liu, D. R. (2004) DNA-templated organic synthesis: Nature's strategy for controlling chemical reactivity applied to synthetic molecules. *Angew. Chem., Int. Ed. 43*, 4848–4870.
(13) Luo, P., Leitzel, J. C., Zhan, Z.-Y. J., and Lynn, D. G. (1998) Analysis of the structure and stability of a backbone-modified oligonucleotide: implications for avoiding product inhibition in catalytic template-directed synthesis. *J. Am. Chem. Soc. 120*, 3019–3031.
(14) Sokolova, N. I., Ashirbekova, D. T., Dolinnaya, N. G., and Shabarova, Z. A. (1988) Chemical reactions within DNA

duplexes. Cyanogen bromide as an effective oligodeoxyribonucleotide coupling agent. *FEBS Lett. 232*, 153–155.
(15) Ashley, G. W., and Kushlan, D. M. (1991) Chemical synthesis of oligodeoxynucleotide dumbbells. *Biochemistry 30*, 2927–2933.
(16) Zhan, Z.-Y. J., and Lynn, D. G. (1997) Chemical amplification through template-directed synthesis. *J. Am. Chem. Soc. 119*, 12420–12421.
(17) Liu, J., and Taylor, J.-S. (1998) Template-directed photoligation of oligodeoxyribonucleotides via 4-thiothymidine. *Nucleic Acids Res. 26*, 3300–3304.
(18) Fujimoto, K., Matsuda, S., Takahashi, N., and Saito, I. (2000) Template-directed photoreversible ligation of deoxyoligonucleotides via 5-vinyldeoxyuridine. *J. Am. Chem. Soc. 122*, 5646–5647.
(19) Gartner, Z. J., Kanan, M. W., and Liu, D. R. (2002) Expanding the reaction scope of DNA-templated synthesis. *Angew. Chem., Int. Ed. 41*, 1796–1800.
(20) Gryaznov, S. M., Schultz, R., Chaturvedi, S. K., and Letsinger, R. L. (1994) Enhancement of selectivity in recognition of nucleic acids via chemical autoligation. *Nucleic Acids Res. 22*, 2366–2369.
(21) Gryaznov, S. M., and Letsinger, R. L. (1993) Chemical ligation of oligonucleotides in the presence and absence of a template. *J. Am. Chem. Soc. 115*, 3808–3809.
(22) Gartner, Z. J., and Liu, D. R. (2001) The generality of DNA-templated synthesis as a basis for evolving non-natural small molecules. *J. Am. Chem. Soc. 123*, 6961–6963.
(23) Chladek, S., and Nagyvary, J. (1972) Nucleophilic reactions of some nucleoside phosphorothioates. *J. Am. Chem. Soc. 94*, 2079–2785.
(24) Herrlein, M. K., Nelson, J. S., and Letsinger, R. L. (1995) A covalent lock for self-assembled oligonucleotide conjugates. *J. Am. Chem. Soc. 117*, 10151–10152.
(25) Xu, Y., Karalkar, N. B., and Kool, E. T. (2001) Nonenzymatic autoligation in direct three-color detection of RNA and DNA point mutations. *Nat. Biotechnol. 19*, 148–152.
(26) Xu, Y., and Kool, E. T. (2000) Rapid and selective selenium-mediated autoligation of DNA strands. *J. Am. Chem. Soc. 122*, 9040–9041.
(27) Herrlein, M. K., and Letsinger, R. L. (1994) Selective chemical autoligation on a double-stranded DNA template. *Nucleic Acids Res. 22*, 5076–5078.
(28) Rapozzi, V., and Xodo, L. E. (2004) Efficient silencing of bcr/abl oncogene by single- and double-stranded siRNAs targeted against b2a2 transcripts. *Biochemistry 43*, 16134–16141.
(29) Abe, H., and Kool, E. T. (2004) Destabilizing universal linkers for signal amplification in self-ligating probes for RNA. *J. Am. Chem. Soc. 126*, 13980–13986.
(30) Ficht, S., Mattes, A., and Seitz, O. (2004) Single-nucleotide-specific PNA-peptide ligation on synthetic and PCR DNA templates. *J. Am. Chem. Soc. 126*, 9970–9981.
(31) Luther, A., Brandsch, R., and von Kiedrowski, G. (1998) Surface-promoted replication and exponential amplification of DNA analogs. *Nature (London) 396*, 245–248.
(32) Ma, Z., and Taylor, J.-S. (2003) PNA-based RNA-triggered drug-releasing system. *Bioconjugate Chem. 14*, 679–683.
(33) Ma, Z., and Taylor, J. S. (2001) Nucleic acid triggered catalytic drug and probe release: A new concept for the design of chemotherapeutic and diagnostic agents. *Bioorg. Med. Chem. 9*, 2501–2510.
(34) Brunner, J., Mokhir, A., and Kraemer, R. (2003) DNA-templated metal catalysis. *J. Am. Chem. Soc. 125*, 12410–12411.
(35) Grossmann, T. N., and Seitz, O. (2006) DNA-catalyzed transfer of a reporter group. *J. Am. Chem. Soc. 128*, 15596–15597.

BC700244S

Preparation, Characterization, and Application of Biotinylated and Biotin−PEGylated Glucagon-Like Peptide-1 Analogues for Enhanced Oral Delivery

Su Young Chae,[†] Cheng-Hao Jin,[†] Han Jong Shin,[†] Yu Seok Youn,[‡] Seulki Lee,[#] and Kang Choon Lee*[,†]

Drug Targeting Laboratory, College of Pharmacy, SungKyunKwan University, 300 Chonchon-dong, Jangan-ku, Suwon City 440–746, Korea, College of Pharmacy, Pusan National University, Busan 609–735, Korea, and Biomedical Research Center, Korea Institute of Science and Technology, Seoul 136–791, Korea. Received August 2, 2007; Revised Manuscript Received October 28, 2007

Glucagon-like peptide-1 (GLP-1) (7–36) is a type of incretin hormone with unique antidiabetic potential. The introduction of orally active GLP-1 offers substantial benefits in the treatment of type 2 diabetes over conventional injection-based therapies. Because the intestinal absorption of GLP-1 is restricted by its natural characteristics, we developed a series of GLP-1 analogues via the site-specific conjugation of biotin−NHS and/or of biotin−poly(ethylene glycol)−NHS at Lys^{26} and Lys^{34} of GLP-1 (7–36), respectively, in order to improve oral delivery. The resultant GLP-1 analogues, $Lys^{26,34}$-DiBiotin-GLP-1 (DB-GLP-1) and Lys^{26}-Biotin-Lys^{34}-(Biotin-PEG)-GLP-1 (DBP-GLP-1), were prepared and studied in terms of their chemical, structural, and biological properties. DBP-GLP-1 demonstrated superior proteolytic stability against trypsin, intestinal fluid, and the major GLP-1 inactivation enzyme (dipeptidyl peptidase-IV (DPP-IV)) to native GLP-1 or DB-GLP-1 ($p < 0.001$). The in vitro insulinotropic effects of DB-GLP-1 and DBP-GLP-1 showed potent biological activity in a dose-dependent manner, which resembled that of native GLP-1 in terms of stimulating insulin secretion in isolated rat islets of Langerhans. Intraperitoneal glucose tolerance tests (IPGTT) after the oral administration of GLP-1 analogues in diabetic db/db mice demonstrated that DB-GLP-1 and DBP-GLP-1 significantly reduced the $AUC_{0-180\ min}$ of glucose for 3 h by 14.9% and 24.5% compared to that of native GLP-1, respectively ($p < 0.01$). In particular, DBP-GLP-1 concentration in plasma rapidly increased 30 min after oral administration in rats, presumably due to improved intestinal absorption. These findings revealed that site-specific biotinylated and biotin−PEGylated GLP-1 is absorbed by intestine and that it has biological activity in vivo. Therefore, we propose that this orally active bioconjugated GLP-1 might be considered as a potential oral antidiabetic agent for type 2 diabetes mellitus.

INTRODUCTION

Glucagon-like peptide-1 (GLP-1) is the product of the glucagon gene, and is secreted from enteroendocrine L-cells of the intestinal mucosa in response to orally ingested nutrients (*1, 2*) GLP-1 is viewed as an interesting antidiabetic agent for the treatment of type 2 diabetes because of its marked glucose-dependent insulinotropic effect. GLP-1 has a number of beneficial effects in type 2 diabetes; for example, it inhibits glucagon secretion and gastric emptying and suppresses appetite (*3–6*) In addition, GLP-1 has strong disease-modifying possibilities in type 2 diabetes, as it inhibits β-cell apoptosis and stimulates β-cell proliferation and/or neogenesis (*7, 8*). Overall, GLP-1 is viewed as a potent therapeutic agent for type 2 diabetic patients, but its short half-life in physiological environments and limited oral bioavailability remain critical hurdles to its successful clinical application (*3, 9*).

The short biological half-life (∼2 min) of GLP-1 is mainly due to its rapid inactivation by the ubiquitous protease (dipeptidyl peptidase-IV (DPP-IV)), which acts on its two N-terminal amino acids, histidine and alanin (*10–12*). To overcome this limitation, several GLP-1 receptor agonists have been developed and investigated to improve the therapeutic value of GLP-1 (*13,14*). However, although these injectable GLP-1 receptor agonists have produced promising results, there is a continuous demand for an orally active GLP-1, as such an agent offers significant advantages in terms of therapeutic and patient acceptability. Furthermore, since the absorption of orally active GLP-1 occurs in the intestine, a DPP-IV resistant GLP-1 efficiently absorbed in the intestine would have the potential to mimic the physiological effects of native GLP-1, which is secreted by intestinal L-cells.

However, the development of such an orally active peptide drug presents an arduous challenge, due to the low intestinal absorption and proteolytic stability of GLP-1 in the gastrointestinal (GI) track (*15, 16*). Thus, the successful oral delivery of this peptide involves increasing its intestinal membrane permeability and overcoming the barrier of enzymatic degradation. Site-specific bioconjugation offers a convenient means of developing orally active peptide drugs. Many different types of peptide bioconjugation, with vitamins, fatty acids, bile acids, and PEG, have been used to develop orally active peptide agents (*16–19*).

Here, we describe new strategies for producing orally active GLP-1 derivatives using site-specific biotinylation and biotin−PEGylation. As a member of the vitamin B family, biotin can be recognized and absorbed through the Na^+-dependent multivitamin transporter (SMVT) systems (*20–22*). Moreover, the natural physicochemical properties of biotins have been utilized to facilitate the intestinal absorption of peptide drugs through passive transport via enhanced hydrophobicity resulting from biotin conjugation and a predominant SMVT absorption

* Corresponding author. E-mail: kclee@skku.edu. Tel: +82-31-290-7704, Fax: +82-31-290-7724.
[†] SungKyunKwan University.
[‡] Pusan National University.
[#] Korea Institute of Science and Technology.

10.1021/bc700292v CCC: $40.75 © 2008 American Chemical Society
Published on Web 12/14/2007

system (*22–24*). We previously reported that site-specific PEGylated GLP-1 at the Lys^{34} position profoundly improves its enzymatic stability while retaining its biological activities, and thus enhances its therapeutic potential in type 2 diabetic db/db mice (*25–27*). The conjugation of water soluble polymers on the lysine residues GLP-1 also showed the preserved insulinotropic activity on pancreatic islets (*28, 29*). In view of these observations that site-specific PEGylated GLP-1 can increase enzymatic stability but retain biological activity, we hypothesized that site-specific biotinylation and biotin−PEGylation might enhance the intestinal absorption of GLP-1 due to its increased permeability and stability without prominent activity loss. In this study, we prepared and characterized site-specifically bioconjugated GLP-1s using sequential biotin and biotin−PEG conjugations on Lys^{26} and Lys^{34} of GLP-1, respectively. The therapeutic potentials of these bioconjugated GLP-1s were then investigated by examining their metabolic stabilities and insulinotropic activities in vitro and their hypoglycemic effects and intestinal absorptions in type 2 diabetic db/db mice.

MATERIALS AND METHODS

Materials. GLP-1 was purchased from Bachem (Torrance, CA, USA), Fmoc-GLP-1 from the American Peptide Company (Sunnyvale, CA), and biotin−poly(ethylene glycol) *N*-hydroxysuccinimide ester (biotin−PEG, MW 3400) from Nektar Therapeutics (Huntsville, AL). Dipeptidyl peptidase inhibitor and GLP-1 radioimmunoassay (RIA) kits were purchased from Linco Research (St. Charles, MO), and insulin enzyme immunoassay (EIA) kits from Mercodia (Uppsala, Sweden). All other reagents, unless otherwise indicated, were purchased from Sigma-Aldrich Co. (Saint Louis, MO) and were used as received. Type 2 diabetic C57BL/6 db/db mice (male, 7–8 weeks old) were obtained from the Korea Research Institute of Bioscience and Biotechnology (Daejon, Korea), and male Sprague–Dawley (SD) rats (150–200 g) were purchased from the Hanlim Experimental Animal Laboratory (Seoul, Korea).

Preparation of $Lys^{26,34}$-DiBiotin-GLP-1 (DB-GLP-1). DB-GLP-1 was synthesized by a coupling reaction between N-hydrosuccinimide-activated biotin (biotin−NHS) and the lysine residues (Lys^{26} and Lys^{34}) of GLP-1 in organic solvent. Briefly, 20 μL of biotin−NHS (2 mg/mL in dimethylsulfoxide (DMSO) containing 0.3% triethylamine (TEA)) was reacted with 380 μL of GLP-1 (5 mg/mL in DMSO with 0.3% TEA) (GLP-1/biotin−NHS molar ratio of 2) with gentle mixing at room temperature for 1 h. The reaction was then stopped by adding 100 μL of stop solution (deionized water containing 1% trifluoroacetic acid (TFA)). DB-GLP-1 was finally obtained by preparative high-performance liquid chromatography (HPLC).

Preparation of Lys^{26}-Biotin-Lys^{34}-(Biotin-PEG)-GLP-1 (DBP-GLP-1). DBP-GLP-1 was prepared by the stepwise conjugation of biotin−PEG and biotin on Lys^{34} and Lys^{26} of GLP-1, respectively, using procedures similar to that described above for DB-GLP-1 synthesis. Detailed of the procedures used are illustrated in Scheme 1. First, N^{ter}-FMOC-GLP-1 (FMOC-GLP-1, 1 mg/mL in DMF with 0.3% TEA) was reacted with a 1.5 times molar excess of biotin−PEG−NHS (6 mg/mL in DMF with 0.3% TEA) for 1 h at room temperature. After stopping the reaction with stop solution, Lys^{34}-(Biotin-PEG)-FMOC-GLP-1 was separated by reverse-phase HPLC (RP-HPLC). The product was obtained from the collected fraction by lyophilization. Second, Lys^{34}-(Biotin-PEG)-FMOC-GLP-1 (2 mg/mL in DMF containing 0.3% TEA) was further reacted with a 3-fold molar excess of biotin−NHS for 1 h at room temperature, as described above, following deprotection of the FMOC group of the final product by adding piperidine to a final concentration of 5% for 20 min, and then stopping the reaction with stop solution. DBP-GLP-1 was obtained by preparative HPLC.

Scheme 1. Schematic Diagram of the Preparations of Site-Specific Biotinylated and Biotin−PEGylated GLP-1

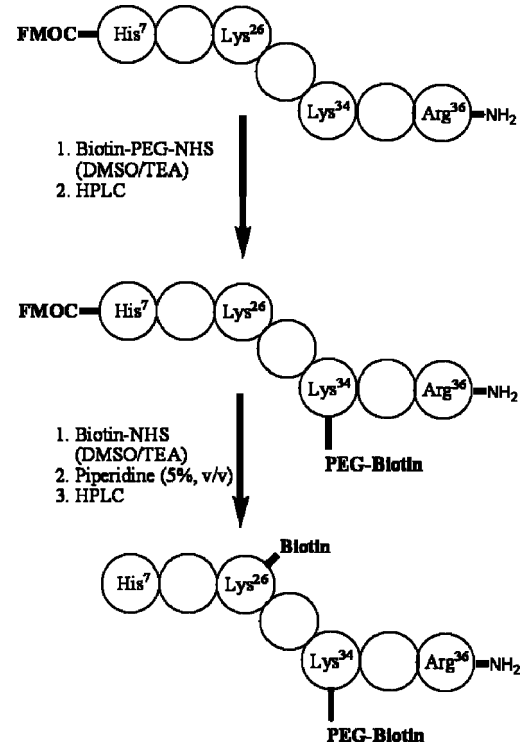

Purification of DB-GLP-1, Lys^{34}-(Biotin-PEG)-FMOC-GLP-1, and DBP-GLP-1. The bioconjugated GLP-1 analogues mentioned above were isolated and purified from their reaction mixtures by preparative RP-HPLC using a Capcell-pak RP-18 column (250 × 4 mm, 5 μm, Shiseido, Japan) at ambient temperature at a constant flow rate of 1.0 mL/min under UV absorbance monitoring at 215 nm. The mobile phase consisted of 0.1% TFA in deionized water (eluent A) and acetonitrile (AN) containing 0.1% TFA (eluent B), and these were as linear gradients, as follows: DB-GLP-1, 35−42% B for 20 min; Lys^{34}-(Biotin-PEG)-FMOC-GLP-1, 40−43% B for 20 min; DBP-GLP-1, 38−43% B for 15 min. HPLC fractions corresponding to respective peaks were collected separately, flushed off with nitrogen, and concentrated using an ultrafiltration unit (Ultracel YM3, MWCO 3000, Millipore, Billerica, MA). The products obtained were characterized by HPLC and MALDI-TOF mass spectroscopy, and stored at −70 °C until required for further experiments.

Characterization of Bioconjugated GLP-1s. Bioconjugation and site-specific modification were confirmed by MALDI-TOF MS of GLP-1 analogues before and after lysyl endoproteinase Lys-C digestion, as reported previously (*25*). Bioconjugations were confirmed using MALDI-TOF-MS molecular weight measurements using a Voyager-RP Biospectrometry workstation (PerSeptive Biosystems, Cambridge, MA). Briefly, the sample−matrix solution was prepared by mixing 1 μL of aliquot with 2 L of the matrix solution (a saturated solution of α-cyanohydroxycinnamic acid (CHCA) in 50% of water/ACN containing 0.1% (v/v) TFA). 1 μL of the sample−matrix solution was then deposited onto a well of a sample plate and dried by rapid vacuum evaporation. Data generated by 2 ns pulses of the 337 nm nitrogen laser were averaged for each spectrum in linear mode; positive-ion TOF detection was performed using on accelerating voltage of 25 kV.

To determine the locations of the biotinylation and PEGylation sites, Lys-C digestion experiments were performed, as described previously (*27*). Briefly, 10 μL of Lys-C (10 μg/mL,

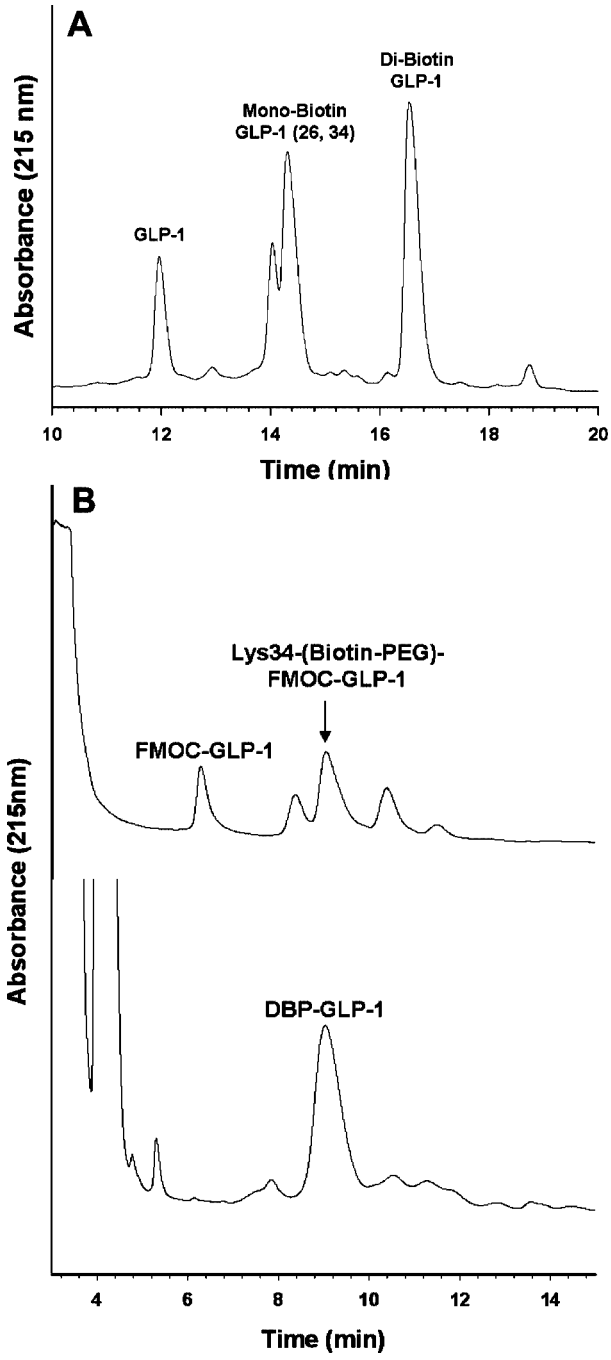

Figure 1. RP-HPLC analysis of DB-GLP-1 and DBP-GLP-1. (A) Chromatogram of the biotinylation reaction mixture; and (B) Lys^{26}-(biotin-PEG)-FMOC-GLP-1 and DBP-GLP-1.

pH 7.4) was added to 20 μL of sample solution (50 mM Tris−HCl, buffer pH 8.5) containing each positional isomer of bioconjugated GLP-1s (10 μg/mL). Reaction mixes were incubated at 37 °C for 60 min, and after digestion, individual samples were analyzed by MALDI-TOF-MS.

Proteolytic Stability Studies of the Bioconjugated GLP-1s. The proteolytic stabilities of the bioconjugated GLP-1s against trypsin, DPP IV, and intestinal fluid were evaluated as previously described with slight modification (*25*). Intestinal fluid was obtained from 24 h prefasted SD rat intestine (jejunum) by flushing with PBS and centrifugation. A portion (20 μL) of either GLP-1 or bioconjugated GLP-1s (200 μg/mL each) were mixed with the same volume of enzyme solution (2 mM trypsin in PBS pH 6.5, 25 mU/mL DPP IV in Tris−HCl buffer pH 7.4, and intestinal fluid, preincubated at 37 °C for 30 min), and

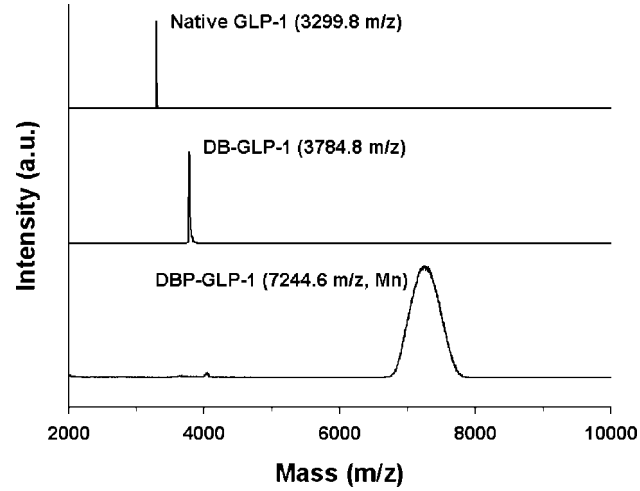

Figure 2. MALDI-TOF mass spectra of native GLP-1, DB-GLP-1, and DBP-GLP-1.

further incubated at 37 °C. At predetermined times, the incubations were stopped by adding 100 μL of chilled stop solution (1% TFA in DW). The mixtures were then centrifuged at 12 000 rpm for 5 min, and supernatants were analyzed by RP-HPLC. Degradation half-lives were then calculated, assuming first-order kinetics.

Biological Activities of the Bioconjugated GLP-1s. Insulinotropic activities of GLP-1 and bioconjugated GLP-1s on rat pancreatic islets were assessed as previously described (*25*–*27*). Briefly, male SD rats (250–270 g) were anesthetized with ketamine and xylazine (90/10 mg/kg, i.p.). The donor pancreas was swollen by injecting cold Hank's balanced buffered salt solution (HBSS, pH 7.4, Sigma) containing 1.5 mg/mL of type V collagenase (Sigma). Isolated islets were purified by centrifugation in a discontinuous Ficoll (Amersham Biosciences AB, Uppsala, Sweden) gradient at 2400 rpm for 25 min. Purified islets were cultured in RPMI-1640 culture medium (Sigma) supplemented with 10% fetal bovine serum (Gibco, Carlsbad, CA) and 1% penicillin−streptomycin (Gibco) at 37 °C in a 95% air/5% CO_2 atmosphere for 2 days. The islets were then washed, incubated in Krebs-Ringer bicarbonate (KRB) buffer, seeded at 20 islet/well on a 24 well plate in 1 mL of KRB containing 16.8 mM glucose, and incubated with various concentrations of GLP-1 and bioconjugated GLP-1s (0.1, 1, 10, and 100 nM) for 2 h. Insulinotropic activities were evaluated by measuring the amount of insulin released to media using an enzyme immunoassay kit (Rat insulin ELISA kit, Mercodia AB, Uppsala, Sweden).

The in vivo bioactivities of the bioconjugated GLP-1s were evaluated using oral glucose tolerance tests (OGTT) in type 2 diabetic db/db mouse (8−10 weeks old), after intraperitoneal drug administration (*26*, *27*). In brief, 18 h fasted mice were administered bioconjugated GLP-1s (10 nmol/kg, i.p., at 30 min prior to oral glucose administration). A 1.0 g/kg dose of glucose was then administered orally to each mouse. At predetermined times, blood glucose levels were monitored using a glucometer (Accu-Chek Sensor, Roche Diagnostics Corp., Mannheim, Germany).

Evaluation of the Hypoglycemic Efficacies of the Bioconjugated GLP-1s. The hypoglycemic efficacies of the bioconjugated GLP-1s administered orally were investigated using an intraperitoneal glucose tolerance test (IPGTT). Briefly, 18 h fasted mice were injected with a glucose solution (1.0 g/kg, 100 μL, at time 0 min, i.p.), and then orally administered gastric neutralizer (0.1 mL of 3% $NaHCO_3$) and bioconjugated GLP-1s (15 nmol/mouse, 200 mL, in a PBS/propylene glycol 50/50 mixture) at 30 min before glucose injection. Blood glucose levels

Table 1. Molecular Masses of Site-Specific Biotinylated and Biotin−PEGylated GLP-1 after Lys-C Protease Digestion, as Determined by MALDI-TOF

samples	possible Lys-C fragments		
	fragments	molecular mass	observed mass
GLP-1	His^{7}-Lys^{26}	2098.2	2099.6
	Glu^{27}-Lys^{34}	1005.2	1005.8
	Gly^{35}-Arg^{37}	231.2	N.D.[a]
DB-GLP-1	$Lys^{26,34}$-Biotin-GLP-1	3784.2	3784.6
Lys^{34}-(Biotin-PEG)-FMOC-GLP-1	FMOC-His^{7}-Lys^{26}	2322.8	2332.5
	Gln^{27}-Lys^{34}-(Biotin-PEG)-Arg^{36}	4876.5 (Mn)	4926.7 (Mn)
DBP-GLP-1	Lys^{26}-Biotin-Lys^{34}-(Biotin- PEG)-GLP-1	7192.3 (Mn)	7244.5 (Mn)

[a] Not determined.

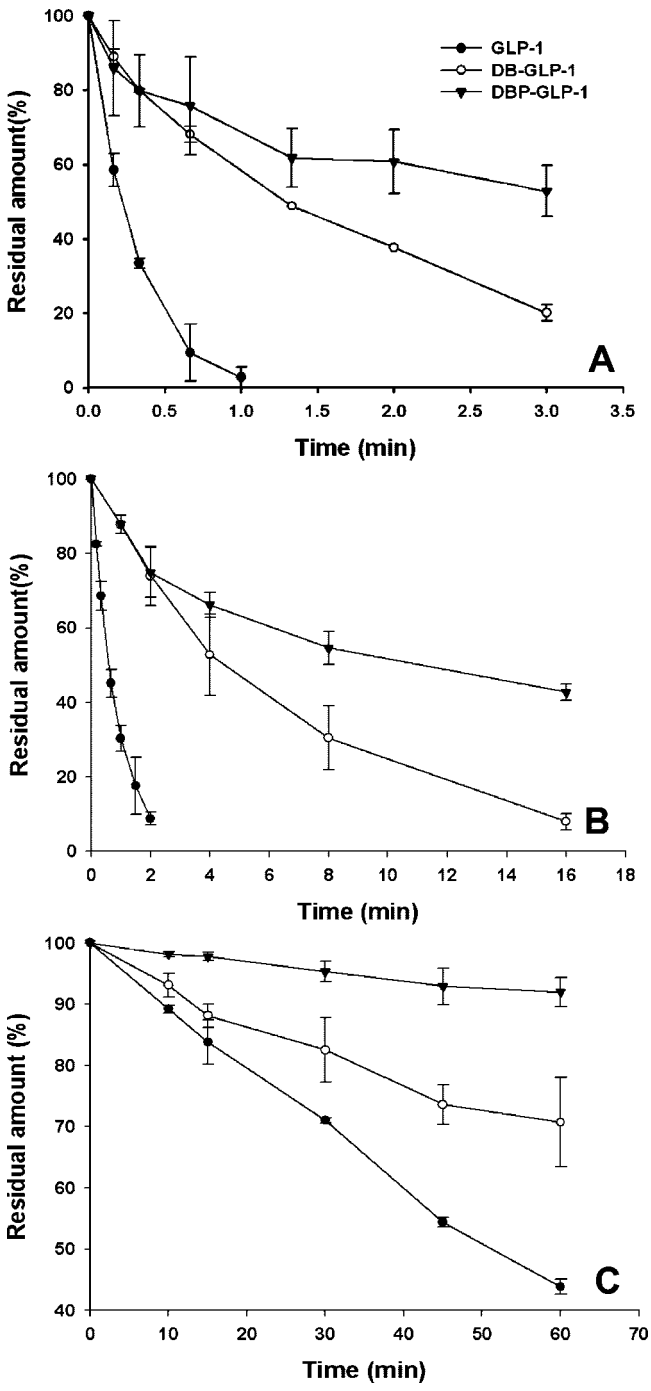

Figure 3. The degradation profiles of GLP-1, DB-GLP-1 and DBP-GLP-1 incubated with (A) trypsin, (B) intestinal fluid, and (C) isolated DPP IV enzyme. Residues were quantified by RP-HPLC. Data are the means ± SD of three determinations.

were then monitored using the above-mentioned glucometer. As controls, vehicle or GLP-1 were administered in an identical manner. Areas under the curve (AUC) were calculated in concentration per minute for the total experimental periods (0−180 min).

Pharmacokinetics in Vivo. To investigate oral absorption, pharmacokinetic profiling of the bioconjugated GLP-1s was performed, as described previously (*25*). For this study, a jugular vein was cannulated in male SD rats at one day before the experiment. The animals were randomly divided into three groups and GLP-1 mol equiv amount of the bioconjugated GLP-1s (DB-GLP-1 and DBP-GLP-1) was dissolved in PBS (20 nmol/rat) and administered i.v. or perorally (p.o.), respectively. Blood samples, drawn at predetermined times, were placed in ice-cold polyethylene tubes containing DPP IV inhibitor (10 μL per mL of blood; Linco Research Inc., St. Charles, MO). Plasma samples were obtained by centrifugation and stored at −70 °C until required for assay. Concentrations of GLP-1 in rat plasma were analyzed using a commercial GLP-1 radioimmunoassay kit (active GLP-1 RIA kit, Linco Research Inc., St. Charles, MO).

RESULTS AND DISCUSSION

Preparation and Characterization of Bioconjugated GLP-1s. Unlike chemical conjugations to proteins where the degree of substitution plays a major role in their biological and pharmaceutical characteristics, peptide drug modifications, such as PEGylation, biotinylation, acylation, and other conjugations, show stronger relationships between conjugate position and therapeutic efficacy and potential (*27*, *30*, *31*). In particular, the chemical attachment of functional moieties to the primary amine groups of GLP-1 resulted in position-dependent characteristics. GLP-1 possesses three different sites for nucleophilic substitution via a primary amine group located at the N-terminal, i.e., His^{7}, Lys^{26}, and Lys^{34}. In previous, we monitored the effect of the PEGylated GLP-1 on biological activity. Compared to the native GLP-1, the in vitro insulinotropic activity of Nter-PEG-GLP-1 and Lys-PEG-GLP-1 were 44.1% and 83.1%, respectively (100 nM peptide, 16.8 mM glucose) (*25*, *26*). More detailed investigations revealed that the PEGylation on Lys^{34} of GLP-1 resulted in 93% activity remaining (*27*). On the basis of these results, we concluded that conjugation of bulky biotin−PEG on the Lys^{34} and small m.w. of biotin on the Lys^{26} position could minimize the loss of GLP-1's activity among the various combinations.

To prepare the described bioconjugated GLP-1s, Lys-amine specific conjugation reactions were conducted in an organic medium, as described previously (*25–27*). The biotin modification of GLP-1 resulted in a mixture of biotinylated GLP-1 isomers, as illustrated in the RP-HPLC chromatogram shown in Figure 1A. Of the four distinct HPLC peaks observed in the biotinylated reaction mixture, the first three peaks were attributed to native GLP-1 (elution time 11.96 min) and monobiotin-GLP-1 (14.03 and 14.30 min), which had mass values of 3299.8 *m*/*z* and 3542.8 *m*/*z*, respectively. The fourth peak (16.53 min)

Table 2. Summary of GLP-1, DB-GLP-1, and DBP-GLP-1 Stabilities in Various Digestive Systems

	trypsin		intestinal fluid		DPP IV	
samples	half-life (s)	folds increase	half-life (s)	folds increase	half-life (s)	folds increase
GLP-1	11.6 ± 0.8		0.57 ± 0.06		49.8 ± 3.6	
DB-GLP-1	85.6 ± 1.4	7.4	4.38 ± 0.79	7.7	117.4 ± 9.4	2.4
DBP-GLP-1	210.0 ± 5.3	18.1	13.94 ± 1.14	24.5	495.0 ± 9.3	9.9

represented $Lys^{26,34}$-Dibiotinylated GLP-1 (DB-GLP-1), which had a mass of 3784.8 *m/z*, as illustrated in Figure 2. Further investigations of DB-GLP-1 using Lys-C digestion assays and following MALDI-TOF confirmed the biotinylation of GLP-1 at Lys^{26} and Lys^{34} (Table 1).

To prepare heterogeneously bioconjugated GLP-1 with biotin and biotin−PEG at different lysine residues, N-terminal protected GLP-1 was utilized to improve reaction yield and selectivity (*30*, *31*). Of the various N-terminal protected GLP-1s examined, 9-fluorenylmethyl carbamate (FMOC) protected GLP-1 was found to have several advantages, e.g., superior stability in acidic HPLC conditions and ease of deprotection under mild basic conditions. By using FMOC-GLP-1, heterogeneous bioconjugations were conducted using sequential coupling reactions between lysine residues and biotin−PEG−NHS and biotin−NHS. As illustrated in Figure 1B, biotin−PEG conjugation on FMOC-GLP-1 resulted in the formation of monoconjugated positional isomers (second and third peaks) and diconjugated GLP-1 on at Lys^{26} and Lys^{34}. MALDI-TOF and Lys-C digestion assays revealed that the third peak was Lys^{34}-(Biotin-PEG)-FMOC-GLP-1 (Table 1). The Lys^{34}-conjugated portion was separated, purified, and used as a substrate for further bioconjugation with biotin−NHS. Biotinylation at Lys^{26} and removal of the FMOC protecting group were conducted by sequentially reacting Lys^{34}-(Biotin-PEG)-FMOC-GLP-1 with biotin-NHS for 1 h and then treating with piperidine (final concentration 5%). HPLC of the reaction mixtures revealed that heterobioconjugated GLP-1 had been formed in high yield (Figure 1B, about 90% yield). MALDI-TOF and Lys-C digestion analysis confirmed the successful heterobioconjugations by biotin and biotin−PEG at Lys^{26} and Lys^{34}, respectively. The observed mass of Lys^{26}-Biotin-Lys^{34}-(Biotin-PEG)-GLP-1 (DBP-GLP-1) was 7244.5 (Mn, calcd. 7192.3). Moreover, DBP-GLP-1 did not produce fragments when treated with Lys-C (Figure 2 and Table 1).

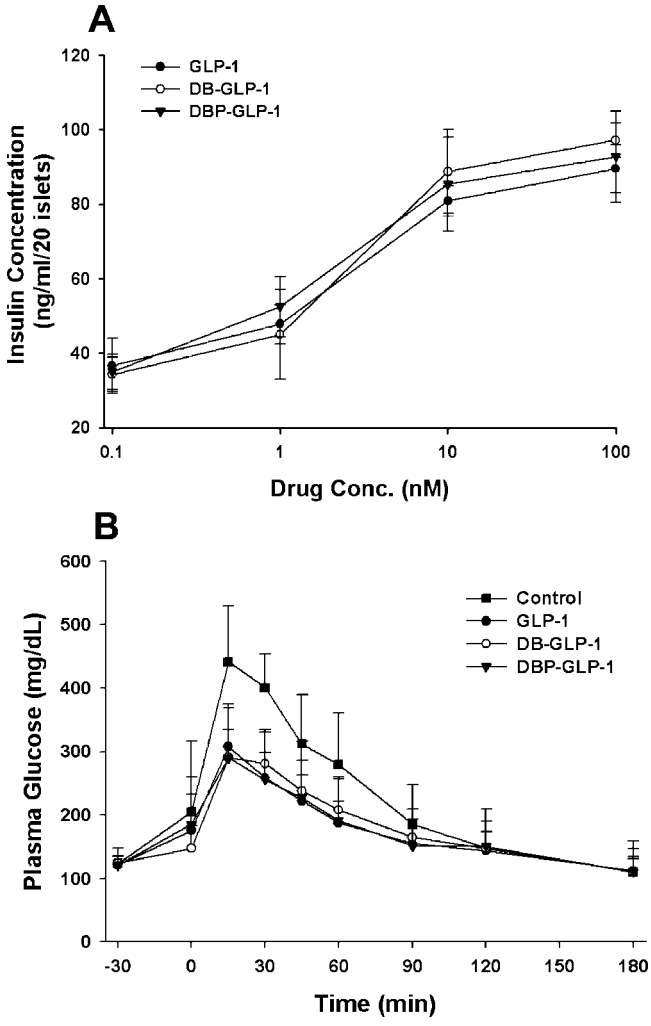

Figure 4. In vitro (A) and in vivo (B) biological activities of GLP-1, DB-GLP-1, and DBP-GLP-1. (A) Dose-dependent insulinotropic activities of GLP-1, DB-GLP-1, and DBP-GLP-1 on isolated rat pancreatic islets at a glucose concentration of 16.8 mM. (B) Glucose stabilizing of the three agents in type 2 diabetic db/db mice (fasted for 18 h), after i.p. administration (−30 min, 10 nmol/kg) and oral glucose (0 min, 1.0 g/kg).

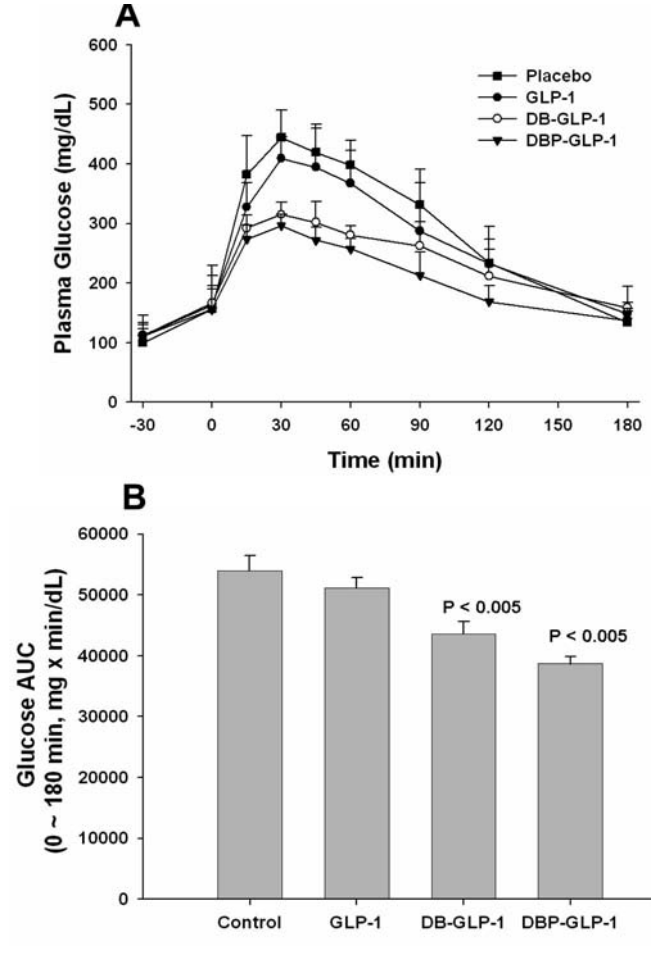

Figure 5. (A) Glucose clearance kinetics after the oral administrations of GLP-1, DB-GLP-1, or DBP-GLP-1 prior to intraperitoneal glucose injections. 18 h fasted db/db mice were administered the drugs orally (−30 min, 15 nmol/kg) followed by glucose (0 min, 1.0 g/kg), and plasma glucose levels were monitored for 180 min. (B) Calculated glucose AUCs of the experimental groups. * $p < 0.05$ vs DB-GLP-1 administered rats.

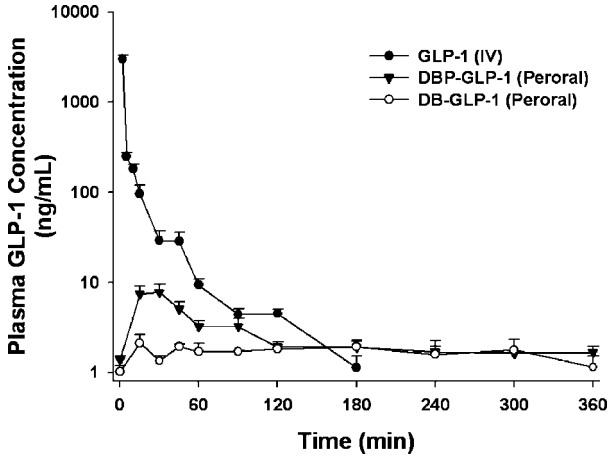

Figure 6. Plasma concentrations of GLP-1 (20 nmol/kg, i.v.), DB-GLP-1 (20 nmol/kg, p.o.), and DBP-GLP-1 (20 nmol/kg, p.o.). Values are means ± SD ($n = 4$).

Proteolytic Stabilities of GLP-1 and Bioconjugated GLP-1s. The protection of peptide drugs from enzymatic digestion in the intestinal compartment must be accomplished to realize oral peptide drug delivery (*1011*). To investigate the effect of the described bioconjugations on the enzymatic stability of the GLP-1, a series of enzyme stability tests were conducted.

Bioconjugations to the lysine residues of GLP-1 enhanced its gastrointestinal stability (Figure 3 and Table 2). In case of the trypsin, one of the most abundant pancreatic digestive enzymes, bioconjugation resulted in a dramatic improvement in proteolytic stability (Figure 3A), and this was further improved by introducing PEG in DBP-GLP-1. DB-GLP-1 and DBP-GLP-1 were found to have more than 7 and 18 times better proteolytic stabilities, respectively, than GLP-1 according to our trypsin degradation tests. Moreover, similar enhancements of proteolytic resistance (7- and 24-fold, respectively) were observed in the presence of intestinal fluid, which more closely represents intestinal enzymatic digestion.

For GLP-1-based incretin mimetics, stability in the systemic circulation is also key for an efficient oral delivery system. The instability of GLP-1 in the circulation is mainly attributable to its degradation by DPP IV (*1011*). As shown in Figure 3, native GLP-1 was rapidly degraded by DPP IV with a half-life of 49.8 min. As previously reported, DPP IV mediated GlP-1 degradation resulted in the truncation of the two N-terminal amino acids and destroyed its insulinotropic activity (*25*). However, biotinylation and biotin−PEGylation enhanced the proteolytic resistances of DB-GLP-1 and DBP-GLP-1 against DPP IV by 2.4- and 9.9-fold, respectively, as compared with native GLP-1.

Biological Activities of the Bioconjugated GLP-1s. Chemical modifications of protein or peptide biopharmaceuticals invariably alter their biological and pharmacological characteristics (*17–19*), and thus, such chemical modifications require meticulous investigation. One of the most prominent biological effects of GLP-1 is that it stimulates insulin secretion by pancreatic β-cells. Furthermore, this insulinotropic activity is strongly dependent on glucose concentration, and in fact, it has no effect on insulin secretion at glucose concentrations below 4.5 mM (*32*). Therefore, we performed experiments using isolated pancreatic islets in high-glucose media (16.8 mM glucose in KRH buffer). As shown in Figure 4A, GLP-1 and the bioconjugated GLP-1s showed concentration-dependent insulinotropic activity on pancreatic islets. As we reported previously for PEGylated GLP-1 derivatives (*26, 27*), GLP-1 and the two bioconjugated GLP-1s potentiated insulin secretion in a concentration-dependent manner and reached saturation at around 10 nM. Moreover, our results demonstrated that DB-GLP-1 and DBP-GLP-1 robustly retained biological activity, and that they have insulinotropic effects on pancreatic islets.

The in vivo bioactivities of GLP-1, DB-GLP-1, and DBP-GLP-1 administered intraperitoneally into diabetic db/db mice were evaluated by performing oral glucose tolerance tests, as described previously (*27*). As was found by in vitro bioactivity testing, all three agents showed similar kinetic patterns of glucose clearance. As shown in Figure 4B, blood glucose levels in the placebo group (saline i.p. injection) rapidly increased to ca.450 mg/dL at 15 min after glucose administration and then decreased slowly. On the other hand, mice pretreated with GLP-1, DB-GLP-1, or DBP-GLP-1 showed rapid glucose clearance kinetics and maximum plasma glucose levels of ca. 300 mg/dL, mainly due to stimulated insulin secretion. Therefore, the in vitro insulinotropic activity tests and in vivo hypoglycemic activity tests performed during this study show that DB-GLP-1 and DBP-GLP-1 substantially maintained the biological activity of native GLP-1.

Oral Hypoglycemic Effects of DB-GLP-1 and DBP-GLP-1. To evaluate the therapeutic efficacies of orally administered (p.o.) DB-GLP-1 and DBP-GLP-1, we used the intraperitoneal glucose tolerance test (IPGTT). Unlike the results described above after i.p. administration, p.o. administrations of GLP-1, DB-GLP-1, or DBP-GLP-1 had remarkably different glucose clearance kinetics. As illustrated in Figure 5A, the saline (placebo) and GLP-1 administered groups (30 min prior to glucose administration) showed a rapid increase in plasma glucose levels after the i.p. administration of glucose solution (0 min). 30 min after i.p. glucose administration, plasma glucose levels in saline and GLP-1 treated animals reached ca. 440 and 410 mg/dL, respectively, whereas in DB-GLP-1 and DBP-GLP-1 treated animals, they reached only 315 and 296 mg/dL, respectively.

Moreover, DB-GLP-1 and DBP-GLP-1 both enhanced glucose tolerance during the experimental periods, which we attribute to enhanced intestinal absorption, and although DBP-GLP-1 treated animals showed initial blood glucose elevations that were similar to those observed for DB-GLP-1, DBP-GLP-1 treated animals achieved the normal glycemic state more quickly. Statistical analysis revealed that the mean glucose levels in DBP-GLP-1 treated animals at 90 and 120 min after glucose injection were significantly lower than in DB-GLP-1 treated animals ($p < 0.05$, t test). We attribute this enhanced stability of DBP-GLP-1 vs DB-GLP-1 to its enhanced proteolytic stability and biotin-facilitated intestinal absorption. Owing to the absence of a natural biotin synthesis system, humans and other mammals must obtain the vitamin exogenously through intestinal absorption (*20, 21*). Although the exact molecular mechanism is still unsolved, it is evident that the biotin intake is reliant on the carrier-mediated mechanism (SMVT system).

Table 3. Pharmacokinetic Parameters after Administering GLP-1, DB-GLP-1, or DBP-GLP-1 to SD Rats[a]

sample	AUC (ng × min × mL^{-1})	C_{max}(ng/mL)	T_{max}(min)	$t_{1/2}$(min)
GLP-1 (i.v.)	9892 ± 913	N.A.[b]	N.A.	5.33 ± 0.76
DB-GLP-1	507 ± 81	N.A.	N.A.	N.A.
DBP-GLP-1	998 ± 104	7.72 ± 1.54	28.0 ± 3.1	39.45 ± 10.15

[a] Data are means ± SD ($n = 4$). AUC, area under the curve; C_{max}, maximal plasma concentration; T_{max}, time to reach maximum plasma concentration; $t_{1/2}$, half-life. [b] Not available.

The enhanced cellular and intestinal absorption of biotin-based peptides also have been reported (*22–24*). Sinco et al. reported that more than 3-fold enhanced absorption of R.I.-K-Tat9 peptide was achieved by biotin conjugation through passive and predominantly SMVT pathway (*22*). On the basis of these ideas, it can be expected that the effect of enhanced intestinal absorption and the following antidiabetic effect of DBP-GLP-1 is related to the SMVT system; however, the relationship between DBP-GLP-1 and the SMVT system should be elucidated.

Pharmacokinetic Profiles of DB-GLP-1 and DBP-GLP-1 in the Rat. The pharmacokinetic characteristics of orally administered bioconjugated GLP-1s were also investigated, and the results are illustrated in Figure 6 and Table 3. As a control experiment, native GLP-1 was administered i.v., and its plasma concentrations were then monitored vs time. The plasma concentrations of GLP-1 rapidly reduced and reached the basal level at 3 h after injection, which we attribute to the rapid systemic clearance and DPP IV mediated inactivation. Orally administered DB-GLP-1 showed the maintenance of basal levels around 1−2 ng/mL. Compared to the blank plasma levels of GLP-1 (1.28 ± 0.32 ng/mL, time 0 point), the plasma GLP-1 concentrations observed by oral DB-GLP-1 administration revealed the negligible intestinal absorptions, except at the 15 min point (2.12 ± 0.35 ng/mL). Typical intestinal absorption patterns were observed for orally administered DBP-GLP-1. Active GLP-1 plasma concentrations in rats peaked at 7.72 ng/mL (C_{max}) at 28 min (T_{max}) after DBP-GLP-1 oral administration. After 120 min, the plasma levels of DBP-GLP-1 groups also returned to the basal level. On the basis of their pharmacokinetic profiles, the calculated average AUCs for i.v. GLP-1, oral DB-GLP-1, and oral DBP-GLP-1 were 9892, 507, and 998 $ng \cdot min \cdot mL^{-1}$, respectively. Although oral administration might provoke the intestinal secretion of natural GLP-1, the existence of apparent absorption peaks in plasma and the higher AUC value of DBP-GLP-1 strongly support its enhanced intestinal absorption. Moreover, the introduction of PEG molecules in DBP-GLP-1 also appeared to significantly increase plasma half-life, which concurs with our previous investigations (*25–27*). Moreover, as compared with GLP-1 administered i.v., orally administered DBP-GLP-1 had a plasma half-life that was more than 7-fold greater.

CONCLUSION

In this report, we found that DB-GLP-1 and DBP-GLP-1 show enhanced GLP-1 intestinal absorption. $Lys^{26,34}$-DiBiotin-GLP-1 (DB-GLP-1) and Lys^{26}-Biotin-Lys^{34}-(Biotin-PEG)-GLP-1 (DBP-GLP-1) were prepared using lysine-specific coupling reactions following HPLC separations. Both DB-GLP-1 and DBP-GLP-1, but especially DBP-GLP-1, had markedly better proteolytic stabilities than native GLP-1. Derivatization also preserved the biological and pharmacological activities of DB-GLP-1 and DBP-GLP-1. Furthermore, DBP-GLP-1 showed typical intestinal absorption patterns by pharmacokinetic profiling and a dramatically enhanced oral hypoglycemic effect versus native GLP-1. On the basis of these findings, we believe that DBP-GLP-1 is a good candidate antidiabetic peptide drug.

ACKNOWLEDGMENT

This work was supported by a grant from the Ministry of Science and Technology of Korea (M10414030001-05N1403-00140).

LITERATURE CITED

(1) Kieffer, T. J., and Habener, J. F. (1999) The glucagon-like peptides. *Endocr. Rev. 20*, 876–913.

(2) Meier, J. J., and Nauck, M. A. (2005) Glucagon-like peptide 1 (GLP-1) in biology and pathology. *Diabetes Metab. Res. Rev. 21*, 91–117.

(3) Deacon, C. F. (2004) Therapeutic strategies based on glucagon-like peptide 1. *Diabetes 53*, 2181–2189.

(4) Gutniak, M. K., Linde, B., Holst, J. J., and Efendic, S. (1995) Subcutaneous injection of the incretin hormone glucagon-like peptide 1 abolishes postprandial glycemia in NIDDM. *Diabetes Care 17*, 1039–1044.

(5) Dupre, J., Ross, S. A., Watson, D., and Brown, J. C. (1973) Stimulation of insulin secretion by gastric inhibitory polypeptide in man. *J. Clin. Endocrinol. Metab. 37*, 826–828.

(6) Turton, M. D., O'Shea, D., Gunn, I., Beak, S. A., Edwards, C. M., Meeran, K., Choi, S. J., Taylor, G. M., Heath, M. M., Lambert, P. D., Wilding, J. P., Smith, D. M., Ghatei, M. A., Herbert, J., and Bloom, S. R. (1996) A role for glucagon-like peptide-1 in the central regulation of feeding. *Nature (London) 379*, 69–72.

(7) Xu, G., Stoffers, D. A., Habener, J. F., and Bonner-Weir, S. (1999) Exendin-4 stimulates both beta-cell replication and neogenesis, resulting in increased beta-cell mass and improved glucose tolerance in diabetic rats. *Diabetes 48*, 2270–2276.

(8) Stoffers, D. A., Kieffer, T. J., Hussain, M. A., Drucker, D. J., Egan, J. M., Bonner-Weir, S., and Habener, J. F. (2000) Insulinotropic glucagon-like peptide-1 agonists stimulate expression of homeodomain protein IDX-1 and increase islet size in mouse pancreas. *Diabetes 49*, 741–748.

(9) Zander, M., Madsbad, S., Madsen, J. L., and Holst, J. J. (2002) Effect of 6-week course of glucagon-like peptide 1 on glycaemic control, insulin sensitivity, and beta-cell function in type 2 diabetes: a parallel-group study. *Lancet 359*, 824–830.

(10) Kieffer, T. J., McIntosh, C. H., and Pederson, R. A. (1995) Degradation of glucose-dependent insulinotropic polypeptide and truncated glucagon-like peptide 1 in vitro and in vivo by dipeptidyl peptidase IV. *Endocrinology 136*, 3585–3596.

(11) Mentlein, R., Gallwitz, B., and Schmidt, W. E. (1993) Dipeptidyl-peptidase IV hydrolyses gastric inhibitory polypeptide, glucagon-like peptide-1(7–36) amide, peptide histidine methionine and is responsible for their degradation in human serum. *Eur. J. Biochem. 214*, 829–835.

(12) Vilsbøll, T., Agerso, H., Krarup, T., and Holst, J. J. (2003) Similar elimination rates of glucagon-like peptide-1 in obese type 2 diabetic patients and healthy subjects. *J. Clin. Endocrinol. Metab. 88*, 220–224.

(13) Yoo, B. K., Triller, D. M., and Yoo, D. J. (2006) Exenatide: a new option for the treatment of type 2 diabetes. *Ann. Pharmacother. 40*, 1777–1784.

(14) Madsbad, S., Schmitz, O., Ranstam, J., Jakobsen, G., and Matthews, D. R. (2004) Improved glycemic control with no weight increase in patients with type 2 diabetes after once-daily treatment with the long-acting glucagon-like peptide 1 analog liraglutide (NN2211): a 12-week, double-blind, randomized, controlled trial. *Diabetes Care 27*, 1335–1342.

(15) Hamman, J. H., Enslin, G. M., and Kotzé, A. F. (2005) Oral delivery of peptide drugs: barriers and developments. *BioDrugs 19*, 165–177.

(16) Goldberg, M., and Gomez-Orellana, I. (2003) Challenges for the oral delivery of macromolecules. *Nat. Rev. Drug Discovery 2*, 289–295.

(17) Lee, Y., Nam, J. H., Shin, H. C., and Byun, Y. (2001) Conjugation of low-molecular-weight heparin and deoxycholic acid for the development of a new oral anticoagulant agent. *Circulation 104*, 3116–3120.

(18) Kim, S. K., Lee, E. H., Vaishali, B., Lee, S., Lee, Y. K., Kim, C. Y., Moon, H. T., and Byun, Y. (2005) Tricaprylin microemulsion for oral delivery of low molecular weight heparin conjugates. *J. Controlled Release 105*, 32–42.

(19) Chalasani, K. B., Russell-Jones, G. J., Yandrapu, S. K., Diwan, P. V., and Jain, S. K. (2007) A novel vitamin B12-nanosphere conjugate carrier system for peroral delivery of insulin. *J. Controlled Release 117*, 421–429.

(20) Balamurugan, K., Ortiz, A., and Said, H. M. (2003) Biotin uptake by human intestinal and liver epithelial cells: role of the SMVT system. *Am. J. Physiol. Gastrointest. Liver Physiol. 285*, G73–77.

(21) Chatterjee, N. S., Kumar, C. K., Ortiz, A., Rubin, S. A., and Said, H. M. (1999) Molecular mechanism of the intestinal biotin transport process. *Am. J. Physiol. 277*, C605–613.

(22) Ramanathan, S., Pooyan, S., Stein, S., Prasad, P. D., Wang, J., Leibowitz, M. J., Ganapathy, V., and Sinko, P. J. (2001) Targeting the sodium-dependent multivitamin transporter (SMVT) for improving the oral absorption properties of a retro-inverso Tat nonapeptide. *Pharm. Res. 18*, 950–956.

(23) Minko, T., Paranjpe, P. V., Qiu, B., Lalloo, A., Won, R., Stein, S., and Sinko, P. J. (2002) Enhancing the anticancer efficacy of camptothecin using biotinylated poly(ethylene glycol) conjugates in sensitive and multidrug-resistant human ovarian carcinoma cells. *Cancer Chemother. Pharmacol. 50*, 143–150.

(24) Ramanathan, S., Qiu, B., Pooyan, S., Zhang, G., Stein, S., Leibowitz, M. J., and Sinko, P. J. (2001) Targeted PEG-based bioconjugates enhance the cellular uptake and transport of HIV-1 TAT nonapeptide. *J. Controlled Release 77*, 199–212.

(25) Lee, S. H., Lee, S., Youn, Y. S., Na, D. H., Chae, S. Y., Byun, Y., and Lee, K. C. (2005) Synthesis, characterization, and pharmacokinetic studies of PEGylated glucagon-like peptide-1. *Bioconjugate Chem. 16*, 377–382.

(26) Lee, S., Youn, Y. S., Lee, S.-H., Byun, Y., and Lee, K. C. (2006) PEGylated glucagon-like peptide-1 displays preserved effects on insulin release in isolated pancreatic islets and improved biological activity in db/db mice. *Diabetologia 49*, 1608–1611.

(27) Youn, Y. S., Chae, S. Y., Lee, S., Jeon, J. E., Shin, H. G., and Lee, K. C. (2007) Evaluation of therapeutic potentials of site-specific PEGylated glucagon-like peptide-1 isomers as a type 2 anti-diabetic treatment: Insulinotropic activity, glucose-stabilizing capability, and proteolytic stability. *Biochem. Pharmacol. 73*, 84–93.

(28) Kim, S., and Bae, Y. H. (2004) Long-term insulinotropic activity of glucagon-like peptide-1/polymer conjugate on islet microcapsules. *Tissue Eng. 10*, 1607–16.

(29) Kim, S., Kim, S. W., and Bae, Y. H. (2005) Synthesis, bioactivity and specificity of glucagon-like peptide-1 (7–37)/polymer conjugate to isolated rat islets. *Biomaterials 26*, 3597–606.

(30) Youn, Y. S., and Lee, K. C. (2007) Site-specific PEGylation for high-yield preparation of Lys(21)-amine PEGylated growth hormone-releasing factor (GRF) (1–29) using a GRF(1–29) derivative FMOC-protected at Tyr(1) and Lys(12). *Bioconjugate Chem. 18*, 500–506.

(31) Youn, Y. S., Na, D. H., and Lee, K. C. (2007) High-yield production of biologically active mono-PEGylated salmon calcitonin by site-specific PEGylation. *J. Controlled Release 117*, 371–379.

(32) Jia, X., Brown, J. C., Ma, P., Pederson, R. A., and McIntosh, C. H. (1995) Effects of glucose-dependent insulinotropic polypeptide and glucagon-like peptide-I-(7–36) on insulin secretion. *Am. J. Physiol. 268*, E645–651.

BC700292V

Reversible Pegylation Prolongs the Hypotensive Effect of Atrial Natriuretic Peptide

Maoz Nesher,[†] Yelena Vachutinsky,[‡] Gil Fridkin,[§] Yehuda Schwarz,[†] Keren Sasson,[‡] Mati Fridkin,[§] Yoram Shechter,[‡] and David Lichtstein*,[†]

Department of Physiology, The Hebrew University-Hadassah Medical School, Jerusalem, Israel, and Departments of Biological Chemistry and of Organic Chemistry, The Weizmann Institute of Science, Rehovot, Israel. Received August 5, 2007; Revised Manuscript Received October 30, 2007

Natriuretic peptides (NP), including atrial natriuretic peptide (ANP), induce potent natriuresis and vasodilation and thereby generate hypotension *in vivo*. Despite intensive efforts, clinical application of NP as an antihypertensive agent is limited because of their short biological half-life and poor bioavailability. Recently, we have developed a strategy that facilitates slow release of peptides from PEG−peptide inactive conjugates, based on reversible pegylation. Peptides prepared by this approach undergo slow, spontaneous chemical hydrolysis at physiological conditions, releasing the native active peptide/protein drug from the inactive conjugates over prolonged periods. A PEG chain of 30 kDa was linked covalently to the α-amino side chain of the hormone via a MAL-Fmoc-NHS spacer, yielding PEG_{30}-Fmoc-ANP, a prodrug that releases the native hormone upon incubation at physiological conditions. Bolus administration of native ANP to Wistar rats receiving adrenaline yields a short, transitory effect in lowering blood pressure (BP), reaching a maximum at 2 min, and then returning to control values after 12 to 25 min. In contrast, administration of PEG_{30}-Fmoc-ANP lowered BP following a lag period of 50 min, and maintained low BP for a period exceeding 60 min. Saline or PEG_{30}-Fmoc-Alanine were not effective in lowering BP in Wistar rats. These results show that the novel compound, PEG_{30}-Fmoc-ANP, is a reversible pegylated prodrug derivative that facilitates a prolonged BP lowering effect in rats and may be considered as a candidate for development into an antihypertensive drug.

INTRODUCTION

Natriuretic peptides (NP), including atrial natriuretic peptide (ANP), brain natriuretic peptide (BNP), and C-type natriuretic peptide (CNP) induce potent natriuresis and vasodilation and thereby generate hypotension *in vivo* both in humans and in other mammals (*1*, *2*). ANP stimulates natriuresis by increasing renal glomerular filtration rate and inhibiting Na^+ reabsorption at the collecting duct. ANP also suppresses secretion of aldosterone, vasopressin, and renin, thereby stimulating both natriuresis and diuresis (*3*, *4*). In the vasculature, ANP relaxes norepinephrine-, angiotensin II-, and K^+-induced vascular smooth muscle contraction causing an immediate hypotensive effect (*5*). Consequently, ANP plays a central role in controlling blood pressure (BP) and volume regulation (*6*). Despite intensive efforts, clinical application of the natriuretic peptide family members as antihypertensive agents is limited because of their short biological half-life and poor bioavailability. The $t_{1/2}$ of ANP is 2 to 5 min in human and even less in the rat (*7*). Of the three major natriuretic peptide receptors, natriuretic peptide receptors A, B, and C (NPR-A, -B, -C, respectively), NPR-A and NPR-B are guanylyl cyclase-linked, which utilize cGMP as the intracellular messenger (*7*). The third receptor, NPR-C, is not linked to guanylyl cyclase but appears to act as clearance receptor of the peptides from the circulation (*8*). Inactivation of circulating ANP also involves neutral endopeptidase (NEP), a membrane-bound metallopeptidase widely expressed in the vasculature (*9*). NPR-C and NEP rapidly eliminate ANP from the circulation leading to its short $t_{1/2}$ and, therefore, limit its suitability as a drug. Nevertheless, intravenous administration of ANP or BNP reduces arterial BP and improves central hemodynamics in patients with chronic heart failure (*10*, *11*). Furthermore, preliminary results indicate that combined inhibition of angiotensin converting enzyme (ACE) and NEP by vasopeptidase inhibitors is an effective strategy in the treatment of hypertension and other cardiovascular diseases including heart failure (*12*). In addition, Nesiritide (Natrecor; SCIOS, Sunnyvale, CA), a recombinant form of human BNP, has been approved for the treatment of acutely decompensated heart failure by the US Food and Drug Administration since 2001 (*13*), and ANP is commercially available in Japan under the brand name Carperitide (Astellas Pharma, Fujisawa, Japan) (*14*). Unfortunately, clinical data suggest that the incidence of angioedema may increase upon vasopeptidase inhibition (*15*). Moreover, Sackner-Bernstein and co-workers showed that Nesiritide treatment may be associated with increased risk of worsening renal function (*16*) and even death (*17*) after treatment of acutely decompensated heart failure. Thus, the development of stable-prolonged-acting ANP is of significant therapeutic value.

Modifications of peptide/protein can lead to prolonged plasma half-life times. One common method of peptide modification is the covalent attachment of poly(ethylene glycol) (PEG) chain to peptides and proteins (*18*, *19*). Pegylation was shown to improve delivery of drugs and reduce adverse effects (*18*). Pegylated peptides are shielded from proteolytic enzymes, antibodies, or antigen processing cells (*18*). The feature gained by pegylation is predominantly a significant lifetime prolongation, in some instance from minutes to hours or even days (*20*).

* Dr. David Lichtstein, Department of Physiology, The Hebrew University - Hadassah Medical School, Jerusalem, 91120, Israel. Phone: 972-2-6758522; Fax: 972-2-6439736; E-mail: davidli@ekmd.huji.ac.il.

[†] The Hebrew University-Hadassah Medical School.

[‡] Department of Biological Chemistry, The Weizmann Institute of Science.

[§] Department of Organic Chemistry, The Weizmann Institute of Science.

10.1021/bc700294w CCC: $40.75 © 2008 American Chemical Society
Published on Web 12/11/2007

The major obstacle, however, is the inactivation that often takes place upon the covalent attachment of PEG chain to a protein and moreso to peptide drugs.

Recently, we developed a strategy, named reversible pegylation, for prolonging the lifetime of peptides and proteins (*21*). Conjugate prepared by this approach turn into a "prodrug" which undergoes slow, spontaneous hydrolysis at physiological conditions, releasing the native active peptide/protein drug from the inactive conjugate over prolonged periods. This approach was successfully applied to protract the action of exendin-4 (*21*), interferon α2 (*22*), peptide YY_{3-36} (*23*) and insulin (in preparation). In this study, we initially found that conventional (irreversible) pegylation inactivates ANP. We, therefore, applied the strategy of reversible pegylation to this hormone and investigated its characteristic features *in vitro* and its potency of facilitating a long-lasting hypotensive effect *in vivo*.

EXPERIMENTAL PROCEDURES

Materials. *N*-α-9-Fluorenylmethoxycarbonyl (Fmoc)-protected amino acids, Fmoc-Tyr(tBu)-preloaded Wang resins, *N*-hydroxybenzotriazole (HOBt), and benzotriazol-1-yl-oxytripyrrolidinophosphonium hexafluorophosphate (PyBOP) were purchased from Novabiochem (Laufelfingen, Switzerland). *N*,*N*-dimethylformamide (DMF), dichloromethane (DCM), *N*-methyl-2-pyrrolidone (NMP), *t*-butylmethyl ether, and HPLC-grade acetonitrile and trifluoroacetic acid (TFA) were from JT Baker (Phillipsburg, NJ). Dicyclohexylcarbodiimide (DCC) and piperidine were from Merck (Darmstadt, Germany). *N*-methylmorpholine (NMM) and triethylsilane (TES) were from Fluka (Buchs, Switzerland). PEG_{30}-SH (MPEG-SH-30K) was purchased from Nektar Transforming Therapeutics and contained 0.4 ± 0.03 mol SH per mole solid material as determined by 5,5′-dithiobis(2-nitrobenzoic acid) (DTNB). BSA, SDS, urethane, and dialysis bags were from Sigma (Rehovot, Israel) and adrenaline from Teva (Debrecen, Hungary). All other materials used in this study were of analytical grade.

Solid-Phase ANP Synthesis. ANP was synthesized using manual Fmoc-solid-phase methodology on Wang resin preloaded with the Fmoc-protected C-terminal amino acid, i.e., Tyr. DMF and NMP were used as solvents. Double couplings were achieved by reacting 3 Fmoc-AA-OH equivalents with either 3 equiv of PyBOP and 6 equiv of NMM or 3 equiv of HOBT and DCC. The completion of the coupling reaction was indicated by a negative ninhydrin test. N^{α}-Fmoc deprotection was carried out with 20% piperidine in dimethylformamide. Cleavage of the peptides from the solid support and simultaneous side chain deprotection was achieved by a 4 h treatment with trifluoroacetic acid in the presence of triethylsilane, thioanisole, and water (85/5/5/5, v/v). After 24 h at room temperature, the cleavage solution was collected and the crude peptides were precipitated from the solution with *t*-butylmethyl ether at 0 °C. After several washings with ether, the precipitated peptides were dissolved in a solution of water/acetonitrile with 1% TFA and then lyophilized.

The peptide containing cysteine residues was cyclized by intramolecular oxidation. This peptide (0.2 mg/mL) was dissolved at high dilution in 0.1 M ammonium acetate containing potassium ferricyanide (0.01 mM; 1.4 equiv) and stirred overnight. Reduction in the content of cysteine moieties was followed using DTNB. The crude peptide was purified by reversed-phase HPLC (see below) on a semipreparative C18 column and characterized by ESMS and amino acid analysis. The product appeared as a single peak on analytical HPLC chromatography (R_t = 3.3 min), having identical R_t value as that of commercially available human ANP, indicating that the synthesis, cyclization, and purification yielded the desired product. Amino acid analysis following acid hydrolysis showed the expected amino acid composition. Mass spectrometry analysis (see below) revealed a mass $[M - H]^+$ of 3081.21 ± 0.43 Da. Calcd. 3081.44 Da.

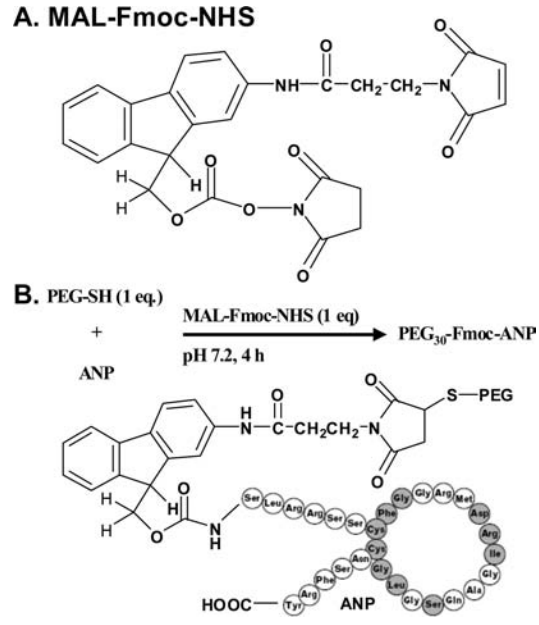

Figure 1. Structure of 9-hydroxymethyl-2-(amino-3-maleimidopropionate)-7-*N*-hydroxysuccinimide (MAL-Fmoc-NHS) (A). Schematic presentation of the steps involved in the preparation of PEG_{30}-Fmoc-ANP (B).

ANP Conjugates Preparation. *Preparation of PEG_{30}-Fmoc-ANP.* MAL-Fmoc-NHS (Figure 1A) is a heterobifunctional agent consisting of fluorenemethoxycarbonyl *N*-hydroxysuccinimide ester that reacts with amino groups of peptides and proteins. A maleimide group, attached to the fluorenyl backbone, enables its coupling to any sulfhydryl-containing compound. Figure 1B shows the optimal procedure found for preparing PEG_{30}-Fmoc-ANP. Accordingly, to a stirred solution of ANP (1 mg) in 100 μL of 0.1 M phosphate buffer, pH 7.2 (3.24 mM), 10 mg of PEG_{30}-SH in 100 μL phosphate buffer was added to obtain a final concentration of 3.33 mM. MAL-Fmoc-NHS (15 μL) from a fresh solution of MAL-Fmoc-NHS (10 mg/mL in DMF, 150 μg) was then added. The reaction was carried out for 4 h followed by dialysis for 2 days against distilled H_2O to remove residual DMF, phosphate buffer, and free ANP. Alternatively, the product was purified by HPLC. The product was characterized by MALDI-TOF mass spectrometry. Effective molecular weight of the conjugate was obtained by SDS gel electrophoresis (see below). The amount of ANP in the conjugate was determined by acid hydrolysis of a 20 μL of 2 mg/mL aliquot, followed by amino acid analysis. ANP concentration was calculated according to alanine (1 residue), tyrosine (1 residue), isoleucine (1 residue), leucine (2 residues), and phenylalanine (2 residues). MALDI-TOF mass spectral analysis showed 1:1 PEG_{30}-Fmoc/ANP stoichiometry. The molecular mass ($[M - H]^+$) of synthesized ANP was 3081.21 Da as determined by ESMS. PEG_{30}-SH had an average molecular mass of 32 300 Da. The spacer molecule following conjugation had a MW of 387 Da, and the conjugate yielded a major peak corresponding to a molecular mass of 35 675 Da. PEG_{30}-Fmoc-ANP migrates on analytical HPLC column (see below) as a wide peak with R_t value of 43 min.

Nonreversible Pegylation of ANP. A stable, nonreversible PEG−ANP conjugate was prepared using the same procedure described for PEG_{30}-Fmoc-ANP, except for the use of 3-maleimidobenzoate-*N*-hydroxysuccinimide ester (MIB-NHS, Pierce, Rockford, USA) to link PEG_{30}-SH to ANP.

High Performance Liquid Chromatography (HPLC) and Mass Spectrometry. Reverse-phase HPLC was performed with a Spectra-Physics SP8800 liquid chromatography system (Spectro-Physics, San Jose, CA) equipped with an Applied Biosystem 757 variable-wavelength absorbance detector. The column effluents were monitored by UV absorbance at 220 nm, and chromatograms were recorded on a chromJet integrator (Thermo-Separation, Riviera Beach, FL). Compounds were analyzed by analytical reversed-phase HPLC using an RP-18, 100 × 4.6 mm Chromolith column (Merck, Darmstadt, Germany). HPLC prepacked columns were either Vydac RP-18, 250 × 22 mm, bead size 10 μm for ANP purification, or Vydac RP-4, 250 × 22 mm, bead size 10 μm, for pegylated ANP derivative purification (Bucher Biotec AG, Basel, Switzerland). Linear gradients were formed between solution A (0.1% TFA in H_2O) and solution B (0.1% TFA in acetonitrile−H_2O 75:25). The analytical column was eluted with a binary gradient of 10–100% solution B over 14 min at a flow rate of 3 mL. Purifications were achieved with a 10–100% B gradient over 50 min, with a flow of 10.0 mL/min.

Mass spectra were determined using matrix-assisted laser-desorption/ionization time-of-flight (MALDI-TOF) mass spectroscopy (Micromass UK Ltd.) and electrospray ionization mass spectra (ESMS) techniques, performed on a Micromass Platform LCZ 4000 (Manchester, UK). Amino acid composition was analyzed following acid hydrolysis in 6 N HCl at 110 °C for 24 h by Dionex amino acid analyzer (Dionex Corporation, CA. USA).

SDS-PAGE Electrophoresis. To determine effective molecular weight of PEG_{30}-Fmoc-ANP/PEG-ANP conjugates, SDS-PAGE was performed using 15% polyacrylamide slab gel according to the Laemmeli method. 10 μg of each sample and a standard protein solution were boiled for 3 min, centrifuged, and loaded on a SDS-PAGE. Pegylated ANPs were specifically stained with a barium iodide solution according to the method of Kurfurst (*24*). This specific staining is based on the formation of a barium iodide complex with the poly(ethylene glycol) molecule. After electrophoresis, the gel was soaked in a 5% glutaraldehyde solution for 15 min at room temperature for fixation and then immersed in 20 mL of 0.1 M perchloric acid for 15 min. After these washes, 10 mL of a 5% barium chloride solution was added, followed by 4 mL of 0.1 M iodine solution. The stained PEG bands appeared within a few minutes. After 15 min, the staining solution was replaced and the gel was put into water.

Biological Methods.*[^{125}I]-ANP Binding to HeLa Cells.*

Cell Culture. NPR-A expressing HeLa cells were obtained from Professor Haim Garty (Departments of Biological Chemistry, The Weizmann Institute of Science, Rehovot, Israel) and grown at 35 °C in a 5% CO_2 humidified incubator in Dulbecco's modified Eagle's medium (DMEM) containing 10% fetal calf serum, penicillin, and streptomycin (100 U/mL of each). The binding assay was performed on subconfluent cell monolayers in 24-well dishes at a density of $4 \cdot 10^5$ cells/well preincubated for 24 h.

[^{125}I]-ANP Binding. ANP was iodinated by the chloramine T procedure of Hunter and Greenwood (*25*). HeLa cell monolayers were washed twice with PBS buffer (pH 7.4) containing 1% bovine serum albumin and then incubated in the same buffer containing [^{125}I]-ANP (100 000 cpm/well) and increasing concentrations (0.74 to 37 nM) of either native ANP or PEGylated ANP derivatives for 2 h at 4 °C. Nonspecific binding was measured in the presence of excess, unlabeled ANP (1.5 μM). The cells were then washed twice with ice-cold buffer and solubilized with 0.2% w/v sodium dodecylsulphate (SDS). Following incubation (37 °C for 30 min), the solubilized cells were transferred to counting vials, and radioactivity was counted (γ-counter, Packard Cobra, GMI, USA). All experiments were performed in duplicate, and each experiment was repeated at least three times. Specific binding is defined as total radioactive content (in the absence of native ANP) minus that obtained at high (1.5 μM) concentration of unlabeled ANP. Receptor binding capacity was determined by calculating the concentration of unlabeled ANP or its derivative that was required to displace 50% of specifically bound [^{125}I]-ANP.

Table 1. Molecular Weight of PEG_{30}-Fmoc-ANP, as Determined by MALDI-TOF and by SDS Gel Electrophoresis[a]

mass (g/mol) (calculated)	$[M + H^+]$ (g/mol) (found by MALDI-TOF)	effective MW according to SDS gel electrophoresis
35 768	35 675	~68 000

[a] Molecular mass was determined by MALDI-TOF and by SDS gel electrophoresis as described in the Experimental Procedures section.

In Vivo Studies.*Animals.* Experiments were performed on male Wistar rats weighing 300–350 g. The rats were housed according to a 12 h light/dark cycle and were allowed at least a 3 day acclimatization period with normal rat chow and tap water *ad libitum*. All procedures were carried out according to the guidelines of the Hebrew University-Hadassah Medical School Animal Care Committee for the use and care of laboratory animals.

Experimental Methods. Animals were anesthetized with urethane (1 g/kg, i.p.) and placed on a heated pad. Rectal temperature was adjusted to 37.5–38 °C by a rectal probe. Following tracheotomy (PE260 catheter), the two femoral veins and the right femoral artery were cannulated with a PE50 heparanized tube. Blood pressure (BP) was recorded from the right femoral artery using SP 844 pressure transducer (MEMSCAP, Skoppum, Norway) coupled to an amplifier (Laboratory linc V, Coulbourn instruments, Allentown, PA). The analog signal was converted to a digital recording by a PowerLab 16SP integration system, and the data were stored on a personal computer by *Chart 4.0* software (Adinstruments, Castle Hill, Australia). Heart rate (HR) was calculated from the BP beats. All animals received an infusion of 3.3 μg/kg/min of adrenaline throughout the experiment using syringe pump (Stoelting, IL). After 30 min, the test compounds (3 μg/kg ANP, 100 μg/kg ANP, 200 μg/kg PEG_{30}-Fmoc-alanine, and PEG_{30}-Fmoc-ANP 96 ± 7 μg covalently linked ANP/kg) were administered by a bolus injection through the second femoral vein cannula in 100 μL saline. In some experiments, 0.83 μg/kg ANP, in 30 μL saline/min, was administered by infusion. The animals were monitored for 120 min after the treatments and then sacrificed. Animals manifesting unstable BP, irregular heart beats, or breathing abnormalities during the experiments were excluded.

Statistical Analysis. Mean arterial blood pressure (MAP), systolic blood pressure (SBP), and HR were calculated by *Chart 4.0* software. Statistical analysis was performed for the changes in BP parameters between sequential measurements and time 0 (just before compound administration) of the experiment in 2 min intervals. This allowed for direct comparison of the responses to treatment between groups when baselines differed (*26*). One-way analysis of variance (ANOVA) was used to compare differences among groups, and two-way ANOVA for repeated measures, followed by Tukey posthoc test. Student's paired *t* test was used to compare differences in the same group. *SPSS 11.5* for windows (SPSS Inc., Chicago, IL) was used to perform the statistical analyses.

RESULTS

ANP Conjugates Syntheses. Table 1 summarizes several characteristic features of the PEG_{30}-Fmoc-ANP conjugate. ANP contains N-terminal α-amino group available for acylation by

Table 2. Receptor Binding Capacities of ANP and Its Conjugates[a]

	IC_{50} (nM)	biological potency (%)
ANP	1.31 ± 0.01	100
PEG_{30}-ANP (nonreversibly PEGylated)	$127^b \pm 7.4$	1.03
PEG_{30}-Fmoc-ANP	$89^b \pm 10.37$	1.47
PEG_{30}-Fmoc-ANP incubated in PBS-1% BSA pH = 7.4 (2 d, 37 °C)	$12^b \pm 0.51$	10.91
PEG_{30}-Fmoc-ANP incubated in 0.1 M borate buffer, pH = 8.5 (2 d, 37 °C)	$11^b \pm 0.44$	11.9

[a] [^{125}I]-ANP binding to HeLa cells was performed as described in Experimental Section. [b] ANP concentration was calculated based on the amount of covalently linked ANP in the conjugate, as measured by amino acid analysis following acid hydrolysis. IC_{50} are expressed as mean ± SD of 4 experiments. Biological potency was calculated as (IC_{50} of ANP/IC_{50} of test compound) × 100.

MAL-Fmoc-NHS. Since our heterobifunctional agent (MAL-Fmoc-NHS) is highly specific to amino side chains in non-SH-containing peptides and proteins (*21–23*) and ANP is a non-lysine-containing peptide agonist (*3*), only the N-terminal α-amino group of ANP is available for acylation. The synthetic procedure applied (Experimental Procedures section) was followed by extensive dialysis and HPLC purification to remove any residual ANP expected, thus yielding a monomodified homogeneous conjugate. Indeed, MALDI-TOF mass spectral analysis shows a main peak having 1:1 PEG_{30}-Fmoc/ANP stoichiometry. The molecular mass of synthesized ANP was 3081 Da as determined by ESMS. PEG_{30}-SH had an average molecular mass of 32 300 Da. The spacer molecule following conjugation has a MW of 387 Da, and the conjugate yielded a major peak corresponding to a molecular mass of 35 675 Da. Acid hydrolysis and amino acid analysis of PEG_{30}-Fmoc-ANP revealed the content of 31 ± 3 μg ANP rather than 86 μg ANP per mg solid material as has been calculated for this molecular weight. This suggests that our preparation also contains PEG_{30}-Fmoc that has not been linked to ANP. Further dosage calculations, however, were based on the value of 31 ± 3 μg ANP per mg solid material, namely, that determined by amino acid analysis following acid hydrolysis.

Receptor Binding Capacity of ANP Conjugates. HeLa cells bind [^{125}I]-ANP with high affinity and the displacement of the ligand by unlabeled ANP yielded an IC_{50} value of 1.3 ± 0.096 nM (data not shown). Previous studies demonstrated that this binding is associated with elevation in the cellular cGMP level (*27, 28*). Table 2 summarizes the receptor binding capacities of the native and pegylated derivatives of ANP in HeLa cells. Relative IC_{50} values obtained revealed that both conventional pegylated ANP and PEG_{30}-Fmoc-ANP have ~1% of the receptor binding affinity of the native peptide. PEG_{30}-Fmoc-ANP, however, undergoes reactivation upon incubation at physiological conditions. This was valid for PEG_{30}-Fmoc-ANP incubated either in 0.1 M borate buffer (pH 8.5, 37 °C) or in PBS buffer containing 1% w/v BSA (pH 7.4, 37 °C).

Release of ANP upon Incubation at Physiological Conditions. PEG_{30}-Fmoc-ANP (322 μg/mL, 10 μg covalently linked ANP/mL) was incubated in 0.1 M borate buffer, pH 8.5, at 37 °C (see Discussion). Aliquots were withdrawn at different time points and analyzed both for the amount of ANP released and for receptor-binding potency using the [^{125}I]-ANP displacement assay in HeLa cells (Figure 2). Under these incubation conditions, peptides are hydrolyzed from PEG-Fmoc-peptide conjugates at a rate that is nearly identical to that obtained in normal human serum at 37 °C (*21, 22*). Upon incubation, ANP has been hydrolyzed from the conjugate in a nearly linear fashion with the concomitant increase in receptor binding potency (Figure 2). About 7% (0.78 ± 0.03 μg) of ANP has been released on day 1 (Figure 2). Based on this value and preliminary results, we calculated that 1 mg of PEG_{30}-Fmoc-ANP (namely, 31 ± 3 μg covalently linked ANP) per rat or more is required for the *in vivo* experiments.

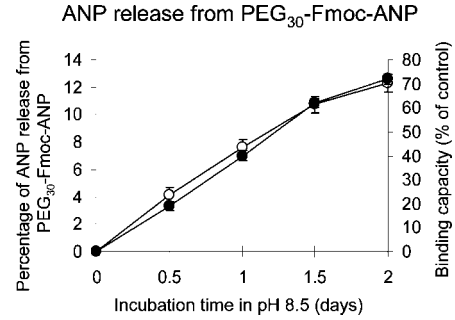

Figure 2. Rate of ANP release from PEG_{30}-Fmoc-ANP. PEG_{30}-Fmoc-ANP (10 μg covalently linked ANP) was incubated in borate buffer (pH 8.5) at 37 °C. Aliquots were withdrawn at the indicated time points and analyzed for the amount of ANP released (○) and for receptor binding capacity (•) (Experimental Procedures section). Binding capacity is calculated as the IC_{50} for the ANP released, versus the IC_{50} of the same quantity of the native hormone. The data are presented as mean ± SD of 4 experiments.

Effect of ANP on Mean Arterial and Systolic BP. Following infusion of adrenaline (3.3 μg/kg/min) for 30 min, rats were injected with native ANP at a dose of 3 and 100 μg/kg. These treatments elicited significant reductions in mean arterial and systolic BP (Figure 3A,B). As expected, ANP effects were transient, and even at the high dose (100 μg/kg), BP returned to control values 20–25 min after the injection. These reductions in mean arterial and systolic BP were accompanied with insignificant, minor changes in diastolic BP and HR (data not shown). These results are in agreement with many studies demonstrating the hypotensive transient effects of ANP (*29, 30*). Notably, a fall in BP at the lower ANP dose (3 μg/kg) was not detected in rats that were not pretreated with adrenaline (data not shown). Therefore, the increase in sensitivity to ANP and its derivatives following adrenaline pretreatment has been subsequently applied.

Prolonged Hypotensive Effects Following Administration of PEG_{30}-Fmoc-ANP. Mean arterial and systolic BP of control animals receiving only adrenaline infusion (3.3 μg/kg/min) decreased slightly by about 10 mmHg within 2 h (Figure 4A,B). This reduction is probably due to time-dependent desensitization of the adrenergic receptors as reported previously (*31*). The administration of PEG_{30}-Fmoc-ANP at a dose of 96 ± 7 μg covalently linked ANP/kg body weight did not change the mean arterial and systolic BP until about 50 min after injection. Mean arterial and systolic BPs decreased markedly and remained low over a period exceeding 60 min (Figure 4A,B). For comparison, the effect of continous infusion of native ANP at a rate of 0.83 μg/kg/min is demonstrated as well (Figure 4A,B). As shown previously (*30, 32*), this treatment yields an immediate effect on lowering both mean and systolic BP in rats, which persists as long as ANP is being infused. Indeed, as reported here, a marked reduction in BP is obtained over a period of 10 to 95 min. Bolus injection of PEG_{30}-Fmoc-alanine at a dose of 200 μg/kg body weight showed insignificant effect on BP that did not differ from that obtained in a saline-treated group (data not shown). Thus, a single administration of PEG_{30}-Fmoc-ANP at a dose of ~100 μg covalently linked ANP/kg facilitates a marked and prolonged BP lowering action in rats,

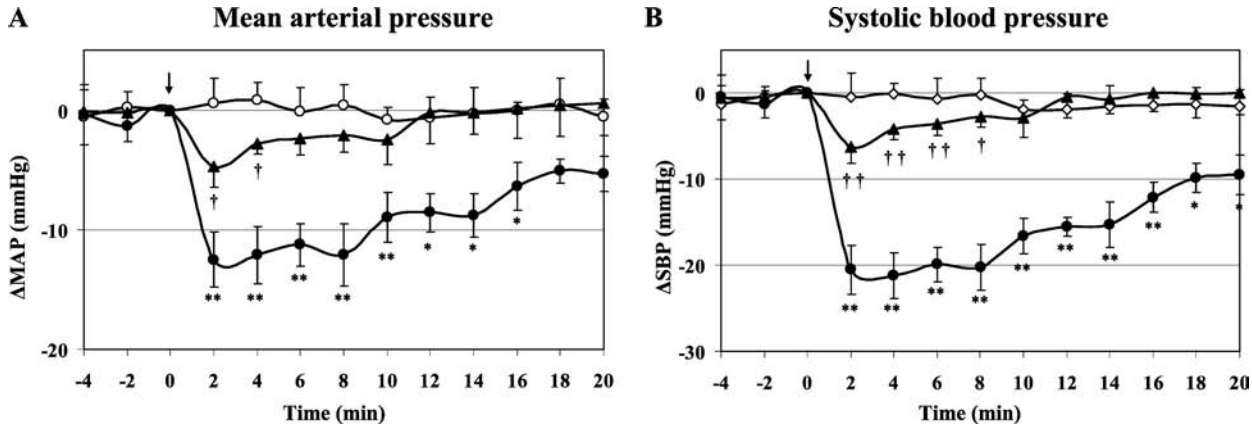

Figure 3. Effect of ANP on BP parameters in anesthetized rats. Animals were anesthetized with urethane, and BP was recorded from the right femoral artery as described in the Experimental Procedures section. All animals received an infusion of 3.3 μg/kg/min of adrenaline throughout the experiment. After 30 min (indicated by an arrow), saline (○), 100 μg/kg ANP (•), and 3 μg/kg ANP (▲) were administered intravenously by 100 μL bolus injection. Values are expressed as mean ± SE ($n = 6$). *$P < 0.05$ vs control; **$P < 0.01$ vs control; $^{\dagger}P < 0.05$ vs baseline; $^{\dagger\dagger}P < 0.01$ vs baseline.

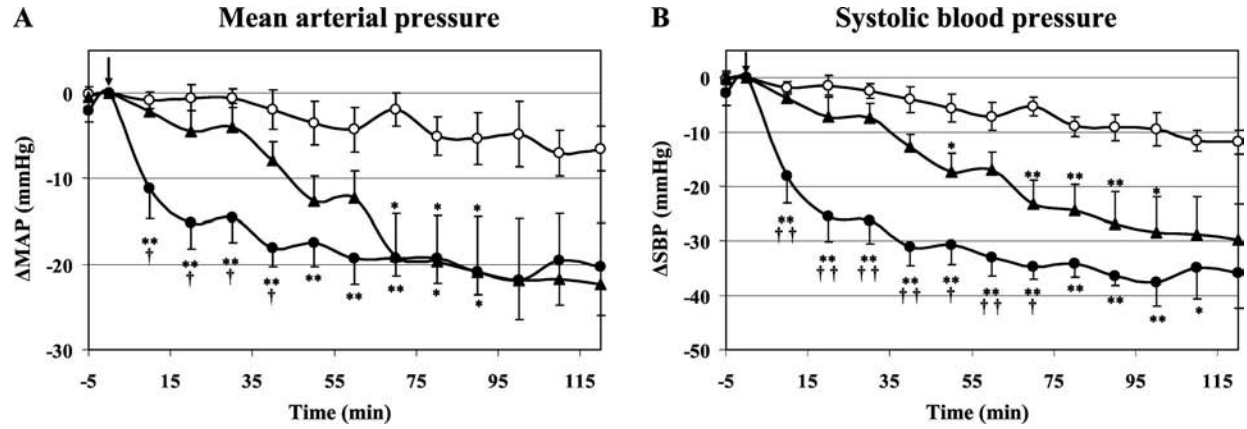

Figure 4. Effect of PEG_{30}-Fmoc-ANP on BP in anesthetized rats. Animals were anesthetized with urethane and BP was recorded from the right femoral artery as described in the Experimental Procedures section. All animals received an infusion of 3.3 μg/kg/min of adrenaline throughout the experiment. After 30 min (indicated by an arrow), the animals received 100 μL bolus injection of saline (○), 96 ± 7 μg/kg covalently linked PEG_{30}-Fmoc-ANP (▲), or infusion of 0.83 μg/kg/min ANP (•). Values are expressed as mean ± SE ($n = 6$). *$P < 0.05$ vs control; **$P < 0.01$ vs control; $^{\dagger}P < 0.05$ vs PEG_{30}-Fmoc-ANP; $^{\dagger\dagger}P < 0.01$ vs PEG_{30}-Fmoc-ANP.

which starts at 50 min after administration and resembles the pattern obtained by continuous infusion of ANP.

DISCUSSION

Since the pioneering work of de Bold and his colleagues (*29*), demonstrating the natriuretic response to atrial extracts in rats, many attempts were made to utilize the active substance from that extract (i.e., ANP) as a natural hypotensive agent. It has become clear that continuous infusion of ANP yields natriuresis, diuresis, and hypotension in animal models and in humans (*1, 7*), indicating that this natural peptide may have a significant therapeutic value. However, ANP is a short-lived species *in vivo*, as it undergoes proteolysis in the circulatory system by NEP and NPR-C and is rapidly cleared by the kidneys (*3, 8, 9*). Therefore, the hypotensive effect of ANP is a transient phenomenon (*29*). The rapid degradation of ANP in the serum poses a serious limitation on its practical use. Therefore, developing a long-acting version of this hormone is a prerequisite for its therapeutic application in the future.

The covalent attachment of PEG to peptides/proteins (pegylation) was shown to dramatically prolong the lifetime of the PEG−peptide conjugate and shield them from proteolysis *in vivo* (*18–20, 33*). Therefore, we first attempted this strategy by covalently linking PEG_{30}-SH to ANP through the nonreversible linker MIB-NHS. A PEG chain of 30 kDa has been selected, since lower molecular weight PEG chains are considerably less effective in preventing clearance by kidney filtration (*34*). Indeed, PEG_{30}-Fmoc and PEG_{30}-Benz-ANP, having calculated molecular weights of ∼36 kDa, migrated as a ∼68 kDa species on SDS gel electrophoresis (Table 1 A), indicating a substantial enlargement in the hydrodynamic volume and therefore in the effective molecular weight of these conjugates. This value is very close to the ∼70 kDa cutoff for glomerular filtration of native globular proteins (*35*).

In spite of those profound advantages, a major obstacle of conventional pegylation is the inactivation that often takes place, particularly with regard to short peptide agonists upon derivatization. A proportionally larger section of low MW peptide agonists participate in and must be accessible to receptor binding. Indeed, as found here, irreversible pegylation of ANP nearly fully abolished its receptor binding to HeLa cells (Table 2).

The remaining alternative was therefore to apply the strategy of reversible pegylation. In this study, we have linked PEG_{30}-SH to the single α-amino side chain of ANP via the heterobifunctional spacer MAL-Fmoc-NHS (Figure 1A). The latter was designed on the basis of the Fmoc principle by which the peptide is released from the conjugate in its native active form. The Fmoc group is used in organic and peptide synthesis for the protection of amino groups and can be removed following basic

treatment, such as with piperidine, within several minutes (*36, 37*). In neutral, aqueous solutions, Fmoc moieties undergo slow, spontaneous hydrolysis, resulting in the regeneration of the native proteins. Since ANP is a non-lysine-containing peptide, an homogeneous 1:1 monomodified PEG-Fmoc-ANP conjugate, where the PEG chain is linked exclusively to the α-amino function of the hormone, has been obtained (Table 1).

As expected, PEG_{30}-Fmoc-ANP is an inactive conjugate as well, and therefore a classical prodrug. This derivative, however, releases ANP and is reactivated upon incubation at physiological conditions (Figure 2). Although this process takes place at a slow rate, receptor binding capacity showed a nearly 7-fold increase within two days of incubation at pH 8.5 and 37 °C (Table 2). Previously, we have shown that the rate of hydrolysis of Fmoc-derived species at pH 8.5, 37 °C, is nearly similar to that obtained at pH 7.4 in the presence of physiological conditions of albumin. We did attribute this finding to the catalytic function of albumin (*21–23*). A linear relationship was obtained between receptor binding potency and the amount of ANP detached from the conjugate (Figure 2). Following the completion of these *in vitro* studies, we investigated whether this conjugate could facilitate a prolonged effect *in vivo.*

Administration of ANP at a dose of 0.1–3 μg/kg to normotensive rats failed to lower BP at any time point following injection (data not shown). Thus, native rats do not provide a suitable experimental pharmacological model to study ANP-induced hypotension. We therefore took advantage of the observation that ANP effects can be intensified by catecholamines (*38–40*). Accordingly, we infused adrenaline to all our animal groups to elevate BP and sensitize the effect of ANP. Indeed, the administration of 3 μg/kg of ANP, which by itself does not affect BP in naive animals, reduced it significantly in rats receiving constant infusion of adrenaline (Figure 3). Notably, this *in vivo* experimental system appears to reflect well the short half-life of ANP ($t_{1/2}$ = 2–5 min, (*7*)). Even with the intravenous administration of a relatively high dosage of ANP (100 μg/kg, 30 μg/rat), BP returned to control levels within 20–25 min following administration (Figure 3). This is in complete agreement with other studies (*29, 30*).

The protracted action of PEG_{30}-Fmoc-ANP in lowering BP is demonstrated in Figure 4. Note should be taken that our *in vivo* experimental system limits the measurement of BP up to a period of 2 h. BP, however, has reached its lowest value 2 h after PEG_{30}-Fmoc-ANP administration. Extrapolation of these data reveals that a low level of BP could be maintained for a period well exceeding ∼10 h as we previously documented with related PEG_{30}-Fmoc-peptide analogues (*21, 23*). Rough calculation based on (1) the administration of 30 μg covalently linked ANP/rat, with a 10× dilution shortly after administration, and (2) the rate of ANP released found *in vitro* (Figure 2) reveals that a level of about 6–10 ng/mL of free ANP is expected to be maintained in the circulatory system at any time point following a lag period of ∼1 h. This ANP level is well within the K_d value for *in vitro* ANP binding affinity to intact cellular systems, ($K_d \approx 2$ nM, (*28*)).

CONCLUSION

In summary, we managed to overcome several obstacles that prevent the designing of prolonged, continuous, therapeutically active ANP. The strategy of conventional pegylation has been replaced by reversible pegylation, an approach that resembles a continuous ANP infusion by the continuous release of the hormone over a prolonged period following administration. Our results show that the novel compound PEG_{30}-Fmoc-ANP release ANP under physiological conditions prolonging the action of the active peptide.

ACKNOWLEDGMENT

We thank Dr. U. Shpolansky for his help in setting up the *in vivo* experimental system. M.F. is the Lester Pearson Professor of Protein Chemistry. Y.S. is the incumbent of the C.H. Hollenberg Chair in Metabolic and Diabetes Research, established by the friends and associates of Dr. C.H. Hollenberg of Toronto, Canada.

LITERATURE CITED

(1) Silver, M. A. (2006) The natriuretic peptide system: kidney and cardiovascular effects. *Curr. Opin. Nephrol. Hypertens. 15*, 14–21.
(2) Nakayama, T. (2005) The genetic contribution of the natriuretic peptide system to cardiovascular diseases. *Endocr. J. 52*, 11–21.
(3) Levin, E. R., Gardner, D. G., and Samson, W. K. (1998) Natriuretic peptides. *N. Engl. J. Med. 339*, 321–328.
(4) McGrath, M. F., de Bold, M. L., and de Bold, A. J. (2005) The endocrine function of the heart. *Trends Endocrinol. Metab. 16*, 469–477.
(5) Ahluwalia, A., MacAllister, R. J., and Hobbs, A. J. (2004) Vascular actions of natriuretic peptides. Cyclic GMP-dependent and -independent mechanisms. *Basic Res. Cardiol. 99*, 83–89.
(6) Antunes-Rodrigues, J., de Castro, M., Elias, L. L., Valenca, M. M., and McCann, S. M. (2004) Neuroendocrine control of body fluid metabolism. *Physiol. Rev. 84*, 169–208.
(7) Potter, L. R., Abbey-Hosch, S., and Dickey, D. M. (2006) Natriuretic peptides, their receptors, and cyclic guanosine monophosphate-dependent signaling functions. *Endocr. Rev. 27*, 47–72.
(8) Anand-Srivastava, M. B. (2005) Natriuretic peptide receptor-C signaling and regulation. *Peptides 26*, 1044–1059.
(9) Corti, R., Burnett, J. C., Jr., Rouleau, J. L., RuschitzkaF., and Luscher, T. F. (2001) Vasopeptidase inhibitors: a new therapeutic concept in cardiovascular disease. *Circulation 104*, 1856–1862.
(10) Maisel, A. S. (2003) Nesiritide: a new therapy for the treatment of heart failure. *Cardiovasc. Toxicol. 3*, 37–42.
(11) Suwa, M., Seino, Y., Nomachi, Y., Matsuki, S., and Funahashi, K. (2005) Multicenter prospective investigation on efficacy and safety of carperitide for acute heart failure in the 'real world' of therapy. *Circ. J. 69*, 283–290.
(12) Quaschning, T. (2005) Vasopeptidase inhibition for blood pressure control: emerging experience. *Curr. Pharm. Des. 11*, 3293–3299.
(13) Burger, A. J., and Burger, M. R. (2002) Nesiritide (Scios). *IDrugs 5*, 703–709.
(14) Vesely, D. L. (2006) Which of the cardiac natriuretic peptides is most effective for the treatment of congestive heart failure, renal failure and cancer? *Clin. Exp. Pharmacol. Physiol. 33*, 169–176.
(15) Messerli, F. H., and Nussberger, J. (2000) Vasopeptidase inhibition and angio-oedema. *Lancet 356*, 608–609.
(16) Sackner-Bernstein, J. D., Skopicki, H. A., and Aaronson, K. D. (2005) Risk of worsening renal function with nesiritide in patients with acutely decompensated heart failure. *Circulation 111*, 1487–1491.
(17) Sackner-Bernstein, J. D., Kowalski, M., Fox, M., and Aaronson, K. (2005) Short-term risk of death after treatment with nesiritide for decompensated heart failure: a pooled analysis of randomized controlled trials. *JAMA 293*, 1900–1905.
(18) Veronese, F. M., and Pasut, G. (2005) PEGylation, successful approach to drug delivery. *Drug Discovery Today 10*, 1451–1458.
(19) Werle, M., and Bernkop-Schnurch, A. (2006) Strategies to improve plasma half life time of peptide and protein drugs. *Amino Acids 30*, 351–367.
(20) Roberts, M. J., Bentley, M. D., and Harris, J. M. (2002) Chemistry for peptide and protein PEGylation. *Adv. Drug Delivery Rev. 54*, 459–476.

(21) Tsubery, H., Mironchik, M., Fridkin, M., and Shechter, Y. (2004) Prolonging the action of protein and peptide drugs by a novel approach of reversible polyethylene glycol modification. *J. Biol. Chem. 279*, 38118–38124.

(22) Peleg-Shulman, T., Tsubery, H., Mironchik, M., Fridkin, M., Schreiber, G., and Shechter, Y. (2004) Reversible PEGylation: a novel technology to release native interferon alpha2 over a prolonged time period. *J. Med. Chem. 47*, 4897–4904.

(23) Shechter, Y., Tsubery, H., Mironchik, M., Rubinstein, M., and Fridkin, M. (2005) Reversible PEGylation of peptide YY3–36 prolongs its inhibition of food intake in mice. *FEBS Lett. 579*, 2439–2444.

(24) Kurfurst, M. M. (1992) Detection and molecular weight determination of polyethylene glycol-modified hirudin by staining after sodium dodecyl sulfate-polyacrylamide gel electrophoresis. *Anal. Biochem. 200*, 244–248.

(25) Hunter, W. M., and Greenwood, F. C. (1962) Preparation of iodine-131 labelled human growth hormone of high specific activity. *Nature (London) 194*, 495–496.

(26) Rybczynska, A., Boblewski, K., Lehmann, A., Orlewska, C., Foks, H., Drewnowska, K., and Hoppe, A. (2005) Calcimimetic NPS R-568 induces hypotensive effect in spontaneously hypertensive rats. *Am. J. Hypertension 18*, 364–371.

(27) Kort, J. J., and Koch, G. (1990) Receptors for atrial natriuretic peptide (ANP) and cyclic GMP responses in HeLa cells. *Biochem. Biophys. Res. Commun. 168*, 148–154.

(28) Watt, V. M., and Yip, C. C. (1989) HeLa cells contain the atrial natriuretic peptide receptor with guanylate cyclase activity. *Biochem. Biophys. Res. Commun. 164*, 671–677.

(29) de Bold, A. J., Borenstein, H. B., Veress, A. T., and Sonnenberg, H. (1981) A rapid and potent natriuretic response to intravenous injection of atrial myocardial extract in rats. *Life Sci. 28*, 89–94.

(30) Sasaki, A., Kida, O., Kangawa, K., Matsuo, H., and Tanaka, K. (1985) Hemodynamic effects of alpha-human atrial natriuretic polypeptide (alpha-hANP) in rats. *Eur. J. Pharmacol. 109*, 405–407.

(31) Guimaraes, S., and Moura, D. (2001) Vascular adrenoceptors: an update. *Pharmacol. Rev. 53*, 319–356.

(32) Hirata, Y., Ishii, M., Sugimoto, T., Matsuoka, H., Fukui, K., Sugimoto, T., Yamakado, M., Tagawa, H., Miyata, A., and Kangawa, K. (1988) Hormonal and renal effects of atrial natriuretic peptide in patients with secondary hypertension. *Circulation 78*, 1401–1410.

(33) Shepherd, J., Jones, J., Takeda, A., Davidson, P., and Price, A. (2006) Adefovir dipivoxil and pegylated interferon alfa-2a for the treatment of chronic hepatitis B: a systematic review and economic evaluation. *Health Technol. Assess. 10*, 1–183, iii-iv, xi-xiv.

(34) Rosendahl, M. S., Doherty, D. H., Smith, D. J., Carlson, S. J., Chlipala, E. A., and Cox, G. N. (2005) A long-acting, highly potent interferon alpha-2 conjugate created using site-specific PEGylation. *Bioconjugate Chem. 16*, 200–207.

(35) Caliceti, P., and Veronese, F. M. (2003) Pharmacokinetic and biodistribution properties of poly(ethylene glycol)-protein conjugates. *Adv. Drug Delivery Rev. 55*, 1261–1277.

(36) Carpino, L., and Han, G. (1972) The 9-fluorenylmethoxycarbonyl amino-protecting group. *J. Org. Chem. 37*, 3404–3409.

(37) Carpino, L., and Han, G. (1970) The 9-fluorenylmethoxycarbonyl function, a new base-sensitive amino-protecting group. *J. Am. Chem. Soc. 92*, 5748–5749.

(38) Yasujima, M., Abe, K., Kohzuki, M., Tanno, M., Kasai, Y., Sato, M., Omata, K., Kudo, K., Tsunoda, K., and Takeuchi, K., et al. (1985) Atrial natriuretic factor inhibits the hypertension induced by chronic infusion of norepinephrine in conscious rats. *Circ. Res. 57*, 470–474.

(39) Badalamenti, S., Borroni, G., Lorenzano, E., Incerti, P., and Salerno, F. (1992) Renal effects in cirrhotic patients with avid sodium retention of atrial natriuretic factor injection during norepinephrine infusion. *Hepatology 15*, 824–829.

(40) Parkes, D. G., Coghlan, J. P., McDougall, J. G., and Scoggins, B. A. (1990) Effects of atrial natriuretic factor on pressor responsiveness to angiotensin II, norepinephrine, and vasopressin in conscious sheep. *J. Cardiovasc. Pharmacol. 15*, 16–21.

BC700294W

Flurbiprofen Derivatives in Alzheimer's Disease: Synthesis, Pharmacokinetic and Biological Assessment of Lipoamino Acid Prodrugs

Rosario Pignatello,*[,†] Valentina Pantò,[†] Stefano Salmaso,[§] Sara Bersani,[§] Venerando Pistarà,[‡] Vladimir Kepe,[||] Jorge R. Barrio,[||] and Giovanni Puglisi[†]

Dipartimento di Scienze Farmaceutiche and Dipartimento di Scienze Chimiche, Università degli Studi di Catania, Viale A. Doria, 6 - 95125 Catania, Italy, Dipartimento di Scienze Farmaceutiche, Università degli Studi di Padova, Via F. Marzolo, 5 - 35131 Padova, Italy, and Department of Molecular and Medical Pharmacology, The David Geffen School of Medicine at UCLA, Los Angeles, California 90095. Received August 18, 2007; Revised Manuscript Received October 27, 2007

Flurbiprofen (FLU) lipophilic prodrugs with lipoamino acids (LAA) **6a**−**e** were synthesized for brain delivery. Chemical and plasmatic stability of prodrugs **6a**−**e** as well as pharmacokinetic distribution studies for the prodrugs **6b** and **6d** were carried out. FLU prodrugs **6a**−**e** were compared to the parent drug for their ability to inhibit binding of [F-18]FDDNP to *in vitro* formed *β*-amyloid protein (A*β* fibrils). FLU−LAA conjugates showed a typical prodrug stability profile, being stable in PBS at pH 7.4 and releasing the active drug in plasma. Compound **6d** yielded a slow accumulation of FLU in the brain. In the *in vitro* inhibition assay, all prodrugs except for the prodrug with the longest alkyl side chain (**6e**) were effective as inhibitors of [F-18]FDDNP binding to A*β* fibrils with EC50 values in the 10−300 nM range. The different brain accumulation kinetics shown by FLU and its LAA conjugate **6d** suggested a possible slow-releasing activity of FLU by these prodrugs in the brain or a differential pharmacological effect deserving further, detailed studies on their biodistribution and pharmacological profile.

INTRODUCTION

Brain inflammation is one of the biochemical processes contributing to neurodegeneration in Alzheimer's disease (AD) (*1*). Recent studies have demonstrated that mediators of inflammatory reaction in AD, such as cytokines, free radicals, adhesion molecules, and prostaglandins, were neurotoxic in experimental models (*2*). These compounds were hypothesized to act as extracellular signals promoting neuronal degeneration (*3, 4*). The formation of extracellular senile plaques, neuropathological fibrillar deposits of *β*-amyloid protein (A*β*), has been associated with a variety of proteins which may also be potential propagators of inflammation (*5*).

A possible role of inflammation in AD pathogenesis and development is also supported by clinical evidence indicating that administration of nonsteroidal anti-inflammatory agents (NSAIDs) to AD patients slows deterioration of cognitive functions (*6*), reduces the incidence of AD (*7*), and exerts a neuroprotective effect (*8, 9*). Direct NSAID interaction with fibrillar *β*-amyloid protein (A*β*) has also been shown *in vitro* (*10*).

Since cyclooxygenase-2 inducible isoform (COX-2), one of the target enzymes of NSAIDs, has been detected at high levels in the brain of AD patients (*11*), it has been hypothesized that NSAIDs primarily exert their neuroprotective effect by inhibition of COX-2 mediated synthesis of pro-inflammatory prostanoids (*8*). Experimental evidence further suggests that inhibition of high expression levels of both COX-1 and COX-2 isoforms produces beneficial effects against brain inflammation (*12*).

Some NSAIDs have been shown to decrease the production of A*β*42, the major component of senile plaques of AD brain, and counteract the progression of A*β*42 pathology in transgenic mouse models of AD (*13*). The proposed mechanism for this activity is an allosteric modulation of *γ*-secretase activity, the enzyme responsible for the formation of *β*-amyloid. The inhibition of A*β*42 production is independent from the anti-COX activity and is related to the chemical structure of the compounds, with some NSAIDs being active (ibuprofen, sulindac, flurbiprofen, indomethacin, diclofenac) and others not (naproxen, aspirin, celecoxib) (*14, 15*).

NSAID availability in the brain is crucial to the efficiency of these drugs as neuroprotective agents. In order to enhance brain availability of NSAIDs, we investigated amphiphilic conjugates with lipoamino acids (LAA). In this report, we focus our interest on flurbiprofen (FLU, **1**) a drug that, because of its anti-inflammatory and analgesic activities attributed to the inhibition of both COX isoforms, has been considered as a potential neuroprotective agent in AD therapy (*16–21*). Furthermore, FLU reduced the secretion of both A*β*42 and A*β*40 peptides in Neuro-2a cells and rat primary cortical neurons (*12, 22*) as well as in the brain of tg2576 *β*-amyloid transgenic mice (*13, 14*).

FLU was modified with LAA residues; this was aimed at increasing its availability in the brain. LAA are α-amino acids bearing alkyl side chains, whose length and structure can be modified to achieve the desired physicochemical properties (*23*). Because of the presence of an alkyl chain and a polar amino acid head, LAA conjugation yields amphiphilic derivatives, with a membrane-like character that can favor their interaction with and penetration through biological membranes and barriers (*24–26*).

Recent pharmacological studies have focused attention on the *R*-enantiomer of FLU (*R*-FLU) as a possible agent for AD treatment. *R*-FLU, in fact, lacks the side effects of NSAIDs mediated by their inhibition of COX. However, both *S*- and *R*-FLU have been shown to be equipotent in lowering A*β*42 levels in mouse brain and share the same mechanism of

* Corresponding author. Prof. Rosario Pignatello, Phone: +39 0957384021; Fax: +39 095222239; email: r.pignatello@unict.it.

[†] Dipartimento di Scienze Farmaceutiche, Università degli Studi di Catania.

[‡] Dipartimento di Scienze Chimiche, Università degli Studi di Catania.

[§] Università degli Studi di Padova.

[||] The David Geffen School of Medicine at UCLA.

10.1021/bc700312y CCC: $40.75 © 2008 American Chemical Society
Published on Web 12/12/2007

interaction with the γ-secretase complex (*13*). In this first study, we thus chose to perform the chemical derivatization using the racemic form of FLU; a further exploitation of the potentiality of FLU−LAA prodrugs could be made using pure *R*-FLU.

LAA with different alkyl side chains ranging from 4 to 12 carbon atoms were linked to FLU through an ethanolamine spacer via an ester bond between FLU and the spacer and an amide bond between the LAAs and the spacer. The chemical stability profiles of all synthesized conjugates (**6a**−**e**) were determined in pH 7.4 phoshate buffer, while the pharmacokinetic and biodistribution patterns were evaluated for **6b** and **6d** after intravenous administration to mice.

The capacity of FLU and prodrug **6** to interact with the insoluble fibrillar aggregates of β-amyloid (1–40) protein was also tested using radiofluorinated [F-18]FDDNP in a competition assay with *in vitro* formed β-amyloid (1–40) fibrils. [F-18] FDDNP (2-(1-{6-[(2-[F-18]fluoroethyl)(methyl)amino]-2-naphthyl}ethylidene)malononitrile) is a positron-emitting radiofluorinated molecular imaging probe with binding affinity for neuropathological lesions found in AD, β-amyloid senile plaques, and neurofibrillary tangles, used for *in vivo* positron emission tomography (PET) imaging of the neuropathology load in AD patients' brains (*27*).

EXPERIMENTAL PROCEDURES

Materials. FLU (racemic form), (±)*N*-Boc-2-aminohexanoic acid (**4a**), (±)2-aminoalkanoic acids, and the other reactants and solvents were purchased from Sigma-Aldrich Chimica Srl (Milan, Italy). The 2-aminoalkanoic acids were Boc-protected before use following a published procedure (*28*) to give compounds **4b**−**e**. All solvents were dried by distillation according to standard methods (*29*) and stored over 4 Å molecular sieves activated at 400 °C for at least 24 h.

[F-18]FDDNP was prepared by tosyloxy-to-fluorine nucleophilic substitution from cyclotron-produced [F-18]fluoride anion and 2-{[6-(2,2-dicyano-1-methylvinyl)-2-naphthyl](methyl) amino}ethyl 4-methylbenzenesulfonate as described elsewhere (*30*) and immediately used for competitive binding assays with FLU and prodrugs **6a**−**e**.

The male Balb/c mice weighing 22 ± 2 g used for the *in vivo* studies had free access to food and were housed at the Department of Pharmaceutical Sciences, University of Padua. Animal experiments were performed in accordance with Italian law (D.L. 116/92) and European guidelines (EEC n. 86/609).

Instrumentation. TLC analysis was used to check the purity of compounds using silica gel aluminum plates (Merck $F_{254-366}$); the spots were detected by spraying the plate with ninhydrin or an acid–base reactant. Elemental analysis was carried out on a Carlo Erba 1106 analyzer; samples were kept under vacuum for 24 h over P_2O_5 before analysis. FT-IR spectra were recorded as nujol mulls with a Perkin-Elmer 1600 spectrophotometer. ^{1}H NMR spectra were obtained in $CDCl_3$ at 200 MHz using a Varian Innova instrument. Chemical shifts are reported in ppm, using TMS as internal standard. Mass spectra were measured with a triple quadripole instrument (IPE sciex API 3000) operating in SIM mode with positive ion electrospray.

The partition and distribution coefficients (cLog *P* and cLog $D_{7.4}$) of FLU and prodrugs were calculated using the *ACD/LogP 5.15* software (Advanced Chemistry Development Inc., Toronto, Canada) and the *Pallas 3.0* software package (CompuDrug International, Inc., Sedona, AZ), respectively (Table 1).

Synthesis of FLU−EA Intermediate (3). FLU (**1**) (0.82 mmol, 200 mg) was dissolved in 20 mL of anhydrous dichloromethane (DCM), and 1-hydroxybenzotriazole (HOBt) (0.82 mmol, 123 mg) and triethylamine (TEA) (1.64 mmol, 227 μL) were added. The solution was treated with 1.64 mmol (232 mg) of 1-ethyl-3-(3-dimethylaminopropyl)carbodiimide hydrochloride (EDAC) and the mixture was kept at 0 °C in an ice–water bath for 2 h. *N*-Boc-ethanolamine [*tert*-butyl-*N*-(2-hydroxyethyl)carbamate] (190 μL, 1.23 mmol) in 10 mL of DCM was added to the reaction mixture and stirred at 0 °C for 2 h. The mixture was brought to room temperature and stirred for an additional 4–6 h. The solvent was removed under vacuum, and the oily residue was dissolved in 20 mL DCM, washed twice with 20 mL aliquots of water, followed by 5% $NaHCO_3$ solution, 5% aqueous acetic acid, and finally brine. The organic phase was separated, dried over anhydrous sodium sulfate, and evaporated. The final residue was purified by flash chromatography on silica gel with ethyl acetate/cyclohexane, 40:60 (v/v) to obtain compound **2**.

Table 1. General Structure and Properties of FLU−EA−LAA Conjugates 6a−e

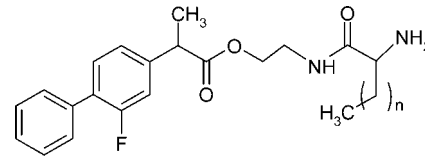

					HPLC method	
compound	*n*	cLog *P*[a]	cLog *P*[b]	cLog $D_{7.4}$[b]	eluent (ACN/water, % v/v)	R_T (min)
6a	3	4.82 ± 0.56	4.67	3.88	60:40	7.1
6b	5	5.88 ± 0.56	5.69	4.83	60:40	13.3
6c	7	6.94 ± 0.56	6.71	5.78	75:25	8.1
6d	9	8.01 ± 0.56	7.73	6.80	90:10	9.6
6e	11	9.07 ± 0.56	8.75	7.74	90:10	15.8
FLU	–	*4.11 ± 0.37*	*4.24*	*0.18*	*75:25*	*1.3*
3	–	–	–	–	*75:25*	*5.9*

[a] Predictions were made using the *ACD LogP 5.15* software. [b] Calculated using the *Pallas 3.0* software.

The Boc protective group was finally removed with 10% (v/v) solution of TFA in DCM for 30 min at room temperature. The solvents were evaporated under a nitrogen flow, and the residue was treated with 20 mL of 5% sodium hydrogen carbonate and extracted with 20 mL DCM. The organic phase was separated, dried as described above, and evaporated to dryness to give FLU−EA [**3**; 2-(2-fluoro-4-biphenyl)propionic acid 2-aminoethyl ester] (Scheme 1). The oily compound was kept refrigerated until use. Elemental analysis for $C_{17}H_{18}FNO_2$, % found (theoretical): C 70.70 (71.06), H 6.22 (6.31), N 4.86 (4.87). IR (cm^{-1}): 1733.7 (ester *C*=O), 3302.2 (amine); MS (*m*/*z*): 288 $[M + 1]^+$ (100%); ^{1}H NMR (ppm): 7.49–7.30 (m, 6H, aromatic), 7.08 (m, 1H, ∅-H), 7.04 (s, 1H, ∅-H), 4.26 (t, 2H, OCH_2), 3.68–3.54 (q, 1H, $\underline{CH}$-CH_3), 3.08 (m, 2H, $\underline{CH_2}$-NH_2), 1.39 (d, 3H, CH_3).

Synthesis of FLU−EA−LAA Derivatives (6a−e): General Procedure (Scheme 1). A Boc-LAA derivative (**4a**−**e**, 0.25 mmol) was dissolved in 10 mL DCM, and HOBt (0.16 mmol, 24.5 mg) and TEA (0.32 mmoles, 44 μL) were added. The chosen LAA was then activated by adding EDAC (0.32 mmol, 45.4 mg) and stirring the mixture for 2 h in an ice–water bath. A solution of **3** (0.25 mmol, 68.9 mg) in 10 mL DCM was then added, and the mixture was kept at 0 °C for 2 h and then at room temperature for 18–24 h. Upon completion of the conjugation (TLC), the mixture was extracted as reported above, and the waxy residue was purified by column chromatography, using an ethyl acetate/cyclohexane gradient from 50:50 to 60:40 (v/v) to isolate compounds **5a**−**e**. The obtained product was deprotected by 20% TFA in DCM, and the residue was purified by semipreparative TLC (0.5 mm layer silica gel plates, SIL G-50, Macherey-Nagel GmbH & Co., Düren, Germany) eluted with an 80:20 DCM/methanol mixture. Compounds **6** were stored in closed amber glass containers at 4 °C.

Analytical Characterization of Compounds 6a−e. 6a (n = 3): 2-(2-fluoro-4-biphenyl)propionic acid 2-(2-aminohexanoyl)aminoethyl ester. Elemental analysis for $C_{23}H_{29}FN_2O_3$, % found (theoretical): C 69.21 (68.98), H 7.31 (7.30), N 7.00 (6.99). IR (cm^{-1}): 1678.9 (amide *C*=O), 1750.1 (ester *C*=O). MS (*m*/*z*, %): 401.6 $[M + H]^+$ (100), 313 (13), 288 (7). ^{1}H NMR (ppm): 7.99 (broad, 1H, NH), 7.76–7.40 (m, 6H, aromatic), 7.22 (m, 1H, ∅-H), 7.15 (s, 1H, ∅-H), 4.41 (m, 2H, OCH_2), 3.72 (q, 1H, CH-CH_3), 3.42 (m, 2H, CH_2-NH_2), 1.79 (m, 2H, CH_2), 1.61 (d, 3H, CH_3), 1.35–1.24 (t, 4H, CH_2), 0.85 (t, 3H, ω-CH_3).

6b (n = 5): 2-(2-fluoro-4-biphenyl)propionic acid 2-(2-aminooctanoyl)aminoethyl ester. Elemental analysis for $C_{25}H_{33}FN_2O_3$, % found (theoretical): C 69.80 (70.07), H 7.77 (7.76), N 6.50 (6.54). IR (cm^{-1}): 1679.8 (amide *C*=O), 1741.8 (ester *C*=O). MS (*m*/*z*, %): 429.5 $[M + H]^+$ (100), 368 (4), 340 (5). ^{1}H NMR (ppm): 7.97 (broad, 1H, NH), 7.52–7.34 (m, 5H, aromatic), 7.26 (s, 1H, ∅-H), 7.11 (m, 1H, ∅-H), 7.05 (s, 1H, ∅-H), 4.10 (m, 2H, OCH_2), 3.72 (q, 1H, CH-CH_3), 3.45 (m, 2H, CH_2-NH_2), 1.77 (m, 2H, CH_2), 1.48 (d, 3H, CH_3), 1.25–1.21 (t, 8H, CH_2), 0.82 (t, 3H, ω-CH_3).

6c (n = 7): 2-(2-fluoro-4-biphenyl)propionic acid 2-(2-aminodecanoyl)aminoethyl ester. Elemental analysis for $C_{27}H_{37}FN_2O_3$, % found (theoretical): C 70.80 (71.02), H 8.16 (8.17), N 6.11 (6.14). IR (cm^{-1}): 1679.6 (amide *C*=O), 1739.3 (ester *C*=O). MS (*m*/*z*, %): 457.7 $[M + H]^+$ (100), 396 (8), 368 (7). ^{1}H NMR (ppm): 8.04 (broad, 1H, NH), 7.62–7.38 (m, 5H, aromatic), 7.56 (s, 1H, ∅-H), 7.09 (m, 1H, ∅-H), 7.02 (s, 1H, ∅-H), 4.30 (broad m, 2H, OCH_2), 3.90 (q, 1H, CH-CH_3), 3.49 (m, 2H, CH_2-NH_2), 1.66 (m, 2H, CH_2), 1.56 (d, 3H, CH_3), 1.32–1.17 (t, 12H, CH_2), 0.88 (t, 3H, ω-CH_3).

6d (n = 9): 2-(2-fluoro-4-biphenyl)propionic acid 2-(2-aminododecanoyl)aminoethyl ester. Elemental analysis for $C_{29}H_{41}FN_2O_3$, % found (theoretical): C 71.59 (71.87), H 8.56 (8.53), N 5.81 (5.78). IR (cm^{-1}): 1667.1 (amide *C*=O), 1734.1 (ester *C*=O). MS (*m*/*z*, %): 485.6 $[M + H]^+$ (100), 486 (35), 396 (9). ^{1}H NMR (ppm): 7.98 (broad, 1H, NH), 7.54–7.39 (m, 6H, aromatic), 7.21 (m, 1H, ∅-H), 6.88 (s, 1H, ∅-H), 4.34 (m, 2H, OCH_2), 3.76 (q, 1H, CH-CH_3), 3.48 (m, 2H, CH_2-NH_2), 1.77 (m, 2H, CH_2), 1.63 (d, 3H, CH_3), 1.32–1.21 (m, 16H, CH_2), 0.86 (t, 3H, ω-CH_3).

6e (n = 11): 2-(2-fluoro-4-biphenyl)propionic acid 2-(2-aminotetradecanoyl)aminoethyl ester. Elemental analysis for $C_{31}H_{45}FN_2O_3$, % found (theoretical): C 72.88 (72.62), H 8.88 (8.85), N 5.45 (5.46). IR (cm^{-1}): 1664 (amide *C*=O), 1728 (ester *C*=O). MS (*m*/*z*, %): 513.9 $[M + H]^+$ (100), 485 (55), 457 (20), 420 (12). ^{1}H NMR (ppm): 8.04 (broad, 1H, NH), 7.50–7.26 (m, 5H, aromatic), 7.46 (s, 1H, ∅-H), 7.12 (m, 1H, ∅-H), 6.97 (s, 1H, ∅-H), 4.24 (m, 2H, OCH_2), 3.75 (q, 1H, CH-CH_3), 3.46 (m, 2H, CH_2-NH_2), 1.79 (m, 2H, CH_2), 1.60 (d, 3H, CH_3), 1.30–1.22 (t, 20H, CH_2), 0.88 (t, 3H, ω-CH_3).

Chemical Stability Assay. Each prodrug **6a**−**e** (1 mg) was dissolved in DMSO (100 μL) and diluted to 1 mL with isotonic phosphate buffer (PBS, pH 7.4). The mixture was incubated at 37 ± 1 °C, and 100 μL aliquots were withdrawn at regular time intervals (every 7–8 days). HPLC analysis was performed to determine the amount of intact prodrugs as well as the amounts of released FLU (**1**) and FLU−EA (**3**), products of hydrolytic cleavage of the FLU−EA ester bond or the EA−LAA amide bond, respectively. A Varian ProStar chromatograph equipped with a Varian 410 autosampler and a Waters C18 Symmetry column (5 μm, 4.6 × 150 mm), connected to a Waters C18 Symmetry precolumn, was used for the analysis. The UV detector was set at 247 nm. 10 μL aliquots were injected by means of a Varian 410 autosampler and the compounds eluted at 1 mL/min under isocratic conditions with different water/acetonitrile (ACN) mixtures, as summarized in Table 1.

Scheme 1. General Procedure for the Synthesis of FLU−EA−LAA Prodrugs

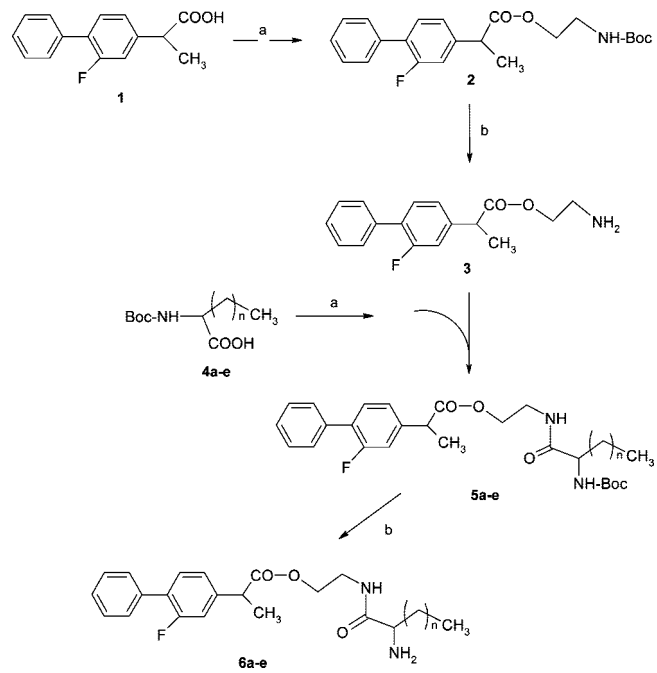

Plasma Stability Evaluation. Three heparinized mouse whole blood samples (300 μL) were mixed with 150 μL of 50:50 water/ACN containing 9 μg of either FLU, **6b** or **6d**, and kept at 37 °C. At scheduled times (30, 60, 120, 180, 240, and 300 min), 50 μL of the samples were withdrawn and added of 100 μL of ACN to precipitate proteins. The samples were centrifuged for 5 min at 4 °C and 14 000 rpm, and the supernatant was analyzed according to the procedure reported below. The drug and prodrug contents were referred to the standard titration curves.

Analytical Procedure. The content of FLU, FLU−EA (**3**), and prodrugs **6b** and **6d** in the tissue extraction samples was evaluated by reverse-phase HPLC using an analytical C-18 column (Luna, Phenomenex, 250 × 4.6 mm). NAP standard solution (50 μL) was added to the samples as an internal standard. The column was eluted with a gradient of water (eluent A) and ACN (eluent B), both containing 0.05% TFA, according to the following gradient scheme: 40% eluent B for 3 min, up to 60% eluent B in 20 min, to 90% eluent B in 2 min, and back to the initial conditions in 2 min. The UV detector was set at 247 nm. FLU, **6b**, **6d**, and NAP retention times were 20.5, 14.7, 25.5, and 13.9 min, respectively. Standard curves were calculated for each compound in the range 0.08–40 μg/mL with r^2 = 0.996 – 0.999. The amounts of the compounds **6b** and **6d** and their hydrolysis products FLU and FLU−EA were determined from the standard curves using the corresponding peak areas.

In the case of solid tissues, the blood contribution was evaluated and subtracted according to the procedure reported in the literature (*31*).

Extraction Tests from Plasma and Organs. The recovery of compounds **1**, **6b**, and **6d** from mouse liver, kidney, brain, spleen, and plasma was evaluated.

100 μL of heparinized whole blood was withdrawn from mice by retrobulbar puncture and added to 100 μL of 50:50 (v/v) ACN/water mixture containing different amounts (1, 2, and 3 μg) of FLU or FLU equivalent amounts of prodrugs, and 50 μL of naproxen standard solution (NAP) (0.1 μg/μL in the same solvent mixture). The samples were mixed and centrifuged for 3 min at 3000 rpm. Aliquots of 50 μL of clear supernatant were

withdrawn, mixed with 100 μL of ACN, vortex-mixed, and finally centrifuged for 3 min at 14 000 rpm. The supernatants containing the extracted compounds were analyzed by HPLC as reported above.

Liver, kidney, brain, and spleen taken from the same mouse were washed with physiological solution and gently dried on paper. Different volumes (10, 20, 30, 40, and 50 μL) of ACN solutions containing 50 ng/μL of each compound were added to 50 mg of liver, kidney, brain, and spleen samples. The samples were mixed with 50 μL of NAP standard solution (0.1 μg/μL) and 1 mL of 50:50 (v/v) ACN/water mixture. The samples were homogenized and then centrifuged for 5 min at 4000 rpm. The supernatants were collected by suction and the pellets treated three times with 1 mL of ACN/water mixture and once with 1 mL of ACN. All five supernatants were combined and centrifuged for 3 min at 14 000 rpm. The final volume was lyophilized, and the residue was dissolved in 200 μL of 50:50 (v/v) ACN/water mixture, centrifuged for 5 min at 14 000 rpm, and finally analyzed by reverse-phase HPLC according to the gradient elution reported above.

Pharmacokinetic Assay. Solutions containing 4 mg of FLU (**1**) or FLU equivalent compounds **6b** or **6d** in 1 mL of DMSO were diluted with 3 mL of phosphate-buffered saline (0.15 M NaCl, 20 mM phosphate buffer), pH 7.4. 110 mice were divided into 3 groups of 35 animals (test groups) and 1 group of 5 animals (control group). Each group received one of the above solutions; the animals were injected via the tail vein with 100 μL of the respective solution. The 5 animals in the control group were intravenously injected with 100 μL of the vehicle (1:3 DMSO/saline solution). At scheduled times, 50 μL of blood samples were randomly withdrawn by retrobulbar puncture; at least three animals were used per each time point. The blood samples were immediately mixed with 50 μL of a NAP standard solution (0.1 μg/μL). Aliquots of the supernatant (50 μL) were mixed with 50 μL of ACN, centrifuged for 5 min at 14 000 rpm to precipitate proteins, and analyzed by reverse-phase HPLC as described above.

At scheduled times (30, 60, 180, 420, and 560 min) seven animals/group were bled and sacrificed and liver, spleen, kidney, and brain were taken. The collected blood was processed as described above. The whole organs were washed in saline and gently dried with absorbent paper, weighed, spiked with 50 μL of the above standard NAP solution, and processed according to the procedure previously reported. The amounts of recovered FLU−EA−LAA prodrugs, FLU−EA (**3**), and free FLU were determined by HPLC analysis as described above.

Radioactive [F-18]FDDNP Competitive Binding Assay with Aβ(1–40) Fibrils. Aβ(1–40) Fibril Formation. β-amyloid(1–40) fibrils were prepared *in vitro* from the commercially available Aβ(1–40) peptide (Biosource, Camarillo, CA) according to published methods (*30*). Briefly, 1.0 mg of Aβ(1–40) peptide was dissolved in 1 mL of phosphate buffered saline (PBS), pH 7.4, and stirred with a magnetic stirring bar for 3–4 days at 37 °C, after which a visibly cloudy solution was obtained. This mixture was further diluted to 10 mL with PBS, pH 7.4, and used as such for competitive binding assays of FLU and prodrugs **6a**−**e** against [F-18]FDDNP. The fibril formation was confirmed using Congo red (*32*) and Thioflavine T (*33*) UV spectrophotometric assays. Fibrils were used immediately after their production was confirmed.

Competition Binding Assays. The methodology published for determination of competition binding assays with NAP and ibuprofen (IBU) was used (*10*). Fresh 5 mM ethanol solutions of FLU and of all prodrugs were prepared for each competitive binding assay. Solutions of each compound in 1% ethanol/PBS, pH 7.4, in the range from 0.1 pM to 300 nM were incubated with 9.25 MBq/mL of [F-18]FDDNP (specific activity >74 GBq/μCi) and with 0.875 μg/mL of Aβ(1–40) fibrils for 60 min. The fibrils were isolated by filtration through Anodisc 25 alumina membrane filters (0.2 μm particle retention; Whatman International Ltd., Maidstone, England) in a 1225 sampling manifold (Millipore, Bradford, MA) that was modified with stainless steel support screens (Millipore) and glass sample chambers. Each filter was washed twice with 3 mL of PBS, pH 7.4. The radioactivity retained by the filters was measured and decay-corrected to a common reference time with a Packard Cobra II Auto-Gamma gamma counter (Packard, Meriden, CT). The binding of [F-18]FDDNP to Aβ(1–40) fibrils without a competitor determined 100% specific binding.

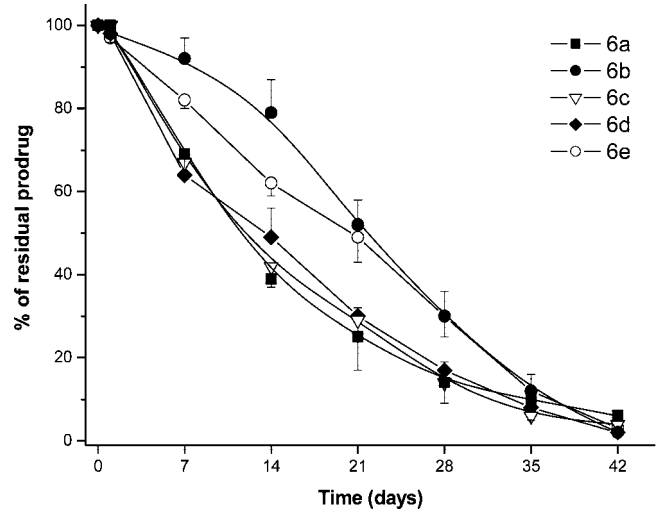

Figure 1. Degradation profiles of compounds **6a**−**e** in isotonic phosphate buffered saline at pH 7.4.

Competition results were analyzed and K_i values then calculated using the ligand binding module for *SigmaPlot 2001* (SPSS, Chicago, IL). The comparison of one- and two-site models for binding involved calculating the *F* statistic with a significance level of $P < 0.05$. All radioactive binding assays were performed in triplicate.

RESULTS AND DISCUSSION

Chemistry and Stability Tests. The lipophilic prodrugs of FLU were synthesized according to a procedure used for the preparation of other LAA conjugates, using water-soluble carbodiimide-assisted coupling reactions (*34–36*). Compounds **6a**−**e** were obtained in 50–80% yield and with high purity using semipreparative TLC. No attempt was made at this level to separate the eventual diastereomers formed by using racemic FLU and Boc-LAA as starting compounds.

Spectroscopic and mass analyses confirmed the assigned structure; in particular, IR spectroscopy showed the disappearance of the stretching peak of the FLU carboxyl group (at 1697 cm^{-1} in nujol) and appearance of two new peaks, around 1720–1750 cm^{-1}, due to the FLU−EA ester bond, and 1665–1680 cm^{-1}, related to the EA−LAA amide bond. The increasing lipophilicity of prodrugs with the increasing length of the side alkyl chain of the LAA residue is shown by the calculated Log *P* and Log $D_{7.4}$ values (Table 1).

The chemical stability of compounds **6a-e** was tested in phoshate buffered saline at 37 °C and pH 7.4 (Figure 1). Lengthening of the LAA alkyl side chain, and therefore of compound lipophilicity, was associated with an increasing stability to chemical hydrolysis, except for compound **6b**, which showed the highest stability. Hydrolytic cleavage of all prodrugs was completed after 7 weeks. The HPLC analysis showed that all the prodrugs **6** were hydrolyzed predominantly into FLU

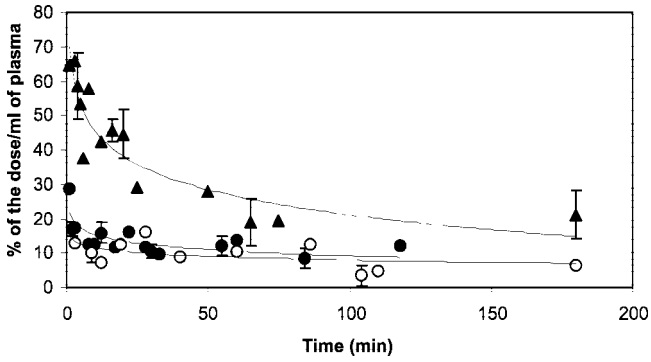

Figure 2. Plasma FLU levels after i.v. administration of the free drug (▲) or conjugates **6b** (○) and **6d** (•) (100 μg FLU equivalent/mouse). In the case of **6b** and **6d**, FLU levels refer to the amount of injected FLU equivalents.

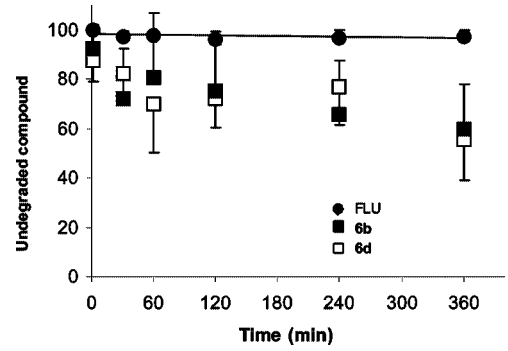

Figure 3. Stability of FLU or prodrugs **6b** and **6d** after incubation in mouse plasma at 37 °C.

from the earliest incubation times on, since the intermediate FLU-EA (**3**) was detected only at very low concentrations. Compound **3** was also very susceptible to hydrolysis in PBS, and a very rapid conversion into FLU was observed within 24 h of incubation (data not shown). As expected, the ester bond in the prodrugs **6a**−**e** was more susceptible to hydrolysis than the amide link between the spacer and the LAA residue.

The sensitivity to chemical hydrolysis of the ester bond in the prodrugs was verified by incubating compounds **6a**−**e** in a 3:1 (v/v) 2 M KOH/methanol mixture at 37 °C. After 15 min, the complete hydrolysis of the prodrugs into the parent FLU was observed (HPLC) (data not shown).

***In Vivo* Biodistribution Tests.** Based on their alkyl side chain length, prodrugs **6b** and **6d** were chosen as representatives of the short- and long-chain LAA conjugates to carry out pharmacokinetic and biodistribution tests.

Preliminary validation studies demonstrated the reliability of the extraction and analytical procedures adopted in the experimental protocols. The recovery of FLU and prodrugs **6b** and **6d** from blood spiked with these compounds was 89.7 ± 4.3%, 91.5 ± 6.8%, and 94.9 ± 4.2%, respectively. The recovery from the homogenized tissues was in the range 86–94% for all analyzed organs (liver, kidney, brain, lungs, and spleen). These values were used in the elaboration of the pharmacokinetic data to normalize the value of recovered products. Neither FLU nor FLU−EA were detected in blood and homogenized organ samples supplemented with **6b** and **6d**, indicating that these prodrugs were not hydrolyzed during the extraction procedure.

Figure 2 shows the time-course FLU levels in plasma after i.v. administration of the parent drug or prodrugs **6b** and **6d** to mice. In the case of the latter compounds, no intact prodrug was detected in blood 2 min after injection. After the same amount of time, low levels of free FLU were observed after administration of both **6b** and **6d**.

The fast disappearance of the prodrugs (Figure 2) can be only partially ascribed to their plasma degradation, since preliminary studies demonstrated that both conjugates are relatively stable upon *in vitro* incubation in plasma (about 25% degradation after 2 h and 40% degradation after 6 h) (Figure 3). The absence of the prodrug in plasma and the low FLU levels in liver and kidneys can thus be ascribed to a quick partition into peripheral compartments, namely, endothelial tissue, from which the following hydrolysis by endothelial lipases justifies the prolonged and stable drug levels observed in the circulation. A more likely alternative is the liver release of the hydrophobic compounds via the bile, release into the small intestine, and reabsorption prior to hydrolysis via endothelial lipases. A detailed pharmacokinetic or radiolabeled prodrug study would answer the question and is planned as a further step of this research.

In contrast, after i.v. injection, free FLU did not undergo a rapid partition into the peripheral compartments and maintained prolonged high plasma drug levels compared with the drug levels reached after the administration of prodrugs **6b** and **6d**.

To get information about the *in vivo* fate of **6b** and **6d**, prodrug and free FLU contents in the main organs were measured. The experiments were carried out for 9 h, since prodrug degradation made longer time evaluations difficult.

Figure 4 shows the extracellular accumulation of FLU in the main organs after FLU, **6b**, or **6d** i.v. administration to mice. After i.v. administration, free FLU rapidly distributed to the various tissues with concentration distributions in the order liver > brain > kidney > spleen. FLU concentration in these organs was almost constant up to 3 h, follow by a slow decline. Only negligible amounts of the drug were detected after 7 h.

In the case of prodrugs **6b** and **6d**, only the released parent FLU was observed. The intact prodrugs could not be detected in the homogenized tissues, similarly to what was observed in the blood. The two prodrugs, however, displayed a markedly different behavior with regard to FLU availability to various organs. From the first times after administration of **6b**, only small amounts of FLU were detected in the liver, kidneys, and spleen, while negligible disposition was observed in the brain. Conversely, the higher homologue **6d** led to accumulation of higher amounts of released FLU in the various organs. In general, after **6d** administration the maximal FLU concentration in the main tissues was reached later than after free FLU injection. The **6d** derivative yielded maximal FLU accumulation in the liver and spleen after 1 and 3 h after administration, respectively. The FLU levels in the kidneys also increased throughout 9 h, indicating that the drug was constantly released from the peripheral compartments and possibly eliminated by glomerular filtration or distributed to other kidney tissues. Again, more detailed studies are required to determine the exact elimination routes of the drug after i.v. administration of these prodrugs, for instance, by determining their concentration vs time in urine or feces.

Concerning the presence of FLU in the brain, injection of the parent drug led to constant brain levels for 3 h; therafter, the drug rapidly disappeared from this area. Such a pattern conforms to the levels of FLU in plasma, where the drug was detectable only for 3 h (Figure 2). After injection of compound **6d**, the released FLU appeared in the brain after 1 h, and the intracerebral FLU levels continued to rise up to the ninth hour, reaching higher values than those observed in the first 3 h after the injection of free FLU. The maximum brain/liver ratio (about 12% brain/plasma concentration) was reached 1 h after injection.

These pharmacokinetic findings suggest that the prodrugs dispersed rapidly and massively into a peripheral compartment. In the case of **6b**, which was found to be more stable than the upper homologues in plasma, the parent drug was not released into the brain; with **6d**, free FLU was released and accumulated

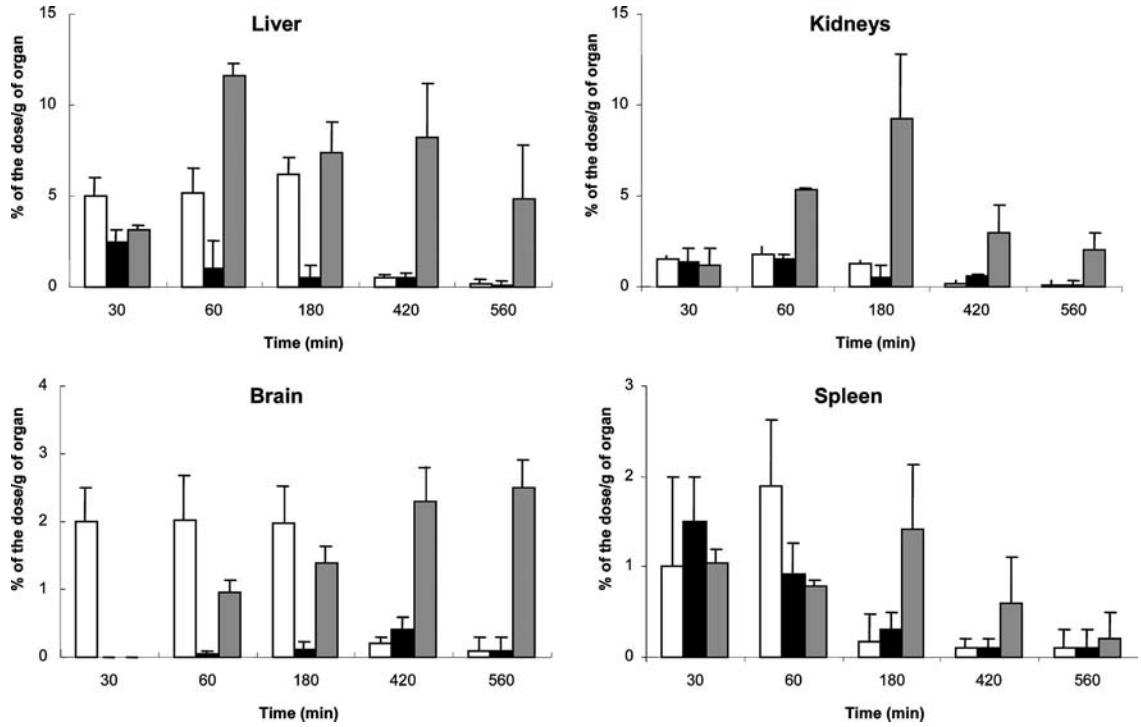

Figure 4. FLU concentrations in liver, brain, kidneys, and spleen after i.v. administration (100 μg FLU equiv/mouse) of the free drug (white) or conjugates **6b** (black) and **6d** (gray). In the case of the latter compounds, FLU levels were referred to the amount of FLU released from the prodrugs *in vivo*.

preferentially in the brain tissue; actually, the brain/plasma FLU concentration obtained with **6d** increased over time to reach about 30% 420 min from injection.

The different tissue distribution obtained with the various FLU derivatives is probably due to their dissimilar *in vivo* pathway/metabolism, such as the previously mentioned enterohepatic reticulation or association with vessel endothelium. However, a profound characterization of the pharmacokinetic profile of prodrugs **6** was beyond the intent of this paper; thus, further *in vivo* pharmacological studies will be started to elucidate the fate of these compounds.

The stark differences observed in the *in vivo* behavior between the two prodrugs highlight the effect that the LAA residue can exert on their biopharmaceutical profiles. In particular, a relatively small difference in the chain length (four methylene groups) in the side alkyl chain of the LAA promoiety of **6b** and **6d** led to a considerably different distribution profile.

The combined analysis of the chemical and plasmatic stability tests confirmed the validity of these conjugates as possible prodrugs for FLU. Compounds **6**, in fact, showed good stability in aqueous buffer and a slow release of the active drug in plasma.

[F-18]FDDNP Binding Assay. IBU and NAP showed competitive inhibition of [F-18]FDDNP binding with *in vitro* β-amyloid fibrils, with weak binding for IBU ($K_i = 11.3 \pm 5.2$ μM for *S*-IBU and 44.4 ± 17.4 μM for *R*-IBU) and with 3 orders of magnitude higher binding affinity for NAP ($K_i = 2.76 \pm 0.95$ nM for *S*-NAP and $K_i = 5.71 \pm 1.31$ nM for *R*-NAP) (*10*, *30*, *37*). In contrast to NAP and IBU, FLU proved to be ineffective in blocking [F-18]FDDNP from binding to its two specific binding sites on *in vitro* formed Aβ(1–40) fibrils in the concentration range of competitors used (0.1 pM to 300 nM). This apparent lack of binding can be better understood if structural factors are taken into consideration. The structure of FLU is related to that of IBU, i.e., they both have a central phenyl ring and propanoic acid residue. However, while IBU possesses an isobutyl group in the para position to the alkyl carboxilic acid chain, FLU has a phenyl ring in the para position and a fluorine meta substitution. Such an arrangement of substituents in FLU most likely pushes both phenyl rings out of plane due to steric and electrostatic interactions between the para phenyl ring and the meta fluorine atom.

The consequent lack of planarity may then decrease the probability of FLU interaction with the [F-18]FDDNP binding site. FLU−EA, the intermediate FLU ester with 2-aminoethanol, also showed no apparent competition in the *in vitro* assays.

The FLU prodrugs **6a** (C4 alkyl chain), **6b** (C6 alkyl chain), **6c** (C8 alkyl chain), and **6d** (C10 alkyl chain), on the other hand, demonstrated competitive inhibition of [F-18]FDDNP binding to β-amyloid(1–40) fibrils. Prodrug **6e** (C12 alkyl chain) did not compete with [F-18]FDDNP binding. Prodrugs **6a**, **6b**, and **6d** competed with [F-18]FDDNP for low-affinity binding (K_i values: **6a** 0.386 μM; **6b** 3.65 μM; and **6d** 0.017 μM), prodrug **6c**, on the other hand, showed competition for both high- and low-affinity binding sites with $K_i = 25.3$ pM and 0.396 μM, respectively. The results are shown in Figure 5.

Conjugation of the LAA residues to FLU changes the nature of its interaction with the Aβ(1–40) fibril surface. Hydrophobic interaction between the alkyl side chain with the hydrophobic areas on the surface of the fibrils becomes important and may overcome the effects of steric hindrance allowing the prodrugs to bind to the [F-18]FDDNP binding site(s). We also cannot underestimate interactions of the free amino group with the anionic side chains on the fibril. There are several aspartate and glutamate residues in the structure of the Aβ protein which can form strong electrostatic interactions and anchor the prodrugs **6a**−**d** on the surface.

The capacity of prodrug **6c** to bind to both [F-18]FDDNP binding sites on the fibrils and also the complete absence of competition suggested different hypotheses. The processes involved may include micellization of the hydrophobic prodrugs at higher concentrations (high nanomolar) under the conditions used for the competition assays (1% ethanol in PBS) and interactions of the micelles with the fibril surface. Formation

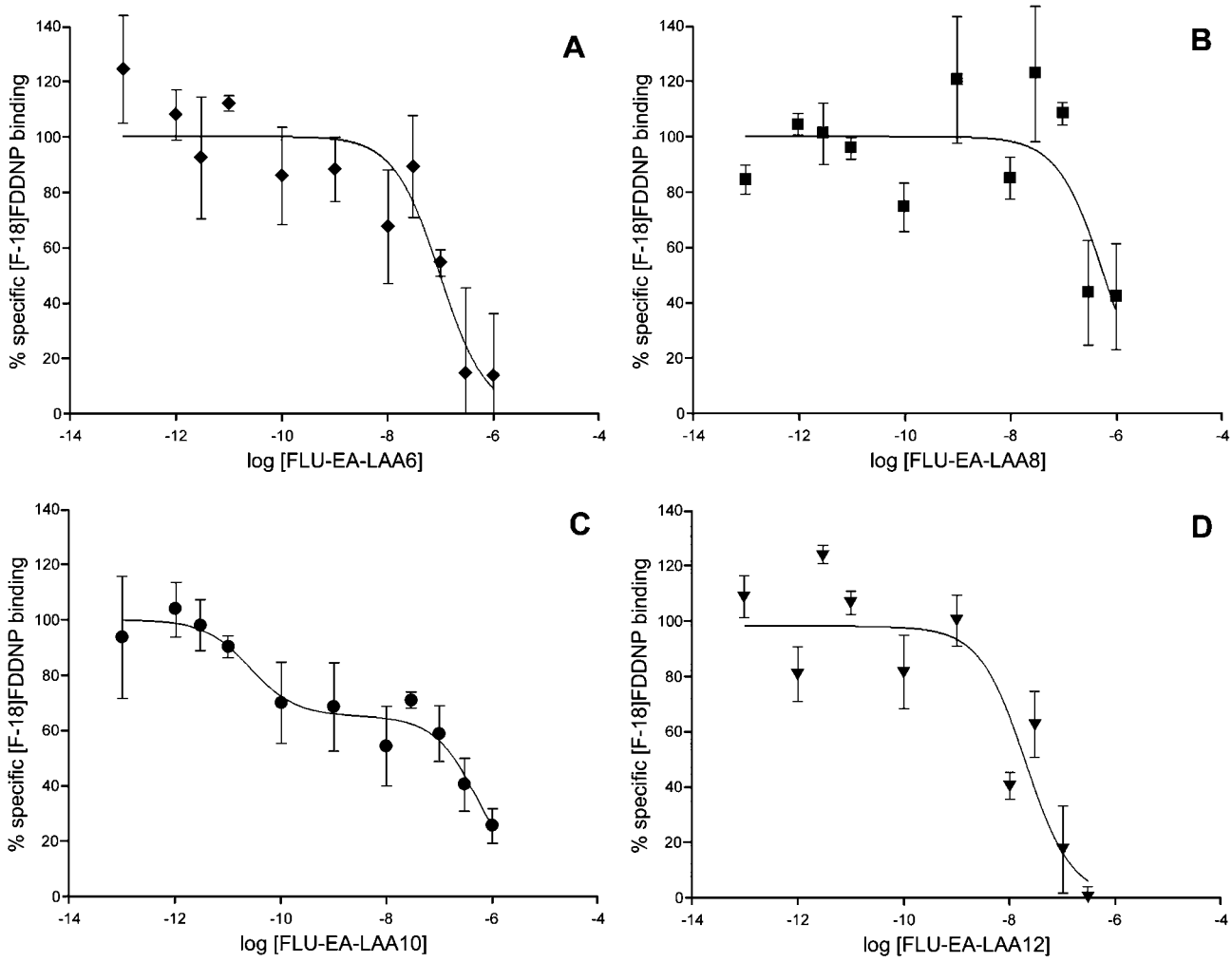

Figure 5. Prodrugs **6a**−**d** inhibition [F-18]FDDNP binding profile to the *in vitro* formed β-amyloid(1–40) fibrils. Compounds **6a** (A), **6b** (B), and **6d** (D) competed with [F-18]FDDNP for one binding site. Compound **6c** (C) blocked [F-18]FDDNP from both binding sites.

of micelles or other types of lipophilic aggregates can also be taken into consideration to explain the pharmacokinetic profile observed for prodrugs **6** and discussed previously. This statement implies that the amount injected in these studies is large and the pharmacokinetics would be altered by a mass effect. The amount administered for the present studies had to be reasonably high to permit chemical analysis, but *in vivo* studies using radiolabeled derivatives of these compounds (e.g., subnanogram/kg injected) may produce different and more reliable (e.g., mass independent) results.

CONCLUSIONS

The combined analysis of chemical and plasmatic stability data indicate these conjugates as possible prodrugs for FLU. They showed, in fact, good stability in buffer solution and a gradual release of the active drug in plasma, most probably upon enzymatic intervention. Compound **6d**, in particular, behaved as a slow-release FLU prodrug of FLU.

Even though their physicochemical properties were not optimized, it is possible to speculate that selected structural changes, e.g., the kind of spacer between the drug and the LAA promoiety, could lead to novel, more selective compounds for brain delivery of FLU. The inhibitory activity of [F-18]FDDNP binding to *in vitro* formed β-amyloid protein fibrils confered a structure−binding affinity relationship to these compounds; this study demonstrates that, if any differential pharmacological effect was observed with respect to FLU, it is not because of direct binding to the fibrils, but rather to other mechanisms (e.g., anti-inflammatory mechanisms), suggesting FLU−EA−LAA derivatives as potential prodrugs for AD treatment.

Experimental results showed that only FLU was found in specific organs even when prodrugs **6b** and **6d** were injected. A possible explanation is that the lipophilic prodrugs accumulated in a specific peripheral compartment, e.g., bile and following enterohepatic recirculation, from where FLU was released; thereafter, it entered the brain and was slowly eliminated by kidneys and liver. In addition, compounds **6b** and **6d** possess different lipophilic/hydrophilic balance and structure that may affect their pharmacokinetic properties and stability, in particular, the high stability in buffer that seems unusual for an ester linkage.

Similarly, the different distribution kinetics recorded in the brain after the administration of either the prodrugs or parent FLU deserve a detailed pharmacological study, for instance, by using radiolabeled forms of FLU−LAA conjugates.

As discussed above, the probable development of this study will be to apply the same synthetic strategy to *R*-FLU, e.g., the drug enantiomer that is currently under clinical trial as a potential agent in AD therapy. The issue of FLU−LAA prodrug stereochemistry, in fact, deserves attention, since their stability in plasma and organs can also be affected by stereochemical differences related to the enzymes involved in the metabolism and/or bioconversion to FLU.

ACKNOWLEDGMENT

Professor Istvan Toth, at the School of Pharmacy, University of Queensland, Brisbane (Australia), is gratefully acknowledged for mass analysis. We would like to thank Gerald Timbol at the David Geffen School of Medicine at UCLA, Los Angeles (USA), for performing the Aβ fibril binding assays and Professor Paolo Caliceti, at the University of Padua (Italy), for his helpful discussion in the manuscript preparation. This work was partially supported by the USA Department of Energy grant DE-FC03-02ER63420.

LITERATURE CITED

(1) Akiyama, H., Barger, S., Barnum, S., Bradt, B., Bauer, J., Cole, G. M., Cooper, N. R., Eikelenboom, P., Emmerling, M., Fiebich, B. L., Finch, C. E., Frautschy, S., Griffin, W. S. T., Hampel, H., Hull, M., Landreth, G., Lue, L.-F., Mrak, R., Mackenzie, I. R., McGeer, P. L., O'Banion, M. K., Pachter, J., Pasinetti, G., Plata-Salaman, C., Rogers, J., Rydel, R., Shen, Y., Streit, W., Strohmeyer, R., Tooyoma, I., van Muiswinkel, F. L., Veerhuis, R., Walker, D., Websterm, S., Wegrzyniak, B., Wenk, G., and Wyss-Coray, T. (2000) Inflammation and Alzheimer's disease. *Neurobiol. Aging 21*, 383–421.

(2) Mrak, R. E., Sheng, J. G., and Griffin, W. S. (1995) Glial cytokines in Alzheimer's disease: review and pathogenic implications. *Hum. Pathol. 26*, 816–823.

(3) Mrak, R. E., and Griffin, W. S. (2005) Potential inflammatory biomarkers in Alzheimer's disease. *J. Alzheimer Dis. 8*, 369–375.

(4) Bate, C., Kempster, S., Last, V., and Williams, A. (2006) Interferon-gamma increases neuronal death in response to amyloid-beta1–42. *J. Neuroinflammation 3*, 7.

(5) Siegel, D. A., Davies, P., Dobrenis, K., and Huang, M. (2006) Tomoregulin-2 is found extensively in plaques in Alzheimer's disease brain. *J. Neurochem. 98*, 34–44.

(6) Prasad, K. N., Cole, W. C., and Prasad, K. C. (2002) Risk factors for Alzheimer's disease: role of multiple antioxidants, non-steroidal anti-inflammatory and cholinergic agents alone or in combination in prevention and treatment. *J. Am. Coll. Nutr. 21*, 506–522.

(7) Yip, A. G., Green, R. C., Huyck, M., Cupples, L. A., Farrer, L. A., and MIRAGE Study Group. (2005) Nonsteroidal anti-inflammatory drug use and Alzheimer's disease risk: the MIRAGE Study. *BMC Geriatr. 5*, 2

(8) Martyn, C. (2003) Anti-inflammatory drugs and Alzheimer's Disease. *BMJ 327*, 353–354.

(9) Price, D. (2003) Effect of NSAIDs on risk of Alzheimer Disease. *BMJ 327*, 752.

(10) Agdeppa, E. D., Kepe, V., Petrič, A., Satyamurthy, N., Liu, J., Huang, S. C., Small, G. W., Cole, G. M., and Barrio, J. R. (2003) In vitro detection of (S)-naproxen and ibuprofen binding to plaques in the Alzheimer's brain using the positron emission tomography molecular imaging probe 2-(1-[6-[(2-[(18)F]fluoroethyl)(methyl)amino]-2-naphthyl]ethylidene) malononitrile. *Neuroscience 117*, 723–730.

(11) Pasinetti, G. M. (2002) From epidemiology to therapeutic trials with anti-inflammatory drugs in Alzheimer's disease: the role of NSAIDs and cyclooxygenase in beta-amyloidosis and clinical dementia. *J. Alzheimer Dis. 4*, 435–445.

(12) Gasparini, L., Ongini, E., and Wenk, G. (2004) Non-steroidal anti-inflammatory drugs (NSAIDs) in Alzheimer's disease: old and new mechanism of action. *J. Neurochem. 91*, 521–536.

(13) Eriksen, J. L., Sagi, S. A., Smith, T. E., Weggen, S., Das, P., McLendon, D. C., Ozols, V. V, Jessing, K. W., Zavitz, K. H., Koo, E. H., and Golde, T. E. (2003) NSAIDs and enantiomers of flurbiprofen target γ-secretase and lower Aβ42 in vivo. *J. Clin. Invest. 112*, 440–449.

(14) Weggen, S., Eriksen, J. L., Das, P., Sagi, S. A., Wang, R., Pietrzik, C. U., Findlay, K. A., Smith, T. E., Murphy, M. P., Bulter, T., Kang, D. E., Marquez-Sterling, N., Golde, T. E., and Koo, E. H. (2001) A subset of NSAIDs lower amyloidogenic Aβ42 independently of cyclooxygenase activity. *Nature 414*, 212–216.

(15) Imbimbo, B. P. (2004) The potential role of non-steroidal anti-inflammatory drugs in treating Alzheimer's disease. *Exp. Opin. Invest. Drugs 13*, 1469–1481.

(16) Avramovich, Y., Amit, T., and Youdim, M. B. (2002) Non-steroidal anti-inflammatory drugs stimulate secretion of non-amyloidogenic precursor protein. *J. Biol. Chem. 277*, 31466–31473.

(17) Gasparini, L., Ongini, E., Wilcock, D., and Morgan, D. (2005) Activity of flurbiprofen and chemically related anti-inflammatory drugs in models of Alzheimer's disease. *Brain Res. Brain Res. Rev. 48*, 400–408.

(18) Hirohata, M., Ono, K., Naiki, H., and Yamada, M. (2005) Non-steroidal anti-inflammatory drugs have anti-amyloidogenic effects for Alzheimer's beta-amyloid fibrils in vitro. *Neuropharmacol. 49*, 1088–1099.

(19) Townsend, K. P., and Praticò, D. (2005) Novel therapeutic opportunities for Alzheimer's disease: focus on nonsteroidal anti-inflammatory drugs. *FASEB J. 19*, 1592–1601.

(20) Doraiswamy, P. M., and Xiong, G. L. (2006) Pharmacological strategies for the prevention of Alzheimer's disease. *Exp. Opin. Pharmacother. 7*, 1–10.

(21) Stock, N., Munoz, B., Wrigley, J. D., Shearman, M. S., Beher, D., Peachey, J., Williamson, T. L., Bain, G., Chen, W., Jiang, X., St-Jacques, R., and Prasit, P. (2006) The geminal dimethyl analogue of flurbiprofen as a novel Abeta(42) inhibitor and potential Alzheimer's disease modifying agent. *Bioorg. Med. Chem. Lett. 16*, 2219–2322.

(22) Gasparini, L., Rusconi, L., Xu, H., Del Soldato, P., and Ongini, E. (2004) Modulation of beta-amyloid metabolism by non-steroidal anti-inflammatory drugs in neuronal cell cultures. *J. Neurochem. 88*, 337–348.

(23) Toth, I. (1994) A novel chemical approach to drug delivery: lipid amino acid conjugates. *J. Drug Targeting 2*, 217–239.

(24) Wong, A., and Toth, I. (2001) Lipid, sugar and liposaccharide based delivery systems. *Curr. Med. Chem. 8*, 1123–1136.

(25) Pignatello, R., Guccione, S., Castelli, F., Sarpietro, M. G., Giurato, L., Lombardo, M., and Puglisi, and Toth, I. (2006) Enhancement of drug affinity for cell membranes by conjugation with lipoamino acids. II. *Int. J. Pharm. 310*, 53–63.

(26) Pignatello, R., Maltese, A., Maugeri, F., and Bucolo, C. (2006) Enhancement of availability of cloricromene at brain level by a lipophilic prodrug. *J. Pharm. Pharmacol. 58*, 1001–1005.

(27) Small, G. W., Kepe, V., Ercoli, L. M., Siddarth, P., Bookheimer, S. Y., Miller, K. J., Lavretsky, H., Burggren, A. C., Cole, G. M., Vinters, H. V., Thompson, P. M., Huang, S.-C., Satyamurthy, N., Phelps, M. E., and Barrio, J. R. (2006) PET of brain amyloid and tau in mild cognitive impairment. *N. Engl. J. Med. 355*, 2652–2663.

(28) Gibbons, W. A., Hughes, R. A., Choralambous, M., Christodoulou, M., Szeto, A., Aulobaugh, A. E., Mascagni, P., and Toth, I. (1990) Synthesis, resolution and tructural elucidation of lipidic amino acids and their homo- and hetero-oligomers. *Liebigs Ann. Chem.* 1175–1183.

(29) Perrin, D. D., Armarego, W. L. F., and Perrin, D. R. (1980) *Purification of Laboratory Chemicals* 2nd ed., Pergamon Press, Oxford.

(30) Liu, J., Kepe, V., žabjek, A., Petrič, A., Padgett, H. C., Satyamurthy, N., and Barrio, J. R. (2007) High-yield, automated radiosynthesis of 2-1-{6-(2-(18)F-fluoroethyl)(methyl)amino-2-naphthyl}ethylidene)malononitrile (18)F-FDDNP) ready for animal or human administration. *Mol. Imaging Biol. 9*, 6–16.

(31) Caliceti, P., Schiavon, O., and Veronese, F. M. (1999) Biopharmaceutical properties of uricase conjugated to neutral amphiphilic polymers. *Bioconjugate Chem. 10*, 638–646.

(32) Klunk, W. E., Jacob, R. F., and Mason, R. P. (1999) Quantifying amyloid β-peptide (Aβ) aggregation using the Congo red-Aβ (CR-Aβ) spectrophotometric assay. *Anal. Biochem. 26*, 66–76.

(33) LeVine, H. (1993) Thioflavine T interaction with synthetic Alzheimer's disease β-amyloid peptides: detection of amyloid aggregation in solution. *Protein Sci. 2*, 404–410.

(34) Pignatello, R., Jansen, G., Kathmann, I., Puglisi, G., and Toth, I. (1998) Lipoamino acid conjugates of methotrexate with antitumor activity. *J. Pharm. Sci. 87*, 367–371.

(35) Pignatello, R., Puleo, A., Giustolisi, S., Cuzzocrea, S., Dugo, L., Caputi, A. P., and Puglisi, G. (2002) Cloricromene conjugates with short-chain alkylamino acids: synthesis and biological evaluation. *Drug Dev. Res. 57*, 115–121.

(36) Pignatello, R., Puleo, A., Campisi, A., Acquaviva, R., and Puglisi, G. (2004) Improved antioxidant activity of lipophilic conjugates of idebenone with short and medium alkylamino acids. *J. Drug Delivery Sci. Technol. 14*, 181–186.

(37) Agdeppa, E. D., Kepe, V., Liu, J., Flores-Torres, S., Satyamurthy, N., Petric, A., Cole, G. M., Small, G. W., Huang, S.-C., and Barrio, J. R. (2001) Binding characteristics of radiofluorinated 6-dialkylamino-2-naphthylethylidene derivatives as positron emission tomography imaging probes for b-amyloid plaques in Alzheimer's disease. *J. Neurosci. 21*, RC189.

BC700312Y

Selection of Reaction Additives Used in the Preparation of Monomeric Antibody−Calicheamicin Conjugates

Irwin Hollander, Arthur Kunz, and Philip R. Hamann*

Wyeth Research, 401 N. Middletown Road, Pearl River, New York 10965. Received August 24, 2007; Revised Manuscript Received September 24, 2007

The formation of protein aggregates can be a major problem during the preparation of antibody−drug conjugates. Herein is described the methods by which reaction additives were selected, which reduce the tendency of antibodies to aggregate during the attachment of the cytotoxic agent calicheamicin to form an immunoconjugate. Reaction conditions were delineated that produced optimized yields of monomeric conjugates. These conditions were used in the preclinical preparations of gemtuzumab ozogamicin (Mylotarg), the first commercially available chemotherapeutic immunoconjugate.

INTRODUCTION

In the more than thirty years since the development of methods for preparing monoclonal antibodies, there have been numerous attempts to use these proteins as effective vehicles for targeting cytotoxic agents to human cancers. Although there are now six antibodies and two radioimmunoconjugates approved for cancer treatment in the United States, the only conjugate of a cytotoxic agent, such as a phytotoxin, a cytotoxic oncology agent, or a natural product analogue, is gemtuzumab ozogamicin (gem-ozo[1] , Mylotarg, **2** (Figure 1), antibody = hP67.6) (*1*), in spite of numerous agents being examined in the clinic (*2*). Gem-ozo is a conjugate of the anti-CD33 antibody hP67.6 and NAc-gamma calicheamicin DMH, a derivative of the naturally occurring gamma calicheamicin. The calicheamicins are members of the enediyne family of antitumor antibiotics that, even at subpicomolar concentrations, produce double-stranded DNA cleavage (*3, 4*).

In gem-ozo, the antibody and calicheamicin derivative are covalently attached by a bifunctional linker referred to as the AcBut linker (*5*). This linker allows for attachment of the calicheamicin to the lysines on the antibody and forms an acyl hydrazone with the calicheamicin derivative that supplies a site of hydrolytic release in the lysosomes of the CD33-positive target cells. In preclinical models of acute myeloid leukemia, for which gem-ozo is approved, a hydrazone linkage was required for potent, selective cytotoxicity and gave conjugates superior to the amide conjugate (**4**), which does not contain that linkage (*6*). This is not required for all calicheamicin conjugates (*7*). Unfortunately, the introduction of the AcBut linker made conjugation to antibodies problematic, in that the maximum usable amount of the cosolvent DMF produced only modest yields of low-loaded, monomeric conjugates because of aggregation (Figure 2A). Although this material was used in the initial biological characterization of gem-ozo, scale up for development activities required a dramatic improvement in the loading and yield of monomeric conjugates. This article details how the use of various unique additives in the conjugation reaction solved this problem.

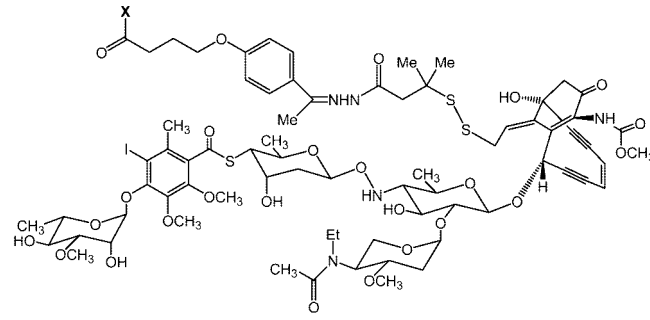

1 NAc-gamma calicheamicin DMH AcBut OSu, **X** = N-hydroxysuccinimide ("AcBut OSu")
2 NAc-gamma calicheamicin DMH AcBut conjugate, **X** = antibody ("AcBut Conjugate")

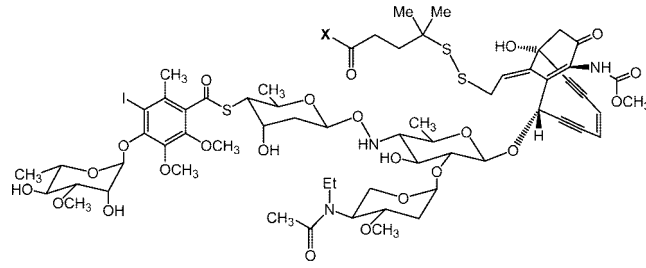

3 NAc-gamma calicheamicin DM OSu, **X** = N-hydroxysuccinimide ("DM OSu")
4 NAc-gamma calicheamicin DM conjugate, **X** = antibody ("Amide Conjugate")

Figure 1. Structures of calicheamicin derivatives and conjugates. In both conjugates, the natural product, gamma calicheamicin, is modified to contain an NAc group and a disulfide stabilized by two methyl groups (DM = dimethyl). The conjugates differ in the presence of the hydrolyzable hydrazone bond in the AcBut conjugates.

EXPERIMENTAL PROCEDURES

Reagents. Antibody hP67.6 (CDP771/2, anti-CD33 humanized IgG_4) was produced by cell culture in CHO cells and purified with affinity and ion exchange column chromatography by Lonza Biologics. The purity of the antibody was greater than 95%.

The synthesis of NAc-gamma calicheamicin DMH AcBut OSu (**1**; see Figure 1 for structures) and the original procedures for making conjugates have been published (*5*).

* To whom correspondence should be addressed. Phone: (845) 602-3423. Fax: (845) 602-5561. E-mail: hamannp@wyeth.com.

[1]Abbreviations: gem-ozo, gemtuzumab ozogamicin (Mylotarg); NAc, N-acetyl; DMF, *N*,*N*-dimethylformamide; DMH, dimethyl hydrazide; gamma, calicheamicin γ_1^I; OSu (ester), ester of *N*-hydroxysuccinimide; PBS, phosphate-buffered saline; SDS−PAGE, sodium dodecyl sulfate−polyacrylamide gel electrophoresis; SEC, size-exclusion chromatography.

10.1021/bc700321z CCC: $40.75 © 2008 American Chemical Society
Published on Web 11/10/2007

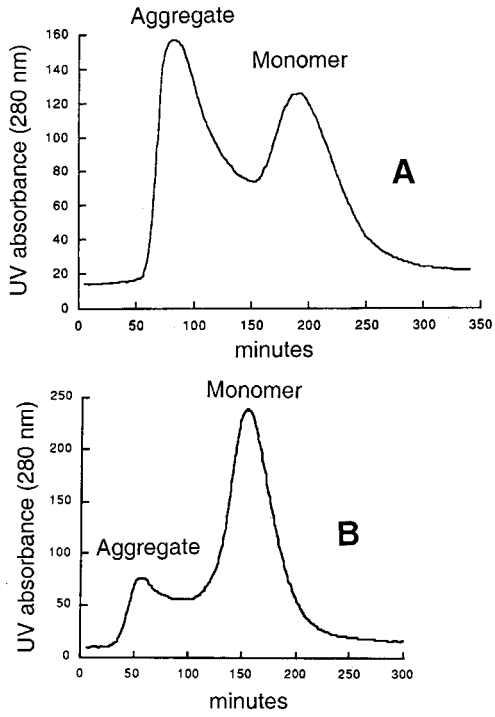

Figure 2. Size-exclusion chromatography trace of conjugation reactions. Representative profiles of conjugation reactions performed on 30 mg of antibody hP67.6 and 6 equivalents of the AcBut OSu (**1**) with 20% DMF and no additives (A) or with 5% DMF, 20% propylene glycol, and 80 mM octanoic acid (B). Pooled monomer for the conjugation shown in A was about 1 mol/mol, while in B, the loading was 2.5 mol/mol.

Tween-80, glycine, maltose, histidine, Pluronic F-68, octanoic acid, *N*-acetyl tryptophan, benzyl alcohol, propylene glycol, glycerol, benzoic acid, isopropanol, and *t*-butanol were all reagent grade (Sigma Chemical).

The PBS used is 50 mM sodium phosphate and 100 mM NaCl at pH 7.4, prepared using reagent grade mono and dibasic sodium phosphate salts and sodium chloride (Sigma Chemical).

Aggregated Conjugate. Aggregated antibody−calicheamicin conjugate with the AcBut linker (**2**) was prepared using the published procedure as follows (*5*).

To a 10 mg/mL solution of antibody hP67.6 in PBS was added additional buffer and the cosolvent DMF to give a solution of 5 mg/mL antibody and 20% DMF. To this solution was added 6 mol equiv of NAc-gamma calicheamicin DMH AcBut OSu (**1**) in DMF at 10 mg/mL. The mixture was shaken gently at room temperature for 16 h and then purified by size-exclusion chromatography on a Sephacryl S-200 (GE Healthcare) column eluted with PBS. The eluted protein was fractionated on the basis of its 280 nm absorbance. Fractions were further analyzed by high-performance liquid chromatography on a Zorbax GF-250 column (Dupont) in 0.2 M sodium phosphate and 25% propylene glycol at pH 7.0. Fractions containing aggregate (Figure 2A) were selected to give conjugate (**2**) having approximately 25% aggregated protein as measured by peak areas at 280 nm. This material was concentrated to ∼1 mg/mL using Amicon Centriprep 30 ultrafiltration devices.

Aggregate Dissociation Assay. Each additive was aliquoted as a 10X concentrate to a 50 μL aliquot of the aggregate fraction prepared as described above, to give the desired percent of additive as listed in Table 1. The mixtures were incubated overnight at room temperature and then analyzed by size-exclusion chromatography (SEC). SEC was performed both on a Zorbax (Dupont) GF-250 column eluted with 0.2 M sodium phosphate containing 25% propylene glycol and on a Superose 12 HR (Pharmacia) column eluted with PBS. Both columns were monitored by UV absorbance at 280 and 333 nm to determine protein and calicheamicin profiles.

Table 1. Additives Examined and Their Concentrations

additive	concentration
Tween-80	1%
glycine	300 mM
glycine maltose	200 mM/2%
glycine histidine	100 mM/100 mM
Pluronic F-68	1%
octanoic acid	80 mM
octanoic acid *N*-acetyl tryptophan	40 mM/6 mM
benzyl alcohol	1%
sodium benzoate	0.5%
propylene glycol	33%
glycerol	25%

Conjugation Experiments. To a 10 mg/mL solution of antibody hP67.6 in PBS was added additional buffer and one or more of the additives to give a solution of 3.25 mg/mL antibody (∼250 μL). To this solution was added 6 mol equiv of NAc-gamma calicheamicin DMH AcBut OSu (1) in DMF at 10 mg/mL (5% DMF final concentration). The mixture was shaken gently at room temperature for 16 h and then purified by size-exclusion chromatography on a Superose 200 (Pharmacia) column eluted with PBS. The eluted protein was fractionated on the basis of its 280 nm absorbance. Fractions were further analyzed by high-performance liquid chromatography on a Zorbax GF-250 column (Dupont) in 0.2 M sodium phosphate and 25% propylene glycol at pH 7.0. Fractions containing predominantly monomer were pooled to give the final conjugate (**2**).

Optimized Large-Scale Conjugation Conditions. To 30 mg of hP67.6 antibody at 6.5 mg/mL in PBS was added propylene glycol (30% final concentration) and 1 M octanoic acid (final concentration 60 mM). The pH was then adjusted to ∼7.75 with 1 M NaOH. Six molar equivalents of NAc-gamma calicheamicin DMH AcBut OSu (**1**) in propylene glycol at 6 mg/mL was then added. The mixture was shaken gently at 25 °C for 3 h before filtering through a Millex HV filter to remove particulates and purifying by SEC on a Sephacryl S-200 column eluted with PBS (Figure 2B). Monomeric fractions were then pooled to give conjugate (**2**) with <4% dimer and a loading of 2.5 mol/mol in 60% protein yield.

RESULTS

The agents chosen for this study were chosen, to a significant extent, from a list of FDA-approved excipients for protein formulation. This was done because it was not known if the additives found to be effective in preventing aggregate formation would need to be present to keep the final purified, monomeric conjugate from aggregating and because it was anticipated that some of these agents would be difficult to remove completely. The concentrations chosen for initial screening were consistent with their normal usage and are shown in Table 1.

The AcBut OSu (**1**) derivative is poorly utilized in conjugations of the hP67.6 antibody with DMF as the cosolvent, that is, much of the OSu ester is hydrolyzed instead of conjugated. Because some of the additives might, hopefully, increase the efficiency of the conjugation, it was anticipated that comparing conjugation reactions might be difficult and time-consuming. Therefore, it was decided to see initially if the selected additives would function to disassociate the aggregate that had been isolated from a previous conjugation. That this was possible was supported by the previous observation that diluting conjugate fractions containing aggregate led to a slow conversion of some of the aggregate to monomer and that reconcentration

Table 2. Results of the Deaggregation Experiment

additive	loading M/M	Zorbax G-250% aggregate	Superose 12% aggregate
control	2.9	26	28
Tween-80	3.9	49	34
glycine	3.0	26	24
glycine/maltose	3.7	24	22
glycine/histidine	3.4	25	21
Pluronic F-68	4.3	22	20
octanoic acid	2.7	4	11
octanoic/*N*-acetyl Trp	4.3	15	22
benzyl alcohol	4.1	22	9
benzoic acid	4.3	23	21
propylene glycol	3.0	7	5
glycerol	2.6	12	11

Table 3. Results of Small-Scale Conjugation Experiments

additive	% aggregate in reaction	loading on monomeric product	protein recovery (%)
control (25% DMF)	50	2.9	26
25% propylene glycol	15	4.0	43
80 mM octanoic acid	11	2.6	74
25% propylene glycol/80 mm octanoic acid	3	3.6	80
25% glycerol	0	0	99
25% *t*-butanol	10	3.6	54
25% isopropanol	17	2.6	64

increased the aggregate content again. Also, it had been shown by SDS−PAGE that the aggregates were noncovalent.

Pooled conjugate fractions containing about 25% dimer, the fraction considered to be the easiest to disassociate, and a smaller amount of higher-ordered aggregate were treated overnight as indicated in Table 2 at room temperature and assessed for the amount of remaining aggregate. The amount of aggregate seen by the two methods was relatively consistent, but with some unexplained deviations for certain additives. All the additives had either no effect or reduced the amount of aggregate except for Tween-80, which, surprisingly, caused increased aggregation. The three most successful agents were octanoic acid, glycerol, and propylene glycol, which decreased the amount of aggregate by as much as 90%.

On the basis of this experiment, it was decided to use the top three candidates in small-scale conjugation reactions to see if they would prevent aggregation during conjugation. Two alcohols, *t*-butanol and isopropanol, were added to these possibilities at this time, and the results are shown in Table 3. All the additives used alone had very significant effects on the amount of aggregate and the yield. Most of them improved the loading, except for glycerol, which led to no detectable conjugation for unknown reasons. A combination of the two best additives, propylene glycol and octanoic acid, was also used, leading to an almost 95% reduction in the amount of aggregation, more than 15% increase in the final loading, and a 3-fold increase in the protein yield. Subsequent experiments (results not included) showed that *t*-butanol was incompatible with octanoic acid at the concentrations used and that isopropanol was less effective than propylene glycol.

Although at this point in time a basic conjugation procedure using a combination of propylene glycol and octanoic acid was in hand that was suitable for initial development work, further variables were examined (detailed comparative results not included). It had been observed that the conjugation reactions with octanoic acid took much longer to go to completion than the *t*-butanol or propylene glycol reactions (16 h vs 3 h), presumably because of a shift in pH from 7.4 to ~6.9 upon adding the octanoic acid. Readjusting the pH to 7.4 before addition of the AcBut OSu ester increased the rate of these conjugation reactions, and increasing the pH to 7.9 increased it even more. At the same time, the total amount of calicheamicin attached to antibody (monomer and aggregate) increased. However, when the amount of AcBut OSu ester was adjusted to give comparable loading to that seen at the lower reaction pH, there was little difference in the amount of aggregate formed or the ultimate yield of conjugate.

DMF had been used for the stock of the AcBut OSu ester and hence as a reaction cosolvent because of its successful use in conjugation procedures prior to the development of the AcBut linker (*6*). However, when the use of DMF was examined with the new additives, reducing or eliminating DMF was found to give somewhat higher conjugation efficiency. The AcBut OSu stocks were thereafter made in either propylene glycol or ethanol, either one performing equally well. Finally, only minor differences in the conjugation results were seen when the concentration of propylene glycol was varied from 20 to 30% or when the octanoic acid concentration was varied from 50 to 80 mM. Below these concentrations, the beneficial effects were slowly lost, and incompatibilities were seen in some cases at higher concentrations. The final optimized procedure for this antibody as detailed in the Experimental Procedures section is 30% propylene glycol at pH 7.75, 60 mM octanoic acid, and 6 equiv of NAc-gamma calicheamicin DMH AcBut OSu, which gives a 60% yield (protein) of monomeric antibody conjugate containing 2.5 mol/mol of calicheamicin (Figure 2B).

DISCUSSION

The conjugation of low molecular weight, hydrophobic, cytotoxic agents (such as the calicheamicins) to large hydrophilic antibodies is complicated by their dramatically different physical properties. While antibodies prefer their natural, buffered, aqueous environment and only tolerate limited amounts of certain organic cosolvents, agents such as the calicheamicins have severely limited or no aqueous solubility and prefer polar organic solvents (*8*). Even after conjugation has been accomplished, the same solubility issues still present themselves in the tendency of the conjugates to form aggregates by the lipophilic association of the calicheamicins conjugated to the surface of the antibody. Although sometimes low-order aggregates such as a dimerized conjugate retain antibody binding activity, they have unacceptable pharmacokinetic properties in vivo and must be minimized or removed because of the possible increase in toxicity they may cause if present in larger amounts.

The formation of these aggregates during the conjugation reaction also leads to a reduction in yield of both protein and calicheamicin due to the consumption of materials in nonuseful forms and by the loss of monomers during the necessary process of aggregate removal. Unfortunately, it is the more highly loaded species that have the greatest tendency to aggregate, which leads to lower loading on the monomeric conjugate. This aggregation tendency for calicheamicin conjugates was greatly exacerbated when using the AcBut linker, and therefore, an improved procedure was needed that would minimize these aggregates during conjugation.

Our starting point for the hybrid linker reaction was taken from the successful conditions established for the conjugation for the previous NAc-gamma calicheamicin DM OSu (**3**) derivative (*6*). This derivative readily reacted with antibodies in the presence of 25% of an organic cosolvent such as DMF to give over 80% yield of both protein and calicheamicin and with a loading on monomeric conjugate (**4**) of 2 to 3 mole of drug/mol antibody with low aggregate. When these conditions were used with the AcBut linker, unacceptable levels of aggregate were formed, and, subsequently, poor loadings and yields of monomeric conjugate (**2**) were obtained. Variations in the reaction conditions in terms of the concentration of antibody, temperature, equivalents of calicheamicin, and the

concentration of DMF were of little help. Attempts to make the calicheamicin derivative more soluble, such as by using HEPES instead of phosphate buffer or adding the salting-in salt perchlorate also did not improve conjugation. It was therefore decided to investigate the use of different reaction additives that might help dissolve or disassociate calicheamicin so that it could react more efficiently with the antibody while at the same time preventing the aggregation of the product.

Since aggregate formation was one obvious problem in the conjugation reaction, it was decided to use as the first screening method an analysis wherein preformed aggregate was tested for dissociation by a variety of additives. The additives were selected on the basis of their potential for solublizing hydrophobic moieties, compatibility with proteins, and their status as FDA-approved parenteral additives since there was the possibility that an effective excipient would need to be present in the conjugates to prevent reaggregation. It was noted that the deaggregation process was relative slow, requiring hours to see any effects and overnight treatment to reach apparent completion. It was also noted that the untreated control conjugate responded less to the additives as it was aged, that is, that aggregation appears to become stronger with time. The lower amount of aggregate indicated in Table 2 may, therefore, represent the minimum deaggregation possible.

On the basis of these results, octanoic acid, propylene glycol, and glycerol were used during trial conjugations in place of most of the DMF. In addition, isopropanol and *t*-butanol were also tested because of their similarity to propylene glycol and glycerol in chemical properties and previous use as cosolvents for proteins. A combination of propylene glycol and octanoic acid was tested, combining what seemed to be the best two deaggregators. Interestingly, the ability of these additives to give a clear conjugation reaction did not seem to correlate with the outcome, as *t*-butanol gave the clearest reaction but not the best conjugation results. The final results indicate that the combination of propylene glycol and octanoic acid produced the least aggregate and highest protein recovery with excellent drug loading. Conditions for conjugating an AcBut-linked calicheamicin derivative to antibodies were determined, which gave a yield of monomeric conjugate of up to 90% and with drug loadings of around 3 mol/mol. (See the Experimental Procedures section for details.)

When these specific conditions were varied within a reasonably narrow range, minor variations in the amount of aggregate, the loading, and the efficiency of conjugation occurred with respect to the crude product. However, the amount of calicheamicin isolated on monomer remained relatively constant. Experience has shown that higher calicheamicin loading is offset by a somewhat higher aggregate and lower monomer yield. Further testing indicated that these conditions did not affect immunoreactivity or specific cytotoxicity (data not included) and were used in preclinical preparations of Mylotarg. These conditions were applicable to larger scale conjugation reactions (30 mg) with only slight increases in the amount of aggregate seen, and the results were dramatically improved compared with that obtained with DMF alone (Figure 2).

The ultimate question is why these additives greatly improve the conjugation reaction to make the AcBut conjugates. The AcBut OSu derivative (**1**) is less soluble in buffer containing 25% DMF than the DM OSu derivative (**3**), but the difference is not dramatic enough to offer a satisfying explanation. However, it is very possible that these calicheamicin derivatives do not exist as a true solution during the conjugation but as some sort of aggregated state (*8*). Perhaps one effect of the additives is to alter any aggregated state of the calicheamicins in solution to make the OSu ester more accessible for conjugation.

The final conjugates remain as monomer constructs even after purification and concentration, even though the additives have been removed to the limit of detection. In the conjugate, the AcBut linker itself, which is the new part of the conjugate, is closest to the antibody and, therefore, may not be as solvent exposed as the calicheamicin portion of the conjugates, which is the portion that the amide and AcBut conjugates have in common. Perhaps the AcBut linker forces this calicheamicin portion to be a little farther away from the protein surface and to be more solvent exposed. It would, therefore, be more likely to interact with any unconjugated calicheamicin that exists in an associated state, and multiple conjugate molecules could interact with the same cluster of unconjugated calicheamicin, leading to aggregation. The aggregate would, therefore, have unusually high, partially noncovalent loading, and that has indeed been observed.

Whatever the reasons for the benefit of these additives, these conjugation conditions have proven applicable to the AcBut-linked conjugates of other antibodies, even though some adjustment of conditions is necessary for each new antibody. Those further adjustments and additional optimizations will be reported in due course. It is hoped that the process used in this study to find acceptable additives may prove useful in the development of other protein−drug conjugates, for which significant problems have been reported (*9*).

ACKNOWLEDGMENT

We are grateful to Marty Kunstmann for useful discussions and suggestions.

LITERATURE CITED

(1) Bross, P. F., Beitz, J., Chen, G., Chen, X. H., Duffy, E., Kieffer, L., Roy, S., Sridhara, R., Rahman, A., Williams, G., and Pazdur, R. (2001) Approval summary: Gemtuzumab ozogamicin in relapsed acute myeloid leukemia. *Clin. Cancer Res. 7*, 1490. *Clin. Cancer Res.* (2002) *8*, 300; correction.

(2) Meyers, D. L., and Senter, P. D. (2003) Recent advances in antibody drug conjugates for cancer therapy. *Annu. Rep. Med. Chem. 38*, 229–236.

(3) Ellestad, G. A., Ding, W-D., Zein, N., and Townsend, C. A. (1995) DNA-cleaving properties of calicheamicin γ_1^I. *Enediyne Antibiotics as Antitumor Agents* (Borders, D. B., and Doyle T. W., Eds.) pp 137–160, Marcel Dekker, NY.

(4) Lee, M. D., Ellestad, G. A., and Borders, D. B. (1991) Calicheamicins: discovery, structure, chemistry, and interaction with DNA. *Acc. Chem. Res. 24*, 235–243.

(5) Hamann, P. R., Hinman, L. M., Hollander, I., Beyer, C. F., Lindh, D., Holcomb, R., Hallett, W., Upeslacis, J., Shochat, D., Mountain, A., Flowers, D. A., and Bernstein, I. (2002) A potent and selective anti-CD33 antibody-calicheamicin conjugate for treatment of acute myeloid leukemia. *Bioconjugate Chem. 13*, 47–58.

(6) Hamann, P. R., Hinman, L. M., Beyer, C. F., Lindh, D., Upeslacis, J., Flowers, D. A., and Bernstein, I. (2002) An anti-CD33 antibody-calicheamicin conjugate for treatment of acute myeloid leukemia, choice of linker. *Bioconjugate Chem. 13*, 40–46.

(7) Hamann, P. R., Hinman, L. M., Beyer, C. F., Greenberger, L., Lin, C., Lindh, D., Menendez, A. T., Upeslacis, J., and Wallace, R. (2005) An anti-MUC1 antibody-calicheamicin conjugate for treatment of solid tumors, choice of linker and overcoming drug resistance. *Bioconjugate Chem. 16*, 346–353.

(8) Myers, A. G., Cohen, S. B., and Kwon, B. M. (1994) A study of the reaction of Calicheamicin γ with glutathione in the presence of double-stranded DNA. *J. Am. Chem. Soc. 116*, 1255–1271.

(9) Zhao, R. Y., Sun, D., Cavanagh, E., et al. (2007) Design and Synthesis of PEG-Containing CC-1065 Analogs for Targeted Therapy of Cancer. ACS 233rd National Meeting, Chicago, IL, Poster MEDI-138.

BC700321Z

Novel Single-Chain Fv′ Formats for the Generation of Immunoliposomes by Site-Directed Coupling

Sylvia K. E. Messerschmidt,[†] Anke Kolbe,[†] Dafne Müller,[†] Michael Knoll,[‡] Jürgen Pleiss,[‡] and Roland E. Kontermann*,[†]

Institut für Zellbiologie und Immunologie, Universität Stuttgart, Allmandring 31, 70569 Stuttgart, Germany, and Institut für Technische Biochemie, Universität Stuttgart, Allmandring 31, 70569 Stuttgart, Germany. Received September 10, 2007; Revised Manuscript Received October 2, 2007

Immunoliposomes generated by coupling of antibodies to the liposomal surface allow for an active targeting of entrapped compounds to diseased areas. Single-chain Fv fragments (scFv) represent the smallest part of an antibody containing the entire antigen-binding site. They can be coupled in a defined and site-directed manner through genetically engineered cysteine residues, for example, those added at the C-terminus. Here, we have performed a comparative analysis of various scFv′ variants with cysteine residues present at the end of a C-terminal extension of varying length and composition (HC variants) or introduced in the linker sequence connecting the variable heavy and light chain domain (LC variants). Using a scFv fragment directed against fibroblast activation protein (FAP) as a model antibody, we could show that all variants can be employed for the generation of active immunoliposomes, although the presence of three additional cysteine residues in one scFv′ molecule resulted in decreased binding of immunoliposomes compared to that of immunoliposomes generated with scFv′ molecules containing only one additional cysteine residue. In order to further improve the scFv′ format by reducing the number of additional amino acid residues, we also generated molecules with the hexahistidyl-tag incorporated into the linker sequence together with a cysteine residue either at position 1 or 3 of the linker sequence (LCH variants). These newly designed scFv′ molecules may be particularly suitable for the generation of immunoliposomes and other antibody conjugates, limiting the number of additional residues in these antibody molecules to a minimum.

INTRODUCTION

Immunoliposomes have been developed for targeted drug delivery, for example, the delivery of chemotherapeutic drugs to tumor tissues (*1*). These immunoliposomes are generated by coupling antibodies or antibody fragments to the surface of liposomal drugs (*2*). Initially, whole antibodies were used for this purpose. However, several studies have shown that whole antibodies, for example, monoclonal antibodies of murine origin, induce immune responses, which can lead to neutralization (*3, 4*). Furthermore, immunoliposomes composed of whole antibodies are rapidly cleared from circulation because of Fc-receptor mediated uptake by cells of the reticulo-endothelial system (*5*). Hence, new approaches have emerged that employ antibody fragments, such as Fab′ fragments, which can be obtained from whole antibodies by proteolytic cleavage and subsequent reduction or by production in recombinant form, for example, in bacteria (*6*). Immunoliposomes composed of Fab′ fragments have shown reduced immunogenicity and improved therapeutic effects compared to IgG immunoliposomes (*7*).

Progress in antibody engineering technologies has led to the establishment of various methods to obtain antibodies with desired binding properties from combinatorial antibody libraries, for example, using phage display technology (*8*). These approaches also allow for the isolation of human antibody molecules, which further reduce or even avoid immunogenicity in humans. Thus, a large variety of such antibodies has been already isolated and is available for the generation of targeted therapeutics. Routinely, these antibodies are present as single-chain Fv (scFv) fragments. This format represents the smallest part of an antibody with full antigen-binding activity and is therefore sufficient for the generation of targeted therapeutics. Hence, scFv molecules are ideally suited for the generation of immunoliposomes, and various studies have already demonstrated their feasibility (*6*).

To achieve site-directed and defined coupling, one or more additional cysteine residues have been introduced into the scFv molecule, mainly at the C-terminus, which allow conjugation to sulfhydryl-reactive reagents (*9, 10*). Such scFv′ molecules, that is, scFv possessing free sulfhydryl groups, have been successfully employed for the generation of immunoliposomes (*9–11*) but also for other applications, for example, site-directed PEGylation to improve pharmacokinetic properties and the generation of immunosensors and targeted gold nanoparticles (*12–16*).

Different scFv′ formats have been described in the literature, differing in the position and number of additional cysteine residues. Thus, up to three cysteine residues have been added to the C-terminus of a scFv molecule (*9, 10, 16–20*). These scFv′ molecules also varied in the length and composition of the C-terminal extension. In addition, a few studies have described monovalent or bivalent scFv molecules with an additional cysteine residue introduced in the linker sequence connecting the variable domains (*14, 21*).

Recent studies have shown that the position and number of the cysteine residues incorporated can influence the coupling efficiency and functionality of the generated immunoliposomes (ref *10*; unpublished observations). Here, we performed a comparative analysis of scFv′ variants with one or three additional cysteine residues introduced either at a C-terminal extension of varying length or at different positions in the linker peptide using a scFv fragment directed against fibroblast activation protein (FAP) as model antibody (*22*). The novel

* Corresponding author. Tel: +49 711 685-66989. Fax: +49 711 685-67484. E-mail: roland.kontermann@izi.uni-stuttgart.de.
[†] Institut für Zellbiologie und Immunologie.
[‡] Institut für Technische Biochemie.

10.1021/bc700349k CCC: $40.75 © 2008 American Chemical Society
Published on Web 11/08/2007

finding that scFv′ molecules with a linker cysteine can be used for the generation of immunoliposomes prompted us to generate optimized scFv′ molecules with a hexahistidyl-tag sequence as well as the additional cysteine located in the linker sequence, thus reducing the number of additional residues in a scFv′ molecule to a minimum.

MATERIALS AND METHODS

Materials. All lipids were purchased from Avanti Polar Lipids (Alabaster, USA). DiI was purchased from Sigma (Taufkirchen, Germany). HRP-conjugated anti-His-tag antibody was purchased from Santa Cruz Biotechnology (USA) and FITC-conjugated anti-His antibody from Dianova (Hamburg, Germany). Human plasma (stabilized with citrate/phosphate/dextrose solution (CPD)) was kindly provided by the blood center of Katharinenhospital (Stuttgart, Germany). The stably transfected human FAP-expressing fibrosarcoma cell line HT1080-13.8 (HT1080-FAP_{mo}) expressing mouse FAP as well as HT1080 wild-type cells was grown in RPMI, 5% FCS, and 2 mM glutamine.

Cloning and Expression of scFv′ Variants. The scFv′ 36 HC constructs (HC2–4) were generated by PCR amplification of scFv′ 36-encoding DNA present in bacterial expression vector pABC4 (*22*) using primers LMB3 (5′-CAG GAA ACA GCT ATG ACC-3′) and HC2-Eco-For (5′-GCG CAT CAT CAC CAT CAC CAT GGC GGA TCG AGT GGC TCA GGA TGC TAA GAA TTC CAC TGG-3′), HC3-Eco-For (5′-GCG CAT CAT CAC CAT CAC CAT GGC GGA TCG AGT GGC TCA TGC GGA TGT AGT TGC TAA GAA TTC CAC TGG-3′), or HC4-Eco-For (5′-CAT CAT CAC CAT CAC CAC GGC GGA TCC AGC GGC GGA TCC AGC GGC TCC GGA TGC TAA GAA TTC CGG-3′), respectively. The resulting PCR products were digested with SfiI and *Eco*RI and cloned into vector pAB1 digested with the same enzymes. For generating the LC variants (LC1–3), scFv′ molecules were amplified from pAB1-scFv36 with primer LMB2 (5′-GTA AAA CGA CGG CCA GT-3′) and LC1-Xho-Back (5′-ACC GTC TCG AGT TGC GGA GGC GGT TCA GGC GGA GGT GGC TCT-3′), LC2-Xho-Back (5′-ACC GTC TCG AGT GGT TGC GGC GGT TCA GGC GGA GGT GGC TCT-3), and LC3-Xho-Back (5′-ACC GTC TCG AGT GGT GGA TGC GGT TCA GGC GGA GGT GGC TCT-3′), respectively. PCR products were digested with XhoI and NotI and cloned into pAB1-scFv36 digested with the same enzymes. LCH variants were generated in the same manner using primers LCH1-Xho-Back (5′-ACC GTC TCG AGT TGC GGA GGC GGT CAT CAT CAC CAT CAC CAT GGA GGC GGT AGT GCA CAA ATT CTG ATG-3′) and LCH3-Xho-Back (5′-ACC GTC TCG AGT GGT GGA TGC GGT CAT CAT CAC CAT CAC CAT GGA GGC GGT AGT GCA CAA ATT CTG ATG-3′) as back primers. Antibody fragments were purified by immobilized metal ion affinity chromatography (IMAC) as described elsewhere (*23*). Protein concentration was determined by measuring the absorbance at 280 nm. scFv′ were analyzed by SDS−PAGE under reducing and nonreducing conditions and stained with Coomassie brilliant blue R250 or immunoblotted with a HRP-conjugated anti-His-tag antibody.

Generation of scFv Immunoliposomes by the Postinsertion Method. Immunoliposomes were generated by postinsertion of scFv′-conjugated micelles into preformed PEG-liposomes. All liposomes were prepared by the film hydration−extrusion method and were composed of EPC/Chol/mPEG-DSPE at a molar ratio of 6.5:3:0.5. In addition, all liposomes contained 0.3 mol % DiI as fluorescent dye. Lipids and DiI were dissolved in chloroform, and a thin lipid film was formed by removing the chloroform in a rotary evaporator at 42 °C and drying under vacuum for at least 1 h. The lipid film was hydrated with 1 mL of 10 mM Hepes buffer at pH 6.7. The final lipid concentration was 10 μmol lipid per mL of buffer. The resulting multilamellar vesicle dispersion was extruded 21 times through 50 nm polycarbonate membranes using a LiposoFast extruder (Avestin, Ottawa, Canada). For the preparation of Mal-PEG-DSPE micelles, chloroform was removed by incubation at RT and lipid dissolved in ddH_2O to a final concentration of 10 mg/mL. For the coupling of scFv′ to Mal-PEG-DSPE micelles, purified scFv were reduced in 2 mM tris(2-carboxyethyl)phosphine (TCEP) for 2 h at room temperature followed by the removal of TCEP by dialysis against O_2 free 10 mM Na_2HPO_4/NaH_2PO_4 buffer, 0.2 mM EDTA, and 30 mM NaCl (pH 6.7) overnight at 4 °C. Micellar lipid and reduced scFv′ were mixed at a molar ratio of 4.67:1 (*24*). The coupling reaction was performed at room temperature for 30 min The reaction was quenched with 1 mM L-cysteine and 0.02 mM EDTA at pH 5.5. The scFv′-coupled micelles were inserted into preformed PEGylated liposomes by incubation at 55 °C for 30 min (0.6 mol % and 2 mol % micellar lipid with respect to liposomal lipid). Unbound scFv molecules were removed by gel filtration using a Sepharose CL4B column (Amersham, Braunschweig, Germany). Liposome size and ζ-potenial were measured using a ZetaSizer Nano ZS (Malvern, Herrenberg, Germany).

Analysis of Coupling Efficiency. The scFv′-coupled micelles were analyzed by SDS−PAGE under reducing conditions and stained with Coomassie Brilliant Blue R250. The coupling efficiency was determined by quantifying the intensity of the protein bands before and after coupling to micelles using the software ImageQuant (GE Healthcare, Germany).

Determination of Protein Melting Points. The melting point of the scFv′ 36 variants was determined with ZetaSizer Nano ZS (Malvern, Herrenberg, Germany). Approximately 150 μg of purified scFv′ protein was diluted in PBS to a total volume of 1 mL and sterile filtered into a quartz cuvette. Dynamic laser light scattering intensity was measured while the temperature was increased in 1 °C intervals from 30 to 70 °C with 2 min equilibration for each temperature step. The melting point was defined as the temperature at which the light scattering intensity dramatically increased.

Flow Cytometry. Cells were detached from cell culture dishes using 0.05% trypsin and 0.02% EDTA (GIBCO). Approximately 250,000 cells were incubated with DiI-labeled immunoliposomes (10 nmol lipid) in PBS containing 2% FCS and 0.02% sodium azide (PBA) for 1 h at room temperature. After washing cells three times with PBA buffer (4 °C), cells were resuspended in 500 μL of PBA buffer and analyzed by flow cytometry (Epics XL-MCL, Beckmann). The binding of purified scFv′ molecules was determined by incubating detached cells with antibody molecules (10 μg/mL) in PBA buffer for 1 h at room temperature. Cells were then washed three times as described and incubated with FITC-conjugated anti-His-tag antibody diluted 1/200. Data were evaluated with WinMDI, version 2.8.

In Vitro Plasma Stability. To analyze plasma stability, immunoliposomes (10 nmol lipid) were preincubated in the presence of 50% human plasma for 4 days at 37 °C in a total volume of 50 μL. Subsequently, the binding of immunoliposomes to cells was analyzed by flow cytometry as described above.

Modeling of scFv 36 Variants. A model of scFv 36 without the linker was generated using the Web Antibody Modeling (WAM) server (*25*). A linker of 14 amino acids connecting the V_H and V_L subunits was modeled using MODELER 6v2 (*26*). The linker region did not contain secondary structure as expected from the distance between the C-terminus of V_H and the N-terminus of V_L along the surface of the protein. The quality of the scFv 36 model was checked by PROSA2003's knowledge-

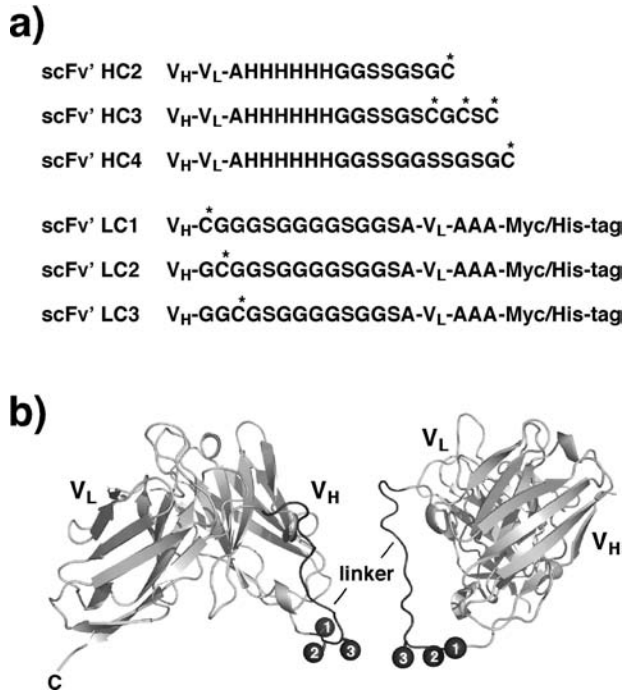

Figure 1. Composition of scFv′ variants. (a) C-terminal sequences of constructs HC2, HC3, and HC4 as well as the linker sequences of constructs LC1, LC2, and LC3. Cysteine residues are marked with an asterisk. The Myc/His-tag has the sequence -EQKLISEEDLNGAAH-HHHHH-. (b) Model structure of anti-FAP scFv′ 36 with the positions of the three linker modifications LC1–3 shown from two sides. Sulfur atoms of the three cysteine residues incorporated into the linker peptide are shown as spheres (*1–3*).

based potentials (*27*), and stereochemical checks were carried out with the PROCHECK package (*28, 29*).

RESULTS

Generation and Characterization of scFv′ Variants. Six different scFv′ variants of anti-FAP scFv 36 were designed (Figure 1a). The variants HC2 and HC4 contain one additional cysteine residue at the C-terminus and vary in the length of the C-terminal extension, which also contains a hexahistidyl-tag for purification. Variant HC3 contains three additional cysteine residues at the C-terminal extension. In addition, we designed three scFv′ variants (LC1–3) containing an additional cysteine residue in the peptide linker (position 1, 2, or 3, respectively). These variants are also provided with a vector-encoded Myc-tag and hexahistidy-tag at the C-terminus. In order to show that the cysteine side chains are accessible for coupling reactions, a model of scFv′ 36 including the linker connecting the variable domains was generated. This model structure of scFv′ 36 indicated that the linker modifications are located at the bottom of the scFv′ molecule opposite the antigen-binding site and that the side-chain sulfhydryl groups are accessible for coupling (Figure 1b).

All six scFv′ variants could be expressed in bacteria and purified from periplasmic preparations by IMAC. Yields of 0.2–0.8 mg of purified protein per liter culture were obtained. These yields are similar to yields typically obtained for unmodified scFv 36 (0.3–0.7 mg/L culture). A single band with an apparent molecular weight of 32 kDa was detected in SDS−PAGE under reducing conditions (Figure 2a). Two bands of 30 and 60 kDa were seen under nonreducing conditions for the HC constructs, while the LC constructs showed only one prominent band of 30 kDa (Figure 2c). The identity of these protein bands was further confirmed by immunoblotting with an anti-His-tag antibody (Figure 2b and d). This experiment

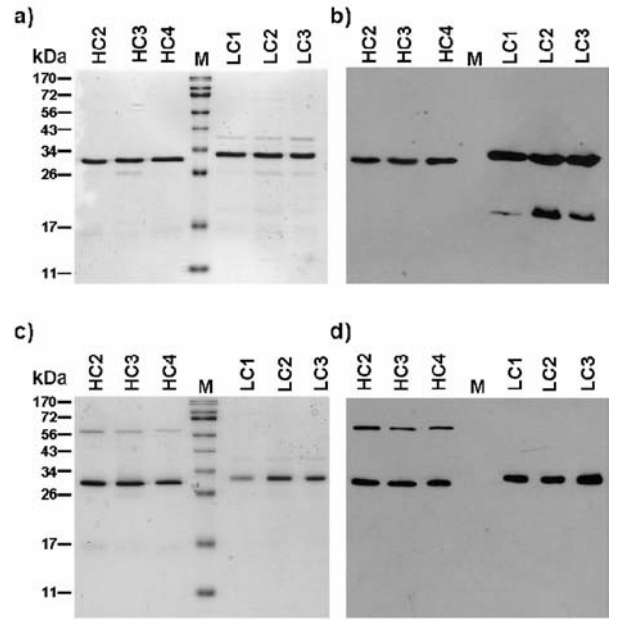

Figure 2. SDS−PAGE and immunoblot analysis of purified scFv′ variants. Purified scFv′ variants HC2–4 and LC1–3 were analyzed by 15% SDS−PAGE under nonreducing (c and d) or reducing (a and b) conditions and either stained with Coomassie or immunoblotted with an anti-His-tag antibody (2 μg/lane were used for Coomassie staining and 1 μg/lane for immunoblotting).

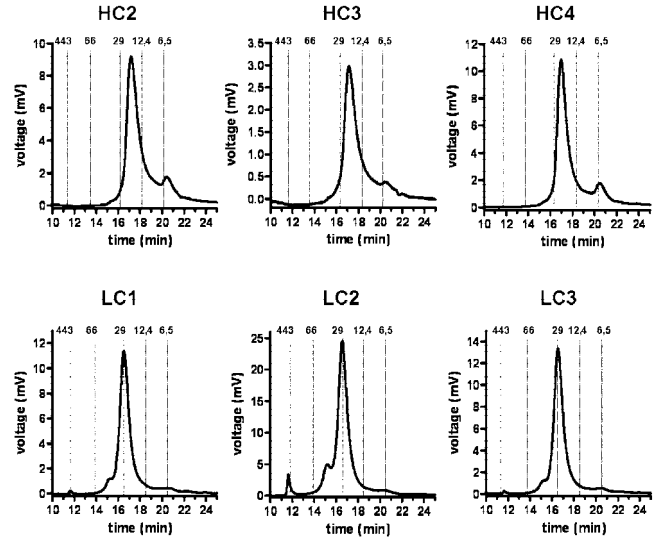

Figure 3. Size exclusion chromatography. scFv′ molecules were analyzed by HPLC size exclusion chromatography using a BioSep-Sec-2000 column. Peak positions of standard proteins are indicated.

also revealed for the LC1–3 preparations a second protein band of approximately 20 kDa, probably due to proteolytic cleavage. Therefore, LC variants appeared to be more susceptible to proteolytic cleavage than the HC variants. The cleavage band was strongest for the LC2 variant.

All scFv′ variants showed a single major peak in size exclusion chromatography (Figure 3). The three HC variants eluted with an apparent molecular mass of 22.5 kDa (calculated molecular mass, 28 kDa), while all LC variants eluted with an apparent molecular mass of 29 kDa (calculated molecular mass, 28 kDa).

The thermal stability of the scFv′ variants was deduced from their melting points as measured by dynamic light scattering (Figure 4). For all HC constructs, the melting point was

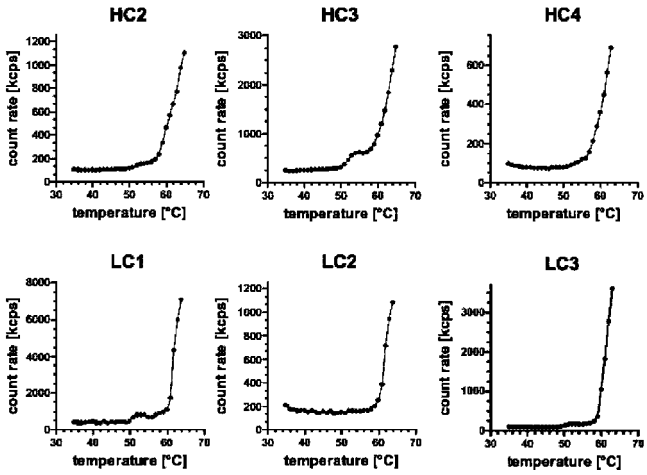

Figure 4. Thermal stability. Protein melting curves of the scFv′ variants were determined by dynamic light scattering using 1 °C intervals.

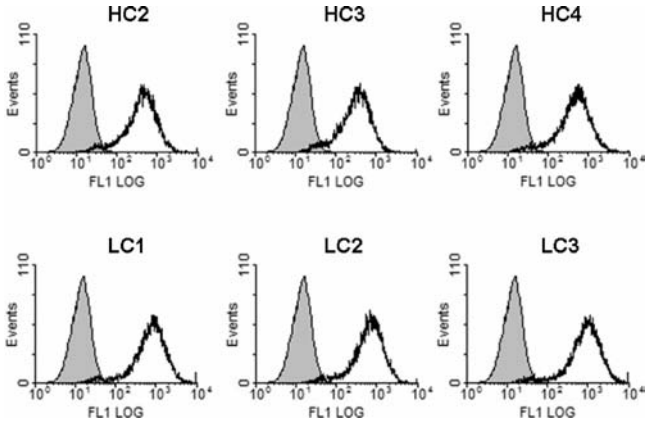

Figure 5. Binding of scFv′ variants to FAP-expressing cells. scFv′ molecules were analyzed by flow cytometry for binding to HT1080-FAP_{mo} cells. Gray areas, cells incubated without scFv′; solid line, cells incubated with scFv′ molecules.

determined to be around 56–57 °C. The LC constructs showed a slightly higher melting point with 58–59 °C.

All scFv′ variants specifically recognized FAP-expressing cells (HT1080-FAP_{mo}) in flow cytometry experiments, indicating that the incorporation of additional cysteine residues at the C-terminus or linker region does not interfere with antigen binding activity (Figure 5).

Coupling of scFv′ Fragments to Mal-PEG-DSPE Micelles. Next, we analyzed the coupling of the scFv′ fragments to Mal-PEG-DSPE micelles using a molar scFv′ to lipid ratio of 1:4.67. The coupling reaction was performed at room temperature for 30 min. SDS−PAGE analysis demonstrated efficient coupling of all constructs (Figure 6). Coupling efficiency was in the range of 80–98% as determined by densitometric quantification (Table 1). Highest coupling efficiency was achieved with construct HC3. All constructs possessing one additional cysteine showed after coupling an increase in apparent molecular mass of approximately 3 kDa, while the mass of HC3 was increased by approximately 10 kDa. This finding indicates that one Mal-PEG-DSPE chain is conjugated to HC2, HC4, and LC1–3, while three chains are conjugated to HC3.

Generation of scFv Immunoliposomes by the Post-insertion Method. scFv′-coupled micelles were used to generate scFv immunoliposomes, applying the postinsertion method. In this method, scFv′-coupled micelles are inserted into preformed PEGylated liposomes by incubation at 55 °C for 30 min (*30, 31*). Two different micelle to liposome ratios (0.6 mol % and 2 mol % micellar lipid with respect to liposomal lipid) were used for the preparation of immunoliposomes. In both cases, the generated immunoliposomes had a size of 90–106 nm, similar to the size of the acceptor liposomes used for the postinsertion of micelles (108 nm) (Table 2). All immunoliposomes had a slightly negative ζ-potential, while the ζ-potential of plain liposomes was slightly positive (Table 2). ScFv density was calculated to be in the range of 1.1–1.2 nmol scFv/μmol lipid at 0.6 mol % micellar lipid and 3.7–3.9 nmol scFv/μmol lipid at 2 mol % micellar lipid.

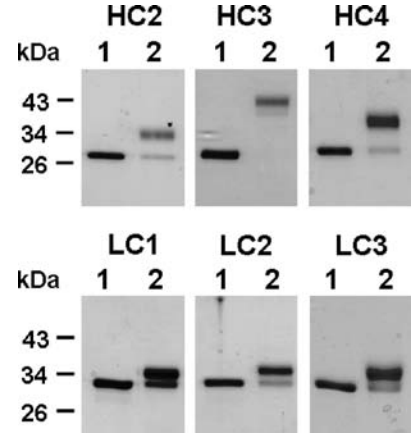

Figure 6. Coupling of scFv′ variants to Mal-PEG-DSPE micelles. SDS−PAGE analysis of scFv′ fragments before (1) and after (2) coupling to Mal-PEG_{2000}-DSPE micelles at a molar ratio of antibody to lipid of 1:4.67. Gels were stained with Coomassie. Coupling of the antibody molecules to the lipid is indicated by reduced mobility.

Table 1. Coupling Efficiencies of scFv′ Variants[a]

construct	coupling efficiency (%)
scFv′ 36-HC2	86.7 ± 4.5
scFv′ 36-HC3	97.8 ± 0.2
scFv′ 36-HC4	82.0 ± 7.5
scFv′ 36-LC1	79.7 ± 4.7
scFv′ 36-LC2	81.8 ± 3.9
scFv′ 36-LC3	90.2 ± 2.4

[a] Coupling efficiencies were determined by quantitative analysis of scFv′ fragments before and after coupling to micelles (see Figure 6).

Table 2. Size, Polydispersity Index (PDI) and ζ-Potential of scFv Immunoliposomes[a]

construct	size (nm)	PDI	ζ-potential (mV)
	108 ± 2.3	0.123 ± 0.038	5.2 ± 3.5
scFv′ 36-HC2	90 ± 1.5	0.159 ± 0.058	−12.6 ± 5.4
scFv′ 36-HC3	96 ± 1.2	0.134 ± 0.032	−12.5 ± 2.8
scFv′ 36-HC4	102 ± 2.8	0.156 ± 0.034	−15.0 ± 0.5
scFv′ 36-LC1	106 ± 3.7	0.178 ± 0.021	−8.8 ± 1.5
scFv′ 36-LC2	105 ± 7.6	0.149 ± 0.004	−11.2 ± 7.9
scFv′ 36-LC3	105 ± 7.7	0.112 ± 0.054	−2.8 ± 2.3

[a] Immunoliposomes were generated by postinsertion of scFv-conjugated micelles (2 mol % lipid) into preformed PEG-liposomes.

All immunoliposomes specifically bound FAP-expressing HT1080-FAP_{mo} cells (Figure 7). No binding to these cells was observed for plain (untargeted) liposomes. None of the liposomes showed binding to FAP-negative HT1080 cells. Binding was stronger when higher micellar concentrations were used for postinsertion. Binding intensity was similar for all immunoliposomes, except for scFv HC3-derived immunoliposomes, which showed a reduced binding activity (approximately 50% of the other immunoliposomes based on the mean fluorescence intensity) (Table 3). Furthermore, the binding of all immunoliposomes to HT1080-FAP_{mo} cells could be completely blocked by soluble scFv36 (10 μg/mL), while no blocking was seen with an irrelevant scFv molecule directed against another antigen

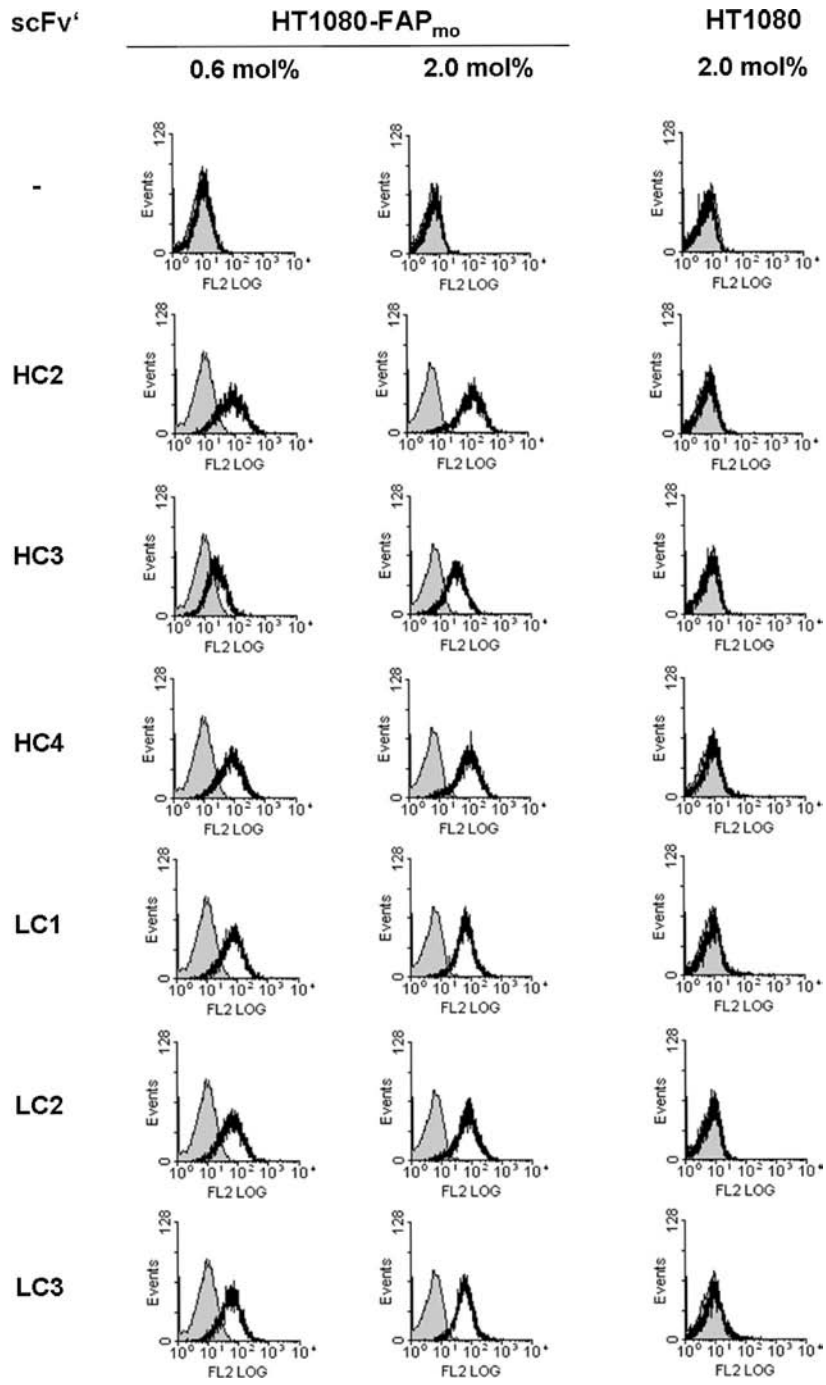

Figure 7. Binding of scFv-immunoliposomes to FAP-expressing cells. Micelle-coupled scFv′s were inserted at two concentrations (0.6 mol % and 2 mol % micellar lipids) into preformed PEGylated liposomes and analyzed for binding to FAP-expressing HT1080 cells (HT1080-FAP$_{mo}$) or to wild-type HT1080 cells. Plain liposomes (-), i.e., untargeted liposomes, were included as the negative control. Gray areas, cells alone; thick line, cells incubated with liposomes at 10 nmol lipid per 250.000 cells.

expressed by these cells (not shown). All immunoliposomes were highly stable in human plasma, showing no or only marginal reduction in binding after incubation in human plasma at 37 °C for 4 days (not shown).

scFv′ Formats Combining a Cysteine Residue and Hexahistidyl-Tag in the Linker. In order to reduce the number of additional amino acids in the scFv′ molecule, we generated new scFv′ variants with the hexahistidyl-tag incorporated into the linker sequence together with an additional cysteine residue either at position 1 or 3 of the linker sequence (Figure 8a). These LCH variants (LCH1 and LCH3) terminate at the C-terminus with residue Arg107 of the V_L domain, thus containing only 14 amino acid residues of the linker sequence as additional residues. Both variants could be expressed in bacteria and purified by IMAC with yields of 0.3 mg/L culture, similar to the HC and LC variants (Figure 8b and c). For both variants, SDS−PAGE analysis showed a predominant band of 26 kDa under reducing and nonreducing conditions. Both variants also formed dimers. In addition, some proteolytic cleavage products were observed (corresponding to 15–25% of the intact molecules). Although detection with anti-His-tag antibodies of cell-bound scFv′ LCH variants was strongly reduced (not shown), immunoliposomes generated with both LCH variants (size, 103.0 ± 2.1 nm for LCH1 and 105.6 ± 1.7 nm for LCH3) showed strong and specific binding to FAP-expressing cells (Figure

Table 3. Binding of scFv Immunoliposomes to FAP-Expressing Cells[a]

construct	MFI
	9.0 ± 3.1
scFv′ 36-HC2	104.8 ± 20.5
scFv′ 36-HC3	48.5 ± 10.4
scFv′ 36-HC4	108.2 ± 35.4
scFv′ 36-LC1	97.7 ± 35.5
scFv′ 36-LC2	109.8 ± 52.2
scFv′ 36-LC3	96.8 ± 41.8

[a] Binding is shown as mean fluorescence intensity (MFI) derived from four preparations of each immunoliposome.

8d). Binding was similar to that observed for LC variants (Figure 8d) and could be blocked with soluble anti-FAP scFv (not shown).

DISCUSSION

Here, we investigated two strategies for the generation of scFv′ molecules suitable for site-directed coupling via reactive sulfhydryl groups. Strategy 1 is based on scFv′ molecules having one or more additional cysteine residues at the end of a C-terminal extension of varying length. These C-terminal extensions introduce some additional spacing as well as flexibility between the antibody molecule and the reactive partner. Strategy 2 is based on molecules having one additional cysteine residue incorporated into the peptide linker connecting the V_H and V_L domains, thus not requiring any additional C-terminal extension.

Using an anti-FAP scFv as the model antibody, we could show that all these scFv′ derivatives could be expressed in *E. coli* and purified in soluble form with the majority of the molecules present in monomeric form. Yields of the scFv′ molecules were similar to those obtained for the unmodified scFv 36. Thus, the addition of one or three cysteine residues either to the C-terminus or to the linker sequences does not lead to reduced expression levels of this scFv molecule, as described for other scFv′ molecules that showed markedly reduced expression levels (*32*). Some scFv′ dimers could be observed in SDS−PAGE and immunoblotting analysis, especially for the three HC constructs but also for the LCH constructs, indicating that the cysteine residues are accessible for the formation of disulfide-linked homodimers. Furthermore, all molecules were functional, active, and possessed similar melting points. These findings demonstrate that the addition of one or three cysteine residues as well as C-terminal extensions does not influence expression, conformation, stability, and binding activity.

All scFv′ constructs could be coupled to maleimide-containing lipids. Coupling efficiencies and binding activity of the resulting immunoliposomes were similar for all constructs containing one additional cysteine residue, irrespective of whether it is present at the C-terminus or in the linker sequence. In contrast, the presence of three cysteine residues at the C-terminus resulted in immunoliposomes with reduced binding activity. SDS−PAGE analysis indicated that this variant (HC3) reacts with three Mal-PEG-DSPE molecules. After insertion into liposomes, this might lead to unfavorable orientation on the lipid bilayer, resulting in reduced accessibility and cell binding.

All scFv immunoliposomes described in the literature so far have been prepared from scFv′ molecules with the additional cysteine(s) located at the C-terminus (*9, 10, 18, 20, 22, 33, 34*) or have been conjugated through amino-reactive coupling reagents (*35, 36*). The use of cysteine residues engineered into the recombinant antibody molecule allows for a site-directed and oriented coupling compared to coupling to amino groups, which is undirected and might thus influence antigen-binding activity. Because the C-terminus of a scFv molecule is located

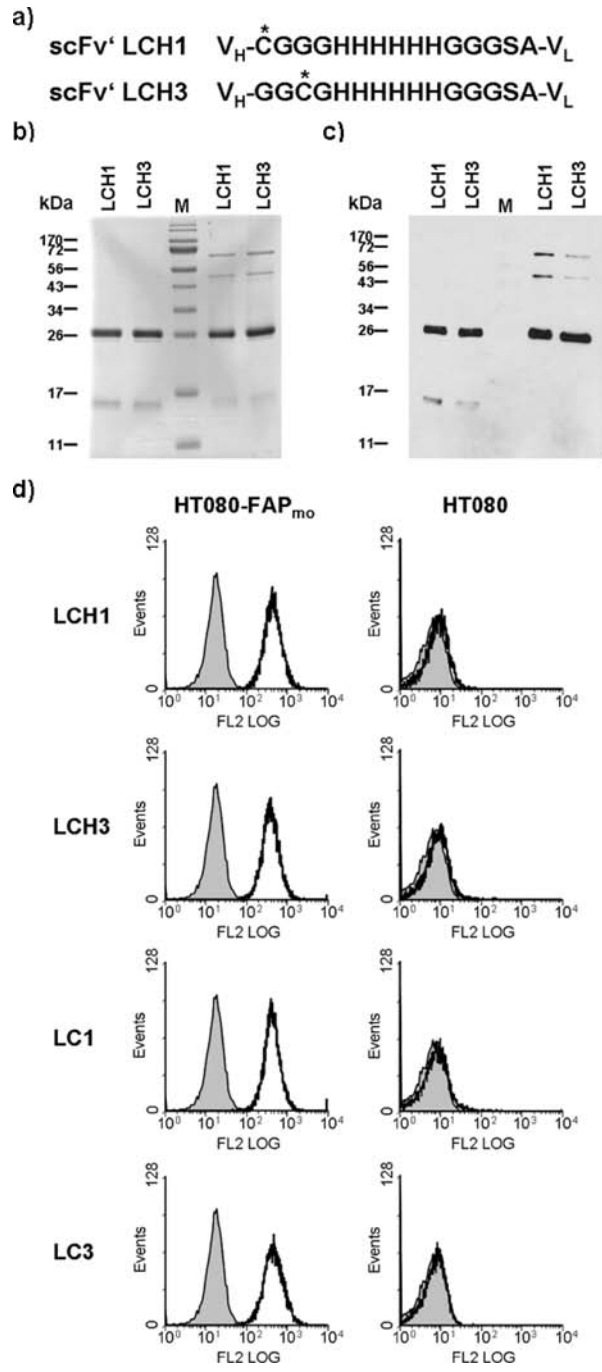

Figure 8. LCH variants. (a) Sequence of the linker of constructs LCH1 and LCH3 with the additional cysteine and the hexahistidyl-tag present in the linker peptide. (b) Coomassie-stained SDS−PAGE (2 μg/lane) and (c) immunoblot experiments (1 μg/lane) with the anti-His-tag antibody of purified LCH1 and LCH3 analyzed under reducing (left side of marker) or nonreducing (right side of marker) conditions. (d) Flow cytometry analysis of binding of LCH1 and LCH3 immunoliposomes to FAP-expressing HT1080 cells or FAP-negative HT1080 wild-type cells. The binding of LC1 and LC3 immunoliposomes was included for direct comparison. Gray areas, cells alone; thick line, cells incubated with liposomes at 10 nmol lipid per 250.000 cells.

opposite the antigen-binding site, coupling to reactive lipids or PEG chains should not interfere with the recognition of target cells. This was further confirmed in our study applying three constructs with C-terminal cysteines.

Interestingly, functional immunoliposomes could also be prepared with scFv′ molecules with an additional cysteine residue present in the linker sequence. For this approach, we compared three positions (1–3) of the linker peptide. No

differences in coupling efficiency and binding to target cells were observed between these three constructs or in comparison to the HC2 and HC4 constructs. The structural models of the anti-FAP scFv′ molecules indicate that these three positions are located at the bottom of the scFv′ molecule opposite the antigen-binding site. Recently, a similar scFv′ fragment possessing an additional cysteine residue at position 1 of a 15 residue linker was applied for the generation of a piezoimmunosensor for the detection of low concentrations of antigen in complex samples (*14*). Our study confirmed the suitability of site-directed coupling and has extended the application of scFv′ linker variants for the generation of targeted nanoparticulate carrier systems.

This approach was further developed by applying scFv′ molecules with the additional cysteine residue and the hexahistidyl-tag present in the linker sequence. These novel molecules have the advantage that except for the linker sequence no additional amino acid residues are present. Thus, these scFv′ molecules are reduced to the minimal length and composition required for easy one-step purification via IMAC and site-directed coupling to sulfhydryl-reactive molecules. Indeed, we could show that these LCH variants are produced in soluble and active forms in bacteria and that these molecules could be efficiently purified from periplasmic extracts by IMAC. Although recognition by anti-His-tag antibodies is impaired, they could be used to generate immunoliposomes that bind strongly to target cells. These newly designed scFv′ molecules may be particularly suitable for the generation of immunoliposomes and other antibody conjugates, limiting the number of additional residues in these antibody molecules. Instead of the hexahistidyl sequence, one can envisage that other short purification and/or detection tags, such as Strep-tag, poly Arg-tag, or FLAG-tag, may be integrated into the linker sequence, thus implementing further approaches for detection and purification (*37*).

In summary, we performed a comparative study of various scFv′ molecules designed for defined and oriented conjugation to sulfhydryl-reactive molecules. We could show that both genetically introduced single C-terminal cysteine residues as well as single cysteine residues in the linker sequence are equally suitable for the generation of scFv immunoliposomes for target-cell-specific binding and delivery.

ACKNOWLEDGMENT

We would like to thank Ronny Rüger (University of Jena) for helpful suggestions and discussions. This work was supported by a grant from Landesstiftung Baden-Württemberg ("Kompetenznetz funktionelle Nanostrukturen", project C11).

LITERATURE CITED

(1) Allen, T. M., and Cullis, P. R. (2004) Drug delivery systems: entering the mainstream. *Science 303*, 1818–1822.

(2) Mastrobattista, E., Koning, G. A., and Storm, G. (1999) Immunoliposomes for the targeted delivery of antitumor drugs. *Adv. Drug Delivery Rev. 40*, 103–127.

(3) Philipps, N. C., and Dahman, J. (1995) Immunogenicity of immunoliposomes: reactivity against species-specific IgG and liposomal phospholipids. *Immunol. Lett. 45*, 149–152.

(4) Bendas, G., Rothe, U., Scherphof, G. L., and Kamps, J. A. A. M. (2003) The influence of repeated injections on pharmacokinetics and biodistribution of different types of sterically stablized immunoliposomes. *Biochim. Biophys. Acta 1609*, 63–70.

(5) Koning, G. A., Morselt, H. W. M., Gorter, A., Allen, T. M., Zalipsky, S., Scherphof, G. L., and Kamps, J. A. A. M. (2003) Interaction of differently designed immunoliposomes with colon cancer cells and Kupffer cells. An in vitro comparison. *Pharm. Res. 20*, 1249–1257.

(6) Kontermann, R. E. (2006) Immunoliposomes for cancer therapy. *Curr. Opin. Mol. Ther. 8*, 39–45.

(7) Sapra, P., Moase, E. H., Ma, J., and Allen, T. M. (2004) Improved therapeutic responses in a xenograft model of human B lmyphoma (Namalwa) for liposomal vincristine versus liposomal doxorubicin targeted via anti-CD19 IgG2a or Fab′ fragments. *Clin. Cancer Res. 10*, 1100–1111.

(8) Kim, S. J., Park, Y., and Hong, H. J. (2005) Antibody engineering for the development of therapeutic antibodies. *Mol. Cells 20*, 17–29.

(9) Marty, C., Scheidegger, P., Ballmer-Hofer, K., Klemenz, R., and Schwendener, R. A. (2001) Production of functionalized single-chain Fv antibody fragments to the ED-B domain of the B-isoform of fibronectin in *Pichia pastoris*. *Protein Expression Purif. 21*, 156–164.

(10) Völkel, T., Hölig, P., Merdan, T., Müller, R., and Kontermann, R. E. (2004) Targeting of immunoliposomes to endothelial cells using a single-chain Fv fragment directed agaisnt human endoglin (CD105). *Biochim. Biophys. Acta 1663*, 158–166.

(11) Park, J. W., Kirpotin, D. B., Hong, K., Shalaby, R., Shao, Y., Nielsen, U. B., Marks, J. D., Papahadjopoulos, D., and Benz, C. C. (2001) Tumor targeting using anti-HER2 immunoliposomes. *J. Controlled Release 74*, 95–113.

(12) Nataranja, A., Xiong, C.-Y., Albrecht, H., DeNardo, G. L., and DeNardo, S. J. (2005) Characterization of site-specific scFv PEGylation for tumor-targeting pharmaceuticals. *Bioconjugate Chem. 16*, 113–121.

(13) Krimner, E. M., Hepp, J., Hoffmann, P., Bruckmaier, S., Petersen, L., Petsch, S., Parr, L., Schuster, I., Mangold, S., Lorenczewski, G., Lutterbüse, P., Buziol, S., Hochheim, I., Volkland, J., Molhoj, M., Sriskandarajah, M., Strasser, M., Itin, C., Wolf, A., Basu, A., Yang, K., Filupa, D., Sorensen, P., Kufer, P., Baeuerle, P., and Raum, T. (2006) A highly stable polyenthylene glycol-conjugated human single-chain antibody neutralizing granulocyte-macrophage colony stimulating factor at low nanomolar concentration. *Protein Eng., Des. Sel. 19*, 461–470.

(14) Shen, Z., Stryker, G. A., Mernaugh, R. L., Yu, L., Yan, H., and Zeng, X. (2005) Single-chain fragment variable antibody piezoimmunosensors. *Anal. Chem. 77*, 797–805.

(15) Backmann, N., Zahnd, C., Huber, F., Bietsch, A., Plückthun, A., Lang, H.-P., Güntheroldt, H.-J., Hegner, M., and Gerber, C. (2005) A label-free immunosensor array using single-chain antibody fragments. *Proc. Natl. Acad. Sci. U.S.A. 102*, 14587–14592.

(16) Ackerson, C. J., Jadzinsky, P. D., Jensen, G. J., and Kornberg, R. D. (2006) Rigid, specific, and discrete gold nanoparticle/antibody conjugates. *J. Am. Chem. Soc. 128*, 2635–2640.

(17) McCartney, J. E., Tai, M. S., Hudziak, R. M., Adams, G. P., Weiner, L. M., Jin, D., Stafford III, W. F., Liu, S., Bookman, M. A., Laminet, A. A., Fand, I., Houston, L. L., Oppermann, H., and Huston, J. S. (1994) Engineering disulfide-linked single-chain Fv dimers [$(sFv')_2$] with improved solution and targeting properties: anti-digoxin 26–10 $(sFv')_2$ and anti-c-erbB-2 741F8 $(sFv')_2$ made by protein folding and bonded through C-terminal cysteinyl peptides. *Protein Eng. 8*, 301–314.

(18) Nielsen, U. B., Kirpotin, D. B., Pickering, E. M., Hong, K., Park, J. W., Shalaby, M. R., Shao, Y., Benz, C. C., and Marks, J. D. (2002) Therapeutic efficacy of anti-ErbB2 immunoliposomes targeted by a phage antibody selected for cellular endocytosis. *Biochim. Biophys. Acta 1591*, 109–108.

(19) Albrecht, H., Burke, P. A., Natarajan, A., Xiong, C. Y., Kalicinsky, M., DeNardo, G. L., and DeNardo, S. J. (2004) Production of soluble scFvs with C-terminal-free thiol for site-specific conjugation or stable dimeric scFvs on demand. *Bioconjugate Chem. 15*, 16–26.

(20) Rubio Demirovic, A., Marty, C., Console, S., Zeisberger, S. M., Ruch, C., Jaussi, R., Schwendener, R. A., and Ballmer-Hofer, K. (2005) Targeting human cancer cells with VEGF receptor-2-directed liposomes. *Oncol. Rep. 13*, 319–324.

(21) Albrecht, H., DeNardo, G. L., and DeNardo, S. J. (2006) Monospecific bivalent scFv-SH: effects of linker length and location of an engineered cysteine on production, antigen binding

activity and free SH accessibility. *J. Immunol. Methods 310*, 100–116.
(22) Baum, P., Müller, D., Rüger, R., and Kontermann, R. E. (2007) Single-chain Fv immunoliposomes for the targeting of fibroblast activation protein-expressing tumor stromal cells. *J. Drug Target. 15*, 399–406.
(23) Rüger, R., Müller, D., Fahr, A., and Kontermann, R. E. (2005) Generation of immunoliposomes using recombinant single-chain Fv fragment bound to Ni-NTA-liposomes. *J. Drug Target. 13*, 399–406.
(24) Nellis (2005) Preclinical manufacture of an anti-HER2 scFv-PEG-DSPE liposome-inserting conjugate. 1. Gram-scale production and purification. *Biotechnol. Prog. 21*, 205–220.
(25) Whitelegg, N. R. J., and Rees, A. R. (2000) WAM - an improved algorithm for modelling antibodies on the Web. *Protein Eng. 13*, 819–824.
(26) Sali, A., and Blundell, T. L. (1993) Comparative protein modelling by satisfaction of spatial restraints. *J. Mol. Biol. 234*, 779–815.
(27) Sippl, M. J. (1993) Recognition of errors in three-dimensional structures of proteins. *Proteins 17*, 355–362.
(28) Laskowski, R. A., MacArthur, M. W., Moss, D. S., and Thornton, J. M. (1993) PROCHECK: a program to check the stereochemical quality of protein structures. *J. Appl. Crystallogr. 26*, 283–291.
(29) Morris, A. L., MacArthur, M. W., Hutchinson, E. G., and Thornton, J. M. (1992) Stereochemical quality of protein structure coordinates. *Proteins 12*, 345–364.
(30) Ishida, T., Iden, D. L., and Allen, T. M. (1999) A combinatorial approach to producing sterically stabilized (stealth) immunoliposomal drugs. *FEBS Lett. 460*, 129–133.
(31) Allen, T. M., Sapra, P., and Moase, E. (2002) Use of the post-insertion method for the formation of ligand-coupled liposomes. *Cell. Mol. Biol. Lett. 7*, 889–894.
(32) Schmiedl., A., Breitling, F., Winter, C. H., Queitsch, I., and Dübel, S. (2000) Effects of unpaired cyteines on yield, solubility and activity of different recombinant antibody constructs expressed in *E. coli*. *J. Immunol. Methods 242*, 101–114.
(33) Mamot, C., Drummond, D. C., Greiser, U., Hong, K., Kirpotin, D. B., Marks, J. D., and Park, J. W. (2003) Epidermal growth factor receptor (EGFR)-targeted immunoliposomes mediate specific and efficient drug delivery to EGFR- and EGFRvIII-overexpressing tumor cells. *Cancer Res. 63*, 3154–3161.
(34) Cheng, W. W. K., Das, D., Suresh, M., and Allen, T. M. (2007) Expression and purification of two anti-CD19 single chain Fv fragments for targeting of liposomes to CD19-expressing cells. *Biochim. Biophys. Acta 1768*, 21–29.
(35) Gosk, S., Gottstein, C., and Bendas, G. (2005) Targeting of immunoliposomes to endothelial cells expressing VCAM: a future strategy in cancer therapy. *Int. J. Clin. Pharmacol. Ther. 43*, 581–582.
(36) Hu, H., Chen, D., Liu, Y., Deng, Y., Yang, S., Qiao, M., Zhao, J., and Zhao, X. (2006) Target ability and therapy efficacy of immunoliposomes using a humanized antihepatoma disulfide-stabilized Fv fragment on tumor cells. *J. Pharm. Sci. 95*, 192–199.
(37) Terpe, K. (2003) Overview of tag protein fusions: from molecular and biochemical fundamentals to commercial systems. *Appl. Microbiol. Biotechnol. 60*, 523–533.

BC700349K

A Novel Class of Intrinsic Proteasome Inhibitory Gene Transfer Peptides

Molly E. Martin and Kevin G. Rice*

Division of Medicinal and Natural Products Chemistry, College of Pharmacy, University of Iowa, Iowa City, Iowa 52242.
Received September 21, 2007; Revised Manuscript Received October 30, 2007

Proteasomes are multisubunit enzymes responsible for the degradation of many cytosolic proteins. The inhibition of the proteasome has been the subject of intense interest in the development of drug therapies. We have previously demonstrated that simultaneous administration of a tripeptide aldehyde proteasome inhibitor (MG115 or MG132) with a peptide (Cys-Trp-Lys_{18}) DNA condensate boosted gene expression by 30-fold in cell culture. In the present study, we have developed a convergent synthesis to allow the incorporation of a proteasome inhibitor tripeptide into the C-terminal end of a gene delivery peptide. The resulting peptides formed DNA condensates that mediated a 100-fold enhancement in gene expression over a control peptide lacking all or part of the tripeptide inhibitor. Gene transfer peptides possessing intrinsic proteasome inhibitors were also found to be nontoxic to cells in culture. These results suggest that intrinsic proteasome inhibition may also be used to boost the efficiency of peptide-mediated nonviral gene delivery systems in vivo.

INTRODUCTION

The proteasome is a multisubunit complex that is responsible for the degradation of many cytosolic proteins such as damaged or misfolded proteins (*1, 2*), degradation of cyclins for cell cycle control (*3, 4*), destruction of transcription factors that control cell differentiation (*3, 4*), and processing of foreign proteins for the generation of cellular immune responses (*1, 5*). The 26S proteasome complex is composed of the barrel-like 20S catalytic core capped at the ends by the 19S regulatory subunits (*2, 6*). The 19S regulatory particles are responsible for substrate recognition, unfolding, and translocation of proteins into the catalytic core. The proteolytic sites of the proteasome are contained inside the core of the 20S complex (*7, 8*). Unlike many other proteolytic enzymes, the proteasome has multiple peptidase activities that can be classified into three main groups: cleavage after hydrophobic side chains (chymotrypsin-like), cleavage after basic residues (trypsin-like), and cleavage after acidic residues (peptidylglutamyl peptide hydrolysis or PGPH) (*6, 7*).

Previous work by Duan et al. established the proteasome to be a key route of metabolism for viral gene delivery vectors (*9*). In studies of airway epithelial cells, it was found that the adeno-associated virus (AAV) vector was ubiquitinated after endocytosis and targeted for degradation by the proteasome. Coadministration of tripeptide proteasome inhibitors increased gene expression from the apical surface by over 200-fold in cell culture and also increased AAV-mediated gene transfer in the liver and lung (*9*).

Nonviral vectors are often composed of cationic peptides, polymers, and lipids that interact with the negatively charged backbone of DNA to form nanometer sized particles that spontaneously transfect cells in culture (*10*). The intracellular dissociation and subsequent metabolism of a cationic peptide polymer leads to the release and premature metabolism of plasmid DNA by DNase leading to a low level and short duration of expression (*11*). The enzymes responsible for the metabolism of peptide-mediated nonviral delivery systems are believed to be in the lysosomes (*12*); however, recent evidence has implicated the involvement of the proteasome (*13*).

Kim et al. hypothesized that peptide−DNA condensates could follow a route of metabolism similar to that of viruses because of their comparable size and susceptibility to serine proteases (*13*). Transfection of HepG2 cells in the presence of tripeptide proteasome inhibitors resulted in a 30-fold increase in luciferase expression for peptide−DNA condensates, whereas lipofectamine and polyethylenimine transfections were not enhanced. However, simultaneous uptake of condensate and inhibitor can be difficult, and these tripeptide inhibitors are very cytotoxic, with an LD_{50} of approximately 2 μM (*13*).

Peptide vinyl esters are a new class of proteasome inhibitors that are suggested to work through a mechanism similar to that of the well-known peptide vinyl sulfone inhibitors such as NLVS (*14–17*). The C-terminal vinyl ester covalently modifies the active site of the proteasome by serving as a substrate for a Michael addition with the catalytic threonine residue at the N-terminus of the β subunit (*14*). We hypothesize that gene delivery peptides containing an intrinsic C-terminal vinyl ester moiety may resist metabolism by the proteasome and thereby increase the gene transfer efficiency of peptide−DNA condensates. Here, we describe the synthesis and testing of gene delivery peptides containing a variety of intrinsic peptide vinyl ester sequences that condense DNA, mediate cellular uptake, inhibit the proteasome, and boost gene transfer efficiency. Incorporation of the peptide inhibitor sequence into the DNA condensate provides a mechanism for cointernalization of the proteasome inhibitor with the peptide−DNA condensate without the cytotoxic effects of giving a separate inhibitor.

MATERIALS AND METHODS

(Benzotriazol-1-yloxy)tris(dimethylamino)phosphonium hexafluorophosphate, *N*-terminal Fmoc-protected amino acids, *N*-terminal Boc-protected amino acids, 1-hydroxybenzotriazole, diisopropylcarbodiimide, and 2-chlorotrityl chloride resin for peptide synthesis were obtained from Advanced ChemTech (Lexington, KY). Triethylamine, ether, trifluoroacetic acid, hexane, ethyl acetate, and acetonitrile were purchased from Fisher. Dichloromethane, *N*,*O*-dimethylhydroxylamine hydro-

* To whom correspondence should be addressed. Kevin G. Rice, College of Pharmacy, University of Iowa, 115 South Grand Avenue, Iowa City, IA 52242. Tel: 319-335-9903. Fax: 319-335-8766. E-mail: kevin-rice@uiowa.edu.

10.1021/bc700362b CCC: $40.75 © 2008 American Chemical Society
Published on Web 12/21/2007

chloride, lithium aluminum hydride, tetrahydrofuran, triethylphosphonoacetate, potassium *tert*-butoxide, acetic acid, 2,2,2-trifluoroethanol, diisopropylethylamine, and thiazole orange were purchased from Sigma-Aldrich Chemical Co. (St. Louis, MO). HepG2 cells were provided by the Center for Gene Therapy of CF in the University of Iowa. DMEM, Hams-F12, sodium pyruvate, penicillin/streptomycin, and inactivated fetal bovine serum (FBS) were from Invitrogen Life Technologies Inc. (Carlsbad, CA). A 5.6 kbp plasmid (pCMVL) encoding the reporter gene luciferase was a gift from Dr. Hickman at the University of California (Davis, CA). Endotoxin-free plasmids were purified from *Escherichia coli* on a Qiagen ultrapure column according to the manufacturer's instructions. Luciferase from *Photinus pyralis*, D-luciferin, and ATP were purchased from Roche Diagnostics Corporation (Indianapolis, IN). The BCA assay kit was from Pierce Biotechnology Inc. (Rockford, IL). MG 115 (Z-Leu-Leu-Nva-CHO) was purchased from Calbiochem (San Diego, CA).

Synthesis of Leu-ve and Nva-ve. Leu-ve and Nva-ve were synthesized by modification of methods by Fehrentz and Castro (*18*). The peptide aldehyde was converted to the vinyl ester according to the procedure of Hover et al. (*19*). Briefly, triethylamine (2.2 g, 22 mmol) was added to a solution of Boc-amino acid **1** (5.0 g, 22 mmol) in 90 mL of dichloromethane (DCM), followed by the addition of (benzotriazol-1-yloxy)tris-(dimethylamino)phosphonium hexafluorophosphate (BOP; 9.6 g, 22 mmol). After 5 min, *N*,*O*-dimethylhydroxylamine hydrochloride (2.3 g, 24 mmol) and triethylamine (2.4 g, 24 mmol) were added, and the reaction was stirred at RT under nitrogen. Approximately 0.5 mL of additional triethylamine was added to the reaction to raise the pH to 7. The reaction was monitored by TLC (1:1 ethyl acetate/hexane, $R_f = 0.52$) and reached completion within 45 min. The mixture was diluted to 150 mL with DCM and washed successively with 3 N HCl (3 × 50 mL), saturated $NaHCO_3$ (3 × 50 mL), and saturated NaCl (3 × 50 mL). The organic layer was dried over $MgSO_4$ and evaporated to give **2**.

Lithium aluminum hydride (LAH; 0.95 g, 25 mmol, 5 equiv) was added to 150 mL of tetrahydrofuran (THF) under nitrogen. The LAH slurry was then added dropwise to **2** in 50 mL of THF and mixed for 20 min under nitrogen. The mixture was hydrolyzed with potassium hydrogen sulfate (4.77 g, 35 mmol) in 100 mL of water, and THF was evaporated. Ether (200 mL) was added, and the aqueous layer was separated and extracted with 3 × 50 mL ether. The organic phases were combined, washed with 3 N HCl (3 × 50 mL), saturated $NaHCO_3$ (3 × 50 mL), and saturated NaCl (3 × 50 mL), and dried over $MgSO_4$. The solvent was then evaporated to give **3**.

Triethylphosphonoacetate (3.11 g, 15.5 mmol) was added to 58 mL of THF and cooled to 0 °C. Potassium *tert*-butoxide (1.56 g, 13.9 mmol) in 14 mL of THF was added and stirred at room temperature for 1 h. The mixture was then cooled to 5 °C, aldehyde **3** was added in 23 mL of THF, and the reaction was stirred for 2 h at room temperature until the reaction was shown to be complete by TLC (9:1 hexane/ethyl acetate, $R_f = 0.25$). The solvent was evaporated, and the residue was dissolved in 200 mL of 50% ether in water. The aqueous phase was then extracted with ether (2 × 100 mL), the combined organic layers were dried over $MgSO_4$, and the solvent was evaporated. The residue was then purified by flash chromatography using 9:1 hexane/ethyl acetate to give **4**. The Boc-protected vinyl ester **4** was then treated with 90% trifluoroacetic acid (TFA) in water for 40 min followed by evaporation of TFA. The residue was precipitated with ether, and the resulting solid was separated by centrifugation to give vinyl ester **5** in an overall yield of 40%.

The product was characterized by proton NMR (300 MHz, acetone-d_6): $\delta = 6.98$ (dd, $J = 7.2$ Hz, 15.9 Hz, 1H), 6.17 (dd, $J = 1.2$ Hz, 15.9 Hz, 1H), 4.90 (m, 1H), 4.16 (q, $J = 7.2$ Hz, 2H), 1.98–2.10 (m, 1H), 1.64–1.76 (m, 2H) 1.24 (t, $J = 7.2$ Hz, 3H), 0.95 (dd, $J = 3.6$ Hz, 6.3 Hz, 6H). MS: $M + H^+ = 186.1$.

Nva-ve was synthesized by an identical approach with an overall yield of 48%. ^{1}H NMR (300 MHz, acetone-d_6): $\delta = 6.99$ (dd, $J = 6.9$ Hz, 15.9 Hz, 1H), 6.14 (dd, $J = 0.9$ Hz, 15.9 Hz, 1H), 4.86 (m, 1H), 4.16 (q, $J = 7.2$ Hz, 2H), 1.80–1.95 (m, 2H), 1.35–1.50 (m, 2H), 1.25 (t, $J = 7.2$ Hz, 3H), 0.93 (t, $J = 7.5$ Hz, 3H). MS: $M + H^+ = 172.1$.

Intrinsic Proteasome Inhibitory Gene Transfer Peptide Synthesis. Peptides of the following sequences WK_{18}, WK_{18}LL, WK_{18}VS, WK_{18}VQ, WK_{18}FQ, WK_{18}YVQ, and WK_{18}FVQ were synthesized on 2-chlorotrityl chloride resin at a 30 μmol scale. Standard Fmoc procedures were used with 1-hydroxybenzotriazole and diisopropylcarbodiimide double couplings on an Apex 396 Advanced ChemTech solid-phase peptide synthesizer. *N*-terminal and side-chain protected peptides were cleaved from the resin by reaction with acetic acid/2,2,2-trifluoroethanol/DCM (1:1:8 (v/v/v)) for 30 min at RT. Fifteen volumes of hexane were then added, and the solvent was evaporated to give the crude protected peptide.

Each protected peptide (4 μmol) was dissolved in THF, and diisopropylethylamine (DIPEA; 4 μmol), BOP (12 μmol), and HOBt (24 μmol) were added. Vinyl ester **5** (20 μmol) and DIPEA (20 μmol) were added, and the reaction was stirred at room temperature for 1.5 h. The solvent was then evaporated, and the peptide was deprotected with 90% TFA for 1 h. Following evaporation, the peptide was dissolved in water for purification. Peptides were purified on RP-HPLC by injection onto a Vydac C_{18} semipreparative column (2 × 25 cm) eluted at 10 mL/min with 0.1% TFA and a 20–30% gradient of acetonitrile over 30 min while monitoring absorbance at 280 nm. The major peak was collected and pooled from multiple runs, concentrated by rotary evaporation, and lyophilized. Purified peptides were reconstituted in water and quantified by absorbance ($\varepsilon_{280} = 5600\ M^{-1}\ cm^{-1}$) to determine the isolated yield, which ranged from 18 to 45%. The peptides were characterized on an Agilent 1100 LC-ESI-ion trap by injecting 2 nmol onto a Vydac C_{18} analytical column (0.47 × 25 cm) eluted at 0.7 mL/min with 0.1% TFA and a 5–55% gradient of acetonitrile over 30 min The RP-HPLC eluent was directly infused into the electrospray ionization source, and mass spectral data were obtained in the positive mode for all peptides. Peptides containing a *C*-terminal nor-Val vinyl ester (Nva-ve) were also synthesized using the same method described above.

Preparation and Characterization of Peptide−DNA Condensates. Peptide−DNA condensates were prepared by combining 50 μg of pCMVL in 500 μL of Hepes-buffered mannitol (HBM; 5 mM Hepes, 0.27 M mannitol at pH 7.5) with 20 nmol of peptide in 500 μL of HBM while vortexing to create DNA condensates possessing a charge ratio (NH_4^+/PO_4^-) of approximately 2:1. The particle size of DNA condensates was measured by quasi-elastic light scattering (QELS) on a Brookhaven ZetaPlus particle sizer (Brookhaven Instruments Corporation, NY). The relative binding affinity of the peptides for DNA was monitored by two methods. In the first method, peptide−DNA condensates (40 μL) of varying stoichiometries were added to 960 μL of HBM containing 0.1 μM thiazole orange. The fluorescence of the intercalated dye was measured using a LS50B fluorometer (Perkin-Elmer) by exciting at 498 nm while monitoring emission at 546 nm with both the excitation and emission slit widths set at 8.5 (*20*). Peptide-mediated condensation was also monitored by a band-shift assay. Condensates with increasing peptide to DNA ratios (0–1 nmol

peptide per μg of DNA) were electrophoresed on an agarose gel (1 μg DNA per well) and visualized by ethidium bromide staining (*21*).

In Vitro Gene Expression. HepG2 cells (5×10^5) were plated on 6 × 35 mm wells and grown to 40–70% confluency in DMEM supplemented with 50% Hams-F12, 10% FBS, 250 U/mL penicillin, and 250 μg/mL streptomycin at 37 °C in a humidified 5% CO_2 incubator. Transfections were performed in DMEM (1 mL/35 mm well) supplemented with 2% FBS, sodium pyruvate (1 mM), penicillin, and streptomycin (100 U and 100 μg/mL). Peptide−DNA condensates (10 μg of DNA in 0.2 mL of HBM) were added dropwise to triplicate wells. After a 4 h incubation at 37 °C, the medium was replaced with 2 mL of fresh culture medium (DMEM containing 50% Hams-F12 and 10% FBS). Following a total of 24 h of incubation, the cells were washed twice with 2 mL of ice-cold PBS (calcium- and magnesium-free) and then treated with 0.5 mL of lysis buffer (25 mM Tris hydrochloride at pH 7.8, 1 mM EDTA, 8 mM magnesium chloride, and 1% Triton X-100) for 10 min at 4 °C. The cell lysate was scraped, transferred to a 1.5 mL microcentrifuge tube, and centrifuged for 10 min at 13,000*g* at 4 °C to pellet the cell debris. Lysis buffer (300 μL), sodium-ATP (4.3 μL of a 165 mM solution at pH 7, 4 °C), and cell lysate (100 μL, 4 °C) were combined in a test tube, briefly mixed, and immediately placed in the luminometer. Luciferase relative light units were measured by Lumat LB 9501 (Berthold Systems, Germany) with 10 s integration after automatic injection of 100 μL of 0.5 mM D-luciferin. The relative light units were converted to fmol using a standard curve generated by adding a known amount of luciferase to 35 mm wells containing 40–70% confluent HepG2 cells. The resulting standard curve had an average slope of 1×10^5 relative light units/fmol of enzyme. Protein concentrations were measured by BCA assay using bovine serum albumin as a standard (*22*). The amount of luciferase recovered in each sample was normalized to milligrams of protein and reported as the mean and standard deviation obtained from triplicate transfections.

Cytotoxicity Assay. The in vitro toxicity of the vinyl ester peptides was evaluated by the MTT reduction assay (*23*). HepG2 cells were plated on 6 × 35 mm wells at 5×10^5 cells/well and grown to 40–70% confluency. The culture media was then replaced with 1 mL of fresh DMEM supplemented with 2% FBS, and the cells were treated with either 0.4 nmol peptide/μg DNA condensates or varying concentrations of peptide alone. After 4 h of incubation with condensates or peptide, the media was removed and replaced with 2 mL of the original growth media, and the cells were allowed to incubate for another 20 h. The media were then removed and replaced with 2 mL fresh culture media, and 500 μL of 0.5% (w/v) MTT in PBS solution was added and allowed to incubate at 37 °C for 1 h to promote the formation of formazan crystals. The media containing MTT were removed, and the crystals were dissolved by the addition of 1 mL of DMSO and 250 μL of Sorenson's glycine buffer (0.1 M glycine, 0.1 M NaCl at pH 10.5) and measured spectrophotometrically at 595 nm on a microplate reader (Bio-Rad, Bethesda, MD). The percent viability was determined relative to untreated cells.

RESULTS

Proteasomes play a major role in the degradation of intracellular proteins and peptides (*2, 8*). Previous studies by Kim et al. demonstrated that simultaneous administration of peptide−DNA condensates and a proteasome inhibitor, such as the peptide aldehyde MG115, could increase gene expression by 30-fold over that of the control (*13*). The proposed mechanism involves blocking the premature metabolism of the peptide−DNA condensates in the cell.

Although tripeptide aldehydes such as MG115 or MG132 were shown to increase gene transfer, they simultaneously induced apoptosis and produced dose-dependent cell toxicity. In an effort to inhibit the proteasome to increase gene transfer while avoiding cell toxicity, we hypothesized that a single DNA condensing peptide containing an intrinsic proteasome inhibitor would potentially block the proteasome, avoid cellular toxicity, and could be used to increase gene transfer efficiency in vivo.

We first attempted the synthesis of WK_{18} with a *C*-terminal LLnV-aldehyde similar to MG115 using a Weinreb-amide resin. Although the synthesis was successful, the purified WK_{18}-LLnV-aldehyde formed intramolecular Schiff's-bases with the K_{18} side chains resulting in a mixture of isomers. The mixture of peptides was also found to be a poor inhibitor of the proteasome that did not provide enhanced gene transfer.

The strategy was refined by incorporating a less reactive *C*-terminal vinyl ester proteasome inhibitor sequence into the gene delivery peptide (*14, 15*). Tripeptide analogues possessing a *C*-terminal vinyl ester have been shown to act as a Michael acceptor for the nucleophilic hydroxyl group of the catalytic threonine residue at the active site of the proteasome (*14, 15*).

We first approached the synthesis of WK_{18}LLnV-vinyl ester (ve) by releasing the fully protected WK_{18}LLnV-aldehyde from the Weinreb-amide resin with LAH, followed by its direct conversion to the vinyl ester using a Horner−Wadsworth−Emmons reaction (*19, 24–26*). This strategy was successful but only afforded 1% yields of the desired WK_{18}LLnV-ve and proved difficult to optimize.

A higher yielding more general strategy involved the solid-phase synthesis of WK_{18}LL on a 2-chlorotrityl chloride resin followed by a mild acid cleavage to release the fully protected peptide from the resin (Scheme 1). Subsequent coupling of the *N*-terminus of a chemically synthesized Leu-ve or Nva-ve to the *C*-terminus of the protected peptide, followed by deprotection and purification, established a general convergent high-yielding pathway to the desired WK_{18}LLnV-ve (42%) and related peptides (18–45%) (Table 1). During the coupling of the head group to the protected peptide with BOP, it was essential to use excess HOBt to suppress racemization at the α-carbon of the *C*-terminal leucine of the WK_{18}LL. Without the excess HOBt, the reaction produced two products of identical mass that represent the L−D isomerization.

The chemical synthesis of the Leu-ve and Nva-ve head groups proved to be efficient, high yielding, and general for most amino acid starting materials (Scheme 2). Using a commercially available Boc amino acid (**1**), the *C*-terminus was converted into the Weinreb amide (**2**), then reduced with LAH to give the aldehyde (**3**). This intermediate was converted via the Horner−Wadsworth−Emmons reaction to Boc-Leu-ve (**4**) and finally deprotected to provide the desired Leu-ve (**5**) with an overall 40% yield. The same synthetic strategy was also applied to the synthesis of the Nva-ve head group resulting in a 48% overall yield.

Preparative HPLC-purified peptides were rechromatographed on analytical RP-HPLC to determine yield and establish structure on the basis of mass determined by LC-MS. The RP-HPLC analysis of purified WK_{18}LLL-ve demonstrates purity analysis based on monitoring Trp in eluting peaks by absorbance and fluorescence (Figure 1). For each purified peptide, a single major peak demonstrated >95% purity that also produced a doubly charged positive ion in the ESI-MS (Figure 1, inset) corresponding to the calculated mass of the desired peptide (Table 1).

Seven different peptides were prepared containing different head groups and subterminal amino acids (Table 1). Since it is not known which site is responsible for the degradation of gene delivery peptides, a variety of head groups were designed to

Scheme 1. Convergent Synthesis of WK_{18}LLL-ve Gene Transfer Peptide[a]

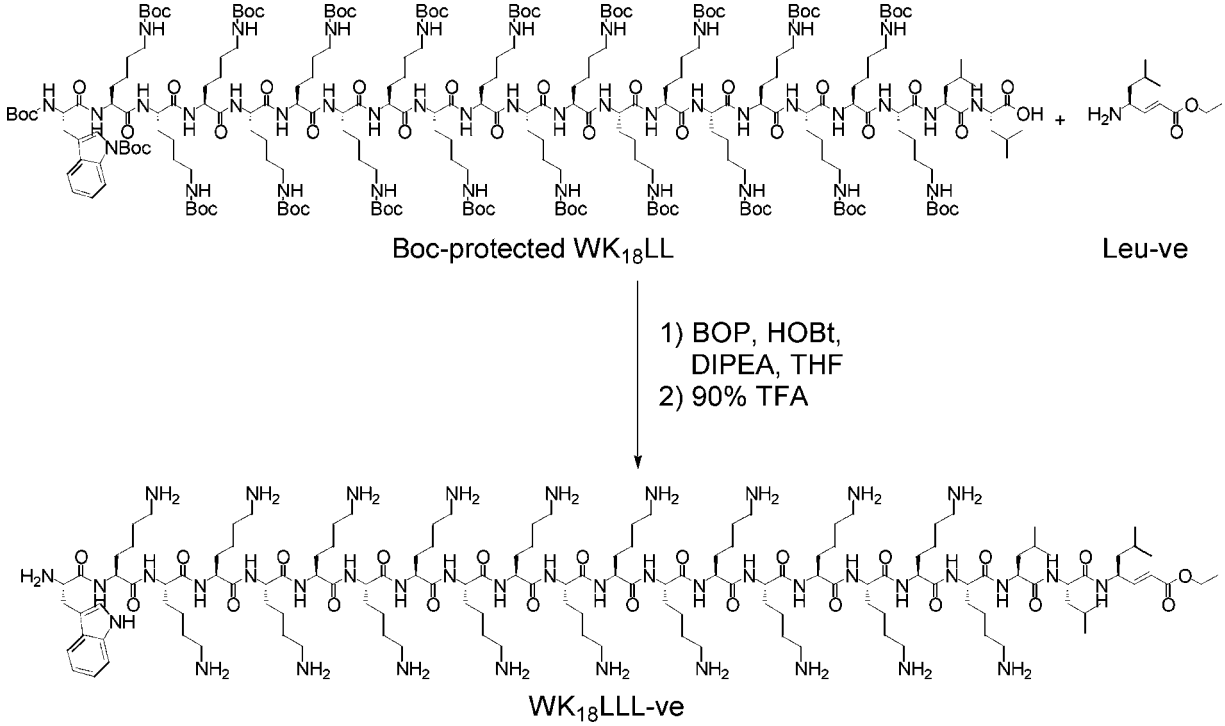

[a] The *C*-terminus of the fully protected WK_{18}LL peptide prepared on chlorotrityl resin is conjugated with the *N*-terminus of Leu-ve, then deprotected to form WK_{18}LLL-ve.

Table 1. Vinyl Ester Peptides

sequence	mass (obs/calc)	particle size (nm)[a]
WK_{18}LLL-ve	2904.9/2904.8	100 ± 20
WK_{18}LLnV-ve	2890.0/2891.6	112 ± 26
WK_{18}VSL-ve	2864.8/2866.0	103 ± 18
WK_{18}VQL-ve	2905.8/2906.8	182 ± 45
WK_{18}FQL-ve	2953.9/2955.0	104 ± 23
WK_{18}YVQL-ve	3069.0/3070.0	110 ± 24
WK_{18}FVQL-ve	3053.0/3054.2	117 ± 22

[a] Particle size determined by QELS at 50 μg/mL in HBM. Mean diameter determination is from the average of 10 measurements ± standard deviation, which is the half-width of the population at the half-height of the peak.

act at either the chymotrypsin- or trypsin-like site of the proteasome. The first two peptides with the LLL-ve and LLnV-ve head group sequences were designed on the basis of the sequences of the commercially available peptide−aldehyde inhibitors MG132 (Z-LLL-H) and MG115 (Z-LLnV-H). Both the MG132 and MG115 tripeptide inhibitors are known to selectively inhibit the chymotrypsin-like site of the proteasome and were synthesized for this purpose. The other five head groups, VSL-ve, VQL-ve, FQL-ve, YVQL-ve, and FVQL-ve, have been shown by Marastoni et al. to selectively inhibit the trypsin-like site of the proteasome when used as tri and tetrapeptide inhibitor sequences (*14, 15*).

We have previously shown that WK_{18} is sufficient to condense DNA and form small condensates (*27*). Each proteasome inhibitor gene transfer peptide was compared for its ability to bind DNA by thiazole orange displacement and gel retardation. The thiazole orange exclusion assay was performed by titrating increasing amounts of peptide with a constant amount of DNA. The displacement of the thiazole orange intercalator dye leads to a decrease in fluorescence intensity until an asymptote is reached, representing the stoichiometry for complete condensation (Figure 2). WK_{18} and WK_{18}FQL-ve each reached an asymptote at 0.4 nmol peptide/μg DNA, indicating complete condensation of the DNA. Each proteasome inhibitor

Scheme 2. Chemical Synthesis of the Leu-ve Head Group[a]

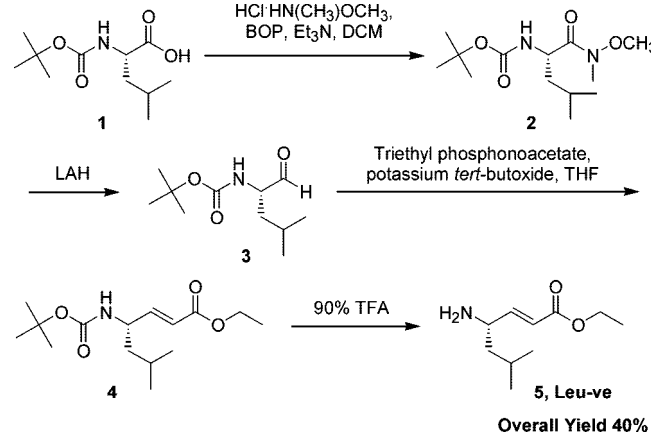

[a] Starting with Boc-Leu (**1**), the *C*-terminus is converted into the Weinreb amide (**2**). Reduction leads to the formation of aldehyde (**3**), and Horner−Wadsworth−Emmons coupling results in the formation of vinyl ester (**4**). Final deprotection of Boc results in an overall yield of 40% for Leu-ve (**5**). The same approach was utilized to synthesize nor-Val vinyl ester (Nva-ve) with comparable yields.

gene transfer peptide illustrated in Table 1 had a result comparable with that of WK_{18}FQL-ve.

The migration of DNA on an agarose gel was compared following the addition of increasing amounts of WK_{18}FQL-ve (Figure 2). Complete retardation of DNA was observed for both WK_{18} and WK_{18}FQL-ve at 0.2 nmol peptide/μg DNA.

To examine the influence of intrinsic proteasome inhibition on gene expression, HepG2 cells were transfected with DNA condensates prepared with each peptide in Table 1. Luciferase expression was measured for each of the vinyl ester peptides and compared to the controls WK_{18} and PEI. As illustrated in Figure 3, each peptide−DNA condensate mediated a significant increase in expression relative to WK_{18}, with WK_{18}FQL-ve

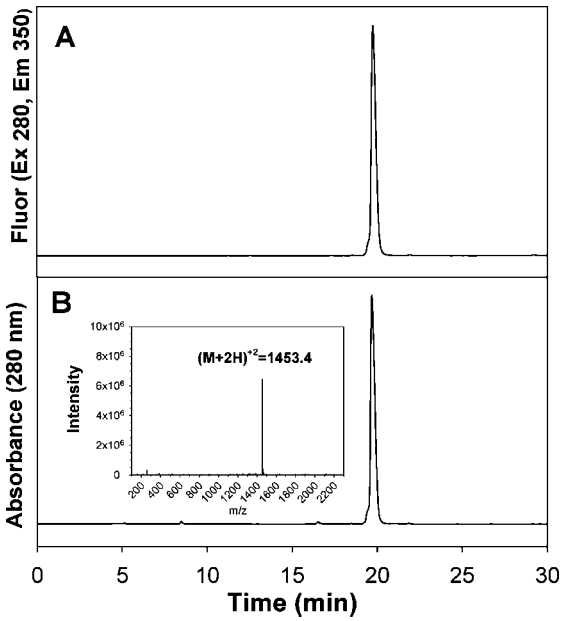

Figure 1. LC-MS characterization of purified WK_{18}LLL-ve. The rechromatograph of purified WK_{18}LLL-ve on RP-HPLC eluted with 0.1% TFA and acetonitrile is illustrated. The chromatogram was monitored by fluorescence (panel A), absorbance (panel B), and by ESI-MS. The major peak (>95%) at 19.8 min produced a doubly charged positive ion at 1453.4 *m*/*z* (inset) corresponding to a mass of 2904.8 amu.

having a 100-fold increase over WK_{18} and transfection efficiency similar to that of PEI.

Since other proteasome inhibitors are known to be cytotoxic, each vinyl ester peptide was examined for cytotoxic effects using the MTT assay. HepG2 cells were treated with either peptide−DNA condensates or varying concentrations of free peptide or proteasome inhibitor for 4 h to model the exposure during gene transfer experiments. The results established that a peptide−DNA condensate dose of 4 nmol of peptide and 10 μg of DNA was not cytotoxic to HepG2 cells (Figure 4A). A similar result was obtained when treating HepG2 cells with varying concentrations of either WK_{18} or WK_{18}FQL-ve, which established the lack of toxicity even at the highest concentration of 8 μM (Figure 4B). These results are in contrast to the peptide inhibitor MG115 that produces an LD_{50} of 2 μM.

DISCUSSION

The proteasome is an important enzyme that degrades cellular proteins and has recently been implicated in the metabolism of both viral and nonviral gene delivery systems (*9*, *13*). It was first shown that proteasome inhibitors could enhance gene expression mediated by an adeno-associated virus in CF/T1 cells (*9*). More recently, the addition of a tripeptide aldehyde proteasome inhibitor, such as MG115 or MG132, resulted in a significant increase in gene expression when cells were transfected with peptide−DNA condensates (*13*). This increase in gene transfer was not observed for nonpeptide systems, such as PEI or lipofectamine, or in the presence of lysosomal enzyme–inhibitors, therefore indicating the proteasome's involvement in the degradation of the peptide delivery systems. However, these peptide−aldehyde inhibitors are cytotoxic with an LD_{50} of 2 μM or less. Therefore, we hypothesized that an intrinsic proteasome inhibitor sequence could be built into the gene delivery peptide to inhibit the proteasome, reduce the cytotoxicity of the inhibitor, and increase gene transfer efficiency.

In support of this hypothesis, several peptides were designed with an *N*-terminal cationic region for DNA binding and a

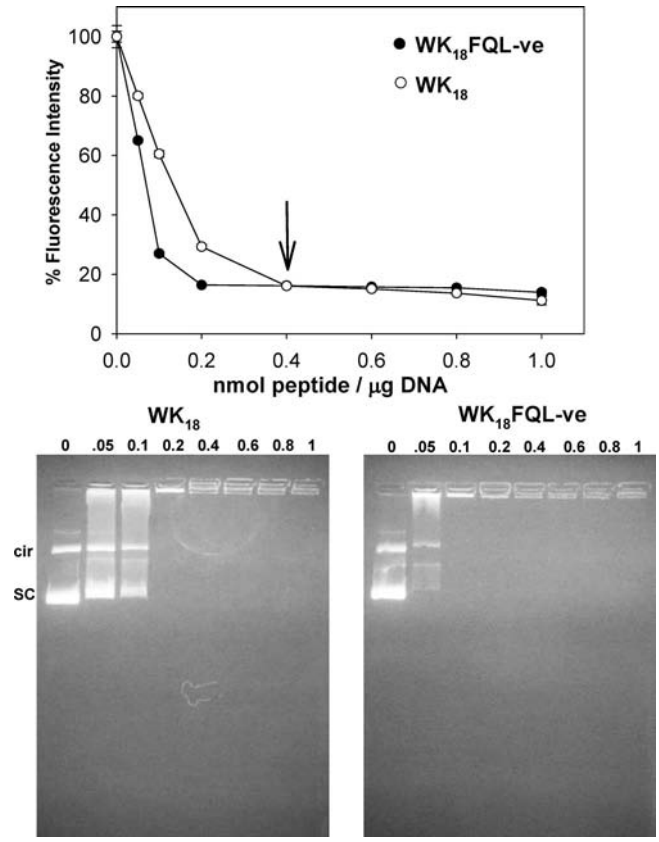

Figure 2. DNA condensation with proteasome inhibitor gene transfer peptides. DNA condensates were formed in triplicate by the addition of 0–1 nmol of WK_{18} or WK_{18}FQL-ve to 1 μg of plasmid DNA in 1 μM thiazole orange. The fluorescence intensity of thiazole orange was measured (ex 498, em 546) at each ratio of peptide to DNA (upper panel). An asymptote in the fluorescent intensity was observed at a ratio of 0.4 nmol peptide/μg DNA, indicating complete condensation. The results observed for WK_{18} and WK_{18}FQL-ve are representative of those observed for each peptide in Table 1. Similarly, peptide-mediated condensation of DNA was monitored by a band shift assay (lower panels). Complete retardation of DNA was observed at 0.2 nmol of peptide per μg of DNA.

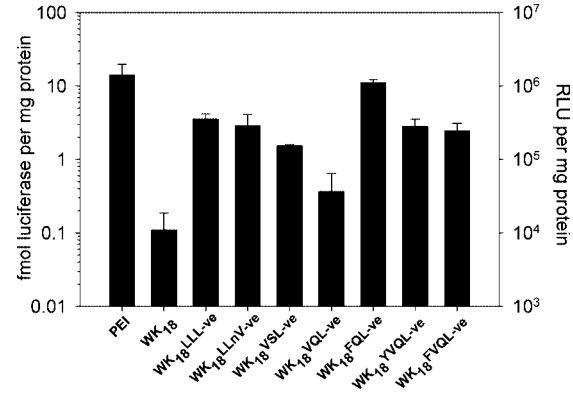

Figure 3. Efficiency of proteasome inhibitor gene transfer peptides. HepG2 cells were transfected in triplicate with 10 μg of DNA condensed with 4 nmol of each proteasome inhibitory gene transfer peptide and compared to transfections with dose-matched controls of PEI:DNA (N/P 9:1) and WK_{18}:DNA. The results establish that WK_{18}FQL-ve mediated a 100-fold increase in gene transfer relative to WK_{18}.

C-terminal head group sequence for proteasome inhibition. Originally, this design included an aldehyde at the *C*-terminus of the peptide in an effort to build in either the MG115 or MG132 proteasome inhibitor sequence. However, the aldehyde proved to be difficult to synthesize in high yields along with

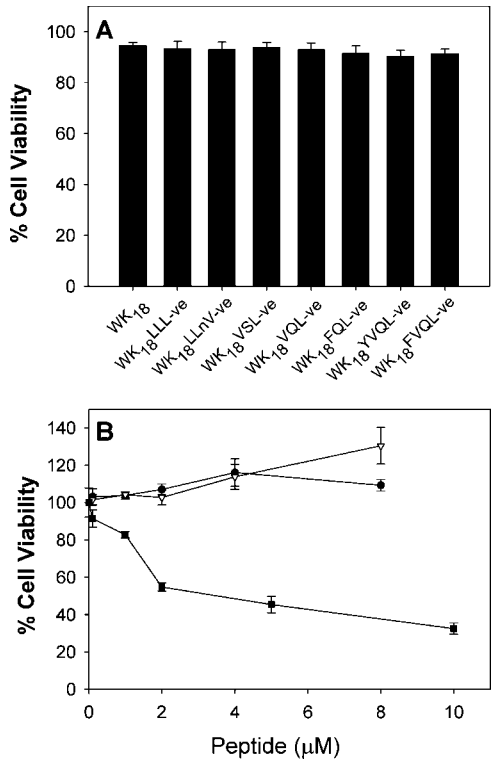

Figure 4. Relative toxicity of proteasome inhibitory gene transfer peptides. HepG2 cells were treated for 4 h with 10 μg of DNA condensed with 4 nmols of each proteasome inhibitory gene transfer peptide. The cell toxicity was assessed by the MTT assay. The results illustrated in panel A demonstrate a lack of cytotoxicity on HepG2 cells. Similarly, the results presented in panel B demonstrate that treatment of HepG2 cells with increasing concentrations of $WK_{18}FQL$ (•) or WK_{18} (▲) results in no toxicity up to 8 μM, where the tripeptide MG115 (■) is toxic to cells at 2–5 μM.

being quite reactive with the side chain amines of the lysine residues in forming a variety of intramolecular Schiff's bases. To solve this problem, we incorporated a vinyl ester inhibitor sequence recently developed by Marastoni et al. (Schemes 1 and 2, and Figure 1) (*14–17*). The vinyl ester head group is similar to the well-known vinyl sulfone class of proteasome inhibitors and is believed to function through a similar mechanism of Michael addition with the γ-hydroxyl group of the threonine side chain on the proteasome. Marastoni's group synthesized several tri and tetrapeptide sequences optimizing the P2−P4 positions and the *N*-terminal protecting group for potent and selective inhibition at the trypsin-like site of the proteasome. They concluded that a glutamine in the P2 position was favorable for trypsin-like selectivity, along with the presence of aromatic and hydrophobic residues in the P3 and P4/*N*-terminal-protecting group position. Another important discovery is that the vinyl ester inhibitors are nontoxic and do not affect cell proliferation, unlike other classes of proteasome inhibitors (*14*).

The enhanced gene transfer by cationic peptides was dependent on the presence of a vinyl ester head group (Figure 3). These results in HepG2 cells were consistent with a similar enhancement in gene transfer observed when treating cells with an MG115, a known tripeptide proteasome inhibitor. There is no direct evidence that cationic peptides containing a vinyl ester are exclusive in their inhibition of the intracellular proteasome. The inhibition of other proteolytic enzymes could also result in enhanced gene transfer.

Since three types of proteolytic acitivites within the proteasome are known, we synthesized several different sequences targeting both the trypsin-like and chymotrypsin-like catalytic activities. On the basis of Marastoni's results, we designed peptides that incorporated the most potent vinyl ester tri and tetrapeptide inhibitor sequences aimed at targeting the trypsin-like activity of the proteasome. We also included two sequences based on those of MG115 (Leu-Leu-Nva) and MG132 (Leu-Leu-Leu) to target chymotrypsin-like activity, as they are both selective for this site in the form of a peptide−aldehyde inhibitor and are weakly inhibitory at the trypsin-like and PGPH sites (*28*). However, the proteasome is a complex enzyme with allosteric interactions between its subunits (*29, 30*). Inhibition of one site within the enzyme can lead to activation and/or inhibition of either of the other sites. The gene delivery peptides contain multiple lysine residues, which would suggest that degradation would most likely occur by the trypsin-like site that cleaves after basic residues. As seen in Figure 3, the peptide $WK_{18}FQL$-ve gives over 100-fold increase in gene expression over that of the control, suggesting that inhibition presumably at the trypsin-like site leads to the highest levels of gene expression. However, there are many interactions within the proteasome between the subunits that could be inhibiting other catalytic activities as well that could be contributing to this increase in expression. Also, the two peptides targeting the chymotrypsin-like site, $WK_{18}LLL$-ve and $WK_{18}LLnV$-ve, both gave significant levels of increased gene expression over that of the control, indicating that inhibition of the chymotrypsin-like site also positively affects peptide-mediated gene expression.

In agreement with the data presented by Marastoni, the gene delivery peptides containing a vinyl ester head group were not toxic to cells as determined by the MTT assay (Figure 4). The peptides were tested in the MTT assay as condensates with DNA and dosed as free peptide at increasing concentrations. Both the condensates and free peptide gave no toxicity, unlike MG115, which had an IC_{50} of 2–5 μM. The peptide−aldehydes are highly potent at inhibiting the chymotrypsin-like activity of the proteasome (*8*) but are also very toxic to cells (*13*). By changing to a vinyl ester head group, we are able to significantly decrease the cytotoxicity of the proteasome inhibitor. Even though Michael addition-type inhibitors are thought to be less potent than MG115, they bind covalently to the catalytic threonine residue for long-term inhibition unlike the reversible aldehyde that only provides transient inhibition (*8*). However, when used to condense DNA at a 0.4 nmol peptide per μg DNA ratio, a 1 μM concentration of the inhibitor is present in the transfection media. Data by Kim et al. showed that a 10 μM dose of MG115 is needed to achieve maximal luciferase expression in HepG2 cells (*13*). Therefore, less of the inhibitor may be required to achieve the inhibition needed to see a significant increase in gene expression. In addition, MG115 only mediated a 30-fold increase in expression over that of the control, while the most potent vinyl ester derivative could produce a 100-fold increase in luciferase expression.

Proteasome inhibitors are able to prevent premature degradation of peptide−DNA condensates and give over a 30-fold increase in luciferase expression. However, these inhibitors are highly toxic and induce apoptosis in cells. Incorporation of an intrinsic proteasome inhibitor sequence into a gene delivery peptide results in a nonviral vector that is able to condense DNA, transfect cells, inhibit the proteasome, and increase gene transfer over control peptides without the cytotoxic effects seen with other inhibitors. With these capabilities, the vinyl ester gene delivery peptides may be able to boost the efficiency of peptide-mediated nonviral gene delivery systems in vivo.

ACKNOWLEDGMENT

We gratefully acknowledge support for this work from the National Institutes of Health, Bethesda, MD (grant DK066212)

as well as the AFPE Predoctoral Fellowship in the Pharmaceutical Sciences (to M.E.M.).

LITERATURE CITED

(1) Groll, M., Ditzel, L., Lowe, J., Stock, D., Bochtler, M., Bartunik, H. D., and Huber, R. (1997) Structure of 20S proteasome from yeast at 2.4 A resolution. *Nature 386*, 463–471.

(2) Voges, D., Zwickl, P., and Baumeister, W. (1999) The 26S proteasome: a molecular machine designed for controlled proteolysis. *Annu. Rev. Biochem. 68*, 1015–1068.

(3) Hershko, A., and Ciechanover, A. (1998) The ubiquitin system. *Annu. Rev. Biochem. 67*, 425–479.

(4) Hochstrasser, M. (1996) Ubiquitin-dependent protein degradation. *Annu. Rev. Genet. 30*, 405–439.

(5) Craiu, A., Gaczynska, M., Akopian, T., Gramm, C. F., Fenteany, G., Goldberg, A. L., and Rock, K. L. (1997) Lactacystin and clasto-lactacystin beta-lactone modify multiple proteasome beta-subunits and inhibit intracellular protein degradation and major histocompatibility complex class I antigen presentation. *J. Biol. Chem. 272*, 13437–13445.

(6) Orlowski, M. (1990) The multicatalytic proteinase complex, a major extralysosomal proteolytic system. *Biochemistry 29*, 10289–10297.

(7) Coux, O., Tanaka, K., and Goldberg, A. L. (1996) Structure and functions of the 20S and 26S proteasomes. *Annu. Rev. Biochem. 65*, 801–847.

(8) Kisselev, A. F., and Goldberg, A. L. (2001) Proteasome inhibitors: from research tools to drug candidates. *Chem. Biol. 8*, 739–758.

(9) Duan, D., Yue, Y., Yan, Z., Yang, J., and Engelhardt, J. F. (2000) Endosomal processing limits gene transfer to polarized airway epithelia by adeno-associated virus. *J. Clin. Invest. 105*, 1573–1587.

(10) Bloomfield, V. A. (1996) DNA condensation. *Curr. Opin. Struct. Biol. 6*, 334–341.

(11) Liu, D., and Knapp, J. E. (2001) Hydrodynamics-based gene delivery. *Curr. Opin. Mol. Ther. 3*, 192–197.

(12) Wiethoff, C. M., and Middaugh, C. R. (2003) Barriers to nonviral gene delivery. *J. Pharm. Sci. 92*, 203–217.

(13) Kim, J., Chen, C.-P., and Rice, K. G. (2005) The proteasome metabolizes peptide-mediated nonviral gene delivery systems. *Gene Ther. 12*, 1581–1590.

(14) Marastoni, M., Baldisserotto, A., Cellini, S., Gavioli, R., and Tomatis, R. (2005) Peptidyl vinyl ester derivatives: new class of selective inhibitors of proteasome trypsin-like activity. *J. Med. Chem. 48*, 5038–5042.

(15) Marastoni, M., Baldisserotto, A., Trapella, C., Gavioli, R., and Tomatis, R. (2006) P3 and P4 position analysis of vinyl ester pseudopeptide proteasome inhibitors. *Bioorg. Med. Chem. Lett. 16*, 3125–3130.

(16) Marastoni, M., Baldisserotto, A., Trapella, C., Gavioli, R., and Tomatis, R. (2006) Synthesis and biological evaluation of new vinyl ester pseudotripeptide proteasome inhibitors. *Eur. J. Med. Chem. 41*, 978–984.

(17) Baldisserotto, A., Marastoni, M., Trapella, C., Gavioli, R., Ferretti, V., Pretto, L., and Tomatis, R. (2007) Glutamine vinyl ester proteasome inhibitors selective for trypsin-like (beta2) subunit. *Eur. J. Med. Chem. 42*, 586–592.

(18) Fehrentz, J.-A., and Castro, B. (1983) An efficient synthesis of optically active α-(t-butoxycarbonylamino)-aldehydes from α-amino acids. *Synthesis 8*, 676–678.

(19) Hover, J. A., Bock, C. W., and Bhat, K. L. (2003) Synthesis of chiral 3,4-disubstituted pyrroles from L-amino acids. *Heterocycles 60*, 791–798.

(20) McKenzie, D. L., Kwok, K. Y., and Rice, K. G. (2000) A potent new class of reductively activated peptide gene delivery agents. *J. Biol. Chem. 275*, 9970–9977.

(21) Adami, R. C., Collard, W. T., Gupta, S. A., Kwok, K. Y., Bonadio, J., and Rice, K. G. (1998) Stability of peptide-condensed plasmid DNA formulations. *J. Pharm. Sci. 87*, 678–683.

(22) Smith, P. K., Krohn, R. I., Hermanson, G. T., Mallia, A. K., Gartner, F. H., Provenzano, M. D., Fujumoto, E. K., Goeke, N. M., Olson, B. J., and Klenk, D. C. (1985) Measurement of protein using bicinchoninic acid. *Anal. Biochem. 150*, 76–85.

(23) Mosmann, T. (1983) Rapid colorimetric assay for cellular growth and survival: application to proliferation and cytotoxicity assays. *J. Immunol. Methods 65*, 55–63.

(24) Dinh, T. Q., and Armstrong, R. W. (1996) Synthesis of ketones and aldehydes via reactions of Weinreb-type amides on solid support. *Tetrahedron Lett. 37*, 1161–1164.

(25) Fehrentz, J. A., Paris, M., Heitz, A., Velek, J., Winternitz, F., and Martinez, J. (1997) Solid phase synthesis of C-terminal peptide aldehydes. *J. Org. Chem. 62*, 6792–6796.

(26) Fehrentz, J.-A., Paris, M., Heitz, A., Velek, J., Liu, C.-F., Winternitz, F., and Martinez, J. (1995) Improved solid phase synthesis of C-terminal peptide aldehydes. *Tetrahedron Lett. 36*, 7871–7874.

(27) Wadhwa, M. S., Collard, W. T., Adami, R. C., McKenzie, D. L., and Rice, K. G. (1997) Peptide-mediated gene delivery: influence of peptide structure on gene expression. *Bioconjugate Chem. 8*, 81–88.

(28) Rock, K. L., Gramm, C., Rothstein, L., Clark, K., Stein, R., Dick, L., Hwang, D., and Goldberg, A. L. (1994) Inhibitors of the proteasome block the degradation of most cell proteins and the generation of peptides presented on MHC class I molecules. *Cell 78*, 761–771.

(29) Kisselev, A. F., Garcia-Calvo, M., Overkleeft, H. S., Peterson, E., Pennington, M. W., Ploegh, H. L., Thornberry, N. A., and Goldberg, A. L. (2003) The caspase-like sites of proteasomes, their substrate specificity, new inhibitors and substrates, and allosteric interactions with the trypsin-like sites. *J. Biol. Chem. 278*, 35869–35877.

(30) Kisselev, A. F., Akopian, T. N., Castillo, V., and Goldberg, A. L. (1999) Proteasome active sites allosterically regulate each other, suggesting a cyclical bite-chew mechanism for protein breakdown. *Mol. Cell 4*, 395–402.

BC700362B

TECHNICAL NOTES

Application of an Environmentally Sensitive Fluorophore for Rapid Analysis of the Binding and Internalization Efficiency of Gene Carriers

Jamie M. Bergen, Ester J. Kwon, Tammy W. Shen, and Suzie H. Pun*

Department of Bioengineering, University of Washington, 1705 NE Pacific Street, Seattle, Washington 98195. Received August 20, 2007; Revised Manuscript Received October 3, 2007

Nonviral gene carriers must associate with and become internalized by cells in order to mediate efficient transfection. Methods to quantitatively measure and distinguish between cell association and internalization of delivery vectors are necessary to characterize the trafficking of vector formulations. Here, we demonstrate the utility of nitro-2,1,3-benzoxadiazol-4-yl (NBD)-labeled oligonucleotides for discrimination between bound and internalized gene carriers associated with cells. Dithionite quenches the fluorescence of extracellular NBD-labeled material, but is unable to penetrate the cell membrane and quench internalized material. We have verified that dithionite-mediated quenching of extracellular materials occurs in both polymer- and lipid-based gene delivery systems incorporating NBD-labeled oligonucleotides. By exploiting this property, the efficiencies of cellular binding and internalization of lipid- and polymer-based vectors were studied and correlated to their transfection efficiencies. Additionally, spatiotemporal information regarding binding and internalization of NBD-labeled gene carriers can be obtained using conventional wide-field fluorescence microscopy, since dithionite-mediated quenching of extracellular materials reveals the intracellular distribution of gene carriers without the need for optical sectioning. Hence, incorporation of environmentally sensitive NBD−oligos into gene carriers allows for facile assessment of binding and internalization efficiencies of vectors in live cells.

INTRODUCTION

Nonviral gene carriers offer the potential to safely and efficiently mediate the delivery of nucleic acid based therapeutics into targeted cells (*1*, *2*). Nonviral vectors are typically based on cationic polymers or lipids, which upon self-assembly with plasmid DNA form complexes termed polyplexes or lipoplexes, respectively. Despite efforts to design more efficient nonviral gene carriers, viral vectors remain the leading candidates for gene therapy due to their significantly higher gene transfer efficiencies compared to synthetic vectors. A number of physical barriers hinder the progress of gene carriers from the cell surface to the nucleus (*3*). Toward the design of more efficient nonviral gene carriers, it is important to quantitatively compare various vectors and formulations for their abilities to overcome each of the intracellular barriers. The initial barrier encountered upon arrival at targeted cells, cellular internalization, is a prerequisite to achieving transgene expression. A technique to reliably measure the degree of internalization of gene carriers into cells would facilitate the establishment of structure–function relationships in the development of improved nonviral gene carriers.

Here, a strategy is described for differentiating between extra- and intracellular gene carriers using 7-nitro-2,1,3-benzoxadiazol-4-yl (NBD)-labeled oligonucleotides as environmentally sensitive probes. NBD is a highly fluorescent compound that is irreversibly quenched by exposure to the reducing agent dithionite (Scheme 1). It was previously demonstrated that NBD-labeled lipids are useful tools to monitor lipid asymmetry at the plasma membrane

Scheme 1. Dithionite-Mediated Reduction of the Fluorophore Nitro-2,1,3-benzoxadiazol-4-yl (NBD) to a Nonfluorescent Derivative

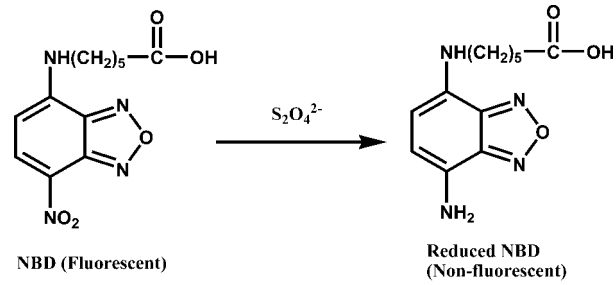

since cell membranes are relatively impermeable to dithionite (*4*). By the same principles, we demonstrate here that NBD-labeled oligonucleotides can be incorporated into polymer- or lipid-based nonviral gene carriers to distinguish between extra- and intracellular materials. Current protocols to quantify vector internalization include cell treatment with polyion wash buffers to remove cell-associated materials or cell exposure to antifluorophore antibodies or Trypan blue to quench extracellular fluorescence. The NBD/dithionite approach presented here offers a reliable, cost-effective alternative that is compatible with downstream analysis by flow cytometry, fluorescence microscopy, and fluorimetry in whole cells or lysates.

To demonstrate the utility of NBD-labeled oligonucleotides, the internalization efficiencies of a series of lipoplex and polyplex formulations were evaluated in a high-throughput, fluorescence-based assay and compared to overall transfection efficiency. Additionally, we show that dithionite-mediated

* To whom correspondence should be addressed. E-mail: spun@u.washington.edu, Tel: (206) 685-3488, Fax: (206) 616-3928.

10.1021/bc700315v CCC: $40.75 © 2008 American Chemical Society
Published on Web 12/07/2007

quenching of extracellular NBD-labeled gene carriers enables discrimination between bound and internalized materials associated with small-diameter neurites using wide-field fluorescence microscopy, an application that was previously hindered by technical limitations. Hence, NBD-labeled oligonucleotides are a useful tool for investigating the binding and internalization profiles of nonviral gene carriers.

EXPERIMENTAL PROCEDURES

2.1. Incorporation of NBD-Labeled Oligonucleotides into Nonviral Gene Delivery Systems. *2.1.1. Synthesis of NBD−Oligos and TR−Oligos.* Oligonucleotides with a 5′ amino group (5′-NH_2-TTC TCC GAA CGT GTC ACG TT-3′) were synthesized and desalted by Integrated DNA Technologies (Coralville, IA). Oligonucleotides were conjugated to succinimidyl ester derivatives of either 6-(*N*-(7-nitrobenz-2-oxa-1,3-diazol-4-yl)amino)hexanoate (NBD-X) or Texas Red-X (TR) (Invitrogen, Carlsbad, CA) following guidelines provided by the manufacturer. Briefly, oligonucleotides were purified by chloroform extraction to remove interfering compounds such as tris(hydroxymethyl) aminomethane (Tris). 100 μg of purified oligonucleotide was then diluted in 0.1 M sodium tetraborate buffer, pH 8.5, and the dye, freshly dissolved in DMSO, was added to this solution at a 40:1 or 20:1 dye/oligo ratio for NBD and TR, respectively. The conjugation reaction proceeded overnight at room temperature, and then free dye was separated from oligonucleotides by ethanol precipitation. Yields and conjugation efficiencies were determined on the basis of absorbance measurements at 260, 465, and 595 nm to measure oligonucleotide, NBD, and TR concentrations, respectively. The NBD-labeled oligonucleotide was recovered with a 90% yield, and the labeling efficiency was 81%. For the TR-labeled oligonucleotide, the yield and labeling efficiency were 75% and 85%, respectively.

2.1.2. Formulation of Lipoplexes and Polyplexes Incorporating Labeled Oligonucleotides. Lipofectamine 2000 (L2K) was purchased from Invitrogen (Carlsbad, CA) and poly(ethylenimine) (PEI; 25 000 MW, branched) was obtained from Sigma (St. Louis, MO). Lipoplexes were formulated by condensing labeled oligonucleotides with L2K according to the manufacturer's instructions. Briefly, oligonucleotides were diluted in phosphate-buffered saline (PBS) (for fluorimeter-based quenching studies) or in OptiMEM (Invitrogen) (for cell binding and internalization studies) to a concentration of 0.01 μg/μL, and were added to an equal volume of L2K diluted in PBS or OptiMEM. The ratio of DNA (μg) to L2K (μL) was varied from 1:0.5 to 1:3. The mixture was incubated for 20 min at room temperature to allow lipoplex self-assembly. To formulate polyplexes, oligonucleotides were diluted to a concentration of 0.02 μg/μL in PBS or F12-K medium with no supplements (ATCC; Manassas, VA), and an equal volume of PEI diluted in PBS or F12-K medium was added. This mixture was incubated for 20 min at room temperature to allow particle formation. PEI amine to DNA phosphate (N/P) ratios were calculated on the basis of the monomer molecular weights of 43 and 330 Da for PEI and DNA, respectively, and polyplexes were formulated at N/P ratios from 3 to 10.

2.1.3. Fluorescence Measurements of Dithionite-Mediated NBD Quenching in Gene Carriers. Lipoplexes and polyplexes were formulated as described in the previous section using NBD-labeled oligonucleotides. To evaluate dithionite-mediated quenching of NBD-labeled gene carriers, lipoplexes were formulated at a L2K/DNA ratio of 3 and polyplexes were formulated at an N/P ratio of 5. Sodium dithionite was purchased from EMD Chemicals (Gibbstown, NJ), and was prepared as a 1 M stock solution in 1 M Tris, pH 10, immediately prior to use. Fluorescence measurements were obtained using a TECAN Safire II microplate reader (Tecan Systems, Inc., San Jose, CA). NBD was excited at a wavelength of 465 nm, and emission was read at 535 nm. Initial fluorescence measurements were taken in wells containing 100 μL of the lipoplex solution, polyplex solution, or a solution containing an equivalent amount of free oligonucleotide. Subsequently, 9.6 μL of either 1 M dithionite in 1 M Tris (for a final dithionite concentration of 88 mM) or 9.6 μL of 1 M Tris alone (as a negative control) was added to the wells containing lipoplexes or polyplexes and incubated for 2 min at room temperature prior to repeating NBD fluorescence measurements. The pH sensitivity of NBD emission was tested by measuring the emission intensities of NBD−oligos in PBS (pH 7.4), Tris buffer (pH 10.0), and acetate buffer (pH 4.5). To verify that dithionite-mediated quenching was specific to NBD, lipoplexes formulated using a 90/10 mixture of NBD/TR were also analyzed. TR samples were excited at 595 nm, and emission was read at 615 nm.

2.2. Binding and Uptake of NBD-Labeled Lipoplexes and Polyplexes in Cultured Cells. *2.2.1. Cell Culture.* HeLa cells were purchased from ATCC (CCL-2) and cultured in minimum essential medium (MEM) supplemented with 10% fetal bovine serum and antibiotics. Cells were passaged every 3–4 days.

2.2.2. Microscopy-Based Binding and Uptake Assay. HeLa cells were seeded on a 24-well plate at 5×10^4 cells/0.5 mL/well and allowed to attach overnight. NBD-labeled polyplexes (N/P = 5) and lipoplexes (L2K/DNA = 3) were formulated as described in section 2.1.2. Cells were rinsed with PBS, and medium was replaced with 500 μL/well OptiMEM. Polyplexes or lipoplexes incorporating 1 μg NBD−oligo were added to each well and incubated for either 1 h at 4 °C or for 3 h at 37 °C. Following the specified incubation period, medium was removed and the cells were rinsed once with PBS. Then, dithionite in Tris buffer or an equivalent volume of Tris buffer was diluted to a concentration of 88 mM in PBS and incubated with the cells for 5 min. Following incubation, cells were rinsed three times with PBS and imaged immediately by bright-field and fluorescence microscopy using a standard FITC filter set.

2.3. Measurement of Internalization and Transfection Efficiencies. *2.3.1. Validation of Internalization Measurements by Fluorimetry and Flow Cytometry.* HeLa cells were seeded at 8×10^4 cells/well on a 24-well plate for fluorimetry or at 3×10^5 cells/well on a 6-well plate for flow cytometry and allowed to attach overnight. Cells were rinsed with PBS and preincubated in OptiMEM at 4 or 37 °C for 1 h. NBD-labeled polyplexes (N/P = 5) were formulated as described in section 2.1.2., with the exception that polyplexes were formulated in water. After polyplex addition, cells were incubated at 4 or 37 °C for an additional hour. Medium was removed and cells were incubated with cold 10 mM Tris in PBS with or without 10 mM dithionite for 2 min. Cells were then rinsed 2 times with PBS. For flow cytometry, cells were harvested by trypsinization, and cell populations in each sample were analyzed for mean fluorescence using a BD FACScan analyzer. Cell lysate was prepared for fluorimetry by resuspending cells in 0.1% Triton X-100 in water. After one freeze–thaw cycle, 10× PBS was added to the lysate for a final concentration of 1× prior to fluorescence measurements. Experiments were performed in triplicate, and values are reported in relative fluorescence units.

2.3.2. Measurement of Internalization and Transfection Efficiencies for Polyplexes and Lipoplexes. HeLa cells were seeded at 8×10^4 cells/well on a 24-well plate and allowed to attach overnight. Cells were rinsed with PBS and preincubated with OptiMEM at 37 °C for 1 h. Polyplexes (N/P ratios of 10,

7, 5, and 3) and lipoplexes (L2K/DNA ratios of 3:1, 1:1, and 0.5:1) were formulated using NBD-labeled oligonucleotides or gWiz Luciferase plasmid (Aldevron; Fargo, ND) as described previously. Cells were incubated with polyplex or lipoplex solutions at 37 °C for 5 h. For internalization measurements, dithionite treatment and lysate preparation were performed as described in section 2.3.1. For transfection efficiency measurements, media was replaced after 5 h and reporter gene expression was measured 48 h later. To measure luciferase reporter gene expression, cells were lysed with Reporter Lysis Buffer (Promega; Madison, WI) and luciferase activity was measured using Promega's luciferase assay system. Total protein in lysate samples was measured using a Micro BCA Protein Assay Kit (Pierce; Rockford, IL). Values are reported in relative light units (RLU)/mg protein and are the mean ± standard deviation of triplicate samples.

2.4. Ratiometric Imaging To Differentiate between Intracellular and Extracellular Material in Neuron-Like Cells. *2.4.1. Culture of Neuron-Like PC-12 Cells.* PC-12 cells were obtained from ATCC (CRL-1721) and were cultured in F12-K medium supplemented with 15% horse serum, 2.5% fetal bovine serum, and antibiotics in a 37 °C, 5% CO_2 environment. Cells were fed by replacing the growth medium every 2–3 days and were passaged when ~80% confluent. Cells were detached from the flask by exposure to trypsin-EDTA for 2 min and were collected in 1 mL of F12-K medium. To obtain a single-cell suspension, cells were passed through a series of fire-polished glass pipettes of decreasing diameter. For differentiation to a neuron-like phenotype, cells were plated on a poly(D-lysine)-coated flask in differentiation medium consisting of F12-K medium supplemented with 1% horse serum, antibiotics, and NGF at a concentration of 100 ng/mL.

2.4.2. Ratiometric Imaging To Differentiate between Intracellular and Extracellular Material. NBD/TR-double-labeled oligonucleotides were complexed with L2K at an L2K/DNA ratio of 3 as described in previous sections. Lipoplexes were adsorbed to the surface of wells of a 96-well plate by incubation for 1 h at room temperature. Dithionite was added to samples at a final concentration of 88 mM and incubated for 5 min at room temperature before rinsing with PBS. As a negative control for NBD quenching, an equivalent volume of Tris buffer was added to lipoplexes in separate wells. Green and red fluorescence images were taken in each sample using identical image acquisition settings. Ratio analysis was performed using *MetaMorph* software to measure the green/red signal ratio for individual particles in dithionite-treated and untreated wells. Specifically, a particle was selected in the red image, and the integrated pixel intensity was measured using the Region Measurements function in *MetaMorph*. The integrated pixel intensity for the particle was corrected for background fluorescence based on the integrated pixel intensity of a background region near the particle. Background-subtracted integrated pixel intensity values measured in both the green and red channels were used to calculate the green/red signal ratio.

Six-day differentiated, neuron-like PC-12 cells were plated sparsely on a poly(L-lysine)-coated 24-well plate to allow separation between cells and were allowed to attach overnight. TR/NBD-double-labeled lipoplexes were formulated using a 90/10 NBD−/TR−oligo mixture. Cells were incubated with lipoplexes for 3 h at 37 °C. Cells were then rinsed with PBS, incubated with PBS containing 88 mM dithionite for 5 min, rinsed 3 times, and imaged by bright-field and fluorescence microscopy. Internalized material was confirmed using the image analysis techniques described above.

RESULTS

3.1. Packaged NBD-Labeled Oligonucleotides Are Quenched by Dithionite. NBD fluorescence is irreversibly quenched upon exposure to dithionite by the reaction illustrated in Scheme 1. It was previously demonstrated that brief exposure to dithionite at concentrations up to 100 mM is nontoxic to cells, and that the NBD nitro group reduction occurs efficiently at a dithionite concentration of 88 mM (*4*). As shown in Figure 1A, brief exposure of NBD-labeled oligonucleotides to 88 mM dithionite quenched their fluorescence by 99%.

NBD-labeled oligonucleotides were also examined for their susceptibility to dithionite-mediated quenching when incorporated into lipid- or polymer-based gene delivery systems, termed "lipoplex" and "polyplex", respectively (Figure 1A). Condensation of NBD-labeled oligonucleotides by cationic lipids or polymers caused slight fluorescence quenching prior to the addition of dithionite. Quenching is commonly observed upon condensation of fluorophore-labeled DNA with polycations, as tight packing leads to fluorophore self-quenching. Still, the remaining NBD fluorescence was readily detectable above background. Dithionite exposure reduced the fluorescence signal by 99% and 98% for lipoplexes and polyplexes, respectively, and the resulting fluorescence levels were only slightly above background.

To serve as a useful probe that discriminates between extra- and intracellular gene carriers, NBD−oligos must be insensitive to pH fluctuations such as the acidification that occurs when gene carriers are transported through the endo/lysosomal pathway. The fluorescence emission from NBD−oligos was compared at pH values of 4.5, 7.4, and 10.0 to determine the effect of pH on fluorescence emission. Exposure to acidic or basic environments did not significantly influence the NBD emission intensity (Figure 1B).

3.2. NBD-Labeled Gene Carriers Exposed To Cells Function as an Environmentally Sensitive Probe. To validate NBD-labeled gene carriers as a tool for distinguishing between bound and internalized material in cells, polyplexes incorporating NBD-labeled oligonucleotides were incubated with HeLa cells at either 4 or 37 °C and were subsequently exposed to dithionite to quench extracellular fluorescence. Since endocytosis is inhibited at 4 °C, it was expected that the labeled material would bind to, but remain outside of, cells. In contrast, it was expected that the gene carriers would be internalized by cells during incubation at 37 °C. As shown in Figure 2A,B, the fluorescence signal from NBD-labeled polyplexes that bound to cells at 4 °C was quenched by exposure to dithionite. In contrast, when cells were incubated with NBD-labeled polyplexes at 37 °C, polyplexes underwent internalization into cells, and the signal from internalized polyplexes was not quenched due to the inability of dithionite to penetrate cellular membranes (Figure 2C,D). Similar results were obtained for NBD-labeled lipoplexes (data not shown).

3.3. Validation of Internalization Measurements Based on Quenching of Extracellular NBD Fluorescence. The degree of cellular internalization of gene carriers, determined the amount of unquenched NBD−oligo in dithionite-treated cell populations, was measured both by flow cytometry and by fluorescence measurements in cell lysates. To validate internalization measurements based on NBD fluorescence remaining after dithionite treatment, internalization was also measured by inhibiting endocytosis in samples that were not treated with dithionite (Figure 3). Since endocytosis is inhibited at 4 °C, the fluorescence of internalized polyplexes can be calculated by subtracting total cell-associated fluorescence. The fluorescence of internalized polyplexes is calculated by subtracting total cell-associated fluorescence of cells incubated with polyplexes at 4 °C from total cell-associated fluorescence of cells incubated

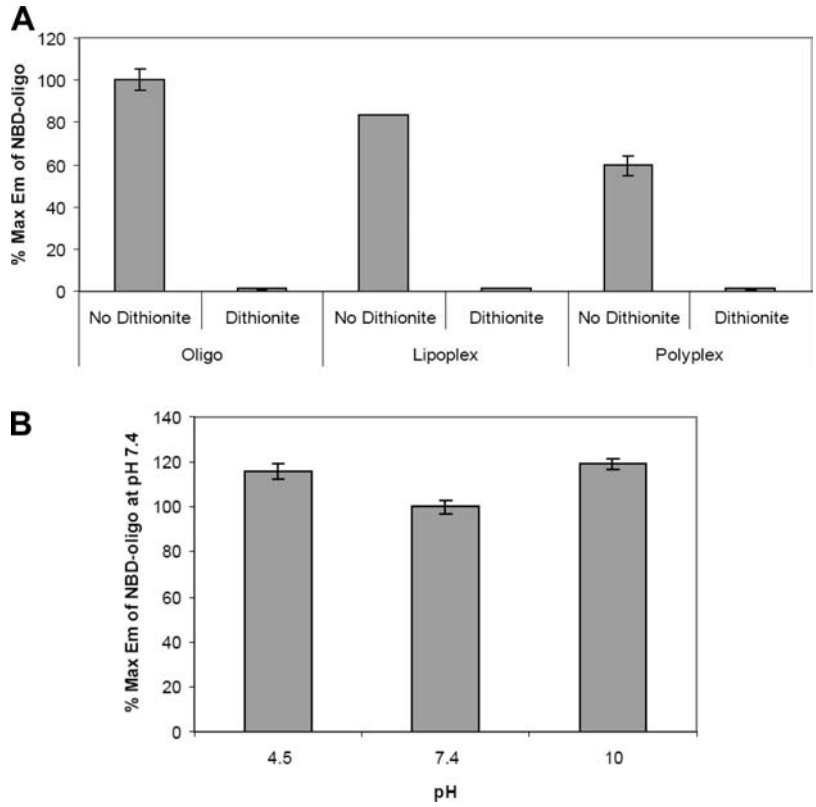

Figure 1. Effect of dithionite treatment and pH on NBD fluorescence emission intensity. (A) Fluorescence emission of NBD-labeled oligonucleotides and lipid- and polymer-based gene carriers incorporating NBD-labeled oligonucleotides was measured in the presence and absence of dithionite. Values are presented as the percentage fluorescence emission compared to an equivalent amount of uncomplexed, unquenched NBD−oligo ± standard deviation. (B) Fluorescence emission of NBD−oligos was measured in acidic, neutral, and basic buffers. Values are presented as the percentage fluorescence emission compared to an equivalent amount of NBD−oligo in PBS (pH 7.4) ± standard deviation.

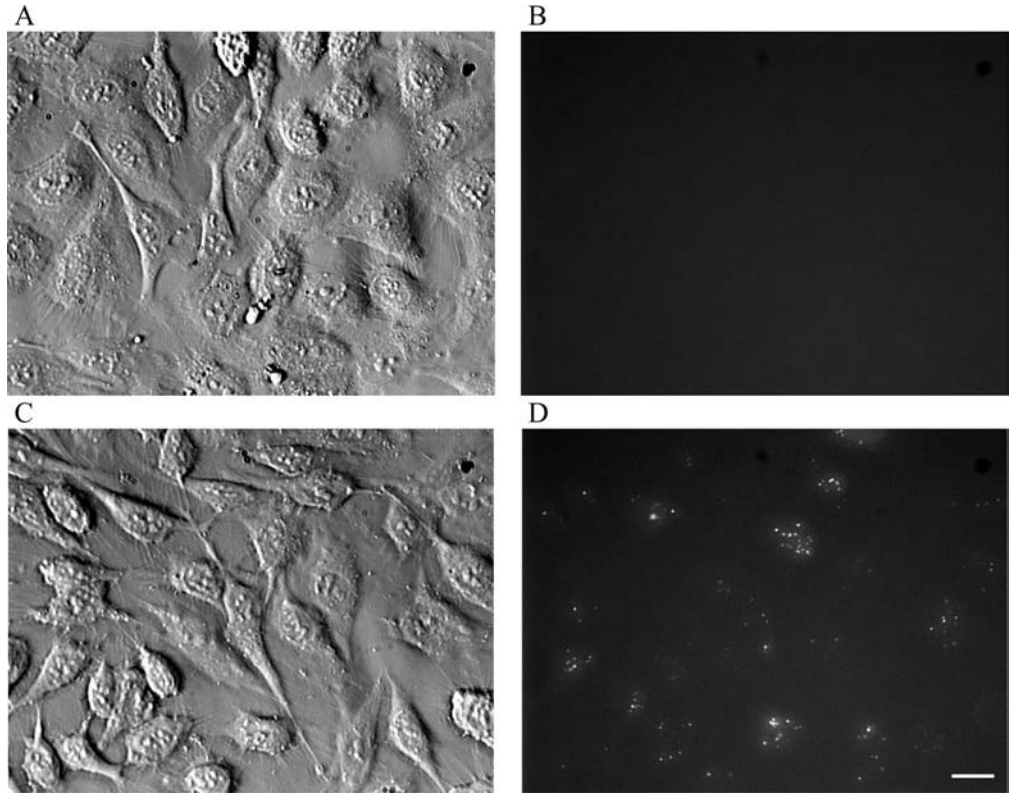

Figure 2. Selective quenching of cell-associated, uninternalized gene carriers in HeLa cells. NBD-labeled polyplexes that were bound to HeLa cells at 4 °C, but not internalized, were quenched by dithionite (A,B), while polyplexes incubated with cells for 3 h at 37 °C were internalized and protected from dithionite-mediated quenching (C,D). Bright-field and corresponding fluorescence images are shown (scale bar = 20 μm).

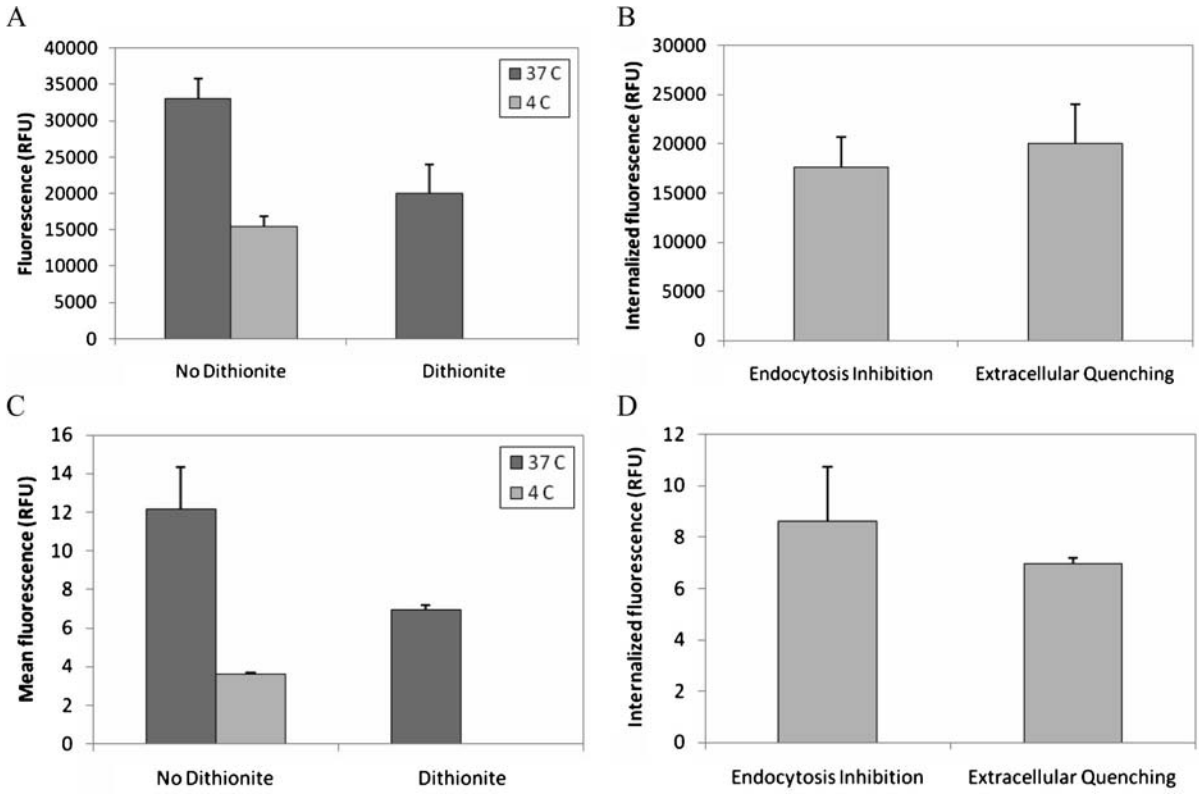

Figure 3. Quantification of vector internalization by endocytosis inhibition vs extracellular quenching with dithionite treatment. Cells were incubated with NBD-labeled polyplexes at 37 °C to allow binding and endocytosis of gene carriers. For endocytosis inhibition, a separate cell sample was incubated with polyplexes at 4 °C. For extracellular quenching with dithionite treatment, cells were incubated with polyplexes at 37 °C and then briefly treated with dithionite to quench extracellular fluorescence. NBD fluorescence was measured in cell lysates using a plate reader (A) and in suspensions of whole cells based on flow cytometry analysis (C). The degree of cellular internalization of polyplexes was measured either by subtracting cell-associated fluorescence at 4 °C from cell-associated fluorescence at 37 °C (No Dithonite) or by measuring unquenched fluorescence associated with cells following dithionite treatment (Dithionite). Differences in the degree of polyplex internalization measured on the basis of endocytosis inhibition vs dithionite quenching were not statistically significant using either fluorescence measurements in lysate (B) or flow cytometry data (D).

with polyplexes at 37 °C. Dithionite treatment of cells incubated with polyplex at 4 °C abolishes all fluorescence (Figure 3A,C). Therefore, it was hypothesized that the amount of internalized polyplex can also be determined quantitatively by simply measuring the total cell fluorescence from dithionite-treated cells. As shown in Figure 3B,D, internalization measurements derived from dithionite-treated cells were in close agreement with those based on a comparison between cell-associated fluorescence in samples incubated with polyplexes at 37 °C with those incubated at 4 °C ($p > 0.05$) with both flow cytometry and fluorescence measurements of cell lystates. Similar data were obtained when cells were treated with NBD-labeled lipoplexes (data not shown). Thus, dithionite treatment of cells exposed to NBD-labeled vectors can be used as a rapid method to quantify internalization. It should be noted that, for studies involving the quantification of internalized vectors, dithionite treatment methods were modified to reduce the extent of exposure of cells to dithionite. Specifically, the dithionite concentration was reduced from 88 mM to 10 mM and the incubation time was reduced from 5 min to 2 min. Under these conditions, extracellular materials were efficiently quenched, while the quenching of internalized materials due to leakage of dithionite across the cell membrane was minimized.

3.4. Degree of Internalization of Gene Carriers Varies with Formulation Parameters. The degree of internalization of various polyplex and lipoplex formulations was compared to the transfection efficiency mediated by the same formulation. As shown in Figure 4, both internalization and transfection efficiencies differed significantly between lipoplexes and polyplexes. Interestingly, while lipoplex internalization by cells was at least 4-fold less efficient than polyplex internalization, reporter gene expression in the lipoplex-treated samples was 2 orders of magnitude higher. Although some fluorescence quenching occurs upon condensation of NBD−oligos by cationic polymers and lipids (Figure 1), exposure of NBD-labeled lipoplexes and polyplexes to cell lysate containing 150 mM NaCl resulted in full vector unpackaging and fluorescence recovery (data not shown). Hence, the internalization data reported here are not confounded by differences in the degree of NBD−oligo self-quenching.

3.5. NBD/Texas Red Double-Labeled Gene Carriers Enable Discrimination between Internalized and Cell-Associated Materials in Neuron-Like Cells. In order to simultaneously image surface-bound and internalized vectors, lipoplexes were double-labeled with the nonquenchable, pH-insensitive dye, Texas Red (TR), along with NBD. As expected, the NBD signal in double-labeled lipoplexes was quenched by dithionite, while the TR signal remained unaffected (Figure 5). To quantitatively differentiate between uninternalized and internalized particles, ratiometric analysis methods were established using microscopy images of NBD/TR-double-labeled lipoplexes. A comparison of dithionite-treated versus untreated lipoplexes revealed that the green/red fluorescence emission ratios obtained were significantly different between treated and untreated lipoplexes (Figure 6A). By applying ratiometric analysis to images NBD/TR-lipoplex-exposed, dithionite-treated cells and by comparing green/red fluorescence ratios of individual particles to the values obtained from quenched or unquenched particles in Figure 6A, it was possible to confirm internalization

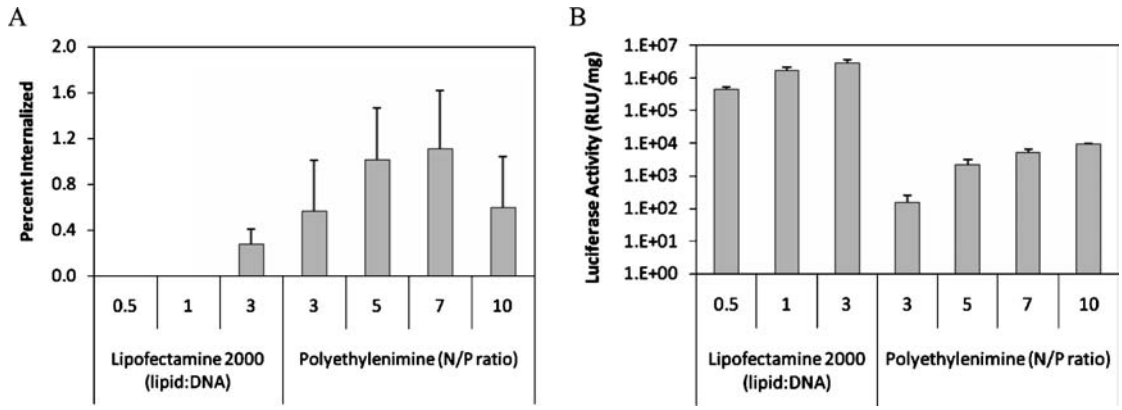

Figure 4. Correlation between the degree of vehicle internalization and transfection efficiency. (A) The degree of cellular internalization of various lipoplex and polyplex formulations incorporating NBD−oligos was determined on the basis of the amount of unquenched NBD fluorescence following dithionite treatment, and was normalized by the total NBD fluorescence added to the cells. (B) Transfection efficiencies of identical formulations incorporating luciferase-encoding plasmid DNA are presented as mean RLU/mg protein ± standard deviation.

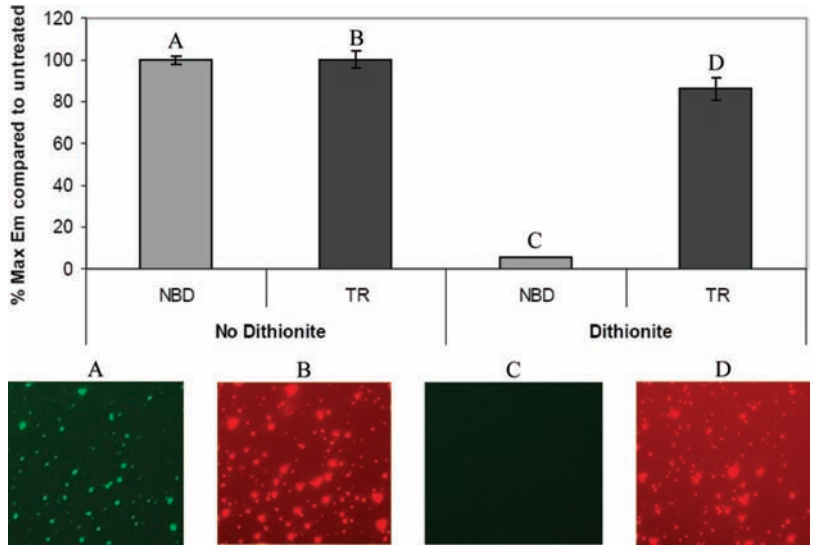

Figure 5. Selective quenching of NBD in double-labeled lipoplexes. NBD/TR-double-labeled lipoplexes were examined by fluorimetry and fluorescence microscopy.

of a fraction of the lipoplexes that bound to neuron-like PC-12 cells (Figure 6B,C).

DISCUSSION

Efficient intracellular delivery of DNA or RNA is critical for the success of nucleic acid based therapies. A method to rapidly determine the efficiency of delivery vector uptake in mammalian cells would contribute toward the design and selection of promising delivery vehicles. For example, screening of polymer suites and libraries has yielded new materials with improved delivery efficiencies (*5–7*). Subsequent determination of the efficiency of specific cellular trafficking steps would provide valuable insights on structure–function relationships. Since most carriers form positively charged nanoparticles upon complexation with nucleic acids, and since these particles are known to bind robustly to the cell membrane through electrostatic interactions, methods are necessary to distinguish between carriers that are internalized by cells and those which remain associated with the cell surface but fail to internalize. Additionally, the ability to discriminate between extra- and intracellular materials would enable evaluation of the spatiotemporal distribution of gene carriers in cells using standard wide-field microscopy.

Various methods have been described to discriminate between surface-bound and internalized materials. Notably, several dye/quencher combinations have been employed to eliminate fluorescence from uninternalized materials associated with cells. For example, antibodies raised against fluorescent dye molecules, such as fluorescein, can selectively quench extracellular fluorescence due to tight binding of the antibody to the dye (*8, 9*). Additionally, treatment of cells with Trypan Blue eliminates extracellular green fluorescence through an energy transfer mechanism (*10, 11*). This technique has been employed to quench extracellular fluorescence associated with gene carriers and fluorescent microspheres (*12–14*). Finally, washing cells with buffers containing high salt concentrations has been utilized to dissociate complexes adsorbed to the cell surface through electrostatic interactions (*15, 16*). While implementation of these quenching techniques has provided important insight into the internalization efficiencies of various macromolecules, these techniques have limitations for the analysis of gene carrier internalization. First, it is unclear how efficiently antibodies can access fluorophores that are packaged within nanoparticles consisting of cationic lipids or polymers and nucleic acids. Additionally, the efficiency of quenching with Trypan Blue has been shown to depend on the specific brand of Trypan Blue used (*17*). Finally, since previous methods to quench extracellular fluorescence have employed fluorescein-labeled gene carriers, it is important to consider that the pH sensitivity of fluorescein can confound measurements of internalization, since

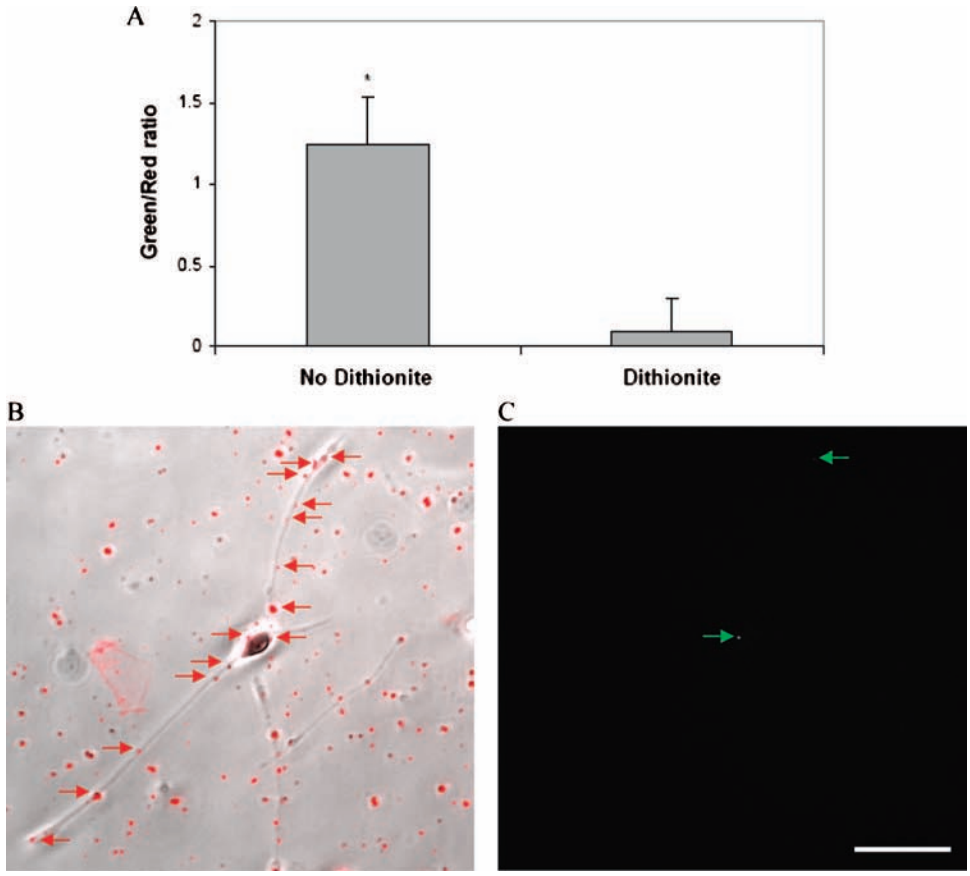

Figure 6. Ratiometric analysis distinguishes between intracellular and extracellular lipoplexes in neuron-like PC-12 cells. (A) The ratio of NBD to TR fluorescence signals is significantly different between dithionite-treated and untreated particles (*$p < 0.001$). NBD/TR-double-labeled lipoplexes that associated with the cell are indicated by red arrows in the bright-field/fluorescence overlay image (B), while lipoplexes that were internalized retained NBD fluorescence and are indicated by green arrows (C) (scale bar = 50 μm).

its fluorescence may also be reduced in acidic intracellular compartments. The NBD/dithionite combination described here offers a reliable and cost-effective alternative.

In this work, NBD-labeled oligonucleotides were incorporated into polymer- and lipid-based nonviral gene carriers to differentiate between internalized vehicles and uninternalized vehicles associated with the cell plasma membrane. NBD-labeled gene carriers were quenched by exposure to dithionite but retained their fluorescence in the intracellular milieu due to the relative impermeability of the cell plasma membrane to dithionite. As a demonstration of the utility of NBD−oligos in formulation screening, the internalization efficiencies of various polyplex and lipoplex formulations were measured. Internalization measurements were then compared to the efficiency of reporter gene expression mediated by the same formulation. Interestingly, while lipoplexes were internalized less efficiently than polyplexes, they mediated significantly higher transfection efficiencies in the cell line tested. This phenomenon was previously observed by Varga et al. (*18*) and is likely due to the enhanced intracellular trafficking efficiency of lipoplexes compared to polyplexes. Consequently, while internalization measurements may serve as an initial, rapid screen to identify formulations with high binding and internalization efficiencies, transfection screening should also be performed to uncover differences in the intracellular trafficking efficiencies of internalized materials.

It should be noted that slow diffusion of dithionite through cell membranes has been observed and can result in intracellular fluorescence quenching (*4*). However, NBD quenching of extracellular material occurs within seconds, whereas leakage through the cell membrane takes place on the order of minutes. The timing of fluorescence measurements may require optimization, especially for systems where perturbations to the integrity of the cell membrane can occur. Protocols have been described to account for the permeability of cellular membranes by measuring the initial rate of quenching, rather than the extent of quenching, and could be utilized if a highly precise determination of gene carrier internalization were required (*19*). Nonetheless, the NBD/dithonite combination described here offers a means for facile evaluation of gene carrier internalization that does not suffer from the limitations of previously described approaches.

NBD−oligos are also useful to distinguish between extracellular and internalized materials by fluorescence microscopy. Confocal laser scanning microscopy is routinely employed to study the intracellular distribution of nonviral gene carriers in cells. By taking optical slices as thin as 0.5 μm, confocal imaging has revealed the intracellular distribution of fluorescently labeled gene carriers in fibroblasts and other cell types with subcellular detail (*20*). However, this technique is not reliable for imaging gene carriers in neuronal projections, where the depth of field is similar in size to the typical neurite diameter. This limitation was encountered by Suk et al. (*21*) in a study of the intracellular transport of PEI/DNA polyplexes in rat primary neurons. Although it is possible to narrow the slice depth in confocal images by applying digital deconvolution algorithms, it would be beneficial to develop an alternative method for differentiating between internalized and surface-bound gene carriers that can be implemented using conventional wide-field fluorescence microscopy. By incorporating mixtures of NBD- and TR-labeled oligonucleotides into gene carriers and employing ratiometric imaging, it was possible to reliably differentiate

between extra- and intracellular lipoplexes in the neurites of NGF-differentiated PC-12 cells. This concept is similar to ratiometric imaging of fluorescein/Cy5-labeled gene vectors to measure the pH environments of gene carriers in the cell, which has been described previously (*8*, *22*), but it investigates a different step in the delivery pathway.

In future applications, the NBD/dithionite system can potentially be exploited to measure the efficiency and dynamics of cell binding, internalization, and vesicular escape of gene carriers. While brief exposure of cells to dithionite quenches primarily extracellular NBD fluorescence, exposure beyond 30 s begins to slowly quench cytoplasmic fluorescence at a rate of approximately 4% per minute due to slow leakage of dithionite across the outer plasma membrane (*4*). However, NBD enclosed by intracellular vesicles such as endosomes remains largely unquenched by dithionite that leaks into the cytoplasm (*23*). By exposing cells to NBD-labeled gene carriers and measuring the quenching kinetics of NBD, it may be possible to measure the percentages of surface-bound, vesicle-enclosed, and cytosolic gene carriers. Since it is of interest to compare different gene vectors for their abilities to escape from endosomes, comparative studies using NBD-labeled oligonucleotides condensed by various polymers or lipids would elucidate structure–function relationships, while avoiding more time-consuming techniques such as subcellular fractionation.

ACKNOWLEDGMENT

This work was funded by the NIH/NINDS (R21 NS052030) and an NSF CAREER Award (BES-0454324). JMB acknowledges the Whitaker Foundation and the University of Washington's Engineered Biomaterials Training Program (T32 GM065098) for graduate fellowship support. Flow cytometry studies were conducted at the UW Department of Immunology Cell Analysis Facility.

Supporting Information Available: Raw flow cytometry plots are provided corresponding to the data presented in Figure 3C. This material is available free of charge via the Internet at http://pubs.acs.org/BC.

LITERATURE CITED

(1) Pack, D. W., Hoffman, A. S., Pun, S., and Stayton, P. S. (2005) Design and development of polymers for gene delivery. *Nat. Rev. Drug Discovery 4*, 581–93.

(2) Gao, X., Kim, K. S., and Liu, D. (2007) Nonviral gene delivery: what we know and what is next. *AAPS J. 9*, E92–104.

(3) Medina-Kauwe, L. K., Xie, J., and Hamm-Alvarez, S. (2005) Intracellular trafficking of nonviral vectors. *Gene Ther. 12*, 1734–51.

(4) McIntyre, J. C., and Sleight, R. G. (1991) Fluorescence assay for phospholipid membrane asymmetry. *Biochemistry 30*, 11819–27.

(5) Akinc, A., Lynn, D. M., Anderson, D. G., and Langer, R. (2003) Parallel synthesis and biophysical characterization of a degradable polymer library for gene delivery. *J. Am. Chem. Soc. 125*, 5316–23.

(6) Hwang, S. J., Bellocq, N. C., and Davis, M. E. (2001) Effects of structure of beta-cyclodextrin-containing polymers on gene delivery. *Bioconjugate Chem. 12*, 280–90.

(7) Liu, Y., and Reineke, T. M. (2007) Poly(glycoamidoamine)s for gene delivery. structural effects on cellular internalization, buffering capacity, and gene expression. *Bioconjugate Chem. 18*, 19–30.

(8) Forrest, M. L., and Pack, D. W. (2002) On the kinetics of polyplex endocytic trafficking: implications for gene delivery vector design. *Mol. Ther. 6*, 57–66.

(9) Mallender, W. D., Carrero, J., and Voss, E. W., Jr (1996) Comparative properties of the single chain antibody and Fv derivatives of mAb 4–4-20. Relationship between interdomain interactions and the high affinity for fluorescein ligand. *J. Biol. Chem. 271*, 5338–46.

(10) Hed, J., Hallden, G., Johansson, S. G., and Larsson, P. (1987) The use of fluorescence quenching in flow cytofluorometry to measure the attachment and ingestion phases in phagocytosis in peripheral blood without prior cell separation. *J. Immunol. Methods 101*, 119–25.

(11) Sun, B., Eckhardt, E. R., Shetty, S., van der Westhuyzen, D. R., and Webb, N. R. (2006) Quantitative analysis of SR-BI-dependent HDL retroendocytosis in hepatocytes and fibroblasts. *J. Lipid Res. 47*, 1700–13.

(12) Bengali, Z., Rea, J. C., and Shea, L. D. (2007) Gene expression and internalization following vector adsorption to immobilized proteins: dependence on protein identity and density. *J Gene Med 9*, 668–78.

(13) Rejman, J., Bragonzi, A., and Conese, M. (2005) Role of clathrin- and caveolae-mediated endocytosis in gene transfer mediated by lipo- and polyplexes. *Mol. Ther. 12*, 468–74.

(14) Rejman, J., Oberle, V., Zuhorn, I. S., and Hoekstra, D. (2004) Size-dependent internalization of particles via the pathways of clathrin- and caveolae-mediated endocytosis. *Biochem. J. 377*, 159–69.

(15) Dailey, L. A., Kleemann, E., Merdan, T., Petersen, H., Schmehl, T., Gessler, T., Hanze, J., Seeger, W., and Kissel, T. (2004) Modified polyethylenimines as non viral gene delivery systems for aerosol therapy: effects of nebulization on cellular uptake and transfection efficiency. *J. Controlled Release 100*, 425–36.

(16) Ruponen, M., Ronkko, S., Honkakoski, P., Pelkonen, J., Tammi, M., and Urtti, A. (2001) Extracellular glycosaminoglycans modify cellular trafficking of lipoplexes and polyplexes. *J. Biol. Chem. 276*, 33875–80.

(17) Van Amersfoort, E. S., and Van Strijp, J. A. (1994) Evaluation of a flow cytometric fluorescence quenching assay of phagocytosis of sensitized sheep erythrocytes by polymorphonuclear leukocytes. *Cytometry 17*, 294–301.

(18) Varga, C. M., Tedford, N. C., Thomas, M., Klibanov, A. M., Griffith, L. G., and Lauffenburger, D. A. (2005) Quantitative comparison of polyethylenimine formulations and adenoviral vectors in terms of intracellular gene delivery processes. *Gene Ther. 12*, 1023–32.

(19) Angeletti, C., and Nichols, J. W. (1998) Dithionite quenching rate measurement of the inside-outside membrane bilayer distribution of 7-nitrobenz-2-oxa-1,3-diazol-4-yl-labeled phospholipids. *Biochemistry 37*, 15114–9.

(20) Akita, H., Ito, R., Khalil, I. A., Futaki, S., and Harashima, H. (2004) Quantitative three-dimensional analysis of the intracellular trafficking of plasmid DNA transfected by a nonviral gene delivery system using confocal laser scanning microscopy. *Mol. Ther. 9*, 443–51.

(21) Suk, J. S., Suh, J., Lai, S. K., and Hanes, J. (2007) Quantifying the intracellular transport of viral and nonviral gene vectors in primary neurons. *Exp. Biol. Med. (Maywood) 232*, 461–9.

(22) Akinc, A., and Langer, R. (2002) Measuring the pH environment of DNA delivered using nonviral vectors: implications for lysosomal trafficking. *Biotechnol. Bioeng. 78*, 503–8.

(23) Pomorski, T., Herrmann, A., Zimmermann, B., Zachowski, A., and Muller, P. (1995) An improved assay for measuring the transverse redistribution of fluorescent phospholipids in plasma membranes. *Chem. Phys. Lipids 77*, 139–46.

BC700315V

Well-Defined Nanoassemblies Using Gold Nanoparticles Bearing Specific Number of DNA Strands

Wei Jie Qin and Lin Yue Lanry Yung*

Department of Chemical and Biomolecular Engineering, National University of Singapore, 10 Kent Ridge Crescent, Singapore 119260. Received May 18, 2007; Revised Manuscript Received October 10, 2007

The accurate assembly of nanoparticles into specially designed structures is important for the application of nanoparticle-based materials. Here we report the fabrication of well-defined nanoparticle assemblies via the grouping of gold nanoparticles bearing a specific number of short DNA per particle. Furthermore, we explored various conditions that affect the grouping. Our results show that direct linkage of two nanoparticle-bound DNA without the use of linker DNA yields 80% grouping, which is the highest of all conditions tested. Longer hybridization times and buffer conditions with higher ionic strength also increase grouping formation. These results provide key knowledge that controls the hybridization of nanoparticle-bound DNA for achieving well-defined nanoassemblies with high yield.

INTRODUCTION

Driven by the need from nanotechnology, materials science, and biological and biomedical applications, various approaches for the fabrication of defined nanostructures have been developed in recent years (*1, 2*). Among them, the bottom up approach in which nanometer-scaled building blocks are assembled into larger entities attract the most attention (*3*). Within these areas, great efforts have been directed to the self-assembly of hybrid materials from inorganic nanoparticles and biomolecules, such as DNA, RNA, and proteins (*4, 5*). Metallic, semiconductor, and magnetic nanoparticles are commonly used components in the bottom up self-assembly. Because of their small size, nanoparticles show unique chemical and physical properties and have great potential in the development of functional nanoassembly (*6–9*), chemical sensors (*10*), biomolecular electronics (*11, 12*), and biological applications (*3, 13*).

The realization of above applications requires deliberate and accurate arrangement of nanoparticles into predesigned structures. DNA molecules, which possess unique molecular recognition capability and mechanical rigidity as well as high-precision enzyme processibility, are particular attractive for applications demanding accurate arrangement and a high degree of structural control (*14–16*). Furthermore, DNA molecules can be synthesized readily in a predesigned length and sequence with various functional groups for the conjugation or fluorescent detection. Thus, DNA is a highly promising molecule for directing programmable self-assembly and has been extensively used to fabricate nanostructured scaffolds as well as position proteins, metal, or semiconductor nanoparticles and other molecular devices (*17–19*). The combination of DNA molecules with inorganic nanoparticles has led to the development of novel hybrid materials that incorporate the sequence specific recognition capability of DNA molecules with the size-dependent optical, electrical, magnetic, and catalytic properties of nanoparticles.

The collective properties of nanoparticles are mainly dependent on their hierarchical arrangements and interparticle distance. For example, noble metallic nanoparticles have plasmon resonances in the visible range and do not blink or bleach. The wavelength of this plasmon resonance shifts upon varying the distance between nanoparticles. Applying the shifting of plasmon resonance as the nanoscale distance monitoring tool requires precise control over the distance between nanoparticles to allow the propagation of light along a defined path efficiently (*20, 21*). However, there have been only a limited number of studies focused on fabricating nanoparticle−DNA assemblies with very well-defined structure, such as dimer, trimer, and other higher order multimers (*22, 23*).

Previously we have shown that gold nanoparticle−DNA (nAu-DNA) conjugates bearing specific number of short DNA can be prepared by gel electrophoresis isolation followed by restriction endonuclease manipulation of the nanoparticle (nAu)-bound DNA (*24*). Here, we further demonstrate how these conjugates can be used to construct well-defined nanogroupings. The effects of interparticle spacing as well as nAu−linker DNA interactions on the final conjugate grouping were studied. In our approach, two sets of specially designed nAu-DNA conjugates are first modified with a specific number (1, 2, 3. . .) of short single stranded DNA (ssDNA) that are not directly complementary to each other. These conjugates do not recognize each other until a complementary linker DNA, which hybridizes to the DNA on both sets of conjugates, is introduced. Only conjugate groupings with defined structure (dimer or trimer) can form due to the fixed number of DNA on each nAu. The resulting conjugate groupings are analyzed and quantified by agarose gel electrophoresis. The size differentiation ability of gel electrophoresis enables separation and identification of different nAu grouping structures, such as monomers, dimers, and trimers.

MATERIALS AND METHODS

Materials. Hydrogen tetrachloroaurate (III) trihydrate, trisodium citrate dihydrate, tannic acid, 4,4′-(phenylphosphinidene) bis-(benzenesulfonic acid) (PPBS), dithiothreitol (DTT), NaCl, $MgCl_2$, and tris-borate-EDTA (TBE) buffer were purchased from Sigma-Aldrich. The synthetic DNA (modified with thiol linker at the 5′ end) was purchased from Integrated DNA Technologies (IDT). Restriction endonuclease EcoR V (500000 unit/mL) was obtained from New England Biolabs. Acrylamide/Bis solution (30%) (29:1) and ethidium bromide were obtained from Bio-Rad Laboratories. Agarose was purchased from

* Corresponding author. E-mail: cheyly@nus.edu.sg.

10.1021/bc700178f CCC: $40.75 © 2008 American Chemical Society
Published on Web 12/07/2007

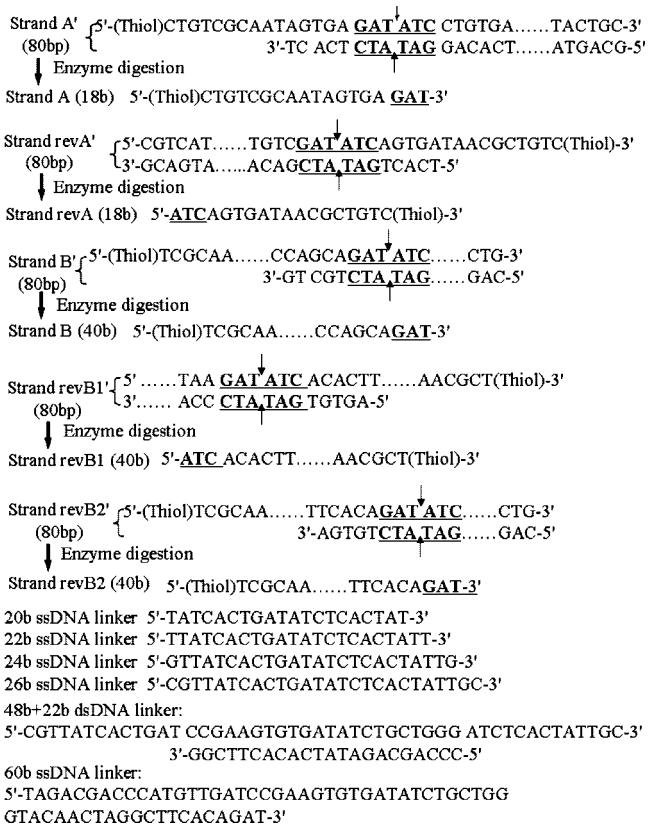

Figure 1. DNA sequences used in this study. For Strands A′, revA′, B′, revB1′, and revB2′, the underlined sequences are the recognition site of EcoR V, and the arrows indicate the enzyme cleavage site.

Cambrex. Dialysis tubing (Float-A-lyzer, MWCO: 3500) was obtained from Spectra/Por. Milli-Q water with resistance >18 MΩ/cm was used throughout the experiments.

Synthesis and Characterization of Gold Nanoparticles. Gold nanoparticles (nAu) were synthesized by the reduction of hydrogen tetrachloroaurate (III) trihydrate by trisodium citrate dihydrate and tannic acid (*25*). In order to determine the size and size distribution of the resulting nAu, TEM characterization was performed on a Philips CM300 FEG system operating at 200 kV. At least 200 particles were sized from TEM micrographs via the graphics software Image-Pro Express (Media Cybernetics). The mean particle diameter was 10 nm, and the size distribution was within 15% of the mean diameter.

Preparation of nAu-DNA Conjugates. The DNA sequences used in this study are shown in Figure 1 (complete sequences are shown in Figure S1, Supporting Information). Two complementary single-stranded DNA (ssDNA), one modified with a thiol linker, were allowed to hybridize to form a double-stranded DNA (dsDNA). Strand A′, strand B′, and strand revB2′ were modified with a 5′ thiol linker, whereas strand revA′ and strand revB1′ were with a 3′ thiol linker. These dsDNA were used to prepare different sets of conjugates (nAu-A′ and nAu-revA′, nAu-B′ and nAu-revB1′, and nAu-B′ and nAu-revB2′) for grouping studies. The detailed procedure of conjugate preparation can be found in our previous work (*24*). Briefly, 2 μM dsDNA was mixed with nAu for 2 h followed by 5-T ssDNA for surface passivation. Excess reagents were then removed by repeated washing and centrifuging the conjugates with 0.5× TBE.

Agarose Gel Electrophoresis Isolation and Extraction of nAu-DNA Conjugates. Agarose gel electrophoresis (3% agarose at 5 V/cm and 0.5× TBE as running buffer) was carried out for 4 h to separate the conjugates bearing from one to three dsDNA molecules. Discrete bands can easily be identified because of the wine-red color of nAu. Desired bands were extracted from the gel, and the conjugates were then recovered by electrophoretic dialysis (*26*). After recovery from agarose gel, the conjugates were purified by repeated washing (with 50 mM tris buffer, pH 8.0) and centrifuging to ensure the complete removal of EDTA, which may deactivate the restriction endonuclease.

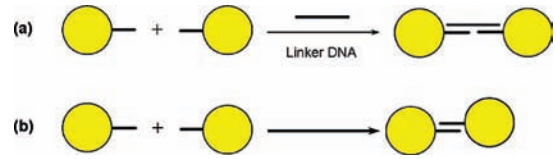

Figure 2. Schematic picture of the formation of nAu-DNA conjugate groupings. (a) Either the pair nAu-A + nAu-revA or nAu-B + nAu-revB1 with linker DNA. (b) Direct pairing of nAu-DNA conjugate using nAu-B + nAu-revB2 without linker DNA.

Enzyme Manipulation of nAu-Bound DNA and Digestion Efficiency. The restriction endonuclease digestion of nAu-bound dsDNA (strand A′ to strand A, strand revA′ to strand revA, etc.) was performed by incubating the conjugates with 100 units of EcoR V at 37 °C in a 200 μL reaction buffer for 20 h. After incubation, the enzyme was deactivated by adding 50 mM EDTA. As shown previously, the digested conjugates (nAu-A, nAu-revA, etc.) were analyzed by polyacrylamide gel electrophoresis (PAGE) to confirm the digestion efficiency and yield of nAu conjugates with a specific number of DNA strands (*24*). Briefly, the digested samples were first centrifuged (13000*g* for 15 min) to separate digested DNA from nAu, and the digested DNA was loaded into a 12% gel for electrophoresis (0.5× TBE as running buffer). The DNA bands were stained with ethidium bromide and visualized by a Syngene GeneGenius UV/white light gel documentation system. The enzyme digestion efficiency was calculated by quantifying digested DNA fragments using gel analysis software from the manufacturer.

Formation and Analysis of nAu-DNA Conjugate Groupings. A pair of nAu-DNA conjugates (nAu-A with nAu-revA, nAu-B with nAu-revB1, etc.), each carrying a single DNA strand (1.5 pmol of each), were mixed in a buffer containing 50 mM tris at pH 8.0, 100 mM NaCl, and 2 mM $MgCl_2$ at a 1:1 molar ratio. Different linker DNA molecules (Figure 1) were then added to the mixture to allow the hybridization of linker DNA with the complementary strands attached to the nAu surface in a tail-to-tail configuration (Figure 2a). The hybridization of cDNA to link nAu conjugates was carried out by first heating the sample to 70 °C for 2 min to ensure complete melting of the DNA strands followed by slow cooling down to 25 °C at a rate of 0.2 °C/min. After the formation of conjugate groupings, agarose gel electrophoresis (3% agarose at 5 V/cm, 0.5× TBE as running buffer) was carried out at 4 °C to characterize and quantify the conjugate groupings. Desired bands of conjugate groupings were visualized by a Syngene GeneGenius UV/white light gel documentation system or a Bio-Rad GS-800 calibrated densitometer. The grouping percentage of nAu-DNA conjugates was calculated by quantifying the relative optical intensity of the gel bands using gel analysis software from the manufacturer, more specifically, dividing the amount of conjugate groupings by the total amount of conjugates in the same lane (unbound conjugates + conjugate groupings). Each value reported was the average of three individual tests. For the study on the relative mobility of conjugate groupings in 3% agarose gel, the elapsed time and the corresponding position of the conjugate groupings were monitored and recorded during electrophoresis. The positions of the gel bands from seven different electrophoretic durations (1 to 5 h) were then measured. The conjugate

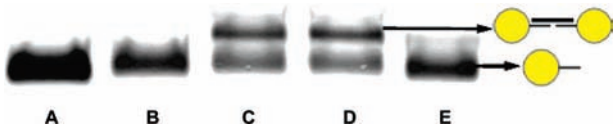

Figure 3. Conjugate grouping of nAu-DNA conjugates with various lengths of DNA linker. Lane A corresponds to the conjugate without DNA modification, and lanes B, C, D, and E correspond to conjugates nAu-A + nAu-revA with no linker, with 26-, 24-, and 22-base linker DNA respectively. The stoichiometric ratio of nAu-A, nAu-revA, and linker DNA is 1:1:1.

groupings were next extracted from the gel and recovered by electrophoretic dialysis (*26*) for TEM characterization.

RESULTS AND DISCUSSION

Grouping percentage of nAu-DNA conjugates using linker DNA of different lengths. As reported earlier by Alivisatos and co-workers (*27*), agarose gel electrophoresis can only be used to isolate nAu-DNA conjugates bearing specific numbers of long DNA molecules. For DNA with 50 bases or less, electrophoresis fails since the electrophoretic mobility difference between conjugates bearing different numbers of DNA strands is insignificant. To obtain nAu-DNA conjugates bearing specific numbers of short DNA, we have used an approach that combines both agarose gel electrophoresis and endonuclease digestion (*24*). First, agarose gel electrophoresis is used to isolate nAu-DNA conjugates bearing different numbers of long DNA strands. Subsequently, the conjugates with specific numbers of DNA strands are treated with EcoR V digestion to cleave DNA into shorter strands. In this way, the number, length, and sequence of the DNA strands on the resultant conjugates are precisely controlled. Restriction endonucleases are enzymes that recognize short specific DNA sequences and cleave the DNA (*28*). Their use on nAu-bound DNA has been reported by several groups (*29–32*) including us (*24, 33*). The enzyme digestion efficiency of 10 nm nAu-bound DNA obtained from PAGE (data not shown) shows that above 90% digestion can be achieved for all of the five dsDNA (strands A′, revA′, B′, revB1′, and revB2′). The high digestion efficiency leads to short and homogeneous DNA on nAu that is critical for the subsequent conjugate assembly formation.

When nAu-A and nAu-revA conjugates were mixed with linker DNA, a tail-to-tail dimer configuration (Figure 2a) was formed to reduce the steric hindrance and allow maximum grouping. Since both nAu-A and nAu-revA were bound with only a single DNA strand, other higher order structures (trimers, tetramers, etc.) were not obtained. The identification of these conjugate groupings is shown in Figure 3. The stoichiometric ratio of nAu-A, nAu-revA, and linker DNA used for assembling is 1:1:1. Since strand A and strand revA are not complementary to each other, a linker is needed for the formation of conjugate groupings. Lane A corresponds to the conjugates without strand A or revA modification (control). Lanes B, C, D, and E correspond to conjugates nAu-A and nAu-revA with no linker, 26-, 24-, and 22-base linker DNA, respectively. Using the band in lane B, which contains only nAu-DNA conjugate monomers, we can identify that the bands on the bottom of lanes C and D correspond to the unbound conjugate monomers (share exactly the same mobility with the band in lane B), and the bands on the top (with slower mobility) correspond to the conjugate dimers. The dimers with two nAu particles exhibit slower mobility due to the overall larger size that slows their movement through the gel. Dimer formation using two different sizes of nAu can also be achieved (see Figure S2 in Supporting Information). The presence of a single band in lane B also indicates no dimer formation due to nonspecific binding among the conjugates. Therefore, the hybridization of the cDNA linker with nAu-A and nAu-revA drives this dimer formation.

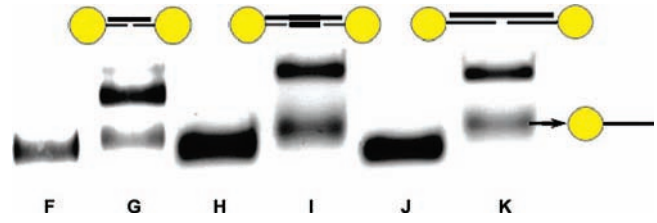

Figure 4. Conjugate grouping of nAu-DNA conjugates with various lengths of DNA linker. Lanes F, H, and J correspond to the conjugate without DNA modification, and lanes G, I, and K correspond to conjugates nAu-A and nAu-revA with 26-base, 48b + 22 bp, and nAu-B and nAu-revB1 with 60-base linker DNA, respectively. The gel pictures shown are combined results from different sets of experiments.

Inherently, cDNA hybridization is highly efficient; however, for dimerization of nAu conjugates via linker DNA, a mixture of monomers and dimers is found in the gel. As seen in lanes C and D in Figure 3, with linker DNA of different lengths, the yields of groupings using the 26- and 24-base linkers are only 55.6% and 55.3%, respectively, and even the nAu-A/nAu-revA/linker ratio is 1:1:1. Similar results were previously reported by Alivisatos and co-workers in which a complete grouping of nAu-DNA conjugates could not be achieved when a linker with a complementary sequence of 100 bases was used (*22, 23*). In addition, we have recently demonstrated in a separate study that using linkers to form dimer conjugates exhibits a linear relationship that allows quantitative measurement of the amount of linkers (*34*). However, this linear relationship only holds at a linker ratio of 0.5 or lower. At higher linker ratios, the grouping efficiency of the dimers starts to drop.

There are a number of factors that may affect the grouping efficiency (and percentage) of nAu conjugates, such as the length of the complementary bases of nAu-bound DNA to linker DNA, the length of linker DNA (distance between nAu conjugates in the resultant groupings), and the ways of formation of linkage (either through linker DNA or via direct hybridization of two nAu-bound DNA as shown in Figure 2b). Determining the dominant factor controlling the nAu grouping is crucial for achieving precisely organized nanoassemblies with high yield. The assembly of nAu conjugates using various kinds of linker DNA is shown in Figure 4. Lanes F, H, and J correspond to nAu without DNA conjugation (control), and lanes G and I correspond to conjugates nAu-A and nAu-revA with 26-base and 48b + 22 bp linkers (see Figure 1), respectively. Lane K is nAu-B and nAu-revB1 with the 60-base linker. Note that the 48 + 22 bp linker is a double stranded DNA with sticky ends that are complementary to the nAu-bound strands A and revA. The use of 48b + 22 bp dsDNA and 60-base ssDNA linkers (Lanes I and K) yields similar gel band distribution and grouping percentage compared with conjugates linked by 26-base ssDNA (lane G). All three conjugate dimer bands yield the maximum grouping percentages of approximately 55%. Increasing interparticle distance (Lane I) should reduce the charge repulsion between nAu conjugates, and increasing the number of complementary base pairing (Lane K) should lead to more stable grouping structure. However, higher grouping percentage is not found in Figure 4 for both cases.

Interestingly, an improved grouping percentage is obtained when direct hybridization between nAu-bound DNA is adopted without the linker DNA. In lanes M, N, and O of Figure 5, conjugate grouping structures (dimers, trimers, and tetramers) appear to be the primary product, and the monomer bands are extremely faint, implying a higher consumption of the monomers. The grouping percentages are found to be 70–80% for lanes M, N, and O, which are obviously higher than those

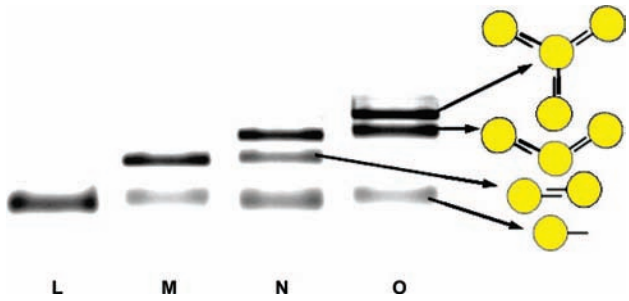

Figure 5. Conjugate grouping formation via the direct linkage of two nAu-bound DNA. Lanes L, M, N, and O correspond to nAu-B, nAu-B + nAu-revB2, nAu-B + nAu-2XrevB2, and nAu-B + nAu-3XrevB2, respectively. 2XrevB2, two strand revB2 per nAu; 3XrevB2, three strand revB2 per nAu.

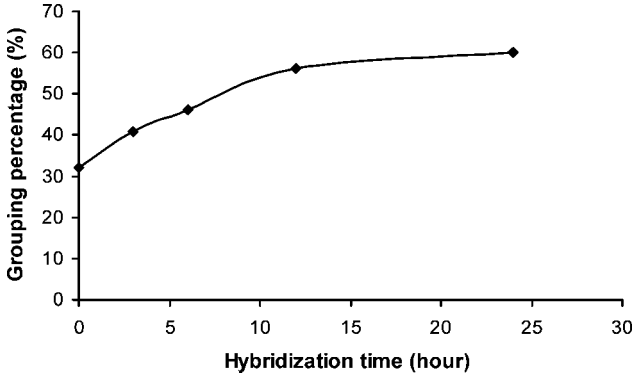

Figure 6. Study on the grouping percentage of nAu-DNA conjugates under various hybridization times.

obtained in the three-strand hybridization system shown in Figure 4. We attribute this increased grouping efficiency to two possible reasons: (1) Compared with free DNA in solution, the translational mobility of nAu-bound DNA is relatively low. This may lead to a low collision rate between cDNA. In addition, the low number of DNA bound on nAu (1–3 DNA per nAu) relative to more than 100 DNA strands per nAu reported previously (*35*) may further reduce the collision probability with complementary nAu-bound DNA to form linkage. Direct linkage between two nAu-bound DNA may be more favorable since it may require shorter collision time compared with grouping via linker DNA, where the linkage of two nAu-bound DNA to the same complementary linker DNA is required. (2) A high salt buffer condition (100 mM NaCl and 2 mM $MgCl_2$) was used in the grouping experiments to screen the charge repulsion between nAu and to facilitate grouping formation. At the same time, however, the linker DNA may tend to form a self-dimer and compete with the conjugate grouping formation. Therefore, a higher grouping percentage cannot be reached when linker DNA is involved.

Effect of Hybridization Conditions on Final Grouping Percentage. A further study on the grouping efficiency under different postannealing hybridization period at 25 °C was carried out using nAu-B, nAu-revB1, and 60-base linker DNA (ratio of 1: 1: 1), and the results are shown in Figure 6. It can be found that the grouping percentage is proportional to the length of hybridization time. With increasing hybridization time, the grouping percentage increases, and the maximum grouping of approximately 60% is obtained after 24 h. This percentage almost doubles compared with the case without postannealing hybridization (hybridization time of zero). This increase in grouping percentage further confirms the low collision rate argument described in the previous section. Longer times allow more collision and therefore facilitate the correct grouping

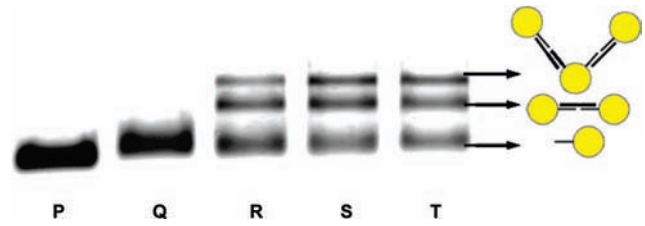

Figure 7. Study on the effect of the ion strength of the hybridization buffer on the nAu-DNA conjugate grouping percentage. Lane P corresponds to the conjugate without DNA modification, and lanes Q−T correspond to the hybridization buffer with 0, 2, 10, and 30 mM $MgCl_2$.

Table 1. Relative Mobility of Conjugate Groupings Linked by Different Linker DNA

DNA linker	26-base ssDNA	48 + 22 bp dsDNA	direct linkage without linker DNA	60-base ssDNA
relative mobility of conjugate dimer	0.66	0.60	0.57	0.54
relative mobility of conjugate trimer	0.45	0.41	0.39	0.35

formation. However, prolonged hybridization does not further improve the grouping percentage much. For example, less than 4% increase is observed as the hybridization time extends from 12 to 24 h.

Ion strength in the hybridization buffer is another important factor that affects the nAu conjugate grouping efficiency. Buffer with high ion strength is commonly used to screen the electrostatic repulsion between nAu conjugates and facilitate the assembly process. To determine the effect of ion strength on the grouping of DNA-linked nAu conjugates, we investigated the grouping percentage as a function of $MgCl_2$ concentration in hybridization buffer. In this test, nAu-A, nAu-2XrevA (two strand revA per nAu), 26-base linker DNA (nAu-A/nAu-2XrevA/linker DNA = 2:1:2), and 50 mM NaCl were used in all samples. As shown in Figure 7, when 2 mM or more $MgCl_2$ is used, the nAu conjugates assemble into dimer and trimer structures, and at least a 50% grouping percentage can be achieved. However, no grouping structure is formed when the salt concentration drops to 50 mM NaCl and no $MgCl_2$ (lane Q). In contrast, cDNA of the same sequences in the absence of nAu hybridizes into dsDNA well in 50 mM NaCl or less and without $MgCl_2$. Such a significant difference in grouping percentage was not unexpected. The 5-T ssDNA passivation of nAu leads to a highly negatively charged surface and stronger electrostatic repulsion among nAu when they come close to each other during DNA hybridization. Bivalent ions, such as Mg^{2+}can efficiently screen this electrostatic repulsion and allow more hybridization events to take place, leading to an improved grouping percentage. Our results clearly show that electrostatic repulsion between nAu-nAu conjugates and nAu-linker DNA play a critical role in the assembly process of the conjugates. The repulsion can be easily tailored by adjusting the ion strength in the hybridization buffer to reversibly control the grouping and ungrouping of nAu-DNA conjugates. Two millimolar $Mg^{2+}$is found to be sufficient for efficiently screening electrostatic repulsion. Less than 10% further improvement in grouping percentage is obtained when Mg^{2+}concentration increases from 2 mM to 30 mM (lanes R−T).

Electrophoretic Mobility of Conjugate Groupings Linked by Various Lengths of Linker DNA. The electrophoretic mobilities of conjugate dimers and trimers linked by different lengths of linkers were compared using the relative mobility of gel bands containing different conjugate groupings (see Figure S3 in Supporting Information). The relative mobility is deter-

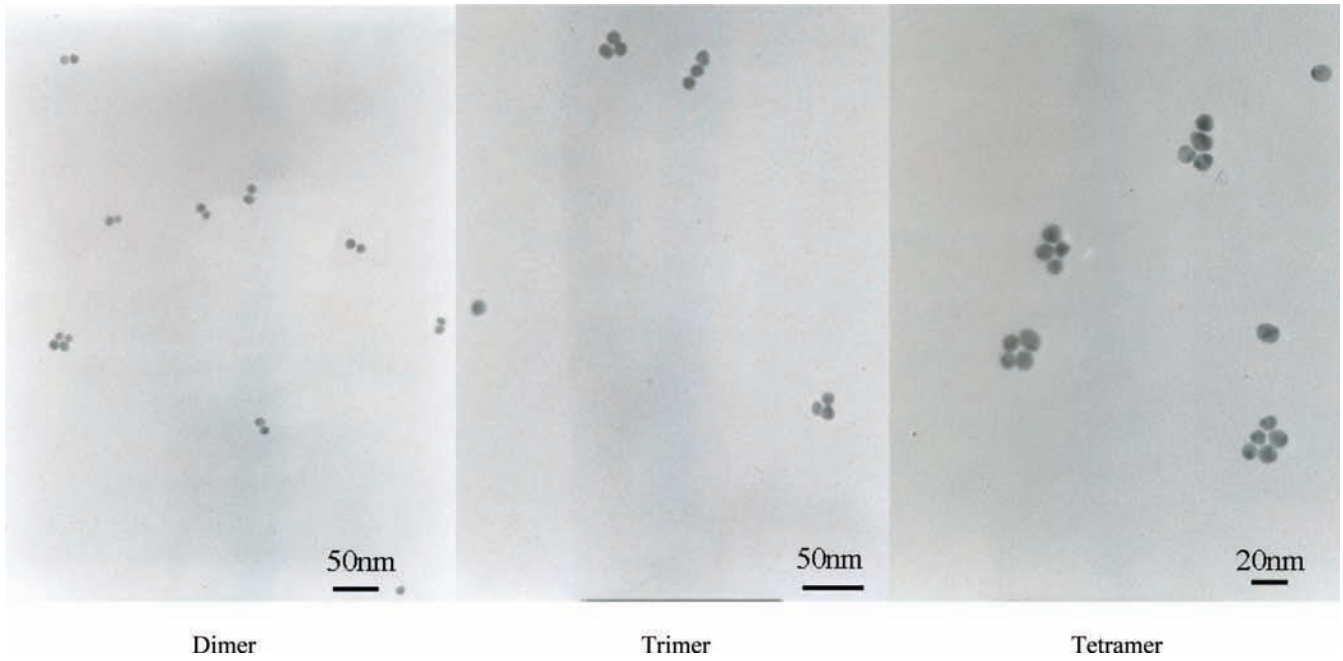

Figure 8. TEM images of nAu-DNA conjugate groupings.

mined as the ratio of migration distance of conjugate groupings relative to that of the nAu without DNA modification. The relative mobility of the groupings can be considered as an indicator of the size of each grouping and is found to be a function of the length of linker DNA and the number of nAu involved in the grouping. Longer linker DNA or a higher number of nAu results in an enlarged size of the grouping and therefore slower relative mobility. However, as shown in Table 1, the difference in the relative mobility between the 26-base and 60-base linker DNA linked grouping dimers/trimers is only 0.1, even though there is a 34 base difference in linker length (approximately 11 nm on the basis of Watson–Crick pairing). The addition of an extra 10 nm nAu and the formation of higher order of structure is more effective in reducing the mobility than using a longer DNA linker because of the bulky size and rigid shape of nAu. This can be seen from the approximately 0.2 relative mobility difference between conjugate dimers and trimers among the same linker cases. It is worth pointing out that conjugate groupings via the direct linkage of nAu-bound DNA (nAu-B and nAu-revB2) have an actual spacing of 50b between two nAu; however, they exhibit slower mobility compared with conjugate groupings linked by 48 + 22 bp dsDNA (actual spacing between two nAu is 58b). These phenomena can be seen for both conjugate dimer or trimer cases. As reported by previous studies, the mobility of conjugate groupings in agarose gel is decided by their size (*22, 27*). This abnormal mobility behavior may be attributed to the formation of a more rigid DNA duplex by direct linkage compared with the use of linker DNA. The presence of linker DNA results in additional hinges in the middle of the DNA duplex and may make the resultant conjugate grouping more flexible in going in between pores of the gel during electrophoresis.

To give a direct correlation between conjugates with different electrophoretic mobility and their actual structure, conjugate groupings were recovered from the gel and visualized by TEM. Figure 8 shows the structures of conjugate dimer, trimer, and tetramer extracted from corresponding gel bands. A large majority of the conjugates participated in the same grouping structure, indicating that each discrete gel band does contain a single type of grouping and not a mixture of several conjugate structures. A small number of monomers and high-order groupings observed in the TEM images may be due to the interruption by the extraction of conjugate samples from the gel as well as TEM preparation processes (See Figure S4 in Supporting Information for more TEM images of the nAu-DNA conjugate groupings.).

CONCLUSIONS

In this work, nAu conjugates bearing specific numbers of short DNA were used to construct nanoassemblies with well-defined structure. Various factors that affect the grouping percentages of nAu-DNA conjugates were investigated. The conjugate groupings were analyzed by gel electrophoresis, and discrete gel bands corresponding to groupings with defined structures were observed. The results show that the direct linkage of two nAu-bound DNA, longer hybridization times, and higher ion strength buffer lead to a higher grouping percentage of nAu-DNA conjugates. Furthermore, the number of nAu involved in the grouping structure is more effective in deciding its electrophoretic mobility than the length of linker DNA. TEM characterization further demonstrates that conjugate groupings extracted from each gel band consist of the expected grouping structure. This confirms that gel electrophoresis is an efficient tool for the isolation of small grouping structures of nAu-DNA conjugates. The results obtained in this study provide additional characteristics of the hybridization pattern of nAu-bound DNA and can be useful toward achieving a more defined and complex assembly of nanoparticles. Finely tailored nanoparticle assemblies can find application in a wide range of areas, such as fabrication of nanomaterials, nanoelectronics, and nanomechanical systems.

ACKNOWLEDGMENT

We thank the National University of Singapore for providing the doctoral scholarship for W.J.Q. and the research funding (R-279-000-125-112 and R-279-000-205-112) for this work.

Supporting Information Available: Complete sequences of the DNA used in this study, dimer formation of different sizes of conjugates, agarose gel image for electrophoretic mobility study on nAu-DNA groupings, and more TEM images of nAu-

DNA groupings. This material is available free of charge via the Internet at http://pubs.acs.org.

LITERATURE CITED

(1) Katz, E., and Willner, I. (2004) Integrated nanoparticle-biomolecule hybrid systems: synthesis, properties, and applications. *Angew. Chem., Int. Ed. 43*, 6042–6108.

(2) Dawn, A., and Nandi, A. K. (2006) Formation of silver nanoparticles in deoxyribonucleic acid-poly(o-methoxyaniline) hybrid: A novel nano-biocomposite. *J. Phys. Chem. B 110*, 18291–18298.

(3) Mirkin, C. A. (2000) Programming the assembly of two- and three-dimensional architectures with DNA and nanoscale inorganic building blocks. *Inorg. Chem. 39*, 2258–2272.

(4) Zheng, J. W., Constantinou, P. E., Micheel, C., Alivisatos, A. P., Kiehl, R. A., and Seeman, N. C. (2006) Two-dimensional nanoparticle arrays show the organizational power of robust DNA motifs. *Nano Lett. 6*, 1502–1504.

(5) Verma, A., Srivastava, S., and Rotello, V. M. (2005) Modulation of the interparticle spacing and optical behavior of nanoparticle ensembles using a single protein spacer. *Chem. Mater. 17*, 6317–6322.

(6) Mitchell, G. P., Mirkin, C. A., and Letsinger, R. L. (1999) Programmed assembly of DNA functionalized quantum dots. *J. Am. Chem. Soc. 121*, 8122–8123.

(7) Fu, A. H., Micheel, C. M., Cha, J., Chang, H., Yang, H., and Alivisatos, A. P. (2004) Discrete nanostructures of quantum dots/Au with DNA. *J. Am. Chem. Soc. 126*, 10832–10833.

(8) Wang, G. L., and Murray, R. W. (2004) Controlled assembly of monolayer-protected gold clusters by dissolved DNA. *Nano Lett. 4*, 95–101.

(9) Zhang, J. P., Liu, Y., Ke, Y. G., and Yan, H. (2006) Periodic square-like gold nanoparticle arrays templated by self-assembled 2D DNA nanogrids on a surface. *Nano Lett. 6*, 248–251.

(10) Elghanian, R., Storhoff, J. J., Mucic, R. C., Letsinger, R. L., and Mirkin, C. A. (1997) Selective colorimetric detection of polynucleotides based on the distance-dependent optical properties of gold nanoparticles. *Science 277*, 1078–1081.

(11) Braun, E., Eichen, Y., Sivan, U., and Ben-Yoseph, G. (1998) DNA-templated assembly and electrode attachment of a conducting silver wire. *Nature 391*, 775–778.

(12) Park, S. J., Lazarides, A. A., Mirkin, C. A., Brazis, P. W., Kannewurf, C. R., and Letsinger, R. L. (2000) The electrical properties of gold nanoparticle assemblies linked by DNA. *Angew. Chem., Int. Ed. 39*, 3845–3848.

(13) Parak, W. J., Gerion, D., Pellegrino, T., Zanchet, D., Micheel, C., Williams, S. C., Boudreau, R., Le Gros, M. A., Larabell, C. A., and Alivisatos, A. P. (2003) Biological applications of colloidal nanocrystals. *Nanotechnology 14*, 15–27.

(14) Niemeyer, C. M.,and Mirkin, C. A. (2004) *Nanobiotechnology: Concepts, Applications and Perspectives*, John Wiley & Sons, Weinheim, Germany.

(15) Dillenback, L. M., Goodrich, G. P., and Keating, C. D. (2006) Temperature-programmed assembly of DNA: Au nanoparticle bioconjugates. *Nano Lett. 6*, 16–23.

(16) Pinto, Y. Y., Le, J. D., Seeman, N. C., Musier-Forsyth, K., Taton, T. A., and Kiehl, R. A. (2005) Sequence-encoded self-assembly of multiple-nanocomponent arrays by 2D DNA scaffolding. *Nano Lett. 5*, 2399–2402.

(17) Tang, Z. Y., and Kotov, N. A. (2005) One-dimensional assemblies of nanoparticles: Preparation, properties, and promise. *Adv. Mater. 17*, 951–962.

(18) Loweth, C. J., Caldwell, W. B., Peng, X. G., Alivisatos, A. P., and Schultz, P. G. (1999) DNA-based assembly of gold nanocrystals. *Angew. Chem., Int. Ed. 38*, 1808–1812.

(19) Manzanera, M., Frankel, D. J., Li, H. T., Zhou, D. J., Bruckbauer, A., Kreutzmann, P., Blackburn, J. M., Abell, C., Rayment, T., Klenerman, D., and Barker, P. D. (2006) Macroscopic 2D networks self-assembled from nanometer-sized protein/DNA complexes. *Nano Lett. 6*, 365–370.

(20) Sonnichsen, C., Reinhard, B. M., Liphard, J., and Alivisatos, A. P. (2005) A molecular ruler based on plasmon coupling of single gold and silver nanoparticles. *Nat. Biotechnol. 23*, 741–745.

(21) Reinhard, B. M., Siu, M., Agarwal, H., Alivisatos, A. P., and Liphardt, J. (2005) Calibration of dynamic molecular rule based on plasmon coupling between gold nanoparticles. *Nano Lett. 5*, 2246–2252.

(22) Zanchet, D., Micheel, C. M., Parak, W. J., Gerion, D., Williams, S. C., and Alivisatos, A. P. (2002) Electrophoretic and structural studies of DNA-directed Au nanoparticle groupings. *J. Phys. Chem. B 106*, 11758–11763.

(23) Claridge, S. A., Goh, S. L., Frechet, J. M. J., Williams, S. C., Micheel, C. M., and Alivisatos, A. P. (2005) Directed assembly of discrete gold nanoparticle groupings using branched DNA scaffolds. *Chem. Mater. 17*, 1628–1635.

(24) Qin, W. J., and Yung, L. Y. L. (2005) Nanoparticle-DNA conjugates bearing a specific number of short DNA strands by enzymatic manipulation of nanoparticle-bound DNA. *Langmuir 21*, 11330–11334.

(25) Handley, D. A. (1989) Colloidal Gold, *Principles Methods and Applications*, Academic Press, NY.

(26) Sambrook, J.,and Russell, D. W. (2001) *Molecular Cloning: A Laboratory Manual*, 3 ed., Cold Spring Harbor Laboratory Press, NY.

(27) Zanchet, D., Micheel, C. M., Parak, W. J., Gerion, D., and Alivisatos, A. P. (2001) Electrophoretic isolation of discrete Au nanocrystal/DNA conjugates. *Nano Lett. 1*, 32–35.

(28) Pingoud, A., and Jeltsch, A. (1997) Recognition and cleavage of DNA by type-II restriction endonucleases. *Eur. J. Biochem. 246*, 1–22.

(29) He, L., Musick, M. D., Nicewarner, S. R., Salinas, F. G., Benkovic, S. J., Natan, M. J., and Keating, C. D. (2000) Colloidal Au-enhanced surface plasmon resonance for ultrasensitive detection of DNA hybridization. *J. Am. Chem. Soc. 122*, 9071–9077.

(30) Yun, C. S., Khitrov, G. A., Vergona, D. E., Reich, N. O., and Strouse, G. F. (2002) Enzymatic manipulation of DNA - Nanomaterial constructs. *J. Am. Chem. Soc. 124*, 7644–7645.

(31) Kanaras, A. G., Wang, Z. X., Bates, A. D., Cosstick, R., and Brust, M. (2003) Towards multistep nanostructure synthesis: Programmed enzymatic self-assembly of DNA/gold systems. *Angew. Chem., Int. Ed. 42*, 191–194.

(32) Wang, Z. X., Kanaras, A. G., Bates, A. D., Cosstick, R., and Brust, M. (2004) Enzymatic DNA processing on gold nanoparticles. *J. Mater. Chem. 14*, 578–580.

(33) Qin, W. J., and Yung, L. Y. L. (2006) Efficient manipulation of nanoparticle-bound DNA via restriction endonuclease. *Biomacromolecules 7*, 3047–3051.

(34) Qin, W. J., and Yung, L. Y. L., (2007) Nanoparticle-based detection and quantification of DNA with single nucleotide polymorphism (SNP) discrimination selectivity, *Nucleic Acids Res. 35*, e111.

(35) Demers, L. M., Mirkin, C. A., Mucic, R. C., Reynolds, R. A., Letsinger, R. L., Elghanian, R., and Viswanadham, G. (2000) A fluorescence-based method for determining the surface coverage and hybridization efficiency of thiol-capped oligonucleotides bound to gold thin films and nanoparticles. *Anal. Chem. 72*, 5535–5541.

BC700178F

FEBRUARY 2008
Volume 19, Number 2

© *Copyright 2008 by the American Chemical Society*

Bioconjugate Chemistry

REVIEWS

The Synthesis and Chelation Chemistry of DOTA−Peptide Conjugates

Luis M. De León-Rodríguez and Zoltan Kovacs*

University of Texas Southwestern Medical Center, Advanced Imaging Research Center, 2201 Inwood Road NE 4.2, Dallas, Texas 75390-8568. Received August 28, 2007; Revised Manuscript Received October 11, 2007

Metal complexes of DOTA (1,4,7,10-tetraazacyclododecane-1,4,7,10-tetraacetic acid)−peptide conjugates are increasingly used as targeted imaging and therapeutic radiopharmaceuticals and MRI contrast agents. This review covers the bifunctional derivatives of DOTA, the solution and solid-phase synthesis of DOTA−peptide conjugates, their coordination and chelation chemistry, and the biomedical applications of various DOTA−peptide conjugate metal complexes.

INTRODUCTION

Peptide-based targeting vectors are becoming increasingly popular for diagnostic and therapeutic applications. They offer several advantages over antibodies including more favorable pharmacokinetics and better tumor penetration. Peptide sequences that are capable of binding to their target with affinities comparable to those of monoclonal antibodies can be generated by chemical or phage display libraries. Affinity selection of random phage display peptide libraries is a very powerful way of identifying novel targeting sequences for a receptor from billions of peptides (*1*).

While diagnostic nuclear imaging is currently dominated by ^{99m}Tc, there is no single isotope that is perfectly suitable for the treatment of all cancers. The half-lives and energies of the available radioisotopes cover a wide range, and the best-suited therapeutic isotope has to be selected according to the size, type, and stage of the tumor (*2*). Due to their favorable nuclear properties, ^{90}Y and radiolanthanide isotopes such as ^{177}Lu and ^{153}Sm are frequently chosen for therapeutic applications. Unlike their nuclear properties, the chemical behavior of all lanthanide and yttrium isotopes is quite similar. The most stable oxidation state of these elements is 3+, and the solution chemistry of the hard, trivalent Ln(III) cations is characterized by their strong tendency to form complexes with hard donor atoms (O, F^-, and N). Their coordination number is usually 8 or 9, and they form thermodynamically very stable complexes with polyamino polycarboxylate-type ligands that have 8 or 9 donor atoms (Figure 1). Among these ligands, the macrocyclic 1,4,7,10-tetraazacyclododecane-1,4,7,10-tetraacetic acid (DOTA) (**1**) stands out, as it forms complexes with Ln(III) ions with extraordinary thermodynamic stability and kinetic inertness. It should be emphasized that DOTA complexes are significantly more inert kinetically than chelates of DTPA (*3*–*6*), and although both DOTA and DTPA complexes have been used as imaging agents and radiopharmaceuticals, DTPA complexes have been shown to dissociate and release metal under physiological conditions. This may not be of concern in the case of an MRI exam with Gd-DTPA when clearance of the contrast agent is rapid (*7*, *8*), but for targeted radiopharmaceutical applications, when the clearance of the complex is slow, DOTA (**1**) and not DTPA (**3**) should be the ligand of choice.

* Corresponding author. UT Southwestern Medical Center, Advanced Imaging Research Center, 2201 Inwood Road NE 4.2, Dallas, TX 75390-8568 USA. Tel. +1 2146452755, e-mail: zoltan.kovacs@utsouthwestern.edu.

10.1021/bc700328s CCC: $40.75 © 2008 American Chemical Society
Published on Web 12/12/2007

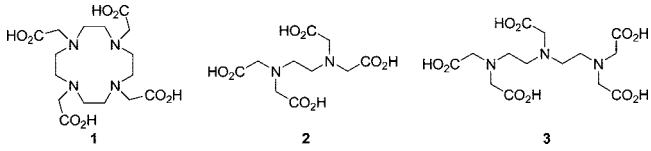

Figure 1. Polyamino polycarboxylate ligands.

A large number of DOTA−peptide conjugates have been synthesized so far, and some of them are already in clinical applications (*9*). Some reviews (see references cited in the Applications section) have covered the nuclear medicine applications of DOTA−peptide conjugate based radiopharmaceuticals, while their synthetic and coordination chemistry has not been reviewed in detail. Therefore, this review is focused on the synthesis and chelation chemistry of DOTA−peptide conjugates.

BIFUNCTIONAL LIGANDS AND LINKERS

Construction of a targeted radiopharmaceutical involves the covalent attachment (conjugation) of the chelate of the radioactive isotope to the targeting vector using a bifuctional chelator. Bifunctional ligands therefore have a reactive functionality, usually an aromatic isothiocyanate group or an activated ester, which will react with nucleophilic sites (-NH_2, -SH, or -OH) of the targeting vector (*10*). A linker may be incorporated between the chelator and the targeting vector to influence the pharmacokinetic properties of the conjugate (*10*). Hydrocarbon, PEG, or polypeptide linkers can alter the pharmacokinetics and biodistribution by changing the overall charge and hydrophilicity of the drug (*11–13*). Peptide-based linkers can also incorporate specific metabolizable sequences. An elegant method based on an "on-demand cleavable" peptide sequence has been developed recently to minimize the radiation delivered to normal tissues. A short peptide linker (rqYKYkf) identified from combinatorial peptide libraries was incorporated between the DOTA moiety and the targeting vector (ChL6 monoclonal antibody) of a targeted radiopharmaceutical. This sequence can specifically be cleaved by the thrombolytic enzyme TNKase that is restricted to the blood pool. After adequate tumor localization of the drug, the enzyme was administered intravenously. Since the enzyme stayed in the blood pool, it released the radioactive DOTA chelate only from the circulating radiopharmaceutical. The rapid renal clearance of the small-molecule DOTA complex resulted in diminished radiation dose to normal tisssues (*14*).

SYNTHESIS OF DOTA PEPTIDES

Conjugating DOTA to Antibodies. Initial strategies to attach DOTA to peptides emerged from earlier methodologies developed for antibody labeling. Proteins are most commonly modified on the primary amino groups of lysine sidechains. Due to their polar and hydrophilic nature, these are usually located on the surface of proteins and thus are easily functionalized. *p*-Isothiocyanatobenzyl DOTA (**4**) was the first DOTA bifunctional chelator developed for protein labeling and continues to be the most widely used DOTA bifunctional for antibody labeling (*15–17*). It is water-soluble and reacts easily with lysine side chains in slightly basic solutions (pH 8–9) (*18*). Encouraged by the success of this bifunctional, other DOTA derivatives with an aromatic SCN group have been developed (**5**−**9**) (Figure 2), but these do not show significant improvements in labeling yield or in vivo stability (*19–21*).

The synthesis of these SCN derivatives, especially the backbone substituted compounds, is fairly lengthy and tedious, and so other approaches based on the in situ activation of the much more readily available DOTA have been developed. A simple procedure is based on the activation of one of the acetic acid sidearms of DOTA with isobutyl chloroformate in the presence of tetramethyl guanidine to form a mixed anhydride derivative (*22*). In situ preparation of NHS and sulfo-NHS esters of DOTA were also reported (*23, 24*). Although proteins were successfully labeled with these mixtures under very mild conditions, this approach has two disadvantages. First, in order to suppress the cross-linking due to the activation of more than one acetate sidearm, a large excess of DOTA has to be used. Second, these activated esters are quite sensitive to hydrolysis, and thus the labeling results are unpredictable.

Both problems can be overcome by using preformed DOTA−NHS ester (**10**) (Figure 3) that can be standardized before conjugation (*25*). Since the preformed DOTA−NHS is synthesized using a selective protection−functionalization−deprotection approach to ensure that only one of the acetate sidearms be activated, the formation of cross-linked side products during bioconjugation is eliminated. While DOTA−NHS can label proteins at neutral pH under milder conditions than *p*-isothiocyanatobenzyl DOTA (*26*), it hydrolyzes rapidly in water (*27*). To minimize the hydrolysis problems mentioned above, several DOTA phenolic-activated ester derivatives were prepared (**11**−**18**) from the corresponding phenol, DOTA, and EDC or DCC, followed by HPLC purification (*28*) (Figure 3). Some of these derivatives showed higher hydrolitic stabilities (**11**, **14**, and **17**) compared to DOTA−NHS (**10**) (*28*), as well as good labeling efficiencies with albumin (*29*).

Although in proteins the lysine side chain amino groups are the most commonly labeled, conjugation of DOTA through the thiol groups of cystein residues with DOTA maleimide derivatives under relatively mild conditions (pH ∼7) has also been reported (*30, 31*).

Solution-Phase Conjugation. In solution, peptides and peptide derivatives can be conjugated to DOTA in the same manner as antibodies using water-soluble bifunctional ligands. For example, an *E. coli* heat-stable peptide analogue was conjugated in aqueous solution at pH 8.5 with the isothiocyanate derivative **6** through an aminocaproic acid linker (*32*). In situ prepared DOTA−NHS ester was also used to conjugate DOTA to the N-terminus of protected octreotide and octreotate derivatives in a water−DMF mixture in which both DOTA and the protected peptide were soluble (*33, 34*). This method can be especially advantageous when the peptide is not available in the protected form as was the case with certain cyclic RDG peptide derivatives. Good coupling yields (up to 79%) of DOTA to RGD peptide monomers and multimers were obtained by using an excess of a mixture of DOTA/EDC/sulfo-NHS (10:5:4). Activation of DOTA in the form of the sulfo-NHS ester was allowed to run for 30 min at 4 °C in water followed by the addition of the peptide. The pH was adjusted to 8.5 for the coupling (*35, 36*).

A new DOTA derivative, α-amino-DOTA (**19**) (Figure 4) was prepared with the objective of attaching DOTA to the C-terminus of a peptide, since in some scenarios, the peptide function might be compromised because of DOTA conjugation to the N-terminus or to lysine side chains. Thus, (**19**) was conjugated through the NH_2 group to the C-terminus of a MMP-2 targeting heptamer oligopeptide in NMP solution using HBTU/HOBT in the presence of triethylamine (*37*). However, usage of (**19**) might be problematic for peptide sequences containing amino or carboxylic functional groups in the lateral chains. Additionally, the racemic nature of (**19**) will result in the formation of a mixture of enantiomers after conjugation, which may adversely affect the bioactivity of the conjugate.

Solid-Phase Conjugation. Since most peptides are generated by solid-phase peptide synthesis (SPPS), it is much more convenient to perform the conjugation step on the solid support. While this approach offers the advantages of the solid-phase

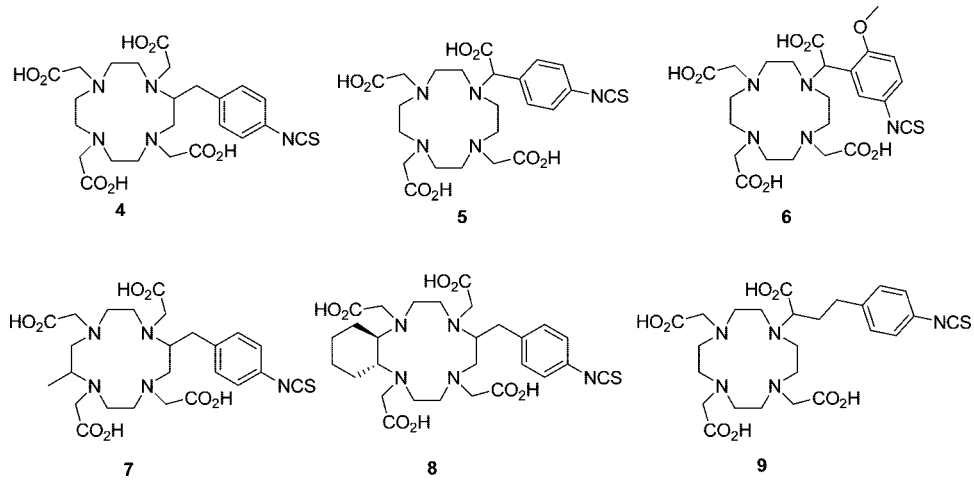

Figure 2. Bifunctional DOTA derivatives with an aromatic isothiocyanate group.

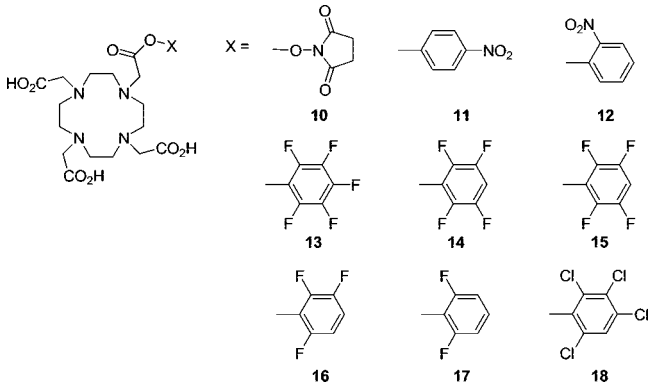

Figure 3. Activated esters of DOTA.

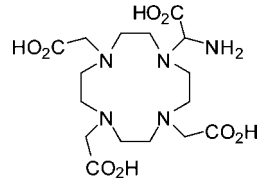

Figure 4. The structure of α-amino-DOTA.

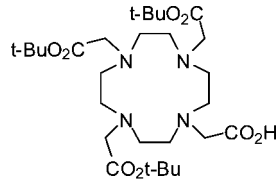

Figure 5. DOTA-tris(*tert*-butyl ester).

synthesis technique, it also presents special challenges for the bifunctional ligand. Most importantly, the ligand has to be compatible with the chemistry used for the peptide synthesis and should preferably be soluble under the conditions of SPPS. The tris-*tert*-butyl ester of DOTA (**20**) (Figure 5) satisfies these requirements. This bifunctional ligand (in the salt free, zwitterionic form) is readily soluble in most organic solvents and the *tert*-butyl ester protection is fully compatible with standard SPPS techniques.

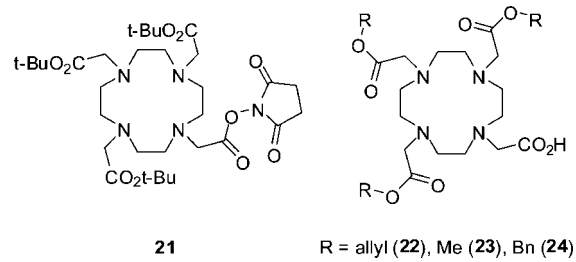

Figure 6. DOTA−tris(*tert*-butyl)-NHS ester and other DOTA−tris(protected) derivatives.

First reported in 1999 (*38*), DOTA−tris(*tert*-butyl ester) is now commercially available and has become the most popular bifunctional ligand for attaching a DOTA unit to a peptide on solid support. It can easily be coupled to free amino groups using tetramethyluronium-type coupling agents such as HBTU or HATU. The most convenient way of conjugation comprises the addition of DOTA−tris(*tert*-butyl ester) to the N-terminus of the protected peptide chain as the last amino acid in an automated peptide synthesizer followed by cleavage from the resin and removal of the acid-labile protecting groups. It can also be attached to Lys side chains, but this requires the use of orthogonal protection strategies (see later). The preformed activated NHS ester of DOTA−tris(*tert*-butyl ester) (**21**) (Figure 6) has also been synthesized (*25*), and this reagent does not require a coupling agent to couple DOTA to free amino groups (*39*). A disadvantage of DOTA−tris(*tert*-butyl ester) is the problems associated with the relatively long deprotection times necessary for the complete cleavage of the *tert*-butyl esters (*40*). There have been several attempts to improve upon this bifunctional chelator by replacing the *tert*-butyl with other groups that can be removed under milder or different conditions. Thus, the following derivatives have been reported: DOTA−tris (allyl ester) (**22**) (can be cleaved with a Pd catalyst) (*40*), DOTA−tris(methyl ester) (**23**) (can be cleaved by basic treatment) (*41*), and DOTA−tris(benzyl ester) (**24**) (can be deprotected with H_2, Pd on C) (*42*). However, these DOTA derivatives have not found widespread applications yet. Unprotected DOTA in the form of its tris(tetrabutyl ammonium) salt, which is soluble in some organic solvents, has also been coupled to peptides in SPPS (*43*). In all these derivatives, the DOTA unit is linked to peptides through one of the acetate sidearms, and the conjugate has four amino, three carboxylates, and one amide group available for metal binding. The ligand forms neutral complexes with lanthanides and Y(III), and the amide oxygen of the conjugating sidearm also coordinates. DOTA derivatives that leave all four acetate sidearms intact

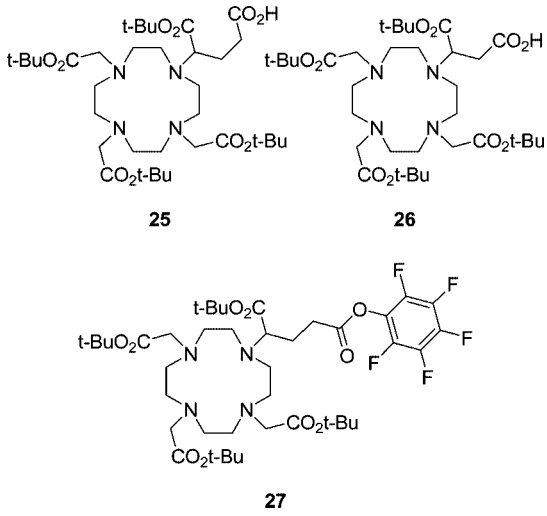

Figure 7. Structures of DOTAGA, DOTASA, and DOTAGA pentafluorophenyl ester.

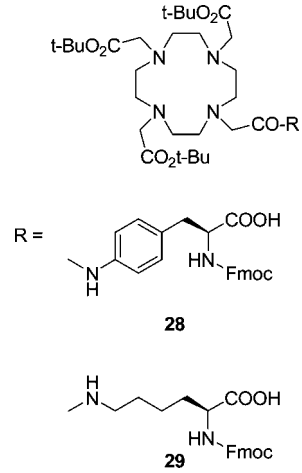

Figure 8. Fmoc-protected DOTA−Phe and DOTA−Lys derivatives.

Scheme 1. DOTA Construction in SPPS

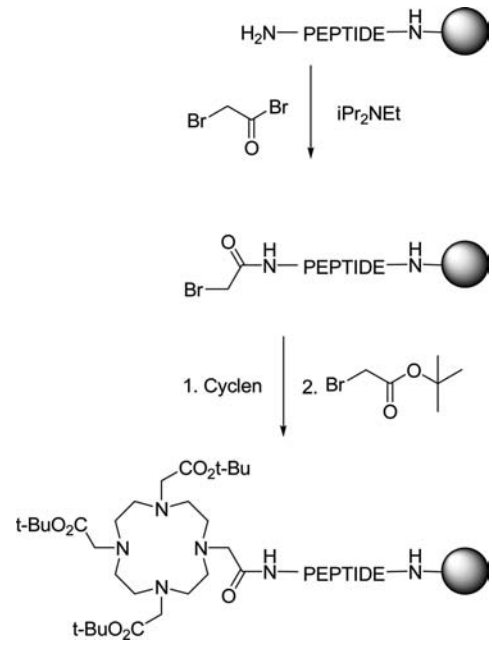

have also been synthesized and conjugated to peptides (Figure 7). These include DOTAGA (**25**) and DOTASA (**26**) as well as the pentafluorophenyl ester of DOTAGA (**27**) (*44–46*).

While with DOTA−tris(*tert*-butyl ester) it is relatively easy to conjugate DOTA to the N terminus of the peptide chain attached to the solid support, attaching a DOTA moiety to Lys side chains requires the synthesis of orthogonally protected peptides. Peptides with Dde [1-(4,4-dimethyl-2,6-dioxocyclohex-1-ylidene)ethyl] or, more preferably, ivDde [1-(4,4-dimethyl-2,6-dioxocyclohex-1-ylidene)-3-methylbutyl] protected lysine in the desired position were synthesized using Fmoc chemistry. Selective removal of the Dde or ivDde protection with hydrazine afforded the resin-bound peptide with the free Lys ϵ-NH_2, which were coupled to DOTA−tris(*tert*-butyl ester) (*47–49*). Using this approach, octreotate derivatives with up to nine Lys residues were synthesized and subsequently labeled with DOTA (*49*). Obviously, conjugation of DOTA by this method is limited to the N-terminal position or Lys side chains. DOTA can be conjugated to other positions using amino acid derivatives and/or novel SPPS techniques designed specifically for the desired target peptides as was demonstrated by the C and N functionalization of Tyr^3-octreotate with DOTA (*50*) and the use of a *p*-formylamido phenylalanine for the specific conjugation of DOTA to Phe residues (*51*). However, these approaches are limited in scope. A more general method involves the use of preformed DOTA−amino acid derivatives which allows the introduction of a DOTA unit into any desired position in the peptide sequence without the need of orthogonal protection (*52, 53*). Protected DOTA−Lys (**28**) (*52, 53*) and DOTA−Phe (**29**) (Figure 8) derivatives that are fully compatible with standard SPPS conditions (*N*-α-Fmoc protection, free carboxyl for the coupling, and acid-labile *tert*-butyl protection of the remaining acetate sidearms of the DOTA unit) have been synthesized. These DOTA−amino acids can be used in SPPS to build peptides that incorporate the DOTA moiety in any desired position (*52*). Interestingly, the type of solid support appears to have a significant effect on the coupling efficiency of the subsequent amino acid beyond the DOTA−amino acid. When Rink amide resin was used, successful coupling after the DOTA amino acid was achieved only with Fmoc amino acid pentafluorophenyl (OPfp) esters (*52*), but HBTU-type activating agents worked satisfactorily on an XAL−PEG−PS solid support (*53*). PEG−PS resins have polar poly(ethylene glycol) (PEG) chains grafted onto microporous styrene−divinyl benzene copolymer and have been shown to be superior to conventional supports for the synthesis of hydrophobic peptides, suggesting that the *tert*-butyl ester groups of DOTA may cause the aggregation of the protected peptide chain.

DOTA−tris(*tert*-butyl ester) can also be used for solution-phase couplings if the peptide is soluble in nonaqueous solvents such as DMF or NMP. A recent Nature Protocol gives a detailed procedure on the small-scale (1–5 mg peptide) solution-phase conjugation of (**20**) (*54*).

Instead of using DOTA bifunctional or DOTA amino acid derivatives, an alternative approach to DOTA peptides involves the construction of the DOTA unit on the resin-bound peptide chain as outlined in Scheme 1 (*55*). Expensive bifunctional ligands are not needed, but it requires three consecutive steps on the solid support to build the DOTA moiety, and the yields were somewhat low, probably due to slow cyclen derivatization.

Protected α-amino−DOTA loaded Wang resin (**30**) (Figure 9) was used to obtain a DOTA−peptide conjugate (NH_2-Asp-Glu-Val-Asp-DOTA) in which the chelator is conjugated to the C-terminus. This methodology can also be adapted to the

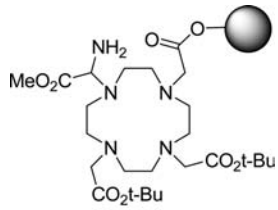

30

Figure 9. α-Amino-DOTA−loaded Wang resin.

synthesis of peptide derivatives that contain the DOTA moiety at an *endo* position of the peptide chain (*56*).

COORDINATION AND CHELATION CHEMISTRY

Coordination Chemistry. There are relatively few reports on the structural features of metal complexes of DOTA−peptide conjugates. Y(III) and the lanthanides are most likely coordinated by the four N and four O atoms, including the amide oxygen with the macrocyclic ring adopting a square [3333] conformation. Isostructural complexes of lanthanide(III) ions and yttrium(III) with the parent ligand DOTA crystallize with a capped square antiprism geometry where the basal plane is occupied by four amine nitrogens of the macrocycle, the capped plane is occupied by four carboxylate oxygens of the acetate sidearms, and the capping position is occupied by a water molecule (*57, 58*). In aqueous solution, the relative orientation of the acetate sidearms and the macrocyclic ring results in two coordination isomers that differ in the torsion or twist angle between the basal N4 and capped O4 squares. A torsion angle around 39° defines a square antiprismatic while an angle of –29° defines a twisted square antriprismatic coordination geometry. These coordination isomers can interconvert by arm rotation or ring inversion (*59*). Lanthanide(III) chelates of other DOTA derivatives also exist in the two interconverting diastereomeric forms of square antiprism and twisted square antiprism. The ratio of the two forms depends on the size of the lanthanide cation as well as the stereochemistry of the ligand (*60, 61*).

The Y(III) complex of the model ligand DOTA−D-PheNH_2 has been prepared, and the X-ray crystal structure revealed that the metal is eight-coordinated and the complex exists in the twisted square antiprismatic form (*38*). On the other hand, the complex with the much smaller Ga(III) appears to have a completely different structure with a distorted octahedral geometry. The macrocyclic ring adopts a [2424] conformation, and only two carboxylates coordinate leaving the amide oxygen and a carboxylate free (*38*). The In(III) complex of the mono(*p*-aminoanilide) derivative of DOTA was shown to have the twisted square antiprismatic geometry in the solid state, but NMR studies indicated that in solution the amide oxygen does not coordinate and the complex exhibits a fluxional behavior (*62*). The major difference between Y(III) and In(III) or Ga(III) is the size. While yttrium(III) (ionic radii ∼1.02 Å) fits perfectly in the cavity of the octadentate ligand, Ga(III) and In(III) are significantly smaller and they prefer ligands with fewer donor atoms. The experimentally observed differences in the biodistribution, clearance, and lipophilicity of the Y, In, and Ga complexes of the same DOTA peptide may in fact be due to the different coordination geometries (*62*).

Chelation Chemistry. The chelation of the radioactive metal ion by the DOTA−peptide conjugate (radiolabeling) is an integral part of the construction of the radiopharmaceutical. The formation rates of the Ln^{3+} complexes with macrocyclic ligands, especially with DOTA, are typically slow. Kinetic measurements suggest the first step in the formation of Ln complexes with DOTA derivatives involves the rapid formation of a mono- or diprotonated intermediate, and the rate-determining step is the base assisted rearrangement of this intermediate (*63*). In some cases, these protonated intermediates have directly been observed by UV–vis, luminescence, and NMR spectroscopy. The slow formation kinetics of DOTA-based ligands can be a significant disadvantage that may limit the practical use of DOTA-based radiopharmaceuticals (*64*). To speed up the chelation process, high temperatures have often been used during the complexation (*18, 65*). For example, DOTA-conjugated somatostatin analogues have been labeled with ^{111}In, ^{90}Y or ^{177}Lu by heating the solution at 95 °C for 25 min or at 80 °C for 20 min, and DOTA−affibodies have been labeled with ^{90}Y and ^{177}Lu at 60 °C for 15 min, giving nearly 100% labeling efficiency (*66–68*). The ^{166}Ho complex of DOTA was prepared in less than a minute by microwave-assisted synthesis, suggesting that this method may be useful for the labeling of DOTA peptides as well (*69*). As one might expect, the pH plays a critical role in the chelation. The rate of complex formation increases with pH, but above pH 6, the lanthanide ions start to form insoluble hydroxo complexes. Thus, the optimal pH for the labeling is between pH 5 and 6. The pH is usually maintained by a sodium acetate or ammonium acetate buffer (50 mM to 0.5 M), and the acetate buffer does not appear to have a significant effect on the complexation (as long as the pH is controlled) even when its concentration is very high (0.5 M) (*70*). Very often, only a small fraction of the available chelator sites is labeled, and the large excess of ligand prevents the formation of insoluble metal−hydroxo species through the rapid formation of intermediary complexes, and the complexation can be performed at higher pH values (pH 7–8) (*71*).

The activity of a radiopharmaceutical is characterized by the specific activity, which refers to the number of radioactive disintegrations per second (Bq, becquerel) per unit amount (grams or moles) of material. For receptor imaging and especially for therapeutic applications, high specific activity is preferred, since the number of receptors as well as their affinity to the radiopharmaceutical is limited (*65*).

Metal ion contaminants coming from the radiometal stock solution or from other reagents and glassware can have a significant effect on the radiolabeling yield if they compete with the desired radiometal for the ligand. These are mainly transition metals or other lanthanides (Al, Ce, Co, Cr, Cu, Fe, La, Ni, Pb, Zn) present as trace metals in the radiolanthanide stock solution, and the total concentration of trace metals can be much higher than that of the desired radiometal. Zr(IV) and Hf (IV), which are the decay products of ^{90}Y and ^{177}Lu, respectively, have been reported to have no effect on the chelation of these radiometals (*65, 72–74*). Often, free radical scavengers such as ascorbic acid or gentisic acid are added as stabilizers to the chelation mixture to prevent radiolytic degradation of the product (*75*).

Certain peptide sequences can bind Ln(III) ions with surprisingly high affinity (50 nM) (*76, 77*), and this may interfere with the complexation in spite of the fact that the thermodynamic stability of the DOTA chelates is several orders of magnitude higher than that of the peptide−metal complexes.

In summary, it is possible to label DOTA−peptide conjugates with radiometal ions such as ^{90}Y(III) or ^{177}Lu(III) to high specific activity, but in each case, the conditions such as pH, temperature, ligand to metal ratio, and choice of buffer have to be carefully optimized.

APPLICATIONS

Complexes of DOTA peptides, depending on the metal ion, have found applications in three major areas: magnetic resonance imaging [GdIII), Eu(III)], nuclear imaging [^{111}In(III), ^{68}Ga(III), $^{64/67}$Cu(II)], and therapeutic radiopharmaceuticals [^{90}Y(III), ^{177}Lu(III)].

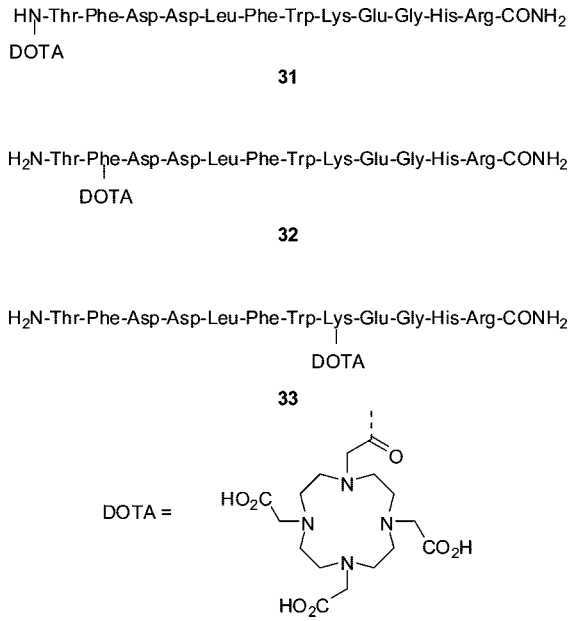

Figure 10. DOTA−Gal80 binding peptide conjugates.

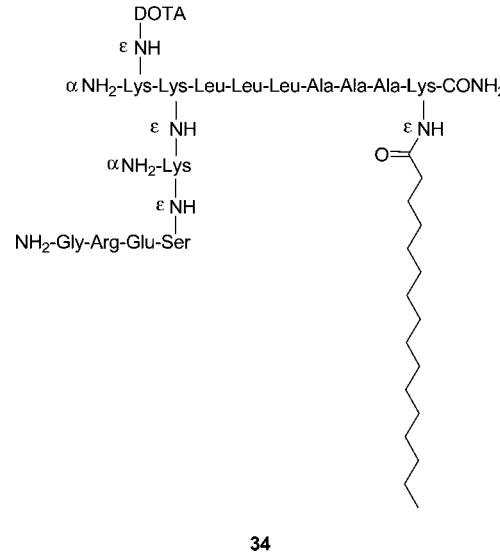

Figure 11. DOTA-labeled peptide amphiphile.

Gd(III)-Labeled DOTA−Peptide Conjugates as MRI Contrast Agents. Although MRI has excellent spatial and temporal resolution, its sensitivity is significantly lower than that of nuclear imaging methods, and so targeted and molecular imaging is still not feasible with MRI (*78*). Early attempts were aimed at increasing the number of DOTA chelates conjugated on antibodies to achieve target-specific contrast enhancement. Thus, DOTA was linked to polylysine using the mixed anhydride method, and the Gd(III)-labeled polylysine was conjugated to human serum albumin (*22*). However, it was estimated that over a hundred Gd−DOTA units per targeting protein is necessary to reach detectable concentrations, which undoubtedly would significantly alter the targeting properties of any biological vector. A much more promising approach is based on the dependence of relaxivity of a gadolinium agent on the rotational correlation time (tumbling rate) of the molecule. According to the Solomon−Bloembergen theory, the rotational correlation times for small Gd chelates are much shorter than optimal for maximum relaxivity, and it has been shown that slowing down the tumbling rate can dramatically improve relaxivity. This can be achieved by covalently linking the chelate to a macromolecule such as a dendrimer or, more advantageously, exploiting noncovalent binding of small, specific chelates to high molecular weight substrates. The latter mechanism is the basis of the receptor-induced magnetization enhancement (RIME) (*79*). Because of their potentially high binding affinities for their targets, Gd−DOTA−peptide derivatives are excellent candidates for this approach.

This concept is well-illustrated by the MRI detection of the specific binding of the Gd−DOTA−Gal80 binding peptide (**31**) (Figure 10) to the galactose regulatory protein Gal80. The binding event results in about 5-fold relaxivity increase and was successfully demonstrated by MRI at concentration levels as low as 10 μM (*80*). The Gal80 binding peptide was previously identified by phage display (*81*). Additionally, a small DOTA−Gal80 peptide library was created by SPPS using compounds (**28**) and (**29**) (Figure 8), and it was shown that conjugates (**32**) and (**33**) (Figure 10) did not show specific binding to Gal80 (*52*). This approach can obviously be adapted to the detection of other proteins by simply generating the specific peptide sequence.

DOTA−peptide conjugates with peptide sequences cleavable by proteolytic enzymes have also been synthesized. Short sequences that are substrates of certain matrix metalloproteinases are preferentially cleaved between an Ala and Leu residue by the enzyme. Thus, Gd-DOTA peptides like Gd-DOTA-Pro-Met-Ala-Leu-Trp-Met-Arg will be cleaved by the enzyme yielding Gd-DOTA-Pro-Met-Ala. It was suggested that the resultant shorter Gd−DOTA−peptide conjugates have faster water exchange rates and thereby higher relaxivities than the original complexes, and therefore the agent will be turned on in the presence of the enzyme (*82*). The change in relaxivity, however, is not nearly as dramatic as in the case of Gd-(**31**).

Interesting self-assembling branched DOTA−peptide conjugate amphiphiles such as (**34**) (Figure 11) were synthesized by SPPS. The branching points were introduced using an orthogonal protection strategy with Fmoc-Lys(Mtt)-OH (Mtt = 4-methyltrityl). Due to the β-sheet forming sequence $(Leu)_3$-$(Ala)_3$ and the hydrophobic palmitoyl tail, the Gd complex of (**34**) gives rise to long cylindrical nanostructures (nanofibers) in aqueous solution that trap water and form a hydrogel. Gd-(**34**) formed homogeneous gels with other peptide amphiphiles, and the relaxivity of Gd-(**34**) gels was about three times higher than that of a control gel mixed with Gd-DTPA as the tumbling rate of the peptide bound Gd complex slows down (*83*).

Since small Gd complexes are ionic and do not cross cell membranes, Gd-DOTA has also been conjugated to transmembrane peptides such as HIV-tat or varying-length polyarginine oligomers that successfully delivered the ionic contrast agent inside the cell (*47, 48, 84*).

DOTA−Peptide Conjugates as Radiopharmaceuticals. Over the past decade, a large number of DOTA peptides have been synthesized and labeled with various radioactive metal ions for both diagnostic and therapeutic purposes, and a comprehensive review of these compounds is well beyond the scope of this article. Instead, we will focus on some of the highlights of this dynamically developing field and will give a brief summary on the latest results on DOTA-labeled somatostain analogues, RGD peptides, and affibody derivatives.

There has been considerable activity in the area of radiolabeled somatostatin analogues, as clinical trials are in progress in Europe with ^{90}Y- and ^{177}Lu-labeled DOTA derivatives for the therapy of neuroendocrine tumors and other cancers (*85*). Octreotide, octreotate, and lanreotide somatostatin analogues are agonists of the somatostatin receptor, and they mimic the action of somatostatin (*86, 87*). Therefore, the binding event triggers the internalization of the ligand–receptor complex, which so far has been believed necessary for successful targeting. This

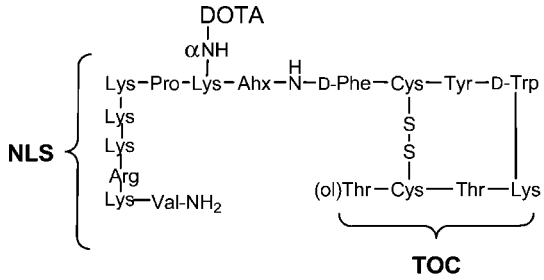

DOTA-Lys(NLS-NH_2)-TOC, **35**

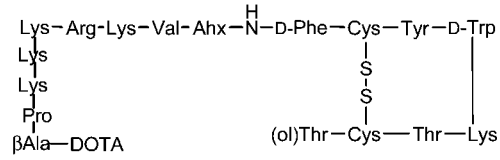

DOTA-βAla-NLS-Ahx-TOC, **36**

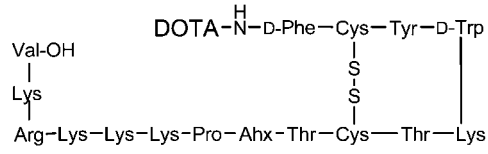

DOTA-TOC-Ahx-NLS(COOH), **37**

Figure 12. Trifunctional DOTATOC conjugates (Ahx = 6-aminohexanoic acid).

may not be the case, as it has been shown recently that ^{111}In-DOTA labeled sst3-ODN-8, [DOTA-*cyclo*(DCys-Phe-Tyr-DAgl^8(Me,2-naphthoyl)-Lys-Thr-Phe-Cys)-OH] and sst2-ANT, [DOTA-(p-NO_2-Phe)-*cyclo*(DCys-Tyr-DTrp-Lys-Thr-Cys)-DTyr-NH_2] antagonists, compounds that bind to the receptor without producing the biochemical effects of somatostatin, have significantly higher tumor uptake than the DOTA-labeled agonists (*88*). These results suggest that radiolabeled antagonists of other receptors, such as cholecystokinin, gastrin-releasing peptide, vasoactive intestinal peptide, and neurotensin receptors, could also offer higher tumor uptake and improved in vivo stability and, therefore, could be used advantageously as diagnostic and therapeutic radiopharmaceuticals (*88*).

A new generation of DOTA−somatostatin analogues capable of performing three different functions have been reported recently (*89*, *90*). They consist of a somatostatin analogue (Tyr^3-octreotide, TOC) that is capable of receptor binding and internalization in sstr-positive tissues, a heptapeptide (Pro-Lys-Lys-Lys-Arg-Lys-Val-OH) nuclear localization signal (NLS) that targets the cell nucleus and the DOTA unit that chelates the Auger emitter ^{111}In(III) (Figure 12). These conjugates were designed to enhance cellular and nuclear uptake, to have prolonged retention time in tumors and to localize in the cell nucleus to improve the efficiency of cell killing by the low-energy Auger electrons. Compounds (**35**), (**36**), and (**37**) have been synthesized by SPPS on 2-chlorotrityl chloride resin by coupling DOTA−tris(*tert*-butyl ester) to the N-terminus of the growing peptide chain with HATU in the presence of *i*Pr_2NEt. During the synthesis of (**35**), a protected fragment [Fmoc-Lys(ivDde)-Ahx-Tyr^3-octreotide] was assembled by stepwise elongation and DOTA−tris(*tert*-butyl ester) was coupled to the N-terminus after the removal of Fmoc. The ivDde was then removed with hydrazine, and the peptide synthesis was continued by branching off the Lys side chain. Alternatively, (**35**) was also synthesized following a convergent approach that involved the solution-phase coupling of Tyr^3-Lys^5(ivDde)-octreotide and an appropriately protected DOTA(t-Bu)$_3$-Lys(NLS)-Ahx-OH fragment (*90*). This mixed solid-phase−solution-phase approach did not offer any advantages, presumably because the coupling of the two large fragments was not very efficient. The location of the chelate moiety had a significant effect on the bioactivity: modification of DOTATOC at the C-terminus (compound **37**), resulting in a significant loss of binding affinity for both rat and human sstr2 receptors, but N-terminal functionalization (**35** and **36**) preserved the pharmacological activity.

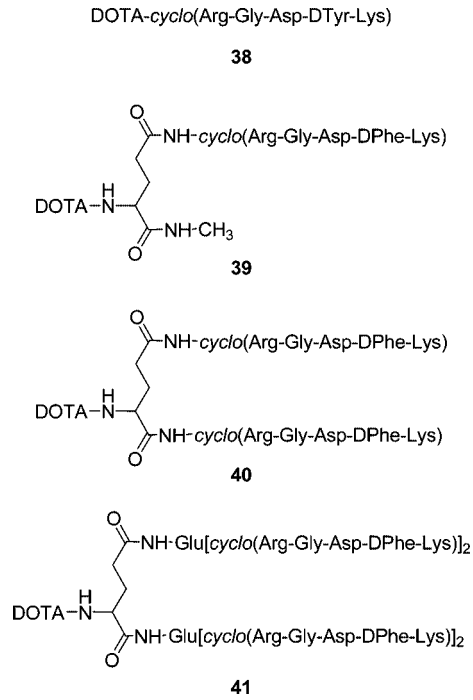

Figure 13. DOTA−RGD peptide conjugates.

Integrin receptors are a group of transmembrane proteins that participate in many vital biochemical processes including signal transduction and the interaction with the extracellular matrix. It has been shown that $\alpha_V\beta_3$ integrin plays a key role in the angiogenesis of growing solid tumors by supporting endothelial cell growth (*91*). Ligands of integrin receptors include the matrix proteins such as fibronectin, tenascin, vitronectin, and collagen, and receptor binding is mediated by a three amino acid sequence (RGD). Short peptides with RGD motif are powerful antagonists of the integrin receptors and inhibit angiogenesis and induce apoptosis by blocking the interaction with the extacellular matrix proteins (*92, 93*). Cyclic RGD peptides have higher selectivity than the linear analogues, and inclusion of D amino acids will increase the biological stability. Cyclopentapeptides like *cyclo*(Arg-Gly-Asp-DPhe-Lys) or *cyclo*(Arg-Gly-Asp-DTyr-Lys) can easily be functionalized at the Lys side chain amino group. Dimers and tetramers of *cyclo*(Arg-Gly Asp-DPhe-Lys) attached together by Glu linkers have also been synthesized (Figure 13). DOTA conjugation to the Lys side chain (**38**) or α-NH_2 of the Glu linker (**39**) was achieved in reasonable yields by using either in situ prepared DOTA−sulfo-NHS (*35*, *36*) or DOTA−tris(*tert*-butyl ester) and a coupling agent (*71*).

The in vitro binding affinity of the monomer (**39**) and dimer (**40**) for $\alpha_V\beta_3$ integrin is six and four times lower, respectively, than that of the tetramer (**41**) (19.6 nM). Tumor uptake of the ^{111}In-labeled tetramer was significantly higher than that of the monomer and dimer (*94*) probably due to multivalent interaction (*95*, *96*)

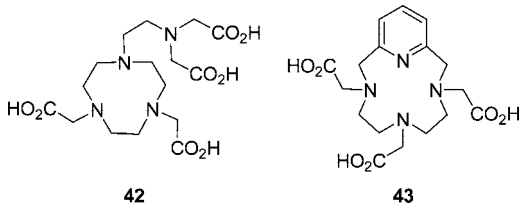

42 **43**

Figure 14. Ligands with fast complex formation kinetics.

with the receptor. The ^{90}Y-DOTA-labeled cyclopentapeptide dimer induced significant tumor growth delay in the mouse xenograft model and has potential as a therapeutic radiopharmaceutical for solid tumors (*97*).

Monomeric, dimeric, and tetrameric dendrimers of *cyclo*(Arg-Gly-Asp-DPhe-Lys) have been synthesized by click chemistry using the N-ϵ-azido derivative of the cyclopentapeptide. As expected, the ^{111}In-DOTA labeled multimeric derivatives have shown enhanced uptake in tumors overexpressing $\alpha_V\beta_3$ integrins (*98*).

The cyclic RGD peptide *cyclo*(Arg-Gly-Asp-DTyr-Lys) was also labeled with ^{64}Cu-DOTA, and microPET imaging revealed receptor-specific tumor accumulation; but the agent also had persistent activity accumulation in liver and kidneys (*35*). Inclusion of a poly(ethylene glycol) linker significantly improved the pharmacokinetics, and ^{64}Cu-DOTA-PEG-*cyclo*(Arg-Gly-Asp-DTyr-Lys) conjugate has been used to image brain and lung tumors (*12, 99, 100*).

Affibodies are small proteins that display binding surfaces similar to antibodies, and by varying the amino acids in their recognition site, affibodies targeting a specific protein can be identified by phage display. Affibodies can be synthesized by standard SPPS, and they rapidly and spontaneously fold after synthesis. They have been proposed for therapy of tumors with nonreceptor markers and imaging of receptors that do not have naturally occurring ligands (*101–104*). Recently, a HER2 receptor-specific 58 amino acid affibody modified with DOTA at the N-terminus was synthesized (*105*). The DOTA-labeled derivative binds to the HER2 cell surface receptor in the picomolar range. In vivo molecular imaging of HER2 expressing carcinomas has been demonstrated with the ^{111}In- and ^{68}Ga-labeled derivatives and the ^{90}Y/^{177}Lu-labeled conjugates showing high antigen binding capacity and cellular retention in HER2/neu expressing urinary bladder carcinoma (*68*).

Many other radiolabeled DOTA−peptide conjugates have been developed for imaging and therapeutic purposes. These have been reviewed elsewhere, and the reader is referred to several excellent recent reviews (*106–119*).

CONCLUSION AND FUTURE PROSPECTS

Due to the high thermodynamic stability and kinetic inertness of DOTA complexes, DOTA-based bifunctional chelators will continue to be the ligand of choice for labeling peptides and antibodies with ^{90}Y and radiolanthanides. Future research efforts will focus on new DOTA-like bifunctional derivatives with improved formation kinetics while retaining satisfactory kinetic inertness for biomedical applications. New approaches to site- or residue-specific labeling will be developed. Compounds (**42**−**47**) represent interesting new ideas, and although originally they have not been intended for peptide conjugation, it is easy to realize their potential for attaching DOTA-based ligands and chelates to appropriately modified peptides. Chelator (**42**) (Figure 14) has the same number of donor atoms as DOTA, but it consists of a macrocyclic triazacyclonane-diacetic acid and an acyclic iminodiacetic acid moiety connected together by an ethylene bridge. Preliminary data showed that this ligand chelated Y(III) much faster than DOTA while the ^{88}Y complex

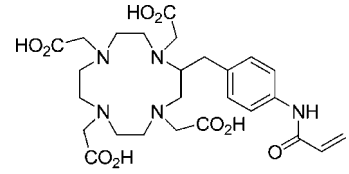

44

Figure 15. Acryloylamidobenzyl DOTA.

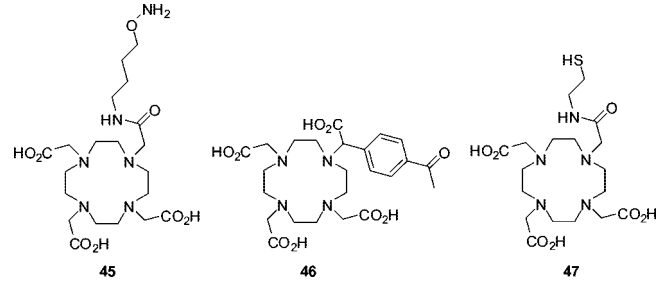

45 **46** **47**

Figure 16. Aminooxy- and mercapto-functionalized DOTA derivatives.

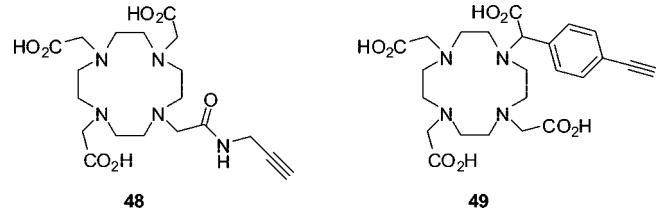

48 **49**

Figure 17. DOTA propargylamide.

appeared stable in serum for 14 days. The cooperative binding of the macrocyclic and acyclic components to the metal ion speeds up the complexation without compromising the stability of the complex (*64*). Detailed kinetic studies on the chelation properties of the ligand PCTA (**43**) (Figure 14) revealed that this interesting chelator has the fastest formation rates with Ln(III) ions among all the 9–14-membered tri- or tetraazamacrocyclic ligands (*120*). The fast formation kinetics is probably due to preorganization of the ligand by the pyridine ring, which also serves as a built-in chromophore sensitizer for luminescent lanthanides such as Eu(III) and Tb(III). The extremely long luminescent lifetimes (milliseconds) of these ions allow the separation of the lanthanide emission from the background fluorescence by time-gating imaging techniques (*121*). Thus, PCTA−peptides could be useful in the construction of in vivo optical imaging probes as well.

The yttrium complex of acryloylamido derivative (**44**) (Figure 15) represents a conceptually different approach to protein labeling. This complex binds to monoclonal antibody 2D12.5 with a K_d approximately 10^{-8} M. When a Gly residue in the proximity of the binding site is substituted for a Cys, the acryloyl group on the DOTA will form a covalent bond through a Michael-type addition, converting a weak binder into and infinite binder (*122–124*).

Ligands (**45**–**49**) (Figures 16 and 17) have functional groups that selectively react with other groups, potentially allowing chemoselective labeling at specific positions. The aminooxy functional group selectively reacts with aldehydes and ketones to form oximes, and so the aminooxy-functionalized DOTA derivative (**45**) can be used to label biomolecules through a carbonyl group (*125*). Alternatively, a DOTA derivative with a ketone functional group (**46**) has been reported to label aminooxy-modified peptides (*126*). Although (**46**) maintains all four acetate arms for metal complexation, conjugation results

in the formation of enantiomeric mixtures. Peptides with dehydroalaninyl residues, formed by base-catalyzed β-elimination of the phosphate group from the corresponding phosphorylated serine analogues, react with DOTA mercaptoethyl amide (**47**) in a Michael addition (*127*).

DOTA propargylamide (**48**) (Figure 17) and its *tert*-butyl ester have recently been reported (*128*) to specifically label azidophenylalaline residues in a Cu(I) catalyzed [3 + 2] cycloaddition ("click chemistry") (*129*). In a similar concept, an alkyne-functionalized DOTA derivative (**49**) with the four acetate arms was reported and applied to label azido-modified peptides (*126*). However, the "click chemistry" involved in these couplings has two disadvantages: first, a Cu(I) catalyst is required, which in turn complicates the purification of the final product due to the complexation of this metal by DOTA; second, the cycloaddition between the alkyne and azide can lead to the formation of two triazol isomers.

Finally, we believe that the trend of designing and synthesizing DOTA conjugates of more complex structures such as multimers, multifunctional constructs, protein fragments, and nanoparticles will continue, eventually leading to the creation of more efficient diagnostic and therapeutic agents.

LITERATURE CITED

(1) Smith, G. P., and Petrenko, V. A. (1997) Phage display. *Chem. Rev. 97*, 391–410.

(2) Lewis, M. R., Zhang, J., Jia, F., Owen, N. K., Cutler, C. S., Embree, M. F., Schultz, J., Theodore, L. J., Ketring, A. R., Jurisson, S. S., and Axworthy, D. B. (2004) Biological comparison of ^{149}Pm-, ^{166}Ho-, and ^{177}Lu-DOTA-biotin pretargeted by CC49 scFv-streptavidin fusion protein in xenograft-bearing nude mice. *Nucl. Med. Biol. 31*, 213–223.

(3) Woods, M., Kovacs, Z., Kiraly, R., Brücher, E., Zhang, S., and Sherry, A. D. (2004) Solution dynamics and stability of lanthanide(III) (S)-2-(p-nitrobenzyl)DOTA complexes. *Inorg. Chem. 43*, 2845–2851.

(4) Duncan, J. R., Franano, F. N., Edward, W. B., and Welch, M. J. E. (1994) Evidence of gadolinium dissociation from protein-DTPA-gadolinium complexes. *Invest. Radiol. 29*, S58–S61.

(5) Sarka, L., Burai, L., and Brücher, E. (2000) The rates of the exchange reactions between [Gd (DTPA)]$^{2-}$ and the endogenous ions Cu^{2+} and Zn^{2+}: a kinetic model for the prediction of the in vivo stability of [Gd (DTPA)]$^{2-}$, used as a contrast agent in magnetic resonance imaging. *Chem.—Eur. J. 6*, 719–724.

(6) Bousquet, J. C., Saini, S., Stark, D. D., Hahn, P. F., Nigam, M., Wittenberg, J., and Ferrucci, J. T., Jr. (1988) Gd-DOTA: characterization of a new paramagnetic complex. *Radiology 166*, 693–698.

(7) Weinmann, H. J., Laniado, M., and Mützel, W. (1984) Pharmacokinetics of gadolinium-DTPA/dimeglumine after intravenous injection into healthy volunteers. *Physiol. Chem. Phys. Med. NMR 16*, 167–172.

(8) Zangos, S., Hammerstingl, R., Mack, M. G., Straub, R., Engelmann, K., Eichler, K., Balzer, T., and Vogl, T. J. (2001) Renal enhancement and excretion of the hepatobiliary contrast agent Gd-EOB-DTPA. *Rofo-Fortschr. Röntg. 173*, 1034–1040.

(9) Cremonesi, M., Ferrari, M., Bodei, L., Tosi, G., and Paganelli, G. (2006) Dosimetry in peptide radionuclide receptor therapy: a review. *J. Nucl. Med. 47*, 1467–1475.

(10) Liu, S., and Edwards, D. S. (2001) Bifunctional chelators for therapeutic lanthanide radiopharmaceuticals. *Bioconjugate Chem. 12*, 7–34.

(11) Parry, J. J., Kelly, T. S., Andrews, R., and Rogers, B. E. (2007) In vitro and in vivo evaluation of ^{64}Cu-labeled DOTA-linker-bombesin(7–14) analogues containing different amino acid linker moieties. *Bioconjugate Chem. 18*, 1110–1117.

(12) Dijkgraaf, I., Liu, S., Kruijtzer, J. A. W., Soede, A. C., Oyen, W. J. G., Liskamp, R. M. J., Corstens, F. H. M., and Boerman, O. C. (2007) Effects of linker variation on the in vitro and in vivo characteristics of an ^{111}In-labeled RGD peptide. *Nucl. Med. Biol. 34*, 29–35.

(13) Li, L., Yazaki, P. J., Anderson, A.-L., Crow, D., Colcher, D., Wu, A. M., Williams, L. E., Wong, J. Y. C., Raubitschek, A., and Shively, J. E. (2006) Improved biodistribution and radioimmunoimaging with poly(ethylene glycol)-DOTA-conjugated anti-CEA diabody. *Bioconjugate Chem. 17*, 68–76.

(14) Kumaresan, P. R., Natarajan, A., Song, A., Wang, X., Liu, R., DeNardo, G., DeNardo, S., and Lam, K. S. (2007) Development of tissue plasminogen activator specific "on demand cleavable" (ODC) linkers for radioimmunotherapy by screening one-bead-one-compound combinatorial peptide libraries. *Bioconjugate Chem. 18*, 175–182.

(15) Deshpande, S. V., DeNardo, S. J., Kukis, D. L., Moi, M. K., McCall, M. J., DeNardo, G. L., and Meares, C. F. (1990) Yttrium-90-labeled monoclonal antibody for therapy: labeling by a new macrocyclic bifunctional chelating agent. *J. Nucl. Med. 31*, 473–479.

(16) Renn, O., and Meares, C. F. (1992) Large-scale synthesis of the bifunctional chelating agent 2-(p-nitrobenzyl)-1,4,7,10-tetraazacyclododecane-N,N′,N″,N‴-tetraacetic acid, and the determination of its enantiomeric purity by chiral chromatography. *Bioconjugate Chem. 3*, 563–569.

(17) McMurry, T. J., Brechbiel, M., Kumar, K., and Gansow, O. A. (1992) Convenient synthesis of bifunctional tetraaza macrocycles. *Bioconjugate Chem. 3*, 108–117.

(18) Cooper, M. S., Sabbah, E., and Mather, S. J. (2006) Conjugation of chelating agents to proteins and radiolabeling with trivalent metallic isotopes. *Nat. Protoc. 1*, 314–317.

(19) Chappell, L. L., Ma, D., Milenic, D. E., Garmestani, K., Venditto, V., Beitzel, M. P., and Brechbiel, M. W. (2003) Synthesis and evaluation of novel bifunctional chelating agents based on 1,4,7,10-tetraazacyclododecane-N,N′,N″,N‴-tetraacetic acid for radiolabeling proteins. *Nucl. Med. Biol. 30*, 581–595.

(20) Chappell, L. L., Rogers, B. E., Khazaeli, M. B., Mayo, M. S., Buchsbaum, D. J., and Brechbiel, M. W. (1999) Improved synthesis of the bifunctional chelating agent 1,4,7,10-tetraaza-N-(1-carboxy-3-(4-nitrophenyl)propyl)-N′,N″,N-tris(acetic acid) cyclododecane (PA-DOTA). *Bioorg. Med. Chem. 7*, 2313–2320.

(21) Cheng, R. C., Fordyce, W. A., Goeckeler, W. F., Kruper, W. J., Baughman, S., Garlich, J. R., Kiefer, G. E., McMillan, K., Simon, J., Wilson, D. A., and Frank, R. K. (1989) Tetraazacyclododecane macrocyclic bifunctional chelants, complexes thereof and their antibody conjugates. WO Patent No. 8912631.

(22) Sieving, P. F., Watson, A. D., and Rocklage, S. M. (1990) Preparation and characterization of paramagnetic polychelates and their protein conjugates. *Bioconjugate Chem. 1*, 65–71.

(23) Lewis, M. R., Raubitschek, A., and Shively, J. E. (1994) A facile, water-soluble method for modification of proteins with DOTA. Use of elevated temperature and optimized pH to achieve high specific activity and high chelate stability in radiolabeled immunoconjugates. *Bioconjugate Chem. 5*, 565–576.

(24) Lewis, M. R., Kao, J. Y., Anderson, A.-L., Shively, J. E., and Raubitschek, A. (2001) An improved method for conjugating monoclonal antibodies with N-hydroxysulfosuccinimidyl DOTA. *Bioconjugate Chem. 12*, 320–324.

(25) Kovacs, Z., Mudigonda, D. S., and Sherry, A. D. (2005) Preparation of cyclic tertiary amine chelating agents for labeling biomolecules using preformed active esters. US Patent No. 6838557.

(26) Mohsin, H., Fitzsimmons, J., Shelton, T., Hoffman, T. J., Cutler, C. S., Lewis, M. R., Athey, P. S., Gulyas, G., Kiefer, G. E., Frank, R. K., Simon, J., Lever, S. Z., and Jurisson, S. S. (2007) Preparation and biological evaluation of ^{111}In-, ^{177}Lu- and ^{90}Y-labeled DOTA analogues conjugated to B72.3. *Nucl. Med. Biol. 34*, 493–502.

(27) Lu, S. X., Takach, E. J., Solomon, M., Zhu, Q., Law, S.-J., and Hsieh, F. Y. (2005) Mass spectral analyses of labile DOTA-NHS and heterogeneity determination of DOTA or DM1 conjugated anti-PSMA antibody for prostate cancer therapy. *J. Pharm. Sci. 94*, 788–797.

(28) Mier, W., Hoffend, J., Krämer, S., Schuhmacher, J., Hull, W. E., Eisenhut, M., and Haberkorn, U. (2005) Conjugation of DOTA using isolated phenolic active esters: the labeling and biodistribution of albumin as blood pool marker. *Bioconjugate Chem. 16*, 237–240.

(29) Mukai, T., Namba, S., Arano, Y., Ono, M., Fujioka, Y., Uehara, T., Ogawa, K., Konishi, J., and Saji, H. (2002) Synthesis and evaluation of a monoreactive DOTA derivative for indium-111-based residualizing label to estimate protein pharmacokinetics. *J. Pharm. Pharmacol. 54*, 1073–1081.

(30) Lewis, M. R., and Shively, J. E. (1998) Maleimidocysteineamido-DOTA derivatives: new reagents for radiometal chelate conjugation to antibody sulfhydryl groups undergo pH-dependent cleavage reactions. *Bioconjugate Chem. 9*, 72–86.

(31) Li, L., Tsai, S.-W., Anderson, A.-L., Keire, D. A., Raubitschek, A. A., and Shively, J. E. (2002) Vinyl sulfone bifunctional derivatives of DOTA allow sulfhydryl- or amino-directed coupling to antibodies. Conjugates retain immunoreactivity and have similar biodistributions. *Bioconjugate Chem. 13*, 110–115.

(32) Gali, H., Sieckman, G. L., Hoffman, T. J., Owen, N. K., Chin, D. T., Forte, L. R., and Volkert, W. A. (2001) In vivo evaluation of an ^{111}In-labeled ST-peptide analog for specific-targeting of human colon cancers. *Nucl. Med. Biol. 28*, 903–909.

(33) Albert, R., Smith-Jones, P., Stolz, B., Simeon, C., Knecht, H., Bruns, C., and Pless, J. (1998) Direct synthesis of [DOTA-DPhe^1]-octreotide and [DOTA-DPhe1,Tyr^3]-octreotide (SMT487): two conjugates for systemic delivery of radiotherapeutical nuclides to somatostatin receptor positive tumors in man. *Bioorg. Med. Chem. Lett. 8*, 1207–1210.

(34) Schottelius, M., Schwaiger, M., and Wester, H.-J. (2003) Rapid and high-yield solution-phase synthesis of DOTA-Tyr^3-octreotide and DOTA-Tyr^3-octreotate using unprotected DOTA. *Tetrahedron Lett. 44*, 2393–2396.

(35) Chen, X., Park, R., Tohme, M., Shahinian, A. H., Bading, J. R., and Conti, P. S. (2004) MicroPET and autoradiographic imaging of breast cancer α_v-integrin expression using ^{18}F- and ^{64}Cu-labeled RGD peptide. *Bioconjugate Chem. 15*, 41–49.

(36) Wu, Y., Zhang, X., Xiong, Z., Cheng, Z., Fisher, D. R., Liu, S., Gambhir, S. S., and Chen, X. (2005) microPET imaging of glioma integrin $\alpha_v\beta_3$ expression using ^{64}Cu-labeled tetrameric RGD peptide. *J. Nucl. Med. 46*, 1707–1718.

(37) Yoo, B., and Pagel, M. (2006) A facile synthesis of α-amino-DOTA as a versatile molecular imaging probe. *Tetrahedron Lett. 47*, 7327–7330.

(38) Heppeler, A., Froidevaux, S., Mäcke, H. R., Jermann, E., Béhé, M., Powell, P., and Hennig, M. (1999) Radiometal-labelled macrocyclic chelator-derivatized somatostatin analogue with superb tumour-targeting properties and potential for receptor-mediated internal radiotherapy. *Chem.—Eur. J. 5*, 1974–1981.

(39) Rosseto, R., and Hajdu, J. (2005) A rapid and efficient method for migration-free acylation of lysophospholipids: synthesis of phosphatidylcholines with sn-2-chain-terminal reporter groups. *Tetrahedron Lett. 46*, 2941–2944.

(40) Wängler, B., Beck, C., Wagner-Utermann, U., Schirrmacher, E., Bauer, C., Rösch, F., Schirrmacher, R., and Eisenhut, M. (2006) Application of tris-allyl-DOTA in the preparation of DOTA-peptide conjugates. *Tetrahedron Lett. 47*, 5985–5988.

(41) Jaakkola, L., Ylikoski, A., and Hovinen, J. (2006) Simple synthesis of a building block for solid-phase labeling of oligonucleotides with 1,4,7,10-tetraazacyclododecane-1,4,7,10-tetraacetic acid (DOTA). *Bioconjugate Chem. 17*, 1105–1107.

(42) Anelli, P. L., Lattuada, L., Gabellini, M., and Recanati, P. (2001) DOTA tris(phenylmethyl) ester: a new useful synthon for the synthesis of DOTA monoamides containing acid-labile bonds. *Bioconjugate Chem. 12*, 1081–1084.

(43) Hsieh, H. P., Wu, Y. T., Chen, S. T., and Wang, K. T. (1999) Direct solid-phase synthesis of octreotide conjugates: precursors for use as tumor-targeted radiopharmaceuticals. *Bioorg. Med. Chem. 7*, 1797–1803.

(44) Eisenwiener, K. P., Powell, P., and Mäcke, H. R. (2000) A convenient synthesis of novel bifunctional prochelators for coupling to bioactive peptides for radiometal labelling. *Bioorg. Med. Chem. Lett. 10*, 2133–2135.

(45) Mäcke, H. R., Eisenwiener, K., and Powell, P. (2002) Prochelators for the preparation of radiometal labeled molecules having improved biological properties. PCT Int. Appl. WO Patent No. 2002024235.

(46) Amedio, J. C., Caravan, P. D., Jacques, V., Zhou, K. L., Levy, S., Kalageropoulos, S., and Greenfield, M. (2005). Preparation of optically pure and enriched isomers of DOTA-type chelating ligands, and contrast agents. PCT Int. App. WO Patent No. 2005001415.

(47) Bhorade, R., Weissleder, R., Nakakoshi, T., Moore, A., and Tung, C. H. (2000) Macrocyclic chelators with paramagnetic cations are internalized into mammalian cells via a HIV-tat derived membrane translocation peptide. *Bioconjugate Chem. 11*, 301–305.

(48) Prantner, A. M., Sharma, V., Garbow, J. R., and Piwnica-Worms, D. (2003) Synthesis and characterization of a Gd-DOTA-D-permeation peptide for magnetic resonance relaxation enhancement of intracellular targets. *Mol. Imaging 2* 333–341.

(49) Mier, W., Graham, K. A. N., Wang, Q., Krämer, S., Hoffend, J., Eisenhut, M., and Haberkorn, U. (2004) Synthesis of peptide conjugated chelator oligomers for endoradiotherapy and MRT imaging. *Tetrahedron Lett. 45*, 5453–5455.

(50) Graham, K. A. N., Wang, Q., Eisenhut, M., Haberkorn, U., and Mier, W. (2002) A general method for functionalising both the C- and N-terminals of Tyr^3-octreotate. *Tetrahedron Lett. 43*, 5021–5024.

(51) De León-Rodríguez, L. M., Kovacs, Z., and Sherry, A. D. (2005) Chemistry for DOTA peptide labeling at phenylalanine residues: on the road to preparing peptide ligand tagged libraries. *Lett. Org. Chem. 2*, 160–164.

(52) De León-Rodríguez, L. M., Kovacs, Z., Dieckmann, G. R., and Sherry, A. D. (2004) Solid-phase synthesis of DOTA-peptides. *Chem.—Eur. J. 10*, 1149–1155.

(53) Gallazzi, F., Wang, Y., Jia, F., Shenoy, N., Landon, L. A., Hannink, M., Lever, S. Z., and Lewis, M. R. (2003) Synthesis of radiometal-labeled and fluorescent cell-permeating peptide-PNA conjugates for targeting the bcl-2 proto-oncogene. *Bioconjugate Chem. 14*, 1083–1095.

(54) Sosabowski, J. K., and Mather, S. J. (2006) Conjugation of DOTA-like chelating agents to peptides and radiolabeling with trivalent metallic isotopes. *Nat. Protoc. 1*, 972–976.

(55) Peterson, J. J., Pak, R. H., and Meares, C. F. (1999) Total solid-phase synthesis of 1,4,7,10-tetraazacyclododecane-N,N′,N″,N‴-tetraacetic acid-functionalized peptides for radioimmunotherapy. *Bioconjugate Chem. 10*, 316–320.

(56) Yoo, B., and Pagel, M. D. (2007) Peptidyl molecular imaging contrast agents using a new solid-phase peptide synthesis approach. *Bioconjugate Chem. 18*, 903–911.

(57) Benetollo, F., Bombieri, G., Calabi, L., Aime, S., and Botta, M. (2003) Structural variations across the lanthanide series of macrocyclic DOTA complexes: insights into the design of contrast agents for magnetic resonance imaging. *Inorg. Chem. 42*, 148–157.

(58) Chang, C. A., Francesconi, L. C., Malley, M. F., Kumar, K., Gougoutas, J. Z., Tweedle, M. F., Lee, D. W., and Wilson, L. J. (1993) Synthesis, characterization, and crystal structures of M(DO3A) (M = Fe, Gd) and Na[M(DOTA)] (M = Fe, Y, Gd). *Inorg. Chem. 32*, 3501–3508.

(59) Meyer, M., Dahaoui-Gindrey, V., Lecomte, C., and Guilard, R. (1998) Conformations and coordination schemes of carboxylate and carbamoyl derivatives of the tetraazamacrocycles cyclen and cyclam, and the relation to their protonation states. *Coord. Chem. Rev. 178–180*, 1313–1405.

(60) Howard, J. A. K., Kenwright, A. M., Moloney, J. M., Parker, D., Woods, M., Port, M., Navet, M., and Rousseau, O. (1998) Structure and dynamics of all of the stereoisomers of europium complexes of tetra(carboxyethyl) derivatives of dota: ring inversion is decoupled from cooperative arm rotation in the RRRR and RRRS isomers. *Chem. Commun. 13*, 1381–1382.

(61) Woods, M., Kovacs, Z., Zhang, S., and Sherry, A. D. (2003) Towards the rational design of magnetic resonance imaging contrast agents: isolation of the two coordination isomers of lanthanide DOTA-type complexes. *Angew. Chem., Int. Ed. 42*, 5889–5892.

(62) Liu, S., He, Z., Hsieh, W.-Y., and Fanwick, P. E. (2003) Synthesis, characterization, and X-ray crystal structure of In-(DOTA-AA) (AA = p-aminoanilide): a model for ^{111}In-labeled DOTA-biomolecule conjugates. *Inorg. Chem. 42*, 8831–8837.

(63) Szilágyi, E., Tóth, E., Kovács, Z., Platzek, J., Radüchel, B., and Brücher, E. (2000) Equilibria and formation kinetics of some cyclen derivative complexes of lanthanides. *Inorg. Chim. Acta 298*, 226–234.

(64) Chong, H.-S., Garmestani, K., Ma, D., Milenic, D. E., Overstreet, T., and Brechbiel, M. W. (2002) Synthesis and biological evaluation of novel macrocyclic ligands with pendent donor groups as potential yttrium chelators for radioimmunotherapy with improved complex formation kinetics. *J. Med. Chem. 45*, 3458–3464.

(65) Breeman, W. A. P., de Blois, E., Bakker, W. H., and Krenning, E. P. (2006) *Radionuclide Peptide Cancer Therapy*, (Chinol, M., and Paganelli, G., Eds.) pp 119–125, Taylor & Francis, New York.

(66) Wild, D., Schmitt, J. S., Ginj, M., Mäcke, H. R., Bernard, B. F., Krenning, E., De Jong, M., Wenger, S., and Reubi, J.-C. (2003) DOTA-NOC, a high-affinity ligand of somatostatin receptor subtypes 2, 3 and 5 for labelling with various radiometals. *Eur. J. Nucl. Med. Mol. Imaging 30*, 1338–1347.

(67) Laznicek, M., Laznickova, A., Mäcke, H. R., Eisenwiener, K., Reubi, J.-C., and Wenger, S. (2002) Octreotide and octreotate derivatives radiolabeled with yttrium: pharmacokinetics in rats. *Cancer Biother. Radiopharm. 17*, 527–533.

(68) Fortin, M.-A., Orlova, A., Malmström, P. U., and Tolmachev, V. (2007) Labelling chemistry and characterization of [^{90}Y/^{177}Lu]-DOTA-ZHER2:342–3 affibody molecule, a candidate agent for locoregional treatment of urinary bladder carcinoma. *Int. J. Mol. Med. 19*, 285–291.

(69) Park, S. H., Gwon, H. J., and Jang, S. H. (2007) Microwave-assisted rapid synthesis of ^{166}Ho-1,4,7,10-tetraazacyclododecane-N,N′,N″,N‴-tetraacetic acid: a bifunctional chelating agent for radiopharmaceuticals. *Asian J. Chem. 19*, 391–395.

(70) Giblin, M. F., Sieckman, G. L., Shelton, T. D., Hoffman, T. J., Forte, L. R., and Volkert, W. A. (2006) In vitro and in vivo evaluation of ^{177}Lu- and ^{90}Y-labeled E. coli heat-stable enterotoxin for specific targeting of uroguanylin receptors on human colon cancers. *Nucl. Med. Biol. 33*, 481–488.

(71) Liu, S., Cheung, E., Ziegler, M. C., Rajopadhye, M., and Edwards, D. S. (2001) ^{90}Y and ^{177}Lu labeling of a DOTA-conjugated vitronectin receptor antagonist useful for tumor therapy. *Bioconjugate Chem. 12*, 559–568.

(72) Breeman, W. A. P., de Jong, M., Visser, T. J., Erion, J. L., and Krenning, E. P. (2003) Optimizing conditions for radiolabeling of DOTA-peptides with ^{90}Y, ^{111}In and ^{177}Lu at high specific activities. *Eur. J. Nucl. Med. Mol. Imaging 30*, 917–920.

(73) Stimmel, J. B., and Kull, F. C., Jr. (1998) Samarium-153 and lutetium-177 chelation properties of selected macrocyclic and acyclic ligands. *Nucl. Med. Biol. 25*, 117–125.

(74) Stimmel, J. B., Stockstill, M. E., and Kull, F. C., Jr. (1995) Yttrium-90 chelation properties of tetraazatetraacetic acid macrocycles, diethylenetriaminepentaacetic acid analogues, and a novel terpyridine acyclic chelator. *Bioconjugate Chem. 6*, 219–225.

(75) Liu, S., and Edwards, D. S. (2001) Stabilization of ^{90}Y-labeled DOTA-biomolecule conjugates using gentisic acid and ascorbic acid. *Bioconjugate Chem. 12*, 554–558.

(76) Nitz, M., Sherawat, M., Franz, K. J., Peisach, E., Allen, K. N., and Imperiali, B. (2004) Structural origin of the high affinity of a chemically evolved lanthanide-binding peptide. *Angew. Chem., Int. Ed. 43*, 3682–3685.

(77) Su, X.-C., Huber, T., Dixon, N. E., and Otting, G. (2006) Site-specific labeling of proteins with a rigid lanthanide-binding tag. *ChemBioChem 7*, 1599–1604.

(78) Nunn, A. D., Linder, K. E., and Tweedle, M. F. (1997) Can receptors be imaged with MRI agents? *Q. J. Nucl. Med. 41*, 155–162.

(79) Caravan, P., Ellison, J. J., McMurry, T. J., and Lauffer, R. B. (1999) Gadolinium(III) chelates as MRI contrast agents: structure, dynamics, and applications. *Chem. Rev. 99*, 2293–2352.

(80) De León-Rodríguez, L. M., Ortiz, A., Weiner, A. L., Zhang, S., Kovacs, Z., Kodadek, T., and Sherry, A. D. (2002) Magnetic resonance imaging detects a specific peptide-protein binding event. *J. Am. Chem. Soc. 124*, 3514–3515.

(81) Han, Y., and Kodadek, T. (2000) Peptides selected to bind the Gal80 repressor are potent transcriptional activation domains in yeast. *J. Biol. Chem. 275*, 14979–14984.

(82) Meade, T. J., and Allen, M. J. (2004) Functional MRI agents for cancer imaging. PCT Int. App. WO Patent No. 2004037210.

(83) Bull, S. R., Guler, M. O., Bras, R. E., Venkatasubramanian, P. N., Stupp, S. I., and Meade, T. J. (2005) Magnetic resonance imaging of self-assembled biomaterial scaffolds. *Bioconjugate Chem. 16*, 1343–1348.

(84) Allen, M. J., MacRenaris, K. W., Venkatasubramanian, P. N., and Meade, T. J. (2004) Cellular delivery of MRI contrast agents. *Chem. Biol. 11*, 301–307.

(85) Chinol, M., and Paganelli, M., Eds. (2006) *Radionuclide Peptide Cancer Therapy*, Taylor & Francis, New York.

(86) Dasgupta, P. (2004) Somatostatin analogues: multiple roles in cellular proliferation, neoplasia, and angiogenesis. *Pharmacol. Ther. 102*, 61–85.

(87) Janecka, A., Zubrzycka, M., and Janecki, T. (2001) Somatostatin analogs. *J. Pept. Res. 58*, 91–107.

(88) Ginj, M., Zhang, H., Waser, B., Cescato, R., Wild, D., Wang, X., Erchegyi, J., Rivier, J., Mäcke, H. R., and Reubi, J. C. (2006) Radiolabeled somatostatin receptor antagonists are preferable to agonists for in vivo peptide receptor targeting of tumors. *Proc. Natl. Acad. Sci. U.S.A. 103*, 16436–16441.

(89) Ginj, M., Hinni, K., Tschumi, S., Schulz, S., and Maecke, H. R. (2005) Trifunctional somatostatin-based derivatives designed for targeted radiotherapy using auger electron emitters. *J. Nucl. Med. 46*, 2097–2103.

(90) Ginj, M., and Maecke, H. R. (2005) Synthesis of trifunctional somatostatin based derivatives for improved cellular and subcellular uptake. *Tetrahedron Lett. 46*, 2821–2824.

(91) Tucker, G. C. (2006) Integrins: molecular targets in cancer therapy. *Curr. Oncol. Rep. 8*, 96–103.

(92) Tucker, G. C. (2003) α_V integrin inhibitors and cancer therapy. *Curr. Opin. Invest. Drugs 4*, 722–731.

(93) Meyer, A., Auernheimer, J., Modlinger, A., and Kessler, H. (2006) Targeting RGD recognizing integrins: drug development, biomaterial research, tumor imaging and targeting. *Curr. Pharm. Des. 12*, 2723–2747.

(94) Dijkgraaf, I., Kruijtzer, J. A. W., Liu, S., Soede, A. C., Oyen, W. J. G, Corstens, F. H. M., Liskamp, R. M. J., and Boerman, O. C. (2007) Improved targeting of the $\alpha_V\beta_3$ integrin by multimerisation of RGD peptides. *Eur. J. Nucl. Med. Mol. Imaging 34*, 267–273.

(95) Kiessling, L. L., Gestwicki, J. E., and Strong, L. E. (2006) Synthetic multivalent ligands as probes of signal transduction. *Angew. Chem., Int. Ed. 45*, 2348–2368.

(96) Mammen, M., Chio, S.-K., and Whitesides, G. M. (1998) Polyvalent interactions in biological systems: implications for design and use of multivalent ligands and inhibitors. *Angew. Chem., Int. Ed. 37*, 2755–2794.

(97) Janssen, M. L., Oyen, W. J., Dijkgraaf, I., Massuger, L. F., Frielink, C., Edwards, D. S., Rajopadhye, M., Boonstra, H.,

Corstens, F. H., and Boerman, O. C. (2002) Tumor targeting with radiolabeled $\alpha_V\beta_3$ integrin binding peptides in a nude mouse model. *Cancer Res. 62*, 6146–6151.
(98) Dijkgraaf, I., Rijnders, A. Y., Soede, A., Dechesne, A. C., Van Esse, G. W., Brouwer, A. J., Corstens, F. H. M., Boerman, O. C., Rijkers, D. T. S., and Liskamp, R. M. J. (2007) Synthesis of DOTA-conjugated multivalent cyclic-RGD peptide dendrimers via 1,3-dipolar cycloaddition and their biological evaluation: implications for tumor targeting and tumor imaging purposes. *Org. Biomol. Chem. 5*, 935–944.
(99) Chen, X., Hou, Y., Tohme, M., Park, R., Khankaldyyan, V., Gonzales-Gomez, I., Bading, J. R., Laug, W. E., and Conti, P. S. (2004) Pegylated Arg-Gly-Asp peptide: ^{64}Cu labeling and PET imaging of brain tumor $\alpha_V\beta_3$-integrin expression. *J. Nucl. Med. 45*, 1776–1783.
(100) Chen, X., Sievers, E., Hou, Y., Park, R., Tohme, M., Bart, R., Bremner, R., Bading, J. R., and Conti, P. S. (2005) Integrin $\alpha_V\beta_3$-targeted imaging of lung cancer. *Neoplasia 7*, 271–279.
(101) Nilsson, F. Y., and Tolmachev, V. (2007) Affibody molecules: new protein domains for molecular imaging and targeted tumor therapy. *Curr. Opin. Drug Discovery Dev. 10*, 167–175.
(102) Tolmachev, V., Orlova, A., Nilsson, F. Y., Feldwisch, J., Wennborg, A., and Abrahmsen, L. (2007) Affibody molecules: potential for in vivo imaging of molecular targets for cancer therapy. *Exp. Opin. Biol. Ther. 7*, 555–568.
(103) Tolmachev, V., Orlova, A., Pehrson, R., Galli, J., Baastrup, B., Andersson, K., Sandström, M., Rosik, D., Carlsson, J., Lundqvist, H., Wennborg, A., and Nilsson, F. Y. (2007) Radionuclide therapy of HER2-positive microxenografts using a ^{177}Lu-labeled HER2-specific affibody molecule. *Cancer Res. 67*, 2773–2782.
(104) Tran, T., Engfeldt, T., Orlova, A., Widström, C., Bruskin, A., Tolmachev, V., and Karlström, A. E. (2007) In vivo evaluation of cysteine-based chelators for attachment of ^{99m}Tc to tumor-targeting affibody molecules. *Bioconjugate Chem. 18*, 549–558.
(105) Orlova, A., Tolmachev, V., Pehrson, R., Lindborg, M., Tran, T., Sandström, M., Nilsson, F. Y., Wennborg, A., Abrahmsén, L., and Feldwisch, J. (2007) Synthetic affibody molecules: a novel class of affinity ligands for molecular imaging of HER2-expressing malignant tumors. *Cancer Res. 67*, 2178–2186.
(106) Wängler, C., Buchmann, I., Eisenhut, M., Haberkorn, U., and Mier, W. (2007) Radiolabeled peptides and proteins in cancer therapy. *Protein Pept. Lett. 14*, 273–279.
(107) Breeman, W. A., Kwekkeboom, D. J., de Blois, E., de Jong, M., Visser, T. J., and Krenning, E. P. (2007) Radiolabelled regulatory peptides for imaging and therapy. *Anti-cancer Agents Med. Chem. 7*, 345–357.
(108) Reubi, J. C., Mäcke, H. R., and Krenning, E. P. (2005) Candidates for peptide receptor radiotherapy today and in the future. *J. Nucl. Med. 46, Suppl. 1* 67S–75S.
(109) Milenic, D. E., Brady, E. D., and Brechbiel, M. W. (2004) Antibody-targeted radiation cancer therapy. *Nat. Rev. Drug Discovery 3*, 488–499.
(110) Liu, S., Robinson, S. P., and Edwards, D. S. (2005) Radiolabeled integrin $\alpha_v\beta_3$ antagonists as radiopharmaceuticals for tumor radiotherapy. *Top. Curr. Chem. 252* (Contrast Agents III), 193–216.
(111) de Jong, M., Kwekkeboom, D., Valkema, R., and Krenning, E. P. (2003) Radiolabelled peptides for tumour therapy: current status and future directions. Plenary lecture at the EANM 2002. *Eur. J. Nucl. Med. Mol. Imaging 30*, 463–469.
(112) Heppeler, A., Froidevaux, S., Eberle, A. N., and Maecke, H. R. (2000) Receptor targeting for tumor localisation and therapy with radiopeptides. *Curr. Med. Chem. 7*, 971–994.
(113) Weiner, R. E., and Thakur, M. L. (2006) Developments of radiolabeled peptides. *Radionuclide Peptide Cancer Therapy*, (Chinol, M., and Paganelli, M., Eds.) pp 41–85, Taylor & Francis, New York.
(114) Weiner, R. E., and Thakur, M. L. (2005) Radiolabeled peptides in oncology: role in diagnosis and treatment. *BioDrugs 19*, 145–163.
(115) Smith, C. J., Volkert, W. A., and Hoffman, T. J. (2005) Radiolabeled peptide conjugates for targeting of the bombesin receptor superfamily subtypes. *Nucl. Med. Biol. 32*, 733–740.
(116) Aloj, L., and Morelli, G. (2004) Design, synthesis and preclinical evaluation of radiolabeled peptides for diagnosis and therapy. *Curr. Pharm. Des. 10*, 3009–3031.
(117) Smith, C. J., Volkert, W. A., and Hoffman, T. J. (2003) Gastrin releasing peptide (GRP) receptor targeted radiopharmaceuticals: a concise update. *Nucl. Med. Biol. 30*, 861–868.
(118) Fichna, J., and Janecka, A. (2003) Synthesis of target-specific radiolabeled peptides for diagnostic imaging. *Bioconjugate Chem. 14*, 3–17.
(119) Hoffman, T. J., Quinn, T. P., and Volkert, W. A. (2001) Radiometallated receptor-avid peptide conjugates for specific in vivo targeting of cancer cells. *Nucl. Med. Biol. 28*, 527–539.
(120) Tircso, G., Kovacs, Z., and Sherry, A. D. (2006) Equilibrium and formation/dissociation kinetics of some Ln(III)PCTA complexes. *Inorg. Chem. 45*, 9269–9280.
(121) Faulkner, S., Pope, S. J. A., and Burton-Pye, B. P. (2005) Lanthanide complexes for luminescence imaging applications. *Appl. Spectrosc. Rev. 40*, 1–31.
(122) Butlin, N. G., and Meares, C. F. (2006) Antibodies with infinite affinity: origins and applications. *Acc. Chem. Res. 39*, 780–787.
(123) Corneillie, T. M., Whetstone, P. A., and Meares, C. F. (2006) Irreversibly binding anti-metal chelate antibodies: Artificial receptors for pretargeting. *J. Inorg. Biochem. 100*, 882–890.
(124) Corneillie, T. M., Lee, K. C., Whetstone, P. A., Wong, J. P., and Meares, C. F. (2004) Irreversible engineering of the multielement-binding antibody 2D12.5 and its complementary ligands. *Bioconjugate Chem. 15*, 1392–1402.
(125) Hovinen, J. (2006) Synthesis of aminooxy-functionalized lanthanide(III) chelates for carbonyl-group conjugation. *Chem. Biodivers. 3*, 296–303.
(126) Knör, S., Modlinger, A., Poethko, T., Schottelius, M., Wester, H.-J., and Kessler, H. (2007) Synthesis of novel 1,4,7,10-tetraazacyclodecane-1,4,7,10-tetraacetic acid (DOTA) derivatives for chemoselective attachment to unprotected polyfunctionalized compounds. *Chem.—Eur. J. 13*, 6082–6090.
(127) Mattila, K., Siltainsuu, J., Balaspiri, L., Ora, M., and Lönnberg, H. (2005) Derivatization of phosphopeptides with mercapto- and amino-functionalized conjugate groups by phosphate elimination and subsequent Michael addition. *Org. Biomol. Chem. 3*, 3039–3044.
(128) Prasuhn, D. E., Jr., Yeh, R. M., Obenaus, A., Manchester, M., and Finn, M. G. (2007) Viral MRI contrast agents: coordination of Gd by native virions and attachment of Gd complexes by azide-alkyne cycloaddition. *Chem. Commun.* 1269–1271.
(129) Mindt, T. L., Struthers, H., Brans, L., Anguelov, T., Schweinsberg, C., Maes, V., Tourwé, D., and Schibli, R. (2006) "Click to chelate": synthesis and installation of metal chelates into biomolecules in a single step. *J. Am. Chem. Soc. 128*, 15096–15097.

BC700328S

COMMUNICATIONS

Tumor-Targeted Gene Delivery Using Molecularly Engineered Hybrid Polymers Functionalized with a Tumor-Homing Peptide

Kris C. Wood,[†] Samira M. Azarin,[†] Wadih Arap,[§] Renata Pasqualini,[§] Robert Langer,*[,†,‡] and Paula T. Hammond*[,†]

Department of Chemical Engineering, Biological Engineering Division, Massachusetts Institute of Technology, Cambridge, Massachusetts 02139, Department of Genitourinary Medical Oncology, University of Texas M.D. Anderson Cancer Center, Houston, Texas 77030. Received November 3, 2007; Revised Manuscript Received December 12, 2007

Before gene therapy can be used in clinical settings, safe and efficient DNA delivery systems must be developed to overcome a range of extra- and intracellular transport barriers. As a step toward the development of a modular, multifunctional gene delivery system to overcome these diverse barriers, we have developed a family of linear−dendritic "hybrid" polymers which contain functionalities for tissue targeting, minimization of nonspecific interactions, endosomal buffering, and DNA binding. Here, we demonstrate the rapid three-step, room-temperature, aqueous synthesis of hybrid polymers, as well as the functionalization of these polymers with a peptide targeting ligand that specifically binds to glucose-regulated protein-78 kDa (GRP-78), a clinically relevant tumor antigen identified in human cancer patients. These polymer systems can condense plasmid DNA into small nanoparticle structures (<210 nm) and transfect cells expressing GRP-78 with efficiencies that exceed that of branched polyethylenimine (bPEI), one of the best commercially available polymers for *in vitro* transfections. The synthetic approach described here may be useful for the rapid synthesis and optimization of polymer gene delivery systems bearing a range of diverse functional domains, and the specific GRP-78-targeted systems developed in this study may potentially have clinical applications in cancer gene therapy.

One approach toward the development of improved nonviral nucleic acid delivery systems involves the rational design of integrated, multifunctional systems containing domains which can be used to impart diverse functions such as DNA binding, endosomal buffering, and tissue or intracellular targeting (*1, 2*) Unfortunately, many early attempts to build such multifunctional systems have been unsuccessful because the addition of new domains results in the direct modification of existing domains, adversely affecting their properties. For example, the conjugation of poly(ethylene glycol) (PEG) to polyethylenimine (PEI) via primary and secondary amines, while improving the colloidal stability of polymer−DNA complexes, also dramatically decreases transfection efficiency by directly altering the polymer's DNA binding and endosomal buffering properties (*3*).

In response to these well-established problems, we set out to design a gene delivery system possessing multiple functional domains arranged together in a modular fashion, such that new domains could be added, modified, or removed while only minimally affecting existing properties. In order to make this possible, we required that all domains be physically separated from one another, that no domains possess overlapping functions, and that domains be assembled using complementary (orthogonal) chemistries (Figure S1a). Here, we demonstrate the rapid synthesis and *in vitro* validation of a system which fulfills all of the above criteria. This system, based on linear−dendritic "hybrid" polymers consisting of linear PEG and dendritic poly(amidoamine) (PAMAM), possesses functional domains for electrostatic DNA condensation, endosomal escape (via the proton sponge mechanism), reduction of nonspecific tissue interactions, and tissue targeting (Figure S1b) (*4*). In order to functionalize hybrid polymers with sensitive biological functional domains such as peptides, antibodies, and nucleic acids, we have developed a synthetic scheme that uses commercially available starting materials and a rapid (three reaction steps, two days), aqueous chemical conjugation (*1, 5*). To examine the utility of this approach, we synthesize hybrid polymers modified with a peptide ligand (denoted peptide **1**, sequence = WIFPWIQL) capable of selectively targeting glucose-regulated protein-78 kDa (GRP-78) (*6*). GRP-78 is a functional tumor antigen identified in human cancer patients, and peptide **1** has been used to target GRP-78 in tumors *in vitro*, *in vivo* (in mouse models of breast and prostate cancer), and in human patient-derived tumor samples (*6, 7*). We show here that peptide **1** functionalized hybrid polymer systems can electrostatically condense DNA into small nanoparticle structures with low, positive zeta potentials and the ability to transfect cells expressing GRP-78 more efficiently than branched polyethylenimine (bPEI), one of the best commercially available polymers for *in vitro* transfections.

* To whom correspondence should be addressed. 77 Massachusetts Avenue, Room 66-546, Cambridge, MA 02139. Tel: 617-258-7577; Fax: 617-258-5766; Email: hammond@mit.edu. 77 Massachusetts Avenue, Room E25-342, Cambridge, MA 02139; Tel: 617-253-3123; Fax: 617-258-8827; Email: rlanger@mit.edu.

[†] Department of Chemical Engineering, Massachusetts Institute of Technology.

[‡] Biological Engineering Division, Massachusetts Institute of Technology.

[§] University of Texas M.D. Anderson Cancer Center.

10.1021/bc700408r CCC: $40.75 © 2008 American Chemical Society
Published on Web 01/12/2008

Scheme 1. Synthesis of Peptide-Functionalized Hybrid Polymers

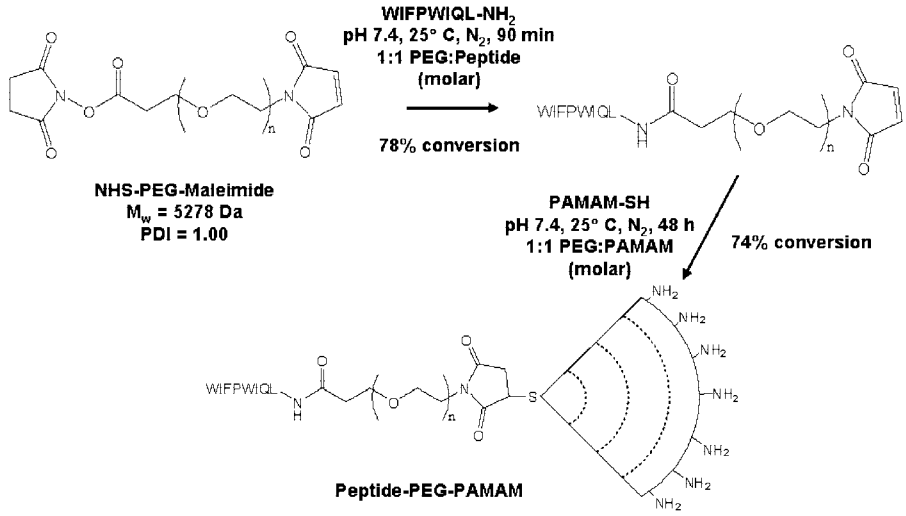

The aqueous synthetic approach developed in this work is shown in Scheme 1. Critical to this approach is the availability of cystamine-core PAMAM dendrimers (generation 4.0), which can be reduced to yield dendrons with a single, free thiol in the interior (*8*). Briefly, dendrimers were first reduced by addition to a molar excess of dithiothreitol (DTT) with overnight stirring under N_2 gas, followed by dialysis against pure water to remove the reducing agent. Ellman's assay was used to quantify the fraction of dendrimers reduced prior to the PEG conjugation (see Supporting Information). In a separate vessel, peptide **1** was added to a bifunctional maleimide-PEG-NHS ester for 90 min, followed by addition of a molar equivalent of reduced dendrimer at pH 7.4 (phosphate buffered saline) with stirring for 24–48 h to yield the final conjugate. Note that peptide **1** was dissolved in dimethylsulfoxide (DMSO) prior to the PEG conjugation reaction only because it is insoluble in water.

Quantitatively, PAMAM reduction proceeded at conversions of 95–100% (based on total thiol concentration as measured by Ellman's method). The peptide−PEG conjugation reaction proceeded at 78% conversion (Figure S2), and the final PEG−PAMAM conjugation step went at 74% conversion (based on the disappearance of thiols; see Table S1). To ensure that the disappearance of free thiols during the PEG−PAMAM conjugation step was a result of a reaction with the PEG maleimide group instead of the reformation of dendritic disulfides, a sample of the final product was incubated overnight with a 10-fold molar excess of DTT, dialyzed, and analyzed again for thiol content. No additional thiols were observed, suggesting that all originally reacted thiols had formed stable thioether linkages with the maleimide group. Additionally, each conjugate was also verified using NMR (see Supporting Information).

A range of techniques was used to measure the physical properties of polymer−DNA complexes. In Figure 1a, gel electrophoresis demonstrates binding and charge neutralization of plasmid DNA (pCMV-Luciferase) by hybrid polymers at polymer/DNA mass ratios greater than 1:1 (N:P 0.8:1), with complete charge neutralization occurring at mass ratios equal to or greater than 5:1 (N:P 3.9:1). Zeta potential measurements indicate that complexes formed at polymer/DNA ratios of up to 40:1 (N:P 31:1) have low, positive zeta potentials, and dynamic light scattering shows that small particles (<210 nm) are formed with diameters equal to or less than the reported cutoff of ~200 nm for efficient cellular uptake *in vivo* (Figure 1b) (*9*). Particle size showed some sensitivity to the polymer/DNA mass ratio, with small ratios yielding smaller (~140–150 nm) particles and larger ratios yielding slightly larger particles (180–210 nm), likely due to increased steric or charge repulsion in complexes formed at high mass ratios.

To test for the ability of these peptide-functionalized hybrid polymers to target and deliver plasmid DNA to cells expressing GRP-78, we transfected DU145 prostate carcinoma cells, which have been shown to bind and internalize peptide **1** in a GRP-78-dependent manner (*6*). As shown in Figure 2, peptide-functionalized hybrid polymers can transfect DU145 cells at levels nearly 10-fold higher than an optimized formulation of

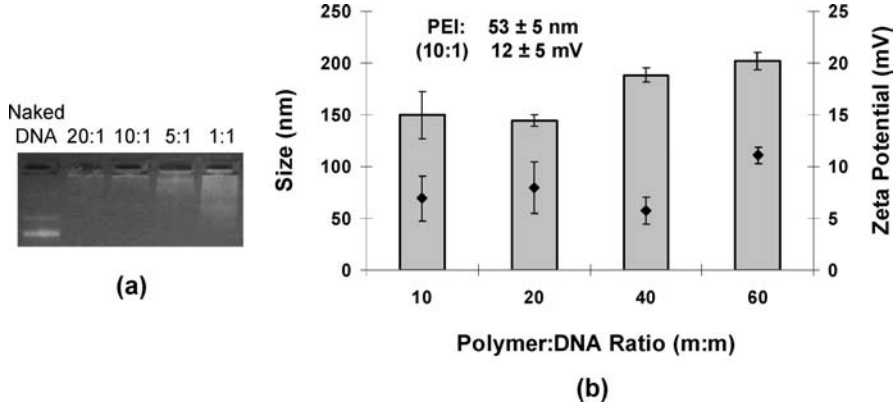

Figure 1. Physical properties of hybrid polymer−DNA complexes. (a) 1% agarose gel electrophoresis demonstrates DNA binding at indicated mass ratios. (b) Size (nm, bars) and zeta potential (mV, diamonds) of polymer/DNA complexes measured by dynamic light scattering (DLS). Error bars indicate 1 standard deviation in measured values.

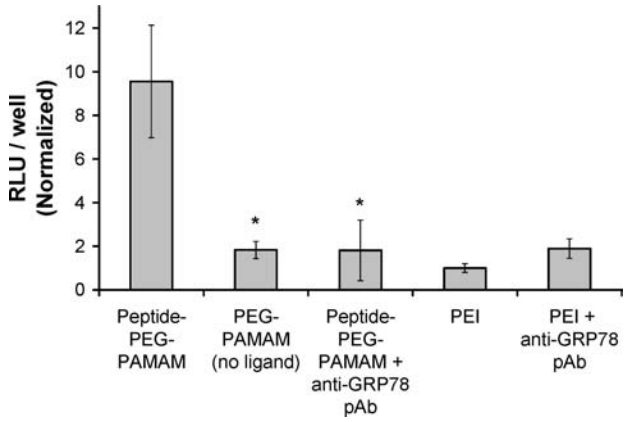

Figure 2. Transfection of DU145 prostate carcinoma cells expressing GRP-78 using peptide-modified hybrid polymers. Polymers with and without the peptide ligand, and peptide-modified polymers transfected in the presence of polyclonal anti-GRP-78 antiserum to block receptor binding, are shown (*6*). * indicates $p < 0.1$. Results normalized to an optimized formulation of PEI (2:1 PEI/DNA ratio (m:m)). All results are given as average +/− standard error.

branched PEI (25 kDa). Moreover, this process is receptor-mediated, as evidenced by the fact that cells transfected using polymers lacking a peptide ligand, as well as cells transfected with peptide-functionalized polymers in the presence of polyclonal anti-GRP-78 antiserum (to block receptor–ligand binding), yielded significantly lower levels of transfection (Figure 2). (For more information on serum stability and cytotoxicity of hybrid polymer systems, see ref (*4*).)

In conclusion, we have developed a rapid and simple aqueous synthesis to construct multidomain, biomolecule-functionalized polymers for nonviral gene delivery applications. Unlike previous efforts to functionalize spherical dendrimers with PEG, targeting groups, or other moieties through DNA binding peripheral amines, this approach allows for the synthesis of asymmetric polymers with well-controlled architectures whose DNA binding and endosomal buffering properties are not directly altered in the functionalization process (*10–12*). As a demonstration of this design and its utility, we synthesized hybrid polymers functionalized with short peptides which efficiently target and transfect cells expressing GRP-78, a clinically relevant tumor antigen. Preliminary *in vivo* bioluminescence imaging experiments performed using mice bearing EF43-*FGF4* tumors demonstrate that a single, intravenous injection of these GRP-78-targeted systems can also lead to transient, tumor-specific transgene expression (data not shown). In the future, the peptide-functionalized hybrid polymers developed in this study may potentially find use in clinical applications involving the targeted delivery of "suicide" transgenes to solid tumors (*13*). More broadly, the general synthetic approach described here could be a useful tool for the rapid synthesis and optimization of next-generation gene delivery systems bearing biological functional domains such as nuclear localization sequences, adjuvants, and protein transduction domains (*2*).

ACKNOWLEDGMENT

This work was supported by the National Institutes of Health (R01-EB00244 and R21-EB004122) and the Division of Materials Research of the National Science Foundation (DMR 9903380). K.C.W. thanks the National Cancer Institute and the MIT Center for Cancer Research for a Ludwig Research Fellowship. We thank Drs. Gregory Zugates and Amin Hajitou for helpful discussions and Drs. Donald Tomalia and Ryan Hayes (Dendritic Nanotechnologies, Inc.) for assistance in obtaining cystamine-core PAMAM dendrimers.

Supporting Information Available: Schematic of hybrid polymers, conjugation of peptide 1 to Maleimide-PEG-NHS as monitored by the fluoraldehyde assay, table of reaction conversions, detailed experimental methods, and NMR characterization. This information is available free of charge via the Internet at http://pubs.acs.org/BC.

LITERATURE CITED

(1) Luo, D. and Steiner, W. (2000) Synthetic DNA delivery systems. *Nat. Biotechnol. 18*, 33–37.
(2) Wagner, E. (2004) Strategies to improve DNA polyplexes for *in vivo* gene transfer: Will "artificial viruses" be the answer? *Pharm. Res. 21*, 8–14.
(3) Sung, S.-J., Min, S., Cho, K., Lee, S., Min, Y.-J., Yeom, Y.-I., and Park, J.-K. (2003) Effect of polyethylene glycol on gene delivery of polyethylenimine. *Biol. Pharm. Bull. 26*, 492–500.
(4) Wood, K. C., Little, S. R., Langer, R., and Hammond, P. T. (2005) A family of hierarchically self-assembling linear-dendritic hybrid polymers for highly efficient targeted gene delivery. *Angew. Chem. Int. Ed. 44*, 6704–6708.
(5) Putnam, D. (2006) Polymers for gene delivery across length scales. *Nat. Mater. 5*, 439–51.
(6) Arap, M. A., Lahdenranta, J., Mintz, P. J., Hajitou, A., Sarkis, A. S., Arap, W., and Pasqualini, R. (2004) Cell surface expression of the stress response chaperone GRP78 enables tumor targeting by circulating ligands. *Cancer Cell 6*, 275–84.
(7) Mintz, P. J., Kim, J., Do, K. A., Wang, X., Zinner, R. G., Cristofanilli, M., Arap, M. A., Hong, W. K., Troncoso, P., Logothetis, C. J., Pasqualini, R., and Arap, W. (2003) Fingerprinting the circulating repertoire of antibodies from cancer patients. *Nat. Biotechnol. 21*, 57–63.
(8) Tomalia, D. A., Huang, B., Swanson, D. R., Brothers, H. M., and Klimash, J. W. (2003) Structure control within poly(amidoamine) dendrimers: size, shape and regio-chemical mimicry of globular proteins. *Tetrahedron 59*, 3799–3813.
(9) Rejman, J., Oberle, V., Zuhorn, I. S., and Hoekstra, D. (2004) Size-dependent internalization of particles via the pathways of clathrin-and caveolae-mediated endocytosis. *Biochem. J. 377*, 159–169.
(10) Huang, R. Q., Qu, Y. H., Ke, W. L., Zhu, J. H., Pei, Y. Y., and Jiang, C. (2007) Efficient gene delivery targeted to the brain using a transferrin-conjugated polyethyleneglycol-modified polyamidoamine dendrimer. *FASEB J. 21*, 1117–25.
(11) Luo, D., Haverstick, K., Belcheva, N., Han, E., and Saltzman, W. M. (2002) Poly(ethylene glycol)-conjugated PAMAM dendrimer for biocompatible, high-efficiency DNA delivery. *Macromolecules 35*, 3456–3462.
(12) Choi, J. S., Nam, K., Park, J., Kim, J. B., Lee, J. K., and Park, J. (2004) Enhanced transfection efficiency of PAMAM dendrimer by surface modification with L-arginine. *J. Controlled Release 99*, 445–456.
(13) Hajitou, A., Trepel, M., Lilley, C. E., Soghomonyan, S., Alauddin, M. M., Marini, F. C., Restel, B. H., Ozawa, M. G., Moya, C. A., Rangel, R., Sun, Y., Zaoui, K., Schmidt, M., von Kalle, C., Weitzman, M. D., Gelovani, J. G., Pasqualini, R., and Arap, W. (2006) A hybrid vector for ligand-directed tumor targeting and molecular imaging. *Cell 125*, 385–98.

BC700408R

Toward Multivalent Signaling across G Protein-Coupled Receptors from Poly(amidoamine) Dendrimers

Yoonkyung Kim,[†] Béatrice Hechler,[‡] Athena M. Klutz,[†] Christian Gachet,[‡] and Kenneth A. Jacobson*[,†]

Molecular Recognition Section, Laboratory of Bioorganic Chemistry, National Institute of Diabetes and Digestive and Kidney Diseases, National Institutes of Health, Bethesda, Maryland 20892, INSERM U.311, EFS-Alsace, and Université Louis Pasteur, Strasbourg, France. Received August 28, 2007; Revised Manuscript Received November 3, 2007

Activation of the A_{2A} receptor, a G protein-coupled receptor (GPCR), by extracellular adenosine, is antiaggregatory in platelets and anti-inflammatory. Multiple copies of an A_{2A} agonist, the nucleoside CGS21680, were coupled covalently to PAMAM dendrimers and characterized spectroscopically. A fluorescent PAMAM-CGS21680 conjugate **5** inhibited aggregation of washed human platelets and was internalized. We envision that our multivalent dendrimer conjugates may improve overall pharmacological profiles compared to the monovalent GPCR ligands.

Small-molecule ligands for a G protein-coupled receptor (GPCR) generally bind within its heptahelical transmembrane domain to trigger intracellular signaling pathways (*1, 2*). Accordingly, the surface contact of a distal structural unit of a bound ligand, away from the pharmacophore region, with a GPCR at/near its extracellular domain (i.e., a secondary interaction) may impart additional selectivity and affinity. An approach to designing ligands for GPCRs by applying structural modification at their permissive distal sites has led to the concept of functionalized congeners (*3, 4*). For instance, ligands for GPCRs may require attachment to a carrier molecule for delivery, and the chemical functional groups and geometry of a linker moiety can be varied, as guided by receptor affinity.

Dendrimers (*5–7*) are treelike macromolecules which possess favorable characteristics: structural integrity, control of the component functional groups and their corresponding physical properties by chemical synthesis, feasibility to conjugate multiple functional units at the periphery and the interior, and a low enzymatic degradation rate. For the past 15 years, dendrimers have been used for biomedical research (*8–12*) including gene transfection (polycationic nature) (*13–16*), drug delivery (targeted/controlled release, encapsulation, or covalent/electrostatic attachment) (*17–21*), protein−carbohydrate interactions (multivalent effect) (*22–27*), medical diagnostics (signal amplification) (*12, 28*), and tissue engineering (*29–31*). Poly(amidoamine) (PAMAM) dendrimer is composed of aliphatic amino and amido groups, and its relatively biocompatible nature has found many applications in biomedicine (*32–35*). Although the heterogeneity of commercial PAMAM dendrimers may hinder the structural characterization at the monomolecular level (*36*), usage of PAMAM dendrimers may provide quick and easy access to gauge the applicability of dendrimers as advanced therapeutic agents before progressing to tailor-made dendrimers.

Here, we report the first example of dendrimer applications to induce the multivalent intracellular signal transduction across GPCRs. Adenosine receptors (ARs) are members of the Group A GPCR family that are involved in various disease states such as inflammation, cancer, cardiovascular damage, and nervous system disorders (*37–39*). Four subtypes of ARs, A_1, A_{2A}, A_{2B}, and A_3, have been identified to date, with each manifesting a unique pharmacological profile, tissue distribution, and effector coupling. To test the feasibility of our approach, the carboxylic acid derivative CGS21680[1](**1** (*40–42*)), an A_{2A} AR agonist, was selected as a ligand for the attachment to the peripheral amino groups of a third generation (G3) PAMAM dendrimer with an ethylenediamine core (**2**). Here, the PAMAM dendrimer linked to CGS21680 through its aliphatic amino end group can be considered a part of the distal modification under the functionalized congener concept to modulate the biological activity of the original ligand (*3, 4*).

Our plan for the conjugation of CGS21680 to the PAMAM dendrimer was to utilize its distal carboxylic acid group extending from the C-2 position of the adenine base, which was shown to be a site suitable for attachment that is tolerated in receptor binding (*3*). The synthetic feasibility to make PAMAM-CGS21680 conjugates through a peptide coupling method was first examined at a monomeric level using CGS21680 in its unprotected form. For peptide coupling, PyBOP[1] was adopted as a coupling reagent. PyBOP generally allows rapid condensation in high yield unless a significant steric challenge is involved. Unlike a somewhat sluggish and unselective carbodiimide-mediated coupling, which acts essentially through dehydration (i.e., forming urea as a byproduct), PyBOP does not generate any esterified products between a free hydroxyl and a carboxylic acid. Thus, CGS21680 **1** was treated with an excess of base, followed by an equimolar amount of *N*-Boc-ethylenediamine[1] in DMF[1] (Scheme 1). PyBOP (0.8 equiv) was added to this mixture to form an activated intermediate in situ and to achieve the coupling exclusively at the primary aliphatic amine. Thus, the preactivation step of the carboxylic acid group commonly applied before the addition of amine was avoided in order to minimize the formation of intra- or intermolecular cross-coupled products involving the adenine N^6amine. Indeed, neither the ^{1}H NMR nor the mass spectrum of the crude mixture showed the formation of any unwanted side products, and this reaction produced the desired compound **3** in 90% isolated yield.

* Author to whom correspondence should be addressed. Phone: 301-496-9024, fax: 301-480-8422; e-mail: kajacobs@helix.nih.gov.

[†] National Institutes of Health.

[‡] INSERM U.311, EFS-Alsace, and Université Louis Pasteur.

[1]Abbreviations: CGS21680, 2-[4-(2-carboxylethyl)phenylethylamino]-5′-*N*-ethylcarboxamidoadenosine; PyBOP, benzotriazol-1-yl-oxytripyrrolidinophosphonium hexafluorophosphate; Boc, *tert*-butoxycarbonyl; DIEA, *N*,*N*-diisopropylethylamine; Et_3N, triethylamine; DMF, *N*,*N*-dimethylformamide; DMSO, dimethyl sulfoxide; DHB, 2,5-dihydroxybenzoic acid; THAP, 2,4,6-trihydroxyacetophene; ADP, adenosine 5′-diphosphate.

10.1021/bc700327u CCC: $40.75 © 2008 American Chemical Society
Published on Web 01/05/2008

Scheme 1

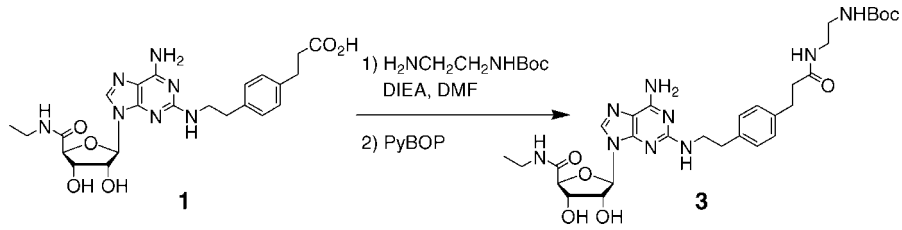

Scheme 2

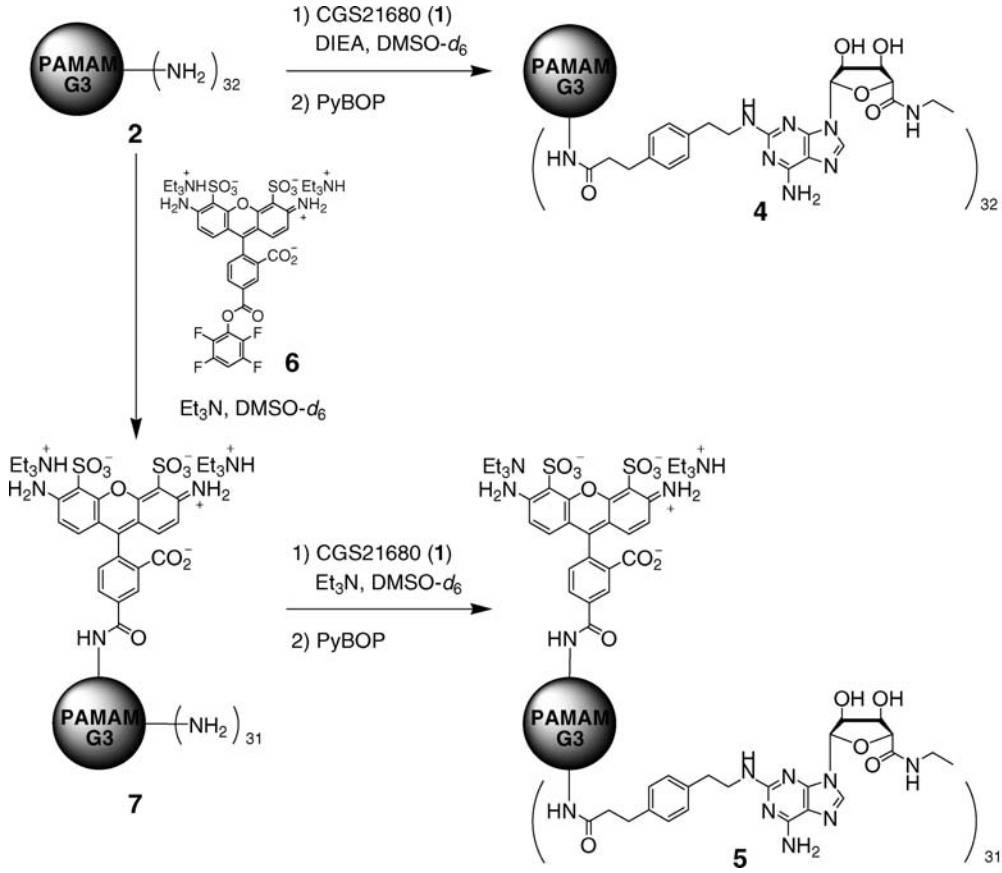

Next, this PyBOP coupling strategy was applied to the PAMAM dendrimer. We began by preparing the dendrimer conjugate **4**, which was fully amide-coupled with CGS21680 (Scheme 2). A slight excess of CGS21680 was added to a basic solution of PAMAM **2**, which was then treated with 32 equiv of PyBOP as a DMSO-d_6[1] solution. Deuterated DMSO was used as the reaction solvent in order to avoid later complications in the NMR analysis based on integration in DMSO-d_6. The reaction continued for 22 h, and the product was purified by size exclusion chromatography (SEC) in DMF to give the desired compound **4** in quantitative yield as confirmed by ^{1}H NMR. Here, the peak corresponding to the methylene α- to the carbonyl at the CGS21680 linker terminus was well-resolved at 2.33 ppm and exhibited the maximal shift upon coupling, similar to the result observed for the monomeric analogue **3**. The integration value of a methyl peak from CGS21680 at 0.95 ppm (96.3 H) relative to a PAMAM methylene peak "c" at 2.18 ppm (120 H)—an internal standard of PAMAM G3 for characterization by integration—indicated that the reaction proceeded completely to produce the desired product **4** bearing 32 CGS21680 groups.

To aid in the microscopic visualization in biological assays, a fluorescent dendrimer derivative **5** was then prepared. We chose Alexa Fluor 488 as a fluorophore, which has similar absorption/emission maxima to those of fluorescein, but is reported to have a higher photostability, pH insensitivity, and good water solubility (*43*, *44*). Thus, an equimolar amount of Alexa Fluor 488 was added to PAMAM dendrimer **2** as a 5-carboxy tetrafluorophenyl ester **6** in DMSO-d_6 (Scheme 2). A small amount of red precipitate was observed almost instantly upon addition of **6**. However, removal of this precipitate by filtration did not affect the recovery of an anticipated mass balance when calculated after the full conjugation of the ligands in the next step to prepare **5**. Analysis of the fluorescent intermediate **7** by ^{1}H NMR integration was difficult, and thus, the conjugation of 1 equiv of Alexa Fluor 488 was assumed on the basis of the stoichiometry of addition. The filtered crude mixture **7** was used for the next step without any purification. Subsequent attachment of CGS21680 to **7** was carried out using the same PyBOP coupling strategy as for **4**, but by adding 31 equiv of PyBOP instead. The fluorescent PAMAM-GS21680 conjugate **5** was purified by SEC and was similarly characterized by ^{1}H NMR integration to confirm that, on average, 31 CGS21680 groups were attached to the dendrimer (Supporting Information).

PAMAM-CGS21680 conjugates **4** and **5** were then characterized by matrix-assisted laser desorption ionization time-of-flight (MALDI-TOF) mass spectrometry (see Supporting Information).

Table 1. Comparison of Molecular Weights and the Number of CGS21680 Groups Attached Determined by NMR and MALDI MS

			MALDI							
	NMR		DHB matrix				THAP matrix			
cmpd	no. of CGS21680	MW[b]	M_n[c]	M_w[d]	PDI[e]	no. of CGS21680[f]	M_n[c]	M_w[d]	PDI[e]	no. of CGS21680[f]
2	0	6909	5772	5909	1.02	0	5956	6085	1.02	0
4	32	22317	18839	19391	1.03	28	19789	20449	1.03	30
5[a]	31	22352	19050	19502	1.02	27	19576	20044	1.02	28

[a] Counterions of sulfate groups for Alexa Fluor 488 were assumed to be protons. [b] PAMAM dendrimer **2** used for calculation here was assumed to have 32 peripheral amino groups and no structural defects. [c] Number-average molar mass. [d] Weight-average molar mass. [e] Polydispersity index. [f] No matrix adduct was considered for the estimation.

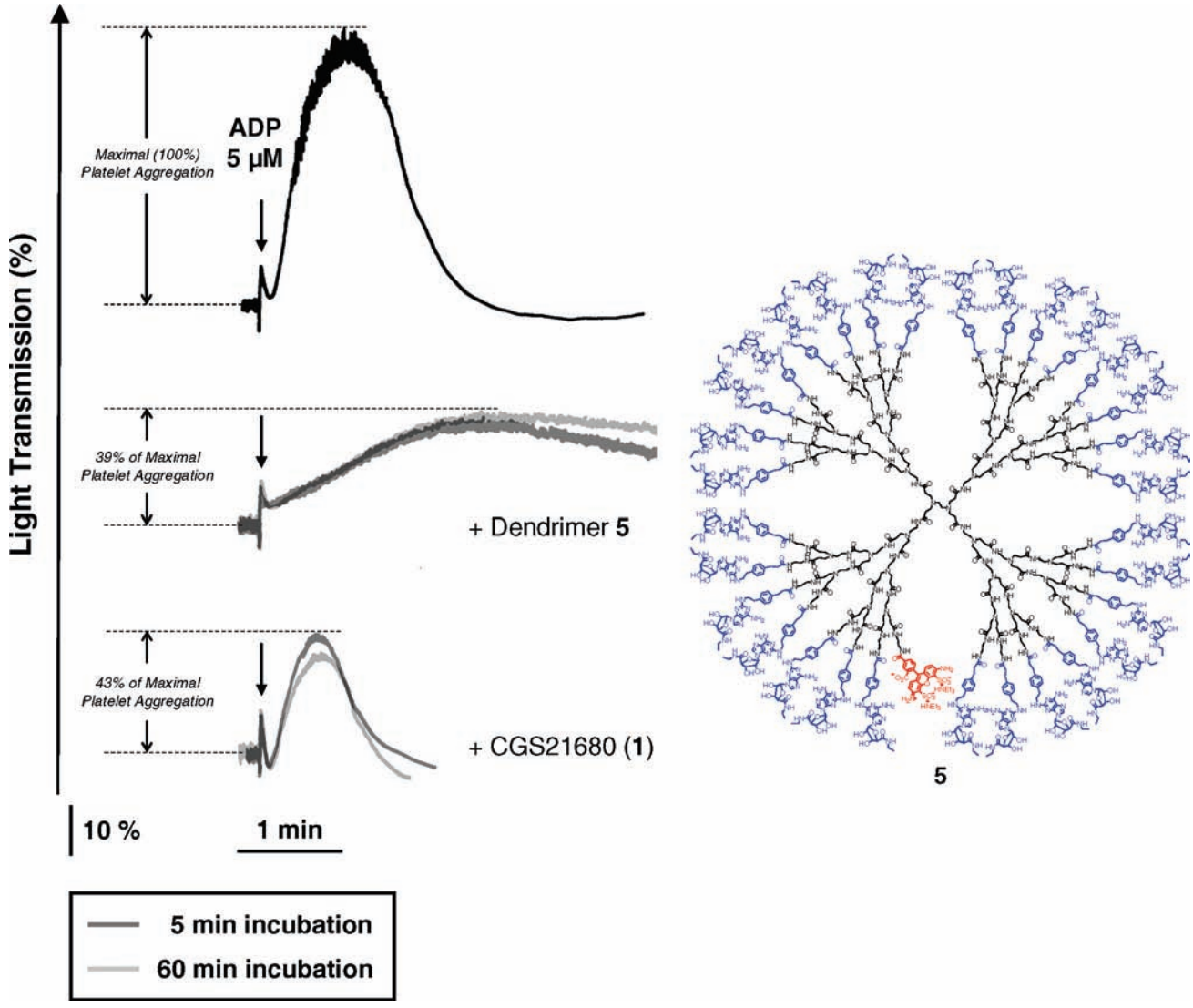

Figure 1. Platelet aggregation studies at 37 °C in the presence or absence of dendrimer **5** (Supporting Information). A suspension of human washed platelets was incubated with DMSO (top), dendrimer **5** (middle), or CGS21680 **1** (bottom) (each added as a DMSO solution), to which ADP was then added to induce the platelet aggregation. An increase in light transmission indicates increased aggregation. The final concentration of dendrimer **5** or CGS21680 **1** in the media was 2 μM, and the total content of DMSO in the media was 0.4% (v/v) in all cases.

Various MALDI matrices were attempted; however, in all cases, the intensity of the desired peak was generally weak, and the peak shape was overly broad due to the heterogeneity and possible fragmentation of PAMAM under the applied MALDI condition. Among those attempted matrices, DHB[1] and THAP[1] gave the best results for analysis. A broad peak corresponding to the half-size of the desired compound **4** or **5** was detected, which may have originated from either a doubly charged species or the fragmentation of the desired compound at the middle of the ethylenediamine core as suggested previously (*45*). In comparison to the ^{1}H NMR integration-based characterization, MALDI underestimated the average molecular weights (MWs) for both **4** and **5** in either matrix when the broad peak region above the MW of a half-size dendrimer was considered for calculations (Table 1). MALDI of a commercial PAMAM dendrimer **2** obtained under similar conditions also underestimated the average MW by ca. 1000 Da. When the MALDI-estimated average MW of PAMAM **2** was subtracted from those of **4** and **5**, dendrimers **4** and **5** were found to have 28–30 and 27–28 CGS21680 attachments, respectively, thus a slight underestimation when compared to those calculated by NMR. The deviations in MALDI-estimated MWs from those determined by NMR integration may have resulted from the difference in the tendency to form multiple matrix-adducts

between **2**, with many free amino groups, and the fully conjugated dendrimer **4** or **5**. In either matrix, the polydispersity of PAMAM-CGS21680 conjugate **4** or **5** was relatively low, ca. 1.02–1.03, and was similar to the value obtained for PAMAM dendrimer **2**. This result further supports that the conjugation of CGS21680 was nearly complete for both **4** and **5**, by reacting at most of the available peripheral amino groups of the PAMAM dendrimer.

Preliminary conformational studies of PAMAM-CGS21680 conjugate **4** were performed by nuclear Overhauser enhancement (NOE) experiments and computer modeling (see Supporting Information). PAMAM interiors were predicted to maintain a relatively compact structure by forming exchangeable multiple hydrogen bonds in water or methanol (*32*). Unlike water molecules, which may interact mostly with the charged ammonium ions at the surface of PAMAM, polar aprotic DMSO may be more likely to penetrate into the PAMAM interior to disrupt the hydrogen-bonded network. Indeed, NOE cross-peaks were observed between methylene groups of PAMAM ("b" and "c") and the protons from the ribose moiety (i.e., methyl, H-1′, H-2′, H-3′, and H-4′) of CGS21680 in DMSO-d_6 (Supporting Information), suggesting a possible internalization of the ligand into the PAMAM interior. In addition, the energy-minimized structure of **4** (*HyperChem7.5.2*, Amber force field) exhibited a relatively large volume in the interior, which is sufficiently spacious to accommodate several internalized ligands simultaneously (*46*). Eighteen hydrogen bonds were detected in the interior of the PAMAM-CGS21680 conjugate **4**. The overall shape of **4** was somewhat ellipsoidal (*32*), with the diameter ranging ca. 65–85 Å.

Next, our fluorescent PAMAM-CGS21680 conjugate **5** was subjected to in vitro functional assays. We specifically chose the platelet aggregatory system (*47–49*) to examine the potential pharmacological value of our dendrimer-based multivalent ligand carriers for GPCR signaling. CGS21680, an A_{2A} AR agonist, is already known to display a potent antiaggregatory effect in human platelet preparations (*48*, *49*). The degree of platelet aggregation was determined by aggregometry after addition of ADP[1] to a washed human platelet suspension (*50*) containing either the PAMAM-CGS21680 dendrimer conjugate **5** or CGS21680 monomer **1** as a DMSO solution (2 μM) or the same volume of pure DMSO as a control (Figure 1) (Supporting Information). Our preliminary findings indicated that ADP-induced platelet aggregation, which occurs through the nucleotide binding to P2Y receptors on the platelet surface, was inhibited in the platelet suspension containing either dendrimer **5** or monomer **1** to a similar degree (i.e., 61% inhibition by **5**; 57% inhibition by **1**, both at 2 μM), whereas platelets treated with DMSO alone aggregated in response to ADP. The inhibitory effect was the same whether the dendrimer conjugate was incubated for 5 or 60 min. Interestingly, the platelet aggregation response in the presence of dendrimer **5** exhibited a slower onset in comparison to that of control or the platelet suspension treated with monovalent CGS21680. Moreover, the fluorescent dendrimer conjugate **5** was clearly observed inside the platelets under a fluorescent confocal microscope (Figure 2), when the platelet suspension was incubated with dendrimer **5** and washed to remove any free dendrimer **5** in the extracellular medium. Thus, the extracellularly administered dendrimer conjugate is effectively internalized in platelets. The internalization of intravenously injected macromolecules into platelet granules has been described (*53*). Future studies will be directed toward determining the structural features of the dendrimer conjugates that affect internalization.

In summary, in an effort to develop highly potent agonists acting through multivalent signaling across GPCRs, PAMAM dendrimer conjugates **4** and **5** loaded with multiple copies of

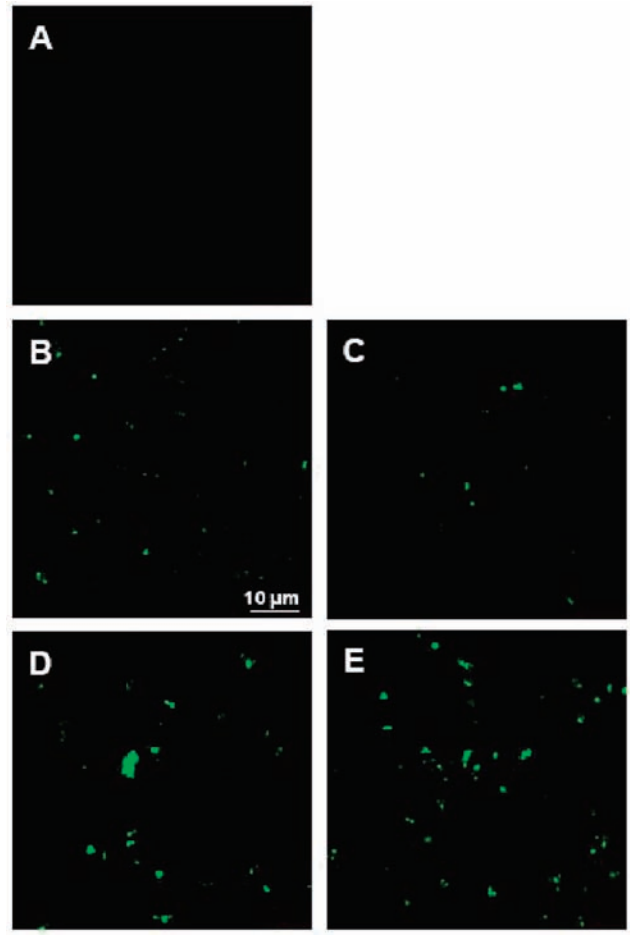

Figure 2. Fluorescence confocal microscopy of human washed platelets incubated with either (A) DMSO or (B−E) dendrimer **5** (Supporting Information). Incubation time: (B) 5 min, (C) 15 min, (D) 30 min, and (E) 60 min. The final concentration of dendrimer **5** in the media was 2 μM, and the total content of DMSO in the media was 0.4% (v/v) in all cases.

CGS21680 were synthesized using a peptide coupling method and purified by SEC. The average MWs and the degree of ligand attachments for dendrimers **4** and **5** were determined by ^{1}H NMR integration and MALDI. Both analyses support the formation of nearly fully loaded dendrimers. Our preliminary functional assay clearly demonstrated a potent antiaggregatory effect of the PAMAM-CGS21680 dendrimer **5** on the platelet aggregation induced by ADP. In addition, the fluorescent dendrimer **5** was found to be internalized into the platelet as shown by the fluorescent confocal microscopy studies. The approach described here to develop multivalent ligands for GPCRs can be extended to create a dendrimer containing a set of heterogeneous agonists/antagonists, in order to induce combined synergistic biological effects via binding to different receptor subtypes simultaneously on a cellular membrane (*51*, *52*). A detailed investigation on the pharmacological effects of our dendrimers on platelet aggregation will be reported in due course.

ACKNOWLEDGMENT

This research was supported in part by the Intramural Research Program of the NIH, NIDDK. We thank Dr. Herman Yeh for the helpful advice on the NMR experiments. We are grateful to Drs. Ratna Dutta and Haijun Yao at the Mass Spectrometry Laboratory of the University of Illinois, for numerous attempts to obtain MALDI spectra of our PAMAM

dendrimer derivatives. Y.K. thanks the Can-Fite Biopharma for financial support.

Supporting Information Available: Experimental procedures, ^{1}H NMR, NOESY, and MALDI spectra, and the energy-minimized structure. This material is available free of charge via the Internet at http://pubs.acs.org/BC.

LITERATURE CITED

(1) Landry, Y., Niederhoffer, N., Sick, E., and Gies, J. P. (2006) Heptahelical and other G-protein-coupled receptors (GPCRs) signaling. *Curr. Med. Chem. 13*, 51–63.

(2) Ratnala, V. R., Kiihne, S. R., Buda, F., Leurs, R., de Groot, H. J., and DeGrip, W. J. (2007) Solid-state NMR evidence for a protonation switch in the binding pocket of the H1 receptor upon binding of the agonist histamine. *J. Am. Chem. Soc. 129*, 867–872.

(3) Jacobson, K. A., and Daly, J. W. (1991) Purine functionalized congeners as molecular probes for adenosine receptors. *Nucleosides Nucleotides 10*, 1029–1038.

(4) Jacobson, K. A., Kirk, K. L., Padgett, W. L., and Daly, J. W. (1985) Functionalized congeners of adenosine: preparation of analogues with high affinity for A_1-adenosine receptors. *J. Med. Chem. 28*, 1341–1346.

(5) Tomalia, D. A. (2005) Birth of a new macromolecular architecture: dendrimers as quantized building blocks for nanoscale synthetic polymer chemistry. *Prog. Polym. Sci. 30*, 294–324.

(6) Grayson, S. M., and Fréchet, J. M. J. (2001) Convergent dendrons and dendrimers: from synthesis to applications. *Chem. Rev. 101*, 3819–3867.

(7) Zeng, F., and Zimmerman, S. C. (1997) Dendrimers in supramolecular chemistry: from molecular recognition to self-assembly. *Chem. Rev. 97*, 1681–l712.

(8) Lee, C. C., MacKay, J. A., Fréchet, J. M. J., and Szoka, F. C. (2005) Designing dendrimers for biological applications. *Nat. Biotechnol. 23*, 1517–1526.

(9) Svenson, S., and Tomalia, D. A. (2005) Dendrimers in biomedical applications-reflections on the field. *Adv. Drug Delivery Rev. 57*, 2106–2129.

(10) Shabat, D., Amir, R. J., Gopin, A., Pessah, N., and Shamis, M. (2004) Chemical adaptor systems. *Chem. Eur. J. 10*, 2626–2634.

(11) Boas, U., and Heegaard, P. M. H. (2004) Dendrimers in drug research. *Chem. Soc. Rev. 33*, 43–63.

(12) Stiriba, S.-E., Frey, H., and Haag, R. (2002) Dendritic polymers in biomedical applications: from potential to clinical use in diagnostics and therapy. *Angew. Chem., Int. Ed. 41*, 1329–1334.

(13) Zhou, J., Wu, J., Hafdi, N., Behr, J.-P., Erbacher, P., and Peng, L. (2006) PAMAM dendrimers for efficient siRNA delivery and potent gene silencing. *Chem. Commun.* 2362–2364.

(14) Luo, D., Haverstick, K., Belcheva, N., Han, E., and Saltzman, W. M. (2002) Poly(ethylene glycol)-conjugated PAMAM dendrimer for biocompatible, high-efficiency DNA delivery. *Macromolecules 35*, 3456–3462.

(15) Tang, M. X., Redemann, C. T., and Szoka, F. C., Jr. (1996) In vitro gene delivery by degraded polyamidoamine dendrimers. *Bioconjugate Chem. 7*, 703–714.

(16) Haensler, J., and Szoka, F. C., Jr. (1993) Polyamidoamine cascade polymers mediate efficient transfection of cells in culture. *Bioconjugate Chem. 4*, 372–379.

(17) Gillies, E. R., and Fréchet, J. M. J. (2005) Dendrimers and dendritic polymers in drug delivery. *Drug Discovery Today 10*, 35–43.

(18) D'Emanuele, A., and Attwood, D. (2005) Dendrimer-drug interactions. *Adv. Drug Delivery Rev. 57*, 2147–2162.

(19) Haag, R. (2004) Supramolecular drug delivery systems based on polymeric core-shell architectures. *Angew. Chem., Int. Ed. 43*, 278–282.

(20) Patri, A. K., Majoros, I. J., and Baker, J. R., Jr. (2002) Dendritic polymer macromolecular carriers for drug delivery. *Curr. Opin. Chem. Biol. 6*, 466–471.

(21) Liu, M., and Fréchet, J. M. J. (1999) Designing dendrimers for drug delivery. *Pharm. Sci. Tech. Today 2*, 393–401.

(22) Woller, E. K., Walter, E. D., Morgan, J. R., Singel, D. J., and Cloninger, M. J. (2003) Altering the strength of lectin binding interactions and controlling the amount of lectin clustering using mannose/hydroxyl-functionalized dendrimers. *J. Am. Chem. Soc. 125*, 8820–8826.

(23) Woller, E. K., and Cloninger, M. J. (2002) The lectin-binding properties of six generations of mannose-functionalized dendrimers. *Org. Lett. 4*, 7–10.

(24) Jayaraman, N., Nepogodiev, S. A., and Stoddart, J. F. (1997) Synthetic carbohydrate-containing dendrimers. *Chem. Eur. J. 3*, 1193–1199.

(25) Page, D., and Roy, R. (1997) Synthesis and biological properties of mannosylated starburst poly(amidoamine) dendrimers. *Bioconjugate Chem. 8*, 714–723.

(26) Kieburg, C., and Lindhorst, T. K. (1997) Glycodendrimer synthesis without using protecting groups. *Tetrahedron Lett. 38*, 3885–3888.

(27) Mammen, M., Choi, S.-K., and Whitesides, G. M. (1998) Polyvalent interactions in biological systems: implications for design and use of multivalent ligands and inhibitors. *Angew. Chem., Int. Ed. 37*, 2754–2794.

(28) Krause, W., Hackmann-Schlichter, N., Maier, F. K., and Müller, R. (2000) Dendrimers in diagnostics. *Top. Curr. Chem. 210*, 261–308.

(29) Wathier, M., Jung, P. J., Carnahan, M. A., Kim, T., and Grinstaff, M. W. (2004) Dendritic macromers as in situ polymerizing biomaterials for securing cataract incisions. *J. Am. Chem. Soc. 126*, 12744–12745.

(30) Grinstaff, M. W. (2002) Biodendrimers: new polymeric biomaterials for tissue engineering. *Chem. Eur. J. 8*, 2838–2846.

(31) Carnahan, M. A., Middleton, C., Kim, J., Kim, T., and Grinstaff, M. W. (2002) Hybrid dendritic-linear polyester-ethers for in situ photopolymerization. *J. Am. Chem. Soc. 124*, 5291–5293.

(32) Lee, H., Baker, J. R., Jr., and Larson, R. G. (2006) Molecular dynamics studies of the size, shape, and internal structure of 0% and 90% acetylated fifth-generation polyamidoamine dendrimers in water and methanol. *J. Phys. Chem. B 110*, 4014–4019.

(33) Maiti, P. K., Çağın, T., Wang, G., and Goddard, W. A. (2004) Structure of PAMAM dendrimers: generations 1 through 11. *Macromolecules 37*, 6236–6254.

(34) Lee, I., Athey, B. D., Wetzel, A. W., Meixner, W., and Baker, J. R., Jr. (2002) Structural molecular dynamics studies on polyamidoamine dendrimers for a therapeutic application: effects of pH and generation. *Macromolecules 35*, 4510–4520.

(35) Esfand, R., and Tomalia, D. A. (2001) Poly(amidoamine) (PAMAM) dendrimers: from biomimicry to drug delivery and biomedical applications. *Drug Discovery Today 6*, 427–436.

(36) Shi, X., Majoros, I. J., Patri, A. K., Bi, X., Islam, M. T., Desai, A., Ganser, T. R., and Baker, J. R., Jr. (2006) Molecular heterogeneity analysis of poly(amidoamine) dendrimer-based mono- and multifunctional nanodevices by capillary electrophoresis. *Analyst 131*, 374–381.

(37) Jacobson, K. A., and Gao, Z.-G. (2006) Adenosine receptors as therapeutic targets. *Nat. Rev. Drug Discovery 5*, 247–264.

(38) Yan, L., Burbiel, J. C., Maass, A., and Müller, C. E. (2003) Adenosine receptor agonists: from basic medicinal chemistry to clinical development. *Exp. Opin. Emerging Drugs 8*, 537–576.

(39) Fredholm, B. B., IJzerman, A. P., Jacobson, K. A., Klotz, K.-N., and Linden, J. (2001) International Union of Pharmacology. XXV. Nomenclature and classification of adenosine receptors. *Pharmacol. Rev. 53*, 527–552.

(40) Hutchison, A. J., Williams, M., de Jesus, R., Yokoyama, R., Oei, H. H., Ghai, G. R., Webb, R. L., Zoganas, H. C., Stone, G. A., and Jarvis, M. F. (1990) 2-(Arylalkylamino)adenosinuronamides: A new class of highly selective adenosine A_2 receptor ligands. *J. Med. Chem. 33*, 1919–1924.

(41) Jarvis, M. F., Schulz, R., Hutchison, A. J., Do, U. H., Sills, M. A., and Williams, M. (1989) [^{3}H]CGS 21680, A selective A_2 adenosine receptor agonist directly labels A_2 receptors in rat brain. *J. Pharm. Exp. Therap. 251*, 888–893.

(42) Hutchison, A. J., Webb, R. L., Oei, H. H., Ghai, G. R., Zimmerman, M. B., and Williams, M. (1989) CGS 21680C an A_2 selective adenosine receptor agonist with preferential hypotensive activity. *J. Pharm. Exp. Therap. 251*, 47–55.

(43) Haugland, R. P. (2002) *Handbook of Fluorescent Probes and Research Products*, 9th ed., Molecular Probes, Invitrogen, pp 20–35.

(44) Panchuk-Voloshina, N., Haugland, R. P., Bishop-Stewart, J., Bhalgat, M. K., Millard, P. J., Mao, F., Leung, W.-Y., and Haugland, R. P. (1999) Alexa dyes, a series of new fluorescent dyes that yield exceptionally bright, photostable conjugates. *J. Histochem. Cytochem. 47*, 1179–1188.

(45) Peterson, J., Allikmaa, V., Subbi, J., Pehk, T., and Lopp, M. (2003) Structural deviations in poly(amidoamine) dendrimers: a MALDI-TOF MS analysis. *Eur. Polym. J. 39*, 33–42.

(46) Petkova, V., Parvanova, V., Tomaliab, D., Swansonb, D., Bergstromb, D., and Vogt, T. (2005) 3D structure of dendritic and hyper-branched macromolecules by X-ray diffraction. *Solid State Commun. 134*, 671–675.

(47) Gachet, C. (2006) Regulation of platelet functions by P2 receptors. *Annu. Rev. Pharmacol. Toxicol. 46*, 277–300.

(48) Gessi, S., Varani, K., Merighi, S., Ongini, E., and Borea, P. A. (2000) A_{2A} adenosine receptors in human peripheral blood cells. *Br. J. Pharmacol. 129*, 2–11.

(49) Ledent, C., Vaugeois, J.-M., Schiffmann, S. N., Pedrazzini, T., Yacoubi, M. E., Vanderhaeghen, J.-J., Costentin, J., Heath, J. K., Vassart, G., and Parmentier, M. (1997) Aggressiveness, hypoalgesia and high blood pressure in mice lacking the adenosine A2a receptor. *Nature 388*, 674–678.

(50) Gurden, M. F., Coates, J., Ellis, F., Evans, B., Foster, M., Hornby, E., Kennedy, I., Martin, D. P., Strong, P., and Vardey, C. J. (1993) Functional characterization of three adenosine receptor types. *Br. J. Pharmacol. 109*, 693–698.

(51) Jacobson, K. A., Xie, R., Young, L., Chang, L., and Liang, B. T. (2000) A novel pharmacological approach to treating cardiac ischemia: binary conjugates of A_1 and A_3 adenosine receptor agonists. *J. Biol. Chem. 275*, 30272–30279.

(52) Jacobson, K. A., Lipkowski, A. W., Moody, T. W., Padgett, W., Pijl, E., Kirk, K. L., and Daly, J. W. (1987) Binary drugs: conjugates of purines and a peptide that bind to both adenosine and substance P receptors. *J. Med. Chem. 30*, 1529–1532.

(53) Handagama, P. J., Shuman, M. A., and Bainton, D. F. (1989) Incorporation of intravenously injected albumin, immunoglobulin G, and fibrinogen in guinea pig megakaryocyte granules. *J. Clin. Invest. 84*, 73–82.

BC700327U

MRI Detection of Thrombin with Aptamer Functionalized Superparamagnetic Iron Oxide Nanoparticles

Mehmet Veysel Yigit,[†,‡] Debapriya Mazumdar,[‡,§] and Yi Lu*[,†,‡,§,△]

Center for Biophysics and Computational Biology, Beckman Institute for Advanced Science and Technology, Department of Chemistry and Department of Biochemistry, University of Illinois at Urbana–Champaign, 600 S. Mathews Avenue, Urbana, IL 61801. Received October 22, 2007; Revised Manuscript Received November 27, 2007

Design of smart MRI contrast agent based on superparamagnetic iron oxide nanoparticles and aptamers has been described for the detection of human α-thrombin protein. The contrast agent is based on the assembly of the aptamer functionalized nanoparticles in the presence of thrombin. A detectable change in MRI signal is observed with 25 nM thrombin in human serum. Changes were neither observed with control analytes, streptavidin, or bovine serum albumin, nor with inactive aptamer functionalized nanoparticles.

Magnetic resonance imaging (MRI) is advancing rapidly, as it provides noninvasive, three-dimensional examination of biological events in living organisms. A particularly active area of research in the MRI field is the development of MRI contrast agents for image enhancement (*1–9*). Superparamagnetic iron oxide nanoparticles (SPIOs) are attractive, since they are shown to be effective in enhancing magnetic resonance image contrast (*4*). The applications of SPIOs in MRI have ranged from nontargeted detection of diseases by accumulating at certain tissues to targeted detection of biomolecular markers in cells (*10–16*). Target-specific MRI detection using SPIOs is particularly interesting, as it helps monitor several cellular or molecular processes (*16–18*). For example, cross-linked dextran-coated superparamagnetic iron oxide (CLIO) nanoparticles have been functionalized with different biomolecules and used for detection of different targets including oligonucleotides (*19, 20*) proteins (*17, 20, 21*), enzymatic activities (*22*), viruses (*23*), and enantiomeric impurities (*24*). It has been shown that CLIO nanoparticle assemblies create a distinctive magnetic phenomenon called magnetic relaxation switching (MRS), where the core of a single nanoparticle in the assemblies becomes more effective in enhancing T2 relaxation time of adjacent water protons, when compared to dispersed nanoparticles (*4, 19*). This mechanism has been widely used in many magnetic detection schemes either going from a disperse state to an assembled state of nanoparticles or visa versa (*19, 20, 22, 24*). For instance, it has been shown that oligonucleotide functionalized dispersed CLIO nanoparticles can be used for the sequence-specific detection of complementary oligonucleotides simply by hybridizing oligonucleotides and assembling CLIO nanoparticles into clusters (*19*). This process enhances the T2 relaxation of the nearby water protons and can be detected by MRI. While this approach is effective in oligonucleotide detection, it would be very interesting if this nucleic acid-based approach could be expanded beyond nucleic acid detection to MRI of even broader classes of targets.

Aptamers are single-stranded functional nucleic acid molecules which can bind a variety of chemical and biological molecules with high affinity and selectivity (*25–28*). They are obtained through a combinatorial biology technique called systematic evolution of ligands by exponential enrichment (SELEX), by isolating the active species from a large random pool of DNA or RNA molecules (*25, 26*). They are often analogous to antibodies due to their selectivity and sensitivity in binding to a broad range of molecules (*29–32*). When compared to antibodies, aptamers serve several advantages such as the relative ease with which they can be selected for any target analyte and their stability against biodegradation and denaturation. Due to these properties, aptamers are good candidates for building chemical and biological sensors in many fields such as medical diagnostics and environmental monitoring. Therefore, these aptamers have been transformed into fluorescent (*33–47*), colorimetric (*48–57*), and electrochemical sensors (*58–60*). Although these aptamer sensors have been widely investigated *in vitro*, their applications *in vivo* remain a significant challenge because light penetration through skin is difficult and signal interference from cellular components is common. Recently, we reported a method for combining adenosine aptamer and CLIO nanoparticles into a system to detect adenosine in the micromolar range via MRI. The contrast in MR image of the nanoparticle solution increases as the adenosine concentration increases in the environment (*61*). Herein, we describe a new method for combining magnetic relaxation switching properties of CLIO nanoparticles with aptamer technology in order to create MRI contrast agents with nanomolar detection limit. The advantage of this technique over other sensing methods is that MRI signal is much less vulnerable to changes in background colors or fluorescence from biological media, such as serum and cell suspensions. In contrast to our previously reported system with adenosine, which depends on analyte-induced disassembly of particles to produce an increase in brightness, this method is based on assembly of particles leading to a decrease in brightness of MR image. This change in signal from bright to dark is a significant advantage, as this is preferred in T2-weighted MR imaging. Furthermore, instead of a metabolite, we demonstrate the detection of a protein in the current system, as proteins constitute most enzymes and biomolecular markers in living systems.

To demonstrate the use of aptamer functionalized CLIO nanoparticles for protein detection we chose to detect thrombin

* Fax: (+1) 217-333-2685. Tel: (+1) 217-333-2619. E-mail yi-lu@uiuc.edu.

† Center for Biophysics and Computational Biology.

‡ Beckman Institute for Advanced Science and Technology.

§ Department of Chemistry.

△ Department of Biochemistry.

10.1021/bc7003928 CCC: $40.75 © 2008 American Chemical Society
Published on Web 01/04/2008

Scheme 1. Schematic Illustration for Thrombin Detection Using MRI[a]

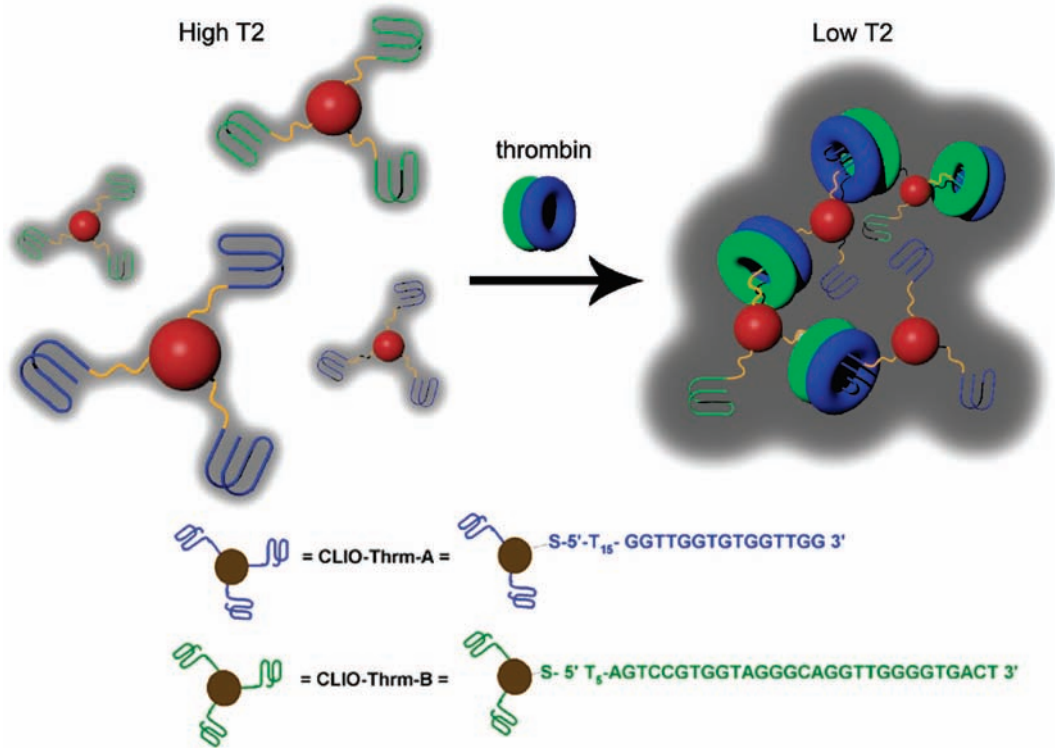

[a] The CLIO nanoparticles (shown as red spheres) have been modified with either Thrm-A, a DNA aptamer (shown as blue lines) that binds to fibrinogen-recognition exosite of thrombin, or Thrm-B, a DNA aptamer (shown as green lines) that binds to the heparin-binding exosite of thrombin. Addition of thrombin consisting of both fibrinogen (as blue donuts) and heparin (as green donuts) exosites resulted in aggregation of CLIO nanoparticle assembly, reducing the T2 relaxation time. The DNA sequences are shown at the bottom. The drawing is not to scale.

via MRI . We combined the CLIO nanoparticles with thrombin aptamers, Thrm-A, which binds to the fibrinogen-recognition exosite of thrombin, and Thrm-B, which binds to the heparin-binding exosite of thrombin, as shown in Scheme 1 (*62*, *63*).

Materials: All DNA samples were purchased from Integrated DNA Technologies Inc. (Coralville, IA). The thiol-modified DNA molecules were purified by the standard desalting method. Human alpha thrombin was purchased from Haematologic Technologies Inc. (Essex Junction, VT). BSA was purchased from Aldrich (St. Louis, MO). Streptavidin was purchased from SouthernBiotech (Birmingham, AL). N-Succinimidyl-3-(2-pyridylthio)-propionate (SPDP) was purchased from Molecular Biosciences (Boulder, CO). Cross-linked dextran coated superparamagnetic iron oxide nanoparticles (CLIO, 500 μg Fe mL^{-1}) were synthesized and coupled to SPDP according to literature procedure and purified with PD-10 column (*17*). The thiol modified oligos, Thrm-A (5′ SH-T_{15}-GGTTGGTGTGGTTGG 3′), Thrm-B (5′ SH-TTTTTAGTC-CGTGGTAGGGCAGGTTGGGGTGACT 3′), CNT-Thrm-A (5′ TCA-CAGATGAGT-A_{12}-SH 3′), and CNT-Thrm-B (5′ SH-CCCAGGT-TCTCT 3′) were activated by incubating with eight equivalent of tris (2-carboxyethyl) phosphine hydrochloride (TCEP). Excess TCEP was removed by desalting using a SepPak C-18 catridge. TCEP-activated thiol modified DNA (50 μM final concentration) was mixed with CLIO-SPDP (400 μg Fe mL^{-1}) in 100 mM phosphate buffer at pH 8.0 overnight. Excess DNA was removed by magnetic separation column (Miltenyi Biotec, Auburn, CA) from CLIO-DNA conjugates. Sample preparation and MRI detection: CLIO-Thrm-A and CLIO-Thrm-B were mixed in 1:1 ratio and diluted in 100 mM NaCl, 25 mM KCl, and 25 mM tris-HCl buffer at pH 7.4. 250 μL of sample (12 μg Fe mL^{-1}) was aliquoted into the wells of a microplate and varying amounts of analyte was added in each well. T2-weighted MR images were obtained on a 4.7 T NMR instrument using a spin–echo pulse sequence with variable echo time (TE = 25–100 ms) and repetition time (TR) of 3000 ms. Light-scattering experiments: DLS measurements were performed using Nicomp 380 ZLS Particle Sizer (Particle Sizing Systems, Santa Barbara, CA). An intensity-weighted value was used to report the average particle diameter.

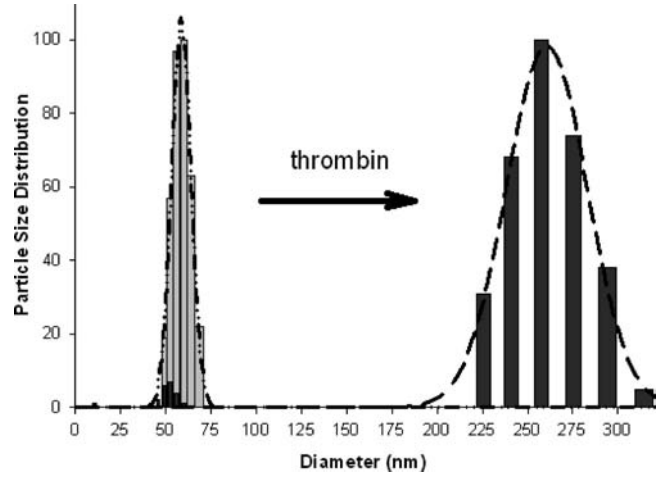

Figure 1. Particle size distribution of 1:1 CLIO-Thrm-A and CLIO-Thrm-B mixture before (light gray bars) and after (dark gray bars) addition of 50 nM thrombin.

The contrast agent designed for thrombin detection is composed of a 1:1 mixture of Thrm-A and Thrm-B functionalized CLIO nanoparticles (CLIO-Thrm-A and CLIO-Thrm-B, respectively) in aqueous solution. In the presence of thrombin, aptamer sequences fold into a G-quadruplex arrangement in order to bind to thrombin (*64*, *65*). After attachment of the CLIO nanoparticles to thrombin, the disperse nanoparticles assemble into aggregates, changing the magnetic relaxation properties of nearby water protons, thereby reducing the T2 relaxation time. This event can be monitored as a decrease in brightness of T2-weighted MR image of the solution via MRI (*24*).

To confirm that the aptamer functionalized nanoparticles bind to thrombin, 1 μM thrombin was added into the 1:1 homoge-

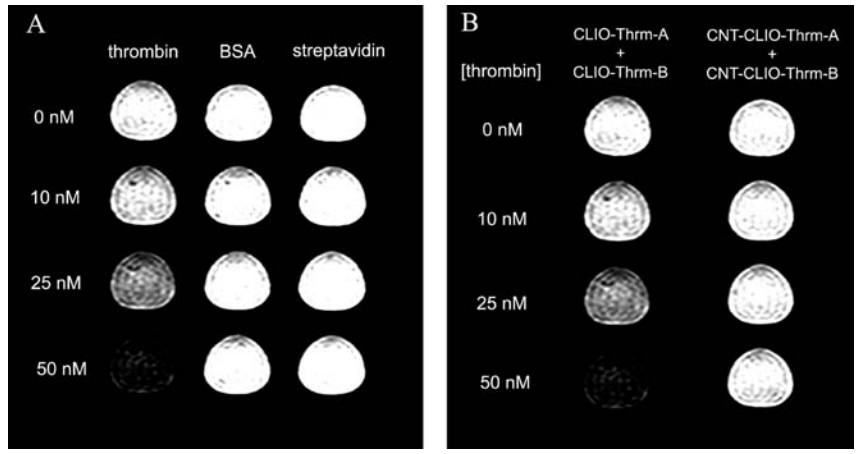

Figure 2. (A) Contrast change in T2-weighted MR image in 1:1 CLIO-Thrm-A and CLIO-Thrm-B mixture with 0, 10, 25, and 50 nM thrombin (first column), BSA (second column), and streptavidin (third column). (B) Contrast change in T2-weighted MR image with 0, 10, 25, and 50 nM thrombin in CLIO-Thrm-A and CLIO-Thrm-B mixture (first column), and in CNT-CLIO-Thrm-A and CNT-CLIO-Thrm-B mixture (second column).

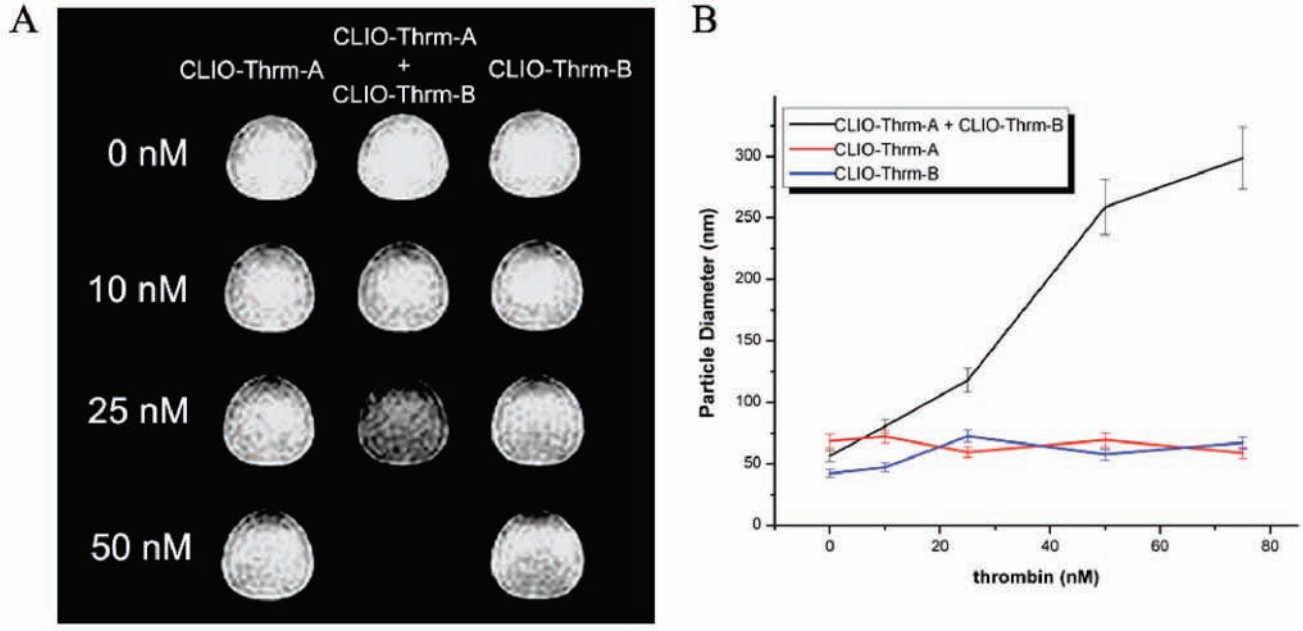

Figure 3. (A) Contrast change in T2-weighted MR image with 0, 10, 25, and 50 nM thrombin in CLIO-Thrm-A (first column), CLIO-Thrm-A and CLIO-Thrm-B mixture. (Note: The image is completely dark at 50 nM thrombin) (second column) and in CLIO-Thrm-B (third column). (B) Particle diameter change with CLIO-Thrm-A, 1:1 CLIO-Thrm-A and CLIO-Thrm-B mixture, or CLIO-Thrm-B with addition of thrombin.

Figure 4. T2-weighted MR image of 1:1 CLIO-Thrm-A and CLIO-Thrm-B mixture in human serum.

neous mixture of CLIO-Thrm-A and CLIO-Thrm-B (150 μg Fe mL^{-1}), which resulted in rapid precipitation in seconds (data not shown). Similar behavior was not observed when bovine serum albumin (BSA) or streptavidin was used as an analyte. This result indicates that the precipitation of nanoparticles is due to the binding event of analyte and its aptamer. Particle size analysis also showed that, upon addition of 50 nM thrombin into a mixture of CLIO-Thrm-A and CLIO-Thrm-B (12 μg Fe mL^{-1}), the average diameter of CLIO nanoparticles immediately increased from 58.9 $\pm$ 4.4 nm to 259.5 $\pm$ 22.5 nm. Figure 1 shows the intensity-weighted particle size distribution of CLIO nanoparticles obtained with dynamic light scattering (DLS), which indicates that the nanoparticles are cross-linked by thrombin molecules, therefore increasing the average diameter. At this CLIO nanoparticle concentration, precipitation of nanoparticles was not observed (*19*). These results strongly suggest that thrombin binding to aptamers on CLIO nanoparticles induces the assembly of nanoparticles.

After confirming thrombin-induced assembly of nanoparticles via DLS, we proceeded to check its utility as an MRI contrast agent. The binding of CLIO-Thrm-A and CLIO-Thrm-B to thrombin, assembled the nanoparticles into clusters, resulting in a decrease of the T2 relaxation time of the neighboring water protons in the medium. We have tested the system at different thrombin concentrations from 0 to 50 nM. A decrease in brightness of the MR image of the samples was observed as the concentration of thrombin was increased (Figure 2A), which was attributed to a decrease in T2 relaxation time (*24*). A

noticeable change in contrast was observed even as low as 10 nM thrombin, and a significant change was observed at 50 nM thrombin.

To ensure that the contrast is solely due to the binding event and not any other artifact, the system was tested with BSA and streptavadin. The MR images obtained with these two analytes did not show a difference in contrast when their concentration was increased from 0 to 50 nM. This result suggests that the change in contrast is due to thrombin and not any other effect. In order to check if the change in contrast is due to aptamer and analyte binding and not thrombin molecule itself, we have tested random DNA sequences of different lengths that do not bind to thrombin. To do so, we prepared a 1:1 mixture of random DNA sequence (CNT-Thrm-A and CNT-Thrm-B) functionalized CLIO nanoparticles (CNT-CLIO-Thrm-A and CNT-CLIO-Thrm-B). The control samples were subjected to the same procedure as was used in preparing CLIO-Thrm-A and CLIO-Thrm-B, and then placed into the wells of a microplate. Thrombin was added to both systems with an increasing concentration from 0 to 50 nM. The obtained MR images showed a change in brightness for samples with CLIO-Thrm-A and CLIO-Thrm-B, but no change with CNT-CLIO-Thrm-A and CNT-CLIO-Thrm-B (see Figure 2B). This result suggests that the change in the MR signal is due to active thrombin binding aptamers and not any other nonspecific interaction of DNA with thrombin. The two control experiments taken together strongly indicate that the change in MR signal is solely due to the binding event of thrombin to the aptamers, which results in assembly of CLIO nanoparticles into clusters, decreasing the T2 relaxation time of the environment.

In order to demonstrate that thrombin molecule requires a mixture of CLIO-Thrm-A and CLIO-Thrm-B to generate a MR signal, we tried to use only CLIO-Thrm-A or CLIO-Thrm-B to detect thrombin. As seen in Figure 3A, the MR signal did not change with neither of these nanoparticle suspensions, but a clear change in MR signal was observed with the 1:1 mixture of nanoparticles. The particle size analysis confirms this result, as an increase in particle diameter was observed when thrombin was added into the 1:1 mixture of nanoparticles, but such an increase was not observed with CLIO-Thrm-A or CLIO-Thrm-B alone (see Figure 3B). MR data and particle size analysis together suggest that both CLIO-Thrm-A and CLIO-Thrm-B are necessary for detection of thrombin with magnetic relaxation switching.

To check the utility of this system in biological fluids, we tested our sample in 50% human serum. A clear change in the MR signal was observed with 25 nM, and a significant change was seen with 75 nM thrombin (Figure 4). This result demonstrates that the system works in human serum without interference of biological components in serum.

In conclusion, we demonstrated aptamer functionalized superparamagnetic iron oxide nanoparticles for detection of an analyte, which is dependent upon the binding event of aptamer conjugated CLIO nanoparticles and the target molecule. The system demonstrated here is specific to thrombin and the sensitivity is as low as 10 nM. Similar approaches can be applied to other aptamer and CLIO nanoparticle systems.

ACKNOWLEDGMENT

The authors thank Natasha Yeung for helpful discussions and for comments on the manuscript and Dr. Boris Odintsov for his help in operating the MRI equipment. This material is based upon work supported by the National Science Foundation (DMR-0117792, DMI-0328162, and CTS-0120978), the U.S. Army Research Office (DAAD19-03-1-0227), and Biomedical Imaging Center of the Beckman Institute for Advanced Science and Technology and University of Illinois at Urbana–Champaign.

LITERATURE CITED

(1) Carr, D. H., Brown, J., Bydder, G. M., Steiner, R. E., Weinmann, H. J., Speck, U., Hall, A. S., and Young, I. R. (1984) Gadolinium-DTPA as a contrast agent in MRI: initial clinical experience in 20 patients. *Am. J. Roentgenol. 143*, 215–224.

(2) Kabalka, G., Buonocore, E., Hubner, K., Moss, T., Norley, N., and Huang, L. (1987) Gadolinium-labeled liposomes: targeted MR contrast agents for the liver and spleen. *Radiology 163*, 255–258.

(3) Weissleder, R., Hahn, P. F., Stark, D. D., Rummeny, E., Saini, S., Wittenberg, J., and Ferrucci, J. T. (1987) MR imaging of splenic metastases: ferrite-enhanced detection in rats. *Am. J. Roentgenol. 149*, 723–726.

(4) Josephson, L., Lewis, J., Jacobs, P., Hahn, P. F., and Stark, D. D. (1988) The effects of iron oxides on proton relaxivity. *Magn. Reson. Imaging 6*, 647–653.

(5) Saeed, M., Wagner, S., Wendland, M. F., Derugin, N., Finkbeiner, W. E., and Higgins, C. B. (1989) Occlusive and reperfused myocardial infarcts: differentiation with Mn-DPDP–enhanced MR imaging. *Radiology 172*, 59–64.

(6) Li, W.-h., Fraser, S. E., and Meade, T. J. (1999) A calcium-sensitive magnetic resonance imaging contrast agent. *J. Am. Chem. Soc. 121*, 1413–1414.

(7) Harisinghani, M. G., Barentsz, J., Hahn, P. F., Deserno, W. M., Tabatabaei, S., van de Kaa, C. H., de la, R. J., and Weissleder, R. (2003) Noninvasive detection of clinically occult lymph-node metastases in prostate cancer. *N. Engl. J. Med. 348*, 2491–2499.

(8) Lee, J., Zylka, M. J., Anderson, D. J., Burdette, J. E., Woodruff, T. K., and Meade, T. J. (2005) A steroid-conjugated contrast agent for magnetic resonance imaging of cell signaling. *J. Am. Chem. Soc. 127*, 13164–13166.

(9) Frullano, L., Tejerina, B., and Meade, T. J. (2006) Synthesis and characterization of a doxorubicin-Gd(III) contrast agent conjugate: A new approach toward prodrug-procontrast complexes. *Inorg. Chem. 45*, 8489–8491.

(10) Kresse, M., Wagner, S., Pfefferer, D., Lawaczeck, R., Elste, V., and Semmler, W. (1998) Targeting of ultrasmall superparamagnetic iron oxide (USPIO) particles to tumor cells in vivo by using transferrin receptor pathways. *Magn. Reson. Med. 40*, 236–242.

(11) Enochs, W. S., Harsh, G., Hochberg, F., and Weissleder, R. (1999) Improved delineation of human brain tumors on MR images using a long-circulating, superparamagnetic iron oxide agent. *J. Magn. Reson. Imaging 9*, 228–232.

(12) Dodd, C. H., Hsu, H.-C., Chu, W.-J., Yang, P., Zhang, H.-G., Mountz, J. D., Zinn, K., Forder, J., Josephson, L., Weissleder, R., Mountz, J. M., and Mountz, J. D. (2001) Normal T-cell response and in vivo magnetic resonance imaging of T cells loaded with HIV transactivator-peptide-derived superparamagnetic nanoparticles. *J. Immunol. Methods 256*, 89–105.

(13) Kooi, M. E., Cappendijk, V. C., Cleutjens, K. B. J. M., Kessels, A. G. H., Kitslaar, P. J. E. H. M., Borgers, M., Frederik, P. M., Daemen, M. J. A. P., and van Engelshoven, J. M. A. (2003) Accumulation of ultrasmall superparamagnetic particles of iron oxide in human atherosclerotic plaques can be detected by in vivo magnetic resonance imaging. *Circulation 107*, 2453–2458.

(14) Artemov, D., Mori, N., Okollie, B., and Bhujwalla, Z. M. (2003) MR molecular imaging of the Her-2/neu receptor in breast cancer cells using targeted iron oxide nanoparticles. *Magn. Reson. Med. 49*, 403–408.

(15) Corot, C., Petry, K. G., Trivedi, R., Saleh, A., Jonkmanns, C., Le, B. J.-F., Blezer, E., Rausch, M., Brochet, B., Foster-Gareau, P., Baleriaux, D., Gaillard, S., and Dousset, V. (2004) Macrophage imaging in central nervous system and in carotid atherosclerotic plaque using ultrasmall superparamagnetic iron

oxide in magnetic resonance imaging. *Invest. Radiol. 39*, 619–625.
(16) Nitin, N., LaConte, L. E. W., Zurkiya, O., Hu, X., and Bao, G. (2004) Functionalization and peptide-based delivery of magnetic nanoparticles as an intracellular MRI contrast agent. *J. Biol. Inorg. Chem. 9*, 706–712.
(17) Josephson, L., Tung, C.-H., Moore, A., and Weissleder, R. (1999) High-efficiency intracellular magnetic labeling with novel superparamagnetic-Tat peptide conjugates. *Bioconjugate Chem. 10*, 186–191.
(18) Lewin, M., Carlesso, N., Tung, C.-H., Tang, X.-W., Cory, D., Scadden, D. T., and Weissleder, R. (2000) Tat peptide-derivatized magnetic nanoparticles allow in vivo tracking and recovery of progenitor cells. *Nat. Biotechnol. 18*, 410–414.
(19) Josephson, L., Perez, J. M., and Weissleder, R. (2001) Magnetic nanosensors for the detection of oligonucleotide sequences. *Angew. Chem., Int. Ed. 40*, 3204–3206.
(20) Perez, J. M., Josephson, L., and Weissleder, R. (2004) Use of magnetic nanoparticles as nanosensors to probe for molecular interactions. *ChemBioChem 5*, 261–264.
(21) Zhao, M., Kircher, M. F., Josephson, L., and Weissleder, R. (2002) Differential conjugation of Tat peptide to superparamagnetic nanoparticles and its effect on cellular uptake. *Bioconjugate Chem. 13*, 840–844.
(22) Zhao, M., Josephson, L., Tang, Y., and Weissleder, R. (2003) Magnetic sensors for protease assays. *Angew. Chem., Int. Ed. 42*, 1375–1378.
(23) Perez, J. M., Simeone, F. J., Saeki, Y., Josephson, L., and Weissleder, R. (2003) Viral-induced self-assembly of magnetic nanoparticles allows the detection of viral particles in biological media. *J. Am. Chem. Soc. 125*, 10192–10193.
(24) Tsourkas, A., Hofstetter, O., Hofstetter, H., Weissleder, R., and Josephson, L. (2004) Magnetic relaxation switch immunosensors detect enantiomeric impurities. *Angew. Chem., Int. Ed. 43*, 2395–2399.
(25) Ellington, A. D., and Szostak, J. W. (1990) In vitro selection of RNA molecules that bind specific ligands. *Nature (London) 346*, 818–822.
(26) Tuerk, C., and Gold, L. (1990) Systematic evolution of ligands by exponential enrichment: RNA ligands to bacteriophage T4 DNA polymerase. *Science 249*, 505–510.
(27) Wilson, D. S., and Szostak, J. W. (1999) In vitro selection of functional nucleic acids. *Annu. Rev. Biochem. 68*, 611–647.
(28) Famulok, M., Mayer, G., and Blind, M. (2000) Nucleic acid aptamers-from selection in vitro to applications in vivo. *Acc. Chem. Res. 33*, 591–599.
(29) Drolet, D. W., Moon-McDermott, L., and Romig, T. S. (1996) An enzyme-linked oligonucleotide assay. *Nat. Biotechnol. 14*, 1021–1025.
(30) Wang, Y., Killian, J., Hamasaki, K., and Rando, R. R. (1996) RNA molecules that specifically and stoichiometrically bind aminoglycoside antibiotics with high affinities. *Biochemistry 35*, 12338–12346.
(31) Jayasena, S. D. (1999) Aptamers: an emerging class of molecules that rival antibodies in diagnostics. *Clin. Chem. 45*, 1628–1650.
(32) Liss, M., Petersen, B., Wolf, H., and Prohaska, E. (2002) An aptamer-based quartz crystal protein biosensor. *Anal. Chem. 74*, 4488–4495.
(33) Yamamoto, R., Baba, T., and Kumar, P. K. (2000) Molecular beacon aptamer fluoresces in the presence of Tat protein of HIV-1. *Genes Cells 5*, 389–96.
(34) Jhaveri, S. D., Kirby, R., Conrad, R., Maglott, E. J., Bowser, M., Kennedy, R. T., Glick, G., and Ellington, A. D. (2000) Designed signaling aptamers that transduce molecular recognition to changes in fluorescence intensity. *J. Am. Chem. Soc. 122*, 2469–2473.
(35) Stojanovic, M. N., de Prada, P., and Landry, D. W. (2000) Fluorescent sensors based on aptamer self-assembly. *J. Am. Chem. Soc. 122*, 11547–11548.
(36) Li, J., and Lu, Y. (2000) A highly sensitive and selective catalytic DNA biosensor for lead ions. *J. Am. Chem. Soc. 122*, 10466–10467. .
(37) Hamaguchi, N., Ellington, A., and Stanton, M. (2001) Aptamer beacons for the direct detection of proteins. *Anal. Biochem. 294*, 126–131.
(38) Fang, X., Cao, Z., Beck, T., and Tan, W. (2001) Molecular aptamer for real-time oncoprotein platelet-derived growth factor monitoring by fluorescence anisotropy. *Anal. Chem. 73*, 5752–5757.
(39) Stojanovic, M. N., de Prada, P., and Landry, D. W. (2001) Aptamer-based folding fluorescent sensor for cocaine. *J. Am. Chem. Soc. 123*, 4928–4931.
(40) Li, J. J., Fang, X., and Tan, W. (2002) Molecular aptamer beacons for real-time protein recognition. *Biochem. Biophys. Res. Commun. 292*, 31–40.
(41) Nutiu, R., and Li, Y. (2003) Structure-switching signaling aptamers. *J. Am. Chem. Soc. 125*, 4771–4778.
(42) Nutiu, R., and Li, Y. (2004) Structure-switching signaling aptamers: Transducing molecular recognition into fluorescence signaling. *Chem.—Eur. J. 10*, 1868–1876.
(43) Chen, Y., Wang, M., and Mao, C. (2004) An autonomous DNA nanomotor powered by a DNA enzyme. *Angew. Chem., Int. Ed. 43*, 3554–3557.
(44) Nutiu, R., Mei, S., Liu, Z., and Li, Y. (2004) Engineering DNA aptamers and DNA enzymes with fluorescence-signaling properties. *Pure Appl. Chem. 76*, 1547–1561.
(45) Liu, Y., Lin, C., Li, H., and Yan, H. (2005) Aptamer-directed self-assembly of protein arrays on a DNA nanostructure. *Angew. Chem., Int. Ed. 44*, 4333–4338.
(46) Tian, Y., and Mao, C. (2005) DNAzyme amplification of molecular beacon signal. *Talanta 67*, 532–537.
(47) Navani, N. K., and Li, Y. (2006) Nucleic acid aptamers and enzymes as sensors. *Curr. Opin. Chem. Biol. 10*, 272–281.
(48) Stojanovic, M. N., and Landry, D. W. (2002) Aptamer-based colorimetric probe for cocaine. *J. Am. Chem. Soc. 124*, 9678–9679.
(49) Liu, J., and Lu, Y. (2003) A colorimetric lead biosensor using DNAzyme-directed assembly of gold nanoparticles. *J. Am. Chem. Soc. 125*, 6642–6643.
(50) Pavlov, V., Xiao, Y., Shlyahovsky, B., and Willner, I. (2004) Aptamer-functionalized Au nanoparticles for the amplified optical detection of thrombin. *J. Am. Chem. Soc. 126*, 11768–11769.
(51) Liu, J., and Lu, Y. (2004) Adenosine-dependent assembly of aptazyme-functionalized gold nanoparticles and its application as a colorimetric biosensor. *Anal. Chem. 76*, 1627–1632.
(52) Ho, H.-A., and Leclerc, M. (2004) Optical sensors based on hybrid aptamer/conjugated polymer complexes. *J. Am. Chem. Soc. 126*, 1384–1387.
(53) Huang, C.-C., Huang, Y.-F., Cao, Z., Tan, W., and Chang, H.-T. (2005) Aptamer-modified gold nanoparticles for colorimetric determination of platelet-derived growth factors and their receptors. *Anal. Chem. 77*, 5735–5741.
(54) Liu, J., and Lu, Y. (2006) Fast colorimetric sensing of adenosine and cocaine based on a general sensor design involving aptamers and nanoparticles. *Angew. Chem., Int. Ed. 45*, 90–94.
(55) Liu, J., and Lu, Y. (2007) Non-base pairing DNA provides a new dimension for controlling aptamer-linked nanoparticles and sensors. *J. Am. Chem. Soc. 129*, 8634–8643.
(56) Lu, Y., and Liu, J. (2006) Functional DNA nanotechnology: emerging applications of DNAzymes and aptamers. *Curr. Opin. Biotechnol. 17*, 580–588.
(57) Lu, Y., and Liu, J. (2007) Smart nanomaterials inspired by biology: dynamic assembly of error-free nanomaterials in response to multiple chemical and biological stimuli. *Acc. Chem. Res. 40*, 315–323.
(58) Xu, D., Xu, D., Yu, X., Liu, Z., He, W., and Ma, Z. (2005) Label-free electrochemical detection for aptamer-based array electrodes. *Anal. Chem. 77*, 5107–5113.

(59) Xiao, Y., Piorek, B. D., Plaxco, K. W., and Heeger, A. J. (2005) A reagentless signal-on architecture for electronic, aptamer-based sensors via target-induced strand displacement. *J. Am. Chem. Soc. 127*, 17990–17991.

(60) Xiao, Y., Lubin, A. A., Heeger, A. J., and Plaxco, K. W. (2005) Label-free electronic detection of thrombin in blood serum by using an aptamer-based sensor. *Angew. Chem., Int. Ed. 44*, 5456–5459.

(61) Yigit, M. V., Mazumdar, D., Kim, H.-K., Lee, J. H., Odintsov, B., and Lu, Y. (2007) Smart "turn-on" magnetic resonance contrast agents based on aptamer-functionalized superparamagnetic iron oxide nanoparticles. *ChemBioChem 8*, 1675–1678.

(62) Bock, L. C., Griffin, L. C., Latham, J. A., Vermaas, E. H., and Toole, J. J. (1992) Selection of single-stranded DNA molecules that bind and inhibit human thrombin. *Nature (London) 355*, 564–566.

(63) Tasset, D. M., Kubik, M. F., and Steiner, W. (1997) Oligonucleotide inhibitors of human thrombin that bind distinct epitopes. *J. Mol. Biol. 272*, 688–698.

(64) Macaya, R. F., Schultze, P., Smith, F. W., Roe, J. A., and Feigon, J. (1993) Thrombin-binding DNA aptamer forms a unimolecular quadruplex structure in solution. *Proc. Natl. Acad. Sci. U.S.A. 90*, 3745–3749.

(65) Padmanabhan, K., Padmanabhan, K. P., Ferrara, J. D., Sadler, J. E., and Tulinsky, A. (1993) The structure of a-thrombin inhibited by a 15-mer single-stranded DNA aptamer. *J. Biol. Chem. 268*, 17651–17654.

BC7003928

Lipophilic Peptides for Gene Delivery

Carla A. H. Prata,[†] Xiao-Xiang Zhang,[†] Dan Luo,[‡] Thomas J. McIntosh,[§] Philippe Barthelemy,[||] and Mark W. Grinstaff*,[†]

Departments of Biomedical Engineering and Chemistry, Boston University, Boston, Massachusetts 02215, Department of Biological and Environmental Engineering, Cornell University, Ithaca, New York 14853, Department of Cell Biology, Duke University Medical Center, Durham, North Carolina 27710, and INSERM U869, Université Victor Segalen, Bordeaux, F-33076, France. Received December 10, 2007; Revised Manuscript Received December 21, 2007

DNA transfections are widely performed in research laboratories and *in vivo* gene delivery holds the promise for curing many diseases. The synthetic carriers or vectors for DNA are typically cationic lipids. However, in biology, the recognition of nucleic acids by proteins involves both electrostatic and stacking contributions. As such we have prepared a series of new lipophilic peptide vectors that possess lysine and tryptophan amino acids for evaluation. These lipophilic peptides show minimal cytotoxicity and enhanced *in vitro* gene transfection activity.

The complexation of cationic amphiphiles with DNA or RNA and the resulting supramolecular structures are of interest for the delivery of nucleic acids to cells. As such, a means to correct a defective gene, introduce a new gene, or knock-down a gene is provided for a specific *in vitro* or *in vivo* application (*1–7*). This complexation between cationic amphiphiles and nucleic acids is governed by electrostatic interactions between the positively charged amphiphiles and the negatively charged phosphate backbone of the nucleic acid and the hydrophobic chain−chain packing forces between the individual assembled amphiphiles. In biology, the recognition of nucleic acids by proteins involves more than electrostatic interactions (*8–10*). Examination of these protein nucleic acid recognition motifs typically reveals structures rich in basic and aromatic amino acids that provide important electrostatic and stacking contributions to binding. With this inspiration in mind, we are designing peptide-based amphiphiles for gene delivery. Herein we describe a series of lipophilic peptides including the synthesis, physiochemical properties, cytotoxicity, and *in vitro* gene transfection activity.

To mimic structural characteristics present in nucleic acid binding proteins, we selected the tripeptide Lys-Trp-Lys, **KWK**, to be the headgroup for the amphiphile because it possesses cationic charges and an aromatic side chain and is relatively small in size. Moreover, this peptide is known to bind DNA with a binding constant on the order of 10^4 M and is a model peptide used to study protein−nucleic acid interactions, and lysine and tryptophan provide important interactions in a number of structurally characterized DNA binding domains of proteins (*11–14*). In addition, lysine-based small molecule amphiphiles and macromolecules (e.g., polylysine) are being explored and used for gene transfection (*15–24*). In order to perform a systematic study to identify the key molecular components responsible for transfection activity with these new lipophilic peptides, we prepared a series of amphiphiles where the headgroup (charge, aliphatic content, aromatic content) and fatty acid chain length (C12:0, C14:0, C16:0, and C18:0) were varied. As shown in Figure 1, fourteen different lipophilic peptides were synthesized and investigated. The lipophilic peptides were synthesized in good yield. First, the fatty acids were coupled to 3-*t*-butyldiphenylsilylglycerol using EDCI and DMAP in CH_2Cl_2. The silyl protecting group was removed with TBAF and then the corresponding Boc-protected amino acids were coupled to the free primary hydroxyl. The complete synthetic and characterization details as well as the reaction scheme can be found in the Supporting Information document.

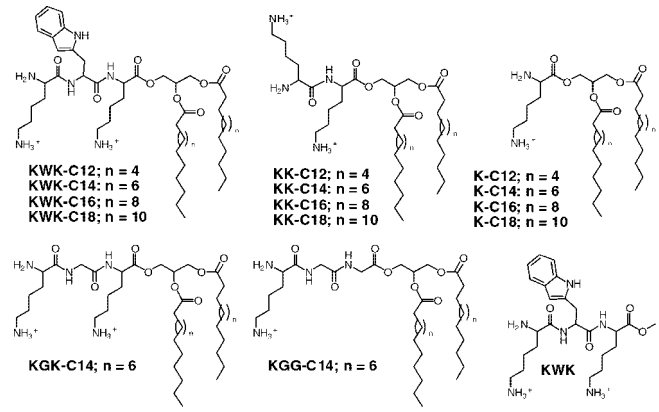

Figure 1. Lipophilic peptides under investigation for gene delivery.

To determine whether the lipophilic peptides bind DNA, we performed a standard ethidium bromide-DNA displacement fluorescence assay. All of the lipophilic peptides bind DNA with approximately the same affinity 10^6 M as measured by displacement of ethidium bromide. Most of the lipophilic peptides form DNA complexes with a cation to anion ratio between 1.5 and 2, except for the C18:0 analogues which have a cation to anion ratio of 3. Binding curves for all of the lipophilic peptides can be found in the SI.

These lipophilic peptides are likely to form bilayer vesicles in aqueous solution, given the polar headgroup and long hydrophobic acyl chains present in the structure. We prepared liposome solutions of all the lipophilic peptides with and without DNA by sonicating a hydrated film of the lipid in an aqueous solution (see SI for details). Dynamic light scattering measurements revealed the average diameter to range from 170 to 850 nm for the various lipophilic peptides. As expected, vesicles were not observed with the tripeptide alone, **KWK**. Next, X-ray

* Correspondence should be addressed to M.W.G.; author E-mail: mgrin@bu.edu.
[†] Boston University.
[‡] Cornell University.
[§] Duke University Medical Center.
[||] INSERM U869.

10.1021/bc700451b CCC: $40.75 © 2008 American Chemical Society
Published on Web 01/11/2008

diffraction experiments were performed at 25 °C on samples in the absence and presence of DNA to characterize the supramolecular structure (see SI). A hydrated vesicle pellet was obtained for all samples except **K-C14**, **KK-C16**, **K-C16**, and **KGG-C14**. For the specimens that formed pellets, oriented multilayers were prepared for X-ray analysis by placing the pellets on a curved glass substrate and incubating at 66% relative humidity. All of the samples that did diffract showed multiple reflections indexing as orders of lamellar repeat periods, characteristic of lipid bilayers. For a specific headgroup the lamellar repeat period systematically increased with increasing fatty acid chain length. For example, the repeat periods for **KK-C12**, **KK-C14**, and **KK-C18** were 3.7 nm, 4.1 nm, and 5.1 nm, respectively. For these **KK** samples the repeat period did not increase appreciably upon the addition of DNA, indicating that DNA was not present within the multilayers. The lipophilic peptides **KWK-C14** and **KWK-C16**, possessing the tripeptide headgroup and either the C14:0 or C16:0 acyl chains, gave larger lamellar repeat periods in the presence of DNA. The addition of DNA increased the repeat periods from 4.4 to 7.3 nm and 6.6 to 7.1 nm for **KWK-C14** and **KWK-C16**, respectively. For **KGK-C14** a repeat period of 4.1 nm was obtained without DNA and a satisfactory pellet with DNA was not obtained. For **KGG-C14** the repeat period in the presence of DNA was 6.8 nm. These data with the tripeptide headgroups are consistent with a structural model where a smectic phase is formed with the DNA chains located between the adjacent lipid bilayers within the multilamellar liposome. This structural model has been reported for complexes of DNA with DOTAP (*25*) and cationic triesters of phosphatidylcholine (*26*).

Transfection experiments using the reporter gene, β-galactosidase (β-gal, pVax-LacZ1, Invitrogen), were performed with chinese hamster ovarian (CHO) and NIH 3T3 cells (see SI for details). Gene transfection results were determined after 48 h as a function of both lipophilic peptides and cation/anion ratio. Only those lipophilic peptides possessing the tripeptide headgroup afforded significant transfection of the reporter gene. The peptide itself does not transfect. As shown in Figure 2 for the CHO cells, lipophilic peptides **KWK-C14** and **KWK-C16** were more effective synthetic vectors than the **KWK-C12** and **KWK-C18** based lipids. To assess the role of the aromatic tryptophan and lysine in the headgroup, we tested peptidic amphiphile **KGK-C14** where the W was replaced with a glycine (G) residue and **KGG-C14** where the alpha K was also replaced with a G. As shown in Figure 2, good transfection activity was observed with **KGK-C14**, and higher levels were obtained with the **KGG-C14** transfection agent. The lipophilic peptide **KGG-C14** was comparable to our positive control. Successful transfection was also observed with the NIH 3T3 cells as shown in Figure 2 with the **KWK-C16** being the most active. The lipophilic peptides transfected a large number of cells in the population as confirmed by histochemical staining (Figure 3). Cytotoxity experiments performed with all the tripeptide lipophilic peptides showed no significant cytotoxicity, similar to nontreated cells and significantly better than Lipofectamine 2000 when exposed to chinese hamster ovarian (CHO) or NIH 3T3 cells (see SI).

In summary, a series of new lipophilic peptides are reported and those possessing a cationic tripeptide headgroup are effective nonviral vectors for gene delivery. A number of observations can be made for these lipophilic peptides including (1) the necessity for lipophilicity in the vector as the tripeptide itself does not form vesicular structures nor afford transfection (**KWK-C14** vs **KWK**); (2) more cationic charges are not the sole contributor to efficient transfection (**K-C16** vs **KK-C16** vs **KWK-C16**); (3) a peptide-based headgroup containing an aromatic residue capable of DNA intercalation is not required as substitution by an aliphatic residue gives activity; (4) spacing

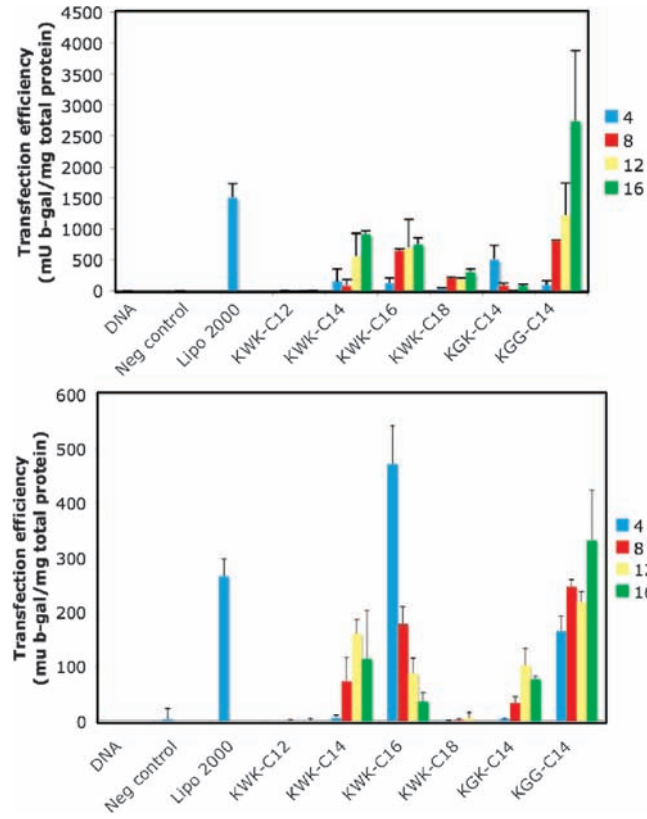

Figure 2. Gene transfection results after 48 h in CHO cells (top) and in NIH 3T3 (bottom) as a function of lipophilic peptide and mole ratio. $N = 3$.

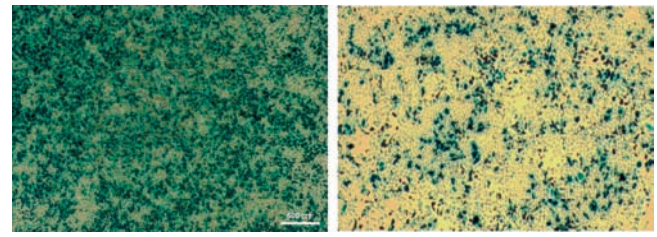

Figure 3. Photograph of CHO cells transfected with the reporter gene, β-galactosidase (β-gal) using **KWK-C14** (right) and Lipofectamine 2000 (left).

of the cationic charges within the headgroup affords better transfection performance (**KWK-C14** vs **KK-C14**); and (5) lipoplexes forming a lamellar structure with DNA which possess >6 nm repeat periods perform better compared to the structures that do not (**KWK-C14** vs **KK-C14**). These results highlight the sensitivity of gene transfection to subtle changes in chemical structure and the importance of identifying the optimized noncovalent interactions between the transfection agent and DNA. Importantly, these results with the lipophilic peptides expand the current repertoire of efficient transfection vectors available for use. Continued research with synthetic nonviral vectors will facilitate the design, development, and subsequent *in vitro* and *in vivo* evaluation toward the goal of efficient and safe delivery of nucleic acids.

ACKNOWLEDGMENT

This work was supported by the National Institutes of Health (EB005658 to M.W.G. and GM27278 to T.J.M.).

Supporting Information Available: Complete experimental details, synthesis, characterization data, and cytotoxicity experiments can be found. This material is available free of charge via the Internet at http://pubs.acs.org.

LITERATURE CITED

(1) Saltzman, W. M., and Luo, D. (2000) Synthetic DNA delivery systems. *Nat. Biotechnol. 18*, 33–37.
(2) Davis, M. E. (2002) *Curr. Opin. Biotechnol. 13*, 128–131.
(3) Kabanov, A. V., Felgner, P. L. ,and Seymour, L. W. (1998) Self-assembling complexes for gene delivery, *From laboratory to clinical trial*, John Wiley and Sons, New York.
(4) Putnam, D. (2006) Polymers for gene delivery across length scales. *Nat. Mater. 5*, 439–451.
(5) Behr, J. P. (1994) Gene transfer with synthetic cationic amphiphiles: Prospects for gene therapy. *Bioconjugate Chem. 5*, 382–389.
(6) Yan, W., and Huang, L. (2007) Recent advances in liposome-based nanoparticles for antigen delivery. *Polym. Rev. 47*, 329–344.
(7) Karmali, P. P., and Chaudhuri, A. (2007) Cationic liposomes as non-viral carriers of gene medicines: Resolved issues, open questions, and future promises. *Med. Res. Rev. 27*, 696–722.
(8) Nadassy, K., Wodak, S. J., and Janin, J. (1999) Structural features of protein-nucleic acid recognition sites. *Biochemistry 38*, 1999–2017.
(9) Jones, S., van Heyningen, P., Berman, H. M., and Thornton, J. M. (1999) Protein-DNA interactions: A structural analysis. *J. Mol. Biol. 287*, 877–896.
(10) Ahmad, S., Gromiha, M. M., and Sarai, A. (2004) Analysis and prediction of DNA-binding proteins and their binding residues based on composition, sequence and structural information. *Bioinformatics 20*, 477–486.
(11) Brun, F., Toulmé, J. J., and Hélène, C. (1975) Interactions of aromatic residues of proteins with nucleic acids. Fluorescence studies of the binding of oligopeptides containing tryptophan and tyrosine residues to polynucleotides. *Biochemistry 14*, 558–563.
(12) Behmoaras, T., Toulmé, J. J., and Hélène, C. (1982) Specific recognition of apurinic sites in DNA by a tryptophan containing peptide. *Proc. Nat. Acad. Sci. 78*, 926–930.
(13) Masse, J. E., Wong, B., Yen, Y.-M., Allain, F. H.-T., Johnson, R. C., and Feigon, J. (2002) The s. Cerevisiae architectural hmgb protein nhp6a complexed with DNA: DNA and protein conformational changes upon binding. *J. Mol. Biol. 323*, 263–284.
(14) Redinbo, M. R., Champoux, J. J., and Hol, W. G. J. (2000) Novel insights into catalytic mechanism from a crystal structure of human topoisomerase i complex with DNA. *Biochemistry 39*, 6832–6840.
(15) Kabanov, A. V., and Kabanov, V. A. (1995) DNA complexes with polycations for the delivery of genetic material into cells. *Bioconjugate Chem. 6*, 7–20.
(16) Karmali, P. P., Kumar, V. V., and Chaudhuri, A. (2004) Design, syntheses, and in vitro gene delivery efficacies of novelmono, d-, and trilysinated cationic lipids: A structure-activity investigation. *J. Med. Chem. 47*, 2123–2132.
(17) Choi, J. S., Joo, D. K., Kim, C. H., Kim, K., and Park, J. S. (2000) Synthesis of barbell-like tri-block copolymers, poly(l-lysine)dendrimer-block-poly(ethylene glycol)-block-poly(l-lysine) dendrimers and its self-assembly with plasmid DNA. *J. Am. Chem. Soc. 122*, 474–480.
(18) Zauner, W., Ogris, M., and Wagner, E. (1998) Polylysine-based transfection systems utilizing receptor-mediated delivery. *Adv. Drug. Delivery Rev. 30*, 97–113.
(19) Deshmukh, H. M., and Huang, L. (1997) Liposome and polylysine mediated gene transfer. *New. J. Chem. 21*, 113–124.
(20) Slimani, H., Guenin, E., Briane, D., Coudert, R., Charnaux, N., Starzec, A., Vassy, R., Lecouvey, M., Perret, Y. G., and Cao, A. (2006) Lipopeptide-based liposomes for DNA delivery into cells expressing neuropilin-1. *J. Drug Targeting 14*, 694–706.
(21) Murphy, E. A., Waring, A. J., Murphy, J. C., Willson, R. C., and Longmuir, K. J. (2001) Development of an effective gene delivery system: A study of complexes composed of a peptide-based amphiphilic DNA compaction agent and phospholipid. *Nucleic Acid Res. 29*, 3694–3704.
(22) Gopal, V., Prasad, T. K., Rao, N. M., Takafuji, M., Rahman, M. M., and Ihara, H. (2006) Synthesis and in vitro evaluation of glutamide-containing cationic lipids for gene delivery. *Bioconjugate Chem. 17*, 1530–1536.
(23) Chan, E., Amon, M., Marano, R. J., Wimmer, N., Kearns, P. S., Manolios, N., Rakoczy, P. E., and Toth, I. (2007) Novel cationic lipophilic peptides for oligodeoxynucleotide delivery. *Bioorg. Med. Chem. 15*, 4091–4097.
(24) Waterhouse, J. E., Harbottle, R. P., Keller, M., Kostarelos, K., Coutelle, C., Jorgensen, M. R., and Miller, A. D. (2005) Synthesis and application of integrin targeting lipopeptides in targeted gene delivery. *ChemBioChem 6*, 1212–1223.
(25) Radler, J. O., Koltover, I., Salditt, T., and Safinya, C. R. (1997) Structure of DNA-cationic liposome complexes: DNA intercalation in multilamellar membranes in distinct interhelical packing regimes. *Science 275*, 810–814.
(26) MacDonald, R. C., Ashley, G. W., Shida, M. M., Rakhmanova, V. A., Tarahovsky, Y. S., Kennedy, M. T., Pozharski, E. V., Baker, K. A., Jones, R. D., Rosenzweig, H. S., Choi, K. L., Qiu, R., and McIntosh, T. J. (1999) Physical and biological properties of cationic triesters of phosphatidylcholine. *Biophys. J. 77*, 2612–2629.

BC700451B

ARTICLES

Applications of Mesenchymal Stem Cells Labeled with Tat Peptide Conjugated Quantum Dots to Cell Tracking in Mouse Body

Yun Lei,[†,‡] Haiyang Tang,[§] Lide Yao,[†] Richeng Yu,[‡] Meifu Feng,*[,§] and Bingsuo Zou*[,†]

Micro-Nano Technologies Research Center and State Key Lab of CBSC, Hunan University, Changsha 410082, China, Institute of Physics and Institute of Zoology, Chinese Academy of Sciences, Beijing 100080, China. Received February 28, 2007; Revised Manuscript Received September 15, 2007

Fluorescent quantum dots have great potential in cellular labeling and tracking. Here, PEG encapsulated CdSe/ZnS quantum dots have been conjugated with Tat peptide, and introduced into living mesenchymal stem cells. The Tat peptide conjugated quantum dots in mesenchymal stem cells were assessed by fluorescent microscopy, laser confocal microscope and. flow cytometry. The result shows that Tat peptide conjugated quantum dots could enter mesenchymal stem cells efficiently. The Tat-quantum dots labeled stem cells were further injected into the tail veins of NOD/SCID beta2 M null mice, and the tissue distribution of these labeled cells in nude mice were examined with fluorescence microscope. The result shows that characteristic fluorescence of quantum dots was observed primarily in the liver, the lung and the spleen, with little or no quantum dots accumulation in the brain, the heart, or the kidney.

INTRODUCTION

Stem cells have generated a great deal of excitement as a potential source of cell-based therapies (*1, 2*). The development of stem cell therapies requires a quantitative and qualitative assessment of stem cell fate and their distribution in the host organism. The uses of traditional organic fluorophores and green fluorescent protein are subject to certain limitations in living cells. Quantum dots (QDs) as a new generation of fluorescent markers have shown tremendous advantage in biological research, especially cellular labeling and imaging (*3, 4*). Many efforts have been directed toward introducing QDs into cells. Strategies have been used such as microinjection (*5*), electroporation (*6*), phagocytosis (*7, 8*), cationic lipid transportation (*9*), and peptide-mediated transfection (*10–15*). Therefore, peptide-mediated transfection has attracted more and more attention for the efficient cellular transmembrane delivery and labeling (*16, 17*). Though the mechanism of peptide-mediated membrane translocation remains unclear, increasing evidence indicates the involvement of several types of endocytosis (*18–20*).

Here, we used the cell-penetrating peptide Tat modified with a linker and the C-terminus followed by a reactive cysteine, which was covalently attached to QDs via the cross-linking reagent. Moreover, considering the cytotoxicity of QDs in the biological system, CdSe/ZnS QDs have been investigated for different surface modification (*21*) such as coating with mercaptoacid, silane, and polymer. Recently, PEG-coated QDs were investigated (*22, 23*), and the results show that PEG-coated QDs have minimal impact on cells. Thus, in our work, 1,2-distearoyl-*sn*-glycero-3-phosphoethanolamine-*N*-[amino(poly(ethylene glycol)) 2000] (DSPE-PEG 2000 amine) was selected to coat QDs with amine groups as functional groups for further covalent bonding to the cysteine-modified Tat peptide. PEG-coated QD-Tat peptide complexes were transported into living mesenchymal stem cells (MSCs) and assessed by fluorescent microscopy, laser confocal microscopy, and flow cytometry. The QD–Tat peptide labeled MSCs were further assessed with stem cell engraftment in nude mice, and the result shows that Tat peptide covalently conjugated QDs may not only act as an effective probe for stem cell observation in vitro, but also serve as a long-term tracer for stem cell based transplantation in the mouse body. Thus, the purpose of our study was to evaluate the internalization of Tat peptide conjugated QDs MSCs and the tissue distribution of these labeled stem cells in a nude mouse.

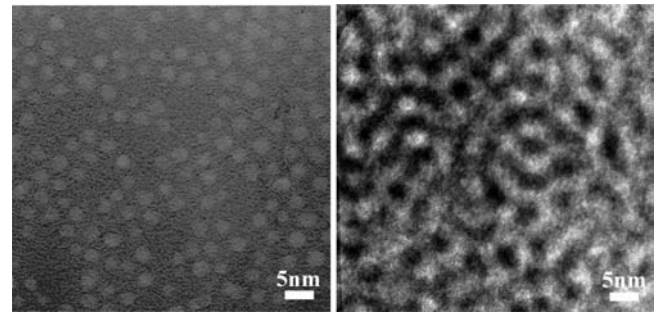

Figure 1. TEM images of the as-prepared TOPO-capped CdSe/ZnS QDs (left, about 3 nm) and DSPE-PEG-coated QDs (right, about 4 nm).

MATERIALS AND METHODS

Materials. *n*-Trioctylphosphine oxide (TOPO) (90%), bis(trimethylsilyl) sulfide (95%), $Cd(CH_3)_2$ (97% hexane solution), $Zn(CH_3)_2$ (1.0 M heptane solution), and *n*-trioctylphosphine (TOP) were purchased from Acros Chemicals Corporation. Se

* E-mail: zoubs@aphy.iphy.ac.cn (B.Z.); fengmf@ioz.ac.cn (M.F.).
[†] Hunan University.
[‡] Institute of Physics, Chinese Academy of Sciences.
[§] Institute of Zoology, Chinese Academy of Sciences.

10.1021/bc0700685 CCC: $40.75 © 2008 American Chemical Society
Published on Web 12/15/2007

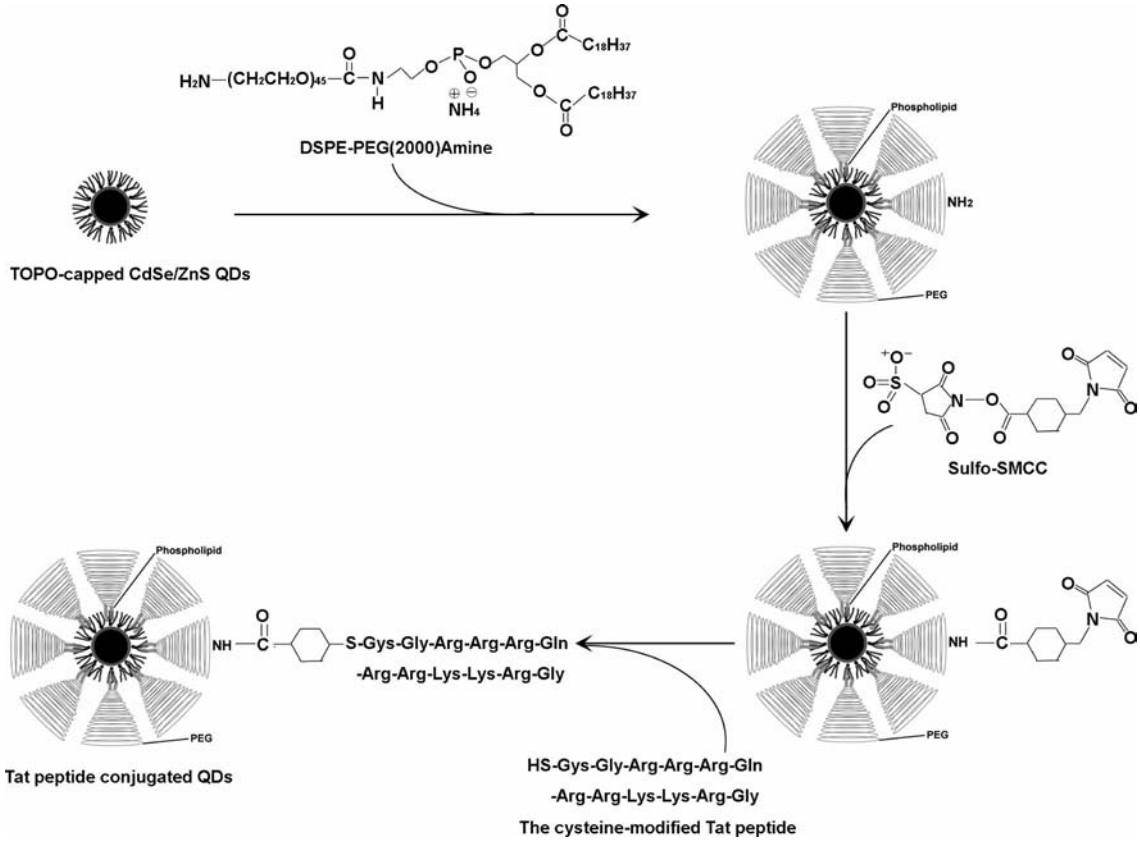

Figure 2. Schematic illustration of peptide-conjugated QDs for stem cell targeting and imaging. The first step involves the coating of TOPO-capped QDs with DSPE-PEG 2000 NH_2. After coating, DSPE-PEG-coated QDs are water-soluble with amine on the surface. Then, the DSPE-PEG-coated CdSe/ZnS QDs were reacted overnight with the cysteine-modified Tat peptides via the Sulfo-SMCC cross-linker. Sulfo-SMCC has an *N*-hydroxysuccinimide (NHS) ester at one end, which reacts with a primary amine on the QDs to form an amide bond and a maleimide group at the other, which reacts with a thiol on the cysteine-modified Tat peptide to form a thioether.

powder (99%), $CHCl_3$ (AR), and methanol (AR) were purchased from Beijing Chemical Reagents Corporation. Sulfosuccinimidyl 4-(*N*-maleimidomethyl)cyclohexane-1-carboxylate (Sulfo-SMCC) were purchased from Pierce Biotechnology. Cell-penetrating peptide Tat custom-modified with a linker at the C-terminus followed by a reactive cysteine was purchased from Beijing Scilight Biotechnology Limited Corporation. 1,2-Distearoyl-*sn*-glycero-3-phosphoethanolamine-*N*-[amino(poly(ethylene glycol)) 2000] (DSPE-PEG 2000 amine) was purchased from Avanti Polar Lipids Inc.

Preparation of DSPE-PEG-Coated CdSe/ZnS QDs. An encapsulation strategy was used for hydrophobic CdSe/ZnS QDs. This approach exploits the hydrophobic nature of the nanoparticle surface by utilizing an amphiphilic poly(ethylene glycol)-phospholipid (PEG-phospholipid), whose hydrophobic portion interacts with the nanoparticle surface to create micelles, resulting in a self-assembled monolayer coating. The PEG portion of the coating confers them aqueous solubility and biocompatibility, at the same time the use of modified PEG allows for bioconjugation (*24*).

CdSe/ZnS QDs were prepared using a synthetic route reported earlier (*25, 26*). Since the quality of TOPO affected the nucleation and growth process seriously, TOPO was purified at the temperature of 400 °C in argon before use. All other reagents were used without any further purification. The prepared TOPO-capped QDs were added with equal volume of methanol and cooled to −10 °C for 2 h. After vigorous centrifugation, the precipitation from the cold solution was collected for the further use.

50 mg DSPE-PEG 2000 amine was dissolved in 2 mL chloroform, and 2.5 mg TOPO-capped CdSe/ZnS QDs were added. QDs coated with DSPE-PEG 2000 amine was dried under argon gas and left in a vacuum desiccator for 48 h to remove all trace of organic solvent.

Bioconjugation of DSPE-PEG-Coated CdSe/ZnS QDs. To functionalize CdSe/ZnS QDs for bioconjugation and subsequent delivery and imaging studies, we used the cysteine-modified Tat peptide and heterobifunctional cross-linking reagent Sulfo-SMCC. First, Sulfo-SMCC was dissolved in 500 μL phosphate-buffered saline (PBS, pH 7.4, NaCl 50 mM) at a concentration of 20 μM, and then DSPE-PEG-coated CdSe/ZnS QDs were dispersed in the PBS solution of Sulfo-SMCC cross-linker at a concentration of 1 μM. After incubating for 60 min at room temperature, excess cross-linker molecules were removed by using a Sephadex G-25 column. The 10-fold concentration of Tat peptide (10 μM) was added to the above PBS solution and reacted overnight with the DSPE-PEG-coated CdSe/ZnS QDs via the Sulfo-SMCC cross-linker.

Cell Cultures. MSCs were isolated from fetal bone marrow. The cells were grown in complete Dulbecco's Modified Eagle'S Medium—high glucose (10% fetal bovine serum, 100 U/mL penicillin, and 100U/mL streptomycin sulfate) on a 6-well plate predeposited with a slide.

Cell Labeling with Bioconjugated CdSe/ZnS QDs. 500 μL Tat peptide-conjugated QDs were added to the culture of MSCs (5×10^6). The Tat peptide-conjugated QDs and MSCs were incubated at 37 ° for 60 min.

MSC Transplantation and Bioluminescent Imaging. For studies on systemic distribution and engraftment of QD–Tat peptide labeled stem cells, approximately 10^6 labeled stem cells suspended in 0.2 mL PBS were injected intravenously into the tail veins of NOD/SCID beta2 M null mice (male, 8 weeks of

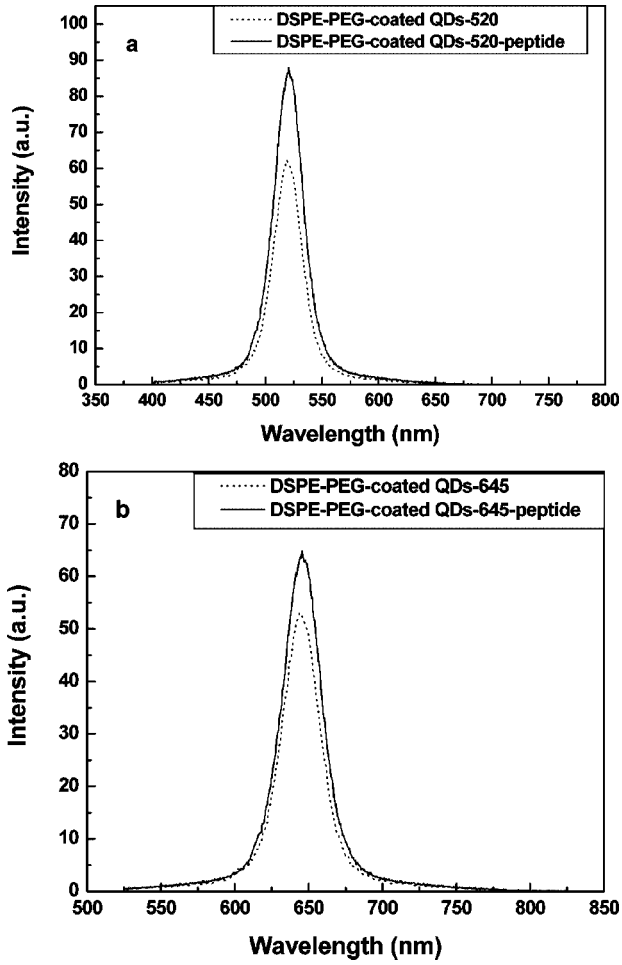

Figure 3. PL spectra of DSPE-PEG-coated QDs and Tat peptide-conjugated QDs. The PL intensity of Tat peptide-conjugated QDs-520 (solid line) enhances by 41% compared to simple DSPE-PEG-coated QDs-520 (dotted line). Similarly, the PL intensity of Tat peptide-conjugated QDs-645 (solid line) increases by 22% as compared to simple DSPE-PEG-coated QDs-645 (dotted line). The PL spectra were recorded with an excitation at 380 nm.

age). Mice were killed after 24 h, and major organs (heart, lung, spleen, liver, kidney, and brain) were removed and washed three times with PBS to remove retained erythrocytes. Collected tissues were frozen in liquid nitrogen and embedded into paraffin. To assess histological QD uptake and distribution of transplanted stem cells, tissue collections were cryosectioned into sections 5–10 μm thick, fixed with acetone at 0 °C, and examined with a fluorescence microscope.

Characterizations. The morphologies of CdSe/ZnS QDs were observed on a JEM2010 transmission electron microscope. The photoluminescence (PL) spectra were recorded on a PTI-601 fluorescence spectrophotometer. The fluorescence images were taken on a fluorescence microscope (Olympus IX71) excited by an ultraviolet source, and the confocal images were recorded on a Zeiss LSM510 laser confocal microscope excited by an argon laser (488 nm).

To investigate the location of QD–Tat peptides into MSCs, the MSCs were treated for transmission electron microscope (TEM) observation. MSCs were fixed with 2.5% glutaraldehyde for 4 h at room temperature and rinsed with phosphate-buffered saline (PBS), and then the cells were fixed with 1% osmium tetraoxide for 1 h and washed with distilled water. The samples were dehydrated through a graded ethanol and acetone series, and finally embedded with epoxy resin. The epoxy resin samples were polymerized at 60 °C for 24 h. Thin sections were made using an ultramicrotome and collected on copper grids. The samples on copper grids were observed on a Philips CM200 transmission electron microscope (TEM) at 80 KV.

To assess the labeling efficiency of QD–Tat peptides, the MSCs incubated with QD–Tat peptides were trypinized and washed with PBS three times, and then analyzed using flow cytometry (FACSCaliblur, BD Biosciences, San Diego, CA, USA) with a 488 nm Ar laser.

RESULTS AND DISCUSSION

Monodispersed CdSe/ZnS QDs capped with TOPO were characterized by transmission electron microscopy (Figure 1 left), and the corresponding size distribution (σ) is 2.72%. After coating with DSPE-PEG 2000 amine (Figure 1 right), the size distribution of DSPE-PEG-coated QDs is 11.3% due to the effect of the solvent polarity.

The scheme of DSPE-PEG coating and Tat peptide conjugation for cellular targeting and imaging is shown in Figure 2. The first step involves the coating of TOPO-capped QDs with DSPE-PEG 2000 amine. After coating, DSPE-PEG-coated QDs are water-soluble with amine on the surface. Then, the DSPE-PEG-coated CdSe/ZnS QDs reacted overnight with the cysteine-modified Tat peptides via the Sulfo-SMCC cross-linker.

Tat peptide conjugated QDs were prepared with two distinct QDs (QDs-520 and QDs-645). The PL spectra were measured after the first reaction with DSPE-PEG 2000 amine, and the PL intensity of QDs changed during the peptide coupling process. As shown in Figure 3a, the PL intensity of QDs-520 was enhanced remarkably after the secondary coupling with the Tat peptides, increasing by 41%. Clearly, this increase was also observed in QDs-645 (Figure 3b) after conjugating with Tat peptides, enhanced by 22%. The enhancement might be attributed to the covalent bonding between the thiol groups of cysteine-modified Tat peptides and the amide groups of DSPE-PEG 2000 amine capped QDs. Coating QD with a high molecular weight polymer such as polypeptides might prohibit electron leakage through the surface NH_2 groups and might contribute to the continuously electron-rich condition of whole QDs (*10*).

MSCs were incubated with Tat peptide-conjugated QDs and observed by fluorescent microscopy. The fluorescent microscopy images (Figure 4a–c) show that MSCs incubated with QD–Tat peptides emit fluorescence. A punctate and vesicular QD fluorescence pattern was observed within perinuclear spaces. For comparison, DSPE-PEG-coated QDs were directly incubated with MSCs without the assistance of Tat peptides. The fluorescent microscopy images are shown in Figure 4d–f. No intracellular QD fluorescence was observed in MSCs. Similarly, control experiments performed with a random peptide resulted in no noticeable cellular uptake (Figure 4g–i). The results suggest that Tat peptide is an effective vehicle for labeling QDs entering stem cells. The reactive cysteine sequence allows Tat peptides to conjugate with DSPE-PEG-coated QDs via cross-linking reagent while the oligoarginine sequence allows QD delivery across the cellular membrane and intracellular labeling.

The QD–Tat peptide labeled stem cells were further studied on a laser confocal microscope (Figure 5). In contrast to our previous observations using fluorescence microscopy, the more sensitive confocal observation technique used here indicated a higher intensity of intracellular QD fluorescence than what was previously measured above (a punctate and vesicular QD fluorescence pattern in Figure 4). The fluorescent QD–Tat peptides dispersed nearly homogeneously throughout the cytoplasm in the periphery of the nucleus. To demonstrate the use of QD–Tat peptides in a multiplexing experiment, two color quantum dots (QDs-520 and QDs-645) are designed to bind to

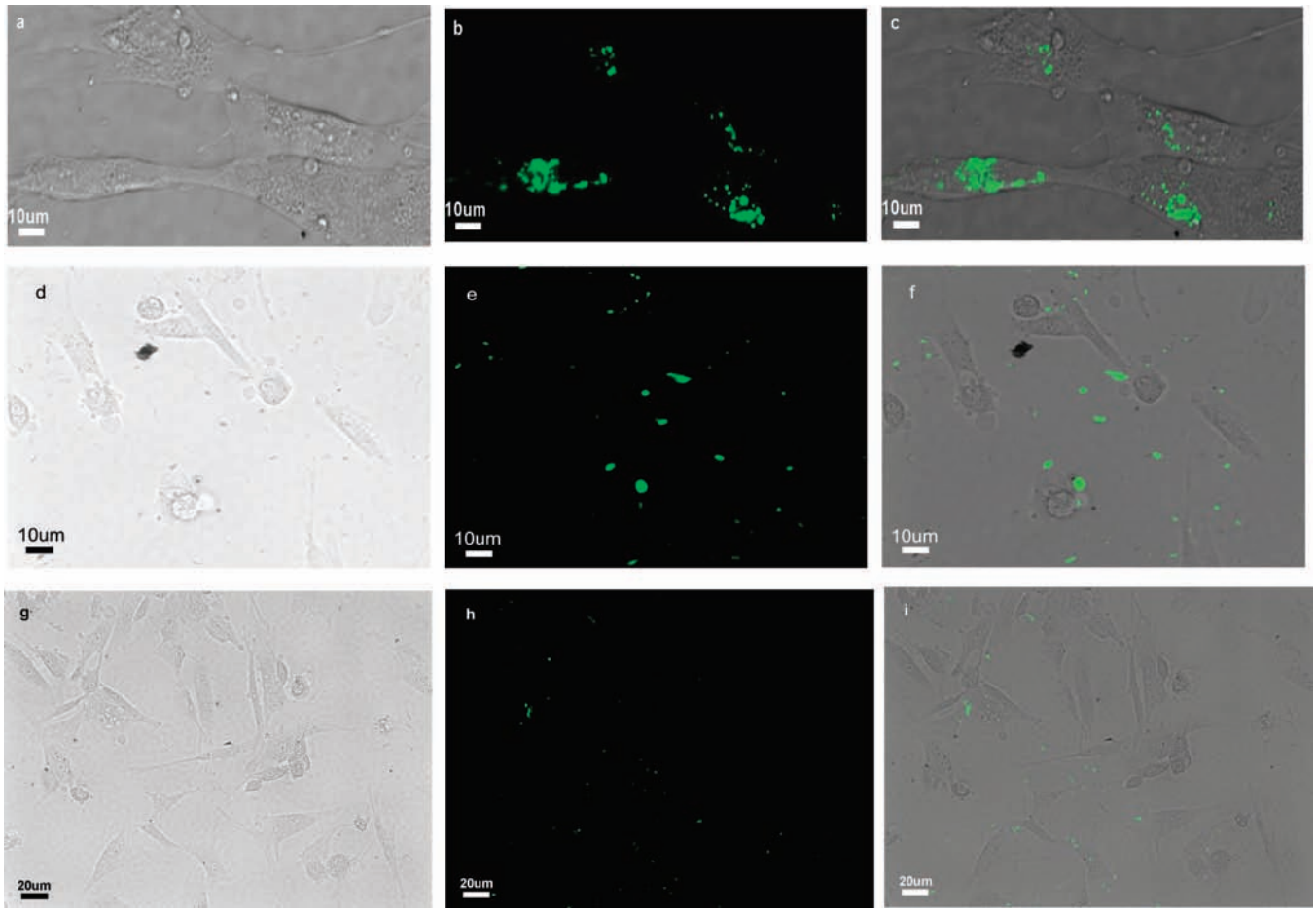

Figure 4. Fluorescent microscopy images of MSCs incubated with DSPE-PEG-coated QDs. With the use of Tat peptides, MSCs labeled by the green QD–Tat peptides are shown in parts a–c. As compared, DSPE-PEG-coated QDs were directly incubated with MSC without the assistance of Tat peptides, and the images are shown in parts d–f. A control experiment was performed to use QDs with a random peptide, and the images are shown in parts g–i. Therefore, a, d, and g are the images in the bright field; b, e, and h are the corresponding fluorescent images; and c, f, and I are the merged images.

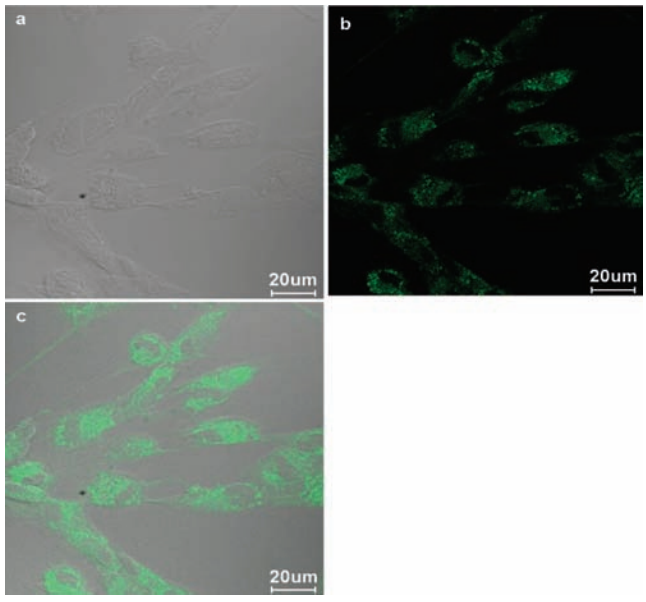

Figure 5. Confocal images of MSCs labeled by QD–Tat peptides. (a) MSCs labeled by green QD–Tat peptides in bright field. (b) Green fluorescent image. (c) Merged image of parts a and b.

Tat peptides and introduced into the same stem cells simultaneously. After excitation with a 488 nm laser line, both populations of bioconjugated QDs were identified in stem cells using confocal laser microscopy. The confocal images of MSCs labeled with two color QD–Tat peptides are shown in the Supporting Information. The green (Figure S1a) and red (Figure S1b) fluorescence of QD–Tat peptides are superimposed as yellow dots, which are shown in the merged fluorescent image of Figure S1d.

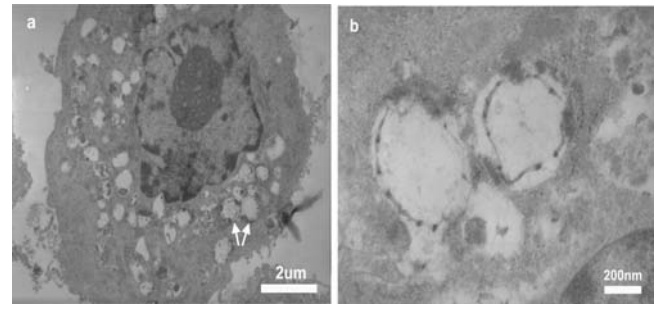

Figure 6. TEM analysis of the internalized QD–Tat peptides in MSCs. (a) TEM images of MSCs labeled by QD–Tat peptides, and the white arrowheads indicate endosomes. (b) A magnified view of endosomes in (a). QD–Tat peptides are seen as black dots surrounding the interior of the vesicles.

The internalization of QD–Tat peptides was further observed by transmission electron microscopy, which provided an even higher resolution than confocal microscopy. Figure 6a,b provides TEM images of intracellular QD–Tat peptides. The white arrowheads in Figure 6a indicate endosomes, which are magni-

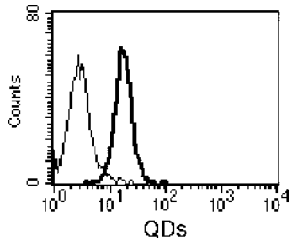

Figure 7. Flow cytometry analysis for the Tat peptide-conjugated QDs in MSCs. The left curve represents MSCs treated as control, and the right curve represents the responding sample treated with Tat peptide-conjugated QDs.

fied in Figure 6b. QD–Tat peptides are seen as black dots, surrounding the interior of the endosomes. The electron micrographs provide direct evidence that at least a portion of the internalized QD–Tat peptides were colocalized within endosomes. This result is consistent with the work reported by Delehanty et al. (*12*). They not only confirmed that QD signal dispersed nearly homogeneously throughout the cytoplasm on confocal microscopy, but also observed partial colocalization of QDs within endosomes. The partial colocalization of QDs within endosomes suggests a role for endocytosis in the uptake of the QD–Tat peptides. Other reports using live-cell imaging and FACS analysis have also established the role of endocytosis in the uptake of arginine-rich cell-penetrating peptides and their cargos (*27–29*).

The MSCs incubated with Tat peptide-conjugated QDs were trypinized and washed with PBS three times, and then analyzed using flow cytometry. Flow cytometry analysis (Figure 7) in the left curve represents the MSCs treated as control, and that in the right curve represents the responding sample treated with green QD–Tat peptides emitted at 520 nm. The flow cytometry data indicate that Tat peptide-conjugated QDs could enter MSCs with high efficiency (>95%). Although flow cytometry cannot distinguish between surface-bound and intracellular QD–Tat peptides, confocal and TEM data do confirm the uptake of the QD–Tat peptides by the MSCs. Furthermore, steps were taken to wash away the surface-bound QD–Tat peptides and ensure that data from flow cytometry were from the internalized QD–Tat peptides.

The internalized QD–Tat peptides in MSCs were further assessed with stem cell engraftment in nude mouse. Because red luminescent QDs were easier to distinguish from the

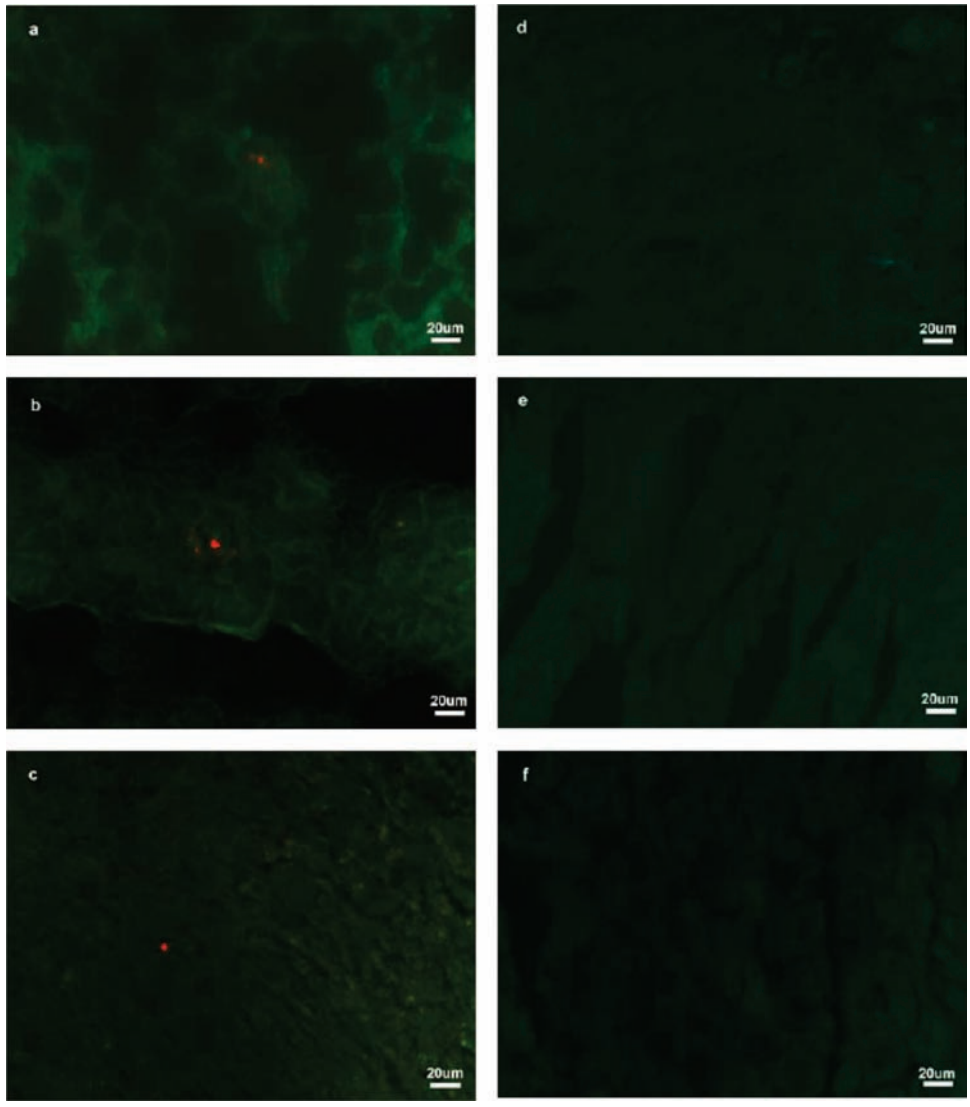

Figure 8. Intracellular labeling of stem cells by QD–Tat peptides permits in vivo imaging despite tissue autofluorescence. MSCs labeled with Tat peptide-conjugated QDs were intravenously injected into mice, and tissue sections of six normal host organs were observed via fluorescent microscopy. The characteristic red fluorescence of QD–Tat peptides were detected primarily in the lung (a), the liver (b), and the spleen (c), with little or no QD accumulation in the brain (d), the heart (e), or the kidney (f). All other signals were due to background autofluorescence.

autofluorescent tissue background than the green luminescent QDs, we injected the tail veins of NOD/SCID beta2 M null mice with QD-645-Tat peptide-labeled MSCs. After 24 h, the mice were killed and major organs (heart, lung, spleen, liver, kidney, and brain) were extracted and fixed in formalin. Representative images (Figure 8a) were obtained from 5 to 10 μm optical tissue sections on a fluorescence microscope excited by an ultraviolet source. The characteristic red fluorescence shows the presence of labeled MSCs in the lung. Tissues from other organs including liver (Figure 8b) and spleen (Figure 8c) were examined for the presence of QD-645-Tat peptide labeled stem cells. The presence of QD–Tat peptide labeled stem cells in other tissues indicated that not all the stem cells are trapped in the lung. A population of stem cells is able to circumnavigate the lung capillary network and seed other organs. However, the number of stem cells per field labeled with red QD–Tat peptide tracer was lower in the spleen and liver than in the lung tissues. The sections of the brain (Figure 8d), the heart (Figure 8e), or the kidney (Figure 8f) were also observed in fluorescence microscopy; no red luminescent spots appeared on these three kinds of organs. The results are in line with the report by Simon et al. after injecting QDs-labeled tumor cells into the tail vein of a rat (*9*).

CONCLUSIONS

In summary, PEG-QDs with covalently coupled Tat peptides produce nanometer-sized materials with biological function, which can penetrate the cellular membrane for cellular labeling and imaging. To assess the technique qualitatively and quantitatively, we combined the use of laser confocal microscopy and transmission electron microscopy to evaluate intracellular quantum dot localization in single cells and flow cytometry to quantify the delivery efficiency over a population of live mesenchymal stem cells. The result shows that Tat peptide-conjugated quantum dots could enter MSCs efficiently. The QD–Tat peptide labeled stem cells were injected intravenously into the tail veins of NOD/SCID beta2 M null mice, and the tissue distribution of these labeled stem cells in nude mice was examined by fluorescence microscopy. The result shows that characteristic fluorescence of QD–Tat peptides was observed primarily in the liver, the lung, and the spleen, with little or no QD accumulation in the brain, the heart, or the kidney. The labeled stem cells can be visualized by fluorescent imaging at the single-cell level, which offers a promising approach in stem cell transplantation and will hold a significant impact on the advancement of stem cell based therapy.

ACKNOWLEDGMENT

The authors would like to thank the 973 projects of MOST (Grant No. 2002CB713802 and No. 2005CB623602) and NSFC fund (No. 30370383, 90606001, and 90406024) of China for financial supports.

Supporting Information Available: Additional information as described in the text. This material is available free of charge via the Internet at http://pubs.acs.org.

LITERATURE CITED

(1) Meinel, L., Hofmann, S, Karageorgiou, V., Zichner, L., Langer, R., Kaplan, D., and Vunjak-Novakovic, G. (2004) Engineering cartilage-like tissue using human mesenchymal stem cells and silk protein scaffolds. *Biotechnol. Bioeng. 88*, 379–391.

(2) Gronthos, S., Mrozik, K., Shi, S., and Bartold, P. M. (2006) Ovine periodontal ligament stem cells: Isolation, characterization, and differentiation potential. *Calcified Tissue Int. 79*, 310–317.

(3) Jaiswal, J. K., Mattoussi, H., Mauro, J. M., and Simon, S. M. (2003) Long-term multiple color imaging of live cells using quantum dot bioconjugates. *Nat. Biotechnol. 21*, 47–51.

(4) Zahavy, E., Freeman, E., Lustig, S., Keysary, A., and Yitzhaki, S. (2005) Double labeling and simultaneous detection of b- and t cells using fluorescent nano-crystal (q-dots) in paraffin-embedded tissues. *J Fluoresc. 15*, 661–665.

(5) Dubertret, B., Skourides, P., Norris, D. J., Noireaux, V., Brivanlou, A. H., and Libchaber, A. (2002) In vivo imaging of quantum dots encapsulated in phospholipid micelles. *Science 298*, 1759–1762.

(6) Derfus, A. M., Chan, W. C. W., and Bhatia, S. N. (2004) Intracellular delivery of quantum dots for live cell labeling and organelle tracking. *Adv. Mater. 16*, 961–966.

(7) Chan, W. C. W., and Nie, S. M. (1998) Quantum dot bioconjugates for ultrasensitive nonisotopic detection. *Science 281*, 2016–2018.

(8) Parak, W. J., Boudreau, R., Le, G. M., Gerion, D., Zanchet, D., Micheel, C. M., Williams, S. C., Alivisatos, A. P., and Larabell, C. (2002) Cell motility and metastatic potential studies based on quantum dot imaging of phagokinetic tracks. *Adv. Mater. 14*, 882–885.

(9) Voura, E. B., Jaiswal, J. K., Mattoussi, H., and Simon, S. M. (2004) Tracking metastatic tumor cell extravasation with quantum dot nanocrystals and fluorescence emission-scanning microscopy. *Nat. Med. 10*, 993–998.

(10) Hoshino, A., Fujioka, K., Oku, T., Nakamura, S., Suga, M., Yamaguchi, Y., Suzuki, K., Yasuhara, M., and Yamamoto, K. (2004) Quantum dots targeted to the assigned organelle in living cells. *Microbiol. Immunol. 48*, 985–994.

(11) Chen, F. Q., and Gerion, D. (2004) Fluorescent CdSe/ZnS nanocrystal-peptide conjugates for long-term, nontoxic imaging and nuclear targeting in living cells. *Nano Lett. 4*, 1827–1832.

(12) Delehanty, J. B., Medintz, I. L., Pons, T., Brunel, F. M., Dawson, P. E., and Mattoussi, H. (2006) Self-assembled quantum dot-peptide bioconjugates for selective intracellular delivery. *Bioconjugate Chem. 17*, 920–927.

(13) Smith, A. M., Ruan, G., Rhyner, M. N., and Nie, S. M. (2006) Engineering luminescent quantum dots for In vivo molecular and cellular imaging. *Ann Biomed Eng. 34*, 3–14.

(14) Silver, J., and Ou, W. (2005) Photoactivation of quantum dot fluorescence following endocytosis. *Nano Lett. 5*, 1445–1449.

(15) Lagerholm, B. C., Wang, M. M., Ernst, L. A., Ly, D. H., Liu, H. J., Bruchez, M. P., and Waggoner, A. S. (2004) Multicolor coding of cells with cationic peptide coated quantum dots. *Nano Lett. 4*, 2019–2022.

(16) Zhao, M., Kircher, M. F., Josephson, L., and Weissleder, R. (2002) Differential conjugation of tat peptide to superparamagnetic nanoparticles and its effect on cellular uptake. *Bioconjugate Chem. 13*, 840–844.

(17) Lewin, M., Carlesso, N., Tung, C. H., Tang, X. W., Cory, D., Scadden, D. T., and Weissleder, R. (2000) Tat peptide-derivatized magnetic nanoparticles allow in vivo tracking and recovery of progenitor cells. *Nat. Biotechnol. 18*, 410–414.

(18) Richard, J. P., Melikov, K., Brooks, H., Prevot, P., Lebleu, B., and Chernomordik, L. V. (2005) Cellular uptake of unconjugated TAT peptide involves clathrin-dependent endocytosis and heparan sulfate receptors. *J. Biol. Chem. 280*, 15300–15306.

(19) Drin, G., Cottin, S., Blanc, E., Rees, A. R., and Temsamani, J. (2003) Studies on the internalization mechanism of cationic cellpenetrating peptides. *J. Biol. Chem. 278*, 31192–311201.

(20) Fittipaldi, A., Ferrari, A., Zoppe, M., Arcangeli, C., Pellegrini, V., Beltram, F., and Giacca, M. (2003) Cell membrane lipid rafts mediate caveolar endocytosis of HIV-1 Tat fusion proteins. *J. Biol. Chem. 278*, 34141–34149.

(21) Kirchner, C., Liedl, T., Kudera, S., Pellegrino, T., Javier, A. M., Gaub, H. E., Stolzle, S., Fertig, N., and Parak, W. J. (2005) Cytotoxicity of colloidal CdSe and CdSe/ZnS nanoparticles. *Nano Lett. 5*, 331–338.

(22) Zhang, T. T., Stilwell, J. L., Gerion, D., Ding, L. H., Elboudwarej, O., Cooke, P. A., Gray, J. W., Alivisatos, A. P.,

and Chen, F. F. (2006) Cellular effect of high doses of silica-coated quantum dot profiled with high throughput gene expression analysis and high content cellomics measurements. *Nano Lett. 6*, 800–808.

(23) Ballou, B., Lagerholm, B. C., Ernst, L. A., Bruchez, M. P., and Waggoner, A. S. (2004) Noninvasive imaging of quantum dots in mice. *Bioconjugate Chem. 15*, 79–86.

(24) Nitin, N., LaConte, L. E. W., Zurkiya, O., Hu, X., and Bao, G. (2004) Functionalization and peptide-based delivery of magnetic nanoparticles as an intracellular MRI contrast agent. *J. Biol. Inorg. Chem. 9*, 706–712.

(25) Dabbousi, B. O., RodriguezViejo, J., Mikulec, F. V., Heine, J. R., Mattoussi, H., Ober, R., Jensen, K. F., and Bawendi, M. G. (1997) (CdSe)ZnS core-shell quantum dots: Synthesis and characterization of a size series of highly luminescent nanocrystallites. *J. Phys. Chem. B 101*, 9463–9475.

(26) Hashizume, K., Matsubayashi, M., Vacha, M., and Tani, T. (2002) Individual mesoscopic structures studied with submicrometer optical detection techniques: CdSe nanocrystals capped with TOPO and ZnS-overcoated system. *J. Lumin. 98*, 49–56.

(27) Wadia, J. S., Stan, R. V., and Dowdy, S. F. (2004) Transducible TAT-HA fusogenic peptide enhances escape of TAT-fusion proteins after lipid raft macropinocytosis. *Nat. Med. 10*, 310–5.

(28) Kaplan, I. M., Wadia, J. S., and Dowdy, S. F. (2005) Cationic TAT peptide transduction domain enters cells by macropinocytosis. *J. Controlled Release 102*, 247–53.

(29) Richard, J. P., Melikov, K., Vives, E., Ramos, C., Verbeure, B., Gait, M. J., Chernomordik, L. V., and Lebleu, B. (2003) Cellpenetrating peptides. A reevaluation of the mechanism of cellular uptake. *J. Biol. Chem. 278*, 585–590.

BC0700685

General Structure–Activity Relationship for Poly(glycoamidoamine)s: The Effect of Amine Density on Cytotoxicity and DNA Delivery Efficiency

Chen-Chang Lee, Yemin Liu, and Theresa M. Reineke*

Department of Chemistry, University of Cincinnati, Cincinnati, Ohio 45221-0172. Received May 8, 2007; Revised Manuscript Received October 5, 2007

Herein, two new series of poly(glycoamidoamine)s (branched and linear) have been synthesized by polycondensation. The polymer repeat units have been designed to contain D-glucaramide, *meso*-galactaramide, D-mannaramide, or L-tartaramide structures and five or six ethyleneamine units to investigate the amine density effects on the bioactivity as compared to a similar series of poly(glycoamidoamine)s previously described that contain four ethyleneamines. These delivery vehicles were created to examine the effects that the number of secondary amines in the polymer repeat unit and the polymer structure (branched and linear) have on plasmid DNA (pDNA) binding affinity, polyplex formation, cell viability, and gene expression in the absence and presence of serum in the culture medium. The results reveal that the new polymers with higher amine density in the repeat unit do not significantly enhance the transfection efficiency compared to that of previous models containing four ethyleneamines, but an increase in cytotoxicity is noticed. Linear polymers reveal higher pDNA neutralization efficacy, gene expression, and toxicity than the branched versions containing a similar chemical structure, which may be caused by a higher protonation of the amine groups. With these new vectors, some interesting trends emerged. The galactaramide and tartaramide analogues revealed higher delivery efficiency than the glucaramide and mannaramide structures. In addition, the branched and linear structures containing five ethyleneamines in the repeat unit formed polyplexes at higher N/P ratios, which had lower zeta potential and lower delivery efficacy than the analogues with six ethyleneamines, and also the linear structures generally revealed higher delivery efficiency and toxicity when compared to those of their branched analogues.

INTRODUCTION

Viral vectors and nonviral vectors are currently being explored for genetic drug delivery. Nonviral systems are gaining widespread attention due to the many issues that have surfaced with viral-based systems (*1–6*). Theoretically, there are many advantages of using synthetic polymers. For example, their versatility allows them to be tailored to carry various types and sizes of nucleic acids for a variety of delivery applications (*5, 7*). However, it is well-known that small changes in the polymer chemical and structural properties can affect efficiency, toxicity, and the cellular mechanisms involved in delivery (*8–10*). Also, the delivery efficiency is often cell-type dependent (*11–13*), which also may be related to the polymer structure. To find a proper synthetic vector for a particular therapeutic target, medicinal chemistry-like studies will help determine the proper efficacious delivery system.

Among the many cationic vectors with amine functionalities, poly(ethylenimine) (PEI) (*14, 15*), PAMAM dendrimer (*16*), poly L-lysine (PLL) (*17*), and chitosan (*18*) are widely studied DNA carriers. The amines within these materials enable them to form tight and small complexes (termed polyplexes or dendriplexes) with DNA through electrostatic binding and neutralization of the DNA backbone (*19*). The amine groups within these materials also play important roles in delivery efficiency; they facilitate cell-membrane binding and internalization via various endocytotic routes. In addition, it has been hypothesized that the amine groups, which can be protonated at physiological pH, enable the systems to escape from the endosomes via the "proton sponge" effect (*14*). Unfortunately, the high amine density in polymers such as PEI can cause cytotoxicity *in vitro* and *in vivo* because highly charge-dense materials can likely destabilize the cellular membrane (*20, 21*). In addition, previous studies also have found that the transfection efficiency of PEI is dependent on several factors including the physical structure (branched or linear) and the molecular weight (*22–26*). For example, Colledge et al. found that the gene delivery efficiency of branched and linear PEI is significantly dependent on the polymer structure where linear PEI was generally found to be more efficient (*24*). Conversely, vectors that have a lower amine density are typically better tolerated in biological systems. A well-known example is chitosan, a copolymer of glucosamine and *N*-acetyl-D-glucosamine, and a commonly studied DNA carrier. However, the poor solubility of chitosan, lack of buffering capacity, and high polydispersity are major drawbacks for its use as a nucleic acid carrier (*27*). A series of polymers inspired by the structures of PEI and chitosan, termed poly(glycoamidoamine)s, has been previously designed and synthesized by our research group as shown in Figure 1. This polymer series has allowed us to understand how subtle chemical properties can profoundly affect polymer bioactivity. For example, we have shown that as the secondary amine number increases from one to four, the transfection increases significantly, while retaining similar biocompatibility (*28–31*). We have also found that altering the hydroxyl number and stereochemistry displayed by the carbohydrate moieties (either D-glucarate, *meso*-galactarate, D-mannarate, or L-tartarate) results in dissimilar gene expression profiles, which is likely related to differences in the polymer−pDNA binding affinity, the ability of the vector to decrease nuclease degradation, and/or cellular internalization efficiency (*31*).

Herein, our aim was to further investigate the amine density effect by increasing the secondary amine number in the poly(glycoamidoamine) repeat unit to five and six and examine

* To whom correspondence should be addressed. E-mail: theresa.reineke@uc.edu.

10.1021/bc7001659 CCC: $40.75 © 2008 American Chemical Society
Published on Web 01/16/2008

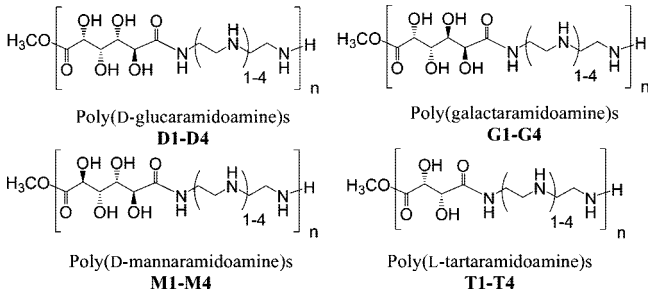

Figure 1. Library of 16 poly(glycoamidoamine)s previously studied (*24–26*). The polymers are divided into four families and are named according to the carbohydrate moieties and the number of secondary amines per repeat unit.

the bioactivity profiles in the absence and presence of serum in the medium. In addition, we have synthesized both branched and linear versions of these structures to compare how the polymer geometry affects the biological properties. To synthesize the target polymers, we have employed four esterified carbohydrate units (D-glucarate (**D**), *meso*-galactarate (**G**), D-mannarate (**M**), and L-tartarate (**T**)) in a manner similar to that in our previous studies and polymerized them with 4 novel oligoethyleneamine monomers (by utilizing protected and deprotected versions of hexaethyleneheptamine and heptaethyleneoctamine) to obtain 16 different polymer structures (8 branched and 8 linear). We have analyzed the structural properties of each polymer by ^{1}H NMR, gel permeation chromatography (GPC), light scattering, and viscometry studies. To compare these data with the results obtained from the poly(glycoamidoamine)s previously synthesized (containing 1 to 4 secondary amines per repeat unit (*28–30*)), the novel polymers synthesized herein have been made with a similar degree of polymerization (between 9 and 15). We have observed through dynamic light scattering (DLS) and gel electrophoresis experiments that there are considerable differences in the binding and compaction of pDNA when polymers containing five and six ethyleneamine units are compared. In addition, the polymer geometry appears to significantly affect bioactivity. It was also discovered that the gene expression level appears to reach a plateau with the polymers that have four ethyleneamine groups in the repeat unit. This work presents our continued efforts to understand the structure−bioactivity relationships with these poly(glycoamidoamine) models, which will advance the knowledge in this field toward the rational design of novel synthetic polymers for effective nucleic acid delivery.

EXPERIMENTAL PROCEDURES

1. General. The carbohydrate monomers (dimethyl *meso*-galactarate, D-mannaro-1,4:6,3-dilactone, esterified D-glucaric acid) used in the polymerization were synthesized according to previous reported methods (*32–34*). Dimethyl L-tartarate used in the polymerization was obtained from Acros Chemical Co. (Morris Plains, NJ). All reagents used in the synthesis, if not specified, were obtained from Aldrich Chemical Co. (Milwaukee, WI) and used without further purification. Methanol, triethylamine (TEA), and dichloromethane (CH_2Cl_2) were purified according to conventional methods. Plasmid DNA (pDNA), pCMVβ (7.2 kbp), was purchased from Plasmidfactory (Bielefeld, Germany), and gWiz-luc (6.7 kbp) was purchased from Aldevron (Fargo, ND). Mass spectra were obtained with an IonSpec ESI mass spectrometer in positive ion mode. IR spectra were measured with a Perkin-Elmer Spectrum One Fourier transform infrared spectrometer, and the samples were prepared as KBr pellets. ^{1}H and ^{13}C NMR were recorded on a Bruker AV-400 MHz spectrometer. The ^{1}H NMR data were reported as follows: chemical shift (δ ppm), multiplicity, J coupling constant (Hz), and peak integration. Cell culture media and supplements were purchased from Gibro/Invitrogen (Carlsbad, CA). pCMVβ was labeled with a Cy5 nucleic acid labeling kit (Mirus, Madison, WI), and purified by QIAquick PCR purification kit (QIAGEN, Valencia, CA). HeLa cells were purchased from ATCC (Rockville, MD). The luciferase assays were completed with a Promega Luciferase Assay Kit (Madison, WI). The toxicity assays were performed with a Bio-Rad DC Protein Assay Kit (Hercules, CA).

2. Monomer Synthesis. *2.1. Synthesis of Hexaethyleneheptamine. 2.1.1. N^1,N^5-Dibenzyl-N^2,N^3,N^4-tris(tert-butoxycarbonyl)-tetraethylenepentamine (***2a***).* Compound **1a** (4.08 g, 8.40 mmol), synthesized according to a previously reported procedure (*35, 36*), was dissolved in 70 mL of methanol and stirred in an ice bath for 10 min. Benzaldehyde (1.69 mL, 16.7 mmol) was added dropwise at 0 °C to produce the imines, and the mixture was stirred for another 30 min. TLC was used to monitor reaction completion. Next, $NaBH_4$ (0.63 g, 16.7 mmol) was added slowly over 30 min to the solution at 0 °C to reduce the imines to amines, and the mixture was stirred for another 2 h at 0–5 °C. The solvent was then evaporated under reduced pressure, the residue was thoroughly mixed with 50 mL of EtOAc and 30 mL saturated sodium bicarbonate, and the mixture was separated. The water portion was extracted with 2 × 20 mL of EtOAc, and the combined organic layers were dried with anhydrous $MgSO_4$. The drying agent was filtered and the product concentrated *in vacuo*. The residue was purified via flash column chromatography ($CH_3OH/CH_2Cl_2/NH_4OH$ = 10/100/1; R_f = 0.31) to yield the titled compound as a light yellow oil (4.75 g, 84%). ^{1}H NMR ($CDCl_3$): δ = 1.40 (s, 9H, C(C$\underline{H}_3$)$_3$), 1.44 (s, 18H, C(C$\underline{H}_3$)$_3$), 2.77 (brs, 4H, NHC$\underline{H}_2$CH$_2$N), 3.33 (brs, 12H, NHCH$_2$C$\underline{H}_2$N, NC$\underline{H}_2$C$\underline{H}_2$N), 3.78 (s, 4H, C$\underline{H}_2$Ph), 7.19–7.23 (m, 2H), 7.24–7.32 (m, 8H). ^{13}C NMR ($CDCl_3$): δ = 28.35, 28.39, 45.34, 45.62, 47.02. 47.33, 47.62, 53.47, 53.57, 79.53, 79.55, 126.87, 127.63, 128.28, 139.98, 140.18, 155.26, 155.45. FT-IR (KBr pellet, cm^{-1}): 3459.6, 2972.5, 2923.1, 1695.5, 1473.3, 1415.7, 1160.5. ESI-MS: calcd. for $(M + H)^+$ $C_{37}H_{60}N_5O_6$, 670.4543; found, 670.4535.

*2.1.2. N^1,N^5-Dibenzyl-N^1,N^5-bis(ethylphthalimido)-N^2,N^3,N^4-tris(tert-butoxycarbonyl) tetraethylenepentamine (***3a***).* To a stirred solution of KF-celite (4.24 g) and **2a** (4.75 g, 7.10 mmol) in CH_3CN (30 mL) at room temperature, *N*-bromoethyl phthalimide (14.4 g, 56.8 mmol) was added in one portion and refluxed for 14 h. The KF-celite was then filtered with celite after reaction completion. The solvent was removed under reduced pressure, and the residue was purified via flash chromatography (EtOAc/Hex = 1/1; R_f = 0.57) to yield **3a** as a waxy solid (5.25 g, 73%). ^{1}H NMR ($CDCl_3$): δ = 1.41 (s, 18H, C(C$\underline{H}_3$)$_3$), 1.45 (s, 9H, C(C$\underline{H}_3$)$_3$), 2.73 (t, J = 6.4 Hz, 8H, NC$\underline{H}_2$C$\underline{H}_2$N), 3.21–3.36 (m, 12H, NC$\underline{H}_2$C$\underline{H}_2$N, Ph(CO)$_2$NCH$_2$C$\underline{H}_2$N), 3.60–3.65 (m, 4H, C$\underline{H}_2$Ph), 3.74 (t, J = 6.4 Hz, 4H, Ph(CO)$_2$NC$\underline{H}_2$CH$_2$N), 7.02–7.14 (m, 10H), 7.71 (s, 4H), 7.79 (s, 4H). ^{13}C NMR ($CDCl_3$): δ = 28.25, 35.78, 44.43, 44.83, 45.01, 45.42, 45.83, 46.08, 51.27, 51.40, 51.84, 58.41, 58.59, 79.08, 79.20, 79.26, 122.84, 126.58, 126.67, 127.79, 127.89, 128.45, 128.48, 131.96, 133.56, 138.86, 154.94, 155.08, 167.76. FT-IR (KBr pellet, cm^{-1}): 3472.5, 2972.5, 2934.1, 1769.6, 1711.9, 1695.5, 1467.8, 1418.4, 1163.3. ESI-MS: calcd. for $(M + H)^+$ $C_{57}H_{74}N_7O_{10}$, 1016.5419; found, 1016.5497.

*2.1.3. N^2,N^3,N^4-Tris(tert-butoxycarbonyl)-hexaethyleneheptamine (***4a***).* To a solution of compound **3a** (5.22 g, 5.10 mmol) in MeOH (47 mL), hydrazine monohydrate (5.90 mL) was added and refluxed for 3 h yielding the primary amines. Then, CH_3Cl (45 mL) and 4 N NH_4OH (45 mL) were added to the reaction, and the mixture was stirred for another 30 min at room temperature. The organic and aqueous layers were separated, and the aqueous layer was extracted with 3 × 25 mL CH_3Cl.

The combined organic layers were dried with anhydrous $MgSO_4$. The drying agent was then filtered, and the filtrate was evaporated to yield the crude product as a viscous liquid (3.49 g, 90%). The next step to deprotect the benzyl groups was carried out without further purification. The product from the previous step (3.49 g, 4.60 mmol) was dissolved in MeOH (40 mL) and $Pd(OH)_2$ (0.40 g) was added to the solution. The reaction was shaken in a Parr hydrogenator under 50 psi of H_2(g) for 48 h, and reaction completion was monitored via TLC. The $Pd(OH)_2$ was then filtered with celite, and the solvent was evaporated. The residue was purified via flash chromatography (EtOAc/MeOH/NH_4OH = 3/1/1; R_f = 0.40) to obtain the waxy solid product **4a** (1.90 g, 71%). ^{1}H NMR (DMSO-d_6): δ = 1.38 (s, 27H, C(C$\underline{H}_3$)$_3$), 2.55–2.80 (brs, 8H, $NH_2C\underline{H}_2C\underline{H}_2NH$), 2.61–2.68 (brs, 4H, $NHC\underline{H}_2CH_2N$), 3.10–3.28 (m, 12H, $NC\underline{H}_2C\underline{H}_2N$). ^{13}C NMR (DMSO-$d_6$): δ = 28.49, 41.74, 45.09, 45.24, 45.38, 47.78, 48.23, 52.43, 78.89, 79.12, 154.91, 154.94, 155.00. FT-IR (KBr pellet, cm^{-1}): 3423.1, 3274.7, 2978.0, 1709.2, 1690.0, 1465.0, 1415.7, 1163.3. ESI-MS: calcd. for (M + H)$^+$ $C_{27}H_{58}N_7O_6$, 576.4449; found, 576.4174.

*2.1.4. Hexaethyleneheptamine (***5a***).* Compound **4a** (2.60 g, 4.50 mmol) was dissolved in 4 N HCl in dioxane (50 mL) and stirred for 3 h in an ice bath to remove the Boc protecting groups. The final product was dried *in vacuo* and purified via exhaustive dialysis (100 MW cutoff membrane) against ultra pure H_2O for 24 h. The final deprotected oligoamine was lyophilized to dryness to yield a fluffy white solid (0.478 g, 39%). ^{1}H NMR (D_2O with one drop of DCl): δ = 3.44 (t, J = 7.2 Hz, 4H, $NH_2C\underline{H}_2CH_2NH$), 3.54 (t, J = 7.2 Hz, 4H, $NH_2CH_2C\underline{H}_2NH$), 3.59–3.64 (m, 16H, $NHC\underline{H}_2C\underline{H}_2NH$). ^{13}C NMR ($D_2O$ with one drop of DCl): δ = 38.24, 46.20, 46.32, 47.59. FT-IR (KBr pellet, cm^{-1}): 3413.1, 2980.6, 2948.9, 2688.9, 2436.0, 1059.9. ESI-MS: calcd. for (M + H)$^+$ $C_{12}H_{34}N_7$, 276.2876; found, 276.2977.

*2.2. Synthesis of Heptaethyleneoctamine. 2.2.1. N^1,N^6-Dibenzyl-N^2,N^3,N^4,N^5-tetra(tert-butoxycarbonyl)-pentaethylene-hexamine (***2b***).* Compound **1b** (16.3 g, 25.8 mmol), synthesized according to a reported procedure (*35*, *36*), was dissolved in 165 mL of MeOH/CH_2Cl_2 (10:1) and stirred in an ice bath for 10 min. Benzaldehyde (0.78 mL, 77.3 mmol) was added dropwise at 0 °C to produce the imines, and the mixture was stirred for another 30 min. Reaction completion was monitored via TLC. Next, $NaBH_4$ (2.93 g, 77.3 mmol) was added slowly over 30 min to the previous solution at 0 °C to reduce the imines to amines, and the mixture was stirred for another 2 h at 0–5 °C. The solvent was then evaporated under reduced pressure, the residue was thoroughly mixed with 120 mL of EtOAc and 100 mL of saturated sodium bicarbonate, and the mixture was separated. The water portion was then extracted with 2 × 60 mL of EtOAc, and the combined organic layers were dried with anhydrous $MgSO_4$. The drying agent was filtered and the product concentrated *in vacuo*. The residue was purified via flash column chromatography ($CH_3OH/CH_2Cl_2/NH_4OH$ = 10/100/1; R_f = 0.37) to yield the desired compound as a light yellow oil (8.06 g, 62%). ^{1}H NMR ($CDCl_3$): δ = 1.36 (s, 36H, C(C$\underline{H}_3$)$_3$), 2.69 (brs, 4H, $NHC\underline{H}_2CH_2N$), 3.23 (brs, 16H, $NHCH_2C\underline{H}_2N$, $NC\underline{H}_2C\underline{H}_2N$), 3.87 (s, 4H, $\underline{CH}_2$Ph), 7.11–7.13 (m, 2H), 7.17–7.21 (m, 8H). ^{13}C NMR ($CDCl_3$): δ = 28.38, 28.40, 45.43, 45.78, 47.56, 53.55, 79.55, 126.83, 127.96, 128.26, 140.22, 155.18, 155.46. FT-IR (KBr pellet, cm^{-1}): 3439.6, 2978.0, 2928.6, 1687.3, 1467.8, 1418.4, 1168.8. ESI-MS: calcd. for (M + H)$^+$ $C_{44}H_{73}N_6O_8$, 813.5490; found, 813.5494.

*2.2.2. N^1,N^6-Dibenzyl-N^1,N^6-bis(ethylphthalimido)-N^2,N^3,N^4,N^5-tetra(tert-butoxycarbonyl)-pentaethylenehexamine (***3b***).* To a stirred solution of KF-celite (3.20 g) and **2b** (3.72 g, 4.60 mmol) in CH_3CN (32 mL) at room temperature, *N*-bromoethyl phthalimide (9.29 g, 36.6 mmol) was added in one portion and refluxed for 14 h. After reaction completion (monitored via TLC), the KF-celite was removed via filtration with celite. The filtrate was removed under reduced pressure, and the residue was purified via flash chromatography (EtOAc/Hex = 1/1; R_f = 0.57) to yield **3b** as a waxy solid (2.21 g, 48%). ^{1}H NMR ($CDCl_3$): δ = 1.39 (s, 9H, C(C$\underline{H}_3$)$_3$), 1.40 (s, 9H, C(C$\underline{H}_3$)$_3$), 1.43 (s, 18H, Boc), 2.60–2.70 (brs, 4H, $NC\underline{H}_2CH_2N$), 2.70 (t, J = 5.2 Hz, 4H, $NCH_2C\underline{H}_2N$), 3.15–3.33 (m, 16H, $NC\underline{H}_2C\underline{H}_2N$, Ph(CO)$_2$-$NCH_2C\underline{H}_2N$), 3.60 (brs, 4H, $\underline{CH}_2$Ph), 3.71 (t, J = 5.2 Hz, 4H, Ph(CO)$_2$$NC\underline{H}_2CH_2NH$), 6.98–7.14 (m, 10H), 7.69 (s, 4H), 7.77 (s, 4H). ^{13}C NMR ($CDCl_3$): δ = 28.43, 36.00, 45.17, 45.55, 45.97, 51.41, 51.60, 52.01, 52.11, 58.57, 58.78, 79.35, 79.55, 123.08, 126.75, 126.83, 126.92, 127.98, 128.08, 128.65, 132.18, 133.74, 139.04, 155.17, 155.29, 168.04. FT-IR (KBr pellet, cm^{-1}): 3467.0, 2972.5, 2939.6, 1775.0, 1711.9, 1692.7, 1465.0, 1415.7, 1166.0. ESI-MS: calcd. for (M + H)$^+$ $C_{64}H_{87}N_8O_{12}$, 1159.6365; found, 1159.6443.

*2.2.3. N^1,N^6-Dibenzyl-N^2,N^3,N^4,N^5-tetra(tert-butoxycarbonyl)-heptaethyleneoctamine (***4b***).* To a solution of compound **3b** (2.08 g, 1.80 mmol) in MeOH (16 mL), hydrazine monohydrate (2.10 mL) was added, and the mixture was refluxed for 3 h to yield the primary amines. Next, CH_3Cl (14 mL) and 4 N NH_4OH (14 mL) were added to the reaction, and the mixture was stirred for another 30 min at room temperature. The organic and aqueous layers were separated, the aqueous layer was extracted with 3 × 8 mL CH_3Cl, and the combined organic layers were dried with anhydrous $MgSO_4$. The drying agent was filtered, and the solvent was evaporated to yield the crude product as an oil (1.44 g, 89%). The resulting product (1.33 g, 1.47 mmol), utilized without further purification, was then dissolved in MeOH (20 mL), and $Pd(OH)_2$ (0.30 g) was added to the solution. The reaction was shaken in a Parr hydrogenator under 50 psi of H_2(g) for 48 h to remove the benzyl groups. After reaction completion (monitored via TLC), the $Pd(OH)_2$ was removed via filtration with celite, and the solution was evaporated. The residue was purified via flash chromatography (EtOAc/MeOH/NH_4OH = 3/1/1; R_f = 0.21) to obtain compound **4b** as a waxy solid (0.823 g, 68%). ^{1}H NMR (DMSO-d_6): δ = 1.39 (s, 36H, C(C$\underline{H}_3$)$_3$), 2.00–2.40 (brs, 6H, N$\underline{H}_2$, N$\underline{H}$C$\underline{H}_2$-CH_2N), 2.48–2.52 (m, 4H, $NH_2C\underline{H}_2CH_2NH$), 2.56–2.64 (m, 8H, $NH_2CH_2C\underline{H}_2NH$, $NHC\underline{H}_2C\underline{H}_2N$), 3.10–3.33 (brs, 16H, $NC\underline{H}_2C\underline{H}_2N$). ^{13}C NMR (DMSO-$d_6$): δ = 28.46, 41.89, 44.83, 45.30, 45.34, 45.40, 45.45, 45.73, 47.17, 47.86, 48.30, 52.69, 78.91, 79.14, 154.89, 155.01. FT-IR (KBr pellet, cm^{-1}): 3434.1, 3263.7, 2978.0, 1692.7, 1481.5, 1415.66, 1166.0. ESI-MS: calcd. for (M + H)$^+$ $C_{34}H_{71}N_8O_8$, 719.5317; found, 719.5087.

*2.2.4. Heptaethyleneoctamine (***5b***).* Compound **4b** (2.08 g, 2.9 mmol) was dissolved in 4 N HCl in dioxane (30 mL) and stirred for 3 h in an ice bath to remove the Boc groups. The final product was dried *in vacuo* and purified via exhaustive dialysis (100 MW cutoff membrane) against ultra pure H_2O for 24 h. The final deprotected oligoethyleneamine was lyophilized to dryness to yield a fluffy white solid (0.516 g, 56%). ^{1}H NMR (one drop of DCl in D_2O): δ = 3.42–3.46 (m, 4H, $NH_2C\underline{H}_2CH_2NH$), 3.54 (t, J = 7.2 Hz, 4H, $NH_2CH_2C\underline{H}_2NH$), 3.59–3.65 (m, 20H, $NHC\underline{H}_2C\underline{H}_2NH$). ^{13}C NMR (one drop of DCl in D_2O): δ = 38.25, 46.21, 46.32, 47.60. FT-IR (KBr pellet, cm^{-1}): 3435.1, 2980.4, 2951.0, 2680.9, 2432.8, 1285.3. ESI-MS: calcd. for (M + H)$^+$ $C_{14}H_{39}N_8$, 319.3219; found, 319.3609.

3. Polymerization. *3.1. Branched Polymer Synthesis. 3.1.1.* **G5$_B$.** Dimethyl *meso*-galactarate (20.0 mg, 0.08 mmol) was mixed with a methanol solution (0.42 mL) containing triethylamine (60 μL) and **5a** (23.2 mg, 0.08 mmol) and stirred at room temperature for 48 h. The solution was exhaustively dialyzed in ultrapure water and solution was lyophilized to dryness, yielding the final polymer product (10.9 mg, 29%). ^{1}H NMR (D_2O): δ = 2.95 (brs, 18H), 3.47 (brs, 6H), 3.95 (s, 1H), 4.00

(s, 1H), 4.04 (s, 1H), 4.24–4.27 (m, 1H), 4.45 (s, 2H). IR (KBr pellet, cm^{-1}): 3374.2, 2945.0, 2846.1, 1652.9, 1644.8, 1547.1, 1415.3, 1045.2.

3.1.2. **G6$_B$.** Dimethyl *meso*-galactarate (20.0 mg, 0.08 mmol) was mixed with a methanol solution (0.34 mL) containing triethylamine (60 μL) and **5b** (27.0 mg, 0.08 mmol) and stirred at room temperature for 48 h. The solution was exhaustively dialyzed in ultrapure water, and the solution was lyophilized to dryness, yielding the final polymer product (11.5 mg, 28%). ^{1}H NMR (D_2O): δ = 2.93 (brs, 22H), 3.47 (brs, 6H), 3.95 (s, 1H), 4.00 (s, 1H), 4.03–4.06 (m, 1H), 4.24–4.26 (m, 1H), 4.45 (s, 2H). IR (KBr pellet, cm^{-1}): 3388.9, 2954.2, 2852.3, 1642.8, 1602.6, 1541.8, 1417.5, 1048.5.

3.1.3. **D5$_B$**. Esterified D-glucaric acid (20.0 mg, 0.08 mmol) was mixed with a methanol solution (0.34 mL) containing triethylamine (68 μL) and **5a** (23.2 mg. 0.08 mmol) and stirred at room temperature for 36 h. The solution was exhaustively dialyzed in ultrapure water, and the solution was lyophilized to dryness, yielding the final polymer product (9.50 mg, 25%). ^{1}H NMR (D_2O): δ = 2.96 (brs, 16H), 3.46 (brs, 8H), 3.91–3.98 (m, 2H), 4.05–4.07 (m, 1H), 4.10–4.15 (m, 2H), 4.26–4.31 (m, 1H), 4.34–4.37 (m, 1H). IR (KBr pellet, cm^{-1}): 3357.4, 2964.3, 1646.8, 1543.2, 1123.3.

3.1.4. **D6$_B$.** Esterified D-glucaric acid (20.0 mg, 0.08 mmol) was mixed with a methanol solution (0.34 mL) containing triethylamine (68 μL) and **5b** (26.7 mg. 0.08 mmol) and stirred at room temperature for 36 h. The solution was exhaustively dialyzed in ultrapure water, and the solution was lyophilized to dryness, yielding the final polymer product (13.7 mg, 36%). ^{1}H NMR (D_2O): δ = 2.96 (brs, 20H), 3.46 (brs, 8H), 3.92–3.95 (m, 1H), 3.96–4.00 (m, 2H), 4.06–4.09 (m, 1H), 4.12–4.15 (m, 2H), 4.25–4.31 (m, 2H), 4.34–4.39 (m, 2H). IR (KBr pellet, cm^{-1}): 3390.8, 2945.4, 2848.4, 1645.1, 1540.3, 1125.1.

3.1.5. **M5$_B$.** D-Mannaro-1,4:6,3-dilactone (20.0 mg, 0.11 mmol) was mixed with a methanol solution (0.60 mL) containing triethylamine (78 μL) and **5a** (35.0 mg, 0.11 mmol) and stirred at room temperature for 72 h. The solution was exhaustively dialyzed in ultrapure water, and the solution was lyophilized to dryness, yielding the final polymer product (10.5 mg, 32%). ^{1}H NMR (D_2O): δ = 3.02 (brs, 16H), 3.52 (brs, 8H), 3.96 (s, 2H), 4.05–4.07 (m, 1H), 4.11–4.13 (m, 1H), 4.20–4.28 (m, 2H). IR (KBr pellet, cm^{-1}): 3393.8, 2932.1, 2868.1, 1643.9, 1580.2, 1539.1, 1361.5, 1123.5.

3.1.6. **M6$_B$.** D-Mannaro-1,4:6,3-dilactone (12.8 mg, 0.07 mmol) was mixed with a methanol (0.73 mL) solution containing triethylamine (65 μL) and **5b** (25.0 mg, 0.09 mmol) and stirred at room temperature for 72 h. The solution was exhaustively dialyzed in ultrapure water, and the solution was lyophilized to dryness, yielding the final polymer product (19.5 mg, 39%). ^{1}H NMR (D_2O): δ = 2.93 (brs, 20H), 3.45 (brs, 8H), 3.94–3.98 (m, 2H), 4.03–4.06 (m, 1H), 4.09–4.13 (m, 1H), 4.21–4.27 (m, 2H). IR (KBr pellet, cm^{-1}): 3366.5, 2834.1, 1645.7, 1541.8, 1410.0, 1122.2.

3.1.7. **T5$_B$.** Dimethyl L-tartarate (20.0 mg, 0.11 mmol) was added to a methanol solution (0.17 mL) containing triethylamine (89 μL) and **5a** (30.0 mg, 0.11 mmol) and stirred at room temperature for 96 h. The solution was exhaustively dialyzed in ultrapure water, and the solution was lyophilized to dryness, yielding the final polymer product (6.70 mg, 16%). ^{1}H NMR (D_2O): δ = 2.98 (br, 16H), 3.50 (br, 8H), 4.10–4.12 (m, 1H), 4.33–4.35 (m, 1H), 4.59 (s, 2H). IR (KBr pellet, cm^{-1}): 3411.5, 2931.6, 2856.1, 1650.9, 1539.0, 1121.3.

3.1.8. **T6$_B$.** Dimethyl L-tartarate (20.0 mg, 0.11 mmol) was added to a methanol solution (0.17 mL) containing triethylamine (89 μL) and **5b** (35.0 mg, 0.11 mmol) and stirred at room temperature for 96 h. The solution was exhaustively dialyzed in ultrapure water, and the solution was lyophilized to dryness, yielding the final polymer product (7.40 mg, 16%). ^{1}H NMR (D_2O): δ = 2.91 (br, 20H), 3.45 (br, 8H), 4.32–4.33 (m, 1H), 4.57 (s, 2H). IR (KBr pellet, cm^{-1}): 3393.5, 2933.4, 2848.1, 1653.1, 1536.6, 1133.1.

3.2. Linear Polymer Synthesis. 3.2.1. **G5$_L$.** Dimethyl *meso*-galactarate (27.0 mg, 0.11 mmol) was mixed with a methanol solution (0.57 mL) containing triethylamine (81 μL) and **4a** (66.0 mg, 0.11 mmol) and stirred at room temperature for 48 h. The product was dialyzed against methanol using a 1000 MW cutoff membrane and dried under vacuum, yielding 53.4 mg (0.06 mmol, 53%) of protected polymer. The resulting polymer was then treated with 1 mL of dry 4 N HCl in dioxane for 3 h to remove the Boc groups. The final polymer product was dialyzed against ultra pure water using a 100 MW cutoff membrane and lyophilized to dryness, yielding 19.6 mg (0.06 mmol, 72%) of polymer. ^{1}H NMR (D_2O): δ = 3.36 (br, 4H), 3.68 (br, 20H), 4.06 (s, 2H), 4.49 (s, 2H). FT-IR (KBr pellet, cm^{-1}): 3515.5, 2976.2, 1763.8, 1577.6, 1308.5.

3.2.2. **G6$_L$.** Dimethyl *meso*-galactarate (20.7 mg, 0.09 mmol) was mixed with a methanol solution (0.35 mL) containing triethylamine (62 μL) and **4b** (62.4 mg, 0.09 mmol) and stirred at room temperature for 48 h. The product was dialyzed against methanol using a 1000 MW cutoff membrane and dried under vacuum, yielding 53.4 mg (0.02 mmol, 28%) of protected polymer. The resulting polymer was then treated with 1 mL of dry 4 N HCl in dioxane for 3 h to remove the Boc groups. The final polymer product was dialyzed against ultra pure water using a 100 MW cutoff membrane and lyophilized to dryness, yielding 27.6 mg (0.06 mmol, 94%) of polymer. ^{1}H NMR (D_2O with one drop of DCl): δ = 3.32–3.39 (m, 4H), 3.51–3.72 (m, 24H), 4.06 (s, 2H), 4.48 (s, 2H). FT-IR (KBr pellet, cm^{-1}): 3791.7, 3087.0, 1668.5, 1548.8, 1331.1.

3.2.3. **D5$_L$.** Esterified D-glucaric acid (23.0 mg, 0.1 mmol) was mixed with a methanol solution (0.32 mL) containing triethylamine (68 μL) and **4a** (55.8 mg. 0.1 mmol) and stirred at room temperature for 24 h. The product was dialyzed against methanol using a 1000 MW cutoff membrane and dried under vacuum, yielding 24.1 mg (0.03 mmol, 33%) of protected polymer. The resulting polymer was then treated with 1 mL of dry 4 N HCl in dioxane for 3 h to remove the Boc groups. The final polymer product was dialyzed against ultra pure H_2O using a 100 MW cutoff membrane and lyophilized to dryness, yielding 7.90 mg (0.02 mmol, 55%) of polymer. ^{1}H NMR (D_2O with one drop of DCl): δ = 3.35 (t, J = 5.6 Hz, 4H), 3.54–3.67 (m, 20H), 3.98 (t, J = 5.2 Hz, 1H), 4.28 (m, 1H), 4.18 (d, J = 5.2 Hz, 1H), 4.30 (m, 1H). FT-IR (KBr pellet, cm^{-1}): 3264.4, 3022.2, 1666.1, 1549.1, 1329.5.

3.2.4. **D6$_L$.** Esterified D-glucaric acid (22.6 mg, 0.1 mmol) was mixed with a methanol solution (0.38 mL) containing triethylamine (67 μL) and **4b** (68.1 mg. 0.1 mmol) and stirred at room temperature for 36 h. The product was dialyzed against methanol using a 1000 MW cutoff membrane and dried under vacuum, yielding 43.9 mg (0.05 mmol, 52%) of protected polymer. The resulting polymer was then treated with 1 mL of dry 4N HCl in dioxane for 3 h to remove the Boc groups. The product was dialyzed against ultra pure water using a 100 MW cutoff membrane and lyophilized to dryness, yielding 22.9 mg (0.05 mmol, 95%) of polymer. ^{1}H NMR (D_2O with one drop of DCl): δ = 3.35 (t, J = 6.0 Hz, 4H), 3.52–3.68 (m, 24H), 4.00 (t, J = 5.2 Hz, 1H), 4.15–4.16 (m, 1H), 4.13 (d, J = 5.2 Hz, 1H), 4.42–4.43 (m, 1H). FT-IR (KBr pellet, cm^{-1}): 3398.1, 3012.2, 1665.9, 1548.6, 1333.7.

3.2.5. **M5$_L$.** D-Mannaro-1,4:6,3-dilactone (17.0 mg, 0.11 mmol) was mixed with a methanol solution (0.65 mL) containing triethylamine (20 μL) and **4a** (56.0 mg, 0.11 mmol) and stirred at room temperature for 72 h. The product was dialyzed against methanol using a 1000 MW cutoff membrane and dried

under vacuum, yielding 27.2 mg (0.04 mmol, 37%) of protected polymer. The resulting polymer was then treated with 1 mL of dry 4 N HCl in dioxane for 3 h to remove the Boc groups. The final polymer product was dialyzed against ultra pure water using a 100 MW cutoff membrane and lyophilized to dryness, yielding 8.0 mg (0.02 mmol, 50%) of polymer. ^{1}H NMR (D_2O with one drop of DCl): $\delta = 3.35$ (t, $J = 5.6$ Hz, 4H), 3.53–3.65 (m, 20H), 3.98 (d, $J = 6.4$ Hz, 2H), 4.28 (d, $J = 6.4$ Hz, 2H). FT-IR (KBr pellet, cm^{-1}): 3407.4, 3011.2, 1653.1, 1561.3, 1330.3.

3.2.6. **M6$_L$.** D-Mannaro-1,4:6,3-dilactone (13.9 mg, 0.08 mmol) was mixed with a methanol (0.40 mL) solution containing triethylamine (18 μL) and **4b** (58.0 mg, 0.08 mmol) and stirred at room temperature for 72 h. The product was dialyzed against methanol using a 1000 MW cutoff membrane and dried under vacuum, yielding 27.9 mg (0.03 mmol, 39%) of protected product. The resulting polymer was then treated with 1 mL of dry 4 N HCl in dioxane for 3 h to remove the Boc groups. The final polymer product was dialyzed against ultra pure H_2O using a 100 MW cutoff membrane and lyophilized to dryness, yielding 8.90 mg (0.02 mmol, 60%) of polymer. ^{1}H NMR (D_2O with one drop of DCl): $\delta = 3.35$ (t, $J = 5.6$ Hz, 4H), 3.54–3.67 (m, 24H), 3.98 (d, $J = 6.4$ Hz, 2H), 4.28 (d, $J = 6.4$ Hz, 2H). FT-IR (KBr pellet, cm^{-1}): 3398.6, 3012.2, 1666.2, 1554.9, 1330.5.

3.2.7. **T5$_L$.** Dimethyl L-tartarate (15.0 mg, 0.08 mmol) was added to a methanol solution (0.13 mL) containing triethylamine (68 μL) and **4a** (48.3 mg, 0.08 mmol) and stirred at room temperature for 96 h. The product was dialyzed against methanol using a 1000 MW cutoff membrane and dried under vacuum, yielding 22.8 mg (0.03 mmol, 39%) of protected polymer. The resulting polymer was then treated with 1 mL of dry 4 N HCl in dioxane for 3 h to remove Boc groups. The final polymer product was dialyzed against ultra pure H_2O using a 100 MW cutoff membrane and lyophilized to dryness, yielding 8.40 mg (0.02 mmol, 67%) of polymer. ^{1}H NMR (D_2O with one drop of DCl): $\delta = 3.31$–3.38 (m, 4H), 3.51–3.64 (m, 18H), 3.65–3.71 (m, 2H), 4.64 (s, 2H). FT-IR (KBr pellet, cm^{-1}): 3398.2, 3010.2, 1665.8, 1547.4, 1333.9.

3.2.8. **T6$_L$.** Dimethyl L-tartarate (15.6 mg, 0.09 mmol) was added to a methanol solution (0.135 mL) containing triethylamine (71 μL) and **4b** (63.1 mg, 0.09 mmol) and stirred at room temperature for 96 h. The product was dialyzed against methanol using a 1000 MW cutoff membrane and dried under vacuum, yielding 40.3 mg (0.05 mmol, 55%) of protected polymer. The resulting polymer was then treated with 1 mL of 4 N HCl in dioxane for 3 h to remove the Boc groups. The final polymer product was dialyzed against ultra pure water using a 100 MW cutoff membrane and lyophilized to dryness, yielding 18.1 mg (0.04 mmol, 87%) of polymer. ^{1}H NMR (D_2O with one drop of DCl): $\delta = 3.31$–3.40 (m, 4H), 3.52–3.73 (m, 24H), 4.63 (s, 2H). IR (KBr pellet, cm^{-1}): 3398.8, 3011.2, 1666.4, 1547.2 1330.3.

4. Polymer and Polyplex Characterization. *4.1. Gel Permeation Chromatography (GPC).* The molecular weight, polydispersity index, and the Mark–Houwink-Sakurada (MHS) parameter (α) for the two series of polymers were measured with a Viscotek GPCmax instrument equipped with a GMPW$_{XL}$ column coupled to a triple detection system (static light scattering, viscometry, and refractive index). A solution of 0.5 M sodium acetate containing 20% acetonitrile was used as the mobile phase. Each sample was dissolved in the mobile phase, injected into the column (100 μL), and eluted at 0.8 mL/min. A PEO ($M_w = 22$ kDa) standard was used for calibration.

4.2. Gel Electrophoresis Shift Assays. The ability of these polymers to bind pDNA (pCMVβ) was measured by gel electrophoresis at 60 V. Agarose gel (0.6%, w/v) containing SYBR Safe DNA gel stain was prepared in TAE buffer (40 mM Tris-acetate, 1 mM EDTA). Each polymer was dissolved in nuclease-free water (Gibco, Carlsbad, CA). Plasmid DNA (10 μL, 0.1 μg/μL) was mixed with the same volume of polymer solution at *N*/*P* ratios between 0 and 50 (N = moles of polymer amine groups that can be protonated; P = moles of phosphate groups on the pDNA) and incubated for 30 min at room temperature before the addition of loading buffer (2 μL of Blue Juice, Invitrogen, Carlsbad, CA). An aliquot of each sample was loaded into the well of the gel. A stable polymer−DNA complex is shown by the lack of migration of the pDNA in the electrophoretic field.

4.3. Dynamic Light Scattering and Zeta Potential Measurements. Polyplex sizes were measured at 633 nm on a Zetasizer (Nano ZS) dynamic light scattering instrument (Malvern Instruments, Malvern, UK) at room temperature. Polyplexes were formed at an *N*/*P* ratio of 20 (150 μL) by incubating each polymer with pCMVβ (150 μL, 0.02 μg/μL) for 30 min. The z-average particle size was determined by cumulant fit of the data with a detection angle of 173°. Each sample was diluted to 0.9 mL with nuclease-free water or supplemented Dulbecco's modified eagle medium (DMEM) (containing 10% FBS), and the particle size was measured at intervals of 0, 20, and 60 min after DMEM addition in triplicate. The zeta potential measurements were also performed using the same instrument with a detection angle of 17°. The polyplexes were formed in water using the same procedure described above. After 45 min of incubation time, each sample was then diluted to 0.9 mL with nuclease-free water, and the zeta potential was measured.

4.4. Flow Cytometry. HeLa cells were seeded on 12-well plates at 1.0×10^5 cells/well and allowed to incubate in supplemented DMEM at 37 °C and 5% CO_2 for 24 h. The polyplexes were prepared by combining 100 μL of Cy5-labeled pDNA (0.02 μg/μL) and 100 μL of **M4**, **M5$_B$**, **M6$_B$**, **M5$_L$**, **M6$_L$**, **T4**, **T5$_B$**, **T6$_B$**, **T5$_L$**, or **T6$_L$** at an *N*/*P* of 20. The cells were then transfected with 0.5 mL of polyplex solution (2 μg of pDNA/well) in 0.4 mL of serum-free media (Opti-MEM) or DMEM containing 10% FBS. The cells were incubated with each solution for 4 h to allow endocytosis and internalization of the polyplexes. After transfection, the cells were rinsed with PBS multiple times to remove the cell-surface-bound polyplexes. Supplemented DMEM was then added, and the cells were incubated for another 30 min to allow further polyplex internalization. Four and half-hours after initial transfection, the cells were rinsed again with PBS, trypsinized, pelleted, the supernatant aspirated off, and the cells again resuspended in PBS containing 2% FBS for fluorescent activated cell sorting (FACS) analysis. A FACSCanto II (Becton Dickenson, San Jose, CA) equipped with an helium−neon laser to excite Cy5 (633 nm) was used. Ten thousand events were collected in duplicate for each sample. The positive fluorescence level was established by visual inspection of the histogram of negative control cells such that less than 1% appeared in the positive region.

4.5. Luciferase Reporter Gene Expression and Cell Viability Assays. HeLa cells were seeded on 24-well plates at 5×10^4 cells/well and allowed to incubate in supplemented Dulbecco's modified Eagle medium (DMEM, supplemented with 10% FBS, 100 units/mg penicillin, 100 μg/mL streptomycin, and 0.25 μg/mL amphotericin) at 37 °C and 5% CO_2 for 24 h. Polymer solutions (150 μL) were incubated with gWiz-Luc (150 μL, 0.02 μg/μL) at *N*/*P* ratios of 10, 20, and 30 at room temperature for 1 h to form the polyplexes. The mixtures were then diluted to 900 μL with serum-free media (Opti-MEM) or DMEM containing 10% FBS. Each well of cells was transfected with 300 μL of the polyplex solution containing 1 μg of gWiz-Luc pDNA complexed with each poly(glycoamidoamine). Each sample was tested in triplicate. Untransfected

cells and cells transfected with naked gWiz-Luc (1 μg pDNA, $N/P = 0$) were used as negative controls. Four hours after the transfection, 800 μL of the supplemented DMEM was added to each well. Twenty-four hours after transfection, the media was replaced with fresh supplemented DMEM (1 mL). Forty-seven hours after initial transfection, the media was removed, and the cells were washed with 500 μL of PBS and treated with cell culture lysis buffer (Promega, Madison, WI). The amount of protein in the cell lysates (as mg of protein) was determined against a standard curve of bovine serum albumin (98%, Sigma, St. Louis, MO), using a Bio-Rad DC protein assay kit (Hercules, CA).

Cell lysates were analyzed for luciferase activity with Promega's luciferase assay reagent (Madison, WI). For each sample, luminescence was measured over 10 s in duplicate with a luminometer (GENios Pro, TECAN US, Research Triangle Park, NC), and the average was utilized. The cell viability profiles were characterized by the amount of protein in the cell lysates. The protein levels of the transfected cells were normalized to the protein amount obtained for untransfected cells.

RESULTS AND DISCUSSION

Synthesis and Characterization of the Poly(glycoamidoamine)s. Here, we have synthesized two series of poly(glycoamidoamine)s, both branched and linear, based on a variety of carbohydrate comonomers and an oligoethyleneamine moiety containing five or six amines in the polymer repeat unit. This study was undertaken to examine how the amine stoichiometry and polymer physical structure affects cell viability and transfection efficiency. From our previous studies (*28–31*), we have discovered that increasing the number of secondary amines in the polymer repeat unit from one to four significantly increases the cellular uptake and gene expression. Many other studies in this field have also revealed that amines with a buffering capacity may play an important role in increasing the transfection efficiency; however, in general, the higher amine density and positive charge usually results in higher cytotoxicity (*22,23,37*). Previous studies in this field have also shown that the polymer structure can also significantly affect bioactivity (*22–26*). For example, Wightman and co-workers found that linear PEI usually reveals higher transfection efficiency than branched PEI *in vitro* (in Neuro 2a, MCA-38, and C26 cells) (*25*).

The current polymers were designed to investigate whether further increasing the amine number to five and six can further increase the cellular uptake and transfection efficiency without increasing the toxicity associated with poly(glycoamidoamine)s. To this end, 16 new polymers, based on our original carbohydrate monomers, were created to investigate the role of amine number and branching. As shown in Scheme 1, four new oligoethyleneamine monomers with five and six secondary amines were synthesized by first protecting the primary amine end groups of tetraethylenepentamine or pentaethylenehexamine with trifluoroacetyl units and then protecting the internal secondary amines with *tert*-butoxycarbonyl (Boc) according to a previously published method (*35, 36*). The trifluoroacetyl units were removed under mildly basic conditions to liberate the terminal primary amines, which were then protected again with benzyl (Bn) groups. By using Gabriel synthesis, the total amine number in the oligoethyleneamines was increased by two, yielding the Boc-protected monomers **4a** and **4b** (utilized to synthesize the linear polymers). To obtain the deprotected monomers (**5a** and **5b**) for the synthesis of the branched structures, the protecting groups on **4a** and **4b** were cleaved by a conventional method.

The four esterified carbohydrate monomers were then polymerized with these four new oligoethyleneamines via two different methods highlighted in Schemes 2 and 3 to yield the small library of 16 new structures. The first method, shown in Scheme 2, uses the fully deprotected oligoethyleneamines (monomers **5a** and **5b**), and the second method, shown in Scheme 3, uses the partial-Boc-protected oligoethyleneamines (monomers **4a** and **4b**) in the polymerization. In Scheme 2, both the primary and secondary amine groups can theoretically react with the esterified carbohydrate monomers, which results in slightly branched polymers. Conversely, as shown in Scheme 3, there are less free secondary amines in the oligoethyleneamines monomers (**4a** and **4b**), and the polymerization proceeds to yield linear polymers. Although there are still two free secondary amines in the oligoethyleneamines in Scheme 3, the steric hindrance of the neighboring Boc groups likely discourages polymerization from these functional groups.

Scheme 1. Synthesis of the Four Oligoethyleneamine Monomers 4a, 4b, 5a, and 5b[a]

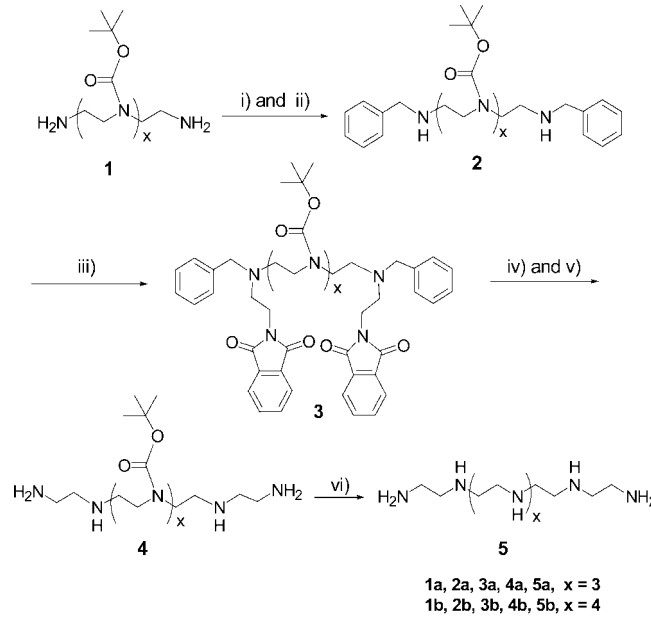

[a] Conditions: (i) PhCHO, MeOH, (ii) $NaBH_4$, (iii) *N*-(2-bromoethyl) phthalimide, KF-celite, CH_3CN, (iv) $H_2NNH_2.H_2O$, MeOH (v) $Pd(OH)_2$/C, H_2 (50 psi), MeOH, (vi) 4N HCl in dioxane.

The polymerization reactions to create the linear and branched polymers were monitored via GPC containing a triple detection system (static light scattering, viscometry, and refractive index). The reaction conditions were optimized to yield polymers with similar degrees of polymerization (n_w, Table 1). The n_w values were between 9 to 15, thus ensuring that the biological properties of these polymers could be accurately compared to the previous polymers synthesized by our group. GPC/light scattering/viscometry results confirmed that the final polymers synthesized via Scheme 2 (branched) had lower Mark–Houwink−Sakurada (MHS) α values than the polymers synthesized via Scheme 3 (linear), as shown in Table 1. The lower α values shown in Table 1a, calculated from the MHS equation ($[\eta] = KM^{\alpha}$), reveal that the polymers synthesized via Scheme 2 appear to be more branched than the polymers synthesized via Scheme 3 (Table 1b). It is interesting to note that the polymers formed with the tartarate and galactarate monomers appear to be less branched than their mannarate and glucarate analogues because of the higher α values in Table 1a. In general, all of the linear polymers synthesized via Scheme 3 had higher MHS values than their branched analogues synthesized via Scheme 2. It should also be noted here that the linear polymers could have higher α values because HCl was used during the deprotection step. This could cause a higher amine fraction in the polymer backbone to be protonated, causing

Scheme 2. Synthesis of the Branched Poly(glycoamidoamine) Analogues with Monomers 5a or 5b[a]

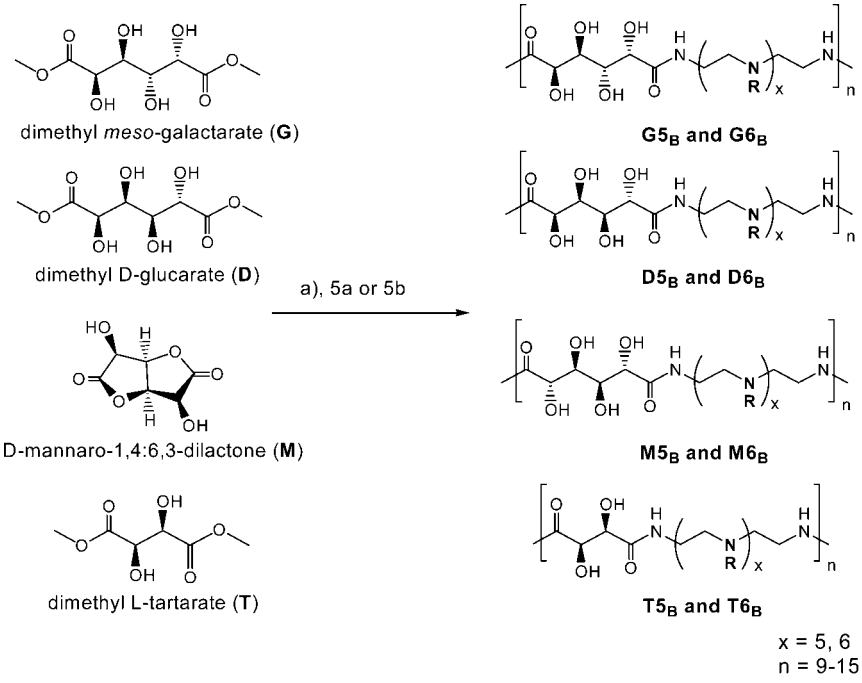

[a] Conditions: (a) TEA, MeOH, R = H or point of branching.

Scheme 3. Synthesis of the Linear Poly(glycoamidoamine) Analogues with Monomers 4a or 4b[a]

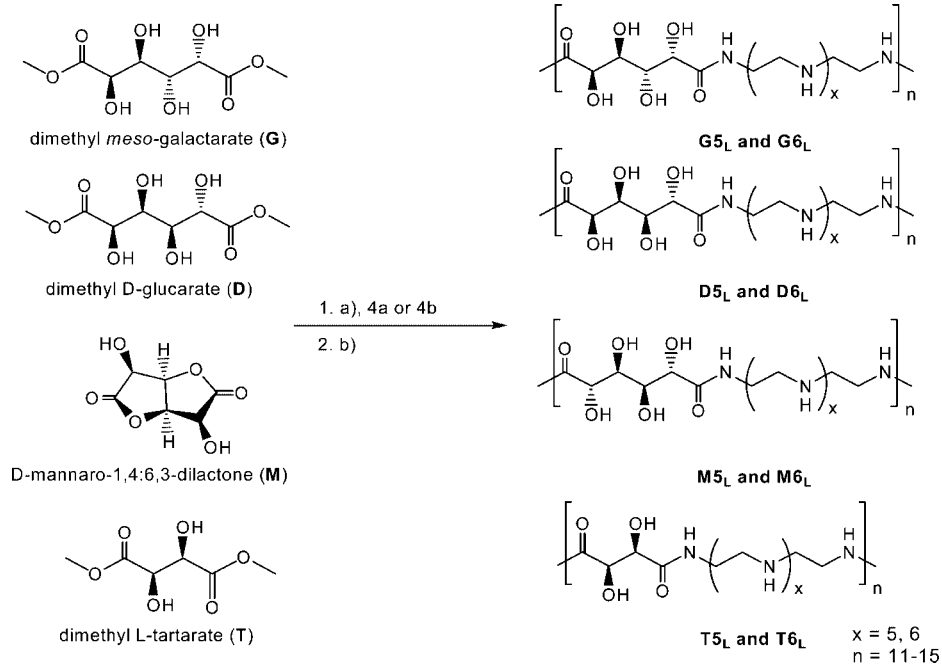

[a] Conditions: (a) TEA, MeOH; (b) 4 N HCl in dioxane.

an electrostatic repulsion effect, thus discouraging random-coil solution morphologies and encouraging stiff-chain solution structures (yielding higher α values). Studies to understand the degree of protonation via titration are currently in progress to investigate this possibility.

When comparing the ^{1}H NMR spectra of the analogous structures, several interesting features were observed. For example, it was noticed that there are more peaks in the spectrum of **G5$_B$** than the spectrum of **G5$_L$** in the carbohydrate region of ^{1}H NMR (shown in Figure 2), which indicated a higher degree of branching in the **G5$_B$** structure. Also, in the spectra of all of the linear structures, the peaks were all sharper than the peaks in the spectra of the branched structures, which revealed broader peak widths. In addition, the methylene protons between the secondary amines and the methylene protons adjacent to the amides in the linear polymers had different chemical shift values in the ^{1}H NMR spectrum as compared to the branched polymers (Figure 2). The methylene protons adjacent to the amines in the linear analogues (likely to be more protonated) are shifted further downfield than the methylene protons adjacent to the amines in the branched polymers (less protonated). Lastly, it was also interesting to find that the linear polymers had a different final

Table 1. Molecular Weight (M_w), Polydispersity (M_w/M_n), MHS Parameter (α), Degree of Polymerization (n_w), and the *N*/*P* Ratios of Polymer−pDNA Binding and Charge Neutralization Obtained from Gel Electrophoresis Assays for the (a) Branched ($G5_B$–$T6_B$) and (b) Linear ($G5_L$–$T6_L$) Poly(glycoamidoamine)s

(a)

polymers	M_w (kDa)	M_w/M_n	MHS (α)	n_w	*N*/*P*
$G5_B$	4.4	1.8	0.58	10	5
$G6_B$	5.4	2.2	0.53	11	4
$D5_B$	3.8	1.5	0.45	9	5
$D6_B$	4.8	1.8	0.46	10	4
$M5_B$	4.3	1.4	0.50	9	10
$M6_B$	5.3	1.8	0.47	11	7
$T5_B$	5.9	1.3	0.69	15	3
$T6_B$	6.4	1.4	0.62	15	3

(b)

polymers	M_w (kDa)	M_w/M_n	MHS (α)	n_w	*N*/*P*
$G5_L$	4.8	1.1	0.73	11	2
$G6_L$	7.4	1.3	0.76	15	2
$D5_L$	4.7	1.1	0.79	10	2
$D6_L$	4.9	1.2	0.69	10	2
$M5_L$	4.8	1.4	0.83	11	3
$M6_L$	5.3	1.1	0.70	11	3
$T5_L$	4.7	1.1	0.72	12	2
$T6_L$	5.3	1.1	0.66	12	2

material form as compared to their branched analogues. For instance, after lyophilizing the final products, **$G5_B$** resulted in a fluffy powder, while **$G5_L$** was a sticky solid.

Polymer−DNA Binding, Particle Size, and Zeta Potential. The efficient compaction of pDNA into nanoparticles is an essential process that mediates the endocytosis of polyplexes, where cells typically uptake polyplexes ranging from 50 to several hundred nanometers (*7*, *38*). The ability of each polymer to bind, charge neutralize, and compact pDNA is typically dependent on the *N*/*P* ratio and the degree of branching. The 16 structures presented here were examined for their ability to bind and compact pDNA via gel electrophoresis shift assays and dynamic light scattering (DLS). Because there are less amines capable of being protonated in the branched polymers (due to the formation of amides during branching) than in the linear series of polymers, the linear structures may have stronger electrostatic interactions with the negative phosphate groups on the pDNA. Table 1 summarizes the results of the gel electrophoresis shift assays (*N*/*P* ratios of polymer−pDNA binding and charge neutralization). As shown, the linear polymers bind and neutralize pDNA at lower *N*/*P* ratios than the branched polymers. It should be noted that the degree of branching for these polymers is very difficult to determine and is not known at this time.

As shown in Figure 3, most of the polymers synthesized here can form nanoparticles with pDNA with less than 250 nm as determined via DLS at $N/P = 20$ in nuclease-free water. However, it was interesting to find that most polyplexes formed with the linear polymers yielded larger particle sizes than the branched polymers, which could be related to their high amine (cation) density and polycation repulsions. Zeta potential measurements were conducted on aqueous solutions containing the polyplexes formed at $N/P = 20$. Figure 3 (lines) reveals that all of the polyplexes have high positive surface charge, especially, polyplexes formed with the linear polymers (in excess of 40 mV). The high zeta potentials observed with the polyplexes formed with the linear polymers may be due to the protonated amines caused by the acid-mediated deprotection step (Scheme 3).

To understand the stability of polyplexes formed with this new series of polymers in the presence of media containing serum, polyplex size (for all polymers analogs) at $N/P = 20$ was examined via DLS at 0, 20, and 60 min after dilution with DMEM (supplemented with 10% FBS), as shown in Figure 4. Upon the addition of DMEM, most of the polyplexes grew in size to about 250 nm. After 20 min, the polyplexes formed with the **D_B** and **M_B** series further increased in size to about 700–800 and 400–600 nm, respectively. After exposure in serum-containing media, the polyplex size in the **D_B** and **M_B** series continued to grow, especially in the **D_B** series (increase to over 1000 nm). These data revealed that polyplexes formed with the **T_B** and **G_B** polymers were more stable from aggregation than the polyplexes formed with the **M_B** and **D_B** series. These results supported our previously published results that the stereochemistry of carbohydrate can affect polyplex stability from aggregation (*39*). In the linear analogues, the DLS data indicated that the polyplexes also were more stable from aggregation after dilution with DMEM (containing 10% FBS). It was found that polyplexes formed with the linear polymers followed a different trend than the branched analogues (polyplexes formed with the **D_L** and **G_L** polymers appeared to be slightly more stable from aggregation than polyplexes formed with the **M_L** and **T_L** polymers).

Cellular Delivery and Toxicity Studies. The cellular uptake facilitated by the new series of poly(glycoamidoamine)s based on mannarate and tartarate (**M4**, **$M5_B$**, **$M6_B$**, **$M5_L$**, **$M6_L$**, **T4**, **$T5_B$**, **$T6_B$**, **$T5_L$**, and **$T6_L$**) were investigated by flow cytometry. This study quantifies both the number of cells that uptake Cy5-labeled pDNA and the average intensity of Cy5 fluorescence (relative amount of pDNA) in the cell population. This experiment was performed in both serum-free (Opti-MEM) and DMEM containing 10% serum at an *N*/*P* ratio of 20. HeLa cells were incubated with each polyplex solution for 4 h to allow endocytosis. After removing the cell-surface-bound polyplexes and further incubating for 30 min, the cells were trypsinized and isolated for FACS analysis. The mean fluorescence intensity and the percentage of positive cells in both transfection conditions are shown in Figure 5. It was found that all of the polymers significantly enhanced the cellular uptake of pDNA in both conditions, with the exception of **$M5_B$**, whose result may be due to the fact that **$M5_B$** appears to have a low binding affinity to pDNA (Table 1a). The polyplexes formed with **$M5_B$** may dissociate during cell surface binding to the negatively charged glycosaminoglycans, which would result in low cellular uptake profiles. When comparing the bioactivity of polyplexes formed with both the linear and branched **M** and **T** series of polymers in the serum-free condition (Figure 5a), it was observed that the linear polymers facilitated much higher cellular entry than the branched versions of the same structure with the exception of polymer **T6** (statistical significance shown by the symbol * on the top of linear version in Figure 5a). For example, the mean fluorescence intensity of the cells transfected by **$M6_L$** was twice as high as that of **$M6_B$**, and the number of transfected cells also increased from 85% to almost 100%. Second, polymers that carry six amine functionalities demonstrated higher cellular uptake profiles than polymers with five amine groups in the polymer repeat unit (with the exception of polymer **$T6_L$**, statistical significance shown by the symbol ◇ in Figure 5a). Third, polyplexes formed with the **T** series of polymers were shown to enter the cell membrane more efficiently than the **M** series of polyplexes (statistical significance shown by the symbol ^ for the **T** series in Figure 5a). This could be due to the more efficient binding between the **T** series of polymers and pDNA shown by the gel shift assays (Table 1). When comparing the cellular entry facilitated by both the **M** and **T** series of polymers in DMEM containing 10% serum (Figure 5b), a systematic trend was not noticed. However, the mean fluorescence intensity data correlated well to the polyplex sizes formed with these polymers (Figure 4). For example, polyplexes

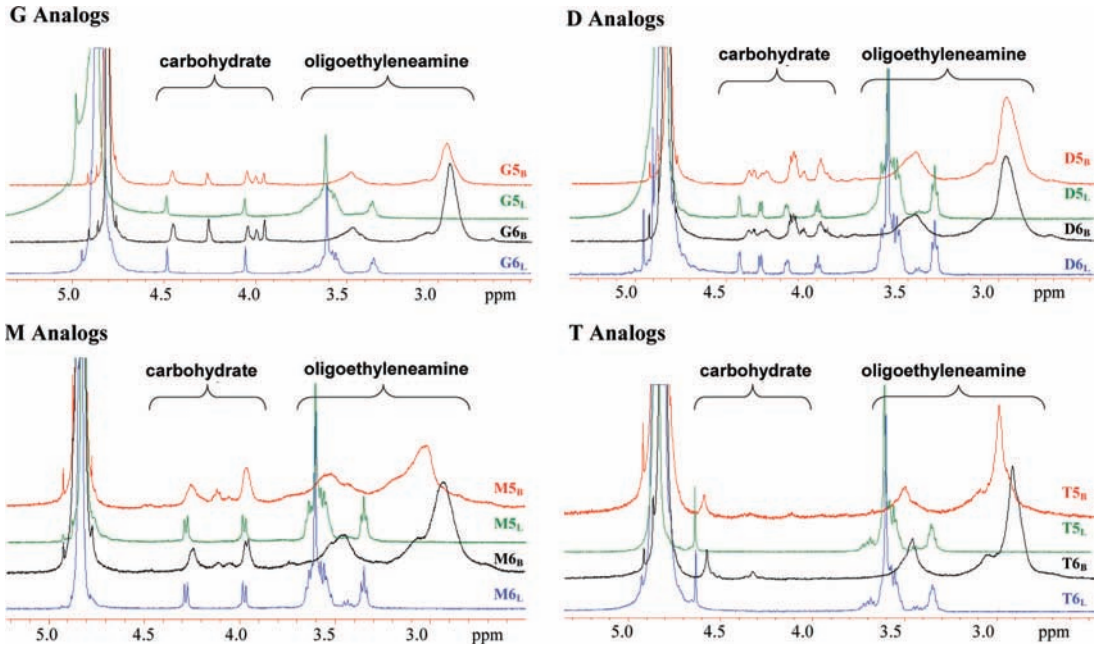

Figure 2. [1]H NMR for the branched and linear poly(glycoamidoamine)s. The spectra are labeled as follows: red, branched polymers obtained from **5a**; green, linear polymers obtained from **4a**; black, branched polymers obtained from **5b**; and blue, linear polymers obtained from **4b**. All spectra were taken in D_2O (large HOD peak at 4.85 ppm), and the region between 3.9 to 4.7 ppm represents the carbohydrate proton resonances, and the region between 2.8 to 3.7 ppm represents the oligoethyleneamine resonances.

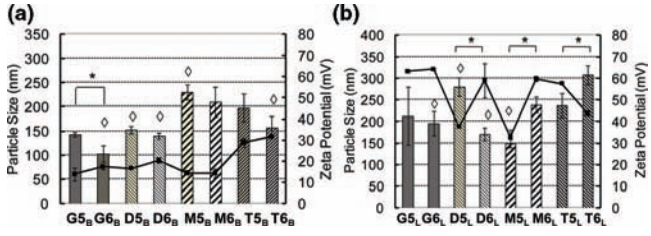

Figure 3. Polyplex size (bars) and the zeta potential (line) for the polyplexes formed with (a) branched and (b) linear polymers at $N/P = 20$ in nuclease-free water. Data are reported as the mean ± standard of deviation of three replicates. Statistical significances of particle size are shown with * or ◊ as $p < 0.05$. The symbol * shows that a significant difference in particle size was observed between polymers with the same carbohydrate moiety but with a variation of amine number in the repeat unit (e.g., $G5_B$ vs $G6_B$). The symbol ◊ indicates a significant difference with the same amine number and same carbohydrate but different physical structures (e.g., $G5_B$ vs $G5_L$).

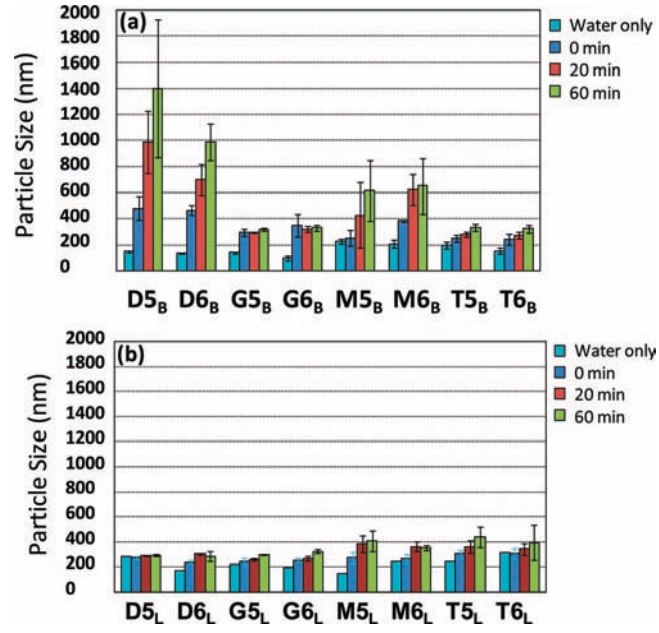

Figure 4. Polyplex size for the polymer−pDNA complexes formed with (a) branched and (b) linear polymers at $N/P = 20$ in water only and then at 0 min, 20 min, and 60 min after dilution with DMEM (containing 10% FBS). Data are reported as the mean ± standard of deviation of three replicates.

formed with $\mathbf{T5_B}$ and $\mathbf{T6_B}$ were shown to be smaller and more stable in DMEM containing 10% serum than polyplexes formed with $\mathbf{M5_B}$ and $\mathbf{M6_B}$, which correlated to the higher cellular uptake facilitated by polymers $\mathbf{T5_B}$ and $\mathbf{T6_B}$. Polymers $\mathbf{M5_L}$ and $\mathbf{M6_L}$ delivered a similar amount of Cy5-pDNA into the cells as did polymers $\mathbf{T5_L}$ and $\mathbf{T6_L}$, which could be also attributed to the similar size and stability of these polyplexes. Polymers $\mathbf{T5_B}$ and $\mathbf{T6_B}$ were shown to have the highest cellular uptake profile in DMEM containing 10% serum.

To promote the intracellular delivery of genetic materials, nucleic acids need to bypass many destructive obstacles besides cellular entry (*40*). Hence, luciferase reporter gene expression experiments were also performed within HeLa cells to examine the gene expression levels of the polyplexes formed with the linear and branched polymers containing either five or six amines per repeat unit. In this experiment, the previously synthesized polymers with four secondary amines in the polymer repeat unit (**G4**, **D4**, **M4**, and **T4**) (*28–31*) were used as positive controls, and naked pDNA was used as a negative control. Luciferase reporter gene expression results showed that the *N*/*P* ratio that displayed optimal transfection efficiency with these polyplexes was at $N/P = 20$ (considering both gene expression and cytotoxicity). As shown in Figure 6a, in serum-free transfection conditions, we first noticed that the analogues with six ethyleneamines (in both the linear and branched series) yielded higher gene expression than the analogues with five ethyleneamines (statistical significance was shown by the symbol ◇ in Figure 6a). Second, the linear analogues facilitated higher gene expression than the branched analogues with the exception of $\mathbf{T6_L}$ (statistical significance shown by the symbol * in Figure 6a). In addition, there was no obvious enhancement in the gene expression levels when comparing the branched and linear

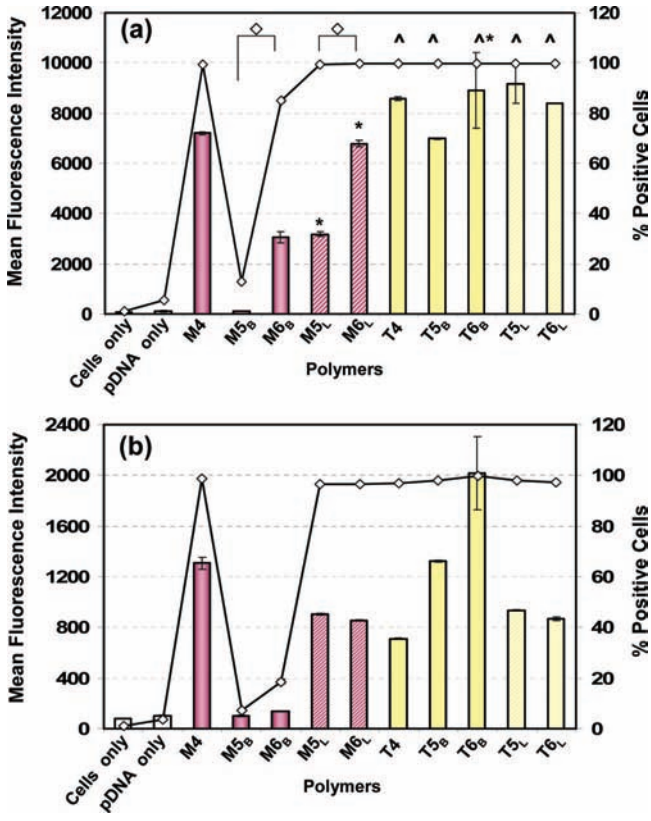

Figure 5. Cellular uptake of Cy5-labeled pDNA complexed with **M4**, $\mathbf{M5_B}$, $\mathbf{M6_B}$, $\mathbf{M5_L}$, $\mathbf{M6_L}$, **T4**, $\mathbf{T5_B}$, $\mathbf{T6_B}$, $\mathbf{T5_L}$, and $\mathbf{T6_L}$ in HeLa cells. (a) Mean fluorescence intensity (bars) and the percentage of cells positive for Cy5 (line) in serum-free transfection. Statistical significances in the mean fluorescence intensity are shown with *, ◇, or ^ as $p < 0.05$. The symbol * indicates that a significant difference in the mean fluorescence intensity was observed between the linear and the branched version of the polymers (e.g., $\mathbf{M5_L}$ vs $\mathbf{M5_B}$). The symbol ◇ indicates that a significant difference in the mean fluorescence intensity was observed between polymers with the same carbohydrate moieties but different amine stoichiometry (e.g., $\mathbf{M6_L}$ vs $\mathbf{M5_L}$). The symbol ^ indicates that a significant difference in the mean fluorescence intensity was observed between polymers with the same amine stoichiometry but different carbohydrate moieties (e.g., $\mathbf{T6_L}$ vs $\mathbf{M6_L}$). (b) Mean fluorescence intensity (bars) and the percentage of cells positive for Cy5 (line) in serum-containing transfection.

polymers to the previously published positive controls (**D4**, **G4**, **M4**, and **T4**). This may be due to the fact that the gel shift assays indicate that these new systems (with higher amine stoichiometry) do not appear to bind pDNA with higher affinity. This was especially true for the branched vectors, where high *N*/*P* ratios were needed to bind and charge neutralize pDNA. Previous work in our group has indicated a relationship between poly(glycoamidoamine) binding affinity and transfection efficiency (*28–31*). Polymers that bind pDNA in a stronger manner can protect it more efficiently from the nuclease degradation and premature release (polyplex dissociation) by negatively charged cell-surface glycosaminoglycans. It was also interesting to observe a similar hydroxyl stereochemistry effect on the gene delivery efficiency (that was noticed in previous studies) when comparing the results obtained with the analogues containing the same amine stoichiometry but different carbohydrate units (*28–31, 39*). Both the linear and branched polymers created with the tartarate and galactarate moieties generally facilitated higher gene expression than the polymers synthesized with the glucarate and mannarate monomers (with the exception of $\mathbf{D6_L}$). These results support our previous studies that the hydroxyl number and hydroxyl stereochemistry can play a role in delivery efficacy. This trend was very pronounced with the branched polymers where $\mathbf{D5_B}$, $\mathbf{D6_B}$, $\mathbf{M5_B}$, and $\mathbf{M6_B}$ yielded very low delivery efficacy. This effect could be partially due to their lower amine density because of branching. As shown in Table 1, the α values for $\mathbf{D5_B}$, $\mathbf{D6_B}$, $\mathbf{M5_B}$, and $\mathbf{M6_B}$ were lower than those for $\mathbf{G5_B}$, $\mathbf{G6_B}$, $\mathbf{T5_B}$, and $\mathbf{T6_B}$, indicating a higher degree of branching in the analogues synthesized with glucarate and mannarate. In addition, the linear analogues in this study obviously had higher gene expression levels than the branched versions, which may be attributed to their higher zeta potential values (Figure 3) and their stronger pDNA binding as suggested by the gel shift assays (Table 1). Better binding affinity may prevent pDNA from nuclease degradation during intracellular transport (*39*), and higher zeta potentials may enable polyplexes to strongly interact with the negatively charged cell-surface proteoglycans (*43*), leading to an increase in cellular uptake and DNA delivery. For the transfection performed in DMEM containing 10% serum (Figure 6b), we have noticed that almost all of these new poly(glycoamidoamine)s can significantly enhance gene delivery over the previously published analogues with four ethyleneamines (with the exception of polymers $\mathbf{D5_B}$, $\mathbf{D6_B}$, $\mathbf{M5_B}$, and $\mathbf{M6_B}$). Also, the linear versions of these polymers generally yielded higher gene expression than the branched analogues with serum (statistical significance is shown by the symbol * in Figure 6b). Gene expression appeared to also be affected by the carbohydrate type in the branched polymers, where the tartarate and galactarate series generally facilitated higher gene expression than the glucarate and mannarate series. This may be related to the stability of the tartarate and galactarate polyplexes in the serum-containing media (Figure 4a). Also in the 10% serum, the polymers with six ethyleneamines (in both the linear and branched series) did not show higher gene delivery profiles compared to their analogues with five ethyleneamines, except for $\mathbf{D6_B}$ and $\mathbf{T6_B}$, which demonstrated significantly higher gene expression than $\mathbf{D5_B}$ and $\mathbf{T5_B}$.

In both the presence and absence of serum, we have noticed that the luciferase gene expression level promoted by **M** and **T** polymers correlate to their cellular internalization (shown by the Cy5 fluorescence intensity in Figure 5). The polymer that facilitates better cell membrane internalization generally yields higher luciferase gene expression. This observation implies that the cellular uptake of the polyplexes formed with these new series of polymers is the key step that determines the efficacy of the pDNA delivery process.

The cell viability of HeLa cells exposed to polyplexes formed with both the linear and branched polymers in two transfection conditions is shown in Figure 7a and 7b. Cell viability in the experiment was characterized by the fraction of cell survival normalized to the untransfected cells. In general, the new series of poly(glycoamidoamine)s appeared to yield high cell viability at high $N/P = 20$. In addition, it was noticed that HeLa cell viability after exposure to polyplexes formed with the branched polymers was generally higher (between 70 and 100%) as compared to the linear analogues, particularly in the absence of serum. These results indicated that increasing the amine stoichiometry within the branched structures does not increase cytotoxicity, which is likely a result of the lower number of secondary amines (due to the formation of amides from branching units) (*28–31*). The exception was $\mathbf{T6_B}$ (60% cell survival), which may be related to the lower number of hydroxyl groups and thus increased amine density. The higher cytotoxicity of the linear analogues in the absence of serum may be attributed to the higher zeta potential of polyplexes formed with the linear polymers and the higher number of free amines in these structures, which may cause disruptions in the negatively charged cell membrane. Previous work in this area has shown that a high density of positive charges may cross-bridge cell-surface receptors, interfering with critical intracellular processes

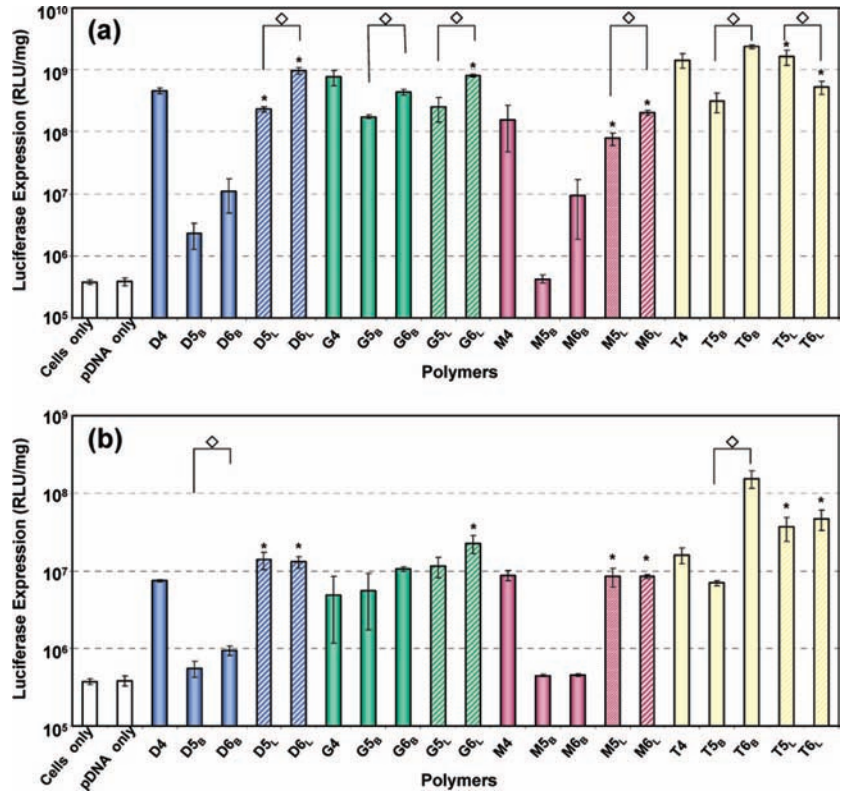

Figure 6. Luciferase gene expression observed with polyplexes formed with pDNA and each poly(glycoamidoamine) at $N/P = 20$. (a) Transfection in the absence of serum (Opti-MEM). (b) Transfection in DMEM containing 10% serum. The gene expression values are shown as relative light units (RLU) per milligram of protein. The data are reported as the mean ± standard of deviation of three replicates. Statistical significances in luciferase expression are shown with * or ◇ as $p < 0.05$. The symbol * indicates that a significant difference in gene expression was observed between the linear and the branched version of the polymers (e.g., $\mathbf{D5_L}$ vs $\mathbf{D5_B}$). The symbol ◇ indicates that a significant difference in gene expression was observed between polymers with the same carbohydrate moieties but different amine stoichiometry (e.g., $\mathbf{D6_L}$ vs $\mathbf{D5_L}$).

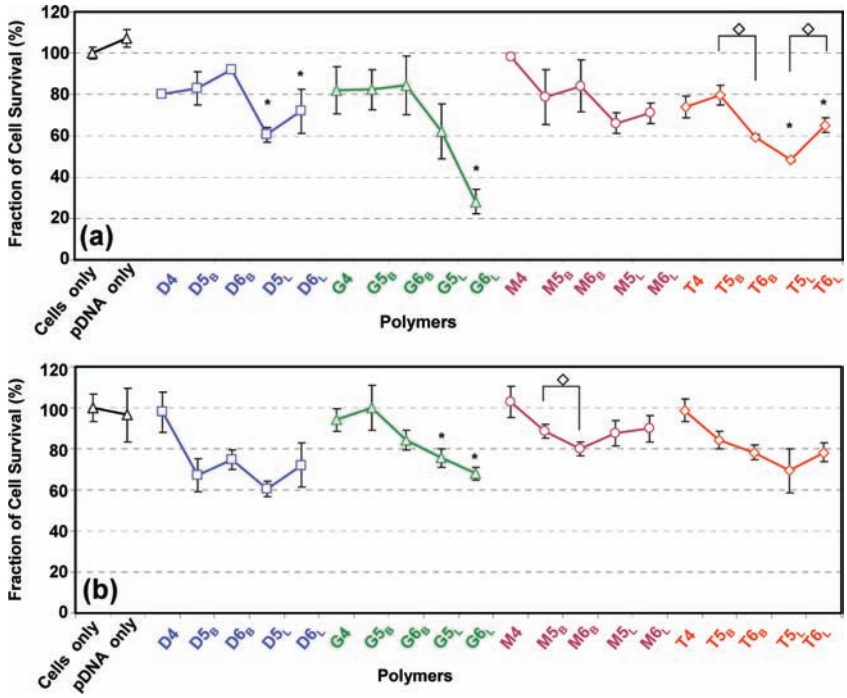

Figure 7. Fraction of cell survival in HeLa cells transfected with polyplexes formed with pDNA and each poly(glycoamidoamine) at $N/P = 20$. (a) Transfection in the absence of serum (Opti-MEM). (b) Transfection in DMEM containing 10% of serum. The fraction of cell survival values were normalized to untransfected cells. The data are reported as the mean ± standard of deviation of three replicates, and statistical significances are shown with * or ◇ as $p < 0.05$. The symbol * indicates that a significant difference in cell survival was observed between the linear and the branched analogues (e.g., $\mathbf{D5_L}$ vs $\mathbf{D5_B}$). The symbol ◇ indicates that a significant difference in cell survival was observed between polymers with the same carbohydrate moieties but different amine stoichiometry (e.g., $\mathbf{D6_L}$ vs $\mathbf{D5_L}$).

(*21*, *41*, *42*). For example, with L929 cells exposed to polycations, Fischer et al. showed that membrane leakage and a decrease in the metabolic activity occurs (*37*), which are initialized by the electrostatic interactions between cationic macromolecules and the negatively charged cell membrane. When comparing the polymers with six ethyleneamines and their analogues with five ethyleneamines in the repeat unit, a significant difference in the cell viability profiles was not observed even though polymers with six ethyleneamines seemed to facilitated higher gene expression (Figure 6).

CONCLUSIONS

The poly(glycoamidoamine) nucleic acid delivery vectors were originally designed by our group as models that combine the structural characteristics of chitosan (carbohydrate) and PEI (ethyleneamine). Several prior works by our group have shown that these structures have high delivery efficiency and biocompatibility (*28–31*). In a related examination, Nagasaki and co-workers synthesized a modified chitosan derivative that contained an additional primary amine in the C-6 position of the repeat unit, which revealed higher gene expression than chitosan while retaining low cytotoxicity (*44*). Another similar copolymer with increasing amine density, PEI-g-chitosan, yielded higher gene expression than branched PEI (25 kDa) and retained low cytotoxicity as compared to branched PEI (25 kDa) (*44*). Conversely, Kim and co-workers found that increasing the amine stoichiometry in their reducible poly(amidoethyleneimine) repeat unit, decreased the gene expression profile because of the increase of cytotoxicity (*45*). Here, this new series of poly(glycoamidoamine)s with higher amine stoichiometry has shown that the transfection efficiency remains about the same in serum-free media but is higher in the presence of serum. However, similar to that in the study by Kim et al., an increase in cytotoxicity was observed with the increase in amine density (Figures 6 and 7).

With this study, we have learned that significant differences in delivery efficacy are noticed between branched and linear polymers of similar chemical structure in both the absence and presence of serum. In general, similar to PEI, branched structures tend to be less toxic but have lower delivery efficacy than linear analogues in both conditions. This is likely due to a decrease in secondary amine density from branching units. We also noted that the $\mathbf{T_B}$ series had higher transfection profiles than the $\mathbf{M_B}$ series in both the absence and presence of serum, which is likely due to the higher cellular uptake and serum stability of the $\mathbf{T_B}$ polymers when compared to those of the $\mathbf{M_B}$ series. It was also interesting to find that even though the $\mathbf{T_L}$ series has serum stability and cellular uptake similar to those of the $\mathbf{M_L}$ series, the $\mathbf{T_L}$ series still has significantly higher transfection efficiency than that of the $\mathbf{M_L}$ analogues. Moreover, we have discovered that a certain limitation in amine density exists with our poly(glycoamidoamine) vectors. Our previous work has shown that as the amine stoichiometry increases from one secondary amine in the repeat unit to four, the delivery efficiency is significantly enhanced without compromising biocompatibility. With the poly(glycoamidoamine) models created herein, we have observed that as amine stoichiometry is further increase to five and six, gene expression reaches a certain point, and cytotoxicity starts to increase. Our studies with these poly(glycoamidoamine) models reveal that there is a fine balance between delivery efficiency and toxicity. Overcoming this issue will likely be a challenge in the field of nucleic acid delivery and efficacious vector design.

ACKNOWLEDGMENT

The funding of this work was provided by NSF CAREER (CHE-0449774) and the Beckman Young Investigators programs. T.M.R. is a Fellow of the Alfred P. Sloan Foundation.

LITERATURE CITED

(1) Mahato, R. I. (2005) Water insoluble and soluble lipids for gene delivery. *Adv. Drug Delivery Rev. 57*, 699–712.

(2) Luo, D., and Saltzman, W. M. (2000) Synthetic DNA delivery systems. *Nat. Biotechnol. 18*, 33–37.

(3) Borchard, G. (2001) Chitosans for gene delivery. *Adv. Drug. Delivery Rev. 52*, 145–150.

(4) Kircheis, R., Wightman, L., and Wagner, E. (2001) Design and gene delivery activity of modified polyethylenimines. *Adv. Drug Delivery Rev. 53*, 341–358.

(5) Anwer, K., Rhee, B. G., and Mendiratta, S. K. (2003) Recent progress in polymeric gene delivery systems. *Crit. Rev. Ther. Drug Carrier Syst. 20*, 249–293.

(6) Stefanidakis, M., and Koivunen, E. (2004) Peptide-mediated delivery of therapeutic and imaging agents into mammalian cells. *Curr. Pharm. Des. 10*, 3033–3044.

(7) Garnett, M. C. (1999) Gene-delivery systems using cationic polymers. *Crit. Rev. Ther. Drug Carrier Syst. 16*, 147–207.

(8) Zelikin, A. N., Putnam, D., Shastri, P., Langer, R., and Izumrudov, V. A. (2002) Aliphatic ionenes as gene delivery agents: elucidation of structure-function relationship through modification of charge density and polymer length. *Bioconjugate Chem. 13*, 548–553.

(9) van de Wetering, P., Moret, E. E., Schuurmans-Nieuwenbroek, N. M. E., van Steenbergen, M. J., and Hennink, W. E. (1999) Structure-activity relationships of water-soluble cationic methacrylate/methacrylamide polymers for nonviral gene delivery. *Bioconjugate Chem. 10*, 589–597.

(10) Plank, C., Tang, M. X., Wolfe, A. R., and Szoka, F. C., Jr (1999) Branched cationic peptides for gene delivery: role of type and number of cationic residues in formation and in vitro activity of DNA polyplexes. *Hum. Gene Ther. 10*, 319–332.

(11) Behr, J.-P. (1993) Synthetic gene-transfer vector. *Acc. Chem. Res. 26*, 274–278.

(12) Davis, M. E. (2002) Non-viral gene delivery systems. *Curr. Opin. Biotechnol. 13*, 128–131.

(13) Nishikawa, M., and Huang, L. (2001) Nonviral vectors in the new millennium: delivery barriers in gene transfer. *Hum. Gene Ther. 12*, 861–870.

(14) Boussif, O., Lezoualc'h, F., Zanta, M. A., Mergny, M. D., Scherman, D., Demeneix, B., and Behr, J.-P. (1995) A versatile vector for gene and oligonucleotide transfer into cells in culture and in vivo: polyethylenimine. *Proc. Natl. Acad. Sci. U.S.A 92*, 7297–7301.

(15) Erbacher, P., Bettinger, T., Belguise-Valladier, P., Zou, S., Coll, J. L., Behr, J.-P, and Remy, J. -S. (1999) Transfection and physical properties of various saccharide, poly(ethylene glycol), and antibody-derivatized polyethylenimines (PEI). *J. Gene Med. 1*, 210–222.

(16) Tang, M. X., and Szoka, F. C. (1997) The influence of polymer structure on the interactions of cationic polymers with DNA and morphology of the resulting complexes. *Gene Ther. 4*, 823–832.

(17) Wolfert, M. A., and Seymour, L. W. (1996) Atomic force microscopic analysis of the influence of the molecular weight of poly-L-lysine on the size of polyelectrolyte complexes formed with DNA. *Gene Ther. 3*, 269–273.

(18) Leong, K. W., Mao, H. -Q., Truong-Le, V. L., Roy, K., Walsh, S. M., and August, J. T. (1998) DNA-polycation nanospheres as non-viral gene delivery vehicles. *J. Controlled Release 53*, 183–193.

(19) Dunlap, D. D., Maggi, A., Soria, M. R., and Monaco, L. (1997) Nanoscopic structure of DNA condensed for gene delivery. *Nucleic Acids Res. 25*, 3095–3101.

(20) Moghimi, S. M., Symonds, P., Murray, J. C., Hunter, A. C., Debska, G., and Szewczyk, A. (2005) A two-stage poly(ethylenimine)-mediated cytotoxicity: implications for gene transfer/therapy. *Mol. Ther. 11*, 990–995.

(21) Ryser, H. J. (1967) A membrane effect of basic polymers dependent on molecular size. *Nature 215*, 934–936.

(22) Fischer, D., Bieber, T., Li, Y., Elsasser, H-P., and Kissel, T. (1999) A novel non-viral vector for DNA delivery based on low molecular weight, branched polyethylenimine: effect of molecular weight on transfection efficiency and cytotoxicity. *Pharm. Res. 16*, 1273–1279.

(23) Godbey, W. T., Wu, K. K., and Mikos, A. G. (1999) Size matters: molecular weight affects the efficiency of poly(ethylenimine) as a gene delivery vehicle. *J. Biomed. Mater. Res. 45*, 268–275.

(24) Wiseman, J. W., Goddard, C. A., McLelland, D., and Colledge, W. H. (2003) A comparision of linear and branched polyethylenimine (PEI) with DCChol/DOPE lisosomes for gene delivery to epithelial cells in vitro and in vivo. *Gene Ther. 10*, 1654–1622.

(25) Wightman, L., Kircheis, R., Rössler, V., Carotta, S., Ruzicka, R., Kursa, M., and Wagner, E. (2001) Different behavior of branched and linear polyethylenimine for gene delivery *in vitro* and *in vivo*. *J. Gene Med. 3*, 362–372.

(26) Seib, F. P., Jones, A. T., and Duncan, R. (2007) Comparison of the endocytic properties of linear and branched PEIs, and cationic PAMAM dendrimers in B16f10 melanoma cells. *J. Controlled Release 117*, 291–300.

(27) Erbacher, P., Zou, S., Bettinger, T., Steffan, A-M., and Remy, J-S. (1998) Chitosan-based vector/DNA complexes for gene delivery: biophysical characteristics and transfection ability. *Pharm. Res. 15*, 1332–1339.

(28) Liu, Y., Wenning, L., Lynch, M., and Reineke, T. M. (2006) Gene Delivery with Novel Poly(L-tartaramidoamine)s, in *Polymeric Drug Delivery Volume I: Particulate Drug Carriers* (Svenson, S., Ed.) Vol. 913, pp 216–227, American Chemical Society, Washington DC.

(29) Liu, Y., and Reineke, T. M. (2005) Hydroxyl stereochemistry and amine number within poly(glycoamidoamine)s affect intracellular DNA delivery. *J. Am. Chem. Soc. 127*, 3004–3015.

(30) Liu, Y., Wenning, L., Lynch, M., and Reineke, T. M. (2004) New poly(D-glucaramidoamine)s induce DNA nanoparticle formation and efficient gene delivery into mammalian cells. *J. Am. Chem. Soc. 126*, 7422–7423.

(31) Liu, Y., and Reineke, T. M. (2007) Poly(glycoamidoamine)s for gene delivery. Structural effects on cellular internalization, buffering capacity, and gene expression. *Bioconjugate Chem. 18*, 19–30.

(32) Kiely, D. E., Chen, L., and Lin, L. H. (1994) Hydroxylated nylons based on unprotected esterified D-glucaric acid by simple condensation reactions. *J. Am. Chem. Soc. 116*, 571–578.

(33) Kiely, D. E., Chen, L., and Lin, T. H. (2000) Synthetic polyhydroxypolyamides from galactaric, xylaric, D-glucaric, and D-mannaric acids and alkylenediamine monomers-some comparisons. *J. Polym. Sci. A 38*, 594–603.

(34) Linstead, R. P., Owen, L. N., and Webb, R. F. (1953) Elimination reactions of esters. III. Derivatives of dibasic polyhydroxy acids. *J. Chem. Soc.* 1225–1231.

(35) Koscova, S., Budesinsky, M., and Hodacova, J. (2003) A facile synthesis of selectively protected linear oligoamines. *Collect. Czech. Chem. Commun. 68*, 744–750.

(36) Srinivasachari, S., Liu, Y., Zhang, G., Prevette, L., and Reineke, T. M. (2006) Trehalose click polymers inhibit nanoparticle aggregation and promote pDNA delivery in serum. *J. Am. Chem. Soc. 128*, 8176–8184.

(37) Fischer, D., Li, Y., Ahlemeyer, B., Krieglstein, J., and Kissel, T. (2003) In vitro cytotoxicity testing of polycations: influence of polymer structure on cell viability and hemolysis. *Biomaterials 24*, 1121–1131.

(38) Mukherjee, S., Ghosh, R. N., and Maxfield, F. R. (1997) Endocytosis. *Phys. Rev. 77*, 759–803.

(39) Liu, Y., and Reineke, T. M. (2006) Poly(glycoamidoamine)s for gene delivery. Stability of polyplexes and efficacy with cardiomyoblast cells. *Bioconjugate Chem. 17*, 101–108.

(40) Aziz, S. M., Gosland, M. P., Crooks, P. A., Olson, J. W., and Gillespie, M. N. (1995) A novel polymeric spermine conjugate inhibits polyamine transport in pulmonary artery smooth muscle cells. *J. Pharmacol. Exp. Ther. 274*, 181–186.

(41) Bottega, R., and Epand, R. M. (1992) Inhibition of protein kinase C by cationic amphiphiles. *Biochemistry 31*, 9025–9030.

(42) Medina-Kauwe, L. K., Xie, J., and Hamm-Alvarez, S. (2005) Intracellular trafficking of nonviral vectors. *Gene Ther. 12*, 1734–1751.

(43) Mislick, K. A., and Baldeschwieler, J. D. (1996) Evidence for the role of proteoglycans in cation-mediated gene transfer. *Proc. Natl. Acad. Sci. U.S.A. 93*, 12349–12354.

(44) Satoh, T., Kano, T., Nakatani, M., Sakairi, N., Shinkai, S., and Nagasaki, T. (2006) 6-Amino-6-deoxy-chitosan. Sequential chemical modifications at the C-6 positions of N-phthaloyl-chitosan and evaluation as a gene carrier. *Carbohydr. Res. 341*, 2406–2413.

(45) Christensen, L. V., Chang, C.-W., Kim, W. J., Kim, W. S., Zhong, Z., Lin, C., Engbersen, J. F. J., and Feijen, J. (2006) Reducible poly(amido ethylenimine)s designed for triggered intracellular gene delivery. *Bioconjugate Chem. 17*, 1233–1240.

BC7001659

Synthesis and Evaluation of ^{18}F- and ^{11}C-Labeled Phenyl-Galactopyranosides as Potential Probes for *in Vivo* Visualization of LacZ Gene Expression using Positron Emission Tomography

Sofie Celen,[†] Christophe Deroose,[‡] Tjibbe de Groot,[‡] Satish K. Chitneni,[†] Rik Gijsbers,[§] Zeger Debyser,[§] Luc Mortelmans,[‡] Alfons Verbruggen,[†] and Guy Bormans*[,†]

Laboratory for Radiopharmacy, Faculty of Pharmaceutical Sciences, and Department of Nuclear Medicine, U.Z. Gasthuisberg, and Division of Molecular Medicine, Katholieke Universiteit Leuven, Leuven, Belgium. Received June 18, 2007; Revised Manuscript Received October 22, 2007

3-Hydroxy-2-nitrophenyl 2,3,4,6-tetra-*O*-acetyl-β-D-galactopyranoside, a derivative of the chromogenic β-galactosidase (β-gal) substrate *o*-nitrophenyl β-D-galactopyranoside (ONPG) was synthesized using a Koenigs−Knorr glycosylation reaction. It was alkylated with 2-[^{18}F]fluoroethyl triflate or [^{11}C]methyl triflate, followed by deacetylation of the sugar hydroxyl groups to obtain radiolabeled 3-(2′-[^{18}F]fluoroethoxy)-2-nitrophenyl β-D-galactopyranoside ([^{18}F]-**2c**) and 3-[^{11}C]methoxy-2-nitrophenyl β-D-galactopyranoside ([^{11}C]-**3c**), which were evaluated as potential reporter probes for *in vivo* visualization of LacZ gene expression with positron emission tomography (PET). *In vitro*, [^{18}F]-**2c** and [^{11}C]-**3c** were good substrates of β-gal and showed, respectively, a 7.5- and 2.5-fold higher uptake into β-gal expressing cells (LacZ cells) compared to control cells. However, reversed-phase HPLC analysis of the LacZ cell lysate and supernatant showed that labeled 3-(2′-[^{18}F]fluoroethoxy)-2-nitrophenol, the hydrolysis product formed by β-gal-mediated cleavage of [^{18}F]-**2c**, substantially leaked out of the cells, which would lead to loss of PET signal. In a μPET study of [^{18}F]-**2c** in a mouse with a β-gal expressing tumor, high retention was observed in liver and kidneys, but only negligible accumulation was seen in the tumor. As a general conclusion, it can be stated that the synthesized PET tracers [^{18}F]-**2c** and [^{11}C]-**3c** are not suitable for use as LacZ reporter probes. Further structural modifications to improve the diffusion over the tumor cell membrane and to increase retention in β-gal expressing cells may lead to more favorable *in vivo* imaging probes.

INTRODUCTION

Given progress in molecular biology and genetics as well as advances in imaging technology, it is possible to visualize cellular processes in space and time at a molecular or genetic level (*1*). One of the most studied molecular imaging targets to date is the expression of genes. *In vivo* imaging of the location, the magnitude, and the time variation of gene and transgene expression is important in the development of transgenic animal models of disease, in trafficking and targeting of cells, and in gene therapy (*2, 3*). Many promising methods are being developed to image gene expression by using an appropriate combination of a reporter transgene and a reporter probe (*4, 5*). The most commonly used reporter systems include β-galactosidase (*6–8*), β-glucuronidase (*6, 9*), chloramphenicol acetyltransferase (*6,10*), green fluorescent protein (*6,11,12*), and luciferases (*6, 13–15*). Among these, the LacZ gene, which encodes *E. coli* β-galactosidase (β-gal), is one of the most attractive reporter genes due to its widespread use in different vectors, convenient *in vitro* and histological detection methods, split protein systems, and its presence in many transgenic mouse models (*16*). Up to now, this reporter system has been frequently used for *in vitro* evaluation of gene expression using substrates allowing colorimetric (*17, 18*), fluorescence (*19–22*), chemiluminescence (*23*), or bioluminescence (*24*) detection. All these optical imaging modalities are very useful in superficial tissues and have extensive applications in small animals, but application to larger animals is limited by the depth of light penetration.

Monitoring reporter gene expression in larger animals and ultimately in humans is possible with the use of specific radiotracers combined with nuclear imaging techniques like positron emission tomography (PET *2, 25*) or single-photon emission computed tomography (SPECT (*26*)) and magnetic resonance imaging (MRI) in combination with paramagnetic reporter probes (*27–29*). The group of Mason et al. (*30, 31*) have been developing MRI probes by introducing a fluorine atom or a trifluoromethyl group in the colorimetric indicator *ortho*-nitrophenyl β-D-galactopyranoside (ONPG) and demonstrated the usefulness of these fluorogalactopyranosides to detect β-gal activity *in vitro* with ^{19}F NMR spectroscopy.

Well-known and established PET and SPECT reporter systems are herpes simplex virus type 1 thymidine kinase (HSV1-tk) in combination with ^{18}FHBG, human dopamine type 2 receptor (hD_2R) in combination with [^{18}F]fluoroethylspiperone, and human sodium iodide symporter (hNIS) in combination with $^{124}I^-$, $^{123}I^-$, or $^{99m}TcO_4^-$ (*4, 5*). However, little progress has been made in the development of radioprobes that target LacZ gene expression. Lee et al. (*32*) described the use of a radiolabeled competitive inhibitor 2-(4-[^{125}I/^{123}I]iodophenyl) ethyl 1-thio-β-D-galactopyranoside to detect β-gal activity in mice bearing LacZ expressing tumors using SPECT. The disadvantage of this system is the low sensitivity using an inhibitor probe and the poor cell membrane permeability. Bormans et al. (*33*) synthesized 2′-[^{18}F]fluorodeoxylactose (^{18}FDL) using an enzymatic method starting from 2-[^{18}F]fluoro-2-deoxy-D-glucose (^{18}FDG). The yield of the enzymatic synthesis was rather low, and a biodistribution study in Rosa-26

* Corresponding author. Address: Herestraat 49 bus 821 BE-3000 Leuven Belgium. Tel: +32 16 330447. Fax: +32 16 330449. E-mail: guy.bormans@pharm.kuleuven.be.

[†] Laboratory for Radiopharmacy, Faculty of Pharmaceutical Sciences.

[‡] Department of Nuclear Medicine, U.Z. Gasthuisberg.

[§] Division of Molecular Medicine.

10.1021/bc700216d CCC: $40.75 © 2008 American Chemical Society
Published on Web 01/08/2008

mice compared to control mice showed a lack of tissue retention, probably due to the inability of ^{18}FDL to cross the cell membrane.

In our study, a derivative of ONPG was synthesized, labeled with ^{18}F or ^{11}C, and both radiolabeled agents were evaluated as potential reporter probes for *in vivo* visualization of LacZ gene expression with PET.

MATERIALS AND METHODS

General. All reagents and solvents were obtained commercially from Acros (Geel, Belgium), Aldrich, Fluka, Sigma (Sigma-Aldrich, Bornem, Belgium), Merck (Darmstadt, Germany), or Fischer Bioblock Scientific (Tournai, Belgium) unless otherwise specified. For ascending thin layer chromatography (TLC), precoated aluminum-backed plates (silica gel 60 with fluorescent indicator, 0.2 mm thickness; Macherey-Nagel, Düren, Germany) were used and developed using mixtures of ethyl acetate and hexane, CH_2Cl_2 and hexane, or acetonitrile as mobile phase. After evaporation of the solvent, compounds were detected under UV light (254 nm). The sugar compounds were additionally visualized by staining in oxidative medium (5% H_2SO_4 in ether), followed by heating. ^{1}H and ^{13}C NMR spectra were recorded on a Gemini 200 MHz spectrometer (Varian, Palo Alto, CA, USA) using $CDCl_3$ or DMSO-d_6 as solvent. Chemical shifts are reported in parts per million relative to tetramethylsilane ($\delta = 0$). Coupling constants are reported in hertz. Splitting patterns are defined by s (singlet), br s (broad singlet), d (doublet), dd (double–doublet), t (triplet), dt (double triplet), or m (multiplet). High-performance liquid chromatography (HPLC) analysis was performed on an XTerra RP C_{18} column (5 μm, 4.6 mm × 250 mm; Waters, Milford, USA) eluted with mixtures of water or 0.1 M ammonium acetate pH 4 and acetonitrile. The column effluent was monitored for absorbance with a UV-spectrometer (Waters 2487 Dual γ absorbance detector) set at 254 nm and for radioactivity using a 2 in. NaI(Tl) scintillation detector coupled to a single-channel analyzer (Medilab-Select, Mechelen, Belgium). Output of both detectors was analyzed using RaChel analysis software (Lablogic, Sheffield, UK). The radioactivity counting for biodistribution studies, log *P* determinations, and cell-uptake studies was done using an automated gamma counter equipped with a 3 in. NaI(Tl) well crystal coupled to a multichannel analyzer (Wallac 1480 Wizard 3″, Wallac, Turku, Finland). Exact mass measurements were performed on a time-of-flight spectrometer (LCT, Micromass, Manchester, UK) equipped with a standard electrospray ionization (ESI) interface. Samples were infused in acetonitrile/water mixtures with a Harvard 22 syringe pump (Harvard Apparatus, Holliston, Massachusetts, USA). Accurate mass determination was done by coinfusion with a 10 μg/mL solution of ONPG in acetonitrile/water as an internal calibration mass in positive mode (ES+). Acquisition and processing of the data were done with *Masslynx* software (version 3.5, Waters). Melting points (mp) were determined using an IA9000 digital melting point apparatus (Electrothermal, Southend-on-Sea, England).

The experiments in mice were carried out in compliance with the national laws relating to the conduct of animal experimentation and with approval of the local ethical committee for animal experiments.

Synthesis.*3-Hydroxy-2-nitrophenyl 2,3,4,6-tetra-O-acetyl-β-D-galactopyranoside (**1**).* To a solution of 0.42 g (2.7 mmol) 2-nitroresorcinol in a mixture of 10 mL quinoline and 5 mL CH_2Cl_2 was added 1 g (3.65 mmol) Ag_2CO_3 and 1 g (2.43 mmol) 2,3,4,6-tetra-*O*-acetyl-α-D-galactopyranosyl bromide. The flask was shielded from light, and the suspension was stirred for 3 h. The reaction mixture was poured into 50 mL methanol/dichloromethane (1:9 v/v) followed by filtration over celite. The filtrate was successively washed with 50 mL HCl (1 M), 50 mL water, 50 mL saturated $NaHCO_3$ solution, and 50 mL brine. After drying over $MgSO_4$, the solution was filtered and the filtrate was concentrated in vacuo and applied on a silica gel column eluted with ethyl acetate/hexane (1:1 v/v). Yield: 0.37 g (0.76 mmol, 31%) of a yellow solid.

^{1}H NMR ($CDCl_3$) δ 2.02, 2.07, 2.12, 2.19 (12H, 4× s, 4× *CH$_3$CO*), 4.09 (1H, t, $^3J_{H5\text{-}H6} = 6$ Hz, *H-5*), 4.17–4.28 (2H, m, 2× *H-6*), 5.10 (2H, d, $^3J_{H1\text{-}H2} = 8$ Hz, *H-1*; dd, $^3J_{H3\text{-}H2} = 10.6$ Hz, $^3J_{H3\text{-}H4} = 3$ Hz, *H-3*), 5.48 (1H, d, $^3J_{H4\text{-}H3} = 3$ Hz, *H-4*), 5.58 (1H, dd, $^3J_{H2\text{-}H3} = 10.6$ Hz, $^3J_{H2\text{-}H1} = 8$ Hz, *H-2*), 6.82 (1H, d, $^3J = 8.4$ Hz, *H$_{ar}$-4*), 6.86 (1H, d, $^3J = 8.4$ Hz, *H$_{ar}$-6*), 7.39 (1H, t, $^3J = 8.4$ Hz, *H$_{ar}$-5*).

^{13}C NMR ($CDCl_3$) δ 20.52, 61.28, 66.68, 67.80, 70.56, 71.42, 100.31 (*anomeric C-1*), 109.05, 113.73, 134.97, 154.64, 170.24.

Exact Mass (ESI-MS) for $C_{20}H_{22}NO_{13}Na$ $[M + Na]^+$: found 508.1048, calculated 508.1062. mp: 167–169 °C.

3-(2′-Fluoroethoxy)-2-nitrophenol (2a). A solution of 0.25 g (1.6 mmol) 2-nitroresorcinol, 0.094 mL (1.6 mmol) 2-fluoroethanol, and 0.42 g (1.6 mmol) triphenylphosphine in 15 mL tetrahydrofuran was stirred for 10 min at room temperature under an atmosphere of nitrogen, and 0.32 mL (1.6 mmol) diisopropylazodicarboxylate was added in one portion. After stirring for 4 h at room temperature under nitrogen, a small amount of silica gel was added, and the solvent was evaporated. The silica gel impregnated with the crude product was applied on a silica gel column that was eluted with a mixture of ethyl acetate/hexane (3:7 v/v), yielding 0.18 g (0.9 mmol, 56%) of a yellow solid.

^{1}H NMR ($CDCl_3$) δ 4.26 (2H, dt, $^3J_{H\text{-}F} = 26.8$ Hz, $^3J = 4.2$ Hz, -*C$\underline{H_2}$CH$_2$F*), 4.74 (2H, dt, $^2J_{H\text{-}F} = 46.8$ Hz, $^3J = 4.2$ Hz, -*CH$_2$C$\underline{H_2}$F*), 6.47 (1H, d, $^3J = 8.4$ Hz, *H$_{ar}$-6*), 6.68 (1H, d, $^3J = 8.4$ Hz, *H$_{ar}$-4*), 7.32 (1H, t, $^3J = 8.4$ Hz, *H$_{ar}$-5*), 10.1 (br s, OH).

^{13}C NMR ($CDCl_3$) δ 70.05, 83.01, 105.02, 111.54, 135.39, 156.46.

3-(2′-Fluoroethoxy)-2-nitrophenyl 2,3,4,6-tetra-O-acetyl-β-D-galactopyranoside (2b). The title compound was prepared from 3-(2′-fluoroethoxy)-2-nitrophenol (**2a**) using the same procedure as described for compound **1**. Yield: 0.19 g (0.35 mmol, 31%) of a white solid.

^{1}H NMR ($CDCl_3$) δ 2.01, 2.08, 2.13, 2.18 (12H, 4× s, 4× *CH$_3$CO*), 4.1 (1H, t, $^3J_{H5\text{-}H6} = 6$ Hz, *H-5*), 4.18–4.40 (4H, m, 2× *H-6*; -*C$\underline{H_2}$CH$_2$F*), 4.72 (2H, dt, $^2J_{H\text{-}F} = 46.8$ Hz, $^3J = 4.2$ Hz, -*CH$_2$C$\underline{H_2}$F*), 5.02 (1H, d, $^3J_{H1\text{-}H2} = 8$ Hz, *H-1*), 5.07 (1H, dd, $^3J_{H3\text{-}H2} = 10.6$ Hz, $^3J_{H3\text{-}H4} = 3.2$ Hz, *H-3*), 5.42–5.52 (2H, m, $^3J_{H2\text{-}H3} = 10.6$ Hz, $^3J_{H2\text{-}H1} = 8$ Hz, *H-2*; *H-4*), 6.8 (1H, d, $^3J = 8.4$ Hz, *H$_{ar}$-6*), 6.93 (1H, d, $^3J = 8.4$ Hz, *H$_{ar}$-4*), 7.34 (1H, t, $^3J = 8.4$ Hz, *H$_{ar}$-5*).

^{13}C NMR ($CDCl_3$) δ 20.39, 61.25, 66.65, 67.71, 68.74, 70.47, 71.36, 82.98, 100.88 (*anomeric C-1*), 108.84, 110.72, 131.09, 149.03, 150.69, 170.15.

3-(2′-Fluoroethoxy)-2-nitrophenyl β-D-galactopyranoside (2c). To a solution of 0.136 g (0.26 mmol) 3-(2′-fluoroethoxy)-2-nitrophenyl 2,3,4,6-tetra-*O*-acetyl-β-D-galactopyranoside (**2b**) in 14 mL methanol was added 0.385 mL of a solution of 100 mg sodium in 20 mL methanol, and stirring was continued for 30 min. A small amount of silica gel was added, and the solvent was evaporated. The silica gel impregnated with the crude product was applied on a silica gel column that was eluted with acetonitrile, yielding 0.065 g (0.178 mmol, 70%) of a white solid.

^{1}H NMR (DMSO) δ 3.45–3.69 (6H, m, *H-2*; *H-3* ; *H-4*; *H-5*; 2× *H-6*), 4.38 (2H, dt, $^3J_{H\text{-}F} = 30.2$ Hz, $^3J = 3.6$ Hz, -*C$\underline{H_2}$CH$_2$F*), 4.69 (2H, dt, $^2J_{H\text{-}F} = 47.6$ Hz, $^3J = 3.6$ Hz, -*CH$_2$C$\underline{H_2}$F*), 4.99 (1H, d, $^3J_{H1\text{-}H2} = 7.4$ Hz, *H-1*), 6.95 (1H, d,

^3J = 8.4 Hz, H_{ar}-*6*), 6.98 (1H, d, ^3J = 8.4 Hz, H_{ar}-*4*), 7.45 (1H, t, ^3J = 8.4 Hz, H_{ar}-*5*).

^{13}C NMR (DMSO) δ 60.33, 68.1, 69.07, 70.04, 73.54, 75.9, 83.551, 101.09 (*anomeric C-1*), 107.07, 108.53, 131.63, 149.29, 150.12.

Exact Mass (ESI-MS) for $C_{14}H_{17}FNO_9Na$ $[M + Na]^+$: found 386.0844, calculated 386.0858. mp: 123–125 °C.

3-Methoxy-2-nitrophenol (3a). The same procedure was used as described for compound **2a**, using methanol instead of 2-fluoroethanol. Yield 0.17 g (1 mmol, 62%) of a yellow solid.

^{1}H NMR ($CDCl_3$) δ 3.95 (3H, s, -*OCH*$_3$), 6.55 (1H, d, ^3J = 8.4 Hz, H_{ar}-*6*), 6.71 (1H, d, ^3J = 8.4 Hz, H_{ar}-*4*), 7.41 (1H, t, ^3J = 8.4 Hz, H_{ar}-*5*), 10.22 (s, *OH*).

3-Methoxy-2-nitrophenyl 2,3,4,6-tetra-O-acetyl-β-D-galactopyranoside (3b). The title compound was prepared from 3-methoxy-2-nitrophenol (**3a**) using the same procedure as described for compound **1**. Yield: 0.13 g (0.26 mmol, 39%) of a yellow solid.

^{1}H NMR ($CDCl_3$) δ 2.1 (12H, 4× s, 4× *CH*$_3$*CO*), 3.82 (3H, s, -*OCH*$_3$), 4.01 (1H, t, $^3J_{H5\text{-}H6}$ = 6.2 Hz, *H-5*), 4.1–4.24 (2H, m, 2× *H-6*), 4.92 (1H, d, $^3J_{H1\text{-}H2}$ = 8 Hz, *H-1*), 5.0 (1H, dd, $^3J_{H3\text{-}H2}$ = 10.6 Hz, $^3J_{H3\text{-}H4}$ = 3.2 Hz, *H-3*), 5.36–5.45 (2H, m, $^3J_{H2\text{-}H3}$ = 10.6 Hz, $^3J_{H2\text{-}H1}$ = 8 Hz, $^3J_{H4\text{-}H3}$ = 3.2 Hz, *H-2*; *H-4*), 6.71 (1H, d, ^3J = 8.4 Hz, H_{ar}-*6*), 6.82 (1H, d, ^3J = 8.4 Hz, H_{ar}-*4*), 7.27 (1H, t, ^3J = 8.4 Hz, H_{ar}-*5*).

^{13}C NMR ($CDCl_3$) δ 20.55, 56.51, 61.28, 66.65, 67.65, 70.47, 71.29, 100.83 (*anomeric C-1*), 107.35, 109.78, 131.12, 151.73, 170.42.

3-Methoxy-2-nitrophenyl-β-D-galactopyranoside (3c). The same procedure was used as described for compound **2c**, using 3-methoxy-2-nitrophenyl 2,3,4,6-tetra-*O*-acetyl-β-D-galactopyranoside (**3b**) as starting material. Yield 0.03 g (0.09 mmol, 45%) of a yellow solid.

^{1}H NMR (DMSO) δ 3.38–3.7 (6H, m, *H-2*; *H-3*; *H-4*; *H-5*; 2× *H-6*), 3.86 (3H, s, -*OCH*$_3$), 4.58 (d, *OH*), 4.66 (t, *OH*), 4.87 (d, *OH*), 4.98 (1H, d, $^3J_{H1\text{-}H2}$ = 7.4 Hz, *H-1*), 5.11 (d, *OH*), 6.92 (1H, d, ^3J = 8.4 Hz, H_{ar}-*6*), 6.96 (1H, d, ^3J = 8.4 Hz, H_{ar}-*4*), 7.45 (1H, t, ^3J = 8.4 Hz, H_{ar}-*5*).

^{13}C NMR (DMSO) δ 56.81, 60.33, 68.13, 70.04, 73.54, 75.9, 101.06 (*anomeric C-1*), 106.07, 108.14, 131.69, 149.2, 150.21.

Exact Mass (ESI-MS) for $C_{13}H_{16}NO_9Na$ $[M + Na]^+$: found 354.0823, calculated 354.0796. mp: 130.5–132 °C.

Radiolabeling. *Production of [^{18}F]fluoride and Radiosynthesis of [^{18}F]-2c using 2-[^{18}F]fluoroethyl Triflate ([^{18}F]FEtOTf).* $[^{18}F]F^-$ was obtained using an $^{18}O(p,n)^{18}F$ reaction by irradiation of 0.5 mL of 97% enriched $[^{18}O]H_2O$ (Rotem HYOX^{18}, Rotem Industries, Beer Sheva, Israel) in a niobium target with 18 MeV protons from a Cyclone 18/9 cyclotron (Ion Beam Applications, Louvain-la-Neuve, Belgium). After the irradiation, $[^{18}F]F^-$ was separated from $[^{18}O]H_2O$ using a SepPak Light Accell plus QMA anion exchange cartridge (Waters). The $[^{18}F]F^-$ was then eluted from the cartridge with a solution containing 2.47 mg potassium carbonate and 27.92 mg Kryptofix 222 dissolved in 0.75 mL of H_2O/CH_3CN (5:95 v/v) into a reaction vial.

After evaporation with a stream of helium of the solvent from the reaction vial, $[^{18}F]F^-$ was further dried by azeotropic distillation using 1 mL of dry acetonitrile. A volume of 5 μL 2-bromoethyl triflate in 0.7 mL *o*-dichlorobenzene was added to the vial containing $[^{18}F]F^-$. The resulting 2-[^{18}F]fluoroethyl bromide was then distilled at 120 °C with a helium flow (3–4 mL/min) and subsequently passed over a silver triflate column (6 mm × 50 mm) at 250 °C to obtain [^{18}F]FEtOTf. The resulting [^{18}F]FEtOTf was bubbled into another reaction vial containing 1 mg of the precursor (**1**) and 5 μL NaOH 1 M in 0.3 mL acetone. After distillation of a sufficient amount of radioactivity in the solution, the reaction vial was closed and heated at 90 °C for 10 min. After cooling, deprotection of the sugar hydroxyl groups was done by addition of 0.3 mL NaOH 33 mM and incubation for 5 min at room temperature. The reaction mixture was subsequently neutralized with 0.5 mL 0.5 M phosphate buffer pH 5, and the mixture was heated at 90 °C for 4 min with a flow of helium to remove the unreacted [^{18}F]FEtOTf or [^{18}F]FEtOH which is formed as a side product. The resulting mixture was purified by HPLC on a μBondapak C_{18} column (10 μm, 7.8 mm × 300 mm; Waters), eluted with 0.05 M sodium acetate buffer pH 5.5/ethanol (85:15 v/v) at a flow rate of 4 mL/min. The radiolabeled compound [^{18}F]-**2c** eluted after 6.35 min and was obtained with a decay-corrected radiochemical yield of approximately 59% relative to starting activity of [^{18}F]FEtOTf. Radiochemical purity and specific activity were assayed using HPLC on an XTerra RP C_{18} column (5 μm, 4.6 mm × 250 mm; Waters) eluted with gradient mixtures of water/acetonitrile (0 min, 90:10 v/v; 20 min, 30:70 v/v; linear gradient) at a flow rate of 1 mL/min. [^{18}F]-**2c** elutes after 11 min and was obtained with an average specific activity of 64.6 GBq/μmol at the end of synthesis (EOS) and a radiochemical purity of >99%.

Production of [^{11}C]methyl Triflate ([^{11}C]MeOTf) and Radiosynthesis of [^{11}C]-3c. Carbon-11 was produced by a $^{14}N(p,\alpha)^{11}C$ nuclear reaction. The target gas (a mixture of 95% N_2 and 5% H_2) was irradiated using 18 MeV protons at a beam current of 25 μA for about 30 min, to yield $[^{11}C]CH_4$. The $[^{11}C]CH_4$ was then reacted with vaporous I_2 at 650 °C in a home-built recirculation synthesis module to convert it to [^{11}C]MeI. Subsequently, [^{11}C]MeOTf was obtained by passage of the [^{11}C]MeI over a silver triflate column (6 mm × 50 mm) at 180 °C. The resulting [^{11}C]MeOTf was bubbled through a solution of 1 mg precursor (**1**) in a mixture of 5 μL NaOH 1 M and 0.3 mL acetone. When the amount of radioactivity in the vial had stabilized, the sugar hydroxyl groups were deprotected by addition of 0.3 mL NaOH 33 mM and incubation for 5 min at room temperature. The reaction mixture was subsequently neutralized with 0.5 mL 0.5 M phosphate buffer pH 5 and purified by HPLC on a μBondapak C_{18} column (Waters), eluted with 0.1 M ammonium acetate pH 4/ethanol (90:10 v/v) at a flow rate of 4 mL/min. [^{11}C]-**3c** eluted after 10.2 min and was obtained with a decay-corrected radiochemical yield of approximately 94% relative to [^{11}C]MeOTf starting activity. The product was analyzed by HPLC on an XTerra RP C_{18} column (Waters) eluted with gradient mixtures of water/acetonitrile (0 min, 90:10 v/v; 20 min, 30:70 v/v; linear gradient) at a flow rate of 1 mL/min. [^{11}C]-**3c** elutes after 10.5 min and was obtained with an average specific activity of 26.1 GBq/μmol at the end of synthesis (EOS) and a radiochemical purity of >99%.

Log *P* (*n*-Octanol/Phosphate Buffer pH 7.4). The partition coefficient was determined using a modification of the method described by Vanbilloen et al. (*34*). An aliquot of 30 μL of RP-HPLC purified tracer solution containing 185 kBq of [^{18}F]-**2c** or 555 kBq [^{11}C]-**3c** was added to a polypropylene tube (Sarstedt, Nümbrecht, Germany) containing 2 mL 0.025 M sodium phosphate buffer pH 7.4 and 2 mL *n*-octanol (density = 0.827 g/mL). The tube was vortexed at room temperature for 2 min, followed by centrifugation at 3000 rpm (1837 g) for 5 min (Eppendorf centrifuge 5810, Eppendorf, Westbury, USA). Aliquots of 50 μL and 500 μL were drawn from the *n*-octanol and aqueous phases, respectively, taking care to avoid cross-contamination between the two phases. The samples were weighed, and radioactivity was counted using an automated gamma counter. The experiments were performed at least in triplicate.

***In Vitro* Hydrolysis of [^{18}F]-2c and [^{11}C]-3c by β-gal.** An aliquot of 0.4 mL HPLC purified [^{18}F]-**2c** (5.9 MBq) or 0.4 mL HPLC purified [^{11}C]-**3c** (9.6 MBq) was added to 0.6 mL of a solution containing HEPES buffer pH 7.0 (120 mM),

$MgSO_4$ (4 mM), NaCl (180 mM), and 6 μg (1 U) β-gal (*E. coli*, E.C.3.2.1.23, 165 U/mg, Fluka). The solution was incubated at 37 °C in an oil bath, and 50 μL samples were collected at different time points ranging from 30 s to 45 min after the start of the incubation. Enzymatic activity was stopped by cooling the samples in ice. Each sample was analyzed for release of the radiolabeled aglycon using HPLC coupled to radiometric detection using an XTerra RP C_{18} column eluted with mixtures of 40% acetonitrile ([^{18}F]-**2c**) or 30% acetonitrile ([^{11}C]-**3c**) in 0.1 M ammonium acetate pH 4 at a flow rate of 1 mL/min. Intact [^{11}C]-**3c** elutes at 4 min, the carbon-11 labeled aglycon 3-[^{11}C]methoxy-2-nitrophenol ([^{11}C]-**3a**) resulting from enzymatic hydrolysis elutes at 11.5 min. Intact [^{18}F]-**2c** elutes at 3.5 min and the fluorine-18 labeled hydrolysis product 3-(2′-[^{18}F]fluoroethyl)-2-nitrophenol ([^{18}F]-**2a**) at 8 min. The percentage of conversion of [^{18}F]-**2c** and [^{11}C]-**3c** as a function of the incubation period was calculated from the integrated HPLC chromatograms.

Biodistribution Study in Normal Mice. Solutions of [^{18}F]-**2c** and [^{11}C]-**3c** obtained after RP-HPLC purification were diluted using 0.9% NaCl for injection to concentrations of 3.7 MBq/mL and 37 MBq/mL, respectively. The biodistribution of both tracers was determined in male NMRI mice (body mass 30–40 g). The mice were anesthetized by intraperitoneal injection of 0.1 mL of a solution containing 3 mg ketamine and 0.225 mg xylazine. A volume of 0.1 mL of the diluted tracer solution was then injected via a tail vein, and the mice were sacrificed by decapitation at 2 or 60 min postinjection (p.i., $n = 3$ per time point). All organs and body parts were dissected. Blood was collected in tared tubes, and the masses of all organs and body parts were determined. The radioactivity in each organ was counted using a 3 in. NaI(Tl) well counter, corrected for background radioactivity and expressed as a percentage of the injected dose (% ID) or as a percentage of the injected dose per gram tissue (% ID/g). For the calculation of total radioactivity in blood, blood mass was assumed to be 7% of the body mass.

Metabolism of [^{18}F]-2c and [^{11}C]-3c in Normal Mice. The metabolic stability of [^{18}F]-**2c** and [^{11}C]-**3c** was studied in normal mice by determination of the relative amounts of the parent tracer and metabolites in plasma. An aliquot of 3.7 MBq of [^{18}F]-**2c** or 18 MBq of [^{11}C]-**3c** was injected intravenously via a tail vein of anesthetized mice. The animals ($n = 2$ per tracer) were sacrificed by decapitation at 30 min p.i., and blood was collected into a BD vacutainer (containing lithium heparin; BD, Franklin Lakes, USA). After centrifugation at 3000 rpm (1837 g) for 5 min (Eppendorf centrifuge 5810), plasma was collected, diluted with an equal volume of acetonitrile, and again centrifuged for 5 min at 3000 rpm. The plasma was filtered through a 0.22 μm filter (Millipore, Bedford, USA), and the filter was rinsed with an equal volume of water. Finally, the filtered plasma was mixed with authentic **2a** and **2c** or authentic **3a** and **3c** and analyzed using HPLC on an XTerra RP C_{18} column eluted with mixtures of 40% acetonitrile ([^{18}F]-**2c**) or 30% acetonitrile ([^{11}C]-**3c**) in 0.1 M ammonium acetate pH 4 at a flow rate of 1 mL/min. After passing through an inline UV detector, the HPLC-eluate was collected in 1 mL fractions, and their radioactivity was measured using a gamma counter.

Cell Uptake Studies. A lentiviral vector (LV) encoding the cDNA of β-gal linked to the puromycin-N-acetyl transferase (*pac*) gene from *Streptomyces alboniger* through an encephalomyocarditis virus internal ribosome entry site (IRES) was produced as described (*35*) and denominated LV-LacZ-I-P. A similar vector encoding the firefly luciferase (fluc) gene or the varicella zoster virus thymidine kinase (VZV-tk) was used as the control (LV-fluc-I-P and LV-VZV-tk-I-P).

Human embryonic kidney cells (293T) transduced with LV-LacZ-I-P and with LV-fluc-I-P were maintained in culture in medium containing 1 μg/mL puromycin. They were plated in triplicate at a density of 200 000 cells per well in 24-well plates. After 24 h, the medium was discarded, and 0.25 mL of fresh medium with HPLC-purified tracer (185 kBq of [^{18}F]-**2c** or 1.11 MBq of [^{11}C]-**3c** per well) was added. The cells were then incubated at 37 °C in a 5% CO_2 atmosphere for time intervals of 30, 60, 90, or 120 min ($n = 3$ per time point, per vector). Earlier time points were not investigated. Following incubation and removal of the medium, the cells were washed three times with 0.4 mL of ice−cold phosphate-buffered saline (PBS). The cells were then lysed with 0.25 mL of Cell Culture Lysis Reagent 1× solution (Promega Corporation, Madison, USA) for 10 min, after which the lysate was collected, followed by a 0.125 mL rinse using the same solution. The cell fractions (lysate and rinse) as well as the wash fractions (medium and PBS) were collected separately for each well, and the radioactivity was measured using a gamma counter. This procedure was repeated for each incubation period. The protein concentration of each cell fraction was determined using the Bio-Rad Protein Assay (Biorad, München, Germany) and a spectrophotometer (Bio Synchron-Anthos 2010, Anthos LabTec Instruments, Austria) at 595 nm. Tracer uptake was normalized for total protein content in the cell fraction for each individual well and expressed as percentage of total radioactivity per milligram protein.

HPLC Analysis of Cell Lysates and Supernatants of LacZ Gene- and VZV-tk Gene-Transduced Cells after 30 min Incubation with [^{18}F]-2c. Cells expressing β-gal or VZV-TK as control were grown to near confluency in 75 cm^2 flasks, in the conditions described above. The medium was discarded, and the monolayer was incubated with 4 mL of fresh medium containing 22 MBq of [^{18}F]-**2c** for each flask. After 30 min incubation at 37 °C and removal of the medium, the cells were washed with cold PBS (3 × 5 mL). Intracellular components from the cells in both flasks were harvested by treatment with 1.5 mL of Cell Culture Lysis Reagent solution, followed by a rinse with 1 mL of the same solution. An aliquot of 1 mL of the cell suspension was diluted with an equal volume of acetonitrile, and the mixture was centrifuged at 3000 rpm (1837 g) for 5 min (Eppendorf centrifuge 5810). 1.5 mL of the centrifuged cell suspension was filtered through a 0.22 μM filter (Millipore), and the filter was rinsed with an equal volume of water. Finally, the filtrate was mixed with authentic **2a** and **2c** and analyzed using HPLC on an XTerra RP C_{18} eluted with a mixture of 30% acetonitrile in 0.1 M ammonium acetate pH 4 at a flow rate of 1 mL/min. After passing through an inline UV detector, the HPLC eluate was collected in 1 mL fractions, and the radioactivity of all fractions was measured using a gamma counter. The supernatant from both flasks was analyzed in the same way, with the only difference that these fractions were first centrifuged (prior to addition of acetonitrile) to remove the small number of cells that might have been detached from the bottom of the flask during the rinse steps.

μPET Imaging in a β-gal Expressing Tumor Mouse Model. Five million SHSY5Y (human neuroblastoma) cells stably transduced with LV-LacZ-I-P were implanted in the flank of female nude mice. Tumor growth and body mass were monitored on a regular basis. The mice were housed on a 12 h/12 h light/darkness cycle and had access to food and water ad libitum. When the tumor reached a volume over 500 mm^3, imaging was performed. Dynamic μPET imaging was performed with a Focus 220 micro-PET scanner (Concorde Microsystems, Knoxville, TN, USA). The mouse was anesthetized with isoflurane (2%) in oxygen at a flow rate of 1 L/min and subsequently injected with 13 MBq [^{18}F]-**2c** via a lateral tail vein. A μPET image was acquired for 215 min, and reconstruc-

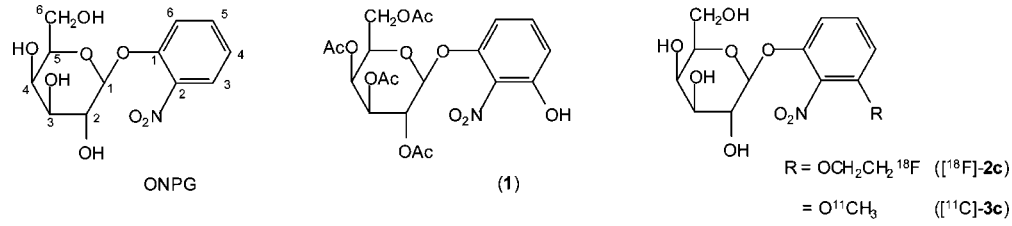

Figure 1. Structure of ONPG, 3-hydroxy-2-nitrophenyl 2,3,4,6-tetra-*O*-acetyl-*β*-D-galactopyranoside (**1**) and the radiolabeled probes 3-(2′-[^{18}F]fluoroethoxy)-2-nitrophenyl *β*-D-galactopyranoside ([^{18}F]-**2c**) and 3-[^{11}C]methoxy-2-nitrophenyl *β*-D-galactopyranoside ([^{11}C]-**3c**).

Scheme 1. Radiolabeling of Precursor 1 and Subsequent Deprotection Yielding [^{18}F]-2c and [^{11}C]-3c

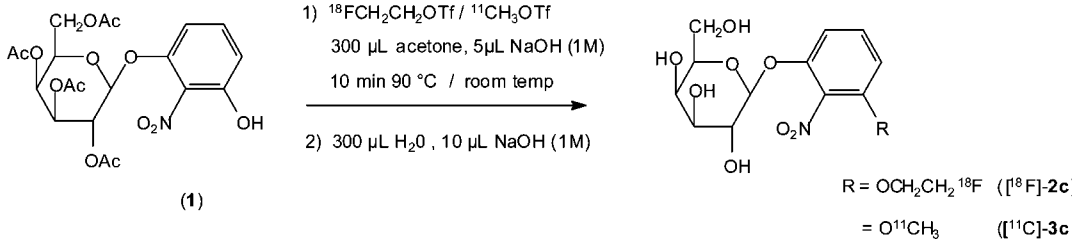

tion was done using filtered back-projection with a RAMP 0.5 filter. The images were displayed in AMIDE (*36*).

RESULTS AND DISCUSSION

β-Galactosidase (*β*-gal), the enzyme encoded by the LacZ gene, catalyzes hydrolysis of galactopyranosides by cleavage of the C−O bond between the sugar and the aglycon with overall retention of anomeric configuration (*37, 38*). As indicated by the diversity of substrates that can be used to detect *β*-gal activity, this enzyme has a broad substrate specificity. The only prerequisite is the conservation of the galactose structure, since it has been observed that hydrogen bonding between the active site of the enzyme and the hydroxyl groups of the glycosidic substrate is important in the formation of the enzyme–substrate complex (*37–40*). On the basis of these findings, we derivatized in the present study *o*-nitrophenyl *β*-D-galactopyranoside (ONPG) in the phenyl moiety in order to minimize interference with its binding affinity, labeled it using [^{18}F]FEtOTf or [^{11}C]MeOTf and evaluated the two tracers as potential reporter probes for *in vivo* visualization of LacZ gene expression with PET. The structures of ONPG, the precursor **1**, and the PET-tracers [^{18}F]-**2c** and [^{11}C]-**3c** are shown in Figure 1.

The ONPG-derived precursor **1** was synthesized following the procedure described by Oyama et al. (*41*), which involved a Koenigs−Knorr glycosylation reaction of 2-nitroresorcinol with acetobromo-α-D-galactose in the presence of silver carbonate in quinoline at room temperature. Inversion of the configuration at the anomeric center resulted in the sole formation of the *β*-anomer in a 30% yield. Compound **1** was identified using mass spectrometry, and its structure was confirmed with ^{1}H and ^{13}C NMR. The presence of the anomeric H-1 at 5.1 ppm as a doublet with an axial−axial coupling ($^{3}J_{H1\text{-}H2}$) of 8 Hz, the coupling of H-2 with H-3 with a coupling constant ($^{3}J_{H2\text{-}H3}$) of 10.6 Hz in the ^{1}H NMR spectrum, and the resonance of the anomeric carbon atom at 100.31 ppm in the ^{13}C NMR spectrum proved the *β*-configuration of the precursor (*42*). To prevent alkylation of the sugar hydroxyl groups, hydrolysis of the protective acetate groups was performed after radiolabeling. Since the synthesis of the cold reference compounds by alkylation of **1** with 2-fluoroethyl tosylate or methyl triflate and subsequent deprotection failed or resulted in a negligible yield, we first synthesized the alkylated phenols (**2a** and **3a**) via a Mitsunobu coupling between 2-nitroresorcinol and the corresponding alcohol (2-fluoroethanol or methanol) using triphenylphosphine and diisopropylazodicarboxylate in tetrahydrofuran. The structure of these compounds was confirmed with ^{1}H and ^{13}C NMR. In a second step, the alkylated phenols were coupled to acetobromo-α-D-galactose in the same way as described for the synthesis of **1**, yielding **2b** and **3b** in a moderate yield. Subsequent deprotection of the sugar hydroxyl groups using sodium methoxide resulted in the desired reference compounds **2c** and **3c**. The anomeric *β*-configuration, essential for substrate affinity for *β*-galactosidase, was again confirmed by the characteristic chemical shifts (**2c**, $\delta_{H\text{-}1} = 4.99$ ppm, $\delta_{C\text{-}1} = 101.09$ ppm; **3c**, $\delta_{H\text{-}1} = 4.98$ ppm, $\delta_{C\text{-}1} = 101.06$ ppm) and coupling constants ($^{3}J_{H1\text{-}H2} = 7.4$ Hz) in the ^{1}H and ^{13}C NMR spectra. High-resolution mass spectrometry (HRMS) yielded the exact mass as calculated for the precursor (**1**) and the reference compounds (**2c**, **3c**).

Previous attempts to label a derivative of ONPG bearing a tosyl-ethoxy substituent in ortho position of the nitro group directly with [^{18}F]fluoride failed because of decomposition of the precursor under the applied labeling conditions (Kryptofix 222 in combination with K_2CO_3 or $KHCO_3$ at 110 or 60 °C). These failures prompted us to use the secondary labeling agents 2-[^{18}F]fluoroethyl triflate ([^{18}F]FEtOTf) and [^{11}C]methyl triflate ([^{11}C]MeOTf), which do not require the use of a strongly alkaline solution of kryptofix and a potassium salt at elevated temperatures. [^{18}F]FEtOTf and [^{11}C]MeOTf were synthesized following reported procedures (*43, 44*). Labeling with carbon-11 was done by alkylation of precursor **1** with [^{11}C]MeOTf in acetone in the presence of NaOH at room temperature. Labeling with fluorine-18 was done in a similar way with [^{18}F]FEtOTf as alkylating agent. However, heating to 90 °C was required to effect the reaction. At 70 °C, slightly lower yields were obtained, and at room temperature, less than 20% of the protected tracer was formed (Scheme 1). For both tracers, labeling was followed by deprotection of the sugar hydroxyl groups under basic conditions. For the fluorine-18 labeled tracer, the unreacted [^{18}F]EtOTf or [^{18}F]EtOH was evaporated, and both tracers were purified using preparative RP-HPLC. Chemical and radiochemical purity of both HPLC purified tracers was examined on an analytical RP C_{18} column and were found to be >99%. The identity of the tracers was confirmed by coelution with authentic nonradioactive compounds after coinjection on analytical RP-HPLC.

The lipophilicity of the tracers was determined by measuring their *n*-octanol/water partition coefficients, which were found

Scheme 2. Schematic Representation of Enzymatic Cleavage of the Galactopyranosides into Their Corresponding Phenol−Aglycons and D-Galactose

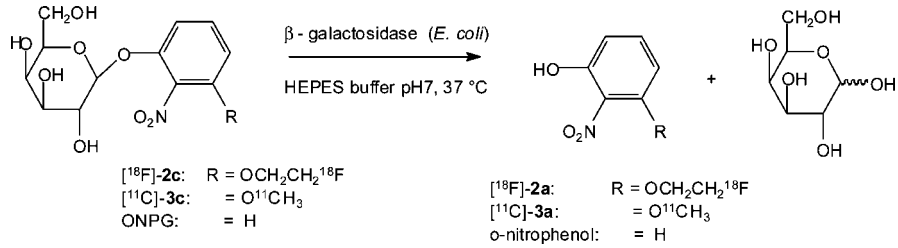

to be −0.8 and −0.7, respectively, for [^{18}F]-**2c** and [^{11}C]-**3c**. This reflects the polarity of the sugar backbone. The optimal theoretical log *P* value of a compound for passive diffusion over the blood−brain barrier is situated within the range 1–2.5 (*45*, *46*). Extrapolating this to diffusion over a cell membrane suggests that the labeled galactose derivatives may not be lipophilic enough to efficiently enter the cells through passive diffusion. In literature, no evidence of active transport for this type of galactose derivative was found. However, the cell uptake studies (*vide infra)* suggest that [^{18}F]-**2c** and [^{11}C]-**3c** do enter the cells.

In an *in vitro* test (Scheme 2), both tracers were found to be good substrates of β-gal with results in a comparable range as reported by Cui et al. (*30*) for a similar compound (Figure 2). After 30 s of incubation at 37 °C, already 89% of [^{18}F]-**2c** was hydrolyzed. Complete hydrolysis was reached after about 15 min. For the C-11 labeled tracer, the enzymatic conversion was somewhat slower. After 30 s of incubation, 60% of [^{11}C]-**3c** was hydrolyzed, and almost complete hydrolysis (90%) was reached after 15 min. In a similar test with the reference substrate ONPG (1 mg), 100% conversion was also reached within 15 min (results not shown). In a control experiment under identical conditions, but in the absence of β-gal, no hydrolysis of the labeled galactose derivatives was observed.

These results suggest that the labeled galactose derivatives were specifically hydrolyzed by β-gal, with a rate comparable to that for ONPG.

The biodistribution of [^{18}F]-**2c** and [^{11}C]-**3c** was evaluated in normal male NMRI mice at 2 and 60 min p.i. for both tracers. Data are shown in Tables 1 and 2. Both tracers have a similar behavior *in vivo*, but the clearance from blood, defined as the 2-min-to-60-min ratio of the blood activity, was slower for [^{18}F]-**2c** than for [^{11}C]-**3c** (1.7 and 4.7, respectively). Blood clearance occurred mainly through the renal pathway with 33.2% of the injected dose (ID) ([^{18}F]-**2c**) and 45.8% ID ([^{11}C]-**3c**) in the urine at 60 min p.i. Negligible uptake was seen in the brain, which was expected in view of the negative log *P* value. The slow blood clearance may interfere with successful *in vivo* imaging.

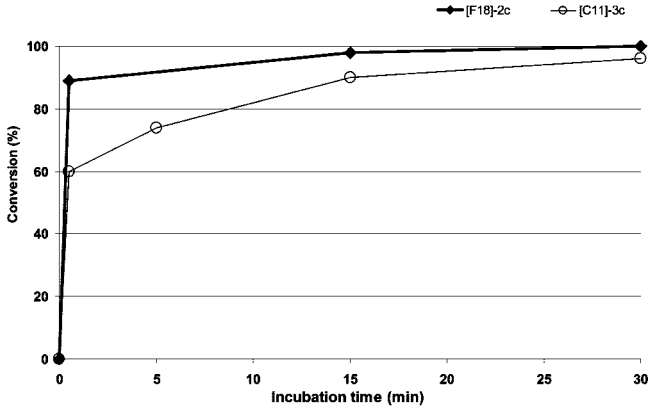

Figure 2. *In vitro* hydrolysis of [^{18}F]-**2c** (♦) and [^{11}C]-**3c** (○) by β-gal (1U) in HEPES buffered solution at 37 °C.

Table 1. Biodistribution of [^{18}F]-2c in Normal NMRI Mice 2 and 60 min p.i.[a]

	% ID[b]		% ID/g[c]	
[^{18}F]-**2c**	2 min	60 min	2 min	60 min
urine	0.3 ± 0.1	33.2 ± 0.9		
kidneys	10.1 ± 1.1	3.3 ± 1.2	21.3 ± 3.6	7.0 ± 2.8
liver	20.0 ± 2.3	5.1 ± 0.7	10.7 ± 0.9	2.9 ± 0.1
intestines	8.9 ± 0.4	14.3 ± 0.9	3.0 ± 0.3	4.9 ± 0.7
spleen + pancreas	0.9 ± 0.1	0.5 ± 0.0	3.6 ± 0.1	2.2 ± 0.3
lungs	1.5 ± 0.0	0.5 ± 0.0	7.2 ± 0.6	3.0 ± 0.3
heart	0.5 ± 0.1	0.4 ± 0.0	5.2 ± 0.6	4.6 ± 0.5
stomach	1.1 ± 0.2	0.6 ± 0.1	2.1 ± 0.7	1.1 ± 0.3
brain	0.1 ± 0.0	0.4 ± 0.0	0.5 ± 0.1	1.9 ± 0.2
blood	21.4 ± 2.2	11.6 ± 3.0	8.0 ± 0.8	4.6 ± 1.4

[a] Data are expressed as mean ± SD; $n = 3$ per time point; p.i. = post injection. [b] Percentage of injected dose calculated as cpm in organ/total cpm recovered. [c] Percentage of injected dose per gram tissue.

Table 2. Biodistribution of [^{11}C]-3c in Normal NMRI Mice 2 and 60 min p.i.[a]

	% ID[b]		% ID/g[c]	
[^{11}C]-**3c**	2 min	60 min	2 min	60 min
urine	0.3 ± 0.2	45.8 ± 7.9		
kidneys	7.8 ± 1.6	3.5 ± 2.2	14.4 ± 4.5	5.8 ± 3.7
liver	22.0 ± 1.5	14.9 ± 2.6	9.9 ± 1.3	6.8 ± 0.9
intestines	10.1 ± 1.0	10.2 ± 2.2	3.0 ± 0.4	3.0 ± 0.9
spleen + pancreas	1.0 ± 0.2	0.6 ± 0.1	3.2 ± 0.7	1.9 ± 0.2
lungs	1.4 ± 0.1	0.3 ± 0.0	5.9 ± 0.2	1.2 ± 0.2
heart	0.6 ± 0.1	0.2 ± 0.0	3.6 ± 0.4	1.2 ± 0.2
stomach	1.0 ± 0.1	0.6 ± 0.1	1.3 ± 0.1	0.7 ± 0.1
brain	0.1 ± 0.0	0.1 ± 0.0	0.3 ± 0.0	0.4 ± 0.1
blood	19.5 ± 2.5	4.3 ± 0.8	7.4 ± 0.9	1.6 ± 0.4

[a] Data are expressed as mean ± SD; $n = 3$ per time point; p.i. = post injection. [b] Percentage of injected dose calculated as cpm in organ/total cpm recovered. [c] Percentage of injected dose per gram tissue.

The metabolic stability was determined in normal mice, having low levels of endogenous β-galactosidase (*47*). Plasma analysis of [^{18}F]-**2c** and [^{11}C]-**3c** at 30 min p.i. revealed that, respectively, 98% and 97% of the activity was present as intact tracer, indicating high *in vivo* stability. Negligible traces of hydrolysis product were found, indicating little degradation by endogenous mammalian β-galactosidase.

The results of the cell uptake studies are shown in Figure 3a ([^{18}F]-**2c**),b ([^{11}C]-**3c**). A maximal uptake was observed after 30 min incubation for [^{18}F]-**2c** with a 7.5-fold higher uptake in the β-gal-expressing cells (3.2%/mg protein) compared to the control cells (0.4%/mg protein). This uptake ratio is comparable with the maximal uptake ratio of the iodine-123 labeled β-gal inhibitor of the group of Lee et al. (*32*).

For [^{11}C]-**3c**, the maximal uptake was reached after 90 min of incubation with a 2.5-fold higher uptake in the β-gal expressing cells (5.2%/mg protein) compared to the control cells (2.1%/mg protein). [^{18}F]-**2c** was further evaluated *in vitro* and *in vivo*.

The uptake of [^{18}F]-**2c** in the β-gal-expressing cells decreases significantly as a function of time, from 3.2%/mg protein after

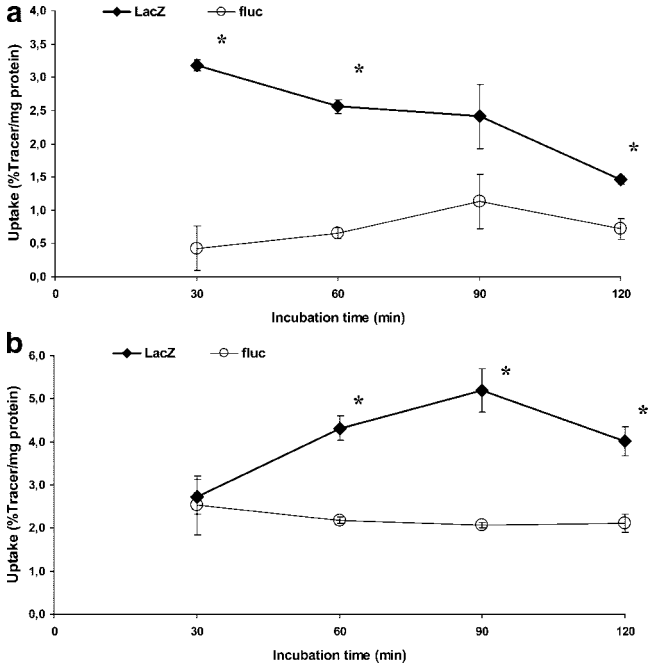

Figure 3. a. Time-dependent uptake levels of [^{18}F]-**2c** in LacZ gene (♦)- and fluc gene (○)-transduced 293T cells. Data are expressed as % tracer/mg protein and are mean values of triplicate samples. Values with asterisk are significant different; $p < 0.006$, unpaired bidirectional Student *t* test. b. Time-dependent uptake levels of [^{11}C]-**3c** in LacZ gene (♦)- and fluc gene (○)-transduced 293T cells. Data are expressed as % tracer/mg protein and are mean values of triplicate samples. Values with asterisk are significant different; $p < 0.005$, unpaired bidirectional Student *t* test.

30 min of incubation to 1.5%/mg protein after 120 min of incubation (Figure 3a). This may be due to leakage of the radiolabeled aglycon ([^{18}F]-**2a)** out of the transduced cells. To test this hypothesis and to check the nature of the metabolites present in the transduced cells, the cell lysates and supernatant fractions of both the β-gal expressing cells as well as the control cells were analyzed using RP-HPLC, after incubation with [^{18}F]-**2c** for 30 min. The HPLC chromatograms of the supernatants and cell lysates of the LV-LacZ-I-P and LV-VZV-tk-I-P transduced cells are shown in Figure 4a (supernatants) and b (cell lysates). The cold intact (**2c**) and hydrolyzed (**2a**) reference compounds were added to the cell lysates and supernatant fractions prior to HPLC analysis. In this way, the signals in the reconstructed radiometric HPLC chromatogram could be assigned by correlation to the signals in the UV absorption chromatogram. The component eluting in fractions 4 to 6 is the intact tracer [^{18}F]-**2c**. The metabolite eluting in fractions 14 to 16 is the aglycon 3-(2′-[^{18}F]fluoroethoxy)-2-nitrophenol ([^{18}F]-**2a**). In the LacZ cell lysate, 63.5% of the radioactivity was recovered as radiolabeled aglycon (Table 3). In the VZV-tk control cells, only negligible amounts of hydrolysis product were found in the cells and in the supernatants. This suggests that the labeled aglycon (50.7%) found in the supernatant fraction of the β-gal expressing cells must have leaked out of the LacZ expressing cells, which would result in loss of PET-signal. This back-diffusion can be explained in terms of the pK_a of the hydrolysis product ([^{18}F]-**2a**). The pK_a of nonsubstituted *o*-nitrophenol is 7.23 (*48*); the dissociation constant of [^{18}F]-**2a** is therefore estimated to be in a similar range. Ideally, the dissociation constant should be an order of magnitude lower than 7.4 (physiological pH) to direct the equilibrium to the dissociated form, resulting in a higher retention of the ionized aglycon in LacZ transduced cells.

To test the potential of [^{18}F]-**2c** as a PET reporter probe for detecting LacZ gene expression *in vivo*, a mouse growing

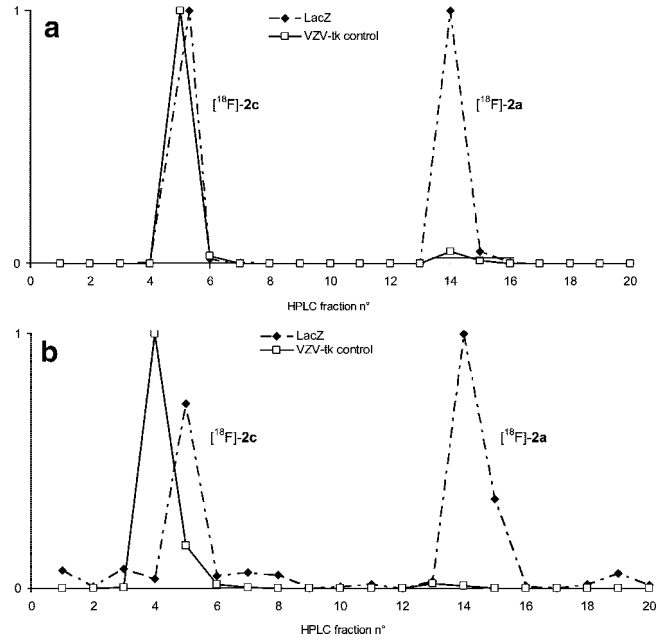

Figure 4. a. Analysis of the supernatants of LacZ gene- and VZV-tk gene-transduced 293T cells after 30 min incubation with [^{18}F]-**2c**. b. Analysis of the cell lysates of LacZ gene- and VZV-tk gene-transduced 293T cells after 30 min incubation with [^{18}F]-**2c**.

Table 3. Results of the RP-HPLC Analysis of the Cell Lysate and Supernatant Fractions of LacZ Gene- and VZV-tk Gene-Transduced Cells Recovered after 30 min Incubation with [^{18}F]-2c

	cell lysate[a]		supernatant[a]	
	LacZ	VZV-tk	LacZ	VZV-tk
[^{18}F]-**2c** (intact)	36.5	97.8	49.3	94.4
[^{18}F]-**2a** (aglycon)	63.5	2.2	50.7	5.6

[a] Data are expressed as % of recovered activity.

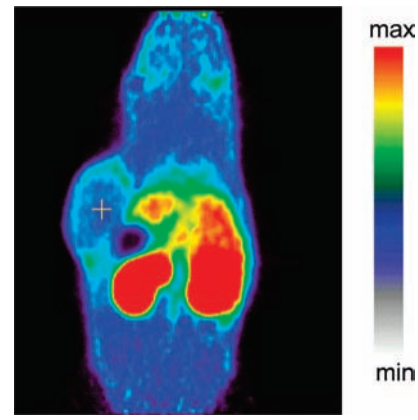

Figure 5. μPET image, selected from a 3D data set (summed image from 0 to 215 min p.i.), of the distribution of [^{18}F]-**2c** in a β-gal-expressing tumor mouse model. The position of the tumor is marked with a cross.

β-galactosidase-expressing SHSY5Y-LacZ-I-P xenografts was injected with [^{18}F]-**2c** and a μPET image was acquired for 215 min. Figure 5 shows the summed image from 0 to 215 min. In analogy with the mice biodistribution study, high uptake is seen in the liver and the kidneys. Only negligible accumulation is observed in the LacZ-transduced tumor, despite the pronounced difference in uptake between β-gal expressing cells and control cells *in vitro*. The absence of tracer accumulation in the LacZ tumor can be due to poor passive diffusion over the tumor cell membrane. This would be in accordance with the results of Liu

et al. (*49*) who needed to perform direct intratumoral injection of their fluoronitrophenyl galactopyranoside MRI probe to observe any contrast.

CONCLUSION

A derivative of the chromogenic β-gal substrate ONPG was efficiently synthesized and labeled with [^{18}F]FEtOTf or [^{11}C]MeOTf to obtain [^{18}F]-**2c** and [^{11}C]-**3c**, which were evaluated as reporter probes for detection of LacZ gene expression with PET. Metabolic stability analysis of plasma collected 30 min after injection of [^{18}F]-**2c** or [^{11}C]-**3c** in mice showed high *in vivo* stability for both tracers. In an in *vitro* experiment, [^{18}F]-**2c** and [^{11}C]-**3c** were found to be good substrates with complete conversion after about 15 min of incubation with β-galactosidase. Cell uptake studies revealed that [^{18}F]-**2c** had a 7.5-fold higher uptake into LacZ gene-transduced cells compared to control cells. For [^{11}C]-**3c**, this difference was only 2.5. RP-HPLC analysis of the cell lysates and supernatant fractions from β-gal expressing cells and control cells after 30 min of incubation with [^{18}F]-**2c** showed substantial leakage of the β-gal cleavage product of [^{18}F]-**2c** out of the transduced cells, which would lead to loss of PET signal. In a μPET study of [^{18}F]-**2c** in a LacZ expressing tumor mouse model, only negligible accumulation was observed in the LacZ transduced tumor, despite the significant difference in uptake between β-gal expressing cells and control cells *in vitro*. As a general conclusion, it can be stated that the synthesized PET tracers [^{18}F]-**2c** and [^{11}C]-**3c** are not suitable for use as LacZ reporter probes. Further modifications to improve diffusion over the tumor cell membrane and to increase the retention in β-gal expressing cells may lead to better *in vivo* imaging results.

ACKNOWLEDGMENT

We gratefully thank Marva Bex and Sigrid Ruymen for their assistance in the labeling experiments and Christelle Terwinghe, Kim Deliège, and Peter Vermaelen for their help in the *in vivo* studies. This work was supported by SBO grant (IWT-30 238) of the Flemisch Institute supporting Scientific-Technological Research in industry (IWT), the IDO grant (IDO/02/012) of the Katholieke Universiteit Leuven, and by the EC-FP6-project DiMI, LSHB-CT-2005-512146.

LITERATURE CITED

(1) Doubrovin, M., Serganova, I., Mayer-Kuckuk, P., Ponomarev, V., and Blasberg, R. G. (2004) Multimodality *in vivo* molecular-genetic imaging. *Bioconjugate Chem. 15*, 1376–1388.

(2) Herschman, H. R. (2004) PET reporter genes for noninvasive imaging of gene therapy, cell tracking and transgenic analysis. *Crit. Rev. Oncol. Hematol. 51*, 191–204.

(3) Acton, P. D., and Zhou, R. (2005) Imaging reporter genes for cell tracking with PET and SPECT. *Q. J. Nucl. Med. Mol. Imaging 49*, 349–360.

(4) Gambhir, S. S., Barrio, J. R., Herschman, H. R., and Phelps, M. E. (1999) Assays for noninvasive imaging of reporter gene expression. *Nucl. Med. Biol. 26*, 481–490.

(5) Serganova, I., and Blasberg, R. (2005) Reporter gene imaging: potential impact on therapy. *Nucl. Med. Biol. 32*, 763–780.

(6) Wood, K. V. (1995) Marker proteins for gene expression. *Curr. Opin. Biotechnol. 6*, 50–58.

(7) Lin, W. C., Pretlow, T. P., Pretlow, T. G., and Culp, L. A. (1990) Bacterial lacZ gene as a highly sensitive marker to detect micrometastasis formation during tumor progression. *Cancer Res. 50*, 2808–2817.

(8) Cui, C., Wani, M. A., Wight, D., Kopchick, J., and Stambrook, P. J. (1994) Reporter genes in transgenic mice. *Transgenic Res. 3*, 182–194.

(9) Jefferson, R. A., Bevan, M., and Kavanagh, T. (1987) The use of the *Escherichia coli* β-glucuronidase gene as a gene fusion marker for studies of gene expression in higher plants. *Biochem. Soc. Trans. 15*, 17–18.

(10) Gorman, C. M., Moffat, L. F., and Howard, B. H. (1982) Recombinant genomes which express chloramphenicol acetyltransferase in mammalian cells. *Mol. Cell. Biol. 2*, 1044–1051.

(11) Chalfie, M., Tu, Y., Euskirchen, G., Ward, W. W., and Prasher, D. C. (1994) Green fluorescent protein as a marker for gene expression. *Science 263*, 802–805.

(12) Hoffman, R. M. (2002) Green fluorescent protein imaging of tumour growth, metastasis, and angiogenesis in mouse models. *Lancet Oncol. 3*, 546–556.

(13) O'Connell-Rodwell, C. E., Burns, S. M., Bachmann, M. H., and Contag, C. H. (2002) Bioluminescent indicators for *in vivo* measurements of gene expression. *Trends Biotechnol. 20*, S19–S24.

(14) Rehemtulla, A., Stegman, L. D., Cardozo, S. J., Gupta, S., Hall, D. E., Contag, C. H., and Ross, B. D. (2000) Rapid and quantitative assessment of cancer treatment response using *in vivo* bioluminescence imaging. *Neoplasia 2*, 491–495.

(15) Williams, T. M., Burlein, J. E., Ogden, S., Kricka, L. J., and Kant, J. A. (1989) Advantages of firefly luciferase as a reporter gene: application to the interleukine-2 gene promoter. *Anal. Biochem. 176*, 28–32.

(16) Rossi, F., Charlton, C. A., and Blau, H. M. (1997) Monitoring protein–protein interactions in intact eukaryotic cells by β-galactosidase complementation. *Proc. Natl. Acad. Sci. U.S.A. 94*, 8405–8410.

(17) Sanchez-Ramos, J., Song, S., Dailey, M., Cardozo-Pelaez, F., Hazzi, C., Stedeford, T., Willing, A., Freeman, T. B., Saporta, S., Zigova, T., Sanberg, P. R., and Snyder, E. Y. (2000) The X-gal caution in neural transplantation studies. *Cell Transplant. 9*, 657–667.

(18) Aamlid, K. H., Lee, G., Smith, B. V., Richardson, A. C., and Price, R. G. (1990) New colorimetric substrates for the assay of glycosidases. *Carbohydr. Res. 205*, c5–c9.

(19) Tung, C.-H., Zeng, Q., Shah, K., Kim, D.-E., Schellingerhout, D., and Weissleder, R. (2004) *In vivo* imaging of β-galactosidase activity using far red fluorescent switch. *Cancer Res. 64*, 1579–1583.

(20) Rotman, B., Zderic, J. A., and Edelstein, M. (1963) Fluorogenic substrates for β-D-galactosidases and phosphatases derived from fluorescein (3,6-dihydroxyfluoran) and its monomethyl ether. *Proc. Natl. Acad. Sci. U.S.A. 50*, 1–6.

(21) Nolan, G. P., Fiering, S., Nicolas, J.-F., and Herzenberg, L. A. (1988) Fluorescence activated cell-analysis and sorting of viable mammalian cells based on β-D-galactosidase activity after transduction of *Escherichia coli* lacZ. *Proc. Natl. Acad. Sci. U.S.A. 85*, 2603–2607.

(22) Zhang, Y.-Z., Naleway, J. J., Larison, K. D., Huang, Z., and Haugland, R. P. (1991) Detecting lacZ gene expression in living cells with new lipophilic, fluorogenic β-galactosidase substrates. *FASEB J. 5*, 3108–3113.

(23) Jain, V. K., and Magrath, I. T. (1991) A chemiluminescent assay for quantitation of β-galactosidase in the femtogram range. Application to quantitation of β-galactosidase in lacZ-transfected cells. *Anal. Biochem. 199*, 119–124.

(24) Wehrman, T. S., Von Degenfeld, G., Krutzik, P. O., Nolan, G. P., and Blau, H. M. (2006) Luminescent imaging of β-galactosidase activity in living subjects using sequential reporter-enzyme luminescence. *Nat. Methods 3*, 295–301.

(25) Gambhir, S. S. (2002) Molecular imaging of cancer with positron emission tomography. *Nat. Rev. Cancer 2*, 683 693.

(26) Bailey, D. L., and Parker, J. A. (2004) Single photon emission computed tomography, *Nuclear Medicine in Clinical Diagnosis and Treatment*, 3rd ed., Vol. 2 (Ell, P. J., and Gambhir, S. S., Eds.) pp 1815–1826,Chapter 128, Churchill Livingstone, Edinburgh, GB.

(27) Bogdanov, A., and Weissleder, R. (1998) The development of *in vivo* imaging systems to study gene expression. *Trends Biotechnol. 16* (1), 5–10.

(28) Weissleder, R., Moore, A., Mahmood, U., Bhorade, R., Benveniste, H., Chiocca, E. A., and Basilion, J. P. (2000) *In vivo* magnetic resonance imaging of transgene expression. *Nat. Med. 6*, 351–354.

(29) Louie, A. Y., Hüber, M. M., Ahrens, E. T., Rothbächer, U., Moats, R., Jacobs, R. E., Fraser, S. E., and Meade, T. J. (2000) In vivo visualization of gene expression using magnetic resonance imaging. *Nat. Biotechnol. 18*, 18321–325.

(30) Cui, W., Otten, P., Li, Y., Koeneman, K. S., Yu, J., and Mason, R. P. (2004) Novel NMR approach to assessing gene transfection: 4-fluoro-2-nitrophenyl-β-D-galactopyranoside as a prototype reporter molecule for β-galactosidase. *Magn. Res. Med. 51*, 616–620.

(31) Yu, J., Liu, L., Kodibagkar, V. D., Cui, W., and Mason, R. P. (2006) Synthesis and evaluation of novel enhanced gene reporter molecules: Detection of β-galactosidase activity using ^{19}F NMR of trifluoromethylated aryl β-D-galactopyranosides. *Bioorg. Med. Chem. 14*, 326–333.

(32) Lee, K.-H., Byun, S. S., Choi, J. H., Paik, J.-Y., Choe, Y. S., and Kim, B.-T. (2004) Targeting of LacZ reporter gene expression with radioiodone-labelled phenylethyl-β-D-thiogalactopyranoside. *Eur. J. Nucl. Med. Mol. Imaging 31*, 433–438.

(33) Bormans, G., and Verbruggen, A. (2001) Enzymatic synthesis and biodistribution in mice of β-O-D-galactopyranosyl-(1,4′)-2′-[^{18}F]fluoro-2′-deoxy-D-glucopyranose (2′-[^{18}F]fluorodeoxylactose). *J. Labelled Cmpd. Radiopharm. 44*, 417–423.

(34) Vanbilloen, H. P., Kieffer, D., Cleynhens, B. J., Bormans, G., Mortelmans, L., and Verbruggen, A. M. (2005) Development and biological evaluation of ^{99m}Tc-BAT-tropane esters. *Nucl. Med. Biol. 32*, 607–612.

(35) Geraerts, M., Michiels, M., Baekelandt, V., Debyser, Z., and Gijsbers, R. (2005) Upscaling of lentiviral vector production by tangential flow filtration. *J. Gene Med. 7*, 1299–1310.

(36) Andreas Loening, Crump Institute for Molecular Imaging, UCLA School of Medicine, CA, USA, http://sourceforge.net/projects/amide/.

(37) Withers, S. G., and Aebersold, R. (1995) Approaches to labeling and identification of active site residues in glycosidases. *Protein Sci. 4*, 361–372.

(38) McCarter, J. D., Adam, M. J., and Withers, S. G. (1992) Binding energy and catalysis. Fluorinated and deoxygenated glycosides as mechanistic probes of Escherichia coli (LacZ) β-galactosidase. *Biochem. J. 286*, 721–727.

(39) Namchuk, M. N., and Withers, S. G. (1995) Mechanism of *Agrobacterium* β-glucosidase: Kinetic analysis of the role of noncovalent enzyme/substrate interactions. *Biochemistry. 34*, 16194–16202.

(40) Yoon, S., Kim, H. G., Chun, K. H., and Shin, J. E. N. (1996) 4-Deoxy-analogs of p-nitrophenyl β-D-galactopyranosides for specificity study with β-galactosidase from *Escherichia coli*. *Bull. Korean Chem Soc. 17*, 599–604.

(41) Oyama, K. I., and Kondo, T. (2004) Total synthesis of apigenin 7,4′-di-O-β-glucopyranoside, a component of blue flower pigment of Salvia patens, and seven chiral analogues. *Tetrahedron. 60*, 2025–2034.

(42) Yu, J., Otten, P., Ma, Z., Cui, W., Liu, L., and Mason, R. P. (2004) Novel NMR approach to assessing gene transfection: Synthesis and evaluation of fluorinated phenyl-β-D-galactosides with potential application for assessing LacZ gene expression. *Bioconjugate Chem. 15*, 1334–1341.

(43) Zhang, M. R., Furutsuka, K., Yoshida, Y., and Suzuki, K. (2003) How to increase the reactivity of [F-18]fluoroethyl bromide: [F-18]fluoroethylation of amine, phenol and amide functional groups with [F-18]FEtBr, [F-18]FEtBr/NaI and [F-18]FEtOTf. *J. Labelled Cmpd. Radiopharm. 46*, 587–598.

(44) Jewett, D. M. (1992) A simple synthesis of [C-11]methyl triflate. *Appl. Radiat. Isot. 43*, 1383–1385.

(45) Dishino, D. D., Welch, M. J., Kilbourn, M. R., and Raichle, M. E. (1983) Relationship between lipophilicity and brain extraction of C-11-labeled radiopharmaceuticals. *J. Nucl. Med. 24*, 1030–1038.

(46) Young, R. C., Mitchell, R. C., Brown, T. H., Ganellin, C. R., Griffiths, R., Jones, M., Rana, K. K., Saunders, D., Smith, I. R., Sore, N. E., and Wilks, T. J. (1998) Development of a new physicochemical model for brain penetration and its application to the design of centrally acting H-2-receptor histamine-antagonists. *J. Med. Chem. 31*, 656–671.

(47) Weiss, D. J., Liggitt, D., and Clark, J. G. (1999) Histochemical discrimination of endogenous mammalian β-galactosidase activity from that resulting from lac-Z gene expression. *Histochem. J. 31*, 231–236.

(48) pK_a data compiled by Williams, R. http://research.chem.psu.edu/brpgroup/pKa_compilation.pdf.

(49) Liu, L., Kodibagkar, V. D., Yu, J.-X., and Mason, R. P. (2007) ^{19}F-NMR detection of lacZ gene expression via the enzymatic hydrolysis of 2-fluoro-4-nitrophenyl β-D-galactopyranoside *in vivo* in PC3 prostate tumor xenografts in the mouse. *FASEB J. 21*, 2014–2019.

BC700216D

Labeling of Fatty Acid Ligands with the Strong Electrophilic Metal Fragment $[^{99m}Tc(N)(PNP)]^{2+}$ (PNP = Diphosphane Ligand)

Emiliano Cazzola,[†] Elisa Benini,[†] Micol Pasquali,[†] Peter Mirtschink,[‡] Martin Walther,[§] Hans-Jurgen Pietzsch,[‡] Licia Uccelli,[†] Alessandra Boschi,[†] Cristina Bolzati,[△] and Adriano Duatti*[,†]

Laboratory of Nuclear Medicine, Department of Radiological Sciences, University of Ferrara, 44100 Ferrara, Italy, Institute of Physiology, Medical Faculty Carl Gustav Carus, Technical University Dresden, 01307 Dresden, Germany, Institute of Radiopharmacy, Forschungszentrum Dresden-Rossendorf, PF 510119, 01314 Dresden, Germany, and ICIS-CNR, Corso Stati Uniti, 4, 35127 Padova, Italy. Received June 25, 2007; Revised Manuscript Received November 28, 2007

The electrophilic metal fragment $[^{99m}Tc(N)(PNP)]^{2+}$ (PNP = diphosphane ligand) has been employed for the labeling of fatty acid chains of different lengths. To provide a site-specific group for the attachment of the metallic moiety, the fatty acid derivatives were functionalized by appending a bis-mercapto or, alternatively, a dithiocarbamato π-donor chelating systems to one terminus of the carbon chain to yield both dianionic and monoanionic bifunctional ligands (L). The resulting complexes, $[^{99m}Tc(N)(PNP)(L)]^{0/+}$, exhibited the usual asymmetrical structure in which a Tc≡N group was surrounded by two different bidentate chelating ligands. Dianionic ligands gave rise to neutral complexes, while monoanionic ligands afforded monocationic species. Biodistribution studies were carried out in rats. An isolated perfused rat heart model was employed to assess how strucural changes in the radiolabeled fatty acid compound affect the myocardial first pass extraction. Results showed that only monocationic complexes accumulated in myocardium to a significant extent. Conversely, neutral complexes were not efficiently retained into the heart region and rapidly washed out. In isolated perfused rat heart experiments, monocationic complexes exhibited a behavior similar to that of the monocationic flow tracers ^{99m}Tc-MIBI and ^{99m}Tc-DBODC with almost identical extraction values, a result that could be attributed to the presence of the monopositive charge. Instead, a slightly lower myocardial extraction was found for neutral complexes. Comparison of the observed kinetic behavior of neutral complexes in the isolated perfused rat heart model with that of the myocardial metabolic tracer [^{123}I]IPPA revealed that the introduction of the metallic moiety partially hampers recognition of the labeled fatty acids by cardiac enzymes, and consequently, their behavior did not completely reflect myocardial metabolism.

INTRODUCTION

The search for a Tc-99m labeled fatty acid derivative has been actively pursued in the past years in the attempt to find a suitable alternative to radiopharmaceuticals labeled with positron emitter radionuclides or iodine radioisotopes for monitoring heart metabolism (*1, 2*). A Tc-99m imaging agent sensitive to alterations in fatty acid metabolism in myocardium would be highly desirable because of the ideal nuclear properties of this radionuclide and its easy availability through the ^{99}Mo/^{99m}Tc generator system. A number of different Tc-99m complexes incorporating fatty acid chains of different lengths have been reported, but none of them were shown to have potential use in clinical practice (*3, 9*).

An ideal Tc-99m agent for heart imaging should possess some key features that are essential for visualizing the cardiac region. For instance, one of the most critical requirements is a rapid and quantitative washout of activity from nontarget organs surrounding the heart, such as blood, lungs, and liver, to avoid interference with the activity localized into the myocardium. In particular, liver uptake always constitutes a rather difficult problem, which may become even more important when the radioactive agent is employed for targeting some subtle metabolic process. Indeed, a common drawback plaguing the biodistribution behavior of Tc-99m tracers for imaging fatty acid metabolism proposed so far is attributable to high and persistent liver uptake. A few years ago, we discovered that a large class of Tc-99m complexes, having the general structure sketched in Figure 1b, are easily extracted by the myocardium, but rapidly and quantitatively washed out from nontarget organs, in particular, from the liver (*10, 12*). These complexes can be thought to be composed essentially by two parts: (a) a metal-containing fragment, $\{[^{99m}Tc(N)(PNP)]^{2+}\}$, formed by the technetium atom coordinated to a terminal nitride group (N^{3-}) and a bidentate diphosphane ligand (PNP), and (b) a bidentate ligand having a suitable set, (X,Y), of coordinating donor atoms. In this representation, the metallic portion $[^{99m}Tc(N)(PNP)]^{2+}$ can be viewed as a strong electrophilic molecular fragment capable of selectively interacting with bidentate electron-rich ligands (XY) through the overlap of its empty π-antibonding orbitals with the filled π-orbitals of the donor ligand (*13, 14*).

The favorable properties for cardiac imaging of this new category of Tc-99m complexes were particularly apparent in the study of the biological behavior of the complex $[^{99m}Tc(N)(PNP5)(DBODC)]^{+}$ {PNP5 = bis[(dimethoxypropylphosphanyl)ethyl]ethoxyethylamine; DBODC = *N,N′*-bis(ethoxyethyl)dithiocarbamato}. It was found that this complex rapidly accumulates in myocardium of various animal species and in humans, and washout from nontarget organs was extremely fast and quantitative. In particular, heart/liver ratio was 1 order of magnitude higher than those observed for commercial Tc-99m heart imaging agents (*15, 16*).

* dta@unife.it.
[†] University of Ferrara.
[‡] Technical University Dresden.
[§] Institute of Radiopharmacy.
[△] ICIS-CNR.

10.1021/bc7002378 CCC: $40.75 © 2008 American Chemical Society
Published on Web 01/19/2008

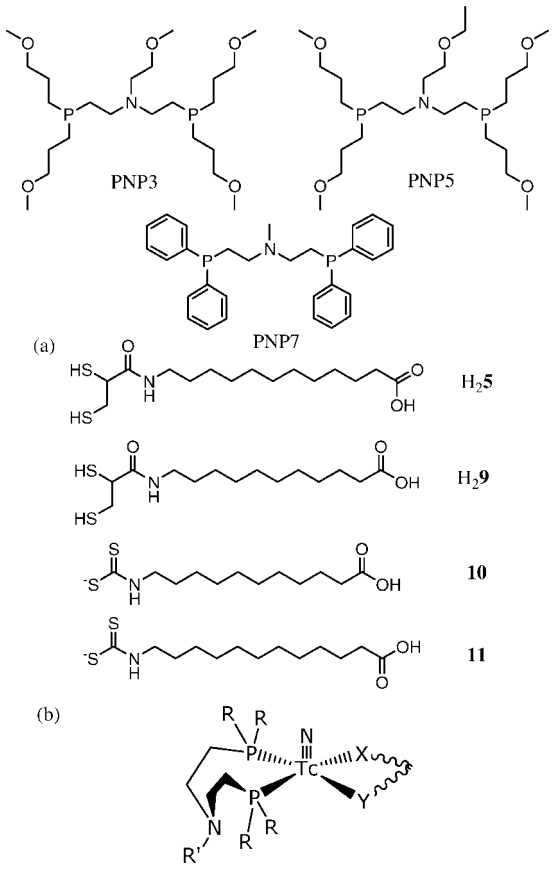

Figure 1. (a) The ligands utilized in this study and (b) general structure of asymmetrical nitride Tc(V) complexes.

Based on these findings, we speculated that, presumably, the $[^{99m}Tc(N)(PNP)]^{2+}$ basic molecular motif characterizing this class of complexes might be a key factor favoring the fast liver elimination. This consideration prompted us to exploit this chemistry for designing new Tc-99m radiopharmaceuticals for in vivo monitoring of cardiac metabolism, which should incorporate the $[^{99m}Tc(N)(PNP)]^{2+}$ building block together with a suitable bidentate ligand bearing a lateral fatty acid chain. In our strategy, the combination of these two molecular pieces would allow the development of myocardial tracers targeting fatty-acid-heart metabolism while concomitantly showing a fast liver clearance.

This paper describes the synthesis of new bifunctional ligands (L) derived from fatty acids having different lengths in their carbon backbone and their reactions with the metal synthon $[^{99m}Tc(N)(PNP)]^{2+}$ to afford new asymmetrical complexes of the type $[^{99m}Tc(N)(PNP)(L)]^{0/+}$. The chemical characterization and full biological evaluation in animals of these new Tc-99m agents will be also reported.

EXPERIMENTAL SECTION

Materials. Technetium-99m was eluted from a $^{99}Mo/^{99m}Tc$ generator provided by Amersham Sorin (Saluggia, Italy). The diphosphane ligands bis[(dimethoxypropylphosphanyl)-ethyl]methoxyethylamine (PNP3), bis[(dimethoxypropyl-phosphanyl)ethyl]ethoxyethylamine (PNP5), and bis[(diphe-nylphosphanyl)ethyl]methylamine (PNP7) (Figure 1a) were purchased from Argus Chemicals (Florence, Italy) or prepared according to literature procedures (*17*). All commercially available compounds and solvents were reagent grade and were used without further purification.

Labeling of *p*-iodophenylpentadecanoic acid (EMKA-CHE-MIE, Markgröningen, Germany) with ^{123}I was performed through Cu(I)-assisted nucleophilic exchange to give the final [^{123}I]IPPA radiocompound as described previously (*18*).

Table 1. Cromatographics Results

	TLC (R_f)	(R_t, min)	
complex	^{99m}Tc	Re	^{99m}Tc
syn, anti-[M(N)(PNP3)(5)]	0.33, 0.43[a]	14.50, 15.23[d]	15.37, 16.02[d]
syn, anti-[M(N)(PNP3)(9)]	0.25, 0.360[a]	15.28, 15.85[d]	16.13, 16.68[d]
$[M(N)(PNP3)(10)]^+$	0.42[b]		14.60[d]
$[M(N)(PNP3)(11)]^+$	0.31[b]		15.18[d]
$[M(N)(PNP5)(10)]^+$	0.37[c]		14.97[d]
$[M(N)(PNP5)(11)]^+$	0.27[c]	14.80[d]	15.34[d]

[a] C_{18}, CH_3CN/0.1-M Et_3N (pH =3 adjusted with 1 M H_3PO_4) (70:30). [b] SiO_2, ETOH/CH_3Cl/toluene/0.5 M NH_4OAc (l.5:3:3:0.5). [c] C_{18}, saline/CH_3OH/THF/HOAc (glacial) (2:8:1:1). [d] Reversed-phase C_{18} column, gradient: A = MeOH, B = phosphate buffer (0.01 M, pH 7.4), t = 0 min, A = 50%, t = 15 min, A = 100%.

Instruments. FT IR spectra were recorded on a Nicolet 510P Fourier transform spectrometer, in the range 4000−400 cm^{-1} and in KBr mixture using a Spectra-Tec diffuse reflectance collector accessory. Elemental analyses (C, H, N, S) were performed on a Carlo Erba 1106 elemental analyzer. ^1H, ^{13}C, and ^{31}P NMR spectra were collected on a Brucker 400 instrument using $SiMe_4$ as internal reference (^1H, ^{13}C) and 85% aqueous H_3PO_4 as external reference (^{31}P).

Chromatography. The radiochemical purity (RCP) of the final Tc-99m compounds were determined by thin-layer chromatography (TLC) on SiO_2 plates and reversed-phase C18 plates (Merck). The activity on the plates were located and measured by a Cyclone instrument (Packard). High-performance liquid chromatography (HPLC) was performed on a Beckman System Gold instrument equipped with a radioisotope detector (model 170). HPLC analysis was carried out using a reversed-phase ODS precolumn (45 × 4.6 mm) and a reversed-phase ODS column (250 × 16 mm) (Beckman) at flow rate of 1 mL/min. Chromatographic results are reported in Table 1.

Synthesis of ω-[(2,3-Dimercaptopropanoyl)amino] Fatty Acid Ligands. In the following the symbol, **H_2n** (where **n** = **5**, **9**) stands for the protonated dimercapto fatty acid ligand, while **n** represents the resulting deprotonated dianionic ligand. When applied, the standard workup procedure for product isolation involved quenching of the reaction mixture in aqueous solution followed by extraction thoroughly with chloroform and washing of the extracts with saturated saline. The combined extracts were then dried over $MgSO_4$, filtered, and the solvent removed under reduced pressure.

Preparation of 11-{[2,3-Bis(acetylthio)propanoyl]amino}undecanoic Acid ($H_2$5). The synthesis of this ligand was conducted according to the reaction scheme illustrated in Figure 2.

*Methyl-11-[(2,3-dibromopropanoyl)amino]undecanoate (***3***).* Dibromopropionic acid (**1**) (1.00 g, 4.31 mmol) and DCC (890 mg, 4.31 mmol) were dissolved in 80 mL of iced chloroform (0 °C). Another solution, prepared separately by dissolving the ω-amino fatty acid ester hydrochloride **2** (1.10 g, 4.37 mmol) and ethyldiisopropylamine (738 μL, 4.31 mmol) in 20 mL of chloroform, was added dropwise to the first solution under stirring. The reaction mixture was stirred overnight without further cooling and then weakly acidified (pH ∼ 3.5) with a few drops 2 M hydrobromic acid. Finally, it was filtered off and evaporated under reduced pressure to remove the solvent. After completing the standard workup procedure for product isolation, purification was carried out by column chromatography (silicagel, $CHCl_3$/Et_2O/HOAc (150/10/0.15)] yielding 1.41 g (76%) of a colorless solid (**3**).

^1H NMR (δ ppm, $CDCl_3$). 6.28 (br, 1H, N*H*), 4.46 (dd, $^3J_1$ = 4.5 Hz, $^3J_2$ = 8.3 Hz, 1H, C*H*Br), 3.97 (dd, $^3J_1$ = 8.4 Hz,

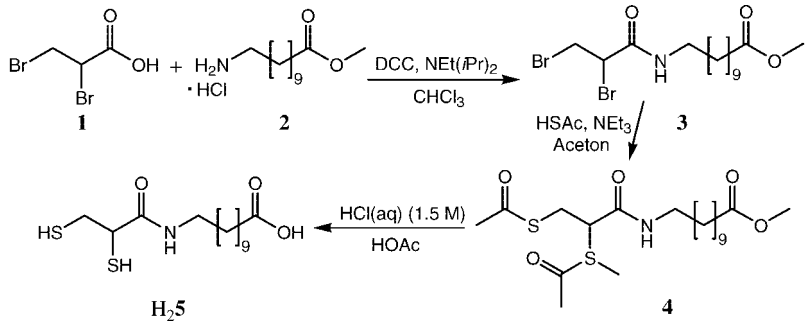

Figure 2. Reaction diagram for the synthesis of the ligand $\mathbf{H_2 5}$.

$^2J_2$ = 10.2 Hz, 1H, ½CH_2Br), 3.82 (dd, $^3J_1$ = 4.5 Hz, $^2J_2$ = 10.3 Hz, 1H, ½CH_2Br$_2$), 3.66 (s, 3H, OCH_3), 3.31 (q, ^3J = 6.7 Hz, 2H, CH_2N), 2.29 (t, ^3J = 7.5 Hz, 2H, CH_2COO), 1.65–1.49 (m, 4H, 2CH_2), 1.38–1.22 (m, 12H, 6CH_2).

^{13}C NMR (δ ppm, $CDCl_3$) 174.4, *C*OO, 165.9, *C*ONH, 51.4, O*C*H$_3$, 46.4, *C*HBr, 40.3, *C*H$_2$N, 34.1, *C*H$_2$COO, 32.3, *C*H$_2$Br, 29.3, 29.2(2C), 29.1(2C), 29.0, 26.7, 24.9.

IR (cm^{-1}, KBr). 3289, 3076 ν(NH), 1727 ν(*C*═O, ester), 1654 ν(*C*═O, amide), 1558 δ(NH), 1178 ν(C−O), 594 ν(C−Br).

Elemental analysis for $C_{15}H_{27}Br_2NO_3$ (mm = 429.19). Calcd: C, 41.9, H, 6.34, N, 3.26. Found: C, 42.00, H, 6.08, N, 3.27.

*Methyl-11-{[2,3-bis(acetylthio)propanoyl]amino}undecanoate (**4**).* Triethylamine (785 μL, 5.63 mmol) was added to a solution of thioacetic acid (440 mg, 5.78 mmol) in acetone (25 mL) at –78 °C. To the resulting mixture, a solution of the dibromide derivative **3** (1.20 g, 2.80 mmol) in acetone (15 mL) was further added dropwise. After slowly warming up to room temperature, the mixture was stirred for 16 h. Then, the solvent was removed under reduced pressure, and the crude product was obtained by applying the standard workup procedure. Purification, carried out by column chromatography [silicagel, mobile phase, *n*-hexane/Et_2O/HOAc (100:100:0.2)] yielded 738 mg of the protected fatty acid ligand **4** as a colorless solid (yield, 63%).

^{1}H NMR (δ ppm, $CDCl_3$). 6.14 (br, 1H, N*H*), 4.08 (dd, $^3J_1$ = 6.3 Hz, $^3J_2$ = 8.7 Hz, 1H, C*H*S), 3.65 (s, 3H, OCH_3), 3.36 (dd, $^3J_1$ = 8.7 Hz, $^2J_2$ = 13.7 Hz, 1H, ½CH_2S), 3.23 (dd, $^3J_1$ = 6.1 Hz, $^2J_2$ = 13.7 Hz, 1H, ½CH_2S), 3.25–3.16 (m, 2H, CH_2N), 2.38 (s, 3H, CCH_3), 2.33 (s, 3H, CCH_3), 2.29 (t, ^3J = 7.6 Hz, 2H, CH_2COO), 1.65–1.55 (m, 2H, CH_2), 1.50–1.40 (m, 2H, CH_2), 1.33–1.21 (m, 12H, 6CH_2).

^{13}C NMR (δ ppm, $CDCl_3$). 195.7 (*C*OS), 195.2 (*C*OS), 174.3 (*C*OO), 169.3 (*C*ONH), 51.4 (O*C*H$_3$), 45.5 (*C*HS), 39.7 (*C*H$_2$N), 34.1 (*C*H$_2$COO), 30.4 (*C*CH$_3$), 30.3 (C*C*H$_3$), 29.4, 29.3(2C), 29.2, 29.1(2C), 29.0, 26.7, 24.9.

IR (cm^{-1}, KBr). 3278, 3094 ν(NH), 1739 ν(*C*═O, ester), 1692 ν(*C*═O, thioester), 1647 ν(*C*═O, amide), 1564 δ(NH), 1176 ν(C−O).

Elemental analysis for $C_{19}H_{33}NO_5S_2$ (mm, 419.61). Calcd: C, 54.39, H, 7.93, N, 3.34, S, 15.28. Found: C, 54.35, H, 8.02, N, 3.31, S, 15.28.

*11-[(2,3-Dimercaptopropanoyl)amino]undecanoic Acid (**H$_2$5**).* Hydrochloric acid (1.5 M, 3 mL) was added to a solution of **4** (500 mg, 1.19 mmol) in glacial acetic acid (6 mL), and the resulting mixture was heated for 45 min at 100 °C. After cooling to room temperature, the reaction mixture was diluted with 75 mL of water and the crude product was extracted according to the standard workup procedure. Purification was carried out by column chromatography [silicagel, mobile phase, $CHCl_3$/EtOAc/HOAc (80:20:1)] yielding the fatty acid ligand $\mathbf{H_2 5}$ as a colorless solid (298 mg, yield, 78%).

^{1}H NMR (δ ppm, $CDCl_3$). 6.48 (br, 1H, N*H*), 3.44 (ddd, $^3J_1$ = 4.7 Hz, $^3J_2$ = 6.6 Hz, $^3J_3$ = 10.6 Hz, 1H, C*H*SH), 3.28 (dq, $^3J_1$ = 1.4 Hz, $^3J_2$ = 7.2 Hz, 2H, CH_2N), 3.15 (ddd, $^3J_1$ = 4.8 Hz, $^3J_2$ = 8.6 Hz, $^2J_3$ = 13.7 Hz, 1H, ½CH_2SH), 2.95 (ddd, $^3J_1$ = 6.8 Hz, $^3J_2$ = 9.6 Hz, $^2J_3$ = 13.8 Hz, 1H, ½CH_2SH), 2.42 (d, ^3J = 10.6 Hz, 1H, CHS*H*), 2.34 (t, ^3J = 7.5 Hz, 2H, CH_2COO), 1.68 (dd, $^3J_1$ = 8.5 Hz, $^3J_2$ = 9.6 Hz, 1H, CH$_2$S*H*), 1.67–1.58 (m, 2H, CH_2), 1.57–1.48 (m, 2H, CH_2), 1.38–1.22 (m, 12H, 6CH_2).

^{13}C NMR (δ ppm, $CDCl_3$). 179.2 (*C*OO), 170.4 (*C*ONH), 46.0 (*C*HS), 40.3 (*C*H$_2$N), 34.1 (*C*H$_2$COO), 30.7 (*C*H$_2$S), 29.6, 29.5, 29.4, 29.3 (2C), 29.1, 27.0, 24.9.

IR (cm^{-1}, KBr). 3300, 3092 ν(NH), 2547 ν(SH), 1713 ν(*C*═O, acid), 1641 ν(*C*═O, amide), 1558 δ(NH).

Elemental analysis for $C_{14}H_{27}NO_3S_2$ (mm, 321.51). Calcd: C, 52.30, H, 8.46, N, 4.36, S, 19.95. Found: C, 52.33, H, 8.41, N, 4.31, S, 19.91.

ESI MS (*m*/*z*). 344 (100%) ($C_{14}H_{27}NO_3S_2Na^+$).

Preparation of 12-{[2,3-Bis(acetylthio)propanoyl]amino}dodecanoic Acid ($\mathbf{H_2 9}$). The synthesis of this ligand was conducted according to the reaction scheme illustrated in Figure 3.

*2,3-Bis(acetylthio)propionic Acid (**7**).* Triethylamine (3.65 mL, 26.2 mmol) and dibrompropionic acid (**1**) (3.00 g, 12.9 mmol), dissolved in acetone (10 mL), were added to a solution of thioacetic acid (2.05 g, 26.9 mmol) in acetone (20 mL), at –78 °C. After warming up slowly to room temperature, the mixture was stirred for 16 h, and then filtered off to eliminate precipitated ammonium salt. Finally, the solvent was removed under reduced pressure, and the resulting crude product was purified by column chromatography [silicagel, mobile phase, *n*-hexane/Et_2O/HOAc (60:40:1)] to afford a highly viscous, light yellow oil (**6**). Yield, 52% (1.49 g).

^{1}H NMR (δ ppm, $CDCl_3$). 4.34 (t, ^3J = 7.0 Hz, 1H, C*H*S), 3.42 (dd, $^3J_1$ = 7.8 Hz, $^2J_2$ = 13.9 Hz, 1H, ½CH_2S), 3.28 (dd, $^3J_1$ = 6.3 Hz, $^2J_2$ = 14.1 Hz, 1H, ½CH_2S), 2.40 (s, 3H, CH_3), 2.35 (s, 3H, CH_3).

^{13}C NMR (δ, $CDCl_3$). 194.5 (*C*OS), 192.8 (*C*OS), 175.1 (*C*OO), 45.1 (*C*HS), 30.4 (*C*H$_3$), 30.1 (*C*H$_3$), 29.9 (*C*H$_2$S).

*Methyl-12-{[2,3-bis(acetylthio)propanoyl]amino}dodecanoate (**8**).* To a solution of **6** (795 mg, 3.58 mmol) in dry tetrahydrofuran (25 mL), 1-hydroxybenzotriazole (535 mg, 3.96 mmol) was first added at –10 °C, then followed by a solution of DCC (775 mg, 3.76 mmol) in tetrahydrofuran (5 mL). The resulting mixture was stirred for 30 min at −10 °C. A solution composed of the ω-amino-fatty-acid-ester hydrochloride **7** (1.00 g, 3.76 mmol) and ethyl diisopropylamine (625 μL, 3.65 mmol) dissolved in chloroform (5 mL) was added slowly to the reaction mixture. After warming up slowly to room temperature, the mixture was further stirred for 16 h, and then the solvent was removed under reduced pressure. Purification of the crude product, carried out by column chromatography [silicagel, mobile phase, *n*-hexane/Et_2O/HOAc (100:100:0.2)], yielded 1.18 g of the protected fatty acid **8** as a colorless solid. (Yield, 76%).

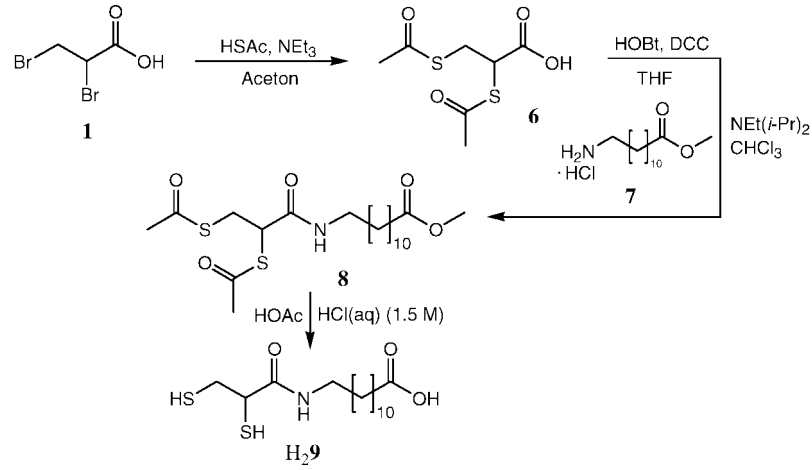

Figure 3. Reaction diagram for the synthesis of the ligand $\mathbf{H_2 9}$.

^{1}H NMR (δ ppm, $CDCl_3$). 6.14 (br, 1H, N*H*), 4.08 (dd, $^3J_1 = 6.1$ Hz, $^3J_2 = 8.7$ Hz, 1H, C*H*S), 3.65 (s, 3H, OCH_3), 3.36 (dd, $^3J_1 = 8.7$ Hz, $^2J_2 = 13.7$ Hz, 1H, ½CH_2S), 3.23 (dd, $^3J_1 = 6.2$ Hz, $^2J_2 = 13.6$ Hz, 1H, ½CH_2S), 3.25–3.16 (m, 2H, CH_2N), 2.38 (s, 3H, CCH_3), 2.33 (s, 3H, CCH_3), 2.29 (t, $^3J = 7.6$ Hz, 2H, CH_2COO), 1.66–1.55 (m, 2H, CH_2), 1.50–1.40 (m, 2H, CH_2), 1.34–1.20 (m, 14H, 7CH_2).

^{13}C NMR (δ ppm, $CDCl_3$). 195.7 (*C*OS), 195.2 (*C*OS), 174.3 (*C*OO), 169.3 (*C*ONH), 51.4 (O*C*H$_3$), 45.5 (*C*HS), 39.8 (*C*H$_2$N), 34.1 (*C*H$_2$COO), 30.4 (C*C*H$_3$), 30.3 (C*C*H$_3$), 29.4 (2C), 29.3 (2C), 29.2, 29.1 (2C), 29.0, 26.7, 24.9.

IR (cm^{-1}, KBr). 3293, 3091 ν(NH), 1736 ν(*C*═O, ester), 1715, 1703 ν(*C*═O, thioester), 1641 ν(*C*═O, amid), 1561 δ(NH), 1173 ν(C−O) cm^{-1}.

Elemental analysis for $C_{20}H_{35}NO_5S_2$ (mm, 433.63). Calcd: C, 55.40, H, 8.14, N, 3.23, S, 14.79. Found: C, 55.22, H, 8.09, N, 3.21, S, 15.16.

*12-{[2,3-Bis(acetylthio)propanoyl]amino}dodecanoic Acid (***$\mathbf{H_2 9}$***).* Conversion of **8** (800 mg, 1.84 mmol), carried out as described above for the ligand $\mathbf{H_2 5}$ afforded $\mathbf{H_2 9}$ as a colorless solid. Yield, 80% (496 mg).

^{1}H NMR (δ ppm, $CDCl_3$). 6.50 (br, 1H, N*H*), 3.45 (ddd, $^3J_1 = 4.7$ Hz, $^3J_2 = 6.7$ Hz, $^3J_3 = 10.6$ Hz, 1H, C*H*SH), 3.28 (dq, $^3J_1 = 1.1$ Hz, $^3J_2 = 7.1$ Hz, 2H, CH_2N), 3.15 (ddd, $^3J_1 = 4.8$ Hz, $^3J_2 = 8.4$ Hz, $^2J_3 = 13.8$ Hz, 1H, ½CH_2SH), 2.95 (ddd, $^3J_1 = 6.9$ Hz, $^3J_2 = 9.6$ Hz, $^2J_3 = 13.7$ Hz, 1H, ½CH_2SH), 2.42 (d, $^3J = 10.6$ Hz, 1H, CHS*H*), 2.34 (t, $^3J = 7.5$ Hz, 2H, CH_2COO), 1.68 (dd, $^3J_1 = 8.4$ Hz, $^3J_2 = 9.5$ Hz, 1H, CH$_2$S*H*), 1.66–1.58 (m, 2H, CH_2), 1.57–1.48 (m, 2H, CH_2), 1.38–1.22 (m, 14H, 7CH_2).

^{13}C NMR (δ ppm, $CDCl_3$). 179.2 (*C*OO), 170.2 (*C*ONH), 45.7 (*C*HS), 40.1 (*C*H$_2$N), 33.9 (*C*H$_2$COO), 30.4 (*C*H$_2$S), 29.4, 29.3 (3C), 29.1 (2C), 28.9, 26.8, 24.6.

IR (cm^{-1}, KBr). 3304, 3091 ν(NH), 2552 ν(SH), 1699 ν(*C*═O, acid), 1643 ν(*C*═O, amid), 1559 δ(NH).

Elemental analysis for $C_{15}H_{29}NO_3S_2$ (mm, 335.53).Calcd: C, 53.70, H, 8.71, N, 4.17, S, 19.11. Found:C, 53.90, H, 8.47, N, 4.03, S, 18.83.

ESI MS (*m*/*z*). 359 (100%) ($C_{15}H_{31}NO_3S_2Na^+$).

Synthesis of ω-[(Dithiocarbamato)amino] Fatty Acid Ligands. In the following, the symbol $\mathbf{Xn^\bullet}$ (where $\mathbf{X = Ba, 2K}$ and $\mathbf{n^\bullet = 10^\bullet, 11^\bullet}$) stands for the salt of the doubly deprotonated dithiocarbamato fatty acid ligand as represented by $\mathbf{n^\bullet}$. The monoanionic form of $\mathbf{n^\bullet}$, involving only a deprotonated sulfur atom at the dithiocarbamato group, is represented by the symbol **n** (**10**, **11**). The preparation of dithiocarbamato derivatives of fatty acid ligands was performed according to reactions reported in Figure 4.

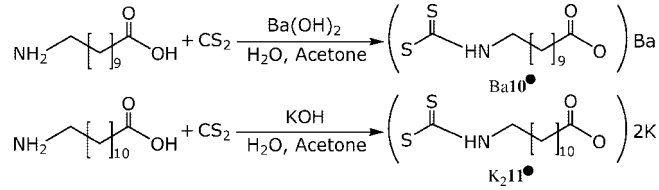

Figure 4. Reaction diagram for the synthesis of the ligands $\mathbf{Ba10^\bullet}$ and $\mathbf{K_2 11^\bullet}$.

*Barium 11-(carbodithioatoamino)undecanoate (***$\mathbf{Ba10^\bullet}$***).* Barium hydroxide (1.85 g, 5.88 mmol) was dissolved in 100 mL of water and, to the resulting solution, 11-aminoundecanoic acid (1.00 g, 4.9 mmol) and acetone (50 mL) were added under stirring. The reaction mixture was cooled at 0 °C, and carbon disulfide (0.50 mL, 6.37 mmol) was then added dropwise under stirring. The reaction was kept at 0 °C and stirred overnight. Precipitation of a colorless solid was observed, which was filtered off. Additional precipitate was collected after evaporation of the solvent under reduced pressure. The combined solids were then washed with CH_2Cl_2, ethanol, and diethyl ether to afford 1.1 g of $\mathbf{Ba10^\bullet}$ as a colorless solid. (Yield, 80%).

^{1}H NMR (δ ppm, D_2O). 3.76 (t, $^3J = 7.1$ Hz, 2H, CH_2COO), 3.68 (br, 1H, N*H*), 2.45 (t, $^3J = 7.4$ Hz, CH_2N), 1.81 (br, 2H, CH_2CH$_2$COO), 1.80 (br, 2H, CH_2CH$_2$NH), 1.57 (br, 6H, CH$_2$CH_2CH$_2$).

^{13}C NMR (δ ppm, D_2O). 209.7 (*C*S2), 184.6 (*C*OO), 48.4 (*C*H$_2$N), 40.7 (*C*H$_2$COO), 37.8, 31.9, 28.9, 28.8, 28.8, 28.7, 28.7, 27.8 (*C*H$_2$).

IR (cm^{-1}, KBr). 3280, 3070 ν(NH), 1706 ν(*C*═O, acid), 1501 δ(NH), 1471 ν(CNS, dithiocarbamate).

Elemental analysis for $C_{12}H_{21}NO_2S_2Ba$ (mm, 412.76). Found: C, 51.95, H, 8.36, N, 5.05, S, 23.11. Found: C, 52.04, H, 8.41, N, 5.31, S, 22.91.

ESI MS (*m*/*z*). 301 (100%) ($C_{12}H_{21}NO_2S_2$ Na^+). ES$^-$ MS (*m*/*z*). 277 (100%) ($C_{12}H_{21}NO_2S_2$).

*Dipotassium 12-(carbodithioatoamino)dodecanoate (***$\mathbf{K_2 11^\bullet}$***).* Potassium hydroxide (0.65 g, 10.2 mmol) was dissolved in 70 mL of water. To this solution, 12-aminoundecanoic acid (1.00 g, 4.64 mmol) and acetone (30 mL) were added under stirring. The solution was cooled at 0 °C, and carbon disulfide (0.5 mL, 6.37 mmol) was added dropwise under stirring. The resulting yellow solution was stirred overnight at 0 °C and then evaporated under reduced pressure to give a pale yellow solid. After washing with CH_2Cl_2, ethanol, and diethyl ether, $\mathbf{K_2 11^\bullet}$ (1.0 g) was collected as a colorless solid. (Yield, 75%).

^{1}H NMR (δ ppm, D_2O): 3.75 (t, $^3J = 7.1$ Hz, 2H, CH_2COO), 3.66 (br, 1H, N*H*), 2.41 (t, $^3J = 7.4$ Hz, CH_2N), 1.85 (br, 2H,

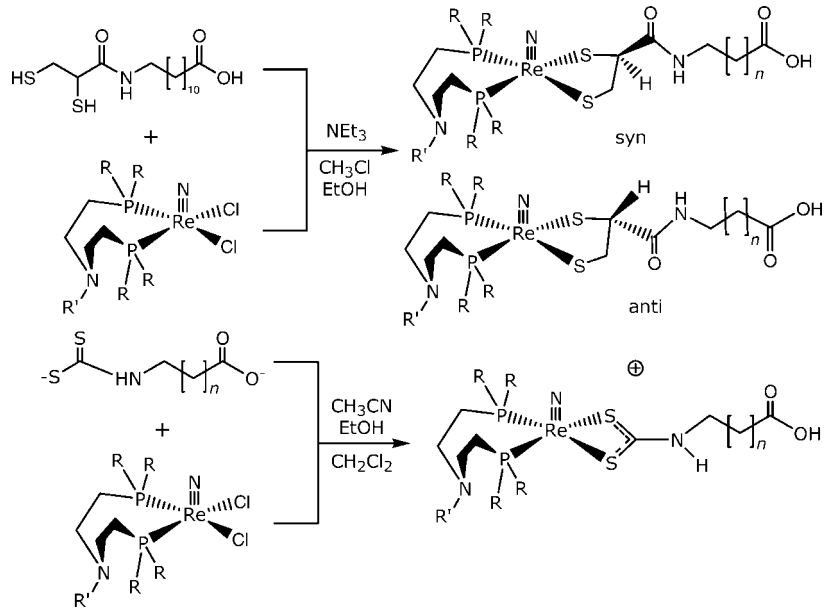

Figure 5. Reaction diagram for the synthesis of rhenium complexes with fatty acid ligands.

C*H*$_2$CH$_2$COO), 1.82 (br, 2H, C*H*$_2$CH$_2$NH), 1.55 (br, 7H, CH$_2$C*H*$_2$CH$_2$). ^{13}C NMR (δ ppm, D$_2$O). 209.7 (*C*S2), 184.5 (*C*OO), 48.4 (*C*H$_2$NH), 37.7 (*C*H$_2$COO), 29.2, 28.8, 28.7, 28.6, 27.8, 27.6, 26.3, 26.2 (*C*H$_2$).

IR (KBr). 3193, 2998 ν(NH), 1702 ν(*C*═O, acid), 1518 ν(NH), 1470 δ(CN) cm^{-1}.

Elemental analysis for $C_{13}H_{23}NO_2S_2K_2$ (327.64). C, 53.57, H, 8.65, N, 4.81, S, 22.00. Found: C, 53.90, H, 8.47, N, 4.83, S, 21.83.

ESI MS (*m*/*z*). MS (ES$^-$) 290 (100%) ($C_{13}H_{24}NO_2S_2$).

Synthesis of Rhenium Complexes with Fatty Acid Ligands. Rhenium complexes with fatty acid ligands were prepared at the macroscopic concentration level (>10^{-6} mol dm^{-3}) starting from the precursor complex [Re(N)(PNP7)Cl$_2$] and following the reaction scheme described in Figure 5. The precursor complex [Re(N)(PNP7)Cl$_2$] was obtained according to procedures reported previously (*13, 17*).

Re(N)(PNP7)(L) (L = **5**, **9***; PNP = PNP7).* A 2-fold molar excess of the appropriate dimercapto fatty acid ligand was added to 75 mg of the precursor complex [Re(N)(PNP7)Cl$_2$] suspended in a mixture of chloroform (10 mL) and ethanol (10 mL) containing triethylamine (55.0 μL, 395.0 μmol). The reaction mixture was heated under reflux and the course of the reaction monitored by TLC [silicagel, CHCl$_3$/EtOAc (1:1)]. Approximately after 2 h, the conversion of the precursor complex was almost complete. Then, the mixture was neutralized by 2 M citric acid, and the solvent removed under reduced pressures. The crude precipitate was washed with CH$_2$Cl$_2$, EtOH, and Et$_2$O. The resulting complexes were further purified through steps, *a* and *b*, carried out by column chromatography [(*a*) silicagel, mobile phase, CHCl$_3$/MeOH (10:1), (*b*) silicagel, CHCl$_3$/MeOH/acetone (20:1:1)]. After purification, the resulting product was washed with diethyl ether.

*[Re(N)(PNP7)(***5***)].* Yield, 72% (72 mg). Light-yellow solid collected as *syn*/*anti* stereoisomeric mixture.

^{1}H NMR (δ ppm, CDCl$_3$). 7.95–7.82 (m, 8H, C*H*$_{ar}$), 7.80 (t, ^3J = 5.6 Hz, 1H, N*H*$_{syn}$), 7.46–7.20 (m, 20H, C*H*$_{ar}$), 7.07–6.97 (m, 4H, C*H*$_{ar}$), 6.96–6.86 (m, 8H, C*H*$_{ar}$), 6.36 (t, ^3J = 5.8 Hz, 1H, N*H*$_{anti}$), 3.78 (dd, J_1 = 3.1 Hz, J_2 = 6.0 Hz, 1H, C*H*S$_{syn}$), 3.70 (dd, J_1 = 4.8 Hz, J_2 = 11.8 Hz, 1H, C*H*S$_{anti}$), 3.41–3.21 (m, 4H, ½C*H*$_2$S$_{syn}$, ½C*H*$_2$S$_{anti}$, C*H*$_2$NH$_{syn}$), 3.17 (q, ^3J = 6.6 Hz, 2H, C*H*$_2$NH$_{anti}$), 3.13–2.52 (m, 17H, 4C*H*$_2$N, 4C*H*$_2$P, ½C*H*$_2$S$_{syn}$), 2.52–2.43 (m, 1H, ½C*H*$_2$S$_{anti}$), 2.34 (t, ^3J = 6.9 Hz, 2H, C*H*$_2$COO$_{anti}$), 2.32 (t, ^3J = 6.9 Hz, 2H, C*H*$_2$COO$_{syn}$), 2.10 (s, 3H, NC*H*$_{3anti}$), 2.01 (s, 3H, NC*H*$_{3syn}$), 1.67–1.56 (m, 6H, 2C*H*$_{2syn}$, C*H*$_{2anti}$), 1.47–1.18 (m, 26H, 6C*H*$_{2syn}$, 7C*H*$_{2anti}$).

^{13}C NMR (δ ppm, CDCl$_3$). 177.3 (2C, 2*C*OO), 174.8 (*C*ONH$_{syn}$), 174.6 (*C*ONH$_{anti}$), 135–127 (48C$_{ar}$), 60.6 (d, $^3J_{CP}$ = 13.0 Hz, *C*HS$_{anti}$), 55.5 (d, $^3J_{CP}$ = 13.0 Hz, *C*HS$_{syn}$), 53.8 (*C*H$_2$NCH$_{2anti}$), 53.6 (3C, CH$_2$N*C*H$_{2,anti}$, *C*H$_2$NCH$_{2syn}$), 46.6 (N*C*H$_{3anti}$), 45.9 (N*C*H$_{3syn}$), 42.9 (d, $^3J_{CP}$ = 9.9 Hz, *C*H$_2$S$_{syn}$), 39.7 (*C*H$_2$NH$_{syn}$), 39.4 (*C*H$_2$NH$_{anti}$), 38.9 (d, $^3J_{CP}$ = 6.9 Hz, *C*H$_2$S$_{anti}$), 33.9 (*C*H$_2$COO$_{syn}$), 33.8 (*C*H$_2$COO$_{anti}$), 29.3, 29.2, 29.1, 29.0 (4C), 28.8 (4C), 28.7, 26.7, 26.6, 25.5 (d, $^1J_{CP}$ = 33.6 Hz, *C*H$_2$P$_{syn}$), 25.3 (d, $^1J_{CP}$ = 32.8 Hz, *C*H$_2$P$_{anti}$), 24.9 (d, $^1J_{CP}$ = 32.0 Hz, *C*H$_2$P$_{anti}$), 24.7 (2C), 24.0 (d, $^1J_{CP}$ = 32.0 Hz, *C*H$_2$P$_{syn}$).

^{31}P NMR (δ ppm, CDCl$_3$). 17.0 (d, $^2J_{PP}$ = 8.5 Hz, *syn*), 16.5 (d, $^2J_{PP}$ = 8.6 Hz, *anti*), 14.7 (d, $^2J_{PP}$ = 7.3 Hz, *syn*), 14.5 (d, $^2J_{PP}$ = 8.6 Hz, *anti*).

IR (cm^{-1}, KBr). 1723 ν(*C*═O, acid), 1627 ν(*C*═O, amide), 1531 δ(NH), 1436 ν(P-Ph), 1100 ν(Re-P), 1051 ν(Re≡N) cm^{-1}.

Elemental analysis for $C_{43}H_{56}N_3O_3P_2ReS_2$ (mm, 975.22). Calcd: C, 52.96, H, 5.79, N, 4.31, S, 6.58. Found: C, 52.70, H, 5.89, N, 4.21, S, 6.49.

*[Re(N)(PNP7)(***9***)].* Yield, 68% (67 mg). Light-yellow solid collected as a *syn*/*anti* stereoisomeric mixture.

^{1}H NMR (δ ppm, CDCl$_3$). 7.95–7.81 (m, 8H, C*H*$_{ar}$), 7.80 (t, ^3J = 5.8 Hz, 1H, N*H*$_{syn}$), 7.46–7.20 (m, 20H, C*H*$_{ar}$), 7.08–6.97 (m, 4H, C*H*$_{ar}$), 6.96–6.86 (m, 8H, C*H*$_{ar}$), 6.39 (t, ^3J = 5.6 Hz, 1H, N*H*$_{anti}$), 3.78 (dd, J_1 = 3.0 Hz, J_2 = 6.0 Hz, 1H, C*H*S$_{syn}$), 3.70 (dd, J_1 = 4.9 Hz, J_2 = 12.2 Hz, 1H, C*H*S$_{anti}$), 3.42–3.21 (m, 4H, ½C*H*$_2$S$_{syn}$, ½C*H*$_2$S$_{anti}$, C*H*$_2$NH$_{syn}$), 3.17 (q, ^3J = 6.6 Hz, 2H, C*H*$_2$NH$_{anti}$), 3.14–2.53 (m, 17H, 4C*H*$_2$N, 4C*H*$_2$P, ½C*H*$_2$S$_{syn}$), 2.53–2.44 (m, 1H, ½C*H*$_2$S$_{anti}$), 2.34 (t, ^3J = 7.4 Hz, 2H, C*H*$_2$COO$_{anti}$), 2.32 (t, ^3J = 7.3 Hz, 2H, C*H*$_2$COO$_{syn}$), 2.11 (s, 3H, NC*H*$_{3,anti}$), 2.02 (s, 3H, NC*H*$_{3syn}$), 1.68–1.56 (m, 6H, 2C*H*$_{2,syn}$, C*H*$_{2anti}$), 1.47–1.20 (m, 30H, 7C*H*$_{2syn}$, 8C*H*$_{2anti}$).

^{13}C NMR (δ ppm, CDCl$_3$). 177.1 (2C, 2*C*OO), 174.9 (*C*ONH$_{syn}$), 174.6 (*C*ONH$_{anti}$), 135–127 (48C$_{ar}$), 60.5 (d, $^3J_{CP}$ = 13.7 Hz, *C*HS$_{anti}$), 55.5 (d, $^3J_{CP}$ = 12.2 Hz, *C*HS$_{syn}$), 53.8 (*C*H$_2$NCH$_{2anti}$), 53.6 (3C; CH$_2$N*C*H$_{2anti}$, *C*H$_2$NCH$_{2syn}$), 46.6 (N*C*H$_{3anti}$), 45.9 (N*C*H$_{3syn}$), 42.9 (d, $^3J_{CP}$ = 9.9 Hz, *C*H$_2$S$_{syn}$), 39.8 (*C*H$_2$NH$_{syn}$), 39.5 (*C*H$_2$NH$_{anti}$), 38.9 (d, $^3J_{CP}$ = 6.1 Hz, *C*H$_2$S$_{anti}$), 33.8 (*C*H$_2$COO$_{syn}$), 33.7 (*C*H$_2$COO$_{anti}$), 29.4, 29.2,

29.1 (2C), 29.0 (2C), 28.9 (3C), 28.8 (2C), 28.7 (3C), 26.7, 26.5, 25.5 (d, $^1J_{CP}$ = 32.8 Hz, *C*H_2P_{syn}), 25.4 (d, $^1J_{CP}$ = 33.6 Hz, *C*H_2P_{anti}), 24.9 (d, $^1J_{CP}$ = 32.0 Hz, *C*H_2P_{anti}), 24.6 (2C), 24.0 (d, $^1J_{CP}$ = 32.0 Hz, *C*H_2P_{syn}).

^{31}P NMR (δ ppm, $CDCl_3$). 17.0 (d, $^2J_{PP}$ = 8.5 Hz, *syn*), 16.5 (d, $^2J_{PP}$ = 8.6 Hz, *anti*), 14.7 (d, $^2J_{PP}$ = 8.6 Hz, *syn*), 14.5 (d, $^2J_{PP}$ = 8.5 Hz, *anti*).

IR (cm^{-1}, KBr). 1724 ν(*C*═O, acid), 1630 ν(*C*═O, amide), 1529 δ(NH), 1435 ν(P-Ph), 1099 ν(Re-P), 1051, ν(Re≡N).

Elemental analysis for $C_{44}H_{58}N_3O_3P_2ReS_2$ (mm, 989.25). Calcd: C, 53.42, H, 5.91, N, 4.25, S, 6.48. Found: C, 53.00, H, 6.01, N, 4.1, S, 6.33.

*[Re(N)(PNP7)(**11**)]*$^+$. 23 mg (70.2 mmol) of the dithiocarbamate fatty acid ligand **$K_2$11$^•$** were added to a chloroform (10 mL)/ethanol (10 mL) mixture containing 150.0 mg (195.7 μmol) of [Re(N)(PNP7)Cl_2]. This mixture was refluxed for 1 h and then neutralized by addition of 2 M citric acid. After removal of the solvent under reduced pressure, the crude product was isolated by applying the standard workup procedure. The resulting light yellow solid was dissolved in acetone followed by addition of an ethanolic solution of [BF_4]Na (2.0 mg in 10 mL). The final product was recovered as BF_4 salt by slow evaporation of the solvent. Yield, 77% (80 mg).

^{1}H NMR (δ ppm, $CDCl_3$). 7.95–7.80 (m, 8H, CH_{ar}), 7.46–7.20 (m, 20H, CH_{ar}), 7.06–6.98 (m, 4H, CH_{ar}), 6.96–6.86 (m, 8H, CH_{ar}), 4.21 (br, 1H, N*H*), 3.73 (t, ^3J = 7.1 Hz, 2H, CH_2COO), 2.88 (t, ^3J = 7.4 Hz, CH_2N), 2.08 (s, 3H, NCH_3), 2.01 (br, 2H, CH_2CH_2NH), 1.85 (br, 2H, CH_2CH_2COO), 1.61 (br, 7H, CH_2CH_2CH_2).

^{13}C NMR (δ ppm, $CDCl_3$). 25.5 (d, $^1J_{CP}$ = 32.4 Hz, *C*H_2P), 24.9 (d, $^1J_{CP}$ = 32.0 Hz, *C*H_2P), 24.7 (2C), 24.0 (d, $^1J_{CP}$ = 32.0 Hz, *C*H_2P).

^{13}C NMR (δ ppm, D_2O). 317.7 (*C*S2), 184.5 (*C*OO), 58.7 (*C*H_2NH), 38.3 (*C*H_2COO), 30.2, 29.6, 29.0, 28.8, 27.1, 26.5, 26.0, 25.5 (*C*H_2).

^{31}P NMR (δ ppm, $CDCl_3$). 13.22 (d, $^2J_{PP}$ = 8.7 Hz), 12.5 (d, $^2J_{PP}$ = 8.9 Hz).

IR (cm^{-1}, KBr). 1725 ν(*C*═O, acid), 1632 ν(*C*═O, amide), 1524 δ(NH), 1099 ν(Re-P), 1051, ν(Re≡N) cm^{-1}.

Elemental analysis for $C_{42}H_{55}N_3O_2P_2ReS_2BF_4$ (mm, 1033.01). Calcd: C, 48.83, H, 5.37, N, 4.07, S, 6.21. Found: C, 48.22, H, 5.30, N, 3.98, S, 6.03.

Preparation of ^{99m}Tc-Complexes. A three-step procedure was employed for the preparation of ^{99m}Tc-complexes.

In all preparations, the first two steps were carried out as follows. Freshly generator eluted [$^{99m}TcO_4$]Na (0.250 mL, 50.0 MBq to 3.0 GBq) was added to a vial containing 5.0 mg of succinic dihydrazide (SDH) and 0.1 mg of $SnCl_2$ suspended in a mixture of 0.1 mL of saline and 1.0 mL of ethanol. The reaction solution was kept at room temperature for 30 min. Then, 1.0 mg of the appropriate diphosphane ligand (PNP = PNP3, PNP5), dissolved in 0.2 mL of ethanol was further added to the reaction vial, which was left at room temperature for an additional 30 min to afford the precursor metal fragment [^{99m}Tc(N)(PNP)]$^{2+}$.

The third step was conducted according to the procedure detailed below for each category of ^{99m}Tc-nitride complexes.

*[^{99m}Tc(N)(PNP)(L)] (L = **5**, **9**, PNP = PNP3).* The intermediate precursor [^{99m}Tc(N)(PNP)]$^{2+}$ was almost immediately converted into the final neutral complex [^{99m}Tc(N)(PNP)(L)] by adding an ethanolic solution of the appropriate dithiol ligand (**$H_2$5**, **$H_2$9**) (1.0 mg in 0.2 mL) to the reaction vial heated at 50 °C. Chromatographic characterization revealed the formation of an isomeric pair (**a** and **b**) of the same complex. Total yield determined by HPLC chromatography was approximately 95% (**a**, 45%; **b**, 50%). A representative HPLC chromatogram for this class of complexes is reported in Figure 6a.

[^{99m}Tc(N)(PNP)(L′)]$^+$ *(L′ = **10**, **11**, PNP = PNP3, PNP5).* Conversion of the precursor [^{99m}Tc(N)(PNP)]$^{2+}$ into the final monocationic complex [^{99m}Tc(N)(PNP)(L′)]$^+$ was similarly obtained by adding an ethanolic solution of the appropriate dithiocarbamate ligand (**Ba10$^•$**, **$K_2$11$^•$**) (1.0 mg in 0.2 mL) to the reaction vial heated at 60 °C. Yield, 96% (determined by HPLC). A representative HPLC chromatogram for this class of complexes is reported in Figure 6b.

Purification. To avoid interference of excess of reagents and free ligands on the biological evaluation of the new ^{99m}Tc-complexes, the following purification procedures were applied.

[^{99m}Tc(N)(PNP)(L)] Complexes. The reaction mixture was diluted with 8.0 mL of water and loaded onto a C18 SepPak cartridge (Waters) previously activated with ethanol (95%, 5.0 mL) and water (5.0 mL). The cartridge was rinsed with water (20.0 mL) and ethanol (60%, 3.0 mL). Finally, the desired ^{99m}Tc-complex was recovered by repeated elution with ethanol (0.4 mL followed by 3 × 1.0 mL). The first fraction was not utilized for biological studies. The remaining fractions were combined, and the total radiochemical purity (RCP) (measured by HPLC) was approximately 100% (**a**, 48%; **b**, 52%).

[^{99m}Tc(N)(PNP)(L′)]$^+$ *Complexes.* The reaction mixture was diluted with 8.0 mL of water and loaded onto a C18 SepPak cartridge (Waters) previously activated with ethanol (95%, 5.0 mL) and water (5.0 mL). The cartridge was rinsed with water (20 mL) and an ethanolic solution containing [N(*n*-Bu)$_4$]Br (10% w/w, 1.0 mL). The final ^{99m}Tc-complex was eluted by repeated elution with the same [N(*n*-Bu)$_4$]Br solution (1 × 0.4 mL followed by 3 × 1.0 mL). The first fraction was not utilized for biological studies. The remaining fractions were combined, and RCP (measured by HPLC) was approximately 100%.

Serum Stability. The selected ^{99m}Tc-complex (100 μL), purified as described above, were added to a propylene test tube (5.0 mL) containing rat serum (900 μL) or, alternatively, saline (900 μL). The resulting mixture was incubated at 37 °C for 2 h. RCP changes in time were monitored by TLC at 15, 30, 60, and 120 min. No significant changes of RCP were observed in saline. Conversely, a slow decrease of RCP occurred in rat serum (RCP, 82% at 15 min and 45% at 120 min after incubation).

In Vitro Reaction with Glutathione (GSH) and Cysteine. An aliquot of a stock aqueous solution of GSH (50.0 μL, 10.0 mM) was added to a propylene test tube (5.0 mL) containing a phosphate buffer (250.0 μL, 0.2 M, pH = 7.4), water (100.0 μL), and the appropriate ^{99m}Tc-complex (100.0 μL) purified as described above. The mixture was incubated at 37 °C for 2 h. For the blank, an equal volume of water was added in place of GSH solution. Aliquots of the resulting mixtures were withdrawn at 15, 30, 60, and 120 min after incubation, and analyzed by TLC chromatography. The complexes were found to be inert toward substitution by GSH.

An identical procedure was employed with aqueous solutions of cysteine hydrochloride (10.0 mM and 1.0 mM). ^{99m}Tc-complexes were found to be stable toward transchelation by cysteine.

Biological Evaluation. Animal experiments were performed according to the animal welfare regulations of the Italian and German local authorities.

Biodistribution Studies. Female Sprague–Dawley rats, weighing 200−250 g, were housed for 1 week under a 12 h light/12 h dark cycle with free access to food and water for subsequent biodistribution studies. Animals were fasted before experiments for 12 h and then anesthetized with an intramuscular injection of a mixture of ketamine (80 mg kg^{-1}) and xilazine (19 mg kg^{-1}). After purification, the selected ^{99m}Tc-complex was diluted with a physiological solution containing 5% human serum albumin (HSA). The final solution was less than 5% ethanol

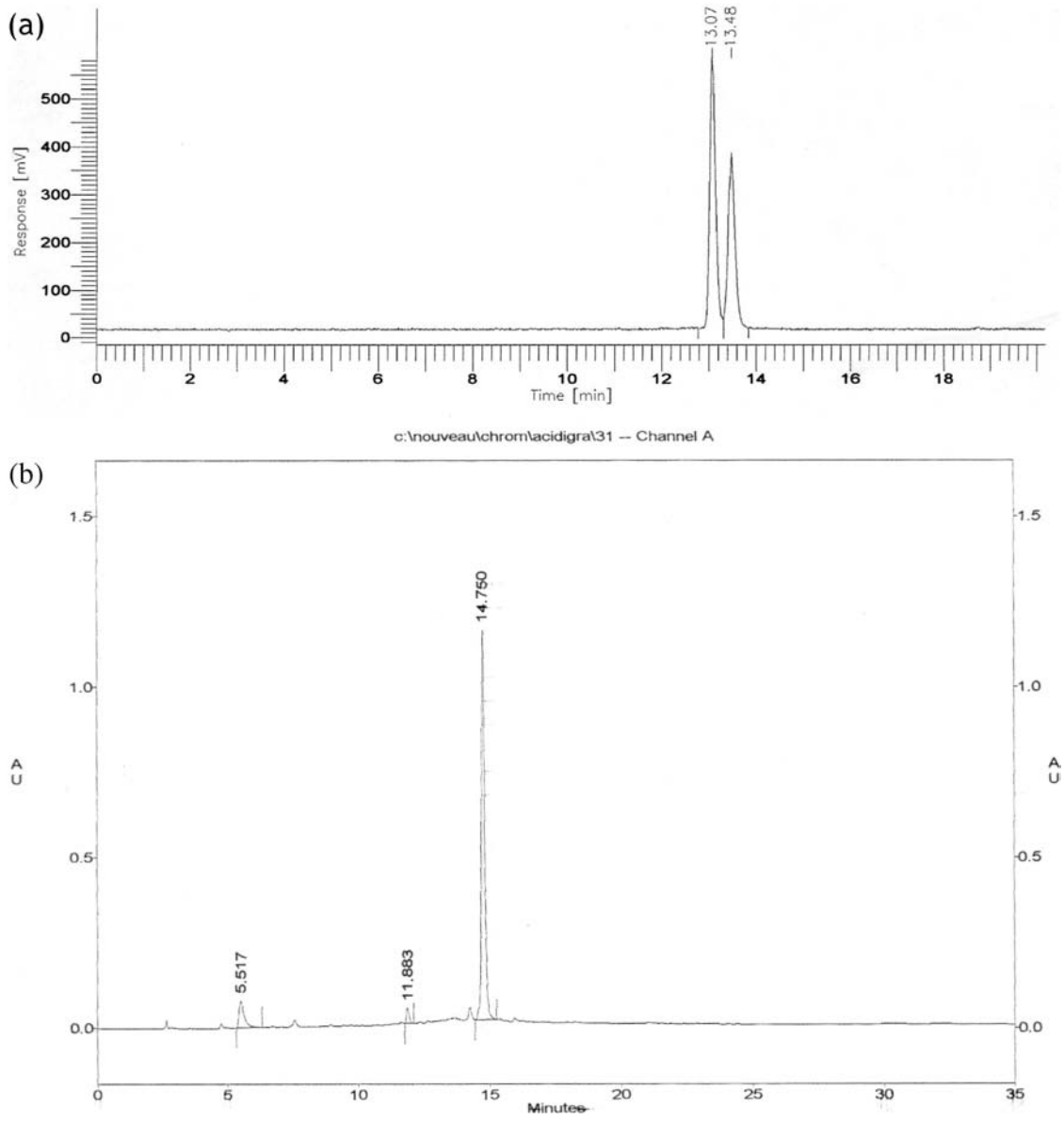

Figure 6. Representative HPLC chromatograms of complexes (a) [^{99m}Tc(N)(PNP3)(**9**)] and (b) [^{99m}Tc(N)(PNP5)(**10**)]$^{+}$.

content. Radioactivity (100 μL, 300−370 kBq) was administered through the jugular vein. The animals ($n = 3$) were sacrificed by dislocation at 5, 30, and 60 min time intervals postinjection. The blood was withdrawn from the heart through a syringe immediately after sacrifice and counted for the radioactivity. Organs were excised, rinsed with saline, weighed, and radioactivity determined with a NaI well counter. The percent injected dose per gram (%ID g^{-1}) for each organ and blood was calculated and results are reported in Tables 2 and 3.

Isolated Perfused Rat Heart Experiments. Female Wistar rats (250−350 g) were obtained from Charles River Laboratories, Sulzfeld, Germany.

Anesthesia was performed in two steps as follows. After resting for a short time in a chamber flushed with diethyl ether, deep anesthesia was achieved by intraperitoneal (i.p.) injection of 2–3 mL of urethane (15%). In addition, 1000 U/kg i.p. heparin was injected before opening the peritoneal cavity. Hearts were rapidly removed during continuous cooling and mounted vertically via the aorta on a perfusion cannula (this operation required less than 1 min after removal). Perfusion was immediately started according to the Langendorff technique with a modified KHB containing NaCl (116.0 mmol L^{-1}), KCl (4.6 mmol L^{-1}), $MgSO_4$ (1.2 mmol L^{-1}), KH_2PO_4 (1.2 mmol L^{-1}), $NaHCO_3$ (25.0 mmol L^{-1}), $CaCl_2$ (2.5 mmol L^{-1}), glucose (11.0 mmol L^{-1}), and pyruvate (2.0 mmol L^{-1}). The buffer was continuously bubbled with a mixture of 95% O_2/5% CO_2 (pH, 7.38−7.43), equilibrated with fatty-acid-free bovine serum albumin (BSA 0.1%, 14.9 μmol L^{-1}), and maintained at 37 °C in a water bath. Total coronary flow was measured using an ultrasonic transit-time flow-meter (T206 Transonic Systems Inc., Ithaca, NY) inserted in the arterial perfusion line and kept constant at 10 mL/min. Coronary perfusion pressure (CPP) was measured through a pressure transducer (Gould Statham, USA) connected to the perfusion cannula. Heart rate was calculated manually from a CPP printout. "Arterial" and "venous" perfusate samples collected anaerobically were analyzed for pO_2, pCO_2, pH, and HCO_3^- (AVL 990S, AVL Scientific Corporation, Roswell, GA) before each intervention.

The experimental procedure was performed as already described (*7*, *19*). In brief, Tc-99m labeled fatty acids were diluted in a ratio of 1:2 with KHB enriched with 6% BSA and left to equilibrate at room temperature for 30 min. After a period of 30 min to achieve hemodynamic stabilization of the beating heart, the selected ^{99m}Tc-labeled fatty acid complex was infused proximal to the perfusion cannula in a 1:1000 ratio. Starting with the infusion, the venous effluent perfusate was completely

Table 2. Biodistribution of [^{99m}Tc(N)PNP3)(L)]$^{0/+}$ Complexes in Normal Rats[a]

organ	time after injection (min) 5	30	60
	L = **5**		
blood	0.30 ± 0.05	0.12 ± 0.00	0.09 ± 0.01
heart	0.11 ± 0.03	0.03 ± 0.01	0.02 ± 0.00
lungs	0.22 ± 0.08	0.05 ± 0.01	0.04 ± 0.01
liver	3.10 ± 0.92	0.39 ± 0.00	0.29 ± 0.11
kidneys	0.74 ± 0.45	0.17 ± 0.09	0.08 ± 0.02
intestine	19.45 ± 2.17	14.25 ± 9.53	21.90 ± 14.99
	L = **9**		
blood	0.22 ± 0.08	0.08 ± 0.00	0.06 ± 0.01
heart	0.10 ± 0.03	0.02 ± 0.00	0.02 ± 0.00
lungs	0.13 ± 0.07	0.03 ± 0.01	0.03 ± 0.01
liver	9.92 ± 0.25	3.49 ± 1.14	2.38 ± 0.45
kidneys	1.38 ± 0.34	0.34 ± 0.07	0.38 ± 0.23
intestine	18.77 ± 0.86	20.77 ± 3.20	22.21 ± 10.97
	L = **10**		
blood	0.21 ± 0.01	0.06 ± 0.00	0.09 ± 0.05
heart	0.37 ± 0.00	0.23 ± 0.03	0.19 ± 0.01
lungs	0.30 ± 0.04	0.14 ± 0.01	0.15 ± 0.02
liver	14.55 ± 0.76	7.22 ± 0.08	2.90 ± 0.40
kidneys	2.07 ± 0.63	0.65 ± 0.04	0.42 ± 0.05
intestine	8.24 ± 0.50	17.42 ± 2.54	19.93 ± 0.48
	L = **11**		
blood	0.23 ± 0.01	0.04 ± 0.00	0.02 ± 0.00
heart	1.07 ± 0.02	0.97 ± 0.04	0.59 ± 0.03
lungs	0.37 ± 0.05	0.13 ± 0.01	0.10 ± 0.01
liver	18.28 ± 0.54	5.77 ± 0.09	1.75 ± 0.16
kidneys	3.35 ± 0.13	0.88 ± 0.06	0.49 ± 0.03
intestine	6.26 ± 0.80	20.62 ± 3.01	23.70 ± 0.39

[a] Values are expressed as % injected dose/gram (%ID/g) ± standard deviations (n = 5).

Table 3. Biodistribution of [^{99m}Tc(N)PNP5)(L)]$^{0/+}$ Complexes in Normal Rats[a]

organ	time after injection (min) 5	30	60
	L = **5**		
blood	0.34 ± 0.03	0.10 ± 0.02	0.07 ± 0.01
heart	0.13 ± 0.02	0.02 ± 0.00	0.01 ± 0.00
lungs	0.21 ± 0.09	0.04 ± 0.01	0.03 ± 0.00
liver	3.26 ± 0.52	0.41 ± 0.06	0.23 ± 0.08
kidneys	0.84 ± 0.25	0.27 ± 0.07	0.10 ± 0.02
intestine	20.45 ± 2.03	16.15 ± 6.50	19.90 ± 12.25
	L = **9**		
blood	0.28 ±0.05	0.06 ± 0.01	0.04 ± 0.01
heart	0.12 ± 0.04	0.04 ± 0.00	0.01 ± 0.00
lungs	0.17 ± 0.09	0.08 ± 0.01	0.02 ± 0.01
liver	8.72 ± 0.13	3.69 ± 0.09	2.59 ± 0.25
kidneys	1.55 ± 0.22	0.45± 0.06	0.32 ± 0.19
intestine	19.28 ± 0.80	23.02 ±5.08	20.96 ± 12.11
	L = **10**		
blood	0.15 ± 0.01	0.02 ± 0.00	0.02 ± 0.05
heart	0.48 ± 0.02	0.22 ± 0.01	0.18 ± 0.01
lungs	0.34 ± 0.06	0.16 ± 0.02	0.10 ± 0.03
liver	6.98 ± 0.76	3.22 ± 0.09	2.73 ± 0.17
kidneys	2.17 ± 0.23	0.51 ± 0.05	0.41 ± 0.01
intestine	19.88 ± 0.35	20.78 ± 3.01	19.07 ± 0.27
	L = **11**		
blood	0.15 ±0.02	0.03 ± 0.02	0.02 ± 0.00
heart	0.89 ± 0.00	0.53 ± 0.10	0.40 ± 0.00
lungs	0.30 ± 0.04	0.28 ± 0.10	0.19 ± 0.03
liver	5.31 ± 0.40	1.03 ± 0.22	0.30 ± 0.07
kidneys	2.18 ± 0.09	0.87 ± 0.10	0.36 ± 0.06
intestine	21.00 ± 0.43	17.73 ± 3.95	17.95 ± 8.08

[a] Values are expressed as % injected dose/gram (%ID/g) ± standard deviations (n = 5).

recovered in successive 15 s collecting periods. Infusion was stopped after 180 s, while continuing the collection of venous effluate for further 60 s to rinse out the residual radiolabeled substance from the coronary vessels, which were not taken up into the extravasal space. Then, perfusion was stopped and hearts instantaneously removed and separated into ventricles and atria. For input calculation (A_{in}) five 15-s perfusate samples were collected under identical radioactivity infusion and flow settings directly from the perfusion cannula in the absence of a heart. All perfusate and heart samples were measured with a gamma counter (Wallac 1470 Wizard, Perkin-Elmer, Freiburg, Germany). Only experiments in which the calculated amounts of counts per minute were in the expected experimental range (±20%) were included in the final analysis. Measurements were corrected for radionuclide decay.

Metabolic Analysis. After intravenous administration of ^{99m}Tc fatty acid complexes (50 MBq) into normal rats, the animals were sacrificed at 60 min postinjection, and intestine homogenates were obtained. Analysis was performed by HPLC as detailed before.

RESULTS AND DISCUSSION

Neutral and monocationic nitride Tc(V) complexes of the type ^{99m}Tc(N)(PNP)(L)]$^{0/+}$ (PNP = PNP3, PNP5; L = **5**, **9**, **10**, **11**) were successfully obtained by reacting the strong electrophilic precursor [^{99m}Tc(N)(PNP)]$^{2+}$ with bidentate chelating ligands bearing lateral fatty acid chains of different lengths (Figure 1a). These bifunctional ligands were prepared by appending a dimercapto or, alternatively, a dithiocarbamato chelating group to one terminus of a fatty acid chain containing eleven or twelve carbon atoms following the reaction schemes illustrated in Figures 2–4. Dimercapto derivatives (**5**, **9**) coordinated to the [^{99m}Tc(N)(PNP)]$^{2+}$ metal fragment as dianionic bidentate ligands, thus affording neutral complexes. Instead, dithiocarbamato derivatives (**10**, **11**) bound to the same fragment as monoanionic bidentate ligand, and consequently, the resulting complexes were monocationic. Structural characterization of Tc-99m complexes was carried out by comparison with the corresponding rhenium complexes. These compounds were synthesized starting from the mixed halogeno−phosphino complex [Re(N)(PNP)Cl$_2$]. The reaction scheme utilized for the synthesis of rhenium complexes is illustrated in Figure 5. In particular, rhenium complexes with the diphosphane ligand PNP7 were used as model compounds because of their ability to precipitate in a microcrystalline form that allowed an easier characterization by spectroscopic methods. Conversely, the diphosphane ligands PNP3 and PNP5 usually gave rise to oily compounds, which were difficult to isolate and characterize after chromatographic purification. Analytical and spectroscopic data, conjoined with results obtained previously with other similar dimercapto and dithiocarbamato complexes (*12, 20*), clearly showed that these complexes possess the usual asymmetrical structure with two different bidentate ligands coordinated to the same M≡N (M = Tc, Re) group as illustrated in Figure 5. Specifically, one diphosphane ligand PNP binds to the M≡N core through the two π-donor phosphorus atoms, while one dimercapto (or dithiocarbamato) ligand is linked to the same core through the two π-donor sulfur atoms. At both macroscopic and tracer levels, dimercapto complexes were isolated as a *syn*/*anti* isomeric pair. This isomerism arises from the relative orientation of the pendant fatty acid chain with respect to the M≡N group, and is related to the sp^3 tetrahedral hybridization of the carbon atom of the ethyl bridge connecting the two sulfur atoms and also linked to the fatty acid chain (Figure 5). When the fatty acid chain is tethered to the planar sp^2 carbon atom through the amino nitrogen atom of the dithiocarbamato moiety,

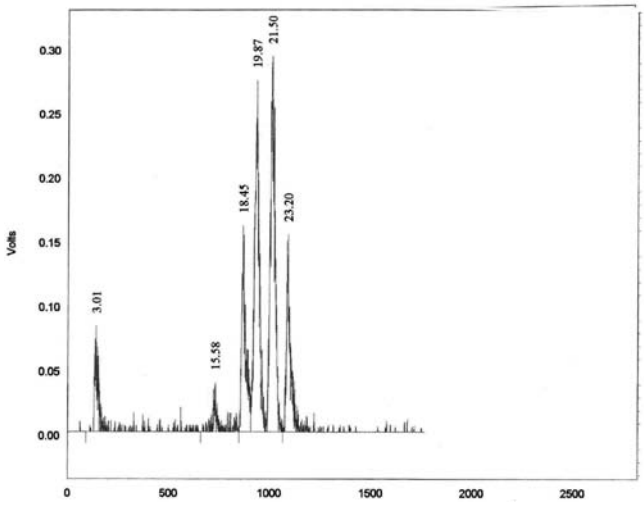

Figure 7. Representative HPLC analysis of intestine homogenates 60 min after intravenous administration of [^{99m}Tc(N)(PNP3)(**9**)] in normal rats.

this isomerism cannot be generated, and only a single species was isolated (Figure 5). Representative chromatographic profiles of these two types of fatty acid asymmetrical nitride Tc-99m complexes are reported in Figure 6.

Stability studies demonstrated that the Tc-99m complexes reported here are highly stable in solution and in human plasma, and resistant to transchelation by cysteine and glutathione.

Since liver washout was considered as a key issue for developing a suitable metabolic myocardial imaging agent, derivatives containing the ligand PNP7, bearing two phenyl groups on each of the two phosphorus atoms, were not further evaluated because of the poor liver washout showed by this category of complexes. Biological evaluation in animals was conducted only for Tc-99m complexes containing the diphosphane ligands PNP3 and PNP5. After purification, the resulting Tc-99m complexes were dissolved in saline containing 5% HSA. Biodistribution data (Tables 2 and 3) confirmed the fast and quantitative liver washout usually exhibited by this type of complexes. Elimination of liver activity into the intestine was relevant for all complexes as well as the rapid washout from lungs and blood. However, some significant heart uptake was found only for monocationic complexes with dithiocarbamato ligands, with neutral complexes being only slightly retained by the myocardium at 5 min post injection, and then completely washed out from this tissue after 30 min from injection. On the contrary, a slow elimination of myocardial activity was observed for monocationic complexes, and approximately 50% of the activity found in the myocardium at 5 min postinjection was still retained after 60 min from administration (Table 3).

In view of the facts that most of the radioactivity was excreted via the hepatobiliary pathway and concentration of radioactivity in urine was too low for a reliable metabolic analysis, we focused on metabolites in intestine homogenates. Metabolic stability of both neutral and monocationic Tc-99m fatty acid complexes described here was studied by HPLC analysis of intestine homogenates collected at 60 min postinjection. Results showed that these complexes undergo a significant metabolic transformation in the liver as illustrated in the representative example reported in Figure 7.

The monocationic complexes [^{99m}Tc(N)(PNP)(L)]$^+$ (PNP = PNP3; L = **10**, **11**) and the neutral complex [^{99m}Tc(N)(PNP5)(**9**)] were evaluated on the isolated heart model. As a reference, the ventricular extractions of the well-established iodinated metabolic cardiac tracer [^{123}I]IPPA, and of the monocationic myocardial flow tracers ^{99m}Tc-MIBI and the recently reported

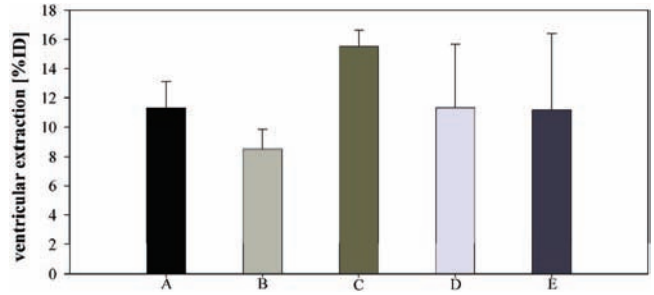

Figure 8. Ventricular extractions of the dodecanoic fatty acid complexes [^{99m}Tc(N)(PNP3)(**11**)]$^+$ (A) and [^{99m}Tc(N)(PNP5)(**9**)] (B), and of the metabolic tracer [^{123}I]IPPA (C) and flow tracers ^{99m}Tc-MIBI (D) and ^{99m}TcN-DBODC (E) as determined in the same isolated perfused rat heart model.

agent ^{99m}TcN-DBODC (*15*, *16*), were determined. As shown in Figure 8, the monocationic dodecanoic fatty acid derivative [^{99m}Tc(N)(PNP3)(**11**)]$^+$ achieved the highest ventricular extraction (11.33 ± 1.79% ID) among the newly synthesized compounds. For the undecanoic fatty acid complex [^{99m}Tc(N)(PNP3)(**10**)]$^+$ only a slightly lower extraction (10.24% ID) was obtained. As compared to the corresponding PNP3 analogue, the neutral PNP5 derivative [^{99m}Tc(N)(PNP5)(**9**)] clearly showed a lower ventricular extraction (8.52 ± 1.3% ID). The highest ventricular extraction was measured for the tracer [^{123}I]IPPA (15.51 ± 1.10% ID) (*7*). The myocardial extractions of the new agent ^{99m}TcN-DBODC and of ^{99m}Tc-MIBI were 11.20 ± 5.19% ID and 11.34 ± 4.33% ID, respectively and, thus, fall in the same range of the monocationic Tc-99m fatty acid complexes reported here.

The so-called "metal fragment approach" may be worth consideration as an extension of the original concept of the "bifunctional approach", which is commonly used for designing new radiolabeled diagnostic probes, when applied to the labeling of bioactive molecules with metallic radioisotopes. The introduction of this more sophisticated chemical method was mostly prompted by the need to obtain high specific activity labeling in preparations of radiotracers for monitoring in vivo receptor density. The key feature of the metal fragment approach lies in the use of metallic functional groups possessing an intrinsically high electronic stability but that display a selective reactivity toward specific classes of coordinating atoms and ligands through substitution reactions. The metallic group [^{99m}Tc(N)(PNP)]$^{2+}$, composed of a Tc≡N core bound to a bidentate diphosphane ligand, nicely represents this category of molecular moieties that can be conveniently employed for the high specific activity labeling of bioactive molecules. It is highly stable toward redox reactions but interacts selectively only with ligands containing soft π-donor atoms as a result of its strong electrophilic character. This means that a biomolecule having a suitable set of π-donor atoms is capable of coordinating readily to this fragment.

In the present study, the above strategy was applied to the design and synthesis of a new class of Tc-99m radiopharmaceuticals for monitoring fatty acid metabolism in myocardial tissue. Since similar studies on Tc-99m-labeled fatty-acid complexes with different chelating systems showed that derivatives incorporating a C12 carbon chain exhibited the highest myocardial uptake (*7*, *9*, *20*), C11 and C12 chain lengths were selected here as the most appropriate. A possible explanation for this observation could be found by considering the greater sterical size of the chelating system containing the metal atom as compared to iodophenyl substituents. In fact, it was calculated that ^{99m}Tc compounds substituted with C11 or C12 fatty acids ligands have approximately the same size of ω-(*p*-[^{123}I]iodophenyl fatty acids. Furthermore, it should be noted that prolongation

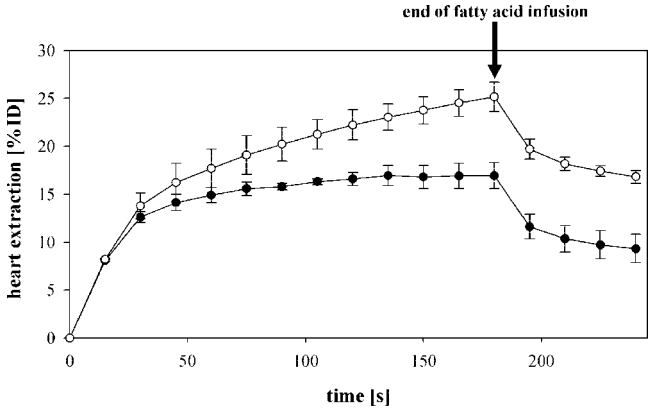

Figure 9. Extraction kinetic curves of the dodecanoic fatty acid neutral complex [^{99m}Tc(N)(PNP5)(**9**)] (•) and [^{123}I]IPPA (○).

of the carbon chain length usually does not prevent the competitive fast and high liver uptake of labeled fatty acids.

The choice of the specific diphosphane ligand was dictated by the requirement to achieve a rapid and quantitative liver washout necessary to improve target-to-background ratio. All biological data available so far on Tc-99m complexes with PNP3 and PNP5 (*10*, *11*, *14*, *16*, *20*, *22*) clearly indicate that these ligands usually impart to the resulting complexes the property of being rapidly washed out from the liver.

Biodistribution studies on [^{99m}Tc(N)(PNP)(L)]$^{0/+}$ (PNP = PNP3, PNP5) complexes reported here sharply confirmed this prediction. Both neutral and monocationic species exhibit a fast liver elimination associated with a rapid washout from blood and lungs. Unfortunately, these favorable properties were counteracted by the relatively low heart uptake of these complexes, which did not exceed 1.07% of injected activity. In particular, only monocationic derivatives showed some significant myocardial accumulation and retention. Conversely, neutral complexes were rapidly washed out from the heart after a first slight accumulation at 5 min postinjection. Generally, dodecanoic fatty acid derivatives showed higher cardiac uptake than undecanoic analogues.

The above findings contrasted with results obtained in isolated perfused rat heart experiments. This model provides a suitable method for evaluating the uptake and extraction of radiolabeled compounds without the presence of disturbing effects always occurring in whole animal studies, e.g., effects of stress having an influence on the endocrinological system that regulates metabolic processes. Based on bidistribution results, the two monocationic complexes [^{99m}Tc(N)(PNP3)(**10**)]$^+$ and [^{99m}Tc(N)(PNP3)(**11**)]$^+$, which showed the highest heart accumulation, and the neutral complex [^{99m}Tc(N)(PNP5)(**9**)] were evaluated in the isolated rat heart model. Even though the well-established iodinated fatty acid tracer [^{123}I]IPPA achieved the highest outcome, some of the new Tc-99m fatty acid complexes showed remarkable values of myocardial extraction. In particular, there was almost no difference in the incorporated activity between the monocationic fatty acid complexes [^{99m}Tc(N)(PNP3)(**11**)]$^+$ and [^{99m}Tc(N)(PNP3)(**10**)]$^+$ and the recently discovered flow tracer ^{99m}TcN-DBODC. The similarity between the extraction values of ^{99m}Tc-MIBI and ^{99m}TcN-DBODC had been demonstrated previously in animal studies (*15*, *16*).

The present study on the isolated heart also offered a simple possibility to investigate myocardial first pass extraction kinetics. This is demonstrated in Figure 9, which reports a more detailed analysis of the uptake and extraction kinetics of the neutral derivative [^{99m}Tc(N)(PNP5)(**9**)] as compared to [^{123}I]IPPA. In the rapid, almost linear initial uptake occurring during the first 30 s of tracer infusion, both radiolabeled compounds showed a similar amount of uptake (12.60 ± 0.56% ID for [^{99m}Tc(N)(PNP5)(**9**)] vs 13.78 ± 1.32% ID for [^{123}I]IPPA). In the subsequent period of tracer infusion, corresponding to the net accumulation by the myocardium including influx, efflux, and intracellular metabolism (*23*), the extraction kinetic curve of [^{99m}Tc(N)(PNP5)(**9**)] continued to increase but with a perceptible lower slope as compared to [^{123}I]IPPA. This fact points to an accelerated efflux of the evaluated Tc-99m fatty acid analogue, which could be, presumably, attributed to a disturbed recognition by intracellular enzymes of fatty acid transport and metabolism. The observed increased efflux was also evidenced by a faster washout of the radiolabeled ^{99m}Tc compound out of the myocardium at the end of infusion. Whereas during the first 60-s period of labeled fatty acid perfusion only 8.35% ID of [^{123}I]IPPA left the infused heart, this value increased up to 7.62% ID for [^{99m}Tc(N)(PNP5)(**9**)]. Thus, at the end of the infusion process, only 33.17% of [^{123}I]IPPA activity washed out from perfused heart, while this washout was 44.97% for [^{99m}Tc(N)(PNP5)(**9**)].

The apparently altered metabolic behavior of ^{99m}Tc-labeled fatty acid was also confirmed by metabolic studies performed on intestine samples. These data revealed that these complexes are quantitatively metabolized in the liver. Interestingly, this process did not transform each Tc-99m complex to a single metabolite, but rather to a mixture of undetermined species, a result that is difficult to be attributed to a specific metabolic pathway.

The comparative analysis of the kinetic behavior of [^{99m}Tc(N)(PNP5)(**9**)] and [^{123}I]IPPA may allow a tentative interpretation of biodistribution data in rats. As mentioned above, the fast washout of [^{99m}Tc(N)(PNP5)(**9**)] suggests that the resulting radiolabeled fatty acid has partially lost its original biological properties, thus becoming a poor substrate for cardiac enzymatic activity. This may readily explain the in vivo behavior of neutral complexes characterized by some initial uptake followed by a rapid washout. Evidently, this behavior is mostly driven only by passive diffusion as a consequence of the lack of an efficient metabolic trapping. Conversely, the situation appears substantially different for monocationic complexes in which the presence of a positive charge permits their blockage on the mitochondrial membrane of myocites through the action of a well-established mechanism (*24*, *25*). However, further studies are required to assess whether this retention could favor an easier recognition of the labeled fatty acid by cardiac enzymes and promote some metabolic activity.

CONCLUSIONS

The design and preparation of a new class of asymmetrical nitride Tc-99m complexes incorporating a lateral fatty acid chain have been successfully carried out. The selective affinity of the strong electrophilic metal fragment [^{99m}Tc(N)(PNP)]$^{2+}$ allowed us to obtain the final radiopharmaceuticals in high specific activity and almost quantitative yields (>95%), thus giving further support to previous studies showing the strong efficiency of this fragment as a labeling moiety for small biomolecules.

However, biological evaluation of the resulting complexes in an isolated perfused heart model showed that the tethering of the metal fragment to the fatty acid chain caused some significant perturbation of its original biological properties. In particular, the comparison between the behavior of the metabolic tracer [^{123}I]IPPA and the neutral complex [^{99m}Tc(N)(PNP5)(**9**)], in which the potential effect of the presence of a monopositive charge on the heart uptake mechanism was ruled out, clearly demonstrated that recognition of the labeled fatty acid as a substrate for β-oxidation was partially hampered, presumably as a result of some steric hindrance brought about by the metallic moiety onto the bioactive molecule. Additional studies are

required to assess whether the metabolic activity could be restored by increasing the separation between the metal fragment and the fatty acid chain through the insertion of some suitable linker.

ACKNOWLEDGMENT

Financial support for this work by Nihon Medi-Physics, Tokyo, Japan is gratefully acknowledged.

LITERATURE CITED

(1) Corbett, J. R. (1999) Fatty acid for imaging myocardial metabolism. *Semin. Nucl. Med. 29*, 237–258.

(2) Schelbert, H. R. (2000) PET contributions to understanding normal and abnormal cardiac perfusion and metabolism. *Ann. Biomed. Eng. 28*, 922–929.

(3) Mach, R. H., Kung, H. F., Jungwiwattanaporn, P., and Guo, Y. Z. (1991) Synthesis and bioditribution of a new class of 99mTc-labeled fatty acid analogs for myocardial imaging. *Int. J. Appl. Radiat. Instrum. B 18*, 215–226.

(4) Magata, Y., Kawaguchi, T., Ukon, M., Yamamura, N., Uehara, T., Ogawa, K., Arano, Y., Temma, T., Mukai, T., Tadamura, E., and Saji, H. (2004) A Tc-99m labeled long fatty ac-id derivative for myocardial imaging. *Bioconjugate Chem. 15*, 389–393.

(5) Chu, T., Zhang, Y., Liu, X., Wang, Y., Hu, S., and Wang, X. (2004) Synthesis and biodis-tribution of 99mTc-carbonyltechnetium-labeled fatty acid. *Appl. Radiat. Isot. 60*, 845–850.

(6) Jung, C. M., Kraus, W., Leibnitz, P., Pietzsch, J., Kropp, J., and Spies, H. (2002) Synthe-ses and first crystal structures of rhenium complexes derived from ϖ-functionalized fatty acid as model compounds of technetium tracers for myocardial metabolism imaging. *Eur. J. Inorg. Chem. 7*, 1219–1225.

(7) Walther, M., Jung, C. M., Bergmann, R., Pietzsch, H. J., Rode, K., Fahmy, K., Mirtschink, P., Stehr, S., Heintz, A., Wunderlich, G., Kraus, W., Pietzsch, H. J., Kropp, J., Deußen, A., and Spies, H. (2007) Synthesis and biological evaluation of a new type of 99mTechnetium-labeled fatty acid for myocardial metabolism imaging. *Bioconjugate Chem. 18*, 216–230.

(8) Mirtschink, P., Stehr, S. N., Pietzsch H-J., Bergmann, R., Pietzsch, J., Wunderlich, G., Heintz, A. C., Kropp, J., Spies, H., Kraus, W., Deussen, A. and Walther, M. (2007) Modified "4 + 1" mixed ligand technetium labeled fatty acids for myocardial imaging: evaluation of myocardial uptake and biodistribution. *Bioconjugate Chem.* Accepted for publication.

(9) Uehara, T., Uemura, T., Hirabayashi, S., Adachi, S., Odaka, K., Akizawa, H., Magata, Y., Irie, T., and Arano, Y. (2007) Technetium-99m labeled long chain fatty acid analogues metabolized by beta oxidation in the heart. *J. Med. Chem. 50*, 543–549.

(10) Boschi, A., Bolzati, C., Uccelli, L., Duatti, A., Benini, E., Refosco, F., Tisato, F., and Pif-fanelli, A. (2002) A class of asymmetrical nitrido technetium-99m complexes as heart imaging agents with improved biological properties. *Nucl. Med. Commun. 23*, 689–693.

(11) Boschi, A., Uccelli, L., Bolzati, C., Duatti, A., Sabba, N., Moretti, E., Di Domenico, G., Zavattini, G., Refosco, F., and Giganti, M. (2003) Synthesis and biological evaluation of monocationic asymmetric 99mTc-nitride heterocomplexes showing high heart uptake and improved imaging properties. *J. Nucl. Med. 44*, 806–814.

(12) Bolzati, C., Refosco, F., Cagnolini, A., Tisato, F., Boschi, A., Duatti, A., Uccelli, L., Dolmella, A., Marotta, E., and Tubaro, M. (2004) Synthesis, solution-state and solid-state structural characterization of monocationic nitrido heterocomplexes [M(N)(DTC)(PNP)]22 (M = 99Tc, Re; DTC = dithiocarbamate; PNP = heterodiphos-phane). *Eur. J. Inorg. Chem. 9*, 1902–1913.

(13) Bolzati, C., Boschi, A., Uccelli, L., Tisato, F., Refosco, F., Cagnolini, A., Duatti, A., Prakash, S., Bandoli, G., and Vittadini, A. (2002) Chemistry of the strong electrophilic metal fragment $[^{99}Tc(N)(PXP)]^{2+}$ (PXP = diphosphine ligand). A novel tool for the se-lective labeling of small molecules. *J. Am. Chem. Soc. 124*, 11468–11479.

(14) Boschi, A., Duatti, A., and Uccelli, L. (2005) Development of technetium-99m and rhe-nium-188 radiopharmaceuticals containing a terminal metal-nitrido multiple bond for diagnosis and therapy. *Top. Curr. Chem. 252*, 85–101.

(15) Hatada, K., Riou, L. M., Ruiz, M., Yamamichi, Y., Duatti, A., Lima, R. L., Goode, A. R., Watson, D. D., Beller, G. A., and Glover, D. K. (2004) 99mTc-N-DBODC5, a new myocardial perfusion imaging agent with rapid liver clearance: comparison with 99mTc-sestamibi and 99mTc-tetrofosmin in rats. *J. Nucl. Med. 45*, 2095–2101.

(16) Hatada, K., Ruiz, M., Riou, L. M., Lima, R. L., Goode, A. R., Watson, D. D., Beller, G. A., and Glover, D. K. (2006) Organ biodistribution and myocardial uptake, washout, and redistribution kinetics of Tc-99m N-DBODC5 when injected during vasodilator stress in canine models of coronary stenoses. *J. Nucl. Cardiol. 13*, 779–790.

(17) Tisato, F., Refosco, F., Porchia, M., Bolzati, C., Bandoli, G., Dolmella, A., Duatti, A., Boschi, A., Jung, C. M., Pietzsch, H-J., and Kraus, W. (2004) The crucial role of the di-phosphine heteroatom X in the stereochemistry and stabilization of the substitution-inert $[M(N)(PXP)]^{2+}$ m etal fragments (M = Tc, Re; PXP = diphosphine ligand). *Inorg. Chem. 43*, 8617–8625.

(18) Mertens, J., Eersels, J., and Vanryckeghem, W. (1987) New high yield Cu(I) assisted ^{123}I radioiodination of 15(p-I-phenyl)-9-methyl pentadecanoic acid, a potential myocar-dial tracer. *Eur. J. Nucl. Med. 13*, 159–60.

(19) Heintz, A. C., Jung, C. M., Stehr, S. N., Mirtschink, P., Walther, M., Pietzsch, J., Berg-mann, R., Pietzsch, H-J., Spies, H., Wunderlich, G., Kropp, J., and Deussen, A. (2007) Myocardial uptake and biodistribution of newly designed technetium labeled fatty acid analogues. *Nucl. Med. Commun. 28*, 637–647.

(20) Bolzati, C., Benini, E., Cazzola, E., Jung, C, Tisato, F., Refosco, F., Pietzsch, H. J., Spies, H., Uccelli, L., and Duatti, A. (2004) Synthesis, characterization, and biological evaluation of neutral nitrido technetium(V) mixed ligand complexes containing di-thiolates and aminodiphosphines. A novel system for linking technetium to bio-molecules. *Bioconjugate Chem. 15*, 628–637.

(21) Boschi, A., Uccelli, L., Duatti, A., Bolzati, C., Refosco, F., Tisato, F., Romagnoli, R., Baraldi, P. G., Varani, K., and Borea, P. A. (2003) Asymmetrical nitrido tc-99m hetero-complexes as potential imaging agents for benzodiazepine receptors. *Bioconjugate Chem. 14*, 1279–1288.

(22) Bolzati, C., Mahmood, A., Malago, E., Uccelli, L., Boschi, A., Jones, A. G., Refosco, F., Duatti, A., and Tisato, F. (2003) The [(99m)Tc(N)(PNP)](2+) metal fragment: a techne-tium-nitrido synthon for use with biologically active molecules. The N-(2-methoxyphenyl)piperazyl-cysteine analogues as examples. *Bioconjugate Chem. 14*, 1231–1242.

(23) Stremmel, W., and Berk, P. D. (1986) Hepatocellular influx of [^{14}C]oleate reflects mem-brane transport rather than intracellular metabolism or binding. *Proc. Natl. Acad. Sci. U.S.A 83*, 3086–3090.

(24) Piwnica-Worms, D., Kronauge, J. F., and Chiu, M. L. (1990) Uptake and retention of hexakis (2 methoxyisobutyl isonitrile) technetium(I) in cultured chick myocardial cells. Mitochondrial and plasma membrane potential dependence. *Circulation 82*, 1826–1838.

(25) Piwnica-Worms, D. P., Kronauge, J. F., LeFurgey, A., Backus, M., Hockett, D., Ingram, P., Lieberman, M., Holman, B. L., Jones, A. G., and Davison, A. (1994) Mitochondrial localization and characterization of 99Tc-sestamibi in heart cells by electron probe X-ray microanalysis and 99Tc-NMR spectroscopy. *Magn. Reson. Imaging 12*, 641–652.

BC7002378

PEGylated Dendrimers with Core Functionality for Biological Applications

Steven J. Guillaudeu,[†] Megan E. Fox,[†] Yarah M. Haidar,[†] Edward E. Dy,[‡] Francis C. Szoka,[‡] and Jean M. J. Fréchet*,[†]

College of Chemistry, University of California, Berkeley, California 94720-1460, and Department of Biopharmaceutical Sciences and Pharmaceutical Chemistry, University of California, San Francisco, California 94143-0446. Received July 14, 2007; Revised Manuscript Received November 29, 2007

The synthesis of a variety of core functionalized PEGylated polyester dendrimers and their in vitro and in vivo properties are described in this report. These water-soluble dendrimers have been designed to carry eight functional groups on their dendritic core for a variety of biological applications such as drug delivery and in vivo imaging as well as eight solubilizing groups. Using a common symmetrical aliphatic ester dendritic core and trifunctional amino acid moieties, a library of dendrimers with phenols, alkyl alcohols, alkynes, ketones, and carboxylic acid functionalities has been synthesized without the need for column chromatography. The amines were PEGylated, leaving the other functionality of the amino acid available for further manipulation such as the attachment of drugs and/or labels. Radiolabeling experiments with the PEGylated dendrimers showed that they had a long circulation half-life in mice, confirming the potential of this class of dendrimers for therapeutic and/or diagnostic applications. A carboxylic acid functionalized dendrimer was elaborated to carry doxorubicin bound via a hydrazone bond. The drug-loaded carrier accumulated more in tumors and less in healthy organs than the clinically used PEGylated liposomal formulation Doxil. The efficient synthesis, high versatility, and favorable biological properties make these PEGylated polyester dendrimers promising structures for therapeutic and/or imaging applications.

INTRODUCTION

Dendritic polymers are currently being evaluated for many in vivo biological applications including drug delivery, tissue growth scaffolding, imaging (magnetic resonance, near-infrared, positron emission), and boron−neutron capture therapy (*1–4*). PEGylated dendrimers, in which a multifunctional dendritic core is conjugated to polyethylene glycol (PEG, or polyethylene oxide) chains, are an interesting subclass of dendritic polymers for these applications (*5*). Various PEG−dendrimer hybrids have shown lower toxicity and hemolytic properties, long blood circulation times, low organ accumulation, and high accumulation in tumor tissue due to the enhanced permeation and retention (EPR) effect (*6–14*).

PEG−dendrimer hybrids can be constructed by two basic architectures: PEG (linear or branched) can be attached to the apex (*10*) (Figure 1a) or the peripheral groups (*15*) (Figure 1b and c) of dendrimers. In the former, the dendrimer periphery (if compatible with the solvent) is more exposed to the surrounding environment, while in the latter, a PEG shell is the most solvent accessible. From the reported works cited above, it appears that both show great promise for biotechnological applications, but the latter has shown the best performance with respect to long blood circulation half-lives and low organ accumulation (*7–9, 12, 16*). In our previous work exploring PEG−dendrimer hybrids (*10, 12, 15–21*), we have found that a nontoxic, biodegradable, asymmetric polyester dendrimer with eight PEG chains of 5000 Da molecular weight and multiple sites for drug attachment, a bow-tie dendrimer, is efficient at delivering the chemotherapeutic agent doxorubicin (Dox) to C26 tumors in mice; this led to complete tumor regression in all of the treated mice with only a single dose (*16*). The effective tumor therapy with the bow-tie is believed to stem from the highly branched dendritic architecture that lowers the rate of filtration through renal membranes and the PEG−shell/drug−core structure that shields the therapeutic from recognition by the reticuloendothelial system (*12, 16*). Such a system, with a PEG shell and functional core, may prove useful in many of the above applications where a long circulation time, accumulation at leaky blood vessel sites such as in tumors, inflammation sites, or arterial injuries, and biocompatibility and biodegradability are desired. Dendrimers with a PEGylated periphery that have accessible functionality on the dendrimer have been produced by substoichiometrically PEGylating amine-terminated dendrimers such as PAMAM or polylysine (*7–9, 22–28*), by using elegant control of the reactivity on melamine dendrimers (*6*), through ether formation on bifunctional polyether dendrimers (*18, 19*), and by PEGylating an asymmetrically protected ester dendrimer (*15*).

We now describe the high-yielding column-free synthesis of a family of PEGylated ester dendrimers bearing some analogy in terms of functionality and architecture to the bow-tie dendrimer. However, these new dendrimers are symmetric about the core, with different multifunctional handles easily incorporated at their periphery, thereby increasing their ease of preparation and versatility for potential biomedical applications. One generation of bis-2,2-hydroxymethylpropanoic acid (bisH-MPA) building block was attached to a pentaerythritol core, followed by eight copies of a trifunctional amino acid molecule via EDCI-mediated coupling of their carboxylic acid functionality. Following deprotection, the terminal amines were PEGylated using a carbamate linkage, leaving the third functionality of the amino acid available for further elaboration. Because the amino acid-terminated dendrimers do not require column chromatography for purification, these compounds are more readily accessed than the functionally analogous bow-tie dendrimers we have successfully used in cancer chemotherapy. In this article, we demonstrate the versatility of this approach by presenting structures with ketones, alkynes, carboxylic acids, alkyl alcohols, and phenols present at the core of the macro-

* Corresponding author. Tel: (510)-643-3077. Fax: (510)-643-3079. E-mail: frechet@berkeley.edu.
[†] University of California, Berkeley.
[‡] University of California, San Francisco.

10.1021/bc700264g CCC: $40.75 © 2008 American Chemical Society
Published on Web 01/04/2008

molecule. Because of our interest in the potential of these compounds for drug delivery to tumors, the stability of these PEGylated dendrimers in buffer and plasma was studied, and biodistributions of the radiolabeled phenolic dendrimer in nontumored mice and of the carboxylate dendrimer conjugated to Dox in tumored mice were determined.

MATERIAL AND METHODS

Materials. Materials were used as obtained from commercial sources unless otherwise noted. Dimethylformamide (DMF), pyridine, and CH_2Cl_2 for syntheses were purged for 1 h with nitrogen and further dried by passing them through commercially available push stills (Glass Contour). Benzene was distilled from CaH_2. Monomethoxy polyethyleneglycol *p*-nitrophenyl carbonate (PEO-PNP) (*29*) and **1** (*30*) were synthesized according to published procedures. Solvents were removed under reduced pressure using a rotary evaporator or by vacuum pump evacuation.

Characterization. NMR spectra were recorded on Bruker AV 300, AVB 400, AVQ 400, or DRX 500 MHz instruments. Fourier transform infrared (FTIR) spectroscopic analyses were performed using a thin film cast from an appropriate solvent on a NaCl plate. Elemental analyses were performed at the UC Berkeley Mass Spectrometry Facility. MALDI-TOF MS was performed on a PerSeptive Biosystems Voyager-DE, generally using the following matrices: *trans*-3-indoleacrylic acid (IAA) for *tert*-butyloxycarbonyl (Boc)-protected dendrimers or 2,5-dihyroxybenzoic acid (DHB) for amine-terminated dendrimers. Samples were prepared by diluting dendrimer solutions (~1 M) 40-fold in 100 mM matrix solutions in tetrahydrofuran and spotting 0.5 μL on the sample plate. Size exclusion chromatography (SEC) system A consisted of a Waters 515 pump, a Waters 717 autosampler, a Waters 996 Photodiode Array detector (210–600 nm), and a Waters 2414 differential refractive index (RI) detector. SEC was performed at 1.0 mL/min in a PLgel Mixed B (10 μm) and a PLgel Mixed C (5 μm) column (Polymer Laboratories, both 300 × 7.5 mm), in that order, using DMF with 0.2% LiBr as the mobile phase and linear PEO (4,200–478,000 MW) as the calibration standards. The columns were kept at 70 °C. SEC system B consisted of the same equipment as that in system A and was performed at 1.0 mL/min in two SDV Linear S (5 μm) columns (Polymer Standards Service, 300 × 8 mm) using DMF with 0.2% LiBr as the mobile phase. The columns were kept at 70 °C. SEC system C consisted of a Waters Alliance separation module 2695 and a Waters 410 differential RI detector. SEC was performed in a G2500 PWXL (6 μm) and a G3000 PWXL (6 μm) column (TosoHaas, both 300 × 7.8 mm), in that order, at ambient temperature using phosphate buffered saline (pH 7.4) as the mobile phase. Radioactivity from ^{125}I was quantified with 1480 Wallac Wizard 3 Automatic Gamma Counter. Counts emitted from samples contained in screw-cap scintillation vials were measured over the course of 1 min and were recorded as counts per minute (cpm).

Animal Experiments. All animal experiments were performed in compliance with the National Institutes of Health guidelines for animal research under a protocol approved by the Committee on Animal Research at University of California (San Francisco, CA) (UCSF). C-26 colon carcinoma cells obtained from the UCSF cell culture facility were cultured in RPMI medium 1640 containing 10% FBS.

Nomenclature. A pentaerythritol core (PE) with one generation of *bis*-2,2-hydroxymethylpropanoic acid (G1) and serine protected as a benzyl ether for the side chain and with a Boc on the amine (Ser(Bn)Boc) is abbreviated PE-G1-(Ser(Bn)Boc)$_8$ because there are eight serines. Standard nomenclature is used for other amino acids Xaa and their protecting groups (PG). The PEGylated versions are abbreviated as PE-G1-(Xaa(PG)-PEO)$_8$. In the title of this article, we term the final polymers core functionalized because the reactive functionalities used to attach the drugs and or imaging labels are located near the core of the macromolecules, which is surrounded and engulfed by long PEG linear chains.

General Procedure for the Acylation of 1 with Amino Acids. Synthesis of PE-G1-(Ser(Bn)Boc)$_8$ (3b). Compound **1** (201 mg, 0.334 mmol), L-Boc-Ser(Bn)-OH (946 mg, 3.20 mmol), and 4-dimethylaminopyridine (DMAP) (195 mg, 1.60 mmol) were dissolved in DMF (2.7 mL), and then 1-ethyl-3-[3-dimethylaminopropyl]carbodiimide hydrochloride (EDCI) (613.3 mg, 3.20 mmol) was added. After 4 h, the reaction was complete as determined by MALDI. The solution was diluted with diethyl ether (75 mL) and washed with 1 M $NaHSO_4$ (3 × 50 mL), 1 M NaOH (3 × 50 mL), and water (2 × 50 mL). The organic layer was dried with $MgSO_4$, and filtered, and the solvent was removed to yield a white solid (903 mg, quant). ^{1}H NMR (400 MHz, $CDCl_3$): δ 1.16 (s, 12), 1.41 (s, 72), 3.64 (m, 8), 3.81 (m, 8), 4.01 (d, 4, J = 11.1), 4.10 (d, 4, J = 11.1), 4.19 (dd, 8, J = 10.6, 11.2), 4.44 (m, 32), 5.47 (s, 8), 7.28 (m, 40). ^{13}C NMR (100 MHz, $CDCl_3$): δ 17.52, 28.36, 46.78, 53.97, 61.73, 65.30, 65.46, 69.91, 73.25, 79.87, 127.72, 127.80, 128.44, 137.59, 155.39, 170.14, 171.59. MALDI-TOF MS. $[M + Na]^+$ ($C_{145}H_{196}N_8O_{48}Na$) Calcd: m/z = 2840.3. Found: m/z = 2839.9. Anal. ($C_{145}H_{196}N_8O_{48}$) C, H, N.

PE-G1-(Tyr(Bn)Boc)$_8$ (3a). Yield 92%. ^{1}H NMR (400 MHz, $CDCl_3$): δ 1.12 (s, 12), 1.35 (s, 72), 2.87 (m, 8), 3.04 (m, 8), 4.18–4.37 (m, 24), 4.51 (m, 8), 4.93 (s, 16), 5.16 (s, 8), 6.84 (d, 16, J = 7.0), 7.04 (d, 16, J = 7.0), 7.28–7.38 (m, 40). ^{13}C NMR (100 MHz, $CDCl_3$): δ 17.70, 28.36, 37.15, 46.68, 54.59, 65.61, 69.97, 70.65, 79.79, 115.00, 127.51, 127.92, 128.41, 128.56, 130.36, 137.12, 155.20, 157.93, 171.76. MALDI-TOF MS. $[M + Na]^+$ ($C_{193}H_{228}N_8O_{48}Na$) Calcd: m/z = 3449.6. Found: m/z = 3446.3. Anal. ($C_{193}H_{228}N_8O_{48}$) C, H, N.

PE-G1-(Asp(Bn)Boc)$_8$ (3c). The synthesis was performed as described in the general procedure. Following the extractions, a small amount of benzyl alcohol was present; it was removed by two precipitations of the dendrimer from ether into excess hexanes. Because the product stuck to the glass surfaces as a white gummy material, the hexanes were decanted, and the residual solvent was removed under vacuum to yield a white solid (95%). ^{1}H NMR (400 MHz, $CDCl_3$): δ 1.19 (s, 12), 1.40 (s, 72), 2.88 (m, 16), 4.13–4.38 (m, 24), 4.61 (br s, 8), 5.09 (m, 16), 5.61 (s, 8), 7.31 (br s, 40). ^{13}C NMR (100 MHz, $CDCl_3$): δ 17.74, 28.32, 36.62, 43.01, 46.48, 50.02, 62.25, 65.71, 66.85, 79.98, 128.32, 128.57, 135.54, 155.31, 170.55, 170.78, 171.74. MALDI-TOF MS. $[M + Na]^+$ ($C_{153}H_{196}N_8O_{56}Na$) Calcd: m/z = 3064.3. Found: m/z = 3065.1. Anal. ($C_{153}H_{196}N_8O_{56}$) C, H, N.

PE-G1-(PropargylGlyBoc)$_8$ (3d). ^{1}H NMR (300 MHz, $CDCl_3$): δ 1.31 (s, 12), 1.45 (s, 72), 2.14 (d, 8, J = 2.5), 2.72 (s, 16), 4.13–4.48 (m, 28), 5.45 (d, 8, J = 7.9). ^{13}C NMR (100 MHz, $CDCl_3$): δ 17.19, 22.58, 28.30, 46.62, 52.02, 62.10, 65.74, 72.15, 78.70, 80.20, 155.01, 170.25, 171.62. MALDI-TOF MS. $[M + Na]^+$ ($C_{105}H_{148}N_8O_{40}Na$) Calcd: m/z = 2185.4. Found: m/z = 2183.6. Anal. ($C_{105}H_{148}N_8O_{40}$) C, H, N.

PE-G1-((4-AcetylPhe)Boc)$_8$ (3e). ^{1}H NMR (300 MHz, $CDCl_3$): δ 1.19 (s, 12), 1.35 (s, 72), 2.55 (d, 24, J = 1.8), 3.01 (br s, 8), 3.19 (m, 8), 4.16–4.35 (m, 24), 4.59 (br s, 8), 5.30 (br s, 8), 7.25 (d unresolved from solvent, 16, J = 7.5), 7.86 (d, 16, J = 8.1). ^{13}C NMR (100 MHz, $CDCl_3$): δ 17.69, 28.28, 37.85, 46.55, 54.17, 61.93, 65.66, 77.26, 80.08, 128.65, 129.53, 135.97, 141.91, 155.15171.42, 171.76, 197.78. MALDI-TOF MS. $[M + Na]^+$ ($C_{153}H_{196}N_8O_{48}Na$) Calcd: m/z = 2936.3. Found: m/z = 2934.3. Anal. ($C_{153}H_{196}N_8O_{48}$) C, H, N.

General Deprotection by Anhydrous HCl. PE-G1-(Ser(Bn)NH$_3$Cl)$_8$ (b). Compound **3b** (98.8 mg, 0.35 mmol) was dissolved in ethanol (0.5 mL) and cooled to 0 °C. Acetyl chloride (0.4 mL) was added dropwise over 2 min. After 30 min, the reaction was complete as determined by MALDI (IAA). The solvents and remaining acetyl chloride were removed by rotary evaporation, and the white solid product was dried under high vacuum.

General Deprotection by Trifluoroacetic Acid. PE-G1-(Asp(Bn)NH$_3$TFA)$_8$ (c). Compound **3c** (251.2 mg, 82.6 μmol) was dissolved in a 1:1 mixture of trifluoroacetic acid (TFA) and CH_2Cl_2. After 30 min, deprotection was complete as determined by MALDI (DHB). The solvents were removed under vacuum.

General PEGylation Reaction. PE-G1-(Asp(Bn)PEO)$_8$ (4c). PEO-PNP (3.678 g, 700 μmol), DMAP (38 mg, 310 μmol), *N*,*N*-diisopropylethylamine (520 μL, 3.0 mmol), pyridine (2.5 mL), and benzene (5 mL) were added to deprotected **3b** (described above, 82.6 μmol). After 3 days, piperidine (600 μL, 6.1 mmol) was added to quench excess PEO-PNP, and the reaction was stirred for an additional 16 h. The solution was diluted with benzene (25 mL) and the product was precipitated into ether (600 mL). The white solid was collected by filtration, rinsed with ether, and dialyzed against water in 3500 molecular weight cutoff (MWCO) regenerated cellulose membranes (Spectra-Por) for 18 h. The retained water solution was lyophilized to yield a white powder (3.15 g). ^{1}H NMR (400 MHz, $CDCl_3$): δ 1.13 (br s, 12), 2.9 (m, 16), 3.38 (s, 24), 3.65 (br m, ~4300), 4.2–4.4 (br m, 42), 4.62 (br s, 8), 5.07 (m, 16), 5.9 (br s, ~6), 7.31 (m, unresolved from solvent, ~40).

PE-G1-(Tyr(Bn)PEO)$_8$ (4a). ^{1}H NMR (500 MHz, $CDCl_3$): δ 1.16 (s, 12), 2.88 (br s, 8), 3.03 (br s, 8), 3.38 (s, 24), 3.65 (br m, ~4380), 4.0–4.4 (br m, 42), 4.53 (br s, 8), 4.93 (s, 16), 5.45 (br s, ~6), 6.84 (d, 16, J = 6.5), 7.02 (d, 16, J = 7.6), 7.2–7.4 (m, unresolved from solvent, ~40).

PE-G1-(Ser(Bn)PEO)$_8$ (4b). ^{1}H NMR (500 MHz, $CDCl_3$): δ 1.13 (s, 12), 3.38 (s, 24), 3.65 (br m, ~3900), 4.1–4.5 (br m, 55), 5.74 (br s, ~5), 7.20–7.35 (br m, unresolved from solvent, ~40).

PE-G1-(PropargylGlyPEO)$_8$ (4d). ^{1}H NMR (500 MHz, $CDCl_3$): δ 1.30 (s, 12), 2.15 (s, unresolved from residual water, ~8), 2.74 (s, 16), 3.38 (s, 24), 3.65 (br m, ~4500), 4.1–4.6 (br m, 38), 5.78 (br s, ~4).

PE-G1-((4-AcetylPhe)PEO)$_8$ (4e). ^{1}H NMR (500 MHz, $CDCl_3$): δ 1.14 (s, 12), 2.54 (s, 24), 3.02 (br s, 8), 3.17 (br s, 8), 3.38 (s, 24), 3.65 (br m, ~4100), 4.0–4.3 (br m, 42), 4.6 (br s, 8), 5.66 (br s, ~5), 7.28 (m, unresolved from solvent), 7.86 (br s, 16).

PE-G1-(AspPEO)$_8$ (5). Compound **4c** (96.4 mg) was deprotected in CH_3OH (5 mL) by hydrogenolysis using Pd/C (10 wt%, 10 mg) at 1 atm for 16 h. The solution was filtered through celite, and the solvent was removed under reduced pressure. ^{1}H NMR (500 MHz, $CDCl_3$): δ 1.27 (s, 12), 2.80 (br s, 8), 2.97 (br s, 8), 3.38 (s, 24), 3.64 (br m, ~3600), 4.0–4.4 (br m, 42), 4.62 (br s, 8), 6.22 (br s, ~4).

***N*′-(4-Hydroxymethyl-benzyl)-hydrazinecarboxylic Acid *tert*-Butyl Ester (6).** 4-(Hydroxymethyl) benzoic acid (0.760 g, 5 mmol), HOBt (0.341 g, 2.5 mmol, 0.5 equiv), and *tert*-butyl carbazate (0.925 g, 7 mmol, 1.4 equiv) were suspended in CH_2Cl_2 (25 mL) at 0 °C. EDCI (1.06 g, 5.5 mmol, 1.1 equiv) was added, and the mixture was stirred for 24 h. The mixture became almost homogeneous after a few hours, and the product later precipitated. The white solid was filtered, rinsed with CH_2Cl_2 (3 × 5 mL), and dried (790 mg, 59%). ^{1}H NMR (MeOD-d_3): δ 1.49 (s, 9), 4.66 (s, 2), 7.45 (d, 2, J = 8), 7.83 (d, 2, J = 8). ^{13}C NMR (MeOD-d_3): δ 27.34, 63.19, 80.63, 126.40, 127.37, 131.00, 146.02, 156.63, 168.34. IR (cm^{-1}): 3726.8, 1720.2, 1664.1, 860.3. mp = 159–160 °C (dec.). Calcd: $[M + H]^+$ ($C_{13}H_{19}N_2O_4$) m/z = 267.1345. Found: FABHR MS: $[M + H]^+$ m/z = 267.1350. Anal. ($C_{13}H_{18}N_2O_4$) C, H, N.

PE-G1-(Asp(BnCONNBoc)PEO)$_8$ (7). Coumpound **5** (200 mg, 38 μmol COOH) was dissolved in DMF (0.75 mL). Coumpound **6** (300 mg, 1.13 mmol), *N*,*N*′-dicyclohexylcarbodiimide (245 mg, 1.19 mmol), and DMAP *p*-toluenesulfonate salt (13 mg, 44 μmol) were added. After 24 h, the solution was diluted with water (10 mL), filtered through celite, and dialyzed against water in 3500 MWCO membranes for 18 h. The retained water solution was lyophilized to yield a white powder (172 mg). By ^{1}H NMR, comparing the OMe peak at δ 3.38 to the Boc peak at δ 1.48, it was determined that ca. 50% of the COOH groups reacted with the linker. ^{1}H NMR (400 MHz, $CDCl_3$): δ 1.11 (s, 12), 1.49 (s, 37), 2.34 (unresolved from residual water in solvent), 2.95 (br m, ~12), 3.38 (s, 24), 3.65 (br m, ~3100), 4.0–4.4 (br m, 25), 4.63 (br s, 3), 4.75 (s, 1), 5.11 (br s, ~5), 6.1 (br s, ~2), 7.81 (br m, ~8).

PE-G1-(Asp(BnCONNDox)PEO)$_8$ (8). Coumpound **7** (15.2 mg, 1.5 μmol NNBoc) was dissolved in 1:1 TFA/CH_2Cl_2 for 2 h. The solvent was removed under a stream of N_2. Residual TFA was removed by dissolving the solid in CH_3OH and evaporating it under a stream of N_2. The polymer was then dissolved in CH_3OH (1 mL) and Dox (4.5 mg, 7.8 μmol) was added. The reaction was stirred at 60 °C in the dark for 16 h. The polymer was eluted on an LH-20 column with CH_3OH. The first dark red band (high MW material) was collected, the solvent was removed by evaporation under a stream of N_2, and the product was further purified on a PD-10 column using water as the eluent. The collected dark red fraction was lyophilized to yield a red powder (10 mg). The loading of Dox was determined by the absorbance at 486 nm (ε = 11,500) (*31*) to be 2.9 wt %, or ~50% of the maximum theoretical loading.

PE-G1-TyrPEO$_8$ (9a). Compound **4a** (195 mg) was dissolved in a mixture of TFA (2 mL) and thioanisole (0.25 mL). After 16 h, TFA was removed under reduced pressure, and NEt_3 (0.5 mL) was added. The solution was diluted with CH_3OH (6 mL) and dialyzed 24 h against CH_3OH in a 3500 MWCO regenerated cellulose membrane. After removing the retentate solvent under reduced pressure, the product was purified on a PD-10 column and lyophilized (yield: 135 mg, 69%). ^{1}H NMR (400 MHz, $CDCl_3$): δ 1.03 (s, 12), 2.95 (br s, 16), 3.38 (s, 24), 3.65 (br m, ~4350), 3.9–4.3 (br m, 34), 4.49 (br s, 8), 5.55 (br s, ~6), 6.76 (br s, 16), 6.94 (br s, 16), 7.52 (br s, ~6).

Polymer Aqueous Buffer Hydrolysis Study. Compound **4b** was dissolved at a concentration of 1 mg/mL in a solution of PBS, pH 7.4, with 30 mM $NaNO_3$. The polymer solutions were incubated at 37 °C, and samples were taken periodically over a period of 20 days. Samples were frozen at −80 °C until they could be prepared for molecular weight determination by SEC. Samples were prepared for SEC (system B) by running solutions through PD-10 desalting columns in distilled water, followed by lyophilization.

Polymer Plasma Degradation Study. A stock polymer solution of **4a** in PBS with 30 mM $NaNO_3$, pH 7.4, was made at a concentration of 20 mg polymer/mL. Lyophilized human plasma (Sigma) was reconstituted in PBS, and the pH was adjusted to 7.4 using 1 M HEPES containing 9 g/L NaCl and 13.5 g/L NaOH. The choice of buffer is important to prevent a change in plasma pH over the course of the experiment. For each time point, 40 μL of polymer solution was added to 160 μL of preheated human plasma in a 1.5 mL centrifuge vial and vortexed briefly. Samples were incubated at 37 °C. At the desired time point, 200 μL of a 1:1 methanol/water with 2 wt % $ZnSO_4$ solution was added to the vial to precipitate the proteins. The sample was briefly vortexed, centrifuged at 14,100 rcf for 5 min, then frozen at −80 °C until it could be prepared

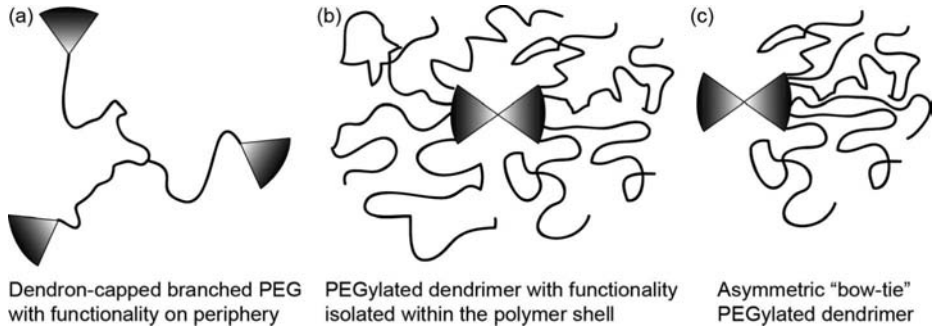

Figure 1. Schematic representations of the PEG−dendrimer hybrid structures. PEG can be attached (a) at the dendrimer apex or the periphery of (b) symmetric or (c) asymmetric bow-tie dendrimers.

for molecular weight determination by SEC. Individual samples were prepared for SEC (system C) by filtering the supernatant through 0.2 μm pore size PTFE syringe filters.

Radioiodination of the Free Phenols on Tyrosine (Tyr)-Functionalized PE Dendrimers (9b). For tracing of the dendrimer in biodistribution studies, the free phenols of **9a** were radiolabeled with ^{125}I using a published procedure (*32*). Briefly, **9a** (3 mg, 75 pmol) was dissolved in 0.49 mL of boric acid buffer (0.1 M, pH 8.5). A solution of potassium iodide in water (1 μM) was added (136 μL), followed by chloramine T in boric acid buffer (1 μM, 272 μL). The mixture was allowed to react for 15 min, then sodium bisulfite solution (50 μM, 6.8 μL) was added to stop the reaction. The material was purified on a PD-10 column and lyophilized overnight to yield 3 mg of iodinated polymer. The polymer was iodinated at 1 μCi per PEGylated dendrimer. A solution of iodinated polymer was combined with a solution of non-iodinated polymer, resulting in a final solution of 5 mg polymer/mL and with an activity of 14.2 μCi/mL.

Biodistribution Studies in Nontumored Mice. Radioiodinated polymer solutions (200 μL, ~6.5 million cpm/mouse) were injected intravenously in the tail vein of 6–8 week old female CD-1 mice. The mice were sacrificed at three different times following injection for biodistribution analyses: 30, 540, and 2880 min postinjection (three mice per experimental group). The blood (collected by heart puncture), heart, lungs, liver, stomach, spleen, intestines, kidneys, and carcass (divided into three portions) were collected for analyses. Each were weighed, and the amount of radioactivity present in each organ was quantified. For the 2880 min time point, the mice were housed in metabolic cages and the urine and feces collected. Additionally, retro-orbital (RO) bleeds were taken at four different time points to construct a blood concentration curve. A 10 min RO bleed was taken from the 30 min sacrifice mice, 60 and 1440 min RO were taken from the 2880 min sacrifice mice, and a 180 min RO bleed was taken from the 540 min sacrifice mice. All samples were weighed and the amount of radioactivity present quantified.

Urine was analyzed by running 1 mL of urine from each polymer biodistribution through a G-50 Sephadex column (column volume ~10 mL). Fractions were collected and analyzed for radioactivity to determine whether radioactivity in the urine was polymer-associated or low MW-associated. A set of PEO polymers with known MW polymers was also run on the G-50 column for comparison.

The % injected dose per gram (%ID/g) of blood versus time curve was analyzed using a two compartment model described by eq 1. The two compartment model (*33*) was chosen as the blood concentration curve showed two distinct rates of decay. The pharmacokinetic parameters *A*, α, *B*, and β for the two-compartment model were estimated using the residuals model. All pharmacokinetic quantities were calculated from these parameters.

$$C_p = Ae^{-\alpha t} + Be^{-\beta t} \quad (1)$$

Biodistribution Studies in Tumored Mice. Six to eight week old female Balb/C mice were injected in the right rear flank with C26 colon carcinoma cells by subcutaneous administration (3×10^5 cells in 50 μL media). Tumors were allowed to grow 13 days.

Mice were injected intravenously in the tail vein with one of the following solutions in PBS: **8** (8 mg Dox equiv/kg), DOXIL (8 mg Dox equiv/kg), or free Dox (8 mg/kg) (three mice per experimental group). Two control mice were also injected with 200 μL of PBS. The mice were sacrificed 2880 min postinjection. The blood (collected by heart puncture), heart, lungs, liver, spleen, kidney, muscle, and tumor were collected for analyses. Each organ was weighed, and 200–300 mg of the collected organs were combined with ~0.6 mL zirconia beads and 1 mL of acidified isopropyl alcohol (0.075 M HCl, 90% IPA) in 2.0 mL centrifuge tubes. The samples were homogenized for 30 s and incubated at 4 °C for 24 h. Samples were then frozen at −80 °C in a freezer until quantification of Dox content by fluorescence measurements could be made. At measurement time, samples were thawed and centrifuged for 5 min at 14,000 rpm (15,400*g*). Then, 80 μL of supernatant was combined with 920 μL of acidified IPA for fluorescence measurements. Dox fluorescence (ex 485 nm, em 595 nm) was measured on a Spex Fluorolog fluorimeter. Calibration curves were made from organ samples collected from the control mice.

RESULTS AND DISCUSSION

Synthesis of the PEGylated Dendrimers. The synthesis of the core functional PEGylated dendrimers is straightforward and nearly quantitative at all dendronization steps (Scheme 1). The first generation pentaerythritol bisHMPA dendrimer **1** (PE-G1-OH_8) was synthesized as previously described (*30*). This molecule was chosen as a core because a large number of radially emanating functional groups could be attained in a minimum number of steps on a large scale, and the biodegradable ester backbone is desirable for biological applications. Attachment of the amino acids **2a**−**e** using DMAP catalyzed EDCI coupling provided analytically pure dendrimers (**3**), requiring only an extractive workup for most versions. None of the dendrimers required column chromatography for analytically pure material, thus facilitating scale up. The reaction was monitored by MALDI-TOF MS to detect incomplete couplings (Figure 2a for **3c**). In all cases, the reaction went to completion, normally within 4 h. Occasionally, loss of either a single *tert*-butyl group or a number of Boc groups was seen in the MALDI-TOF spectrum, but the peaks associated with a loss of 8 Boc groups, however, were higher than those associated with 7 or 6, indicating that this was an artifact of the ionization process because of the use of an acidic matrix. In the workup of **3c**, some benzyl alcohol was produced, likely due to the ester

Scheme 1. Synthesis of PEGylated Ester Dendrimers with Core Functionality[a]

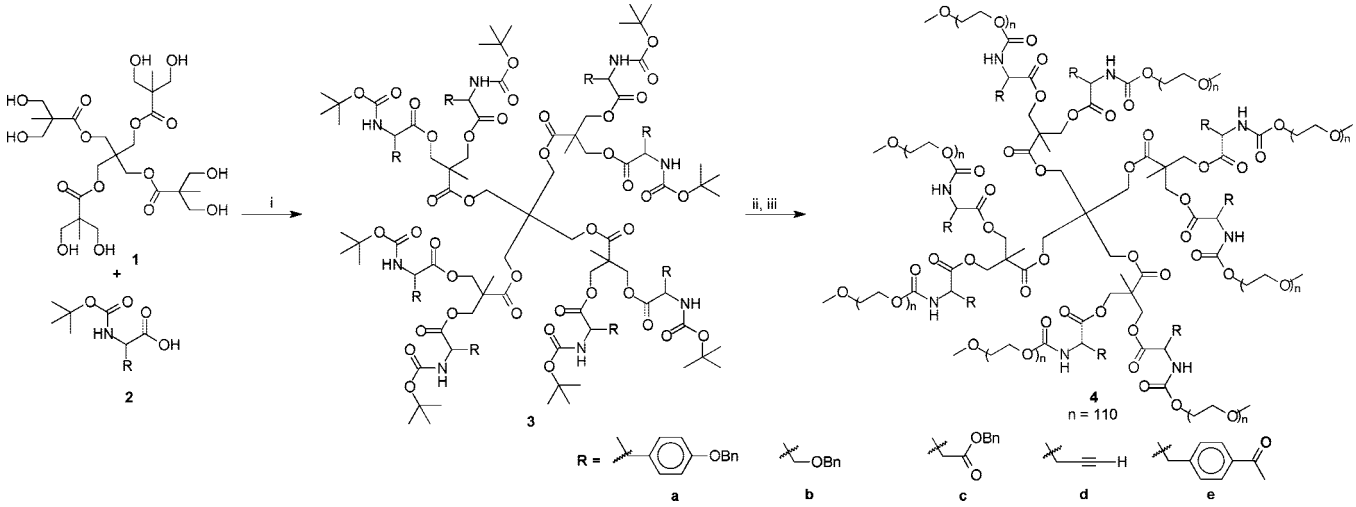

[a] (i) EDC, DMAP, DMF; (ii) TFA/DCM or AcCl/EtOH; (iii) PEO-PNP, DMAP, Pyr, PhH, DIPEA.

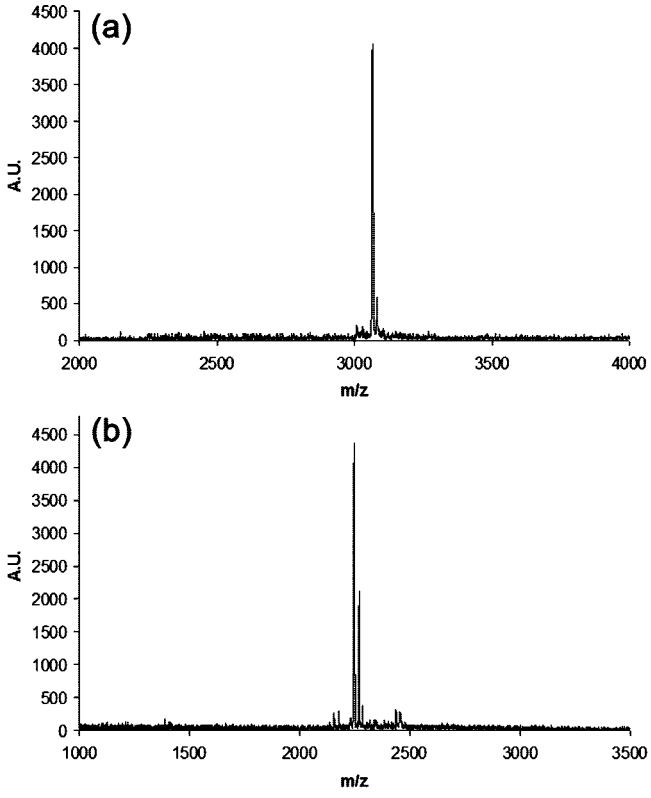

Figure 2. MALDI-TOF spectra of (a) **3c** and (b) **3c** after Boc deprotection. Note that the deprotected product was isolated as the octa(trifluoroacetate) salt.

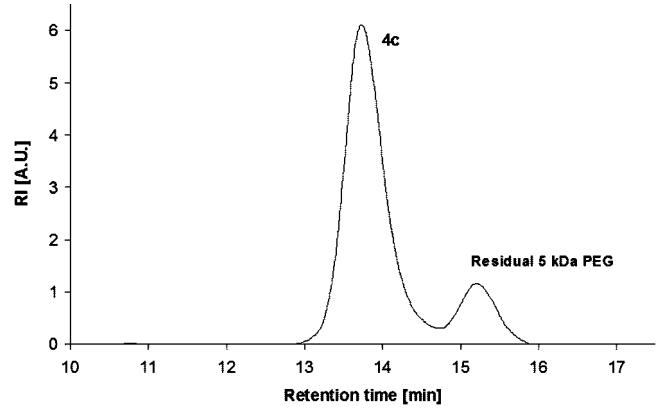

Figure 3. Size exclusion chromatogram (SEC) of **4c** and residual linear PEG in DMF solvent.

hydrolysis of some of the water-soluble starting amino acid. This was removed by precipitation of the material into hexanes. These dendrimers are soluble in a variety of common organic solvents (CH_2Cl_2, $CHCl_3$, CH_3OH, EtOAc, etc.). Dialysis in 3500 molecular weight cutoff regenerated cellulose membranes against methanol is an alternative purification procedure to extractive workups, generally producing yields greater than 80%. All of the amino acids attached are commercially available, although the unnatural amino acids are more expensive and may not be readily available on a large scale. By using this variety of amino acids, PEGylated dendrimers ready for radiolabeling, esterification, amidation (with limitations, vida infra), click reactions, Pd coupling, and hydrazone/oxime formation are easily accessible.

Deprotection of the amine-protecting Boc groups could be monitored by MALDI-TOF MS (Figure 2b for **3c**). Products were isolated by the removal of the solvent and used in the next step without further purification. In the MALDI-TOF spectrum of **3a**, the loss of a single benzyl group was seen, but this was a minor event that did not interfere with the PEGylation reaction. Monomethoxy-PEO-*p*-nitrophenyl carbonate (PEO-PNP, 5000 MW) (*29*) was used in ~5% excess to fully cover the amine periphery of the dendritic core. After 3 days, size exclusion chromatography in DMF showed a peak around 38,000 Da, and another at 6,000 Da corresponding to the excess PEO-PNP (Figure 3 for **4c**). A ninhydrin test indicated that all primary amines were reacted in each case. For applications where excess PEO-PNP could be problematic, the addition of a slight excess of piperidine to the crude reaction mixture, followed by 12 h of stirring, effectively capped the remaining activated 5000 Da PEO. At this stage, the products could be purified from small molecules by dialysis in water. We have shown previously (*15*) that excess linear PEG can be removed from the PEGylated dendrimer by careful dialysis, but in this work, no such purification was attempted as it leads to a significant lowering of the yield of the PEGylated dendrimer, and the small amount of lower molecular weight linear PEG impurity should not alter the in vivo characteristics of the PEGylated dendrimers.

Scheme 2. Linker Synthesis, Attachment, and Dox Loading[a]

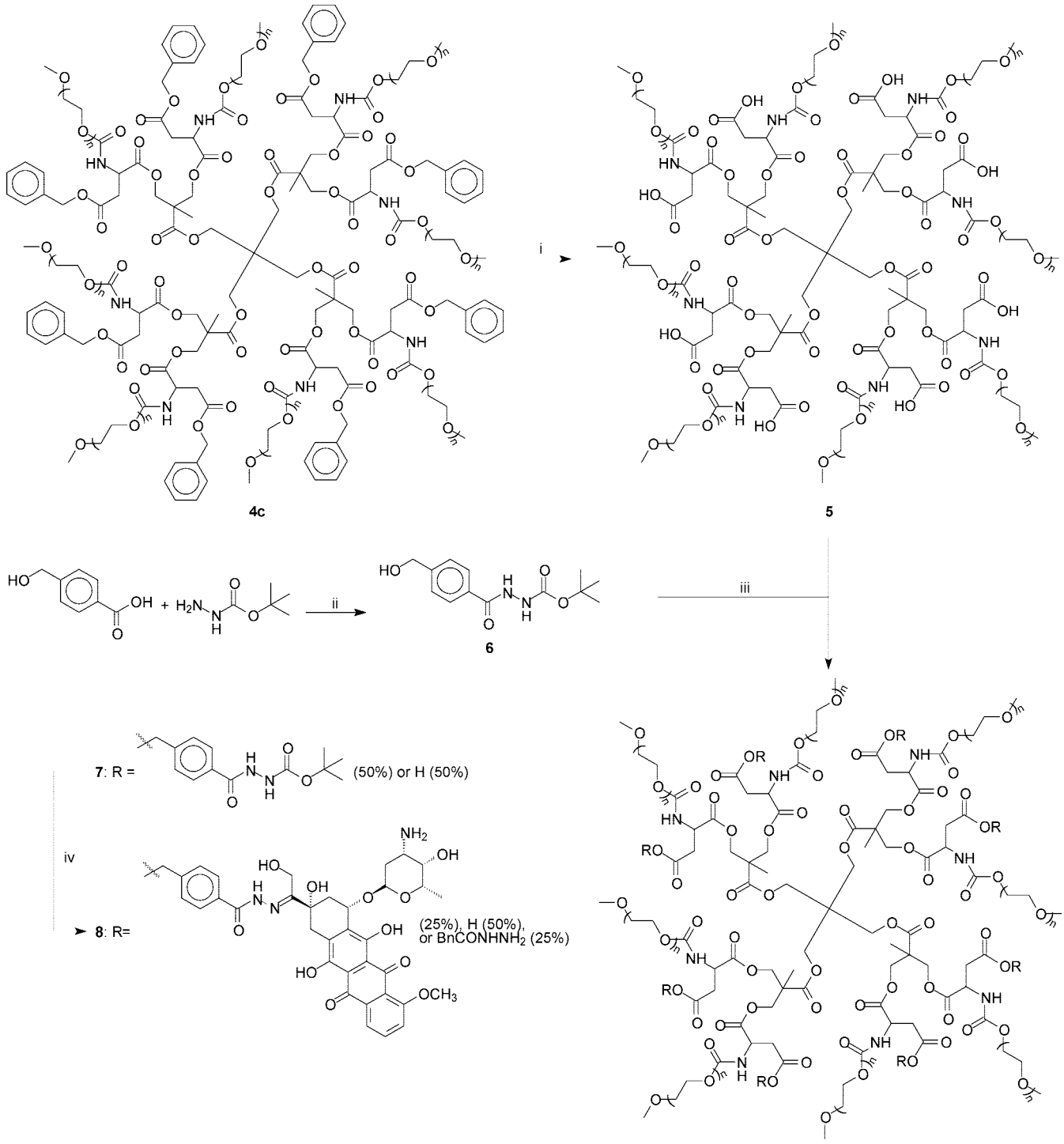

[a] (i) H_2, Pd/C, ME OH; (ii) EDCl, HOBt, DCM; (iii) DMF, DCC, DPTS; (iv) TFA, DCM, then MeOH, Dox, 60 °C.

Dox Loading of the PEGylated Dendrimers. To demonstrate that the dendritic cores are accessible for further chemical manipulation, **4c** was elaborated to contain Dox conjugated through a hydrazone bond (Scheme 2). This linkage shows promise for releasing Dox in its biologically active form after endocytosis but is stable at physiological pH 7.4 (*34–37*). Although the most straightforward route to a hydrazide-containing polymer would be attachment of *tert*-butylcarbazate directly to the aspartate moiety, we found that the α-amido ester bonds were not completely stable in the presence of excess amine and some degradation of the dendrimer occurred. It should be noted that piperidine, the secondary amine used to deactivate excess PEO-PNP, does not cause ester degradation. Similar results were seen when deprotecting the ε-Cbz of a lysine version of the dendrimer (data not shown). No further attempts were made to optimize the conditions to amidate with primary amines. To circumvent this degradation by a nucleophilic amine, hydroxyl-hydrazide linker **6** was synthesized and, following hydrogenolysis of the benzyl ester-protecting group of **4c** to afford **5**, was attached to the dendrimer. A comparison of the Boc peak at 1.48 ppm against the OMe of the PEG chains at 3.38 ppm in the ^{1}H NMR spectrum indicated that roughly 50% coverage (4 molecules of **6** attached to **7**) is achieved under these conditions. Such coverage is sufficient for the intended application.

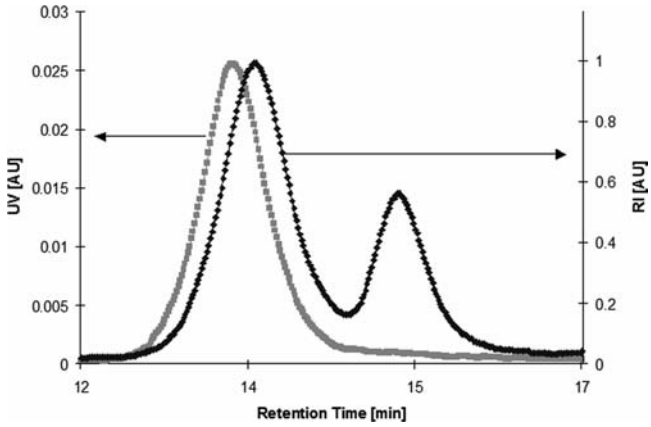

Figure 4. SEC of **8** in DMF. The delay between the UV (abs 584 nm) and RI traces is due to the sequential placement of the detectors.

Deprotection of the hydrazide Boc group followed by hydrazone formation with Dox in methanol afforded polymer **8** containing 2.9 wt % Dox. This value is 50% of the theoretical loading, consistent with previous work in our laboratories (*16*). Such partial loading may result from the presence of residual trifluoroacetic acid in the reaction mixture from the deprotection step, which lowers the pH of the solution below the ideal level for hydrazone formation. Optimization of the reaction conditions for linker attachment and drug conjugation should result in significantly higher (∼4-fold) loadings. Although some linear PEG was still present in the reaction mixture, the absorbance at 584 nm (in 0.2% LiBr in DMF) in the size exclusion chromatogram shows that, as expected, Dox was only attached to the PEGylated dendrimer and not to free PEG (Figure 4). The refractive index (RI) trace of the drug-loaded carrier (Figure 4) appeared different from that of the initial PEGylated dendrimer (Figure 3) and all the intermediates in terms of the amount of excess linear PEG. Initially, when the carboxylate groups were protected, ca. 5% excess PEG was seen, as expected. As the core was deprotected, linker added, and drug added, the ratio of the PEGylated dendrimer peak area to the linear PEG area decreased. The peaks were eluted at the same retention time for each, indicating that the molecular weight did not change and that degradation had not occurred. Therefore, we believe this was an artifact related to the changing refractive index of the material and that the amount of residual free PEG did not actually change. The drug-loaded material **8** was highly water soluble.

In Vitro Biodegradability of the PEGylated Dendrimers. While prior work has shown that PEGylated ester dendrimers can be hydrolyzed in aqueous solutions (*12*), we carried out experiments to determine if these PEGylated dendrimers could be degraded by enzymes since it has been suggested that PEGylation can inhibit access of enzymes and physiological fluids to a dendritic core (*38*). The properties of **4a** in biologically relevant situations was evaluated by tracking its stability in pH 7.4 buffer and in human plasma at 37 °C. As expected, over the course of 20 days in buffer, the PEG chains were hydrolyzed leading to a mixture of molecules with lower overall molecular weight and higher polydispersity than that of the starting **4a**. However, a significant portion of the material was still of higher molecular weight, suggesting that it had remained intact. Initial studies in plasma reconstituted using distilled water, as instructed by the manufacturer, showed that complete degradation of the ester dendrimer took place within only 48 h, leading to a product in which the largest molecules appeared to be 5 kDa PEG chains. However, it was found that the reconstituted plasma had a pH of ∼9, and thus, the high level of ester degradation seen was likely a result of the basic pH and not enzymatic degradation. After careful adjustment of the pH to 7.4 using a nonvolatile buffer such as HEPES buffer, the plasma samples showed degradation profiles essentially identical to those in PBS, pH 7.4. Therefore, this preliminary work does not shed light on the accessibility of the polyester dendritic core itself to enzymes.

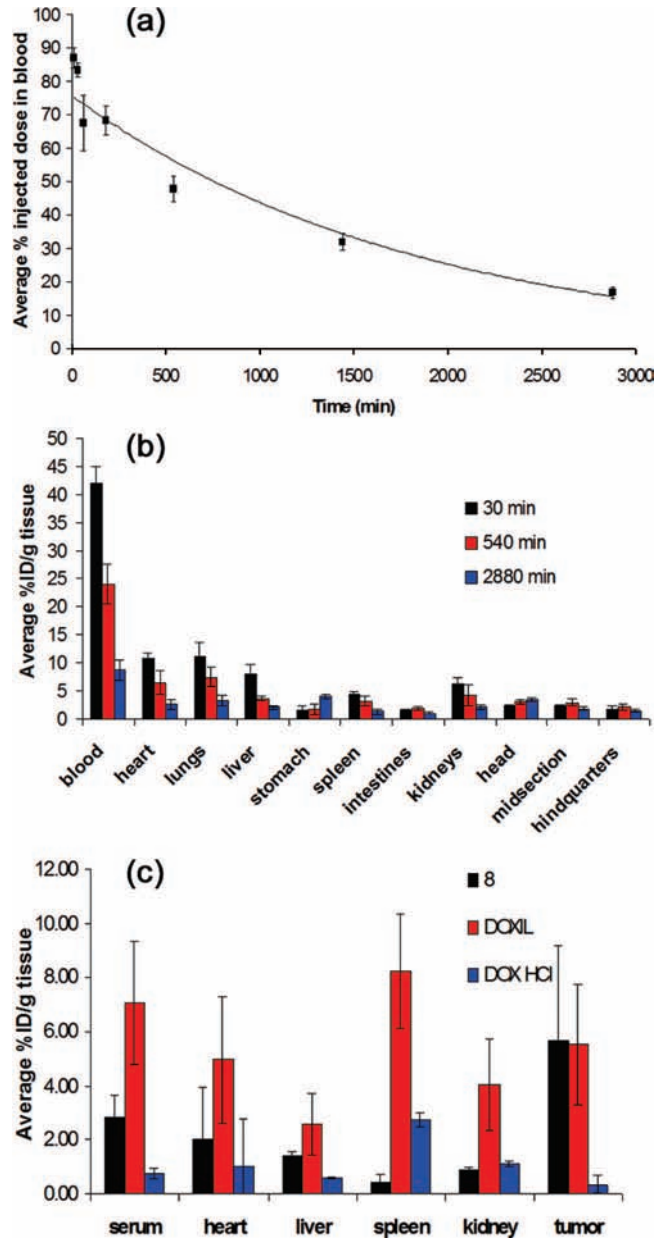

Figure 5. (a) Blood circulation profile of radiolabeled **9b** given as the average percent ID of polymer in the blood over time (three mice per time point). The line represents the fit curve resulting from the calculated pharmacokinetic parameters detailed in Table 1. (b) Biodistribution of radiolabeled **9b** in nontumored mice taken at three time points: 30, 540, and 2880 min postinjection (three mice per time point). (c) Forty-eight hour biodistribution, given as the average %ID Dox/g tissue, of **8** in mice tumored subcutaneously in the right flank with C26 colon carcinoma. DOXIL and Dox HCl were run as controls (three mice per treatment group).

Biodistribution Studies of Radiolabeled Polymer. To follow the fate of the PEGylated dendrimer in vivo, the phenolic groups of **4a** were deprotected and radiolabeled with ^{125}I (compound **9b**, not shown). Six to eight week old female Balb/C mice were injected intravenously with polymer solutions, and the distribution of the radiolabel in tissues was followed over time. The blood concentration profile (Figure 5a), given as the

Table 1. Pharmacokinetic Data for Radiolabeled 9b

$t_{1/2,\alpha}$ (h)	0.32 ± 0.11
$t_{1/2,\beta}$ (h)	23.8 ± 2.5
V_1 (g blood)	1.94 ± 0.07
$AUC_{0\rightarrow\infty}$ (%ID·h/g)	$1{,}200 \pm 100$
k_{21} (L/min)	0.024 ± 0.012
k_{12} (L/min)	0.01 ± 0.02
k_{el} (L/min)	0.0007 ± 0.0004

average %ID of radioactivity, shows >16%ID remained in the blood after 48 h. A two-compartment pharmacokinetic model (*33*) was fitted to the data, and from this the pharmacokinetic parameters were determined. In particular, the blood circulation half-life $t_{1/2\beta}$ was found to be 23.8 ± 2.5 h (Table 1), and the area under the curve, $AUC_{0\rightarrow\infty}$, was determined to be $1{,}200 \pm 100$%ID·h/g blood. The long circulation half-life and large $AUC_{0\rightarrow\infty}$ are indicative of high levels of polymer in the blood and increased opportunity for accumulation in a tumor due to the EPR effect. This is consistent with previously reported results for PEGylated bow-tie dendrimers of similar molecular weight (*12*) and is more favorable than results obtained with linear 50 kDa PEO (*39*). The biodistribution study of **9b** (Figure 5b) showed low levels of polymer in all vital organs after 48 h, less than 5%ID/g tissue.

However, despite the long blood circulation half-life, 28.5%ID and 5.0%ID were found in the urine and feces, respectively, after 48 h. To determine whether this radioactivity was polymer-associated (>5,000 Da) or low MW-associated (<5,000 Da), urine samples were run on a G-50 size exclusion column. The results showed that 35% of the radioactivity eluted was polymer-associated, and 65% of the radioactivity eluted was low-MW-associated (data not shown). While some whole polymer can be filtered from the blood by the kidneys, it is likely that the excreted radioactivity can be attributed to the hydrolysis of the polymer in the blood. It was unclear, however, what the radiolabeled low MW material might be. Li et al. observed a similar phenomenon with their radiolabeled antibody single-chain Fv, where the radioactivity in the urine was dissociated from the antibody, and believed that radioactive iodine was being removed by deiodinases present in the plasma membrane of renal tubule cells, which recognize iodinated tyrosine (*40*). As little iodine was found in the thyroid (<0.5%ID) (data not shown), it is most likely that iodine was being removed preferentially from the tyrosine handles of **9b** as it passed through the kidneys before excretion. Therefore, we believe the biodistribution reflects the polymer distribution and not the distribution of free iodine.

Biodistribution Studies of Dox-Loaded Polymer. A biodistribution of the Dox-loaded **8** was completed to confirm that its distribution behavior had not changed significantly by the change of the functional handle at the core and the attachment of a drug payload. Six to eight week old female Balb/C mice were tumored with the C26 murine colon carcinoma in their right flank. Mice were injected with **8** at a dose of 8 mg Dox/kg. After 48 h, less than 5%ID/g tissue had accumulated in the vital organs, similar to what was seen with radiolabeled **9b**. Furthermore, the Dox-loaded polymer **8** (Figure 5c) delivered 5.7 ± 3.5%ID/g tissue, or 1.2 ± 0.5%ID, to the tumor. This was comparable with the Dox delivered to the tumor from the clinically used PEGylated liposomal formulation DOXIL, both of which delivered approximately 20 times more drug to the tumor than is achieved without carrier. In addition, dendritic carrier **8** showed lower accumulation in the spleen than that observed with free Dox and, in all tested vital organs, than that observed with DOXIL. Lower accumulation of Dox in the vital organs should result in less toxicity, while the high concentration in the tumor may result in chemotherapy treatment as effective as that of DOXIL.

CONCLUSIONS

A variety of biodegradable PEGylated dendrimers with various core functionalities has been synthesized in a scalable process. The use of trifunctional amino acids on the biologically tolerated ester dendrimers is a simple way of incorporating functionality at the core of PEGylated dendritic macromolecules and tailoring them for different applications. This method is general and can be applied to any of the common amine-terminated dendrimers such as the polyamidoamines, polylysine, polypropyleneimine, etc. Clearly, it can also be adapted for use with other families of dendrimers with other types of terminal groups. The core functionalities, if protected during synthesis, are easily deprotected and elaborated further. Radiolabeling the phenolic version facilitated the determination of in vivo biodistribution and pharmacokinetics. It was found that this system has a long circulation half-life and does not accumulate in normal tissue, as was also the case for previous PEGylated dendrimers (*10*, *12*, *15*, *16*). A hydrazide linker was attached to the carboxylate version, and Dox was conjugated to it by a hydrazone. The drug carrier was found to deliver as much Dox to a tumor as the clinically used PEGylated liposomal formulation DOXIL, while less drug was found in healthy tissue. Explorations of the efficacy of the Dox-loaded carrier in tumor therapy, the use of these systems in imaging, and the reactivities of the variants of this system (such as alkyne or ketone functionalized dendrimers) are currently underway.

ACKNOWLEDGMENT

Financial support of this research by the National Institutes of Health (GM 65361 and EB 002047) is gratefully acknowledged. We thank Dr. Marian Snauko (UC Berkeley) for assistance with size exclusion chromatography and Dr. Cameron Lee (UC Berkeley) for insightful discussions.

LITERATURE CITED

(1) Lee, C. C., Mackay, J. A., Fréchet, J. M. J., and Szoka, F. C. (2005) Designing dendrimers for biological applications. *Nat. Biotechnol. 23*, 1517–1526.

(2) Boas, U., Christensen, J. B., and Heegaard, P. M. H. (2006) *Dendrimers in Medicine and Biotechnology: New Molecular Tools*, RSC Publishing, Cambridge, U.K.

(3) Tomalia, D. A., Reyna, L. A., and Svenson, S. (2007) Dendrimers as multi-purpose nanodevices for oncology drug delivery and diagnostic imaging. *Biochem. Soc. Trans. 35*, 61–67.

(4) Paleos, C. M., Tsiourvas, D., and Sideratou, Z. (2007) Molecular engineering of dendritic polymers and their application as drug and gene delivery systems. *Mol. Pharmaceutics 4*, 169–188.

(5) Gajbhiye, V., Kumar, P. V., Tekade, R. K., and Jain, N. K. (2007) Pharmaceutical and biomedical potential of PEGylated dendrimers. *Curr. Pharm. Des. 13*, 415–429.

(6) Chen, H. T., Neerman, M. F., Parrish, A. R., and Simanek, E. E. (2004) Cytotoxicity, hemolysis, and acute in vivo toxicity of dendrimers based on melamine, candidate vehicles for drug delivery. *J. Am. Chem. Soc. 126*, 10044–10048.

(7) Okuda, T., Kawakami, S., Akimoto, N., Niidome, T., Yamashita, F., and Hashida, M. (2006) PEGylated lysine dendrimers for tumor-selective targeting after intravenous injection in tumor-bearing mice. *J. Controlled Release 116*, 330–336.

(8) Okuda, T., Kawakami, S., Maeie, T., Niidome, T., Yamashita, F., and Hashida, M. (2006) Biodistribution characteristics of amino acid dendrimers and their PEGylated derivatives after intravenous administration. *J. Controlled Release 114*, 69–77.

(9) Margerum, L. D., Campion, B. K., Koo, M., Shargill, N., Lai, J. J., Marumoto, A., and Sontum, P. C. (1997) Gadolinium(III) DO3A macrocycles and polyethylene glycol coupled to dendrimers - Effect of molecular weight on physical and biological properties of macromolecular magnetic resonance imaging contrast agents. *J. Alloys Compd. 249*, 185–190.

(10) De Jesús, O. L. P., Ihre, H. R., Gagne, L., Fréchet, J. M. J., and Szoka, F. C. (2002) Polyester dendritic systems for drug delivery applications: In vitro and in vivo evaluation. *Bioconjugate Chem. 13*, 453–461.

(11) Malik, N., Wiwattanapatapee, R., Klopsch, R., Lorenz, K., Frey, H., Weener, J. W., Meijer, E. W., Paulus, W., and Duncan, R. (2000) Dendrimers: Relationship between structure and biocompatibility in vitro, and preliminary studies on the biodistribution of I-125-labelled polyamidoamine dendrimers in vivo. *J. Controlled Release 65*, 133–148.

(12) Gillies, E. R., Dy, E., Fréchet, J. M. J., and Szoka, F. C. (2005) Biological evaluation of polyester dendrimer: Poly(ethylene oxide) "bow-tie" hybrids with tunable molecular weight and architecture. *Mol. Pharmaceutics 2*, 129–138.

(13) Matsumura, Y., and Maeda, H. (1986) A new concept for macromolecular therapeutics in cancer-chemotherapy: Mechanism of tumoritropic accumulation of proteins and the antitumor agent Smancs. *Cancer Res. 46*, 6387–6392.

(14) Iyer, A. K., Khaled, G., Fang, J., and Maeda, H. (2006) Exploiting the enhanced permeability and retention effect for tumor targeting. *Drug Discovery Today 11*, 812–818.

(15) Gillies, E. R., and Fréchet, J. M. J. (2002) Designing macromolecules for therapeutic applications: Polyester dendrimer-poly(ethylene oxide) "bow-tie" hybrids with tunable molecular weight and architecture. *J. Am. Chem. Soc. 124*, 14137–14146.

(16) Lee, C. C., Gillies, E. R., Fox, M. E., Guillaudeu, S. J., Fréchet, J. M. J., Dy, E. E., and Szoka, F. C. (2006) A single dose of doxorubicin-functionalized bow-tie dendrimer cures mice bearing C-26 colon carcinomas. *Proc. Natl. Acad. Sci. U.S.A. 103*, 16649–16654.

(17) Ihre, H. R., De Jesús, O. L. P., Szoka, F. C., and Fréchet, J. M. J. (2002) Polyester dendritic systems for drug delivery applications: Design, synthesis, and characterization. *Bioconjugate Chem. 13*, 443–452.

(18) Gitsov, I., Wooley, K. L., Hawker, C. J., Ivanova, P. T., and Fréchet, J. M. J. (1993) Synthesis and properties of novel linear dendritic block-copolymers: Reactivity of dendritic macromolecules toward linear-polymers. *Macromolecules 26*, 5621–5627.

(19) Gitsov, I., Wooley, K. L., and Fréchet, J. M. J. (1992) Novel polyether copolymers consisting of linear and dendritic blocks. *Angew. Chem., Int. Ed. Engl. 31*, 1200–1202.

(20) Liu, M. J., Kono, K., and Fréchet, J. M. J. (1999) Water-soluble dendrimer-poly(ethylene glycol) starlike conjugates as potential drug carriers. *J. Polym. Sci. Part A: Polym. Chem. 37*, 3492–3503.

(21) Liu, M. J., Kono, K., and Fréchet, J. M. J. (2000) Water-soluble dendritic unimolecular micelles: Their potential as drug delivery agents. *J. Controlled Release 65*, 121–131.

(22) Bhadra, D., Bhadra, S., and Jain, N. K. (2006) PEGylated peptide dendrimeric carriers for the delivery of antimalarial drug chloroquine phosphate. *Pharm. Res. 23*, 623–633.

(23) Bhadra, D., Bhadra, S., and Jain, N. K. (2005) Pegylated lysine based copolymeric dendritic micelles for solubilization and delivery of artemether. *J. Pharm. Pharm. Sci. 8*, 467–482.

(24) Bhadra, D., Bhadra, S., and Jain, N. K. (2005) PEGylated peptide-based dendritic nanoparticulate systems for delivery of artemether. *J. Drug Delivery Sci. Technol. 15*, 65–73.

(25) Bhadra, D., Bhadra, S., Jain, S., and Jain, N. K. (2003) A PEGylated dendritic nanoparticulate carrier of fluorouracil. *Int. J. Pharm. 257*, 111–124.

(26) Luo, D., Haverstick, K., Belcheva, N., Han, E., and Saltzman, W. M. (2002) Poly(ethylene glycol)-conjugated PAMAM dendrimer for biocompatible, high-efficiency DNA delivery. *Macromolecules 35*, 3456–3462. .

(27) Kobayashi, H., Kawamoto, S., Saga, T., Sato, N., Hiraga, A., Ishimori, T., Konishi, J., Togashi, K., and Brechbiel, M. W. (2001) Positive effects of polyethylene glycol conjugation to generation-4 polyamidoamine dendrimers as macromolecular MR contrast agents. *Magn. Reson. Med. 46*, 781–788.

(28) Pan, G. F., Lemmouchi, Y., Akala, E. O., and Bakare, O. (2005) Studies on PEGylated and drug-loaded PAMAM dendrimers. *J. Bioact. Comp. Polym. 20*, 113–128.

(29) Veronese, F. M., Largajolli, R., Boccu, E., Benassi, C. A., and Schiavon, O. (1985) Surface modification of proteins: Activation of monomethoxy-polyethylene glycols by phenylchloroformates and modification of ribonuclease and superoxide-dismutase. *Appl. Biochem. Biotechnol. 11*, 141–152.

(30) Parrott, M. C., Marchington, E. B., Valliant, J. F., and Adronov, A. (2005) Synthesis and properties of carborane-functionalized aliphatic polyester dendrimers. *J. Am. Chem. Soc. 127*, 12081–12089.

(31) Gabbay, E. J., Grier, D., Fingerle, R. E., Reimer, R., Levy, R., Pearce, S. W., and Wilson, W. D. (1976) Interaction specificity of anthracyclines with deoxyribonucleic-acid. *Biochemistry 15*, 2062–2070.

(32) Larwood, D. J., and Szoka, F. C. (1984) Synthesis, characterization, and in vivo disposition of iodinatable polyethyleneglycol derivatives - Differences in vivo as a function of chain-length. *J. Labelled Compd. Radiopharm. 21*, 603–614.

(33) Welling, P. G. (1997) *Pharmacokinetics: Processes, Mathematics, and Applications* pp 271–282, American Chemical Society, Washington, DC.

(34) Ulbrich, K., Etrych, T., Chytil, P., Jelínková, M., and Øíhová, B. (2003) HPMA copolymers with pH-controlled release of doxorubicin - In vitro cytotoxicity and in vivo antitumor activity. *J. Controlled Release 87*, 33–47.

(35) Chytil, P., Etrych, T., Koòák, C., Šírová, M., Mrkvan, T., Øíhová, B., and Ulbrich, K. (2006) Properties of HPMA copolymer-doxorubicin conjugates with pH-controlled activation: Effect of polymer chain modification. *J. Controlled Release 115*, 26–36.

(36) Bae, Y., Jang, W. D., Nishiyama, N., Fukushima, S., and Kataoka, K. (2005) Multifunctional polymeric micelles with folate-mediated cancer cell targeting and pH-triggered drug releasing properties for active intracellular drug delivery. *Mol. BioSyst. 1*, 242–250.

(37) Bae, Y., Nishiyama, N., Fukushima, S., Koyama, H., Yasuhiro, M., and Kataoka, K. (2005) Preparation and biological characterization of polymeric micelle drug carriers with intracellular pH-triggered drug release property: Tumor permeability, controlled subcellular drug distribution, and enhanced in vivo antitumor efficacy. *Bioconjugate Chem. 16*, 122–130.

(38) Yang, H., and Lopina, S. T. (2006) In vitro enzymatic stability of dendritic peptides. *J. Biomed. Mater. Res. 76A*, 398–407.

(39) Yamaoka, T., Tabata, Y., and Ikada, Y. (1994) Distribution and tissue uptake of poly(ethylene glycol) with different molecular-weights after intravenous administration to mice. *J. Pharm. Sci. 83*, 601–606.

(40) Li, Q. Z., Hudson, W., Wang, D., Berven, E., Uckun, F. M., and Kersey, J. H. (1998) Pharmacokinetics and biodistribution of radioimmunoconjugates of anti-CD19 antibody and single-chain Fv for treatment of human B-cell malignancy. *Cancer Immunol. Immunother. 47*, 121–130.

BC700264G

Molecular Scale Architecture: Engineered Three- And Four-Way Junctions

Stephanie Wilkinson,[†] Michael Diechtierow,[§] R. August Estabrook, Falk Schmidt,[||] Michael Hüben,[||] Elmar Weinhold,[||] and Norbert O. Reich*[,†,‡]

Department of Chemistry and Biochemistry and Biomolecular Science and Engineering Program, University of California at Santa Barbara, 93106-9510, University of Heidelberg, Germany, and Institute of Organic Chemistry, RWTH Aachen University, Germany. Received July 18, 2007; Revised Manuscript Received October 18, 2007

Biomolecular self-assembly provides a basis for the bottom-up construction of useful and diverse nanoscale architectures. DNA is commonly used to create these assemblies and is often exploited as a lattice or an array. Although geometrically rigid and highly predictable, these sheets of repetitive constructs often lack the ability to be enzymatically manipulated or elongated by standard biochemical techniques. Here, we describe two approaches for the construction of position-controlled, molecular-scale, discrete, three- and four-way DNA junctions. The first approach for constructing these junctions relies on the use of nonmigrating cruciforms generated from synthetic oligonucleotides to which large, biologically generated, double-stranded DNA segments are enzymatically ligated. The second approach utilizes the DNA methyltransferase-based SMILing (sequence-specific methyltransferase-induced labeling of DNA) method to site-specifically incorporate a biotin within biologically derived DNA. Streptavidin is then used to form junctions between unique DNA strands. The resultant assemblies have precise and predetermined connections with lengths that can be varied by enzymatic or hybridization techniques, or geometrically controlled with standard DNA functionalization methods. These junctions are positioned with single nucleotide resolution on large, micrometer-length templates. Both approaches generate DNA assemblies which are fully compatible with standard recombinant methods and thus provide a novel basis for nanoengineering applications.

INTRODUCTION

Diverse materials including nanotubes (*1*), organic molecules (*2*), and biomolecules (*3*) are being employed to form novel nanoscale devices. Of these approaches, biomolecules offer a promising route to form complex and well-defined structures due to their highly convergent, self-assembling capabilities. DNA-based constructs provide many unique properties which make them ideal candidates for nanoscale devices. First, the self-assembling nature of DNA provides a bottom-up approach for synthesis with exquisite specificity and selection. Second, the physical dimensions of DNA, 2 nm in diameter and anywhere from 5 to 5000 nm in length, make this biomolecule an attractive template for wires in the nanometer regime despite its intrinsically poor conductivity (*4*). Third, commercially available DNA modifying enzymes (e.g., polymerases, ligases, endonucleases, and methyltransferases) and DNA binding proteins (e.g., zinc finger containing proteins) are compatible with such architectures facilitating their controlled static and dynamic manipulation.

The specific interactions between base pairs of DNA have been used to create nanostructures and direct the assembly of materials on the angstrom to micrometer scale (*5*–*7*). An emerging application of DNA nanostructures is the development of molecular electronics through the use of bottom-up approaches (*3*) (*8*) (*9*). In this context, the ability to construct discrete three- and four-way junctions will become increasingly important as more complex electronic architectures are sought. Novel DNA architectures for nanotemplating have been prepared, most notably by Seeman and co-workers (*6*). These DNA architectures are most frequently made up of highly repetitive, blocklike lattices or scaffolds (*7*) (*10*). These geometrically defined structures are repetitive and relatively rigid in both structure and sequence, making further recombinant manipulation problematic. For example, it is extremely difficult to introduce site-specific modifications to a small number of positions in such highly repetitive assemblies. Similarly, restriction enzymes, DNA ligases, and DNA polymerases are not always able to gain access to these highly interwoven assemblies. The methods described here can be used in conjunction with lattices or arrays in order to increase their versatility, or as a stand-alone assembly method yielding flexible constructs.

DNA-based molecular electronics have included conductive nanowires as well as electroless plating techniques (*3*) (*4*). An important electronic feature common to many devices relies on the use of junctions for signal splitting and amplification as well as for control gates. To this end, we have constructed isolated three-way and four-way DNA junctions at predetermined positions. One approach uses a nonmigrating cruciform as the core structure to which long, flexible DNA arms are enzymatically ligated (Figure 1). This recombinant approach differs from a similar method where 5′-biotinylated DNA was joined together by a streptavidin linkage to create a discrete four-way junction (*11*). Such structures are readily positioned onto metal electrodes via 5′ or 3′ functionalization to the ends of DNA (*3*) (*4*). Another approach positions one or more biotins or other labels *within biologically isolated DNA*. This position-controlled and selective placement of biotin was achieved with the SMILing DNA method (sequence-specific methyltransferase-induced labeling of DNA) (*12*) (*13*), which uses modified AdoMet analogues

* To whom correspondence should be addressed: reich@chem.ucsb.edu, (805) 893-8368; FAX (805) 893-4120.

[†] Department of Chemistry and Biochemistry, University of California at Santa Barbara.

[‡] Biomolecular Science and Engineering Program, University of California at Santa Barbara.

[§] University of Heidelberg.

[||] RWTH Aachen University.

10.1021/bc700270k CCC: $40.75 © 2008 American Chemical Society
Published on Web 12/11/2007

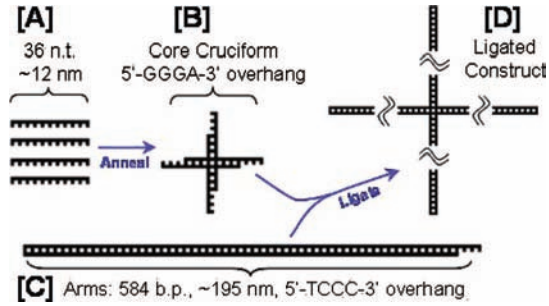

Figure 1. Cartoon of cruciform construction. (A) Four single strands of DNA are annealed to form the core cruciform. (B) Core cruciform. (C) Large DNA arms constructed by PCR with subsequent BsmBI digestion to create 5′-TCCC-3′ overhangs. (D) DNA arms were ligated to the core cruciform to form the final cruciform construct.

and sequence-specific DNA methyltransferases to deliver the biotin moiety.

EXPERIMENTAL PROCEDURES

Cruciform Preparation. Large DNA cruciforms were constructed by ligating PCR-derived DNA molecules to a small synthetic core junction. The small core cruciform was constructed by annealing four synthetic 36 bp DNA molecules (5′-GGGAGGTAGGACCGCAATCCTGAGCACGTCTCAACG-3′, 5′-GGGACCACCAGTGCCATAGTGGATTGCGGTCCT-ACC-3′, 5′-GGGAGGAACTGTGCATTCGGACTATGGCAC-TGGTGG-3′, and 5′-GGGACGTTGAGACGTGCTCACCGAAT-GCACAGTTCC-3′) with a 5′ overhang of 5′-GGGA-3′ on each arm. Oligonucleotides purchased from Midlands DNA were HPLC purified and kinased with dATP (Sigma) and T4 DNA kinase (NEB) extensively to ensure that all strands were fully phosphorylated at the 5′ end. These oligos were then repurified by phenol−chloroform extraction and annealed by boiling a mixture of equal molar ratios of each strand in STE buffer (100 mM NaCl, 10 mM Tris pH 8.0, 1 mM EDTA) for 5 min before being slowly cooled to room temperature. Proper annealing was confirmed by PAGE stained with SYBR gold (Invitrogen).

Large cruciform arms were made using pBR322 as a template for PCR. Amplicons 899 bp in length were generated with the primers 5′-CCCCCTTACACGGAGGCATCAGTGACC-3′ and 5′-GCTATGAGAAAGCGCCACGCTTCCCGAAGG-3′, respectively. The resulting amplicon had a single BsmBI recognition site 226 bp from one end. Up to 10 mL of PCR mixture was made using Taq DNA polymerase, 2.5 mM dNTPs, 2 ng/μL of each primer, 1 ng/μL of template, and was thermocycled: (1) 30 s at 95 °C, (2) 30 s at 95 °C, (3) 1 min at 55 °C, (4) 2 min at 74 °C, (5) repeat 30 times from step 2. PCR product was purified using the Qiaquick PCR Clean-up Kit (Qiagen) followed by phenol−chloroform precipitation. The concentration of the amplicon in TE (10 mM Tris, pH = 8.0, 1 mM EDTA) buffer was determined by A_{260}. Purified amplicon was digested with BsmBI (NEB) for up to 12 h to ensure completion. Once fully cut, the two fragments were isolated and purified by agarose gel extraction. DNA bands were cut from an agarose gel run in TBE buffer (10 mM Tris pH 8.0, 10 mM boric acid, 1 mM EDTA) and placed into 10 000 MWC dialysis tubing (Spectrum) for further electrophoresis. After 1 h, the current was reversed for 30 s and the TBE buffer within the dialysis tubing, which contained the isolated DNA fragments, was removed and ethanol precipitated. The concentration of amplicon fragments in TE buffer was determined by A_{260}.

Ligation reactions were made between synthetic core cruciforms and PCR-derived arms with T4 DNA ligase (NEB) at 4 °C. These reactions were usually done in large amounts so small aliquots could be removed and analyzed by agarose gel to monitor progress. Initially, PCR fragments had a 5-fold higher molar concentration than core cruciforms. As the reaction progressed, additional arm, core cruciform, or ligase could be added. Core cruciforms with four ligated arms were isolated from an agarose gel in the same manner as the PCR fragments. Construction was confirmed by digestion with T7 endonucleases I (NEB), which specifically cleaves DNA junctions (data not shown).

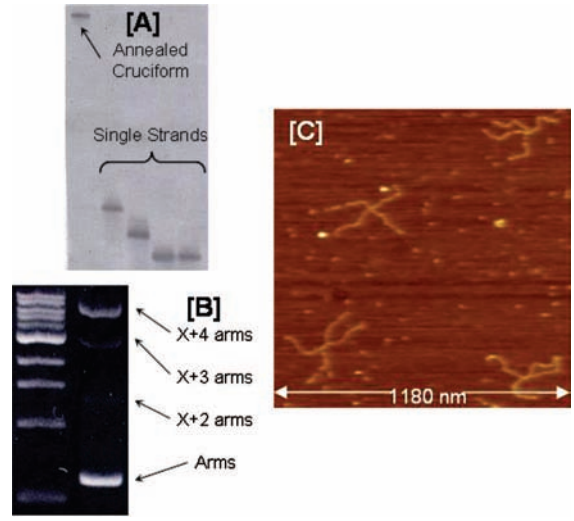

Figure 2. Data from cruciform construction. (A) 12% PAGE showing the annealing of single strands to form the core cruciform. (B) Ligated constructs were identified and isolated from 1% agarose gel. (C) Constructs were imaged by AFM on mica.

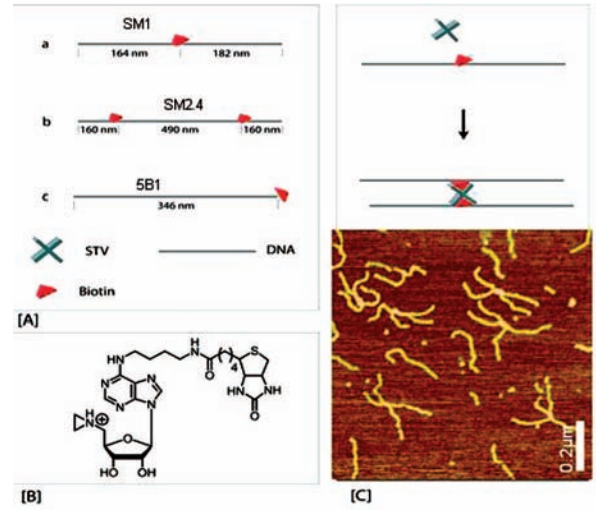

Figure 3. Schematic and AFM of four-way SMILing junctions. (A) Schematic showing the materials and design for assembling junctions. (B) Chemical structure of the modified methyltransferase cofactor 6BAz used in the SMILing DNA reactions. (C) Schematic and AFM image of four-way junctions created by incubating SM1 and STV at a ratio of 1:1.

SMILing DNA Preparation. Plasmid pBR322 (NEB) was used as a template for PCR amplifications, using the forward primer 5′-CCAAGTCATTCTGAGAATAGTGTA-3′ and reverse primer 5′-CGCCGAAACAAGCGCTCATGAGCCCG-3′, respectively, to generate a 1017 bp dsDNA fragment (SM1, Figure 3A(a)) with one centrally located (164 and 182 nm away from each end) recognition sequence for the DNA methyltransferase M.BseCI. This amplicon was also formed with a 5′-biotin (5B1, Figure 3A(c)) by using the forward primer listed above with the reverse biotinylated primer 5′-[BioTEG]CGCCGAAA-CAAGCGCTCATGAGCCCG-3′. Plasmid pUC19 (NEB) was

also used as a template for PCR using the primers 5′-AGGCATGCAAGCTTGGCGTAATCATGG-3′ and 5′-CCC-CGACACCCGCCAACACC-3′, respectively, to generate a 2383 bp dsDNA fragment (SM2.4, Figure 3A(b)) with two recognition sequences for the DNA methyltransferase M.TaqI, 160 nm from either end. All primers were ordered from Operon. Each PCR amplicon was purified with a Qiagen QIAquick PCR purification kit followed by phenol−chloroform extraction and ethanol precipitation.

SMILing DNA Modification. SM1 (1 μg), with one recognition site for M.BseCI at position 531–536 (30 nM), M.BseCI (303 nM), and 6BAz (80 μM, Figure 3B) were incubated in buffer (50 μL containing 10 mM Tris/HCl, pH 7.4, 20 mM $MgCl_2$, 50 mM NaCl, 50 μM EDTA, and 2 mM 2-mercaptoethanol) at 55 °C for 3 h. The reaction mixture was then heated to 70 °C for 20 min. Control reactions without M.BseCI and 6BAz were performed in parallel. After analysis by agarose gel electrophoresis, SM1 was purified using QIAquick PCR purification kits (QIAGEN) according to the instructions of the manufacturer. Similar protocols were used to create SM2.4.

To test the integrity of the DNA, aliquots of the SMILing reaction and the control reactions (10 μL, 0.2 μg DNA) were treated with Proteinase K (1 μL, 20 mg/mL in 10 mM Tris/HCl, pH 7.5, QIAGEN Proteinase K) and incubated at 37 °C for 1 h. Afterward, 6× loading buffer (2.2 μL, 30% glycerin, and 0.25% bromophenol blue) was added to each aliquot and the DNA was visualized by agarose gel electrophoresis (data not shown). Restriction analysis was performed by taking aliquots of the SMILing reaction and the control reactions (10 μL, 0.2 μg DNA) supplemented with water (1.3 μL), BSA (1.0 μL, 1.5 mg/mL), 10× NEB 2 buffer (1.5 μL, 100 mM Tris/HCl, pH 7.9, 100 mM $MgCl_2$, 500 mM NaCl, 10 mM DTT), and R.ClaI (1.2 μL, 4 units in NEB 2 buffer) and incubated at 37 °C for 1 h. Afterward, Proteinase K (1 μL, 20 mg/mL in 10 mM Tris/HCl, pH 7.5, QIAGEN Proteinase K) was added to each aliquot and the solutions were incubated at 37 °C for 1 h. Finally, 6× loading buffer (3.2 μL) was added to each aliquot. Results of the restriction digest were visualized by agarose gel electrophoresis (Supporting Information). To ensure biotin function, aliquots of the SMILing reaction and the control reactions (10 μL, 0.2 μg DNA) were supplemented with streptavidin (5 μL, 5 mg/mL in PBS buffer: 100 mM sodium phosphate, 100 mM NaCl, 2 mM sodium azide, pH 7.5) and incubated at 37 °C for 1 h. Afterward, 6× loading buffer (3.2 μL) was added to each aliquot. DNA mobility was visualized on a 0.8% agarose gel (Supporting Information).

Four-Way SMILing Junctions. These junctions were constructed using SM1 and streptavidin (STV) (Figure 3C) at a molar ratio of 1:1. DNA samples (150 nM) were incubated for 48 h at 4 °C. The long incubation time maximized the assembly of the desired junction, which was slow to form in solution. The desired construct was confirmed by both agarose gel electrophoresis and AFM analysis (Figure 3C and Supporting Information). Further distance analysis by AFM also showed that the location of the four-way junction is consistent with the SMILing DNA-directed placement of the biotin group onto SM1 (Figure 3).

Three-Way SMILing Junctions. These junctions were constructed with SM1, 5B1, and STV (Figure 4A,C). The highest yields were obtained with a stepwise addition of STV to SM1 in a ratio of SM1:STV of 1:5, followed by the addition of 5B1. AFM analysis verified that the location of the three-way junction is consistent with the SMILing DNA-directed placement of the biotin onto SM1 (Figure 4A,C). To create a double-three-way junction (Figure 4B,D), 5B1 and STV were incubated at a ratio of 1:5 followed by addition of SM2.4 at a ratio of 5B1/SM2.4 of 2:1. The anticipated placements of the three-way junctions on this larger element are also consistent with the SMILing DNA-directed placement of the two biotin moieties on SM2.4 (Figure 4A).

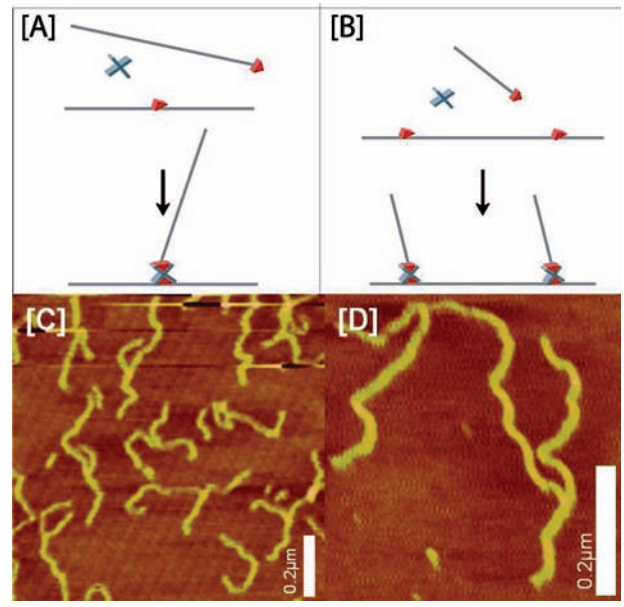

Figure 4. Schematic and AFM of three-way junctions. (A) Schematic of a single three-way junction formation. STV was preincubated with SM1 at a 5:1 ratio with subsequent addition of 5B1 to achieve the desired construct. (B) Schematic of double three-way junction formation. 5B1 was preincubated with 5-fold molar excess STV. SM2.4 was added at half the concentration of 5B1 to form junctions. (C) Tapping-mode AFM image of single three-way junctions described in A. (D) AFM image of a double three-way junction described in B.

AFM Sample Preparation. Desired DNA constructs were assembled in solution prior to immobilization for AFM. The resulting DNA (10 ng) was incubated in 20 μL of 1 mM $MgCl_2$ for 30 min at 22 °C. The resulting 20 μL solution was then deposited on freshly cleaved mica and left for 5 min. The sample was then washed using 3 mL of filtered and doubly distilled deionized water. Water remaining on the mica was wicked away and further dried with nitrogen. All AFM imagining was done on a Digital Instrument Multimode Dimension 3000.

RESULTS AND DISCUSSION

Cruciform-Based Junctions. Our initial four-way DNA junction was constructed by using a core, immobile cruciform from a set of previously published sequences (Figure 1) (*14*). These sequences were modified slightly to incorporate additional four base overhangs on the 5′ ends. The annealing of this cruciform showed a few aberrant secondary structures by PAGE, but the correct cruciform was still the most abundant form (Figure 2A). The successful ligation of the long arms to the core cruciform required several purification steps. PCR amplicons that formed the basis of the arm were purified away from residual primers which showed inhibitory affects toward the DNA ligase. The resulting purified amplicons were then digested with BsmBI to yield small (315 b.p.) and large (584 b.p.) DNA fragments. The large DNA fragment was isolated by gel purification followed by phenol−chloroform extraction and ethanol precipitation. The large DNA fragment was ligated back to the small DNA fragment to confirm the presence of the 5′ overhang (5′-TCCC-3′) essential for cruciform ligation.

Large four-way DNA junctions were successfully assembled by T4 DNA ligase as shown by agarose gel in Figure 2B. Initial cruciform ligation reactions contained roughly 5-fold molar excess of arm to core cruciform. As the reaction progress was monitored over time, subsequent additions of either core or arm

were made to the reaction mixture. The addition of free arm, although already in excess, led to more of the 4-way junctions. Isolation and purification of the large cruciforms was accomplished by gel excision. Due to the nature of this technique and the cruciform structure, large quantities of ligated cruciform were often required in order to recover a discernible amount. Various methods including the QIAquick Gel Extraction Kit (Qiagen) were attempted, but electrophoresis followed by concentration by ethanol precipitation gave the best results. Once purified, the final product was confirmed by successful digestion with T7 endonucleaseI, which exclusively cleaves DNA junctions.

The long, flexible DNA arms may find novel nanotechnology applications due to their extended linear nature and ability to be modified at unique and predetermined positions. For example, we have placed single metallic nanoparticles at specific positions on such structures with a goal toward creating electronic components (*36*). Although the structure of the DNA is not novel (*11*), our procedure to create the cruciform is unique. We have exploited the convergent capabilities of using DNA and DNA modifying enzymes in order to achieve higher-order structures. In this regard, using PCR-derived DNA that is manipulated by a restriction endonuclease is much more cost-effective than ordering synthetic arms or 5′ biotinylated primers. Further, we have shown that the immobile cruciform can be manipulated by enzymatic means. The construction approach demonstrated here should also be applicable for three-way junctions and junctions involving arms of various lengths.

SMILing-Based Junctions. The SMILing approach relies on cofactor analogues that deliver a small molecule from modified S-adenosylmethionine (AdoMet) to a site-specific location on the DNA (*12*) (*13*). This DNA methyltransferase-directed assembly of DNA junctions is schematically shown in Figures 3 and 4. DNA methyltransferases are responsible for many biological functions in prokaryotes and eukaryotes, including prokaryotic restriction-modification systems (*15*), DNA mismatch repair (*16*), chromosome replication (*17*), gene regulation (*18*), mammalian development (*19*), oncogenesis (*20*), and the organization of chromatin structure (*21*). Because these enzymes are structurally and mechanistically well-understood, they provide a sound basis for the types of bionanoengineering described here.

The SMILing method's replacement of an aziridine ring for the amino acid in AdoMet allows for the covalent incorporation of diverse ligands (*12*) (*13*) (*22*). Here, we applied the SMILing DNA approach to form novel, branching DNA structures. M.BseCI and M.TaqI use the natural cofactor AdoMet to methylate the amino group of the starred adenine residue in the sequences 5′-ATCGA*T-3′ and 5′-TCGA*-3′, respectively. In our studies, these enzymes were used to catalyze a nucleophilic aziridine ring opening of the cofactor analog 6BAz (Figure 3B) and covalently attach a single biotin at the target adenine in their respective recognition sequences (Figure 3A). The reaction of M.BseCI with the AdoMet analogue 6BAz results in the selective placement of biotin at one position within the 1017 bp dsDNA fragment (164 and 182 nm from each end). The M.TaqI reaction incorporated a biotin at two positions on the 2383 bp dsDNA (160 nm from either end). Biotin incorporation was verified by showing that the corresponding restriction endonuclease was incapable of digesting the modified DNA (Supporting Information).

The tetravalent binding capacity of streptavidin (STV) (*23*) suggests that the reaction between SM1 molecules and STV can lead to four-, six-, and eight-way junctions. However, we saw no evidence for six- or eight-way junctions (Supporting Information). Further, the formation of the four-way junction occurred after a 48 h incubation at 4 °C. The lengthy reaction time for four-way junctions and lack of six- and eight-way junctions is most likely due to the steric hindrance and electrostatic repulsion between the negatively charged DNA phosphate groups. To optimize the assembly of the desired four-way junction, we varied both the STV to biotinylated DNA ratio and a prebound DNA-STV to biotinylated DNA ratio. There was a clear dependence on these two ratios and how well junctions were formed (Supporting Information). At high concentrations of STV, few junctions were formed most likely due to all biotins being bound by individual STV. Conversely, high DNA concentrations yielded more junctions. In the case of the four-way junction, a 1:1 ratio of STV to biotinylated DNA gave the best results for formation of the desired DNA construct.

Contrary to the single incubation for four-way junctions, two reaction steps were necessary for the assembly of three-way junctions. For a single three-way junction, excess STV was allowed to bind to SM1 followed by the addition of the 5B1 to the reaction mixture (Figure 4A). Junction formation of the STV to the 5′-biotinylated DNA occurred much faster in comparison with the SMILing-modified DNA alone (data not shown), suggesting that steric interactions between DNA molecules may play a significant role in determining the rate and extent of reaction. A stepwise addition was also used for the construction of the double three-way junction (Figure 4B). 5B1 was preincubated with excess STV followed by addition of SM2.4.

The use of biotin−streptavidin linkages to form DNA structures is well-understood (*11*) (*24–27*); however, we have used a DNA-modifying enzyme to incorporate a biotin site specifically within long, native DNA derived from PCR. Li et al. reports a 2.1-fold increase in height upon STV binding to bare DNA (*28*). Cross-section analyses of our biotin−streptavidin linkages reveal a similar change in height; however, this is not easily seen in the SMILing DNA figures. We propose that this could be due to dehydrating AFM conditions that have been previously seen with DNA (*29*) and DNA binding proteins (*30*) or differences in tips used for AFM. However, the presence of the STV in our images can be further validated by the lengths of the DNA branches seen in Figures 3 and 4. The lengths correlate well with the site-specific positioning of the biotin and are consistent throughout many structures. The mere probability of this occurrence is highly unlikely.

Our current ability to assemble DNA junctions via biotin−streptavidin linkages provides constructs which are topologically but not geometrically defined. The lack of geometric constraint comes from the long DNA "arms" which extend from the junctions and go well beyond the persistence length of double-stranded DNA. Importantly, any approach making use of DNA junctions (*31*) will be faced by the breakdown of the geometric constraints when used with long DNA "arms". However, this may be overcome by using surfaces to which the complementary oligonucleotides are directed, forcing the hybridization of specific arms to particular surfaces in a geometrically defined manner. Additionally, PCR-derived DNA retains the ability to be end-functionalized, enabling placement of arms across electrodes or other devices.

Recent studies have described novel methods of creating finite DNA structures (*10*) (*27*) (*32*) (*33*). Although successful, these studies are still dependent on tightly packed, non-native forms of DNA, which make further manipulation by recombinant methods difficult. Our approach is further distinguished from DNA tiling and DNA array methods (*6*) (*27*) (*34*) (*35*), which normally result in assemblies with variable lengths or dimensions. Notably, Tian et al. recently described a long, flexible 4-way DNA junction (*11*). However, their approach relied solely upon 5′-biotinylated DNA brought together by the tetravalent binding capability of streptavidin. Our approaches use enzymatic manipulation (ligation, SMILing) independent of 5′ modifications to achieve similar higher-order structures. We argue that

our approaches offer more control with site-specific biotin incorporations within DNA in addition to the versatility associated with recombinant methods of manipulating biomolecules. Furthermore, the use of biologically derived DNA is more cost-effective and does not require the types of purification normally needed for synthetic DNA. Finally, the relative homogeneity of synthetic DNA oligonucleotide sequences means that kinetic traps may interfere with the assembly of a particular structure; this is less likely to be a problem with the highly heterogeneous biologically derived DNA.

Our construction of a set of novel, discrete nucleic acid architectures shows promise for directing the assembly of a variety of nanomaterials into higher-order structures using bottom-up assembly. This approach shows a level of molecular control which is essential for the construction of robust nanomaterials. Additionally, this approach also incorporates the use of recombinant techniques such as PCR and the use of DNA-modifying enzymes to achieve novel DNA architectures. The application of this approach to fabricate hybrid structures using carbon nanotubes and nanoparticles is being pursued. Ultimately, the retention of DNA molecules that can be manipulated by recombinant DNA methods provides a further basis for subsequent design and functionalization.

ACKNOWLEDGMENT

We thank Dr. Nadrian Seeman for insights into cruciform construction. This work was supported by a grant from the Institute for Collaborative Biotechnologies (DAAD19-03-D-0004), U.S. Army Research Office (Reich), and a UC GREAT Grant (Reich). This work made use of MRL Central Facilities supported by the MRSEC Program of the National Science Foundation under award No. DMR00-80034. We thank Basar Gider for helping in the initial synthesis of 6BAz, Kerstin Glensk for performing the SMILing reactions, and Prof. Dr. Michalis Kokkinidis for providing M.BseCI. We also thank Dr. Debra Fygenson for her suggestions.

Note Added after ASAP Publication: The author's name has changed since the original Web posting on December 11, 2007. The correction was made and the article reposted on January 9, 2008.

Supporting Information Available: Details on the SMILing modified DNA and the concentration and ratio dependencies on junction formation are given. This material is available free of charge via the Internet at http://pubs.acs.org.

LITERATURE CITED

(1) Martin, C. R., and Kohli, P. (2003) The emerging field of nanotube biotechnology. *Nat. Rev. Drug Discovery 2*, 29–37.
(2) Rosei, F., Schunack, M., Naitoh, Y., Jiang, P., Gourdon, A, Laegsgaard, E., Stensgaard, I., Joachim, C., and Besenbacher, F. (2003) Properties of large organic molecules on metal surfaces. *Prog. Surf. Sci. 71*, 95–146.
(3) Braun, E., and Keren, K. (2004) From DNA to transistors. *Adv. Phys. 53*, 441–96.
(4) Taniguchi, M., and Kawai, T. (2006) DNA electronics. *Phys. E 33*, 1–12.
(5) Brucale, M., Zuccheri, G., and Samori, B. (2006) Mastering the complexity of DNA nanostructures. *Trends Biotechnol. 5*, 235–43.
(6) Seeman, N. C., and Lukeman, P. S. (2005) Nucleic acid nanostructures: bottom-up control of geometry on the nanoscale. *Rep. Prog. Phys. 68*, 237–70.
(7) Gothelf, K. V., and LaBean, T. H. (2005) DNA-programmed assembly of nanostructures. *Org. Biomol. Chem. 3*, 4023–37.
(8) Katz, E., and Willner, I. (2004) Integrated nanoparticle-biomolecule hybrid systems: synthesis, properties, and applications. *Angew. Chem., Int. Ed. 43*, 6042–108.
(9) Seeman, N. C. (2003) DNA in a material world. *Nature (London) 421*, 427–31.
(10) Rothemund, P. W. K. (2006) Folding DNA to create nanoscale shapes and patterns. *Nature (London) 440*, 297–302.
(11) Tian, Y., He, Y., Ribbe, A. E., and Mao, C. D. (2006) Preparation of branched structures with long DNA duplex arms. *Org. Biomol. Chem. 4*, 3404–5.
(12) Pljevaljcic, G., Schmidt, F., and Weinhold, E. (2004) Sequence-specific methyltransferase-induced labeling of DNA (SMILing DNA). *ChemBioChem 5*, 265–9.
(13) Pljevaljcic, G., Schmidt, F., Peschlow, A., and Weinhold, E. (2004) Sequence-specific DNA labeling using methyltransferases. *Methods Mol. Biol. 283*, 145–61.
(14) Kallenbach, N. R., Ma, R. I., and Seeman, N. C. (1983) An immobile nucleic-acid junction constructed from oligonucleotides. *Nature (London) 305*, 829–31.
(15) Wilson, G. G., and Murray, N. E. (1991) Restriction and modification systems. *Annu. Rev. Genet. 25*, 585–627.
(16) Palmer, B. R., and Marinus, M. G. (1994) The dam and dcm strains of *Escherichia coli*–a review. *Gene 143*, 1–12.
(17) Reisenauer, A., Kahng, L. S., McCollum, S., and Shapiro, L. (1999) Bacterial DNA methylation: a cell cycle regulator? *J. Bacteriol. 181*, 5135–9.
(18) Jaenisch, R., and Bird, A. (2003) Epigenetic regulation of gene expression: how the genome integrates intrinsic and environmental signals. *Nat. Genet. 33*, 245–54.
(19) Reik, W., and Walter, J. (2001) Genomic imprinting: parental influence on the genome. *Nat. Rev. Genet. 2*, 21–32.
(20) Jones, P. A., and Baylin, S. B. (2002) The fundamental role of epigenetic events in cancer. *Nat. Rev. Genet. 3*, 415–28.
(21) Jackson-Grusby, L., and Jaenisch, R. (1996) Experimental manipulation of genomic methylation. *Semin. Cancer Biol. 7*, 261–8.
(22) Pljevaljcic, G., Pignot, M., and Weinhold, E. (2003) Design of a new fluorescent cofactor for DNA methyltransferases and sequence-specific labeling of DNA. *J. Am. Chem. Soc. 125*, 3486–92.
(23) Hendrickson, W. A., Pahler, A., Smith, J. L., Satow, Y., Merritt, E. A., and Phizackerley, R. P. (1989) Crystal structure of core streptavidin determined from multiwavelength anomalous diffraction of synchrotron radiation. *Proc. Natl. Acad. Sci. U.S.A. 86*, 2190–4.
(24) Niemeyer, C. M., Adler, M., Gao, S., and Chi, L. (2001) Nanostructured DNA-protein aggregates consisting of covalent oligonucleotide-streptavidin conjugates. *Bioconjugate Chem. 12*, 364–71.
(25) Niemeyer, C. M. (2004) Semi-synthetic DNA-protein conjugates: novel tools in analytics and nanobiotechnology. *Biochem. Soc. Trans. 32*, 51–3.
(26) Park, S. H., Yin, P., Liu, Y., Reif, J. H., LaBean, T. H., and Yan, H. (2005) Programmable DNA self-assemblies for nanoscale organization of ligands and proteins. *Nano Lett. 5*, 729–33.
(27) Park, S. H., Pistol, C., Ahn, S. J., Reif, J. H., Lebeck, A. R., Dwyer, C., and LaBean, T. H. (2006) Finite-size, fully addressable DNA tile lattices formed by hierarchical assembly procedures. *Angew. Chem., Int. Ed. 45*, 735–9.
(28) Li, H. Y., Park, S. H., Reif, J. H., LaBean, T. H., and Yan, H. (2004) DNA-templated self-assembly of protein and nanoparticle linear arrays. *J. Am. Chem. Soc. 126*, 418–9.
(29) Bezanilla, M., Manne, S., Laney, D. E., Lyubchenko, Y. L., and Hansma, H. G. (1995) Adsorption of DNA to mica, silylated mice, and minerals - characterization by atomic-force microscopy. *Langmuir 11*, 655–9.
(30) Allison, D. P., Kerper, P. S., Doktycz, M. J., Spain, J. A., Modrich, P., Larimer, F. W., Thundat, T., and Warmack, R. J. (1996) Direct atomic force microscope imaging of EcoRI endonuclease site specifically bound to plasmid DNA molecules. *Proc. Natl. Acad. Sci. U.S.A. 93*, 8826–9.

(31) He, Y., Chen, Y., Liu, H., Ribbe, A. E., and Mao, C. (2005) Self-assembly of hexagonal DNA two-dimensional (2D) arrays. *J. Am. Chem. Soc. 127*, 12202–3.
(32) Liu, Y., Ke, Y. G., and Yan, H. (2005) Self-assembly of symmetric finite-size DNA nanoarrays. *J. Am. Chem. Soc. 127*, 17140–1.
(33) Lund, K., Liu, Y., Lindsay, S., and Yan, H. (2005) Self-assembling a molecular pegboard. *J. Am. Chem. Soc. 127*, 17606–7.
(34) Feldkamp, U., and Niemeyer, C. M. (2006) Rational design of DNA nanoarchitectures. *Angew. Chem., Int. Ed. 45*, 1856–76.
(35) O'Neill, P., Rothemund, P. W., Kumar, A., and Fygenson, D. K. (2006) Sturdier DNA nanotubes via ligation. *Nano Lett. 6*, 1379–83.
(36) Braun, G., Diechtierow, M., Wilkinson, S., Schmidt, F., Lugowski, M., Weinhold, E., and Reich, N. Unpublished results.

BC700270K

Enzyme-Directed Positioning of Nanoparticles on Large DNA Templates

Gary Braun,[†] Michael Diechtierow,[†] Stephanie Wilkinson,[†] Falk Schmidt,[§] Michael Hüben,[§] Elmar Weinhold,[§] and Norbert O. Reich*[,†,‡]

Department of Chemistry and Biochemistry, Biomolecular Science and Engineering Program, University of California, Santa Barbara, California 93106-9510, and Institute of Organic Chemistry, RWTH Aachen University, Germany. Received July 20, 2007; Revised Manuscript Received November 5, 2007

A method to position nanoparticles onto DNA with high resolution using an enzyme-based approach is described. This provides a convenient route to assemble multiple nanoparticles (e.g., Au and CdSe) to specific positions with a high level of control and expandability to more complex assemblies. Atomic force microscopy is used to analyze the nanostructures, which have potential interest for biosensor, optical waveguide, molecular electronics, and energy transfer studies.

INTRODUCTION

The ability to position nanoparticles and quantum dots onto molecular scaffolds with nanometer control has potential applications for biosensors, optical waveguides, molecular electronics, energy transfer, and surface-enhanced Raman spectroscopy (SERS) (*1, 2*). The development of nanoscale molecular electronics is being pursued using nanowires, nanotubes (*3–6*), conducting organic molecules, as well as biomolecular approaches (*7–13*). Many of these approaches rely on the incorporation of nanoparticles (NPs) to enhance the electronic features of the particular nanoarchitecture. For example, the construction of nanoparticle-based single electron tunneling devices requires the positioning of a single nanoparticle within nanometer distance to the conducting wires and, to work at room temperature, a NP size small enough that the Coulomb charging energy exceeds the thermal energy. Several biomolecular routes to controlling electronic elements rely on DNA structures that spontaneously self-assemble into repeating polymeric patterns that can direct nanoparticles (*14–17*). Depositing the DNA between electrodes on a substrate is a separate challenge, although promising strategies include incorporating thiol groups to bind gold surfaces, using hybridization through terminal single stranded overhangs onto short complimentary DNA coatings (*18*), or using electric fields to orient and stretch long DNA across an electrode gap in solution (*19*). In this article, we complement these methods by enabling targeted placement of single or multiple chemical modifications onto large DNA templates and show their capacity to control the positioning of nanoparticles. We used biotin−streptavidin interactions to drive a gold NP to the biotinylated nucleotide(s) and electrostatic assembly of a separate NP type, small metallic, or semiconductor quantum dots to fill in the remaining DNA backbone. These hybrid materials are of particular interest for studying electronic interactions through controlled spacing and geometry. Multiple enzymes, each recognizing a unique recognition sequence, may be used to further extend this approach.

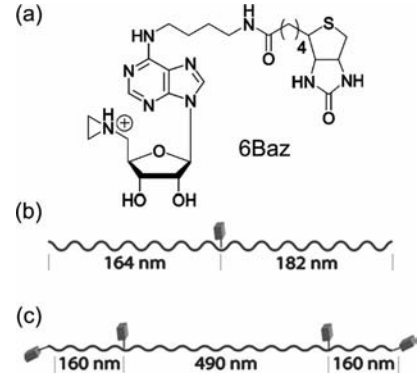

Figure 1. Design of DNA templates. (a) The 6BAz artificial cofactor used to biotinylate DNA with M.*Taq*I and M.BseCI. (b) SM1 and (c) SM2. Biotin modification is shown by a grey box at the position being modified.

RESULTS AND DISCUSSION

We used the SMILing DNA approach to incorporate biotin molecules at predetermined positions for binding NPs within stretches of thousands of base pairs (*20–23*). The approach relies on the use of bacterial DNA methyltransferases known to methylate specific DNA sites using the natural cofactor *S*-adenosyl-L-methionine (AdoMet). SMILing DNA uses aziridine-modified AdoMet analogues to deliver a desired functionality in place of the methyl group. The synthetic analogue 6Baz allows the site-specific incorporation of biotin through an ∼2 nm linker composed of the opened aziridine ring (attached to the targeted position of the nucleotide) and the extended adenosyl structure with an aminobutyl group attached to the 6 position of the adenine ring (Figure 1a and Supporting Information). Binding to streptavidin (STV) was recently demonstrated after DNA biotinylation with a related aziridine cofactor giving a similar linker length (*23*). In addition, this linker length is similar to amine-reactive PEG-biotin labeling reagents commonly used for protein modification and is expected to lower steric hindrance when binding STV while negligibly affecting the positional resolution of the method. The DNA methyltransferases M.*Taq*I and M.BseCI recognize the sequences 5′-TCGA-3′ and 5′-ATCGAT-3′, respectively (the modified adenine is

* Corresponding author. E-mail: reich@chem.ucsb.edu.
[†] Department of Chemistry and Biochemistry, University of California, Santa Barbara.
[‡] Biomolecular Science and Engineering Program, University of California, Santa Barbara.
[§] RWTH Aachen University.

10.1021/bc700275h CCC: $40.75 © 2008 American Chemical Society
Published on Web 12/19/2007

underlined). Successful biotinylation of the DNA with both enzymes was verified using agarose gel analysis and showed quantitative coupling efficiency (Supporting Information).

Biotinylated binding sites were incorporated within two lengths of DNA templates to demonstrate versatility in the positioning of nanoparticles. Plasmid pBR322 was used to generate a 1017 bp DNA fragment (~346 nm) with one recognition site for M.BseCI positioned 164 and 182 nm away from the ends (SM1, Figure 1b and Supporting Information). Plasmid pUC19 was used to create a 2.4 kb fragment (~810 nm, SM2) with two internal recognition sites for M.*Taq*I positioned 160 nm inward from each end (*21*). In addition, 5′-biotinylated primers were used during the PCR amplification for SM2, yielding a total of four sites (Figure 1c). (For targeting the DNA to substrate-surface features, one would make use of unique functional groups conjugated to the primers, or their hybridization sequence, as the primers reside at the ends of the DNA template.) In each system, STV linkages were used to attach biotinylated gold nanoparticles (AuNP).

AuNP were prepared with a passivating layer for stability in buffer and for resisting nonspecific interactions with DNA by coating them with the anionic bis(*p*-sulfonatophenyl)phenylphosphine (BSP, Strem). Small numbers of biotin ligands were introduced through the use of the disulfide moiety *N*-[6-(biotinamido)hexyl]-3′-(2′-pyridyldithio)propionamide (Biotin-HPDP, Pierce), functionalizing the Au at a ratio of 1:3 biotin/NP. A low ratio was used to minimize the cross-linking of DNA when combined with STV and DNA in solution, while the anionic ligand BSP was expected to reduce nonspecific interactions.

Biotinylated SM1 DNA was incubated with a 3-fold excess of STV, combined with a 20-fold excess of biotin-AuNP and then deposited onto mica for AFM visualization (Figure 2a). A low concentration of $ZnCl_2$ (1 mM) was added for depositing the DNA onto freshly cleaved mica while minimizing the background level of free NPs. The DNA constructs in Figure 2b clearly show the central positioning of NPs (Supporting Information). The bent conformation of the construct is most likely due to the liquid flow during washing.

Anticipated uses of such NP−DNA constructs for nanoelectronics could require immobilization onto SiO_2/Si surfaces (*14, 25*). We therefore tested SiO_2/Si substrates derivatized with hexamethyldisilizane (HMDS) for the bottom-up assembly of DNA−NP structures. HMDS functionalizes the SiO_2 surface with trimethylsilyl groups, which are useful for molecular combing of double stranded DNA, a common immobilization and alignment strategy, while the hydrophobic passivation layer also limits nonspecific deposition of NPs (*14, 26, 27*). In Figure 2c, a single 13 nm biotin-AuNP is bound to the center of combed STV-SM1. The incubation with biotin-AuNP does not appear to significantly disrupt the combed DNA template. Figure 2 parts d and e present the height analyses of the 6 and 13 nm NP constructs on mica and HMDS-SiO_2/Si, respectively.

To explore metal/semiconductor heterostructure assembly, nanoparticles were deposited stepwise onto STV-SM1 templates previously combed onto HMDS-SiO_2/Si. The templates were first modified with a 13 nm biotin-AuNP (as in Figure 2c) followed by electrostatically coating the rest of the DNA with cationic 2-aminoethanethiol 3.3 nm CdSe/ZnS core/shell QD (AET-CdSe/ZnS) prepared by ligand exchange of hexadecylamine-passivated CdSe/ZnS (*28*). The anionic phosphate backbone of the DNA attracts the cationic QD similar to previous studies with positively charged AuNP and DNA (*27, 29–31*). The large difference in size between the two is evident through AFM analysis (Figure 2f) indicating successful assembly. The ability to pattern hybrid nanostructures, for example, metal, insulator, and semiconductor quantum dots (QD) onto the same

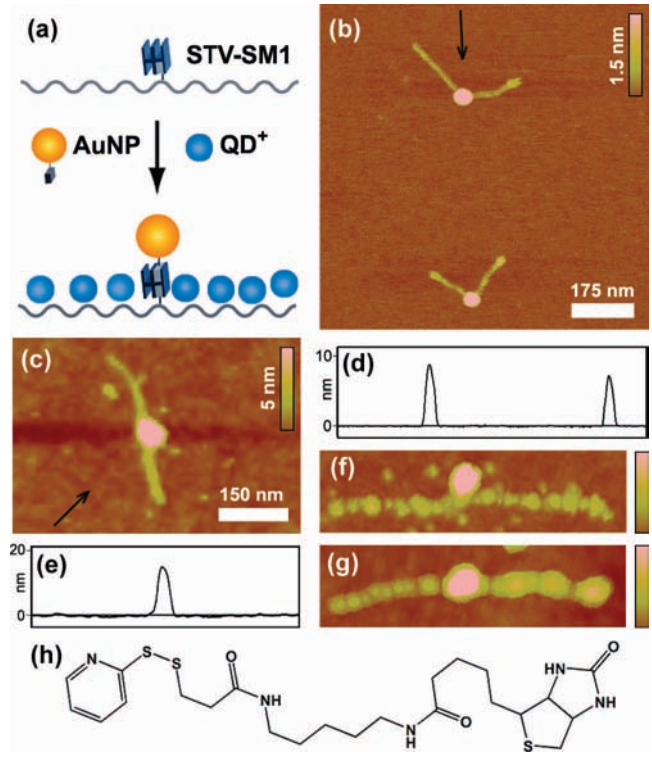

Figure 2. (a) General strategy for assembling biotinylated AuNP and cationic quantum dots (QD^{+}) onto STV-SM1 DNA. (b) AFM image of 6 nm AuNP-DNA formed by solution-based assembly of all components, deposited on mica. (c) Biotin-AuNP (13 nm) placement on SM1 carried out by immobilization of STV-DNA on Si/SiO_2 followed by binding by biotin-AuNP. (d) Height analysis of b along arrow. (e) Height analysis of c along arrow. (f) DNA with 13 nm AuNP with electrostatically assembled QD. (g) Electrostatic assembly of 3.5 nm thiocholine AuNP followed by 13 nm biotin-AuNP. The height bar is 10 nm, and the image is 400 nm across in f and g. (h) Structure of the biotin-HPDP disulfide.

template is of interest for exploring novel plasmonic materials. For example, QD coupling with localized metal surface plasmons has been shown to occur for closely spaced metal nanoparticles near a single QD, where the characteristic optical feature of the plasmon was detected in the QD emission spectrum (*32–34*). Similar structures could be achieved using a directed-assembly approach by using a STV-functionalized QD at the central position and cationic gold nanoparticles along the DNA.

To further test the binding site integrity of the SMILing approach, STV-SM1 was combed onto the HMDS-Si/SiO_2 surface and nonspecifically coated with cationic thiocholine 3.5 nm AuNP (tcAuNP) (*27*). This was followed by a back-filling at the central STV with a 13 nm biotin-AuNP (Figure 2g). Apparently, the initial electrostatic NP coating step does not affect the biotin binding capability of STV-SM1 nor significantly affect the specificity of the interaction. Because of the large size difference of the particles, it is clear that biotin-AuNP binds only at the center of the template.

We also tested the ability for STV-AuNP to bind to the biotin site within combed DNA, as a variation of stepwise assembly. Here, 6 nm STV-functionalized AuNP binds to biotin-SM1, which had been deposited on SiO_2 by combing. This scheme and resultant structure are presented in Figures S1 and S2 (Supporting Information). We conclude that the spacer connecting the biotin to the DNA base is indeed sufficient for attachment of STV postcombing. Metal nanowires with a height of ~20 nm were grown from these templates using a tcAuNP coating as a seed layer (Figure S3, Supporting Information) (*10, 27*).

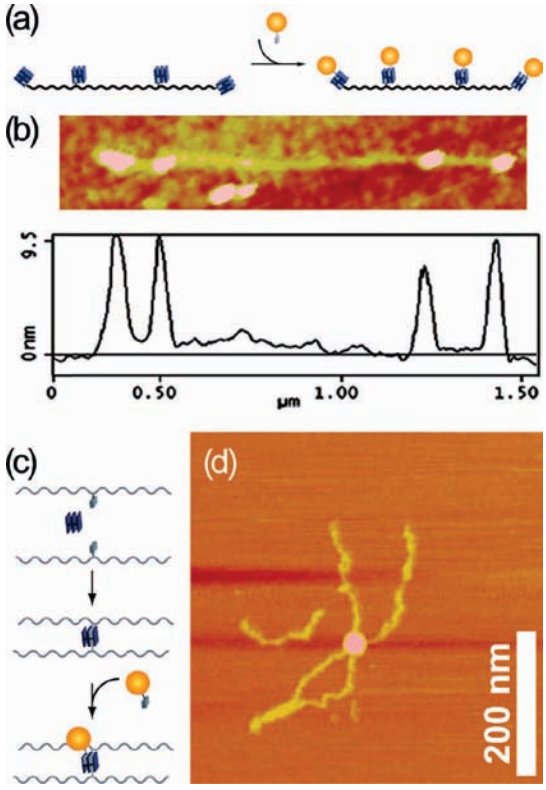

Figure 3. (a) Scheme for SM2 templating of AuNP. (b) AFM image and cross-section of SM2 bound with four 6 nm biotin-AuNP, taken along the structure axis. Two sites obtained by enzymatic biotinylation are internal, and two sites are external 5′ biotins from the synthetic primers. (c) Four-way junction scheme using STV with central AuNP. (d) Junction decorated with 6 nm biotin-AuNP on mica.

We could not discern a central gap by AFM, although this may be due to tip resolution limits (∼10–20 nm tip radius). We note that TEM imaging has previously been used to show that STV masking of reductively grown NP seeds is possible on a DNA template, and such analysis is underway (*10*).

A DNA template with two internally positioned biotins and biotins at the ends was generated by enzymatic SMILing modification of a PCR product created with biotinylated primers (SM2). This 810 nm construct was designed with recognition sites 160 nm inward from each end. Templates were incubated with excess STV and combed onto HMDS/Si/SiO_2, and then reacted with 6 nm biotin-AuNP. Figure 3b shows AFM height and cross-section analysis of a complete construct, while Figure S4 (Supporting Information) shows an example of a defect structure bound with only one AuNP (Supporting Information). The template appears stretched due to combing (*35*), as the overall length is ∼1075 nm compared to the theoretical 810 nm. The stretched center-to-center distance between the right two particles is measured at 195 nm rather than 160 nm (∼120% of theoretical), which is consistent with an overall DNA stretching of ∼130%.

Formation of intricate nanostructures through molecular lithography is likely to require interconnecting junctions (*14*,*36*,*37*). Using the SMILing DNA approach, novel four-way junctions can be created using STV (*24*). SM1 and STV combined at a molar ratio of 1:1 was used to form four-way junctions. A single NP was positioned at the junction by incubation with biotinylated 6 nm AuNP (Figure 3d). This template could be envisioned as an electronic junction if the DNA arms are directed to bind to separate surface electrodes, metallized, and a functional nanomaterial (e.g., semiconductor) attached at the central streptavidin (*10*, *36*).

In summary, we have demonstrated a new method for controlling the placement of nanoparticles onto DNA scaffolds. This enzymatic approach may be extended to position NPs onto biological or synthetic DNA constructs. More complex DNA constructs may be designed by using multiple enzymes, each recognizing a unique recognition sequence and delivering one of a variety of chemical groups through synthetic cofactors. As such, this approach shows promise for directing the assembly of a variety of nanomaterials into organized structures with applications including nanoelectronics, biosensors, plasmon wave guides, and SERS-active materials.

ACKNOWLEDGMENT

This work was supported by a grant from the Institute for Collaborative Biotechnologies (DAAD19-03-D-0004, U.S. Army Research Office (Reich) and NIH (5RO1EB000832). This work made use of MRL Central Facilities supported by the MRSEC Program of the National Science Foundation under award No. DMR00-80034. We thank Kerstin Glensk for performing the SMILing reactions and Professor Michaelis Kokkinidis for supplying M.BseCI. We also thank Daniel Neuman for providing hexadecylamine-CdSe/ZnS.

Supporting Information Available: Details of DNA and nanomaterial preparation with supporting figures. This information is available free of charge via the Internet at http://pubs.acs.org.

LITERATURE CITED

(1) Maier, S. A., Kik, P. G., Atwater, H. A., Meltzer, S., Harel, E., Koel, B. E., and Requicha, A. A. A. (2003) Local detection of electromagnetic energy transport below the diffraction limit in metal nanoparticle plasmon waveguides. *Nat. Mater. 2*, 229–232.

(2) Gearheart, L. A., Ploehn, H. J., and Murphy, C. J. (2001) Oligonucleotide adsorption to gold nanoparticles: A surface-enhanced raman spectroscopy study of intrinsically bent DNA. *J. Phys. Chem. B 105*, 12609–12615.

(3) Hu, J. T., Min, O. Y., Yang, P. D., and Lieber, C. M. (1999) Controlled growth and electrical properties of heterojunctions of carbon nanotubes and silicon nanowires. *Nature 399*, 48–51.

(4) Tans, S. J., Devoret, M. H., Dai, H. J., Thess, A., Smalley, R. E., Geerligs, L. J., and Dekker, C. (1997) Individual single-wall carbon nanotubes as quantum wires. *Nature 386*, 474–477.

(5) Odom, T. W., Huang, J. L., Kim, P., and Lieber, C. M. (2000) Structure and electronic properties of carbon nanotubes. *J. Phys. Chem. B 104*, 2794–2809.

(6) Yao, Z., Postma, H. W. C., Balents, L., and Dekker, C. (1999) Carbon nanotube intramolecular junctions. *Nature 402*, 273–276.

(7) Braun, E., and Keren, K. (2004) From DNA to transistors. *Adv. Phys. 53*, 441–496.

(8) Mao, C. D., Labean, T. H., Reif, J. H., and Seeman, N. C. (2000) Logical computation using algorithmic self-assembly of DNA triple-crossover molecules. *Nature 407*, 493–496.

(9) Seeman, N. C. (2003) DNA in a material world. *Nature 421*, 427–431.

(10) Griffin, F., Ongaro, A., and Fitzmaurice, D. (2004) DNA-templated assembly of nanoscale wires and protein-functionalized nanogap contacts. *Analyst 129*, 1171–1175.

(11) Mao, C. B., Solis, D. J., Reiss, B. D., Kottmann, S. T., Sweeney, R. Y., Hayhurst, A., Georgiou, G., Iverson, B., and Belcher, A. M. (2004) Virus-based toolkit for the directed synthesis of magnetic and semiconducting nanowires. *Science 303*, 213–217.

(12) Park, S. H., Yan, H., Reif, J. H., Labean, T. H., and Finkelstein, G. (2004) Electronic nanostructures templated on self-assembled DNA scaffolds. *Nanotechnology 15*, S525–S527.

(13) Liu, D., Park, S. H., Reif, J. H., and Labean, T. H. (2004) DNA nanotubes self-assembled from triple-crossover tiles as templates for conductive nanowires. *Proc. Natl. Acad. Sci. U.S.A. 101*, 717–722.
(14) Keren, K., Berman, R. S., Buchstab, E., Sivan, U., and Braun, E. (2003) DNA-templated carbon nanotube field-effect transistor. *Science 302*, 1380–1382.
(15) Katz, E., and Willner, I. (2004) Integrated nanoparticle-biomolecule hybrid systems: Synthesis, properties, and applications. *Angew. Chem., Int. Ed. 43*, 6042–6108.
(16) Zhang, S. G. (2003) Fabrication of novel biomaterials through molecular self-assembly. *Nat. Biotechnol. 21*, 1171–1178.
(17) Tanaka, S., Fritzsche, W., Sako, Y., and Yanagidal, T. (2006) Synthesis of Long-template DNA Using Enzymatic Reaction for Regular Alignment of Au-nanoparticles. *Chem. Lett. 35* (11), 1290–1291.
(18) Csáki, A., Maubach, G., Born, D, Reichert, J., and Fritzsche, W. (2002) DNA-based molecular nanotechnology. *Single Mol.* (5–6), 275–280.
(19) Dewarrat, F., Calame, M., and Schönenberger, C. (2002) Orientation and positioning of DNA molecules with and electric field technique. *Single Mol. 3* (4), 189–193.
(20) Pljevaljcic, G., Pignot, M., and Weinhold, E. (2003) Design of a new fluorescent cofactor for DNA methyltransferases and sequence-specific labeling of DNA. *J. Am. Chem. Soc. 125*, 3486–3492.
(21) Pljevaljcic, G., Schmidt, A., Peschlow, A., and Weinhold, E. (2004) Sequence-specific DNA labeling using methyltransferases. *Methods Mol. Biol. 283*, 145–161.
(22) Pljevaljcic, G., Schmidt, F., and Weinhold, E. (2004) Sequence-specific methyltransferase-induced labeling of DNA (SMILing DNA). *ChemBioChem 5*, 265–269.
(23) Pljevaljcic, G., Schmidt, F., Scheidig, A. J., Lurz, R., and Weinhold, E. (2007) Quantitative labeling of long plasmid DNA with nanometer precision. *ChemBioChem 8*, 1516–1519.
(24) Wilkinson, S., Diechtierow, M., Estabrook, A. E., Schmidt, F., Lugowski, M., Weinhold, E., and Reich, N. O. (2007) Molecular scale architecture: engineered three- and four-way junctions. *Bioconjugate Chem.*, submitted for publication.
(25) Braun, E., Eichen, Y., Sivan, U., and Ben-Yoseph, G. (1998) DNA-templated assembly and electrode attachment of a conducting silver wire. *Nature 391*, 775–778.
(26) Allemand, J. F., Bensimon, D., Jullien, L., Bensimon, A., and Croquette, V. (1997) pH-dependent specific binding and combing of DNA. *Biophys. J. 73*, 2064–2070.
(27) Braun, G., Inagaki, K., Estabrook, R. A., Wood, D. K., Levy, E., Cleland, A. N., Strouse, G. F., and Reich, N. O. (2005) Gold nanoparticle decoration of DNA on silicon. *Langmuir 21*, 10699–10701.
(28) Cumberland, S. L., Berrettini, M. G., Javier, A., and Strouse, G. F. (2003) Synthesis and characterization of a 1: 6 Au-CdSe nanocomposite. *Chem. Mater. 15*, 1047–1056.
(29) Nakao, H., Shiigi, H., Yamamoto, Y., Tokonami, S., Nagaoka, T., Sugiyama, S., and Ohtani, T. (2003) Highly ordered assemblies of Au nanoparticles organized on DNA. *Nano Lett. 3*, 1391–1394.
(30) Warner, M. G., and Hutchison, J. E. (2003) Linear assemblies of nanoparticles electrostatically organized on DNA scaffolds. *Nat. Mater. 2*, 272–277.
(31) Wang, G. L., and Murray, R. W. (2004) Controlled assembly of monolayer-protected gold clusters by dissolved DNA. *Nano Lett. 4*, 95–101.
(32) Gryczynski, I., Malicka, J., Jiang, W., Fischer, H., Chan, W. C. W., Gryczynski, Z., and Lakowicz, J. R. (2005) Surface-plasmon-coupled emission of quantum dots. *J. Phys. Chem. B 109*, 1088–1093.
(33) Shimizu, K. T., Woo, W. K., Fisher, B. R., Eisler, H. J., and Bawendi, M. G. (2002) Surface-enhanced emission from single semiconductor nanocrystals. *Phys. Rev. Lett. 89* (11), 117401.
(34) Song, J., Atay, T., Shi, S., Urabe, H., and Nurmikko, A. V. (2005) Large enhancement spatially controlled plasmons. *Nano Lett. 5* (8), 1557–1561.
(35) Liu, Y. Y., Wang, P. Y., Dou, S. X., Wang, W. C., Xie, P., Yin, H. W., and Zhang, X. D. (2004) Ionic effect on combing of single DNA molecules and observation of their force-induced melting by fluorescence microscopy. *J. Chem. Phys. 121*, 4302–4309.
(36) Chung, S. W., Ginger, D. S., Morales, M. W., Zhang, Z. F., Chandrasekhar, V., Ratner, M. A., and Mirkin, C. A. (2005) Top-down meets bottom-up: Dip-pen nanolithography and DNA-directed assembly of nanoscale electrical circuits. *Small 1*, 64–69.
(37) Mizuno, R., Haruta, H., Morii, T., Okada, T., Asakawa, T., and Hayashi, K. (2004) Synthesis and AFM visualization of DNA nanostructures. *Thin Solid Films* (Proceedings of the 7th International Symposium an Atomically Controlled Surfaces, Interfaces and Nanostructures), *464–465*, 459–463.

BC700275H

Semisynthetic Analogues of PSC-RANTES, a Potent Anti-HIV Protein

Hubert Gaertner, Robin Offord,[†] Paolo Botti,[‡] Gabriel Kuenzi, and Oliver Hartley*

Department of Structural Biology and Bioinformatics, Centre Médical Universitaire, 1 rue Michel Servet, 1211 Geneva 4, Switzerland. Received August 13, 2007; Revised Manuscript Received October 8, 2007

New HIV prevention methods are needed, and among those currently being explored are "microbicides", substances applied topically to prevent HIV acquisition during sexual intercourse. The chemokine analogue PSC-RANTES (N^{α}(*n*-nonanoyl)-*des*-Ser^{1}-[L-thioprolyl^{2}, L-cyclohexylglycyl^{3}]-RANTES(4–68)) is a highly potent HIV entry inhibitor which has shown promising efficacy in its initial evaluation as a candidate microbicide. However, a way must be found to produce the molecule by cheaper means than total chemical synthesis. Since the only noncoded structures are located at the N-terminus, a possible solution would be to produce a protein fragment representing all but the N-terminal region using low-cost recombinant production methods and then to attach, site specifically, a short synthetic fragment containing the noncoded N-terminal structures. Here, we describe the evaluation of a range of different conjugation chemistries in order to identify those with potential for development as economical routes to production of a PSC-RANTES analogue with antiviral activity as close as possible to that of the parent protein. The strategies tested involved linkage through oxime, hydrazone/hydrazide, and $\Psi[CH_2-NH]$ bonds, as well as through a peptide bond obtained either by a thiazolidine rearrangement or by direct α-amino acylation of a protein fragment in which 4 of the 5 lysine residues of the native sequence were replaced by arginine (the fifth lysine is essential for activity). Where conjugation involved replacement of one or more residues with a linker moiety, the point in the main chain at which the linker was introduced was varied. The resulting panel of 22 PSC-RANTES analogues was evaluated for anti-HIV activity in an entry inhibition assay. The [Arg^{25,45,56,57}] PSC-RANTES analogue has comparable potency to PSC-RANTES, and one of the oxime linked analogues, 4L-57, has potency only 5-fold lower, with scope for improvement. Both represent promising leads for development as microbicide compounds that could be produced at low cost via semisynthesis.

INTRODUCTION

New prevention methods are urgently required to combat the HIV/AIDS pandemic, which is currently running at a rate of approximately 5 million new infections per year (*1*). One of the strategies currently being developed relates to the use of "microbicides"—antiviral products that can be applied topically to genital mucosa prior to sexual intercourse, thereby preventing HIV transmission from person to person (*2*).

PSC-RANTES (*3*) is a chemokine analogue that has shown promising efficacy in preclinical studies related to its use as a microbicide (*4*). In its totally synthetic form, however, PSC-RANTES is likely to be impossibly expensive for worldwide use (*5*). Since the non-natural structures in PSC-RANTES are all located within an N-terminal pharmacophore, semisynthetic strategies could be envisaged in which a protein fragment representing all but the N-terminus of the sequence is produced by low-cost microbial fermentation, followed by site-specific conjugation of a short synthetic peptide containing the N-terminal pharmacophore.

One strategy to produce PSC-RANTES semisynthetically would involve the use of native chemical ligation (*6*) between a protein fragment beginning at Cys^{10} and an N-terminal fragment with a C-terminal thioester that contains the noncoded pharmacophore. We chose not to consider this route, however, since it would involve the production of a long and relatively expensive thioester peptide, as well as a folding step (formation of disulfide bridges) after the ligation. Instead, we chose to focus on approaches involving conjugation conditions that are compatible with the presence of the native disulfide bonds in the protein fragment and which could be adapted to the use of shorter, less expensive synthetic N-terminal fragments. Hence, the first set of strategies we envisaged involved the formation of oxime, hydrazone/hydrazide, and $\Psi[CH_2-NH]$ bonds. These require N-terminal Ser or Thr residues to be engineered into the protein fragment (see linker-based strategy in Figure 1). With N-terminal Ser or Thr, periodate oxidation of the amino alcohol to a glyoxylic acid residue, O=CH—CO-, allows the specific conjugation to an aminooxy- or hydrazide-functionalized peptide through the formation of an oxime or hydrazone bond. In an another linker strategy, reductive amination under slightly acidic conditions was used to conjugate the short synthetic N-terminal peptide fragment functionalized with an aminoacetaldehyde moiety to the protein fragment. This approach, though less specific because it is only based on the difference of reactivity between α- and ε-amine groups toward aldehydes, has the advantage of generating the shortest linker—involving the substitution of only one amino acid residue—but the disadvantage of introducing a positively charged group into the protein backbone (Scheme 1). All of the linker-based strategies lead to modification to both the backbone and the side chains of the

* Corresponding author. Tel. +41 22 379 54 75. Fax +41 22 379 55 02.

[†] Present address Mintaka Foundation for Medical Research, 14 chemin des Aulx, 1228 Plan-les-Ouates, Geneva, Switzerland.

[‡] Present address ArisGen, 14 chemin des Aulx, 1228 Plan-les-Ouates, Geneva, Switzerland.

[1] Abbreviations: 4L-5,7H, etc., see description of linker terminology in the Discussion section; AOP-RANTES, the aminooxypentane oxime of [glyoxylyl^{1}]RANTES (2-68); Apm, aspartimide; Chg, cyclohexylglycine; EDC, *N*-(3-dimethylaminopropyl)-*N*′-ethylcarbodiimide; HM-Thiaz, 2-hydroxymethylthazolididine; MES, morpholinoethanesulfonic acid; NHS, *N*-hydroxysuccinimide; NNY-RANTES, N^{α}(*n*-nonanoyl)-RANTES(2-68); PrS, thioproline; Pse, 2-(phenylsulphonyl)ethyl; PSC-RANTES, (N^{α}(*n*-nonanoyl)-*des*-Ser^{1}-[L-thioprolyl^{2}, L-cyclohexylglycyl^{3}]-RANTES(4-68)); RANTES, the traditional name for the chemokine CCL5 (Swissprot: CCL5_HUMAN).

10.1021/bc7003044 CCC: $40.75 © 2008 American Chemical Society
Published on Web 01/08/2008

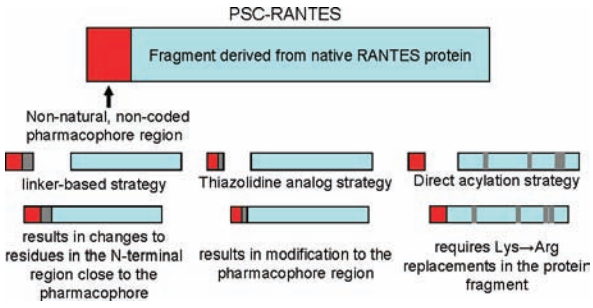

Figure 1. Schematic representation of the semisynthetic strategies used in this study. PSC-RANTES (upper panel) can be considered to consist of a protein fragment derived from native RANTES (cyan), and which could be produced cheaply by biosynthesis, to which a short, synthetic N-terminal pharmacophore region containing non-natural, noncoded structures (red) is joined. All three of the semisynthesis strategies we evaluated in this study necessitate the introduction of modifications (indicated in gray) to the PSC-RANTES protein.

protein at the linkage site, and some of them also change the register of the backbone by adding atoms (Scheme 1). Hence, we opted to create panels of analogues for each linkage type, varying the site at which the linkage was introduced (Table 1).

Yet another possible strategy requires the protein fragment to have N-terminal cysteine. The resulting 1-amino, 2-thiol structure at the N-terminus can be specifically conjugated to a glycolaldehyde-functionalized ester of the short synthetic N-terminal fragment through formation of a thiazolidine, which can be further rearranged to a 2-hydroxymethyl-thioproline with the generation of an authentic peptide bond (Scheme 2). The drawback here is that the structure of the pharmacophore unit of PSC-RANTES cannot be precisely reproduced (see thiazolidine analogue strategy in Figure 1).

Our last strategy involved direct acylation of the amino terminus of protein fragments in which either four or five of the five lysine residues present in native RANTES had been replaced by arginine (see direct acylation strategy in Figure 1). This approach has the advantage of generating a natural peptide bond at the linker site but the disadvantage of changing structures elsewhere in the protein that may be important for activity.

The PSC-RANTES analogues from the different groups were evaluated for their anti-HIV activity. We discuss the results obtained with regard to structure–activity relationships at the anti-HIV pharmacophore of PSC-RANTES and suggest that two of the above strategies have potential for development as economic routes to production of semisynthetic PSC-RANTES analogues that could be effective microbicides.

EXPERIMENTAL PROCEDURES

Reagents and Chemicals. Unless otherwise specified, all solvents and reagents were obtained from Fluka (Buchs, Switzerland), were of analytical or higher grade, and were used without further purification. All amino acids were purchased from Orpegen (Heidelberg, Germany). The resins were from NeoMPS (Strasbourg, France) or Bachem (Bubendorf, Switzerland). Water was repurified using a Milli-Q system (Millipore, Inc., Bedford, MA).

HPLC. Analytical RP-HPLC (reverse-phase high-performance liquid chromatography) was performed using a column 250 × 4 mm i.d. packed with Nucleosil 300-A, 5 μm C8 particles. The flow rate was 0.7 mL/min, and effluent was monitored at 214 nm. Peptides were purified on a C8 semi-preparative column (250 × 10 mm i.d. Nucleosil 300-A, 5 μm particle size) at a flow rate of 4 mL/min monitored at 214 nm, or purified on a Vydac C8 preparative column (250 × 22 mm i.d., 10 μm particle size) at 15 mL/min monitored at 214 nm. Solvents used in RP-HPLC were as follows: A, 0.1% TFA (1 g TFA in 1 L H_2O); B, 0.1% TFA in 90% acetonitrile (1 g of TFA mixed with 100 mL of H_2O and then brought to 1 L with acetonitrile). Generally, the conditions used in analytical work were 2 min isocratic at 20% B followed by a linear gradient to 65% B over 45 min. In preparative work, a linear gradient (usually of the same slope) was used after 2 min at initial conditions. All peptide components were collected manually at the detector exit, evaporated at room temperature under reduced pressure, frozen, and then recovered by lyophilization.

Mass Spectrometry. Electrospray ionization mass spectrometry (ESI-MS) was performed in positive ion mode on a Platform-II instrument (Micromass, Manchester, England). Samples were introduced at 10 μL/min in solvent acetonitrile/water/formic acid (49.9:49.9:0.2). MALDI-TOF mass spectrometry was performed in linear mode using sinapinic acid as the matrix on a Voyager Elite machine (Applied Biosystems, Foster City, CA) equipped with delayed extraction. External calibration was performed on the electrospray machines using a solution of horse heart apomyoglobin and on the MALDI-TOF machine using the mixture of peptides supplied by the manufacturer.

Synthesis of RANTES Fragments. Although the route to bulk manufacture of the larger RANTES fragments would ultimately be biosynthesis, for exploratory experimental purposes it was more rapid and convenient to prepare them by total chemical synthesis. The two proteins and ten protein fragments described in Table S1 of the Supporting Information were prepared by polymer-supported organic synthesis of the two segments that would have been formed if they had been cleaved between residues 33 and 34. *t*-Butoxycarbonyl chemistry was used, as described in ref (*7*). The segments were coupled in a native chemical ligation (*6*). Folding of the resulting molecule with concomitant disulfide formation was carried out in the presence of a Cys-SH/$(Cys\text{-}S)_2$ redox couple except for [Cys^2]-RANTES(2-68), where conjugation to the N-terminal peptide fragment was performed before the folding step. Purity and integrity of the resulting analogues were routinely verified by HPLC and mass spectrometry.

Synthesis of *n*-Nonanoyl Peptides. The short N-terminal synthetic fragments that contain the pharmacophore all possess an N-terminal *n*-nonanoyl group as in PSC-RANTES (Scheme 1). These *n*-nonanoyl peptides were synthesized as described in ref (*8*). Crude material obtained after ether precipitation (following HF resin cleavage) was used without HPLC purification for further C-terminal functionalization. For synthesis of *n*-nonanoyl-PrS-Chg-Ser-Ser-Asp^6, Boc-Asp(OPse)-OH was used to maintain side-chain protection during further C-terminal modification of the peptide. Because of difficulties with the deprotection, this peptide was also synthesized using Fmoc chemistry, using 2-chlorotrityl chloride resin and cleaving the fully protected peptide with acetic acid/trifluoroethanol/dichloromethane (2:2:6) for 2 h.

Synthesis of Heterobifunctional Spacer Reagents Containing Aminooxy Groups (Scheme 3). *I. 2-(Boc-aminooxy)ethylamine (III). N-[2-(Tert-butyl-N-hydroxycarbamoyl)ethyl]phthalimide (I).* Conditions of synthesis are similar to those described in ref (*9*). *tert*-Butyl *N*-hydroxycarbamate (1.32 g, 10 mmol) was dissolved in anhydrous DMF (7 mL), NaH (380 mg, 60% dispersion in mineral oil, 9.5 mmol) was added at room temperature, and the mixture stirred for 1 h, then cooled to 0 °C, treated with 2-bromoethylphthalimide (2.03 g, 8 mmol) for 2 h at 0 °C, and then left at room temperature overnight. The material was precipitated in cold water (100 mL) and the precipitate redissolved in EtOAc. The organic layer was

Scheme 1. Backbone Structure of PSC-RANTES Analogues Resulting from the Use of Different Linker-Based Strategies

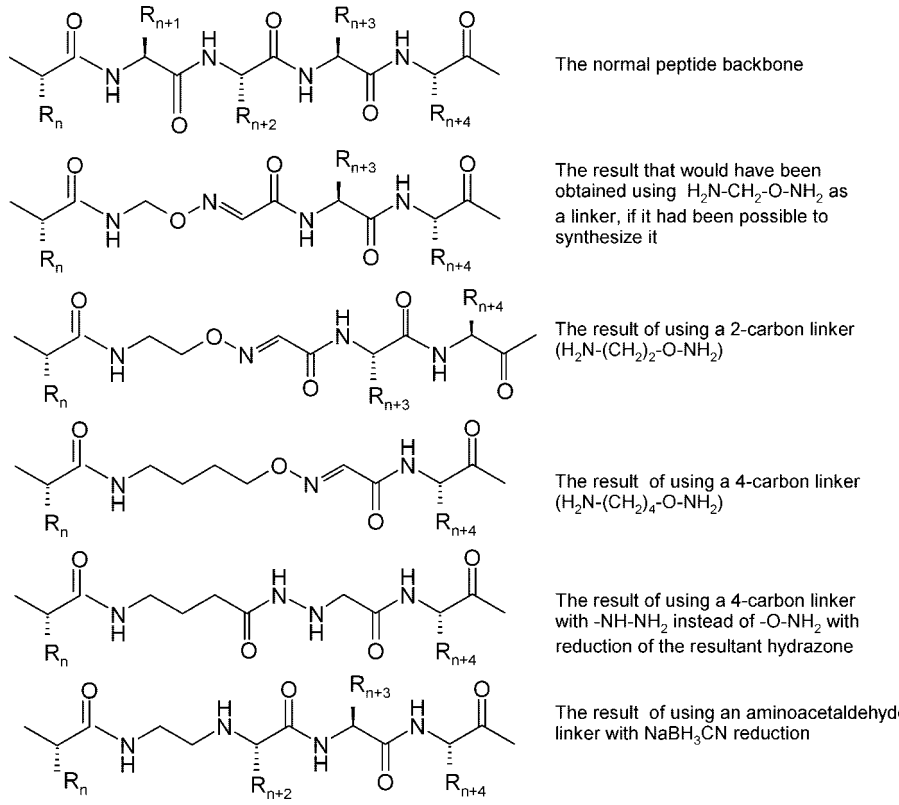

Table 1. N-Terminal Structures of PSC-RANTES Analogues Produced Using Linker-Based Strategies[a]

Compound	N-terminal structure	Linker used
2L-45	*n*-nonanoyl-PrS-Chg-^^^^^^^-Asp-Thr-Thr-Pro	2-carbon oxime
2L-56	*n*-nonanoyl-PrS-Chg-Ser-^^^^^^^-Thr-Thr-Pro	2-carbon oxime
2L-67	*n*-nonanoyl-PrS-Chg-Ser-Ser-^^^^^^^-Thr-Pro	2-carbon oxime
2L-78	*n*-nonanoyl-PrS-Chg-Ser-Ser-Asp-^^^^^^^-Pro	2-carbon oxime
4L-46	*n*-nonanoyl-PrS-Chg-^^^^^^^^^^-Thr-Thr-Pro	4-carbon oxime
4L-57	*n*-nonanoyl-PrS-Chg-Ser-^^^^^^^^^^-Thr-Pro	4-carbon oxime
4L-68	*n*-nonanoyl-PrS-Chg-Ser-Ser-^^^^^^^^^^-Pro	4-carbon oxime
4L-46H	*n*-nonanoyl-PrS-Chg-^^^^^^^^^^-Thr-Thr-Pro	4-carbon hydrazone
4L-57H	*n*-nonanoyl-PrS-Chg-Ser-^^^^^^^^^^-Thr-Pro	4-carbon hydrazone
4L-68H	*n*-nonanoyl-PrS-Chg-Ser-Ser-^^^^^^^^^^-Pro	4-carbon hydrazone
4L-46HR	*n*-nonanoyl-PrS-Chg-^^^^^^^^^^-Thr-Thr-Pro	4-carbon methyl-hydrazine
4L-57HR	*n*-nonanoyl-PrS-Chg-Ser-^^^^^^^^^^-Thr-Pro	4-carbon methyl-hydrazine
4L-68HR	*n*-nonanoyl-PrS-Chg-Ser-Ser-^^^^^^^^^^-Pro	4-carbon methyl-hydrazine
1L-4	*n*-nonanoyl-PrS-Chg-^^^-Ser-Asp-Thr-Thr-Pro	1-carbon ψ[CH_2-NH]
1L-5	*n*-nonanoyl-PrS-Chg-Ser-^^^-Asp-Thr-Thr-Pro	1-carbon ψ[CH_2-NH]
1L-6	*n*-nonanoyl-PrS-Chg-Ser-Ser-^^^-Thr-Thr-Pro	1-carbon ψ[CH_2-NH]
1L-7	*n*-nonanoyl-PrS-Chg-Ser-Ser-Asp-^^^-Thr-Pro	1-carbon ψ[CH_2-NH]
1L-7 *des*	*n*-nonanoyl-PrS-Chg-Ser-Ser-Apm-Thr-^^^-Pro	1-carbon ψ[CH_2-NH]

[a] The residues substituted by the linkers are indicated using ∧∧∧; the structures of the different linkers can be found in Scheme 1. See the appropriate footnote for the abbreviations for noncoded amino acids.

successively washed with a saturated NaCl solution and then water. The crude product (**I**) was dried over $MgSO_4$ and solvent removed. Yield 1.3 g (53%).

N-[2-(tert-butyl-N-hydroxycarbamoyl)ethyl]amine (III). A mixture of 1.1 g of *N*-[2-(*tert*-butyl-*N*-hydroxycarbamoyl)ethyl]phthalimide (**I**) and 1.4 mL hydrazine hydrate in 20 mL ethanol was refluxed overnight at 90 °C. The solution was cooled, and the precipitated phthalyl hydrazide was separated by centrifugation. The supernatant was diluted with water and acidified with 10% TFA. A further precipitate was separated by centrifugation and the deprotected material isolated from the supernatant by preparative HPLC (yield 215 mg, 0.75 mmol, 21%), showing the expected mass (ESI-MS M + H found 177.2, theor. M + H 177.0).

II. 4-(Boc-aminooxy)butylamine (IV). The same protocol was used starting from *tert*-butyl *N*-hydroxycarbamate (400 mg, 3 mmol), NaH (114 mg, 2.85 mmol), and 4-bromobutylphthalimide (675 mg, 2.4 mmol). The recovered *N*-[4-(*tert*-butyl-*N*-hydroxycarbamoyl)butyl]phthalimide (**II**) (630 mg, 1.7 mmol, 70%) was treated with a 2-fold molar excess of hydrazine

Scheme 2. Ligation through Thiazolidine Ring Formation

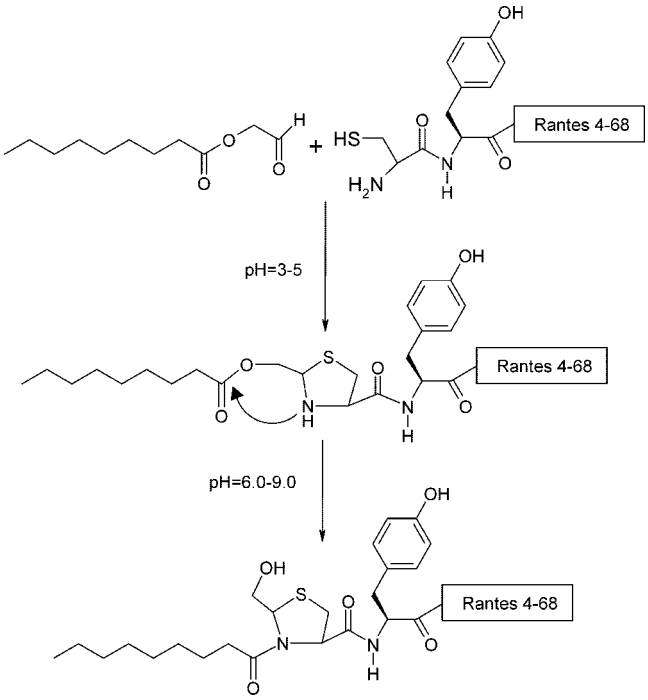

Scheme 3. Synthesis of Heterobifunctional Spacer Reagents Containing Aminooxy Groups

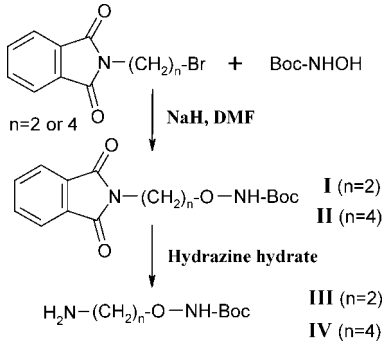

hydrate to afford, after isolation and HPLC purification as above, an oily product (**IV**) (105 mg, 0.33 mmol, 19%) with the expected mass (ESI-MS M + H found 204.8, theor. M + H 205.0).

Synthesis of Aminooxy-Functionalized n-Nonanoyl Peptides. Coupling of the 2- and 4-Carbon Linkers to the C-Termini of the n-Nonanoyl Peptides. *n*-Nonanoyl peptide (25 μmol) was dissolved in 50 μL DMF and mixed with equimolar amounts of solid NHS and diisopropylcarbodiimide. A 3-fold molar excess of Boc-aminooxy-linker (**III** or **IV**) was dissolved in 50 μL DMF and added to the *n*-nonanoyl peptide solution, and diisopropylethylamine, equivalent to a 4-fold molar excess over *n*-nonanoyl peptide, was added to the reaction mixture which was then incubated overnight at room temperature. The mixture was then acidified with 10 μL acetic acid and the conjugation product isolated by preparative HPLC using a gradient of 30−70% B over 40 min. In the case of *n*-nonanoyl-PrS-Chg-Ser-Ser-Asp(OPse)-OH, the (OPse) protecting group was removed afterward by 2 h treatment at 37 °C in 3 mL of 0.1 M $NaHCO_3$, 10% α-mercaptoethanol, 40%CH_3CN, pH 9.0 (*10*). The lyophilized material was deprotected by a 5 min treatment in 1 mL neat TFA. The TFA was evaporated under N_2, the material redissolved in CH_3CN/water and freeze-dried.

Synthesis of Hydrazide-Functionalized *n*-Nonanoyl Peptides. These were made manually at the 0.1 mmol scale according to standard techniques of Fmoc peptide chemistry (*11*) starting with 2-methoxy-4-alkoxybenzyloxycarbonyl hydrazide resin (Bachem, Switzerland). The *n*-nonanoyl peptides were deprotected and cleaved from the resin by vortexing with 1.5 mL of a mixture consisting of TFA (95%), 2.5% H_2O, and 2.5% triisopropylsilane (v/v) for 1 h at room temperature and filtered to remove resin. The solution was evaporated under N_2, and the oily material taken up in CH_3CN−water and lyophilized. The resulting *n*-nonanoyl peptides could be used in the conjugation reaction without any further purification.

Synthesis of Aldehyde-Functionalized Reagents and *n*-Nonanoyl Peptides. *n*-Nonanoyl-2,2′-dimethoxyethyl ester was prepared by reaction of *n*-nonanoic acid cesium salt with bromoacetaldehyde dimethylacetal in dimethylformamide (DMF) at 60 °C for 48 h (*12*). *n*-Nonanoyl peptide (25 μmol) dissolved in 200 μL DMF was mixed with a 5-fold excess of aminoacetaldehyde diethylacetal and an equimolar amount of (benzotriazol-1-yloxy)tripyrrolidinophosphonium hexafluorophosphate (PyBOP) reagent. The solution was incubated for 3 h at room temperature, acidified, and the conjugation product isolated by preparative HPLC using a gradient of 30–70% B over 40 min. The acetal group was cleaved by a 5 min treatment in 1 mL neat TFA. The TFA was evaporated under N_2, the *n*-nonanoyl glycoaldehyde ester was redissolved in CH_3CN/ water, freeze-dried, and used immediately for the conjugation step. In the case of the aldehyde derivative of the fully protected peptide, *n*-nonanoyl-PrS-Chg-Ser(tBu)-Ser(tBu)-Asp(OtBu), the protecting groups were removed all at once by a 1 h treatment in neat TFA.

Conjugation through Oxime and Hydrazone Bonds. The truncated proteins with N-terminal serine residues were dissolved in water at 2 mg/mL, mixed with an equal volume of 2% (w/v) NH_4HCO_3 buffer, containing 40 mM methionine, pH 8.3, and oxidized in the presence of a 20-fold excess of sodium metaperiodate. After 10 min incubation in the dark, the reaction was quenched by the addition of a 10 000-fold excess of ethylene glycol. The oxidized protein was retained on a Sep-Pack cartridge, eluted with 80% CH_3CN in 0.1% TFA, and freeze-dried. The protein was redissolved (4 mg/mL) in a 0.1 M acetate (Na) buffer containing 20 mM methionine, 40% CH_3CN, apparent pH 4.6, and either a 2-fold excess of aminooxy-functionalized *n*-nonanoyl peptide or a 6-fold excess of hydrazide-functionalized *n*-nonanoyl peptide was added, dissolved in the same buffer at a concentration of 4 mg/mL. After overnight incubation, the conjugation product was isolated by semipreparative HPLC, using a 1 × 25 cm Macherey-Nagel column at 4 mL/min. In the case of hydrazone conjugates, the hydrazone bond could be reduced by incubation of the recovered and lyophilized material in 400 μL of 0.4 M $NaBH_3CN$ in the same buffer as used previously for 4 days in the dark (*13*), before HPLC purification.

Conjugation through a Thiazolidine Analogue. Unfolded [Cys^2]RANTES(2-68) was dissolved in 0.1 M sodium phosphate, 6 M GnCl, pH 6.0, to a concentration of approximately 5 mg/mL, a 50 molar excess of freshly TFA-deprotected *n*-nonanoyl glycolaldehyde ester was added and the pH readjusted to 5.0. After a 1 h incubation, the conjugation product was isolated by preparative HPLC and freeze-dried. The thiazolidine conjugate was then redissolved in 0.1 M sodium phosphate, 6 M GnCl, pH 7.5, at 4 mg/mL and the solution incubated for 4 days at 37 °C, with daily readjustment of the pH to 7.5. The solution was acidified to pH 3.0 and further incubated with 5 mg tris(2-carboxyethyl)phosphine for 1 h, before isolation of the rearranged thiazolidine analogue by

semipreparative HPLC. The material was then refolded under the same conditions as given above.

Conjugation through a Methylene Amino, Ψ[CH_2−NH] Bond. Truncated RANTES (2 mg/mL in water) was reacted at a molar ratio of 1:10 with 5 mg/mL solution freshly deprotected *n*-nonanoyl aminoacetaldehyde peptide in 80% acetonitrile and mixed with an equal volume of 0.2 M acetate(Na) buffer containing 50% acetonitrile, pH 5.2. The reaction took place at room temperature for 15 h. Sodium cyanoborohydride (1 M) dissolved in the same buffer was added to the reaction to a final cyanoborohydride concentration of 0.3 M. The reaction medium was further incubated at room temperature for at least 6 h before isolation of the conjugation product by semipreparative HPLC.

Conjugation via N-Terminal Acylation of Protein Fragments in Which Lysine Residues Had Been Replaced by Arginines. The complementary short N-terminal peptide, *n*-nonanoyl-PrS-Chg, was activated with NHS by a 1 h incubation with equimolar amounts of HO-Su and EDC in DMSO. The modified protein fragment, [$Arg^{25,45,56,57}$] RANTES-(4–68) (see Table S1 in the Supporting Information), was dissolved in 0.1 M MES buffer containing 50% DMSO, apparent pH 5.5, to a concentration of approximately 4 mg/mL, a 20 molar excess of freshly activated peptide was added, and the solution stirred over 15 h. The solution was then acidified with acetic acid, diluted 10-fold with water, and the conjugation product isolated by semipreparative HPLC using a 1 × 25 cm Macherey-Nagel column at 4 mL/min.

HIV Entry Inhibition Assay. Envelope-mediated cell fusion assays were carried out as described in ref (*14*) with HeLa-P5L (*15*) and HeLa-Env-ADA (*16*) cell lines. Experiments were performed in triplicate, and dose-inhibition curves were fitted by using *Prism* software (GraphPad, CA).

RESULTS

Production of Oxime Analogues. Construction of the oxime analogues was driven by the idea of synthesizing the shortest possible stable linker, functionalized with an amine and an aminooxy group. Our initial strategy involved using a one-carbon linker, which would have entailed the replacement of only two residues and would have kept the backbone of the semisynthetic protein in register with that of PSC-RANTES (Scheme 1). However, these compounds proved inaccessible due to their high instability (data not shown), and it was therefore necessary to investigate linkers with two or more carbon atoms. As shown in Scheme 1, incorporation of a two- or four-carbon linker results in the replacement of two or three residues, respectively. While the two-carbon linker has the advantage of substituting one less residue that the four-carbon linker, it has the disadvantage of introducing a one-atom shift, relative to PSC-RANTES, of the register of the backbone of the N-terminal region of the semisynthetic protein (Scheme 1). Since it is likely that linker position will influence the biological activity of the resulting protein, we opted to generate a panel of analogues for each linker, moving the site of the linker within the N-terminal region of the protein. The nomenclature used for this series of analogues was 2L-*x*,*y* for the two-carbon linker and 4L-*x*,*y* for the four-carbon linker, with *x* and *y* denoting the positions of the first and last substituted residue (Table 1).

We chose to produce the aminooxy-functionalized *n*-nonanoyl peptides through reaction of N-(bromoalkyl)phthalimides with *tert*-butyl *N*-hydroxycarbamates. A 2-fold excess of aminooxy-functionalized peptide was sufficient to drive the conjugation reaction to completion. All intermediates in the construction of the different conjugates were characterized by mass spectrometry and described in Table S1 in the Supporting Information.

Production of Hydrazone and Hydrazide Analogues. We used 2-methoxy-4-alkoxybenzyloxycarbonyl-hydrazide resin to produce a range of *n*-nonanoyl peptides hydrazide-functionalized with a two-carbon linker. These could be reacted with N-terminal Ser or Thr protein fragments that had been oxidized with periodate to generate a range of hydrazone-linked PSC-RANTES analogues. Reduction of the hydrazone bond with $NaBH_3CN$ gave us easy access to the corresponding methyl hydrazine linked analogues, which allow more backbone flexibility at the linkage site. The nomenclature used for this group of compounds is 4L-*x*,*y*H for the hydrazone analogues and 4L-*x*,*y*HR for the reduced methyl hydrazine analogues, with *x* and *y* denoting the positions of the first and last substituted residue (Table 1).

Production of Ψ[CH_2−NH] Analogues. Reductive amination, in which an aldehyde reacts with the N-terminal α-amino group of a target protein in the presence of sodium cyanoborohydride as a reducing agent, has been recently explored as a route to selectively modify proteins at the α-amino group without protecting the ϵ-amino groups on lysine residues (*17*–*19*). This approach is less restrictive than other established semisynthetic strategies, since it does not require the presence of an N-terminal residue such as Ser, Thr, or Cys. Under only slightly acidic conditions, the α-amino group (pK_a in the region of 8) is deprotonated to a significantly greater extent than the ϵ-amino groups of lysine residues (pK_a in the region of 10). Reaction of a peptide aldehyde with the α-amino group results in the replacement of one residue in the peptide chain by an aminoethylene moiety (Scheme 2).

We opted to test this conjugation approach using the same group of protein fragments that was used to generate the oxime and hydrazone analogues, together with a corresponding group of aminoacetaldehyde-conjugated *n*-nonanoyl peptides. The nomenclature used for this series of analogues was 1L-*x*, with *x* and *y* denoting the positions of the substituted residues (Table 1). It was necessary to change the strategy for the functionalization of one of the *n*-nonanoyl peptides, namely, *n*-nonanoyl-PrS-Chg-Ser-Ser-Asp(OPse)-OH, since the Asp deprotection step carried out under basic conditions resulted in an almost quantitative dehydration of the compound with the formation of an aspartimide. While we opted to retain the *n*-nonanoyl peptide carrying the aspartimide modification and use it to produce an extra analogue (1L-7 *des*, Table 1), it was possible to obtain the desired Asp analogue by using the orthogonal (OtBu) protecting group for the Asp side chain, with the fully protected peptide being cleaved from the 2-chlorotrityl chloride resin with acetic acid.

Not unexpectedly, given the limited selectivity of the approach, each conjugation reaction gave rise to detectable overreaction products resulting from the conjugation of the aminoacetaldehyde-functionalized *n*-nonanoyl peptides with the ϵ-amino groups of the protein (Figure 2).

Production of Thiazolidine Analogues. Proteins carrying an N-terminal cysteine residue can be site-specifically modified at the N-terminus with an aldehyde under acidic conditions (*20*), and the use of a glycolaldehyde ester opens the way to a rearrangement that regenerates a true peptide bond (*21*), although both the condensation and rearranged products give a mixture of two diastereoisomers due to the creation of a new asymmetric carbon at position 2 of the thiazolidine ring. We chose to use this approach to generate two PSC-RANTES analogues. First, conjugation of an *n*-nonanoyl glycolaldehyde ester to [Cys^2]-RANTES(2-68) generates as the final product N^{α}*n*-nonanoyl-[2-hydroxymethythiazolidine^2]RANTES(2-68), an analogue very similar in structure to N^{α}(*n*-nonanoyl)-RANTES(2-68), the molecule known as NNY-RANTES. This was a lead compound, already quite potent in itself, identified during the development of PSC-RANTES (*3*). Second, since the technology developed by the group of Schultz (*22*) enables a single noncoded amino

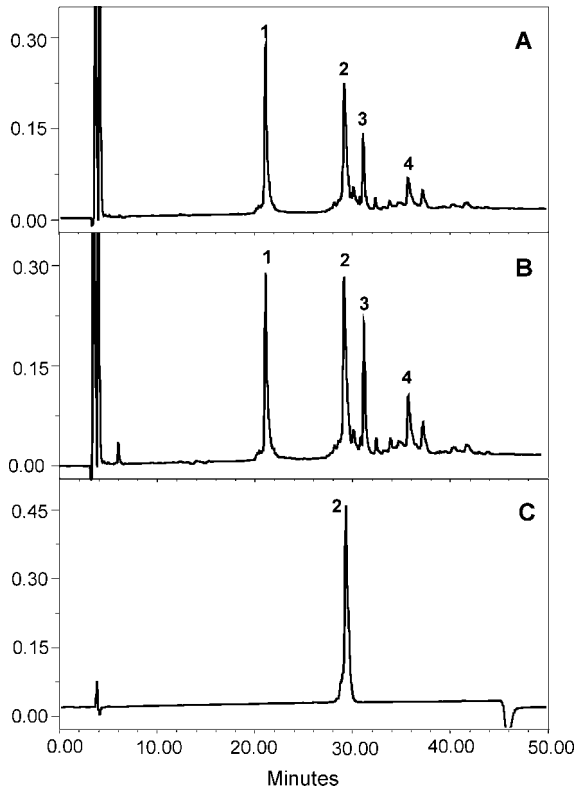

Figure 2. Analytical HPLC of the reductive amination reaction of *n*-nonanoyl-PrS-Chg-Ser^4-NH-CH_2-CHO with [Asp^6]RANTES(6-68). (A) Reaction mixture 2 h after addition of $NaBH_3CN$ following an overnight incubation. (B) Reaction mixture 20 h after addition of $NaBH_3CN$. (C) *n*-Nonanoyl-PrS-Chg-Ser^4-NH-CH_2-CH_2-RANTES(6-68), after semipreparative HPLC purification. Peak 1, [Asp^6]RANTES(6-68); Peak 2, the formed conjugate, *n*-nonanoyl-PrS-Chg-Ser^4-NH-CH_2-CH_2-RANTES(6-68); Peak 3, excess *n*-nonanoyl-PrS-Chg-Ser^4-NH-CH_2-CHO; Peak 4, the overreaction bisubstituted conjugate.

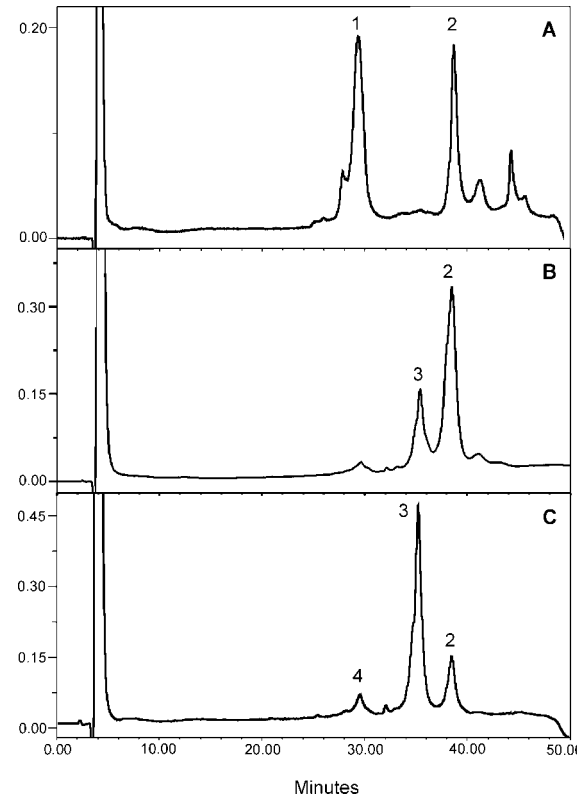

Figure 3. Progress in the construction of *n*-nonanoyl-HMThiaz^2-Chg^3-RANTES(4-68). (A) Reaction of [Cys^2, Chg^3]RANTES(2-68) with *n*-nonanoyl glycolaldehyde ester after 45 min incubation at pH.5.0. (B,C) The O to N acyl transfer at pH 7.5 after 1 and 4 days incubation at 37 °C, respectively. Peak 1, [Cys^2, Chg^3]RANTES(2-68); Peak 2, the thiazolidine conjugate; Peak 3, the O,N acyl rearranged conjugate; Peak 4, the hydrolyzed condensation product [HMThiaz^2, Chg^3]RANTES(2-68).

acid to be site-specifically incorporated into recombinant proteins and works particularly well with aromatic or cyclic residues, we opted to perform the same reaction on [Cys^2, Chg^3]RANTES(2-68), in order to produce the analogue N^{α}(*n*-nonanoyl)-[2-hydroxymethylthazolidide^2, Chg^3]RANTES(2-68), an analogue for which the only structural difference relative to PSC-RANTES is a hydroxymethyl side chain (present in two diastereisomeric forms) on the carbon at position 2 of the thiazolidine ring. If the latter analogue were found to have useful biological properties, the methods of Schultz and co-workers could presumably be adapted to the production of the [Cys^2, Chg^3]RANTES(2-68) as a totally recombinant molecule, onto which, as we have just seen, the *n*-nonanoyl 2-hydroxymethythazoline moiety could be introduced with total site specificity.

For the purposes of this part of the study, the folding of the protein with concomitant formation of disulfide bridges was performed after conjugation of the peptide to enable us to avoid the need to develop the new folding conditions for totally synthetic protein fragments carrying an N-terminal cysteine residue. For both conjugation reactions, incubation with a 50-fold excess of the *n*-nonanoyl glycolaldehyde ester resulted in an HPLC shift of the protein of more than 8 min, as shown in Figure 3A for the [Cys^2, Chg^3]RANTES(2-68). The isolated thiazolidine ester derivatives were resolubilized in a sodium phosphate buffer pH 7.5 to allow O to N acyl rearrangement, as previously described (*21*). This reaction was stopped after 4 days of incubation (Figure 3C), since no improvement could be observed over a longer period of time (data not shown). The incomplete reaction may be related to the presence of contaminating *n*-nonanoyl glycolaldehyde ester, which is difficult to detect and totally eliminate after the first reaction step due to its very low optical absorbance, and which would be highly reactive with the protein's ϵ-amino groups under the more basic conditions of the second reaction. Starting with 15 mg unfolded protein, 5 mg of condensation product were isolated, which finally gave 1 mg of the rearranged compound.

Anti-HIV Activity of PSC-RANTES Analogues. The anti-HIV activity of the full set of PSC-RANTES analogues, together with reference compounds AOP-RANTES, NNY-RANTES, and PSC-RANTES, was determined in a series of cell fusion assays. Each compound was assayed in at least four independent experiments, with PSC-RANTES used as an internal standard in each experiment. Results are shown in Figure 5. The measured potency of PSC-RANTES across the total of 41 independent assays (mean IC_{50} value of 24 pM) is in agreement with previously published values (*3*), as are those for AOP-RANTES and NNY-RANTES (mean IC_{50} values of 0.96 nM and 190 pM, respectively).

Oxime-Based Analogues. In general, the oxime-based analogues with two-carbon linkers were less potent than the corresponding analogues with four-carbon linkers (both 2L-45 and 2L-56 are less potent than 4L-46; both 2L-56 and 2L-67 are less potent than 4L-57; both 2L-67 and 2L-78 are less potent than 4L-68). While a number of the analogues in this series show anti-HIV activity that compares well to the earlier lead molecules, AOP-RANTES and NNY-RANTES, the best analogue in this series, 4L-57 (IC_{50} value of 130 pM), is still approximately 5-fold less potent than PSC-RANTES.

Hydrazone/Methyl Hydrazine-Based Analogues. Each of the hydrazone analogues showed comparable (4L-46H) or lower

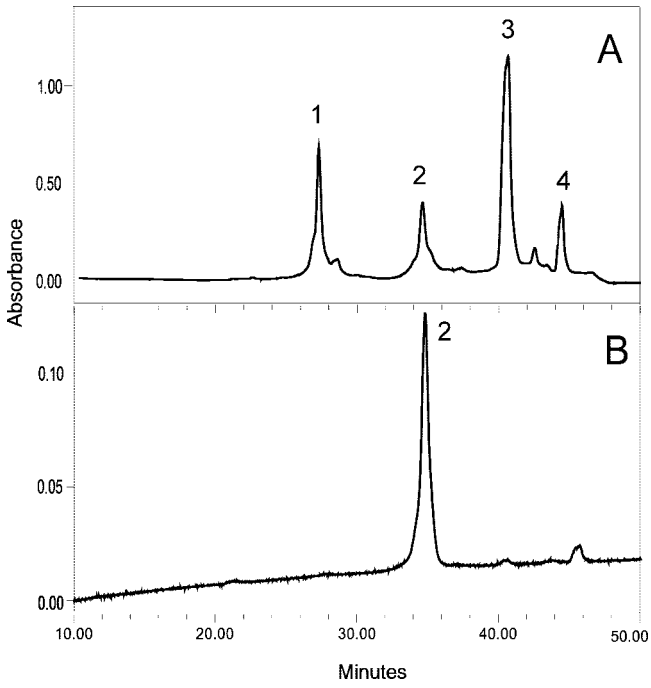

Figure 4. Production of PSC-RANTES[$Arg^{25,45,56,57}$] via direct acylation of [$Arg^{25,45,56,57}$]RANTES(4-68) with *n*-nonanoyl-PrS-Chg. Analytical HPLC of the reaction medium after 15 h incubation at room temperature (A) and after isolation of the conjugation product (B). Peak 1, unreacted [$Arg^{25,45,56,57}$]RANTES(4-68); Peak 2, PSC-RANTES[$Arg^{25,45,56,57}$]; Peak 3, excess *n*-nonanoyl-PrS-Chg. Peak 4 is presumed to be the product of over-reaction, with acylation of both the α- and ϵ-amino groups of the protein fragment.

activity (4L-57H, 4L-68H) to the corresponding four-carbon linker oxime analogues. Reduction to methyl hydrazide did not affect the activity of two of the analogues (4L-57HR, 4L68HR), but strongly reduced the activity of a third (4L-46HR).

Ψ[CH_2−NH] Analogues. The use of the reductive amination approach gave us access to a one-carbon linker strategy, which has the advantages of retaining backbone register while requiring replacement of only one residue. Interestingly, this strategy provided little advantage over the four-carbon linker oxime approach, which also retained backbone register but necessitated the replacement of three residues. While 1L-4 shows slightly higher potency than 4L-46, 1L-5 was less potent than any of the 4L oxime compounds, 1L-6 showed lower potency than 4L-57, and 1L-7 showed lower potency than both 4L-57 and 4L-68.

Thiazolidine Analogues. The protein N^{α}(*n*-nonanoyl)-[HMThiaz^2]RANTES(2-68) shows considerable anti-HIV activity (IC_{50} value of 120 pM), a value comparable to that of our earlier lead compound, NNY-RANTES, to which it has a strong structural resemblance (see Discussion section). When in addition to the substitution of 2-hydroxymethyl thiazolidine for Pro^2 we replaced Tyr^3 by cyclohexylglycine, the potency of the new analogue was less (IC_{50} value of 0.98 nM) by an approximately 40-fold reduction compared to the lead compound PSC-RANTES in spite of the close structural resemblance of the two proteins.

"All-Arg" Analogues. If the protein fragment were to contain no lysine residues, acylation by the short N-terminal fragment would be totally site-specific onto the α-amino group of the protein fragment. This could be achieved by replacing all the lysine residues in the native sequence of the protein fragment (positions 25, 33, 45, 56, and 57) with arginine. Had the properties of the resulting protein [$Arg^{25,33,45,56,57}$]PSC-RANTES been as attractive as those of PSC-RANTES itself, it might well have led to a highly economic production process, in spite of the noncoded residues. However, upon synthesis and testing of this analogue, we found that, despite its having an N-terminal region identical to that of PSC-RANTES, it has an approximately 15-fold reduction in potency relative to PSC-RANTES (Figure 5, IC_{50} value of 380 pM). This prompted us to speculate that one or more of the lysine residues in the protein, although distant in the linear sequence of the protein from its putative pharmacophore, may play an important role in its anti-HIV activity. On the basis of ongoing studies of a different group of PSC-RANTES analogues (*23*), as well as studies in which Lys residues of native RANTES were substituted (*24*), we postulated that Lys^{33} might be a key component of the PSC-RANTES pharmacophore. We found, in agreement with this hypothesis, that [$Arg^{25,45,56,57}$]PSC-RANTES showed potency indistinguishable from that of PSC-RANTES (IC_{50} value of 35 pM). It was therefore desirable to see if, despite the presence of one ϵ-amino group in the relevant protein fragment as well as the α-amino group, acylation by the short N-terminal peptide

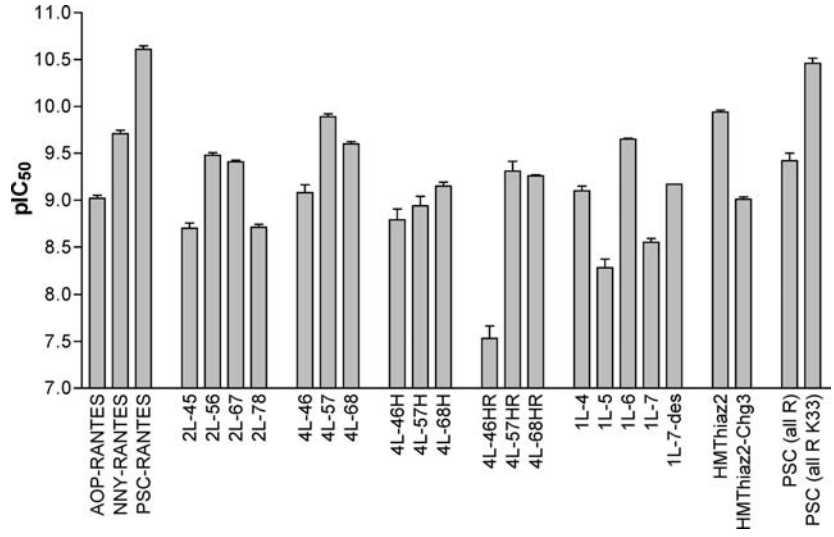

Figure 5. Anti-HIV potency of semisynthetic PSC-RANTES analogues and reference compounds. At least four independent dose–response experiments were performed for each compound using a cell fusion assay, Bars represent the mean potency from the group of experiments performed (pIC_{50}; −log(molar IC_{50} value)), with error bars representing the SEM. See text for the definition of the linker nomenclature. HMThiaz2 = N^{α}(*n*-nonanoyl)-[HMThiaz^2]RANTES(2-68), HMThiaz2-Chg3 = N^{α}(*n*-nonanoyl)-[HMThiaz^2, Chg^3]RANTES(2-68).

could be directed to the α-amino group alone by an appropriate choice of reaction conditions (see below).

Production of Analogues by N-Terminal Acylation of Protein Fragments Having No, Or Few, Lysines. The satisfactory potency of [$Arg^{25,45,56,57}$]PSC-RANTES, mentioned above, led us to consider a pH-controlled acylation of the α-amino group of [$Arg^{25,45,56,57}$]RANTES(4-68) with *n*-nonanoyl-PrS-Chg to produce the full-length construct. The reaction had to be performed in a semiorganic medium to solubilize the highly hydrophobic N-terminal peptide. DMSO turned out to be the most appropriate cosolvent for this reaction, leading to the formation of the wanted product, eluting at approximately 35 min (Figure 4A). The other solvents investigated (DMF, THF) resulted in the formation of a double peak in this region (data not shown). However, even in DMSO, while the higher reactivity of the α-amino group was clearly responsible for a high yield of the wanted product, under the reaction conditions investigated there was some formation of overreaction products, eluting at approximately 44 min (Figure 4A).

DISCUSSION

In this study, we set out to identify strategies with potential for development as economical routes to production of a PSC-RANTES analogue with antiviral activity as close as possible to that of the parent protein. The bulk of the protein would be produced at low cost by biosynthesis prior to attachment to a short N-terminal pharmacophore region that contains the non-natural, noncoded structures and which would be synthesized separately. High-yield production of recombinant RANTES fragments has been demonstrated using *E. coli* with expression methods directed toward inclusion body formation (*24*), and we have successfully used this approach to produce samples of N-terminally truncated derivatives of RANTES (O.H. et al., unpublished results). While expression of proteins via inclusion body formation often leads to incomplete cleavage of the initiating methioine (e.g., ref *25*), this problem can be overcome by the use of N-terminal peptide tags featuring specific enzymatic cleavage sites (e.g., ref *26*). The criteria we chose to adopt when exploring the suitability of the different ligation strategies were as follows: ease and cost of production of the N-terminal fragment, ease and yield of the conjugation reaction, and anti-HIV activity of the resulting analogue. These considerations led us to decide not to explore semisynthesis of PSC-RANTES via native chemical ligation; while it would certainly be a feasible approach, it would necessitate the production of a long and relatively expensive thioester peptide, as well as a folding step after the ligation.

We therefore considered several semisynthesis approaches, some of which necessitate the introduction of a nonpeptide linker region into the protein. Since incorporation of the linker leads to the replacement of backbone and side chain atoms of the protein, and the likelihood of inactivation of a protein increases with the number of substitutions introduced into key regions, we attempted to keep the linkers as short as possible. We varied the site of introduction of the linker, and hence the site at which atoms of the original protein would be changed.

Taken together, study of the three linker-based strategies that we used shows that certain parts of the N-terminal region would appear to be more amenable to the introduction of linker moieties than others. We found overall that substitution at positions 4 and 8 led to a greater reduction in biological activity than substitution at positions 5, 6, and 7. Finally, we did not find that use of a shorter linker necessarily leads to better retention of activity. Indeed, the most potent protein that we constructed with a linker, the oxime-linked analogue 4L-57, has the longest linker region tested, one which requires three residues to be replaced. This four-carbon oxime linker performed generally better than the shorter two-carbon linker that we tested, perhaps because the two-carbon linker modifies the backbone register of the semisynthetic protein with respect to PSC-RANTES.

It was not our purpose in this exploratory study to completely optimize the processes evaluated. In the case of the four-carbon linkers, a useful next step might be to use molecular diversity (library) methods to change the pharmacophore: it is possible that changes there could offset the effect of the linker on activity.

It was possible to directly compare the four-carbon linker oxime linkage strategy with the corresponding one using hydrazones. The activity of the hydrazone analogues was generally lower than that of the corresponding oxime ones, indicating that the activity of the protein is influenced by either the composition or flexibility of the linkers, or both. Reducing the hydrazone linker to methyl hydrazide would be expected to increase linker flexibility, and at certain positions in the protein, this led to a slight increase in activity. In the case of 4L-46HR, however, reduction to a hydrazide led to a more than 10-fold loss in potency. This loss might be related to the fact that in this case the secondary -NH- group in the reduced linker could, when ionized, place a positive charge in proximity to the negative charge of the Asp^6 side chain in the native protein and a strong ionic interaction here might distort the configuration of the whole pharmacophore.

Further evidence that introduction of a positive charge into the backbone can affect activity is provided by results obtained with Ψ[CH−NH] analogues. While these analogues have the shortest linker region that we tested, one which requires the replacement of only one residue, they introduce a full positive charge into the backbone, since reduction of the Schiff base results in a secondary amine with a pK_a in the 10.0–11.0 range. Once again, 1L-5, the analogue in the Ψ[CH_2−NH] series in which the backbone charge is introduced adjacent to Asp^6, shows the greatest reduction in activity. The highest activity in this series of conjugates was obtained for 1L-6, which means that replacement of Asp^6 by an aminoethylene moiety with concomitant alkylation of the nitrogen of Thr^7 is better tolerated. Overall, however, the performance of the Ψ[CH_2−NH] analogues suggests that use of a cumbersome but uncharged linker region does less harm to activity than introduction of a shorter linker carrying a positive charge.

Ligation According to Tam's Thiazolidine Strategy. This method (*21*) yields a native peptide bond in the backbone structure with, however, the introduction of a hydroxymethyl thiazolidine residue immediately C-terminal to the junction site. This residue can be thought of as an analogue of proline (present at position 2 of RANTES and of the earlier lead protein NNY-RANTES) and of thioproline (present at this position in the current lead PSC-RANTES). We therefore used the strategy to incorporate 2-hydroxymethyl thiazolidine at position 2 of NNY-RANTES, and it was encouraging to find that it retains the potency (IC_{50} value of 120 pM) of the parent molecule. We also produced a 2-hydroxymethyl thiazolidine^2 analogue of our best protein lead PSC-RANTES using the same chemistry. This time the protein fragment was [Cys^2-Chg^3]RANTES(2-68), which should be possible to obtain in recombinant form using the Schultz technology (*22*). The conjugation was successful, but the resulting molecule exhibited a significant loss of activity (IC_{50} value of 0.98 nM) compared to the parent PSC-RANTES (IC_{50} value of 24 pM). This apparently paradoxical result recalls previous observations that certain modifications at position 3 of RANTES analogues that are normally beneficial lead to a significant loss in potency when made in the presence of normally beneficial or neutral changes at position 2 (*3*). Thus, PSC-RANTES itself is the result of simultaneously replacing Pro^2 of NNY-RANTES ((*N*$^{\alpha}$(*n*-nonanoyl)-*des*-Ser^1-RANTES(2-

68)) with thioproline and Tyr^3 by cyclohexylglycine. Substitution of position 2 alone in NNY-RANTES had given only a slight improvement in potency, substitution of position 3 alone had given a 3.4-fold improvement, while in PSC-RANTES substitution of both together gave a 5-fold improvement. However, if position 2 was substituted by 4-hydroxyproline, which also gave no significant change in potency if introduced alone into NNY-RANTES, the simultaneous introduction of cyclohexylglycine in position 3 led neither to an improvement nor to the maintenance of potency, but to an approximately 100-fold decrease (*3*).

All-Arg Analogues. Had [$Arg^{25,33,45,56,57}$]PSC-RANTES (in which all the lysines in the sequence are replaced by arginines) shown comparable activity to PSC-RANTES itself, it would have been possible to use the short N-terminal pharmacophore peptide to acylate with complete specificity the sole amino group of the corresponding protein fragment, namely, the α-amino group. Unfortunately, it showed a significant loss in activity relative to PSC-RANTES. However, [$Arg^{25,45,56,57}$]PSC-RANTES showed activity comparable with that of PSC-RANTES, confirming earlier indications as to the importance of Lys^{33} for the anti-HIV activity of PSC-RANTES (*23*). [$Arg^{25,45,56,57}$]PSC-RANTES therefore represents a potent candidate molecule that could be produced by semisynthesis given sufficient selectivity of acylation between the protein fragment's one α-amino group and its one ϵ-amino group. In an initial practical test of this strategy, we obtained a sufficient degree of selectivity to offer the hope that optimization might lead to a practically useful process. We would not expect the replacement of the four lysines by arginine to increase the immunogenicity of the protein, but this point would need to be investigated experimentally.

We conclude that, in particular, both the four-carbon oxime linker and the direct acylation of [$Arg^{25,45,56,57}$]RANTES (4-68) represent routes to powerful semisynthetic anti-HIV compounds that show potential for optimization.

ACKNOWLEDGMENT

This work was supported by the Mintaka Foundation for Medical Research, Geneva, and the Foundation Dormeur Vaduz. We thank Dr. Reto Stöcklin of Atheris SA (Geneva) for giving us access to the Micromass Platform instrument.

Supporting Information Available: Supplementary Table S1. This material is available free of charge via the Internet at http://pubs.acs.org.

LITERATURE CITED

(1) Who, U. A. (2006) *AIDS Epidemic Update*, UN AIDS/World Health Organisation, Geneva, Switzerland.

(2) Lederman, M. M., Offord, R. E., and Hartley, O. (2006) Microbicides and other topical strategies to prevent vaginal transmission of HIV. *Nat. Rev. Immunol. 6*, 371–382.

(3) Hartley, O., Gaertner, H., Wilken, J., Thompson, D., Fish, R., Ramos, A., Pastore, C., Dufour, B., Cerini, F., Melotti, A., Heveker, N., Picard, L., Alizon, M., Mosier, D., Kent, S., and Offord, R. (2004) Medicinal chemistry applied to a synthetic protein: development of highly potent HIV entry inhibitors. *Proc. Natl. Acad. Sci. U.S.A. 101*, 16460–5.

(4) Lederman, M. M., Veazey, R. S., Offord, R., Mosier, D. E., Dufour, J., Mefford, M., Piatak, M., Jr., Lifson, J. D., Salkowitz, J. R., Rodriguez, B., Blauvelt, A., and Hartley, O. (2004) Prevention of vaginal SHIV transmission in rhesus macaques through inhibition of CCR5. *Science 306*, 485–7.

(5) Moore, J. P. (2005) Topical microbicides become topical. *N. Engl. J. Med. 352*, 298–300.

(6) Dawson, P. E., Muir, T. W., Clark-Lewis, I., and Kent, S. B. (1994) Synthesis of proteins by native chemical ligation. *Science 266*, 776–9.

(7) Wilken, J., and Kent, S. B. (1998) Chemical protein synthesis. *Curr. Opin. Biotechnol. 9*, 412–26.

(8) Wilken, J., Hoover, D., Thompson, D. A., Barlow, P. N., McSparron, H., Picard, L., Wlodawer, A., Lubkowski, J., and Kent, S. B. (1999) Total chemical synthesis and high-resolution crystal structure of the potent anti-HIV protein AOP-RANTES. *Chem. Biol. 6*, 43–51.

(9) Carrasco, M. R., Brown, R. T., Serafimova, I. M., and Silva, O. (2003) Synthesis of N-Fmoc-O- (N′-Boc-N′-methyl)-aminohomoserine, an amino acid for the facile preparation of neoglycopeptides. *J. Org. Chem. 68*, 195–7.

(10) Villain, M., Gaertner, H., and Botti, P. (2003) Native chemical ligation with aspartic and glutamic acids as C-terminal residues: scope and limitations. *Eur. J. Org. Chem. 2003*, 3267–3272.

(11) McNamara, J. F., Lombardo, H., Pillai, S. K., Jensen, I., Albericio, F., and Kates, S. A. (2000) An efficient solid-phase strategy for the construction of chemokines. *J. Pept. Sci. 6*, 512–8.

(12) Wang, S. S., Gisin, B. F., Winter, D. P., Makofske, R., Kulesha, I. D., Tzougraki, C., and Meienhofer, J. (1977) Facile synthesis of amino acid and peptide esters under mild conditions via cesium salts. *J. Org. Chem. 42*, 1286–90.

(13) Gaertner, H. F., Offord, R. E., Cotton, R., Timms, D., Camble, R., and Rose, K. (1994) Chemo-enzymic backbone engineering of proteins. Site-specific incorporation of synthetic peptides that mimic the 64–74 disulfide loop of granulocyte colony-stimulating factor. *J. Biol. Chem. 269*, 7224–30.

(14) Sabbe, R., Picchio, G. R., Pastore, C., Chaloin, O., Hartley, O., Offord, R., and Mosier, D. E. (2001) Donor- and ligand-dependent differences in C-C chemokine receptor 5 reexpression. *J. Virol. 75*, 661–71.

(15) Simmons, G., Clapham, P. R., Picard, L., Offord, R. E., Rosenkilde, M. M., Schwartz, T. W., Buser, R., Wells, T. N. C., and Proudfoot, A. E. (1997) Potent inhibition of HIV-1 infectivity in macrophages and lymphocytes by a novel CCR5 antagonist. *Science 276*, 276–9.

(16) Pleskoff, O., Treboute, C., Brelot, A., Heveker, N., Seman, M., and Alizon, M. (1997) Identification of a chemokine receptor encoded by human cytomegalovirus as a cofactor for HIV-1 entry. *Science 276*, 1874–8.

(17) Basu, A., Yang, K., Wang, M., Liu, S., Chintala, R., Palm, T., Zhao, H., Peng, P., Wu, D., Zhang, Z., Hua, J., Hsieh, M. C., Zhou, J., Petti, G., Li, X., Janjua, A., Mendez, M., Liu, J., Longley, C., Zhang, Z., Mehlig, M., Borowski, V., Viswanathan, M., and Filpula, D. (2006) Structure-function engineering of interferon-beta-1b for improving stability, solubility, potency, immunogenicity, and pharmacokinetic properties by site-selective mono-PEGylation. *Bioconjugate Chem. 17*, 618–30.

(18) Lee, H., Jang, I. H., Ryu, S. H., and Park, T. G. (2003) N-terminal site-specific mono-PEGylation of epidermal growth factor. *Pharm. Res. 20*, 818–25.

(19) Nie, Y., Zhang, X., Wang, X., and Chen, J. (2006) Preparation and stability of N-terminal mono-PEGylated recombinant human endostatin. *Bioconjugate Chem. 17*, 995–9.

(20) Zhang, L., and Tam, J. P. (1996) Thiazolidine formation as a general and site-specific conjugation method for synthetic peptides and proteins. *Anal. Biochem. 233*, 87–93.

(21) Liu, C. F., and Tam, J. P. (1994) Peptide segment ligation strategy without use of protecting groups. *Proc. Natl. Acad. Sci. U.S.A. 91*, 6584–8.

(22) Wang, L., Xie, J., and Schultz, P. G. (2006) Expanding the genetic code. *Annu. Rev. Biophys. Biomol. Struct. 35*, 225–49.

(23) Gaertner, H., Lebeau, O., Borlat, I., Cerini, F., Kuenzi, G., Melotti, M., Fish, R., Offord, R., Springael, J.-Y., Marc Parmentier, M., and Hartley, O. (2008) *Protein Eng. Des. Sel.*, in press.

(24) Martin, L., Blanpain, C., Garnier, P., Wittamer, V., Parmentier, M., and Vita, C. (2001) Structural and functional analysis of the RANTES-glycosaminoglycans interactions. *Biochemistry 40*, 6303–18.

(25) Proudfoot, A. E., Power, C. A., Hoogewerf, A. J., Montjovent, M. O., Borlat, F., Offord, R. E., and Wells, T. N. (1996) Extension of recombinant human RANTES by the retention of the initiating methionine produces a potent antagonist. *J. Biol. Chem. 271*, 2599–603.

(26) Shin, N. K., Kim, D. Y., Shin, C. S., Hong, M. S., Lee, J., and Shin, H. C. (1998) High-level production of human growth hormone in *Escherichia coli* by a simple recombinant process. *J. Biotechnol. 62*, 14351.

BC7003044

DNA Binding, Cleavage, and Cytotoxic Activity of the Preorganized Dinuclear Zinc(II) Complex of Triazacyclononane Derivatives

Xin Sheng,[†] Xun Guo,[†] Xiao-Min Lu,[‡] Guo-Yuan Lu,*[,†] Ying Shao,[†] Fang Liu,*[,†] and Qiang Xu[‡]

Department of Chemistry, State Key Laboratory of Coordination Chemistry, Nanjing University, Nanjing 210093, People's Republic of China, and State Key Laboratory of Pharmaceutical Biotechnology, Nanjing University, Nanjing 210093, People's Republic of China. Received August 26, 2007; Revised Manuscript Received November 24, 2007

A preorganized cleft dinuclear zinc(II) complex of 2,6-bis(1-methyl-1,4,7-triazacyclonon-1-yl)pyridine **1** as an artificial nuclease was prepared via an improved method. The interactions of **1**, **2** [1,4,7-triazacyclononane (TACN)], and their zinc(II) complexes with calf thymus DNA were studied by spectroscopic techniques, including fluorescence and CD spectroscopy. The results indicate that the DNA binding affinities of these compounds are in the following order: Zn^{II}_2−**1** > Zn^{II}−**2** > **1** > **2**. The binding constants of the Zn^{II}_2−**1** and Zn^{II}−**2** complexes are 3.57×10^6 and 1.43×10^5 M^{-1}, respectively. Agarose gel electrophoresis was used to assess the plasmid pUC 19 DNA cleavage activities in the presence of the dinuclear Zn^{II}_2−**1** complex, which exhibits powerful DNA cleavage efficiency. Kinetic data for DNA cleavage promoted by the Zn^{II}_2−**1** complex under physiological conditions give the observed rate constant (k_{obs}) of 0.136 h^{-1}, which shows an 10^7-fold rate acceleration over uncatalyzed supercoiled DNA. The comparison of the dinuclear Zn^{II}_2−**1** complex with the mononuclear zinc(II) complex of 1,4,7-triazacyclononane indicates that the DNA cleavage acceleration promoted by the Zn^{II}_2−**1** complex is due to the efficient cooperative catalysis of the two proximate zinc(II) cation centers. A hydrolytic mechanism of the cleavage process was suggested, and a preliminary study of the antitumor activity was also conducted.

INTRODUCTION

Artificial nucleases have recently received considerable interest for their potential applications in the fields of molecular biological technology and drug development (*1–10*). Among them, transition metal complexes as synthetic metallonucleases have been studied extensively due to their diversity in structure and reactivity (*11–26*), and some of them also exhibit antitumor or anti-HIV activities (*27–32*). Dinuclear or multinuclear complexes have especially attracted attention as artificial nucleases (*33–37*) since dinuclear or multinuclear metal centers are often found in natural nucleases and the metal centers may demonstrate synergistic effects in the activation and recognition of the active phosphodiesters and nuclear acids (*38, 39*). In Nature, there are many phosphoesterases that are activated by two or more metal ions, such as the 3′,5′-exonuclease from the Klenow fragment of DNA polymerase I (*40*), Rnase H from HIV reverse transcriptase (*41*), P1 nuclease (*42*), alkaline phosphatase (*43*), and phospholipase C (*44*). *Tetrahymena* ribozyme (*45, 46*) is also thought to be activated by at least two metal ions. Over the years, interesting dinuclear Cu(II), Co(III), and La(III) complexes that cleave activated phosphate esters and RNA have been reported (*33–39*). Especially, the dinuclear zinc(II) complexes of bis(1,4,7-triazacyclononane) [bis(TACN)] exhibit an excellent ability to cleave the phosphate ester bond of active phosphodiesters and RNA model compounds (*38, 39, 47–49*). Breslow (*50*) first prepared the dinuclear Zn(II) complex of bis(TACN) with a rigid spacer (4,4′-biphenyl group) and demonstrated that its cleaving activity toward active phosphodiester BNP (bis-*p*-nitrophenyl phosphate), RNA model HPNP (2-hydroxypropyl-*p*-nitrophenyl phosphate), and UpU dinucleoside is 5 times more effective than that of the corresponding mononuclear zinc(II) complex. The dizinc complex of bis(TACN) with a pyrazolate bridge reported by Kaden and Richard (*51*) has a 200-fold rate acceleration for BNP hydrolysis over the background reaction. The dinuclear zinc(II) complex of bis(TACN) containing a 2,2′-dimethylbipyridine bridge reported by Bencini, Lippolis, and co-workers (*52*) has a 350-fold rate acceleration for BNP hydrolysis. However, DNA-cleaving dinuclear metallic systems based on zinc(II) are scare (*26*). It is well-known that phosphodiester backbones in DNA are enormously stable, and their half-life under physiological conditions is estimated to be 200 million years (*53–57*). Therefore, DNA hydrolysis promoted by artificial nucleases is still a challenging subject. Recently, Scrimin and co-workers (*58*) reported that the dinuclear TACN zinc(II) complex of heptapeptide exhibits a remarkable hydrolytic cleavage activity of plasmid DNA with a first-order rate constant of 1.0×10^{-5} s^{-1} under physiological conditions, which is 20 times more reactive than its monometallic counterpart. Inspired by Scrimin's work, we synthesized a preorganized cleft molecule 2,6-bis(1-methyl-1,4,7-triazacyclonon-1-yl)pyridine **1** and investigated the DNA cleavage activity promoted by **1** and its bisnuclear zinc complex (Zn^{II}_2−**1**) under physiological conditions. We report here the detailed studies of the DNA binding and plasmid DNA hydrolysis process promoted by the Zn^{II}_2−**1** complex, including the complex concentration dependence, pH dependence, ionic strength dependence, cleavage kinetics, and comparison of the activity of the dinuclear zinc(II) Zn^{II}_2−**1** complex and the mononuclear TACN **2**−zinc(II) complex (Scheme 1). The mechanism of the cleavage process is suggested, and a preliminary study of the antitumor activity was also conducted.

EXPERIMENTAL PROCEDURES

Materials. All reagents and chemicals were of analytical grade and used without further purification. Plasmid pUC 19 DNA was purchased from TaKaRa Biotechnology Co. Ltd., and

* To whom correspondence should be addressed. Telephone: +86-25-8368-5613. Fax: +86-25-8332-1884. E-mail: lugyuan@nju.edu.cn.

[†] State Key Laboratory of Coordination Chemistry, Nanjing University.

[‡] State Key Laboratory of Pharmaceutical Biotechnology, Nanjing University.

10.1021/bc700322w CCC: $40.75 © 2008 American Chemical Society
Published on Web 01/08/2008

Scheme 1. Synthesis of Dinuclear Ligand 1

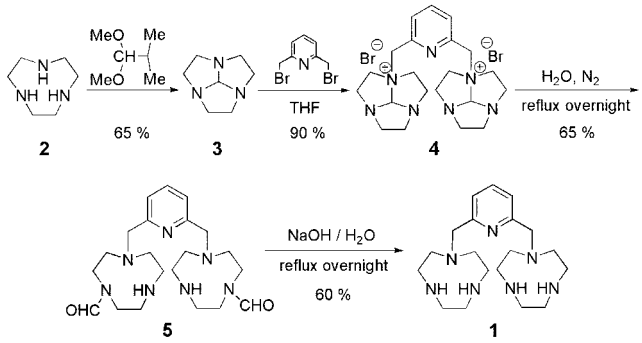

the purity was checked by agarose gel electrophoresis; their concentrations were determined by UV spectroscopy using the extinction coefficient appropriate for double-stranded DNA (1.0 OD_{260} = 50 μg/mL). Agarose was from Oxoid Limited (Basingstoke, U.K.). Ethidium bromide (EB) was from Amresco Inc. Tris(hydroxymethyl)aminomethane (Tris-Base) was from Robiot Co. Ltd. Bromophenol blue, glycerol, and ethyldiaminetetraacetic acid (EDTA) were commercially available. Deionized water was obtained from an ionized column from doubly distilled water. All solvents were purified by the standard procedure.

Apparatus. ^{1}H NMR and ^{13}C NMR data were recorded on a Brucker AM 300 spectrometer. Elemental analyses were performed on a Perkin-Elmer 240C instrument. Mass spectra were obtained on an electrospray mass spectrometer (LCQ, Finnigan) in positive mode. The pH value was confirmed with an ORION868 pH meter with an Ag/AgCl electrode as the reference electrode in a saturated KCl solution at room temperature. Agarose gel electrophoresis was conducted with a DYY-5 electrophoresis apparatus. Bands were visualized by UV light and photographed using a DigiDoc-It gel imaging and documentation system (version 1.1.23, UVP, Inc., Unpland, CA). The intensity of the DNA bands was estimated by TotalLab image analysis software (version 2.01).

Fluorescence Measurements. The fluorescent spectral studies were performed by the measurement of the emission intensity of ethidium bromide (EB) on an AMINCO Bowman Series 2 luminescence spectrometer. The experiments were carried out by adding 0−21 μM **2**, **1**, Zn^{II}−**2**, or Zn^{II}_2−**1** into the EB (1.0 μM)-bound CT-DNA (30 μM) solution in 5 mM Tris-HCl buffer (pH 6.8), and the fluorescence was measured and normalized to 100% relative fluorescence.

Circular Dichroism Measurements. All CD spectroscopic studies were carried out with a continuous flow of nitrogen purging the polarimeter, and the measurements were performed at room temperature with 1 cm pathway cells. The CD spectra were run from 320 to 220 nm at a speed of 20 nm/min, and the buffer background was automatically subtracted. Data were recorded at an interval of 0.1 nm. The CD spectrum of CT-DNA alone (50 μM) was recorded as the control.

DNA Cleavage Assays. Cleavage reactions of supercoiled pUC 19 DNA (0.05 mM bp) were carried out at 37 °C in 50 mM Tris-HCl/10 mM NaCl buffer in a total volume of 15 μL. The results of cleavage reactions were monitored by agarose gel electrophoresis (80 V for 1.5 h), and the supercoiled plasmid DNA values were corrected by a factor of 1.3 on the basis of average literature estimates of weakened binding of EB to this structure.

Synthesis of 1,4,7-Triazacyclononane (2). The synthesis of 1,4,7-triazacyclononane was achieved according to the literature method (*59*): ^{1}H NMR (300 MHz, $CDCl_3$) δ 2.00 (s, 3H, NH_2), 2.79 (s, 12H, CH_2); ^{13}C NMR (75 MHz, D_2O) δ 41.2 (CH_2).

Synthesis of 1,4,7-Triazatricyclo[5.2.1.0^{4,10}]decane (3). A stirred solution of 1,4,7-triazacyclononane **2** (1 g, 7.75 mmol) and $HC(OMe)_2NMe_2$ (0.93 g, 7.83 mmol) in anhydrous benzene (12.5 mL) was heated at 90 °C for 6 h. The mixture was then allowed to cool to room temperature and filtered. After the solvent was removed, the residue (0.70 g, 5.04 mmol) was distilled at 4 mmHg and the fraction boiling at 56 °C was collected: yield 65%; ^{1}H NMR (300 MHz, $CDCl_3$) δ 2.40–2.52 (m, 6H, $3CH_2$), 2.70–2.77 (m, 6H, $3CH_2$), 4.66 (s, 1H, CH); ESI-MS *m*/*z* $[M + H]^+$ calcd 140.1, found 140.4.

Synthesis of 2,6-Bis(1-methyl-1-azonia-4,7-diazatricyclo [5.2.1^{4,10}]decane)pyridine dibromide (4). A stirred solution of compound **3** (0.33 g, 2.37 mmol) in anhydrous THF (1 mL) was cooled to 0 °C, and then a solution of 2,6-bis(bromomethyl)pyridine (0.30 g, 1.13 mmol) in anhydrous THF (1.5 mL) was added slowly. The mixture was stirred at 0 °C for 48 h. Then, the mixture was filtered, and the residue was washed with THF (2 × 1 mL) and ether (1 mL). A white solid (0.39 g, 1.01 mmol) was obtained: yield 90%; ^{1}H NMR (300 MHz, D_2O) δ 2.99–3.09 (m, 8H, $4CH_2$), 3.32–3.54 (m, 8H, $4CH_2$), 3.86–3.93 (m, 8H, $4CH_2$), 4.54 (s, 4H, $2ArCH_2$), 5.89 (s, 2H, 2CH), 7.69 (d, J = 7.8 Hz, 2H, 2ArH), 7.82 (t, J = 7.8 Hz, 1H, ArH); ESI-MS *m*/*z* $[M - Br]^+$ calcd 462.2, found 462.2.

Synthesis of 2,6-Bis(1-carboxaldehyde-4-methyl-1,4,7-triazacyclonon-4-yl)pyridine (5). Compound **4** (0.55 g, 1.01 mmol) was dissolved in water (6 mL) and the mixture stirred overnight at room temperature under an atmosphere of dry N_2. The mixture was filtered, and the filtrate was extracted with $CHCl_3$ (3 × 10 mL). The organic layer was treated with charcoal and filtered. Then, the solvent was removed under vacuum to give compound **5** as a pale yellow oil (0.27 g, 0.65 mmol): yield 65%; ^{1}H NMR (300 MHz, $CDCl_3$) δ 2.52–2.83 (m, 8H, $4CH_2$), 3.10–3.37 (m, 8H, $4CH_2$), 3.44 (s, 2H, 2NH), 3.50–3.71 (m, 8H, $4CH_2$), 3.82 (s, 4H, $2ArCH_2$), 7.15–7.24 (m, 2H, 2ArH), 7.51–7.80 (m, 1H, ArH), 8.03 (s, 2H, CHO); ^{13}C NMR (75 MHz, D_2O) δ 45.1 (CH_2), 46.7 (CH_2), 48.3 (CH_2), 48.8 (CH_2), 53.9 (CH_2), 62.3 ($ArCH_2$), 123.4 (Ar C), 138.8 (Ar C), 158.7 (Ar C), 166.5 (CHO); ESI-MS *m*/*z* $[M + H]^+$ calcd 418.3, found 418.5.

Synthesis of 2,6-Bis(1-methyl-1,4,7-triazacyclonon-1-yl)-pyridine (1). Compound **5** (0.27 g, 0.65 mmol) was dissolved in a sodium hydroxide solution (20 mL, 2.5 M) and the mixture stirred overnight at room temperature under an atmosphere of dry N_2. The mixture was filtered, and the residue was extracted with $CHCl_3$ (3 × 10 mL). All of the organic layers (including the filtrate and the extractant) were merged and dried. The solvent was removed under vacuum to give compound **1** as a pale yellow oil (0.14 g, 0.39 mmol): yield 60%; ^{1}H NMR (300 MHz, $CDCl_3$) δ 2.58–2.62 (m, 8H, $4CH_2$), 2.66–2.74 (s, 16H, $8CH_2$), 3.23 (br s, 4H, 4NH), 3.82 (s, 4H, $2ArCH_2$), 7.17 (d, J = 7.6 Hz, 2H, 2ArH), 7.54 (t, J = 7.6 Hz, 1H, ArH); ^{13}C NMR (75 MHz, D_2O) δ 43.8 (CH_2), 48.3 (CH_2), 50.6 (CH_2), 61.7 ($ArCH_2$), 123.6 (Ar C), 138.7 (Ar C), 158.2 (Ar C); ESI-MS *m*/*z* $[M + H]^+$ calcd 362.3, found 362.4. Anal. Calcd for $C_{19}H_{35}N_7$: C, 63.12; H, 9.76; N, 27.12. Found: C, 63.36; H, 9.63; N, 27.01.

Preparation of the Zinc(II) Complex Storage Solution. A mixture of ligand **1** (or **2**) and $ZnCl_2$ at a 2:1 (or 1:1) molar ratio in methanol (10 mL) was stirred for 5 h at room temperature and then evaporated to remove the solvent. The residue was dissolved in deionized water as the zinc(II) complex storage solution.

Materials and Methods of Cytotoxic Assays. *Cell Lines.* A murine B16 melanoma cell line and a human HL-60 promyelocytic leukemia cell line were obtained from American Type Culture Collection (ATCC, Rockville, MD), maintained in DMEM (Life Technologies Inc., Grand Island, NY) and

RPMI 1640 (Gibco, Scotland, U.K.), respectively, supplemented with penicillin (100 units/mL), streptomycin (100 μg/mL), and 10% fetal bovine serum (Life Technologies) at 37 °C in a humidified atmosphere containing 5% CO_2 in air.

MTT Assays for Cell Viability. Cells were cultured in 96-well plates for 72 h with various compounds. Cell viability was evaluated with a modified MTT assay (*60*). Briefly, 20 μL of 4 mg/mL 3-(4,5-dimethyl-2-thiazolyl)-2,5-diphenyl-2*H*-tetrazolium bromide (MTT, Sigma) in medium was added for a further 4 h incubation. After the supernatant had been removed, 200 μL of DMSO was added to dissolve the formazan crystals. The absorbance was read on an ELISA reader (Tecan) at 540 nm. The relative survival rate was determined in relation to that of untreated cells, which was set as 100%.

RESULTS AND DISCUSSION

General Aspects. Compound **1** is a bis-triazacrown ether, in which the rigid 2,6-dimethylenepyridine is employed as the bridging group to construct a preorganized cleft receptor for phosphodiester. The cleft zinc(II) complex affords a cavity to accommodate, recognize, and bind the phosphodiesters of DNA because the two zinc(II) ion centers are kept at a certain distance. On the other hand, the proximate pyridyl nitrogen atom can coordinate to one of the two metal ions (*61, 62*), which makes the zinc(II) ion center more immovable for the efficient binding and recognizing of the DNA phosphodiester backbone. Therefore, high DNA cleavage activity can be expected due to the quite efficient cooperative catalysis of two zinc(II) ions in a rigid cleft molecule system.

The organic ligand **1** was prepared according to the literature method (*63*) with some modifications in good yield via a four-step reaction starting from **2** (Scheme 1). The reaction of 2 equiv of the 1,4,7-triazacyclononane orthoamide with 2,6-bis(bromomethyl)pyridine in THF followed by hydrolysis gave a new intermediate product **5**. Then, compound **5** was treated with an aqueous NaOH solution to give ligand **1**. The zinc(II) complexes of **1** and **2** were prepared by mixing methanol solutions of the organic ligands and $ZnC1_2$. The metal-bound chlorides in Zn^{II}_2−**1** and Zn^{II}−**2** complexes can be displaced spontaneously by water molecules in aqueous solvents (*64–66*). The ESI-MS spectrum (Figure S1, Supporting Information) of the zinc(II) complex of ligand **1** demonstrates that **1** coordinates two zinc(II) ions in water when 2 equiv of $ZnCl_2$ is added.

DNA Binding Assays. DNA binding is the critical step for DNA cleavage in most cases. Therefore, the binding of the ligands (**1** and **2**) and their complexes (Zn^{II}_2−**1** and Zn^{II}−**2**) to CT-DNA was studied by using fluorescence and circular dichroism spectroscopy. UV–vis absorption spectroscopy is also one of the convenient tools for examining the interaction between small molecules and nucleic acids, but these complexes have very UV absorbances similar to that of calf thymus (CT-DNA) at 260 nm; thus, the DNA binding studies were not carried out by using UV–vis absorption spectroscopy.

Fluorescence Spectroscopic Studies. The binding of the compounds to CT-DNA was studied by evaluating the fluorescence emission intensity of the ethidium bromide (EB)−DNA system upon the addition of the four compounds. If these compounds added to the EB−DNA system replace the bound EB, the emission intensity will be reduced. The fluorescence quenching of EB bound to DNA by **2**, **1**, Zn^{II}−**2**, and Zn^{II}_2−**1** is shown in Figure S2 (Supporting Information), in which the fluorescence intensity at 610 nm (λ_{ex} = 518 nm) of EB in the bound form was plotted against the compound concentration. The relative binding propensity of the compounds to CT-DNA was determined by the classical Stern−Volmer equation $I_0/I = 1 + Kr$ (*67–70*), where I_0 and I are the fluorescence intensities in the absence and presence of the quencher, respectively, K is the linear Stern−Volmer quenching constant dependent on the ratio of r_{bE} (the ratio of the bound concentration of EB to the concentration of DNA), and r is the ratio of the total concentration of the quencher to that of DNA (*67–70*). Figure 1 is the plot of I_0/I versus [quencher]/[DNA], and quenching constant K is given by the slope. The K values obtained for **2**, **1**, Zn^{II}−**2**, and Zn^{II}_2−**1** are 0.053 ± 0.010, 0.157 ± 0.015, 0.259 ± 0.005, and 0.827 ± 0.022, respectively. These results demonstrate that Zn^{II}−**2** and Zn^{II}_2−**1** complexes have stronger affinity for DNA than the corresponding ligands **2** and **1**. Moreover, the dinuclear Zn^{II}_2−**1** complex possesses much better DNA binding ability than the mononuclear Zn^{II}−**2** complex. The apparent binding constant (K_{app}) was also calculated from the equation K_{EB}[EB] = K_{app}[complex], where the complex concentration was the value at a 50% reduction of the fluorescence intensity of EB and $K_{EB} = 1.0 \times 10^7$ M^{-1} ([EB] = 1.0 μM) (*71*). The K_{app} values are 1.43×10^5 M^{-1} for Zn^{II}−**2** and 3.57×10^6 M^{-1} for Zn^{II}_2−**1** (Figure S3, Supporting Information). It is noticed that the binding constant of Zn^{II}_2−**1** is 30-fold higher than that of Zn^{II}−**2**.

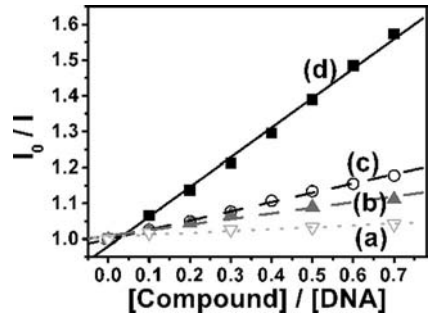

Figure 1. Stern−Volmer quenching plots of EB bound to DNA by (a) **2**, (b) **1**, (c) Zn^{II}−**2**, and (d) Zn^{II}_2−**1**, which give the quenching constants K. The experiments were conducted by adding 0−21 μM **2**, **1**, Zn^{II}−**2**, or Zn^{II}_2−**1** to the EB-bound CT-DNA solution in 5 mM Tris-HCl buffer (pH 6.8).

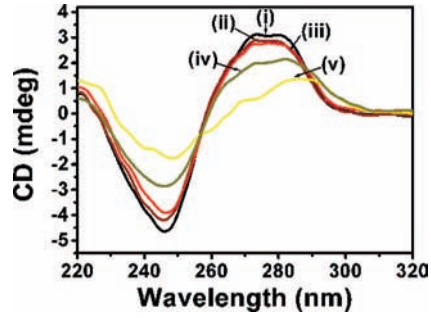

Figure 2. Circular dichroism spectrum of (i) CT-DNA (5.0×10^{-5} M) and the interaction with (ii) **2**, (iii) **1**, and (iv) Zn^{II}−**2** at a [compound]/[CT-DNA] ratio of 1 and (v) Zn^{II}_2-**1** at a [compound]/[CT-DNA] ratio of 0.5. All the spectra were recorded in Tris-HCl buffer at pH 6.8.

Circular Dichroism Studies. CD spectroscopy is a useful technique for assessing whether nucleic acids undergo conformational changes as a result of complex formation or changes in the environment. Figure 2 displays the CD spectra of CT-DNA treated with **2**, **1**, and Zn^{II}−**2** with a ratio ([compound]/[DNA]) of 1 and Zn^{II}_2−**1** with the ratio of 0.5. Both the positive (~275 nm) band and the negative (~245 nm) band decreased in intensity in the presence of the zinc(II) complexes except for those with ligands **2** and **1**. Both the positive and negative CD bands decreased in intensity with the increase in the concentrations of the added complexes Zn^{II}−**2** and Zn^{II}_2−**1** (Figure S4, Supporting Information). This suggests that Zn^{II}−**2** and Zn^{II}_2−**1** can unwind the DNA helix and lead to the loss of

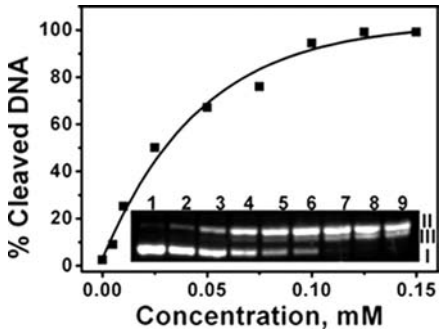

Figure 3. Plot of percent cleaved DNA vs different concentrations of Zn^{II}_2−**1**. The inset is the agarose gel (1%) of the concentration-variable reaction products [incubated in Tris-HCl buffer (pH 6.8) for 15 h at 37 °C]: lane 1, DNA control; and lanes 2–9, concentrations of Zn^{II}_2−**1** of 0.005, 0.010, 0.025, 0.050, 0.075, 0.100, 0.125, and 0.150 mM, respectively.

helicity (*72, 73*). The largest decrease in the CD band intensity caused by Zn^{II}_2−**1** (each triaza-crown ether unit) compared to those of the other compounds at the same concentration implies that Zn^{II}_2−**1** is more effective than **1**, **2**, and Zn^{II}−**2** in perturbing the secondary structure of DNA.

From the results of these fluorescence and CD spectroscopic studies, we conclude that the abilities of the compounds to bind to CT-DNA are in the following order: Zn^{II}_2−**1** > Zn^{II}−**2** > **1** ≈ **2**.

Cleavage of Plasmid DNA. The affinities of 1,4,7-triazacyclononane (TACN) **2** and compound 2,6-bis(1-methyl-1,4,7-triazacyclonon-1-yl)pyridine **1** for zinc(II) ion have been reported by Kimura (*74*) and Beneini (*62*), respectively. The stability constant of the 1:1 complex of **2** (TACN) and zinc(II) is 11.3 (*74*), indicating a very high stability. In Bencini and Lippolis's work (*62*), two TACN units of compound **1** can simultaneously coordinate zinc(II) ions to form a 1:2 dinuclear complex with an extremely large stability constant (log K = 26.2) in aqueous solution at pH 6−7. Therefore, in this investigation, when the ratios of ligands **1** and **2** to zinc(II) are 1:2 and 1:1, respectively, the dinuclear Zn^{II}_2−**1** and mononuclear Zn^{II}−**2** complexes are main species existing under the experimental pH condition, respectively.

To assess the DNA cleaving behavior of Zn^{II}_2−**1**, cleavage reactions of supercoiled pUC 19 DNA (0.05 mM bp) were carried out at 37 °C in 50 mM Tris-HCl/10 mM NaCl buffer in a total volume of 15 μL. The results of cleavage reactions were monitored by agarose gel electrophoresis (80 V for 1.5 h), and the supercoiled plasmid DNA values were corrected by a factor of 1.3 on the basis of average literature estimates of weakened binding of EB to this structure (*75, 76*). The inset of Figure 3 is the agarose gel of the DNA cleavage promoted by Zn^{II}_2−**1**, which indicates that Zn^{II}_2−**1** cleaves DNA efficiently. The supercoiled DNA (form I) relaxes to form a nicked circular DNA (form II) in the presence of Zn^{II}_2−**1**, and then the linear DNA (form III) forms when the complex concentration increases. The concentration dependence plot exhibits a saturation profile (Figure 3), which suggests that the DNA cleavage activity of Zn^{II}_2−**1** is increased with the increase in the complex concentration, and it is closed to be saturated at a complex concentration of 0.10 mM. To improve our understanding of whether the metal ions or ligand **1** alone is able to cleave DNA, control assays were carried out under the same conditions with the metal ions alone or ligand **1** alone, respectively. Figure S5 and Table S1 (Supporting Information) show the results of pUC 19 DNA cleavage (incubated for 12 h at 37 °C) in the presence of different metal ions (0.20 mM). Little cleavage (15%) was found. A similar result was reported by Barton (*77*). On the other hand, when DNA was incubated for 12 h at 37 °C in the

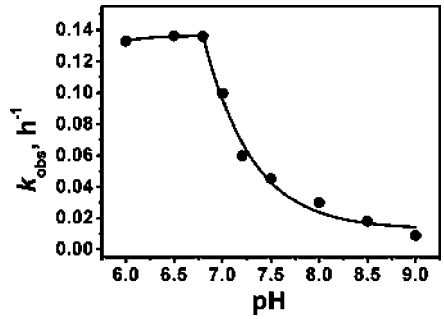

Figure 4. pH-dependent profile for DNA cleavage promoted by Zn^{II}_2−**1** (0.10 mM) at 37 °C.

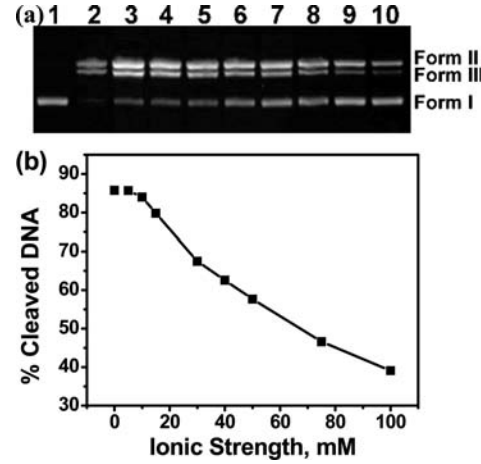

Figure 5. (a) Agarose gel (1%) of the DNA cleavage reaction products promoted by Zn^{II}_2−**1** (0.10 mM) for 12 h at 37 °C and pH 6.8 under different ionic strength conditions: lane 1, DNA control; lane 2, no NaCl; and lanes 3–9, ionic strengths of 5, 10, 15, 30, 40, 50, 75, and 100 mM, respectively. (b) Ionic strength-dependent profile for DNA cleavage promoted by Zn^{II}_2−**1** (0.10 mM).

presence of ligand **1** (0.10 mM) alone, only 12% supercoiled DNA was cleaved (see the Supporting Information, page S12), indicating that ligand **1** alone can hardly cleave DNA, while the Zn^{II}_2−**1** complex (0.10 mM) caused 80% cleavage of DNA under the same conditions (Supporting Information, page S16).

Figure 4 presents the pH-dependent profile for DNA cleavage promoted by Zn^{II}_2−**1** (0.10 mM) at 37 °C, which indicates that a pH range of 6.0−6.8 is the optimal pH condition, and the cleavage rate decreases with an increase in the pH value (pH 6.8−9.0). The species distribution diagrams of the Zn(II)-bound water for the dimetallic Zn^{II}_2−**1** complex was reported by Bencini (*62*), which shows that two and three hydroxide anions can be bound to zinc(II) ion with the increasing pH condition (pH >6.8). Indeed, the decrease in reactivity above pH 6.8 may be related to the deprotonation of a second water molecule on the complex, which may result in a competition for the complexation of the substrate phosphodiester anion. As a result, the Tris-HCl buffer at pH 6.8 was used for all of the DNA cleavage reactions. Ionic strength always affects the DNA cleavage significantly. Ionic strength dependence assays show that the cleavage activity decreases with an increase in the ionic strength (Figure 5a,b), which implies that the positively charged zinc(II) centers bind with the anionic sites in the phosphodiester of DNA, rather than with the DNA bases, via electrostatic interactions (*78*). Thus, a relatively low NaCl concentration (10 mM) was selected to control the ionic strength in all experiments.

Kinetics of DNA degradation have been studied. Figure 6a shows the agarose gel of the supercoiled plasmid DNA cleavage promoted by Zn^{II}_2−**1** (0.10 mM) in Tris-HCl/NaCl buffer (pH 6.8) at 37 °C into nicked and linear forms. The time course

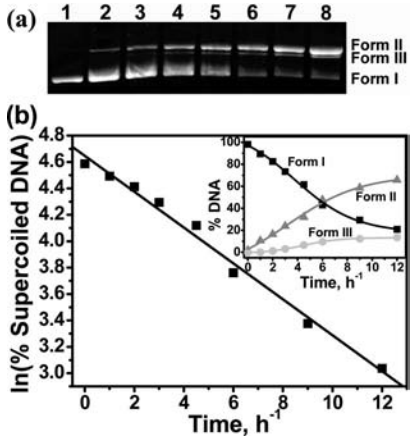

Figure 6. Time course of pUC 19 DNA (0.05 mM bp) cleavage promoted by Zn^{II}_2−**1** (0.10 mM). (a) Agarose gel (1%) of the time-variable reaction products: lanes 1–8, reaction times of 0, 1.0, 2.0, 3.0, 4.5, 6.0, 9.0, and 12.0 h, respectively. (b) Plot of ln(% supercoiled DNA) vs reaction time. The inset of Figure 4b is the plot of percent DNA vs time.

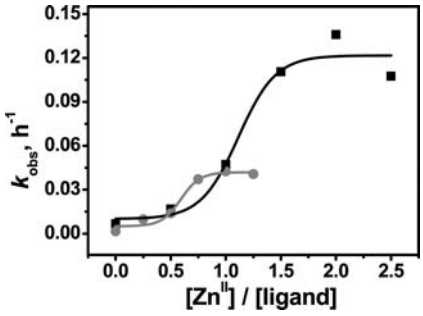

Figure 7. Dependence of the rate of DNA cleavage on the [Zn^{II}]/[ligand] ratio at a constant ligand concentration (0.10 mM) at 37 °C (pH 6.8, 50 mM Tris-HCl/10 mM NaCl buffer): **1** () and **2** (•).

plot indicates that the extension of supercoiled DNA cleavage varies exponentially with reaction time, giving pseudo-first-order kinetics with an apparent first-order rate constant of 0.136 ± 0.005 h^{-1} (Figure 6b), which shows 10^7-fold rate acceleration over that of uncatalyzed supercoiled DNA (*53–57, 60*).

To confirm that the cooperative catalysis of the dinuclear complex is an efficient strategy as expected, the dependence of the DNA cleavage rate on the [Zn^{II}]/[ligand] ratio at a constant ligand concentration (0.10 mM) has been measured (Figure 7). For ligand **2**, the rate of DNA hydrolysis increases to a plateau that is reached when 1 equiv of zinc(II) ion has been added, indicating that one zinc(II) ion per ligand **2** is required for maximum activity; for ligand **1**, limiting reactivity is reached at 2 equiv of zinc(II) ion. The observed maximum cleavage rate constants of **1** and **2** in the presence of zinc(II) ion (2:1 and 1:1) are 0.136 ± 0.005 h^{-1} (k_{obs}^1) and 0.0425 ± 0.0014 h^{-1} (k_{obs}^2), respectively (Table S2, Supporting Information). We notice that the DNA cleavage efficiency of 1 equiv of Zn^{II}_2−**1** is higher than that of 2 equiv of Zn^{II}−**2** (k_{obs}^1 is 3 times greater than k_{obs}^2), which indicates that the acceleration by Zn^{II}_2−**1** is due to the efficient cooperative catalysis of the two proximate zinc(II) cation centers (*38, 39, 79*). That is to say, having two preorganized metal ion centers connected by a rigid bridging structure in one system is a more efficient strategy for DNA cleavage.

Mechanism. To verify if reactive oxygen species (ROS) are, at least in part, responsible for the cleavage of DNA promoted by Zn^{II}_2−**1**, reactions were carried out in the presence of typical scavengers (*37, 80*) for singlet oxygen (NaN_3, 10 mM), for superoxide (KI, 10 mM), and for hydroxyl radical (1 mM DMSO and 1 mM *t*-BuOH) (see Figure S6 and Table S3 of the Supporting Information). Figure 8 shows that there is no evident inhibition effect on the DNA cleavage in the presence of all scavengers (NaN_3, DMSO, *t*-BuOH, and KI), which rules out the involvement of these reactive oxygen species, at least in a free and diffusible form. On the other hand, zinc(II) complexes generally cleave DNA by the hydrolytic pathway (*81*). Therefore, DNA cleavage promoted by Zn^{II}_2−**1** might not occur by an oxidative pathway but takes place by a hydrolytic pathway.

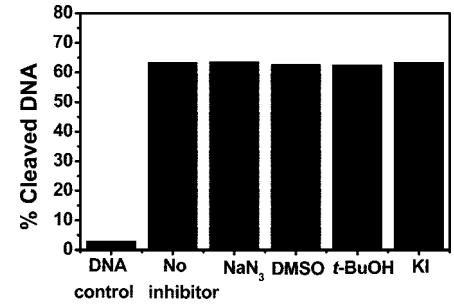

Figure 8. Histogram representing of pUC19 plasmid DNA (0.05 mM bp) cleaved by Zn^{II}_2−**1** (0.10 mM) in the presence of standard radical scavengers incubated for 8 h at 37 °C in pH 6.8 buffer (50 mM Tris-HCl/10 mM NaCl).

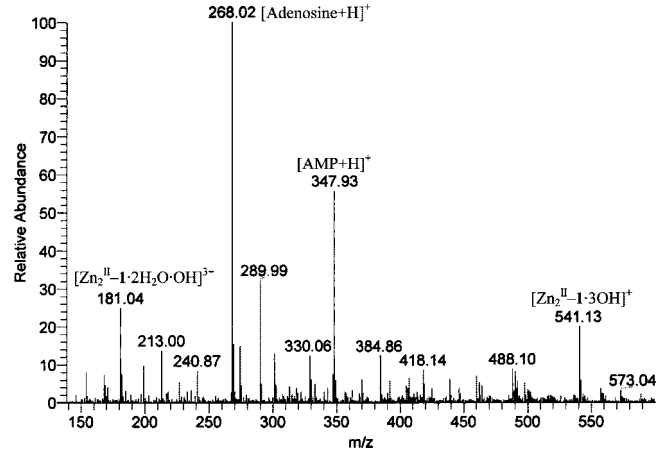

Figure 9. ESI-MS analysis of ApA hydrolysis promoted by Zn^{II}_2−**1**.

To further prove the hydrolysis pathway, a small dinucleotide model system adenylyl(3′–5′)phosphoadenine (ApA) was used as the nucleic acid mimic. ApA (0.10 mM) and Zn^{II}_2−**1** (0.01 mM) were dissolved in deionized water, and after equilibration for 8 h at room temperature, ESI-MS analysis was carried out. In the ESI-MS spectrum (Figure 9), the signals at *m*/*z* 268.02 and 347.93 show the presence of ApA cleavage products adenosine (calcd *m*/*z* 268.10) and adenine monophosphate (AMP, calcd *m*/*z* 348.06). The generation of the adenosine and AMP indicates that the phosphodiester bonds of ApA were cleaved by Zn^{II}_2−**1** via the hydrolysis pathway (*38*). Therefore, as in ApA, the hydrolysis pathway should be the possible mechanism for DNA cleavage promoted by Zn^{II}_2−**1**. As a comparison, ESI-MS analysis of ApA treated with ligand **1** was also carried out under the same conditions (Figure S7, Supporting Information), and there were no signs of cleavage products (adenosine and AMP). Therefore, it is concluded that the hydrolysis of ApA was caused by the cooperativity of the two zinc(II) ions in Zn^{II}_2−**1**.

In the ESI-MS spectrum of Zn^{II}_2−**1** in a neutral aqueous solution (Figure S1, Supporting Information), the peaks at *m*/*z* 540.90 and 180.96 show the signals of species **a** ([Zn_2^{II}−

Scheme 2. Equilibration between a and b

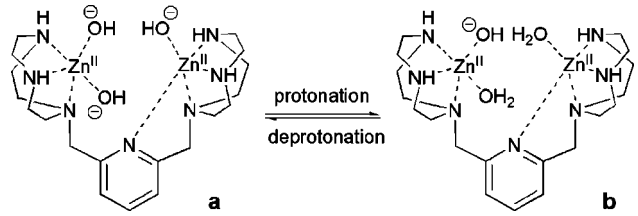

Scheme 3. A Plausible Mechanism for DNA Cleavage Promoted by Zn^{II}_2···C1

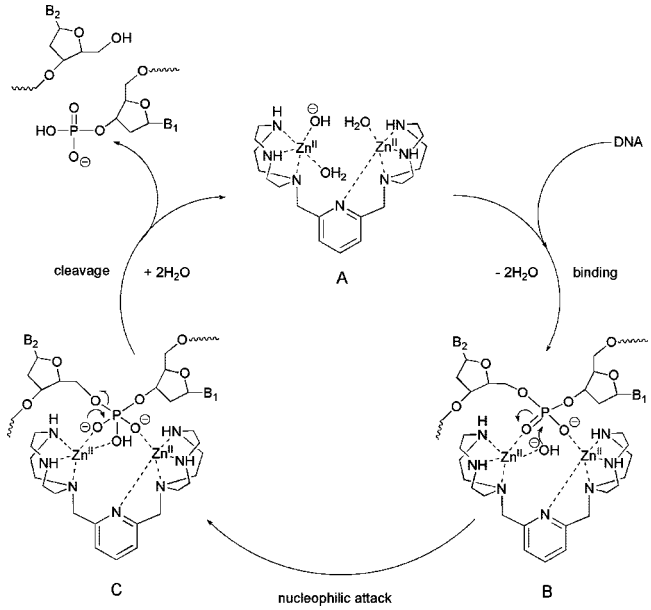

1·3OH]$^+$, calcd *m*/*z* 540.16) and **b** ([Zn_2^{II}−**1**·2H_2O·OH]$^{3+}$, calcd *m*/*z* 180.73), respectively (Scheme 2), which indicates the existence of the zinc(II)-bound OH in the aqueous solution. This fact is also consistent with the result reported by Beneini and Lippolis (*62*). In addition, Chuburu and co-workers (*61*) reported that the N atom of the pyridine is involved in the coordination of one copper(II) ion in the monocrystal structures of the dinuclear copper(II) complex of 2,6-bis(1,4,7,10-tetraazacyclododecylmethyl)pyridine. Therefore, a similar status is achieved in the dinuclear zinc(II) complex presented here. According to the ESI-MS spectrum of Zn^{II}_2−**1** and some reports from the literature (*33–37, 61, 62*), a plausible mechanism for DNA cleavage promoted by Zn^{II}_2−**1** is schematically depicted in Scheme 3. It is well-known that dinuclear metal complexes bind the phosphodiester backbone of DNA much more tightly than 2 equiv of the corresponding mononuclear complex due to the two-point DNA binding mechanism (*82*). Therefore, the first step of DNA cleavage promoted by Zn^{II}_2−**1** is that in which two zinc(II) cations recognize and bind the phosphodiester bond of DNA through the coordinate linkage and electrostatic interaction, and the synergistic effect between the two zinc(II) ions activates the central phosphorus atom. Then, the activated phosphorus atom is nucleophilically attacked by the proximate zinc(II)-bound OH, resulting in the formation of the trigonal bipyramidal phosphorus intermediate. Finally, one of the P−O ester bonds of the phosphodiester is broken by the intramolecular charge delivery to complete the DNA cleavage and the catalyst regeneration.

Consequently, DNA cleavage promoted by Zn^{II}_2−**1** takes place via a hydrolytic pathway with the observed maximum rate constant k_{obs}^1 of 0.136 ± 0.005 h^{-1}. This value is comparable to the value of 1×10^{-5} s^{-1} (0.36 h^{-1}) reported by Scrimin and co-workers (*58*) for the dinuclear zinc(II) complexes with a heptapeptide as the artificial nuclease. Recently, Yu and co-workers (*83*) reported that dimetallic zinc(II) complexes made by linking two cyclen ligands with pyridinic or phenolic moieties can completely cleave plasmid DNA to give form II after only 5 min. However, the complexes appear active only in the presence of the reducing agent vitamin C, and thus, the cleavage mechanism could be a nonhydrolytic pathway (*26*).

Table 1. Percentage of Growth Inhibition

	B16 cells[a]			HL-60 cells[a]		
	10^{-3} M	10^{-4} M	10^{-5} M	10^{-4} M	10^{-5} M	10^{-6} M
Zn^{II}	89	13	0	8	4	0
1	61	8	0	32	3	0
2	23	2	0	16	2	0
Zn^{II}_2−**1**	91	88	36	97	97	3
Zn^{II}−**2**	89	13	0	23	3	0

[a] Tumor cells were treated with different compounds for 72 h and incubated with 4 mg/mL MTT for 4 h. The amount of MTT formazan produced was determined by measuring the absorbance at 540 nm.

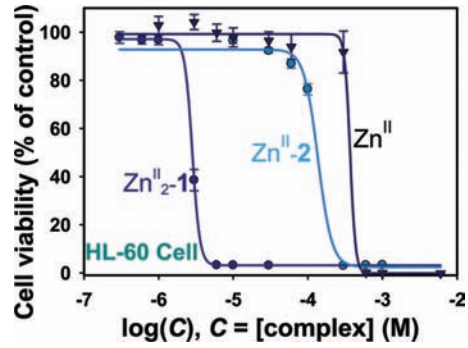

Figure 10. Inhibitory effect of zinc(II) ion, Zn^{II}−**2**, and Zn^{II}_2−**1** on the proliferation of HL-60 cells. Cells were exposed to the compounds for 72 h. The relative survival rate was determined in relation to that of untreated control cells, which was set to 100%. Data are means ± the standard deviation of three experiments, and each experiment included triplicate wells.

Cytotoxic Activities. To evaluate the antitumor activity, B16 and HL-60 cells were exposed to different concentrations of ligand **1**, **2**, zinc(II) ion, and the zinc(II) Zn^{II}_2−**1** and Zn^{II}−**2** complexes for 72 h. Cell viability was determined by MTT assays (*84*). The inhibition percentages are listed in Table 1. According to these results of the cytotoxic assays, we conclude that the two zinc(II) complexes (Zn^{II}_2−**1** and Zn^{II}−**2**) exhibit much stronger cytotoxic effects than the corresponding ligands (**1** and **2**), and HL-60 cells prove to be more sensitive to these compounds than B16 cells. The antitumor activities are shown to follow the order **2** < **1** < Zn^{II}−**2** < Zn^{II}_2−**1**. Heavy metal ions are cytotoxic to cells at 10^{-3} M (*85*). Table 1 and Figure 10 show that zinc(II) ions also exhibit antitumor activity at this level, but when zinc(II) ions are diluted to 3×10^{-4} M, the percentage inhibition decreases sharply ($IC_{50} = 3.70 \times 10^{-4}$ M). On the other hand, Zn^{II}_2−**1** still kept its antitumor activity toward HL-60 cells even at 10^{-6} M. To further evaluate the antitumor activity of the Zn^{II}_2−**1** and Zn^{II}−**2** complexes, IC_{50} values against HL-60 cells were calculated as shown in Figure 10. The IC_{50} values are 1.36×10^{-4} M for Zn^{II}−**2** and 2.54×10^{-6} M for Zn^{II}_2−**1**. We notice that the IC_{50} value against HL-60 cells of Zn^{II}_2−**1** is 50-fold larger than that of Zn^{II}−**2**.

CONCLUSIONS

In conclusion, a preorganized cleft bis(1,4,7-triazacyclononane)−Zn^{II} complex Zn^{II}_2−**1** as an artificial nuclease was prepared via an improved method. The interactions of **1**, **2**, and

their zinc(II) complexes with calf thymus DNA were studied by spectroscopic techniques (fluorescence and CD spectroscopy). The results indicate that the DNA binding affinities of these compounds are ordered as follows: Zn^{II}_2−**1** > Zn^{II}−**2** > **1** > **2**. The binding constant of Zn^{II}_2−**1** is 3.57×10^6 M^{-1}. Complex concentration, pH, and ionic strength dependences of the DNA cleavage promoted by Zn^{II}_2−**1** were studied by agarose gel electrophoresis. Kinetic data of DNA cleavage promoted by Zn^{II}_2−**1** (0.10 mM) under physiological conditions give an observed rate constant k_{obs} of 0.136 h^{-1}, which shows 10^7-fold rate acceleration over that of uncatalyzed supercoiled DNA. The DNA cleavage rate versus different [Zn^{II}]/[ligand] ratios at a constant ligand concentration was also studied to compare the DNA cleavage efficiencies between mononuclear **2** and dinuclear **1** zinc(II) complexes, and the result shows that the acceleration of the DNA cleavage promoted by Zn^{II}_2−**1** is due to the efficient cooperative catalysis of the preorganized two-proximate zinc(II) cation centers. ESI-MS analysis of the dinucleotide hydrolysis and radical scavengers' inhibition studies indicates the hydrolytic mechanism of the cleavage process. Furthermore, a preliminary study of the antitumor activity shows that the antitumor activity of the dinuclear zinc(II) complex is 50-fold higher than that of the mononuclear complex. The IC_{50} value against HL-60 cells of Zn^{II}_2−**1** is 2.54×10^{-6} M.

ACKNOWLEDGMENT

We acknowledge support of this work by the National Basic Research Program of China (Grant 2007CB925103) and the National Science Foundation of China (Grant 20774039).

Supporting Information Available: Spectra for compound **1**, fluorescence and CD spectroscopy, photographs of the agarose gels, and kinetic data. This information is available free of charge via the Internet at http://pubs.acs.org.

LITERATURE CITED

(1) Liu, C., Wang, M., Zhang, T., and Sun, H. (2004) DNA hydrolysis promoted by di- and multi-nuclear metal complexes. *Coord. Chem. Rev. 248*, 147–168.

(2) Burger, R. M. (1998) Cleavage of nucleic acids by bleomycin. *Chem. Rev. 98*, 1153–1169.

(3) Pogozelski, W. K., and Tullius, T. D. (1998) Oxidative strand scission of nucleic acids: Routes initiated by hydrogen abstraction from the sugar moiety. *Chem. Rev. 98*, 1089–1107.

(4) Armitage, B. (1998) Photocleavage of nucleic acids. *Chem. Rev. 98*, 1171–1200.

(5) Rajski, S. R., and Williams, R. M. (1998) DNA crosslinking agents as antitumor drugs. *Chem. Rev. 98*, 2723–2795.

(6) Hegg, E. L., and Burstyn, J. N. (1998) Toward the development of metal-based synthetic nucleases and peptidases: A rationale and progress report in applying the principles of coordination chemistry. *Coord. Chem. Rev. 173*, 133–165.

(7) Cowan, J. A. (2001) Chemical nucleases. *Curr. Opin. Chem. Biol. 5*, 634–642.

(8) Morrow, J. R., and Iranzo, O. (2004) Synthetic metallonucleases for RNA cleavage. *Curr. Opin. Chem. Biol. 8*, 192–200.

(9) Perreault, D. M., and Anslyn, E. V. (1997) Unifying the current data on the mechanism of cleavage: Transesterification of RNA. *Angew. Chem., Int. Ed. 36*, 433–450.

(10) Corneillie, T. M., Whetstone, P. A., Lee, K. C., Wong, J. P., and Meares, C. F. (2004) Converting weak binders into infinite binders. *Bioconjugate Chem. 15*, 1389–1391.

(11) Erkkila, K. E., Odom, D. T., and Barton, J. K. (1999) Recognition and reaction of metallointercalators with DNA. *Chem. Rev. 99*, 2777–2795.

(12) McMillin, D., and McNett, K. M. (1998) Photoprocesses of copper complexes that bind to DNA. *Chem. Rev. 98*, 1201–1219.

(13) Ren, R., Yang, P., Zheng, W., and Hua, Z. (2000) A simple copper(II)-L-histidine system for efficient hydrolytic cleavage of DNA. *Inorg. Chem. 39*, 5454–5463.

(14) Branum, M. E., Tipton, A. K., Zhu, S., and Que, L., Jr. (2001) Double-strand hydrolysis of plasmid DNA by dicerium complexes at 37 °C. *J. Am. Chem. Soc. 123*, 1898–1904.

(15) Komiyama, M., Kina, S., Matsumura, K., Sumaoka, J., Tobey, S., Lynch, V. M., and Anslyn, E. (2002) Trinuclear copper(II) complex showing high selectivity for the hydrolysis of 2′–5′ over 3′–5′ for UpU and 3′–5′ over 2′–5′ for ApA ribonucleotides. *J. Am. Chem. Soc. 124*, 13731–13736.

(16) Yang, M.-Y., Richard, J. P., and Morrow, J. R. (2003) Substrate specificity for catalysis of phosphodiester cleavage by a dinuclear Zn(II) complex. *Chem. Commun.*, 2832–2833.

(17) Worm, K., Chu, F., Matsumoto, K., Best, M. D., Lynch, V., and Anslyn, E. V. (2003) Preorganized bis-zinc phosphodiester cleavage catalysts possessing natural ligands: A lesson pertinent to bimetallic artificial enzymes. *Chem.—Eur. J. 9*, 741–747.

(18) Gupta, T., Dhar, S., Nethaji, M., and Chakravarty, A. R. (2004) Bis(dipyridophenazine)copper(II) complex as major groove directing synthetic hydrolase. *Dalton Trans.*, 1896–1900.

(19) Boseggia, E., Gatos, M., Lucatello, L., Mancin, F., Moro, S., Palumbo, M., Sissi, C., Tecilla, P., Tonellato, U., and Zagotto, G. (2004) Toward efficient Zn(II)-based artificial nucleases. *J. Am. Chem. Soc. 126*, 4543–4549.

(20) An, Y., Tong, M.-L., Ji, L.-N., and Mao, Z.-W. (2006) Double-strand DNA cleavage by copper complexes of 2,2′-dipyridyl with electropositive pendants. *Dalton Trans.*, 2066–2071.

(21) Jin, Y., and Cowan, J. A. (2005) DNA cleavage by copper-ATCUN complexes. Factors influencing cleavage mechanism and linearization of dsDNA. *J. Am. Chem. Soc. 127*, 8408–8415.

(22) Hamma, T., and Miller, P. S. (2003) 4-(2-Aminooxyethoxy)-2-(ethylureido)-quinoline-oligonucleotide conjugates: Synthesis, binding interactions, and derivatization with peptides. *Bioconjugate Chem. 14*, 320–330.

(23) Feng, G., Mareque-Rivas, J. C., Torres Martin de Rosales, R., and Williams, N. H. (2005) A highly reactive mononuclear Zn(II) complex for phosphodiester cleavage. *J. Am. Chem. Soc. 127*, 13470–13471.

(24) Sheng, X., Lu, X.-M., Zhang, J.-J., Chen, Y.-T., Lu, G.-Y., Shao, Y., Liu, F., and Xu, Q. (2007) Synthesis and DNA cleavage activity of artificial receptor 1,4,7-triazacyclononane containing guanidinoethyl and hydroxyethyl side arms. *J. Org. Chem. 72*, 1799–1802.

(25) Li, Q.-L., Huang, J., Wang, Q., Jiang, N., Xia, C.-Q., Lin, H.-H., Wu, J., and Yu, X.-Q. (2006) Monometallic complexes of 1,4,7,10-tetraazacyclododecane containing an imidazolium side: Synthesis, characterization, and their interaction with plasmid DNA. *Bioorg. Med. Chem. 14*, 4151–4157.

(26) Mancina, F., and Tecilla, P. (2007) Zinc(II) complexes as hydrolytic catalysts of phosphate diester cleavage: From model substrates to nucleic acids. *New J. Chem. 31*, 800–817.

(27) Zhang, C. X., and Lippard, S. J. (2003) New metal complexes as potential therapeutics. *Curr. Opin. Chem. Biol. 7*, 481–489.

(28) Michaelis, K., and Kalesse, M. (1999) Selective cleavage of the HIV-1 TAR-RNA with a peptide-cyclen conjugate. *Angew. Chem., Int. Ed. 38*, 2243–2245.

(29) Parker, L. L., Lacy, S. M., Farrugia, L. J., Evans, C., Robins, D. J., O'Hare, C. C., Hartley, J. A., Jaffar, M., and Stratford, I. J. (2004) A novel design strategy for stable metal complexes of nitrogen mustards as bioreductive prodrugs. *J. Med. Chem. 47*, 5683–5689.

(30) Fichna, J., and Janecka, A. (2003) Synthesis of target-specific radiolabeled peptides for diagnostic imaging. *Bioconjugate Chem. 14*, 3–17.

(31) Liang, F., Wan, S., Li, Z., Xiong, X., Yang, L., Zhou, X., and Wu, C. (2006) Medical applications of macrocyclic polyamines. *Curr. Med. Chem. 13*, 711–727.

(32) Kikuta, E., Murata, M., Katsube, N., Koike, T., and Kimura, E. (1999) Novel recognition of thymine base in double-stranded DNA by zinc(II)-macrocyclic tetraamine complexes appended with aromatic groups. *J. Am. Chem. Soc. 121*, 5426–5436.

(33) Rey, N. A., Neves, A., Bortoluzzi, A. J., Pich, C. T., and Terenzi, H. (2007) Catalytic promiscuity in biomimetic systems: Catecholase-like activity, phosphatase-like activity, and hydrolytic DNA cleavage promoted by a new dicopper(II) hydroxo-bridged complex. *Inorg. Chem. 46*, 348–350.

(34) Fry, F. H., Moubaraki, B., Murray, K. S., Spiccia, L., Warren, M., Skelton, B. W., and White, A. H. (2003) Asymmetry in endogenously bridged dinuclear copper(II) and zinc(II) complexes formed by 1,2-bis[1,4,7-triazacyclonon-1-yl]propan-2-ol. *Dalton Trans.,* 866–871.

(35) Feng, G., Mareque-Rivas, J. C., and Williams, N. H. (2006) Comparing a mononuclear Zn(II) complex with hydrogen bond donors with a dinuclear Zn(II) complex for catalysing phosphate ester cleavage. *Chem. Commun.*, 1845–1847.

(36) Qian, J., Gu, W., Liu, H., Gao, F., Feng, L., Yan, S., Liao, D., and Cheng, P. (2007) The first dinuclear copper(II) and zinc(II) complexes containing novel Bis-TACN: Syntheses, structures, and DNA cleavage activities. *Dalton Trans.*, 1060–1066.

(37) Zhao, Y., Zhu, J., He, W., Yang, Z., Zhu, Y., Li, Y., Zhang, J., and Guo, Z. (2006) Oxidative DNA cleavage promoted by multinuclear copper complexes: Activity dependence on the complex structure. *Chem.—Eur. J. 12*, 6621–6629.

(38) Young, M. J., and Chin, J. (1995) Dinuclear copper(II) complex that hydrolyzes RNA. *J. Am. Chem. Soc. 117*, 10577–10578.

(39) Iranzo, O., Elmer, T., Richard, J. P., and Morrow, J. R. (2003) Cooperativity between metal ions in the cleavage of phosphate diesters and RNA by dinuclear Zn(II) catalysts. *Inorg. Chem. 42*, 7737–7746.

(40) Beese, L. S., and Steitz, T. A. (1991) Structural basis for the 3′–5′ exonuclease activity of *Escherichia coli* DNA polymerase I: A two metal ion mechanism. *EMBO J. 10*, 25–33.

(41) Davies, J. F., Hostomska, Z., Hostomsky, Z., Jordan, S. R., and Matthews, D. A. (1991) Crystal structure of the ribonuclease H domain of HIV-1 reverse transcriptase. *Science 252*, 88–95.

(42) Lahm, A., Volbeda, S., and Suck, D. (1990) Crystallisation and preliminary crystallographic analysis of P1 nuclease from *Penicillium citrinum*. *J. Mol. Biol. 215*, 207–210.

(43) Kim, E. E., and Wyckoff, H. W. (1991) Reaction mechanism of alkaline phosphatase based on crystal structures. Two-metal ion catalysis. *J. Mol. Biol. 218*, 449–464.

(44) Hough, E., Hansen, L. K., Birknes, B., Jynge, K., Hansen, S., Hordvik, A., Little, C., Dodson, E. J., and Derewenda, Z. (1989) High-resolution (1.5 Å) crystal structure of phospholipase C from *Bacillus cereus*. *Nature 338*, 357–360.

(45) Sleitz, T. A., and Steitz, J. A. (1993) A general two-metal-ion mechanism for catalytic RNA. *Proc. Natl. Acad. Sci. U.S.A. 90*, 6498–6502.

(46) Piccirilli, J. A., Vyle, J. S., Caruthers, M. H., and Cech, T. R. (1993) Metal ion catalysis in the *Tetrahymena* ribozyme reaction. *Nature 361*, 85–88.

(47) Aoki, S., and Kimura, E. (2004) Zinc-nucleic acid interaction. *Chem. Rev. 104*, 769–787.

(48) Rossi, P., Felluga, F., Tecilla, P., Formaggio, F., Crisma, M., Toniolo, C., and Scrimin, P. (2000) An azacrown-functionalized peptide as a metal ion based catalyst for the cleavage of a RNA-model substrate. *Biopolymers 55*, 496–501.

(49) Williams, N. H., Lebuis, A. M., and Chin, J. (1999) A structural and functional model of dinuclear metallophosphatases. *J. Am. Chem. Soc. 121*, 3341–3348.

(50) Chapman, W. H., Jr., and Breslow, R. (1995) Selective hydrolysis of phosphate esters, nitrophenyl phosphates and UpU, by dimeric zinc complexes depends on the spacer length. *J. Am. Chem. Soc. 117*, 5462–5469.

(51) Vichard, C., and Kaden, T. A. (2002) Phosphate and phosphonate ester hydrolysis promoted by dinuclear metal complexes. *Inorg. Chim. Acta 337*, 173–180.

(52) Arca, M., Bencini, A., Berni, E., Caltagirona, C., Devillanova, F. A., Isaia, F., Garau, A., Giorgi, C., Lippolis, V., Perra, A., Tei, L., and Valtancoli, B. (2003) Coordination properties of new bis(1,4,7-triazacyclononane) ligands: A highly active dizinc complex in phosphate diester hydrolysis. *Inorg. Chem. 42*, 6929–6939.

(53) Westheimer, F. H. (1987) Why nature chose phosphates. *Science 235*, 1173–1178.

(54) Williams, N. H., Takasaki, B., Wall, M., and Chin, J. (1999) Structure and nuclease activity of simple dinuclear metal complexes: Quantitative dissection of the role of metal ions. *Acc. Chem. Res. 32*, 485–493.

(55) Sigman, D. S., Mazumder, A., and Perrin, D. M. (1993) Chemical nucleases. *Chem. Rev. 93*, 2295–2316.

(56) Chin, J., Banaszczyk, M., Jubian, V., and Zou, X. (1989) Cobalt(III) complex-promoted hydrolysis of phosphate diesters: Comparison in reactivity of rigid cis-diaquo(tetraaza)cobalt(III) complexes. *J. Am. Chem. Soc. 111*, 186–190.

(57) Chen, W., Kitamura, Y., Zhou, J.-M., Sumaoka, J., and Komiyama, M. (2004) Site-selective DNA hydrolysis by combining Ce(IV)/EDTA with monophosphate-bearing oligonucleotides and enzymatic ligation of the scission fragments. *J. Am. Chem. Soc. 126*, 10285–10291.

(58) Sissi, C., Rossi, P., Felluga, F., Formaggio, F., Palumbo, M., Tecilla, P., Toniolo, C., and Scrimin, B. (2001) Dinuclear Zn^{2+} complexes of synthetic heptapeptides as artificial nucleases. *J. Am. Chem. Soc. 123*, 3169–3170.

(59) Hoye, R. C., Richman, J. E., Dantas, G. A., Lightbourne, M. F., and Shinneman, L. S. (2001) Synthesis of polyazamacrocyclic compounds via modified Richman-Atkins cyclization of β-trimethylsilylethanesulfonamides. *J. Org. Chem. 66*, 2722–2725.

(60) Sargent, J. M., and Taylor, C. G. (1989) Appraisal of the MTT assay as a rapid test of chemosensitivity in acute myeloid leukaemia. *Br. J. Cancer 60*, 206–210.

(61) El Ghachtouli, S., Cadiou, C., Déchamps-Olivier, I., Chuburu, F., Aplincourt, M., Turcry, V., Le Baccon, M., and Handel, H. (2005) Spectroscopy and redox behaviour of dicopper(II) and dinickel(II) complexes of bis(cyclen) and bis(cyclam) ligands. *Eur. J. Inorg. Chem.*, 2658–2668.

(62) Bazzicalupi, C., Bencini, A., Faggi, E., Garau, A., Giorgi, C., Lippolis, V., Perra, A., and Valtancoli, B. (2006) Encapsulation of metal cations and anions within the cavity of bis(1,4,7-triazacyclononane) receptors. *Dalton Trans.*, 1409–1418.

(63) Wang, H. J., and Wu, C. T. (1997) Synthesis of bis(macrocyclic) polyamines containing rigid bridging groups. *Chin. Chem. Lett. 8*, 209–212.

(64) Schwarzenbach, G., and Moser, P. (1953) Metal complexes with polyamines. X. With tetrakis(2-aminoethyl)ethylenediamine ("penten"). *Helv. Chim. Acta 36*, 581–597.

(65) Sacconi, L., Paoletti, P., and Ciampolini, M. (1961) Thermochemical studies. VI. Heats and entropies of reaction of transition-metal ions with triethylenetetramine. *J. Chem. Soc.*, 5115–5120.

(66) Ng, C. Y., Motekaitis, R. J., and Martell, A. E. (1979) New multidentate ligands. 18. Synthesis of 1,4-bis(bis(2-aminoethyl)aminomethyl)benzene: Binuclear chelating tendencies and mixed-ligand binuclear chelate formation. *Inorg. Chem. 18*, 2982–2986.

(67) Lakowicz, J. R., and Weber, G. (1973) Quenching of fluorescence by oxygen. Probe for structural fluctuations in macromolecules. *Biochemistry 12*, 4161–4170.

(68) Lee, M., Rhodes, A. L., Wyatt, M. D., Forrow, S., and Hartley, J. A. (1993) GC base sequence recognition by oligo(imidazolecarboxamide) and C-terminus-modified analogues of distamycin deduced from circular dichroism, proton nuclear magnetic resonance, and methidiumpropylethylenediaminetetraacetate-iron(II) footprinting studies. *Biochemistry 32*, 4237–4245.

(69) Childs, L. J., Malina, J., Rolfsnes, B. E., Pascu, M., Prieto, M. J., Broome, M. J., Rodger, P. M., Sletten, E., Moreno, E. V., Rodger, A., and Hannon, M. J. (2006) A DNA-binding copper(I) metallosupramolecular cylinder that acts as an artificial nuclease. *Chem.—Eur. J. 12*, 4919–4927.

(70) Liu, J., Zhang, T., Lu, T., Qu, L., Zhou, H., Zhang, Q., and Ji, L. (2002) DNA-binding and cleavage studies of macrocyclic copper(II) complexes. *J. Inorg. Biochem. 91*, 269–276.

(71) Dhar, S., Nethaji, M., and Chakravarty, A. R. (2005) N,N-Bis[2-(2-pyridyl)ethyl]-2-phenylethylamine-copper(II) bowl that enhances red light-induced DNA cleavage activity. *Inorg. Chem. 44*, 8876–8883.

(72) Pasternack, R. F. (2003) Circular dichroism and the interactions of water soluble porphyrins with DNA. *Chirality 15*, 329–332.

(73) Karidi, K., Garoufis, A., Hadjiliadis, N., and Reedijk, J. (2005) Solid-phase synthesis, characterization and DNA binding properties of the first chloro(polypyridyl)ruthenium conjugated peptide complex. *Dalton Trans.*, 728–734.

(74) Kodama, M., and Kimura, E. (1978) Equilibra of complex formation between several bivalent metal ions and macrocyclic between several bivalent metal ions and macrocyclic tri- and penta-amines. *J. Chem. Soc., Dalton Trans.*, 1081–1085.

(75) González-Álvarez, M., Alzuet, G., Borrás, J., Macías, B., and Castiñeiras, A. (2003) Oxidative cleavage of DNA by a new ferromagnetic linear trinuclear copper(II) complex in the presence of H_2O_2/sodium ascorbate. *Inorg. Chem. 42*, 2992–2998.

(76) Rammo, J., Hettich, R., Roigk, A., and Schneider, H.-J. (1996) Catalysis of DNA cleavage by lanthanide complexes with nucleophilic or intercalating ligands and their kinetic characterization. *Chem. Commun.*, 105–107.

(77) Basile, L. A., Raphael, A. L., and Barton, J. K. (1987) Metal-activated hydrolytic cleavage of DNA. *J. Am. Chem. Soc. 109*, 7550–7551.

(78) Nomura, A., and Sugiura, Y. (2004) Sequence-selective and hydrolytic cleavage of DNA by zinc finger mutants. *J. Am. Chem. Soc. 126*, 15374–15375.

(79) Peng, W., Liu, P.-Y., Jiang, N., Lin, H.-H., Zhang, G.-L., Liu, Y., and Yu, X.-Q. (2005) Dinuclear macrocyclic polyamine zinc(II) complexes linked with flexible spacers: Synthesis, characterization, and DNA cleavage. *Bioorg. Chem. 33*, 374–385.

(80) Sissi, C., Mancin, F., Gatos, M., Palumbo, M., Tecilla, P., and Tonellato, U. (2005) Efficient plasmid DNA cleavage by a mononuclear copper(II) complex. *Inorg. Chem. 44*, 2310–2317.

(81) Tan, J., Wang, B., and Zhu, L. (2007) Hydrolytic cleavage of DNA by quercetin zinc(II) complex. *Bioorg. Med. Chem. Lett. 17*, 1197–1199.

(82) Humphry, T., Forconi, M., Williams, N. H., and Hengge, A. C. (2002) An altered mechanism of hydrolysis for a metal-complexed phosphate diester. *J. Am. Chem. Soc. 124*, 14860–14861.

(83) Xiang, Q.-X., Zhang, J., Liu, P.-Y., Xia, C.-Q., Zhou, Z.-Y., Xie, G., and Yu, X. Q. (2005) Dinuclear macrocyclic polyamine zinc(II) complexes: Syntheses, characterization and their interaction with plasmid DNA. *J. Inorg. Biochem. 99*, 1661–1669.

(84) Alley, M. C., Scudiero, D. A., Monks, A., Hyrsey, M. L., Czerwinski, M. J., Fine, D. L., Abbott, B. J., Mayo, J. G., Shoemaker, R. H., and Boyd, M. R. (1988) Feasibility of drug screening with panels of human tumor cell lines using a microculture tetrazolium assay. *Cancer Res. 48*, 589–601.

(85) Liang, F., Wu, C., Lin, H., Li, T., Gao, D., Li, Z., Wei, J., Zheng, C., and Sun, M. (2003) Copper complex of hydroxyl-substituted triazamacrocyclic ligand and its antitumor activity. *Bioorg. Med. Chem. Lett. 13*, 2469–2472.

BC700322W

Disulfide Cross-Linked Polyethylenimines (PEI) Prepared via Thiolation of Low Molecular Weight PEI as Highly Efficient Gene Vectors

Qi Peng, Zhenlin Zhong,* and Renxi Zhuo

Key Laboratory of Biomedical Polymers of Ministry of Education, Department of Chemistry, Wuhan University, Wuhan 430072, P. R. China. Received August 26, 2007; Revised Manuscript Received November 30, 2007

Ring-opening reaction of low molecular weight polyethylenimine with an M_w of 800 Da (800 Da PEI) with methylthiirane produced thiolated polyethylenimine (PEI−SH_X). The thiolation degree X, which is the average number of thiol groups on a PEI molecule, was readily adjusted by the methylthiirane/PEI ratio. Oxidation of the thiolated PEIs with DMSO afforded disulfide cross-linked PEIs (PEI−SS_X). The molecular weights of PEI−SS_X were estimated by viscosity measurement to be 7100, 8000, and 8400 for $X = 2.6$, 6.5, and 9.4, respectively. The PEI−SS_X series can bind and condense plasmid DNAs effectively forming nanosized polyplexes. The size of dry polyplexes is less than 100 nm on the TEM pictures. In solution, the size of the polyplexes was measured by DLS to be about 400 nm. In vitro experiments showed that the PEI−SS_X series have a lower cytotoxicity and higher gene transfection efficiency compared with the high molecular weight PEI with M_w of 25 KDa. The presence of fetal bovine serum did not decrease the transfection efficiency. The results proved the hypothesis that reductively degradable disulfide-containing PEIs could possesses simultaneously higher gene transfection efficiency and lower cytotoxicity than the nondegradable ones.

INTRODUCTION

Recent years have witnessed rapid development of nonviral vectors based on polyethylenimine (PEI) and derivatives associated with gene therapy (*1–3*). The cationic polymer PEI has been widely used for nonviral transfection in vitro and in vivo and has an advantage over other polycations in that it combines strong DNA compaction capacity with an intrinsic endosomolytic activity. It is one of the most effective vectors among the synthetic polycations due to its proton sponge effect (*4–7*). High molecular weight PEI (HMW PEI) can form tight complexes with DNA. It attracts special interest due to its lysosomal buffering capacity and potential ability to protect DNA from degradation by lysosomal enzymes. Although gene delivery efficiency increases with the molecular weight of PEI, cytotoxicity also increases. HMW PEI/DNA polyplexes can exist in very small dense particles, thereby limiting the unpacking of DNA once inside the nucleus (*8*). On the other hand, low molecular weight PEI (LMW PEI), which has demonstrated a low toxicity in cell culture studies (*9, 10*), can not effectively condense DNA and displays very poor transfection activity (*11*).

To circumvent these problems, it is supposed that enhancement in gene delivery efficiency with minimal cytotoxicity may be achieved by cross-linking small PEIs with linkages that are potentially biodegradable (*12–14*). Such linkages include esters, amides, orthoesters, acetals, glycosides, and disulfides. Almost all these synthetic degradable PEIs have been designed to solve the following two problems: first, the contradiction between tight complex formation outside cells and the easy dissociation of complexes inside cells; second, preparation of the nonviral gene vector with high transfection efficiency and low cytotoxicity (*15*).

The strategy of reversible cross-linking of small PEIs with disulfide bonds that are cleavable in intracellular reductive environments is especially attractive. A disulfide bond could be cleaved by reduced glutathione, and the intracellular glutathione concentration is 50–1000 times higher than that in extracellular milieu (*16, 17*). It provides a way to maintain stability of the cross-linked polymer and form compact polyplexes with pDNA in the extracytoplasmic environment, while inducing the efficient release of entrapped pDNA from the polyplexes after their movement into the reductive cytoplasmic compartment. This would achieve efficient gene expression in vivo while limiting effects of toxicity. The disulfide bond has been successfully applied in preparation of environmentally sensitive polycations such as modified PEIs (*12, 18–20*), PLL (*21, 22*), and peptides (*23, 24*) for gene delivery. In the first report describing the transfection properties of cross-linked LMW PEI by disulfide bonds, branched PEI with an M_w of 800 Da was cross-linked by the reaction with either dithiobis(succinimidylpropionate) (DSP) or dimethyl 3,3′-dithiobispropionimidate dihydrochloride (DTBP), resulting in greatly increased gene transfection efficiency (*12*). The DTBP cross-linked LMW PEI has showed a significantly lower cytotoxicity compared to a HMW PEI (*18*). More recently, disulfide-connected linear polyethylenimines were reported to have gene transfection efficiency close to nondegradable high molecular linear PEI, while their cytotoxicity is very low or negligible compared to the latter (*20*).

Though the results in the literature are very encouraging, no disulfide-containing PEI was reported to have a gene transfection efficiency surpassing an unmodified HMW PEI. Moreover, early cytoplasmic DNA release might result in gene digestion by cytosolic nucleases (*25*). So, it is still unclear whether a disulfide-containing PEI possesses an advantage in gene transfection efficiency over the normal nondegradable PEIs. This paper would introduce a new strategy for preparation of disulfide-containing PEIs by oxidation of thiolated LMW PEI with the polyethylenimine structure intact. The results proved the hypothesis that reductively degradable disulfide-containing

* To whom correspondence and reprint requests should be addressed. Phone: +86-27-6875-4061. Fax: +86-27-6875-4509. E-mail: zlzhong@yahoo.com.

10.1021/bc7003236 CCC: $40.75 © 2008 American Chemical Society
Published on Web 01/19/2008

PEIs could possess simultaneously higher gene transfection efficiency and lower cytotoxicity than the nondegradable ones.

MATERIALS AND METHODS

Materials. PEIs with M_W of 800 Da and 25 KDa were purchased from Aldrich. Methylthiirane was synthesized by literature procedure (*26*). pEGFP-5.3 kb, a plasmid DNA containing the green fluorescent protein gene under the control of human cytomegalovirus (CMV) immediate early promoter, and encoding a red-shifted variant of wild-type green fluorescent protein (GFP), was purchased from Clontech, Mountain View, CA. Plasmid pGL3 under the control of SV40 promoter and with enhancer sequences encoding luciferase was obtained from Promega, Madison, WI. Plasmids were propagated in *Escherichia colia* in Luria–Bertani (LB) medium containing 50 μg/mL kanamycin or 60 μg/mL ampicillin at 37 °C. The mixture was shaken overnight at 250 rpm. The plasmid was purified using E. Z. N. A. Fastfilter Endofree Plasmid Midi kits (Omega) according to the manufacturer's instruction. The DNA concentration was determined by measuring the UV absorbance at 260 nm. The purity of DNA was assessed spectrophotometrically by measuring absorbance at wavelengths of 260 and 280 nm (OD_{260}/OD_{280} 1.8 or greater). Concentration and purity of DNA were confirmed using 0.7% agarose gel electrophoresis containing GelRed. DNA aliquots were stored at −20 °C prior to use. Dubelcco's Modified Eagle's Medium (DMEM), penicillin−streptomycin, trypsin, Dubelcco's phosphate buffered saline, and 3-(4,5-dimethylthiazol-2-yl)-2,5-diphenyltetrazolium bromide (MTT) were purchased from Sigma. Other commercially available reagents were used as received.

Synthesis of Thiolated LMW PEI (PEI−SH_X). In a 25 mL flask, 1.00 g of PEI (800 Da) was dissolved in 5 mL of deionized water. Next, 0.1 N HCl was added dropwise to the PEI solution while stirring until pH was regulated to 7.2. After removal of water by evaporation under reduced pressure, the yellow solid thus obtained was dispersed in 3 mL of CH_3OH in an ampule. After the sample was purged with argon for 5 min, a calculated amount of methylthiirane was added to the ampule. The ampule was sealed and kept in a 50 °C oil bath for 24 h with magnetic stirring. The content of the ampule was transferred to a flask and evaporated to dryness under reduced pressure and kept under argon. The thiol group content was determined by Ellman's method (*27*, *28*). ^{1}H NMR (300 MHz, D_2O): δ 3.15–2.55 (m, NCH_2CH_2N, NCH_2CHMeS), 1.18–1.05 (m, CH_3).

Synthesis of Disulfide Cross-Linked PEI (PEI−SS_X). A solution of 1.50 g of PEI−SH_X in 3 mL of methanol and 1.5 mL of dimethyl sulfoxide (DMSO) was stirred for 48 h. The reaction solution was precipitated in diethyl ether three times, and dried under high vacuum to give a light yellow viscous glue. ^{1}H NMR (300 MHz, D_2O): δ 3.14–2.66 (m, NCH_2CH_2N, NCH_2CHMeS), 1.25–1.05 (m, CH_3).

Cytotoxicity Assay of PEI−SS_X. The cytotoxicity assay was carried out on the basis of an MTT assay on HeLa cells. HeLa cells were seeded in 96-well plates at an initial density of 5000 cells/well in 200 μL of DMEM complete medium. The cells were allowed to grow for 24 h. The original media were replaced with 100 μL of fresh media. The PEI−$SS_{2.6}$, PEI−$SS_{6.5}$, PEI−$SS_{9.4}$, or 25 KDa PEI solution was added to the media at concentrations ranging from 0.001 to 0.5 mg/mL. Each dosage was replicated in 4 wells. Treated cells were incubated at 37 °C under a humidified atmosphere of 95% air and 5% CO_2 for 24 h. MTT reagent (20 μL in PBS, 5 mg/mL) was added to each well, and the cells were incubated for another 4 h at 37 °C. 100 μL of DMSO was added to each well until all crystals dissolved. The absorbance at 570 nm of the solution in each well was recorded using a Microplate Reader (Bio-Rad model 550). Cell viability was calculated according to the following equation: cell viability (%) = $(OD_{sample} - OD_{blank})/(OD_{control} - OD_{blank}) \times 100$ where OD_{sample} is the absorbance of the solution of the cells cultured with the polymer and PEI; OD_{blank} is the absorbance of the medium; and $OD_{control}$ is the absorbance of the solution of the cells cultured with the medium only.

Viscosity Measurements. Capillary viscosity measurements were carried out to estimate molecular weights (*29*, *30*). The polyamine polymers were neutralized with hydrochloric acid and dissolved in 150 mM NaCl at concentration from 20 mg/mL to 5 mg/mL. Viscosity measurements were carried out using a capillary viscometer at 25 °C. The molecular weights of cross-linked polymers were calculated using the Mark–Houwink equation $[\eta] = KM^{\alpha}$ where M is the molecular weight and K and α are Mark–Houwink parameters determined from PEI standards of known molecular weights.

Preparation of PEI−SS_X/pDNA Polyplexes and Agarose Gel Retardation. A 0.1 mg/mL aqueous solution of plasmid DNA (pEGFP or pGL3) was diluted to designed concentration (usually 20 μg/mL) using 150 mM NaCl solution under vortexing. Designed aqueous solutions of PEI−SS_X were added slowly to the pDNA solutions. The amount of polymer added was calculated on the basis of chosen N/P ratios of PEI−SS_X/DNA (nitrogen atoms of the polymer over phosphates of pDNA). The mixture was incubated at room temperature for 30 min for the complex formation. A 5 μL sample of the polyplex solution mixed with 1 μL of 6× loading buffer was loaded to agarose gel. The polyplexes were electrophoresed on a 0.7% agarose gel containing GelRed with Tris-acetate (TAE) running buffer (pH 8) at 80 V for 80 min. DNA bands were visualized by an UV (254 nm) illuminator and photographed with a Vilber Lourmat imaging system (France). The shapes of the complexes of polymer/DNA were observed at 25 °C using a transmission electron microscope.

DTT Reduction of Disulfides and its Impact on Stability of the PEI Polyplexes. To the solution of PEI−$SS_{2.6}$/pDNA polyplex at N/P ratio of 10 prepared as described above was added 1,4-dithio-DL-threitol (DTT) at different concentrations from 0.1 to 310 mM. Polyplexes were incubated at room temperature for 30 min. Then the polyplexes were electrophoresed on a 0.7% agarose gel containing GelRed with Tris-acetate (TAE) running buffer at 80 V for 80 min.

Particle Size and Zeta Potential Measurements. The particle size and zeta potential were measured on a Nano-ZS ZEN3600 (Malvern) instrument at room temperature. The polyplexes at various N/P ratios were prepared by adding appropriate volume of pEGFP DNA solution (0.1 mg/mL in 40 mM Tris−HCl buffer) to appropriate volumes of PEI−SS_X solution (in 150 mM NaCl). Then the polyplexes were incubated at room temperature for 30 min. After that, the polyplexes were diluted with 150 mM NaCl solution or pure water to 1.0 mL volume prior to measure. The final sample containing 1 μg of pDNA is in 150 mM NaCl for size measurements or in 10 mM NaCl for zeta potential measurements.

Determination of in Vitro Transfection Efficiency. The in vitro transfection efficiency of PEI−SS_X was evaluated in 293T and HeLa cells, using the polyplexes of PEI−SS_X with pGL3 or pEGFP DNA.

As for pGL3, a typical procedure is as follows: Cells were seeded at a density of 70 000–80 000 cells/well into 24-well plates. They were incubated at 37 °C in a humidified atmosphere of 95% air and 5% CO_2 until the cells reached about 70% confluence. At the time of transfection, the medium in each well was replaced with 1 mL of DMEM without containing FBS. The polyplexes of polymer/DNA at N/P ratios ranging from 10:1 to 40:1 prepared as described above were added and incubated with cells for 4 h at 37 °C. The amount of DNA added

Scheme 1. Schematic Representation of the Preparation of the Disulfide-Cross-Linked LMW PEIs (PEI−SS$_X$)

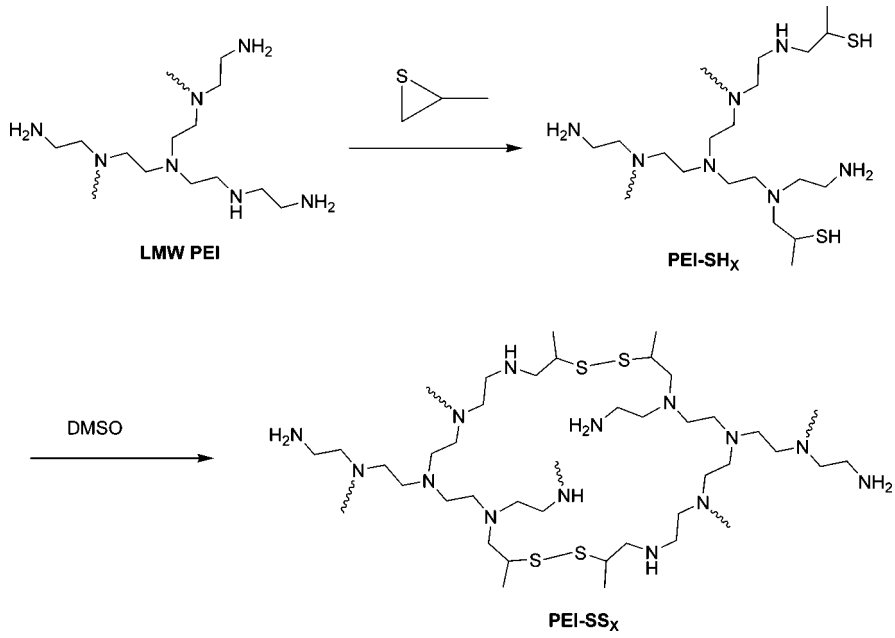

to each well was 1 μg. The medium was replaced with 1 mL of fresh complete medium, and the cells were further incubated for 48 h. After incubation, cells were permeabilized with 200 μL of cell lysis buffer. After two cycles of freezing and thawing, the lysate was transferred into microtubes and centrifuged for 5 min. Then the luciferase activity of the supernatants were measured using 100 μL of luciferase assay reagent on a Lumat LB 9507 tube luminometer (Berthold) for 30 s. The light units (LU) measured using a protein assay kit (Pierce) were normalized against protein concentration in the cell extracts. Luciferase activity was expressed as relative light units (RLU/mg protein). The data were reported for triplicate samples.

pEGFP transfection efficiency was estimated using a flow cytometry (Beckman Coulter XL, USA). HeLa cells were seeded at a density of 70 000–80 000 cells/well in a 24-well tissue culture plate. The cells were incubated at 37 °C in a humidified atmosphere of 95% air and 5% CO_2 until the cells reached about 70% confluence. The cells were transfected with polymer/pEGFP polyplexes at N/P ratios ranging from 10:1 to 40:1 prepared as described above. For comparison, cells transfected with naked pEGFP and branched 25 KDa PEI were used as a control at the N/P ratio of 10. The total amount of plasmid in each well was kept at 1.0 μg. The process of transfection is as described above. After the transfection, cells were separately harvested from each well by the trypsin-EDTA treatment, and suspended in 1 mL of PBS in microcentrifuge tubes. The cells expressing green fluorescent protein were enumerated by the fluorescence-activated cell sorting. The nontransfected cells were used as a negative control.

In Vitro Transfection Experiment in Serum. The process of transfection experiments was the same as described above, except that the medium at the time of transfection was replaced with DMEM containing 10% FBS (fetal bovine serum).

Preparation of PEI−SS$_{2.6}$/pDNA Polyplexes by in Situ Air Oxidation and Determination of in Vitro Transfection Efficiency. At designed time intervals prior to the transfection experiments, calculated amounts of PEI−SH$_{2.6}$ and pDNA were mixed in 150 mM NaCl at pDNA concentration of 20 μg/mL in a 1.5 mL centrifuge tube. The mixed solutions in the tubes were incubated in air at room temperature for in situ oxidation of the thiol groups and polyplex formation. The transfection efficiency of the polyplexes thus prepared with different oxidation times was determined parallel on a 24-well plate by the previously described process.

RESULTS AND DISCUSSION

Design and Preparation of PEI−SS$_X$ via Thiolation and Cross-Linking of 800 Da PEI. The strategy for preparation of the disulfide cross-linked PEIs is shown in Scheme 1 in two steps. First, a LMW PEI is thiolated by ring-opening reaction with methylthiirane. Second, the thiolated PEI is cross-linked into higher molecular weight structures by disulfide-forming oxidation of the thiol groups. Langer et al. (*7*) have proven that the high transfection efficiency of PEI is greatly attributed to the high buffering capacity in the endosomal pH range 5–7. Therefore, it is important to keep the buffering property of PEI unaffected during disulfide cross-linking. The disulfide-containing cross-linking reagents DSP and DTBP (*12*) or thiolation reagents iminothiolane (*19*) and *N*-succinimidyl-3-(2-pyridyldithio)propionate (*22*) used in the literature, however, would transfer an amino group to either a neutral amide group or a strong basic α-amino imino group, inevitably affecting the polyamine structure and lowering the endosomal buffer capacity of PEI. We designed the two-step route as shown in Scheme 1 using methylthiirane as a thiolation reagent based on the consideration that the thiolation reaction would not significantly change the acid–base property of the PEI, because it only transfers a primary or second amine group into a higher order amine by adding a mercaptoalkyl group without causing a significant change in pK_a.

Thiolation of LMW PEI (M_w = 800 Da) was achieved through the ring-opening reaction of methylthiirane with the primary and secondary amino groups of PEI at pH 7.2, resulting in the introduction of 2-mercaptopropyl groups on the amine groups (Scheme 1). The products with variable thiol group contents thus prepared were presented as PEI−SH$_X$, where X stands for the average number of thiol groups on each 800 Da PEI molecule. The thiolation degree X was determined by Ellman's test (*28*, *29*). With methylthiirane/PEI feed ratios (mol/mol) of 3, 8, and 12, the thiolation degree (X) of the product PEI−SH$_X$ were found to be 2.6, 6.5, and 9.4, respectively.

It was found that keeping a neutral or slightly acidic pH is critical for this reaction. The thiol-generating ring-opening

reaction of a thiirane with an amine group is always competed by the sulfide-generating ring-opening polymerization reaction. Under the basic condition of a free PEI, the main reaction is ring-opening polymerization of methylthiirane resulting in a polysulfide with very few thiol groups only at the chain ends, because a thiol group is deprotonated as a thiolate anion that is a much more active nucleophile than an amine group. Under a condition of neutral or slightly acidic, a great portion of amine groups exist in the active free form while most thiol groups remain in a less active neutral form. Therefore, the thiolate-initiated ring-opening polymerization reaction would be negligible under the neutralized condition.

Thiolated LMW PEIs were cross-linked by oxidation with DMSO at room temperature, and the final products PEI−SS_X were subjected to Ellman's test for the estimation of residual thiol groups. After 2 days of the cross-linking reaction in DMSO, the amount of remained thiol groups was found to be less than 10% of the initial value for all samples, indicating the formation of covalent disulfide bonds.

All the three oxidized products PEI−SS_X ($X = 2.6$, 6.5, and 9.4) were water-soluble, indicating that the cross-linking is constrained within a definite number of LMW PEI molecules. For PEI−$SH_{2.6}$ and PEI−$SH_{6.5}$, the reaction mixtures were clear solutions during the whole oxidation process. For PEI−$SH_{9.4}$, however, gelation was observed during the cross-linking process. The gel became a clear solution again gradually in one to two days at room temperature. This phenomenon may be explained by the interchange of intramolecular and intermolecular disulfide bonds. At a high thiolation degree, a cross-linked network might be formed through intermolecular disulfide bonds resulting in gelation. The gel gradually dissolved with the destruction of the infinite network, probably because some intermolecular disulfide bonds transferred into intramolecular ones under the experimental conditions.

Molecular weights of the disulfide cross-linked PEI−SS_X were estimated by viscosity measurements using a capillary viscometer. In 150 mM NaCl aqueous solution (pH 7.4, 20 °C), the intrinsic viscosities of PEI−$SS_{2.6}$, PEI−$SS_{6.5}$, and PEI−$SS_{9.4}$ were measured to be 6.96, 7.16, and 7.22 L/g, respectively; while those of 800 Da PEI and 25 KDa PEI purchased from Aldrich were measured to be 4.22 and 7.29 L/g, respectively. Thus, the molecular weights of PEI−$SS_{2.6}$, PEI−$SS_{6.5}$, and PEI−$SS_{9.4}$ were estimated to be 7100, 8000, and 8400, respectively. Surprisingly, the disulfide cross-linked PEIs have very similar intrinsic viscosities regardless of their thiolation degree in the range from 2.6 to 9.4. This result suggests that the majority of disulfide cross-links are intramolecular when the thiolation degree is high. It should be noted that the molecular weights of the PEI−SS_X, especially those with high thiolation degrees, might be underestimated because of their more compact structure compared to the non-cross-linked PEI.

As expected, the acid–base titration curves of the PEI−SS_X series are almost identical with that of 25 KDa PEI, showing good buffering capacity in the pH range 5−7.

Cytotoxicity of PEI−SS_X. MTT assay was carried out to determine the cytotoxicity of the PEI−SS_X series. Figure 1 shows that the PEI−SS_X series, regardless of the thiol group content, had a lower cytotoxicity compared to 25 KDa PEI in HeLa cells. Their IC_{50} values are all about 25 μg/mL being around nearly four times higher than the IC_{50} of 7 μg/mL of 25 KDa PEI, though greatly lower than the IC_{50} of 800 Da PEI (>200 μg/mL). The cytotoxicity of cationic polymers was probably caused by polymer aggregation on cell surfaces impairing the important membrane function (*31*). Also, polymers may interfere with critical intracellular processes of cells. PEI−SS_X has an amine constitution similar to 25 KDa PEI; therefore, its relatively low cytotoxicity should be caused by

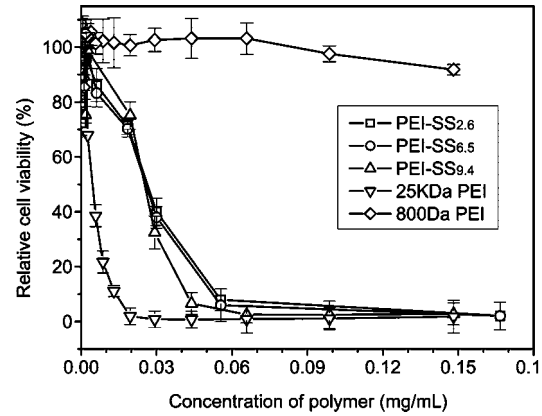

Figure 1. Relative cell viability at 24 h after the addition of PEI−SS_X and 25 KDa PEI.

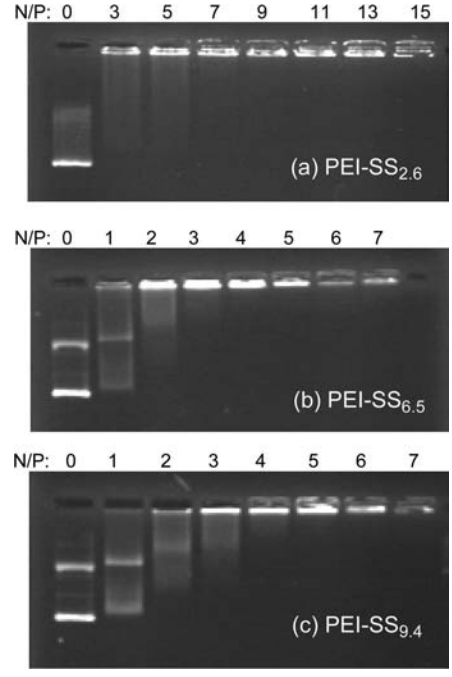

Figure 2. The effect of increasing concentration of PEI−SS_X on the electrophoretic migration of pEGFP through an agarose gel. The polyplex composition (N/P ratio) was expressed as PEI nitrogen atoms per DNA phosphate.

the lower molecular weight as reported for lower molecular weight PEI and the lower amine content (*12*). In addition, PEI−SS_X should degrade into low molecular weight PEI with low toxicity. Therefore, the biocompatibility and long-term safety of PEI−SS_X should be improved significantly as compared to the widely used 25 KDa PEI.

Formation and Charaterization of PEI−SS_X/pDNA Polyplexes. The polyplex of a disulfide cross-linked LMW PEI with a pDNA was prepared by adding PEI−SS_X aqueous solution slowly to the pDNA solution. The amount of polymer added was calculated on the basis of chosen N/P ratios, nitrogen atoms of the polymer over phosphates of pDNA, in PEI−SS_X/DNA. Formation of the polyplexes was investigated by agarose gel retardation and TEM measurements.

As shown in Figure 2, as the concentration of the polycation increased, the mobility of pEGFP was reduced by increasing DNA condensation and compaction. PEI with M_w of 800 Da used for the preparation of PEI−SS_X could not form stable complexes with DNA, even at N/P ratios higher than 20 (data not shown). In contrast, 25 KDa PEI was the most efficient

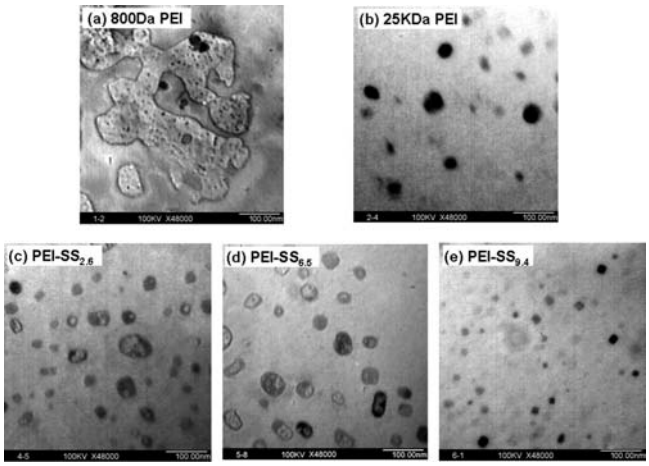

Figure 3. Transmission electron microscope of polyplexes of pEGFP with (a) 800 Da PEI, (b) 25 KDa PEI, (c) PEI−$SS_{2.6}$, (d) PEI−$SS_{6.5}$, and (e) PEI−$SS_{9.4}$ at N/P = 30.

that it could completely retard DNA migration at a N/P ratio of 1, while the required N/P ratios were 7, 3, and 5, for PEI−$SS_{2.6}$, PEI−$SS_{6.5}$, and PEI−$SS_{9.4}$ to completely retard the pDNA, respectively. These results demonstrated that this kind of disulfide cross-linked LMW PEI can bind a pDNA effectively in a wide range of thiol group contents. While the DNA binding capacity of these disulfide cross-linked polymers is not very sensitive to the thiol group content, PEI−$SS_{6.5}$, the one with 6.5 disulfide bonds on each 800 Da PEI, showed a higher binding capacity than PEI−$SS_{2.6}$ and PEI−$SS_{9.4}$. This result suggests that a disulfide bond density that is too low or too high is not good for DNA binding.

The size and shape of the polyplexes were then evaluated by TEM measurements (Figure 3). All of the polyplexes, regardless of the cross-linking and charge densities, have diameters below 100 nm at N/P ratio of 30. In the pictures, very few nanosized spherical structures and mainly anomalous congeries with a size of several micrometers were observed in 800 Da PEI/DNA (Figure 3a). In contrast, small granules mainly with a short axis of 30–60 nm were found in 25 KDa PEI/DNA (Figure 3b). It illustrates that 25 KDa PEI forms compact polyplex particles with plasmid DNA, in good agreement with earlier reports (*32*, *33*). Oval structures in the size range 10–100 nm in the PEI−SS_X/DNA polyplexes were shown in Figure 3c−e. They did not show obvious differences in their morphology as compared to 25 KDa PEI/DNA polyplex. PEI−$SS_{9.4}$/DNA particles were found to be smaller than those of PEI−$SS_{2.6}$ and PEI−$SS_{6.5}$ on the TEM photographs.

The particle sizes of the polyplexes in 150 mM NaCl solution were determined by DLS as shown in Figure 4. At N/P ratios above 10, the pDNA polyplexes of the three PEI−SS_X polymers all have a size of about 400 nm. 25 KDa PEI forms the most compact pDNA polyplex with a size about 200 nm, and 800 Da PEI forms the loosest polyplex with a size of about 1000 nm. The trend of the sizes is in accordance with the results of molecular weight measurements and gel retardation experiments.

Zeta potentials of the polyplexes were measured in 10 mM NaCl solutions and shown in Figure 5. At N/P ratios below 3, the zeta potentials are negative showing an incomplete complexation. With increasing N/P ratio, zeta potentials of the polyplexes rapidly increase and reach plateaus at N/P ratios between 10 and 20. The 25 KDa PEI polyplex has the highest zeta potential of 35 mV, and the 800 Da PEI polyplex has the lowest zeta potential of 10 mV. All three PEI−SS_X (X = 2.6, 6.5, and 9.4) polyplexes have very similar zeta potentials of about 25 mV.

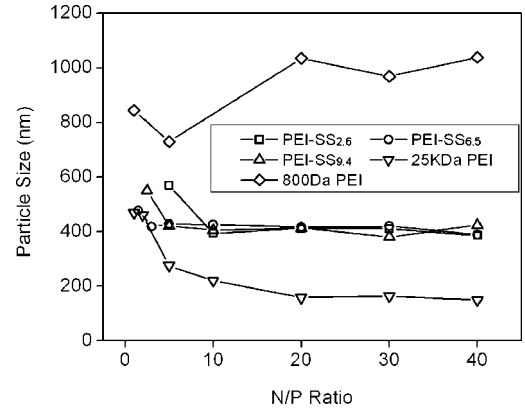

Figure 4. Particle size of the PEI/pDNA polyplexes measured by DLS in 150 mM NaCl solution.

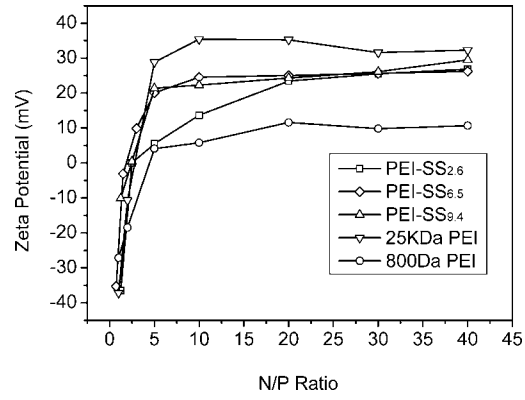

Figure 5. Surface charge of the PEI/pDNA polyplexes in 10 mM NaCl solution at various N/P ratios.

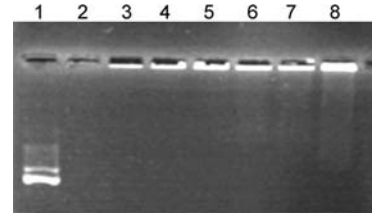

Figure 6. Gel retardation analysis of PEI−$SS_{2.6}$/pEGFP (N/P = 10) complex pretreated with various concentration of DTT. Lane 1, pEGFP only; lane 2, PEI−$SS_{2.6}$/pEGFP; lanes 3–8, PEI−$SS_{2.6}$/pEGFP pretreated with 0.1, 0.5, 2.5, 12.5, 62.5, and 310 mM DTT for 30 min.

Effect of DTT on Stability of PEI−SS_X/pDNA Polyplex. The stability of the PEI−SS_X/pDNA polyplexes in reductive media was investigated using 1,4-dithio-DL-threitol (DTT) as a reductive reagent. PEI−$SS_{2.6}$/pEGFP polyplex at N/P ratio of 10 was added pretreated for 30 min with DTT at a wide concentration range from 0.1 to 310 mM, and then checked by gel retardation analysis. As shown in Figure 6, with the increase of DTT concentration, the DNA band at the sample loading hole became more and more bright. At high DTT concentration, a "tail" outside the hole was visible. No band of the free pDNA, however, was observed even when the DTT concentration was as high as 310 mM. Therefore, it is not clear whether or to what extent the intracellular reductive environments with several millimolars of glutathione can help the release of pDNA from the disulfide cross-linked polyplexes.

In Vitro Transfection Efficiency. The gene delivery efficiency of the disulfide cross-linked LMW PEIs was evaluated by in vitro transfection experiments of pGL3 and pEGFP into HeLa and 293T cells. Branched 25 KDa PEI, which is the most

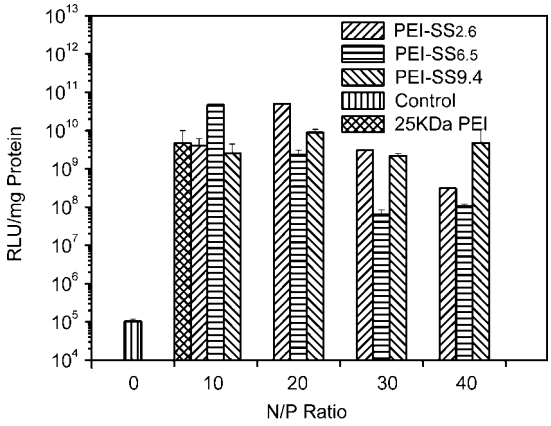

Figure 7. In vitro transfection efficiency of the polyplexes of pGL3 with PEI−SS_X series in HeLa cells in comparison with 25 KDa PEI. The transfection efficiency of 25 KDa PEI was obtained at an optimal N/P ratio of 10:1. Data are averages of three parallel experiments.

widely used polycation gene vector and considered highly efficient, was used for comparison. Our own experiments (data not shown) and literature report (*12*) showed that 25 KDa PEI yields optimal gene expression at N/P ratio around 10.

The transfection results of pGL3 to cultured HeLa cells were presented in Figure 7. The polyplexes of PEI−SS_X series showed transfection efficiencies comparable to or even significantly higher than that of 25 KDa PEI. Within the range of N/P ratios tested, PEI−$SS_{6.5}$ showed a maximum efficiency at an N/P ratio of 10, while PEI−$SS_{2.6}$ and PEI−$SS_{9.4}$ showed their maxima at a relatively higher N/P ratio of 20. This result is consistent with the gel retardation results showing that PEI−$SS_{6.5}$ has the highest DNA binding capacity among the three. At their own optimal N/P ratios, the PEI−$SS_{2.6}$ and PEI−$SS_{6.5}$ systems achieved nearly 10 times higher luciferase expression as compared with the optimal value of 25 KDa PEI. This result is notable compared with the literature reports in which the gene transfection efficiency of either branched or linear low molecular weight PEI was greatly enhanced by disulfide linkages but still significantly lower than that of their high molecular weight analogues (*12, 20*).

Excellent transfection ability of the PEI−SS_X series was further confirmed in the transfection of pEGFP to 293 T and HeLa cells.

The transfection of pEGFP in 293T and HeLa cells by PEI−SS_X was first visualized with a fluorescent microscope (Figure 8). 25 KDa PEI was also used for comparison, and naked pEGFP was used as a control. The cells transfected with PEI−SS_X/pEGFP and 25 KDa PEI/pEGFP showed many bright green fluorescent spots, while the 293T control transfected with naked pEGFP had only a few dim fluorescent spots. As shown in Figure 8, both 293T and HeLa cells with PEI−$SS_{2.6}$ as a pEGFP gene vector expressed much more fluorescent proteins than those with 25 KDa PEI. Moreover, PEI−$SS_{2.6}$ showed much lower cytotoxicity than 25 KDa PEI even at a higher N/P ratio. Under a microscope (pictures not shown), the appearance of the cells transfected with PEI−SS_X/pEGFP at N/P ratio of 30 was as normal as those with naked pEGFP, while the cells with 25 KDa PEI/pEGFP had a decreased cell density with some cells lumped together.

The transfection efficiency of pEGFP in HeLa was further quantified using a flow cytometry in terms of cell population expressing GFP. Figure 9 shows the percentage of the HeLa cells expressing GFP. It reveals again that the PEI−SS_X has apparently higher transfection efficiency than 25 KDa PEI. Within the N/P ratios of 10, 20, 30, and 40 tested, all the three PEI−SS_X/pEGFP polyplexes (X = 2.6, 6.5, and 9.4) showed

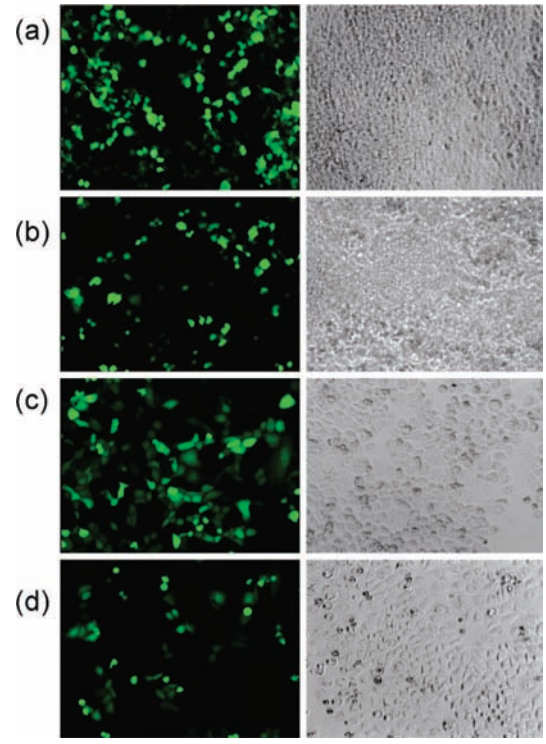

Figure 8. Fluorescent microscope images of pEGFP-transfected cells: (a) PEI−$SS_{2.6}$ in 293T at N/P = 30, (b) 25 KDa PEI in 293T at N/P = 10, (c) PEI−$SS_{2.6}$ in HeLa at N/P = 30, and (d) 25 KDa PEI in HeLa at N/P = 10.

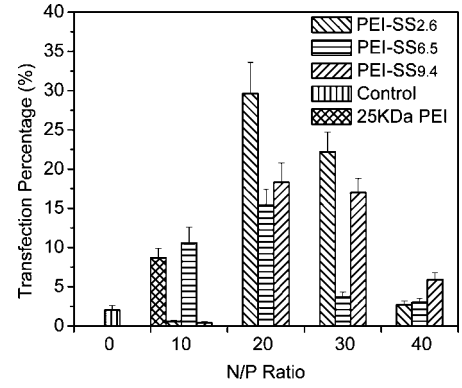

Figure 9. Transfection efficiency of the pEGFP polyplexes with PEI−SS_X to HeLa cells in terms of the percentage of cells expressing GFP.

their maximum efficiency values at N/P ratio of 20, with 15–30% cells expressing detectable GFP. In the case of 25 KDa PEI/pEGFP at an optimal N/P ratio of 10, the percentage of the cells expressing detectable GFP was 9%.

It is proven that the high buffering capacity in the endosomal pH range 5–7 originating from the unique polyamine structure is very important for the high transfection efficiency of PEI (*7*). Also, it is reported that reductive agents such as glutathione at an intracellular concentration can help the release of pDNAs from the polyplexes with disulfide-containing PEIs (*12, 20*). Therefore, the remarkably higher transfection efficiency of PEI−SS_X compared with 25 KDa PEI might be attributed to the introduction of reductively cleavable disulfide bonds, while the high density polyamine structure and buffering property of PEI are almost intact.

Since therapeutic gene transfection is in vivo, it is important to investigate the influence of serum on the transfection efficiency. For comparison, parallel transfection experiments of

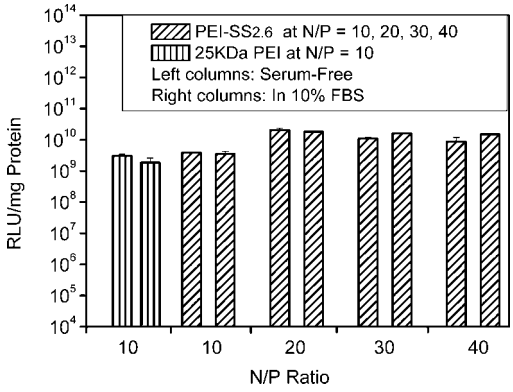

Figure 10. Comparison of transfection efficiency pGL3 to HeLa cells in serum-free and serum-supplemented DMEM media.

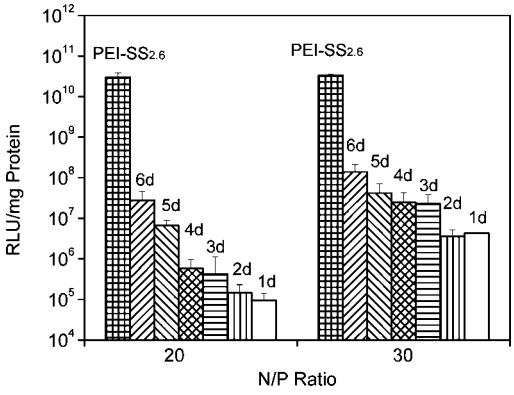

Figure 11. Comparison of the polyplexes prepared by in situ air oxidation of PEI−$SH_{2.6}$ for 1 to 6 days with the polyplexes prepared from DMSO-preoxidized PEI−$SS_{2.6}$ for transfection of pGL3 to HeLa cells.

pGL3 to HeLa cells in the absence or presence of 10% FBS were performed using PEI−$SS_{2.6}$ as a vector (Figure 10). For PEI−$SS_{2.6}$ at an N/P ratio of 10 and 20, no significant difference could be observed between the efficiencies in serum-free medium and serum-supplemented medium. At N/P ratio of 30 and 40, the efficiency in the serum-supplemented medium was even slightly higher than that in serum-free medium. For 25 KDa PEI at an N/P ratio of 10, however, the presence of 10% FBS decreased the efficiency slightly by about 50% of luciferase expression level. These results imply that PEI−SS_X might be suitable for in vivo gene transfection.

It was reported that monomolecular pDNA nanoparticles were successfully prepared through in situ air-oxidation of amphiphilic thiol compounds (*34*, *35*). Therefore, it is attractive to investigate whether the polyplexes prepared by in situ air oxidation of thiol PEI with pDNA possess any advantage over those prepared with the pre-cross-linked PEI−SS_X. Comparative transfection experiments about PEI−$SH_{2.6}$/DNA polyplexes oxidized in air for a different period of time with PEI−$SS_{2.6}$/DNA polyplexes were performed (Figure 11). The efficiency of the in situ air-oxidized polyplexes increased gradually with the oxidation time from 1 to 6 days, suggesting a very slow oxidation process. Even after oxidation for six days, the efficiency was still a few orders of magnitude lower than the polyplexes from the PEI−$SH_{2.6}$ preoxidated in DMSO at both N/P ratios of 20 and 30.

CONCLUSION

Designed amounts of thiol groups were readily introduced to LMW PEI using methylthiirane as an effective thiolation agent cross-linking reagent. Since thiol groups and amino groups are competent in the ring-opening reaction of a thiirane, it is important to adjust the basic reaction medium to a neutral pH in order to preventing the thiol groups from sulfide-forming polymerization. The thiolated LMW PEIs were transferred to disulfide cross-linked polyethylenimines, PEI−SS_X, by oxidation of the thiol groups with DMSO. The structure and buffering property of PEI were kept almost intact in PEI−SS_X because the thiol groups were introduced by the ring-opening alkylation on amino groups which does not significantly change the acid–base property. In vitro experiments demonstrated that the PEI−SS_X series have lower cytotoxicity and much higher gene transfection efficiency than 25 KDa PEI. The results proved that reductively degradable disulfide cross-linked low molecular weight PEIs could possess simultaneously higher gene transfection efficiency and lower cytotoxicity than their nondegradable high molecular weight analogues.

ACKNOWLEDGMENT

This research was financially supported by National Natural Science Foundation of China (20574054), "973 Programme" of the Ministry of Science and Technology of China (2005CB623903), and Program for New Century Excellent Talents in Universities (NCET) of the Minister of Education of China.

LITERATURE CITED

(1) Lungwitz, U., Breunig, M., Blunk, T., and Gopferich, A. (2005) Polyethylenimine-based non-viral gene delivery system. *Eur. J. Pharm. Biopharm. 60*, 247–266.

(2) Godbey, W. T., Wu, K. K., and Mikos, A. G. (1999) Tracking the intracellular path of poly(ethylenimine)/DNA complexes for gene delivery. *Proc. Natl. Acad. Sci. U.S.A. 96*, 5177–5181.

(3) Guo, W. J., and Lee, R. J. (2001) Efficient gene delivery via non-covalent complexes of folic acid and polyethylenimine. *J. Controlled Release 77*, 131–138.

(4) Boussif, O., Lezoualc'ht, F., Zanta, M. A., Mergnyt, M. D., Schermant, D., Demeneixt, B., and Behr, J. P. (1995) A versatile vector for gene and oligonucleotide transfer into cells in culture and in vivo: Polyethylenimine. *Proc. Natl. Acad. Sci. U.S.A. 92*, 7297–7301.

(5) Michael, N., Dagmar, F., and Thomas, K. (2005) Recent advances in rational gene transfer vector design based on poly(ethylene imine) and its derivatives. *J. Gene Med. 7*, 992–1009.

(6) Boussif, O., Zanta, M. A., and Behr, J. P. (1996) Optimized galenics improve in vitro gene transfer with cationic molecules up to 1000-fold. *Gene Ther. 3*, 1074–1080.

(7) Akinc, A., Thomas, M., Klibanov, A. M., and Langer, R. (2005) Exploring polyethylenimine-mediated DNA transfection and the proton sponge hypothesis. *J. Gene Med. 7*, 657–663.

(8) Schaffer, D. V., Fidelman, N. A., Dan, N., and Lauffenburger, D. A. (2000) Vector unpacking as a potential barrier for receptor-mediated polyplex gene delivery. *Biotechnol. Bioeng. 67*, 598–606.

(9) Godbey, W. T., Barry, M. A., and Saggau, P. (2000) Poly. (ethylenimine)-mediated transfection: a new paradigm for gene delivery. *J. Biomed. Mater. Res. 51*, 321–328.

(10) Funhoff, A. M., Van Nostrum, C. F., and Koning, G. A. (2004) Endosomal escape of polymeric gene delivery complexes is not always enhanced by polymers buffering at low pH. *Biomacromolecules 5*, 32–39.

(11) Kunath, K., Harpe, A. V., Fischer, D., Petersen, H., and Kissel, T. (2003) Low-molecular-weight polyethylenimine as a non-viral vector for DNA delivery: comparison of physicochemical properties, transfection efficiency and in vivo distribution with high-molecular-weight polyethylenimine. *J. Controlled Release 89*, 113–125.

(12) Gosselin, M. A., Guo, W., and Lee, R. J. (2001) Efficient gene transfer using reversibly crosslinked low molecular weight polyethylenimine. *Bioconjugate Chem. 12*, 989–994.

(13) Thomas, M., Ge, Q., Lu, J. J., Chen, J. Z., and Klibanov, A. M. (2005) Crosslinked small polyethylenimine: while still nontoxic, deliver DNA efficiently to mammalian cells in vitro and in vivo. *Pharm. Res. 22*, 373–380.

(14) Ahn, C. H., Chae, S. Y., Bae, Y. H., and Kim, S. W. (2002) Biodegradable poly(ethylenimine) for plasmid DNA delivery. *J. Controlled Release 80*, 273–282.

(15) Tang, G. P., Guo, H. Y., Alexis, F., Wang, X., Zeng, S., Lim, T. M., Ding, J., Yang, Y. Y., and Wang, S. (2006) Low molecular weight polyethylenimines linked by β-cyclodextrin for gene transfer into the nervous system. *J. Gene Med 8*, 736–744.

(16) Meister, A., and Anderson, M. E. (1983) Glutathione. *Annu. Rev. Biochem. 52*, 711–760.

(17) Bellomo, G., Vairetti, M., Stivala, L., Mirabelli, F., Richelmi, P., and Orrenius, S. (1992) Demonstration of nuclear compartmentalization of glutathione in hepatocytes. *Proc. Natl. Acad. Sci. U.S.A. 89*, 4412–4416.

(18) Wang, Y. X., Chen, P., and Shen, J. C. (2006) The development and characterization of a glutathione-sensitive crosslinked polyethylenimine gene vector. *Biomaterials 27*, 5292–5298.

(19) Carlisle, R. C., Etrych, T., Briggs, S. S., Preece, J. A., Ulbrich, K., and Seymour, L. W. (2004) Polymer-coated polyethylenimine/DNA complexes designed for triggered activation by intracellular reduction. *J. Gene Med. 6*, 337–344.

(20) Lee, Y., Mo, H. J., Koo, H., Park, J. Y., Cho, M. Y., Jin, J. W., and Park, J. S. (2007) Visualization of the degradation of a disulfide polymer, linear poly(ethylenimine sulfide), for gene delivery. *Bioconjugate Chem. 18*, 13–18.

(21) Kakizawa, Y., Harada, A., and Kataoka, K. (1999) Environment-sensitive stabilization of core-shell structured polyion complex micelle by reversible crosslinking of the core through disulfide bond. *J. Am. Chem. Soc. 121*, 11247–11248.

(22) Miyata, K., Kakizawa, Y., Nishiyama, N., Harada, A., Yamasaki, Y., Koyama, H., and Kataoka, K. (2004) Block catiomer polyplexes with regulated densities of charge and disulfide cross-linking directed to enhance gene expression. *J. Am. Chem. Soc. 126*, 2355–2361.

(23) McKenzie, D. L., Smiley, E., Kwok, K. Y., and Rice, K. G. (2000) Low molecular weight disulfide crosslinking peptides as nonviral gene delivery carriers. *Bioconjugate Chem. 11*, 901–909.

(24) McKenzie, D. L., Kwok, K. Y., and Rice, K. G. (2000) A potent new class of reductively activated peptide gene delivery agents. *J. Biol. Chem. 275*, 9970–9977.

(25) Pollard, H., Toumaniantz, G., Amos1, J.-L., Avet-Loiseau, H., Guihard, G., Behr, J.-P., and Escande, D. (2001) Ca^{2+}-sensitive cytosolic nucleases prevent efficient delivery to the nucleus of injected Plasmids. *J. Gene Med. 3*, 153–164.

(26) Bordwell, F. G., and Andersen, H. M. (1953) The reaction of epoxides with thiourea. *J. Am. Chem. Soc. 75*, 4959–4962.

(27) Eyer, P., Worek, F., Kiderlen, D., Sinko, G., Stuglin, A., Rudolf, V. S., and Reiner, E. (2003) Molar absorption coefficients for the reduced Ellman reagent: reassessment. *Anal. Biochem. 312*, 224–227.

(28) Riddles, P. W., Blakeley, R. L., and Zerner, B. (1979) Ellman's reagent: 5, 5′-dithiobis(2-nitrobenzoic acid)-a reexamination. *Anal. Chem. 94*, 75–81.

(29) von Harpe, A., Petersen, H., Li, Y., and Kissel, T. (2000) Characterization of commercially available and synthesized polyethylenimines for gene delivery. *J. Controlled Release 69*, 309–322.

(30) Dong, W., Jin, G. H., Li, S. F., Sun, Q. M., Ma, D. Y., and Hua, Z. C. (2006) Cross-linked polyethylenimine as potential DNA vector for gene delivery with high efficiency and low cytotoxicity. *Acta Biochim. Biophys. Sin. 38*, 780–787.

(31) Ryser, H. J. P. (1967) A membrane effect of basic polymers dependent on molecular size. *Nature 215*, 934–936.

(32) Merdan, T., Kunath, K, Petersen, H., Bakowsky, U., Voigt, K. H., Kopecek, J., and Kissel, T. (2005) PEGylation of poly(ethyleneimine) affects stability of complexes with plasmid DNA under in vivo conditions in a dose-dependent manner after intravenous injection into mice. *Bioconjugate Chem. 16*, 785–792.

(33) Petersen, H., Fechner, P. M., Martin, A. L., Stolnik, S., Roberts, C. J., Fischer, D., Davies, M. C., and Kissel, T. (2002) Polyethylenimine-graft-poly(ethylene glycol) copolymers: influence of copolymer block structure on DNA complexation and biological activities as gene delivery system. *Bioconjugate Chem. 13*, 845–854.

(34) Dauty, E., Remy, J. S., Blessing, T., and Behr, J. P. (2001) Dimerizable cationic detergents with a low cmc condense plasmid DNA into nanometric particles and transfect cells in culture. *J. Am. Chem. Soc. 123*, 9227–9234.

(35) Chittimalla, C., Zammut-Italiano, L., Zuber, G., and Behr, J.-P. (2005) Monomolecular DNA nanoparticles for intravenous delivery of genes. *J. Am. Chem. Soc. 127*, 11436–11441.

BC7003236

Enhanced Cellular Uptake of Virus-Like Particles through Immobilization on a Sialic Acid-Displaying Solid Surface

Noriko Ohtake,[†] Kenichi Niikura,*[,‡] Tadaki Suzuki,[§] Keita Nagakawa,[†] Hirofumi Sawa,[§,||] and Kuniharu Ijiro[‡,⊥]

Graduate School of Science, Hokkaido University N21W10, Sapporo 001-0021, Japan, Research Institute for Electronic Science, Hokkaido University N21W10, Sapporo 001-0021, Japan, Department of Molecular Pathobiology, Research Center for Zoonosis Control, Hokkaido University N20W10, Sapporo 001-0020, Japan, 21st Century COE Program for Zoonosis Control, Hokkaido University N20W10, Sapporo 001-0020, Japan, and CREST, JST, 4-1-8 Honcho Kawaguchi, Saitama 332-0012, Japan. Received September 10, 2007; Revised Manuscript Received November 13, 2007

Herein, we present the efficient cellular uptake of immobilized virus-like particles (VLPs) made of recombinant JC virus capsid proteins. VLPs expressed in *Escherichia coli* were labeled with fluorescein isothiocyanate (FITC). We compared two approaches for the cellular uptake of the FITC-VLPs. In the first approach, FITC-VLPs were immobilized on a polystyrene substrate, and then NIH3T3 cells were cultured on the same substrate. In the second approach, cells were cultured on a polystyrene substrate, and FITC-VLPs were then added to the cell culture medium. Flow cytometric analysis and confocal laser microscopic observation revealed that immobilized VLPs were incorporated into the cells with higher efficiency than were the diffusive VLPs suspended in solution. The cellular uptake of VLPs on the substrate was increased in a VLP density-dependent manner. As a control, disassembling VLPs to form VP1 pentamers abolished incorporation into the cells. Displaying sialic acid on the substrate enhanced VLP density through the specific affinities between the VLPs and sialic acid, resulting in efficient incorporation into the seeded cells. These techniques can be applied to the development of novel drug delivery systems and cell microarrays not only of nucleic acids but also of small molecules and proteins through their encapsulation in VLPs.

INTRODUCTION

Recently, much emphasis has been placed on the use of cell microarrays as effective tools for the study of a range of phenomena in mammalian cells, as they provide a rapid and simple method for the high-throughput analysis of multiple gene functions (*1*–*3*). Cell microarray technology is based on a "reverse transfection" (*4*) or "substrate-mediated drug delivery" (*5*) system, in which preimmobilized plasmid DNAs are transfected directly from the substrate into seeded cells. Compared with the conventional method, in which cells are cultured in a medium containing plasmid DNAs, the reverse transfection method has advantages such as easy handling, low cytotoxicity, and enhanced gene expression even in the presence of serum (*6*, *7*). Several problems, however, remain to be solved with regard to drug-immobilization techniques. For example, in the initial method of reverse transfection established by Sabatini et al. (*4*), usage was limited to gene delivery, as only DNAs could be coated onto the substrate by mixing with gelatin. Microarrays of small molecules, such as drugs and peptides, have also been constructed through the use of biodegradable polymers or chemolabile linkers as drug reservoirs on the surface of the substrates (*8*, *9*). These methods, however, were limited in that the drugs were only incorporated into cells through a passive (and sometimes time-consuming) process because their release from the substrates depended on free diffusion. To prevent cross-contamination of compounds, immobilization at low density and concentration was required, thus affording only a small number of samples spotted in the array and decreased cellular uptake. The future application of cell microarrays requires a high-performance drug carrier that can be uniformly immobilized on the substrates, while providing active and efficient entry of various drugs into a broad variety of cells.

Therefore, we propose a new substrate-mediated delivery approach using virus-like particles (VLPs) as potential carriers of various drug components (Figure 1). We focused on the JC virus (*10*), which belongs to the Polyomavirus family and can enter a broad range of mammalian cells (*11*). Since it is a

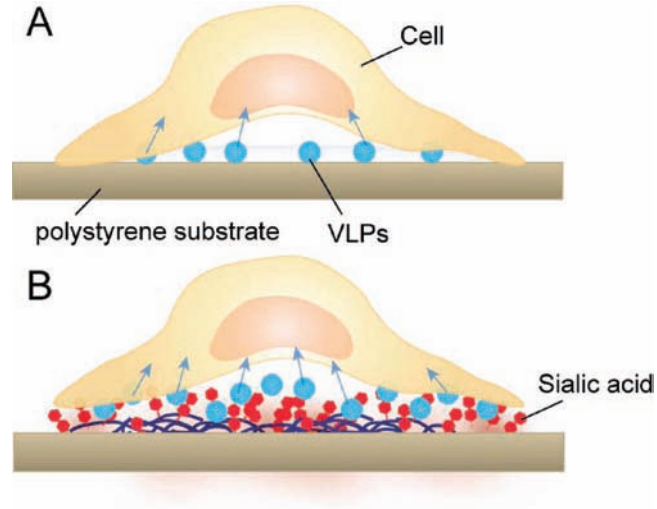

Figure 1. Schematic illustration of the substrate-mediated delivery approach using virus-like particles (VLPs). (A) Immobilization of VLPs on a polystyrene surface. (B) Enhanced immobilization of VLPs on a synthetic sialic acid-appended polymer (PV-Sia)-coated surface.

* Corresponding author. Tel: +81-11-706-9370. Fax: +81-11-706-9370. E-mail: kniikura@poly.es.hokudai.ac.jp.
[†] Graduate School of Science, Hokkaido University.
[‡] Research Institute for Electronic Science, Hokkaido University.
[§] Research Center for Zoonosis Control, Hokkaido University.
[||] 21st Century COE Program for Zoonosis Control.
[⊥] CREST.

10.1021/bc700348g CCC: $40.75 © 2008 American Chemical Society
Published on Web 01/08/2008

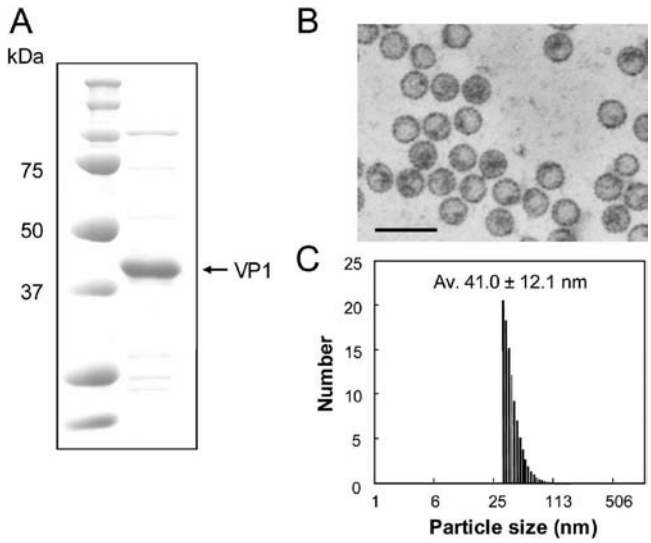

Figure 2. Characterization of VLPs expressed in *E. coli*. (A) SDS−PAGE analysis of purified VLPs. The VLPs were subjected to SDS−PAGE, and the resulting gel was stained with Coomassie Brilliant Blue. (B) STEM images of purified VLPs (dark field, negatively stained) at 200 kV. The scale bar is 100 nm. (C) Particle size analysis by dynamic light scattering (DLS), performed at 25 °C.

nonenveloped virus, it is better able to tolerate dry conditions than enveloped viruses; thus, it is suitable for immobilization and preservation on the substrates. The capsid of the JC virus is composed of three capsid proteins: VP1, VP2, and VP3. VP1, the 39 kDa major capsid protein of the JC virus, can be expressed recombinantly in *E. coli* or insect cells. It is known that recombinant VP1 pentamers self-assemble to form VLPs (*12*). Since VP1 is known to recognize sialic acid receptors on the cellular surface (*13, 14*), cellular uptake of VLPs through receptor-mediated endocytosis can be expected. Moreover, VLPs are capable of internalizing not only genes but also proteins, small molecules, and peptides (*15, 16*). For example, the encapsidation of green fluorescent protein (GFP) and methotrexate (MTX) into Polyoma VLPs has been carried out using VP2 as an anchor molecule (*17*). In this way, VLPs have a potential as carriers of various drug components to several kinds of mammalian cells.

Although some cell microarray systems employing adenoviruses or lentiviruses solely as carriers of DNAs and RNAs have been developed (*18, 19*), there has been no detailed study of cellular uptake efficiency that compares diffusive viruses in solution with those immobilized on substrates. Herein, as a first step in the fabrication of a cell microarray based on VLPs, we report the efficient cellular uptake of immobilized VLPs on a substrate, compared with that of diffusive VLPs in solution, by means of flow cytometric analyses and confocal laser microscopic observations. We also report the effective immobilization of VLPs using the specific affinity between the VLPs and sugar moieties, which enhanced the cellular incorporation of VLPs.

EXPERIMENTAL PROCEDURES

General Methods. Fluorescein isothiocyanate (FITC), fetuin, and asialo fetuin were obtained from Sigma-Aldrich Corp. (USA). Poly(*N-p*-vinylbenzyl-6-*O*-carboxymethyl-6′-*O*-carboxymethyl-*O*-*β*-D-galactopyranosyl-(1→4)-D-gluconamide) (PV-LACOOH) and Poly(*N-p*-vinylbenzyl-*O*-2-acetoamide-2-deoxy-*β*-D-glucopyranosyl-(1→4)-2-acetoamide-2-deoxy-D-gluconamide) (PV-GlcNAc) were purchased from Seikagaku Corp. (Japan). UDP-galactose (UDP-Gal) and CMP-*N*-acetylneuraminic acid disodium salt (CMP-NANA, 2Na) were obtained from Yamasa Corp. (Japan) and Nacalai Tesque, Inc. (Japan), respectively, and *β*1,4-galactosyltransferase (GalT) and α2,6-sialyltransferase (SiaT) were obtained from Toyobo Co. Ltd. (Japan), and Japan Tobacco, Inc. (Japan), respectively. All samples were prepared with ultrapure water (Milli-Q, Millipore, USA) and used without further purification.

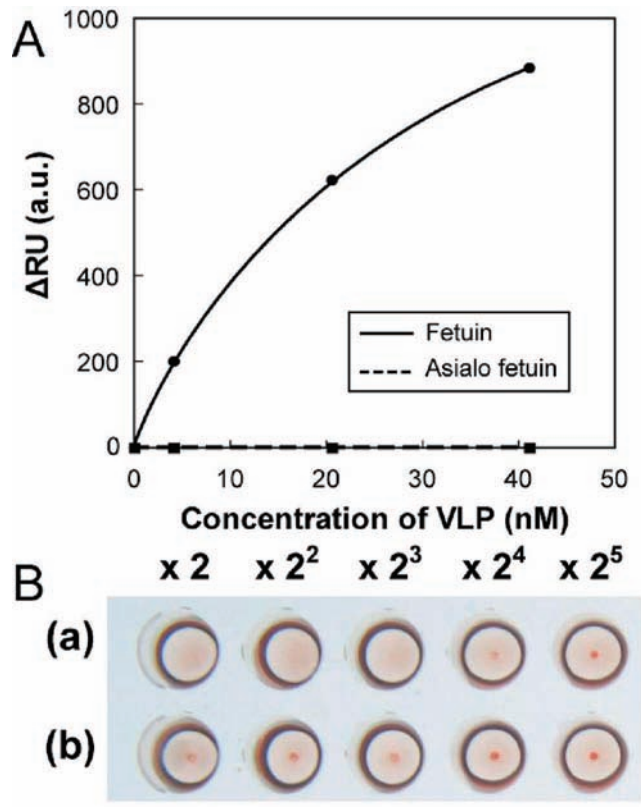

Figure 3. Measurements of the binding affinity between the VLPs and sialo-glycoprotein using surface plasmon resonance (SPR) and hemagglutination (HA) assay. (A) Concentration dependence of maximum response units obtained from the SPR measurements. Fetuin (—) or asialo fetuin (---) were immobilized on the sensor chip. (B) HA assay of (a) original and (b) predissociated VLPs. Twenty-five micoliters of serially diluted aqueous solutions of VLPs were examined. The number represents the reciprocal of the dilution factor.

Expression and Purification of JC VLPs. JC VLPs were prepared as previously described (*11*). Briefly, the pET15b plasmid (Novagen, USA) including the JC virus VP1 DNA was transformed into *E. coli*, BL21 (DE3) pLysS (Stratagene, USA). After overnight colony culture at 37 °C in Terrific broth, the expression of VP1 was induced with 1.0 mM isopropyl-*β*-D-thiogalactopyranoside (IPTG) for 4 h at 30 °C, and the mixture was collected by centrifugation at 4,000*g* for 15 min. The pellet was resuspended in reassociation buffer (pH 7.4, 20 mM Tris-HCl, 150 mM NaCl, and 1 mM $CaCl_2$) containing 1 mg of lysozyme/mL and kept on ice for 30 min, and then 1% sodium deoxycholate was added. After incubation for 10 min on ice, the sample was treated with DNaseI (100 U/mL) for 30 min at 30 °C and lysed by five cycles of sonication for 30 s. After centrifugation of the lysate at 10,000*g* for 20 min at 4 °C, the supernatant was centrifuged at 25,000 rpm (SW28 rotor, OptimaL, Beckman Coulter, USA) for 3 h at 4 °C. The white layer in the tube was lysed in a reassociation buffer containing CsCl at a final concentration of 1.29 g/mL and then centrifuged at 32,000 rpm (SW41 rotor, OptimaL, Beckman Coulter, USA) for 16 h at 4 °C. The resultant fractions were dialyzed in reassociation buffer at 4 °C overnight.

Dissociation of VLPs/FITC Labeling of VLPs. For the dissociation of particle structures, VLPs were mixed in PBS

Scheme 1. Cellular Uptake of (a) Immobilized or (b) Diffusive FITC-VLPs through the Two Approaches

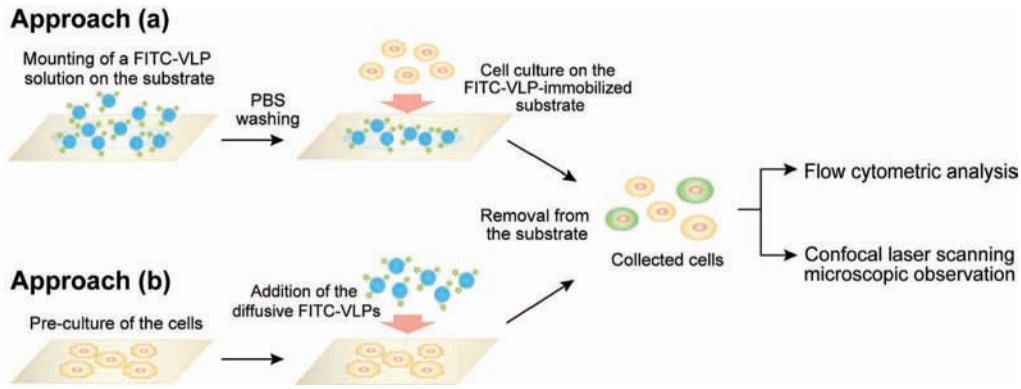

containing 3 mM dithiothreitol (DTT) and 10 mM EGTA at 4 °C overnight.

For the conjugation of VLPs with FITC, 2.5 mg of VLPs was dissolved in 0.1 M carbonate−bicarbonate buffer (pH 9.0), mixed with 250 μg of FITC, and incubated at room temperature for 2 h. The mixture was dialyzed twice in PBS (pH 7.4) containing 1 mM $CaCl_2$.

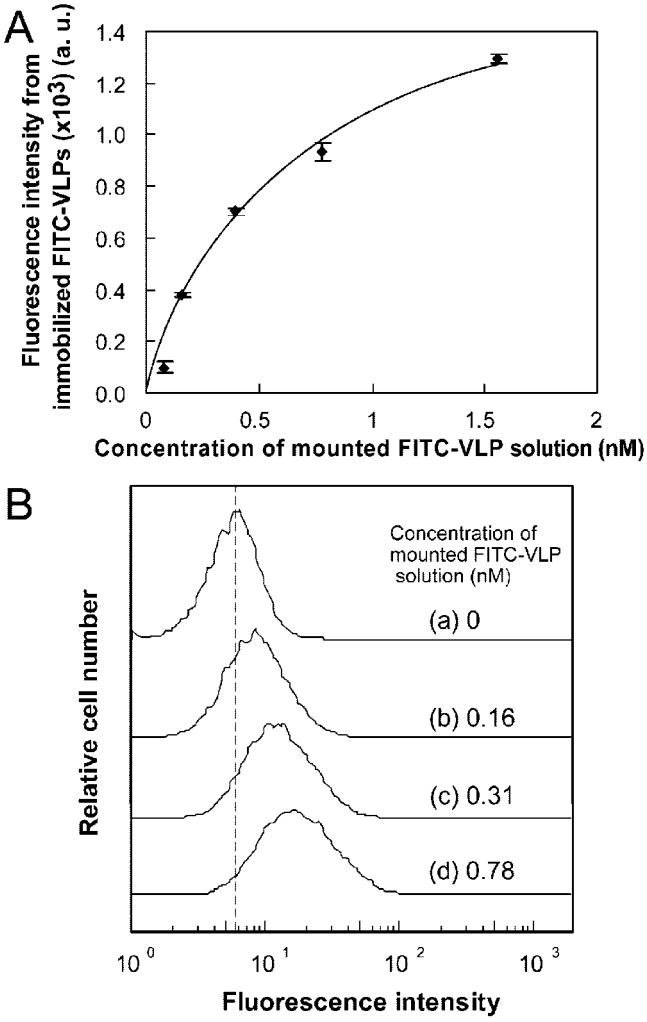

Figure 4. Immobilization of FITC-VLPs and their subsequent cellular uptake via the substrate-mediated approach using polystyrene substrates. (A) Measurement of the fluorescence intensity of immobilized FITC-VLPs at various concentrations. (B) Flow cytometric analysis of NIH3T3 cells cultured on the FITC-VLP-coated substrates. The histograms of the cellular uptake of FITC-VLPs are shown. The initial concentration of the mounted FITC-VLP solution was (a) 0 nM, (b) 0.16 nM, (c) 0.31 nM, and (d) 0.78 nM.

Electron Microscopy/Dynamic Light Scattering (DLS) Analysis. Before observation, 2 μL of the samples was dropped on carbon-coated TEM grids and then negatively stained with 2% phosphotungstic acid. After desiccation overnight, the morphology of the VLPs was confirmed by scanning transmission electron microscopy (STEM) (HD-2000, Hitachi, Japan).

Particle size analysis of the VLPs in reassociation buffer was performed by dynamic light scattering (FDLS-3000, Otsuka Electronics, Japan) with measurements taken at 25 °C.

Surface Plasmon Resonance (SPR) Measurement. The measurement of the interactions between the VLPs and glycoproteins were carried out using SPR techniques (Biacore X, Biacore, USA). The sensor chip was equilibrated with a running buffer (pH 7.4, 10 mM Tris-HCl, 150 mM NaCl, and 1 mM $CaCl_2$). Fetuin and asialo fetuin were adsorbed onto an Au-coated sensor chip (SIA Kit Au, Biacore, USA) prior to measurement. The buffer solution containing various VLP concentrations (4−40 nM) was then injected onto the glycoprotein-coated sensor chip, and the signal was recorded.

Hemagglutination (HA) Assay. The hemagglutination assay was performed to estimate the functional efficiency of VLPs, as described elsewhere (*20*). Briefly, 25 μL of serially diluted aqueous solutions of VLPs were prepared in a 96-well V-shaped microplate, using 25 μL of PBS (pH 7.15) containing 0.2% bovine serum albumin (BSA). After incubation at 37 °C for 1 h, 25 μL of 0.5% type-O red blood cells were added to each well. The 96-well plate was kept at 4 °C for 3 h and the end point attained. The HA titer was defined as the reciprocal of the greatest dilution of VLP suspension for which complete hemagglutination was observed.

Synthesis of Sugar-Displaying Polymers. Enzymatic synthesis of PV-LacNAc was carried out in 10 mM Hepes-NaOH (pH 7.4), 10 mM $MnCl_2$, 50 mM NaCl, 6.8 mM PV-GlcNAc, 20 mM UDP-Gal, and β1,4-galactosyltransferase (170 mU/mL). The enzymatic reaction mixture was slowly rotated at 30 °C overnight. The prepared crude PV-LacNAc solution was next applied to a glycosyltransferase reaction after simple purification using spin filtration. Then, the sialic acid-displaying polymer (PV-Sia) was synthesized in 20 mM cacodylate buffer (pH 7.5), 3.4 mM PV-LacNAc, 5 mM CMP-NANA, and 50 mU/mL α2,6-sialyltransferase. The enzymatic reaction mixture was slowly rotated at 30 °C overnight.

Preparation of FITC-VLP-Coated Substrates. PV-LACOOH, PV-LacNAc, and PV-Sia were diluted to 0.17 mM with ultrapure water. After sonication for 1 min, 2 mL of each solution was applied to a 6-well cell culture plate (Nunc, USA). The plate was incubated at room temperature for 1 h and then rinsed twice with PBS. The FITC-VLP solution was diluted with PBS to a final concentration of 0−1.57 nM and added to the plate pretreated with PBS or PV-sugar. The plate was incubated in the dark for 1 h and washed twice with PBS.

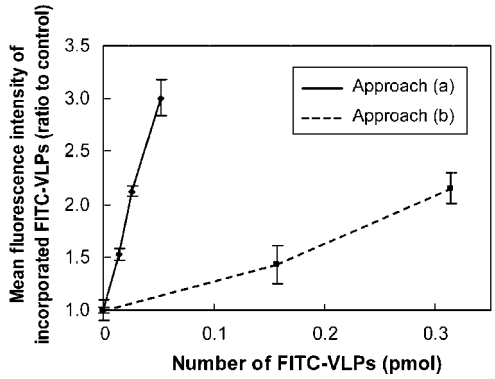

Figure 5. Mean fluorescence intensity of incorporated FITC-VLPs in NIH3T3 cells through approaches (a) and (b). The relative fluorescence intensity was estimated by taking the intensity of untreated cells as 1.0. The solid line represents the mean cellular uptake of immobilized FITC-VLPs on the substrates (approach (a)), and the dashed line represents that of diffusive FITC-VLPs in culture medium (approach (b)).

Plate Reader Measurements. The fluorescence intensities of each sample were measured by a plate reader (Ex. 485 nm/Em. 535 nm, Infinite 2000, Tecan, Switzerland) using an optical bottom plate (Nunc, USA) with a clear bottom and black side walls. The fluorescence intensity derived from the FITC-VLPs was estimated by taking the intensity of PBS as a baseline.

Cell Culture. NIH3T3 cells were seeded on the FITC-VLP-coated substrate and grown in Dulbecco's modified essential medium (DMEM) supplemented with 10% fetal bovine serum (FBS) and 1% antibiotics (penicillin/streptomycin) (Sigma-Aldrich, USA) in 5% CO_2 for 4 h. After rinsing several times with PBS, the cells were treated with trypsin (Gibco, USA) and collected by centrifugation.

Flow Cytometry/Confocal Laser Microscopy. The cells were resuspended in PBS and analyzed using a fluorescence-activated cell sorter (FACS canto, Becton Dickinson, USA). For each analysis, 10,000 events were monitored.

The collected cells were also seeded onto an 8-well chamber slide (Nunc, USA) and cultured for 4 h under the same conditions. After rinsing with PBS, the chambers were removed, and the cells were fixed with 4% paraformaldehyde for 10 min. For staining the cell nuculei, 4′,6′-diamidino-2-phenylindole (DAPI) dihydrochloride solution (Dojindo, Japan) was added to a final concentration of 1 μg/mL. The slides were observed using a confocal laser scanning microscope (FV-300, Olympus, Japan).

RESULTS

A. Characterization of Virus-Like Particles (VLPs). JC virus VP1 recombinantly expressed in *E. coli* spontaneously self-assembles into virus-like particles (VLPs) in the presence of calcium ions. Assembled VLPs were purified by CsCl density gradient centrifugation. The purified VLPs were electrophoresized on 5% SDS−polyacrylamide gels (Figure 2A). The main band was observed at around 40 kDa, which is in good agreement with the molecular weight of native JC virus VP1 (39 kDa). The morphology of the VLPs was examined by electron microscopy after negative staining (Figure 2B). A relatively homogeneous population of particles of around 40 nm in diameter was observed. Particle size analysis was also performed by dynamic light scattering (DLS). The mean diameter of the VLPs was estimated to be 41.0 ± 12.1 nm (Figure 2C). These results were similar to those reported in previous literature (*21*).

Although it has been reported that JC VLPs preferentially bind to *N*-linked glycoproteins containing terminal sialic acid (*22*), the quantitative binding constant has not yet been determined. Therefore, we measured the binding affinity between the VLPs and sialo-glycoprotein by surface plasmon resonance (SPR) measurements on a Biacore instrument. As a target glycoprotein, we chose fetuin, which is a 48-kDa-protein possessing 8.9 wt% of sialic acid moieties (*23, 24*). Asialo fetuin, a sialic acid-free protein, was used as a negative control. The two glycoproteins were separately adsorbed onto an Au-coated sensor chip through hydrophobic interactions. Different

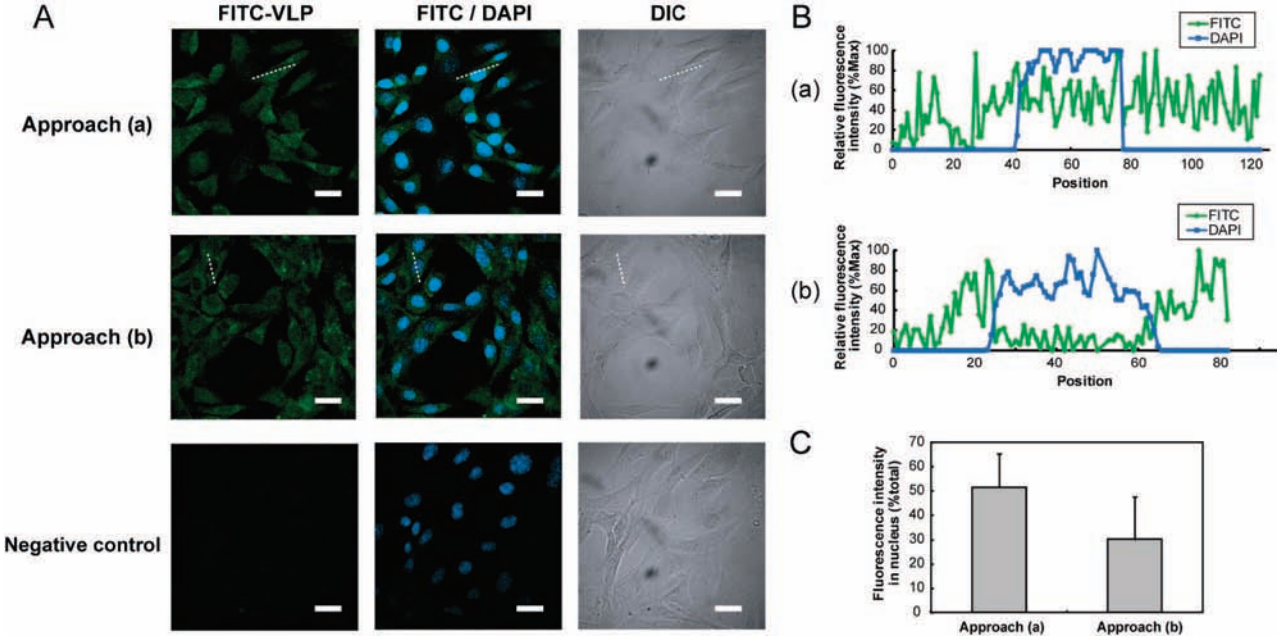

Figure 6. Comparision of the localization of FITC-VLPs incorporated into NIH3T3 cells through approaches (a) and (b). (A) Fluorescence images (left), merged fluorescence and nuclear staining images (middle), and differential interference contrast images (right) showing cells after FITC-VLP incorporation through approaches (a) and (b). Images of the negative control using untreated cells are also displayed. The cells were observed by confocal laser scanning microscopy. The scale bars are 20 μm. (B) Relative fluorescence intensities of FITC and DAPI along the dotted lines drawn on the images for approaches (a) and (b) in (A), respectively. (C) Ratio of fluorescence intensities of FITC in the nucleus. The total fluorescence intensity of FITC in the cell was taken as 100%.

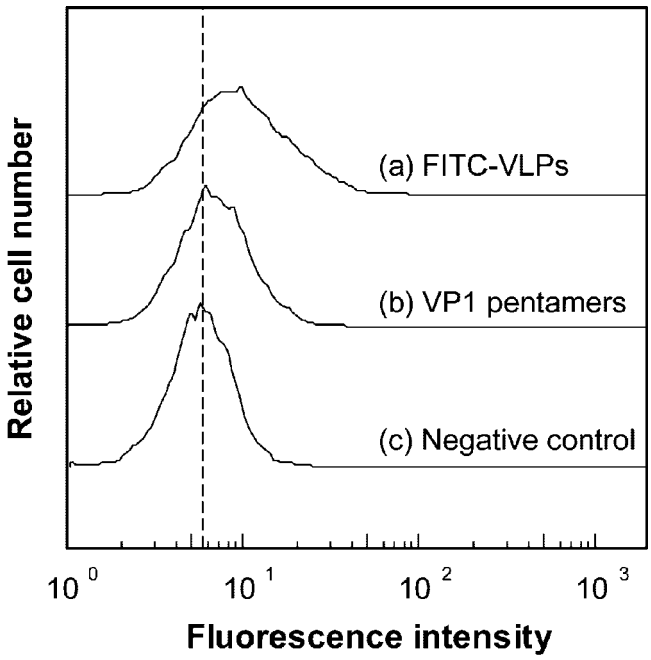

Figure 7. Flow cytometric analyses of substrate-mediated cellular uptake of (a) FITC-VLPs and (b) FITC-VLPs disassembled to form VP1 pentamers. The histogram of the negative control using untreated cells is shown as (c).

concentrations of the VLPs were passed over the surface to determine the concentration-dependent maximum response units (ΔRU) (Figure 3A). The binding constant of 4.1×10^7 M^{-1} estimated from the ΔRU curve demonstrates the high selectivity of the VLPs to the sialic acids. This value was similar in order to that of another lectin, SSA (1.4×10^7 M^{-1}) (*25*). To confirm the ability of our recombinant VLPs to recognize sialic acid, we also performed the hemagglutination (HA) assay (Figure 3B). The HA titer of VLPs obtained from *E. coli* was 512 HA/μL, suggesting a relatively high binding affinity between the VLPs and sialic acids present in red blood cells. The samples that were predissociated to VP1 pentamers by treatment with EGTA and DTT did not show any HA activity, probably because they no longer had the ability to bridge blood cells (Figure 3B).

B. Introduction of VLPs Deposited on a Polystyrene-Based Substrate. In order to quantify cellular uptake, VLPs were conjugated with FITC through a stable covalent linkage with the amine group on the VLPs, and the reaction mixture was then dialyzed to remove the unreacted FITC. The two approaches to the cellular uptake of FITC-labeled VLPs are illustrated in Scheme 1. In our novel approach (a), the FITC-VLPs were first immobilized on the substrate and washed with PBS, and then the cells were seeded onto the substrate. In this approach, the immobilized FITC-VLPs were directly introduced from the substrate to the cultured cells. Approach (b) represents a conventional method, in which the cells were cultured on the substrate prior to the addition of FITC-VLPs into the culture medium.

First, we investigated the immobilization of FITC-VLPs and their subsequent cellular uptake in approach (a). We employed a tissue culture polystyrene plate to immobilize the FITC-VLPs for cell culture. An aqueous solution of FITC-VLPs was mounted on a polystyrene substrate and incubated for 1 h, and then the substrate was rinsed well with PBS. The fluorescence intensities of the substrate before and after rinsing with PBS were measured using a fluorescence plate reader. Approximately 1/10 of FITC-VLPs in the mounted solution were deposited on the substrate even after rinsing with PBS (data not shown).

Various concentrations of FITC-VLP in aqueous solutions were also mounted on the substrate, followed by washing with PBS and measurement of fluorescence intensities (Figure 4A). The fluorescence intensity curve shows that the number of FITC-VLPs immobilized on the substrate increased exponentially with increases in the initial concentration of FITC-VLPs in the aqueous solution, up to the saturation of the FITC-VLP binding sites on the polystyrene substrate.

NIH3T3 cells were cultured on the FITC-VLP-coated substrate in DMEM containing 10% FBS for 4 h and then removed from the substrate by treatment with trypsin. After collection, the cellular uptake of FITC-VLPs was analyzed by flow cytometry. The histogram shown in Figure 4B indicates the introduction of FITC-VLPs into the cells cultured on the FITC-VLP-coated substrates. The cellular uptake of FITC-VLPs increased with increases in the initial concentration of FITC-VLPs because of an increase in the number of VLPs immobilized on the substrate.

We next compared the efficiency of cellular uptake of FITC-VLP through approaches (a) and (b). Mean cellular uptake using various quantities of FITC-VLPs (0−0.32 pmol) is plotted in Figure 5. The number of FITC-VLPs used in the two approaches was calculated as follows. Aqueous solutions of FITC-VLPs at identical concentrations were first mounted in both approaches. In approach (a), as the substrate was rinsed with PBS, some of the FITC-VLPs in the mounted solution were washed out. Therefore, the number of FITC-VLPs immobilized on the substrate was estimated from the relative fluorescence intensity at each concentration as previously determined by plate reader measurement. However, in approach (b), the number of FITC-VLPs was estimated only by culture volume of the mounted solution. We used 2 mL of FITC-VLP-containing DMEM for approach (b), which is the minimum volume required for cell culture, and the number of FITC-VLPs in solution was considered to be sufficient compared with that in previous reports (*26*). Surprisingly, the introduction of FITC-VLPs through approach (a) was possible at a much lower quantity than was possible through approach (b). While approach (b) requires more than 0.1 pmol of FITC-VLPs for the detection of cellular uptake, less than 0.1 pmol of FITC-VLPs was sufficient for high cellular uptake in approach (a). This result suggests that immobilization on the substrate leads to efficient cellular uptake of FITC-VLPs.

Cellular uptake of FITC-VLPs was further confirmed by confocal laser scanning microscopy (Figure 6A). To eliminate the fluorescence derived from FITC-VLPs retained on the substrate, the cells were removed from the substrate by trypsin treatment and cultured again on new glass slides for a further 4 h. The observation of cells prepared by approaches (a) and (b) showed that FITC-VLPs were internalized into the cells, not just attached to the cell surface. Interestingly, the VLPs from the substrate were more dispersed into the nucleus than were those from the solution (Figure 6B and C).

As a control, FITC-VLPs were disassembled to VP1 pentamers by the addition of DTT and EGTA prior to immobilization on the substrate (Figure 7). In this case, there was little incorporation of the disassembled sample from the substrate as compared to that of the original VLPs, suggesting that VLP formation is necessary for cellular uptake from the substrate.

C. Increased Cellular Uptake Using Sialic-Acid Displaying Substrate. On the basis of our results using polystyrene-based substrates, deposition of a large number of VLPs on the substrate was significant enough to increase the cellular uptake of the immobilized VLPs. Therefore, we sought to enhance cellular uptake through increasing the number of VLPs immobilized on the substrate using their specificity to sialic acid (*22*).

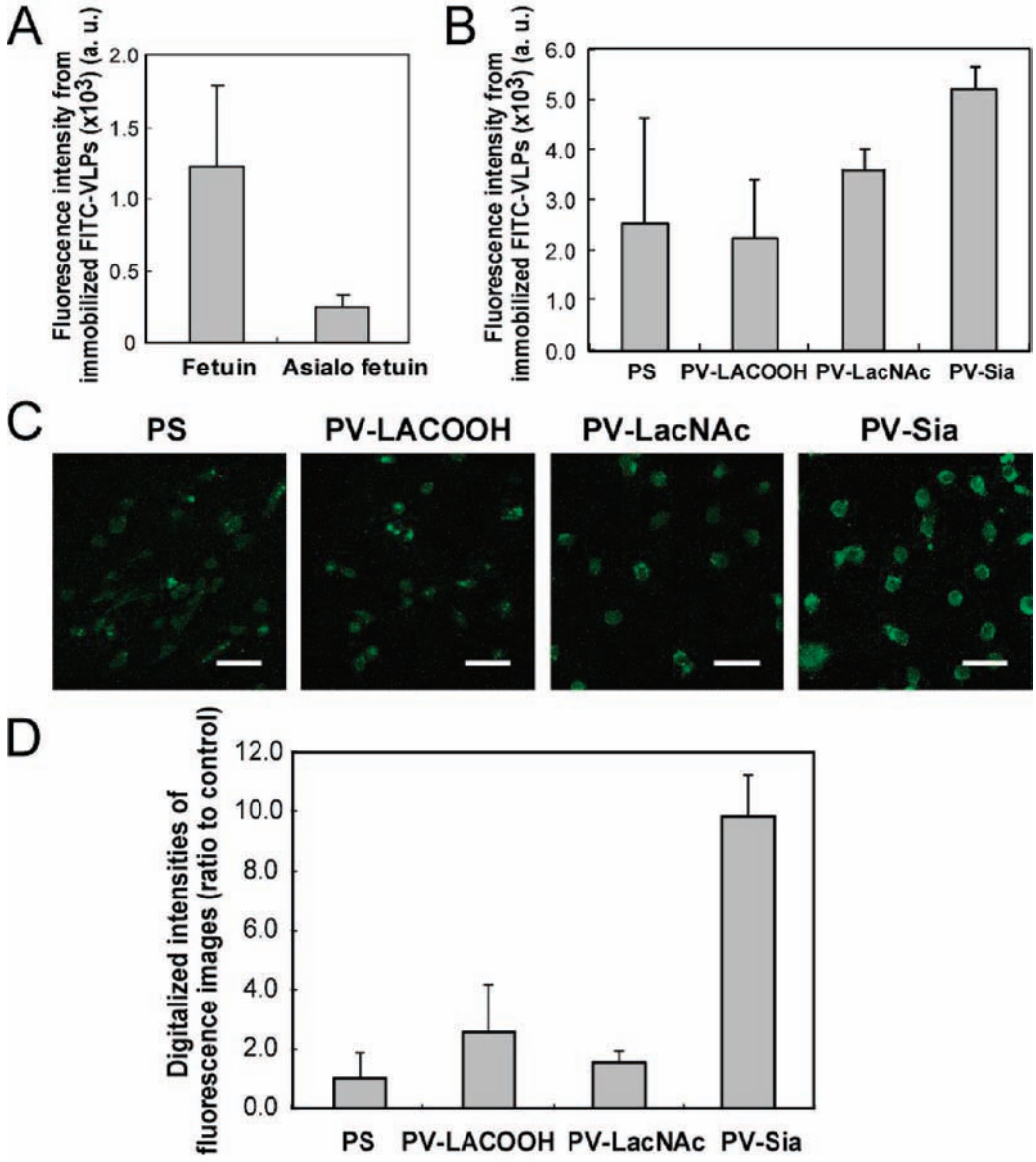

Figure 8. Immobilization of FITC-VLPs and subsequent cellular uptake via the substrate-mediated approach using sugar-displaying substrates. (A) Fluorescence intensities of FITC-VLPs attached to the substrate precoated with 0.5 mg/mL fetuin and asialo fetuin. (B) Comparison of the fluorescence intensities of FITC-VLPs immobilized on the polystyrene (PS) and sugar-displaying substrates. (C) Fluorescence images of NIH3T3 cells cultured on the FITC-VLP-coated sugar-displaying substrates. The cells were observed by confocal laser scanning microscopy. The scale bars are 50 μm. (D) Comparison of the NIH3T3 cellular uptake of FITC-VLPs attached to the sugar-displaying substrates. Whole fluorescence intensities of the confocal images were estimated using image analysis, and the mean values obtained from three images are shown. The relative fluorescence intensity was estimated by taking the intensity of PS as 1.0.

Using fetuin and asialo fetuin, we initially confirmed that displaying sialic acid from the polystyrene substrate could increase the number of immobilized FITC-VLPs (Figure 8A). The result shows that the FITC-VLPs were more effectively immobilized onto the fetuin-coated substrate than that coated with asialo fetuin, which is in good agreement with the results of the SPR measurement. This suggests that displaying sialic acid from a polystyrene substrate is effective in increasing FITC-VLP immobilization.

For the preparation of a sugar-displaying substrate more appropriate for cell culture, we next used PV-sugars, which are synthetic sugars grafted to polystyrene (*27, 28*). PV-sugars are reported to dissolve in water, forming a characteristic bottlebrush conformation composed of a polystyrene backbone covered with sugar brushes (*29*). Mounting aqueous solutions of PV-sugars onto substrates can provide a uniform glycopolymer-coated surface, which has good biocompatibility for cell culture (*30, 31*).

The synthesis of PV-sugar containing sialic acid (PV-Sia) was performed by two-step glycosyltransferase reaction (Scheme 2). In the first stage, an aqueous solution of PV-GlcNAc was treated with β1,4-galactosyltransferase (GalT) in the presence of UDP-Gal, providing the formation of PV-LacNAc. The product was further treated with α2,6-sialyltransferase (SiaT) in the presence of CMP-NANA, generating the final product PV-Sia. Since the polymers formed a micelle structure, they were not identifiable by NMR. Therefore, glycosylation was confirmed both by the specific binding of lectins for galactose and by resorcinol assay sensitive to sialic acid. FITC-labeled RCA120, which is a lectin that specifically associates with Galβ1-4GlcNAc (*32, 33*), did not bind to the PV-GlcNAc-coated substrate but strongly bound after the galactosyltransferase reaction (see Supporting Information). Subsequent sialylation of the polymer by sialyltransferase caused a large decrease in RCA120 binding since the lectin only slightly associates with

Scheme 2. Enzymatic Syntheses of Sialic Acid-Displaying PV-Sugars

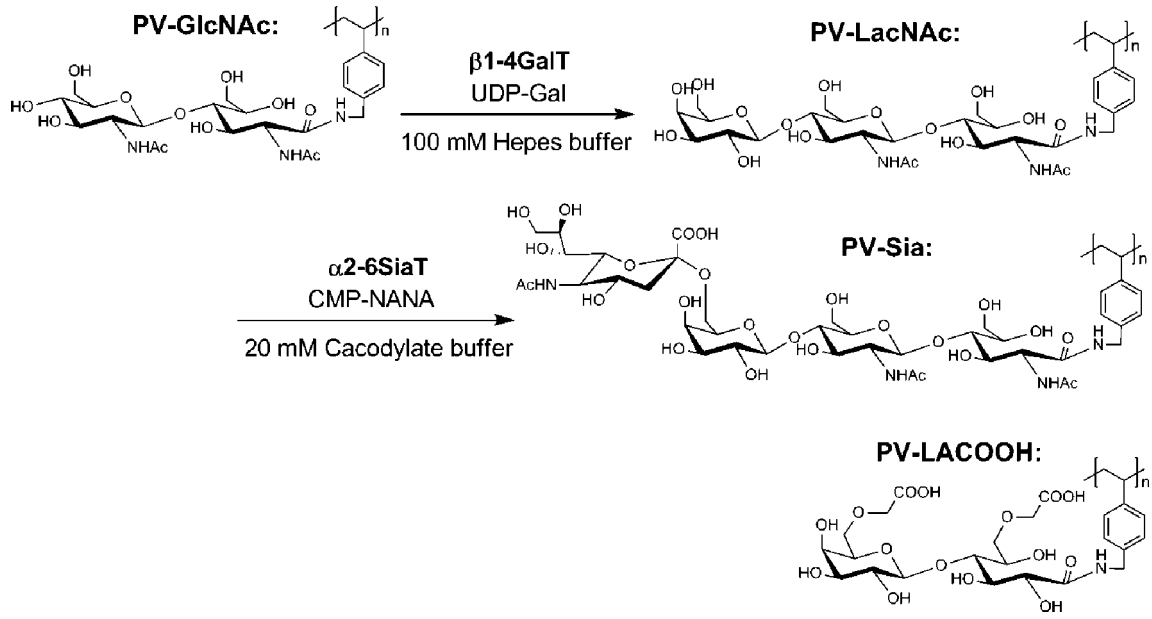

sialic acid (*34*). The content of sialic acid in the polymer was then determined by colorimetry using the resorcinol assay (*35*). The sialic acids released from glycosidic linkage by heating in a strong aqueous acid solution were quantified by absorption at 580 nm. The ratio of side chains possessing a sialic acid in PV-Sia was estimated to be around 19% (see Supporting Information). These experiments showed that carbohydrates were transferred step by step, and that almost 20% of sialic acids were finally displayed on the polymer chain. We otherwise used PV-LACOOH as a control for the electrostatic interaction of PV-Sia. Ellipsometric measurements were carried out in order to detect the film thickness of each polymer (see Supporting Information). Glass slides were spin-coated with PV-sugars and washed well with water. After drying overnight, the thickness of the films was examined. The thicknesses of the PV-LACOOH, PV-LacNAc, and PV-Sia films were 79.3 ± 3.7, 77.7 ± 4.3, and 79.6 ± 3.7 nm, respectively, indicating that the polymers were tightly fixed to the surface of the substrates.

Plate reader measurements after the binding of the FITC-VLPs showed that the fluorescence intensity obtained from the PV-Sia-coated substrate was 2-fold higher than that obtained from the polystyrene substrate (Figure 8B). The difference in fluorescence intensity between the PV-Sia-coated and the polystyrene substrates was in good agreement with that between the substrates coated with fetuin and asialo fetuin (Figure 8A). The PV-LacNAc-coated substrate provided a moderate increase in FITC-VLP immobilization. FITC-VLP immobilization onto the PV-LACOOH-coated substrate was approximately equivalent to that onto the polystyrene substrate. These results indicate that FITC-VLPs were effectively immobilized on the PV-Sia-displaying substrate because of their specific interaction with sialic acid, not because of electrostatic interaction.

Finally, the introduction of FITC-VLPs from sugar-displaying substrates was investigated using confocal laser scanning microscopy as described above. Fluorescence images of NIH3T3 cells cultured on the FITC-VLP-coated sugar-displaying substrates are shown in Figure 8C. Seeded cells adhered well to all sugar-displaying substrates showing no cytotoxicity (data not shown). The cellular uptake of FITC-VLPs was also observed on all sugar-displaying substrates. The digitalized intensities of the fluorescence images demonstrate that the cells cultured on the PV-Sia-displaying substrate provided the significantly highest fluorescence intensity (Figure 8D). Our results show that coating the substrate with sialic acid-displaying biomaterials leads to more effective cellular uptake of VLPs.

DISCUSSION

JC virus VP1 recombinantly expressed in *E. coli* spontaneously self-assembles into virus-like particles (VLPs), which can be isolated by CsCl density gradient centrifugation. Surface plasmon resonance (SPR) measurements indicated that the VLPs have specific affinity to the sialic acid moiety of glycoprotein. We investigated the immobilization of VLPs and their subsequent cellular uptake in approach (a) using a tissue culture polystyrene plate. A comparison of this approach with the control, approach (b), revealed that immobilized VLPs were incorporated into the cells with higher efficiency than were the diffusive VLPs suspended in solution. When VLPs are added to a solution, a limited number of VLPs can access the cell surface because of their Brownian movements. However, when introduced from a substrate, a large number of VLPs can spontaneously come into contact with the cellular surface, leading to more effective uptake. Another possible explanation of this enhanced cellular uptake from the substrate is cell adhesion. There have been some reports on reverse transfection showing that increased cell adhesiveness through the addition of an extracellular matrix (ECM) enhances gene expression (*36, 37*). In our study, cell adhesion to the VLP-coated substrates was actually increased in comparison to that to the untreated substrates (data not shown). This indicates that VLPs themselves acted as an ECM and strengthened cell adhesion, resulting in the enhanced cellular uptake of the VLPs.

Subsequent confocal laser microscopic observation indicated that VLPs introduced from the substrate were more dispersed into the nucleus than were those from the solution (Figure 6). In this study, we used JC virus-derived VLPs, containing a nuclear localizing signal at the C-terminus, known to localize in the nucleus after cellular uptake (*26*). We speculated that FITC-VLPs from the substrate could be localized into the nucleus faster than those from the solution since the cellular uptake from the substrate occurred more rapidly. Previously, Shea et al. demonstrated that the expression of immobilized DNAs leveled up to 100-fold greater than bulk delivery of DNAs (*38*). Our results showing rapid cellular uptake of VLPs from the substrate and subsequent dispersion into the nucleus could

explain the fact that substrate-mediated transfection induces efficient and enhanced gene expression.

We next proved that VLP formation was necessary for cellular uptake from the substrate. Even if VP1 pentamers bind to the receptors on the cell surface, they might be incapable of inducing structural change in the receptor, thus they cannot induce endocytosis. In addition, size effect is also important for the incorporation of VLPs. According to the report of Aoyama et al., the optimal size of nanoparticles for endocytosis is around 50 nm (*39*), which is almost the same size as that of the VLPs in this study.

Finally, PV-Sia was enzymatically synthesized and used for the immobilization of FITC-VLPs, resulting in enhancement of the cellular uptake of FITC-VLPs. Two factors are thought to be mainly responsible for this enhancement using PV-Sia: increased FITC-VLP immobilization and strengthened adhesion of seeded cells. Akaike et al. reported that PV-LA, a PV-sugar, acts as an ECM and enables progressive hepatocyte adhesion (*40*). This function of PV-sugar as an ECM might be crucial to the enhancement of cell adhesion. Though various factors are thought to contribute to the efficiency of cellular uptake, we demonstrated that increased VLP immobilization using sialic acid significantly increased the incorporation of VLPs from the substrate.

In conclusion, we report the efficient cellular uptake of immobilized VLPs. VLPs expressed in *E. coli* were labeled with FITC and immobilized on the substrate. Flow cytometric analysis and confocal laser microscopic observation revealed that immobilized VLPs were incorporated into the cells with higher efficiency than were diffusive VLPs suspended in solution. Our approach was extended to sialic acid-displaying surfaces aimed at increasing the number of FITC-VLPs immobilized on the substrate via the specific affinity between VLPs and sialic acid. These techniques have potential applications to the fabrication of cell microarray systems using VLPs as multiple carriers of nucleic acids, small molecules, and proteins.

ACKNOWLEDGMENT

We appreciate Associate Professor Yoshiko Miura of JAIST for kindly providing a PV-sugar sample. We also thank Professor Kohei Uosaki and Assistant Professor Satoru Takakusagi of Hokkaido University for their help with ellipsometric measurements. Noriko Ohtake and Tadaki Suzuki appreciate the financial support provided by JSPS. This study was supported in part by grants from the Program of Founding Research Centers for Emerging and Reemerging Infectious Diseases, MEXT, Japan.

Supporting Information Available: Details of experimental procedures and results for the characterization of synthetic polymers. This material is available free of charge via the Internet at http://pubs.acs.org.

LITERATURE CITED

(1) Wu, R. Z., Bailey, S. N., and Sabatini, D. M. (2002) Cell-biological applications of transfected-cell microarrays. *Trends Cell Biol. 12*, 485–488.

(2) Baghdoyan, S., Roupioz, Y., Pitaval, A., Castel, D., Khomyakova, E., Papine, A., Soussaline, F., and Gidrol, X. (2004) Quantitative analysis of highly parallel transfection in cell microarrays. *Nucleic Acids Res. 32*, e77.

(3) Fujimoto, H., Yoshizako, S., Kato, K., and Iwata, H. (2006) Fabrication of cell-based arrays using micropatterned alkanethiol monolayers for the parallel silencing of specific genes by small interfering RNA. *Bioconjugate Chem. 17*, 1404–1410.

(4) Ziauddin, J., and Sabatini, D. M. (2001) Microarrays of cells expressing defined cDNAs. *Nature 411*, 107–110.

(5) Segura, T., Volk, M. J., and Shea, L. D. (2003) Substrate-mediated DNA delivery: role of the cationic polymer structure and extent of modification. *J. Controlled Release 93*, 69–84.

(6) Bengali, Z., Pannier, A. K., Segura, T., Anderson, B. C., Jang, J. H., Mustoe, T. A., and Shea, L. D. (2005) Gene delivery through cell culture substrate adsorbed DNA complexes. *Biotechnol. Bioeng. 90*, 290–302.

(7) Okazaki, A., Jo, J., and Tabata, Y. (2007) A reverse transfection technology to genetically engineer adult stem cells. *Tissue Eng. 13*, 245–251.

(8) Bailey, S. N., Sabatini, D. M., and Stockwell, B. R. (2004) Microarrays of small molecules embedded in biodegradable polymers for use in mammalian cell-based screens. *Proc. Natl. Acad. Sci. U.S.A. 101*, 16144–16149.

(9) Hoff, A., Andre, T., Fischer, R., Voss, S., Hulko, M., Marquardt, U., Wiesmuller, K. H., and Brock, R. (2004) Chemolabile cellular microarrays for screening small molecules and peptides. *Mol. Diversity 8*, 311–320.

(10) Eash, S., Manley, K., Gasparovic, M., Querbes, W., and Atwood, W. J. (2006) The human polyomaviruses. *Cell. Mol. Life Sci. 63*, 865–876.

(11) Suzuki, S., Sawa, H., Komagome, R., Orba, Y., Yamada, M., Okada, Y., Ishida, Y., Nishihara, H., Tanaka, S., and Nagashima, K. (2001) Broad distribution of the JC virus receptor contrasts with a marked cellular restriction of virus replication. *Virology 286*, 100–112.

(12) Goldmann, C., Petry, H., Frye, S., Ast, O., Ebitsch, S., Jentsch, K. D., Kaup, F. J., Weber, F., Trebst, C., Nisslein, T., Hunsmann, G., Weber, T., and Luke, W. (1999) Molecular cloning and expression of major structural protein VP1 of the human polyomavirus JC virus: Formation of virus-like particles useful for immunological and therapeutic studies. *J. Virol. 73*, 4465–4469.

(13) Gee, G. V., Dugan, A. S., Tsomaia, N., Mierke, D. F., and Atwood, W. J. (2006) The role of sialic acid in human polyomavirus infections. *Glycoconjugate J. 23*, 19–26.

(14) Liu, C. K., Wei, G., and Atwood, W. J. (1998) Infection of glial cells by the human polyomavirus JC is mediated by an N-linked glycoprotein containing terminal alpha(2–6)-linked sialic acids. *J. Virol. 72*, 4643–4649.

(15) Garcea, R. L., and Gissmann, L. (2004) Virus-like particles as vaccines and vessels for the delivery of small molecules. *Curr. Opin. Biotechnol. 15*, 513–517.

(16) Georgens, C., Weyermann, J., and Zimmer, A. (2005) Recombinant virus like particles as drug delivery system. *Curr. Pharm. Biotechnol. 6*, 49–55.

(17) Abbing, A., Blaschke, U. K., Grein, S., Kretschmar, M., Stark, C. M. B., Thies, M. J. W., Walter, J., Weigand, M., Woith, D. C., Hess, J., and Reiser, C. O. A. (2004) Efficient intracellular delivery of a protein and a low molecular weight substance via recombinant polyomavirus-like particles. *J. Biol. Chem. 279*, 27410–27421.

(18) Bailey, S. N., Ali, S. M., Carpenter, A. E., Higgins, C. O., and Sabatini, D. M. (2006) Microarrays of lentiviruses for gene function screens in immortalized and primary cells. *Nat. Methods 3*, 117–122.

(19) Honma, K., Miyata, T., and Ochiya, T. (2004) The role of atelocollagen-based cell transfection array in high-throughput screening of gene functions and in drug discovery. *Curr. Drug Discovery Technol. 1*, 287–294.

(20) Nukuzuma, S., Yogo, Y., Guo, J., Nukuzuma, C., Itoh, S., Shinohara, T., and Nagashima, K. (1995) Establishment and characterization of a carrier cell culture producing high titres of polyoma JC virus. *J. Med. Virol. 47*, 370–377.

(21) Viscidi, R. P., Rollison, D. E. M., Viscidi, E., Clayman, B., Rubalcaba, E., Daniel, R., Major, E. O., and Shah, K. V. (2003) Serological cross-reactivities between antibodies to simian virus 40, BK virus, and JC virus assessed by virus-like-particle-based enzyme immunoassays. *Clin. Diagn. Lab. Immunol. 10*, 278–285.

(22) Komagome, R., Sawa, H., Suzuki, T., Suzuki, Y., Tanaka, S., Atwood, W. J., and Nagashima, K. (2002) Oligosaccharides as receptors for JC virus. *J. Virol. 76*, 12992–13000.

(23) Spiro, R. G. (1960) Studies on fetuin, a glycoprotein of fetal serum. I. Isolation, chemical composition, and physiochemical properties. *J. Biol. Chem. 235*, 2860–2869.

(24) Nilsson, B., Norden, N. E., and Svensson, S. (1979) Structural studies on the carbohydrate portion of fetuin. *J. Biol. Chem. 254*, 4545–4553.

(25) Okazaki, I., Hasegawa, Y., Shinohara, Y., Kamasaki, T., and Bhikhabhai, R. (1995) Determination of the interactions between lectins and glycoproteins by surface plasmon resonance. *J. Mol. Recognit. 8*, 95–99.

(26) Qu, Q., Sawa, H., Suzuki, T., Semba, S., Henmi, C., Okada, Y., Tsuda, M., Tanaka, S., Atwood, W. J., and Nagashima, K. (2004) Nuclear entry mechanism of the human polyomavirus JC virus-like particle: role of importins and the nuclear pore complex. *J. Biol. Chem. 279*, 27735–27742.

(27) Kobayashi, K., Sumitomo, H., and Ina, Y. (1985) Synthesis and functions of polystyrene derivatives having pendant oligosaccharides. *Polym. J. (Tokyo) 17*, 567–575.

(28) Miura, Y., Ikeda, T., Wada, N., Sato, H., and Kobayashi, K. (2003) Chemoenzymatic synthesis of glycoconjugate polymers: greening the synthesis of biomaterials. *Green Chem. 5*, 610–614.

(29) Wataoka, I., Urakawa, H., Kobayashi, K., Akaike, T., Schmidt, M., and Kajiwara, K. (1999) Structural characterization of glycoconjugate polystyrene in aqueous solution. *Macromolecules 32*, 1816–1821.

(30) Tobe, S., Takei, Y., Kobayashi, K., and Akaike, T. (1992) Receptor-mediated formation of multilayer aggregates of primary cultured adult rat hepatocytes on lactose-substituted polystyrene. *Biochem. Biophys. Res. Commun. 184*, 225–230.

(31) Lee, J. S., Kim, S. H., Kim, Y. J., Akaike, T., and Kim, S. C. (2005) Hepatocyte adhesion on a poly[N-p-vinylbenzyl-4-O-beta-D-galactopyranosyl-D-glucoamide]-coated poly(L-lactic acid) surface. *Biomacromolecules 6*, 1906–1911.

(32) Kornfeld, K., Reitman, M. L., and Kornfeld, R. (1981) The carbohydrate-binding specificity of pea and lentil lectins. Fucose is an important determinant. *J. Biol. Chem. 256*, 6633–6640.

(33) Yamasaki, N., Absar, N., and Funatsu, G. (1985) Ultraviolet difference spectroscopic analysis of the saccharide-binding properties of Ricinus communis agglutinin. *Biochim. Biophys. Acta 828*, 155–161.

(34) Shinohara, Y., Sota, H., Kim, F., Shimizu, M., Gotoh, M., Tosu, M., and Hasegawa, Y. (1995) Use of a biosensor based on surface plasmon resonance and biotinyl glycans for analysis of sugar binding specificities of lectins. *J. Biochem. (Tokyo) 117*, 1076–1082.

(35) Peters, B. P., and Aronson, N. N., Jr (1976) Reactivity of the sialic acid derivative 5-acetamido-3, 5-dideoxy-L-arabino-heptulosonic acid in the resorcinol and thiobarbituric acid assays. *Carbohydr. Res. 47*, 345–353.

(36) Yoshikawa, T., Uchimura, E., Kishi, M., Funeriu, D. P., Miyake, M., and Miyake, J. (2004) Transfection microarray of human mesenchymal stem cells and on-chip siRNA gene knockdown. *J. Controlled Release 96*, 227–232.

(37) Uchimura, E., Yamada, S., Uebersax, L., Yoshikawa, T., Matsumoto, K., Kishi, M., Funeriu, D. P., Miyake, M., and Miyake, J. (2005) On-chip transfection of PC12 cells based on the rational understanding of the role of ECM molecules: efficient, non-viral transfection of PC12 cells using collagen IV. *Neurosci. Lett. 378*, 40–43.

(38) Segura, T., and Shea, L. D. (2002) Surface-tethered DNA complexes for enhanced gene delivery. *Bioconjugate Chem. 13*, 621–629.

(39) Osaki, F., Kanamori, T., Sando, S., Sera, T., and Aoyama, Y. (2004) A quantum dot conjugated sugar ball and its cellular uptake. On the size effects of endocytosis in the subviral region. *J. Am. Chem. Soc. 126*, 6520–6521.

(40) Hoshiba, T., Cho, C. S., Murakawa, A., Okahata, Y., and Akaike, T. (2006) The effect of natural extracellular matrix deposited on synthetic polymers on cultured primary hepatocytes. *Biomaterials 27*, 4519–4528.

BC700348G

Multifunctional Chimeric Proteins for the Sequential Regulation of Neural Stem Cell Differentiation

Tadashi Nakaji-Hirabayashi, Koichi Kato, Yusuke Arima, and Hiroo Iwata*

Institute for Frontier Medical Sciences, Kyoto University, 53 Kawahara-cho, Shogoin, Sakyo-ku, Kyoto 606-8507, Japan.
Received September 13, 2007; Revised Manuscript Received October 30, 2007

Controlling the dynamics of growth factor signaling is a challenge in regenerative medicine for various tissues including the central nervous system. Here, we report on the development of the biomolecular system that facilitates sequential regulation of growth factor signals acting on neural stem/progenitor cells. Recombinant technology was employed to synthesize the multifunctional chimeric protein that contained multiple domains, including epidermal growth factor (EGF), ciliary neurotrophic factor (CNTF), globular capping domain, thrombin-cleavable sequence, and substrate-binding domain with affinity for Ni(II) ions. The chimeric protein is expected to expose CNTF upon elimination of the capping domain by digestion with endogenous thrombin in vivo. When the multifunctional chimeric protein was immobilized onto a substrate through the coordination of the substrate-binding domain with surface-immobilized Ni(II) ions, the substrate served to proliferate neural stem cells, maintaining the population of undifferentiated cells at 85%. This effect is primarily due to the activity of EGF, while CNTF activity is temporally veiled with the capping domain. Upon digesting the thrombin-cleavable sequence to remove the capping domain, the activity of CNTF emerged to induce differentiation of astrocytes in situ from the proliferated neural stem cells. The fraction of differentiated astrocytes reached 68% of total cells. These results demonstrate the feasibility of the system for controlling the dynamics of growth factor signals.

INTRODUCTION

Transplantation of neural progenitor cells is considered a potential modality for the structural and functional restoration of the central nervous system (CNS) (*1, 2*). An alternative strategy is to recruit and stimulate endogeneous neural stem cells (NSCs) by the local administration of appropriate agents (*3*). In these approaches, the tight regulation of transplanted or recruited cell behavior is a challenging task because cell proliferation, migration, differentiation, and network formation must be regulated temporally and spatially for orchestrating the chronological processes toward tissue reconstruction (*4, 5*).

In the mammalian CNS, a variety of neurotrophins and mitogens operate in a time-dependent manner to modulate the dynamics of cellular differentiation and tissue organization (*6*). Toward the regeneration of neural tissues, the transplantation of cells with biomaterials that provide microenvironments mimicking natural extracellular stimuli may improve the outcome after transplantation. To date, biodegradable scaffolds that incorporate adhesive peptides (*7, 8*), growth factors (*9*), and Notch ligands (*10*) were reported for this purpose. However, the biomaterials that facilitate the temporal regulation of multiple signal presentation remain to be developed for more precisely modulating the hierarchically complex process of tissue reorganization.

In this study, we aimed at establishing the chimeric protein system that permits the switching of growth factor presentation for the tightly regulated proliferation and differentiation of NSCs. Our approach is to utilize the multifunctional chimeric protein (MCP) that contains two different growth factors fused to each other. To sequentially regulate the signaling of two growth factors, the terminal of the second growth factor is capped by a globular polypeptide with a protease-cleavable linker peptide in between so that the capping polypeptide temporally hinders the active site of the second growth factor until the linker is cleaved by protease. The MCP further contains a peptide sequence that binds specifically to substrates for the oriented presentation of the protein. Such a MCP was rationally designed and synthesized using recombinant technology.

Our future goal is to extend this system for use in tissue engineering of the central nervous system. The MCP will be incorporated into biodegradable polymer networks carrying its binding site and used as a scaffold for neural stem/progenitor cells. Because the sequential administration of multiple growth factors requires repeated intervention to the brain, a single component system such as MCP will have an advantage in such an application. As a key component, a thrombin-cleavable peptide is incorporated to the MCP. To optimize the dynamics of growth factor actions, the peptide sequence can be readily replaced with peptides cleavable with other proteases involved in tissue reconstruction processes such as matrix metalloproteinases.

To examine the feasibility of our approach, we synthesized the chimeric protein that contains epidermal growth factor (EGF) and ciliary neurotrophic factor (CNTF). It is reported that EGF exhibits mitogenic activity for NSCs (*11*), while CNTF promotes the glial specification of NSCs (*11*). To elicit the effects of growth factor switching, several types of control proteins were synthesized, and all of these proteins were subjected to biological assays using the cell-based microarray method (*12*). The MCP was further immobilized onto glass-based substrates for quantitative assays. The results of these assays provided a proof of principle for our approach toward the sequential regulation of NSC differentiation.

EXPERIMENTAL PROCEDURES

Chimeric Proteins. Figure 1 shows the domain structure of MCP and control proteins synthesized in this study. The MCP contains full length sequences of human CNTF (200 aa) and human EGF (53 aa). These polypeptides were linked with a

* To whom correspondence should be addressed. Tel: +81-75-751-4119. Fax: +81-75-751-4119. E-mail: iwata@frontier.kyoto-u.ac.jp.

10.1021/bc700355t CCC: $40.75 © 2008 American Chemical Society
Published on Web 01/11/2008

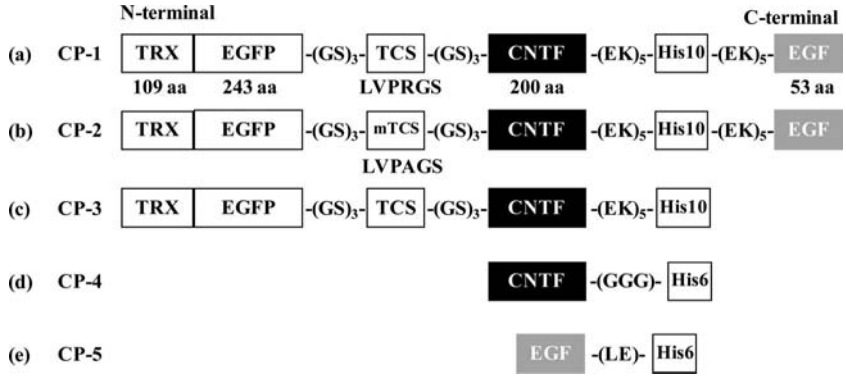

Figure 1. Domain structure of multifunctional chimeric proteins (CP-1) and control proteins (CP-2 to CP-5) synthesized in this study. TRX, thioredoxin; EGFP, enhanced green fluorescent protein; TCS, thrombin cleavage site; mTCS, mutated-TCS; CNTF, ciliary neurotrophic factor; EGF, epidermal growth factor.

decahistidine linker sequence (His10) that facilitates specific binding of the chimeric protein to the substrates carrying Ni(II) ions through coordination (*13*). As a capping polypeptide, enhanced green fluorescent protein (EGFP; 243 aa) was fused to the N-terminal of CNTF with a thrombin-cleavable site (TCS; LVPRGS) (*14*) incorporated in between. At the N-terminal of EGFP, thioredoxin (TRX; 109 aa) was further added because this polypeptide is frequently used to enhance the solubility of fusion partners (*15*). In addition, amino acid sequences, $(GS)_3$ and $(EK)_5$ (*16*), were inserted at both ends of TCS and His10, respectively, as flexible linkers. The total number of amino acid residues reached 668 aa. The MCP protein is referred to as CP-1. The other control proteins include a MCP with a mutated TCS (mTCS; LVPAGS) instead of the authentic TCS described above (Figure 1b; CP-2), a MCP lacking EGF (Figure 1c; CP-3), and either EGF or CNTF fused with a hexahistidine sequence (Figure 1d and e; CP-4 and CP-5, respectively).

Outline of the preparation of chimeric genes is depicted in Figure S1 (Supporting Information). Sequences of primers and oligonucleotides used for the construction of the CP-1 gene are shown in Table S1 (Supporting Information). The conditions of thermal cycling employed in polymerase chain reaction (PCR) amplification are shown in Table S2 (Supporting Information). First, synthetic oligonucleotides were subjected to overlap extension and PCR to prepare DNA encoding an $(EK)_6$-His10-$(EK)_6$ sequence containing an EcoR I site at the 5′-end and 22-mer oligonucleotides at the 3′-end that overlapped with the 5′-region of the EGF gene. The EGF gene was amplified by PCR from pET-22b-EGF (*12*) using specific primer sets (Table S1). The 5′-end of the forward primer was flanked with 20-mer oligonucleotides that overlapped with the 3′-region of $(EK)_6$-His10-$(EK)_6$. In addition, the reverse primer contained the Xho I site at the 5′-end. The products of overlap extension PCR were annealed, extended again by overlap extension, and amplified by PCR to obtain the $(EK)_6$-His10-$(EK)_6$-EGF gene. The chimeric gene was digested with EcoR I and Xho I and unidirectionally ligated to the pET-32b vector (Novagen) previously digested with the same restriction enzymes. The plasmid (pET-32b-His10-EGF) was cloned in *Escherichia coli* (*E. coli*) strain DH5α and purified with Qiagen MiniPrep Purification Kit. The correctness of the chimeric gene was checked by sequencing.

At the second step, cDNAs for EGFP and CNTF were amplified by PCR from pEGFP-C1 (Clontech) and pET-16b-NidLBD-CNTF (*18*), respectively. The forward primer used for the EGFP gene contained the Msc I site, while the reverse primer contained a sequence for $(GS)_3$-TCS-$(GS)_3$ and a 21-mer sequence that overlapped with the 5′-region of the CNTF gene. Similarly, the forward primer used for the CNTF gene contained a 22-mer sequence that overlapped with 3′-region of the EGFP gene and a sequence for $(GS)_3$-TCS-$(GS)_3$, while the reverse primer contained the EcoR I site. The PCR products were annealed, extended by overlap extension, and amplified by PCR to obtain the EGFP-$(GS)_3$-TCS-$(GS)_3$-CNTF gene. The chimeric gene was digested with Msc I and EcoR I and unidirectionally ligated downstream of the TRX sequence in pET-32b-His10-EGF linearized by digesting with the same restriction enzymes. The plasmid was cloned in *E. coli* strain DH5α and purified with Qiagen MiniPrep Purification Kit. The correctness of the chimeric gene was checked by sequencing.

For constructing the plasmid for CP-2, the EGFP-$(GS)_3$-mTCS-$(GS)_3$-CNTF gene was prepared using primers with mutation in the TCS site. First, EGFP-$(GS)_3$-mTCS and mTCS-$(GS)_3$-CNTF genes were amplified using pET-32b-EGFP-TCS-CNTF-His10-EGF as a template. Amplified DNAs were extended by overlap extension PCR to obtain EGFP-$(GS)_3$-mTCS-$(GS)_3$-CNTF and inserted into the Msc I-EcoR I site of pET-32b-His10-EGF. For CP-3, EGFP-$(GS)_3$-TCS-$(GS)_3$-CNTF was inserted downstream of TRX in original pET-32b. The gene for CP-4 was amplified by PCR from pET-16b-NidLBD-CNTF (*18*) and ligated to Nde I-Xho I sites in pET-22b (Novagen). For CP-5, previously constructed pET-22b-EGF (*12*) was used.

The MCP (CP-1) and control proteins (CP-2 to CP-5) were expressed in *E. coli* strain BL21-CodonPlus (Stratagene) using Overnight Express Autoinduction System (Novagen). The MCP and control proteins obtained as inclusion bodies were extracted with 8 M urea and purified by Ni-chelated affinity chromatography (His Trap HP column; Amersham) using a Prime AKTA chromatography system (Amersham). These proteins were refolded by dialyzing against a solution of reduced and oxidized forms of glutathione. The details of dialysis conditions are provided in Table S3 (Supporting Information). The purity and the molecular size of MCP and control proteins were analyzed by sodium dodecylsulfate−polyacrylamide gel electrophoresis (SDS−PAGE). The biological activity of EGF contained in MCP and control proteins was assessed from the mitogenic activity in neurosphere culture (*19*). The biological activity of CNTF contained in CP-1, CP-3, and CP-4 was assessed from the efficiency of glial induction from NSCs cultured on fibronectin-coated dishes (*19*). The assays for CNTF activity in CP-1 and CP-3 were conducted after the capping domain was removed by thrombin digestion.

Thrombin Digestion. MCP and control proteins (MCP with mTCS and EGF-deficient MCP) were separately dissolved to the concentration of 50 μg/mL in 20 mM tris-HCl buffer (pH 8.4) containing 0.6 unit/mL thrombin from bovine serum (POLA Pharma, Tokyo, Japan), 150 mM NaCl, and 2.5 mM $CaCl_2$. The mixed solutions were kept at 37 °C for typically 45 min to allow for the digestion of TCS. The reaction was stopped by adding an equal volume of SDS−PAGE sample buffer contain-

ing 10% β-mercaptoethanol. The digestion products were analyzed by SDS−PAGE with coomassie brilliant blue (CBB) staining.

Microarray Preparation. Microarrays were prepared as reported previously (*10*). In brief, a thin gold film was deposited on two types of glass plates: glass slides (26 × 22 × 0.5 mm; Matsunami Glass Ind., Ltd., Osaka, Japan) for cell culture and S-LAL10 glass plates (25 × 25 × 1 mm, reflective index = 1.720) for surface plasmon resonance (SPR) imaging. The self-assembled monolayer (SAM) of 1-hexadecanethiol was prepared on gold and photolytically micropatterned to create an array of 4 × 4 circular spots (2 mm in diameter and 4 mm in center-to-center distance) presenting bare gold. Then, the SAM of 11-mercapto-1-undecanoic acid was formed within the spots. The carboxylic acid within spots was derivatized with *N*-(5-amino-1-carboxypentyl) iminodiacetic acid and then chelated with Ni(II) ions. Solutions of MCP and control proteins (7 μM) in phosphate buffered saline (PBS) were manually pipetted (1.2 μL per spot) to separate spots on a single plate under sterile conditions. The plate was kept at room temperature for 2 h to allow the binding of decahistidine or hexahistidine sequence to the surface-immobilized Ni(II) ions. Finally, the plate was washed with PBS to remove unreacted proteins. Prior to cell culture experiments, the protein-immobilized plates were blocked with 2% Pluronic F127 (Sigma) solution.

Surface Plasmon Resonance (SPR). SPR imaging was performed to detect immobilized proteins on the microarray. The details of a homemade SPR imaging apparatus are reported elsewhere (*20*). A protein-immobilized array prepared as described above was mounted on a triangular glass prism. A p-polarized, collimated white light was radiated to the back of the array through the prism (Kretschmann configuration) at a constant incident angle ca. 0.5° smaller than the angle for the occurrence of surface plasmon resonance at the region between spots on the array. To obtain a two-dimensional (2D) reflection image, reflected light was passed through a narrow band interference filter (center wavelength: 905 nm) and then collected with a charge-coupled device (CCD; C2400–79, Hamamatsu Photonics). The reflection image represents local changes in the reflective index in the vicinity of the sample surface and hence reflects the distribution of protein over the microarray. Imaging was carried out under PBS at 30 °C.

For monitoring protein immobilization and thrombin digestion, a homemade SPR sensor (*21*) was used. A Ni(II)-chelated surface was prepared using mixed SAM consisting of 16-mercapto-1-hexadecanoic acid and (1-mercaptoundec-11-yl) triethyleneglycol (molar ratio, 1:9) formed on the entire surface of a BK7 glass plate (25 × 25 × 1 mm, reflective index = 1.515) by chemistry similar to that described above. The plate was mounted to the SPR sensor with a flow cell, and the resonance angular shift was continuously monitored during the following procedures. After equilibrating with PBS, the surface was exposed to 10 mg/mL bovine serum albumin solution in PBS in a flow cell for 10 min, and then pure PBS was circulated for 5 min to wash the surface. PBS was switched with 20 mM sodium phosphate buffer (pH 7.4) containing 20 mM imidazole (binding buffer) and circulated for 7 min, then 50 μg/mL MCP solution in binding buffer was circulated for 45 min followed by washing with pure binding buffer for 10 min. The surface was then exposed to 0.5 unit/mL thrombin solution in binding buffer for 50 min and washed with pure binding buffer. Finally, 20 mM sodium phosphate buffer (pH 7.4) containing 500 mM imidazole was circulated for 25 min to desorb protein fragments remaining on the surface and then switched with fresh PBS. The resonance angular shift was converted to the surface density of protein, assuming the unit angular shift of 0.5 μg/cm^2/DA (*22*).

Cell Isolation and Culture. The striatum was isolated from the fetuses (E16) of Fischer344 rats according to the guidelines of the Animal Welfare Committee of the institute and dissociated into single cells by treating with 0.05% trypsin solution containing 0.53 mM ethylenediamine-*N*,*N*,*N*′,*N*′-tetraacetic acid (EDTA). The single cells obtained were suspended in DMEM/F12 (1:1) (Gibco) containing 5 μg/mL heparin, 100 unit/mL penicillin, and 100 μg/mL streptomycin (base medium), supplemented with 2% B27 supplement (Gibco), 20 ng/mL basic fibroblast growth factor (bFGF), and 20 ng/mL EGF, and cultured for 4–5 days to form neurospheres.

Neurospheres at passage 2 were dissociated into single cells by treating with 0.05% trypsin-EDTA solution. The cells were suspended in the base medium containing 2% B27 supplement and then seeded onto the microarrays or the protein-immobilized glass plates at 3.0 × 10^4 cells/cm^2. The cells were cultured in an incubator at 37 °C under 5% CO_2. After 3 days, 1 unit/μL thrombin solution was added to the medium to a final concentration of 0.6 unit/mL and incubated for 45 min at 37 °C under 5% CO_2, followed by washing with base medium to remove thrombin. Then, fresh base medium containing 2% B27 supplement was added to the culture, and cells were incubated for an additional 2–3 days at 37 °C under 5% CO_2. Finally, cells were washed gently with DMEM/F12 (1:1) to remove weakly adhering cells and observed with a phase-contrast optical microscope (DP51, Olympus Optical CO., Ltd., Tokyo, Japan).

Immunocytochemistry. Cells on the substrate were fixed with PBS containing 4% paraformaldehyde and 0.1% glutaraldehyde, and permeabilized by treating with 0.5% TritonX-100 solution at room temperature for 20 min. Then, the cells were treated with 2% skim milk solution for 2 h to block nonspecific adsorption of antibodies, followed by binding of primary antibodies against nestin (1:200, mouse monoclonal Rat 401, BD Pharmingen), glial fibrillary acidic protein (GFAP, mouse monoclonal, MAB3402, Chemicon), or class III β-tubulin (βIII; 1:600, rabbit polyclonal, Covance, Princeton, NJ) for 1 h at room temperature. After washing with PBS containing 0.05% Tween-20, cells were treated by Alexa Fluor 594 antimouse IgG and Alexa Fluor 488 antirabbit IgG (both from Molecular Probes) at a dilution of 1:500 for 1 h at room temperature and washed with PBS containing 0.05% Tween-20. Then, cell nuclei were counterstained with 1 mg/mL Hoechst33258. The localization of secondary antibodies was analyzed with an epifluorescent microscope (DP70, Olympus). Cells reactive for antibodies against nestin, GFAP, and βIII were counted on the microphotographs for the area of 340 × 460 μm^2, which contained at most approximately 500 total cells. Cells were counted on five different microphotographs obtained from the same sample, and these data were averaged. The data are shown as the mean ± standard deviation for five independent samples.

Gene Expression Analysis. Total RNA was isolated from cells cultured on the protein-immobilized surfaces using the SV Total RNA Isolation system (Promega), and 100 ng RNA was used per reverse transcription (RT) reaction using Ready-to-Go You-Prime First-Strand Beads (Amersham) primed by oligo(dT)$_{15}$ (Promega). First-strand cDNA was then amplified by PCR using the specific primers listed in Table S4 (Supporting Information). The number of thermal cycles was determined so as to maintain the targeted sample population in the exponential amplification phase for each gene. All samples were run in triplicate, and the products were analyzed by electrophoresis in 2% agarose gel with ethidium bromide staining. Glyceraldehyde-3-phosphate dehydrogenase (GAPDH) was also

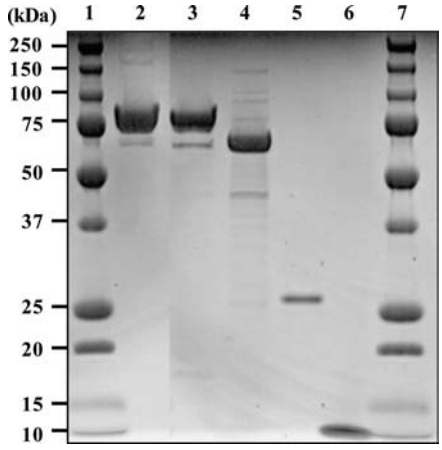

Figure 2. SDS−PAGE analysis of MCP and control proteins expressed in *E. coli* and purified by metal chelate chromatography. Proteins were electrophoresed in 12.5% polyacrylamide gel at 200 V for 40 min and visualized by CBB staining. Lanes 1 and 7, molecular weight standard; lane 2, CP-1; lane 3, CP-2; lane 4, CP-3; lane 5, CP-4; and lane 6, CP-5.

amplified as the reference gene. The electrophoresed DNA was imaged with Gel Doc 2000 and Integration Control Unit (Bio-Rad).

RESULTS

Characterization of Chimeric Proteins. Figure 2 shows the result of SDS−PAGE analysis for the MCP and control proteins. The molecular weight estimated from the mobility of protein bands are as follows: CP-1 (79 kDa), CP-2 (79 kDa), CP-3 (63 kDa), CP-4 (26 kDa), and CP-5 (7.5 kDa). Because low molecular weight CP-5 could not be separated appropriately with 12.5% polyacrylamide gel (Figure 2, lane 6), SDS−PAGE was additionally performed for CP-5 with 16% polyacrylamide gel to more precisely determine the molecular size (Figure S2, Supporting Information). The molecular weights estimated for CP-1 to CP-5 are in accordance with those expected from the theoretical amino acid numbers. These chimeric proteins exhibited the bioactivity of CNTF and/or EGF when qualitatively assessed in proliferation and differentiation assays with NSCs (data not shown). In CP-5, hexahistidine sequence was fused to the C-terminal of EGF, whereas decahistidine sequence was fused to the N-terminal of EGF in CP-1 and CP-2. Our separate experiments showed that the differences in the length and the position of a histidine tag had minor effects on the bioactivity of EGF fusions (data not shown).

CP-1, CP-2, and CP-3 were digested with 0.6 unit/mL thrombin at 37 °C for 45 min. Digested products were analyzed by SDS−PAGE (Figure 3). As shown in Figure 3A, digestion of CP-1 resulted in the formation of protein fragments of approximately 40 and 35 kDa, corresponding to the N- and C-terminal regions spanning from TCS, respectively. Similarly, CP-3 produced approximately 40 kDa (from N-terminal to TCS) and 25 kDa fragments (from TCS to C-terminal) (Figure 3C). In contrast, CP-2 containing mTCS (LVPAGS) remained intact even after treatment with thrombin (Figure 3B). These results are reasonable because thrombin recognizes the TCS (LVPRGS) to hydrolyze the peptide bond between arginine and glycine (*14*). There is no consensus sequence in the other regions of CP-1. Thrombin digestion of CP-1, CP-2, and CP-3 in a culture medium gave results similar to those in buffer solution (Figure S3, Supporting Information). The higher concentration of thrombin (5 unit/mL) or prolonged reaction (90 min at 0.6 unit/mL) gave rise to the formation of much smaller fragments (data not shown), probably because of nonspecific hydrolysis at other arginine−glycine linkages contained in the proteins. In addition, NSCs cultured on the CP-1-immobilized surface (see below for immobilization) were totally detached from the substrate upon contacting with 1.5 unit/mL thrombin. From these findings, we decided to digest the TCS with 0.6 unit/mL thrombin for 45 min in the later experiments.

Immobilization of Chimeric Proteins. Chimeric proteins were immobilized on the micropatterned surface through the coordination of His10 with Ni(II) ions fixed on the spots. A microarray thus obtained was analyzed with the SPR imaging technique (Figure 4A). As can be seen, brightness is higher in all of the protein-immobilized spots than in the control spot, confirming the immobilization of proteins. The intensity of reflected light is varied depending on the amount of chimeric proteins immobilized (Figure 4B), with a linear correlation to the molecular size of immobilized proteins.

To examine whether the capping domain can be removed from the immobilized chimeric protein by thrombin digestion, the immobilization of CP-1 and its digestion were performed in a flow cell of the SPR sensor while resonance angular shift was monitored. As can be seen from the sensorgram (Figure 5), CP-1 was immobilized to the Ni(II)-chelated surface pretreated with BSA. The resonance angular shift due to CP-1 immobilization reaches 1.4 DA, which corresponds to the surface density of 0.7 μg/cm^2 (*22*). The resonance angle was gradually reduced by exposing the surface to thrombin solution ($g \rightarrow h$ in Figure 5). The ratio of the resonance angular shifts due to decapping and total recovery of decapped CP-1 by imidazole exposure was determined to be 0.57, which is in accordance with the ratio (0.54) of the numbers of amino acid residues corresponding to N- and C-terminal regions spanning from TCS. These results indicate that TCS was cleaved by thrombin, leaving decapped CP-1 on the surface.

Microarray-Based Assay. NSCs were cultured on the microarray that displayed MCP and control proteins. The microarray also contained spots onto which CP-3 and CP-5 or CP-4 and CP-5 were coimmobilized from their equimolar mixture. After a 3-day culture, an entire array was treated with 0.6 unit/mL thrombin for 45 min, and then cells were cultured for an additional 2 days. Markers for undifferentiated cells (nestin) and differentiated neurons (βIII) and astrocytes (GFAP) were immunologically stained, while nuclei were stained with Hoechst dye (Figure 6). The microarray-based method facilitated parallel and rapid assays under the same conditions for every experimental variation. Furthermore, the planar surface of the microarrays enabled us to distinguish reasonably small differences in marker expression, in marked contrast to the conventional culture systems with plastic dishes or microplates.

As shown in Figure 6A, substantial numbers of cells are seen on the spots with immobilized CP-1, CP-2, and CP-5. In contrast, a few cells are seen on the spots with CP-3, CP-4, CP-3/CP-5, and CP-4/CP-5, being similar to the spot with bare SAM. Taking into account the structure of chimeric proteins, these results indicate that the presence of the EGF domain is crucial for the effective adhesion and proliferation of the cells. This is reasonable because NSCs are considered to be trapped initially on the surface by EGF−EGF receptor (EGFR) interactions, receiving the EGF signal for proliferation (*17*). However, the coimmobilization of CP-5 could not improve cell adhesion and proliferation on the spots with CP-3/CP-5 and CP-4/CP-5. Because coimmobilization requires separate binding sites for each component, the surface density of coimmobilized CP-5 on the spots with CP-3/CP-5 and CP-4/CP-5 may be smaller than that on the spot with CP-5 alone. This is confirmed by the observation (Figure 4B) that the total amount of proteins on spots with CP-3/CP-5 and CP-4/CP-5 was approximately half

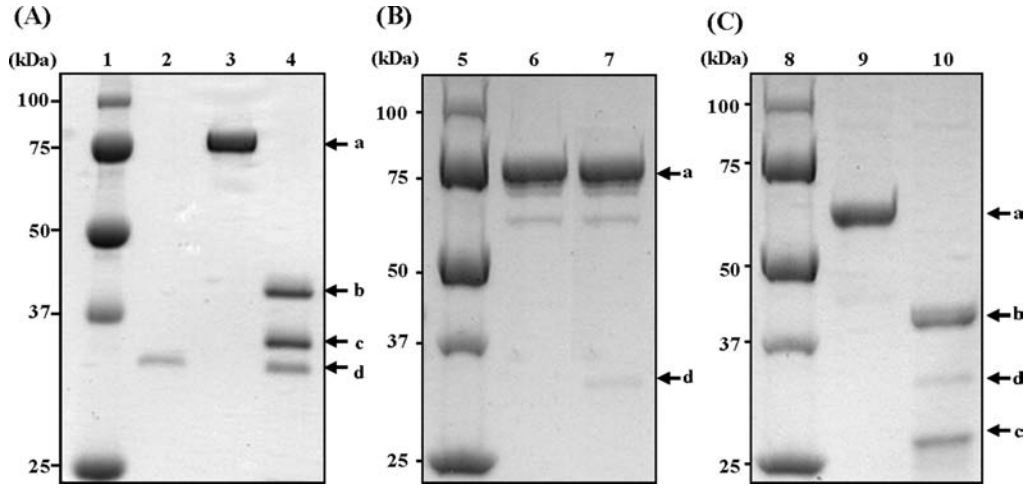

Figure 3. SDS−PAGE analysis of chimeric proteins digested by thrombin. (A) CP-1, (B) CP-2, and (C) CP-3 were digested with 0.6 unit/mL thrombin at 37 °C for 45 min. Then the products were analyzed with SDS−PAGE with 12.5% polyacrylamide gels with CBB staining. Lanes 1, 5, and 8, molecular weight standard; lane 2, thrombin; lane 3, 6, and 9, intact protein; lane 4, 7, and 10, proteins digested with thrombin. Arrows represent the protein band for (a) intact protein, (b and c) digested fragments, and (d) thrombin.

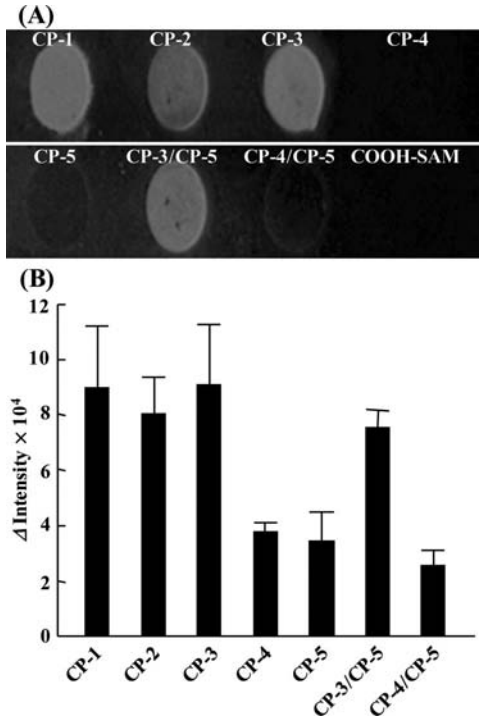

Figure 4. Surface plasmon resonance (SPR) imaging of the microarray. (A) SPR image of the microarray onto which various chimeric proteins were immobilized. Protein identification was indicated on the image. CP-3/CP-5 and CP-4/CP-5 represent the fact that equimolar mixtures of these proteins were used for immobilization. COOH-SAM represents a control spot without immobilized protein. (B) Intensity of reflected light determined on the spots. The difference from the intensity on the control spot (COOH-SAM) was plotted. The data are expressed as the mean ± standard deviation for three independent experiments.

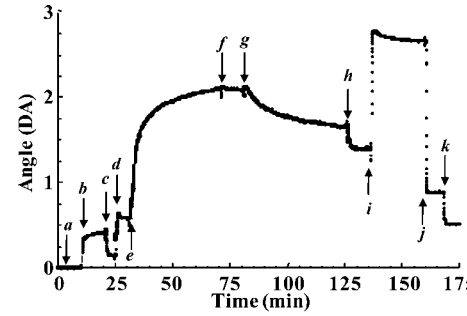

Figure 5. Surface plasmon resonance (SPR) analysis for the immobilization and thrombin treatment of multifunctional chimeric protein. Arrows (a−k) represent the time when the following solutions were injected to the Ni(II)-chelated surface: (a) PBS, (b) 1% BSA in PBS, (c) PBS, (d) 20 mM sodium phosphate containing 20 mM imidazole (pH 7.4; binding buffer), (e) 50 μg/mL CP-1 in binding buffer, (f) binding buffer, (g) 0.6 unit/mL thrombin solution in binding buffer, (h) binding buffer, (i) 20 mM sodium phosphate containing 500 mM imidazole (pH 7.4), (j) binding buffer, and (k) PBS.

of the sum on the spots with CP-3 and CP-5 and on the spots with CP-4 and CP-5, respectively.

The results of immunocytochemical staining are shown in Figure 6B and C. The comparison between Figure 6A and B shows that the majority of cells expressed nestin regardless of the spots. A striking result is that GFAP expression is most notable on the spot with CP-1 and moderate to negligible on the other spots (Figure 6C). Given the fact that CNTF strongly induces astrocytic differentiation from NSCs (*11*), the result just described gives evidence that the CNTF domain in the immobilized CP-1 was unveiled upon decapping to act effectively on the cells.

Quantitative Assay of Differentiation. Cells were cultured on the glass substrate onto which CP-1 was immobilized (Figure 7). In this experiment, the entire surface of a glass plate was modified with the protein for precise quantification. The results of comparable experiments for the CP-5-immobilized substrate are given in Figure S4 (Supporting Information). From these microphotographs, the total number of cells and the fraction of cells positive for nestin, βIII, and GFAP were determined (Figure 8). On the CP-5-immobilized surface, cells proliferated rapidly, and more than 95% of total cells expressed nestin with negligible expression of βIII and GFAP (<5% for both markers), being in good agreement with our previous study (*17*). Cells on the CP-1-immobilized surfaces reduced their proliferation rate and the level of nestin expression (85%). This is probably due to the effect that a large globular polypeptide (TRX-EGFP-TCS-CNTF) in CP-1 reduces the surface density of the EGF domain, compared to the surface with CP-5 alone. On the CP-1-immobilized surface, the expression of βIII was at a low level, similar to the surface with CP-5. However, a large number of cells expressed GFAP when the substrate was treated with thrombin (68 ± 3.9%). This result suggests that a large part of

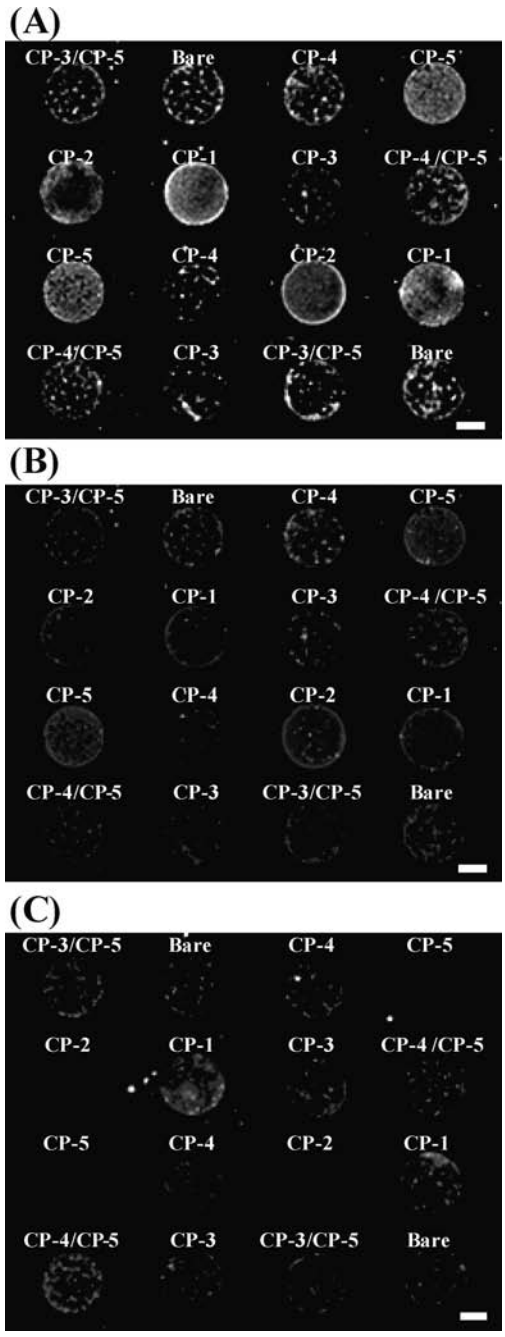

Figure 6. Fluorescent microphotographs of cells cultured for 6 days on the microarray that displayed various chimeric proteins. (A) Nuclear staining with Hoechst. Immunocytochemical staining of (B) nestin and (C) GFAP. The immobilized proteins are indicated above each spot. Bare represents spots with a pristine SAM terminated with carboxylic acid. Scale bar: 1 mm.

cells expressed both nestin and GFAP. In contrast, a smaller number of cells expressed GFAP (18 ± 2.4%), when thrombin treatment was omitted. These results again demonstrate that CNTF action can be temporally controlled by thrombin digestion. However, the number of GFAP-expressing cells is significantly larger than that for the surface with immobilized CP-5 (2.7 ± 1.8%).

Analysis of Gene Expression. In Figure 9, the results of semiquantitative RT-PCR are shown for cells obtained after a 6-day culture on the CP-1-immobilized surfaces with and without thrombin treatment. For comparison, data are further shown for cells cultured on the CP-5-immobilized surface for 5 days and for cells immediately after neurosphere culture.

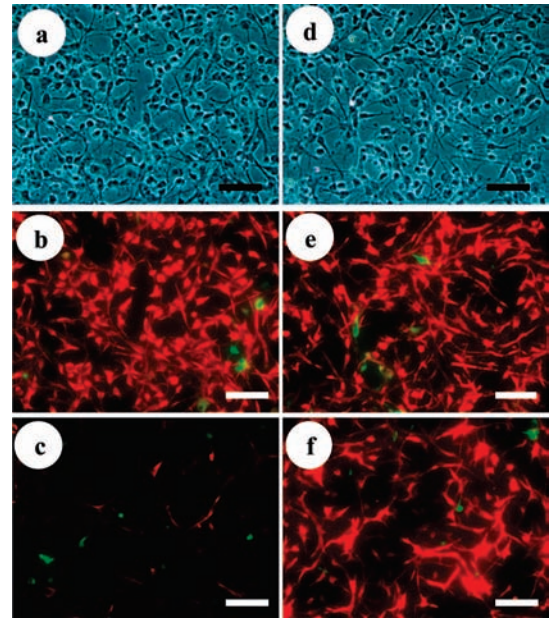

Figure 7. Immunocytochemistry of NSCs cultured on the CP-1-immobilized surfaces with or without thrombin digestion. (a−c) Cells were stained 6 days after cell seeding without thrombin treatment. (d−f) Cells were cultured for 3 days, treated with 0.6 unit/mL thrombin at 37 °C for 45 min, and then additionally cultured for 3 days. Images a and d are recorded at the same view as that for b and e, respectively. Cells were stained with antibodies against (b and e) nestin (red) and βIII (green), and (c and f) GFAP (red) and βIII (green). Scale bar: 100 μm.

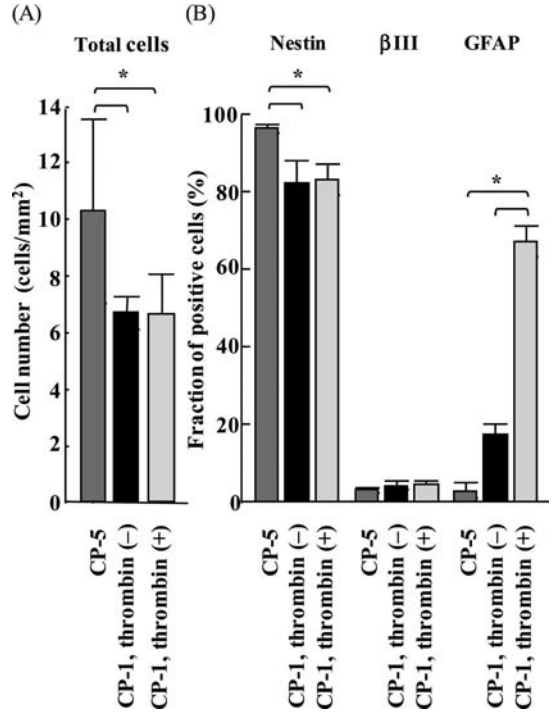

Figure 8. Quantitative evaluation for (A) total number of cells and (B) the fraction of cells expressing nestin, GFAP, and βIII. Cells were cultured on the surface with immobilized (gray) CP-5, (closed) CP-1 without thrombin treatment, and (light gray) CP-1 with thrombin treatment. The data are expressed as the mean ± standard deviation for $n = 6$. The asterisk indicates the statistical significance ($P < 0.05$, true significant difference test) compared to the CP-5 spot.

No difference was observed for every sample in the expression of mRNA for EGFR, CNTF receptor (CNTFR), leukemia inhibitory factor receptor (LIFR), and gp130. EGFR is a tyrosine

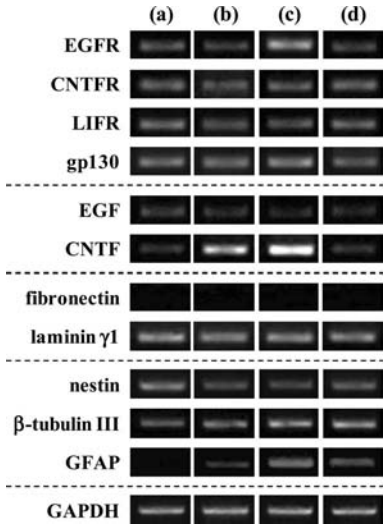

Figure 9. RT-PCR analysis of genes expressed in cells cultured for 5–6 days on the surface with immobilized (a) CP-5, (b) CP-1 (without thrombin treatment), and (c) CP-1 (with thrombin treatment). Cells were cultured for 3 days followed by treatment with 0.6 unit/mL thrombin at 37 °C for 45 min. Then cells were additionally cultured for 3 days. (d) Cells obtained from neurosphere culture.

kinase receptor for EGF (*23*), while CNTFR forms a complex with LIFR and gp130 to bind CNTF (*24*). These results suggest that cells are always ready for receiving the signals from EGF and CNTF if they are available.

A similar level of mRNA for βIII is seen for all types of cells. mRNA for nestin was expressed at a slightly higher level in cells on CP-5-immobilized surface among the sample studied. The expression of mRNA for GFAP is seen most abundantly in the cells on the CP-1-immobilized surface with thrombin treatment, with moderate expression on CP-1 without thrombin treatment and neurosphere cells. No mRNA for GFAP was amplified from cells on the CP-5-immobilized surface. These results are in accordance with those obtained by the immunostaining of marker proteins.

mRNA for EGF was expressed at a similar level regardless of the type of spots, suggesting that EGF-responsive self-renewing cells produce EGF by themselves. CNTF mRNA expression increased in cells at the CP-1-immobilized surface after thrombin treatment, though low but significant expression was also observed even without thrombin treatment. The difference in the expression level between these two conditions was obvious when assessed from the band intensities analyzed using an imaging software (data not shown). Since astrocytes are known to synthesize CNTF (*25*), the result supports our observation that CNTF stimulation triggers astrocytic differentiation, as described in the earlier sections.

mRNA for fibronectin was not detected in any samples tested, while mRNA for the laminin γ1 chain was abundantly expressed. The laminin γ1 chain is a component of laminin subtypes 1, 2, and 4 (*26*) and is present in a variety of tissues including the brain (*27*). The results of RT-PCR suggest that cells, initially attached through interactions of EGFR with the immobilized EGF, secreted laminin by themselves to enhance cell adhesion to the surface.

DISCUSSION

Controlling the dynamics of growth factor signaling is a challenge in regenerative medicine for various tissues including the CNS (*6*). For this purpose, the biomolecular engineering approach is promising, because artificial proteins with multiple functions can be rationally designed using recombinant technology. In this study, we designed the conjugate of two different growth factors, EGF and CNTF, with the removable capping system. The results presented here demonstrate that the sequential actions of EGF and CNTF could be achieved because of the capping domain being removable upon protease treatment (Figures 6, 7, and 8). The temporal capping of CNTF and the subsequent decapping were shown to be effective for inducing the glial differentiation of NSCs previously expanded by the mitogenic activity of a fusion partner, EGF. These processes could be simply demonstrated here by microarray-based assays as well as a more-detailed quantitative analysis.

In a protease-cleavable capping system, a thrombin-susceptible TCS sequence (LVPRGS) was located between the capping domain and CNTF. Our results showed that thrombin specifically digested the TCS sequence to eliminate the TRX-EGFP domain, leaving the CNTF-His10-EGF domain (Figures 3 and 5). The result of temporally controlled glial differentiation indicates that a relatively large domain of TRX-EGFP effectively hinders the accessibility of the CNTFR-LIFR-gp130 complex toward CNTF. Thrombin is a member of serine proteases and plays a key role in the coagulation cascade (*28*). Investigators have reported that thrombin is implicated in neurodegeneration (*29*), especially in Alzheimer's disease microvessels (*30*), though the local concentration of thrombin in the CNS lesion is not available. From these investigations, we expect that CNTF is decapped in response to the availability of endogenous thrombin in degenerative lesion sites, as in the case with fibrin gels (*31*). Different kinetics of growth factor switching may be achieved by replacing the TCS with a cleavage site for matrix metalloproteinase (MMP). For example, Kim et al. reported that the active form of MMP-3 was released from stressed dopamine neurons in Parkinson's disease (*32*).

It is well recognized that EGF is a strong activator for the self-renewal of NSCs in vitro (*11, 19*). Our previous study (*17*) showed that the oriented immobilization of CP-5 provided substrates for the efficient propagation of NSCs. Comparable results were obtained with CP-1 without thrombin treatment (Figure 8). The presence of GFAP-positive cells on the CP-1 surface without thrombin digestion ($18 \pm 2.4\%$; Figure 8) suggests incomplete hindrance by the globular capping domain or protease cleavage during the course of the assay. Upon thrombin digestion, cells started to receive a stimulus from CNTF, giving rise to directed specification into GFAP-positive astrocytes, with the low level of neuronal differentiation. CNTF is known to bind to a specific, nonsignaling receptor (CNTF receptor alpha) as well as signaling receptors including LIFR and gp130 to transmit signals into cells (*25*). It was shown that the exposure of rat embryonic CNS stem cells to CNTF led to their differentiation into type 1 astrocytes via tyrosine phosphorylation of STAT1 and STAT3 (*25*). In addition, a 2-fold increase in the rate of astrocytic differentiation was reported in CNTF-exposed cells derived from human neurospheres (*11*). The results obtained in our study are in accordance with these previous observations. In our system, EGF is present at the surface even after decapping. The incorporation of a protease-cleavable site between the His10 and EGF domains may improve the clear switching of growth factor actions.

The MCP developed in this study provides the biomolecular means to achieve the sequential actions of two growth factors. Different types of growth factors will be required depending on clinical settings for cell replacement therapy in the CNS. The biomolecular systems for these purposes can be engineered rationally with recombinant technology, taking advantage of our design concept for MCP. The chimeric protein can be incorporated into the scaffolds made of synthetic or natural biodegradable polymers that possess metal ions for chelate formation with His10 in the protein. The combination of the scaffold

materials and progenitor cells will provide an efficient strategy for cell-based therapy in the CNS. A study on such an intelligent scaffold system is currently underway.

CONCLUSIONS

Recombinant technology was employed to synthesize the MCP consisting of two growth factor domains (EGF and CNTF), a globular capping domain (TRX-EGFP), a protease-cleavable domain (TCS), and a substrate-binding domain (His10). When immobilized to the surface of the substrate through the coordination of His10, the MCP served NSCs for proliferation, maintaining their undifferentiated state. This effect is due to the activity of EGF, while CNTF activity is temporally veiled with the capping domain. Upon digesting TCS with thrombin, the activity of CNTF emerged to induce the differentiation of astrocytes in situ from previously expanded NSCs. These results demonstrate the feasibility of the system for controlling the dynamics of growth factor signals.

ACKNOWLEDGMENT

This study was supported by Kobe Cluster, the Knowledge-Based Cluster Creation Project and Grant-in-Aid for Scientific Research (19300171, 19·6117), MEXT. T.N.-H. acknowledges JSPS for a research fellowship.

Supporting Information Available: Outline of plasmid construction is provided in Figure S1. The sequences of primers and oligonucleotides used for the synthesis of chimeric genes are provided in Table S1. The conditions for overlap extension PCR is provided in Table S2. Conditions for dialysis are provided in Table S3. Primers and thermal cycling conditions for RT-PCR are provided in Table S4. The results of SDS−PAGE analysis for CP-5 with 16% polyacrylamide gel are provided in Figure S2. The results of SDS−PAGE analysis for MCP digested by thrombin in a medium are provided in Figure S3. Immunostaining of cells on the CP-5-immobilized surface is provided in Figure S4. This material is available free of charge via the Internet at http://pubs.acs.org.

LITERATURE CITED

(1) Björklund, A., and Lindvall, O. (2000) Cell replacement therapies for central nervous system disorders. *Nat. Neurosci. 3*, 537–544.

(2) Goldman, S. (2005) Stem and progenitor cell-based therapy of the human central nervous system. *Nat. Biotechnol. 23*, 862–871.

(3) Grimaldi, P., and Rossi, F. (2006) Lack of neurogenesis in the adult rat cerebellum after Purkinje cell degeneration and growth factor infusion. *Eur. J. Neurosci. 23*, 2657–2668.

(4) Boockvar, J. A., Kapitonov, D., Kapoor, G., Schouten, J., Counelis, G. J., Bogler, O., Snyder, E. Y., McIntosh, T. K., and O'Rourkea, D. M. (2003) Constitutive EGFR signaling confers a motile phenotype to neural stem cells. *Mol. Cell. Neurosci. 24*, 1116–1130.

(5) Teixeira, A. I., Duckworth, J. K., and Hermanson, O. (2007) Getting the right stuff: Controlling neural stem cell state and fate in vivo and in vitro with biomaterials. *Cell Res. 17*, 56–61.

(6) Lessmann, V., Gottmann, K., and Malcangio, M. (2003) Neurotrophin secretion: current facts and future prospects. *Prog. Neurobiol. 69*, 341–374.

(7) Silva, G. A., Czeisler, C., Niece, K. L., Beniash, E., Harrington, D. A., Kessler, J. A., and Stupp, S. I. (2004) Selective differentiation of neural progenitor cells by high-epitope density nanofibers. *Science 303*, 1352–1355.

(8) Yokoi, H., Kinoshita, T., and Zhang, S. (2005) Dynamic reassembly of peptide RADA16 nanofiber scaffold. *Proc. Natl. Acad. Sci. U.S.A. 102*, 8414–8419.

(9) Moore, K., Macsween, M., and Shoichet, M. S. (2006) Immobilized concentration gradients of neurotrophic factors guide neurite outgrowth of primary neurons in macroporous scaffolds. *Tissue Eng. 12*, 267–278.

(10) Liu, C. Y., Apuzzo, M. L. J., and Tirrell, D. A. (2003) Engineering of the extracellular matrix: Working toward neural stem cell programming and neurorestoration - Concept and progress report. *Neurosurgery 52*, 1154–1165.

(11) Caldwell, M. A., He, X., Wilkie, N., Pollack, S., Marshall, G., Wafford, K. A., and Svendsen, C. N. (2001) Growth factors regulate the survival and fate of cells derived from human neurospheres. *Nat. Biotechnol. 19*, 475–479.

(12) Kato, K., Sato, H., and Iwata, H. (2005) Immobilization of histidine-tagged recombinant proteins onto micropatterned surfaces for cell-based functional assays. *Langmuir 21*, 7071–7015.

(13) Gershon, P. D., and Khilko, S. (1995) Stable chelating linkage for reversible immobilization of oligohistidine tagged proteins in the BIAcore surface plasmon resonance detector. *J. Immunol. Methods 183*, 65–76.

(14) Pryor, K. D., and Leiting, B. (1997) High-level expression of soluble protein in *Escherichia coli* using a His(6)-tag and maltose-binding-protein double-affinity fusion system. *Protein Expr. Purif. 10*, 309–319.

(15) LaVallie, E. R., DiBlasio, E. A., Kovacic, S., Grant, K. L., Schendel, P. F., and McCoy, J. M. (1993) A thioredoxin gene fusion expression system that circumvents inclusion body formation in the *E. coli* cytoplasm. *Biotechnology 11*, 187–193.

(16) Ghosh, T., Garde, S., and García, A. E. (2003) Role of backbone hydration and salt-bridge formation in stability of α-helix in solution. *Biophys. J. 85*, 3187–3193.

(17) Nakaji-Hirabayashi, T., Kato, K., Arima, Y., and Iwata, H. (2007) Oriented immobilization of epidermal growth factor onto culture substrates for the selective expansion of neural stem cells. *Biomaterials 28*, 3517–3529.

(18) Kato, K., Sato, H., and Iwata, H. (2006) Differentiation of neural stem cells cultured on extracellular matrices with growth factor chimeras. *Polymer Preprints, Japan 55*, 1971.

(19) Reynolds, B. A., Tetzlaff, W., and Weiss, S. A. (1992) A multipotent EGF-responsive striatal embryonic progenitor cell produces neurons and astrocytes. *J. Neurosci. 12*, 4565–4574.

(20) Arima, Y., Ishii, R., Hirata, I., and Iwata, H. (2006) Development of surface plasmon resonance imaging apparatus for high-throughput study on protein-surface interactions. *J. Surf. Sci. Nanotechnol. 4*, 201–207.

(21) Hirata, I., Morimoto, Y., Murakami, Y., Iwata, H., Kitano, E., Kitamura, H., and Ikada, Y. (2000) Study of complement activation on well-defined surfaces using surface plasmon resonance. *Colloids. Surf., B 18*, 285–292.

(22) Knoll, W. (1991) Polymer thin films and interfaces characterized with evanescent light. *Makromol. Chem. 192*, 2827–2856.

(23) Starbuck, C., and Lauffenburger, D. A. (1992) Mathematical-model for the effects of epidermal growth-factor receptor trafficking dynamics on fibroblast proliferation responses. *Biotechnol. Prog. 8*, 132–143.

(24) Kallen, K. J., Grotzinger, J., and Rose-John, S. (2000) New perspectives on the design of cytokines and growth factors. *Trends Biotechnol. 18*, 455–461.

(25) Dallner, C., Woods, A. G., Deller, T., Kirsch, M., and Hofmann, H.-D. (2002) CNTF and CNTF receptor alpha are constitutively expressed by astrocytes in the mouse brain. *Glia 37*, 374–378.

(26) Patton, B. L. (2000) Laminins of the neuromuscular system. *Microsc. Res. Tech. 51*, 247–261.

(27) Grimpe, B., Dong, S., Doller, C., Temple, K., Malouf, A. T., and Silver, J. (2002) The critical role of basement membrane-

independent laminin γ1 chain during axon regeneration in the CNS. *J. Neurosci. 22*, 3144–3160.

(28) Bode, W. (2006) The structure of thrombin: A janus-headed proteinase. *Semin. Thromb. Hemostasis 32*, 16–31.

(29) Lee, D. Y., Park, K. W., and Jin, B. K. (2006) Thrombin induces neurodegeneration and microglial activation in the cortex in vivo and in vitro: proteolytic and non-proteolytic actions. *Biochem. Biophys. Res. Commun. 346*, 727–738.

(30) Grammas, P., Samany, P. G., and Thirumangalakudi, L. (2006) Thrombin and inflammatory proteins are elevated in Alzheimer's disease microvessels: implications for disease pathogenesis. *J. Alzheimer's Dis. 9*, 51–58.

(31) Ju, Y.-E., Janmey, P. A., McCormick, M. E., Sawyer, E. S., and Flanagan, L. A. (2007) Enhanced neurite growth from mammalian neurons in three-dimensional salmon fibrin gels. *Biomaterials 28*, 2097–2108.

(32) Kim, Y. S., Choi, D. H., Block, M. L., Lorenzl, S., Yang, L., Kim, Y. J., Sugama, S., Cho, B. P., Hwang, O., Browne, S. E., Kim, S. Y., Hong, J. S., Beal, M. F., and Joh, T. H. (2007) A pivotal role of matrix metalloproteinase-3 activity in dopaminergic neuronal degeneration via microglial activation. *FASEB J. 21*, 179–187.

BC700355T

Synthesis, Characterization, Antitumor Activity of Pluronic Mimicking Copolymer Micelles Conjugated with Doxorubicin via Acid-Cleavable Linkage

Yuhan Lee, Sung Young Park, Hyejung Mok, and Tae Gwan Park*

Department of Biological Sciences, Korea Advanced Institute of Science and Technology, Daejeon 305-701, Republic of Korea.
Received October 15, 2007; Revised Manuscript Received November 12, 2007

Pluronic mimicking poly(ethylene oxide)-poly(propylene oxide)-poly(ethylene oxide) (PEO-PPO-PEO) triblock copolymer having multiple hydroxyl groups in the PPO middle segment (core-functionalized Pluronic: CF-PLU) was synthesized for conjugation of doxorubicin (DOX). DOX was conjugated on the multiple hydroxyl groups of CF-PLU via an acid-labile hydrazone linkage (CF-PLU-DOX). In aqueous solution, CF-PLU-DOX copolymers self-assembled to form a core/shell-type micelle structure consisting of a hydrophobic DOX-conjugated PPO core and a hydrophilic PEO shell layer. The conjugated DOX from CF-PLU-DOX micelles was released out more rapidly at pH 5 than pH 7.4, indicating that the hydrazone linkage was cleaved under acidic condition. CF-PLU-DOX micelles exhibited greatly enhanced cytotoxicity for MCF-7 human breast cancer cells compared to naked DOX, while CF-PLU copolymer itself showed extremely low cytotoxicity. Flow cytometry analysis revealed that the extent of cellular uptake for CF-PLU-DOX micelles was greater than free DOX. Confocal image analysis also showed that CF-PLU-DOX micelles had a quite different intracellular distribution profile from free DOX. CF-PLU-DOX micelles were mainly distributed in the cytoplasm, endosomal/lysosomal vesicles, and nucleus, while free DOX was localized mainly within the nucleus, suggesting that CF-PLU-DOX micellar formulation might be advantageously used for overcoming the multidrug resistance (MDR) effect, which gradually develops in many tumor cells during repeated drug administration.

INTRODUCTION

Doxorubicin (DOX), a topoisomerase inhibitor, is a widely used anticancer drug in the treatment of many types of cancer (*1–4*). However, systemic administration of DOX itself elicits severe cardiac toxicity due to the lack of ability to target cancer cells, and also shows the multidrug resistance (MDR) effect (*5–7*). To improve pharmacokinetic/dynamic profiles, enhance passive tumor targeting, and alleviate the MDR effect, various nanoscale DOX formulations such as polymeric nanoparticles, polymer conjugates, liposomes, polymeric micelles, and dendrimer conjugates have been reported to maximize its therapeutic efficacy (*8–22*). Polymeric and lipid nanoparticles containing DOX, when they are injected systemically, significantly alter their biodistribution profiles, thereby preferably targeting to the tumor tissue in a passive manner by the "enhanced permeation and retention (EPR)" effect (*23*). DOX has been physically encapsulated and/or chemically conjugated within poly(ethylene glycol) (PEG)-decorated biodegradable polymeric nanoparticles and micelles to prolong circulation time in the bloodstream as well as to increase the extent of extravascular accumulation in the tumor region. As an attempt to overcome the MDR effect that continuously pumps out intracellular free DOX molecules through the P-glycoprotein (P-gp) pump on the cell membrane, DOX was chemically conjugated onto water-soluble polymers, nanoparticles, and micelles via an acid-cleavable linkage, to change subcellular trafficking of DOX within cells (*24, 25*). Free DOX is taken up by cells via a passive diffusion mechanism, which is highly susceptible for the MDR effect. In contrast, DOX-conjugated nanoparticles and micelles are transported into cells via an endocytosis process, possibly reducing the concentration of cytosolic free DOX for the P-gp pumping action. It is conceivable that DOX molecules conjugated to nanoparticles and micelles are cleaved within the acidic endosomal vesicles and then transported into the cytosol, resulting in bypassing the MDR effect to some extent (*26, 27*).

Poly(ethylene oxide)-poly(propylene oxide)-poly(ethylene oxide) (PEO-PPO-PEO) triblock copolymers (Pluronic) have been widely used as biocompatible drug carriers (*28, 29*). In aqueous solution, Pluronic copolymers self-assemble to form a spherical micelle above a critical micelle concentration and temperature. Pluronic micelles with ~40 nm in diameter are composed of a hydrophobic PPO core and hydrophilic PEO corona. Various hydrophobic anticancer drugs have been physically entrapped within the PPO core of the Pluronic micelles to increase the drug solubility as well as enable passive targeting to the solid tumor. However, Pluronic copolymer micelles are not stable enough to maintain structural integrity for loading the moderately hydrophobic DOX within the inner core. This is partly due to the fact that hydrophobic self-association of PPO middle blocks in the core is not so strong in comparison to other polymeric micelles such as biodegradable poly(lactic acid)-*b*-PEG copolymer micelles. As a result, Pluronic copolymer micelles are easily disintegrated upon dilution below the critical micelle concentration after injection in the bloodstream, limiting their practical uses for systemic delivery of DOX. Nevertheless, it was recently demonstrated that Pluronic copolymer micelles, when administered together with various anticancer drugs, showed enhanced cytotoxic activities by sensitization of MDR cells (*30–32*). The sensitization effect to MDR cancer cells by Pluronic copolymers was attributed to the inhibition of P-gp activity by depletion of ATP.

In this study, a Pluronic-mimicking copolymer having multiple hydroxyl groups on the PPO middle segment was

* Corresponding author. T. G. Park, Tel +82-42-869-2621; Fax +82-42-869-2610; E-mail address: tgpark@kaist.ac.kr.

10.1021/bc700382z CCC: $40.75 © 2008 American Chemical Society
Published on Web 12/29/2007

synthesized and chemically conjugated with DOX via an acid-labile linkage. DOX was conjugated on the multiple hydroxyl groups on the PPO segment via a hydrazone linkage to form a more stable self-assembled micellar structure through $\pi-\pi^*$ interaction between polyaromatic ring structures in DOX buried in the core. It was expected that DOX was specifically released out in an intact form from the copolymer carrier under acidic physiological conditions such as an intracellular endosomal compartment within the tumor cells. The synthesized Pluronic F127 mimicking copolymer micelles were characterized using ^{1}H NMR, transmission electron microscopy (TEM), and light scattering. In vitro cytotoxicity and cellular uptake behavior of the DOX-conjugated copolymer micelles were evaluated for the MCF-7 human breast cancer cell line using free DOX as a control.

EXPERIMENTAL PROCEDURES

Materials. Doxorubicin hydrochloride was purchased from Wako Chemicals (Japan). Epichlorohydrin, anhydrous 1,4-dioxane, methoxy-poly(ethylene glycol) (mPEG) (MW: 5000), poly(propylene oxide) (PPO) (Mw: 2000), *N*,*N*′-dimethylethylenediamine, sodium chloride, triethylamine, anhydrous dimethylsulfoxide (DMSO), deutrium oxide (D_2O), and dimethylsulfoxide-d_6 (DMSO-d_6) were purchased from Sigma-Aldrich (Milwaukee, WI). Sodium sulfate and sodium hydroxide were purchased from Junsei (Japan). *p*-Nitrophenyl chloroformate (*p*-NPC) was purchased from TCI (Japan). The MCF-7 cell line of human breast cancer cells was obtained from Korean Cell Line Bank (Seoul, Korea).

Synthesis of PEO-PPO-PEO Triblock Copolymer Having Hydroxyl Groups on PPO Segment. *Synthesis of Epoxide-Terminated PPO and Epoxide-Terminated mPEG.* Epichlorohydrin (7.44 g, 0.08 mol) was added dropwise to a mixture of PPO (40 g, 0.04 mol) and pulverized NaOH (5 g, 0.25 mol) in 50 mL of anhydrous 1,4-dioxane. The reaction mixture was heated to 65 °C and stirred magnetically for 6 h. The cooled reaction mixture was filtered, and the product was extracted in methylene chloride. The organic layer was dried over Na_2SO_4, concentrated by evaporation of methylene chloride, and further dried under vacuum. Synthesis of epoxide-terminated mPEG was also carried out similarly using the method described in the preparation of epoxide-terminated PPO.

^{1}H NMR ($CDCl_3$): δ = 3.88–3.08 (br, 2H of PPO), 3.08 (m, oxirane), 2.78 (m, OCH_2), 2.42 (m, oxirane), and 1.16−1.03 (br, 3H of PPO).

Synthesis of PPO Multiblock Having Multiple Hydroxyl Groups on the Chain. A PPO multiblock copolymer having multiple hydroxyl groups in the backbone was prepared by step-growth polymerization of epoxide-terminated PPO (21.1 g, 0.01 mol) and *N*,*N*′-dimethylethylenediamine (0.088 g, 0.01 mol) in refluxing ethanol (200 mL) for 40 h. After reacting for 40 h, an excess amount of *N*,*N*′-dimethylethylenediamine was added to introduce terminal amine groups in the PPO multiblock copolymer, and further reacted overnight in the refluxing solvent. After the reaction, the solvent was removed under vacuum and the remaining viscous solution was dissolved in methylene chloride (80 mL) followed by washing with saturated NaCl solution (10 mL). The organic phase was dried over $MgSO_4$ and the solvent was evaporated under vacuum. The product was dissolved in deionized water, dialyzed to remove unreacted diamine, and lyophilized for 48 h.

^{1}H NMR ($CDCl_3$): δ = 3.88–3.06 (br, 2H of PPO), 2.3–2.25 (br, (CH_3)CH_2CH_2N(CH_3)), and 1.14−1.04 (br, 3H of PPO).

Synthesis of PEO-PPO-PEO Triblock Copolymer. A triblock copolymer having multiple hydroxyl groups in the PPO backbone (core-functionalized Pluronic, CF-PLU) was prepared by reacting the amine-terminated multiblock PPO (15 g, 0.0036 mol) to the epoxide-terminated mPEG (55 g, 0.01 mol) in refluxing ethanol (100 mL) for 40 h. The product was precipitated in excess cold diethyl ether. The triblock copolymer was purified by dialysis (molecular weight cutoff 6000–8000, Spectrum Laboratories, Inc., USA) in a cold room for 2 days, and lyophilized.

^{1}H NMR (D_2O): δ = 5.21–5.14 (br, 1H of lactide), 3.88–3.06 (br, 2H of PPO and PEO), 2.3–2.25 (br, (CH_3)CH_2CH_2N(CH_3)), and 1.2−1.05 (br, 3H of PPO).

Synthesis of DOX-Conjugated PEO-PPO-PEO Copolymer via a Hydrazone Bond. *Synthesis of Amine-Reactive PEO-PPO-PEO Copolymer.* PEO-PPO-PEO copolymer was activated using *p*-NPC. Briefly, PEO-PPO-PEO copolymer (1 g, 0.071 mmol) was dissolved in distilled methylene chloride (20 mL), and triethylamine (0.049 mL, 0.071 mmol) was added in the solution. The copolymer solution was dropped into *p*-NPC (0.049 mg, 3 equiv) solution in methylene chloride (5 mL) for 1 h and reacted for 48 h with vigorous stirring. After evaporating methylene chloride, an excess amount of methanol was added to remove unreacted *p*-NPC. After removing methanol, the product was purified by extraction with sodium chloride saturated deionized water and precipitated in cold diethyl ether (−20 °C) and dried in vacuo.

Conjugation of Hydrazine on PEO-PPO-PEO Copolymer. Amine-reactive PEO-PPO-PEO copolymer (1 g, 0.07 mmol) dissolved in methylene chloride (20 mL) was slowly dropped into hydrazine monohydrate (0.22 mL, 10 equiv) solution in methylene chloride (5 mL) and reacted for 24 h. After evaporating methylene chloride, the product was dissolved in deionized water and dialyzed against water and then lyophilized.

Conjugation of DOX on PEO-PPO-PEO Copolymer. Hydrazine-conjugated PEO-PPO-PEO copolymer (100.58 mg) and DOX (10 mg, 1 equiv) were dissolved in anhydrous DMSO (10 mL). The reaction was kept for 48 h at 60 °C. Unreacted DOX and DMSO were removed using dialysis for 12 h at 4 °C against pH 9.0 distilled–deionized water adjusted with 0.1 M NaOH, and the product was lyophilized. All reactions were performed in a dark room. DOX conjugation was confirmed by gel permeation chromatography (GPC, Waters) detected by both an RI detector (RI-71, Shodex) and a UV detector (Waters 486 tunable absorbance detector, Waters) at absorbance 480 nm using chloroform as an eluant. The degree of substitution of DOX was determined using a spectrophotometer (Shimadzu UV-1601, Japan) at 480 nm.

NMR Spectroscopy. Micelle formation of DOX-conjugated PEO-PPO-PEO copolymer via a hydrozone bond (core-functionalized Pluronic conjugated with DOX, CF-PLU-DOX) was confirmed by ^{1}H NMR spectroscopy (Bruker Avance 400 spectrometer operating at 400 MHz). D_2O and DMSO-d_6 were used as solvents to compare the NMR spectra of DOX containing micelles and free DOX, which were prepared at a concentration of 0.1 (w/v) %.

Transmission Electron Microscopy (TEM) Image Analysis. Transmission electron microscopy (TEM, CM-20, Philips, The Netherlands) was used to visualize the morphology of CF-PLU and CF-PLU-DOX micelles. For comparison, Pluronic F127 micelles were used as controls. Each sample was dropped onto a TEM copper grid covered with a carbon film (300 mesh, Ted Pella, U.S.A.) for 10 min and air-dried overnight.

Size Distribution Using Dynamic Light Scattering. Dynamic laser light scattering (DLS) measurement was carried out using a Brookhaven laser light scattering instrument (ZetaPlus, Brookhaven Instruments Corporation, New York, USA), with a He−Ne laser operating at a wavelength of 677 nm at required temperature. A scattering angle of 90° was used for all measurements. The concentration of the sample was 0.005 (w/

Scheme 1. Synthesis of Core-Functionalized PEO-PPO-PEO Copolymer (CF-PLU)

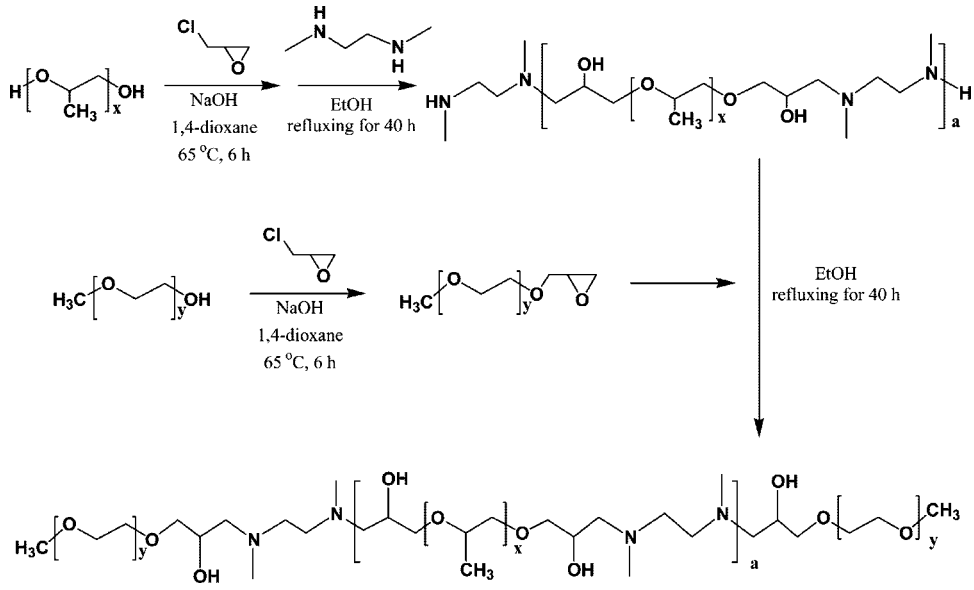

v) % in deionized water, and the solution temperature was equilibrated for more than 30 min before measurement.

DOX Release Experiment. pH-dependent DOX release profiles from CF-PLU-DOX micelles were determined using a previously described method (*27*). Briefly, CF-PLU-DOX micelles (1 mg/mL) were prepared in pH 5.0 and pH 7.4 phosphate buffered saline (PBS) solutions. One milliliter of the solution was placed inside a dialysis membrane (molecular weight cutoff 3500, Spectrum Laboratories, Inc., USA) and dialyzed against 10 mL of pH 5.0 and pH 7.4 PBS solutions. The outer buffer solution containing released DOX was collected at predetermined time points and replaced with 10 mL of fresh buffer solutions. The amount of the released DOX was measured using UV–vis spectroscopy (Shimadzu, Japan) at a 480 nm wavelength and calculated on the basis of a calibration curve using DOX solutions with various concentrations as standards. The experiment was carried out in triplicate.

In Vitro Cell Cytotoxicity, Confocal Image Analysis, and Flow Cytometry Studies. MCF-7 breast cancer cell line was used in this study. Cells were maintained in DMEM media containing 10% fetal bovine serum (FBS) in humidified air containing 5% CO_2. Cells in each culture dish were exposed to various concentrations of free DOX and CF-PLU-DOX for 48 h and cell viability was examined. Cell viability was determined using the conventional MTT assay method. For confocal laser microscopy (Zeiss, Germany) images, cells on a slide glass were exposed to an equivalent DOX concentration of 5 μM for 15 min, washed out thoroughly, and visualized to observe the early stage of cellular uptake. The extent of cellular uptake was also quantified by flow cytometry (FACSCalibur, NJ) after exposure of the cells to the equivalent DOX concentration of 5 μM for 15 min.

RESULTS AND DISCUSSION

Core-functionalized PEO-PPO-PEO (CF-PLU) was synthesized using an epoxide−amine reaction method as shown in Scheme 1. Two terminally functionalized epoxide groups in the precursor PPO chain were reacted with secondary amine groups of *N*,*N*′-dimethylethylenediamine as a chain extender, producing a multiblock PPO chain with six hydroxyl groups on the backbone. Using GPC, it was confirmed that two epoxide-terminated PPO chains (Mw 2000) were chain-extended via the epoxide−amine reaction, producing the multiblock PPO chain having weight-average molecular weight of 4090 (number of precursor PPO: 2). By conjugating an epoxide-terminated mPEG to the two terminal amine groups of the multiblock PPO chain, Pluronic-mimicking PEO-PPO-PEO copolymer with multiple hydroxyl groups on the PPO segment was synthesized. The weight-average molecular weight of the synthesized triblock copolymer was 14 348 (Mw of PPO segment 4090 and Mw of PEO segment 10 258) as determined by GPC. The balance of molecular weight between the PPO and PEO segments in the copolymer was similar to that in Pluronic F127. The copolymer had six hydroxyl groups in the PPO segment in total, resulting from four hydroxyl groups in the multiblock PPO chain (two epoxide-terminated PPO chains in series) and two hydroxyl groups in the two end-capped mPEG chains that had terminal epoxide groups before reaction. The multiple hydroxyl groups on the PPO segment of the CF-PLU copolymer were further modified with DOX via a hydrazone linkage, an acid-labile bond, using a sequential *p*-NPC-mediated hydroxyl−amine coupling reaction followed by an amine−ketone reaction as shown in Scheme 2. The degree of substitution (DS) for DOX was 67.9% (~4.1 DOX per CF-PLU) as determined using a UV–vis spectrometric method. The conjugation of DOX to CF-PLU was confirmed by GPC analysis as shown in Figure 1. CF-PLU-DOX as detected by UV absorbance at 480 nm was eluted earlier than CF-PLU that was detected by RI, suggesting that DOX was covalently conjugated onto the PPO backbone of CF-PLU.

The formation of a core/shell-type micelle structure for CF-PLU-DOX copolymer in aqueous solution was confirmed by ^{1}H NMR spectra using two different solvents (D_2O and DMSO-d_6). For the spectra of CF-PLU-DOX copolymer using DMSO-d_6 as the solvent (Figure 2a), characteristic peaks of DOX (multiple peaks at 4.5–5.4 ppm and 0.8–1 ppm) were detected, indicating that the copolymer molecules were fully dissolved in the solvent while exposing the conjugated DOX in the solvent. In contrast, in the spectra taken in D_2O as a solvent, the DOX peaks disappeared while characteristic PEO and PPO peaks still appeared, suggesting that DOX molecules conjugated to the hydrophobic PPO segment were buried within the core. The results supported that the CF-PLU-DOX copolymers self-assembled into core/shell-type micelles in aqueous solution. The effective diameter of CF-PLU-DOX micelles measured by dynamic light scattering was 164.9 ± 34.4 nm, while that of CF-PLU micelles was 88.5 ± 6.8 nm, indicating that the conjugated DOX in the core increased micelle size. The

Scheme 2. Synthesis of Doxorubicin-Conjugated Core-Functionalized PEO-PPO-PEO Copolymer via a Hydrazone Bond (CF-PLU-DOX)

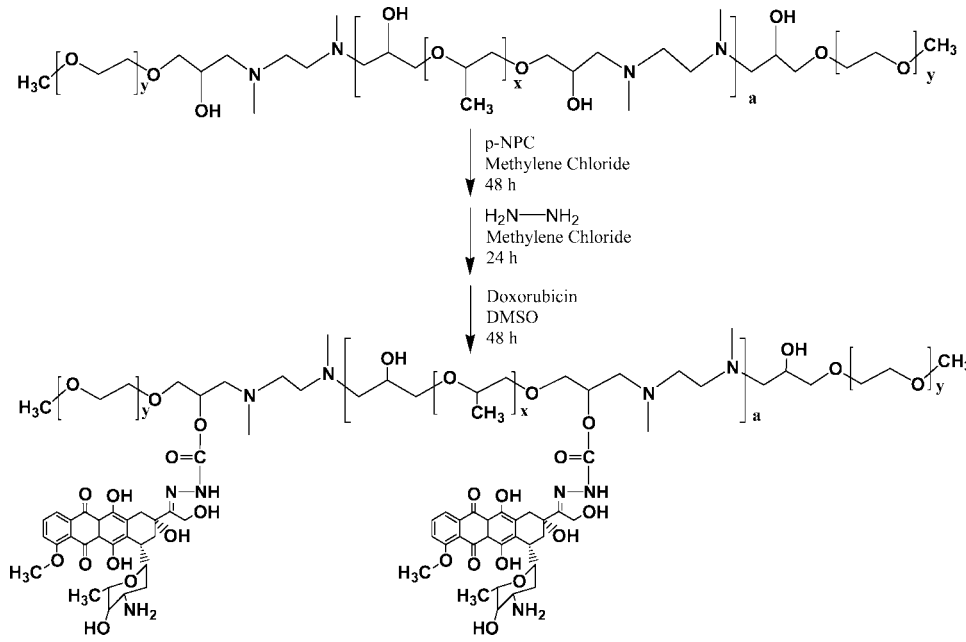

theoretical drug loading efficiency was 13.7% as calculated on the basis of the degree of substitution of CF-PLU-DOX (67.9%).

To further investigate the morphology of core/shell-type CF-PLU-DOX micelles, TEM images of CF-PLU-DOX or CF-PLU micelles were taken. Figure 3a,b clearly shows the core/shell structure of CF-PLU-DOX copolymer micelles in aqueous solution, which were composed of a dark core (average diameter: ca. 90 nm) surrounded by a relatively bright shell layer (average thickness: ca. 15 nm). At lower magnification (Figure 3c), tightly packed nanospheres having an average size of about 120 nm were observed. On the other hand, CF-PLU copolymer micelles were irregular in shape and showed an average size of about 90 nm, consistent with the size obtained from the DLS study. The irregular morphology with multiple nuclei might be caused by interfering hydrophobic interactions of PPO segments by multiple hydroxyl groups present in the synthesized PEO-PPO-PEO copolymer. It was likely that water molecules associated with the hydroxyl groups could not be completely removed from the core during the self-assembly process of the copolymers, resulting in the inner nuclei-like water pockets. Considering that Pluronic F127 micelles are about 40 nm in diameter in aqueous solution, the increased micelle sizes of CF-PLU and CF-PLU-DOX could be attributed to the modified and core-functionalized PEO-PPO-PEO structure. It was likely that hydrophobic interaction and/or $\pi-\pi^*$ stacking of conjugated DOX molecules in the core were responsible for the self-assembling core/shell structure of CF-PLU-DOX micelles. This core/shell structure is promising for cancer therapy, because the PEG shell can provide a stealth property with prolonged circulation time in the bloodstream, while the stabilized inner core can prevent early DOX release from the micelles during the circulation.

DOX release from CF-PLU-DOX micelles was evaluated at pH 5.0 and pH 7.4 conditions. CF-PLU-DOX micelles are expected to exhibit pH-responsive DOX release profile due to the acid-labile nature of the hydrazone linkage between DOX and PPO middle backbone. As shown in Figure 4, CF-PLU-

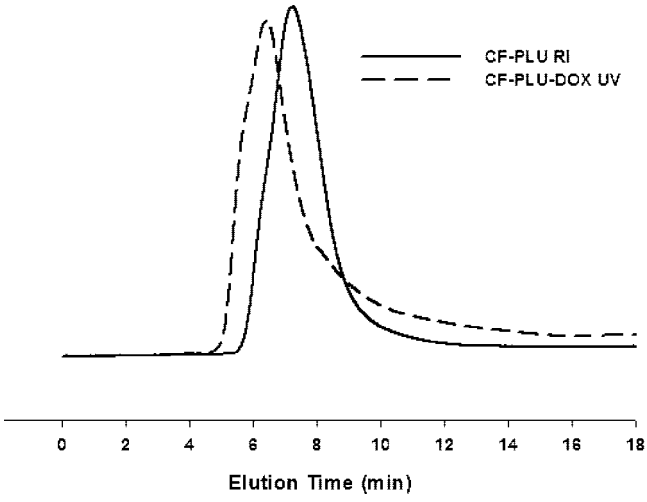

Figure 1. Gel permeation chromatography profiles before and after DOX conjugation. Solid line indicates CF-PLU copolymer before DOX conjugation using RI detector, and dotted line indicates CF-PLU-DOX copolymer after DOX conjugation using UV detector.

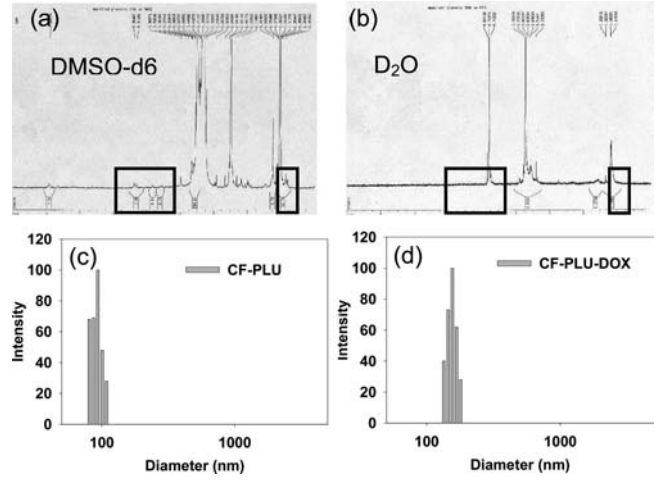

Figure 2. Micellization of DOX-conjugated PEO-PPO-PEO copolymer as confirmed by ^{1}H NMR spectroscopy using (a) DMSO-d_6 and (b) D_2O as solvents. The size was determined by dynamic light scattering (DLS) analysis: (c) CF-PLU and (d) CF-PLU-DOX at a concentration of 0.05 (w/v) %.

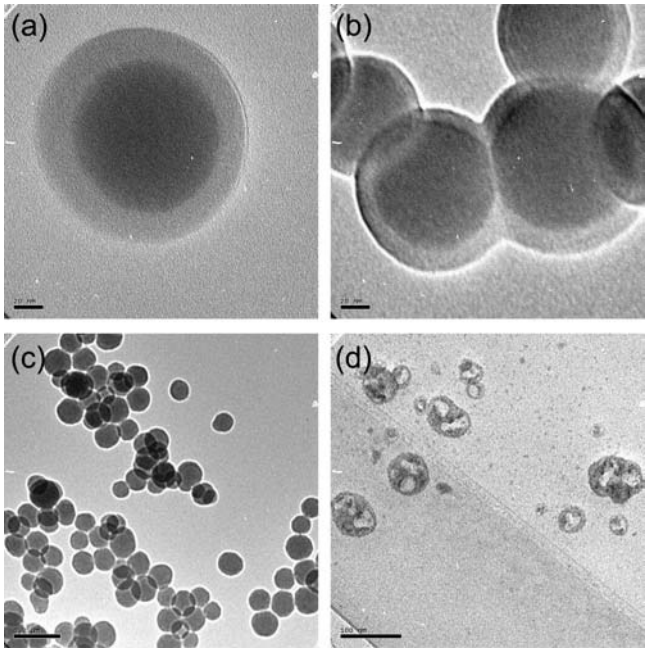

Figure 3. TEM images of CF-PLU-DOX (a−c) and CF-PLU (d).

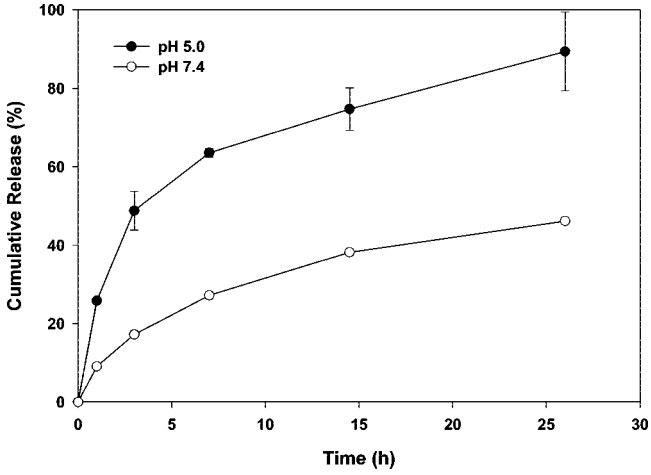

Figure 4. In vitro release profiles of DOX from CF-PLU-DOX micelles at pH 7.4 (○) and pH 5 (•).

DOX micelles showed much faster DOX release at pH 5.0 than at pH 7.4. At pH 5.0, CF-PLU-DOX micelles released out about 50% of the initially loaded DOX for the first 3 h, and liberated 84% after 26 h. However, at pH 7.4, the micelles released out only 15% of DOX for 3 h and less than 40% after 26 h. The accelerated DOX release in acidic pH condition is highly desirable for effective treatment of cancer. It is conceivable that CF-PLU-DOX micelles are passively targeted to the tumor tissue through the enhanced permeation and retention (EPR) effect with minimized DOX release during circulation in the bloodstream. There would be two beneficial effects for the acid-sensitive DOX release: (1) after accumulation in the vicinity of the tumor cells, DOX could be cleaved and released from the CF-PLU-DOX micelles selectively in the acidic solid tumor microenvironment for passive cellular uptake (*27, 29, 30*); (2) and more importantly, intact CF-PLU-DOX micelles would be taken up by tumor cells through nonspecific endocytosis, and located preferentially in the acidic endosome compartments, where DOX could be cleaved, escaped from the endosome, and released out in the cytosol. The second cellular uptake mechanism of DOX conjugated to CF-PLU micelles via endocytosis

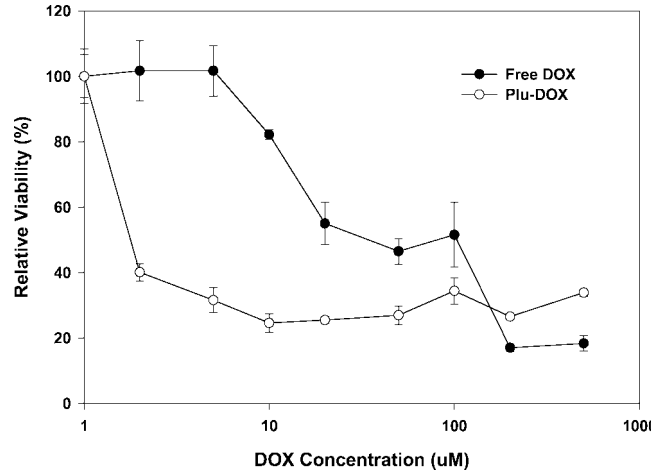

Figure 5. Cytotoxicities of CF-PLU-DOX micelles (○) and free DOX (•) using MCF-7 cell line.

could bypass the MDR effect often observed for the cellular uptake of free DOX bypassive diffusion.

Cytotoxicity effects of CF-PLU-DOX micelles were evaluated using the MCF-7 human breast cancer cell line. Cells were treated with free DOX or CF-PLU-DOX micelles with an equivalent concentration of DOX. As shown in Figure 5a, CF-PLU-DOX micelles exhibited far greater cytotoxicity than free DOX. The inhibition concentration (IC_{50}) of CF-PLU-DOX micelles was 1.2 μM, which is 15-fold lower than that of free DOX (18.5 μM). In addition, it was evident that the enhanced cytotoxicity of CF-PLU-DOX micelles was not due to the cytotoxicity of the carrier polymer (CF-PLU). The CF-PLU copolymer exhibited very low cytotoxicity (more than 90% of the cells survived) over the same polymer concentration range (data not shown).

To further investigate the cellular uptake efficiency of CF-PLU-DOX micelles, FACS analysis and confocal laser microscopy were used to quantitatively evaluate and visualize CF-PLU-DOX micelles internalized within cells. As shown in Figure 6a, FACS analysis taken after treating for 15 min clearly showed that the cellular uptake extent of CF-PLU-DOX micelles was greater than that of free DOX, indicating that the enhanced cellular uptake of CF-PLU-DOX micelles was responsible for the increased cytotoxicity as shown in Figure 5a. Figure 6b,c shows confocal images of the cells treated with free DOX and CF-PLU-DOX micelles for 15 min. MCF-7 cells treated with free DOX showed that DOX was predominantly accumulated in the nuclei (left panel), while the cells treated with CF-PLU-DOX micelles showed scattered intense small red dots and red fluorescence in the cytosol and nuclei (right panel). The different confocal images clearly suggested that the CF-PLU-DOX micelles were taken up by endocytosis-mediated cellular uptake, while free DOX was transported into cells via a passive diffusion mechanism. The intense DOX accumulation only in the nuclei for free DOX, not in the cytosol, was because intracellular DOX molecules in the cytosol were rapidly transported to the nucleus and avidly bound to the chromosomal DNA. In contrast, it appears that CF-PLU-DOX micelles were initially located within the endosome vesicles, releasing cleaved DOX in the cytosol region in a sustained manner. This suggests that the enhanced cytotoxicity for CF-PLU-DOX micelles was mainly due to their endocytic intracellular transport (*33*), increasing the extent of cellular uptake.

Lastly, it should be noted that Pluronic-mimicking copolymers used in this study might also contribute to the sensitization of MCF7 cells, additionally influencing the extent of DOX-induced apoptotic cell death. Earlier studies reported that a physical

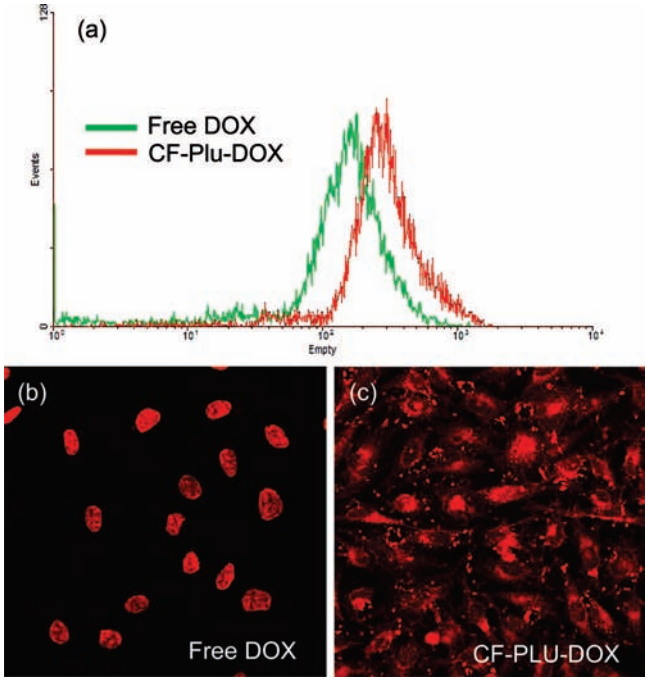

Figure 6. Cellular uptake of CF-PLU-DOX micelles. (a) FACS analysis using MCF-7 cells treated with free DOX (green line) and CF-PLU-DOX (red line). Confocal laser microscopy images for HeLa cells treated with (b) free DOX, and (c) CF-PLU-DOX micelles.

mixture formulation of DOX and Pluronic copolymers treated to MCF7 cells significantly changed its genome expression patterns: up-regulating the ATP-associated genes involved in the respiratory chain and genes involved in the apoptotic signal transduction pathway. In addition, Pluronic copolymers are known to suppress the overexpression of MDR-related genes for various non-MDR cancer cells (*34*, *35*). Structurally similar to Pluronic copolymers, CF-PLU copolymers are also expected to exhibit the similar MDR suppression effect in MCF7 cells with initiation of apoptotic signal transduction. Thus, it is likely that the CF-PLU-DOX micelles might have significant effects on overcoming the MDR barrier in cancer cells. We are currently investigating the anticancer effect of CF-PLU-DOX micelles using MDR cells.

In conclusion, a new class of Pluronic mimicking micelles was synthesized to release DOX in a pH-responsive manner. PEO-PPO-PEO copolymer having multiple hydroxyl groups on the PPO segment was synthesized and DOX molecules were conjugated via an acid-labile hydrazone linkage. The DOX-conjugated copolymer self-assembled in aqueous solution to form tightly packed spherical micelles or micellar aggregates having a core–shell structure composed of a DOX core and PEG shell. The copolymer micelles released DOX to a greater extent under acidic condition. The cytotoxicity of CF-PLU-DOX micelles was 15-fold greater than that of free DOX for MCF-7 human breast cancer cells. The enhanced cytotoxicity was mainly due to the increased cellular uptake of DOX-conjugated micelles that were taken up by endocytosis. It was possible that core-functionalized Pluronic mimicking copolymers synthesized in this study could be similarly conjugated with other hydrophobic anticancer drugs such as paclitaxel. Self-assembled nanoscale CF-PLU micelles conjugated with potent antitumor agents are expected not only to improve solubility in aqueous solution, but also to enhance targeting capacity to the solid tumor.

ACKNOWLEDGMENT

This study was supported by the grant from the National Research Laboratory project from the Ministry of Science and Technology, Republic of Korea.

LITERATURE CITED

(1) Momparlor, R. L., Karon, M., Siegel, S. E., and Avila, F. (1976) Effect of adriamycin on DNA, RNA, and protein synthesis in cell-free systems and intact cells. *Cancer Res. 36*, 2891–2895.
(2) Laginha, K. M., Verwoert, S., Charrois, G. J. R., and Allen, T. M. (2005) Determination of doxorubicin levels in whole tumor and tumor nuclei in murine breast cancer tumors. *Clin. Cancer Res. 11*, 6944–6949.
(3) Frederick, C. A., Williams, L. D., Ughetto, G., van der Marel, G. A., van Boom, J. H., Rich, A., and Wang, A. H.-J. (1990) Structural comparison of anticancer drug-DNA complexes: adriamycin and daunomycin. *Biochemistry 29*, 2538–2549.
(4) Etrych, T., Jelinkova, M., Rihova, B., and Ulbrich, K. (2001) New HPMA copolymers containing doxorubicin bound via pH-sensitive linkage: synthesis and preliminary in vitro and in vivo biological properties. *J. Controlled Release 73*, 89–102.
(5) Marchi, N., Hallene, K. L., Kight, K. M., Cucullo, L., Moddel, G., Bingaman, W., Dini, G., Vezzani, A., and Janigro, D. (2004) Significance of MDR1 and multiple drug resistance in refractory human epileptic brain. *Biomed. Central Medicine 2*, 37.
(6) Batrakova, E. V., Kelly, D. L., Li, S., Li, Y., Yang, Z., Xiao, L., Alakhova, D. Y., Sherman, S., Alakhov, V. Yu., and Kabanov, A. V. (2006) Alteration of genomic responses to doxorubicin and prevention of MDR in breast cancer cells by a polymer excipient: Pluronic P85. *Mol. Pharm. 3*, 113–123.
(7) Marin, A., Sun, H., Husseini, G. A., Pitt, W. G., Christensen, D. A., and Rapoport, N. Y. (2002) Drug delivery in pluronic micelles: effect of high-frequency ultrasound on drug release from micelles and intracellular uptake. *J. Controlled Release 84*, 39–47.
(8) Vasey, P. A., Kaye, S. B., Morrison, R., Twelves, C., Wilson, P., Duncan, R., Thomson, A. H., Murray, L. S., Hilditch, T. E., Murray, T., Burtles, S., Fraier, D., Frigerio, E., and Cassidy, J. (1999) Phase I clinical and pharmacokinetic study of PK1 [N-(2-Hydroxypropyl)methacrylamide copolymer doxorubicin]: first member of a new class of chemotherapeutic agents - drug-polymer conjugates. *Clin. Cancer Res. 5*, 83–94.
(9) Lee, E. S., Na, K., and Bae, Y. H. (2005) Doxorubicin loaded pH-sensitive polymeric micelles for reversal of resistant MCF-7 tumor. *J. Controlled Release 103*, 405–418.
(10) Hruby, M., Konak, C., and Ulbrich, K. (2005) Polymeric micellar pH-sensitive drug delivery system for doxorubicin. *J. Controlled Release 103*, 137–148.
(11) Bae, Y., Nishiyama, N., Fukushima, S., Koyama, H., Yasuhiro, M., and Kataoka, K. (2005) Preparation and biological characterization of polymeric micelle drug carriers with intracellular pH-triggered drug release property: tumor permeability, controlled subcellular drug distribution, and enhanced in vivo antitumor efficacy. *Bioconjugate Chem. 16*, 122–130.
(12) Furgeson, D. Y., Dreher, M. R., and Chilkoti, A. (2006) Structural optimization of a "smart" doxorubicin-polypepide conjugate for thermally targeted delivery to solid tumors. *J. Controlled Release 110*, 362–369.
(13) Zhou, X., Chang, Y.-C., Oyama, T., McGuire, M. J., and Brown, K. C. (2004) Cell-specific delivery of a chemotherapeutic to lung cancer cells. *J. Am. Chem. Soc. 126*, 15656–15657.
(14) Yoo, H. S., and Park, T. G. (2004) Folate receptor targeted delivery of doxorubicin nano-aggregates stabilized by doxorubicin-PEG-folate conjugate. *J. Controlled Release 100*, 247–256.
(15) Yoo, H. S., and Park, T. G. (2004) Folate receptor targeted biodegradable polymeric doxorubicin micelles. *J. Controlled Release 96*, 273–283.
(16) Yoo, H. S., and Park, T. G. (2001) Biodegradable polymeric micelles composed of doxorubicin conjugated PLGA-PEG block copolymer. *J. Controlled Release 70*, 63–70.

(17) Burke, P. J., Kalet, B. T., and Koch, T. H. (2004) Antiestrogen binding site and estrogen receptor mediate uptake and distribution of 4-hydroxytamoxifen-targeted doxorubicin-formaldehyde conjugate in breast cancer cells. *J. Med. Chem. 47*, 6509–6518.

(18) Cogan, P. S., and Koch, T. H. (2004) Studies of targeting and intracellular trafficking of an anti-androgen doxorubicin-formaldehyde conjugate in PC-3 prostate cancer cells bearing androgen receptor-GFP chimera. *J. Med. Chem. 47*, 5690–5699.

(19) Chytil, P., Etrych, T., Konak, C., Sirova, M., Mrkvan, T., Rihova, B., and Ulbrich, K. (2006) Properties of HPMA copolymer-doxorubicin conjugates with pH-controlled activation: effect of polymer chain modification. *J. Controlled Release 115*, 26–36.

(20) Mino, T., Batrakova, E. V., Li, S., Li, Y., Pakunlu, R. I., Alakhov, V. Yu., and Kabanov, A. V. (2005) Pluronic block copolymers alter apoptotic signal transduction of doxorubicin in drug-resistant cancer cells. *J. Controlled Release 105*, 269–278.

(21) Greco, F., Vicent, M. J., Gee, S., Jones, A. T., Gee, J., Nicholson, R. I., and Duncan, R. (2007) Investigating the mechanism of enhanced cytotoxicity of HPMA copolymer-Dox-AGM in breast cancer cells. *J. Controlled Release 117*, 28–39.

(22) Minko, T., Kopeckova, P., Pozharov, V., and Kopecek, J. (1998) HPMA copolymer bound adriamycin overcomes MDR1 gene encoded resistance in a human ovarian carcinoma cell line. *J. Controlled Release 54*, 223–233.

(23) Leroux, J.-C., Roux, E., Le Garrec, D., Hong, K., and Drummond, D. C. (2001) N-isopropylacrylamide copolymrs for the preparation of pH-sensitive liposomes and polymeric micelles. *J. Controlled Release 72*, 71–84.

(24) Torchilin, V. P. (2005) Recent advanced with liposomes as pharmaceutical carriers. *Nat. Rev. Drug Discovery 4*, 145–160.

(25) Miller, D. W., Batrakova, E. V., Waltner, T. O., Alakhov, V. Yu., and Kabanov, A. V. (1997) Interactions of Pluronic block copolymers with brain microvessel endothelial cells: evidence of two potential pathways for drug absorption. *Bioconjugate Chem. 8*, 649–657.

(26) Alakhov, V. Yu., Moskaleva, E. Yu., Batrakova, E. V., and Kabanov, A. V. (1996) Hypersensitization of multidrug resistant human ovarian carcinoma cells by Pluronic P85 block copolymer. *Bioconjugate Chem. 7*, 209–216.

(27) Yoo, H. S., Lee, E. A., and Park, T. G. (2002) Doxorubicin-conjugated biodegradable polymeric micelles having acid-cleavable linkages. *J. Controlled Release 82*, 17–27.

(28) Tomlinson, R., Heler, J., Brocchini, S., and Duncan, R. (2003) Polyacetal-doxorubicin conjugates designed for pH-dependent degradation. *Bioconjugate Chem. 14*, 1096–1106.

(29) Gillies, E. R., and Frechet, J. M. J. (2005) pH-Responsive copolymer assemblies for controlled release of doxorubicin. *Bioconjugate Chem. 16*, 361–368.

(30) Lee, C. C., Cramer, A. T., Jr., and Frechet, J. M. J. (2006) An intramolecular cyclization reaction is responsible for the in vivo inefficacy and apparent pH insensitive hydrolysis kinetics of hydrazone carboxylate derivatives of doxorubicin. *Bioconjugate Chem. 17*, 1364–1368.

(31) Ahmed, F., Pakunlu, R. I., Brannan, A., Bates, F., Minko, T., and Discher, D. E. (2006) Biodegradable polymersomes loaded with both paclitaxel and doxorubicin permeate and shrink tumors, including apoptosis in proportion to accumulated drug. *J. Controlled Release 116*, 150–158.

(32) Yang, S. R., Lee, H. J., and Kim, J.-D. (2006) Histidine-conjugated poly(aminoacid) derivatives for the novel endosomolytic delivery carrier of doxorubicin. *J. Controlled Release 114*, 60–68.

(33) Janes, K. A., Fresneau, M. P., Marazuela, A., Fabra, A., and Alonso, M. J. (2001) Chitosan nanoparticles as delivery systems for doxorubicin. *J. Controlled Release 73*, 255–267.

(34) Kabanov, A. V. (2006) Polymer genomics: an insight into pharmacology and toxicology of nanomedicines. *Adv. Drug Delivery Rev. 58*, 1597–1621.

(35) Kabanov, A. V., Batrakova, E. V., and Alakhov, V. Yu. (2002) Pluronic block copolymers for overcoming drug resistance in cancer. *Adv. Drug Delivery Rev. 54*, 759–779.

BC700382Z

Retrograde Delivery of Photosensitizer (TPPp-O-β-GluOH)$_3$ Selectively Potentiates Its Photodynamic Activity

Mohamed Amessou,[†] Danièle Carrez,[‡,§] Delphine Patin,[†] Marianne Sarr,[†] David S. Grierson,[‡,||,⊥] Alain Croisy,[‡,§] Antonio C. Tedesco,[@] Philippe Maillard,*[,‡,||,#] and Ludger Johannes[†,#]

Institut Curie, Centre de Recherche, 26 rue d'Ulm, F-75248 Paris Cedex 05, France, CNRS UMR144, 26 rue d'Ulm, F-75248 Paris Cedex 05, France, Institut Curie, Centre de Recherche, Centre Universitaire, Université Paris-Sud, F-91405 Orsay Cedex, France, INSERM U759, Centre Universitaire, Université Paris-Sud, F-91405 Orsay Cedex, France, CNRS UMR176, Centre de Recherche, Centre Universitaire, Université Paris-Sud, F-91405 Orsay, France, and Departamento de Química, Laboratório de Fotobiologia e Fotomedicina, Faculdade de Filosofia Ciências e Letras de Ribeirão Preto, Universidade de São Paulo, Av. Bandeirantes 3900, CEP, 14040-901 Ribeirão Preto, Brazil. Received October 29, 2007; Revised Manuscript Received November 15, 2007

Photodynamic therapy involves administration of a photosensitizing drug and its subsequent activation by visible light of the appropriate wavelength. Several approaches to increasing the specificity of photosensitizers for cancerous tissues and, in particular, through their conjugation to ligands that are directed against tumor-associated antigens have been investigated. Here, we have studied the delivery of the photocytotoxic porphyrin compound TPP(p-O-β-D-GluOH)$_3$ into tumor cells that overexpress the glycosphingolipid Gb3, using the Gb3-binding nontoxic B-subunit of Shiga toxin (STxB) as a vector. To allow for site-directed chemical coupling, an STxB variant carrying a free sulfhydryl moiety at its C-terminal end has been used. Binding affinity, cellular uptake, singlet oxygen quantum yield, and phototoxicity of the conjugate have been examined. Despite some effect of coupling on both the photophysical properties of TPP(p-O-β-D-GluOH)$_3$ and the affinity of STxB for its receptor, the conjugate exhibited a higher photocytotoxic activity than the photosensitizer alone and was exquisitely selective for Gb3-expressing tumor cells. Furthermore, our data strongly suggest that STxB-mediated retrograde delivery of the photosensitizer to the biosynthetic/secretory pathway is critical for optimal cytotoxic activity. In conclusion, a strong rationale for using retrograde delivery tools such as STxB in combination with photosensitizing agents for the photodynamic therapy of tumors is presented.

INTRODUCTION

Anticancer therapy often relies on the use of chemotherapeutic agents that efficiently eliminate dividing cancer cells. However, in many cases, chemotherapy fails to eradicate tumors, and even when chemotherapy is successful, systemic cytotoxicity often results in deleterious side effects. To overcome these limitations, novel strategies have been developed that aim at increasing the selectivity of tumor treatment. In this context, antibodies, hormones, growth factors, lectins, and toxins have been explored as tools for delivering therapeutic compounds to cancer cells (*1*, *2*).

The bacterial Shiga toxins and verotoxins (or Shiga-like toxins) share a cellular receptor, the glycosphingolipid globotriaosylceramide (Gb3[1] or CD77), that is expressed on a number of human malignancies, such as Burkitt's lymphoma (*3*) and cancers of the breast (*4*), brain (*5*), ovary (*6*), colon (*7*), and testis (*8*). Shiga toxin is produced by *Shigella dysenteria*, and verotoxins are produced by enterohemorrhagic strains of *Escherichia coli* (*9*). These toxins are composed of an enzymatic component (A subunit) that inhibits protein biosynthesis by modifying rRNA and a nontoxic homopentameric component (B subunit or STxB). The A subunit cannot enter cells by itself. For plasma membrane binding and internalization, it requires a noncovalent interaction with STxB. In toxin sensitive cells, STxB delivers the holotoxin from the plasma membrane to the endoplasmic reticulum, via the early endosome and the Golgi apparatus, a transport pathway termed the retrograde route (*10*, *11*). Trafficking through the retrograde route allows STxB to escape degradation in lysosomes and recycling to the plasma membrane, resulting in its stable association with cells.

Recently, the possibility of using STxB as a delivery tool for Gb3-expressing tumors has been addressed. It was shown that upon oral uptake or intravenous injection, STxB targets adenocarcinomas of the intestine in a transgenic mouse model (*12*). In the context of the holotoxin, an antineoplasic activity has been detected upon injection of verotoxin-1 into xenografted tumors (*5*, *13–15*), and verotoxin-1 eliminates clonogenic tumor cells in purging applications (*16*). However, the use of holotoxin as a therapeutic agent in humans may be limited by the fact that the catalytic effect of the A subunit is not tumor specific. STxB has therefore directly been linked to therapeutic com-

* To whom correspondence should be addressed. Phone: +33 1-69 86 31 71. Fax: +33 1-69 07 53 27. E-mail: philippe.maillard@curie.u-psud.fr.

[†] Institut Curie, Centre de Recherche, and CNRS UMR144.

[‡] Institut Curie, Centre de Recherche, Centre Universitaire, Université Paris-Sud.

[§] INSERM U759, Centre Universitaire, Université Paris-Sud.

[||] CNRS UMR176, Centre de Recherche, Centre Universitaire, Université Paris-Sud.

[⊥] Present address: Faculty of Pharmaceutical Sciences, University of British Columbia, 2146 East Mall, Vancouver, BC, Canada V6T 123.

[@] Universidade de São Paulo.

[#] Principal investigators.

[1] Abbreviations: Gb3, globotiaosyl ceramide; STxB, Shiga toxin B subunit; PDT, photodynamic therapy; PPMP, 1-phenyl-2-hexadecanoyl-amino-3-morpholino-1-propanol; MTT, 3-(4,5-dimethylthiazol-2-yl)-2,5-diphenyltetrazolium bromide; TPP, tetraphenylporphyrin; LD, lethal dose; BFA, brefeldin A.

10.1021/bc7003999 CCC: $40.75 © 2008 American Chemical Society
Published on Web 01/19/2008

pounds that have selective antitumor activity (*17*) or that can be activated locally (*18*).

Photodynamic therapy (PDT) is based on the preferential accumulation of a photosensitizing molecule in malignant tissue after its systemic administration. Illumination using light of an appropriate wavelength excites the photosensitizer, and subsequent photoactivation results in the release of cytotoxic species such as singlet oxygen and free radicals which are responsible for the destruction of target tissue (*19*). Several major issues continue to limit the wider application of PDT as a cancer treatment modality, including deleterious effects related to accumulation of the photosensitizer in normal tissue as well as in tumor tissue. To overcome this problem, one strategy which is receiving considerable attention is to covalently link the photosensitizer to a carrier molecule to localize the PDT effect (for reviews, see refs *20* and *21*).

In this work, we have synthesized a new glycoporphyrin that was covalently linked to STxB. We have demonstrated that the photocytotoxic properties of the conjugate depend critically on its subcellular delivery via the retrograde route.

MATERIALS AND METHODS

Materials. All solvents were reagent grade. Dry MeOH was kept over 3 Å sieves; methylene chloride was distilled from calcium hydride and kept over 4 Å sieves, and chloroform was distilled from calcium chloride and kept over 4 Å sieves. Column chromatography was performed with the indicated solvents and using E. Merck silica gel 60 (particle size of 0.035–0.070 mm). Macherey-Nagel precoated plates (SIL G-200, 2 mm) were used for preparative thin layer chromatography. Yields refer to chromatographically and spectroscopically pure compounds. ^{1}H spectra were recorded on a Bruker AC-300 spectrometer at room temperature using an internal deuterium lock. Acidic impurities in $CDCl_3$ were removed by treatment with anhydrous K_2CO_3. Mass spectrometry analysis was performed using a MALDI-TOF mass spectrometer (PerSeptive Biosystem Voyager Elite, PerSeptive Biosystem, Framingham, MA). Quantitative UV–visible spectra were obtained using a Varian DMS 200 spectrometer. Microanalyses were performed by the ICSN-CNRS Elemental Analysis Center at Gif-sur-Yvette, France. STxB-Cys and STxB-Glyc-KDEL were prepared as previously described (*28*, *36*). PD-10 gel exclusion columns (Amersham Pharmacia Biotech), 1-phenyl-2-hexadecanoylamino-3-morphorpholin-1-propanol (PPMP) (Calbiochem), secondary fluophore-coupled antibodies (Jackson Immunresearch), and 3-(4,5-dimethylthiazol-2-yl)-2,5-diphenyltetrazolium bromide (MTT) (Sigma Aldrich) were obtained from the indicated commercial sources. The protein concentration was determined by the Bio-Rad assay (Bio-Rad Laboratories). HeLa cells were cultured as published previously (*28*).

Synthesis of TPP(p-O-β-D-GluOH)$_3$(p-CH$_2$Br). *5,10,15-Tris[4-(2′,3′,4′,6′-tetraacetyl-O-β-D-glucosyloxyphenyl)]-20-(4-bromomethylphenyl)porphyrin (**3**).* Freshly distilled pyrrole (205 μL, 2.9 mmol) in chloroform (7.50 mL), 4-O-(2′,3′,4′,6′-tetraacetyl-β-D-glucopyranosyloxy)benzaldehyde (1 g, 2.2 mmol), and 4-bromomethylbenzaldehyde (0.147 g, 0.74 mmol) in chloroform (7.5 mL) were added to chloroform (750 mL) purged with argon for 30 min. The mixture was stirred under argon for a further 10 min. Then a BF_3-etherate solution in chloroform (317 μL, 0.5 M) was added, and the mixture was stirred under argon. The mixture was stirred at room temperature for 2 h. Triethylamine (305 μL) was added, and the mixture was stirred at room temperature 15 min. *o*-Chloranil (1.385 g, 5.6 mmol) was added, and the solution was stirred at room temperature for 2 h. Silica gel (10 g) was added to the dark solution, and the solvent was evaporated. The absorbed crude products were placed on the top of a chromatographic silica gel column. The porphyrin mixture was eluted with methylene chloride and acetone (10/1, v/v). The third red fraction was collected and purified again by preparative thin layer silica gel chromatography eluted with methylene chloride and acetone (10/1, v/v). The titled pure triglycosylated porphyrin **3** was obtained as red crystals after crystallization from methylene chloride and heptane (300 mg, 31% yield). Anal. $C_{87}H_{85}BrN_4O_{30}\cdot 3H_2O$. Calcd: C, 58.03; H, 5.09; N, 5.09. Found: C, 58.07; H, 4.77; N, 2.74. UV–visible spectrum in methylene chloride: λ_{max} (nm) [ϵ (mmol^{-1} cm^{-1})] 419.5 (414.3), 516 (17.9), 552 (10.5), 591 (6.9), 647 (5.9). ^{1}H NMR spectrum in $CDCl_3$: δ 8.88 (s, 8 H, pyrrole), 8.26 (d, 2 H, *o*-phenyl), 8.16 (d, 6 H, *o*-phenoxy), 7.82 (d, 2 H, *m*-phenyl), 7.42 (d, 6 H, *m*-phenoxy), 5.50 (m, 9 H, H "ose"), 5.33 (m, 3 H, H "ose"), 4.88 (s, 2 H, CH_2Br), 4.45 (dd, 3 H, H_aC_6 "ose"), 4.33 (d, 3 H, H_bC_6 "ose"), 4.08 (m, 3 H, HC_5 "ose"), 2.24 (s, 9 H, acetyl), 2.14 (s, 9 H, acetyl), 2.13 (s, 18 H, acetyl), −2.79 (s, 2 H, NH).

*5,10,15-Tris(4-O-β-D-glucosyloxyphenyl)-20-(4-bromomethylphenyl)porphyrin (**4**).* To a solution of **3** (50 mg, 28.6 μmol) in dry MeOH (10 mL) and dry CH_2Cl_2 (10 mL) was added a solution of NaOMe in MeOH (100 μL, 1 M), and the mixture was stirred for 1.5 h at room temperature. IWT TMD-8 ion-exchange resin (0.310 g) was then added, and gentle stirring was continued for 1.5 h. The reaction mixture was filtered, and the recovered resin was washed with MeOH. The combined filtrate and washings were then evaporated to dryness and crystallized from MeOH and 1,2-dichloroethane. Product **6** (33 mg, 93%) was obtained as a red powder. Anal. $C_{63}H_{61}BrN_4O_{18}\cdot 11H_2O$. Calcd: C, 52.54; H, 5.81; N, 3.89. Found: C, 52.77; H, 4.81; N, 4.08. UV–visible spectrum in DMSO: λ_{max} (nm) [ϵ (mmol^{-1} cm^{-1})] 422 (373.7), 517.5 (16.2), 554 (11.5), 592.5 (6.7), 649 (6.6). ^{1}H NMR spectrum in DMSO-d_6: δ 8.87 (s, 6 H, pyrrole), 8.82 (s, 2 H, pyrrole), 8.24 (d, 2 H, *o*-phenyl, J = 7.9 Hz), 8.13 (d, 6 H, *o*-phenoxy, J = 7.9 Hz), 7.89 (d, 2 H, *m*-phenyl, J = 8.3 Hz), 7.48 (d, 6 H, *m*-phenoxy, J = 8 Hz), 5.7 (s, 2 H, CH_2Br), 5.23 (d, 3 H, HC_1 "ose"), 3.82 (d broad, 3 H, H_aC_6 "ose"), 3.54 (m, 3 H, H_bC_6 "ose"), 3.42 (m, 3 H, HC_3 "ose"), −2.91 (s, 2 H, NH). ^{13}C NMR spectrum in DMSO-d_6: δ 157.4 (*p*-C phenoxy), 141 (*meso*-C phenyl), 137 (*p*-C phenyl), 135.1 (*meso*-C and *m*-C phenoxy), 134.5 (*o*-C phenyl), 131 (C-H pyrrole), 127 (*m*-C phenyl), 120 (*meso*-C), 114.3 (*o*-C or *m*-C phenoxy), 100.5 (C_1 "ose"), 73.5 (C_2 "ose"), 60.7 (C_6 "ose"), 45.7 (CH_2Br). MALDI-TOF ($C_{63}H_{61}BrN_4O_{18}$): calcd 1240.32, found M + 1 1241.48.

Chemical Coupling of STxB with TPP(p-O-β-D-GluOH)$_3$(p-CH$_2$Br). STxB-Cys (5 mg/mL) in 20 mM borate buffer (pH 9) and 150 mM NaCl was incubated volume to volume with a 5-fold molar excess of TPP(p-O-β-D-GluOH)$_3$(p-CH$_2$Br) dissolved in DMSO. The reaction was carried out in the dark for 2 h at room temperature. The TPP(p-O-β-D-GluOH)$_3$(p-CH$_2$)−STxB conjugate was separated from monomeric TPP(p-O-β-D-GluOH)$_3$(p-CH$_2$Br) by gel filtration chromatography using PD-10 columns equilibrated with PBS and 10 mM EDTA buffer (pH 8.0).

Mass Spectrometry Analysis. All analyses were performed on a Voyager-DE PRO MALDI-TOF mass spectrometer (Applied Biosystems, Framingham, MA) operated in the delayed extraction and linear mode. A solution of sinapinnic acid in acetonitrile and TFA (30%/0.1%) was used as a matrix. Samples were prepared by mixing them with the matrix at a sample: matrix ratio of 1:1. The mixture (1 μL) was spotted onto a MALDI plate and allowed to dry.

Immunofluorescence Analysis. Immunofluorescence experiments were performed as previously described (*28*). Briefly, cells were incubated for 30 min at 4 °C with 1 μM STxB or TPP(p-O-β-D-GluOH)$_3$(p-CH$_2$)−STxB conjugate, washed, incubated for 45 min at 37 °C, fixed in 4% *p*-formaldehyde for 15 min at

room temperature, quenched with ammonium chloride, and permeabilized with 0.05% saponin. STxB was labeled with the monoclonal anti-STxB antibody (13C4) and revealed by the Cy3-coupled secondary antibody. Then coverslips were mounted and analyzed on a Leica wide field fluorescence microscope.

Receptor Binding Assay. STxB-Glyc-KDEL was iodinated using iodobeads as previously described (*28*). The binding affinities of the TPP(p-O-β-D-GluOH)$_3$(p-CH$_2$)−STxB conjugate and STxB-Cys for cells were compared in competition experiments. These were performed in 24-well plates (10^5 cells per well). Briefly, HeLa cells in triplicate were incubated for 30 min at 4 °C in complete DMEM medium with 20 nM [^{125}I]STxB-Glyc-KDEL (6000 cpm/ng) in the absence or presence of increasing concentrations (4 nM to 2.5 μM) of TPP(p-O-β-D-GluOH)$_3$(p-CH$_2$)−STxB conjugate or STxB-Cys. Cells were washed three times with complete DMEM medium and lysed in 2 × 0.5 mL of 0.1 M KOH buffer. Cell-associated radioactivity was determined using a gamma counter.

Assessment of Singlet Oxygen Formation. The singlet measurements were based on the direct determination by luminescence measurement at 1270 nm of the amount of photosensitizer-generated singlet oxygen [$\Phi_\Delta(^1O_2)$] (*37*). A frequency double Nd:YAG laser (Continuum, Santa Clara, CA) was used for excitation (8 ns half-life), and the luminescence decay kinetics were detected using a germanium detector operating at liquid nitrogen temperature. A silicon filter was used to prevent any fluorescence signal from interfering with the singlet oxygen measurement. Transient decays were averaged using a Tektronix TDS 340 digital oscilloscope and analyzed with software from Edinburgh Instruments. The experiments were conducted using pheophorbide-*a* in deuterated ethanol as a reference [$\Phi_\Delta(^1O_2) = 0.59$] (*38*). Quantum yields of singlet molecular oxygen were determined in oxygen-saturated solutions.

Phototoxicity Assay. HeLa cells were seeded in 96-well plates at a density of 10^5 cells/mL (0.2 mL/well) and allowed to grow for 24 h in an incubator (5% CO_2, 37 °C, humidified atmosphere). On the day of the experiment, the culture medium was removed, and 200 μL of fresh DMEM medium with 2% FCS containing photosensitizers at a final concentration between 1 and 6 μM was added to each well. Cells were incubated at 37 °C for 24 h and then washed before fresh complete medium was added. Illumination was performed in sterile form for 15 min (1.8 J/cm^2) through the bottom of the culture plates using a "light box" made of six Philips TL 13 W tubes (total fluence of 3.8 mW/cm^2) covered by a diffusing glass fitted with an orange filter (0% T at 520 nm and 80% T at 590 nm), leading to a final fluence of 2 mW/cm^2. Controls were as follows: wells containing cells treated with the photosensitizer but not exposed to light, wells containing cells without photosensitizer and without light, and wells containing cells without photosensitizer and exposed to light. Cell viability was measured after 24 h by determination of mitochondrial activity using the MTT assay. At the time of counting, 100 μL of a DMEM/MTT (0.5 mg/mL) solution was added to each well and replaced 4 h later with 200 μL of DMSO. Optical densities of microplates were determined at 540 nm with a Bio-Rad microplate reader (model 450); survival was expressed as a percentage of untreated controls. Each experiment was carried out in triplicate.

Brefeldin A Treatment. Cells were incubated with the TPP(p-O-β-D-GluOH)$_3$(p-CH$_2$)−STxB conjugate (64 μg/mL) for 1 h, alone or in the presence of brefeldin A (BFA, 5 μg/mL). Cells were then washed three times at 4 °C with ice-cooled medium and illuminated as described above before reincubation at 37 °C for 24 h. Cell survival was assessed as described above and compared to unirradiated cultures as well as to BFA-treated cells without photosensitizer and untreated controls.

Statistical Analysis. Results are expressed as the means ± the standard error of the mean. Comparisons were made using an unpaired *t* test; a p of <0.05 was considered to be significant.

RESULTS

Synthesis of Glycoconjugated Photosensitizer. The triglucosylated porphyrin **3** (Scheme 1) is prepared by condensing pyrrole, *p*-2,3,4,6-tetraacetyl-O-β-D-glucosyloxybenzaldehyde (*22*), and bromo-*p*-tolualdehyde (*23*) (4, 3, and 1 equiv, respectively) in moderate yield (31%), using Lindsey's method (*24*). Compound **3** was purified by preparative thin layer chromatography on silica gel and characterized by physical methods. The unprotected glucoconjugated compound **4** (Scheme 1) was obtained quantitatively from **3** by treatment with MeONa and MeOH (*25*) (for experimental details, see Materials and Methods). TPP(p-O-β-D-GluOH)$_3$ (Scheme 1), the unconjugated analogue of the TPP(p-O-β-D-GluOH)$_3$(p-CH$_2$)−STxB conjugate was prepared using Oulmi's method (*26*).

Preparation of Glycoporphyrin−STxB Conjugates. To couple the photosensitizer **4** via its *p*-bromobenzyl substituent to a defined acceptor site on STxB, a cysteine residue was added to the C-terminal part of the protein, yielding STxB-Cys (*27*). The coupling reaction was carried out at room temperature for 2 h using a 5-fold molar excess of glycoporphyrin **4** over STxB-Cys pentamer in borate buffer containing 50% DMSO to minimize glycoporphyrin aggregation. The TPP(p-O-β-D-GluOH)$_3$(p-CH$_2$)−STxB conjugate was separated from nonconjugated compound **4** using gel filtration chromatography and analyzed using MALDI-TOF mass spectrometry. The MALDI-TOF mass spectra displayed two major peaks, one at *m*/*z* 8956 and the other at *m*/*z* 7792 corresponding to the conjugate and the nonmodified STxB-Cys, respectively (Figure 1A). Other, much less intense peaks were observed at *m*/*z* 10120, which could correspond to the coupling of two glycoporphyrin molecules to STxB, and at *m*/*z* 10389, which probably results from the reaction of the double conjugate with the sinapinnic acid matrix used for MALDI-TOF analysis.

In the next step, we examined the intracellular trafficking of the conjugate. Using immunofluorescence analysis, we could show that TPP(p-O-β-D-GluOH)$_3$(p-CH$_2$)−STxB accumulated as efficiently in the Golgi apparatus as STxB-Cys (Figure 1B), demonstrating that the functional properties of STxB were preserved.

Characterization of the Gb3 Binding Capacity of the Conjugate. The immunofluorescence experiment indicated that the TPP(p-O-β-D-GluOH)$_3$(p-CH$_2$)−STxB conjugate could still efficiently bind to its cellular receptor, despite the drastic coupling conditions using high DMSO concentrations and the hydrophobic nature of the glycoporphyrin. To obtain a quantitative measure of receptor binding, we performed in vitro displacement assays using an iodinated Gb3 ligand, termed [^{125}I]STxB-Glyc-KDEL (*28*). The iodinated ligand was incubated with cells in the presence of increasing concentrations of STxB-Cys or TPP(p-O-β-D-GluOH)$_3$(p-CH$_2$)−STxB conjugate (Figure 2). The conjugate was an efficient competitor, albeit with an IC$_{50}$ that was 5-fold higher than that of STxB-Cys. However, this slight decrease in affinity is not specific to the TPP(p-O-β-D-GluOH)$_3$(p-CH$_2$)−STxB conjugate, as it is also observed with STxB conjugates that involve antigenic proteins (not shown).

Quantum Yield of Singlet Oxygen Formation. Light-triggered generation of singlet oxygen by porphyrins, and other tetrapyrrole-based molecules, is the basis for the photodynamic therapy approach to eradicating cancer cells. We compared the photoefficiency of the TPP(p-O-β-D-GluOH)$_3$(p-CH$_2$)−STxB conjugate to that of analogous unconjugated TPP(p-O-β-D-GluOH)$_3$ and found that the singlet oxygen producing ability

Scheme 1. Structure of TPP(p-O-β-D-GluOH)$_3$ and Reaction Scheme for the Synthesis of Glycoconjugated Porphyrin 4

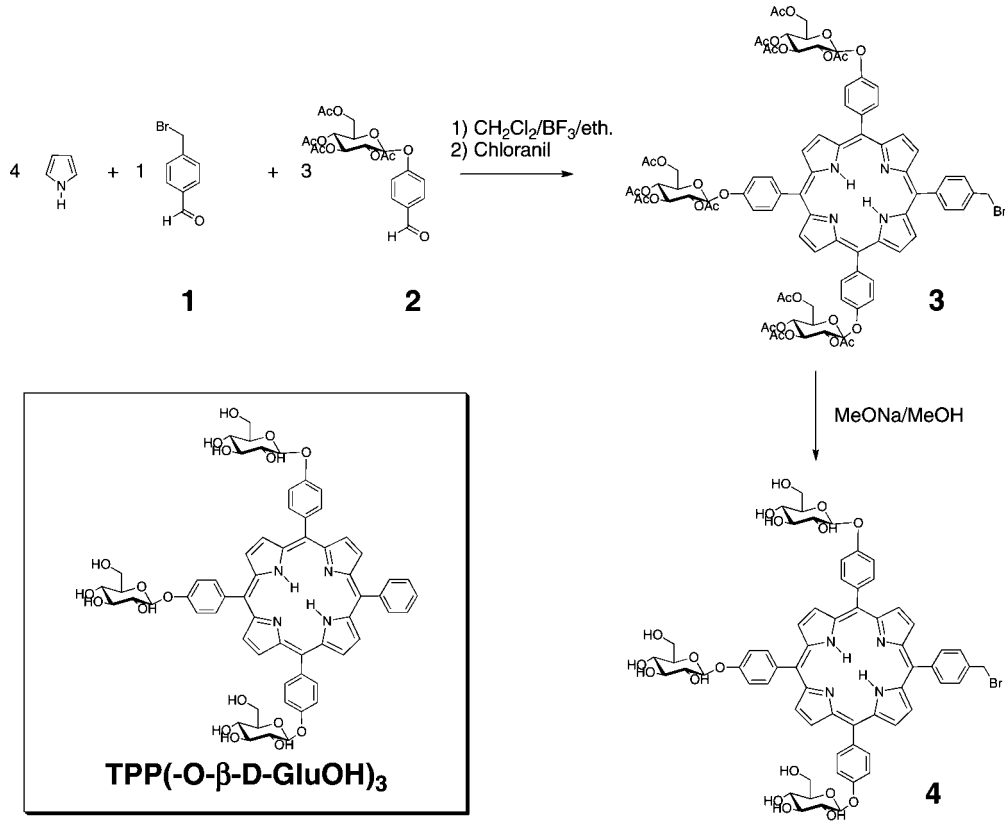

of the conjugate (0.13) was 3 times lower than that of the reference molecule (0.4). It appears that chemical coupling of **4** to STxB induces a reduction of the glycoporphyrin singlet oxygen quantum yield.

Cellular Phototoxicity. The phototoxicity of the free photosensitizer TPP(p-O-β-D-GluOH)$_3$ and the TPP(p-O-β-D-GluOH)$_3$(p-CH$_2$)−STxB conjugate was determined on HeLa cells after exposure to >540 nm light with a fluence of 1.8 J/cm^2. The presence of the STxB receptor in this cell line is well established and was confirmed using receptor binding experiments. Cells were treated with equimolar concentrations of free TPP(p-O-β-D-GluOH)$_3$ and the TPP(p-O-β-D-GluOH)$_3$(p-CH$_2$)−STxB conjugate. We observed that the conjugate was more efficient at photodynamic cell killing than TPP(p-O-β-D-GluOH)$_3$ (Figure 3). Expressed in molar concentration of photosensitizer, the LD$_{50}$ for the conjugate was 0.6 μM, and that of free TPP(p-O-β-D-GluOH)$_3$ was 3 μM, corresponding to a 5-fold sensitization. In the absence of light, toxicity was found to be negligible in all cases, with a survival fraction close to 100% (not shown). Similarly, in the absence of the TPP(p-

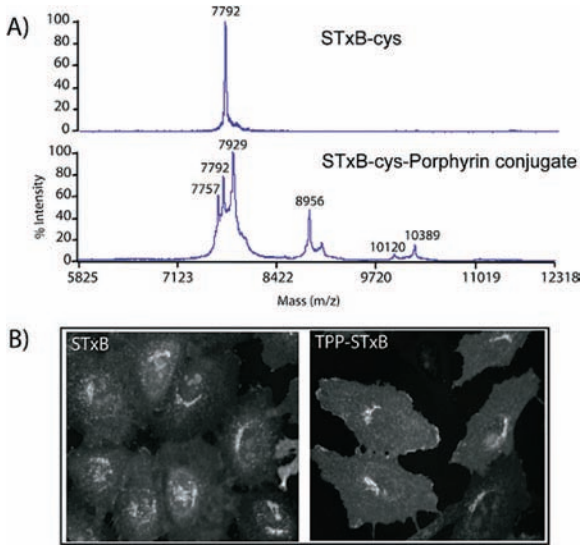

Figure 1. (A) MALDI-TOF mass spectra of STxB-Cys and the TPP(p-O-β-D-GluOH)$_3$(p-CH$_2$)−STxB conjugate. STxB-Cys: *m/z* 7793 (calcd) and 7792 (found). TPP(p-O-β-D-GluOH)$_3$(p-CH$_2$)−STxB conjugate: *m/z* 8954 (calcd) and 8956 (found). Note that in conjugated STxB-Cys, statistically at least one B fragment per homopentamer is modified by a TPP(p-O-β-D-GluOH)$_3$(p-CH$_2$) group. (B) Cellular uptake of STxB-Cys and the TPP(p-O-β-D-GluOH)$_3$(p-CH$_2$)−STxB conjugate. After binding at 4 °C, HeLa cells were washed and incubated at 37 °C for 45 min. The subcellular localization of STxB was determined using a mouse monoclonal anti-STxB antibody (13C4). Note that in both cases, STxB can be detected in perinuclear Golgi membranes.

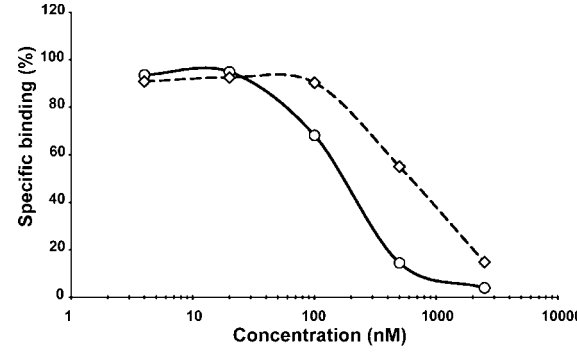

Figure 2. Displacement of [^{125}I]STxB-Glyc-KDEL from binding to Gb3-expressing cells by increasing concentrations of unlabeled STxB-Cys or TPP(p-O-β-D-GluOH)$_3$(p-CH$_2$)−STxB conjugate. HeLa cells were incubated for 30 min at 4 °C with 20 nM [^{125}I]STxB-Glyc-KDEL (6000 cpm/ng) either in the presence or in the absence of the indicated concentrations of unlabeled proteins. Means of two experiments carried out in triplicate: STxB-Cys (○) and TPP(p-O-β-D-GluOH)$_3$(p-CH$_2$)−STxB conjugate (◇).

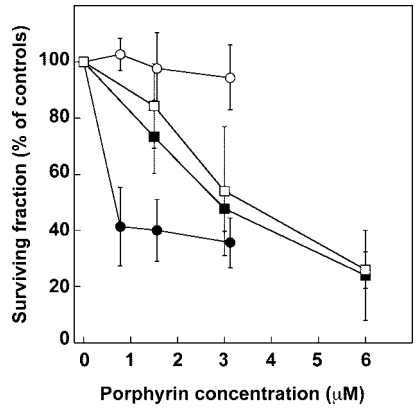

Figure 3. Photodynamic killing of HeLa cells with free TPP(p-O-β-D-GluOH)$_3$ or the TPP(p-O-β-D-GluOH)$_3$(p-CH$_2$)−STxB conjugate. Control or PPMP-treated HeLa cells were incubated for 24 h at 37 °C in the dark with increasing concentrations of free TPP(p-O-β-D-GluOH)$_3$ or TPP(p-O-β-D-GluOH)$_3$(p-CH$_2$)−STxB conjugate. The cells were washed three times, followed by irradiation (λ > 540 nm) at a fluence rate of 2 mW/cm^2 and a light dose of 1.8 J/cm^2. The extent of cell death was measured by determination of mitochondrial activity using the MTT assay. The error bars represent the standard error of the mean of at least three experiments. Reported are effects of free TPP(p-O-β-D-GluOH)$_3$ in control (■) or PPMP-treated HeLa cells (□) and effects of the TPP(p-O-β-D-GluOH)$_3$(p-CH$_2$)−STxB conjugate in control (●) or PPMP-treated HeLa cells (○).

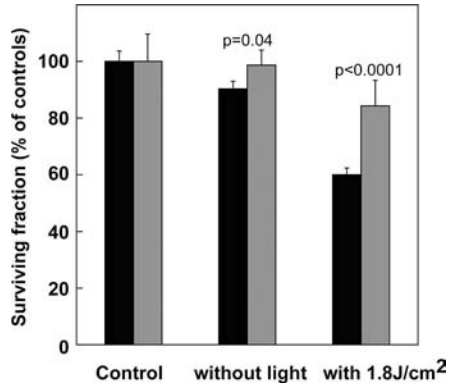

Figure 4. Effect of brefeldin A (BFA, 5 μg/mL) on the photocytotoxicity (1.8 J/cm^2) of the TPP(p-O-β-D-GluOH)$_3$(p-CH$_2$)−STxB conjugate (64 μg/mL, corresponding to 0.3 μM free porphyrin): (black bars) without BFA and (gray bars) BFA-treated.

O-β-D-GluOH)$_3$(p-CH$_2$)−STxB conjugate, cell survival was 100%, a value independent of light exposure (not shown).

To determine whether the phototoxicity of the conjugate was receptor-mediated, we performed the same experiment described above in HeLa cells in which Gb3 expression was inhibited using 1-phenyl-2-hexadecanoyl-amino-3-morphorpholin-1-propanol (PPMP) (*29*). We found that the unconjugated TPP(p-O-β-D-GluOH)$_3$ induced cell death to the same extent in Gb3-expressing and Gb3-deficient cells (Figure 3). In contrast, the conjugate induced a toxic effect in only Gb3-expressing cells, indicating that coupling to STxB provides selective means for the delivery of the photosensitizer to tumor cells (Figure 3).

Intracellular Compartmentalization of Phototoxicity. To measure the importance of optimal phototoxicity of retrograde delivery of TPP(p-O-β-D-GluOH)$_3$ to membranes of the biosynthetic/secretory pathway, we exploited our previous findings that treatment of cells with brefeldin A induces the accumulation of STxB in early endosomes (*30*). As shown in Figure 4, the light-induced phototoxicity of TPP(p-O-β-D-GluOH)$_3$(p-CH$_2$)-STxB was significantly higher in cells in which the conjugate was accumulated in the Golgi apparatus (column 5), when compared to cells in which the conjugate was accumulated in endosomes (column 6). In the absence of light (columns 3 and 4), the difference was much lower, and in the absence of conjugate (columns 1 and 2), it was inexistant. These data strongly suggest that the targeting of the conjugate to Golgi membranes places the photosensitizer in a molecular environment that is optimal for transducing its phototoxic effect.

DISCUSSION

Classical cancer treatments, including surgery, radiation therapy, and chemotherapy, all cause serious side effects by the loss of normal cell function. These phenomena arise because of the lack of unambiguous, identifiable biochemical differences between normal and malignant cells. Even antibody-based approaches are confronted with severe problems that limit their use (*31*). This includes the fact that antibodies are large proteins and do not penetrate well into the tumor mass. Furthermore, antibodies remain in many cases at the cell surface or are degraded in lysosomes, thereby reducing the efficiency by which the active principle reaches intracellular sites of action. To start addressing these limitations, we have developed a PDT approach that exploits the naturally evolved capacity of STxB, a small protein, to target specific intracellular sites (*10*).

The most innovative contribution of our study consists of the demonstration that the phototoxic effect of the glycoconjugated photosensitizer directly depends on its retrograde delivery to membranes of the biosynthetic/secretory pathway. While at this stage we do not have a molecular interpretation of this finding, it is an established fact that many critical cellular functions are regulated on Golgi membranes, such as cell migration (*32*) and signaling (*33*). The localized production of short-lived singlet oxygen species and free radicals may therefore have a profound effect. Retrograde transport also provides access to the endoplasmic reticulum, which has recently been identified as a potential target for anticancer therapy (*34*). The reduced cytotoxic activity of the endosomal photosensitizer may also stem from nonoptimal pH conditions or from exposure to degrading conditions in late endosomes and/or lysosomes.

In a previous study, Tarrago-Trani et al. began exploring the use of STxB for the delivery of the photosensitizing compound chlorin e6 (*18*). However, this work was limited by the fact that no receptor-free condition was tested. In our work, we could demonstrate that the conjugated photosensitizer to Gb3-expressing cells is highly selective in that the phototoxic effect is totally lost on cells in which receptor expression has been inhibited.

As glycoporphyrins are poorly water soluble compounds, one of the principle challenges resides in making them amenable for biodistribution. Toward this end, we first exploited the fact that STxB is a very stable molecule that retains its structural integrity under extreme medium conditions and that readily recovers its native state after unfolding (*35*). Coupling and purification could therefore be conducted in 50% DMSO without significant loss of cell binding and intracellular trafficking activity. Furthermore, STxB resists extracellular inactivation and is capable of crossing tissue barriers (*12*), which should also facilitate the in vivo distribution of photosensitizers onto tumors.

The solubilization effect likely also explains why the TPP(p-O-β-D-GluOH)$_3$(p-CH$_2$)−STxB conjugate is more potent than the glycoporphyrin alone. The immunofluorescence results show that the TPP(p-O-β-D-GluOH)$_3$(p-CH$_2$)−STxB conjugate still efficiently binds to the cellular receptor Gb3. Remarkably, TPP(p-O-β-D-GluOH)$_3$ alone did not provoke any toxicity at the same dose at which the conjugate induced 50% cell death. We notice that the photosensitizing activity of the conjugated glycoporphyrin is 5 times higher than that of the parent molecule, and this despite a reduction in quantum yield after coupling.

In conclusion, our study establishes a strong rational for the use of STxB as a delivery tool for photosensitizing molecules in the development of PDT applications for the treatment of human cancers.

ACKNOWLEDGMENT

Wolfgang Faigle, Jean-Marc Clavel, Damarys Loew (Institut Curie), and Vincent Guérineau (ICSN, CNRS) are acknowledged for their technical assistance. This work was supported by grants from Institut Curie (PIC Vectorisation), Association pour la Recherche sur le Cancer (3105 and 5177), and Fondation de France.

LITERATURE CITED

(1) Dubowchik, G. M., and Walker, M. A. (1999) Receptor-mediated and enzyme-dependent targeting of cytotoxic anticancer drugs. *Pharmacol. Ther. 83*, 67–123.

(2) Dyba, M., Tarasova, N. I., and Michejda, C. J. (2004) Small molecule toxins targeting tumor receptors. *Curr. Pharm. Des. 10*, 2311–2334.

(3) Mangeney, M., Richard, Y., Coulaud, D., Tursz, T., and Wiels, J. (1991) CD77: An antigen of germinal center B cells entering apoptosis. *Eur. J. Immunol. 21*, 1131–1140.

(4) LaCasse, E. C., Bray, M. R., Patterson, B., Lim, W. M., Perampalam, S., Radvanyi, L. G., Keating, A., Stewart, A. K., Buckstein, R., Sandhu, J. S., Miller, N., Banerjee, D., Singh, D., Belch, A. R., Pilarski, L. M., and Gariepy, J. (1999) Shiga-like toxin-1 receptor on human breast cancer, lymphoma, and myeloma and absence from CD34(+) hematopoietic stem cells: Implications for *ex vivo* tumor purging and autologous stem cell transplantation. *Blood 94*, 2901–2910.

(5) Arab, S., Rutka, J., and Lingwood, C. (1999) Verotoxin induces apoptosis and the complete, rapid, long-term elimination of human astrocytoma xenografts in nude mice. *Oncol. Res. 11*, 33–39.

(6) Arab, S., Russel, E., Chapman, W. B., Rosen, B., and Lingwood, C. A. (1997) Expression of the verotoxin receptor glycolipid, globotriaosylceramide, in ovarian hyperplasias. *Oncol. Res. 9*, 553–563.

(7) Kovbasnjuk, O., Mourtazina, R., Baibakov, B., Wang, T., Elowsky, C., Choti, M. A., Kane, A., and Donowitz, M. (2006) The glycosphingolipid globotriaosylceramide in the metastatic transformation of colon cancer. *Proc. Natl. Acad. Sci. U.S.A. 102*, 19087–19092.

(8) Ohyama, C., Fukushi, Y., Satoh, M., Saitoh, S., Orikasa, S., Nudelman, E., Straud, M., and Hakomori, S. (1990) Changes in glycolipid expression in human testicular tumor. *Int. J. Cancer 45*, 1040–1044.

(9) O'Brien, A. D., Tesh, V. L., Donohue-Rolfe, A., Jackson, M. P., Olsnes, S., Sandvig, K., Lindberg, A. A., and Keusch, G. T. (1992) Shiga toxin: Biochemistry, genetics, mode of action, and role in pathogenesis. *Curr. Top. Microbiol. Immunol. 180*, 65–94.

(10) Johannes, L., and Decaudin, D. (2005) Protein toxins: Intracellular trafficking for targeted therapy. *Gene Ther. 16*, 1360–1368.

(11) Sandvig, K., and van Deurs, B. (2005) Delivery into cells: Lessons learned from plant and bacterial toxins. *Gene Ther. 12*, 865–872.

(12) Janssen, K.-P., Vignjevic, D., Boisgard, R., Falguières, T., Bousquet, G., Decaudin, D., Dollé, F., Louvard, D., Tavitian, B., Robine, S., and Johannes, L. (2006) *In vivo* tumor targeting using a novel intestinal pathogen-based delivery approach. *Cancer Res. 66*, 7230–7236.

(13) Ishitoya, S., Kurazono, H., Nishiyama, H., Nakamura, E., Kamoto, T., Habuchi, T., Terai, A., Ogawa, O., and Yamamoto, S. (2004) Verotoxin induces rapid elimination of human renal tumor xenografts in SCID mice. *J. Urol. 171*, 1309–1313.

(14) Heath-Engel, H. M., and Lingwood, C. A. (2003) Verotoxin sensitivity of ECV304 cells *in vitro* and *in vivo* in a xenograft tumour model: VT1 as a tumour neovascular marker. *Angiogenesis 6*, 129–141.

(15) Salhia, B., Rutka, J. T., Lingwood, C., Nutikka, A., and Van Furth, W. R. (2002) The treatment of malignant meningioma with verotoxin. *Neoplasia 4*, 304–311.

(16) LaCasse, E. C., Saleh, M. T., Patterson, B., Minden, M. D., and Gariepy, J. (1996) Shiga-like toxin purges human lymphoma from bone marrow of severe combined immunodeficient mice. *Blood 88*, 1561–1567.

(17) El Alaoui, A., Schmidt, F., Amessou, M., Florent, J. C., and Johannes, L. (2007) Shiga toxin-mediated retrograde delivery of a topoisomerase I inhibitor prodrug. *Angew. Chem., Int. Ed. 46*, 6469–6472.

(18) Tarrago-Trani, M. T., Jiang, S., Harich, K. C., and Storrie, B. (2006) Shiga-like toxin subunit B (SLTB)-enhanced delivery of chlorin e6 (Ce6) improves cell killing. *Photochem. Photobiol. 82*, 527–537.

(19) MacDonald, I. J., and Dougherty, T. J. (2001) Basic principles of photodynamic therapy. *J. Porphyrins Phthalocyanines 5*, 105–129.

(20) Wojtyk, J. T., Goyan, R., Gudgin-Dickson, E., and Pottier, R. (2006) Exploiting tumour biology to develop novel drug delivery strategies for PDT. *Med. Laser Appl. 21*, 225–238.

(21) Sharman, W. M., van Lier, J. E., and Allen, C. M. (2004) Targeted photodynamic therapy via receptor mediated delivery systems. *Adv. Drug Delivery Rev. 56*, 53–76.

(22) Halazy, S., Berges, V., Ehrhard, A., and Danzin, C. (1990) *Ortho*- and *para*-(difluoromethyl)aryl-β-image-glucosides: A new class of enzyme-activated irreversible inhibitors of β-glucosidases. *Bioorg. Chem. 18*, 330–344.

(23) Wen, L., Li, M., and Schlenoff, J. B. (1997) Polyporphyrin thin films from interfacial polymerization of mercaptoporphyrins. *J. Am. Chem. Soc. 119*, 7726–7733.

(24) Lindsey, J. S., Schreiman, I. C., Hsu, H. C., Kearney, P. C., and Marguerettaz, A. M. (1987) Rothemund and Adler-Longo reactions revisited: Synthesis of tetraphenylporphyrins under equilibrium conditions. *J. Org. Chem. 52*, 827–836.

(25) Zemplén, G. (1927) Abbau der reduzierenden biosen. *Ber. Dtsch. Chem. Ges.* 1555–1564.

(26) Oulmi, D., Maillard, P., Guerquin-Kern, J.-L., Huel, C., and Momenteau, M. (1995) Glyconjugated porphyrins. 3 Synthesis of flat amphiphilic meso-(glycosylated-aryl)-aryl porphyrins and mixed meso-(glycosylated-aryl)-alkyl porphyrins bearing some mono and disaccharide groups. *J. Org. Chem. 60*, 1554–1564.

(27) Haicheur, N., Benchetrit, F., Amessou, M., Leclerc, C., Falguières, T., Fayolle, C., Bismuth, E., Fridman, W. H., Johannes, L., and Tartour, E. (2003) The B-subunit of Shiga toxin coupled to full-size protein elicits humoral and cellular immune responses associated with a TH1 dominant polarization. *Int. Immunol. 15*, 1161–1171.

(28) Johannes, L., Tenza, D., Antony, C., and Goud, B. (1997) Retrograde transport of KDEL-bearing B-fragment of Shiga toxin. *J. Biol. Chem. 272*, 19554–19561.

(29) Abe, A., Inokuchi, J., Jimbo, M., Shimeno, H., Nagamatsu, A., Shayman, J. A., Shukla, G. S., and Radin, N. S. (1992) Improved inhibitors of glucosylceramide synthase. *J. Biochem. 111*, 191–196.

(30) Mallard, F., Tenza, D., Antony, C., Salamero, J., Goud, B., and Johannes, L. (1998) Direct pathway from early/recycling endosomes to the Golgi apparatus revealed through the study of Shiga toxin B-fragment transport. *J. Cell Biol. 143*, 973–990.

(31) Sharkey, R. M., and Goldenberg, D. M. (2006) Targeted therapy of cancer: New prospects for antibodies and immunoconjugates. *CA Cancer J. Clin. 56*, 226–243.

(32) Mellor, H. (2004) Cell motility: Golgi signalling shapes up to ship out. *Curr. Biol. 14*, R434–R435.

(33) Mor, A., and Philips, M. R. (2006) Compartmentalized Ras/MAPK signaling. *Annu. Rev. Immunol. 24*, 771–800.

(34) Boelens, J., Lust, S., Offner, F., Bracke, M. E., and Vanhoecke, B. W. (2007) Review. The endoplasmic reticulum: A target for new anticancer drugs. *In Vivo 21*, 215–226.

(35) Pina, D. G., Gomez, J., Villar, E., Johannes, L., and Shnyrov, V. L. (2003) Thermodynamic analysis of the structural stability of Shiga toxin B-subunit. *Biochemistry 42*, 9498–9506.

(36) Mallard, F., and Johannes, L. (2003) Shiga toxin B-subunit as a tool to study retrograde transport. In *Methods in Molecular Medicine: Shiga Toxin Methods and Protocols* (Philpott, D., and Ebel, F., Eds.), Vol. 73, Chapter 17, pp 209–220.

(37) Bautista-Sanches, A., Kasselouri, T., Desroches, M. C., Blais, J., Maillard, P., de Oliveira, D. M., Tedesco, A. C., Prognon, P., and Delaire, J. (2005) Photophysical properties of glucoconjugated chlorins and porphyrins and their associations with cyclodextrins. *J. Photochem. Photobiol., B 81*, 154–162.

(38) Spiller, W., Kliesch, H., Wohrle, D., Hackbarth, S., Roder, B., and Schnurpfeil, G. (1998) Singlet oxygen quantum yields of different photosensitizers in polar solvents and micellar solutions. *J. Porphyrins Phthalocyanines 2*, 145–158.

BC7003999

^{111}In-Labeled Lactam Bridge-Cyclized α-Melanocyte Stimulating Hormone Peptide Analogues for Melanoma Imaging

Yubin Miao,*[,†,‡] Fabio Gallazzi,[§] Haixun Guo,[†] and Thomas P. Quinn[§,△,⊥]

College of Pharmacy, Cancer Research Treatment Center, and Department of Dermatology, University of New Mexico, Albuquerque, New Mexico 87131, Departments of Biochemistry and Radiology, University of Missouri, Columbia, Missouri 65211, and Harry S. Truman Memorial Veteran Hospital, Columbia, Missouri 65201. Received August 21, 2007; Revised Manuscript Received November 27, 2007

The purpose of this study was to examine the influence of the lactam bridge cyclization on melanoma targeting and biodistribution properties of the radiolabeled conjugates. Two novel lactam bridge-cyclized α-MSH peptide analogues, DOTA-CycMSH (1,4,7,10-tetraazacyclododecane-1,4,7,10-tetraacetic acid-c[Lys-Nle-Glu-His-DPhe-Arg-Trp-Gly-Arg-Pro-Val-Asp]) and DOTA-GlyGlu-CycMSH (DOTA-Gly-Glu-c[Lys-Nle-Glu-His-DPhe-Arg-Trp-Gly-Arg-Pro-Val-Asp]), were synthesized and radiolabeled with ^{111}In. The internalization and efflux of ^{111}In-labeled CycMSH peptides were examined in B16/F1 melanoma cells. The melanoma targeting properties, pharmacokinetics, and SPECT/CT imaging of ^{111}In-labeled CycMSH peptides were determined in B16/F1 melanoma-bearing C57 mice. Both ^{111}In-DOTA-CycMSH and ^{111}In-DOTA-GlyGlu-CycMSH exhibited fast internalization and extended retention in B16/F1 cells. The tumor uptake values of ^{111}In-DOTA-CycMSH and ^{111}In-DOTA-GlyGlu-CycMSH were 9.53 ± 1.41% injected dose/gram (% ID/g) and 10.40 ± 1.40% ID/g at 2 h postinjection, respectively. Flank melanoma tumors were clearly visualized with ^{111}In-DOTA-CycMSH and ^{111}In-DOTA-GlyGlu-CycMSH by SPECT/CT images at 2 h postinjection. Whole-body clearance of the peptides was fast, with greater than 90% of the radioactivities cleared through urinary system by 2 h postinjection. There was low radioactivity (<0.8% ID/g) accumulated in blood and normal organs except kidneys at all time points investigated. Introduction of a negatively charged linker (-Gly-Glu-) into the peptide sequence decreased the renal uptake by 44% without affecting the tumor uptake at 4 h postinjection. High receptor-mediated melanoma uptakes coupled with fast whole-body clearance in B16/F1 melanoma-bearing C57 mice demonstrated the feasibility of using ^{111}In-labeled lactam bridge-cyclized α-MSH peptide analogues as a novel class of imaging probes for receptor-targeting melanoma imaging.

INTRODUCTION

Skin cancer is the most commonly diagnosed cancer in the United States. Malignant melanoma is the most lethal form of skin cancer and the most commonly diagnosed malignancy among young adults with an increasing incidence. It is predicted that there will be 59 940 cases of malignant melanoma newly reported and 8110 fatalities in 2007 (*1*). There is a great need to develop novel imaging probes and treatment approaches for melanoma detection and therapy since early diagnosis and prompt surgical removal are a patient's best hope for a cure. Although 2-[^{18}F]fluoro-2-deoxy-D-glucose ([^{18}F]FDG) is commonly used for positron emission tomography (PET) diagnosis and staging of melanoma, [^{18}F]FDG is not melanoma-specific and some melanoma cells are not detected by [^{18}F]FDG since they use substrates other than glucose as energy sources (*2, 3*). Alternatively, the G-protein-coupled melanocortin-1 (MC1) receptors have been used as targets for melanoma imaging peptides due to their overexpression on human and mouse melanoma cells (*4–8*). Radiolabeled α-melanocyte stimulating hormone (α-MSH) peptide analogues, derived from wild-type α-MSH, are very promising candidates for melanoma imaging and therapy due to their nanomolar MC1 receptor binding affinities and high receptor-mediated tumor uptakes in murine melanoma-bearing mice and human melanoma xenografts (*9–13*).

The strategy of peptide cyclization was used to improve binding affinity, *in vivo* stability, and receptor selectivity of the α-MSH peptides (*14–16*). Compared to the linear peptides, the cyclic peptides possess less conformational freedom due to the stabilization of secondary structures such as beta turns, which results in greater receptor binding affinities. Furthermore, the constrained cyclic peptides confer higher stability against the proteolytic degradations *in vivo* (*17*). Peptide cyclization strategies can be generally classified into four types, namely, (1) backbone to backbone; (2) N-terminus to C-terminus; (3) one side chain to C-terminus or N-terminus; (4) two side chains via disulfide or lactam bridges. Over the past several years, peptide cyclization through metal coordination has been successfully employed in developing radiolabeled cyclic α-MSH peptide analogues for melanoma imaging and therapy. Metal cyclization made the α-MSH peptide analogues resistant to chemical and proteolytic degradation *in vivo* (*18, 19*). ^{111}In-DOTA-Re[Cys^{3,4,10}, D-Phe^{7}]-α-MSH$_{3-13}$} (^{111}In-DOTA-ReCCMSH) exhibited 11.4 ± 2.89% injected dose/gram (% ID/g) tumor uptake 2 h postinjection in the B16/F1 murine melanoma mouse model (*19*). A comparison of biodistribution data between ^{111}In-labeled DOTA-conjugated metal-cyclized and disulfide bridge-cyclized α-MSH peptide analogues demonstrated that the metal cyclization resulted in more favorable pharmacokinetics

* Corresponding author. Yubin Miao, 2502 Marble NE, MSC09 5360, College of Pharmacy, University of New Mexico, Albuquerque, NM 87131-0001. Phone: (505) 925-4437; Fax: (505) 272-6749 ; E-mail: ymiao@salud.unm.edu.

† College of Pharmacy, University of New Mexico.

‡ Cancer Research Treatment Center and Department of Dermatology, University of New Mexico.

§ Department of Biochemistry, University of Missouri.

△ Department of Radiology, University of Missouri.

⊥ Harry S. Truman Memorial Veteran Hospital.

10.1021/bc700317w CCC: $40.75 © 2008 American Chemical Society
Published on Web 01/16/2008

of radiolabeled peptides, such as higher tumor uptake and lower renal uptake values (*19*), indicating that the different cyclization strategies might dramatically affect the biodistribution properties of peptides with comparable *in vitro* binding affinities.

In this study, Lys-Asp lactam bridge cyclization was employed to the α-MSH peptides to examine its effect on melanoma targeting and pharmacokinetics of the radiolabeled peptides. Two novel DOTA-conjugated lactam bridge-cyclized α-MSH peptide analogues, namely, DOTA-CycMSH and DOTA-GlyGlu-CycMSH, were synthesized and characterized by liquid chromatography–mass spectrometry (LC-MS). A negatively charged linker of -Gly-Glu- was introduced between DOTA and CycMSH sequences to determine its effect in reducing the renal uptake value of the radiolabeled peptide. The pharmacokinetics and SPECT/CT imaging of ^{111}In-labeled lactam bridge-cyclized α-MSH peptides were determined in B16/F1 melanoma-bearing C57 mice to evaluate their potential as SPECT imaging probes for melanoma detection.

EXPERIMENTAL PROCEDURES

Chemicals and Reagents. Amino acid and resin were purchased from Advanced ChemTech Inc. (Louisville, KY) and Novabiochem (San Diego, CA). DOTA-tri-*t*-butyl ester was purchased from Macrocyclics Inc. (Richardson, TX). $^{111}InCl_3$ was purchased from Mallinckrodt, Inc. (St. Louis, MO). All other chemicals used in this study were purchased from Thermo Fischer Scientific (Waltham, MA) and used without further purification. B16/F1 murine melanoma cells were obtained from American Type Culture Collection (Manassas, VA).

Peptide Synthesis. Intermediate scaffold of H_2N-Lys(Dde)-Nle-Glu(OtBu)-His(Trt)-DPhe-Arg(Pbf)-Trp(Boc)-Gly Arg(Pbf)-Pro-Val was synthesized on Val-2-Chlorotrityl Chloride (Val-2ClTrt) resin using standard 9-fluorenylmethyloxycarbonyl (Fmoc) chemistry by an Advanced ChemTech multiple-peptide synthesizer (Louisville, KY). A small aliquot of the scaffold material was cleaved and characterized by LC-MS. Gly Glu-(OtBu) and DOTA-tri-*t*-butyl ester were manually attached to the intermediate scaffold using standard Fmoc chemistry, respectively. Protected branched peptide was cleaved from the resin treating with 25% hexafluoroisopropanol (HFIP) and 5% triisopropylsilane (TIS) in dichloromethane (DCM) and characterized by LC-MS. Peptide cyclization between the acid moiety of Val and the amino group of Asp coupled to the Lys side chain was achieved by overnight reaction in DMF in the presence of 1 mM 1-hydroxybenzotriazole (HOBT), 2-(1*H*-benzotriazole-1-yl)-1,1,3,3-tetranethyluronium hexafluorophosphate (HBTU), and *N*,*N*-diisopropylethylamine (DIEA) mixture. The protecting groups were totally removed by treating with a mixture of trifluoroacetic acid (TFA), thioanisole, phenol, water, ethanedithiol, and triisopropylsilane (87.5:2.5:2.5:2.5:2.5:2.5) for 2 h at room temperature (25 °C). The peptides were precipitated and washed with ice-cold ether for four times. The final products were purified by RP-HPLC and characterized by LC-MS.

***In Vitro* Competitive Binding Assay.** The IC_{50} values of DOTA-CycMSH and DOTA-GlyGlu-CycMSH were determined by using methods described previously (*8*). B16/F1 cells were harvested and seeded into a 24-well cell culture plate (5×10^5/well) and incubated at 37 °C overnight. After being washed once with binding media (MEM with 25 mM HEPES, pH 7.4, 0.2% BSA, 0.3 mM 1,10-phenathroline), the cells were incubated at room temperature (25 °C) for 2 h with approximately 50 000 cpm of ^{125}I-Tyr^2-[Nle^4, D-Phe^7]-α-MSH {NDP-MSH} (GE HealthCare, Piscataway, NJ) in the presence of increasing concentrations of DOTA-CycMSH or DOTA-GlyGlu-CycMSH in 0.3 mL of binding media. The reaction media were aspirated after incubation. Cells were rinsed with 0.5 mL of ice-cold pH 7.4, 0.2% BSA/0.01 M PBS twice and lysed in 0.5 mL of 1 N NaOH for 5 min. The activities in cells were measured in a gamma counter. The IC_{50} values for the peptides were calculated by using the Grafit software (Erithacus Software Limited, UK).

Complexation of the Peptide with ^{111}In. ^{111}In-DOTA-CycMSH and ^{111}In-DOTA-GlyGlu-CycMSH were prepared using a 0.5 M NH_4OAc-buffered solution at pH 5.4. Briefly, 50 μL of $^{111}InCl_3$ (18.5–37.0 MBq in 0.05 M HCl), 10 μL of 1 mg/ml DOTA-CycMSH or DOTA-GlyGlu-CycMSH aqueous solution, and 400 μL of 0.5 M NH_4OAc (pH 5.4) were added into a reaction vial and incubated at 75 °C for 45 min. After the incubation, 20 μL of 0.5% EDTA aqueous solution was added into the reaction vial to scavenge potential unbound ^{111}In. The radiolabeled complexes were purified to single species by Waters RP-HPLC (Milford, MA) on a Grace Vadyc C-18 reverse-phase analytical column (Deerfield, IL) using a 20 min gradient of 16–26% acetonitrile in 20 mM HCl aqueous solution with a flow rate of 1 mL/min. Purified peptide samples were purged with N_2 gas for 20 min to remove the acetonitrile. The pH of final solution was adjusted to 7.4 with 0.1 N NaOH and normal saline for animal studies. The stability of ^{111}In-DOTA-CycMSH and ^{111}In-DOTA-GlyGlu-CycMSH was determined by incubation in mouse serum at 37 °C according to the published procedure (*20*) for various time periods, and monitored for degradation by RP-HPLC.

Cellular Internalization and Efflux of ^{111}In-labeled Peptides. Cellular internalization and efflux of ^{111}In-DOTA-CycMSH and ^{111}In-DOTA-GlyGlu-CycMSH were evaluated in B16/F1 cells as described by Miao et al. (*21*). After being washed once with binding media (MEM with 25 mM HEPES, pH 7.4, 0.2% BSA, 0.3 mM 1,10-phenathroline), B16/F1 cells in cell culture plates were incubated at 25 °C for 20, 40, 60, 90, and 120 min ($n = 4$) in the presence of approximately 200 000 counts per minute (cpm) of HPLC-purified ^{111}In-DOTA-CycMSH (0.019 pmol) or ^{111}In-DOTA-GlyGlu-CycMSH (0.019 pmol). After incubation, the reaction media were aspirated and cells were rinsed with 2×0.5 mL of ice-cold pH 7.4, 0.2% BSA/0.01 M PBS. Cellular internalization of radiolabeled peptides was assessed by washing the cells with acidic buffer [40 mM sodium acetate (pH 4.5) containing 0.9% NaCl and 0.2% BSA] to remove the membrane-bound radioactivity. The remaining internalized radioactivity was obtained by lysing the cells with 0.5 mL of 1 N NaOH for 5 min. Membrane-bound and internalized ^{111}In activities were counted in a gamma counter. Cellular efflux of radiolabeled peptides was determined by incubating B16/F1 cells with ^{111}In-DOTA-CycMSH and ^{111}In-DOTA-GlyGlu-CycMSH for 2 h at 25 °C, removing nonspecific-bound activity with 2×0.5 mL of ice-cold pH 7.4, 0.2% BSA/0.01 M PBS rinse, and monitoring radioactivity released into cell culture media. At time points of 20, 40, 60, 90, and 120 min, the radioactivities in media, on cell surface, and in cells were separately collected and counted in a gamma counter.

Biodistribution Studies. All the animal studies were conducted in compliance with Institutional Animal Care and Use Committee approval. The pharmacokinetics of ^{111}In-DOTA-CycMSH and ^{111}In-DOTA-GlyGlu-CycMSH were determined in B16/F1 murine melanoma-bearing C57 female mice (Harlan, Indianapolis, IN). C57 mice were inoculated subcutaneously with 1×10^6 B16/F1 murine melanoma cells in the right flank. After 10 days, when the weight of tumors reached approximately 0.2 g, 0.037 MBq of ^{111}In-DOTA-CycMSH or ^{111}In-DOTA-GlyGlu-CycMSH was injected into each mouse through the tail vein. Groups of 5 mice were sacrificed at 2, 4, and 24 h postinjection, and tumors and organs of interest were harvested, weighed, and counted. Blood values were taken as 6.5% of the whole-body weight. The tumor uptake specificity of ^{111}In-DOTA-CycMSH and ^{111}In-DOTA-GlyGlu-CycMSH was de-

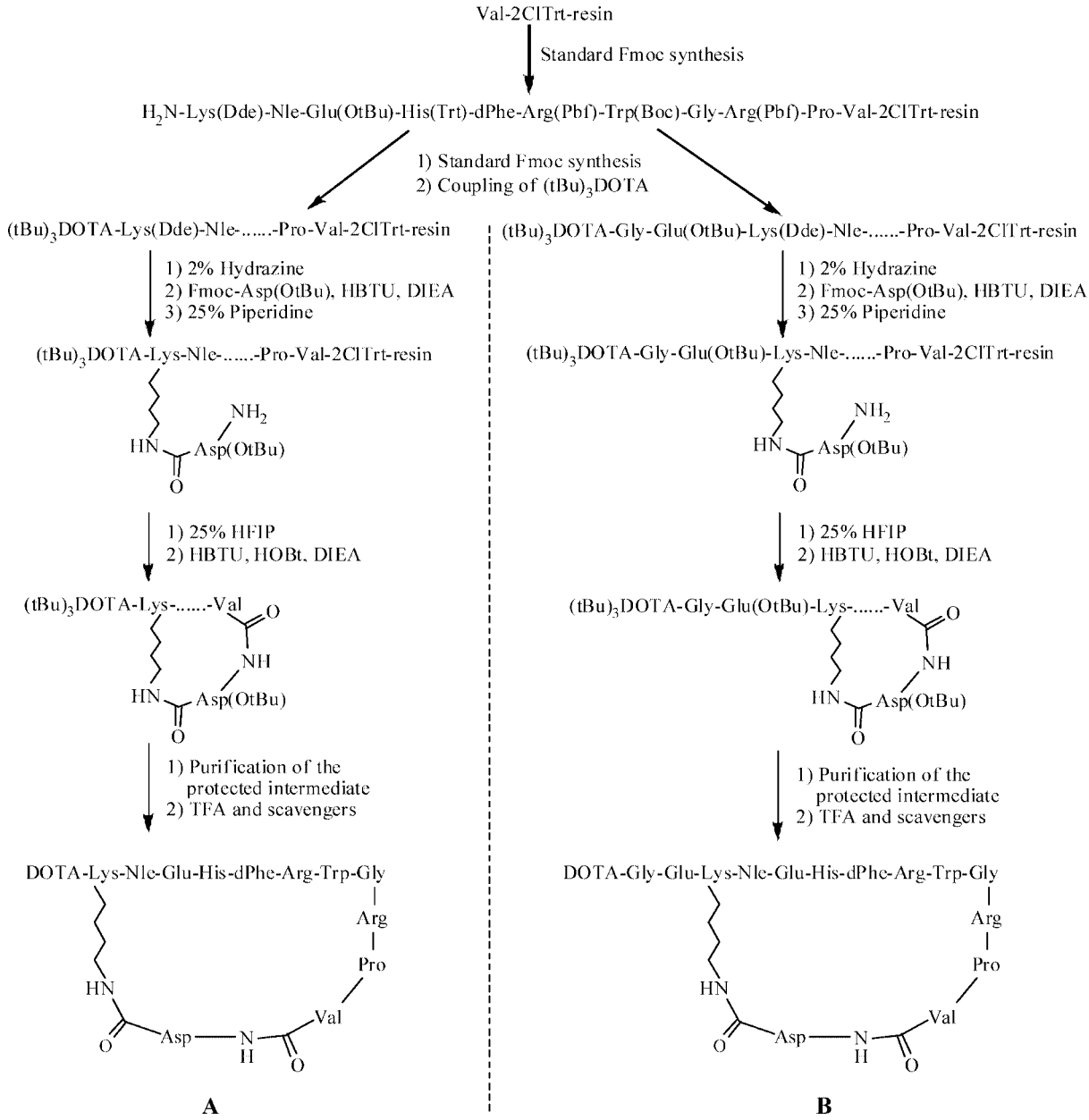

Figure 1. Synthetic schemes of DOTA-CycMSH (A) and DOTA-GlyGlu-CycMSH (B).

termined by blocking tumor uptake with the coinjection of 10 μg (6.07 nmol) of unlabeled NDP-MSH, a linear α-MSH peptide analogue with picomolar affinity for the MC1 receptors present on murine melanoma cells. Statistical analysis was performed using the Student's *t* test for unpaired data. A 95% confidence level was chosen to determine the significance between radiolabeled compounds, with $p < 0.05$ being significantly different.

Imaging Melanoma with ^{111}In-DOTA-CycMSH and ^{111}In-DOTA-GlyGlu-CycMSH. Two B16/F1 melanoma-bearing C57 mice were injected with 13.7 MBq of ^{111}In-DOTA-CycMSH or ^{111}In-DOTA-GlyGlu-CycMSH via the tail vein, respectively. The mice were euthanized for micro-CT imaging immediately followed by micro-SPECT imaging at 2 h postinjection. Micro-SPECT scans of 60 frames for each animal were acquired and total counts acquisitions of 524 672 and 278 242 counts (2 h acquisition) were achieved for both SPECT scans, respectively. The micro-SPECT images were obtained using the Micro-CAT II CT/SPECT (Siemens) unit equipped with high-resolution 2 mm pinhole collimators (*22*). Reconstructed data from SPECT and CT were visualized and coregistered using Amira 3.1 (Ascent Media System & Technology Service, Northvale, NJ).

Urinary Metabolites of ^{111}In-DOTA-CycMSH and ^{111}In-DOTA-GlyGlu-CycMSH. 100 μL of HPLC-purified ^{111}In-DOTA-CycMSH (0.74–1.11 MBq, 0.82–1.12 ng) or ^{111}In-DOTA-GlyGlu-CycMSH (0.74–1.11 MBq, 0.90–1.35 ng) was injected into each B16/F1 murine melanoma-bearing C57 mouse through the tail vein. At 2 h after dose administration, mice were sacrificed and the urine was collected. The radioactive metabolites in the urine were analyzed by injecting aliquots of urine into HPLC. A 20 min gradient of 16–26% acetonitrile/20 mM HCl was used for the urine analysis.

RESULTS

DOTA-CycMSH and DOTA-GlyGlu-CycMSH were synthesized and purified by RP-HPLC, and the identities of peptides were confirmed by electrospray ionization mass spectrometry. The synthetic schemes are presented in Figure 1. The competitive binding curves of DOTA-CycMSH and DOTA-GlyGlu-CycMSH are shown in Figure 2. The IC_{50} values of DOTA-

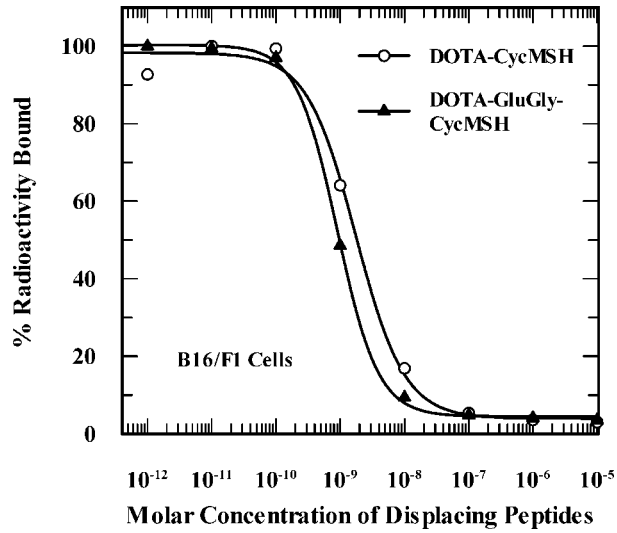

Figure 2. The competitive binding curves of DOTA-CycMSH and DOTA-GlyGlu-CycMSH in B16/F1 murine melanoma cells. The IC_{50} values of DOTA-CycMSH and DOTA-GlyGlu-CycMSH were 1.75 nM and 0.90 nM.

CycMSH and DOTA-GlyGlu-CycMSH were 1.75 nM and 0.90 nM in B16/F1 cells. The peptides were labeled with ^{111}In using a 0.5 M NH_4OAc-buffered solution at pH 5.4. The radiolabeling yields were greater than 95% for both peptides. ^{111}In-DOTA-CycMSH and ^{111}In-DOTA-GlyGlu-CycMSH were completely separated from their excess nonlabeled peptides by RP-HPLC. The retention times of ^{111}In-DOTA-CycMSH and ^{111}In-DOTA-GlyGlu-CycMSH were 15.4 and 18.0 min, respectively. The specific activities of ^{111}In-DOTA-CycMSH and ^{111}In-DOTA-GlyGlu-CycMSH were 9.03×10^8 and 8.23×10^8 MBq/g, respectively. ^{111}In-DOTA-CycMSH and ^{111}In-DOTA-GlyGlu-CycMSH were stable in mouse serum at 37 °C. Only the ^{111}In-labeled peptides were detected by RP-HPLC after 24 h of incubation (Figure 3).

Cellular internalization and efflux of ^{111}In-DOTA-CycMSH and ^{111}In-DOTA-GlyGlu-CycMSH were evaluated in B16/F1 cells at 25 °C. Figure 4 illustrates cellular internalization and efflux of ^{111}In-DOTA-CycMSH and ^{111}In-DOTA-GlyGlu-CycMSH. Both ^{111}In-DOTA-CycMSH and ^{111}In-DOTA-GlyGlu-CycMSH exhibited rapid cellular internalization and extended cellular retention. There were 73.71 ± 1.71% of the ^{111}In-DOTA-CycMSH and 66.19 ± 2.12% of the ^{111}In-DOTA-GlyGlu-CycMSH activity internalized in the B16/F1 cells 40 min postincubation. There were 81.98 ± 2.02% of the ^{111}In-DOTA-CycMSH and 78.93 ± 0.64% of the ^{111}In-DOTA-GlyGlu-CycMSH activity internalized in the cells after 2 h incubation. Cellular efflux experiments demonstrated that 90.26 ± 1.71% of the ^{111}In-DOTA-CycMSH activity and 90.00 ± 1.10% of the ^{111}In-DOTA-GlyGlu-CycMSH activity remained inside the cells 2 h after incubating cells in culture media at 25 °C.

The pharmacokinetics and tumor targeting properties of ^{111}In-DOTA-CycMSH and ^{111}In-DOTA-GlyGlu-CycMSH were determined in B16/F1 murine melanoma-bearing C57 mice. The biodistribution of ^{111}In-DOTA-CycMSH and ^{111}In-DOTA-GlyGlu-CycMSH are shown in Table 1. Both ^{111}In-DOTA-CycMSH and ^{111}In-DOTA-GlyGlu-CycMSH exhibited very rapid and high tumor uptakes. At 2 h postinjection, ^{111}In-DOTA-CycMSH and ^{111}In-DOTA-GlyGlu-CycMSH reached their peak tumor uptake values of 9.53 ± 1.41 and 10.40 ± 1.40% ID/g, respectively. There were 7.54 ± 0.70% ID/g of the ^{111}In-DOTA-CycMSH and 7.40 ± 0.43% ID/g of the ^{111}In-DOTA-GlyGlu-CycMSH activity remained in the tumors 4 h postinjection. The tumor uptake values of ^{111}In-DOTA-CycMSH and ^{111}In-DOTA-GlyGlu-CycMSH decreased to 2.22 ± 0.51 and 2.37 ± 0.28% ID/g at 24 h postinjection. In competition studies, the tumor uptakes of ^{111}In-DOTA-CycMSH and ^{111}In-DOTA-GlyGlu-CycMSH with 10 μg (6.07 nmol) of nonradiolabeled NDP coinjection were only 3.0% and 2.6% of the tumor uptake without NDP coinjection at 2 h after dose administration ($p < 0.01$), demonstrating that the tumor uptakes were specific and receptor-mediated. Whole-body clearance of ^{111}In-DOTA-CycMSH and ^{111}In-DOTA-GlyGlu-CycMSH was very rapid, with approximately 90% of the injected radioactivity cleared through the urinary system by 2 h postinjection (Table 1).

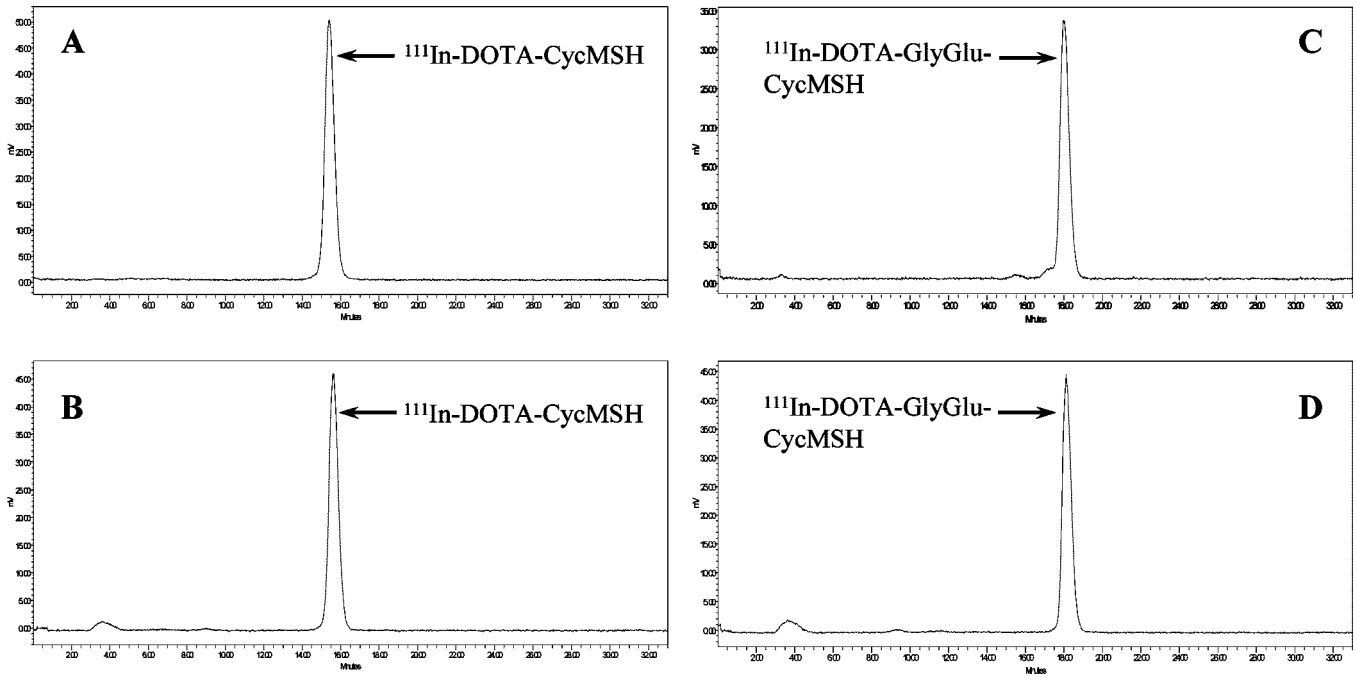

Figure 3. HPLC profiles of radioactive ^{111}In-DOTA-CycMSH (A), ^{111}In-DOTA-GlyGlu-CycMSH (C) and mouse serum stability of ^{111}In-DOTA-CycMSH (B), ^{111}In-DOTA-GlyGlu-CycMSH (D) after 24 h incubation at 37 °C, respectively. The retention times of ^{111}In-DOTA-CycMSH and ^{111}In-DOTA-GlyGlu-CycMSH were 15.4 and 18.0 min, respectively.

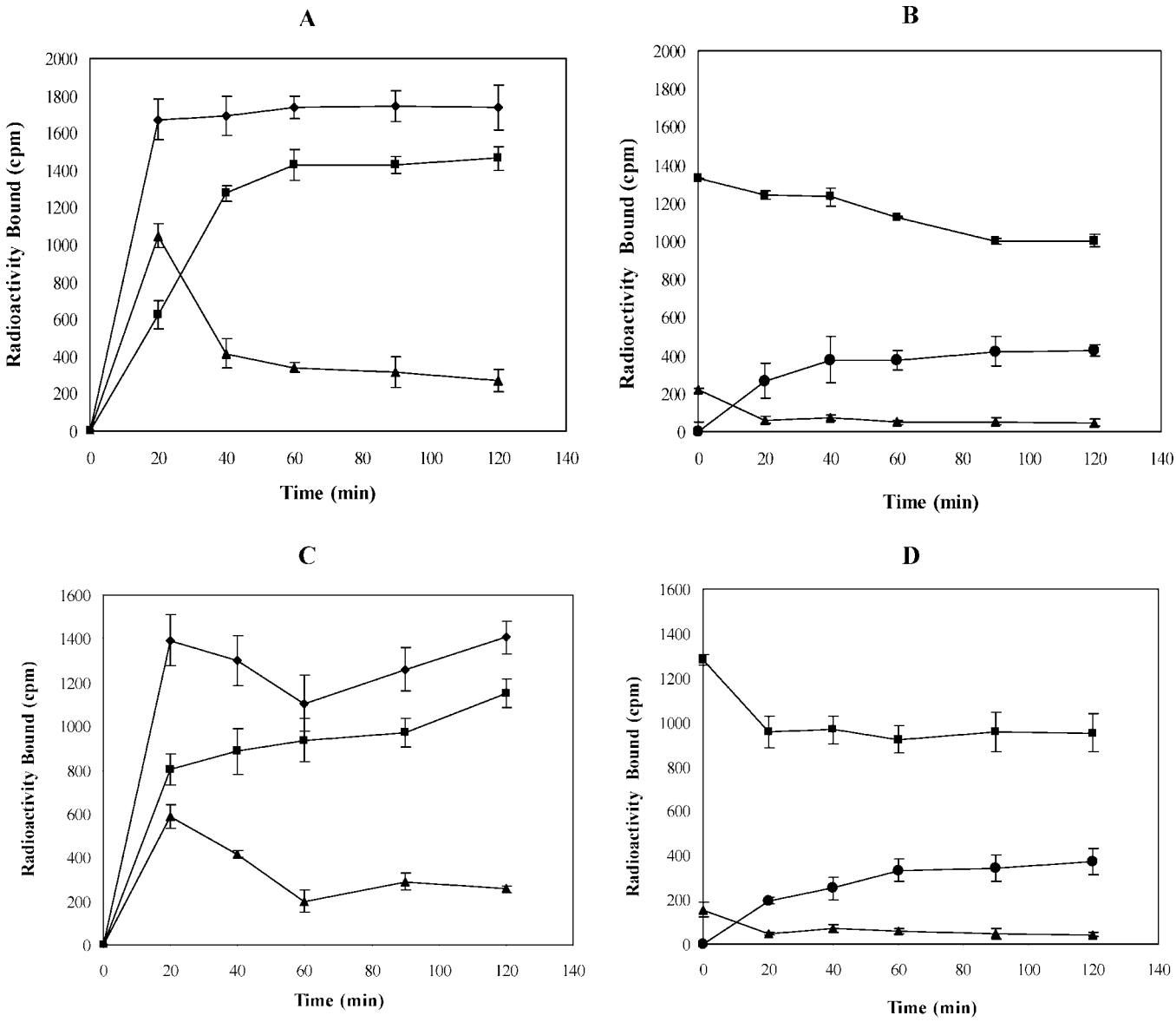

Figure 4. Cellular internalization and efflux of ^{111}In-DOTA-CycMSH (A and B) and ^{111}In-DOTA-GlyGlu-CycMSH (C and D) in B16/F1 murine melanoma cells at 25 °C. Total bound radioactivity (♦), internalized activity (■), cell membrane activity (▲), and cell culture media activity (●) were presented as counts per minute (cpm).

Normal organ uptakes of ^{111}In-DOTA-CycMSH and ^{111}In-DOTA-GlyGlu-CycMSH were generally very low (<0.8% ID/g) except for the kidneys at all time points investigated in this study. High tumor/blood and tumor/normal organ uptake ratios were demonstrated 2 h postinjection (Table 1). Although there was no statistical difference in tumor uptake between ^{111}In-DOTA-CycMSH and ^{111}In-DOTA-GlyGlu-CycMSH, the renal uptake of ^{111}In-DOTA-GlyGlu-CycMSH was significantly lower ($p < 0.05$, Table 1) than that of ^{111}In-DOTA-CycMSH at 2, 4, and 24 h postinjection. ^{111}In-DOTA-GlyGlu-CycMSH displayed 44% lower renal uptake than ^{111}In-DOTA-CycMSH at 4 h postinjection. At 24 h after dose administration, the kidney uptake values of ^{111}In-DOTA-CycMSH and ^{111}In-DOTA-GlyGlu-CycMSH decreased to 16.00 ± 2.30 and 9.06 ± 1.82% ID/g, respectively. Bone uptake values of ^{111}In-DOTA-CycMSH and ^{111}In-DOTA-GlyGlu-CycMSH were low (<0.2% ID/g) at all time points investigated in this study.

Two B16/F1 murine melanoma-bearing C57 mice were separately injected with ^{111}In-DOTA-CycMSH (13.7 MBq, 15.2 ng) and ^{111}In-DOTA-GlyGlu-CycMSH (13.7 MBq, 16.6 ng) through the tail vein to visualize the tumors at 2 h after dose administration. The whole-body SPECT images of the mice were fused with CT images, respectively. The transaxial tumor images and the whole-body images are presented in Figure 5. Flank melanoma tumors were visualized clearly by both ^{111}In-DOTA-CycMSH and ^{111}In-DOTA-GlyGlu-CycMSH at 2 h postinjection. Both ^{111}In-DOTA-CycMSH and ^{111}In-DOTA-GlyGlu-CycMSH exhibited high tumor to normal organ uptake ratios except for the kidney, which was coincident with the trend observed in the biodistribution results. In view of the substantial renal uptake values of ^{111}In-DOTA-CycMSH and ^{111}In-DOTA-GlyGlu-CycMSH in the biodistribution results, the urinary metabolites of ^{111}In-DOTA-CycMSH and ^{111}In-DOTA-GlyGlu-CycMSH were analyzed by RP-HPLC at 2 h postinjection. The HPLC elution profiles of ^{111}In-DOTA-CycMSH and ^{111}In-DOTA-GlyGlu-CycMSH are shown in Figure 6. All of ^{111}In-DOTA-CycMSH and ^{111}In-DOTA-GlyGlu-CycMSH were transformed to two more polar metabolites at 2 h postinjection, respectively.

DISCUSSION

Previous publications have demonstrated that the cyclization of α-MSH peptide analogues was able to improve the binding affinities and *in vivo* stability of peptides (*14–16*). The cyclic

Table 1. Biodistribution of ^{111}In-DOTA-CycMSH and ^{111}In-DOTA-GlyGlu-CycMSH in B16/F1 Murine Melanoma-Bearing C57 Mice[a]

	^{111}In-DOTA-CycMSH				^{111}In-DOTA-GlyGlu-CycMSH			
tissue	2 h	2 h blockade	4 h	24 h	2 h	2 h blockade	4 h	24 h
				Percent Injected Dose/Gram (% ID/g)				
tumor	9.53 ± 1.41	0.29 ± 0.14	7.54 ± 0.70	2.22 ± 0.51	10.40 ± 1.40	0.27 ± 0.10	7.40 ± 0.43	2.37 ± 0.28
brain	0.06 ± 0.02	0.05 ± 0.04	0.05 ± 0.04	0.02 ± 0.03	0.10 ± 0.07	0.01 ± 0.02	0.02 ± 0.03	0.05 ± 0.04
blood	0.09 ± 0.14	0.11 ± 0.11	0.01 ± 0.00	0.05 ± 0.06	0.14 ± 0.05	0.12 ± 0.11	0.02 ± 0.04	0.09 ± 0.14
heart	0.20 ± 0.18	0.17 ± 0.15	0.06 ± 0.05	0.07 ± 0.13	0.16 ± 0.18	0.04 ± 0.06	0.00 ± 0.00	0.09 ± 0.17
lung	0.22 ± 0.18	0.10 ± 0.10	0.11 ± 0.10	0.03 ± 0.06	0.04 ± 0.03	0.12 ± 0.14	0.01 ± 0.00	0.06 ± 0.05
liver	0.17 ± 0.03[b]	0.12 ± 0.00	0.09 ± 0.07[b]	0.11 ± 0.01[b]	0.27 ± 0.03	0.25 ± 0.05	0.21 ± 0.02	0.24 ± 0.08
spleen	0.39 ± 0.41	0.42 ± 0.37	0.80 ± 0.39	0.22 ± 0.39	0.16 ± 0.33	0.15 ± 0.14	0.27 ± 0.40	0.15 ± 0.25
stomach	0.10 ± 0.06	0.08 ± 0.10	0.13 ± 0.15	0.02 ± 0.04	0.06 ± 0.07	0.03 ± 0.05	0.02 ± 0.03	0.04 ± 0.07
kidneys	16.16 ± 1.86[b]	16.21 ± 2.33	21.69 ± 0.34[b]	16.00 ± 2.30[b]	13.07 ± 2.49	8.61 ± 1.34	12.13 ± 1.17	9.06 ± 1.82
muscle	0.14 ± 0.10	0.28 ± 0.32	0.01 ± 0.01	0.03 ± 0.04	0.06 ± 0.12	0.13 ± 0.13	0.05 ± 0.06	0.05 ± 0.06
pancreas	0.07 ± 0.06	0.13 ± 0.04	0.03 ± 0.05	0.07 ± 0.06	0.07 ± 0.10	0.09 ± 0.15	0.05 ± 0.08	0.02 ± 0.02
bone	0.20 ± 0.16	0.16 ± 0.14	0.04 ± 0.05	0.18 ± 0.13	0.14 ± 0.07	0.42 ± 0.37	0.00 ± 0.00	0.06 ± 0.05
				Percent Injected Dose (%ID)				
intestines	0.34 ± 0.11	0.23 ± 0.06	0.25 ± 0.08	0.05 ± 0.02	0.27 ± 0.15	0.27 ± 0.06	0.15 ± 0.01	0.07 ± 0.02
urine	91.70 ± 0.62	94.53 ± 0.65	92.34 ± 0.80	94.69 ± 0.49	90.32 ± 1.64	96.52 ± 0.20	92.36 ± 0.74	95.04 ± 0.84
				Uptake Ratio of Tumor/Normal Tissue				
tumor/blood	105.89	2.64	754.00	44.40	74.29	2.25	370.00	26.33
tumor/kidneys	0.59	0.02	0.35	0.14	0.80	0.0.3	0.61	0.26
tumor/lung	43.32	2.90	68.55	74.00	260.00	2.25	740.00	39.50
tumor/liver	56.06	2.42	83.78	20.18	38.52	1.08	35.24	9.88
tumor/muscle	68.07	1.04	754.00	74.00	173.33	2.08	148.00	47.40

[a] The data were presented as percent injected dose/gram or as percent injected dose (mean ± SD, $n = 5$). [b] $P < 0.05$, significance comparison between ^{111}In-DOTA-CycMSH and ^{111}In-DOTA-GlyGlu-CycMSH at 2, 4 and 24 h postinjection.

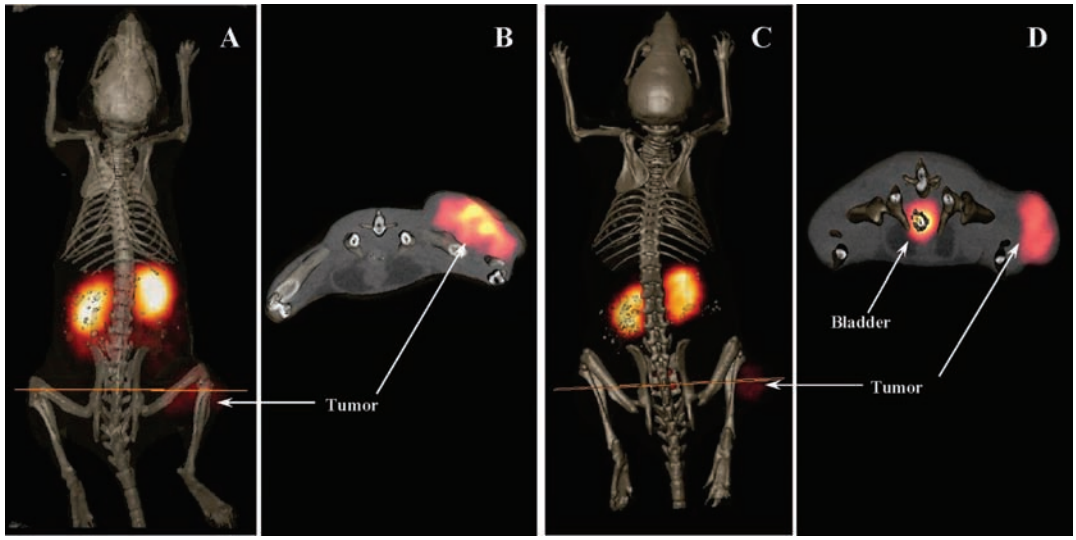

Figure 5. Whole-body and transaxial images of ^{111}In-DOTA-CycMSH (A,B) and ^{111}In-DOTA-GlyGlu-CycMSH (C,D) in B16/F1 flank melanoma-bearing C57 mice at 2 h postinjection.

peptides possess less conformational freedom and higher stability than the linear peptides due to the stabilization of secondary structures, such as beta turns. The stabilization of secondary structures makes the cyclic peptides a better fit to the receptor binding pocket, enhancing the binding affinities of the cyclic peptides. Peptide cyclization can be achieved through disulfide bridges, lactam bridges, covalent bonds such as N−N and N−C bonds, or metal coordination. Site-specific bond formation or metal coordination allows one to control the ring size of the cyclic peptide, which is critical for optimal receptor binding. Over the past several years, we have successfully employed radiometal to cyclize CCMSH peptides through radiolabeling processes (*6*, *7*, *18*). Labeling the CCMSH peptides with ^{99m}Tc or ^{188}Re simultaneously completed the peptide cyclization and the coupling of radionuclides to the peptides for melanoma imaging or therapy. The metal cyclization made α-MSH peptide analogues resistant to chemical and proteolytic degradation *in vivo* (*18*, *19*). Furthermore, the metal cyclization resulted in greater tumor uptake and lower renal uptake values of the radiolabeled peptides compared to the disulfide bridge cyclization (*19*), demonstrating that the different cyclization strategies affect the biodistribution properties of radiolabeled peptides with similar *in vitro* receptor binding affinities.

Two novel lactam bridge-cyclized α-MSH peptide analogues were synthesized to examine the effect of lactam bridge cyclization on the tumor targeting and pharmacokinetics of the radiolabeled peptides. DOTA-CycMSH and DOTA-GlyGlu-CycMSH displayed IC_{50} values of 1.75 and 0.9 nM, that were comparable to metal- and disulfide-cyclized α-MSH peptide analogues previously reported (*19*). The lactacm bridge cyclization remained the nanomolar receptor binding affinities of the peptides, demonstrating its suitability and feasibility as a strategy to cyclize the peptides. Both ^{111}In-DOTA-CycMSH and ^{111}In-DOTA-GlyGlu-CycMSH exhibited rapid cellular internalization and extended cellular retention in B16/F1 cells, with approximately 70% of the activity internalized in the cells 40 min

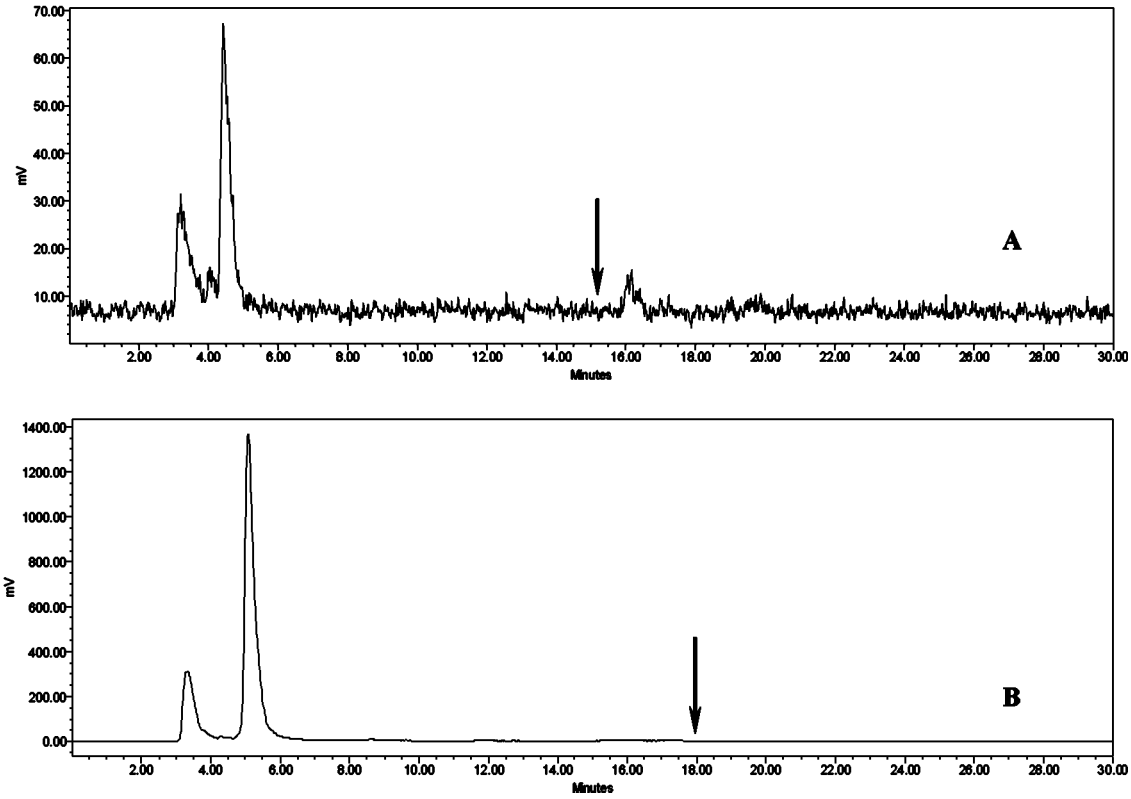

Figure 6. HPLC profiles of radioactive urine samples of B16/F1 murine melanoma-bearing C57 mice at 2 h postinjection of ^{111}In-DOTA-CycMSH (A) and ^{111}In-DOTA-GlyGlu-CycMSH (B). Arrows indicate retention time of the original compound of ^{111}In-DOTA-CycMSH and ^{111}In-DOTA-GlyGlu-CycMSH prior to the tail vein injection.

postincubation and 90% of internalized activity remained in the cells after 2 h incubation in culture media. Efficient cellular internalization coupled with extended retention made the lactam bridge-cyclized α-MSH peptide analogues suitable for melanoma imaging and therapy (*6, 23*).

Both ^{111}In-DOTA-CycMSH and ^{111}In-DOTA-GlyGlu-CycMSH exhibited high receptor-mediated tumor uptakes of 9.53 ± 1.41 and 10.40 ± 1.40% ID/g at 2 h postinjection, respectively. The tumor uptakes of ^{111}In-DOTA-CycMSH and ^{111}In-DOTA-GlyGlu-CycMSH (lactam bridge-cyclized α-MSH peptides) were comparable to that of ^{111}In-DOTA-ReCCMSH (a metal-cyclized α-MSH peptide), but slightly higher than the tumor uptake of ^{111}In-DOTA-[Cys^{4,10}, D-Phe^{7}]-α-MSH$_{4-13}$ (^{111}In-DOTA-CMSH, a disulfide bridge-cyclized α-MSH peptide) (*19*). Two novel ^{111}In-labeled DOTA-conjugated linear α-MSH peptide analogues, [Nle^{4}, Asp^{5}, D-Phe^{7}, Lys^{11}(DOTA)-^{111}In]-α-MSH$_{4-11}$ (^{111}In-DOTA-NAPamide) and ^{111}In-DOTA-[β-Ala^{3}, Nle^{4}, Asp^{5}, D-Phe^{7}, Lys^{10}]-α-MSH$_{3-10}$ (^{111}In-DOTA-MSH$_{oct}$), were reported for melanoma imaging (*11, 12*). ^{111}In-DOTA-NAPamide displayed greater tumor uptake values and better pharmacokinetics than ^{111}In-DOTA-MSH$_{oct.}$ The tumor uptake values of ^{111}In-DOTA-NAPamide were 7.56 ± 0.51% ID/g at 4 h and 2.32 ± 0.28% ID/g at 24 h postinjection in the B16/F1 melanoma mouse model (*12*). Both ^{111}In-DOTA-CycMSH and ^{111}In-DOTA-GlyGlu-CycMSH exhibited comparable tumor uptake values with ^{111}In-DOTA-NAPamide at 4 and 24 h postinjection. Flank melanoma tumors were clearly visualized with ^{111}In-DOTA-CycMSH and ^{111}In-DOTA-GlyGlu-CycMSH at 2 h postinjection by SPECT/CT images (Figure 5). The SPECT imaging of tumors accurately matched the anatomical information from CT images. ^{111}In-DOTA-CycMSH and ^{111}In-DOTA-GlyGlu-CycMSH displayed high tumor to normal organ uptake ratios except for the kidney, which was coincident with the trend observed in biodistribution results. The high receptor-mediated tumor uptake and tumor to normal organ uptake ratios highlighted the potential of radiolabeled lactam bridge-cyclized α-MSH peptides as a novel class of peptide radiopharmaceuticals for melanoma imaging.

Both biodistribution results and SPECT/CT images demonstrated that the kidney was primary excretion pathway of the radiolabeled lactam bridge-cyclized α-MSH peptides. The strategy of infusing basic amino acids such as lysine or arginine has been employed to decrease the renal uptakes of radiolabeled peptides by shielding the electrostatic interaction between positively charged peptides and negatively charged surface of tubule cells (*7, 24, 25*). Recently, it has been reported that different pathways may play roles in the mechanism of the renal uptake of radiolabeled peptides besides the electrostatic interaction between the positively charged peptides and negatively charged tubule cells (*26, 27*). For instance, the use of colchicine, which prevents endocytosis in tubular cells, has successfully decreased the renal uptake up to 25% in a rat model (*27*). Moreover, transmembrane glycoproteins, such as megalin, have been reported to be involved in the renal uptakes of radiolabeled somatostatin analogues (*28*). Since the extracellular domains of megalin can accommodate a variety of ligands, megalin may be involved in the renal uptakes of other radiolabeled peptides. Glutamic acid has been introduced into the peptide sequences to reduce the renal uptakes of radiolabeled metal-cyclized α-MSH peptides (*29*), as well as a PKM linker to modify the biodistribution of radiolabeld RGD peptides (*30–35*). In this study, the structural modification of increasing the overall negative charge of the peptide (introducing a glutamic acid) was investigated to demonstrate whether the structural modification could reduce the renal uptake values of the radiolabeled peptides. As a matter of fact, the introduction of a negatively charged glutamic acid as a linker significantly ($p < 0.05$) decreased the renal uptake of ^{111}In-DOTA-GlyGlu-CycMSH by 44% compared to ^{111}In-DOTA-CycMSH (Table 1) 4 h postinjection, suggesting that the electrostatic interaction played an important role in the renal uptakes of ^{111}In-DOTA-CycMSH

and ^{111}In-DOTA-GlyGlu-CycMSH. The urine analysis showed that both ^{111}In-DOTA-CycMSH and ^{111}In-DOTA-GlyGlu-CycMSH were metabolized into two moieties that might be responsible for the activity retention in kidneys. The kidney uptake value of ^{111}In-DOTA-GlyGlu-CycMSH was 29% higher than ^{111}In-DOTA-ReCCMSH at 4 h postinjection. However, the renal uptake value of ^{111}In-DOTA-GlyGlu-CycMSH was only 34% of that of ^{111}In-DOTA-CMSH at 4 h postinjection, demonstrating that the lactam cyclization was better than the disulfide cyclization in terms of less renal uptake value. Introduction of one more negatively charged glutamic acid or lysine coinjection might further decrease the renal uptake of ^{111}In-DOTA-GlyGlu-CycMSH. Another potential strategy to further reduce the kidney uptake would be to use shorter lactam bridge-cyclized α-MSH peptide, since lower molecular weight ^{111}In-DOTA-NAPamide exhibited less kidney uptake than ^{111}In-DOTA-GlyGlu-CycMSH. Further reduction of the renal uptakes will facilitate the clinical evaluations of this novel class of radiolabeled α-MSH peptides as melanoma imaging probes, as well as promote the potential use of this novel class of radiolabeled α-MSH peptides as therapeutic agents for peptide-targeted radionuclide therapy of melanoma.

In conclusion, ^{111}In-labeled DOTA-conjugated lactam bridge-cyclized α-MSH peptides exhibited high receptor-mediated tumor uptake coupled with fast whole-body clearance in B16/F1 murine melanoma model. Introduction of a negatively charged linker (-Gly-Glu-) into the peptide sequence decreased the renal uptakes by 44% without affecting the tumor uptakes 4 h postinjection. ^{111}In-labeled lactam bridge-cyclized α-MSH peptide analogues appear to be a novel class of very promising peptide radiopharmaceuticals for receptor-targeting melanoma imaging.

ACKNOWLEDGMENT

The authors express their gratitude to Drs. Wynn A. Volkert and Susan L. Deutscher for their helpful discussions. The authors thank Drs. Said D. Figueroa, Timothy J. Hoffman and Ms. Tiffani Shelton, Katherine Benwell for their assistance. Grant support: UNM-LANL MOU on Research and Education Grant 2R76T (Y.M), American Foundation for Pharmaceutical Education Grant 3R48E (Y.M) and American Cancer Society Institutional Research Grant IRG-92–024 (Y.M) and National Cancer Institute P50 Imaging Center Grant P50-CA-103130 (T.P.Q).

LITERATURE CITED

(1) Jemal, A., Siegel, R., Ward, E., Murray, T., Xu, J., and Thun, M. J. (2007) Cancer statistics, 2007. *Ca Cancer J. Clin. 57*, 43–66.

(2) Nabi, H. A., and Zubeldia, J. M. (2002) Clinical application of 18F-FDG in oncology. *J. Nucl. Med. Technol. 30*, 3–9.

(3) Dimitrakopoulou-Strauss, A., Strauss, L. G., and Burger, C. (2001) Quantitative PET studies in pretreated melanoma patients: A comparison of 6-[18F]fluoro-L-DOPA with 18F-FDG and 15O-water using compartment and non-compartment analysis. *J. Nucl. Med. 42*, 248–256.

(4) Tatro, J. B., and Reichlin, S. (1987) Specific receptors for alpha-melanocyte-stimulating hormone are widely distributed in tissues of rodents. *Endocrinology 121*, 1900–1907.

(5) Siegrist, W., Solca, F., Stutz, S., Giuffre, L., Carrel, S., Girard, J., and Eberle, A. N. (1989) Characterization of receptors for alpha-melanocyte-stimulating hormone on human melanoma cells. *Cancer Res. 49*, 6352–6358.

(6) Chen, J., Cheng, Z., Hoffman, T. J., Jurisson, S. S., and Quinn, T. P. (2000) Melanoma-targeting properties of 99mTechnetium-labeled cyclic α-melanocyte-stimulating hormone peptide analogues. *Cancer Res. 60*, 5649–5658.

(7) Miao, Y., Owen, N. K., Whitener, D., Gallazzi, F., Hoffman, T. J., and Quinn, T. P. (2002) In vivo evaluation of 188Re-labeled alpha-melanocyte stimulating hormone peptide analogs for melanoma therapy. *Int. J. Cancer 101*, 480–487.

(8) Miao, Y., Whitener, D., Feng, W., Owen, N. K., Chen, J., and Quinn, T. P. (2003) Evaluation of the human melanoma targeting properties of radiolabeled alpha-Melanocyte stimulating hormone peptide analogues. *Bioconjugate Chem. 14*, 1177–1184.

(9) Miao, Y., Owen, N. K., Fisher, D. R., Hoffman, T. J., and Quinn, T. P. (2005) Therapeutic efficacy of a 188Re labeled α-melanocyte stimulating hormone peptide analogue in murine and human melanoma-bearing mouse models. *J. Nucl. Med. 46*, 121–129.

(10) Miao, Y., Hylarides, M., Fisher, D. R., Shelton, T., Moore, H., Wester, D. W., Fritzberg, A. R., Winkelmann, C. T., Hoffman, T. J., and Quinn, T. P. (2005) Melanoma therapy via peptide-targeted α-radiation. *Clin. Cancer Res. 11*, 5616–5621.

(11) Froidevaux, S., Calame-Christe, M., Tanner, H., Sumanovski, L., and Eberle, A. N. (2002) A novel DOTA-α-melanocyte-stimulating hormone analog for metastatic melanoma diagnosis. *J. Nucl. Med. 43*, 1699–1706.

(12) Froidevaux, S., Calame-Christe, M., Schuhmacher, J., Tanner, H., Saffrich, R., Henze, M., and Eberle, A. N. (2004) A Gallium-labeled DOTA-α-melanocyte-stimulating hormone analog for PET imaging of melanoma metastases. *J. Nucl. Med. 45*, 116–123.

(13) Froidevaux, S., Calame-Christe, M., Tanner, H., and Eberle, A. N. (2005) Melanoma targeting with DOTA-alpha-melanocyte-stimulating hormone analogs: structural parameters affecting tumor uptake and kidney uptake. *J. Nucl. Med. 46*, 887–895.

(14) Sawyer, T. K., Hruby, V. J., Darman, P. S., and Hadley, M. E. (1982) [half-Cys4,half-Cys10]-α-melanocyte-stimulating hormone: a cyclic α-melanotropin exhibiting superagonist biological activity. *Proc. Natl. Acad. Sci. U.S.A. 79*, 1751–1755.

(15) Al-Obeidi, F., Hadley, M. E., Pettitt, B. M., and Hruby, V. J. (1989) Design of a new class of superpotent cyclic a-melanotropins based on quenched dynamic simulations. *J. Am. Chem. Soc. 111*, 3413–3416.

(16) Al-Obeidi, F., de L. Castrucci, A. M., Hadley, M. E., and Hruby, V. J. (1989) Potent and prolonged-acting cyclic lactam analogs of a-melanotropin: design based on molecular dynamics. *J. Med. Chem. 32*, 2555–2561.

(17) Fung, S., and Hruby, V. J. (2005) Design of cyclic and other templates for potent and selective peptide α-MSH analogues. *Curr. Opin. Chem. Biol. 9*, 352–358.

(18) Giblin, M. F., Wang, N. N., Hoffman, T. J., Jurisson, S. S., and Quinn, T. P. (1998) Design and charaterization of α-melanotropin peptide analogs cyclized through rhenium and technetium metal coordination. *Proc. Natl. Acad. Sci. U.S.A. 95*, 12814–12818.

(19) Chen, J., Cheng, Z., Owen, N. K., Hoffman, T. J., Miao, Y., Jurisson, S. S., and Quinn, T. P. (2001) Evaluation of an 111In-DOTA-rhenium cyclized α-MSH analog: a novel cyclic-peptide analog with improved tumor-targeting properties. *J. Nucl. Med. 42*, 1847–1855.

(20) Aloj, L., Panico, M., Caraco, C., Del Vecchio, S., Arra, C., Affuso, A., Accardo, A., Mansi, R., Tesauro, D., De Luca, S., Pedone, C., Visentin, R., Mazzi, U., Morelli, G., and Salvatore, M. (2004) In vitro and in vivo characterization of Indium-κ and Technetium-99m labeled CCK-8 derivatives for CCK-B receptor imaging. *Cancer Biother. Radiopharm. 19*, 93–98.

(21) Miao, Y., Hoffman, T. J., and Quinn, T. P. (2005) Tumor-targeting properties of ^{90}Y and ^{177}Lu-labeled α-melanocyte stimulating hormone peptide analogues in a murine melanoma model. *Nucl. Med. Biol. 32*, 485–493.

(22) Miao, Y., Benwell, K., and Quinn, T. P. (2007) ^{99m}Tc and ^{111}In labeled alpha-melanocyte stimulating hormone peptides as imaging probes for primary and pulmonary metastatic melanoma detection. *J. Nucl. Med. 48*, 73–80.

(23) Volkert, W. A., and Hoffman, T. J. (1999) Therapeutic radiopharmaceuticals. *Chem. Rev. 99*, 2269–2292.

(24) Behr, T. M., Sharkey, R. M., Juweid, M. E., Blumenthal, R. D., Dunn, R. M., Bair, H. J., Wolf, F. G., Becker, W. S., and Goldenberg, D. M. (1995) Reduction of the renal uptake of radiolabeled monoclonal antibody fragments by cationic amino acids and their derivatives. *Cancer Res. 55*, 3825–3834.

(25) Behr, T. M., Becker, W. S., Sharkey, R. M., Juweid, M. E., Dunn, R. M., Bair, H. J., Wolf, F. G., and Goldenberg, D. M. (1996) Reduction of renal uptake of monoclonal antibody fragments by amino acid infusion. *J. Nucl. Med. 37*, 829–833.

(26) Béhé, M., Kluge, G., Becker, W., Gotthardt, M., and Behr, T. M. (2005) Use of polyglutamic acids to reduce uptake of radiometal-labeled minigastrin in the kidneys. *J. Nucl. Med. 46*, 1012–1015.

(27) Rolleman, E. J., Krenning, E. P., Van Gameren, A., Bernard, B. F., and De Jong, M. (2004) Uptake of [^{111}In-DTPA0]octreotide in the rat kidney is inhibited by colchicine and not by fructose. *J. Nucl. Med. 45*, 709–713.

(28) De Jong, M., Barone, R., Krenning, E. P., Bernard, B. F., Melis, M., Vissor, T., Gekle, M., Willnow, T. E., Walrand, S., Jamar, F., and Pauwels, S. (2005) Megalin is essential for renal proximal tubule reabsorption of ^{111}In-DTPA-Octreotide. *J. Nucl. Med. 46*, 1696–1700.

(29) Miao, Y., Fisher, D. R., and Quinn, T. P. (2006) Reducing renal uptake of ^{90}Y and ^{177}Lu labeled alpha-melanocyte stimulating hormone peptide analogues. *Nucl. Med. Biol. 33*, 723–733.

(30) Liu, S., He, Z., Hsieh, W. Y., Kim, Y. S., and Jiang, Y. (2006) Impact of PKM linkers on biodistribution characteristics of the ^{99m}Tc-labeled cyclic RGDfK dimer. *Bioconjugate Chem. 17*, 1499–1507.

(31) Dijkgraaf, I., Liu, S., Kruijtzer, J. A., Soede, A. C., Oyen, W. J., Liskamp, R. M., Corstens, F. H., and Boerman, O. C. (2007) Effects of linker variation on the in vitro and in vivo characteristics of an ^{111}In-labeled RGD peptide. *Nucl. Med. Biol. 34*, 29–35.

(32) Liu, S., Hsieh, W. Y., Jiang, Y., Kim, Y. S., Sreerama, S. G., Chen, X., Jia, B., and Wang, F. (2007) Evaluation of a ^{99m}Tc-labeled cyclic RGD tetramer for noninvasive imaging integrin $\alpha_v\beta_3$-positive breast cancer. *Bioconjugate Chem. 18*, 438–446.

(33) Wu, Y., Zhang, X., Xiong, Z., Cheng, Z., Fisher, D. R., Liu, S., Gambhir, S. S., and Chen, X. (2005) MicroPET imaging of glioma integrin $\alpha_v\beta_3$ expression using ^{64}Cu-labeled tetrameric RGD peptide. *J. Nucl. Med. 46*, 1707–1718.

(34) Li, Z. B., Cai, W., Cao, Q., Chen, K., Wu, Z., He, L., and Chen, X. (2007) ^{64}Cu-labeled tetrameric and octameric RGD peptides for small-animal PET of tumor $\alpha_v\beta_3$ integrin expression. *J. Nucl. Med. 48*, 1162–1171.

(35) Dijkgraaf, I., Kruijtzer, J. A., Liu, S., Soede, A. C., Oyen, W. J., Corstens, F. H., Liskamp, R. M., and Boerman, O. C. (2007) Improved targeting of the alpha(v)beta(3) integrin by multimerisation of RGD peptides. *Eur. J. Nucl. Med. Mol. Imaging 34*, 267–273.

BC700317W

Characterization of PLL-g-PEG-DNA Nanoparticles for the Delivery of Therapeutic DNA

Markus Rimann,[†,△] Tessa Lühmann,[†,△] Marcus Textor,[†,‡] Barbara Guerino,[†] Joëlle Ogier,[†,§] and Heike Hall*[,†]

Cells and BioMaterials, Department of Materials, ETH Zurich, Switzerland, BioInterfaceGroup, Oberflächentechnik/Laboratory for Surface Science and Technology, Department of Materials, ETH Zurich, Switzerland, and INSERM U 424, Bat 3, 7 ème étage11, rue Humann, 67085 Strasbourg CEDEX, France. Received September 5, 2007; Revised Manuscript Received November 20, 2007

Local and controlled DNA release is a critical issue in current gene therapy. As viral gene delivery systems are associated with severe security problems, nonviral gene delivery vehicles were developed. Here, DNA-nanoparticles using grafted copolymers of PLL and PEG to increase their biocompatibility and stealth properties were systematically studied. Ten different PLL-based polymers with no, low, and high PEG grafting and PEG molecular weights as well as different PLL backbone lengths were complexed with plasmids containing 3200 to 10,100 base pairs. Stable complexes were formed and selected for cytotoxicity and transfection efficiency. Predominantly, PLL-g-PEG-DNA nanoparticles grafted with 4 or 5% PEG moieties of 5 kDa transfected 40% COS-7 cells without reduction of cell viability when formed at N/P ratios between 0.1 and 12.5. The molecular weight of PLL did not significantly affect transfection efficiency or cytotoxicity indicating that a specific cationic charge-density-to-PEG-ratio is important for efficient transfection and low cytotoxicity. The PLL-g-PEG-DNA nanoparticles were spherical with a diameter of ∼100 nm and did not aggregate over 2 weeks. Moreover, they protected included plasmid DNA against serum components and DNase I digestion. Therefore, such storage stable and versatile PLL-g-PEG-DNA nanoparticles might be useful to deliver differently sized therapeutic DNA for *in vivo* applications.

1. INTRODUCTION

Gene transfer using nonviral vectors is a promising approach for the safe delivery of therapeutic DNA in genetic and acquired human diseases (*1–6*). In contrast to viral vectors, nonviral vectors benefit from low immunogenecity, the absence of endogenous recombination, low production costs, and reproducibility (*2*). Furthermore, they have no size limitation in DNA packaging. Unfortunately, nonviral DNA delivery vehicles often affect cell viability and have poor transfection efficiency. Gene expression only results when the DNA is delivered into the cell nucleus of the target cell. On its way, the DNA has to pass several biological barriers beginning with the plasma membrane, followed by avoidance of the endosomal pathway, and finally passage through the nuclear pores (*1, 2*). Today, there is still a huge need for carriers that transport DNA quickly and efficiently and release it in a controlled manner. Moreover, the storage stability of such carriers becomes an issue.

Currently, three different strategies for nonviral application of therapeutic DNA have been developed. The simplest way is the use of naked DNA, which is injected directly into the target tissue (*7*), applied via electroporation or ultrasound (*8*), or loaded onto nanosize particles of heavy metal and brought into the cell by gene gun applications (*9*). Enzymatic degradation of the unprotected DNA and poor cell transfection efficiencies are the major drawbacks (*7*). Another approach is the use of lipoplexes that are lipid-based DNA vehicles, entering the cytoplasm by cell membrane fusion (*10, 11*). Many different modifications for specific cell targeting and intracellular routing have been developed (*12, 13*). However, the primary drawback is the rapid clearance of lipoplexes in the blood system and their short-term stability (*14*). The third approach is to use polycationic substances, such as poly L-lysine (PLL), poly L-ornithin, polyethyleneimine (PEI), and chitosan, to complex plasmid DNA (*2, 15–21*). Although polymers with high cationic charge density condense the DNA into structures amenable to cellular internalization, the high charge density is one factor that contributes to their cytotoxicity as interactions of polycations with cell membranes induce nanoscale hole formation and enhance membrane permeability (*22–24*). To reduce cytotoxicity, different block copolymers between PEG and PLL, PEG and PEI, and PEG and chitosan as well as PEG and poly aspartic acid were used to form DNA vehicles (*15, 18–21, 23, 25*). Moreover, peptide-based DNA vectors or covalent complexes between PEG−peptides and PEG−glycopeptides were developed (*17, 26–29*). However, low cationic charge density can reduce or eliminate DNA condensation capability. The balance between cationic charge density and DNA condensation is complicated even further when endosomal escape moieties and nuclear translocation sites are considered (*30–32*).

Here, a systematic and quantitative study of grafted PLL-PEG copolymers is presented, illustrating how PLL backbone length, PEG molecular weight, and degree of PLL grafting with PEG affect (a) PLL-g-PEG-DNA nanoparticle formation for *in vitro* transfection; (b) size and stability of the formed nanoparticles; and (c) cytotoxicity of the transfection vehicle. Furthermore, the stability of such DNA-containing nanoparticles with time and the release of functional plasmid DNA were investigated as it is crucial for any medical application.

* Corresponding author. Heike Hall, ETH Zurich, Department of Materials, HCI E415, Cells and BioMaterials, Wolfgang-Pauli-Strasse 10, CH-8093 Zürich, Switzerland. Phone: +41 44 633 69 75. Fax: +41 44 632 1073. E-mail: heike.hall@mat.ethz.ch.

† Cells and BioMaterials, ETH Zurich.

‡ BioInterfaceGroup, ETH Zurich.

§ INSERM U 424.

△ Both authors contributed equally well to this work and should be regarded as first authors.

10.1021/bc7003439 CCC: $40.75 © 2008 American Chemical Society
Published on Web 01/04/2008

Table 1. Names and Composition of the PLL-g-PEG-Copolymers Used Here to Form PLL-g-PEG-DNA Condensates[a]

polymer name	PLL (kDa)	PEG (kDa)	PEG/PLL (absolute number)	PEGylation (g) (%)
PLL_{300}	300 (=1435 lysine residues)			
PLL_{300}-g_4-PEG_1	300	1	55.8	4
PLL_{300}-g_{24}-PEG_1	300	1	341.7	24
PLL_{300}-g_4-PEG_5	300	5	59.5	4
PLL_{300}-g_{20}-PEG_5	300	5	287.0	20
PLL_{20}	20 (=96 lysine residues)			
PLL_{20}-g_7-PEG_1	20	1	6.7	7
PLL_{20}-g_{24}-PEG_1	20	1	23.2	24
PLL_{20}-g_5-PEG_5	20	5	5.1	5
PLL_{20}-g_{28}-PEG_5	20	5	27.1	28

[a] Molecular weights of PLL and PEG are indicated in (kDa), whereas the ratio between PEG and PLL (PEGylation, g) is indicated in percent. PEGylation was calculated using the absolute numbers of PEG moieties per lysine of the PLL-molecule.

2. MATERIALS AND METHODS

2.1. Polymer Synthesis. Eight different PLL-g-PEG-polymers (Table 1) were used in this study. They were synthesized using poly L-lysine hydrobromide with molecular weights of 20 and 300 kDa (Sigma), referred to as PLL_{20} and PLL_{300}, respectively, and the *N*-hydroxysuccinimidyl ester of methoxy-terminated poly(ethylene glycol) (Nektar, USA, molecular weights 1 and 5 kDa). PLL_{20} contains 96 lysine residues, and PLL_{300} contains 1435. The grafting ratio (g) was calculated using the absolute number of PEG moieties per lysine of the PLL backbone, expressed in percent form. Synthesis and analysis were performed as described previously (*33*). Reaction rates were determined by ^{1}H NMR (D_2O) (β, γ, and δ CH_2 peaks of lysine at 1–2 ppm, CH_2CH_2O of PEG at 3.3–3.9 ppm). The polymers were stored at −20 °C until further use.

2.2. Formulation of PLL-g-PEG-DNA Condensates. Transfection studies were performed in 24 well plates (TPP, Switzerland). PLL-g-PEG-DNA condensates were formed by using either a vector expressing enhanced green fluorescent protein (pEGFP-N1, Clontech), β-galactosidase (pSV-β-galactosidase, Promega), pHisTrx (*34*), or plasmid #343 (kindly provided by Markus Kuenzler, Institute for Microbiology, ETH Zurich, Switzerland) at a final DNA concentration of 1 μg/150 μL (=6.7 μg/mL) in PBS and a PLL-g-PEG concentration according to NH_4^+/PO_4^{3-} (amino group in PLL/phosphate group in DNA; N/P) charge ratios between 0.1 to 25. PLL-g-PEG was provided in 75 μL of PBS (0.01 M phosphate buffered saline, pH 7.4, Sigma), and DNA dissolved in 75 μL of PBS was added dropwise into the polymer solution. The complexes were equilibrated for 30 min at room temperature and were always freshly prepared prior to use.

2.3. Plasmid Propagation. The vectors pEGFP-N1, pSV-β-galactosidase, pHISTrx, and #343 used in this study were transformed into *E. coli* strain Top10 (Invitrogen), grown in LB media supplemented either with 30 μg/mL kanamycin for pEGFP-N1 and pSV-β-galactosidase or with 50 μg/mL ampicillin for all other plasmids. The plasmid DNA was purified using a Maxiprep kit (Qiagen), and the concentration was determined photometrically at 260 nm.

2.4. Stability of Condensates: Release of DNA by Heparin Replacement, DNase I Protection Assay, and Serum Stability. The stability of PLL_{20}-g_5-PEG_5-DNA complexes was analyzed, and the release of the plasmid DNA by heparin displacement was studied. PLL_{20}-g_5-PEG_5-DNA condensates were made at a final DNA concentration of 1 μg/150 μL (=6.7 μg/mL) in PBS and PLL_{20}-g_5-PEG_5-DNA with N/P ratios = 3.125 and 25. After 30 min of incubation, 750 μg of heparin (15 μL of a 50 mg/mL stock solution, 181 USP units/mg, H-9399 Sigma) and 5 μL of 5 M NaCl were added. The samples were analyzed on a 1% agarose gel containing 0.5 μg/mL ethidium bromide in TAE buffer (40 mM Tris, 40 mM acetic acid, 1 mM EDTA) for 1 h and visualized on an UV-transilluminator. As controls, PLL_{20}-g_5-PEG_5-DNA nanoparticles (N/P ratio = 3.125 and 25) without heparin and NaCl addition were treated in an analogous manner.

The stability of PLL_{20}-g_5-PEG_5-DNA and PLL_{20}-DNA condensates against DNase I (New England Biolabs) and serum compounds was analyzed. For both, 5 μg of pEGFP-N1 plasmid was complexed with PLL_{20} (Sigma) and PLL_{20}-g_5-PEG_5 with the N/P charge ratios ranging from 0.1 to 25. For the determination of DNase I stability, $MgCl_2$ (2.5 mM final concentration) and 5 U DNase I were added to the condensates. After 10 min of incubation at 37 °C, the enzyme reaction was stopped by the addition of 10 μL of 0.3 M EDTA (15 mM final concentration), and the samples were transferred on ice. As controls, 5 μg of naked DNA was digested with DNase I, and PLL_{20}-g_5-PEG_5-DNA nanoparticles (N/P ratio = 3.125) without DNase I were treated in the same way. In order to release the DNA from the nanoparticles, 150 μL of heparin (stock solution 50 mg/mL) and 5 μL of 5 M NaCl were added to the condensates for 30 min at 4 °C. The samples were analyzed on 1% agarose gels as described above.

To determine the serum stability of the polymer−DNA condensates, 150 μL of DMEM (Cat. No. 21885, GibcoBRL) containing 10% fetal bovine serum (F7524, Sigma) was added and incubated at 4 and 37 °C for 7 days. The DNA of the PLL_{20}-g_5-PEG_5 nanoparticles was released and analyzed as stated for DNase I protection assays.

2.5. Cells and Cell Culture. COS-7 (SV 40 transformed kidney cells of African green monkey, ATCC CRL 1651, ATCC Rocksville, MA) cells were cultured as exponentially growing subconfluent monolayers at 37 °C containing 5% CO_2. The cell culture was maintained in 25 cm^2 culture flasks in DMEM (Cat. No. 21885, low glucose, glutamax I, GibcoBRL) supplemented with 10% heat inactivated FBS (F7524, Sigma) and 1% ABAM (Cat. No.: 15240, GibcoBRL). COS-7 cells were seeded at a constant density of 7500 cells/cm^2 on 8-well chamber slides (Labtek), 24-, and 96 well plates. For all experiments, cells were used 24 h post seeding.

2.6. *In Vitro* Gene Expression in COS-7 Cells. Polymer−DNA condensates were prepared as described above. Briefly, 1 μg of pEGFP-N1 plasmid per well (24-well plate) was complexed with PLL_{20}, PLL_{300}, and all PLL-g-PEG polymers using N/P charge ratios 0.1 to 25, yielding a volume of 150 μL. After removing the tissue culture medium and rinsing the cells with PBS once, the polymer−DNA condensates were added onto the cells and incubated for 30 min at 37 °C and 5% CO_2, then 450 μL DMEM, containing 2% FBS, was added for 24 h. The transfection medium was replaced with DMEM supplemented with 10% FBS, and the cells were incubated for another 24 h before the cells were analyzed for GFP expression by fluorescence microscopy. Hoechst 33342 nuclear stain (Invitrogen) was used to identify the total cell number, and ethidium bromide (AppliChem) was used to determine the potential cytotoxicity of the polymer−DNA condensates. Briefly, the cells were incubated for 2 min in DMEM with 10% FBS containing 4 μg/mL Hoechst 33342 and 10 μg/mL ethidium bromide. After rinsing the cells three times with PBS, the transfection efficiency was analyzed by counting the GFP-expressing cells in 3 nonoverlapping areas of 500 mm^2 in relation to the total cell number as determined by Hoechst nuclear stain. The software ImageJ 1.2 was used. As positive control, DEAE dextran (Cat. No.: 30461, Fluka) transfection was performed: 1.25 μg of pEGFP-N1 DNA was complexed

with 50 μg of DEAE dextran in 150 μL of PBS and added to the cells that were rinsed with PBS and incubated for 30 min at 37 °C and 5% CO_2. Then, 450 μL of DMEM with 10% FBS and 0.9 μL of chloroquine (Sigma) from a stock solution of 50 mM in PBS were added. Cells were incubated for 2.5 h at 37 °C and 5% CO_2, and subsequently, they were treated with 10% DMSO in DMEM with 10% FBS for 2.5 min. The DMSO-containing medium was removed, and the cells were cultured for 48 h in DMEM containing 10% FBS. Transfection efficiency was analyzed by fluorescence microscopy as described above.

2.7. Determination of Nanoparticle Cytotoxicity. In order to quantify the cytotoxicity of the PLL-g-PEG-DNA nanoparticles, WST-1 proliferation assay (Roche) was performed. The following polymers and controls have been used to form polymer−DNA condensates containing 0.167 μg of pEGFP-N1 per well of a 96-well plate: PLL_{20}-g_5-PEG_5, PLL_{300}-g_4-PEG_1, PLL_{300}-g_4-PEG_5, PLL_{20}, and PLL_{300} with the N/P ratios 0.1−25. As controls, COS-7 cells were transfected with naked DNA (0.167 μg pEGFP-N1 per 96-well plate), DEAE dextran, and incubated with PBS alone. COS-7 cells were transfected in 96-well plates. Forty-eight hours after transfection, 20 μL of WST-1 reagent was applied to each well containing 200 μL of DMEM supplemented with 10% FBS, and the cells were incubated for another hour at 37 °C and 5% CO_2. Absorption at 440 nm was measured using a microplate reader, Infinite M200 (Tecan). Each condition was performed in quadruple and repeated three times.

2.8. Particle Size Analysis. The particle size of the PLL_{20}-g_5-PEG_5-DNA nanoparticles was measured with dynamic light scattering (DLS) at a scattering angle of 90° on a Brookhaven BI-SM200 instrument. The wavelength of the laser beam was $\lambda = 532$ nm, emitted from a Laser Quantum (UK) ventus LP 532. The nanoparticles were prepared as stated for the transfection studies with a final DNA concentration of 10 μg/mL. The PLL_{20}-g_5-PEG_5-to-DNA concentration corresponded to an N/P ratio of 3.125, 6.25, 12.5, and 25. Plasmids pEGFP-N1, pSV-β-galactosidase (Promega), pHISTrx (*34*), and #343 were used for DLS analysis (N/P ratio = 3.125). Each measurement was performed for 5 min, and the hydrodynamic diameters of three independent samples for each condition were analyzed. To obtain the 7 and 14 day values, PLL_{20}-g_5-PEG_5-DNA nanoparticles were stored at 4 °C between the measurements.

2.9. Fluorescence Dye Exclusion Assay. The maximal condensation of polymers and DNA was assayed using PicoGreen (Invitrogen), which binds to soluble double-stranded DNA. Nanoparticles with either PLL_{20}-g_5-PEG_5 or PLL_{20} were produced as stated above using pEGFP-N1 and pSV-β-galactosidase vectors at a concentration of 10 μg/mL. The polymer-to-DNA ratios corresponded to the N/P charge ratios of 0.1 to 25. Nanoparticles were mixed with 100 μL of PicoGreen solution (PicoGreen stock solution diluted 1:200 in PBS) and incubated for 5 min at room temperature in the dark. The fluorescence of PicoGreen was determined according to the manufacturer's protocol using a microplate reader, Infinite M200 (Tecan), with excitation at 480 nm while monitoring emission at 520 nm. Decreasing fluorescence indicated less free double-stranded DNA and was regarded as the amount of DNA that was incorporated into the polymer−DNA nanoparticles. The measurements were performed in duplicate and repeated three times.

2.10. Negative Stain Transmission Electron Microscopy (TEM). For the visualization of the polymer−DNA condensates, negative staining TEM was performed. PLL_{20}-g_5-PEG_5-DNA condensates were prepared in ddH_2O using 5 μg of pEGFP-N1 plasmid complexed at the N/P ratio = 3.125. A twenty microliter nanoparticle solution was applied for 2 min on Formvar and carbon-coated 300 mesh copper-grids, which were freshly glow discharged. The remaining ddH_2O was removed by suction with filter paper, and the condensates were negative stained for 3 × 15 s on drops of 2% phosphor tungsten acid in ddH_2O. Finally, the excess staining solution was removed by suction with filter paper, and the grid was air-dried. The samples were analyzed with a transmission electron microscope (Philips 208) using high voltage (80 kV) at magnifications of 44,000 to 110,000. Samples with either polymer or DNA only were prepared in a similar way.

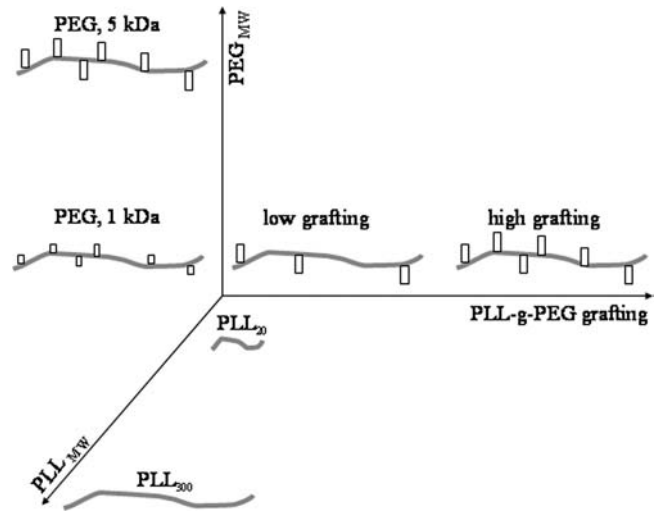

Figure 1. Schematic of the composition of PLL-g-PEG-copolymers used in this study. Eight different PLL-g-PEG polymers that varied in the molecular weight of the PLL-backbone, the amount of PLL grafting with PEG, and the molecular weight of PEG were used to form PLL-g-PEG-DNA condensates.

3. RESULTS

3.1. *In Vitro* Transfection Efficiencies of DNA-Containing Condensates Formed with Different PLL-g-PEG Copolymers. The aim of this study was to systematically analyze different grafted PLL-g-PEG copolymers and determine their potential in the formation of DNA-containing condensates. For this purpose, 10 different polymers were selected that varied in their PLL backbone length, PEG molecular weight, and the amount of PLL grafting (Figure 1 and Table 1). Two different PLL molecular weights (20 and 300 kDa) were chosen to determine the influence of PLL backbone length on the formation of DNA-containing condensates. The PLL backbone was grafted with short and long PEG-moieties (1 and 5 kDa, respectively), and different amounts of grafted PEG moieties were studied. Nongrafted PLL_{20} and PLL_{300} were compared to low grafted (4–7%) and high grafted (20–28%) PLL_{20} and PLL_{300}. PLL-g-PEG condensates were formed using an NH_4^+/PO_4^{3-} (N/P) ratio of 3.125, and the *in vitro* transfection efficiency of COS-7 cells was determined. Figure 2A compares transfection efficiencies of all 10 polymers condensed with plasmid DNA encoding the information for the expression of enhanced green fluorescent protein (pEGFP-N1). Polymers PLL_{300}-g_4-PEG_1, PLL_{300}-g_4-PEG_5 (Figure 2A, a) and PLL_{20}-g_5-PEG_5 (Figure 2A, b) showed the best transfection efficiencies. All three polymers had a low amount of PEGylation (4 and 5%, respectively). PLL_{300}-g_4-PEG_1 contained the low molecular weight PEG (1 kDa), resulting in ~10% transfection efficiency, whereas PLL_{300}-g_4-PEG_5 and PLL_{20}-g_5-PEG_5 were grafted with high molecular weight PEG (5 kDa) leading to 20 and 40% transfection efficiency, respectively. These results indicate a strong influence of the amount and molecular weight of PEG moieties on transfection efficiency, less so of the molecular weight of the PLL backbone. Highly PEGylated polymers containing 20–28%

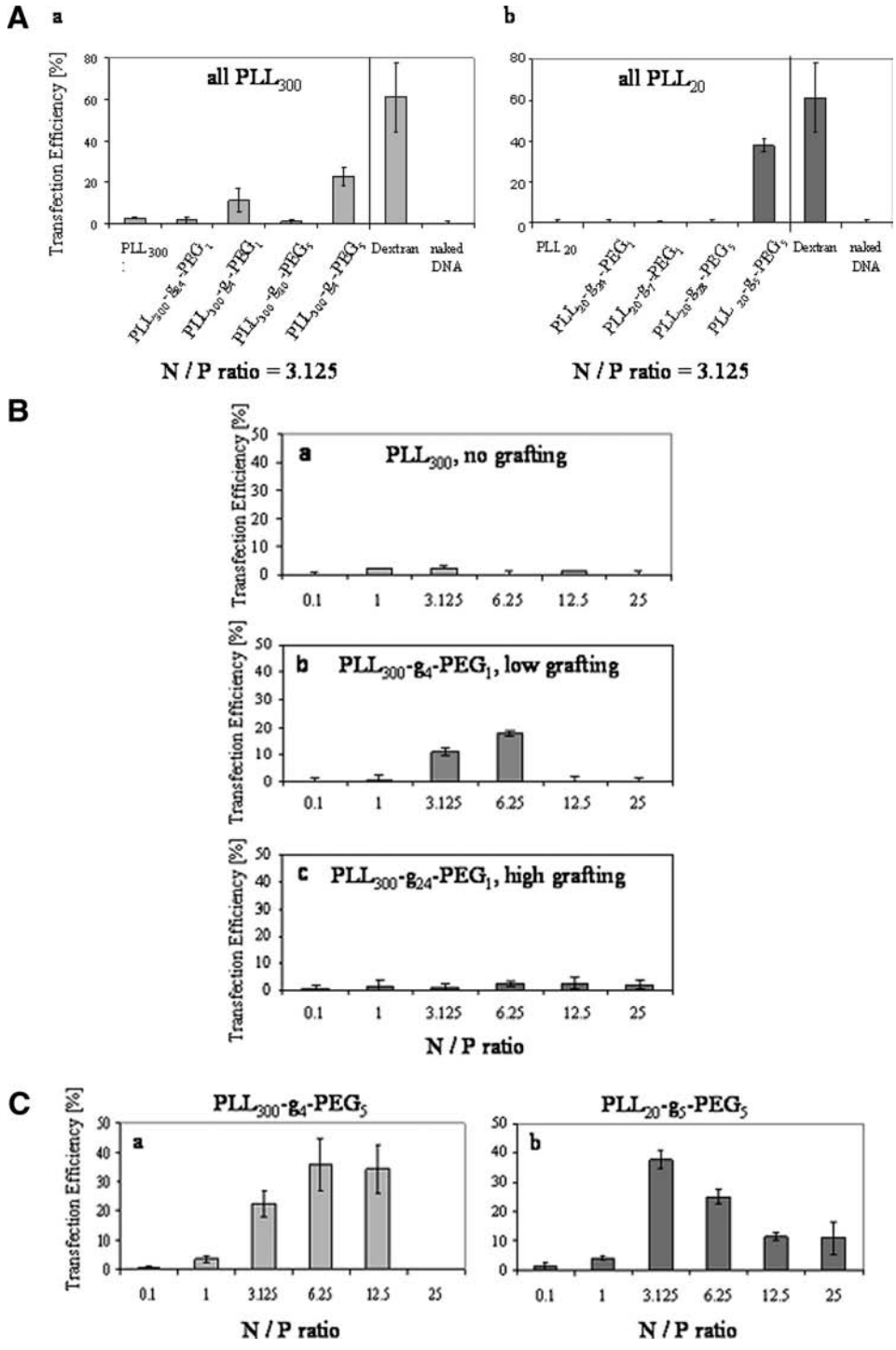

Figure 2. Transfection efficiencies of PLL-g-PEG-DNA condensates with different PLL backbones (A), PEG grafting (B), and N/P ratios (C). (A) (a) Grafted and nongrafted PLL with a molecular weight of 300 kDa (PLL_{300}) was used to form polymer−DNA condensates for transfection of COS-7 cells with a plasmid coding for the expression of green fluorescent protein (pEGFP-N1). All PLL_{300}-based PLL-g-PEG condensates were compared. The N/P ratio was 3.125 for all condensates. DEAE-dextran transfection and naked DNA applied in PBS were used as control. (A) (b) Grafted and nongrafted PLL with a molecular weight of 20 kDa (PLL_{20}) was used to form polymer−DNA condensates for transfection of COS-7 cells. All PLL_{20}-containing PLL-g-PEG condensates were compared. The N/P ratio used was 3.125 for all condensates. DEAE-dextran transfection and naked DNA were used as controls. (B) Polymer−DNA condensates formed with PLL_{300} displaying different grafting ratios were compared for their transfection capability. (B) (a) Nongrafted PLL_{300} was used to form PLL-DNA condensates; (b) PLL_{300}-g_4-PEG_1 with 4% PEG grafting was used to form PLL-g-PEG-DNA; and (c) PLL_{300}-g_{24}-PEG_1 with 24% PEG grafting was used. For a, b, and c, the N/P ratios to form the polymer−DNA condensates were 0.1 to 25. COS-7 cells were cultured on tissue culture polystyrene for 24 h and transfected with DNA-containing condensates. Transfection efficiencies were determined after a total of 48 h by fluorescence microscopy. The ratio between the total cell numbers as determined by Hoechst nuclear stain to the numbers of green fluorescent cells was analyzed. The data represent mean values ± SD of three independent experiments carried out in duplicate. (C) Comparison of transfection efficiencies of PLL-g-PEG-DNA condensates formed with PLL_{20} and PLL_{300} polymers with low grafting (4 and 5% PEG) but high molecular weight of the grafted PEG moiety (5 kDa). (a) Shows the transfection efficiency of PLL_{300}-g_4-PEG_5-DNA condensates formed with PLL_{300} grafted with 4% of 5 kDa PEG moieties. (b) Demonstrates the transfection efficiencies of DNA-containing polymer condensates formed with PLL_{20} grafted with 5% of 5 kDa PEG moieties (PLL_{20}-g_5-PEG_5-DNA). For (a) and (b), six different N/P ratios were used to form the condensates.

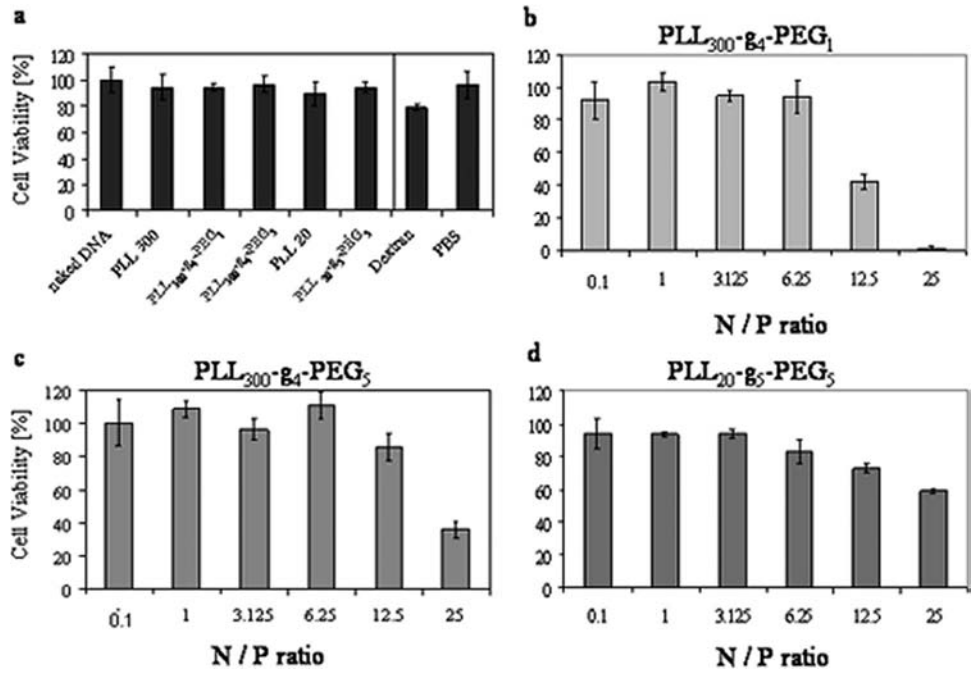

Figure 3. Cell viability of COS-7 cells after transfection with PLL-DNA and PLL-g-PEG-DNA condensates. Cell viability of COS-7 cells 48 h after transfection was determined by analysis of the mitochondrial activity using a WST-1 cell proliferation assay. (a) Nongrafted PLL_{300}- and PLL_{20}-, as well as all grafted PLL-g-PEG-DNA condensates that showed significant transfection efficiencies in COS-7 cells (in Figure 2A, a and b) were compared. The N/P ratio for all condensates was 3.125. Transfection with DEAE dextran and PBS only treatment were used as controls. Cell viability was determined 48 h after transfection with PLL_{300}-g_4-PEG_1-DNA (b), PLL_{300}-g_4-PEG_5-DNA (c), and PLL_{20}-g_5-PEG_5-DNA condensates (d). N/P ratios between 0.1 to 25 were used to form the condensates.

PEG showed poor transfection rates (below 2%) independent from the grafted PEG molecular weight. DEAE dextran complexed with plasmid DNA and transfection with naked DNA were performed in parallel. DEAE dextran showed transfection efficiencies of 61 ± 17%, whereas the application of naked DNA did not result in any GFP expression.

Different PLL_{300}-containing polymers with no, low (4%), and high (24%) PEG grafting were used to form DNA condensates with N/P ratios between 0.1 and 25. For all grafted polymers, PEG with 1 kDa was used (Figure 2B). Only when COS-7 cells were exposed to low PEGylated PLL_{300} (PLL_{300}-g_4-PEG_1), significant expression of green fluorescent protein could be observed (Figure 2B, b). The transfection efficiencies were found to be 10% for N/P ratio 3.125 and 20% for N/P ratio 6.25. Highly grafted PLL_{300} (Figure 2B, c) and non-PEGylated PLL_{300} (Figure 2B, a) were used to form polymer−DNA condensates; however, transfection resulted in very poor (<2%) expression of green fluorescent protein for all N/P ratios tested. These experiments indicate that not only the amount of PEG grafting is decisive for the transfection of COS-7 cells but also the formation of condensates with a medium charge ratio.

Since transfection efficiency is related to low PEGylation, the influence of the PLL backbone length (20 kDa vs 300 kDa PLL) was determined (Figure 2C). Interestingly, the polymers PLL_{300}-g_4-PEG_5 and PLL_{20}-g_5-PEG_5 showed comparable transfection efficiencies when PLL-g-PEG-DNA condensates were formed with N/P ratios between 0.1 and 25. The transfection efficiencies were found to be around 40% for PLL_{300}-g_4-PEG_5 formed at N/P ratio = 6.25 (Figure 2C, a) and for PLL_{20}-g_5-PEG_5 formed at N/P ratio = 3.125 (Figure 2C, b).

3.2. Determination of Cell Viability after Transfection with Polymer−DNA Condensates. Cell viability of COS-7 cells was analyzed using a proliferation assay that monitors mitochondrial activity as an indication for living cells (Figure 3). Cell viability was determined 48 h after transfection with different PLL_{300}- and PLL_{20}-containing DNA condensates formed at an N/P ratio of 3.125 (Figure 3a). Cell viability was not affected (>95% living cells) and was comparable to cell viability without any transfection. However, when COS-7 cells were transfected with DEAE dextran−DNA condensates, cell viability was impaired as only 78 ± 2% cells remained alive. Transfection with PLL_{300}-g_4-PEG_1, PLL_{300}-g_4-PEG_5, and PLL_{20}-g_5-PEG_5 containing DNA-condensates formed at N/P ratios between 0.1 and 25 demonstrated that cell viability depends strongly on the N/P ratio used to form the polymer−DNA condensates. Figure 3b and c shows that when condensates were formed with N/P ratios higher than 12.5 cell viability is significantly impaired, whereas cell viability remained significantly higher when PLL_{20}-g_5-PEG_5-DNA condensates were formed with N/P ratios higher than 12.5 (Figure 3d).

All findings displayed in Figures 2 and 3 indicated that polymer PLL_{20}-g_5-PEG_5 performed best with respect to transfection efficiency and cell viability over a wide range of N/P ratios as well as in ease of synthesis. In all further experiments, PLL_{20}-g_5-PEG_5 was used to form DNA-containing condensates, and particle size distribution and storage stability were characterized.

3.3. Determination of Size and Storage Stability of PLL_{20}-g_5-PEG_5-DNA Condensates. Particle size and storage stability of PLL_{20}-g_5-PEG_5-DNA condensates formed with N/P ratio = 3.125 were determined. To investigate the diameter of the condensates as a function of the size of the condensed plasmid, four different plasmids with 3200 to 10,100 base pairs (bp) were used. The hydrodynamic diameter of the polymer−DNA condensates was measured using dynamic light scattering (DLS) at a scattering angle of 90 ° (Figure 4a). The condensates displayed a mean diameter between 90 and 110 nm independent of the plasmid size used. The size of PLL_{20}-g_5-PEG_5-DNA condensates was determined after different storage times at 4 °C by DLS and found to be stable for at least 14 days in PBS (Figure 4b). When condensates were formed between PLL_{20}-g_5-PEG_5-DNA and plasmid DNA (pEGFP-N1) at N/P ratios increasing from 3.125 to 25, the hydrodynamic diameter remained at around 90 nm (Figure 4c).

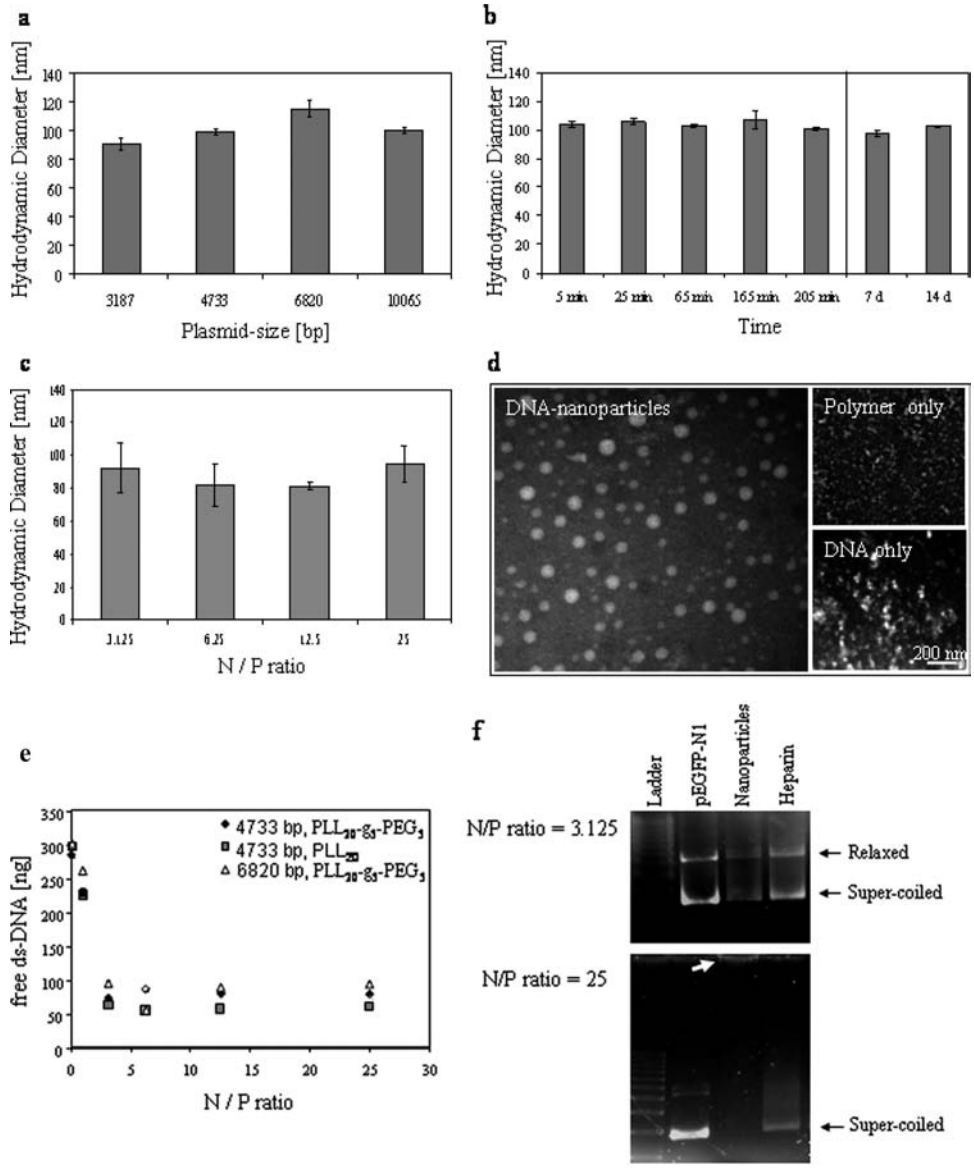

Figure 4. Size and storage stability of PLL_{20}-g_5-PEG_5-DNA condensates. (a) The size of PLL_{20}-g_5-PEG_5-DNA condensates was analyzed by dynamic light scattering. The hydrodynamic diameter of the condensates was determined as a function of the number of base pairs (bp) of the complexed plasmid DNA. PLL_{20}-g_5-PEG_5-DNA was used to form nanoparticles with an N/P ratio of 3.125 in PBS with four different plasmids: pHisTrx (3187 bp), pEGFP-N1 (4733 bp), pSV-β-galactosidase (6820 bp), and #343 (10065 bp). The data represent mean values ± SD of three independent experiments carried out in triplicate. (b) Size stability with time of PLL_{20}-g_5-PEG_5-DNA condensates formed with pEGFP-N1 (4733 bp) at an N/P ratio = 3.125 in PBS. The hydrodynamic diameter was determined during a time period of 0–14 days as indicated. The data represent the mean values ± SD of three independent experiments carried out in triplicate. (c) Hydrodynamic diameters of DNA-containing condensates formed with pEGFP-N1 (4733 bp) were determined. PLL_{20}-g_5-PEG_5-DNA condensates were formed with N/P ratios = 3.125, 6.25, 12.5, and 25 in PBS. The data represent the mean values ± SD of three independent experiments. (d) Negative stain transmission electron microscopy (TEM) images of PLL_{20}-g_5-PEG_5-DNA condensates (DNA-nanoparticles) formed with an N/P ratio of 3.125, PLL_{20}-g_5-PEG_5 polymer only (polymer only), and pEGFP-N1 plasmid only (DNA only). (e) Determination of the polymer-to-DNA ratio to form maximal condensed polymer−DNA condensates. The optimal N/P ratio between the polymers and DNA moieties was determined by PicoGreen, which binds to soluble double-stranded DNA. Polymer−DNA condensate formation was measured as a decrease in fluorescence intensity. Two different polymers, nongrafted PLL_{20} and PLL_{20}-g_5-PEG_5-DNA, were complexed with pEGFP-N1 (4733 bp). PLL_{20}-g_5-PEG_5 was also condensed with the plasmid pSV-β-galactosidase (6820 bp). N/P ratios between 0.1 and 25 were analyzed. The figure represents mean values ± SD of three independent experiments carried out in duplicate. (f) Determination of the stability of PLL_{20}-g_5-PEG_5-DNA nanoparticles formed with pEGFP-N1 (4733 bp) at N/P ratios = 3.125 and 25. Plasmid DNA was released from the nanoparticles by the addition of 750 μg of heparin separated by 1% agarose gel electrophoresis. The arrow indicates large particles in the loading slot.

To visualize the PLL_{20}-g_5-PEG_5-DNA nanoparticles, negative stain transmission electron microscopy was used. The particles were found to be spherical and homogeneously distributed, and they did not aggregate (Figure 4d). For controls, naked plasmid DNA and plain polymer were analyzed indicating that distinct DNA-containing nanoparticles form only when PLL_{20}-g_5-PEG_5 and plasmid DNA were combined.

In order to determine the polymer-to-DNA ratio for optimal DNA condensation, the interaction of PicoGreen with soluble double-stranded plasmid DNA was measured. By increasing the amount of polymer, the availability of free DNA for binding with PicoGreen was reduced as DNA was incorporated into the condensates, and a decrease in fluorescence intensity was observed. Condensates were formed between PLL_{20}-g_5-PEG_5 and plasmid pEGFP-N1 (4733 bp), and PLL_{20} and pEGFP-N1 as well as for PLL_{20}-g_5-PEG_5 and pSV-β-galactosidase (6820 bp). The N/P ratios equal to and higher than 3.125 showed maximal DNA condensation as indicated by stable low fluo-

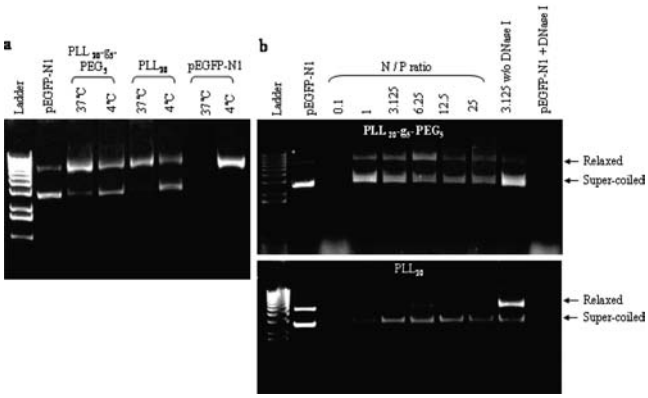

Figure 5. Serum stability of PLL_{20}-g_5-PEG_5-DNA nanoparticles and protection against DNase I digestion. (a) Stability of DNA-containing nanoparticles, consisting of PLL_{20} and PLL_{20}-g_5-PEG_5-DNA nanoparticles (formed with N/P ratio = 3.125). Particles and naked DNA were incubated for 7 days either at 4 °C or at 37 °C in 10% serum-containing tissue culture medium. DNA was released from the condensates by the addition of 15 μL of 50 mg/mL heparin and 5 μL of 5 M NaCl and separated by 1% agarose gel electrophoresis. (b) DNase I protection assay of PLL_{20}-g_5-PEG_5-DNA- and PLL_{20}-DNA-containing nanoparticles formed with different N/P ratios as indicated. Five micrograms of the pEGFP-N1 plasmid was used as a control. The nanoparticles were incubated for 10 min with 5 U DNase I, which was stopped by the addition of 0.3 M EDTA. DNA was released by 50 mg/mL heparin and 5 M NaCl addition and separated by gel electrophoresis as described above.

rescence (Figure 4e). Maximal plasmid condensation seems to be independent of the size of the incorporated plasmid as both plasmids with 4733 and 6820 bp performed equally well. These findings were in good agreement with data obtained for DLS. Furthermore, the release of plasmid DNA from the condensates was determined by heparin replacement (Figure 4f). Condensates were formed between PLL_{20}-g_5-PEG_5 and plasmid pEGFP-N1 at N/P ratios = 3.125 and 25. The DNA was released by 750 μg heparin and analyzed by agarose gel electrophoresis. Interestingly, even at such high heparin concentrations released plasmid DNA from condensates formed with N/P ratio = 25 appeared only as supercoiled structures, whereas plasmid DNA released from condensates formed at N/P ratio = 3.125 released relaxed and supercoiled plasmids to a similar extent. These findings might be relevant for transfection studies where plasmid DNA needs to be released in the nucleus to become physiologically active.

A gene delivery system should not only deliver DNA but also protect the incorporated DNA; therefore, polymer−DNA nanoparticles and naked plasmid DNA were exposed to serum components and DNase I treatment. Nanoparticles formed by PLL_{20}, PLL_{20}-g_5-PEG_5, and naked plasmid DNA were exposed to 10% fetal bovine serum (FBS) for 7 days at 4 and 37 °C, respectively (Figure 5a). Naked plasmid DNA was degraded at 37 °C, whereas DNA-containing nanoparticles formed with PLL_{20}-g_5-PEG_5 or PLL_{20} protected the incorporated plasmid DNA efficiently. In order to test the functionality of the complexes after storage at 4 and 37 °C in the presence of serum components, COS-7 cells were transfected with the nanoparticles and showed successful expression of green fluorescent protein (data not shown).

When nanoparticles formed with PLL_{20}-g_5-PEG_5 or PLL_{20} were exposed to DNase I, plasmid DNA remained intact for particles produced with N/P ratios between 1 to 25 (Figure 5b). Especially, the supercoiled form of the plasmids was preserved. Plasmid DNA was completely degraded when DNA-containing nanoparticles were formed with N/P ratio = 0.1. To confirm DNase I activity, naked DNA was completely digested during the time of the experiment. These findings suggest that plasmid DNA incorporated into the nanoparticles is protected by the structure and positive charge of PLL_{20}-g_5-PEG_5 and partially by PLL_{20} polymers.

4. DISCUSSION

Gene transfer using polymer-based DNA condensates is a promising approach for the safe delivery of therapeutic DNA in genetic and acquired human diseases. Many studies have been performed, but poor *in vivo* and *in vitro* transfection efficiencies and high cytotoxicity are still important issues (*2*, *11*, *35*). For these reasons, this project aimed to circumvent the inherent cytotoxicity of polycationic DNA condensates by forming polymer−DNA nanoparticles using grafted copolymers of poly L-lysine (PLL) and poly(ethylene glycol) (PEG). PEGylation improves the solubility and stability of PLL-g-PEG-DNA nanoparticles in watery solutions, and the steric effects of exposed PEG chains result in nanoparticles with reduced nonspecific protein adsorption as compared to charged polymer−DNA complexes (*36*). In addition, PEGylation might contribute to their cellular uptake (*23*, *25*, *31*, *37*, *38*).

Several studies using grafted PLL-g-PEG copolymers to form DNA complexes were carried out; however, a systematic analysis of the influences of PLL backbone length, the molecular weight of grafted PEG, and the amount of PEG grafting is still lacking. Here, eight different grafted PLL-g-PEG copolymers were explored for their capability to complex plasmid DNA and transfect COS-7 cells *in vitro*. The polymers were selected to have very different molecular weights of the PLL backbone (20 and 300 kDa), as low molecular weight PLL with less than 3 kDa do not form stable complexes with DNA (*26*), and very high molecular weight PLL-DNA (<700 kDa) complexes demonstrated high cytotoxicity and a tendency to aggregate and precipitate depending on the ionic strength (*39*). Here, the molecular weight of grafted PEG was 1 and 5 kDa, respectively, and no, low, and high grafting were compared. Successful gene expression combined with high cell viability (>94% living cells) was observed only when PLL was grafted with a low amount (4 or 5%) of PEG at medium N/P ratios of 3.125–12.5. The molecular weight of the PEG moieties seemed to be important (5 kDa), whereas the molecular weight of PLL did not affect transfection efficiency. Cell viability was only affected when condensates were formed at N/P ratios higher than 12.5 where low molecular weight PLL (PLL_{20}) showed lower cytotoxicity than high molecular weight PLL (PLL_{300}). However, these findings were not relevant for N/P ratios 3.125 and 6.25 where transfection efficiencies were best. Therefore, we could identify two polymers that performed best in the formation of polymer−DNA condensates, namely, PLL_{300}-g_4-PEG_5 and PLL_{20}-g_5-PEG_5. Other studies that used PLL of 20 kDa grafted with 5, 12, and 30 kDa PEG at 5 or 10% grafting ratio (*37*, *38*, *40*) demonstrated the highest cell viability and transfection efficiency for complexes formed between PLL_{20} grafted with 10% PEG of molecular weight of 5 kDa (*37*), whereas Mannistö et al. (*40*) found similar values for 20 kDa PLL grafted with 5 or 12 kDa PEG at 5% or 10% grafting. In our hands, high grafting of 20–28% PEG (1 or 5 kDa) on PLL_{20} or PLL_{300} did not show any successful transfection of COS-7 cells. These studies indicate that the equilibrium between lengths and probably the flexibility of the attached PEG moieties contribute to high transfection efficiency and stealth properties of the DNA-containing nanoparticles. Our study demonstrated that effective transfection and low cytotoxicity were correlated to a well-defined N/P ratio, which ranges from 3.125 to 12.5 for PLL_{300}-g_4-PEG_5 and from 3.125 to 6.25 for PLL_{20}-g_5-PEG_5, as polymer−DNA complexes formed with lower or higher N/P ratio did not transfect COS-7 cells. With increasing N/P ratios, especially for PLL_{300}-g_4-PEG_5, cytotoxicity increased signifi-

cantly, leaving no living cells at N/P ratio = 25. Efficiently transfecting and nontoxic polymer−DNA condensates contain 3–6 times more amino groups from PLL as compared to phosphate groups from DNA. At physiological conditions, these amino groups are positively charged and mediate maximal DNA condensation, shown here by fluorescence dye exclusion as well as cell surface attachment. These findings correlate nicely with the data of other authors that have found positive zeta potentials (∼40 mV) for condensates formed between cationic polymers and DNA (*20*, *24*, *37*, *40*).

Transfection efficiencies of PLL_{20}-g_5-PEG_5 at N/P ratio 3.125 and of PLL_{300}-g_4-PEG_5 at N/P ratio 6.25 were comparable to those of DNA complexes formed with DEAE-dextran; however, our PLL-g-PEG condensates formed at N/P ratio = 3.125 were found to be 20% less toxic. DEAE-dextran transfection is not suitable for *in vivo* applications as efficient transfection requires a toxic fusogeneic substance such as chloroquine and an osmotic shock to let the DNA condensates enter into COS-7 cells (*41*, *42*). In contrast, PLL_{20}-g_5-PEG_5 and PLL_{300}-g_4-PEG_5 might be well suited for bolus injections for DNA vaccines or other *in vivo* applications.

As PLL_{20}-g_5-PEG_5 performed best when transfection rate, cytotoxicity over a wide range of N/P ratios, and simplicity of polymer synthesis and DNA condensate production are considered, we performed our further studies with PLL_{20}-g_5-PEG_5-DNA condensates.

PLL_{20}-g_5-PEG_5-DNA condensates displayed a hydrodynamic diameter of ∼100 nm that was stable for at least 14 days. Interestingly, the diameter seems to be independent of the size of the incorporated plasmid DNA, as it remains almost constant for condensed plasmids between 3200 and 10100 bp. Values found in the literature vary between 80 to 200 nm when using standard plasmids (∼5000 bp) (*2*, *15*, *38*). When PLL_{20}-g_5-PEG_5-DNA condensates were visualized by negative stain transmission electron microscopy, particles appeared uniformly distributed and not aggregated. These findings were in accordance with our DLS measurements. Similar data were obtained for PLL_{20} grafted with 12 kDa PEG at 10% grafting when polymer−DNA complexes were analyzed by atomic force microscopy (*37*).

A particle diameter of ∼100 nm is able to circulate in the blood stream and lies within the favorable range for cellular uptake (*2*, *27*, *40*, *43*, *44*). This very interesting characteristic provides a clear advantage toward the limited packaging size of viral gene delivery systems and is an important criterion to consider when choosing such polymer−DNA condensates for further gene delivery applications. Similar studies have been performed by Mao et al. (*45*), when PEG chain length of poly(ethylene glycol) to grafted poly ethyleneimine (PEI) was analyzed for the delivery of siRNA. Their findings underline that the stability and size of the complexes are clearly influenced by the polymer-to-PEG structure, and high degrees of substitution resulted in larger, diffuse complexes that showed condensation only at high N/P ratios. Condensates formed with PEI at 25 kDa grafted with PEG at 2 kDa were very similar to the polymer structures used in our study. Condensation was complete when N/P ratios of 3 were reached. Interestingly, their polymer-to-siRNA condensates were larger in diameter (150 nm) as compared to our findings. These results might be explained by other studies that showed that siRNA, although being very short (21–23 bp), is very stiff an does not allow further condensation (*32*). However, in our study we were able to condense plasmid DNA between 3200 and 10,100 bp, which formed very homogeneous condensates between 90 and 110 nm. These findings suggest that condensation properties, capabilities, and necessities of siRNA and plasmid DNA are very different as siRNA needs to be released from the condensate already in the cytosol, whereas plasmids need to be delivered to the cell nucleus to be physiologically active (*32*). Therefore, our study selected specifically for DNA-containing nanoparticles that are stable, well condensed, nontoxic, and able to transfect cells efficiently.

As it is important for plasmid gene delivery systems to provide protection of therapeutic DNA in biological systems, for example, within the blood stream of a patient or when exposed to endogenous DNases in the vicinity of ruptured cells in a wound site, the polymer−DNA nanoparticles developed here and naked plasmid DNA were exposed to serum components at 37 and 4 °C for 7 days and to DNase I treatment in an *in vitro* setup. The DNA, incorporated in PLL_{20} and PLL_{20}-g_5-PEG_5 complexes, remained stable at 4 and 37 °C for 7 days, whereas naked DNA was degraded at 37 °C. It could be shown that polymer−DNA complexes were stable against DNase I treatment from N/P ratios 1 to 25. These findings indicate the high tolerance of PLL_{20}-g_5-PEG_5-polymer-DNA condensates against enzymatic degradation and serum proteins, which makes them suitable for direct injection into the blood stream or a wound site. These findings might be explained by reduced protein adsorption due to PEGylation of the DNA−polymer nanoparticles. Systematic studies on serum protein adsorption on differentially PEGylated-PLL adsorbed onto Nb_2O_5 surfaces demonstrated that the higher the PEG content of the surface the lower the amount of serum proteins adsorbed (*33*, *36*). Future studies might reveal a correlation between the amount of adsorbed serum proteins or DNase I on the surface of polymer−DNA nanoparticles and their stability.

5. CONCLUSIONS

In summary, the PLL-g-PEG-DNA nanoparticles used here showed excellent transfection efficiency combined with low cytotoxicity in COS-7 cells. Furthermore, we demonstrated that the PLL_{20}-g_5-PEG_5-DNA condensates displayed outstanding long-term stability that allows for their preparation a few weeks before actual use. Moreover, this study provides new insights into the rational design of novel DNA delivery vehicles that can be used to package DNA of different sizes without a change in DNA condensation, the final particle diameter, and their storage stability. All of these characteristics are advantageous compared to plasmid size limitations in viral gene delivery systems and stability issues in lipid-based gene delivery systems.

Future work will have to address surface functionalization with cell recognition and/or intracellular routing molecules as well as nuclear localization sequences (*2*, *38*, *43*, *46*). In addition, recent work with cationic polymer-based DNA delivery vehicles illustrated the importance of specific modification for cell targeting (*47*, *48*) as the treatment of many diseases could benefit from local application and transient expression of therapeutic proteins.

ACKNOWLEDGMENT

We thank Stéphanie Pasche, BioInterfaceGroup, Oberflächentechnik/Laboratory for Surface Science and Technology, Department of Materials, ETH Zurich, Switzerland for the synthesis of the polymers, Cornelius Gauer, Institute for Chemistry and Bioengineering, ETH Zurich, Switzerland for help and advice with DLS size distribution measurements and Anne Greet Bittermann, ZMB, Center for Microscopy and Imaging Analysis, University of Zurich, Switzerland for helping with TEM imaging. The Gebert Rüf Foundation (GRS-053/05), Switzerland, is acknowledged for financial support.

LITERATURE CITED

(1) Dinçer, S., Türk, M., and Pişkin, E. (2005) Intelligent polymers as nonviral vectors. *Gene Ther. 12* (Suppl. 1), 39–45.

(2) Park, T. G., Jeong, J. H., and Kim, S. W. (2006) Current status of polymeric gene delivery systems. *Adv. Drug Delivery Rev. 58*, 467–486.

(3) Rosenecker, J., Huth, S., and Rudolph, C. (2006) Gene therapy for cystic fibrosis lung disease: current status and future perspectives. *Curr. Opin. Mol. Ther. 8*, 439–445.

(4) Pietersz, G. A., Tang, C. K., and Apostolopoulos, V. (2006) Structure and design of polycationic carriers for gene delivery. *Mini Rev. Med. Chem. 6* (12), 1285–1298.

(5) Romano, G. (2007) Current development of nonviral-mediated gene transfer. *Drug News Perspect. 20* (4), 227–231.

(6) Heyde, M., Partridge, K. A., Oreffo, R. O., Howdle, S. M., Shakesheff, K. M., and Garnett, M. C. (2007) Gene therapy used for tissue engineering applications. *J. Pharm. Pharmacol. 59* (3), 329–350.

(7) Liu, F., Shollenberger, L. M., Conwell, C. C., Yuan, X., and Huang, L. (2007) Mechanism of naked DNA clearance after intravenous injection. *J. Gene Med. 9*, 613–619.

(8) Kusumanto, Y. H., Mulder, N. H., Dam, W. A., Losen, M. H., Meijer, C., and Hospers, G. A. (2007) Improvement of in vivo transfer of plasmid DNA in muscle: Comparison of electroporation versus ultrasound. *Drug Delivery 14*, 273–277.

(9) Kuriyama, S., Mitoro, A., Tsujinoue, H., Nakatani, T., Yoshiji, H., Tsujimoto, T., Yamazaki, M., and Fukui, H. (2000) Particle-mediated gene transfer into murine livers using a newly developed gene gun. *Gene Ther. 7*, 1132–1136.

(10) Felgner, P. L., Gadek, T. R., Holm, M., Roman, R., Chan, H. W., Wenz, M., Northrop, J. P., Ringold, G. M., and Danielsen, M. (1987) Lipofection: a highly efficient, lipid-mediated DNA-transfection procedure. *Proc. Natl. Acad. Sci. U.S.A. 84*, 7413–7417.

(11) Lv, H., Zhang, S., Wang, B., Cui, S., and Yan, J. (2006) Toxicity of cationic lipids and cationic polymers in gene delivery. *J. Controlled Release 114*, 100–109.

(12) Vandenbroucke, R. E., De Smedt, S. C., Demeester, J., and Sanders, N. N. (2007) Cellular entry pathway and gene transfer capacity of TAT-modified lipoplexes. *Biochim. Biophys. Acta 1768*, 571–579.

(13) Kawakami, S., Sato, A., Nishikawa, M., Yamashita, F., and Hashida, M. (2000) Mannose receptor-mediated gene transfer into macrophages using novel mannosylated cationic liposomes. *Gene Ther. 7*, 292–299.

(14) Lai, E., and van Zanten, J. H. (2002) Evidence of lipoplex dissociation in liquid formulations. *J. Pharm. Sci. 91*, 1225–1232.

(15) Ramsay, E., Hadgraft, J., Birchall, J., and Gumbleton, M. (2000) Examination of the biophysical interaction between plasmid DNA and the polycations, polylysine and polyornithine, as a basis for their differential gene transfection in-vitro. *Int. J. Pharm. 210*, 97–107.

(16) Lee, M., Nah, J. W., Kwon, Y., Koh, J. J., Ko, K. S., and Kim, S. W. (2001) Water-soluble and low molecular weight chitosan-based plasmid DNA delivery. *Pharm. Res. 18*, 427–431.

(17) Pichon, C., Goncalves, C., and Midoux, P. (2001) Histidine-rich peptides and polymers for nucleic acids delivery. *Adv. Drug Delivery Rev. 53*, 75–94.

(18) Davis, M. E. (2002) Non-viral gene delivery systems. *Curr. Opin. Biotechnol. 13*, 128–131.

(19) Zaitsev, S., Cartier, R., Vyborov, O., Sukhorukov, G., Paulke, B. R., Haberland, A., Parfyonova, Y., Tkachuk, V., and Bottger, M. (2004) Polyelectrolyte nanoparticles mediate vascular gene delivery. *Pharm. Res. 21*, 1656–1661.

(20) Zhang, X., Pan, S. R., Hu, H. M., Wu, G. F., Feng, M. , Zhang, W. , and Luo, X. (2007) Poly(ethylene glycol)-block-polyethyleneimine copolymers as carriers for gene delivery: Effects of PEG molecular weight and PEGylation degree. *J. Biomed. Mater. Res. A*, in press.

(21) Zhang, Y., Chen, J., Zhang, Y., Pan, Y., Zhao, J., Ren, L., Liao, M., Hu, Z., Kong, L., and Wang, J. (2007) A novel PEGylation of chitosan nanoparticles for gene delivery. *Biotechnol. Appl. Biochem. 46*, 197–204.

(22) Wagner, E., Ogris, M., and Zauner, W. (1998) Polylysine-based transfection systems utilizing receptor-mediated delivery. *Adv. Drug Delivery Rev. 30*, 97–113.

(23) Lee, H., Jeong, J. H., and Park, T. G. (2002) PEG grafted polylysine with fusogenic peptide for gene delivery: high transfection efficiency with low cytotoxicity. *J. Controlled Release 79*, 283–291.

(24) Hong, S., Leroueil, P. R., Janus, E. K., Peters, J. L., Kober, M. M., Islam, M. T., Orr, B. G., Baker, J. R., Jr., and Banaszak Holl, M. M. (2006) Interaction of polycationic polymers with supported lipid bilayers and cells: nanoscale hole formation and enhanced membrane permeability. *Bioconjugate Chem. 17*, 728–734.

(25) Choi, Y. H., Liu, F., Kim, J. S., Choi, Y. K., Park, J. S., and Kim, S. W. (1998) Polyethylene glycol-grafted poly-L-lysine as polymeric gene carrier. *J. Controlled Release 54*, 39–48.

(26) Kwok, K. Y., Park, Y., Yang, Y., McKenzie, D. L., Liu, Y., and Rice, K. G. (2003) In vivo gene transfer using sulfhydryl cross-linked PEG-peptide/glycopeptide DNA co-condensates. *J. Pharm. Sci. 92*, 1174–1185.

(27) Trentin, D., Hubbell, J., and Hall, H. (2005) Non-viral gene delivery for local and controlled DNA release. *J. Controlled Release 102*, 263–275.

(28) Trentin, D., Hall, H., Wechsler, S., and Hubbell, J. A. (2006) Peptide-matrix-mediated gene transfer of an oxygen-insensitive hypoxia-inducible factor-1alpha variant for local induction of angiogenesis. *Proc. Natl. Acad. Sci. U.S.A. 103*, 2506–2511.

(29) Chen, C. P., Kim, J. S., Liu, D., Rettig, G. R., McAnuff, M. A., Martin, M. E., and Rice, K. G. (2007) Synthetic PEGylated glycoproteins and their utility in gene delivery. *Bioconjugate Chem. 18*, 371–378.

(30) Ogris, M., Brunner, S., Schuller, S., Kircheis, R., and Wagner, E. (1999) PEGylated DNA/transferrin-PEI complexes: reduced interaction with blood components, extended circulation in blood and potential for systemic gene delivery. *Gene Ther. 6*, 595–605.

(31) Mishra, S., Webster, P., and Davis, M. E. (2004) PEGylation significantly affects cellular uptake and intracellular trafficking of non-viral gene delivery particles. *Eur. J. Cell Biol. 83*, 97–111.

(32) Gary, D. J., Puri, N., and Won, Y. Y. (2007) Polymer-based Si RNA delivery: perspectives on the fundamental and phenomenological distinctions from polymer-based DNA delivery. *J. Controlled Release 121*, 64–73.

(33) Pasche, S., De Paul, S. M., Voros, J., Spencer, N. D., and Textor, M. (2003) Poly(L-lysine)-graft-poly(ethylene glycol) assembled monolayers on niobium oxide surfaces: A quantitative study of the influence of polymer interfacial architecture on resistance to protein adsorption by ToF-SIMS and in situ OWLS. *Langmuir 19*, 9216–9225.

(34) Kammerer, R. A., Schulthess, T., Landwehr, R., Lustig, A., Fischer, and Engel, J. (1998) Tenascin-C hexabrachion assembly is a sequential two-step process initiated by coiled-coil alpha-helices. *J. Biol. Chem. 273* (17), 10602–10608.

(35) Labhasetwar, V. (2005) Nanotechnology for drug and gene therapy: the importance of understanding molecular mechanisms of delivery. *Curr. Opin. Biotechnol. 16*, 674–680.

(36) Michel, R., Pasche, S., Textor, M., and Castner, D. C. (2005) Influence of PEG architecture on protein adsorption and conformation. *Langmuir 21*, 12327–12332.

(37) Toncheva, V., Wolfert, M. A., Dash, P. R., Oupicky, D., Ulbrich, K., Seymour, L. W., and Schacht, E. H. (1998) Novel vectors for gene delivery formed by self-assembly of DNA with poly(L-lysine) grafted with hydrophilic polymers. *Biochim. Biophys. Acta 1380*, 354–368.

(38) Lee, M., and Kim, S. W. (2005) Polyethylene glycol-conjugated copolymers for plasmid DNA delivery. *Pharm. Res. 22*, 1–10.

(39) Kwok, K. Y., McKenzie, D. L., Evers, D. L., and Rice, K. G. (1999) Formulation of highly soluble poly(ethylene glycol)-peptide DNA condensates. *J. Pharm. Sci. 88*, 996–1003.

(40) Mannistö, M., Vanderkerken, S., Toncheva, V., Elomaa, M., Ruponen, M., Schacht, E., and Urtti, A. (2002) Structure-activity relationships of poly(L-lysines): effects of pegylation and molecular shape on physicochemical and biological properties in gene delivery. *J. Controlled Release 83*, 169–182.

(41) Zobel, H. P., Kreuter, J., Werner, D., Noe, C. R., G, K., and Zimmer, A. (1997) Cationic polyhexylcyanoacrylate nanoparticles as carriers for antisense oligonucleotides. *Antisense Nucleic Acid Drug Dev. 7*, 483–493.

(42) Pari, G., and Xu, Y. (2004) Gene transfer into mammalian cells using calcium phosphate and DEAE-dextran. *Methods Mol. Biol. 245*, 25–32.

(43) Kleemann, E., Neu, M., Jekel, N., Fink, L., Schmehl, T., Gessler, T., Seeger, W., and Kissel, T. (2005) Nano-carriers for DNA delivery to the lung based upon a TAT-derived peptide covalently coupled to PEG-PEI. *J. Controlled Release 109*, 299–316.

(44) Vijayanathan, V., Thomas, T., and Thomas, T. J. (2002) DNA Nanoparticles and development of DNA delivery vehicles for gene therapy. *Biochemistry 41*, 14085–14094.

(45) Mao, S., Neu, M., Germershaus, O., Merkel, O., Sitterberg, J., Bakowsky, U., and Kissel, T. (2006) Influence of polyethylene glycol chain length on the physicochemical and biological properties of poly(ethyleneimine)-graft-poly(ethylene glycol) block copolymer/SiRNA polyplexes. *Bioconjugate Chem. 17*, 1209–1218.

(46) Trehin, R., and Merkle, H. P. (2004) Chances and pitfalls of cell penetrating peptides for cellular drug delivery. *Eur. J. Pharm. Biopharm. 58*, 209–223.

(47) Bikram, M., Ahn, C. H., Chae, S. Y., Lee, M., Yockman, J. W., and Kim, S. W. (2004) Biodegradable poly(ethylene glycol)-co-poly(L-lysine)-g-histidine multiblock copolymers for nonviral gene delivery. *Macromolecules 37*, 1903–1916.

(48) Kim, S. H., Jeong, J. H., Chun, K. W., and Park, T. G. (2005) Target-specific cellular uptake of PLGA nanoparticles coated with poly(L-lysine)-poly(ethylene glycol)-folate conjugate. *Langmuir 21*, 8852–8857.

BC7003439

Enhancement of Star Vector-Based Gene Delivery to Endothelial Cells by Addition of RGD-Peptide

Ayaka Ishikawa,[†] Yue-Min Zhou,[†] Nobuaki Kambe,[‡] and Yasuhide Nakayama*[,†]

Department of Bioengineering, Advanced Medical Engineering Center, National Cardiovascular Center Research Institute, Osaka, Japan and Department of Applied Chemistry, Graduate School of Engineering, Osaka University, Osaka Japan. Received October 17, 2007; Revised Manuscript Received December 1, 2007

This study aimed to investigate the feasibility of using a cationic nonviral gene carrier in endothelial cells for enhancing gene expression by the addition of an integrin-binding RGD peptide. A 4-branched cationic polymer of poly(*N*,*N*-dimethylaminopropylacrylamide) (star vector), developed as a gene carrier, could complex with the luciferase-encoding plasmid DNA under a charge ratio of 5 (vector/pDNA) to form polymer/DNA complexes (polyplexes). The addition of the RGD-containing peptide (GRGDNP) to the polyplex solution led to a decrease in the ζ-potential from ca. +30 to +20 mV along with the reduction in the particle size from ca. 300 to 200 nm. Additionally, a marked inhibition of polyplex aggregation was observed, indicating the coating of the polyplex surface with RGD peptides. A transfection study on endothelial cells showed that the luciferase activity increased with the amount of RGD peptides added to the polyplexes and exhibited minimal cellular cytotoxicity. The transfection activity further increased when cyclic RGD peptides (RGDFV) were used; the activity with RGD peptide addition was approximately 8-fold compared to that without RGD peptide addition. Gene delivery to endothelial cells was significantly enhanced by only the addition of RGD peptides to star vector-based polyplexes.

INTRODUCTION

Cationic polymers such as poly(ethylenimine) (PEI) (*1–4*) and poly(*N*,*N*-dimethylaminopropyl acrylamide) (PDMAPAAm) (*5–8*) can generate nanoparticles by the formation of polyion complexes, i.e., "polyplexes" with DNA. These polymers are highly expected to be among the major carriers in nonviral gene delivery systems due to the many advantages they offer over viral systems (*9–13*). These advantages include blocking of specific immune responses, no restrictions in DNA size, and ease of large-scale production.

We attempted to investigate the usefulness of star-shaped cationic polymers as a base chemical structure for a novel high-performance gene carrier (*5–8*). These polymers, known as star vectors, were prepared by initiator-transfer agent-terminator (iniferter)-based living radical polymerization (*14*, *15*) of DMAPAAm, using the respective multidithiocarbamate-derivatized benzenes (multifunctional iniferters) (*5*, *7*). The gene expression efficiency was enhanced with the increase in the number of branching in COS-1 cells. Recently, it was shown that grafting of each cationic branch in the star vector with nonionic block chain resulted in a considerable improvement in the gene transfection efficiency (*7*). On the other hand, it was shown that introducing a ligand to the star vector was effective in delivering the target to specific cells. For example, for targeting resting macrophages, the star vector was incorporated with C45D18 peptide, which is an oligopeptide with an active site derived from Vpr of human immunodeficiency virus type-1 (*6*).

The vitronectin receptor $\alpha_V\beta_3$ is highly upregulated in endothelial cells of tumors, while it is minimally expressed in resting or normal blood vessels (*16*). The tripeptide sequence, arginine (Arg)-glycine (Gly)-aspartic acid (Asp) (RGD) found in the active site of vitronectin binds to $\alpha_V\beta_3$ and almost half of the 22 known integrins (*17*). RGD peptides are exploited for cell entry by pathogenic microorganisms such as the foot-and-mouth disease virus (*18*). A great advantage of integrin targeting is that internalization occurs by a "zippering" mechanism (*19*) that allows the uptake of relatively large structures such as bacteria. Therefore, several cationic polymer vectors combined with RGD peptides were developed for tumor-targeted gene delivery (*20–23*). For example, RGD-containing peptides were coupled with PEI with or without a PEG spacer. The RGD-modified PEI showed a significant increase in transfection efficiency as compared to only PEI in endothelial cells. Almost all RGD-mediated gene delivery systems have been described with the chemical derivatization of RGD peptides to vector compounds.

In this paper, we report the influence of the addition of RGD to star vector-based polyplexes on the physicochemical and biological properties of the polyplexes that comprised plasmid DNA and 4-branched cationic star vector with a molecular weight of ca. 18 000. As a model, an RGD-containing peptide GRGDNP and cyclic RGD peptides were used. We strongly believed that if the coating of the polyplex surface with the RGD peptides occurs only by the addition of these peptides, then the gene transfection efficiency to endothelial cells would be enhanced, similar to that in the case of chemical derivatization of the RGD peptides.

MATERIALS AND METHODS

Materials. RGD-containing peptide (GRGDNP) was purchased from Wako Pure Chemical Industry (Osaka, Japan) and cyclic RGD peptide (RGDFV) were from Peptide Institute, Inc. (Osaka, Japan).

Synthesis of Cationic 4-Branched Polymer. The cationic 4-branched polymer, 1,2,4,5-tetrakis(*N*,*N*-diethyldithiocarbamyl(poly(*N*-[3-(dimethylamino)propyl]acrylamide)benzene was synthesized by iniferter-based living radical photopolymerization from 1,2,4,5-tetrakis(*N*,*N*-diethyldithiocarbamylmethyl)benzene

* To whom correspondence should be addressed: Department of Bioengineering, Advanced Medical Engineering Center, National Cardiovascular Center Research Institute, 5-7-1 Fujishiro-dai, Suita, Osaka 565-8565, Japan. Telephone: (+81) 6-6833-5012 (ex. 2624). Fax: (+81) 6-6872-8090. E-mail: nakayama@ri.ncvc.go.jp.

[†] National Cardiovascular Center Research Institute.

[‡] Osaka University.

10.1021/bc700385r CCC: $40.75 © 2008 American Chemical Society
Published on Web 01/19/2008

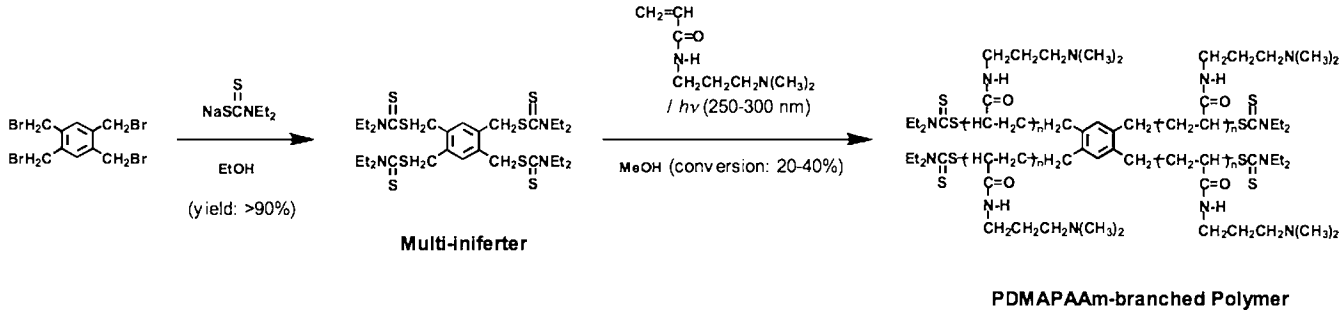

Figure 1. Synthesis of PDMAPAAm 4-branched polymer (star vector).

as a multifunctional iniferter with DMAPAAm as cationic monomer, according to the method previously reported by us (*5, 7*). Brifely, to 6 mL of a benzene solution of 1,2,4,5-tetrakis(*N,N*-diethyldithiocarbamylmethyl)benzene (72 mg, 0.1 mmol) DMAPAAm (72 mg, 0.1 mmol) was added; this was diluted to a final volume of 20 mL with methanol and placed into a 50-mL quartz crystal tube. After bubbling with dry N_2 gas for 5 min to exclude air, the solution was irradiated for 90 min with a 200-W high-pressure mercury lamp (SPOT CURE; USHIO, Tokyo, Japan) under an N_2 atmosphere at room temperature. The light intensity was set to 1 mW/cm^2 at a wavelength of 250 nm (UVR-1; TOPCON, Tokyo, Japan). The reaction mixture was concentrated and adjusted to an appropriate concentration in order to facilitate purification by precipitation in a large volume of ether. Reprecipitation was carried out in a methanol−ether system. The final precipitate was dried under vacuum to yield a PDMAPAAm 4-branched polymer (conversion, 13%). The molecular weight (Mn) as determined by GPC analysis was 18 000 g·mol^{-1}. ^{1}H NMR: δ 1.7–1.5 (br, 3H, -C$\underline{H}_2$-CH- and -CH$_2$-C$\underline{H}_2$-CH$_2$-), 2.0–1.8 (br, 1H, -C$\underline{H}$-CO), 2.2–2.1 (br, 6H, -N-C$\underline{H}_3$), 2.4–2.2 (br, 2H, -C$\underline{H}_2$-N(CH$_3$)$_2$), 3.2–3.0 (br, 2H, -NH-C$\underline{H}_2$-), 7.8–7.4 (br, 1H, -NH).

Preparation of Polyplexes. The cationic 4-branched polymer was dissolved in a saline solution. Aliquots of these solutions (60 μL) were added to the plasmid DNA (pGL3-control) dissolved in 90 μL of Tris-HCl buffer (pH 7.4) to obtain polymer/DNA ratios of 5 or 10, which correspond to cation/anion (C/A) ratios. The solutions (total volume, 150 μL; plasmid concentration, 20 mg/mL) were mixed using a pipet. After 10 min of complex formation, 25 μL of the complex solutions were added into each well of 24-well plates for transfection (the amount of DNA added to a well, 0.5 μg/well).

Biophysical Characterization of Polyplexes. The ζ-potentials and mean diameters of the polyplexes in a saline solution having the same concentration that was used for transfection at a C/A ratio of 5 were determined by employing DLS on an ELS-8000 system (Otuska Co., Osaka, Japan) equipped with a 10-mW He-Ne laser.

***In Vitro* Transfection and Cell Viability Assays.** COS-1 cells (approximately 3 × 10^4 cells per well) were seeded prior to treatment in 24-well plates and grown for 24 h in DMEM (Gibco, Invitrogen Corp., Carlsbad, CA) containing 10% fetal calf serum (Hyclone Laboratories Inc., Logan, UT), penicillin (200 units/mL; ICN Biomedicals Inc., Aurora, OH), and streptomycin (200 mg/mL; ICN) in an atmosphere of 5% CO_2 at 37 °C. Transfections were performed with 0.5 μg of the DNA in 24-well plates in 0.2 mL of OPTI-MEM I (Gibco). After 3 h of incubation, the cells were washed once with PBS(−) and cultured in 1 mL of DMEM containing 10% fetal calf serum for an additional 48 h. The medium was removed and the cells were washed twice with PBS(−). The cells were lysed with 0.2 mL of cell lysis buffer (Promega, Madison, WI) and mixed by vortexing. The lysate was centrifuged at 15 000 rpm for 1 min at 4 °C and 5 μL of the supernatant was analyzed for luciferase activity using a Luminous CT-9000D (Dia-Iatron, Tokyo, Japan) luminometer. The relative light unit/s (RLU) were converted into the amount of luciferase (pg) using a luciferase standard curve, which was obtained by diluting recombinant luciferase (Promega) in lysis buffer. The protein concentrations of cell lysates were measured by performing a Bio-Rad protein assay (BIO-RAD, Hercules, CA) using bovine serum albumin as a standard. The expressed luciferase represented the amount (mole quantity), which is standardized for the total protein content of the cell lysate. The data are presented as means ± SD (n = 5).

Cytotoxicity was assessed by performing a cell viability assay using the WST-8 method (Dojindo, Kumamoto, Japan). COS-1 cells were seeded 24 h prior to treatment in 96-well plates at 5000 cells per well. Cells were treated under the same conditions used for luciferase assay with 6.2 μL of the transfection mixture including 0.124 μg of pDNA added to each well. They were treated under appropriate conditions for 3 h, washed once with PBS, and cultured in 50 μL of DMEM (Gibco) containing 10% fetal calf serum for an additional 24 h. To each well, 10 μL of WST-8 reagent (5 mmol/l) was added. After 2 h of incubation at 37 °C, absorbance at 450 nm was read in a BIO-RAD microplate reader (model 680). The data are presented as means ± SD (n = 5).

RESULTS AND DISCUSSION

Interaction of Polyplex and RGD Peptide. The cationic 4-branched polymer with a molecular weight of ca. 18 000 was prepared by iniferter-based living radical polymerization (*5, 7*). The polymer had an extremely low polydispersity of less than 1.7. When the saline solution of cationic 4-branched polymer (7.9 μg/60 μL) was mixed with a tris-HCl buffer of luciferase-encoding pDNA (3 μg/90 μL) under a charge ratio of 5 (polymer/DNA), polyplexes in the form of approximately 300-nm nanoparticles were formed by electrostatic affinity (Figures 1, 2); this observation was similar to that of our previous study (*5, 7*).

First, we evaluated the interaction between the polyplexes and GRGDNP by measuring the change in the particle size. When the solution of the polyplexes, which were formed by mixing the polymer and the pDNA, was allowed to stand at 37 °C, the particle size significantly increased with time due to the aggregation of the polyplexes (Figure 2). The nanosized particles became microsized ones within 10 min. On the other hand, when the saline solution of RGD peptide was added to the polyplex solution immediately after preparation, the size of polyplexes reduced to approximately 200 nm. When the obtained polyplex solution was allowed to stand at 37 °C, the aggregation of the polyplexes was prevented depending on the amount of RDG peptide added. This indicated the interaction between the RGD peptide and the polyplexes. The saturation of the prevention effect was observed at approximately 30 μg.

To examine the surface electric property of the polyplexes, their ζ-potential in the presence or absence of RGD peptide

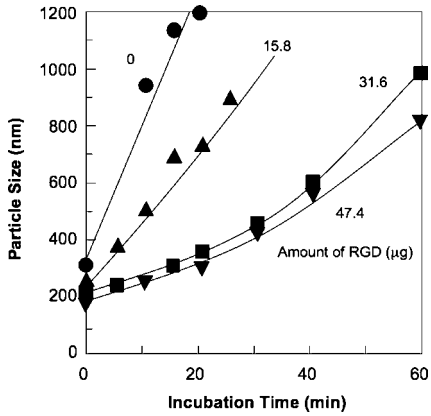

Figure 2. Incubation time-dependent cumulant diameter changes in aqueous solutions of polyplexes prepared by mixing DNA (pGL3-control, 3 μg) and PDMAPAAm 4-branched polymer (star vector, 7.9 μg) under a charge ratio of 5 at pH 7.4 in the presence of RGD peptides, whose amounts ranged from 0 to 47.7 μg.

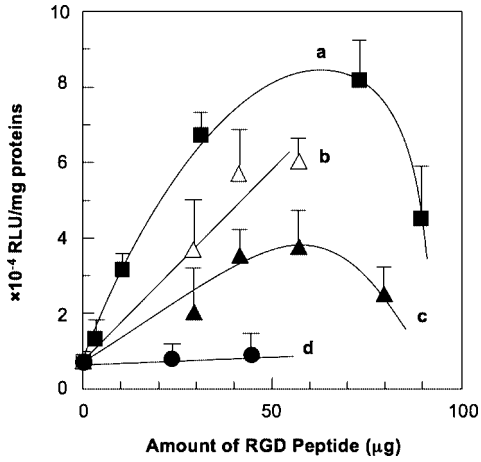

Figure 3. Transfection efficiency to endothelial cells of the polyplexes prepared by mixing DNA (pGL3-control, 3 μg) and PDMAPAAm 4-branched polymer (star vector, 7.9 μg) under a charge ratio of 5 in the presence of GRGDNP peptides (**b**, **c**, **d**) or cyclic RGD peptide (**a**) under charge ratio of 5 (vector/pDNA) in **a**, **c**, and **d**, or 10 in **b**. The RGD peptide was added before contact of the polyplexes with the endothelial cells (**c**).

was measured using DLS. In the RGD peptide-free polyplexes, the ζ-potential was approximately +30 mV, whereas it was decreased to approximately +20 mV after the addition of the RGD peptide (47.4 μg). The reduced surface potential might be due to the coating of the polyplex surface with the peptide. Although the driving force for the binding between the polyplexes with a positive charge and the RGD peptide with a lower electrical potential is still unknown, it was estimated that the surface coating occurred due to a physical interaction such as adsorption of the RGD peptide on the polyplexes without any chemical binding. These particle size and ζ-potential data lead to the conclusion that the aggregation of the polyplexes was prevented by the coating of the polyplexes with the RGD peptide in order to reduce the positive charge of the surface and to use almost all of the 30 μg of the RGD peptide added. The amount was about 4 times of that of cationic polymer used to form the polyplexes completely.

***In Vitro* Transfection Efficiency.** The gene transfection efficiency of the polyplexes coated or not coated with the RGD peptide was tested on model cell line of mice vascular endothelial cells (ECs). The result is summarized in Figure 3. The cells transfected with the luciferase-encoding plasmid (pGL3) in the absence of the RGD peptide exhibited a low luciferase expression, whereas those transfected with polyplexes + RGD peptide exhibited a higher luciferase expression and this expression increased with the amount of RGD peptide added (curve **c** in Figure 3). Upon an increase in C/A ratio from 5 to 10 further increase in the luciferase expression was observed (curve **b** in Figure 3). The highest luciferase expression occurred when approximately 50 μg RGD peptide was added. However, further addition of the RGD peptide led to a decrease in the luciferase expression.

The enhancement of luciferase expression by the addition of the RGD peptide was considered to be due to 2 major reasons—the stabilization of the polyplex particles and the RGD-mediated internalization of the polyplexes into the cells. The DNA expression observed using polyplexes occurred via the following 5 sequential steps: (1) attachment of the polyplexes onto the cell surface, (2) internalization of the polyplexes into the cell, (3) endosomal escape of polyplexes, (4) DNA release from polyplexes, and (5) internalization of the DNA into the nucleus. Almost all of the cationic polymers, including PEI, can conjugate with DNA to form nanosized polyplexes by an electrostatic affinity immediately after mixing. However, the polyplexes gradually aggregate with the increase in incubation time to grow from nanosized to macrosized particles by a similar electrostatic affinity, as demonstrated in Figure 2. In general, it was reported that the transfection efficiency was low in large particles because such particles could not easily internalize into the cells, which is the above-mentioned second step. In this study, indeed, polyplex particles became stable by the addition of the RGD peptide and synchronously, the transfection efficiency increased. However, the enhancement of gene transfection by the stabilization effect of the polyplex particles was eliminated by the following experiment.

When approximately 50 μg of RGD peptide was added to the cultured cells before the addition of the solution containing the RGD peptide-coated polyplexes, little change in the luciferase expression was observed (curve **d** in Figure 3). This indicated that little internalization of the polyplexes into the cells occurred even by polyplex stabilization. The reason for such an observation was considered to be that integrin receptors on the cellular membrane were capped and as a result little polyplex was recognized by the cells. Therefore, we believed that the enhancement of the gene transfection efficiency was due to the RGD-mediated internalization. The changes in cellular morphology and motility were not noticed even after RGD capping of integrin receptors within our observation period including medium change after 3 h of incubation with the polyplexes, although it was reported that integrins regulate several cellular functions including cell migration, growth, and differentiation (*25*, *26*).

On the other hand, when cyclic RGD (cRGD) peptide was added to the polyplexes, a further increase in gene transfection efficiency was observed (curve **a** in Figure 3). Cyclization of the RGD peptides is known to increase receptor affinity and selectivity by providing a conformational restraint (*17*). In addition, we observed that compared to the noncyclic RGD peptide, the use of the cRGD peptide increased the gene transfection efficiency by approximately 3 times. For both RGD and cRGD peptides, excessive addition of the peptides led to a decrease in the transfection efficiency. From the result presented in Figure 2, the amount of RGD peptide required for completely coating the polyplexes was approximately 30–50 μg. The surplus amount of RGD peptide might bind to the integrin receptor and prevent binding with the RGD peptide coating the polyplexes.

Cytotoxicity of Polyplexes with RGD Peptide. By using the WST-8 assay, the *in vitro* cytotoxicity of the RGD-added polyplexes for the EC cells was studied as a function of the amount of the RGD peptide added. The polyplexes with a charge

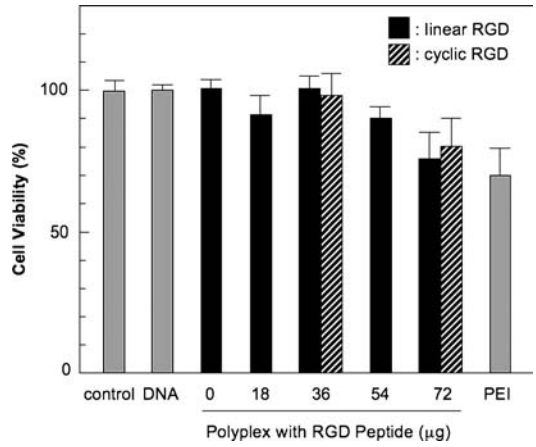

Figure 4. Cytotoxicity of the polyplexes prepared by mixing DNA (pGL3-control, 3 μg) and PDMAPAAm 4-branched polymer (star vector, 7.9 μg) when different amount of linear RGD or cyclic RGD peptides are added. For comparison, the cytotoxicity data of polyplexes of linear PEI (ExGen 500) at the charge ratio of 5 are also provided. Cell viability was determined by the WST assay.

ratio of 5 exhibited little toxicity (Figure 4). The addition of up to approximately 40 μg of RGD peptide also demonstrated little toxicity. At higher amounts of RGD peptide (72 μg), permissible viability, which was higher than that with PEI at a charge ratio of 6, was observed. Very low cytotoxicity was also demonstrated in cRGD peptide (Figure 4). There was little difference in cytotoxicity between RGD and cRGD peptides.

CONCLUSIONS

Our study is the first to report that cationic polymer-based gene transfer to EC cells is markedly enhanced in the presence of the RGD peptide. This peptide was only added to the solution of the polyplexes, which was prepared by mixing the cationic polymer and pDNA, without derivatization of the peptide to the polymer by chemical binding, as demonstrated in almost all other reports. The enhancement of gene transfer by the addition of the RGD peptide may be applied even for other cationic polymer vectors because the RGD peptide could coat the cationic surface of the polyplexes. The surface coating ability may be enhanced by the introduction of anionic amino acids such as aspartic acid or glutamic acid to the RGD peptide.

LITERATURE CITED

(1) Boussif, O., Lezouclc'h, F., Zanta, M., Mergny, M. D., Scherman, D., Demeneix, B., and Behr, J. P. (1995) A versatile vector for gene and oligonucleotide transfer into cells in culture and *in vivo*: polyethylenimine. *Proc. Natl. Acad. Sci. U.S.A. 92*, 7297–7301.

(2) Godbey, W. T., Wu, K. K., and Mikos, A. G. (1999) Poly(ethyleneimine) and its role in gene delivery. *J. Controlled Release 60*, 149–160.

(3) Kichler, A. (2004) Gene transfer with modied polyethyleneimine. *J. Gene Med. 6 Suppl. 1* S3–S10.

(4) Demeneix, B., Hassani, Z., and Behr, J. P. (2004) Towards multifunctional synthetic vectors. *Curr. Gene Ther. 4*, 445–455.

(5) Nakayama, Y., Masuda, T., Nagaishi, M., Hayashi, M., Ohira, M., and Harada-Shiba, M. (2005) High performance gene delivery polymeric vector: nano-structured cationic star polymers (star vector). *Curr. Drug Delivery 2*, 53–57.

(6) Mizuguchi, F., Ooe, Y., Hoshino, S., Shimura, M., Kasahara, T., Kano, S., Ohta, T., Takaku, F., Nakayama, Y., and Ishizaka, Y. (2005) Improved gene expression in resting macrophages using an oligopeptide derived from Vpr of human immunodeficiency virus type-1. *Biochem. Biophys. Res. Commun. 338*, 1499–1506.

(7) Nakayama, Y., Kakei, C., Ishikawa, A., Zhou, Y. M., Nemoto, Y., Uchida, K. (2007) Synthesis and *in vitro* eveluation of novel star-shaped block copolymers (blocked star vectors) for efficient gene delivery. *Bioconjugate Chem.* [Epub shead of print].

(8) Zhou, Y. M., Ishikawa, A., Okahashi, R., Uchida, K., Nemoto, Y., Nakayama, M., and Nakayama, Y. (2007) Deposition transfection technology using a DNA complex with a thermoresponsive cationic star polymer. *J. Controlled Release 123*, 239–246.

(9) Li, S., and Huang, L. (2000) Gene therapy progress and prospects: non-viral gene therapy by systemic delivery. *Gene Ther. 7*, 31–34.

(10) Luo, D., and Saltzman, W. M. (2000) Enhancement of transfection by physical concentration of DNA at the cell surface. *Nat. Biotechnol. 18*, 33–37.

(11) Gebhart, C. L., and Kabanov, A. K. (2001) Evaluation of polyplexes as gene transfer agents. *J. Controlled Release 73*, 401–416.

(12) Thomas, M., and Klibanov, A. M. (2003) Non-viral gene therapy: polycation-mediated DNA delivery. *Appl. Microbiol. Biotechnol. 62*, 27–34.

(13) Dubruel, P., and Schacht, E. (2006) Vinyl polymers as non-viral gene delivery carriers: current status and prospects. *Macromol. Biosci. 6*, 789–810.

(14) Otsu, T., Yoshida, M., and Tazaki, T. (1982) A model for living radical polymerization. *Makromol. Chem. Rapid Commun. 3*, 133–140.

(15) Otsu, T., Matsunaga, T., Doi, T., and Matsumoto, A. (1995) Features of living radical polymerization of vinyl monomers in homogeneous system using *N,N*-diethyldithiocarbamate derivatives as photoiniferters. *Eur. Polym. J. 31*, 67–78.

(16) Varner, J. A., and Cheresh, D. A. (1996) Integrins and cancer. *Curr. Opin. Cell Biol. 8*, 724–730.

(17) Rouslahti, E. (1996) RGD and other recognition sequences for integrins. *Annu. Rev. Cell Dev. Biol. 12*, 697–715.

(18) Logan, D., Abu-Ghazaleh, R., and Blakemore, W., et al. (1993) Structure of a major immunogenic site on foot-and mouth disease virus. *Nature 362*, 566–568.

(19) Isberg, R. R. (1991) Discrimination between interacellular uptake and surface adhesion of bacterial pathogens. *Science 252*, 934–938.

(20) Hart, S. L., Harbottle, R. P., and Cooper, R., et al. (1995) Gene delivery and expression mediated by an intergrin-binding peptide. *Gene Ther. 2*, 552–554.

(21) Erbacher, P., Remy, J.S., and Behr, J. P. (1999) Gene transfer with synthetic virus-like particles via the integrin-mediated endocytosis pathway. *Gene Ther. 6*, 138–145.

(22) Kim, W. J., Yockman, J. W., Lee, M., Jeong, J. H., Kim, Y. H., and Kim, S. W. (2005) Soluble Flt-1 gene delivery using PEI-g-PEG-RGD conjugate for anti-anigiogenesis. *J. Contolled Release 106*, 224–234.

(23) Suh, W., Han, S. O., Yu, L., and Kim, S. W. (2002) An anigiogenetic, endothelial-cell-targeted polymeric gene carrier. *Mol. Ther. 6*, 664–672.

(24) Klaus, K., Merdan, T., Hegener, O., Haberlein, H., and Kissel, T. (2003) Integrin targeting using RGD-PEI conjugates for in vitro gene transfer. *J. Gene Med. 5*, 588–599.

(25) Ruoslahti, E., and Reed, J. C. (1994) Anchorage dependence, integrins and apotosis. *Cell 77*, 477–478.

(26) Damsky, C. H., and Werb, Z. (1992) Signal transduction by integrin receptors for extracellular matrix: cooperative processing of extracellular information. *Curr. Opin. Cell Biol. 5*, 864–868.

BC700385R

TECHNICAL NOTES

Effect of Ligand Density on the Spectral, Physical, and Biological Characteristics of CdSe/ZnS Quantum Dots

Samuel J. Clarke,[†] C. A. Hollmann,[†] Faisal A. Aldaye,[‡] and Jay L. Nadeau*[,†]

Department of Biomedical Engineering, McGill University, Montreal, QC Canada H3A 2B4, Department of Chemistry, McGill University, Montreal, QC Canada H3A 2K6. Received March 8, 2007

Chemical modification of the surface of CdSe/ZnS quantum dots (QDs) with small molecules or functional ligands often alters the characteristics of these particles. For instance, dopamine conjugation quenches the fluorescence of the QDs, which is a property that can be exploited for sensing applications if the conjugates are taken up into living cells. However, different sizes and/or preparations of mercaptocarboxylic acid solubilized QDs show very different properties when incubated with cells. It is unknown what physical parameters determine a QDs ability to interact with a cell surface, be endocytosed, escape from endosomes, and/or enter the nucleus. In this study, we examine the surface chemistry of QD−dopamine conjugates and present an optimized method for tracking the attachment of small biomolecules to the surface. It is found that the fluorescence intensity, surface charge, colloidal stability, and biological interactions of the QDs vary as a function of the density of dopamine on the surface. Successful targeting of QD−dopamine to dopamine receptor positive PC12 cells correlates with greater homogeneity of particle thiol layer, and a minimum number of ligands required for specific association can be estimated. These results will enable users to develop methods for screening QD conjugates for biological activity before proceeding to experiments with cell lines and animals.

INTRODUCTION

Quantum dots (QDs) are growing in popularity for use in biological systems. A survey of recent scientific literature is a testimony to the enormous research effort devoted to these types of studies (for reviews, see *1–5*). Part of the reason for the immense popularity of QDs, and to a lesser extent other nanoparticles (NPs), is that their unique optical properties are vastly superior to the properties of more conventional biological fluorophores. Indeed, the wide absorption spectrum, narrow emission, and large extinction coefficients are some of the most attractive characteristics. There has been much work toward engineering stable QD coatings that are biologically compatible and that possess a high number of functional groups such as amino (*6*), hydroxyl (*7*), carboxyl (*8*), and thiol (*9*). Despite this, most of these functionalization strategies increase the hydrodynamic radius of the particles by an order of magnitude, significantly lower the quantum yield, or are appropriate only for certain types of particles (e.g., cysteamine is stable on CdTe particles but not on CdSe/ZnS).

In our work, we have used short chain thiol-terminated molecules in order to preserve the small intrinsic size of the particles and their ability to transfer energy and electrons to neighboring or covalently bound molecules (*10–12*). These minimally passivated particles are extremely environmentally sensitive in ways that are potentially useful, such as in their ability to indicate cellular redox potential (*13*). However, this sensitivity also means that great variability is seen among different sizes of QDs, different synthetic batches, and among different bioconjugation reactions. Such variability makes biological experiments often "hit or miss" and leads to loss of time and costly reagents. We have chosen the ligand dopamine (DA) and its receptor as a model system to evaluate the effect of the conjugation of DA to QDs and the resulting biological activity of the functionalized particles. The primary amino reactive compound *o*-phthaldialdehyde (OPA) is used to quantify the number of dopamine (DA) ligands that can be bound to QDs of different sizes and under different incubation conditions. The relationship between ligand density and efficient cellular association is established, providing guidelines for the number of ligands needed to create a high-affinity small-molecule−QD conjugate. These results demonstrate the usefulness of this protocol to characterize QD conjugates before they are used in biological experiments.

EXPERIMENTAL SECTION

Chemicals. All chemicals were of the highest grade available and were purchased from Sigma-Aldrich Canada unless otherwise noted. Solvents were purchased from Fisher Scientific. Sodium phosphate buffer was used at a final reaction concentration of 50 mM at pH 7.2.

Synthesis of QDs. CdSe/ZnS QDs were synthesized using a method adapted from Asokan et al. (*14*), and based on the noncoordinating solvent 1-octadecene (ODE). Briefly, 0.05 g of cadmium oxide (CdO) and 2 mL oleic acid (OA) were added to a three-neck flask containing 20 mL of ODE. This mixed was degassed and heated under an atmosphere of nitrogen to 250 °C. The mixture turned colorless around 150 °C. The

* To whom correspondence should be addressed: Jay Nadeau, Department of Biomedical Engineering, McGill University, 3775 University St., Montreal QC Canada H3A 2B4. Phone: 514-398-8372. Fax: 514-398-7461. E-mail: jay.nadeau@mcgill.ca.

[†] Department of Biomedical Engineering.

[‡] Department of Chemistry.

10.1021/bc700404v CCC: $40.75 © 2008 American Chemical Society
Published on Web 01/18/2008

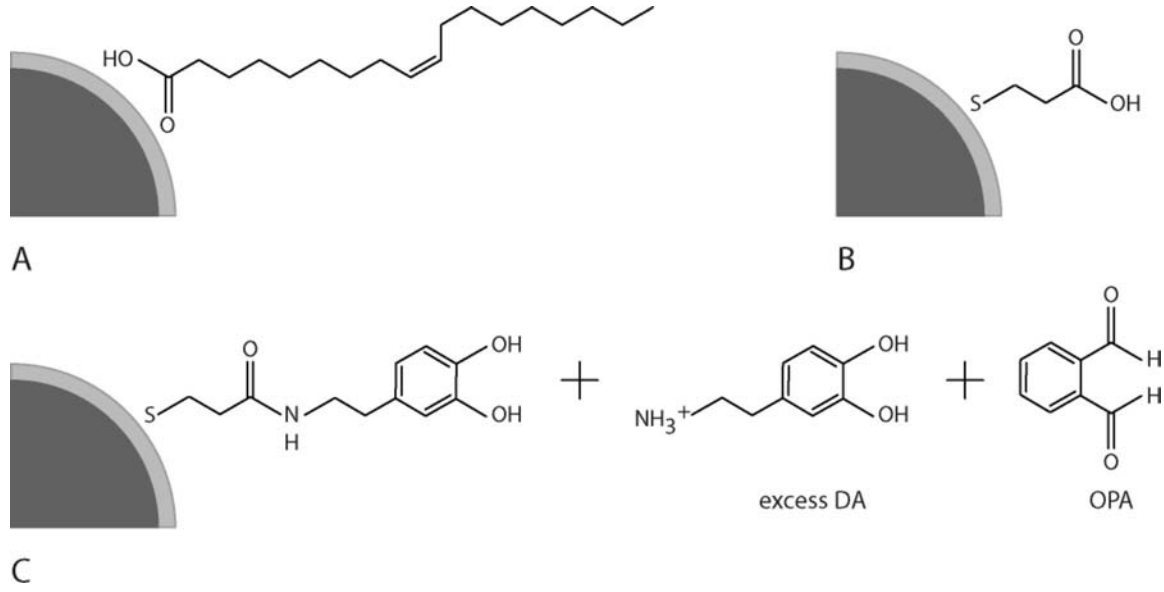

Figure 1. QD modification scheme. (A) As-synthesized QDs are stabilized with hydrophobic OA ligands. (B) A thiol-exchange reaction replaces the OA with hydrophilic MPA ligands. (C) DA is attached to the QDs through an EDC-mediated coupling reaction. OPA reacts with the free amines of unreacted dopamine and forms a fluorescent moiety that can be quantified through spectrometry and used to determine the extent of surface modification.

selenium (Se) precursor was prepared by mixing 0.016 g of Se with 0.75 mL trioctylphoshine (TOP), under inert atmosphere, followed by sonication until the solution became transparent. The zinc sulfide (ZnS) precursors were prepared as follows: 0.75 mL of TOP was combined with 0.2 mL hexamethyldisilathiane [$(TMS)_2S$] and 0.3 mL dimethylzinc [$Zn(CH_3)_2$] under inert atmosphere and diluted to 5 mL with ODE. Once the CdO/OA/ODE mixture reached 250 °C, the heat was turned off, and the Se precursor was injected rapidly using a needled syringe. The ZnS precursor was injected over a time course of 5 min during the desired stage of QD growth. Afterward, the temperature was allowed to drop to 100 °C and it was maintained at this temperature for several hours. To purify the quantum dots, repeated extractions with equivolume hexanes/methanol were performed. The purified QDs were finally stored in the ODE/hexanes phase until further use.

Mercaptocarboxylic Acid Functionalization of QDs. Mercaptopropionic acid (MPA) was used to replace the OA surfactant by a thiol-exchange reaction. One milliliter of concentrated QDs (OD > 5 at first exciton peak) in ODE/hexanes was diluted to 5 mL using methanol. MPA was added to a final concentration of 1 M and the pH was adjusted to 10 using tetramethylammonium hydroxide pentahydrate (TMAH). This solution was stirred at room temperature for 72 h. The thiol-modified QDs were separated from excess MPA ligand by precipitation and several washings with ethyl acetate. The QDs were dried at room temperature for several hours under air and resuspended in Milli-Q water (Millipore).

EDC Coupling of Dopamine. Dopamine hydrochloride (DA) was coupled to the QDs by a 1-ethyl-3-(3-dimethylaminopropyl)carbodiimide hydrochloride (EDC) mediated reaction. During a typical reaction, QDs in water were dialyzed against phosphate buffer for 1 h and diluted to a final concentration of 1 μM in 20 mM phosphate buffer. EDC and DA were added to the reaction mixture at a final ratio of 5000:1000:1 (EDC:DA:QD). These numbers are typical, as we varied the ratio of EDC in order to obtain different levels of QD modification. Reactions were performed under inert atmosphere or ascorbic acid (AA) was added to the reaction solution at an equivalent ratio to the DA to prevent the autoxidation of DA. The mixture was reacted for 30 min under gentle shaking and purified from excess DA and EDC side products by precipitation with THF and resuspension in phosphate buffer.

Quantum Yield Estimation. Quantum yields (QY) were obtained by comparing the integrated emission value of the QDs to a standard dye, Rhodamine 6G (QY = 0.95) in ethanol. The sample absorbance were matched to 0.030 ± 0.003 at the excitation wavelength of 480 nm. The concentrations of our QD solutions were determined from published (*15*) extinction coefficients based on the CdSe core.

Gel Electrophoresis. Gel electrophoresis was performed on 0.5% agarose gels in 0.5× TAE buffer (20 mM Tris, 20 mM acetate, 0.5 mM EDTA, pH 8.3). QD samples were diluted to 100 nM in 3% glycerol loading buffer immediately before use. A 20 V/cm electric field was applied for 20 s followed by 10 V/cm electric field for 15 min. Gels were imaged by fluorescence detection using a model 120 Electrophorisis Analysis System (Kodak, Rochester, NY).

OPA Assay. An *o*-phthaldialdehyde (OPA) stock solution was prepared by dissolving 1 mg/mL of OPA in phosphate buffer and the addition of 2 μL/mL β-mercaptoethanol (βME). The assay was adapted for use in a 96 well microplate by mixing 250 μL of OPA stock with 25 μL of the desired sample and allowing the solution to react for 1 min. Emission spectra were excited at 350 nm and collected at 460 nm. In order to calculate the amount of bound DA to each of the NPs surface, control experiments with no EDC were conducted and compared to equivalent reactions containing EDC (Figure 2). The difference in fluorescence intensity from the OPA reagent was used to calculate the number of bound DA to the particle surface. Controls for interference from the QDs and EDC showed negligible interactions or quenching (Supporting Information Figure S1).

Cell Culture and Treatment. PC12 cells with D2 DA receptors were a generous gift from Stuart Sealfon, Mount Sinai School of Medicine. The cells were confirmed to have D2 receptors by immunofluorescence staining (available in Supporting Information Figure S2). PC12 cells were maintained at 37 °C /5% CO_2 in Dulbecco's Modified Eagle's Medium (DMEM) supplemented with 5% fetal bovine serum and 10% horse serum with 500 μg/mL G418, 100 U/mL penicillin, 100 μg/mL streptomycin, and 2 mM L-glutamine. Control cells

Table 1. Quantum Dot Parameters

	quantum yield (%)			
sample	oleic acid	MPA	diameter (nm)	extinction coefficient (*15*)
QD560	36.1	19.3	3.21 ± 0.21	87 600
QD600	26.2	5.7	4.68 ± 0.54	230 000

without dopamine receptors were HEK293T cells, mouse A9 epithelial cells, and 3T3 fibroblasts. Control cell lines were maintained at 37 °C/5% CO_2 in Dulbecco's Modified Eagle's Medium (DMEM) supplemented with 10% fetal bovine serum, 100 U/mL penicillin, 100 μg/mL streptomycin, and 2 mM L-glutamine.

For QD labeling experiments, the cell medium was replaced with Optimem serum-free medium. QDs were added to the cells at a concentration of 5 nM. Cells were incubated for 45 min at 37 °C/5% CO_2. Before analysis, cells were washed extensively with phosphate buffered saline (PBS) pH 7.4 and imaged in PBS.

Spectroscopy and Microscopy. Absorbance and emission spectra were recorded on SpectraMax Plus and SpectraMax Gemini readers from Molecular Devices. Cells were examined and imaged with an Olympus IX-71 microscope and a Nuance multispectral imaging system. The objective lens was a Nikon LCPlanF 40× (NA = 0.60). UV illumination was through a "quantum dot" filter cube set (excitation = 380–460 nm, dichroic = 475 nm, emission = 500 LP).

RESULTS AND DISCUSSION

Properties of QDs and Degree of Surface Passivation. Synthesis of CdSe/ZnS QDs using the solvent ODE is advantageous over methods that use trioctylphoshine oxide (TOPO) (*14*). This is because TOPO is a waxy solid at room temperature, complicating preparative and purification steps. The combination of OA and ODE provide a safer and easier synthetic route that yields high-quality QDs with OA as the surfactant (Figure 1A). In this work, we prepared two distinct batches of QDs with emission maxima at 560 and 600 nm, denoted as QD560 and QD600, with QY values of >25% in organic solvent (Table 1).

Specific association of a QD probe with target cells depends on numerous factors, which include both efficiency of specific binding (receptor–ligand interactions) and reduction in nonspecific binding. Nonspecific binding of QDs is a problem that has been poorly addressed, particularly because uptake of nonfunctionalized QDs is sometimes desired. However, in order to target specific cell populations such as cancer cells (*16*, *3*), uptake of QDs without a targeting ligand is undesirable. Our hypothesis in this work is that the specificity of the QD probe to its target is related to the number of available functionalized groups on the QD particle surface and also the degree of thiol layer homogeneity. Historically these parameters have not been measured or controlled for in QD experiments.

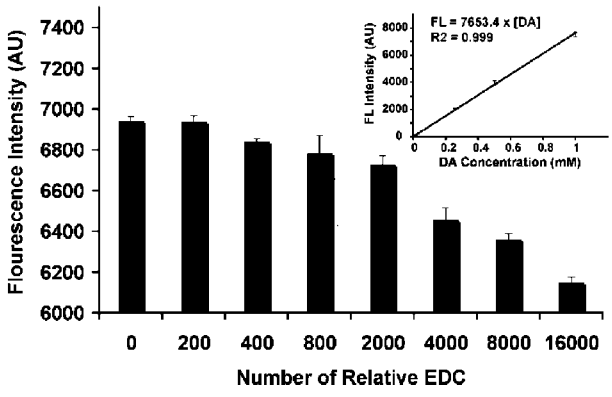

Figure 2. Reaction of QD600-DA with OPA. For a fixed ratio of QD:DA (1:2500), increasing levels of EDC lead to a reduction in OPA intensity due to covalent binding of the DA to the surface of the QDs. Inset: The fluorescent emission of OPA increases linearly with the amount of DA in solution. Data are an average of four experiments with error bars indicating the standard error of the mean.

We found that ligand exchange reactions with MPA for at least 72 h were required to reduce nonspecific binding. Replacement of the OA surfactant with MPA (Figure 1B) resulted in a significant reduction in quantum yields due to hole-trapping (46.5% for QD560 and 78.2% for QD600, Table 1) on the thiols (*17*) without significant changes in peak location or shape (absorbance and emission spectra are available in Supporting Information Figure S3). This reduction in brightness was also correlated with lack of nonspecific binding to all cell lines tested (293T, 3T3, A9, and PC12). QDs showing <90% reduction in QY, or solubilized for less than 72 h, showed extensive binding to cell membranes with formation of large clusters, typical of nonspecific adhesion (*13*) (Supporting Information Figure S5). These results indicate the importance of a well-passivated, homogeneous surfaces before the binding of biomolecules to the QDs. It is likely that the hydrophobic ligands (in this case OA) were not completely displaced; a residual fraction of the original surfactant remains on the surface of the nanoparticle during most ligand-exchange reactions (*18*). However, after sufficient reaction time (i.e., 72 h) it is assumed that a few enough of such ligands remain so that adhesion of the long carbon chains to the cell's membrane is minimized.

Surface Modification by Dopamine. Carbodiimide based reactions are useful zero-length cross-linkers that form amino-reactive intermediates on carboxylate groups (*19*). EDC reagents have been particularly popular for cross-linking NPs to a range of biomolecules. Despite its widespread use, there is a lack of techniques for the assessment of the reaction product that are bound to particles. UV–vis absorption measurements can be used to qualitatively assess molecules bound to a particle surface (*20*, *21*). However, a drawback of absorbance measurements is that many small molecules do not absorb light sufficiently in order to qualify for this analysis.

We have used the compound OPA to characterize several aspects of the EDC reaction. OPA in the presence of βME reacts rapidly with primary amino groups in order to form highly fluorescent products. Ninhydrin and fluorescamine reagents have a similar reactivity toward primary amines, but OPA is more stable in aqueous solution and more sensitive (*22*). Rosenthal and co-workers (*23*) have used fluorescamine to characterize the binding of poly(ethylene glycol) (PEG) to commercially produced amphiphilic QDs. For assays that contain QDs, OPA has an additional advantage over colormetric measures. QDs absorb strongly in the visible range and are likely to interfere with these reagents. The fluorescence emission of OPA is in the blue region (ca. 460 nm) and sufficiently far away from the emission of the QDs in this study (ca. >560 nm) to avoid interference. Because DA contains a primary amine, it causes OPA to react and fluoresce with an intensity that is linear in emission intensity over a wide range. For our experimental setup, the emission was linear over the range 0–1 mM DA (inset, Figure 2). Thus, in order to estimate the number of DA molecules that bound to the QDs, OPA was reacted with the coupling reaction in the presence and absence of EDC. As expected, there was a reduction in the intensity of the OPA signal in the presence of EDC resulting from the conversion of the DA amino groups to an amide bond with the carboxylate group on MPA (Figure 2). The amount by which the OPA signal

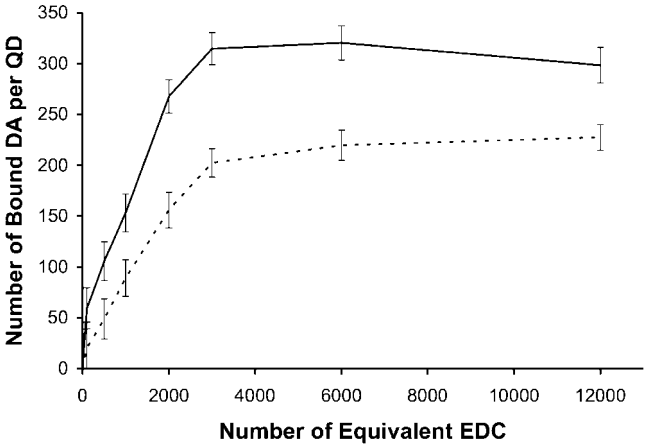

Figure 3. Number of bound DA molecules as a function of the number of equivalent EDC molecules added to the coupling reaction for QD560 (dashed line) and QD600 (solid line) as measured by OPA assay. Data are an average of four experiments with error bars indicating the standard error of the mean.

difference from the EDC negative samples was used to calculate the number of DA ligands that have bound to the surface of the QDs.

The relationship between the relative number of EDC molecules, in the reaction, along with the number of DA molecules that are bound to the QDs is depicted in Figure 3. A similar trend for both QD560 and QD600 is observed. The number of bound DA ligands increases almost linearly with the number of EDC molecules added to the reaction until a plateau is reached. The plateau can be interpreted as a saturation of the available carboxylate groups on the QD surface with DA and this is an indirect measure of the number of carboxylate groups that occupy the surface of the QD. In these calculations, the error reported along with the estimation of bound DA is related to the variation of the OPA reagent rather than an actual distribution of modification within the sample.

If the QD is modeled as a sphere using the TEM sizing parameters (Table 1 and Supporting Information Figure S4), the surface area of QD560 and QD600 are 32.35 nm^2 and 68.77 nm^2, respectively. Since the sulfur group on a short-chain thiol has a molecular area of 0.025 nm^2 (*24*), QD560 has a theoretical capacity to bind approximately 647 MPA molecules and QD600 has a capacity for 1375 MPA molecules on the surface of the particle through Zn−S bonds. Our results from Figure 3 suggest that the number of available MPA molecules on the surface of the QDs is considerably lower than what the physical size permits. There are a number of reasons to account for this. The conformation of the MPA molecule on the surface of the QD may not always have its carboxylate group oriented in a position that is favorable or accessible for reaction with the EDC molecule. Steric limitations can be excluded, as both the DA and EDC molecules are small and unlikely to hinder the reaction based on their size. Surface defects are present on the surface of QDs and since larger particles have a higher number of surface defects (*25*) this may explain why the larger red QD600 has a lower density of MPA molecules to surface area than the green QD560. Finally, the accuracy of our method to calculate the QD concentration cannot be eliminated as a source of error. This absorbance-based method is widely used and is based on published extinction coefficients (*15*).

Interestingly, the most heavily modified particles (ca. 200 DA molecules for QD560 and ca. 300 DA molecules for QD600) were not as stable as those with only partial modification and these particles visibility precipitated out of solution after a short time. MPA passivated QDs are stabilized in solution by the negatively charged carboxylate groups on the surface of the

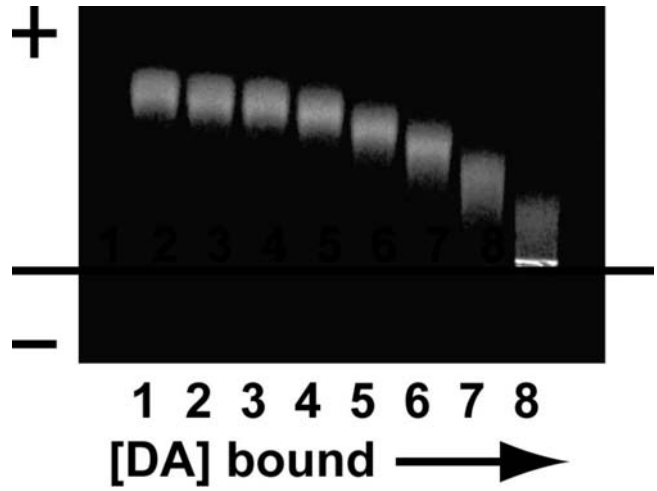

Figure 4. Agarose gel electrophoresis showing the change in QD600 surface charge with increasing levels of bound DA. Lane 1, 0; lane 2, 1.0 ± 4.9; lane 3, 28.8 ± 3.2; lane 4, 45.1 ± 12.4; lane 5, 61.6 ± 6.7; lane 6, 139.6 ± 8.9l; lane 7, 167.4 ± 4.9; lane 8, 228.1 ± 4.4. Loss of stability correlates with broadening of the gel band and aggregation (particles remain in the loading well). The horizontal black line indicates the loading postion.

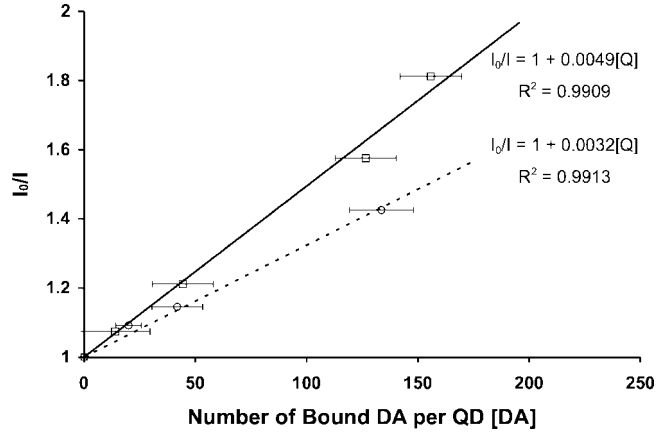

Figure 5. Relationship between the number of DA particles bound to the surface of the QD and the resulting emission intensity. For both QD560 (dashed line, cross marker) and QD600 (black line, square marker) the relationship can be fitted to the linear equations depicted on the graph. Data are an average of four experiments with error bars indicating the standard error of the mean.

particles. Modification of these carboxylate groups by an uncharged small molecule such as DA (it is uncharged when the amino group is blocked by conjugation) has the effect of neutralizing the surface charge. We used gel electrophoresis to investigate the effect of the density of DA on the surface charge of QD600. As expected, the negatively charged QDs migrate toward the positive electrode in a single narrow band consistent with a homogeneous and monodisperse population of QDs (Figure 4, lane 1). Increasing modification of the particles leads to a corresponding shift in the mobility of the particles under the influence of an electric field. In the samples with the highest levels of DA, broadening of the fluorescent bands and aggregation is evident (Figure 4, lanes 7 and 8) due to loss of colloidal stability following the loss in surface charge. Conjugation of DA to a QD population is expected to lead some distribution of modification by DA within the sample. However, in the samples that were stable (Figure 4, lanes 1–6), conjugation of DA did not lead to observable broadening of the bands in the gel and indicates a mostly uniform distribution of DA modification across the samples.

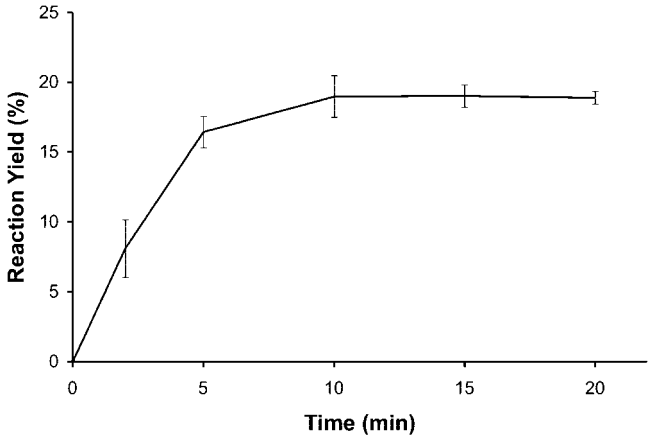

Figure 6. Time scale of the EDC coupling reaction as measured by OPA assay. Results are typical; data shown are from a coupling reaction with a ratio of 12000:1000:1 EDC:DA:QD. Data are an average of three experiments with error bars indicating the standard error of the mean.

Effect on Spectral Characteristics. Manipulating the extent of ligand coverage of the QD surface can be an effective way to modulate its fluorescent properties. In Figure 5, we demonstrate the effect of the number of bound DA ligands and the subsequent reduction in the fluorescent emission intensity of the QDs. Fluorescence static quenching can be modeled using the Stern-Volmer equation:

$$\frac{I_0}{I} = 1 + K[Q] \quad (1)$$

In this equation, I_0 and I are the fluorescent intensity in the absence and presence of the quencher Q and K is the quenching constant. Deviations from this linear relationship are often attributed to a combination of static and dynamic quenching (collisional) (*26*) and this type of relationship is not suitable for fitting to a linear Stern-Volmer model. To eliminate the effect of collisional dynamic quenching by free DA, EDC, or AA, we purified the conjugates from excess unbound ligand and reaction products. Static quenching remains as the predominant quenching mechanism (*27*). In Figure 3, the quenching data for QD560 and QD600 were fitted to a linear equation over the full range of DA modification. The quenching constant for QD560 was $K = 0.0032$ molecules^{-1} and $K = 0.0049$ molecules^{-1} for QD600. These results indicate that the larger QD600 particles were more efficiently quenched than QD560. When we repeated these experiments using QDs from different synthetic batches we found that the quenching data was quite unique for each QD and generally independent of size (data not shown). The chemical and physical properties of QDs are known to vary widely across different synthetic reactions and these data further underscore the importance of characterizing a QD-conjugate. Knowledge of the ligand-quenching relationship is useful for designing a QD bioprobe. Our recent work has utilized these particles in the region of high modification by DA and maximum emission quenching and these particles behaved as efficient cellular sensors of redox conditions (*13*). However, if the QD bioprobe were to be designed as a static fluorescent marker, then it would be more practical to modify the surface with a smaller number of DA ligands in order to preserve the fluorescent intensity of the QDs.

Optimization of the Coupling Reaction. In addition to quantifying the number of DA ligands on the surface of the particles, we have also utilized the OPA assay to measure the kinetics of the coupling reaction. The thiol surfactant layer is quite sensitive to even mild reaction conditions (*28*); therefore, we have used these results to maximize the yield and minimize the reaction time. Figure 6 demonstrates the rate of reaction for a typical reaction with 1000 DA equivalents and QD560. The reaction was largely complete after 10 min, consistent with a recent report (*29*) demonstrating a similar reaction time scale. In the literature, there is a wide disparity among the suggested reaction conditions for the EDC mediated reaction. Most protocols have reported incubation times of several hours, while some even perform the reaction overnight. These results imply that shorter duration reaction times are just as effective as much longer times. In addition, we observed that the efficiency of the coupling reaction was drastically reduced when our QD samples had small levels of free MPA due to incomplete purification of the QDs. Washing of the particles with ethyl acetate and dialysis against phosphate buffer was required to eliminate these free thiol molecules. Short chain thiols are typically used to quench the EDC reaction (*19*), so it is no surprise that the free thiolate groups hinder the desired reaction.

Incubation with Cells. We investigated the effect of DA ligand coverage and corresponding association to D2 receptor expressing PC12 cells. As expected, cells that were treated with

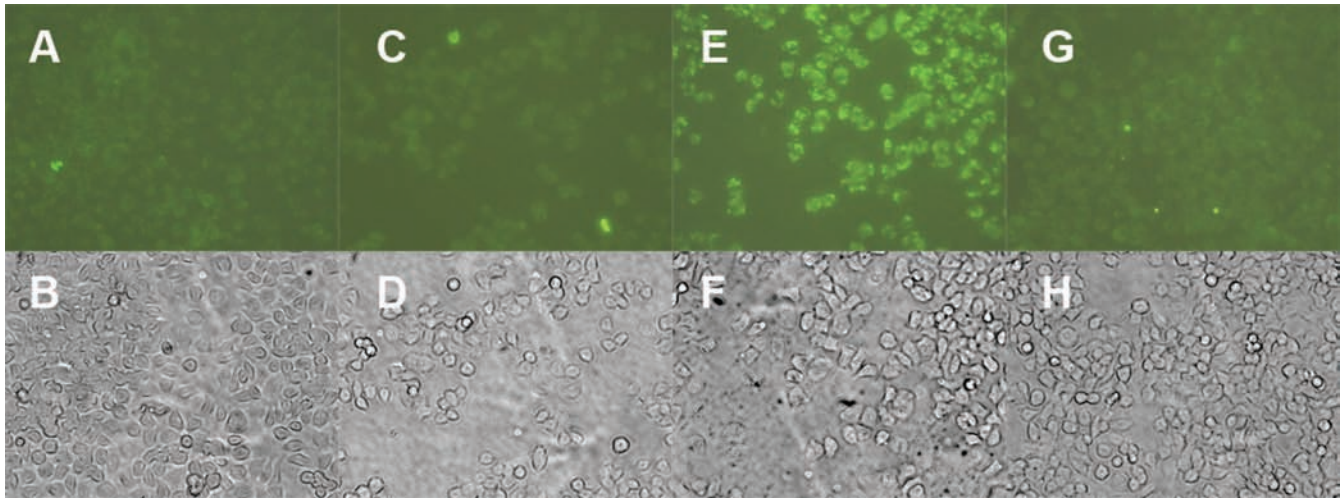

Figure 7. Cellular uptake of QD560 by dopamine-receptor-expressing PC12 cells as investigated by fluorescence microscopy. Scale bar = 20 μm and applies to all panels. (A,B) Unmodified MPA QD560 does not associate with cells. (C,D) QD560 with 50 ± 8.6 DA ligands has little specificity for cells. (E,F) With 100 ± 9.3 DA ligands, QD560 had a high specificity for the surface DA receptors. (G.H) 1 mM free DA is an effective competitor for QD560 with ca. 100 DA ligands. QD association was seen within 30 min of treatment.

QDs alone did not show any visible QD association when examined by fluorescence microscopy (Figure 7A,B). Again, little association was seen with QD560−DA conjugates with ca. 50 ligands (Figure 7C,D). A striking difference was visible with QD conjugates bearing ca. 100 DA ligands (Figure 7E,F). These QDs were visible as bright green fluorescence on the surface of the cells and the labeling is consistent with the targeting of the surface receptors. To further confirm the specificity of this reaction, we also incubated this sample in the presence of 1 mM free DA. No QD association was seen (Figure 7G,H) indicating the ability of free DA to compete for receptor binding on the cell surface. As a further control, no QD association was apparent in HEK293T cells lacking D2 receptors (Supporting Information Figure S5). A striking improvement in targeting was seen when we compare the cellular association of QD560 with 50 and 100 DA ligands. This data is consistent with recent experiments where an increase in the density of the ligands was sufficient to improve the affinity of the probes by several orders of magnitude (*17*). The enhancement was attributed to a multivalent interaction involving multiple ligands interacting with multiple cell receptors to greatly enhance the affinity of a nanoparticle conjugate. An estimate of the number of molecules that are required for efficient cell association can serve to maximize the efficiency of existing QD conjugates as well as design future probes. The requirement for efficient displacement of the hydrophobic surfactant as well as binding of 100 DA ligands explains the failure of labeling experiments with QDs of low surface quality or minimal DA coverage. It will be interesting to observe the relationship between the initial number of bound ligands and the number of ligands that persist under high-intensity UV or blue light irradiation, which causes photoenhancement and possibly surfactant decay (*13, 30*). Some preparations or colors of QDs may show faster degradation (*31*) and thus loss of biological activity resulting in limited absolute cellular association. It is also apparent, however, that 100 DA ligands represent only a portion of the available surface sites, and that some of the functional groups on the surface are available for alternative purposes. Indeed, we have also demonstrated that free carboxylate groups on the surface of the particles are required for a stable colloidal solution. Most QD probes in the literature are simple configurations based on a single ligand. With these results in mind, we can begin to design smarter probes with multiple ligands that may serve several purposes such as recognition and drug delivery (*32*).

This study has shown that OPA is a sensitive assay for characterizing the surface of QDs when they are decorated with a simple molecule such as DA. Manipulating the degree of ligand coverage is important for exploiting changes in the spectral properties of the QDs, for preserving the colloidal stability of the particles and optimizing cellular association by receptor-mediated processes. These results suggest important guidelines for designing NP based probes. Although this study focused strictly on CdSe/ZnS particles, the results and techniques are valid for a host of different particle compositions ranging from gold to iron to synthetic NPs.

ACKNOWLEDGMENT

This research is funded by U.S. EPA—Science to Achieve Results (STAR) program Grant #R831712 and by the National Science and Engineering Research Council of Canada (NSERC) Individual Discovery #RGPIN 312970 and NanoInnovation Platform.

Supporting Information Available: Control experiments for OPA interference, immunofluorescence staining of PC12 cells for DA receptors, full QD absorption and emission spectra, TEM images of QDs and size distributions, nonspecific binding and control cell experiments. This material is available free of charge via the Internet at http://pubs.acs.org/BC.

LITERATURE CITED

(1) Weng, J., and Ren, J. (2006) Luminescent quantum dots: a very attractive and promising tool in biomedicine. *Curr. Med. Chem. 13*, 897–909.

(2) Smith, A. M., Dave, S., Nie, S., True, L., and Gao, X. (2006) Multicolor quantum dots for molecular diagnostics of cancer. *Exp. Rev. Mol. Diagn. 6*, 231–44.

(3) Samia, A. C., Dayal, S., and Burda, C. (2006) Quantum dot-based energy transfer: perspectives and potential for applications in photodynamic therapy. *Photochem. Photobiol. 82*, 617–25.

(4) Smith, A. M., Ruan, G., Rhyner, M. N., and Nie, S. (2006) Engineering luminescent quantum dots for in vivo molecular and cellular imaging. *Ann. Biomed. Eng. 34*, 3–14.

(5) Medintz, I. L., Uyeda, H. T., Goldman, E. R., and Mattoussi, H. (2005) Quantum dot bioconjugates for imaging, labelling and sensing. *Nat. Mater. 4*, 435–46.

(6) Lovric, J., Bazzi, H. S., Cuie, Y., Fortin, G. R., Winnik, F. M., and Maysinger, D. (2005) Differences in subcellular distribution and toxicity of green and red emitting CdTe quantum dots. *J. Mol. Med. 83*, 377–85.

(7) Pathak, S., Choi, S. K., Arnheim, N., and Thompson, M. E. (2001) Hydroxylated quantum dots as luminescent probes for in situ hybridization. *J. Am. Chem. Soc. 123*, 4103–4.

(8) Bruchez, M., Jr., Moronne, M., Gin, P., Weiss, S., and Alivisatos, A. P. (1998) Semiconductor nanocrystals as fluorescent biological labels. *Science 281*, 2013–6.

(9) Wolcott, A., Gerion, D., Visconte, M., Sun, J., Schwartzberg, A., Chen, S., and Zhang, J. Z. (2006) Silica-coated CdTe quantum dots functionalized with thiols for bioconjugation to IgG proteins. *J. Phys. Chem. B 110*, 5779–89.

(10) Kloepfer, J. A., Mielke, R. E., Wong, M. S., Nealson, K. H., Stucky, G., and Nadeau, J. L. (2003) Quantum Dots as Strain- and Metabolism-Specific Microbiological Labels. *Appl. Environ. Microbiol. 69*, 4205–4213.

(11) Kloepfer, J. A., Cohen, N., and Nadeau, J. L. (2004) FRET between CdSe quantum dots in lipid vesicles and water- and lipid-soluble dyes. *J. Phys. Chem. B 108*, 17042–17049.

(12) Kloepfer, J. A., Mielke, R. E., and Nadeau, J. L. (2005) Uptake of CdSe and CdSe/ZnS quantum dots into bacteria via purine-dependent mechanisms. *Appl. Environ. Microbiol. 71*, 2548–57.

(13) Clarke, S. J., Hollmann, C. A., Zhang, Z. J., Suffern, D., Bradforth, S. E., Dimitrijevic, N. M., Minarik, W. G., and Nadeau, J. L. (2006) Photophysics of dopamine-modified quantumdots and effects on biological systems. *Nat. Mater. 5*, 409–417.

(14) Asokan, S., Krueger, K. M., Alkhawaldeh, A., Carreon, A. R., Mu, Z. Z., Colvin, V. L., Mantzaris, N. V., and Wong, M. S. (2005) The use of heat transfer fluids in the synthesis of high-quality CdSe quantum dots, core/shell quantum dots, and quantum rods. *Nanotechnology 16*, 2000–2011.

(15) Yu, W. W., Qu, L. H., Guo, W. Z., and Peng, X. G. (2003) Experimental determination of the extinction coefficient of CdTe, CdSe, and CdS nanocrystals. *Chem. Mater. 15*, 2854–2860.

(16) Bakalova, R., Ohba, H., Zhelev, Z., Nagase, T., Jose, R., Ishikawa, M., and Baba, Y. (2004) Quantum dot anti-CD conjugates: Are they potential photosensitizers or potentiators of classical photosensitizing agents in photodynamic therapy of cancer? *Nano Lett. 4*, 1567–1573.

(17) Hong, S., Leroueil, P. R., Majoros, I. J., Orr, B. G., Baker, J. R., Jr., and Banaszak Holl, M. M. (2007) The binding avidity of a nanoparticle-based multivalent targeted drug delivery platform. *Chem. Biol. 14*, 107–15.

(18) Kuno, M., Lee, J. K., Dabbousi, B. O., Mikulec, F. V., and Bawendi, M. G. (1997) The band edge luminescence of surface modified CdSe nanocrystallites: Probing the luminescing state. *J. Chem. Phys. 106*, 9869–9882.

(19) Hermanson, G. T. (1996) *Bioconjugate Techniques*, Academic Press, San Diego.
(20) Weilin, S., and Xiying, M. (2006) The detection application of CdS quantum dots in labeling DNA molecules. *Biomed. Mater. 1*, 81.
(21) Santra, S., Liesenfeld, B., Dutta, D., Chatel, D., Batich, C. D., Tan, W. H., Moudgil, B. M., and Mericle, R. A. (2005) Folate conjugated fluorescent silica nanoparticles for labeling neoplastic cells. *J. Nanosci. Nanotechnol. 5*, 899–904.
(22) Benson, J. R., and Hare, P. E. (1975) ortho-Phthalaldehyde - fluorogenic detection of primary amines in picomole range - comparison with fluorescamine and ninhydrin. *Proc. Natl. Acad. Sci. U.S.A. 72*, 619–622.
(23) Bentzen, E. L., Tomlinson, I. D., Mason, J., Gresch, P., Warnement, M. R., Wright, D., Sanders-Bush, E., Blakely, R., and Rosenthal, S. J. (2005) Surface modification to reduce nonspecific binding of quantum dots in live cell assays. *Bioconjugate Chem. 16*, 1488–1494.
(24) Sui, G., Orbulescu, J., Ji, X. J., Gattas-Asfura, K. M., Leblanc, R. M., and Micic, M. (2003) Surface chemistry studies of quantum dots (QDs) modified with surfactants. *J. Cluster Sci. 14*, 123–133.
(25) Dabbousi, B. O., RodriguezViejo, J., Mikulec, F. V., Heine, J. R., Mattoussi, H., Ober, R., Jensen, K. F., and Bawendi, M. G. (1997) (CdSe)ZnS core-shell quantum dots: Synthesis and characterization of a size series of highly luminescent nanocrystallites. *J. Phys. Chem. B 101*, 9463–9475.
(26) Laferriere, M., Galian, R. E., Maurel, V., and Scaiano, J. C. (2006) Non-linear effects in the quenching of fluorescent quantum dolts by nitroxyl free radicals. *Chem. Commun.* 257–259.
(27) Yiidiz, I., Tomasulo, M., and Raymo, F. M. (2006) A mechanism to signal receptor-substrate interactions with luminescent quantum dots. *Proc. Natl. Acad. Sci. U.S.A. 103*, 11457–11460.
(28) Aldana, J., Wang, Y. A., and Peng, X. G. (2001) Photochemical instability of CdSe nanocrystals coated by hydrophilic thiols. *J. Am. Chem. Soc. 123*, 8844–8850.
(29) Jin, T., Fujii, F., Sakata, H., Tamura, M., and Kinjo, M. (2005) Calixarene-coated water-soluble CdSe-ZnS semiconductor quantum dots that are highly fluorescent and stable in aqueous solution. *Chem. Commun.* 2829–2831.
(30) Silver, J., and Ou, W. (2005) Photoactivation of quantum dot fluorescence following endocytosis. *Nano Lett. 5*, 1445–1449.
(31) Aldana, J., Lavelle, N., Wang, Y. J., and Peng, X. G. (2005) Size-dependent dissociation pH of thiolate ligands from cadmium chalcogenide nanocrystals. *J. Am. Chem. Soc. 127*, 2496–2504.
(32) Gao, X., Yang, L., Petros, J. A., Marshall, F. F., Simons, J. W., and Nie, S. (2005) In vivo molecular and cellular imaging with quantum dots. *Curr. Opin. Biotechnol. 16*, 63–72.

BC700404V

Convenient Preparation of ^{68}Ga-Based PET-Radiopharmaceuticals at Room Temperature

I. Velikyan,*[,†] H. Maecke,[‡] and B. Langstrom[†,§]

Uppsala Applied Science Lab, GEMS PET Systems AB, GE Healthcare, SE-752 29 Uppsala, Sweden, Division of Radiological Chemistry, University Hospital, CH-4031 Basel, Switzerland, and Department of Biochemistry and Organic Chemistry, BMC, Uppsala University, SE-75124 Uppsala, Sweden. Received September 5, 2007; Revised Manuscript Received November 13, 2007

A straightforward labeling using generator produced positron emitting ^{68}Ga, which provides high quality images, may result in kit type production of PET radiopharmaceuticals and make PET examinations possible also at centers lacking accelerators. The introduction of macrocyclic bifunctional chelators that would provide fast ^{68}Ga-complexation at room temperature would simplify even further tracer preparation and open wide possibilities for ^{68}Ga-labeling of fragile and potent macromolecules. Gallium-68 has the potential to facilitate development of clinically practical PET and to promote PET technique for individualized medicine. The macrocyclic chelator, 1,4,7-triazacyclononanetriacetic acid (NOTA), and its derivative coupled to an eight amino acid residue peptide (NODAGA-TATE, [NODAGA^0, Tyr^3]Octreotate) were labeled with ^{68}Ge/^{68}Ga-generator produced positron emitting ^{68}Ga. Formation kinetics of ^{68}Ga-NOTA was studied as a function of pH and formation kinetics of ^{68}Ga-NODAGA-TATE was studied as a function of the bioconjugate concentration. The nearly quantitative radioactivity incorporation (RAI > 95%) for ^{68}Ga-NOTA was achieved within less than 10 min at room temperature and pH 3.5. The concentrations of NODAGA-TATE required for RAI of >90% and >95% were, respectively, 2–5 and 10 μM. In both cases the purification of the ^{68}Ga-labeled products was not necessary since the radiochemical purity was >95% and the preparation buffer, 4-(2-hydroxyethyl) piperazine-1-ethanesulfonic acid (HEPES) is suitable for human use. In order to confirm the identity of the products, complexes comprising ^{nat}Ga were synthesized and analyzed by mass spectrometry. The complex was found to be stable in the reaction mixture, phosphate buffer, and human plasma during 4.5 h incubation. Free and peptide conjugated NOTA formed stable complexes with ^{68}Ga at room temperature within 10 min. This might be of special interest for the labeling of fragile and potent macromolecules and allow for kit type preparation of ^{68}Ga-based radiopharmaceuticals.

INTRODUCTION

The long shelf life generator produced positron-emitting ^{68}Ga ($T_{1/2}$ = 68 min) is of potential interest for clinical PET. It is readily available on demand and it decays by 89% through positron emission resulting in images with high resolution and potential accurate quantification. Its half-life of 68 min might be sufficient for production and application of tracers and it minimizes the radiation dose to the patient. It also allows repetitive examinations. The only stable chemical form in solution at physiological conditions is Ga (III) cation that can form stable complexes with chelators, naked or conjugated with macromolecules or small organic molecules. It is established that macrocyclic chelator, 1,4,7,10-tetraazacyclododecanetetraacetic acid (DOTA), either free or coupled to macromolecules forms very stable complexes with ^{68}Ga. However, the complex formation with DOTA derivatives requires elevated temperature (*1*, *2*). A fast, reliable method comprising preconcentration and purification of the ^{68}Ge/^{68}Ga generator eluate and microwave heating was developed for automated production of peptide based tracers with higher specific radioactivity (*2–4*). The introduction of macrocyclic chelators that would provide fast ^{68}Ga-complexation at room temperature would simplify even further the tracer preparation and allow for kit type labeling analogous to one carried out with the SPECT isotope ^{99m}Tc in addition–offering the sensitivity and quantification advantages of the PET technique. The fast ^{68}Ga-labeling reaction at room temperature might also become an attractive tool when producing fragile temperature sensitive macromolecular tracers. The recognized potential of PET technique and ^{68}Ga-based radiopharmaceuticals for use in oncology, cardiology, neurology, and infection diseases strongly motivates the development of such a production procedure (*5–10*). The worldwide interest toward ^{68}Ga is increasing quickly and, for example, in Europe at least 40 centers have already introduced the generator. Moreover, the struggle for more efficient authorization of radiopharmaceuticals by legislative institutions is progressing steadily (*11*). The introduction of ^{68}Ga-based radiopharmaceutical kit production that would not require cyclotron and qualified chemists would make the PET radiopharmaceuticals readily available and might accelerate the expansion of nuclear medicine and promote PET examinations for personalized medicine worldwide.

Macrocyclic chelators that form very stable complexes with metal cations are of paramount interest for radiopharmaceutical design. Gallium complexes with NOTA (*12–14*) and its various derivatives, namely, 1,4,7-tris(2-mercaptoethyl)-1,4,7-triazacyclononane (TACN-TM) (*15*), 1,4,7-triazacyclononane-1-succinic acid-4,7-deacetic acid (NODASA) (*16*), 1,4,7-triazacyclononane-*N*,*N*′,*N*″-tris(methylenephosphonic) acid (NOTP) (*17*, *18*), 1,4,7-triazacyclononane-*N*,*N*′,*N*″-tris(methylenephosphonate-monoethylester) (NOTPME) (*17*, *18*) have demonstrated octahedral coordination geometry, high thermodynamic stability and similar plasma and *in vivo* stability. It has been reported that the

* Address for correspondence: Irina Velikyan, Uppsala Applied Science Lab, GEMS PET Systems AB, GE Healthcare, Husbyborg, SE-75229 Uppsala, Sweden, Phone: +46 18 180917, Fax: +46 18 180912, E-mail: Irina.Velikyan@ge.com.

† GE Healthcare.

‡ University Hospital.

§ Uppsala University.

10.1021/bc700341x CCC: $40.75 © 2008 American Chemical Society
Published on Web 01/19/2008

biodistribution and clearance pattern of ^{67}Ga-NOTA phosphonate analogues depend on the overall charge of the complexes (*17*). The thermodynamic stability constant (log *K*) of Ga(III)-DOTA (*19*) and Ga(III)-NOTA (*12*, *14*) complexes was determined, respectively, to be 21.33 and 30.98. It is the compactness of the triazanonane ring and the steric efficiency of the pendant acetate groups that lead to the formation of complexes of unusually high stability and selectivity for the Ga(III) (*14*). However, it should be stressed that the high stability of macrocyclic complexes is provided by the extremely slow dissociation reactions. Typical dissociation constant values are 10^5 to 10^7 times lower than those of open-chain analogues. The hole-size effects influence both thermodynamics and kinetics of macrocyclic complexes. This is because a chelator in its minimum energy metal-binding conformation will be optimized for a particular size of a metal ion, and when other metal ions are bound, the chelator conformational energy will rise with a resultant decrease in stability of the complex. Thus, macrocycles are selective for metal ions (*20–22*). For a given ionic size the stability of the complex increases with increasing charge. Another factor which influences the complexation rate and the stability is the presence of pendant arms, which help to achieve the full coordination number of the metal ion. The above-mentioned characteristics make NOTA very attractive for radiopharmaceutical development. In this work we investigated the potential of ^{68}Ga in combination with NOTA for a simple kit type production of radiopharmaceuticals at room temperature.

EXPERIMENTAL PROCEDURES

Materials. HEPES (4-(2-hydroxyethyl)piperazine-1-ethanesulfonic acid), sodium acetate, and double distilled hydrochloric acid (Riedel de Haën) were obtained from Sigma-Aldrich Sweden (Stockholm, Sweden). Sodium dihydrogen phosphate, disodium hydrogen phosphate, and trifluoroacetic acid (TFA) were obtained from Merck (Darmstadt, Germany). The purchased chemicals were used without further purification. Deionized water (18.2 MΩ), produced with a Purelab Maxima Elga system (Bucks, UK) was used in all reactions.

^{68}Ga Production. ^{68}Ga ($T_{1/2}$ = 68 min, β^+ = 89%, and EC = 11%) was available from a ^{68}Ge/^{68}Ga-generator-system (Cyclotron Co., Ltd., Obninsk, Russia) where ^{68}Ge ($T_{1/2}$ = 270.8 d) was attached to a column of an inorganic matrix based on titanium dioxide. The ^{68}Ga was eluted with 6 mL of 0.1 M hydrochloric acid.

^{68}Ga-Labeling of NOTA. HEPES (7–14 mg) or sodium acetate (16 mg) buffering agents was added to 200 μL of ^{68}Ga and the pH was adjusted with HCl and NaOH to give pH values between 2 and 7. NOTA (50 nmol, synthesized at Grove Centre, GB) was added and the reaction mixture was incubated at room temperature. The reaction mixture was analyzed by thin layer chromatography (TLC) applying the analyte to a polyethyleneimine cellulose plate (PEI-Cellulose F, Merck, Germany) and using 0.4 M NaH_2PO_4 (pH = 3.5) as running buffer. Autoradiography was employed to image the TLC strips. A phosphor storage plate (Molecular Dynamics, Amersham Biosciences, U.K.) was placed on top of the strips. The plate was scanned with PhosphorImager (PI) SI unit (Molecular Dynamics, Amersham Biosciences, U.K.) and analyzed using *ImageQuant 5.1* software. The nonincorporated (free) ^{68}Ga stayed at the origin and R_F of the ^{68}Ga-complex was 0.9.

^{68}Ga-Labeling of NODAGA-TATE. The pH of the ^{68}Ge/^{68}Ga-generator eluate was adjusted to 3.5–5.0 by adding either HEPES to give finally a 1.0 M solution with regard to HEPES or sodium acetate to give finally a 0.4 M solution with regard to sodium acetate. Then 0.2–20 nmol of NODAGA-TATE (received as lyophilized powder from Helmut Maecke, Division of Radiological Chemistry, University Hospital, Basel, Switzerland, and dissolved in deionized water to give stock solutions of 0.1 mM and 1 mM concentration) were added and the reaction mixture was incubated at room temperature. The reaction mixture was analyzed on an HPLC system from Beckman (Fullerton, CA) consisting of a 126 pump, a 166 UV detector, and a radiation detector coupled in series. Data acquisition and handling was performed using the Beckman System Gold Nouveau Chromatography software package. The column used was a Vydac RP 300 Å HPLC column (Vydac, USA) with the dimensions 150 mm × 4.6 mm, 5 μm particle size. The applied gradient elution was as follows: A = 10 mM TFA; B = 70% acetonitrile (MeCN), 30% H_2O, 10 mM TFA with UV-detection at 220 nm; flow was 1.2 mL/min; 0–2 min isocratic 20% B, 20–90% B linear gradient 8 min, 90–20% B linear gradient 2 min.

LC-ESI-MS Analysis. Electrospray ionization mass spectrometry (ESI-MS) was performed using a Fisons Platform (Micromass, Manchester, UK) with positive mode scanning and detecting $[M + 1H]^{1+}$, $[M + 2H]^{2+}$, $[M + 3H]^{3+}$, and $[M + NH_4]^+$ species. NOTA was detected at m/z = 304 for $[M + 1H]^{1+}$. The analysis of ^{69,71}Ga-NOTA was performed by direct infusion. Two different systems, namely, formic acid and ammonium acetate, were used resulting in the detection of m/z = 370.23, m/z = 372.1 for $[M + H]^+$ and m/z = 387.16, m/z = 389.26 for $[M + NH_4]^+$, respectively. NODAGA-TATE was detected at m/z = 704 for $[M + 2H]^{2+}$ and 470 for $[M + 3H]^{3+}$, and ^{69,71}Ga-NODAGA-TATE was detected at m/z = 738 for $[M + 2H]^{2+}$. The ^{69,71}Ga-NOTA and ^{69,71}Ga-NODAGA-TATE were synthesized under conditions indentical to radiolabeling and were used for the identification of the radio-HPLC chromatogram signals. The coupled HPLC system was from Alliance (Waters 2695, UK) with photodiode array UV detector. The column used was an Atlantis, dC 18, HPLC column with the dimensions 100 mm × 2.1 mm, 3 μm particle size. Isocratic elution was applied with the following parameters: A = 10 mM formic acid; B = 100% acetonitrile (MeCN), with UV-detection at 210–400 nm; flow was 0.3 mL/min, A/B = 80/20.

Stability in Human Plasma. The reaction mixture of ^{68}Ga-NOTA (RAI > 95%, 50 μL) was added to the prewarmed (37 °C) plasma (500 μL) and incubated for 270 min. The samples (100 μL) were taken at 10, 30, 60, 120, and 270 min time points and acetonitrile (400 μL) was added to sediment the proteins present. Then the samples were centrifuged at 14 000 rpm for 10 min at +4 °C (Allegra X-22R Centrifuge, Beckman Coulter, USA). The supernatant was collected and filtered through a 0.2 μm nylon membrane at 13 200 rpm for 1 min at +4 °C. The radioactivity of the pellets, supernatant, and filters was measured in a well counter and ionization chamber. The data was used to calculate the extraction efficiency. The supernatant was analyzed by TLC applying the analyte to a polyethyleneimine cellulose plate (PEI-Cellulose F, Merck, Germany) and using 0.4 M NaH_2PO_4 (pH = 3.5) as running buffer. Autoradiography was employed to image the TLC strips.

Stability in Reaction Mixture and PBS. The stability of the ^{68}Ga-NOTA and ^{68}Ga-NODAGA-TATE complexes was monitored in PBS and reaction mixture. The samples (5–20 μL) were taken at 10, 30, 60, 120, and 240 min time points. ^{68}Ga-NOTA was analyzed by PEI-cellulose F TLC followed by autoradiography imaging of the strips. ^{68}Ga-NODAGA-TATE was analyzed by UV-radio-HPLC.

RESULTS AND DISCUSSION

The general structure of NOTA derivative chelators is given in Figure 1 and consists of three macrocyclic amine groups and three carboxylic groups for coordination to Ga(III) and an additional functional group (Y_1) such that the chelate can be conjugated to a vector, e.g., preferably alkylamine, alkylsulfide, alkoxy, alkyl carboxylate, arylamine, aryl sulfide, or α-halo-

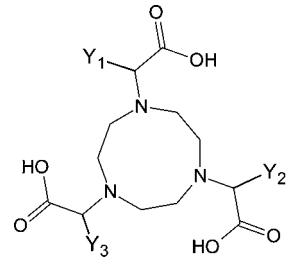

Figure 1. Basic structure of macrocyclic chelator, NOTA, and its derivatives.
NOTA: $Y_1=Y_2=Y_3=H$
NODASA: $Y_1=Y_2=H$; Y_3= CH2CH2COOH
NODAGA-TATE: $Y_1=Y_2=H$; Y_3= CH2CH2C(O)R;

where R = D-Phe-Cys-Tyr-D-Trp-Lys-Thr-Cys-Thr

Figure 1

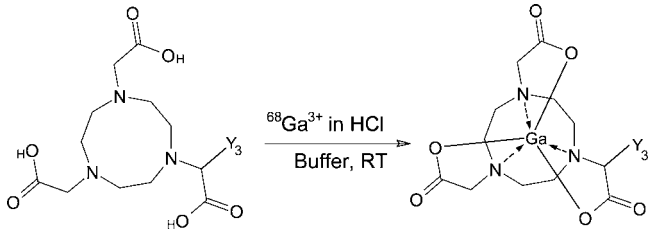

Figure 2. Reaction scheme for the complexation of ^{68}Ga(III) with NOTA (Y_3=H) and NODAGA-TATE (Y_3 = $CH_2CH_2C(O)R$, where R = Tyr^3-octreotate).

acetyl; Y_2 and Y_3 can be H or contain one or more functional moieties that would on one hand improve the complexation depending on a particular metal cation and on the other hand change the overall charge and hydrophilicity of the complex in order to modify the pharmacokinetics and blood clearance rates, e.g., alkylamine, alkoxy, alkyl carboxylate, phenol, hydroxamate, aryl sulfide, and alkyl.

In this particular work, ^{68}Ga-labeling of 1,4,7-triazacyclononanetriacetic acid (NOTA) and its derivative coupled to an eight amino acid residue peptide (NODAGA-TATE, [NODAGA^0, Tyr^3] octreotate) was performed at room temperature considering the possibility for a simple kit type tracer production as well as preparation of tracers based on temperature sensitive fragile macromolecules (Figure 2). Formation kinetics of ^{68}Ga-NOTA was studied during 1 h at room temperature as a function of pH values covering the range from 2 to 7. The aliquots of the reaction mixture sampled at 1, 3, 10, 30, and 60 min time points were analyzed by thin layer chromatography (TLC) both directly after the aspiration and later after the reaction was first quenched in water. The radioactivity incorporation at early time points was slightly higher in the case of the quenched samples, indicating most probably that the complexation reaction continued even after 200–1000-fold dilution of the reaction mixture. In addition, the reproducibility of the direct analysis was higher with relative standard deviation (RSD) values of ~1% and ~4%, respectively, for the direct and quenched cases. Thus the TLC analysis performed directly after the aspiration of the aliquots was preferred. The nonincorporated (free) ^{68}Ga stayed at the origin and R_F of the ^{68}Ga-complex was 0.9.

The time course of ^{68}Ga complexation reaction with NOTA at room temperature for varied buffer and pH conditions is presented in Figure 3A. Radioactivity incorporation reached a plateau within 10 min independent of the pH. The radioactivity incorporation (RAI > 95%) for ^{68}Ga-NOTA was achieved within less than 10 min at room temperature and pH 3.5 using HEPES buffer (Figure 3B).

In order to confirm the identity of the product, the complex comprising stable gallium isotopes (^{69,71}Ga) was synthesized and analyzed by mass spectrometry (ESI-MS). ^{69,71}Ga-NOTA was synthesized under the same conditions as its radioactive counterpart, but using a mixture of ^{68}Ga and ^{69,71}Ga cations. The aim of the use of a mixture of radioactive and stable gallium isotopes was twofold: (1) to create a reaction condition identical to the labeling procedure; (2) to allow following the reaction.

The formed neutral complex was expected to be difficult to protonate in order to observe it by ESI-MS. However, it was possible to optimize the analysis conditions and confirm the formation of ^{69,71}Ga-NOTA using two different systems, namely, formic acid and ammonium acetate and detecting respectively m/z = 370.23, m/z = 372.1 for $[M + H]^+$ and m/z = 387.16, m/z = 389.26 for $[M + NH_4]^+$. The production of the complex was also indirectly verified by the consumption of NOTA and the drastic decrease of the corresponding signal at m/z = 304 for $[M + 1H]^{1+}$. The stability of the ^{68}Ga-NOTA complex was monitored in PBS, reaction mixture, and human plasma and was found stable and in agreement with literature data (*12–15, 18, 23*). The complex extraction efficiency from the plasma was 65 ± 4% at 10, 30, 60, 120, and 270 min time points, and the only intact complex was detected after the incubation at 37 °C during 4.5 h. The choice of the time frame was dictated by the half-life of ^{68}Ga and consequent useful tracer application time ($4 \times T_{1/2}$).

Formation kinetics of ^{68}Ga-NODAGA-TATE was studied for varied concentration of the bioconjugate. The graph (Figure 4) presents the time course of ^{68}Ga complexation reaction with NOTA conjugated peptide at room temperature in sodium acetate buffer for varied concentration of the bioconjugate. Radioactivity incorporation reached a plateau within 10 min. The nearly quantitative radioactivity incorporation (>95%) required 10 μM and higher concentration of the bioconjugate. This concentration exceeded 4× the one required when using microwave heating (*2*).

The formation of ^{68}Ga-NODAGA-TATE was monitored by HPLC with UV- and Radio-detection (Figure 5). The authentic reference substance (^{69,71}Ga-NODAGA-TATE) was synthesized under the same conditions as its radioactive counterpart, but using a mixture of ^{68}Ga and ^{69,71}Ga cations for the same reason as described above for ^{69,71}Ga-NOTA.

The identity of the authentic reference substance (^{69,71}Ga-NODAGA-TATE) was confirmed by LC-ESI-MS detecting m/z = 704 for $[M + 2H]^{2+}$, m/z = 470 for $[M + 3H]^{3+}$ of NODAGA-TATE, and m/z = 738 for $[M + 2H]^{2+}$ of ^{69,71}Ga-NODAGA-TATE. The stability of the ^{68}Ga-NODAGA-TATE was monitored in the reaction mixture and PBS. The UV and radio signals corresponded to the tracer and no additional signals were detected indicating the stability of the molecule.

In both cases of ^{68}Ga-NOTA and ^{68}Ga-NODAGA-TATE the purification of the product was not necessary since the radiochemical purity was >95% and the preparation buffer, 4-(2-hydroxyethyl)piperazine-1-ethanesulfonic acid (HEPES) is suitable for intravenous injections. For example, HEPES is currently used as an ingredient of indium(In-111)oxin GE Healthcare radiopharmaceutical (manufacturer, GE Healthcare Limited; registration number, 800820; approval date, 1990–06–21; Medical Products Agency, Sweden).

Previously, the high similarity of the geometry of gallium complexes with NOTA and NODASA independent of the pendant arm modification has been demonstrated by X-ray

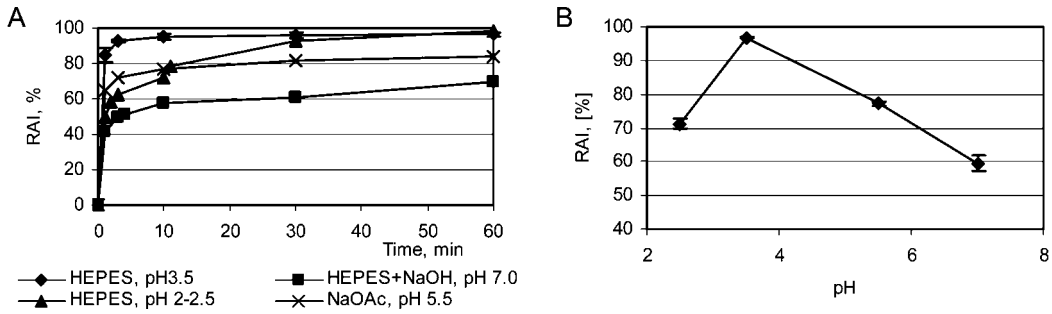

Figure 3. (A) Time course of ^{68}Ga complexation reaction with NOTA at room temperature and varied pH conditions ($N = 2–3$, the error bars are omitted for simplicity). (B) Radioactivity incorporation after 10 min incubation at room temperature as a function of pH.

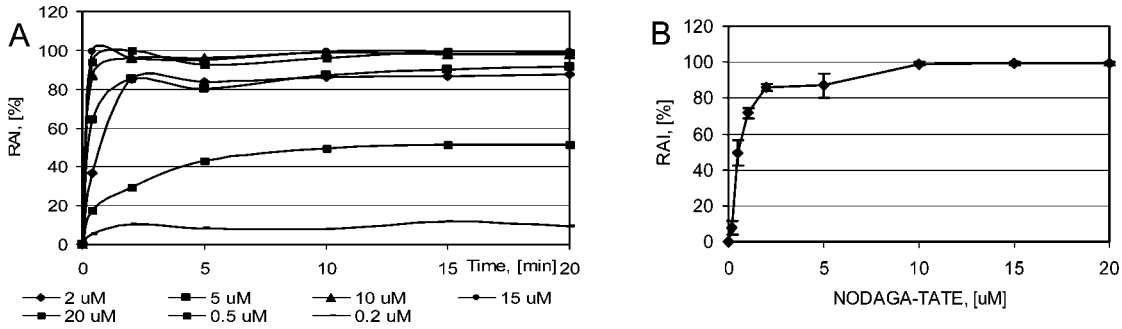

Figure 4. (A) Time course of ^{68}Ga complexation reaction at room temperature for varied concentration of NODAGA-TATE ($N = 2–3$, the error bars are omitted for simplicity). (B) Radioactivity incorporation as a function of the bioconjugate concentration (10 min incubation, RT).

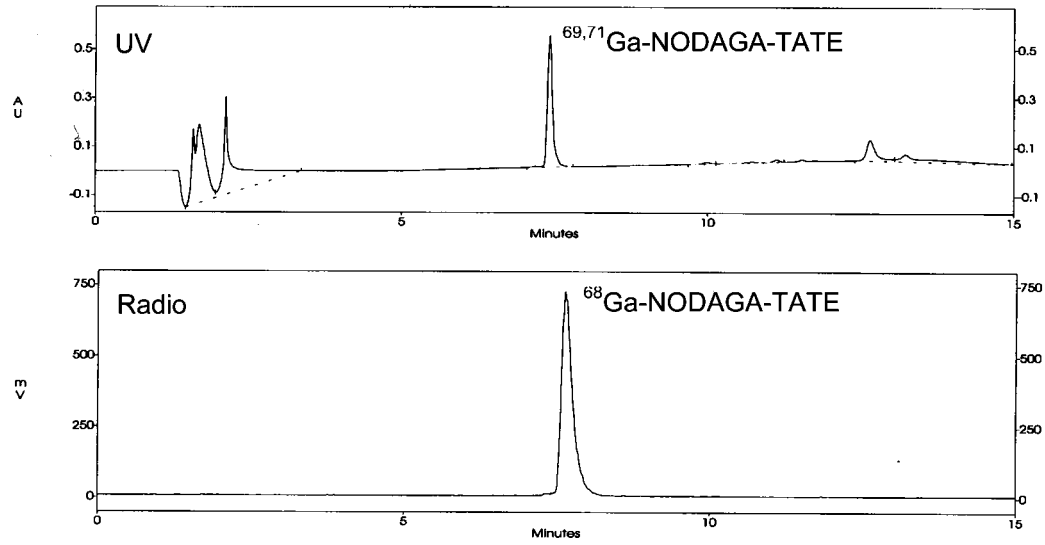

Figure 5. A typical example of an UV- and radio-HPLC chromatograms, respectively, for ^{69,71}Ga-NODAGA-TATE and ^{68}Ga-NODAGA-TATE. The reaction mixture was spiked with the stable reference. (The UV-signals at R_t of 12.66 and 13.33 are systematic and not related to the analyte.)

crystallography (*12*, *13*, *16*). In this study the complexation yields and conditions were similar for NOTA and NODAGA-TATE indicating that most probably the labeling is affected only by the macrocyclic chelator and consequently the latter might be coupled to a number of biologically active vectors resulting in a simple production of wide range of PET radiopharmaceuticals. The fast and nearly quantitative labeling results in higher specific radioactivity which might be crucial for the accurate quantification of PET examinations as well as in the application of expensive and highly potent macromolecular tracers. The labeling at room temperature allows the production of tracers comprising temperature sensitive and fragile macromolecules like antibodies. The nearly quantitative radioactivity incorporation at room temperature and reaction solution constitution compatible with human use promise a very simple kit type production.

CONCLUSIONS

The complexation of ^{68}Ga with NODAGA-TATE and NOTA was observed at RT and pH 3.5 within 10 min with the yield of >95%. The product purification was not necessary since the incorporation was nearly quantitative and the HEPES buffer is suitable for human use. Formation of ^{68}Ga-NOTA and ^{68}Ga-NODAGA-TATE was confirmed by the synthesis and subsequent ESI-LC-MS analysis of the counterparts comprising stable gallium isotopes.

^{68}Ga-NOTA was confirmed to be stable in human plasma at 37 °C during 4.5 h. The suggested ^{68}Ga and NOTA based labeling procedure might be of special interest for the labeling of fragile and potent macromolecules and might allow for a simple kit type preparation of ^{68}Ga-based radiopharmaceuticals.

ACKNOWLEDGMENT

Professor Vaughan Griffiths and Dr. Philip Duncanson (Queen Mary, University of London) and Dr. Peter Iveson (GE Healthcare) are acknowledged for the provision with NOTA and Medical Diagnostics, GE Healthcare, for partial financial support.

LITERATURE CITED

(1) Meyer, G. J., Macke, H., Schuhmacher, J., Knapp, W. H., and Hofmann, M. (2004) ^{68}Ga-labelled DOTA-derivatised peptide ligands. *Eur. J. Nucl. Med. Mol. Imaging 31*, 1097–104.

(2) Velikyan, I., Beyer, G. J., and Langstrom, B. (2004) Microwave-supported preparation of ^{68}Ga-bioconjugates with high specific radioactivity. *Bioconjugate Chem. 15*, 554–60.

(3) Velikyan, I., and Långström, B. (2004) Microwave method for preparing radiolabelled gallium complexes. WO 2004/089425, USA.

(4) Velikyan, I., Långström, B., and Beyer, G. (2004) Method of obtaining gallium-68 and use thereof and device for carrying out said method. WO 2004/089517, USA.

(5) Maecke, H. R. (2005) Radiolabeled peptides in nuclear oncology: influence of peptide structure and labeling strategy on pharmacology, In *Ernst Schering Research Foundation Workshop*, pp 43–72.

(6) Green, M. A. (1990) The potential for generator-based PET perfusion tracers. *J. Nucl. Med. 31*, 1641–5.

(7) Cutler, C. S., Giron, M. C., Reichert, D. E., Snyder, A. Z., Herrero, P., Anderson, C. J., Quarless, D. A., Koch, S. A., and Welch, M. J. (1999) Evaluation of gallium-68 tris(2-mercaptobenzyl)amine: a complex with brain and myocardial uptake. *Nucl. Med. Biol. 26*, 305–16.

(8) Anderson, C. J., and Welch, M. J. (1999) Radiometal-labeled agents (non-technetium) for diagnostic imaging. *Chem. Rev. 99*, 2219–2234.

(9) Maecke, H., and André, J. (2007) ^{68}Ga-PET radiopharmacy: a generator-based alternative to ^{18}F-radiopharmacy. *Ernst Schering Res. Found. Workshop 62*, 215–42.

(10) Hoffend, J., Mier, W., Schuhmacher, J., Schmidt, K., Dimitrakopoulou-Strauss, A., Strauss, L. G., Eisenhut, M., Kinscherf, R., and Haberkorn, U. (2005) Gallium-68-DOTA-albumin as a PET blood-pool marker: experimental evaluation in vivo. *Nucl. Med. Biol. 32*, 287–292.

(11) Breeman, W. A., and Verbruggen, A. M. (2007) The ^{68}Ge/^{68}Ga generator has high potential, but when can we use ^{68}Ga-labelled tracers in clinical routine? *Eur. J. Nucl. Med. Mol. Imaging 34*, 978–981.

(12) Broan, C. J., Cox, J. P. L., Craig, A. S., Kataky, R., Parker, D., Harrison, A., Randall, A. M., and Ferguson, G. (1991) Structure and solution stability of indium and gallium complexes of 1,4,7,-triazacyclononanetriacetate and yttrium complexes of 1,4,7,10-tetraazacyclododecanetetraacetate and related ligands: kinetically stable complexes for use in imaging and radioimmunotherapy. X-ray molecular structure of the indium and gallium complexes of 1,4,7,-triazacyclononane-1,4,7-triacetic acid. *J. Chem. Soc., Perkin Trans. 21*, 87–99.

(13) Craig, A. S., Parker, D., Adams, H., and Bailey, N. A. (1989) Stability, Ga-71 NMR, and crystal-structure of a neutral gallium(III) complex of 1,4,7-triazacyclononanetriacetate - a potential radiopharmaceutical. *J. Chem. Soc.: Chem. Commun.* 1793–1794.

(14) Clarke, E. T., and Martell, A. E. (1991) Stabilities of the Fe(III), Ga(III) and In(III) chelates of N,N′,N″-triazacyclononanetriacetic acid. *Inorg. Chim. Acta 181*, 273–280.

(15) Ma, R., Welch, M. J., Reibenspies, J., and Martell, A. E. (1995) Stability of metal-ion complexes of 1,4,7-tris(2-mercaptoethyl)-1,4,7-triazacyclononane (Tacn-Tm) and molecular-structure of in($C_{12}H_{24}N_3S_3$). *Inorg. Chim. Acta 236*, 75–82.

(16) Andre, J. P., Maecke, H. R., Zehnder, M., Macko, L., and Akyel, K. G. (1998) 1,4,7-Triazacyclononane-1-succinic acid-4,7-diacetic acid (NODASA): A new bifunctional chelator for radio gallium-labelling of biomolecules. *Chem. Commun.* 1301–1302.

(17) Prata, M. I., Santos, A. C., Geraldes, C. F., and de Lima, J. J. (1999) Characterisation of $^{67}Ga^{3+}$ complexes of triaza macrocyclic ligands: biodistribution and clearance studies. *Nucl. Med. Biol. 26*, 707–10.

(18) Prata, M. I., Santos, A. C., Geraldes, C. F., and de Lima, J. J. (2000) Structural and in vivo studies of metal chelates of Ga(III) relevant to biomedical imaging. *J. Inorg. Biochem. 79*, 359–63.

(19) Clarke, T. E., and Martell, A. E. (1991) Stabilities of trivalent metal ion complexes of the tetraacetate derivatives of 12-, 13- and 14-membered tetraazamacrocyles. *Inorg. Chim. Acta 190*, 37–46.

(20) Hancock, R. (1990) Molecular mechanics calculations and metal ion recognition. *Acc. Chem. Res. 23*, 253–257.

(21) Harris, W. R. (1986) Thermodynamics of gallium complexation by human lactoferrin. *Biochemistry 25*, 803–8.

(22) Umetani, S., Le, Q., and Matsui, M. (1996) Molecular design of chelating ligands with highly selective recognition and separation functions for group 13 metal ions. *ICR Annu. Rep. 3*, 14–15.

(23) Eisenwiener, K. P., Prata, M. I., Buschmann, I., Zhang, H. W., Santos, A. C., Wenger, S., Reubi, J. C., and Macke, H. R. (2002) NODAGATOC, a new chelator-coupled somatostatin analogue labeled with [$^{67/68}$Ga] and [^{111}In] for SPECT, PET, and targeted therapeutic applications of somatostatin receptor (hsst2) expressing tumors. *Bioconjugate Chem. 13*, 530–41.

BC700341X

Two-Photon Excitation Fluorescence Resonance Energy Transfer with Small Organic Molecule as Energy Donor for Bioassay

Lingzhi Liu,[†] Genghui Wei,[†] Zhihong Liu,*[,†] Zhike He,[†] Si Xiao,[‡] and Ququan Wang*[,‡]

College of Chemistry and Molecular Sciences and Key Laboratory of Acoustic and Photonic Materials and Devices of Ministry of Education, Wuhan University, Wuhan 430072, P. R. China. Received October 4, 2007; Revised Manuscript Received November 7, 2007

A fluorescence resonance energy transfer (FRET) model using two-photon excitable small organic molecule DMAHAS as energy donor has been constructed and tried in an assay for avidin. In the FRET model, biotin was conjugated to the FRET donor, and avidin was labeled with a dark quencher DABS-Cl. Binding of DABS-Cl labeled avidin to biotinylated DMAHAS resulted in the quenching of fluorescence emission of the donor, based on which a competitive assay for free avidin was established. With using such donors that are excited in IR region, it is capable of overcoming some primary shortcomings of conventional one-photon FRET methods, especially in bioassays, such as the interference from background fluorescence or scattering light, the coexcitation of the energy acceptor with the donor. And such small molecules also show advantages over inorganic up-converting particles that also give anti-Stokes photoluminescence and have been applied as FRET donor recently. The results of this work suggest that two-photon excitable small molecules could be a promising energy donor for FRET-based bioassays.

INTRODUCTION

Fluorescence resonance energy transfer (FRET)[1]is defined as the nonradiative transfer of the excited-state energy from a fluorescent donor to an acceptor, which may be fluorescent or not. FRET is considered as a sensitive and reliable "ruler" over distances of 10—100 Å (*1*) and has broad applications in studying interactions of biological macromolecules (*2*), in immunoassay (*3*), and so on. However, it is often seen that the energy acceptor is coexcited with the energy donor because of the overlap of their excitation spectra (*4, 5*). Meanwhile, autofluorescence or scattering light always arises from biomolecules upon the excitation of energy donor. Therefore, new pairs of energy donor–acceptor are desired for FRET methods, especially in bioassays.

Recently, two-photon (TP) excitation has attracted a lot of attention in biological applications. In such a nonlinear optical process, two low-energy photons are simultaneously absorbed to reach the excited state (*6*). TP excitable materials can be excited in IR region to give emission in the visible region. Under TP excitation with IR light, the autofluorescence of biomolecules and the scattered excitation light could be eliminated, thus the sensitivity is significantly improved. Besides, the IR light causes much less photobleaching off the focal plane and less photodamage to biological samples (*7, 8*). The above unique features have led to the wide use of TP excitation, notably in microscopic imaging (*9, 10*). Because of the anti-Stokes photoluminescence nature of TP excitation which avoids the direct excitation of energy acceptor, one can expect two-photon excitable materials to be promising energy donors for FRET microscopy. TP-FRET microscopy has been used to characterize the intranuclear dimerization of protein molecules in living cells (*11*) and to illuminate protein interactions in tissue (*12*). In biological imaging applications combined with microscopy, TP-FRET has shown higher energy transfer efficiency, less background, and deeper imaging depth than confocal FRET. TP-FRET also has advantages over wide-field FRET as there is less photodamage above and below the focal plane (*13*).

While efforts are being made to apply the anti-Stokes photoluminescence in biological imaging, TP-FRET based quantitative bioassays in homogeneous solutions have been studied much less. So far there have been several reports on FRET bioassays using up-converting phosphors (UCPs) as donors. UCPs are kinds of inorganic particles that give anti-Stokes photoluminescence via the sequential absorption of two or more low-energy photons, which is similar to TP excitation. Kuningas et al. (*14, 15*) and Li et al. (*16*) have developed bioassays based on upconversion fluorescence resonance energy transfer (UC-FRET). Most recently, luminescent quantum dots (QDs)-based FRET driven by a two-photon process, which eliminates the direct excitation of the acceptor and thus results in a near-zero background, has also been reported (*17*). The significance of using the IR light excitable UCPs as energy donor in bioassays has been proved in these papers. Nevertheless, the relatively large size of UCPs has caused some negative effects (*15, 18*), such as signal variation, reabsorptive energy transfer of ions in the core, instability of the phosphor bioconjugates, and nonspecific binding interactions. These have reduced the sensitivity of UC-FRET and restricted its applications.

Therefore, TP excitable small organic molecules would be a better alternative to UCPs in some aspects as the FRET donor, especially when the nonspecific binding/adsorbing of target

* Corresponding authors. Zhihong Liu, E-mail: zhhliu.whu@163.com, Tel: 86-27-87218754, Fax: 86-27-68754067, Address: College of Chemistry and Molecular Sciences, Wuhan University, Wuhan 430072, China. Ququan Wang, E-mail: qqwang@whu.edu.cn, Tel: 86-27-6875-2989-8445, Fax: 86-27-6875-2569, Address: Key Laboratory of Acoustic and Photonic Materials and Devices of Ministry of Education, Wuhan University, Wuhan 430072, China.

[†] College of Chemistry and Molecular Sciences.

[‡] Key Laboratory of Acoustic and Photonic Materials and Devices of Ministry of Education.

[1]Abbreviations: DABS-Av, DABS-Cl conjugated avidin; DABS-BSA, DABS-Cl labeled bovine serum albumin; DABS-Cl, 4-(Dimethylamino)azobenzene-4′-sulfonyl chloride; DMAHAS, *trans*-4-(*N*-2-hydroxyethyl-*N*-ethyl amino)-4′-(dimethyl amino)stilbene; FRET, fluorescence resonance energy transfer; QDs, quantum dots; TP, two-photon; TP-FRET, two-photon excitation fluorescence resonance energy transfer; UCPs, up-converting phosphors.

10.1021/bc700369q CCC: $40.75 © 2008 American Chemical Society
Published on Web 01/16/2008

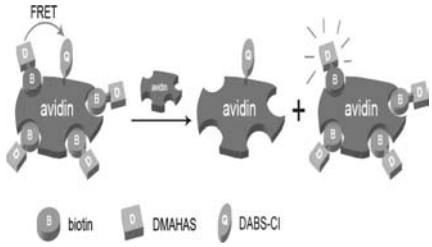

Figure 1. Schematic representation of the model FRET system with biotinylated DMAHAS as donor and DABS-Cl conjugated avidin as acceptor. FRET occurred upon the binding of DABS-Av to biotinylated DMAHAS, resulting in the quenching of the donor. With the addition of free avidin, the labeled avidin was partially replaced due to the competition towards biotin, which led to partial recovery of the fluorescence of donor.

molecules on the surface of particles, which always causes false positive results, is considered. Small molecules are capable of overcoming the problems resulted from the size effect of UCPs and thus improve the sensitivity and specificity of quantitative assays. What's more, organic molecules are structurally more flexible so that it is much easier to configure the molecules and motifs for the purpose of improving FRET efficiency and conjugating with biomolecules. Herein in this work, we have constructed a model assay for avidin (see Figure 1) to demonstrate the merits of TP excitation in FRET-based bioassays. Organic molecule *trans*-4-(*N*-2-hydroxyethyl-*N*-ethyl amino)-4′-(dimethyl amino)stilbene (DMAHAS) was employed as energy donor since it is convenient to conjugate with biotin through the reactive hydroxyl group. 4-(Dimethylamino)azobenzene-4′-sulfonyl chloride (DABS-Cl) is a nonfluorescent quencher with high molar extinction coefficient, which makes it a good acceptor in FRET. It was chosen as the acceptor in this work because it has a maximum absorption around 470 nm (*19*), which matches well with the emission spectrum of DMAHAS. To the best of our knowledge, such TP excitation FRET model for bioassay using small organic molecule as energy donor has not yet been reported in literature.

EXPERIMENTAL PROCEDURES

Synthesis of DMAHAS and Biotinylated DMAHAS. DMAHAS was synthesized according to a reported pathway (*20*), and then biotinylated DMAHAS was prepared with a normal labeling method (*21*). Biotin (29.3 mg, 0.12 mmol), DMAHAS (31 mg, 0.1 mmol), *N*,*N*′-dicyclohexylcarbodiimide (24.8 mg, 0.12 mmol), and 4-dimethylaminopyridine (1.23 mg, 0.01 mmol) were dissolved in anhydrous dichloromethane (10 mL). The mixture was stirred at room temperature for 5 days under argon atmosphere, after which the solution was filtered and the filtrate was evaporated. The residue was purified by column chromatography on silica gel using a 20:1 (v/v) ethyl acetate/methanol as eluent, and a yellow crystal was obtained (structures shown in Figure 2).^{1}H NMR ($CDCl_3$), δ: 7.35 (m, 4H), 6.83 (s, 2H), 6.71 (m, 4H), 5.20 (s, 1 H, NH), 4.87 (s, 1 H, NH), 4.44 (m, 1H), 4.25 (m, 3H), 3.56 (m, 2H), 3.41 (m, 2H), 3.08 (m, 1H), 2.96 (s, 6H), 2.90—2.67 (m, 2H), 2.31 (t, 2H), 1.63 (m, 4H), 1.38 (m, 2H), 1.17 (t, 3H). HRMS (ESI-TOF) calcd for $C_{30}H_{40}N_4O_3S$ $[M + H]^+$ 537.2899, found 537.2901.

Preparation of DABS-Cl Conjugated Avidin. DABS-Av conjugate was prepared using a method analogous to others (*22*). Avidin was dissolved in 0.1 M sodium carbonate-sodium bicarbonate buffer, pH 9.1, at a concentration of 1 mg/mL. DABS-Cl was dissolved in DMF at a concentration of 1 mg/mL. The DABS-Cl solution was protected from light and used immediately. With gentle shaking, 30 μL of the DABS-Cl solution was slowly added to the avidin solution. After reacting

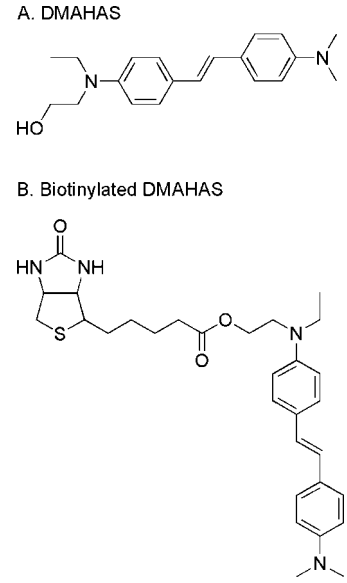

Figure 2. Structures of (A) DMAHAS, (B) biotinylated DMAHAS.

at room temperature for 2 h in the dark, the unbound DABS-Cl molecules were removed by exhaustive dialysis against the above buffer overnight at 4 °C.

The dye to protein ratio was estimated as follows: the concentration of DABS-Cl was determined by the absorbance at 474 nm, using the molar extinction coefficient of 3.3×10^4 M^{-1} cm^{-1}. Since DABS-Cl has a contribution to the absorbance at 280 nm, the concentration of avidin was determined by the absorbance at 280 nm after deducting the contribution of DABS-Cl at this wavelength, using the molar extinction coefficient of 8.88×10^4 M^{-1} cm^{-1} (*23*).

Preparation of DABS-BSA Conjugate. Similar to the process for making DABS-Av, BSA was dissolved in 0.1 M sodium carbonate-sodium bicarbonate buffer, pH 9.1, at a concentration of 1 mg/mL. And DABS-Cl was also dissolved in DMF at a concentration of 1 mg/mL, which was protected from light and used immediately. With gentle shaking, 100 μL of the DABS-Cl solution was slowly added to the BSA solution. After reacting at room temperature for 2 h in the dark, the unbound DABS-Cl molecules were removed by exhaustive dialysis against the above buffer overnight at 4 °C.

The dye-to-protein ratio was determined with the same manner as DABS-to-avidin ratio described above.

Measurement of TP Excited Fluorescence. Two-photon excited fluorescence detection system included two parts. The excitation light was provided by a mode-locked pulsed laser (Mira 900, Coherent) to provide high instantaneous photon flux density. The photoluminescence was recorded on a liquid-nitrogen cooled CCD detector (SPEC-10, Princeton) through a monochromator (Spectrapro 2500i, Acton). Two-photon fluorescence was excited at 800 nm with ~3 ps pulse width and 76 MHz repetition rate. The fluorescence intensity was given in normalized form, i.e., the maximum emission of each group of data was set as 1, and others were calculated proportionally. A LS 55 fluorometer (Perkin-Elmer) equipped with 1 cm cell was used for one-photon fluorescence measurements.

In a typical FRET experiment, 1×10^{-4} M biotinylated DMAHAS in DMF was diluted to 1×10^{-6} M with phosphate buffer, thus the solvent was a mixture of aqueous buffer (0.1 M phosphate buffer, pH 7.4) and 1% DMF (v/v). Under room temperature, DABS-Cl labeled avidin (0.145 μM avidin with the dye-to-protein ratio as 1.6) was added to the solution, which was then vortexed and incubated for 15 min. Then the fluorescence emission of biotinylated DMAHAS was recorded under excitation at 800 nm. For the fluorescence recovery, $1 \times$

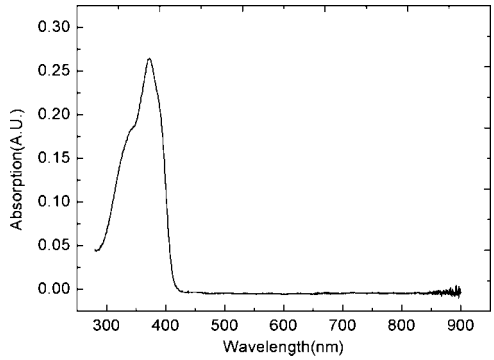

Figure 3. Linear absorption spectrum of DMAHAS (1×10^{-5} M in DMF).

10^{-6} M free avidin was added to another tube containing the same amount of biotinylated DMAHAS and DABS-Cl labeled avidin, which had been allowed to react for 15 min. After thoroughly mixing and incubating for another 15 min, the mixture was subjected to fluorescence measurement.

In the control experiments which were performed to exclude nonspecific interactions of biomolecules, 1×10^{-6} M biotinylated DMAHAS was incubated, also for 15 min under room temperature, with DABS-Cl labeled BSA (0.122 μM BSA with the dye-to-protein ratio as 1.6) and 0.18 μM free avidin, respectively. And the fluorescence of the donor was detected likewise.

For competitive assay of avidin, varying concentrations of free avidin (0, 0.1 μM, 0.4 μM, 0.8 μM, 1.3 μM, 1.9 μM, and 2.6 μM) were incubated with 1×10^{-5} M biotinylated DMAHAS and DABS-Cl labeled avidin (concentration fixed at 2.4 μM) for 15 min, and then the same fluorescence detecting procedure as above was followed for each sample.

RESULTS

Spectral Properties of the Donor. In order to confirm the TP excitation luminescence of the donor, the linear absorption spectrum of DMAHAS was examined first. From Figure 3, it is seen that its maximum absorption locates at 372 nm and there is no linear absorption in the range from 430 to 900 nm, which indicates that the photoluminescence of DMAHAS excited with 800 nm is purely the two-photon induced fluorescence. The TP excited fluorescence of the organic molecule is structurally originated from its symmetrical D-π-D conjugate motif. The biotinylation on the terminal hydroxyl group does not destroy the symmetrical charge transfer within the conjugated chain or the rigid plane of the molecule. Therefore, the biotinylation did not alter the nonlinear photoluminescence of DMAHAS. The fluorescence emission of both DMAHAS and biotin-conjugated DMAHAS under TP excitation model at 800 nm are presented in Figure 4, which shows that the TP fluorescence emission of biotinylated DMAHAS did not differ much from that of DMAHAS.

Optimization of the DABS-to-Avidin Ratio. The FRET efficiency can be adjusted by altering the dye-to-protein ratio. Generally speaking, increasing the dye-to-protein ratio will enhance the overall FRET efficiency due to the increased overlap integral (*24*). However, high dye-to-protein ratio does not always work well because labeling with more than one fluorophore may also result in problems, like concentration-dependent quenching, which will limit the detection sensitivity. Besides, the solubility and activity of the complex may be decreased in cases when coupling water-insoluble molecules to the surface of proteins owing to the hydrophobicity of the conjugate (*22*). In our experiments, we also found that adding excessive DABS-Cl to avidin solution would cause severe aggregation of the protein.

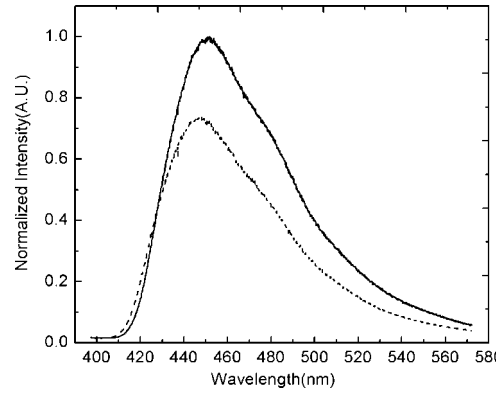

Figure 4. Two-photon excitation fluorescence spectra. (—) DMAHAS (1×10^{-2} M in DMF), (□) biotinylated DMAHAS (1×10^{-2}M in DMF). Excitation wavelength = 800 nm.

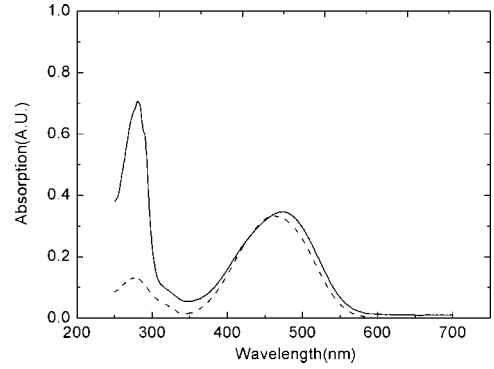

Figure 5. UV–vis absorption spectra for the calculation of DABS-to-avidin ratio. (—) the DABS-Av conjugate, (□) DABS-Cl (1×10^{-5} M in acetonitrile).

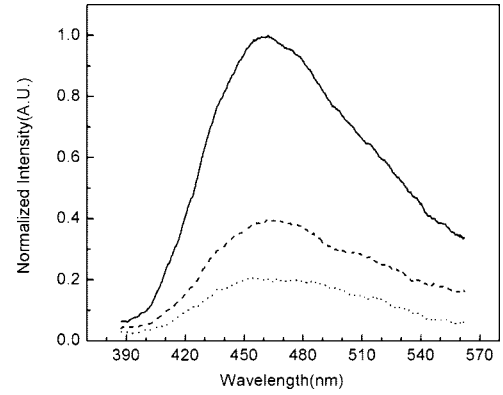

Figure 6. Two-photon excitation fluorescence spectra of the FRET model. (—) biotinylated DMAHAS (1×10^{-6} M), (. . .) biotinylated DMAHAS + DABS-Av (0.145 μM avidin with the dye-to-protein ratio as 1.6), (□) biotinylated DMAHAS + DABS-Av + unlabeled avidin (1×10^{-6} M). Excitation wavelength = 800 nm.

In this case, the dye-to-protein ratio should be scaled back. The UV–vis absorption spectra of pure DABS-Cl and the DABS-Av complex are illustrated in Figure 5, based on which the DABS-to-avidin ratio was calculated as 1.6.

Construction of the TP Excitation FRET Model. FRET occurred upon the addition of DABS-Cl conjugated avidin to the biotinylated DMAHAS solution, since DMAHAS and DABS-Cl were in proximity due to the specific binding of biotin and avidin. As is shown in Figure 6, when avidin conjugate was present, the two-photon excited fluorescence of biotinylated DMAHAS, the donor, was quenched by the acceptor. With adding free avidin to the above system, the fluorescence intensity

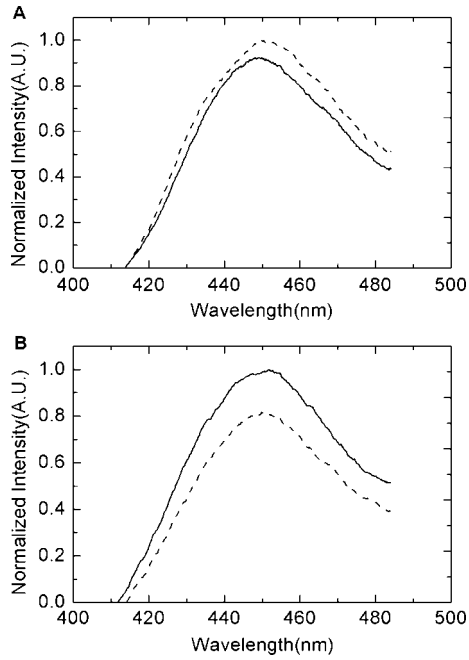

Figure 7. Two-photon excitation fluorescence spectra of control experiments. (A) (—) biotinylated DMAHAS (1×10^{-6} M), (□) biotinylated DMAHAS + DABS-Cl labeled BSA (0.122 μM BSA with the dye-to-protein ratio as 1.6). (B) (—) biotinylated DMAHAS (1×10^{-6} M), (□) biotinylated DMAHAS + unlabeled avidin (0.18 μM). Excitation wavelength = 800 nm.

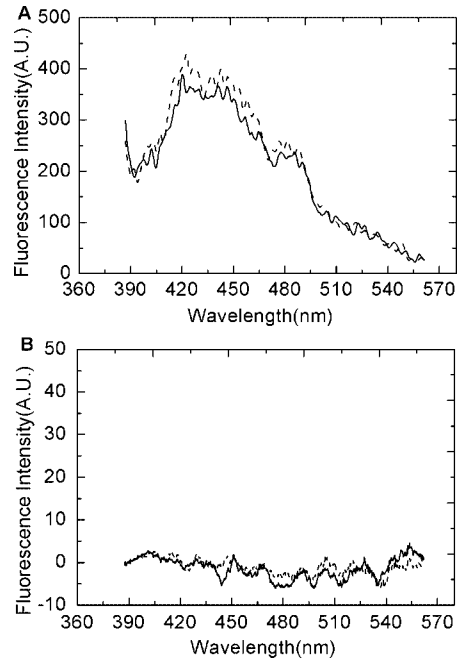

Figure 8. Comparison on the background signal under one-photon and two-photon excitation. (A) one-photon excitation. (—) DABS-Cl labeled avidin (0.145 μM avidin with the dye-to-protein ratio as 1.6), (□) avidin (1×10^{-6} M). Excitation wavelength = 372 nm, Excitation slit = 5 nm, Emission slit = 15 nm. (B) two-photon excitation. (—) DABS-Cl labeled avidin (0.145 μM avidin with the dye-to-protein ratio as 1.6), (□) avidin (1×10^{-6} M). Excitation wavelength = 800 nm.

recovered partially, which resulted from the competition between the labeled and unlabeled avidin toward biotin. The replacement of labeled avidin with free avidin is due to the stronger biotin binding ability of the latter (*25*).

Examination on the Specificity of the TP-FRET Model. Two control experiments were performed to exclude nonspecific interactions of biomolecules, in which biotinylated DMAHAS was incubated with DABS-Cl labeled BSA or with free avidin. DABS-BSA conjugate was prepared with the same method as DABS-Av. The dye-to-protein ratio was also determined to be 1.6. The fluorescence of biotinylated DMAHAS was not quenched by DABS-Cl labeled BSA which had almost the same concentration as avidin used to quench the fluorescence of biotinylated DMAHAS in the FRET model, i.e., 0.122 μM BSA versus 0.145 μM avidin (Figure 7A). And in another experiment, the fluorescence of biotinylated DMAHAS was not directly enhanced with 0.18 μM free avidin either (Figure 7B). These results indicated that the quenching and the recovery of the fluorescence of the donor were not induced by any nonspecific interactions of macromolecules, which is always a troublesome problem in large-size-particle-based biosensors (nanometer to micrometer magnitude), such as the UCPs described above.

In order to illustrate the ability of TP excitation FRET to exclude interferences from autofluorescence or scattering light, the background signal of biomolecules under one-photon and two-photon excitation was compared. Figure 8A indicates that in the case of one-photon excitation, when exciting avidin and DABS-Cl labeled avidin at the optimum excitation wavelength of DMAHAS at 372 nm, the background light around 420–480 nm could not be ignored, which would interfere the luminescence of DMAHAS and thus reduce the sensitivity. While under two-photon excitation at 800 nm there was only noise signal from the instrument, which could be negligible (Figure 8B).

Competitive Assay for Avidin. Finally, the TP-FRET model was tried to investigate the dependence of the relative fluorescence intensity (FL/FL_0) of the donor on the concentration of free avidin (where FL_0 represents the fluorescence intensity in the absence of free avidin and FL represents the fluorescence intensity under different concentrations of free avidin). As shown in Figure 9, the FL/FL_0 of the donor is dependent on avidin concentration and is linear to the concentration in a certain range (0.4−2.6 μM) with a correlation coefficient of 0.9947, which suggests that the two-photon FRET model could be a candidate for quantitative bioassay.

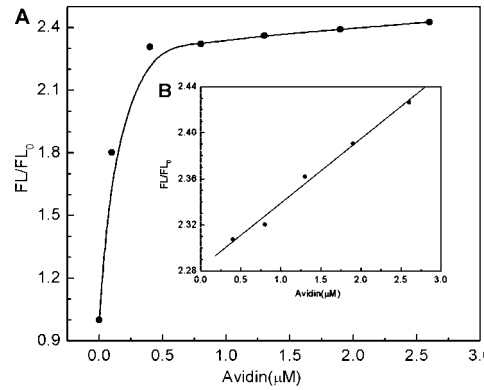

Figure 9. Competitive assay for avidin. (A) The dependence of FL/FL_0 of biotinylated DMAHAS on the concentration of free avidin. (B) The linear calibration curve of FL/FL_0 to the concentration of free avidin within the range 0.4−2.6 μM.

DISCUSSION

The results show that TP-FRET bioassays can overcome the shortcomings of conventional one-photon-FRET and that small organic molecules have advantages over the newly reported inorganic particles as the energy donor in bioassays. They have supported the hypothesis that TP excitable small organic molecules could be a kind of competent energy donor for FRET in homogeneous bioassays. However, it must be pointed out that, as a start of investigating the applicability of TP-FRET

with small molecule as energy donor in bioassay, the biocompatibility of the donor molecule used here and the analytical performance of the model have not been considered intensively. As a quantitative bioassay, the linear range for avidin is somewhat narrow, and the sensitivity is not as good as the reported UCPs-based biosensors. This might be mainly caused by the rather poor solubility of biotinylated DMAHAS in aqueous solution, which results in aggregation or precipitation out of water at high concentrations. Besides, the moderate TP absorption cross section of DMAHAS also restricted the detection sensitivity. An ideal TP-FRET donor molecule is expected to have large TP absorption cross section, high fluorescence quantum yield as well as good biological compatibility such as water solubility. Although the investigations on the relationship between molecular structure and TP absorption property over the past few years have enabled people to design and synthesize molecules with large TP absorption cross section (*26*, *27*), most of them have poor solubility in water preventing them from biological applications. Whereas many of the water soluble fluorophores commonly used as fluorescent tags in biological samples, if TP excitable, only have a small TP absorption cross section (*28*, *29*), for example, the value for fluorescein in water at pH 13 is only 36 GM (*30*) (1 GM = 1×10^{-50} cm^4 s $photon^{-1}$). Therefore for further research concerning TP-FRET methods in quantitative bioassay, emphasis should be put on development of donor molecules with both high water solubility and larger TP absorption cross section. It seems there is a conflict between the two aspects because, generally speaking, a larger absorption cross section requires a larger hydrophobic conjugated motif within the molecule, which always leads to the decrease of water solubility. Nevertheless, great efforts are being made and some exciting results have already been obtained in most recent years. For instance, by encapsulating the hydrophobic TP excitable molecules into the hydrophobic interior of micelles, large TP absorption cross section in water is achieved (*31*–*33*). Recently, a new type of fluorescent chromophores with efficient TP absorption cross sections and high fluorescence quantum yield in aqueous medium as well as in organic medium have been successfully developed (*34*). As such examples are so limited, it remains a challenge for scientists to investigate the effect of solvent especially water on the properties of two-photon excited molecules and to develop molecules with large TP absorption cross section in aqueous solutions.

ACKNOWLEDGMENT

This work was supported by the National Natural Science Foundation of China (No. 20675059) and the Science Fund for Creative Research Groups (No. 20621502), NSFC and The National Key Scientific Program-Nanoscience and Nanotechnology (No. 2006CB933103). Authors thank Dr. Song Wu and Dr. Bao-Ping Zhai for helping in synthetic work.

LITERATURE CITED

(1) dos Remedios, C. G., and Moens, P. D. J. (1995) Fluorescence resonance energy transfer spectroscopy is a reliable "ruler" for measuring structural changes in proteins. *J. Struct. Biol. 115*, 175–185.

(2) Graham, D. L., Lowe, P. N., and Chalk, P. A. (2001) A method to measure the interaction of Rac/Cdc42 with their binding partners using fluorescence resonance energy transfer between mutants of green fluorescent protein. *Anal. Biochem. 296*, 208–217.

(3) Oswald, B., Lehmann, F., Simon, L., Terpetschnig, E., and Wolfbeis, O. S. (2000) Red laser-induced fluorescence energy transfer in an immunosystem. *Anal. Biochem. 280*, 272–277.

(4) Schmid, J. A., Scholze, P., Kudlacek, O., Freissmuth, M., Singer, E. A., and Sitte, H. H. (2001) Oligomerization of the human serotonin transporter and of the rat GABA transporter 1 visualized by fluorescence resonance energy transfer microscopy in living cells. *J. Biol. Chem. 276*, 3805–3810.

(5) Willard, D. M., Carillo, L. L., Jung, J., and Orden, A. V. (2001) CdSe-ZnS quantum dots as resonance energy transfer donors in a model protein-protein binding assay. *Nano Lett. 1*, 469–474.

(6) Dyer, J., Jockusch, S., Balsanek, V., Sames, D., and Turro, N. J. (2005) Two-photon induced uncaging of a reactive intermediate. Multiphoton in situ detection of a potentially valuable label for biological applications. *J. Org. Chem. 70*, 2143–2147.

(7) Lakowicz, J. R. (1999) Instrumentation for fluorescence spectroscopy. *Principles of Fluorescence Spectroscopy*,2nd ed., pp 57–59, Chapter 2, Kluwer Academic, New York.

(8) Thomas, T. P., Myaing, M. T., Ye, J. Y., Candido, K., Kotlyar, A., Beals, J., Cao, P., Keszler, B., Patri, A. K., Norris, T. B., and Baker Jr, J. R. (2004) Detection and analysis of tumor fluorescence using a two-photon optical fiber probe. *Biophys. J. 86*, 3959–3965.

(9) Potter, S. M., Wang, C.-M., Garrity, P. A., and Fraser, S. E. (1996) Intravital imaging of green fluorescent protein using two-photon laser-scanning microscopy. *Gene 173*, 25–31.

(10) Miller, E. W., Albers, A. E., Pralle, A., Isacoff, E. Y., and Chang, C. J. (2005) Boronate-based fluorescent probes for imaging cellular hydrogen peroxide. *J. Am. Chem. Soc. 127*, 16652–16659.

(11) Chen, Y., and Periasamy, A. (2004) Characterization of two-photon excitation fluorescence lifetime imaging microscopy for protein localization. *Microsc. Res. Tech. 63*, 72–80.

(12) Mills, J. D., Stone, J. R., Rubin, D. G., Melon, D. E., Okonkwo, D. O., Periasamy, A., and Helm, G. A. (2003) Illuminating protein interactions in tissue using confocal and two-photon excitation fluorescent resonance energy transfer microscopy. *J. Biomed. Opt. 8*, 347–356.

(13) Chen, Y., Mills, J. D., and Periasamy, A. (2003) Protein localization in living cells and tissues using FRET and FLIM. *Differentiation 71*, 528–541.

(14) Kuningas, K., Rantanen, T., Ukonaho, T., Lövgren, T., and Soukka, T. (2005) Homogeneous assay technology based on upconverting phosphors. *Anal. Chem. 77*, 7348–7355.

(15) Kuningas, K., Ukonaho, T., Päkkilä, H., Rantanen, T., Rosenberg, J., Lövgren, T., and Soukka, T. (2006) Upconversion fluorescence resonance energy transfer in a homogeneous immunoassay for estradiol. *Anal. Chem. 78*, 4690–4696.

(16) Wang, L., Yan, R., Huo, Z., Wang, L., Zeng, J., Bao, J., Wang, X., Peng, Q., and Li, Y. (2005) Fluorescence resonant energy transfer biosensor based on upconversion-luminescent nanoparticles. *Angew. Chem., Int. Ed. 44*, 6054–6057.

(17) Clapp, A. R., Pons, T., Medintz, I. L., Delehanty, J. B., Melinger, J. S., Tiefenbrunn, T., Dawson, P. E., Fisher, B. R., O'Rourke, B., and Mattoussi, H. (2007) Two-photon excitation of quantum-dot-based fluorescence resonance energy transfer and its applications. *Adv. Mater. 19*, 1921–1926.

(18) Heer, S., Kömpe, K., Güdel, H.-U., and Haase, M. (2004) Highly efficient multicolour upconversion emission in transparent colloids of lanthanide-doped $NaYF_4$ nanocrystals. *Adv. Mater. 16*, 2102–2105.

(19) Lin, J.-K., and Chang, J.-Y. (1975) Chromophoric labeling of amino acids with 4-dimethylaminoazobenzene-4′-sulfonyl chloride. *Anal. Chem. 47*, 1634–1638.

(20) Yan, Y. (2003) Synthesis and nonlinear optical properties of new symmetrically substituted stilbenes. *J. Solid State Chem. 172*, 364–369.

(21) Cosnier, S., Stoytcheva, M., Senillou, A., Perrot, H., Furriel, R. P. M., and Leone, F. A. (1999) A biotinylated conducting polypyrrole for the spatially controlled construction of an amperometric biosensor. *Anal. Chem. 71*, 3692–3697.

(22) Hermanson, G. T. (1996) Avidin-biotin systems. *Bioconjugate Techniques*, pp 586–587, Chapter 13, Academic Press, San Diego.

(23) Hulspas, R., Krijtenburg, P. J., Keij, J. F., and Bauman, J. G. J. (1993) Avidin-EITC: an alternative to avidin-FITC in confocal scanning laser microscopy. *J. Histochem. Cytochem. 41*, 1267–1272.

(24) Medintz, I. L., Trammell, S. A., Mattoussi, H., and Mauro, J. M. (2004) Reversible modulation of quantum dot photoluminescence using a protein-bound photochromic fluorescence resonance energy transfer acceptor. *J. Am. Chem. Soc. 126*, 30–31.

(25) Fan, W., Guhlke, S., Qian, J. H., Zhu, B. X., and Biersack, H. (2003) Reactivity comparison of biological material after radiolabeling with avidin-biotin system. *J. Nucl. Radiochem. 25*, 49–51.

(26) Reinhardt, B. A., Brott, L. L., Clarson, S. J., Dillard, A. G., Bhatt, J. C., Kannan, R., Yuan, L., He, G. S., and Prasad, P. N. (1998) Highly active two-photon dyes: design, synthesis, and characterization toward application. *Chem. Mater. 10*, 1863–1874.

(27) Chung, S.-J., Rumi, M., Alain, V., Barlow, S., Perry, J. W., and Marder, S. R. (2005) Strong, low-energy two-photon absorption in extended amine-terminated cyano-substituted phenylenevinylene oligomers. *J. Am. Chem. Soc. 127*, 10844–10845.

(28) Xu, C., and Webb, W. W. (1996) Measurement of two-photon excitation cross sections of molecular fluorophores with data from 690 to 1050 nm. *J. Opt. Soc. Am., B 13*, 481–491.

(29) Song, J. M., Inoue, T., Kawazumi, H., and Ogawa, T. (1999) Determination of two photon absorption cross section of fluorescein using a mode locked titanium sapphire laser. *Anal. Sci. 15*, 601–603.

(30) Albota, M. A., Xu, C., and Webb, W. W. (1998) Two-photon fluorescence excitation cross sections of biomolecular probes from 690 to 960 nm. *Appl. Opt. 37*, 7352–7356.

(31) Woo, H. Y., Korystov, D., Mikhailovsky, A., Nguyen, T.-Q., and Bazan, G. C. (2005) Two-photon absorption in aqueous micellar solutions. *J. Am. Chem. Soc. 127*, 13794–13795.

(32) Tian, Y., Chen, C.-Y., Cheng, Y.-J., Cody Young, A., Tucker, N. M., and Jen, A. K.-Y. (2007) Hydrophobic chromophores in aqueous micellar solution showing large two-photon absorption cross sections. *Adv. Funct. Mater. 17*, 1691–1697.

(33) Chen, C.-Y., Tian, Y., Cheng, Y.-J., Cody Young, A., Ka, J.-W., and Jen, A. K.-Y. (2007) Two-photon absorbing block copolymer as a nanocarrier for porphyrin: energy transfer and singlet oxygen generation in micellar aqueous solution. *J. Am. Chem. Soc. 129*, 7220–7221.

(34) Hayek, A., Bolze, F., Nicoud, J.-F., Baldeck, P. L., and Mély, Y. (2006) Synthesis and characterization of water-soluble two-photon excited blue fluorescent chromophores for bioimaging. *Photochem. Photobiol. Sci. 5*, 102–106.

BC700369Q

MARCH 2008
Volume 19, Number 3

© *Copyright 2008 by the American Chemical Society*

Bioconjugate Chemistry

COMMUNICATIONS

O_2 Binding to Human Serum Albumin Incorporating Iron Porphyrin with a Covalently Linked Methyl-L-Histidine Isomer

Akito Nakagawa,[†] Teruyuki Komatsu,*[,†,‡] Makoto Iizuka,[†] and Eishun Tsuchida*[,†]

Research Institute for Science and Engineering, Waseda University, 3-4-1 Okubo, Shinjuku-ku, Tokyo 169-8555, Japan, and PRESTO, Japan Science and Technology Agency (JST), 4-1-8 Honcho, Kawaguchi-shi, Saitama 332-0012, Japan. Received October 30, 2007; Revised Manuscript Received December 1, 2007

We describe the significant difference in the O_2 binding affinities of human serum albumin (HSA) incorporating 5,10,15,20-tetrakis{α,α,α,α-*o*-(1′-methylcyclohexanamido)phenyl}porphinatoiron(II) with a covalently linked 1-methyl-L-histidine or 3-methyl-L-histidine [HSA-FeP(1-MHis), HSA-FeP(3-MHis)]. The HSA-FeP(3-MHis) showed an extraordinarily high O_2 binding affinity ($P_{1/2}$ = 0.2 Torr, 25 °C, pH 7.4), which is close to those of relaxed-state hemoglobin and myoglobin. However, replacement of the 3-methyl-L-histidine moiety in FeP(3-MHis) by 1-methyl-L-histidine caused a 35-fold reduction in O_2 affinity; the $P_{1/2}$ value of HSA-FeP(1-MHis) (22 Torr, 37 °C, pH 7.4) is almost identical to that of human red blood cells. Results of kinetic studies indicate that the low O_2 binding affinity of FeP(1-MHis) is predominantly manifested in the high O_2 dissociation rate constant. In a toluene solution, an identical relationship in the O_2 binding property was similarly observed for FeP(1-MHis) and FeP(3-MHis). The axial Fe-N(1-MHis) coordination might be restrained by steric interaction between the 4-methylene group of the histidine and the porphyrin plane.

Numerous synthetic model hemes have been prepared to mimic the O_2 binding capability of hemoglobin (Hb) and myoglobin (Mb) over the past few decades (*1*–*3*). In these highly modified iron(II) porphyrins, axial coordination of the nitrogenous base plays a crucial role in regulating O_2 binding affinity. Collman and co-workers demonstrated that picket-fence porphyrin[1] ligating a 1,2-dimethylimidazole (1,2-DMIm) showed a 70-fold lower O_2 binding affinity [$P_{1/2}$ (O_2 partial pressure at which 50% of porphyrin was dioxygenated) = 38 Torr, 25 °C] than that of the complex with 1-methylimidazole (1-MIm) (*4*, *5*). This reduction was ascribed to the steric interaction between the 2-methyl group of the imidazole and the porphyrin plane. Furthermore, they showed that the replacement of imidazole by pyridine in the tailed picket-fence porphyrin lowered the O_2-binding affinity by a factor of 40 (*6*). The weaker π-basicity of pyridine and the increased steric repulsion of the six-atom pyridine ring compared to that of the five-atom imidazole reduced the O_2 binding of the iron(II) porphyrins (*7*–*10*). We previously reported that 2-[{8-*N*-(methylimidazolyl)octanoyloxy}methyl]-5,10,15,20-tetrakis{α,α,α,α-*o*-(1′-methylcyclohexanamido)phenyl}porphinatoiron(II) [FeP(2-MIm)] formed a stable O_2 adduct in toluene solution, and human serum albumin (HSA) incorporating FeP(2-MIm) [HSA-FeP(2-MIm)]

* Corresponding author. Tel: +81-3-5286-3120. Fax: +81-3-3205-4740. E-mail: eishun@waseda.jp (E.T.). E-mail: teruyuki@waseda.jp (T.K.).
[†] Waseda University.
[‡] Japan Science and Technology Agency (JST).

[1] Picket-fence porphyrin: 5,10,15,20-tetrakis{(α,α,α,α-o-pivalamido)-phenyl}porphinatoiron.

10.1021/bc700400n CCC: $40.75 © 2008 American Chemical Society
Published on Web 01/19/2008

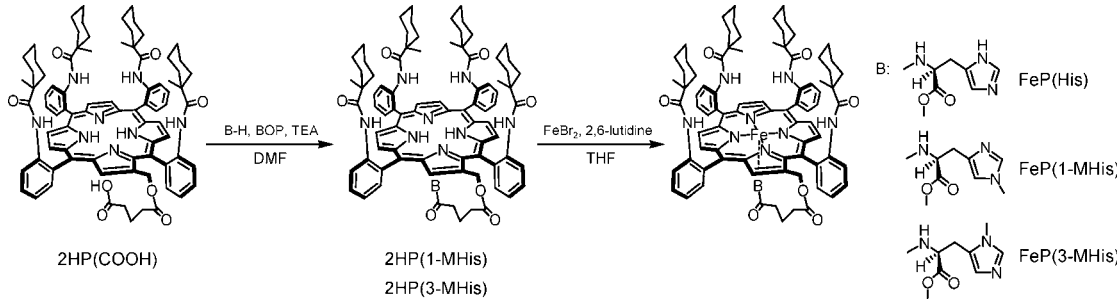

Figure 1. Synthetic scheme of iron(II) porphyrin bearing a covalently linked histidine derivative as an axial base at the β-pyrrolic position.

can bind O_2 not only in aqueous media (pH 7.4) but also in the blood stream as an artificial red blood cell (RBC) substitute (*11, 12*). For practical biomedical applications of the synthetic iron(II) porphyrin as an O_2 carrier, two physiological requirements exist. First, O_2 binding affinity should be close to that of human RBC ($P_{1/2}$ = 27 Torr, 37 °C). Second, it is favorable to use natural histidine as an axial base because some imidazole and pyridine derivatives show toxicity to respiratory organs and the central nervous system (*13*). Nevertheless, few studies have addressed O_2 binding of the synthetic model heme having a histidyl group (*14–16*). We have demonstrated the O_2 binding equilibrium and kinetics of 5,10,15,20-tetrakis{α,α,α,α-*o*-(1′-methylcyclohexanamido)phenyl}porphinatoiron(II) with an ω-histidylalkyl chain [FeP(His)[2]] (*17*). A new class of biocompatible O_2 carriers would be realized if we can regulate O_2 binding affinity by changing the steric and electronic natures of the attached histidine. We now report a significant difference in the O_2 binding properties of HSA hybrid with synthetic iron(II) porphyrin bearing a covalently linked 1-methyl-L-histidine or 3-methyl-L-histidine [HSA-FeP(1-MHis) and HSA-FeP(3-MHis)] (Figure 1) under physiological conditions (pH 7.4, 37 °C).

The 1-methyl-L-histidine methylester or 3-methyl-L-histidine methylester was introduced into the carboxyl group of the parent free-base porphyrin, 2-{(4-carboxybutanoyloxy)methyl}-5,10,15,20-tetrakis{α,α,α,α-*o*-(1′-methylcyclohexanamido)phenyl}porphin [2HP(COOH)] (*11*), via an amide linkage, yielding histidine-terminated porphyrins (>60% yield) (Figure 1). The cyclohexanoyl substituents stabilized the O_2 adduct complex rather than the pivaloy group (*11*). The central iron was inserted as iron(II) using $FeBr_2$ and 2,6-lutidine in anhydrous THF. The analytical data of all compounds were satisfactorily obtained (see Supporting Information).

Both FeP(1-MHis) and FeP(3-MHis) are readily incorporated into HSA (Mw: 66.5 kDa), producing stable artificial hemoproteins: HSA-FeP(1-MHis) and HSA-FeP(3-MHis) [in phosphate-buffered saline (PBS) solution at pH 7.4, [porphyrin]/[HSA] = 4 (mol/mol)]. The UV–vis absorption spectra of the aqueous HSA-FeP(1-MHis) and HSA-FeP(3-MHis) solutions under an N_2 atmosphere showed a similar feature of HSA-FeP(2-MIm) and HSA-FeP(His) (Figure 2) (Table S1) (*11, 17*). The spectral shapes resembled those of the five-N-coordinate high-spin ferrous complex of picket-fence porphyrin and other tetraphenylporphyrin derivatives (*5*). These results indicated that FeP(1-MHis) and FeP(3-MHis) formed a five-N-coordinate high-spin complex with an intramolecularly coordinated methyl-

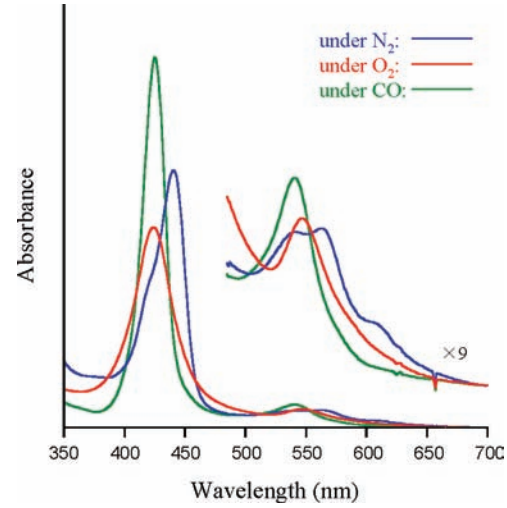

Figure 2. UV–vis absorption spectral changes of HSA-FeP(1-MHis) in PBS solution at 25 °C.

L-histidine moiety in the protein matrix. Upon bubbling of O_2 gas into the solution, the absorption pattern changed immediately to that of the O_2 adduct complex. The dioxygenations of these artificial hemoproteins have been observed reversibly under physiological conditions (pH 7.4, 37 °C). After passing the CO gas, the absorption maxima shifted to that of the carbonyl complex.

The O_2 binding affinities [$K = (P_{1/2})^{-1}$] of HSA-FeP(1-MHis) and HSA-FeP(3-MHis) were determined by the absorption spectral changes at various O_2 concentrations (eq 1).

$$\mathrm{FeP(B)} + \mathrm{O_2} \underset{k_{off}}{\overset{k_{on}}{\rightleftharpoons}} \mathrm{FeP(B)\text{-}O_2} \quad [K = (P_{1/2})^{-1}] \tag{1}$$

The HSA-FeP(3-MHis) showed an extraordinarily high O_2 binding affinity ($P_{1/2}$ = 0.2 Torr, 25 °C), which is 5-fold greater than that of HSA-FeP(His), which was close to the values of the relaxed-state Hb(α) and Mb (Table 1) (*18–20*). However, replacement of the 3-methyl-L-histidine moiety in FeP(3-MHis) by the 1-methyl-L-histidine isomer [FeP(1-MHis)] caused a 35-fold reduction of O_2 binding affinity ($P_{1/2}$ = 7 Torr, 25 °C); the $P_{1/2}$ value of 22 Torr at 37 °C was almost identical to that of human RBC (27 Torr) (*21*).

Laser flash photolysis experiments gave the association and dissociation rate constants for O_2 (k_{on}, k_{off}) (*5, 11*). The time course of the absorption change accompanying the O_2 recombinations to HSA-FeP(1-MHis) and HSA-FeP(3-MHis) after the laser pulse irradiation comprised two phases of first-order kinetics (Figure S1a). The decay was fitted by a double exponential profile, which provided the fast and slow association rate constants of O_2 (k_{on} and k'_{on}) (Table 1). This behavior was similarly observed in HSA-

[2] Abbreviations: FeP(His), 2-{(4-methoxycarbonyl-histidinamidobutanoyloxy)methyl}-5,10,15,20-tetrakis{α,α,α,α-o-(1′-methylcyclohexanamido)phenyl}porphinatoiron; FeP(1-MHis), 2-[{4-methoxycarbonyl(1-methyl)histidinamidobutanoyloxy}methyl]-5,10,15,20-tetrakis{α,α,α,α-o-(1′-methylcyclohexanamido)phenyl}porphinatoiron; FeP(3-MHis), 2-[{4-methoxycarbonyl(3-methyl)histidinamidobutanoyloxy}methyl]-5,10,15,20-tetrakis{α,α,α,α-o-(1′-methylcyclohexanamido)phenyl}porphinatoiron.

Table 1. O_2 Binding Parameters of Human Serum Albumin Hybrid with Iron(II) Porphyrin Bearing a Methyl-L-Histidine Isomer in PBS Solution (pH 7.4) at 25 °C

HSA-iron(II) porphyrin	k_{on} (M^{-1} s^{-1})	k'_{on} (M^{-1} s^{-1})	k_{off} (s^{-1})	k'_{off} (s^{-1})	$P_{1/2}$[a] (Torr)
HSA-FeP(1-MHis)	5.4×10^7	8.1×10^6	620	93	7 (22)
HSA-FeP(3-MHis)	5.4×10^7	6.8×10^6	20	2.4	0.2 (1)
HSA-FeP(His)[b]	5.4×10^7	8.8×10^6	89	14	1 (3)
Hb(α) (R-state)[c]	3.3×10^7[d]		13[e]		0.24
Mb[f,g]	1.4×10^7		12		0.51
RBC[h]					8 (27)

[a] At 37 °C in parenthesis. [b] Ref *11*. [c] Human Hb α-subunit. [d] In 0.1 M phosphate buffer (pH 7.0, 21.5 °C); ref *18*. [e] In 10 mM phosphate buffer (pH 7.0, 20 °C); ref *19*. [f] Sperm whale Mb. [g] In 0.1 M phosphate buffer (pH 7.0, 20 °C); ref *20*. [h] Human red blood cell suspension. In isotonic buffer (pH 7.4); ref *21*.

Table 2. O_2 Binding Parameters of Iron(II) Porphyrin Bearing a Methyl-L-Histidine in Toluene Solution at 25 °C

iron(II) porphyrin	k_{on} (M^{-1} s^{-1})	k_{off} (s^{-1})	$P_{1/2}$ (Torr)
FeP(1-MHis)	9.8×10^7	3.5×10^4	27
FeP(3-MHis)	1.6×10^8	5.2×10^2	0.3
FeP(His)[a]	2.0×10^8	4.3×10^3	1.7

[a] In benzene solution, ref *17*.

FeP(His) and HSA-FeP(2-MIm) (*11*). It has been interpreted that the O_2 associations to the iron(II) porphyrins in HSA were affected by microenvironments around the accommodation site (steric hindrance of the amino acid residue and difference in polarity) (*22*). The kinetic data indicated that the low O_2 binding affinity of HSA-FeP(1-MHis) is predominantly manifested in the high O_2 dissociation rate constant (Table 1).

To evaluate the significant differences in FeP(1-MHis) and FeP(3-MHis), their O_2 binding parameters in toluene solution were determined. The UV–vis absorption spectra of ferrous FeP(1-MHis) (λ_{max}, 440, 542, 563 nm) and FeP(3-MHis) (λ_{max}, 440, 540, 565 nm) under an N_2 atmosphere showed the formation of a five-N-coordinate high spin complex. Dioxygenation was sufficiently stable and reversible at 25 °C depending on O_2 partial pressure. The recombination process of O_2 to the iron(II) porphyrins in toluene solution after laser flash photolysis was fitted by a single exponential (Figure S1b). FeP(3-MHis) exhibited a 6-fold higher O_2 binding affinity ($P_{1/2}$ = 0.3 Torr, 25 °C) compared to that of FeP(His) (Table 2) (*11*). Kinetically, this high O_2 binding affinity is attributable to the low O_2 dissociation rate. The high σ-basicity of 3-methyl-L-histidine (p*K*a, 6.48) in comparison to that of histidine (p*K*a, 6.00) (*23*) can serve to increase the electron density on the central metal, which would enhance O_2 uptake. FeP(1-MHis) showed a 90-fold lower O_2 affinity ($P_{1/2}$ = 27 Torr, 25 °C) relative to FeP(3-MHis), which is mainly caused by the high k_{off} value, as observed in aqueous media. In general, the steric hindrance to the axial base coordination deforms the six-coordinate structure of the iron(II) porphyrin and increases the O_2 dissociation rate constant (*1, 2*). For example, the 1,2-DMIm complexes showed 11–58-fold higher k_{off} values than the 1-MIm ligated complexes (*3, 5, 24*).

We simulated the geometry of histidine coordination in dioxygenated porphyrin.[3] The bond angle of N(por)−Fe−N(His) was 90° for FeP(His) and FeP(3-MHis), but it was markedly tilted in FeP(1-MHis) (a maximum of 98°) (Figure 3). On the basis of these results, it can be concluded that the axial coordination of 1-methyl-L-histidine to the central iron is

[3] The esff forcefield simulation was performed using an Insight II system (Molecular Simulations Inc.). The structure was generated by alternative minimizations and annealing dynamic calculations from 1,000 to 100 K.

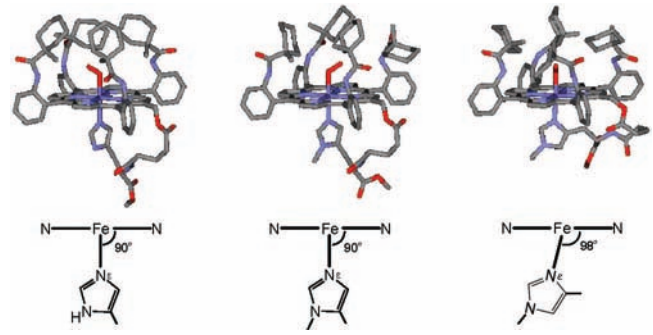

Figure 3. Simulated structures of the O_2 adduct complexes of FeP(His), FeP(3-MHis), and FeP(1-MHis). In FeP(His) and FeP(3-MHis), the bond angles of N(por)−Fe−N(His) were 90°, but 98° in FeP(1-MHis) because of the steric interaction between the 4-methylene group of histidine and the porphyrin plane. Molecular dynamics and minimization (force field: esff) were performed using an Insight II system. Hydrogens were omitted for clarification.

restrained by the steric interaction between the 4-methylene group of the histidine and the porphyrin plane, which significantly increased the dissociation rate of O_2.

In conclusion, a variation in the methyl-L-histidine isomer covalently linked at the porphyrin periphery changed the O_2 binding affinity of the iron(II) porphyrin by a factor of 90 in toluene. This difference is greater than the previous finding for a picket-fence porphyrin (2-MIm) complex-bound O_2 with a 70-fold lower affinity than that of the 1-MIm complex (*4*). The increased k_{off} value of FeP(1-MHis) is caused by steric repulsion between the 4-methylene group of histidine and the porphyrin plane. In aqueous media, the O_2 binding ability of HSA incorporating the iron(II) porphyrin can also be modulated by structural isomerization of the axial methyl-L-histidine. HSA-FeP(1-MHis) with a $P_{1/2}$ value similar to that of human RBC under physiological conditions can become a promising O_2 carrier, which satisfies both the biocompatibility and clinical requirements for efficient O_2 delivery to the tissue cells.

ACKNOWLEDGMENT

This work was partially supported by Grant-in-Aid for Young Scientists (B) (No. 18750156) from JSPS, PRESTO from JST, and Health Science Research Grants from MHLW, Japan.

Supporting Information Available: Experimental details, absorption maximum wavelengths of the iron(II) porphyrins, and absorption change accompanying O_2 rebinding to FeP(3-MHis) and HSA-FeP(3-MHis) after laser flash photolysis. This material is available free of charge via the Internet at http://pubs.acs.org.

LITERATURE CITED

(1) Collman, J. P., Boulatov, R., Sunderland, C. J., and Fu, L. (2004) Functional analogues of cytochrome c oxidase, myoglobin, and hemoglobin. *Chem. Rev. 104*, 561–588.
(2) Collman, J. P., and Fu, L. (1999) Synthetic Models for Hemoglobin and Myoglobin. *Acc. Chem. Res. 32*, 455–463.
(3) Momenteau, M., and Reed, C. A. (1994) Synthetic heme-dioxygen complexes. *Chem. Rev. 94*, 659–698.
(4) Collman, J. P., Brauman, J. I., Doxsee, K. M., Halberd, T. M., and Suslick, K. S. (1978) Model compounds for the T state of hemoglobin. *Proc. Natl. Acad. Sci. U.S.A. 75*, 564–568.
(5) Collman, J. P., Brauman, J. I., Iverson, B. L., Sessler, J. L., Morris, R. M., and Gibson, Q. H. (1983) O_2 and CO binding to iron(II) porphyrins: A comparison of the "picket fence" and "pocket" porphyrins. *J. Am. Chem. Soc. 105*, 3052–3064.

(6) Collman, J. P., Brauman, J. I., Doxsee, K. M., Sessler, J., Morris, R. M., and Gibson, Q. H. (1983) Effect of axial base on dioxygen and carbon monoxide affinities of iron(II) porphyrins. Imidazole vs. pyridine. *Inorg. Chem. 22*, 1427–1432.

(7) Chang, C. K., and Traylor, T. G. (1975) Kinetics of oxygen and carbon monoxide binding to synthetic analogs of the myoglobin and hemoglobin active sites. *Proc. Nat. Acad. Sci. U.S.A. 72*, 1166–1170.

(8) Linard, J. E., Ellis, P. E., Jr., Budge, J. R., Jones, R. D., and Basolo, F. (1980) Oxygenation of iron(II) and cobalt(II) "capped" porphyrins. *J. Am. Chem. Soc. 102*, 1896–1904.

(9) Momenteau, M., Mispelter, J., Loock, B., and Lhoste, J.-M. (1985) Both-faces hindered porphyrins. Part 3. Synthesis and characterization of internally five-co-ordinated iron(II) basket handle porphyrins derived from 5,10,15,20-tetrakis(o-aminophenyl)porphyrin. *J. Chem. Soc., Perkin Trans.1* 221–231.

(10) Lavalette, D., Tetreau, C., Mispelter, J., Momenteau, M., and Lhoste, J.-M. (1984) Linear free-energy relationships in binding of oxygen and carbon monoxide with heme model compounds and heme proteins. *Eur. J. Biochem. 145*, 555–565.

(11) Komatsu, T., Matsukawa, Y., and Tsuchida, E. (2002) Effect of heme structure on O_2-binding properties of human serum albumin-heme hybrids: Intramolecular histidine coordination provides a stable O_2-adduct complex. *Bioconjugate Chem. 13*, 397–402.

(12) Komatsu, T., Huang, Y., Yamamoto, H., Horinouchi, H., Kobayashi, K., and Tsuchida, E. (2004) Exchange transfusion with synthetic oxygen-carrying plasma protein "albumin-heme" into an acute anemia rat model after seventy-percent hemodilution. *J. Biomed. Mater. Res. 71A*, 644–651.

(13) Sax, N. I., and Lewis, R. J. (1987) *Hazardous Chemicals Desk Reference*, Van Nostrand Reinhold Company, Inc., New York.

(14) Van der Heijden, A., Peter, H. G., and Van der Oord, A. H. A. (1971) Coupling of L-histidine methyl ester and L-histidine-containing peptide esters to ferric protoporphyrin IX chloride. *J. Chem. Soc. D* 369–370.

(15) Warme, P. K., and Hager, L. P. (1970) Heme sulfuric anhydrides. I. Synthesis and reactions of mesoheme sulfuric anhydride. *Biochemistry 9*, 1599–1606.

(16) Momenteau, M., Rougee, M., and Loock, B. (1976) Five-coordinate iron-porphyrin as a model for the active site of hemoproteins. Characterization and coordinating properties. *Eur. J. Biochem. 71*, 63–76.

(17) Komatsu, T., Matsukawa, Y., Miyatake, K., and Tsuchida, E. (2001) O_2-adduct complex of meso-tetrakis(α,α,α,α-o-pivalamidophenyl)porphinatoiron(II) with an intramolecularly coordinated proximal histidine. *Chem. Lett.* 668–669.

(18) Gibson, Q. H. (1970) The reaction of oxygen with hemoglobin and the kinetic basis of the effect of salt on binding of oxygen. *J. Biol. Chem. 245*, 3285–3288.

(19) Olson, J. S., Andersen, M. E., and Gibson, Q. H. (1971) The Dissociation of the first oxygen molecule from some mammalian oxyhemoglobins. *J. Biol. Chem. 246*, 5919–5923.

(20) Rohlfs, R., Mathews, A. J., Carver, T. E., Olson, J. S., Springer, B. A., Egeberg, K. D., and Sligar, S. G. (1990) The effects of amino acid substitution at position E7 (residue 64) on the kinetics of ligand binding to sperm whale myoglobin. *J. Biol. Chem. 265*, 3168–3176.

(21) Imai, K., Morimoto, H., Kotani, M., Watari, H., Hirata, W., and Kuroda, M. (1979) Studies on the function of abnormal hemoglobins I. An improved method for automatic measurement of the oxygen equilibrium curve of hemoglobin. *Biochim. Biophys. Acta 200*, 189–1967.

(22) Komatsu, T., Matsukawa, Y., and Tsuchida, E. (2000) Kinetics of CO and O_2 binding to human serum albumin-heme hybrid. *Bioconjugate Chem. 11*, 772–776.

(23) Lide, R. D., Eds. (2000) *CRC Handbook of Chemistry and Physics*, 81st ed., Section 7, CRC Press, Boca Raton, FL.

(24) Momenteau, M., Loock, B., Tetreau, C., Lavalette, D., Croisy, A., Schaeffer, C., Huel, and Lhoste, J.-M. (1987) Synthesis and characterization of a new series of iron(II) single-face hindered porphyrins. Influence of central steric hindrance upon carbon monoxide and oxygen binding. *J. Chem. Soc., Perkin Trans. 2* 249–257.

BC700400N

Small-Molecule Reagents for Cellular Pull-Down Experiments

Xiang Wang, Brandon S. Imber, and Stuart L. Schreiber*

Howard Hughes Medical Institute, Broad Institute of Harvard and MIT, 7 Cambridge Center, Cambridge, Massachusetts 02142, and Department of Chemistry and Chemical Biology, Harvard University, 12 Oxford Street, Cambridge, Massachusetts 02138. Received August 7, 2007; Revised Manuscript Received December 1, 2007

Affinity purification of interacting proteins from cellular extracts is a powerful technique for identifying the cellular targets of small molecules. Affinity matrix-based small-molecule reagents are usually prepared by conjugating small molecules of interest to a solid support such as agarose. This protocol describes an efficient and robust method to immobilize small molecules containing a primary alcohol, a common functional group in small molecules, especially in small molecules prepared using diversity-oriented synthesis. This method comprises one element of a systematic approach to the target identification problem in chemical biology.

Small molecules that modulate protein function are valuable tools for studying cell circuitry, among others (*1*, *2*). These small-molecule probes are increasingly being identified in cell-based, phenotypic screens (*3*). This discovery route requires effective methods for identifying cellular targets, and the technique of affinity chromatography (*4*), which requires small-molecule-based affinity reagents, has proven to be the most effective approach to accomplish this goal (*5*, *6*).

Many methods have been developed to attach small molecules covalently to beaded agarose containing such functional groups as acids, amines, and so forth (*7*). A complementary pair of functional groups on the beads and small molecules is required for selective immobilization. Recently, Finn and co-workers have shown that small molecules bearing a terminal alkyne or azide can be covalently attached to agarose using a Cu(I)-catalyzed 1,3-dipolar cycloaddition reaction (*8*) with high efficiency and specificity (*9*). Amino- or hydroxyl-containing small molecules are extremely common in modern collections of compounds used in high-throughput screening. Whereas amino-containing small molecules are routinely conjugated to beaded agarose for use in affinity chromatography, hydroxyl-containing small molecules have proven to be more challenging. Although methods exist to immobilize hydroxyl-containing ligands using oxiranes (*10*) or vinyl sulfones (*11*), these suffer from either the poor reactivity of oxiranes or the poor stability of the sulfones.

Diversity-oriented synthesis (DOS, Figure 1) yields small molecules well-suited for the discovery of probes, the optimization of them, and the eventual efficient manufacturing of the optimized variants (*12*, *13*). In our own studies, we have incorporated a hydroxymethyl group into *every* product, resulting from our diversity syntheses. This functional group is poised for further modifications, such as immobilization on the glass surface for small-molecule microarray screens (*14*), covalent modification with biasing elements for targeting classes of proteins (*15*), and, as described here, conjugation to beaded agarose for the identification of cellular targets.

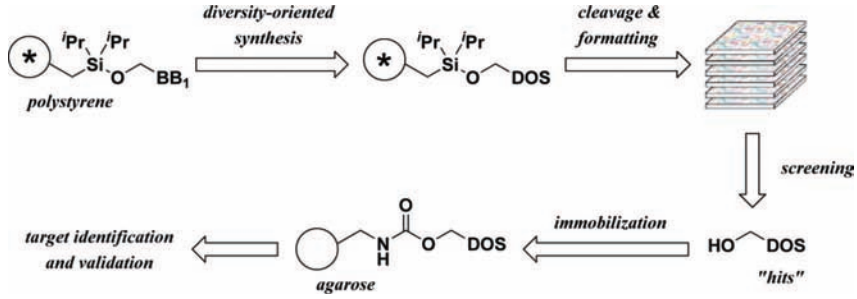

Figure 1. General strategy for identifying the targets of biologically active small molecules.

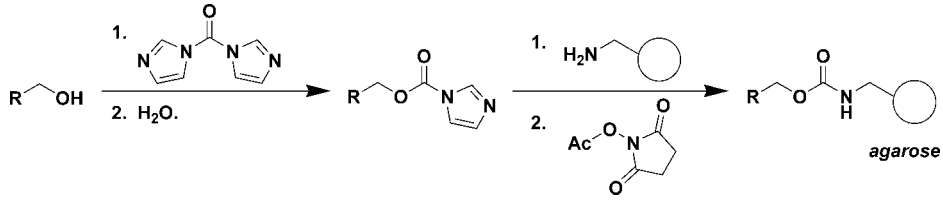

Figure 2. Scheme for immobilizing primary alcohol-containing small molecules on beaded agarose.

* To whom correspondence should be addressed. Phone: (617) 324-9603. Fax: (617) 324-9601. E-mail: stuart_schreiber@harvard.edu.

10.1021/bc700297j CCC: $40.75 © 2008 American Chemical Society
Published on Web 01/15/2008

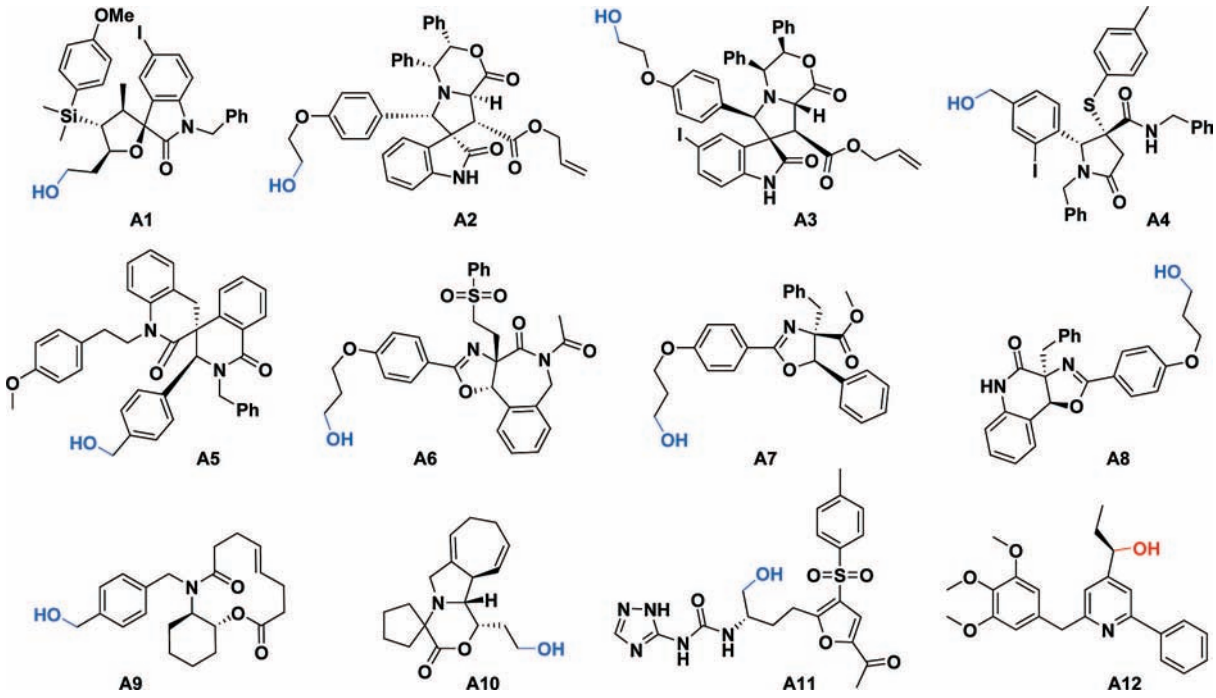

Figure 3. Representative immobilized alcohol-containing small molecules.

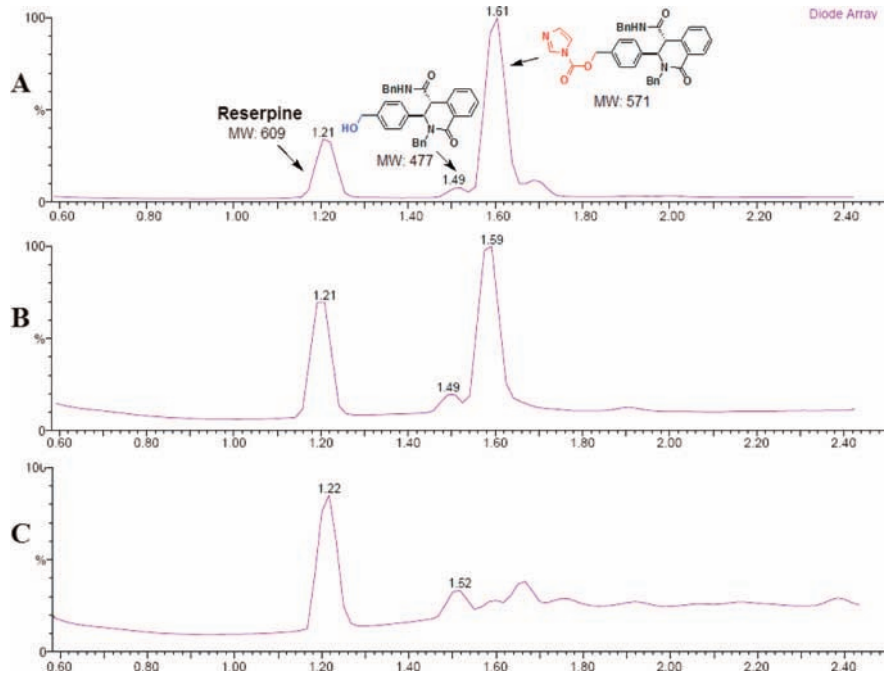

Figure 4. Determination of the loading efficiency using HPLC-MS with reserpine as an internal standard. (A) LC trace of the mixed imidazolide and reserpine in DMF. (B) LC trace of the immobilization reaction mixture after incubation at room temperature for 2 days. (C) LC trace of the immobilization reaction mixture after incubation at 50 °C for 16 h. (a) HPLC method: 5–95% acetonitrile in water with 0.1% formic acid over 2.5 min. Diode array wavelength: 210–500 nm.

RESULTS AND DISCUSSION

Here, we report an efficient and robust method to immobilize hydroxyl-containing small molecules to beaded agarose. 1,1′-Carbonyldiimidazole (CDI *16*−*18*) reagent has been used to immobilize amino-containing small molecules (*19*). We recognized that the mixed imidazolide intermediate resulting from reaction of this reagent with hydroxyl-containing compounds is inert to most functional groups and stable to a wide range of solvents and temperatures. We reasoned that the resulting carbamate bond would be noncharged and highly stable under conditions used in cellular pull-downs, and thus well-suited for many target identification applications. Hence, we chose to use CDI to activate the hydroxyl-containing compounds. The resulting mixed imidazolide was immobilized on amino-containing beaded agarose after the excess CDI was quenched with water (Figure 2). The excess amine on the agarose surface was blocked by acetylation using *N*-acetoxysuccinamide.

This protocol has been used to synthesize dozens of primary alcohol-containing small molecules (see Figure 3 for representa-

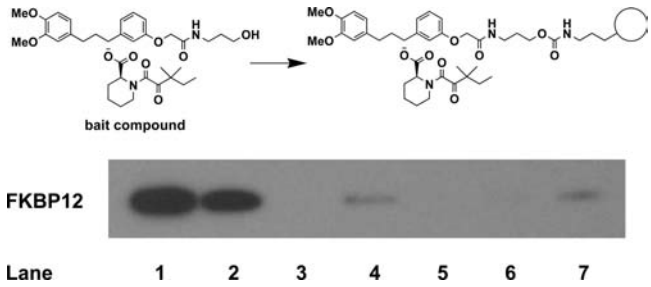

Figure 5. Immobilization of a compound known to bind immunophilin proteins and the affinity purification of FKBP12 from A549 whole cell lysate using the immobilized bait. In the Western blot, lane **1**, affinity-purified protein sample 1 using immobilized bait compound; lane **2**, affinity purified protein sample 2 using immobilized bait compound; lane **3**, affinity purified protein sample 3 using blocked blank beads; lane **4**, A549 whole cell lysate; lane **5**, residue cell lysate 1 after affinity purification using immobilized bait compound; lane **6**, residue cell lysate sample 2 after affinity purification using immobilized bait compound; lane **7**, residue cell lysate sample 3 after affinity purification using blocked blank beads.

tive molecules A1−A11) conjugated to beaded agarose with over 85% loading efficiency. Secondary alcohol-containing small molecules such as A12 (Figure 3) may also be conjugated to beaded agarose, albeit with significantly lower efficiency (<40%). The loading efficiency can be determined by high-performance liquid chromatography–mass spectroscopy (HPLC-MS) when a nonreactive small molecule is used as an internal standard. Figure 4 shows the typical LC trace before and after the conjugation reaction in the presence of reserpine. This protocol can tolerate a variety of functional groups, such as esters, amides, acids, phenols, tertiary alcohols, and so forth.

A small molecule known to bind members of the FKBP family of proteins (*20*) (scheme of Figure 5) was conjugated with carboxylink coupling gel using the protocol described above. The conjugate was next used to affinity purify a cellular target of this compound, FKBP12, from the lysate of A549 lung epithelial cells. Electrophoresis followed by Western immunoblotting experiments showed most of FKBP12 (lanes 1 and 2 of Figure 5) was retained by the affinity reagent. The blank beads did not pull down any FKBP12 protein (lane 3 of Figure 5).

In summary, we have developed an efficient and robust method to immobilized primary alcohol-containing small molecules to beaded agarose. Further optimization for secondary alcohols and applications of this method for the target identification of hit molecules derived from high-throughput screenings are in progress and will be reported in due course.

ACKNOWLEDGMENT

We thank the National Cancer Institute (2PO1 CA-78048) for support of this research, Drs. J. Shaw, A. Franz, C. Neumann, R. Looper, R. Mazitschek, N. Kumagai, D. Pizzirani, and Mr. B. Gray for donation of the compounds, and Drs. J. Yang and A. N. Koehler for helpful discussion. S.L.S. is an Investigator of Howard Hughes Medical Institute at the Broad Institute of Harvard and MIT.

Supporting Information Available: Experimental procedures. This material is available free of charge via the Internet at http://pubs.acs.org.

Note Added after ASAP Publication: This paper was published ASAP on January 15, 2008 with an incomplete Acknowledgment. The correct version reposted on February 8, 2008.

LITERATURE CITED

(1) Schreiber, S. L. (2003) The small-molecule approach to biology: chemical genetics and diversity-oriented organic synthesis make possible the systematic exploration of biology. *Chem. Eng. News 81*, 51–61.
(2) Schreiber, S. L. (2005) Small Molecules: The missing link in the central dogma. *Nat. Chem. Biol. 1*, 64–66.
(3) Khersonsky, S. M., and Chang, Y. T. (2004) Strategies for facilitated forward chemical genetics. *ChemBioChem 5*, 903–908.
(4) Cuatrecasas, P. (1972) Affinity chromatography and purification of the insulin receptor of liver cell membranes. *Proc. Natl. Acad. Sci. U.S.A. 69*, 1277–1281.
(5) Harding, M. W., Galat, A., Uehling, D. E., and Schreiber, S. L. (1989) A receptor for the immunosuppressant FK506 is a *cis-trans* peptidyl-prolyl isomerase. *Nature (London) 341*, 758.
(6) Taunton, J., Hassig, C. A., and Schreiber, S. L. (1996) A mammalian histone deacetylase related to the yeast transcriptional regulator Rpd3p. *Science 272*, 408–411.
(7) Carlsson, J., Janson, J.-C., and Sparrman, M. (1998) *Protein Purification* (JansonJ.-C., and Ryden, L., Eds.), pp 335–442.
(8) Huisgen, R (1984) 1,3-Dipolar cycloaddition-introduction, survey, mechanism, In *1,3-Dipolar Cycloaddition Chemistry* (Padwa, A., Ed.) pp 1–176, Wiley, New York.
(9) Punna, S., Kaltgrad, E., and Finn, M. G. (2005) "Clickable" agarose for affinity chromatography. *Bioconjugate Chem. 16*, 1536–1541.
(10) Lowe, C. R. L. (1974) *Affinity Chromatography*, p 28, John Wiley, New York.
(11) Porath, J. (1974) *Methods Enzymology* (Jakoby, B., and Wilchek, M., Eds.) pp 34−30, Vol *34*, Academic Press, New York.
(12) Burke, M. D., and Schreiber, S. L. (2004) A planning strategy for diversity-oriented synthesis. *Angew. Chem., Int. Ed. Engl. 43*, 46–58.
(13) Franz, A. K., Dreyfuss, P. D., and Schreiber, S. L. (2007) Synthesis and cellular profiling of diverse organosilicon small molecules. *J. Am. Chem. Soc. 129*, 1020–1021.
(14) MacBeath, G., Koehler, A. N., and Schreiber, S. L. (1999) Printing small molecules as microarrays and detecting protein-ligand interactions en masse. *J. Am. Chem. Soc. 121*, 7967–7968.
(15) Sternson, S. M., Wong, J. C., Grozinger, C. M., and Schreiber, S. L. (2001) Synthesis of 7200 small molecules based on a substructural analysis of the histone deacetylase inhibitors trichostatin and trapoxin. *Org. Lett. 3*, 4239–4242.
(16) Staab, H. A. (1957) Reactive heterocyclic diamides of carbonic acid. *Ann. 609*, 75–83.
(17) Stollner, D., Scheller, F. W., and Warsinke, A. (2002) Activation of cellulose membranes with 1,1′-carbonyldiimidazole or 1-cyano-4-dimethylaminopyridinium tetrafluoroborate as a basis for the development of immunosensors. *Anal. Biochem. 304*, 157–165.
(18) Wu, X. Q., Wu, C., and He, R. Q. (2002) Immobilized earthworm fibrinolytic enzyme III-1 with carbonyldiimidazole activated-agarose. *Protein Pept. Lett. 9*, 75–80.
(19) Hearn, M. T. W. (1987) *Methods Enzymology* Mosbach, K., Ed. pp 102−117, Vol *135*, Part B.
(20) Keenan, T., et al. (1998) Synthesis and activity of bivalent FKBP12 ligands for the regulated dimerization of proteins. *Bioorg. Med. Chem. 6*, 1309–1335.

BC700297J

Lanthanide-Binding Tags with Unnatural Amino Acids: Sensitizing Tb^{3+} and Eu^{3+} Luminescence at Longer Wavelengths

Anne M. Reynolds, Bianca R. Sculimbrene, and Barbara Imperiali*

Departments of Chemistry and Biology, Massachusetts Institute of Technology, 77 Massachusetts Avenue, Cambridge, Massachusetts 02139. Received November 19, 2007; Revised Manuscript Received February 1, 2008

Lanthanide-binding tags (LBTs) are small, genetically encoded, versatile protein fusion partners that selectively bind lanthanide ions with high affinity. The LBT motif features a strategically positioned tryptophan residue that sensitizes Tb^{3+} luminescence upon excitation at 280 nm. Herein, we describe the preparation of new LBT peptides that incorporate unnatural amino acids in place of tryptophan, and which sensitize both Tb^{3+} and Eu^{3+} luminescence at lower energies. We also report the semisynthesis of proteins tagged with these new LBTs using native chemical ligation. This expands the scope of LBTs and will enable their wider use in luminescence applications.

Understanding the localization and fate of proteins *in vivo* is a key research objective in cell biology. Toward this end, fluorescence spectroscopy has become a widely used technique, with much effort devoted toward the development and incorporation of suitable fluorophores into biological molecules. Lanthanide ions represent attractive complements to the more commonly used organic fluorophores, as these species exhibit long-lived (millisecond) luminescence lifetimes, large Stokes shifts, unpolarized luminescence, and sharp emission peaks. Due to these advantages, the use of lanthanide-based probes is becoming more common in applications such as luminescence spectroscopy (*1, 2*) and luminescence resonance energy transfer (LRET) (*3, 4*). To overcome the inherently low absorption of lanthanide ions, researchers have developed sensitizing fluorophores that, upon excitation, transfer energy to the lanthanide (*5, 6*). However, few general methods to incorporate lanthanide-based probes into proteins exist, and these are generally limited to substitution of lanthanides at native calcium-binding sites (*7–9*), incorporation of unnatural amino acids with side-chain chelators (*10*), and covalent labeling of reactive side chains using lanthanide chelates (*11, 12*).

Recent work in our laboratory has been focused on the development of lanthanide-binding tags (LBTs), which are short peptides (17–20 amino acids) that selectively and avidly bind lanthanide ions (*13–16*). Originally based on EF-hand Ca^{2+}-binding loops, LBTs have been optimized for Tb^{3+} binding through multiple rounds of split-and-pool peptide library synthesis (*14, 16*). In these motifs, the indole ring of a strategically positioned tryptophan residue sensitizes Tb^{3+} luminescence (*17*). These multitasking tags have been appended to various proteins and used to detect peptide–protein interactions using LRET (*18*). The paramagnetic lanthanides have also been used to aid in the determination of protein structure by NMR spectroscopy (*19, 20*), and the heavy atoms provide scattering power for phasing X-ray crystallographic data (*21*). While clearly advantageous for these *in vitro* studies, the UV light necessary for tryptophan excitation (280 nm) is not ideal in cellular systems (*22*), and the ability to sensitize only Tb^{3+} limits their more general use in luminescence applications. Herein, we report the development of new LBTs that incorporate non-natural amino acids as sensitizers, which feature lower-energy excitation and sensitize Eu^{3+} as well as Tb^{3+} luminescence.

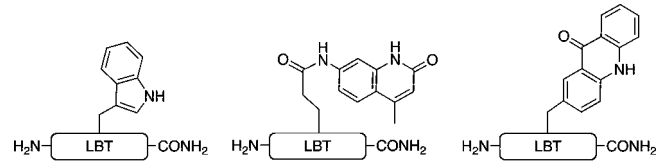

H_2N-FITDNNDG**X**IEGDELLLEEG-$CONH_2$

Figure 1. Sequences of peptides LBT(Trp), LBT(cs124), and LBT(Acd), where the side chain of the amino acid denoted **X** is illustrated.

In these studies, we targeted two unnatural amino acids as potential lanthanide sensitizers in LBTs. The first is based on carbostyril 124 (cs124), which has been used as a sensitizer of both Tb^{3+} and Eu^{3+} luminescence in the context of polyaminocarboxylate chelates (*23, 24*). The second is based on the acridone (Acd) fluorophore, which has been previously used to sensitize Eu^{3+} luminescence in small molecules (*25–28*). These fluorophores were selected because they are known to sensitize lanthanide luminescence, making them attractive initial targets in the context of LBTs, and they are excited at lower energies (337 and 390 nm, respectively). Finally, the acridone fluorophore is highly photostable, making it particularly attractive for potential *in vivo* applications. For our studies, both of the sensitizers were incorporated into amino acid building blocks for use in solid-phase peptide synthesis (SPPS). The cs124 moiety was coupled to the side chain of glutamic acid via the aniline nitrogen (*29*), while the acridone-containing amino acid was prepared via a literature procedure (*30*). Both of the amino acids were N_α-Fmoc-protected and incorporated into LBT peptides at the optimal position for sensitizing lanthanide luminescence *via* standard SPPS (Figure 1) (*17*). The parent LBT containing tryptophan was also prepared for comparison (*16*).

Luminescence spectra of all three LBT peptides in the presence of lanthanide ions are illustrated in Figure 2. LBT(cs124) sensitizes Tb^{3+} luminescence upon excitation at 337 nm, and the intensity of the emission at 544 nm is higher than that of LBT(Trp) (Figure 2a). The presence of the new sensitizer does not significantly alter the Tb^{3+} affinity, as the dissociation constant (K_D), determined by direct titration, is 34 nM (Table 1) compared to 19 nM for LBT(Trp) (*16*). LBT(cs124) also

* To whom correspondence should be addressed. Tel: 1-617-253-1838. Fax: 1-617-452-2419 . E-mail: imper@mit.edu.

10.1021/bc700426c CCC: $40.75 © 2008 American Chemical Society
Published on Web 02/15/2008

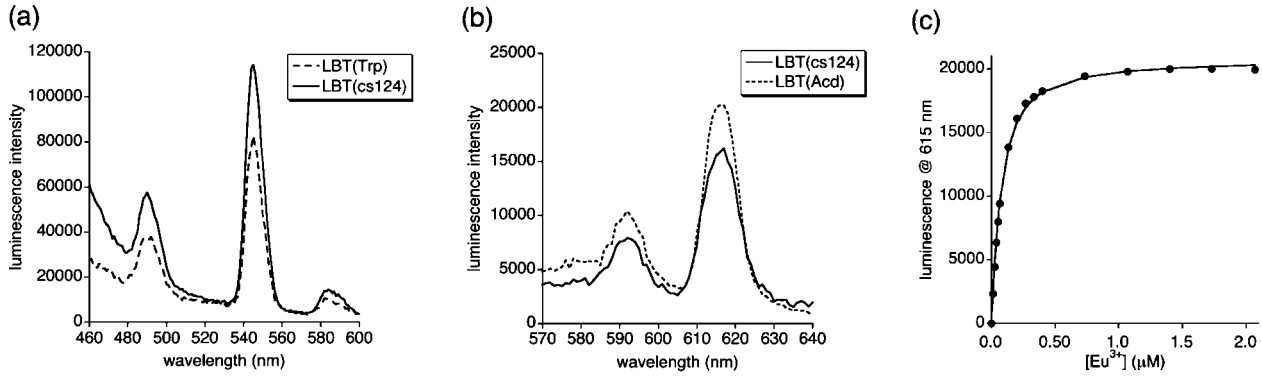

Figure 2. (a) Emission spectra of LBTs (50 nM) in the presence of Tb^{3+} (200 nM) with excitation at 280 nm for LBT(Trp) (---) and 337 nm for LBT(cs124) (—). (b) Emission spectra of LBTs (50 nM) in the presence of Eu^{3+} (200 nM) with excitation at 337 nm for LBT(cs124) (—) and 390 nm for LBT(Acd) (••••). (c) Titration of LBT(Acd) (50 nM) with Eu^{3+} (•), and fit derived from SPECFIT/32 (—).

Table 1. Comparison of Ln^{3+} Binding Affinities of LBT Peptides and Tagged Proteins[a]

construct	$K_D(Tb^{3+})$	$K_D(Eu^{3+})$
LBT(Trp)	19 nM[b]	
LBT(cs124)	34 ± 3 nM	10 ± 2 nM
LBT(Acd)		52 ± 2 nM
LBT(Trp)-Crk(SH2)	35 ± 5 nM	
LBT(cs124)-Crk(SH2)	46 ± 12 nM	69 ± 4 nM
LBT(Acd)-Crk(SH2)		54 ± 17 nM

[a] Titrations performed at a peptide/protein concentration of 50 nM. [b] From ref (*16*).

effectively sensitizes Eu^{3+} luminescence, and titration with Eu^{3+}provides a dissociation constant of 10 nM. This slightly tighter binding of Eu^{3+} versus $Tb^{3+}$was unexpected based on our previous observations that a similar LBT sequence binds lanthanides other than Tb^{3+} with lower affinity (*15*), though the difference is not large between these two lanthanide ions. The cs124-containing amino acid thus allows for the synthesis of new LBTs that sensitize both Tb^{3+} and Eu^{3+} luminescence. The only disadvantage of the cs124 sensitizer in this context is the sensitivity of the fluorophore to photobleaching. Under constant illumination, the luminescence intensities decrease 10–15% over 60 s, but remain nearly constant when O_2 has been removed (Figure S1). Additionally, the initial luminescence intensities nearly double when deoxygenated buffers are used. We therefore used deoxygenated buffers in all experiments with this sensitizer.

LBT(Acd) also sensitizes Eu^{3+} luminescence upon excitation at 390 nm, with a higher overall luminescence intensity than LBT(cs124) (Figure 2b). The spectrum was collected using a 570 nm long-pass filter to reduce interference from acridone fluorescence. The dissociation constant, determined by direct titration of LBT(Acd) with Eu^{3+}, is 52 nM (Figure 2c), which is only slightly weaker than the other LBTs (Table 1). No luminescence was observed in the presence of other lanthanides including Nd^{3+}, Tb^{3+}, Er^{3+}, Tm^{3+}, and Yb^{3+}. Finally, because the acridone moiety is extremely photostable (Figure S1), LBTs featuring this sensitizer such as LBT(Acd) will be extremely useful in applications where continuous irradiation is required; this characteristic was also reported in previous studies in which the acridone amino acid was used as a fluorophore (*31*).

As is the case for other lanthanide-based probes, the luminescence intensities of these new LBTs are lower than typical organic fluorophores, with detection limits in the low-nanomolar range in the case of the peptides sensitizing Eu^{3+} and the picomolar range for peptides sensitizing Tb^{3+}. However, the long-lived lanthanide luminescence provides the ability to perform time-gated experiments that minimize background autofluorescence (*1, 2*), increasing the overall sensitivity.

With these promising results, we next targeted the assembly of full-length proteins tagged with the new LBTs. We chose the SH2 domain of the Crk adaptor protein as the test case, as this is a protein that has been previously tagged with LBTs for LRET experiments (*18*). While several methods exist for incorporating unnatural amino acids into proteins (*32, 33*), we chose to prepare the LBT-tagged proteins *via* semisynthesis using native chemical ligation (NCL) (*34*). In this approach, one fragment bearing a C-terminal thioester is reacted with a second fragment containing an N-terminal cysteine residue. Reversible thioester exchange leads to an S-to-N acyl rearrangement to form a native amide bond. Using the NCL strategy, the desired LBT can be appended to the N-terminus of Crk(SH2), which requires the peptide to be prepared with a C-terminal thioester and the protein to be expressed with an N-terminal cysteine.

Toward this end we synthesized LBTs containing either tryptophan or the unnatural amino acids at the sensitizing position on highly acid-labile TGT resin. This allows the completed peptides to be released from the resin using 0.5% TFA in CH_2Cl_2, while leaving the side-chain protecting groups intact (Figure S2). The free carboxyl termini were then coupled to benzyl mercaptan to generate the protected thioester peptides (*35, 36*). The side-chain protecting groups were removed under standard cleavage conditions to provide the LBT-thioesters, which were purified by reverse-phase HPLC and confirmed by ESI-MS.

Crk(SH2) was overexpressed in *E. coli* as a GST fusion protein construct with a tobacco etch virus (TEV) protease recognition site (ENLYFQC) (*37*), such that proteolytic cleavage affords the desired protein with an N-terminal Cys residue (Figure 3a). After purification on Glutathione Sepharose and subsequent TEV cleavage, the appropriate peptide thioester was added directly to the crude reaction mixture along with sodium 2-mercaptoethanesulfonate (MESNA, 150 mM) to facilitate rapid thioester exchange. From gel electrophoresis analysis, the ligations proceeded to 80–90% completion, and did not progress further after 16 h (Figure 3b). The excess thiol and peptide were removed by dialysis, while the GST and His_6-tagged TEV were removed with Glutathione Sepharose and Ni-NTA agarose, respectively. The LBT-tagged proteins were isolated with >90% purity, with a small amount of unligated protein as the major byproduct.

An advantage of the new sensitizers, particularly in the case of Acd, is that they can be used to visualize the tagged proteins. For example, visualization of an SDS-PAGE gel on a shortwave UV transilluminator (300 nm) reveals a very weak fluorescence signal from the tryptophan residues in LBT(Trp)-Crk(SH2), a stronger signal from the cs124 moiety in LBT(cs124)-Crk(SH2), and very intense fluorescence from the acridone moiety in

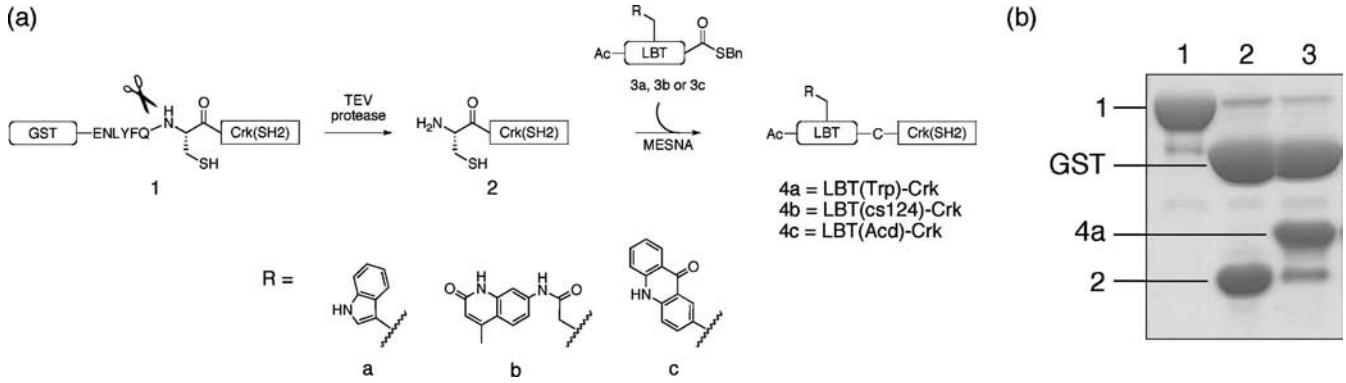

Figure 3. (a) Semisynthesis of LBT-tagged Crk(SH2) proteins. (b) Coomassie-stained SDS-PAGE gel showing GST-TEV-Crk(SH2) (lane 1), products of TEV cleavage (lane 2), and products of NCL with peptide 3a (lane 3). Similar results were observed in the semisynthesis of 4b and 4c.

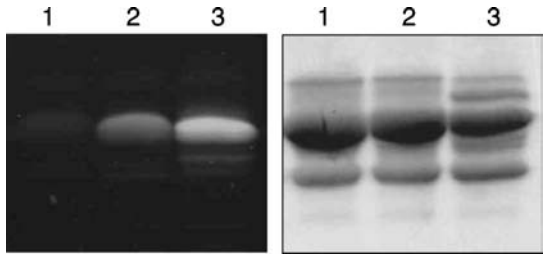

Figure 4. SDS-PAGE gel of semisynthetic LBT-tagged Crk(SH2) proteins, visualized on a transilluminator (300 nm, left), then stained with Coomassie Brilliant Blue (right). Lane 1 = LBT(Trp)-Crk(SH2); Lane 2 = LBT(cs124)-Crk(SH2); Lane 3 = LBT(Acd)-Crk(SH2).

LBT(Acd)-Crk(SH2) (Figure 4). Staining the same gel with Coomassie Brilliant Blue reveals that all proteins are present in approximately the same quantities. The emission of the acridone amino acid was detected with as little as 4.5 μg of protein and is comparable to detection of protein with the Coomassie stain. This provides a simple method for monitoring the ligations using SDS-PAGE using standard laboratory equipment; the sensitivity could likely be significantly improved by using a high-tech imaging instrument.

The luminescence properties of the new LBTs were quite similar in the context of the full proteins, where LBT(Trp)-Crk(SH2) sensitizes Tb^{3+} luminescence, LBT(cs124)-Crk(SH2) sensitizes both Tb^{3+} and Eu^{3+} luminescence, and LBT(Acd)-Crk(SH2) sensitizes only Eu^{3+} luminescence. The trends in overall luminescence intensities are the same, with cs124 being brighter than tryptophan for Tb^{3+} and acridone being brighter than cs124 for Eu^{3+} (Figure S3). Titrations revealed that the binding constants for the respective lanthanides are all in the low nanomolar range and are similar to those of the peptides (Table 1).

An important feature of LBTs is that water molecules are completely excluded from the inner coordination sphere of the bound lanthanide (*15*). This is important for the luminescence properties, as bound water molecules lead to luminescence quenching via energy transfer to the O−H bonds. To ensure that the change of sensitizer and lanthanide has not affected this coordination, luminescence decay experiments were performed in varying ratios of H_2O and D_2O. The luminescence lifetimes obtained from these decay experiments were used to calculate the number of water molecules, q, bound to Eu^{3+} in the new LBT-proteins using a literature procedure (*38*, *39*). The results provided q values of 0.006 for LBT(Acd)-Crk(SH2) and −0.06 for LBT(cs124)-Crk(SH2). (Uncertainties in q values are estimated to be ±0.5, owing to errors in the measured luminescence decay rates and the calculated proportionality constants (*39*).) These results provide further evidence that the coordination environment around Eu^{3+} is similar to that for Tb^{3+} in the optimized LBTs studied to date.

In summary, we have developed LBTs featuring two new sensitizers that are excited at lower energy and sensitize luminescence of Tb^{3+} and Eu^{3+}. Other advantageous photophysical properties of LBTs have not been affected, as these LBTs bind lanthanides tightly and exclude water molecules from their inner coordination spheres. We have established a general method for appending LBTs with lower-energy excitation to the N-terminus of a target protein using native chemical ligation and semisynthesis. This expands the utility of this class of lanthanide-based probes and current work is aimed at using them *in vivo*.

ACKNOWLEDGMENT

This research was supported by the NSF-CRC program (CHE-0304832). A.M.R. and B.R.S. acknowledge the NIH for Ruth L. Kirschstein National Research Service Awards. We also thank Prof. Martin Schwarz (University of Virginia) for a generous gift of the clone expressing the Crk SH2 domain, and Emi Sei for initial synthetic contributions.

Supporting Information Available: Figures S1−S3, plus detailed experimental procedures and characterization data. This material is available free of charge via the Internet at http://pubs.acs.org.

LITERATURE CITED

(1) Hemmilä, I., and Laitala, V. (2005) Progress in lanthanides as luminescent probes. *J. Fluoresc. 15*, 529–542.
(2) Bünzli, J.-C. G. (2006) Benefiting from the unique properties of lanthanide ions. *Acc. Chem. Res. 39*, 53–61.
(3) Selvin, P. R. (2000) The renaissance of fluorescence resonance energy transfer. *Nat. Struct. Biol. 7*, 730–734.
(4) Heyduk, T. (2002) Measuring protein conformational changes by FRET/LRET. *Curr. Opin. Biotechnol. 13*, 292–296.
(5) Gudgin Dickson, E. F., Pollak, A., and Diamandis, E. P. (1995) Time-resolved detection of lanthanide luminescence for ultrasensitive bioanalytical assays. *J. Photochem. Photobiol., B 27*, 3–19.
(6) Richardson, F. S. (1982) Terbium (III) and europium(III) ions as luminescent probes and stains for biomolecular systems. *Chem. Rev. 82*, 542–552.
(7) Barbieri, R., Bertini, I., Cavallaro, G., Lee, Y. M., Luchinat, C., and Rosato, A. (2002) Paramagnetically induced residual dipolar couplings for solution structure determination of lanthanide binding proteins. *J. Am. Chem. Soc. 124*, 5581–5587.

(8) Burroughs, S. E., Horrocks, W. D., Ren, H., and Klee, C. B. (1994) Characterization of the lanthanide ion-binding properties of calcineurin-B using laser-induced luminescence spectroscopy. *Biochemistry 33*, 10428–10436.

(9) Pidcock, E., and Moore, G. R. (2001) Structural characteristics of protein binding sites for calcium and lanthanide ions. *J. Biol. Inorg. Chem. 6*, 479–489.

(10) Becker, C. F. W., Clayton, D., Shapovalov, G., Lester, H. A., and Kochendoerfer, G. G. (2004) On-resin assembly of a linkerless lanthanide(III)-based luminescence label and its application to the total synthesis of site-specifically labeled mechanosensitive channels. *Bioconjugate Chem. 15*, 1118–1124.

(11) Purdy, M. D., Ge, P. H., Chen, J. Y., Selvin, P. R., and Wiener, M. C. (2002) Thiol-reactive lanthanide chelates for phasing protein X-ray diffraction data. *Acta Crystallogr., Sect. D 58*, 1111–1117.

(12) Rodriguez-Castaneda, F., Haberz, P., Leonov, A., and Griesinger, C. (2006) Paramagnetic tagging of diamagnetic proteins for solution NMR. *Magn. Reson. Chem. 44*, S10–S16.

(13) Franz, K. J., Nitz, M., and Imperiali, B. (2003) Lanthanide-binding tags as versatile protein coexpression probes. *ChemBioChem 4*, 265–271.

(14) Nitz, M., Franz, K. J., Maglathlin, R. L., and Imperiali, B. (2003) A powerful combinatorial screen to identify high-affinity terbium(III)-binding peptides. *ChemBioChem 4*, 272–276.

(15) Nitz, M., Sherawat, M., Franz, K. J., Peisach, E., Allen, K. N., and Imperiali, B. (2004) Structural origin of the high affinity of a chemically evolved lanthanide-binding peptide. *Angew. Chem., Int. Ed. 43*, 3682–3685.

(16) Martin, L. J., Sculimbrene, B. R., Nitz, M., and Imperiali, B. (2005) Rapid combinatorial screening of peptide libraries for the selection of lanthanide-binding tags (LBTs). *QSAR Comb. Sci. 24*, 1149–1157.

(17) Macmanus, J. P., Hogue, C. W., Marsden, B. J., Sikorska, M., and Szabo, A. G. (1990) Terbium luminescence in synthetic peptide loops from calcium-binding proteins with different energy donors. *J. Biol. Chem. 265*, 10358–10366.

(18) Sculimbrene, B. R., and Imperiali, B. (2006) Lanthanide-binding tags as luminescent probes for studying protein interactions. *J. Am. Chem. Soc. 128*, 7346–7352.

(19) Wöhnert, J., Franz, K. J., Nitz, M., Imperiali, B., and Schwalbe, H. (2003) Protein alignment by a coexpressed lanthanide-binding tag for the measurement of residual dipolar couplings. *J. Am. Chem. Soc. 125*, 13338–13339.

(20) Martin, L. J., Hahnke, M. J., Nitz, M., Wohnert, J., Silvaggi, N. R., Allen, K. N., Schwalbe, H., and Imperiali, B. (2007) Double-lanthanide-binding tags: design, photophysical properties, and NMR applications. *J. Am. Chem. Soc. 129*, 7106–7113.

(21) Silvaggi, N. R., Martin, L. J., Schwalbe, H., Imperiali, B., and Allen, K. N. (2007) Double-lanthanide-binding tags for macromolecular crystallographic structure determination. *J. Am. Chem. Soc. 129*, 7114–7120.

(22) Goda, N., Tenno, T., Inomata, K., Iwaya, N., Sasaki, Y., Shirakawa, M., and Hiroaki, H. (2007) LBT/PTD dual tagged vector for purification, cellular protein delivery and visualization in living cells. *Biochim. Biophys. Acta 1773*, 141–146.

(23) Li, M., and Selvin, P. R. (1995) Luminescent polyaminocarboxylate chelates of terbium and europium: the effect of chelate structure. *J. Am. Chem. Soc. 117*, 8132–8138.

(24) Li, M., and Selvin, P. R. (1997) Amine-reactive forms of a luminescent diethylenetriaminepentaacetic acid chelate of terbium and europium: attachment to DNA and energy transfer measurements. *Bioconjugate Chem. 8*, 127–132.

(25) Dadabhoy, A., Faulkner, S., and Sammes, P. G. (2000) Small singlet-triplet energy gap of acridone enables longer wavelength sensitisation of europium(III) luminescence. *J. Chem. Soc., Perkin Trans. 2* 2359–2360.

(26) Dadabhoy, A., Faulkner, S., and Sammes, P. G. (2002) Long wavelength sensitizers for europium(III) luminescence based on acridone derivatives. *J. Chem. Soc., Perkin Trans. 2* 348–357.

(27) Bretonnière, Y., Cann, M. J., Parker, D., and Slater, R. (2002) Ratiometric probes for hydrogencarbonate analysis in intracellular or extracellular environments using europium luminescence. *Chem. Commun.* 1930–1931.

(28) Bretonnière, Y., Cann, M. J., Parker, D., and Slater, R. (2004) Design, synthesis and evaluation of ratiometric probes for hydrogencarbonate based on europium emission. *Org. Biomol. Chem. 2*, 1624–1632.

(29) See the Supporting Information for experimental details.

(30) Szymanska, A., Wegner, K., and Lankiewicz, L. (2003) Synthesis of N-[(tert-butoxy)carbonyl]-3-(9,10-dihydro-9-oxo-acridin-2-yl)-L-alanine, a new fluorescent amino acid derivative. *Helv. Chim. Acta 86*, 3326–3331.

(31) Hamada, H., Kameshima, N., Szymanska, A., Wegner, K., Lankiewicz, L., Shinohara, H., Taki, M., and Sisido, M. (2005) Position-specific incorporation of a highly photodurable and blue-laser excitable fluorescent amino acid into proteins for fluorescence sensing. *Bioorg. Med. Chem. 13*, 3379–3384.

(32) Hahn, M. E., and Muir, T. W. (2005) Manipulating proteins with chemistry: a cross-section of chemical biology. *Trends Biochem. Sci. 30*, 26–34.

(33) Hendrickson, T. L., de Crecy-Lagard, V., and Schimmel, P. (2004) Incorporation of nonnatural amino acids into proteins. *Annu. Rev. Biochem. 73*, 147–176.

(34) Muir, T. W. (2003) Semisynthesis of proteins by expressed protein ligation. *Annu. Rev. Biochem. 72*, 249–289.

(35) Futaki, S., Sogawa, K., Maruyama, J., Asahara, T., Niwa, M., and Hojo, H. (1997) Preparation of peptide thioesters using Fmoc-solid-phase peptide synthesis and its application to the construction of a template-assembled synthetic protein (TASP). *Tetrahedron Lett. 38*, 6237–6240.

(36) Mezo, A. R., Cheng, R. P., and Imperiali, B. (2001) Oligomerization of uniquely folded mini-protein motifs: Development of a homotrimeric beta beta alpha peptide. *J. Am. Chem. Soc. 123*, 3885–3891.

(37) Kapust, R. B., Tozser, J., Copeland, T. D., and Waugh, D. S. (2002) The P1′ specificity of tobacco etch virus protease. *Biochem. Biophys. Res. Commun. 294*, 949–955.

(38) Horrocks, W. D., and Sudnick, D. R. (1979) Lanthanide ion probes of structure in biology - laser-induced luminescence decay constants provide a direct measure of the number of metal-coordinated water-molecules. *J. Am. Chem. Soc. 101*, 334–340.

(39) Beeby, A., Clarkson, I. M., Dickins, R. S., Faulkner, S., Parker, D., Royle, L., de Sousa, A. S., Williams, J. A. G., and Woods, M. (1999) Non-radiative deactivation of the excited states of europium, terbium and ytterbium complexes by proximate energy-matched OH, NH and CH oscillators: an improved luminescence method for establishing solution hydration states. *J. Chem. Soc., Perkin Trans. 2* 493–504.

BC700426C

ARTICLES

Conjugation of (*E*)-5-[2-(Methoxycarbonyl)ethenyl]cytidine to Hydrophilic Microspheres: Development of a Mobile Microscale UV Light Actinometer

Shiyue Fang,[‡,§,#] Yousheng Guan,[‡,△] Ernest R. Blatchley III,[†] Chengyue Shen,[†,⊥] and Donald E. Bergstrom*[,‡,§]

School of Civil Engineering, Purdue University, West Lafayette, Indiana 47907-2051, Birck Nanotechnology Center, Department of Medicinal Chemistry and Molecular Pharmacology and the Purdue Cancer Center, Purdue University, West Lafayette, Indiana 47907, and The Walther Cancer Institute, Indianapolis, Indiana 46208. Received September 3, 2007; Revised Manuscript Received December 18, 2007

(*E*)-5-[2-(Methoxycarbonyl)ethenyl]cytidine was biotinylated through a diisopropylsilylacetal linkage and attached to the surface of hydrophilic streptavidin-coated microspheres through the high-affinity noncovalent interaction between biotin and streptavidin. The functionalized microspheres form a stable suspension in water. Upon UV irradiation, the nonfluorescent (*E*)-5-[2-(methoxycarbonyl)ethenyl]cytidine on the microspheres undergoes photocyclization to produce highly fluorescent 3-β-D-ribofuranosyl-2,7-dioxopyrido[2,3-*d*]pyrimidine. The fluorescence intensity of the microspheres can be correlated to the particle-specific UV doses applied at different suspension concentrations. The microspheres allow one to measure the UV dose (fluence) distribution in high-throughput water disinfection systems.

INTRODUCTION

Several years ago, we initiated a multidisciplinary project aimed at developing a means for experimentally characterizing continuous-flow UV light disinfection photoreactors. For this project, a mobile UV light actinometer based on a microsphere that has the following three features is required: (i) Under UV irradiation at 254 nm (and other germicidally active wavelengths), the microsphere produces fluorescence when excited with a lower energy light, and the fluorescent intensity on the microsphere is correlated to the dose of germicidal UV light applied to the microspheres over a broad range. (ii) The functionalized microsphere has a hydrophilic surface and forms a relatively stable suspension in water. (iii) The physical properties of the microspheres such as size, shape, and density resemble those of relevant waterborne microbial pathogens. The use of microspheres for measurement of UV dose (fluence) distribution has been reported, but the microspheres were coated with a fluorescent dye whose absorption maximum fell at a much higher wavelength than required for germicidal action, and the measured effect was photobleaching (*1*). Moreover, the magnitude of the change in fluorescence signal was relatively small for the doses of UV radiation that are relevant in disinfection applications. In order to achieve maximum sensitivity and range, a system in which the UV irradiation transforms a nonfluorescent molecule with an absorption maximum in the wavelength range of germicidal lamps to a light-stable fluorescent molecule would be preferable. There are many examples of fluorescent photochromic compounds (*2*–*5*), but relatively few examples of compounds that when irradiated with UV light of wavelength less than 300 nm lead to a single product that is both UV-stable and fluorescent.

In 1982, we reported the preparation and characterization of (*E*)-5-[2-(methoxycarbonyl)ethenyl]cytidine (**1**) (*6*). This cytidine nucleoside analogue is not fluorescent; however, under UV irradiation at 254 nm, its trans-double bond is presumed to undergo trans–cis isomerization to form the intermediate **2**, which cannot be isolated or even observed. In intermediate **2**, the amino group would now be positioned in close proximity to the methyl ester group, which facilitates rapid cyclization through nucleophilic attack to give the stable and highly fluorescent product 3-β-D-ribofuranosyl-2,7-dioxopyrido[2,3-*d*]pyrimidine (**3**, Scheme 1). We have previously reported the use of compound **1** as a chemical actinometer for germicidal UV irradiation (*7*). We reasoned that attaching **1** to 5 μm diameter hydrophilic microspheres would provide mobile actinometers with the desired properties for application in the measurement of UV fluence distribution in flowthrough UV disinfection systems. This manuscript describes the chemistry to accomplish the construction of the derivatized microsphere, while the dosimetry application is described elsewhere (*8*).

EXPERIMENTAL PROCEDURES

General. All reactions were performed under a blanket of dry dinitrogen or argon. Reagents and solvents available from commercial sources were used as received unless otherwise noted. Pyridine and triethylamine were distilled over CaH_2. Acetone was dried over anhydrous Na_2SO_4 and filtered. Thin layer chromatography (TLC) was performed using silica gel on

* Correspondence to Donald E. Bergstrom, Purdue University, Room 2042, Birck Nanotechnology Center, 1205 West State Street, West Lafayette, IN 47907-2057, Telephone: 765-494-6275, E-mail: bergstrom@purdue.edu.

† School of Civil Engineering, Purdue University.

‡ Department of Medicinal Chemistry and Molecular Pharmacology, Purdue University.

§ The Walther Cancer Institute.

△ Current address: Anthill Technologies, Woburn, MA.

⊥ Current address: HydroQual, Inc., Johnstown, NY.

Current address: Department of Chemistry, Michigan Tech University, Houghton, MI.

10.1021/bc700336x CCC: $40.75 © 2008 American Chemical Society
Published on Web 02/12/2008

Scheme 1. Photochemical Reaction of Nucleoside 1

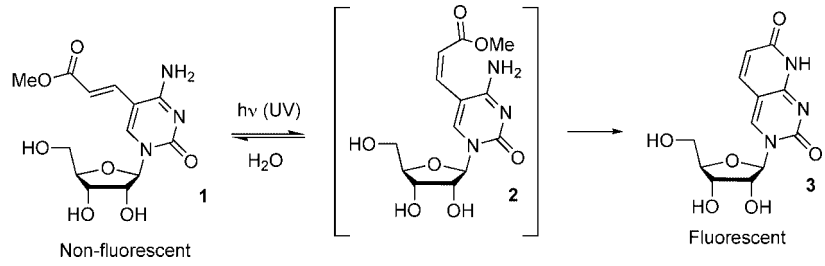

aluminum 60F-254, 200 μm thickness TLC plates. Flash column chromatography was performed using 40 μm silica gel. NMR spectra were obtained using 250 and 500 MHz NMR spectrometers. Chemical shifts (δ) are reported relative to residual CD_3OH ($\delta = 4.87$ ppm for ^1H and 49.15 ppm for ^{13}C). Infrared spectra were recorded on a FTIR spectrophotometer. Melting points were determined using a Mel-Temp melting point apparatus and are uncorrected. Streptavidin-coated microspheres (1.0% solid content in 100 mM borate, pH 8.5 + 0.1% BSA + 0.05% Tween 20 + 10 mM EDTA buffer with 0.1% NaN_3 antimicrobial agent; mean diameter 5.5 μm; number of microspheres per gram 2.038×10^{10}; number of microspheres per milliliter 2.040×10^8; surface area 1.240×10^{12} μm^2) were manufactured by Polysciences, Inc. (Warrington, PA). TTL buffer: 100 mM Tris−HCl, pH 8.0, and 0.1% Tween 20, 1.0 M LiCl. PBS buffer: 0.1 M, pH 7.0.

2′,3′-Propylidinonyl-(*E*)-5-[2-(methoxycarbonyl)ethenyl] cytidine (4). A one-neck round-bottom flask was charged with **1** (1.2 g, 3.6 mmol), *p*-toluenesulfonic acid monohydrate (2.1 g, 11.0 mmol), and acetone (20 mL). To this suspension was added DMF (about 5 mL) until insoluble materials were dissolved, forming a light yellow solution. After stirring at room temperature overnight, the reaction mixture was partitioned between saturated Na_2CO_3 solution (20 mL) and CH_2Cl_2 (20 mL × 3). The organic phase was washed with water (20 mL × 2), dried over $MgSO_4$, and solvents were removed under reduced pressure. Flash column chromatography (9:1 EtOAc/MeOH) gave **4** as a white solid (1.16 g, 88%): mp 162–3 °C; $R_f = 0.45$ (9:1 EtOAc/MeOH); IR (KBr, cm^{-1}) ν 3350, 2984, 1646, 1625, 1207; ^1H NMR (CD_3OD, 500 MHz) δ 1.38 (s, 3H), 1.58 (s, 3H), 3.76–3.89 (m, 2H), 3.79 (s, 3H), 4.32 (s, 1H), 4.76–4.95 (m, 2H), 5.95 (s, 1H), 6.37 (d, 1H, $J = 15.8$ Hz), 7.62 (d, 1H, $J = 15.8$ Hz), 8.51 (s, 1H); ^{13}C NMR (CD_3OD, 500 MHz) δ 25.7, 27.7, 52.3, 63.1, 82.2, 87.1, 89.5, 95.7, 104.2, 115.0, 118.4, 137.0, 144.3, 157.2, 165.6, 168.8; HRMS (ESI, M + H^+) Calcd for $C_{16}H_{22}N_3O_7$368.1458, found 368.1476.

Biotinyl Alcohol 7. Biotin (2.00 g, 8.19 mmol), triethylamine (1.72 mL, 12.29 mmol), and DMF (10 mL) were combined in a one-neck round-bottom flask and cooled to 0 °C. To this white suspension, *iso*-butylchloroformate (1.70 mL, 13.10 mmol) was added via syringe, and the reaction mixture was stirred at 0 °C for 1 h. The white suspension was then cooled to −60 °C. A solution of 6-amino-1-hexanol (**6**, 1.55 g, 13.10 mmol) and triethylamine (1.37 mL, 9.83 mmol) in DMF (5 mL) was added slowly via syringe, and the suspension was stirred overnight while gradually warming to room temperature. Anhydrous ether (100 mL) was added; the resulting white precipitate washed with ether (10 mL × 2) and then dissolved in methanol (50 mL) and stirred with Rexyn 201 (OH) resin (10 g) for 1 h. After filtration to remove the resin, the light yellow solution was concentrated under reduced pressure. Addition of ether (30 mL) produced the product as a white solid (2.40 g, 85%): mp 159–60 °C; IR (thin film, cm^{-1}) ν 3301, 2931, 2854, 1684, 1633; ^1H NMR (CD_3OD, 500 MHz) δ 1.36–1.75 (m, 14H), 2.20 (t, 2H, $J = 7.4$ Hz), 2.71 (d, 1H, $J = 12.7$ Hz), 2.93 (dd, 1H, $J = 12.8$, 5.0 Hz), 3.15–3.31 (m, 3H), 3.54 (t, 2H, $J = 6.6$ Hz), 4.31 (dd, 1H, $J = 7.8$, 4.4 Hz), 4.50 (dd, 1H, $J = 7.8$, 5.0 Hz); ^{13}C NMR (CD_3OD, 500 MHz) δ 26.6, 26.9, 27.8, 29.5, 29.8, 30.4, 33.6, 36.8, 40.3, 41.0, 57.0, 61.6, 62.9, 63.4, 166.1, 175.9; EIMS *m/z* 343 (M^+), 299, 283, 226, 179, 124; HRMS (EI) Calcd for $C_{16}H_{29}N_3O_3S$ 343.1930, found 343.1914.

Biotinylated Nucleoside Derivative 8. To a suspension of **7** (1.20 g, 3.48 mmol) in DMF (7.0 mL) and pyridine (2.0 mL) was added diisopropyldichlorosilane (630 μL, 3.48 mmol) via syringe at −60 °C. The colorless solution was stirred for about 5 h while warming to room temperature, and then cooled to −60 °C again. A solution of **4** (427 mg, 1.16 mmol) in DMF (3.0 mL) was added via syringe, and stirred overnight while warming to rt. Addition of ether (50 mL) gave a white precipitate, which was partitioned between sat $NaHCO_3$ (25 mL) and *n*-butanol (20 mL × 5). The organic phase was dried over $MgSO_4$, solvents removed, and the product purified by flash column chromatography (9:1 CH_2Cl_2/MeOH). The product was obtained as a light yellow foam (433 mg, 45%): $R_f = 0.25$ (9:1 CH_2Cl_2/MeOH); IR (thin film, cm^{-1}) ν 2928, 2860, 1699, 1648; ^1H NMR (CD_3OD, 500 MHz) δ 0.88–1.77 (m, 34H), 2.19 (t, 2H, $J = 6.6$ Hz), 2.71 (d, 1H, $J = 12.7$ Hz), 2.92 (dd, 1H, $J = 12.7$, 5.0 Hz), 3.10–3.21 (m, 4H), 3.31 (d, 2H, $J = 1.4$ Hz), 3.54 (t, 1H, $J = 6.6$ Hz), 3.75 (t, 2H, $J = 6.3$ Hz), 3.77 (s, 3H, -OMe), 3.97–4.06 (m, 2H), 4.30 (dd, 1H, $J = 7.8$, 4.4 Hz), 4.36–4.37 (m, 1H), 4.48–4.51 (m, 1H), 4.95 (dd, 1H, $J = 6.2$, 1.8 Hz), 5.81 (d, 1H, $J = 1.7$ Hz), 6.30 (d, 1H, $J = 16.3$ Hz), 7.60 (d, 1H, $J = 15.8$ Hz), 8.19 (s, 1H); ^{13}C NMR (CD_3OD, 500 MHz) δ 13.3, 13.4, 17.9, 17.9, 18.0, 25.7, 26.8, 27.1, 27.6, 28.0, 29.7, 29.9, 30.6, 33.9, 37.0, 40.5, 41.2, 52.4, 57.2, 61.8, 63.5, 64.4, 64.8, 82.6, 87.2, 90.0, 96.8, 104.1, 114.8, 118.6, 137.3, 144.1, 157.1, 165.6, 166.2, 168.6, 176.1; HRMS (ESI, M + H^+) Calcd for $C_{38}H_{63}N_6O_{10}SSi$ 823.4096, found 823.4087.

Biotinyl Nucleoside Derivative 10. Following the procedure for preparation of **8**, biotin derivative **9** (255 mg, 0.52 mmol), DMF (6 mL), imidazole (87 mg, 1.25 mmol), diisopropyldichlorosilane (113 μL, 0.63 mmol) and **4** (230 mg, 0.63 mmol) gave **10** as a white foam after flash column chromatography (9:1 CH_2Cl_2/MeOH, 255 mg, 51%): $R_f = 0.3$ (9:1 CH_2Cl_2/MeOH); IR (thin film, cm^{-1}) ν 3187, 2941, 2862, 1648, 1068; ^1H NMR (CD_3OD, 500 MHz) δ 0.94–1.04 (m, 14H), 1.29–1.31 (m, 6H), 1.36 (s, 3H), 1.43–1.45 (m, 2H), 1.56 (s, 3H), 1.64–1.68 (m, 2H), 1.69–1.80 (m, 2H), 1.82 (t, 2H, $J = 8.3$ Hz), 2.62 (t, 2H, $J = 7.4$ Hz), 2.34–2.37 (m, 2H), 2.76 (d, 1H, $J = 12.7$ Hz), 2.95 (dd, 1H, $J = 12.7$, 7.9 Hz), 3.22–3.24 (m, 1H), 3.38 (t, 4H, $J = 5.4$ Hz), 3.57 (t, 4H, $J = 5.7$ Hz), 3.63 (s, 4H), 3.78 (s, 3H), 4.00–4.05 (m, 2H), 4.36–4.38 (m, 2H), 4.56 (dd, 1H, $J = 7.7$, 5.1 Hz), 4.88 (dd, 1H, $J = 6.3$, 3.3 Hz), 5.03 (dd, 1H, $J = 6.4$, 1.4 Hz), 5.90 (s, 1H), 6.35 (d, 1H, $J = 15.7$ Hz), 7.63 (d, 1H, $J = 15.5$ Hz), 8.22 (s, 1H); ^{13}C NMR (CD_3OD, 500 MHz) δ 14.5, 14.7, 18.27, 18.30, 18.33, 18.4, 25.7, 26.9, 27.6, 29.6, 29.8, 30.3, 30.5, 32.5, 35.5, 36.8, 40.3, 40.4, 41.2, 41.6, 50.0, 52.4, 52.5, 57.0, 61.7, 63.4, 64.5, 70.7, 71.3, 74.9, 82.2, 86.7, 89.5, 95.8, 104.7, 115.0, 119.4, 136.7, 143.6, 165.2, 168.2, 176.2, 176.3; HRMS (ESI, M + H^+) Calcd for $C_{41}H_{74}N_7O_{13}SSi$ 968.4835, found 968.4830.

Scheme 2. Strategies for Directly Linking Compounds 1 and 3 to Microspheres

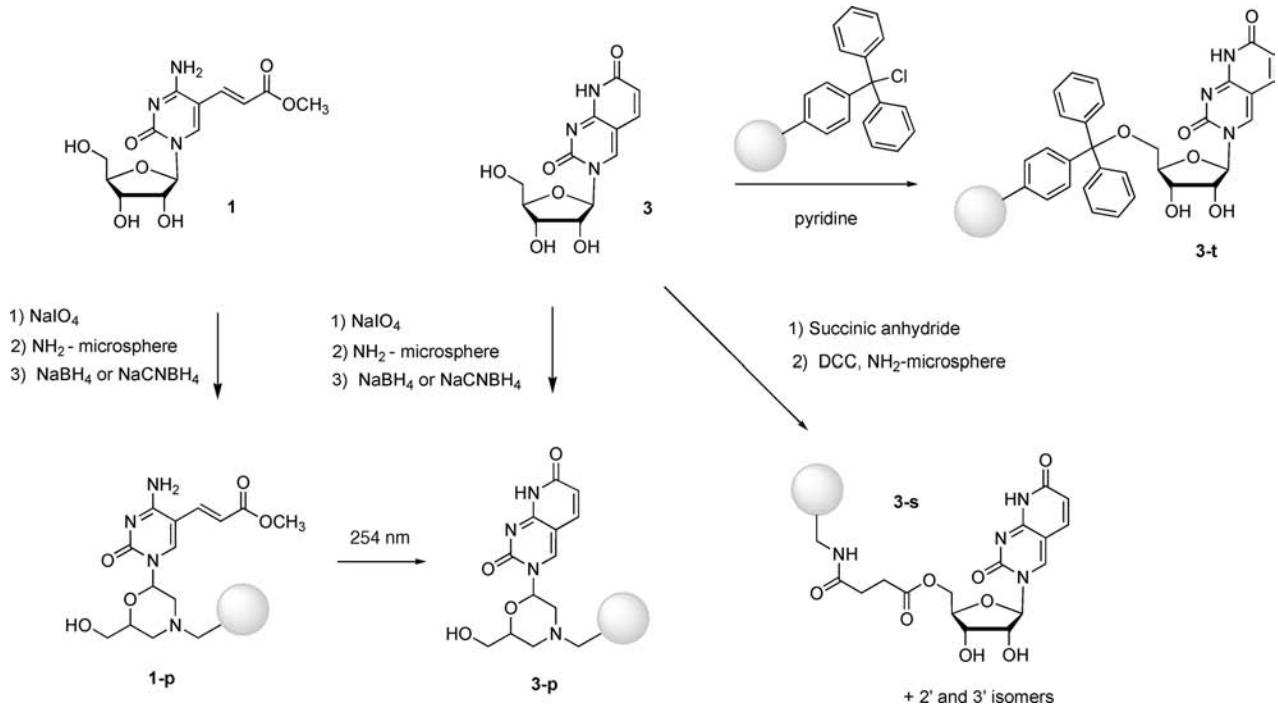

Attachment of Biotinylated Nucleoside Analogues to Streptavidin-Coated Microspheres. The microsphere suspension (1.0 mg, 0.1 mL) was transferred to a centrifuge tube. The storage buffer was removed by first centrifuging and removing the supernatant, leaving the white microspheres, which were washed with 200 μL TTL buffer. The biotinylated nucleosides (**8** or **10**, ~80μg in 25 μL TTL buffer) were added to the microspheres, and incubated at room temperature for 20 min with occasional gentle shaking. The buffer was removed after centrifuging, and the microspheres were washed with PBS buffer (1 mL × 3) and water (1 mL × 3) and stored as a suspension in water at 0 °C in the dark. Microspheres coated with **8** were found to be unstable, even after repeated additional washings with PBS buffer (1 mL × 2) and water (1 mL × 2), fluorescence in the buffer or water was observed under UV light, and fluorescence on the washed microspheres became less and less intense. Microspheres coated with **10** were stable under these washing conditions, after storing at 0 °C for several days in the dark, and no adverse effects were observed in fluorescence studies. Following UV irradiation, the excitation maximum of the fluorescent microsphere suspension in water was 336 nm and the emission maximum fell at 381 nm, which closely matches the excitation and emission maxima of compound **3** (*6*). The determination of the relationship between UV dose and fluorescent intensity of the microsphere suspension in water is reported elsewhere (*8*).

RESULTS AND DISCUSSION

To tether nucleosides **1** and **3** to microspheres, we initially explored the strategies outlined in Scheme 2. Microspheres with nucleoside **1** directly attached would serve as the sensor, but we also required microspheres with compound **3** for calibration. It became clear after considerable effort that simple direct methods for tethering would not yield microspheres with the fluorescence response required for quantification of UV dose. In all cases, the conjugation reaction was either inefficient or there was considerable quenching of the photoreaction and/or fluorescence. Problems associated with quenching when fluorophores are closely spaced within a matrix or on a surface are well-recognized (*9–11*).

Scheme 3. Preparation of Compound 4

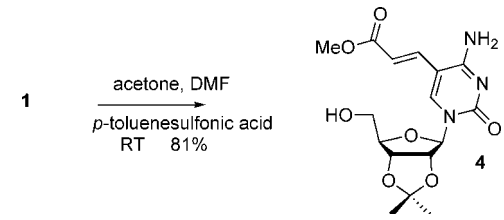

As outlined in Scheme 2, the conjugation methods attempted included periodate oxidation followed by borohydride (*12*) or cyanborohydride (*13*) mediated reductive amination to amine-coated polystyrene and silica microspheres. This method has been shown to enable the conjugation of ribonucleotides, including cytidine derivatives, to solid supports (*12, 14, 15*). However, we were not able to obtain fluorescent microspheres either by attachment of compound **1** to give derivatized beads **1-p** followed by UV irradiation (254 nm) or by direct attachment of fluorescent nucleoside **3**. The final product in both cases should be **3-p**. A variety of solvents (H_2O, DMF, and DMSO), both sodium borohydride and sodium cyanoborohydride, and a number of different silica and polystyrene amine-substituted microbeads were investigated without success. Seela and co-workers have attached ribonucleosides to sepharose beads by first synthesizing 2′,3′-ethylidene derivatives from levulinic acid and then coupling the pendant carboxylic group to 6-amino-hexylagarose using the water-soluble carbodiimide EDC (*16–18*). We attempted a number of variations on this approach (not shown), but were not able to obtain fluorescent microspheres.

Alcohols can be directly linked to polystyrene trityl chloride resin (*19*). However, fluorescent nucleoside **3** did not yield fluorescent microspheres with a polystyrene trityl resin. It is possible that resin **3-t** was formed but we were unable to detect fluorescence. Finally, we attempted to link nucleoside **3** by way of a succinic acid linker (Scheme 2) to give **3-s**, but this approach also failed to give fluorescent microspheres. As a result of these failures, we chose to pursue a biotin−streptavidin conjugation strategy that would significantly reduce the density of nucleoside **1** while at the same time placing each molecule

Scheme 4. Preparation of Biotinyl Cytidine Analogue 8

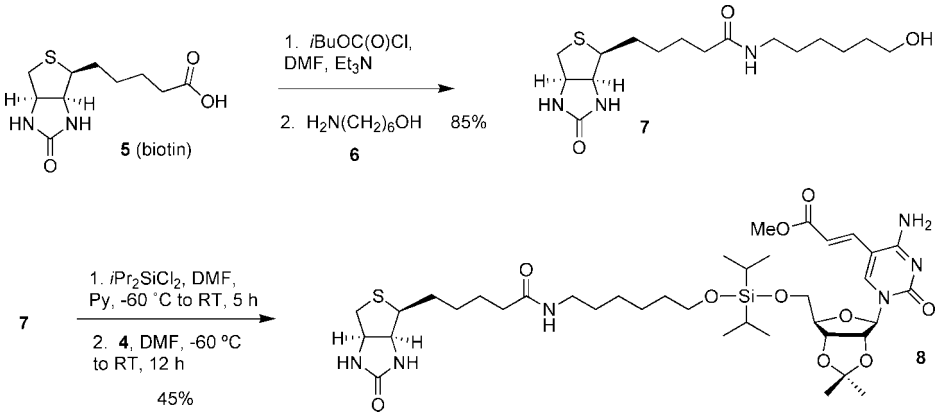

further from the surface of the microsphere. Streptavidin-coated microspheres with a wide range of physical properties are commercially available; and these microspheres are hydrophilic because streptavidin is relatively hydrophilic. The microspheres chosen for this study have a diameter of ~5.5 μm and a specific gravity of 1.05, which would allow them to mimic the movement and trajectories of waterborne microbial pathogens. A study by Buranda et al. on 6.2 μm diameter streptavidin-coated microspheres yielded an estimate of 10^6 binding sites per microsphere (*20*). This translates to an average density of less than one binding site per 100 nm^2.

However, there was yet another issue to be resolved. It has been observed that biotin−fluorophore conjugates are also subject to quenching. When Gruber et al. examined biotin conjugates of fluorescein, tetramethylrhodamine, Cy3, and Cy5, they found that fluorescein and tetramethyrhodamine bound through a 14 atom spacer showed considerable quenching (*21*). With longer spacers (PEG800 and PEG1900), there was considerably less quenching. We chose to investigate a 20 atom spacer that was both more rigid and sterically hindered than simple PEG spacers, rationalizing that the steric bulk and rigidity would function more effectively to separate chromophores than simple incorporation of very long, but highly flexible spacers. It was necessary to link the spacer through the ribose group, since the methoxycarbonyl and 4-amino groups are required for the photochemical reaction. Moreover, the 2′- and 3′-OH groups are conveniently protected by acetal formation, which leaves a single site, the 5′-hydroxy available for attachment of the spacer to biotin. At the same time, a 2′,3′-acetal would be anticipated to considerably increase solubility in organic solvents thereby facilitating the chemistry necessary to functionalize the molecule at the 5′-OH. When nucleoside **1** was stirred in a mixture of acetone and DMF in the presence of *p*-toluenesulfonic acid, compound **4** was obtained in 83% yield as a white solid (Scheme 3) (*22*).

In order to achieve selective coupling between a biotin containing moiety and compound **4** at the 5′-hydroxyl group in the presence of the unprotected cytosine amino group, we pursued a strategy based on the generation of silyl ether linkers. We first prepared biotinyl alcohol **7** by coupling biotin (**5**) to aminoalcohol **6** using *i*BuOC(O)Cl as the carboxylic acid activating agent (*23*). Then, 1 equiv of dichlorodiisopropylsilane was allowed to react with the hydroxyl group in the biotinyl alcohol **7**. The intermediate was not isolated but allowed to then react directly with the cytidine analogue **4** through the formation of a diisopropylsilylacetal functionality as shown in Scheme 4 to give the biotinylated cytidine analogue **8**.

Next, attempts were made to attach **8** to streptavidin-coated microspheres. The microspheres were first washed with two portions of TTL buffer (100 mM Tris−HCL, pH 8.0, and 0.1% Tween 20, 1.0 M LiCl), and then suspended in a TTL buffer containing **8**. The suspension was incubated at room temperature for 20 min with occasional gentle shaking in the dark. The microspheres were then collected by centrifuging, and washed sequentially with PBS buffer and deionized water, and then suspended in deionized water. After exposure of the microspheres to UV light, fluorescence was observed on the microspheres. However, fluorescence was also observed in the washing buffer and continued to appear in the wash solution on repeated washing. Concomitantly, the fluorescence on the microspheres became less and less intense with washing. From these observations, it appeared that the silyl acetal linkage in **8** was not stable in aqueous buffer and water. This was confirmed by shaking **8** in a mixture of water and *n*-butanol, whereupon after 2 h, **8** could no longer be detected in the *n*-butanol phase by TLC.

Scheme 5. Conjugation of Biotin Derivative 9to Nucleoside 4

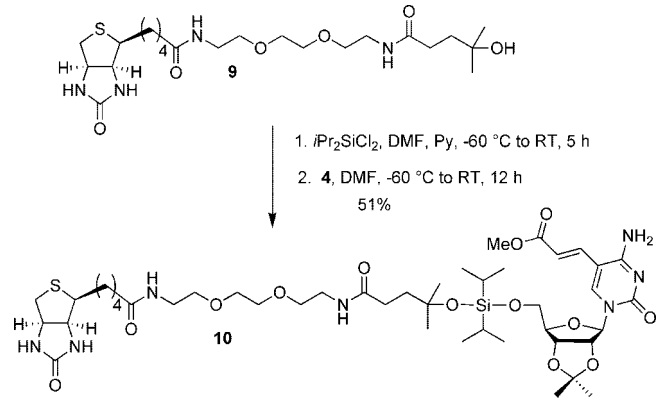

Since the stability of silyl acetal linkage is dependent on the bulkiness of the alkyl groups attached to silicon (*24, 25*), we also investigated *t*Bu(Ph)$SiCl_2$ as a reagent for linking the nucleoside to biotin (*24, 25*). However, this strategy generated complex mixtures that may be attributed to the generation of a new chiral silicon center as well as less complete transformation because of the lower reactivity of *t*Bu(Ph)$SiCl_2$. Attempts to isolate the desired product in pure form failed. This led us to ultimately design compound **10**. The silyl acetal linkage in this molecule is expected to be more stable than that in **8**, because of the bulky tertiary carbon attached to one of the two oxygen atoms in the linkage. Moreover, in comparison to *t*Bu(Ph)$SiCl_2$, *i*Pr_2SiCl_2 is more reactive, and does not generate a new chiral silicon center. As shown in Scheme 5, under reaction conditions similar to those used to prepare compound **8**, **4** was linked to biotin derivative **9** (*26*) with *i*$Pr_2SiCl_2$to give the target molecule **10** in 51% yield after flash chromatography purification.

We found that only 1.2 equiv of compound **9** were required to achieve effective conversion of nucleoside **4** to compound

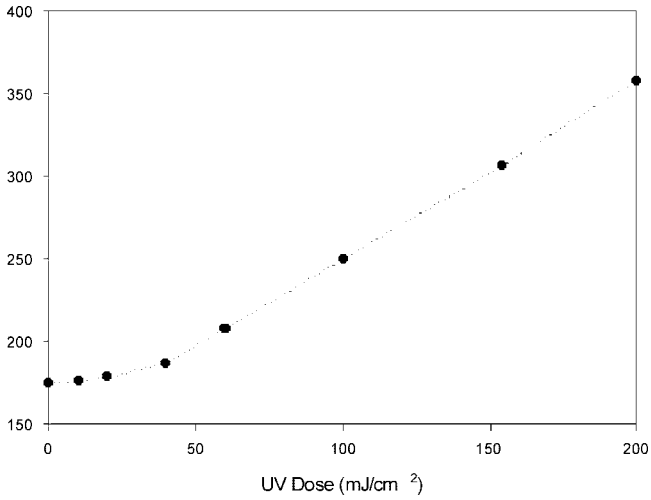

Figure 1. Mean fluorescence intensity (FI) of microspheres as a function of applied UV_{254} dose. Reported FI values represent the mean of measurements collected for roughly 10 000 particles by flow cytometry.

10. The biotinylated nucleoside **10** was obtained as a clean white foam and its structure established by ^1H, ^{13}C NMR, UV, IR, and high-resolution mass spectroscopy. It is stable in air, water, and other commonly used organic solvents, and no decomposition was observed during chromatography on silica gel and storage in desiccator for several months.

With the more stable **10** in hand, attachment to streptavidin-coated microspheres was investigated. Using a procedure similar to that used for attaching **8** to the microspheres, **10** was found to be irreversibly attached. Even after washing extensively with PBS buffer and water, UV irradiation of the microspheres still promoted the cyclization reaction to yield fluorescent microspheres when excited at 320 nm. The relationship between the fluorescence intensity (FI) of a population of microspheres (~10 000) was determined by flow cytometery (Figure 1). Flow cytometry was performed on an Epics Altra cell sorter (Beckman-Coulter) using a 351 nm line of the Argon 5 W Enterprise laser (Coherent, Inc.) with power set at 60 mW for the UV line. FI measurements were collected in linear mode with a band-pass filter at 380 nm. As illustrated in Figure 1, the FI of the population of microspheres increased monotonically with increasing UV dose. The cause of the lag in FI in the limit of low UV dose is unknown; however, this lag is overcome in application of microspheres for measurement of UV dose distribution delivery by preirradiation of microspheres at a dose of 50 mJ/cm^2 or more (*8*).

In conclusion, by using the unique diisopropylsilyacetal linkage and the strong noncovalent interaction between biotin and streptavidin, we successfully attached the highly functionalized cytidine analogue to microspheres. Because of their hydrophilic surface, the microspheres can form a stable suspension in water. The fluorescence intensity of the suspension of these microspheres responds monotonically to applied UV light dose, which demonstrates their suitability for use as a mobile UV light actinometer.

ACKNOWLEDGMENT

This work was funded by the Water Environment Research Foundation (Grant 99-CTS-2-UR) the Showwalter Trust, and the National Institutes of Health (GM53155). Assistance from the Purdue University Cytometry Laboratories and from Eric Cox is greatly appreciated. Support from the National Cancer Institute Grant (P30 CA23168) awarded to Purdue University is also gratefully acknowledged

Supporting Information Available: UV, IR, ^1H-NMR, and ^{13}C-NMR spectra for compounds **8** and **10** (Figures **S1–S8**). This material is available free of charge via the Internet at http://pubs.acs.org.

LITERATURE CITED

(1) Bohrerova, Z., Bohrer, G., Mohanraj, S. M., Ducoste, J., and Linden, K. G. (2005) Experimental measurements of fluence distribution in a UV reactor using fluorescent microspheres. *Environ. Sci. Technol. 39*, 8925–8930.

(2) Bouas-Laurent, H., and Durr, H. (2001) Organic photochromism. *Pure Appl. Chem. 73*, 639–665.

(3) Horaguchi, T., Hosokawa, N., Tanemura, K., and Suzuki, T. (2002) Photocyclization reactions. Part 8 [1]. Synthesis of 2-quinolone, quinoline and coumarin derivatives using trans-cis isomerization by photoreaction. *J. Heterocycl. Chem. 39*, 61–67.

(4) Li, H., Yang, J. H., and Porter, N. A. (2005) Preparation and photochemistry of *o*-aminocinnamates. *J. Photochem. Photobiol. A: Chem. 169*, 289–297.

(5) Terrian, D. L., Mohammad, T., and Morrison, H. (1995) Photocyclization of ortho-substituted cinnamic-acids. *J. Org. Chem. 60*, 1981–1984.

(6) Bergstrom, D. E., Inoue, H., and Reddy, P. A. (1982) Pyrido[2,3-d]pyrimidine nucleosides - synthesis via cyclization of C-5 substituted cytidines. *J. Org. Chem. 47*, 2174–2178.

(7) Shen, C. Y., Fang, S. Y., Bergstrom, D. E., and Blatchley, E. R. (2005) (*E*)-5-[2-(Methoxycarbonyl)ethenyl]-cytidine as a chemical actinometer for germicidal UV radiation. *Environ. Sci. Technol. 39*, 3826–3832.

(8) Blatchley, E. R., Shen, C. Y., Naunovic, Z., Lin, L. S., Lyn, D. A., Robinson, J. P., Ragheb, K., Gregori, G., Bergstrom, D. E., Fang, S. Y., Guan, Y. H., Jennings, K., and Gunaratna, N. (2006) Dyed microspheres for quantification of UV dose distributions: Photochemical reactor characterization by Lagrangian actinometry. *J. Environ. Eng. Div. Am. Soc. Civ. Eng. 132*, 1390–1403.

(9) Deka, C., Lehnert, B. E., Lehnert, N. M., Jones, G. M., Sklar, L. A., and Steinkamp, J. A. (1996) Analysis of fluorescence lifetime and quenching of FITC-conjugated antibodies on cells by phase-sensitive flow cytometry. *Cytometry 25*, 271–279.

(10) Imhof, A., Megens, M., Engelberts, J. J., de Lang, D. T. N., Sprik, R., and Vos, W. L. (1999) Spectroscopy of fluorescein (FITC) dyed colloidal silica spheres. *J. Phys. Chem. B 103*, 1408–1415.

(11) Tirri, M. E., Wahlroos, R., Meltola, N. J., Toivonen, J., and Hanninen, P. E. (2006) Effect of polystyrene microsphere surface to fluorescence lifetime under two-photon excitation. *J. Fluoresc. 16*, 809–816.

(12) Gilham, P. T. (1971) The covalent binding of nucleotides, polynucleotides, and nucleic acids to cellulose, in *Nucleic Acids, Part D* (Grossman, L., and Moldave, K., Eds.) pp 191–197, Academic Press, New York.

(13) Hileman, R. E., Parkhurst, K. M., Gupta, N. K., and Parkhurst, L. J. (1994) Synthesis and characterization of conjugates formed between periodate-oxidized ribonucleotides and amine-containing fluorophores. *Bioconjugate Chem. 5*, 436–444.

(14) Ermolinsky, B. S., and Mikhailov, S. N. (2000) Periodate oxidation in chemistry of nucleic acids: Dialdehyde derivatives of nucleosides, nucleotides, and oligonucleotides (review). *Bioorg. Khim. 26*, 483–504.

(15) Tullius, M. V., Vann, W. F., and Gibson, B. W. (1999) Covalent modification of Lys19 in the CTP binding site of cytidine 5′-monophosphate N-acetylneuraminic acid synthetase. *Protein Sci. 8*, 666–675.

(16) Rosemeyer, H., and Seela, F. (1979) Polymer-linked 6-azauridine 5′-monophosphate, a resin of high bioaffinity to orotidine-5′-phosphate decarboxylase. *J. Med. Chem. 22*, 1545–1547.

(17) Seela, F., Ott, J., and Rosemeyer, H. (1979) Immobilization of adenosine-acetals with variable alkylidene residues - function of the spacer during enzymatic deamination. *Z. Naturforsch., C:*

J. Biosci. 34, 350–358.

(18) Seela, F., and Rosemeyer, H. (1978) Immobilization of cytidine and uridine via 2′,3′-O-cyclic acetal derivatives to agarose. *Z. Naturforsch., C: J. Biosci. 33*, 56–60.

(19) Leznoff, C. C., and Hall, T. W. (1982) The synthesis of a soluble, unsymmetrical phthalocyanine on a polymer support. *Tetrahedron Lett. 23*, 3023–3026.

(20) Buranda, T., Jones, G. M., Nolan, J. P., Keij, J., Lopez, G. P., and Sklar, L. A. (1999) Ligand receptor dynamics at streptavidin-coated particle surfaces: A flow cytometric and spectrofluorimetric study. *J. Phys. Chem. B 103*, 3399–3410.

(21) Gruber, H. J., Marek, M., Schindler, H., and Kaiser, K. (1997) Biotin-fluorophore conjugates with poly. (ethylene glycol) spacers retain intense fluorescence after binding to avidin and streptavidin. *Bioconjugate Chem. 8*, 552–559.

(22) Schmitt, L., and Tampe, R. (1996) ATP-lipids - Protein anchor and energy source in two dimensions. *J. Am. Chem. Soc. 118*, 5532–5543.

(23) Keana, J. F. W., Ogan, M. D., Lu, Y. X., Beer, M., and Varkey, J. (1986) Functionalized Keggin-type and Dawson-type cyclopentadienyltitanium heteropolytungstate anions - small, individually distinguishable labels for conventional transmission electron-microscopy. 2. Reactions. *J. Am. Chem. Soc. 108*, 7957–7963.

(24) Gillard, J. W., Fortin, R., Morton, H. E., Yoakim, C., Quesnelle, C. A., Daignault, S., and Guindon, Y. (1988) Symmetrical alkoxysilyl ethers - a new class of alcohol-protecting groups - preparation of *tert*-butoxydiphenylsilyl ethers. *J. Org. Chem. 53*, 2602–2608.

(25) Tamao, K., and Kawachi, A. (1995) Reduction of phenylchlorosilanes with lithium 1-(dimethylamino)naphthalenide - a new access to functionalized silyllithiums. *Organometallics 14*, 3108–3111.

(26) Fang, S. Y., and Bergstrom, D. E. (2003) Fluoride-cleavable biotinylation phosphoramidite for 5′-end-labeling and affinity purification of synthetic oligonucleotides. *Nucleic Acids Res. 31*, 708–715.

BC700336X

Labeling of Adenovirus Particles with PARACEST Agents

Olga Vasalatiy,[†] Robert D. Gerard,[‡] Piyu Zhao,[†] Xiankai Sun,[§] and A. Dean Sherry*[,†,§,||]

Department of Chemistry, University of Texas at Dallas, P.O. Box 830688, Richardson, Texas 75083, Department of Internal Medicine, University of Texas Southwestern Medical Center, 6000 Harry Hines Boulevard, Dallas, Texas 75390, Department of Radiology, University of Texas Southwestern Medical Center, 5323 Harry Hines Blvd, Dallas, Texas 75390, and Advanced Imaging Research Center, University of Texas Southwestern Medical Center, 5323 Harry Hines Blvd, NE 4.2, Dallas, Texas 75390. Received July 12, 2007; Revised Manuscript Received December 4, 2007

Recombinant adenovirus type 5 particles (AdCMVLuc) were labeled with two different bifunctional ligands capable of forming stable complexes with paramagnetic lanthanide ions. The number of covalently attached ligands varied between 630 and 1960 per adenovirus particle depending upon the chemical reactivity of the bifunctional ligand (NHS ester versus isothiocyanide), the amount of excess ligand added, and the reaction time. The bioactivity of each labeled adenovirus derivative, as measured by the ability of the virus to infect cells and express luciferase, was shown to be highly dependent upon the number of covalently attached ligands. This indicates that certain amino groups, likely on the surface of the adenovirus fiber protein where cell binding is known to occur, are critical for viral attachment and infection. Addition of $^{177}Lu^{3+}$ to chemically modified versus control viruses demonstrated a significant amount of nonspecific binding of $^{177}Lu^{3+}$ to the virus particles that could not be sequestered by addition of excess DTPA. Thus, it became necessary to implement a prelabeling strategy for conjugation of preformed lanthanide ligand chelates to adenovirus particles. Using preformed Tm^{3+}-**L2**, a large number of chelates having chemical exchange saturation transfer (CEST) properties were attached to the surface residues of AdCMVLuc without nonspecific binding of metal ions elsewhere on the virus particle. The potential of such conjugates to act as PARACEST imaging agents was tested using an on-resonance WALTZ sequence for CEST activation. A 12% decrease in bulk water signal intensity was observed relative to controls. This demonstrates that viral particles labeled with PARACEST-type imaging agents can potentially serve as targeted agents for molecular imaging.

INTRODUCTION

Magnetic resonance imaging (MRI), one of the most widely used noninvasive imaging modalities, provides contrast in images of soft tissues that depend upon the proton density of tissues and inherent differences tissue water relaxation rates. In the early 1980s, it was discovered that paramagnetic metal chelates could accelerate proton spin–lattice relaxation rates and thereby enhance image contrast. More recently, another method for altering MR image contrast was reported that relies on selective presaturation of chemically exchanging protons involving either endogenous molecules or exogenous probes which then exchange with bulk water protons to reduce its intensity. This new class of contrast media is referred to as CEST agents (*1*). There are numerous types of exchangeable protons in tissue, but the most common are -OH and -NH groups. Unfortunately, the chemical shift difference between these types of exchanging protons and water protons is small, and consequently selective saturation can be problematical. However, the potential advantages of CEST agents over conventional T_1 agents, including the ability to switch contrast "on" and "off" and the sensitivity of CEST to environmental effects such as pH and temperature, provide incentives for continued development of such agents. The concentration of any single chemically exchanging proton or water molecule that is required to produce significant CEST contrast is quite high, but this limitation can partially be compensated for by optimizing the chemical exchange rate (k_{ex}) between the agent and bulk water and by maximizing the number of exchangeable sites available on each agent. A successful example of the latter was reported recently (*2*) where glycogen in mouse liver was imaged by presaturation of the exchanging glycogen -OH protons (glycoCEST) that lie ~1 ppm downfield of tissue water.

Paramagnetic metal complexes having a single, slowly exchanging bound water molecule can function by a CEST mechanism as well (*3*). As the chemical shift of lanthanide-bound water molecules can be shifted as much as 700 ppm away from the bulk water resonance, this offers the possibility of selectively saturating the Ln^{3+}-bound water proton signal with less chance of inadvertently saturating bulk water protons. This large chemical shift difference between the Ln^{3+}-bound and bulk water signals makes this class of CEST contrast agents unique. For this reason, the term "PARACEST" is now used to differentiate such paramagnetic complexes from diamagnetic CEST compounds (*4*). Although paramagnetic systems have this attractive advantage, they do suffer from the same lack of sensitivity as diamagnetic CEST molecules on a proton concentration basis. One obvious method that could be used to increase the sensitivity of a CEST agent is to increase the number of exchangeable sites per molecule (*5*). High molecular weight platforms such as proteins, liposomes, linear and branched polymers, and spherical polymers based on core–shell morphology offer the opportunity to accumulate higher numbers of exchangeable sites per particle and thereby increase their "effective" concentration.

* To whom correspondence should be addressed. Tel: (214) 645-2730, e-mail: dean.sherry@utsouthwestern.edu.

[†] University of Texas at Dallas.

[‡] Department of Internal Medicine, University of Texas Southwestern Medical Center.

[§] Department of Radiology, University of Texas Southwestern Medical Center.

[||] Advanced Imaging Research Center, University of Texas Southwestern Medical Center.

10.1021/bc7002605 CCC: $40.75 © 2008 American Chemical Society
Published on Web 02/07/2008

Scheme 1

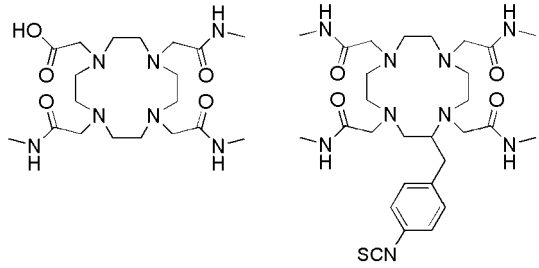

L1 **L2**

There is interest in using viral particles as biodelivery platforms due to their structural and architectural diversity and biological properties. The architecture of the viral particles consists of interior and exterior regions that can be chemically or genetically modified. The interior compartment of the viral particle can provide a naturally constrained cage for encapsulation of inorganic or organic materials (*6*), while chemical modifications of exterior surface capsid proteins have included specific nucleation of inorganic materials on the surface of the particles, and derivatization with PEG (polyethylene glycol) (*7*), fluorescent labels (*8, 9*), peptides (*10*), or MRI contrast agents (*11*). Studies by Allen et al. (*12*) have shown that the naturally occurring, endogenous metal binding sites of cowpea chlorotic mottle virus bind Gd^{3+} ions with a dissociation constant of $K_d = 31\ \mu M$ yielding a nanoparticle template for MRI applications. Anderson and co-workers (*11*) have extended this strategy by labeling the MS2 virus capsid with over 500 GdDTPA moieties (DTPA = diethylenetriaminepentaacetic acid) but did not test the viral bioactivity of the resulting modified nanoparticles.

Human adenovirus is a nonenveloped, double-stranded DNA-containing particle approximately 130 nm in diameter with icosahedral symmetry (*13*). Although over 50 types and 6 subgroups of human adenovirus have been identified, adenovirus type 2 and 5 of subgroup C are most commonly used as vectors in gene transfer. The adenovirus binds to cell surface receptors with high affinity *via* a COOH-terminal globular knob domain of the fiber protein. The recombinant knob domain binds about 4700 sites per HeLa cell with an affinity of $3 \times 10^9\ M^{-1}$ and is capable of blocking adenovirus infection of human cells (*14*). Each capsid protein of the adenovirus particle contains multiple exposed functional groups that can be chemically modified. Adenovirus 5 knob protein chemically modified with succinidyl 6-hydrozinonicotinate (HYNIC) and subsequently radiolabeled with ^{99m}Tc shows high-affinity binding to cells ($K_d = 1.4$ nM) (*15*). Replacement of the E1 region of the viral genome with a foreign gene generates a recombinant vector capable of efficiently infecting a wide variety of cells *in vitro* and tissues *in vivo*. These properties have prompted our interest in the use of adenoviral particles as drug delivery platforms.

The goal of this study was to compare the chemical reactivity of two bifunctional chelating agents **L1** and **L2** (Scheme 1) with replication-defective adenovirus particles and to optimize the labeling of viral particles with PARACEST agents derived from thulium (Tm^{3+}) and **L2** under conditions where viral activity is not totally disrupted. The AdCMVLuc virus (*20*) containing the luciferase reporter gene was chosen for this study so we could follow the infectious activity of the virus using a standard luciferase chemiluminescent assay after chemical modification with either reactive metal-free bifunctional ligands or metal ion preloaded chelates with favorable exchange properties for CEST imaging. Our goal was to create PARACEST-labeled viral particles that retain their infectious biological activity for potential use as tissue targeting agents for combined optical (luciferase) and MR (PARACEST) molecular imaging.

EXPERIMENTAL PROCEDURES

Materials and Methods. All starting reagents and solvents were obtained from commercial sources and used as received unless otherwise indicated. ^1H and ^{13}C NMR spectra were acquired using a JEOL Eclipse 270 operating at 270 and 67.5 MHz, respectively. Chemical shifts are reported in parts per million (δ) relative to TMS at 0 ppm. Infrared spectra were obtained on a Nicolet Avatar 360 FT-IR spectrometer either as KBr pellets or as thin films. UV–vis absorption spectra were recorded using a Pharmacia LKB-Ultrospec III single beam spectrometer. Hydrogenation was performed using a Parr hydrogenation apparatus. Electrospray ionization mass spectroscopy (ESI MS) was performed by HT Laboratories, San Diego, California. Fast atom bombardment mass spectroscopy (FAB MS) was performed by the Mass Spectrometry Facility at the University of Alabama at Tuscaloosa. Elemental analyses and inductively coupled plasma mass spectrometry (ICP MS) measurements were completed by Galbraith Laboratories, Knoxville, Tennessee. Luciferase (relative light units) was quantified using a SIRUS Luminometer V3.1. ^{177}Lu (0.05 N HCl) was obtained from the Research Reactor Center, University of Missouri at Columbia, Missouri. All buffers and reagent solutions for radiolabeling were prepared in Millipore deionized (DI) water and treated with Chelex 100 resin (100–200 mesh, Na^+ form, Bio-Rad Laboratories) for at least 4 h, followed by filtration through 0.22 μm CA membrane (Corning Inc.). Metal-free plastic ware used for all labeling experiments was soaked in 15% HNO_3 for 12 h and rinsed with Millipore DI water prior to use. Quantification of radioactivity was determined using a Rita Star Radioisotope TLC analyzer (Straubenhardt, Germany). Virus concentrations are expressed in particles/mL as measured by absorbance at 260 nm. CEST spectra and T_2 measurements were acquired using Varian INOVA-500 spectrometer at 500 MHz. Prior to data acquisition, samples were allowed to warm to room temperature and equilibrated in the probe at 25 °C for at least 10 min.

Synthetic Methods. 1,4,7-tris(*tert*-butyloxycarbonyl)-1,4,7,10-tetraazacyclo dodecane (*16*), 2-bromo-*N*-methylacetamide, 2-*p*-isothiocyanatobenzyl-1,4,7,10-tetraazacyclododecane-1,4,7,10-tetra (methylcarbonylamide) (*17*), and 1,4,7,10-tetraazacyclododecane-1,4,7,10-tetra(methylcarbonylamide) (referred to as DTMA) (*18*) were prepared as described previously.

1,4,7-Tris(*tert*-butyloxycarbonyl)-1,4,7,10-tetraazacyclododecane-10-benzyl acetate (4). K_2CO_3 (1.54 g, 11.1 mmol) was added to an acetonitrile (20 mL) solution of tris-Boc-protected cyclen 3 (4.3 g, 9.09 mmol). The suspension was heated for 10 min at 60 °C, followed by addition of benzyl bromoacetate (1.76 mL, 11.2 mmol). The reaction mixture was heated for 12 h at 60–70 °C, then filtered, and the solvents removed under reduced pressure. The residue was purified by column chromatography over silica gel eluting with 10% methanol in chloroform to afford the title compound as a colorless solid (5.2 g, 92% yield). $R_f = 0.5$ (SiO_2, MeOH/$CHCl_3$, 1:9). ^1H NMR (270 MHz, $CDCl_3$): $\delta = 1.42$ (18H, s, C $(CH_3)_3$), 1.44 (9H, s, $C(CH_3)_3$), 2.9–3.2 (16H, s br, ring CH_2), 3.5 (2H, s, CH_2CO_2), 5.1 (2H, s, OCH_2Ph), 7.3 (5H, m, Ph). ^{13}C NMR (67.5 MHz, CDCl3) $\delta =$ 28.4 $C(CH_3)_3$, 28.7 $C(CH_3)_3$, 47.3 (CH_2 ring), 49.8 (CH_2 ring), 51.3(CH_2 ring), 53.7(CH_2 ring), 55.0 (NCH_2CO), 66.1 (OCH_2Ph), 79.1 ($C(CH_3)_3$), 79.4 ($C(CH_3)_3$), 128.4 (Ph), 128.5 (Ph), 135.6 (Ph), 155.2 (CONH), 155.7 (CONH), 155.9 (CONH), 170.3 (COO). FTIR (KBr): 3010, 2979, 2932, 2448, 1689, 1464, 1417, 1363, 1243, 1167, 1025, 982, 912 cm^{-1}. *m*/*z* (ESI+) ([M + H]$^+$ 621, [M + Na]$^+$ 643, [M + K]$^+$ 659). Anal. Found C = 60.7%, H = 8.4%, N = 8.8% $C_{32}H_{52}N_4O_8 \cdot H_2O$. Theory: C = 60.6%, H = 8.8%, N = 8.8%.

1,4,7,10-Tetraazacyclododecane1-1-benzyl Acetate Trihydrochloride Salt (5). HCl (12 M, 5 mL) was added dropwise to a solution of **4** (5.0 g, 8.1 mmol) in ethanol (10 mL). The resulting solution was stirred for 3 h at room temperature. The reaction mixture was concentrated to 5–6 mL and the precipitates were filtered. The residue was crystallized from a mixture of water and tetrahydrofuran to afford a colorless crystalline compound (3.0 g, 81% yield).[1] H NMR (270 MHz, D_2O, (pD = 2): δ = 2.9 (16H, s br, ring CH_2), 3.6 (2H, s, CH_2COO), 5.2 (2H, s, OCH_2Ph), 7.4 (5H, m, Ph). ^{13}C NMR (67.5 MHz, D_2O, dD = 2) δ = 41.7 (CH_2 ring), 42.3 (CH_2 ring), 44.3 (CH_2 ring), 49.4 (CH_2 ring), 54.1 (NCH_2CO), 68.0 (OCH_2Ph), 128.9 (Ph), 129.2 (Ph), 135.3 (Ph), 173.3 (CO_2). FTIR (KBr): 3398, 2974, 2645, 2435, 1743, 1611, 1565, 1480, 1460, 1440, 1375, 1351, 1277, 1188, 1167, 1070, 940 cm^{-1}. *m/z* (ESI+) 321 (100% [M + H]$^+$). Anal. Found C = 45.5%, H = 7.7%, N = 12.9% $C_{17}H_{28}N_4O_2 \cdot 3HCl \cdot H_2O$. Theory: C = 45.6%, H = 7.4%, N = 12.5%.

1,4,7,10-Tetraazacyclododecane-1,4,7-tris(methylcarbonylamide), 10-Benzyl Acetate (6). K_2CO_3 (9.0 g, 65 mmol) was added to monoprotected cyclen **5** (2.9 g, 6.5 mmol) in acetonitrile (50 mL). The suspension was heated for 20 min at 60 °C. 2-Bromo-*N*-methylacetamide (2.96 g, 19.6 mmol) was then added in one portion. The reaction mixture was heated overnight at 60 °C then cooled, filtered, and washed with cold acetonitrile (2 × 50 mL). The solids were dissolved in DI water (30 mL), extracted with dichloromethane (3 × 250 mL), and the combined organic fractions dried over Na_2SO_4. The solvents were removed under reduced pressure to afford a colorless product (3.29 g, 95% yield).[1]H NMR (270 MHz, $CDCl_3$): δ = 2.1–2.6 (16H, m br, CH_2 ring), 2.7 (3H, s, CH_3), 2.75 (6H, s, CH_3), 3.11–3.17 (8H, m, CH_2CO), 5.1 (2H, s, OCH_2Ph), 7.3 (5H, m, Ph), 7.8 (4H, s br, $NHCH_3$). ^{13}C NMR (67.5 MHz, $CDCl_3$) δ = 26.1 (CH_3), 26.2 (CH_3), 50.5 (CH_2 ring), 51.5–51.7 (CH_2 ring), 55.2 (CH_2CONH), 57.2 (CH_2CONH), 57.6 (CH_2CO), 67.0 (CH_2Ph), 128.5 (Ph), 128.7 (Ph), 135.5 (Ph), 171.6 (CONH), 171.9 (CONH), 172.4 (COO). FTIR (KBr): 3258, 3076, 2970, 2948, 2823, 1732, 1654, 1553, 1449, 1410, 1370, 1304, 1235, 1192, 1103, 990 cm^{-1}. *m/z* (ESI+) 556 (100% [M + Na]$^+$); Anal. Found C = 46.8%, H = 8.5%, N = 15.0% $C_{26}H_{43}N_7O_5 \cdot 7.5\ H_2O$. Theory: C = 46.7%, H = 8.8%, N = 14.7%.

1,4,7,10-Tetraazacyclododecane-1,4,7-tris(methylcarbonylamide)-10-acetate (1). 10 % palladium on carbon (0.8 g) was added to a solution of **5** (4.3 g, 8.1 mmol) in ethanol (30 mL). The reaction mixture was placed in a hydrogenation vessel for 24 h with the H_2 pressure of 45 psi. The catalyst was filtered through filter agent (Celite545, Aldrich) and the solvents were removed under reduced pressure to afford a colorless solid (2.9 g, 81% yield). ^{1}H NMR (270 MHz, D_2O): δ = 2.7 (6 H, s, CH_3), 2.8 (3H, s, CH_3), 3.0 (4H, s br, ring CH_2), 3.18 (4H, s br, ring CH_2), 3.4 (8H, s br, ring CH_2), 3.5 (4H, s, CH_2CONH), 3.8 (2H, s, CH_2CONH), 4.0 (2H, s, CH_2CO_2). ^{13}C NMR (67.5 MHz, D_2O): δ = 26.2 (CH_3), 26.3 (CH_3), 48.1–51.5 (CH_2 ring, br), 51.9 (CH_2CONH), 54.6 (CH_2CONH), 56.1 (CH_2CO_2), 166.2 (CONH), 169.9 (CONH), 172.4 (CO_2). FTIR (KBr): 3262, 3095, 2967, 2843, 1654, 1561, 1452, 1394, 1157, 1087, 1046, 909 cm^{-1}. *m/z* (ESI−) 442 (100% [M − H]$^-$).

Preparation of Thulium Complexes. An aqueous solution of the ligand **L2** was adjusted to pH = 5.5 using 1 M NaOH. A stoichiometric quantity of a standardized aqueous thulium chloride solution was added and the reaction mixture stirred at room temperature with constant adjustment of pH to 5.0–5.5 using 1 M NaOH. After approximately 1 h, no further drop in pH was observed and the final pH was adjusted to 7 followed by filtration. The absence of free thulium was verified by adding a small aliquot of this equilibrium mixture to a solution of 0.15 M acetate buffer, pH 5.5, containing a drop of xylenol orange as indicator. Once verified, the Tm**L2** solution was freeze-dried and stored in powdered form at −20 °C. Tm-**L2**: FTIR (KBr): 2120 (N═C═S) cm^{-1}; *m/z* (FAB+) 770 [Tm^{3+}**L2 - 2H**]$^+$.

1,4,7,10-Tetraazacyclododecane-1,4,7-tris(methylcarbonylamide)-10-1-*N*-hydroxy Succinimidyl Acetate (7). Acetate (**7**) was obtained by the method of Lewis et al. (*19*). Compound **L1** (2.9 mg, 6.6 μmol) was dissolved in water (1.043 mL, 4 °C), and the pH of the solution adjusted to 5 with 15 μL of 1 M HCl. *N*-Hydroxysuccinimide (0.76 mg, 6.6 μmol) was dissolved in water (0.06 mL, 4 °C) and added. The reaction mixture was stirred for 5 min, followed by addition of 0.05 mL solution of 1-ethyl-3-[3-dimethylaminopropyl]carbodiimide hydrochloride (EDC) (0.63 mg, 3.3 μmol) at 4 °C. The reaction mixture was stirred for 30 min on ice (at 0 °C) and the final pH of the reaction mixture adjusted to 7.4 by addition of 50 μL of 0.2 M Na_2HPO_4. The active ester was used for modification of adenovirus particles without further purification.

Cell Lines. Cell lines were cultured in Dulbecco's Modified Eagle's Medium (DMEM) supplemented with 10% (vol/vol) fetal bovine serum (FBS). Standard cell culture conditions were incubation at 37 °C and 5% CO_2. The 911 cell line used for propagation of recombinant adenovirus is derived from a human embryonic retinoblast and contains an integrated copy of the leftmost portion of the adenovirus 5 genome that complements the defect in E1 replacement vectors. The HT1080 cells used for *in vitro* bioactivity determination of viral particles are a human fibrosarcoma tumor cell line.

Preparation of Purified Recombinant Adenovirus. The AdCMVLuc virus (*20*) used here was chosen for ease of bioactivity analysis. 911 cells were cultured in DMEM containing 10% FBS grown to near 100% confluency. The growth medium was removed, and cells were infected by adding virus stock solution diluted into 2.5 mL DMEM, 2% FBS. The plate was rocked at 15 min intervals for 1 h. DMEM, 2% FBS (15 mL) was added to the dish, followed by incubation at 37 °C for 3–5 days. The cell were lysed by addition of 10% Nonidet P-40 (US Biochemical), and the cell lysate was centrifuged at 10 000 rpm for 10 min at 4 °C in a Sorvall GSA rotor to separate the cell debris. The supernatant was saved and one-half volume of 20% PEG 8000, 2.5 M NaCl, was added to each bottle. The bottles were incubated on ice for 1 h to precipitate the virus particles. The precipitated virus was collected by centrifugation at 10 000 rpm for 10 min at 4 °C. The viral pellet was resuspended in 5 mL of CsCl (d = 1.10 g/mL) in 20 mM Tris HCl pH 8.0 buffer. The suspension was centrifuged for 5 min at 8000 *g* at 4 °C in a Sorval SS-34 rotor. CsCl gradients were prepared as follows: 2.0 mL CsCl (d = 1.40 g/mL) in 20 mM Tris HCl (pH 8.0) buffer on the bottom of a centrifuge tube, and 3.0 mL CsCl (d = 1.30 g/mL) in 20 mM Tris HCl (pH 8.0) buffer on the top of the previous layer. The viral CsCl supernatant in 20 mM Tris HCl (pH 8.0) buffer was layered on the top of the CsCl step gradient and centrifuged at 20 000 rpm for 2 h at 20 °C in a Beckman SW41 swinging bucket ultracentrifuge rotor. The white viral opalescent band, which appeared as a band between the 1.3/1.4 CsCl layers, was collected. Virus was further purified by gel permeation chromatography using Sepharose CL-4B equilibrated with isotonic phosphate (PBS, 137 mM NaCl, 2.74 mM KCl, 4.3 mM Na2HPO4, 1.4 mM KH_2PO_4, pH 7.5) or carbonate (0.05 M Na_2CO_3/$NaHCO_3$, 140 mM NaCl, pH 8.6) buffers. Virus was stored at −80 °C after addition of glycerol to 10% final concentration until use.

Conjugation of L1 to Adenovirus. To a 0.1 mL aliquot of adenovirus particles (1.0 × 10^{13} particles/mL, 1.66 pmol) in PBS buffer was added a solution of active ester **7** in phosphate buffer (2.7 mM) at different molar ratios. Additional buffer was

added as necessary to keep the volume in all vials constant. The reaction mixture was incubated at 4 °C for 4 h on the rocker. Spin columns were prepared for gel permeation chromatography as follows: a 3 mL disposable syringe was plugged with cotton and filled with Sepharose CL-4B equilibrated in acetate buffer (0.15 M CH_3COONH_4, 0.14 M NaCl, pH 7). Those columns were washed by centrifugation at 3000 rpm for 3 min at least 5 times until a constant volume of eluent was obtained prior to conjugate purification. Each reaction mixture was placed on a spin column and centrifuged at 3000 rpm for 3 min in an Eppendorf Centrifuge model 5810 R. After viral loading, the spin column was washed once with 0.2 mL acetate buffer. The two fractions were collected, vortexed, centrifuged, and the absorbance at 260 nm was measured. The samples were analyzed to determine the ligand/adenovirus ratio and bioactivity.

Conjugation of L2 to Adenovirus. L2 (5 mg, 8.3 μmol) was dissolved in water (0.1 mL), followed by addition of 2.86 mL of carbonate buffer previously cooled to 4 °C. To 0.2 mL of adenovirus (1×10^{13} particles/mL, 3.32 pmol) in carbonate buffer (0.05 M $Na_2CO_3/NaHCO_3$, 140 mM NaCl, pH 7.9) were added different amounts of **L2**. The volume of each reaction mixture was adjusted to keep it constant in all vials. The reaction mixtures were placed in a cooled room (4 °C) on the continuous mixing rocker for 6 h. The **L2**-AdCMVLuc conjugates were purified in a manner identical to that of **L1**-AdCMVLuc.

Kinetics of L1 and L2 Conjugation to Adenovirus Particles. To 0.4 mL of adenovirus in PBS (4×10^{12} particles/mL) or carbonate (5×10^{12} particles/mL) buffer was added 61 μL (2.71 mM) of freshly prepared active ester **7** or 49 μL (2.8 mM) of isothiocyanate (**L2**). The reaction mixtures were incubated at 4 °C on the continuous mixing rocker, and at different time intervals 100 μL of each reaction mixture was taken and purified to evaluate the ligand/adenovirus ratio and bioactivity.

Determination of Ligand/Adenovirus Ratio. The number of ligands per adenovirus particle was determined by using Pb(II) as a colorimetric indicator as previously described (*21*). Briefly, the method is based on the decrease in absorbance at 656 nm that occurs upon transchelation of Pb^{2+} from arsenazo III to the virus-bound chelate sites. Experimentally, 100 μL of each conjugate solution was incubated with Pb(II)-Arzenaso III for 30 min to allow sufficient time for binding of Pb^{2+} into all chelate sites on the virus (*21*) prior to measuring the absorbance at 656 nm.. A calibration curve was established by mixing known concentrations of the parent ligand **L1** or **L2** (0.0–2.5 μM) with the lead reagent and measuring the absorbance at 656 nm. The virus concentration was obtained by measuring absorbance at 260 nm (1 OD unit corresponds to 1×10^{12} particles/mL).

Cell Infection and Bioactivity. The bioactivity of the viral preparations and viral conjugates was assessed by infection of HT1080 cells with an adenovirus vector that expresses firefly luciferase from the cytomegalovirus (CMV) promoter. The expression of luciferase activity in the cells infected with adenovirus is directly proportional to the number of infecting virus particles. HT1080 cells were cultured in DMEM with 10% FBS in 12 well plates. The growth medium was removed and 0.5 mL fresh (warmed to 37 °C) medium was added to each well. Aliquots (1, 3, and 10 μL) of a purified adenovirus conjugate or control unmodified adenovirus were added to wells in duplicate. After a 1 h incubation period at 37 °C to allow the virus to bind and infect cells, the infection medium was removed and replaced by 1 mL of fresh medium (warmed to 37 °C). The plates were then incubated for 15–19 h at 37 °C to allow luciferase expression (*22*).

Luciferase Assay. Infected HT1080 cells were assayed for luciferase expression as previously described (*14*). Briefly, cells were lysed by addition of 0.5 mL of lysis buffer (25 mM Tris−phosphate buffer pH 7.8, 2 mM dithiothreitol (DDT), 2 mM 1,2-diaminocyclohexane-*N*,*N*,*N*′,*N*′-tetraacetic acid 10% glycerol, 1% Triton X-100). Extracts (10 μL) were mixed with 0.1 mL of lysis buffer, and to that 50 μL of luciferin reagent (20 mM tricine, pH 7.8, 1.07 mM $(MgCO_3) \times 4Mg(OH)_2$, 2.67 mM $MgSO_4$, 0.1 mM EDTA, 33.3 mM DTT, 270 μM coenzyme A, 470 μM luciferin, 530 μM ATP) was added. Luminescence was measured for 10 s and expressed in relative light units (RLU).

Adenovirus Stability as a Function of Time. To 0.2 mL adenovirus (4×10^{12} particles/mL) in PBS (pH 7.4) or carbonate buffer (pH 7.9) was added 150 μL of PBS (pH 7.4) or carbonate buffer (pH 8.6) and viruses were incubated in the cold room at 4 °C. At different time intervals, aliquots were taken and samples used to infect HT1080 cells in duplicate. After 24 h, cells were extracted and assayed for luciferase expression as a measure of viral infectivity.

^{177}Lu-Adenovirus Binding Assays. The amount of complexed versus free $^{177}Lu^{3+}$ was determined by radio-TLC. 0.5 μL sample of a virus or virus−conjugate solution was spotted onto silica gel 60 TLC plates (EDM Chemicals Inc.) and, after drying with a stream of cold air, eluted with 10% ammonium acetate in methanol (1:3 v/v). Prior to TLC, excess DTPA was added to each virus sample to quantify the amount of radioactivity not associated with the adenovirus. As free uncomplexed $^{177}Lu(Ac)_3$ and $^{177}Lu^{3+}$-conjugated virus particles remain at the origin while $^{177}LuDTPA^{2-}$ moves with the solvent front, it was easy to distinguish $^{177}Lu^{3+}$-conjugated virus and $^{177}Lu^{3+}$ associated with the virus nonspecifically (R_f = 0–0.12) from $^{177}LuDTPA^{2-}$, which migrated with the solvent front (R_f = 0.48–0.50).

The virus conjugates were loaded with $^{177}Lu^{3+}$ as follows: 5 μL of $^{177}Lu^{3+}$ in 0.05 N HCl (11–12 μCi) was mixed with 15 μL of acetate buffer (0.15 M ammonium acetate, pH 8) then added to 50 μL of adenovirus (1.15×10^{12} particles/mL) in acetate buffer (0.15 M ammonium acetate, 140 mM NaCl). The reaction mixture was incubated at 25 °C for various selected time intervals, then 10 μL of the mixture was challenged with 20 000-fold excess DTPA (10 mM, pH 8). After an equilibration period of 30 min, the samples were analyzed by radio-TLC.

Preparation of TmL2−Adenovirus Conjugates. Adenovirus (2.4 mL, 5×10^{12} particles/mL) in Tris buffer was placed on a Sepharose CL-4B column equilibrated with HEPES buffer (pH 8.6 10 mM HEPES, 135 mM NaCl, 7 mM KCl). Adenovirus (3.1 mL, 3.85×10^{12} part/mL) was mixed with 355 μL of Tm**L2** (2.8 mM) in HEPES buffer (pH 8.6). The reaction mixture was incubated in a cold room at 5 °C with continuous stirring for 3 h, followed by quenching with 1 mL of 10 mM Tris HCl buffer pH 7.4. The adenovirus conjugate was concentrated by CsCl gradient centrifugation (on a discontinuous CsCl gradient of 1.3 and 1.4 g/mL CsCl as before) and gel filtered on a Sepharose CL-4B column equilibrated with HEPES buffer (pH 7.4, 10 mM HEPES, 135 mM NaCl, 7 mM KCl).

RESULTS AND DISCUSSION

Synthesis. L1 was synthesized as outlined in Scheme 2. Tris-Boc-protected cyclen **3** was obtained by published methods (*16*) followed by monoalkylation of the free amine with benzyloxybromoacetate under standard conditions (K_2CO_3/MeCN). Excess alkylating agent was removed by column chromatography to yield intermediate **4** followed by smooth removal of the Boc groups using an ethanolic hydrochloric acid to generate monobenzyl protected cyclen **5** as the HCl salt. The free amines of **5** were alkylated with 2-bromo-*N*-methylacetamide and 10 equiv of K_2CO_3 to produce **6**. It was not necessary to isolate the monobenzyl protected cyclen **5** in the free base form to perform

Scheme 2

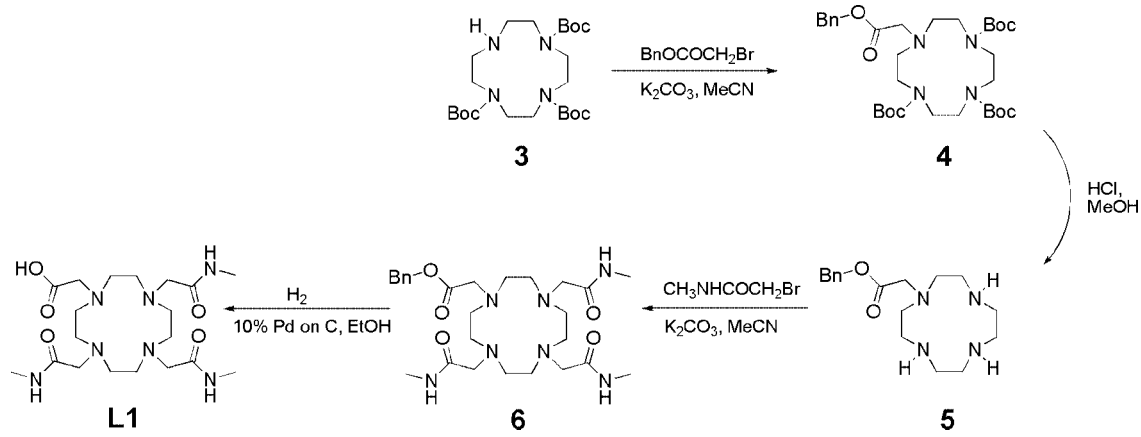

Scheme 3

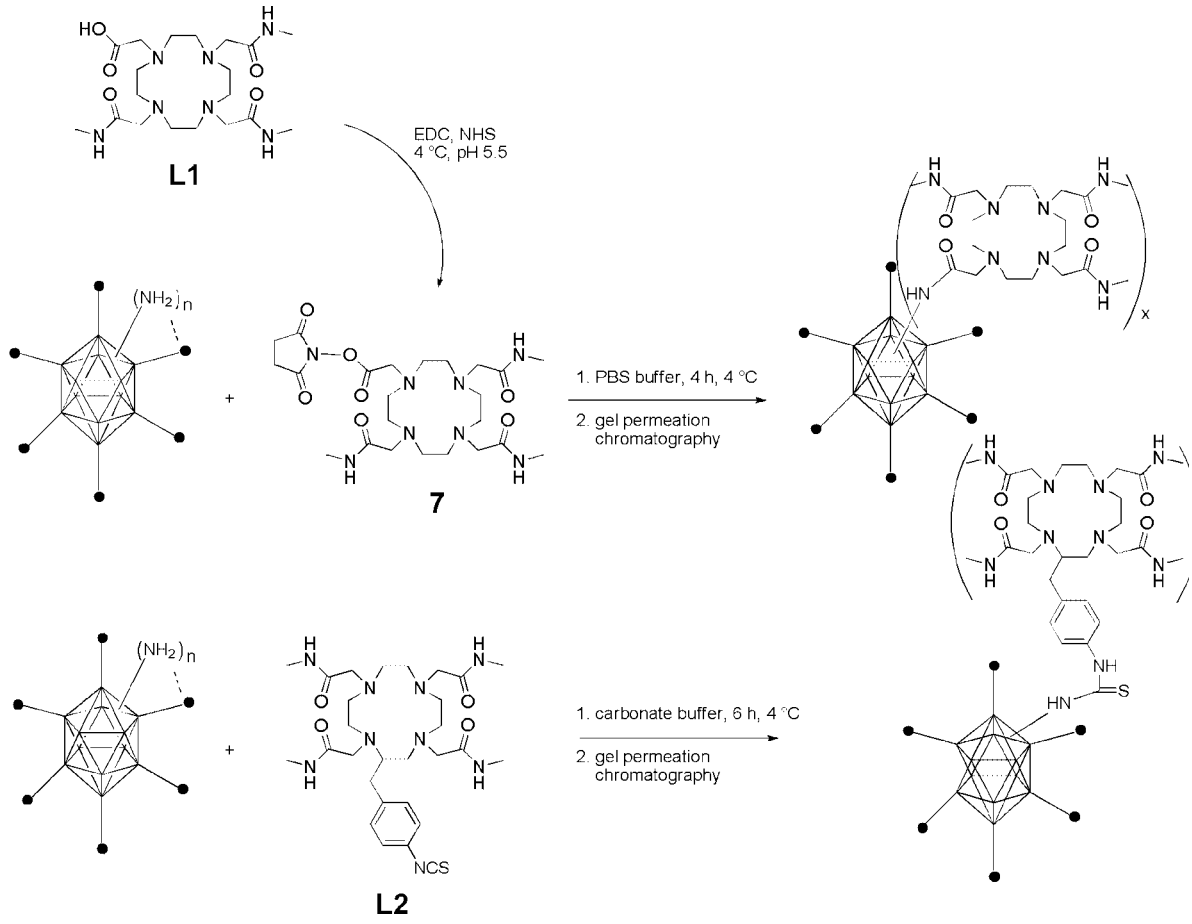

this reaction. Compound **6** was conveniently isolated in analytically pure form by precipitation from acetonitrile. **L1** was obtained by removal of benzyl protective group by hydrogenolysis with H_2 and 10% palladium on carbon in ethanol. The *N*-hydroxysuccinimide ester of **L1** was generated *in situ* according to a previously published method (*19*). Ligand **2** was synthesized using a previously published method (*17*).

Conjugation of L2 to Adenovirus. The isothiocyanate of DOTA-tetraamide reacts with the ϵ-amino group of viral surface lysine residues to produce a thiourea linkage under basic conditions (Scheme 3). The method of Mirzadeh et al. (*23*) was adapted to generate the **L2**−adenovirus conjugates. To estimate the number of reactive surface lysine residues per adenoviral particle, a set of reactions were run where the amount of added ligand **L2** was varied while the virus concentration was kept constant. Ligand **2** was reacted with adenovirus at [**L2**]:adenovirus ratios ranging from 10^3:1 to 10^6:1. Unreacted bifunctional chelator was removed from the viral conjugates by gel permeation chromatography, which removed >99% of the unreacted bifunctional agent as indicated by ^{177}Lu radiolabeling studies. Incubation of each virus conjugate with $^{177}Lu^{3+}$ and consequent analysis by radio-TLC showed that most of the radioactivity was associated with a fraction having an R_f of ∼0.1 The number of chelates on the adenovirus surface was established using a published Pb^{2+}-arsenazo III colorimetric method (*21*) and the adenovirus concentration was obtained by UV absorbance. Figure 1 shows that the reaction conditions

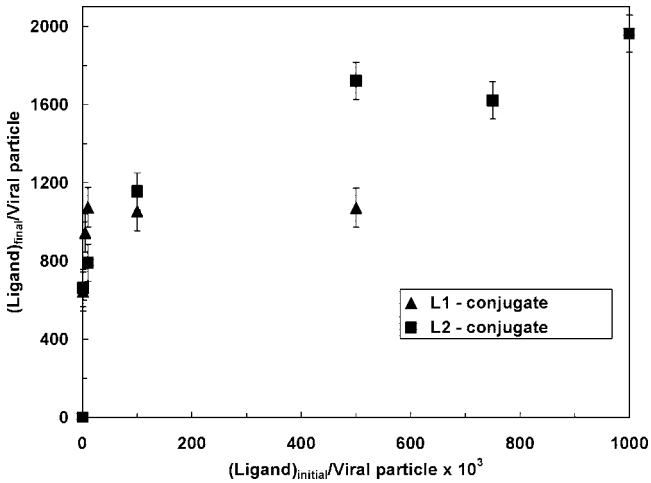

Figure 1. Plot showing the number of ligands attached per virus particle as a function of initial ligand concentration. Ligands **L1** and **L2** were incubated at 4 °C for 4 h (**L1**) and 6 h (**L2**) to allow for virus modification.

described above yielded virus particles with up to ~2000 **L2** chelates per adenovirus particle.

Conjugation of L1 to Adenovirus. The **L1** activated ester (compound **7**) was used to react with surface lysine residues of the adenovirus particles to form amide linkages (Scheme 3). Since the **L1** active ester was not isolated prior to its reaction with virus, the theoretical concentration of bifunctional agent is based on the concentration of EDC as the limiting reagent. To establish the maximum loading number of modified lysine residues with **7**, a similar strategy as described above for ligand **L2** was undertaken. However, due to complete loss in adenovirus bioactivity when using a 5×10^5:1 ratio of **L2**:AdCMVLuc, the reaction stoichiometry was reduced to **7**:AdCMVLuc ratios of 10^3:1, 5×10^4:1, 10^4:1, 10^5:1, and 5×10^5:1. The reaction mixtures were purified by gel permeation chromatography and analyzed by radio-TLC showing >99% radioactivity associated with the fraction having $R_f = 0.07$–0.11. Figure 1 shows that the number of attached chelates gradually increased to a maximum of ~1100 with increasing concentrations of the active ester, **7**. A comparson of the two conjugation experiments shows that the number of attached **L1** ligands maximizes near ~1100 chelators with no significant increase in the number of chelators observed beyond this point, whereas the number of attached **L2** ligands approached a maximum of ~2000. This difference most likely reflects the tendency of the more reactive NHS ester to hydrolyze under these experimental conditions, although the reduced steric demand of **L2** relative to **L1** may also play a role at the higher conjugation efficiency of **L2**.

Optimal Reaction Times for Lower Concentrations of Reactive Bifunctional Agents. In a second series of experiments, the active ester of **L1** (ligand **7**) or **L2** was added to adenovirus in 50 000-fold excess at 4 °C, and after various incubation periods (Figure 2), the reactions were terminated by rapid gel permeation chromatography using spin columns. Although the active ester **7** reacts more rapidly with lysine amino groups initially (Figure 2), after 2 h there was no significant difference in the total number of **L1** versus **L2** ligands attached likely due to competitive hydrolysis of NHS ester at this reaction pH. In separate experiments, it was shown that the active ester **7** was consumed within 2 h. These data show that both reagents modify an equal number of surface lysine groups (~1200) after a 2 h incubation time at 4 °C.

Bioactivity (Luciferase) Assay. In order to be considered useful as a vector for optical imaging, the modified virus must

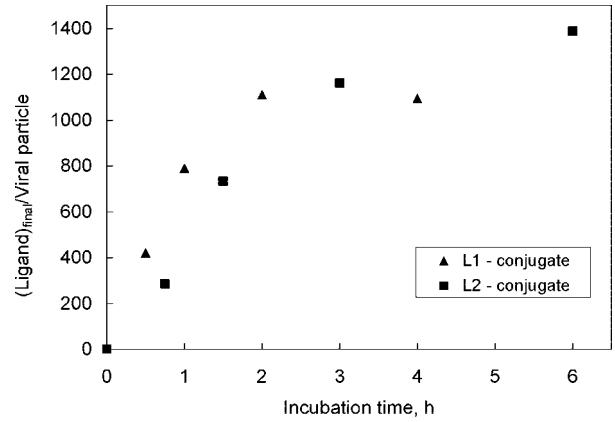

Figure 2. Plot showing the number of ligands attached per virus particle as a function of incubation time for ligands **L1** and **L2**. All modifications were performed at 4 °C.

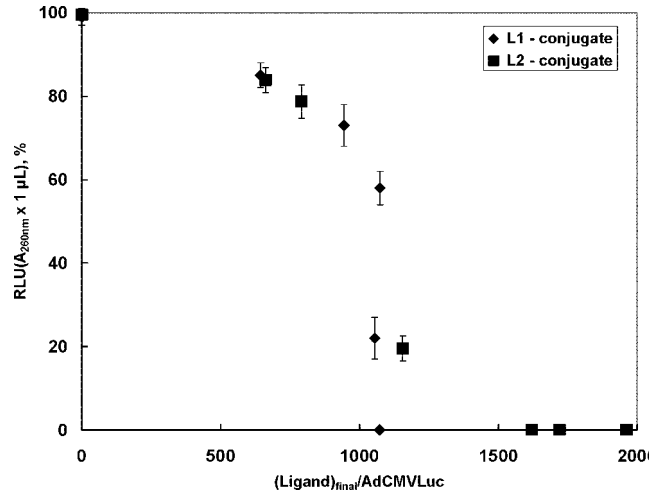

Figure 3. Plot showing the reduction in viral infectivity as a function of the number of ligands attached to virus particles. At each time point shown in Figure 2, an aliquot of modified virus was purified and used to infect HT1080 cells. Unmodified virus was used as a control and the extent of luciferase expression (in RLU) was set to 100%. Luciferase activity measured in each modified virus sample was expressed as a percentage of control.

maintain an ability to infect cells and express luciferase. To evaluate the effects of chemical modification, viral bioactivity was assessed by infecting HT 1080 cells with modified adenovirus particles. As shown in Figure 3, a significant decline in viral bioactivity was observed upon modification of surface lysines with either reactive ligand **L1** or **L2**. Viral bioactivity deceased almost linearly with increasing number of conjugated ligands until about 800 ligands were attached. When the number of attached ligands reached ~1000 per viral particle, viral infectivity dropped precipitously, as these conjugation reactions derivatize not only reactive lysine groups on the hexon capsid proteins of the core viral particle but also the fiber proteins which are responsible for the attachment of the virus to the host cell. The results shown in Figure 3 suggest that 800–900 sites can be modified without a dramatic loss in bioactivity, but further modification has a much more dramatic effect on the ability of the virus to infect cells. In samples where ~1100 molecules of **L1** or 1200 molecules of **L2** were conjugated, viral bioactivity decreased to ~20% of control values (20% residual activity). This amount of residual activity could reflect a subpopulation of particles that are substituted at a fractionally lower level than the average particle in the population, but there is little reason to assume such an anisotropic distribution in the extent of

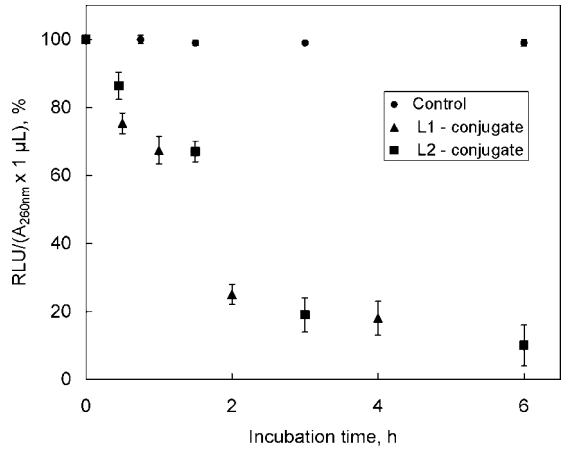

Figure 4. Plot showing the loss in bioactivity as a function of time after addition of 50 000-fold excess ligand (either **L1** or **L2**) to viral particles.. The initial time points (0 h) correspond to the bioactivity of unmodified adenovirus in the corresponding buffer . Control represents the ability of unmodified adenovirus to infect HT1080 cells after incubation at 4 °C.

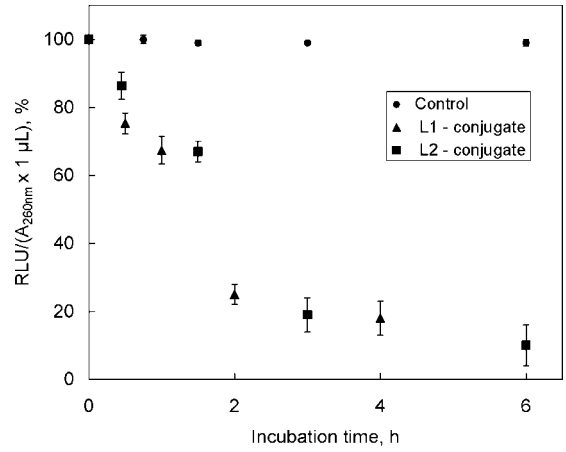

Figure 5. Residual $^{177}Lu^{3+}$ bound to adenovirus particles as a function of incubation time. At the indicated time-points, 20 000-fold excess of DTPA (pH 8) was added to remove weakly bound $^{177}Lu^{3+}$ and the virus was purified by gel filtration chromatography and counted.

substitution across the population of particles given that there are hundreds to thousands of potential substitutions per particle, and a trillion particles per milliliter in the solution. We assume that average level of substitution is reflective of the average level of bioactivity, some with more substitution per particle (and less infectivity), some with less (and more infectivity). For the purposes of this study, a goal of creating labeled virus particles with a minimum of 50% bioactivity was considered acceptable.

To achieve this target, another set of experiments was performed where the amount of excess **L1** or **L2** was lowered to 50 000-fold excess and aliquots of sample were removed as a function of time to follow the progression of the chemical reactions. Those results are reported in Figure 4. After a 1 h conjugation reaction using the active ester **7**, 790 chelators were attached and at the same time ~70% of bioactivity was retained. In comparison, the isothiocyanate, **L2**, showed 730 chelators were loaded per adenoviral particle after a 1.5 h incubation time and this virus maintained ~72% bioactivity. This indicates that, when using an initial excess of 50 000 bifunctional chelators per virus particle, the conjugation reaction should be terminated at 1 and 1.5 h for **L1** and **L2**, respectively, to achieve optimal results. Any potential loss of bioactivity arising from instability of the virus in PBS or carbonate buffer was eliminated by running a set of control reactions. Indeed, the adenovirus maintained a full ability to infect cells upon incubation in PBS (pH 7.4) and carbonate (pH 7.9) for 9 h at 4 °C (Figure 4).

Radiolabeling of Adenovirus. Initial attempts to fill only the conjugated ligand sites on the surface of the adenovirus with either Eu^{3+} or $^{177}Lu^{3+}$ proved unsuccessful because of nonspecific binding of these metal ions at other virus particle locations. To better understand this initial observation, unmodified adenovirus particles were incubated with $^{177}Lu^{3+}$ and then challenged with an excess of DTPA to quantify the amount of radioactivity associated with the viral particle through nonspecific binding. Figure 5 shows that the amount of nonspecific binding of $^{177}Lu^{3+}$ to the virus particles increases with incubation time and maximizes at ~10% after 9 h. This shows that $^{177}Lu^{3+}$ gets trapped by the viral particle, perhaps internally, by binding sites that are inaccessible to DTPA. Similar observations were made by Basu et al. (*24*). where they identified 180 metal binding sites based on the crystal structure of cowpea chlorotic mottle virus. Each binding site is thought to be composed of five amino acid residues from two adjacent protein subunits. Tb^{3+} binding, as measured by fluorescence, was tested both on the wild-type virus and a mutant virus where the RNA had been removed. In both cases, metal binding displayed very similar K_d values (K_d = 19 μM and 17 μM, respectively) suggesting that the encapsidated RNA does not contribute to the metal binding. Even though adenovirus represents a very different class of virus, it is tempting to speculate that the DNA in its interior does not bind metal ions nonspecifically. Heavy metal binding sites have been identified using the crystal structure of hexon, the major coat protein of adenovirus (*25*). These sites are located close to the loops l_1, l_2, or l_3 on the surface of the protein molecule or l_4 which lies underneath the hexon. The loop l_4 of each hexon protein might be particularly inaccessible to DTPA. Since this nonspecific binding of heavy metals might complicate the interpretation of any subsequent imaging experiments, an alternative prelabeling approach was adopted for the **L2** system where the ligand itself could be preloaded with the desired metal ion prior to labeling the virus. This strategy could not be used for the more reactive activated ester form of **L1**.

Conjugation of TmL2 to Virus Particles. Given that the detection limit of thulium-based PARACEST agents has been reported to be in the micromolar range (*26*), adenovirus particles were labeled with the prelabeled reagent, Tm**L2**, to evaluate whether CEST can be detected from samples of surface-labeled virus particles. The Tm**L2**−adenovirus conjugate was prepared using techniques similar to that of the parent ligand (Scheme 3). Two control experiments were run; first, an unmodified adenovirus was prepared in HEPES buffer and incubated with $TmDTMA^{3+}$ (1,4,7,10-tetra(methylcarbonylamide)-1,4,7,10-tetraaza cyclododecane), a nonbifunctional version of Tm**L2**. This control was performed to estimate the effect of entrapment or strong electrostatic interactions of positively charged complexes with viral particles. The control samples were treated in a similar fashion to that of Tm**L2**−adenovirus conjugates. The concentrations of the viral particles were adjusted to maintain a constant 2.5×10^{13} particles/mL, and the thulium concentrations were determined by inductively coupled plasma mass spectrometry (ICP-MS). The Tm**L2**−adenovirus conjugates were found to contain 1140 thulium ions per adenovirus particle, indicating that a result similar to conjugation with nonprelabeled **L2** was obtained (Figure 3). Somewhat unexpectedly, adenovirus particles incubated in the presence of $TmDTMA^{3+}$ for 3 h and consequently purified also contained ~280 entrapped $TmDTMA^{3+}$ complexes. This indicates that the tripositive complex, $TmDTMA^{3+}$, is tightly bound by virus particles and is not removed by simple gel purification procedures. Even though the stability of $TmDTMA^{3+}$ (log K_{TmL} = 14.08) is

Table 1. Experimental T_2 Relaxation Times and M_Z/M_0 for Adenovirus Particles

	T_2, s	M_Z/M_0, %	[Tm^{3+}], μM	[virus], 10^{-7} M
adenovirus	0.244 ± 0.002	80	N/D	0.42
adenovirus−TmDTMA	0.220 ± 0.002	82	11.8	0.42
adenovirus−Tm**L2**	0.127 ± 0.002	68	48	0.42

considerably lower than the parent chelate, $TmDOTA^-$, it has been shown that other lanthanide cations (Ln^{3+}) dissociate much more slowly from tetraamide ligands such as DTMA, **L1**, or **L2** than from DOTA (*26*), so the possibility of Tm^{3+} release from any of these chelates on the adenovirus particle is unlikely. Thus, we feel confident that thulium, as measured by ICP-MS for both the control and conjugation products, reflects Tm-$DTMA^{3+}$ and Tm**L2** and not free Tm^{3+} released from these chelates. The results of the control and radiolabeling experiments show that a significant level of nonspecific binding by any positively charged species, whether it be a simple cation such as $^{177}Lu^{3+}$ or a chelated cation such as $TmDTMA^{3+}$, is difficult to avoid.

CEST Studies. Recently, Vinogradov et al. (*27*) reported that Tm^{3+}-based PARACEST agents can be detected by imaging in the μM (micromolar) range by using a modified on-resonance low-power WALTZ-16 pulse train for activation. To apply this technique to labeled virus particles, the intensity of the solvent–water signal was measured after application of WALTZ-16 pulse train directly on the water resonance and compared to a spectrum collected by placing the WALTZ-16 pulse train far off resonance. Any differences in intensities between those two spectra should then reflect rapid water exchange on and off the viral-bound Tm^{3+} PARACEST agent (*27*). The modified WALTZ-16 pulse sequence depends on the number of parameters including T_1 and T_2 relaxation times of bulk water and the lifetime of water molecule coordinated to thulium ion in the complex (τ_M). Considering the relatively short bulk water transverse relaxation time (T_2, Table 1) of the adenovirus solution (~0.22 ms at [virus] = $(2.5 \pm 0.1) \times 10^{13}$ particles/mL), a WALTZ pulse length of 856 μs and irradiation power of 291 Hz was chosen (*27*).

The solvent–water T_1 relaxation times for these samples were on the order of 2 s, a value considered adequate for this type of WALTZ-16 experiment (*27*). The experimental T_2 values were however considerably shorter, in the range 0.12–0.24 s, and as predicted by theory, the biggest effect on the magnetization will occur whenever T_2 is ~0.4 s. On the basis of those predictions and to subtract out the influence of T_2, the WALTZ-16 experiment was performed first on an unmodified adenovirus

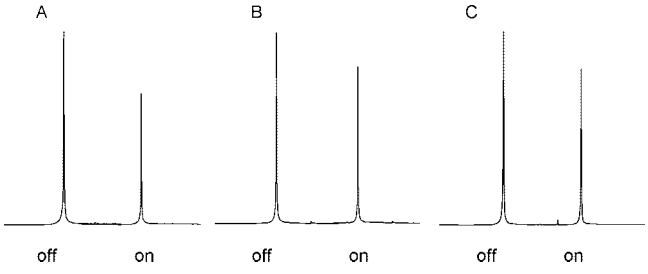

Figure 6. Residual bulk water signal intensities after applying WALTZ-16 pulse train (B_0 = 500 MHz, B_1 = 291 Hz, pulse length 0.856 ms, 25 °C) either "off" resonance where the carrier frequency is set to 1986 Hz away from the water resonance or "on" resonance where the carrier frequency is set at the water frequency. (A) corresponds to a sample containing Tm**L2**−adenovirus in the HEPES buffer (10 mM HEPES, 135 mM NaCl, 7 mM KCl); the total concentration of Tm**L2** in the sample was 48 μM. (B) 48 μM $TmDTMA^{3+}$ in HEPES buffer. (C) an equivalent amount of unmodified adenovirus (as in A) in HEPES buffer.

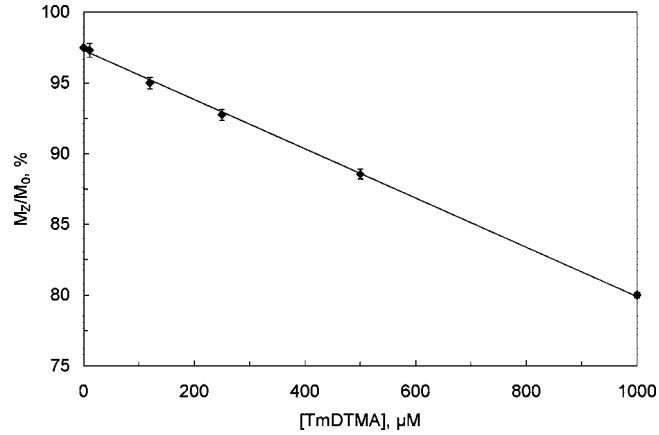

Figure 7. Plot of the decrease in water magnetization (M_Z/M_0) using the WALTZ-16 pulse sequence as a function of $TmDTMA^{3+}$ concentration. The WALTZ-16 pulse train was applied on resonance (B_0 = 500 MHz, B_1 = 291 Hz, pulse length 0.856 ms, 25 °C).

sample (as control) and the Tm**L2**−adenovirus sample. As shown in Figure 6, the water intensity was reduced by ~20% for the unmodified virus sample (Figure 6b) and 18% for adenovirus incubated in the presence of $TmDTMA^{3+}$ (Figure 6c), compared to buffer alone. Although there was considerable entrapment of $TmDTMA^{3+}$ (noncovalent interactions) when incubated with the adenovirus, the presence of this compound did not change M_Z/M_0 compared to unmodified virus. This suggests that the entrapped $TmDTMA^{3+}$ is not exchanging protons rapidly with bulk water and furthermore shows that the adenovirus alone causes a decrease in water intensity using the WALTZ-16 pulse train due to its short T_2. The T_2 of the adenovirus−$TmDTMA^{3+}$ sample was somewhat shorter than adenovirus alone, likely due to the presence of ~280 entrapped $TmDTMA^{3+}$ complexes per adenovirus particle. Interestingly, a substantially larger effect was measured for the TmL2 - adenovirus conjugate, in which a 32% decrease in solvent–water intensity was observed. The 12% difference in water intensity between these two samples can be directly attributed to the presence of the conjugated PARACEST agent on the surface of the adenovirus.

The dependence of $TmDTMA^{3+}$ concentration on the reduction of observed magnetization (M_Z/M_0) using WALTZ 16 pulse train was also investigated as a positive control. Figure 7 summarizes the results and clearly shows that 48 μM Tm-$DTMA^{3+}$ (equivalent to the concentration of Tm**L2** in the virus sample used in Figure 6) produces a modest 2% reduction in signal intensity. Thus, 12% difference in water intensity observed for the Tm**L2** virus particle is not simply due to the presence of conjugated Tm**L2** in solution, but must reflect some exchange advantage of viral-conjugated Tm**L2** compared to the nonconjugated parent complex, $TmDTMA^{3+}$. This suggests that water exchange in Tm**L2** is altered when bound to the surface of virus particles (compared to that seen for $TmDTMA^{3+}$) and this change is advantageous for CEST. Whether this reflects an increased or decreased water exchange rate for the viral-bound Tm**L2** (both could result in a CEST advantage if operating in certain water exchange regimes (*28*)) will require more detailed studies that are beyond the scope of the present investigation.

CONCLUSIONS

Labeling of virus particles with two different bifunctional ligands resulted in diminished viral bioactivity that decreased in proportion to the number of the attached ligands. For in vivo applications where it is desirable to have at least 50% viral bioactivity, it was found that the number of attached ligands

needed to be fewer than ~800 to maintain 75–80% bioactivity. Labeling experiments with $^{177}Lu^{3+}$ and $TmDTMA^{3+}$ at 4 °C (as a free chelate control) showed nonspecific binding of positively charged species to the adenovirus. To circumvent nonspecific metal ion binding to the adenovirus, the isothiocyanate bifunction ligand (**L2**) was preloaded with Tm^{3+} and the resulting chelate was used to label the adenovirus with a conjugation efficiency similar to that of free **L2**. The resulting Tm**L2**−adenovirus conjugate showed a 12% decrease of water signal intensity using a WALTZ-16 sequence for CEST activation. These results demonstrate that PARACEST-labeled virus particles can be prepared that retain high viral infectivity and expression of luciferase activity and, at the same time, are sufficiently sensitive to be detected by WALTZ-16 initiated CEST imaging.

ACKNOWLEDGMENT

This work was supported in parts by grants from the National Institutes of Health (CA-115531 and RR-02584) and the Robert A. Welch Foundation (AT-584). We also thank Julie Poirot for her assistance with the adenovirus preparation.

LITERATURE CITED

(1) Ward, K. M., Aletras, A. H., and Balaban, R. S. (2000) New class of contrast agents for MRI based on proton chemical exchange dependent saturation transfer (CEST). *J. Magn. Reson. 143*, 79–87.

(2) van Zijl, P. C. M., Jones, C. K., Ren, J., Malloy, C. R., and Sherry, A. D. (2007) MRI detection of glycogen in vivo by using chemical exchange saturation transfer imaging (glycoCEST). *Proc. Natl. Acad. Sci. U.S.A 104*, 4359–4364.

(3) Zhang, S., Winter, P., Wu, K., and Sherry, A. D. (2001) A novel europium(III)-based MRI contrast agent. *J. Am. Chem. Soc. 123*, 1517–1518.

(4) Zhang, S., Merritt, M., Woessner, D. E., Lenkinski, R. E., and Sherry, A. D. (2003) PARACEST agents: Modulating MRI contrast via water proton exchange. *Acc. Chem. Res. 36*, 783–790.

(5) Goffeney, N., Bulte, J. W. M., Duyn, J., Bryant, L. H., and van Zijl, P. C. M. (2001) Sensitive NMR detection of cationic-polymer-based gene delivery systems using saturation transfer via proton exchange. *J. Am. Chem. Soc. 123*, 8628–8629.

(6) (a) Douglas, T., and Young, M. (1998) Host-guest encapsulation of materials by assembled virus protein cages. *Nature 393*, 152–155. (b) Douglas, T., Strable, E., Willits, D., Aitouchen, A., Libera, M., and Young, M. (2002) Protein engineering of a viral cage for constrained nanomaterials synthesis. *Adv. Mater. 14*, 415–418.

(7) Raja, K. S., Wang, Q., Gonzalez, M. J., Manchester, M., Johnson, J. E., and Finn, M. G. (2003) Hybrid virus-polymer materials. 1. Synthesis and properties of PEG-decorated cowpea mosaic virus. *Biomacromolecules 4*, 472–476.

(8) Wang, Q., Lin, T., Johnson, J. E., and Finn, M. G. (2002) Natural supramolecular building blocks cysteine-added mutants of cowpea mosaic virus. *Chem. Biol. 9*, 813–819.

(9) Wang, Q., Kaltgrad, E., Lin, T., Johnson, J. E., and Finn, M. G. (2002) Natural supramolecular building blocks: Wild-type cowpea mosaic virus. *Chem. Biol. 9*, 805–811.

(10) Johnson, J., Lin, T., and Lomonossoff, G. (1997) Presentation of heterologous peptides on plant viruses: genetics, structure, and function. *Annu. Rev. Phytopathol. 35*, 67–86.

(11) Anderson, E. A., Isaacman, S., Peabody, D. S., Wang, E. Y., Canary, J. W., and Kirshenbaum, K. (2006) Viral nanoparticles donning a paramagnetic coat: conjugation of MRI contrast agents to the MS2 capsid. *Nano Lett. 6*, 1160–1164.

(12) Allen, M., Bulte, J. W. M., Liepold, L., Basu, G., Zywicke, H. A., Frank, J. A., Young, M., and Douglas, T. (2005) Paramagnetic viral nanoparticles as potential high-relaxivity magnetic resonance contrast agents. *Magn. Reson. Med. 54*, 807–812.

(13) Gerard, R. D., Meidell, R. S. (1995) *Adenovirus vectors. DNA cloning: a practical approach.* (Hames, B. D., and Glover, D., Eds.) pp. 285–307, Oxford University, Press, Oxford, UK.

(14) Henry, L. J., Xia, D., Wilke, M. E., Deisenhofer, J., and Gerard, R. D. (1994) Characterization of the knob domain of the adenovirus type 5 fiber protein expressed in Escherichia coli. *J. Virol. 68*, 5239–5246.

(15) Zinn, K. R., Douglas, J. T., Smyth, C. A., Liu, H. G., Wu, Q., Krasnykh, V. N., Mountz, J. D., Curiel, D. T., and Mountz, J. M. (1998) Imaging and tissue distribution of 99mTc-labeled adenovirus knob (serotype 5). *Gene Ther. 5*, 798–808.

(16) Woods, M., Kiefer, G. E., Botta, S., Castillo-Muzquiz, A., Eshelbrenner, C., Michaudet, L., McMillan, K., Mudigunda, S. D. K., Ogrin, D., Tircso, G., Zhang, S., Zhao, P., and Sherry, A. D. (2004) Synthesis, relaxometric and photophysical properties of a new pH-responsive MRI contrast agent: The effect of other ligating groups on dissociation of a p-nitrophenolic pendant arm. *J. Am. Chem. Soc. 126*, 9248–9256.

(17) Vasalatiy, O. (2007) PhD Thesis, Chapter 1, University of TX at Dallas, USA.

(18) Bianchi, A., Calabi, L., Giorgi, C., Losi, P., Mariani, P., Paoli, P., Rossi, P., Valtancoli, B., and Virtuani, M. (2000) Thermodynamic and structural properties of Gd^{3+} complexes with functionalized macrocyclic ligands based upon 1,4,7,10-tetraazacyclododecane. *Dalton Trans. 5*, 697–705.

(19) Lewis, M. R., Kao, J. Y., Anderson, A. L. J., Shively, J. E., and Raubitschek, A. (2001) An improved method for conjugating monoclonal antibodies with N-hydroxysulfo succinimidyl DOTA. *Bioconjugate Chem. 12*, 320–324.

(20) Herz, J., and Gerard, R. D. (1993) Adenovirus-mediated transfer of low density lipoprotein receptor gene acutely accelerates cholesterol clearance in normal mice. *Proc. Natl. Acad. Sci. U.S.A. 90*, 2812–2816.

(21) Dadachova, E., Chappell, L. L., and Brechbiel, M. W. (1999) Spectrophotometric method for determination of bifunctional macrocyclic ligands in macrocyclic ligand-protein conjugates. *Nucl. Med. Biol. 26*, 977–982.

(22) De Wet, J. R., Wood, K V, DeLuca, M., Helinsli, D. R., and Subramani, S. (1987) Firefly luciferase gene: structure and expression in mammalian cell. *Mol. Cell. Biol. 7*, 725–737.

(23) Mirzadeh, S., Brechbiel, M. W., Atcher, R. W., and Gansow, O. A. (1990) Radiometal labeling of immunoproteins: covalent linkage of 2(4-isothiocyanatobenzyl) diethylenetriamine pentaacetic acid ligands to immunoglobulin. *Bioconjugate Chem. 1*, 59–65.

(24) Basu, G., Allen, M., Willits, D., Young, M., and Douglas, T. (2003) Metal binding to cowpea chlorotic mottle virus using terbium(III) fluorescence. *J. Biol. Inorg. Chem. 8*, 721–725.

(25) Athappilly, F. K., Murali, R., Rux, J. J., Cai, Z., and Burnett, R. M. (1994) The refined crystal structure of hexan, the major coat protein of adenovirus type 2 at 2.9 Å resolution. *J. Mol. Biol. 242*, 430–455.

(26) Pasha, A., Tircso, G., Tircsone Benyo, E., Brucher, E., and Sherry, A. D. (2007) Synthesis and characterization of DOTA-(amide) 4 derivatives: equilibrium and kinetic behavior of their lanthanide (III) complexes. *Eur. J. Inorg. Chem. 27*, 4340–4349.

(27) Vinogradov, E., Zhang, S., Lubag, A., Balschi, J. A., Sherry, A. D., and Lenkinski, R. E. (2005) On-resonance low B1 pulses for imaging of the effects of PARACEST agents. *J. Magn. Reson. 176*, 54–63.

(28) Woessner, D. E, Zhang, S., Merritt, M. E., and Sherry, A. D. (2005) Numerical solution of the Bloch equations provides insights into the optimum design of PARACEST agents for MRI. *Magn. Reson. Med. 53*, 790–799.

BC7002605

Synthesis, Biophysical Characterization, and Anti-HIV Activity of Glyco-Conjugated G-Quadruplex-Forming Oligonucleotides

Jennifer D'Onofrio,[†] Luigi Petraccone,[‡] Luigi Martino,[‡] Giovanni Di Fabio,[†] Alfonso Iadonisi,[†] Jan Balzarini,[§] Concetta Giancola,*[,‡] and Daniela Montesarchio*[,†]

Dipartimento di Chimica Organica e Biochimica and Dipartimento di Chimica "Paolo Corradini", Università degli Studi di Napoli "Federico II", Via Cintia 4, I-80126 Napoli, Italy, and Rega Institute for Medical Research, Katholieke Universiteit Leuven, 10 Minderbroederstraat, B-3000 Leuven, Belgium. Received September 4, 2007; Revised Manuscript Received December 11, 2007

Novel hybrid oligonucleotides carrying the G-quadruplex-forming d($^{5'}$TGGGAG$^{3'}$) sequence, conjugated with mono- or disaccharides at the 3′ or 5′-end through phosphodiester bonds, have been synthesized as potential anti-HIV agents, *via* a fully automated, online phosphoramidite-based solid-phase strategy. CD-monitored thermal denaturation studies on the resulting quadruplexes indicated the insertion of a single monosaccharide at the 3′-end as the optimal modification, conferring improved stability to the quadruplex complex. In addition, the 3′-conjugation with glucose or mannose converted the anti-HIV inactive unmodified oligomer into active compounds. On the contrary, the 5′-tethering with these monosaccharides, as well as the conjugation, either at the 5′ or 3′-end, with sucrose, were in all cases detrimental to quadruplex stability and did not improve the biological activity. On the basis of the assumption that the kinetically and thermodynamically favored formation of the quadruplex complex is a prerequisite for efficient antiviral activity, a novel bis-conjugated oligonucleotide was designed. This combined a mannose residue at the 3′-phosphate end with bulky aromatic *tert*-butyldiphenylsilyl (TBDPS) group at the 5′-end, previously shown to markedly favor the formation of quadruplex complexes. The 5′,3′-bis-conjugated 6-mer, for which a detailed biophysical characterization has been carried out, resulted in 3-fold greater antiviral activity against HIV-1 than the sole 3′-glyco-conjugated oligonucleotide.

INTRODUCTION

Glyco-conjugates participate in a variety of biological processes of paramount importance, including molecular recognition, signal trafficking, and recognition of cell surface through carbohydrate-binding proteins, as well as intracellular lectins in a sugar-dependent manner (*1*–*3*). Synthetic glyco-conjugates are therefore useful diagnostic tools to identify and characterize endogenous sugar-binding proteins, but they can also show high potential in several therapeutic applications for specific drug delivery (*4, 5*). Methods to obtain glyco-conjugates—such as neoglycoproteins, glycosylated polymers, or glycopeptides—have been largely developed; on the contrary, synthetic strategies to prepare glyco-oligonucleotides are still far from being fully optimized (*6*).

Indeed, for several *in vivo* applications of oligonucleotides (ODNs), end derivatization with carbohydrates can result in a very convenient strategy to improve their otherwise poor internalization, eliciting specific sugar-binding processes to cell membranes and thus finally enhancing their cellular uptake by endocytosis. Through glyco-conjugation, further desirable properties can be conveyed to oligonucleotide-based drugs, as increased bioavailability, due to protection toward nucleases, and reduction of unwanted aggregation. DNA−carbohydrate conjugates have been prepared by direct, online solid-phase glycosidation of the 5′-end of oligonucleotides with suitable trichloroacetimidate sugar scaffolds (*7, 8*). A convenient procedure involved the use of unprotected carbohydrates, conjugated to 5′-amino-modified oligonucleotides by exploiting a reductive amination procedure (*9*). Recently, site-specifically galactosylated oligonucleotides, obtained from a 2′-deoxyuridine phosphoramidite carrying one galactose unit on the base, were synthesized, and periodic glycoclusters using a half-sliding oligonucleotide strategy could be obtained (*10, 11*). An alternative strategy to efficiently conjugate carbohydrates to ODNs was first explored by Akhtar and co-workers, who synthesized a suitable phosphoramidite derivative of mannose, incorporated onto the 5′-OH terminus of the solid-supported ODN by standard phosphoramidite chemistry (*12*). A similar approach has been recently proposed also by Joyce et al., who designed a new class of DNA−carbohydrate conjugates, called nucleo-glycoconjugates, based on the synthesis of three new phosphoramidite carbohydrate derivatives, inserted at the extremities or at defined, internal positions of the growing oligonucleotide chain (*13, 14*). In this frame, we recently synthesized suitably protected phosphoramidite derivatives of model mono- or disaccharides. When used in conjunction with DMT[1]-protected sugars immobilized on solid supports, they allowed us to prepare, through an online automated oligonucleotide synthesis protocol, a variety of 5′- and 3′-glycoconjugates of ODNs with stable phosphodiester linkages connecting the saccharide residues to one or both OH termini of the oligonucleotide chain (*15, 16*). In all the studied cases, the presence of the saccharide dangling ends was

* Corresponding author. Prof. Daniela Montesarchio, PhD, Dipartimento di Chimica Organica e Biochimica, Complesso Universitario di Monte S.Angelo, Via Cynthia, 4, I-80126 Napoli, Italy, FAX number: +39-081-674393, e-mail address: daniela.montesarchio@unina.it.

[†] Dipartimento di Chimica Organica e Biochimica, Università degli Studi di Napoli "Federico II".

[‡] Dipartimento di Chimica "Paolo Corradini", Università degli Studi di Napoli "Federico II".

[§] Katholieke Universiteit Leuven.

[1]Abbreviations: Ac = acetyl; CE = 2-cyanoethyl; CPG = controlled pore glass; DBB = 3,4-dibenzyloxybenzyl; DCC = *N*,*N*-dicyclohexylcarbodiimide; DIPEA = *N*,*N*-diisopropylethylamine; DMAP = 4-dimethylaminopyridine; DMT = 4,4′-dimethoxytriphenylmethyl; LCAA = long chain alkylamine; TBDPS = *tert*-butyldiphenylsilyl; TEA = triethylamine; TEAB = triethylammonium bicarbonate.

10.1021/bc7003395 CCC: $40.75 © 2008 American Chemical Society
Published on Web 02/07/2008

Scheme 1. Synthetic Scheme for the Preparation of Phosphoramidite Building Blocks 16, 17, and 18, and of Functionalized CPG Solid Supports 19, 20, and 21

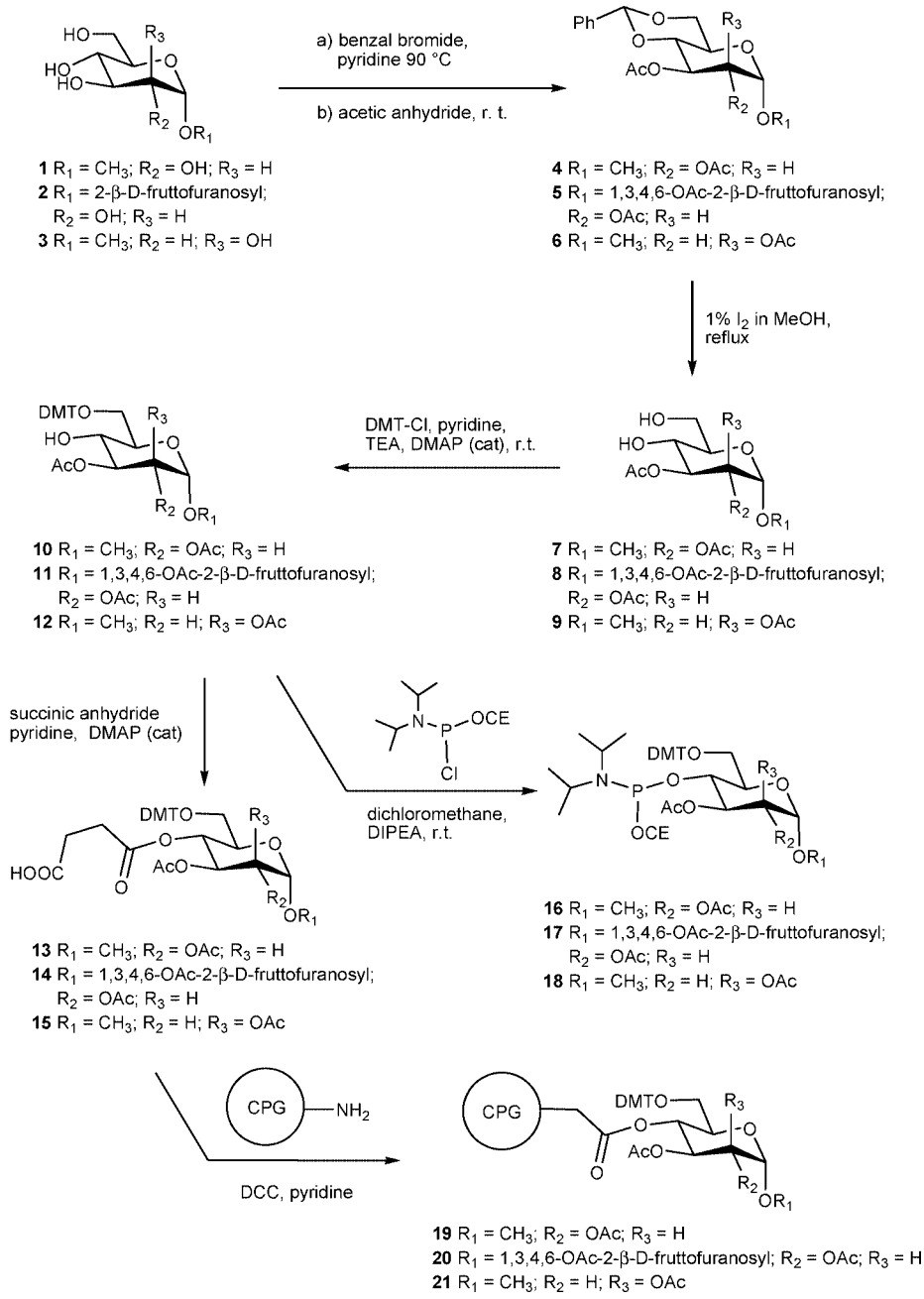

shown to protect the ODN chains from nuclease digestion, while not hampering their specific recognition properties.

In the search for ODNs endowed with significant antiviral properties, Hotoda and his group recently investigated a series of G-quadruplex-forming ODNs, finally focusing their research interest on modified oligonucleotides of sequence d($^{5\prime}$TGGGAG$^{3\prime}$). These were found to exhibit potent anti-HIV activity associated with low cytotoxicity when carrying at the 5′-end bulky aromatic residues, as the 3,4-dibenzyloxybenzyl (DBB) or *tert*-butyldiphenylsilyl (TBDPS) groups (*17, 18*). Structure–activity relationship analysis indicated that G-quadruplex formation, as well as the presence of large aromatic substituents at the 5′-end, were both essential for their antiviral activity. In this frame, we studied a selected set of Hotoda's 5′-modified ODNs: our data, combining CD, DSC, and molecular modeling studies on the modified G-quadruplexes in comparison with the unmodified one, showed that the overall stability of the investigated complexes correlated well with the reported IC_{50}values, thus furnishing quantitative evidence, even if still indirect, to the hypothesis that the G-quadruplex structures are the ultimate active species, effectively responsible for the desired antiviral effects (*19*).

Aiming at the preparation of novel oligonucleotide-based antivirals, we adopted the d($^{5\prime}$TGGGAG$^{3\prime}$) sequence as a suitable platform to investigate the effect of glyco-conjugation on both quadruplex formation and biological properties of G-rich ODNs. Here, we here describe the synthesis, biophysical characterization, and biological properties of d($^{5\prime}$TGGGAG$^{3\prime}$) oligomers, carrying a monosaccharide or disaccharide tail (with glucose, mannose, and sucrose chosen here as model carbohydrates) at either the 5′ or 3′-end. The best modification, in terms of both quadruplex formation and antiviral activity enhancement, i.e., the 3′-conjugation with a mannose residue, was then combined with the insertion of TBDPS at the 5′-end. The resulting 5′,3′-bis-conjugated TBDPS-$^{5\prime}$TGGGAG$^{3\prime}$-*p*-mannose was found to be 3-fold more active than the sole 3′-conjugated

Scheme 2. Synthetic Scheme for the Preparation of Glyco-Conjugated Oligonucleotides II-VII

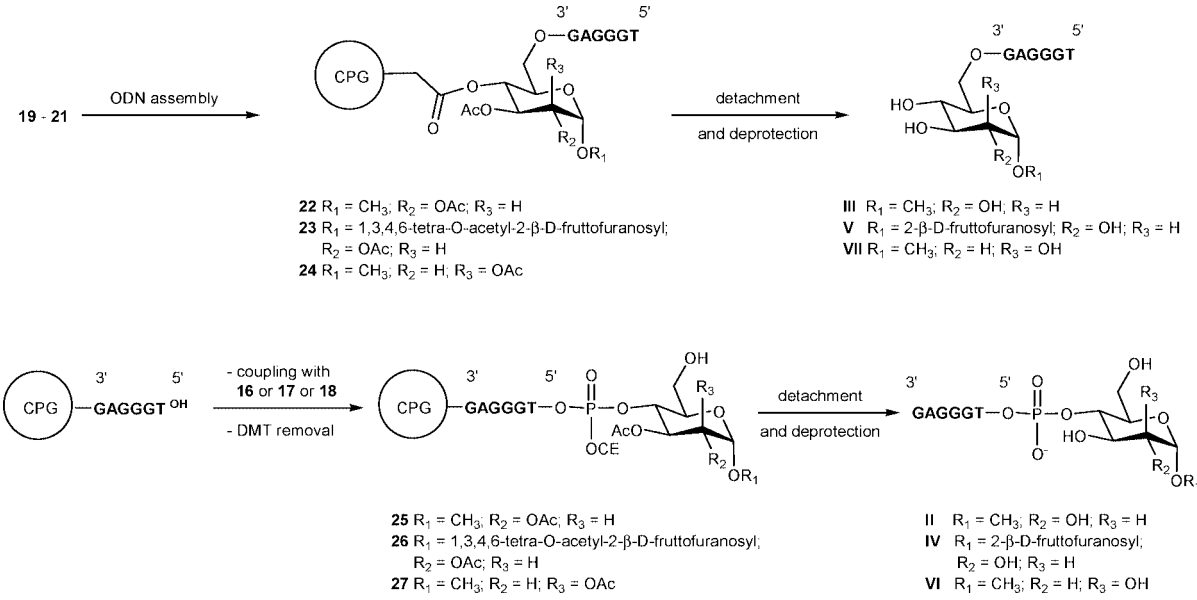

$^{5'}$TGGGAG$^{3'}$-*p*-mannose oligonucleotide. To gain a deeper insight into the thermodynamic and kinetic parameters governing the quadruplex association/dissociation processes in solution, detailed CD analysis and CD-monitored thermal denaturation studies for the 5′,3′-bis-conjugated d($^{5'}$TGGGAG$^{3'}$) have been carried out and discussed.

EXPERIMENTAL PROCEDURES

Synthesis and Characterization of Oligonucleotides I−IX. DMT-protected succinylated sugars **13**, **14**, and **15**; phosphoramidite building blocks **16**, **17**, and **18**; and functionalized solid supports **19**, **20**, and **21** were synthesized following the reactions described in Scheme 1, according to previously reported protocols (*15*, *16*). Oligonucleotides **I**−**IX** were synthesized using standard solid-phase β-cyanoethyl phosphoramidite chemistry on a 15 μmol scale, in all cases adopting DMT-off protocols. In the case of oligomer **I**, starting from 100 mg of commercially available 2′-deoxyguanosine-functionalized controlled pore glass (CPG-dG) support with 0.10 mequiv/g initial loading, the sequence $^{5'}$d(TGGGAG)$^{3'}$was assembled by exploiting standard commercially available 3′-phosphoramidite 2′-deoxynucleoside monomers. As depicted in Scheme 2, the synthesis of oligomers **III**, **V**, and **VII** was realized starting from 100 mg of functionalized CPG supports **19**, **20**, and **21**, respectively, with 0.06–0.08 mequiv/g initial loading, on which the sequence $^{5'}$d(TGGGAG)$^{3'}$ was assembled in a standard manner. In the case of oligomers **II**, **IV**, and **VI**, starting from 100 mg of commercially available CPG-dG support with 0.10 mequiv/g initial loading, after the assembly of the sequence $^{5'}$d(TGGGAG)$^{3'}$, an additional coupling with phosphoramidite building blocks **16**, **17**, or **18**, respectively, was then realized. The synthesis of oligomer **IX** was achieved starting from functionalized support **21**, as described in Scheme 3, which was first used in the solid-phase assembly of the sequence $^{5'}$d(GGGAG)$^{3'}$, then coupled with 5′-TBDPS-thymidine-3′-phosphoramidite building block **29**, synthesized as previously described (*19*). Once the chain elongation was complete, target oligomers **I**−**IX** were detached from the solid support and deprotected by standard treatment with conc aq ammonia at 55 °C for 12 h.

The combined filtrates and washings were concentrated under reduced pressure, redissolved in H_2O, and analyzed and purified by HPLC. Purification of the crude natural oligomer **I** and of conjugated oligonucleotides **II**−**VII** was carried out on an

Scheme 3. Synthetic Scheme for the Preparation of 5′,3′-Bis-Conjugated Oligonucleotide IX

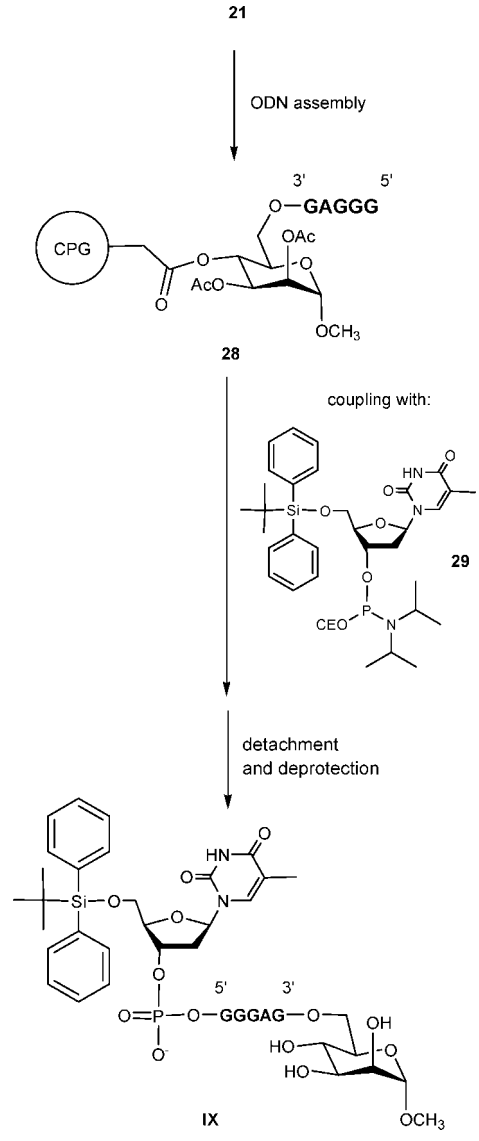

Table 1. Oligonucleotide Characterization

sequence (5′−3′)	HPLC[a] retention time, min	MS data calcd	ESI-MS data found
$^{5'}$TGGGAG$^{3'}$ (**I**)	15.5; 26.7	$C_{60}H_{74}N_{27}O_{34}P_5$: 1872.26	1872.01
Glucose-*p*-$^{5'}$TGGGAG$^{3'}$ (**II**)	16.9; 24.8	$C_{67}H_{86}N_{27}O_{42}P_6$: 2127.40	2128.08
$^{5'}$TGGGAG$^{3'}$-*p*-glucose (**III**)	17.5; 22.3	$C_{67}H_{86}N_{27}O_{42}P_6$: 2127.40	2128.27
sucrose-*p*-$^{5'}$TGGGAG$^{3'}$(**IV**)	16.6; 27.2	$C_{72}H_{95}N_{27}O_{47}P_6$: 2276.52	2277.10
$^{5'}$TGGGAG$^{3'}$-*p*-sucrose (**V**)	16.0; 21.8	$C_{72}H_{95}N_{27}O_{47}P_6$: 2276.52	2276.88
mannose-*p*-$^{5'}$TGGGAG$^{3'}$(**VI**)	15.9; 26.4	$C_{67}H_{86}N_{27}O_{42}P_6$:2127.40	2127.88
$^{5'}$TGGGAG$^{3'}$-*p*-mannose (**VII**)	16.2; 23.8	$C_{67}H_{86}N_{27}O_{42}P_6$:2127.40	2127.79
TBDPS-$^{5'}$TGGGAG$^{3'}$(**VIII**)	14.0	$C_{76}H_{92}SiN_{27}O_{34}P_5$: 2109.48	2110.96
TBDPS-$^{5'}$TGGGAG$^{3'}$-*p*-mannose (**IX**)	9.2; 11.5	$C_{83}H_{105}SiN_{27}O_{42}P_6$:2366.81	2366.28

[a] For HPLC conditions, see Experimental Procedures.

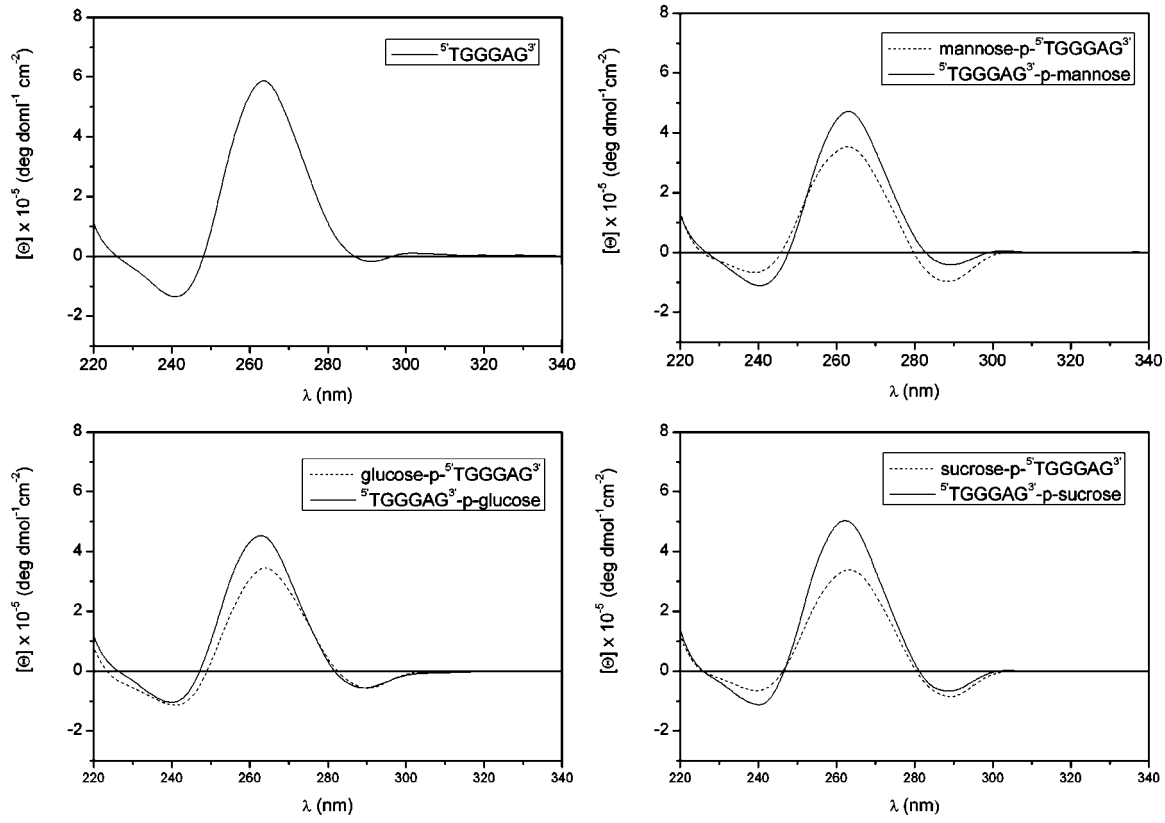

Figure 1. CD spectra of the natural ODN $^{5'}$TGGGAG$^{3'}$ (**I**) and of glyco-conjugated oligonucleotides **II**−**VII**. The spectra were recorded at 20 °C in a 10 mM potassium phosphate buffer (pH 7.0), supplemented with 200 mM KCl, at 5×10^{-5} M quadruplex concentration.

analytical anion exchange Nucleogel SAX column (Macherey-Nagel, 1000–8/46, 4.6 × 50 mm, 5 μm), adopting the following eluents: buffer A, 20 mM KH_2PO_4/K_2HPO_4 aq solution (pH 7.0), containing 20% (v/v) CH_3CN; buffer B, 1 M KCl, 20 mM KH_2PO_4/K_2HPO_4 aq solution (pH 7.0), containing 20% (v/v) CH_3CN. In all cases, using a linear gradient from 0% to 100% B in 40 min, flow rate 0.8 mL/min, and detection at $\lambda = 260$ nm, two main peaks were observed. As previously found (*18, 19*), in all the purification attempts on an anionic exchange HPLC column, the fastest eluting peak, attributed to the single-strand 6-mer, was always accompanied by a major peak, having a higher retention time, due to G-quadruplex aggregates generated under HPLC elution conditions.

Oligonucleotide **VIII**, synthesized as previously described (*19*), was purified by HPLC on a NUCLEOSIL RP18 column (Supelco, 100–5, C18, 4.6 × 250 mm, 7 μm), using a linear gradient of CH_3CN in 0.1 M TEAB in H_2O, pH 7.0, from 20% to 100% in 20 min, flow rate 0.8 mL/min, with detection at $\lambda = 260$ nm. Oligonucleotide **IX** was purified by HPLC on a RP18 Eclipse column (Agilent, XD8-C18); buffer A, 0.1 M TEAB in H_2O, pH 7.0; buffer B, CH_3CN; a linear gradient from 20% to 100% B in 20 min, flow rate 0.8 mL/min, with detection at $\lambda = 260$ nm, was used. The isolated oligomers had the retention times reported in Table 1. After HPLC purification, the oligonucleotide samples were desalted on a Sephadex G25 column eluted with H_2O/EtOH (4:1, v/v). Successively, HPLC analysis of the desalted oligomers **I**−**IX** on a Partisphere Whatman RP18 analytical column (125 × 4.0 mm, 5 μm), eluted with a linear gradient from 0% to 100% in 60 min of CH_3CN in TEAB buffer (0.1 M, pH 7.0), flow = 0.8 mL/min, confirmed the expected purity for all the samples (higher than 98%). The modified oligonucleotides were characterized by ESI-MS mass spectrometry in the negative mode, in all cases giving masses in accordance with the expected values (Table 1).

In a typical experiment, starting from 100 mg of commercially available CPG-dG supports, or of sugar-functionalized supports **19**, **20**, or **21**, 80–120 OD units of purified **I**−**IX** could be obtained.

Quadruplex Preparation. The quadruplex complexes were obtained by dissolving the lyophilized oligonucleotide in the appropriate buffer, annealed by heating at 95 °C for 5 min and slow cooling to room temperature. The buffer used was 10 mM

Table 2. Melting Temperatures of the Quadruplexes Formed by ODNs I−IX[a]

oligonucleotide sequence (5′−3′)	T_m (°C)
$^{5'}$TGGGAG$^{3'}$ (**I**)	41 ± 1
Glucose-*p*-$^{5'}$TGGGAG$^{3'}$ (**II**)	26 ± 1
$^{5'}$TGGGAG$^{3'}$-*p*-glucose (**III**)	44 ± 1
sucrose-*p*-$^{5'}$TGGGAG$^{3'}$(**IV**)	35 ± 1
$^{5'}$TGGGAG$^{3'}$-*p*-sucrose (**V**)	36 ± 1
mannose-*p*-$^{5'}$TGGGAG$^{3'}$(**VI**)	31 ± 1
$^{5'}$TGGGAG$^{3'}$-*p*-mannose (**VII**)	45 ± 1
TBDPS-$^{5'}$TGGGAG$^{3'}$ (**VIII**)	75 ± 1[b]
TBDPS-$^{5'}$TGGGAG$^{3'}$-*p*-mannose (**IX**)	81 ± 1

[a] As determined by CD-monitored thermal denaturation studies (see also Figure 1 in Supporting Information). [b] Data from ref (*19*).

Table 3. Anti-HIV-1 and Anti-HIV-2 Activity and Cytostatic Properties of Oligonucleotides II-VII in Human T-Lymphocyte (CEM) Cells

oligonucleotide	EC_{50}[a] (μM) HIV-1(III_B)	EC_{50}[a] (μM) HIV-2(ROD)	CC_{50}[b] (μM)	S.I.[c]
glucose-*p*-$^{5'}$TGGGAG$^{3'}$ (**II**)	87 ± 4.9	99 ± 70	110	1.30
$^{5'}$TGGGAG$^{3'}$-*p*-glucose (**III**)	21 ± 9.8	140	>140	>6.7
sucrose-*p*-$^{5'}$TGGGAG$^{3'}$ (**IV**)	>30	>30	57 ± 13	<1.9
$^{5'}$TGGGAG$^{3'}$-*p*-sucrose (**V**)	≥30	>30	74 ± 34	≤2.5
mannose-*p*-$^{5'}$TGGGAG$^{3'}$ (**VI**)	>30	>30	41 ± 34	<1.4
$^{5'}$TGGGAG$^{3'}$-*p*-mannose (**VII**)	14 ± 3.9	≥30	70 ± 3.2	5.0

[a] EC_{50} = effective concentration or concentration required to protect CEM cells against the cytopathicity of HIV by 50%. [b] CC_{50} = cytostatic concentration or concentration required to inhibit CEM cell proliferation by 50%. [c] S.I. = selectivity index for HIV-1, calculated as the ratio of CC_{50}/EC_{50}.

Table 4. Anti-HIV-1 RT Activity for the Glyco-Conjugates Using Poly rC/dG as the Template and dGTP as the Substrate

oligonucleotide	IC_{50}[a]
Glucose-*p*-$^{5'}$TGGGAG$^{3'}$ (**II**)	>140
$^{5'}$TGGGAG$^{3'}$-*p*-glucose (**III**)	>140
sucrose-*p*-$^{5'}$TGGGAG$^{3'}$(**IV**)	≥140
$^{5'}$TGGGAG$^{3'}$-*p*-sucrose (**V**)	64.9 ± 9.5
mannose-*p*-$^{5'}$TGGGAG$^{3'}$(**VI**)	>140
$^{5'}$TGGGAG$^{3'}$-*p*-mannose (**VII**)	>140
TBDPS-$^{5'}$TGGGAG$^{3'}$-*p*-mannose (**IX**)	≥140

[a] IC_{50} = 50% inhibitory concentration or compound concentration required to inhibit the HIV-1 RT-catalyzed reaction by 50%.

potassium phosphate, 200 mM KCl, 0.1 mM EDTA at pH = 7.0. The concentration of the dissolved oligonucleotides **I**−**VII** was determined by UV measurements at 260 nm and at 95 °C, using, as the molar extinction coefficients, the values calculated by the nearest neighbor model (*20*) for the sequence $^{5'}$d(TGGGAG)$^{3'}$, assuming the contribution of the terminal sugar residues to be negligible at this wavelength. For oligonucleotide **IX**, the contribution of the TBDPS group at the 5′-end was taken into account, as previously described in the case of **VIII** (*19*).

CD Experiments. All circular dichroism (CD) experiments were registered on a JASCO J-715 spectrophotometer equipped with a thermostatically controlled cuvette holder (JASCO PTC-348), in a 0.2 cm or 0.5 path length cuvette. CD spectra were collected from 220 to 340 nm, at 20 nm/min, with a response time of 4 s and at 1 nm bandwidth. The molar ellipticity was calculated from the equation $[\theta] = 100 \cdot \theta / cl$ where θ is the ellipticity value, c is the quadruplex concentration (5.0×10^{-5} M), and l is the path length of the cell in cm. Thermal dissociation of the studied quadruplexes was monitored by following the CD signal at 263 nm upon increasing the temperature.

The quadruplex dissociation kinetics was measured by rapidly increasing the temperature and following the change of the CD signal at 263 nm with time. All the experiments were performed in a temperature and concentration range where the reassociation reaction can be neglected. The kinetic constants were obtained by fitting the recorded time-dependent decrease in CD signal with a single exponential function. For each sequence, the kinetic constant was determined at five different temperatures.

The structural transition from the single strands to the tetramolecular quadruplex was monitored in the temperature range 10–30 °C by recording the CD spectra as a function of time. The samples were incubated at 90 °C for 5 min and then rapidly cooled. The kinetic constant and reaction order were obtained by analyzing the CD vs time profiles as previously described (*21*).

Biological Assays. For the anti-HIV assays, CEM cells (4.5×10^5 cells/mL) were suspended in fresh culture medium and infected with HIV-1 at 100 $CCID_{50}$ per mL of cell suspension in the presence of appropriate dilutions of the test compounds. After 4 to 5 days incubation at 37 °C, giant cell formation was recorded microscopically in the CEM cell cultures. The 50% effective concentration (EC_{50}) corresponds to the compound concentrations required to prevent syncytium formation by 50% in the virus-infected CEM cell cultures.

To determine the cytostatic activity, all assays were performed in 96-well microtiter plates. To each well were added (5–7.5) $\times 10^4$ CEM cells and a given amount of the test compound. The cells were allowed to proliferate for 72 h at 37 °C in a humidified CO_2-controlled atmosphere. At the end of the incubation period, the cells were counted in a Coulter counter. The CC_{50} (50% inhibitory concentration) was defined as the concentration of the compound that inhibited CEM cell proliferation by 50%.

In the cocultivation assays, 5×10^4 persistently HIV-1-infected HUT-78 cells (designated HUT-78/HIV-1) were mixed with 5×10^4 Sup-T1 cells, along with appropriate concentrations of the test compounds. After 16 to 20 h, marked syncytium formation was noted in the control cell cultures, and the number of syncytia was determined under a microscope.

For determination of the 50% inhibitory concentration (IC_{50}) of the test compounds against HIV-1 RT, the RNA-dependent DNA polymerase assay was performed as follows: the reaction mixture (50 μL) contained 50 mM Tris·HCl (pH 7.8), 5 mM DTT, 300 μM glutathione, 500 μM EDTA, 150 mM KCl, 5 mM $MgCl_2$, 1.25 μg of bovine serum albumin, a fixed concentration of the labeled substrate [^{3}H]dGTP (1.6 μM, 1 μCi; specific activity, 12.6 Ci/mmol; Amersham Pharmacia Biotech), a fixed concentration of the template/primer poly(rC)·oligo(dG)$_{12–18}$ (0.1 mM; Amersham Pharmacia Biotech), 0.06% Triton X-100, 5 μL of the inhibitor solution [containing various concentrations (5-fold dilutions) of the compounds], and 5 μL of the RT preparations. The reaction mixtures were incubated at 37 °C for 30 min, at which time 200 μL of yeast RNA (2 mg/mL) and 1 mL of trichloroacetic acid (5%, v/v) in water were added. The solutions were kept on ice for at least 30 min, after which the acid-insoluble material was filtered over Whatman GF/C glass-fiber filters and washed 10 times with 2 mL of 5% trichloroacetic acid in water and once with 70% ethanol. The filters were then analyzed for radioactivity in a liquid scintillation counter (Canberra Packard, Zellik, Belgium). The

Table 5. Anti-HIV-1 and Anti-HIV-2 Activity and Cytostatic Properties of Oligonucleotide IX in Human T-Lymphocyte (CEM) and MT-4 Cells[a]

oligonucleotide	EC_{50}[b] (μM)				CC_{50}[c] (μM)		S.I.[d]
	MT-4		CEM				
	HIV-1	HIV-2	HIV-1 (III_B)	HIV-2 (ROD)	MT-4	CEM	
TBDPS-$^{5'}$TGGGAG$^{3'}$-*p*-mannose (**IX**)	6.7 ± 0.1	>70	4.2 ± 2.0	>70	>70	>70	>17 on CEM; >10 on MT-4
TBDPS-$^{5'}$TGGGAG$^{3'}$ (**VIII**)	0.88 ± 0.070[e]		1.8 ± 0.5	>14	>40[e]	>14	>8 on CEM; >45 on MT-4

[a] For comparison, data from ref (*18*) for oligonucleotide **VIII**, determined using MT-4 cells, are also reported. [b] EC_{50} = effective concentration or concentration required to protect CEM cells against the cytopathicity of HIV by 50%. [c] CC_{50} = cytotoxic concentration or concentration required to reduce CEM or MT4 cell viability by 50%. [d] S.I. = selectivity index for HIV-1, calculated as the ratio of CC_{50}/EC_{50}. [e] Data from ref (*18*).

Table 6. Inhibitory Activity of the Glyco-Conjugates against Syncytia Formation between Persistently HIV-1-Infected HUT-78/HIV-1 Cells and Uninfected SupT1 Cells

oligonucleotide	EC_{50}[a] (μM)
II	>140
III	>140
IV	>30
V	>140
VI	>140
VII	>140
VIII	>14
IX	1.3 ± 0.49

[a] EC_{50} = 50% effective concentration or compound concentration required to prevent giant (syncytium) cell formation between HUT-78/HIV-1 and SupT1 cells by 50%.

IC_{50} for each test compound was determined as the compound concentration that inhibited HIV-1 RT activity by 50%.

RESULTS

Several modified oligonucleotides have been shown to inhibit HIV-1 in cell culture. If, in most cases, a non-sequence-specific inhibition is hypothesized, sequence-specific effects are also invoked for aptamers (*22*). Particularly, for G-rich ODNs the putative mechanism of action is based on the interference/inhibition of both cell-to-cell and virus-to-cell transmission of HIV-1 by interaction with the V3 loop and the CD4 binding site on viral gp120 (*23–25*). As it is accepted that G-rich ODNs exert their anti-HIV activity through formation of G-quadruplex complexes, the correlation between thermodynamic stability and rate of formation of the quadruplexes, on one end, and the antiviral properties, on the other, was assumed here as the basis for the rational design of novel oligonucleotide-based antivirals.

Starting from the model oligonucleotide d($^{5'}$TGGGAG$^{3'}$), indicated here as **I**, a small library of 5′- and 3′-glyco-conjugates carrying the same sequence was synthesized and their ability to generate four-stranded quadruplexes analyzed by CD-monitored thermal denaturation experiments. 5′- and 3′-conjugated 6-mers **II**−**VII**, as well as unmodified 6-mer **I** (Scheme 2 and Table 1), were synthesized using standard solid-phase β-cyanoethyl phosphoramidite chemistry protocols on a 15 μmol scale (*26*). Glucose and sucrose-containing-phosphoramidites **16** and **17**, as well as sugar-functionalized supports **19** and **20**, were prepared essentially as previously reported (*15, 16*). Novel mannose building block **18** and mannose-functionalized support **21** were synthesized in analogy with the corresponding glucose and sucrose derivatives and exploited for the synthesis of mannose-containing oligomers **VI** and **VII**, respectively, here chosen as examples of glyco-conjugates which can find a direct application for lectin recognition. In all cases, starting from 100 mg of commercially available DMT-protected guanosine-functionalized CPG support (0.10 mequiv/g, used in connection with phosphoramidites **16**–**18** for the synthesis of 5′-conjugated oligomers) or from LCAA-CPG functionalized with the appropriate DMT-protected sugar residue (**19**–**21**, 0.06–0.08 mequiv/g, used for the 3′-conjugation), on average, 80–120 OD units of pure **I**−**VII** could be isolated, after HPLC purification, and characterized by ESI-MS data (Table 1).

CD spectra at 20 °C for all the studied sequences were diagnostic of parallel-stranded quadruplex structures showing a positive band at 263 nm and a negative band at 243 nm (Figure 1) (*18, 19, 27*). The melting temperatures and melting profiles for each system were largely influenced by the scan rate, revealing kinetic control of the quadruplex dissociation process. From the CD-monitored melting profiles for all the samples, registered at 263 nm (see Supporting Information) at the slowest heating rate investigated (0.05 °C/min), the corresponding melting temperature values were determined (see Table 2). Inspection of Table 2 reveals that 6-mers **III** and **VII**, carrying a monosaccharide residue at their 3′-end, formed quadruplex complexes with moderately increased stability with respect to unmodified sequence **I** ($\Delta T_m = +3/+4$ °C). Remarkably, the same modifications at the 5′-end of the ODN chain caused a dramatic destabilization, with ΔT_m of −15 and −10 °C for **II** and **VI**, respectively. When inserted at either the 5′ or 3′-end of the sequence, the disaccharide tail produced quadruplex complexes with comparable thermal stability; however, both **IV** and **V** showed lower melting temperature values than unmodified oligomer **I** ($\Delta T_m = -6/-5$ °C).

The activity of the synthesized glyco-conjugated oligonucleotides against-HIV-1 and HIV-2 was evaluated in human T-lymphocyte (CEM) cell cultures, as well as their cytotoxic properties. Interestingly, the EC_{50} values of the glyco-conjugated oligonucleotides were found to correlate well with the thermal stabilities of the corresponding quadruplex complexes, and activity against HIV-1 in the 10–20 μM range for 3′-glyco-conjugated ODNs **III** and **VII** was observed (Table 3). No obvious correlation was found between the lack of anti HIV RT activity, reported in Table 4, and the anti-HIV activity. These data further confirmed that specific antiviral activity of G-quadruplex-forming ODNs, with well-defined three-dimensional structures, is not due to HIV-1 reverse transcriptase inhibition, but can be attributed to efficient interaction with the viral entry process. From the data in our hands, we concluded that, among the investigated conjugations, the insertion of a monosaccharide, and more specifically, of a mannose residue at the 3′-phosphate end of the studied ODN sequence, was the most promising modification in terms of both quadruplex formation and biological activity.

Assuming **VII** as the best candidate for further drug optimization, we thought of combining the 3′-glyco-conjugation present in this oligomer with an additional 5′-tethering, chosen among the ones previously demonstrated by Hotoda et al. to convert the anti-HIV inactive $^{5'}$TGGGAG$^{3'}$ into an active drug, effective at micromolar concentration (*18*). In our previous work, the *tert*-butyldiphenylsilyl (TBDPS) group at the 5′-end of the $^{5'}$TGGGAG$^{3'}$ sequence (**VIII**) was shown to markedly enhance both the equilibrium and the rate of formation of the quadruplex complexes, in comparison with the unmodified sequence (*19*). In an effort to improve the biophysical and pharmacological profile of this G-rich oligonucleotide, we synthesized the oligonucleotide containing both the TBDPS residue at the 5′-

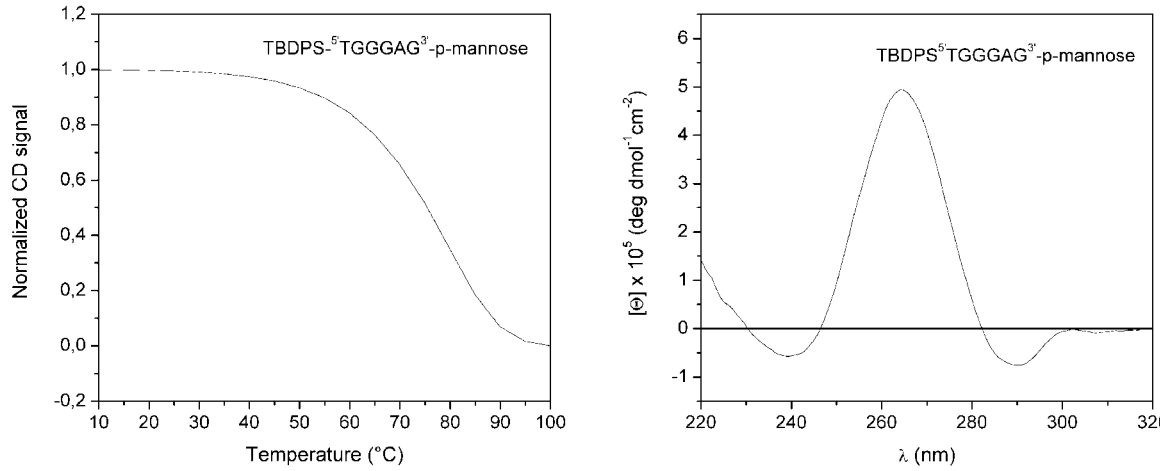

Figure 2. CD melting profile (on the left) and CD spectrum at 20 °C (on the right) of the 5′,3′-bis-conjugated oligonucleotide **IX**, at 5×10^{-5} M quadruplex concentration.

end and the mannose moiety at the 3′-phosphate end, thus obtaining the oligomer TBDPS-$^{5'}$TGGGAG$^{3'}$-*p*-mannose **IX**. The synthetic procedure to obtain **IX**, described in Scheme 3, is based on the usage of functionalized solid support **21** in conjunction with 5′-TBDPS-thymidine-3′-phosphoramidite building block **29** (*18, 19*), exploited in the last coupling of the solid-phase ODN assembly. Antiviral evaluation on **IX** showed that the insertion of the TBDPS group at the 5′-end of $^{5'}$TGGGAG$^{3'}$-*p*-mannose notably affected its biological activity, with a 3-fold increase in the anti-HIV potency, with respect to ODN **VII**, carrying the sole mannose as the tethering group (Table 5). However, bis-conjugate **IX** was found to be 2.3-fold less active than TBDPS-$^{5'}$TGGGAG$^{3'}$ (**VIII**) on HIV-infected CEM cells. When the series of compounds were examined for their inhibitory activity against syncytium formation between persistently HIV-1-infected HUT-78/HIV-1 cells and uninfected SupT1 cells, only **IX** was measurably inhibitory (Table 6). In order to gain a critical insight into the peculiar structural features of bis-conjugated ODN **IX**, a detailed physicochemical characterization of the corresponding quadruplex complex was therefore carried out and comparison with previously studied TBDPS-$^{5'}$TGGGAG$^{3'}$ (**VIII**), to better investigate the role of the mannose−phosphate appendage at the 3′-end on the quadruplex structure, is reported here.

The CD spectrum of TBDPS-5′-TGGGAG-3′-*p*-mannose **IX** is consistent with the formation of a parallel quadruplex structure (Figure 2). From the CD melting profile obtained at 0.05 °C/min, shown in Figure 2, the melting temperature of the quadruplex complex was found to be 81 °C, with a ΔT_m of +40 °C with respect to unmodified **I**, and of +36 °C with respect to the quadruplex formed by **VII**, bearing mannose−phosphate tails at the 3′-ends (Table 2). In order to especially focus on the kinetic aspects, recognized to primarily affect the *in vivo* existence of four-stranded quadruplex complexes, a complete biophysical characterization of the quadruplex formed by ODN **IX** was carried out. The obtained data were compared with those previously determined for TBDPS-$^{5'}$TGGGAG$^{3'}$ **VIII** (*19*). The kinetics of TBDPS-$^{5'}$TGGGAG$^{3'}$-*p*-mannose quadruplex association was investigated in detail. The rate of the association reaction was studied by monitoring the ellipticity at 263 nm as a function of time after heating the sample at 95 °C for 5 min followed by fast cooling. The molar ellipticity vs time profiles are shown in Figure 3. The experimental curves were fitted following a previously described procedure (*21*). All the data were consistent with a reaction order of 4.0. The kinetic experiments were performed over the temperature range 15–30 °C. The activation energy (E_{on}) was derived from the slope of the Arrhenius plot (see Supporting Information). The kinetic parameters are summarized in Table 7. We found that the association rate decreased upon increasing the temperature, due to a negative value for the activation energy, in accordance with previously obtained data for the TBDPS-$^{5'}$TGGGAG$^{3'}$ quadruplex. The activation energy for the formation of the quadruplex complex of **IX** is about half the activation energy determined in the case of **VIII**. In the 15–30 °C temperature range, the kinetic constants for the TBDPS-$^{5'}$TGGGAG$^{3'}$ and TBDPS-$^{5'}$TGGGAG$^{3'}$-*p*-mannose quadruplexes are comparable. However, when the values are extrapolated at higher temperatures, the association reaction for quadruplex formation in **IX** is much faster in comparison to **VIII**, due to the difference in the absolute value of their activation energies. The kinetics of quadruplex dissociation for TBDPS-$^{5'}$TGGGAG$^{3'}$-*p*-mannose was also investigated by performing temperature-jump experiments. In each experiment, the temperature of the sample was rapidly increased and the rate of quadruplex dissociation was monitored by following the change of CD signal with time. The kinetic profiles at different temperatures are shown in Figure 4. The dissociation rate constants were then obtained by fitting these kinetic profiles with a single exponential curve. The activation energy (E_{off}) was derived from the corresponding Arrhenius plot (see Supporting Information). The kinetic parameters for quadruplex dissociation are summarized in Table 8. The quadruplex formed by **IX** has k_{off} values comparable with those previously determined for **VIII**. The E_{off} value for the quadruplex formed by **IX** is about 130 kJ mol^{-1} higher than the value found for **VIII**.

Taken together, these data showed that bis-conjugated TBDPS-$^{5'}$TGGGAG$^{3'}$-*p*-mannose **IX** formed more kinetically and thermodynamically stable four-stranded quadruplex structures than TBDPS-$^{5'}$TGGGAG$^{3'}$(**VIII**). Therefore, we can conclude that the presence of mannose residues at the 3′-phosphate end of the G-rich oligonucleotide chain, in addition to providing several desirable properties for the *in vivo* activity, as increased resistance toward nucleases and improved cellular uptake, also significantly contributes to the overall stabilization of the quadruplex complex. However, contrarily to what we have found for monoconjugated 6-mers **II**−**VII** when referred to unmodified oligonucleotide **I**, in the comparison of **IX** vs **VIII**, the higher thermal stability for the quadruplex complex did not result in improved biological activity.

Further experiments, including a detailed NMR-based conformational analysis study, are currently underway to further

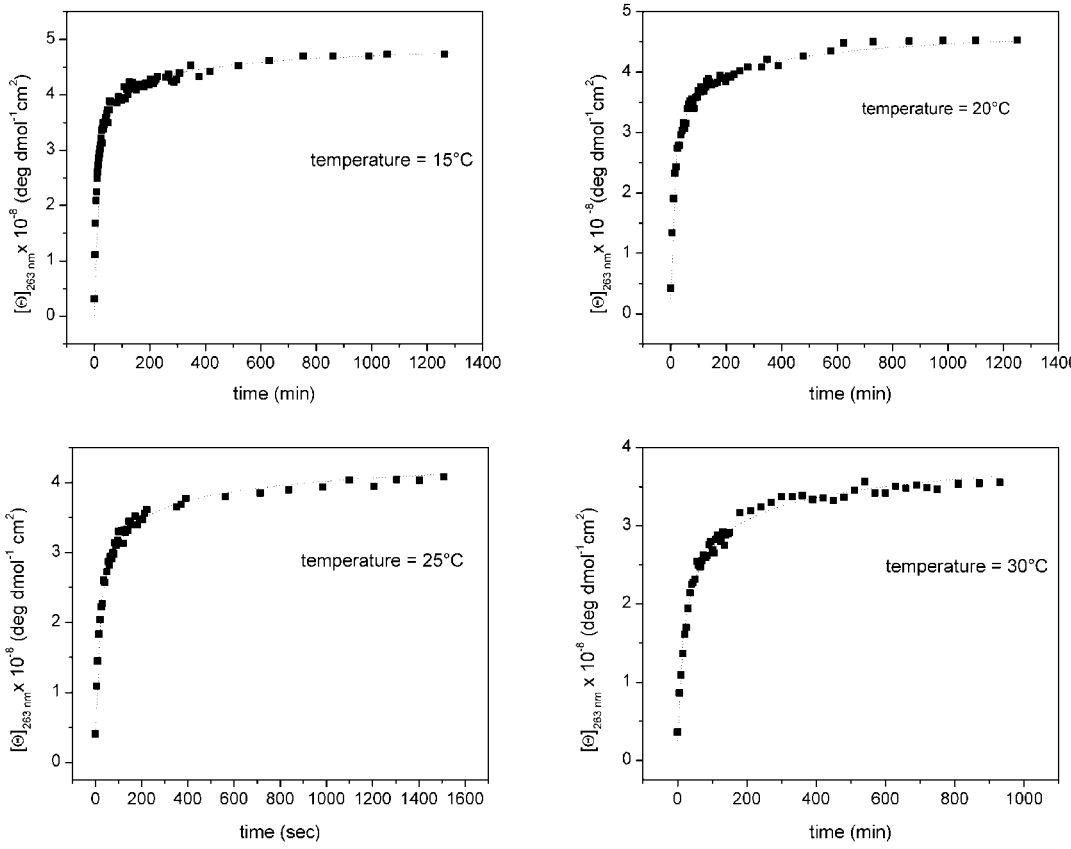

Figure 3. Kinetics of quadruplex formation for 5′,3′-bis-conjugated **IX** at different temperatures. Quadruplex formation leads to an increase of molar ellipticity at 263 nm. Mathematical fits are showed in dotted lines. All the experiments were performed in 10 mM potassium phosphate buffer (pH 7.0), supplemented with 200 mM KCl, at 5×10^{-6} M quadruplex concentration.

Table 7. Kinetic Parameters for the Quadruplex Formation of IX with Respect to VIII[a]

quadruplex	temp (°C) ± 1	*n*	k_{on} $(M^3\ s^{-1})^b$	E_{on} (kJ mol^{-1})
TBDPS-$^{5'}$TGGGAG$^{3'}$-*p*-mannose	15	4	$(9.8 \pm 0.5) \times 10^{10}$	
	20	4	$(5.1 \pm 0.6) \times 10^{10}$	
	25	4	$(3.6 \pm 0.5) \times 10^{10}$	-70 ± 19
	30	4	$(2.3 \pm 0.8) \times 10^{10}$	
TBDPS-$^{5'}$TGGGAG$^{3'}$[c]	15	4	$(2.9 \pm 0.5) \times 10^{11}$	
	20	4	$(1.5 \pm 0.6) \times 10^{11}$	-125 ± 19
	25	4	$(8.6 \pm 0.5) \times 10^{10}$	
	30	4	$(2.3 \pm 0.8) \times 10^{10}$	

[a] All the values have been determined in a 200 mM KCl, 10 mM potassium phosphate, pH 7.0 buffer. [b] k_{on} is defined as $d[S]/dt = -4d[S_4]/dt = -k_{on}[S]^4$. [c] Data from ref (*19*).

clarify the structure–activity relationships of these short, four-stranded G-quadruplex-forming oligonucleotides.

DISCUSSION

After more than two decades, the search for new chemically modified ODNs is a very active field of research, and novel structures are continuously being proposed. Aiming at ODNs endowed with potential anti-HIV activity, end-conjugation with sugars was investigated here as a strategy to improve the pharmacological profile of the oligonucleotide $^{5'}$TGGGAG$^{3'}$, chosen as a model compound. G-rich oligonucleotides are thought to be active against HIV-1 through interactions of the corresponding G-quadruplex complexes with viral gp120 protein. Our results, furnishing an in-depth analysis of the stability and biological activity of the quadruplex structures formed by modified $^{5'}$TGGGAG$^{3'}$ oligonucleotides, further corroborated this hypothesis, showing a good correlation between thermal stability of the corresponding quadruplex complexes and antiviral activity. In detail, the presence of a monosaccharide (glucose or mannose) at the 3′-phosphate end of the ODN chain was identified as the best modification, stabilizing the quadruplex structures and also converting the anti-HIV inactive natural oligomer into moderately active compounds. On the contrary, the same modification, when present at the 5′-end, led to a dramatic destabilization of the quadruplex structure. Still unclear is the reason behind this behavior, but a plausible explanation could be related to the fact that, in the case of 3′-conjugation, the sugar directly interacts with the G-quartet at the 3′-end of the sequence, which in the natural oligonucleotide would be exposed to the solvent. Therefore, in this case, stabilization of the quadruplex complex might arise from removal of the hydration spheres covering the hydrophobic surface of the G quartet due to the presence of the sugar. In the case of 5′-conjugation, this effect is not operative, since the sugar is attached to a dangling thymidine, not directly involved in the four-stranded quadruplex complex, and in turn other steric effects may be effective.

Starting from the most promising modified oligonucleotide investigated here, i.e., oligomer **VII**, further optimization of the target was obtained by conjugating the bulky aromatic group *tert*-butyldiphenylsilyl (TBDPS) group at its 5′-end, previously shown to markedly enhance the formation of quadruplex complexes. The 5′,3′-bis-conjugated TBDPS-$^{5'}$TGGGAG$^{3'}$-*p*-mannose **IX**, onto which a detailed biophysical characterization has been carried out, has been shown to form a four-stranded quadruplex complex with remarkably improved stability, and was 3-fold more active than the sole 3′-glyco-conjugated oligonucleotide **VII**. The mechanism of antiviral action of TBDPS-$^{5'}$TGGGAG$^{3'}$-*p*-mannose is most likely inhibition of

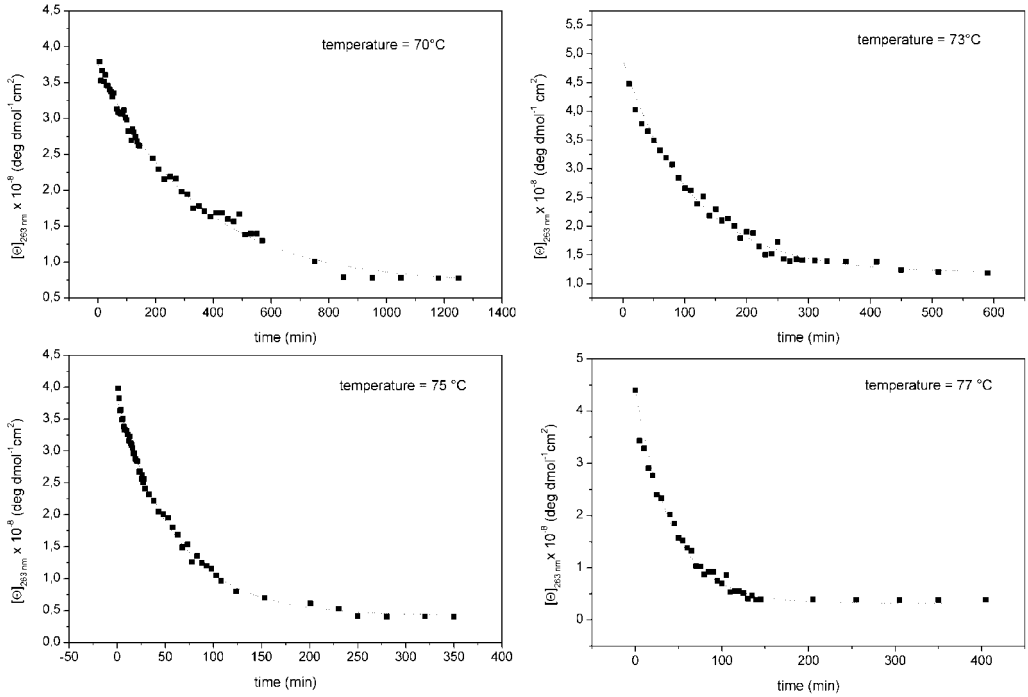

Figure 4. Kinetics of quadruplex dissociation for 5′,3′-bis-conjugated **IX** at different temperatures. Quadruplex dissociation leads to a decrease of molar ellipticity at 263 nm. Mathematical fits are showed in dotted lines. All the experiments were performed at 5×10^{-5} M quadruplex concentration.

Table 8. Kinetic Parameters for the Quadruplex Dissociation of IX with Respect to VIII[a]

quadruplex	temp (°C) ± 1	$k_{off} \times 10^4$ (s^{-1})[b]	E_{off} (kJ mol^{-1})
TBDPS-$^{5'}$TGGGAG$^{3'}$-*p*-mannose	70	0.55 ± 0.03	
	73	1.5 ± 0.02	
	75	2.6 ± 0.4	250 ± 20
	77	4.0 ± 0.1	
	80	6.5 ± 0.3	
TBDPS-$^{5'}$TGGGAG$^{3'}$[c]	70	0.50 ± 0.03	
	73	0.83 ± 0.02	
	75	1.4 ± 0.4	220 ± 20
	77	2.3 ± 0.1	
	80	3.5 ± 0.3	

[a] All the values have been determined in a 200 mM KCl, 10 mM potassium phosphate, pH 7.0 buffer. [b] k_{off} is defined as $d[S]/dt = d[S_4]/dt + k_{off}[S_4]$. [c] Data from ref (*19*).

viral entry (fusion), as is evident from coculture experiments. When compared to the sole 5′-conjugated TBDPS-$^{5'}$TGGGAG$^{3'}$**VIII**, we determined that the 5′,3′-bis-conjugation sensibly favored—both kinetically and thermodynamically—the quadruplex formation, still **IX** exhibited lower anti-HIV activity.

This last result indicates that the antiviral properties of short G-quadruplex forming oligonucleotides are indeed subordinate to the formation of tetrameric complexes, but the *in vivo* picture is obviously much more complicated than simply expected on the basis of a single point of view. In all cases, the quadruplex formation can be considered as a fundamental prerequisite for the *in vivo* biological activity of G-rich oligomers; however, their activity does not exclusively rely on a favored equilibrium between single strands and quadruplex structures, with other mechanisms also successively involved. Therefore, in the search for antiviral properties in the libraries of modified G-rich oligonucleotides, the correlation between thermal stability of the corresponding quadruplex complexes and their anti-HIV activity can be helpful, but this has to be strictly intended only for a first level of prediction, since a variety of different, complex processes may eventually affect their *in vivo* behavior.

Taken together, these findings further expand the repertoire of known anti-HIV active oligonucleotides and can be useful for the future design of novel modified G-rich ODNs with improved antiviral activity.

ACKNOWLEDGMENT

We acknowledge MUR (PRIN) for grants in support of this investigation. We also thank C.I.M.C.F., Università degli Studi di Napoli "Federico II", for the NMR, MS, and CD facilities, and the Rega Centers of Excellence of the K.U.Leuven. This work is dedicated to Prof. Guido Barone and Matteo Adinolfi on the occasion of their 70th birthdays.

Supporting Information Available: General experimental methods; CD melting profiles for ODNs **II**−**VII**; Arrhenius plots for the association and for the dissociation of the 5′,3′-bis-conjugated quadruplex formed by ODN **IX**. This material is available free of charge via the Internet at http://pubs.acs.org.

LITERATURE CITED

(1) Varki, A. (1993) Biological roles of oligosaccharides: all of the theories are correct. *Glycobiology 3*, 97–130.
(2) Koeller, K. M., and Wong, C. H. (2000) Emerging themes in medicinal glycoscience. *Nat. Biotechnol. 18*, 835–841.
(3) Varki, A., Cumming, R., Esko, J., Freeze, H., Hart, G., and Marth, J., Eds. (1999) *Essentials of Glycobiology*, pp 1–331, Chapters 1–21, Cold Spring Harbor Laboratory Press, Cold Spring Harbor, NY, USA.
(4) Lee, Y. C., and Lee, R. T. (1995) Carbohydrate-protein interactions: basis of glycobiology. *Acc. Chem. Res. 28*, 321–327.
(5) Burkhalter, N. F., Dimick, S. M., and Toone, E. J. (2000) Protein-carbohydrate interactions: fundamental considerations. *Carbohydrates in Chemistry and Biology* (Ernst, B., Hart, G. W., and Sinaÿ, P., Eds.) pp 863–911, Chapter 31, Part I, Vol. 2, Wiley-VCH, Weinheim, Germany.
(6) Zatsepin, T. S., and Oretskaya, T. S. (2004) Synthesis and applications of oligonucleotide - carbohydrate conjugates. *Chem. Biodiv. 1* (10), 1401–1417.

(7) Adinolfi, M., Barone, G., De Napoli, L., Guariniello, L., Iadonisi, A., and Piccialli, G. (1999) Solid phase glycosidation of oligonucleotides. *Tetrahedron Lett. 40*, 2607–2610.

(8) Adinolfi, M., De Napoli, L., Di Fabio, G., Guariniello, L., Iadonisi, A., Messere, A., Montesarchio, D., and Piccialli, G. (2001) Solid-phase synthesis of glyco-oligonucleotide conjugates. *Synlett 6*, 745–748.

(9) Sando, S., Matsui, K., Niinomi, Y., Sato, N., and Aoyama, Y. (2003) Facile preparation of DNA-tagged carbohydrates. *Bio. Med. Chem. Lett. 13*, 2633–2636.

(10) Matsuura, K., Hibino, M., Yamada, Y., and Kobayashi, K. (2001) Construction of glyco-clusters by self-organization of site-specifically glycosylated oligonucleotides and their cooperative amplification of lectin-recognition. *J. Am. Chem. Soc. 123*, 357–358.

(11) Matsuura, K., Hibino, M., Ikeda, T., Yamada, Y., and Kobayashi, K. (2004) Self-organized glycoclusters along DNA: effect of the spatial arrangement of galactoside residues on cooperative lectin recognition. *Chem. Eur. J. 10*, 352–359.

(12) Akhtar, S., Routledge, A., Patel, R., and Gardiner, J. M. (1995) Synthesis of mono- and dimannoside phosphoramidite derivatives for solid-phase conjugation to oligonucleotides. *Tetrahedron Lett. 36*, 7333–7336.

(13) Sheppard, T. L., Wong, C.-H., and Joyce, G. F. (2000) Nucleoglycoconjugates: design and synthesis of a new class of DNA - carbohydrate conjugates. *Angew. Chem., Int. Ed. Engl. 39*, 3660–3663.

(14) Wang, Y., and Sheppard, T. L. (2003) Chemoenzymatic synthesis and antibody detection of DNA glycoconjugates. *Bioconjugate Chem. 14*, 1314–1322.

(15) Adinolfi, M., De Napoli, L., Di Fabio, G., Iadonisi, A., Montesarchio, D., and Piccialli, G. (2002) Solid phase synthesis of oligonucleotides tethered to oligo-glucose phosphate tails. *Tetrahedron 58*, 6697–6704.

(16) Adinolfi, M., De Napoli, L., Di Fabio, G., Iadonisi, A., and Montesarchio, D. (2004) Modulating the activity of oligonucleotides by carbohydrate conjugation: solid phase synthesis of sucrose-oligonucleotide hybrids. *Org. Biol. Mol. 2*, 1879–1886.

(17) Koizumi, M., Kaneko, M., Ohmine, T., Furukawa, H., and Nishigaki T. 1999. Patent no. JP98/04625; PCT/WO99/19474.

(18) Hotoda, H., Koizumi, M., Koga, R., Kaneko, M., Momota, K., Ohmine, T., Furukawa, H., Agatsuma, T., Nishigaki, T., and Sone, J. (1998) Biologically active oligodeoxyribonucleotides. 5. 5′-End-substituted d(TGGGAG) possesses anti-human immunodeficiency virus type 1 activity by forming a G-quadruplex structure. *J. Med. Chem. 41*, 3655–3663.

(19) D'Onofrio, J., Petraccone, L., Erra, E., Martino, L., Di Fabio, G., De Napoli, L., Giancola, C., and Montesarchio, D. (2007) 5′-Modified G-quadruplex forming oligonucleotides endowed with anti-HIV activity: synthesis and biophysical properties. *Bioconjugate Chem. 18* (4), 1194–1204.

(20) Cantor, C. R., Warshaw, M. M., and Shapiro, H. (1970) Oligonucleotide interactions. 3. Circular dichroism studies of the conformation of deoxyoligonucleotides. *Biopolymers 9*, 1059–1077.

(21) Petraccone, L., Pagano, B., Esposito, V., Randazzo, A., Piccialli, G., Barone, G., Mattia, C. A., and Giancola, C. (2005) Thermodynamics and kinetics of PNA-DNA quadruplex-forming chimeras. *J. Am. Chem. Soc. 127*, 16215–16223.

(22) Van Aerschot, A. (2006) Oligonucleotides as antivirals: dream or realistic perspective? *Antiviral Res. 71*, 307–316.

(23) Agatsuma, T., Furukawa, H., Hotoda, H., Koizumi, M., Koga, R., and Kaneko, M. (1997) Anti-human immunodeficiency virus type 1 activity of R-95288, a phosphodiester hexadeoxyribonucleotide modified by dibenzyloxybenzyl and hydroxyethyl residues at the 5′ and 3′-ends. *Antivir. Chem. Chemother. 8* (5), 429–438.

(24) Cherepanov, P., Este, J. A., Rando, R. F., Ojwang, J. O., Reekmans, G., Steinfeld, R., David, G., De Clercq, E., and Debyser, Z. (1997) Mode of interaction of G-quartets with the integrase of human immunodeficiency virus type 1. *Mol. Pharmacol. 52*, 771–780.

(25) Suzuki, J., Miyano-Kurosaki, N., Kuwasaki, T., Takeuchi, H., Kawai, G., and Takaku, H. (2002) Inhibition of human immunodeficiency virus type 1 activity in vitro by a new self-stabilized oligonucleotide with guanosine-thymidine quadruplex motifs. *J. Virol. 76*, 3015–3022.

(26) Brown, T., and Brown, D. J. S. (1991) Modern machine-aided methods of oligodeoxyribonucleotide synthesis. In *Oligonucleotides and analogues: a practical approach*, (Eckstein, F., Ed.) pp 1–23, IRL Press, Oxford, UK.

(27) Petraccone, L., Erra, E., Esposito, V., Randazzo, A., Mayol, L., Nasti, L., Barone, G., and Giancola, C. (2004) Stability and structure of telomeric DNA sequences forming quadruplexes containing four G-tetrads with different topological arrangements. *Biochemistry 43*, 4877–4884.

BC7003395

Synthesis of Multifunctional Polyvinylsaccharide Containing Controllable Amounts of Biospecific Ligands

V. Korzhikov,[†] S. Roeker,[‡] E. Vlakh,[†] C. Kasper,[‡] and T. Tennikova*,[†]

Institute of Macromolecular Compounds, Russian Academy of Science, Bolshoy pr. 31, 199004, St. Petersburg, Russia, and Institut für Technische Chemie der Universität Hannover, Callinstr. 3, 30167 Hannover, Germany. Received October 16, 2007; Revised Manuscript Received December 20, 2007

In the present study, the attempt to synthesize a multibiofunctional polymeric vector to be used for construction of composite scaffolds for bone tissue engineering has been undertaken. The polymers based on 2-deoxy-2-methacrylamido-D-glucose were functionalized by a growth factor (BMP-2), GRGDSP peptide, and poly(L-lysine) using aldehyde chemistry. The covalent modification process was quantitatively studied, and a polymer conjugate containing all these ligands was formed. In addition, the impacts of coupled ligands toward the adsorption of polymers on the commercial mineral macroporous matrix Sponceram used in cell culture applications were studied.

1. INTRODUCTION

For a long time, biomaterials used for surgical purposes were generally intended to remain inert, thus, unaffected by the reactions with surrounding tissues (*1–7*). While these approaches were useful in many applications, numerous investigators have been currently addressing the means by which biological recognition might be imported (*3, 8–15*). Therefore, it may be possible to utilize such biologically active materials to control cellular interactions and cell function. For example, the new approach for construction of three-dimensional (3-D) composite scaffolds for bone tissue engineering (*16*) supposes the use of biofunctional polymers. In this case, a suitable mineral support should be adsorptively covered by a biocompatible but nondegradable macromolecular compound bearing covalently coupled special ligands responsible for cell adhesion, growth, and differentiation. In this manner, the general idea of this work is the functionalization of the matrix surface in order to intensify *in vitro* or/and *in vivo* tissue formation.

The biomolecules of interest are growth factors (*17–19*) and adhesive peptides (*20–23*). The former are polypeptides involved in the regulation of a variety of cellular activities such as growth and differentiation. Bone morphogenetic proteins (BMP) belonging to the transforming growth factor-β (TGF-β) family and regulating main cellular functions can be proposed as the most probable candidates for our goals. The latter are the so-called RGD peptides. They represent integrin-binding mediators and contain the Arg-Gly-Asp sequence in their chemical structure. Modification of the scaffold surface with RGD peptides may enhance cell adhesion to the matrix and activate integrin signaling pathways. Additionally, different oligo- and polycations, such as poly(L-lysine), could be used to simplify a nonspecific electrostatic cell adhesion.

There are few basic requirements that should be met while designing the polymer for the purpose described in ref (*24*). First, the polymer has to be biocompatible. Second, it has to possess the required molecular mass (MM). This means that, on one hand, the polymer has to be of sufficient MM to exhibit a tendency to be adsorbed on the mineral matrix, and on the other hand, the polymer MM should not hinder its removal from the body (usually, MM = (20–30) $\times$ 10^3). Finally, the polymer has to have sufficient adsorption capability with regard to the mineral supports and contain reactive groups for ligands covalent conjugating.

For these purposes, the use of a new type of polymer known as polyvinylsaccharides (PVS) (*25–31*), which are carbon backbone polymers containing carbohydrate residues as side groups, looks very promising. The presence of saccharide groups in such polymers gives the possibility of forming a structure that may induce a significant increase of specific interactions (*32–39*) in cells with a scaffold surface. As the reactions of bioligand covalent coupling should proceed at mild conditions without yielding toxic byproducts and considering the fact that proteins and peptides contain amino groups, aldehyde chemistry was chosen for this purpose.

In our previous studies, the new hydrophilic polymers based on 2-deoxy-*N*-methacrylamido-D-glucose (MAG) with a controllable amount of aldehyde groups and the evidence for those to be adsorbed on several mineral supports were obtained (*40*). Nevertheless, the important issue in our studies is the supervised functionalization of the mineral matrix surface, which could be achieved by quantitatively controllable coupling of special ligands to the polymer prior to its adsorption on a solid matrix. Thus, the biological response of the system might be governed. Moreover, the combination of several bioligands with different functions on one polymer chain is of special interest.

In the present work, the detailed study of the obtained polymer modification with the bone morphogenetic protein (BMP-2) model, namely, RNase, RGD-peptide, and poly(L-lysine), as well as the synthesis of a polymeric conjugate containing all these ligands on one polymer chain were carried out. The impact of the introduced ligands on the adsorption parameters of polymers was evaluated. In addition, in order to assay the applicability of synthesized conjugates in bone tissue engineering, the cytotoxicity of the initial and modified polymers was examined.

2. EXPERIMENTAL SECTION

2.1. Materials and Instruments. All buffer salts and other reagents of pro analysi (p.a.) quality were purchased from Fluka (Buchs, Switzerland) and Sigma (Taufkirchen, Germany). The

* Correspondence to: Prof. Dr. Chem. Sci. Tennikova T. B. Bolshoy pr. 31, 199004, St. Petersburg, Russia, tel: (812) 323-10-50, fax: (812) 323-68-69, e-mail: tennikova@mail.ru.

[†] Russian Academy of Science.

[‡] Institut für Technische Chemie der Universität Hannover.

10.1021/bc700383w CCC: $40.75 © 2008 American Chemical Society
Published on Web 03/04/2008

dialysis bags Spectra/Pore (MWCO: 1000) used for polymer desalting were purchased from Spectra (USA). The separation of nonreacted low- and high-molecular ligands from polymer conjugates was performed in spin-columns (VIVASCIENCE, Sartorius Group, Göttingen, Germany)—membrane MWCO: 3000, 30 000.

For adsorption studies, the macroporous monolithic Sponceram (Sp) (doped ZrO_2 ceramic material; pore size 600 μm; surface area ~1.4 m^2/g) kindly donated by Zellwerk GmbH (Germany) was used as a mineral support.

Poly(L-lysine) (pLL) of MM 15 000 and ribonuclease A (RNase) were the products of Sigma (Germany). Bone morphogenetic protein-2 (BMP-2) was a kind gift of Prof. Dr. W. Sebald (Institut für Physiologische Chemie, Universität Würzburg, Germany).

For UV–vis measurements, the full-spectrum UV/vis spectrophotometer NANO-DROP ND-1000 (peQLab Biotechnologie GmbH, Germany) was used. The fluorescence measurements were performed using Multiscan Fluorimeter FLUOROSCAN ASCENT (Thermo Electron Corp., UK).

2.2. Methods. *2.2.1. Polymer Synthesis and Aldehyde Group Generation.* The samples of water-soluble 2-deoxy-2-methacrylamido-D-glucose (MAG) homopolymer (pMAG) and its copolymer with 1-vinyl-2-pyrrolidone (VP) and acrolein diethylacetal (DAAc) (p(MAG-co-VP-co-DAAc)) were used as functional vectors.

2.2.1.1. Synthesis of pMAG. The synthesis of MAG polymer was performed similarly to a previously published procedure (*31*, *40*). MAG (6 g, 0.024 mol) was dissolved in 57 mL of DMF, and 0.3 g (5 wt % from MAG amount) of AIBN was added. The reaction mixture was purged with nitrogen. Polymerization was carried out in a sealed ampule at 60 °C for 24 h. The product was precipitated in diethyl ether. After filtration and vacuum drying, 5.7 g (95%) of polymer was obtained. The specific viscosity was measured in 0.1 M Na_2SO_4 at 25 °C and was found to be equal to 0.11 dL/g that corresponded to MM_η = 21 000 ($[\eta]^{25\ °C} = 8.29 \times 10^{-4}$. $M^{0.49}$). MM_w(light-scattering) was equal to 25 800.

2.2.1.2. Synthesis of p(MAG-co-VP-co-DAAc). The samples of p(MAG-*co*-VP-*co*-DAAc) were synthesized by free radical polymerization of comonomers in the presence of AIBN in DMF (*40*) as described above. The comonomers ratio was [MAG]:[VP]:[DAAc] = 15:45:40 mol %. The copolymerization proceeded for 72 h. The resulting polymer product was purified *via* dialysis for 24 h against water and then lyophilized. MM_w (light-scattering) was found to be equal to 13 500.

2.2.1.3. Oxidation of pMAG. The synthesis of dialdehyde derivatives of pMAG was carried out as follows (*40*): 0.5 g (0.002 mol) of pMAG was dissolved in 80 mL of water and cooled down to 5 °C. Then, the sodium periodate was added in an amount corresponding to the desirable amount of aldehyde groups to be obtained. Generally, $[NaIO_4]$:[MAG] = 0.5 and 0.7 mol were used to obtain 20 and 30 mol % of aldehyde groups. The reaction was allowed to proceed for 24 h in the dark at 5 °C. Then, the product was purified by dialysis against water (24 h) and dried by lyophilization. The appearance of aldehyde groups in oxidized polymer was registered via IR spectra measurements. There are two small peaks, 1755 and 1735 cm^{-1}, at the foot of wide amide carbonyl band, which might be referred to the absorption of two aldehyde groups arising from α-glycol cleavage.

2.2.1.4. Activation of p(MAG-co-VP-co-DAAc). The activation, e.g., the removal of blocking acetal groups, of p(MAG-*co*-VP-*co*-DAAc) was carried out in aqueous solution of hydrochloric acid containing 5 mg/mL of polymer at 50–60 °C for 2 h, pH 2.0. After the reaction completed, the solution of activated polymer was dialyzed for 12 h against water and lyophilized. In the IR-spectra of activated p(MAG-*co*-VP-*co*-DAAc), the evident swell (in comparison with pMAG spectra) at the foot of the amide carbonyl band is observed that might be referred with confidence to the absorption of aldehyde groups.

2.2.2. Analytical Methods. 2.2.2.1. Quantification of Aldehyde Groups (Schiff'S Test). The molar amount of aldehyde groups was determined by a reaction of polymers with fuchsinsulfite reagent (Shiff's reagent). For this purpose, the calibration curve was plotted using glutaric dialdehyde as a standard, and the extinction coefficient of CHO-groups was calculated. The analytical procedure was carried out as follows: to a sample of 0.5 mL of aldehyde containing substance, 2.5 mL of Shiff reagent was added, and the absorbance of colored complex was measured at 550 nm in 40 min.

2.2.2.2. Iodine test. The molar amount of VP in p(MAG-*co*-VP-*co*-DAAc) and the concentration of this copolymer at adsorption studies was determined using iodine test. For that, 3 mL of 3 mM iodine in 0.2 M sodium acetate buffer, pH 4.6, was added to 0.5 mL of polymer solution. The absorbance of the colored complex was measured immediately at 460 nm.

2.2.2.3. UV Measurements. In addition to the Schiff's test, the direct measurements at 265–270 nm were used to quantify the amount of the polymers and their conjugates with high- and low-molecular mass ligands.

2.2.3. Polymer Modification. All covalent coupling reactions were allowed to proceed at room temperature for 2 h with stirring (400–700 rpm). After polymer functionalization, all modified samples were treated with sodium borohydride, then purified by spin-column dialysis (membrane MWCO: 3000, 30 000) and stored in a refrigerator at 4 °C.

2.2.3.1. Coupling of Low-Molecular Mass Ligand (GRGDSP–Peptide). In this case, the molar proportions of polymer CHO groups and NH_2 groups of peptide were used. 1, 2, 5, and 10 equiv (in the case of p(MAG-*co*-VP-*co*-Ac) modification) and 1 and 2 equiv (in the case of oxidized pMAG modification) of GRGDSP—peptide, calculated according to the molar content of polymer CHO groups, were dissolved in 0.5 mL 0.01 M sodium borate buffer, pH 10.0, and added to the same volume of activated polymer containing 1 equiv of aldehyde groups (aqueous solution, pH 10.0).

To prove quantitatively the covalent coupling of peptide to the polymer, a fluorescent test was carried out. For that, 5 equiv of dansylcadaverine were dissolved in 2 mL of 7 M urea solution containing 7.5% MeOH and added to 1 equiv of polymer—peptide conjugate dissolved in 2 mL of sodium borate buffer, pH 10.0. Then, 10 equiv of water-soluble 1-ethyl-3-(3-dimethylaminopropyl) carbodiimide hydrochloride (EDC) dissolved in 1 mL of urea was introduced. The reaction proceeded for 40 min at room temperature. Low-molecular mass components of the reaction mixture were separated by spin-column dialysis, and the determination of fluorescent emission of bound to the peptide marker was carried out at 485 nm (corresponding to excitation wavelength of 355 nm). The preliminary calibration curve for free dansylcadaverine allowed quantitative determination of peptide amount bound to the polymer.

2.2.3.2. Coupling of Macromolecular Ligands. In the case of coupling of proteins and pLL, both containing numerous amino groups, for the reaction mixture preparation the mass proportions were used.

SDS-PAGE characterization of modified products was carried out using 16% gels prepared according to the standard procedure (*41*). Silver staining was used for oxidized pMAG, proteins, and conjugate zone detection (*16*, *41*).

(a) Poly(L-Lysine). To study the coupling of pLL to the polymers, the following model experiment was performed. First, the labeling of pLL with FITC was done. For this, 6 μL of fresh FITC aqueous solution, 1 mg/mL, was added to 1 mg/

mL solution of pLL in 0.01 M sodium borate buffer, pH 10.0. The reaction proceeded for 1 h, and the product was then purified from nonreacted FITC by spin-column dialysis (membrane MWCO: 3000). After that, the calibration curve from fluorescence measurement for the detection of pLL labeled with FITC was plotted. In the second stage of this experiment, the reaction of pLL−FITC with activated polymers at different mass proportions was carried out. 1 mass equiv of pLL−FITC conjugate dissolved in 0.01 M sodium borate buffer, pH 10.0, was added to 1 mL solution containing 5, 10, 20, or 40 mass equiv of activated polymer (borate buffer, pH 10.0). The reaction was allowed to proceed for 2 h with slight stirring (550 rpm). The resulting polymer conjugate was purified from nonreacted pLL−FITC via spin-column dialysis (membrane MWCO: 30 000), and the amount of Lys units coupled to the polymer was evaluated by fluorescence measurement.

(b) Ribonuclease A and BMP-2. RNase A was chosen as a cheap BMP-2 model because of their similar isoelectric points and close molecular masses. Quantitative studies of RNase coupling to aldehyde-bearing polymers were carried out using the same model experiment as was made in the case of pLL. 10 μL of FITC aqueous solution, 1 mg/mL, was added to 2 mg/mL solution of protein in 0.01 M sodium borate buffer, pH 10.0. The labeling reaction was allowed to proceed for 1 h, and the product was purified by spin-column dialysis (membrane MWCO: 3000). For polymer modification, 1 mass equiv of protein−FITC conjugate dissolved in 0.01 M sodium borate buffer, pH 10.0, was added to 1 mL solution containing 2, 5, 10, and 20 mass equiv of activated polymer (borate buffer, pH 10.0). After the spin-column dialysis (membrane MWCO: 30 000), the fluorescence of polymer−(protein−FITC) conjugates was measured, and the molar amount of protein coupled was evaluated using the previously plotted calibration curve.

For construction of composite matrices for cell culture experiments, about 400 mass excess of aldehyde-bearing polymer per amount of BMP-2 was used.

2.2.2.3. Synthesis of Triple Conjugate. The construction of multifunctional polymer conjugate containing RNase, pLL, and RGD−peptide was performed via "step-by-step" addition of ligands to the polymer solution and using the quantitative methods described above. All reactions were carried out in 0.01 M sodium borate buffer, pH 10.0. On the final step, the excess of sodium borohydride was added in order to reduce Schiff's bases and possibly unreacted aldehyde groups.

(a) Coupling of RNase−FITC to Oxidized pMAG. In the first step, 1 mL of oxidized polyMAG solution, 2 mg/mL, was added to 0.1 mL of RNase−FITC solution, 1 mg/mL ([pMAG]:[RNase] = 20:1 mass proportion). The reaction proceeded with slight stirring for 1 h. The product was purified by spin-column dialysis (membrane MWCO: 30 000) and two 0.1 mL aliquots were taken for fluorescence measurements.

(b) Coupling of pLL–FITC to pMAG–(RNase–FITC) Conjugate. In the second step, 1 mg/mL, 1 mL of polyMAG–(RNase–FITC) conjugate solution, 1.6 mg/mL, was added to 0.08 mL of pLL–FITC solution ([pMAG]:[pLL] = 20:1 mass proportion). In all cases, the concentration of polymer was considered to be the concentration of the whole conjugate. The reaction, purification, and fluorescence measurements were realized in the same way as in the case of RNase.

(c,d) Coupling of RNase−FITC and pLL−FITC to p(MAG-co-VP-co-Ac). The modification of p(MAG-VP-Ac) with RNase and pLL was carried out in the same way as was done with oxidized pMAG. The only difference consisted of a larger excess of polymer used in each step, namely, [p(MAG-*co*-VP-*co*-Ac)]:[ligand]=30:1 mass proportion.

(e) Coupling of RGD−Peptide. 0.2 mL of RGD−peptide solution, 1 mg/mL, was added to both conjugates of polymers with RNase−FITC and pLL−FITC. The reaction proceeded for 1.5 h with slight stirring. The product was purified by spin-column dialysis, and the residual solution passed through membrane (MWCO: 3000) was measured at 226 nm. Thus, the amount of nonreacted peptide was evaluated, and the molar quantity of peptide coupled to the polymer was calculated using the previously plotted calibration curve.

2.2.4. Adsorption Studies. In all cases, the study of adsorption kinetics and isotherms building were performed at static conditions. Despite the experiments on covalent modification of aldehyde-bearing polymers by amino-containing ligands being carried out in 0.01 M sodium borate buffer, pH 10.0, it is essential for adsorption studies to be performed at physiological conditions, e.g., at pH 7.0. Therefore, 0.01 M sodium borate buffer, pH 10.0, adjusted to pH 7.0 by boric acid (called borate solution, pH 7.0) was used in all experiments.

2.2.4.1. Adsorption Kinetics and Desorption Studies. 1.5 mL of polymer (or conjugate) solution with concentration 1 mg/mL in borate solution, pH 7.0, was added to 50 mg of mineral support. The adsorption proceeded with slight stirring (300–400 rpm) at 25 °C for 3 h. At regular intervals, the content was centrifuged, and the amount of adsorbed polymer was estimated by measuring its concentration in the supernatant using the methods described above (reaction with Shiff's reagent, iodine test, and UV measurements).

The control of possible polymer desorption was carried out by incubation of mineral supports in 0.01 M PBS 7.0 over 14 days using the same quantitative methods to evaluate the desorbed amount of polymer derivatives.

2.2.4.2. Isotherm Building. For this purpose, several samples containing 50 mg of mineral support each were used. The concentrations of polymers (conjugates) solutions in borate solution, pH 7.0, varied from 0.25 to 3.5 mg/mL. The samples of Sponceram were incubated for 2 h (the time corresponding to the plateau on the kinetics curves) at 25 °C in polymer solution, and the amount of adsorbed polymer at fixed concentration was determined as mentioned above.

2.2.4.3. Statistics. For each point, both for kinetics measurements and isotherm building, the set of three equivalent experiments ($n = 3$), with a pure Sponceram as a control, were performed and three UV–vis measurements were done for each sample. The presented results are given as a mean values and the average deviation is 5%.

2.2.4.4. Adsorption of Polymers and Conjugates for Cell Culture Experiments. For cell culture experiments, the adsorption of initial polymers was performed in 15 mL tubes containing 20 pieces of Sponceram 15–20 mg each, and 5 mL of sterilized (0.2 μm filter) polymer solution in sodium borate buffer, pH adjusted to 7.0, with concentration 0.5 mg/mL was added to the tubes. The tubes were slightly stirred (300 rpm) or rotated (1 rpm) at least overnight. Then, the solution of the polymer was removed, and the pieces of Sponceram were washed twice with phosphate buffering saline (PBS), pH 7.0. Subsequently, the composite materials were incubated with cell culture medium for 2 h at room temperature or overnight at 4 °C.

The conjugates adsorption was carried out in a similar way, except the 2 mL tubes and 1.5 mL of 1.0 mg/mL or 0.5 mg/mL solutions were used.

2.2.5. Cell Culture Experiments. 2.2.5.1. Cultivation of MC3T3-E1 Cells. MC3T3-E1 cells were stored in Dulbecco's modified eagle medium (DMEM), supplemented with 10% fetal bovine serum and antibiotics. For assays in 96-well plates, 5000 cells per well were seeded. For cell seeding onto Sponceram, 15–20 mg pieces of Sponceram were shaken (350 rpm) with 20 μL of a cell suspension (1 mio cells/mL) for 30 min at 37 °C, 5% CO_2. The Sponceram pieces were sterilized by auto-

Table 1. Modification of pMAG (30 mol % CHO groups, MM 20 000) and p(MAG-*co*-VP-*co*-Ac) (7 mol % CHO groups, MM 13 500) with GRGDSP−Peptide[a]

$[CHO]_{polym}$:$[NH_2]_{GRGDSP}$ mol ratio	[CHO] group conversion, mol %
pMAG	
1	75
0.5	94
p(MAG-co-VP-co-Ac)	
1	40
0.5	50
0.2	63
0.1	93

[a] Reaction conditions: 0.01 M sodium borate buffer, pH 10.0, 25 °C, 2 h stirring (550 rpm). Purification: spin-column dialysis (MWCO: 3000). The aldehyde groups conversion (the amount of peptide bound to the polymer) was determined by fluorescent test with use of dansylcadaverine as a fluorescent label ($\lambda_{ex.}$= 355 nm, $\lambda_{em.}$= 485 nm).

claving and incubated with cell culture medium for at least 2 h before cell seeding.

2.2.5.2. MTT Assay. MTT assays were performed with n = 5 and one negative control. The matrices were placed into new wells to measure exclusively the viability of the cells adherent to the Sponceram but not those on the bottom of the well. Cells/matrices were incubated with 100 μL of cell culture medium and 10 μL MTT (5 mg/mL in PBS) for 4 h at 37 °C, 5% CO_2. Formazan crystals were dissolved overnight with 10% SDS in 0.01 M HCl. The formazan absorption was measured at 570 nm subtracted by the 630 nm absorption.

2.2.5.3. Statistical Analysis. A p value of <0.05 was considered statistically significant. In order to confirm the dependence of one variable on another (e.g., whether cell viability is dependent on polymer concentration), a linear regression was performed, considering a p value of <0.01 statistically significant.

3. RESULTS AND DISCUSSION

3.1. Polymer Modification. Following the main idea of this work, the mineral matrix has to be covered by a nondegradable polymer vector covalently modified with ligands which impart bifunctionality to. The water-soluble 2-deoxy-2-methacrylamido-D-glucose (MAG) homopolymer (pMAG) and its copolymer with *N*-vinylpyrrolidone (VP) and acroleyn diethylacetal (DAAc) [p(MAG-*co*-VP-*co*-DAAc)] were used as functional vectors. Also, having the final aim of creating a multifunctional conjugate containing the mixture of several ligands on one polymer chain, we were intending to study the possibility of controlled introduction of these ligands. For this purpose, the analysis of covalent coupling of single ligands to the polymers under investigation was performed.

3.1.1. GRGDSP−Peptide Coupling. Both oxidized pMAG and p(MAG-*co*-VP-*co*-Ac) were modified with GRGDSP–peptide at different molar proportions of aldehyde groups of polymers and amino groups of peptide (Table 1). The idea of this model experiment is presented in Figure 1. The coupling of GRGDSP–peptide was determined by treatment of the conjugate with dansylcadaverine fluorescent label in the presence of water-soluble carbodiimide (EDC). Then, the polymeric conjugate was purified from low-molecular compounds by spin-column dialysis, and the fluorescence of the sample was detected.

The results obtained for oxidized pMAG and those for p(MAG-*co*-VP-*co*-Ac) are shown in Table 1. As this reaction was supposed to be controlled by the diffusion of peptide to the aldehyde groups of polymer, in most cases, an excess of peptide was used. Besides, some steric hindrance caused by glucose side residues and polymer microstructure might occur. One can see that, in the case of oxidized pMAG, containing 30

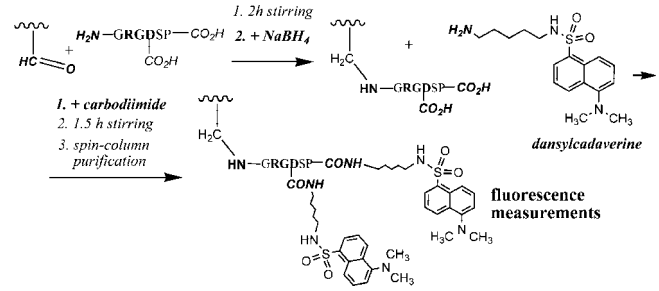

Figure 1. Polymer modification with RGD peptide and evaluation of the molar amount of peptide coupled.

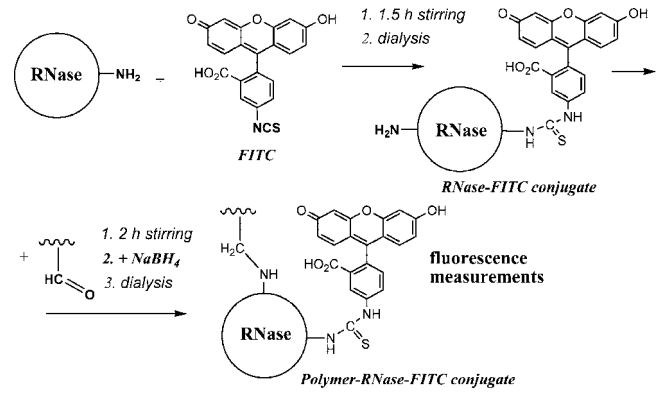

Figure 2. Polymer modification with RNase.

mol % of CHO groups, close to 100% conversion occurs as early as the [CHO]:[NH_2] = 1:2 molar proportion of initial reaction mixture is used. This is not so for p(MAG-*co*-VP-*co*-Ac), which contains much fewer aldehyde groups (7 mol %). In the latter case, the high conversion occurs only at [CHO]:[NH_2] = 1:10 molar proportion of a reaction mixture.

Thus, generally we can conclude that the reactions of GRGDSP peptide with polymers are really controlled by diffusion of peptide to the polymer aldehyde groups; consequently, the increase of peptide concentration leads to higher conversion.

3.2.2. Modification with Macromolecular Ligands. 3.2.2.1. RNase and BMP-2. For qualitative confirmation of pMAG−RNase conjugate formation, SDS-PAGE in 16% gel was used. While the pMAG itself does not move in the gel, the oxidized pMAG and its conjugate with RNase migrates across the gel layer demonstrating a continuous band due to polymer molecular weight distribution. After silver staining of the gel, the bands corresponding to the formation of conjugate were observed.

The quantitative studies of RNase coupling were performed by use of fluorometrical detection. For that, fluorescent labeling with FITC was carried out before coupling to the polymer (Figure 2). As was mentioned above, the use of RNase A as a model of BMP-2 was reasonable because these proteins have nearly the same isoelectric points and molecular mass.

Observing the data in Table 2, one can see that the reaction between polymers and RNase takes place. As the reaction proceeds between two macromolecular compounds, some steric hindrance effects occur. Thus, in order to magnify the protein conversion, the excess of polymers and, consequently, of aldehyde groups, in most cases was applied. Besides, there is the evidence for the fact that RNase binds to p(MAG-*co*-VP-*co*-Ac) to a greater extent than to oxidized pMAG. This result might be explained by p(MAG-*co*-VP-*co*-DAAc) structure peculiarities which provides the greater accessibility of aldehyde groups for protein coupling.

Table 2. Modification of pMAG and p(MAG-*co*-VP-*co*-Ac) with RNase[a]

[Polymer]:[RNase], mass ratio	[CHO]:[RNase], mol ratio	protein conversion, mol %
	pMAG	
2	33	4
5	83	7
10	166	31
20	337	43
	p(MAG-co-VP-co-Ac)	
2	9	13
5	23	25
10	45	37
20	93	85

[a] Reaction conditions: 0.01 M sodium borate buffer, pH 10.0, 25 °C, 2 h stirring (550 rpm). Purification: spin-column dialysis (MWCO: 3000). The aldehyde group conversion (the amount of peptide bound to the polymer) was determined by fluorescent test with use of FITC as fluorescent label ($\lambda_{ex.}$= 485 nm, $\lambda_{em.}$= 538 nm).

Table 3. Modification of pMAG and p(MAG-*co*-VP-*co*-Ac) with pLL[a]

[Polymer]:[pLL], mass ratio	[CHO]: [Lys-unit], mol ratio	[NH_2] conversion, mol %
	pMAG	
5	0.85	49
10	1.70	59
20	3.39	75
40	6.78	82
	p(MAG-co-VP-co-Ac)	
5	0.23	23
10	0.47	29
20	0.94	64
40	1.87	68

[a] Reaction conditions: 0.01 M sodium borate buffer, pH 10.0, 25 °C, 2 h stirring (550 rpm). Purification: spin-column dialysis (MWCO: 3000). The aldehyde group conversion (the amount of peptide bound to the polymer) was determined by fluorescent test with use of FITC as fluorescent label ($\lambda_{ex.}$ = 485 nm, $\lambda_{em.}$ = 538 nm).

3.2.2.2. Poly(L-Lysin) (pLL). For investigation of quantitative coupling of pLL to the polymers, the same model experiment as in the case with RNase was performed. The data obtained for polyMAG and p(MAG-*co*-VP-*co*-Ac) are presented in Table 3. Likewise to the case with proteins, an excess of polymer per amount of pLL was used. Note that, when less than a 5-fold mass excess of polymer was used, the formation of an insoluble part occurred, which is most likely due to intermolecular cross-linking of aldehyde-containing polymers by polyamino-containing molecules of pLL. Also, it is important to point out that, apart from the cases with proteins, the calculations were carried out not to the molecule of pLL, but to the molar quantity of L-lysine units, because the molecular mass of pLL (like other synthetic polymers) represents a mean value.

Observing the data obtained (Table 3), one can see that the maximum conversion of amino groups was reached in the case of oxidized pMAG that bears greater amount of aldehyde groups. Interestingly, while considering molar ratios of aldehyde groups and amino-bearing lysine units (Table 3), it is becoming evident that amino group conversion and, thus, the reactivity of aldehyde groups are nearly equal for both polymers. This might be explained by the high amount of easily accessible amino groups in pLL, which allows one to overcoming the diffusion limitations occurring in the case of RNase. So, the use of pMAG here might be preferable only due to higher quantity of aldehyde groups in its structure.

3.2.3. Triple Conjugate Formation. As was mentioned above, the final aim of this part of work was to create a polymeric vector containing the so-called "cocktail" of ligands on one polymer chain. Therefore, using the data obtained in single-ligand coupling experiments, the attempt to construct the mixed

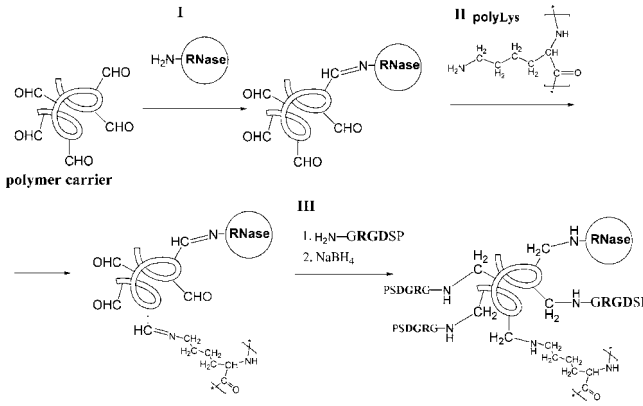

Figure 3. Triple conjugate synthesis.

conjugate was made. The synthesis was performed via "step-by-step" introduction of ligands (Figure 3) to the polymer using the same quantitative methods described above. First, the macromolecular ligands (RNase and then pLL) were added, because their coupling is affected by steric hindrance and an excess of aldehyde groups is required. After that, an excess of RGD−peptide was added, and its coupled amount was qualified by evaluation of the quantity of unreacted peptide. Finally, the conjugate was treated with sodium borohydride to turn Shiff's bases into more stable single bonds and to convert unreacted aldehyde groups to hydroxyls. The latter point is important to prevent subsequent reactions and possible toxic effect for the cells.

The data obtained are collected in Table 4. It is obvious that the conversion of ligands taking place at each step proves the successful construction of the desired triple conjugates.

3.2. Adsorption Studies. As was pointed out in the Introduction, this work was aimed toward obtaining polymers that can be used as the organic part of composite scaffolds for bone tissue regeneration. An important issue in such composites is the interfacial bonding between ceramics and polymer. If the adhesion of the two phases is poor, the biological properties of polymeric conjugates with biomolecules suffer. Thus, it was important to determine the adsorption characteristics of the obtained conjugates and compare them with those of initial polymers.

The mineral support used in our experiments, namely, Sponceram (Sp), has the anionic character of its surface. This fact was also taken into account at the construction of the polymeric part of composite.

3.2.1. Adsorption of Initial Polymers. 3.2.1.1. Adsorption Kinetics and Desorption Studies. The resulting kinetic curves of adsorption of the polymers under study on Sponceram are shown in Figure 4. It is seen that the adsorption process is quite intensive, and it achieves its maximum, the plateau on the curves, within about 100 min. As the shapes of all kinetic curves are nearly the same, for further comparison of adsorption kinetics of conjugates on Sponceram only oxidized pMAG was used.

The data obtained in desorption studies are demonstrated in Table 5. There is evidence for the fact that the polymers in the study do not desorb in noticeable amounts within 14 days, which in turn indicates the adsorption strength.

3.2.1.2. Isotherms Building. The plotted isotherms of adsorption are shown in Figure 5. The acquired values of $Q_{a\ max}$, for which the amount of adsorbed polymer corresponding to the plateau on the isotherm curve was accepted, are presented in Table 5.

Thus, considering the results of adsorption kinetics studies and plotted isotherms, one can see that there are no significant

Table 4. Construction of Triple Conjugate

step I		step II		step III	
[polymer]:[RNase], mass ratio	protein conversion, mol %	[polymer]:[pLL], mass ratio	[NH_2] conversion, mol %	[MAG]:[RGD], mol ratio	RGD conversion, mol %
		pMAG			
20:1	47	20:1	33	7:1	39
		p(MAG-co-VP-co-Ac)			
30:1	58	30:1	15	8:1	25

Table 5. Adsorption/Desorption Parameters of Polymers and Their Conjugates

		desorption, mg/g sorb.	
sample	Q_{max} mg/g sorb.	8 days	14 days
oxidized pMAG	16.5	0.2	0.3
p(MAG-*co*-VP-*co*-Ac)	14.1	0.3	0.5
pMAG−pLL	18.2	0.3	0.4
pMAG−RNase	17.0	0.2	0.3
pMAG−RGD	6.1	0.0	0.1

differences both in the trends of curves and in the quantity of polymers adsorbed. Obviously, the MAG residue seems to be a major cause for all polymers to be adsorbed. This effect might be explained by the ability of MAG to form a large amount of hydrogen bonds with negatively charged oxygen atoms on the surfaces of the mineral matrix.

The absence of significant desorption measured within 14 days at physiological pH confirms the strength of adsorption and, thereafter, a possibility of using such polymers for construction of composite scaffolds for cell culture applications without any risk of polymer leakage from a mineral surface.

3.2.2. Adsorption of Conjugates. The adsorption study of conjugates was performed in the same way and via the same quantitative methods as in the case of aldehyde-containing polymers. Considering the fact that the adsorption characteristics of two pMAG samples and p(MAG-*co*-VP-*co*-Ac) are very similar, in this study we used only pMAG (20 mol % of aldehyde) conjugates.

The obtained kinetics curves and isotherms are demonstrated in Figure 6 and Figure 7, respectively. The observation of kinetic curves approves only a slight difference in their shape, whereas the amounts of conjugates adsorbed are remarkably different. We can suppose that kinetics curves trends are determined by pMAG structure, whereas the Q_{max} at a certain concentration is influenced by the presence of different ligands. This is likely

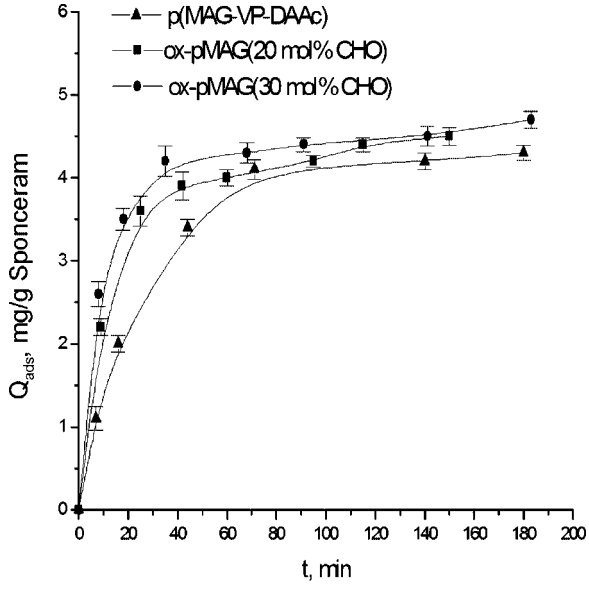

Figure 4. Kinetic curves of oxidized pMAG (20 and 30 mol % [CHO]) and p(MAG-*co*-VP-*co*-Ac) adsorption on Sponceram. The experiment was performed in 0.01 M sodium borate solution, pH 7.0, at 25 °C and with slight stirring, 300 rpm. The concentrations of initial solutions were 1 mg/mL.

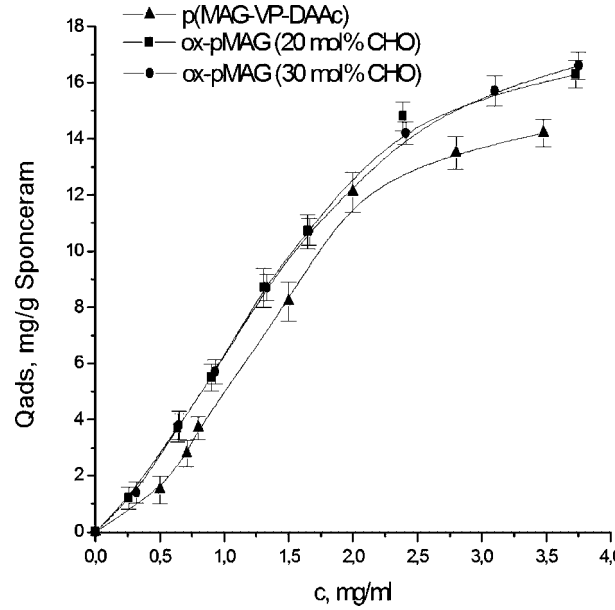

Figure 5. Isotherms of oxidized pMAG (20 and 30 mol % [CHO]) and p(MAG-*co*-VP-*co*-Ac) adsorption on Sponceram. The experiment was performed in 0.01 M sodium borate solution, pH 7.0, at 25 °C and slight stirring, 300 rpm. The reaction time was 4 h.

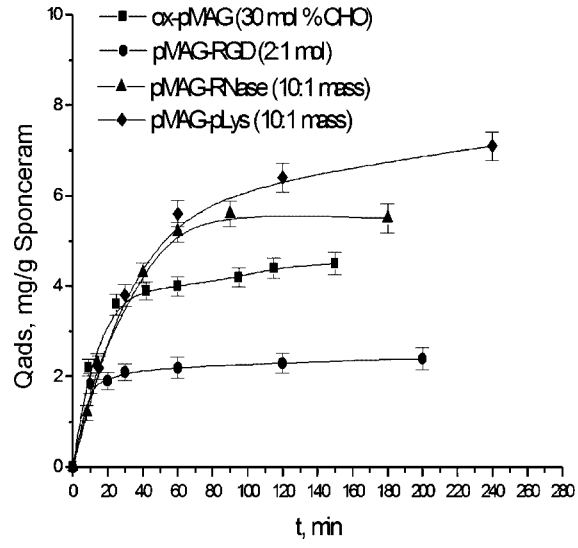

Figure 6. Adsorption kinetic curves of oxidized pMAG and its conjugates with RGD−peptide, RNase, and pLL on Sponceram. The experiment was performed in 0.01 M sodium borate solution, pH 7.0, at 25 °C and at slight stirring, 300 rpm. The concentrations of initial solutions were 1 mg/mL.

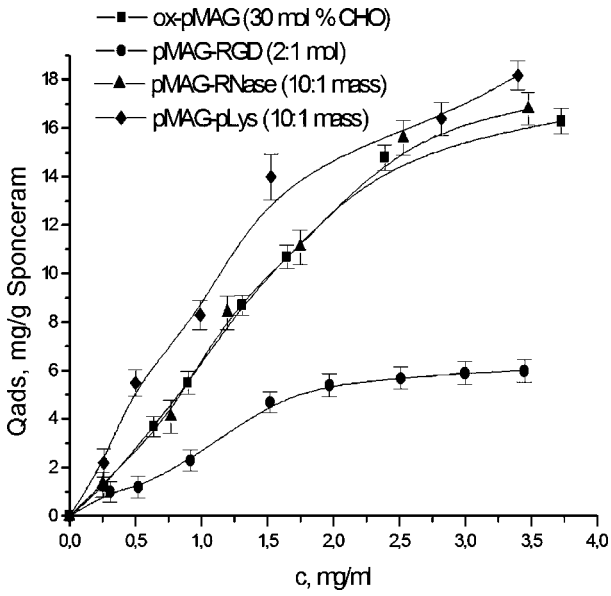

Figure 7. Isotherms of oxidized pMAG and its conjugates with RGD−peptide, RNase, and pLL adsorption on Sponceram. The experiment was performed in 0.01 M sodium borate solution, pH 7.0, at 25 °C and at slight stirring, 300 rpm. The reaction time was 4 h.

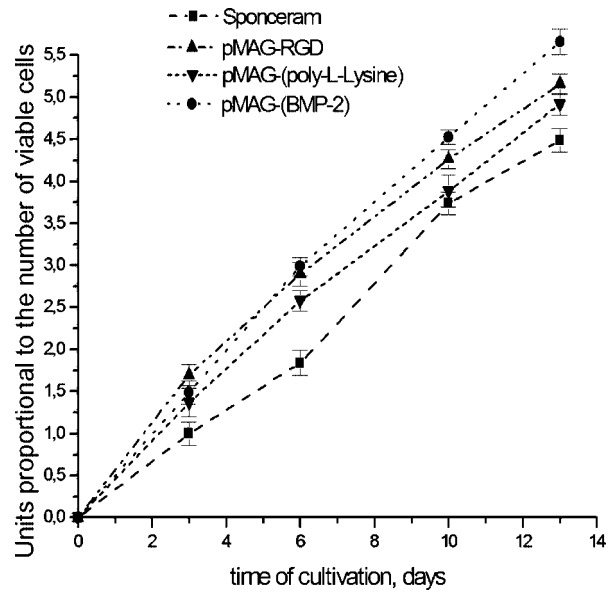

Figure 8. MTT assay−pMAG modified with BMP-2, GRGDSP peptide, and pLL adsorbed on Sponceram.

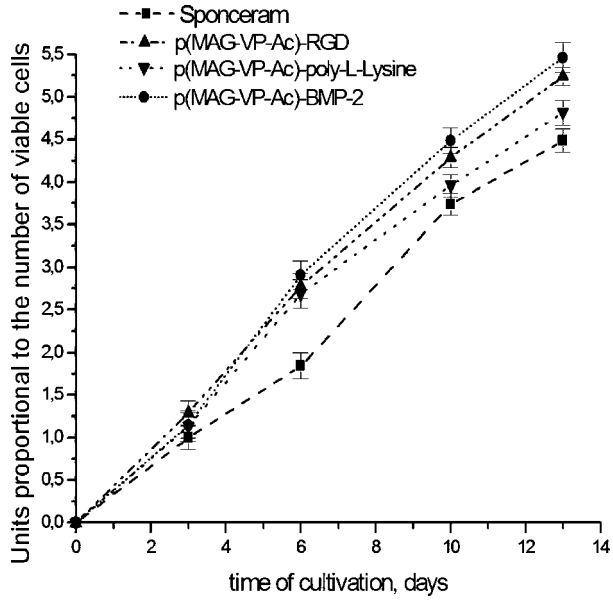

Figure 9. MTT assay−p(MAG-*co*-VP-*co*-Ac) modified with BMP-2, GRGDSP, and pLL adsorbed on Sponceram.

to be true when watching the isotherms of adsorption. A considerable amount of pMAG−pLL conjugate adsorbed is due to the positive charge of poly(L-lysine) causing the ionic interactions with the negatively charged surface of Sponceram. In the latter case, there is no well-marked plateau on the isotherm curve, that might be due to the formation of multilayers. Besides, it is obvious that coupling of RGD−peptide affects the conformation and polymer macrostructure that results in adsorption behavior.

Desorption parameters of adsorbed conjugates are shown in Table 5. It is seen that, as in aldehyde polymer derivatives, the desorption within 14 days is practically equal to zero.

In addition to building the isotherm, the approximate calculations of the polymer coverage on the mineral matrix surface were made by considering the polymers to be adsorbed more or less as stretched threads. The results of these calculations allow to say that at Q_{max} on the isotherm curves the surface of Sponceram is overfilled with polymer.

3.3. Cytotoxicity. Initially, every polymer that was considered for adsorption on the mineral matrix was tested for its cytotoxicity in cell culture medium. MC3T3-E1 cells were used for this purpose. In these studies, the aldehyde forms of the polymers [oxidized pMAG and p(MAG-*co*-VP-*co*-Ac)] were shown to decrease cell viability in comparison with the standard cell culture. At the same time, the nonaldehyde forms of polymers [pMAG and p(MAG-*co*-VP-*co*-DAAc)] did not display such an effect (*40*).

After that, pMAG, oxidized pMAG, and p(MAG-*co*-VP-*co*-Ac) were adsorbed on Sponceram, and the viability of MC3T3-E1 cells on these modified materials was investigated. Sponceram incubated with borate buffer, which was used for the polymer adsorption, served as a control. Cell viability was roughly the same for all tested samples. Unlike the experiments with polymers supplementing the cell culture medium, there was no significant cytoxicity or any difference between polymers containing aldehyde groups and those without (*40*).

Nevertheless, the polymers modified with biospecific ligands, not the initial polymers, were of the primary interest in this work. Herewith, it is essential to note that in target conjugates there are no aldehyde groups, because they are used for the reactions with macromolecules and small ligands and, finally, should be reduced to hydroxylic groups when treated with sodium borohydride.

To test the cytotoxicity of the obtained conjugates, the polymers oxidized pMAG and p(MAG-VP-Ac) were coupled to BMP-2, RGD peptide, and pLL, respectively, and then adsorbed on Sponceram. The viability of the MC3T3-E1 cells was observed on these composite materials over a time period of two weeks and compared to the cell viability on Sponceram treated with borate buffer (Figures 8 and 9). The results showed that the amount of cells adhered onto composite materials was increased in all measurements when compared to pure Sponceram. The investigation of the impact of ligands on cell behavior—cell adhesion pLL and RGD peptide) and differentiation (BMP-2)—is in progress.

CONCLUSIONS

The quantitatively controllable functionalization of polymers based on 2-deoxy-2-methacrylamido-D-glucose with GRGDSP-

peptide, Ribonuclease A (physical model of BMP-2), and poly(L-lysine) was carried out; and the conjugate containing all these ligands was synthesized. The study of adsorption characteristics of initial polymers and their conjugates with the foregoing ligands allows us to conclude that the adsorption process is strong enough for all polymers and their conjugates. Moreover, the first experiments on the viability of cells on the Sponceram covered with polymers and their conjugates with RGD peptide, pLL, and BMP-2 clearly showed that the polymers in use are not cytotoxic when adsorbed on the mineral surface and tend to increase cell adhesion when modified with special ligands. Thus, we can suggest this type of conjugate for development of scaffolds for bone tissue engineering.

ACKNOWLEDGMENT

This work was financially supported by the grants of Russian Foundation of Basic Research (RFBR, 05-03-32310) and German Scientific Society (DFG, KA 1784/4–1). The authors are grateful to the German Academic Exchange Service (DAAD) for providing the scholarship for PhD student Victor Korzhikov for six months work at the Institute of Technical Chemistry, University of Hannover (ITC UH). We are also grateful Prof. Dr. Thomas Scheper for kind cooperation and positive discussions.

LITERATURE CITED

(1) Mano, F., Sousa, A., Boesel, F., Neves, M., and Reis, L. (2004) Bioinert, biodegradable and injectable polymeric matrix composites for hard tissue replacement: state of the art and recent developments. *Compos. Sci. Technol. 64*, 789–817.

(2) Liu, X., Chu, K., and Ding, C. (2004) Surface modification of titanium, titanium alloys and re-lated biomaterials for biomedical applications. *Mater. Sci. Eng., R 47*, 49–121.

(3) Agrawal, C. M. (1998) Reconstructing the human body using biomaterials. *J. Miner. Met. Mater. Soc. 50*, 31–35.

(4) (Scheftler, M.; Colombo, P., Eds.) (2006) *Cellular Ceramics: Manufacturing, Properties and Applications*, pp 548–z549, Wiley-VCH.

(5) Prime, K. L., and Whitesides, G. M. (2005) Self-assembled organic monolayers: model sys-tems for studying adsorption of proteins at surfaces. *Science 252*, 1164–1167.

(6) Chapman, R. G., Ostuni, E., Takayama, S., Holmlin, R. E., Yan, L., and Whitesides, G. M. (2000) Surveying for surfaces that resist the adsorption of proteins. *J. Am. Chem. Soc. 122*, 8303–8304.

(7) Catanese, J., Cooke, D., Maas, C., and Bumpous, J. (1999) Mechanical properties of medi-cal grade expanded polytetrafluoroethylene: the effects of internodal distance, density and displacement rate. *J. Biomed. Mater. Res. 48*, 187–192.

(8) Matsumoto, T., and Mooney, J. D. (2006) Cell instructive polymers. *Adv. Biochem. Eng./Biotechnol. 102*, 113–137.

(9) Mistry, A. S., and Mikos, A. G. (2005) Tissue engineering strategies for bone regeneration. *Adv. Biochem. Eng./Biotechnol. 94*, 2–22.

(10) Hern, D. L., and Hubbel, J. A. (1998) Incorporation of adhesion peptides into nonadhesive hy-drogels useful in tissue engineering. *J. Biomed. Mater. Res. 39*, 266–276.

(11) Mann, B. K., Tsai, A. T., Scott-Burden, T., and West, J. L. (1999) Modification of surfaces with cell adhesion peptides alters extracellular matrix deposition. *Biomaterials. 20*, 2281–2286.

(12) Schmedlen, R. H., Masters, K. S., and West, J. L. (2002) Photocrosslinkable PVA hydrogels that can be modified with cell adhesion peptides for use in tissue engineering. *Biomaterials 23*, 4325–4332.

(13) Rowley, J. A., Madlambayan, G., and Mooney, D. J. (1999) Alginate hydrogels as synthetic extracellular matrix materials. *Biomaterials 20*, 45–53.

(14) Sakiyama-Elbert, S. E., and Hubbell, J. A. (2000) Development of fibrin derivatives for controlled release of growth factors. *J. Controlled Release 65*, 389–402.

(15) Lee, K. Y., Peters, M. C., Anderson, K. W., and Mooney, D. J. (2000) Controlled growth factor release from synthetic extracellular matrices. *Nature 408*, 998–1000.

(16) Vlakh, E., Panarin, E., Tennikova, T., Suck, K., and Kasper, C. (2005) Development of multi-functional polymer-mineral composite materials for bone tissue engineering. *J. Biomed. Mater. Res. 75*, 333–341.

(17) Park, M. S., Kim, S-S., Cho, S-W., Choi, C. Y., and Kim, B-S. (2006) Enhancement of osteo-genic efficacy of osteoblasts transplantation by the sustained delivery of basic fibroblast growth factor. *J. Biomed. Mater. Res. 79B*, 353–359.

(18) Xu, X. L., Lou, J., Tang, T., Ng, K. W., Zhang, J., Yu, Ch., and Dai, K. (2006) Evaluation of different scaffolds for BMP-2 genetic orthopedic tissue engineering. *J. Biomed. Mater. Res. 75B*, 289–303.

(19) Kim, J., Kim, I. S., Cho, T. H., Lee, K. B., Hwang, S. J., Tae, G., Noh, I., Lee, S. H., Park, Y., and Sun, K. (2007) Bone regeneration using hyaluronic acid-based hydrogel with bone morphogenetic protein-2 and human mesenchymal stem cells. *Biomaterials 28*, 1830–1837.

(20) Massia, S. P., and Hubbell, J. A. (1990) Covalent surface immobilization of Arg-Gly-Asp- and Tyr-Ile-Gly-Ser-Arg-containing peptides to obtain well-defined cell-adhesive substrates. *Anal. Biochem. 187*, 292–301.

(21) Lin, H-B., Sun, W., Mosher, D. F., Garcia-Echeverria, C., Schaufelberger, K., Lelkes, P. I., and Cooper, S. L. (1994) Synthesis, surface, and cell-adhesion properties of polyurethanes containing covalently grafted RGD-peptides. *J. Biomed. Mater. Res. 28*, 329–342.

(22) Drumheller, P. D., Hubbell, J. A. (1995) Surface immobilization of adhesive ligands for investigations of cell-substrate interactions. *The Biomedical Engineering Handbook* (Bronzino, J. D., Ed.) pp 1583–1596, CRC Press Inc., Boca Raton, Florida.

(23) Scaffner, P., and Dard, M. M. (2003) Structure and function of RGD peptides involved in bone biology. *Cell. Mol. Life Sci. 60*, 119–132.

(24) Moulinex, J. (1984) Water Soluble Synthetic Polymers: Properties and Behaviour, pp 135–146, Vol. 3, CRC Press, Boca Raton, FL.

(25) Klein, J., and Herzog, D. (1987) Poly. (vinylsacharide)s 2: Synthesis of some poly. (vinylsacharide)s of the amide type and investigation of their solution properties. *Macromol. Chem. 188*, 1217–1232.

(26) Klein, J., and Blumenberg, K. (1988) Synthesis and polymerization of 6-O-methylallylgalactose derivatives. *Makromol. Chem. 189*, 805–813.

(27) Wulf, G., Schmid, J., and Venhoff, Th. (1996) The synthesis of polymerizable vinylsugars. *Makromol. Chem. Phys. 197*, 259–274.

(28) Garcia-Martin, M. G., Jimenez-Hidalgo, G., Al-Kass, S. S. J., Caraballo, I., de Paz, M. V., and Galbis, J. A. (2000) Synthesis and characterization of some new homo- and co-poly. (vinylsaccharides). Some preliminary studies as drug delivery. *Polymer 41*, 821–826.

(29) D'Agosto, F., Charreyre, M-T., Pichot, Ch., and Mandrand, B. (2002) Polymer of controlled chain length carrying hydrophilic galactose moieties for immobilization of DNA probes. *Macromol. Chem. Phys. 203*, 146–154.

(30) Wulff, G., and Clarkson, G. (1994) On the synthesis of C-glycosyl compounds containing dou-ble bonds without the use of protecting groups. *Carbohydr. Res. 257*, 81–95.

(31) Panarin, E. F., and Ivanova, N. P. (2005) Synthesis of copolymers of vinylformamide with N-methacryloylglucosamine. *Russ. J. Appl. Chem. 78*, 1316–1319.

(32) Miyata, T., Ootsuki, N., Nakamae, K., Okumura, M., and Kinomura, K. (1994) Protein adsorp-tion on a copolymer having pendant monosaccharide groups. Relationship between surface

free energy and protein adsorption. *Makromol. Chem. Phys. 195*, 3597–3607.
(33) Stanek, L. G., Heilmann, S. M., and Gleason, W. B. (2006) Preparation and copolymerization of a novel carbohydrate containing monomer. *Carbohydr. Polym. 65*, 552–556.
(34) Nakaya, R., Nishio, K., Memita, M., and Imoto, M. (1993) Polymeric glycolipid analogues, 3. Polymethylacrylates containing glucose moieties attached to the polymer backbones via n-alkyl chains of various length. *Makromo. Chem. Rapid Commun. 14*, 77–83.
(35) Ma, Q., and Feng, Sh. (2006) Synthesis of a new kind of carbohydrate-modified polysiloxanes and its morphological transition of molecular aggregates in water. *Carbohydr. Polym. 65*, 321–326.
(36) Lin, W-J., and Chen, M. H. (2007) Synthesis of multifunctional chitosan with galactose as tar-geting ligand for glycoprotein receptor. *Carbohydr. Polym. 67*, 474–480.
(37) Cuervo-Rodriguez, R., Bordege, V., and Fernandez-Garcia, M. (2007) Synthesis and characteri-zation of novel glycopolymers based on ethyl α-hydroxy-methacrylate. *Carbohydrate Po-lym. 68*, 89–94.
(38) Kobayashi, K., Sumitomo, H., and Ina, Y. (1985) Synthesis and functions of polystyrene deriva-tives having pendant oligosaccharide. *Polym. J. 17*, 567–575.
(39) Nazarova, O. V., Fomina, N. G., Afanas'eva, E. V., and Panrin, E. F. (2003) N-methacryloylaminodeoxyglucose copolymers containig unsaturated acid and activated ester units. *Russ. J. Appl. Chem. 76*, 1647–1650.
(40) Korzhikov, V. A., Diederichs, S., Nazarova, O. V., Vlakh, E. G., Kasper, C., Panarin, E. F., TennikovaT. B. Water-soluble aldehyde bearing polymers of 2-deoxy-2-methacrylamido-D-glucose for bone tissue engineering, *J. Appl. Polym. Sci.* 2008, *108*, 2386–2397.
(41) Rosenberg, I. M., (1996) Protein analysis and purification. *Benchtop techniques*, pp 55–79, Chapter 4, Birkhauser, Boston.

BC700383W

Novel Biodegradable Poly(disulfide amine)s for Gene Delivery with High Efficiency and Low Cytotoxicity

Mei Ou,[†] Xu-Li Wang,[‡] Rongzuo Xu,[‡] Chien-Wen Chang,[†] David A. Bull,[§] and Sung Wan Kim*[,†]

Center for Controlled Chemical Delivery (CCCD), Department of Pharmaceutics and Pharmaceutical Chemistry, 421 Wakara Way, Suite 318, University of Utah, Salt Lake City, Utah 84112, and Division of Cardiothoracic Surgery, Room 3C127, School of Medicine, 30N 1900E, University of Utah, Salt Lake City, Utah 84132. Received October 25, 2007; Revised Manuscript Received December 13, 2007

Novel biodegradable poly(disulfide amine)s with defined structure, high transfection efficiency, and low cytotoxicity were designed and synthesized as nonviral gene delivery carriers. Michael addition between *N*,*N*′-cystaminebisacrylamide (CBA) and three *N*-Boc protected diamines (*N*-Boc-1,2-diaminoethane, *N*-Boc-1,4-diaminobutane, and *N*-Boc-1,6-diaminohexane) followed by *N*-Boc deprotection under acidic condition resulted in final cationic polymers with disulfide bonds, tertiary amine groups in main chains, and pendant primary amine groups in side chains. Polymer structures were confirmed by ^{1}H NMR, and their molecular weights were in the range 3.3−4.7 kDa with narrow polydispersity (1.12−1.17) as determined by size exclusion chromatography (SEC). Acid–base titration assay showed that the poly(disulfide amine)s possessed superior buffering capacity to branched PEI 25 kDa in the pH range 7.4−5.1, which may facilitate the escape of DNA from the endosomal compartment. Gel retardation assay demonstrated that significant polyplex dissociation was observed in the presence of 5.0 mM DTT within 1 h, suggesting rapid DNA release in the reduction condition such as cytoplasm due to the cleavage of disulfide bonds. Genetic transfections mediated by these poly(disulfide amine)s were side-chain spacer length dependent. The poly(disulfide amine) with a hexaethylene spacer, poly(CBA-DAH), had comparable transfection efficiency to bPEI 25 kDa in the tested cell lines, i.e., 293T cells, Hela cells, and NIH3T3 cells. This same poly(disulfide amine) mediated 7-fold higher luciferase expression than bPEI 25 kDa in C2C12 cells (mouse myoblast cell line), a cell line difficult to transfect with many cationic polymers. Furthermore, MTT assay indicated that all three poly(disulfide amine)s/pDNA polyplexes were significantly less toxic than bPEI/pDNA complexes.

INTRODUCTION

Gene therapy has broad potential in the treatment of human genetic and acquired diseases through the delivery and application of therapeutic gene-based drugs. The use of safe, efficient, and controllable gene carriers is a requirement for the success of clinical gene therapy (*1, 2*). Although viral vectors are very efficient in gene delivery, their potential safety and immunogenicity concerns raise their risk in clinical applications (*3*). As an alternative to viral vectors, cationic polymers such as poly(L-lysine) (PLL), poly(ethylenimine) (PEI), poly(amidoamine)s dendrimers, and cationic liposomes have been synthesized as gene delivery carriers. The advantages of these cationic polymer carriers include safety, stability, large DNA and RNA loading capacity, and easy and large-scale production (*4–6*). The cationic polymers can condense negatively charged DNA into nanosized particles through electrostatic interactions, and the polymer/pDNA polyplexes can enter cells via endocytosis (*7–9*). As a result, the polymers can protect pDNA from nuclease degradation and facilitate cellular uptake to induce high gene transfection (*10, 11*).

The currently available cationic polymers, however, have significant cytotoxicity concerns, mostly due to their poor biocompatibility and nondegradability under physical conditions. Consequently, the development of hydrolyzable cationic polymers was proposed, such as poly(*β*-amino ester)s (*12–14*), poly(amino ester)s (*15, 16*), and poly(amido amine)s (*17, 18*). For example, the library of poly(*β*-amino ester)s, containing ester bonds in structures, have been reported to improve biodegradability and transfection efficiency and decrease cytotoxicity (*19, 20*). However, their degradation via hydrolysis or enzymatic cleavage is relatively slow in both extracellular oxidizing and intracellular reducing environments. At this point, disulfide bonds are preferred in the design and synthesis of biodegradable polymers. First, disulfide bonds are more hydrolytically stable than ester bonds in the extracellular environment, so the polycations with disulfide bonds can be used to prepare stable complexes with plasmid DNA. Second, disulfide bonds can be cleaved rapidly by glutathione and thioredoxin reductases in cytoplasm. As a result, DNA can be rapidly released from polyplexes to mediate efficient gene expression. Also, cytotoxicity will be decreased by avoiding high charge density and long-term polymer accumulation (*21*). Lin and co-workers have recently synthesized various linear poly(amido amine)s containing repetitive disulfide linkages in structures, which were proven to have significantly increased transfection efficiency and decreased cytotoxicity in COS-7 cells (*22*). However, poly(amido amine)s incorporated only tertiary amine groups, hydroxyl groups, and/or imidazole groups. The tertiary amine groups have limited DNA binding affinity due to steric hindrance, while hydroxyl and imidazole groups contribute little to binding of DNA. Consequently, transfection efficiencies would be decreased by their reduced ability to complex DNA. Therefore, we proposed to incorporate primary or secondary amine groups in such biodegradable

* Correspondence to Dr. Sung Wan Kim, Center for Controlled Chemical Delivery (CCCD), Department of Pharmaceutics and Pharmaceutical Chemistry, University of Utah, Salt Lake City, Utah 84112, Phone: 801 581-6654, Fax: 801 581-7848, Email: rburns@pharm.utah.edu.

[†] CCCD.

[‡] Department of Pharmaceutics and Pharmaceutical Chemistry.

[§] School of Medicine.

10.1021/bc700397x CCC: $40.75 © 2008 American Chemical Society
Published on Web 03/04/2008

polymers to increase nucleic acid binding affinity and following transfection efficiency. Our laboratory has previously synthesized a new form of poly(amido ethylenimine)s containing disulfide bonds and secondary amine groups in their structures (*23*). Those polymers have been proven to have significant transfection efficiency and low cytotoxicity for both DNA and siRNA delivery (*23, 24*). During the synthesis, however, these polymers will form branches randomly, resulting in significant structural cross-linking and therefore poor solubility in water and some organic solvents.

In this paper, we propose to synthesize and evaluate poly(disulfide amine)s, a novel series of linear cationic polymers with many of the characteristics of ideal polymeric gene delivery carriers that can mediate high gene transfection with low cytotoxicity. The advantages of these polymers are as follows: (1) Defined and improved polymer structures. Prepared by Michael addition and *N*-Boc deprotection under acidic condition, these polymers contain disulfide bonds, tertiary amine groups, and pendant primary amine groups in structures, and they do not form uncontrollable branches and cross-linking in synthesis. These structures aim to meet the fundamental design criteria of good gene carriers: reasonable biodegradability, strong DNA condensation ability, efficient gene transfection and low cytotoxicity. (2) Biodegradability. Poly(disulfide amine)s contain disulfide bonds in main chain, and are relatively stable in the extracellular oxidizing environment while being rapidly degraded in the intracellular reducing environment. Therefore, genetic materials in polyplexes will be released efficiently in the cytoplasm to allow for efficient gene expression. Meanwhile, cytotoxicity will decrease due to polymer degradation. (3) High nucleic acid binding affinity. Introducing unique primary amine side groups into poly(disulfide amine)s improves water solubility and enhances positive charge density. This allows plasmid DNA and other genetic materials, such as antisense oligonucleotides, peptide nucleic acids, and siRNA, to be stably condensed into nanosized particles under physiological pH, which will contribute to endocytosis and consequently efficient gene transfection. (4) High buffering capacity. The combination of tertiary and primary amine groups in poly(disulfide amine)s can promote endosomal−lysosomal escape based on the "proton sponge hypothesis". This characteristic gives poly(disulfide amine)s great potential in gene delivery. In this study, we synthesized poly(disulfide amine)s via Michael addition and *N*-Boc deprotection. Polymers were characterized by ^{1}H NMR, SEC, and acid–base titration. The properties of polymer/pDNA complexes were studied by dynamic light scattering and gel electrophoresis. *In vitro* transfection as well as *in vitro* cytotoxicty of polymer/pDNA complexes were evaluated by luciferase assay, BCA protein assay, and MTT assay using 293T cells (human renal epithelial cell line), Hela cells (human cervical cancer cell line), NIH3T3 (mouse embryonic fibroblasts), and C2C12 cells (mouse myoblast cell line).

MATERIALS AND METHODS

1. Materials. *tert*-Butyl-*N*-(2-aminoethyl)carbamate (*N*-Boc-1,2-diaminoethane, *N*-Boc-DAE), *tert*-butyl-*N*-(4-aminobutyl) carbamate (*N*-Boc-1,4-diaminobutane, *N*-Boc-DAB), *tert*-butyl-*N*-(6-aminohexyl)carbamate (*N*-Boc-1,6-diaminohexane, *N*-Boc-DAH), hyperbranched polyethylenimine (bPEI, M_w = 25 kDa), trifluoroacetic acid (TFA), triisobutylsilane (TIS), dithiothreitol (DTT), ethidium bromide (EtBr), and 3-(4,5-dimethyl-2-thiazolyl)-2,5-diphenyl-2*H*-tetrazolium bromide (MTT) were purchased from Sigma-Aldrich (St. Louis, MO). *N,N′*-Cystaminebisacrylamide (CBA) was purchased from PolySciences, Inc. (Warrington, PA). The plasmid pCMV-Luc, containing a firefly luciferase reporter gene which was inserted into a pCI plasmid vector driven by the CMV promoter (Promega, Madison, WI),

Scheme 1. Synthesis of Biodegradable Poly(disulfide amine)s

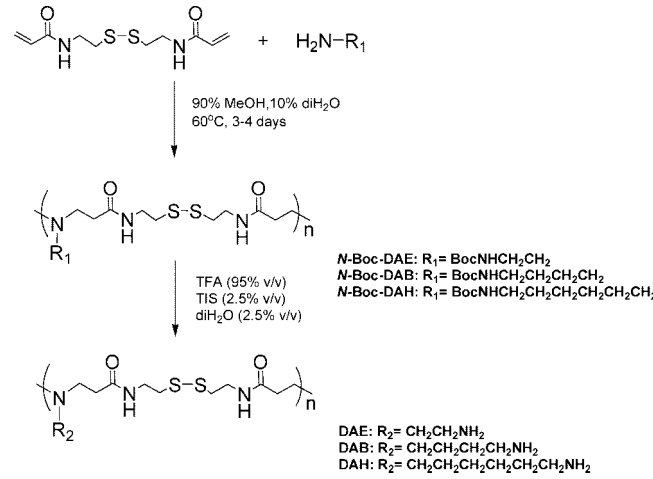

was amplified in *E. coli* DH5α and isolated by standard Maxiprep kit (Invitrogen, Carlsbad, CA) according to manufacture's instruction. Dulbecco's Modified Eagle's Medium (DMEM), penicillin−streptomycin, fetal bovine serum (FBS), trypsin-like enzyme (TrypLE Express), and Dulbecco's phosphate buffered saline (PBS) were purchased from Invitrogen-Gibco (Carlsbad, CA). Luciferase assay system with reporter lysis buffer was purchased from Promega (Madison, WI). All materials and solvents were used as received without further purification.

2. Polymer Synthesis. The synthetic route of poly(disulfide amine)s was illustrated in Scheme 1. Here, the synthesis of poly(CBA-DAE) is described as the representative procedure. Briefly, *N*-Boc-DAE (0.160 g, 1 mmol) and CBA (0.260 g, 1 mmol) were added into a flask and dissolved in 1 mL MeOH/H_2O mixture (9/1 v/v). Polymerization was conducted in an oil bath at 60 °C in the dark under nitrogen atmosphere for 4 days. Then, 10% mol excess *N*-Boc-DAE was added into the reaction solution to consume any unreacted acrylamide functional groups, and the reaction was performed at 60 °C for at least additional 2 h. After that, the product was precipitated with 40 mL anhydrous diethyl ether and dried. Subsequently, the acid-liable *N*-Boc protection group was removed with a TFA/TIS/H_2O mixture (95/2.5/2.5 v/v) for 30 min. The crude was precipitated in 40 mL anhydrous diethyl ether and dried under vacuum. It was further purified by dialysis (MWCO = 1000) against MilliQ deionized water overnight, followed by lyophilization to obtain poly(CBA-DAE) as a solid powder. Poly(CBA-DAB) and poly(CBA-DAH) were synthesized similarly, except the polymerization took 3 days for them. The poly(disulfide amine)s were analyzed by ^{1}H NMR (400 MHz, D_2O) and the data are listed below.

Poly(CBA-DAE): 2.91 ($NCH_2CH_2NH_2$, 2H), 2.64 ($NCH_2CH_2NH_2$, 2H), 2.63 (NCH_2CH_2CO, 4H), 2.22 (NCH_2CH_2CO, 4H), 3.34 ($CONHCH_2CH_2SS$, 4H), 2.62 (CH_2SSCH_2, 4H).

Poly(CBA-DAB): 3.08 ($NCH_2CH_2CH_2CH_2NH_2$, 2H), 1.58 ($NCH_2CH_2CH_2CH_2NH_2$, 2H), 1.58 ($NCH_2CH_2CH_2CH_2NH_2$, 2H), 2.91 ($NCH_2CH_2CH_2CH_2NH_2$, 2H), 2.82 (NCH_2CH_2CO, 4H), 2.48 (NCH_2CH_2CO, 4H), 3.38 ($CONHCH_2CH_2SS$, 4H), 2.63 (CH_2SSCH_2, 4H).

Poly(CBA-DAH): 3.15 ($NCH_2CH_2CH_2CH_2CH_2CH_2NH_2$, 2H), 1.48 ($NCH_2CH_2CH_2CH_2CH_2CH_2NH_2$, 2H), 1.19 ($NCH_2CH_2CH_2CH_2CH_2CH_2NH_2$, 2H), 1.19 ($NCH_2CH_2CH_2CH_2CH_2CH_2NH_2$, 2H), 1.48 ($NCH_2CH_2CH_2CH_2CH_2CH_2NH_2$, 2H), 2.85 ($NCH_2CH_2CH_2CH_2CH_2CH_2NH_2$, 2H), 2.81 ($NCH_2CH_2CO$, 4H), 2.52 ($NCH_2CH_2CO$, 4H), 3.35 ($CONHCH_2CH_2SS$, 4H), 2.65 ($CH_2SSCH_2$, 4H). The ^{1}H NMR spectra of poly(disulfide amine)s are given in the Supporting Information.

3. Polymer Characterization. The molecular weights of the polymers were determined by size exclusion chromatography (SEC) on an AKTA FPLC system (Amersham Biosciences, Piscataway, NJ) equipped with a Superose 12 column, and UV and refractive index detectors, eluted with Tris buffer (20 mM, pH 7.4) at a rate of 0.5 mL/min. Molecular weights were calibrated with standard poly[*N*-(2-hydroxypropyl)methacrylamide] (pHPMA). The FPLC data of polymers are given in the Supporting Information.

4. Buffering Capacity. The buffering capacities of the poly(disulfide amine)s were determined by acid–base titration. Briefly, 10 mL polymer solution was adjusted initially to pH 11.0 by 0.1 M NaOH. Then, the basic polymer solutions were titrated to pH 3.0 with aliquots of 0.01 M HCl. pH values of the solutions were measured after each addition. The buffering capacity is defined as the percentage of amine groups becoming protonated from pH 7.4 to 5.1 and can be calculated from the following equation (*22*):

$$\text{Buffering capacity (\%)} = \Delta V_{\text{HCl}} \times 0.01M/N \text{ mol} \times 100\%$$

Here, ΔV_{HCl} is the volume of 0.01 M HCl solution which brought the pH value of the polymer solution from 7.4 to 5.1, and N mol is the total moles of amine groups in the known amount of poly(disulfide amine)s.

5. Particle Size Measurement. Polyplexes were prepared by vortexing 1 μg pDNA (25 μL, 40 μg/mL) solution with an equal volume of polymer solution at predetermined nitrogen/phosphate (N/P) ratios, followed by 30 min incubation. The polyplexes were then diluted in 2 mL of dustfree diH_2O and the average particle sizes of polyplexes were measured using a BI-200SM dynamic light scattering instrument (DLS, Brookhaven Instrument Corporation, Holtsville, NY) at a 633 nm incident beam. Measurements were made at 25 °C at an angle of 90°. Measurements for each sample were repeated three times and reported as mean values ± standard deviations.

6. Gel Retardation Assay. Agarose gel (1%, w/v) containing 0.5 μg/mL ethidium bromide (EtBr) was prepared in TAE (Tris−acetate−EDTA) buffer. Poly(disulfide amine)/DNA complexes at predetermined N/P ratios were prepared in HEPES buffer as described above. The samples were mixed with 6 × loading dye and the mixtures were loaded onto an agarose gel. The gel was run at 100 V for 30 min and the location of DNA bands was visualized with a UV illuminator using a Gel Documentation Systems (Bio-Rad, Hercules, CA). The DNA release from poly(disulfide amine)s/DNA polyplexes was evaluated by incubating polyplexes with 5 mM DTT at 37 °C for 1 h. The samples were then analyzed by gel electrophoresis as described above.

7. *In Vitro* Transfection. Synthetic poly(disulfide amine)s mediated transfection was evaluated on 293T cells (human renal epithelial cell line, ATCC), HeLa cells (human cervical cancer cell line, ATCC), NIH3T3 (mouse embryonic fibroblasts, ATCC), and C2C12 cells (mouse myoblast cell line, ATCC) by using the plasmid pCMV-Luc as reporter gene. Cells were maintained in DMEM containing 10% FBS, streptomycin (100 μg/mL), and penicillin (100 units/mL) at 37 °C in a humidified atmosphere with 5% CO_2. Cells were seeded 24 h prior to transfection in 24-well plates at initial density of 8.0×10^4, 4.0×10^4, 4.0×10^4, and 3.5×10^4 cells/well for 293T, HeLa, NIH3T3, and C2C12, respectively. DNA was complexed with the poly(CBA-DAE), poly(CBA-DAB), poly(CBA-DAH), and bPEI at predetermined N/P ratios in HEPES buffer and incubated for 30 min before use. At the time of transfection, the medium in each well was replaced with fresh serum-free medium. Polyplexes (0.5 μg DNA/well) were incubated with the cells for 4 h at 37 °C. The medium was then replaced with 500 μL of fresh complete medium, and cells were incubated for additional 44 h. The cells were then washed with prewarmed PBS, treated with 200 μL cell lysis buffer, and subjected to a freezing−thawing cycle. Cellular debris was removed by centrifugation at 14 000 *g* for 5 min. The luciferase activity in the cell lysate (25 μL) was measured using a luciferase assay kit (100 μL luciferase assay buffer) on a luminometer (Dynex Technologies Inc., Chantilly, VA). The relative luminescent unit (RLU) of luciferase expression was normalized against protein concentration in the cell extracts, measured by a BCA protein assay kit (Pierce, Rockford, IL). All transfection assays were carried out in triplicate.

Table 1. Characteristics of Biodegradable Poly(disulfide amine)s[a]

polymers	M_n (kDa)	M_w (kDa)	PDI	buffering capacity in pH range 7.4–5.1 (%)
poly(CBA-DAE)	2.85	3.34	1.17	52.61
poly(CBA-DAB)	4.23	4.72	1.12	61.20
poly(CBA-DAH)	3.12	3.52	1.13	55.65

[a] FPLC conditions: poly(disulfide amine)s are dissolved in 0.5 mL Tris buffer (pH 7.4) as a concentration of 25 mg/mL. Superose 12 column is used to measure the molecular weight and polydispersity. Flow rate is 0.5 mL/min. Standard calibration is calculated using poly[*N*-(2-hydroxypropyl)methacrylamide] (pHPMA). Acid−base titration conditions: 10 mL of polymer solutions in 0.1 M NaCl was titrated with 0.01 M HCl from pH 11.0 to 3.0.

8. Cytotoxicity. NIH3T3 cells were seeded in a 24-well plate at a density of 4.0×10^4 cells/well and incubated for 24 h. DNA was complexed with the poly(CBA-DAE), poly(CBA-DAB), poly(CBA-DAH), and bPEI at predetermined N/P ratios in HEPES buffer and incubated for 30 min before use. Polyplexes (0.5 μg DNA/well) were incubated with the cells for 4 h in serum-free medium followed by 20 h in complete medium. MTT solution (50 μL, 2 mg/mL) was then added, and cells were further incubated for 2 h. The medium was removed, and 300 μL DMSO was then added to each well. The absorption was measured at 570 nm using a microplate reader (model 680, Bio-Rad Laboratory, Hercules, CA). The percentage relative cell viability was determined relative to control (untreated) cells, which were not exposed to transfection system and taken as 100% cell viability. All cytotoxicity experiments were performed in triplicate.

RESULTS AND DISCUSSION

1. Synthesis and Characterization of Biodegradable Poly(disulfide amine)s. Three novel biodegradable poly(disulfide amine)s were synthesized by Michael addition between *N*,*N*′-cystaminebisacrylamide (CBA) and three different *N*-Boc protected diamine monomers, *N*-Boc-DAE, *N*-Boc-DAB, and *N*-Boc-DAH. After removing *N*-Boc protection groups, three linear comblike polymers, poly(CBA-DAE), poly(CBA-DAB), and poly(CBA-DAH), were synthesized with one disulfide bond, one tertiary amine group in the main chain, and one pendant primary amine group in a side chain in each repeating unit (Scheme 1). All three poly(disulfide amine)s were purified by dialysis and lyophilized as a solid powder and were readily soluble in water, PBS buffer, HEPES buffer, Tris buffer, dimethyl sulfoxide (DMSO), and methanol, but not in chloroform, diethyl ether, and tetrahydrofuran. The final structures of poly(disulfide amine)s were confirmed by ^{1}H NMR (400 MHz, D_2O). The disappearance of signal peaks between δ 5 and 7 ppm indicated that the acrylamide end groups no longer existed in the final polymer products. Additionally, the two-step synthetic procedure avoided the possibility of forming branches or cross-links. These ^{1}H NMR results confirmed that our polymers have defined structures as expected and no branches were observed.

The molecular weight of polymers were measured by fast protein liquid chromatography (FPLC) and calibrated by pHPMA standards (Table 1). The range of the weight average

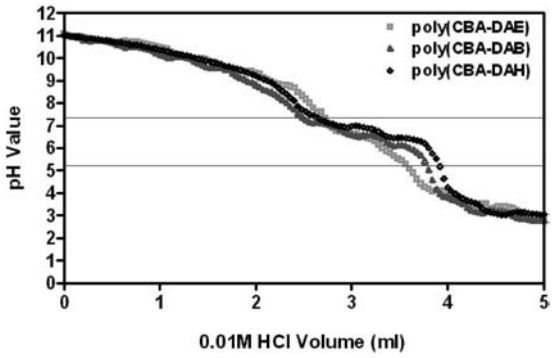

Figure 1. Titration curves were obtained by titrating poly(disulfide amine)s aqueous solutions in 10 mL 0.1 M NaCl from pH 11.0 (initially adjusted by 0.1 M NaOH) to pH 3.0 using 0.01 M HCl. pH of the solutions was measured after each addition.

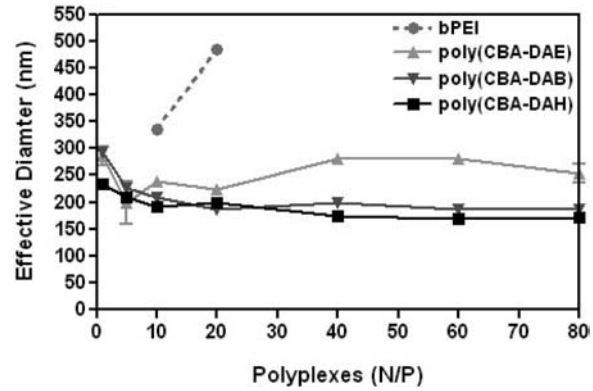

Figure 2. Average particle sizes of poly(disulfide amine)s/pDNA complexes were measured at varying nitrogen/phosphate (N/P) ratios from 1:1 to 80:1, while bPEI (25 kDa)/pDNA complexes were measured at N/P ratios of 10:1 and 20:1. (●) bPEI; (▲) poly(CBA-DAE); (▼) poly(CBA-DAB); (■) poly(CBA-DAH).

molecular weight (M_w) of these polymers was from 3.34 to 4.72 kDa, while the range of the number average molecular weight (M_n) was from 2.85 to 4.23 kDa. The polydispersity index (PDI), ranging from 1.12 to 1.17, indicates that these poly(disulfide amine)s have a narrow molecular weight distribution.

Buffering capacity is an important factor for cationic gene carriers according to "proton sponge hypothesis" proposed by Behr et al. (*10*). It helps polymeric carriers to effectively compact and protect DNA after endocytosis and helps DNA escape from endosomes/lysosomes (*25–27*). Buffering capacities of poly(disulfide amine)s, measured by acid–base titration, were expressed as the percentage of amine groups being protonated from pH 7.4 to 5.1, mimicking the change from the high pH extracellular environment to the low pH endosomal environment (*22, 23, 28*). The results (Table 1 and Figure 1) show that all poly(disulfide amine)s have excellent buffering capacity, ranging from 52.61% to 61.20% protonation, which is much higher than the previously reported results of bPEI 25 kDa, 24% (*22*) and 13.5% (*23*). The high buffering capacities enable poly(disulfide amine)s to facilitate endosomal escape, contributing to an increase in gene transfection efficiency.

There are several attributes of linear poly(disulfide amine)s that make them particularly attractive for the development of new polymeric gene carriers: (1) the polymers contain disulfide bonds for fast degradation; (2) primary and tertiary amine groups can self-assemble with DNA, facilitating endosomal escape and release of DNA to the nucleus efficiently; (3) the presence of primary amine groups at each repeating units for high nucleic acid binding affinity and good water solubility; (4) the capacity to synthesize a variety of analogues directly from commercial available monomer materials; (5) amine concentration can be evaluated for more accurate and efficient gene transfection for the future library of poly(disulfide amine)s.

2. Characterization of Polymer/Plasmid DNA Complexes. To mediate endocytosis through cell membrane, cationic polymers need to condense DNA into nanosized particles via electrostatical interactions between the positively charged polymers and the negatively charged phosphates on DNA backbones (*11, 29*). Dynamic light scattering (DLS) studies showed that three poly(disulfide amine)s can condense plasmid DNA into small particles with effective diameters of less than 300 nm at polymer/pDNA nitrogen/phosphate (N/P) ratios of 1:1 and above. In contrast, the diameters of bPEI/pDNA particles were larger at N/P ratios of 10:1 and 20:1 (336.5 and 484.5 nm) under the same conditions (Figure 2).

Gel retardation assay further verified that poly(disulfide amine)s can condense plasmid DNA at low N/P ratios. All poly(disulfide amine)s were dissolved in HEPES buffer solution (20 mM HEPES, pH 7.4, 5% glucose). One microgram samples of plasmid DNA (pCMV-Luc) with varying amounts of polymers were mixed and incubated at desired N/P ratios followed by performing agarose gel electrophoresis stained with EtBr (Figure 3). In the absence of DTT (Figure 3A), poly(CBA-DAE), poly(CBA-DAB), and poly(CBA-DAH) can completely retard plasmid DNA migration from N/P ratios of 5:1, 3:1, and 3:1, respectively. When the polyplexes were incubated with 5.0 mM DTT at 37 °C for 1 h, mimicking the intracellular reducing environment containing 0.1–10 mM glutathione, pDNA was released from all three poly(disulfide amine)s at all N/P ratios, with bands migrating toward the positive electrode in gel electrophoresis (Figure 3B). For the nondegradable control polymer bPEI 25 kDa, there was no pDNA released from bPEI/pDNA complexes in the presence of DTT. This gel retardation assay proved that all three poly(disulfide amine)s can release pDNA efficiently from polyplexes via disulfide bond cleavage, leading to increased DNA release and increased gene expression.

To facilitate efficient gene expression, cationic polymers should not only strongly condense plasmid DNA extracellularly, but also efficiently release DNA from polyplexes intracellulary. Previously, the hydrolyzable polymers, such as poly(β-amino amine)s and poly(amido amine)s, were synthesized by one-step Michael addition and only contained tertiary amines, hydroxyl, and/or imidazole groups (*12, 22*). The tertiary amine groups have limited DNA binding affinity due to steric hindrance, while hydroxyl and imidazole groups contribute little in binding DNA. As a result, relatively high N/P ratios were required to completely condense DNA. For example, to retard DNA migration in gel electrophoresis, weight ratios equal to or higher than 40:1 were needed for poly(β-amino amine)s (*20*). Similarly, weight ratios of 24:1 or higher are required for poly(amido amine)s, such as pAPOL (*22*). For the poly(disulfide amine)s, on the contrary, the results of the gel retardation assay showed that they can form stable complexes with pDNA at N/P ratios as low as 3:1, suggesting that poly(disulfide amine)s with primary amines have stronger nucleic acid binding affinities than those hydrolyzable polycations as mentioned above. In addition, pendant primary amine groups are more nucleophilic than tertiary amine groups, which will facilitate more efficient gene transfection and expression (*19*). It is also well-known that disulfide bonds can be cleaved rapidly in the presence of a high intracellular concentration of glutathione and thioredoxin reductases. This rapid cleavage of disulfide bonds will ensure DNA release from complexes efficiently to facilitate nuclear import, gene transcription, and gene expression (*22, 23, 30, 31*). In the presence of the reducing agent DTT, the cleavage of disulfide bonds of polymers was expected to dissociate polyplexes and release free DNA which were monitored by the agarose gel electrophoresis. Our poly(disulfide amine)s also

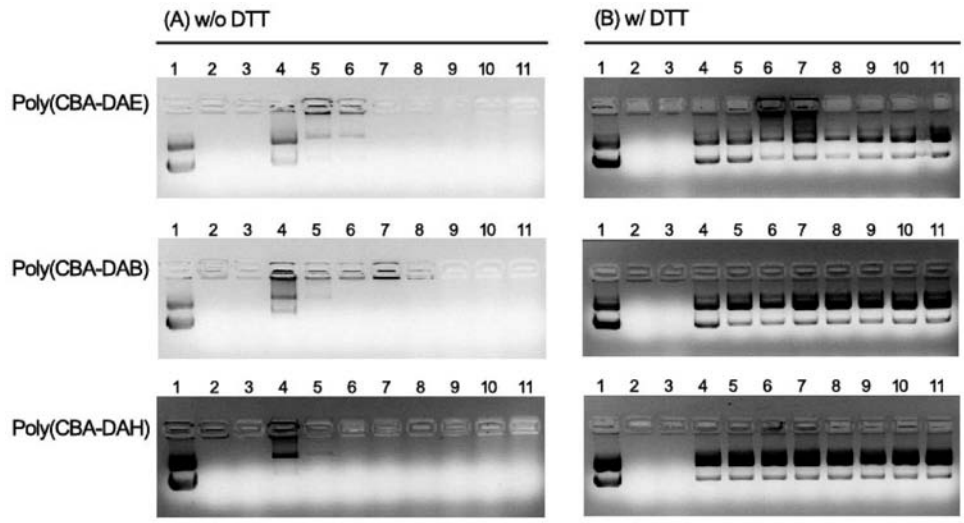

Figure 3. Agarose gel electrophoresis of poly(CBA-DAE), poly(CBA-DAB), and poly(CBA-DAH) with plasmid DNA polyplexes at different nitrogen/phosphate (N/P) ratios at the conditions of (A) without DTT and (B) with 5.0 mM DTT incubation (37 °C, 1 h). Lane 1, naked pDNA; lanes 2 and 3, bPEI/pDNA at N/P ratios of 10:1 and 20:1; lanes 4–11, poly(disulfide amine)s/pDNA at N/P ratios of 1:1, 2:1, 3:1, 5:1, 10:1, 15:1, 20:1, and 40:1.

showed the ability of rapid cleavage in the presence of DTT, mimicking the intracellular reducing environment. In summary, poly(disulfide amine)s demonstrated strong DNA condensing abilities by forming nanosized particles at low N/P ratios. They also showed rapid DNA releasing abilities by rapid disulfide bond cleavage in a reducing environment, which will facilitate the following gene expression (*32–35*).

3. *In Vitro* Transfection and Cytotoxicity of Poly(disulfide amine)s/Plasmid DNA Complexes. To evaluate *in vitro* transfection efficiency of biodegradable poly(disulfide amine)s, their complexes with reporter gene pCMV-Luc (0.5 μg/well) expressing luciferase were produced on four different cell lines, 293T, HeLa, NIH3T3, and C2C12, at five N/P ratios ranging from 5:1 to 80:1 in the absence of serum. bPEI (25 kDa)/pDNA complexes at an N/P ratio of 20:1 was used as a positive control. At this N/P ratio, bPEI showed the highest gene transfection efficiency while maintaining at least 70% cell viability. The transfection efficiency was quantitatively measured as the luciferase enzyme activity and normalized as the total cell protein concentration by BCA protein assay (Figure 4). Among these poly(disulfide amine)s, poly(CBA-DAH) showed the highest level of gene expression in all four cell lines. In 293T, HeLa and NIH3T3 cell lines, poly(CBA-DAH) had a comparable luciferase gene expression level to bPEI 25 kDa, at varying N/P ratios from 5:1 to 80:1. Interestingly, poly(CBA-DAH) expressed up to 7-fold higher gene transfection efficiency than bPEI in the C2C12 cell line at all N/P ratios, which was statistically different. The other two polymers showed overall lower luciferase expression than poly(CBA-DAH), while poly(CBA-DAB) was N/P ratio dependent for gene expression in these four cell lines, suggesting that optimal N/P ratios for gene transfection are different for these three polymers. Until now, many biodegradable polymers containing disulfide bonds have been reported to reduce cytotoxicity; however, most of them have less or only comparable transfection efficiency compared to bPEI 25 kDa (*22, 23, 34, 36, 37*). These results of high transfection efficiency of poly(disulfide amine)s, especially poly(CBA-DAH), support our future studies, since the primary mouse myoblast cell line (C2C12) is generally a cell line which is difficult to transfect with cationic polymers.

It is well-established that polymers containing disulfide bonds have good stability in an oxidative extracellular environment while they are efficiently degraded in reducing intracellular environment. Previous studies indicated that the better dissociation of plasmid DNA from polymers with disulfide bonds will facilitate gene expression (*30, 38, 39*). This characteristic gives our poly(disulfide amine)s a good ability to unpack DNA in the cells and improve transfection efficiency. Additionally, the primary amines are introduced into side chains of poly(disulfide amine)s, which can not only improve water solubility but is also expected to enhance stable complexation of plasmid DNA to mediate highly efficient gene delivery (*31, 40*).

For the three poly(disulfide amine)s, the transfection efficiency sequence is poly(CBA-DAH) > poly(CBA-DAB) > poly(CBA-DAE). The main difference among the three polymers is their side chain lengths. Poly(CBA-DAH) has the longest alkyl side chain and may be more flexible and more hydrophobic than the other two polymers. It was observed previously that the polymers containing more hydrophobic side chains had higher transfection efficiency (*22*), which suggested that the side chains would influence gene delivery (*20, 22, 31*). While the exact mechanisms to explain and the precise methods to measure how side chain structures of polymers affect transfection are unknown, the more flexible and hydrophobic characteristics may assist pDNA complexation or some other unknown transfection steps (*20*). Some hypothesis indicated that the polymers with longer alkyl chains are more flexible and hydrophobic than stiffer polymers, which may contribute to more stable binding of nucleic acids (*31, 41*). It is suggested that these more stable polyplexes will be distracted less by specific negatively charged cell surface proteins (proteoglycans), and therefore these polyplexes will remain intact during cellular endocytosis and consequently induce higher transfection efficiency (*40, 42*).

In vitro cytotoxicity of poly(disulfide amine)s was evaluated by a standard MTT assay on NIH3T3 cells (Figure 5). The experiments were performed in the same manner as the transfection experiments described above, except that the MTT assay was performed at 24 h instead of 48 h post-transfection. As expected, poly(disulfide amine)s showed much lower cytotoxicity than bPEI 25 kDa. The overall profile in Figure 5 showed that bPEI 25 kDa has increasing cytotoxicity with increasing N/P ratios, while cell viability decreased to 7.7% at an N/P ratio of 80:1. In contrast, poly(disulfide amine)s showed no significant toxicity for cells even at an N/P ratio of 80:1, retaining 90% or higher cell viability relative to control cells (nontreated NIH3T3 cells). The results are consistent with the other three cell lines: 293T, HeLa, and C2C12. Reduced cytotoxicity is apparently a significant benefit of poly(disulfide

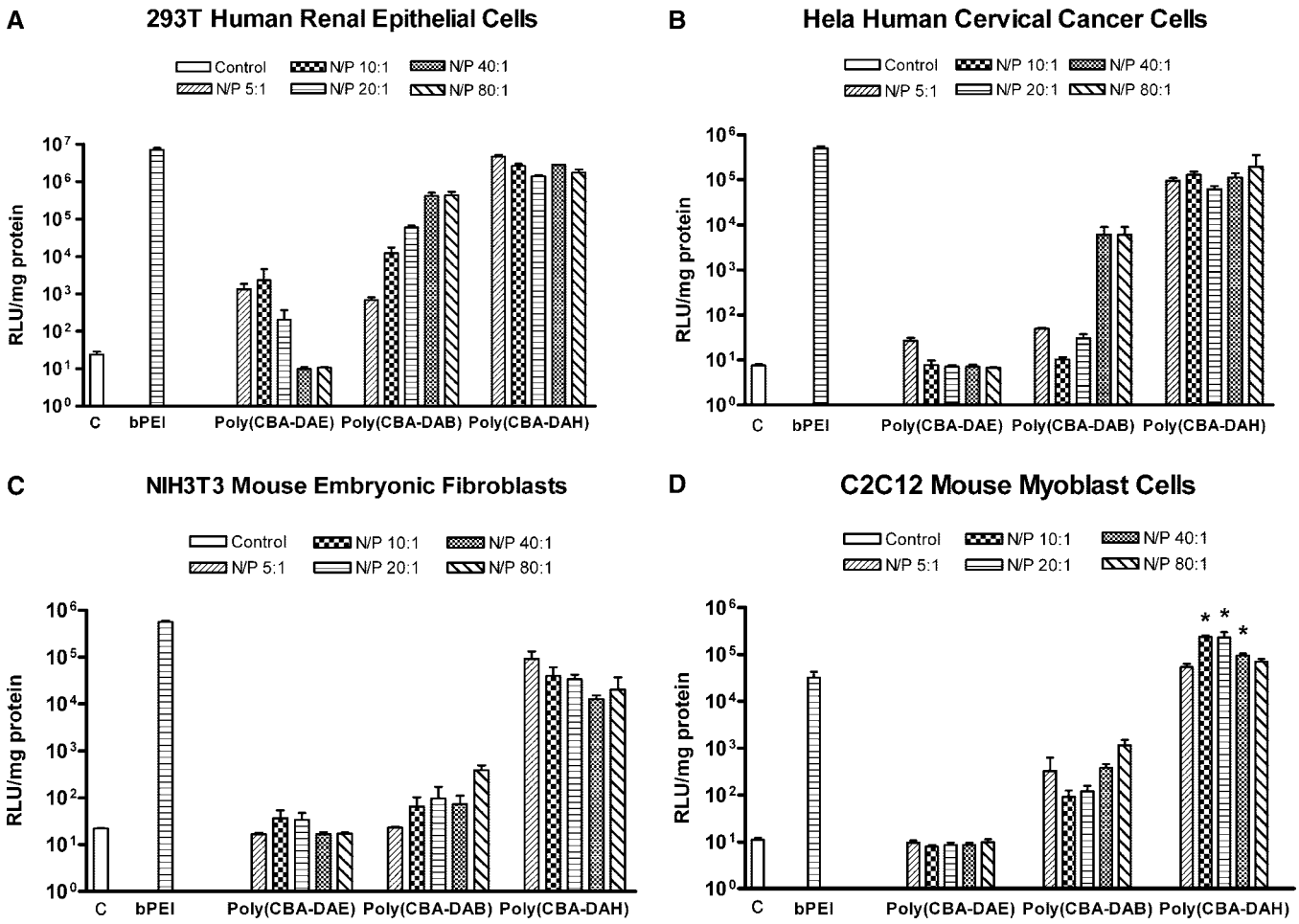

Figure 4. Transfection efficiency of poly(disulfide amine)/pDNA polyplexes in four different cell lines at varying nitrogen/phosphate (N/P) ratios (0.5 μg pDNA/well). Negative control (C): nontreated cells group. Positive control: a bPEI 25 kDa group at N/P ratio of 20:1. The N/P ratios of poly(disulfide amine)/pDNA complexes were 5:1, 10:1, 20:1, 40:1, and 80:1, respectively. Transfection results are expressed in triplicate as the relative luminescent unit (RLU) of luciferase reporter gene expression normalized by the total cell protein content in each well as mean values ± standard deviations. (A) 293T cells: human renal epithelial cell line. (B) HeLa cells: human cervical cancer cell line. (C) NIH3T3: mouse embryonic fibroblasts cell line. (D) C2C12 cells: mouse myoblast cell line.

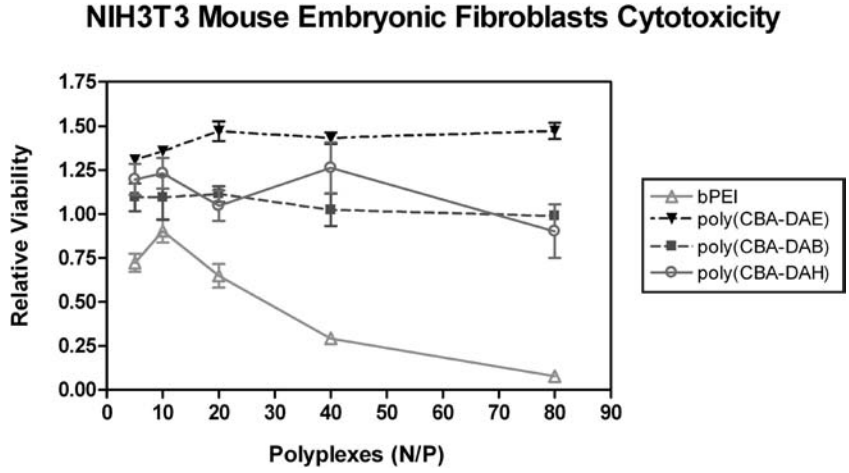

Figure 5. Relative cell viabilities of poly(disulfide amine)s/pDNA polyplexes in NIH3T3 cells at varying nitrogen/phosphate (N/P) ratios compared to a nontreated control group and a bPEI 25 kDa treated group (0.5 μg pDNA/well): (Δ) bPEI, (▼) poly(CBA-DAE), (■) poly(CBA-DAB), and (○) poly(CBA-DAH). Cytotoxicity was determined by MTT assay and represented triplicate as mean values ± standard deviations.

amine)s, though only poly(CBA-DAH) showed superior transfection efficiency compared to bPEI 25 kDa. It suggested that the reduced toxicity is related to polymer degradation. bPEI 25 kDa would accumulate intracellularly, leading to undesirable toxicity. Introducing disulfide bonds into polymers would alleviate these concerns, because they will be degraded to nontoxic, small molecules through cleavage of disulfide bonds. Therefore, DNA would be released to mediate efficient gene transfection, and those low molecular weight fragments of polymers will be cleared easily from the body (*30*). Our transfection and cytotoxicity results of poly(disulfide amine)s accomplish the previous studies.

In summary, these novel poly(disulfide amine)s, especially poly(CBA-DAH), have high gene transfection efficiency and low cytotoxicity and great potential for gene delivery *in vitro*. From the above data, poly(CBA-DAH) has a significantly high gene transfection in primary mouse myoblast cell line (C2C12). This novel poly(disulfide amine) is a promising gene carrier in many other primary cells and stem cells. We have shown that poly(CBA-DAH) has high gene transfection efficiency on SVR cells (mouse pancreatic islet endothelial cells). Besides delivery plasmid DNA, poly(disulfide amine)s can be used as gene carriers to deliver other types of genetic material into human cells, such as antisense oligonucleotides, therapeutic genes, and small interfering RNA (siRNA). Furthermore, poly(disulfide amine)s can be modified with targeting moieties to specifically delivery genetic materials into certain cell types.

CONCLUSION

In this work, we have synthesized and investigated three novel linear and structurally defined poly(disulfide amine)s: poly(CBA-DAE), poly(CBA-DAB), and poly(CBA-DAH). Those poly(disulfide amine)s are readily biodegraded in a reducing environment, releasing DNA rapidly due to the cleavage of disulfide bonds. They also have superior buffering capacity and nucleic acid binding ability based on acid–base titration and gel electrophoresis assay. In addition, all poly(disulfide amine)s showed much lower cytotoxicity than bPEI 25 kDa in NIH3T3 cells. The gene transfection efficiency of these polymers is side-chain spacer length dependent. Among the three polymeric carriers, poly(CBA-DAH), which contains a hexaethylene spacer, has the highest transfection efficiency in 293T cells, HeLa cells, NIH3T3 cells, and C2C12 cells. Specifically, it has a higher transfection efficiency than bPEI 25 kDa in C2C12 cells, a mouse primary myoblast cell line that is otherwise difficult to transfect. These poly(disulfide amine)s, especially poly(CBA-DAH), are promising for delivery of other genetic materials, such as therapeutic genes and siRNA. They also have potential in stem cell gene delivery. We are going to establish *in vivo* models using these poly(disulfide amine)s to further study their potential as gene carriers for gene delivery.

ACKNOWLEDGMENT

This work is supported by National Institutes of Health (NIH) grant HL065477 and HL071541. We thank Dr. Zheng-Rong Lu (University of Utah, SLC, UT) for the generous use of equipments and facilities.

Supporting Information Available: FPLC data, ^{1}H NMR spectra, and experimental procedures. This information is available free of charge via the Internet at http://pubs.acs.org.

LITERATURE CITED

(1) Mulligan, R. C. (1993) The basic science of gene therapy. *Science 260*, 926–32.
(2) Verma, I. M., and Somia, N. (1997) Gene therapy–promises, problems and prospects. *Nature 389*, 239–42.
(3) Baum, C., Kustikova, O., Modlich, U., Li, Z., and Fehse, B. (2006) Mutagenesis and oncogenesis by chromosomal insertion of gene transfer vectors. *Hum. Gene Ther. 17*, 253–63.
(4) Li, S., and Huang, L. (2000) Nonviral gene therapy: promises and challenges. *Gene Ther. 7*, 31–4.
(5) Liu, F., Shollenberger, L. M., and Huang, L. (2004) Non-immunostimulatory nonviral vectors. *FASEB J. 18*, 1779–81.
(6) Niidome, T., and Huang, L. (2002) Gene therapy progress and prospects: nonviral vectors. *Gene Ther. 9*, 1647–52.
(7) Cho, Y. W., Kim, J. D., and Park, K. (2003) Polycation gene delivery systems: escape from endosomes to cytosol. *J. Pharm. Pharmacol. 55*, 721–34.
(8) De Laporte, L., Cruz Rea, J., and Shea, L. D. (2006) Design of modular non-viral gene therapy vectors. *Biomaterials 27*, 947–54.
(9) Piskin, E., Dincer, S., and Turk, M. (2004) Gene delivery: intelligent but just at the beginning. *J. Biomater. Sci. Polym. Ed. 15*, 1181–202.
(10) Boussif, O., Lezoualc'h, F., Zanta, M. A., Mergny, M. D., Scherman, D., Demeneix, B., and Behr, J. P. (1995) A versatile vector for gene and oligonucleotide transfer into cells in culture and in vivo: polyethylenimine. *Proc. Natl. Acad. Sci. U.S.A. 92*, 7297–301.
(11) Pack, D. W., Hoffman, A. S., Pun, S., and Stayton, P. S. (2005) Design and development of polymers for gene delivery. *Nat. Rev. Drug Discovery 4*, 581–93.
(12) Anderson, D. G., Lynn, D. M., and Langer, R. (2003) Semi-automated synthesis and screening of a large library of degradable cationic polymers for gene delivery. *Angew. Chem., Int. Ed. Engl. 42*, 3153–8.
(13) Lynn, D. M., Amiji, M. M., and Langer, R. (2001) pH-responsive polymer microspheres: rapid release of encapsulated material within the range of intracellular pH. *Angew. Chem., Int. Ed. Engl. 40*, 1707–1710.
(14) Lynn, D. M., Anderson, D. G., Putnam, D., and Langer, R. (2001) Accelerated discovery of synthetic transfection vectors: parallel synthesis and screening of a degradable polymer library. *J. Am. Chem. Soc. 123*, 8155–6.
(15) Lim, Y. B., Kim, S. M., Suh, H., and Park, J. S. (2002) Biodegradable, endosome disruptive, and cationic network-type polymer as a highly efficient and nontoxic gene delivery carrier. *Bioconjugate Chem. 13*, 952–7.
(16) Liu, Y., Wu, D., Ma, Y., Tang, G., Wang, S., He, C., Chung, T., and Goh, S. (2003) Novel poly(amino ester)s obtained from Michael addition polymerizations of trifunctional amine monomers with diacrylates: safe and efficient DNA carriers. *Chem. Commun. (Cambridge, UK)* 2630–1.
(17) Lavignac, N., Lazenby, M., Foka, P., Malgesini, B., Verpilio, I., Ferruti, P., and Duncan, R. (2004) Synthesis and endosomolytic properties of poly(amidoamine) block copolymers. *Macromol. Biosci. 4*, 922–9.
(18) Richardson, S. C., Pattrick, N. G., Man, Y. K., Ferruti, P., and Duncan, R. (2001) Poly(amidoamine)s as potential nonviral vectors: ability to form interpolyelectrolyte complexes and to mediate transfection in vitro. *Biomacromolecules 2*, 1023–8.
(19) Akinc, A., Anderson, D. G., Lynn, D. M., and Langer, R. (2003) Synthesis of poly. (beta-amino ester)s optimized for highly effective gene delivery. *Bioconjugate Chem. 14*, 979–88.
(20) Anderson, D. G., Akinc, A., Hossain, N., and Langer, R. (2005) Structure/property studies of polymeric gene delivery using a library of poly. (beta-amino esters). *Mol. Ther. 11*, 426–34.
(21) Bulmus, V., Woodward, M., Lin, L., Murthy, N., Stayton, P., and Hoffman, A. (2003) A new pH-responsive and glutathione-reactive, endosomal membrane-disruptive polymeric carrier for intracellular delivery of biomolecular drugs. *J. Controlled Release 93*, 105–20.
(22) Lin, C., Zhong, Z., Lok, M. C., Jiang, X., Hennink, W. E., Feijen, J., and Engbersen, J. F. (2007) Novel bioreducible poly(amido amine)s for highly efficient gene delivery. *Bioconjugate Chem. 18*, 138–45.
(23) Christensen, L. V., Chang, C. W., Kim, W. J., Kim, S. W., Zhong, Z., Lin, C., Engbersen, J. F., and Feijen, J. (2006) Reducible poly(amido ethylenimine)s designed for triggered intracellular gene delivery. *Bioconjugate Chem. 17*, 1233–40.
(24) Jeong, J. H., Christensen, L. V., Yockman, J. W., Zhong, Z., Engbersen, J. F., Jong Kim, W., Feijen, J., and Kim, S. W. (2007) Reducible poly(amido ethylenimine) directed to enhance RNA interference. *Biomaterials 28*, 1912–7.
(25) Park, T. G., Jeong, J. H., and Kim, S. W. (2006) Current status of polymeric gene delivery systems. *Adv. Drug Delivery Rev. 58*, 467–86.

(26) Sonawane, N. D., Szoka, F. C., Jr., and Verkman, A. S. (2003) Chloride accumulation and swelling in endosomes enhances DNA transfer by polyamine-DNA polyplexes. *J. Biol. Chem. 278*, 44826–31.

(27) Zhong, Z., Feijen, J., Lok, M. C., Hennink, W. E., Christensen, L. V., Yockman, J. W., Kim, Y. H., and Kim, S. W. (2005) Low molecular weight linear polyethylenimine-*b*-poly. (ethylene glycol)-*b*-polyethylenimine triblock copolymers: synthesis, characterization, and in vitro gene transfer properties. *Biomacromolecules 6*, 3440–8.

(28) Akinc, A., Lynn, D. M., Anderson, D. G., and Langer, R. (2003) Parallel synthesis and biophysical characterization of a degradable polymer library for gene delivery. *J. Am. Chem. Soc. 125*, 5316–23.

(29) Oupicky, D., Parker, A. L., and Seymour, L. W. (2002) Laterally stabilized complexes of DNA with linear reducible polycations: strategy for triggered intracellular activation of DNA delivery vectors. *J. Am. Chem. Soc. 124*, 8–9.

(30) Pichon, C., LeCam, E., Guerin, B., Coulaud, D., Delain, E., and Midoux, P. (2002) Poly[Lys-(AEDTP)]: a cationic polymer that allows dissociation of pDNA/cationic polymer complexes in a reductive medium and enhances polyfection. *Bioconjugate Chem. 13*, 76–82.

(31) Wang, X. L., Jensen, R., and Lu, Z. R. (2007) A novel environment-sensitive biodegradable polydisulfide with protonatable pendants for nucleic acid delivery. *J. Controlled Release 120*, 250–8.

(32) McKenzie, D. L., Kwok, K. Y., and Rice, K. G. (2000) A potent new class of reductively activated peptide gene delivery agents. *J. Biol. Chem. 275*, 9970–7.

(33) Byk, G., Wetzer, B., Frederic, M., Dubertret, C., Pitard, B., Jaslin, G., and Scherman, D. (2000) Reduction-sensitive lipopolyamines as a novel nonviral gene delivery system for modulated release of DNA with improved transgene expression. *J. Med. Chem. 43*, 4377–87.

(34) Gosselin, M. A., Guo, W., and Lee, R. J. (2001) Efficient gene transfer using reversibly cross-linked low molecular weight polyethylenimine. *Bioconjugate Chem. 12*, 989–94.

(35) Oupicky, D., Carlisle, R. C., and Seymour, L. W. (2001) Triggered intracellular activation of disulfide crosslinked polyelectrolyte gene delivery complexes with extended systemic circulation in vivo. *Gene Ther. 8*, 713–24.

(36) Putnam, D., Gentry, C. A., Pack, D. W., and Langer, R. (2001) Polymer-based gene delivery with low cytotoxicity by a unique balance of side-chain termini. *Proc. Natl. Acad. Sci. U.S.A. 98*, 1200–5.

(37) Lee, Y., Mo, H., Koo, H., Park, J. Y., Cho, M. Y., Jin, G. W., and Park, J. S. (2007) Visualization of the degradation of a disulfide polymer, linear poly. (ethylenimine sulfide), for gene delivery. *Bioconjugate Chem. 18*, 13–8.

(38) Schaffer, D. V., Fidelman, N. A., Dan, N., and Lauffenburger, D. A. (2000) Vector unpacking as a potential barrier for receptor-mediated polyplex gene delivery. *Biotechnol. Bioeng. 67*, 598–606.

(39) Forrest, M. L., Koerber, J. T., and Pack, D. W. (2003) A degradable polyethylenimine derivative with low toxicity for highly efficient gene delivery. *Bioconjugate Chem. 14*, 934–40.

(40) Liu, Y., and Reineke, T. M. (2005) Hydroxyl stereochemistry and amine number within poly. (glycoamidoamine)s affect intracellular DNA delivery. *J. Am. Chem. Soc. 127*, 3004–15.

(41) Anderson, D. G., Peng, W., Akinc, A., Hossain, N., Kohn, A., Padera, R., Langer, R., and Sawicki, J. A. (2004) A polymer library approach to suicide gene therapy for cancer. *Proc. Natl. Acad. Sci. U.S.A. 101*, 16028–33.

(42) Tseng, W. C., and Jong, C. M. (2003) Improved stability of polycationic vector by dextran-grafted branched polyethylenimine. *Biomacromolecules 4*, 1277–84.

BC700397X

^{99m}Tc-Labeling of HYNIC-Conjugated Cyclic RGDfK Dimer and Tetramer Using EDDA as Coligand

Jianjun Wang, Young-Seung Kim, and Shuang Liu*

School of Health Sciences, Purdue University. Received November 15, 2007; Revised Manuscript Received January 1, 2008

In this study, EDDA (ethylenediamine-*N*,*N*′-diacetic acid) was used as the coligand for ^{99m}Tc-labeling of cyclic RGDfK conjugates: HYNIC−dimer (HYNIC = 6-hydrazinonicotinamide; dimer = E[c(RGDfK)]$_2$) and HYNIC−tetramer (tetramer = E{E[c(RGDfK)]$_2$}$_2$). First, HYNIC−dimer was allowed to react with $^{99m}TcO_4^-$ in the presence of excess tricine and stannous chloride to form the intermediate complex [^{99m}Tc(HYNIC−dimer)-(tricine)$_2$], which was then allowed to react with EDDA to afford [^{99m}Tc(HYNIC−dimer)(EDDA)] with high yield (>90%) and high specific activity (~8.0 Ci/μmol). Under the same radiolabeling conditions, the yield for [^{99m}Tc(HYNIC−tetramer)(EDDA)] was always <65%. The results from a mixed-ligand experiment show that there is only one EDDA bonding to the ^{99m}Tc-HYNIC core in [^{99m}Tc(HYNIC−dimer)(EDDA)]. The athymic nude mice bearing subcutaneous U87MG human glioma xenografts were used to evaluate the impact of EDDA coligand on the biodistribution characteristics and excretion kinetics of the ^{99m}Tc-labeled HYNIC−dimer and HYNIC−tetramer. Surprisingly, [^{99m}Tc(HYNIC−dimer)(EDDA)] and [^{99m}Tc(HYNIC−tetramer)(EDDA)] had almost identical tumor uptake over the 2 h period. The use of EDDA as coligand to replace tricine/TPPTS (TPPTS = trisodium triphenylphosphine-3,3′,3″-trisulfonate) did not significantly change the uptake of the ^{99m}Tc-labeled HYNIC-dimer in noncancerous organs, such as the liver, kidneys, and lungs; but it did result in a significantly lower kidney uptake for the ^{99m}Tc-labeled HYNIC−tetramer due to faster renal excretion. It was also found that the radiotracer tumor uptake decreases in a linear fashion as the tumor size increases. The smaller the tumors are, the higher the tumor uptake is regardless of the identity of radiotracer.

INTRODUCTION

Radiolabeled RGD peptides represent a new class of radiotracers with the potential for both early tumor detection and monitoring of tumor metastasis and therapeutic response in cancer patients. In the past several years, many radiolabeled RGD peptides have been evaluated as the integrin $\alpha_v\beta_3$-targeted radiotracers for tumor imaging by SPECT or PET in preclinical animal models and human clinical trials (*1–14*). They have been reviewed extensively (*15–21*). Among several promising radiotracers, [^{18}F]Galacto-RGD has become the first PET radiotracer for noninvasive imaging of integrin $\alpha_v\beta_3$-positive tumors in cancer patients (*22–24*). The results from imaging studies in metastatic melanoma patients clearly show that there is a sufficient integrin $\alpha_v\beta_3$ expression for PET imaging. Although radiotracers based on the cyclic RGD monomer are able to target tumors by binding to the integrin $\alpha_v\beta_3$ expressed on tumor cells and endothelial cells of tumor neovasculature, their tumor uptake is relatively low, which may limit their application as tumor imaging agents in clinics.

We have been using multivalent cyclic RGD peptides, such as E[c(RGDfK)]$_2$ (dimer) and E{E[c(RGDfK)]$_2$}$_2$ (tetramer), for development of integrin $\alpha_v\beta_3$-targeted radiotracers (*25–35*). These multimeric cyclic RGD peptides are used as such that the radiotracer tumor uptake can be improved due to their higher integrin $\alpha_v\beta_3$ binding affinity. Recently, we reported the ^{111}In- and ^{64}Cu-labeled cyclic RGDfK tetramer as SPECT and PET radiotracers, respectively (*28, 32*). It was also found that both ^{111}In(DOTA−tetramer) (DOTA = 1,4,7,10-tetraazacyclododecane-1,4,7,10-tetraacetic acid; tetramer = E{E[c(RGDfK)]$_2$}$_2$) and ^{64}Cu(DOTA−tetramer) have a significantly higher tumor uptake due to their higher integrin $\alpha_v\beta_3$ binding affinity than their dimeric analogues (*28, 32*). Similar results were obtained for the ^{99m}Tc-labeled HYNIC−tetramer (HYNIC = 6-hydrazinonicotinamide) using tricine/TPPTS (trisodium triphenylphosphine-3,3′,3″-trisulfonate) as coligands (*27, 31*). However, the kidney uptake of the ternary ligand complex [^{99m}Tc(HYNIC−tetramer)(tricine)(TPPTS)] was very high (>25% ID/g) over the 2 h study period, probably due to the negative charges on the TPPTS coligand (*31*).

EDDA (EDDA = ethylenediamine-*N*,*N*′-diacetic acid) has been used for ^{99m}Tc-labeling of the HYNIC-conjugated somatostatin analogues (*36–38*) and RGD peptide (*39*). It was found that [^{99m}Tc(HYNIC−RGD)(EDDA)] had a high tumor uptake, along with the rapid renal excretion, and low uptake in the liver and muscle. The tumor uptake studies also showed specific targeting of integrin $\alpha_v\beta_3$ in the mice bearing small cell lung tumors. All tumors could be readily visualized by scintigraphic imaging. It was claimed that [^{99m}Tc(HYNIC−RGD)(EDDA)] had tumor/organ ratios comparable to those of [^{18}F]Galato-RGD (*39*). These promising results lead us to explore the use of EDDA as the coligand for ^{99m}Tc-labeling of the HYNIC−dimer and HYNIC−tetramer conjugates. The main objective is to demonstrate whether EDDA is useful for minimizing the kidney uptake of ^{99m}Tc-labeled cyclic RGD dimer and tetramer.

In this study, we used EDDA as coligand for ^{99m}Tc-labeling of both HYNIC−dimer and HYNIC−tetramer. A mixed-ligand experiment was used to determine the number of EDDA ligands bonding to the ^{99m}Tc-HYNIC core. The athymic nude mice bearing U87MG human glioma xenografts were used to evaluate the impact of EDDA coligand on biodistribution properties of the ^{99m}Tc-labeled HYNIC−dimer and HYNIC−tetramer. In addition, we also examined the relationship between the size and tumor uptake of [^{99m}Tc(HYNIC−dimer)(EDDA)], [^{99m}Tc

* To whom correspondence should be addressed: School of Health Sciences, Purdue University, 550 Stadium Mall Drive, West Lafayette, IN 47907. Phone: 765-494-0236; Fax: 765-496-1377; Email: lius@pharmacy.purdue.edu.

10.1021/bc7004208 CCC: $40.75 © 2008 American Chemical Society
Published on Web 02/19/2008

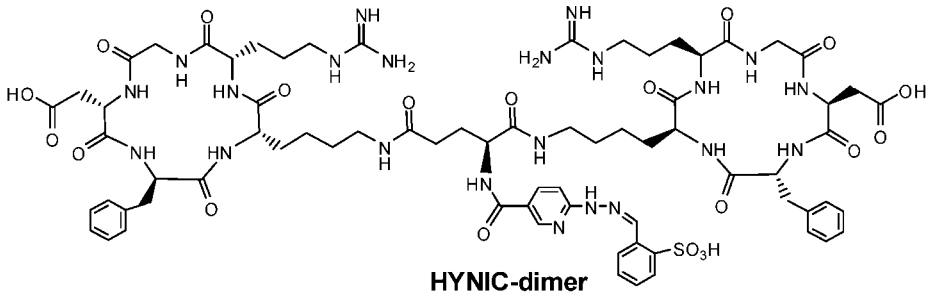

HYNIC-dimer

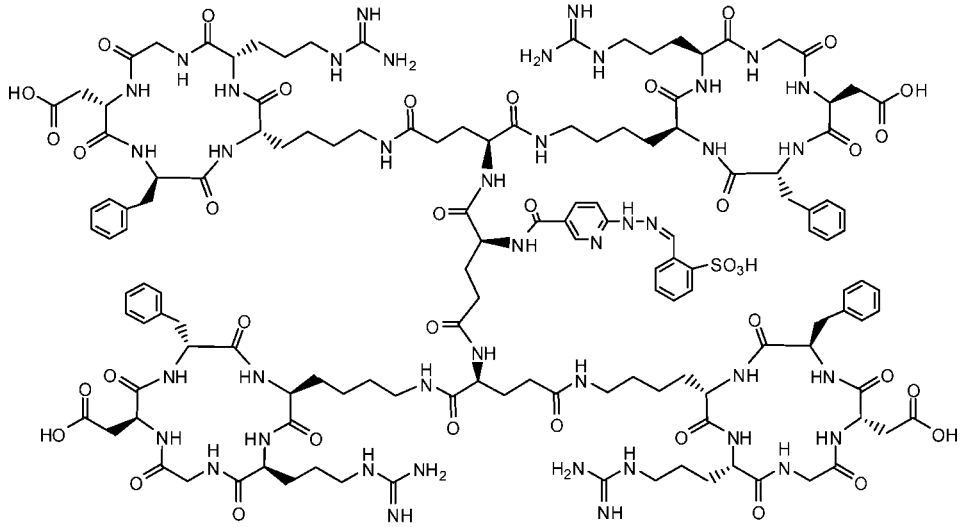

HYNIC-tetramer

Figure 1. HYNIC-conjugated cyclic RGDfK dimer (HYNIC−dimer) and tetramer (HYNIC−tetramer).

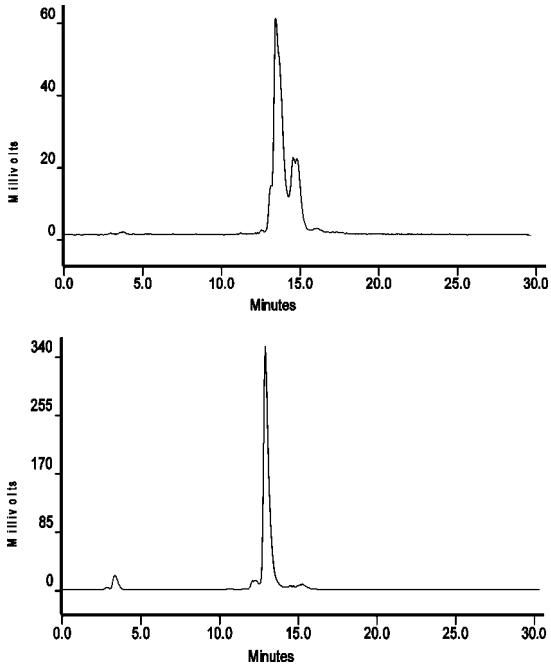

Figure 2. Typical radio-HPLC chromatograms (method 1) of [^{99m}Tc(HYNIC−dimer)(tricine)$_2$] (top) and [^{99m}Tc(HYNIC−dimer)(EDDA)] (bottom).

(HYNIC−tetramer)(EDDA)], and [^{99m}Tc(HYNIC−tetramer)(tricine)(TPPTS)].

EXPERIMENTAL SECION

Materials. Ethylenediamine-*N*,*N*′-diacetic acid (EDDA) and tricine were purchased from Sigma/Aldrich (St. Louis, Missouri). Pentapeptide c(RGDfK) was purchased from Peptides International, Inc. (Louisville, Kentucky). HYNIC−E-[c(RGDfK)]$_2$ (HYNIC−dimer), HYNIC−E{E[c(RGDfK)]$_2$}$_2$ (HYNIC−tetramer), and [^{99m}Tc(HYNIC−tetramer)(tricine)-(TPPTS)] were prepared according to the literature procedures (*29*,*31*). *N*,*N*′-Bis(benzyl)ethylenediamine-*N*,*N*′-diacetic acid (Bn_2EDDA) was prepared according to the literature method (*40*). $Na^{99m}TcO_4$ was obtained from a commercial DuPont Pharma ^{99}Mo/^{99m}Tc generator (N. Billerica, MA).

Instruments and Methods. The radio-HPLC method (method 1) used the LabAlliance HPLC system equipped with a β-ram IN-US detector and Zorbax C_{18} column (4.6 mm × 250 mm, 300 Å pore size). The flow rate was 1 mL/min. The mobile phase was isocratic with 90% solvent A (25 mM NH_4OAc buffer, pH = 5.0) and 10% solvent B (acetonitrile) at 0–2 min, followed by a gradient mobile phase going from 10% solvent B at 2 min to 15% solvent B at 5 min and to 20% solvent B at 20 min. Method 2 was almost identical to method 1 except that the gradient mobile phase was used from 20% solvent B at 5 min and to 40% solvent B at 20 min.

Synthesis of [^{99m}Tc(HYNIC−dimer)(EDDA)]. To a 5 cc vial containing tricine (20 mg in 1 mL of succinate buffer (pH = 5) was added 0.2 mL of HYNIC−dimer solution (100 μg/mL), 0.3 mL of $^{99m}TcO_4^-$ solution in saline, and 25 μL $SnCl_2$ solution (1 mg/mL) in 1 N HCl. The vial containing the reaction mixture was heated at 100 °C for 20 min. A sample of the resulting solution was analyzed by HPLC (method 1). To the vial above was added 0.5 mL of EDDA solution (10 mg/mL, pH ∼ 7.4). The resulting mixture was heated at 100 °C for 20 min. After cooling to room temperature, a sample from the solution was analyzed by HPLC (method 1). The radiochemical purity (RCP) was >95%. The HPLC retention time was 13.2 min.

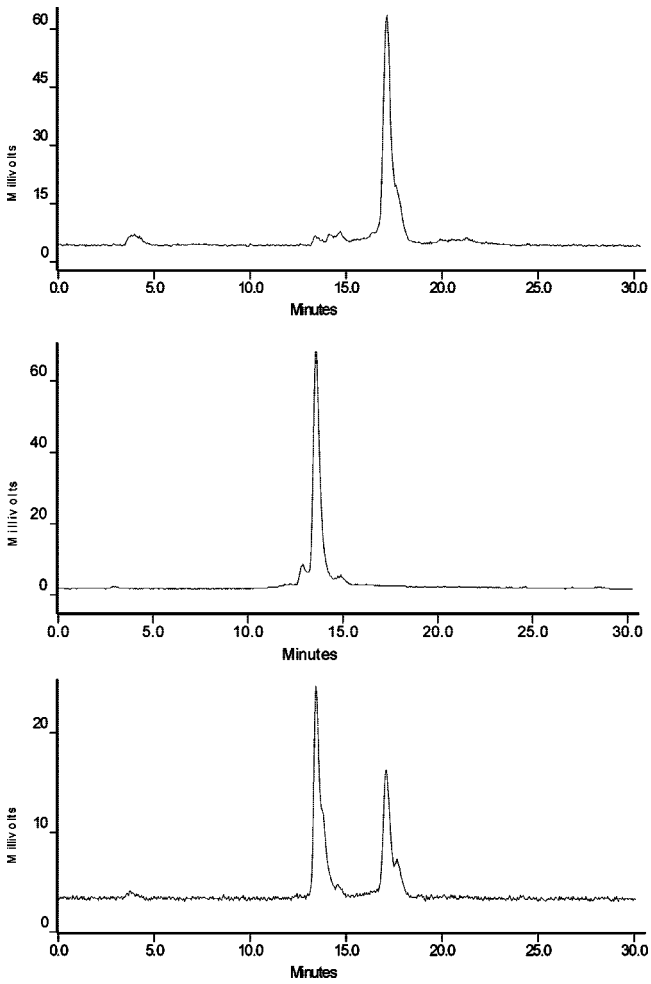

Figure 3. Radio-HPLC chromatograms (method 1) of [^{99m}Tc-(HYNIC−dimer)(Bz$_2$EDDA)] (top), [^{99m}Tc(HYNIC−dimer)-(EDDA)] (middle), and the reaction solution (bottom) containing [^{99m}Tc(HYNIC−dimer)(Bz$_2$EDDA)] and [^{99m}Tc(HYNIC−dimer)-(EDDA)]. The presence of only two sets of peaks at 13.5 and 17.0 min from [^{99m}Tc(HYNIC−dimer)(EDDA)] and [^{99m}Tc(HYNIC−dimer)(Bn$_2$EDDA)], respectively, clearly demonstrated that there is only one EDDA bonded to the ^{99m}Tc-HYNIC core.

Table 1. Stability Data for [^{99m}Tc(HYNIC−dimer)(EDDA)] and [^{99m}Tc(HYNIC−tetramer)(EDDA)] in the Presence of Cysteine and Histidine (1 mg/mL in 25 mM phosphate buffer, pH = 7.5)

time post purification	RCP (%) in histidine solution (1 mg/mL, pH = 7.4)		RCP (%) in cysteine solution (1 mg/mL, pH = 7.4)	
	dimer	tetramer	dimer	tetramer
0.5 h	100	99	100	99
1.0 h	100	99	100	99
2.0 h	99	98	98	98
4.0 h	97	98	98	96
6.0 h	95	97	95	96

Synthesis of [^{99m}Tc(HYNIC−dimer)(Bn$_2$EDDA)]. To a clean 5 cc vial containing tricine (20 mg in 1 mL succinate buffer, pH = 5) was added 0.2 mL of HYNIC−dimer solution (100 μg/mL), 0.3 mL of $^{99m}TcO_4^-$ solution in saline, and 25 μL $SnCl_2$ solution (1 mg/mL) in 1 N HCl. The vial containing the reaction mixture was heated at 100 °C for 20 min. To the vial was added 0.5 mL of Bn$_2$EDDA solution (10 mg/mL, pH ~ 7.4). The vial was heated at 100 °C for another 20 min. After cooling to room temperature, a sample from the solution was analyzed by radio-HPLC (method 1). The RCP was >95%. The HPLC retention time was 17.2 min.

Synthesis of [^{99m}Tc(HYNIC−tetramer)(EDDA)]. To a 5 cc vial containing tricine (20 mg in 1 mL succinate buffer, pH = 5) was added 0.2 mL of HYNIC−tetramer solution (100 μg/mL), 0.3 mL of $^{99m}TcO_4^-$ solution, and 25 μL $SnCl_2$ solution (1 mg/mL) in 1 N HCl. The vial containing the reaction mixture was heated at 100 °C for 20 min. To the vial above was added 0.5 mL of EDDA solution (10 mg/mL, pH ~ 7.4). The resulting mixture was heated at 100 °C for 20 min. After cooling to room temperature, a sample from the solution was analyzed by radio-HPLC (method 2). The RCP was ~65%. The HPLC retention time was 15.2 min.

Doses Preparation and Solution Stability. [^{99m}Tc(HYNIC−dimer)(EDDA)] and [^{99m}Tc(HYNIC−tetramer)(EDDA)] were prepared. Doses were prepared by dissolving the purified radiotracer in saline to give a concentration of 20 μCi/mL for biodistribution studies and 1.0 mCi/mL for metabolism studies. Each animal was injected with 0.1 mL of the dose solution. For cysteine and histidine challenging experiments, the radiotracer was purified by HPLC. Volatiles in mobile phases were removed under vacuum. The residue was dissolved in the cysteine or histidine solution (1 mg/mL, pH = 7.4). Samples of the resulting solution were analyzed by radio-HPLC (method 1 for [^{99m}Tc(HYNIC−dimer)(EDDA)] and method 2 for [^{99m}Tc-(HYNIC−tetramer)(EDDA)]) at 0, 2, 4, and 6 h.

Determination of Log *P* Values. Log *P* values were determined using the following procedure: The radiotracer was purified by HPLC. Volatiles were removed completely under vacuum. The residue was dissolved in a equal volume (3 mL/3 mL) mixture of *n*-octanol and 25 mM phosphate buffer (pH = 7.4). After stirring vigorously for ~20 min, the mixture was centrifuged at a speed of 8000 rpm for 5 min. Samples (in triplets) from both *n*-octanol and aqueous layers were counted in a gamma counter (Perkin-Elmer Wizard - 1480). The log *P* value was measured three different times and reported as an average of three different measurements plus the standard deviation. The log *P* values were −3.59 ± 0.11 and −3.26 ± 0.08 for [^{99m}Tc(HYNIC−dimer)(EDDA)] and [^{99m}Tc(HYNIC−tetramer)(EDDA)], respectively.

Mixed-Ligand Experiment. To a clean 5 cc vial containing tricine (20 mg in 1 mL of succinate buffer, pH = 5) was added 0.2 mL of HYNIC−dimer solution (100 μg/mL), 0.3 mL of $^{99m}TcO_4^-$ solution in saline, and 25 μL $SnCl_2$ solution (1 mg/mL) in 1 N HCl. The reaction mixture was heated at 100 °C for 20 min. To the mixture above was added 0.5 mL of the solution containing EDDA (10 mg/mL, pH ~7.4) and Bn$_2$EDDA (10 mg/mL, pH ~7.4). The resulting mixture was heated at 100 °C for another 20 min. After cooling to room temperature, a sample of the resulting solution was analyzed by the radio-HPLC (method 1).

Animal Model. Biodistribution studies were performed according to the literature procedures (*30*). These studies were carried out using the athymic nude mice bearing U87MG human glioma xenografts in compliance with NIH animal experiment guidelines (*Principles of Laboratory Animal Care*, NIH Publication No. 86–23, revised 1985). The animal protocol for the animal studies has been approved by the Purdue University Animal Care and Use Committee (PACUC). U87MG human glioma cells were grown at 37 °C in Minimal Essential Medium (Alpha Modification) containing 3.7 g of sodium bicarbonate/L, 10% fetal bovine serum v/v, in a humidified atmosphere of 5% carbon dioxide. Female athymic nu/nu mice were purchased from Harlan (Indianapolis, IN) at 4–5 weeks of age. Each mouse was orthotopically implanted with 5×10^6 U87MG human glioma cells into the mammary fat pad. Four to five weeks after inoculation, animals with tumors in the range 0.1–1.5 g were used for biodistribution studies.

Table 2. Biodistribution Data of [^{99m}Tc(HYNIC−dimer)(EDDA)] in the Athymic Nude Mice Bearing the U87MG Human Glioma Xenografts ($n = 5$ for each time point) unless Specified

organ (% ID/gram)	5 min	30 min	60 min ($n = 8$)	120 min ($n = 6$)
blood	4.41 ± 0.48	1.56 ± 0.33	1.17 ± 0.12	0.57 ± 0.25
brain	0.25 ± 0.05	0.15 ± 0.02	0.15 ± 0.03	0.10 ± 0.02
heart	3.20 ± 0.34	1.62 ± 0.22	1.33 ± 0.17	0.86 ± 0.15
intestine	7.58 ± 2.05	7.55 ± 3.43	4.63 ± 1.18	3.03 ± 0.54
kidney	25.25 ± 5.64	11.70 ± 2.25	8.42 ± 1.33	5.97 ± 0.94
liver	5.29 ± 0.29	4.03 ± 0.55	3.97 ± 0.39	2.98 ± 0.48
lungs	6.36 ± 0.91	4.32 ± 0.30	3.32 ± 0.27	2.10 ± 0.36
muscle	3.85 ± 0.60	2.60 ± 1.14	2.66 ± 0.46	2.02 ± 0.23
spleen	2.30 ± 0.19	1.43 ± 0.45	1.26 ± 0.30	0.77 ± 0.11
tumor	4.17 ± 2.35	5.44 ± 1.54	4.07 ± 2.02	6.44 ± 1.76
tumor/blood	1.47 ± 0.88	4.45 ± 1.29	5.28 ± 0.92	12.55 ± 5.33
tumor/brain	30.79 ± 18.32	46.37 ± 10.37	36.56 ± 7.43	66.33 ± 23.53
tumor/liver	1.35 ± 0.59	1.69 ± 0.40	1.38 ± 0.40	2.21 ± 0.70
tumor/lung	1.11 ± 0.43	1.58 ± 0.28	1.64 ± 0.42	3.10 ± 0.85
tumor/muscle	1.85 ± 0.80	2.78 ± 0.60	2.07 ± 0.61	3.24 ± 1.02

Table 3. Biodistribution Data of [^{99m}Tc(HYNIC−tetramer)(EDDA)] in the Athymic Nude Mice Bearing the U87MG Human Glioma Xenografts ($n = 5$ for Each Time Point unless Specified)

organ	5 min	30 min	60 min	120 min ($n = 6$)
blood	3.16 ± 0.78	1.47 ± 0.32	0.54 ± 0.11	0.45 ± 0.18
brain	0.28 ± 0.03	0.18 ± 0.04	0.13 ± 0.02	0.11 ± 0.02
heart	4.10 ± 0.53	2.87 ± 0.91	1.72 ± 0.22	1.51 ± 0.39
intestine	21.38 ± 4.86	14.47 ± 2.08	8.01 ± 1.31	8.27 ± 1.92
kidney	26.69 ± 2.48	17.84 ± 2.82	11.01 ± 0.88	9.54 ± 2.23
liver	7.56 ± 1.48	5.67 ± 1.23	4.22 ± 0.70	4.60 ± 0.82
lungs	6.07 ± 0.86	4.67 ± 1.00	3.76 ± 0.58	3.23 ± 0.99
muscle	2.11 ± 0.37	1.66 ± 0.27	0.96 ± 0.15	0.92 ± 0.26
spleen	3.97 ± 0.80	3.28 ± 1.10	2.77 ± 0.73	2.44 ± 0.35
tumor	4.39 ± 1.00	5.13 ± 3.10	4.70 ± 0.82	6.57 ± 1.63
tumor/blood	1.43 ± 0.30	3.38 ± 2.70	8.98 ± 1.35	15.89 ± 4.77
tumor/brain	15.44 ± 1.98	26.44 ± 6.78	34.82 ± 6.11	60.43 ± 7.53
tumor/liver	0.59 ± 0.17	0.58 ± 0.22	1.09 ± 0.31	1.47 ± 0.50
tumor/lung	0.75 ± 0.27	0.98 ± 0.62	1.22 ± 0.19	2.11 ± 0.44
tumor/muscle	2.13 ± 0.62	2.77 ± 0.07	4.89 ± 0.88	7.43 ± 2.03

Biodistribution Protocol. 20 tumor-bearing mice (20–25 g) were anesthetized with intraperitoneal injection of a mixture containing Ketamine (40–100 mg/kg) and Xylazine (2–5 mg/kg). Once the animal was in the surgical plane of anesthesia, as noted by the lack of pain response, the radiotracer (∼2 μCi) dissolved in 0.1 mL saline was administered via tail vein. Five animals were sacrificed by sodium pentobarbital overdose (100 mg/kg) at 5, 30, 60, and 120 min postinjection (p.i.). Blood samples were withdrawn from the heart through a syringe. Organs (tumor, brain, eyes, spleen, lungs, liver, kidneys, muscle, and intestine) were excised, washed with saline, weighed, and counted on a gamma counter. The organ uptake was calculated as a percentage of the injected dose per organ (% ID/organ) and a percentage of the injected dose per gram of organ tissue (% ID/g). The biodistribution data and target-to-background (T/B) ratios are reported as an average plus the standard variation. Comparison between two different radiotracers was also made using the one-way ANOVA test (*GraphPad Prism 5.0*, San Diego, CA). The level of significance was set at $p < 0.05$.

Metabolism. Two normal mice were used for metabolism studies. Each mouse was administered the radiotracer at a dose of 100 μCi/mouse. The urine samples were collected at 30 min and 2 h p.i. by manual void, and were mixed with equal volume of acetonitrile. The mixture was centrifuged at 8000 rpm. The supernatant was collected and filtered through a 0.20 μm Millex-LG syringe driven filter unit. The filtrate was analyzed by radio-HPLC (method 1 for [^{99m}Tc(HYNIC−dimer)(EDDA)] and method 2 for [^{99m}Tc(HYNIC−tetramer)(EDDA)]). The feces samples were collected at ∼120 min p.i. The sample was suspended in a mixture of 50% acetonitrile aqueous solution, and the resulting mixture was vortexed for 5–10 min. After centrifuging, the supernatant was collected and passed through a 0.20 μm Millex-LG syringe driven filter unit. The filtrate was analyzed by radio-HPLC.

RESULTS

Radiochemistry. [^{99m}Tc(HYNIC−dimer)(EDDA)]and[^{99m}Tc-(HYNIC−tetramer)(EDDA)] (Figure 1) were prepared in two steps. HYNIC−dimer was first allowed to react with $^{99m}TcO_4^-$ in the presence of excess tricine and stannous chloride to form the [^{99m}Tc(HYNIC−dimer)(tricine)$_2$] intermediate, which was then reacted with EDDA to form [^{99m}Tc(HYNIC−dimer)-(EDDA)]. [^{99m}Tc(HYNIC−tetramer)(EDDA)] was prepared in the same fashion using HYNIC−tetramer. Attempts to prepared [^{99m}Tc(HYNIC−dimer)(EDDA)] and [^{99m}Tc(HYNIC−tetramer)-(EDDA)] in one step by directly reacting the HYNIC−dimer or HYNIC−tetramer with $^{99m}TcO_4^-$ in the presence of EDDA and stannous chloride were not successful due to their low yield (<50%).

Figure 2 shows representative HPLC chromatograms of [^{99m}Tc-(HYNIC−dimer)(tricine)$_2$] (top) and [^{99m}Tc(HYNIC−dimer)-(EDDA)] (bottom). The key to achieving high RCP for [^{99m}Tc-(HYNIC−dimer)(EDDA)] was the high-yield formation of the intermediate complex [^{99m}Tc(HYNIC−dimer)(tricine)$_2$]. Successful ligand exchange was evidenced by disappearance of multiple peaks at ∼14 min from [^{99m}Tc(HYNIC−dimer)(tricine)$_2$] (Figure 2: top) and formation of a single peak at 13 min (Figure 2: bottom). Small peaks at ∼3 min (Figure 2: bottom) were formed during ligand exchange process due to the instability of [^{99m}Tc(HYNIC−dimer)(tricine)$_2$]. The radiolabeling yield was >90% using 20 μg of HYNIC−dimer (∼1.2 × 10^{-8} mol) and 20 mCi of $^{99m}TcO_4^-$ (∼1.5 × 10^{-10} mol of ^{99m}Tc/^{99}Tc for 24 h generator). The specific activity was ∼8.0 Ci/μmol for [^{99m}Tc(HYNIC−dimer)(EDDA)]. In contrast, the radiolabeling yield was always <65% for [^{99m}Tc(HYNIC−tetramer)(EDDA)] even though the [^{99m}Tc(HYNIC−tetramer)(tricine)$_2$] intermediate was prepared in 95% yield. The log P values were determined to be −3.59 ± 0.11 and −3.26 ± 0.08 for [^{99m}Tc(HYNIC−dimer)(EDDA)] and [^{99m}Tc(HYNIC−tetramer)(EDDA)], respectively.

In order to determine the number of EDDA in [^{99m}Tc(HYNIC−dimer)(EDDA)] and [^{99m}Tc(HYNIC−tetramer)(EDDA)], a mixed-ligand experiment was carried out using EDDA and Bn_2EDDA as the competing ligands to react with [^{99m}Tc(HYNIC−dimer)-(tricine)$_2$]. If there is only one EDDA in [^{99m}Tc(HYNIC−dimer)(EDDA)], the radio-HPLC chromatogram of the resulting reaction mixture is expected to show two sets of radiometric peaks: one set from [^{99m}Tc(HYNIC−dimer)(EDDA)] and the other from [^{99m}Tc(HYNIC−dimer)(Bn_2EDDA)]. If there were two EDDA ligands bonding to the ^{99m}Tc-HYNIC core, a third

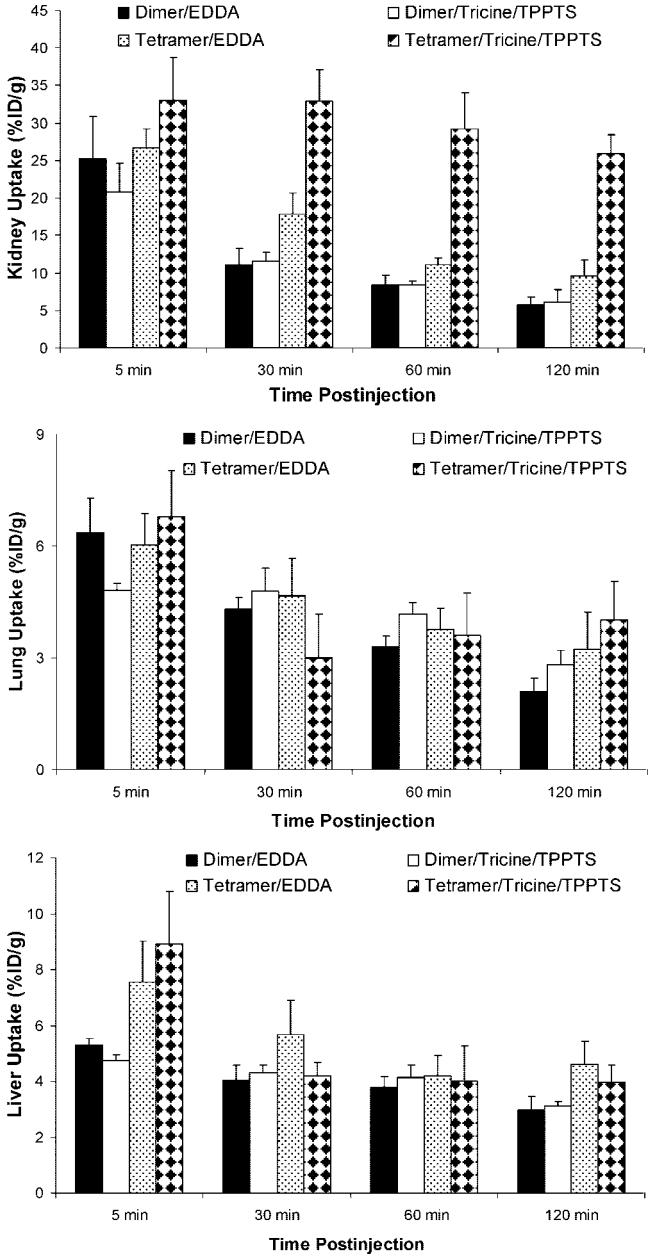

Figure 4. Direct comparison of the organ uptake between [^{99m}Tc(HYNIC−dimer)(EDDA)][^{99m}Tc(HYNIC−dimer)(tricine)(TPPTS)][^{99m}Tc(HYNIC−tetramer)(EDDA)], and [^{99m}Tc(HYNIC−tetramer)(tricine)(TPPTS)] in kidneys, liver, and lungs.

set of peaks from the mixed-ligand complex [^{99m}Tc(HYNIC−dimer)(EDDA)(Bn_2EDDA)] would have been expected. The presence of only two sets of radiometric peaks from [^{99m}Tc-(HYNIC−dimer)(EDDA)] and [^{99m}Tc(HYNIC−dimer)(Bn_2-EDDA)] in the chromatogram (Figure 3) clearly shows that there is only one EDDA bonded to the ^{99m}Tc-HYNIC core in [^{99m}Tc-(HYNIC−dimer)(EDDA)].

It is important to emphasize that EDDA is tetradentate, and an additional monodentate ligand, such as Cl^-, is required to complete the octahedral Tc coordination sphere. This will result in formation of isomers for [^{99m}Tc(HYNIC−dimer)(EDDA)] when EDDA bonds to Tc. Thus, it is not surprising that [^{99m}Tc-(HYNIC−dimer)(EDDA)] shows 2–3 small satellite peaks in the 12–15 min region of its HPLC chromatogram (Figure 3). Similar results have been reported for a ^{99m}Tc-labeled monomeric cyclic RGD peptide (*40*).

Solution Stability. Their solution stability was studied using the cysteine and histidine challenge experiments. Table 1 summarizes the solution stability data for the HPLC purified [^{99m}Tc(HYNIC−dimer)(EDDA)] and [^{99m}Tc(HYNIC−tetramer)-(EDDA)] and 6 h in the presence of excess histidine or cysteine (1 mg/mL, pH = 7.4). Obviously, [^{99m}Tc(HYNIC−dimer)-(EDDA)] and [^{99m}Tc(HYNIC−tetramer)(EDDA)] remained stable for >6 h, suggesting that they are intact before being injected into animals.

Biodistribution Characteristics. The athymic nude mice bearing U87MG glioma xenografts were used to study biodistribution properties of [^{99m}Tc(HYNIC−dimer)(EDDA)] and [^{99m}Tc(HYNIC−tetramer)(EDDA)]. Both [^{99m}Tc(HYNIC−dimer)(EDDA)] and [^{99m}Tc(HYNIC−tetramer)(EDDA)] were prepared, and purified by HPLC to remove excess "unlabeled" HYNIC conjugate that may compete with the radiotracer in binding to the integrin $\alpha_v\beta_3$ expressed on tumor cells and in normal tissues. Biodistribution data for [^{99m}Tc(HYNIC−dimer)(EDDA)] and [^{99m}Tc(HYNIC−tetramer)(EDDA)] are summarized in Tables 2 and 3, respectively.

In general, [^{99m}Tc(HYNIC−dimer)(EDDA)] and [^{99m}Tc-(HYNIC−tetramer)(EDDA)] have a rapid blood clearance. Their tumor uptake was comparable within the experimental error over the 2 h study period. Their lung uptake also compared favorably during the same study period. The liver uptake of [^{99m}Tc-(HYNIC−dimer)(EDDA)] was 5.29 ± 0.29% ID/g and 2.98 ± 0.48% ID/g at 5 and 120 min p.i., respectively, and was significantly lower ($p < 0.01$) than that of [^{99m}Tc(HYNIC−tetramer)(EDDA)] (7.56 ± 1.48% ID/g and 4.60 ± 0.82% ID/g at 5 and 120 min p.i., respectively). The initial kidney uptake of [^{99m}Tc(HYNIC−dimer)(EDDA)] (25.25 ± 5.64% ID/g at 5 min p.i.) was almost identical to that of [^{99m}Tc(HYNIC−tetramer)(EDDA)] (26.69 ± 2.48% ID/g at 5 min p.i.); but this similarity disappeared at >30 min p.i. The kidney uptake of [^{99m}Tc(HYNIC−dimer)(EDDA)] was 11.70 ± 2.25% ID/g and 5.97 ± 0.94% ID/g at 30 and 120 min p.i., respectively, while the kidney uptake of [^{99m}Tc(HYNIC−tetramer)(EDDA)] was 17.84 ± 2.82% ID/g at 5 min p.i. and 9.54 ± 2.23% ID/g at 120 min p.i. The muscle uptake of [^{99m}Tc(HYNIC−dimer)-(EDDA)] (3.85 ± 0.60% ID/g and 2.02 ± 0.23% ID/g at 5 and 120 min p.i., respectively) was significantly higher than that of [^{99m}Tc(HYNIC−tetramer)(EDDA)] (2.11 ± 0.37% ID/g and 0.92 ± 0.26% ID/g at 5 and 120 min p.i., respectively).

Figure 4 compares the organ uptake (% ID/g) of [^{99m}Tc-(HYNIC−dimer)(EDDA)], [^{99m}Tc(HYNIC−dimer)(tricine)-(TPPTS)], [^{99m}Tc(HYNIC−tetramer)(EDDA)], and [^{99m}Tc-(HYNIC−tetramer)(tricine)(TPPTS)] in the liver, kidneys, and lungs. The biodistribution data for [^{99m}Tc(HYNIC−dimer)-(tricine)(TPPTS)] and [^{99m}Tc(HYNIC−tetramer)(tricine)(TPPTS)] were obtained from our previous studies in the same tumor-bearing animal model (*29*, *31*). Replacing tricine/TPPTS with EDDA did not change the uptake of the ^{99m}Tc-labeled HYNIC−dimer in kidneys, liver, or lungs. [^{99m}Tc(HYNIC−tetramer)(EDDA)] also had the liver and lung uptake very similar to that of [^{99m}Tc(HYNIC−tetramer)(tricine)(TPPTS)]; but it had a much lower kidney uptake than [^{99m}Tc(HYNIC−tetramer)(tricine)(TPPTS)] over the 2 h period (Figure 4).

During biodistribution studies, we noticed a large variation in the tumor uptake for both [^{99m}Tc(HYNIC−dimer)(EDDA)] and [^{99m}Tc(HYNIC−tetramer)(EDDA)], and their tumor uptakes were largely dependent upon the tumor size. Similar behavior was reported for the ^{99m}Tc-labeled cyclic RGDfK monomer (*11*). To further clarify this relationship, we added extra tumor-bearing mice into the 60 and 120 min groups for both radiotracers. We also performed a biodistribution study on [^{99m}Tc-(HYNIC−tetramer)(tricine)(TPPTS)] at 120 min p.i. The biodistribution data at 60 and 120 min were used for all three

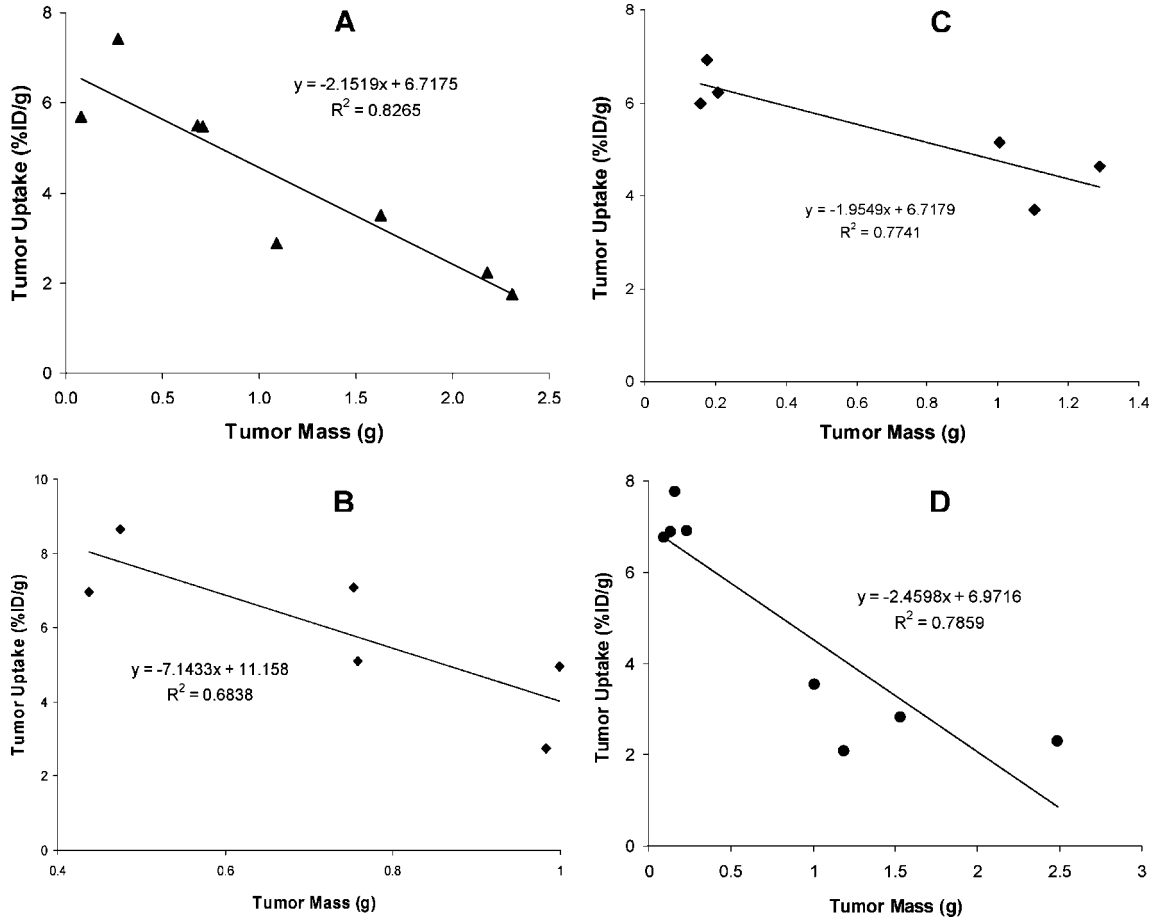

Figure 5. The relationship between the tumor size and tumor uptake (expressed as (% ID/g) for [[99m]Tc(HYNIC−dimer)(EDDA)] at 60 min p.i. (A: $n = 8$) and 120 min p.i. (B: $n = 5$), [[99m]Tc(HYNIC−tetramer)(EDDA)] at 120 min p.i. (C: $n = 6$), and [[99m]Tc(HYNIC−tetramer)(tricine)(TPPTS)] at 120 min p.i. (D: $n = 8$) in the athymic nude mice bearing the U87MG human glioma xenografts.

radiotracers to minimize the interference from their blood activity. Figure 5 shows the inverse linear relationship between the tumor size and tumor uptake (expressed as % ID/g) of [[99m]Tc(HYNIC−dimer)(EDDA)] at 60 min (A) and 120 min (B) p.i., [[99m]Tc(HYNIC−tetramer)(EDDA)] (C), and [[99m]Tc(HYNIC−tetramer)(tricine)(TPPTS)] (D) at 120 min p.i. in the same model. It is clear that the radiotracer tumor uptake (% ID/g) decreases as the tumor size increases. Smaller tumors (<0.5 g) always show higher radiotracer uptake (>5% ID/g) that large tumors (>1.0 g) regardless of the identity of radiotracer.

Metabolic Properties. Normal athymic mice were used to examine metabolic stability of [[99m]Tc(HYNIC−dimer)-(EDDA)] and [[99m]Tc(HYNIC−tetramer)(EDDA)]. Since >85% of [[99m]Tc(HYNIC−dimer)(EDDA)] and [[99m]Tc(HYNIC−tetramer)(EDDA)] was excreted from the renal and hepatobiliary routes by 2 h p.i., we used radio-HPLC to analyze urine and feces samples from the mice administered with the radiotracer (∼100 μCi/mouse). Figure 6 shows radio-HPLC chromatograms of [[99m]Tc(HYNIC−dimer)(EDDA)] (left) and [[99m]Tc(HYNIC−tetramer)(EDDA)] (right) in saline (A), in the urine at 30 min p.i. (B), in the urine at 120 min p.i. (C), and in the feces at 120 min p.i. (D). There were no metabolites detected in the urine at 30 and 120 min p.i. for both radiotracers, indicating that they have a high metabolic stability during excretion from the renal system. Only 35% of [[99m]Tc(HYNIC−dimer)-(EDDA)] and 15% of [[99m]Tc(HYNIC−tetramer)(EDDA)] remained intact in the feces samples, suggesting that they underwent significant metabolism during excretion from the hepatobiliary system.

DISCUSSION

Recently, Decristoforo et al. (*39*) reported the [99m]Tc-labeled cyclic RGD monomer, HYNIC-c(RGDyK) (HYNIC-RGD). It was found that HYNIC-RGD could be labeled with [99m]Tc in high specific activity (∼100 GBq/μmol or 2.7 Ci/ μmol) using EDDA as coligand. Despite the fact that [[99m]Tc(HYNIC-RGD)(EDDA)] had a high tumor uptake, along with the rapid renal excretion, and low uptake in the liver and muscle, it is not known about the composition of [99m]Tc radiotracer even though the LC-MS data suggested that there were two EDDA ligands binding to the [99m]Tc-HYNIC core (*41*). In this study, we used EDDA as the coligand to prepare [[99m]Tc(HYNIC−dimer)(EDDA)] and [[99m]Tc(HYNIC−tetramer)(EDDA)]. The specific activity was ∼300 GBq/μmol or 8 Ci/μmol for [[99m]Tc-(HYNIC−dimer)(EDDA)] using the two-step radiolabeling procedure. Both [[99m]Tc(HYNIC−dimer)(EDDA)] and [[99m]Tc-(HYNIC−tetramer)(EDDA)] have very high *in vitro* solution stability (Table 1).

There are several important findings from this study. The results from a mixed-ligand experiment clearly demonstrate that there is only one EDDA bonding to the [99m]Tc-HYNIC core in [[99m]Tc(HYNIC−dimer)(EDDA)] and [[99m]Tc(HYNIC−tetramer)-(EDDA)] (Figure 3). To our surprise, [[99m]Tc(HYNIC−dimer)-(EDDA)] and [[99m]Tc(HYNIC−tetramer)(EDDA)] have almost identical tumor uptake (Tables 2 and 3). There is no advantage of the [99m]Tc-labeled HYNIC−tetramer over its dimeric analogue when EDDA is used as the coligand. This seems to contradict

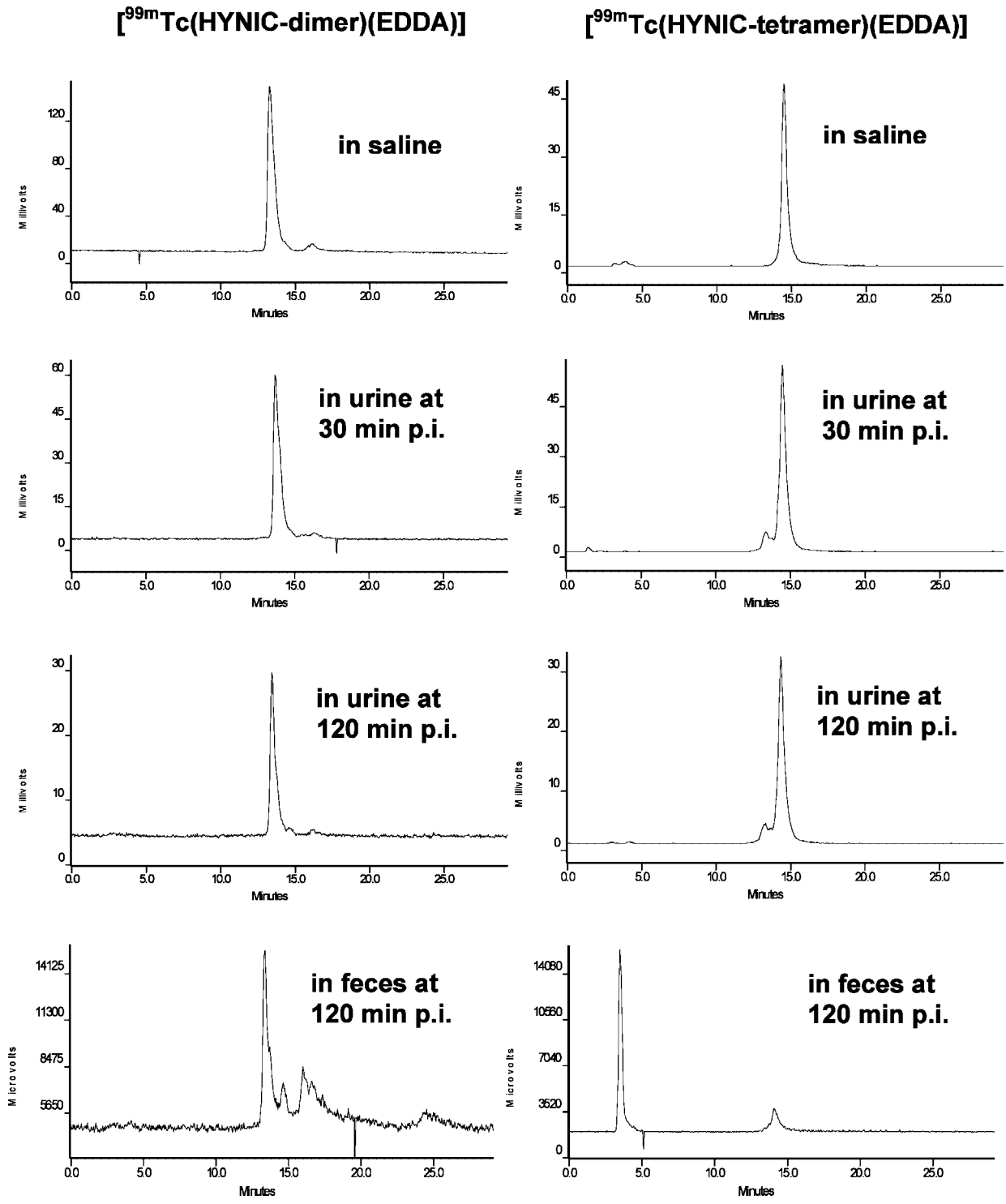

Figure 6. Typical radio-HPLC chromatograms of the HPLC-purified [^{99m}Tc(HYNIC−dimer)(EDDA)] and [^{99m}Tc(HYNIC−tetramer)(EDDA)] in saline before injection, in urine at 30 min p.i., in urine at 120 min p.i., and in feces at 120 min p.i. Each mouse was administered with ∼ 100 μCi radiotracer. Two normal mice were used for each radiotracer.

the results obtained from ^{111}In(DOTA−tetramer) (*33*), ^{64}Cu(DOTA−tetramer) (*26, 28*), and [^{99m}Tc(HYNIC−tetramer)-(tricine)(TPPTS)] (*29, 31*) over their dimeric analogues. There is no clear explanation for this observation. Replacing tricine/TPPTS with EDDA did not significantly change the uptake of the ^{99m}Tc-labeled HYNIC−dimer in kidneys, liver, and lungs; but it did result in a significantly lower kidney uptake for [^{99m}Tc(HYNIC−tetramer)(EDDA)] due to its faster renal excretion (Figure 4) than [^{99m}Tc(HYNIC−tetramer)(tricine)(TPPTS)]. Apparently, coligands have a significant impact on excretion kinetics of the ^{99m}Tc-labeled HYNIC−tetramer.

It is very important to note that the tumor growth rate varies significantly even though each mouse receives the same number of tumor cells for the same inoculation time. The radiotracer tumor uptake decreases as the tumor size increases in a linear fashion. The smaller the tumors are, the higher the tumor uptake (% ID/g) is regardless of the identity of radiotracer (Figure 5). Since Chen and co-workers have elegantly demonstrated that

the radiotracer tumor uptake is well-correlated with the integrin $\alpha_v\beta_3$ expression levels in tumors (*42*), we believe that the reduced radiotracer uptake (% ID/g) might be related to the integrin $\alpha_v\beta_3$ density.

The radiotracer tumor uptake expressed as %ID reflects the total number of integrin $\alpha_v\beta_3$ receptors expressed on both tumor cells and endothelial cells, while the tumor uptake expressed as %ID reflects the integrin $\alpha_v\beta_3$ density. In small tumors, the microvessel density and the integrin $\alpha_v\beta_3$ density are high. The tumor uptake expressed as % ID/g is high (Figure 5) even though the radiotracer tumor uptake expressed as %ID is low (Supporting Information). As the tumor grows, the total number of integrin $\alpha_v\beta_3$ receptors expressed on tumor cells becomes larger, and the tumor uptake expressed as %ID increases (Supporting Information). In contrast, the microvessel density decreases because of maturity of blood vessels, and the integrin $\alpha_v\beta_3$ density also decreases due to larger interstitial space and higher collagen concentrations (*43*). In addition, part of the tumor tissue may also become necrotic, which may also lead to lower the integrin $\alpha_v\beta_3$ density in larger tumors. As a result, the radiotracer tumor uptake expressed as % ID/g in larger tumors is significantly lower than that of smaller ones (Figure 5). Thus, it is important to select the mice bearing tumors of the same or similar size for biological evaluations. This may become more important when comparing radiotracers for their tumor uptake and tumor-targeting capability. However, this will, to a certain degree, compromise the "random nature" of the evaluation process.

Radiolabeled small peptides often accumulate in kidneys and liver (*44*). Extensive metabolic degradation was observed for the ^{99m}Tc-labeled cyclic RGDfK monomer (*10*), dimer (*29*), and tetramer (*31*), and the ^{64}Cu-labeled cyclic RGDfK tetramer in kidneys and urine samples (*28*). In this study, [^{99m}Tc(HYNIC−dimer)(EDDA)] and [^{99m}Tc(HYNIC−tetramer)(EDDA)] (Figure 6) show very high metabolic stability during their excretion from the renal system and significant metabolism during their excretion from the hepatobiliary system, probably due to rapid enzymatic degradation of the cyclic RGD peptide and/or the ^{99m}Tc chelate. The difference in the metabolic fate between [^{99m}Tc-(HYNIC−tetramer)(EDDA)] described in this study and [^{99m}Tc-(HYNIC−tetramer)(tricine)(TPPTS)] (*31*) seems to be related to coligands (EDDA vs tricine/TPPTS) in the Tc chelate.

CONCLUSION

In summary, we have described the synthesis and evaluation of [^{99m}Tc(HYNIC−dimer)(EDDA)] and [^{99m}Tc(HYNIC−tetramer)(EDDA)] as potential radiotracers for tumor imaging using athymic nude mice bearing the U87MG glioma xenografts. The key findings of this study are as follows: (1) there is only one EDDA binding to the ^{99m}Tc-HYNIC core; (2) the use of EDDA as coligand to replace tricine/TPPTS does not significantly change the uptake of the ^{99m}Tc-labeled HYNIC-dimer in liver, kidneys, and lungs; but it results in a significantly lower kidney uptake for the ^{99m}Tc-labeled HYNIC−tetramer due to faster radiotracer renal excretion; and (3) the radiotracer tumor uptake decreases as the tumor size increases in a linear fashion.

ACKNOWLEDGMENT

We would like to thank Dr. Sulma I. Mohammed, the Director of Purdue Cancer Center Drug Discovery Shared Resource, Purdue University, for her assistance with the tumor-bearing animal model. This work is supported, in part, by Purdue University and research grants: R01 CA115883 A2 (S.L.) from National Cancer Institute (NCI), BCTR0503947 (S.L.) from Susan G. Komen Breast Cancer Foundation, R21 EB003419-02 (S.L.) from National Institute of Biomedical Imaging and Bioengineering (NIBIB) and R21 HL083961-01 from National Heart, Lung, and Blood Institute (NHLBI).

Supporting Information Available: Additional figure. This material is available free of charge via the Internet at http://pubs.acs.org.

LITERATURE CITED

(1) Sivolapenko, G. B., Skarlos, D., Pectasides, D., Stathopoulou, E., Milonakis, A., Sirmalis, G., Stuttle, A., Courtenay-Luck, N. S., Konstantinides, K., and Epenetos, A. A. (1998) Imaging of metastatic melanoma utilizing a technetium-99m labeled RGD-containing synthetic peptide. *Eur. J. Nucl. Med. 25*, 1383–1389.

(2) Chen, X., Park, R., Shahinian, A. H., Tohme, M., Khankaldyyan, V., Bozorgzadeh, M. H., Bading, J. R., Moats, R., Laug, W. E., and Conti, P. S. (2004) ^{18}F-labeled RGD peptide: initial evaluation for imaging brain tumor angiogenesis. *Nucl. Med. Biol. 31*, 179–189.

(3) Chen, X., Park, R., Tohme, M., Shahinian, A. H., Bading, J. R., and Conti, P. S. (2004) MicroPET and autoradiographic imaging of breast cancer α_v-integrin expression using ^{18}F- and ^{64}Cu-labeled RGD peptide. *Bioconjugate Chem. 15*, 41–49.

(4) Chen, X., Tohme, M., Park, R., Hou, Y., Bading, J. R., and Conti, P. S. (2004) MicroPET imaging of breast cancer αv-integrin expression with ^{18}F-labeled dimeric RGD peptide. *Mol. Imaging 3*, 96–104.

(5) Chen, X., Park, R., Shahinian, A. H., Bading, J. R., and Conti, P. S. (2004) Pharmacokinetics and tumor retention of ^{125}I-labeled RGD peptide are improved by PEGylation. *Nucl. Med. Biol. 31*, 11–19.

(6) Chen, X., Sievers, E., Hou, Y., Park, R., Tohme, M., Bart, R., Bremner, R., Bading, J. R., and Conti, P. S. (2005) Integrin $\alpha_v\beta_3$-targeted imaging of lung cancer. *Neoplasia 7*, 271–279.

(7) Zhang, X., and Chen, X. (2007) Preparation and characterization of ^{99m}Tc(CO)$_3$-BPy-RGD complex as $\alpha_v\beta_3$ integrin receptor-targeted imaging agent. *Appl. Radiat. Isot. 65*, 70–78.

(8) Haubner, R., Wester, H. J., Reuning, U., Senekowitsch-Schmidtke, R., Diefenbach, B., Kessler, H., Stöcklin, G., and Schwaiger, M. (1999) Radiolabeled $\alpha_v\beta_3$ integrin antagonists: a new class of tracers for tumor imaging. *J. Nucl. Med. 40*, 1061–1071.

(9) Haubner, R., Wester, H. J., Burkhart, F., Senekowitsch-Schmidtke, R., Weber, W., Goodman, S. L., Kessler, H., and Schwaiger, M. (2001) Glycolated RGD-containing peptides: tracer for tumor targeting and angiogenesis imaging with improved biokinetics. *J. Nucl. Med. 42*, 326–336.

(10) Haubner, R., Bruchertseifer, F., Bock, M., Schwaiger, M., and Wester, H. J. (2004) Synthesis and biological evaluation of ^{99m}Tc-labeled cyclic RGD peptide for imaging the $\alpha_v\beta_3$ expression. *Nuklearmedizin 43*, 26–32.

(11) Fani, M., Psimadas, D., Zikos, C., Xanthopoulos, S., Loudos, G. K., Bouziotis, P., and Varvarigou, A. D. (2006) Comparative evaluation of linear and cyclic ^{99m}Tc-RGD peptides for targeting of integrins in tumor angiogenesis. *Anticancer Res. 26*, 431–434.

(12) Alves, S., Correia, J. D. G., Gano, L., Rold, T. L., Prasanphanich, A., Haubner, R., Rupprich, M., Alberto, R., Decristoforo, C., Snatos, I., and Smith, C. J. (2007) In vitro and in vivo evaluation of a novel ^{99m}Tc(CO)$_3$-pyrazolyl conjugate of cyclo-(Arg-Gly-Asp-D-Tyr-Lys). *Bioconjugate Chem. 18*, 530–537.

(13) Janssen, M., Oyen, W. J. G., Massuger, L. F. A. G., Frielink, C., Dijkgraaf, I., Edwards, D. S., Rajopadhyhe, M., Corsten, F. H. M., and Boerman, O. C. (2002) Comparison of a monomeric and dimeric radiolabeled RGD-peptide for tumor targeting. *Cancer Biother. Radiopharm. 17*, 641–646.

(14) Janssen, M., Oyen, W. J. G., Dijkgraaf, I., Massuger, L. F. A. G., Frielink, C., Edwards, D. S., Rajopadyhe, M., Boonstra, H., Corsten, F. H., and Boerman, O. C. (2002) Tumor targeting with radiolabeled integrin $\alpha_v\beta_3$ binding peptides in a nude mice model. *Cancer Res. 62*, 6146–6151.

(15) Weber, W. A., Haubner, R., Vabuliene, E., Kuhnast, B., Webster, H. J., and Schwaiger, M. (2001) Tumor angiogenesis targeting using imaging agents. *Q. J. Nucl. Med. 45*, 179–182.

(16) van de Wiele, C., Oltenfreiter, R., De Winter, O., Signore, A., Slegers, G., and Dieckx, R. A. (2002) Tumor angiogenesis pathways: related clinical issues and implications for nuclear medicine imaging. *Eur. J. Nucl. Med. 29*, 699–709.

(17) Liu, S., Robinson, S. P., and Edwards, D. S. (2003) Integrin $\alpha_v\beta_3$ directed radiopharmaceuticals for tumor imaging. *Drugs of the Future 28*, 551–564.

(18) McDonald, D. M., and Choyke, P. (2003) Imaging Angiogenesis: from microscope to clinic. *Nat. Med. 9*, 713–725.

(19) Haubner, R., and Wester, H. J. (2004) Radiolabeled tracers for imaging of tumor angiogenesis and evaluation of anti-angiogenic therapies. *Curr. Pharm. Des. 10*, 1439–1455.

(20) Chen, X. (2006) Multimodality imaging of tumor integrin $\alpha_v\beta_3$ expression. *Mini-Rev. Med. Chem. 6*, 227–234.

(21) Liu, S. (2006) Radiolabeled multimeric cyclic RGD peptides as integrin $\alpha_v\beta_3$-targeted radiotracers for tumor imaging. *Mol. Pharm. 3*, 472–487.

(22) Haubner, R., Wester, H. J., Weber, W. A., Mang, C., Ziegler, S. I., Goodman, S. L., Senekowitsch-Schmidtke, R., Kessler, H., and Schwaiger, M. (2001) Noninvasive imaging of $\alpha_v\beta_3$ integrin expression using ^{18}F-labeled RGD-containing glycopeptide and positron emission tomography. *Cancer Res. 61*, 1781–1785.

(23) Beer, A. J., Haubner, R., Goebel, M., Luderschmidt, S., Spilker, M. E., Wester, H. J., Weber, W. A., and Schwaiger, M. (2005) Biodistribution and pharmacokinetics of the $\alpha_v\beta_3$-selective tracer ^{18}F-Galacto-RGD in cancer patients. *J. Nucl. Med. 46*, 1333–1341.

(24) Haubner, R., Weber, W. A., Beer, A. J., Vabulience, E., Reim, D., Sarbia, M., Becker, K. F., Goebel, M., Hein, R., Wester, H. J., Kessler, H., and Schwaiger, M. (2005) Noninvasive visuallization of the activiated $\alpha_v\beta_3$ integrin in cancer patients by positron emission tomography and [^{18}F]Galacto-RGD. *PLOS Med. 2*, e70.

(25) Liu, S., Edwards, D. S., Ziegler, M. C., Harris, A. R., Hemingway, S. J., and Barrett, J. A. (2001) ^{99m}Tc-Labeling of a hydrazinonictotinamide-conjugated vitronectin receptor antagonist useful for imaging tumors. *Bioconjugate Chem. 12*, 624–629.

(26) Chen, X., Liu, S., Hou, Y., Tohme, M., Park, R., Bading, J. R., and Conti, P. S. (2004) MicroPET imaging of breast cancer integrin $\alpha_v\beta_3$ expression with ^{64}Cu-labeled dimeric RGD-containing cyclic peptides. *Mol. Imag. Biol.* 350–359.

(27) Liu, S., Hsieh, W. Y., Kim, Y. S., and Mohammed, S. I. (2005) Effect of coligands on biodistribution characteristics of ternary ligand ^{99m}Tc complexes of a HYNIC-conjugated cyclic RGDfK dimer. *Bioconjugate Chem. 16*, 1580–1588.

(28) Wu, Y., Zhang, X., Xiong, Z., Cheng, Z., Fisher, D. R., Liu, S., Gambhir, S. S., and Chen, X. (2005) MicroPET imaging of glioma integrin $\alpha_v\beta_3$ expression using ^{64}Cu-labeled tetrameric RGD peptide. *J. Nucl. Med. 46*, 1707–1718.

(29) Liu, S., He, Z. J., Hsieh, W. Y., Kim, Y. S., and Jiang, Y. (2006) Impact of PKM linkers on biodistribution characteristics of the ^{99m}Tc-labeled cyclic RGDfK dimer. *Bioconjugate Chem. 17*, 1499–1507.

(30) Jia, B., Shi, J., Yang, Z., Xu, B., Liu, Z., Zhao, H., Liu, S., and Wang, F. (2006) ^{99m}Tc-labeled cyclic RGDfK dimer: initial evaluation for SPECT imaging of glioma integrin $\alpha_v\beta_3$ expression. *Bioconjugate Chem. 17*, 1069–1076.

(31) Liu, S., Hsieh, W. Y., Jiang, Y., Kim, Y. S., Sreerama, S. G., Chen, X., Jia, B., and Wang, F. (2007) Evaluation of a ^{99m}Tc-labeled cyclic RGD tetramer for non-invasive imaging integrin $\alpha_v\beta_3$-positive breast cancer. *Bioconjugate Chem. 18*, 438–446.

(32) Dijkgraaf, I., Kruijtzer, J. A. W., Liu, S., Soede, A. C., Oyen, W. J. G., Corstens, F. H. M., Liskamp, R. M. J., and Boerman, O. C. (2007) Improved targeting of the $\alpha_v\beta_3$ integrin by multimerization of RGD peptides. *Eur. J. Nucl. Med. Mol. Imaging 34*, 267–273.

(33) Dijkgraaf, I., Liu, S., Kruijtzer, J. A. W., Soede, A. C., Oyen, W. J. G., Liskamp, R. M. J., Corstens, F. H. M., and Boerman, O. C. (2007) Effect of linker variation on the in vitro and in vivo characteristics of an ^{111}In-labeled RGD peptide. *Nucl. Med. Biol. 34*, 29–35.

(34) Liu, S., Kim, Y. S., Sreerama, S. G. (2007) Coligand effects on solution stability, biodistribution and metabolism of ^{99m}Tc-labeled cyclic RGDfK tetramer, Nucl. Med. Biol. ASAP.

(35) Jia, B., Liu, Z., Yu, Z., Yang, Z., Zhao, H., He, Z. J., Liu, S., Wang, F. (2007) Linker effects on biological properties of ^{111}In-labeled DTPA conjugates of a cyclic RGDfK dimer Bioconjugate Chem. ASAP.

(36) Bangard, M., Béhé, M., Guhlke, S., Otte, R., Bender, H., Maecke, H. R., and Biersack, H. J. (2000) Detection of somatostatin receptor-positive tumors using the new ^{99m}Tc-tricine-HYNIC-D-Phe1-Tyr3-octreotide: first results in patients and comparison with ^{111}In-DTPA-D-Phe1-octreotide. *Eur. J. Nucl. Med. 27*, 628–637.

(37) Decristoforo, C., Melendez-Alafort, L., Sosabowski, J. K., and Mather, S. J. (2000) ^{99m}Tc-HYNIC-[Tyr3]-octreotide for imaging somatostatin-receptor-positive tumors: preclinical evaluation and comparison with ^{111}In-Octreotide. *J. Nucl. Med. 41*, 1114–1119.

(38) Decristoforo, C., Mather, S. J., Cholewinski, W., Donnemiller, E., Riccabona, G., and Moncayo, R. (2000) ^{99m}Tc-EDDA/HYNIC-TOC: a new ^{99m}Tc-labeled radiopharmaceutical for imaging somatostatin receptor-positive tumors: first clinical results and intrapatient comparison with ^{111}In-labeled octreotide derivatives. *Eur. J. Nucl. Med. 27*, 1318–1325.

(39) Decristoforo, C., Faintuch-Linkowski, B., Rey, A., von Guggenberg, E., Rupprich, M., Hernandez-Gonzales, I., Rodrigo, T., and Haubner, R. (2006) [^{99m}Tc]HYNIC-RGD for imaging integrin $\alpha_v\beta_3$ expression. *Nucl. Med. Biol. 33*, 945–952.

(40) Liu, S., Edwards, D. S., Looby, R. J., Harris, A. R., Poirier, M. J., Barrett, J. A., Heminway, S. J., and Carroll, T. R. (1996) Labeling a hydrazinonicotinamide-modified cyclic IIb/IIIa receptor antagonist with ^{99m}Tc using aminocarboxylates as co-ligands. *Bioconjugate Chem. 7*, 63–70.

(41) Von Guggenberg, E., Sarg, B., Lindner, H., Alafort, L. M., Mather, S. J., Moncayo, R., and Decristoforo, C. (2003) Preparation via coligand exchange and characterization of [^{99m}Tc-EDDA-HYNIC-D-Phe1,Tyr3]Octreotide (^{99m}Tc-EDDA/HYNIC-TOC). *J. Label. Compd. Radiopharm. 46*, 307–318.

(42) Zhang, X., Xiong, Z., Wu, Y., Cai, W., Tseng, J. R., Gambhir, S. S., and Chen, X. (2006) Quantitative PET imaging of tumor integrin $\alpha_v\beta_3$ expression with ^{18}F-FRGD2. *J. Nucl. Med. 47*, 113–121.

(43) Jain, R. K. (1987) Transport of molecules in the tumor interstitium: a review. *Cancer Res. 47*, 3039–3051.

(44) Trejtnar, F., Laznicek, M., Laznickova, A., and Mather, S. J. (2000) Pharmacokinetics and renal handling of ^{99m}Tc-labeled peptides. *J. Nucl. Med. 41*, 177–182.

BC7004208

Modulation of Antibody Pharmacokinetics by Chemical Polysialylation

Antony Constantinou,[†,§] Agamemnon A. Epenetos,[†] Dale Hreczuk-Hirst,[‡,△] Sanjay Jain,[‡] and Mahendra P. Deonarain*[,†]

Division of Cell and Molecular Biology, Faculty of Natural Sciences, Imperial College London, Exhibition Road, London, SW7 2AZ, United Kingdom, Lipoxen plc, 2 Royal College Street, London NW1 0NH. Received May 16, 2007; Revised Manuscript Received December 14, 2007

Chemical coupling of a variety of polymers to therapeutic proteins has been studied as a way of improving their pharmacokinetics and pharmacodynamics *in vivo*. Conjugates have been shown to possess greater stability, lower immunogenicity, and a longer blood circulation time due to the chemicophysical properties of these hydrophilic long chain molecules. Naturally occurring colominic acid (polysialic acid, PSA) has been investigated as an alternative to synthetic polymers such as poly(ethylene glycol) (PEG) due to its lower toxicity and natural metabolism. Antibodies and their fragments are a good example of the types of proteins which benefit from pharmacokinetic engineering. Here, we chemically attached differing amounts and differing lengths of short (11 kDa) and longer (22 kDa) chain colominic acid molecules to the antitumor monoclonal antibody H17E2 Fab fragment. Different coupling ratios and lengths were seen to alter the electrophoretic mobility of the Fab fragment but have a minor effect on the antibody immunoreactivity toward the placental alkaline phosphatase (PLAP) antigen. Polysialylation generally increased Fab fragment blood half-life resulting in higher tumor uptake in a KB human tumor xenograft mouse model. One H17E2 Fab-PSA conjugate had over a 5-fold increase in blood exposure and over a 3-fold higher tumor uptake with only a marginal decrease in tumor/blood selectivity ratio compared to the unconjugated Fab. This conjugate also had a blood bioavailability approaching that of a whole immunoglobulin.

INTRODUCTION

The use of polymers to modulate the *in vivo* pharmacokinetics of proteins and drugs for therapeutic applications has been shown for many conjugates to enhance their efficacy (*1, 2*). The primary objective of such conjugation is normally to extend the longevity of therapeutic agents in circulation that would otherwise be cleared too rapidly by renal clearance to give a larger therapeutic window. However, other advantages in polymer conjugation include the masking of antigenic sites that would cause clearance by a variety of immune responses, as well as providing stabilizing features that reduce the risk of degradation under physiological conditions or by protease activity (*3, 4*).

The synthetic polymer poly(ethylene glycol) (PEG) represents the most extensively used and investigated form of polymer conjugation for pharmacokinetic engineering of small proteins or drugs (reviewed in (*1*)). Successful examples in the clinic include Oncaspar (PEG-asparaginase) for the treatment of lymphoblastic leukemia (*5*), PEGasys (PEG-interferon α−2a) for the treatment of chronic Hepatitis C infections (*6*), and Macugen (PEG-aptanib sodium), for the treatment macular degeneration (*7*).

Although considered biologically inert moieties, there have been concerns regarding the long-term safety of PEG *in vivo*, and whether chronic accumulation of PEG over prolonged use could lead to toxicity (*4, 8, 9*). Small length polymers of PEG have demonstrated renal clearance; however, larger molecular weight conjugates cannot be easily broken down through any known natural pathway, and there is evidence to suggest that they can accumulate in tissues once they have been taken up by cells through phagocytic processes. Furthermore, exposure from repeat and/or high doses has been shown to elicit an immune response which may lead to problems where long-term treatment is required (*10, 11*).

Recently, polysialic acid (PSA) has been investigated as an alternative to PEG (reviewed in (*12*)). Naturally occurring PSA polymers are carbohydrate chains that have been identified on the surface of a variety of cells from microbes to vertebrates. A specific form of this polymer, colominic acid, is a homopolymer of α-2,8-linked 5-*N*-acetylneuraminic acid (Neu5Ac) residues normally associated with the bacterial capsule of neuroinvasive bacteria such as *Escherichia coli* K1 (*13*). Gregoriadis et al. was the first to postulate and pioneer the use of PSA (colominic acid) as an alternative to PEGylation for conjugation to improve the stability and *in vivo* pharmacokinetics of small drugs and proteins (*14, 15*). Reductive amination of the nonreducing end of the polymer allowed chemical conjugation via the primary amine groups on proteins. In this manner, the therapeutic benefits of PSA conjugation have been demonstrated with aspariginase (*16*) and insulin (*17*) for the treatment of leukemia and diabetes, respectively, and both have shown an increase in enzyme stability and increased serum half-lives. The prolonged residency of polysialylated conjugates increases the potential of the species to reach its target and provide a therapeutic effect before being cleared from circulation, hence extending the duration of action. It has also been demonstrated that, by varying the length of the PSA chain, the number of PSA chains per conjugate, and the PSA conformation used, the half-life of the of the conjugate can be modulated for

* Corresponding author. Dr. M. P. Deonarain, Division of Cell and Molecular Biology, Faculty of Natural Sciences, Imperial College London, Exhibition Road, London, SW7 2AZ, Tel: +44 207 594 5318, Fax: +44 207 594 4560, E-mail: m.deonarain@imperial.ac.uk.

† Imperial College London.

§ Current address: John Wayne Cancer Institute, 2200 Santa Monica Blvd, Santa Monica, CA 90404.

‡ Lipoxen plc.

△ Current address: Glycoform Ltd, Unit 44C, Milton Park, Abingdon, Oxon, OX14 4RU.

10.1021/bc700319r CCC: $40.75 © 2008 American Chemical Society
Published on Web 02/29/2008

optimal therapeutic affect (*17*). Furthermore, a study of immunogenicity involving PSA-conjugated and native asparaginase demonstrated that only the native enzyme elicited an immune response in mice, while polysialylated asparaginase. despite having a 3–4-fold longer clearance rate, did not elicit an immune response, suggesting that PSA conjugation can mask antigenic epitopes (*18*). In addition, given that the source of PSA consists of α-2,8-linked 5-*N*-acetylneuraminic acid, which is the natural component of PSA in mammals, it is not thought that the polymer on its own would elicit an immune response in humans.

Although Siglec and Selectin receptors that recognize sialic acid containing glycans are known to exist, ligand recognition appears to be dependent on neighboring sugar residues within the glycan, and as yet, no receptors with PSA specificity have been identified (reviewed in (*19*)). The apparent lack of PSA receptors and low immunogenicity provides molecular stealth and adds to the nontoxic properties of PSA. PSA conjugates must be desialylated by neuraminidase-like enzymes before they can be cleared via the hepatic asialoglycoprotein receptor and metabolized (*20*).

The biodegradable, nontoxic, and highly hydrophilic properties of PSA are therefore being exploited to increase the serum half-life and consequently the action of small peptides and drugs. These observations are of particular pharmaceutical interest, since polysialylation offers a potentially superior method over current conjugation methods using PEGylation. Potentially, the greatest advantage in increasing the longevity of therapeutic agents would be where long-term specific activity was desired, and could be of immediate benefit to already commercially available therapeutic agents such as the neutralizing antibodies Remicade (Infliximab), used to treat rheumatoid arthritis (*21*), and Avastin (*22*), used in many solid cancers. Also, the conjugation technology could be applied to other common therapeutic agents where improved longevity pharmacokinetics would be beneficial such as insulin (*23*) and erythropoietin (*24*) for the treatment of diabetes and anemic conditions, respectively.

In this study, an analysis of the effect of protein polysialylation was investigated using a Fab antibody fragment. This fragment, which is specific for the placental-like alkaline phosphatase (PLAP) antigen associated with germ cell carcinomas (*25, 26*), was modified and immunoconjugates compared *in vitro* and *in vivo*. Our results indicate polysialylation can extend the half-life of antibody fragments leading to improved tumor uptake without compromising on tumor to tissue specificity.

EXPERIMENTAL PROCEDURES

Materials. H17E2 IgG was a gift from Professor Lemoine (CRUK). Polysialic acid (colominic acid) was from Marukin, Japan, supplied by Sigma, UK, and Camida, Ireland. PLAP antigen was supplied by Calzyme, Inc.; PLAP positive KB cell-line supplied by the EACC and grown in Dulbecco's modified Eagle medium (DMEM) supplemented with 10% fetal calf serum and 50 IU/mL of penicillin and streptomycin (Invitrogen). Unless stated, immunochemicals were from Sigma. Mouse anti-PSA-NCAM monoclonal IgM was from Chemicon. Carrier-free ^{125}I-NaCl was supplied by GE Healthcare, UK.

Production and Purification of H17E2 Fab. H17E2 Fab fragments were derived by papain cleavage using the Immuno Pure Fab preparation kit (Pierce), following the manufacturers instructions. The solublized Fab and Fc fragments were recovered and separated by Protein A. Proteins were further purified using a HiLoad 16/10 Superdex-200 HR 10/30 gel filtration column equilibrated with PBS and compared to previously run protein standards. Samples were further analyzed for the presence of protein by Coomassie staining and Western blotting.

Chemical Polysialylation. The PSA used in this work was colominic acid (linear α-(2,8) linked *N*-acetylneuraminic acid) purified from the capsular coating of *E. coli* K1, supplied in alternative different lengths, 11 and 22 kDa (average molecular weights), which are equivalent to ∼35 and 71 units of sialic acid, respectively. The average molecular weight (nominal mass) of these polymers was determined independently by Viscotek Europe Ltd. (Lipoxen, unpublished; (*17*)).

For the purpose of protein−PSA conjugation by reductive amination, PSA was oxidized with 0.1 M periodate as described (*17*). The oxidized material was dialyzed extensively against a 0.01% ammonium carbonate buffer (pH 7.4) at 4 °C, concentrated by reverse dialysis on a bed of poly(ethylene glycol) (8 kDa), lyophilized, and stored at −80 °C until required. Oxidized PSA was added to 5 mL protein samples to give a 25-fold molar excess in a glass tube. For lower coupling ratios, a 2- to 5-fold molar excess was used. The mixture was mixed gently and supplemented with 20 mg $NaCNBH_3$. The tube was sealed and rotated at 37 °C for 48 h to allow the conjugation reaction to take place whereupon ∼100% conjugation was expected. After incubation, the sample was allowed to cool and the conjugated material was purified from free PSA by addition of $(NH_4)_2SO_4$ to give a 70% saturated solution. The sample was rotated for 5 min at room temperature followed by 30 min on ice. The mixture was then centrifuged at 5000 rpm for 5 min and the resulting pellet resuspended in 1 mL 100% $(NH_4)_2SO_4$. The precipitation procedure was then repeated and the pellet resuspended in minimal PBS. Finally, the conjugated sample was analyzed by PAGE and characterized for polysialylation degree by a resorcinol assay.

Determination of PSA/Fab Ratios. The resorcinol assay, based on the method by Svennerholm (*27*), allowed the amount of colominic acid present in a sample relative to known standards to be measured. The resorcinol agent (0.25 mM cupric sulfate, 0.2% resorcinol, 80% conc HCl made up with dH_2O) was freshly prepared, and at least five colominic acid standards were prepared within the 40–400 μg/mL range. In triplicate, 100 μL of standard and test samples were added to 100 μL of resorcinol agent. The tubes were sealed and the mixture heated for 30 min at 95 °C. Once the tubes had cooled down, 400 μL of ethanol was mixed in. Finally, the absorbance at 560 nm was measured for 250 μL of each sample and standards in a microplate assay. The standard values were used to construct a calibration curve from which the colominic acid content of the test samples could be extrapolated. A molar value was determined according to the PSA length used in test samples, and similarly a protein molar value determined for samples using the Coomassie Plus protein assay kit compared to protein standards. Using these values, a PSA to protein molar ratio was calculated.

Western Blot Analyses. Protein gels for Western blot analysis were transferred to nitrocellulose membrane, blocked in PBS/5% Marvel milk protein made, and then incubated with either anti-mouse Fc-specific or anti-mouse Fab-specific one-step HRP-conjugated antibody. The blot was developed using enhanced chemiluminescence (ECL, GE Healthcre, UK) and exposed to high-performance autoradiography film.

Protein Radio-Iodination. Protein samples were iodinated using the IODO-GEN Iodination Reagent. To precoated tubes, 100 μL of the Tris iodination buffer was added, followed by 10 μL (1.0 mCi) $Na^{125}I$. The activated iodide was then removed and added directly to the protein solution for iodination. The reaction was allowed to take place for 8 min. To end the reaction, 50 μL of scavenging buffer (10 mg/mL tyrosine in PBS) was added and mixed. After 5 min incubation, the iodinated sample was dialyzed against PBS.

Conjugate Stability Assay. Blood was collected from mice, centrifuged at 13 000 rpm for 30 min, and serum was siphoned off for use in protein stability assays. ^{125}Iodine-labeled samples were mixed with an equal volume of serum and incubated at 37 °C over a 24 h period. Aliquots were taken at 0, 0.5, 2, 6, and 24 h points, mixed with SDS-PAGE loading buffer, and frozen until all samples were ready for analysis by SDS-PAGE and autoradiography.

Bioactivity by ELISA Analysis. Flat-bottom 96-well ELISA plates coated with PLAP antigen at 1 μg/mL in PBS were used. After three washes with PBS, one wash with PBS/0.1% Tween, and three more PBS washes, the plate was then blocked with 5% Marvel for 1 h at 37 °C and washed again. Binding activity of the anti-PLAP Fab and conjugates was established by serially diluting samples across test wells in 1% Marvel/PBS for 1 h at 37 °C. For the purpose of testing Fab purity following papain cleavage of whole H17E2 antibody, the plate was then washed as above and incubated with the either antimouse Fc-specific or antimouse Fab-specific one-step HRP-conjugated antibody. For the purpose of PSA detection, the plate was incubated first with primary anti-PSA IgM followed by secondary anti-IgM HRP for 1 h 37 °C. In both cases, incubation with detection antibodies was terminated by washing the plates as described above and binding detected using BM Blue POD substrate (Roche, UK). The reaction was stopped with 10 μL of acid (1 M H_2SO_4) and the absorbance measured at 450 nm.

Sigmoidal curves (four-parameter logistic) were fitted to ELISA data to determine K_d values using *SigmaPlot* using the one-site saturation ligand binding equation.

Pharmacokinetic and Biodistribution Studies. Female nude BALB/C mice, 6–8 weeks old, used for *in vivo* studies were from Harlan UK. All *in vivo* research was carried out under a UK Home Office project license PPL 70/5833. Tumour xenografts were set up by injecting mice subcutaneously into the left flank with 0.1 mL containing up to 10 million KB cells. Tumor growth was monitored and took 3–4 weeks to reach the required 6–8 mm diameter for subsequent work. For tissue analyses, up to 100 μL radiolabeled samples were injected intravenously into the mouse tail vein. At the appropriate time points (typically 0.5, 2, 6, 24, and 48 h), mice were culled by exsanguination under terminal anesthesia. Immediately, blood was collected by cardiac puncture and transferred to a sample tube. The mouse was then dissected, and tissues were collected for biodistribution analysis. Radioactivity was counted using a gamma counter. Values were expressed as a percentage of the initial injected dose per gram of tissue (% id/g). For studying *in vivo* blood clearance pharmacokinetics, data values were fitted using *SigmaPlot* to curves that conform to the two-compartmental intravenous model of clearance, which takes into account the biexponential clearance phases, distribution phase and elimination phase, of single intravenous doses. This is described by the exponential decay, double, four-parameter equation $y = ae^{-bx} + ce^{-dx}$, where the distribution phase clearance rate ($t_{1/2\alpha}$) can be determined by ln 2/b, and the elimination clearance rate ($t_{1/2\beta}$) can be determined by ln 2/d. The area under the curve values were determined using the macros available within *SigmaPlot*.

RESULTS

H17E2 Fab Polysialylation. H17E2 Fab that was free from contaminating Fc portion was used for polysialylation (Figure 1A). Anti-Fab and anti-Fc Western blot confirmed that pure Fab fragment had been obtained (Figure 1B,C). Polysialylations were performed with the 11 and 22 kDa polymers. The PSA/Fab molar ratios for each set of immunoconjugates are shown in Table 1. There are 26 lysine residues available, but not all were expected to be accessible. PAGE analyses of the Fab, Fab-PSA11, and Fab-PSA22H under native conditions showed that both immunoconjugates migrated as a polydispersed smear of higher molecular weight species compared to the unmodified Fab (Figure 1D). This was confirmed by the anti-Fab Western blot which showed a small amount of free noncoupled antibody not visible by Coomassie staining (Figure 1E). A different result was seen when detected with the anti-PSA antibody (Figure 1F): the polydispersed species was again evident, but the larger mass PSA immunoconjugate seemed to migrate more rapidly, possibly due to the higher charge. It is clear from these analyses that polysialylation had altered the size and migration properties of the H17E2 Fab, but their polydispersity and heterogeneity hindered a quantitative analysis of the mass and charge properties.

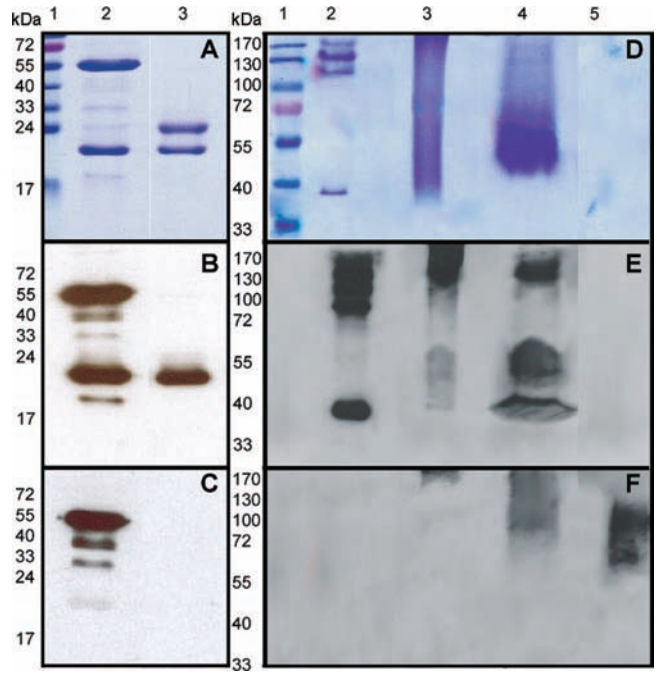

Figure 1. Electrophoretic analyses of H17E2 IgG, Fab, and PSA-Fab conjugates. Left panel: SDS PAGE of markers (lane 1), whole IgG (lane 2), and papain-derived Fab fragments (lane 3) under reducing conditions were analyzed by (A) Coomassie staining, (B) Anti-Fab Western detection, and (C) Anti-Fc Western detection. Right panel: Markers (lane 1), Fab alone (lane 2), and Fab-PSA conjugates (FabPSA11 (lane 3), FabPSA22H (lane 4), and Free PSA22 (lane 5)) were compared by PAGE under native conditions and analyzed by (D) Commassie staining, (E) Anti-Fab Western detection, and (F) Anti-PSA Western detection. Long trail lines observed in conjugates reflect the polydisperse nature of PSA content.

Table 1. Nomenclature and Coupling Ratios of H17E2 Fab-PSA Conjugates[a]

PSA (kDa)	average PSA/Fab molar ratio	abbreviated name
11	9	Fab-PSA11
22	1	Fab-PSA22L (low)
22	5	Fab-PSA22H (high)

[a] The ratios were determined from the resorcinol (PSA) and Coomassie (protein) assays.

Antigen Binding of Immunoconjugates. ELISAs confirmed that the unmodified H17E2 IgG and Fab had binding affinities (K_ds) similar to that already published (*28*). These were compared to the affinities of the PSA immunoconjugates (Figure 2, Table 2). Binding was detected using anti-Fab (Figure 2A) and anti-PSA detection (Figure 2B) antibodies. For the Fab-PSA11 and Fab-PSA22H immunoconjugates detected by anti-Fab antibody, the affinities were slightly reduced by 3.7- and 2.7-fold, respectively.

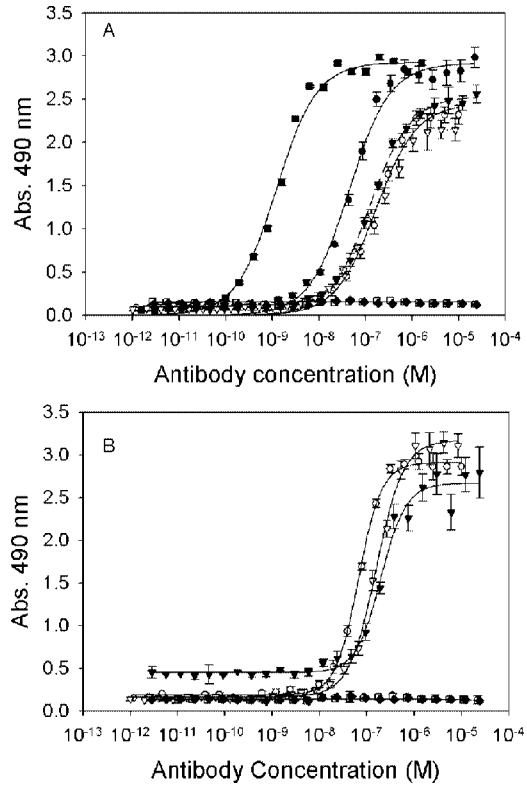

Figure 2. Antigen-binding activity of H17E2 IgG, Fab, and Fab-PSA conjugates. Whole IgG (■), Fab-PSA11 (▽), Fab-PSA22L (○), and Fab-PSA22H (▼) were compared against unconjugated Fab (○) by ELISA. (A) Binding activity was detected by anti-Fab and (B) the presence of PSA on conjugates detected by anti-PSA. Samples were analyzed in triplicate and included control samples MFE-23 (♦), a nonanti-PLAP scFv (detected anti-His), and free PSA22 (□). K_d values were determined by *Sigma Plot*.

Table 2. Immunoreactivity of the H17E2 Fab and PSA Conjugates[a]

antibody	anti-Fab detection K_d (nM)	anti-PSA detection K_d (nM)
unmod. Fab	45	NA
Fab-PSA11	149	61
Fab-PSA22L	145	127
Fab-PSA22H	122	153

[a] The equilibrium dissociation constants for H17E2-PLAP binding were determined by ELISA with both the protein and carbohydrate moieties being detected (Figure 2).

Detection by anti-PSA antibody confirmed that polysialylation had occurred showing a small (1.3–3.4-fold) decrease in affinity. Overall, the addition of long polymers of PSA did not significantly affect the affinity of the Fab antibodies, and the K_ds of the species under study were all very similar among themselves.

Serum Stability. In order to rule out the possibility of protein or carbohydrate degradation occurring, a serum stability assay was carried out *in vitro* using murine serum incubated with a radiolabeled immunoconjugate at 37 °C. Over a 24 h period, no change in the SDS-PAGE banding profile was observed for either the Fab or Fab-PSA22H immunoconjugate, indicating that they were stable in serum (Figure 3).

***In Vivo* Pharmacokinetics.** The effect of polysialylation on the pharmacokinetic behavior of the H17E2 Fab was studied by analyzing blood samples at various time points after IV injection of Fab-PSA conjugates. Data from nude BALB/C mice and tumor-bearing nude BALB/C mice were obtained and pooled. Due to the nature of the coupling chemistry, it was not possible to produce exactly matched immunoconjugates of

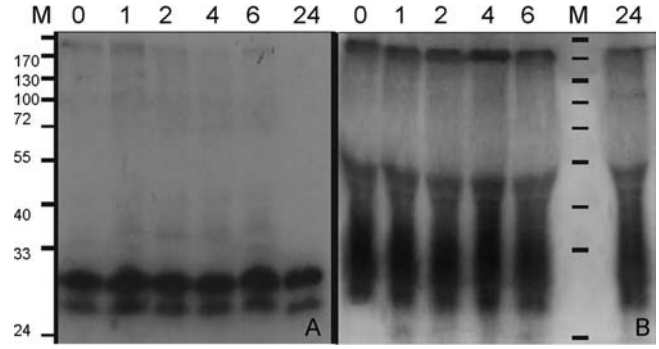

Figure 3. Stability assay of ^{125}I- radiolabeled (A) Fab and (B) Fab-PSA22H samples were incubated with mouse serum at 37 °C. Samples were taken at 0, 1, 2, 4, 6, and 24 h time points and analyzed by SDS-PAGE under reducing conditions. Protein was visualized by exposure of the gel to autoradiographic film.

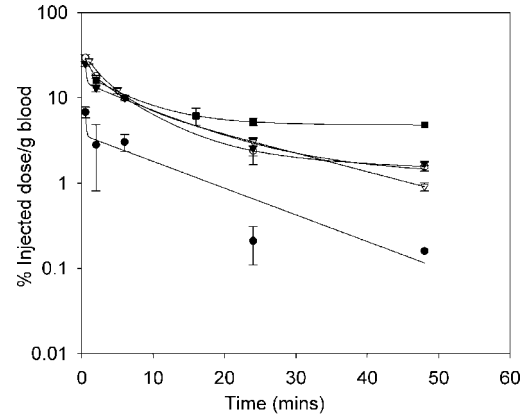

Figure 4. Blood clearance analyses of H17E2 IgG, Fab, and Fab-PSA conjugates. Radioactive cpm values for each sample were measured and calculated as a percentage of the injected dose per gram of blood. Each time point is represented by the mean ± SD of between 3 and 6 mice. The blood clearance of H17E2 (■) whole IgG and (•) Fab is compared graphically with (○) Fab-PSA11, (▽) Fab-PSA22L, and (▼) Fab-PSA22H.

predefined coupling ratios (Table 1). The immunoconjugate present in the blood calculated as the percentage of remaining radioactivity per gram of blood was plotted against time (Figure 4). Pharmacokinetic parameters such as beta-phase clearance rates and total blood exposure (as measured by the area under the curve) were determined and are summarized in Table 3. The stability of the conjugate in serum indicated that the radioactivity represented the intact Fab-PSA conjugate. The results show that, in all cases, polysialylation generally leads to longer blood clearance times compared to the unmodified Fab, resulting in higher blood exposure and hence greater bioavailability. This modulatory effect was generally related to increasing degree of polysialylation, with the Fab-PSA11 having the greater $t_{1/2b}$ (3.2-fold increase compared to Fab) and a high tumor exposure (2.8-fold increase compared to Fab). Similar mass immunoconjugates (Fab-PSA11–150 kDa and Fab-PSA22H-160 kDa) had broadly similar pharmacokinetic properties. Increasing the degree of polysialylation 5-fold using the same length polymer chain (22 kDa) led to an almost 2-fold increase in beta-phase blood clearance half-life with little change in antibody affinity (Figure 2, Table 2). Compared to whole immunoglobulin, which has a very slow blood clearance profile, the immunoconjugates compared favorably, with blood bioavailability (exposure) almost as high as the whole antibody but with better tissue specificity ratios (see below) and potentially lower cross-reactivity. The alpha (distribution) blood

Table 3. Summary of the Pharmacokinetic and Biodistribution Data[a]

antibody	$t_{½(\alpha)}$ (h)	rel. to Fab	$t_{½(\beta)}$ (h)	rel. to Fab	blood AUC (% h/g)	rel. to Fab	tumor AUC (%h/g)	rel. to Fab	tumor/blood ratio @ 48 h	rel. to Fab
IgG	4.6	46	>72 h	>7.5	324	6.8	343	3.5	1.5	0.14
Fab	0.1	1	9.6	1.0	48	1.0	98	1.0	10.8	1.00
Fab-PSA11	1.7	17	30.5	3.2	249	5.2	273	2.8	5.3	0.49
Fab-PSA22L	2.0	20	17.1	1.8	223	4.7	178	1.8	2.6	0.24
Fab-PSA22H	0.7	7	29.1	3	201	4.2	319	3.3	3.5	0.32

[a] Pharmacokinetic beta-elimination constant, total blood exposure (blood area under the curve), total tumor exposure (tumor area under the curve), and tumor/blood selectivity (ratio) were determined from plots of the biodistribution data in Figures 4 and 5.

clearance rates are presented for guidance and are approximate, as only a few early time points were recorded.

Tumour and Tissue Biodistribution. The uptake or retention of the different immunoconjugates in tumors and tissues, measured as the percentage of injected radioactive material per gram, was determined and presented as an absolute value and a tissue/blood ratio (Figure 5). The key parameters are summarized in Table 3 with total tumor exposure as determined from the area under the curve. These were compared to whole IgG and unmodified Fab. As seen for other whole immunoglobulins, the H17E2 IgG exhibited at least a 7.5-fold increase in blood retention resulting in a 3.5-fold increase in tumor uptake compared to the H17E2 Fab. The tumor/blood ratios, typical for IgGs, were poor with a value greater than 1 not being reached until after 16 h. The Fab demonstrated rapid clearance leading to lower absolute uptake with high tumor/blood ratios (greater than 10) by 24 h.

The Fab-PSA22H immunoconjugate, which had one of the slowest blood clearances, yielded the highest absolute uptake, 3.3-fold higher than the unmodified Fab and approaching that of the whole IgG. The tumor/blood ratio was superior to that of whole IgG and only one-third that of Fab (3.5:1), demonstrating improved selectivity (compared to whole immunoglobulin) toward the tumor with almost as good tumor exposure as whole immunoglobulin. The Fab-PSA11 conjugate, although not as effective as the Fab-PSA22H immunoconjugate, still had higher tumor uptake and better specificity ratios compared to the Fab, resulting from the altered blood pharmacokinetics, which was slightly slower than that of the Fab-PSA22H immunoconjugate. Generally, increased blood exposure led to increased tumor uptake. Increasing the PSA content 5-fold (Fab-PSA22L and Fab-PSA22H) led to an almost 2-fold increase in beta-phase blood clearance rate and a 1.8-fold increase in tumor exposure.

There was no significant uptake by any of the normal tissues, showing that polysialylation had not resulted in undesirable and nonspecific cross-reaction.

DISCUSSION

This research showed that antibody fragments such as the anti-PLAP H17E2 Fab species can be polysialylated to different degrees with little significant change to the binding affinities. The polysialylated immunoconjugates migrated as highly charged heterogeneous species by gel electrophoresis. This is due to the highly heterogenic nature of the naturally isolated colominic acid. Further refinement of the colominic acid purification process to generate species with a smaller range of molecular weights should lead to the generation of more defined immunoconjugates. Polysialylation led to a modulation in the *in vivo* pharmacokinetics demonstrated by decreased blood clearance rates and increased blood bioavailability, tumor uptake, and tumor exposure values. This outcome is similar in principle to the effects of conjugation to other polymers (*29–31*).

The H17E2 anti-PLAP antibody/KB tumor xenograft model was chosen because of our past experience and the reliability of the antigen expression. The affinity of the monovalent Fab was approximately 40 nM, which is deemed moderate for typical recombinant antibodies. This affinity value, not being excessively high, permitted a study of the pharmacokinetic influence of polysialylation. It has been shown that very high affinity antibodies reach a ceiling in terms of tumor uptake at around 1 nM (*32*). The degree of polysialylation was determined using the resorcinol assay after repeated ammonium sulfate precipitation to remove the free, unconjugated PSA. Conjugations were performed at higher molar ratios giving higher subsitituted immunoconjugates, but this also resulted in a high degree of noncovalently associated PSA, which was difficult to remove by repeated ammonium sulfate precipitation. Polysialylation did have a small affect on the affinity of the Fab, but the affinities of the immunoconjugates being compared were all similar in value, allowing a valid comparison between the polysialylated species. Site-specific conjugation is an obvious extension of this approach, especially in cases where there are lysine residues in key positions (such as CDRs) where their modification could lead to loss of function (*33*). This was not a problem for the H17E2 antibody, but we have employed our approach with other antibody fragments and found a loss of binding (Constantinou et al., manuscript in preparation). Recombinant antibodies can easily be engineered to replace lysines which are detrimental to coupling (*33*) or engineered to possess one or more residues for site-specific coupling. One example is the use of cysteine residues for thiol coupling onto therapeutic Fab antibodies (*34*).

Gel electrophoresis suggested that the immunoconjugates' mobility was more influenced by the PSA charge properties than the Fab size and charge. The PSA polymers were supplied as polydispersed mixtures of an average molecular weight, which is reflected in the range of different mobilities when observed by gel electrophoresis. Anti-PSA Western blot again confirmed that the Fab had been covalently modified with the PSA polymer.

Prior to any *in vivo* analyses, it was important to show that the polysialylated immunoconjugates were stable in serum at 37 °C. This was indeed the case, as there was no change in the banding pattern across the times analyzed. During the time of the incubation, serum glycosidases did not remove the PSA chains from the conjugate, which would have been seen as a reduction in the banding pattern back to that of the unmodified Fab. The linkage of the PSA chain to the lysine residue of the protein was expected to be robust, as it consists of the stable secondary amine bond and is attached in the reverse orientation to that of naturally occurring PSA.

The pharmacokinetic values obtained for the control proteins such as the unmodified Fab and whole IgG were comparable to what had been published already (*28*). The immunoconjugates showed an up to 3.2-fold decrease in the blood clearance beta-rate compared to the Fab. This slower clearance leads to greater bioavailability (as measured by the area under the curve, AUC), key to prolonging the action of some drugs. However, the greatest blood bioavailability was seen for the Fab-PSA22L, 5.2-fold higher than for unmodified Fab and 80% that of the whole antibody. This was due to the much slower alpha clearance phase.

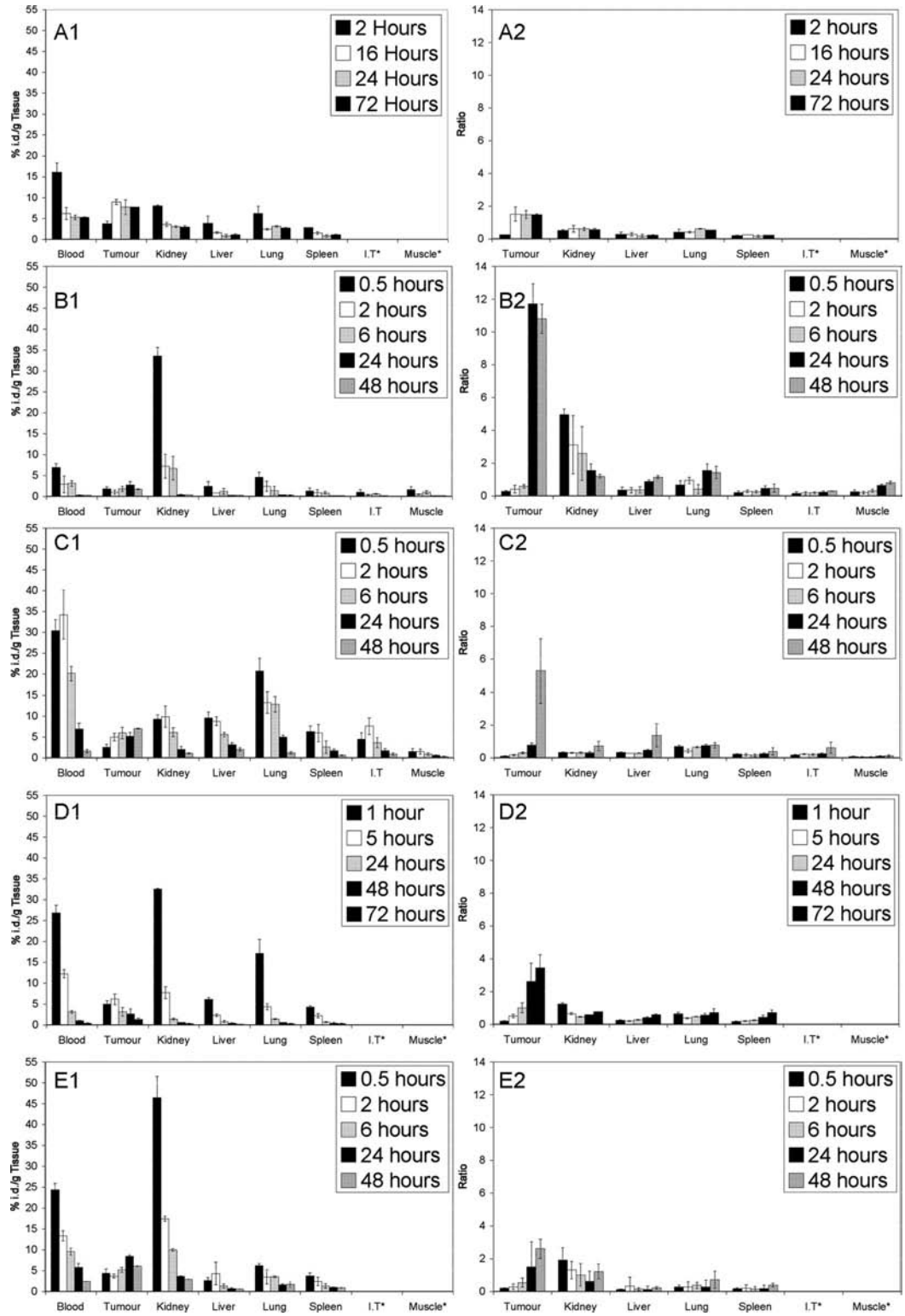

Figure 5. Biodistribution analyses of H17E2 IgG, Fab, and Fab-PSA conjugates. Radioactive cpm values for each sample were measured and calculated as a percentage of the injected dose per gram of tissue. Each bar represents the mean ± SD for three or four mice. Bar charts on the left show the absolute uptake values by each tissue over time, while bar charts on the right show the uptake by each tissue as a ratio to the amount of sample remaining in the blood over time. The bar charts show the biodistributions for **(**A) whole IgG, (B) unconjugated Fab, (C) Fab-PSA11, (D) Fab-PSA22L, and (E) Fab-PSA22H. IT* = intestinal tract.

In general, increased polysialylation led to increased bioavailability, which led to increased tumor exposure approaching that of whole immunoglobulin. The heterogenic nature of these conjugates makes it difficult to identify clear trends; therefore, this work points the way toward site-specific conjugation with polymers of a more defined nature. Polymer conjugation of antibody fragments is seen as a way to increase protein stability and bioavailability (*5–7*, *29–31*) without the limitations of Fc-mediated cross reaction. In addition, less expensive protein production methods available for recombinant fragments such as *E. coli*- and *Pichia pastoris*-expressed single-chain Fvs and Fabs makes polymer conjugation more attractive practically and commercially. However, polysialylation may supersede PEGylation due to its more favorable properties.

Like PEGylation, polysialylation may achieve the observed effects by allowing the protein to possess large hydrodynamic radii by formation of a hydrophilic "watery cloud" (*35*, *36*). This property slows down the blood clearance and prevents excretion through the kidneys. The *in vivo* data did show some high kidney radioactivity at the early time points, which could be attributed to free radioactive iodine which may have been complexed with the PSA and not removed during dialysis. This level quickly reduced. Polysialylation did not lead to aggregate formation, which would have been seen by high liver and spleen uptake caused by metabolism through the reticulo-endothelial system (Figure 5).

The increased blood residency time seen with all immunoconjugates all lead to a corresponding increase in tumor uptake without significant cross-reaction with normal tissues (Figure 5). This supports the premise that PSA is an inert polymer with no natural receptor. The pharmacokinetic distribution (alpha)-phase was not investigated, and it is likely that polysialylation has an effect on how the antibody species distributes within the blood compartment. This needs further investigation.

In conclusion, this study has shown that Fab antibody fragments can be successfully polysialylated with little detriment to its *in vitro* binding properties. We have shown that polysialylation leads to increased blood bioavailability by modulating the clearance rates resulting in increased tumor uptake. Although polysialylation has been used successfully to manipulate drug and protein behavior, this study marks the start of a program of work leading to the better design of PSA antibody conjugates.

ACKNOWLEDGMENT

This work was funded by a Lipoxen Technologies-BBSRC/Case studentship to M.P.D. and A.C. We would like to thank Dr. Peter Laing and Prof. Gregory Gregoriadis for useful discussions and members of the Imperial College CBS Unit for advice and technical help with the *in vivo* experiments.

LITERATURE CITED

(1) Hamidi, M., Azadi, A., and Rafiei, P. (2006) Pharmacokinetic consequences of pegylation. *Drug Delivery 13*, 399–409.

(2) Mehvar, R. (2000) Dextrans for targeted and sustained delivery of therapeutic and imaging agents. *J. Controlled Release 69*, 1–25.

(3) Cantin, A. M., Woods, D. E., Cloutier, D., Dufour, D. E., and Leduc, R. (2002) Polyethylene glycol conjugation at Cys232 prolongs the half-life of alpha1 proteinase inhibitor. *Am. J. Respir. Cell Mol. Biol. 27*, 659–65.

(4) Conover, C. D., Gilbert, C. W., Shum, K. L., and Shorr, R. G. (1997) The impact of polyethylene glycol conjugation on bovine hemoglobin's circulatory half-life and renal effects in a rabbit toploaded transfusion model. *Artif. Organs 21*, 907–15.

(5) Hawkins, D. S., Park, J. R., Thomson, B. G., Felgenhauer, J. L., Holcenberg, J. S., Panosyan, E. H., and Avramis, V. I. (2004) Asparaginase pharmacokinetics after intensive polyethylene glycolconjugated L-asparaginase therapy for children with relapsed acute lymphoblastic leukemia. *Clin. Cancer Res. 10*, 5335–41.

(6) Grace, M. J., Cutler, D. L., and Bordens, R. W. (2006) Pegylated IFNs for chronic hepatitis C: an update. *Exp. Opin. Drug Delivery 2*, 219–26.

(7) Ng, E. W., Shima, D. T., Calias, P., Cunningham, E. T., Jr., Guyer, D. R., and Adamis, A. P. (2006) Pegaptanib, a targeted anti-VEGF aptamer for ocular vascular disease. *Nat. Rev. Drug Discovery 5*, 123–32.

(8) Beranova, M., Wasserbauer, R., Vancurova, D., Stifter, M., Ocenaskova, J., and Mara, M. (1990) Effect of cytochrome P-450 inhibition and stimulation on intensity of polyethylene degradation in microsomal fraction of mouse and rat livers. *Biomaterials 11*, 521–4.

(9) Caliceti, P., Schiavon, O., and Veronese, F. M. (1999) Biopharmaceutical properties of uricase conjugated to neutral and amphiphilic polymers. *Bioconjugate Chem. 10*, 638–46.

(10) Cheng, T. L., Wu, P. Y., Wu, M. F., Chern, J. W., and Roffler, S. R. (1999) Accelerated clearance of polyethylene glycol-modified proteins by anti-polyethylene glycol IgM. *Bioconjugate Chem. 10*, 520–8.

(11) Sroda, K., Rydlewski, J., Langner, M., Kozubek, A., Grzybek, M., and Sikorski, A. F. (2005) Repeated injections of PEG-PE liposomes generate anti-PEG antibodies. *Cell Mol. Biol. Lett. 10*, 37–47.

(12) Gregoriadis, G., Jain, S., Papaioannou, I., and Laing, P. (2005) Improving the therapeutic efficacy of peptides and proteins; a role for polysialic acids. *Int. J. Pharm. 300*, 125–30.

(13) Muhlenhoff, M., Eckhardt, M., and Gerardy-Schahn, R. (1998) Polysialic acid: three-dimensional structure, biosynthesis and function. *Curr. Opin. Struct. Biol. 8*, 558–64.

(14) Gregoriadis, G., McCormack, B., Wang, Z., and Lifely, R. (1993) Polysialic acids: potential in drug delivery. *FEBS Lett. 315*, 271–6.

(15) Gregoriadis, G., Fernandes, A., Mital, M., and McCormack, B. (2000) Polysialic acids: potential in improving the stability and pharmacokinetics of proteins and other therapeutics. *Cell. Mol. Life Sci. 57*, 1964–9.

(16) Fernandes, A., and Gregoriadis, G. (1997) Polysialylated asparaginase: preparation, activity and pharmacokinetics. *Biochem. Biophys. Acta 1341*, 26–34.

(17) Jain, S., Hreczuk-Hirst, D. H., McCormack, B., Mital, M., Epenetos, A. E., Laing, P., and Gregoriadis, G. (2003) Polysialylated insulin: synthesis, characterization and biological activity in vivo. *Biochem. Biophys. Acta 1622*, 42–9.

(18) Fernandes, A. I., and Gregoriadis, G. (2001) The effect of polysialylation on the immunogenicity and antigenicity of asparaginase: implication in its pharmacokinetics. *Int. J. Pharm. 217*, 215–24.

(19) Crocker, P. R., and Varki, A. (2001) Siglecs, sialic acids and innate immunity. *Trends Immunol. 22*, 337–42.

(20) Stockert, R. J. (1995) The asialoglycoprotein receptor: relationships between structure, function, and expression. *Physiol. Rev. 75*, 591–609.

(21) Siddiqui, M. A., and Scott, L. J. (2005) Infliximab: a review of its use in Crohn's disease and rheumatoid arthritis. *Drugs 65*, 2179–208.

(22) Kramer, I., and Lipp, H. P. (2007) Bevacizumab a humanized anti-angiogenic monoclonal antibody for the treatment of colorectal cancer. *J. Clin. Pharm. Ther. 32*, 1–14.

(23) Cefalu, W. T. (2004) Evolving strategies for insulin delivery and therapy. *Drugs 64*, 1149–61.

(24) Sharples, E. J., Thiemermann, C., and Yaqoob, M. M. (2006) Novel applications of recombinant erythropoietin. *Curr. Opin. Pharmacol. 6*, 184–9.

(25) Travers, P., and Bodmer, W. F. (1984) Preparation and characterization of monoclonal antibodies against placental alkaline phosphatase and other human trophoblast-associated determinants. *Int. J. Cancer 33*, 633–41.

(26) Epenetos, A. A., Travers, P., Gatter, K. C., Oliver, R. D., Mason, D. Y., and Bodmer, W. F. (1984) An immunohistological study of testicular germ cell tumours using two different monoclonal antibodies against placental alkaline phosphatase. *Br. J. Cancer 49*, 11–5.

(27) Svennerholm, L. (1957) Quantitative estimation of sialic acids. II. A colorimetric resorcinol hydrochloric acid method. *Biochem. Biophys. Acta 24*, 604–11.

(28) Deonarain, M. P., Rowlinson-Busza, G., George, A. J., and Epenetos, A. A. (1997) Redesigned anti-human placental alkaline phosphatase single-chain Fv: soluble expression, characterization and *in vivo* tumour targeting. *Protein Eng. 10*, 89–98.

(29) Yang, K., Basu, A., Wang, M., Chintala, R., Hsieh, M. C., Liu, S., Hua, J., Zhang, Z., Zhou, J., Li, M., Phyu, H., Petti, G., Mendez, M., Janjua, H., Peng, P., Longley, C., Borowski, V.,

Mehlig, M., and Filpula, D. (2003) Tailoring structure-function and pharmacokinetic properties of single-chain Fv proteins by site-specific PEGylation. *Protein Eng. 16*, 761–70.

(30) Natarajan, A., Xiong, C. Y., Albrecht, H., DeNardo, G. L., and DeNardo, S. J. (2005) Characterization of sitespecific ScFv PEGylation for tumor-targeting pharmaceuticals. *Bioconjugate Chem. 16*, 113–21.

(31) Knauf, M. J., Bell, D. P., Hirtzer, P., Luo, Z. P., Young, J. D., and Katre, N. V. (1988) Relationship of effective molecular size to systemic clearance in rats of recombinant interleukin-2 chemically modified with water-soluble polymers. *J. Biol. Chem. 263*, 15064–70.

(32) Adams, G. P., Schier, R., McCall, A. M., Simmons, H. H., Horak, E. M., Alpaugh, R. K., Marks, J. D., and Weiner, L. M. (2001) High affinity restricts the localization and tumor penetration of single-chain Fv antibody molecules. *Cancer Res. 61*, 4750–5.

(33) Adams, G. P., Shaller, C. C., Chappell, L. L., Wu, C., Horak, E. M., Simmons, H. H., Litwin, S., Marks, J. D., Weiner, L. M., and Brechbiel, M. W. (2000) Delivery of the alpha-emitting radioisotope bismuth-213 to solid tumors via single-chain Fv and diabody molecules. *Nucl. Med. Biol. 27*, 339–46.

(34) Kaushik, V. V., and Moots, R. J. (2005) CDP-870 (certolizumab) in rheumatoid arthritis. *Exp. Opin. Biol. Ther. 5*, 601–6.

(35) Nakaoka, R., Tabata, Y., Yamaoka, T., and Ikada, Y. (1997) Prolongation of the serum half-life of superoxide dismutase by poly. (ethylene) glycol) modification. *J. Controlled Release 46*, 253–261.

(36) Dhalluin, C., Ross, A., Leuthold, L. A., Foser, S., Gsell, B., Muller, F., and Senn, H. (2005) Structural and biophysical characterization of the 40 kDa PEG-interferon-alpha 2a and its individual positional isomers. *Bioconjugate Chem. 16*, 504–17.

BC700319R

Conjugation of a Water-Soluble Gadolinium Endohedral Fulleride with an Antibody as a Magnetic Resonance Imaging Contrast Agent

Chun-Ying Shu,[†] Xin-Yong Ma,[†] Jian-Fei Zhang,[‡] Frank D. Corwin,[§] Jae Hyun Sim,[‡] Er-Yun Zhang,[†] Harry C. Dorn,[‡] Harry W. Gibson,[‡] Panos P. Fatouros,[§] Chun-Ru Wang,*[,†] and Xiao-Hong Fang*[,†]

Beijing National Laboratory for Molecular Sciences (BNLMS), Institute of Chemistry, Chinese Academy of Sciences, Beijing 100080, China, Department of Chemistry, Virginia Polytechnic Institute and State University, Blacksburg, Virginia 24060-0212, and Department of Radiology, Virginia Commonwealth University, Richmond, Virginia 23298.
Received July 20, 2007; Revised Manuscript Received December 13, 2007

Water-soluble gadofullerides exhibited high efficiency as magnetic resonance imaging (MRI) contrast agents. In this paper, we report the conjugation of the newly synthesized gadofulleride, $Gd@C_{82}O_6(OH)_{16}$-$(NHCH_2CH_2COOH)_8$, with the antibody of green fluorescence protein (anti-GFP), as a model for "tumor targeted" imaging agents based on endohedral metallofullerenes. In this model system, the activity of the anti-GFP conjugate can be conveniently detected by green fluorescence protein (GFP), leading to *in vitro* experiments more direct and facile than those of tumor antibodies. Objective-type total internal reflection fluorescence microscopy revealed that each gadofulleride aggregate conjugated on average five anti-GFPs, and the activity of anti-GFPs was preserved after conjugation. In addition, the gadofulleride/antibody conjugate exhibited higher water proton relaxivity (12.0 mM^{-1} s^{-1}) than the parent gadofulleride aggregate (8.1 mM^{-1} s^{-1}) in phosphate buffered saline at 0.35 T, as also confirmed by T_1-weighted images of phantoms. These observations clearly indicate that the synthesized gadofulleride/antibody conjugate not only has targeting potential, but also exhibits higher efficiency as an MRI contrast agent.

INTRODUCTION

Magnetic resonance imaging (MRI) as a noninvasive and convenient imaging technique has been widely applied in clinical diagnosis. Since paramagnetic materials can efficiently reduce the nuclear spin relaxation time of water protons, they have been widely used in clinical MRI to enhance the image contrast and improve the image resolution (*1, 2*). Because clinical MRI contrast agents are administered intravenously to living patients, the basic criteria for designing them are biological safety and high efficiency. Current commercial MRI contrast agents are mainly Gd^{3+} poly(aminocarboxylate) complexes (*1–3*), whose biosafety with reasonable dosages (0.1–0.2 mmol/kg body weight) has been proven by extensive clinical use. However, their proton-relaxing efficiency is far from optimal.

Recently, the application of water-soluble gadolinium-containing endohedral fullerides as MRI contrast agents has been extensively investigated (*4–18*). Besides the high proton relaxivity (up to 20 times (*6*) and 35 times (*16*) larger than the most popular commercial Gd^{3+}-complex contrast agent), low toxicity is expected for them due to the toxic heavy Gd^{3+} ion being protected by the biocompatible fullerene cage. Therefore, the water-soluble gadolinium-containing endohedral fullerides (gadofullerides) are promising next-generation MRI contrast agents. In addition to high efficiency and low toxicity, metallofullerenes are expected to be modified by various functional groups to endow some novel properties, such as Diels–Alder reaction (*19–21*), Bingel reactions (*16, 22*), Prato reactions (*23–26*), and so on. For traditional Gd-chelates, the chelates indeed are easy to modify, but the limited number of sites for H_2O to complex with Gd-chelated agents (e.g., Omniscan) hampers any dramatic increase in water proton relaxivity.

Recently, gadofullerides were observed to aggregate in aqueous solution, and the large size of gadofulleride aggregates is closely related to their high efficiency as MRI contrast agents, e.g., $Gd@C_{60}[C(COOH)_2]_{10}$ (*9, 11, 12, 18*), $Gd@C_{82}(OH)_x$, $Gd@C_{60}(OH)_x$ (*7,9,10,18*), and $Gd@C_{82}O_6(OH)_{16}$-$(NHCH_2CH_2COOH)_8$ (*13, 14*).Our newly synthesized gadofulleride, $Gd@C_{82}O_6(OH)_{16}(NHCH_2CH_2COOH)_8$ (abbreviated AAD-EMF) (*13, 14*), exhibited relatively uniform ~30 nm nanoaggregates in aqueous solution under biological conditions at pH = 7 and displayed high efficiency for enhancing the proton relaxation rates. In addition, AAD-EMF has two types of functional groups on the molecular surface, i.e., -OH and $-NHCH_2CH_2COOH$; the $-NHCH_2CH_2COOH$ groups provide the active -COOH moieties for conjugation with antibodies (*14*). We consider the AAD-EMF as a protypical MRI contrast agent to explore its conjugation with antibodies.

Regarding the choice of antibody, we did not use a tumor antibody, but rather selected the antibody of the green fluorescence protein (anti-GFP) as a prototype biomolecule to conjugate with the AAD-EMF. However, all immune antibodies have similar Y-type structures and active sites, so the successful conjugation of AAD-EMF with anti-GFP should be extended to tumor antibodies in future studies. Most importantly, the activity of anti-GFP can be conveniently detected by using the GFP as a powerful probe, leading to *in vitro* experiments more facile than those with tumor antibodies.

MATERIALS AND METHODS

Materials. Anti-GFP-biotin was bought from Abcam Ltd. Cambridge, UK; GFP was from the Upstate Company, USA; streptavidin was from Molecular Probes, Eugene, OR, USA; BSA-biotin was from Sigma, St. Louis, MO, USA. All the glass slides (no. 1, 24 × 60 mm^2) and cover glasses (no. 1, 22 × 22

* E-mail: crwang@iccas.ac.cn; xfang@iccas.ac.cn.
[†] Chinese Academy of Sciences.
[‡] Virginia Polytechnic Institute and State University.
[§] Virginia Commonwealth University.

10.1021/bc7002742 CCC: $40.75 © 2008 American Chemical Society
Published on Web 02/07/2008

Scheme 1. Step 1. EDC Reacting with Carboxylic Groups in AAD-EMF Aggregates to Create the Active Ester Intermediate. Step 2. Intermediate Reacts with the Antibodies by Formation of Amide Bonds via Reaction with the Amine Nucleophiles

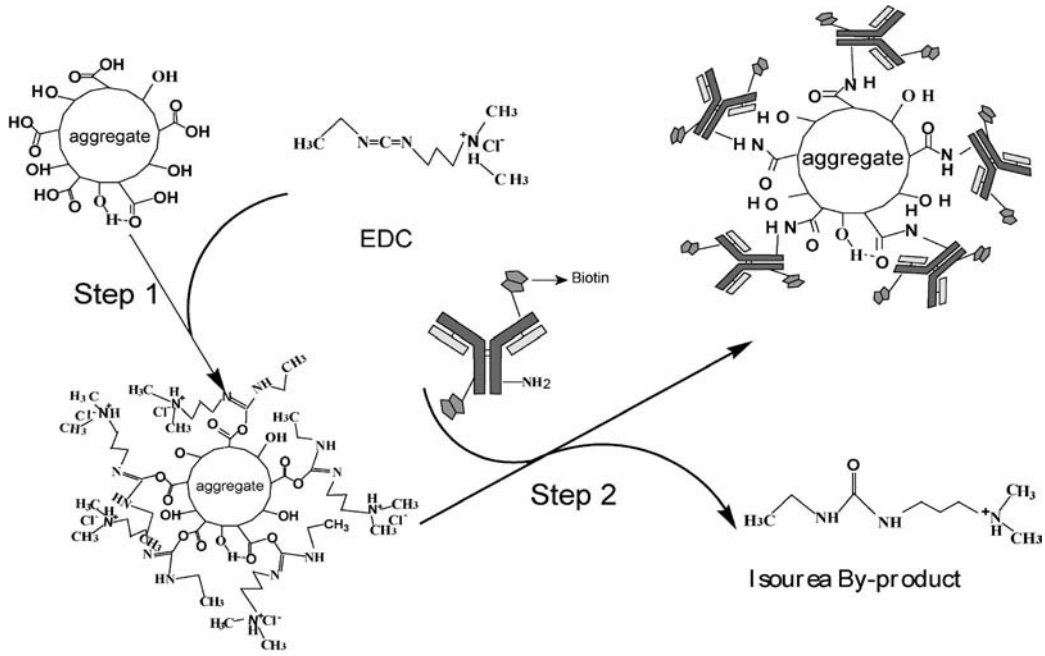

mm^2) were purchased from VWR Scientific Inc. (West Chester, PA, USA). Milli-Q purified water (18.2 MΩ) was used to prepare various aqueous solutions.

A 10^{-8} M stock solution of anti-GFP-biotin was prepared in phosphate buffered saline (PBS) solution (pH = 7.4) and stored at 4 °C. A fresh 0.1 M solution of 1-ethyl-3-(dimethylaminopropyl)carbodiimide hydrochloride (EDC) was prepared with deionized water. The AAD-EMF was prepared and isolated as previously described (*13*). The concentration of the gadolinium in the aqueous solution was 2×10^{-7} M, which was measured by inductively coupled plasma atomic emission spectroscopy (ICP-AES, Prodigy, Leeman Laboratories Inc., 342.247 nm).

Methods. *Synthesis of Gadofulleride/Antibody Conjugate.* The conjugation reaction is shown in Scheme 1. In step 1, 10 μL EDC was added to 40 μL AAD-EMF solution, and the resultant solution was shaken for 15 min under ambient conditions to produce the AAD-EMF/EDC intermediate. In step 2, a 10-fold molar excess of the stock solution of anti-GFP-biotin was added to the AAD-EMF/EDC intermediate at room temperature. After 4 h, the AAD-EMF/antibody conjugate was expected to be formed (*27*). Unfortunately, we could not characterize the conjugate in detail due to the complexity and limited size of the sample. However, the following control experiment supports the formation of the AAD-EMF/antibody conjugate by covalent bonding.

Sample Preparation for the Detection of Antibody Activity. The stock solutions of biotinylated BSA, streptavidin, anti-GFP-biotin, and GFP were stored at 4 °C before use. To avoid self-aggregation of GFP and antibodies, a highly concentrated NaCl solution (600 mM) was used to dilute them to 3.38×10^{-9} M and 1.5×10^{-9} M, respectively.

The sample preparation of the gadofulleride/antibody conjugate for single molecule fluorescence characterization involves four steps as shown in Scheme 2. It is in fact a standard procedure (*28*) to immobilize the antibody-relevant aggregates on a channeled glass plate for further single-molecule fluorescence characterizations. The procedure was performed as follows:

(1) Fix Bovine Serum Albumin (BSA) on the Glass Plate. Biotinylated BSA (1.5 mg/mL, 20 μL) was tiled on a clean glass flow cell to react for 10 min (*28*); then, PBS (pH = 7.4) was used to wash the glass plate thoroughly. In this step, some BSA molecules were deposited in the channels on the glass plate, and the unfixed BSA was washed away by the PBS.

(2) Fix Streptavidin on the Glass Plate. A streptavidin solution (0.25 mg/mL, 20 μL) was dropped onto the glass flow cell to conjugate with biotin of the tiled BSA for 10 min, and the excess streptavidin was washed off by PBS.

(3) Fix Gadofulleride/Antibody Conjugate on the Glass Plate. The aqueous solution of gadofulleride/antibody conjugate prepared in Scheme 1 was dropped onto the glass flow cell and washed off by PBS after 10 min. In this process, the fixed streptavidin on glass plate conjugated with the biotin on the gadofulleride/antibody conjugate and captured the latter tightly. After reaction, the PBS washing removed the unfixed gadofulleride/antibody conjugate.

(4) Add GFP to Gadofulleride/Antibody Conjugate on the Glass Plate. GFP (3.38×10^{-9} M, 15 μL) was dropped on the glass flow cell to react specifically with the active anti-GFP-biotin on the glass plate; after 10 min, the uncoupled GFP was washed off by PBS.

With the above four steps, the gadofulleride/antibody conjugate was fixed to the glass plate; each conjugate captures several GFP molecules. For comparison, three control experiments on samples with only the anti-GFP-biotin (**I**), only the AAD-EMF aggregates (**II**), and the mixture of anti-GFP-biotin and AAD-EMF aggregates without EDC involvement (**III**) were also prepared following similar four-step procedures except step 3, as shown above.

Detection of Antibody Activity via Fluorescent Probe. An objective-type total internal reflection fluorescence microscope (TIRFM) (*29*) was applied to image the gadofulleride/antibody conjugate on the glass plate at the single-molecule level by using the GFP as a probe. The laser beam (488 nm, Ar^+ laser, 65 w/cm^2, Melles Griot, USA) was introduced into an inverted microscope (IX71, Olympus) through an oil-immersion objective (PlanApo 60×, NA1.45, Olympus) to irradiate the sample on the glass plate, and the fluorescence signals emitting from the GFP were collected by the intensified charge coupled device (ICCD) camera (I-Pentamax, Rofer Scientific, USA). Two filters, i.e., BA510IF (long-pass filter, Chroma, USA) and HQ525/50 (band-pass filter, Chroma, USA), were used to block the

Scheme 2. Flow Chart of Sample Preparation for Fluorescence Measurement

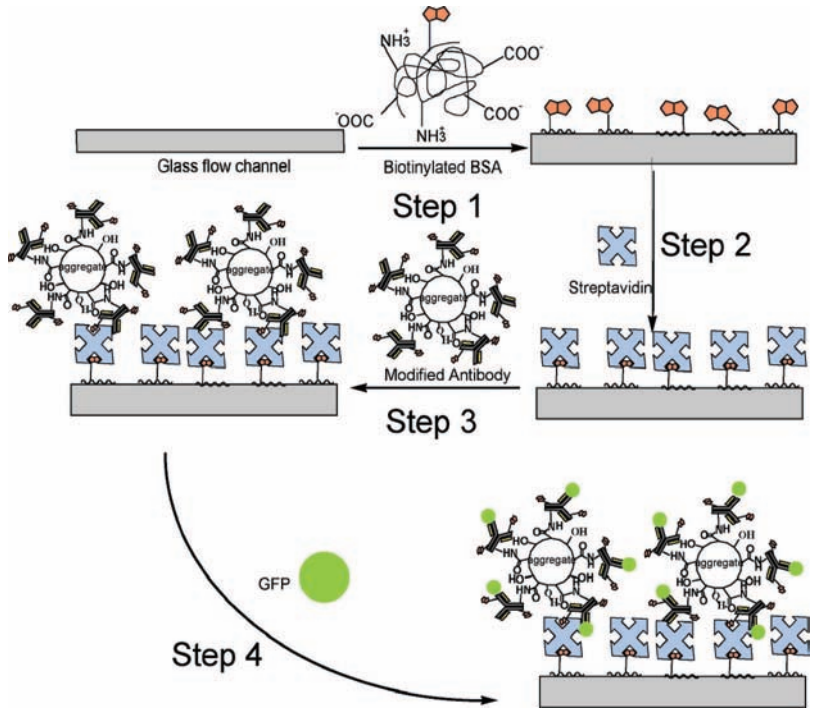

deflected and diffracted laser light. The exposure time of ICCD was set to 100 ms with a gain at 80. The fluorescence images were acquired and analyzed with *MetaMorph 6.0* software (Molecular Devices Corp., USA).

RESULTS AND DISCUSSION

Figure 1 shows a comparison of the fluorescence images of GFP coupled to antibody control (**I**) and the gadofulleride/antibody conjugates. The observed fluorescent signals for the gadofulleride/antibody conjugate revealed that the conjugation was successful and the activity of the anti-GFP-biotin in the gadofulleride/antibody conjugate was preserved. On the contrary, the AAD-EMF control (**II**) had no fluorescent signal (not shown), since the GFP molecules could not be captured without anti-GFP on the glass plate (Scheme 2). Notably, control **III** exhibited fluorescence images similar to that of control **I**, which indicated that PBS wash removes the gadofulleride attached on the anti-GFP-biotin via physical adsorption. This provided indirect evidence for the formation of covalent gadofulleride/antibody conjugates rather than physical adsorption (*30*).

In the experiment, we deliberately maintained low concentrations of BSA and streptavidin. The sparse and irregular patterns of the fluorescent spots in Figure 1 revealed that very few anti-GFPs (in control) or gadofulleride/antibody conjugate were randomly immobilized on the glass plates. Therefore, the probability for two or more fluorescent molecules to locate closely adjacent on the glass surface would be very low, and each fluorescent spot in the images must represent a single molecule. To confirm this supposition, a photobleaching experiment was performed, and the results are shown in Figure 2. The clear-cut one-step bleaching characteristics unambiguously confirmed the single molecular property of each fluorescent spot (*31*).

The AAD-EMF was reported to form minimum aggregates of 30.0 nm in aqueous solution at pH = 7, in which lots of -$NHCH_2CH_2COOH$ chains are located on the aggregate surface and directed outward. In PBS solution, a dynamic light scattering (DLS) experiment demonstrated that the minimum size of the AAD-EMF aggregates was 25.0 nm; the average hydrodynamic radius shifted a little from 72.7 nm in pure water (*14*) to 68.0 nm, indicating that phosphate changed the aggregation size to some extent. If we consider that each -$NHCH_2CH_2COOH$ chain can conjugate one antibody, it is reasonable to deduce that each AAD-EMF aggregate can conjugate several antibodies. In Figure 1, the fluorescence spots corresponding to gadofulleride/antibody conjugate (Figure 1b) show much higher intensity than that of the antibody control (Figure 1a), indicating that in practice each gadofulleride/antibody conjugate may capture several GFPs.

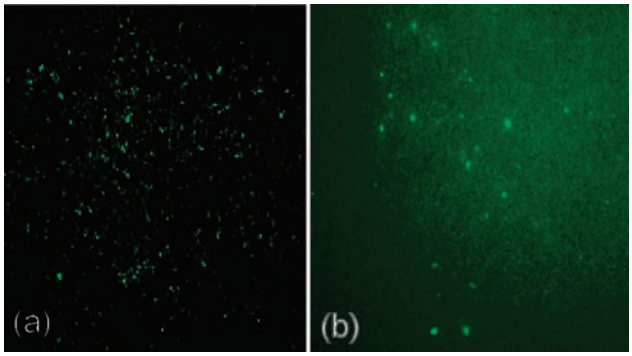

Figure 1. Fluorescence images of (a) the antibody control and (b) gadofulleride/antibody conjugate.

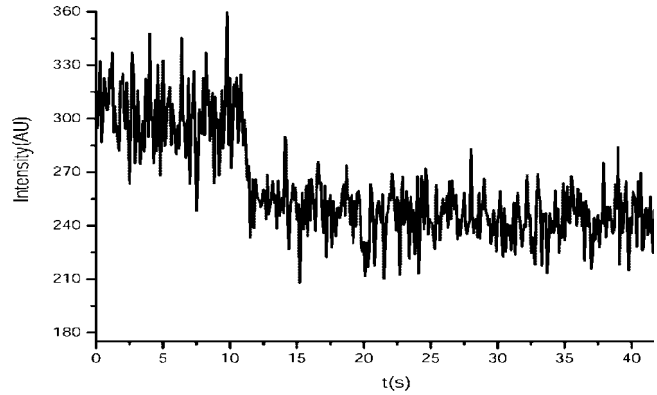

Figure 2. One-step photobleaching curves of single GFP on glass flow cell.

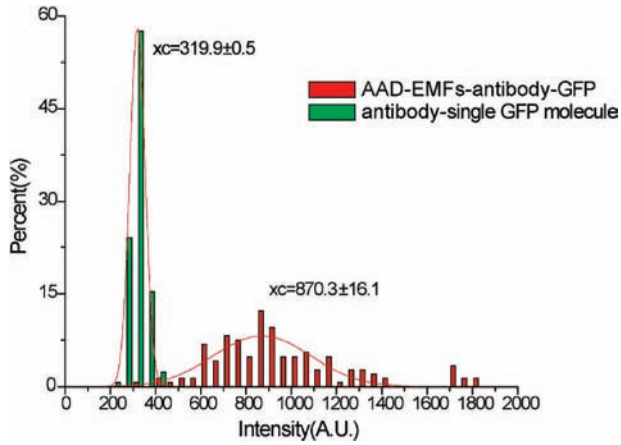

Figure 3. Distribution of fluorescence intensity of the antibody control (green columns) and gadofulleride/antibody conjugate (red columns).

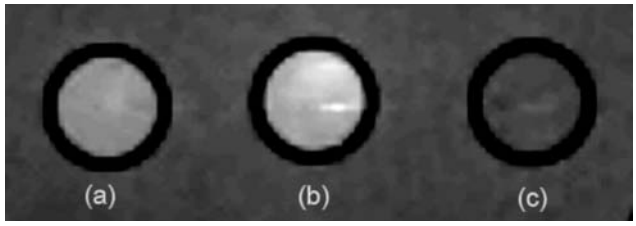

Figure 4. T_1-weighted MRI phantoms of (a) AAD-EMF, (b) gadofulleride/antibody conjugate at a Gd concentration of 17.8 μM, and (c) antibody in PBS at 2.4 T using a spin–echo method with $T_R/T_E = 700$ ms/10 ms, FOV = 3.0 × 3.0 cm^2 at 24 °C.

Because the GFP is greatly overfed in the reactions mentioned above, nearly 100% of the anti-GFPs in the samples were consumed. We then may calculate how many anti-GFPs were conjugated with an AAD-EMF aggregate.

The average number of antibodies conjugated to gadofullerides can be estimated *via* the measured fluorescence intensity. The statistical distribution of fluorescence intensity of antibodies (control **I**) and gadofulleride/antibody conjugates are shown in Figure 3; then, according to eq 1

$$N = (I_{sample} - B_{sample})/(I_{sm} - B_{sm}) \quad (1)$$

the average number of anti-GFPs conjugated with an AAD-EMF aggregate is concluded to be 5. In eq 1, I_{sample} and I_{sm} are the fluorescent intensity of the gadofulleride/antibody conjugate and the antibody control, respectively; B_{sample} and B_{sm} are the measured backgrounds of the two relevant images. Moreover, some fluorescent spots in Figure 1b were observed to have nearly double fluorescence intensity compared with others (Figure 3), which should correspond to dimers of the AAD-EMF aggregates as we already observed in a previous paper (*14*).

Besides confirming the activity of gadofulleride/antibody conjugates, we also measured and compared their water proton relaxivity with unconjugated gadofulleride on a per Gd^{3+} ion basis. In PBS (pH = 7.4) solution, the longitudinal relaxivity (R_1) of AAD-EMF was 8.1 mM^{-1} s^{-1} at 0.35 T with a TEACH SPIN PS1-B instrumentation, whereas after gadofulleride/antibody conjugation, the relaxivity was 12.0 mM^{-1} s^{-1} at the same field strength. In addition, the *in vitro* MRI phantom studies of AAD-EMF and gadofulleride/antibody conjugate at 17.8 μM Gd together with PBS solution were also performed by the T_1-weighted spin–echo method. As shown in Figure 4, the MRI phantom of the gadofulleride/antibody conjugate (Figure 4b) at 2.4 T with a Bruker/Biospec instrumentation indicates enhanced MRI signal efficiency relative to AAD-EMF (Figure 4a), which is consistent with above proton relaxivity analysis of the two contrast agents. These results indicate that gadofulleride/antibody conjugation can improve water proton relaxivity relative to the unconjugated gadofulleride.

Recent studies (*9, 11, 12, 18*) indicate that, besides the number of hydroxyl groups, aggregate size and distance of interaction between the carbon cage and water molecules play predominant roles in proton relaxivity. Recently, Fatouros et al. (*16*) reported an MRI contrast agent based on a trimetallic nitride templated metallofullerene (TNT EMF), $Gd_3N@C_{80}$, which was PEGylated and hydroxylated for medical applications. This compound possessed the highest relaxivity reported so far; this may be due to the cocontribution of three paramagnetic Gd(III) ions in one carbon cage and fast water proton exchange rate together with the slow rotational time caused by the attachment of large moieties in the form of two poly(ethylene glycol) chains via the Bingel cyclopropanation reaction. In contrast, our synthesized gadofulleride/antibody conjugate will possess increased size relative to the unconjugated gadofulleride due to the attachment of the antibody, which leads to slower rotational time and correspondingly higher relaxivity. Notably, the water proton relaxivity of unconjugated gadofulleride in pure water (16.0 mM^{-1} s^{-1}) is higher than that in PBS (8.1 mM^{-1} s^{-1}) at 0.35 T. Laus et al. (*11*) reported that phosphate can disrupt the aggregation of $Gd@C_{60}(OH)_x$ and $Gd@C_{60}[C(COOH)_2]_{10}$ by intercalation of $H_2PO_4^-$ and HPO_4^{2-} ions into the hydrogen-bond network around the malonate or hydroxyl groups of the gadofullerenes. Therefore, the decrease of the relaxivity of the AAD-EMF in PBS can be ascribed to the decrease in aggregate size, as the DLS measurement proved.

As for the relaxivity of the conjugate, although its relaxivity is still too low to image tumor cells, in which antibody receptor sites are typically present at only nanomolar (nM) concentrations (*17, 32*), we can apply the conjugation technique to other analogues with higher relaxivity (*16*) due to the similarity of structure (metal atoms encapsulated in carbon cages), producing targeted, highly efficient MRI contrast agents.

CONCLUSIONS

In summary, we have demonstrated a gadofulleride/antibody conjugate as an MRI contrast agent. By tracing the fluorescent intensity, we concluded that each AAD-EMF aggregate on average captures five antibodies, and the antibody activity is preserved after conjugation. In addition, the gadofulleride/antibody conjugate exhibits higher water proton relaxivity than the parent gadofulleride due to the increased molecular size, which is also confirmed by T_1-weighted imaging. This study represents substantial progress in the development of carbon nanostructures in medicine. Of course, the relaxivity of this material is still far from optimal, but we can extend the conjugation process to functional groups on other analogues with much higher relaxivity, e.g., $Gd_3N@C_{80}$ (*16*). Once this type of conjugated MRI contrast agent with tumor antibody is realized, it will not only greatly improve early tumor diagnosis, but also increase the probability for treatment based on a recent discovery that some gadofullerides can efficiently inhibit tumor cells (*33*).

ACKNOWLEDGMENT

The authors thank Lesley S. Owens and Prof. Gary L. Long in Virginia Tech for the help of measurement of the Gd concentration. C.R.W. thanks the National Natural Science Foundation of China (Nos. 20573121, 20121301), the Major State Basic Research Program of China "Fundamental Investigation on Micro-Nano Sensors and Systems based on BNI Fusion" (Grant 2006CB300402), and the Royal Society in the UK. H.C.D., H.W.G., and P.P.F. are thankful for support from the US National Science Foundation (NIRT, DMR-0507083). F.D.C., H.C.D., H.W.G., H.F., and P.P.F. also gratefully acknowledge support from the US National Institutes of Health (1 RO1 CA119371).

LITERATURE CITED

(1) Lauffer, R. B. (1987) Paramagnetic metal complexes as water proton relaxation agents for NMR imaging: Theory and design. *Chem. Rev. 87*, 901–927.

(2) Toth, E., and Merbach, A. E. (2001) *The Chemistry of Contrast Agents in Medical Magnetic Resonance Imaging*, Wiley, Chichester.

(3) Caravan, P., Ellision, J. J., McMurry, T. J., and Lauffer, R. B. (1999) Gadolinium(III) chelates as MRI contrast agents: Structure, dynamics, and applications. *Chem. Rev. 99*, 2293–2352.

(4) Zhang, S. R., Sun, D. Y., Li, X. Y., Pei, F. K., and Liu, S. Y. (1997) Synthesis and solvent enhanced relaxation property of water-soluble endohedral metallofullerenols. *Fullerene Sci. Technol. 5*, 1635–1643.

(5) Wilson, L. J. (1999) Medical Application of Fullerenes and Metallofullerenes. *Electrochem. Soc. Interface* 24–28. Winter.

(6) Mikawa, M., Kato, H., Okumura, M., Narazaki, M., Kanazawa, Y., Miwa, N., and Shinohara, H. (2001) Paramagnetic water-soluble metallofullerenes having the highest relaxivity for MRI contrast agents. *Bioconjugate Chem. 12*, 510–514.

(7) Kato, H., Kanazawa, Y., Okumura, M., Taninaka, A., Yokawa, T., and Shinohara, H. (2003) Lanthanoid endohedral metallofullerenols for MRI contrast agents. *J. Am. Chem. Soc. 125*, 4391–4397.

(8) Bolskar, R. D., Benedetto, A. F., Husebo, L. O., Price, R. E., Jackson, E. F., Wallace, S., Wilson, L. J., and Alford, J. M. (2003) First soluble M@C_{60} derivatives provide enhanced access to metallofullerenes and permit in vivo evaluation of Gd@C_{60}[$C(COOH)_2$]$_{10}$ as a MRI contrast agent. *J. Am. Chem. Soc. 125*, 5471–5478.

(9) Sitharaman, B., Bolskar, R. D., Rusakova, I., and Wilson, L. J. (2004) Gd@C_{60}[$C(COOH)_2$]$_{10}$ and Gd@$C_{60}(OH)_x$: Nanoscale aggregation studies of two metallofullerene MRI contrast agents in aqueous solution. *Nano Lett. 4*, 2373–2378.

(10) Lu, X., Xu, J. X., Shi, Z. J., Sun, B. Y., Gu, Z. N., Liu, H. D., and Han, H. B. (2004) Studies on the relaxivities of novel MRI contrast agents two water-soluble derivatives of Gd@C_{82}. *Chem. J. Chinese U. 25*, 697–700.

(11) Laus, S., Sitharaman, B., Toth, V., Bolskar, R. D., Helm, L., Asokan, S., Wong, M. S., Wilson, L. J., and Merbach, A. E. (2005) Destroying gadofullerene aggregates by salt addition in aqueous solution of Gd@$C_{60}(OH)_x$ and Gd@C_{60}[$C(COOH)_2$]$_{10}$. *J. Am. Chem. Soc. 127*, 9368–9369.

(12) Toth, E., Bolskar, R. D., Borel, A., Gonzalez, G., Helm, L., Merbach, A. E., Sitharaman, B., and Wilson, L. J. (2005) Water-soluble gadofullerenes: Toward high-relaxivity, pH-responsive MRI contrast agents. *J. Am. Chem. Soc. 127*, 799–805.

(13) Shu, C. Y., Gan, L. H., Wang, C. R., Pei, X. L., and Han, H. B. (2006) Synthesis and characterization of a new water-soluble endohedral metallofullerene for MRI contrast agents. *Carbon 44*, 496–500.

(14) Shu, C. Y., Zhang, E. Y., Xiang, J. F., Zhu, C. F., Wang, C. R., Pei, X. L., and Han, H. B. (2006) Aggregation studies of the water-soluble gadofullerene magnetic resonance imaging contrast agent: [Gd@$C_{82}O_6(OH)_{16}(NHCH_2CH_2COOH)_8$]$_x$. *J. Phys. Chem. B 110*, 15597–15601.

(15) Anderson, S. A., Lee, K. K., and Frank, J. A. (2006) Gadolinium-fullerenol as a paramagnetic contrast agent for cellular imaging. *Invest. Radiol. 41*, 332–338.

(16) Fatouros, P. P., Corwin, F. D., Chen, Z. J., Broaddus, W. C., Tatum, J. L., Kettenmann, B., Ge, Z., Gibson, H. W., Russ, J. L., Leonard, A. P., Duchamp, J. C., and Dorn, H. C. (2006) In vitro and in vivo imaging studies of a new endohedral metallofullerene nanoparticle. *Radiology 240*, 756–764.

(17) Sitharaman, B., Tran, L. A., Pham, Q. P., Bolskar, R. D., Muthupillai, R., Flamm, S. D., Mikos, A. G., and Wilson, L. J. (2007) Gadofullerenes as nanoscale magnetic labels for cellular MRI. *Contrast Media Mol. Imaging 2*, 139–146.

(18) Laus, S., Sitharaman, B., Toth, E., Bolskar, R. D., Helm, L., Wilson, L. J., and Merbach, A. E. (2007) Understanding paramagnetic relaxation phenomena for water-soluble gadofullerenes. *J. Phys. Chem. C 111*, 5633–5639.

(19) Iezzi, E. B., Duchamp, J. C., Harich, K., Glass, T. E., Lee, H. M., Olmstead, M. M., Balch, A. L., and Dorn, H. C. (2002) A symmetric derivative of the trimetallic nitride endohedral metallofullerene, $Sc_3N@C_{80}$. *J. Am. Chem. Soc. 124*, 524–525.

(20) Stevenson, S., Stephen, R. R., Amos, T. M., Cadorette, V. R., Reid, J. E., and Phillips, J. P. (2005) Synthesis and purification of a metallic nitride fullerene bisadduct: Exploring the reactivity of $Gd_3N@C_{80}$. *J. Am. Chem. Soc. 127*, 12776–12777.

(21) Maeda, Y., Miyashita, J., Hasegawa, T., Wakahara, T., Tsuchiya, T., Nakahodo, T., Akasaka, T., Mizorogi, N., Kobayashi, K., Nagase, S., Kato, T., Ban, N., Nakajima, H., and Watanabe, Y. (2005) Reversible and regioselective reaction of La@C_{82} with cyclopentadiene. *J. Am. Chem. Soc. 127*, 12190–12191.

(22) Cardona, C. M., Kitaygorodskiy, A., and Echegoyen, L. (2005) Trimetallic nitride endohedral metallofullerenes: Reactivity dictated by the encapsulated metal cluster. *J. Am. Chem. Soc. 127*, 10448–10453.

(23) Cardona, C. M., Kitaygorodskiy, A., Ortiz, A., Herranz, M. A., and Echegoyen, L. (2005) The first fulleropyrrolidine derivative of $Sc_3N@C_{80}$: Pronounced chemical shift differences of the geminal protons on the pyrrolidine ring. *J. Org. Chem. 70*, 5092–5097.

(24) Yamada, M., Wakahara, T., Nakahodo, T., Tsuchiya, T., Maeda, Y., Akasaka, T., Yoza, K., Horn, E., Mizorogi, N., and Nagase, S. (2006) Synthesis and structural characterization of endohedral pyrrolidinodimetallofullerene: $La_2@C_{80}(CH_2)_2$NTrt. *J. Am. Chem. Soc. 128*, 1402–1403.

(25) Cai, T., Xu, L., Anderson, M. R., Ge, Z., Zuo, T., Wang, X., Olmstead, M. M., Balch, A. L., Gibson, H. W., and Dorn, H. C. (2006) Structure and enhanced reactivity rates of the $D_{5\,h}$ $Sc_3N@C_{80}$ and $Lu_3N@C_{80}$ metallofullerene isomers: the importance of the pyracylene motif. *J. Am. Chem. Soc. 128*, 8581–8589.

(26) Chen, N., Zhang, E. Y., Tan, K., Wang, C. R., and Lu, X. (2007) Size effect of encaged clusters on the exohedral chemistry of endohedral fullerenes: A case study on the pyrrolidino reaction of $Sc_xGd_{3-x}N@C_{80}$ (x=0–3). *Org. Lett. 9*, 2011–2013.

(27) Hermanson, G. T. (1996) *Bioconjugate Techniques*, Pierce Chemical Company, Rockford, IL, P170–172..

(28) Yao, G., Fang, X. H., Yokota, H., Yanagida, T., and Tan, W. (2003) Monitoring molecular beacon DNA probe hybridization at the single-molecule level. *Chem. Eur. J. 9*, 5686–5692.

(29) Mashanov, G. I., Tacon, D., Knight, A. E., Peckham, M., and Molloyc, J. E. (2003) Visualizing single molecules inside living cells using total internal reflection fluorescence microscopy. *Methods 29*, 142–152.

(30) Ashcroft, J. M., Tsyboulski, D. A., Hartman, K. B., Zakharian, T. Y., Marks, J. W., Weisman, R. B., Rosenblum, M. G., and Wilson, L. J. (2006) Fullerene (C_{60}) immunoconjugates: interaction of water-soluble C_{60} derivatives with the murine anti-gp240 melanoma antibody. *Chem. Commun.* 3004–3006.

(31) Tokunaga, M., Kitamura, K., Saito, K., Iwane, A. H., and Yanagida, T. (1997) Single molecule imaging of fluorophores and enzymatic reactions achieved by objective-type total internal reflection fluorescence microscopy. *Biochem. Biophys. Res. Commun. 235*, 47–53.

(32) Nunn, A. D., Linder, K. E., and Tweedle, M. F. (1997) Can receptors be imaged with MRI agents? *Q. J. Nucl. Med. 41*, 155–162.

(33) Chen, C. Y., Xing, G. M., Wang, J. X., Zhao, Y. L., Li, B., Tang, J., Jia, G., Wang, T. C., Sun, J., Xing, L., Yuan, H., Gao, Y. X., Meng, H., Chen, Z., Zhao, F., Chai, Z. F., and Fang, X. H. (2005) Multi hydroxylated [Gd@$C_{82}(OH)_{22}$]$_n$ nanoparticles: Antineoplastic activity of high efficiency and low toxicity. *Nano Lett. 5*, 2050–2057.

BC7002742

Cellular Internalization and Distribution of Arginine-Rich Peptides as a Function of Extracellular Peptide Concentration, Serum, and Plasma Membrane Associated Proteoglycans

Michie Kosuge,[†] Toshihide Takeuchi,[†] Ikuhiko Nakase,[†] Arwyn Tomos Jones,[§] and Shiroh Futaki*[,†,‡]

Institute for Chemical Research, Kyoto University, Uji, Kyoto 611-0011, Japan, SORST, Japan Science and Technology Agency (JST), Kawaguchi, Saitama 332-0012, Japan, and Welsh School of Pharmacy, Cardiff University, Cardiff, CF10 3XF, Wales, United Kingdom. Received July 31, 2007; Revised Manuscript Received December 22, 2007

The exact mechanisms by which arginine-rich cell-penetrating peptides enter cells are still the subject of debate. Here, we have analyzed in detail the effects of serum and extracellular concentration on the internalization of oligoarginines (R*n*; $n = 4, 8, 12, 16$). The presence of serum in the incubation medium had a major influence on the uptake of R12 and R16 peptides but did not affect the uptake of R4 and R8 significantly. Incubation of cells at 37 °C with R12 and R16 peptides in serum-containing medium showed that the majority of labeling was confined to punctate endocytic structures. Performing the same experiments in serum-free media led to a dramatic increase in cytosolic labeling, and similarly diffuse R12 and R16 labeling was observed in cells treated with peptides at 4 °C. This suggests, in both cases, that the peptides were entering via a nonendocytic mechanism. Further studies on R12 peptide suggest that the initiation of nonendocytic uptake and cytosolic labeling is also dependent on serum concentration and extracellular peptide concentration. At relatively low concentrations, the peptide labels endocytic structures, but upon raising the peptide concentration, the fraction labeling the cytosol increases dramatically and this accompanies a nonlinear increase in total cellular fluorescence. Membrane-associated proteoglycans also contribute to increasing the peptide concentration at the cell surface by enhancing their recruitment via electrostatic interactions. These results demonstrate that uptake mechanisms of these compounds are highly dependent on both the presence of serum and the effective extracellular peptide concentration.

INTRODUCTION

The use of cell-penetrating peptides (CPPs, or protein transduction domains, PTDs) for enhancing delivery of molecules across biological barriers has received widespread attention, as they offer a diverse range of therapeutic applications (*1–6*). Among them, arginine-rich peptides including oligoarginine and HIV-1 Tat (48–60) peptides are regarded as one representative class and show high efficiency of translocation through biological membranes (*1–8*). Recent work has shown the applicability of these peptides as intracellular delivery vectors for a wide range of bioactive cargo including synthetic small molecules, peptides, proteins, oligonucleotides, and liposomes. This has been shown in both in vitro and in vivo applications through to clinical trials targeting cancer and allergy (*4, 5*).

Despite their promise and effectiveness, the exact mechanisms by which they breach biological barriers such as the plasma membrane remains to be elucidated. The internalization of HIV-Tat peptide and other arginine-rich peptides, concluded from observations in fixed cells, was thought to occur through temperature- and energy-independent, nonendocytic mechanisms (*8*). However, more recent experiments using intact living cells highlight the importance of endocytic pathways as major routes of internalization (*9, 10*). We and others have proposed that macropinocytosis may be stimulated in cells treated with CPPs (*11, 12*). We have also highlighted the fact that interaction of arginine-rich peptides with membrane-associated proteoglycans such as heparan sulfate and chondroitin sulfate may activate intracellular signals to induce actin organization and thus promote macropinocytosis (*13*). Similar observations were reported in the cellular uptake of oligomers of β-amino acids bearing guanidino moieties (*14*) and amphiphilic peptide vectors (MPG) using a noncovalent complex-formation approach (*15*). Macropinocytosis may therefore be an important uptake mechanism for arginine-rich peptides, but as previously described (*16*), there is strong evidence that other pathways are also utilized including those employing clathrin coats (*10*) and caveolae (*17*); associated cargo is also likely to affect the entry mechanism.

There is, however, accumulating evidence that arginine-rich peptides in particular enter cells in the absence of energy and thus endocytosis (*11, 18, 19*). Fluorescent R8 peptide incubated on ice with a variety of different cell types shows diffuse and often uniform labeling throughout the cytosol and nucleus; the D-R8 isoform also has a strong tendency to label the nucleolus (*11, 18, 19*). In contrast, fluorescent microscopy observations of cells treated with the R8 peptide at 37 °C yield punctate signals that have been identified as endocytic structures. This phenotype is similar to that observed when cells have been fixed following incubation at 37 °C (*8*). This is however an artifact caused by disturbance of plasma membrane during fixation (*9, 11*); arginine-rich peptides have a high tendency to adsorb to cell surface and enter cells through damaged plasma membranes caused by fixation. However, our observation of 4 °C internalization of R8 peptides was using living cells, and the integrity of the plasma membranes was confirmed by the absence of nuclear staining of the membrane-impermeable dye propidium iodide (PI) (*11*). These results strongly suggest that

* To whom correspondence should be addressed: Institute for Chemical Research, Kyoto University, Uji, Kyoto 611-0011, Japan. Tel: +81-774-38-3210, Fax: +81-774-32-3038, E-mail: futaki@scl.kyoto-u.ac.jp.

[†] Kyoto University.

[‡] JST.

[§] Cardiff University.

10.1021/bc700289w CCC: $40.75 © 2008 American Chemical Society
Published on Web 02/13/2008

endocytosis is not the sole internalization mechanism for arginine-rich peptides.

Although the effects of various factors, including temperature (*9, 11, 12, 19*), membrane-associated proteoglycans (*10, 13, 20–25*), and membrane potential (*26*), have been shown to affect the internalization of arginine-rich peptides, very few studies have investigated the influence of serum proteins and culture media components. For example, the influence of serum needs to be carefully assessed if these in vitro models are designed to more closely represent in vivo studies (*27*).

In this report, we examine the effect of serum on the internalization of oligoarginines (R*n*) having different numbers of arginines ($n = 4, 8, 12, 16$). We show that the internalization of the longer R12 and R16 peptides is significantly reduced in the presence of serum. This is a likely consequence of their higher capacity to bind serum proteins. We also show that the peptides can enter cells via at least two mechanisms, and at low concentrations, this leads to labeling of endocytic structures, but at higher concentrations, extensive cytosolic labeling is observed. The prominence of this labeling is dependent on whether incubations are performed in the presence or absence of serum, and finally we confirm that, under defined conditions, energy-independent, direct translocation across the plasma membrane represents a major route of entry for peptides R8, R12, and R16.

EXPERIMENTAL PROCEDURES

Peptides and Proteins. All the peptides used in this study were chemically synthesized by Fmoc (9-fluorenylmethyloxycarbonyl) solid-phase peptide synthesis as reported (*28*). Actual sequences of the synthesized peptides: R*n* ($n = 4, 8, 12, 16$), R*n*-amide; R*n*−Alexa488 ($n = 4, 8, 12, 16$), R*n*-GC(Alexa488)-amide; R12−PAD, RRRRRRRRRRRRGC-CG-D-(KLAKLAK)$_2$-amide. The EGFP protein bearing a $(His)_6$ segment was also prepared as previously reported (*28*). Details of the preparation of peptides and proteins are described in the Supporting Information.

Cell Culture. Human cervical cancer-derived HeLa cells were cultured as exponentially growing subconfluent monolayers on 60 mm dishes in alpha-minimum essential medium (α-MEM) (Invitrogen) supplemented with 10% (v/v) bovine serum (Invitrogen). Chinese hamster ovary (CHO) cells including wild-type CHO-K1, and all glycosaminoglycan-deficient pgsA-745 (A-745) were purchased from the American Type Culture Collection (ATCC) and maintained in F-12 nutrient mixture (Ham's F-12) (Invitrogen) supplemented with 10% (v/v) fetal bovine serum (Biological Industries). Cells were maintained at 37 °C in a humidified 5% CO_2 incubator, and a subculture was performed every 3–4 days.

Confocal Microscopy. Two × 10^5 cells were plated into 35 mm glass-bottomed dishes (Iwaki) and cultured for 48 h. The cells were washed twice with one of three types of incubation buffers (serum-containing medium, serum-free medium, or PBS supplemented with 100 mg/L $CaCl_2$ and $MgCl_2 \cdot 6H_2O$), prior to addition and incubation with peptides and propidium iodide (PI), the latter to assess cell integrity. Intracellular distribution of the fluorescently labeled peptides was immediately analyzed (less than 3 min) *without washing and fixing* using an Olympus FV300 confocal scanning laser system consisting of an Olympus IX81 microscope equipped with a 0.85 NA UPlanApo 40× objective lens. For 4 °C experiments, cells were preincubated in a refrigerator (4 °C) for 1 h; washing and incubation of the cells was then conducted using ice-cold incubation buffer and the 4 °C refrigerator, respectively, prior to observation of the cells, *without washing,* by confocal microscopy. For experiments investigating the role of membrane potential, a buffer PBS(K^+), where the sodium salts in PBS were replaced with equimolar amounts of the equivalent potassium salts, was used (*26, 29*). For experiments employing transferrin, cells were washed twice with an incubation buffer prior to a 30 min incubation with peptides and rhodamine-labeled transferrin (Rho–Tf, 25 μg/mL) (Molecular Probes) diluted with the respective incubation buffer. For the experiments with mitochondrial membrane potential probe JC-1 (Molecular Probes—this exhibits a red-to-green color shift in accordance with depolarization of mitochondrial membrane potential), cells were washed twice with an incubation buffer prior to treatment with R12–PAD (4 μM) for 1 h. After washing twice with PBS and staining with JC-1 (5 μM) for 30 min in α-MEM containing 10% bovine serum, the cells were analyzed by confocal microscopy.

Flow Cytometry. Five × 10^4 HeLa cells were plated into 24 well microplates (Iwaki) and cultured for 48 h. The cells were washed twice with an incubation buffer prior to incubation with peptides in the respective buffers. The cells were then washed twice with PBS containing 0.5 mg/mL heparin and then incubated with 0.01% trypsin for 10 min at 37 °C. The cells were harvested and centrifuged at 3000 rpm for 5 min. The cell pellet was suspended and washed twice with PBS and finally resuspended in PBS for fluorescence analysis with a FACS Calibur flow cytometer (BD Biosciences) using a 488 nm laser excitation and a 515–545 nm emission filter. Each sample was analyzed for 10 000 events.

Cytotoxicity Test. The MTT [3-(4,5-dimethylthiazol-2-yl)-2,5-diphenyl-2*H*-tetrazolium bromide] assay and the lactate dehydrogenase (LDH) release assay were conducted essentially as previously reported (*29*). Briefly, 5 × 10^3 cells were plated into 96 well microplates (Iwaki) and cultured for 48 h. The cells were washed twice with an incubation buffer and treated with peptides (10 μM) for 30 min at 37 °C. After incubation, cytotoxicity was evaluated with MTT assay and LDH release assay as reported (see Supporting Information).

Interaction of Oligoarginine Peptides with Serum Proteins. R12−Alexa488 was diluted (0–20 μM) with serum-containing medium [α-MEM(+)] or serum-free medium [α-MEM(−)] and incubated for 5 min at room temperature prior to analysis by nondenaturing gel electrophoresis using a 5–20% native polyacrylamide gel (SuperSep, purchased from Wako). Bovine serum albumin (0.25 μg) and EGFP (0.5 μg) were respectively used as protein and fluorescent-protein standards. The gel was analyzed with FluorImager595 (Molecular Dynamics) to obtain fluorescence images using 488 nm laser excitation and 515–545 nm emission filter. Staining for proteins with Coomassie Brilliant Blue (CBB) was then conducted. For the experiment to evaluate the amount of the peptides adsorbed to serum proteins, R8−Alexa488, R12−Alexa488, and R16−Alexa488 were diluted to 10 μM in α-MEM(+), α-MEM(−), or PBS and incubated for 5 min at room temperature. Each peptide solution was then subjected to ultrafiltration using Microcon YM-30 centrifugal filter (Millipore) (molecular weight cutoff 30 000) at 14 000 × *g* for 12 min to separate the "free" peptide (unbound with serum) from the peptide adsorbed with serum proteins. Fractional ratios of peptides (*F*) were calculated using the following equation:

$$F = A/(A + B) \quad (1)$$

where *A* is the number of moles of the peptide adsorbed to serum proteins (the peptide remaining on the ultrafilter membrane) and *B* is the number of moles of the unbound peptide (i.e., the peptide in the filtrate). Concentration of a peptide in each fraction was determined by using extinction coefficient of Alexa488 ($\epsilon = 72\,000$, Molecular Probes).

RESULTS

Effects of Serum on the Internalization of Oligoarginine Peptides. Typically, qualitative and quantitative analysis of CPP uptake is performed after they have been incubated with cells

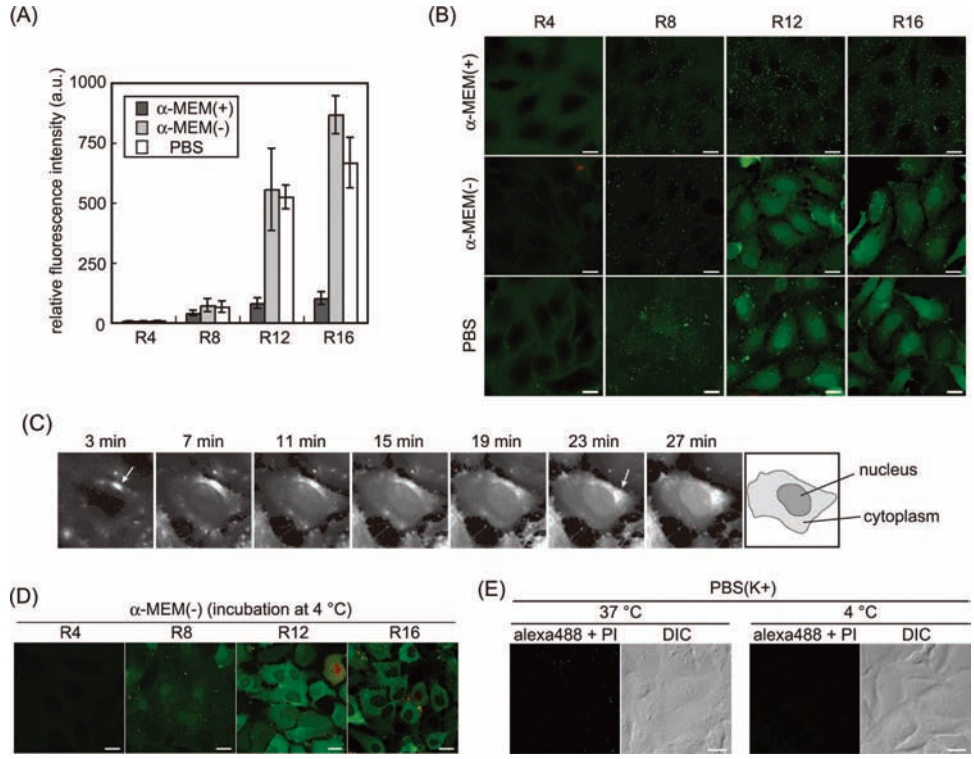

Figure 1. Effects of serum on the internalization of oligoarginine peptides. (A) HeLa cells were incubated with Alexa488-labeled oligoarginine peptides (5 μM) for 15 min in medium containing 10% serum [α-MEM(+)], serum free medium [α-MEM(−)], or PBS prior to trypsin treatment and quantification by flow cytometry. Error bars represent the mean ± standard deviation (SD) of 3 separate experiments. (B) HeLa cells were incubated with oligoarginine peptides (5 μM) for 30 min in α-MEM(+), α-MEM(−), or PBS in the presence of propidium iodide (PI, 1.5 μM) and immediately analyzed by confocal microscopy without washing. All images are merged fluorescence images derived from analysis of Alexa488 (green) and PI (red) labeling. (C) Time course study of R12 (5 μM) internalization in HeLa cells in α-MEM(−) at 37 °C. Arrows indicate the initiation points of the internalization of the R12 peptide. To avoid saturation of the fluorescence signals, the photomultiplier voltage was decreased during the incubation. (D) Confocal microscopic images of HeLa cells incubated with oligoarginine peptides (5 μM) in α-MEM(−) for 30 min at 4 °C in the presence of PI (1.5 μM). (E) Effects of membrane potential on cellular uptake of R12. HeLa cells were incubated with R12−Alexa488 (5 μM) and PI using PBS(K^+) at 37 or 4 °C. Scale bars, 20 μm.

in complete media, serum-free media, or simple buffers such as PBS. Initially, we investigated what effects the addition of serum to the incubation media has on the internalization of peptides of different chain lengths R4, 8, 12, and 16. HeLa cells were treated with Alexa488-conjugated peptides in α-minimal essential medium containing [α-MEM(+)] or lacking [α-MEM(−)] 10% (v/v) bovine serum; phosphate-buffered saline (PBS) was also employed as an alternative incubation buffer. The cells were treated at 37 °C with 5 μM of each respective peptide for 15 min, and the amount of internalized peptides was then quantified by flow cytometry (Figure 1A). R4 showed minimal cellular uptake in both the absence and presence of serum. In the presence of serum, we observed a small increase in internalization R16 > R12 > R8. Performing identical experiments in media lacking serum resulted in a 1.8-fold increase in R8 uptake but a much higher 6.9- and 9.0-fold increase in R12 and R16 uptake, respectively. Performing the same experiments in PBS had effects similar to that of depleting serum from the media.

The presence of serum also had a major impact on the distribution of the peptide inside cells with the greatest effects noted for R12 and R16 (Figure 1B). Earlier studies have shown that fixation prior to microscopic observation, using agents such as paraformaldehyde and acetone/methanol, causes redistribution in the localization of oligoarginine peptides and other arginine-rich peptides (*9, 11*). Additionally, extensive washing with PBS may damage the plasma membrane to affect the cellular localization of these peptides (data not shown). To avoid these experimental artifacts, immediate and direct confocal microscopic observation was conducted in this study *without cell washing and fixation* after incubation of the cells with oligoarginine peptides for 30 min. In complete media incubations, all the peptides typically labeled punctate, endolysosomal-like structures (Figure 1B). However, the R12 and R16 peptides in serum-free incubations displayed marked cytosolic and nuclear labeling together with punctate signals. Time-course imaging of the cells revealed that the initial translocation of the R12 peptide did not occur throughout the cell but at defined locations, and this labeling then diffused through the cytosol and nucleus (Figure 1C). This phenomenon was observed in of the majority of cells, and similar observations were recently reported utilizing a FITC-conjugated R9 peptide (20 μM) incubated with the same HeLa line (*30*).

Provided stringent care is taken to remove surface bound peptide, there is evidence that internalization at 4 °C is marginal or negligible compared with experiments performed at 37 °C (*9–12*). However, we and others have shown significant internalization at 4 °C, but the peptide was localized diffusely through the cytosol and nucleus (*11*, *18*, *19*, *31*, *32*). We similarly incubated HeLa cells with all the peptides at 4 °C and observed significant cytosolic labeling, most notably of R8, R12, and R16 (Figure 1D). Similarly with Figure 1C, internalization of the peptide started at defined locations of the cells followed by the diffusion through cytosol and nucleus (data not shown). Interestingly, nuclear labeling of R12 and R16 peptides in serum-free incubations was less intense at 4 °C as compared with 37 °C and implies that, under these conditions, energy is required for nuclear delivery.

The data so far suggested that, in the absence of serum and at 5 μM concentration, a large fraction of both R12 and R16 peptide was internalized via an energy-independent nonendocytic mechanism. This was not due to peptide-mediated membrane disruption, as all the experiments shown in Figure

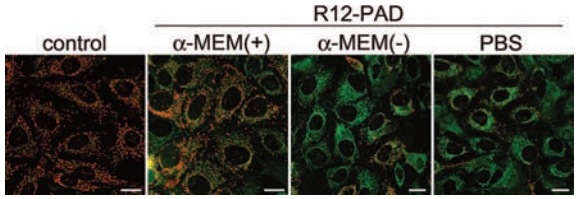

Figure 2. Inhibition of mitochondrial membrane potential by the apoptosis-inducing peptide R12−PAD. HeLa cells were incubated with R12−PAD (4 μM) for 1 h at 37 °C using α-MEM(+), α-MEM(−), or PBS prior to staining with mitochondrial membrane potential-sensitive dye, JC-1 (5 μM). A red-to-green shift of color represents depolarization in membrane potential of mitochondria. Scale bars, 20 μm.

1B,D were conducted in the presence of the membrane-impermeable probe, propidium iodide (PI), that, under all conditions, did not enter the cells.

Since the heterologous distribution of ions on either side of the plasma membrane gives rise to a membrane potential keeping the interior of the cell more negative than the exterior, this may be a driving force for positively charged peptides to translocate across the plasma membrane (*26*, *29*, *33*, *34*). We therefore investigated this further by conducting the same experiments in PBS containing equimolar concentrations of K^+ [PBS(K^+)] rather than Na^+; PBS(K^+) is an isotonic buffer containing potassium concentrations equivalent to that found inside cells, and incubation with this buffer eliminates the membrane potential (*26*). The presence of very few PI-positive cells suggested that eliminating membrane potential had no effect on membrane integrity, but additionally, we found that the internalization and consequent diffuse labeling of the R12 peptide that we observed at 37 °C (Figure 1B) and 4 °C (Figure 1D) was completely blocked under these conditions (Figure 1E). Therefore, membrane potential contribute as a major driving force for the diffuse labeling that we observed at both temperatures.

We next investigated whether the plasma membrane translocating ability of R12 in the absence of serum could be utilized to deliver biologically active cargo. For this, we conjugated R12 to an apoptosis-inducing peptide (pro-apoptotic domain, PAD) (*35*). PAD is an amphiphilic basic peptide that includes 14 residues of D-amino acids, D-$(KLAKLAK)_2$. We previously reported that cytosolic delivery of the PAD peptide using oligoarginine peptides induces mitochondrial membrane disruption and eventual apoptosis (*11*, *28*). Depolarization of mitochondrial membrane potential that accompanies the early stages of apoptosis (*36*) can be monitored using a mitochondrial membrane potential-sensitive probe, JC-1 (*37*). This probe forms aggregates in intact mitochondrial membranes to give a red fluorescence, whereas depolarization of mitochondrial membrane potential induces JC-1 dissociation and green fluorescence. The efficiency of cytosolic delivery of PAD by the R12 peptide was therefore assessed using this probe (Figure 2). In the absence of R12−PAD conjugate, red staining of mitochondria was predominantly observed, suggesting the intactness of mitochondria (Figure 2). When the cells were treated with 4 μM R12-PAD in α-MEM(+) (37 °C, 1 h), a slight shift in JC-1 emission (red to yellow) was observed. However, a dramatic red-to-green shift in fluorescence corresponding to depolarization in mitochondrial membrane potential was observed when the cells were treated with R12−PAD in α-MEM(−) or PBS. These results are in good agreement with an increase in cellular uptake of R12 peptide under serum-free conditions as shown in Figure 1. This suggests that bioactive cargos as well as R12 peptide itself are also efficiently delivered into the cytosol in serum-free conditions.

The absence of PI staining of nucleus after a 30 min incubation with R12 in serum-free medium suggested that there was no significant damage to the plasma membranes when cells were incubated in serum-free conditions (Figure 1B). Incubation of cells in the absence of serum or in PBS could, however, have more long-term detrimental effects. We tested this using an MTT [3-(4,5-dimethylthiazol-2-yl)-2,5-diphenyl-2*H*-tetrazolium bromide] viability assay (*38*) and lactate dehydrogenase (LDH) release assay (*39*). Figure 3A,B demonstrates that treatment of cells in the absence of serum under these defined conditions had no significant effects on cell integrity or viability.

Transferrin is a marker for endocytosis via clathrin-coated vesicles, and we investigated whether R12 incubations in serum-free conditions affected the uptake of transferrin into endocytic vesicles. Cells were coincubated with R12 peptide and rhodamine-labeled transferrin (Rho–Tf) for 30 min, and the cellular distribution of both labels was monitored by confocal microscopy. Figure 3C shows that the diffuse cytosolic and nuclear labeling of the R12 peptide under serum-depleted conditions does not affect Rho–Tf distribution and this labels, as in control cells, distinct vesicular structures. Thus, under serum-free conditions, R12 peptide at this concentration can be internalized by at least two mechanisms: temperature-dependent endocytic uptake with prominence of peptide in vesicular structures, and temperature-independent direct translocation of the peptide through the membranes yielding the characteristic, diffuse cytosolic labeling.

Interaction of Oligoarginine Peptides with Serum Proteins. From the above experiments, we found that the absence of serum in the medium gives distinct intracellular distribution of the R12 peptide, i.e., diffuse cytosolic, together with the punctate cytoplasmic distribution that we typically observe in the presence of serum. It is known that HIV-1 Tat peptide, another typical arginine-rich CPP, interacts with bovine serum albumin (BSA), a major acidic protein in serum (*40*). Although adsorption of the arginine-rich peptides used here may be expected, there have been no detailed examination of the extent or importance of this to their interaction with cells and cellular distribution.

To assess the extent of the peptide−serum interaction, increasing quantities of R12−Alexa488 was diluted in α-MEM(−) or α-MEM(+), and the samples were incubated for 5 min prior to separating the proteins via *nondenaturing* gel electrophoresis. The gels were then stained with Coomassie Brilliant Blue (CBB) that as expected highlighted the presence of multiple bands including a prominent albumin band (Figure 4A).

These experiments were repeated but the gels analyzed on the FluorImager that allowed detection of proteins associated with the fluorescent peptide; EGFP was also loaded and provided a positive control. Figure 4B demonstrates that a number of fluorescent bands were detected in the α-MEM(+) lanes, and their intensity was increased with increasing peptide concentration. A major fluorescent band, indicated by the arrow, migrated at the same position as the band in the BSA−R12 mixture lane (BSA+R12), suggesting that a significant amount of R12 was binding to this protein. In the control experiment, using α-MEM alone, neither R12-derived fluorescence signals nor CBB staining was detected.

The amount of oligoarginine peptide adsorbing to serum proteins was then evaluated using an ultrafiltration method. R8−, R12−, and R16−Alexa488 peptides were incubated as described above with α-MEM(−), α-MEM(+), or PBS prior to passing the samples through a 30 000 molecular weight ultrafiltration unit. The relative amounts of filtered peptide were then compared with the bound unfiltered fraction (Table 1). The data revealed that a considerable fraction of all these arginine peptides bound to serum proteins, and in the case of R16, this represented 97% of the total peptide load. Together with the previous data, this explains why there is such a difference in

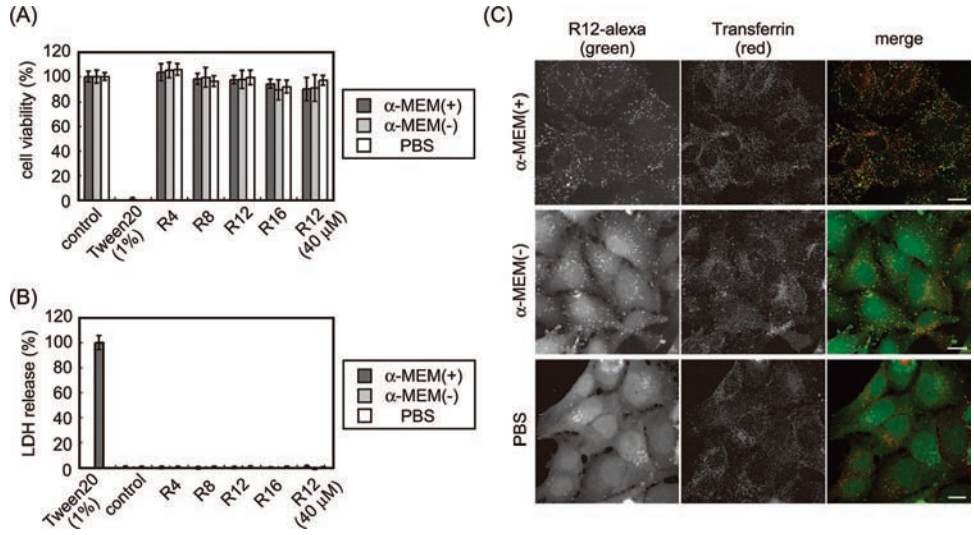

Figure 3. Incubation of cells with oligoarginine peptides in serum-free medium does not affect cell viability, plasma membrane integrity, or endocytosis of transferrin. (A,B) HeLa cells were incubated with nonlabeled oligoarginine peptides (10 μM) for 30 min in α-MEM(+), α-MEM(−), or PBS prior to assessing cell viability (A) and plasma membrane integrity (B). Error bars represent the mean ± SD of a single experiment performed in triplicate. (C) HeLa cells were coincubated with Alexa488-labeled R12 peptide (5 μM) and Rho–Tf (25 μg/mL) for 30 min in α-MEM(+), α-MEM(−), or PBS prior to analysis by confocal microscopy. Scale bars, 20 μm.

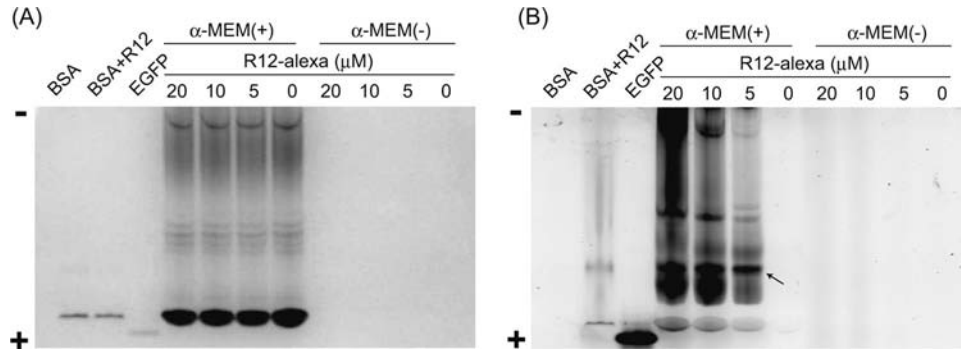

Figure 4. Interaction of oligoarginine peptides with serum proteins. Alexa488-labeled R12 (0–20 μM) was incubated with α-MEM(+) or α-MEM(−) for 5 min at room temperature prior to analysis by *nondenaturing* gel electrophoresis. (A) Proteins detected with CBB. (B) Detection of fluorescently labeled peptide (R*n*−Alexa) as protein complexes. EGFP was used as a positive fluorescent control, and a faint EGFP band is also detected by CBB. The + and − show the direction of the electric field.

Table 1. Percentage of Peptide Bound to Serum Proteins[a]

	R8−Alexa488	R12−Alexa488	R16−Alexa488
α-MEM(+)	64.4 ± 6.8	75.4 ± 11.2	97.4 ± 3.0
α-MEM(−)	0	0	0
PBS	0	0	0

[a] These data represent mean and standard deviation from a single experiment performed in triplicate.

cellular peptide distribution in experiments performed in the absence of serum.

Cytosolic Labeling of R12 Peptide and Concentration of the Peptide Actually Interacting with Plasma Membranes. It is postulated that positive charges on arginine-rich CPPs are one of the most important determining factors for their cellular uptake. This may be due to strong electrostatic interaction with membrane-associated proteoglycans thus concentrating the peptides on cell surfaces. Serum binding of oligoarginine peptides would decrease the effective concentration of the peptides in the medium, and less would be then available to interact with cell surfaces; this could significantly affect the amount internalized. We tested this by incubating R12 peptide with medium supplemented with various concentration of serum (0–10%) and then utilized ultrafiltration to quantify the bound and unbound fraction as described above. Figure 5B shows that decreasing the serum concentration resulted in an increase in the ratios of unbound R12 peptide over serum-bound peptide, and this resulted in an absolute increase in the amount of R12 peptide that was internalized into the cells. This effect was more prominent in experiments performed with the R12 and R16 peptides compared with the R4 and R8 peptides. A 6- to 8-fold increase in cellular uptake of R12 and R16 was observed in the absence of serum in comparison with experiments performed in the presence of 10% serum, whereas only a 1.5-fold increase was observed for the R8 peptide (Figure 5A). Microscopic observations of the cells treated with the R12 peptide in the presence of varying amounts of serum showed that diffuse labeling of the cytosol by the R12 peptide was prominent at lower concentration of serum, especially at ≤2% (Figure 5C). Interestingly, there was only a slight increase (~10%) in the amount of serum-unbound peptide at serum concentration 2% compared with 4%; however, this manifested as a doubling of the amount of internalized peptide (Figure 5B). A marked difference in the distribution of the R12 peptide (diffuse vs punctate) was also observed between serum concentration of 2% and 4% (Figure 5C). These results further support the importance of the effective extracellular peptide concentration on both the internalization mechanism and the final peptide distribution in cells.

Recent published analysis (*19*, *30*) and data presented here suggest that there is a threshold peptide concentration for

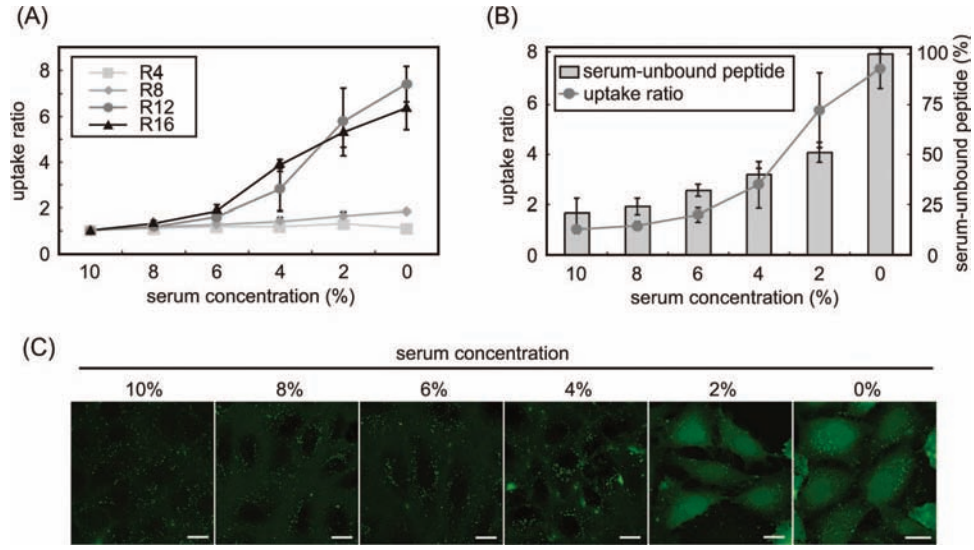

Figure 5. Serum concentration plays a major role in the cytosolic labeling of R12 peptide. (A) HeLa cells were incubated with oligoarginine peptides (5 μM) for 30 min at 37 °C in α-MEM supplemented with various concentration of serum (0–10%) prior to analyzing cell fluorescence by flow cytometry. The data are expressed as the ratio of fluorescence of each condition over the fluorescence of experiments performed in 10% serum. (B) Cells were incubated for 30 min in the presence of α-MEM containing increasing serum concentration. Data show a positive correlation between serum-unbound R12 peptide (columns) and cellular uptake (circles, same data as in (A)). Error bars represent the mean ± SD of 3 separate experiments. (C) HeLa cells were treated with R12−Alexa488 (5 μM) as in (A) and immediately analyzed by confocal microscopy. Scale bars, 20 μm.

cytosolic diffuse labeling. To quantify this threshold value, we measured fluorescence in cells after they had been incubated with increasing concentrations (0.1–40 μM) of R12−Alexa488 in the presence and absence of serum for 30 min. The data in Figure 6A show that in the absence or presence of serum there is a gradual increase in peptide uptake up to 2 μM [α-MEM(−)] and 10 μM [α-MEM(+)], and thereafter fluorescence increased rapidly. Time course study of peptide uptake also suggests the presence of a threshold concentration for diffuse cytosolic labeling (see Supporting Information Figure S1). Following incubation of cells in α-MEM(−) or α-MEM(+) at peptide concentration just below this threshold concentration, we see by fluorescence microscopy that labeling is confined to punctate endocytic structures. However, at higher than threshold concentrations, the labeling is both diffuse/cytosolic and vesicular (Figure 6B). This suggested that endocytic uptake is a dominant pathway for internalization of R12 peptide at lower than the threshold concentration, and diffuse cytosolic labeling is observed when the peptide concentration exceeds this value.

Importance of Membrane-Associated Proteoglycans to Increase Cell-Surface Concentration of the Oligoarginine Peptides. The importance of plasma membrane associated proteoglycans for endocytic uptake of a number of arginine-rich peptides has been reported in several publications (*10, 13, 20–25*). It is assumed that these positively charged peptides accumulate on the cell surfaces by electrostatic interaction with carbohydrate sulfate groups. The ubiquitous occurrence of membrane-associated proteoglycans on the cell surface together with their tight and rapid interaction with the arginine-rich peptides has been considered a primary step in the internalization of these peptides (*22*). We therefore examined whether surface proteoglycans have any role in mediating the difference in distribution of fluorescence that we observed at peptide concentrations lower and higher than the threshold. For this, we utilized two types of Chinese hamster ovary CHO cell lines; the wild-type CHO-K1 line, and its mutant variant, A-745, that is defective in proteoglycan biosynthesis (*13, 21*).

Both cell lines were incubated with increasing concentrations of R12 peptide in the absence of serum at 37 °C for 15 min prior to quantifying cell fluorescence using flow cytometry or analysis by confocal microscopy. Figure 7A shows that internalization of the peptide at ≤1 μM is similar in both cell lines but at higher concentration the mutant cell line accumulates significantly less peptide. Confocal microscopy images of arrowheads a−d in Figure 7A show that diffuse labeling of the cytosol can be achieved in both cell lines but at noticeably different peptide concentrations (Figure 7B). Punctate signals from the R12 peptide suggestive of endocytosis were predominantly observed for A745 cells at 5 μM peptide concentration. Increasing in the concentration to 30 μM yielded the diffuse labeling of cytosol, suggesting that a similar concentration-dependent two-phase internalization of the peptides occurs in this proteoglycan-deficient cell line. In the case of the wild-type CHO-K1 cell line, diffuse cytosolic staining was observed even at the relatively low 5 μM concentration, whereas at 2.5 μM, only punctate structures were visible. The presence of membrane-associated proteoglycans was therefore effective to enhance R12 translocation to give diffuse cytosolic staining, and this we attribute to the increased concentration of the peptides in the vicinity of the cell surfaces.

DISCUSSION

A variety of endocytic pathways have been shown to be utilized by CPP to gain access to cells (*9, 11, 14*). We have however provided evidence that predominantly arginine-rich peptides as used in this study have a propensity to translocate across the plasma membrane when experiments are performed on ice, when defined endocytic pathways cease to function (*11, 18, 19, 41*).

In this study, we have explored the methods of internalization and intracellular distribution of oligoarginine peptides in PBS and medium containing or lacking supplemented serum. We show that serum proteins have considerable effect on the internalization of oligoarginine peptides, especially in the case of the longer R12 and R16 peptides. Incubation of cells with these peptides in serum-free medium significantly enhanced the fraction of the cytosolic peptides that was in marked contrast to the punctate labeling that we observe in identical experiments performed in complete medium. This highlights further the fact that internalization of these peptides can proceed via at least two mechanisms, and we rationalize that only one is dependent

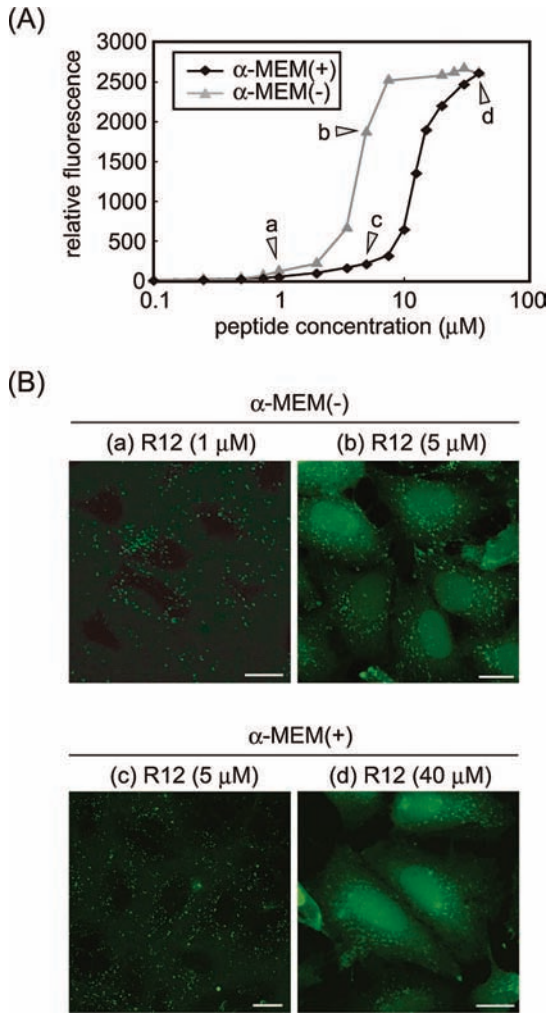

Figure 6. Concentration-dependent two-phase internalization of R12 peptide. (A) HeLa cells were incubated with R12−Alexa488 (0.1–40 μM) for 30 min in α-MEM(+) or α-MEM(−) prior to analysis by flow cytometry. The data represent average values from 2 to 3 separate experiments. (B) Intracellular distributions of the R12 peptide corresponding to a−d in (A). Scale bars, 20 μm.

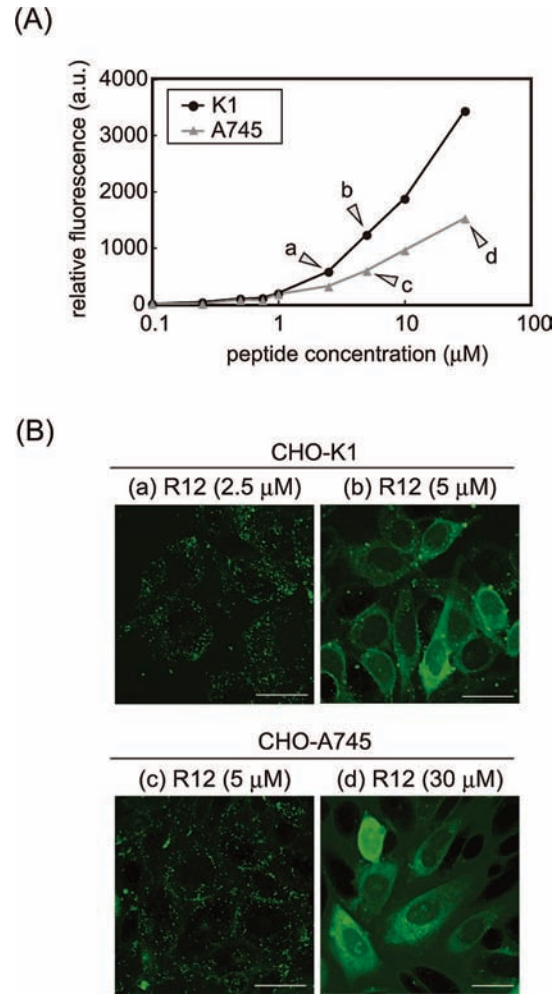

Figure 7. Contribution of surface proteoglycans to intracellular distribution of R12 peptide (A) CHO-K1 cells and proteoglycan-deficient A745 cells were incubated with R12 (0.1–30 μM) in serum-free medium [F-12(-)] at 37 °C for 15 min prior to analysis by flow cytometry. The data represent average values from 2 to 3 separate experiments. (B) Intracellular distribution of the R12 peptide corresponding to arrowheads a−d in (A). Scale bars, 20 μm.

on typical and characterized endocytic pathways. The presence of serum, because it quenches the effective peptide concentration, significantly increases this threshold concentration.

In our previous study, we observed a similar cytosolic labeling of the R8 peptide in PBS in the presence of counteranions such as pyrenebutyrate (*29, 42, 43*). In the presence of pyrenebutyrate, R8 peptide was internalized with high efficiency in a very short period of time to label the cell cytosol, and we proposed that this was via direct translocation through the plasma membrane. Since this efficient internalization was not observed in the absence of the membrane potential, this was proposed as the driving force for peptide translocation. Pyrenebutyrate is sequestered in the membranes via complex formation with the peptides through its carboxylate moiety, and it would neutralize the positive charges of the oligoarginine peptides to decrease the energy barrier on the translocation of the peptides through the membranes. Alternatively, the pyrenebutyrate carboxylate moiety may work to increase the interaction of the peptides with cell surfaces via hydrogen-bond formation with the arginine guanidino moiety.

The internalization of the R12 peptides shown in this study has many aspects in common with translocation of the R8 peptide in the presence of pyrenebutyrate, namely, nonendocytic uptake via plasma membrane translocation, diffuse cytosolic labeling initiating from specific cell locations, internalization at 4 °C, and a dependency on membrane potential (*29*). R12 and R16 peptides would have higher affinities both to serum proteins and cell surfaces than R8 and R4 due to their higher valency of interaction. Oligomerization of 12 residues of arginine may acquire enough affinity to interact with the plasma membrane to achieve direct translocation through the membrane and also to lead a marked increase in their cellular uptake, as is seen for R8 in the presence of pyrenebutyrate. We previously showed that the R8 peptide can partition into chloroform in the presence of the negatively charged phospholipid, phosphatidylglycerol (*44, 45*). Such negatively charged counteranions in the membrane may similarly aid R12 translocation.

It has been reported that membrane-associated proteoglycans are important for the cellular uptake of arginine-rich peptides (*10, 13, 20–25*). We and others also reported that these are critical for peptide-induced actin reorganization and macropinocytosis (*11, 13, 14*). The results obtained here suggest that they have additional roles in enhancing peptide uptake and this is via their capacity to increase the local peptide concentration. Even though oligoarginine peptides may have a higher affinity for sulfate moieties on proteoglycans than plasma membranes (*23*), the increase in local concentration of the arginine-rich peptides in the vicinity of the cell surface would be beneficial to increasing gradient formation across the membranes.

More recently, we reported that a similar diffuse R8 labeling of the cytosol was observed in KG1a leukemia cells, even in the presence of serum, when their plasma membrane cholesterol levels were depleted by methyl-β-cyclodextrin (*19*). In a more recent study, Duchardt et al. showed that depetion of plasma membrane cholesterol promoted the cellular uptake and cytosolic labeling of R9 peptide, but only when the cells were incubated at peptide concentrations ≥ 5 μM (*30*). It could therefore be postulated that endocytic uptake inhibits the accumulation of the peptides on the plasma membrane to reach the threshold levels that then promote translocation to the cytosol. *Inhibitors of endocytic uptake of oligoarginine peptides could therefore contribute to increase the peptide concentration on plasma membrane* and thus promote diffuse cytosolic labeling. Indeed, diffuse cytosolic labeling of R8 peptide was observed when the cells were incubated with peptides at low temperatures (*11, 18, 19*) and, in the presence of the macropinocytosis inhibitor, 5-(*N*-ethyl-*N*-isopropyl)amiloride (EIPA) (*30, 46*).

We previously showed that there is a threshold concentration that needed to be exceeded before visual cytosolic labeling of R8 peptide in nonadherent carcinoma KG1a cells was observed (*19*); similar observations were later shown in adherent cells (*30*). In the present study, detailed analysis of cellular uptake at varying concentration of the peptides similarly showed that the extent of R12 cytosolic labeling is highly dependent on peptide concentration, but we also found that a relatively small increase in peptide concentration beyond this threshold results in a marked increase in cellular uptake and change in intracellular distribution of peptides.

The sigmoidal relationship between R12 peptide concentration and cellular uptake also supports the existence of this threshold concentration that is likely to be different for different cell types. Here, we also discover that a considerable amount of the oligoarginines is associated with serum proteins and the presence of serum in the incubation promotes a right-side shift of the sigmoidal curve, suggesting that adsorption of the peptide with serum protein decreases the concentration of the peptides that can actually interact with the plasma membrane. Curve plateaus at higher peptide concentrations suggest that saturation of the amount internalized can be achieved in the presence and absence of serum, though of different values. The determining factor may be the intracellular peptide concentration that eliminates the peptide gradient between the outside and inside of the cells in the presence of membrane potentials.

The number of arginine residues in the peptide sequence is a major determining factor for interaction with cells and consequent internalization. Diffuse cytosolic labeling was clearly observed with R12 peptide at 5 μM in the absence of serum but not by the R8 peptide; however, in leukemia cells this same peptide was cytosolic at this concentration in serum, whereas only vesicular labeling was observed at 2 μM (*19*). In the present study, the addition of four arginine residues caused a dramatic change in intracellular distribution. The R12 peptide will have a higher propensity to bind negative charge on the cell surface, and its higher concentration on the cell surface will promote comparatively higher membrane translocation compared with R8.

A major goal in our laboratories and many others is to develop novel methods for efficient, direct, and easy delivery of exogenous biofunctional molecules initially to the cell and then to cytosol under serum-containing condition. We have found that the R12 peptide achieves this cytosolic labeling with a threshold concentration of $\sim$20 μM, a value that renders this approach unsuitable for in vivo delivery. However, the design of peptides with minimal interaction with serum proteins and maximal interaction with cell surfaces could lead to the establishment of CPPs with decreased threshold concentrations for cytosolic delivery. Efforts to develop peptides with optimized molecular structures to achieve efficient cytosolic localization with bioactive cargo molecules in low concentration are now ongoing. In addition, as CPP conjugates have shown in vivo responses such as cell transformation (*5, 6*) it could be argued that binding to serum proteins may be favorable for extending the half-life of the peptide and associated therapeutic cargo.

ACKNOWLEDGMENT

This work was supported in part by Grants-in-Aid for Scientific Research from the Ministry of Education, Culture, Sports, Science and Technology of Japan. T.T. is grateful for a JSPS Research Fellowship for Young Scientists. A.T.J. was partly supported by BBSRC grant BB/D013038/1.

Supporting Information Available: Methods of peptide synthesis and fluorescence labeling, preparation of EGFP protein, MTT and LDH release assays, and Figure S1. This material is available free of charge via the Internet at http://pubs.acs.org/BC.

LITERATURE CITED

(1) Joliot, A., and Prochiantz, A. (2004) Transduction peptides: from technology to physiology. *Nat. Cell Biol. 6*, 189–196.
(2) Futaki, S. (2006) Oligoarginine vectors for intracellular delivery: design and cellular-uptake mechanisms. *Biopolymers 84*, 241–249.
(3) Gupta, B., and Torchilin, V. P. (2006) Transactivating transcriptional activator-mediated drug delivery. *Expert Opin. Drug Delivery 3*, 177–190.
(4) Goun, E. A., Pillow, T. H., Jones, L. R., Rothbard, J. B., and Wender, P. A. (2006) Molecular transporters: synthesis of oligoguanidinium transporters and their application to drug delivery and real-time imaging. *ChemBioChem 7*, 1497–1515.
(5) Snyder, E. L., and Dowdy, S. F. (2005) Recent advances in the use of protein transduction domains for the delivery of peptides, proteins and nucleic acids in vivo. *Expert Opin. Drug Delivery 2*, 43–51.
(6) Langel, Ü., Ed. (2006) *Handbook of Cell-Penetrating Peptides*, 2nd ed., CRC Press, Boca Raton.
(7) Futaki, S., Suzuki, T., Ohashi, W., Yagami, T., Tanaka, S., Ueda, K., and Sugiura, Y. (2001) Arginine-rich peptides. An abundant source of membrane-permeable peptides having potential as carriers for intracellular protein delivery. *J. Biol. Chem. 276*, 5836–4580.
(8) Vivès, E., Brodin, P., and Lebleu, B. (1997) A truncated HIV-1 Tat protein basic domain rapidly translocates through the plasma membrane and accumulates in the cell nucleus. *J. Biol. Chem. 272*, 16010–16017.
(9) Richard, J. P., Melikov, K., Vivès, E., Ramos, C., Verbeure, B., Gait, M. J., Chernomordik, L. V., and Lebleu, B. (2003) Cell-penetrating peptides. A reevaluation of the mechanism of cellular uptake. *J. Biol. Chem. 278*, 585–590.
(10) Richard, J. P., Melikov, K., Brooks, H., Prevot, P., Lebleu, B., and Chernomordik, L. V. (2005) Cellular uptake of unconjugated TAT peptide involves clathrin-dependent endocytosis and heparan sulfate receptors. *J. Biol. Chem. 280*, 15300–15306.
(11) Nakase, I., Niwa, M., Takeuchi, T., Sonomura, K., Kawabata, N., Koike, Y., Takehashi, M., Tanaka, S., Ueda, K., Simpson, J. C., Jones, A. T., Sugiura, Y., and Futaki, S. (2004) Cellular uptake of arginine-rich peptides: roles for macropinocytosis and actin rearrangement. *Mol. Ther. 10*, 1011–1022.
(12) Wadia, J. S., Stan, R. V., and Dowdy, S. F. (2004) Transducible TAT-HA fusogenic peptide enhances escape of TAT-fusion proteins after lipid raft macropinocytosis. *Nat. Med. 10*, 310–315.
(13) Nakase, I., Tadokoro, A., Kawabata, N., Takeuchi, T., Katoh, H., Hiramoto, K., Negishi, M., Nomizu, M., Sugiura, Y., and Futaki,

S. (2007) Interaction of arginine-rich peptides with membrane-associated proteoglycans is crucial for induction of actin organization and macropinocytosis. *Biochemistry 46*, 492–501.
(14) Potocky, T. B., Silvius, J., Menon, A. K., and Gellman, S. H. (2007) HeLa cell entry by guanidinium-rich beta-peptides: importance of specific cation-cell surface interactions. *ChemBioChem 8*, 917–926.
(15) Gerbal-Chaloin, S., Gondeau, C., Aldrian-Herrada, G., Heitz, F., Gauthier-Rouviere, C., and Divita, G. (2007) First step of the cell-penetrating peptide mechanism involves Rac1 GTPase-dependent actin-network remodelling. *Biol. Cell 99*, 223–238.
(16) Jones, A. T. (2007) Macropinocytosis: Searching for an endocytic identity and a role in the uptake of cell penetrating peptides. *J. Cell Molec. Med. 113*, 1–15.
(17) Ferrari, A., Pellegrini, V., Arcangeli, C., Fittipaldi, A., Giacca, M., and Beltram, F. (2003) Caveolae-mediated internalization of extracellular HIV-1 tat fusion proteins visualized in real time. *Mol. Ther. 8*, 284–294.
(18) Al-Taei, S., Penning, N. A., Simpson, J. C., Futaki, S., Takeuchi, T., Nakase, I., and Jones, A. T. (2006) Intracellular traffic and fate of protein transduction domains HIV-1 TAT peptide and octaarginine. Implications for their utilization as drug delivery vectors. *Bioconjugate Chem. 17*, 90–100.
(19) Fretz, M. M., Penning, N. A., Al-Taei, S., Futaki, S., Takeuchi, T., Nakase, I., Storm, G., and Jones, A. T. (2007) Temperature-, concentration- and cholesterol-dependent translocation of L and D-octa-arginine across the plasma and nuclear membrane of $CD34^+$ leukaemia cells. *Biochem. J. 403*, 335–342.
(20) Suzuki, T., Futaki, S., Niwa, M., Tanaka, S., Ueda, K., and Sugiura, Y. (2002) Possible existence of common internalization mechanisms among arginine-rich peptides. *J. Biol. Chem. 277*, 2437–2443.
(21) Tyagi, M., Rusnati, M., Presta, M., and Giacca, M. (2001) Internalization of HIV-1 tat requires cell surface heparan sulfate proteoglycans. *J. Biol. Chem. 276*, 3254–3261.
(22) Ziegler, A., and Seelig, J. (2004) Interaction of the protein transduction domain of HIV-1 TAT with heparan sulfate: binding mechanism and thermodynamic parameters. *Biophys. J. 86*, 254–263.
(23) Goncalves, E., Kitas, E., and Seelig, J. (2005) Binding of oligoarginine to membrane lipids and heparan sulfate: structural and thermodynamic characterization of a cell-penetrating peptide. *Biochemistry 44*, 2692–2702.
(24) Console, S., Marty, C., Garcia-Echeverria, C., Schwendener, R., and Ballmer-Hofer, K. (2003) Antennapedia and HIV transactivator of transcription (TAT) "protein transduction domains" promote endocytosis of high molecular weight cargo upon binding to cell surface glycosaminoglycans. *J. Biol. Chem. 278*, 35109–35114.
(25) Fuchs, S. M., and Raines, R. T. (2004) Pathway for polyarginine entry into mammalian cells. *Biochemistry 43*, 2438–2444.
(26) Rothbard, J. B., Jessop, T. C., Lewis, R. S., Murray, B. A., and Wender, P. A. (2004) Role of membrane potential and hydrogen bonding in the mechanism of translocation of guanidinium-rich peptides into cells. *J. Am. Chem. Soc. 126*, 9506–9507.
(27) Moghimi, S. M. (2002) Chemical camouflage of nanospheres with a poorly reactive surface: towards development of stealth and target-specific nanocarriers. *Biochim. Biophys. Acta 1590*, 131–139.
(28) Futaki, S., Niwa, M., Nakase, I., Tadokoro, A., Zhang, Y., Nagaoka, M., Wakako, N., and Sugiura, Y. (2004) Arginine carrier peptide bearing Ni(II) chelator to promote cellular uptake of histidine-tagged proteins. *Bioconjugate Chem. 15*, 475–481.
(29) Takeuchi, T., Kosuge, M., Tadokoro, A., Sugiura, Y., Nishi, M., Kawata, M., Sakai, N., Matile, S., and Futaki, S. (2006) Direct and rapid cytosolic delivery using cell-penetrating peptides mediated by pyrenebutyrate. *ACS Chem. Biol. 1*, 299–303.
(30) Duchardt, F., Fotin-Mleczek, M., Schwarz, H., Fischer, R., and Brock, R. (2007) A comprehensive model for the cellular uptake of cationic cell-penetrating peptides. *Traffic 8*, 848–866.
(31) Maiolo, J. R., Ferrer, M., and Ottinger, E. A. (2005) Effects of cargo molecules on the cellular uptake of arginine-rich cell-penetrating peptides. *Biochim. Biophys. Acta 1712*, 161–172.
(32) Thoren, P. E., Persson, D., Isakson, P., Goksor, M., Onfelt, A., and Norden, B. (2003) Uptake of analogs of penetratin, Tat(48–60) and oligoarginine in live cells. *Biochem. Biophys. Res. Commun. 307*, 100–107.
(33) Terrone, D., Sang, S. L., Roudaia, L., and Silvius, J. R. (2003) Penetratin and related cell-penetrating cationic peptides can translocate across lipid bilayers in the presence of a transbilayer potential. *Biochemistry 42*, 13787–13799.
(34) Bjorklund, J., Biverstahl, H., Graslund, A., Maler, L., and Brzezinski, P. (2006) Real-time transmembrane translocation of penetratin driven by light-generated proton pumping. *Biophys. J. 91*, L29–31.
(35) Ellerby, H. M., Arap, W., Ellerby, L. M., Kain, R., Andrusiak, R., Rio, G. D., Krajewsky, S., Lombardo, C. R., Rao, R., Ruoslahti, E., Bredesen, D. E., and Pasqualini, R. (1999) Anti-cancer activity of targeted pro-apoptotic peptides. *Nat. Med. 5*, 1032–1038.
(36) Green, D. R., and Reed, J. C. (1998) Mitochondria and apoptosis. *Science 281*, 1309–1312.
(37) Minamikawa, T., Williams, D. A., Bowser, D. N., and Nagley, P. (1999) Mitochondrial permeability transition and swelling can occur reversibly without inducing cell death in intact human cells. *Exp. Cell Res. 246*, 26–37.
(38) Denizot, F., and Lang, R. (1986) Rapid colorimetric assay for cell growth and survival. Modifications to the tetrazolium dye procedure giving improved sensitivity and reliability. *J. Immunol. Methods 89*, 271–277.
(39) Callewaert, D. M., Genyea, J., Mahle, N. H., and Korzeniewski, C. (1983) The effect of lysed and nonviable target cells on the experimentally determined kinetic parameters for natural and antibody-dependent cytotoxicity. *J. Immunol. Methods 65*, 351–367.
(40) Ignatovich, I. A., Dizhe, E. B., Pavlotskaya, A. V., Akifiev, B. N., Burov, S. V., Orlov, S. V., and Perevozchikov, A. P. (2003) Complexes of plasmid DNA with basic domain 47–57 of the HIV-1 Tat protein are transferred to mammalian cells by endocytosis-mediated pathways. *J. Biol. Chem. 278*, 42625–42636.
(41) Iwasa, A., Akita, H., Khalil, I., Kogure, K., Futaki, S., and Harashima, H. (2006) Cellular uptake and subsequent intracellular trafficking of R8-liposomes introduced at low temperature. *Biochim. Biophys. Acta 1758*, 713–720.
(42) Perret, F., Nishihara, M., Takeuchi, T., Futaki, S., Lazar, A. N., Coleman, A. W., Sakai, N., and Matile, S. (2005) Anionic fullerenes, calixarenes, coronenes, and pyrenes as activators of oligo/polyarginines in model membranes and live cells. *J. Am. Chem. Soc. 127*, 1114–1115.
(43) Nishihara, M., Perret, F., Takeuchi, T., Futaki, S., Lazar, A. N., Coleman, A. W., Sakai, N., and Matile, S. (2005) Arginine magic with new counterions up the sleeve. *Org. Biomol. Chem. 3*, 1659–1669.
(44) Sakai, N., and Matile, S. (2003) Anion-mediated transfer of polyarginine across liquid and bilayer membranes. *J. Am. Chem. Soc. 125*, 14348–14356.
(45) Sakai, N., Takeuchi, T., Futaki, S., and Matile, S. (2005) Direct observation of anion-mediated translocation of fluorescent oligoarginine carriers into and across bulk liquid and anionic bilayer membranes. *ChemBioChem 6*, 114–122.
(46) Fretz, M., Jin, J., Conibere, R., Penning, N. A., Al-Taei, S., Storm, G., Futaki, S., Takeuchi, T., Nakase, I., and Jones, A. T. (2006) Effects of Na^+/H^+ exchanger inhibitors on subcellular localisation of endocytic organelles and intracellular dynamics of protein transduction domains HIV-TAT peptide and octaarginine. *J. Controlled Release 116*, 247–254.

BC700289W

Chemical Derivatization of Compact Disc Polycarbonate Surfaces for SNPs detection

María-José Bañuls, Francisco García-Piñón, Rosa Puchades, and Ángel Maquieira*

Instituto de Química Molecular Aplicada, Departamento de Química, Universidad Politécnica de Valencia, Camino de Vera s/n, Valencia, Spain. Received September 7, 2007; Revised Manuscript Received December 7, 2007

Compact discs have been proposed as an efficient analytical platform, with potential to develop high-throughput affinity assays for genomics, proteomics, clinics, and health monitoring. Chemical derivatization of CD surfaces is one of the keys to developing highly efficient microarraying-based assays on discs. Approaches for mild chemical modification of polycarbonate (PC) disc surface based on nitration, reduction, and chloromethylation reactions have been developed. Derivatized surfaces as amino and thiol are obtained for PC, maintaining unchanged the mechanical and optical properties of the discs. Studies of covalent attachment of oligonucleotide probes (5′ Cy5-labeled, 3′ NH_2-ended) on the modified surfaces have been performed to develop microarraying assays based on hybridization of cDNA strands and single nucleotide polymorphism discrimination (SNPs). A demonstration of the applicability to the compact disc audio/video technology for its use as analytical system is performed, including the employment of a commercial CD player to read the results on disc.

INTRODUCTION

Biologists, chemists, material scientists, and engineers have collaborated to develop bioassays, mainly DNA and protein microarraying chips. The development of surface-based assays in which numerous probes are immobilized in a spatially addressable manner has been one of the keys of these technologies. Such assay formats lend themselves well to miniaturization and multiplexing (*1, 2*). Nucleic acids (NAs) chip technology uses microscopic arrays of oligonucleotides immobilized on solid supports, as glass or silicon, for gene expression analysis (*3*), polymorphism (*4, 5*) or mutation detection (*6, 7*), DNA sequencing (*8, 9*), and gene discovery (*10, 11*).

Microarraying technologies have been developed quickly from the 1990s, but there are still a lot of improvements to be achieved. New immobilization ways, different assay formats, and alternative detection modes to improve microarraying methodologies are necessary.

Although glass is a popular support for DNA chip technology (*12*), efforts have led to the use of polymeric materials in the preparation of chip-based devices (*13, 14*). Solid polymers offer attractive mechanical and chemical properties, presentations, low cost, fabrication facility and flexibility, biocompatibility, and so forth. Attention has mainly been focused on the applications of microfluidic devices, and their fabrication techniques (*15*), alternative to glass as integrated platforms accomplishing sample manipulation and other analytical steps. Devices as biomicroelectromechanical systems (BioMEMS), laboratory-on-a-chip, and compact disc (CD) are being proposed for different applications (*16, 17*).

Standard CDs are composed of a polycarbonate (PC) substrate (1.2 mm thick), a reflective metalized layer (100 nm thick), and a poly(methyl methacrylate) (PMMA) protective lacquer (10 μm thick) as the ISO:9660 industry standard describes (*18*). Among the advantages of audio/video CD as analytical platform, one can highlight their big surface to spot thousands of capture probes; a low fluorescent background; the availability of high-quality materials at very low cost; the quadratic, circular, and spiral indexing; the easy handling and manufacture; and the possibility to use the top side for detection and the down side for recording; and further use of CD and DVD audio/video players as detectors making possible their application as point-of-care systems, especially interesting for the developing countries.

From the arraying applications of standard CDs, we must point out the seminal work of Kido et al. (*17*) demonstrating the potential to develop micro-ELISAs by surface adsorption of immunoreagents. Adsorption is a useful mode for protein immobilization; however, for nucleic acids it is necessary to use electrostatic forces (e.g., glass supports) or, more preferably, covalent attachment (*19*). In previous works, we showed the possibilities of using compact disc surfaces as high-throughput screening platforms for DNA microarraying (*20*) and for detection of low-abundancy pesticide residues (*21*). Considering all these features, the chemical derivatization of PC, the main CD constituent, to be applied on raw discs for microarraying-based assays can be achieved by means of different chemical or physical processes; the most common techniques include plasma-ion beam treatment, electric discharge, spin-coating, adsorption (*22*), surface grafting, chemical reaction, photoactivation (*23*), vapor deposition of metals, and flame treatment (*24, 25*). The problem is that most of the methods employed for the chemical surface modification of this polymer affect their optical (transparency) and mechanical (resistance, hardness, roughness, etc.) properties, not being applicable to compact discs without perturbing the original performance. The covalent attachment of probes, on the contrary, offers the advantage of a robust resulting surface while retaining its chemical integrity over an extended period of time. Besides, covalent interactions allow the performance of highly homogeneous and reproducible surfaces as self-assembled monolayers.

There are few works studying the chemical modification of CDs to attach probes on the surface. Remacle (*26*) developed DNA microarrays on CD by surface activation employing basic hydrolysis of polycarbonate. Acid groups generated on the polymeric surface allowed the attachment of DNA after treatment with a diamine. The information regarding this procedure

* Corresponding author. Fax: +34 96 387 93 49; Tel: +34 96 387 73 42; E-mail: amaquieira@qim.upv.es.

10.1021/bc7003457 CCC: $40.75 © 2008 American Chemical Society
Published on Web 02/07/2008

Table 1. Nucleotide Sequence of Probes and Targets Used

name	sequence (5′ to 3′)	5′ end	3′ end
SYM8	AATGCTAGCTAATCAATCGGG	Cy5	none
SYM22	$(T)_{15}$CCCGATTGATTAGCTAGCATT	none	C_7-NH_2
SYM23	TTACGATCGATTAGTTAGCCC$(T)_{15}$	Cy5	C_7-NH_2
SYM25	AATGCTAGCTAATCAATCGGG	biotin	none
SYM26	AATGCTAGATAATCAATCGGG	biotin	none

is limited and fragmentary. LaClair (*27*) proposed a screening method for the recognition between small-molecule ligands and biomolecules. It consists of the phosphorylation of the PC surface employing dichlorophosphate to achieve the covalent attachment of hydroxyl-ended ligands. Recognition between surface-expressed moieties and biomolecules is screened by an error determination routine. This innovative approximation shows the limitation in which each drive manufacturer has its own propietary firmware for error correction displaying a different sensitivity and thus different ability for analysis; thus, it necessary to always employ the same disc player to read the results. Also, they use a PTFE mask to perform the assays in wells on the disc surface.

Recently, Li (*28*) reported a polycarbonate surface-activation protocol by UV/ozone treatment which allows the covalent attachment of DNA microarrays and further hybridization assays. This method employs compact discs but cuts them into sheets and not in their original shape, and for the detection uses conventional optical drives (as microarray scanning).

Other authors performed high-quality self-assembled monolayers of alkanethiols on the gold side of CDs, employing them to fabricate inorganic material microstructures (*29, 30*). Likewise, they proposed the idea of DNA micropatterning by a tip-contact CD printer and water-resistant ink onto the gold CD substrate, and subsequent treatment with aqueous gold-etching reagent (*31*).

Recently, our group has reported the procedure for covalently attaching aminated oligonucleotides on PMMA isocyanate-modified compact discs to perform hybridization assays, carrying out the detection with a CD player (*32*).

In the present work, several approaches of covalent modification of PC discs are carried out, in order to get NH_2- and SH-modified surfaces. Results are applied for DNA probe immobilization, hybridization, and SNP (single nucleotide polymorphisms) discrimination assays on polycarbonate disc surface. A CD player is also integrated as a detection system to demonstrate the feasibility of the developed methodology.

EXPERIMENTAL PROCEDURES

Reagents. Ethylenediamine was purchased from Acros (Barcelona, Spain). Glutaraldehyde, Tween 20, 11-mercaptoundecanoic acid, gold-conjugated streptavidin from *Streptomyces avidinii*, and silver enhancer (solutions A and B) liquid substrate from membranes were purchased from Sigma-Aldrich (Madrid, Spain). Hibridization and SNP oligonucleotides (Table 1) were from Sigma-Genosys (Suffolk, UK). Oligonucleotide solutions were tip-contact printed onto the surfaces using a stamper (6 × 4 pins) from V&P Scientific, Inc. (San Diego, CA, USA).

Buffers employed were as follows: Saline sodium citrate (10xSSC, 0.9 M sodium chloride, 0.09 M sodium citrate, pH 7); carbonate buffer (10xCB, 0.5 M sodium carbonate, pH 9.6); phosphate buffer saline (10xPBS, 0.08 M sodium phosphate dibasic, 0.02 M sodium phosphate monobasic, 1.37 M sodium chloride, 27 M potassium chloride, pH 11); MES buffer (0.1 M 2-morpholinoethanesulfonic acid monohydrate, pH 6.5).

Apparatus. Fluorescent-arrayed probes were detected by both a microarray scanner, Genepix 4000B, from Axon Instruments (Union City, CA) at λ_{exc} 635 nm and λ_{em} 670 nm, and a homemade disc fluorescence reader (DFR) (*33*). Hybridization assays were detected by employing a standard CD player modified as described below.

Sessile drop contact angle measurements were performed with a Data Physics contact angle system OCA (Filderstadt, Germany). Two solvents were employed: water 18 MΩ and glycerol 99.9%.

The attenuated total reflectance Fourier transform infrared (ATR-FTIR) spectra were obtained using a Nicolet-Nexus FTIR with Multi-Bounce HATR, ZnSe 45° (Madrid, Spain). Each spectrum represents the average of 256 scans in 4 cm^{-1} resolution. The energy dispersion spectra (EDS) were collected on scattering electron microscopy JASCO-SEM, resolution 59 eV (Easton, MA).

Compact Discs. Golden CD-Rs partially transparents (30% reflectivity) provided by U-Tech Media Corp. (Tau-Yuan Shien, China) were used as platforms. These low-reflectivity recordable compact discs (L-CD, 1.2 mm thick polycarbonate discs, with a gold reflective layer of 30 nm, 12 cm diameter) allow the laser (780 nm) two functions: (a) reflected light (30%) lets the laser to follow the track, maintaining the rotation of the disc (autotracking) and, (b) transmitted light (70%) reaches the microarray spots located on the upper side of the CD, detecting the hybridization intensities by the amount of precipitate produced by an catalytic marker (gold) and a substrate (silver developer).

Disc Reader. A standard CD player from Plextor LLC (Fremont, CA) was used as the detector. The drive uses the servo control system to center and focus the beam on the spiral data track across the whole disc surface. The CD reader uses the original design of the CD players, taking advantage of the CD driver optical system to illuminate accurately the polycarbonate face of the L-CD (partially reflecting the laser and transmitting the rest through the PC surface to the photodiode). The controlled parameters of the optical disc drive include positioning of the laser toward the disc, scanning the whole disc surface while controlling the spatial resolution, and the linear rotation velocity of the disc. A planar photodiode (SLSD-71N6, Silonex, Montreal, Canada), 25.4 mm long, with a spectral sensitivity of 0.55 A/W at 940 nm and a spectral range between 400 and 1100 nm, absorbs the transmitted laser light and converts it into an analog electrical signal.

A reflective photosensor (EE-SY125, Omron, Scahumburg, USA) used to detect the analytical areas includes an infrared led of 950 nm and a phototransistor, with a sensing distance ranging from 0.5 mm to 2 mm. The operational principle of the photosensor is based on the detection of the different reflectivity between the sensing object and the disc. For that, the analytical areas are marked in the outer rim of the disc by low-reflectivity trigger footprints of 3.5 cm size. Because the unmarked perimeter presents higher reflectivity, the photosensor detects the marked areas, providing a trigger signal to the data acquisition board in order to start capturing data exclusively from those zones.

A custom-built electronic board (DAB) incorporates the planar photodiode and the photosensor. The function of the board is twofold: first, the detection of analytical areas, and second the amplification of the analog signal. Both functions are carried out at the same time the CD drive performs its original function of reading and writing data. In this way, during the data acquisition process only the signals from the detection areas are digitized by the data acquisition board (DAQ), stored in the computer, and deconvoluted into an image to further quantify. A scheme of the developed detection system is shown in Figure 1. The detector system is controlled by software running on a Windows-based computer connected to the PC through a universal serial bus interface (USB2.0) to become portable.

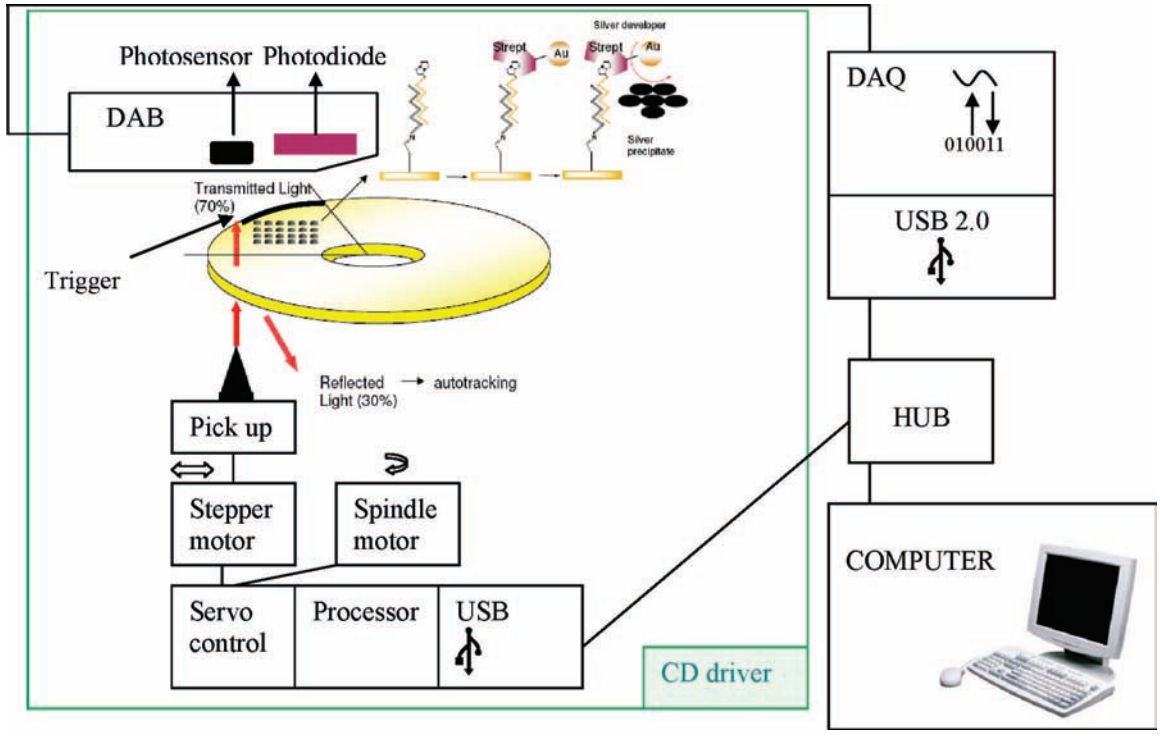

Figure 1. Detection system. The set of servo systems of the CD drive allows disc rotation and laser scanning. The transmitted light through the disc is transformed by the photodiode into an analog electrical signal (RF signal). At the same time, the photosensor detects the trigger footprints, starting the data collection on disc. The amplification/detection board (DAB) is integrated into the CD drive unit and contains the planar photodiode and the photosensor. The data acquisition board (DAQ) digitizes the analog signals and transfers them to the computer for processing.

Custom software was writing in Visual C++. The software provides the control to the CD/DVD driver to scan the surface of the disc, to modulate the disc linear rotation velocity to a specified spatial resolution, and to write data in the CD or DVD. Also, the software provides the control to the data acquisition board to configure the sampling frequency according to the disc rotation speed and desired angular resolution. To scan completely the surface of the L-CD, the software simulates the writing process of a 700 MBytes size file to a controlled disc rotation speed. The scan begins from the inner tracks of the disc, following the continuous spiral toward the outer tracks. The captured data of each detection area are represented within a sector that is formed by a set of arcs centered over a radial direction, starting from the inner toward the outer radio. The software collects the data of each area and stores them in independent files in uncompressed binary format, and displays them into a graphical gray scale code image.

Due to the spatial difference between samples taken horizontally (each 13 μm) and vertically (each 1.6 μm), a graphical horizontal adjustment is done to display a proportional $x-y$ image. This software allows export of the image in a gray-scale code to a compressed tif format or bitmap. Then, the images were processed with *Photoshop 7.0* (Adobe Systems Inc., San Jose, CA), to map the lightest and darkest pixels into black and white before quantifying with *GenePix* software (Axon Inst., Union City, CA). Signal intensities of each spot were calculated by background subtraction.

Disc Surface Modification. *Approach 1. Amination.* Transparent polycarbonate discs (PC1) were stirred in aqueous 30% HNO_3 solution for 30 min at 65 °C. The chips were washed with abundant distilled water (PC2). To reduce the nitro groups, chips were immersed into a solution of $NaBH_4$ 10% in 1xPBS and stirred at room temperature for 6 h, washed first with 1xPBS and finally with distilled water (PC3).

Approach 2. Glutaraldehyde Cross-Linking of Aminated PC. NH_2-functionalized PC discs (PC3, approach 1) were immersed into a solution of aqueous glutaraldehyde (5%, 1xPBS, pH 7) and stirred for 2 h at room temperature. Finally, they were thoroughly washed with 1xPBS and water, and air-dried (PC4). Tollen's and *p*-anisaldehyde tests were used to confirm the presence of aldehyde groups (*34*). Freshly prepared aldehyde-modified discs were always employed for DNA assay.

Approach 3. Thiolation. SH-modified discs were prepared as follows: aminated PC3 chips (approach 1) were immersed into an aqueous solution of 5 mM ethylenecarbodiimide (EDC), 5 mM sulfo-*N*-hydroxysuccinimide (NHSS), and 5 mM 11-mercaptoundecanoic acid in 0.1 M MES buffer, pH 6.5 (100 mL), and stirred at room temperature for 3 h. SH-modified discs were washed with water and ethanol and dried. The presence of SH groups on the treated surface was detected by Ellman's test (*34*). Material obtained was named PC5.

Approach 4. Chloromethylation. In a round-bottomed-flask, 2 g of $ZnCl_2$ and 2 mL of chloromethyl methyl ether were added to polycarbonate slides (PC1) immersed in cyclohexane (80 mL). The mixture was allowed to react at 60 °C for 2 h. Then, the slides were washed with distilled water (PC6).

Oligonucleotide Arraying. Six 5′ Cy5-labeled, 3′ NH_2-ended oligonucleotide (SYM23) solutions (1 and 10 μM) were prepared by employing different solvents: SSC (1x, 10x) pH 7, CB (1x, 10x) pH 9.6, and PBS (1x, 10x) pH 11. Afterward, 3 $\times$ 3 microarrays of each solution were printed onto the PC disc surface and incubated in a wet, dark chamber for 1 h at 42 °C or 4 h at room temperature. Finally, discs were thoroughly rinsed with PBS-T and water and dried. Immobilization results were read with a microarray scanner (cutting the discs in slides of 55 $\times$ 25 mm^2 size) or using the homemade DFR detector (whole disc).

Hybridization Assays. Amino-ended oligonucleotide SYM22 (0.1, 0.5, 1, and 5 μM) was covalently immobilized on the PC

surface as described above. After that, 35 μL of OVA in 1xCB (pH 9.6) was dispensed on each printed area, spread under a coverslip, and incubated for 30 min at room temperature in a moist chamber. After washing 5 min with PBS-T and water (5 min), discs were air-dried. Cy5-labeled target oligonucleotide (SYM8) was serial diluted between 0.001 and 0.2 μM in a mixture containing 6xSSC, 0.6% SDS, 0.1% salmon sperm DNA, and 2% BSA. 35 μL of the complementary oligonucleotide solution was dispensed on the microarrays and spread under a coverslip (22 $\times$ 22 mm^2). The temperature of hybridization was 37 °C, performing the incubation in a dark and humidified chamber for 1 h. After that, the discs were washed with PBS-T for 15 min, then water (5 min), and air-dried to be read.

For hybridization assays employing the CD player as detector, the biotin-ended target oligonucleotide (SYM25) was used following the procedure describe above. After the incubation and washing steps, 35 μL of 10 μg/mL streptavidin−gold in 1xPBS was deposited on each zone of the disc and again incubated for 20 min under a coverslip, in a moist chamber at 37 °C. After rinsing with PBS-T (15 min), water (5 min), and drying, 20 μL of silver developer solution was dispensed, and after 12 min, black spots appeared on the microarrays (*35*, *36*). The transparent polycarbonate disc was placed on a gold metallized CD and read with the CD driver as before.

Single Nucleotide Polymorphism Assays. SYM22 0.1, 0.5, 1, and 5 μM was covalently immobilized on polycarbonate aldehydized discs (PC4). After the OVA blocking step, different solutions (0.05 μM to 0.0005 μM) of SYM25 and SYM26 in 6xSSC, 0.6% SDS, 0.1% salmon sperm DNA, 2% BSA, and 25% formamide were prepared, dispensed on each printing zone, and spread under a coverslip. Discs were incubated for 1 h at 40 °C in a moist, dark chamber, washed with PBS-T then water, and air-dried. Treatment with streptavidin−gold and silver developer was carried out as described before.

RESULTS AND DISCUSSION

All the chemical modifications of chip materials including CD surfaces must consider two key points. First of all, they must maintain the mechanical and optical properties of the raw polymer, as otherwise, optical disc reading and chemical detection using a CD player is inapplicable. Moreover, the functionalization must perform the biomolecule covalent attachment in aqueous media, working at pH and ionic strength values close to the physiological ones, because proteins and nucleic acids can change their behavior in denaturing conditions. These requirements restrict the chemical treatments to mild reaction media.

Amine and thiol functionalizations have been chosen because they offer a well-known chemistry in the conjugation of biomolecules to different surfaces (*37*). They can be converted into suitable moieties for covalent immobilization of amino-ended biomolecules, making use of different cross-linkers such as dialdehydes or diisocyanates. Thiol functionalization is also of interest, because it can directly attach sulfhydryl-ended molecules through the formation of disulfide bridges.

Surface Modifications. Chemical derivatizations successfully developed are divided in four groups: amination, glutaraldehyde cross-linking, thiolation, and chloromethylation. Figure 2 shows the principal steps for each approach and the denomination of the transformed materials as well as the reaction conditions employed for amination, aldehydization, thiolation, and chloromethylation of PC.

The effect of solvents on plastic properties (diethyl ether, dichloromethane, hexane, cyclohexane, methanol, 2-propanol, water) was studied in order to select the most gentle with polycarbonate. It was found that cyclohexane, 2-propanol, and

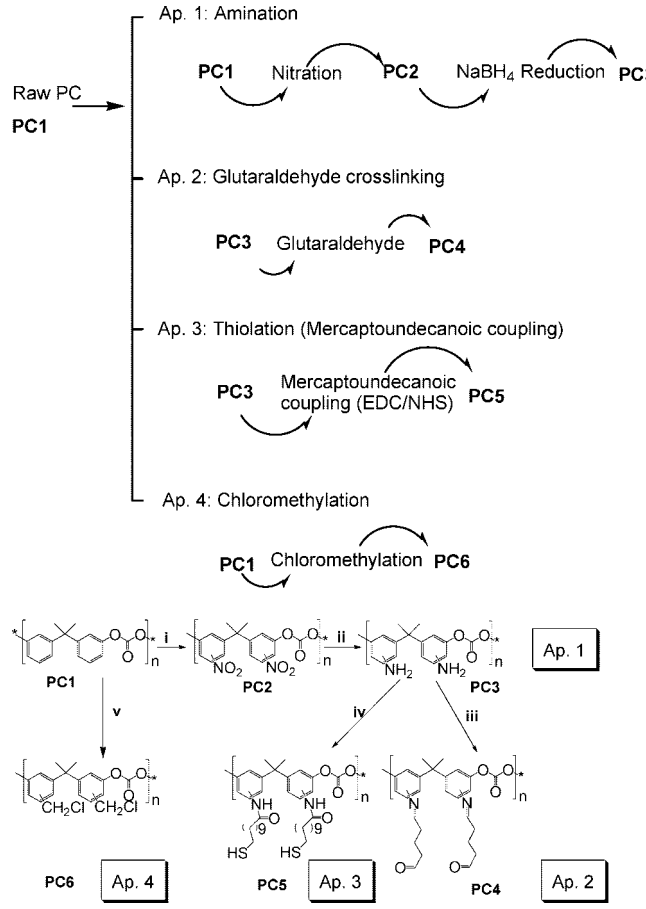

Figure 2. Scheme of surface chemical modifications performed to obtain PC2, PC3, PC4, PC5, and PC6. Reaction conditions employed for approaches 1, 2, 3, and 4.

water maintained the physical properties of PC discs without curling or cracking. Pieces of 55 $\times$ 25 mm^2 were immersed from 3 to 7 days in these solvents, confirming that the slides remained unaltered after these treatments.

In approach 1 (Figure 2), nitration of PC by heating at 65 °C in 30% aqueous HNO_3 for 30 min followed by reduction with $NaBH_4$ afforded an NH_2-modified surface. For approaches 2 and 3, NH_2-modified surfaces (PC3) were treated with glutaraldehyde to give CHO-modified PC and with 11-mercaptoundecanoic acid and EDC/NHSS to give SH-modified PC (approaches 2 and 3, Figure 2).

On the other hand, for the chloromethylation of PC (approach 4, Figure 2), reaction times from 1 to 24 h were studied. It was observed that, applying long exposure times, the roughness of chip surface increased. It resulted in cracking, and the slide became more fragile. Similar effects of fissuring were noticed when working at high temperatures (80–100 °C) for prolonged times (more than 2 h). Although the extent of the surface derivatization was larger when hard conditions were applied, we concluded that 2 h at 60 °C was optimal to reach enough surface modification without alteration of the physical properties of the material (Figure S4 in Supporting Information).

In order to confirm the success of NH_2, CHO, SH, and CH_2Cl modifications, and to study their surface and optical properties, several techniques were employed: contact angle, ATR-FTIR, EDS, and SEM.

Contact Angle. For all the raw and treated polymers, the water and glycerol contact angles were measured. The results are summarized in Table 2. The left and right contact angles of the solvent drops were measured immediately after its placement on the polymeric surface; no differences between contact angles

Table 2. Sessile Drop Contact Angles

surface	θ water	θ glycerol
PC1	78 ± 2	71.6 ± 0.9
PC2	57 ± 2	58 ± 7
PC3	66 ± 2	69 ± 1
PC4	59 ± 2	61.7 ± 0.9
PC5	63 ± 2	74.9 ± 1.5
PC6	53.9 ± 0.6	60.8 ± 1.5

were found. The reported values are the average of five separated water drops on a given substrate, and no significant variation among a set of substrates was found, so we asserted the homogeneity of the modifications carried out.

The measured values correlated well with those found in the literature for unaltered and treated PC surfaces. After chemical modification, a decrease in the water contact angle values was experimentally observed due to the presence of polar groups that increase the hydrophility of the materials.

ATR-FTIR. The attenuated total reflectance−Fourier transform infrared spectra were registered for PC1, PC2, PC3, PC4, PC5, and PC6 (Figure S1 of Supporting Information). PC3 showed a prominent peak around 3200–3400 cm^{-1} characteristic of OH and NH_2 stretching. Because the slides were baked at 40–50 °C before taking the spectra and they remained unaltered after several weeks, the possibility that these peaks were due to the surface solvatation or humidity was discarded. Besides, the derivatized surfaces containing neither amine nor hydroxyl groups (PC1, PC2, PC5, and PC6) did not show any peak around 3200 cm^{-1} after the baking process.

EDS. Energy dispersion spectra were collected for PC1, PC2, PC3, PC4, PC5, and PC6 (Figure S2 of Supporting Information). The successful incorporation of 11-mercaptoundecanoic acid and chloromethyl subunits was clearly observed in PC5 and PC6, respectively, because of the presence of heavy atoms such as S or Cl that are not present in the raw material.

On the other hand, as the reaction with 11-mercaptoundecanoic acid might lead to partial polymerization of the bifunctional acid and to the adsorption of the (hydrophobic) polymer on the substrate, a control experiment was performed to asses the amide formation. For that, PC1 was treated with 11-mercaptoundecanoic acid in a similar manner as PC3. After the reaction, both surfaces were washed exhaustively with a basic aqueous solution (NaOH 0.5 M), then with water, and ED spectra were registered; again for PC5, the existence of S was detected, while in the case of PC1, the presence of S was not observed.

The SEM images of derivatized PC surfaces showed smooth and defect-free surfaces; those images confirmed the homogeneity of the reactions (Figure S2 of Supporting Information).

Oligonucleotide Immobilization Studies. In order to demonstrate the viability of the developed chemical modifications for the covalent attachment of oligonucleotide probes on CD supports, PC discs were treated following the approaches 2 and 4 (Figure 2), because those approaches leave on the surfaces functional moieties (aldehyde and chloromethyl) able to covalently attach aminated probes. Preliminary studies of Cy5-labeled, NH_2-ended oligonucleotides arraying onto PC1, PC2, PC3, and PC4 (approaches 1 and 2, Figure 2) were done employing the above-described method.

Results obtained for every surface showed that no signal was detected for PC1 (raw material) and PC2 (approach 1, Figure 2). For PC3, the fluorescence reading gave some signal, although the oligonucleotide covalent attachment on PC3 was not possible. It was in agreement with the establishment of hydrogen bonds as well as electrostatic interactions between the oligo and the aminated surface.

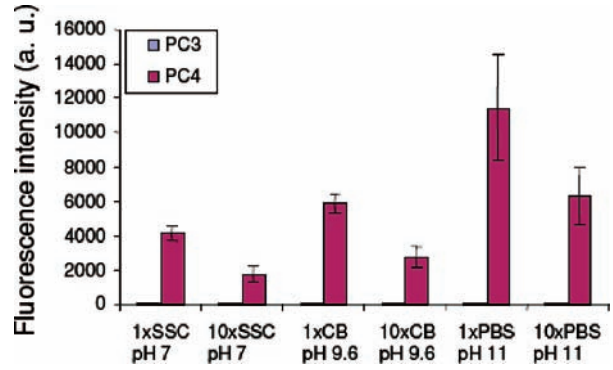

Figure 3. PC3 and PC4 fluorescence emission intensities for 10 μM Cy5-labeled, NH_2-ended oligonucleotide immobilized using different pH and ionic strength conditions. After washings, no significant fluorescence signal was obtained for PC3, while for PC4, the highest-intensity values are obtained for 1xPBS, pH 11.

PC4 provided significant signal (Figure 3); in this case, covalent attachment between NH_2-ended oligonucleotide and aldehydized surface was possible. Theoretically, the reaction should produce a Schiff base. However, the reaction is irreversible. Glutaraldehyde yields polymers in solution (*38*) that at acidic pH are cyclic hemiacetals. At neutral or slightly alkaline pHs at which cross-linking occurs, the α,β-unsaturated aldehyde polymers are formed which increase in length as pH is raised. It is probably the unsaturated polymer that cross-links the amino group of oligonucleotides. The interaction of the Schiff base with adjacent double bonds provides stability toward hydrolysis. With an excess of amino groups, nucleophilic addition of the ethylenic double bond is possible. Thus, it was noted (Figure 3) that the more basic the pH (*11*) is the more effective the covalent attachment.

On the other hand, it was also observed that an increase in the ionic strength of the printing solution decreased the effectiveness of the attachment. In order to eliminate possible electrostatic and hydrophobic/hydrophilic interactions between the surface and Cy5-labeled oligonucleotides, slides were treated with an acidic solution (aq 5% HCl). A 100% signal diminution was observed for PC3, while the signal in PC4 only suffers a reduction between 15% and 30%). This fact also confirmed the existence of covalent attachment for PC4. In all cases, SYM8 was used as a control to test the nonspecific interaction, and a fluorescence signal was almost inexistent for PC1, PC2, PC3, and PC4.

For PC6, derivatized following approach 4, attachment of aminated oligos via nucleophilic attack to the chloromethyl benzene rings was tried. Several times (0, 2, 4, and 16 h) and incubation temperatures (room temperature and 42 °C) were assayed. The best results were obtained for 4 h at 25 °C.

The registered fluorescence signal remained unchanged after washings for PC6 (Figure 4) indicating the existence of covalent interactions. However, the signal of PC1, used as control, was low and disappeared when the chips were exhaustively washed with water. In conclusion, derivatized polycarbonate PC6 seemed to also be appropriate for covalent attachment of the aminated oligonucleotides. This strategy has not been employed before for DNA microarraying, nor on glass. Thus, it is a novel and promising way to develop new surfaces to perform a stable link with DNA probes, and surely with proteins. The main advantage of this approach is that, by using one chemical modification step, the chip is ready for the oligonucleotide covalent attachment. On the other hand, this chemical modification could be successfully applied in other aromatic polymers such as polystyrene. The problem is that the reagents employed are more hazardous than for approach 2: organic solvent is used

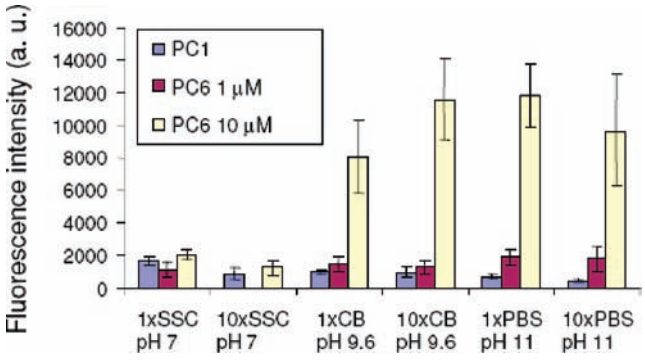

Figure 4. PC1 and PC6 fluorescence emission intensities (neat fluorescence) for 1 μM and 10 μM Cy5-labeled, NH_2-ended oligonucleotide immobilized at different pH and ionic strength conditions. For PC6, the best results are obtained for 1xPBS, pH 11. For PC1, there exists some remaining signal; this signal decreases after exhaustive washings, but not for PC6.

Table 3. Advantages and Disadvantages of Approaches 2 and 4 for Their Employment in Aminated Oligonucleotide Attachment on PC and Application to CD Technology

approach	advantages	disadvantages
2	aqueous solutions mild conditions better signal-to-noise ratio immobilization	three steps functionalization
4	one step functionalization applicable to other aromatic polymers higher neat fluorescence	very toxic reagents employed organic solvent required

instead of aqueous solutions, and chloromethyl ethyl ether is highly toxic. For that, approach 2 providing PC4 was chosen to perform the application to CD supports. In Table 3, the advantages and disadvantages of the proposed approaches are summarized.

Application to CD Supports. *(a) Hybridization Tests.* To demonstrate the applicability of the method to CD technology, PC transparent discs 0.6 mm thick were employed to perform the bioassay. The PC disc was derivatized according to the procedure involving nitration and reduction of the polycarbonate (approach 1), and then treated with glutaraldehyde (approach 3).

Due to the big sample spotting CD surface, eight different zones, each one also with four different probe concentrations, were printed. After the covalent attachment of SYM22, hybridization was performed employing serial dilutions of SYM 25 (0.2 to 0.001 μM). Afterwards, the CD was treated with gold-conjugated streptavidin for 20 min, washed, and revealed with silver enhancer for 12 min. The black precipitate was detected by the CD player. For this, the PC disc was fixed on the metallic layer of a standard gold metallized and unlacquered CD, partially transparent (70% light transmission) to 780 nm laser wavelength (this disc would allow the laser device to follow the track).

To set up the hybridization conditions, different concentrations of probe (from 0.1 to 20 μM) and target (from 0.5 to 100 nM), times, and temperatures were assayed. Black spots were obtained until 2.5 μM of target for all the probe concentrations. Also, several controls were performed avoiding the following: glutaraldehyde treatment, covalent attachment of probe, OVA blocking, hybridization solution, and streptavidin−gold incubation. None of them developed black spots except in the case of the control avoiding the treatment with OVA, as was expected.

Once the hybridization assay was finished, positive spots were obtained for all the target concentrations observable even to the naked eye. Results are shown in Figure 5.

The ammount of precipitate is directly related with the transmitted light of the CD player laser (the greater the precipitate, the less the light transmission). Thus, it is possible to establish a relationship between the hybridization effectiveness and the transmitted (or absorbed) light.

In Figure 6, probe and target saturation curves are shown. The optimal values were found for 5 μM of probe concentration, with it being possible to detect target concentrations of 2.5 nM. Also, it was possible to detect hybridization with probe concentrations as low as 0.1 μM. The sensitivity and efficiency reached with our procedure produced results slightly better than that obtained on PC CD surfaces employing other methodologies such as adsorption immobilization of probes and target hybridization reading with a fluorescence microarray scanner (*20*). In this case, 25 nM of target was detected by employing probe concentrations between 0.5 and 1.0 μM. This demonstrated the feasibility of our detection system, which provides results as good as or even better than those from the standard techniques.

(b) SNPs Assays. Finally, the application of the methodology to discriminate single nucleotide polymorphism was attempted. Two oligonucleotide strands with different sequences were selected: SYM25, the complementary strand of the immobilized probe on the PC disc (SYM22), and SYM26 differs from SYM25 in the base number nine, substituting cytosine for adenine (see Table 1). For that, different conditions were assayed

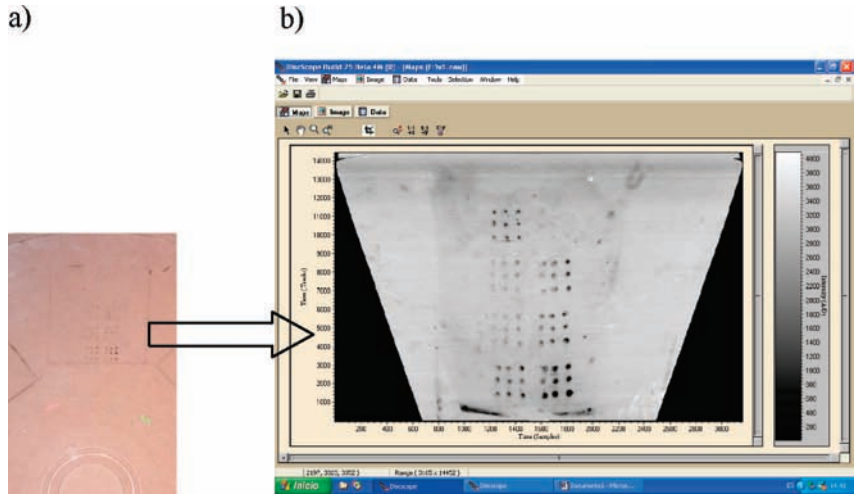

Figure 5. (a) Microarray spots developed on the PC disc after the chemical treatment and the hybridization assays. (b) Computer screen image displayed by the CD reader after the bioassay detection.

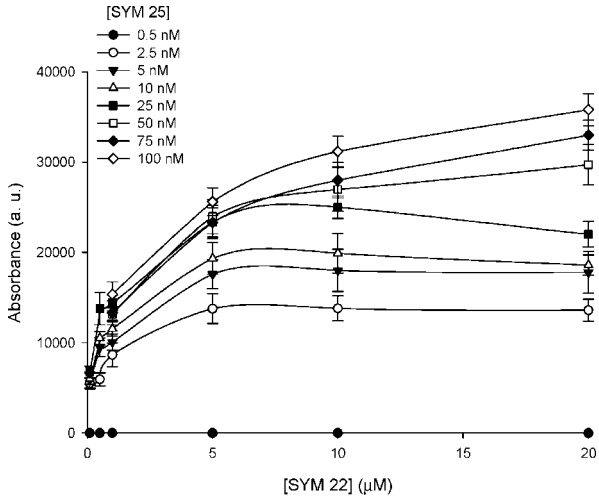

Figure 6. Probe saturation curves for chemically modified polycarbonate discs (approach 1). Reported data are from replicates of nine spots of each oligonucleotide concentration for each CD. (Experiment performed in triplicate).

(concentrations of probe and target; the use of formamide, temperature, and time) to find the optimal discrimination medium.

At the best assay conditions, SNPs resulted at 40 °C, for 1 h and 25% of formamide in the hybridization solution, with it being possible to discriminate between SYM25 and SYM26 at concentrations of 2.5 nM using probe concentrations ranging from 0.1 to 5 μM. These results agreed with our previous equivalent assays employing conventional methodologies.

The conditions employed for these hybridization assays are quite conventional, but they are useful for the aim of this work, that is to prove the principle identified in the introduction: the employment of CDs as suitable analytical platforms and CD players as effective and competitive detection systems. Further work focusing on the improvement of the bioassays to achieve better performance is currently in progress.

CONCLUSION

In this paper, successful modification of the PC surface has been demonstrated in a practical, mild, and clean way to be applied on compact discs as well as other supports that need to maintain their original physical properties. We have shown that modification of PC converts the surface into a suitable platform for covalently building DNA arrays on a standard CD. Among the derivatization approaches, amine-modified discs, by nitration of PC followed by reduction, were selected for the microarraying assays, because it is an easy and clean approach and employs only aqueous solutions, avoiding organic solvents.

One important point to note is that chemical modifications do not affect the general optical properties of the polymeric material, as can be seen from UV–vis or IR spectra of the chip. Also, the fluorescence background remains low. This fact is interesting in order to use different detection devices to read the bioanalytical results obtained on the compact disc.

Considering that polymeric materials can be fabricated into very different presentations and at competitive cost in comparison to glass, this is a promising approach for DNA microarraying chip development also with highly potential applications in fields such as protein, biomedical, genetics, drug discovery, or clinical diagnostic.

The feasibility of the method is fully demonstrated by the successful development of hybridization and SNP assays, which are read employing a standard CD player. The sensitivity and efficiency reached combining polymer chemical activation and CD reader agrees with that obtained for similar assays employing adsorption immobilization methodologies and fluorescence reading detectors.

The described procedure has potencial applications beyond merely the use of biotinylated targets; this strategy has been chosen as a proof of principle, but a big number of potential applications and variations can be easily envissoned; in general, every reaction providing a dark precipitate can be used as developer (e.g., oligonucleotides HRP, phosphatase alkaline, or gold labeling could be used with the proposed methodology). Besides, the employment of DVD technology (650 nm) as detector should allow the reading of fluorescence-labeled (Cy5) targets; in addition, Blu-ray technology (405 nm) could be employed. This work is now in progress. Finally, the search for suitable markers compatible with the CD player wavelength could be of great interest as well.

ACKNOWLEDGMENT

This work was funded by MCYT BQU 2003-02677 and CTQ2007-64735/BQU.

Supporting Information Available: Figure S1. ATR-FTIR of PC1, PC2, PC3, PC4, PC5, and PC6. Figure S2. SEM images and ED spectra of PC1, PC2, PC3, PC4, PC5, and PC6. Figure S3. Preliminary ^{1}H NMR studies for PC5. Figure S4. SEM images of PC6 after chloromethylation at 100 and 60 °C. This material is available free of charge via the Internet at http://pubs.acs.org/BC.

LITERATURE CITED

(1) Schena, M. (2003) *DNA Microarray Analysis*, John Wiley and Sons, Inc., Hoboken, NJ.

(2) Wilson, D. S., and Nock, S. (2002) Functional protein microarrays. *Curr. Opin. Chem. Biol. 6*, 81–85.

(3) Consolandi, C., Severgnini, M., Castiglioni, B., Bordoni, R., Frosini, A., Battaglia, C., Bernardi, L. R., and De Bellis, G. (2006) A structured chitosan-based platform for biomolecule attachment to solid surfaces: application to DNA microarray preparation. *Bioconjugate Chem. 17* (2), 371–377.

(4) Zammatteo, N., Jeanmort, L., Hamels, S., Courtuis, S., Louette, P., Hevesi, L., and Remacle, J. (2000) Comparison between different strategies of covalent attachment of DNA to glass surfaces to build DNA microarrays. *Anal. Biochem. 280* (1), 143–150.

(5) Patnaik, S., Swami, A., Sethi, D., Pathak, A., Garg, B. S., Gupta, K. C., and Kumar, P. (2007) *N*-(Iodoacetyl)-*N*′-(anthraquinon-2-oyl)-ethylenediamine (IAED): a new heterobifunctional reagent for the preparation of biochips. *Bioconjugate Chem. 18* (1), 8–12.

(6) Schena, M., Shalon, D., Davis, R. W., and Brown, P. O. (1995) Quantitative monitoring of gene expression patterns with a complementary DNA microarray. *Science 270*, 467–470.

(7) Vainrub, A., and Pettitt, B. M. (2003) Sensitive quantitative nucleic acid detection using oligonucleotide microarrays. *J. Am. Chem. Soc. 125* (26), 7798–7799.

(8) Becker, H., and Locascio, L. E. (2002) Polymer microfluidic devices. *Talanta 56* (2), 267–287.

(9) Lin, H., Kim, J., Sun, L., and Crooks, R. M. (2006) Replication of DNA microarrays from zip code masters. *J. Am. Chem. Soc. 128* (10), 3268–3272.

(10) Henry, A. C., Tutt, T. J., Galloway, M., Davidson, Y. Y., McWhorter, C. S., Soper, S. A., and McCarley, R. L. (2000) Surface modification of poly. (methyl methacrylate) used in the fabrication of microanalytical devices. *Anal. Chem. 72*, 5331–5337.

(11) Clark, D. T., and Feast, W. J. (1978) *Polymer Surfaces*, Wiley, Chinchester.

(12) Hoheisel, J. D. (2006) Microarray technology: beyond transcript profiling and genotype analysis. *Nat. Rev. Genet. 7* (3), 200–210.

(13) Soper, S. A., Henry, A. C., Vaidya, B., Galloway, M., Wabuyele, M., and McCarley, R. L. (2002) Surface modification of polymer-based microfluidic devices. *Anal. Chim. Acta 470* (1), 87–99.

(14) Reyes, D. R., Iossifidis, D., Auroux, P. A., and Manz, A. (2002) Micro total analysis systems. 1. introduction, theory, and technology. *Anal. Chem. 74* (12), 2623–2636.

(15) Auroux, P. A., Iossifidis, D., Reyes, D. R., and Manz, A. (2002) Micro total analysis systems. 2. analytical standard operations and applications. *Anal. Chem. 74* (12), 2637–2652.

(16) Madou, M., Zoval, J., Jia, G., Kido, H., Kim, J., and Kim, N. (2006) Lab on a CD. *Annu. Rev. Biomed. Eng. 8*, 601–628.

(17) Kido, H., Maquieira, A., and Hammock, B. (2000) Disc-based immunoassay microarrays. *Anal. Chim. Acta 411*, 1–11.

(18) Pohlmann, K. C. (1992) *The Compact Disc Handbook*, A-R Editions, Madison, WI.

(19) Heise, C., and Bier, F. F. (2006) Immobilization of DNA on microarrays. *Top. Curr. Chem. 261*, 1–25.

(20) Morais, S., Marco-Molés, A., Puchades, R., and Maquieira, A. (2006) DNA microarraying on compact disc surfaces. Application to the analysis of single nucleotide polymorphisms in Plum Pox virus. *Chem. Commun. 22*, 2368–2370.

(21) Morais, S., Carrascosa, J., Mira, D., Puchades, R., and Maquieira, A. (2007) Micro-immunoanalysis on standard compact discs to determine low abundant compounds. *Anal. Chem. 79* (20), 7628–7635.

(22) Carion, O., Souplet, V., Olivier, C., Maillet, C., Medard, N., El-Mahdi, O., Durand, J. O., and Melnyk, O. (2007) Chemical micropatterning of polycarbonate for site-specific peptide immobilization and biomolecular interactions. *ChemBioChem 8*, 315–322.

(23) Bora, U., Sharma, P., Kumara, S., Kannanb, K., and Nahar, P. (2006) Photochemical activation of a polycarbonate surface for covalent immobilization of a protein ligand. *Talanta 70*, 624–629.

(24) Garbassi, F., Morra, M., and Occhiello, E. (1994) *Polymer Surfaces*, Wiley, Chichester.

(25) Chan, C. M. (1993) *Polymer Surface Modification and Characterization*, Hanser Publications, Munich.

(26) Remacle, J., Alexandre, I., and Houbion, Y. US Patent 177144, 2002.

(27) La Clair, J. J., and Burkart, M. D. (2003) Molecular screening on a compact disc. *Org. Biol. Chem. 1*, 3244–3249.

(28) Li, Y., Wang, Z., Ou, L. M. L., and Yu, H.-Y. (2007) DNA detection on plastic: Surface activation protocol to convert polycarbonate substrates to biochip platforms. *Anal. Chem. 79*, 426–433.

(29) Yu, H. Z. (2001) Self-assembly on "recordable CDs". *Anal. Chem. 73* (19), 4743–4747.

(30) Yu, H. Z., Rowe, A. W., and Waugh, D. M. (2002) Templated electrochemical deposition of zirconia thin films on "recordable CDs". *Anal. Chem. 74* (22), 5742–5747.

(31) Yu, H.-Z. (2004) New chemistry on old CDs. *Chem. Commun. 23*, 2633–2636.

(32) Bañuls, M. J., Gonzalez-Pedro, M. V., Puchades, R., and Maquieira, A. (2007) PMMA-Isocyanate-modified digital disc as support for oligonucleotide based assays. *Bioconjugate Chem. 18* (5), 1408–1414.

(33) Maquieira, A., Puchades, R., Bañuls M. J., Mira, D., Llorente-Sáez, R., and Martí, J. (2006) System for Chemical Analysis and Data Storage and Treatment on Compact Discs. European Patent Pending, P160ES00, 2006.

(34) Vazquez, J., Qushair, G., and Albericio, F. (2003) Tests for SPS. *Methods Enzym. 369*, 21–27.

(35) Cao, X., Wang, Y. F., Zhang, C. F., and Gao, W. J. (2006) Visual DNA microarrays for simultaneous detection of *Ureaplasma urealyticum* and *Chlamydia trachomatis* coupled with multiplex asymmetrical PCR. *Biosens. Bioelectron. 22*, 393–398.

(36) Alexandre, I., Hamels, S., Dufour, S., Collet, J., Zammatteo, N., De Longueville, F., Gala, J. L., and Remacle, J. (2001) Colorimetric silver detection of DNA microarrays. *Anal. Biochem. 295*, 1–8.

(37) Hermanson, G. T. (1996) *Bioconjugate Techniques*, Academic Press, San Diego, CA.

(38) Wong, S. S. (1991) Homobifunctional cross-linking reagents. In *Chemistry of protein conjugation and cross-linking* pp 75, CRC Press Inc., Boca Raton.

BC7003457

Purification of His-Tagged Proteins with [Desthiobiotin−BSA−EDTA] Conjugates Exhibiting Resistance to EDTA

Guy Patchornik*

Affisink Biotechnology Ltd, 11 Hamaccabee St. Kiryat-Ono 55572, Israel. Received October 2, 2007; Revised Manuscript Received December 5, 2007

Two His-tagged proteins (His_6-P38 and His_6-Protein A) were purified by specific precipitation utilizing nonsoluble macrocomplexes composed of: BSA conjugates (modified with desthiobiotin−NHS and EDTA−dianhydride), tetrameric avidin, and Cu^{2+} ions. The generated pellets containing bound His-tagged proteins are washed with EDTA (25–100 mM) and then eluted in relatively high purity (≥90%) devoid the macrocomplexes. Three different BSA conjugates were synthesized (DB−BSA−EDTA, DB−BSA−EDTA-A, DB−BSA−EDTA-B) and their adsorption capacities (3.8–6.4 μmol/g of BSA conjugate) as well as the recovery yields of His-tagged proteins obtained with them (44–84%) determined. The data demonstrate that capacity is dependent on the stochiometric ratio of modifying reagents (i.e., desthiobiotin−NHS and EDTA−dianhydride) used during the synthesis of the BSA conjugates. Copper ions were found to be significantly superior to Zn^{2+}, Co^{2+}, and Ni^{2+}. BSA conjugates could be regenerated in moderate yields (74–83%) by incubating them at 88 °C in the presence of biotin (10 mM) at pH 7. The absence of resins leads to formation of small pellets (1–5 mg) and utilization of minute volumes of elution buffer (50–100 μL). Hence, concentrated preparations can be obtained, and a reconcentration step may be circumvented.

INTRODUCTION

Immobilized metal-affinity chromatography (IMAC) has become a universal approach for isolation of native as well as recombinant proteins possessing surface-exposed amino acid residues capable of binding immobilized metal ions (Scheme 1, A). The approach was first demonstrated on metalloproteins (*1*) but became widespread after the extensive work of Porath (*2–4*) and Sulkowski (*5–7*).

Specific adsorption is accomplished when stable ternary complexes are formed between electron donor groups from the protein and metal ions bound on different chromatographic supports (Scheme 1, A). Most of these commercial supports are modified with tridentate (e.g., iminodiacetic acid-IDA), tetradentate (e.g., nitriloacetic acid (NTA), carboxymethylated aspartic acid (CM-Asp)), or pentadentate (e.g., *N*,*N*,*N*′-tris-carboxymethyl ethylene diamine (TED)) metal chelators. The terms tridentate, tetradentate, and pentadentate describe the number of occupied coordination bonds formed between a metal ion and a particular chelator; for example, a tridentate chelator would form three bonds with a metal ion leaving five additional coordinating sites (in the octahedral complex) available for binding. These would be generally occupied by water molecules but will be displaced by appropriate electron donor groups from a protein. Whereas tetradentate and pentadentate chelators bind metal ions with high affinity, exhibit low levels of leached metal, and possess low binding capacities (due to the limited number of coordination sites available for protein binding), tridentate chelators bind metal ions with lower affinity, lead to greater metal leakage, but result in greater binding capacities (*8*, *9*).

Although divalent metal ions are generally used (Cu^{2+}, Ni^{2+}, Zn^{2+}, Co^{2+}), trivalent metal cations were found useful as well. For example, Fe^{3+} ions enabled purification of phosphoproteins and organophosphates (*10–12*). Among the different amino acids capable of binding immobilized metal ions (Glu, Asp, Tyr, Cys, Arg, His, Lys, Met, Trp, Tyr), His was found to be the major participant both in proteins (*13, 14*) and in peptides (*15–17*). Nevertheless, it has been shown that the presence of aromatic residues (Trp, Tyr, Phe) in proximity to the histidine residue contribute to the binding affinity (*6, 18*).

The limitation of the approach to naturally surface exposed His residues was circumvented with the advent of recombinant DNA technology which provided a practical route to introduce His residues at defined sites. It was Hochuli et al. (*19, 20*) who demonstrated that expression of proteins with sequential His sequences (i.e., His-tag) at the N or C terminal, together with a resin modified with NTA and loaded with Ni^{2+} ions, leads to a general and efficient isolation process for His-tagged recombinant proteins. Moreover, the observation that the binding affinity increases with the number of water-exposed His residues (*5*) implied that recombinant His-tagged proteins would bind with high affinity and may allow the presence of weak chelators (e.g., imidazole) during the isolation process. The latter would suppress nonspecific binding of impurities containing naturally occurring His residues and increase the purity.

In addition to the compatibility of the His-tag in most prokaryotic and eukaryotic expression systems (*21*), the IMAC approach was found to possess several major advantages over biospecific affinity chromatography: these include high adsorption capacities, high stability of the ligand, mild eluting conditions, applicability to proteins under denaturing conditions, and the capability to regenerate the columns at low cost (*18*).

Scheme 1A illustrates the dependence of the IMAC approach with respect to water-insoluble resins which ideally would exhibit (a) high permeability to the target, (b) hydrophilic characteristics, (c) chemical inertness, and (d) microbiological resistance and cost effectiveness (*4*). Currently, no such ideal resin is available, and the ones which are exhibit some of the above characteristics but not all. For example, silica-based supports provide excellent mechanical properties but tend to lead to irreversible nonspecific adsorption (*22*).

* Corresponding author. E-mail: guy@affisink.com, Tel: 972-8-9302575, Fax: 972-8-9302565.

10.1021/bc700368y CCC: $40.75 © 2008 American Chemical Society
Published on Web 03/01/2008

Scheme 1. Schematic Illustration of His-Tagged Protein Purification Utilizing Modified Resins (A) or Nonsoluble [Desthiobiotinylated-BSA-EDTA: Avidin: Cu^{2+}] Macrocomplexes (B)

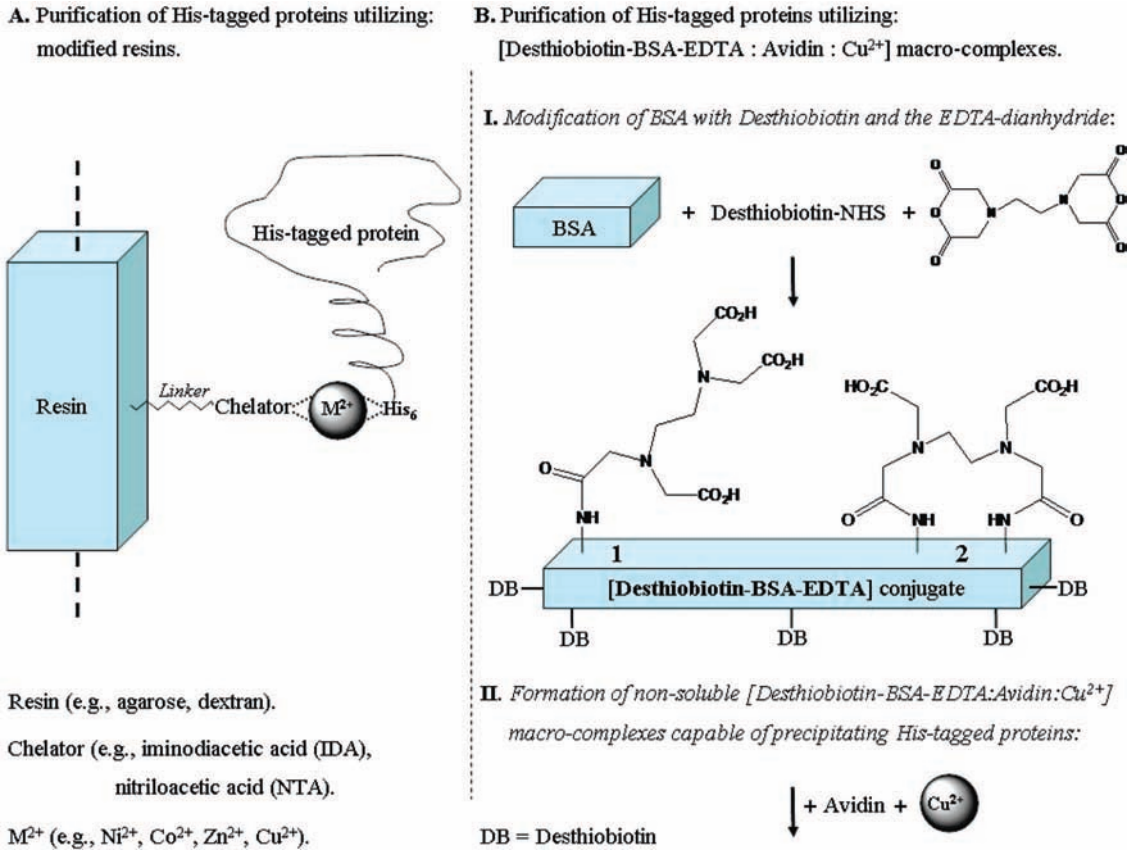

This state of affairs motivated us to initiate the presented study with the objective of developing an alternative platform for IMAC where no resins are utilized and thus no columns are required. The approach is based on specific precipitation of His-tagged proteins together with insoluble macrocomplexes comprising modified BSA[1] conjugates (desthiobiotinylated−BSA−EDTA (DB−BSA−EDTA)), tetrameric avidin, and Cu^{2+} ions. Impurities present in the supernatant are removed by centrifugation; the pellet is washed with EDTA and the His-tagged protein is eluted with imidazole, whereas the [DB−BSA−EDTA: Avidin] macrocomplexes are not.

EXPERIMENTAL PROCEDURES

Materials. For SDS-PAGE, prestained protein markers and Tris were from Bio-Rad. All other reagents were of analytical grade. Avidin, biotin, BSA, ethylenediaminetetraacetic dianhydride, octyl-β-D-glucopyranoside, *n*-dodecyl-β-D-maltopyranoside; urea, and EDTA were from Sigma. Desthiobiotin *N*-hydroxysuccinimidyl ester was from Berry and Associates, Michigan/Illinois. Recombinant His_6-tagged protein A was from BioVision, Inc., Palo Alto, California. Recombinant His_6-tagged P38 was expressed and purified according to Diskin et al. (*23*).

Protein Analysis. Modified BSA conjugates concentration was determined by UV quantitative analysis at 280 nm.

Electrophoresis and Densitometry. Samples were loaded onto a 10% Bis-Tris SDS-polyacrylamide gel (1 mm thickness) according to Laemmli (*24*) and developed for 1 h at constant 120 V. All gels were stained with Coomassie Brilliant Blue R250, and the intensity of bands was measured by densitometry using the Scion Image program. These measurements were used for determining purity and quantification of recovery yields of the target His-tagged proteins.

Preparation of Desthiobiotin−BSA−EDTA (DB−BSA−EDTA) Conjugates. Native BSA (10.6 mg/mL) was modified simultaneously with desthiobiotin *N*-hydroxysuccinimidyl ester (4.2 mg/mL) and ethylenediaminetetraacetic dianhydride (0.85 mg/mL) in the presence of 0.1 M NaPi at pH 8. Both desthiobiotin−NHS and EDTA−dianhydride were first dissolved in DMSO and only then was BSA added slowly to their mixture with constant vortexing. The stochiometric ratio among desthiobiotin−NHS, BSA, and EDTA−dianhydride was 80:1:20, respectively. The mixture was rotated at room temperature for 4 h, the excess of reagents was removed by extensive dialysis in the presence of 50 mM Tris at pH 8, and the preparation was kept at −20 °C until use.

Preparation of DB−BSA−EDTA-A and DB−BSA−EDTA-B Conjugates. These were synthesized according to the above protocol used for DB−BSA−EDTA but with different stochiometric ratios. For the DB−BSA−EDTA-A conjugate, the stoichiometric ratio among the desthiobiotin−NHS, BSA, and EDTA−dianhydride was 50:1:50, and for the DB−BSA−EDTA-B conjugate, the stochiometric ratio was 20:1:80, respectively.

Preparation of Desthiobiotin−BSA (DB−BSA) Conjugates. This protocol is identical to the one described for DB−BSA−EDTA but was performed in the absence of EDTA−dianhydride.

[1] Abbreviations: BSA, Bovine serum albumin; DB, Desthiobiotin; DB-BSA, Desthiobiotinylated BSA conjugate; DB-BSA-EDTA, Desthiobiotinylated-BSA-EDTA conjugate; DDM, *n*-dodecyl-β-D-maltopyranoside; EDTA, Ethylenediamine tetraacetic acid; HMW, high molecular weight; IDA, Iminodiacetic acid; MALDI-TOF, Matrix assisted laser desorption ionization time-of-flight; NTA, Nitriloacetic acid; OG, Octyl-β-D-glucopyranoside; PAGE, polyacrylamide gel electrophoresis; SDS, sodium dodecyl sulfate; TED, Tris(carboxymethyl)ethylene diamine.

General Purification Protocol for His_6-Tagged Proteins Utilizing DB−BSA−EDTA Conjugates. Purification requires four sequential steps. Step I. Preparation of water-insoluble [DB−BSA−EDTA: Avidin: Cu^{2+}] macrocomplexes: Into a medium (100 μL total volume) containing 50 mM Tris at pH 8 and DB−BSA−EDTA (0.75–1.5 mg/mL), a freshly prepared avidin solution (4 mg/mL) was added with constant vortexing. Copper ions (50 mM) were added and a centrifugation step (14K, 1 min) was applied. The supernatant was excluded and the pellet was resuspended again in 50 μL of Tris 50 mM at pH 8. An additional spin (14K, 1 min) was performed, and the supernatant was removed. Step II. Binding: The pellet was resuspended in 50 mM Tris pH 8, 25 mM NaCl, and a cell lysate containing the target His-tagged protein in a total volume of 100 μL. After a short incubation (5–10 min), the supernatant was removed (14K, 1 min). Step III. Washing: The pellet was washed with 50 mM Tris pH 8, 25 mM NaCl, and 25–100 mM EDTA in a total volume of 100 μL. A spin was applied and the supernatant excluded. Step IV. Elution: The His-tagged protein was eluted from the pellet into 50–100 μL of 50 mM imidazole and 100 mM Tris pH 7 within 5–10 min. All steps were performed at 4 °C. Purity may be increased by washing the pellet twice, loading lower concentrations of copper ions during the preparation step of the macrocomplexes or by addition of mild detergents (e.g., 1% of βOG) during the binding and washing steps.

Inhibition of Purification. The purification process was suppressed when (a) no Cu^{2+} was added to the medium, (b) imidazole (25 mM) was present during the binding step, or (c) the DB−BSA conjugate (0.75 mg/mL) was used instead of the DB−BSA−EDTA.

Purification with Other Metal Cations. Isolation was performed according to the general purification protocol but in the presence of 50 mM of Zn^{2+}, Ni^{2+}, or Co^{2+} ions.

The effect of Octyl-β-D-glucopyranoside (βOG) and Urea on Process Efficiency. Into the above general purification protocol, increasing concentrations of βOG (1%, 3%, and 6%) and urea (1 M, 3 M, and 8 M) were added. Both reagents were dissolved in 50 mM Tris pH 8 prior to their use.

Regeneration of DB−BSA−EDTA, DB−BSA−EDTA-A, and DB−BSA−EDTA-B Conjugates. All three BSA conjugates were regenerated in 74–83% yield by incubating the pellet at 88 °C for 5 min in 0.1 M Tris pH 7 and 10 mM of biotin. These recycling conditions are similar to those described earlier with other modified albumins (*25*).

Electron Spray Analysis (ESI). Peptide fingerprinting was performed on a Bruker Reflex III matrix assisted laser desorption ionization time-of-flight mass spectrometer (Bruker, Bremen, Germany) equipped with a delayed extraction ion source, a reflector, and a 337 nm nitrogen laser.

RESULTS

Purification of Recombinant His_6-P38 with [DB−BSA−EDTA: Avidin: Cu^{2+}] Macrocomplexes. Isolation of His-tagged proteins requires the synthesis of DB−BSA−EDTA conjugates from BSA, desthiobiotin−NHS, and EDTA−dianhydride. These conjugates were expected to possess higher molecular weight than the native BSA and to exhibit a different migration pattern. The results in Figure 1 (lanes 1–2) show that the majority of the native BSA was indeed converted into higher molecular weight entities. To bind and precipitate His_6-P38, we prepared insoluble [DB−BSA−EDTA: Avidin: Cu^{2+}] macrocomplexes and added them to the medium. After a short binding step and a spin, the generated pellets were washed with EDTA (25 mM) and the target was eluted with imidazole (50 mM) at pH 7. When we increased the EDTA concentration from 25 mM to 50, 75, and 100 mM, we found that the reductions in the yield relative to the one obtained in the presence of 25 mM EDTA were 23%, 34%, and 48%, respectively (Figure 1, lanes 4–7). Hence, the greater the EDTA concentration during the washing step, the greater the reduction in yield. Nevertheless, it was surprising to find out that, even in the presence of 100 mM of EDTA, 52% of the His_6-P38 was still present in the pellet. It should be noted that when higher NaCl concentrations were employed (e.g., 50–200 mM) the efficiency of the process was decreased due to solubilization of the macrocomplexes (not shown). Yield may be improved by altering the avidin concentration; increasing the BSA conjugate concentration or inclusion of mild detergents (e.g., 1% of βOG) during the elution step.

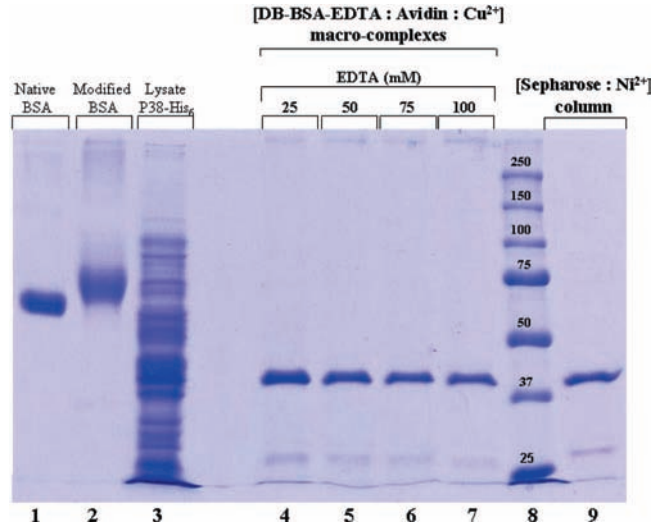

Figure 1. Purification of His_6-P38 with [DB−BSA−EDTA: Avidin: Cu^{2+}] macrocomplexes. Lane 1, native BSA; lane 2, DB−BSA−EDTA conjugates; lane 3, lysate containing His_6-P38; lanes 4–7, recovered protein after washing the pellets with indicated EDTA concentrations followed by elution with 50 mM imidazole; lane 8, Bio-Rad prestained protein markers; lane 9, recovered protein from the same lysate utilizing a [Sepharose: Ni^{2+}] column. The gel is Coomassie stained.

Purification of Recombinant His_6-P38 with a [Sepharose: Ni^{2+}] Column. When the same lysate containing His_6-P38 was applied on a [Sepharose: Ni^{2+}] column, a band with a similar migration pattern to the one observed with the macrocomplexes was observed (Figure 1, lane 9). This was the first indication suggesting that the same His-tagged protein was recovered by the commercial Ni $^{2+}$column and the macrocomplexes.

Electron Spray Ionization (ESI) Analysis. Purified bands obtained via the [DB−BSA−EDTA: Cu^{2+}] macrocomplexes or via the [Sepharose: Ni^{2+}] column were analyzed by ESI. High sequence identity to the known sequence of the MK14_HUMAN Mitogen-activated protein kinase 14 (EC 2.7.11.24) was observed with both approaches (42% for the macrocomplexes and 46% for the [Sepharose: Ni^{2+}] column), thus implying that the same His-tagged protein was isolated.

Requirement for Cu^{2+} Ions and Covalently Bound EDTA. Two independent experiments demonstrated the participation of Cu^{2+} ions in the process: (a) Purification of His_6-P38 was achieved only when Cu^{2+} ions were added to the [DB−BSA−EDTA: Avidin] macrocomplexes (Figure 3A, lanes 3–4). (b) The presence of imidazole (25 mM) during the binding step inhibited the process. Imidazole was expected to compete on immobilized Cu^{2+} ions and inhibit the binding of His_6-P38 to the macrocomplexes. The results obtained in Figure 3A, lane 5 support this speculation. The dependence of the approach on covalently bound EDTA was demonstrated by performing the process with a BSA conjugate (DB−BSA) lacking EDTA. As expected, no band corresponding to the target His_6-P38 was obtained (Figure 3A, lane 6).

Figure 2. Electron spray ionization (ESI) analysis. Purified proteins were analyzed by ESI, and the obtained peptide fragments were compared to the known sequence of the MK14_HUMAN Mitogen-activated protein kinase 14 (EC 2.7.11.24). Isolated proteins recovered via the presented approach (A) or via a [Sepharose: Ni^{2+}] column (B) exhibited 42% and 46% sequence identity, respectively. Matched peptides are shown in bold red.

Comparing Process Efficiency with Other Divalent Cations. Four metal cations are generally utilized in purification of His-tagged proteins; these include Cu^{2+}, Zn^{2+}, Ni^{2+}, and Co^{2+} (*15*). When we tested the above, we found that Cu^{2+} ions were significantly more efficient than Zn^{2+}, Co^{2+}, and Ni^{2+} (Figure 3B, lanes 3–6).

Effect of Octyl-β-D-glucopyranoside (OG) and Urea. The gel in Figure 3C evaluates the effect of a mild detergent (OG) and urea on the process. Whereas the presence of 1–6% of OG did not show any significant effect (Figure 3C, lanes 4–6), the addition of 1 M of urea decreased the process efficiency (Figure 3C, lane 7). When urea concentration was raised to 8 M, the process was quantitatively abolished (Figure 3C, lane 9). This implies that the approach may not be applicable for purification of His-tagged proteins under denaturing conditions.

Binding Capacities of DB−BSA−EDTA, DB−BSA−EDTA-A, and DB−BSA−EDTA-B Conjugates. Capacity experiments were performed by precipitating increasing concentrations of the commercial highly purified His_6-tagged protein A at constant concentrations of the three BSA conjugates (0.4 mg/mL). The presence of His_6-tagged protein A in the supernatant after the precipitation step defined the maximum capacity of the particular BSA conjugate. The data suggest that the higher the EDTA−dianhydride concentration utilized during the synthesis of the BSA conjugates, the greater the capacity value (Table 1).

DISCUSSION

This study investigates an alternative approach for immobilized metal affinity chromatography (IMAC) outlined in Scheme 1A, which does not entail the usage of resins. The approach is based on specific precipitation of His-tagged proteins together with insoluble macrocomplexes composed of BSA conjugates (DB−BSA−EDTA), avidin, and Cu^{2+} ions (Scheme 1B, I−II). The strategy requires preparation of modified BSA conjugates by simultaneous modification of BSA with desthiobiotin−NHS and EDTA−dianhydride. These conjugates possess two unique features: (a) the ability to become water-insoluble in the presence of free avidin (this phenomenon, previously demonstrated with a series of albumins, derives from the capability of free tetrameric avidin to cross-link desthiobiotinylated albumins via their covalently bound desthiobiotins and to generate HMW macrocomplexes which precipitate (*25*)) (b) the capacity to bind His-tagged proteins via immobilized Cu^{2+} ions (Scheme 1B, I−II).

Purification can then be accomplished in four sequential steps. Step I: Synthesized DB−BSA−EDTA conjugates are interconnected with native avidin to form insoluble macrocomplexes of [DB−BSA−EDTA: Avidin] which are then loaded with Cu^{2+} ions. The formation of insoluble macrocomplexes enables efficient removal of free or weakly bound Cu^{2+} ions (by centrifugation) and is equivalent to washing IMAC columns with binding buffer prior to the binding step. Step II: Addition of the [DB−BSA−EDTA: Avidin: Cu^{2+}] macrocomplexes to a medium containing the His-tagged protein will allow specific binding, whereas impurities are removed by centrifugation. Step III: The pellet containing the adsorbed His-tagged protein is washed once to remove nonspecifically adsorbed contaminants. Step IV: The His-tagged protein is eluted in the presence of imidazole. Under these conditions, the [DB−BSA−EDTA: Avidin] macrocomplexes do not dissociate and are kept in the pellet.

Indeed, incubation of [DB-BSA-EDTA: Avidin: Cu^{2+}] macrocomplexes with a cell lysate containing His_6-P38 leads to the recovery of a major band (Figure 1 lane 4) which was shown to be His_6-P38 by two independent experiments: (a) The lysate containing the expressed His_6-P38 was loaded on a commercial [Sepharose: Ni^{2+}] column and a band with a similar migration pattern was observed (Figure 1, lane 9). (b) Electron spray analysis of the protein recovered with DB−BSA−EDTA conjugates (Figure 2A) exhibited high sequence coverage (42%) to the known sequence of the P38 protein kinase (MK14_HUMAN Mitogen-activated protein kinase 14 (EC 2.7.11.24)) and matched as well the amino acid sequence of the recovered protein obtained with the commercial [Sepharose: Ni^{2+}] column (Figure 2B). Hence, both purification approaches recovered the same His-tagged protein.

Unexpected results were observed while searching for conditions postulated to increase the purity of the recovered protein. We found that macrocomplexes with bound His_6-P38 can be washed with EDTA solutions if applied after the precipitation step. For example, a decrease of 23%, 34%, and 48% in yield was observed when the pellets were washed with 50, 75, and 100 mM of EDTA, respectively, in comparison to 25 mM (Figure 1 lanes 4–7). These washing conditions are similar to those generally applied for regeneration of IMAC columns or for total elution of His-tagged proteins (*4*). We speculate that this resistance to EDTA may be the result of the following: I. Possible formation of two different metal chelators on the same BSA (structures **1**–**2** in Scheme 1B). Whereas structure **1** is generated when a single Lys residue attack the EDTA−dianhydride, structure **2** is obtained when two Lys residues from the same BSA participate in the nucleophilic reaction. Structure **1** is the chemical structure of the strong pentadentate chelating ligand TED, known to form octahedral complexes with divalent metal ions (*22*) and is used for isolation of His-tagged proteins (*26*), while structure **2** to the best of our knowledge is novel. It is therefore likely that at least a single strong metal chelator is present. II. Electrostatic effects—the accessibility of EDTA to the ternary complex may be limited by electrostatic repulsions between the negatively charged residues of BSA (pI $\sim$ 4.6) and the carboxylates of EDTA. Moreover, the absence of linkers between the metal chelators and the BSA imply that negatively charged residues of BSA could be in proximity to the ternary complex and may be more efficient in limiting the access of

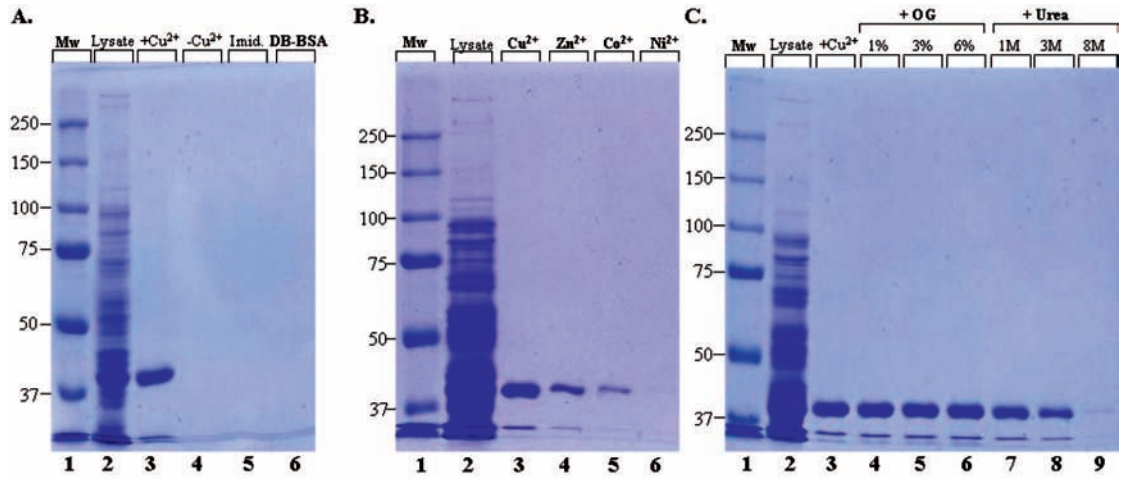

Figure 3. Characterization of BSA conjugates. A. Dependence of the process on Cu^{2+} ions and covalently bound EDTA. Lane 1, Bio-Rad prestained protein markers; lane 2, cell lysate containing His_6-P38; lanes 3 and 4, recovered His_6-P38 in the presence or absence of Cu^{2+} ions, respectively; lane 5, the effect of imidazole (25 mM) during the binding step; lane 6, the effect of replacing BD−BSA−EDTA with DB−BSA conjugates. B. Process efficiency with other metal cations. Lane 1, Bio-Rad prestained protein markers; lane 2, cell lysate containing His_6-P38; lanes 3–6, recovered His_6-P38 with indicated metal cations under identical purification conditions described in the Experimental Procedures. C. Effect of octyl-β-D-glucopyranoside (OG) and urea on the process. Lane 1, Bio-Rad prestained protein markers; lane 2, cell lysate containing His_6-P38; lane 3, control—recovered His_6-P38 in the absence of OG; lanes 4–6, effect of OG at indicated concentrations; lanes 7–9, effect of urea at indicated concentrations. The three gels are Coomassie stained.

Table 1. Characteristics of Different BSA Conjugates

type of BSA conjugate	stochiometric ratios used in the synthesis Desthiobiotin−NHS: BSA:EDTA−dianhy dride	adsorption capacity for His_6-protein A	avidin[a] (mg/mL)	yield[b] at indicated His_6-protein A concentration (mg/mL)		
				0.5	0.18	0.05
DB−BSA−EDTA	80:1:20	3.8 μmol/g	4	44–50%	59–62%	67–72%
DB−BSA−EDTA-A	50:1:50	5.1 μmol/g	2	59–66%	64–69%	74–81%
DB−BSA−EDTA-B	20:1:80	6.4 μmol/g	2.5	71–76%	70–73%	78–84%

[a] Avidin concentration utilized during macrocomplex formation. [b] Range of recovery yields obtained from four independent experiments.

EDTA. III. Increased binding affinity due to additional interactions with BSA and or avidin—this argument is supported by previous studies demonstrating the existence of four types of interactions between His-tagged proteins and metal ions immobilized on membranes (*27*, *28*). We, therefore, speculate that similar interactions may occur between the bound His-tagged protein and residues of BSA and avidin.

A series of experiments demonstrated the dependence of the approach on Cu^{2+} ions and covalently bound EDTA. When Cu^{2+} ions were not added to the medium during the binding step (Figure 3A, lanes 3 vs 4) or when 25 mM of imidazole were present in addition to Cu^{2+} ions, the process was quantitatively suppressed (Figure 3A, lanes 3 vs 5). Furthermore, the requirement for covalently bound EDTA was demonstrated by replacement of DB−BSA−EDTA with DB−BSA conjugates. The latter were prepared by modification of BSA only with desthiobiotin−NHS and represent BSA conjugates lacking covalently bound EDTA. These failed to recover His_6-P38 (Figure 3A, lane 6) and thus provide direct evidence for the presence of covalently bound EDTA in DB−BSA−EDTA conjugates and its participation in the process. A more efficient process to the one presented could be achieved if the binding step would have been performed under homogeneous conditions. For such a scenario, the DB−BSA−EDTA conjugates, Cu^{2+} ions, and His_6-P38 would have to be incubated in the absence of avidin, which would be added at the end of the binding step to initiate specific precipitation. Unfortunately, this preferable route utilizing different metal ions (Cu^{2+}, Zn^{2+}, Co^{2+}, Ni^{2+}) demonstrated that a high contamination background was unavoidable. The major contributors for this observation were free metal ions which promoted nonspecific precipitation even at relatively low concentrations (0.25−5 mM). Hence, formation of insoluble BSA conjugates, prior to the binding step, which enable removal of free or weakly bound metal ions, seems to be a prerequisite for a successful process.

Other metal ions (e.g., Zn^{2+}, Co^{2+}, Ni^{2+}) commonly used in IMAC (*15*) were compared to the performance of Cu^{2+} ions and were found to be significantly less efficient (Figure 3B). The superiority of Cu^{2+} ions seems to be consistent with the order of metal affinities found, for example, with the tridentate chelator IDA (i.e., $Cu^{2+} > Ni^{2+} > Zn^{2+} > Co^{2+}$) (*22*), but fails to explain the dramatic decrease in efficiency with the other cations. The applicability of the approach for isolation of membrane proteins was investigated by addition of mild detergents generally used in purification (*29*) or crystallization (*30*, *31*) of membrane proteins. We found that 1–6% of octyl-β-D-glucopyranoside (OG) had no significant effect on process efficiency (Figure 3C, lanes 4–6) and that *n*-dodecyl-β-D-maltopyranoside leads to similar results (not shown). Therefore, utilization of mild detergents seems to be compatible with the approach. Conversely, high concentrations of urea (8 M) generally applied for purification of His-tagged proteins under denaturing conditions (*32*) had a pronounced negative effect on process efficiency (Figure 3C, lanes 6–9). Since similar results were observed as well with guanidinium–HCL (at 1 M), we conclude that the approach may not be applicable for isolation of His-tagged proteins under denaturing conditions. These results may not be surprising, as both urea and guanidinium–HCL are known chaotropic agents capable of increasing protein solubility (*33*–*35*) and, as such, can promote solubilization of the generated macrocomplexes composed primarily of avidin, BSA, and the His-tagged protein, thereby leading to suppression of the process.

Utilization of proteins rather than synthetic polymers as the insoluble scaffold may possess several limitations deriving from the inherent chemical and physical instability of proteins in

general (*36*). These could include deamidation, disulfide cleavage, oxidation, as well as aggregation, adsorption to surfaces, and protein unfolding. Therefore, one could argue that under harsh purification conditions or after prolonged storage periods, as well as repeated use of the macrocomplexes, the process efficacy would be significantly affected.

Evaluation of the binding capacity of DB−BSA−EDTA conjugates was determined with a commercial highly purified (≥99% by HPLC) recombinant His_6-protein A. The data obtained suggest that each gram of the DB−BSA−EDTA conjugate is capable of adsorbing 3.8 μmol of His_6-protein A (Table 1). In an attempt to increase the binding capacity, two additional BSA conjugates were synthesized: DB−BSA−EDTA-A and DB−BSA−EDTA-B. These were modified under conditions favoring the concentration of EDTA−dianhydride relative to that of the desthiobiotin−NHS (see Experimental Procedures). The data presented in Table 1 show that the binding capacity of the latter BSA conjugates increased in comparison to the DB−BSA−EDTA and that the values obtained (3.8–6.4 μmol/g) are in the range of those generally observed in IMAC (*4*). In addition, the greater recovery yields and lower consumption of avidin of the latter BSA conjugates imply that they should be preferred over DB−BSA−EDTA (Table 1).

Interestingly, whereas IMAC generally requires higher salt concentrations (0.1–1 M NaCl) to suppress nonspecific electrostatic binding (*22*), the presented approach is performed at low ionic strength (25 mM NaCl) and still leads to relatively high purity. This observation can be explained by the (a) absence of resins, (b) absence of linkers between the chelator and the BSA which could provide a site for nonspecific adsorption (*37*), (c) possibility of washing the pellets with EDTA (25–100 mM), or (d) reduction of free metal ions in the medium by BSA, which could suppress nonspecific precipitation. This argument is supported by the findings of Anderson et al. (*26*), who demonstrated the ability of different albumins to abstract immobilized metal ions from chromatographic supports (e.g., Zn^{2+}-IDA or Co^{2+}-IDA) and to lead to the metal ion transfer phenomenon.

CONCLUSIONS

An alternative platform for purification of His-tagged proteins at low ionic strength has been presented. The high purity observed derives from the ability to wash the pellets with EDTA. The absence of resins leads to formation of small pellets (1–5 mg) and the requirement of minute volumes of elution buffer (50–100 μL). Therefore, concentrated preparations of purified His-tagged proteins can be obtained and a reconcentration step may be circumvented. It is hoped that the approach may provide an additional route for isolation of His-tagged proteins.

ACKNOWLEDGMENT

We thank Dr. A. Shainskaya, Weizmann Institute of Science, for kindly providing and analyzing the ESI data.

LITERATURE CITED

(1) Everson, R. J., and Parker, H. E. (1974) Zinc binding and synthesis eight-hydroxy-quinoline-agarose. *Bioinorg. Chem. 4*, 15–20.
(2) Porath, J., Carlsson, J., Olsson, I., and Belfrage, G. (1975) Metal chelate affinity chromatography, a new approach to protein fractionation. *Nature 258*, 598–599.
(3) Porath, J., and Olin, B. (1983) Immobilized metal ion affinity adsorption and metal ion affinity chromatography of biomaterials: serum protein affinities for gel-immobilized iron and nickel ions. *Biochemistry 22*, 1621–1630.
(4) Porath, J. (1992) Immobilized metal ion affinity chromatography. *Protein Expression Purif. 3*, 263–281.
(5) Sulkowski, E. (1985) Purification of proteins by IMAC. *Trends Biotechnol. 3*, 1–7.
(6) Sulkowski, E. (1989) The saga of IMAC and MIT. *Bioessays 10*, 170–175.
(7) Sulkowski, E. (1996) Immobilized metal-ion affinity chromatography: imidazole proton pump and chromatographic sequelae: I. Proton pump. *J. Mol. Recognit. 9*, 389–393.
(8) Gaberc-Porekar, V., and Menart, V. (2005) Potential for using histidine tags in purification of proteins at large scale. *Chem. Eng. Technol. 28*, 1306–1314.
(9) Suen, S. Y., Liu, Y. C., and Chang, C. S. (2003) Exploiting immobilized metal affinity membranes for the isolation or purification of therapeutically relevant species. *J. Chromatogr., B: Anal. Technol. Biomed. Life Sci. 97*, 305–319.
(10) Anderson, L., and Porath, J. (1986) Isolation of phosphoproteins by immobilized metal (Fe^{3+}) affinity chromatography. *Anal. Biochem. 154*, 250–254.
(11) Muszynska, G., Anderson, L., and Porath, J. (1986) Model studies on iron (III) ion affinity chromatography. *Biochemistry 25*, 6850–6853.
(12) Dobrowolska, G., Muszynska, G., and Porath, J. (1991) Selective adsorption of phosphoproteins on gel-immobilized ferric chelate. *J. Chromatogr. 541*, 331–339.
(13) Hemdan, E. S., Zhao, Y. J., Sulkowski, E., and Porath, J. (1989) Surface topography of histidine residues: a facile probe by immobilized metal ion affinity chromatography. *Proc. Natl. Acad. Sci. U.S.A. 86*, 1811–1815.
(14) Sulkowski, E. (1987) Immobilized metal ion affinity chromatography of proteins, In *Protein Purification: Micro to Macro* Liss, A., Ed., pp 149−169.
(15) Below, M., and Porath, J. (1990) Immobilized metal ion affinity chromatography, effect of solute structure, ligand density and salt concentration on the retention of peptides. *J. Chromatogr. 516*, 333–354.
(16) Nakagawa, Y., Yip, T.-T., Belew, M., and Porath, J. (1988) High performance immobilized metal ion affinity chromatography of peptides: Analytical separation of biologically active synthetic peptides. *Anal. Biochem. 168*, 75–81.
(17) Smith, M. C., Furman, T. C., Ingolia, T. D., and Pidgeon, C. (1988) Chelating peptide immobilized metal affinity chromatography. *J. Biol. Chem. 2633*, 7211–7215.
(18) Arnold, F. H. (1991) Metal-affinity separations: a new dimension in protein processing. *Biotechnology 9*, 151–156.
(19) Hochuli, E., Doebeli, H., and Shachar, A. (1987) A new metal chelate adsorbent selective for proteins and peptides containing neighboring histidine residues. *J. Chromatogr. 411*, 177–184.
(20) Hochuli, E., Bannwarth, W., Doebeli, H., Gentz, R., and Stueber, D. (1988) Genetic approach to facilitate purification of recombinant proteins with a novel metal chelate adsorbent. *Bio/Technology* 1321–1325.
(21) Seidler, A. (1994) Introduction of a histidine tail at the N-terminus of a secretory protein expressed in *Escherichia coli*. *Protein Eng. 7*, 1277–1280.
(22) Gaberc-Porekar, V., and Menrat, V. (2001) Perspective of immobilized-metal affinity chromatography. *J. Biochem. Biophys. Methods 49*, 335–360.
(23) Diskin, R., Lebendiker, M., Endgelberg, D., and Livnah, O. (2007) Structures of p38 101 active mutants reveal conformational changes in L16 loop that induce autophosphorylation and activation. *J. Mol. Biol. 365*, 6676.
(24) Laemmli, U. K. (1970) Cleavage of structural proteins during the assembly of the head of bacteriophage T4. *Nature 227*, 680–685.
(25) Patchornik, G. (2007) Double-modified albumins as a tool for antibody purification. *J. Biochem. Biophys. Methods 70*, 671–673.
(26) Anderson, L., Sulkowski, E., and Porath, J. (1991) Immobilized metal ion chromatography of serum albumins. *Bioseparation 2*, 15–22.
(27) Tsai, Y.-H., Wang, M.-Y., and Suen, S.-Y. (2002) Purification of hepatocyte growth factor using polyvinyldiene fluoride-based immobilized metal affinity membranes: equilibrium adsorption study. *J Chromatogr., B 766*, 133–143.

(28) Wu, C.-Y., Suen, S.-Y., Chen, S.-C., and Tseng, J-H. (2003) Analysis of protein adsorption on regenerated cellulose-based immobilized copper ion affinity membranes. *J Chromatogr., A 996*, 53–70.
(29) Cohen, E., Goldshleger, R., Shainskaya, A., Tal, D. M., Ebel, C., Le Maire, M., and Karlish, S. J. (2005) Purification of Na^+,K^+-ATPase expressed in *pichia pastoris* reveals an essential role of phospholipid-protein interactions. *J. Biol. Chem. 280*, 16610–16618.
(30) Michel, H. (1983) Crystallization of membrane proteins. *Trends Biochem. Sci. 8*, 56–59.
(31) Ostermeier, C., and Michel, H. (1997) Crystallization of membrane proteins. *Curr. Opin. Struct. Biol. 7*, 697–701.
(32) Nilsson, J., Ståhl, S., Lundeberg, J., Uhlén, M., and Nygren, P. Å. (1997) Affinity fusion strategies for detection, purification, and immobilization of recombinant proteins. *Protein Expression Purif. 11*, 1–16.
(33) Hatefi, Y., and Hanstein, W. G. (1969) Solubilization of particulate proteins and nonelectrolytes by chaotropic agents. *Proc. Natl. Acad. Sci. U.S.A. 62*, 1129–1136.
(34) Santoro, M. M., and Bolen, D. W. (1988) Unfolding free energy changes determined by the linear extrapolation method. 1. Unfolding of phenylmethanesulfonyl alpha-chymotrypsin using different denaturants. *Biochemistry 27*, 8063–8068.
(35) Shortle, D., Meeker, A. K., and Gerrin, S. L. (1989) Effects of denaturants at low concentrations on the reversible denaturation of staphylococcal nuclease. *Arch. Biochem. Biophys.* 103–113.
(36) Jacob, S., Shirwaikar, A. A., Srinivasan, K. K., Alex, J., Prabu, S. L., Mahalaxmi, R., and Kumar, R. (2006) Stability of proteins in aqueous solution and solid state. *Ind. J. Pharm. Sci. 68*, 154–163.
(37) Lowe, C. R. (1977) The synthesis if several 8 substituted derivatives of adenosine 5′-monophosphate to study the effect of the spacer arm in affinity chromatography. *Eur. J. Biochem. 73*, 265–274.

BC700368Y

Conjugation of the Photoluminescent Silicon Nanoparticles to Streptavidin

Jonghoon Choi,[†,‡] Nam Sun Wang,[†] and Vytas Reipa*[,‡]

Department of Chemical and Biomolecular Engineering, University of Maryland, College Park, Maryland 20742, and Biochemical Science Division, National Institute of Standards and Technology, Gaithersburg, Maryland 20899. Received October 5, 2007; Revised Manuscript Received January 25, 2008

We have covalently attached multiple photoluminescent silicon nanoparticles (SNs) to streptavidin molecules. Conjugation of SNs to a target protein is achieved using the multistage photoassisted procedure. In a first step, the terminal hydrogen in the freshly prepared SNs is substituted with an alkane monolayer that serves as a platform for chemical linkage to a heterobifunctional cross-linker: 4-azido-2,3,5,6-tetrafluorobenzoic acid, succinimidyl ester. A resulting surface coating stabilizes nanoparticles against oxidation and aggregation. Next, an open end of bifunctional cross-linker−diazirine succinimidyl ester is reacted with carboxyl moieties of streptavidin and forms an amide bond. Gel and capillary electrophoresis of the SN−streptavidin complex demonstrated separate elution of the conjugation product and unreacted protein. Then, the number of SNs per protein molecule was determined by measuring complex charge variation by capillary electrophoresis. Conjugate functionality was tested by allowing it to interact with biotinylated polystyrene microbeads. Intense photoluminescence at carefully washed microbeads demonstrated selective binding of silicon nanoparticle bearing streptavidin to biotinylated microbeads. The high quantum yield of streptavidin−SN conjugate in combination with the small size and biocompatibility of silicon nanoparticles presents an attractive platform for the fluorescence labeling in diverse bioassays.

INTRODUCTION

Semiconductor quantum dots were recently recognized to have distinct advantages over organic fluorescent materials in biological tagging applications. Organic dyes are prone to photobleaching under intense laser excitation and are vulnerable to environmental factors such as temperature, oxidation, and acidity, and interaction with certain ions that hamper their application in biological assays. In this regard, stable and efficient binary semiconductor quantum dots offer an attractive platform free of the above problems. Typically, they have size-dependent narrow emission bands and a wide excitation range that permits a multicolor bioanalysis under single-wavelength excitation.

Various approaches of conjugating semiconductor quantum dots to biomolecules have been reported (*1–14*) (for review, see refs *1*−*5*). Water solubility, high fluorescence yield, and compatibility with the analytical protocol media are principal requirements for the practical fluorophore−biomolecule complexes. Binary quantum dot surface modifications for biological applications can be categorized to hydroxyls (*6*), peptides/proteins (*7–9*), thiols (*10, 11*), block copolymers (*12, 13*), and dendrimers (*14*). However, regardless of surface derivatization, the bioapplication of binary quantum dots is hampered by their inherent chemical toxicity (*15–19*) (for review, see ref (*15*)). Consequently, the core materials (Cd/Se, Cd/S, In/P, etc.) require thick, complicated surface coating procedures to prevent content of toxic material with the biosystem. Typically, this leads to a significant increase in the final particle size, and can markedly reduce their application area. Furthermore, such surface modifications often affect the fluorescence quantum yield and spectral properties, both of which hamper the analysis stability and reproducibility. In this context, the need for simple and efficient bioconjugation strategies using nontoxic photoluminescent nanoparticles is evident.

Photoluminescent silicon nanoparticles (SNs) are very appealing in the development of smaller biocompatible probes (*20–23*), as they are expected to be less hazardous than binary semiconductor based quantum dots. Moreover, the silicon surface is open to various chemical functionalizations, thus offering numerous stabilization and bioconjugation options (*24*). Sato et al. (*25*) reacted hydrogen-terminated silicon nanocrystals with acrylic acid to form surface carboxyl functionalities, while Warner et al. used amine termination to ensure SN water solubility (*22*). Such approaches allow engineering of the desired functionality into silicon nanoparticles, increasing nanoparticle monodispersity, and preventing aggregation that may complicate a bioanalysis. Here, we explore a cross-linker-bridged covalent attachment of octane-modified SNs to streptavidin molecules that could be implemented in hybridization-based assays, as these often rely on streptavidin–biotin interactions.

Previously, we reported a conjugation process that describes anchoring of photoluminescent Si nanoparticles to a single-stranded DNA in aqueous solutions (*20*). In this study, we describe the procedure to covalently link SNs to streptavidin molecules that offers access to protein biolabeling, and may find application in *in vitro* assays that rely on antibodies, cell receptors, and cell tracing probes. Covalent bonding between the heterobifunctional cross-linker and a nanoparticle ensures complex stability throughout preparative sample treatments.

We employ 4-azido-2,3,5,6-tetrafluorobenzoic acid, succinimidyl ester (ATFB, SE), which is a bifunctional cross-linker with a photoreactive diazirine and an amine-reactive functionality. The four-step process scheme is shown in Figure 1. Following nanoparticle preparation, hydrogen termination of SNs is substituted with a hydrocarbon moiety using a hydrosilylation reaction. Next, the ATFB bifunctional linker is attached under UV activation and provides a bond to protein amine groups. Subsequently, the SN−succinimidyl ester conjugate is exposed to streptavidin and form a SN−streptavidin complex via amide linkage. Since the cross-linker has the UV-reactive

* Corresponding author. Email: vytas@nist.gov; Telephone: (301) 975-5056; Fax: (301) 330-3447.

[†] University of Maryland.

[‡] National Institute of Standards and Technology.

10.1021/bc700373y CCC: $40.75 © 2008 American Chemical Society
Published on Web 02/22/2008

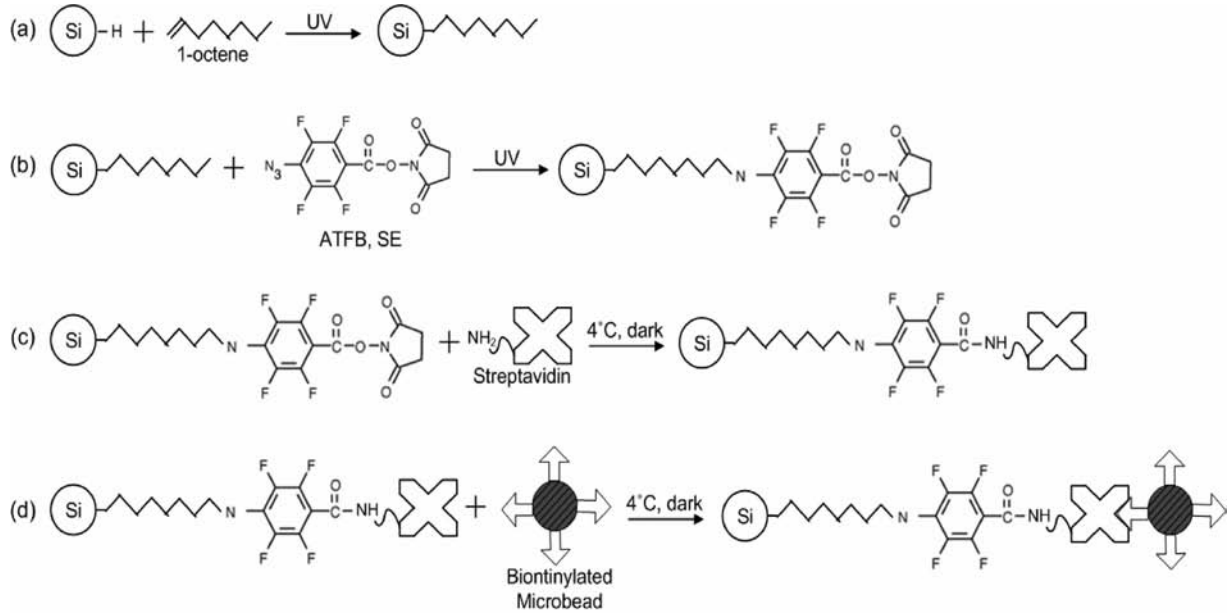

Figure 1. Schematic representation of the silicon nanocrystal and protein molecule covalent conjugation: (a) octane attachment to SNs, (b) bifunctional cross-linker (ATFB, SE) reaction with the octane methyl groups, (c) amide bond formation between the streptavidin and activated cross-linker, (d) test of the SN-streptavidin complex functionality by exposing it to the biotinylated polystyrene microbeads.

end, it allows selective coupling of the diazirine group to the methyl groups of the SN-bound hydrocarbon. SN photoluminescence measurements after each step of the procedure verify both conjugation and photoluminescence efficiency. Finally, we test the tagged streptavidin functionality by reacting the nanoparticle−protein complex with the biotinylated polystyrene microbeads.

The reported straightforward and efficient conjugation strategy and assessment of tagged protein functionality demonstrate silicon nanoparticle potential as an efficient, stable, and biocompatible nanoprobe.

EXPERIMENTAL SECTION

Silicon nanoparticles were prepared using wafer anodic etch in HF-based electrolyte. Both sides of the silicon wafer (As doped, ⟨111⟩ oriented, 0.001 ohm-cm to 0.01 ohm-cm conductivity, Virginia Semiconductor, Inc., Fredericksburg, VA[1]) were electrochemically etched in the HF/H_2O/ethanol (2:1:1, volume ratio) mixture. A lateral etching (*20*, *21*, *26*–*28*) was performed in the Teflon cell that accommodates a 100 mm diameter round Si wafer placed between two Si cathodes. Electric contact was provided to the top edge of the vertically mounted wafer and electrolyte was slowly pumped into the cell, hence providing a solution/air boundary, rising along the wafer surface. Total etch time typically was about 4 h per 100 mm diameter wafer at 120 mA constant current, supplied by a galvanostat (model 363, EG&G Inc., Princeton, NJ). Following anodic etching, the wafer was rinsed several times in deionized water, methanol (HPLC grade, Mallinckrodt Chemicals, Phillipsburg, NJ), and blown dry with nitrogen gas. Dry wafers displayed an intense orange−red luminescence when excited with a 360 nm light. Next, the wafers were sonicated (Neytech, Bloomfield, CT) in a deaerated 10:1 (v/v) mixture of toluene/1-octene for two hours under vigorous N_2 purging. The resulting particle suspension exhibited broadband red−orange photoluminescence under 365 nm excitation.

Following sonication, 20 mL of the Si nanoparticle suspension in toluene/1-octene was placed in the quartz cuvette (Rayonet, Branford,CT) under the N_2 blanket and exposed to 250 nm UV light for 30 min, inside the photochemical reactor (RMR-600) (Rayonet, Branford,CT). The PL color turned to intense blue as a result of the photoassisted hydrosilylation. Finally, the 1-octane derivatized silicon nanoparticle suspension was filtered by passing through the silica gel column.

In the next step of the conjugation protocol, the bifunctional cross-linker 4-azido-2,3,5,6-tetrafluorobenzoic acid succinimidyl ester (ATFB, SE) (Invitrogen, Carlsbad, CA) is attached to the surface of SNs. A 100 μL batch of octane-covered SNs suspension was mixed with 10 μL of 4-azido-2,3,5,6-tetrafluorobenzoic acid succinimidyl ester (ATFB, SE) solution (c = 15 mM) in anhydrous carbon tetrachloride. The reaction mixture was exposed to UV light (λ = 365 nm) inside the UV reactor for 5 min. followed by complete solvent evaporation under N_2 flow. Consequently, fluorinated aryl azide of ATFB reacts with methyl groups of silicon-bound octane and forms a C−N bond (Figure 1b).

The covalent link to the protein molecules was completed by producing the amide bond between the bilinker succinimidyl ester functionality and available streptavidin amine groups (protein molecule has about 100 exposed amines (*29*)). Dry, succinimidyl ester terminated SNs were redissolved in 100 μL of anhydrous DMSO and slowly added to 100 μL of 0.1 M sodium bicarbonate buffer, containing 10 μg of purified streptavidin (Pierce, Rockford, IL). The reaction was carried out in the dark for 1 h under magnetic stirring. Reaction products were analyzed using the native gel electrophoresis. A 15% Tris-HCl polyacrylamide gel (Bio-Rad, Hercules, CA) was injected in 1 μL samples containing the reaction product and the native streptavidin as control in the separate wells. After 2 h of native gel electrophoresis at 150 V in Tris buffer, the gel was dyed using MicrowaveBlue protocol (Protiga, Frederick, MD) for protein staining, and imaged in the MultiImage light cabinet (Alpha Innotech, San Leandro, CA), using both visible light and UV-excited fluorescence modes.

[1] Certain commercial equipment, instruments, materials, or companies are identified in this paper to specify adequately the experimental procedure. Such identification does not imply recommendation nor endorsement by the National Institute of Standards and Technology, nor does it imply that the materials or equipment identified are the best available for the purpose.

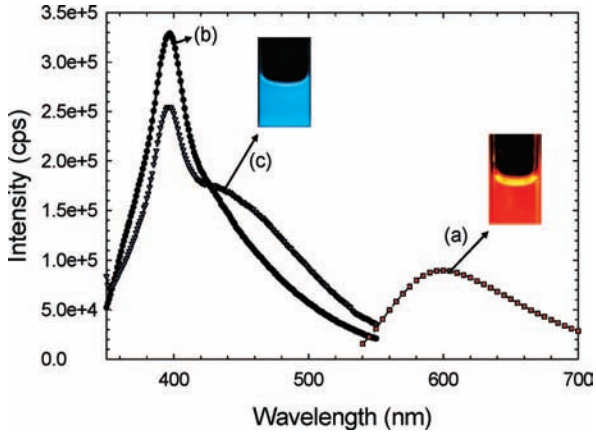

Figure 2. Photoluminescence spectra of freshly prepared silicon nanoparticles in toluene (a), following octane surface derivatization (b), and streptavidin conjugation (c); $\lambda_{exc} = 340$ nm. Insets show the fluorescence images of fresh and derivatized particles under UV excitation.

Functionality of the silicon nanoparticle−streptavidin complex was tested by mixing SN−streptavidin conjugates with a suspension of biotin-coated polystyrene microbeads (average diameter $d = 2$ μm) (Polysciences, Warrington, PA). Prior to mixing, fresh microbeads were separated from their native supernatant by spinning at 10,000 *g* for 5 min. Next, microbeads were washed 3 times by resuspending them in PBS/BSA blocking buffer (0.1 M, pH 7.4), followed by centrifugation. A batch of diluted microbead solution was incubated with the SN−streptavidin conjugate for 30 min at 4 °C, and the supernatant was separated from the mixture by centrifugation. Finally, biotinylated beads were washed in PBS/BSA binding buffer at least three times.

FTIR spectra of reaction products and intermediates were recorded using samples deposited on PTFE IR cards (ICL, Garfield, NJ) on a Bruker IFS 66 (Bruker optics Inc., Billerica, MA) spectrometer.

Fluorescence spectroscopy was used to assess silicon nanoparticle photoluminescent properties after each step of the conjugation procedure. Emission spectra were acquired using 360 nm excitation on a SLM LM800 spectrofluorimeter (SLM Inc., Rochester, NY). Samples were contained in the 3 mm optical path-length quartz cells. Polystyrene microbeads were imaged with fluorescence microscope (Olympus BX50, Tokyo, Japan), using samples spread on glass microscope slides. Images were recorded with SPOT-RT KE digital cameras (Diagnostic Instruments, Sterling Heights, MI) and processed using imaging software (SPOT, version 4.0, Diagnostic Instruments, Sterling Heights, MI).

RESULTS AND DISCUSSION

Fresh silicon nanoparticles, suspended in toluene/octene mixture, displayed red−orange photoluminescence with maximum emission at 600 nm (Figure 2). However, the emission experienced a blue shift with maximum at 400 nm following UV-assisted derivatization with 1-octene. A similar effect was reported previously by Ruckenstein, who suggested a change in emission mechanism upon hydrosilylation (*30*). The blue emission intensity slightly decreased after anchoring to the protein molecule (Figure 2). Decreased intensity at 400 nm, which is typical of octane-derivatized SNs, and the appearance of a new broad feature around 450 nm in the emission spectrum of the final product suggests perturbations in nanocrystal electronic structure due to the covalent bond to the target protein.

Figure 3 shows the FTIR spectra of silicon nanoparticles recorded during various stages of the protein conjugation

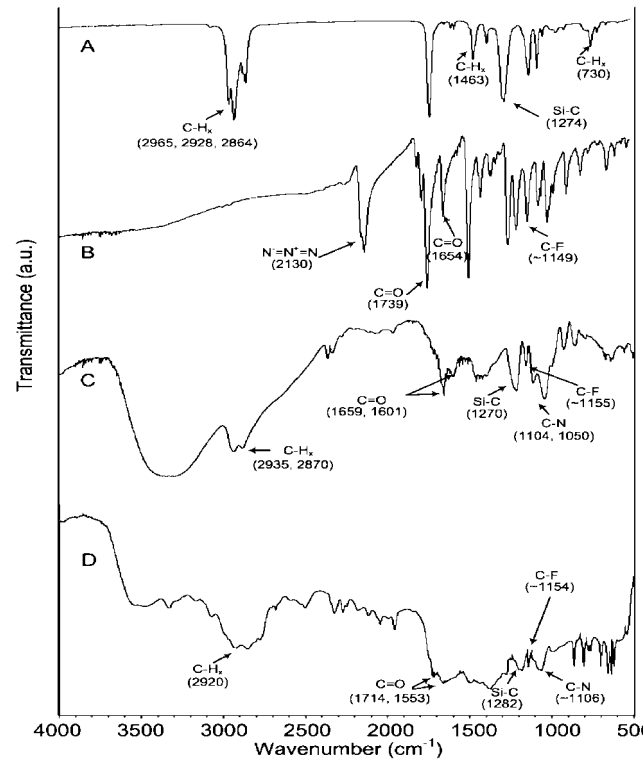

Figure 3. FTIR transmission spectra for dried films of (A) silicon nanoparticles, following the reaction with 1-octene (step a in Figure 1); (B) spectrum of pure bilinker ATFB, SE; (C) silicon nanoparticles subsequent to UV-assisted reaction with bilinker (step b in Figure 1), and (D) product of the conjugation reaction (step c in Figure 1).

procedure. Spectrum recorded following the UV-assisted hydrosilylation (Figure 3A) contains features, assigned to Si−C stretch (1274 cm^{-1}), C−H stretch (2965, 2928, 2964 cm^{-1}), and methylene bending (1463 cm^{-1}) modes, and is consistent with the silicon nanoparticle surface-bound alkane. Vibrational spectrum gets more complicated subsequent to the reaction with the 4-azido-2,3,5,6-tetrafluorobenzoic acid succinimidyl ester (ATFB, SE) (Figure 3C), suggesting the anchoring of the bilinker molecule to the octane-derivatized silicon particles. Notably, the disappearance of the aryl azide stretch at 2130 cm^{-1}, a prominent peak in the pure compound spectrum (Figure 3B) indicates that this group has been converted to nitrene in a photocatalyzed reaction. In addition, several peaks represent the fluorobenzoic acid moiety (1104, 1648, and 1155 cm^{-1}) and octane (1275, 2395 cm^{-1}) that was conjugated in the prior step.

The native electrophoresis gel image in Figure 4 contains separate bands corresponding to the SN−streptavidin complex and free streptavidin. Compared to free streptavidin, the protein−nanoparticle complex elutes earlier and displays an elongated band. The elution time in the native electrophoresis experiment is governed by the analyte morphological shape and charge; therefore, earlier elution of the SN−streptavidin complex is consistent with the extra negative charge due to linked SNs. The polydispersity in the eluted complex charge and molecular weight notably broadens conjugate gel features. One likely source of such polydispersity is silicon nanoparticle size polydispersity prior to conjugation (*26*) that is typical for SNs, produced by breaking up of the nanoporous silicon film. Also, variation in nanoparticle binding efficiency will result in conjugate composition distribution. Complexes with a higher number of SNs per protein molecule will carry a larger net negative charge and, consequently, will elute earlier. Additional experiments will be required to establish a quantitative relationship between the eluted band position and the conjugate molecular weight/charge ratio. Nevertheless, the current gel

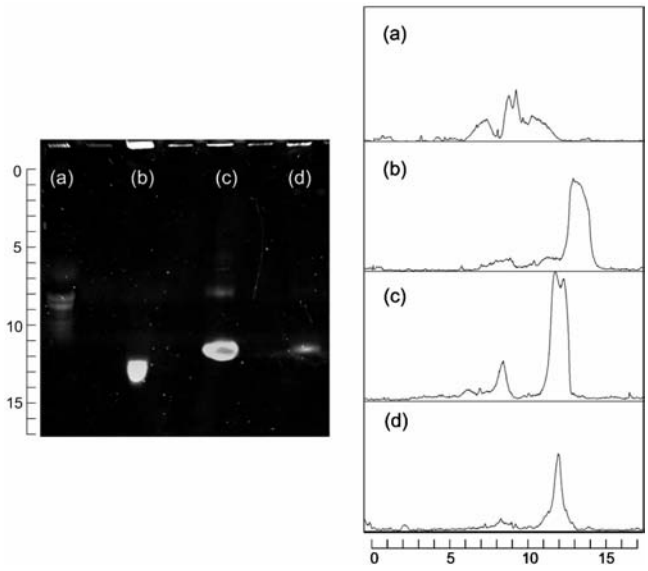

Figure 4. Native gel electrophoresis image and fluorescence intensity profiles from the eluted bands of neat streptavidin (a), and SN−streptavidin conjugates (b,c,d). Variation of elution times among (b), (c), and (d) wells reflect different relative concentrations of the cross-linker tagged SNs to the streptavidin in the final reaction mix (v/v); (b) 1:2, (c) 1:1, and (d) 2:1. Electrophoresis conditions: $U = 200$ V, $t = 2$ h. Mobile buffer: Tris-HCl, pH 8.0. Peaks between 8 and 9 represent neat streptavidin, and from 12 to 14 conjugation products.

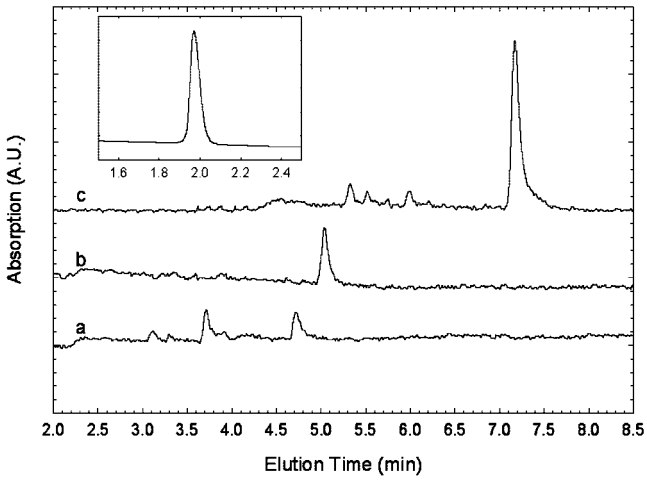

Figure 5. Capillary electrophoresis analysis of silicon nanoparticle/streptavidin conjugation reactants: (a) SNs with attached heterobifunctional cross-linker (ATFB, SE), (b) neat streptavidin, (c) SN−streptavidin conjugate. Inset shows the elution of a neutral molecule (mesityl oxide, see text). Running buffer: Tris−glycine 0.2 M, pH 8, capillary dimensions: $L = 50$ cm, ID = 0.1 mm. Applied voltage: $U = 20$ kV, absorbance detector at $\lambda = 200$ nm.

result confirms the formation of the covalent SN−protein complex and suggests the pathway for further conjugate purification. Gel electrophoresis demonstrates that SN−streptavidin conjugates have higher negative net charge compared to the neat streptavidin (Figure 4).

Further analysis of the conjugation products was performed using capillary electrophoresis (CE). High sensitivity, small samples, and rapid elution facilitated CE application in various fields of analytical chemistry (*31–34*) (for review, see ref (*31*)). Recently, Eckhoff et al. demonstrated CE separation of amine-functionalized silicon nanoparticles, using fluorescence detection (*33*). The analyte surface charge determines its mobility inside the CE capillary and allows charge-based nanoparticle separations. Consequently, the elution time series, produced by UV absorbance detection, can be related to the discrete silicon nanoparticle charges. Separation of surface-derivatized silicon nanoparticles, free streptavidin, and conjugate complex based on their net charge allows assessment of the conjugation efficiency. Given that streptavidin charge varies with the coupled SN number and affects the elution time, it also allows estimatation of the number of conjugated nanoparticles in the protein−SN complex.

Both capillary and gel electrophoresis rely on charge mobility in the electric field; therefore, we have maintained similar conditions in both experiments (buffer, pH, and temperature). In a first step, we have determined the apparent velocities v_{ap} for our sample components: SNs, streptavidin, SN−streptavidin conjugates

$$v_{ap} = \frac{L_{id}}{t_m} \tag{1}$$

where L_{id} is distance from the inlet to the detector, and t_m is travel time of the sample from inlet to the detector point in the capillary. In order to account for the electroosmotic component, we have calibrated our CE system using a neutral molecule, mesityl oxide (SigmaAldrich Inc., St. Lewis, MO), at identical experimental conditions and have estimated the electroosmotic velocity, v_{eo} (eq 2)

$$v_{eo} = \frac{L_{id}}{t_{m,n}} \tag{2}$$

Where v_{eo} is electroosmotic velocity and $t_{m,n}$ is the time for a neutral to arrive at the detector. Consequently, the actual sample velocity inside the capillary (v_{ac}), can be calculated

$$v_{ac} = v_{ap} - v_{eo} = \frac{L_{id}}{t_m} - \frac{L_{id}}{t_{m,n}} \tag{3}$$

Sample mobility μ_{eq} is a product of velocity and electrical field inside the capillary $\mu_{ep} = v_{ac}E$ and can be calculated when the net charge q and Stokes radius r are both known

$$\mu_{ep} = \frac{q}{6\pi\eta r} \tag{4}$$

Here, η is solvent viscosity. By combining eqs 3 and 4, we obtain a relationship between the charge q and sample elution time, t_m

$$q = 6\pi \cdot \eta \cdot r \cdot \left(\frac{L_{id}}{t_m} - \frac{L_{id}}{t_{m,n}}\right) \cdot E \tag{5}$$

where electric field strength $E = V/L_t$; V is total applied voltage, and L_t is total capillary length. Consequently, based on eq 5, we can assign each detected CE peak a net charge value and estimate the number of nanoparticles in the SN−protein complex.

Figure 5 shows the CE trace recorded using the UV absorbance detector ($\lambda = 200$ nm). The capillary inlet was connected to the anode; hence, negative analytes will elute later than neutral or positive molecules. Silanol (Si−OH) groups of the silica capillary interior wall turn into negatively charged silanoates (Si−O−) at pH 8, and attract buffer cations, forming a positive solution layer. This layer is dragged toward the cathode due to the electroosmosis, while negatively charged analytes move in the opposite direction and experience a delayed elution (Figure 5).

Four elution peaks at 3.1, 3.3, 3.7, and 4.8 min (Figure 5a) were analyzed within the range of expected nanoparticle size and surface charge. Based on the photoluminescence emission wavelength and nanocrystal size relationship (*23*), we have estimated that silicon particles with radiuses $r < 0.84$ nm should be responsible for the observed blue photoluminescence of our

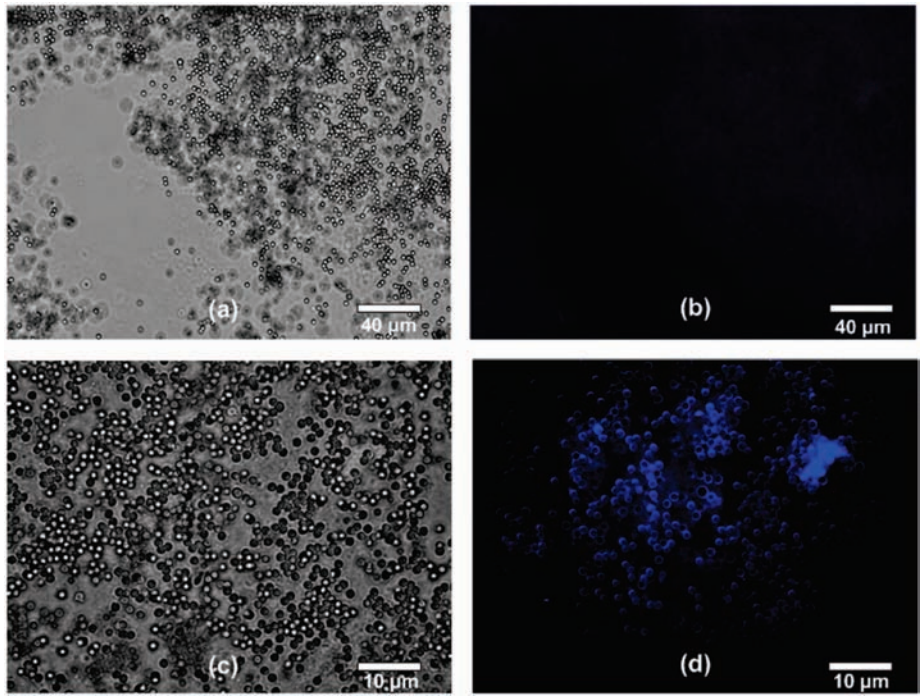

Figure 6. Fluorescence microscopy images of 2 μm diameter biotinylated polystyrene microbeads, following their exposure to silicon nanoparticle−streptavidin complex: (a) biotinylated polystyrene beads, exposed to the neat streptavidin (control) phase image, and (b) fluorescence image; (c) polystyrene beads exposed to a silicon nanoparticle−streptavidin complex phase image, and (d) fluorescence image.

samples (Figure 2). However, a change in emission mechanism due to surface functionalization can markedly affect this relationship (*30*). The two strongest elution peaks at 3.7 and 4.8 min were assigned net charges $q_1 = -1$ and $q_2 = -2$ that correspond to particles with $r_1 = 0.5$ nm and $r_2 = 0.84$ nm, respectively. The elution peak of the neat streptavidin (Figure 5b, at time 5.2 min), corresponds to a net charge of −13 at our experimental conditions (pH 8). Recently, Bradley et al. discussed the possible origin of the net negative streptavidin charge in basic solutions (*29*) and concluded that multiple exposed histidine residues are deprotonated at elevated pH. Notably, our CE derived protein charge estimate ($q_{St} = -13$ at pH 8.0) is consistent with the neat streptavidin zeta potential value (∼50 mV) (*35*).

The strongest feature in Figure 5c ($t = 7.2$ min) corresponds to the net charge from −17 to −18, depending on the associated nanoparticle radius (0.5 or 0.84 nm); therefore, the streptavidin molecule acquires an additional net charge from −4 to −5 due to silicon nanoparticle attachment.

Strong association between streptavidin and biotin is widely exploited in biological assays, and we have to ensure that streptavidin retains its binding capacity after attachment to silicon nanoparticles. The fluorescence microscopy image in the right panel of the Figure 6d displays streptavidin/SN conjugate binding to the biotinylated polystyrene microbeads, following incubation as described in the Experimental Section. Comparison of images on Figure 6 (a,b vs c,d panels) shows that the majority of complex exposed microbeads are associated with the photoluminescent silicon nanoparticles. The photoluminescence intensity variations between biotinylated beads reflect the heterogeneity in nanoparticle brightness and/or binding efficiency. A slight polystyrene bead aggregation, visible in c,d panels of Figure 6 may be caused by the multivalent streptavidin–biotin interactions.

CONCLUSION

We have covalently coupled streptavidin with the photoluminescent silicon nanoparticles using a multistep photoassisted reaction and a bifunctional cross-linker. The characteristic blue nanoparticle photoluminescence was retained in the silicon quantum dot−protein complex. Faster elution of the nanoparticle−streptavidin complex in the native gel electrophoresis indicates extra negative charge of the conjugate due to linked silicon nanoparticles. Typically from 4 to 5 silicon nanoparticles are bound to streptavidin molecule as determined from the capillary electrophoresis analysis. Streptavidin molecules retain their binding capability to the biotin subsequent to the conjugation protocol. Covalent attachment of small, efficient, and nontoxic photoluminescent silicon quantum dots to streptavidin provides a convenient pathway for biomolecule labeling in biotin−streptavidin affinity based assays.

ACKNOWLEDGMENT

Authors thank Dr. Jayne B. Morrow for her assistance with the fluorescence microscopy, and Dr. Karen W. Phinney for capillary electrophoresis. J.C. thanks Dr. Andrea M. Rossi and Mr. Peter Niarhos for helpful discussion.

LITERATURE CITED

(1) Medintz, I. L., Uyeda, H. T., Goldman, E. R., and Mattoussi, H. (2005) Quantum dot bioconjugates for imaging, labelling and sensing. *Nat. Mater. 4*, 435–446.
(2) Klostranec, J. M., and Chan, W. C. W. (2006) Quantum dots in biological and biomedical research: recent progress and present challenges. *Adv. Mater. 18*, 1953–1964.
(3) Hermanson, G. T. (1996) *Bioconjugate techniques*, Academic Press, California.
(4) Alivisatos, P. (2004) The use of nanocrystals in biological detection. *Nat. Biotechnol. 22*, 47–52.
(5) Michalet, X., Pinaud, F. F., Bentolila, L. A., Tsay, J. M., Doose, S., Li, J. J., Sundaresan, G., Wu, A. M., Gambhir, S. S., and Weiss, S. (2005) Quantum dots for live cells, in vivo imaging, and diagnostics. *Science 307*, 538–544.
(6) Pathak, S., Choi, S., Arnheim, N., and Thompson, M. E. (2001) Hydroxylated quantum dots as luminescent probes for in situ hybridization. *J. Am. Chem. Soc. 123*, 4103–4104.

(7) Clarke, S. J., Hollmann, C. A., Zhang, Z., Suffern, D., Bradforth, S. E., Dimitrijevic, N. M., Minarik, W. G., and Nadeau, J. L. (2006) Photophysics of dopamine-modified quantum dots and effects on biological systems. *Nat. Mater. 5*, 409–417.

(8) Bäumle, M., Stamou, D., Segura, J., Hovius, R., and Vogel, H. (2004) Highly fluorescent streptavidin-coated CdSe nanoparticles: Preparation in water, characterization, and micropatterning. *Langmuir 20*, 3828–3831.

(9) Bottini, M., Cerignoli, F., Dawson, M. I., Magrini, A., Rosato, N., and Mustelin, T. (2006) Full-length single-walled carbon nanotubes decorated with streptavidin-conjugated quantum dots as multivalent intracellular fluorescent nanoprobes. *Biomacromolecules 7*, 2259–2263.

(10) Wu, S., Zhao, X., Zhang, Z., Xie, H., Tian, Z., Peng, J., Lu, Z., Pang, D., and Xie, Z. (2006) Quantum-dot labeled DNA probes for fluorescence in situ hybridization (FISH) in the microorganism Escherichia coli. *ChemPhysChem 7*, 1062–1067.

(11) Wolcott, A., Gerion, D., Visconte, M., Sun, J., Schwartzberg, A., Chen, S., and Zhang, J. Z. (2006) Silica-coated CdTe quantum dots functionalized with thiols for bioconjugation to IgG proteins. *J. Phys. Chem. B 110*, 5779–5789.

(12) Pellegrino, T., Manna, L., Kudera, S., Liedl, T., Koktysh, D., Rogach, A. L., Keller, S., Radler, J., Natile, G., and Parak, W. J. (2004) Hydrophobic nanocrystals coated with an amphiphilic polymer shell: A general route to water soluble nanocrystals. *Nano Lett. 4*, 703–707.

(13) Gao, X., Cui, Y., Levenson, R. M., Chung, L. W. K., and Nie, S. (2004) In vivo cancer targeting and imaging with semiconductor quantum dots. *Nat. Biotechnol. 22*, 969–977.

(14) Guo, W., Li, J. J., Wang, Y. A., and Peng, X. (2003) Conjugation chemistry and bioapplications of semiconductor box nanocrystals prepared via dendrimer bridging. *Chem. Mater. 15*, 3125–3133.

(15) Hardman, R. (2006) A toxicologic review of quantum dots: Toxicity depends on physicochemical and environmental factors. *Environ. Health Perspect. 114*, 165–172.

(16) Derfus, A. M., Chan, W. C. W., and Bhatia, S. N. (2004) Probing the cytotoxicity of semiconductor quantum dots. *Nano Lett. 4*, 11–18.

(17) Fischer, H. C., Liu, L. C., Pang, K. S., and Chan, W. C. W. (2006) Pharmacokinetics of nanoscale quantum dots: In vivo distribution, sequestration, and clearance in the rat. *Adv. Funct. Mater. 16*, 1299–1305.

(18) Tsay, J. M., and Michalet, X.,. (2005) New light on quantum dot cytotoxicity. *Chem. Biol. 12*, 1159–1161.

(19) Kirchner, C., Liedl, T., Kudera, S., Pellegrino, T., Javier, A. M., Gaub, H. E., Stolzle, S., Fertig, N., and Parak, W. J. (2005) Cytotoxicity of colloidal CdSe and CdSe/ZnS nanoparticles. *Nano Lett. 5*, 331–338.

(20) Wang, L., Reipa, V., and Blasic, J. (2004) Silicon nanoparticles as a luminescent label to DNA. *Bioconjugate Chem. 15*, 409–412.

(21) Ding, Z., Quinn, M. B., Haram, A. K., Pell, L. E., Korgel, B. A., and Bard, A. L. (2002) Electrochemistry and electrogenerated chemiluminescence from silicon nanocrystal quantum dots. *Science 296*, 1293–1297.

(22) Warner, J. H., Hoshino, A., Yamamoto, K., and Tilley, R. D. (2005) Water-soluble photoluminescent silicon quantum dots. *Angew. Chem., Int. Ed. 44*, 4550–4554.

(23) Warner, J. H., Hoshino, A., Shiohara, A., Yamamoto, K., and Tilley, R. D. (2006) The Synthesis of silicon and germanium quantum dots for biomedical applications. *Proc. SPIE 6069*, 6096071–6096078.

(24) Buriak, J. M. (2002) Organometallic chemistry on silicon and germanium surfaces. *Chem. Rev. 102*, 1271–1308.

(25) Sato, S., and Swihart, M. T.,. (2006) Propionic-acid-terminated silicon nanoparticles: Synthesis and optical characterization. *Chem. Mater. 18*, 4083–4088.

(26) Choi, J., Wang, N. S., and Reipa, V. (2007) Photoassisted tuning of silicon nanocrystal photoluminescence. *Langmuir 23*, 3388–3394.

(27) Jung, K. H., Shih, S., Hsieh, T. Y., Kwong, D. L., and Lin, T. L. (1991) Intense photoluminescence from laterally anodized porous Si. *Appl. Phys. Lett. 59*, 3264–3266.

(28) Belomoin, G., Therrien, J., Smith, A., Rao, S., Twesten, R., Chaieb, S., Nayfeh, M. H., Wagner, L., and Mitas, L. (2002) Observation of a magic discrete family of ultrabright Si nanoparticles. *Appl. Phys. Lett. 80*, 841–843.

(29) Bradley, K., Briman, M., Star, A., and Gruner, G. (2004) Charge transfer from adsorbed proteins. *Nano Lett. 4*, 253–256.

(30) Hua, F. J., Erogbogbo, F., Swihart, M. T., and Ruckenstein, E. (2006) Organically capped silicon nanoparticles with blue photoluminescence prepared by hydrosilylation followed by oxidation. *Langmuir 22*, 4363–4370.

(31) Rodriguez, M. A., and Armstrong, D. W. (2004) Separation and analysis of colloidal/nano-particles including microorganisms by capillary electrophoresis: a fundamental review. *J. Chromatogr., B 800*, 7–25.

(32) Yu, C., Su, C., and Tseng, W. (2006) Separation of acidic and basic proteins by nanoparticle-filled capillary electrophoresis. *Anal. Chem. 78*, 8004–8010.

(33) Eckhoff, D. A., Stuart, J. N., Sutin, J. D. B., Sweedler, J. V., and Gratton, E. (2006) Capillary electrophoresis of ultrasmall carboxylate functionalized silicon nanoparticles. *J. Chem. Phys. 125*, 0811031–0811034.

(34) Huang, X., Weng, J., Sang, F., Song, X., Cao, C., and Ren, J. (2006) Characterization of quantum dot bioconjugates by capillary electrophoresis with laser-induced fluorescent detection. *J. Chromatogr., A 1113*, 251–254.

(35) van Oss, C. J., Giese, R. F., Bronson, P. M., Docoslis, A., Edwards, P., and Ruyechan, W. T. (2003) Macroscopic-scale surface properties of streptavidin and their influence on aspecific interactions between streptavidin and dissolved biopolymers. *Colloids Surf., B 30*, 25–36.

BC700373Y

Noninvasive Optical Imaging of *Staphylococcus aureus* Bacterial Infection in Living Mice Using a Bis-Dipicolylamine-Zinc(II) Affinity Group Conjugated to a Near-Infrared Fluorophore

W. Matthew Leevy,[†] Seth T. Gammon,[‡] James R. Johnson,[†] Andrew J. Lampkins,[†] Hua Jiang,[†,§] Manuel Marquez,[△,⊥] David Piwnica-Worms,[‡] Mark A. Suckow,[#] and Bradley D. Smith*[,†]

Department of Chemistry and Biochemistry and Walther Cancer Research Center, 251 Nieuwland Science Hall, University of Notre Dame, Notre Dame, Indiana 46556, The Molecular Imaging Center, Mallinckrodt Institute of Radiology, Washington University School of Medicine, 510 South Kingshighway Boulevard, Campus Box 8225, St. Louis, Missouri 63110, Key Laboratory of Photochemistry, Institute of Chemistry, Chinese Academy of Sciences, Beijing 100080, China, NIST Center for Theoretical and Computational Nanosciences, Gaithersburg, Maryland 20899, Harrington Department of Bioengineering, Arizona State University, Tempe, Arizona 85287, and Freimann Life Sciences Center, University of Notre Dame, Notre Dame, Indiana 4655. Received October 8, 2007; Revised Manuscript Received December 12, 2007

Optical imaging of bacterial infection in living animals is usually conducted with genetic reporters such as light-emitting enzymes or fluorescent proteins. However, there are many circumstances where genetic reporters are not applicable, and there is a need for exogenous synthetic probes that can selectively target bacteria. The focus of this study is a fluorescent imaging probe that is composed of a bacterial affinity group conjugated to a near-infrared dye. The affinity group is a synthetic zinc (II) coordination complex that targets the anionic surfaces of bacterial cells. The probe allows detection of *Staphylococcus aureus* infection (5×10^7 cells) in a mouse leg infection model using whole animal near-infrared fluorescence imaging. Region of interest analysis showed that the signal ratio for infected leg to uninfected leg reaches 3.9 ± 0.5 at 21 h postinjection of the probe. Ex vivo imaging of the organs produced a signal ratio of 8 for infected to uninfected leg. Immunohistochemical analysis confirmed that the probe targeted the bacterial cells in the infected tissue. Optimization of the imaging filter set lowered the background signal due to autofluorescence and substantially improved imaging contrast. The study shows that near-infrared molecular probes are amenable to noninvasive optical imaging of localized *S. aureus* infection.

INTRODUCTION

Optical imaging of bacterial infection in living animals is emerging as a powerful method to study preclinical models of infectious disease. In most cases, genetic reporter systems such as light-emitting luciferase enzymes, or fluorescent proteins like GFP, have been employed with some notable success (*1*). However, pathogenic bacteria in their native environments do not express endogenous optical reporters. Furthermore, numerous microbes are not amenable to genetic manipulation or DNA transfection. In these cases, alternative optical imaging strategies must be developed such as the use of exogenous synthetic probes that selectively target the bacteria. While the most immediate application of these synthetic probes is the study of preclinical infection models in mice, they also have long-term clinical potential for imaging bacteria in shallow tissue. For example, prosthetic materials like mesh grafts or catheters are common sites of colonization by invasive bacteria such as MRSA (methicillin-resistant *Staphyloccus aureus*) (*2*), but they are difficult systems to image.

To date, only a small number of bacterial targeting probes have been reported for any imaging modality, and very few have been studied in vivo. A key design component is the bacteria targeting group, and previous studies have employed antibodies (*3*), lectins (*4*), sugars (*5*), antibiotic drugs (*6*–*8*), and peptides (*9*). Antibodies are popular, since they can bind tightly to specific molecular targets on the surfaces of both Gram-positive and Gram-negative bacterial cells (*10*). While antibodies have the potential advantage of high specificity, their large molecular size (~150 kD) is a limitation for in vivo imaging because of slow tissue diffusion and blood clearance rates.

A more general way to target bacteria is to employ cationic molecules that are electrostatically attracted to the negatively charged cells (*11*, *12*). The negative surface charge is a characteristic feature of nearly all bacterial membranes, and results from the high fraction of anionic phospholipids and related amphiphiles (*13*). For example, the plasma membrane which surrounds the Gram-positive bacterium *Staphylococcus aureus* is composed of approximately 75% anionic phosphatidylglycerol. Extending from this membrane are anionic glycerophosphate polymers called lipoteichoic acids that weave through and anchor the surrounding peptidoglycan cell wall (*14*). Gram-negative bacteria such as *Escherichia coli* are differentiated by the presence of a second outer bilayer membrane. The external leaflet of this outer membrane is composed of lipopolysaccharide whose core structure, known as lipid A, contains two anionic phosphates (*15*). The anionic surfaces of bacteria are in contrast to the exterior membrane surfaces of most healthy mammalian cells, which contain primarily zwit-

* smith.115@nd.edu, ph: +1 (574) 631 8632, fax: +1 (574) 631 6652.
[†] Department of Chemistry and Biochemistry and Walther Cancer Research Center, University of Notre Dame.
[‡] Washington University School of Medicine.
[§] Chinese Academy of Sciences.
[△] NIST Center for Theoretical and Computational Nanosciences.
[⊥] Arizona State University.
[#] Freimann Life Sciences Center, University of Notre Dame.

10.1021/bc700376v CCC: $40.75 © 2008 American Chemical Society
Published on Web 02/09/2008

terionic phospholipids and thus have a near-neutral charge (*16*). For imaging purposes, a drawback with cationic peptides is their propensity to penetrate (and be retained by) mammalian cells (*17, 18*), while a limitation with antimicrobial peptides is poor signal-to-noise since they actively degrade the bacterial cell membrane target (*19*).

We have discovered that zinc (II) coordination complexes with dipicolylamine (DPA) ligands exhibit remarkably selective affinities for anionic cell membranes (*20*). For example, DPA-Zn(II) based probes allow fluorescent visualization of apoptotic mammalian cells, as they expose anionic phosphatidylserine during the programmed cell death process (*21*). In addition, these DPA-Zn(II) probes are highly selective stains for bacteria even in the presence of human epithelial cells (*22*). The specific focus of this study is fluorescent probe **1** which contains a DPA-Zn(II) affinity group conjugated to a near-infrared (NIR) carbocyanine fluorophore (ex. 794 nm, em. 810 nm). NIR fluorophores are optimal for in vivo imaging purposes given the favorable tissue penetration properties of photons at these wavelengths (*23*). In a preliminary report, we showed that **1** can identify infection sites in living mice, the first demonstration of in vivo bacterial detection using a fluorescent probe (*24*). We now describe a detailed optical imaging investigation of *S. aureus* infection using region of interest analysis to characterize the pharmacokinetics of probe uptake and clearance from the whole animal. We also provide biodistribution and histology data that measures organ and cell selectivity. Overall, we find that **1** is an effective *in vivo* optical imaging probe for localized infection of *S. aureus* in living mice.

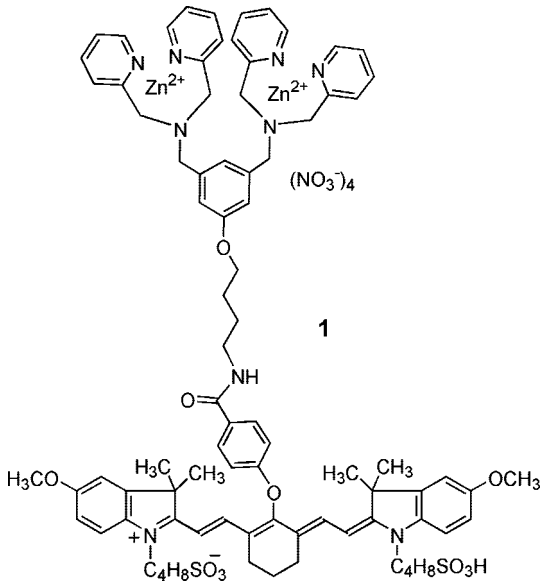

EXPERIMENTAL PROCEDURES

Synthesis. Compound **1** was prepared as previously reported (*24*).

In Vivo Leg Infection Model. An aliquot of *Staphylococcus aureus* NRS11 (5×10^7 colony forming units (CFUs) in 50 μL of Luria–Bertani growth media) was injected intramuscularly into the muscles that overlay the tibia bone in a posterior leg of an athymic nude mouse (strain nu/nu, Taconic, New York). It is worth noting that this anatomical location is not the thigh, which is closer to the body of the mouse. The same location on the contralateral leg was injected with 50 μL of LB media as a vehicle control. The infection was allowed to incubate for 6 h before intravenous injection with probe **1** via the tail vein. After imaging experiments, the mice were anesthetized and euthanized by cervical dislocation.

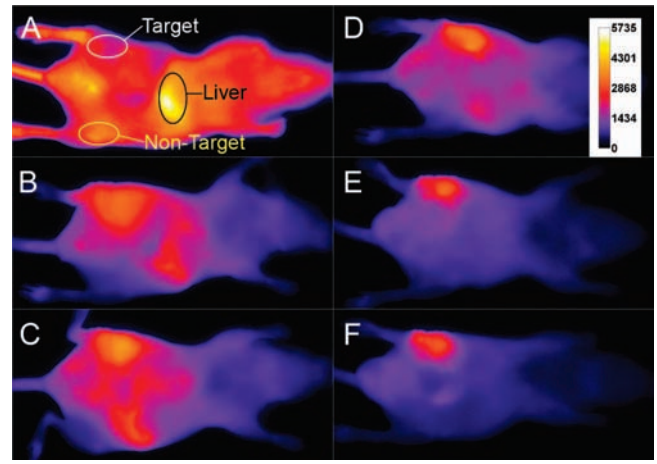

Figure 1. Optical images of a mouse with a *S. aureus* infection in the left posterior leg. Images were acquired following intravenous injection of probe **1** (75 μL of a 1 mM stock) at 0 h (A), 3 h (B), 6 h (C), 12 h (D), 18 h (E), and 21 h (F). Calibration bar (a.u.) applies to all images in the montage. Frame A shows labels for each region of interest (ROI): target (T), non-target (NT), and liver (L).

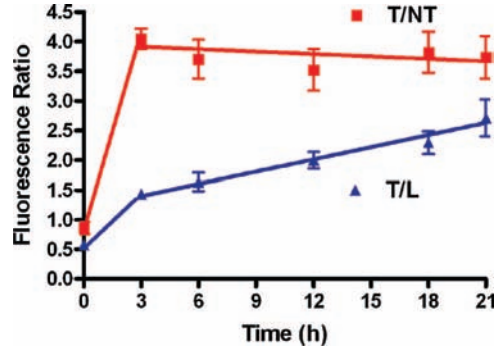

Figure 2. Target to nontarget (T/NT) and target to liver (T/L) fluorescence ratios at each imaging time point ($n = 4$; error bars are standard error of the mean). The lines are provided to guide the eye.

In Vivo Fluorescence Imaging. Imaging was achieved by placing an anesthetized mouse (1.5% isofluorane inhalation) inside a Kodak 4000MM imaging station configured for epi-illumination. The entire animal was irradiated with filtered light of wavelength 755 ± 20 nm, and a 16-bit image of emission intensity at 830 ± 10 nm was collected by a CCD camera during a 60 s acquisition period (F-stop = 2.4, focal plane 2.5 mm, FOV 200 mm no binning). In some cases, the mouse was also imaged using a filter set with excitation at 720 ± 10 nm and emission at 790 ± 35 nm. Mice were imaged before and immediately after injection of **1**, and at subsequent time points as detailed in the text.

Image Preparation and Quantitative Analysis. Images were processed using the *ImageJ 1.37v* program available for free download at http://rsb.info.nih.gov/ij/. Figures 1, 4, 6, and 7 were prepared as follows. First, the original 16-bit images (presented as panels in each figure) were sequentially opened and then converted to an image stack using the "convert images to stack" software command. Next, the stack of images was background-subtracted using the rolling ball algorithm (radius = 500 pixels) that is a feature of the software. This tool calculates the average pixel intensity of any signal emanating from a "non-mouse" region of the image, and then subtracts this calculated value from every pixel in the image. The radius was selected to exceed the maximum width of the mouse; otherwise, the mouse itself will be included in the background calculation. Next, the image stack was set to the "Fire"

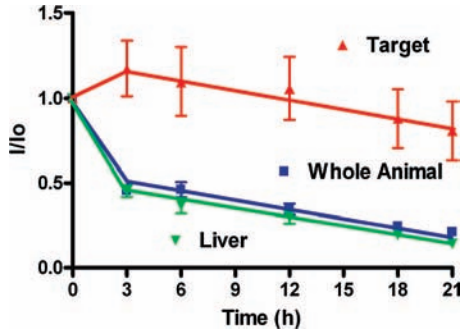

Figure 3. Fluorescence emission time course for the infection target, whole animal, and liver ROIs ($n = 4$; error bars are standard error of the mean). The lines are provided to guide the eye.

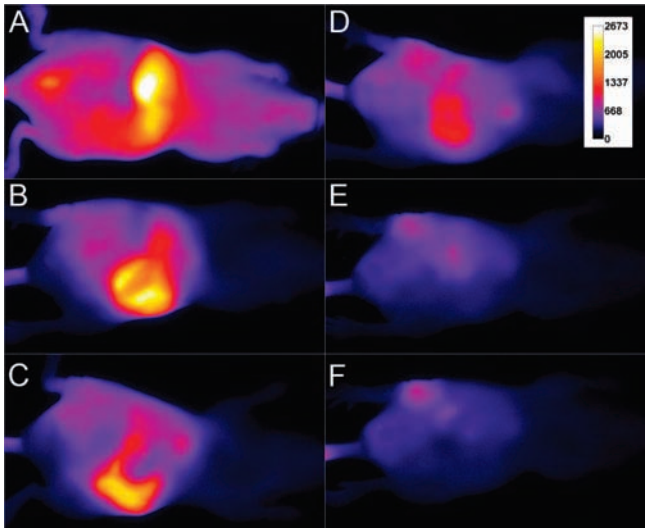

Figure 4. Optical images of a mouse with a *S. aureus* infection in the left posterior leg. Images were acquired following intravenous injection of a low dose of probe **1** (75 μL of a 0.2 mM stock) at 0 h (A), 3 h (B), 6 h (C), 12 h (D), 18 h (E), and 21 h (F). Calibration bar (a.u.) applies to all images in the montage.

fluorescence intensity scale (under "Lookup Tables" menu), which color-codes the fluorescence counts contained in each pixel. After that, the stack of images was converted to a montage using the "convert stack to montage" command. At this point, region of interest (ROI) analysis was performed by selecting a circle ROI from the *ImageJ* tool bar, and drawing it to circumscribe the appropriate anatomical location of each mouse, as shown in Figure 1. The average pixel intensities of the target (T), nontarget (NT), and liver (L) were measured by *ImageJ* (CTRL-M) and recorded for each mouse in *Excel 2003*. In addition, an ROI was drawn around the whole mouse (excluding the target site) and the integrated density recorded. Statistical analysis was performed to acquire the average of each ROI ($n = 4$) with the standard error of the mean (SEM), and the resulting values plotted in *Graphpad Prizm 4*. Two-way ANOVA analysis was also performed in *GraphPad* version 4 to calculate the *p*-values reported in the text. After ROI analysis, a calibration bar was added to the montage using the "calibration bar" command in the *ImageJ* program.

Biodistribution. After imaging studies, the mice were anesthetized by isofluorane inhalation (1.5%) and euthanized by cervical dislocation. The major organs were dissected, placed on a glass plate, and imaged as described above. The biodistribution image was analyzed in *ImageJ* by first subtracting the background (rolling ball method, 100 pixel width). Manual regions of interest (ROIs) were drawn around each organ, and the mean pixel intensity calculated for each. ROIs were drawn around the discrete site of infection. The averages for each organ ($n = 3$) and each infected site ($n = 4$) were calculated and plotted as detailed above.

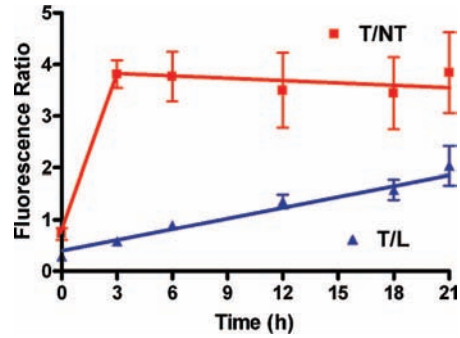

Figure 5. Target to nontarget (T/NT) and target to liver (T/L) fluorescence ratios at each imaging time point after injection with a 0.2 mM stock of **1** ($n = 4$, error bars are standard error of the mean).

Histology. The first analysis used mice with a 9 h infection in one of the posterior legs, but no treatment with probe **1**. Tissue was sampled, including the skin, subcutis, and muscle from the leg which had been administered bacteria; a similar sample was also obtained from the contralateral uninfected leg. The tissue was fixed in 10% neutral buffered formalin for 24 h and then transferred to 70% ethanol. Following embedding in paraffin, tissue was sectioned at 4–5 μm and stained with hematoxylin and eosin. The second analysis used mice that had been infected with bacteria and also injected with probe **1**. Sections at 10 μm from the infected leg and the uninfected contralateral leg were stained with a Texas Red-labeled antibody to *Staphyloccus aureus* protein A (250 μL of a 100 μg/mL solution in buffer: 5 mM TES (*N*-tris(hydroxymethyl)methyl-2-aminoethanesulfonic acid), 145 mM NaCl, pH = 7.4), (Abcam Inc., Goa pAb to protein A (TR) ab7247–1). Microscopy was performed at 600× magnification on a Nikon Eclipse 2000TE microscope with a Photometrics Cascade 512B camera to aquire 16 bit images. Each image was processed using the *ImageJ* software suite. A control in vitro microscopy study confirmed that the Texas-red labeled antibody targets the surface of the *S. aureus*, as expected, with no emission in the Cy7 filter set.

RESULTS AND DISCUSSION

In Vivo Imaging. The bacteria were injected into the muscles that overlay the tibia bone in a posterior leg of athymic nude mice. This infection model was chosen for the following reasons (*1*): (a) The posterior leg is well-separated from all major organs, and bacterial migration from the site is slow, thus reducing any confusion as to the origin of the fluorescent signal. (b) The lack of hair produces less scattering of the light. (c) The inhibited immune system simplifies interpretation of the imaging and histology data.

A cohort of four mice was each infected with a bolus of 5×10^7 colony forming units (CFUs) of *S. aureus* NRS11 in a 50 μL aliquot of Luria–Bertani (LB) growth media. The contralateral leg was injected with LB alone to serve as the vehicle control. After a 6 h incubation, each mouse was injected intravenously, via the tail vein, with probe **1** (75 μL of an aqueous 1 mM stock solution). Assuming a blood volume of 1 mL, the final concentration of **1** in the blood was approximately 75 μM or about 4 mg/kg. Each animal was subsequently imaged on its ventral side at 0, 3, 6, 12, 18, and 21 h using a Kodak 4000MM Imaging Station designed to acquire 16 bit planar fluorescence images. The images were subsequently processed using the *ImageJ* V1.37 software suite (see methods). It is important to note that colors in these images do not represent

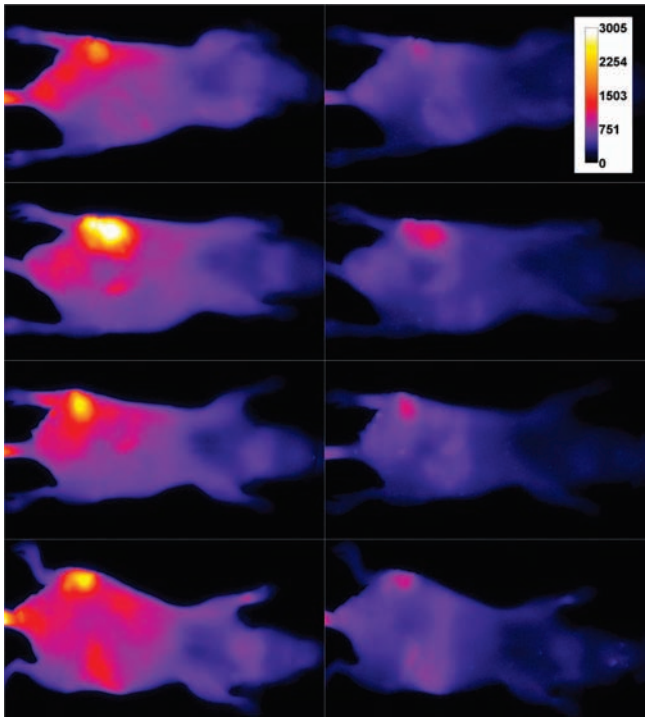

Figure 6. Optical images of four mice each with a *S. aureus* infection in the left posterior leg and acquired 21 h postinjection of probe **1** (75 μL of a 1 mM stock). Left column: animals were imaged using an excitation of 755 nm and emission of 830 nm. Right column: the same animals were imaged using an excitation of 720 nm and emission of 790 nm. Calibration bar (a.u.) applies to all images in the montage.

wavelengths of light, but rather the fluorescence intensity of each pixel in the image.

In Figure 1 are typical fluorescence images (ex: 755, em: 830 nm) obtained for one mouse during the time course of one experiment. Immediately after injection with **1**, there is a bright, confluent fluorescence emanating from most parts of the animal. A region of interest (ROI) analysis was derived from the average pixel intensities at the three anatomical locations shown in frame A: the target leg infection site (T), the contralateral leg as a nontarget site (NT), and the liver (L). At time zero, the target to nontarget (T/NT) fluorescence ratio was 0.85 ± 0.1 ($n = 4$, standard error of the mean), indicating that less probe diffuses through the infected leg relative to the control leg immediately following injection. The cause of this small decrease is unknown, but it may be the result of *S. aureus* induced ischemic damage to the local vasculature, as observed for other Gram-positive microbes (*25*). Localization of **1** can be observed at the target site within 3 h postinjection, and the image continues to sharpen as the probe clears from the mouse body over the subsequent 18 h. Figure 2 shows the average target to nontarget (T/NT) and target to liver (T/L) fluorescence ratios for the cohort of four mice at each imaging time point during the study. The lines that connect the points are to guide the eye and do not represent a mathematical fit. A salient point is that the T/NT ratio reaches a value close to 4 after just 3 h and is sustained for the remainder of the experiment (at 21 h, T/NT $= 3.9 \pm 0.5$, $n = 4$). The T/L ratio also rises quickly during the first 3 h, and then continues to increase slowly with time such that T/L $= 2.7 \pm 0.4$ ($n = 4$) at 21 h.[1]It is important to appreciate the difference between

[1]The values of T/NT and T/L reported here compare favorably with an imaging study that utilized radiolabeled antimicrobial peptides and reported T/NT ratios as high as 4.1 ± 0.7 (*30*). A value for T/L could not be determined, since most of the signal originated from the body of the mouse and not the target site.

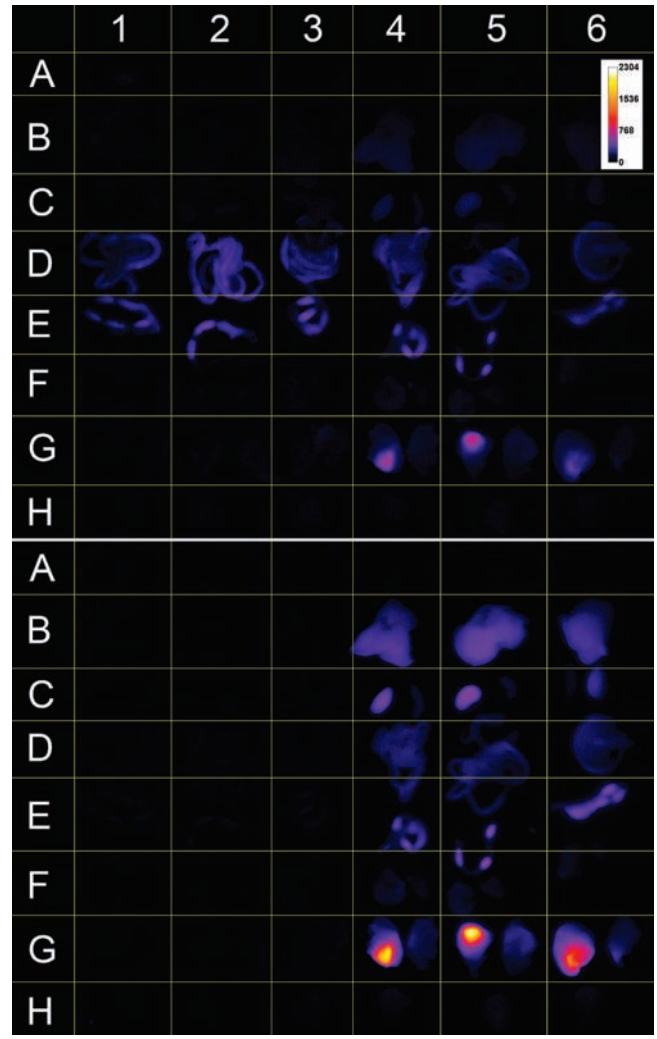

Figure 7. Ex vivo image of mouse tissues from three uninfected mice (columns 1–3) and three infected mice that were injected with **1** (colums 4–6). The organs and blood are given in the following rows of Figure 5: (A) blood, (B) liver, (C) kidney (left) and spleen (right), (D) small intestine, (E) large intestine, (F) lungs (left) and heart (right), (G) left and right posterior leg tissue, and (H) brain. Images were acquired with the 720/790 nm (top frame) and 755/830 nm (bottom) filter sets. Calibration bar (a.u.) set for both frames.

T/NT and T/L. The T/NT ratio is a measure of targeting at the infection site relative to the contralateral control site, whereas the T/L ratio is a measure of the imaging contrast observed between the infection site and the whole mouse. Thus, while the T/NT ratio reaches a maximum in the first 3 h of imaging, the continued linear increase in T/L up to 21 h time reflects the improving contrast that helps identify the infection site relative to the mouse body.

Plotted in Figure 3 are the average changes in total fluorescence emission (I/I_0) from the target site and also the whole animal over the course of the imaging experiment ($n = 4$). These data show that the fluorescence emission from the infection site increased by approximately 20% over the first three hours of the experiment, whereas, the total animal fluorescence decreased by 50% over the same period. This indicates that most of probe **1** binds to the target within the first 3 h, and that after this initial phase, the infection site, liver, and whole animal lose fluorescence at the same apparent linear rate.

In Vivo Imaging with Lower Probe Concentration. Additional in vivo imaging studies were performed to assess the sensitivity of probe **1**. The main goal was to determine whether

useful imaging results could be obtained with a lower dose.[2] Thus, a cohort of four mice were each given a leg infection of *S. aureus* as described above, but this time they received a 5-fold lower intravenous concentration of **1** (15 μM estimated final blood concentration). As shown in Figure 4, the overall signal from the infected leg was less intense. The T/L ratio in Figure 5 increased linearly with time to reach a value of 1.9 $\pm$ 0.4 after 21 h, which is 70% of the value obtained using the higher dose of **1**. Although the signal contrast is lower, the T/NT ratio (Figure 5) mirrors the higher probe dose profile and reaches a value close to 4 after 3 h. These data indicate that the lower probe dose can be used to effectively image a leg infection because this anatomical location has an inherently low background signal that is primarily due to tissue autofluorescence. However, other infection sites, like the kidney and liver which avenues for probe clearance, would be more difficult to image at this lower probe concentration since there is a higher background signal due to some nonselective accumulation of probe.

Optimizing the Imaging Filter Set. A drawback with the popular 2D planar imaging technique used in this study is the attenuation of fluorescence signal with tissue depth. Furthermore, the photophysical properties of carbocyanine fluorophores vary with both solvent polarity and the presence of serum components of blood (*26*). Therefore, it was important to gauge image variability between separate animals and also to check how much the image quality changed with different instrument filter sets. Our previous preliminary study of probe **1** (λ_{max} abs: 794 nm, em: 810 nm) employed a 720/790 nm filter set (excitation at 720 $\pm$ 10 nm, emission at 790 $\pm$ 35 nm) (*24*); however, the imaging data reported above used a more optimal 755 $\pm$ 20/830 $\pm$ 35 nm filter set. The benefit gained by using this longer-wavelength filter set is illustrated in Figure 6, which compares images of four mice at the 21 h time point. With each animal, the *S. aureus* infection site in the left posterior leg is readily discerned, demonstrating the excellent reproducibility of probe **1**. Comparatively, the contrast using the 755/830 nm filter set (Figure 6, left column) is clearly greater for each mouse than that observed with its corresponding image in the 720/790 nm filter set (Figure 6, right column). ROI analysis confirmed that the T/NT ratio for these mice is 3.8 $\pm$ 0.4 with the 755/830 nm set, which is 36% better than the T/NT ratio of 2.8 $\pm$ 0.2 obtained with the 720/790 set ($p = 0.014$). In addition, the T/L ratio values improved from 2.3 $\pm$ 0.2 (720/790 nm set) to 2.8 $\pm$ 0.5 (755/830 nm set) for a 22% average gain ($p = 0.021$). The longer-wavelength filter set enhances contrast for two reasons. First, the deeper red 755/830 nm filter set produces increased probe excitation in deeper tissues, with a corresponding enhancement of fluorescence emission. Second, there is a lower background signal from nonprobe autofluorescence.

Ex Vivo Imaging. Ex vivo fluorescence analysis of the mouse organs was performed to assess the biodistribution of probe **1**. Three mice from the cohort in Figure 3 (i.e., treated with the higher probe concentration) were euthanized by cervical dislocation at the 21 h time point and their organs gathered to determine the distribution of probe **1** (Figure 7, columns 4–6). Three additional mice, that were neither infected nor injected, were used as controls (columns 1–3). The organs and blood were placed on a glass plate and imaged using the Kodak Imaging Station with the 720/790 nm (top frame) and 755/830 nm (bottom frame) filter sets. The fluorescent images are given in the following rows of Figure 5: (A) blood, (B) liver, (C) kidney (left) and spleen (right), (D) small intestine, (E) large intestine, (F) lungs (left) and heart (right), (G) left and right posterior leg muscle, and (H) brain. The infected tissue is immediately obvious upon inspection of row G which shows the left (infected) and right (uninfected) posterior leg muscles. The fluorescence emission emanates from one area of the leg tissue, indicating that probe **1** is localized to the initial site of bacterial injection. Moderate fluorescence intensity also emanated from the liver and small and large intestine, indicating that this is a major excretion pathway for **1**.

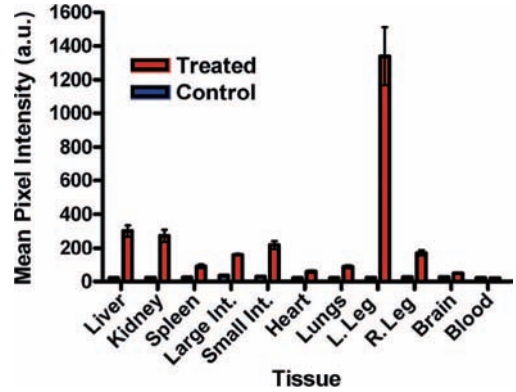

Figure 8. Ex vivo organ quantification of Figure 7 imaged with the 755/830 nm filter set ($n = 3$, error bars are the standard error of the mean).

Inspection of the images in Figure 7 shows that image contrast due to staining by probe **1** is enhanced significantly by changing the 720/790 nm filter set to the longer-wavelength 755/830 nm filter set. In particular, the strong gut autofluorescence (due to food (*27*)) for control mice 1–3 in rows D and E is almost completely eliminated, whereas the fluorescence intensity of every organ containing probe **1** is greater. In other words, the fluorescence ratio of the infected to uninfected leg (T/NT) was increased from 4.5 to 7.8 by changing to the longer-wavelength filter set. Figure 8 shows the average fluorescence intensity of the pixels in each organ as determined by ROI analysis ($n = 3$) from image taken using the optimized 755/830 nm filter set. The left leg gave about 8-fold more signal than the contralateral uninfected leg tissue. Furthermore, the infected leg had a minimum 4-fold greater intensity when compared to other organs like the liver and kidneys. Taken together, the data show that compound **1** selectively targets the leg of each animal that has a localized infection of *S. aureus*.

Histology. Two types of analyses were performed. The first was a general histological comparison of tissue sections from mice with a 9 h infection in one of the posterior legs. After fixation and embedding in paraffin, the tissue samples were sectioned at 4–5 μm and stained with hematoxylin and eosin. As expected, tissue sections from the contralateral uninfected legs were normal and showed no signs of necrosis or inflammation. Tissue sections from infected legs showed evidence of mild to moderate inflammation and some hyaline degeneration; however, there were no pyknotic nuclei or other cellular debris associated with cell death and necrosis.

The second analysis was an immunohistochemical assessment of the selectivity of probe **1** for bacterial cells. Thus, 10 μm sections were processed from the infected and uninfected leg tissue of mice that were injected with **1** (see Experimental Procedures). The sections were counter-stained with a Texas Red labeled antibody with selectivity for protein A (Abcam), an antigen present the surface of *S. aureus*. Microscopy data from one infected tissue section are shown in Figure 9. In the left panel is a phase contrast image. The region containing small dark spots (highlighted in the red box) indicates the presence

[2] A lower probe dose would, of course, lower the chance of chemical toxicity. While a complete toxicity study has not yet been conducted, it is worth noting that the nude mice easily tolerate the presence of probe **1** (4 mg/kg) for at least 24 h, as judged by their continued grooming and nesting activities.

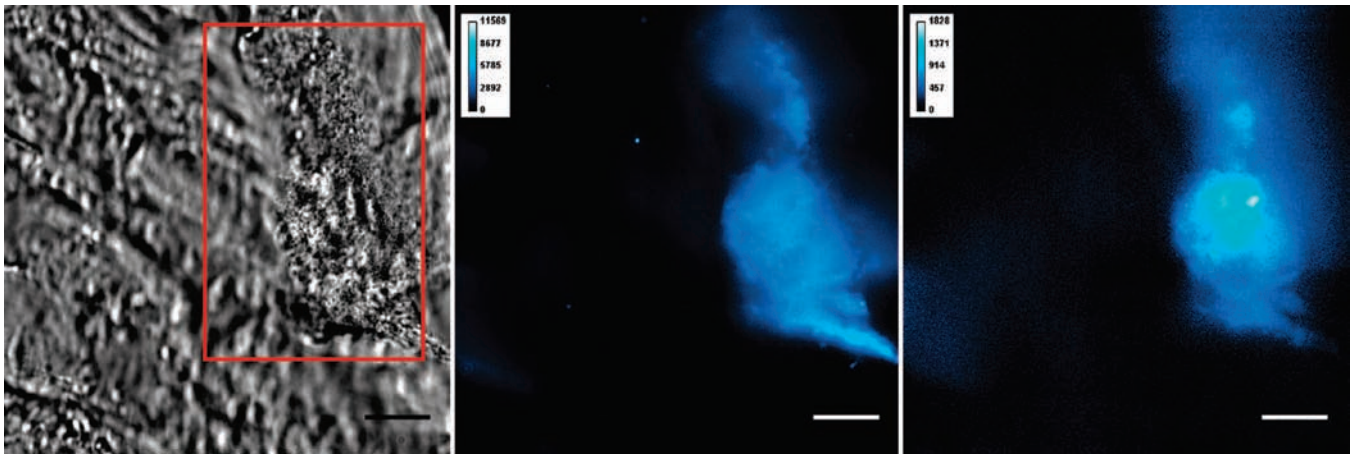

Figure 9. Histological section of infected leg muscle as viewed at 600× in the phase contrast (left), red (center), and NIR Cy7 (right) filter sets. The red box at left designates a patch of spots that mark the presence of bacteria. Infected tissue was sectioned 21 h postinjection of **1**. Scale bar equals 20 μM for each frame. Calibration bar is in arbitrary units.

of bacterial cells. The center picture shows the same section in the red filter set (ex. HQ535/50X, em. HQ610/75m). The colocalized emission from the Texas Red antibody conjugate establishes the presence of *S. aureus*. The right panel shows the section viewed with a NIR Cy7 filter set (ex. 710/75X, em. 810/90m) that selectively detects emission from **1**. The NIR fluorescence intensity in the bacterial cluster was approximately 3-fold higher than in the surrounding tissue. Images of tissue sections from the uninfected contralateral leg of the same mouse were treated with the same antibody stain, but there was no fluorescent signal in the red (antibody) or NIR (probe) channels (data not shown).

The histology data indicate that the DPA-Zn(II) affinity group in compound **1** targets the anionic membrane surfaces of the bacteria cells and not the relatively small number of dead and dying mammalian cells in the leg tissue that surrounds the infection site. Even though the amount of muscle cell death increases as the infection progresses, we expect that probe **1** continues to act as a bacterial imaging agent for two reasons. The first pertains to the increased surface to volume ratio of bacteria compared to mammalian cells. *S. aureus* cells have a diameter of approximately 750 nm, while tubular muscle cells are considerably larger with an effective diameter of over 50 μm and a length of at least 1 mm. Thus, millions of bacteria can occupy the space of one small muscle cell, with over 2 orders of magnitude more cell surface area. Second, bacterial cell surfaces typically have a higher fraction of negatively charged lipids than do mammalian cell surfaces. In the present case, *S. aureus* membranes are about 75% phophatidylglycerol, while the typical mammalian cell has about 15% phophatidylserine (*21*).

CONCLUSIONS

Fluorescent conjugate **1** is a robust imaging probe for the detection of localized *S. aureus* infection. The probe is easily visualized at a leg infection site within 3 h of administration. The probe selectively targets the bacterial cells in the infected tissue, as judged by immunohistochemical analysis. The image contrast was lower with decreased probe dosage; however, this technical limitation can be addressed with new and brighter NIR fluorophores (*28*). The focus of this study was on the Gram-positive *S. aureus*, a common source of secondary infection in healthcare facilities (*29*); however, probe **1** can likely be used to image almost all strains of bacteria because the DPA-Zn(II) affinity group targets the anionic surfaces that are a characteristic feature of nearly all bacterial membranes. One of the future goals of this research is to noninvasively detect and monitor bacterial pathogensis in various infection models, such as the urinary tract, lungs, or brain and spine. Eventually, probe **1**, or the next-generation versions, may have clinical applications. For example, optical imaging would be a useful tool for the clinician seeking information on low-grade infections that occur in mesh grafts or catheter sites, where it is often very difficult to distinguish infection from sterile inflammation.

ACKNOWLEDGMENT

This work was supported by the NIH (GM059078 for B.D.S.) and (P50 CA94056 for D.P-W) and the Walther Cancer Research Center at Notre Dame.

LITERATURE CITED

(1) Leevy, W. M., Serazin, N., and Smith, B. D. (2007) Optical imaging of bacterial infection models. *Drug Discovery Today: Disease Models*, doi: 10.1016/j.ddmod.2007.07.001.

(2) Hirose, K., Marui, A., Nomura, T., Kaneda, K., Kimura, Y., Ikeda, T., Fujita, M., Mitsuyama, M., Tabata, Y., and Komeda, M. (2007) A novel approach to reduce catheter-related infection using sustained-release basic fibroblast growth factor for tissue regeneration in mice. *Heart Vessels 22*, 261–267.

(3) Embleton, M. L., Nair, S. P., Cookson, B. D., and Wilson, M. (2002) Selective lethal photosensitization of methicillin-resistand *Staphylococcus aureus* using a tin(IV) chlorin e6 conjugate. *J. Antimicrob. Chemother. 50*, 857–864.

(4) Holm, C., and Jespersen, L. (2003) A flow-cytometric gram-staining technique for milk-associated bacteria. *Appl. Environ. Microbiol. 69*, 2857–2863.

(5) Qu, L. W., Luo, P. G., Taylor, S., Lin, Y., Huang, W. J., Anyadike, N., Tzeng, T. R. J., Stutzenberger, F., Latour, R. A., and Sun, Y. P. J. (2005) Visualizing adhesion-induced agglutination of *Escherichia coli* with mannosylated nanoparticles. *Nanosci. Nanotechnol. 5*, 319–322.

(6) Metallo, S. J., Kane, R. S., Holmlin, R. E., and Whitesides, G. M. (2003) Using bifunctional polymers presenting vancomycin and fluorescein groups to direct anti-fluorescein antibodies to self-assembled monolayers presenting D-alanine-D-alanine groups. *J. Am. Chem. Soc. 125*, 4534–4540.

(7) Gu, H., Xu, K., Xu, C., and Xu, B. (2006) Biofunctional magnetic nanoparticles for protein separation and pathogen detection. *Chem. Commun.* 941–949.

(8) Gu, H., Ho, P.-L., Tsang, K. W. T., Wang, L., and Xu, B. (2003) Using biofunctional magnetic nanoparticles to capture vancomycin-resistant Enterococci and other gram-positive bacteria at ultralow concentration. *J. Am. Chem. Soc. 125*, 15702–15703.

(9) Lupetti, A., Nibbering, P. H., Welling, M. M., and Pauwels, E. K. J. (2003) Radiopharmaceuticals: new antimicrobial agents. *Trends Biotechnol. 21*, 70–73.
(10) Wing, L., Zhao, W., O'Donoghue, M. B., and Tan, W. (2007) Fluorescent nanoparticles for multiplexed bacteria monitoring. *Bioconjugate Chem. 18*, 297–301.
(11) Hamblin, M. R., O'Donnell, D. A., Murthy, N., Rajagopalan, K., Michaud, N., Sherwood, M. E., and Hasan, T. (2002) Polycationic photosensitizer conjugates: effects of chain length and gram classification on the photodynamice inactivation of bacteria. *J. Antimicrob. Chemother. 49*, 941–951.
(12) Berry, V., Gole, A., Kundu, S., Murphy, C. J., and Saraf, R. F. (2005) Deposition of ctab-terminated nanorods on bacteria to form highly conducting hybrid systems. *J. Am. Chem. Soc. 127*, 17600–17601.
(13) *Microbial Lipids Vol. 1*. Ratledge, C., and Wilkinson, S. G. (Eds.) Academic Press, London, 1988.
(14) Fournier, B., and Philpott, D. J. (2005) Recognition of *Staphylococcus aureus* by the innate immune system. *Clin. Microbiol. Rev. 18*, 521–540.
(15) Meredith, T. C., Aggarwal, P., Mamat, W., Linder, B., and Woodard, R. W. (2006) Redefining the requisite lipopolysaccharide structure in *Escherichia coli*. *ACS Chem. Biol. 1*, 33–42.
(16) Boon, M. J., and Smith, B. D. (2002) Chemical control of phospholipid distribution across bilayer membranes. *Med. Res. Rev. 22*, 251–281.
(17) Nekhotiaeva, N., Elmquist, A., Rajarao, G. K., Hällbrink, M., Langel, Ü., and Good, L. (2004) Cell entry and antimicrobial properties of eukaryotic cell-penetrating peptides. *FASEB J. 18*, 394–396.
(18) Bullok, K., Gammon, S. T., Violini, S., Prantner, A. M., Villalobos, V. M., Sharma, V., and Piwnica-Worms, D. (2006) Permeation peptide conjugates for in vivo molecular imaging applications. *Mol. Imaging 5*, 1–18.
(19) Lupetti, A., Welling, M. M., Mazzi, U., Nibbering, P. H., and Pauwels, E. K. J. (2002) Technetium-99m labelled fluconazole and antimicrobial peptides for imaging of *Candida albicans* and *Aspergillus fumigatus* infections. *Eur. J. Nucl. Med. 29*, 674–679.
(20) Koulov, A. V., Hanshaw, R. G., Stucker, K. A., Lakshmi, C., and Smith, B. D. (2005) Biophysical studies of a synthetic mimic of the apoptosis-detecting protein annexin V. *Isr. J. Chem. 45*, 373–379.
(21) Hanshaw, R. G., and Smith, B. D. (2005) New reagents for phosphatidylserine recognition and detection of apoptosis. *Bioorg. Med. Chem.* 5035–5042.
(22) Leevy, W. M., Johnson, J. R., Lakshmi, C., Morris, J., Marquez, M., and Smith, B. D. (2006) Selective recognition of bacterial membranes by zinc(II)-coordination complexes. *Chem. Commun.* 1595–1597.
(23) Bashkatov, A. N., Genina, E. A., Kochubey, V. I., and Tuchin, V. V. (2005) Optical properties of human skin, subcutaneous and mucous tissues in the wavelength range from 400 to 2000 nm. *J. Phys. D: Appl. Phys. 38*, 2543–2555.
(24) Leevy, W. M., Gammon, S. T., Jiang, H., Johnson, J. R., Maxwell, D. J., Jackson, E. N., Marquez, M., Piwnica-Worms, D., and Smith, B. D. (2006) Optical imaging of a bacterial infection in living mice using a fluorescent near-infrared molecular probe. *J. Am. Chem. Soc. 128*, 16476–16477.
(25) Bryant, A. E., Bayer, C. R., Chen, R. Y. Z., Guth, P. H., Wallace, R. J., and Stevens, D. L. (2005) Vascular dysfunction and ischemic desctruction: the role of streptolysin o-induced platelet/neutrophil complexes. *J. Infect. Dis. 192*, 1014–1022.
(26) Yuan, B., NanGuang, C., and Zhu, Q. (2004) Emission and absorption properties of indocyanine green in intralipid solution. *J. Biomed. Opt. 9*, 497–503.
(27) Mansfield, J. R., Gossage, K. W., Hoyt, C. C., and Levenson, R. M. (2005) Autofluorescence removal, multiplexing, and automated analysis methods for in-vivo fluorescence imaging. *J. Biomed. Opt. 10*, 41207–41215.
(28) Johnson, J. R., Fu, N., Arunkumar, E., Leevy, W. M., Gammon, S. T., Piwnica-Worms, D., and Smith, B. D. (2007) Squaraine Rotaxanes: superior substitutes for Cy-5 molecular probes for near-infrared fluorescence cell imaging. *Angew. Chem., Int. Ed. 119*, 5624–5627.
(29) Dziekan, G., Hahn, A., Thune, K., Schwarzer, G., Schafer, K., Daschner, F. D., and Grundmann, H. (2000) Methicillin-resistant *Staphylococcus aureus* in a teaching hospital: investigation of a nosocomial transmission using a matched case-control study. *J. Hosp. Infect. 46*, 263–270.
(30) Welling, M. M., Lupetti, A., Balter, H. S., Lanzzeri, S., Souto, B., Rey, A. M., Savio, E. O., Paulusma-Annema, A., Pauwels, E. K. J., and Nivvering, P. H. (2001) ^{99m}Tc-labeled antimicrobial peptides for detection of bacterial and *Candida albicans* infections. *J. Nucl. Med. 42*, 788–794.

BC700376V

Extracellular Barriers to *in Vivo* PEI and PEGylated PEI Polyplex-Mediated Gene Delivery to the Liver

Rob S. Burke and Suzie H. Pun*

Department of Bioengineering, University of Washington, 1705 NE Pacific Street, Seattle, Washington 98195. Received October 20, 2007; Revised Manuscript Received November 10, 2007

Polyplex-mediated gene therapy is a promising alternative to viral gene therapy. One challenge to these synthetic carriers is reduced transfection efficiencies *in vivo* compared to those achieved *in vitro*. Many of the intracellular barriers to gene delivery have been elucidated, but similar quantification of extracellular barriers to gene delivery remains a need. In this study, the unpackaging of polyplexes by serum proteins, soluble glycosaminoglycans, and an extracellular matrix extract was demonstrated by a YOYO-1 fluorescence quenching assay. Additionally, exposing polyplexes to serum or proteoglycans before *in vitro* transfection caused decreased cellular uptake of DNA. Lastly, PEI polyplexes and PEGylated PEI polyplexes were injected into the portal vein of mice, and the intrahepatic distributions of labeled DNA and polymer were assessed by confocal microscopy. PEI polyplexes delivered DNA to the liver, but extensive vector unpackaging was observed, with PEI primarily colocalized with the extracellular matrix. PEGylated polyplexes mediated less DNA delivery to the liver, possibly due to premature vector unpackaging in the blood. Through this work, both the blood and the extracellular matrix have been determined to be significant extracellular barriers to polyplex-mediated *in vivo* gene delivery to the liver.

INTRODUCTION

The field of gene therapy first gained momentum with the use of viral gene delivery vectors (*1, 2*). However, interest in the development of nonviral vectors remains high because of challenges associated with the use of viruses in humans, including safety and large-scale production issues (*3, 4*). One of the main classes of nonviral gene delivery vectors that has been extensively investigated is complexes of cationic polymer and DNA, termed polyplexes (*5*). Polycations condense DNA through electrostatic interactions to form particles with sizes on the order of 100 nm. One of the most popular cationic polymers used to form polyplexes is the commercially available polyethylenimine (PEI) (*6*). The use of PEI to deliver DNA has become widespread after several groups showed that it generates particularly high *in vitro* transfection efficiencies compared to those of other nonviral gene delivery vectors by mediating endosomal release (*6–11*).

Branched PEI (bPEI) and linear PEI (lPEI) can both be used effectively for gene delivery. Although lPEI is generally preferred for *in vivo* applications because of its advantageous toxicity profile (*12*), bPEI contains a higher percentage of primary amines and is thus more suitable to modifications. Examples of modifications include incorporation of targeting ligands to increase the specificity of delivery, labeling the polymer with fluorophore to track its location through fluorescence microscopy, or grafting of poly(ethylene glycol) (PEG) to the polymer to increase polyplex stability. Incorporation of PEG in polyplex formulation, a process known as PEGylation, increases the salt stability of the particles and reduces interaction with blood components, resulting in decreased uptake by the reticuloendothelial system and prolonged circulation time of the PEGylated polyplexes (*13*). However, at the same time, PEGylation has been shown to reduce uptake by cells, which in turn reduces the level of gene expression (*14, 15*).

* To whom correspondence should be addressed. Tel: (206) 685-3488. Fax: (206) 616-3928. E-mail: spun@u.washington.edu.

Much of the work investigating the mechanism of nonviral gene delivery has focused on the intracellular barriers that a delivery vector must overcome to deliver its cargo to the nucleus, including binding to the cell surface and internalization (*16–19*), escape from the endosomal pathway (*9, 10, 20, 21*), transport in the cytoplasm (*22–25*), nuclear entry (*26–29*), and vector unpackaging (*30, 31*). However, the extracellular barriers to gene delivery are important to consider for *in vivo* applications. For organ-specific delivery after systemic administration, the vectors must successfully extravasate from the vasculature and maneuver through the extracellular matrix (ECM) to reach the target cells. Because polyplexes are held together electrostatically, other charged species may disrupt the interaction between DNA and polymer. Indeed, Huth et al. showed that polyplexes released from endosomes could unpackage in the cytoplasm by competition with cytosolic RNA (*31*). Additionally, Schaffer et al. found that chromosomal DNA inside the cell nucleus is capable of participating in vector unpackaging (*30*). Taken together, these studies illustrate that polymeric properties such as the molecular weight, which affects how tightly the polymer binds DNA, influence where the polyplexes unpackage after intracellular delivery. However, charged species that are able to compete the polymer off the DNA do not only exist inside cells. Polyplex vector interactions with extracellular and cell surface glycosaminoglycans (GAGs) also result in vector unpackaging and a decrease in gene delivery efficiency (*32–35*).

In vitro transfection studies with PEI polyplexes have shown high gene delivery efficiencies; in contrast, *in vivo* data obtained by various researchers shows that *in vitro* transfection is a poor predictor of *in vivo* success (*12, 36, 37*). The rationale for this work is that, although many polymeric vectors have been optimized *in vitro* to overcome intracellular barriers, there are many extracellular barriers that must be overcome in order to achieve successful *in vivo* gene delivery. An understanding of the limiting barriers to *in vivo* gene delivery will facilitate the design of improved vectors able to overcome these barriers, thus increasing the efficiency of gene delivery. In this work, the integrity of PEI and PEGylated PEI polyplexes is examined both

10.1021/bc700388u CCC: $40.75 © 2008 American Chemical Society
Published on Web 02/23/2008

in vitro and *in vivo* through dual-fluorescence labeling of polymer and DNA. The *in vivo* studies focused on the assessment of intrahepatic distributions of polymer and delivered DNA because other studies have shown that polyplexes accumulate primarily in the liver after injection but that transgene expression is relatively low (*38–41*). Our results reveal that both the serum and the ECM pose barriers to gene delivery. Systemically injected PEI polyplexes are found to be unpackaged in the liver, thus accounting for suboptimal gene delivery efficiencies.

EXPERIMENTAL PROCEDURES

Materials. All materials were purchased from Sigma-Aldrich unless otherwise stated.

Synthesis of PEI-Dinitrophenyl (PEI-DNP). bPEI (25,000 g/mol, 12.7 mg) was dissolved in 0.15 M $NaHCO_3$ at pH 8.3, at 10 mg/mL. To this solution was added 5 mg (25 equiv) of 6-(2,4-dinitrophenyl)aminohexanoic acid, succinimidyl ester (DNP-NHS, from Invitrogen) dissolved at 10 mg/mL in DMF, followed by stirring overnight at room temperature. The polymer was then protonated by the addition of HCl and dialyzed in a Slide-A-Lyzer 10K MWCO dialysis cassette (Pierce) against dH_2O to remove solvent and excess reactants. The solution was lyophilized to yield a fluffy yellow solid. The polymer was redissolved in dH_2O, the PEI concentration was determined by a copper (II) acetate assay as described previously (*42*), and the DNP concentration was measured by absorbance at 360 nm.

Synthesis of PEG-DNP. Thirty-eight milligrams of $HCl \cdot H_2N$-PEG-COOH (5000 g/mol, Nektar Therapeutics) and 1.5 equiv of triethylamine (TEA) were dissolved in 1 mL of anhydrous DMF. DNP-NHS (5.4 mg (1.8 equiv)) was dissolved in 250 μL of anhydrous DMF, added to PEG, and stirred for 48 h. Ten milliliters of dH_2O was added to the reaction mixture, which was then added to a Slide-A-Lyzer 3.5K MWCO dialysis cassette (Pierce) and dialyzed against dH_2O for 2 days to remove unreacted DNP. The reaction solution was recovered from the dialysis cassettes, passed through a glass filter with a piece of grade #50 Whatman filter paper (Fisher), and lyophilized to yield approximately 40 mg of a fluffy yellow solid. ^{1}H NMR (300 MHz Bruker Avance NMR Spectrometer using a BBI inverse probe) was performed on PEG-DNP to determine the labeling ratio of DNP by proton integration of PEG CH_2 next to the terminal carboxyl group (2.5 ppm) and of the DNP CH groups in the aromatic ring (7.1, 8.3, and 9.1 ppm). Integration revealed that 84.1% of the PEG was conjugated to DNP (Supporting Information). The remaining amine groups were reacted with Sulfo-NHS acetate (Pierce), irreversibly capping the amines with an acyl group. Amine blocking was confirmed by a 2,4,6-trinitrobenzenesulfonic acid (TNBS) assay as described in ref *43*.

Synthesis of PEI-PEG-DNP. PEG-DNP (10.5 mg) was dissolved in 400 μL of anhydrous DMF. 1,3-Dicyclohexylcarbodiimide (DCC) (2.0 mg (5 equiv)) was dissolved in 50 μL of anhydrous DMF, and 1.12 mg (5 equiv) of *N*-hydroxysuccinimide (NHS) was dissolved in 50 μL anhydrous DMF. The 50 μL of NHS was added to PEG-DNP, followed immediately by 50 μL of DCC, and the reaction was allowed to stir for 48 h to activate the carboxylic acid group on the PEG with NHS. Then, 6.08 mg of PEI (25,000 g/mol, branched) was dissolved in 608 μL of anhydrous DMF with 150 molar equiv of TEA, and the reaction was stirred for 30 min. The activated PEI solution was added to NHS-PEG-DNP for an 8:1 molar PEG/PEI ratio and allowed to stir for 24 h. Another aliquot of TEA (150 equiv), DCC (5 equiv), and NHS (5 equiv) in anhydrous DMF was added to drive the reaction to completion and stirred for another 24 h. The polymer was protonated by the addition of HCl and dialyzed in a Slide-A-Lyzer 10K MWCO Dialysis Cassette against dH_2O to remove unreacted PEG-DNP from the PEI-PEG-DNP solution. The dialyzed solution was filtered through a 0.22 μm filter and lyophilized to yield a fluffy yellow solid. ^{1}H NMR (300 MHz Bruker Avance NMR Spectrometer using a BBI inverse probe) was performed on PEI-PEG-DNP to determine the labeling ratio of PEG-DNP by proton integration of the PEI main chain CH_2 groups (2.6–3.2 ppm) (*44*) and of the DNP CH groups as described above. The integration of the DNP, the integration of the PEI, and the 0.841 DNP/PEG relationship were used to determine the labeling ratio as 6.84 mol PEG per mol PEI (Supporting Information).

Synthesis of PEI-PEG. bPEI (25,000 g/mol, 6.08 mg) was dissolved in 608 μL of anhydrous DMF with 150 molar equiv of TEA, and the reaction was stirred for 30 min. Then, 10.5 mg of mPEG-SPA (5000 g/mol, Nektar Therapeutics) was dissolved in 400 μL of anhydrous DMF, and the activated PEI solution was added to the mPEG-SPA for an 8:1 molar PEG/PEI ratio and allowed to stir for 48 h. The polymer was protonated by the addition of HCl and dialyzed in a Slide-A-Lyzer 10K MWCO Dialysis Cassette (Pierce) against dH_2O to remove unreacted PEG from the PEI-PEG solution. The dialyzed solution was filtered through a 0.22 μm filter and lyophilized to yield a fluffy white solid. ^{1}H NMR (300 MHz Bruker Avance NMR Spectrometer using a BBI inverse probe) was performed on PEI-PEG to determine the labeling ratio of PEG by proton integration of the PEI main chain CH_2 groups (2.6–3.2 ppm) and of the PEG main chain CH_2 groups (3.6 ppm) (*44*). The integration revealed a labeling ratio of 7.31 mol PEG per mol PEI (Supporting Information).

Labeling Plasmid DNA with Quantum Dots. gWiz-Luciferase plasmid (gWiz-Luc, Endotoxin-free) was purchased from Aldevron, and 1 mg of the DNA plasmid was purified by ethanol precipitation and resuspended in 1× TE buffer (10 mM Tris and 1 mM EDTA) at a concentration of 2 mg/mL. The plasmid was labeled with EZ-Link psoralen-PEO_3-biotin (Pierce) and then linked to streptavidin-conjugated quantum dots (QD-585-SA conjugate from Invitrogen/Molecular Probes) as described by the protocol of Ho et al. (*45*). Briefly, the DNA was biotinylated by photocross-linking psoralen-PEO_3-biotin onto the DNA, and then the QD-585-SA conjugates were attached to the DNA through the biotin. The degree of labeling of the DNA was determined by first creating standard curves of absorbance at 260 nm (A_{260}) versus concentration for both the DNA and the QDs and standard curves of fluorescence (ex ~350 nm, em ~585 nm) versus concentration for both the DNA and QDs. The concentration of the QDs could be determined from the fluorescence measurements, the QD concentration could be used to calculate the QDs' contribution to the A_{260} measurements, and then the corrected A_{260} signal could be used to calculate the DNA concentration. It was determined that the DNA plasmid was labeled with one QD per 2 plasmids.

Formulation of Polyplexes and Testing Salt Stability. The gWiz-Luc plasmid was diluted in water to a concentration of 0.1 μg/μL and mixed with an equal volume of polymer at the desired polymeric nitrogen to DNA phosphate (N/P) ratio. After mixing, the polyplexes were allowed to incubate for 5 min at room temperature. Ten microliters of each polyplex sample was mixed with either 90 μL of dH_2O or PBS, and the 100 μL sample was assayed for particle size by dynamic light scattering (DLS) measured on a Brookhaven Instruments Corp. ZetaPALS instrument. Particle sizing measurements were performed at a wavelength of 659.0 nm with a detection angle of 90° at RT. The samples were then diluted into 1.3 mL dH_2O, and the zeta potential was analyzed on the same ZetaPALS instrument.

Serum and ECM Components Unpackaging Assay. The gWiz-Luc plasmid was mixed with the bis-intercalating dye YOYO-1 iodide (Invitrogen/Molecular Probes) at a dye/base

pair (D:BP) ratio of 1:25 and incubated at 50 °C for 2 h to equilibrate the bis-intercalator complexes with DNA (*46*). Polyplexes were formed at N/P ratios of 0 and 3 by complexing unlabeled or YOYO-labeled DNA with either PEI or PEI-PEG. Type I collagen from rat tail (Upstate/Millipore) was prepared according to the manufacturer's instructions at pH 7.4. Fetal bovine serum (FBS, from Mediatech) was serially diluted with 1:10 dilutions into either dH_2O or OptiMEM I (Invitrogen), while heparan sulfate (HS, from Sigma), collagen, and Matrigel (BD Biosciences) were serially diluted in OptiMEM. Twenty microliters (containing 1 μg DNA) of polyplex was added to each well of a 96-well plate, followed by 80 μL of one dilution of FBS, Matrigel, collagen, or HS. The fluorescence from each well was measured on a Tecan Safire^2 plate reader with excitation at 491 nm and emission at 510–520 nm. The fluorescence signal from the N/P = 3 polyplexes was corrected by subtracting the signal from unlabeled samples and then normalizing to the N/P = 0 (DNA only) signal. For the ECM components, a concentration for 50% unpackaging was determined by fitting a trendline to the data points by linear regression and using the equation of that line to calculate the concentration at 50% unpackaging.

NBD-Oligo Internalization. Mouse fibroblast cells (NIH-3T3, passage 91, ATCC # CRL-1658) were resuspended in complete cell culture medium (DMEM + 10% FBS + 1% antibiotic/antimicrobial) to a concentration of 200,000 cells/mL. The cells were plated at 200,000 cells per well in a 12-well plate. Polyplexes at N/P = 3 with 3 μg of DNA (NBD-labeled oligonucleotide, prepared as described previously (*19*)) in 60 μL were formulated, and the polyplex samples were brought up to 600 μL with OptiMEM or with OptiMEM containing 0.01 μg/μL HS, 10% FBS, or 30% FBS. The cells were incubated with the polyplex solutions for 2 h, and then the cells were washed with 10 mM dithionite/10 mM Tris in cold PBS for 2 min at RT to quench any extracellular NBD fluorescence. The cells were washed with PBS, permeabilized with Triton X-100, and NBD uptake quantified as described previously (*19*).

***In Vitro* Transfection.** Human cervix epithelial adenocarcinoma cells (HeLa, passage 56, ATCC # CCL-2) were resuspended in complete cell culture medium (DMEM + 10% FBS + 1% antibiotic/antimicrobial) to a concentration of 2.5×10^5 cells/mL, and 5×10^5 cells were added to each well of a 6-well plate, each containing a 22 × 22 mm sterilized glass coverslip. The 6-well plates were placed in a 37 °C incubator with 5% CO_2 for 24 h to allow the HeLa cells to attach to the glass coverslips. Polyplexes were formed at an N/P of 3 using 5 μg of DNA-QD and PEI-DNP in 100 μL total volume. Controls containing polymer or DNA only were also prepared. For a polyplex + FBS sample, 300 μL of FBS was added to the 100 μL polyplex (75% v/v FBS), and for a polyplex + HS sample, 100 μL of HS at a concentration of 0.1 μg/μL was added to the 100 μL polyplex (2 μg HS/μg DNA). Each sample was brought up to 1 mL with OptiMEM. The cells were washed twice with PBS, and the transfection mixtures were added. After a 2 h incubation at 37 °C, the cells were fixed with 4% paraformaldehyde (PFA, diluted in PBS) for 7 min, followed by permeabilization with 0.1% Triton X-100 (diluted in PBS) for 7 min and blocking with 10% normal goat serum (Sigma) diluted in PBS + 1% bovine serum albumin (PBS/BSA) for 30 min. The slides were each incubated with 100 μL of a primary rat anti-DNP monoclonal antibody (Zymed) diluted 1:100 (starting concentration 1 mg/mL) in PBS/BSA for 1 h and 100 μL of a secondary antibody (Ab) solution for 30 min. The secondary Ab solution contained goat anti-rat IgG Ab that was labeled with Alexa Fluor 633 (Invitrogen/Molecular Probes) and diluted 1:100 (starting concentration is 2 mg/mL), phalloidin labeled with Alexa Fluor 488 (to stain actin, from Invitrogen/Molecular Probes) diluted 1:10 (starting concentration is 1 unit in 5 μL), and DAPI diluted 1:100 (to stain the nucleus, starting concentration is 1 mM). For the secondary Ab solution, all materials were diluted into PBS/BSA. Cells were washed twice with PBS between all steps. The slides were mounted on Gold Seal Ultra Frost glass microscope slides (Becton Dickinson) with ProLong Antifade reagent (Invitrogen/Molecular Probes) and sealed with nail polish. Cells were imaged on a Zeiss LSM 510 confocal system equipped with an inverted Axiovert 200 motorized microscope using a Zeiss plan-apochromat 63×/1.4 oil objective and taking 2 μm slices in the *z*-plane.

***In Vivo* Liver Delivery.** Polyplexes were prepared at N/P = 3 using 25 μg of DNA-QD per mouse, where both the polymer and DNA were diluted in 5% dextrose to a total volume of 200 μL (400 μL after mixing). The polyplex (PPX) sample was formed using PEI-DNP and the PEGylated polyplex (PEG-PPX) sample was formed using PEI-PEG-DNP. A DNA only sample was made with 25 μg of DNA in 400 μL of 5% dextrose, a PEI only sample was made with an amount of PEI-DNP equivalent to N/P = 3 in 400 μL of 5% dextrose, and a PEG-PEI only sample was made with an amount of PEI-PEG-DNP equivalent to N/P = 3 in 400 μL of 5% dextrose. Each sample was assayed for particle size in dH_2O and PBS before injection into animals. Female BALB/c mice (8 weeks, from Jackson Laboratories) were anesthetized with isoflurane, and the sample solutions were injected into the portal vein. After 20 min or 1 h, a Saf-T-Intima IV catheter (22 GA, 0.75 in, from BD) was inserted into the inferior vena cava, the portal vein was clipped, and the liver was perfused with 10 mL of PBS at a flow rate of 1 mL/min. During perfusion, the liver was periodically gently massaged to enhance the clearance of blood out of the vasculature in the liver. After perfusion, the liver was excised and fixed in 4% PFA for 3 h. The liver was then cut in half, with one-half remaining in 4% PFA overnight. The other half was placed in 25% sucrose (a cryoprotectant) and stored at 4 °C overnight.

Histology, Immunohistochemistry, and Imaging. The livers in PFA were embedded in paraffin, sectioned, and stained with hematoxylin and eosin. The livers in sucrose were snap-frozen in Tissue-Tek Optimal Cutting Temperature embedding medium (OCT, from Sakura Finetek) and sectioned into 8 μm thick sections on a Leica CM 1850 cryostat (Meyer Instruments). Slides were rehydrated in PBS for 10 min, nonspecific Ab binding was blocked by incubating slides in 10% normal goat serum in PBS/BSA for 1 h, and then a primary antibody solution was applied to the slides for 1 h. The primary antibody solution consisted of a 1:100 dilution of rat anti-DNP monoclonal Ab and a 1:100 dilution of rabbit anti-mouse collagen IV polyclonal Ab (Chemicon International) in PBS/BSA. The slides were washed twice with PBS, and a secondary antibody solution was applied to the slides for 30 min. The secondary antibody solution consisted of a 1:100 dilution of goat anti-rat IgG conjugated to Alexa Fluor 633, a 1:100 dilution of goat anti-rabbit IgG conjugated to Alexa Fluor 350, and 2 U per section phalloidin-Alexa488 (stock concentration is 1 Unit/5 μL) with all reagents diluted in PBS/BSA. Glass microscope coverslips were mounted on the tissue sections with ProLong Antifade reagent, then sealed with nail polish. Tissue sections were imaged on a Zeiss LSM 510 confocal system equipped with an inverted Axiovert 200 motorized microscope using either a Zeiss plan-apochromat 63×/1.4 oil objective or an F Fluar 40×/1.3 oil objective and taking 3 μm slices in the *z*-plane.

Colocalization Analysis and DNA Quantification. The 4-channel LSM image files were imported into Volocity Visualization software from Improvision, and the colocalization function was used to assess the colocalization of two channels. A threshold was set on each channel to exclude the low-signal autofluorescence associated with each channel, and then Vo-

locity was used to compute the colocalization coefficients. The calculated colocalization coefficients were M_1 and M_2 as reported by Manders et al., and these coefficients were used because they are proportional to the amount of fluorescence in the colocalizing objects and independent of the signal intensities of each channel (*47*). Volocity software was also used to quantify the amount of DNA in each tissue section. A threshold was set on the DNA channel, and then Volocity was used to calculate the number of voxels in the DNA channel above the threshold.

RESULTS

Polymer and Plasmid Labeling. PEGylated PEI was synthesized by conjugating an activated PEG (PEG-SPA, MW 5000) to PEI (MW 25,000). Graft copolymers with approximately 7 PEG polymers per PEI polymer were synthesized to allow comparisons with previous reports (*39–41*). For fluorescence microscopy studies, polymers were also labeled with 2,4-dinitrophenyl (DNP) for antibody recognition. PEI was tagged with DNP-NHS at a labeling ratio of 23.2 DNP molecules per PEI polymer. PEI-PEG-DNP was synthesized by grafting DNP-PEG-COOH to PEI by DCC/NHS coupling. Graft copolymers with approximately 7 PEG polymers and 5.75 DNP molecules per PEI polymer were synthesized.

Initial experiments were conducted with AlexaFluor568-labeled plasmid DNA. However, the fluorescence quenching observed in condensed DNA resulted in fluorescence levels that were only slightly above background levels in tissue sections. Thus, plasmids were labeled with red fluorescent quantum dots (QDs). DNA was labeled with psoralen-biotin and then reacted with streptavidin-coated QDs, resulting in the incorporation of one QD for every two DNA plasmids. The fluorescence from polyplexes formed with QD-labeled DNA (QD-DNA) at N/P = 3 was approximately 5-fold higher than that from polyplexes formulated with Alexa568-labeled DNA at 6 dye molecules per plasmid (data not shown).

Polyplex Characterization. Polyplexes were formulated at N/P = 3 on the basis of particle size, zeta potential, and gel retardation studies that showed complete DNA condensation at N/P = 3 with only small amounts of free polymer after complex formation (data not shown). The polyplexes used in this study were characterized by measuring particle size in water and physiological salt concentrations and particle surface charge (Supporting Information). Polyplex diameter was ~100–150 nm in water. The unPEGylated polyplex rapidly aggregated to sizes greater than 1 μm in phosphate-buffered saline (PBS), whereas the PEGylation of polyplex conferred improved salt stability. All polyplexes had positive surface charges.

Effect of ECM and Serum Components on Vector Unpackaging. The effect of serum on polyplex stability was assessed using a YOYO-1-based unpackaging assay (Figure 1). The unpackaging assay is based on the properties of YOYO binding to DNA. First, the fluorescence of YOYO is over 1000-fold greater when bound to DNA than when in solution, and second, when YOYO-labeled DNA is condensed with a cationic polymer such as PEI, the dye molecules become closer in proximity and begin to interact electronically, causing a dramatic decrease in fluorescence signal (i.e., YOYO dye self-quenching occurs) (*48*). Complexation of YOYO-labeled plasmid with PEI or PEI-PEG results in a ~75–90% decrease in YOYO fluorescence. Polyplexes incubated with increasing concentrations of fetal bovine serum (FBS) show corresponding increases in YOYO-1 fluorescence until, at 80% FBS, nearly all the fluorescence is recovered, indicating complete unpackaging. Interestingly, the YOYO signal of polyplexes in the absence of serum is significantly higher when diluted in OptiMEM versus water (3-fold higher for unPEGylated and 2-fold higher for PEGylated). The YOYO signal of the polyplexes in the absence of serum is also significantly higher for PEGylated polyplexes versus that for unPEGylated polyplexes (25% of the fluorescence of unpackaged DNA vs 10% for water, and 50% vs 30% for OptiMEM). These data indicate that not only does PEGylation slightly loosen the polyplexes but also the presence of counterions from the salt in OptiMEM loosens the polyplexes.

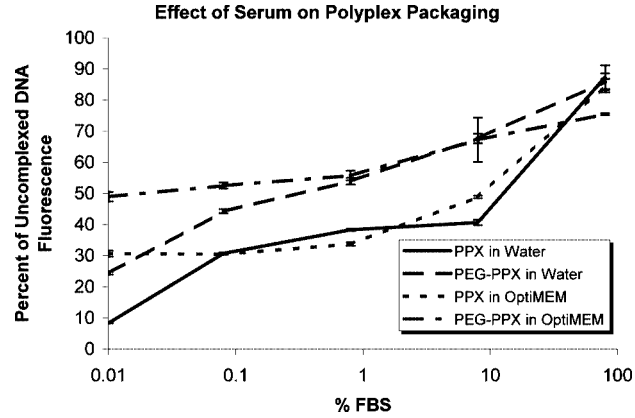

Figure 1. Polyplex (N/P = 3) unpackaging mediated by FBS diluted in water and OptiMEM. The *x*-axis shows the volume percent of FBS in solution. Eighty microliters of the indicated solution was added to 20 μL of polyplex (N/P = 3) containing 1 μg of DNA.

Table 1[a]

	PPX (μg)	PEG-PPX (μg)	fold increase
HS	0.27	0.01	26.3
Matrigel	6.30	0.57	11.0
collagen	301.03	28.50	10.6

[a] Various concentrations of extracellular matrix components (HS, Matrigel and Collagen I) were incubated with PEI and PEGylated PEI polyplex (PPX and PEG-PPX, respectively) labeled with YOYO-1. The amount of the ECM component that was required to unpackage polyplexes containing 1 μg of DNA to recover 50% of uncomplexed DNA fluorescence is reported.

The stability of polyplexes was also assessed in the presence of extracellular matrix proteins. Gene delivery vehicles entering the liver will pass out of the blood vessels and into the hepatic sinusoids that flow past rows of hepatocytes, where they will encounter an extracellular matrix (ECM) composed of both collagen and heparan sulfate proteoglycan (HSPG) (*49–55*). Thus, Matrigel (an ECM extract that contains HSPGs), heparan sulfate (HS, a negatively charged proteoglycan component), and collagen were investigated for their ability to unpackage PEI polyplexes and PEGylated PEI polyplexes (PPX and PEG-PPX, respectively). The amounts of each ECM component required to unpackage polyplexes containing 1 μg of YOYO-1abeled DNA to recover 50% of uncomplexed DNA fluorescence are reported in Table 1. HS most effectively unpackaged the polyplexes, requiring only 0.27 μg of HS and 0.01 μg of HS per μg DNA to unpackage PPX and PEG-PPX, respectively. Comparatively, approximately 25–50 times more Matrigel than HS (by weight) was required to unpackage the polyplexes, with 6.3 μg of Matrigel and 0.57 μg of Matrigel per μg DNA needed to unpackage PPX and PEG-PPX, respectively. Similarly, about 50-fold more collagen than Matrigel (by weight) was required to unpackage the polyplexes, with 301.03 μg of collagen and 28.5 μg of collagen per μg DNA needed to unpackage PPX and PEG-PPX, respectively. A general trend also appears in that approximately 10-fold more ECM component (by weight) is required to unpackage PPX compared to that required to unpackage PEG-PPX. This trend holds true for FBS unpackaging as well, with PEG-PPX unpackaging to 50% of uncomplexed DNA fluorescence around 1% FBS and PPX unpack-

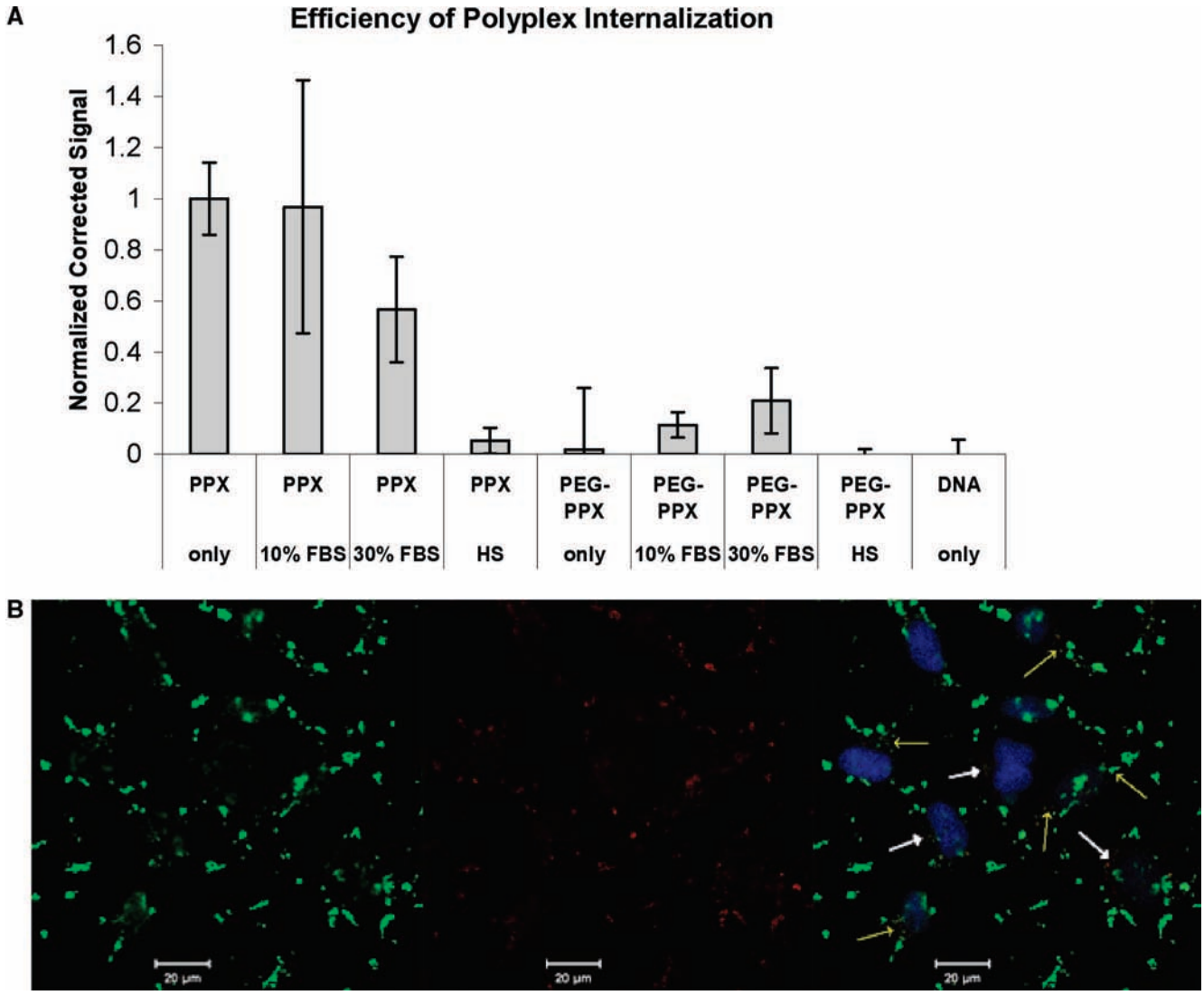

Figure 2. (A) Cellular internalization of PEI and PEGylated PEI polyplexes (PPX and PEG-PPX) incubated in the presence of heparan sulfate or FBS. The amount of internalized DNA for each formulation was normalized to that of cells incubated with PEI polyplex in OptiMEM. The internalization with PEI polyplexes in OptiMEM was statistically significantly different from PEI polyplexes in 30% FBS with $p < 0.05$ and all other samples (except the 10% FBS) with $p < 0.01$. (B) Confocal images from DNA-QD and PEI-DNP polyplex transfections. On the left is the PEI-DNP channel (green), in the middle is the DNA-QD channel (red), and on the right is an overlay of PEI-DNP, DNA-QD, and DAPI (blue). Punctate (yellow, thin arrows) and diffuse (white, thick arrows) fluorescence is observed. Some examples of free DNA are also found near the cell nuclei in the areas of diffuse fluorescence. The scale bars are 20 μm.

aging to 50% of uncomplexed DNA fluorescence around 10% FBS (Figure 1).

Polyplex Internalization. Polyplex-mediated DNA internalization in cultured mammalian cells was quantified in the presence of both FBS and HS by using an environmentally sensitive fluorophore, NBD, conjugated to DNA (Figure 2A). NBD is converted into a nonfluorescent molecule by dithionite, a membrane-impermeable reducing agent. Measurement of fluorescence from internalized NBD-labeled DNA is a facile method to quantify polyplex uptake (*19*). Exposure of cells to polyplexes in OptiMEM or OptiMEM + 10% serum resulted in efficient DNA internalization. However, significantly decreased polyplex uptake was observed in the presence of 30% serum (43% reduction in internalized DNA, $p < 0.05$). Similarly, PPX incubated with HS also led to a statistically significant decrease in the amount of DNA uptake (95% reduction in internalized DNA, $p < 0.01$). As is consistent with previous observations, PEG-PPX did not mediate much internalization of DNA.

HeLa cells were transfected with polyplexes formed with DNA-QD and PEI-DNP to verify dual fluorescence imaging of the polyplexes and to investigate intracellular distributions of polyplexes after internalization. Cells were stained with DAPI to visualize the nucleus and anti-DNP antibodies to visualize PEI and then imaged by confocal microscopy. As can be seen in Figure 2B, PPX were successfully delivered, with both cell-associated polyplexes and internalized polyplexes present. The cell-associated polyplexes are mainly visible as large aggregates attached (primarily through electrostatic interaction between the positively charged particles and the negatively charged cell surface) to the periphery of the actin network. The internalized polyplexes are present in two forms: first (and primarily) in punctate dots characteristic of vesicular localization (yellow, thin arrows) and second in diffuse fluorescence (white, thick arrows). Furthermore, it is clear that much of the PEI is colocalized with DNA, and nearly all of the DNA is colocalized with PEI. Most of the polyplex unpackaging observed occurs in and around the nucleus (in the areas of diffuse fluorescence), indicating that the majority of polyplexes remain intact until the very end stages of delivery. Low uptake of QD-DNA and significant unpackaging was observed with polyplexes incubated

with FBS or HS, consistent with the NBD internalization results (data not shown).

***In Vivo* Liver Delivery.** The intrahepatic distribution of dual-labeled PPX and PEG-PPX after portal vein delivery was next assessed. Eight-week old female BALB/c mice were injected with 400 μL of polyplexes in 5% dextrose, and liver tissue was collected either 20 min or 1 h after injection. The liver tissue was first analyzed by hematoxylin and eosin (H and E) staining for gross morphology. Tissues from a few mice had areas of sinusoidal dilation and hepatocyte death, but most of the tissue in each of the samples was normal and healthy. For fluorescent confocal imaging, tissue sections were stained with phalloidin to visualize actin and an antibody against collagen IV to represent ECM. PEI and PEG-PEI were visualized using an antibody against DNP, and the plasmid was fluorescently labeled with QD. Figure 3A shows confocal images of liver sections harvested 20 min after the portal vein injection of PPX. Both PEI and DNA can be detected in the sections. PEI is primarily colocalized with the collagen lining the sinusoidal structures and rarely colocalized with DNA. DNA was observed to be located near the cell periphery, but no cell-internalized DNA was observed. Figure 3B shows confocal images from liver that was removed 1 h postinjection, and again both PEI and DNA can be detected in the tissue. Similar to the 20 min time point, at 1 h the PEI and DNA are not colocalized with each other; interestingly, intracellular delivery of DNA was observed.

The distribution of PEG-PPX in liver 20 min after administration is shown in Figure 4. The distributions of the polymer and DNA in the tissue are very similar to that of PPX delivery. Again, both polymer and DNA can be detected in the tissue. Notably, with PEG-PPX, much less DNA is observed in the tissue compared to that in PPX (Figures 3 and 4). The relative amount of DNA in the tissues was determined using Volocity software to calculate the number of voxels containing fluorescence in the DNA channel in at least five images from each sample (Figure 5). The amount of DNA fluorescence in the liver 20 min after PPX administration is ~4-fold higher than levels from PEG-PPX or naked DNA injection ($p < 0.01$). Fluorescence from DNA in PPX samples decreases by over 50% between 20 min and 1 h ($p < 0.05$). Interestingly, PEG-PPX did not mediate a statistically significant increase in DNA in the tissue compared to that in the tissue of mice treated with DNA plasmid only, though both PPX time points showed a statistically significant increase in DNA compared to that of the DNA only sample ($p < 0.01$) (Figure 5). Unlike PPX, PEG-PPX does not appear to lead to any observable intracellular DNA delivery, even 1 h after delivery (Supporting Information). With the delivery of plasmid DNA or polymer alone (Supporting Information), it can be seen that very little DNA is present in the tissue when it is not complexed with polymer, although there is a large amount of polymer present in the tissue even when it is not complexed with DNA. No evidence of either DNA or polymer entering cells when delivered alone was found.

Colocalization Analysis. The extent of colocalization between polymer and DNA, collagen, or actin, and DNA and polymer, collagen, or actin was quantified by measuring colocalization coefficients using Volocity image analysis software. The coefficients M_1 and M_2 (as reported by Manders and Aten) are used to represent the degree to which two images overlap because they (i) do not depend on the ratio of the number of objects in both channels, (ii) do not depend on the signal intensities of the channels, and (iii) are proportional to the amount of fluorescence in the colocalizing objects (*47*). For both PPX and PEG-PPX formulations at 20 min and 1 h, DNA is most highly colocalized with actin, with colocalization coefficients ranging from 0.5 to 0.7 as shown in Figure 6. For PPX at 20 min, low colocalization of DNA with PEI or collagen is observed (colocalization coefficients of ~0.2 and ~0.15, respectively). For PPX at 1 h and both PEG-PPX at 20 min and 1 h, the colocalization coefficients of DNA with polymer and collagen are two to three times greater than the respective coefficients from PPX at 20 min. As can be seen in Figure 7, PEI is highly colocalized with collagen IV and actin (with colocalization coefficients ranging from 0.4 to 0.8), while it is only partially colocalized with the DNA (colocalization coefficients of 0.1 or less). Comparing Figures 6 and 7, it can be noted that even when DNA is highly colocalized with PEI, PEI is still not highly colocalized with the DNA, indicating that there is an abundance of free polymer in the tissue not associated with DNA. It should also be noted that the colocalization coefficients for each sample sum to greater than unity because there is colocalization among all the channels; therefore, some colocalized voxels can be counted twice.

DISCUSSION

Electrostatic condensation of polyanionic DNA and polycationic PEI into polyplexes occurs by a polyelectrolyte addition reaction driven by an increase in system entropy due to the displacement of counterions and the final formation of the polyelectrolyte complex, as described by Kabanov and co-workers (*56*). However, the addition of free polyanions can then cause dissociation of the initial complexes as a result of a polyelectrolyte exchange reaction, which is driven by a decrease in free energy due to the redistribution of interpolymeric salt bonds between the complexed polyanion and the free polyanion (*56*). Indeed, unpackaging of polyplexes delivered to cultured mammalian cells has been proposed to occur by competitive binding interactions with RNA in the cytosol or DNA in the nucleus (*30, 31, 57*). Polyplexes administered *in vivo* by systemic injection may be subject to premature unpackaging through interactions with serum proteins or ECM components, which have been shown *in vitro* to bind to and/or unpackage polyplexes (*32, 33, 58–61*).

Rice and co-workers demonstrated that plasmid is rapidly released from cationic peptide vectors in blood unless the vectors are stabilized by cross-linking (*62*). Recently, two reports investigated the biodistribution of PEI and PEGylated PEI polyplexes by radioactive labeling of both DNA and polymer, finding that polyplexes formed with PEGylated PEI or low molecular weight PEI separated in blood in a dose-dependent manner compared to polyplexes formed with high molecular weight PEI, which remained intact (*40, 41*). The studies also showed that PEGylated polyplexes were more likely to unpackage when the PEG grafting on PEI was high or when injected in small quantities but that PEI polyplexes were likely to remain intact even when injected in small quantities (*40, 41*). Additionally, both studies found that large amounts of both DNA and polymer primarily distributed to the liver, with the spleen and lung also having measurable amounts of DNA and polymer (*40, 41*). Although PEI and plasmid were shown to exhibit similar organ distributions and clearance kinetics and therefore assumed to remain packaged, the intrahepatic distributions of the polyplexes has, to date, not been investigated. In this work, the distribution of PEI polyplexes and PEGylated PEI polyplexes in the liver after intravenous delivery was investigated with dual-labeled polymer and plasmid with analysis by fluorescence confocal microscopy.

For systemic administration, the polyplexes will first encounter serum proteins in the blood. The polyplexes will then enter the liver via the portal vein and move into a parallel system of vascular channels called the hepatic sinusoids, which emanate radially from the portal triad (portal vein, hepatic artery, and bile duct) and conform to the surfaces of the hepatic epithelial cell laminae that compose the liver (*51*). The sinusoids

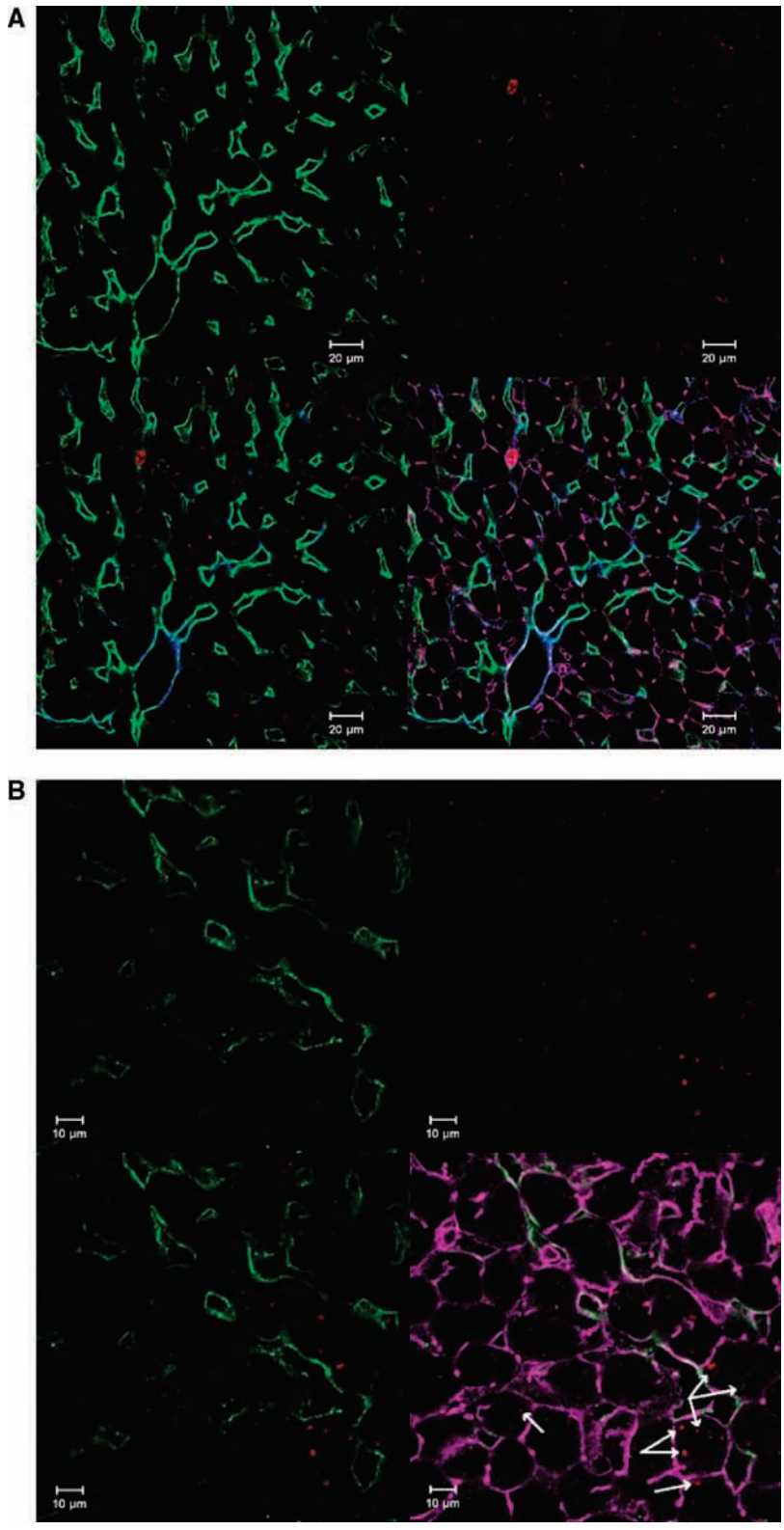

Figure 3. (A) 40× confocal images from a polyplex-injected mouse liver section from a liver that was removed after 20 min. On the top left is the PEI-DNP (green) channel; at the top right is the DNA-QD (red) channel; at the bottom left is the anti-Collagen IV Ab (blue) channel, DNA-QD, and PEI-DNP; and on the bottom right is anti-Collagen, DNA-QD, PEI-DNP, and Phalloidin (anti-actin, colored pink). The scale bars are 20 μm. (B) 63× confocal images from a polyplex-injected mouse liver section from a liver that was removed after 1 h. At the top left is the PEI-DNP (green) channel; at the top right is the DNA-QD (red) channel; on the bottom left is the anti-Collagen IV Ab (blue) channel, DNA-QD, and PEI-DNP; and on the bottom right is anti-Collagen, DNA-QD, PEI-DNP, and Phalloidin (anti-actin, colored pink). The scale bars are 10 μm; the arrows show the internalized DNA-QD.

intercommunicate through fenestrations to form an interconnected system of thin-walled vessels coupled to a large surface area of liver parenchyma to facilitate material transfer from the vessels to the cells (*51*). The hepatic sinusoids are lined with endothelial cells, and hepatic stellate cells lie in the space between the sinusoidal endothelial cells and the parenchymal

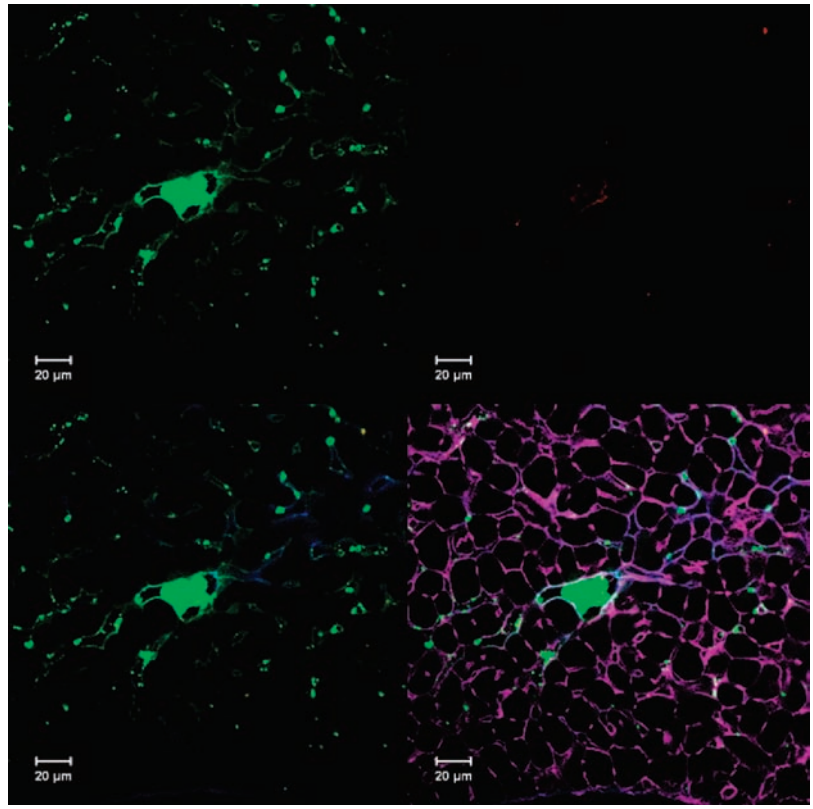

Figure 4. 40× confocal images from PEGylated polyplex-injected mouse liver section from a liver that was removed after 20 min. At the top left is the PEI-DNP (green) channel; on the top right is the DNA-QD (red) channel; on the bottom left is the anti-Collagen IV Ab (blue) channel, DNA-QD, and PEI-DNP; and on the bottom right is anti-Collagen, DNA-QD, PEI-DNP, and Phalloidin (anti-actin, colored pink). The scale bars are 20 μm.

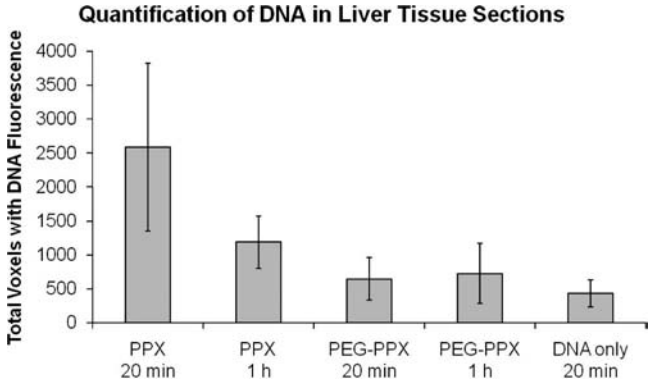

Figure 5. Quantification of DNA in liver tissue sections. Volocity image analysis software was used to quantify the total number of voxels with DNA fluorescence from tissue sections of each sample type. The amount of DNA fluorescence in the liver from PPX administration is ~4-fold higher than levels from PEG-PPX or naked DNA injection ($p < 0.01$). Fluorescence from DNA in PPX samples decreases by over 50% between 20 min and 1 h ($p < 0.05$). PEG-PPX did not mediate a statistically significant increase in DNA in the tissue compared to DNA only. Both PPX time points showed a statistically significant increase in DNA compared to the DNA only sample ($p < 0.01$).

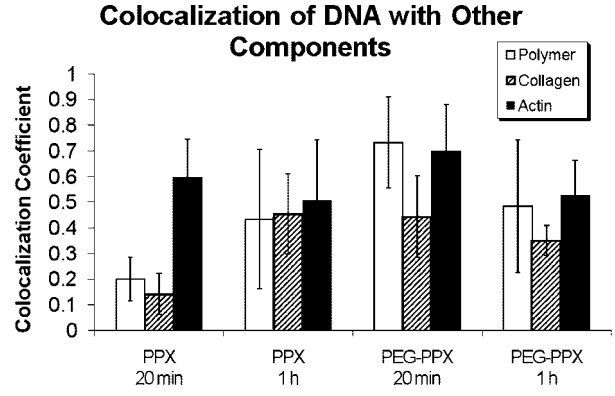

Figure 6. Colocalization coefficients (calculated from images of tissue sections taken 20 min or 1 h after injection) for DNA colocalized with polymer, collagen, or actin, as determined by Volocity. A coefficient value of 1 corresponds to perfect colocalization, while a value of 0 corresponds to no colocalization. For all groups, $n > 3$.

cells, where it has been shown that these stellate cells are mainly responsible for synthesizing the ECM surrounding the sinusoids (*51*, *55*). The ECM associated with the hepatic sinusoids is composed of collagen I, collagen IV, and heparan sulfate proteoglycan (HSPG) (*49*–*55*). Thus, both the serum and the ECM in the hepatic sinusoids present potential threats for premature polyplex unpackaging.

We first determined the ability of serum to unpackage the polyplexes *in vitro*. The assay that was employed uses the quenching of YOYO-labeled DNA fluorescence to report the compaction of DNA in polyplexes. Since YOYO intercalates into DNA before the polyplexes are formed and could potentially affect polyplex structure, it was first confirmed through a secondary approach, ethidium bromide (EtBr) exclusion, that YOYO-1 labeling does not affect polyplex packaging (Supporting Information). Figure 1 clearly shows that increasing the concentration of serum (the composition of FBS is variable, but the main protein components of FBS are albumins, globulins, and fibrinogens) in either water or OptiMEM causes the unpackaging of both PPX and PEG-PPX. The unpackaging of PEG-PPX occurs more readily at lower concentrations of FBS compared to that of PPX, indicating that PPX are more tightly complexed. Next, Table 1 shows the ability of ECM components to unpackage the polyplexes: collagen, Matrigel (the main

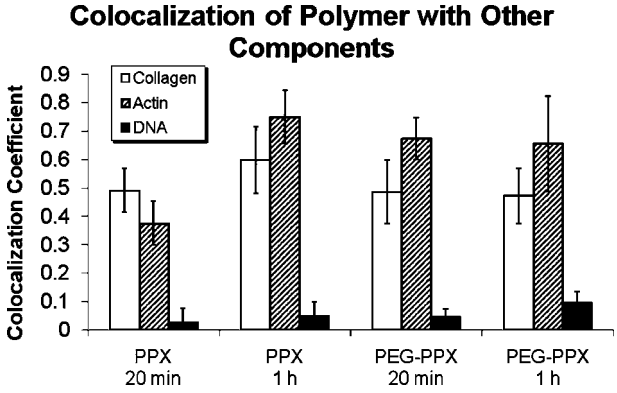

Figure 7. Colocalization coefficients (calculated from images of tissue sections taken 20 min or 1 h after injection) for polymer colocalized with collagen, actin, or DNA, as determined by Volocity. A coefficient value of 1 corresponds to perfect colocalization, while a value of 0 corresponds to no colocalization. For all groups, $n > 3$.

components of Matrigel are laminin, collagen IV, entactin, and heparan sulfate proteoglycans), and HS all effectively unpackage the polyplexes. Again, the unpackaging of PEG-PPX occurs more readily at lower concentrations of ECM components compared to that of PPX. For comparison with Table 1, the weight ratios for 50% unpackaging by FBS are approximately 500 μg FBS protein and 50 μg FBS protein per μg DNA for PPX and PEG-PPX, respectively; thus, the unpackaging mediated by FBS is comparable to that of collagen. In water, collagen I has an isoelectric point around neutral pH, but in the presence of salt, the isoelectric point can change; thus, since the collagen used in these assays was diluted in PBS, the ionic interactions could have shifted the isoelectric point, causing the collagen to be slightly charged (*63*). HS was expected to most effectively unpackage the polyplexes because of its high negative charge density. Matrigel was also expected to mediate the unpackaging of polyplexes because of the fact that it contains HSPG, but its intermediate ability to unpackage is consistent with the fact that its main component is collagen and that HSPG is only a minor component. Neither collagen nor Matrigel was allowed to gel, eliminating the possibility that the unpackaging was caused by the gelation process. Though it was determined that a large excess of FBS protein compared to DNA was required for unpackaging, the ratios necessary are within the physiological range normally found in serum. Thus, soluble GAGs, the GAGs of proteoglycans in the ECM, and serum proteins can all potentially facilitate polyplex unpackaging *in vivo*.

A series of *in vitro* transfections was performed with polyplexes formed from the DNP-labeled polymer and QD-labeled DNA, and the cells were imaged to assess uptake and intracellular distributions. The dual-labeled polyplexes were tested by the same EtBr unpackaging assay as described above, and the labeled PPX were found to be slightly more resistant to unpackaging than unlabeled PPX, while the labeled PEG-PPX were found to unpackage at levels similar to that of unlabeled PEG-PPX (Supporting Information). The dual-labeled polyplexes also exhibited slightly higher zeta potential than the unmodified polyplex, which may be responsible for the higher resistance to unpackaging seen with the labeled PPX (Supporting Information). As can be seen from Figure 2, PPX are efficiently internalized, and most of the internalized of the polymer and DNA are colocalized, while a small fraction has separated intracellularly after escape from endosomes (as evidenced by diffuse fluorescence rather than punctate). In contrast, minimal amounts of internalized DNA is observed with cells treated with plasmid only or with PPX exposed to HS or FBS before delivery, whereas levels of polymer association with cells is similar for all polyplex formulations (data not shown). These results demonstrate that (i) in the absence of serum proteins or ECM components, PPX are efficiently internalized in a packaged state and that (ii) exposure of PPX to serum or HS results in inefficient DNA delivery, likely due to premature vector unpackaging.

The intrahepatic distributions of dual-labeled polyplexes were next assessed. Initial studies used AlexaFluor-labeled plasmid, but the results reported here focus on QD-labeled plasmid because of higher fluorescence yield. However, hepatic distributions were similar for both labeling approaches. The major findings from these studies are that PEI and PEGylated PEI are not colocalized with plasmid DNA in the liver by 20 min postinjection (Figure 3A and 4). The unpackaging of PEG-PPX in the serum has been reported previously, although PEI (25 kD) has been shown to distribute in a manner similar to that of plasmid DNA in the organs (*40*, *41*). On the basis of previous biodistribution studies and these new findings, we propose that PEI polyplexes remain packaged during circulation in serum but unpackage after entering the liver because of competitive binding with ECM components, specifically HS proteoglycans. This conclusion is supported by *in vitro* unpackaging studies that show that HS efficiently unpackages PPX and PEG-PPX and by the observation that PEI is primarily localized around the hepatic sinusoids through collagen IV colocalization (Figure 3 and 4). Published images of HS proteoglycan distribution in the liver show fluorescence lining the hepatic sinusoids that bears a striking resemblance to the images in this work showing PEI lining the sinusoids (*50–53*). Collagen IV has been shown to be present in the space of Disse that lines the hepatic sinusoids, and HSPG has been shown to be present in the same areas. However, antibodies to HS also stain intracellular HS. Because colocalization of PEI with ECM components was quantified in this study by image analysis, collagen IV, which stains in a manner similar to that of extracellular HS was used as an ECM marker instead.

In contrast to PEI, DNA is visualized in intercellular spaces and is associated with the outside of the cells (Figure 3A), which is consistent with other reports (*64*). Previous results combined with the larger amount of DNA observed in the tissue in this study (compared to that in the DNA only sample; see Figure 5) and the fact that DNA disappears from serum very quickly when no PEI protects it (as it has a very short half-life due to nuclease degradation (*65*)) suggest that the polyplexes remain intact in blood. Thus, we propose that bPEI facilitates liver transfection *in vivo* primarily by protecting DNA against nuclease degradation and elimination from circulation, mediating higher levels of delivery to the liver compared with unpackaged DNA. However, because of premature unpackaging of polyplex in the liver, a significant contribution of PEI toward internalization and intracellular trafficking of plasmid DNA is unlikely. The unpackaged DNA was observed to be internalized with kinetics similar to that reported by Wolff and co-workers, who hypothesize that free plasmid DNA can be internalized in hepatocytes by a receptor-mediated process (*66*).

It is worth noting that the colocalization coefficients for DNA with polymer and collagen are higher for PPX at 1 h and PEG-PPX at 20 min and 1 h compared to those for the polyplex at 20 min because of an artifact created by a smaller amount of DNA present in the former samples (Figures 5 and 6). Liver sections acquired 20 min after PPX treatment have considerable amounts of free DNA in the tissue, but the other three samples only have small amounts of DNA remaining because of the fact that most DNA has been unpackaged from the polymeric carrier and degraded. The small amount of DNA that remains does so because it is protected by the polymer from nuclease degradation. Analysis of polymer colocalization in Figure 7 reveals that the polymer has poor colocalization with the DNA in any

sample, thus supporting the hypothesis that the high DNA−polymer colocalization at 1 h and in PEGylated formulations is simply an artifact derived from the presence of a smaller amount of DNA that has been protected by (and so is physically closer to) the PEI.

PEGylation of polyplexes was initially thought to reduce interaction with blood components, thereby increasing the stability of polyplexes in the blood. Subsequent work revealed that the PEGylated polyplexes were actually less stable in blood (*40, 41, 59, 67*). It is likely that a considerable amount of PEG is trapped within the core of the polyplexes after they form, leading to thermodynamic destabilization (*41, 59*). In line with these findings, the *in vitro* unpackaging assay that compared PPX with PEG-PPX showed that PEG-PPX unpackaged more easily. Additionally, it can be seen in Figure 5 that PEG-PPX carry much less DNA into the tissue, most likely due to early unpackaging of polyplexes in blood and DNA degradation by serum nucleases. It should be noted that in the images for PEG-PPX and PEI-PEG only, the amount of polymer seems to be lower than that seen with PPX. This observation may simply be attributed to the fact that the PEI-PEG contains less DNP (approximately 6 DNP per mol of polymer) than PEI (approximately 23 DNP per mol of polymer). However, the decreased amount of PEG-PEI may also be due to an actual change in biodistribution, similar to the report by Fischer et al. indicating that PEI preferentially accumulated in the liver and spleen, while PEG-PEI preferentially accumulated in the spleen and lung (*40*).

Also of interest is the notion that since preconjugating PEG to PEI causes PEG chains to be trapped in the core of the polyplex during formation, which destabilizes the polyplexes and leads to premature unpackaging, it would be beneficial to add PEG onto the polyplexes after they have been formed. However, this method was investigated, and it was found that coating polyplexes with a hydrophilic polymer similar to PEG generated complexes that were also less stable and unpackaged in the blood (*60*). In line with this finding, we have constructed similar postformation PEGylated polyplexes and have shown that they unpackage readily and do not aid in delivering more DNA to the tissue (data not shown). The hepatic DNA and PEG-PEI distributions observed in these studies were similar to those shown for polyplexes formed from PEG-PEI and DNA condensation.

In conclusion, we have demonstrated that both serum proteins and ECM act as extracellular barriers to polyplex-mediated gene delivery because of their ability to unpackage polyplexes. At the same time, polyplexes must unpackage once inside the cell so that transcription of the genes may occur. Thus, a double-edged sword is presented: the polyplexes must be stable enough to resist unpackaging in blood and ECM, but not too stable that they resist unpackaging once reaching their intracellular destination. Polyplexes will no doubt need to change their form in order to reach their full potential and overcome this serious flaw. One can imagine that if PEI and DNA remained associated extracellularly, PEI would be able to mediate much higher gene expression by increasing the amount of DNA taken up by the cells and aiding in DNA escape from endosomes as it does *in vitro*. A potential solution is cross-linking polyplexes with a biodegradable linker that will maintain stability in the blood and degrade in the intracellular environment, as proposed by Neu et al. and Murthy et al. (*68, 69*) or conjugating the nucleic acid cargo directly to the vector, as demonstrated by Rozema et al. (70).

ACKNOWLEDGMENT

Confocal imaging was performed at the NanoTech User Facility (NTUF) at the University of Washington, a member of National Nanotechnology Infrastructure Network supported by NSF, with special thanks to Dr. Dong Qin at NTUF for her training and support on the Zeiss confocal microscope. We also thank Dr. Matthew Yeh, from the Department of Pathology at the University of Washington, for his help with analyzing the liver tissue sections. Paraffin embedding, sectioning, and H & E staining were performed by the Pathology Core Immunocytochemistry Lab at UW. Cryosections were prepared using the cryostat at the UW Engineered Biomaterials (UWEB) histology facility. Jamie Bergen kindly donated the NBD-oligo used in the transfection studies. This work was funded by a National Science Foundation Fellowship awarded to R.S.B., an NSF CAREER Award (CBET-0448547) to S.H.P. and a Young Investigator award to S.H.P. by the National Hemophilia Foundation.

Supporting Information Available: Table S1 shows particle size and zeta potential characterization of the polyplexes. Figure S1 shows the NMR spectrum of PEG-DNP. Figure S2 shows the NMR spectrum of PEI-PEG-DNP. Figure S3 shows the NMR spectrum of unlabeled PEI-PEG. Figure S4 shows polyplex unpackaging as monitored by an EtBr exclusion assay. Figure S5 contains a 63× confocal image of PEG-PPX injected mouse liver removed after 1 h. Figure S6 contains a 40× confocal image from a PEI-only injected mouse liver removed after 20 min. Figure S7 contains a 40× confocal image from PEI-PEG-only injected mouse liver removed after 20 min. Figure S8 contains a 40× confocal image from DNA-only injected mouse liver removed after 20 min. This material is available free of charge via the Internet at http://pubs.acs.org.

LITERATURE CITED

(1) Tomanin, R., and Scarpa, M. (2004) Why do we need new gene therapy viral vectors? Characteristics, limitations and future perspectives of viral vector transduction. *Curr. Gene Ther. 4*, 357–372.

(2) Thomas, C. E., Ehrhardt, A., and Kay, M. A. (2003) Progress and problems with the use of viral vectors for gene therapy. *Nat. Rev. Genet. 4*, 346–358.

(3) Mulligan, R. C. (1993) The basic science of gene therapy. *Science 260*, 926–932.

(4) Glover, D. J., Lipps, H. J., and Jans, D. A. (2005) Towards safe, non-viral therapeutic gene expression in humans. *Nat. Rev. Genet. 6*, 299–310.

(5) Pack, D. W., Hoffman, A. S., Pun, S., and Stayton, P. S. (2005) Design and development of polymers for gene delivery. *Nat. Rev. Drug Discovery 4*, 581–593.

(6) Boussif, O., Lezoualc'h, F., Zanta, M. A., Mergny, M. D., Scherman, D., Demeneix, B., and Behr, J. P. (1995) A versatile vector for gene and oligonucleotide transfer into cells in culture and in vivo: polyethylenimine. *Proc. Natl. Acad. Sci. U.S.A. 92*, 7297–7301.

(7) Godbey, W. T., Wu, K. K., and Mikos, A. G. (1999) Tracking the intracellular path of poly. (ethylenimine)/DNA complexes for gene delivery. *Proc. Natl. Acad. Sci. U.S.A. 96*, 5177–5181.

(8) Kichler, A., Leborgne, C., Coeytaux, E., and Danos, O. (2001) Polyethylenimine-mediated gene delivery: a mechanistic study. *J. Gene. Med. 3*, 135–144.

(9) Akinc, A., and Langer, R. (2002) Measuring the pH environment of DNA delivered using nonviral vectors: implications for lysosomal trafficking. *Biotechnol. Bioeng. 78*, 503–508.

(10) Sonawane, N. D., Szoka, F. C., Jr., and Verkman, A. S. (2003) Chloride accumulation and swelling in endosomes enhances DNA transfer by polyamine-DNA polyplexes. *J. Biol. Chem. 278*, 44826–44831.

(11) Akinc, A., Thomas, M., Klibanov, A. M., and Langer, R. (2005) Exploring polyethylenimine-mediated DNA transfection and the proton sponge hypothesis. *J. Gene. Med. 7*, 657–663.

(12) Gharwan, H., Wightman, L., Kircheis, R., Wagner, E., and Zatloukal, K. (2003) Nonviral gene transfer into fetal mouse livers (a comparison between the cationic polymer PEI and naked DNA). *Gene Ther. 10*, 810–817.

(13) Ogris, M., Brunner, S., Schuller, S., Kircheis, R., and Wagner, E. (1999) PEGylated DNA/transferrin-PEI complexes: reduced interaction with blood components, extended circulation in blood and potential for systemic gene delivery. *Gene Ther. 6*, 595–605.

(14) Mishra, S., Webster, P., and Davis, M. E. (2004) PEGylation significantly affects cellular uptake and intracellular trafficking of non-viral gene delivery particles. *Eur. J. Cell Biol. 83*, 97–111.

(15) Kursa, M., Walker, G. F., Roessler, V., Ogris, M., Roedl, W., Kircheis, R., and Wagner, E. (2003) Novel shielded transferrin-polyethylene glycol-polyethylenimine/DNA complexes for systemic tumor-targeted gene transfer. *Bioconjugate Chem. 14*, 222–231.

(16) Schaffer, D. V., and Lauffenburger, D. A. (1998) Optimization of cell surface binding enhances efficiency and specificity of molecular conjugate gene delivery. *J. Biol. Chem. 273*, 28004–28009.

(17) Mislick, K. A., and Baldeschwieler, J. D. (1996) Evidence for the role of proteoglycans in cation-mediated gene transfer. *Proc. Natl. Acad. Sci. U.S.A. 93*, 12349–12354.

(18) Labat-Moleur, F., Steffan, A. M., Brisson, C., Perron, H., Feugeas, O., Furstenberger, P., Oberling, F., Brambilla, E., and Behr, J. P. (1996) An electron microscopy study into the mechanism of gene transfer with lipopolyamines. *Gene Ther. 3*, 1010–1017.

(19) Bergen, J. M., Kwon, E. J., Shen, T. W., and Pun, S. H. (2008) Application of an environmentally-sensitive fluorophore for rapid analysis of the binding and internalization efficiency of gene carriers. *Bioconjugate Chem. 19*, 377–384.

(20) Bieber, T., Meissner, W., Kostin, S., Niemann, A., and Elsasser, H. P. (2002) Intracellular route and transcriptional competence of polyethylenimine-DNA complexes. *J. Controlled Release 82*, 441–454.

(21) Itaka, K., Harada, A., Yamasaki, Y., Nakamura, K., Kawaguchi, H., and Kataoka, K. (2004) In situ single cell observation by fluorescence resonance energy transfer reveals fast intracytoplasmic delivery and easy release of plasmid DNA complexed with linear polyethylenimine. *J. Gene. Med. 6*, 76–84.

(22) Suh, J., Wirtz, D., and Hanes, J. (2003) Efficient active transport of gene nanocarriers to the cell nucleus. *Proc. Natl. Acad. Sci. U.S.A. 100*, 3878–3882.

(23) Grosse, S., Thevenot, G., Monsigny, M., and Fajac, I. (2006) Which mechanism for nuclear import of plasmid DNA complexed with polyethylenimine derivatives? *J. Gene. Med. 8*, 845–851.

(24) Lukacs, G. L., Haggie, P., Seksek, O., Lechardeur, D., Freedman, N., and Verkman, A. S. (2000) Size-dependent DNA mobility in cytoplasm and nucleus. *J. Biol. Chem. 275*, 1625–1629.

(25) Vaughan, E. E., DeGiulio, J. V., and Dean, D. A. (2006) Intracellular trafficking of plasmids for gene therapy: mechanisms of cytoplasmic movement and nuclear import. *Curr. Gene Ther. 6*, 671–681.

(26) Dean, D. A. (1997) Import of plasmid DNA into the nucleus is sequence specific. *Exp. Cell Res. 230*, 293–302.

(27) Vacik, J., Dean, B. S., Zimmer, W. E., and Dean, D. A. (1999) Cell-specific nuclear import of plasmid DNA. *Gene Ther. 6*, 1006–1014.

(28) Zabner, J., Fasbender, A. J., Moninger, T., Poellinger, K. A., and Welsh, M. J. (1995) Cellular and molecular barriers to gene transfer by a cationic lipid. *J. Biol. Chem. 270*, 18997–19007.

(29) Zanta, M. A., Belguise-Valladier, P., and Behr, J. P. (1999) Gene delivery: a single nuclear localization signal peptide is sufficient to carry DNA to the cell nucleus. *Proc. Natl. Acad. Sci. U.S.A. 96*, 91–96.

(30) Schaffer, D. V., Fidelman, N. A., Dan, N., and Lauffenburger, D. A. (2000) Vector unpacking as a potential barrier for receptor-mediated polyplex gene delivery. *Biotechnol. Bioeng. 67*, 598–606.

(31) Huth, S., Hoffmann, F., von Gersdorff, K., Laner, A., Reinhardt, D., Rosenecker, J., and Rudolph, C. (2006) Interaction of polyamine gene vectors with RNA leads to the dissociation of plasmid DNA-carrier complexes. *J. Gene. Med. 8*, 1416–14124.

(32) Ruponen, M., Yla-Herttuala, S., and Urtti, A. (1999) Interactions of polymeric and liposomal gene delivery systems with extracellular glycosaminoglycans: physicochemical and transfection studies. *Biochim. Biophys. Acta 1415*, 331–341.

(33) Ruponen, M., Ronkko, S., Honkakoski, P., Pelkonen, J., Tammi, M., and Urtti, A. (2001) Extracellular glycosaminoglycans modify cellular trafficking of lipoplexes and polyplexes. *J. Biol. Chem. 276*, 33875–33880.

(34) Ruponen, M., Honkakoski, P., Ronkko, S., Pelkonen, J., Tammi, M., and Urtti, A. (2003) Extracellular and intracellular barriers in non-viral gene delivery. *J. Controlled Release 93*, 213–217.

(35) Moret, I., Esteban Peris, J., Guillem, V. M., Benet, M., Revert, F., Dasi, F., Crespo, A., and Alino, S. F. (2001) Stability of PEI-DNA and DOTAP-DNA complexes: effect of alkaline pH, heparin and serum. *J. Controlled Release 76*, 169–181.

(36) Egilmez, N. K., Iwanuma, Y., and Bankert, R. B. (1996) Evaluation and optimization of different cationic liposome formulations for in vivo gene transfer. *Biochem. Biophys. Res. Commun. 221*, 169–173.

(37) Turunen, M. P., Hiltunen, M. O., Ruponen, M., Virkamaki, L., Szoka, F. C., Jr., Urtti, A., and Yla-Herttuala, S. (1999) Efficient adventitial gene delivery to rabbit carotid artery with cationic polymer-plasmid complexes. *Gene Ther. 6*, 6–11.

(38) Kwok, K. Y., Park, Y., Yang, Y., McKenzie, D. L., Liu, Y., and Rice, K. G. (2003) In vivo gene transfer using sulfhydryl cross-linked PEG-peptide/glycopeptide DNA co-condensates. *J. Pharm. Sci. 92*, 1174–1185.

(39) Kunath, K., von Harpe, A., Petersen, H., Fischer, D., Voigt, K., Kissel, T., and Bickel, U. (2002) The structure of PEG-modified poly. (ethylene imines) influences biodistribution and pharmacokinetics of their complexes with NF-kappaB decoy in mice. *Pharm. Res. 19*, 810–817.

(40) Fischer, D., Osburg, B., Petersen, H., Kissel, T., and Bickel, U. (2004) Effect of poly. (ethylene imine) molecular weight and pegylation on organ distribution and pharmacokinetics of polyplexes with oligodeoxynucleotides in mice. *Drug Metab. Dispos. 32*, 983–992.

(41) Merdan, T., Kunath, K., Petersen, H., Bakowsky, U., Voigt, K. H., Kopecek, J., and Kissel, T. (2005) PEGylation of poly. (ethylene imine) affects stability of complexes with plasmid DNA under in vivo conditions in a dose-dependent manner after intravenous injection into mice. *Bioconjugate Chem. 16*, 785–792.

(42) Park, I. K., Lasiene, J., Chou, S. H., Horner, P. J., and Pun, S. H. (2007) Neuron-specific delivery of nucleic acids mediated by Tet1-modified poly. (ethylenimine). *J. Gene. Med. 9*, 691–702.

(43) Snyder, S. L., and Sobocinski, P. Z. (1975) An improved 2,4,6-trinitrobenzenesulfonic acid method for the determination of amines. *Anal. Biochem. 64*, 284–288.

(44) Sagara, K., and Kim, S. W. (2002) A new synthesis of galactose-poly. (ethylene glycol)-polyethylenimine for gene delivery to hepatocytes. *J. Controlled Release 79*, 271–281.

(45) Ho, Y. P., Chen, H. H., Leong, K. W., and Wang, T. H. (2006) Evaluating the intracellular stability and unpacking of DNA nanocomplexes by quantum dots-FRET. *J. Controlled Release 116*, 83–89.

(46) Carlsson, C., Jonsson, M., and Akerman, B. (1995) Double bands in DNA gel electrophoresis caused by bis-intercalating dyes. *Nucleic Acids Res. 23*, 2413–2420.

(47) Manders, E. M. M., Verbeek, F. J., and Aten, J. A. (1993) Measurement of colocalization of objects in dual-color confocal images. *J. Microsc. (Oxford) 169*, 375–382.
(48) Krishnamoorthy, G., Duportail, G., and Mely, Y. (2002) Structure and dynamics of condensed DNA probed by 1,1′-(4,4,8,8-tetramethyl-4,8-diazaundecamethylene)bis[4-[[3- methylbenz-1,3-oxazol-2-yl]methylidine]-1,4-dihydroquinolinium] tetraiodide fluorescence. *Biochemistry 41*, 15277–15287.
(49) Burkel, W. E., and Low, F. N. (1966) The fine structure of rat liver sinusoids, space of Disse and associated tissue space. *Am. J. Anat. 118*, 769–783.
(50) Stow, J. L., Kjellen, L., Unger, E., Hook, M., and Farquhar, M. G. (1985) Heparan sulfate proteoglycans are concentrated on the sinusoidal plasmalemmal domain and in intracellular organelles of hepatocytes. *J. Cell Biol. 100*, 975–980.
(51) Fawcett, D. W., and Bloom, W. (1986) *A Textbook of Histology*, 11th ed., Saunders, Philadelphia, PA.
(52) Soroka, C. J., and Farquhar, M. G. (1991) Characterization of a novel heparan sulfate proteoglycan found in the extracellular matrix of liver sinusoids and basement membranes. *J. Cell Biol. 113*, 1231–1241.
(53) Zern, M. A., and Reid, L. M. (1993) *Extracellular Matrix: Chemistry, Biology, and Pathobiology with Emphasis on the Liver*, Dekker, New York.
(54) Nerlich, A., Berndt, R., and Schleicher, E. (1991) Differential basement membrane composition in multiple epithelioid haemangioendotheliomas of liver and lung. *Histopathology 18*, 303–307.
(55) Senoo, H. (2004) Structure and function of hepatic stellate cells. *Med. Electron Microsc. 37*, 3–15.
(56) Bakeev, K. N., Izumrudov, V. A., Kuchanov, S. I., Zezin, A. B., and Kabanov, V. A. (1992) Kinetics and mechanism of interpolyelectrolyte exchange and addition-reactions. *Macromolecules 25*, 4249–4254.
(57) Bertschinger, M., Backliwal, G., Schertenleib, A., Jordan, M., Hacker, D. L., and Wurm, F. M. (2006) Disassembly of polyethylenimine-DNA particles in vitro: implications for polyethylenimine-mediated DNA delivery. *J. Controlled Release 116*, 96–104.
(58) Dash, P. R., Read, M. L., Barrett, L. B., Wolfert, M. A., and Seymour, L. W. (1999) Factors affecting blood clearance and in vivo distribution of polyelectrolyte complexes for gene delivery. *Gene Ther. 6*, 643–650.
(59) Oupicky, D., Konak, C., Dash, P. R., Seymour, L. W., and Ulbrich, K. (1999) Effect of albumin and polyanion on the structure of DNA complexes with polycation containing hydrophilic nonionic block. *Bioconjugate Chem. 10*, 764–72.
(60) Oupicky, D., Howard, K. A., Konak, C., Dash, P. R., Ulbrich, K., and Seymour, L. W. (2000) Steric stabilization of poly-L-Lysine/DNA complexes by the covalent attachment of semitelechelic poly[N-(2-hydroxypropyl)methacrylamide]. *Bioconjugate Chem. 11*, 492–501.
(61) Eliyahu, H., Joseph, A., Schillemans, J. P., Azzam, T., Domb, A. J., and Barenholz, Y. (2007) Characterization and in vivo performance of dextran-spermine polyplexes and DOTAP/cholesterol lipoplexes administered locally and systemically. *Biomaterials 28*, 2339–2349.
(62) Collard, W. T., Yang, Y., Kwok, K. Y., Park, Y., and Rice, K. G. (2000) Biodistribution, metabolism, and in vivo gene expression of low molecular weight glycopeptide polyethylene glycol peptide DNA co-condensates. *J. Pharm. Sci. 89*, 499–512.
(63) Freudenberg, U., Behrens, S. H., Welzel, P. B., Muller, M., Grimmer, M., Salchert, K., Taeger, T., Schmidt, K., Pompe, W., and Werner, C. (2007) Electrostatic interactions modulate the conformation of collagen I. *Biophys. J. 92*, 2108–2119.
(64) Lecocq, M., Andrianaivo, F., Warnier, M. T., Wattiaux-De Coninck, S., Wattiaux, R., and Jadot, M. (2003) Uptake by mouse liver and intracellular fate of plasmid DNA after a rapid tail vein injection of a small or a large volume. *J. Gene. Med. 5*, 142–156.
(65) Kawabata, K., Takakura, Y., and Hashida, M. (1995) The fate of plasmid DNA after intravenous injection in mice: involvement of scavenger receptors in its hepatic uptake. *Pharm. Res. 12*, 825–830.
(66) Budker, V., Budker, T., Zhang, G., Subbotin, V., Loomis, A., and Wolff, J. A. (2000) Hypothesis: naked plasmid DNA is taken up by cells in vivo by a receptor-mediated process. *J. Gene. Med. 2*, 76–88.
(67) Mullen, P. M., Lollo, C. P., Phan, Q. C., Amini, A., Banaszczyk, M. G., Fabrycki, J. M., Wu, D., Carlo, A. T., Pezzoli, P., Coffin, C. C., and Carlo, D. J. (2000) Strength of conjugate binding to plasmid DNA affects degradation rate and expression level in vivo. *Biochim. Biophys. Acta 1523*, 103–110.
(68) Neu, M., Sitterberg, J., Bakowsky, U., and Kissel, T. (2006) Stabilized nanocarriers for plasmids based upon cross-linked poly. (ethylene imine). *Biomacromolecules 7*, 3428–3438.
(69) Murthy, N., Campbell, J., Fausto, N., Hoffman, A. S., and Stayton, P. S. (2003) Design and synthesis of pH-responsive polymeric carriers that target uptake and enhance the intracellular delivery of oligonucleotides. *J. Controlled Release 89*, 365–374.
(70) Rozema, D. B., Lewis, D. L., Wakefield, D. H., Wong, S. C., Klein, J. J., Roesch, P. L., Bertin, S. L., Reppen, T. W., Chu, Q., Blokhin, A. V., Hagstrom, J. E., and Wolff, J. A. (2007) Dynamic PolyConjugates for targeted in vivo delivery of siRNA to hepatocytes. *Proc. Natl. Acad. Sci. USA 104*, 12982–12987.

BC700388U

Mitochondria Targeting by Guanidine− and Biguanidine−Porphyrin Photosensitizers

Martha Sibrian-Vazquez, Irina V. Nesterova, Timothy J. Jensen, and M. Graça H. Vicente*

Department of Chemistry, Louisiana State University, Baton Rouge, Louisiana 70803. Received October 23, 2007; Revised Manuscript Received December 3, 2007

We report the syntheses of three new amphiphilic porphyrin derivatives, containing a guanidine, a biguanidine, or an MLS peptide, that were designed to target the cell mitochondria. The guanidine− and biguanidine−porphyrins are poorly soluble in water, forming J-type aggregates in aqueous solutions. On the other hand, the porphyrin−MLS peptide conjugate bearing a low molecular weight PEG spacer is highly water-soluble and does not aggregate in aqueous media. The fluorescence quantum yields determined for all porphyrins were higher at low pH (<6) and the porphyrin−peptide conjugate had the highest quantum yields in aqueous media. All porphyrins showed low dark toxicity toward human carcinoma HEp2 cells, and the guanidine−porphyrin was the most phototoxic (IC_{50} = 4.8 μM at 1 J cm^{-2}), followed by the biguanidine−porphyrin and the porphyrin−MLS (IC_{50} = 8.2 μM and 9.8 μM at 1 J cm^{-2}, respectively). The porphyrin−MLS peptide conjugate accumulated the most within cells of all porphyrins at all times investigated and the biguanidine−porphyrin accumulated the least. Both the guanidine− and biguanidine−porphyrins localized within cell mitochondria and, in addition, were found in the lysosomes and the ER (in the case of the guanidine-porphyrin). In contrast, the porphyrin−MLS peptide conjugate localized mainly within the cell lysosomes.

INTRODUCTION

The preferential accumulation of cancer therapeutic drugs within cell mitochondria as a result of differences in the mitochondrial membrane potential between cancerous and normal cells has been an active area of research (*1*). The mitochondria are considered the "powerhouse" of the cell, playing important roles in the regulation of various biochemical processes, including the TCA and urea cycles, oxidative phosphorylation, beta oxidation of fatty cells, regulation of cell calcium, and apoptotic signaling (*2*). In particular, the role played by mitochondria in apoptosis, the process of programmed cell death, makes these cellular organelles desired targets for therapeutic drugs. The apoptotic changes in mitochondria consist of a loss of the electrochemical gradient across the inner membrane due to the opening of the permeability transition pore, followed by the release of soluble intermembrane proteins into the cytosol. These intermembrane proteins include cytochrome C, apoptosis inducing factor (AIF), and mitochondrially associated caspases that act directly as effectors of the apoptotic process (*1, 2*). Current strategies for the delivery of biologically active molecules to the mitochondria of live mammalian cells are based on (i) the high membrane potential across the inner mitochondrial membrane and the organelle's protein import machinery (*3*) or (ii) the property of certain lipophilic cations for preferential accumulation within mitochondria (*3*). The targeting of cancer cell mitochondria by porphyrin derivatives is an attractive strategy for the development of photodynamic therapy (PDT) photosensitizers with increased biological efficacy. PDT (*4, 5*) is a cancer treatment modality that involves the activation of a tumor-accumulated photosensitizer with light, which generates reactive oxygen species, mainly $^1O_2$, that cause irreversible photodamage to tumor tissues. It has been reported that the phototoxicity of Visudyne, an FDA-approved PDT photosensitizer, and that of other PDT drugs currently in clinical trials, including phthalocyanines Pc4 and ZnPcA1, is partly due to their preferential accumulation within mitochondria (*6, 7*). Previous studies have shown that some cationic porphyrin-based photosensitizers tend to accumulate within cell mitochondria (*8, 9*). Functionalities bearing delocalized positive charges (e.g., the guanidinium and biguanidinium groups) are of particular interest due to their higher lipophilicity compared with groups with localized charges. Several porphyrin derivatives containing delocalized positive charge substituents have been synthesized and some of these compounds were found to be efficient DNA intercalators (*10–15*). On the other hand, porphyrin−peptide conjugates bearing specific organelle-targeting peptide sequences have also been synthesized and investigated (*16–19*), although the use of mitochondrial localization sequences (MLS) has not yet been fully exploited as a targeting strategy for porphyrin-based sensitizers. Mitochondrial proteins bearing a MLS peptide are recognized by the mitochondrial protein import machinery and translocated into the mitochondrial matrix, where the MLS peptide is cleaved by a matrix processing protease (*20, 21*). Several MLS sequences have been identified and used for the specific delivery of drugs to the mitochondria (*22–25*). In a recent study, the sequence MLSLRQSIRFFKGC was used to deliver a cationic Mn-porphyrin to isolated rat liver mitochondria, via a mitochondrial swelling assay (*26*). In our continuing design and investigation of porphyrin-based photosensitizers with specific targeting properties, we report herein the syntheses and properties of a series of amphiphilic cationic porphyrin derivatives aimed at targeting the mitochondria of cancer cells. These compounds contain either a group with delocalized positive charge (guanidinium or biguanidinium) or a MLS peptide attached to the porphyrin via a low molecular weight PEG spacer. We report the photophysical

* E-mail: vicente@lsu.edu.

10.1021/bc700393u CCC: $40.75 © 2008 American Chemical Society
Published on Web 02/13/2008

properties and the *in vitro* biological efficacy of this new series of porphyrins, including their ability for targeting the mitochondria of human carcinoma HEp2 cells.

EXPERIMENTAL PROCEDURES

Synthesis. Unless otherwise indicated, all commercially available starting materials were used directly without further purification. All reactions were monitored by TLC using Sorbent Technologies 0.25 mm silica gel plates with or without UV indicator (60F-254). Silica gel (Sorbent Technologies 32–63 μm) was used for flash column chromatography. ^{1}H NMR spectra were obtained on a ARX-300 Bruker spectrometer. Chemical shifts (δ) are given in ppm relative to d_6-DMSO or $CDCl_3$ (2.49 and 7.26 ppm ^{1}H, respectively,). Electronic absorption spectra were measured on a Perkin-Elmer Lambda 35 UV–vis spectrophotometer. Mass spectra were obtained on an Applied Biosystems QSTAR XL, a hybrid QqTOF mass spectrometer with a MALDI ionization source using CCA as the matrix. HPLC separation and analysis were carried out on a Dionex system including a P680 pump and a UVD340U, detector. Semipreparative HPLC was carried out using a Luna C_{18} 100 Å, 5 μm, 10 × 250 mm (Phenomenex, USA) column and a stepwise gradient; analytical HPLC was carried out using a Delta Pak C_{18} 300 Å, 5 μm, 3.9 × 150 mm (Waters, USA) column and a stepwise gradient.

Guanidinium−Porphyrin 2. To a solution of monoaminoporphyrin **1** (*27*) (0.025 g, 0.039 mmol) in DMF (0.5 mL) was added 12 M HCl (9.9 μL, 0.12 mmol) followed by methanol (0.019 g, 0.59 mmol) and cyanamide (0.0025 g, 0.059 mmol). The reaction mixture was heated at 70 °C for 24 h. The mixture was diluted with ethyl acetate (10 mL) upon which a purple precipitate formed. Complete precipitation was achieved upon addition of hexanes (5 mL). The solid residue was filtered, washed with a mixture of ethyl acetate/hexanes 1:1, and dried under vacuum. The title porphyrin was obtained as the hydrochloride in 42% yield (0.011 g). ^{1}H NMR ($CDCl_3$, 300 MHz): δ 8.81–8.86 (8H, m), 8.20–8.24 (8H, m), 7.98–8.11 2H, m), 7.77 (9H, s), 7.63–7.66 (2H, d), 7.42–7.44 (1H, m), 7.02–7.05(1H, m), −2.75 (2H, s). UV–vis (CH_3OH) λ_{max} (ϵ/M^{-1} cm^{-1}) 419 (251 000), 516 (16 600), 552 (10 800), 588 (8600), 646 (7100). HRMS (MALDI) *m*/*z* 672.2920 (M + H$^+$), calculated for $C_{45}H_{33}N_7$ 672.2875.

Biguanidinium−Porphyrin 3. To a solution of monoaminoporphyrin **1** (*27*) (0.025 g, 0.039 mmol) in DMF (0.5 mL), was added 12 M HCl (9.9 mL, 0.12 mmol) followed by isopropanol (0.036 g, 0.59 mmol) and dicyanamide (0.005 g, 0.059 mmol). The reaction mixture was heated at 90 °C for 18 h. The mixture was diluted with ethyl acetate (10 mL) and hexanes (5 mL). The solid residue was filtered, washed with hexanes, and dried under vacuum. The title porphyrin was obtained as the hydrochloride in 61% yield (0.017 g). ^{1}H NMR (d_6-DMSO, 300 MHz): δ 10.31 (1H, s), 10.24 (1H, s), 8.739.07 (8H, m), 8.16–8.24 (6H, m), 7.86–7.97 (9, m), 7.52 (2H, s), 7.23–7.31 (2H. m), 6.66 (2H, s), −2.89 (2H, s). UV–vis (MeOH) λ_{max} (ϵ/M^{-1} cm^{-1}) 420 (303 000), 516 (23 000), 553 (14 800), 590 (10 600), 647 (9100). HRMS (MALDI) *m*/*z* 714.3063 (M + H$^+$), calculated for $C_{46}H_{35}N_9$ 714.3093.

Porphyrin−MLS 4. The peptide sequence MSVLTPLLLRGLTGSARRLPVPRAKIHSL was prepared on an automated peptide synthesizer (Applied Biosystems Pioneer, Peptide Synthesis System, USA) in a 0.2 mmol scale, using the Fmoc strategy of solid-phase peptide synthesis. A 4-fold excess of the Fmoc-protected amino acids were coupled to the PAL-PEG-PS resin using TBTU/HOBt[1] as the activating agents. After the final coupling and the successive removal of the Fmoc group the resin was washed with DMF and isopropyl alcohol and then dried under vacuum. The dried resin containing the protected amino acid sequence was used in the coupling reaction to the porphyrin precursor. Peptidyl resin (0.025 mmol) was introduced into a glass synthesizer, swelled in DMF for 1 h, and then washed with DMF (2 × 5 mL). To the peptidyl resin was added 500 μL of a solution containing 0.05 mmol of pegylated porphyrin (*16*), 0.150 mmol of DIEA, 0.05 mmol of HOBt, and 0.05 mmol of TBTU. The reaction mixture was shaken overnight at room temperature and then filtered to give a dark purple resin. The resin was washed to remove unreacted porphyrin, first with DMF until the filtrate was colorless, then with dichloromethane and methanol, before being dried under vacuum. Cleavage and deprotection was carried out by treatment of the dried resin with 3 mL of a mixture of TFA/phenol/TIS/H_2O, 88/5/2/5 at room temperature for 4 h. The resin was filtered, washed with TFA (3 × 2 mL), and the filtrates combined and evaporated under vacuum to give a green residue. Addition of cold Et_2O yielded a green precipitate, which was washed repeatedly with Et_2O and dried under vacuum. The purification of the title conjugate was achieved by reverse-phase HPLC on a Luna C_{18} semipreparative column (10 × 250 mm, 5 μm) (Phenomenex, USA) using a solvent system of water/acetonitrile both containing 0.1% TFA, with a stepwise gradient from 60% to 95%. The fraction containing the conjugate was collected and lyophilized to yield pure title conjugate in 23% yield (0.024 g). The purity of the porphyrin−peptide conjugate was >98% as determined by HPLC on an analytical Delta Pak C_{18} (3.9 × 150 mm, 5 μm) column. HPLC t_r = 9.44 min. UV–vis (CH_3OH) λ_{max} (ϵ/M^{-1} cm^{-1}) 415 (295 100), 513 (16 900), 547 (10 500), 588 (8000), 645 (6700). LRMS (MALDI) *m*/*z* (M + H$^+$), 4183.55, calculated for $C_{203}H_{310}N_{51}O_{43}S$ 4182.33.

Photophysical Studies. All absorption spectra were acquired using a Perkin-Elmer Lambda 25 UV–visible Spectrophotometer with 10 mm path length quartz cuvettes. Corresponding diluents were utilized as reference solutions. Emission spectra were obtained using a Florolog 3 spectrofluorimeter. The optical density of solutions used for emission studies was below 0.05 at the excitation wavelength to eliminate inner filter effects. All the measurements were performed within 3 h of solution preparation. Stock solutions (10 mM) of porphyrins **2** and **3** were prepared in DMSO and for porphyrin−peptide conjugate **4** water was used. The aqueous solutions of porphyrins **3** and **4** were prepared by spiking 1.5–2 μL of the corresponding DMSO stock solutions into 1 mL of 100 mM phosphate buffer. The quantum yields were calculated using a secondary standard method (*28*, *29*). Methylene blue was used as a secondary standard. According to the approach, the integrated fluorescence intensity of the analyte (I) and standard (I_R), the optical density of the analyte (OD) and the standard (OD_R), and the refractive index of analyte solvent (n) and standard solvent (n_R) are related to the quantum yield of the analyte (Q) as

$$Q = Q_R \frac{I}{I_R} \frac{OD_R}{OD} \frac{n^2}{n_R^2} \quad (1)$$

[1] Abbreviations: HOBt, 1-hydroxybenzotriazole; DMF, *N*,*N*-dimethylformamide; CCA, α-cyano-4-hydroxycinnamic acid; TFA, trifluoroaectic acid; DIEA, *N*,*N*-diisopropylethylamine; TBTU, 2-(1*H*-benzotriazole-1-yl)-1,1,3,3-tetramethyluronium tetrafluoroborate; DMSO, dimethyl sulfoxide; Boc, *t*-butoxy carbonyl; HEPES, 4-(2-hydroxyethyl)-1-piperazine ethanesulfonic acid; PBS, phosphate buffer saline; FBS, fetal bovine serum; DMEM, Dulbecco's Modified Eagle's Medium; MEM, Minimal Essential Medium; PEG, poly(ethylene glycol); TIS, tri-isopropylsilane; Fmoc, 9-fluorenylmethoxycarbonyl; TCA, tricarboxylic acid cycle; TFE, trifluoroethanol; SDS, sodium dodecylsulfonate.

Scheme 1[a]

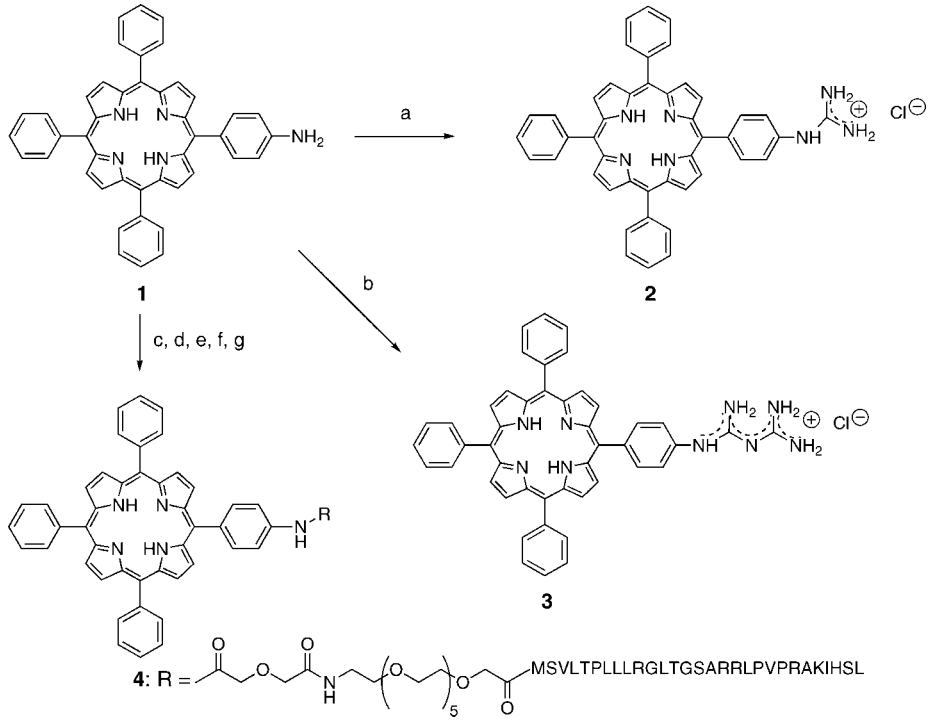

[a] Conditions: (a) $CNNH_2$/HCl/CH_3OH/DMF, 70 °C, 24 h (42%). (b) Dicyanamide/HCl/ isopropanol/DMF, 90 °C, 18 h (61%). (c) Diglycolic anhydride, DMF, rt, 24 h (100%). (d) HOBt/TBTU/DIEA, $NH_2CH_2CH_2(OCH_2CH_2)_5OCH_2CO_2{}^tBu$, rt, 48 h (64%). (e) TFA, rt, 4 h (100%). (f) HOBt/TBTU/DIEA, peptidyl resin, rt, 24 h. (g) TFA/H_2O/Phenol/TIS, 88/5/5/2, rt, 4 h (23%).

where Q_R is a quantum yield of the reference standard (0.03 for Methylene Blue). To account for incomplete spectra, the bands were extrapolated using appropriate fitting models whenever necessary.

Cell Culture. All tissue culture media and reagents were obtained from Invitrogen. Human HEp2 cells were obtained from ATCC and maintained in a 50:50 mixture of DMEM: Advanced MEM containing 5% FBS. The cells were subcultured biweekly to maintain subconfluent stocks.

Time-Dependent Cellular Uptake. HEp2 cells were plated at 10 000 per well in a Costar 96 well plate and allowed to grow for 36 h. Porphyrin stocks were prepared in DMSO or water at a concentration of 10 mM and then diluted into medium to final working concentrations. The cells were exposed to 10 μM of each conjugate for 0, 1, 2, 4, 8, and 24 h. At the end of the incubation time the loading medium was removed and the cells were washed with PBS. The cells were solubilized upon addition of 100 μL of 0.25% Triton X-100 (Calbiochem) in PBS. To determine the porphyrin concentration, fluorescence emission was read at 410/650 nm (excitation/emission) using a BMG FLUOstar plate reader. The cell numbers were quantified using the CyQuant reagent (Molecular Probes).

Dark Cytotoxicity. The HEp2 cells were plated as described above and allowed 36 h to attach. The cells were exposed to increasing concentrations of porphyrin up to 100 μM and incubated overnight. The loading medium was then removed and the cells fed medium containing Cell Titer Blue (Promega) as per manufacturer's instructions. Cell toxicity was then measured by reading the fluorescence at 520/584 nm using a BMG FLUOstar plate reader. The signal was normalized to 100% viable (untreated) cells and 0% viable (treated with 0.2% saponin from Sigma) cells.

Phototoxicity. The HEp2 cells were prepared as described above for the dark cytotoxicity assay and treated with porphyrin concentrations of 0, 0.625, 1.25, 2.5, 5, and 10 μM. After compound loading, the medium was removed and replaced with medium containing 50 mM HEPES pH 7.4. The cells were then placed on ice and exposed to light from a 100 W halogen lamp filtered through a 610 nm long pass filter (Chroma) for 20 min. An inverted plate lid filled with water to a depth of 5 mm acted as an IR filter. The total light dose was approximately 1 J/cm^2. The cells were returned to the incubator for 24 h and assayed for toxicity as described above for the dark cytotoxicity experiment.

Microscopy. The HEp2 cells were plated on LabTek 2 chamber coverslips and incubated overnight, before being exposed to 10 μM of porphyrin. Since the porphyrin macrocycle fluorescences in the red region of the optical spectrum, the images were acquired using standard Texas Red filters. For the colocalization experiments, the cells were incubated for 24 h concurrently with porphyrin and one of the following organelle tracers for 30 min: MitoTracker Green (Molecular Probes) 250 nM, LysoSensor Green (Molecular Probes), BODIPY FL C_5-ceramide at 50 nM (Molecular Probes) and 50 nM, $DiOC_6$-(Molecular Probes) 5 μg/mL. The slides were washed three times with growth medium and new medium containing 50 mM HEPES pH 7.4 was added. By utilizing green fluorescing organelle tracers, it becomes possible to identify the intracellular compartments associated with the porphyrins; when the red and green images are overlaid, areas of colocalization appear as orange−yellow regions. Fluorescent microscopy was performed using a Zeiss Axiovert 200 M inverted fluorescent microscope fitted with standard FITC and Texas Red filter sets (Chroma). The images were aquired with a Zeiss Axiocam MRM CCD camera fitted to the microscope.

RESULTS

Synthesis. The new series of potentially mitochondria-targeting photosensitizers, guanidinium−porphyrin **2**, biguanidinium−porphyrin **3**, and porphyrin−MLS conjugate **4** were synthesized from monoaminoporphyrin **1**, as shown in Scheme 1. The reaction of protonated aminoporphyrin **1** with cyanamide at 70

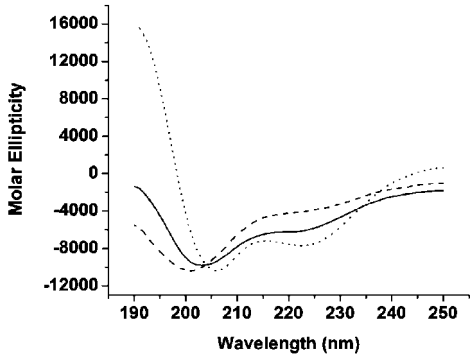

Figure 1. CD spectra in the amide region of conjugate **4** at 20 μM, (full line) TFE/H_2O, pH 7.00, (dash line) 50 mM NaH_2PO_4, pH 5.00, (dot line) 100 mM SDS/H_2O. The ellipticity is given in deg cm^2 dmol^{-1}, the cell path was 0.1 cm, and the temperature 25 °C.

°C in a mixture of DMF/methanol, gave guanidinium−porphyrin **2** in 42% yield. Using a similar procedure, although at 90 °C in a mixture of DMF/isopropanol and in the presence of dicyanamide, biguanidinium−porphyrin **3**, was obtained in 61% yield. The aminoporphyrin **1** was found to be unreactive in the presence of other guanidinylation reagents, including 1*H*-pyrazole-[*N*,*N*′-bis(*tert*-butoxycarbonyl)]-carboxamidine, *N*,*N*′-di-Boc-*N*′-triflyguanidine, and *N*,*N*′-bis(tert-butoxycarbonyl) thiourea, probably as a result of the low nucleophilicity of the amino group of **1**, as we have previously observed (*30*); the use of Mukaiyama's reagent (*31*) in conjunction with *N*,*N*′-bis(tert-butoxycarbonyl)thiourea gave the corresponding *N*-alkylated derivative rather than the targeted guanidinium-porphyrin **2**.

The porphyrin−MLS conjugate **4** was prepared using solid-phase methodology as we have previously reported (*19*). Briefly, aminoporphyrin **1** was converted to the corresponding carboxylate by reaction with diglycolic anhydride followed by pegylation, after deprotection of the terminal carboxylate and activation as the hydroxybenzotriazole ester. The activated pegylated porphyrin was conjugated to the peptidyl resin containing the sequence MSVLTPLLLRGLTGSARRLPVPRAKIHSL, and after cleavage and deprotection from the solid support, conjugate **4** was isolated in 23% yield.

All porphyrins were characterized by ^{1}H NMR, UV–vis, and MS, and in the case of conjugate **4**, also by CD (*vide infra*). Porphyrins **2**−**4** are all soluble in polar solvents, such as CH_3OH, DMSO, and DMF. However, while the porphyrin−peptide conjugate **4** was highly water-soluble, the guanidinium- and biguanidinium-substituted porphyins **2** and **3** were only partially soluble in water.

CD Studies. Conformational studies of the MLS peptide sequence in conjugate **4** were conducted in different media, including aqueous and membrane mimicking environments (in the presence of TFE or SDS). In aqueous solution at pH 5.0, the porphyrin−MLS peptide conjugate **4** shows negative Cotton effects at 198–207 nm as shown in Figure 1, which are characteristic of a random coil conformation. For example, for polylysine at pH 7, [121] = −41 900 deg cm^2 dmol^{-1} at 197 nm (*32*). In membrane mimicking environments, an α-helix structure characterized by two negative bands at 205 and 221 nm, associated with a positive band at 193 nm is induced for conjugate **4**; this conformational change is more clearly observed in the presence of SDS. For example, for polylysine at pH 7, [θ] = 76 900 deg cm^2 dmol^{-1} at 191 nm, [θ] = −32 600 deg cm^2 dmol^{-1} at 208 nm, and [θ] = −35 700 deg cm^2 dmol^{-1} at 222 nm (*32*). These results show that the MLS sequence in conjugate **4** adopts different conformations depending on the nature of the environment, as a result of the number and distribution of the hydrophobic amino acids in the MLS sequence.

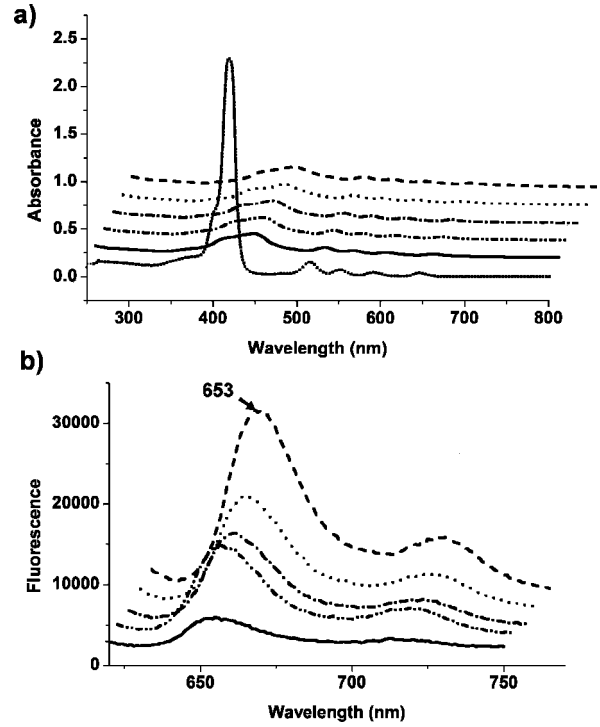

Figure 2. (a) Absorption spectra of 20 μM of porphyrin **2** in DMSO (short dot), and in aqueous solution at different pH. (b) Emission spectra of 2.8 μM porphyrin **2** at different pH (λ_{ex}= 600 nm). pH = 8.00 (full line), pH = 7.4 (dash-dot-dot), pH = 7.00 (dash-dot-dash), pH = 6.00 (large dot), pH = 5.00 (dash).

Photophysical Studies. The absorption and emission spectra in DMSO and in aqueous solutions at different pH values for porphyrins **2** and **3** and peptide conjugate **4** are shown in Figures 2, 3, and 4, respectively. The shape of the absorption spectra for porphyrins **2** and **3** (i.e., wide, poorly resolved bands in aqueous media compared with DMSO) indicate ground-state aggregation of the molecules. The slight red-shift of the Soret band on the absorption spectra (aqueous vs DMSO) and observed fluorescence suggest J-type aggregate formation (*33*). In contrast, the shape of the absorption spectra of the porphyrin−MLS conjugate **4** does not indicate any aggregation in aqueous media or in DMSO. No significant effect of pH on the position and shape of the absorption bands were observed for all porphyrins. The fluorescence quantum yields were found to be pH-dependent as shown in Figure 5. The highest quantum yield determined for porphyrins **2** and **3** and conjugate **4** were 0.0006 (pH = 5.00), 0.0012 (pH = 6.00), and 0.012 (pH = 5.00), respectively. At physiological pH (7.4), the fluorescence of all porphyrins is quenched as determined by the quantum yields determined at this pH. The reduction in quantum yields at pH 7.4 from the maxima observed for porphyrins **2** and **3** and conjugate **4** are 33%, 42%, and 66%, respectively.

Cell Studies. The time-dependent uptake of porphyrins **2** and **3** and conjugate **4** was investigated at a concentration of 10 μM in human HEp2 cells, and the results obtained are shown in Figure 6. The porphyrin−peptide conjugate **4** bearing an amphiphilic MLS sequence accumulated the most within cells at all time points studied, followed by porphyrin **2**. The biguanidinium−porphyrin **3** was the least accumulated within cells (about half as much as porphyrin **2**) of this series of compounds. All porphyrins showed similar uptake kinetics in the first 1–2 h but while porphyrin **2** and conjugate **4** continued

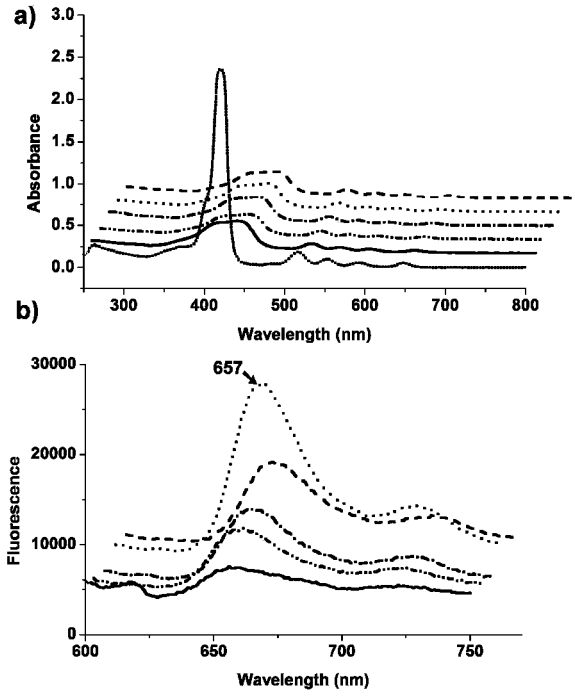

Figure 3. (a) Absorption spectra of 20 μM of porphyrin **3** in DMSO (short dot), and in aqueous solution at different pH. (b) Emission spectra of 2.8 μM porphyrin **3** at different pH (λ_{ex}= 580 nm). pH = 8.00 (full line), pH = 7.4 (dash-dot-dot), pH = 7.00 (dash-dot-dash), pH = 6.00 (large dot), pH = 5.00 (dash).

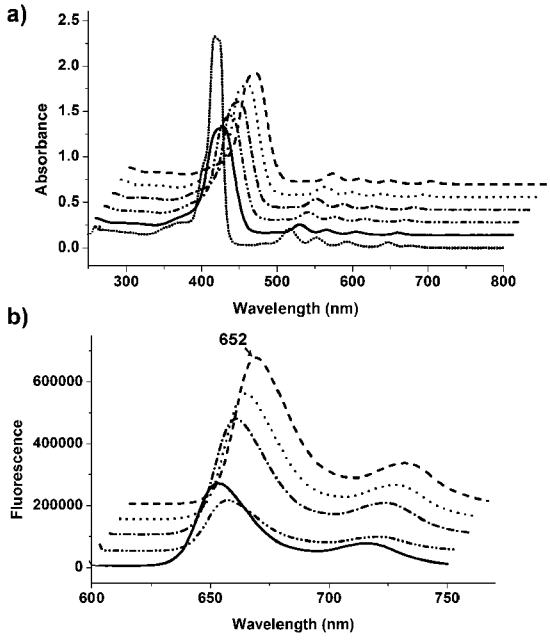

Figure 4. (a) Absorption spectra of 15 μM porphyrin conjugate **4** in DMSO (short dot), and in aqueous solution at different pH. (b) Emission spectra of 4.0 μM porphyrin conjugate **4** at different pH (λ_{ex}= 590 nm). pH = 8.00 (full line), pH = 7.4 (dash-dot-dot), pH = 7.00 (dash-dot-dash), pH = 6.00 (large dot), pH = 5.00 (dash).

to accumulate steadily over time, the biguanidinium−porphyrin **3** exhibited slower uptake.

The dark cytotoxicity and phototoxicity of the new porphyrin conjugates were evaluated upon exposure of HEp2 cells to increasing concentrations of each porphyrin for 24 h. The results obtained are shown in Figures 7 and 8, respectively. While the biguanidinium−porphyrin **3**, the least accumulated within cells, shows no toxicity at concentrations up to 100 μM in the dark,

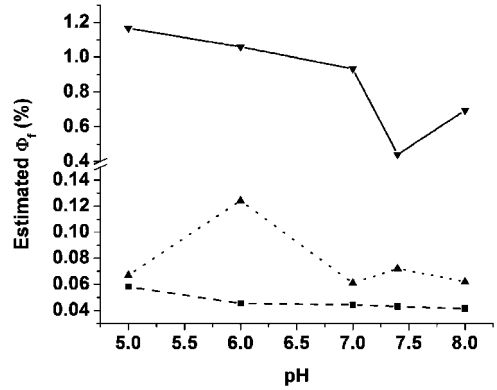

Figure 5. Estimated fluorescence quantum yields (%) at different pH. Porphyrins **2** (dash line), **3** (dot line) and **4** (full line).

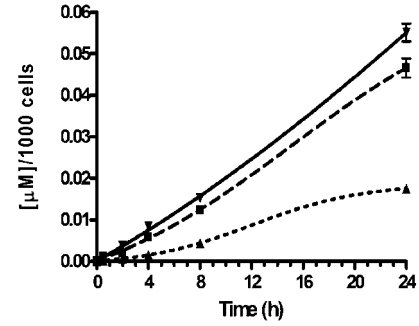

Figure 6. Time-dependent uptake of porphyrins **2** (dash line), **3** (dot line), **4** (full line), at 10 μM by HEp2 cells.

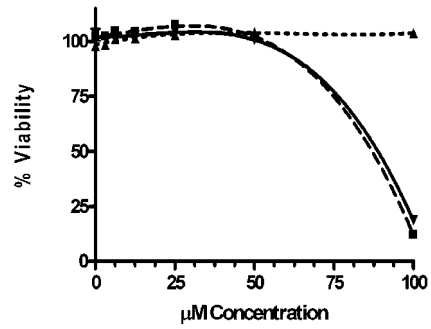

Figure 7. Dark toxicity of porphyrins **2** (dash line), **3** (dot line), and **4** (full line), toward HEp2 cells using the Cell Titer Blue assay.

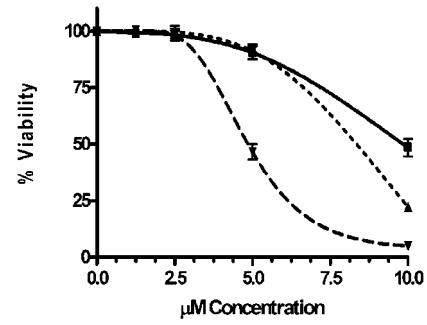

Figure 8. Phototoxicity of porphyrins **2** (dash line), **3** (dot line), **4** (full line) toward HEp2 cells using 1 J/cm^2 dose light.

the guanidinium−porphyrin **2** and conjugate **4** have estimated IC_{50} = 84 and 86 μM, respectively, in the dark (Figure 7). The most phototoxic compound with estimated IC_{50} = 4.8 μM at 1 J cm^{-2} was found to be the guanidinium−porphyrin **2**, followed

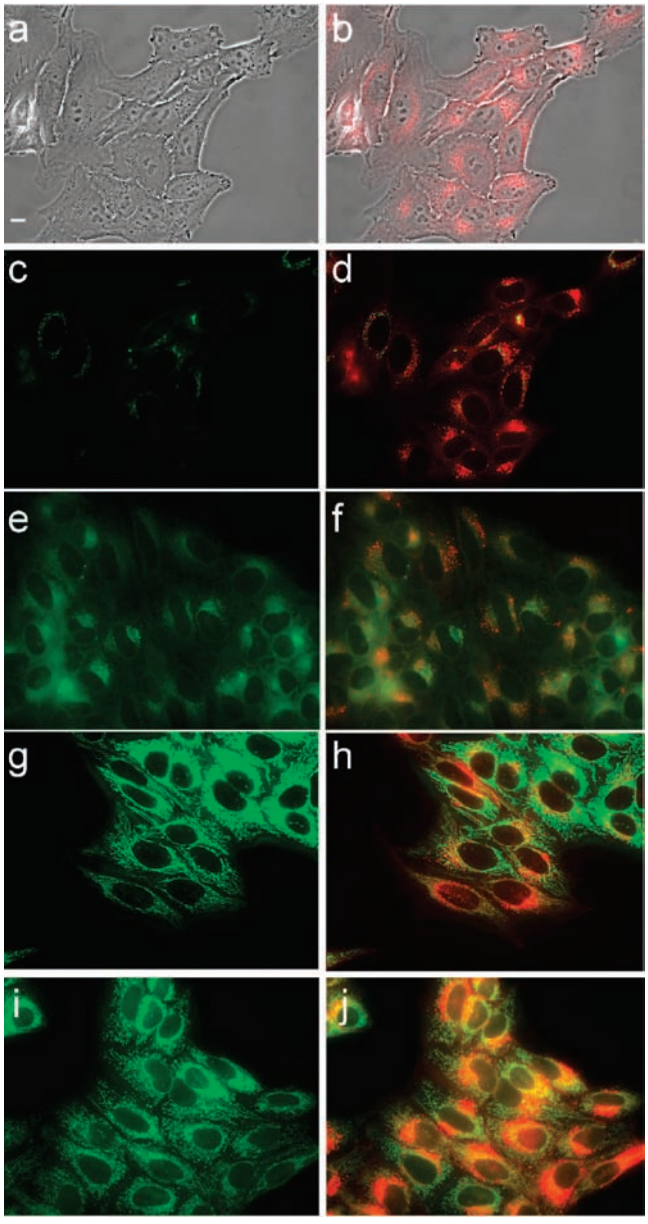

Figure 9. Subcellular localization of porphyrin **2** in HEp2 cells at 10 μM for 24 h. (a) phase contrast, (b) overlay of porphyrin **2** fluorescence and phase contrast, (c) BODIPY Ceramide fluorescence, (e) LysoSensor Green fluorescence, (g) MitoTracker Green fluorescence, (i) $DiOC_6$ fluorescence, (d), (f), (h), (j) overlays of organelle tracers with porphyrin **2** fluorescence. Scale bar: 10 μm.

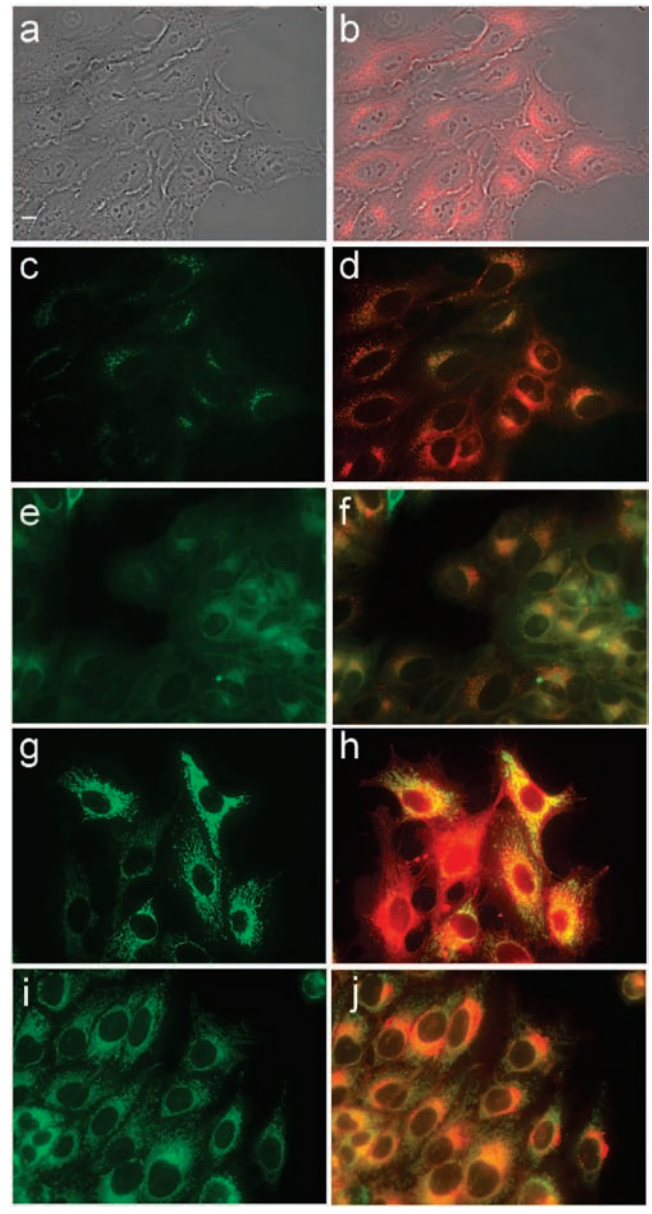

Figure 10. Subcellular localization of porphyrin **3** in HEp2 cells at 10 μM for 24 h. (a) phase contrast, (b) overlay of porphyrin **3** fluorescence and phase contrast, (c) BODIPY Ceramide fluorescence, (e) LysoSensor Green fluorescence, (g) MitoTracker Green fluorescence, (i) $DiOC_6$ fluorescence, (d), (f), (h), (j) overlays of organelle tracers with porphyrin **3** fluorescence. Scale bar: 10 μm.

by the biguanidinium−porphyrin **3** ($IC_{50} = 8.2\ \mu M$ at 1 J cm^{-2}) and conjugate **4** ($IC_{50} = 9.8\ \mu M$ at 1 J cm^{-2}), as shown in Figure 8.

The subcellular localization of the new porphyrin derivatives was investigated in HEp2 cells after 24 h, using fluorescence microscopy. Figures 9, 10, and 11 show the fluorescent patterns observed for porphyrins **2**−**4**, respectively, and their overlay with the organelle specific fluorescent probes BODIPY FL C_5-ceramide (Golgi network), LysoSensor Green (lysosomes), Mitotracker Green (mitochondria), and $DiOC_6$ (ER). The preferential sites of intracellular localization for porphyrin **2** were found to be the mitochondria and the ER (Figure 9h,j). A small amount of **2** was also found in the cell lysosomes. The biguanidinium−porphyrin **3** distributed within cell membranes with a large component in vesicles that correlated to some extent with the lysosomes and, upon longer exposures, in mitochondria and the cytosolic membrane (Figure 10f,h). On the other hand, conjugate **4** was found to localize mainly within the cell lysosomes (Figure 11f).

DISCUSSION

We used two general strategies in the design of mitochondria-targeting photosentizers. The first approach was based on the introduction of a functional group (i.e., guanidine or biguanidine) with a delocalized positive charge, in order to promote preferential accumulation via the high membrane potential across the inner mitochondrial membrane. The guanidinium and biguanidinium groups were chosen because they are strong bases ($pK_a \sim 13$) that are protonated at physiological pH (34–36), and that can form multiple hydrogen bonds and/or electrostatically interact with biological substrates. Since the positive charge is delocalized, guanidinium and biguanidinium groups attached to hydrophobic moieties (such as a porphyrin) form amphiphatic molecules with potentially enhanced affinity for crossing cellular

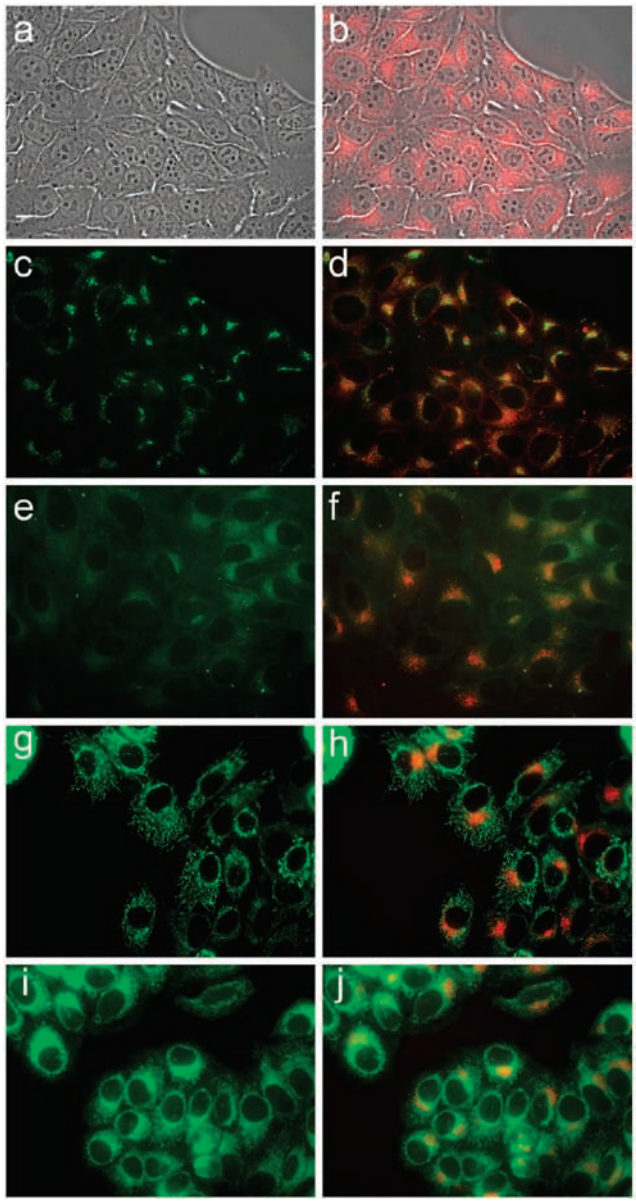

Figure 11. Subcellular localization of conjugate **4** in HEp2 cells at 10 μM for 24 h. (a) phase contrast, (b) overlay of conjugate **4** fluorescence and phase contrast, (c) BODIPY Ceramide fluorescence, (e) LysoSensor Green fluorescence, (g) MitoTracker Green fluorescence, (i) $DiOC_6$ fluorescence, (d), (f), (h), (j) overlays of organelle tracers with conjugate **4** fluorescence. Scale bar: 10 μm.

membranes, for example, via formation of bidentate hydrogen bonds with phosphate groups (*37*). Several methodologies have been developed for the preparation of guanidines in high yield, under mild conditions, typically involving the treatment of an amine with an electrophilic amidine species. The most commonly used reagents include derivatives of pyrazole-1-carboxamidine (*38*), *S*-alkylisothioureas (*39*), protected thiourea derivatives in conjunction with mercury salts or the Mukaiyama reagent (*31*), and protected triflylguanidines (*40*). However, aminoporphyrin **1** was either unreactive to the above guanidinylation reagents or afforded the corresponding *N*-alkylated derivative. We therefore prepared porphyrins **2** and **3** as shown in Scheme 1, by reaction of the anilinium salt of **1** with cyanamide or dicyanamide in DMF/alcohol, using a previously reported procedure (*34*, *41*), in 42–61% yields.

Our second approach involved the conjugation of a MLS peptide sequence to porphyrin **1** via a low molecular weight PEG spacer using a published procedure (*19*), in order to exploit the mitochondrial import machinery. We chose the peptide sequence MSVLTPLLLRGLTGSARRLPVPRAKIHSL, isolated from the subunit VII of human cytochrome c oxidase (*42*), which is encoded in a commercially available expression vector (pShooter) that targets a recombinant protein to the mitochondria of mammalian cells. The PEG spacer was used not only to improve the water solubility of the conjugate, but also to reduce aggregation (*43, 44*) and other possible interactions between the porphyrin macrocycle and the peptide sequence (*30*).

The time-dependent uptake of porphyrins **2** and **3** and conjugate **4** was found to depend significantly on the nature of the substituents at the porphyrin periphery. Conjugate **4** bearing a MLS peptide accumulated the most within cells at all time points studied, while the biguanidinium−porphyrin **3** accumulated the least. The high uptake observed for conjugate **4** is probably due to the presence of the amphiphilic peptide sequence, the low molecular weight PEG spacer, and the low tendency of this conjugate to form aggregates in aqueous media. This result is in agreement with our previous studies showing that conjugation of a peptide to a porphyrin or phthalocyanine macrocycle via a short PEG generally enhances cellular uptake and decreases both intra and intermolecular interactions (*19, 45*). Surprisingly, biguanidinium−porphyrin **3** exhibits significantly lower uptake than guanidinium−porphyrin **2**; this may be attributed to the structural differences between these two groups and their ability to interact with negatively charged groups (e.g., phosphates) on the cell membrane. While the guanidinium group exhibits a planar structure and acts as a bidentate ligand, structural studies on biguanidinium salts indicate that it adopts a nonplanar conformation in order to reduce allylic strain, while still permitting a significant degree of conjugation. Furthermore, structural analyses by X-ray diffraction indicate that arylbiguanidines and their salts can form unique networks bonded by characteristic patterns of hydrogen bonds (*34*), which might have lower affinity for membrane crossing. It is interesting to note that the guanidinium−porphyrin **2** showed similar uptake by the HEp2 cells to that of the peptide conjugate **4**.

All porphyrins showed low dark cytotoxicity, in particular the biguanidinium−porphyrin **3** which was the least taken up by the HEp2 cells. The most phototoxic compound is porphyrin **2**, followed by **3** and the porphyrin peptide conjugate **4**, as a result of both the extent of their uptake and their subcellular distribution. Whereas the preferential sites of intracellular localization of porphyrin **2** are the mitochondria and the ER, porphyrin **3** was mainly found within cellular membranes, the lysosomes, and mitochondria. In contrast, the porphyrin conjugate **4** bearing a MLS peptide sequence localized mainly in the lysosomes rather than in mitochondria, in agreement with our previous studies on porphyrin−peptide conjugates (*19, 30*). Our results show, in agreement with previous reports (*46*), that the nature of the substituents at the porphyrin periphery play an important role in determining their mechanism(s) of cellular uptake and subcellular distribution. Although SAR investigations on mitochondria-targeting molecules (*47, 48*) have indicated that (i) positively charged amphiphilic molecules are delivered into the mitochondria in response to its highly negative membrane potential, and (ii) lipophilic compounds containing delocalized positive charge(s) tend to reduce the free energy change when moving from an aqueous to an hydrophobic environment, not all cationic porphyrin-based sensitizers localize preferentially in mitochondria. We believe that the partial localization in mitochondria observed for porphyrins **2** and **3** is due to the presence of the guanidinium and biguanidinium groups, which play an important role on the lysosomal escape of these photosensitizers as a result of membrane rupture, probably by the proton sponge effect; these photosensitizers are therefore released into the cytoplasm and subsequently delivered into other

organelles, such as the ER and mitochondria (*49–52*). The porphyrin−peptide conjugate **4** containing an MLS peptide sequence was not found in mitochondria, probably as a result of its trapping within endosomes and lysosomes as a result of an endocytotic mechanism of uptake. It is possible that the MLS peptide in conjugate **4** might be cleaved off and degraded to some extent by lysosomal enzymes, as we have recently reported for other porphyrin−peptide conjugates (*53*), before the release of the conjugate from these compartments. As a result of partial mitochondria targeting, porphyrins **2** and **3** were found to be more phototoxic than the peptide conjugate **4**. The highest phototoxicity observed for the guanidinium−porphyrin **2** is probably due to its higher uptake and preferential localization in the mitochondria and ER, as photodamage to these sensitive organelles can lead to rapid cell death via apoptosis (*54–56*).

ACKNOWLEDGMENT

The authors thank Ms. Martha Juban for the MLS peptide sequence synthesis. This work was partially supported by the National Science Foundation, grant number CHE-304833.

Supporting Information Available: HPLC trace for porphyrin−MLS conjugate **4** and conditions. This material is available free of charge via the Internet at http://pubs.acs.org.

LITERATURE CITED

(1) Dias, N., and Bailly, C. (2005) Drugs targeting mitochondrial functions to control tumor cell growth. *Biochem. Pharmacol. 70*, 1–12.

(2) Weissig, V. (2005) Targeted drug delivery to mammalian mitochondria in living cells. *Exp. Opin. Drug Delivery 2*, 89–102.

(3) Rosania, G. R. (2003) Supertargeted chemistry: Identifying relationships between molecular structures and their sub-cellular distribution. *Curr. Topics Med. Chem. 3*, 659–685.

(4) Dougherty, T. J., Gomer, C. J., Henderson, B. W., Jori, G., Kessel, D., Korbelik, M., Moan, J., and Peng, Q. (1998) Photodynamic therapy. *J. Natl. Cancer Inst. 90*, 889–905.

(5) Pandey, R. K., and Zheng, G. (2000). Porphyrins as photosensitizers in photodynamic therapy. *The Porphyrin Handbook. Volume 6: Applications: Past, Present and Future* (Kadish, K. M., Smith, K. M. and Guilard, R. Eds.) pp 157–230, Chapter 43, Academic Press, New York.

(6) Morgan, J., and Oseroff, A. R. (2001) Mitochondria-based photodynamic anti-cancer therapy. *Adv. Drug Delivery Rev. 49*, 71–86.

(7) Trivedi, N. S., Wang, H. W., Nieminen, A. L., Oleinick, N. L., and Izatt, J. A. (2000) Quantitative analysis of Pc 4 localization in mouse lymphoma (LY-R) cells via double-label confocal fluorescence microscopy. *Photochem. Photobiol 71*, 634–639.

(8) Kessel, D., Woodburn, K., Henderson, B. W., and Chang, C. K. (1995) Sites of photodamage in vivo and in vitro by a cationic porphyrin. *Photochem. Photobiol. 62*, 875–881.

(9) Kessel, D., Luguya, R., and Vicente, M. G. H. (2003) Localization and photodynamic efficacy of two cationic porphyrins varying in charge distribution. *Photochem. Photobiol. 78*, 431–435.

(10) Kralova, J., Dvorak, M., and Kral, V. (2003) Novel cationic transport agents for oligonucleotide delivery into primary leukemic cells. *J. Med. Chem. 46*, 2049–2056.

(11) Synytsya, A., Kral, V., Blechova, M., and Volka, K. (2004) Biolocalization and photochemical properties of two novel macrocyclic photosensitizers: a spectroscopic study. *J. Photochem. Photobiol., B 74*, 73–84.

(12) Perree-Fauvet, M., and Gresh, N. (1995) Molecular modeling and chemical synthesis of a bisargynil derivative of a tricationic porphyrin designed to target the major groove of DNA. *Tetrahedron Lett. 36*, 4227–4230.

(13) Mohammadi, S., Perree-Fauvet, M., Gresh, N., Hillairet, K., and Taillandier, E. (1998) Joint molecular modeling and spectroscopic studies of DNA complexes of a bis(arginyl) conjugate of a tricationic porphyrin designed to target the major groove. *Biochemistry 37*, 6165–6178.

(14) Far, S., Kossanyi, A., Verchere-Beaur, C., Gresh, N., Taillandier, E., and Perree-Fauvet, M. (2004) Bis- and tris-DNA intercalting porphyrins designed to target the major groove. Synthesis of acridly-bis-arginyl-porphyrins, molecular modeling of their DNA complexes, and experimental tests. *Eur. J. Org. Chem.* 1781–1797.

(15) Salehi, A., Mei, H-Y., and Bruice, T. C. (1991) Synthesis and DNA-binding studies of new cationic guanidine and betainamide tetraphenylporphyrins. *Tetrahedron Lett. 32*, 3453–3456.

(16) Akhlynina, T. V., Jans, D. A., Rosenkranz, A. A., Statsyuk, N. V., Balashova, I. Y., Toth, G., Pavo, I., Rubin, A. B., and Sobolev, A. S. (1997) Nuclear targeting of chlorin e6 enhances its photosensitizing activity. *J. Biol. Chem. 272*, 20328–20331.

(17) Chaloin, L., Bigey, P., Loup, C., Marin, M., Galeotti, N., Piechaczyk, M., Heitz, F., and Meunier, B. (2001) Improvement of porphyrin cellular delivery and activity by conjugation to a carrier peptide. *Bioconjugate Chem. 12*, 691–700.

(18) Bisland, S. K., Singh, D., and Gariepy, J. (1999) Potentiation of chlorin e6 photodynamic activity in vitro with peptide-based intracellular vehicles. *Bioconjugate Chem. 10*, 982–992.

(19) Sibrian-Vazquez, M., Jensen, T. J., Hammer, R. P., and Vicente, M. G. H. (2006) Peptide-mediated cell transport of water-soluble porphyrin conjugates. *J. Med. Chem. 49*, 1364–1372.

(20) Koehler, C. M. (2000) Protein translocation pathways of the mitochondrion. *FEBS Lett. 476*, 27–31.

(21) Lithgow, T. (2000) Targeting of proteins to mitochondria. *FEBS Lett. 476*, 22–26.

(22) Murphy, M. P. (1997) Selective targeting of bioactive compounds to mitochondria. *Trends Biotechnol. 15*, 326–330.

(23) Chinnery, P. F., Taylor, R. W., Diekert, K., Lill, R., Turnbull, D. M., and Lightowlers, R. N. (1999) Peptide nucleic acid delivery to human mitochondria. *Gene Ther. 6*, 1919–1928.

(24) Muratkovska, A., Lightowlers, R. N., Taylor, R. W., Wilce, J. A., and Murphy, M. P. (2001) Targeting large molecules to mitochondria. *Adv. Drug. Delivery Rev. 49*, 189–198.

(25) Flierl, A., Jackson, C., Cottrell, B., Murdock, D., Siebel, P., and Wallace, D. C. (2003) Targeted delivery of DNA to the mitochondrial compartment via import sequence-conjugated peptide nucleic acid. *Mol. Ther. 7*, 550–557.

(26) Asayama, S., Kawamura, E., Nagaoka, S., and Kawakami, H. (2006) Design of manganese porphyrin modified with mitochondrial signal peptide for a new antioxidant. *Mol. Pharmaceutics 3*, 468–470.

(27) Luguya, R., Jaquinod, L., Fronczek, F. R., Vicente, M. G. H., and Smith, K. M. (2004) Synthesis and reactions of meso-(p-nitrophenyl)porphyrins. *Tetrahedron 60*, 2757–2763.

(28) Fery-Forgues, S., and Lavabre, D. (1999) Are fluorescence quantum yields so tricky to measure? A demonstration using familiar stationery products. *J. Chem. Educ. 76*, 1260–1264.

(29) Lakowicz, J. R. (1999) *Principles of Fluorescence Spectroscopy*, 2nd ed., pp 52–53, Chapter 2, Kluwer Academic/Plenum Publishers, New York.

(30) Sibrian-Vazquez, M., Jensen, T. J., Fronczek, F. R., Hammer, R. P., and Vicente, M. G. H. (2005) Synthesis and characterization of positively charged porphyrin-peptide conjugates. *Bioconjugate Chem. 16*, 852–863.

(31) Yong, Y. F., Kowalsky, J. A., and Lipton, M. A. (1997) Facile and efficient guanylation of amines using thioureas and Mukaiyama's reagent. *J. Org. Chem. 62*, 1540–1542.

(32) Greenfield, N., and Fasman, G. D. (1969) Computed circular dichroism spectra for the evaluation of protein conformation. *Biochemistry 8*, 4108–4116.

(33) Ohno, O., Kaizu, Y., and Kobayashi, H. (1993) J-Aggregate formation of a water-soluble porphyrin in acidic aqueous media. *J. Chem. Phys. 99*, 4128–4139.

(34) LeBel, O., Maris, T., Duval, H., and Wuest, J. D. (2005) A practical guide to arylbiguanidines-Synthesis and structural characterization. *Can. J. Chem. 83*, 615–625.
(35) Kovacevic, B., and Maksic, Z. B. (2001) Basicity of some organic superbases in acetonitrile. *Org. Lett. 3*, 1523–1526.
(36) Fabbrizzi, L., Micheloni, M., Paoletti, P., and Schwarzenbach, G. (1977) Protonation processes of unusual exothermicity. *J. Am. Chem. Soc. 99*, 5574–5576. .
(37) Rothbard, J. B., Jessop, T. C., Lewis, R. S., Murray, B. A., and Wender, P. A. (2004) Role of membrane potential and hydrogen bonding in the mechanism of translocation of guanidinium-rich peptides into cells. *J. Am. Chem. Soc. 126*, 9506–9507.
(38) Bernatowicz, M. S., Wu, Y., and Matsueda, G. R. (1993) Urethane protected derivatives of 1 -guanylpyrazole for the mild and efficient preparation of guanidines. *Tetrahedron Lett. 34*, 3389–3392.
(39) Katritzky, A. R., and Rogoboy, B. V. (2005) Recent developments in guanylating agents. *Arkivoc 4*, 49–87.
(40) Feichtinger, K., Zapf, C., Sings, H. L., and Goodman, M. (1998) Diprotected triflylgunidines: a new class of guanidinylation reagents. *J. Org. Chem. 63*, 3804–3805.
(41) Hughes, J. L., Liu, R. C., and Enkoji, T. (1975) Cardiovascular activity of aromatic guanidine compounds. *J. Med. Chem. 18*, 1077–1088.
(42) Rizzuto, R., Simpson, A. W. M., Brini, M., and Pozzan, T. (1992) Rapid changes of mitochondrial $Ca^{2}+$ revealed by specifically targeted recombinant aequorin. *Nature 358*, 325–327.
(43) Greenwald, R. B. (2001) PEG drugs: an overview. *J. Controlled Release 74*, 159–171.
(44) Greenwald, R. B., Choe, Y. H., McGuire, J., and Conover, C. D. (2003) Effective drug delivery by pegylated drug conjugates. *Adv. Drug Delivery Rev. 55*, 217–250.
(45) Sibrian-Vazquez, M., Ortiz, J., Nesterova, I. V., Fernández-Lázaro, F., Sastre-Santos, A., Soper, S. A., and Vicente, M. G. H. (2007) Synthesis and properties of cell-targeted Zn(II)-phthalocyanine-peptide conjugates. *Bioconjugate Chem. 18*, 410–420.
(46) Kessel, D. (2004) Correlation between subcellular localization and photodynamic efficacy. *J. Porphyrins Phthalocyanines 8*, 1009–1014.
(47) Horobin, R. W. (2001) Uptake, distribution, and accumulation of dyes and fluorescent probes within living cells: a structure-activity modeling approach. *Adv. Colour Sci. Technol. 4*, 101–107.
(48) Horobin, R. W. (2002) Biological staining: mechanisms and theory. *Biotech. Histochem. 77*, 3–13.
(49) Boussif, O., Lezoualc'h, F., Zanta, M. A., Mergny, M. D., Shermann, D., Demeneix, B., and Behr, J.-P. (1995) A versatile vector for gene and oligonucleotide transfer into cells in culture and in vivo: polyethylenimine. *PNAS 92*, 7297–7301.
(50) Goodbey, W. T., Wu, K. K., and Mikos, A. G. (1999) Poly. (ethylenimine) and its role in gene delivery. *J. Controlled Release 60*, 149–160.
(51) Nori, A., and Kaopecek, J. (2005) Intracellular targeting of polymer-bound drugs for cancer therapy. *Adv. Drug Delivery Rev. 57*, 609–636.
(52) Merdam, T., Kaopecek, J., and Kissel, T. (2002) Prospects for cationic polymers in gene and oligonucleotide therapy against cancer. *Adv. Drug Delivery Rev. 54*, 715–758.
(53) Sibrian-Vazquez, M., Jensen, T. J., and Vicente, M. G. H. Synthesis, characterization, and metabolic stability of porphyrin-peptide conjugates bearing bifunctional signaling sequences. *J. Med. Chem.*, accepted for publication.
(54) Luo, Y., Chang, C. K., and Kessel, D. (1996) Rapid initiation of apoptosis by photodynamic therapy. *Photochem. Photobiol. 63*, 528–534.
(55) Kessel, D., and Luo, Y. (1998) Mitochondrial photodamage and PDT-induced apoptosis. *J. Photochem. Photobiol., B 42*, 89–95.
(56) Rao, R. V., Hermel, E., Castro-Obregon, S., del Rio, G., Ellerby, L. M., Ellerby, H. M., and Bredesen, D. E. (2001) Coupling endoplasmic reticulum stress to the cell death program. Mechanism of caspase activation. *J. Biol. Chem. 276*, 33869–33874.

BC700393U

A Doxorubicin Prodrug Activated by the Staudinger Reaction

Remco van Brakel,[‡] Roland C. M. Vulders,[‡] Rembrandt J. Bokdam, Holger Grüll, and Marc S. Robillard*

Department of Bio-Molecular Engineering, Philips Research, Eindhoven, The Netherlands. Received October 24, 2007; Revised Manuscript Received December 19, 2007

Much effort has been devoted to prodrug systems that effect drug release at the tumor through enzymatic action. To widen the scope of prodrug therapy, the use of the selective Staudinger reaction as prodrug activator, instead of relying on enzymatic action, was investigated. Doxorubicin was conjugated to a *p*-azidobenzyl trigger that is cleaved after reacting with the chemical activator, triphenylphosphine. The prodrug activation was confirmed in water, cell growth medium, and serum, using HPLC and LCMS. Next, this approach was tested in a cell proliferation assay with A431 human vulvar skin squamous carcinoma cells. The doxorubicin prodrug was shown to exhibit a 176-fold higher IC_{50} of 15.1 μM vs 0.086 μM for the parent drug, doxorubicin. Addition of triphenylphosphine (5×60 μM in 72 h) to the prodrug in cell culture effected the complete recovery of the activity of the parent drug as evidenced by an IC_{50} value of 0.074 μM. Furthermore, high levels of triphenylphosphine were tolerated well by the cells. The demonstrated usefulness of the Staudinger reaction in cell culture and its in vivo potential opens up new avenues for prodrug therapy.

INTRODUCTION

The lack of selectivity of chemotherapeutic drugs like doxorubicin is a major problem. Dose-limiting toxic side effects can preclude the administration of effective concentrations (*1*). Therefore, much effort has been devoted to drug delivery systems that effect drug release exclusively at the tumor. One way is to activate a systemic prodrug by local or localized enzymatic activity (*2–5*). However, in many cases a target site lacks a suitable overexpressed enzyme or it is present in the cytosol, which requires the prodrug to enter the cell. Targeted enzymatic activity necessitates the use of exogenous enzymes, which are likely to be highly immunogenic, a fact that can hamper repeated administration. A promising alternative achieves tumor targeting and endocytosis of polymer−drug conjugates, followed by drug release through nonspecific (enzymatic) processes (*6*). This approach, however, could be sensitive to unpredictable, inherently slow, or reduced endocytosis. Furthermore, it in general lacks direct temporal and quantitative control over drug release.

To widen the scope of prodrug therapy, we propose here to use the selective Staudinger reaction (Scheme 1) as the prodrug activator in vivo, instead of relying on enzymatic action (*7*). This potentially bioorthogonal reaction occurs between a phosphine (**1a**) and an organic azide (**2a**) to produce an azaylide intermediate **3** that hydrolyzes spontaneously in aqueous conditions to yield the corresponding phosphine oxide (**4a**) and primary amine (**5a**). Very few reactions can be used in a biological environment, and thus far only the Staudinger ligation, a strongly related adaptation of the Staudinger reaction, has proven utility in vivo (*7, 8*). The general usefulness in biological media of the Staudinger reaction itself has remained largely unexplored.

This paper describes for the first time the design and activation of an azido-functionalized prodrug (**2b**, Scheme 2)

Scheme 1. The Staudinger Reaction

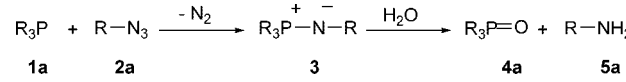

by means of the Staudinger reaction in a cell culture environment. Prodrug **2b** encompasses the anticancer drug doxorubicin **6** linked via the amino group to a *p*-azidobenzyl trigger that is cleaved after reacting with the chemical activator, triphenylphosphine **1b**. The trigger is based on *p*-aminobenzyloxycarbonyl, used in enzyme-activated prodrugs, where unmasking of the amino group leads to an elimination of imino quinone methide, spontaneous decarboxylation, and release of the active drug (*2, 9, 10*). The azide-to-amine reduction in **2b** by **1b** should initiate the same sequence of events. Analogous to the polymer-targeted prodrugs developed by Duncan (*6*) and Shabat (*9*), prodrug **2b** may in a later stage be conjugated to a polymer via the methylene group of the azidobenzyl trigger. After tumor-localization and clearance from the blood of such a polymer construct, a bolus or continuous dose of **1b** may be administered to effect local release of **6**.

EXPERIMENTAL PROCEDURES

General. All solvents and reagents were obtained from Sigma-Aldrich unless stated otherwise and were used as received. Doxorubicin was obtained from Toronto Research Chemicals. NMR spectra were measured on a Bruker Avance DPX 300 spectrometer in the given solvent. Chemical shifts are given in ppm (δ) relative to TMS as an internal standard. Thin layer chromatography (TLC) was performed using Merck ($60F_{254}$) plates. The plates were examined with UV light, iodide, or ninhydrin. Preparative TLC was carried out on Analtech plates 1500 μm (F_{254}). All experiments with the photosensitive azidobenzyl compounds were performed in the dark or in yellow light (TND77385 plastic plate from Takiron with transmittance cut off at 500 nm). HPLC was performed on a Waters system equipped with a Luna Phenyl-Hexyl column (100×4.6 mm, 3 μm). The applied eluents were A, aq NH_4OAc (20 mM, pH 4.5) + 1% AcOH; B, CH_3CN/H_2O (85/15). Flow speed: 0.80 mL/min. LC-MS was performed on an Agilent 1200 HPLC

* Corresponding author. Department of Bio-Molecular Engineering, Philips Research, High Tech Campus 11, 5656 AE Eindhoven, The Netherlands. Fax: (+31) 40 27 44 906; Tel: (+31) 40 27 48 264; E-mail: marc.robillard@philips.com.

[‡] R. van Brakel and R. Vulders contributed equally to this work.

10.1021/bc700394s CCC: $40.75 © 2008 American Chemical Society
Published on Web 02/14/2008

Scheme 2. Prodrug 2b and Its Activation through the Staudinger Reaction by Phosphine 1b, Affording Doxorubicin (6)

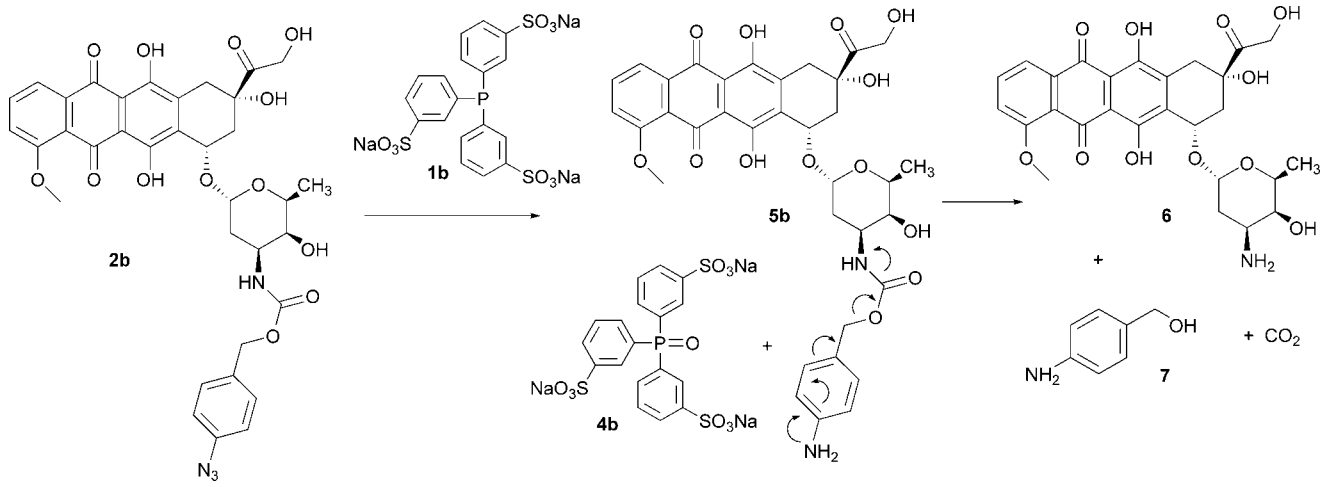

coupled to an Agilent LC MSD Trap XCT Ultra mass spectrometer. A Luna Phenyl-Hexyl column (100 × 4.6 mm, 3.08 μm) was used. The applied eluents were A, aq. NH_4OAc (20 mM, pH 4.5) + 2% CH_3CN; B, CH_3CN. Flow speed: 0.80 mL/min. MALDI TOF MS of **2b** was recorded on the Voyager-DE PRO. Mass spectra of azides **8** and **9** were taken with a Jeol SX102 mass spectrometer using field desorption (FD) (6 kV, 4 mA/min).

HPLC and LCMS Experiments. The cell growth medium used was DMEM (InVitrogen), supplemented with 10% heat-inactivated fetal bovine serum and 0.05% glutamax (InVitrogen). The serum used was 10% heat-inactivated fetal bovine serum.

Appropriate amounts of stock solutions of **2b** (10 mM in DMF) and **1b** (10 mM in DMF) were diluted to 2.5 mL with water, cell growth medium, or 10% serum, and warmed up to 37 °C. Before mixing, samples were withdrawn and analyzed separately. The solutions were mixed and stirred at 37 °C open to atmospheric oxygen. Samples were withdrawn and analyzed without any further sample preparation at the indicated times.

Cell Culture and Proliferation Assay. The A431 squamous carcinoma cells were maintained in a humidified CO_2 (5%) incubator at 37 °C in DMEM (InVitrogen), supplemented with 10% heat-inactivated fetal bovine serum and 0.05% glutamax (InVitrogen) in the presence of penicillin and streptomycin. Compounds **2b** and **6** were, prior to each experiment, freshly dissolved in DMF at 10 mM and subsequently serial-diluted in prewarmed culture medium. Triphenylphosphine-3,3′,3″-trisulfonic acid trisodium salt (**1b**) was dissolved in PBS at 10 mM and serial-diluted in prewarmed medium. Methylthiazolyldiphenyltetrazolium bromide (MTT) was used as described by the manufacturer. Cells were plated out in 96-well plates (Nunc) at a density of 7500 cells/well followed by addition of compounds the next day. Cell culture medium was replaced with 100 μL prewarmed medium containing the different concentrations of **2b** or **6**. Subsequently, 3 μL of appropriate concentrations of **1b** were added to each well twice a day. After 72 h incubation, cell proliferation was assessed by means of a MTT assay (*11*). Briefly, MTT was dissolved in prewarmed medium at 5 mg/mL, passed through a 0.22 μm filter, and 50 μL was added to each well. Following an incubation period of 120 min, the medium was gently aspirated. The formed formazan crystals were dissolved in 100 μL DMSO, and the absorbance was measured with a plate reader (BMG labtech) at 560 nm. IC_{50} values were derived from inhibition curves generated in three independent experiments.

4-Azidobenzyl Alcohol (8). A stirred solution of 4-aminobenzyl alcohol **7** (1.0 g, 8.12 mmol) in aq HCl (5 M, 5 mL) was cooled to 4 °C, and a solution of sodium nitrite (0.62 g, 8.98 mmol) in water (20 mL) was added dropwise in 30 min. Sodium azide (2.1 g, 32.3 mmol) was added in small portions over 30 min with vigorous stirring, while keeping the temperature under 5 °C. After stirring for 1.5 h at 4 °C, the reaction mixture was poured into ice–water, and the pH was adjusted to pH 8 with solid $NaHCO_3$. The water layer was extracted with ethyl acetate, which was then washed with water (2×), dried ($MgSO_4$), and evaporated. Light petroleum ether was poured on the residue, stirred for 30 min, and subsequently kept at 0 °C for 1 night. The resulting cream-colored suspension was filtered, and the residue was washed with 5 mL light petroleum ether, yielding 4-azido benzyl alcohol **8** (932 mg, 6.25 mmol, 77%) as a cream-colored powder (photosensitive). ^1H NMR ($CDCl_3$): δ = 1.89 (s, 1H; OH), 4.65 (s, 2H; CH_2), 7.01 (d, J = 8.3 Hz, 2H; aromatic), 7.34 (d, J = 8.3 Hz, 2H; aromatic). ^{13}C NMR ($CDCl_3$): δ = 64.67, 119.10, 128.51; FD MS: m/z: 149 $[M]^+$.

4-Azidobenzyl 4-Nitrophenyl Carbonate (9). A solution of 4-nitrophenyl chloroformate (204 mg, 1.01 mmol) and pyridine (160 mg, 2.02 mmol) in THF (5 mL) was stirred at 0–4 °C, and a solution of 4-azidobenzyl alcohol **8** (150 mg, 1.01 mmol) in THF (8 mL) was added dropwise in 30 min. The reaction mixture was stirred in the dark at 25 °C for 70 h. The THF solution was evaporated, and 30 mL of ethyl acetate was added. The ethyl acetate layer was washed with water (2×), dried ($MgSO_4$), and evaporated. The residue was recrystallized from light petroleum ether/ethyl acetate yielding 4-azidobenzyl 4-nitrophenyl carbonate **9** (264 mg, 0.84 mmol, 83%) as a yellow powder. IR: 2105 cm^{-1} (azide). ^1H NMR ($CDCl_3$): δ = 5.26 (s, 2H; CH_2), 7.07 (d, J = 8.7 Hz, 2H; aromatic azide), 7.38 (d, J = 9.3 Hz, 2H; aromatic nitro), 7.44 (d, J = 8.7 Hz, 2H; aromatic azide), 8.28 (d, J = 9.3 Hz, 2H; aromatic nitro). ^{13}C NMR ($CDCl_3$): δ = 70.77, 119.79, 122.17, 125.74, 130.91. FD MS: m/z: 314 $[M]^+$.

Azidobenzyl Carbamate Doxorubicin (2b). A solution of 4-azidobenzyl 4-nitrophenyl carbonate **9** (10.3 mg, 33 μmol), triethylamine (9.6 μL, 69 μmol), doxorubicin (**6**, 20.1 mg, 35 μmol) in DMF (2 mL) was stirred in the dark at rt under nitrogen gas for 24 h. After adding more triethylamine (9.6 μL, 69 μmol), the solution was stirred for another 5 days. The DMF was evaporated in vacuo (keeping temperature below 30 °C), and water (50 mL) was added and subsequently extracted with ethyl acetate (3 × 25 mL). The combined organic layers were evaporated to dryness, and the resulting red solid was purified

Scheme 3. Synthesis of Prodrug 2b[a]

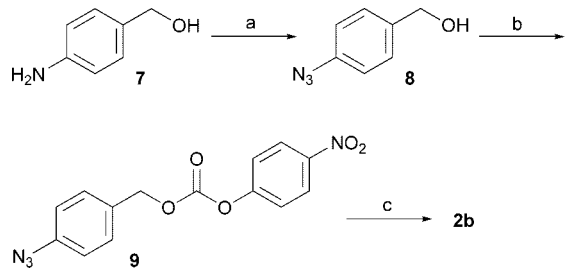

[a] (a) HCl (5 M), $NaNO_2$, NaN_3, 5 °C, 2 h (76%); (b), *p*-nitrophenylchloroformate, pyridine, THF, rt, 70 h (83%); (c) **6**, Et_3N, THF, rt, 30 h (67%).

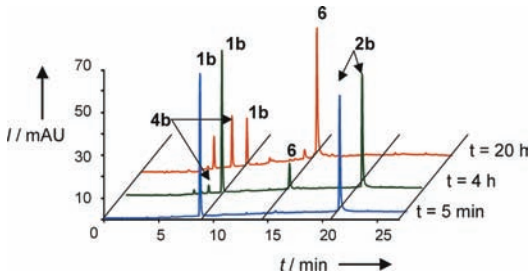

Figure 1. Activation of prodrug **2b** (100 μM) by phosphine **1b** (200 μM) in water followed with HPLC (260 nm).

with preparative TLC (DCM/MeOH; 9/1). The collected fraction at R_f 0.68 was extracted with ethyl acetate/DCM (1/2) and evaporated under reduced pressure to afford **2b** as a red solid (18.3 mg, 77%). IR: 2115 cm^{-1} (azide). ^1H NMR ($CDCl_3$): δ = 1.29 (d, J = 6.6 Hz, 3H; C-CH_3) 1.80–1.90 (m, 2H; CH_2 carbohydrate), 2.17 (dd, J_A = 14.8 Hz, J_B = 4.0 Hz, 1H; CH_2), 2.33 (br dt, J_A = 14.7 Hz, J_B = 1.7 Hz, 1H; CH_2), 3.02 (d, J = 19 Hz, 1H; CH_2), 3.28 (d, J = 19 Hz, 1H; CH_2), 3.66 (br s, 1H; CH carbohydrate), 3.86 (m, 1H; CH carbohydrate), 4.09 (s, 3H; O-CH_3), 4.14 (q, J = 6.4 Hz, 1H; CH-CH_3) 4.76 (s, 2H; CH_2-OH), 4.99 (s, 2H; CH_2 linker), 5.13 (d, J = 8.6 Hz, 1H; amide NH), 5.29 (br m, 1H; CH), 5.50 (d, J = 3.5 Hz, 1H; CH carbohydrate), 6.97 (d, J = 8.3 Hz, 2H; aromatic azide), 7.29 (d, J = 8.3 Hz, 2H; aromatic azide), 7.40 (dd, J_A = 8.5 Hz, J_B = 0.75 Hz, 1H; aromatic dox), 7.80 (dd, J_A = 8.5 Hz, J_C = 7.7 Hz, 1H; aromatic dox), 8.05 (dd, J_B = 0.75 Hz, J_C = 7.7 Hz, 1H; aromatic dox). MALDI TOF MS: m/z 742 $[M + Na]^+$. LCMS: 18.6 min.

RESULTS AND DISCUSSION

Prodrug **2b** was prepared in good yield starting from 4-aminobenzyl alcohol **7** (Scheme 3). Conversion via the diazo intermediate to 4-azidobenzylalcohol **8** was followed by treatment with *p*-nitrophenylchloroformate to afford compound **9** (*12*). Substitution of the *p*-nitrophenyl moiety with doxorubicin **6** yielded prodrug **2b**.

First, the activation of **2b** was studied using HPLC and LCMS. All experiments described below were performed at 37 °C and were open to atmospheric oxygen. When **2b** and **1b** were reacted in water at 37 °C at relatively high concentrations of 100 and 200 μM, respectively, the reaction ran to completion within 20 h as evidenced by HPLC (Figure 1). In general, phosphines are prone to oxidation to phosphine oxides, which are inactive in the Staudinger reaction. Figure 1, however, shows that the phosphine is stable against oxidation in water for 20 h, since there is still a substantial amount of **1b** left after completion of the reaction, confirming stability studies of **1b** alone in water at 37 °C (Figure 2). When the same reaction was performed in cell growth

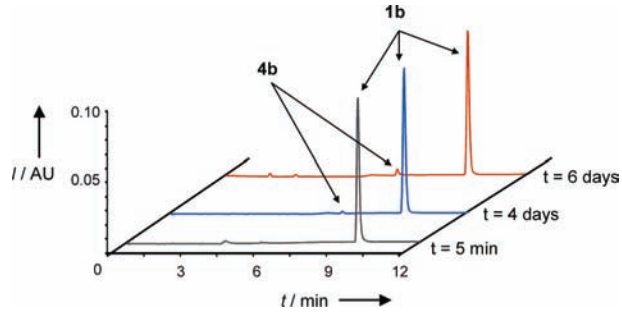

Figure 2. Stability of phosphine **1b** (300 μM) in water followed with HPLC (260 nm).

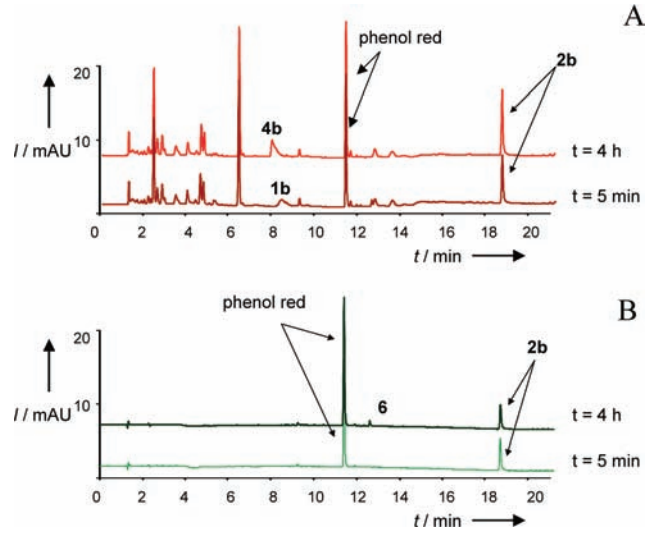

Figure 3. Activation of prodrug **2b** (10 μM) by phosphine **1b** (1 × 20 μM) in cell growth medium followed with LCMS (A, 260 nm; B, 480 nm).

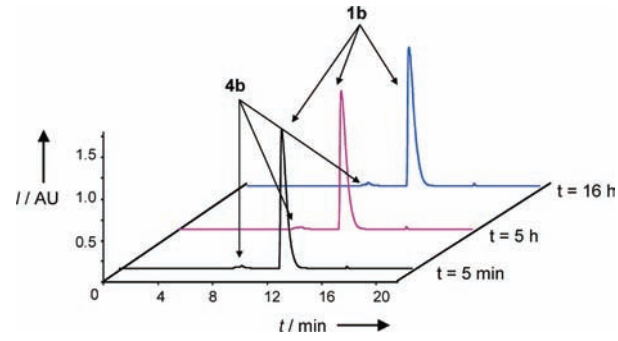

Figure 4. Stability of phosphine **1b** (10 μM) in 10% serum followed with LCMS (254 nm).

medium at 10 and 20 μM, respectively, the amount of free doxorubicin **6** reached 15% within 4 h, after which it stopped increasing as evidenced by LCMS (Figure 3). At the same time, 100% of **1b** was oxidized, demonstrating that the phosphine is rapidly inactivated via another mechanism. Subsequent stability studies in 10% serum showed that **1b** (10 μM) was stable for 16 h (Figure 4). These results indicate that a component specific for cell growth medium was causing the oxidation and that **1b** should be stable enough to be used as activator in vivo. To retain effective use of **1b** as prodrug activator in vitro, the dosing of **1b** was adjusted from single dose to multiple administrations. Additionally, this scheme may be a better mimic of a future clinical application, where clearance from the body or metabolism of the activator needs

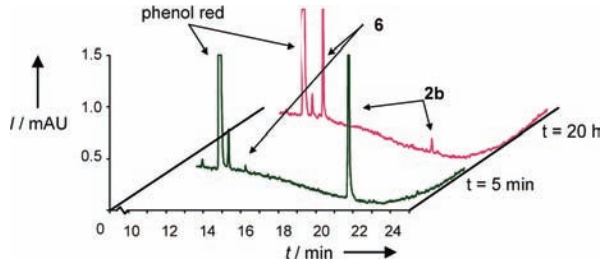

Figure 5. Activation of prodrug **2b** (10 μM) by phosphine **1b** (2 × 60 μM) in cell growth medium followed with LCMS (480 nm).

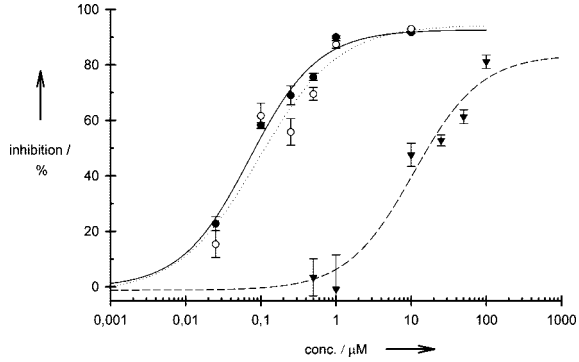

Figure 6. Growth inhibition assay of A431 cells with **2b** (▼), **6** (●), and **2b** with **1b** (5 × 60 μM) (○).

Table 1. IC_{50} Values[a] Determined in the A431 Cell Line Using the MTT Assay (*11*)

entry	compound	IC_{50} (μM)
1	**2b** (prodrug)	15.1 ± 4.00
2	**6** (doxorubicin)	0.086 ± 0.056
3	**2b** with **1b** (5 × 10 μM)	0.320 ± 0.104
4	**2b** with **1b** (5 × 30 μM)	0.110 ± 0.027
5	**2b** with **1b** (5 × 60 μM)	0.074 ± 0.017
6	**1b** (5 × 10/30/60 μM)	[b]
7	**6** with **1b** (5 × 60 μM)	0.119 ± 0.041
8	**7** (aminobenzylalcohol)	[b]
9	**7** with **1b** (5 × 60 μM)	[b]
10	**7** with **6** (1/1)	0.082 ± 0.030

[a] Concentration that results in a reduction of cell proliferation of 50% compared to untreated controls. [b] No reduction in proliferation observed compared to untreated controls.

to be compensated by repeated infusion with fresh phosphine. Activation of prodrug **2b** at 10 μM in cell growth medium was performed by administering two larger doses (60 μM) of **1b** per day. This time, 85% of **2b** was converted to **6** after 8 h, and the reaction was nearly complete after 20 h (Figure 5).

Next, we tested this approach in a cell proliferation assay with A431 human vulvar skin squamous carcinoma cells. Cells were grown in the presence of six different concentrations of **2b** or **6**, with or without two daily doses of **1b** (5 × 10, 30 or 60 μM in 72 h). The antiproliferative effect was determined by quantifying the viable cells 72 h after the addition of **2b** or **6** by means of the MTT assay (Figure 6, Table 1) (*11*). From entries 1 and 2, it is clear that the doxorubicin motif in **2b** is indeed inactivated by the *p*-azidobenzyl trigger: **2b** is much less effective in inhibiting cell growth than **6**, exhibiting an 176-fold higher IC_{50} of 15.1 μM vs 0.086 μM for **6**. To our satisfaction, addition of **1b** (5 × 60 μM in 72 h) to **2b** in cell culture effects the recovery of the activity of the parent drug as evidenced by an IC_{50} value of 0.074 μM. Furthermore, this effect is dose-dependent: reducing the dose of **1b** to 30 or 10 μM leads to a decreased cytotoxicity of 0.110 and 0.320 μM, respectively (entries 3–5). Cells treated only with **1b** did not exhibit any inhibition in cell growth (entry 6). Accordingly, combined treatment with **6** and **1b** afforded the same cytotoxicity as **6** alone (entry 7). Aminobenzylalcohol **7**, the byproduct of prodrug activation, showed no cytotoxicity alone or in combination with **1b**, and no additional cytotoxicity in combination with **6** (entries 8–10). At present, it remains an open question whether the activation takes place extracellularly or intracellularly, or both.

CONCLUSIONS

To summarize, this paper describes the use of the Staudinger reaction in selectively addressing a prodrug in a cell culture environment. High levels of **1b** were shown to be tolerated well by cells, making this the first example of chemical prodrug activation with in vivo potential (*13*). This approach potentially allows an advanced level of temporal and quantitative control over drug release, as it does not rely on the presence of disease-specific or localized enzymes, or on general but heterogeneous mechanisms such as hydrolysis or degradation. The extension of this technology to a polymer-targeted prodrug and its in vivo application will be explored in the near future.

ACKNOWLEDGMENT

We thank Robert-Jan Lamers, Eef Dirksen, Wim Genuit (Shell), Gerard van den Heuvel, Hugo Knobel, and Jeroen Pikkemaat for assistance with HPLC, LCMS, MS, and NMR measurements; and Johan Lub, Dirk Burdinski, and Sander Langereis for useful discussions.

LITERATURE CITED

(1) Minotti, G., Menna, P., Salvatorelli, E., Cairo, G., and Gianni, L. (2004) Anthracyclines: molecular advances and pharmacologic developments in antitumor activity and cardiotoxicity. *Pharmacol. Rev. 56*, 185–229.

(2) Kratz, F., Warnecke, A., Schmid, B., Chung, D. E., and Gitzel, M. (2006) Prodrugs of anthracyclines in cancer chemotherapy. *Curr. Med. Chem. 13*, 477–523.

(3) Bagshawe, K. D. (2006) Antibody-directed enzyme prodrug therapy (ADEPT) for cancer. *Exp. Rev. Anticancer Ther. 6*, 1421–1431.

(4) de Groot, F. M. H., Albrecht, C., Koekkoek, R., Beusker, P. H., and Scheeren, H. W. (2003) "Cascade-release dendrimers" liberate all end groups upon a single triggering event in the dendritic core. *Angew. Chem., Int. Ed. 42*, 4490–4494.

(5) Papot, S., Tranoy, I., Tillequin, F., Florent, J.-C., and Gesson, J.-P. (2002) Design of selectively activated anticancer prodrugs: elimination and cyclization strategies. *Curr. Med. Chem. - Anti-Cancer Agents 2*, 155–185.

(6) Duncan, R. (2006) Polymer conjugates as anticancer nanomedicines. *Nat. Rev. Cancer 6*, 688–701.

(7) Köhn, M., and Breinbauer, R. (2004) The Staudinger Ligation - a gift to chemical biology. *Angew. Chem., Int. Ed. 43*, 3106–3116.

(8) Dube, D. H., Prescher, J. A., Quang, C. N., and Bertozzi, C. R. (2006) Probing mucin-type O-linked glycosylation in living animals. *Proc. Natl. Acad. Sci. U.S.A. 103*, 4819–4824.

(9) Shabat, D., Amir, R. J., Gopin, A., Pessah, N., and Shamis, M. (2004) Chemical adaptor systems. *Chem. Eur. J. 10*, 2626–2634.

(10) Doronina, S. O., Mendelsohn, B. A., Bovee, T. D., Cerveny, C. G., Alley, S. C., Meyer, D. L., Oflazoglu, E., Toki, B. E., Sanderson, R. J., Zabinski, R. F., Wahl, A. F., and Senter, P. D. (2006) Enhanced activity of monomethylauristatin F through monoclonal antibody delivery: effects of linker technology on efficacy and toxicity. *Bioconjugate Chem. 17*, 114–124.

(11) Mossman, T. (1983) Rapid colorimetric assay for cellular growth and survival: application to proliferation and cytotoxicity assays. *J. Immunol. Methods 65*, 55–63.

(12) Griffin, R. J., and Irwin, W. J. (1996) The 4-azidoberazyloxycarbonyl function; application as a novel protecting group and potential prodrug modification for amines. *J. Chem. Soc., Perkin Trans. 1*, 1205–1211.

(13) Recently, a phosphine-doxorubicin conjugate was reported that effects drug release via the traceless Staudinger ligation in aqueous THF: Azoulay, M., Tuffin, G., Sallem, W., and Florent, J.-C. (2006) A new drug-release method using the Staudinger ligation. *Bioorg. Med. Chem. Lett. 16*, 3147–3149.

BC700394S

Synthesis, Copper(II) Complexation, ^{64}Cu-Labeling, and Bioconjugation of a New Bis(2-pyridylmethyl) Derivative of 1,4,7-Triazacyclononane

Gilles Gasser,[†,‡] Linda Tjioe,[†] Bim Graham,*[,§] Matthew J. Belousoff,[†] Stefanie Juran,[‡] Martin Walther,[‡] Jens-Uwe Künstler,[‡] Ralf Bergmann,[‡] Holger Stephan,*[,‡] and Leone Spiccia*[,†]

School of Chemistry, Monash University, Clayton, Vic 3800, Australia, Forschungszentrum Dresden-Rossendorf, Institute of Radiopharmacy, PF 510119, D-01314 Dresden, Germany, and Department of Medicinal Chemistry, Victorian College of Pharmacy, Monash University, Parkville, Vic 3052, Australia. Received October 25, 2007; Revised Manuscript Received November 16, 2007

A new ligand derivative of 1,4,7-triazacyclononane (TACN), 2-[4,7-bis(2-pyridylmethyl)-1,4,7-triazacyclononan-1-yl]acetic acid (**6**), has been synthesized and its complexation behavior toward Cu^{2+} ions investigated. The ligand **6** has been characterized by spectroscopic methods, and a molecular structure of a corresponding Cu(II) complex has been elucidated by single-crystal X-ray analysis. The suitability of **6** for conjugation to peptide substrates has been shown by amide coupling of **6** to the stabilized derivative of bombesin (BN), βAla-βAla-[Cha^{13}, Nle^{14}]BN(7–14), to give the conjugate **8**. The free ligand **6** and the bioconjugate **8** were labeled with $^{64}Cu^{2+}$, and the resulting complexes, **^{64}Cu⊂6** and **^{64}Cu⊂8**, were found to be stable in the presence of a large excess of a competing ligand (cyclam) or copper-seeking superoxide dismutase (SOD), as well as in rat plasma. Biodistribution studies of **^{64}Cu⊂8** in Wistar rats showed a high activity uptake into the pancreas (5.76 ± 0.25 SUV, 5 min p.i.; 3.93 ± 0.25 SUV, 1 h p.i.), which is the organ with high levels of gastrin-releasing peptide receptor (GRPR). This receptor is overexpressed in a large number of breast and prostate carcinomas. The novel **^{64}Cu⊂6** complex had a dominating influence on the nonspecific activity biodistribution of its BN conjugate, since the distribution data of **^{64}Cu⊂6** are similar to those of **^{64}Cu⊂8**. The ^{64}Cu complexes exhibited a low activity accumulation in the liver tissue and an extensive renal clearance, which was distinctively different to the biodistribution of $^{64}CuCl_2$, suggesting that **^{64}Cu⊂6** does not undergo significant demetalation, but rather exhibits high *in vivo* stability.

INTRODUCTION

The selection of potentially useful copper radionuclides in nuclear medicine is wide and includes ^{60}Cu, ^{61}Cu, ^{62}Cu, ^{64}Cu, and ^{67}Cu (*1–6*). However, due to their favorable decay characteristics and the ability to produce them with high specific activity on a biomedical cyclotron, ^{64}Cu ($t_{1/2}$ = 12.7 h; β^+_{max} = 0.653 MeV, 17.4%; β^-_{max} = 0.578 MeV, 39%) and ^{67}Cu ($t_{1/2}$ = 61.8 h; β^-_{max} = 0.576 MeV, 100%) are the preferred copper isotopes for radiopharmaceutical applications. Incorporation of transition metal radionuclides, such as ^{64}Cu and ^{67}Cu, into target-specific radiopharmaceuticals requires the use of chelating ligands to bind the radionuclide to the conjugate (*7–9*). An extremely important requirement is that the resulting radionuclide−ligand complex is both kinetically and thermodynamically stable *in vivo* in order to minimize release of the isotope to normal tissue, thus reducing the background for imaging and minimizing radiation exposure to normal tissue for therapy (*10*). A large variety of amine-based polydentate chelating agents have been investigated in an effort to satisfy this requirement, such as polyaminocarboxylates (*11–14*), cyclic polyamines (azamacrocycles) (*15–17*), cyclic polyaminocarboxylates (*1, 15*) and pyridine-containing polyamines (*18–22*). In general, azamacrocyclic ligands are preferred over acyclic ligands, as the structural features of the macrocyclic Cu(II) complexes render them more kinetically stable under biological conditions (*14, 16, 23–25*). Macrocyclic tetraamines such as 12-N_4 (1,4,7,10-tetraazacyclododecane, "cyclen"), 13-N_4, and 14-N_4 (1,4,8,11-tetraazacyclotetradecane, "cyclam") form very stable complexes with Cu(II) and are resistant to demetalation *in vivo* (*14, 16*). Furthermore, their carboxylate-containing analogues, 1,4,7,10-tetraazacyclododecane-1,4,7,10-tetraacetic acid (DOTA) and 1,4,8,11-tetraazacyclotetradecane-1,4,8,11-tetraacetic acid (TETA), can be coupled to biomolecules. Notably, a copper-based radiopharmaceutical featuring the macrocyclic ligand TETA as a chelating agent has advanced to clinical trials (*26, 27*). Unfortunately, serious problems associated with retention of radioactivity in blood, liver, and bone narrow were found for this bioconjugate (^{64}Cu-TETA-Octreotide), suggesting that dissociation of Cu^{2+} ions from the radiopharmaceutical, and subsequent binding of the ions to proteins such as superoxide dismutase (SOD) in rat livers, is a problem even for this macrocycle (*28*). ^{64}Cu complexes of macrobicyclic tetraaminocarboxylates have shown remarkably improved *in vivo* stability, but harsh labeling conditions has hampered their application (*29–32*).

Another approach to achieve highly stable Cu(II) complexes is through the use of multidentate ligands containing pyridine donor groups, such as *N*,*N*′,*N*″-tris(2-pyridylmethyl)-*cis*,*cis*-1,3,5-triaminocyclohexane (tachpyr), 3,7-diazabicyclo[3.3.1]-nonane (bispidine), and azamacrocycles with pendant pyridyl groups (*10, 18–20, 22, 33, 34*). The latter two ligand structures, in particular, allow the convenient introduction of additional carboxylic groups, enabling their coupling to appropriate biomolecules. Thus, it should be possible to develop new pyridine-containing chelating agents that are able to rapidly form stable radiocopper complexes for targeted imaging and therapeutic purposes. In an effort to address this challenge, we have

* Corresponding authors. Email: bim.graham@vcp.monash.edu.au, Fax: +61 3 9903 9582. Email: h.stephan@fzd.de, Fax: +49 351 260 3232. Email: leone.spiccia@sci.monash.edu.au, Fax: +61 3 9905 4597.
† School of Chemistry, Monash University.
‡ Forschungszentrum Dresden-Rossendorf, Institute of Radiopharmacy.
§ Victorian College of Pharmacy, Monash University.

10.1021/bc700396e CCC: $40.75 © 2008 American Chemical Society
Published on Web 02/07/2008

Scheme 1. Synthesis of 6[a]

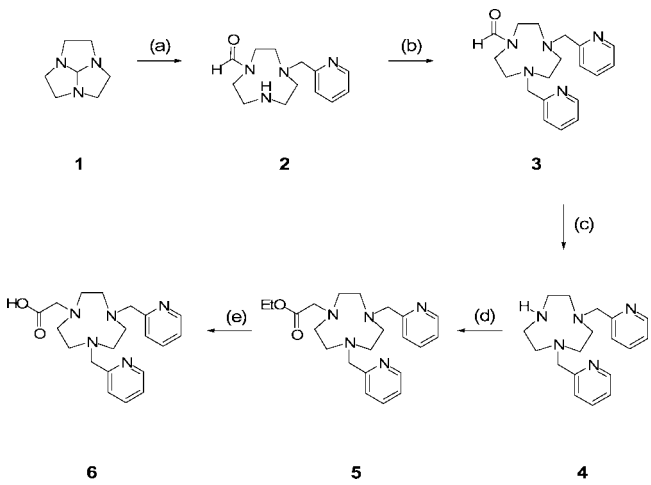

[a] (a) (i) 2-Picolyl chloride, THF, r.t., o/n; (ii) H_2O, reflux, 4 h, 79%; (b) picolyl chloride hydrochloride, K_2CO_3, KI, CH_3CN, reflux, o/n, 77%; (c) 4 M $HCl_{(aq)}$, reflux, 4 h, 85%; (d) Ethylbromoacetate, K_2CO_3, KI, CH_3CN, reflux, o/n, 88%; (f) $LiOH.H_2O$, ethanol/H_2O, 70°C, o/n, 85%.

embarked on a program to develop improved copper-based radiopharmaceuticals featuring pyridyl derivatives of the tridentate macrocycle 1,4,7-triazacyclononane (TACN) as the chelating agent. Due to its small ring size, TACN coordinates facially to metal ions such as Cu^{2+}, with the metal lying out of the plane defined by the three nitrogen atoms. The donor atoms are oriented in such a way as to maximize orbital overlap and thereby produce complexes with very high thermodynamic stabilities (*35*).

Herein, we report the synthesis and copper coordination chemistry of the TACN derivative, 2-[4,7-bis(2-pyridylmethyl)-1,4,7-triazacyclononan-1-yl]acetic acid (**6**) (Scheme 1), that contains two pyridyl pendant groups to increase the stability of the copper complex significantly compared to the parent TACN macrocycle and a carboxylic acid functionality that allows the covalent attachment of **6** to tumor-specific biomolecules via an amide coupling reaction. This possibility for regiospecific coupling is a convincing advantage compared to other previously described pyridine-containing polyamine ligands (*36*).

To demonstrate the utility of **6** in preparing ^{64}Cu-labeled radiotracers, we chose in the first instance to conjugate it to bombesin (BN), a tetradecapeptide that binds with high affinity to the gastrin-releasing peptide receptor (GRPR). The GRPR is overexpressed on a variety of tumors, including commonly diagnosed breast and prostate cancers, and the less common pancreatic and small-cell lung cancers (*37–39*). To date, research investigations have examined BN derivatives radiolabeled mainly with ^{99m}Tc, but also to a lesser extent with ^{64}Cu, ^{18}F, ^{68}Ga, ^{125}I, ^{111}In, ^{177}Lu, ^{188}Re, ^{86}Y, and ^{90}Y (*38–40*). ^{64}Cu conjugates with DOTA-PEG-BN(7–14) (PEG = poly(ethylene glycol)) (*41*), DOTA-[Lys^3]BN (*42, 43*), DOTA-X-BN(7–14) (X = spacer containing 4, 5, 6, 8, or 12 carbon atoms) (*43–46*), DOTA-X-BN(7–14) (X = tripeptide spacer Gly-Gly-Gly, Gly-Ser-Gly, Gly-Ser-Ser, Gly-Glu-Gly, or Gly-Glu-Glu) (*47*), and DOTA-[Pro^1, Tyr^4]BN (*40*) have been described, as well as ^{64}Cu conjugates with CB-TE2A-8-Aoc-BN(7–14) (CB-TE2A, 1,4,8,11-tetraazabicyclo[6.6.2]hexadecane-4,11-diacetic acid; 8-Aoc, 8-aminooctanoic acid) (*46*), or NOTA-X-BN(7–14) (NOTA, 1,4,7-triazacyclononane-1,4,7-triacetic acid; X = single amino acid spacer containing 3, 5, or 8 carbon atoms, Gly-Gly-Gly or Ser-Ser-Ser) (*48*).

The bombesin analogue selected in this work was βAla-βAla-[Cha^{13}, Nle^{14}]BN(7–14) (= βAla-βAla-Gln-Tpr-Ala-Val-Gly-His-Cha-Nle-NH_2), whose ^{99m}Tc-tricarbonyl conjugate (BBS-38) was investigated by García Garayoa et al. (*49, 50*). This BN analogue is characterized by the replacement of the C-terminal natural amino acids Leu^{13} and Met^{14} by Cha^{13}, Nle^{14}, and the further addition of a βAla-βAla spacer group. The Tc-tricarbonyl conjugate of this analogue exhibited an increased metabolic stability in blood plasma and tumor cells, as well as positively affecting the tumor-to-blood/kidney/liver ratio in comparison to the nonstabilized BN(7–14), without a spacer or with other spacers (*49, 50*).

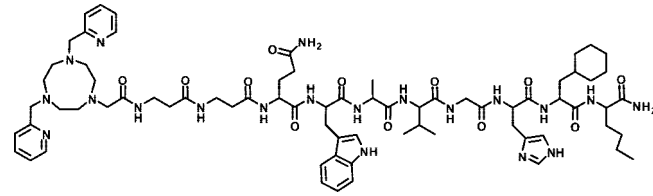

Figure 1. Structure of bioconjugate **8**.

With this in mind, we report herein the conjugation of the TACN derivative **6** to βAla-βAla-[Cha^{13}, Nle^{14}]BN(7–14), resulting in the preparation of the bioconjugate **8** (Figure 1) and present the results of subsequent ^{64}Cu labeling experiments with **6** and **8** to give **^{64}Cu⊂6** and **^{64}Cu⊂8**, respectively. *In vitro* and *in vivo* stability investigations, as well as biodistribution studies, are also presented and discussed.

EXPERIMENTAL SECTION

Materials. All solvents used were of reagent or analytical grade and used as purchased. CH_3CN was dried by standing over activated 4 Å molecular sieves overnight. Distilled water was used for all reactions in aqueous solution. CO_2-free water was prepared by boiling distilled water under nitrogen for 2 h and cooling while bubbling with nitrogen gas. High-purity nitrogen gas was used directly from a reticulated system. βAla-βAla-Gln-Trp-Ala-Val-Gly-His-Cha-Nle-NH_2 (βAla-βAla-[Cha^{13}, Nle^{14}]BN(7–14)) was obtained from Biosyntan GmbH, Germany. Rat blood plasma was prepared from Wistar rats (Harlan Winkelmann GmbH, Borchen, Germany). ^{64}Cu was produced on the PET cyclotron "Cyclone 18/9" of the FZ Dresden-Rossendorf by the ^{64}Ni(p,n) → ^{64}Cu nuclear reaction according to the procedure reported previously (*51, 52*).

Instrumentation and Methods. Infrared spectra were recorded as NaCl plates, nujol, or neat liquids as noted on a Perkin-Elmer 1600 series FTIR spectrophotometer at a resolution of 4.0 cm^{-1}. Diamond ATR spectra were recorded on a Specac "Golden Gate" apparatus. Abbreviations used to describe the peak intensities of IR and ATR spectra are as follows: vs (very strong), s (strong), m (medium), w (weak), sh (shoulder), and br (broad). Microanalytical (C, H, and N) analyses were performed by Campbell Microanalytical Service, Otago, New Zealand. ^{1}H NMR and ^{13}C NMR spectra were measured on a Bruker AC200, DPX300, or DRX400 spectrometer. Tetramethylsilane (TMS) was used as an internal calibrant for spectra recorded in $CDCl_3$ solutions. Abbreviations used to describe the resonances for ^{1}H NMR spectra are as follows: s (singlet), d (doublet), t (triplet), q (quadruplet), m (multiplet), or br (broad singlet). Low-resolution electrospray mass spectra were obtained with a Micromass Platform II Quadrupole Mass Spectrometer fitted with an electrospray source. High-resolution mass spectra were recorded on a Bruker BioApex II 47e FT-ICR MS fitted with an analytical elctrospray source. Samples were introduced by syringe pump at a flow rate of 1 μL/min. The capillary voltage was 200 V. Matrix-assisted laser desorption/ionization time-of-flight mass spectrometry (MALDI-TOF MS) was performed on an Autoflex TOF/TOF instrument from Bruker Daltonics, Germany. HPLC was performed on a Perkin-Elmer device consisting of a Turbo LC System with a quaternary pump

(series 200 LC Pump), a programmable absorbance detector model 785A (Perkin-Elmer Instruments GmbH, Germany), and a homemade γ-ray detector (well-type, NaI(T1) crystal). Eluent A, 0.1% (v/v) TFA in CH_3CN; eluent B, 0.1% (v/v) TFA in H_2O; eluent C, 0.05% (v/v) TFA in CH_3CN; eluent D, 0.04% (v/v) TFA in H_2O. HPLC system 1, Jupiter (Phenomenex) 4 μ Proteo 90Å, 250 × 4.6 mm; gradient elution, 10% to 70% of eluent A in 40 min, 1 mL/min. HPLC system 2, Jupiter (Phenomenex) 4 μ Proteo 90Å, 250 × 10 mm, gradient elution, 10% to 70% of eluent A in 40 min, 3 mL/min. HPLC system 3, Zorbax (Agilent) SB-C18, 300 Å, 5 μm, 250 × 9.4 mm; gradient elution using eluents C and D, 10% to 70% eluent C in 20 min, 3 mL/min, 28 °C. Thin layer chromatography (TLC) was performed using basic alumina (Al_2O_3) plates with detection of species present by $KMnO_4$ oxidation (eluents specified in the synthesis section). TLC of the ^{64}Cu-labeled compounds was performed using neutral alumina plates which were recorded on a Radioisotope Thin Layer Analyzer (Rita Star, Raytest Isotopenmessgerät GmbH, Straubenhardt, Germany). The eluent was a 1:1 mixture by volume methanol/ammonium acetate (5% in water) [$R_f = 0$ (Cu^{2+}); $R_f = 1$ (**^{64}Cu⊂6**)].

1,4,7-Triazacyclo[5.2.1.0^{4,10}]decane (1). 1 was synthesized following the previously reported procedure. Analytical data were in agreement with that described in the literature (*53*, *54*).

1-Formyl-4-(2-pyridylmethyl)-1,4,7-triazacyclononane (2). Picolyl chloride hydrochloride was neutralized with an excess of NaOH, and extraction with DCM yielded neutral picolyl chloride. A sample of this compound (6.02 g, 0.0472 mol) was dissolved in THF (50 mL) and then added dropwise to a solution of **1** (6.35 g, 0.050 mol) in THF (50 mL). The resulting mixture was stirred overnight at room temperature. The orange precipitate which formed was filtered off, washed with THF, and dried under reduced pressure. The solid was dissolved in water (50 mL) and the solution refluxed for 4 h. The solution was cooled to room temperature and aqueous 5 M NaOH added dropwise until a pH of 13 was reached. The compound was then extracted with $CHCl_3$, the organic phase dried with anhydrous $MgSO_4$, filtered, and the solvent removed under vacuum to give **2** as a yellow oil. Yield: 9.21 g (79%). ^{1}H NMR (300 MHz, $CDCl_3$): δ 2.50 (s br, 1H, N*H*), 2.60–2.70 (m, 3H, CH_2TACN ring), 2.85 (m, 1H, CH_2TACN ring), 3.01 (m, 1H, CH_2TACN ring), 3.10–3.25 (m, 4H, CH_2 TACN ring), 3.40–3.50 (m, 3H, CH_2 TACN ring), 3.88 (s, 2H, N-CH_2-pyridyl), 7.18 (m, 1H, C*H* pyridyl), 7.38 (m, 1H, C*H* pyridyl), 7.68 (m, 1H, C*H* pyridyl), 8.12 (s, 1H, C*H*O), 8.54 (m, 1H, C*H* pyridyl). ^{13}C NMR (50.29 MHz, $CDCl_3$): 46.5, 46.6, 47.0, 47.6, 47.9, 49.1, 49.8, 51.7, 52.4, 53.2, 55.1, 56.5 (all *C*H$_2$ TACN ring), 62.9 (N-*C*H$_2$-pyridyl), 121.8, 121.9, 122.7, 122.8, 136.1, 136.3, 136.4, 148.8 (all *C*H pyridyl), 159.3 (*C* pyridyl), 159.4 (*C* pyridyl), 163.4 (*C*HO), 163.5 (*C*HO). IR (KBr disk, cm^{-1}): 3369w ($\nu_{N\text{-}H}$), 3049s ($\nu_{C\text{-}H(Aromatic)}$), 2923br ($\nu_{C\text{-}H}$), 1662s ($\nu_{C=O}$), 1590s ($\nu_{C=N(Pyridyl)}$), 1569s ($\nu_{C=C(Pyridyl)}$), 1435s br ($\nu_{C=C(Pyridyl)}$), 1365s br, 1273s, 1150s, 1047s, 993s, 733s, 700s. ESI-MS electrospray mass spectrum (*m*/*z*): 249.2 (100%) [M + H]$^+$, 261.2 (10%) [M + Na]$^+$. High-resolution ESI mass determination (MeOH): Found, 249.1708; calcd for $C_{13}H_{21}N_4O$, 249.1715.

1-Formyl-4,7-bis(2-pyridylmethyl)-1,4,7-triazacyclononane (3). A solution of picolyl chloride hydrochloride (6.12 g, 0.0371 mol) in CH_3CN (50 mL) was added dropwise to a mixture of **2** (9.21 g, 0.0371 mol) in CH_3CN (50 mL) containing K_2CO_3 (20.50 g, 0.1480 mol) and KI (0.10 g, 0.6020 mmol). The resulting mixture was stirred for 1 h at room temperature and then refluxed overnight. The reaction mixture was cooled to room temperature, filtered, and washed with acetonitrile. The filtrate was evaporated under reduced pressure to yield **3** as a brown oil. Yield: 9.69 g (77%). ^{1}H NMR (300 MHz, $CDCl_3$): δ 2.59 (m, 2H, CH_2TACN ring), 2.81 (m, 2H, CH_2TACN ring), 3.03 (m, 2H, CH_2TACN ring), 3.27 (m, 4H, CH_2TACN ring), 3.42 (m, 2H, CH_2TACN ring), 3.87 (s, 2H, N-CH_2-pyridyl), 3.88 (s, 2H, N-CH_2-pyridyl), 7.14 (m, 2H, C*H* pyridyl), 7.43 (m, 2H, C*H* pyridyl), 7.66 (m, 2H, C*H* pyridyl), 8.05 (s, 1H, C*H*O), 8.53 (m, 2H, C*H* pyridyl). ^{13}C NMR (50.29 MHz, $CDCl_3$): 46.5, 47.0, 50.2, 53.0, 54.2, 57.7 (all *C*H$_2$ TACN ring), 62.9 (N-*C*H$_2$-pyridyl), 63.6 (N-*C*H$_2$-pyridyl), 120.9, 121.8, 122.5, 122.8, 135.6, 135.8, 148.8, 148.9 (all *C*H pyridyl), 159.6 (*C* pyridyl), 159.8 (*C* pyridyl), 163.5 (*C*HO). IR (KBr disk, cm^{-1}): 3052s ($\nu_{C\text{-}H(Aromatic)}$), 3008s ($\nu_{C\text{-}H}$), 2926s br($\nu_{C\text{-}H}$), 2824s br, 2250s, 1666s ($\nu_{C=O}$), 1589s ($\nu_{C=N(Pyridyl)}$), 1569s ($\nu_{C=C(Pyridyl)}$), 1473s ($\nu_{C=C(Pyridyl)}$), 1435s ($\nu_{C=C(Pyridyl)}$), 1371s br, 1314s, 1225s, 1148s, 1047s, 994s, 757s. ESI-MS electrospray mass spectrum (*m*/*z*): 340.1 (100%) [M + H]$^+$. High-resolution ESI mass determination (MeOH): Found, 340.2133; calcd for $C_{19}H_{26}N_5O$, 340.2137.

1,4-Bis(2-pyridylmethyl)-1,4,7-triazacyclononane (4). 3 (9.69 g, 0.0280 mol) was dissolved in aqueous 4 M HCl (50 mL) and the resulting solution refluxed for 4 h. The solution was then allowed to cool to room temperature, and aqueous 5 M NaOH (50 mL) was added dropwise until a pH of 13 was reached. The compound was extracted with $CHCl_3$ (3 × 50 mL), the organic phase washed with anhydrous $MgSO_4$, filtered, and the solvent removed under vacuum to yield **4** as a reddish brown oil. Yield: 7.55 g (85%). Anal. Found (%): C, 69.32; H, 7.76; N, 22.42. Calcd for $C_{18}H_{25}N_5$ (%): C, 69.48; H, 7.65; N, 22.32. ^{1}H NMR (400 MHz, $CDCl_3$): δ 2.75 (m, 4H, CH_2TACN ring), 2.95 (m, 4H, CH_2TACN ring), 3.06 (m, 4H, CH$_2$TACN ring), 3.89 (s, 4H, N-CH_2-pyridyl), 4.71 (s br, 1H, N*H*), 7.14 (m, 2H, C*H* pyridyl), 7.26 (m, 2H, C*H* pyridyl), 7.58 (m, 2H, C*H* pyridyl), 8.61 (m, 2H, C*H* pyridyl). ^{13}C NMR (75.44 MHz, $CDCl_3$): 45.4 (*C*H$_2$ TACN ring), 49.7 (*C*H$_2$ TACN ring), 52.8 (*C*H$_2$ TACN ring), 61.02 (N-*C*H$_2$-pyridyl), 121.7, 122.4, 122.7, 123.1, 136.2, 136.6, 148.8, 149.3 (all *C*H pyridyl), 158.3 (*C* pyridyl). IR (KBr disk, cm^{-1}): 3416w ($\nu_{N\text{-}H}$), 3052s ($\nu_{C\text{-}H(Aromatic)}$), 2919s br ($\nu_{C\text{-}H}$), 1590s ($\nu_{C=N(Pyridyl)}$), 1568s ($\nu_{C=C(Pyridyl)}$), 1472s ($\nu_{C=C(Pyridyl)}$), 1434s ($\nu_{C=C(Pyridyl)}$), 1362s, 1148s, 995s, 752s, 662s. ESI-MS Electrospray mass spectrum (*m*/*z*): 312.3 (100%) [M + H]$^+$.

Ethyl-2-[4,7-bis(2-pyridylmethyl)-1,4,7-triazacyclononan-1-yl]acetate (5). A solution of ethyl bromoacetate (0.50 g, 2.99 mmol) in dry CH_3CN (25 mL) was added dropwise to a mixture of **4** (0.92 g, 3.0 mmol) in dry CH_3CN (25 mL) containing K_2CO_3 (1.64 g, 11.8 mmol) and KI (0.10 g, 0.60 mmol). The resulting mixture was stirred for 1 h at room temperature, and then refluxed overnight. It was subsequently cooled to room temperature, filtered, and the residue washed with dry acetonitrile. The filtrate was collected, and the solvent removed under reduced pressure to yield **5** as a brown oil. Yield: 1.18 g (88%). ^{1}H NMR (200 MHz, $CDCl_3$): δ 1.28 (t, $^3J = 7.1$ Hz, 3H, CH_3-CH$_2$O), 2.45–2.85 (m, 12H, CH_2TACN ring), 3.35 (s, 2H, N-CH_2-COO), 3.86 (s, 4H, N-CH_2-pyridyl), 4.12 (q, $^3J = 7.1$ Hz, 2H, CH$_3$-CH_2O), 7.19 (m, 2H, C*H* pyridyl), 7.46 (m, 2H, C*H* pyridyl), 7.62 (m, 2H, C*H* pyridyl), 8.54 (m, 2H, C*H* pyridyl). ^{13}C NMR (75.44 MHz, $CDCl_3$): δ 13.1 (OCH$_2$-*C*H$_3$), 53.0 (b, *C*H$_2$ TACN ring), 59.0 (N-*C*H$_2$-COO), 59.2 (O*C*H$_2$-CH$_3$), 63.5 (N-*C*H$_2$-pyridyl), 120.9 (*C*H pyridyl), 121.9 (*C*H pyridyl), 134.7 (*C*H pyridyl), 147.6 (*C*H pyridyl), 158.1 (*C* pyridyl), 170.8 (*C*OO). IR (KBr disk, cm^{-1}): 3050s ($\nu_{C\text{-}H(Aromatic)}$), 2930s br ($\nu_{C\text{-}H(TACN)}$), 1732s ($\nu_{C=O}$), 1592s ($\nu_{C=N(Pyridyl)}$), 1568s ($\nu_{C=C(Pyridyl)}$), 1472s ($\nu_{C=C(Pyridyl)}$), 1435s ($\nu_{C=C(Pyridyl)}$), 1372w, 1198w, 1049w, 994s br, 761s. ESI-MS Electrospray mass spectrum (*m*/*z*): 398.3 (100%) [M + H]$^+$.

2-[4,7-Bis(2-pyridylmethyl)-1,4,7-triazacyclononan-1-yl]acetic Acid (6). To **5** (1.18 g, 3.0 mmol) dissolved in ethanol (30 mL) was added LiOH·H_2O (0.45 g, 10.7 mmol) dissolved in water (10 mL). This mixture was stirred at 70 °C overnight. It

was then cooled to room temperature, and the pH was adjusted to 7 by addition of aqueous 1 M HCl. The solvent was removed under reduced pressure and dichloromethane used to extract the solid. The solution was filtered and the filtrate dried with Na_2SO_4. After filtration, the solvent was removed under reduced pressure to yield **6** as a brown oil. Yield: 1.02 g (85%). Anal. Found (%): C, 65.18; H, 7.22; N, 18.88. Calcd for $C_{20}H_{27}N_5O_2$ (%): C, 65.09; H, 7.38; N, 18.98. ^{1}H NMR (75.44 MHz, $CDCl_3$): δ 2.40–2.80 (m, 12H, CH_2TACN ring), 3.19 (s, 2H, N-CH_2-COOH), 3.89 (d, ^2J = 15.2 Hz, 2H, N-CH_2-pyridyl), 3.98 (d, ^2J = 15.2 Hz, 2H, N-CH_2- pyridyl), 7.14 (m, 2H, C*H* pyridyl), 7.28 (m, 2H, C*H* pyridyl), 7.72 (m, 2H, C*H* pyridyl), 8.17 (m, 2H, C*H* pyridyl). ^{13}C NMR (75.44 MHz, $CDCl_3$): δ 49.9 (*C*H_2 TACN ring), 50.0 (*C*H_2 TACN ring), 50.3 (*C*H_2 TACN ring), 59.3 (N-*C*H_2-COOH), 60.5 (N-*C*H_2-pyridyl), 122.1 (*C*H pyridyl), 122.3 (*C*H pyridyl), 136.9 (*C*H pyridyl), 148.6 (*C*H pyridyl), 157.5 (*C* pyridyl), 176.1 (*C*OOH). IR (KBr disk, cm^{-1}): 3390w br ($\nu_{O\text{-}H}$), 3059w ($\nu_{C\text{-}H(Aromatic)}$), 2939m ($\nu_{C\text{-}H}$), 2867s ($\nu_{C\text{-}H}$), 2826s, 2359s, 2192s, 1667s ($\nu_{C=O}$), 1599s ($\nu_{C=N(Pyridyl)}$), 1571s ($\nu_{C=C(Pyridyl)}$), 1481s ($\nu_{C=C(Pyridyl)}$), 1456s ($\nu_{C=C(Pyridyl)}$), 1436s ($\nu_{C=C(Pyridyl)}$), 1365s ($\nu_{C\text{-}O}$), 1149s, 1119s, 1097s, 1046s, 1005s, 978s, 914m, 836s, 727m, 641s. ESI-MS Electrospray mass spectrum (*m*/*z*): 368.3 (100%) $[M - H]^-$.

Ethyl-2-{2-[4,7-bis(2-pyridylmethyl)-1,4,7-triazacyclononan-1-yl]acetamido}acetate (7). 6 (0.65 g, 1.8 mmol) was suspended in acetonitrile (15 mL), and HBTU (0.67 g, 1.8 mmol), DIPEA (1.60 g, 12.4 mmol), and glycine ethyl ester hydrochloride (0.25 g, 1.78 mmol) added. The brown reaction mixture was stirred overnight at room temperature, and thereafter the solvent was removed under reduced pressure. To the residue was added dichloromethane (10 mL), and the mixture was washed with saturated $NaHCO_3$ solution (5 mL) and water (2 × 5 mL). After drying of the organic phase over Na_2SO_4 and subsequent filtration, the solvent was removed under reduced pressure. The crude product was purified by column chromatography on basic alumina with CH_2Cl_2/MeOH (98:2 by volume) as the eluent (R_f = 0.28) to yield **7** as a yellow oil. Yield: 0.32 g (40%). Anal. Found (%): C, 63.55; H, 7.46; N, 18.65. Calcd for $C_{24}H_{34}N_6O_3$ (%): C, 63.49; H, 7.55; N, 18.52. ^{1}H NMR (75.44 MHz, $CDCl_3$): δ 1.19 (t, ^3J = 7.1 Hz, 3H, CH_3-CH_2O), 2.40–2.80 (m, 12H, CH_2TACN ring), 3.40 (s, 2H, N-CH_2-CONH), 3.87 (d, ^2J = 15.3 Hz, 2H, N-CH_2-pyridyl), 3.98 (d, ^2J = 15.3 Hz, 2H, N-CH_2-pyridyl), 4.02 (d, ^3J = 5.8 Hz, 2H, CONH-CH_2-COO), 4.12 (q, ^3J = 7.1 Hz, 2H, OCH_2-CH_3), 7.02 (t, ^3J = 5.8 Hz, 1H, CON*H*), 7.19 (m, 4H, C*H* pyridyl), 7.71 (m, 2H, C*H* pyridyl), 8.07 (m, 2H, C*H* pyridyl). ^{13}C NMR (300 MHz, $CDCl_3$): δ 14.1 (OCH_2-*C*H_3), 41.6 (CONH-*C*H_2-COO), 51.1 (br, *C*H_2 TACN ring), 51.3 (*C*H_2 TACN ring), 59.6 (N-*C*H_2-CONH), 61.3 (N-*C*H_2-pyridyl), 61.7 (COO-*C*H_2-CH_3), 122.9 (*C*H pyridyl), 123.1 (*C*H pyridyl), 137.8 (*C*H pyridyl), 149.1 (*C*H pyridyl), 158.4 (*C* pyridyl), 169.3 (CH_2-*C*OO-CH2), 173.6 (*C*ONH). IR (KBr disk, cm^{-1}): 3406w ($\nu_{N\text{-}H}$), 3035w ($\nu_{C\text{-}H(Aromatic)}$), 2953s ($\nu_{C\text{-}H}$), 2867s ($\nu_{C\text{-}H}$), 2826s, 2359s, 1789s ($\nu_{C=O(ester)}$), 1658s ($\nu_{C=O(amide)}$), 1599s ($\nu_{C=N(Pyridyl)}$), 1571s ($\nu_{C=C(Pyridyl)}$), 1481s ($\nu_{C=C(Pyridyl)}$), 1456s ($\nu_{C=C(Pyridyl)}$), 1436s ($\nu_{C=C(Pyridyl)}$), 1365s ($\nu_{C\text{-}O}$), 1149s, 1097s, 1046s, 978s, 914m, 836s, 727m, 641s. ESI-MS Electrospray mass spectrum (*m*/*z*): 455.3 (100%) $[M + H]^+$.

Bioconjugate 6-βAla-βAla-[Cha^{13}, Nle^{14}]BN(7–14) (8). 6 (2.3 mg, 6.2 μmol), HBTU (4.7 mg, 12 μmol) and βAla-βAla-Gln-Trp-Ala-Val-Gly His-Cha-Nle-NH_2 (5.0 mg, 4 μmol) were dissolved in DMF (2 mL). DIPEA (5.0 μL, 29 μmol) was then added and the mixture stirred for 20 h at room temperature. The DMF was removed under high vacuum and the residual brown oil was purified HPLC (system 2) to yield **8** as a white solid after lyophilization. Yield: 3.6 mg (61%). Electrospray mass spectrum (*m*/*z*): 728 $[M + 2H]^{2+}$, 739 $[M + H + Na]^{2+}$, 1456 $[M + H]^+$, 1478 $[M + Na]^+$. MALDI-TOF MS: Found: 1457.1; calculated for $C_{73}H_{107}N_{20}O_{12}$: 1455.8. HPLC system 1: t_R = 19.2 min.

[Cu(6-H)Cu(NO$_3$)$_2$.MeOH]NO$_3$.MeOH(Cu$_2$⊂6). $Cu(NO_3)_2 \cdot 3H_2O$ (59 mg, 0.24 mmol) was dissolved in MeOH (5 mL) and added to a solution of **6** (89 mg, 0.24 mmol) in MeOH (5 mL). The color changed to dark green and a brown precipitate formed. The solution was filtered to remove the precipitate. Slow diffusion of a ether into this solution produced crystals that were suitable for X-ray crystallography. Yield: 16 mg (18%). Anal. Found (%): C, 37.60; H, 4.43; N, 15.05. Calcd for $Cu_2C_{22}H_{34}N_8O_{13}$ (%): C, 35.43; H, 4.50; N, 15.02. IR (ATR, cm^{-1}): 3049w ($\nu_{C\text{-}H(Aromatic)}$), 2932s ($\nu_{C\text{-}H}$), 2862s ($\nu_{C\text{-}H}$), 1610s ($\nu_{C=O}$), 1573s ($\nu_{C=C(Pyridyl)}$), 1440s ($\nu_{C=C(Pyridyl)}$), 1330s br ($\nu_{NO3\text{-}}$), 1021m, 976m, 826m, 777m.

X-ray Crystallography. Intensity data for a blue crystal of **Cu$_2$⊂6** (0.21 × 0.19 × 0.06 mm^3) was measured at 123 K on a Bruker Apex 2 CCD fitted with graphite-monochromated Mo Kα radiation (0.71073 Å). The data were collected to a maximum 2θ value of 60° and processed using the Bruker *Apex 2* software. Crystal parameters and details of the data collection for **Cu$_2$⊂6** are summarized and presented in the Supporting Information.

The structure was solved by direct methods and expanded using standard Fourier routines in the SHELX-97 (*55, 56*) software package. All hydrogens except for H1M and H2M, which were located on the Fourier-difference map, were placed in idealized positions, and all nonhydrogen atoms were refined anisotropically.

Preparation of ^{64}Cu⊂6 and ^{64}Cu⊂8. An aqueous solution of $^{64}CuCl_2$ (50 MBq, 100 μL, 0.1 M NH_4OAc) was added to ca. 1 mg of **6** or **8** dissolved in 100 μL MeCN/H_2O (1:1 by volume). The reaction mixtures were tempered at 40 °C for 30 min, which results in 90% labeling yield. The crude products were then purified by HPLC (system 2). This results in a radiochemical purity >97%. For *in vivo* studies, the obtained fraction was concentrated to dryness and redissolved in 0.9% aqueous saline solution; t_R = 4.4 min for **^{64}Cu⊂6**, t_R = 19.5 min for **^{64}Cu⊂8** (HPLC system 1).

Concentration Dependence. To 100 μL aqueous solution of ligand **6** (10^{-2} M, 10^{-3} M, 10^{-4} M, and 10^{-5} M in 0.1 M NH_4OAc), 200 kBq of $^{64}CuCl_2$ (100 μL in 0.1 M NH_4OAc) was added. The mixtures were shaken for 10 min and then analyzed by TLC.

Kinetic Studies. 100 μL of an aqueous solution of ligand **6** (10^{-4} M in 0.1 M NH_4OAc) was spiked with $^{64}CuCl_2$ (100 kBq) and stirred. Aliquots of the mixtures were analyzed by TLC to determine the degree of complexation. Samples were taken after 1, 5, 10, and 30 min.

Ligand "Challenge" Experiment. A solution containing 100 kBq $^{64}CuCl_2$ was added to 500 μg of **6** dissolved in 100 μL of 0.1 M NH_4OAc. After 10 min, full complexation of the ligand was checked by TLC. Cyclam (40 mg, more than 100-fold excess) dissolved in 1 mL 0.1 M NH_4OAc was then added to the complex solution, which was stirred for 24 h. Aliquots of the mixtures were assayed by TLC and HPLC (system 1) to determine the degree of decomposition.

SOD "Challenge" Experiment. A solution of 250 kBq $^{64}CuCl_2$ in 0.1 M NH_4OAc was added to 10 μg of **6** dissolved in 100 μL acetonitrile/water (1:5). The full complexation of the ligand was checked via TLC after 15 min. After the removal of acetonitrile, 1.35 mg of SOD (from bovine liver) was dissolved in 200 μL of 0.9 M NaCl solution-representing a more than 1000-fold excess-and added to the prepared complex solution, which was then stirred for 24 h. The degree of decomposition was determined by TLC using aliquots of the mixtures.

Determination of Partition Coefficient log $D_{o/w}$. Ligands **6** or **8** dissolved in 50 μL water ($c_0 = 10^{-3}$ M) were added to a mixture consisting of 390 μL HEPES/NaOH buffer (0.05 M, pH = 7.2, 7.4, 7.8), a 10 μL $^{64}CuCl_2$ solution in 0.1 M NH_4OAc, and 50 μL of a 10^{-4} M aqueous solution of $Cu(NO_3)_2$. The distribution experiments in 1-octanol/buffer system were carried out at 25 ± 1 °C in microcentrifuge tubes (2 cm^3) with mechanical shaking. The phase ratio $V_{(1\text{-octanol})}$:$V_{(aq)}$ was 1:1 (0.5 cm^3 each). The shaking time was 30 min. All samples were centrifuged and the phases separated. The copper concentration in both phases was determined radiometrically using γ-radiation [^{64}Cu, NaI(Tl) scintillation counter automatic gamma counter 1480, Wizard 3″, PerkinElmer]. The results are the average values of three independent experiments.

***In Vitro* Stability.** **^{64}Cu⊂6** or the bioconjugate **^{64}Cu⊂8** were incubated in phosphate buffer (250 μL, Sörensen, pH = 7.4) and rat plasma (250 μL) at 37 °C for 2 h and then at 25 ± 1 °C for 24 h. Cold ethanol (500 μL) was added to the mixture, and after centrifugation for 5 min, the ethanol phase was removed from the protein precipitate. This procedure was repeated another time. The ethanol solution was dried under nitrogen, and a solution of H_2O/CH_3CN (9:1 by volume) (100 μL) was added and acidified with TFA (5 μL). Samples containing **^{64}Cu⊂6** were analyzed using TLC and HPLC (system 1); **^{64}Cu⊂8** samples analyzed only by HPLC. The whole experiment was repeated two times.

***In Vivo* Stability.** The *in vivo* stability of **^{64}Cu⊂8** was analyzed using rat arterial blood samples at various time points (1, 3, 5, 10, 20, 30, and 60 min) after injection of the radiotracer. The samples were centrifuged to precipitate the blood cells. A solution consisting of 50 μL CH_3CN, 45 μL H_2O, and 5 μL TFA was added to 200 μL of the supernatant, and the mixture was then cooled to −20 °C. After centrifugation, the supernatant was analyzed by HPLC (system 3). The chromatogram of **^{64}Cu⊂8** (plasma, 0 min) was obtained by addition of **^{64}Cu⊂8** to rat blood and immediately treating the mixture as described for the *in vivo* samples. Urine and kidney homogenates were treated analogously to the arterial blood samples.

Animals, Feeding, Husbandry and Biodistribution Studies in Rats. The animal research committee of the Regierungspräsidium Dresden approved the animal facilities and the experiments according to institutional guidelines and the German animal welfare regulations. The Wistar rats (Harlan Winkelmann GmbH, Borchen, Germany) were housed under standard conditions with free access to standard food and tap water. Animals were between 7 and 9 weeks of age. The rats were housed in an Animal Biosafety Level 1 (ABSL-1) acclimatized facility with a temperature of 22 ± 2 °C and humidity of 55 ± 5%. Animals were under a 12 h light cycle in temperature (27 ± 1 °C) controlled-airflow cabinets. The animals had free access to standard pellet feed and water.

Four animals (body weight 227 ± 10 g) for each time point were intravenously injected into a tail vein with approximately 8 μCi (0.3 MBq) **^{64}Cu⊂8** conjugate in 0.5 mL electrolyte solution E-153 (Serumwerk Bernburg, Germany) with 5% Tween 80. Animals were euthanized at 5 and 60 min postinjection. Blood and the major organs were collected, weighed, and counted in a Wallac WIZARD Automatic Gamma Counter (PerkinElmer, Germany). The radioactivity of the tissue samples was decay-corrected and calibrated by comparing the counts in tissue with the counts in aliquots of the injected tracer that had been measured in the gamma counter at the same time. The activity in the selected tissues and organs was expressed as percent injected dose per organ (% ID) or as standardized uptake value (SUV). Values are quoted as means ± standard deviation (mean ± SD) for each group of four animals.

PET Imaging. General anesthesia of rats was induced with inhalation of desflurane 9% (v/v) (Suprane, Baxter, Germany) in 40% oxygen/air (gas flow 1 L/min), and was maintained with desflurane 6% (v/v). For arterial blood sampling, a 3.5 Fr umbilical vessel catheter prefilled with heparinized saline was inserted into the right carotid arteria, and 100 μL blood samples were taken at 1, 3, 5, 10, 20, 30, and 60 min after tracer application. In the PET experiments, 0.1 mCi (3.7 MBq) of the **^{64}Cu⊂8** conjugate in 0.5 mL was administered intravenously over 1 min into a tail vein. PET imaging of **^{64}Cu⊂8** in rat was performed over 60 min with a microPET P4 scanner (Siemens CTI Molecular Imaging Inc., Knoxville). Data acquisition was performed in 3D list mode. A transmission scan was carried out prior to the injection of **^{64}Cu⊂8** using a ^{137}Cs point source. Emission data were collected continuously for 60 min after injection of **^{64}Cu⊂8**. The list mode data were sorted into sinograms using a framing scheme of 12 × 10 s, 6 × 30 s, 5 × 300 s, and 5 × 600 s frames. The data were attenuation corrected, and the frames were reconstructed by Ordered Subset Expectation Maximization applied to 3D sinograms (OSEM3D) with 14 subsets, 6 OSEM3D iterations, 2 maximum a posteriori (MAP) iterations, and 0.05 beta-value for smoothing. The pixel size was 0.8 by 0.8 by 1.2 mm^3, and the resolution in the center of field of view was 1.85 mm. No correction for recovery and partial volume effects was applied. The image files were processed using the *ASIPro* software (Siemens, CTI Molecular Imaging Inc. Knoxville) and the *ROVER* software (ABX GmbH, Radeberg, Germany). Summed frames from 30 to 90 s postinjection (p.i.) and 30 to 90 min p.i. were used to define the regions of interest (ROI). The data were normalized to the injected radioactivity by using ^{18}F standards from the injection solution measured in a γ-well counter (Isomed 2000, Dresden, Germany) cross-calibrated to the PET scanner and expressed in SUV.

Statistical Analysis. The data are expressed as means ± SD. One-way analysis of variance (ANOVA) was used for statistical evaluation. Means were compared using Student's *t* test. A *P* value of <0.05 was considered significant and indicated by an asterisk symbol (*).

RESULTS AND DISCUSSION

Ligand Synthesis. The synthesis of the important synthon, 1,4-bis(2-pyridylmethyl)-1,4,7-triazacyclononane (**4**) (see Scheme 1), was reported by our group more than a decade ago (*57*). However, the method published did not afford a pure compound. Purity was not as critical in the previous work as, following complexation, purification of the metal complexes was carried out by cation exchange chromatography. For the present work, however, a pure ligand was required and therefore a new synthetic pathway (Scheme 1) was developed, starting from the known compound 1,4,7-triazatricyclo[5.2.1.0^{4,10}]decane (**1**) (*53, 54*).

Compound **2** was synthesized by first adding 1 equiv of 2-picolyl chloride dropwise to a solution of **1** in THF. The crude orange precipitate obtained was then refluxed in water to give 1-formyl-4-(2-pyridylmethyl)-1,4,7-triazacyclononane (**2**) as a yellow oil in 79% yield. ^{1}H and ^{13}C NMR spectra of compound **2** are complicated by the presence of two rotameric forms in solution due to restricted rotation around the amide bond leading to different proton environments. This phenomenon has been observed for some other TACN-based compounds which possess a formyl group (*58*). Nevertheless, the formation of **2** is confirmed by ^{1}H NMR spectroscopy, with the presence of two singlets at about 8.10 ppm (integrating as one proton in total) corresponding to the proton of the formyl group. The presence of the formyl group was also confirmed by IR spectroscopy, which revealed a strong absorption at 1662 cm^{-1}.

The second pyridyl pendant was introduced by reacting **2** with picolyl chloride hydrochloride in dry CH_3CN. The suc-

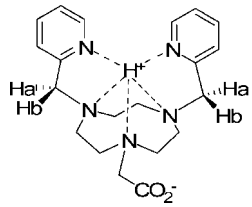

Figure 2. Proposed structure of **6** in $CDCl_3$.

cessful formation of 1-formyl-4,7-bis(2-pyridylmethyl)-1,4,7-triazacyclononane (**3**) was confirmed by ^{1}H NMR spectroscopy in $CDCl_3$, with resonances corresponding to the methylene group of the TACN ring (2.52–3.49 ppm), the methylene protons linking the pyridyl pendant groups to the macrocycle (3.95 ppm), and multiplets due to the pyridyl protons (7.15–8.50 ppm), all integrating in the expected ratio. In contrast to compound **2**, only one resonance for the formyl group was observed for compound **3** (at 8.00 ppm), indicating that the additional pyridyl pendant group restricts the molecule to one rotameric form. The disappearance in the IR spectrum of the ν(N−H) stretching frequency at 3369 cm^{-1} for **2** is a further proof of the formation of **3**.

The cleavage of the formyl group in **3** was achieved by acid hydrolysis in aqueous 4 M HCl solution to give **4** as a brown oil in 85% yield. The ^{1}H and ^{13}C NMR spectra of **4** agreed well with literature data (*57*). The introduction of an acetate pendant arm to facilitate the attachment of a biomolecule was achieved by first reacting **4** with ethyl bromoacetate in the presence of K_2CO_3 and a catalytic amount of KI to give ethyl 2-[4,7-bis(2-pyridylmethyl)-1,4,7-triazacyclononan-1-yl]acetate (**5**) in 88% yield. Formation of the product was confirmed by ESI-MS, with a peak at m/z = 398.3 corresponding to [M + H]$^+$, and a distinctive IR carbonyl stretch at 1732 cm^{-1}. The ^{1}H NMR spectrum of **5** exhibited additional peaks corresponding to the ethyl acetate pendant arm; a triplet at 1.35 ppm with an integration of 3H was assigned to the terminal CH_3 group and a quartet at 4.25 ppm to the ethyl CH_2 group. A singlet at 3.42 ppm corresponding to the methylene protons of the acetate group was also observed. Base-catalyzed hydrolysis of **6** followed by a pH adjustment prior to extraction with dichloromethane yielded 2-[4,7-bis(2-pyridylmethyl)-1,4,7-triazacyclononan-1-yl]acetic acid (**6**). Cleavage of the ester was confirmed by ESI-MS, with a peak at m/z = 368.3 corresponding to [M − H]$^-$. Furthermore, ^{1}H NMR spectroscopy showed the disappearance of the signals corresponding to the ethyl group. Interestingly, when the spectrum was run in $CDCl_3$, two doublets were observed at 3.89 and 3.98 ppm, which were assigned to the four protons of the pyridyl CH_2. An explanation for this observation may be that, in an aprotic solvent like $CDCl_3$, the ligand **6** exists as a zwitterion, with the H$^+$ ion interacting with the five nitrogen atoms present in the ligand (Figure 2). This interaction might cause the pyridyl pendant arms to be locked in one conformation, leading to the two protons of the pyridyl CH_2 residing in different chemical environments. The value of the observed coupling constant (15.2 Hz) is consistent with the geminal coupling that would be predicted between two such nonequivalent pyridyl CH_2 protons. Furthermore, only one signal for the two carbons bearing the four hydrogen atoms was observed in the ^{13}C NMR spectrum, indicating that the two carbons are magnetically equivalent and that only the hydrogens are not. A COSY spectrum subsequently verified that the two doublets seen in the ^{1}H NMR and $CDCl_3$ were due to the methylene protons of the pyridyl arm. The absence of a pair of similar doublets for the pyridyl CH_2 protons in the NMR spectra of the nonzwitterionic compounds **4** and **5** (all ^{1}H NMR spectra were measured in $CDCl_3$) provides evidence of the role that the H$^+$ ion plays in locking the pyridyl arms in one conformation in compound **6**.

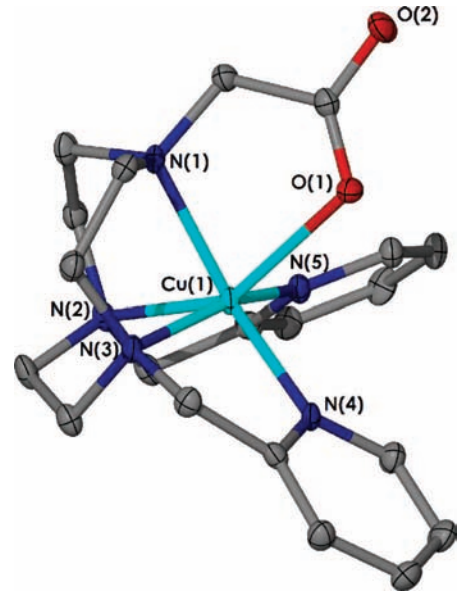

Figure 3. Thermal ellipsoid plot of the Cu(1) unit of **Cu$_2$⊂6** (thermal ellipsoids drawn at 40% probability; hydrogen atoms, nitrate counterions, and a cocrystallized methanol molecule omitted for clarity). The complete binuclear complex is shown in the Supporting Information.

Copper(II) Complex of 6. An attempt to prepare the copper(II) complex of **6** was made by reacting the ligand with copper(II) nitrate in methanol. Instead of a mononuclear complex, dark blue crystals of a binuclear complex, [Cu(**6**-H)Cu(NO$_3$)$_2$.MeOH]NO$_3$·MeOH (**Cu$_2$⊂6**), were obtained when diethyl ether was diffused into a methanol solution of the complex. The infrared spectrum of the complex **Cu$_2$⊂6** showed bands at ca. 1610, 1573, and 1440 cm^{-1}, which can be ascribed to the ν(*C*═N) and ν(*C*═C) stretching frequencies of the 2-pyridylmethyl pendant arms. A thermal ellipsoid plot of the crystal structure of the complex is presented in Figure 3, along with the atomic numbering scheme (see Supporting Information for selected interatomic and hydrogen bonding parameters, and a further figure showing **Cu$_2$⊂6**).

The crystal structure of **Cu$_2$⊂6** reveals that the ligand accommodates two copper(II) ions at a distance of 5.404 Å. However, the formation of a similar binuclear complex is not expected under radiolabeling conditions, where extremely low concentrations of copper ions are added. Of interest to this project is the binding mode of the bioconjugate **8** to the ^{64}Cu radiolabel. Figure 3 highlights the single copper center that has its coordination sphere fully encapsulated by the TACN bioconjugate (**8**). Cu(1) is coordinated facially to three nitrogen atoms of the TACN ring [N(1), N(2), N(3)] with an average Cu−N bond distance of 2.133(4) Å. Two pyridine nitrogen atoms and one oxygen atom from the acetate pendant arm are also involved in the coordination of Cu(1). With the long equatorial bond length (2.381 Å) between the oxygen atom of the acetate and the Cu(II) center, one might consider this center to be in a pseudo-octahedral geometry. The Cu−N$_{pyridine}$ bond distances of the complex fall in the range of those reported for the Cu(II) complexes of pyridyl-containing ligands, (Cu−N$_{pyridine}$ = 2.04–2.06 Å) (*59*). The Cu−N$_{pyridine}$ distances are shorter than Cu−N$_{amine}$ distances due to the better Cu(II) coordination properties of the pyridyl nitrogens. The coordination of TACN was as expected, with, for example, the axial Cu−N$_{TACN}$ distance longer than the others (*59*), viz., the Cu(1)−N(2) distance of 2.204(4) Å is significantly longer than the remaining

Scheme 2. Preparation of 7[a]

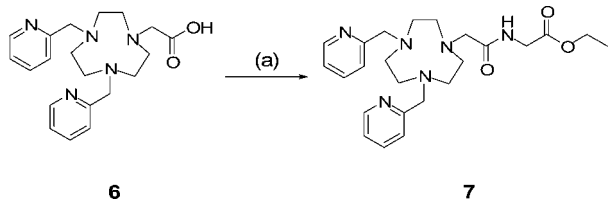

6 **7**

[a] (a) HBTU, DIPEA, glycine ethyl ester·HCl, CH_3CN, r.t., o/n, 40%.

Cu−N interactions, which range from 2.174(4) Å [N(1)] to 2.016(4) Å [N(5)]. The two rings incorporating the pyridine rings are puckered, as seen in the values of the Cu(1)/N(2)/C(9)/C(10) and Cu(1)/N(3)/C(15)/C(16) torsion angles of −42.79 (1)° and −34.10 (1)°, respectively. The second copper(II) center, (Cu(2)), resides in a distorted octahedral geometry (see figure in Supporting Information). The coordination sites are occupied by an oxygen atom from a terminally coordinating methanol molecule, oxygen atoms from two chelating nitrates, and an oxygen from the carboxylate group of **6**. The two axial bonds Cu(2)−O(5N) and Cu(2)−O(2N) of 2.437 and 2.565 Å are very long, and the coordination interaction may be considered weak, hence resulting in a Cu-centered square-planar structure, with weak axial interactions.

Preparation of Bioconjugates 7 and 8. In order to demonstrate that ligand **6** could be coupled to a peptide, a preliminary experiment was conducted to couple **6** to a simple amino acid, glycine ethyl ester hydrochloride, applying standard peptide coupling conditions. Ethyl 2-{2-[4,7-bis(2-pyridylmethyl)-1,4,7-triazacyclononan-1-yl]acetamido}acetate (**7**) was successfully isolated in 40% yield after purification by column chromatography on basic alumina (Scheme 2).

The formation of **7** was confirmed by ESI-MS, with a peak at $m/z = 455.3$ corresponding to $[M + H]^+$. ^1H NMR spectroscopy in $CDCl_3$ showed additional signals corresponding to the amino acid, a triplet at 7.02 ppm due to the amide N*H* proton, a quartet at 4.12 ppm for the protons of the ethyl CH_2 next to the terminal CH_3 group, a doublet at 4.02 ppm for the protons of the glycine CH_2 next to the amide, a singlet peak at 3.54 ppm for the protons of the CH_2 acetate, and a triplet at 1.19 ppm for the terminal CH_3. As was found for compound **6**, two doublets were observed at 3.87 and 3.98 ppm (with a geminal coupling constant of 15.3 Hz) and assigned to the methylene protons of the pyridyl pendant arm. In this case, a possible explanation for the nonequivalence of the methylene protons could be that free rotation around the pyridyl pendant arm is restricted, perhaps as a result of hydrogen-bonding interactions involving the amide-containing pendant.

The bioconjugate **8** (Figure 1) was synthesized by coupling the BN analogue βAla-βAla-Gln-Tpr-Ala-Val-Gly His-Cha-Nle-NH_2 (B1) to **6** in relatively good yield (60%). Similar experimental conditions to those used for the synthesis of **7** were employed. Compound **8** was purified by semipreparative HPLC and its purity checked by analytical HPLC. The presence of **8** was confirmed by ESI-MS, with peaks at 728, 739, 1456, and 1478 corresponding, respectively, to $[M + 2H]^{2+}$, $[M + H + Na]^{2+}$, $[M + H]^+$, and $[M + Na]^+$.

Labeling. To minimize cost, the majority of labeling studies were carried out on the copper complex of **6** rather than that of **8**. Nonetheless, the results obtained with the model compound **6** are representative of those expected for **8**. The first test performed was determination of the lowest concentration of **6** needed to obtain full complexation of $^{64}CuCl_2$ (200 kBq in 10 μL 0.1 M NH_4OAc) to form **^{64}Cu⊂6**. Following shaking of the solution obtained by mixing **6** and $^{64}CuCl_2$ for 10 min, the degree of complexation was monitored by TLC and HPLC. A ligand concentration $>10^{-4}$ M was found to be necessary to obtain complete copper complexation. At a ligand concentration of approximately 10^{-5} M, 10% of free Cu^{2+} ions were still present in solution after 10 min. The rate of copper(II) complexation with **6** was found to be very fast in ammonium acetate buffer solution (*60*) at ambient temperature, viz., the TACN derivative **6** (10^{-4} M) was successfully labeled with ^{64}Cu within 1 min in quantitative yield.

Table 1. Partition Coefficients (log $D_{o/w}$) of the ^{64}Cu Complexes of 6 and 8 at Different pHs

pH	log $D_{o/w}$ (^{64}Cu⊂6)	log $D_{o/w}$ (^{64}Cu⊂8)
7.2	−2.43	−2.39
7.4	−2.45	−2.38
7.8	−2.43	−2.36

Lipophilicity. Information about the lipophilicity of the copper complex **^{64}Cu⊂6** and the bioconjugate **^{64}Cu⊂8** was obtained by measuring their partitioning in a 1-octanol/water system. The partition coefficients (log $D_{o/w}$) were measured at different pH in buffered solution. The results are summarized in Table 1. The copper complexes of both the ligand **6** and the bioconjugate **8** are hydrophilic. This indicates that they should be predestined to show rapid blood clearance and preferential renal excretion. Interestingly, the log $D_{o/w}$ values of the **^{64}Cu⊂8** complex remain unchanged in the pH range investigated, indicating that the protonation state of the peptide does not influence the value of log $D_{o/w}$.

***In Vitro* Stability.** Competition experiments in the presence of the cyclam macrocycle, a ligand that forms one of the most stable Cu(II) complexes known (*14*), were undertaken to check the stability of the ^{64}Cu complexes. **^{64}Cu⊂6** and **^{64}Cu⊂8** were exposed to more than a 100-fold excess of cyclam. No transchelation was observed after 24 h, using HPLC as the detection system [t_R = 4.4 min (**Cu⊂6**), t_R = 5.3 min (**Cu⊂cyclam**), t_R = 19.2 min (**Cu⊂8**), HPLC system 1; see Experimental Section]. The *in vitro* stability of **^{64}Cu⊂6** and **^{64}Cu⊂8** was also assessed in a rat plasma medium after 2 and 24 h. The **^{64}Cu⊂6** complex remained unchanged. In the case of **^{64}Cu⊂8**, after 2 h, another small peak was detected. It was found that this peak was not due to free copper in solution, resulting from dissociation of copper(II) ions from the chelate complex, but instead arose from cleavage of the peptide of **^{64}Cu⊂8**, presumably brought about by the action of peptidases.

Competition experiments were also performed in the presence of SOD (Cu/Zn superoxide dismutase). SOD is a 32 kDa enzyme that is distributed in the cytosol of eukaryotic cells and is particularly abundant in liver, kidney, and red blood cells. This enzyme plays a key role as a copper-binding protein (*28, 30*). Ligand **6** was labeled with ^{64}Cu and spiked with a 1000-fold excess of SOD. After 24 h, the stability of the **^{64}Cu⊂6** complex ($R_f = 1$) was checked via TLC. We could not detect the presence of **^{64}Cu⊂SOD** ($R_f = 0$), which was synthesized for comparison as previously described (*28*). Thus, the absence of protein-bound radioactivity indicates no transchelation of copper(II). Overall, the results of the competition studies showed that both **^{64}Cu⊂6** and **^{64}Cu⊂8** are very stable. This finding is in accordance with our preliminary potentiometric measurements, which indicate that the stability constant for the copper complex is $>10^{25}$ M^{-1}.

***In Vivo* Stability.** The metabolic stability of **^{64}Cu⊂8** was determined in arterial blood samples taken at 1, 3, 5, 10, 20, 30, and 60 min after a single intravenous application of the radiotracer in a rat. The blood samples were centrifuged to obtain the plasma and then treated with acetonitrile to precipitate the proteins. The obtained supernatant was referred to as the plasma extract. The mean relative activity in the plasma was 89 ± 8% of arterial blood activity; the activity of the plasma extract samples contained 66 ± 13% of the plasma activity. The plasma extract was analyzed by RP-HPLC for radiometabolites (Figure

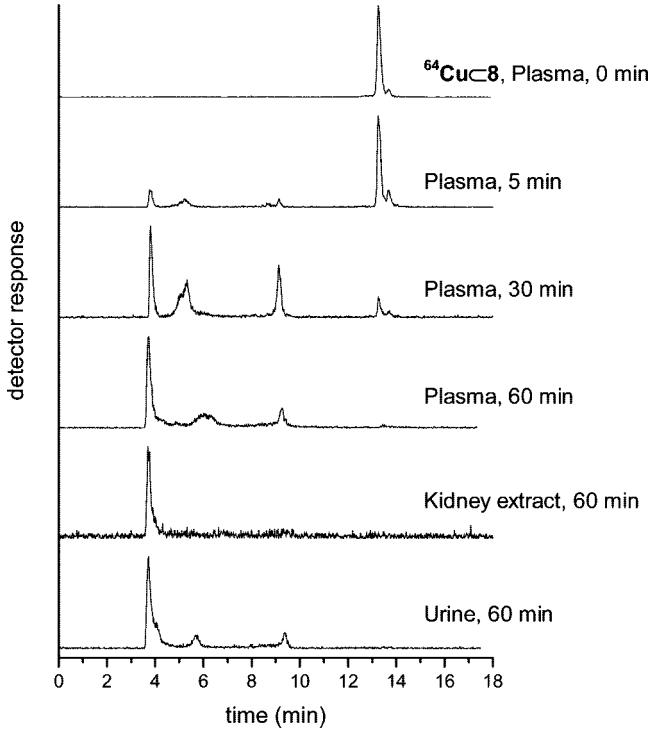

Figure 4. Examples of radiochromatograms (HPLC system 3) of **^{64}Cu⊂8** and rat plasma extract, kidney extract, and urine at various time points after single intravenous application of **^{64}Cu⊂8**.

4). The relative amount of the original compound **^{64}Cu⊂8** (t_R = 12.9 min) decreased from 93% at the time of tracer application (1 min 77%, 3 min 60%, 5 min 50%, 10 min 31%, 20 min 14%, 30 min 6%) to 3% of the total plasma extract activity after one hour (Figure 4). **^{64}Cu⊂8** was converted into three more hydrophilic radiolabeled compounds (t_R = 3.7, 5.3, 9.1 min). The peak at 3.7 min was not caused by $^{64}Cu^{2+}$ since it was eluted at 3.4 min. The residual activity in the kidney extract resulted from only one hydrophilic species (t_R = 3.7 min). The activity of the urine was caused by the same three species detected in the plasma extract. The original compound **^{64}Cu⊂8** could not be detected in the kidney extract or urine. This extensive metabolism of the compound could be species-specific for the rat.

Biodistribution Studies. A summary of the biodistribution and elimination data for the bombesin conjugate **^{64}Cu⊂8**, **^{64}Cu⊂6**, and $^{64}CuCl_2$ in rats is shown in Figures 5 and 6. The values of %ID, %ID/g, and SUV (ID = injected dose; SUV = standardized uptake value) are summarized in the Supporting Information. The SUV was used to normalize the biodistribution data and calculated as followed: SUV = tissue activity concentration (Bq/g) × body weight (g)/injected activity (Bq) (injected and tissue activity were decay-corrected). A high uptake of **^{64}Cu⊂8** was observed in the GRPR-expressing pancreas (5.8 ± 0.7 [SUV] at 5 min after injection, and 3.9 ± 0.3 [SUV] after 1 h). After one hour, the activity concentration was highest in the pancreas of all the organs examined. In contrast to these findings, the activity concentration in the pancreas after injection of **^{64}Cu⊂6** and $^{64}CuCl_2$ was very low, and roughly comparable to the blood activity uptake. The **^{64}Cu⊂8** had a rapid blood clearance, with 2.0 ± 0.3 (SUV) in the circulation at 5 min, followed by a further decrease to 0.23 ± 0.04 (SUV) at 1 h. Liver uptake reached 6.3 ± 0.7% ID at 5 min and declined to 3.7 ± 0.3% ID one hour after injection. The activity detected in the intestine attained 5.3 ± 0.4% ID at 5 min and 9.9 ± 2.4% ID after one hour. In the kidneys, the activity attained 5.3 ± 0.5% ID at 5 min and decreased to 1.6 ± 0.1% ID at one hour. Most activity was eliminated into the urine (13 ± 7% ID at 5 min and 57 ± 4% ID at 1 h). A very similar activity distribution and excretion pattern was observed

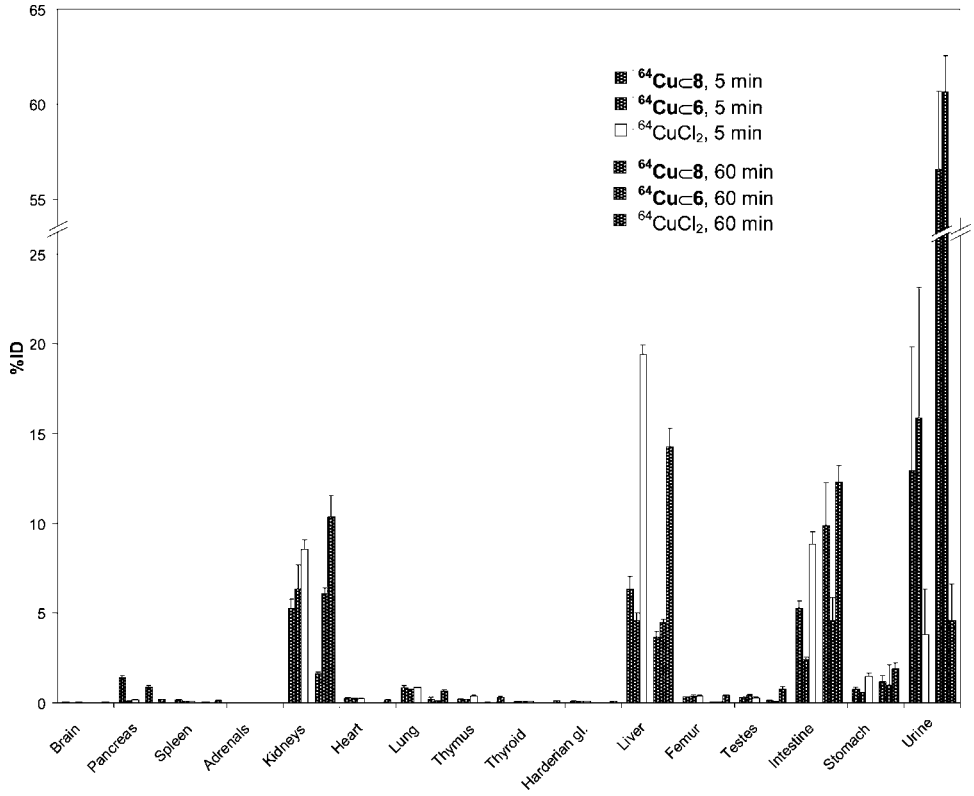

Figure 5. Biodistribution of **^{64}Cu⊂8**, **^{64}Cu⊂6**, and $^{64}CuCl_2$ in male Wistar rats 5 and 60 min after single intravenous application represented as %ID mean ± SD (4 animals per time point). (%ID, %ID/g, and SUV data are given in the Supporting Information).

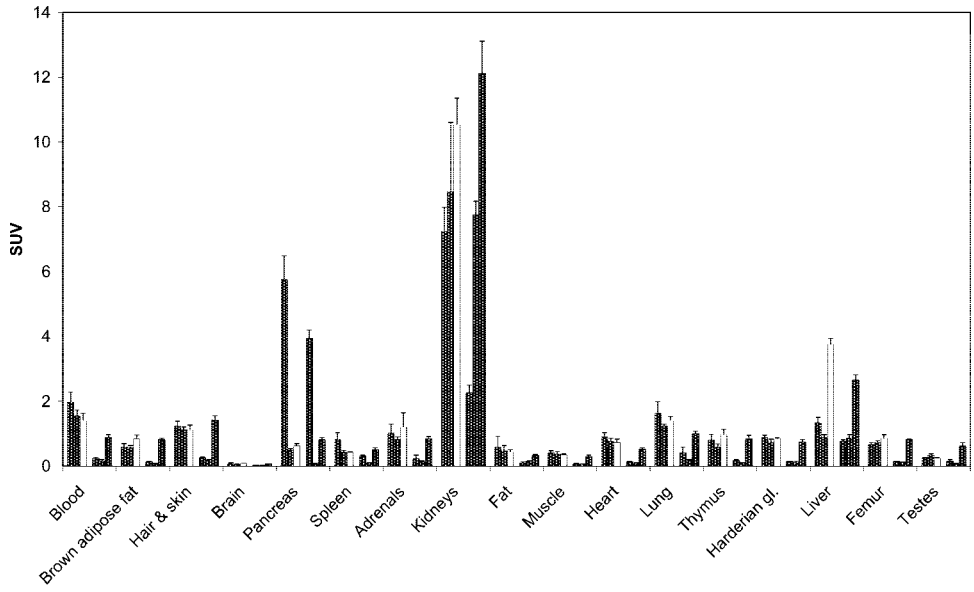

Figure 6. Biodistribution of **^{64}Cu⊂8**, **^{64}Cu⊂6**, and $^{64}CuCl_2$ in male Wistar rats 5 and 60 min after single intravenous application, represented as SUV mean ± SD (4 animals per time point). (%ID, %ID/g, and SUV data are given in the Supporting Information).

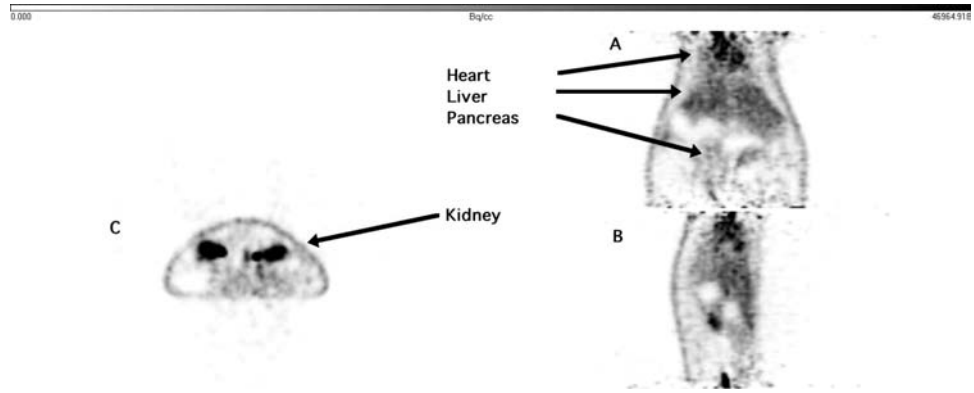

Figure 7. Small animal coronal (A), sagittal (B), and transversal (C) PET images of rat 60 min after single intravenous application of **^{64}Cu⊂8** into a rat tail vein.

after injection of **^{64}Cu⊂6**, which exemplifies the strong influence of the novel ^{64}Cu-TACN chelate to the biodistribution of its bombesin conjugate. In contrast, the activity distribution of $^{64}CuCl_2$ was distinctively different and characterized by a high liver uptake and a very low renal clearance. From the different biodistribution characteristics, it can be deduced that there was only marginal, or no, *in vivo* demetalation of the **^{64}Cu⊂6** unit.

The remarkable kidney uptake of **^{64}Cu⊂8** in comparison to the relatively low liver accumulation is also demonstrated by the small PET images (Figure 7) (note that the pancreas is hard to see due to its proximity to the duodenum of the small intestine).

A variety of radiolabeled bombesin derivatives, or analogues, containing the BN(8–14) sequence have been described in the literature, which show varying pharmacokinetic behavior depending on the radiolabeling approach taken, the spacer between the radiometal chelate, and the peptide N-terminus, and the specific modifications made to the peptide sequence. Since peptides are rapidly metabolized; bombesin derivatives with increased stability toward peptidases have been designed to tackle shortcomings, such as the intermediate or low target uptakes, and high liver and/or kidney uptakes, observed for most of the radiolabeled bombesin conjugates reported so far. Stabilized radiometal-labeled bombesin derivatives include [DPhe^6,βAla^{12},Nle^{14}]BN(6–14) (*61*),[Cha^{13}]BN(7–14) (*49,50,61*), [Nle^{14}]BN(7–14) (*49,50,61,62*),[Cha^{13},Nle^{14}]BN(7–14) (*49,50*), [Pro^1, Tyr^4]BN (*40*), [Pro^1, Tyr^4, Nle^{14}]BN (*62*), [DPhe^6, Leu-NHEt^{13}, des-Met^{14}]BN(6–14) (*63, 64*), and [DTyr^6, βAla^{11}, Thi^{13}, Nle^{14}]BN(6–14) (*64–66*), with the N-terminus conjugated to the radiometal complexes mainly via spacers. The bombesin used in the present work was selected from a study on ^{99m}Tc-tricarbonyl labeled bombesin derivatives in which the radiotracer ^{99m}Tc-BBS-38 was found to show an improved target/nontarget ratio due to the spacer βAla-βAla that stabilized BN(7–14) via Cha^{13} and Nle^{14} (*49, 50*).

The uptake level of **^{64}Cu⊂8** in the pancreas at 1 h p.i. was roughly comparable to the values for ^{99m}Tc-BBS-38 at 1.5 h p.i. The uptake of **^{64}Cu⊂8** in the kidneys and the lungs was significantly higher compared to ^{99m}Tc-BBS-38. The rapid decrease of activity accumulation in the kidneys and the increasing activity in the urine suggest a predominant renal clearance pathway for **^{64}Cu⊂8**, in contrast to the dominant hepatobiliary elimination of ^{99m}Tc-BBS-38 (*49*). The pancreatic uptake of **^{64}Cu⊂8** at 1 h p.i. was roughly in the same range as that described for ^{64}Cu-labeled DOTA bombesin conjugates studied in mice (*41, 42, 44–48*). ^{64}Cu-labeled DOTA-PEG-BN(7–14) (*41*), DOTA-X-BN(7–14) (X = spacer containing 4, 5, 6, 8, or 12 carbon atoms) (*43–46, 48*) and DOTA-X-BN(7–14) (X = Gly-Gly-Gly, Gly-Ser-Gly, or Gly-Ser-Ser) (*47*) resulted in a relatively high liver uptake, which was higher, or nearly the same, as the activity uptake into the kidneys. In contrast, **^{64}Cu⊂8** exhibited a lower uptake in the liver compared to the kidneys. ^{64}Cu-DOTA-[Lys^3]BN (*42, 43*), ^{64}Cu-DOTA-

[Pro[1], Tyr[4]]BN (*40*), ^{64}Cu-CB-TE2A-8-Aoc-BN(7–14) (*46*), and ^{64}Cu-NOTA-8-Aoc-BN(7–14) (*48*) were characterized by a predominant renal excretion pathway comparable to **^{64}Cu⊂8**, which showed an even lower liver uptake than ^{64}Cu-DOTA-[Lys[3]]BN (*42*, *43*) at 21 h p.i.

CONCLUSION

An efficient synthetic strategy has been developed for the preparation of a new TACN derivative, 2-[4,7-bis(2-pyridylmethyl)-1,4,7-triazacyclononan-1-yl]acetic acid (**6**), containing two pyridine pendant arms as well as a carboxylic group for coupling to biomolecules. The X-ray structure of a copper complex of **6** confirmed that the ligand is capable of multidentate coordination to a Cu^{2+} ion. Conjugation of glycine ethyl ester and the bombesin analogue βAla-βAla-[Cha[13], Nle[14]]BN(7–14) to **6** was successfully achieved via amide coupling. Both ligand **6** and the bombesin bioconjugate **8** can readily form radiocopper complexes, **^{64}Cu⊂6** and **^{64}Cu⊂8**, with high stability. *In vitro* ligand competition experiments and stability studies in rat plasma medium gave no evidence of transchelation or demetalation. The ^{64}Cu complexes of **6** and **8** are relatively hydrophilic (log $D_{o/w} < -2.3$). Biodistribution studies of the bombesin conjugate **^{64}Cu⊂8** revealed an accumulation of the compound in the GRPR-expressing pancreas that is roughly comparable to the same bombesin analogue labeled with ^{99m}Tc (^{99m}Tc-BBS-38) (*49*). The bombesin conjugate **^{64}Cu⊂8** showed an extensive renal clearance of the activity, in contrast to ^{99m}Tc-BBS-38 or other BN(7–14) analogues labeled via ^{64}Cu-DOTA (*41*, *43–48*). The ^{64}Cu-TACN unit had a dominating influence on the nonspecific activity biodistribution, since the distribution data of **^{64}Cu⊂6** were very similar to that of **^{64}Cu⊂8**. Comparison with biodistribution data for $^{64}CuCl_2$ indicated that there was only marginal, if any, *in vivo* copper demetalation. The specificity of binding to the GRPR, as well as tumor uptake, will be evaluated in further experiments, and results will be reported in due course.

Our radiopharmacological data support the potential of **^{64}Cu⊂8** for GRPR imaging and indicate that the chelating agent **6** may be an attractive candidate for developing new copper radiopharmaceuticals because it may be efficiently labeled under mild conditions (ambient temperature, aqueous solution) and exhibits fast renal clearance.

ACKNOWLEDGMENT

This work was supported by the Swiss National Science Foundation and the Australian Research Council (ARC) through the Australian Centre for Electromaterials Science (ACES). G.G. was the recipient of a Swiss Fellowship for Prospective Researchers Grant (PBNE2-106771) and acknowledges financial support by the Forschungszentrum Dresden-Rossendorf during his stay in Germany. The authors thank Karin Landrock and Andrea Suhr for excellent technical assistance, and Christina Hultsch for MALDI-TOF measurements.

Supporting Information Available: Crystallographic data for **Cu_2⊂6** is provided in cif format. Figure S1 shows the binuclear structure of **Cu_2⊂6**. Tables of selected bond distances and angles for **Cu2⊂6**, of hydrogen bonds for **Cu2⊂6** and of biodistribution of **^{64}Cu⊂8**, **^{64}Cu⊂6**, and $^{64}CuCl_2$ in rats (mean ± SD of 4 animals per group) after single intravenous application in a tail vein (data in %ID, %ID/g, and SUV) are presented. This material is available free of charge via the Internet at http://pubs.acs.org.

LITERATURE CITED

(1) Blower, P. J., Lewis, J. S., and Zweit, J. (1996) Copper radionuclides and radiopharmaceuticals in nuclear medicine. *Nucl. Med. Biol. 23*, 957–980.

(2) Parker, D. (1996) Imaging and Targeting. *Comprehensive Supramolecular Chemistry* (Atwood, J. L., Davis, J. E. D., MacNicol, D. P., Vögtle, F., and Lehn, J.-M., Eds.) pp 487–536, Pergamon, London.

(3) Anderson, C. J., Green, M. A., and Fujibayashi, Y. (2003) Chemistry of Copper Radionuclides and Radiopharmaceutical Products. *Handbook of Radiopharmaceuticals. Radiochemistry and Applications* (Welch, M. J., and Redvanly, C. S., Eds.) pp 400–422, J. Wiley & Sons, Chichester.

(4) Lever, S. Z., Lydon, J. D., Cutler, C. S., and Jurisson, S. S. (2004) Radioactive Metals in Imaging and Therapy. *Comprehensive Coordination Chemistry II* (McCleverty, J. A., and Meyer, T. J., Eds.) pp 883–911, Elsevier-Pergamon.

(5) Williams, H. A., Robinson, S., Julyan, P., Zweit, J., and Hastings, D. (2005) A comparison of PET imaging characteristics of various copper radioisotopes. *Eur. J. Nucl. Med. Mol. Imaging 32*, 1473–1480.

(6) Anderson, C. J., and Welch, M. J. (1999) *Chem. Rev. 99*, 2219–2234.

(7) Volkert, W. A., and Hoffman, T. J. (1999) Therapeutic Radiopharmaceuticals. *Chem. Rev. 99*, 2269–2292.

(8) Smith, S. V. (2004) Molecular imaging with copper-64. *J. Inorg. Biochem. 98*, 1874–1901, and references therein.

(9) Novak-Hofer, I., and Schubiger, P. A. (2002) Copper-67 as a therapeutic nuclide for radioimmunotherapy. *Eur. J. Nucl. Med. 29*, 821–830.

(10) Ma, D., Lu, F., Overstreet, T., Milenic, D. E., and Brechbiel, M. W. (2002) Novel chelating agents for potential clinical applications of copper. *Nucl. Med. Biol. 29*, 91–105, and references therein.

(11) Hnatowitch, D. J., Layne, W. W., Childs, R. L., Lanteigne, D., and Davis, M. A. (1983) Radioactive labeling of antibody: a simple and efficient method. *Science 220*, 613–615.

(12) Meares, C. F., McCall, M. J., Reardan, D. T., Goodwin, D. A., Diamanti, C. I., and McTigue, M. (1984) Conjugation of antibodies with bifunctional chelating agents: isothiocyanate and bromoacetamide reagents, methods of analysis, and subsequent addition of metal ions. *Anal. Biochem. 142*, 68–78.

(13) Moi, M. K., Meares, C. F., McCall, M. J., Cole, W. C., and DeNardo, S. J. (1985) Copper chelates as probes of biological systems: stable copper complexes with a macrocyclic bifunctional chelating agent. *Anal. Biochem. 148*, 249–253.

(14) Parker, D. (1990) Tumour targeting with radiolabelled macrocycle-antibody conjugates. *Chem. Soc. Rev. 19*, 271–291.

(15) Lukes, I., Kotek, J., Vojtisek, P., and Hermann, P. (2001) Complexes of tetraazacycles bearing methylphosphinic/phosphonic acid pendant arms with copper(II), zinc(II) and lanthanides(III). A comparison with their acetic acid analogues. *Coord. Chem. Rev. 216–217*, 287–312.

(16) Bernhardt, P. V., and Sharpe, P. C. (2000) C-substituted macrocycles as candidates for radioimmunotherapy. *Inorg. Chem. 39*, 4123–4129.

(17) Sun, X., Wuest, J. D., Kovacs, Z., Sherry, A. D., Motekaitis, R., Wang, Z., Martell, A. E., Welch, M. J., and Anderson, C. J. (2003) *In vivo* behavior of copper-64-labeled methanephosphonate tetraaza macrocyclic ligands. *J. Biol. Inorg. Chem. 8*, 217–225.

(18) Tsukube, H., Yamashita, K., Iwachido, T., and Zenki, M. (1991) Sodium-selective macrocyclic polyamine carriers having pyridine-functionalized sidearms. *J. Chem. Soc., Perkin Trans. 1*, 1661–1665.

(19) Sun, Y., Martell, A. E., Reibenspies, J. H., and Welch, M. J. (1991) Syntheses of multidentate ligands containing hydroxypyridyl donor groups. *Tetrahedron 47*, 357–364.

(20) Gateau, C., Mazzanti, M., Pecaut, J., Dunand, F. A., and Helm, L. (2003) Solid-state and solution properties of the lanthanide complexes of a new nonadentate tripodal ligand derived from 1,4,7-triazacyclononane. *Dalton Trans. 12*, 2428–2433.

(21) Bowen, T., and Planalp, R. P., and W., B. M. (1996) An improved synthesis of cis,cis-1,3,5-triaminocyclohexane Synthesis of novel hexadentate ligand derivatives for the preparation

of gallium radiopharmaceuticals. *Biorg. Med. Chem. Lett. 6*, 807–810.

(22) Park, G., Przyborowska, A. M., Ye, N., Tsoupas, N., Bauer, C. B., Broker, G. A., Rogers, R. D., W., B. M., and Planalp, R. P. (2003) Steric effects caused by N-alkylation of the tripodal chelator N,N′,N″-tris(2-pyridylmethyl)-cis,cis-1,3,5-triaminocyclohexane (tachpyr): structural and electronic properties of the Mn(II), Co(II), Ni(II), Cu(II) and Zn(II) complexes. *Dalton Trans.* 318–324.

(23) Anderson, C. J., Connett, J. M., Schwarz, S. W., P. A., R., Guo, L. W., Phillpott, G. W., Zinn, K. R., Meares, C. F., and Welch, M. J. (1992) Copper-64-labeled antibodies for PET imaging. *J. Nucl. Med. 33*, 1685–1690.

(24) Cole, W. C., DeNardo, S. J., Meares, C. F., McCall, M. J., DeNardo, G. L., Epstein, A. L., H.A., O. B., and Moi, M. K. (1986) Serum stability of copper-67 chelates: comparison with indium-111 and cobalt-57. *Nucl. Med. Biol. 13*, 363–368.

(25) Cole, W. C., DeNardo, S. J., Meares, C. F., McCall, M. J., DeNardo, G. L., Epstein, A. L., and O'Brien, H. A., and M. K., M. (1987) Comparative serum stability of radiochelates for antibody radiopharmaceuticals. *J. Nucl. Med. 28*, 83–90.

(26) Rogers, B. E., Anderson, C. J., Connett, J. M., Guo, L. W., Edwards, W. B., Sherman, E. L. C., Zinn, K. R., and Welch, M. J. (1996) Comparison of four bifunctional chelates for radiolabeling monoclonal antibodies with copper radioisotopes: biodistribution and metabolism. *Bioconjugate Chem. 7*, 511–522.

(27) Anderson, C. J., Dehdashti, F., Cutler, P. D., Schwarz, S. W., Laforest, R., Bass, L. A., Lewis, J. S., and McCarthy, D. W. (2001) ^{64}Cu-TETA-octreotide as a PET imaging agent for patients with neuroendocrine tumors. *J. Nucl. Med. 42*, 213–221.

(28) Bass, L. A., Wang, M., Welch, M. J., and Anderson, C. J. (2000) *In vivo* transchelation of copper-64 from teta-octreotide to superoxide dismutase in rat liver. *Bioconjugate Chem. 11*, 527–533.

(29) Sun, X., Wuest, J. D., Weisman, G. R., Wong, E. H., Reed, D. P., Boswell, C. A., Motekaitis, R., Martell, A. E., Welch, M. J., and Anderson, C. J. (2002) Radiolabeling and *in vivo* behavior of copper-64-lavelled cross-bridged cyclam ligands. *J. Med. Chem. 45*, 469–477.

(30) Boswell, C. A., Sun, X., Niu, W. J., Weisman, G. R., Wong, E. H., Rheingold, A. L., and Anderson, C. J. (2004) Comparative *in vivo* stability of copper-64-labeled cross-bridged and conventional tetraazamacrocyclic complexes. *J. Med. Chem. 47*, 1465–1474.

(31) Woodin, K. S., Heroux, K. J., Boswell, C. A., Wong, E. H., Weisman, G. R., Niu, W. J., Tomellini, S. A., Anderson, C. J., Zakharov, L. N., and Rheingold, A. L. (2005) Kinetic inertness and electrochemical behavior of copper(II) tetraazamacrocyclic complexes: Possible implications for in vivo stability. *Eur. J. Inorg. Chem.* 4829–4833.

(32) Anderson, C. J., Wadas, T. J., Wong, E. H., and Weisman, G. R. (2006) Development of chelators for Cu-64 radiopharmaceuticals: Optimizing for *in vivo* stability. *Technecium, Rhenium and other Metals in Chemistry and Nuclear Medicine* (Mazzi, U., Ed.) pp 215–218, SGE Editoriali, Padova, Italy.

(33) Comba, P., Kerscher, M., and Schieck, W. (2007) Bispidine coordination chemistry. *Prog. Inorg. Chem. 55*, 613–704.

(34) Stephan, H., Juran, S., Walther, M., Steinbach, J., Born, K., and Comba, P. (2006) Synthesis, characterization and evaluation of novel chelating agents for copper radionuclides. *Technecium, Rhenium and other Metal in Chemistry and Nuclear Medicine* (Mazzi, U., Ed.) pp 219–222, SGE Editoriali, Padova, Italy.

(35) Chaudhuri, P., and Wieghardt, K. (1987) The chemistry of 1,4,7-triazacyclononane and related tridentate macrocyclic compounds. *Prog. Inorg. Chem. 35*, 329–436.

(36) Chong, H., Torti, S. V., Torti, F. M., and W, B. M. (2002) Synthesis of 1,3,5-cis,cis Triaminocyclo-hexane N-Pyridyl-Derivatives as Potential Antitumor Agents. *J. Org. Chem. 67*, 8072–8078.

(37) Reubi, J. C. (2003) Peptide receptors as molecular targets for cancer diagnosis and therapy. *Endocrine Rev. 24*, 389–427.

(38) Smith, C. J., Volkert, W. A., and Hoffman, T. J. (2005) Radiolabeled peptide conjugates for targeting of the bombesin receptor superfamily subtypes. *Nucl. Med. Biol. 32*, 733–740.

(39) Maina, T., Nock, B., and Mather, S. (2006) Targeting prostate cancer with radiolabelled bombesins. *Cancer Imaging 6*, 153–157.

(40) Biddlecombe, G. B., Rogers, B. E., de Visser, M., Parry, J. J., de Jong, M., Erion, J. L., and Lewis, J. S. (2007) Molecular imaging of gastrin-releasing peptide receptor-positive tumors in mice using 64Cu- and 86Y-DOTA-(Pro1,Tyr4)-bombesin(1–14). *Bioconjugate Chem. 18*, 724–730.

(41) Rogers, B. E., Della Manna, D., and Safavy, A. (2004) *in vitro* and *in vivo* evaluation of a ^{64}Cu-labeled polyethylene glycol-bombesin conjugate. *Cancer Biother. Radiopharm. 19*, 25–34.

(42) Chen, X., Park, R., Hou, Y., Tohme, M., Shahinian, A. H., Bading, J. R., and Conti, P. S. (2004) MicroPET and autoradiographic imaging of GRP receptor expression with ^{64}Cu-DOTA-[Lys^3]bombesin in human prostate adenocarcinoma xenografts. *J. Nucl. Med. 45*, 1390–1397.

(43) Yang, Y.-S., Zhang, X., Xiong, Z., and Chen, X. (2006) Comparative *in vitro* and in vivo evaluation of two ^{64}Cu-labeled bombesin analogs in a mouse model of human prostate adenocarcinoma. *Nucl. Med. Biol. 33*, 371–380.

(44) Rogers, B. E., Bigott, H. M., McCarthy, D. W., Della Manna, D., Kim, J., Sharp, T. L., and Welch, M. J. (2003) MicroPET imaging of a gastrin-releasing peptide receptor-positive tumor in a mouse model of human prostate cancer using a ^{64}Cu-labeled bombesin analogue. *Bioconjugate Chem. 14*, 756–763.

(45) Parry, J. J., Andrews, R., and Rogers, B. E. (2007) MicroPET imaging of breast cancer using radiolabeled bombesin analogs targeting the gastrin-releasing peptide receptor. *Breast Cancer Res.Treat. 101*, 175–183.

(46) Garrison, J. C., Rold, T. L., Sieckman, G., Figueroa, S. D., Volkert, W. A., Jurisson, S. S., and Hoffman, T. J. (2007) *In vivo* evaluation and small-animal PET/DT of a prostate cancer mouse model using ^{64}Cu bombesin analogs: side-by-side comparison of the CB-TE2A and DOTA chelations systems. *J. Nucl. Med. 48*, 1327–1337.

(47) Parry, J. J., Kelly, T. S., Andrews, R., and Rogers, B. E. (2007) *In vitro* and *in vivo* evaluation of ^{64}Cu-labeled DOTA-linker-bombesin(7–14) analogues containing different amino acids linker moieties. *Bioconjugate Chem. 18*, 1110–1117.

(48) Prasanphanich, A. F., Nanda, P. K., Rold, T. L., Ma, L.-J., Lewis, M. R., Garrison, J. C., Hoffman, T. J., Sieckman, G., Figueroa, S. D., and Smith, C. J. (2007) [^{64}Cu-NOTA-8-Aoc-BBN(7–14)NH$_2$] targeting vector for positron-emission tomography imaging of gastrin-releasing peptide receptor-expressing tissues. *Proc. Natl. Acad. Sci. U.S.A 104*, 12462–12467.

(49) García Garayoa, E., Rüegg, D., Bläuenstein, P., Zwimpfer, M., Khan, I. U., Maes, V., Blanc, A., Beck-Sickinger, A. G., Tourwé, D. A., and Schubiger, P. A. (2007) Chemical and biological characterization of new Re(CO)$_3$/[^{99m}Tc](CO)$_3$ bombesin analogues. *Nucl. Med. Biol. 34*, 17–28.

(50) García Garayoa, E., Schweinsberg, C., Maes, V., Rüegg, D, Blanc, A., Bläuenstein, P., Tourwé, D. A., Beck-Sickinger, A. G., and Schubiger, P. A. (2007) New [^{99m}Tc]bombesin analogues with improved biodistribution for targeting gastrin releasing-peptide receptor-positive tumors. *Q. J. Nucl. Med. Mol. Imaging 51*, 42–50.

(51) Szelecsényi, F., Blessing, G., and Qaim, S. M. (1993) Excitation functions of proton induced nuclear reactions on enriched ^{62}Ni and ^{64}Ni: Possibility of production of no-carrier-added ^{62}Cu and ^{64}Cu at a small cyclotron. *Appl. Radiat. Isot. 44*, 575–580.

(52) McCarthy, D. W., Shefer, R. E., Klinkowstein, R. E., Bass, L. A., Margeneau, W. H., Cutler, C. S., Anderson, C. J., and W.J., W. (1997) Efficient production of high specific activity ^{64}Cu using a biomedical cyclotron. *Nucl. Med. Biol. 24*, 35–43.

(53) Atkins, T. J. (1980) Tricyclic trisaminomethanes. *J. Am. Chem. Soc. 102*, 6364–6365.
(54) Erhardt, J. M., Grover, E. R., and Wuest, J. D. (1980) Transfer of hydrogen from orthoamides. Synthesis, structure, and reactions of hexahydro-6bH-2a,4a,6a-triazacyclopenta[cd]pentalene and perhydro-3a,6a,9a-triazaphenalene. *J. Am. Chem. Soc. 102*, 6365–6369.
(55) Sheldrick, G. M. (1997)SHELXS97; Program for crystal structure solution. University of Göttingen, Göttingen, Germany.
(56) Sheldrick, G. M. (1997)SHELXL97; Program for crystal structure refinement. University of Göttingen, Göttingen, Germany.
(57) Mc Lachlan, G. A., Fallon, G. D., Martin, R. L., Moubaraki, B., Murray, K. S., and Spiccia, L. (1994) *Inorg. Chem. 33*, 4663.
(58) Blake, A. J., Fallis, I. A., Parsons, S., Ross, S. A., and Schröder, M. (1996) Asymmetric functionalization of aza macrocycles. Syntheses, crystal structures and electrochemistry of [Ni(Bz[9]aneN3)2][PF6]2 and [Pd(Bz[9]aneN3)2][PF6]2.2MeCN (Bz[9]aneN3 = 1-benzyl-1,4,7-triazacyclononane). *J. Chem. Soc., Dalton Trans. 4*, 525–532.
(59) Karlin, K. D., Hayes, J. C., Juen, S., Hutchinson, J. P., and Zubieta, J. (1982) Tetragonal vs. trigonal coordination in copper(II) complexes with tripod ligands: structures and properties of $[Cu(C_{21}H_{24}N_4)Cl]PF_6$ and $[Cu(C_{18}H_{18}N_4)Cl]PF_6$. *Inorg. Chem. 21*, 4106–4108.
(60) Morphy, J. R., Parker, D., Kataky, R., Eaton, M. A. W., Millican, A. T., Alexander, R., Harrison, A., and Walker, C. (1990) Towards tumour targeting with copper-radiolabelled macrocycle-antibody conjugates: synthesis, antibody linkage, and complexation behaviour. *Chem. Soc., Perkin Trans. 2*, 573–585.
(61) Bläuenstein, P., García-Garayoa, E. G., Rüegg, D., Blanc, A., D., T., Beck-Sickinger, A., and Schubiger, P. A. (2004) Improving the tumor uptake of ^{99m}Tc-labeled neuropeptides using stabilized peptide analogues. *Cancer. Biother. Radiopharm. 19*, 181–188.
(62) Nock, B. A., Nikolopoulou, A., Galanis, A., Cordopatis, P., Waser, B., Reubi, J.-C., and Maina, T. (2005) Potent bombesin-like peptides for GRP-receptor targeting of tumors with ^{99m}Tc: A preclinical study. *J. Med. Chem. 48*, 100–110.
(63) Nock, B., Nikolopoulou, A., Chiotellis, E., Loudos, G., Maintas, D., Reubi, J. C., and Maina, T. (2003) [^{99m}Tc]Demobesin 1, a novel potent bombesin analogue for GRP receptor-targeted tumour imaging. *Eur. J. Nucl. Med. 30*, 247–258.
(64) Maina, T., Nock, B. A., Zhang, H., Nikolopoulou, A., Waser, B., Reubi, J.-C., and Maecke, H. R. (2005) Species differences of bombesin analog interactions with GRP-R define the choice of animal models in the development of GRP-R-targeting drugs. *J. Nucl. Med. 46*, 823–830.
(65) Zhang, H., Chen, J., Waldherr, C., Hinni, K., Waser, B., Reubi, J. C., and Maecke, H. R. (2004) Synthesis and evaluation of bombesin derivatives on the basis of pan-bombesin peptides labeled with indium-111, lutetium-177, and yttrium-90 for targeting bombesin receptor-expressing tumors. *Cancer Res. 64*, 6707–6715.
(66) Dimitrakopoulou-Strauss, A., Hohenberger, P., Haberkorn, U., Mäcke, H. R., Eisenhut, M., and Strauss, L. G. (2007) ^{68}Ga-labeled bombesin studies in patients with gastrointestinal stromal tumors: comparison with ^{18}F-FDG. *J. Nucl. Med. 48*, 1245–1250.

BC700396E

Genetic Engineering, Expression, and Activity of a Chimeric Monoclonal Antibody−Avidin Fusion Protein for Receptor-Mediated Delivery of Biotinylated Drugs in Humans

Ruben J. Boado,[†] Yufeng Zhang,[†] Yun Zhang,[†] Chun-fang Xia,[‡] Yuntao Wang,[‡] and William M. Pardridge*[,‡]

ArmaGen Technologies, Inc., Santa Monica, California 90401, and Department of Medicine, University of California Los Angeles, Los Angeles, California 90024. Received November 2, 2007; Revised Manuscript Received January 7, 2008

The genetic engineering, expression, and validation of a fusion protein of avidin (AV) and a chimeric monoclonal antibody (mAb) to the human insulin receptor (HIR) is described. The 15 kDa avidin monomer was fused to the carboxyl terminus of the heavy chain of the HIRMAb. The fusion protein heavy chain reacted with antibodies specific for human IgG and avidin, and had the same affinity for binding to the HIR extracellular domain as the original chimeric HIRMAb. The fusion protein qualitatively bound biotinylated ligands, but was secreted fully saturated with biotin by COS cells, owing to the high level of biotin in tissue culture medium. Chinese hamster ovary (CHO) cells were permanently transfected with a tandem vector expressing the fusion protein genes, and high expressing cell lines were isolated by methotrexate amplification and dilutional cloning. The product expressed by CHO cells had high binding to the HIR, and migrated as a homogeneous species in size exclusion HPLC and native polyacrylamide gel electrophoresis. The CHO cells were adapted to a 4 week culture in biotin depleted medium, and the HIRMAb-AV fusion protein expressed under these conditions had 1 unoccupied biotin binding site per molecule, based on a [^{3}H]-biotin ultrafiltration assay. The HIRMAb-AV increased biotin uptake by human cells >15-fold, and mediated the endocytosis of fluorescein-biotin, as demonstrated by confocal microscopy. In summary, the HIRMAb-AV fusion protein is a new drug targeting system for humans that can be adapted to monobiotinylated drugs or nucleic acids.

INTRODUCTION

Molecular Trojan horses are genetically engineered receptor-specific monoclonal antibodies (mAb) that undergo receptor-mediated transport through biological membranes, including the blood-brain barrier (BBB) in vivo (*1*). Chimeric and humanized mAb's to the human insulin receptor (HIR) have been genetically engineered, expressed, and shown to have transport properties in vivo comparable to the original murine HIRMAb (*2*). The chimeric or humanized HIRMAb can target to brain, and other organs, recombinant proteins and monoclonal antibodies, and fusion proteins of the HIRMAb and recombinant neurotrophins, single chain Fv antibodies, and lysosomal enzymes have been produced and validated in vivo (*3–5*). However, the fusion protein technology cannot be used to deliver oligopeptides or short interfering RNA (siRNA), because fusion proteins of the HIRMAb and the oligopeptide or siRNA cannot be engineered.

Avidin–biotin technology, in conjunction with the fusion protein technology, can enable the in vivo targeting of peptides and siRNAs. In this approach, a fusion protein of the HIRMAb and avidin is genetically engineered in parallel with the production of a monobiotinylated peptide or siRNA. Recent work shows that siRNAs can be monobiotinylated on either the 5′- or 3′-terminus of the sense strand, and conjugated to streptavidin (SA)-mAb delivery systems without loss of gene siliencing biological activity (*6*). In prior work (*6*), the targeting mAb and the recombinant SA were conjugated with a thioether bond, as described previously (*7*). However, for manufacturing of human therapeutics, what is needed is a eukaryotic expression system for the production of mAb-avidin fusion proteins. Avidin is preferred over SA, because avidin is less immunogenic in humans than is SA (*8*). Previous investigations have demonstrated the feasibility of genetically engineering mAb-avidin fusion proteins, using a murine mAb to the rat transferrin receptor (TfR) (*9*). However, the HIRMAb delivery system is more active than is the TfRMAb delivery system (*1*).

The purpose of the present investigation is to examine the feasibility of the genetic engineering and eukaryotic expression of a fusion protein of avidin and the chimeric HIRMAb, which is designated HIRMAb-AV. The avidin monomer is fused to the carboxyl terminus of the HIRMAb heavy chain constant region (Figure 1). It is assumed that a HIRMAb-avidin (AV) fusion protein that is expressed in eukaryotic expression systems, such as Chinese hamster ovary (CHO) cells, would be fully saturated by the endogenous biotin present in the culture medium, and that this saturation of the fusion protein by the endogenous biotin would effectively eliminate the biotin binding activity of the fusion protein. Once biotin is bound to avidin, it does not readily dissociate off the protein. The dissociation constant (K_D) of avidin binding of biotin is 10^{-15} M, and the dissociation $t_{1/2}$ is 89 days (*10*). Therefore, the present studies examine the feasibility of production of mAb-avidin fusion proteins by CHO cells cultured in biotin-depleted medium.

MATERIALS AND METHODS

Cloning of Avidin cDNA. Avidin cDNA (GenBank X05343) corresponding to amino acids Ala^1-Glu^{128} of the mature chicken avidin protein was cloned by the polymerase chain reaction (PCR) using the oligodexoynucleotides (ODNs) described in Table 1 and an avidin plasmid DNA template. The avidin cDNA was cloned by PCR using 40 ng plasmid cDNA, 0.2 μM avidin

* Correspondence: Dr. William M. Pardridge, UCLA Warren Hall 13-164, 900 Veteran Ave., Los Angeles, CA 90024, Ph: (310) 825-8858, Fax: (310) 206-5163, Email: wpardridge@mednet.ucla.edu.

[†] ArmaGen Technologies, Inc.

[‡] University of California Los Angeles.

10.1021/bc7004076 CCC: $40.75 © 2008 American Chemical Society
Published on Web 02/16/2008

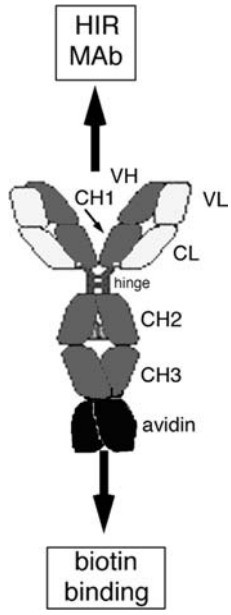

Figure 1. Structure of the fusion protein showing fusion of the amino terminus of the mature avidin monomer to the carboxyl terminus of the CH_3 region of the heavy chain of the chimeric HIRMAb. The fusion protein is a bifunctional molecule with dual functions. The fusion protein binds the HIR, at the BBB, to mediate transport into the brain, and binds biotinylated pharmaceuticals.

Table 1. Oligodeoxynucleotides Primers Used in the Cloning of Avdin cDNA

1) Avidin FWD: 5′-phosphate-CGTCTGCCAGAAAGTGCTCGCTGAC-3′
2) Avidin REV: 5′-phosphate-TCACTCCTTCTGTGTGCGCAGGCGA-3′

forward and reverse ODN primers (Table 1), 0.2 mM deoxynucleosidetriphosphates, and 2.5 U PfuUltra DNA polymerase (Stratagene, San Diego, CA) in a 50 μL Pfu buffer (Stratagene). The amplification was performed in a Mastercycler temperature cycler (Eppendorf, Hamburg, Germany) with an initial denaturing step of 95 °C for 2 min followed by 30 cycles of denaturing at 95 °C for 30 s, annealing at 55 °C for 30 s and amplification at 72 °C for 1 min; followed by a final incubation at 72 °C for 10 min. PCR products were resolved in 0.8% agarose gel electrophoresis, and the expected major single band of ~0.4 kb corresponding to the avidin cDNA was produced (Figure 2).

Engineering of HIRMAb-Avidin Expression Vectors. The ODNs used for PCR are 5′-phosphorylated for direct insertion into the *Hpa*I site of either the pHIRMAb-HC expression plasmid or the pHIRMAb tandem vector (TV) expression plasmid, respectively (Figure 3A,B), as described previously (*3*). The pHIRMAb-HC plasmid encodes the HC of the chimeric HIRMAb, and dual transfection of COS cells with this plasmid and a light chain (LC) expression plasmid, pHIRMAb-LC,

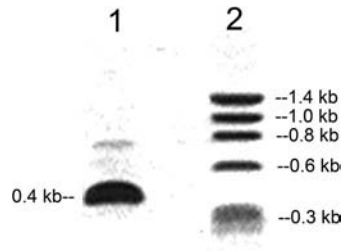

Figure 2. Ethidium bromide stain of agarose gel of avidin cDNA (lane 1), which was produced by PCR with avidin-specific ODN primers (Table 1). Lane 2: molecular weight DNA standards.

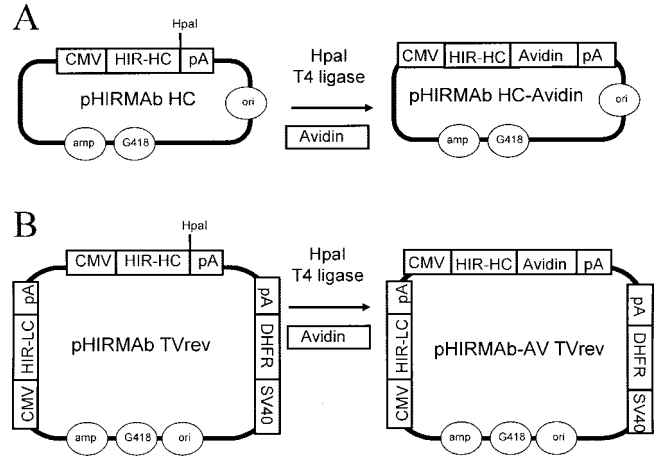

Figure 3. Engineering of the expression plasmid encoding the HIRMAb-AV fusion protein for either COS cells (A) or CHO cells (B). The PCR generated avidin cDNA was ligated into the single *Hpa*I site of either the universal pHIRMAb-HC plasmid (A) or the pHIRMAb tandem vector (B) to form the pHIRMAb-HC-Avidin vector or the pHIRMAb-AV TVrev, respectively. The pHIRMAb-HC plasmid encodes the heavy chain (HC) of the chimeric HIRMAb, and is 5′-flanked by the CMV promoter and is 3′-flanked by the BGH polyA (pA) sequence. The universal pHIRMAb-HC tandem vector (TV) contains expression cassettes, in series, for the HC and LC of the chimeric HIRMAb, and contains the expression cassette for murine DHFR in either forward (for) or reverse (rev) orientation relative to the HC and LC cassettes. In the pHIRMAb-AV TV rev, the DHFR cDNA is 5′-flanked by the hepatitis B virus pA sequence, and is 3′-flanked by the SV40 promoter.

allows for transient expression of either the chimeric HIRMAb, or a fusion protein, in COS cells. The pHIRMAb TV is a tandem vector (TV), which contains multiple genes, each within separate tandem expression cassettes, on a single piece of DNA, and includes the HC expression cassette, the LC expression cassette, and an expression cassette for the murine dihydrofolate reductase (DHFR) gene for amplification of cell lines with methotrexate (MTX). If the DHFR cassette is in the same forward (for) orientation as the HC and LC cassettes, then the TV is designated TVfor; if the DHFR cassette is in reverse (rev) orientation, then the TV is designated TVrev. The TV is engineered for permanent transfection of host cells, such as DG44 Chinese hamster ovary (CHO) cells. Placement of the HC fusion gene, the LC gene, and the genes encoding the selectable markers on a single piece of tandem vector DNA allows for isolation of a high expressing CHO line where the HC fusion gene and LC gene are equally expressed within the host cell. The selectable markers on the TV include the neomycin resistance gene (neo), for selection with G418, and the DHFR gene, for amplification of cell lines with MTX (Figure 3).

The forward avidin PCR primer introduces "CG" nucleotides to maintain the open reading frame and to introduce a Ser-Ser-Ser linker between the carboxyl terminus of the CH3 region of the HIRMAb HC and the amino terminus of the avidin, respectively. The fusion of the avidin monomer to the carboxyl terminus of each HC is depicted in Figure 1. This design sterically restricts the avidin to a dimeric configuration, which replicates the native conformation of avidin, which is a dimer of dimers (*11*). The avidin reverse PCR primer introduces a stop codon, "TGA", immediately after the terminal Glu of the mature avidin protein.

The HIRMAb HC and LC cDNA expression cassettes are driven by the cytomegalovirus (CMV) promoter and contain the bovine growth hormone (BGH) polyadenylation (pA) sequence (Figure 3). The DHFR expression cassette is under the influence of the SV40 promoter and the hepatitis B virus

pA sequence. The engineering of universal pHIRMAb-HC and the pHIRMAb TV vectors was performed by insertion of a single *Hpa*I site at the end of the HIRMAb HC CH3 open reading frame (orf) by site directed mutagenesis (SDM), as described previously (*3*).

Transient Expression of HIRMAb-Avidin Fusion Protein in COS Cells. COS cells were dual transfected with pHIRMAb-LC and pHIRMAb-HC-Avidin, or monotransfected with the pHIRMAb-AV tandem vector, using Lipofectamine 2000, with a ratio of 1:2.5, ug DNA/uL Lipofectamine. Following transfection, the cells were cultured in serum free VP-SFM (Invitrogen, Carlsbad, CA). The conditioned serum free medium was collected at 3 and 7 days. The fusion protein was purified by protein A affinity chromatography.

Permanent Expression of HIRMAb-AV Fusion Protein in Stably Transfected CHO Cells. Serum free medium (SFM) adapted DG44 CHO cells (Invitrogen) were electroporated with 5 ug pHIRMAb-AV TVfor or pHIRMAb-AV TVrev, following linearization with PvuI, using a Gene Pulser Xcell electroporator (BioRad, Hercules, CA). 5×10^6 cells were electroporated with the DNA in 200 uL of phosphate buffered saline (PBS) and 0.2 cm cuvettes using a square wave and 160 V. Cells were suspended in CHO serum free medium (SFM) (Hyclone, Logan, UT) and plated in 4 × 96-well plates. Selection of stable transfectants began 2 days following electroporation with 0.54 mg/mL G418. Aliquots of supernatant were taken for human IgG ELISA when colonies of transfectants were evident, i.e., 21 days. Positive clones were isolated and cultured individually for further characterization. DG44 cells lack endogenous DHFR, and rely on nutrients, hypoxanthine and thymidine (HT) for endogenous folate synthesis. Transfected cells carrying the TV express the exogenous DHFR. Transfected cell lines were further selected by placement in HT-deficient medium. Lines with amplification around the transgene insertion site were selected by subjecting the cells to increasing concentrations of MTX, starting at 20 nM MTX. Following stabilization of the cell line at 80 nM MTX, high producing clones were isolated by limited dilution cloning (DC) at 1 cell per well; a total of 4000 wells were plated at each round of DC, and medium IgG was measured with a human IgG ELISA using a high volume microplate dispenser and a microplate washer (Biotek, Winooski, VT).

SDS-PAGE and Western blotting. The purity of protein A purified fusion protein produced by COS or CHO cells was evaluated with a reducing 12% sodium dodecyl sulfate polyacrylamide gel electrophoresis (SDS-PAGE). Immunoreactivity was tested with a primary rabbit antibody to chicken egg white avidin (Abcam, Cambridge, MA) or a primary goat antiserum against human IgG heavy and light chains (Vector Laboratories, Burlingame, CA).

HIR Receptor Assay. The affinity of the fusion protein for the HIR extracellular domain (ECD) was determined with an ELISA using the lectin affinity purified HIR ECD. CHO cells permanently transfected with the HIR ECD were grown in serum free media (SFM), and the HIR ECD was purified with a wheat germ agglutinin affinity column, as previously described (*12*). The HIR ECD (0.2 ug/well) was plated on Nunc-Maxisorb 96 well dishes and the binding of the chimeric HIRMAb, the HIRMAb-AV fusion protein, or human IgG1 to the HIR ECD was detected with a biotinylated goat antihuman IgG (H+L) antibody (0.3 ug/well), and the ABC Elite detection system (Vector Laboratories). The concentration that caused 50% binding to the HIR ECD, the ED50, was determined by nonlinear regression analysis using the *WinNonlin* software.

Biotinylated BSA ELISA. The qualitative binding of the HIRMAb-AV fusion protein to a biotinylated ligand was assessed with an ELISA using biotinylated bovine serum albumin (BSA, Sigma Chemical Co., St. Louis, MO) as the ligand. The biotinylated BSA was plated to a 96-well ELISA plate (0.4 ug/well). Following aspiration, washing with HBS buffer with 0.05% Tween-20, where HBS = 0.01 M HEPES/0.15 M NaCl/pH = 7.4, and blocking with 2% goat serum in HBS, the HIRMAb-AV fusion protein or the chimeric HIRMAb was added in concentrations ranging from 0 to 3000 ng/mL for 90 min at room termperature. Detection of binding used a alkaline phosphatase conjugate of a goat antihuman kappa light chain antibody and *p*-nitrophenylphosphate.

Table 2. Concentration of HIRMAb-AV in Medium Following Transient Expression in COS Cells[a]

plasmid	IgG at 3 days (μg/mL)	IgG at 7 days (μg/mL)
pHIRMAb HC-avidin + pHIRMAb LC	4.7 ± 0.2	10.7 ± 2.2
pHIRMAb-AV TV-for	1.0 ± 0.2	4.7 ± 1.3
pHIRMAb-AV TV-rev	6.2 ± 0.2	7.8 ± 0.3

[a] Data are mean ± SE (n = 3).

[^{3}H]-Biotin Binding Ultrafiltration Assay. The quantitative binding of biotin to the HIRMAb-AV fusion protein was determined with an ultrafiltration assay, as described previously (*7*). The assay used [^{3}H]-biotin (Perkin-Elmer, Boston, MA), which had a specific activity of 50 uCi/nmol, and an Ultrafree-MC filter unit (Millipore, Billerica, MA), which has a low protein binding regenerated cellulose filter with a 10 kDa molecular weight cutoff. A 100 uL volume of PBS (0.01 M Na_2HPO_4/0.15 M NaCl/pH = 7.4) was added to a microfuge tube (MFT), which contained 0.1 uCi/mL of ^{3}H-biotin (2 nM), various concentrations of unlabeled biotin (25–1000 nM), and a fixed concentration of either avidin (5 ug/mL, 80 nM) or the HIRMAb-AV fusion protein (15 ug/mL, 80 nM). After a 30 min incubation at room temperature, the solution was transferred to the Ultrafree-MC ultrafiltration unit, which was placed in a 1.5 mL MFT, and the unit was centrifuged at 10 000 *g* for 5 min at room temperature. The total biotin binding was determined from the total biotin concentration and the percent binding of the [^{3}H]-biotin, which was determined by sampling the ultrafiltrate for ^{3}H radioactivity using a Perkin-Elmer liquid scintillation counter. The number of biotin binding sites per protein was determined from the ratio of the bound biotin concentration relative to the concentration of the avidin or the HIRMAb-AV fusion protein.

Equilibrium Dialysis of HIRMAb-AV Fusion Protein. The protein A affinity purified HIRMAb-AV fusion protein produced by transfected COS cells was fully saturated by the biotin in the VP-SFM tissue culture medium. The biotin concentration in this medium, 0.75 ug/mL (3100 nM), is in a 55-fold molar excess when the concentration of the HIRMAb-AV fusion protein is 10 ug/mL (Table 2). Therefore, the biotin binding sites on the expressed HIRMAb-AV fusion protein are fully saturated, which would prevent the use of the fusion protein for the drug delivery of biotinylated therapeutics. In an attempt to dissociate the biotin from the HIRMAb-AV fusion protein, the protein was subjected to extensive equilibrium dialysis, using an avidin sequestration technique. The HIRMAb-AV fusion protein was placed in a 1 mL Slide-A-Lyzer dialysis cassette with a 7 kDa molecular weight cutoff (Pierce Chemical Co., Rockford, IL), which was placed in 10 L of PBS, which contained 2 mg/L of avidin and 0.05% sodium azide, and dialysis was performed at 4 °C for 72 h, with a complete change of the 10L dialysis buffer at 36 h. The presence of high concentrations of avidin in the dialysis buffer was intended to sequester in the buffer any biotin that dissociated from the HIRMAb-AV fusion protein during the 72 h. The dialyzed HIRMAb-AV fusion protein was then recovered, and the binding of [^{3}H]-biotin was measured.

Culture of CHO Cells During Biotin Starvation. The CHO cells producing the HIRMAb-AV fusion protein were cultured in HyQ SFM4CHO-utility medium from Hyclone (Logan, UT), which contains 0.194 ug/mL (800 nM) of biotin. The medium biotin is present in a 14-fold molar ratio when the medium HIRMAb-AV fusion protein is 10 mg/L, and it would not be possible to produce fusion protein with unoccupied biotin binding sites. Therefore, the CHO cells were subjected to biotin starvation over a 27 day period. On day 1, CHO cells were centrifuged and resuspended in 25 mL fresh biotin-free serum free medium (SFM), which was supplemented with 20 nM biotin, which is a 40-fold reduction from the usual medium biotin concentration. The cells were cultured in square plastic (polyethylene terephthalate G copolyester, PETG) bottles (Nalge Nunc International, Rochester, NY), on an Innova 200 orbital shaker (New Brunswick Scientific (Edison, NJ) at 120 rpm, which was placed inside a humidified tissue culture incubator at 37 °C, and the cells continued to divide. Fresh SFM with 20 nM biotin was added on days 2 and 4 until the volume of medium was 135 mL. On day 8, fresh medium was added to a total volume of 400 mL and the biotin concentration was reduced to 10 nM. Over the next 18 days, the volume of medium was maintained at 400 mL (135 mL in each of 3 × 500 mL plastic square bottles). During this time, 1500 mL of conditioned medium was harvested from the 3 bottles, and the bottles were replenished with 1500 mL fresh biotin free SFM, so that the medium biotin concentration was successively reduced to 3 nM at day 14, to 1 nM at day 18, to 0.3 nM at day 21, and the culture was terminated at day 26.

HPLC Size Exclusion Chromatography. The presence of aggregates of the HIRMAb-AV fusion protein was evaluated with size exclusion chromatography (SEC) using a 7.8 mm × 30 cm (5 μm) G3000SW high pressure liquid chromatography (HPLC) column (Tosoh Bioscience LLC, Montgomeryville, PA), and a Perkin-Elmer Series 200 pump and UV/vis detector. The HIRMAb-AV fusion protein (100 ug), produced by CHO cells under conditions of biotin starvation, and purified by protein A affinity chromatography, was injected on to the column in a 200 uL volume of PBS, followed by elution in PBS at a flow rate of 0.5 mL/min with detection at 280 nm. The elution profile was recorded with a Servocorder model SR6253 chart recorder (Datamark Corp., Costa Mesa, CA), at 0.5 cm/min, and the chart paper was scanned with a UMAX PowerLook III scanner (Techville, Inc., Dallas, TX) into Adobe Photoshop.

Native Polyacrylamide Gel Electrophoresis. The ability of the HIRMAb-AV fusion protein to migrate into a native polyacrylamide gel was evaluated with native PAGE, using a 15% Ready Gel Tris-HCl Gel (Biorad, Richmond, CA), which was composed of a 8.6 × 6.8 cm 15% resolving gel and a 4% stacking gel. The HIRMAb-AV fusion protein, the chimeric HIRMAb, or human IgG1 was prepared in sample buffer (3 mM histidine, 3 mM MES, pH = 6.1, 30% glycerol), and 5 ug protein per lane was applied, where MES is 2-(*N*-morpholino)-ethanesulfonic acid. The electrophoresis buffer was 30 mM histidine, 30 mM MES, pH = 6.1, and electrophoresis was performed at 150 V for 4 h. Since the HIRMAb-AV fusion protein is cationic with a predicted isoelectric point (pI) of 9.02 (Results), the electrophoresis was performed with reversed electrode polarity. Following electrophoresis, the gel was stained with Coomasie blue, and photographed.

Biotin Uptake Assay. Human renal 293 epithelial cells were obtained from the American type Culture Collection (Rockville, MD), and grown on collagen coated 24-well dishes in DMEM medium with 10% fetal bovine serum. Prior to the uptake assay, the medium was discarded, and 0.4 mL/well of 0.01 M Tris/0.15 M NaCl/pH = 7.4 (TBS) was added, which contained 0.5 uCi/mL (11 nM) of [^{3}H]-biotin (Perkin-Elmer NET721) and either 0 or 5 ug/mL (26 nM) of the HIRMAb-AV fusion protein. After incubation for 2–120 min at 37 °C in a humidified chamber, the incubation was terminated by aspiration of the medium, washing of the wells with cold TBS, and the cell monolayer was solubilized in 0.5 mL/well of 1 N NaOH, followed by determination of ^{3}H radioactivity in the cell lysate and the medium. The cell protein was measured by the bicinchoninic acid (BCA) assay. The ^{3}H-biotin volume of distribution (VD) was determined from the ratio of DPM/mg protein divided by the DPM/uL medium.

Confocal Microscopy. The 293 cells were plated on collagen coated 4-well microscopy slides (Biocoat, Becton Dickinson Labware). Prior to the incubation, the medium was aspirated and replaced with 0.5 mL/well of fresh DMEM, containing 100 nM fluorescein-biotin (Invitrogen B-1370), and either 0 or 60 ug/mL of the HIRMAb-AV fusion protein. The cells were incubated at 37 °C for either 3 or 24 h. Following incubation, the medium was aspirated, the wells were washed well with cold PBS and fixed in 100% methanol for 20 min at −20 °C. The fixative was removed, the cells were washed with cold PBS, the nuclei were stained by incubation in 0.3 ug/mL propidium iodide (Sigma) for 5 min, the wells were washed with PBS, and coverslipped with Vectashield (Vector Laboratories, Burlingame, CA). Confocal microscopy was performed with a Zeiss LSM 5 PASCAL confocal microscope with dual argon and helium/neon lasers equipped with Zeiss LSM software for image reconstruction.

RESULTS

DNA sequencing of the expression cassette of the pHIRMAb-Avidin heavy chain expression plasmid (Figure 3A) encompassed 2,874 nucleotides (nt), including a 714 CMV promoter, a 9 nt Kozak sequence (GCCGCCACC), a 1782 nt coding sequence, and a 369 nt BGH transcription termination sequence. The deduced amino acid sequence showed the heavy chain fusion protein was comprised of 593 amino acids (AA), including a 19 AA signal peptide, a 443 AA chimeric HIRMAb heavy chain, a 3 AA linker (Ser-Ser-Ser), and a 128 AA avidin monomer, which was 100% identical to the AA sequence of avidin, NP_990651 (GenBank). The avidin sequence included a single N-linked glycosylation sequence, and a single internal disulfide bond. The predicted molecular weight of the fusion protein heavy chain, without glycosylation, is 63,191 Da with a pI of 9.02. The pHIRMAb-Avidin expression cassette was used for transient transfection of COS cells as described below. The fusion protein heavy chain (HC) expression cassette, the chimeric HIRMAb light chain (LC) expression cassette, and the DHFR expression cassette were all incorporated into a single tandem vector (TV), designated pHIRMAb-AV TVrev, as shown in Figure 3B; the reverse (rev) designation indicates the orientation of the DHFR cassette was in reverse direction, relative to the HC or LC expression cassettes. DNA sequence analysis showed the 3 expression cassettes were composed of 6332 nt, in the following order: a 731 nt CMV promoter, a 9 nt Kozak sequence, a 705 nt LC open reading frame (orf), a 291 nt BGH sequence, a 23 nt spacer, a 714 CMV promoter, a 9 nt Kozak sequence, a 1782 nt HC orf, a 301 nt BGH sequence, a 940 nt hepatitis B virus (HBV) transcription termination sequence, a 564 nt murine DHFR orf, a 9 nt Kozak sequence, and a 254 nt SV40 promoter. The murine DHFR sequence was 100% identical to nt 857–1510 of NM_010049. The predicted molecular weight of the LC was 23 398 Da with a pI of 5.45.

Dual transfection of COS cells with the pHIRMAb-HC-Avidin plasmid and the chimeric HIRMAb LC expression plasmid, pHIRMAb-LC, resulted in medium levels of fusion protein of the HIRMAb-AV fusion protein of 4.7 ± 0.2 μg/mL

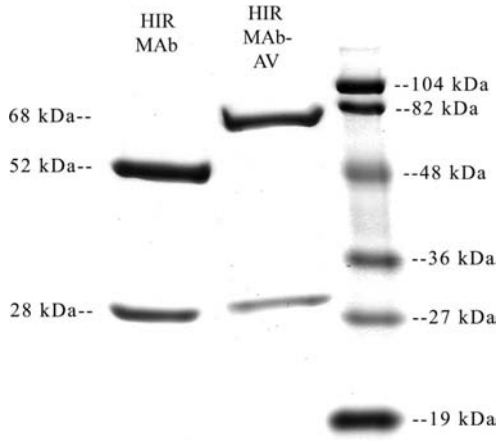

Figure 4. Reducing sodium dodecyl sulfate polyacrylamide gel electrophoresis (SDS-PAGE) of chimeric HIRMAb and the HIRMAb-AV fusion protein. The size of the light chain, 28 kDa, is identical for the chimeric HIRMAb and the fusion protein; the size of the heavy chain of fusion protein is about 16 kDa larger than the chimeric HIRMAb heavy chain, owing to the presence of the avidin monomer. The molecular weights shown for the standards are the actual molecular weights, whereas the molecular weights of the HIRMAb and HIRMAb-AV fusion protein are estimated.

and 10.7 ± 2.2 μg/mL at 3 and 7 days after transfection, respectively. These levels of medium IgG exceed those obtained following transient transfection of COS cells with the chimeric HIRMAb HC and LC genes. COS cells were also lipofected with the CHO cell tandem vectors, pHIRMAb-AV TVfor and pHIRMAb-AV TVrev, which are outlined in Figure 3B. The medium concentrations of the HIRMAb-AV fusion protein with the pHIRMAb-AV TV rev were comparable to that found with dual transfection with the separate HC and LC expression plasmids (Table 2). Lower levels of transient expression were observed with the pHIRMAb AV TVfor (Table 2).

The HIRMAb-AV fusion protein secreted to the serum free medium by transfected COS cells was purified with protein A affinity chromatography. The fusion protein was purified to homogeneity on reduced SDS-PAGE (Figure 4). The HIRMAb-AV fusion protein and the chimeric HIRMAb share the same light chain (LC) (Figure 4), whereas the size of the heavy chain (HC) of the HIRMAb-AV fusion protein is approximately 15 kDa larger than the size of the HC of the chimeric HIRMAb (Figure 4). Western blotting of the purified HIRMAb-AV fusion protein and chimeric HIRMAb was performed with primary antibodies to either human IgG (Figure 5A) or to avidin (Figure 5B). The antihuman IgG antibody reacts with both the HC and the LC of the HIRMAb-AV fusion protein and the chimeric HIRMAb, but not with avidin (AV), and the size of the immunoreactive HC is about 15 kDa larger for the HIRMAb-AV HC as compared to the HIRMAb HC (Figure 5A). The antiavidin antibody reacts with both avidin and the HC of the HIRMAb-AV fusion protein, but not with LC of the HIRMAb-AV fusion protein or chimeric HIRMAb, and the size of the immunoreactive HC is about 15 kDa larger for the HIRMAb-AV HC as compared to the HIRMAb HC (Figure 5B).

The affinity of the HIRMAb-AV fusion protein for the HIR ECD was determined with a binding assay, in parallel with measurements of the binding of the chimeric HIRMAb and human IgG1 (Figure 6). The concentration of chimeric HIRMAb that produced 50% saturation of binding, the ED_{50}, was 0.50 ± 0.06 nM, and the ED_{50} of the COS-cell derived HIRMAb-AV fusion protein was 1.13 ± 0.20 nM; human IgG1 did not bind to the HIR ECD (Figure 6).

An ELISA using biotinylated BSA as the ligand is outlined in Figure 7A. The HIRMAb-AV fusion protein, but not the

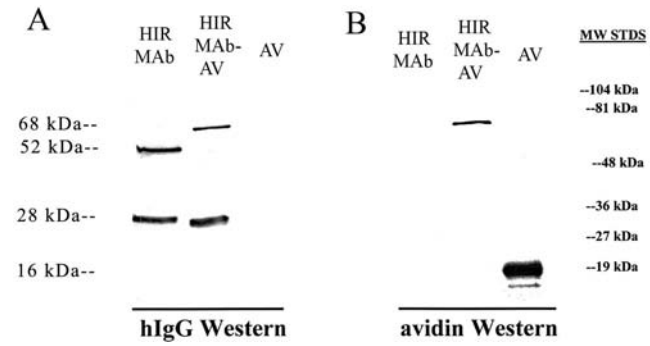

Figure 5. (A) Western blot with antihuman IgG primary antibody. The size of the heavy chain of the fusion protein and the chimeric HIRMAb is 68 kDa and 52 kDa, respectively, and the size of the light chain for either the fusion protein or the chimeric HIRMAb is 28 kDa. (B) Western blot with antiavidin antibody, which reacts with either fusion protein or avidin, but not with chimeric HIRMAb. MW standards (STDS) are shown on the right side. The molecular weights (MW) shown for the standards (STDS) are the actual molecular weights, whereas the molecular weights of the HIRMAb and HIRMAb-AV fusion protein are estimated.

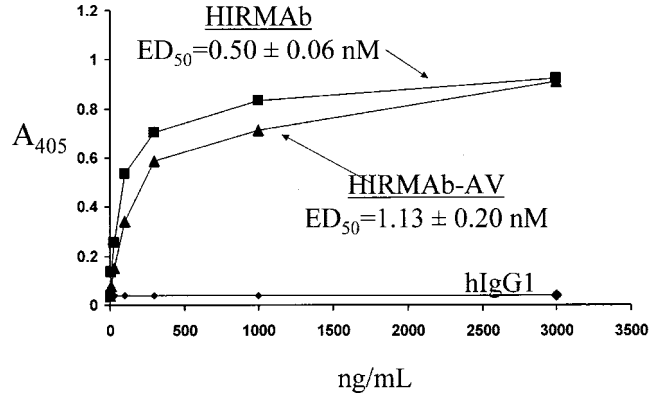

Figure 6. Saturable binding of the chimeric HIRMAb and the HIRMAb-AV fusion protein to the HIR ECD is demonstrated over a range of 0–3000 ng/mL. There is no binding to the HIR by human IgG1. The concentration that produces 50% binding, the ED50, was computed by nonlinear regression analysis with units of ng/ml, and converted to nM, based on the molecular weight of the HIRMAb, 150 000 Da, and the molecular weight of the HIRMAb-AV fusion protedin, 185 000 Da.

chimeric HIRMAb bound to the biotinylated BSA over a concentration range of 0–3000 ng/mL (Figure 7B). This ELISA provides a qualitative index of HIRMAb-AV binding to biotinylated substrate, but does not provide a measure of the number of biotin binding sites on the HIRMAb-AV fusion protein. The latter is determined with a quantitative biotin binding assay using a [^{3}H]-biotin ultrafiltration method (Methods). As shown in Figure 8, 80 nM avidin bound 250 nM biotin, which indicates there are 3 available biotin binding sites per avidin tetramer. However, in this assay, no measureable binding of [^{3}H]-biotin was observed for the COS-derived HIRMAb-AV fusion protein. This was attributed to near complete saturation of the available biotin binding sites on the HIRMAb-AV fusion protein by the endogenous biotin in the tissue culture medium. The medium biotin concentration was 3.1 uM (Methods), as opposed to the concentration of HIRMAb-AV fusion protein, which ranged from 26 nM to 59 nM (Table 2). The HIRMAb-AV fusion protein was subjected to extensive dialysis using an avidin sequestration technique (Methods). However, there were still no measureable biotin binding sites on the fusion protein, as determined with the ultrafiltration assay. These observations suggested that it would not be possible to produce the HIRMAb-AV fusion protein in eukaryotic expression

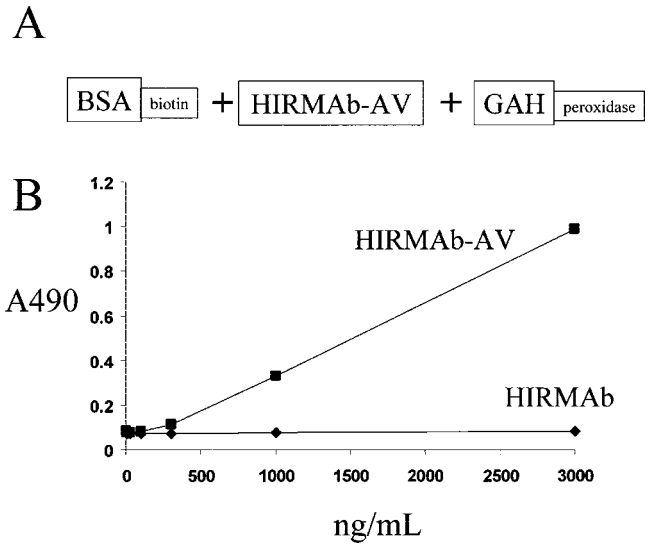

Figure 7. (A) Outline of biotinylated bovine serum albumin (BSA) ELISA. Binding of the HIRMAb-AV fusion protein to the biotinylated BSA is detected with a peroxidase conjugate of a goat antihuman (GAH) IgG. (B) Binding of the HIRMAb-AV fusion protein, but not the chimeric HIRMAb, to biotinylated BSA is demonstrated over a concentration range of 0–3000 ng/mL.

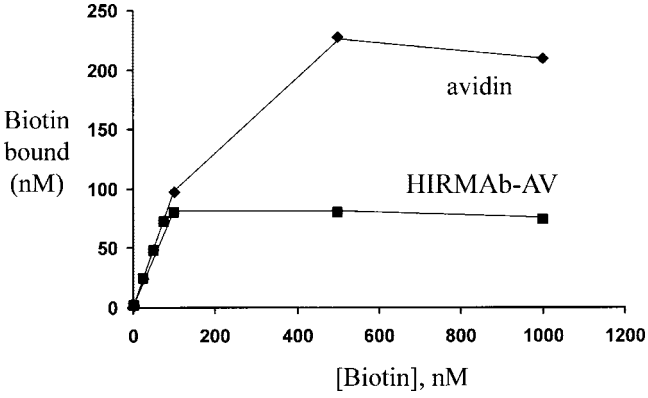

Figure 8. The binding of [^{3}H]-biotin to either avidin or the HIRMAb-AV fusion protein produced in biotin-starved CHO cells is measured with an ultrafiltration assay. The concentration of avidin or the HIRMAb-AV fusion protein in the assay is 80 nM.

systems that retained functional biotin binding sites, unless the host cell line was cultivated in biotin-depleted medium under conditions of biotin starvation over several weeks. This required the availability of a permanently transfected host cell line, such as Chinese hamster ovary (CHO) cells. Following permanent transfection of DG44 CHO cells with linearized pHIRMAb-AV TVrev (Figure 3B), a high producing CHO cell line was isolated following methotrexate amplification and dilutional cloning. The levels of human IgG in the medium of the transfected CHO line grown in serum free medium in shake flasks at a density of (1–2) $\times$ 10^6 cells/mL exceeded 40 mg/L following one round of dilutional cloning. The CHO cells were propagated in square plastic bottles on an orbital shaker, and the medium biotin concentration was reduced from 20 nM to 0.3 nM over a 27 day period (Table 3). During this time, the HIRMAb-AV fusion protein was secreted to the medium and the molar ratio of HIRMAb-AV fusion protein/biotin increased to >300 (Table 3).

The HIRMAb-AV fusion protein produced by the biotin-starved CHO cells was purified by protein A affinity chromatography. The protein eluted as a single homogeneous peak on SEC HPLC, and migrated with a molecular weight of approximately 400 kDa (Figure 9A). The fusion protein migrated as a single homogeneous product in native PAGE gels, and migrated faster than the chimeric HIRMAb or human IgG1, which is consistent with the higher cationic charge of the fusion protein as compared to the HIRMAb alone (Figure 9B).

Table 3. Expression of HIRMAb-AV by CHO Cells under Conditions of Biotin Depletion in Serum Free Medium[a]

day of culture	total cells ($\times 10^6$)	viable cells (%)	biotin (nM)	HIRMAb-Av/ biotin ratio
8	2.7	94	10	2.4
14	1.8	93	3	3.9
18	2.6	83	1	11
21	2.0	69	0.3	41
24	0.8	70	0.3	233
27	1.0	33	0.3	332

[a] Cells were grown in a shake flask on an orbital shaker in serum free medium. The medium biotin was reduced from 800 nM to 20 nM on day 1, and was reduced from 20 nM to 10 nM on day 8.

The affinity of the CHO derived HIRMAb-AV fusion protein for the HIR ECD was measured, and the ED50 of HIRMAb-AV fusion proteing binding was 0.58 $\pm$ 0.09 nM, which was not significantly different from the ED50 for the binding of the chimeric HIRMAb, 0.66 $\pm$ 0.14 nM. The HIRMAb-AV fusion protein produced by the biotin-starved CHO cells quantitatively bound [^{3}H]-biotin, and a 80 nM concentration of fusion protein bound 80 nM biotin (Figure 8), indicating 1 of the 2 biotin binding sites on the fusion protein was unoccupied.

The uptake of ^{3}H-biotin by human renal 293 cells was minimal over a 2 h incubation period at 37C (Figure 10). However, in the presence of the HIRMAb-AV fusion protein, the cell uptake of the ^{3}H-biotin increased over 15-fold, and the biotin VD exceeded 100 uL/mg protein at 120 min of incubation (Figure 10). Confocal microscopy showed no measureable uptake of fluorescein-biotin at 3 or 24 h of incubation in the absence of the HIRMAb-AV fusion protein (Figure 11A). However, in the presence of the HIRMAb-AV fusion protein, there was penetration of the fluorescein-biotin into the intracellular compartment, which was visible in intracellular endosomes, at 3 h (Figure 11B) and 24 h (Figure 11C,D) of incubation.

DISCUSSION

The results of this study are consistent with the following conclusions. First, a fusion gene has been genetically engineered, which encodes a fusion protein wherein the amino terminus of avidin is fused to the carboxyl terminus of the CH_3 region of the HC of the chimeric HIRMAb (Figure 1). Second, following expression in either COS or CHO cells, the HC of the fusion protein is 15 kDa larger than the HC of the chimeric HIRMAb (Figure 4), and the fusion protein HC reacts with antibodies to both human IgG and avidin (Figure 5). Third, the fusion protein is a bifunctional molecule, and binds both the HIR ECD (Figure 6), and binds biotinylated ligands (Figure 7). Fourth, the fusion protein can be produced in CHO cells under conditions of biotin starvation of periods of at least 27 days (Table 3), and the fusion protein retains unoccupied biotin binding sites (Figure 8). Fifth, the HIRMAb-AV fusion protein produced by CHO cells under conditions of biotin starvation is highly stable, does not form aggregates (Figure 9B), and elutes as a monomeric species on HPLC SEC (Figure 9A). Sixth, the HIRMAb-AV fusion protein enhances the cell uptake of biotin (Figure 10) or biotinylated ligands, such as fluorescein-biotin (Figure 11).

The design of the HIRMAb-AV fusion protein places the 15 kDa avidin monomer at the carboxyl terminus of the heavy chain of the chimeric HIRMAb (Figure 1). This places the avidin moiety in a configuration that favors a parallel dimer conformation, which replicates the parallel association of 2 avidin or

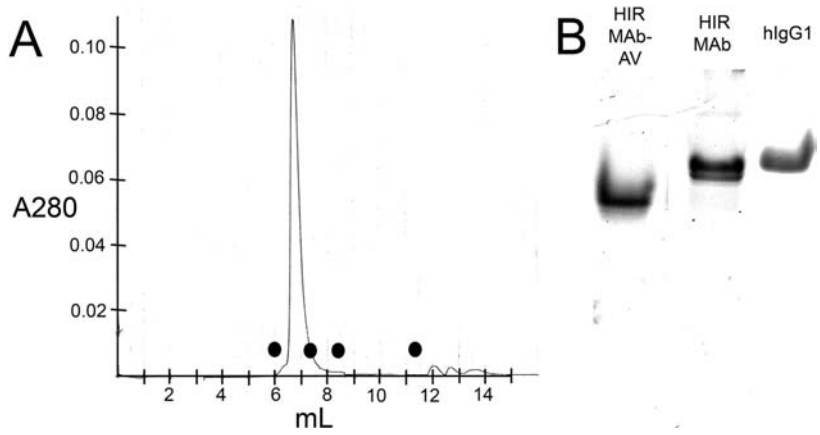

Figure 9. (A) SEC HPLC of the HIRMAb-AV fusion protein produced by biotin-starved CHO cells. The migration of 4 molecular size markers is shown by the solid circles, and in left-to-right order include, blue-dextran-2000 (2 million Da), ferritin (440 kDa), aldolase (158 kDa), and RNase A (14 kDa). (B) Native polyacrylamide gel electrophoresis (PAGE) of the HIRMAb-AV fusion protein, the chimeric HIRMAb, and human IgG1.

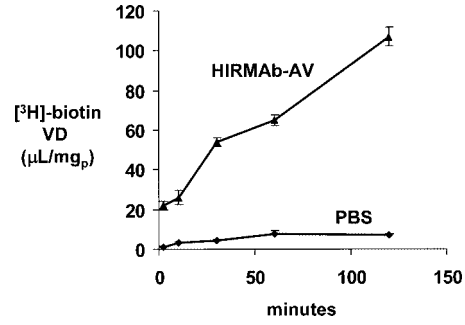

Figure 10. Volume of distribution (VD) of [^{3}H]-biotin in human 293 cells at 2 to 120 min of incubation at 37 °C after comixture of the labeled biotin with either PBS or the HIRMAb-AV fusion protein. Data points are mean ± SE (n = 4 dishes per time point).

streptavidin monomers to form a dimer (*11*). Placement of the avidin monomer at the carboxyl terminus of the heavy chain, as opposed to the amino terminus eliminates interference of antibody binding to the HIR. Avidin is a dimer of dimers (*11*), and the HIRMAb-AV fusion protein may also form a tetrameric structure formed from the association of 2 antiparallel fusion proteins. The evidence for this is the SEC HPLC, which shows the HIRMAb-AV fusion protein migrates with a molecular weight of about 400 kDa, which is twice the expected molecular weight of the glycosylated HIRMAb-AV fusion protein. Avidin has the maximal affinity for biotin when the protein is assembled in the tetrameric configuration. The fact that bound biotin could not be dissociated off the HIRMAb-AV fusion protein despite 72 h of dialysis against a 10 000-fold increase in volume with high concentrations of avidin in the dialysate (Methods) is evidence for the very high affinity of the HIRMAb-AV fusion protein for biotin.

The HIRMAb-AV fusion protein is secreted in high amounts in transfected COS cells (Table 2). The size of the heavy chain (HC) of the fusion protein is about 15 kDa larger than the HC of the chimeric HIRMAb, based on either SDS-PAGE (Figure 4) or Western blotting with an antihuman IgG antibody (Figure 5A). An antiavidin antibody reacts with the fusion protein HC, or with avidin, but not with the HC of the HIRMAb, or the light chain (LC) of either the HIRMAb or the HIRMAb-AV fusion protein (Figure 5B). The COS cell-derived HIRMAb-AV fusion protein binds with high affinity to the HIR, albeit with about 50% reduced affinity as compared to the chimeric HIRMAb (Figure 6). However, the affinity of the CHO-derived HIRMAb-AV fusion protein for the HIR is identical to that of the chimeric HIRMAb (Results), and this may be due to differential glycosylation in CHO and COS cells.

The HIRMAb-AV fusion protein produced by COS cells is fully saturated with biotin, owing to the 50-fold molar excess of biotin over the fusion protein (Results). Nevertheless, the fusion protein reacts with biotinylated BSA in an ELISA (Figure 7). This reactivity is most likely due to the presence of a minor fraction of unoccupied biotin binding sites, perhaps <5% of the total. The biotinylated BSA ELISA only is a qualitative index of biotin binding of the HIRMAb-AV fusion protein. The [^{3}H]-biotin ultrafiltration assay is a quantitative assay of biotin binding sites on the HIRMAb-AV fusion protein, and this assay shows minimal biotin binding by the fusion protein produced by COS cells. Moreover, it is not possible to displace the biotin from the HIRMAb-AV fusion protein with extensive dialysis (Results).

The HIRMAb-AV fusion protein might be produced with unoccupied binding sites if the host cell was subjected to biotin starvation. Therefore, a CHO cell line was permanently transfected with the pHIRMAb-AV TVrev (Figure 3B). Owing to the presence of the HC gene, the LC gene, and the DHFR gene all on a single piece of DNA, it was possible to isolate a high producing cell line following MTX amplification and 1 round of dilutional cloning. The CHO cell-derived fusion protein had high affinity for the HIR, did not form aggregates based on SEC HPLC or native PAGE (Figure 9), and was produced at levels >40 mg/L of human IgG in the serum free conditioned medium in shake flasks at a cell density of (1–2) × 10^6 cells/mL. The HIRMAb-AV fusion protein produced by CHO cells under conditions of biotin starvation bound ^{3}H-biotin, and accelerated biotin uptake into human epithelial cells with a >15-fold increase in VD of the biotin at 2 h of incubation (Figure 10). The HIRMAb-AV fusion protein facilitated cell uptake of fluorescein-biotin, as demonstrated by confocal microscopy (Figure 11). There was no measureable cell uptake of fluorescein-biotin alone (Figure 11A). However, following attachment of the fluorescein-biotin to the HIRMAb-AV fusion protein, there was enhanced cell uptake into the intracellular endosomal compartment at 3 and 24 h of incubation (Figure 11B,C,D).

The expression of avidin, or avidin fusion proteins, in CHO cells has not been previously described, although avidin has been expressed in baculovirus, yeast, and bacterial expression systems (*14*). In order to produce fusion protein with unoccupied biotin binding sites, it was necessary to develop a culture methodology whereby the CHO cells were grown under conditions of biotin depletion. As shown in Table 3, the cells could be maintained for 4 weeks in very low biotin medium,

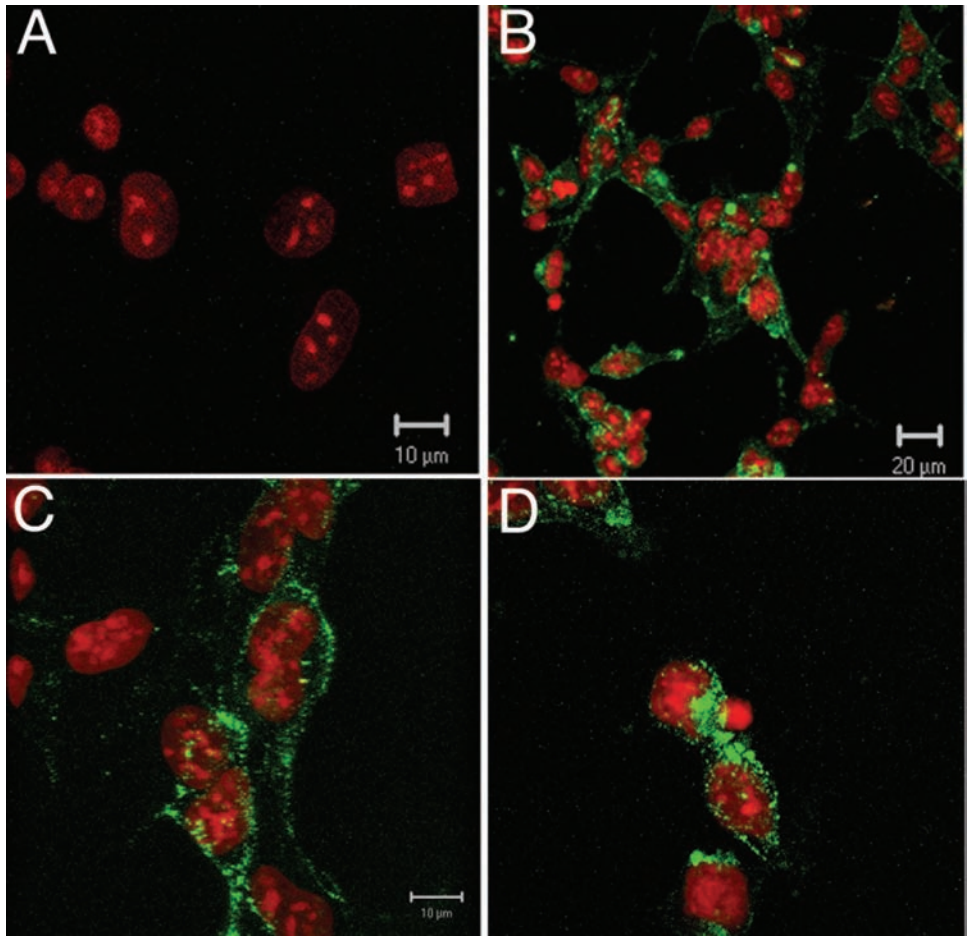

Figure 11. Confocal microscopy of human 293 cells following the addition to the medium of fluorescein-biotin comixed in either PBS (A) or the HIRMAb-AV fusion protein (B,C,D). The cells were incubated for either 3 h (B) or 24 h (A,C,D), and were photographed with either a 40× (B) or 100× (A,C,D) objective. The nuclei are stained red by propidium iodide.

and the HIRMAb-AV fusion protein was continuously produced under these conditions. The biotin ultrafiltration assay demonstrated that there was 1 biotin binding site per antibody molecule (Figure 8). There are 2 predicted biotin binding sites per fusion protein (Figure 1). Therefore, these data show that the HIRMAb-AV fusion protein can be produced in CHO cells under conditions of biotin starvation, to enable production of fusion protein with high affinity biotin binding properties.

In summary, these studies describes the genetic engineering, expression, and validation of a drug delivery system that is active in humans, and is designed to deliver monobiotinylated pharmaceuticals, including siRNA (*6*), across biological membranes via the insulin receptor. The engineering of the HIRMAb-AV fusion protein represents the merger of molecular Trojan horse technology and avidin–biotin technology in drug targeting. Owing to the extremely high affinity of avidin binding of biotin ($K_D = 10^{-15}$ M, dissociation $t_{1/2} = 89$ days), the bond between the Trojan horse HIRMAb and the biotinylated therapeutic is extremely stable in vivo. The avidin–biotin bond does not spontaneously dissociate in vivo, and is disrupted only via the action of tissue enzymatic reactions, particularly in liver and kidney (*15*). Owing to the rapid binding of biotinylated drugs to avidin, the present approach enables "2-vial pharmaceutics," where the HIRMAb-AV fusion protein is formulated in the first vial, and the monobiotinylated therapeutic is formulated in a second vial, and the 2 vials are mixed prior to systemic administration.

The concern with avidin fusion proteins is immunogenicity of the chicken avidin in humans, and a human antiavidin response (HAAR). However, avidin has been administered to humans in 5–10 mg doses intravenously without immunologic reactions (*8, 16, 17*). The human hypo-responsiveness to avidin may arise from oral antigen feeding (*18*). Avidin is abundant in egg whites, and virtually all members of Western societies have consumed dietary eggs, which is a form of oral avidin antigen feeding that could induce immune tolerance in humans to avidin. Support for this hypothesis is the finding that humans have serum antibodies to avidin, and that the titer is lower in subjects on egg-free diets (*19*). Therefore, an avidin fusion protein may be administered to humans without immunological reactions.

ACKNOWLEDGMENT

Winnie Tai and Phuong Tram provided expert technical assistance.

LITERATURE CITED

(1) Pardridge, W. M. (2007) Drug targeting to the brain. *Pharm. Res. 24*, 1733–1744.

(2) Boado, R. J., Zhang, Y., Zhang, Y., and Pardridge, W. M. (2007) Humanization of anti-human insulin receptor antibody for drug targeting across the human blood-brain barrier. *Biotechnol. Bioeng. 96*, 381–391.

(3) Boado, R. J., Zhang, Y., Zhang, Y., and Pardridge, W. M. (2007) Genetic engineering, expression, and activity of a fusion protein of a human neurotrophin and a molecular Trojan horse for delivery across the human blood-brain barrier. *Biotechnol. Bioeng. 97*, 1376–1386.

(4) Boado, R. J., Zhang, Y., Zhang, Y., Xia, C. F., and Pardridge, W. M. (2007) Fusion antibody for Alzheimer's disease with bi-directional transport across the blood-brain barrier transport and Abeta fibril disaggregation. *Bioconjugate Chem. 18*, 447–455.

(5) Boado, R. J., Zhang, Y., Zhang, Y., Xia, C. F., Wang, Y., and Pardridge, W. M. (2008) Genetic engineering of a lysosomal enzyme fusion protein for targeted delivery across the human blood-brain barrier. *Biotechnol. Bioeng. 99*, 475–484.

(6) Xia, C. F., Zhang, Y., Zhang, Y., Boado, R. J., and Pardridge, W. M. (2007) Intravenous siRNA of brain cancer with receptor targeting and avidin-biotin technology. *Pharm. Res. 24*, 2309–2316.

(7) Yoshikawa, T., and Pardridge, W. M. (1992) Biotin delivery to brain with a covalent conjugate of avidin and a monoclonal antibody to the transferrin receptor. *J. Pharmacol. Exp. Ther. 263*, 897–903.

(8) Magnani, P., Paganelli, G., Songini, C., Samuel, A., Sudati, F., Siccardi, A. G., and Fazio, F. (1996) Pretargeted immunoscintigraphy in patients with medullary thyroid carcinoma. *Br. J. Cancer 74*, 825–831.

(9) Penichet, M. L., Kang, Y. S., Pardridge, W. M., Morrison, S. L., and Shin, S. U. (1999) An antibody-avidin fusion protein specific for the transferrin receptor serves as a delivery vehicle for effective brain targeting: initial applications in anti-HIV antisense drug delivery to the brain. *J. Immunol. 163*, 4421–4426.

(10) Green, M. (1975) Avidin. *Adv. Protein Chem. 29*, 85–133.

(11) Hendrickson, W. A., Pahler, A., Smith, J. L., Satow, Y., Merritt, E. A., and Phizackerley, R. P. (1989) Crystal structure of core streptavidin determined from multiwavelength anomalous diffraction of synchrotron radiation. *Proc. Natl. Acad. Sci. U.S.A. 86*, 2190–2194.

(12) Coloma, M. J., Lee, H. J., Kurihara, A., Landaw, E. M., Boado, R. J., Morrison, S. L., and Pardridge, W. M. (2000) Transport across the primate blood-brain barrier of a genetically engineered chimeric monoclonal antibody to the human insulin receptor. *Pharm. Res. 17*, 266–274.

(13) Boado, R. J., and Pardridge, W. M. (1998) Ten nucleotide cis element in the 3′-untranslated region of the GLUT1 glucose transporter mRNA increases gene expression via mRNA stabilization. *Mol. Brain Res. 59*, 109–113.

(14) Hytonen, V. P., Laitinen, O. H., Airenne, T. T., Kidron, H., Meltola, N. J., Porkka, E. J., Horha, J., Paldanius, T., Maatta, J. A. E., Nordlund, H. R., Johnson, M. S., Salminen, T. A., Airenne, K. J., Yla-Herttuala, S., and Kulomaa, M. S. (2004) Efficient production of active chicken avidin using a bacterial signal peptide in Escherichia coli. *Biochem. J. 384*, 385–390.

(15) Wei, R. D., Kou, D. H., and Hoo, S. L. (1971) Dissociation of avidin-biotin complex in vivo. *Experientia 27*, 366–368.

(16) Paganelli, G., Magnani, P., Zito, F., Lucignani, G., Sudati, F., Truci, G., Motti, E., Terreni, M., Pollo, B., Giovanelli, M., Canal, N., Scotti, G., Comi, G., Koch, P., Maecke, H. R., and Fazio, F. (1994) Pre-targeted immunodetection in glioma patients: tumour localization and single-photon emission tomography imaging of [^{99m}Tc]PnAO-biotin. *Eur. J. Nucl. Med. 21*, 314–321.

(17) Samuel, A., Paganelli, G., Chiesa, R., Sudati, F., Calvitto, M., Melissano, G., Grossi, A., and Fazio, F. (1996) Detection of prosthetic vascular graft infection using avidin/indium-111-biotin scintigraphy. *J. Nucl. Med. 37*, 55–61.

(18) Weiner, H. L. (1994) Oral tolerance. *Proc. Natl. Acad. Sci. U.S.A. 91*, 10762–10765.

(19) Bubb, M. O., Green, F., Conradie, J. D., Tchernyshev, B., Bayer, E. A., and Wilchek, M. (1993) Natural antibodies to avidin in human serum. *Immunol. Lett. 35*, 277–280.

BC7004076

Poly(L-lysine)-Modified Iron Oxide Nanoparticles for Stem Cell Labeling

Michal Babič,[†,‡] Daniel Horák,*[,†,‡] Miroslava Trchová,[†] Pavla Jendelová,[‡,§] Kateřina Glogarová,[§] Petr Lesný,[‡,§] Vít Herynek,[‡,||] Milan Hájek,[‡,||] and Eva Syková[‡,§]

Institute of Macromolecular Chemistry, v. v. i., Academy of Sciences of the Czech Republic, Heyrovský Sq. 2, 162 06 Prague 6, Czech Republic, Center for Cell Therapy and Tissue Repair, Charles University, V Úvalu 84, 150 06 Prague 5, Czech Republic, Institute of Experimental Medicine, v. v. i., Academy of Sciences of the Czech Republic, Vídeňská 1083, 142 20 Prague 4, Czech Republic, and Institute of Clinical and Experimental Medicine, Vídeňská 1958/9, 140 21 Prague 4, Czech Republic. Received November 5, 2007; Revised Manuscript Received January 4, 2008

New surface-modified iron oxide nanoparticles were developed by precipitation of Fe(II) and Fe(III) salts with ammonium hydroxide and oxidation of the resulting magnetite with sodium hypochlorite, followed by the addition of poly(L-lysine) (PLL) solution. PLL of several molecular weights ranging from 146 (L-lysine) to 579 000 was tested as a coating to boost the intracellular uptake of the nanoparticles. The nanoparticles were characterized by TEM, dynamic light scattering, FTIR, and ultrasonic spectrometry. TEM revealed that the particles were ca. 6 nm in diameter, while FTIR showed that their surfaces were well-coated with PLL. The interaction of PLL-modified iron oxide nanoparticles with DMEM culture medium was verified by UV–vis spectroscopy. Rat bone marrow stromal cells (rMSCs) and human mesenchymal stem cells (hMSC) were labeled with PLL-modified iron oxide nanoparticles or with Endorem (control). Optical microscopy and TEM confirmed the presence of PLL-modified iron oxide nanoparticles inside the cells. Cellular uptake was very high (more than 92%) for PLL-modified nanoparticles that were coated with PLL (molecular weight 388 00) at a concentration of 0.02 mg PLL per milliliter of colloid. The cellular uptake of PLL-modified iron oxide was facilitated by its interaction with the negatively charged cell surface and subsequent endosomolytic uptake. The relaxivity of rMSCs labeled with PLL-modified iron oxide and the amount of iron in the cells were determined. PLL-modified iron oxide-labeled rMSCs were imaged *in vitro* and *in vivo* after intracerebral grafting into the contralateral hemisphere of the adult rat brain. The implanted cells were visible on magnetic resonance (MR) images as a hypointense area at the injection site and in the lesion. In comparison with Endorem, nanoparticles modified with PLL of an optimum molecular weight demonstrated a higher efficiency of intracellular uptake by MSC cells.

INTRODUCTION

Superparamagnetic iron oxide nanoparticles have been widely used for numerous *in vitro* and *in vivo* biomedical applications (*1*). Such applications exploit two major advantages of magnetic iron oxides: their low toxicity for humans (*2*) and their outstanding magnetic properties, which allow the targeting of drugs to a tumor area through external magnetic fields (*3*). Most *in vitro* applications have focused on immunoassays (*4, 5*), the detection and separation of cells, viruses (*6*), hormones (*7, 8*), oligonucleotides (*9*), DNA (*10*) and proteins (*11*). *In vivo* applications have concentrated on cell and tissue engineering, including cell tagging, tracking, and imaging (*12*) (magnetic resonance imaging, MRI); targeted drug delivery (*13, 14*); gene delivery systems and gene therapy (*15*); as well as targeted hyperthermia of cancers (*16*), tissue repair, and the detoxification of biological fluids (*17*). MRI makes use of the fact that magnetic nanoparticles generate a magnetic field and thus influence their immediate vicinity (*18*). In these applications, there is a growing need for the highly specific, efficient, and rapid internalization of nanoparticles into specific target cells, but this is severely limited by several factors (*19*): (i) nanoparticle aggregation (nanoparticles have a large surface/volume ratio and tend to agglomerate); (ii) the short half-life of the particles in blood circulation (when nanoparticles agglomerate, or adsorb plasma proteins, they are quickly eliminated from the bloodstream by macrophages of the mononuclear phagocyte system before they can reach the target cells); (iii) the low efficiency of the intracellular uptake of nanoparticles; and (iv) nonspecific targeting. Biocompatible polymers and targeting agents are therefore attached to the nanoparticle surface to prevent agglomeration, to make the nanoparticles more biocompatible, and to increase their nonspecific intracellular uptake (*20, 21*). All applications require that the nanoparticles have high magnetization values and a size smaller than 100 nm, with a narrow particle size distribution, so that the particles have uniform physical and chemical properties. Compared with paramagnetics, superparamagnetic iron oxide particles have higher molar relaxivities, and, when used as blood pool and tissue-specific agents, may offer advantages at low concentrations (*22*). The nature of the surface coating on the nanoparticles not only determines the overall size of the colloid, but also plays a significant role in the biokinetics and biodistribution of the nanoparticles in the body. Various biological molecules such as antibodies, proteins, targeting ligands, and so forth may also be bound to the nanoparticle surface to make the particles target-specific.

Since the introduction of particular contrast agents in MRI use in 1987, most superparamagnetic iron oxides (SPIO) and ultrasmall superparamegnetic iron oxides (USPIO) agents, taken up by macrophages, have been prepared using dextran or other types of polymer coatings to achieve good dispersion in water

* Corresponding author. Tel.: +420-296-809-260; Fax: +420-296-809-410; E-mail: horak@imc.cas.cz.

[†] Institute of Macromolecular Chemistry, v. v. i., Academy of Sciences of the Czech Republic.

[‡] Center for Cell Therapy and Tissue Repair.

[§] Institute of Experimental Medicine, v. v. i., Academy of Sciences of the Czech Republic.

[||] Institute of Clinical and Experimental Medicine.

10.1021/bc700410z CCC: $40.75 © 2008 American Chemical Society
Published on Web 02/21/2008

and selectivity (*23*). Dextran-coated nanoparticles, however, do not show sufficient cellular uptake to enable cell tracking, probably because of a relatively inefficient fluid-phase endocytosis pathway. Polymer coatings significantly increase the particle size, which may affect their penetration and metabolic clearance rate in the body. A few recent papers have reported the use of nonpolymer-coated superparamagnetic nanoparticle dispersions in MR imaging (*24*). They were prepared in the water phase and stabilized, e.g., by citrate (*25*) or tetramethylammonium hydroxide (*24*), providing some advantages over those that require additional polymer protection for stabilization. Nanoparticles without a polymer coating have a much smaller size for distinct biodistribution and metabolic clearance profile than conventional polymer-coated-particles. It is, however, not clear whether these particles can be taken up by cells.

Stem cells are the body's master cells and have a unique ability to renew and give rise to other specialized cell types for the development of a tissue (*26*). Cell transplantation is a powerful treatment method for many common diseases, including brain and spinal cord injury; however, current experiments with stem cells do not give information about the behavior of the transplanted cells in the host organism *in vivo*, especially about their migration and fate within the target structures and their potential neoplastic growth. The lack of these data represents a serious obstacle for the clinical use of cell therapy. Human medicine would benefit from the labeling of implanted stem cells and the use of noninvasive methods to image the labeled cells after implantation. Superparamagnetic particles coupled to the cells could target these cells to the desired site in the body.

The preparation of stable iron oxide colloids is not easy. The first paper of this series was focused on the labeling of stem cells with iron oxide nanoparticles coated with D-mannose (*27*). The objective of the present study was to investigate the use of poly(L-lysine) (PLL), which is commonly used to enhance cell adhesion to the surface of a culture dish in *in vitro* cell cultivation, as a prospective vehicle for iron oxide nanoparticle transport into cells. The endocytosis behavior of PLL-modified particles was determined using mesenchymal stem cells (MSCs) and compared with that of control and uncoated superparamagnetic iron oxide nanoparticles.

EXPERIMENTAL SECTION

Materials. $FeCl_2 \cdot 4H_2O$ and $FeCl_3 \cdot 6H_2O$ were purchased from Fluka (Buchs, Switzerland), sodium hypochlorite solution (NaOCl) from Bochemie (Bohumín, Czech Republic), and sodium citrate dihydrate from Lachema (Brno, Czech Republic). All other reagent-grade chemicals were purchased from Aldrich (Milwaukee, WI, USA) and used as received. L-Lysine (LL) and poly(L-lysine) (PLL) hydrobromide (M_w = 9200; 58 900; 93 800; 388 100; and 579 000) and gelatin were from Sigma (St. Louis, MO, USA) and the commercial contrast agent Endorem from Guerbet (Roissy, France). Ultrapure Q water ultrafiltered on a Milli-Q Gradient A10 system (Millipore, Molsheim, France) was used for the preparation of solutions.

Preparation of Uncoated Iron Oxide Nanoparticles and their Treatment with Poly(L-lysine) or L-Lysine. In a typical experiment, 12 mL of 0.2 M $FeCl_3$ aqueous solution was mixed with 12 mL of 0.5 M NH_4OH solution (less than an equimolar amount) under sonication (Sonicator W-385; Heat Systems-Ultrasonics, Inc., Farmingdale, NY, USA) at laboratory temperature for 2 min to form colloid $Fe(OH)_3$. Then, 6 mL of aqueous 0.2 M $FeCl_2$ was added under sonication and the mixture poured into 36 mL of 0.5 M NH_4OH aqueous solution. The resulting magnetite coagulate was left to grow for 15 min, the magnetically separated and repeatedly (7–10×) washed (peptized) with Q-water to remove all impurities (including NH_4Cl) remaining after the synthesis. Finally, 1.5 mL of 0.1 M sodium citrate was added under sonication, and the magnetite was oxidized by the slow addition of 1 mL of 5% sodium hypochlorite solution to the maghemite to enhance the redox stability. The above-described washing procedure was repeated to yield the primary colloid. 0.2 mL of aqueous L-lysine (LL) or poly(L-lysine) solution (concentration 1 mg/mL) was added dropwise with stirring to 10 mL of primary iron oxide colloid, diluted to a concentration of 2.2 mg iron oxide/mL. The obtained mixture was sonicated for 5 min and used in experiments.

Particle Characterization. The morphology of the colloids was observed by transmission electron microscopy (TEM) using a JEOL JEM 200 CX. Particle size distributions were obtained using Atlas image analysis software (Tescan, Brno, Czech Republic) (*27*). For the measurements, a drop of a dilute dispersion was spread on a carbon-coated copper grid, and the grid was air-dried at room temperature before viewing under the microscope. The particle size and distribution were determined by the measurement of at least 300 particles for each sample. Two types of mean particle size were calculated: the number-average particle size (D_n) and the weight-average particle size (D_w; $D_n = \Sigma D_i/N$ and $D_w = \Sigma D_i^4/\Sigma D_i^3$, where N is the number of particles). The particle size distribution was characterized by the polydispersity index (PDI = D_w/D_n). Moreover, the hydrodynamic diameter (*z*-average), polydispersity (from 0 - monodisperse particles - to 1 - polydisperse particles) from the cumulative analysis of time correlation functions, and the surface zeta potential were determined by dynamic light scattering (DLS) using an Autosizer Lo-C (Malvern Instruments Ltd., Malvern, Great Britain).

The PLL coating on the surface of the magnetic nanoparticles was examined using a Thermo Nicolet Nexus 870 FTIR spectrometer (Madison, WI, USA) in an H_2O-purged environment with DTGS (deuterated triglycine sulfate) detector. The Golden Gate single-reflection ATR system (Specac Ltd., Orpington, Great Britain) was used to measure the ATR spectra of powdered samples over a wavenumber range 400–4000 cm^{-1}. Typical parameters were as follows: 256 sample scans, resolution 4 cm^{-1}, Happ-Genzel apodization, KBr beamsplitter. The samples for measurement were prepared by freeze−drying purified PLL-coated nanoparticles (centrifuged four times at 14 000 rpm for 1 h).

Differences in ultrasonic velocity between the reference (water) and the iron oxide colloid were monitored under the slow addition of various amounts of PLL (M_w = 388 100) using an HR-US 102 ultrasonic spectrometer (Ultrasonic Scientific, Dublin, Ireland). In a typical experiment, 1 mL of iron oxide colloid (c = 18 mg/mL) was in the first cell and 1 mL of Q-water in the second cell as a reference. PLL solution (c = 1 mg/mL) was then simultaneously added in 10 μL aliquots to both cells with a Hamilton syringe.

In protein adsorption experiments, 1 mL of the colloid solution with a concentration of 22 mg of iron oxide/mL was mixed with 1 mL of DMEM/10% FBS (fetal bovine serum) on a Vortex-T Genie-2 for 1 h; subsequently, the liquid was separated from the solid by centrifugation (14 000 rpm) for 1 h and measured on a Perkin-Elmer Lambda 20 UV/vis spectrophotometer (Norwalk, CT, USA). An aqueous solution of DMEM/10% FBS (1/1 v/v) served as a standard.

To confirm that PLL was not released from PLL-coated iron oxide nanoparticles during contact with the culture medium, both uncoated (no. 1, Table 1) and PLL-coated iron oxides (no. 4; 22 mg of γ-Fe_2O_3/0.64 mL of water) were mixed with 1 mL of DMEM/10% FBS or 1 mL of 0.15 M NaCl solution for 1 h, and after magnetic separation the supernatant was hydrolyzed in 6 M HCl for 16 h at 115 °C. The concentration of L-lysine in the supernatant was determined by the standard FMOC/*N*-

Table 1. *In Vitro* Bone Marrow Stromal Cell (MSC) Labeling of Surface-Modified Iron Oxide Nanoparticles and Their Characteristics

		concentration					labeled cells[c] (%)	
no.	modification	modifier (mg/mL)	γ-Fe_2O_3 (mg/mL)	PLL/γ-Fe_2O_3 (w/w)	D_n[a] (nm)	PDI[b]	MSC (rat)	MSC (human)
1	none		2.2	0	6.05	1.46	27.9	
2	PLL[d]	0.005	2.2	0.002	6.2	1.32	48.6	
3	PLL[d]	0.01	2.2	0.005	6.2	1.37	65.5	
4	PLL[d]	0.02	2.2	0.009	5.5	1.30	92.2	87.5
Endorem	Dextran		11.2[e]		5.4	1.43	60.0	65.2

[a] D_n – number-average particle diameter determined from TEM. [b] PDI – polydispersity index (ratio of weight- to number-average particle diameter). [c] Average of 10 measurements. [d] M_w = 388 100. [e] mg of iron/mL.

(9-fluorenylmethoxycarbonyl)/ method and reverse-phase HPLC equipped with a Flouromonitor 4100 detector (both LDC Analytical, Riviera Beach, FL, USA) using Macherey-Nagel 125/4 Nucleosil 120-3 C-8 column (Düren, Germany).

Cell Cultures. The isolation of mesenchymal stem cells (MSC) was performed as previously described (*28*). To isolate rat bone marrow mesenchymal stem cells (rMSCs), the femurs of 4-week-old Wistar rats were dissected. The ends of the bones were cut, and the marrow extruded with 5 mL of DMEM with L-glutamine (PAA, Pasching, Austria), using a syringe. Marrow cells were cultivated in DMEM/10% FBS with 100 U/mL of penicillin and 100 U/mL of streptomycin. After 24 h, the nonadherent cells were removed by replacing the medium. The medium was changed every 2–3 days as the cells grew to confluence. The cells were lifted by incubation with 0.25 wt % trypsin.

Human mesenchymal stem cells (hMSC) were obtained from the bone marrows of healthy donors. Bone marrow aspirates were diluted with phosphate-buffered saline (PBS) and centrifuged through a density gradient (Ficoll-Paque Plus, GE Healthcare Life Sciences, Vienna, Austria) for 30 min at 1000 *g* (Hettich, Germany). Nucleated cells from the interface were cultivated in Alpha-Modified Eagle Medium (α-MEM, Gibco BRL, Paisley, Scotland) containing 10% FBS, 100 units/mL penicillin, and 0.1 mg/mL streptomycin. After 48 h, the nonadherent cells were removed by replacing the medium.

Transmission Electron Microscopy of Labeled Cells. For electron microscopic examination, rMSCs were fixed at 4 °C in 2.5% buffered glutaraldehyde for 1 h, then stained with 1% osmium tetroxide for 2 h. The cells were successfully dehydrated with increasing concentrations of ethanol, immersed in propylene oxide, and embedded in Epon 812 resin (Agar Scientific Ltd., Standsted, UK). The samples were cut into ultrathin sections (~60 nm), contrasted with 4% uranyl acetate and Reynold's lead citrate, and examined using a Philips Morgagni 268 electron microscope.

Quantitative Analysis of Labeled Cells. rMSCs were cultivated in duplicate on uncoated 6-well culture plates at a density 10^5 cells/mm^2. Endorem- or poly(L-lysine)-modified nanoparticles were added to the culture medium (10 μL/mL) for 72 h. The culture medium containing excess particles was removed, and the cell were washed with PBS (three times), fixed with 4% paraformaldehyde in 0.1 M PBS, and stained to produce Fe(III) ferrocyanide (Prussian Blue). Labeled and unlabeled cells were quantified using an inverted light microscope (Axiovert 200, Zeiss, Göttingen, Germany) by counting five random fields per well and three wells per run. The cells captured on each image were manually labeled as Prussian Blue positive or negative; the labeled cells were then counted and the staining intensity of the Prussian Blue positive cells was evaluated using the image analysis toolbox in *Matlab 6.1* (The MathWorks, Natick, MA, USA). The threshold was set in the image analysis toolbox for dark blue, and all cells above this threshold were considered intensely stained. Histograms of the intensity of the cytoplasmic staining were constructed.

Comparison of Relaxivity between rMSC Labeled with Endorem or PLL-Modified Iron Oxide. The following suspensions in 4% gelatin were prepared: pure contrast agent (Endorem or PLL-modified iron oxide no. 4), unlabeled rMSC (4000, 1200, and 200 cells per μL), and cells labeled with Endorem or with PLL-modified iron oxide (4000, 2000, 1600, 1200, 800, 400, or 200 cells per μL). MR relaxation times T_1 and T_2 were measured on an 0.5 T Bruker Minispec MQ20 relaxometer (Rheinstetten, Germany). The T_1 and T_2 values were converted to relaxivities r_1 and r_2; relaxation rates $R_1 = 1/T_1$ and $R_2 = 1/T_2$ were related to the actual concentrations of iron or to the cell concentration c: $r_1 = (R_1 - R_{1G})/c$ (l s^{-1} mmol^{-1}), $r_2 = (R_2 - R_{2G})/c$ (l s^{-1} mmol^{-1}), where R_{1G} and R_{2G} are the relaxation rates of pure 4% gelatin.

Iron Analysis. The amount of iron in the cells after mineralization was determined by spectrophotometry. Cell-containing samples were mineralized by the addition of 5 mL HNO_3 and 1 mL H_2O_2 in an ETHOS 900 microwave mineralizator (Millestone, Sydney, Australia). Deionized water was added to reach a total volume of 100 mL. The iron content was determined using Spectroflame M120S apparatus (Spectro, Littleton, MA, USA) calibrated with a standard Astasol solution (Analytika, Prague, Czech Republic). The measurements were repeated four times, and the mean value was determined.

Cell Grafting. Rats were anesthesized with isoflorane and mounted in a stereotactic frame. Using aseptic technique, a hole (1 mm) was drilled in the skull to expose the dura overlying the cortex. Poly(L-lysine)-modified iron oxide-labeled cells or Endorem-labeled cells (1000, 500, or 100 cells suspended in 2 μL of PBS) were slowly injected intracerebrally into the brain over a 10 min period. Unlabeled cells (10 000 in 5 μL of PBS) were injected as a control. The opening was closed by bone wax and the skin was sutured.

MR Imaging. MR images were obtained using a 4.7 T Bruker spectrometer equipped with a homemade surface coil. The rats were anesthesized by passive inhalation of 1.5–2% isoflorane in air. Breathing was monitored during the measurements. Sagittal, coronal, and transversal images were obtained by a fast gradient echo sequence for localizing the following T_2*-weighted axial and coronal images measured by a standard gradient echo sequence. Sequence parameters were as follows: repetition time T_R = 180 ms, echo time T_E = 12 ms, number of acquisitions AC = 48, matrix size 256 × 256, field of view FOV = 3.5 × 3.5 cm (axial images) or 3 × 6 cm (coronal images), slice thickness = 0.75 mm.

Phantoms containing labeled cells were measured by the same sequence with modified geometry parameters to obtain similar spatial resolution as in the *in vivo* measurements.

RESULTS AND DISCUSSION

Chemical Coprecipitation of Fe(II) and Fe(III) Salts and Postsynthesis Iron Oxide Coating with PLL. The key step in the formation of a stable magnetite/maghemite colloid consisted of the careful removal of all the impurities remaining after the synthesis of the magnetite and its oxidation. Purification

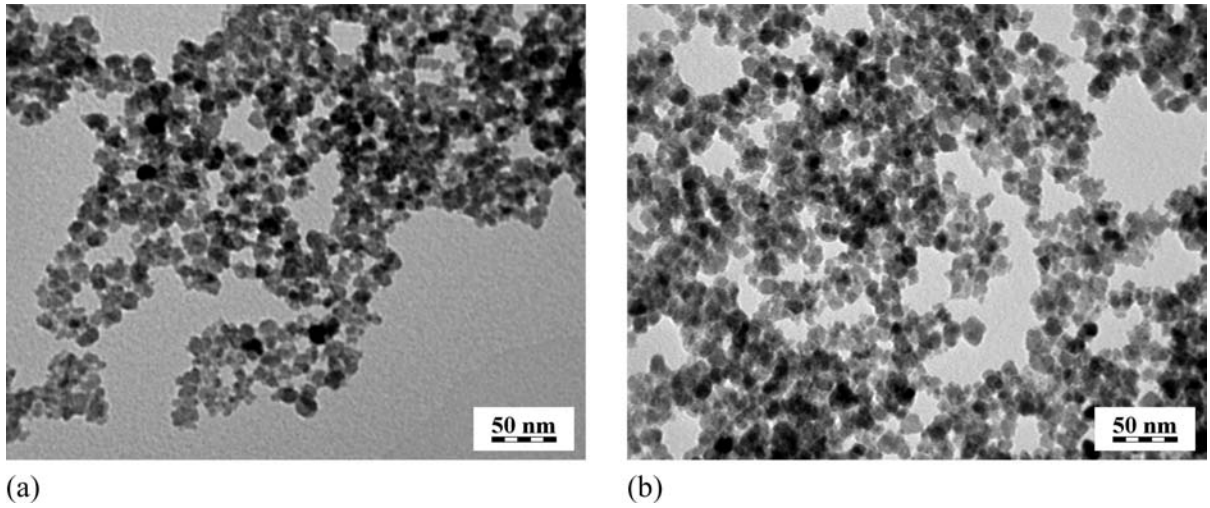

Figure 1. TEM micrographs of (a) uncoated iron oxide nanoparticles no. 1, and (b) PLL-modified iron oxide nanoparticles no. 4.

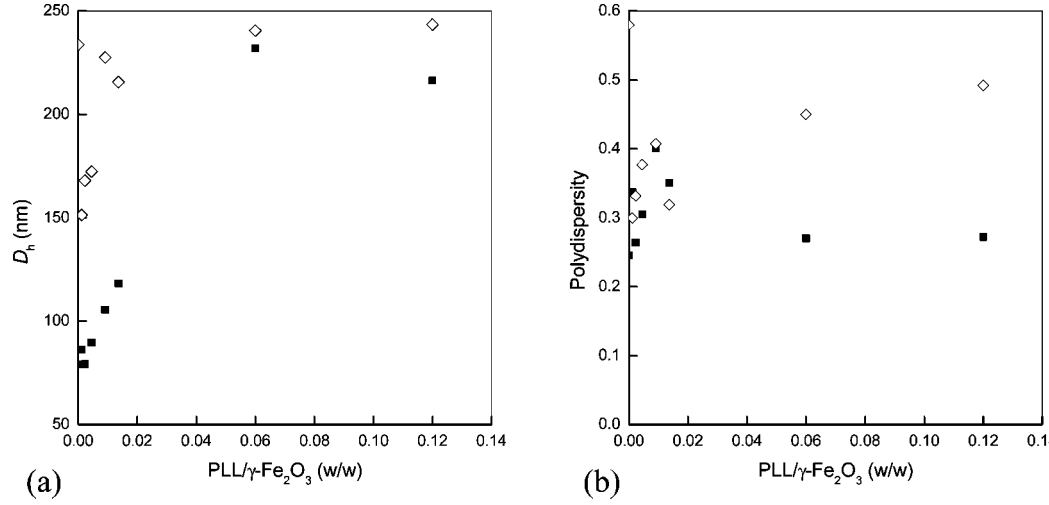

Figure 2. Dependence of (a) hydrodynamic particle diameter D_h and (b) polydispersity, measured by dynamic light scattering, on the PLL/γ-Fe_2O_3 ratio (□) 1 day and (◊) 152 days after synthesis.

was accomplished by magnetic separation in water. Washing with water peptized the particles. Colloidal stability was due to the charges of Fe(III) and citrate ions. Some characteristics of the prepared iron oxides are summarized in Table 1. TEM analysis indicates that dried, uncoated iron oxide particles showed a rather narrow size distribution (Figure 1a). The average size of uncoated nanoparticles no. 1 was about 6.5 nm (Table 1). The colloid showed high stability at neutral pH with no sedimentation observed even after 2 months. The stability is ascribed to the negative charges of the uncoated nanoparticles as documented by their low zeta potential (ca. −46 mV).

The surface modification of nanoparticles is a general strategy for enhancing the cells' permeability to nanoparticles. The transport of nanoparticles can be dramatically altered through the attachment of peptides (*29, 15*). It is expected that the nature of the attached poly(amino acid) strongly influences nanoparticle transport. In this report, the surface of the nanoparticles was modified by PLL (typically of M_w = 388 100) with the aim of promoting cellular uptake. Similarly as in a previous report (*27*), the postsynthesis coating of the primary iron oxide colloid with PLL changed neither the morphology nor the size of the iron oxide crystallites nos. 2–4 (Table 1, Figure 1b).

Figure 2a shows the dependence of the hydrodynamic particle diameter, measured by dynamic light scattering, on the PLL/iron oxide ratio for freshly prepared PLL-modified iron oxide nanoparticles (M_w of PLL = 388 100) and after 5 months of storage. It is normal that the hydrodynamic particle size is larger than the size obtained by TEM (*27*). The hydrodynamic size of freshly prepared particles appears to increase with the PLL/iron oxide ratio up to 0.06, probably due to a thickening of the shell. The hydrodynamic particle size is significantly larger after 5 months of storage, especially at lower PLL/iron oxide ratios,

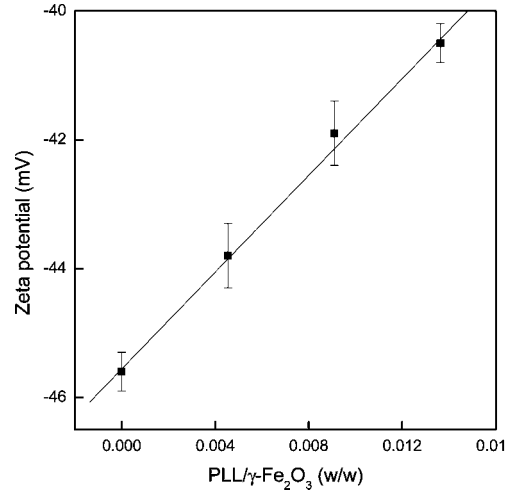

Figure 3. Dependence of zeta potential on the PLL/γ-Fe_2O_3 ratio.

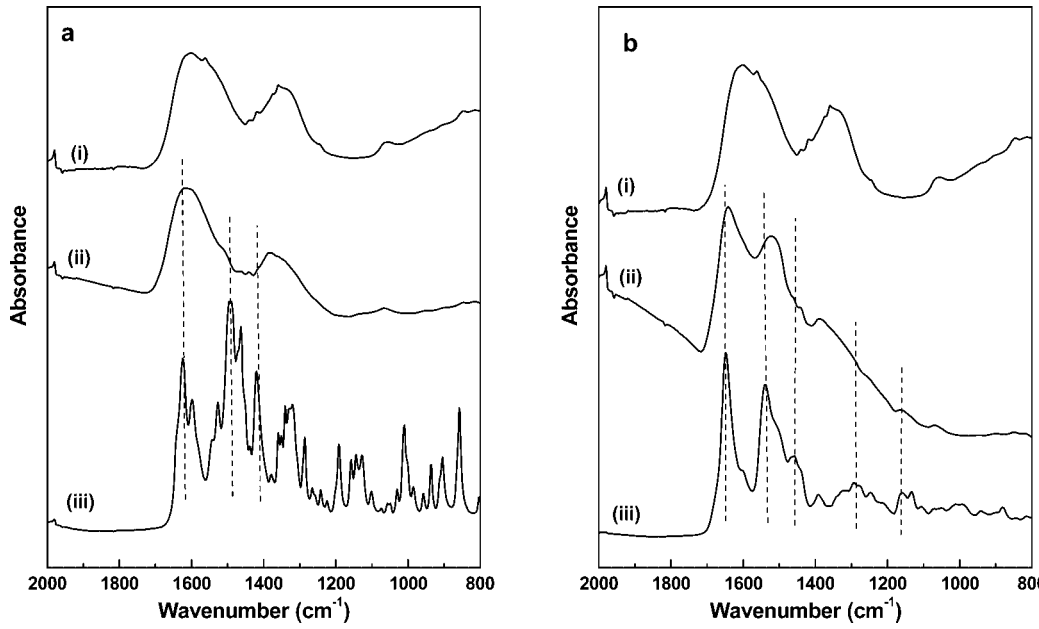

Figure 4. ATR FTIR spectra of magnetic γ-Fe_2O_3 particles before and after surface modification with (a) LL and (b) PLL; (i) iron oxide before modification, (ii) after coating, and (iii) spectrum of neat LL (a) and PLL (b).

Table 2. Concentration of L-Lysine in Hydrolyzed Supernatants after the Separation of Noncoated and PLL-Coated Iron Oxide Nanoparticles from the Medium[a]

sample	coating	medium	LL[b] (mg/mL)
1	PLL	NaCl	0.015
2		DMEM/FBS	0.419
3	PLL	DMEM/FBS	0.281
4[c]		DMEM/FBS	0.613

[a] 0.64 mL of colloid (34.7 mg γ-Fe_2O_3/ml). [b] L-Lysine after hydrolysis. [c] Control (no iron oxide particles in the medium).

because of particle aggregation. This can also be inferred from the analogous dependence of polydispersity (Figure 2b). A very high value of polydispersity was observed particularly in the absence of a PLL shell. Nevertheless, higher polydispersities were typical of all the particles after 5 months of storage (Figure 2b). Figure 3 documents an increase in zeta potential with increasing PLL/γ-Fe_2O_3 ratio, indicating that the negatively charged surface was compensated for by the positively charged PLL. This also shows that at the optimal ratio for cell labeling (0.009, see later) the zeta potential is still sufficiently low to repulse the nanoparticles.

FTIR Spectra. The structure of the surface and the efficiency of the coating of magnetic nanoparticles were analyzed by ATR FTIR spectroscopy. FTIR spectra of magnetic γ-Fe_2O_3 particles before and after surface modification with LL or PLL (M_w = 388 100) are shown in Figure 4. The spectra of pure LL and PLL are included for comparison. Two broad bands of iron oxide dominate the spectrum of the magnetic particles before modification. The spectrum of particles after modification with LL is very close to the spectrum of uncoated iron oxide (Figure 4a), confirming that LL did not coat the nanoparticles. As the molecules of LL have, at the same time, both acidic and basic character, their intermolecular interaction is stronger than the interaction with the particle surface. As a consequence, the particles are then poorly internalized by the cells (see later, Table 2).

The situation was different with PLL coating. The spectrum of particles after modification with PLL differs from the spectrum of uncoated iron oxide (Figure 4b). The main bands of PLL are clearly distinguishable in the spectrum of the modified particles. The Amide I band situated at 1648 cm^{-1} in the spectrum of pure PLL was only slightly shifted to higher wavenumbers by the coating (*30*). The Amide II band was shifted from 1539 cm^{-1} in the spectrum of pure PLL to 1502 cm^{-1} in the coating spectrum. We assume that the bands of -CH_2–NH_3^+ deformation and rocking vibrations influence the spectrum in this region. A broad, strong absorption above 1800 cm^{-1} (only the beginning is shown in Figure 4b) is observed in the spectrum, corresponding most probably to ionic interactions between PLL and the iron oxide particles. This strongly indicates that positive charges of the amine groups at the end of the PLL side chains interact with citrates complexed on the iron oxide surface as schematically illustrated in Figure 5. In contrast to the results observed with LL, the surface of γ-Fe_2O_3 nanoparticles was coated by PLL.

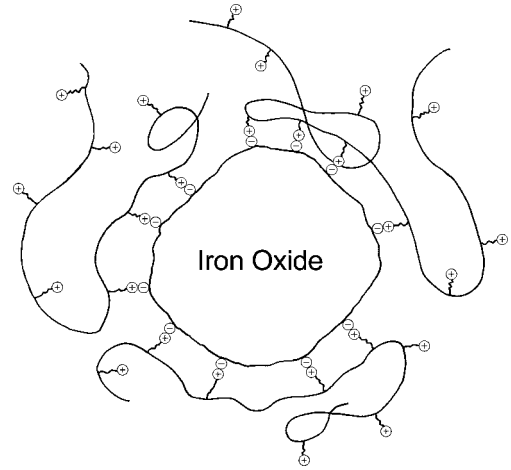

Figure 5. Schematic illustration of the interaction between PLL and a citrate-treated iron oxide nanoparticle.

High-Resolution Ultrasonic Spectroscopy. To investigate the process of PLL coating (M_w = 388 100) of the iron oxide nanoparticles in water, the colloid was monitored by high-resolution ultrasonic spectroscopy. The ultrasonic velocity increased with the addition of PLL. This is caused by an increase in the hydration layer of maghemite particles with hydrophilic PLL molecules, because water molecules are more organized in a hydration shell than in bulk (*31*). Figure 6 illustrates the

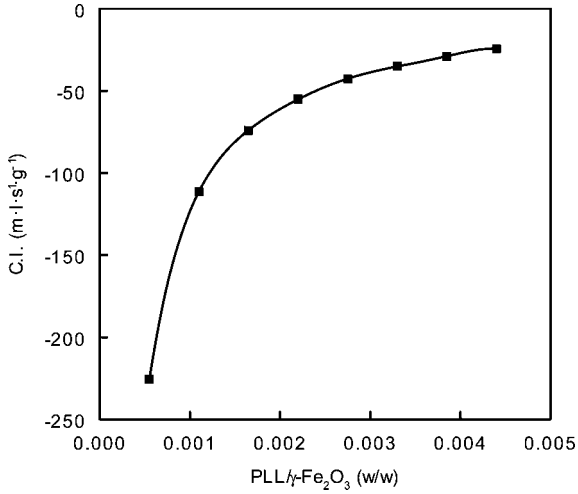

Figure 6. Dependence of the concentration increment of the ultrasonic velocity C.I. on PLL/γ-Fe_2O_3 ratio.

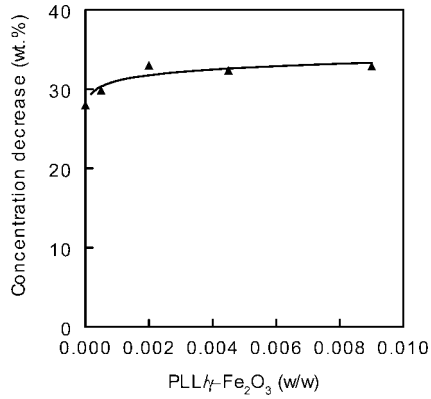

Figure 7. Effect of the PLL/iron oxide ratio on serum protein concentration in culture medium relative to a standard (DMEM/water 1/1 v/v) after adsorption by PLL-modified iron oxide nanoparticles (the concentration of serum proteins was determined by UV spectrometry at 274 nm).

concentration increment of the ultrasonic velocity depending on the amount of PLL added to the iron oxide. The largest increment in ultrasonic velocity was observed at PLL/γ-Fe_2O_3 ratios 0.0005–0.002 (w/w). The further addition of PLL solution did not significantly affect the hydration shell of the maghemite nanoparticles but resulted in a smaller increase in the increment. High-resolution ultrasonic spectroscopy thus provided another confirmation that PLL is indeed adsorbed on the particle surface. Binding is obviously achieved via the electrostatic attraction of opposite charges of PLL and iron oxide surface (Figure 5).

Protein Adsorption from Culture Medium. The adsorption of proteins from culture medium on iron oxide particles is important for elucidating both the transport of iron oxide into the cells and also nanoparticle coagulation. Iron oxide nanoparticles were mixed with serum-containing DMEM medium, the liquid was separated by centrifugation, and the UV spectra of the supernatant were measured against a standard. The relative decrease in the concentration of serum proteins was plotted against the PLL/iron oxide ratio. Figure 7 indicates that even uncoated iron oxide nanoparticles adsorbed some serum proteins from the culture medium. PLL (M_w = 388 100) modification of the iron oxide nanoparticles somewhat increased protein adsorption compared with uncoated iron oxide (Figure 7). The adsorption of serum proteins increased with increasing PLL concentration, reaching a plateau at a PLL/iron oxide ratio of 0.002. It is interesting to note that, while at higher PLL/iron oxide ratios protein adsorption did not increase, the percentage of labeled cells did (Table 1). It might be speculated that the entire PLL chain fully adheres onto the nanoparticle surface at PLL/iron oxide ratios 0.002 or less. The idea is also supported by the ultrasonic measurements. However, at higher ratios, all PLL chains remain attached to the iron oxide surface via their certain segments while their other parts move freely in the medium (Figure 5), facilitating cell labeling (see below). The free chain parts thus do not increase serum protein adsorption, but they can provide contact with the cell membrane.

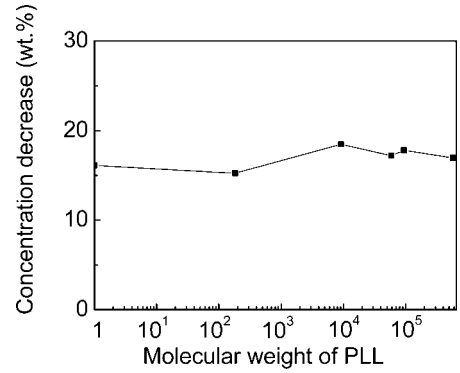

Figure 8. Effect of PLL molecular weight on serum protein concentration in culture medium relative to a standard (DMEM/water 1/1 v/v) after adsorption by PLL-modified iron oxide nanoparticles (the concentration of serum proteins was determined by UV spectrometry at 274 nm; PLL/iron oxide = 0.009 w/w—analogous to nanoparticles no. 4; Table 1).

To exclude the possibility that PLL dissociates from the iron oxide surface once mixed with serum, both uncoated (no. 1, Table 1) and PLL-coated nanoparticles (no. 4) were placed in DMEM/10% FBS medium or 0.15 M NaCl solution, magnetically separated, the supernatants hydrolyzed, and concentration of L-lysine was determined (Table 2). As expected, only traces of L-lysine were found in the supernatant from PLL-modified iron oxide during contact with the 0.15 M NaCl solution (sample 1, Table 2). This documents that PLL strongly associated with the iron oxide nanoparticles. The addition of uncoated iron oxide (sample 2) in DMEM/10% FBS induced a decrease in the amount of L-lysine in the hydrolyzed supernatant as compared with the control (sample 4), while the addition of PLL-coated iron oxide nanoparticles (sample 3) to DMEM/10% FBS led to a more pronounced decrease of L-lysine in the hydrolyzed supernatant. This is in accordance with our protein adsorption experiments (Figure 7). It should be noted that the total amount of L-lysine before hydrolysis and magnetic separation in sample 3 was higher than that in samples 2 and 4 (control), because in addition to serum L-lysine, it also contained L-lysine originating from the PLL coating. These experiments thus did not show the release of PLL from the PLL-coated iron oxide nanoparticles into the culture medium.

The effect of the molecular weight of PLL on the adsorption of FBS serum proteins from DMEM cultivation medium was also investigated by UV–vis spectrometry. The molecular weight of PLL did not significantly influence the adsorption of proteins from the DMEM medium on the surface of PLL-modified maghemite (Figure 8). It should be noted that this experiment was performed with another FBS charge than in the investigation of the effect of the PLL/iron oxide ratio on the concentration decrease in serum proteins, thus explaining the difference in the amount of adsorbed proteins (see Figures 7 and 8).

Cell Labeling. Cell labeling with Fe(III)/Fe(II)/paramagnetic substances is an increasingly common method for *in vivo* cell monitoring and separation (*32*), as the labeled cells can be detected by magnetic resonance imaging. The surface charac-

Table 3. Effect of PLL Molecular Weight on Percentage of rMSC Cells Labeled with PLL-Modified Iron Oxide Nanoparticles[a]

molecular weight	Endorem[b]	146	9200	58 900	93 800	388 100	579 000
percentage of labeled cells[c] (%)	58.6	80.6	87.6	84.7	90.4	92.2	90.5

[a] Concentration 2.2 mg of PLL-modified γ-Fe_2O_3/mL. [b] Control. [c] Average of 15 measurements.

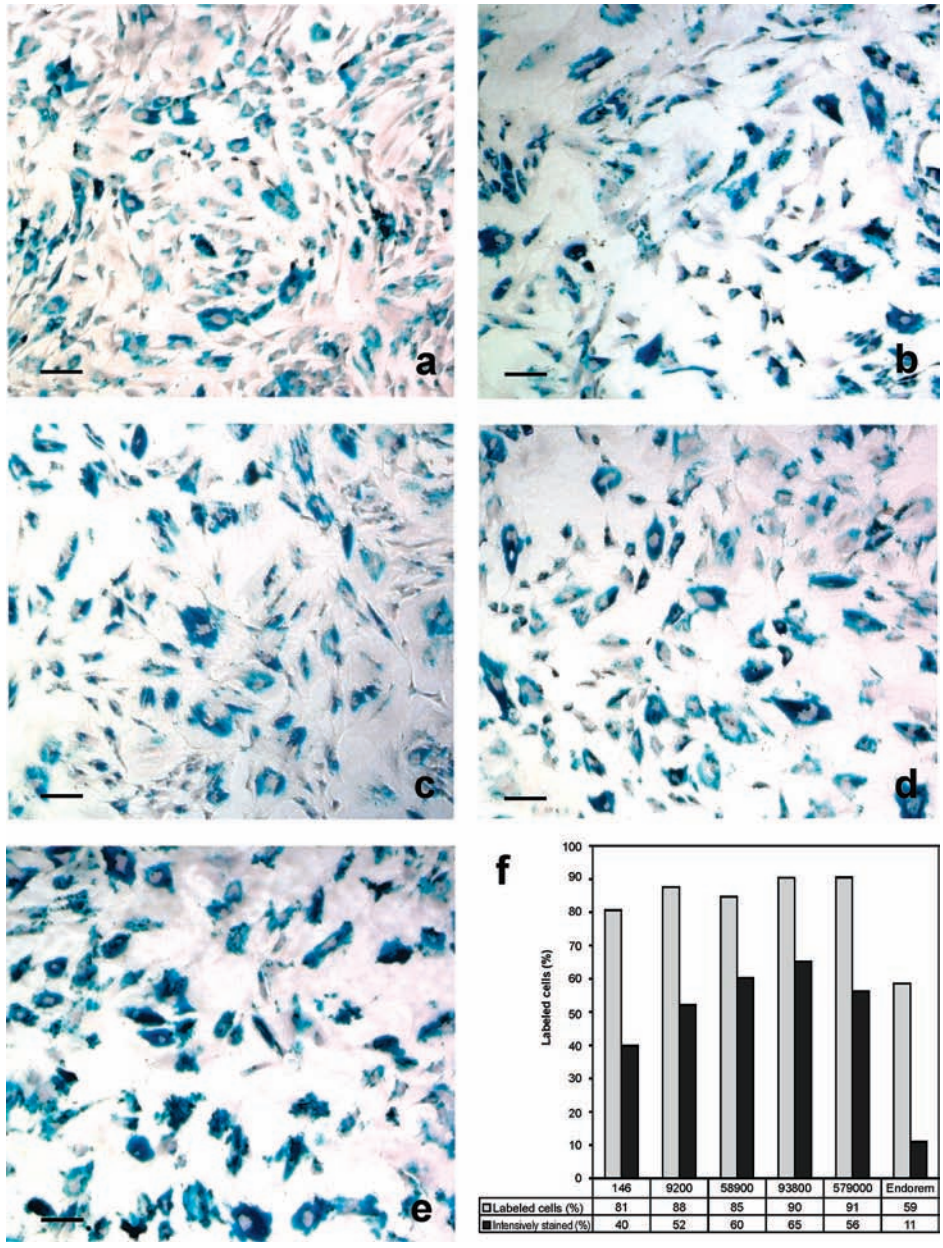

Figure 9. Microscopic observation of rMSCs labeled with PLL-modified iron oxide nanoparticles: effect of PLL molecular weight. M_w = (a) 146, (b) 9200, (c) 58 900, (d) 93 800, and (e) 579 000. Scale bar 50 μm. (f) Histograms of the percentage of the Prussian Blue stained PLL-coated iron oxide nanoparticle- and Endorem-labeled rMSC cells: effect of PLL molecular weight. Grey and black columns represent the percentage of labeled cells and strongly labeled cells, respectively, out of all the cells in the culture medium.

teristic of nanoparticles plays an important role in their internalization in cells. First, rMSCs labeled with either uncoated or surface-modified iron oxide nanoparticles were observed using an optical microscope. Cell labeling with Endorem served as a control. Endorem, however, shows a tendency to adhere on the surface of the cells, in addition to sticking to the bottom of the vessel. Using the Prussian Blue reaction, the cellular iron content was measured in MSCc exposed to the nanoparticles.

Primary Uncoated Iron Oxide. Primary uncoated iron oxide colloid no. 1 (Table 1) was tested for cell labeling to elucidate the importance of iron oxide modification/coating in subsequent experiments. Observation using an optical microscope with phase contrast revealed the iron oxide nanoparticles in rMSCs as dark dots. Cells in contact with the nanoparticles proliferated, and approximately one in every ten cells endocytosed the iron oxide. This might be explained by the formation of aggregates of sterically unstable particles due to the presence of electrolytes in the medium. As the resulting coagulates had a broad size distribution, only the small ones could penetrate into the cells, whereas the large ones were not internalized. In an attempt to increase cell labeling, the iron oxide surface was modified with PLL.

Poly(L-Lysine)-Modified Iron Oxide. PLL is a polycation due to the presence of NH_2 groups, widely used as a nonviral

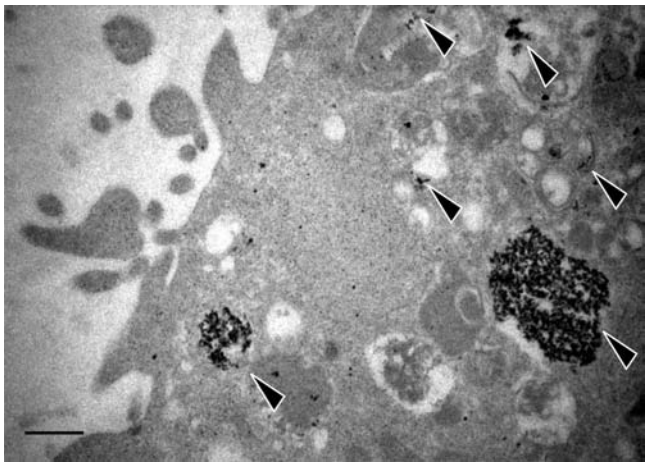

Figure 10. TEM micrographs of rMSC cells labeled with PLL-modified iron oxide nanoparticles (no. 3, Table 1). Scale bar 1 μm.

transfection agent for gene delivery and in DNA complexing thus promoting cell adhesion (*33*) through a positively charged interface clearly possessing an affinity for negatively charged cells. PLL is known to adsorb proteins not only from nutrient solutions, but also from cell membranes.

The results of both rat and human MSC cell labeling with PLL-modified maghemite nanoparticles (M_w of PLL = 388 100) are summarized in Table 1. It is clear that the degree of iron oxide internalization by the cells was PLL concentration-dependent. The higher the PLL concentration, the better the cell labeling (Table 1). The best result in terms of maximum cell labeling was achieved with 0.02 mg PLL per mL of colloid (Table 1, no. 4). The mechanism of PLL-mediated iron oxide uptake by the cells is assumed to be based on endocytosis and/or diffusion through the cell membranes (*34*). Cells took up much more PLL-modified nanoparticles than they did Endorem. Even a relatively low PLL concentration was sufficient for almost complete cell labeling. It can be thus assumed that increased endocytosis was induced by associates formed between PLL-coated nanoparticles and serum proteins. This is in accordance with both our protein adsorption experiments and also the L-lysine analysis of hydrolyzed supernatants (Table 2). The nanoparticles, however, aggregated at concentrations higher than 0.02 mg of PLL/mL. The results document a positive effect of PLL on intracellular nanoparticle uptake. This is in accordance with the published data on the cellular improved uptake of nanoparticles containing amino groups (*35*). Another approach to improve the uptake of nanoparticles into cells using PLL is based on combining a commercially available dextran-coated SPIO, such as Feridex (*36*) or Sinerem (*37*), and a commercially available transfection agent based on PLL (*38*). However, each combination of transfection agent and dextran-coated SPIO nanoparticles has to be carefully titrated and optimized for different cell cultures, since lower concentrations of transfection agent may result in insufficient cellular uptake, whereas higher concentrations may induce the precipitation of complexes or may be toxic for the cells (*39*). Also, magnetite cationic liposomes are known to promote the uptake of magnetic particles by target cells (*18*).

Table 4. Relaxivities r_1 and r_2 of Contrast Agent Suspensions and the Relaxation Rates of Suspensions of rMSCs Labeled with Contrast Agents

	relaxivities of phantoms containing suspension of pure contrast agent (s^{-1}/mmol Fe)		relaxation rates of phantoms containing labeled cells ($s^{-1}/10^6$ cells/mL)	
contrast agent	r_1	r_2	R_1	R_2
PLL-modified iron oxide no. 4	17.36	213	0.32	4.29
Endorem	19.65	126	0.18	1.24

Effect of PLL Molecular Weight. In the next series of experiments, L-lysine and PLL of several molecular weights, ranging up to 579 000, were chosen to test the cellular uptake of PLL-modified iron oxides (Table 3). Maghemite nanoparticles modified with L-lysine (M_w = 146) penetrated into the cells rather poorly, similarly to primary uncoated iron oxide particles, indicating again that LL did not coat the iron oxide (Figure 9). In contrast to LL-modified nanoparticles, the particles modified with PLL were internalized well by the cells. The efficiency of cell labeling increased with the molecular weight of PLL up to M_w = 388 100, which can be considered an optimum PLL molecular weight for γ-Fe_2O_3 nanoparticle modification. This is in accordance with earlier observations of inefficient mammalian cell labeling with low-molecular-weight PLL (*38*). On the other hand, particles coated with high-molecular-weight PLL (M_w = 579 000) showed lower cellular uptake (Table 2) and, moreover, adhered to the cell walls. This was indicated by the fact that the blue-stained areas were larger than the cells (Figure 9e). It is interesting to note that the efficiency of cell labeling with Endorem was higher in the experiments summarized in Table 1 than in those reported in Table 3, probably due to differences in the passage number of the cells used.

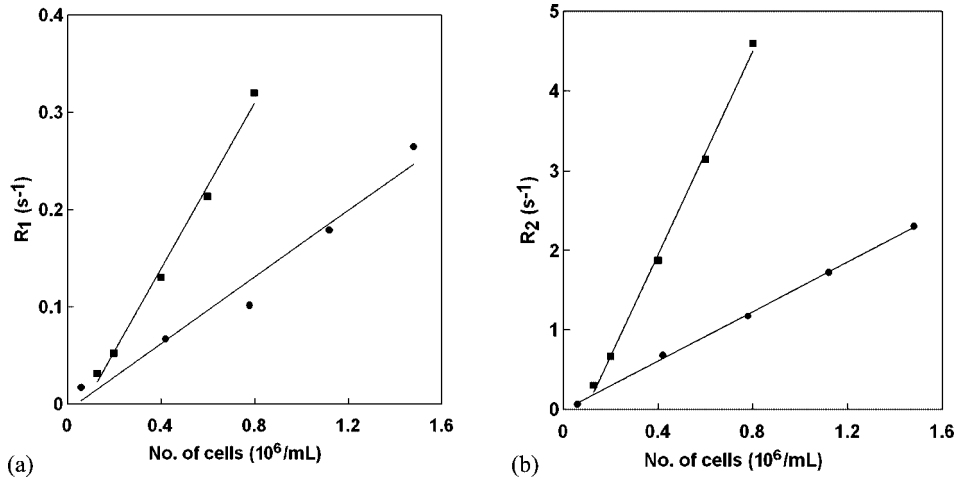

Figure 11. Proton relaxation rates (a) R_1 and (b) R_2 of rMSCs labeled with (•) Endorem and (■) PLL-modified iron oxide nanoparticles (no. 4, Table 1).

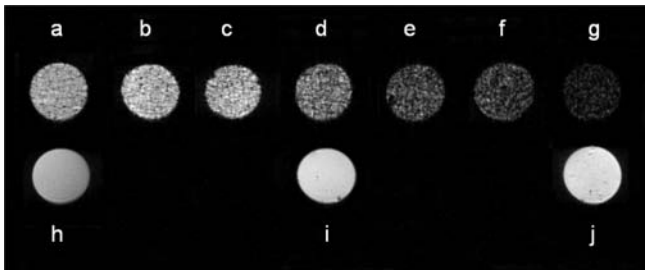

Figure 12. Gelatin phantoms containing (a) 200, (b) 400, (c) 800, (d) 1200, (e) 1600, (f) 2000, and (g) 4000 PLL-modified iron oxide (no. 4)-labeled cells per μL, and control samples with (h) 200, (i) 1200, and (j) 4000 unlabeled cells per μL.

Image analysis tools were used to evaluate not only the percentage of labeled cells, but also the intensity of Prussian Blue staining. The resulting histograms (Figure 9f) confirmed that the cells labeled with particles coated with higher-molecular-weight PLL ($M_w > 58\,900$) were stained to a darker shade of blue, because they contained a greater amount of iron per cell than those labeled with particles coated with low-molecular-weight PLL. However, the intensity of Prussian Blue staining of particles modified with PLL of $M_w = 579\,000$ was slightly decreased.

Transmission Electron Microscopy of Labeled Cells. To confirm the internalization of PLL-coated nanoparticles no. 3 by the cells rather than simply their bonding to the cell surface, and to visualize the location of the nanoparticles inside the cells after internalization, cells were examined by transmission electron microscopy (Figure 10). These observations revealed that the coated nanoparticles indeed crossed cell membranes and were internalized into the cells. They appeared as black dots evenly dispersed in the cell cytoplasm; cell membrane-bound nanoparticle clusters were not detected. The majority of the internalized PLL-coated nanoparticles were located in the lysosomes of the cells, which supports their intracellular trafficking. Nanoparticles are transported in endosomes and finally fused with lysosomes, a process during which the vesicle membranes disappear.

Comparison of Relaxivity between rMSC Labeled with Endorem and PLL-Modified Iron Oxide no. 4. MR relaxometry enables the quantification and proper comparison of relaxation times (and relaxivities), which are responsible for contrast enhancement in T_1-, T_2-, and T_2*-weighted MR images.

In Figure 11, the proton relaxation rates R_1 (a) and R_2 (b) of phantoms with labeled cells suspended in gelatin are plotted against the cell concentration. The relaxation rates of cells loaded with PLL-modified iron oxide nanoparticles were significantly higher than those of cells labeled with Endorem particles. Table 4 compares the relaxivities and relaxation rates of gelatin samples containing suspensions of the contrast agents or labeled cells relative to iron concentration or cell numbers, respectively. Relaxivity r_2 of PLL-modified iron oxide suspended in gelatin was 70% higher than that of Endorem. The difference between the relaxation rates of samples containing cells (related to the number of cells) labeled with PLL-modified nanoparticles and cells labeled with Endorem was much greater. This observation cannot be explained only by the higher relaxivity of the nanoparticles used; it is probably due to the better internalization of PLL-modified iron oxide nanoparticles in the cells. This hypothesis was confirmed by iron analysis of the cell suspensions, the average amounts of iron determined by spectrophotometry after mineralization were 41.5 pg of iron per cell for cells labeled with PLL-modified iron oxide no. 4 and 14.6 pg of iron per cell for Endorem-labeled cells.

***In Vitro* MR Imaging.** To check the sensitivity of the MRI technique and to mimic signal behavior in brain tissue, suspensions of unlabeled cells and cells labeled with PLL-modified iron oxide nanoparticles were imaged *in vitro*. Even the sample containing the lowest concentration (200 cells/μL which corresponds on average to 2 cells per image voxel) still provided visible contrast compared with a control phantom containing the same number of unlabeled cells (Figure 12). A similar set of experiments was performed in our previous work (*40*), in which MR images of gelatin phantoms showed a hypointense signal at the concentrations above 625 labeled cells per μL.

***In Vivo* MR Imaging.** Rats were examined 3 days after transplantation in an MR imager. Figure 13 shows that PLL-modified iron oxide (no. 4)-labeled cells were clearly discernible *in vivo*, even at low concentrations (1000 cells/2 μL). The iron oxide-labeled cell implants were visible as a hypointense area at the injection site. Cells labeled by PLL-modified iron oxide provide a better visible contrast than do Endorem-labeled cells. Labeling with PLL-modified iron oxide thus makes it possible to detect a lower number of cells in the tissue.

CONCLUSIONS

The preparation of new surface-modified iron oxide nanoparticles for stem labeling has been described and their

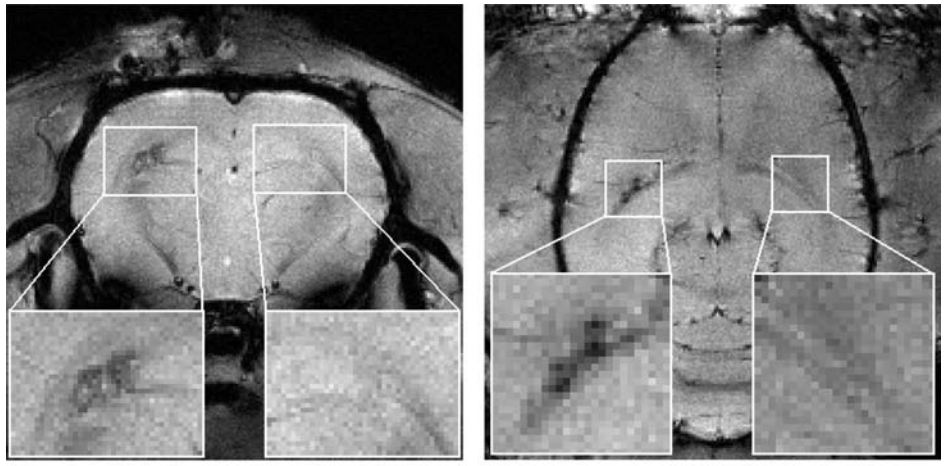

Figure 13. (a) Axial and (b) coronal MR images of a rat brain with 1000 cells labeled with PLL-modified iron oxide implanted into the left hemisphere and 1000 Endorem-labeled cells implanted into the right hemisphere. MR images were taken 3 days after implantation. Enlarged insets clearly show a hypointense signal in the left hemisphere; such a signal is not visible in the right one.

properties optimized. The structure of the polymer shell of the iron oxide core determined the efficacy of the nanoparticles' interaction with cells. A good colloidal stability has been obtained with poly(L-lysine) modifiers. Poly(L-lysine)-modified nanoparticles less than 10 nm in diameter were tested for cell labeling. PLL of high molecular weight ($M_w = 388\,100$) proved to be the most effective surface-modifier for achieving the greatest internalization by rat bone marrow stromal cells. The accumulation of the magnetic particles in the cells was obviously facilitated by PLL-induced modification of the particles' surface charge. TEM examination of PLL-coated nanoparticles showed the successful internalization of the nanoparticles into lysosomes. Nanoparticles were found inside cells, mainly in endosomes. The cellular uptake of iron oxide nanoparticles was dependent on the concentration of PLL used in the iron oxide modification. At high concentrations, the nanoparticles started to aggregate in the culture medium. The cellular iron content was also dependent on the amount of added nanoparticles. Cell labeling with newly developed PLL-modified iron oxide was more efficient than that with a conventionally used agent (Endorem). Compared to Endorem, both the higher r_2 relaxivity of PLL-modified nanoparticles and their better internalization in the cells enabled easier MRI detection and tracking of cells in the tissue after transplantation. Moreover, the viability of PLL-coated iron oxide-labeled cells determined by a colorimetric essay was much higher than in cells labeled with Endorem (*41*). The newly developed PLL-modified iron oxide nanoparticles are expected to be nontoxic, similarly as analogous iron oxide−PLL complexes (*42*), the biodegradation of which and metabolic processes in cells have been reported earlier. The iron is introduced into the normal plasma iron pool and is then incorporated into the hemoglobin of red cells or metabolized (*43*). Compared with PLL modification of dextran-coated iron oxide nanoparticles (*44*), the advantage of our new procedure is that no dextran is necessary to produce the particles, thus simplifying their preparation. The developed nanoparticles are a promising tool for the noninvasive *in vivo* tracking of transplanted cells in the host organism and for monitoring the long-term effects of such transplantation.

ACKNOWLEDGMENT

The financial support of the Center for Cell Therapy and Tissue Repair (No. 1M0021620803), the Grant Agency of the Academy of Sciences of the Czech Republic (grant KAN200200651 and KAN201110651), and the Grant Agency of the Czech Republic (grant 203/05/2256 and 309/06/1594) is gratefully acknowledged.

LITERATURE CITED

(1) Pankhurst, Q. A., Connolly, J., Jones, S. K., and Dobson, J. (2003) Applications of magnetic nanoparticles in biomedicine. *J. Phys. D: Appl. Phys. 36*, R167–R181.

(2) Marchal, G., van Hecke, P., Demaerel, P., Decrop, E., Kennis, C., Baert, A. L., and van der Schueren, E. (1989) Detection of liver metastases with superparamagnetic iron oxide in 15 patients: Results of MR imaging at 1.5 T. *Am. J. Roentgenol. 152*, 771–775.

(3) Lubbe, A. S., Bergemann, C., Riess, H., Schriever, F., Reichardt, P., Possinger, K., Matthias, M., Dorken, B., Herrmann, F., Gurtler, R., Hohenberger, P., Haas, N., Sohr, R., Sander, B., Lemke, A. J., Ohlendorf, D., Huhnt, W., and Huhn, D. (1996) Clinical experiences with magnetic drag targeting: A phase I study with 4′-epidoxorubicin in 14 patients with advanced solid tumors. *Cancer Res. 56*, 4686–4693.

(4) Guesdon, J. L., Thiery, R., and Avrameas, S. (1978) Magnetic enzyme immunoassay for measuring human IgE. *J. Allergy Clin. Immunol. 6*, 23–27.

(5) Druet, E., Mahieu, P., Foidart, J. M., and Druet, P. (1982) Magnetic solid-phase enzyme immunoassay for the detection of anti-glomerular basement membrane antibodies. *J. Immunol. Methods 48*, 149–157.

(6) Gu, H., Ho, P. L., Tsang, K. W. T., Wang, L., and Xu, B. (2003) Using bifunctional magnetic nanoparticles to capture vancomycin-resistant Enterococci and other gram-positive bacteria at ultralow concentration. *J. Am. Chem. Soc. 125*, 15702–15703.

(7) Pazzagli, M., Kohen, F., Sufi, S., Masironi, B., and Cekan, S. Z. (1988) Immunometric assay for lutropin (hLH) based on the use of universal reagents for enzymatic labeling and magnetic separation and monitored by enhanced chemiluminescence. *J. Immunol. Methods 114*, 62–68.

(8) Vonk, G. P., and Schram, J. L. (1991) Dual-enzyme cascade-magnetic separation immunoassay for respiratory syncytial virus. *J. Immunol. Methods 137*, 133–139.

(9) Josephson, L., Perez, J. M., and Weissleder, R. (2001) Magnetic nanosensors for the detection of oligonucleotide sequences. *Angew. Chem., Int. Ed. 40*, 3204–3206.

(10) Patolsky, F., Weizmann, Y., Katz, E., and Willner, I. (2003) Magnetically amplified DNA assays (MADA): Sensing of viral DNA and single-base mismatches by using nucleic acid modified magnetic particles. *Angew. Chem., Int. Ed. 42*, 2372–2376.

(11) Nam, J. M., Thaxton, C. S., and Mirkin, C. A. (2003) Nanoparticle-based bio-bar codes for the ultrasensitive detection of proteins. *Science 301*, 1884–1886.

(12) Lewin, M., Carlesso, N., Tung, C. H., Tang, X. W., Cory, D., Scadden, D. T., and Weissleder, R. (2000) Tat peptide-derivatized magnetic nanoparticles allow in vivo tracking and recovery of progenitor cells. *Nat. Biotechnol. 18*, 410–414.

(13) Torchilin, V. P. (2000) Drug targeting. *Eur. J. Pharm. Sci. 11*, S81–S91.

(14) Häfeli, U. O. Magnetically modulated therapeutic systems. *Int. J. Pharm. 277*, 19–24.

(15) Xiang, J. J., Tang, J.-Q., Zhu, S.-G., Nie, X.-M., Lu, H.-B., Shen, S.-R., Li, X.-L., Tang, K., Zhou, M., and Li, G.-Y. (2003) IONP-PLL: A novel non-viral vector for efficient gene delivery. *J. Gene Med. 5*, 803–817.

(16) Jordan, A., Scholz, R., Maier-Hauff, K., Johannsen, M., Wust, P., Nadobny, J., Schirra, H., Schmidt, H., Deger, S., Loening, S., Lanksch, W., and Felix, R. (2001) Presentation of a new magnetic field therapy system for the treatment of human solid tumors with magnetic fluid hyperthermia. *J. Magn. Magn. Mater. 225*, 118–126.

(17) Gupta, A. K., and Gupta, M. (2005) Synthesis and surface engineering of iron oxide nanoparticles for biomedical applications. *Biomaterials 26*, 3995–4021.

(18) Shinkai, M. (2002) Functional magnetic particles for medical application. *J. Biosci. Bioeng. 94*, 606–613.

(19) Stella, B., Arpicco, S., Peracchia, M. T., Desmaele, D., Hoebeke, J., Renoir, M., D'Angelo, J., Cattel, L., and Couvreur, P. (2000) Design of folic acid-conjugated nanoparticles for drug targeting. *J. Pharm. Sci. 89*, 1452–1464.

(20) Zhang, Y., and Zhang, J. (2005) Surface modification of monodisperse magnetite nanoparticle for improved intracellular uptake to breast cancer cells. *J. Colloid Interface Sci. 283*, 352–357.

(21) Allen, M. J., MacRenaris, K. W., Venktasubramanian, P. N., and Meade, T. J. (2004) Cellular delivery of MRI contrast agents. *Chem. Biol. 11*, 301–307.

(22) Stark, D. D., Weissleder, R., Elizondo, G., Hahn, P. F., Saini, S., Todd, L. E., Wittenberg, J., and Ferrucci, J. T. (1988) Superparamagnetic iron oxide: Clinical application as a contrast agent for MR imaging of the liver. *Radiology 168*, 297–301.

(23) Molday, R. S., and MacKenzie, D. (1982) Immunospecific ferromagnetic iron-dextran reagents for the labeling and magnetic separation of cells. *J. Immunol. Methods 52*, 353–367.

(24) Cheng, F.-Y., Su, C.-H., Yang, Y.-S., Yeh, C.-S., Tsai, C.-Y., Wu, C.-L., Wu, M.-T., and Shieh, D.-B. (2005) Characterization of aqueous dispersions of Fe_3O_4 nanoparticles and their biomedical applications. *Biomaterials 26*, 729–738.

(25) Taupitz, M., Schnorr, J., Wagner, S. A., Abramjuk, C., Pilgrimm, H., Kivelitz, D., Schink, T., Hansel, J., Laub, G., Humogen, H., and Hamm, B. (2002) Coronary MR angiography: Experimental results with a monomer-stabilized blood pool contrast medium. *Radiology 222*, 120–126.

(26) Kiessling, A. A., Anderson, S. C. (2003) *Human embryonic stem cells, an introduction to the science and therapeutic potential*. Jones & Bartlett Publishers, USA.

(27) Horák, D., Babič, M., Jendelová, P., Herynek, V., Trchová, M., Pientka, Z., Pollert, E., Hájek, M., and Syková, E. (2007) D-mannose-modified iron oxide nanoparticles for stem cell labeling. *Bioconjugate Chem. 18*, 635–644.

(28) Azizi, S. A., Stokes, D., Augelli, B. J., DiGirolamo, C., and Prockop, D. J. (1998) Engraftment and migration of human bone marrow stromal cells implanted in the brains of albino rats–similarities to astrocyte grafts. *Proc. Natl. Acad. Sci. U.S.A. 95*, 3908–3913.

(29) Koch, A. M., Reynolds, F., Merkle, H. P., Weissleder, R., and Josephson, L. (2005) Transport of surface-modified nanoparticles through cell monolayers. *ChemBioChem 6*, 337–345.

(30) Socrates, G. (2001) In *Infrared and Raman Characteristic Group Frequencies*, pp 143–145, Wiley, New York.

(31) Van Durme, K., Delellio, L., Kudryashov, E., Buckin, V., and Van Mele, B. (2005) Exploration of high-resolution ultrasonic spectroscopy as an analytical tool to study demixing and remixing in poly(*N*-isopropyl acrylamide)/water solutions. *J. Polym. Sci., Part B: Polym. Phys. 43*, 1283–1295.

(32) Olsvik, O., Popovic, T., Skjerve, E., Cudjoe, K. S., Hornes, E., Ugelstad, J., and Uhlen, M. (1994) Magnetic separation techniques in diagnostic microbiology. *Clin. Microbiol. Rev. 7*, 43–54.

(33) Schatzlein, A. G. (2001) Non-viral vectors in cancer gene therapy: principles and progress. *Anticancer Drugs 12*, 275–304.

(34) Dormer, K., Seeney, C., Lewelling, K., Lian, G., Gibson, D., and Johnson, M. (2005) Epithelial internalization of superparamagnetic nanoparticles and response to external magnetic field. *Biomaterials 24*, 2061–2072.

(35) Petri-Fink, A., Chastellain, M., Juillerat-Jeanneret, L., Ferrari, A., and Hofmann, H. (2005) Development of functional superparamagnetic iron oxide nanoparticles for interaction with human cancer cells. *Biomaterials 26*, 2685–2694.

(36) Frank, J. A., Miller, B. R., Arbab, A. S., Zywicke, H. A., Jordan, E. K., Lewis, B. K., Bryant, L. H., and Bulte, J. W. M. (2003) Clinically applicable labeling of mammalian and stem cells by combining superparamagnetic iron oxides and transfection agents. *Radiology 228*, 480–487.

(37) Hoehn, M., Kustermann, E., Blunk, J., Wiedermann, D., Trapp, T., and Focking, M. (2002) Monitoring of implanted stem cell migration in vivo: A highly resolved in vivo magnetic resonance imaging investigation of experimantal stroke in rat. *Proc. Natl. Acad. Sci. U.S.A. 100*, 1073–1078.

(38) Arbab, A. S., Yocum, G. T., Wilson, L. B., Parwana, A., Jordan, E. K., Kalish, H., and Frank, J. A. (2004) Comparison of transfection agents in forming complexes with ferumoxides, cell labeling efficiency, and cellular viability. *Mol. Imaging 3*, 24–32.

(39) Kalish, H., Arbab, A. S., Miller, B. R., Lewis, B. K., Zywicke, H. A., Bulte, J. W., Bryant, L. H., and Frank, J. A. (2003) Combination of transfection agents and magnetic resonance contrast agents for cellular imaging: Relationship between relaxivities, electrostatic forces, and chemical composition. *Magn. Reson. Med. 50*, 275–282.

(40) Jendelová, P., Herynek, V., DeCroos, J., Glogarová, K., Andersson, B., Hájek, M., and Syková, E. (2003) Imaging the fate of implanted bone marrow stroma cells labeled with superparamagnetic nanoparticles. *Magn. Reson. Med. 50*, 767–776.

(41) Jendelová, P., Horák, D., Babič, M., Glogarová, K., Herynek, V., Hájek, M., and Syková, E. (2007) Modified iron oxide nanoparticles for *in vivo* cell imaging. *Regenerative Med. 2*, 635.

(42) Yocum, G. T., Wilson, L. B., Ashari, P., Jordan, E. K., Frank, J. A., and Arbab, A. S. (2005) Effect of human stem cells labeled with ferumoxides-poly-L-lysine on hematologic and biochemical measurements in rats. *Radiology 235*, 547–552.

(43) Weissleder, R., Stark, D. D., Engelstad, B. L., Bacon, B. R., Compton, C. C., White, D. L., Jacobs, P., and Lewis, J. (1989) Superparamagnetic iron oxide: Pharmacokinetics and toxicity. *Am. J. Roentgenol. 152*, 167–173.

(44) Arbab, A. S., Bashaw, L. A., Miller, B. R., Jordan, E. K., Lewis, B. K., Kalish, H., and Frank, J. A. (2003) Characterization of biophysical and metabolic properties of cells labeled with superparamagnetic iron oxide nanoparticles and transfection agent for cellular MR imaging. *Radiology 229*, 838–846.

BC700410Z

Calix[4]arene Decorated with Four Tn Antigen Glycomimetic Units and P_3CS Immunoadjuvant: Synthesis, Characterization, and Anticancer Immunological Evaluation

Corrada Geraci,*,† Grazia M. L. Consoli,† Eva Galante,† Ennio Bousquet,‡ Maria Pappalardo,‡ and Angelo Spadaro*,‡

Istituto di Chimica Biomolecolare, C.N.R., Via del Santuario 110, I-95028 Valverde (CT), Italy, and Dipartimento di Scienze Farmaceutiche - Università di Catania, Viale A. Doria 6, I-95125 Catania, Italy. Received November 6, 2007; Revised Manuscript Received January 10, 2008

A novel anticancer vaccine candidate built on a nonpeptidic scaffold has been synthesized. Four *S*-Tn tumor-associated glycomimetic antigens have been clustered onto a calix[4]arene scaffold bearing an immunoadjuvant moiety (P_3CS). The immunogenicity of the synthetic construct has been investigated by immunization of mice *in vivo*. ELISA assay has evidenced that the tetravalent construct stimulates a higher production of anti-Tn antigen IgG antibodies when compared to an analogous monovalent compound. This result is ascribable to an antigen cluster effect and makes the reported vaccine candidate a good mimic of the natural motifs present on the mucine surface.

INTRODUCTION

The purpose of cancer vaccination to fight tumors using the patient's own immune system continues to be very attractive and challenging, despite the successes reached during the past few years in conventional anticancer therapy (*1–4*). In fact, several metastatic tumors remain resistant to usual antitumor therapy, such as metastatic melanoma and renal and lung carcinoma. From this, numerous studies have been undertaken to exploit the immune response by successively increasing its strength and specificity in order to oppose the disease with effectiveness. On this concept are based cancer vaccines which generate antibodies capable of recognizing and eliminating circulating cancer cells and micrometastasis.

Mucine are members of a large family of glycoproteins present on the surface of many epithelial cells, where they perform physical (lubrication and moisturization) and protective (against pathogenic microorgamisms and mechanical damage) functions (*5*). The epithelial cancers such as breast, pancreatic, colorectal, ovarian, or prostate cancers are often associated with a dysregulation of the glycosylation processes and consequently with altered carbohydrate patterns expressed on the cancer cell surface (*6*). This determines alteration of the cell adhesion, migration, and communication with the immune system and produces metastatic increase and decrease of the immune response (*7*).

Specific tumor-associated carbohydrate antigens (TAs) such as Globo-H, Tn, TF, and sialyl-Tn, cryptic in normal epithelial cells, are overexpressed on the surface of tumor cells because of an incomplete glycosylation which leads to a block in carbohydrate chain elongation (*8, 9*). Due to the difficulty obtaining these antigens from natural sources, numerous chemical synthetic procedures have been developed to achieve this (*10*).

Unfortunately, TAs are autoantigens or self-antigens (*11*), and hence they are weak immunogens. To circumvent this problem, carrier proteins or macrolipid immunoadjuvants (*12–16*) have been conjugated to the antigen epitope. The elegant studies of Danishefsky et al. are milestones in this research area. Monovalent vaccine constructs composed of a single carbohydrate antigen conjugated to keyhole-limpet hemocyanin (KLH) and coadministered with QS-21 adjuvant have advanced to clinical trials (*17*).

As the carrier protein excess could cause an increased antibody response to the carrier itself and a drop in the immunogenicity of the antigen, a strategy to limit these events has provided the design of multivalent constructs in which the presence of multiple antigenic units results in a more efficient immune response (*18*). In addition, multivalent structures better mimic the mucine surface, wherein Tn antigens are exposed in clusters of 2 to 5. It has been demonstrated that at least two Tn contiguous antigen residues are crucial for the binding of the anti-Tn monoclonal antibodies 83D4 and MLS128, and that MLS128 affinity is greater on a glycopeptide with three successive Tn residues (*19–23*).

In the past ten years, great attention has been paid to the choice of scaffolds for the exposition of multiple antigenic units. Polypeptide fragments, a lysine core extended with peptidic (MAP) (*24*) or glycopeptidic (MAG) (*25*) arms, and a cyclized decapeptide have been selected as backbones to build multivalent vaccines (*26*). Some of them have presented high immunogenicity in mice and in nonhuman primates (*27*).

Following a similar approach, we decided to synthesize a novel fully synthetic cancer vaccine candidate in which a cluster of four Tn antigen glycomimetic units (*S*-Tn) is conjugated to an immunoadjuvant moiety, tripalmitoyl-*S*-glycerylcysteinyl-serine (P_3CS), through a calix[4]arene scaffold (Schemes 1−3). The presence of a rigid platform has provided a tetravalent derivative (**11**) with a definite spatial preorganization of the antigenic moieties.

Biological tests, performed *in vivo* by immunization of mice, showed that the target construct possesses higher immunostimulating activity with respect to the corresponding monovalent

* Corresponding authors. Corrada Geraci: phone +39 095 7212136; fax +39 095 7212141; e-mail corrada.geraci@icb.cnr.it. Angelo Spadaro: phone + 39 095 7384011; fax +39 095 7384250; e-mail angelo.spadaro@unict.it.

† Istituto di Chimica Biomolecolare, C.N.R.

‡ Università di Catania.

10.1021/bc700411w CCC: $40.75 © 2008 American Chemical Society
Published on Web 02/23/2008

Scheme 1. Synthesis of Calixarene Platform 6

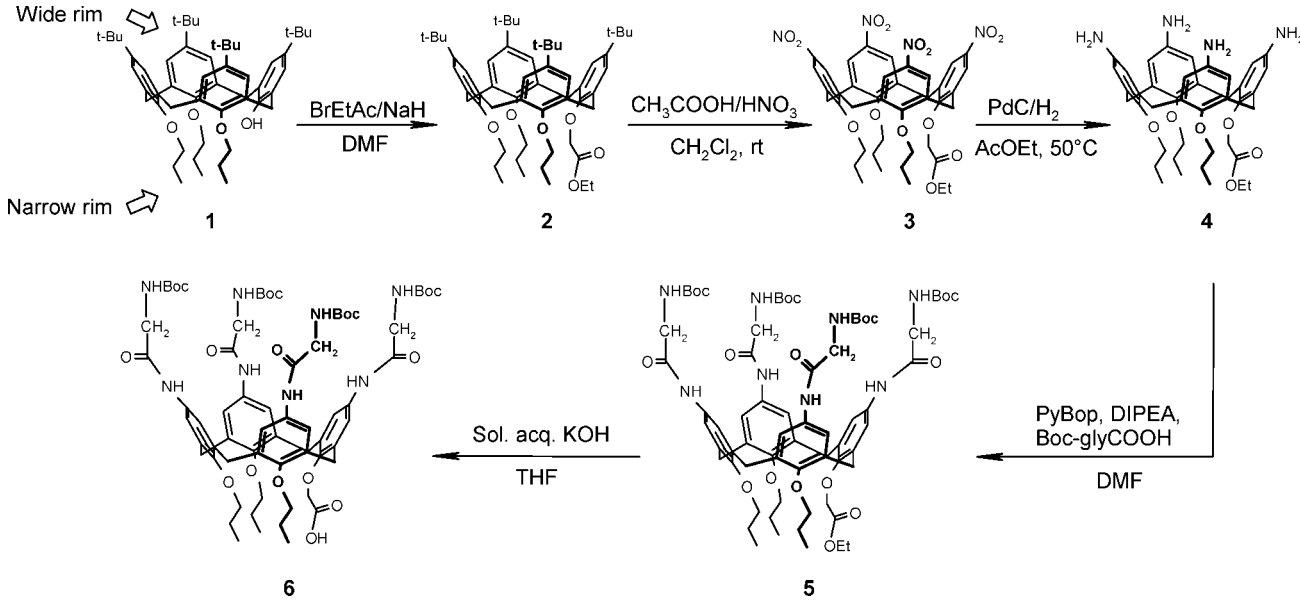

Scheme 2. Synthesis of *S*-TnAg 8

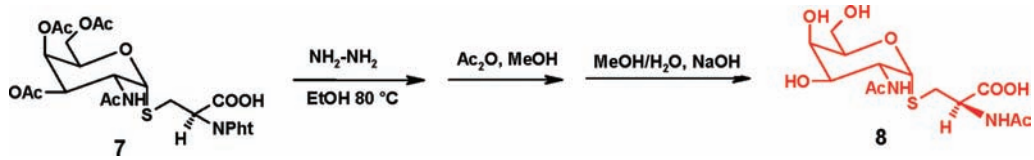

analogous, emphasizing the presence of a cluster effect and the important role of the calixarene macrocycle.

EXPERIMENTAL PROCEDURES

General. All chemical reagents and solvents were obtained from commercial sources and were used without purification. Analytical TLCs were performed on 0.25 mm silica gel 60 coated aluminum foils with F-254 indicator (Merck). Column chromatography was performed on silica gel 60 (230–400 mesh, E. Merck) or on silica gel 100 C18-RP (230–400 mesh, Fluka). Size exclusion column chromatography was carried out on Sephadex LH-20 (Pharmacia Biotech AB, Uppsala Sweden) or Biogel P-2 (Bio-Rad). ^{1}H NMR (400.13 MHz), ^{13}C NMR (100.61 MHz), and 2D-NMR spectra were acquired on a Bruker Avance 400 spectrometer. Chemical shifts (δ) are expressed in parts per million (ppm). Spectra were referenced to the residual proton solvent peaks; coupling constant (J) values are given in Hz. Mass spectra were recorded on a mass spectrometer Waters Micromass ZQ 2000 model ESI-MS (positive ion mode, capillary voltage 3500 V, cone voltage 60 V) or on a MALDI-STR Applied Biosystems instrument (positive ion, reflector mode, accelerating voltage 24000, 256 laser shot). In the ELISA assay, the absorbance was measured on a MDL680 microplate reader (Biorad).

Syntheses. *25,26,27-Tripropoxy-28-hydroxy-p-tert-butylcalix[4]arene (***1***).* was prepared following a literature procedure (*28*).

*25,26,27-Tripropoxy-28-[(ethoxy carbonyl)methoxy]-p-tert-butylcalix[4]arene (***2***).* Compound **1** (1.14 g, 1.5 mmol) was treated with 60% oil-dispersed NaH (62.4 mg, 2.6 mmol) in THF (70 mL)−DMF (18 mL), and then EtBrAc (332 μL, 2.99 mmol) was added. The reaction mixture was stirred for 4 h at room temperature. The mixture was concentrated under vacuum and washed with 0.1 N HCl (50 mL). The suspension obtained was filtered and the gathered white residue was purified by column chromatography (CH_2Cl_2 as eluent) to afford compound **2** (1.21 g, 95%). ^{1}H NMR ($CDCl_3$, 297 K) δ: 0.95–1.05 (overlapped, 9H, 3 × $CH_2CH_2CH_3$), 0.99, 1.16, and 1.17 (s, 18H, 9H, 9H, respectively, 4 × *t*-Bu), 1.29 (t, J = 7.1 Hz, 3H, OCH_2CH_3), 1.96 (q, J = 7.4 Hz, 4H, 2 × $CH_2CH_2CH_3$), 2.09 (q, J = 7.8 Hz, 2H, $CH_2CH_2CH_3$), 3.11 (d, J = 12.6 Hz, 2H, $ArCH_2Ar$), 3.16 (d, J = 12.6 Hz, 2H, $ArCH_2Ar$), 3.70–3.85 (m overlapped, 6H, 3 × $OCH_2CH_2CH_3$), 4.20 (q, J = 7.1 Hz, 2H, OCH_2CH_3), 4.40 (d, J = 12.6 Hz, 2H, $ArCH_2Ar$), 4.60 (d, J = 12.6 Hz, 2H, $ArCH_2Ar$), 4.81 (s, 2H, OCH_2CO), 6.65 (br d, 4H, 4 × ArH), 6.80, 6.90, (s, 2H each, 4 × ArH). ^{13}C NMR ($CDCl_3$, 297 K): 10.1, 10.4, 14.2 (q), 23.3, 23.4, 31.0 (t), 31.4, 31.5, 31.55 (q), 31.6 (t), 33.7, 33.9 (s), 53.4, 60.2, 70.9, 77.1 (t), 124.7, 124.8, 125.1, 125.4 (d), 133.0, 133.2, 134.0, 134.5 (t), 144.1, 144.5, 144.8, 153.3, 153.4, 153.9, 170.7 (s). ES-MS calcd for $C_{57}H_{81}O_6$ (861.6): m/z 861.5 $(M + H)^+$; 883.4 $(M + Na)^+$.

*5,11,17,23-Tetranitro-25,26,27-tripropoxy-28-[(ethoxy carbonyl)methoxy]-calix[4]arene (***3***).* A solution of **2** (1.21 g, 1.4 mmol) in CH_2Cl_2 (25 mL) was mixed with glacial CH_3COOH (25 mL) at room temperature. Then 100% HNO_3 (6.4 mL) was added dropwise under vigorous stirring. After 6 h, the reaction was stopped by addition of water (120 mL). The organic layer was separated and dried and the solvent evaporated in vacuum. The yellow solid was purified by crystallization (CH_2Cl_2/EtOH) to afford the white compound **3** (914 mg, 80%). ^{1}H NMR ($CDCl_3$, 297 K) δ: 0.98 (t, J = 7.4 Hz, 3H, $CH_2CH_2CH_3$), 1.05 (t, J = 7.4 Hz, 6H, 2 × $CH_2CH_2CH_3$), 1.30 (t, J = 7.2 Hz, 3H, OCH_2CH_3), 1.87–1.94 (m overlapped, 6H, 3 × $CH_2CH_2CH_3$), 3.40 (d, J = 14.1 Hz, 2H, $ArCH_2Ar$), 3.46 (d, J = 14.1 Hz, 2H, $ArCH_2Ar$), 3.80–3.97 (m overlapped, 4H, 2 × $OCH_2CH_2CH_3$), 4.00 (t, J = 7.7 Hz, 2H, $OCH_2CH_2CH_3$), 4.23 (q, J = 7.2 Hz, 2H, OCH_2CH_3), 4.53 (d, J = 14.1 Hz, 2H, $ArCH_2Ar$), 4.75 (s, 2H, OCH_2CO), 4.76 (d, J = 14.1 Hz, 2H, $ArCH_2Ar$), 7.34 (br d, 4H, 4 × ArH), 7.84 (s, 4H, 4 × ArH). ^{13}C NMR

Scheme 3. Synthesis of Tetra-*S*-TnAg-Gly-CX-P_3CS (11)

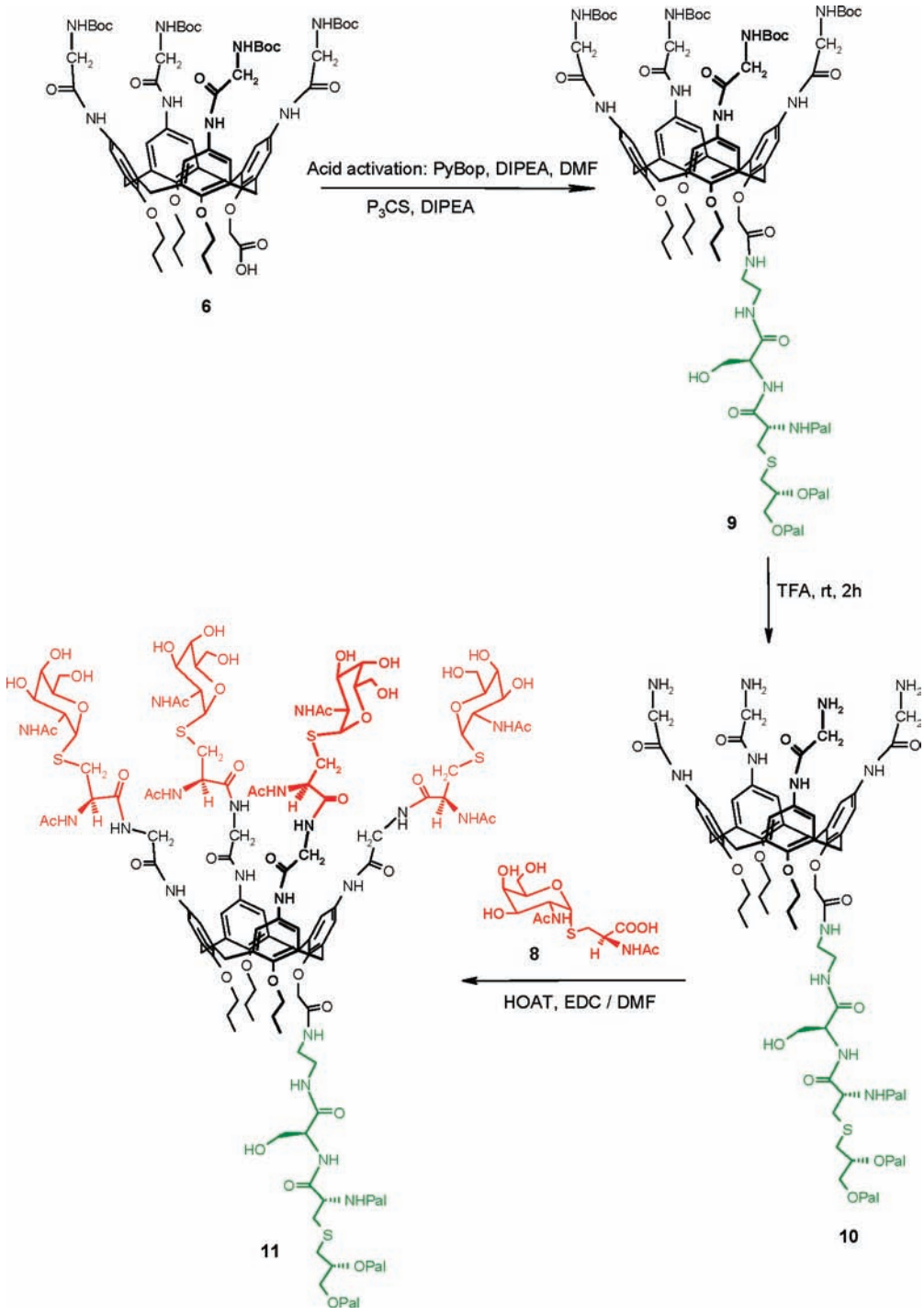

($CDCl_3$, 297 K): 10.3, 14.2 (q), 23.2, 31.1, 31.4 (t), 61.3, 70.7, 77.9 (t), 123.6, 123.7, 124.4, 124.6 (d), 134.7, 134.8, 135.8, 136.0, 143.0, 143.3, 160.9, 161.1, 162.2, 168.5 (s). ES-MS calcd for $C_{41}H_{45}N_4O_{14}$(817.3): *m*/*z* 839.6 $(M + Na)^+$.

*5,11,17,23-Tetraamino-25,26,27-tripropoxy-28-[(ethoxycarbonyl)methoxy]-calix[4]arene (***4***).* Compound **3** (440 mg, 0.54 mmol) was dissolved in AcOEt/MeOH (9:1, v/v) and hydrogenated under atmospheric pressure in the presence of Pd/C at 50 °C. After the hydrogen uptake was completed (12 h), the catalyst was filtered off and the solution was evaporated in vacuum to give pure compound **4** (338 mg, 90%). ^{1}H NMR ($CDCl_3$, 297 K) δ: 0.91 (t, $J = 7.4$ Hz, 3H, $CH_2CH_2CH_3$) 0.98 (t, $J = 7.4$ Hz, 6H, 2 × $CH_2CH_2CH_3$), 1.27 (t, $J = 7.1$ Hz, 3H, OCH_2CH_3), 1.77–1.90 (m overlapped, 6H, 3 × $CH_2CH_2CH_3$), 2.91 (d, $J = 13.3$ Hz, 2H, $ArCH_2Ar$), 2.97 (d, $J = 13.5$ Hz, 2H, $ArCH_2Ar$), 3.14 (br s, 8H, 4 × NH_2), 3.50–3.72 (m overlapped, 4H, 2 × $OCH_2CH_2CH_3$), 3.75 (t, $J = 7.7$ Hz, 2H, $OCH_2CH_2CH_3$), 4.17 (q, $J = 7.1$ Hz, 2H, OCH_2CH_3), 4.31 (d, $J = 13.3$ Hz, 2H, $ArCH_2Ar$), 4.51 (d, $J = 13.5$ Hz, 2H, $ArCH_2Ar$), 4.61 (s, 2H, OCH_2CO), 5.91, 6.22, 6.24 (s, 4H, 2H, 2H, respectively, 8 × ArH). ^{13}C NMR ($CDCl_3$, 297 K): 10.1, 10.4, 14.2 (q), 23.0, 31.1, 31.5, 60.1, 60.3, 70.4, 76.8 (t), 115.8, 115.9, 116.0 (d), 134.8, 134.9, 136.1, 136.4, 140.1, 140.7, 149.5, 149.8, 150.6, 170.6 (s). ES-MS calcd for $C_{41}H_{53}N_4O_6$ (697.4): *m*/*z* 697.3 $(M + H)^+$; 719.3 $(M + Na)^+$.

*5,11,17,23-(Boc-L-glycyl)amino-25,26,27-tripropoxy-28-[(ethoxycarbonyl)methoxy]-calix[4]arene (***5***).* To a solution of compound **4** (200 mg, 0.29 mmol) in dry DMF (15 mL), Boc-glycine

(251.3 mg, 1.43 mmol), PyBop (1.12 g, 2.15 mmol), and DIPEA (0.75 mL, 4.31 mmol) were added. The reaction mixture was stirred overnight at room temperature. The solvent was removed under vacuum; the crude product was washed with 0.1 N HCl and collected by filtration to give a white solid, which was purified by column chromatography eluting with AcOEt/cyclohexane (6:4 v/v) to afford compound **5** (285.3 mg, 75%). ^{1}H NMR ($CDCl_3$, 330 K) δ: 0.94 (t, J = 7.5 Hz, 3H, $CH_2CH_2CH_3$), 0.98 (t, J = 7.5 Hz, 6H, 2 × $CH_2CH_2CH_3$), 1.26 (t, J = 7.2 Hz, 3H, OCH_2CH_3), 1.45, 1.47 (s, 18 H each, 4 × Boc-$(CH_3)_3$), 1.75–1.90 (m overlapped, 6H, 3 × $OCH_2CH_2CH_3$), 3.06 (d, J = 13.2 Hz, 2H, $ArCH_2Ar$), 3.10 (d, J = 13.8 Hz, 2H, $ArCH_2Ar$), 3.72 (m, 2H, $OCH_2CH_2CH_3$), 3.81 (br s overlapped, 8H, 2 × $OCH_2CH_2CH_3$ and 2 × Gly CH_2), 3.89 (br s, 4H, 2 × Gly CH_2), 4.18 (q, J = 7.2 Hz, 2H, OCH_2CH_3), 4.51 (d, J = 13.2 Hz, 2H, $ArCH_2Ar$), 4.58 (d, J = 13.8 Hz, 2H, $ArCH_2Ar$), 4.62 (s, 2H, OCH_2CO), 5.61 (br s, 4H, 4 × Gly N*H*CH_2), 6.54, 6.93 (s, 4H each, 8 × ArH), 8.10 (s, 2H, 2 × Ar-NH), 8.25 (s, 2H, 2 × Ar-NH). ^{13}C NMR ($CDCl_3$, 297 K): 10.1, 10.4, 14.2 (q), 23.1 (t), 28.4 (q), 31.0, 31.3, 44.6, 60.4, 70.4, 76.8, 77.2 (t), 80.2 (s), 121.1 (d), 131.3, 131.5, 132.0, 134.3, 134.4, 135.5, 135.7, 153.0, 153.3, 154.0, 156.5, 168.0, 170.0 (s). ES-MS calcd for $C_{69}H_{97}N_8O_{18}$ (1325.7): *m/z* 1325.9 $(M + H)^+$.

*5,11,17,23-(Boc-L-glycyl)amino-25,26,27-tripropoxy-28-(carbomethoxy)-calix[4]arene (***6***).* Compound **5** (100 mg, 0.075 mmol) was suspended in THF (10 mL) in the presence of water (2 mL) and KOH (50 mg, 0.89 mmol). The resulting mixture was refluxed and stirred for 3 h. The pH was adjusted to 4 with aq 1 N HCl. The product was extracted with CH_2Cl_2, and the organic layer was dried over Na_2SO_4 and evaporated to give pure compound **6** (95.37 mg, 98%). ^{1}H NMR (MeOD, 297 K) δ: 0.95 (t, J = 7.2 Hz, 3H, $CH_2CH_2CH_3$), 1.02 (t, J = 7.5 Hz, 6H, 2 × $CH_2CH_2CH_3$), 1.39, 1.44, 1.46 (s, 9H, 9H, 18H, respectively, 4 × Boc-$(CH_3)_3$), 1.85–2.00 (m overlapped, 6H, 3 × $OCH_2CH_2CH_3$), 3.12 (d, J = 12.9 Hz, 2H, $ArCH_2Ar$), 3.18 (d, J = 13.2 Hz, 2H, $ArCH_2Ar$), 3.68 (br m, 4H, 2 × $OCH_2CH_2CH_3$), 3.81 (br s, 8H, 4 × Gly CH_2), 3.91 (t, J = 7.8 Hz, 2H, $OCH_2CH_2CH_3$), 4.46 (d, J = 12.9 Hz, 2H, $ArCH_2Ar$), 4.62 (d, J = 13.2 Hz, 2H, $ArCH_2Ar$), 4.68 (s, 2H, OCH_2CO), 6.75 (br s, 4H, 4 × ArH), 7.11, 7.13 (s, 2H each, 4 × ArH).

*N-Acetyl-3-S-(2-acetamido-2-deoxy-*α*-D-galactopyranosyl)-L-cysteine (***8***).* Compound **7** (*29*) (56 mg, 0.097 mmol) dissolved in EtOH (40 mL) was reacted with hydrazine hydrate (2.5 mL, 80 mmol) for 2 h under reflux. The mixture was evaporated in vacuum and purified by Biogel P-2 column chromatography (water). An aliquot of 18 mg (0.055 mmol) of the compound obtained was subjected to exhaustive acetylation in the presence of acetic anhydride (12.5 μL, 0.132 mmol) and MeOH as the solvent (2 mL). After 2 h at room temperature, the reaction mixture was concentrated in vacuum to give a solid which was *O*-deacetylated by dissolving in MeOH/H_2O (2:1, v/v, 4 mL) in the presence of aq 1 M NaOH (0.38 mL). After treatment with Amberlite IR-120 (H+) resin until neutralization, the mixture was filtered and the filtrate was concentrated in vacuo to give the white solid **8** (12 mg, 60%). ^{1}H NMR (D_2O, 297 K) δ: 2.02, 2.03 (s, 3H each, 2 × $NHCOCH_3$), 3.00–307 (m, 2H, CysβCHa and CysβCHb), 3.72–3.80 (m, 3H, H-5 and 2 × H-6), 3.84 (dd, $J_{4,3}$ = 3.5 Hz, 1H, H-4), 3.98 (m, 1H, H-2), 4.27 (m, 1H, CysαCH), 4.50 (m, 1H, H-3), 5.52 (d, $J_{1,2}$ = 5.5 Hz, 1H, H-1). ES-MS calcd for $C_{13}H_{23}N_2O_8S$ (367.1): *m/z* 367.2 $(M + H)^+$.

*Boc-Gly-CX-P$_3$CS (***9***).* Compound **6** (19.8 mg, 0.015 mmol) dissolved in dry DMF (2.8 mL) was reacted with PyBop (13.5 mg, 0.026 mmol) and DIPEA (9 μL, 0.05 mmol). After stirring for 4 h at room temperature, a mixture of *N*-{*N*-palmitoyl-*S*-[2,3-bis(palmitoyloxy)-(2*R*)-propyl]-(*R*)-cysteyl-(*S*)-seryl}-1,2 diaminoethane (P_3CS) (*29*) (20.6 mg, 0.019 mmol) and DIPEA (5.6 μL, 0.03 mmol) were added. The reaction mixture was stirred for 24 h at room temperature. After evaporation of the solvent, the residue was washed with water and purified by preparative TLC (MeOH/CH_2Cl_2, 1:9 v/v) to give pure compound **9** (22 mg, 63%). ^{1}H NMR (MeOD/$CDCl_3$, 297 K) δ: 0.77–0.91 (t overlapped, 12H, $CH_2CH_2CH_3$ and 3 × Palmitoyl-CH_3), 0.96 (t, J = 7.0 Hz, 6H, 2 × $CH_2CH_2CH_3$), 1.24 (br s, 60H, 30 × Palmitoyl-CH_2), 1.42, 1.46 (br s, 9H, 27H, respectively, 4 × Boc-$(CH_3)_3$), 1.60 (br m, 18H, 9 × Palmitoyl-CH_2), 1.78 (br s, 6H, 3 × $OCH_2CH_2CH_3$), 2.10–2.40 (m, 6H, 3 × Palmitoyl-CH_2CO), 2.75 (br m, 2H, SCH_2CHOCO), 2.84–3.02 (m, 1H each, Cysβ-CH_2), 3.13 (d, J = 12.8 Hz, 2H, $ArCH_2Ar$), 3.25 (d, J = 14.0 Hz, 2H, $ArCH_2Ar$), 3.49, 3.57 (m, 2H each, NCH_2CH_2N), 3.64 (s, 2H, Gly CH_2), 3.72 (m, 1H, $CHCH_2OH$), 3.84 (br s overlapped, 13H, 3 × $OCH_2CH_2CH_3$, 3 × Gly CH_2, and 1H × $CHCH_2OH$), 4.14 (m, 1H, SCH_2CHCH_2), 4.25–4.45 (overlapped, 6H, 2 × $ArCH_2Ar$, 1H × SCH_2CHCH_2, $CHCH_2OH$), 4.53 (m, 1H, Cysα-CH), 4.83 (s, 2H, OCH_2CO), 5.14 (m, 1H, SCH_2CHOCO), 6.51, 7.19 (br s, 4H each, 8 × ArH). ^{13}C NMR (MeOD/$CDCl_3$, 297 K): 9.5, 9.4, 13.3 (q), 22.3, 22.5, 24.6, 25.5 (t), 27.6 (q), 28.8, 29.0, 29.1, 29.3, 31.1, 31.5, 31.6 (t), 32.2, 33.4, 33.7, 33.9, 35.6, 38.4, 39.2, 39.5, 43.5, 43.7 (t), 52.6, 53.2, 55.2 (d), 61.4, 63.4, 63.5 (t), 70.2 (d), 73.6, 76.1, 77.5 (t), 79.5, 119.9, 120.3, 120.7, 121.2 (s), 132.0, 132.5, 132.7, 133.7, 134.3, 135.9, 151.2, 156.7, 168.0, 168.3, 169.9, 170.9, 172.0, 173.3, 173.5, 175.0 (s). ES-MS calcd for $C_{126}H_{205}N_{12}O_{25}S$ (2318.5): *m/z* 1159.8 $(M + 2H)^{2+}$.

*Gly-CX-P$_3$CS (***10***).* Compound **9** (22 mg, 0.01 mmol) was stirred with TFA (1 mL) for 2 h at rt. The mixture was dried under vacuum by washing three times with ethanol, to give de-Boc derivative **10** in quantitative yield. The CF_3COO^- counterions were replaced with Cl^- anions by repeated treatment of the sample with 0.1 N HCl and removal of the solvent under vacuum. ^{1}H NMR (MeOD, 297 K) δ: 0.88 (t overlapped, 12H, $CH_2CH_2CH_3$ and 3 × Palmitoyl-CH_3), 0.99 (t, J = 7.3 Hz, 6H, 2 × $CH_2CH_2CH_3$), 1.28 (br s, 66H, 33 × Palmitoyl-CH_2), 1.60, 1.60 (m, 6H, 3 × $OCH_2CH_2CH_3$), 1.84 (m, 12H, 6 × Palmitoyl-CH_2), 2.30 (m, 6H, 3 × Palmitoyl-CH_2CO), 2.80 (m, 2H, SCH_2CHOCO), 2.85 and 3.03 (m, 1H each, Cysβ-CH_2), 3.15 (m, 4H, $ArCH_2Ar$), 3.47, 3.56 (m, 2H each, NCH_2CH_2N), 3.68 (s, 4H, OCH_2CO and $CHCH_2OH$), 3.79 (br s, 6H, 3 × $OCH_2CH_2CH_3$), 3.87 (m, 8H, 4 × Gly CH_2), 4.15 (m, 1H, SCH_2CHCH_2), 4.31–4.53 (overlapped, 6H, 2 × $ArCH_2Ar$, 1H × SCH_2CHCH_2, $CHCH_2OH$), 4.56 (m, 1H, Cysα-CH), 5.17 (m, 1H, SCH_2CHOCO), 6.61, 6.62, (s, 2H each, 4 × ArH), 7.17 (m, 4H, 4 × ArH). ES-MS calcd for $C_{106}H_{173}N_{12}O_{17}S$ (1918.3): *m/z* 1918.7 $(M + H)^+$; 960.1 $(M + 2H)^{2+}$; 1940.7 $(M + Na)^+$; 982.6 $(M + 2Na)^{2+}$.

*Tetra-S-TnAg-Gly-CX-P$_3$CS (***11***).* *S*-Tn antigen **9** (15 mg, 41 μmol) was dissolved in dry DMF (1 mL) and reacted with HOAt (410 μL of a solution 0.5 M in DMF) and EDC (39.2 mg, 0.20 mmol). After stirring under argon for a few minutes, a solution of **10** (10.64 mg, 5.12 μmol) and DIPEA (300 μL, 1.72 mmol) in dry DMF (1 mL) was added. The mixture was kept under stirring, for 24 h at room temperature. After evaporation of the solvent (with the addition of a few mL of toluene), the residue was taken up in CH_2Cl_2 and washed with water. The organic layer was dried on Na_2SO_4 and the solvent was evaporated to give a residue that was purified by size-exclusion column chromatography (LH-20, CH_2Cl_2 as eluent). The first fraction was collected and further purified by C18-RP column chromatography (MeOH/CH_2Cl_2 gradient) to give the pure compound **11** as white powder. MALDI-TOF calcd for $C_{158}H_{252}N_{20}O_{45}S_5$ (3310.7): *m/z* 3333.4 $(M + Na)^+$.

Animal Treatment. Five- to eight-week-old female BALB/c mice (Charles River, Calco, Italy) were used in this study. Three

groups of five mice were immunized two times at one-week intervals by intraperitoneal injections of Tetra-*S*-TnAg-Gly-CX-P_3CS **11** (0.030 μM/mouse) or Mono-*S*-TnAg-P_3CS **12** (*29*) at two concentration levels (0.030 and 0.120 μM/mouse) dispersed in 300 μL of a saline solution containing 20 mg/mL of β-HP-CD and 5 mg/mL of HPMC. These additives enhance solubility and physical stability of the dispersion of the constructs tested. Two additional groups were injected with vehicle alone or not treated. After 21 days from the first immunization, sera were collected and stored at −80 °C until ELISA assay.

ELISA End-Point Titers. Total IgG antibodies specific to Tn antigen in sera were detected and quantified by end-point dilution ELISA assay on samples pooled for each group. End-point titers were defined as the highest serum dilution that resulted in an absorbance value two times greater than that of nonimmune control mouse serum with a cutoff value of 0.05 (*30*). 50 μL of 3 mM solution of *S*-Tn antigen (*29*) in water were aliquoted in Nunc CovaLink NH microtiter plate wells (VWR, Italy). An equal volume of coupling reagents NHS (12 mM) and EDC (36 mM) in water was added to each well. Blank control wells, where neither *S*-Tn antigen nor coupling reagents were added, were run in parallel. The plates were shaken at room temperature for 8 h and, after emptying, were washed with water (150 μL × 2), saturated $NaHCO_3$ (2 × 150 μL), SDS (1% in water; 3 × 150 μL), and finally water again (4 × 150 μL). Blocking was done by incubation overnight at 4 °C with bovine serum albumin (BSA, 1% w/v in phosphate-buffered saline (PBS), 200 μL). The plates were washed with PBS containing BSA (1% w/v) and Triton X-100 (0.05%) (2 × 100 μL). 2-fold dilution series of mouse sera prepared in incubation buffer (1% (w/v) BSA, 0.05% (w/v) Tween 20 in PBS) were added in duplicate (100 μL/well) and incubated overnight at 4 °C. The plates were washed with PBS containing 0.05% Tween 20 (150 μL × 3) and 100 μL per well of sheep peroxidase conjugated antimouse IgG (Sigma, Cat-Nr A 6782, 1:2000 in incubation buffer) was added and incubated for 2 h at 37 °C. After washing with PBS containing 0.05% Tween 20 (150 μL × 3), 100 μL per well of substrate TMB (Celbio, Milano, Italy) was added and incubated for 30 min at room temperature in the dark. The enzymatic reaction was stopped with 100 μL of 1 M H_2SO_4 and absorbance at 450 nm was measured in an Elisa microplate reader. Various concentrations of the *S*-Tn antigen and secondary antibody serially diluted in the plates were previously tested in order to optimize the amount of the substance used (data not shown).

Statistical Analysis. Statistical differences of in vivo data are determined using repeated measure analysis of variance (ANOVA) followed by the Bonferroni-Dunn post hoc pairwise comparison procedure. A probability, *P*, of less than 0.05 is considered significant in this study.

RESULTS AND DISCUSSION

Design of the Synthetic Vaccine Candidate. Although the glyco-amino acid GalNAc-O-Ser/Thr is considered the biochemical definition of Tn antigen, experimental evidence confirms that the antigen recognized by the immune system may be more complex. The analysis of the fine specificity of several Tn-binding antibodies demonstrated that clusters of Tn structures were a crucial part of the epitope recognized by the monoclonal antibodies MLS128 and 83D4 (*19–23*) and by the Tn-specific human macrophage C-type lectin (*31*).

In order to mimic the clustered motif of Tn antigen recognized by the immune system, we have designed a vaccine construct where four units of *S*-Tn glycomimetic are covalently linked at the wide rim of a calix[4]arene scaffold bearing, in the narrow rim, an immunoadjuvant moiety (P_3CS).

Calixarene macrocycles (*32–34*) could be suitable molecular platforms for the design of fully synthetic multivalent constructs.

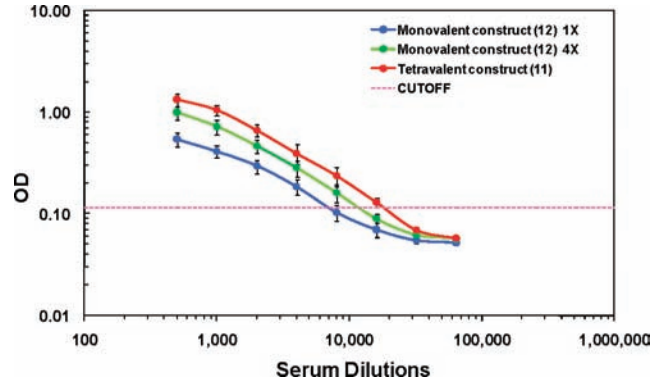

Figure 1. Reactivity of sera of mice immunized with clustered compound **11** or nonclustered monovalent construct **12**. The reference monovalent construct (**12**) was tested at two concentration levels, 1× and 4×, with respect to **11**. Results for total specific anti-Tn IgG antibodies are shown. Data points represent the mean value from group of five animals.

Scheme 4. Covalent Coupling of Tn Ag Glycomimetic to Covalink Plate

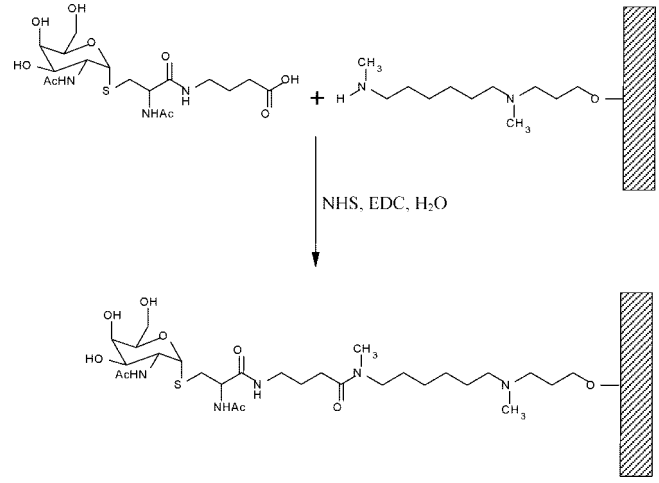

They are synthetically versatile compounds with various applications from inorganic to biological fields. These macrocycles are characterized by [1_n] metacyclophane units that can easily undergo the introduction of functional groups at both their narrow and wide rims (Figure 1), so as to fashion their skeleton in a rigid or mobile conformation and diversify their functional properties. Due to a low toxicity (*35–38*), calixarene derivatives have found large application in the biomedical field as enzyme inhibitors (*39–41*), and anticoagulant and antithrombotic (*42*), antiangiogenic and anticancer (*43*), antiviral (*44*), and antimicrobial and antifungal (*45*) products.

In the designed construct, the four *S*-Tn antigen units are covalently linked by glycine spacers to the calix[4]arene wide rim. Three propyloxy groups and one P_3CS unit introduced at the calixarene narrow rim block the synthetic core in a rigid cone-shaped conformation (*28*) and ensure that the antigenic units will be exposed on the same side with respect to the medium plane of the macrocycle. The all-syn orientation of Tn Ags is crucial to better mimic the cancer cell surface, whereas the presence of a glycine spacer between the calixarene backbone and the antigenic pendants should avoid steric hindrance and ensure flexibility, both advantageous in the antigen—immune system interaction (*29*). The P_3CS moiety, endowed with immunoadjuvant properties, determines the magnitude of the vaccine candidate immune response. This lipopeptide is a potent immunoadjuvant (*46*), derived from the immunologically active *N*-terminal sequence of the principal

Chart 1. Structure of Monovalent Reference Compound (12)

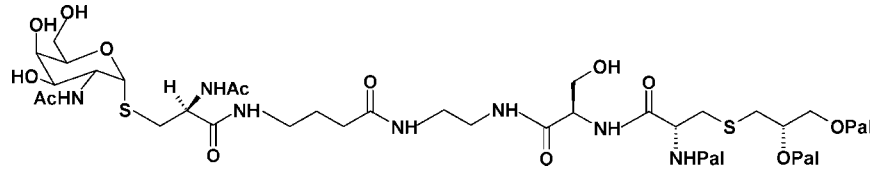

lipoprotein of *Escherichia coli* (*47*). It elicits its activity through the interaction with a Toll-like receptor 2 (*46*). This determines the production of cytokines and chemokines which stimulate the antigen presenting cells with the development and activation of T helper cells.

The glycomimetic *S*-Tn antigen was chosen as antigenic determinant, because of its higher metabolic stability and capability to determine the maximal immunostimulating activity of a construct at lower doses with respect to the natural *O*-Tn analogue (*29*).

Preparation of the Calix[4]arene Platform. Calixarene derivative **1** (*28*) was selected as the starting material and reacted with ethyl bromoacetate in the presence of a strong base (NaH) to obtain the 25,26,27-tripropoxy-28-[(ethoxycarbonyl)methoxy]-*p-tert*-butylcalix[4]arene (**2**) in 95% yield. This compound underwent a direct replacement of the *tert*-butyl groups via an ipso aromatic nitration to give the nitrocalixarene derivative (**3**). Subsequently, reduction of **3** in H_2 atmospheric pressure with Pd-C, as catalyst, supplied the amino derivative (**4**). Afterward, four BOC-glycine spacers were introduced into the macrocycle wide rim, via amide coupling, in the presence of PyBop and DIPEA to give compound **5**. This synthetic procedure (Scheme 1) is easier and more effective than the procedure using NHS and DCC or EDC, and it increases the yield of compound **5** by more than 30%.

TnAg-Calixarene Construct. The treatment of compound **5** with a basic solution removed the protecting ester group at the macrocycle narrow rim and liberated the COOH functionality, which activated by PyBop represents the attachment site for the P_3CS immunoadjuvant unit. The very difficult synthetic step was the simultaneous introduction of four *S*-Tn Ags at the wide rim of the calix[4]arene platform (Scheme 3).

Different synthetic procedures to couple compound **8** (Scheme 2) and **10** via amide bonds were investigated. NHS/EDC, methyl morpholine/triazine, HOBT/EDC, and HOAT/EDC were tested as coupling agents. A better yield of **11** was obtained by activation of the *S*-Tn Ag by means of HOAT/EDC in dry DMF followed by the addition of a solution of compound **10**, drop by drop under argon. MALDI-TOF mass spectrometry revealed a signal at $m/z = 3333.4$ corresponding to the $[M + Na]^+$ ion.

The complex ^1H NMR spectrum of **11** ($CDCl_3$/MeOD mixture) showed overlapping resonances which made difficult the signal assignment. However, the signals relative to the anomeric proton (4.84 ppm, 4H) and acetyl groups of the *N*-acetyl-galactosamine (1.63, 1.68, and 1.72 ppm; 12H) clearly indicated the presence of four *S*-Tn antigen units linked to the calix[4]arene macrocycle.

Biological Assay. The determination of antibodies against saccharides using standard enzyme immunoassay has been more difficult than the assays for detection of antibodies toward proteins, because sugars have very weak passive binding to plastic ELISA plate surface. To circumvent this aspect, different new polar plastic surfaces have been developed with the purpose of increasing the absorption of hydrophilic macromolecules (*48*). Nevertheless, when considering the binding efficiency of adsorbant plastic surfaces for biomacromolecules, it is important to distinguish between the total amount of molecules bonded and molecules that still remain biologically active. As an example, the binding of the carbohydrate moiety of glycopeptidic antigens on a hydrophilic surface can reduce their antibody binding activity, since the carbohydrate moiety normally is the major antigenic determinant. For the Tn antigen, it is reported that the hydrophilic *N*-acetyl-galactosamine is involved in the interaction with the immune system (*49*). To date, for Tn antigen (GalNAc-Ser) no direct absorption binding to ELISA plate has been described.

Table 1. End-Point Titers of Total Specific Anti-Tn IgG Antibodies in Mice after Immunization with Clustered (11) and Nonclustered Monovalent Constructs (12)[a]

construct	end-point titer[b,c]
11	1:16000
12 4×	1:8000
12 1×	1:4000

[a] The reference monovalent construct (**12**) was tested at 1× and 4× molar ratios with respect to **11**. [b] Data points represent the mean value from group of five animals. [c] End-point titers were defined as the highest serum dilution that resulted in an absorbance value two times greater than that of nonimmune control mouse serum.

Recently, a CovaLink NH secondary amine surface has been developed for covalent coupling of carbohydrates and nucleic acids to polystyrene (*50*). The NH functional group of the Covalink plate is spaced 2 nm via alkyl spacers from the polystyrene surface wall to minimize steric hindrance. Covalent binding through a secondary amine group has a number of advantages over passive adsorption such as high binding strength, binding of distinct functional groups, specific orientation of molecules, and improved stability (*49*, *51*). In this paper, we report for the first time the covalent binding of Tn antigen glycomimetic to CovaLink NH microtiter plates (Scheme 4). The resulting functionalized plates were used in the end-point dilution ELISA assay for the specific detection of anti-Tn IgG antibodies.

Immunological Evaluation. We evaluated the immunogenicity of the tetra-Tn mimotope target construct (**11**) using as reference compound a monovalent construct (Chart 1), previously synthesized (*29*) and bearing the same antigen. The reference construct was tested at two concentration levels, 1× and 4×, with respect to compound **11** (0.030 and 0.120 μM/mouse).

The aim was to investigate the role of the "cluster effect" in amplifying the antibody production with respect to a simple concentration increase of Tn antigen units. Sera from the groups of mice were examined for antibody production by the ELISA tests described above.

As reported in Figure 1 and Table 1, all three groups treated with the constructs under examination increased the total Tn-specific IgG antibodies with respect to control animals.

In the serum dilution range considered, mice immunized with compound **11** showed a substantial and significant ($p < 0.05$) production of antibodies. An increase of the end-point titers of 4-fold (1:16000) was measured with respect to the mice immunized using at the equimolar level (0.030 μM/mouse) the reference monovalent construct (1:4000). Even when the concentration of monovalent construct was increased 4-fold with respect to compound **11** (0.120 and 0.030 μM/mouse, respectively), so to compare solutions with the same number of Tn Ag units, the reactivity elicited by the clustered construct was

significantly higher ($p < 0.05$) in the range of serum dilution considered, with a 2-fold increase in the end point titer (1:8000 and 1:16000, respectively). Regarding the monovalent construct, when the molar concentration was quadruplicated the end-point titer increased by only 2-fold (1:4000 and 1:8000, respectively).

Taken together, these data clearly show that a cluster effect determines the higher immunostimulating activity of the tetravalent construct with respect to the monovalent analogue. A cluster effect determining specific lectin-binding ability and amplified lectin affinity has been reported for other glycocalixarene derivatives (*52*). The cluster effect is widely present in natural systems, where it increases strength and specificity in molecular recognition processes (*53–56*). In carbohydrate−protein interaction, the poor association constants for monovalent interactions ($K_a = 10^{3-4}$ M^{-1}) (*57–59*) are amplified by clustering multiple copies of carbohydrates binding multiple receptor sites. Also, the Tn antigens on mucin surface are organized in clusters which represent the preferred targets of many antitumor monoclonal antibodies (*19–23*). Therefore, the efficient antibody production elicited by tetrameric construct **11** evidences the existence of a cluster effect and that the array of Tn Ags assembled on the rigid calix[4]arene scaffold ensures a good mimicking of the natural motif encountered in vivo.

CONCLUSION

A novel, well-defined synthetic multivalent vaccine candidate has been designed. By sequential amide coupling, four *S*-Tn glycomimetic antigens and one P_3CS immunoadjuvant moiety have been anchored at the two different faces (wide and narrow rim) of a calix[4]arene macrocyle. To the best of our knowledge, this construct represents the first example of a vaccine candidate built on a nonpeptidic platform. The results presented in this study demonstrate that the target construct (**11**) induces a more effective immune response when compared to the monovalent reference compound tested both at the same and at 4-fold more concentrated level. The higher production of anti Tn IgG antibodies elicited by tetrameric construct **11** is ascribable to a cluster effect and suggests that the arrangement of Tn Ags on the rigid calix[4]arene scaffold mimics the mucine surface properly. This reveals perspectives for potential applications in cancer immunotherapy.

ACKNOWLEDGMENT

The authors thank Dr. D. Ventura of Etna Biotech (Catania, Italy) for his help in performing the biological study and for sharing his valuable experience and knowledge in working with immune system issues. Thanks are due to Professor S. Sciuto (University of Catania) for helpful discussions.

LITERATURE CITED

(1) Rosenberg, S. A. (2001) Progress in human tumor immunology and immunotherapy. *Nature 411*, 380–384.

(2) Le Poole, I. C., Gerberi, M. A. T., and Kast, W. M. (2002) Emerging strategies in tumor vaccines. Therapeutic modalities. *Curr. Opin. Oncol. 14*, 641–648.

(3) Rosenberg, S. A., Yang, J. C., and Restifo, N. P. (2004) Cancer immunotherapy: moving beyond current vaccines. *Nat. Med. 10*, 909–915.

(4) Hougthon, A. N., Gold, J. S., and Blachere, N. E. (2001) Immunity against cancer: lessons learned from melanoma. *Curr. Opin. Immunol. 13*, 134–140.

(5) Springer, G. F. (1997) Immunoreactive T and Tn epitopes in cancer diagnosis, prognosis, and immunotherapy. *J. Mol. Med. 75*, 594–602.

(6) Hakomori, S. (1989) Aberrant glycosylation in tumor and tumor-associated carbohydrate antigens. *Adv. Cancer Res. 52*, 257–331.

(7) Kuberan, B., and Linhardt, R. J. (2000) Carbohydrate based vaccines. *Curr. Org. Chem. 4*, 653–677.

(8) Freire, T., Lo-Man, R., Piller, F., Piller, V., Leclerc, C., and Bay, S. (2006) Enzymatic large-scale synthesis of MUC6-Tn glyconjugates for antitumor vaccination. *Glycobiology 16*, 390–401.

(9) Kim, Y. J., and Varki, A. (1997) Perspectives on the significance of altered glycosylation of glycoproteins in cancer. *Glyconjugate J. 14*, 569–576.

(10) Svarovsky, S. A., and Barchi, J. J. (2003) Higly efficient preparation of tumor antigen-containing glycopeptide building blocks from novel pentenyl glycosides. *Carbohydr. Res. 338*, 1925–1935 and references therein.

(11) Springer, G. F. (1984) T and Tn, general carcinoma autoantigens. *Science 224*, 1198–1206.

(12) Toyokuni, T., Dean, B., Cai, S., Boivin, D., Hakomori, S.-I., and Singhal, A. K. (1994) Synthetic vaccines: synthesis of a dimeric Tn antigen-lipopeptide conjugate that elicits immune responses against Tn-expressing glycoproteins. *J. Am. Chem. Soc. 116*, 395–396.

(13) Dziadek, S., Kowalczyk, D., and Kunz, H. (2005) Synthetic vaccines consisting of tumor-associated MUC1 glycopeptide antigens and bovine serum albumin. *Angew. Chem., Int. Ed. 44*, 7624–7630.

(14) Kim, J. M., and Roy, R. (1997) Oligomeric glycopeptidomimetics bearing the cancer related TN-antigen. *Tetrahedron Lett. 38*, 3487–3490.

(15) Buskas, T., Ingale, S., and Boons, G.-J. (2005) Towards a fully synthetic carbohydrate-based anticancer vaccine: synthesis and immunological evaluation of a lipidated glycopeptide containing the tumor-associated Tn antigen. *Angew. Chem., Int. Ed. 44*, 5985–5988.

(16) Cipolla, L., Rescigno, M., Leone, A., Peri, F., La Ferla, B., and Nicotra, F. (2002) Novel Tn antigen-containing neoglycopeptides: synthesis and evaluation a anti tumor vaccines. *Bioorg. Med. Chem. 10*, 1639–1646.

(17) Ouerfelli, O., Warren, J. D., Wilson, R. M., and Danishefsky, S. J. (2005) Synthetic carboydrate-based antitumor vaccines: challenges and opportunities. *Expert Rev. Vaccines 4*, 677–685.

(18) Ragupathi, G., Koide, F., Livingston, P. O., Cho, Y. S., Endo, A., Wan, Q., Spassova, M. K., Keding, S. J., Allen, J., Ouerfelli, O., Wilson, R. M., and Danishefsky, S. J. (2006) Preparation and evaluation of unimolecular pentavalent and hexavalent antigenic constructs targeting prostate and breast cancer: a synthetic route to anticancer vaccine candidates. *J. Am. Chem. Soc. 128*, 2715–2725.

(19) Nakada, H., Numata, Y., Inoue, M., Tanaka, N., Kitagawa, H., Funakoshi, I., Fukui, S., and Yamashima, I. (1991) Elucidation of an essential structure recognized by an anti-GalNac-Ser(Thr) monoclonal antibody (MLS 128). *J. Biol. Chem. 266*, 12402–12405.

(20) Nakada, H., Inoue, M., Numata, Y., Tanaka, N., Funakoshi, I., Fukui, S., Mellors, A., and Yamashina, I. (1993) Epitopic structure of Tn glycophorin A for an anti-Tn antibody (MLS 128). *Proc. Natl. Acad. Sci. U.S.A. 90*, 2495–2499.

(21) Reddish, M. A., Jackson, L., Koganty, R. R., Qiu, D. X., Hong, W., and Longenecker, B. M. (1997) Specificities of anti-sialyl-Tn and anti-Tn monoclonal antibodies generated using novel clustered synthetic glycopeptide epitopes. *Glycoconjugate J. 14*, 549–560.

(22) Reis, C. A., Sorensen, T., Mandel, U., David, L., Mirgorodskaya, E., Roepstorff, P., Kihlberg, J., Hansen, J. E., and Clausen, H. (1998) Development and characterization of an antibody directed to an α-N-acetyl-D-galactosamine glycosylated MUC2 peptide. *Glycoconjugate J. 15*, 51–62.

(23) Osinaga, E., Bay, S., Tello, D., Babino, A., Pritsch, O., Assemat, K., Cantacuzène, D., Nakada, H., and Alzari, P. (2000) Analysis of the fine specificity of Tn-binding proteins using synthetic glycopeptide epitopes and a biosensor based on surface plasmon resonance spectroscopy. *FEBS Lett. 469*, 24–28.

(24) Tam, J. P. (1988) Synthetic peptide vaccine design: synthesis and properties of a high-density multiple antigenic peptide system. *Proc. Nat. Acad. Sci. U.S.A. 85*, 5409–5413.

(25) Lo-Man, R., Vichier-Guerre, S., Bay, S., Dériaud, E., Huteau, V., Cantacuzène, D., and Leclerc, C. (2001) Antitumor immunity provided by a synthetic multiple antigenic glycopeptides (MAG) displaying tri-Tn glycotope. *J. Immunol. 166*, 2849–2854.

(26) Grigalevicius, S., Chierici, S, Renaudet, O., Lo-Man, R., Dériaud, E., Leclerc, C., and Dumy, P. (2005) Chemoselectivity assembly and immulogical evaluation of multiepitopic glycoconjugates bearing clustered Tn antigen as synthetic anticancer vaccines. *Bioconjugate Chem. 16*, 1149–1159.

(27) Lo-Man, R., Vichier-Guerre, S., Perraut, R., Dériaud, E., Huteau, V., BenMohamed, L., Diop, O. M., Livingston, P. O., Bay, S., and Leclerc, C. (2004) A fully synthetic therapeutic vaccine candidate targeting carcinoma-associated Tn carbohydrate antigen induces tumor-specific antibodies in nonhuman primates. *Cancer Res. 64*, 4987–4994.

(28) Iwamoto, K., Araki, K., and Shinkai, S. (1991) Conformation and structures of Tetra-*O*-alkyl-*p*-tert-butylcalix[4]arenes. How is the conformation of calix[4]arenes immobilized? *J. Org. Chem. 56*, 4955–4962.

(29) Bousquet, E., Spadaro, A., Pappalardo, M. S., Bernardini, R., Romeo, R., Panza, L., and Ronsisvalle, G. (2000) Synthesis and immunostimulating activity of a thioglycopeptide glycomimetic as a potential anticancer vaccine derived from Tn antigens. *J. Carbohydr. Chem. 19*, 527–541.

(30) Davis, H. L., Mancini, M., Michel, M. L., and Whalen, R. G. (1996) DNA-mediated immunization to hepatitis B surface antigen: longevity of primary response and effect of boost. *Vaccine 14*, 910–915.

(31) Iida, S., Yamamoto, K., and Irimura, T. (1999) Interaction of human macrophage C-type lectin with O-linked and N-acetylgalactosamine residues on mucin glycopeptides. *J. Biol. Chem. 274*, 10697–10705.

(32) Gutsche, C. D. (1989) Calixarenes. In *Monographs in Supramolecular Chemistry* (Stoddart, J. F., Ed.) Royal Society of Chemistry, Cambridge, UK.

(33) Gutsche, C. D. (1998) Calixarenes Revisited. In *Monographs in Supramolecular Chemistry* (Stoddart, J. F., Ed.) Royal Society of Chemistry, Cambridge, UK.

(34) (2001) *Calixarenes 2001* (Asfari, Z., Böhmer, V., Harrowfield, J., and Vicens, J., Eds.) Kluwer, Dordrecht, NL.

(35) Da Silva, E., Shahgaldian, P., and Coleman, A. W. (2004) Haemolytic properties of some water-soluble para-sulphonatocalix[*n*]-arenes. *Int. J. Pharm. 273*, 57–62.

(36) Grote Gansey, M. H. B., de Haan, A. S., Bos, E. S., Verboom, W., and Reinhoudt, D. N. (1999) Conjugation, immunoreactivity, and immunogenicity of calix[4]arene; model study to potential calix[4]arene-based Ac3+ chelators. *Bioconjugate Chem. 10*, 613–623.

(37) Da Silva, E., Lazar, A. N., and Coleman, A. W. (2004) Biopharmaceutical application of calixarenes. *J. Drug Del. Sci. Tech. 14*, 3–20.

(38) Paquet, V., Zumbuehl, A., and Carreira, E. M. (2006) Biologically active amphotericin B-calix[4]arene conjugates. *Bioconjugate Chem. 17*, 1460–1463.

(39) Francese, S., Cozzolino, A., Caputo, I., Esposito, C., Martino, M., Gaeta, C., Troisi, F., and Neri, P. (2005) Transglutaminase surface recognition by peptidocalix[4]arene diversomers. *Tetrahedron Lett. 46*, 1611–1615.

(40) Mecca, T., Consoli, G. M. L., Geraci, C., and Cunsolo, F. (2004) Designed calix[8]arene-based ligands for selective tryptase surface recognition. *Bioorg. Med. Chem. 12*, 5057–5062.

(41) Consoli, G. M. L., Granata, G., Galante, E., Di Silvestro, I., Salafia, L., and Geraci, C. (2007) Synthesis of water-soluble nucleotide-calixarene conjugates and preliminary investigation of their in vitro DNA replication inhibitory activity. *Tetrahedron 63*, 10758–10763.

(42) Hwang, K. M., Qi, Y. M., Liu, S. Y., Lee, T. C., Choy, W., and Chen, J. (1996) U.S. Patent 5,409,959, 1995. *Chem. Abstr. 123*, 959c.

(43) Blaskovich, M. A., Lin, Q., Delarue, F. L., Sun, J., Park, H. S., Coppola, D., Hamilton, A. D., and Sebti, S. M. (2000) Design of GFB-111, a platelet-derived growth factor binding molecule with antiagiogenic and anticancer activity against human tumors in mice. *Nat. Biotechnol. 18*, 1065–1070.

(44) Hwang, K. M., Qi, Y. M., Liu, S. Y., Lee, T. C., Choy, W., and Chen, J. (1996) U.S. Patent 5,441,983, 1995. *Chem. Abstr. 123*, 275992d.

(45) Tanaka, M., and Kikuchi, A. (1996) Jpn. Patent 7,187,930, 1995. *Chem. Abstr. 123*, 220827y.

(46) Aliprantis, A. O., Yang, R.-B., Mark, M. R., Sugett, S., Devaux, B., Radolf, J. D., Klimpel, G, R., Godowsky, P., and Zychlinsky, A. (1999) Cell activation and apoptosis by bacterial lipoproteins through toll-like receptor-2. *Science 285*, 736–739.

(47) Wiesmüller, K. H., Bessler, W., and Jung, G. (1983) Synthesis of the mitogenic S-[2,3-bis. (palmitoyloxy)propyl]-N-palmitoylpentapeptide from *Escherichia coli* lipoprotein. *Hoppe-Seyler's Z. Physiol. Chem. 364*, 593–596.

(48) See: Bulletin No. 6 from "Bulletins and Tech Notes" at www.nuncbrand.com.

(49) Toyokuni, T., Hakomori, S., and Singhal, A. K. (1994) Synthetic carbohydrate vaccines: synthesis and immunogenicity of Tn antigen conjugates. *Bioorg. Med. Chem. 2*, 1119–1132.

(50) See: Tech Note, Vol. 1, No. 9, from "Bulletins and Tech Notes" at www.nuncbrand.com.

(51) Wallner, F. K., Norberg, H. A., Johansson, A. I., Mogemark, M., and Elofsson, M. (2005) Solid-phase synthesis of serine-based glycosphingolipid analogues for preparation of glycoconjugate arrays. *Org. Biomol. Chem. 3*, 309–315.

(52) Consoli, G. M. L., Cunsolo, F., Geraci, C., and Sgarlata, V. (2004) Synthesis and lectin binding ability of glycosamino acid-calixarenes exposing GlcNAc clusters. *Org. Lett. 6*, 4163–4166.

(53) Mammen, M., Choi, S.-K., and Whitesides, G. M. (1998) Polyvalent interactions in biological systems: implications for design and use of multivalent ligands and inhibitors. *Angew. Chem., Int. Ed. Engl. 37*, 2754–2794.

(54) Dam, T. K., Roy, R., Das, S. K., Oscarson, S., and Brewer, C. F. (2000) Binding of multivalent carbohydrates to concanavalin A and Dioclea grandiflora lectin. Thermodynamic analysis of the multivalency effect. *J. Biol. Chem. 275*, 14223–14230.

(55) Gupta, D., Kaltner, H., Dong, X., Gabius, H. J., and Brewer, C. F. (1996) Comparative cross-linking activities oflactose-specific plant and animal lectins and a natural lactose-binding immunoglobulin G fraction from human serum with asialofetuin. *Glycobiology 6*, 843–849.

(56) Hughes, R. C. (2001) Galectins as modulators of cell adhesion. *Biochimie 83*, 667–676.

(57) Bundle, D. R., and Young, N. M. (1992) Carbohydrate-protein interactions in antibodies and lectins. *Curr. Opin. Struct. Biol. 2*, 666–673.

(58) Kiessling, L. L., and Pohl, N. L. (1996) Strength in numbers: Non-natural polyvalent carbohydrate derivatives. *Chem. Biol. 3*, 71–77.

(59) Roy, R., Park, W. K. C., Srivastava, O. P., and Foxall, C. (1996) Combined glycomimetic and multivalent strategies for the design of potent selectin antagonists. *Bioorg. Med. Chem. Lett. 6*, 1399–1402.

BC700411W

Contribution of Linker Stability to the Activities of Anticancer Immunoconjugates

Stephen C. Alley, Dennis R. Benjamin, Scott C. Jeffrey, Nicole M. Okeley, Damon L. Meyer, Russell J. Sanderson, and Peter D. Senter*

Seattle Genetics, Inc., 21823 30th Drive SE, Bothell, Washington 98021. Received November 26, 2007; Revised Manuscript Received January 10, 2008

The linker component of antibody−drug conjugates (ADC) is a key feature in developing optimized therapeutic agents that are highly active at well tolerated doses. For maximal intratumoral drug delivery, linkers are required that are highly stable in the systemic circulation, yet allow for efficient drug release at the target site. In this respect, amide bond-based technologies constitute a technological advancement, since the linker half-lives in circulation ($t_{1/2} \sim 7$ days) are much longer than earlier generation linkers that break down within 1–2 days. The amide linkers, some of which contain peptides, are appended to the mAb carriers through thioether/maleimide adducts. Here, we describe that use of a bromoacetamidecaproyl (bac) in place of the maleimidocaproyl (mc) increases the plasma stability of resulting thioether ADCs. One such ADC, 1F6-C4v2-bac-MMAF, which is directed against the CD70 antigen on lymphomas and renal cell carcinoma, was prepared containing a bac thioether spacer between the drug (MMAF) and the mAb carrier (1F6-C4v2). There was no measurable systemic drug release from this ADC for 2 weeks postadministration in mice. In order to assess the impact of improving linker stability beyond mc containing ADCs, a series of mc and bac-linked 1F6-MMAF conjugates were compared for tolerability, intratumoral drug delivery, and therapeutic efficacy in nude mice with renal cell carcinoma xenografts. There were no statistically significant efficacy differences between sets of mc and bac containing ADCs, although the bac linker technology led to 25% higher intratumoral drug exposure over a 7 day period compared to the corresponding mc linker. The mechanism of drug release from maleimide-adducts likely involves a retro-Michael reaction that takes place in plasma, based on in vitro studies demonstrating that some of the released drug-maleimide derivative became covalently bound to cysteine-34 of serum albumin. In summary, the data indicate that new linkers can be obtained with improved in vivo stability by replacing the maleimide with an acetamide, but the resulting ADCs had similar tolerability and activity profiles.

INTRODUCTION

The toxicity associated with systemically administered anticancer drugs has generated significant interest toward improving drug delivery to tumors while sparing nontarget tissues from chemotherapeutic damage. Antibody−drug conjugates (ADCs), composed of cytotoxic agents fused via conditionally labile linkers to monoclonal antibodies (mAbs) against tumor associated antigens, have figured prominently within this field, with clinically approved drug such as Mylotarg (anti-CD33-calecheamicin) for the treatment of acute myelogenous leukemia (*1–3*) and an array of newer ADCs in various stages of preclinical and clinical development (*4–14*). Studies surrounding these agents have led to the identification of several critical parameters that must be addressed in order to develop targeted drugs with broad applicability for clinical cancer medicine. These include nontarget tissue uptake of ADCs, the heterogeneity of both antigen expression and macromolecular uptake within tumor masses, inappropriate linker stability, inefficient drug release within tumors, and release of drugs with low potency (*6, 15, 16*).

Linker stability plays a central role in ADC efficacy and tolerability. Early generation ADC linkers were commonly derived from disulfides and acid-labile hydrazones, both of which were designed to be cleaved inside target cancer cells, but inevitably underwent cleavage at nontarget sites. Because of this, significant effort has been directed toward balancing the stability of these linkers in the circulation, while still allowing them to be sufficiently labile for activation at the target site. One of the first systematic studies along these lines involved conjugates of ricin A-chain attached to mAbs through differentially hindered disulfide bonds (*17, 18*). The hindered disulfide provided improved conjugate stability in vivo, together with a better therapeutic window in xenograft tumors. These findings were later extended to include ADCs composed of the potent cytotoxin maytansine. Conjugates with sterically hindered disulfides displayed potent antitumor activity and had improved biological stability compared to their less hindered counterparts (*6, 15, 16, 19*). Consistent with this trend is our earlier finding that acid-labile hydrazone linkers provided lower specificity in vitro and higher levels of toxicity in vivo compared to highly stable linkers (*20*). Such studies, together with others (*21, 22*), demonstrate how linker stability can influence ADC activity, specificity, and toxicity.

The approach we have taken toward advancing conditionally labile linker technologies involves the use of intracellular enzymes for drug release. The first example involved valine-citulline (vc) dipeptide derivatives of the potent antimitotic drug, monomethyl auristatin E (MMAE), which were designed to release MMAE upon exposure of the ADCs to lysosomal proteases such as cathepsin B (*20, 23*). While lysosomal enzymes can be detected in the blood, their activities are very low due to endogenous inhibitors and the high pH value of blood compared to lysosomes. Thus, free MMAE was released from vc-linked MMAE ADCs in plasma more slowly ($t_{1/2} > 30$ d) than corresponding acid-labile hydrazone-based ADCs ($t_{1/2} \sim 2$ d) (*20*). This trend in increased ADC stability was also observed in vivo, in that the half-life of drug release from the ADC was 6

* Corresponding author. E-mail psenter@seagen.com.

10.1021/bc7004329 CCC: $40.75 © 2008 American Chemical Society
Published on Web 03/04/2008

days in mice and 10 days in Cynomolgus monkeys for the vc-linked drug (*24*), which is considerably longer than previously reported half-lives of hydrazones and disulfides (*24–26*).

The effects of extending in vivo linker half-life beyond 6–10 days are not known. To investigate this, we describe the generation of new ADCs with drug linkers that show no degradation in the circulation for up to 14 days. Interestingly, this new drug linker does not impact ADC in vivo therapeutic efficacy and tolerability when compared with ADCs that have half-lives of approximately 7 days.

EXPERIMENTAL PROCEDURES

Cell Lines and Reagents. 1F6 (chimeric anti-CD70 (*27*)), 1F6-C4v2 (humanized anti-CD70 with cys to ser heavy chain amino acid substitutions at positions 226 and 229) (*28*) and AC10 (chimeric anti-CD30 (*23*)) are IgG1 mAbs that were isolated as previously described. The human renal cell carcinoma cell lines 786-O, UMRC-3, and Caki-1 were obtained from ATCC. The human lymphoma cell line L428 was obtained from the DSMZ (Braunschweig, Germany). All cell lines were cultured according to the manufacturers suggested protocol. LC/MS and LC/MS/MS spectra were recorded on a MicroMass Q-TOF Ultima mass spectrometer equipped with a Z-spray ion source and a Waters 2795 HPLC system. mc-MMAF, mc-vc-MMAF, bac-MMAF (LC-MS *m/z* (ES^+) 965.8 (M+H)), and bac-vc-MMAF (LC-MS *m/z* (ES^+) 1370.7 (M+H)) were obtained as previously described (*29, 30*).

Preparation of Conjugates. Alkyl-maleimide linked 1F6, 1F6-C4v2, and AC10 ADCs were prepared as previous described (*28, 30*). For the bromoacetamides, the reduced antibodies (*30, 31*) were adjusted to pH 8 with sodium borate and incubated with 2 equiv of bac-vc-MMAF or bac-MMAF per antibody cysteine for 4 h at 25 °C. Subsequent purification and characterization of all ADCs were as previously described (*30*). The conjugated antibodies were unimpaired with respect to affinity for their targets (CD70 for 1F6 and CD30 for AC10) and contained <2% aggregate and <0.5% unconjugated drug.

ELISAs. The concentration of the 1F6-C4v2 component of the ADCs in plasma was measured using a previously described ELISA assay (*24*) using 96-well plates coated with an anti-idiotype-1F6 mAb at a concentration of 1 μg/mL in 100 mM sodium carbonate/bicarbonate (pH 9.6). The plasma samples were then diluted to 500 ng/mL h1F6-C4v2 mAb into PBS with 0.05% Tween 20 containing 1% BSA (PBST/BSA) and added to wells in triplicate. An hour later, the wells were washed, and anti-MMAF mAb SG3.265-biotin (1 μg/mL in PBST/BSA) was added and incubated an additional hour. The wells were washed, and streptavidin-HRP (diluted into PBST/BSA) was added and incubated for 1 h at room temperature. Detection was initiated using TMB substrate added to the washed wells. Reactions were terminated with 1 N H_2SO_4 and absorbance was measured at 450 nm against a reference wavelength of 630 nm. On the same 96-well microtiter plate, samples and standards were also subjected to total mAb ELISA analysis to ensure that the amount of mAb backbone captured to the plate were comparable. The results were compared with standards consisting of purified 1F6-C4v2-mc-$MMAF_n$ or 1F6-C4v2-bac-$MMAF_n$ ADC standards in plasma (n = 1, 2, 3, or 4 drug-linkers per mAb) that were similarly processed. Linear regression analysis of data from the standards was used to obtain an equation relating the average drug/mAb ratio of the relevant ADC to the measured OD_{450}.

Biodistribution. All animal studies were carried out in accordance with Animal Care and Use Committee guidelines. Balb/c nu/nu mice with subcutaneous 786-O tumors xenografts (in vivo passaged, 100–150 mm^3) were treated i.v. with the ADCs at 1.5 mg/kg in PBS. At the time points indicated, mice were sacrificed by CO_2 inhalation, and were then terminally bled. Serum, tumor, and liver were stored at −80 °C until all of the samples were collected. Tumor and liver samples were thawed on ice, 4 mL/gram of tissue of PBS was added, and the tissue was mechanically homogenized on ice. MMAF was extracted from 100 μL homogenate by addition of 100 μL of 0.2% formic acid in water and 400 μL of acetonitrile. After spiking with ^{13}C-MMAF internal standard (*30*), the mixture was incubated at 25 °C for 1 h with occasional vortexing. Following centrifugation to pellet cell debris and precipitated proteins, the supernatant was extracted using a Waters (Milford, MA) Oasis MCX 96-well plate that was conditioned with 0.4 mL (volumes are per well) of 2% ammonium hydroxide in dichloromethane: isopropyl alcohol (80:20), 0.4 mL of methanol, and 0.4 mL of water. The plate was washed with 0.4 mL of 0.2% aqueous formic acid and 0.4 mL of methanol. MMAF was eluted with 2 treatments of 0.4 mL of 2% ammonium hydroxide in dichloromethane/isopropyl alcohol (80:20). The elution solvent was evaporated in a vacuum concentrator and samples were reconstituted in 50 μL of 50% aqueous acetonitrile. For serum samples, serum was mixed with 1 volume of 0.2% aqueous formic acid, spiked with °C-MMAF, and extracted as described above for the tumor and liver samples.

Samples were analyzed by LC-MS/MS by injecting 20 μL of the reconstituted sample onto a 2.1 × 30 mm Agilent (Santa Clara, CA) Zorbax SB C8 column running on a Waters Acquity liquid chromatograph (flow rate 1 mL/minute; column temperature 40 °C; gradient conditions isocratic 5% B (0.1% formic acid in acetonitrile) 95% A (0.1% aqueous formic acid) for 0.5 min, 0.05 min linear gradient to 70% B, isocratic for 0.15 min, 0.05 min linear gradient to 95% B, isocratic 95% B for 0.05 min. The eluted solvent was directed into a Waters Quattro Premier triple quadrupole mass spectrometer operating in multiple reaction monitoring mode. MMAF was analyzed using its 732 *m/z* parent ion and 700 *m/z* fragment ion, while the ^{13}C-MMAF internal standard was analyzed using its 738 *m/z* parent ion and 706 *m/z* fragment ion. Standard curves were generated by spiking MMAF and ^{13}C-MMAF internal standards into tissue homogenates or serum from untreated tumor-bearing animals which were then treated as described above. All data collection and sample analyses were performed using *MassLynx* version 4.0.

Identification of mc-MMAF-Modified Peptides in Plasma. AC10-mc-MMAF was diluted with 50% citrated rat plasma to 5 mg/mL. Half of the reaction was removed and stored at −20 °C as a time zero reference, and the remaining mixture was placed at 37 °C for 5 days. The samples (50 μL) were treated with 8 M urea in 0.5 M ammonium bicarbonate (1.8 mL), dithiothreitol (45 mM, 0.36 mL) was added, and incubation was carried out at 50 °C for 20 min, followed by cooling to room temperature and treatment with iodoacetamide (2.2 mol equiv per mole dithiothreitol) in the dark for 15 min. The samples were then diluted with water to a final urea concentration of 1.9 M, and trypsin (TPCK, Pierce) was added (final concentration 13 μg/mL). After overnight incubation at 37 °C, the solutions were desalted on Pep-Clean C18 spin columns (Pierce), using seven columns for each reaction. The resins were prepared according to manufacturer's instructions and the samples were loaded in 100 μL steps with each sample being reloaded three times to ensure complete capture of peptides. The resin was washed with 5% acetonitrile 0.5% TFA (2 × 200 μL) and then eluted with 70% acetonitrile (2 × 20 μL, 1 × 50 μL). The elutions for each sample were combined and dried under centrifugal vacuum. The peptide residues were dissolved in acetonitrile (87.5 μL) and diluted with PBS (663 μL). Particulates were collected by centrifugation (16 000*g*, 5 min) and were redissolved in DMSO (20 μL) and combined with the super-

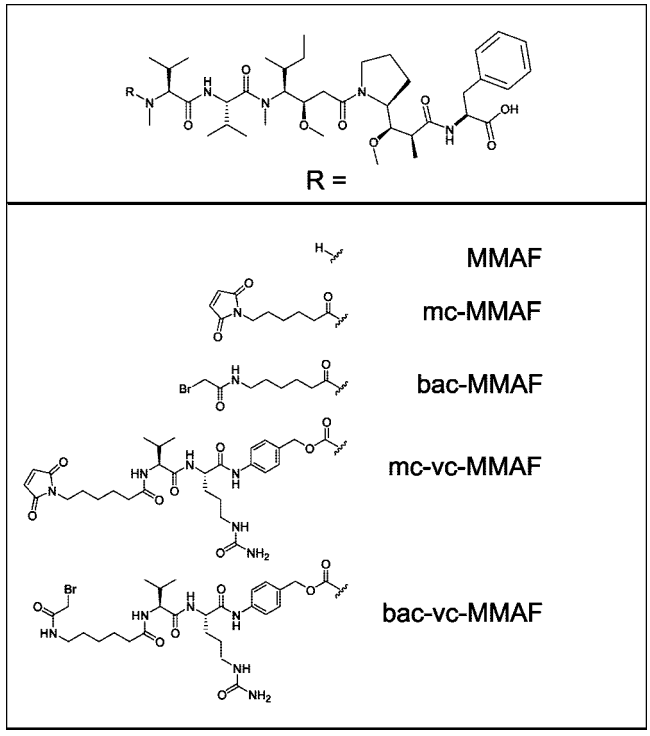

Figure 1. Structures of MMAF and linkers.

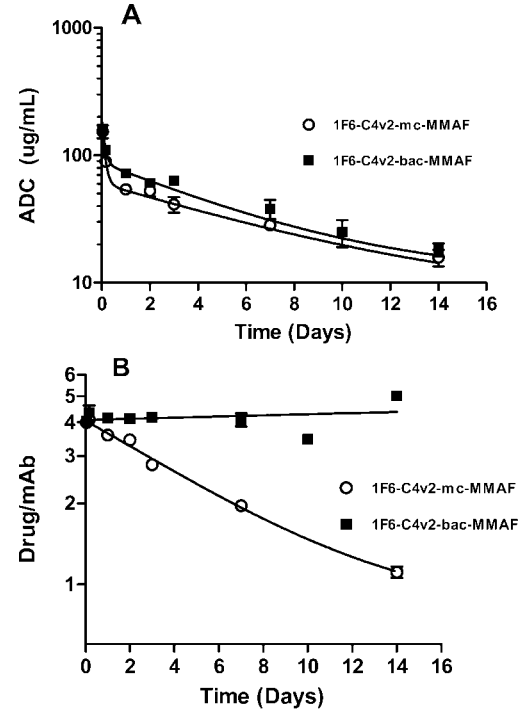

Figure 2. In vivo stability of auristatin ADCs. The mAb concentrations (A) were determined in plasma samples after a single injection of 10 mg/kg of 1F6-C4v2-mc-MMAF and 1F6-C4v2-bac-MMAF (3 animals/group). The drug/mAb ratios (B) were determined using an ELISA whose total signal is proportional to the drug loading of the ADC. The mc-MMAF conjugate shows dissociation of MMAF from the antibody with a half-life of approximately 7 days.

natant. The samples were further diluted with additional PBS to bring the organic solvent composition to 6%.

An Affigel-10 resin coupled to the anti-mc-MMAF antibody SG2.15 was used to capture mc-MMAF-containing peptides from the samples. Each sample was added to 0.9 mL of resin bed and was mixed at 4 °C for 4 h. The slurries were washed with PBS (6 × 2 mL). The bound peptides were eluted by incubation with 5.5 M guanidine hydrochloride (Pierce) in PBS at room temperature for 4 h followed by 20 min at 37 °C. A second elution with fresh guanidine hydrochloride solution was carried out at 37 °C for 30 min. The combined guanidine elutions were desalted on Pep Clean C18 spin columns as previously described using three columns per sample. The eluted peptides were dried by centrifugal vacuum and dissolved in 0.1% TFA. Drug-captured and desalted peptides were examined by LCMS using a Poroshell 300SB-C18 column (Agilent, 2.1 × 75 mm, 5 μm). The samples were separated at 0.2 mL/ minute on a gradient starting at 0% B (0.1% formic acid in acetonitrile), 100% A (0.1% formic acid) for 3 min, then ramping to 15% B over 7 min followed by 15–23% B over 30 min, 23–28% B over 1 min, 28–40% B over 10 min, and finally 40–100% B over 4 min.

In Vitro Cytotoxicity. Log phase cultures of cells were collected and cells were plated at seeding densities ranging from 500 to 10 000 cells/well according to predetermined conditions. After incubating for 24 h, serial dilutions of test molecules were added, and cultures incubated a further 4 days. Assessment of cellular growth was determined using Alamar Blue (Biosource International, Camarillo, CA) dye reduction as previously described (*30*). Briefly, a 40% solution (wt/vol) of freshly prepared Alamar Blue was added to the cells to constitute 10% culture volume. Cells were incubated for 4 h, and dye reduction was measured on a fluorescent plate reader.

In Vivo Efficacy and Tolerability. In vivo efficacy of ADCs were evaluated in female nude mice bearing 786-O xenografts. Once tumors grew to approximately 100 mm^3, test articles in PBS were injected into the tail vein at the indicated doses. Tolerability of ADCs were evaluated using BALB/c mice. The maximum tolerated dose (MTD) is defined as the highest dose that did not induce >20% weight loss, distress, or overt toxicities in any of the animals, and was generally within 20% of doses where such events took place.

Table 1. IC_{50} Values of Immunoconjugates on CD70 Expressing Cell Lines

	IC_{50} (nM)				
ADC	786-O	Caki-1	UMRC-3	L428	LP-1
1F6-C4v2-mc-MMAF	>1000	93	>1000	180	200
1F6-C4v2-bac-MMAF	450	90	490	52	88
1F6-C4v2-mc-vc-MMAF	23	32	87	10	71
1F6-C4v2-bac-vc-MMAF	29	35	37	13	70

Table 2. Percent Weight Change in Treated BALB/c Mice

ADC	day 4	day 9
1F6-C4v2-mc-MMAF 150 mg/kg	3.3	2.0
1F6-C4v2-bac-MMAF 150 mg/kg	−2.6	2.1
1F6-C4v2-mc-vc-MMAF 20 mg/kg	−5	3.0
1F6-C4v2-mc-vc-MMAF 40 mg/kg	−13	not tolerated
1F6-C4v2-mc-vc-MMAF 60 mg/kg	−19	not tolerated
1F6-C4v2-bac-vc-MMAF 20 mg/kg	−9	1.6
1F6-C4v2-bac-vc-MMAF 40 mg/kg	−19	not tolerated
1F6-C4v2-bac-vc-MMAF 60 mg/kg	−22	not tolerated

RESULTS

Auristatin Conjugates. The structures of the previously reported alkyl-maleimide containing drugs vc-MMAF and mc-MMAF (*30*), together with a set of related MMAF derivatives containing bromoacetamides in place of the alkyl-maleimide moieties, are shown in Figure 1. These MMAF-linker derivatives were designed to react with thiols, such as mAb cysteines generated after disulfide bond reduction. The antibodies used were 1F6 (chimeric IgG1 recognizing the CD70 antigen) (*27*), 1F6-C4v2 (humanized IgG1 anti-CD70 mAb with heavy chain

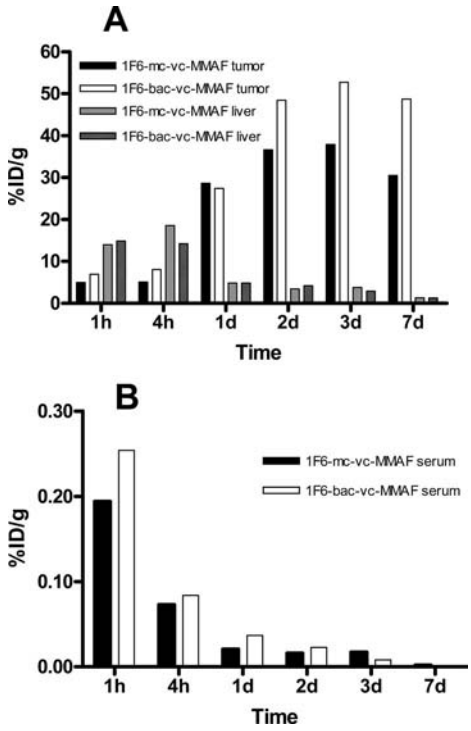

Figure 3. Concentrations of MMAF in (A) tumors and liver, and (B) serum obtained with mc-vc-MMAF and bac-vc-MMAF ADCs (2 animals/group). The results are expressed as the % of the injected dose (%ID) per gram of tissue. The initial weights of the tumors, livers, and blood were approximately 0.1, 1.0, and 1.0 g, respectively.

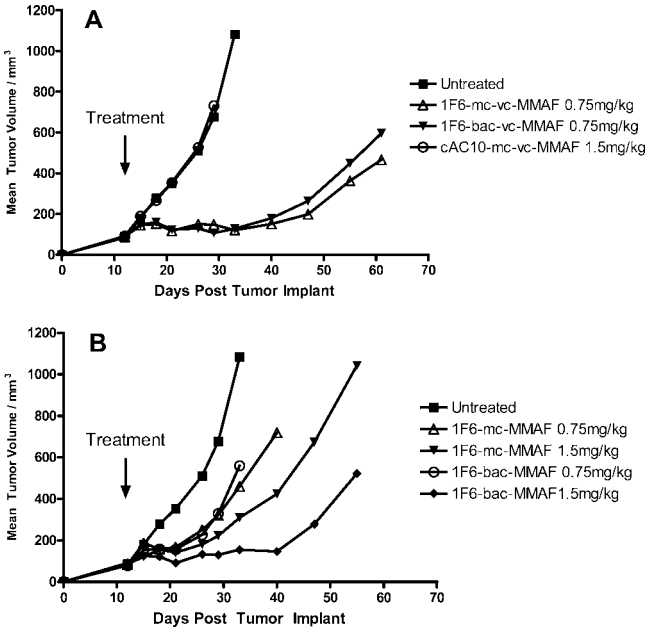

Figure 4. In vivo therapeutic efficacy of the conjugates in SCID mice. Groups of mice (five/group) with subcutaneous 786-O renal cell carcinoma xenografts were treated once (arrow) with conjugates at the doses indicated once the tumors were staged and growing. (A) Comparison of in vivo therapeutic efficacy of vc containing conjugates formed through acetamide (bac) and maleimide (mc) adducts, and (B) similar studies with directly linked ADCs lacking the vc peptide.

cysteine to serine substitutions at positions 226 and 229) (*28*), and AC10 (chimeric IgG1 recognizing the CD30 antigen) (*23*). Reduction of interchain disulfides was accomplished using the reducing agent tris(2-carboxyethyl)phosphine (TCEP), such that an average of two disulfides/mAb were reduced for the 1F6 and AC10 mAbs. Addition of the drug linker complexes led to

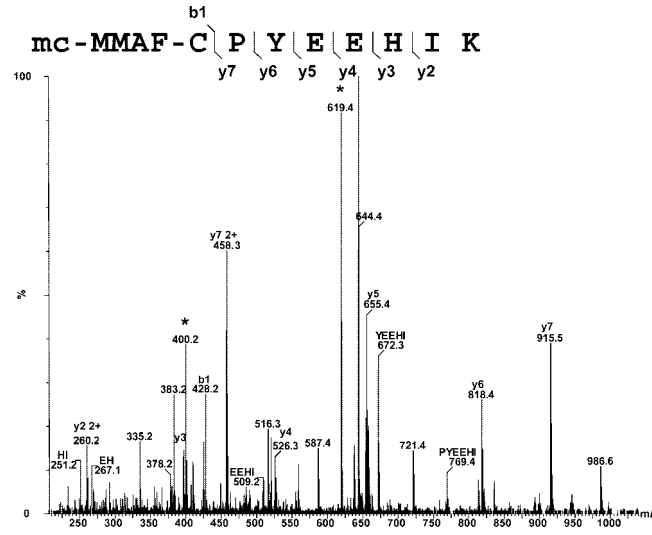

Figure 5. LC/MS/MS spectrum of the rat serum albumin (RSA) peptide-mc-MMAF adduct obtained upon incubation of AC10-mc-MMAF in rat plasma at 37 °C. The *m*/*z* of this peptide (648.4, (m+3)/3) and the MS/MS spectrum are consistent with RSA tryptic peptide T6 (residues 34–41 of the mature protein) modified with mc-MMAF at cysteine-34. Asterisks mark the a1 (400.2) ion containing mc-MMAF and the C-terminal tetrapeptide of MMAF (619.4), which is also a prominent in-source fragmentation ion.

conjugates having an average of four drugs/mAb, with a distribution centered at four drugs/mAb, but ranging between zero and eight. In contrast, the 1F6-C4v2 mAb provided ADCs that were highly homogeneous, since full reduction of the mutated mAb provided only four thiol groups for conjugation (*28*), which led to high yields of 1F6−C4v2-mc-MMAF with four drugs/mAb.

A previously described ELISA assay was used to determine drug to antibody ratios upon prolonged in vitro ADC incubation or after in vivo ADC administration (*24*). The results were compared with a 1F6-C4v2-bac-MMAF conjugate that did not contain a maleimide/thioether adduct. The recombinant mutated mAb was used for all these studies, ensuring that the administered drug was as homogeneous as possible, with initial uniform substitution of four drugs/mAb.

The first step in measuring in vivo ADC stability involved determining ADC concentrations in blood samples of treated animals. An anti-idiotype-based ELISA provided a half-life for clearance of both conjugates in nude mice of approximately 7 days (Figure 2A). Samples from this assay were then subjected to an ELISA using an anti-drug mAb that bound to conjugated drug to an extent that reflected the level of drug substitution on the 1F6 mAb. As shown in Figure 2B, 1F6-C4v2-mc-MMAF lost drug with a half-life of 7 days, which is consistent with an earlier reported half-life of 6–10 days for a maleimide containing auristatin conjugate (*24*). In contrast, the 1F6-C4v2-bac-MMAF conjugate was more stable in vivo, with no apparent drug loss throughout the 14 day assay period.

Cytotoxicity. The 1F6-C4v2 auristatin conjugates were tested on a panel of CD70 expressing renal cell carcinoma cell lines, as shown in Table 1. Cells were exposed to the ADCs continuously for 96 h, and the cytotoxic effects, compared to untreated control cells, were determined by Alamar Blue conversion. Both the dipeptide ADCs with cleavable linkers (bac-vc and mc-vc-MMAF ADCs) exhibited potent and uniform activities against all cell lines tested. The fact that the two conjugates appear to be equally potent is not surprising, given that they release the same drug (MMAF) upon linker cleavage. In contrast, drug release from the 1F6-C4v2-mc-MMAF and bac-MMAF conjugates requires antibody degradation (*30*), and

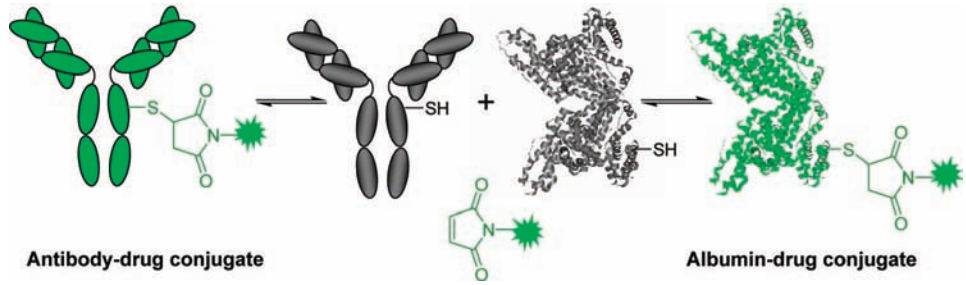

Figure 6. Proposed mechanism of drug transfer from an antibody to albumin through the thioether fragmentation reaction.

the released drugs are not chemically identical, since they contain linker and amino acids from the mAb. Based on previous studies of related ADCs (*30*), the 1F6-C4v2-mc-MMAF conjugate releases cysteine-mc-MMAF upon antibody degradation, and 1F6-C4v2-bac-MMAF should release the corresponding acetamidocysteine adduct. The data in Table 1 show that 1F6-C4v2-bac-MMAF leads to slightly greater potency than 1F6-C4v2-mc-MMAF on all but the Caki-1 cell line, and both ADCs are significantly less potent than the corresponding vc-MMAF ADCs.

Maximum Tolerated Doses. BALB/c nude mice were injected with the conjugates as indicated in Table 2, and the MTDs were determined based on body weight loss and outward signs of toxicity. Both 1F6-mc-MMAF and 1F6-bac-MMAF ADCs were nontoxic at 150 mg/kg, the highest dose tested. On the other hand, the dipeptide-containing ADCs, 1F6-mc-vc-MMAF and 1F6-bac-vc-MMAF, had MTDs of approximately 20 mg/kg. At 40 mg/kg, both ADCs were not tolerated. Therefore, tolerability was not apparently affected when comparing corresponding maleimide and acetamide derived ADCs. The differences in MTDs between the mc and vc-derived ADCs are most likely due to structural differences, as indicated above, between the released drugs.

Drug Delivery. An LC/MS/MS based assay was established to determine the amount of drug present in subcutaneous 786-O renal cell carcinoma xenografts, as well as the liver and serum of BALB/c mice treated with 1F6-mc-vc-MMAF and 1F6-bac-vc-MMAF conjugates at 1.5 mg/kg. The only identifiable drug released from these ADCs was MMAF, consistent with dipeptide cleavage followed by fragmentation of the *p*-aminobenzylcarbamate spacer (*20*). Figure 3A shows that tumor drug levels peaked at approximately 3 days, at which point 1F6-bac-vc-MMAF treated mice had higher intratumoral drug concentrations than those treated with the 1F6-mc-vc-MMAF ADC. Over the period of 7 days, the AUC difference was 25%. The liver (Figure 3A) and serum (Figure 3B) drug concentrations from the two ADCs were similar, consistent with early ADC exposure and lack of drug retention.

Efficacy. The therapeutic effects of the ADCs were determined in nude mice with subcutaneous 786-O tumor xenografts. Since the goal of these experiments was to determine if there were differences between the ADCs, each animal was injected only once at doses that were previously shown to be subcurative (*27*). As expected, 1F6-mc-vc-MMAF displayed significant antitumor activities (Figure 4A). Similar therapeutic effects were obtained with the corresponding 1F6-bac-vc-MMAF ADC, suggesting that the two agents were comparable in activity and potency. The antigen-specific nature of these activities was confirmed through the lack of activity displayed by cAC10-mc-vc-MMAF, an anti-CD30 ADC that does not bind to CD30 antigen negative 786-O cells.

A similar trend of activities was obtained with the ADCs that lacked the dipeptide spacer (Figure 4B). At 0.75 mg/kg, there was a slight delay in tumor outgrowth for both 1F6-mc-MMAF and 1F6-bac-MMAF with no apparent differences between the two groups. The effects at 1.5 mg/kg were more pronounced for both ADCs. Although 1F6-bac-mc-MMAF appears to display a higher degree of antitumor activity than 1F6-mc-MMAF, the difference is not statistically significant (*P* values of 0.10 and 0.11 for days 47 and 55, respectively). These results are consistent with the localization studies which showed comparable levels of drug accumulation for bac and vc-based ADCs (Figure 3A).

Fate of Released Drug. Having established that linker plasma stability was enhanced upon replacement of the maleimide with an acetamide functionality, in vitro experiments were undertaken to identify the fate of the released drug from AC10-mc-MMAF. The ADC was incubated in rat plasma at 37 °C for 5 days, treated with trypsin, and auristatin-conjugated peptide fragments were separated from other plasma proteins by affinity chromatography on a column with an immobilized anti-auristatin mAb. Bound material was eluted, and the resulting peptides were analyzed by LC-MS. The identity of auristatin adducts was facilitated by the prominent in-source auristatin fragmentation peak at *m/z* 619.4. Before incubation, all of the auristatin adducts were comprised of antibody peptides that contained interchain cysteines. Comparison of these traces from the samples obtained after the 5 day plasma incubation revealed a new peak, whose *m/z* and MS/MS spectrum were consistent with a rat serum albumin peptide (residues 34 to 41) modified with the mc-MMAF drug linker (Figure 5). The fragmentation pattern of this peak demonstrated that mc-MMAF was covalently bound to cysteine-34 in albumin. We have confirmed that the same transfer reaction takes place in mice treated with 1F6-C4v2-mc-MMAF (data not shown). Thus, prolonged exposure of alkyl-maleimide auristatin ADCs to plasma proteins may lead to a slow transfer of drug to albumin cysteines. We propose that the mechanism for drug transfer proceeds through the reaction scheme depicted in Figure 6. The first step involves a reversible fragmentation reaction in which the alkyl-maleimide drug product dissociates from the mAb. In buffers such as PBS, this reaction is not observed, since the conjugation reaction is favored. However, in blood or plasma the predominant thiol-containing protein is albumin, which contains a reactive cysteine residue at position 34. The reaction of the maleimide with this cysteine results in the new species observed. The bac-containing ADCs are unable to undergo an analogous fragmentation reaction, and this accounts for their increased plasma stability.

DISCUSSION

Linker stability plays an important role in both the efficacy and toxicity of ADCs. Early generation ADCs often contained unstable linkers with short half-lives (1–2 days) such as disulfides (*17, 18, 26*) and hydrazones (*19, 25, 32*). More recently, attention has turned toward linkers with improved stability characteristics while in the systemic circulation (*15, 30*). Included among them are peptides (*20, 33*), glucuronides (*34*), and nonmetabolizable spacers that remain covalently attached to the drug after the mAb carrier is hydrolyzed in lysosomes of

target cells (*15*, *30*). ADCs incorporating such linkers were formed through the reaction of thiols on one of the components with alkyl-maleimides on the other. In the examples presented here, 1F6-C4v2-mc-MMAF and 1F6−C4v2-mc-vc-MMAF were both stable in buffers, but slowly released drug with approximately 7 day half-lives upon exposure to plasma proteins in vitro and in vivo. We demonstrate that simply by replacement of the maleimide with an acetamide, ADC stability can be significantly increased. There was no apparent drug release from circulating 1F6-C4v2-mc-MMAF in vivo 14 days after administration (Figure 2B). However, in spite of the stability differences between the bromoacetamide and alkyl-maleimide based ADCs, their efficacy, potency, and toxicity characteristics were indistinguishable. This is most likely due to the very similar half-lives (approximately 7 days) of both drug dissociation from the alkyl-maleimide linked conjugates and ADC blood clearance (Figure 2). Extending linker half-life much beyond the pharmacokinetic half-life is not likely to have a pronounced effect on drug exposure, due to reduced ADC concentrations over time. We have calculated a maximum blood AUC difference between the acetamides and maleimide/thioether adducts over 7 days of only 30%, which is in agreement with the 25% difference in tumors shown in Figure 3A. The relative effects on therapeutic efficacy resulting from such small differences are likely to be quite subtle.

The results reported here provide the first direct evidence that maleimide/thioether fragmentation can lead to conjugate instability. The results are similar to a previous report in which a bis-maleimide-linked radiometal immunoconjugate was shown to be unstable in serum, with transfer of the radiometal to albumin taking place (*35*). It was not determined whether the transfer reaction involved maleimide transfer or the formation of noncovalent albumin adducts. Here, we demonstrate that alkyl-maleimides undergo slow dissociation leading to covalent drug transfer to the cysteine-34 residue on serum albumin, the same residue that is thought to be alkylated when maleimide-containing anticancer drug derivatives are systemically administered (*36*–*39*). The transfer mechanism described here most likely involves regeneration of the maleimide through thioether fragmentation, followed by alkylation of the cysteine thiol group on albumin. Experiments to confirm the proposed mechanism include the lack of transfer to S-alkylated albumin, or lack of transfer to albumin in the presence of large excesses of competing thiols (data not shown).

In conclusion, we have demonstrated that ADCs with linker half-lives in the range of 7 days in mice result in nearly optimal safety and efficacy profiles. Attachment of the drug/linker derivatives to mAb thiols through acetamides extends the half-lives significantly by circumventing maleimide transfer. We are currently engaged in studies to more fully explore the activity and toxicity profiles associated with newer generation linker technologies, such as those described here.

ACKNOWLEDGMENT

We wish to thank Drs. Paul Carter, Svetlana Doronina, and Clay Siegall for their valuable input on the studies described, and Martha Anderson, Carol Morris-Tilden, and Jamie Miyamoto for expert experimental assistance.

LITERATURE CITED

(1) Jurcic, J. G. (2005) Immunotherapy for acute myeloid leukemia. *Curr. Oncol. Rep. 7*, 339–46.

(2) Linenberger, M. L. (2005) CD33-directed therapy with gemtuzumab ozogamicin in acute myeloid leukemia: progress in understanding cytotoxicity and potential mechanisms of drug resistance. *Leukemia 19*, 176–82.

(3) Damle, N. K. (2004) Tumour-targeted chemotherapy with immunoconjugates of calicheamicin. *Expert Opin. Biol. Ther. 4*, 1445–52.

(4) Chari, R. V. (2007) Targeted cancer therapy: conferring specificity to cytotoxic drugs. *Acc. Chem. Res.*

(5) Widdison, W. C., Wilhelm, S. D., Cavanagh, E. E., Whiteman, K. R., Leece, B. A., Kovtun, Y., Goldmacher, V. S., Xie, H., Steeves, R. M., Lutz, R. J., Zhao, R., Wang, L., Blattler, W. A., and Chari, R. V. (2006) Semisynthetic maytansine analogues for the targeted treatment of cancer. *J. Med. Chem. 49*, 4392–408.

(6) Wu, A. M., and Senter, P. D. (2005) Arming antibodies: prospects and challenges for immunoconjugates. *Nat. Biotechnol. 23*, 1137–46.

(7) Baker, M. (2005) Upping the ante on antibodies. *Nat. Biotechnol. 23*, 1065–72.

(8) Polson, A. G., Yu, S. F., Elkins, K., Zheng, B., Clark, S., Ingle, G. S., Slaga, D. S., Giere, L., Du, C., Tan, C., Hongo, J. A., Gogineni, A., Cole, M. J., Vandlen, R., Stephan, J. P., Young, J., Chang, W., Scales, S. J., Ross, S., Eaton, D., and Ebens, A. (2007) Antibody-drug conjugates targeted to CD79 for the treatment of non-Hodgkin lymphoma. *Blood 110*, 616–23.

(9) Polakis, P. (2005) Arming antibodies for cancer therapy. *Curr. Opin. Pharmacol. 5*, 382–7.

(10) Chen, Y., Clark, S., Wong, T., Dennis, M. S., Luis, E., Zhong, F., Bheddah, S., Koeppen, H., Gogineni, A., Ross, S., Polakis, P., and Mallet, W. (2007) Armed antibodies targeting the mucin repeats of the ovarian cancer antigen, MUC16, are highly efficacious in animal tumor models. *Cancer Res. 67*, 4924–32.

(11) Ma, D., Hopf, C. E., Malewicz, A. D., Donovan, G. P., Senter, P. D., Goeckeler, W. F., Maddon, P. J., and Olson, W. C. (2006) Potent antitumor activity of an auristatin-conjugated, fully human monoclonal antibody to prostate-specific membrane antigen. *Clin. Cancer Res. 12*, 2591–6.

(12) Tse, K. F., Jeffers, M., Pollack, V. A., McCabe, D. A., Shadish, M. L., Khramtsov, N. V., Hackett, C. S., Shenoy, S. G., Kuang, B., Boldog, F. L., MacDougall, J. R., Rastelli, L., Herrmann, J., Gallo, M., Gazit-Bornstein, G., Senter, P. D., Meyer, D. L., Lichenstein, H. S., and LaRochelle, W. J. (2006) CR011, a fully human monoclonal antibody-auristatin E conjugate, for the treatment of melanoma. *Clin. Cancer Res. 12*, 1373–82.

(13) Dijoseph, J. F., Dougher, M. M., Armellino, D. C., Evans, D. Y., and Damle, N. K. (2007) Therapeutic potential of CD22-specific antibody-targeted chemotherapy using inotuzumab ozogamicin (CMC-544) for the treatment of acute lymphoblastic leukemia. *Leukemia.* .

(14) Dijoseph, J. F., Dougher, M. M., Armellino, D. C., Kalyandrug, L., Kunz, A., Boghaert, E. R., Hamann, P. R., and Damle, N. K. (2007) CD20-specific antibody-targeted chemotherapy of non-Hodgkin's B-cell lymphoma using calicheamicin-conjugated rituximab. *Cancer Immunol. Immunother. 56*, 1107–17.

(15) Erickson, H. K., Park, P. U., Widdison, W. C., Kovtun, Y. V., Garrett, L. M., Hoffman, K., Lutz, R. J., Goldmacher, V. S., and Blattler, W. A. (2006) Antibody-maytansinoid conjugates are activated in targeted cancer cells by lysosomal degradation and linker-dependent intracellular processing. *Cancer Res. 66*, 4426–33.

(16) Xie, H., and Blattler, W. A. (2006) In vivo behaviour of antibody-drug conjugates for the targeted treatment of cancer. *Expert Opin. Biol. Ther. 6*, 281–91.

(17) Thorpe, P. E., Wallace, P. M., Knowles, P. P., Relf, M. G., Brown, A. N., Watson, G. J., Knyba, R. E., Wawrzynczak, E. J., and Blakey, D. C. (1987) New coupling agents for the synthesis of immunotoxins containing a hindered disulfide bond with improved stability in vivo. *Cancer Res. 47*, 5924–31.

(18) Thorpe, P. E., Wallace, P. M., Knowles, P. P., Relf, M. G., Brown, A. N., Watson, G. J., Blakey, D. C., and Newell, D. R. (1988) Improved antitumor effects of immunotoxins prepared with deglycosylated ricin A-chain and hindered disulfide linkages. *Cancer Res. 48*, 6396–403.

(19) Trail, P. A., Willner, D., Lasch, S. J., Henderson, A. J., Hofstead, S., Casazza, A. M., Firestone, R. A., Hellstrom, I., and Hellstrom, K. E. (1993) Cure of xenografted human carcinomas by BR96-doxorubicin immunoconjugates. *Science 261*, 212–5.

(20) Doronina, S. O., Toki, B. E., Torgov, M. Y., Mendelsohn, B. A., Cerveny, C. G., Chace, D. F., DeBlanc, R. L., Gearing, R. P., Bovee, T. D., Siegall, C. B., Francisco, J. A., Wahl, A. F., Meyer, D. L., and Senter, P. D. (2003) Development of potent monoclonal antibody auristatin conjugates for cancer therapy. *Nat. Biotechnol. 21*, 778–84.

(21) Hamann, P. R., Hinman, L. M., Beyer, C. F., Lindh, D., Upeslacis, J., Shochat, D., and Mountain, A. (2005) A calicheamicin conjugate with a fully humanized anti-MUC1 antibody shows potent antitumor effects in breast and ovarian tumor xenografts. *Bioconjugate Chem. 16*, 354–60.

(22) Hamann, P. R., Hinman, L. M., Beyer, C. F., Greenberger, L. M., Lin, C., Lindh, D., Menendez, A. T., Wallace, R., Durr, F. E., and Upeslacis, J. (2005) An anti-MUC1 antibody-calicheamicin conjugate for treatment of solid tumors. Choice of linker and overcoming drug resistance. *Bioconjugate Chem. 16*, 346–53.

(23) Francisco, J. A., Cerveny, C. G., Meyer, D. L., Mixan, B. J., Klussman, K., Chace, D. F., Rejniak, S. X., Gordon, K. A., DeBlanc, R., Toki, B. E., Law, C. L., Doronina, S. O., Siegall, C. B., Senter, P. D., and Wahl, A. F. (2003) cAC10-vcMMAE, an anti-CD30-monomethyl auristatin E conjugate with potent and selective antitumor activity. *Blood 102*, 1458–65.

(24) Sanderson, R. J., Hering, M. A., James, S. F., Sun, M. M., Doronina, S. O., Siadak, A. W., Senter, P. D., and Wahl, A. F. (2005) In vivo drug-linker stability of an anti-CD30 dipeptide-linked auristatin immunoconjugate. *Clin. Cancer Res. 11*, 843–52.

(25) Saleh, M. N., Sugarman, S., Murray, J., Ostroff, J. B., Healey, D., Jones, D., Daniel, C. R., LeBherz, D., Brewer, H., Onetto, N., and LoBuglio, A. F. (2000) Phase I trial of the anti-Lewis Y drug immunoconjugate BR96-doxorubicin in patients with lewis Y-expressing epithelial tumors. *J. Clin. Oncol. 18*, 2282–92.

(26) Xie, H., Audette, C., Hoffee, M., Lambert, J. M., and Blattler, W. A. (2004) Pharmacokinetics and biodistribution of the antitumor immunoconjugate, cantuzumab mertansine (huC242-DM1), and its two components in mice. *J. Pharmacol. Exp. Ther. 308*, 1073–82.

(27) Law, C. L., Gordon, K. A., Toki, B. E., Yamane, A. K., Hering, M. A., Cerveny, C. G., Petroziello, J. M., Ryan, M. C., Smith, L., Simon, R., Sauter, G., Oflazoglu, E., Doronina, S. O., Meyer, D. L., Francisco, J. A., Carter, P., Senter, P. D., Copland, J. A., Wood, C. G., and Wahl, A. F. (2006) Lymphocyte activation antigen CD70 expressed by renal cell carcinoma is a potential therapeutic target for anti-CD70 antibody-drug conjugates. *Cancer Res. 66*, 2328–37.

(28) McDonagh, C. F., Turcott, E., Westendorf, L., Webster, J. B., Alley, S. C., Kim, K., Andreyka, J., Stone, I., Hamblett, K. J., Francisco, J. A., and Carter, P. (2006) Engineered antibody-drug conjugates with defined sites and stoichiometries of drug attachment. *Protein Eng. Des. Sel. 19*, 299–307.

(29) Senter, P. D., Doronina, S. O., Toki, B. E. (2005)Monomethylvaline compounds capable of conjugation to ligands. PatentWO 2005-011711.

(30) Doronina, S. O., Mendelsohn, B. A., Bovee, T. D., Cerveny, C. G., Alley, S. C., Meyer, D. L., Oflazoglu, E., Toki, B. E., Sanderson, R. J., Zabinski, R. F., Wahl, A. F., and Senter, P. D. (2006) Enhanced activity of monomethylauristatin F through monoclonal antibody delivery: effects of linker technology on efficacy and toxicity. *Bioconjugate Chem. 17*, 114–24.

(31) Sun, M. M., Beam, K. S., Cerveny, C. G., Hamblett, K. J., Blackmore, R. S., Torgov, M. Y., Handley, F. G., Ihle, N. C., Senter, P. D., and Alley, S. C. (2005) Reduction-alkylation strategies for the modification of specific monoclonal antibody disulfides. *Bioconjugate Chem. 16*, 1282–90.

(32) Boghaert, E. R., Khandke, K. M., Sridharan, L., Dougher, M., Dijoseph, J. F., Kunz, A., Hamann, P. R., Moran, J., Chaudhary, I., and Damle, N. K. (2007) Determination of pharmacokinetic values of calicheamicin-antibody conjugates in mice by plasmon resonance analysis of small (5 μl) blood samples. *Cancer Chemother. Pharmacol.* .

(33) Dubowchik, G. M., and Walker, M. A. (1999) Receptor-mediated and enzyme-dependent targeting of cytotoxic anticancer drugs. *Pharmacol. Ther. 83*, 67–123.

(34) Jeffrey, S. C., Andreyka, J. B., Bernhardt, S. X., Kissler, K. M., Kline, T., Lenox, J. S., Moser, R. F., Nguyen, M. T., Okeley, N. M., Stone, I. J., Zhang, X., and Senter, P. D. (2006) Development and properties of beta-glucuronide linkers for monoclonal antibody-drug conjugates. *Bioconjugate Chem. 17*, 831–40.

(35) Lewis, M. R., and Shively, J. E. (1998) Maleimidocysteineamido-DOTA derivatives: new reagents for radiometal chelate conjugation to antibody sulfhydryl groups undergo pH-dependent cleavage reactions. *Bioconjugate Chem. 9*, 72–86.

(36) Kratz, F., Muller-Driver, R., Hofmann, I., Drevs, J., and Unger, C. (2000) A novel macromolecular prodrug concept exploiting endogenous serum albumin as a drug carrier for cancer chemotherapy. *J. Med. Chem. 43*, 1253–6.

(37) Chung, D. E., and Kratz, F. (2006) Development of a novel albumin-binding prodrug that is cleaved by urokinase-type-plasminogen activator (uPA). *Bioorg. Med. Chem. Lett. 16*, 5157–63.

(38) Lebrecht, D., Geist, A., Ketelsen, U. P., Haberstroh, J., Setzer, B., Kratz, F., and Walker, U. A. (2007) The 6-maleimidocaproyl hydrazone derivative of doxorubicin (DOXO-EMCH) is superior to free doxorubicin with respect to cardiotoxicity and mitochondrial damage. *Int. J. Cancer. 120*, 927–34.

(39) Unger, C., Haring, B., Medinger, M., Drevs, J., Steinbild, S., Kratz, F., and Mross, K. (2007) Phase I and pharmacokinetic study of the (6-maleimidocaproyl)hydrazone derivative of doxorubicin. *Clin. Cancer. Res. 13*, 4858–66.

BC7004329

Synthesis of Aminoglycoside Conjugates of 2′-*O*-Methyl Oligoribonucleotides

Kaisa Ketomäki and Pasi Virta*

Department of Chemistry, University of Turku, FIN-20014 Turku, Finland. Received November 20, 2007; Revised Manuscript Received January 4, 2008

Aminoglycoside conjugates of 2′-*O*-methyl oligoribonucleotides have been synthesized entirely on a solid phase using conventional phosphoramidate chemistry. For this purpose, appropriately protected neamine-derived phosphoramidites, viz., 2-cyanoethyl [6,3′,4′-tri-*O*-levulinoyl-N^1,N^3,$N^{2'}$,$N^{6'}$-tetra(trifluoroacetyl)neamine-5-*O*-ethyl] *N*,*N*-diisopropylphosphoramidite, **1**, and 2-cyanoethyl [6,3′,4′,2″,3″-penta-*O*-levulinoyl-N^1,N^3,$N^{2'}$,$N^{6'}$-tetra(trifluoroacetyl) ribostamycin-5″-yl] *N*,*N*-diisopropylphosphoramidite, **2**, have been prepared and attached via phosphodiester linkage to an appropriate 2′-*O*-methyl oligoribonucleotide. Levulinoyl esters are used to cap the hydroxyl groups of the aminoglycoside moieties, since they may be selectively removed prior to ammonolysis. In this manner, the potential *O*→*N* acyl migration is excluded. Applicability of the strategy has been demonstrated by the synthesis of eight different aminoglycoside conjugates, in which **1** and **2** are attached directly to the 5′-end (**6** and **10**) or, alternatively, to an inserted non-nucleosidic hydroxyalkyl armed branching unit (**3**, **4**, or **5**), which results in intrachain conjugates (**7**–**9**, **11**–**13**). The potential of these conjugates to act as a sequence-selective artificial nuclease has been studied.

INTRODUCTION

Aminoglycosides are well-known antibiotics having affinity for structural elements of RNA in which the usual base pairing is disrupted. Their bactericidal effect is based on binding to the ribosomal decoding site (A-site), which reduces the fidelity of protein translation (*1–4*), but they additionally have comparable affinities to other structurally related RNA targets. Aminoglycosides are, e.g., able to inhibit several ribozymes (*5, 6*) and, perhaps most interesting for the general public, they bind to important HIV regions, TAR,[1]RRE (*7, 8*), and DIS (*9, 10*), resulting in inhibition of viral replication. However, the known natural aminoglycosides are very diverse RNA binders, which is mainly a consequence of their polycationic nature. To overcome this promiscuity, numerous tailored aminoglycosides have been synthesized in recent years. One approach is conjugation of aminoglycosides to nucleobases (*9, 11–14*), oligonucleotides (*15*), or PNA (*16*), in which affinity to numerous RNA targets may be whittled down by increased sequence selectivity.

In addition to the binding properties discussed above, aminoglycosides show potential for chemical cleavage of RNA. This feature is common to diamines and polyamines in general (*17, 18*), but with aminoglycosides, the more defined spatial positioning of the amino groups, their individual pK_a values, and lowered conformational freedom may further accelerate the hydrolysis. As an example, neomycin hydrolyzes simple adenylyl(3′−5′) adenosine more effectively than an unstructured diamine (*19*). This metal-ion-independent catalytic activity expectedly remains at a marginal level, but remarkable rate acceleration may be obtained by participation of metal cations. Cu^{2+}-complexes of neamine and kanamycin have been reported to be efficient cleaving agents of RNA (*20*), and even of DNA (*21*). These observations give an insight that both requirements (the RNA recognition and the cleavage) for an artificial sequence-specific nuclease may already exist in aminoglycosides (*22–25*), but conjugation to a complementary oligonucleotide or PNA may be a respectable option. A PNA−neamine conjugate has been reported not only to bind to the HIV-1 TAR region, but also to catalyze its hydrolysis (*26, 27*). The conjugate results in relatively fast metal-ion-independent cleavage, enhances cellular uptake, and inhibits viral replication.

With the above goals in mind, aminoglycoside-conjugated oligonucleotides are an attractive subject in organic chemistry, but from the synthetic point of view, they may still need some consideration. Ligation of those two classes of biomolecules in solution has advantages, such as asimple protecting group scheme, but it may be time-consuming to carry out. Fully automated synthesis may, hence, be a more attractive choice. In that case, however, several amino and hydroxyl groups of an appropriate aminoglycoside have to be masked with easily removable protecting groups, which should be compatible with the standard oligonucleotide synthesis and, preferably, be base-labile. Furthermore, the amino groups should not be exposed when the adjacent hydroxyl groups still bear acyl-type protection, since *O*→*N*-acyl migration may take place. Base-modified 2′-deoxyuridine phosphoramidites, conjugated with 2,6-diaminoglucose (*28*) and neomycine units (*29*) have been used for the synthesis of aminoglycoside-modified oligonucleotides. The aminoglycoside moieties have been capped with protecting group combinations, such as acetyl esters with trifluoroacetamides and trifluoroacetylesters with Boc-carbamates. On using the former combination (*28*), a substantial amount of acetamide byproducts have been found in the product mixture. This has been attributed to acetyl capping of the trifluoroacetamide functions upon oligonucleotide assembly, but the possibility of acyl migration has not been excluded. The latter combination (*29*) overcomes acyl migration, but the strategy suffers from potential depurination, when expanded to adenine- and guanine-containing oligonucleotides.

* pasi.virta@utu.fi.

[1]Abbreviations: All, Allyl; Boc, *tert*-butoxycarbonyl; CPG, controlled pore glass; DCA, dichloroacetic acid; DMAP, 4-dimethylaminopyridine; DIS, dimerization initiation site; DMTr, 4,4′-dimethoxytrityl; HEPES, 4-(2-hydroxyethyl)-1-piperazineethanesulfonic acid; *i*Pr, 1-methylethyl; Lev, levulinoyl (4-oxopentanoyl); MMTr, 4-methoxytrityl; RRE, rev-response element, TAR, trans-acting response element, TBDMS, *tert*-butyldimethylsilyl; Tfa, trifluoroacetyl, TMS, tetramethylsilane, TMSTf, trimethylsilyl triflate.

10.1021/bc7004279 CCC: $40.75 © 2008 American Chemical Society
Published on Web 02/19/2008

In the present study, an entirely solid phase synthesis of aminoglycoside conjugates of 2′-*O*-methyl oligoribonucleotides (**6**–**13**) using standard phosphoramidate chemistry has been described. Appropriately tethered neamine-based phosphoramidites, **1** and **2**, were first synthesized using cheap neomycin trisulfate as an initial starting material. The resulted phosphoramidites **1** and **2** were then attached to resin-bound oligonucleotides via a phosphodiester linkage. Inserted non-nucleosidic branching units (**3**–**5**) were utilized to obtain intrachain conjugates (**7**–**9**, **11**–**13**), or alternatively, direct coupling to the 5′-end was performed (**6** and **10**). Prior to ammonolysis, the resins were treated with a mixture of hydrazinium acetate to orthogonally remove the levulinoyl protections. In this manner, acyl migration to the adjacent amino groups on the aminoglycoside moieties (**1** and **2**) was eliminated. Applicability of the strategy was demonstrated by the synthesis of eight different conjugates (**6**–**13**), which all were obtained with acceptable 41–65% purity. A strategy to obtain intrachain conjugates (**7**–**9**, **11**–**13**) was devised to be expanded to the library synthesis, in which various conjugates may readily be obtained by mixing different building blocks, the aminoglycosides (**1** and **2**) with the branching units (**3**–**5**), at an appropriate site in the oligonucleotide sequence. Since a neamine PNA conjugate has been reported to be an efficient artificial nuclease (*26*, *27*), a small library of aminoglycosides (**6**–**13**) bearing the native negatively charged phosphodiester backbone may advisably give further information about the general nuclease activity of these attractive biomolecules. In the present study, conjugates (**6**–**13**) were targeted to chimeric ribo/2′-*O*-methyl oligonucleotides (**14** and **15**), which upon hybridization (excluding experiments with **6** and **10**) constitute triand pentanucleotide bulges (A_3 and A_5) opposite the aminoglycosidic regions. One of the conjugates (**9**) resulted in metal-ion-independent cleavage of the targets [**14** and **15**, $k = (2.7 \pm 0.6) \times 10^{-7}$ s^{-1} and $(2.3 \pm 0.6) \times 10^{-7}$ s^{-1}, respectively], but usually the cleavage obtained by the conjugates (**6**–**8**, **10**–**13**) remained at a marginal level or the conjugates were fully inactive.

EXPERIMENTAL PROCEDURES

General Methods and Materials. The NMR spectra of **1**–**3**, **19**–**31**, and **33**–**36** were recorded at 400 and 500 MHz. The chemical shifts are given in ppm from internal TMS and coupling constants in hertz. Peak assignments were supported by appropriate 2D NMR methods, e.g., COSY, HSQC, and HMBC. The mass spectra of **1**–**3**, **6**–**13**, **20**–**31**, and **33**–**36** were recorded by EI and ESI ionization methods. The 2′-*O*-methyl oligoribonucleotide conjugates (**6**–**13**) and the chimeric target oligonucleotides (**14** and **15**) were assembled by conventional phosphoramidate strategy using a 1 μmol scale and following the standard RNA coupling protocol of Appplied Biosystems 342 DNA synthesizer. LiChroCART Hypersil ODS column (250 × 10 mm, 5 μm) at a flow rate of 3 mL min^{-1} was used for RP HPLC purifications of the 2′-*O*-methyl oligoribonucleotide conjugates (**6**–**13**). In each case, a gradient elution from 20% to 70% acetonitrile in 0.1 mol L^{-1} $Et_3N^+OAc^-$buffer over 30 min was used.

6,3′,4′-Tri-*O*-acetyl-5-*O*-allyl-1,3,2′,6′-tetraazido Neamine (20). 6,3′,4′-tri-*O*-acetyl-1,3,2′,6′-tetraazido neamine (**19**) was synthesized from neomycine trisulfate (**16**) according to the literature (*30*–*32*). Improvements to the selective acylation of **18** may be mentioned. Acetic anhydride (0.50 mL, 51 mmol) in pyridine (2.0 mL) was dropwise added to a mixture of **18** (0.68 g, 16 mmol) and a catalytic amount of DMAP in pyridine (1.0 mL). The reaction was allowed to stir overnight at ambient temperature, quenched by addition of methanol, and evaporated to dryness. The residue was purified by silica gel chromatography (40% EtOAc in petroleum ether) to yield 0.64 g (73%) of the product (**19**) as white foam. All side products, mainly 5,6,3′,4′-tetra-*O*-acetyl-1,3,2′,6′-tetraazido neamine (0.16 g, 17%), were also isolated, combined, and restored to **18** (acetyl groups were removed by 0.1 mol L^{-1} NaOMe in MeOH, 1 h at 25 °C, cf. synthesis of **26** below). The regenerated crude **18** may again be used for the selective acylation, with the same yield. **19**: ^{1}H NMR (500 MHz, $CDCl_3$) δ 5.50 (dd, 1H, J = 10.3 Hz, 9.5 Hz), 5.37 (d, 1H, J = 3.6 Hz), 5.06 (dd, 1H, J = 10.0 Hz, 9.5 Hz), 4.95 (dd, 1H, J = 10.0 Hz, 9.9 Hz), 4.35 (m, 1H), 3.70–3.66 (m, 2H), 3.62 (d, 1H, J = 3.6 Hz), 3.55 (ddd, 1H, J = 12.5 Hz, 10.1 Hz, 4.6 Hz), 3.47–3.37 (m, 3H), 3.34 (dd, 1H, J = 13.5 Hz, 5.1 Hz), 2.42 (ddd, 1H, J = 13.3 Hz, 4.5 Hz, 4.5 Hz), 2.19, 2.11, and 2.07 (each s, each 3H), 1.64 (ddd, 1H, J = 12.9 Hz, 12.9 Hz, 12.9 Hz); ^{13}C NMR ($CDCl_3$, 250 MHz) δ 170.5, 170.2, 169.7, 98.8, 83.7, 75.0, 74.4, 71.2, 69.5, 69.3, 61.7, 58.3, 57.9, 50.8, 31.9, 20.8, 20.7, 20.6. A mixture of **19** (1.1 g, 20 mmol), $Pd(OAc)_2$ (9 mg, 0.04 mmol), Ph_3P (53 mg, 0.20 mmol), and allyl methyl carbonate (0.46 mL, 41 mmol) in THF (5.0 mL) was refluxed for 15 min and evaporated to dryness (*33*). The residue was purified by silica gel chromatography (5% EtOAc in CH_2Cl_2) to yield 0.50 g (42%) of the desired product **20** as white foam and 0.21 g (17%) of 6-*O*-allyl-1,3,2′,6′-tetraazido-5,3′,4′-tri-*O*-acetyl neamine as yellowish oil. **20**: ^{1}H NMR (500 MHz, $CDCl_3$) δ 5.88 (m, 1H), 5.61 (d, 1H, J = 3.9 Hz), 5.50 (dd, 1H, J = 10.6 Hz, 9.4 Hz), 5.26 (m, 1H), 5.17 (m, 1H), 5.04 (dd, 1H, J = 10.0 Hz, 9.5 Hz), 5.02 (dd, 1H, J = 10.0 Hz, 9.9 Hz), 4.51 (m, 1H), 4.34 (m, 1H), 4.17 (m, 1H), 3.63 (dd, 1H, J = 9.6 Hz, 9.6 Hz), 3.51 (dd, 1H, J = 9.5 Hz, 9.4 Hz), 3.50–3.45 (m, 2H), 3.41–3.36 (m, 2H), 3.31 (dd, 1H, J = 13.5 Hz, 5.1 Hz), 2.40 (ddd, 1H, J = 13.3 Hz, 4.6 Hz, 4.6 Hz), 1.63 (ddd, J = 12.7 Hz, 12.7 Hz, 12.7 Hz); ^{13}C NMR ($CDCl_3$, 250 MHz) δ 170.1, 169.7, 169.6, 133.7, 117.0, 97.6, 82.2, 78.0, 75.5, 74.2, 70.2, 69.3, 69.3, 60.9, 58.7, 58.0, 50.8, 50.8, 31.7, 20.9, 20.7, 20.7; HRMS (ESI) $[M + Na]^+$ $C_{21}H_{28}N_{12}NaO_9$ requires 615.1994, found 615.2005. 6-*O*-allyl-1,3,2′,6′-tetraazido-5,3′,4′-tri-*O*-acetyl neamine: ^{1}H NMR (500 MHz, $CDCl_3$) δ 5.60 (m, 1H), 5.16 (dd, 1H, J = 10.8 Hz, 9.2 Hz), 5.01–4.91 (m, 2H), 4.92 (d, 1H, J = 3.9 Hz), 4.88 (dd, 1H, J = 9.7 Hz, 9.7 Hz), 4.75 (dd, 1H, J = 10.1 Hz, 9.4 Hz), 4.19 (ddd, 1H, J = 10.3 Hz, 5.0 Hz, 2.7 Hz), 4.01 (m, 1H), 3.82 (m, 1H), 3.30 (m, 1H), 3.28 (dd, 1H, J = 9.6 Hz, 4.4 Hz), 3.22 (ddd, 1H, J = 12.1 Hz, 9.9 Hz, 4.4 Hz), 3.10 (dd, 1H, J = 13.5 Hz, 2.7 Hz), 3.07 (dd, 1H, J = 10.8 Hz, 3.9 Hz), 3.02 (dd, 1H, J = 13.5 Hz, 5.0 Hz), 2.93 (dd, 1H, J = 9.8 Hz, 9.8 Hz), 2.11 (ddd, 1H, J = 13.4 Hz, 4.6 Hz, 4.6 Hz), 1.86, 1.80, 1.78 (each s, each 3H), 1.23 (ddd, 1H, J = 12.4 Hz, each); ^{13}C NMR ($CDCl_3$, 250 MHz) δ 169.5, 169.5, 168.7, 133.3, 117.7, 98.3, 81.6, 78.3, 74.1, 74.0, 69.4, 69.2, 69.1, 60.3, 59.2, 58.3, 50.4, 31.7, 20.7, 20.4, 20.4; HRMS (ESI) $[M + Na]^+$: $C_{21}H_{28}N_{12}NaO_9$ requires 615.1994, found 615.1966.

1,3,2′,6′-Tetraazido-5-*O*-(2-hydroxyethyl)neamine (21). Osmium tetroxide (2.5 wt % solution in 2-methyl-2-propanol, 0.20 mL, 16 μmol) was added to a mixture of **20** (0.50 g, 0.84 mmol) in water−dioxane (1:4 v/v, 5.0 mL) (*34*). After 1 h stirring, the mixture was cooled to 0 °C, the solvent volume was increased to 20 mL, and $NaIO_4$ (0.36 g, 17 mmol) was slowly added. The reaction was then allowed to warm up, stirred at room temperature for 5 h, and the resulted aldehyde intermediate was then extracted with ethyl acetate (3 × 10 mL). The organic layers were combined, dried with Na_2SO_4, and evaporated to dryness. The residue was dissolved in a mixture of dichloromethane−ethanol (1:2, v/v, 15 mL), and $NaBH_4$ (64 mg, 1.7 mmol) was added. After 5 h stirring, the reaction was quenched by addition of saturated ammonium chloride, and the crude product intermediate was extracted with ethyl acetate (3 × 10 mL). The organic layers were combined, dried with Na_2SO_4, and evaporated to dryness. The residue was dissolved in 0.1

mol L^{-1} methanolic sodium methoxide (5.0 mL). The mixture was stirred at ambient temperature for 1 h, neutralized by addition of strongly acidic cation-exchange resin, and filtered. The filtrate was evaporated to dryness and purified by silica gel chromatography (40% EtOAc in CH_2Cl_2) to yield 0.21 g (53%) of the product (**21**) as a colorless oil. ^{1}H NMR (500 MHz, $CDCl_3$) δ 5.59 (d, 1H, J = 3.7 Hz), 4.24 (m, 1H), 4.04–3.96 (m, 2H), 3.90 (dd, 1H, J = 9.9 Hz, 9.5 Hz), 3.78 (ddd, 1H, J = 11.6 Hz, 7.5 Hz, 3.1 Hz), 3.72 (ddd, 1H, J = 11.5 Hz, 3.7 Hz, 3.4 Hz), 3.55–3.33 (m, 8H), 3.16 (dd, 1H, J = 10.6 Hz, 3.8 Hz), 2.26 (ddd, 1H, J = 12.4 Hz, 4.2 Hz, 4.2 Hz), 1.42 (ddd, 1H, J = 12.2 Hz, 12.2 Hz, 12.2 Hz); ^{13}C NMR ($CDCl_3$, 250 MHz) δ 97.9, 85.8, 77.6, 76.9, 74.4, 71.8, 71.2, 70.8, 62.9, 61.7, 60.0, 59.5, 51.2, 31.8; HRMS (ESI) $[M + Na]^+$ $C_{14}H_{22}N_{12}NaO_7$ requires 493.1627, found 493.1615.

1,3,2′,6′-Tetraazido-5-*O*-[2-(4-methoxytrityloxy)ethyl]neamine (22). Compound **21** (0.20 g, 0.43 mmol) was dissolved in pyridine (2.0 mL), and 4-methoxytrityl chloride (0.20 g, 0.64 mmol) was added to the mixture. Reaction mixture was stirred overnight at ambient temperature, quenched by addition of methanol, and evaporated to dryness. The residue was dissolved in ethyl acetate and washed with saturated $NaHCO_3$. The organic layer was separated, dried with Na_2SO_4, and evaporated to dryness. The residue was purified by silica gel chromatography (20% EtOAc in CH_2Cl_2) to yield 0.32 g (100%) of the product **22** as a white foam. ^{1}H NMR (500 MHz, $CDCl_3$): δ 7.47 (d, 4H, J = 7.6 Hz), 7.35–7.29 (m, 6H), 7.23 (dd, 2H, J = 7.4 Hz, 7.3 Hz), 6.87 (d, 2H, J = 8.9 Hz), 5.94 (d, 1H, J = 3.8 Hz), 4.25 (m, 1H), 4.15 (m, 1H), 4.02 (m, 1H), 3.91 (dd, 1H, J = 10.3 Hz, 10.1 Hz), 3.79 (s, 3H), 3.63 (dd, 1H, J = 9.6 Hz, 9.5 Hz), 3.57–3.33 (m, 9H), 3.27 (m, 1H), 2.94 (dd, 1H, J = 10.5 Hz, 3.8 Hz), 2.23 (ddd, 1H, J = 12.3 Hz, 4.3 Hz, 4.3 Hz), 1.39 (ddd, 1H, J = 12.3 Hz, each). ^{13}C NMR ($CDCl_3$, 250 MHz) δ 158.8, 144.6, 144.5, 135.5, 130.3, 128.4, 127.4, 126.6, 112.7, 97.4, 86.6, 85.2, 77.1, 76.8, 72.1, 71.8, 71.3, 70.8, 63.6, 62.9, 60.5, 60.2, 59.7, 54.3, 51.3, 31.7; HRMS (ESI) $[M + Na]^+$ $C_{34}H_{38}N_{12}NaO_8$ requires 765.2828, found 765.2804.

6,3′,4′-Tri-*O*-levulinoyl-5-*O*-[2-(4-methoxytrityloxy)ethyl]-*N*^{1},*N*^{3},*N*$^{2'}$,*N*$^{6'}$-tetra(trifluoroacetyl) Neamine (23). Trimethyl phosphine (1 mol L^{-1} Me_3P in toluene, 1.41 mL, 14 mmol) was added to a mixture of **22** (0.21 g, 0.28 mmol) in water−dioxane (1:4, v/v, 2.5 mL) under nitrogen. The reaction was stirred for 4 h at ambient temperature, and then concentrated ammonia (1.0 mL) was added. After overnight stirring, volatiles were removed, and the residue was dissolved in dry methanol (2.0 mL). Triethylamine (1.0 mL) and freshly distilled methyl trifluoroacetate (0.23 mL,) were then added to the mixture, the reaction was stirred overnight, and evaporated to dryness. The resulted crude trifluoroacetylated neamine derivative was dissolved in ethyl acetate and washed with saturated $NaHCO_3$. The organic layer was separated, dried with Na_2SO_4, and evaporated to dryness. The residue was dissolved in pyridine (2.0 mL), and then levulinic anhydride and a catalytic amount of DMAP were added to the mixture. After 2 h stirring, the reaction was quenched by addition of methanol. Ethyl acetate was added, and the crude product was washed with saturated $NaHCO_3$. The organic layer was separated, dried with Na_2SO_4, and evaporated to dryness. The crude final product was purified by silica gel chromatography (20% petroleum ether in EtOAc) to yield 0.28 g (74%) of **23** as a white foam. ^{1}H NMR (500 MHz, $CDCl_3$) δ 8.30 (t, 1H, J = 5.5 Hz), 7.75 (d, 1H, J = 9.3 Hz), 7.46 (d, 1H, J = 9.4 Hz), 7.42 (d, 4H, J = 7.5 Hz), 7.32–7.2 (m, 9H), 7.14 (d, 1H, J = 7.8 Hz), 6.85 (d, 2H, J = 9.0 Hz), 5.51 (d, 1H, J = 3.3 Hz), 5.13 (dd, 1H, J = 10.3 Hz, 9.9 Hz), 5.00 (dd, 1H, J = 10.1 Hz, 9.9 Hz), 4.98 (dd, 1H, J = 9.8 Hz, 9.8 Hz), 4.23–4.07 (m, 3H), 4.01 (ddd, 1H, J = 10.1 Hz, 4.5 Hz, 4.5 Hz), 3.91 (dd, 1H, J = 9.9 Hz, 9.6 Hz), 3.86 (m, 1H), 3.81 (s, 3H), 3.74 (dd, 1H, J = 9.2 Hz, 9.2 Hz), 3.73 (m, 1H), 3.60–3.48 (m, 2H), 3.29 (m, 2H), 2.93 (ddd, 1H, J = 18.9 Hz, 9.5 Hz, 4.2 Hz), 2.77–2.45 (m, 8H), 2.42–2.22 (m, 4H), 2.18 (s, 3H), 2.11 (s, 3H), 2.09 (s, 3H), 1.87 (ddd, 1H, J = 12.7 Hz, each); ^{13}C NMR ($CDCl_3$, 250 MHz) δ 208.5, 206.5, 206.1, 173.7, 172.3, 172.2, 158.6, 144.3, 144.3, 135.4, 130.5, 128.5, 127.7, 126.9, 112.1, 96.5, 86.7, 81.3, 76.8, 75.1, 72.5, 70.0, 69.9, 67.9, 63.0, 55.2, 52.7, 49.4, 48.6, 41.7, 38.0, 37.8, 37.7, 31.8, 29.6, 29.5, 29.4, 28.0, 27.7, 27.6 (Tfa related peaks not listed); HRMS (ESI) $[M + Na]^+$ $C_{57}H_{60}F_{12}N_4NaO_{18}$ requires 1339.3603, found 1339.3653.

5-*O*-(2-Hydroxyethyl)-6,3′,4′-tri-*O*-levulinoyl-*N*^{1},*N*^{3},*N*$^{2'}$,*N*$^{6'}$-tetra(trifluoroacetyl)neamine (24). Compound **23** was dissolved in a mixture of dichloroacetic acid in dichloromethane (3:97, v/v, 6.0 mL). The reaction was stirred for 1 h at ambient temperature, quenched by addition of methanol, and then saturated $NaHCO_3$was added to the mixture. The resulted organic layer was separated, dried with Na_2SO_4, and evaporated to dryness. The residue was purified via silica gel chromatography (4% MeOH in CH_2Cl_2) to yield 0.21 g (97%) of the product (**24**) as white foam. ^{1}H NMR (500 MHz, $CDCl_3$) δ 8.74 (d, 1H, J = 6.6 Hz), 8.18–8.15 (b, 2H), 7.62 (d, 1H, J = 9.1 Hz), 5.38 (d, 1H, J = 3.4 Hz), 5.26 (dd, 1H, J = 10.4 Hz, 10.0 Hz), 5.20 (dd, 1H, J = 9.9 Hz, 9.8 Hz), 4.96 (dd, 1H, J = 9.9 Hz, 9.8 Hz), 4.37 (m, 1H), 4.24–4.06 (m, 5H), 3.99 (dd, 1H, J = 9.6 Hz, 9.1 Hz), 3.90 (m, 1H), 3.78–3.75 (m, 3H), 3.60 (m, 1H), 3.43 (m, 1H), 2.84–2.37 (m, 12H), 2.17 (s, 3H), 2.15 (s, 3H), 2.14 (s, 3H), 2.00 (m, 1H), 1.42 (m, 1H); ^{13}C NMR ($CDCl_3$, 250 MHz) δ 208.9, 207.2, 207.1, 174.3, 172.9, 172.0, 97.9, 81.8, 78.9, 77.6, 74.2, 69.8, 69.2, 67.9, 62.0, 53.0, 50.7, 48.7, 47.9, 38.6, 37.7, 37.7, 37.4, 31.6, 29.6, 29.6, 29.4, 28.0, 27.9, 27.8 (Tfa related peaks not listed); HRMS (ESI) $[M + Na]^+$ $C_{37}H_{44}F_{12}N_4NaO_{17}$ requires 1067.2402, found 1067.2416.

2-Cyanoethyl [6,3′,4′-tri-*O*-levulinoyl-*N*^{1},*N*^{3},*N*$^{2'}$,*N*$^{6'}$-tetra(trifluoroacetyl)neamine-5-*O*-ethyl] *N*,*N*-diisopropylphosphoramidite (1). 2-Cyanoethyl *N*,*N*-diisopropylphosphonamidic chloride (53 μL, 0.24 mmol) was added to a mixture of **24** (0.19 g, 0.18 mmol) and triethylamine (0.13 mL, 0.90 mmol) in dichloromethane (2.5 mL) under nitrogen. The mixture was stirred for 1 h at ambient temperature and then subjected directly to a silica gel column. Elution with 2% triethylamine and 20% petroleum ether in ethyl acetate yielded 0.21 g (93%) of the product (**1**) as white foam. ^{1}H NMR (500 MHz, $CDCl_3$) δ 8.16 (t, 0.56H, J = 5.4 Hz), 8.11 (t, 0.44H, J = 5.5 Hz), 7.87 (b, 1H), 7.45 (d, 0.44H, J = 10.0 Hz), 7.42 (d, 0.56H, J = 9.6 Hz), 7.11 (b, 1H), 5.59 (d, 0.56H, J = 3.2 Hz), 5.55 (d, 0.44H, J = 3.4 Hz), 5.22 and 5.21 (both dd, sum 1H, J = 10.7 Hz, 2.5 Hz, and J = 10.5 Hz, 2.4 Hz), 5.10 (dd, 0.56H, J = 9.9 Hz, 9.8), 5.05 (dd, 0.44H, J = 9.9 Hz, 9.8 Hz), 4.99 and 4.97 (both dd, sum 1H, J = 10.1 Hz, 3.9 Hz, and J = 10.1 Hz, 4.3 Hz), 4.40–4.32 (m, 1H), 4.24–4.06 (m, 3H), 3.95–3.71 (m, 8H), 3.64–3.55 (m, 4H), 3.44–3.39 (m, 1H), 2.88 (ddd, 1H, J = 18.8 Hz, 8.9 Hz, 4.5 Hz), 2.79–2.41 (m, 14H), 2.29–2.25 (m, 1H), 2.19 and 2.18 (both s, sum 3H), 2.17 and 2.16 (both s, sum 3H), 2.13 (s, 3H), 1.94–1.86 (m, 1H), 1.20, 1.19, 1.18, 1.17, and 1.15 (each s, sum 12H); ^{13}C NMR ($CDCl_3$, 250 MHz) δ 208.0, 207.9, 206.7, 206.7, 206.4, 206.3, 173.58, 173.56, 172.38, 172.36, 172.2, 172.1, 118.25, 118.22, 96.9, 81.38, 81.34, 75.0, 74.9, 77.4, 75.0, 74.9, 72.7, 72.7, 72.9, 72.8, 70.1, 69.7, 69.5, 68.0, 67.9, 62.6, 62.5, 62.3, 62.2, 58.5, 58.3, 58.3, 58.2, 52.8, 52.8, 49.3, 48.8, 43.0, 42.9, 41.2, 38.0, 37.9, 37.7, 31.6, 29.6, 29.5, 29.5, 28.1, 27.7, 27.6, 27.6, 24.7, 24.6, 24.6, 24.6, 24.5, 24.5, 24.5, 21.0, 20.3, 20.3 (Tfa related peaks not listed); ^{31}P NMR ($CDCl_3$, 200 MHz) δ 149.2, 148.2; HRMS (ESI) $[M + Na]^+$ $C_{46}H_{61}F_{12}N_6NaO_{18}P$ requires 1267.3481, found 1267.3432.

1,3,2′,6′-Tetraazido-5″-*O*-(4-methoxytrityl)ribostamycin (26). 6,3′,4′, 2″, 3″, 5″-Hexa-*O*-acetyl-1,3,2′,6′-tetraazidoribostamycin (**23**) (*35*) was first synthesized from the neamine derivative (**19**). **19** (0.30 g, 0.54 mmol) and 1,2,3,5-tetra-*O*-acetyl-*β*-D-ribofuranose (0.35 g, 1.1 mmol) were dissolved in dry dichloromethane (2.0 mL). The mixture was cooled to 0 °C, trimethylsilyl trifluoromethanesulfonate (0.20 mL, 1.1 mmol) was slowly added, and then the reaction was allowed to stir for 3 h under nitrogen. Saturated $NaHCO_3$ was added to the mixture, and the resulted organic phase was separated, dried with Na_2SO_2, and evaporated to dryness. The residue was purified by silica gel chromatography (from 30% to 40% EtOAc in petroleum ether) to yield 0.26 g (59%) of the product (**25**) as white foam. ^{1}H NMR (500 MHz, $CDCl_3$): δ 5.91 (d, 1H, J = 3.8 Hz), 5.46 (dd, 1H, J = 10.7 Hz, 9.3 Hz), 5.43 (d, 1H, J = 3.9 Hz), 5.20 (dd, 1H, J = 4.9 Hz, 4.8 Hz), 5.10 (dd, 1H, J = 4.9 Hz, 4.1 Hz), 5.02 (dd, 1H, J = 10.0 Hz, 9.6 Hz), 4.97 (dd, 1H, J = 9.9 Hz, 9.9 Hz), 4.49 (ddd, 1H, J = 10.1 Hz, 5.3 Hz, 2.7 Hz), 4.44 (dd, 1H, J = 12.2 Hz, 3.1 Hz), 4.26 (m, 1H), 4.16 (dd, 1H, J = 12.2 Hz, 3.6 Hz), 3.88 (dd, 1H, J = 9.3 Hz, 9.1 Hz), 3.71 (dd, 1H, J = 9.8 Hz, 9.0 Hz), 3.54 (ddd, 1H, J = 12.5 Hz, 10.0 Hz, 4.6 Hz), 3.45 (ddd, 1H, J = 12.5 Hz, 10.2 Hz, 4.4 Hz), 3.38 (dd, 1H, J = 13.5 Hz, 2.8 Hz), 3.32 (dd, 1H, J = 13.5 Hz, 5.4 Hz), 3.24 (dd, 1H, J = 10.7 Hz, 3.8 Hz), 2.40 (ddd, 1H, J = 13.3 Hz, 4.6 Hz, 4.6 Hz), 2.23, 2.12, 2.11, 2.10, 2.07, 2.07 (each s, each 3H), 1.63 (ddd, 1H, J = 13.0 Hz each); ^{13}C NMR ($CDCl_3$, 250 MHz) δ 170.6, 170.1, 169.7, 169.6, 169.5, 169.5, 106.3, 96.4, 80.9, 79.7, 76.4, 74.7, 74.1, 70.9, 70.0, 69.2, 69.2, 63.1, 61.0, 59.1, 58.1, 51.0, 31.6, 20.9, 20.7, 20.7, 20.7, 20.5, 20.4. Compound **25** (0.98 g, 1.2 mmol) was dissolved in 0.1 mol L^{-1} methanolic sodium methoxide (10 mL). The mixture was stirred at ambient temperature for 1 h, neutralized by addition of strongly acidic cation-exchange resin, filtered, and evaporated to dryness. The residue was dissolved in pyridine (3.0 mL), and then a mixture of 4-methoxytrityl chloride (0.49 g, 1.6 mmol) in pyridine (3.0 mL) was slowly added. The reaction was allowed to stir overnight at ambient temperature, quenched by addition of methanol, and evaporated to dryness. The residue was purified by silica gel chromatography (5% MeOH in CH_2Cl_2) to yield 0.71 g (71%) of the product (**26**) as white foam. ^{1}H NMR (500 MHz, $CDCl_3$): δ 7.50 (d, 4H, J = 7.6 Hz), 7.37–7.30 (m, 6H), 7.23 (m, 1H), 6.89 (d, 2H, J = 8.9 Hz), 5.87 (d, 1H, J = 3.8 Hz), 5.35 (d, 1H, J = 1.5 Hz), 4.26–4.22 (m, 2H), 4.16 (ddd, 1H, J = 9.9 Hz, 5.7 Hz, 2.0 Hz), 4.11 (m, 1H), 3.83 (dd, 1H, J = 10.4 Hz, 9.1 Hz), 3.80 (s, 3H), 3.67–3.61 (m, 2H), 3.53–3.39 (m, 5H), 3.33–3.28 (m, 4H), 2.92 (dd, 1H, J = 10.4 Hz, 3.9 Hz, 3.8 Hz), 2.22 (m, 1H), 1.38 (ddd, 1H, J = 12.2 Hz, each); ^{13}C NMR ($CDCl_3$, 250 MHz) δ 158.8, 144.6, 144.5, 135.3, 130.4, 128.3, 128.3, 127.5, 127.5, 126.5, 126.5, 112.8, 109.3, 96.7, 86.4, 84.3, 82.2, 76.3, 76.0, 75.3, 71.5, 71.3, 71.2, 71.0, 64.4, 63.6, 60.3, 59.7, 54.4, 51.3, 31.7; HRMS (ESI) $[M + Na]^+$ $C_{37}H_{42}N_{12}NaO_{11}$ requires 853.2988, found 853.2982.

6,3′,4′, 2″, 3″-Penta-*O*-levulinoyl-5″-*O*-(4-methoxytrityl)-*N*^{1},*N*^{3},*N*$^{2′}$,*N*$^{6′}$-tetra(trifluoroacetyl)ribostamycin (27). Compound **27** was synthesized from **26** using the three-step procedure, as described for **23**, but 10 molar equiv levulinic anhydride was used. After silica gel chromatography (2% MeOH in CH_2Cl_2), product (**27**) was obtained as white foam in a 79% yield (0.45 g). ^{1}H NMR (500 MHz, $CDCl_3$) δ 7.98 (t, 1H, J = 5.4 Hz), 7.68 (d, 1H, J = 8.5 Hz), 7.43–7.40 (m, 5H), 7.32–7.21 (m, 9H), 6.88 (d, 2H, J = 9.0 Hz), 5.80 (b, 1H), 5.36 (d, 1H, J = 4.1 Hz), 5.37–5.32 (m, 2H), 5.12 (dd, 1H, J = 10.3 Hz, 9.9 Hz), 5.00 (dd, 1H, J = 10.2 Hz, 8.6 Hz), 4.93 (dd, 1H, J = 9.9 Hz, 9.8 Hz), 4.26–4.15 (m, 2H), 4.09 (m, 1H), 4.05–3.98 (m, 4H), 3.81 (s, 3H), 3.46–3.35 (m, 2H), 3.29 (dd, 1H, J = 10.5 Hz, 4.0 Hz), 3.24 (dd, 1H, J = 10.5 Hz, 3.1 Hz), 2.89 (ddd, 1H, J = 18.9 Hz, 9.0 Hz, 4.6 Hz), 2.83–2.30 (m, 21H), 2.21, 2.20, 2.17, 2.11, 2.09 (each s, each 3H), 1.89 (ddd, J = 12.7 Hz each); ^{13}C NMR ($CDCl_3$, 250 MHz) δ 208.3, 206.8, 206.8, 206.6, 206.2, 174.6, 172.1, 171.8, 171.8, 171.7, 158.7, 144.1, 144.0, 134.9, 130.7, 130.6, 128.6, 127.8, 127.8, 127.0, 127.0, 113.2, 107.4, 95.5, 86.7, 80.7, 74.7, 73.5, 71.5, 70.4, 69.4, 67.7, 62.7, 55.2, 53.5, 51.9, 49.9, 48.6, 41.7, 38.2, 38.0, 37.8, 37.7, 37.6, 31.4, 29.8, 29.7, 29.7, 29.4, 29.3, 27.9, 27.8, 27.6, 27.5, 27.5 (Tfa related peaks not listed); HRMS (ESI) $[M + Na]^+$ $C_{70}H_{76}F_{12}N_4NaO_{25}$ requires 1623.4499, found 1623.4434.

6,3′,4′, 2″, 3″-Penta-*O*-levulinoyl-*N*^{1},*N*^{3},*N*$^{2′}$,*N*$^{6′}$-tetra(trifluoroacetyl)ribostamycin (28). Compound **28** was synthesized from **27** as described for **24** above. After silica gel chromatography (4% MeOH in CH_2Cl_2), product **28** was obtained as white foam in a 91% yield (0.34 g). ^{1}H NMR (500 MHz, $CDCl_3$) δ 8.10–8.06 (m, 2H), 7.74 (b, 1H), 7.50 (b, 1H), 5.61 (b, 1H), 5.27 (b, 1H), 5.21–5.17 (m, 2H), 5.12 (m, 1H), 4.99 (dd, 1H, J = 9.5 Hz, 9.5 Hz), 4.94 (dd, 1H, J = 9.8 Hz, 9.8 Hz), 4.39 (ddd, 1H, J = 10.4 Hz, 10.0 Hz, 3.8 Hz), 4.26–4.15 (m, 2H), 4.07–4.03 (m, 2H), 4.00 (dd, 1H, J = 8.7 Hz, 8.6 Hz), 3.91 (dd, 1H, J = 9.1 Hz, 8.9 Hz), 3.78 (m, 1H), 3.65 (m, 1H), 3.56 (m, 1H), 3.41–3.38 (m, 2H), 2.88–2.40 (m, 21H), 2.20, 2.19, 2.16, 2.14, 2.13 (each s, each 3H), 1.79 (ddd, 1H, J = 12.7 Hz, each); ^{13}C NMR ($CDCl_3$, 250 MHz) δ 207.9, 207.3, 206.9, 206.8, 206.7, 173.8, 172.4, 172.2, 172.1, 172.0, 107.2, 96.4, 81.8, 80.1, 78.0, 74.6, 73.7, 69.8, 69.7, 69.5, 68.5, 60.7, 52.1, 49.9, 48.6, 40.4, 38.1, 37.8, 37.7, 37.6, 31.6, 29.7, 29.6, 29.6, 29.5, 29.3, 28.0, 27.7, 27.6, 27.6, 27.4 (Tfa related peaks not listed); HRMS (ESI) $[M + Na]^+$ $C_{50}H_{60}F_{12}N_4NaO_{24}$ requires 1351.3298, found 1351.3300.

2-Cyanoethyl [6,3′,4′,2″,3″-penta-*O*-levulinoyl-*N*^{1},*N*^{3},*N*$^{2′}$,*N*$^{6′}$-tetra(trifluoroacetyl)ribostamycin-5″-yl] *N*,*N*-diisopropylphosphoramidite (2). Compound **2** was synthesized from **28** as described for **1** above. After silica gel chromatography (2% Et_3N in EtOAc), product **2** was obtained as white foam in a 92% yield (0.35 g). ^{1}H NMR (500 MHz, $CDCl_3$): δ 8.49 (b, 0.54H), 8.25 (t, 0.46H, J = 5.9 Hz), 7.64 (d, 0.46H, J = 9.3 Hz), 7.53 (d, 0.54H, J = 9.3 Hz), 7.26 (d, 0.46H, J = 9.3 Hz), 7.21 (d, 0.54H, J = 9.3 Hz), 7.05 (m, 1H), 6.00 (d, 0.54H, J = 3.1), 5.90 (d, 0.46H, J = 3.5 Hz), 5.34 (d, 0.54H, J = 4.7 Hz), 5.33 (d, 0.46H, J = 4.6 Hz), 5.29–5.25 (m, 1H), 5.18–4.95 (m, 4H), 4.44 (ddd, 0.46H, J = 10.2 Hz, 10.2 Hz, 3.8 Hz), 4.38 (ddd, 0.56H, J = 10.1 Hz, 10.1 Hz, 3.9 Hz), 4.34–4.25 (m, 1H), 4.18–3.79 (m, 7H), 3.72–3.41 (m, 6H), 2.98–2.32 (m, 23H), 2.21, 2.21, 2.20, 2.19, 2.18, 2.17, 2.14, 2.14 (each s, 12H), 1.86–1.76 (m, 1H), 1.22, 1.21, 1.21, 1.20, 1.18 (each s, 12H); ^{13}C NMR ($CDCl_3$, 250 MHz) δ 208.6, 208.2, 206.7, 206.7, 206.4, 206.4, 206.3, 206.2, 174.3, 174.2, 172.5, 172.2, 171.8, 171.7, 171.7, 171.7, 171.6, 118.8, 118.4, 106.9, 106.5, 95.5, 95.1, 81.4, 81.4, 75.5, 75.3, 74.6, 74.4, 74.1, 74.1, 71.0, 70.8, 70.8, 70.3, 69.8, 66.8, 61.8, 61.6, 58.5, 58.4, 51.9, 51.8, 49.7, 49.6, 48.0, 47.9, 43.0, 42.9, 38.2, 38.0, 38.0, 37.8, 37.7, 37.6, 31.8, 31.6, 29.8, 29.8, 29.8, 29.7, 29.7, 29.6, 29.4, 28.1, 28.0, 27.7, 27.6, 27.5, 27.3, 24.7, 24.6, 24.6, 20.4, 20.3, 20.1, 20.0 (Tfa related peaks not listed); ^{31}P NMR ($CDCl_3$,200 MHz) δ 148.9 and 148.7; HRMS (ESI) $[M + Na]^+$ $C_{59}H_{77}F_{12}N_6NaO_{25}P$ requires 1551.4377, found 1551.4329.

6,3′,4′-Tri-*O*-levulinoyl-*N*^{1},*N*^{3},*N*$^{2′}$,*N*$^{6′}$-tetra(trifluoroacetyl)-neamine (30). *N*^{1},*N*^{3},*N*$^{2′}$,*N*$^{6′}$-tetra(trifluoroacetyl)neamine (**29**) was first synthesized from neamine tetrahydrochloride (**17**) according to the literature (*28*). Levulinic anhydride (13.3 g, 62 mmol) was slowly added to a mixture of **29** (14.6 g, 21 mmol) and a catalytic amount of DMAP in pyridine (60 mL). The mixture was stirred overnight at ambient temperature and evaporated to dryness. The residue was dissolved in ethyl acetate and washed with saturated $NaHCO_3$. The organic layer was separated, dried with Na_2SO_4, and evaporated to dryness. The

crude product was purified by silica gel chromatography (50% EtOAc in CH_2Cl_2) to yield 13.8 g (67%) of **30** as white foam. ^{1}H NMR (500 MHz, $CDCl_3$) δ 8.39 (d, 1H, J = 8.3 Hz), 8.09 (b, 1H), 7.69 (d, 1H, J = 8.4 Hz), 7.65 (d, 1H, J = 7.9 Hz), 5.37 (d, 1H, J = 3.6 Hz), 5.27 (dd, 1H, J = 10.4 Hz, 9.9 Hz), 5.16 (dd, 1H, J = 10.1 Hz, 10.1 Hz), 4.95 (dd, 1H, J = 10.0 Hz, 9.9 Hz), 4.29 (m, 1H), 4.21 (dd, 1H, J = 9.7 Hz, 9.6 Hz), 4.12–4.05 (m, 2H), 3.97–3.94 (m, 2H), 3.83 (ddd, 1H, J = 9.4 Hz, 9.3 Hz, 3.2 Hz), 3.48 (m, 2H), 2.92 (ddd, 1H, J = 19.0 Hz, 9.0 Hz, 4.5 Hz), 2.87–2.40 (m, 12H), 2.34 (ddd, 1H, J = 13.0 Hz, each), 2.20 (s, 3H), 2.19 (s, 3H), 2.18 (m, 1H), 2.14 (s, 3H); ^{13}C NMR ($CDCl_3$, 250 MHz) δ 209.2, 208.4, 206.8, 174.1, 172.7, 172.5, 98.1, 80.0, 75.4, 74.6, 70.3, 69.6, 68.4, 52.9, 49.9, 48.4, 40.4, 38.2, 38.1, 37.7, 30.3, 29.6, 29.5, 29.4, 28.5, 27.9, 27.7 (Tfa related peaks not listed); HRMS (ESI) $[M + Na]^+$ requires 512.1106, found 512.1122.

2-Cyanoethyl [6,3′,4′-tri-*O*-levulinoyl-N^1,N^3,$N^{2'}$,$N^{6'}$-tetra-(trifluoroacetyl)neamine-5-yl] *N*,*N*-diisopropylphosphoramidite (31). Compound **31** was synthesized from **30** as described for **1**, but 3.6 molar equiv 2-cyanoethyl *N*,*N*-diisopropylphosphonamidic chloride and a prolonged reaction time (3 h) were required. After silica gel chromatography (1% Et_3N and 30% petroleum ether in EtOAc), product **31** was obtained as white foam in a 90% yield (0.54 g). ^{1}H NMR (500 MHz, $CDCl_3$) δ7.81 (d, 0.55H, J = 8.8 Hz), 7.76 (d, 0.45H, J = 9.2 Hz), 7.70–7.66 (m, 1H), 7.56 (d, 0.45H, J = 9.7 Hz, 7.50–7.48 (m, 1H), 7.41 (d, 0.55H, J = 9.5 Hz), 5.81 (d, 0.55H, J = 3.7 Hz), 5.45 (b d, 0.45H, J = 2.9 Hz), 5.26 (dd, 0.45H, J = 10.4 Hz, 9.1 Hz), 5.22 (dd, 0.55H, J = 10.2 Hz, 9.4 Hz), 5.11–4.97 (m, 2H), 4.47–4.39 (m, 1H), 4.31–3.34 (m, 11H), 2.80–2.36 (m, 14H), 2.15–2.08 (m, 1H), 2.18, 2.10, 2.10 (each s, sum 9H), 1.97–1.87 (m, 1H); ^{13}C NMR ($CDCl_3$, 250 MHz) δ 207.0, 206.9, 206.6, 206.6, 206.4, 206.3, 172.6, 172.5, 172.1, 172.0, 172.0, 171.9, 118.6, 118.3, 96.3, 94.6, 78.8, 76.5, 76.3, 75.0, 74.7, 73.5, 69.9, 69.8, 68.9, 68.7, 68.6, 68.0, 58.9, 58.8, 58.7, 58.6, 43.2, 43.1, 39.5, 39.5, 37.4, 37.3, 37.3, 31.1, 30.7, 28.8, 28.8, 28.7, 28.6, 28.6, 28.1, 28.1, 27.7, 27.6, 27.6, 23.9, 23.9, 23.8, 23.8, 23.8, 23.7, 23.6, 22.2, 22.2, 22.2, 19.8, 19.8, 19.7, 19.7 (Tfa related peaks not listed); ^{31}P NMR ($CDCl_3$, 200 MHz) δ 150.8, 150.5; HRMS (ESI) $[M + Na]^+$ $C_{44}H_{57}F_{12}N_6NaO_{17}P$ requires 1223.3218, found 1223.3191.

Ethyl 2-{(2*R*,3*S*,5*R*)-3-*tert*-butyldimethylsilyloxy-5-[(4,4′-dimethoxytrityl)oxymethyl] Tetrahydrofuran-2-yl}acetate (33). Compound **32** was synthesized as described earlier (*36*, *37*). *tert*-Butyldimethylsilyl chloride (1.43 g, 9.5 mmol) was added to a mixture of **32** (2.4 g, 4.7 mmol) and a catalytic amount of imidazole in pyridine (20 mL). The reaction was stirred overnight at 40 °C, quenched by addition of methanol, and evaporated to dryness. The residue was dissolved in dichloromethane and washed by saturated $NaHCO_3$. The organic phase was separated, dried with Na_2SO_4, and evaporated to dryness. The product was purified by silica gel chromatography (0.1% Et_3N and 3% MeOH in CH_2Cl_2) to yield 2.9 g (60%) of **33** as a colorless oil. ^{1}H NMR (400 MHz, $CDCl_3$) δ 7.47–7.44 (m, 2H), 7.37–7.17 (m, 7H), 6.84–6.82 (m, 4H), 4.56 (m, 1H), 4.18 (m, 1H), 4.17 (m, 2H), 3.93 (m, 1H), 3.08 (m, 2H), 2.68 (dd, 1H, J = 15.3 Hz, 7.0 Hz), 2.52 (dd, 1H, J = 15.3 Hz, 6.2 Hz), 1.96 (ddd, 1H, J = 12.6 Hz, 5.4 Hz, 2.2 Hz), 1.72 (ddd, 1H, J = 12.6 Hz, 9.8 Hz, 5.8 Hz), 1.27 (t, 3H, J = 7.3 Hz), 0.86 (s, 9H), 0.07 (s, 3H), 0.02 (s, 3H); ^{13}C NMR ($CDCl_3$,100 MHz) δ 171.2, 158.4, 144.9, 136.2, 136.2, 130.1, 128.2, 127.7, 126.6, 113.0, 86.6, 85.9, 74.6, 74.2, 64.1, 60.4, 55.2, 41.1, 40.8, 25.8, 14.2, −4.7, −4.8; MS (EI) M^+ requires 620.3, found 620.

(2*R*,3*S*,5*S*)-3-*tert*-Butyldimethylsilyloxy-2-[(4,4′-dimethoxytrityl)oxymethyl]-5-(2-hydroxyethyl)tetrahydrofuran (34). Lithium aluminum hydride (0.16 g, 4.3 mmol) was slowly added to a cooled (0 °C) mixture of **33** in diethyl ether (20 mL). The mixture was allowed to warm to room temperature, and then the stirring was continued overnight at room temperature. The excess hydride was destroyed by careful addition of water, and then the crude product was extracted with dichloromethane (3 × 20 mL). The organic layers were combined, dried with Na_2SO_4, and evaporated to dryness. The residue was purified by silica gel chromatography (0.1% Et_3N and 3% MeOH in CH_2Cl_2) to yield 1.4 g (83%) of **34** as yellowish oil. ^{1}H NMR (400 MHz, $CDCl_3$) δ 7.50 (d, 2H, J = 8.1 Hz), 7.40–7.24 (m, 7H), 6.88 (d, 4H, J = 8.8 Hz), 4.38 (m, 1H), 4.28 (m, 1H), 3.95 (m, 1H), 3.87 (m, 2H), 3.84 (s, 6H), 3.14 (d, 2H, J = 4.7 Hz), 2.75 (b, 1H), 1.98–1.69 (m, 4H), 0.90 (s, 9H), 0.06 (s, 3H), 0.04 (s, 3H); ^{13}C NMR ($CDCl_3$, 100 MHz) δ 158.4, 144.9, 136.1, 136.1, 130.0, 128.2, 127.7, 126.7, 113.1, 86.9, 86.0, 78.6, 74.0, 64.1, 61.6, 55.2, 41.6, 37.3, 25.8, −4.7, −4.8; MS (EI) M^+ requires 578.3, found 578.

(2*R*,3*S*,5*S*)-3-*tert*-Butyldimethylsilyloxy-2-[(4,4′-dimethoxytrityl)oxymethyl]-5-(2-levulinoyloxyethyl)tetrahydrofuran (35). Levulinic anhydride (1.5 g, 7.1 mmol) was added to a mixture of **34** (1.3 g, 2.4 mmol) in pyridine (20 mL). The mixture was stirred at ambient temperature for 3 h and evaporated to dryness. The residue was dissolved in dichloromethane and washed with saturated $NaHCO_3$. The organic phase was dried with Na_2SO_4 and evaporated to dryness. The crude product was purified by silica gel chromatography (0.1% Et_3N and 3% MeOH in CH_2Cl_2) to yield 1.5 g (86%) of **35** as colorless oil. ^{1}H NMR (500 MHz, $CDCl_3$) δ 7.49–7.46 (m, 2H), 7.37–7.20 (m, 7H), 6.85–6.83 (m, 4H), 4.30–4.18 (m, 4H), 3.90 (m, 1H), 3.81 (s, 6H), 3.12–3.05 (m, 2H), 2.76 (m, 2H), 2.60 (m, 2H), 2.20 (s, 3H), 1.93–1.85 (m, 3H), 1.66 (ddd, 1H, J = 12.6 Hz, 9.8 Hz, 5.8 Hz), 0.86 (s, 9H), 0.02 (s, 3H), 0.00 (s, 3H);^{13}C NMR ($CDCl_3$, 100 MHz) δ 172.7, 158.3, 144.9, 136.2, 136.1, 130.0, 128.2, 127.7, 126.6, 113.0, 86.3, 85.9, 75.2, 74.3, 64.3, 62.1, 55.2, 41.4, 37.9, 34.8, 29.9, 28.0, 25.8, −4.7, −4.8; MS (EI) M^+ requires 676.4, found 676.

(2*R*,3*S*,5*S*)-2-[(4,4′-Dimethoxytrityl)oxymethyl]-5-(2-levulinoyloxyethyl)tetrahydrofuran-3-ol (36). Tetrabutylammonium fluoride monohydrate (1.5 g, 5.7 mmol) was added to a mixture of **35** (1.2 g, 1.8 mmol) in tetrahydrofurane (15 mL). The mixture was stirred for 2 h at room temperature and then volatiles were removed. The residue was dissolved in dichloromethane and washed with water. The organic phase was dried with Na_2SO_4 and evaporated to dryness. The crude product was purified by silica gel chromatography (0.1% Et_3N and 3% MeOH in CH_2Cl_2) to yield 0.90 g (87%) of **36** as colorless oil. ^{1}H NMR (500 MHz, $CDCl_3$) δ 7.47–7.45 (m, 2H), 7.36–7.21 (m, 7H), 6.86–6.83 (m, 4H), 4.32 (b, 1H), 4.29–4.17 (m, 3H), 3.92 (m, 1H), 3.81 (s, 6H), 3.24 (dd, 1H, J = 9.6 Hz, 4.6 Hz), 3.10 (dd, 1H, J = 9.6 Hz, 5.9 Hz), 2.76 (m, 2H), 2.58 (m, 2H), 2.20 (s, 3H), 2.01 (b, 1H), 2.00 (ddd, 1H, J = 13.0 Hz, 7.6 Hz, 2.1 Hz), 1.96–1.89 (m, 2H), 1.79 (ddd, 1H, J = 13.0 Hz, 9.8 Hz, 6.3 Hz); ^{13}C NMR ($CDCl_3$, 250 MHz) δ 206.8, 172.7, 158.5, 144.9, 136.1, 130.1, 128.2, 127.9, 127.8, 126.8, 113.1, 86.1, 85.8, 75.3, 74.7, 64.7, 62.0, 55.3, 55.2, 40.9, 38.0, 34.7, 29.9, 28.0; MS (EI) M^+ requires 562.3, found 562.

2-Cyanoethyl {(2*R*,3*S*,5*S*)-2-[(4,4′-Dimethoxytrityl)oxymethyl]-5-(2-levulinoyloxyethyl)tetrahydrofuran-3-yl} *N*,*N*-Diisopropylphosphoramidite (3). Compound **3** was synthesized from **36** as described for **1**, above. After silica gel chromatography (2% Et_3N and 48% petroleum ether in EtOAc), product **3** was obtained as white foam in an 82% yield (0.54 g). ^{1}H NMR (500 MHz, CD_3CN) δ 7.49–7.46 (m, 2H), 7.38–7.33 (m, 4H), 7.32–7.28 (m, 2H), 7.24–7.20 (m, 1H), 6.86–6.82 (m, 4H), 4.46–4.42 (m, 1H), 4.32–4.21 (m, 3H), 4.09–4.08 (m, 1H), 3.86–3.53 (m, 4H), 3.82 (s, 3H), 3.81 (s, 3H), 3.19–3.09 (m, 2H), 2.78–2.75 (m, 2H), 2.64–2.58 (m, 3H), 2.48–2.45 (m, 1H), 2.20 (s, 3H), 2.20–2.07 (m, 1H), 1.97–1.93 (m, 2H), 1.82–1.75

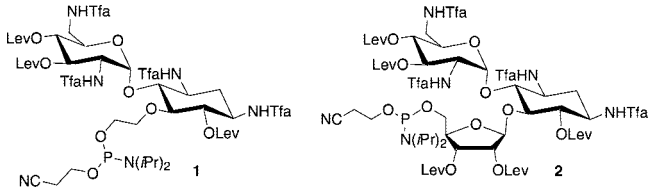

Figure 1. Aminoglycoside phosphoramidites (**1** and **2**) applicable to the automated oligonucleotide synthesis.

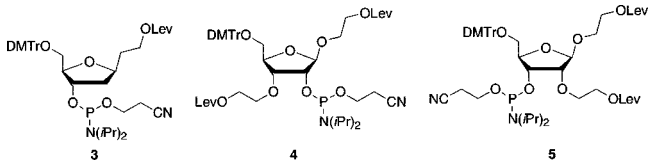

Figure 2. Branching units (**3**–**5**) used for the intrachain conjugation.

(m, 1H), 1.20, 1.19, 1.17, 1.17, 1.15, 1.10, 1.08 (each s, sum 12H); ^{13}C NMR (CD_3CN, 250 MHz) δ 206.8, 206.8, 172.6, 172.6, 158.7, 145.3, 136.1, 136.1, 136.1, 136.0, 130.1, 130.0, 128.1, 128.1, 127.8, 126.8, 126.8, 118.6, 118.4, 113.1, 85.9, 85.3, 85.3, 85.0, 85.0, 75.7, 75.7, 75.6, 75.5, 75.4, 75.2, 64.4, 64.3, 61.6, 58.5, 58.4, 54.9, 43.0, 42.9, 40.0, 40.0, 40.0, 39.9, 37.5, 34.5, 34.4, 29.0, 27.8, 24.0, 24.0, 23.9, 23.9, 20.1, 20.1, 20.0, 20.0; ^{31}P NMR ($CDCl_3$, 200 MHz) δ 148.0, 147.8; HRMS (ESI) $[M + Na]^+$ $C_{42}H_{55}N_2NaO_9P$ requires 785.3537, found 785.3542.

Synthesis of the Aminoglycoside Conjugates of the 2′-*O*-Methyl Oligoribonucleotides (6–13). The 2′-*O*-methyl oligoribonucleotide conjugates (**6**–**13**) were assembled on an Applied Biosystems 392 DNA synthesizer in 1.0 μmol scale using conventional phosphoramidite chemistry and following the standard RNA coupling protocol. The coupling efficiency of the branching units **3**–**5** was equal to that of the commercially available 2′-*O*-methylribonucleoside phosphoramidites (0.1 mol L^{-1} solution of **3**, **4**, or **5** in acetonitrile, 4,5-dicyanoimidazole activation, 600 s coupling time, standard oxidation cycle: 0.02 mol L^{-1} I_2 in mixture of pyridine, H_2O, and THF, 0.4/9.1/90.5 v/v/v, 30 s) (*42*). Once the 2′-*O*-methyl oligoribonucleotide chains were assembled, the orthogonal levulinoyl protections of **40**–**42** were manually removed by conventional hydrazinium acetate treatment [i.e., resins are suspended in a mixture of $NH_2NH_2 \cdot H_2O$, pyridine, and AcOH (0.124/4/1 v/v/v, 1 h at 25 °C), washed with pyridine, MeOH, and acetonitrile, dried, and reset to the DNA synthesizer]. The aminoglycoside phosphoramidites (**1** and **2**) were then coupled to the hydroxyalkyl arms of **43**–**45** or to the exposed 5′-OH group of **37**, using two consecutive standard couplings (0.1 mol L^{-1} solution of **1** or **2** in dry acetonitrile, 4,5-dicyanoimidazole activation, 600 s coupling time, twice, followed by standard oxidation cycle, as above). In order to avoid potential acyl migration, the levulinoyl protections of the amino glycoside moieties of **38**, **39**, and **46**–**51** were selectively removed using the same hydrazinium acetate treatment, as above. Finally, the resins were subjected to concentrated ammonia (15 h at 55 °C) to release the crude 2′-*O*-methyl oligoribonucleotide conjugates (**6**–**13**). The product mixtures were filtered, the filtrates were evaporated to dryness, the residues were dissolved in water, and then the conjugates (**6**–**13**) were subjected to RP HPLC purification (Figure 1, 2, 3, 4). Purity of the crude conjugates ranged from 41% to 66%. Isolated yields of the homogenized conjugates were 15% to 26% (according to UV absorbances of dissolved **6**–**13**). The authenticity of the conjugates was verified by MS(ESI) spectroscopy (properties of the **6**–**13**; see Table 1).

Kinetic Measurements. The reactions were carried out in Eppendorf tubes immersed in a water bath, the temperature being maintained at 35.0 ± 0.1 °C. pH of the samples was adjusted to 7.3 with a HEPES buffer (0.1 mol L^{-1}) prepared in sterilized water. For the metal-ion-dependent experiments, Zn^{2+} ion was added as a nitrate salt to give the overall metal ion concentration of 90 μmol L^{-1}. The ionic strength was adjusted to 0.1 mol L^{-1} with sodium nitrate. The concentrations of the aminoglycoside conjugates (**6**–**13**) and the targets (**14** and **15**) were 18 μmol L^{-1}. 4-Nitrobenzenesulfonate ion was used as an internal standard. The total volume of the reaction mixture was 200 μL in each kinetic run. Aliquots of 20 μL were withdrawn at suitable intervals, cooled to 0 °C, and the reaction quenched by adding of 1.0 mol L^{-1} aqueous hydrogen chloride (1.0 μL). The composition of the samples was quantified by capillary zone electrophoresis (Beckman Coulter P/ACE MDQ CE System) using a fused silica capillary (50 μm, 50 cm). Inverted polarity, citrate buffer (0.2 mol L^{-1}, pH 3.1), and –30 kV voltage were used. The temperature of the capillary was kept at 25 °C. Hydrodynamic injection at 2 psi for 8 s was applied. Between each analytical run, the capillary was flushed for 3 min with water, 10 mmol L^{-1} aqueous hydrogen chloride, and the background electrolyte buffer. The quantification of the target oligonucleotides (**14** and **15**) was based on comparison of their UV absorption at 254 nm to that of internal standard. The peak area was first normalized by dividing it by the migration time and then by the similarly normalized peak area of the internal standard. First-order rate constants for the cleavage of the target oligonucleotides by the conjugates (**6**–**13**) were obtained by applying the integrated first-order rate law to the disappearance of the target oligonucleotide (**14** and **15**).

RESULTS AND DISCUSSION

Synthesis of the Aminoglycoside Phosphoramidites (1, 2, and 31). For the synthesis of aminoglycoside conjugates of 2′-*O*-methyl oligoribonucleotides, three different neamine-based phosphoramidites (**1**, **2**, and **31**) were initially synthesized (outlined in Schemes 1, 2, 3). Commercially available neamine and ribostamycin are rather expensive starting materials to be used for the multistep synthesis. Neomycin trisulfate (**16**) may readily be hydrolyzed to neamine tetrahydrochloride (**17**) (*30*), and, hence, it served as a cheap starting material for each compound. In **1** and **2**, hydroxyethyl and ribose residues were introduced between the phosphoramidite and neamine moieties. In **31**, the O^5 was directly phosphitylated. Synthesis of this reagent was straightforward, but in contrast to **1** and **2**, it turned out be incompatible with the automated RNA synthesis.

Introduction of hydroxyethyl tether to **1** involves ether bond formation, which requires complete protection of the amino functions. In contrast to carbamates or amides (*11*, *38*), azide masking of **18** meets this requirement. This was carried out according to literature by Cu^{2+}-catalyzed diazo transfer (*31*). Three of the four hydroxyl groups were then selectively acetylated with acetic anhydride in pyridine to give **19** (71%) (*31*). In this reaction, all byproducts may be combined and **18** may be regenerated by conventional sodium methoxide treatment (*39*). The reaction may be repeated with crude regenerated **16** in the same yield. The hydroxyethyl moiety was introduced to the O^5-position of neamine via an allyl ether intermediate. The free OH-group of **19** was allylated under neutral condition with allyl methylcarbonate in the presence of $Pd(OAc)_2$ and triphenylphosphine resulting in **20** in 42% yield (*33*). During this reaction, some acyl migration occurred giving 6-*O*-allyl-1,3,2′,6′-tetraazido-5,3′,4′-tri-*O*-acetyl neamine (17%) as a side product. OsO_4 hydroxylation and concomitant $NaIO_4$ oxidation converted the allyl group of **20** to an oxoethyl group, which was subsequently reduced to the hydroxyethyl group with $NaBH_4$ (*34*). Removal of the acetyl protections by sodium methoxide treatment (*39*) gave **21** in 53% overall yield. MMTr-

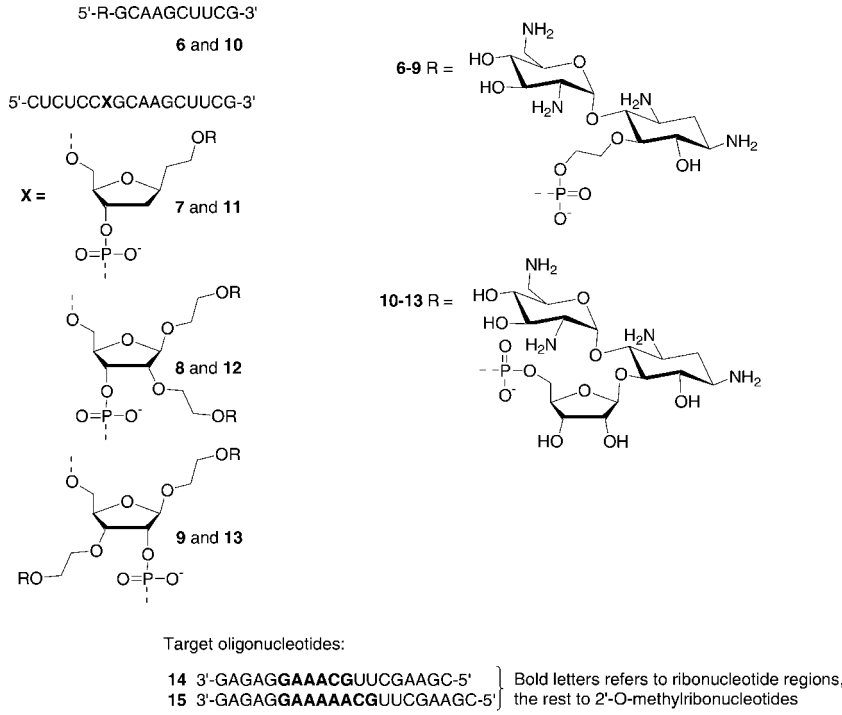

Figure 3. Synthesized neamine (**6**–**9**) and ribostamycin (**10**–**13**) conjugates of 2′-*O*-methyl oligoribonucleotides and the target oligonucleotides (**14** and **15**).

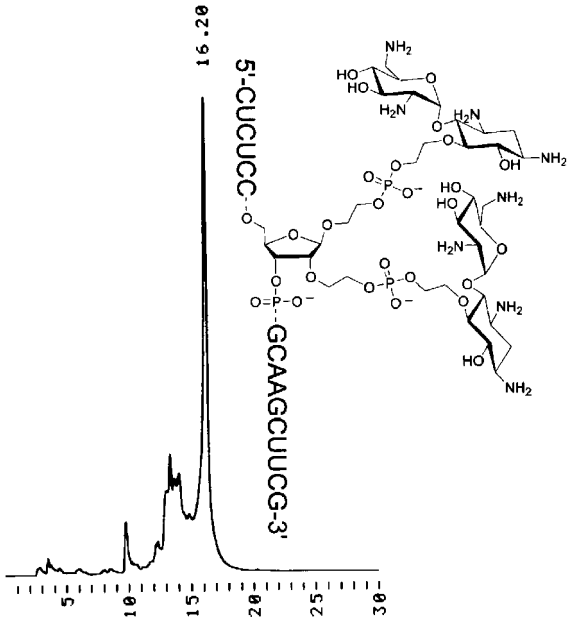

Figure 4. An example of RP HPLC chromatogram of crude product mixture (conjugate **8**).

capping of the primary OH group, in the presence of the secondary ones, gave quantitatively **22**. Staudinger reaction with Me_3P released the amino groups, which were subsequently protected by trifluoroacetyl groups. These two steps may be performed without chromatographic purification, and synthesis was directly continued to the levulinoylation resulting in **23** in 74% overall yield. Finally, the MMTr group was removed with 3% dichloroacetic acid (**24**, 97%) and the exposed primary hydroxyl group was phosphitylated (**1**, 93%).

The azide masked neamine (**19**) was a useful starting material also for the ribostamycin derived phosphoramidite (**2**). The 5-OH of protected neamines is usually only weakly reactive, like in acylations (cf. **16** and **27**), but **17** has turned out to be a good glycosyl acceptor (*35*, *40*, *41*). Analogously to the previously published furanosylation of paromamine (*40*), 1,2,3,5-tetra-*O*-acetyl-*β*-D-ribofuranose was simply used as a donor. The protected ribostamycin (**25**) was obtained in 59% yield. Per-*O*-acetylated phenylthioribofuranoside has recently been used for the same reaction to give **25** in 37% yield (*35*). After deacetylation of **25**, synthesis to obtain **2** was continued analogously to the described preparation of **1** from **21**. The primary hydroxyl group was protected with an MMTr group (**26**, 71%), the azide masks were removed, the trifluoracetyl and levulinoyl protections were introduced (**27**, 79%), the primary hydroxyl group was released (**28**, 91%) and, finally, the phosphitylation was performed to give **2** (92%).

Table 1. Properties of the Synthesized 2′-*O*-Methyl Oligoribonucleotide Conjugates (6–13)

entry	2′-*O*-methyl oligoribonucleotide conjugate	purity of the crude conjugate[a] %	observed mass[b] g mol^{-1}	required mass
1	**6**	64	3727.8	3726.8
2	**7**	66	5868.9	5867.1
3	**8**	51	6372.9	6371.9
4	**9**	61	6372.9	6371.9
5	**10**	65	3815.7	3814.8
6	**11**	65	5956.8	5955.2
7	**12**	44	6550.2	6547.4
8	**13**	41	6550.2	6547.4

[a] Purities according to RP HPLC chromatograms of crude mixtures of **6**–**13**. [b] Masses calculated from $[(M - 3H)/3]^{-3}$.

The phosphoramidite **31** was synthesized from the neamine tetrahydrochloride (**17**). The amino groups were converted to the trifluoroacetamides according to the literature (**29**, 91%) (*28*). The hydroxyl groups were then selectively esterified as levulinoylates (**30**, 67%), and the remained free 5-OH was phosphitylated to give **31** (90%).

Synthesis of Branching Units 3–5. Preparation of the ribose-based branching units **4** and **5**, and their applicability to the automated RNA synthesis have recently been described (*42*). Previously prepared ethyl 2-[(2*R*,3*S*,5*R*)-5-(4,4′-dimethoxytrityloxymethyl)-3-hydroxytetrahydrofuran-2-yl] acetate (**32**) (*36*, *37*)

Scheme 1. Syntheses of the Aminoglycoside Phosphoramidites[a]

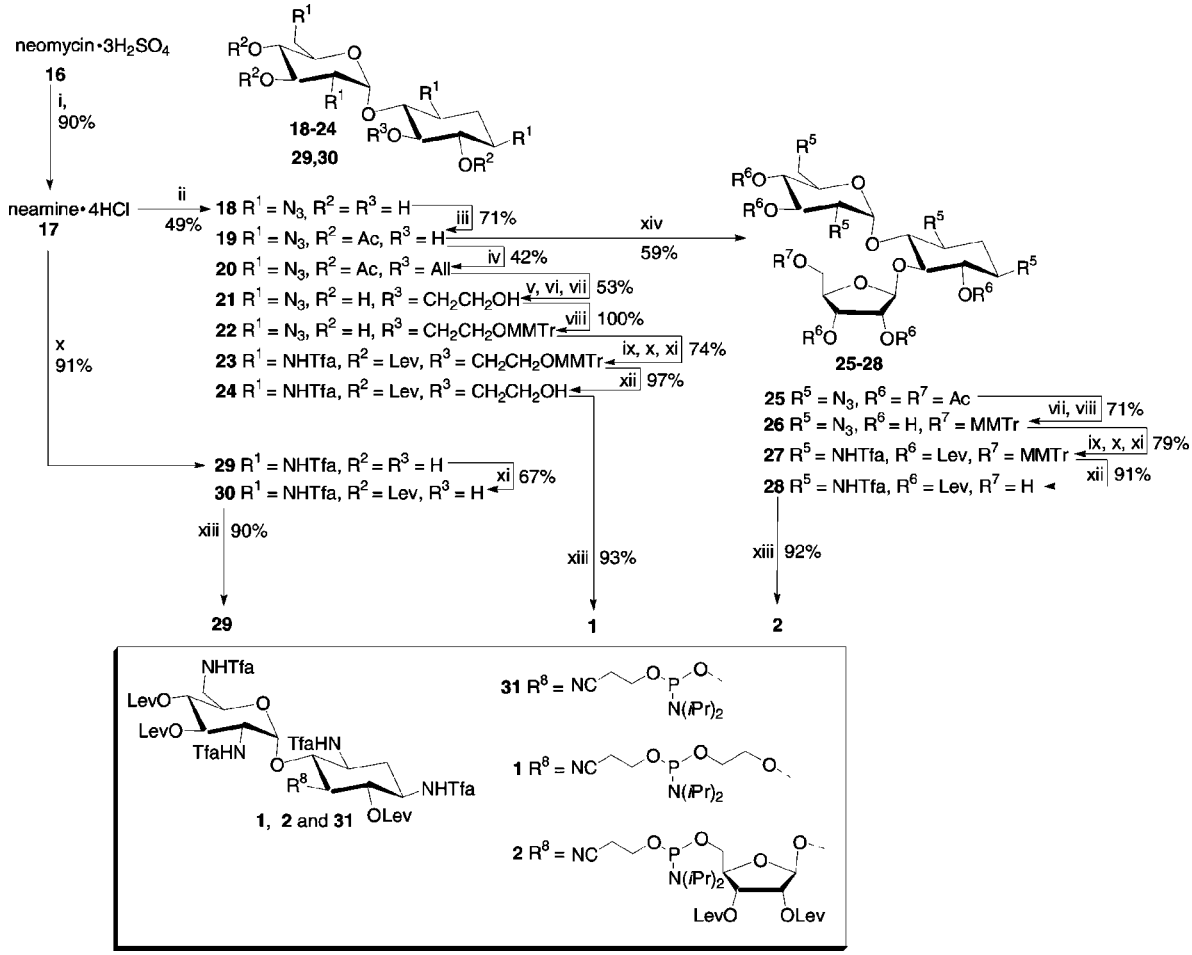

[a] Reagents and conditions: (i) aq HCl, MeOH, reflux; (ii) TfN_3, K_2CO_3, $CuSO_4$, H_2O, MeOH, CH_2Cl_2; (iii) Ac_2O, DMAP, pyridine; (iv) allyl methyl carbonate, $Pd(OAc)_2$, PPh_3, THF, reflux; (v) OsO_4, *i*PrOH, $NaIO_4$, H_2O, dioxane; (vi) $NaBH_4$, EtOH, CH_2Cl_2; (vii) NaOMe, MeOH; (viii) MMTrCl, pyridine; (ix) Me_3P, toluene, H_2O, dioxane, N_2 atm.; (x) TfaOMe, Et_3N, MeOH; (xi) levulinic anhydride, DMAP, pyridine; (xii) DCA, CH_2Cl_2; (xiii) 2-cyanoethyl *N*,*N*-diisopropylphosphonamidic chloride, Et_3N, dichloromethane; (xiv) 1,2,3,5-tetra-*O*-acetyl-*β*-ribofuranose, TMSTf, CH_2Cl_2, 0°C.

Scheme 2. Synthesis of the Branching Unit 3[a]

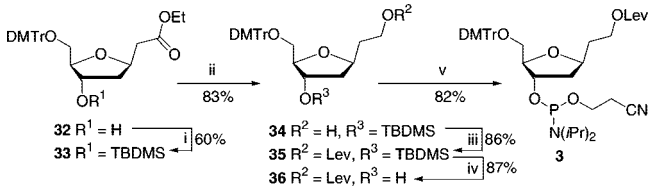

[a] Reagents and conditions: (i) TBDMSCl, imidazole, pyridine, 40 °C; (ii) $LiAlH_4$, THF; (iii) Lev_2O, pyridine; (iv) $Bu_4N^+F^-\cdot H_2O$, THF.

was used as a starting material for the branching unit **3**. The secondary hydroxyl group of **32** was *tert*-butyldimethylsilylated (**33**, 60%) and then the ethyl ester was reduced by lithium aluminum hydride to give **34** (86%). The resultant primary alcohol was capped as a levulinoyl ester (**35**, 86%), the TBDMS protection was removed (**36**, 87%), and the exposed hydroxyl group was phosphitylated to give **3** (82%).

Synthesis of the Aminoglycoside Conjugates of 2′-*O*-Methyl Oligoribonucleotides. To verify and optimize the applicability of the aminoglycoside phosphoramidites (**1**, **2**, and **31**) to the automated oligonucleotide synthesis, they were first coupled to the 5′-end of a simple solid-supported T_5 homooligodeoxyribonucleotide. Coupling efficiencies were evaluated by RP HPLC analysis of the released product mixtures. Use of standard RNA coupling protocol gave ca. 80% coupling yield for **1** and **2**. These couplings were improved to an acceptable 95% yield by using of two consecutive coupling cycles (i.e., 0.1 mol L^{-1} solution of **1** or **2** in dry acetonitrile, 4,5-dicyanoimidazole activation, 600 s coupling time, twice, followed by standard oxidation cycle: 0.02 mol L^{-1} I_2 in mixture of pyridine, H_2O, and THF, 0.4/9.1/90.5 v/v/v, 30 s). This procedure turned out to also give an acceptable yield for the conjugates bearing two aminoglycoside ligands (cf. **8**, **9**, **12**, and **13**). In contrast to **1** and **2**, coupling of **31** remained at a poor level and, hence, this building block was excluded from the synthesis of final conjugates. Coupling of the hydroxyalkyl-armed branching units (**4** and **5**) has recently been shown to be as efficient as that of the commercially available 2′-*O*-methyl-ribonucleoside building blocks; the couplings were quantitative using a standard RNA coupling protocol (*42*). The branching unit **3** behaved similarly. In order to demonstrate the importance of orthogonally removable levulinoyl protections on the aminoglycoside moieties, direct ammonolysis (15 h, 55 °C) without hydrazinium acetate treatment was used for release of the fully protected ribostamycin conjugate (**2**-T_5). In this manner, the yield of the desired conjugate decreased by 22% and *N*-acyl side products appeared (according to RP HPLC chromatograms; see Supporting Information). Thus, the *O*→*N* acylation would be a remarkable problem, especially if two aminoglycoside ligands are to be attached (cf. **8**, **9**, **12**, and **13**). One hour treatment with a mixture of hydrazinium acetate ($NH_2NH_2\cdot H_2O$,

Scheme 3. Synthesis of the Neamine (6–9) and Ribostamycin (10–13) Conjugates of the 2′-*O*-Methyl Oligoribonucleotides[a]

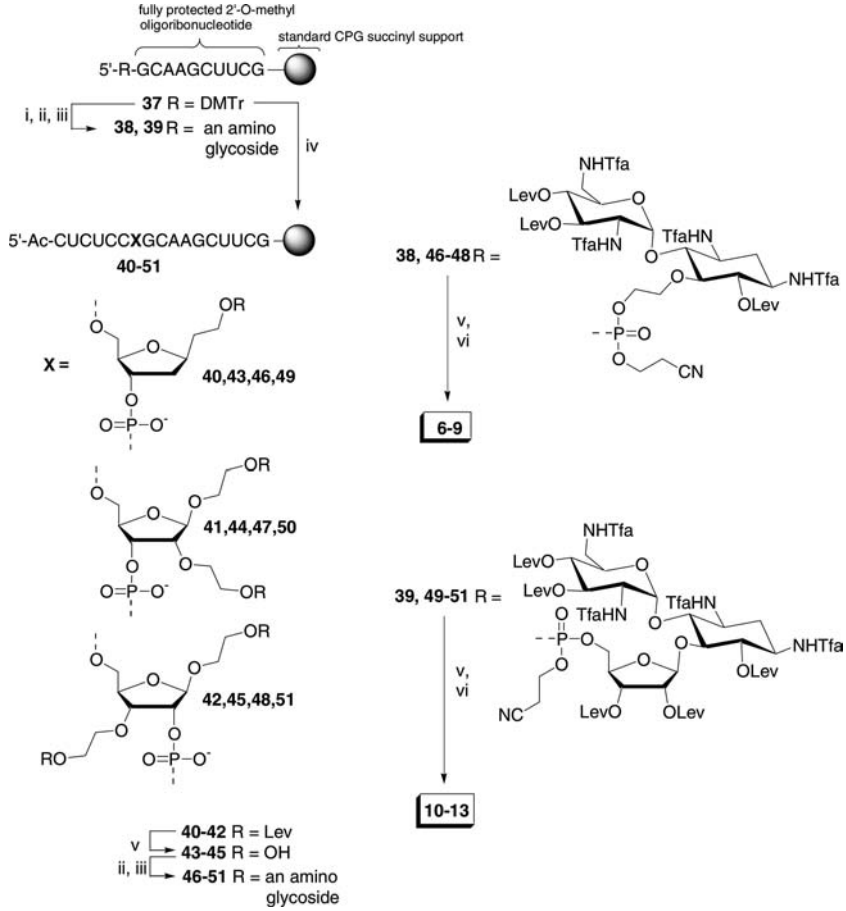

[a] Reagents and conditions: (i) DCA, CH_2Cl_2; (ii) **1** or **2**, 4,5-dicyanoimidazole, acetonitrile; (iii) I_2, pyridine, H_2O, THF; (iv) standard oligoribonucleotide synthesis; (v) hydrazinium acetate, AcOH, pyridine; (vi) aq NH_3, 15 h at 55 °C.

pyridine, AcOH, 0.124/4/1, v/v/v at 25 °C) eliminated acyl migrated products completely. Traces of a defective Tfa removal were found in the product mixure. This small amount of unexpectedly stable Tfa-amides may be slightly decreased (6% to 4% of total absorbance in RP HPLC) by using prolonged ammonolysis (48 h, at 55 °C). With these remarks, conjugates **6**–**13** were synthesized. The 2′-*O*-methyl oligoribonucleotide chains **37**, and **40**–**42** were assembled on a 1 μmol scale following the standard RNA coupling protocol. Levulinoyl protections of the inserted branching units (**40**−**42**) were removed by hydrazinium acetate treatment ($NH_2NH_2 \cdot H_2O$, pyridine, AcOH, 0.124/4/1, v/v/v, 1 h at 25 °C), and then the aminoglycoside phosphoramidites (**1** and **2**) were coupled to the hydroxyalkyl arms of **43**−**45** or to the exposed 5′-end of **37**. Two consecutive standard RNA couplings (0.1 mol L^{-1} solution of **1** or **2** in dry acetonitrile, 600 s coupling time, twice) were used in each case. Levulinoyl protections of the aminoglycoside moieties (**38**, **39**, **46**–**51**) were orthogonally removed by the same hydrazinium acetate treatment as used for the hydroxyalkyl arms above, and then the conjugates were released by ammonia (conc aq NH_3, 15 h at 55 °C). Purity of the conjugates (**6**, **7**, **9**, and **10**) having one aminoglycoside unit was ca. 65%. Attachment of two aminoglycosidic ligands lowered the purity (**8**, **9**, **12**, and **13**) to 41–61% (see Figure 4 and Table 1). Each conjugate was easily purified by RP HPLC (Figure 5). The isolated yield ranged from 15% to 26%. Authenticity of the conjugates **6**–**13** was verified by MS(ESI) (see Table 1). MS(ESI) also showed that the desired conjugates were free from other closely related oligonucleotide derivatives, such as *O*→*N*-acyl migrated side products.

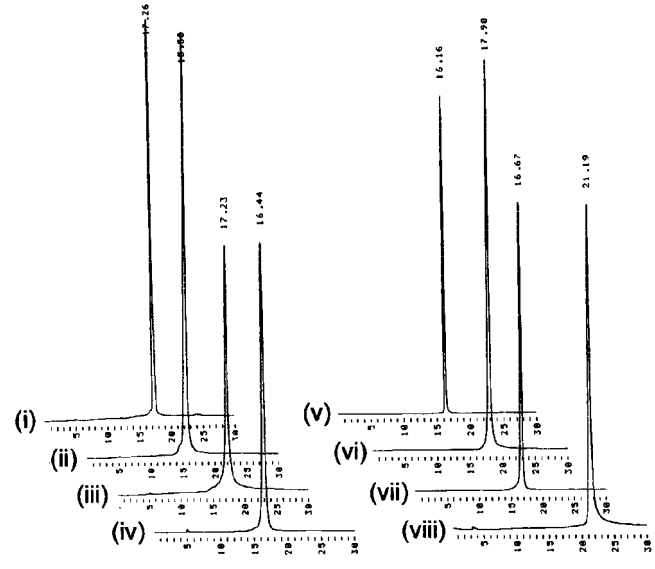

Figure 5. RP HPLC chromatograms (i−viii) of the homogenized conjugates (**6**–**13**), respectively.

RNA Cleavage by the Aminoglycoside Conjugates (6–13). Cleavage activity of the conjugates (**6**–**13**) was studied by using chimeric ribo/2′-*O*-methylribo oligonucleotides (**14** and **15**) as targets. Upon hybridization (excluding experiments with **6** and **10**), a tri- and pentanucleotide bulge (A3 and A5), serving as potential cleaving sites, is formed opposite the aminoglycoside regions. Each aminoglycoside conjugate (**6**–**13**) was

incubated with the target (**14** or **15**) at 18 μmol L^{-1} equimolar concentration (35 °C, pH = 7.3, I = 0.1 mol L^{-1}). Aliquots were withdrawn at appropriate intervals, and their composition was determined by zone capillary electrophoresis. In these metal-ion-independent cleavage studies, one of the conjugates (i.e., conjugate **9**) accelerated the hydrolysis of target oligonucleotides (**14** and **15**), the first-order rate constants being $(2.7 \pm 0.6) \times 10^{-7}$ s^{-1} and $(2.3 \pm 0.6) \times 10^{-7}$ s^{-1}, respectively, while the other conjugates turned out to be almost inactive. Cleavage of **14** by **11** [$k = (1.0 \pm 0.3) \times 10^{-7}$ s^{-1}] may still be noteworthy, but, e.g., target **14** in the presence of conjugates **6**, **7**, **10**, and **12** remained fully intact (100%, $k_{cat} = k_{uncat} = 0$, an aliquot withdrawn after three weeks incubation). Similarly, target **15** remained intact (99–100%) in the presence of **6**−**8** and **10**, and negligible cleavage (under the limits of experimental error) was observed with the other experiments (**14** in the presence of **8** and **13** and **15** in the presence of **11**, **12**, and **13**). All the conjugates contain the same active core, i.e., neamine, but site within the sequence selective motif (**6** and **10** vs **7**–**9**, **11**, **12**, and **13**), number of the cores (**6**, **7**, **10**, and **11** vs **8**, **9**, **12**, and **13**), structural orientations and lengths of the spacers are different. Comparing **9** to **8**, both conjugates have similarly orientated neamine in the 1-*O*-position (branching unit **4** vs **5**), but in contrast to **9**, conjugate **8** is inactive. Comparing **9** to **13**, both conjugates bear the same branching unit (**5**), but ribostamycine (**13**) instead of ethylene glycol derived neamine (**9**) reduces the activity. Hence, the 3-*O*-tethered orientation for the neamine (**4**) together with an appropriate spacer (ethylene glycol in **9**) probably is favorable for the cleavage. We recently described cleavage properties of di(azacrown) conjugated oligonucleotides with the same targets (**14** and **15**). Interestingly, the 3-*O* ribose (**4**) branched azacrown conjugate was even in that case superior to other closely related conjugates (*42*). Metal-ion-independent cleavage of HIV-1 TAR RNA by neamine−PNA conjugates has recently been reexamined by Chaubey et al. (*27*). Consistent with the foregoing, they noted that small structural differences perturbed the activity of the neamine−PNA conjugates; only one of the conjugates resulted in a remarkable cleavage. Chaubey et al. proposed the following mechanism for the neamine catalyzed hydrolysis of RNA (*27*). The deprotonated amino group ($pK_a = 6.9$) at the 3-position of ring I extracts a hydrogen atom from the 2′-OH group of the ribose moiety of the RNA, while the protonated amino group ($pK_a = 9.2$) at the 6′-position of ring II polarizes the phosphate group by electrostatic interaction. These two interactions, together, facilitate intramolecular nucleophilic attack of 2′-OH to the phosphorus atom, which leads to the formation of 2′,3′-cyclic phosphate and cleavage of RNA. In comparison to metal chelate-based nucleases, metal-ion-independent activity, which is based on unprotonated and protonated amino groups in a negatively charged environment, understandably may be perturbed more dramatically by structural differences. In order to study metal-ion dependence of the cleavages by **6**–**13**, each experiment was additionally performed in the presence of Zn^{2+} ion [90 μmol L^{-1} $Zn(NO_3)_2$] keeping the other conditions unchanged. Somewhat increased activities were now found. However, only in one case (conjugate **11** vs target **14**) was the first-order rate constant ($k = 9.0 \times 10^{-7}$ s^{-1}) markedly different from that of the nonspecific cleavage by Zn^{2+} complexes. Otherwise, the accelerations [$k = (1.5–7.0) \times 10^{-7}$ s^{-1}] may be considered to be more or less marginal compared to the background obtained with the targets (**14** and **15**) in 90 μmol L^{-1} Zn^{2+} concentration alone ($k < 1 \times 10^{-6}$ s^{-1}) (*42*, *43*). It is worth noting that cleavage activity of conjugate **9** was not markedly accelerated by addition of the Zn^{2+} ion. The cleavage of **14** by **9** in the presence of the Zn^{2+} ion remained unchanged [$k = (2.7 \pm 0.6) \times 10^{-7}$ s^{-1}] and slight Zn^{2+} promoted acceleration to cleavage of **15** by **9** [$k = (6.0 \pm 0.3) \times 10^{-7}$ s^{-1}] was found.

In the present study, equimolar concentrations of the conjugates (**6**–**13**) with the targets (**14** and **15**) have been used, in which the rate constants for the metal-ion-independent cleavages of **14** and **15** were as low as $k \leq 2.7 \times 10^{-7}$ s^{-1}. Real catalytic activity would require further identification (including experiments, in which a catalytic amount of the conjugate and excess of the targets are used), but as may already be noticed by these rate constants, none of the conjugates met requirements for a real catalyst. An obvious explanation to the modest cleavage activities is restricted access of the neamine cores to the phosphodiester bonds of target RNA bulges. However, this is not necessarily completely caused by structural reasons, such as an inappropriate spacer between the neamine and the 2′-*O*-methyl oligoribonucleotides or the structure of the branching units, but competitive binding of the positively charged aminoglycoside to phosphodiester groups on the same molecule (i.e., intramolecular electrostatic interaction) may also play a role. This explanation is partly consistent with findings that a polyamine−PNA conjugate provides higher catalytic activity compared to its oligonucleotide counterpart (*44*, *45*). Among the metal-ion-independent nucleases, bearing a 2′-deoxy oligoribonucleotide or 2′-*O*-methyl oligoribonucleotide as a sequence-selective motif, only a tris(2-aminobenzimidazole)-based nuclease has been reported to have marked cleaving activity so far (*46*). It should also be noted that the chimeric oligonucleotides **14** and **15** are relatively stable as targets. For example, the Zn^{2+}complexes of the di(azacrown) conjugates of 2′-*O*-methyl oligoribonucleotides, which in an optimal case have equal catalytic activity to the most efficient Zn^{2+} and Cu^{2+}-based artificial nucleases (*47*, *48*), also have moderate cleavage ability [$k = (0.9–1.7) \times 10^{-6}$ s^{-1}] to these targets (**14** and **15**) (*42*). Thus, the real cleavage potential of the aminoglycoside conjugates (**6**–**13**) may still remain obscure, and further studies with different targets are required.

CONCLUSION

In the present study, aminoglycoside conjugates of 2′-*O*-methyl oligoribonucleotides (**6**–**13**) have been successfully synthesized entirely on a solid support. The *O*-levulinoyl and *N*-trifluoroacetyl protecting group combination has been used for the aminoglycoside moieties, which enables elimination of *O*→*N*-acyl migration. The potential of these conjugates to act as a sequence-selective and metal-ion-independent artificial nuclease has been studied with chimeric ribo/2′-*O*-methyl oligonucleotides (**14** and **15**). With these experiments, one of the conjugates (**9**) resulted in metal-ion-independent cleavage of the targets [**14** and **15**, $k = (2.7 \pm 0.6) \times 10^{-7}$ s^{-1} and $(2.3 \pm 0.6) \times 10^{-7}$ s^{-1}, respectively], but usually the cleavage obtained by the conjugates (**6**–**8**, **10**–**13**) remained at a marginal level or the conjugates were fully inactive.

ACKNOWLEDGMENT

The authors thank Professor Harri Lönnberg for advice considering the cleavage studies and corrections in the preparation of the manuscript. The financial support from the Academy of Finland is gratefully acknowledged.

Supporting Information Available: NMR and MS spectral data for **1**–**3**, **6**–**13**, **20**–**31**, and **33**–**36** and RP HPLC chromatographic data as evidence for the *O*→*N*-acyl migration. This material is available free of charge via the Internet at http://pubs.acs.org.

LITERATURE CITED

(1) Davies, J., Gorini, L., and Davis, B. D. (1965) Misreading of RNA codewords induced by aminoglycoside antibiotics. *Mol. Pharmacol. 1*, 93–106.

(2) Moazed, D., and Noller, H. F. (1987) Interaction of antibiotics with functional sites in 16S ribosomal RNA. *Nature 327*, 389–394.

(3) Von Ahsen, U., and Noller, H. F. (1993) Footprinting the sites of interaction of antibiotics with catalytic group I intron RNA. *Science 260*, 1500–1503.

(4) Francois, B., Russell, R. J. M., Murray, J. B., Aboul-ela, F., Masquida, B., Vicens, Q., and Westhof, E. (2005) Crystal structures of complexes between aminoglycosides and decoding site oligonucleotides: role of the number of rings and positive charges in the specific binding leading to miscoding. *Nucleic Acid Res. 33*, 5677–5690.

(5) Von Ahsen, U., Davies, J., and Schroeder, R. (1991) Antibiotic inhibition of group I ribozyme function. *Nature 353*, 368–370.

(6) Herman, T. (2005) Drugs targeting the ribosome. *Curr. Opin. Struct. Biol. 15*, 355–366.

(7) Mei, H.-Y., Galan, A. A., Halim, N. S., Mack, D. P., Morelan, D. W., Sanders, K. B., Truong, H. N., and Czarnik, A. W. (1995) Inhibition of an HIV-1 Tat-derived peptide binding to TAR RNA by aminoglycoside antibiotics. *Bioorg. Med. Chem. Lett. 5*, 2755–2760.

(8) Zapp, M. L., Stern, S., and Green, M. R. (1993) Small molecules that selectively block RNA binding of HIV-1 rev protein inhibit rev function and viral production. *Cell 74*, 969–978.

(9) Tam, V. K., Kwong, D., and Tor, Y. (2007) Fluorescent HIV-1 dimerization initiation site: design, properties, and use for ligand discovery. *J. Am. Chem. Soc. 129*, 3257–3266.

(10) Ennifar, E., Paillart, J.-C., Bodlenner, A., Walter, P., Weibel, J.-M., Aubertin, A.-M., Pale, P., Dumas, P., and Marquet, R. (2006) Targeting the dimerization initiation site of HIV-1 RNA with aminoglycosides: from crystal to cell. *Nucleic Acid Res. 34*, 2328–2339.

(11) Liu, M., Haddad, J., Axucena, E., Kotra, L. P., Kirzhner, M., and Mobashery, S. (2000) Tethered bisubstrate derivatives as probes for mechanism and as inhibitors of aminoglycoside 3′-phosphotransferases. *J. Org. Chem. 65*, 7422–7431.

(12) Yajima, S., Shionoya, H., Akagi, T., and Hamasaki, K. (2006) Neamine derivatives having a nucleobase with a lysine or an arginine as a linker, their synthesis and evaluation as potential inhibitors for HIV TAR-Tat. *Bioorg. Med. Chem. Lett. 14*, 2799–2809.

(13) Blount, K. F., and Tor, Y. (2006) A tale of two targets: Differential RNA selectivity of nucleobase-aminoglycoside conjugates. *ChemBioChem 7*, 1612–1621.

(14) Cai, L., Li, Q., Ren, B., Yang, Z.-J., Zhang, L.-R., and Zhang, L.-H. (2007) Synthesis of aminodisaccharide-nucleoside conjugates for RNA binding. *Tetrahedron 63*, 8135–8144.

(15) Charles, I., Xue, L., and Arya, D. P. (2002) Synthesis of aminoglycoside-DNA conjugates. *Bioorg. Med. Chem. Lett. 12*, 1259–1262.

(16) Hyun, S., Lee, K. H., and Yu, J. (2006) A strategy for the design of selective RNA binding agents. Preparation and RRE RNA binding affinities of a neomycin-peptide nucleic acid heteroconjugate library. *Bioorg. Med. Chem. Lett. 16*, 4757–4759.

(17) Yoshinary, K., Yamasaki, K., and Komiyama, M. (1991) Oligoamines as simple and efficient catalyst for RNA hydrolysis. *J. Am. Chem. Soc. 113*, 5899–5901.

(18) Oivanen, M., Kuusela, S., and Lönnberg, H. (1998) Kinetics and mechanism for the cleavage and isomerization of the phosphodiester bonds of RNA by Brθnsted acids and bases. *Chem. Rev. 98*, 961–990.

(19) Kirk, S. R., and Tor, Y. (1998) Hydrolysis of an RNA dinuclear monophosphate by neomycin B. *Chem. Commun.* 147–148.

(20) Sreedhara, A., Patwardhan, A., and Cowan, J. A. (1999) Novel reagents for targeted cleavage of RNA sequences: towards a new family of inorganic pharmaceuticals. *Chem. Commun.* 1147–1148.

(21) Sreedhara, A., Freed, J. D., and Cowan, J. A. (2000) Efficient inorganic deoxyribonucleases. Greater than 50 million-fold rate enhancement in enzyme-like DNA cleavage. *J. Am. Chem. Soc. 122*, 8814–8824.

(22) Niittymäki, T., and Lönnberg, H. (2006) Artificial ribonucleases. *Org. Biomol. Chem. 4*, 15–25.

(23) Cowan, J. A. (2001) Chemical nucleases. *Curr. Opin. Chem. Biol. 5*, 634–642.

(24) Komiyama, M., Sumaoka, J., Kuzuya, A., and Yamamoto, Y. (2001) Sequence-selective artificial ribonucleases. *Methods Enzymol. 341*, 455–468.

(25) Travick, B. N., Daniher, A. T., and Bashkin, J. K. (1998) Inorganic mimics of ribonucleases and ribozymes: from random cleavage to sequence-specific chemistry to catalytic antisense drugs. *Chem. Rev. 98*, 939–960.

(26) Riguet, E., Tripathi, S., Chaubey, B., Désire, J., Pandey, V. N., and Décout, J.-L. (2004) A peptide nucleic acid-neamine conjugate that targets and cleaves HIV-1 TAR RNA inhibits viral replication. *J. Med. Chem. 47*, 4806–4809.

(27) Chaubey, B., Tripathi, S., Désire, J., Baussanne, I., Décout, J.-L., and Pandey, V. (2007) Mechanism of RNA cleavage by sequence specific polyamide nucleic acid-neamine conjugate. *Oligonucleotides 17*, 302–313.

(28) Tona, R., Bertolini, R., and Hunziker, J. (2000) Synthesis of aminoglycoside-modified oligonucleoties. *Org. Lett. 2*, 1693–1696.

(29) Charles, I., Xi, H., and Arya, D. P. (2007) Sequence-specific targeting of RNA with an oligonucleotide-neomycin conjugate. *Bioconjugate Chem. 18*, 160–169.

(30) Park, W. K. C., Auer, M., Jaksche, H., and Wong, C.-H. (1996) Rapid combinatorial synthesis of aminoglycoside antibiotic mimetics: Use of a polyethylene glycol-linked amine and a neamine-derived aldehyde in multiple component condensation as a strategy for the discovery of new inhibitors of the HIV RNA rev response element. *J. Am. Chem. Soc. 118*, 10150–10155.

(31) Alper, P. B., Hung, S.-C., and Wong, C.-H. (1996) Metal catalyzed diazo transfer. *Tetrahedron Lett. 37*, 6029–6032.

(32) Van den Broek, S. A. M. E., Gruijters, B. W. T., Rutjes, F. P. J. T., van Delft, F. L., and Blaauw, R. H. (2007) A Short and scalable route to orthogonally *O*-protected 2-deoxystreptamine. *J. Org. Chem. 72*, 3577–3580.

(33) Guibe, F., and Saint M'Leux, Y. (1981) The allyloxycarbonyl group for alcohol protection: quantitative removal or transformation into allyl protecting group via π-allyl complexes of palladium. *Tetrahedron Lett. 22*, 3591–3594.

(34) Buskas, T., Söderberg, E., Konradsson, P., and Fraser-Reid, B. (2000) Use of n-pentenyl glycosides as precursor to various spacer functionalities. *J. Org. Chem. 65*, 958–963.

(35) Li, J., Chiang, F., Chen, H.-N., and Chang, C.-W. T. (2007) Investigation of the regioselectivity for the Staudinger reaction and its application for the synthesis of aminoglycosides with N-1 modification. *J. Org. Chem. 72*, 4055–4066.

(36) Hovinen, J., and Salo, H. (1997) C-glycoside phosphoramidite building block for versatile functionalization of oligodeoxyribonucleotides. *J. Chem. Soc., Perkin Trans. 1*, 3017–3020.

(37) Niittymäki, T., Kaukinen, U., Virta, P., Mikkola, S., and Lönnberg, H. (2004) Preparation of azacrown-functionalized 2′-*O*-methyl oligoribonucleotides, potential artificial Rnases. *Bioconjugate Chem. 15*, 174–184.

(38) Haddad, J., Kotra, L. P., Llano-Sotelo, B., Kim, C., Azucena, E. F., Jr., Liu, M., Vakulenko, S. B., Chow, C. S., and Mobashery, S. (2002) Design of novel antibiotics that bind to the ribosomal acyltransfer site. *J. Am. Chem. Soc. 124*, 3229–3237.

(39) Zemplen, G., and Kuntz, A. (1923) The sodium compounds of glucose and the saponification of the acylated sugars. *Brit. 56B*, 1705–1710.

(40) Ding, Y., Swayze, E. E., Hofstadler, S. A., and Griffey, R. H. (2000) Efficient synthesis of neomycin B related aminoglycosides. *Tetrahedron Lett. 41*, 4049–4052.

(41) Nudelman, I., Rebibo-Sabbah, A., Shallom-Shezifi, D., Hainrichon, M., Stahl, I., Ben-Yosef, T., and Baasov, T. (2006) Redesign of aminoglycosides for treatment of human genetic diseases caused by premature stop mutations. *Bioorg. Med. Chem. Lett. 16*, 6310–6315.

(42) Niittymäki, T., Virta, P., Ketomäki, K., and Lönnberg, H. (2007) Di(azacrown) conjugates of 2′-O-methyl oligoribonucleotides as sequence-selective artificial ribonucleases. *Bioconjugate Chem. 18*, 1583–1592.

(43) Niittymäki, T., and Lönnberg, H. (2004) Sequence-selective cleavage of oligoribonucleotides by 3d transition metal complexes of 1,5,9-triazacyclododecane-functionalized 2′-*O*-methyl oligoribonucleotides. *Bioconjugate Chem. 15*, 1275–1280.

(44) Komiyama, M., Inokawa, T., and Yoshinary, K. (1995) Ethylenediamine-oligo DNA hybrid as sequence-selective artificial ribonuclease. *J. Chem. Soc., Chem. Commun.* 77–78.

(45) Verheijen, J. C., Deiman, B. A. L. M., Yeheskiely, E., van der Marel, G. A., and van Boom, J. H. (2000) Efficient hydrolysis of RNA by a PNA-diethylenetriamine adduct. *Angew. Chem., Int. Ed. 39*, 369–372.

(46) Gnaccarini, C., Peter, S., Scheffer, U., Vonhoff, S., Klussmann, S., and Göbel, M. W. (2006) Site-specific cleavage of RNA by a metal-free artificial nuclease attached to antisense oligonucleotides. *J. Am. Chem. Soc. 128*, 8063–8067.

(47) Putnam, W. C., Daniher, A. T., Trawick, B. N., and Bashkin, J. K. (2001) Efficient new ribozyme mimics: direct mapping of molecular design principles from small molecules to macromolecular, biomimetic ctalysis. *Nucleic Acid Res. 29*, 2199–2204.

(48) Åström, H., Williams, N. H., and Strömberg, R. (2003) Oligonucleotide based artificial nuclease (OBAN) systems. Bulge size dependence and positioning of catalytic group in cleavage of RNA-bulges. *Org. Biomol. Chem. I*, 1461–1465.

BC7004279

DNA-Encoded Chemical Libraries for the Discovery of MMP-3 Inhibitors

Jörg Scheuermann, Christoph E. Dumelin,[†] Samu Melkko,[†] Yixin Zhang, Luca Mannocci, Madalina Jaggi, Jens Sobek,[‡] and Dario Neri*

Institute of Pharmaceutical Sciences, Department of Chemistry and Applied Biosciences, ETH Zürich, Wolfgang-Pauli-Strasse 10, CH-8093 Zurich, Switzerland. Received November 27, 2007; Revised Manuscript Received December 3, 2007

Encoded self-assembling chemical (ESAC) libraries are characterized by the covalent display of chemical moieties at the extremity of self-assembling oligonucleotides carrying a unique DNA sequence for the identification of the corresponding chemical moiety. We have used ESAC library technology in a two-step selection procedure for the identification of novel inhibitors of stromelysin-1 (MMP-3), a matrix metalloproteinase involved in both physiological and pathological tissue remodeling processes, yielding novel inhibitors with micromolar potency.

INTRODUCTION

Chemical compounds carrying unique DNA fragments as amplifiable identification "bar codes" may serve as building blocks for the construction and screening of chemical libraries of unprecedented size, with considerable implications for drug discovery (*1–7*). DNA-encoded chemical libraries can be classified as "single pharmacophore" chemical libraries (in which a single chemical structure is covalently attached to a DNA fragment) and as "dual pharmacophore" chemical libraries (in which each complementary DNA strand carries a chemical moiety) (Figure 1) (*6*). In the latter case, the two pharmacophores can simultaneously contact the target protein of interest, thus conferring a high binding affinity by virtue of the chelate effect (*4, 8, 9*).

Dual pharmacophore DNA-encoded chemical libraries (ESAC[1] libraries) may be used for the de novo identification of pairs of synergistic binding molecules to protein targets of interest or for the affinity maturation of known lead compounds, which can eventually be converted into small organic molecules devoid of the DNA portion. The process relies on the preferential enrichment of library compounds binding to the target protein of interest immobilized on a solid support, followed by PCR amplification of the recovered oligonucleotide−compound conjugates and by bar code identification on DNA microarrays (Figure 2) (*4, 10*).

Matrix metalloproteinases (MMPs) are zinc-dependent proteases which are involved in tissue remodeling for a variety of physiological and pathological processes (*11–14*). More than 50 MMP inhibitors have entered clinical trials, 46 of which have been discontinued while 7 are still in the evaluation process (*15*). It is generally accepted that future endeavors for the pharmaceutical targeting of MMPs should aim at the development of more selective inhibitors, and in the identification of those MMPs which play a crucial role in pathogenesis (*13, 16, 17*).

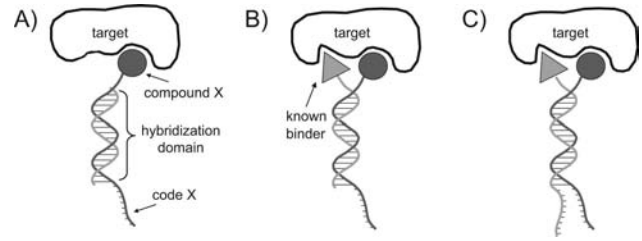

Figure 1. Schematic representation of different formats of encoded self-assembling chemical (ESAC) libraries which can be used for selections against a target antigen. Small molecules are coupled to oligonucleotides, which contain a hybridization domain and (if appropriate) a code revealing the identity of the covalently coupled molecule. After DNA−duplex formation, the oligonucleotide−compound conjugate sublibraries can be used in single pharmacophore selections (A), affinity maturation selections of known binders (B), or de novo selections of binding molecules from a combinatorial library generated by assembling two sublibraries (C).

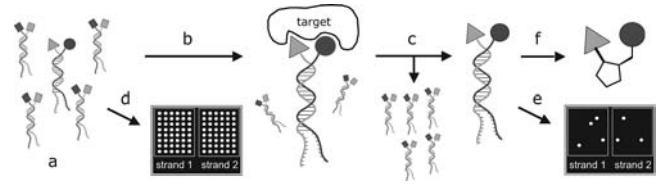

Figure 2. A typical ESAC library selection and readout procedure. The DNA−duplex library (a) is panned against the target protein of interest (b). After washing and removal of unbound molecules (c), the codes of the remaining binders are PCR amplified and compared with the unselected library on oligonucleotide microarrays (d,e). Resulting binding pairs are then validated and positive binding partners are conjugated to suitable scaffolds yielding small druglike molecules (f).

In this article, we present the use of ESAC libraries and technologies for both the identification of a novel MMP-3 inhibitory scaffold and its ESAC technology-assisted affinity maturation, yielding micromolar MMP-3 inhibitors.

EXPERIMENTAL PROCEDURES

Cloning and Expression of Human MMP-3 Catalytic Domain. The gene of human MMP-3 catalytic domain (residues 100–272) (*18*) was subcloned into a pQE12 vector (Qiagen,

* Corresponding author. Dario Neri, Institute of Pharmaceutical Sciences, Department of Chemistry and Applied Biosciences, ETH Zürich, Wolfgang-Pauli-Str. 10, 8093 Zürich, Switzerland. neri@pharma.ethz.ch, Fax: +41 633 13 58, Tel: +41 633 74 01.

[†] Philochem AG, c/o ETH Zürich, Zürich, Switzerland.

[‡] Functional Genomics Center Zurich, ETH Zurich/ University of Zurich, Zurich, Switzerland.

[1]Abbreviations: CAII, carbonic anhydrase II; CPA, carboxypeptidase A; DMSO, dimethyl sulfoxide; EDC, 1-ethyl-3-[3-(dimethylamino) propyl] carbodiimide; ESAC library, encoded self-assembling chemical library; hu-MMP3, human MMP-3; mu-MMP3, murine MMP-3; PBS, phosphate buffered saline; TBS, Tris-buffered saline, TEA, triethylamine; SSC, sodium chloride-sodium citrate; uPA, urokinase-type plasminogen activator.

10.1021/bc7004347 CCC: $40.75 © 2008 American Chemical Society
Published on Web 02/07/2008

Table 1. Compounds Derived from MMP3 Selections

No.	structure	ESAC library No.
I	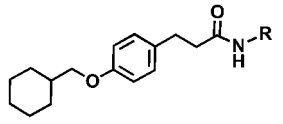	327
II	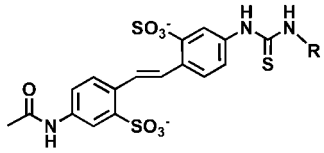	581
III (ctrl)	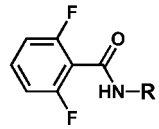	2

Scheme 1. Synthesis of Compounds Linking Pharmacophores I and II[a]

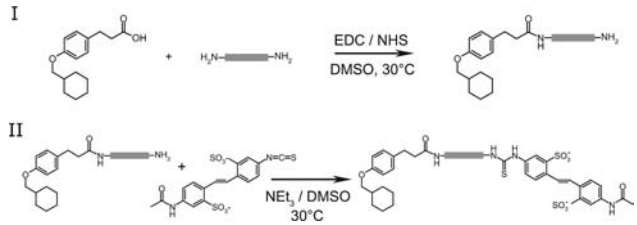

[a] (I) Linkage of **I** precursor carboxylic acid by carbodiimide-mediated activation with a diamino linker. (II) Coupling of **I**-amine with **II** precursor isothiocyanate to a dual pharmacophore compound.

Hombrechtikon, Switzerland) using restriction sites *Eco*RI and *Bgl*II and the primers 5′-ACT GAA TTC ATT AAA GAG GAG AAA TTA ACT ATG TTC AGA ACC TTT CCT GGC ATC-3′ and 5′-ACT AGA TCT CTA TCA GTG ATG GTG ATG GTG ATG GCC ACC GGG GGT CTC AGG GGA GTC AG-3′. The protein containing a C-terminal His_6-tag was purified with a Ni-NTA column (Qiagen) and dialyzed against 50 mM Tris−Cl, 200 mM NaCl, pH 7.3, and stored frozen at −20 °C.

Cloning and Expression of Murine MMP-3 Catalytic Domain. The murine MMP-3 catalytic domain (residues 100–273) was isolated from a murine cDNA library (eye) and cloned into a pQE12 vector (Qiagen, Hombrechtikon, Switzerland) using restriction sites *Eco*RI and *Bgl*II and the primers 5′- CCG GAA TTC ATT AAA GAG GAG AAA TTA ACT ATG TTC AGT ACC TTC CCA GG-3′ and 5′-ACT AGA TCT CTA TCA GTG ATG GTG ATG GTG ATG GCC ACC GAG GAC ATC AGG GGA TGC TGT-3′. The protein containing a C-terminal His_6-tag was purified with a Ni-NTA column (Qiagen) and dialyzed against 50 mM Tris−Cl, 200 mM NaCl, pH 7.3, and stored frozen at −20 °C.

Synthesis of Oligonucleotide Conjugates and Linked Pharmacophores. All chemicals were purchased from Sigma-Aldrich-Fluka (Buchs, Switzerland), unless otherwise denoted. The synthetic principles of the DNA-encoded chemical library of 550 compounds have been described before (*10*). A list of the 550 oligonucleotide-compound conjugates can be found in the Supporting Information (Table 1). In short, 48mer oligonucleotides (IBA GmbH, Göttingen, Germany), carrying a free amino group at the 5′ end (as ω-aminohexyl phosphate diester) were used of the general structure 5′-GGA GCT TCT GAA TTC TGT GTG CTG XXX XXX CGA GTC CCA TGG CGC AGC-3′, where the XXX XXX coding sequence unambiguously codes for the individual chemical compound displayed. The chemical compounds comprising carboxylic acid, carboxylic anhydride, N-hydroxysuccinimide ester, or isothiocyanate groups were coupled to the primary amino group of the oligonucleotides (*4, 10*).

Selection for Binding. The library containing each individual member at a concentration of 1.78 nM was dimerized at a concentration of 100 nM by heteroduplex formation with an unmodified pairing oligonucleotide (for de novo selections) or with a 3′-amino-modified oligonucleotide, which was conjugated to 3-(4-(cyclohexylmethoxy)phenyl) propanoic acid by an amide bond (for affinity maturation selections). Human MMP-3 and control resins were prepared as follows: 317 mg of dry CNBr-modified sepharose (GE Healthcare) were thoroughly washed with cold 1 mM HCl and incubated overnight at 4 °C either with 4 mL of 50 μM MMP-3 in coupling buffer (100 mM $NaHCO_3$, 100 mM NaCl, pH 8.1) or with 1 M Tris−Cl, pH 7.2 (control resin). The MMP-3 resin was washed 5 times with 550 μL of coupling buffer and excess reactive groups on the resin were quenched with 550 μL of 1 M Tris−Cl, pH 7.2, at 4 °C overnight. The resins were then washed at alternating pH with 100 mM sodium acetate, 500 mM NaCl, pH 4.7, and 100 mM Tris−Cl, 500 mM NaCl, pH 8.1 (4 times each) using SpinX columns (Corning Life Sciences, Acton, USA) and resuspended in 2 mL of selection buffer (50 mM Tris−Cl, 200 mM NaCl, 10 mM $CaCl_2$, 1 mM $MgCl_2$, 10 μM $ZnCl_2$, pH 6.7) containing 0.05 mg/mL herring sperm DNA. 10 μL of the DNA duplex library (85 nM total concentration) was then incubated with 200 μL of resin and 200 μL of selection buffer. After incubation for 1 h at 25 °C, the suspension was transferred to a SpinX column (Corning), the supernatant removed, and the resin washed 3 times with 400 μL of selection buffer. The resin was finally resuspended in 400 μL of selection buffer and stored at −20 °C.

Decoding. The codes of the oligonucleotide−compound conjugates were amplified after selection by PCR (50 μL, 25 cycles of 1 min at 94 °C, 1 min at 55 °C, 40 s at 72 °C), using 10 μL of the resuspended resin as template and primers AB_fo_short (GGA GCT TCT GAA TTC TGT GTG CTG) and Elib2_ba (GCT GCG CCA TGG GAC TCG). The product was purified with a PCR purification kit (Qiagen) and subsequently linearly amplified by PCR (as above) using 5′-Cy3-labeled Elib2_ba as primer. The product was precipitated by adding 10% v/v of 3 M sodium acetate, pH 4.7, and 250% v/v of ethanol and redissolved in 120 μL of hybridization buffer (4 × SSC (60 mM sodium citrate, 0.6 M NaCl, pH 7), 50 mM HEPES, 0.2% SDS, pH 7) and hybridized on microarray glass slides (displaying 19-mers with the structure 5′-T GTG CTG XXX XXX CGA GTC-3′) in a Tecan HS 400 instrument for 4 h at 44 °C, followed by successive washing steps with 2 × SSC/0.2% (w/v) SDS, 0.2 × SSC/0.2% (w/v) SDS, and 0.2 × SSC. After hybridization, the microarrays were analyzed by scanning with a Genepix professional 4200A scanner (Molecular Devices, Sunnyvale, CA; $\lambda_{ex} = 532$ nm, 100% laser power, photomultiplier 400). Spot intensities were quantified and evaluated using *Genespotter* software (v 2.4.3, MicroDiscovery, Berlin, Germany). After background subtraction, the mean value was used as spot signal intensity (average of all spots of the same oligonucleotide). Dividing the obtained signal intensities for the MMP-3 selection by the intensities of the control selection (no antigen resin) resulted in a fingerprint of the enrichment profile.

Affinity Chromatography of Enriched ESAC Conjugates. Oligonucleotide 5′-CAG CAC ACA GAA TTC AGA AGC TCC-3′ and the oligonucleotide conjugate 5′-CAG CAC ACA GAA TTC AGA AGC TCC-**I**-3′ were radioactively labeled at the 5′ terminus using γ^{33}P-ATP (GE Healthcare) and T4 polynucleotide kinase (USB, Cleveland, OH) and individually hybridized to enriched ESAC library compounds or controls

Table 2. Inhibition Constants of Dual Pharmacophore Conjugates Derived from MMP3 Selection

R	Linker name	Linker structure	R′	hu-MMP3 / IC_{50}	mu-MMP3 / IC_{50}	CPA / IC_{50}	uPA / IC_{50}	CAII / IC_{50}
I	A	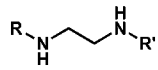	II	48 μM	53 μM	>200 μM	290 μM	>1 mM
I	B	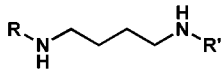	II	31 μM	>1 mM	>200 μM	>1 mM	>1 mM
I	C	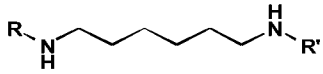	II	37 μM	27 μM	>200 μM	225 μM	>1 mM
I	D	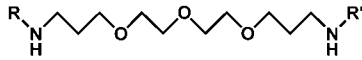	II	52 μM	56 μM	>200 μM	795 μM	>1 mM
I	D	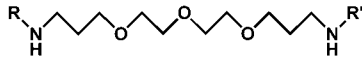	III (ctrl)	>1 mM	ND	ND	ND	ND
I	D	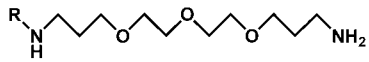	-	>1 mM	ND	ND	ND	ND
II	D	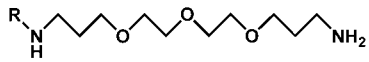	-	>300 μM	ND	ND	ND	ND
I	E	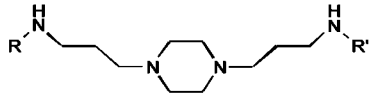	II	91 μM	140 μM	>200 μM	>1 mM	>1 mM
I	F	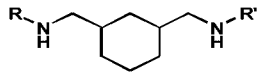	II	50 μM	24 μM	>200 μM	270 μM	>1 mM
I	G	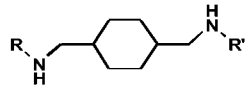	II	24 μM	34 μM	>200 μM	470 μM	>1 mM
I	H	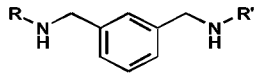	II	23 μM	154 μM	>200 μM	>1 mM	>1 mM
I	J	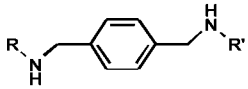	II	10 μM	25μM	>200 μM	>1 mM	>1 mM
I	J	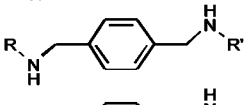	III (ctrl)	>1 mM	ND	ND	ND	ND
I	J	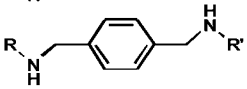	-	>1 mM	ND	ND	ND	ND
I	K	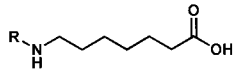	-	>300 μM	ND	ND	ND	ND

at 200 nM final concentration. 15 μL of the hybridization was incubated with 35 μL of selection buffer and 50 μL MMP-3 resin (see above). After 45 min incubation at 25 °C, the resin was washed several times with 400 μL of selection buffer on SpinX columns (Corning). Aliquots of the remaining resin, input, flowthrough, and all washing fractions were subjected to ^{33}P radioactivity counting on a Beckman LS6500 scintillation counter (Beckman Coulter, Fullerton, CA).

Linked Pharmacophores. The synthesis of bidentate conjugates of **I** and **II** was performed according to Scheme 1: 3-(4-(cyclohexylmethoxy)phenyl) propanoic acid (20 μmol) was activated for 30 min at 25 °C with 1-ethyl-3-(3-dimethylaminopropyl)carbodiimide (EDC) (50 μmol) and *N*-hydroxy succinimide (NHS) (100 μmol) in DMSO and subsequently reacted with diaminolinker (200 μmol)/TEA (144 μmol) overnight at 30 °C. The resulting linker conjugate was purified by HPLC, dried, redissolved in 200 μL of DMSO, and reacted after addition of TEA (72 μmol) with 30 μmol of 4-acetamido-4′-isothiocyanostilbene-2,2′-disulfonic acid. After quenching with a molar excess of ethanolamine, the reaction was purified by HPLC, dried, and analyzed by ESI-MS (Quattro Micro, Waters, Milford, CT). ^1H NMR spectra were measured on a Bruker 400 avance instrument (Bruker, Ettlingen, Germany) and concentrations determined using nitromethane as internal standard (compound naming **R-Linker-R′**: cf. Tables 1 and 2).

I-A-II.(*E*)-5-Acetamido-2-(4-(3-(2-(3-(4-(cyclohexylmethoxy) phenyl)propanamido)ethyl)thioureido)-2-sulfostyryl)benzenesulfonic acid. ESI-MS (*m*/*z*): 759.2 ([M + H^+], 100%), calcd: 758.21 Da. ^1H NMR (DMSO-d_6): 7.95 (d, 2.5 Hz, 2H), 7.71 (d, 2.5 Hz, 2H), 7.69 (d, 2.5 Hz, 1H), 7.57–7.47 (m, 3H), 7.09 (d, 8.5 Hz, 2H), 6.80 (d, 8.5 Hz, 2H), 3.71 (d, 6.3 Hz, 2H), 3.24 (m, 2H), 2.74 (t, 7.8 Hz, 2H), 2.40–2.32 (m, 4H), 2.04 (s, 3H), 1.82–1.60 (m, 6H), 1.35–0.96 (m, 5H).

I-B-II. (*E*)-5-(3-(4-(3-(4-(Cyclohexylmethoxy)phenyl)propanamido)butyl)thioureido)-2-(4-ethanamido-2-sulfostyryl)benzenesulfonic acid. ESI-MS (*m*/*z*): 787.2 ([M + H^+], 100%),

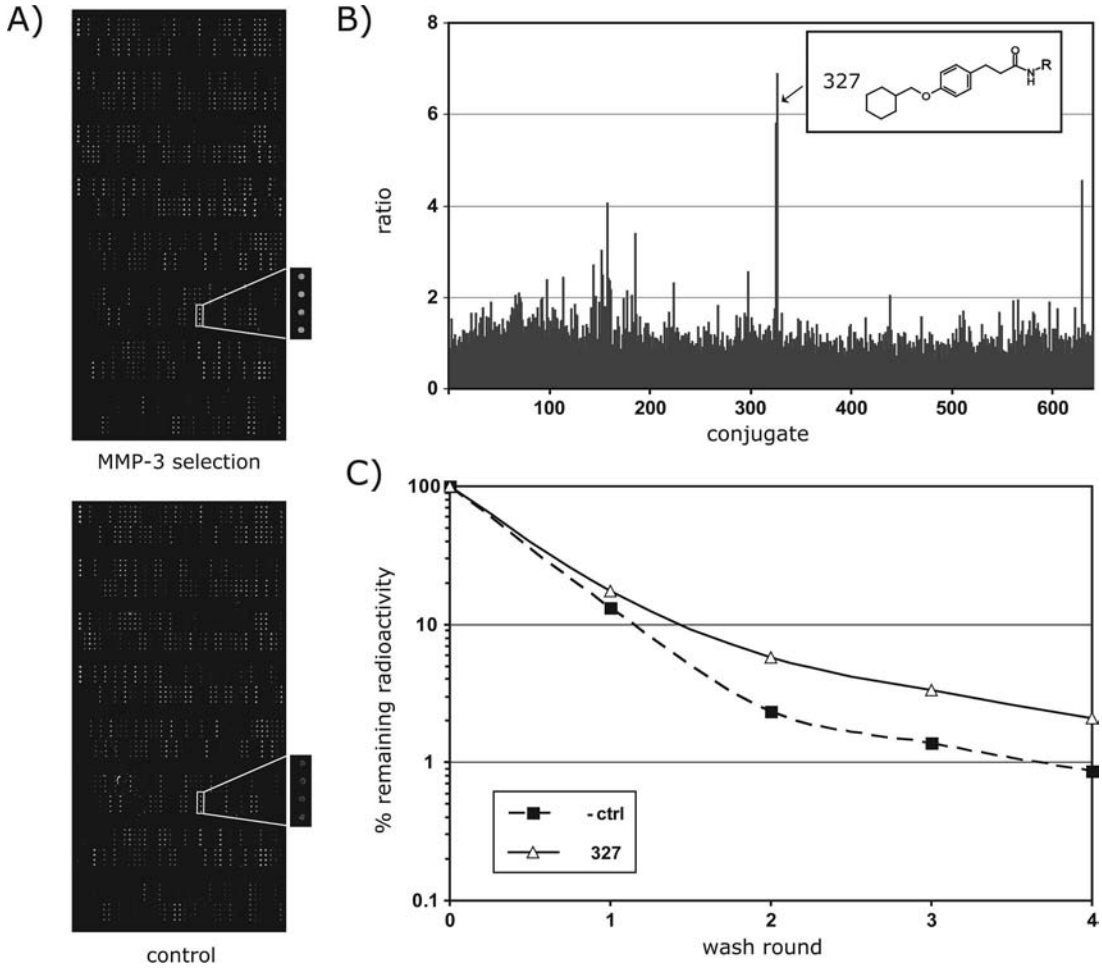

Figure 3. De novo selection of MMP-3 binders using a DNA duplex library consisting of a 3′-unmodified oligonucleotide hybridized to an ESAC library of 550 compounds. (A) Microarray readout after PCR amplification of a selection against MMP-3-displaying resin (upper panel) and control resin (no antigen, lower panel). On the microarrays, ESAC library decoding oligonucleotides are spotted in quadruplicate. The spots encoding the enriched ESAC oligonucleotide−compound conjugate 327 are shown as insets for both MMP-3 and control selection. (B) Quantitative microarray evaluation: Enrichment of ESAC library oligonucleotide−compound conjugates given as ratio of MMP-3 selection versus control selection. The enriched ESAC conjugate 327 is indicated. (C) Affinity chromatography of enriched ESAC conjugate 327 and of nonenriched ESAC conjugate 2 (- ctrl) hybridized each to a radiolabeled unmodified oligonucleotide. The retaining radioactivity was monitored for increasing washing steps.

calcd: 786.24 Da. ^{1}H NMR (partial, DMSO-d_6): 3.72 (d, 6.3 Hz, 2H, R-OCH_2-cyclohexyl of **I**), 2.04 (s, 3H, CH_3-CONHAr of **II**).

I-C-II. (*E*)-5-(3-(6-(3-(4-(Cyclohexylmethoxy)phenyl)propanamido)hexyl)thioureido)-2-(4-ethanamido-2-sulfostyryl)benzenesulfonic acid. ESI-MS (*m*/*z*): 815.2 ([M + H$^+$], 100%), calcd: 814.27 Da. ^{1}H NMR (partial, DMSO-d_6): 3.72 (d, 6.3 Hz, 2H, R-OCH_2-cyclohexyl of **I**), 2.04 (s, 3H, CH_3-CONHAr of **II**).

I-D-II. (*E*)-5-(3-(17-(4-(Cyclohexylmethoxy)phenyl)-15-oxo-4,7,10-trioxa-14-azaheptadecyl)thioureido)-2-(4-ethanamido-2-sulfostyryl)benzenesulfonic acid. ESI-MS (*m*/*z*): 919.3 ([M + H$^+$], 100%), calcd: 918.32 Da. ^{1}H NMR (partial, DMSO-d_6): 3.72 (d, 6.4 Hz, 2H, R-OCH_2-cyclohexyl of **I**), 2.04 (s, 3H, CH_3-CONHAr of **II**).

I-D-III. *N*-(17-(4-(Cyclohexylmethoxy)phenyl)-15-oxo-4,7,10-trioxa-14-azaheptadecyl)-2,6-difluorobenzamide. ESI-MS (*m*/*z*): 605.4 ([M + H$^+$], 100%), calcd: 604.33 Da. ^{1}H NMR (partial, DMSO-d_6): 7.50 (t, 7.5 Hz, 1H, *p-H* of **III**), 3.71 (d, 6.4 Hz, 2H, R-OCH_2-cyclohexyl of **I**).

I-D-NH$_2$. *N*-(3-(2-(2-(3-Aminopropoxy)ethoxy)ethoxy)propyl)-3-(4-(cyclohexylmethoxy)phenyl)propanamide. ESI-MS (*m*/*z*): 465.4 ([M + H$^+$], 100%), calcd: 464.33 Da. ^{1}H NMR (partial, DMSO-d_6): 3.72 (d, 6.4 Hz, 2H, R-OCH_2-cyclohexyl).

II-D-NH$_2$. (*E*)-5-(3-(3-(2-(2-(3-Aminopropoxy)ethoxy)ethoxy)propyl)thioureido)-2-(4-ethanamido-2-sulfostyryl)benzenesulfonic acid. ESI-MS (*m*/*z*): 675.3 ([M + H$^+$], 100%), calcd: 674.18 Da. ^{1}H NMR (partial, DMSO-d_6): 2.04 (s, 3H, CH_3-CONHAr).

I-E-II. (*E*)-5-(3-(3-(4-(3-(3-(4-(Cyclohexylmethoxy)phenyl)-propanamido)propyl)piperazin-1-yl)propyl)thioureido)-2-(4-ethanamido-2-sulfostyryl)benzenesulfonic acid. ESI-MS (*m*/*z*): 899.3 ([M + H$^+$], 100%), calcd: 898.34 Da. ^{1}H NMR (partial, DMSO-d_6): 3.72 (d, 6.4 Hz, 2H, R-OCH_2-cyclohexyl of **I**), 2.04 (s, 3H, CH_3-CONHAr of **II**).

I-F-II. (*E*)-5-(3-((3-((3-(4-(Cyclohexylmethoxy)phenyl)propanamido)methyl)cyclohexyl)methyl)thioureido)-2-(4-ethanamido-2-sulfostyryl)benzenesulfonic acid. ESI-MS (*m*/*z*): 841.2 ([M + H$^+$], 100%), calcd: 840.29 Da. ^{1}H NMR (partial, DMSO-d_6): 3.71 (d, 6.4 Hz, 2H, R-OCH_2-cyclohexyl of **I**), 2.04 (s, 3H, CH_3-CONHAr of **II**).

I-G-II. (*E*)-5-(3-((4-((3-(4-(Cyclohexylmethoxy)phenyl)propanamido)methyl)cyclohexyl)methyl)thioureido)-2-(4-ethanamido-2-sulfostyryl)benzenesulfonic acid. ESI-MS (*m*/*z*): 841.2 ([M + H$^+$], 100%), calcd: 840.29 Da. ^{1}H NMR (partial, DMSO-d_6): 3.71 (d, 6.4 Hz, 2H, R-OCH_2-cyclohexyl of **I**), 2.04 (s, 3H, CH_3-CONHAr of **II**).

I-H-II. (*E*)-5-(3-(3-((3-(4-(Cyclohexylmethoxy)phenyl)propanamido)methyl)benzyl)thioureido)-2-(4-ethanamido-2-sulfostyryl)benzenesulfonic acid. ESI-MS (*m*/*z*): 835.3 ([M + H$^+$], 100%), calcd: 834.24 Da. ^{1}H NMR (partial, DMSO-d_6): 3.72 (d, 6.4 Hz, 2H, R-OCH_2-cyclohexyl of **I**), 2.04 (s, 3H, CH_3-CONHAr of **II**).

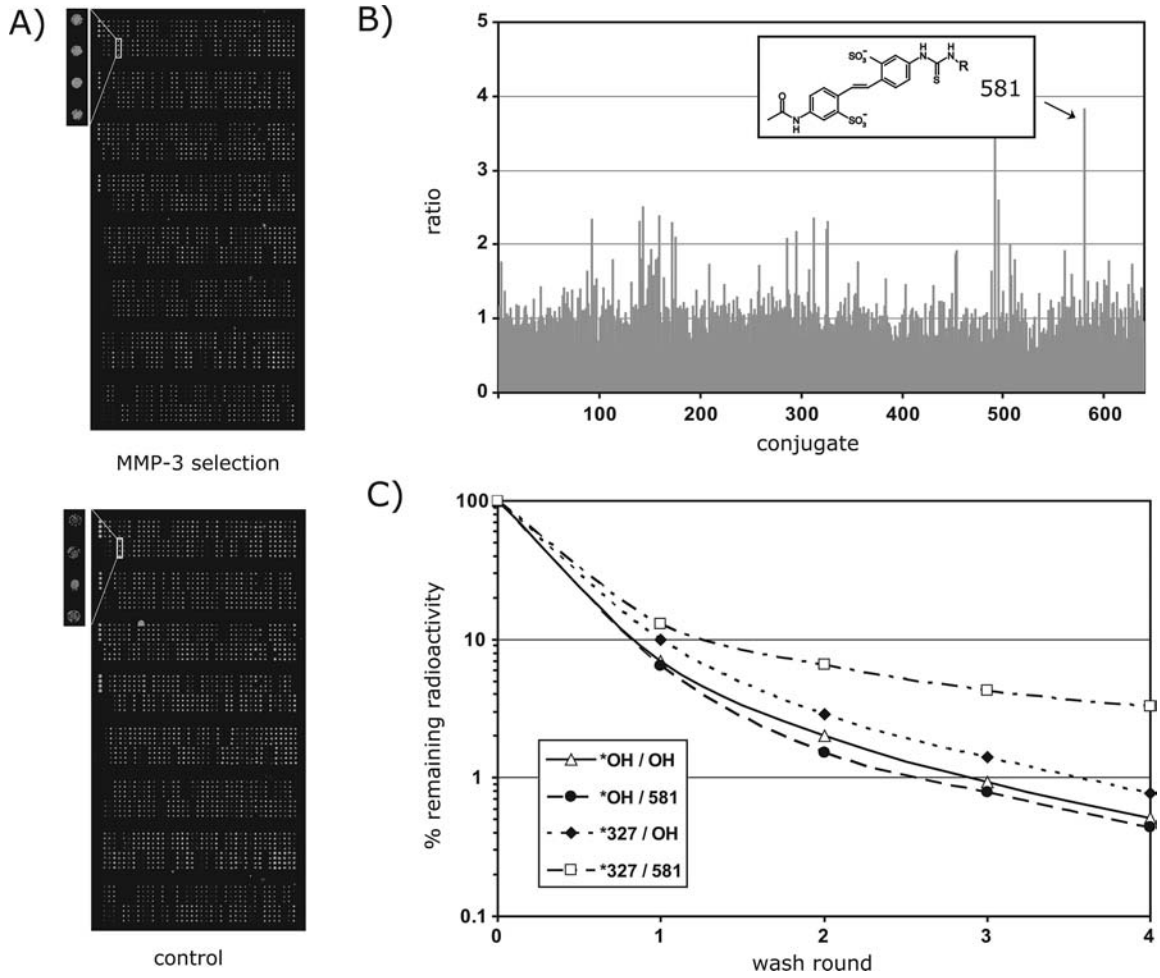

Figure 4. Affinity maturation selection of ESAC conjugate 327 (**I**) using a DNA duplex library consisting of an oligonucleotide displaying **I** on its 3′ terminus hybridized to an ESAC library of 550 compounds. (A) Microarray readout after PCR amplification of affinity maturation selection against MMP-3-displaying resin (upper panel) and control resin (no antigen, lower panel). On the microarrays, ESAC library decoding oligonucleotides are spotted in quadruplicate. The spots encoding the enriched ESAC library conjugate 581 are shown as insets for both MMP-3 and control selection. (B) Quantitative microarray evaluation: Enrichment of ESAC library conjugates given as ratio of MMP-3 selection versus control selection. The enriched ESAC conjugate 581 is indicated. (C) Affinity chromatography of ESAC conjugates 327 and 581 hybridized to an unmodified oligonucleotide (OH/581 and 327/OH), of the combination of both pharmacophores (327/581) and of a unmodified oligonucleotide heteroduplex control (OH/OH). The 5′-radiolabeled oligonucleotide is marked with an asterisk. The retaining radioactivity was monitored for increasing washing steps.

I-J-II. (*E*)-5-(3-(4-((3-(4-(Cyclohexylmethoxy)phenyl)propanamido)methyl)benzyl)thioureido)-2-(4-ethanamido-2-sulfostyryl)benzenesulfonic acid. ESI-MS (*m*/*z*): 835.1 ([M + H^+], 100%), calcd: 834.24 Da. ^{1}H NMR (partial, DMSO-d_6): 3.72 (d, 6.4 Hz, 2H, R-OCH_2-cyclohexyl of **I**), 2.04 (s, 3H, CH_3-CONHAr of **II**).

I-J-III. *N*-(4-((3-(4-(Cyclohexylmethoxy)phenyl)propanamido)methyl)benzyl)-2,6-difluorobenzamide. ESI-MS (*m*/*z*): 521.3 ([M + H^+], 100%), calcd: 520.25 Da. ^{1}H NMR (partial, DMSO-d_6): 7.53 (t, 7.5 Hz, 1H, *p-H* of **III**), 3.73 (d, 6.4 Hz, 2H, R-OCH_2-cyclohexyl of **I**).

I-J-NH$_2$. *N*-(4-(Aminomethyl)benzyl)-3-(4-(cyclohexylmethoxy)phenyl)propanamide. ESI-MS (*m*/*z*): 381.3 ([M + H^+], 100%), calcd: 380.25 Da, ^{1}H NMR (partial, DMSO-d_6): 3.73 (d, 6.4 Hz, 2H, R-OCH_2-cyclohexyl).

I-K-COOH. 7-(3-(4-(Cyclohexylmethoxy)phenyl)propanamido)heptanoic acid. ESI-MS (*m*/*z*): 390.3 ([M + H^+], 100%), calcd: 389.26 Da. ^{1}H NMR (partial, DMSO-d_6): 3.71 (d, 6.4 Hz, 2H, R-OCH_2-cyclohexyl).

MMP-3 Inhibition Assay. 55 μL of MMP-3 in 7.3 mM Tris−Cl, 36.4 mM NaCl, 63.6 mM 2-(*N*-morpholino)ethane sufonate, 1.27 mM $CaCl_2$, 25.5 μM $ZnCl_2$, 0.055% Brij-35, pH 6.1 (final MMP-3 concentration: 417 nM), were incubated in a 384-well microtiter plate (Nunc, Roskilde, Denmark) with a dilution series of inhibitor in DMSO (5 μL) for 20 min at 25 °C. The reaction was started by addition of 10 μL of the fluorogenic substrate Mca-Pro-Leu-Gly-Leu-Dpa-Ala-Arg-NH_2 (OmniMMP, BIOMOL, Exeter, UK, dissolved at 50 μM in 5% DMSO) to 60 μL of MMP-3/inhibitor solution. The change of fluorescence signal (λ_{ex} 328 nm; λ_{em} 393 nm) was recorded over 5 min using a SpectraMax Gemini microplate reader (Molecular Devices). The rate of fluorescence signal increase over time (initial reaction velocity v) was plotted against the corresponding inhibitor concentration, and the IC_{50} value for the inhibitor was obtained by fitting to the equation $v = \alpha/2 \times \{-(I - E_o + IC_{50}) + \mathrm{sqrt}[(I - E_o + IC_{50})^2 + 4 \times IC_{50} \times E_o]\}$ (v = initial velocity, I_o = initial inhibitor concn, E_o = initial enzyme concn) using *SigmaPlot* software (SPSS Inc., Chicago, IL).

uPA Inhibition Assay. 58 μL of 32 nM uPA in TBS were incubated in a 384-well microtiter plate (Nunc, Roskilde, Denmark) with a dilution series of inhibitor in DMSO (5 μL) for 20 min at 25 °C. The reaction was started by addition of 7 μL of the fluorogenic substrate ZGGR-AMC (1 mM in DMSO) (Bachem, Switzerland). The change of fluorescence signal (λ_{ex} 383 nm; λ_{em} 455 nm) was recorded over 4 min using a SpectraMax Gemini microplate reader (Molecular Devices). The rate of fluorescence signal increase over time (initial reaction velocity v) was plotted against the corresponding inhibitor

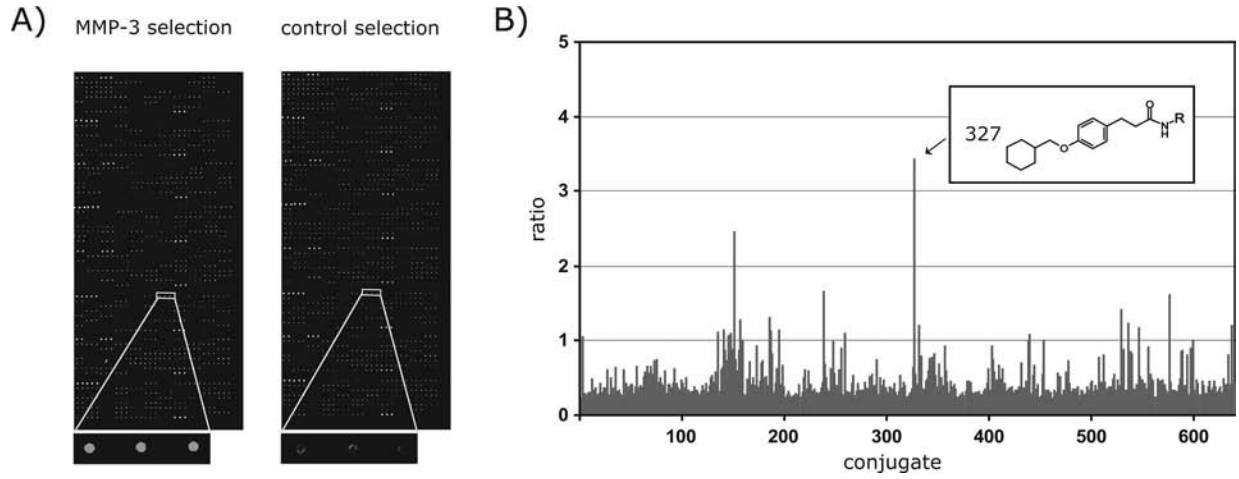

Figure 5. Verification of dual pharmacophore binding: Affinity maturation selection of ESAC conjugate 581 (**II**) using a DNA duplex library consisting of an oligonucleotide displaying **II** on its 3′ terminus hybridized to an ESAC library of 550 compounds. (A) Microarray readout after PCR amplification of an affinity maturation selection against MMP-3-displaying resin (left panel) and control resin (no antigen, right panel). On the microarrays, ESAC library decoding oligonucleotides are spotted in triplicate. The spots coding for the ESAC library conjugate 327 (**I**) are shown as insets for both MMP-3 and control selection. (B) Quantitative microarray evaluation: Enrichment of ESAC library conjugates given as ratio of MMP-3 selection versus control selection. The enriched ESAC library conjugate 327 is indicated.

concentration, and when possible, the IC_{50} value for the inhibitor was obtained by fitting to the above-mentioned equation using *SigmaPlot* software.

CPA Inhibition Assay. 85 μL of 59 nM carboxypeptidase A (cat. no. C9268, Sigma, Buchs, Switzerland) in assay buffer (50 mM Tris−Cl, 1 M NaCl, 1 mM $ZnCl_2$, pH = 7.5) were incubated in a 96-well microtiter plate (Nunclon, Nunc, Roskilde, Denmark) with a dilution series of inhibitor in DMSO (5 μL) for 20 min at 25 °C. The reaction was started by addition of 10 μL of the substrate FA-Phe-Phe-OH (10 mM in DMSO) (cat. no. M1760, Bachem, Switzerland). The change in transmission at 340 nm was recorded over 10 min using a VersaMax microplate reader (Molecular Devices). The signal increase over time (initial reaction velocity v) was plotted against the corresponding inhibitor concentration, and when possible, the IC_{50} value for the inhibitor was obtained by fitting to the above-mentioned equation using *SigmaPlot* software.

CAII Inhibition Assay. 85 μL of 1.2 μg/mL carbonic anhydrase II (cat. no. C3934, Sigma, Buchs, Switzerland) in assay buffer (50 mM Tris−sulfate, 1 mM $ZnCl_2$, pH = 8.5) were incubated in a 96-well microtiter plate (Nunclon, Nunc, Roskilde, Denmark) with a dilution series of inhibitor in DMSO (5 μL) for 20 min at 25 °C. The reaction was started by addition of 10 μL of the substrate *p*-nitrophenyl acetate (10 mM in 1% acetonitril) (cat. no. M1760, Bachem, Switzerland). The change in absorbance at 405 nm was recorded over 10 min using a VersaMax microplate reader (Molecular Devices). The net signal increase over time (initial reaction velocity v) was plotted against the corresponding inhibitor concentration, and when possible, the IC_{50} value for the inhibitor was obtained by fitting to the above-mentioned equation using *SigmaPlot* software.

RESULTS

In an attempt to find novel MMP-3 inhibitors, a library of 550 DNA-encoded chemical compounds was selected for binding to human MMP-3, encouraged by the recent observation that a precursor library of 477 oligonucleotide−compound conjugates could be successfully used in single pharmacophore selections (Figure 1A), yielding specific binders to streptavidin (*10*) and human serum albumin (*30*). Each DNA-encoded compound in the library was prepared by conjugating the chemical compound to the 5′ end of an amino-modified 48-mer oligonucleotide carrying a 6-base code for identification and regions for primer annealing and PCR amplification (*10*). Selection for MMP-3 binding was performed on human MMP-3 covalently coupled to CNBr-activated sepharose resin and on Tris-quenched CNBr-activated sepharose resin (control selection), similar to previously published procedures (*4*, *9*). After thorough washing of the resin, the enriched DNA conjugates were PCR-amplified with a Cy3-labeled primer and hybridized to decoding microarrays (Figure 3A), carrying code-complementary oligonucleotides, spotted in quadruplicate. The ratio of the average fluorescence signal intensity corresponding to each library member from MMP-3 selection and control selection on control resin was determined, giving rise to a fingerprint of enriched binding molecules (Figure 3B). One compound (ESAC library conjugate 327, structure **I** of Table 1) was strongly enriched (7-fold) compared to background.

This 327-oligonucleotide conjugate was then subjected to an affinity chromatography assay, displaying a substantial retention on MMP-3 resin compared to the control (nonenriched ESAC conjugate 2) (Figure 3C). In this assay, a ^{33}P-labeled oligonucleotide was hybridized with the individual ESAC conjugates, incubated with MMP-3 resin and subjected to consecutive washing steps. The radioactivity retained on the resin after the washing steps provided a direct estimate of the MMP-3 binding ability of the individual DNA conjugates, a process which is known to be dependent on the protein density on resin (*8*–*10*).

The newly discovered MMP-3 binder **I** was conjugated to the amino-modified 3′-extremity of a 24-mer oligonucleotide capable of pairing with the 550 member ESAC sublibrary and used as lead for affinity maturation selections (Figure 1B). After affinity capture on immobilized MMP-3, PCR amplification and microarray-based decoding (Figure 4A), enrichment of one synergistic binding moiety was observed (structure **II** of Table 1, corresponding to compound 581 in the ESAC library; Figure 4B). Preferential MMP-3 binding of the bidentate heteroduplex, displaying both compounds **I** and **II**, was confirmed in a radioactivity-based affinity chromatography assay performed as described above (Figure 4C). The bidentate binder was superior compared to DNA conjugates displaying the individual pharmacophores or no pharmacophore at all (Figure 4C).

In order to confirm the results of the ESAC selection, affinity maturation selections were performed, using the DNA conjugate 581 (**II**) as a lead, paired to the 550-member ESAC library. As expected, the corresponding pharmacophore **I** was preferentially

enriched by selections on MMP-3 resin, confirming the synergistic affinity gain offered by the combination of these two pharmacophores (Figure 5).

The newly discovered pharmacophores **I** and **II** were used for the synthesis of low-molecular weight bidentate MMP-3 inhibitors with a series of diamino linkers (A−J, Table 2), according to Scheme 1. The corresponding inhibition constants to MMP-3 were measured, revealing that only the combination of the two pharmacophores yielded compounds of micromolar potency (Table 2). The highest binding affinity was observed for compound **I-J-II**, with an IC_{50} value of 9.9 μM.

The compounds in the series were also characterized in terms of their IC_{50} values for the closely related murine MMP-3, for the Zn-dependent metalloproteinase carboxypeptidase A, for the human serine protease uPA, and for bovine carbonic anhydrase II. As expected, inhibitors of human MMP-3 were also able to inhibit the murine enzyme, but displayed only minor inhibitory activity toward both carboxypeptidase A and uPA, and no detectable activity toward carbonic anhydrase II (Table 2).

DISCUSSION

The experiments presented in this article confirm that a library of 550 compounds, individually coupled to distinct oligonucleotides carrying an identification code, could be used for the identification of novel MMP-3 binding compounds, suitable for subsequent medicinal chemistry optimization. While monodentate MMP-3 binders did not exhibit any substantial inhibitory activity, bidentate inhibitors could be isolated with inhibitory constants in the low micromolar range (*19–23*). The linker connecting the two pharmacophores appeared to play only a moderate contribution to binding affinity, with IC_{50} values for bidentate binders ranging within a factor of 10. The bidentate binders were found to display a good selectivity toward the metalloprotease CPA, the serine protease (uPA) and toward carbonic anhydrase II (Table 2). The production of good-quality catalytic domains of other MMPs, required for the reliable profiling of inhibitory activities, however, remains a major challenge in the field, due to autoproteolytic processes (*24*).

Most of the MMP-3 inhibitors reported so far in the literature featured a zinc-chelating group (e.g., hydroxamate, carboxylate, barbiturate, thiadiazole, thiadiazine, or sulfodiimine *14, 17, 25*). While monodentate zinc-binding groups usually display IC_{50} values in the millimolar range, these moieties can be fused to a peptide mimetic group, thus enhancing both binding affinity and selectivity (*26, 27*). Barbiturate, carboxylates, and thiadiazole derivatives normally display micromolar inhibitory potency to MMP-3 (*28*), but occasionally higher potencies toward gelatinases (*17*). By contrast, hydroxamate derivatives with IC_{50} values for MMP-3 are ranging between 0.27 nM and > 1 μM (*17*).

The present study confirms the potential of ESAC technology for the rapid identification of pairs of pharmacophores which, upon conjugation, display synergistic binding to the target protein of interest. Future directions of this line of research will require the construction of libraries of larger dimensions (e.g., >10 000 compounds) and the implementation of high-throughput decoding methodologies (e.g., by high-throughput sequencing *6, 29*).

ACKNOWLEDGMENT

We thank Dr. Christian Heinis and Stefanie Pfaffen for the construction of the human and murine MMP-3 expression vector, Catharine Aquino Fournier and Dr. Ralph Schlapbach from the Functional Genomics Center Zurich for help with microarray technology. Funding from ETH, SBF (EU Projects STROMA, FluorMMPI), the FP6 (EU Project Immuno-PDT), the Kommission für Technologie and Innovation, and the Swiss National Science Foundation (Project 3100A0-105919) is gratefully acknowledged.

Supporting Information Available: Supplementary table. This material is available free of charge via the Internet at http://pubs.acs.org.

LITERATURE CITED

(1) Brenner, S., and Lerner, R. A. (1992) Encoded combinatorial chemistry. *Proc. Natl. Acad. Sci. U.S.A. 89*, 5381–5383.

(2) Gartner, Z. J., Tse, B. N., Grubina, R., Doyon, J. B., Snyder, T. M., and Liu, D. R. (2004) DNA-templated organic synthesis and selection of a library of macrocycles. *Science 305*, 1601–1605.

(3) Halpin, D. R., and Harbury, P. B. (2004) DNA display II. Genetic manipulation of combinatorial chemistry libraries for small-molecule evolution. *PLoS Biol. 2*, 1022–1030.

(4) Melkko, S., Scheuermann, J., Dumelin, C. E., and Neri, D. (2004) Encoded self-assembling chemical libraries. *Nat. Biotechnol. 22*, 568–574.

(5) Dumelin, C. E., Scheuermann, J., Melkko, S., and Neri, D. (2006) DNA-encoded chemical libraries. *QSAR Comb. Sci. 25*, 1081–1087.

(6) Scheuermann, J., Dumelin, C. E., Melkko, S., and Neri, D. (2006) DNA-encoded chemical libraries. *J. Biotechnol. 126*, 568–581.

(7) Melkko, S., Dumelin, C. E., Scheuermann, J., and Neri, D. (2007) Lead discovery by DNA-encoded chemical libraries. *Drug Discovery Today 12*, 465–471.

(8) Melkko, S., Dumelin, C. E., Scheuermann, J., and Neri, D. (2006) On the magnitude of the chelate effect for the recognition of proteins by pharmacophores scaffolded by self-assembling oligonucleotides. *Chem. Biol. 13*, 225–231.

(9) Melkko, S., Zhang, Y., Dumelin, C. E., Scheuermann, J., and Neri, D. (2007) Isolation of high-affinity trypsin inhibitors from a DNA-encoded chemical library. *Angew. Chem., Int. Ed. 46*, 4671–4674.

(10) Dumelin, C. E., Scheuermann, J., Melkko, S., and Neri, D. (2006) Selection of streptavidin binders from a DNA-encoded chemical library. *Bioconjugate Chem. 17*, 366–370.

(11) Skiles, J. W., Gonnella, N. C., and Jeng, A. Y. (2001) The design, structure, and therapeutic application of matrix metalloproteinase inhibitors. *Curr. Med. Chem. 8*, 425–474.

(12) Overall, C. M., and Lopez-Otin, C. (2002) Strategies for MMP inhibition in cancer: innovations for the post-trial era. *Nat. Rev. Cancer 2*, 657–672.

(13) Coussens, L. M., Fingleton, B., and Matrisian, L. M. (2002) Matrix metalloproteinase inhibitors and cancer: trials and tribulations. *Science 295*, 2387–2392.

(14) Jacobsen, F. E., Lewis, J. A., and Cohen, S. M. (2007) The Design of Inhibitors for Medicinally Relevant Metalloproteins. *ChemMedChem 2*, 152–171.

(15) Peterson, J. T. (2006) The importance of estimating the therapeutic index in the development of matrix metalloproteinase inhibitors. *Cardiovasc. Res. 69*, 677–687.

(16) Peterson, J. T. (2004) Matrix metalloproteinase inhibitor development and the remodeling of drug discovery. *Heart Fail. Rev. 9*, 63–79.

(17) Skiles, J. W., Gonnella, N. C., and Jeng, A. Y. (2004) The design, structure, and clinical update of small molecular weight matrix metalloproteinase inhibitors. *Curr. Med. Chem. 11*, 2911–2977.

(18) Natchus, M. G., Bookland, R. G., Laufersweiler, M. J., Pikul, S., Almstead, N. G., De, B., Janusz, M. J., Hsieh, L. C., Gu, F., Pokross, M. E., Patel, V. S., Garver, S. M., Peng, S. X., Branch, T. M., King, S. L., Baker, T. R., Foltz, D. J., and Mieling, G. E. (2001) Development of new carboxylic acid-based MMP inhibitors derived from functionalized propargylglycines. *J. Med. Chem. 44*, 1060–1071.

(19) Shuker, S. B., Hajduk, P. J., Meadows, R. P., and Fesik, S. W. (1996) Discovering high-affinity ligands for proteins: SAR by NMR. *Science 274*, 1531–1534.

(20) Pellecchia, M., Sem, D. S., and Wuthrich, K. (2002) NMR in drug discovery. *Nat. Rev. Drug Discovery 1*, 211–219.

(21) Blundell, T. L., and Patel, S. (2004) High-throughput X-ray crystallography for drug discovery. *Curr. Opin. Pharmacol. 4*, 490–496.

(22) Erlanson, D. A., Wells, J. A., and Braisted, A. C. (2004) Tethering: fragment-based drug discovery. *Annu. Rev. Biophys. Biomol. Struct. 33*, 199–223.

(23) Hajduk, P. J., and Greer, J. (2007) A decade of fragment-based drug design: strategic advances and lessons learned. *Nat. Rev. Drug Discovery 6*, 211–219.

(24) Tochowicz, A., Maskos, K., Huber, R., Oltenfreiter, R., Dive, V., Yiotakis, A., Zanda, M., Bode, W., and Goettig, P. (2007) Crystal structures of MMP-9 complexes with five inhibitors: contribution of the flexible Arg424 side-chain to selectivity. *J. Mol. Biol. 371*, 989–1006.

(25) Matter, H., and Schudok, M. (2004) Recent advances in the design of matrix metalloprotease inhibitors. *Curr. Opin. Drug Discovery Dev. 7*, 513–535.

(26) Puerta, D. T., and Cohen, S. M. (2004) A bioinorganic perspective on matrix metalloproteinase inhibition. *Curr. Top. Med. Chem. 4*, 1551–1573.

(27) Rao, B. G. (2005) Recent developments in the design of specific matrix metalloproteinase inhibitors aided by structural and computational studies. *Curr. Pharm. Des. 11*, 295–322.

(28) Jacobsen, E. J., Mitchell, M. A., Hendges, S. K., Belonga, K. L., Skaletzky, L. L., Stelzer, L. S., Lindberg, T. J., Fritzen, E. L., Schostarez, H. J., O'Sullivan, T. J., Maggiora, L. L., Stuchly, C. W., Laborde, A. L., Kubicek, M. F., Poorman, R. A., Beck, J. M., Miller, H. R., Petzold, G. L., Scott, P. S., Truesdell, S. E., Wallace, T. L., Wilks, J. W., Fisher, C., Goodman, L. V., Kaytes, P. S., Ledbetter, S. R., Powers, E. A., Vogeli, G., Mott, J. E., Trepod, C. M., Staples, D. J., Baldwin, E. T., and Finzel, B. C. (1999) Synthesis of a series of stromelysin-selective thiadiazole urea matrix metalloproteinase inhibitors. *J. Med. Chem. 42*, 1525–1536.

(29) Margulies, M., Egholm, M., Altman, W. E., Attiya, S., Bader, J. S., Bemben, L. A., Berka, J., Braverman, M. S., Chen, Y. J., Chen, Z., Dewell, S. B., Du, L., Fierro, J. M., Gomes, X. V., Godwin, B. C., He, W., Helgesen, S., Ho, C. H., Irzyk, G. P., Jando, S. C., Alenquer, M. L., Jarvie, T. P., Jirage, K. B., Kim, J. B., Knight, J. R., Lanza, J. R., Leamon, J. H., Lefkowitz, S. M., Lei, M., Li, J., Lohman, K. L., Lu, H., Makhijani, V. B., McDade, K. E., McKenna, M. P., Myers, E. W., Nickerson, E., Nobile, J. R., Plant, R., Puc, B. P., Ronan, M. T., Roth, G. T., Sarkis, G. J., Simons, J. F., Simpson, J. W., Srinivasan, M., Tartaro, K. R., Tomasz, A., Vogt, K. A., Volkmer, G. A., Wang, S. H., Wang, Y., Weiner, M. P., Yu, P., Begley, R. F., and Rothberg, J. M. (2005) Genome sequencing in microfabricated high-density picolitre reactors. *Nature 437*, 376–380.

(30) Dumelin, C. E., Trüssel, S., Buller, F., Trachsel, E., Bootz, F., Beck, S. C., Drumea-Mirancea, M., Seeliger, M. W., Baltes, C., Müggler, T., Rudin, M., Melkko, S., Scheuermann, J., and Neri, D. (2008) Discovery and applications of a portable albumin binder from a DNA-encoded chemical library. *Angew Chem., Int. Ed*, in press.

BC7004347

TECHNICAL NOTES

Efficient Site-Specific Labeling of Proteins via Cysteines

Younggyu Kim,*,† Sam O. Ho,† Natalie R. Gassman,† You Korlann,† Elizabeth V. Landorf,△ Frank R. Collart,△ and Shimon Weiss*,†,‡,§

Department of Chemistry and Biochemistry, Department of Physiology, California NanoSystems Institute, University of California, Los Angeles, 607 Charles E. Young Drive East, Los Angeles, California 90095, and Biosciences Division, Argonne National Laboratory, Argonne, Illinois 60439. Received July 5, 2007; Revised Manuscript Received November 6, 2007

Methods for chemical modifications of proteins have been crucial for the advancement of proteomics. In particular, site-specific covalent labeling of proteins with fluorophores and other moieties has permitted the development of a multitude of assays for proteome analysis. A common approach for such a modification is solvent-accessible cysteine labeling using thiol-reactive dyes. Cysteine is very attractive for site-specific conjugation due to its relative rarity throughout the proteome and the ease of its introduction into a specific site along the protein's amino acid chain. This is achieved by site-directed mutagenesis, most often without perturbing the protein's function. Bottlenecks in this reaction, however, include the maintenance of reactive thiol groups without oxidation before the reaction, and the effective removal of unreacted molecules prior to fluorescence studies. Here, we describe an efficient, specific, and rapid procedure for cysteine labeling starting from well-reduced proteins in the solid state. The efficacy and specificity of the improved procedure are estimated using a variety of single-cysteine proteins and thiol-reactive dyes. Based on UV/vis absorbance spectra, coupling efficiencies are typically in the range 70−90%, and specificities are better than ∼95%. The labeled proteins are evaluated using fluorescence assays, proving that the covalent modification does not alter their function. In addition to maleimide-based conjugation, this improved procedure may be used for other thiol-reactive conjugations such as haloacetyl, alkyl halide, and disulfide interchange derivatives. This facile and rapid procedure is well suited for high throughput proteome analysis.

I. INTRODUCTION

Protein molecules are often targets for chemical modification by covalent conjugation (*1, 2*). These derivatized proteins can specifically recognize and bind target molecules, providing a handle for target detection, quantification, and analysis. Specific and efficient protein labeling techniques are therefore essential for biological research, diagnostics, and therapeutics. Site-specific labeling of proteins is also needed in single molecule fluorescence experiments (*3–5*). Many labeling methods have been developed and utilized, including covalent modification of amino acid side chains (*6–8*), covalent labeling by enzymes (*9–12*), conjugation to unnatural amino acids (*13, 14*), and affinity labeling (*15, 16*).

One of the most common specific covalent coupling methods is the conjugation of a moiety bearing a thiol-reactive group to a solvent-accessible cysteine. This method affords the site-specific labeling of a protein at a unique engineered (or native) surface cysteine. This cysteine could be specifically labeled with dye derivatives of haloacetyl compounds, disulfide, or maleimides. The maleimide is by far the most prevalent functional group to be coupled to a cysteine because the coupling reaction is highly specific and efficient.

The protein must be maintained in a reduced form prior to the maleimide-cysteine coupling reaction to prevent the formation of disulfide bridges and inactivation of the cysteines. Reducing agents such as dithiothreitol (DTT) and tris[2-carboxyethyl]phosphine (TCEP) can be used for this purpose. These reducing agents must be removed before conjugation so that their thiol groups will not compete with target thiols in proteins.

The labeling reaction must be performed shortly after the elimination of reducing agents to prevent reoxidation of the target thiols, resulting in decreased labeling efficiency. In order to circumvent this problem, we developed an alternative, rapid, efficient, and specific cysteine labeling technique; this procedure does not require time-consuming and cumbersome reduction/desalting steps because the labeling reaction is directly performed on highly reduced proteins in the solid state.

We demonstrate our new labeling method, which we dub "solid state-based labeling", or SSL, on two small libraries of model proteins, all containing a single cysteine. The first library consists of mutants of the transcription initiation factor, σ^{70} subunit, of *Escherichia coli* RNA polymerase. The σ^{70} is required for promoter-specific transcription; σ^{70} binds to RNAP coenzyme, interacts with promoter DNA, plays roles in promoter unwinding, promoter escape, early elongation, and is a target for transcription regulators. The *E. coli* sigma factor has been utilized as a target protein for labeling in structural studies of

* Corresponding authors: Younggyu Kim, ykim@chem.ucla.edu; Shimon Weiss, sweiss@chem.ucla.edu, Phone 1-310-794-0093, Fax 1-310-267-4672.

† Department of Chemistry and Biochemistry, UCLA.

‡ Department of Physiology, UCLA.

§ California NanoSystems Institute, UCLA.

△ Argonne National Laboratory.

10.1021/bc7002499 CCC: $40.75 © 2008 American Chemical Society
Published on Web 02/15/2008

bacterial transcription on the ensemble level (*17, 18*) and more recently on the single molecule level (*19–23*). Using SSL, several maleimide-linked dyes have been incorporated specifically and efficiently into single cysteine mutants of σ^{70}, and fluorescence studies have showed that the labeled proteins are fully functional in transcription. The second library consists of a variety of proteins from the organism *Shewanella oneidensis* MR-1 (see (*24–26*) for reviews), either containing a single native surface-exposed cysteine or a single engineered cysteine added at the N-terminal region.

II. EXPERIMENTAL PROCEDURES

II.1. Materials. Alexa-maleimides and tetramethylrhodamine-maleimide were purchased from Invitrogen Corp. (Carlsbad, CA), and Cy3b-maleimide was purchased from GE Healthcare (Piscataway, NJ). *E. coli* RNA polymerase core was purchased from Epicenter Biotechnologies (Madison, WI). Size-exclusion resin HW-50F was purchased from TOSOH Bioscience LLC (Montgomeryville, PA). Disposable polypropylene columns and Nickel-nitrilotriacetic acid (Ni-NTA) Agarose were purchased from Qiagen Inc. (Germany).

II.2. Production and Purification of Proteins. Plasmid pGEMD(-Cys), encoding a σ^{70} derivative with no Cys residues, and plasmids encoding σ^{70} derivatives with single Cys residues were described in Mukhopadhyay et al. (*17*). The expression construct of the single cysteine mutant (A59C) of σ^{70} was created by site-directed mutagenesis. The σ^{70} mutants were expressed and inclusion bodies were prepared according to a published protocol (*17*). The resulting proteins were refolded from the inclusion bodies and further purified by anion exchange chromatography (MonoQ) (GE Healthcare, USA), dialyzed against TGED buffer (20 mM Tris-HCl [pH 7.9]/0.1 mM Ethylenediamine tetraacetic acid [EDTA]/1 mM DTT/5% Glycerol) plus 200 mM NaClBacterial expression constructs for MR-1 σ^{24}, σ^{32}, and the integration host factor (IHF) were provided by Dr. Jeanne Perry of the Protein Expression Laboratory at UCLA and expressed and purified in our laboratory. Single cysteine S*hewanella oneidensis* MR-1 proteins were prepared by amplification of the open reading frame from genomic DNA with KOD DNA polymerase by using conditions and reagents provided by the vendor (Novagen, Madison, WI). The genes were cloned using a modified ligation-independent cloning protocol (*27*). This process generated an expression clone producing a fusion protein with an N-terminal His-tag and a V 5 epitope tag containing a single cysteine. Proteins were purified using immobilized metal affinity chromatography (*28*).

II.3. Ammonium Sulfate Precipitation. The purified proteins in TGED buffer were reduced with 10 mM DTT at 4 °C for 2 h. The 10 mM DTT is sufficient enough to reduce up to several hundred micromolar concentration of the protein sample. Ammonium sulfate powder was added to the reduced protein samples. Final concentration of the ammonium sulfate was 70% so that most proteins were precipitated. After addition of the salt, samples were gently agitated for less than 10 min, and stored at 4 °C. This solid form of proteins in the slurry could be stably stored without losing the structural and functional integrity at 4 °C for years. To estimate the quantity of proteins in the solid state, 50 uL of ammonium sulfate slurry was centrifuged, and the pellet was dissolved in TE buffer (10 mM Tris-HCl [pH 8.0] and 1 mM EDTA). The dissolved sample was quantified by the Bradford assay.

II.4. Dye Conjugation. Four nanomoles of the sample in the slurry were taken and further reduced with 5–10 mM DTT for 2 h at 4 °C. We found that samples stored in the solid state for periods longer than 1 month at 4 °C were not in completely reduced state. Those samples were therefore treated with additional 5–10 mM DTT (at least 2 h incubation at 4 °C) before conjugation. Four nmoles of protein in the slurry were taken and centrifuged at 13 000 *g* for 2–5 min at 4 °C. After removal of the supernatant, the pellet was briefly washed with ice-cold Buffer A (100 mM Na_2PO_4[pH 7.3]/200 mM NaCl/1 mM EDTA) plus 70% $(NH_4)_2SO_4$. Washing was achieved by gently inverting the samples several times and subsequent centrifugation for 2 min. The washed pellet was dissolved in 100 μL of Buffer A containing maleimide-linked fluorophores. Several dye probes were tested: Tetramethylrhodamine (TMR)-6-maleimide (Invitrogen, Eugene); Alexa Fluor488-C5-maleimide (Invitrogen, Eugene); Alexa Fluor647-*C*2-maleimide (Invitrogen, Eugene); and Cy3B-maleimide (GE Healthcare, Piscataway). Each fluorophore was dissolved in dimethyl sulfoxide (DMSO) and mixed with Buffer A. Four nanomoles of the dissolved protein were reacted with 20 nmol of dye (1:5 ratio) for 30 min at room temperature. The conjugation reaction was quenched by adding final 0.5% (72 mM) β-mercaptoethanol to the reaction mixture and incubating for 10 min at room temperature.

To remove excess dye from labeled proteins, 2 mL of resin HW-50F were packed into a disposable column and equilibrated with Buffer B (40 mM Tris-HCl [pH 7.9]/200 mM NaCl/1 mM DTT/0.2 mM EDTA). The reaction mixture was loaded onto the column, eluted with Buffer B and collected in 0.1 mL fractions. Fractions of the labeled protein's peak were pooled together, glycerol was added to a final concentration of 50%, and the sample was stored at −20 °C. The column could be reused if it was thoroughly washed with Buffer C (20 mM Tris-HCl/6 M Guanidine HCl/pH 7.9) followed up by washing with deionized water (to get rid of the free dyes). Washed columns were equilibrated with 20% ethanol and stored at room temperature.

II.5. Determination of Labeling Efficiency and Functional Assays. Desalted proteins were quantified using Lambda 25 UV/vis spectrophotometer (PerkinElmer, Waltham). Dye coupling efficiency was calculated based on the extinction coefficient of each reagent: $\epsilon_{280}(\sigma^{70}) = 41\,370\ M^{-1}\ cm^{-1}$; ϵ_{495}(Alexa Fluor 488) = 71 000 $M^{-1}\ cm^{-1}$; ϵ_{555}(TMR) = 65 000 $M^{-1}\ cm^{-1}$; ϵ_{559}(Cy3B) = 130 000 $M^{-1}\ cm^{-1}$; ϵ_{650}(AlexaFluor 647) = 239 000 $M^{-1}\ cm^{-1}$. Absorbance at 280 nm was corrected by a correction factor (CF) defined as $CF_{280} = A_{280}$ (freedye)/A_{max} (freedye). The CF numerical values for each dye are CF_{280} (AlexaFluor 488) = 0.11; CF_{280}(TetraMethylRhodamine) = 0.03; CF_{280}(Cy3B) = 0.08; and CF_{280}(AlexaFluor 647) = 0.03.

The coupling efficiency (CE) was calculated according to eq 1 (*1*):

$$CE = \frac{\epsilon_{280}(\text{Protein}) \cdot A_{max}}{(A_{280} - CF_{280} \cdot A_{max}) \cdot \epsilon_{dye}} \quad (1)$$

Samples were run on 12% SDS-PAGE gels and visualized by Molecular ImagerFX (Bio-Rad, Hercules). A gel shift assay was carried out to confirm the complex-forming activity of derivatized σ^{70} according to a published protocol (*29*).

III. RESULTS AND DISCUSSION

III.1. Rationale of the Labeling Method. Although the maleimide reactivity toward a free thiol is robust, it is often difficult to achieve high conjugation efficiency due to a variety of issues. Labeling cysteine residues requires proteins be well-reduced by a strong reducing agent, such as dithiothreitol (DTT). However, DTT molecules need to be removed just before conjugation because their thiols are as reactive toward maleimides as cysteines' thiols. Conventional desalting methods include dialysis and size-exclusion chromatography. Dialysis is lengthy and usually results in reoxidation of the free thiols. Size-exclusion chromatography permits faster desalting and is

therefore more commonly used, but has its own drawbacks: (i) desalting is usually accompanied by a loss of proteins and undesired dilution of the sample, especially when a small quantity of proteins is labeled; (ii) desalted proteins need to be quantified before they are reacted with a stoichiometric amount of dye molecules; reoxidation cannot be avoided during this step, resulting in a lower labeling efficiency.

To increase the efficiency, methods for labeling after solid-phase reduction (*17*) and labeling in the presence of thiol-free reductant, tris(2-carboxyethyl)phosphine (TCEP) (*30*, *31*) have been devised. TCEP, a thiol-free trialkylphosphine, was believed to not react with thiol-reactive compounds, thereby obviating the troublesome desalting step. However, it has been shown that TCEP interferes with labeling of proteins with a thiol-reactive dye (*32*). The authors of this report found that the reactivity of thiol-reactive dyes is inhibited by the presence of TCEP, and that dye-TCEP adducts are found in the sample (as evident from HPLC chromatograms). The dye concentration used for the labeling reaction therefore needs to be greater than the TCEP concentration and the concentration of the target cysteine. In the solid-phase reduction protocol, proteins are reduced by immobilized reducing agents (DTT or TCEP), are directly recovered from the reductant column, and are reacted with thiol-reactive dyes after quantification. Although this scheme eliminates the reductant removal step, intrinsic problems still remain: sample loss, dilution, and exposure to reoxidation during the quantitation step.

The improved labeling protocol presented here is based on performing the labeling reaction from a precipitated form of target protein. We reasoned that thiols of protein in the solid state may not be easily oxidized and converted to disulfide forms because of their restricted movement in the state. To test this hypothesis, we chose the well-established ammonium sulfate precipitation through the salting-out effect (*33*). Ammonium sulfate is highly soluble, inexpensive, and apparently unharmful to proteins' function. Target proteins were precipitated by a final concentration of 70–75% ammonium sulfate in a highly reducing environment and stored as a slurry at 4 °C until needed. Precipitation and storage were done in the presence of 5 to 10 mM DTT in order to break any existing disulfide bonds between surface cysteines and to maintain reducing environment. The efficiency of the maleimide-dye conjugation to the protein precipitate was evaluated according to the protocol described in section II.5.

III.2. Labeling of *E. coli* σ^{70} Mutants and *Shewanella oneidensis* MR-1 Proteins. Figure 1 illustrates the labeling strategy. Prior to conjugation, the sample slurry was pelleted by centrifugation and the precipitate was briefly washed with a reductant-free wash buffer (buffer A). The washing step eliminates most of the residual DTT. The wash buffer contains 70% ammonium sulfate to prevent resolubilization of the protein. After washing, the precipitate is immediately reacted with thiol-reactive dyes. Another commonly encountered problem of protein labeling is the separation of labeled proteins from unreacted excess dyes. This step is crucial for fluorescence-based assays since free dyes contribute to a significant background signal that obscures the measurement. However, it is usually not easy to achieve a complete excess dye removal by a single desalting step. We found that the Toyopearl size-exclusion resin (consists of a modified hydrophilic methacrylate polymer) is superior to other commercially available agarose- or polyacrylamide-based resins in separating excess dyes from labeled proteins. The size exclusion separation step was performed using a 2 mL resin volume, under isocratic buffer conditions at neutral pH (pH 7–8) with a moderate ionic strength

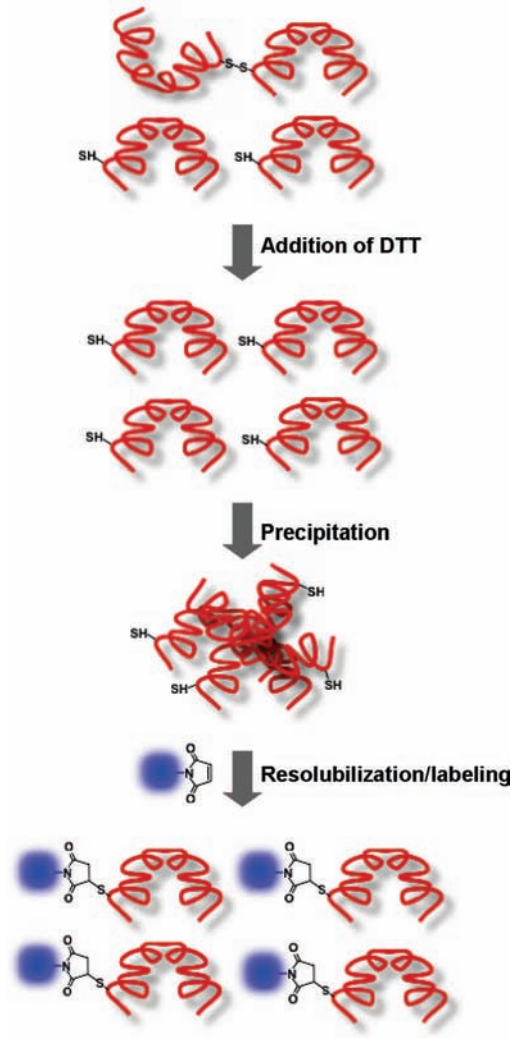

Figure 1. Strategy of solid state-based cysteine labeling. The purified protein is reduced by DTT and stored as an ammonium sulfate precipitate under reducing conditions. A brief centrifugation removes DTT in the supernatant and retrieves the protein as a pellet. Upon redissolving the proteins in a buffer containing thiol-reactive dyes, they are immediately and efficiently labeled.

(100–500 mM NaCl). This desalting step was sufficient in removing >98% of the free-dye in a single step (data not shown).

III.3. Labeling Efficiencies and Specificities. Labeling efficiencies were evaluated by measuring the UV/vis absorbance spectra of the samples (see section II.5.). In a first experiment, several dyes were conjugated to a σ^{70} mutant that has a unique cysteine at residue 596 (arginine to cysteine - R596C) (*18*). Figure 2A shows the absorbance spectra of SSL-labeled σ^{70} (R596C) with Alexa 488 (blue), Cy3b (green), and Alexa 647 (red). The corresponding calculated labeling efficiencies are 91% for Alexa 488 and 70% for Alexa 647. In the case of Cy3b, there was a significant spectral change of the dye after conjugation (appearance of an additional emission peak around 540 nm), precluding an accurate estimation of coupling efficiency to be made. We note that spectral properties of dyes could be significantly altered after conjugation due to their local environment. Nonetheless, the efficiency is likely to be high since the calculated value based on the major peak's absorption only (around 560 nm) is ~65%. SDS-PAGE of these samples analyzed by fluoroimaging and Coomassie-staining indicates the labeling is very specific (Inset of Figure 2A).

In a second experiment, conventional cysteine labeling (*1*) was compared to the SSL method. Maleimide-Cy3b and

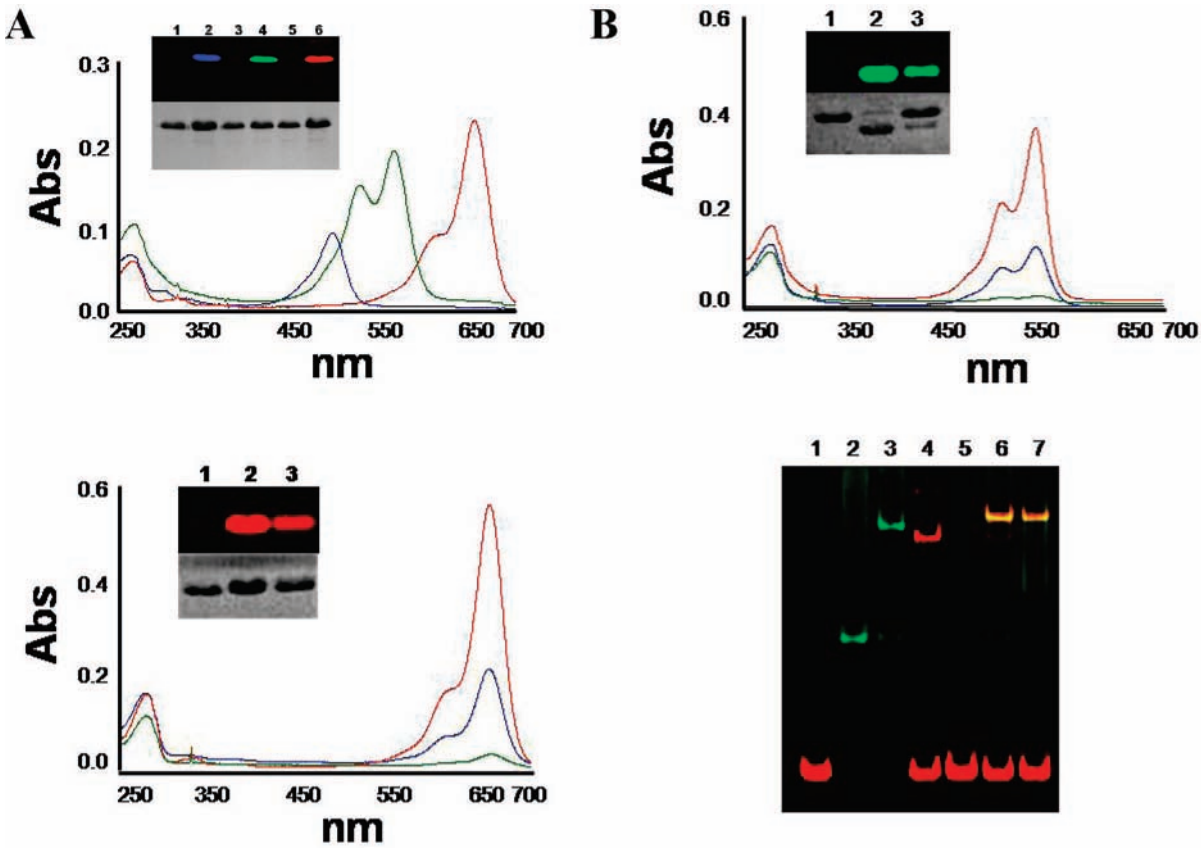

Figure 2. Efficient and specific cysteine labeling: (A) UV/vis spectra of σ^{70} (R596C) labeled with Alexa 488 (blue), Cy3b (green), and Alexa 647 (red). Inset: SDS-PAGE gel of the labeled σ^{70}: the upper panel is a gel image acquired from fluoroimager scan. Each signal, Alexa 488, Cy3b and Alexa 647, was separately imaged by Molecular Imager FX (Bio-Rad, Hercules) and the images were merged: lane 1, 3 and 5 are cysteine-free (Δcys) σ^{70} controls that were subjected to SSL procedure with Alexa 488, Cy3b and Alexa 647, respectively. The fluorescent signals of σ^{70} (R596C) labeled with Alexa 488 (lane 2), Cy3b (lane 4) and Alexa 647 (lane 6) are shown in blue, green and red, respectively. After fluoroimaging, the gel was Coomassie-stained (lower panel). (B) Comparison of SSL to conventional cysteine labeling: UV/vis spectra of Cy3b-σ^{70} (A59C) labeled by SSL (red), conventionally (blue) and a Δcys σ^{70} control (green). Inset: SDS-PAGE gel of the labeled σ^{70}: the upper panel is a gel image from fluoroimager scan: Cy3b-labeled protein bands are shown in green. After fluoroimaging, the gel was Coomassie-stained (lower panel). Lane 1 is cysteine-free (Δcys) σ^{70} control that was subjected to SSL procedure with Cy3b. Lanes 2 and 3 are Cy3b-σ^{70} labeled by SSL and conventional method, respectively. (C) Comparison of SSL to conventional cysteine labeling of Alexa 647-σ^{70} (A59C) (line colors and lane numbers are the same as in B). (D) Electrophoretic mobility shift assay of SSL-labeled Cy3b-σ^{70} (S59C). Holoenzymes were added to Alexa 647-labeled 65 base pairs long *lacCONS-11* promoter DNAs (*17*) (a derivative of the *lacUV5–11* promoter) to a final concentration of 77 nM core, 308 nM Cy3b-σ^{70}, and 77 nM DNA fragment. Following a 30 min incubation at 37 °C, the complexes were challenged with final 0.1 mg/mL heparin, the samples were then incubated for another 5 min at 37 °C before loading onto a 5% polyacrylamide gel (29:1 acrylamide/bisacrylamide; 13.5 × 16 × 0.75 cm) and electrophoresed in 0.5× TBE buffer at 150 V for 2.5 h: lane 1: Alexa 647-DNA only; lane 2: Cy3b-σ^{70} only; lane 3: RNA polymerase core (RNAPc) and Cy3b-σ^{70}; lane 4: RNAPc + Alexa 647-DNA; lane 5: RNAPc + Alexa 647-DNA + heparin; lane 6: RNAPc + Cy3b-σ^{70} + Alexa 647-DNA; lane 7: RNAPc + Cy3b-σ^{70} + Alexa 647-DNA + heparin. Each signal, Cy3b and Alexa 647, was separately imaged, and the images were merged. The yellow bands in lane 6 and 7 are comigrating signals of DNA (red) and Cy3b-σ^{70} (green), indicating that the labeled protein is fully functional for promoter binding.

maleimide-Alexa 647 were conjugated to a σ^{70} mutant that has a unique cysteine at residue 59 (alanine to cysteine - A59C). Normalized spectra of Cy3b-A59C (Figure 2B) and Alexa 647-A59C (Figure 2C) labeled by SSL (red) and conventionally (blue). A cysteine-free Δcys σ^{70} control was also subjected to the same SSL procedure (green). Labeling yields were calculated from these spectra. For SSL labeling, the calculated yields were 76% (Cy3b) and 65% (Alexa 647). For conventional labeling, the calculated yields were 33% (Cy3b) and 24% (Alexa 647).

The specificity of SSL labeling was estimated by a comparison of the UV/vis absorbance spectra of the labeled protein with a cysteine-free protein (Δcys σ^{70}). The labeling of the cysteine-free mutant was less than 5% efficient. The labeling specificity was also confirmed by a cysteine-specific cleavage assay (*29*), which did not cleave the conjugated cysteine residue. Figure S1 shows an example, Cy3b-A59C, that indicates the conjugation is specific to the cysteine residue.

The labeled proteins were also analyzed by SDS-PAGE followed by fluorescence imaging. In the case of Cy3b-maleimide labeling at residue 59, the mobility of the labeled protein was faster than the unlabeled protein (inset of Figure 2B). The reason for the difference in mobilities is unknown. We note, though, that the region containing residue 59 is highly negatively charged, and the hydrophobic Cy3B dye might change some local conformation even in the presence of SDS. Although unexplained, this mobility shift provides another assessment of the labeling efficiency via the intensity ratio of the labeled/unlabeled bands in the Coomassie-stained gel (inset of Figure 2B).

SSL-labeled σ^{70} molecules with Cy3b were analyzed for functionality by a gel-shift assay (Figure 2D). The molecules were added to core enzyme RNA polymerase (RNAP) molecules to form holoenzyme molecules. Holoenzymes were added to promoter DNAs and challenged with heparin to compete off nonspecific protein-DNA interactions (*34*). Lane 3 of Figure 2D clearly shows that the labeled σ^{70} is competent for forming holoenzyme. Lanes 6 and 7 of the same figure clearly show that holoenzyme is fully functional for binding promoter DNA.

Table 1. SSL labeling Efficiencies of Several Single-Cysteine *Shewanella oneidensis* MR-1 Proteins

protein	labeling efficiency	dye
MutT/nudix family proteina[a]	81%	TMR
Nitrogen regulatory protein P-II 1 (glnB-1)[a]	75%	Cy3B
Peptidyl-prolyl cis–trans isomerase FklB[a]	75%	TMR
dnaK, chaperone protein[a]	80%	TMR
rpoE, sigma-24 factor[a]	80%, 94%	Cy3B, Alexa488
rpoH, sigma-32 factor[b]	75%	Cy3B
Integration host factor alpha[a]	90%	Cy3B
Integration host factor beta[a]	85%	Cy3B

[a] A unique single cysteine was introduced near the N-terminus (wild type is cystene-free). [b] Contains a unique surface exposed single cysteine in the wild type.

Labeled σ^{70} proteins have been successfully applied to single molecule and ensemble biophysical assays and showed high activity (*21*). In addition, SSL method was also successfully applied to conjugation of *E. coli*catabolite activator protein (CAP) as well as σ^{70} with benzophenone-maleimide (Y. Kim, Y. Ebenstein and S. Weiss, unpublished result).

To demonstrate the general applicability of the approach, SSL was also used to label a small library of single-cysteine *Shewanella oneidensis* MR proteins with several maleimide dyes (Table 1). σ^{24}, which contained an inaccessible cysteine in the wild-type sequence, was modified such that the inaccessible cysteine was replaced with serine, and an accessible cysteine was added to the N-terminus. σ^{32} contained a unique surfaced exposed cysteine in the wild type sequence that was used for labeling. The remainder of the proteins (originally cysteine-free in the wild type) were labeled via introduction of a unique single cysteine in the N-terminal fusion tag. As shown in Table 1, the proteins were efficiently labeled, and more importantly, multiple samples at a time were labeled simultaneously with high efficiencies because the crucial steps were easily synchronized by the brief centrifugation. These results demonstrate that SSL could be implemented in a titer-plate format, allowing the site-specific and stoichiometric labeling of a large library of proteins in a high throughput fashion.

In conclusion, we developed an improved general procedure for maleimide-based labeling of cysteine containing proteins. This procedure features high labeling efficiency, specificity and simplicity. It is cost-effective and potentially could be used to label a large number of proteins in a high throughput format, offering a platform for proteome-wide analysis. Our approach could be further expanded to other types of thiol labeling such as haloacetyl, alkyl halide, and disulfide interchange derivatives. Current efforts in our laboratory include the utilization of this technique to the studies of protein–protein and protein-DNA interactions of *E. coli* and *Shewanella oneidensis* MR-1 transcription machineries by single molecule fluorescence spectroscopy (*19, 22*).

ACKNOWLEDGMENT

We thank Dr. Ekaterina Korthonjia, Mr. Yun Cheol Kim, Dr. Uljana Mayer-Cumblidge and Dr. Margie Romine for valuable discussions, and Janet Chiang and Dr. Jeanne Perry for the preparation of plasmids for this project. This work was supported by the U.S. Department of Energy, Grant number DE-FG02-04ER63938 and the NIH, Grant number GM069709-01.

Supporting Information Available: Cysteine-specific cleavage results showing the specificity of labeling. This material is available free of charge via the Internet at http://pubs.acs.org/BC.

LITERATURE CITED

(1) Hermanson, G. T. (1996) *Bioconjugate techniques*, Academic Press, San Diego.
(2) Aslam, M., and Dent, A. (1998) *Bioconjugation: Protein coupling techniques for biomedical sciences.*, MacMillan Reference Ltd., London.
(3) Kapanidis, A. N., and Weiss, S. (2002) Fluorescent probes and bioconjugation chemistries for single-molecule fluorescence analysis of biomolecules. *J. Chem. Phys. 117*, 10953–10964.
(4) Schuler, B. (2005) Single-molecule fluorescence spectroscopy of protein folding. *ChemPhysChem 6*, 1206–1220.
(5) Michalet, X., Weiss, S., and Jager, M. (2006) Single-molecule fluorescence studies of protein folding and conformational dynamics. *Chem. Rev. 106*, 1785–1813.
(6) Holmes, K. L., and Lantz, L. M. (2001) Protein labeling with fluorescent probes. *Methods Cell Biol. 63*, 185–204.
(7) Gentle, I. E., De Souza, D. P., and Baca, M. (2004) Direct production of proteins with N-terminal cysteine for site-specific conjugation. *Bioconjugate Chem. 15*, 658–63.
(8) Scheck, R. A., and Francis, M. B. (2007) Regioselective labeling of antibodies through N-terminal transamination. *ACS Chem. Biol. 2*, 247–51.
(9) Lin, C. W., and Ting, A. Y. (2006) Transglutaminase-catalyzed site-specific conjugation of small-molecule probes to proteins in vitro and on the surface of living cells. *J. Am. Chem. Soc. 128*, 4542–3.
(10) Jager, M., Nir, E., and Weiss, S. (2006) Site-specific labeling of proteins for single-molecule FRET by combining chemical and enzymatic modification. *Protein Sci. 15*, 640–646.
(11) Keppler, A., Gendreizig, S., Gronemeyer, T., Pick, H., Vogel, H., and Johnsson, K. (2003) A general method for the covalent labeling of fusion proteins with small molecules in vivo. *Nat. Biotechnol. 21*, 86–9.
(12) Duckworth, B. P., Zhang, Z., Hosokawa, A., and Distefano, M. D. (2007) Selective labeling of proteins by using protein farnesyltransferase. *ChemBioChem 8*, 98–105.
(13) Chin, J. W., Cropp, T. A., Anderson, J. C., Mukherji, M., Zhang, Z., and Schultz, P. G. (2003) An expanded eukaryotic genetic code. *Science 301*, 964–7.
(14) Lin, F. L., Hoyt, H. M., van Halbeek, H., Bergman, R. G., and Bertozzi, C. R. (2005) Mechanistic investigation of the staudinger ligation. *J. Am. Chem. Soc. 127*, 2686–95.
(15) Adams, S. R., Campbell, R. E., Gross, L. A., Martin, B. R., Walkup, G. K., Yao, Y., Llopis, J., and Tsien, R. Y. (2002) New biarsenical ligands and tetracysteine motifs for protein labeling in vitro and in vivo: synthesis and biological applications. *J. Am. Chem. Soc. 124*, 6063–76.
(16) Kapanidis, A. N., Ebright, Y. W., and Ebright, R. H. (2001) Site-specific incorporation of fluorescent probes into protein: hexahistidine-tag-mediated fluorescent labeling with (Ni(2+): nitrilotriacetic Acid (n)-fluorochrome conjugates. *J. Am. Chem. Soc. 123*, 12123–5.
(17) Mukhopadhyay, J., Kapanidis, A. N., Mekler, V., Kortkhonjia, E., Ebright, Y. W., and Ebright, R. H. (2001) Translocation of sigma(70) with RNA polymerase during transcription: fluorescence resonance energy transfer assay for movement relative to DNA. *Cell 106*, 453–63.
(18) Mekler, V., Kortkhonjia, E., Mukhopadhyay, J., Knight, J., Revyakin, A., Kapanidis, A. N., Niu, W., Ebright, Y. W., Levy, R., and Ebright, R. H. (2002) Structural organization of bacterial RNA polymerase holoenzyme and the RNA polymerase-promoter open complex. *Cell 108*, 599–614.
(19) Kapanidis, A. N., Margeat, E., Laurence, T. A., Doose, S., Ho, S. O., Mukhopadhyay, J., Kortkhonjia, E., Mekler, V., Ebright, R. H., and Weiss, S. (2005) Retention of transcription initiation factor s 70 in transcription elongation: single-molecule analysis. *Mol. Cell 20*, 347–356.
(20) Margeat, E., Kapanidis, A. N., Tinnefeld, P., Wang, Y., Mukhopadhyay, J., Ebright, R. H., and Weiss, S. (2006) Direct observation of abortive initiation and promoter escape within

single immobilized transcription complexes. *Biophys. J. 90*, 1419–1431.

(21) Lee, N. K., Kapanidis, A. N., Koh, H. R., Korlann, Y., Ho, S. O., Kim, Y., Gassman, N., Kim, S. K., and Weiss, S. (2007) Three-color alternating-laser excitation of single molecules: monitoring multiple interactions and distances. *Biophys. J. 92*, 303–12.

(22) Kapanidis, A. N., Margeat, E., Ho, S. O., Kortkhonjia, E., Weiss, S., and Ebright, R. H. (2006) Initial transcription by RNA polymerase proceeds through a DNA-scrunching mechanism. *Science 314*, 1144–7.

(23) Kapanidis, A. N., Lee, N. K., Laurence, T. A., Doose, S., Margeat, E., and Weiss, S. (2004) Fluorescence-aided molecule sorting: analysis of structure and interactions by alternating-laser excitation of single molecules. *Proc. Natl. Acad. Sci. U.S.A. 101*, 8936–41.

(24) Gralnick, J. A., and Hau, H. H. (2006) Ecology and biotechnology of the genus *Shewanella*. *Annu. Rev. Microbiol.*

(25) Venkateswaran, K., Moser, D. P., Dollhopf, M. E., Lies, D. P., Saffarini, D. A., MacGregor, B. J., Ringelberg, D. B., White, D. C., Nishijima, M., Sano, H., Burghardt, J., Stackebrandt, E., and Nealson, K. H. (1999) Polyphasic taxonomy of the genus *Shewanella* and description of *Shewanella oneidensis* sp. nov. *Int. J. Syst. Bacteriol. 49*, 705–24.

(26) Tiedje, J. M. (2002) Shewanella--the environmentally versatile genome. *Nat. Biotechnol. 20*, 1118–23.

(27) Dieckman, L. J., Hanly, W. C., and Collart, E. R. (2006) Strategies for high-throughput gene cloning and expression. *Genet. Eng. (NY) 27*, 179–90.

(28) Lin, C. T., Moore, P. A., Auberry, D. L., Landorf, E. V., Peppler, T., Victry, K. D., Collart, F. R., and Kery, V. (2006) Automated purification of recombinant proteins: combining high-throughput with high yield. *Protein Expr. Purif. 47*, 16–24.

(29) Naryshkin, N., Revyakin, A., Kim, Y., Mekler, V., and Ebright, R. H. (2000) Structural organization of the RNA polymerase-promoter open complex. *Cell 101*, 601–11.

(30) Levison, M. E., Josephson, A. S., and Kirschenbaum, D. M. (1969) Reduction of biological substances by water-soluble phosphines: gamma-globulin (IgG). *Experientia 25*, 126–7.

(31) Getz, E. B., Xiao, M., Chakrabarty, T., Cooke, R., and Selvin, P. R. (1999) A comparison between the sulfhydryl reductants tris(2-carboxyethyl)phosphine and dithiothreitol for use in protein biochemistry. *Anal. Biochem. 273*, 73–80.

(32) Tyagarajan, K., Pretzer, E., and Wiktorowicz, J. E. (2003) Thiol-reactive dyes for fluorescence labeling of proteomic samples. *Electrophoresis 24*, 2348–58.

(33) Englard, S., and Seifter, S. (1990) Precipitation techniques. *Methods Enzymol. 182*, 285–300.

(34) Cech, C. L., and McClure, W. R. (1980) Characterization of ribonucleic acid polymerase-T7 romoter binary complexes. *Biochemistry 19*, 2440–2447.

BC7002499

Light-Guided Surface Engineering for Biomedical Applications

Ashwath Jayagopal, Gregory P. Stone, and Frederick R. Haselton*

Department of Biomedical Engineering, Vanderbilt University, 5932 Stevenson Center, Nashville, Tennessee 37232. Received November 1, 2007; Revised Manuscript Received February 1, 2008

Free radical species generated through fluorescence photobleaching have been reported to effectively couple a water-soluble species to surfaces containing electron-rich sites (*1*). In this report, we expand upon this strategy to control the patterned attachment of antibodies and peptides to surfaces for biosensing and tissue engineering applications. In the first application, we compare hydrophobic attachment and photobleaching methods to immobilize FITC-labeled anti-M13K07 bacteriophage antibodies to the SiO_2 layer of a differential capacitive biosensor and to the polyester filament of a feedback-controlled filament array. On both surfaces, antibody attachment and function were superior to the previously employed hydrophobic attachment. Furthermore, a laser scanning confocal microscope could be used for automated, software-guided photoattachment chemistry. In a second application, the cell-adhesion peptide RGDS was site-specifically photocoupled to glass coated with fluorescein-conjugated poly(ethylene glycol). RGDS attachment and bioactivity were characterized by a fibroblast adhesion assay. Cell adhesion was limited to sites of RGDS photocoupling. These examples illustrate that fluorophore-based photopatterning can be achieved by both solution-phase fluorophores or surface-adhered fluorophores. The coupling preserves the bioactivity of the patterned species, is amenable to a variety of surfaces, and is readily accessible to laboratories with fluorescence imaging equipment. The flexibility offered by visible light patterning will likely have many useful applications in bioscreening and tissue engineering where the controlled placement of biomolecules and cells is critical, and should be considered as an alternative to chemical coupling methods.

1. INTRODUCTION

Strategies for the directed patterning of biomolecules at specific sites on diverse material surfaces are highly desired for multiplexed, array-based screening paradigms (*2*), as well as technologies such as tissue engineering, which rely on micro- or nanoscale cell−protein interactions (*3*). Recently, a fluorophore-based immobilization technique was described for the high-resolution, site-specific patterning of proteins such as enzymes within microfluidic channels (*1, 4*). This method utilizes photobleaching, a singlet oxygen-dependent immobilization mechanism, to couple dye-labeled proteins to glass and polydimethylsiloxane (PDMS) surfaces. Visible light patterning has two main advantages over other biomolecular patterning strategies. Nondamaging wavelengths, such as those used in aryl azide and benzophenone chemistries (*5, 6*), are avoided. Second, the reaction can be rapidly carried out in aqueous, neutral buffers preserving protein functionality.

In order to facilitate the implementation of photoattachment chemistry in the development biomolecular and/or cellular arrays, further studies are necessary to expand upon the scope of materials which can be surface engineered using this process, namely, polymer surfaces. Also, efforts to facilitate photopatterning, such as implementation with laser scanning confocal microscopes and software-driven, automated bleach parameters, are relatively unexplored. In addition, a reverse-coupling technique would be desirable. In this case, instead of labeling the soluble protein with a dye, the target surface is conjugated to a fluorophore. This has several advantages. Dye labeling of proteins is not required, and in this scenario, one photoactivable surface could be employed for the patterning of multiple biomolecules.

* Corresponding author. Frederick R. Haselton, VU Station B Box 1510, Nashville, TN 37235, ph: (615)-322-6622. FAX: (615)-343-7919. E-mail: rick.haselton@vanderbilt.edu.

In this study, we explored the utility of visible light-guided surface engineering for site-specific antibody immobilization on a differential capacitance-based viral biosensor (*7*) as well as a polyester filament-based fluorescence detection platform (*8–10*). We then extended this photopatterning technique to couple the cell-adhesion peptide RGDS (*11*) to a surface layer of poly(ethylene glycol)-fluorescein (PEG-FITC) with the intent of developing a substrate for site-specific biomolecular and cellular patterning. This latter example also features low nonspecific adsorption, a limitation not addressed in previous visible-light photopatterning techniques (*4*). In these initial studies, we observed that a variety of surfaces are amenable to photopatterning, and that the simplicity of these techniques makes automated surface patterning readily accessible to biological laboratories with access to a laser scanning confocal microscope. This method may have broad applicability in the field of biosensors which rely on an *a priori* pattern of binding partners as well as tissue engineering applications which rely on spatial control of cells in their construction. Photocoupling can also be used to functionalize nanoparticles and other bioconjugates bearing amine or PEG-FITC moieties.

2. DETAILED EXPERIMENTAL PROCEDURES

Antibodies were photocoupled onto silicon dioxide and polyester surfaces for sandwich immunoassays. In the third portion of this report, peptides were photoimmobilized on PEG-FITC-coated capture substrates in order to modulate cell attachment.

2.1. Photopatterning of Capture Antibody on Capacitive M13K07 Sensor. A previously characterized, capacitive sensor for the detection of the M13K07 bacteriophage (*7*) was prepared for use under dry argon at 25 °C with three rinses of anhydrous acetone (Sigma, St. Louis, MO). The surface was then immersed in a 4% solution of 3-aminopropyltriethoxysilane (United Chemical Technologies, Bristol, PA) in anhydrous

10.1021/bc700406w CCC: $40.75 © 2008 American Chemical Society
Published on Web 03/04/2008

acetone for 10 min, followed by 5 min immersions in anhydrous acetone and ultrapure water, and stored at 25 °C in a desiccator. Successful silanation of capacitor surfaces was verified by comparing the adsorption of fluorescein-conjugated bovine serum albumin (1 mg/mL in borate pH = 8.5) on treated and untreated chips. Immediately prior to use, the silicon dioxide surface was layered by micropipette with 100 μL of a 100 μg/mL FITC-anti-M13K07 monoclonal antibody ((mAb), 2.8 mol FITC/mol IgG) in 100 mM sodium bicarbonate buffer, pH = 8.5.

The FITC-labeled mAb (anti-M13K07 Ms IgG_1, GE Healthcare) was immobilized onto the biosensor surface using an upright laser scanning confocal microscope (LSM 510, Carl Zeiss). The timed bleach function provided in the microscope manufacturer's software package, as used for fluorescence recovery after photobleaching (FRAP) studies (*12*), was used to control the laser intensity of the 488 nm line of a 30 mW Argon laser, as well as the number of scanning iterations. A 4×, 0.1 NA objective was used to scan the 200 μm^2 capacitor surface. Two capacitors were each bleached using different bleach iterations (50 vs 10, using 100% laser intensity). Using the manufacturer's software, the laser was rastered in parallel with the plates of the capacitor, and the bleaching time was less than three minutes. The surface was rinsed three times with PBS, pH = 7.4, for 1 min each. Next, the capacitors were coated with the same amount and concentration of FITC-mouse IgG_1 isotype control mAb (3 mol FITC/mol IgG), and bleached at 100% intensity for 50 iterations.

The functionality of the photoimmobilized surface was ascertained by sandwich immunoassay. The surface was rinsed with PBS, and exposed to a solution of 100 μL of M13K07 bacteriophage (3.3×10^{11} virions/mL) for 30 min at 25 °C. The surface was rinsed with PBS and incubated with 100 μL of Cy5-conjugated anti-M13K07 mAb (1.72 mol Cy5/mol IgG, 50 μg/mL in PBS) for 30 min at 25 °C. The chip was rinsed with PBS and imaged immediately on a Nikon TE2000U inverted fluorescence microscope equipped with a Cy5 fluorescence cube, an Exfo X-Cite 120 metal halide excitation light source, and a C7780 Hamamatsu cooled CCD camera. Mean fluorescence intensities were measured by analyzing ROIs defined along capacitor boundaries using *Image Pro Plus 5.0* (Media Cybernetics), with data plotted using *SigmaPlot 9.0* (SYSTAT).

2.2. Photopatterning of Antibody on Polyester Filament-Based M13K07 Sensing Array. We investigated the utility of photoattachment chemistry in the development of high-throughput biomolecular screening. A previously described polyester monofilament-based system for viral detection based on hydrophobically immobilized capture mAb for multiplexed sandwich immunoassays (*9*) was adapted for the detection of M13K07 bacteriophage, a test virus, based on *photopatterned* mAb. All procedures were carried out at 25 °C. A 120 μm polyester monofilament (Sulky Corp.) was wrapped around a PhastGel sample applicator (GE Healthcare) and inlaid within the concave teeth as previously described (*9*). The filament/comb apparatus was rinsed in successive washes of 70% ethanol, 10% HCl, and Milli-Q water and dried overnight prior to use. A 0.75 μL solution containing 100 μg/mL of anti-M13K07 mAb or mouse IgG_1 isotype control mAb in 100 mM borate buffer, pH = 8.5, was pipetted on each loading tooth for either timed passive incubations or photobleaching sessions. The distance between neighboring teeth is 0.5 cm. For photobleaching, the comb was inverted and suspended within a humidified 60 mm Petri dish upon the Nikon TE2000U microscope stage. For photobleaching, the X-Cite 120 metal halide light source was used in conjunction with a FITC cube and 4× objective at full lamp intensity (1.4 W from microscope emission port, as determined by the manufacturer) for specific durations. Bleaching was monitored by measuring filament mean fluorescence using *Image Pro Plus 5.0*.

To test the functionality of the passively adsorbed and photopatterned surfaces, combs were rinsed three times in PBS, immersed in a multichannel pipet basin containing 3.3×10^{11} virions/mL M13K07 in PBS for 30 min, and rinsed three times with PBS. The combs were subsequently immersed in a basin containing 50 μg/mL Cy5-anti-M13K07 mAb for 30 min and rinsed in PBS.

Filaments were immediately fastened to a standard, precleaned microscope slide with tape, and the fluorescence measured using a Genepix 4000B microarray scanner (Axon Instruments) equipped with a 635 nm laser line as previously described (*9*). The mean fluorescence intensity of ROIs defined along discrete filament spots was measured by *Image Pro Plus* on grayscale 16-bit images, and plotted using *SigmaPlot*.

2.3. Photopatterning of Poly(D-lysine)-Coated Glass Substrate with PEG-RGDS. Poly(D-lysine)-coated 35 mm glass-bottom dishes with no. 1 borosilicate coverglass (MatTek Corp.) were coated with a heterobifunctional PEG spacer (MW = 3400) containing an *N*-hydroxysuccinimide ester (NHS) amine-reactive group and a fluorescein isothiocyanate moiety (NHS-PEG-FITC, Nektar Therapeutics) by incubating the surface with 0.2 mg of NHS-PEG-FITC in 100 mM borate buffer, pH = 8.5, for 1 h. followed by three rinses in borate buffer. Unreacted amine groups were quenched by 20 min incubation with 1 mg of sulfo-NHS-acetate (Pierce Chemical) in borate buffer. This acetylation reaction rendered the remaining amines unreactive. The glass dish was then incubated with with 100 μg/mL of the fibronectin-derived cell-adhesion peptide RGDS (>95% purity, Genscript Corp.) in borate buffer. Photobleaching of 1 mm rectangular areas delineated by taped foil photomasks was achieved using a 10× objective with the aforementioned inverted fluorescence microscope and light source for timed intervals, with mean fluorescence levels monitored to confirm photobleaching. Typically, the time necessary to reduce intensity levels 20% of initial fluorescence was less than 5 min. Photobleaching and RGDS passive adsorptions were followed by three rinses in borate. RGDS presence on the glass substrate was qualitatively assessed using fluorescamine.

Since RGDS has been demonstrated to promote fibroblast adhesion and spreading (*11*), we evaluated the bioactivity of the coupled RGDS using a fibroblast adhesion assay. 3T3 fibroblasts (ATCC) were cultured to 70% confluence in DMEM containing 10% bovine calf serum under incubation at 37 °C, 5% CO_2. The cells were then seeded in each dish at a concentration of 1000 cells/mL and incubated overnight under the same culture conditions. The next day, dishes were rinsed three times with PBS, and fixed for 20 min at 25 °C in 4% paraformaldehyde in PBS. Dishes were incubated with 0.5% trypan blue prior to the fixation step to ascertain cell viability via dye exclusion. The dishes were then rinsed in PBS containing 100 mM glycine and imaged by phase contrast.

2.4. Comparison of Antibody Chemical Crosslinking and Photoattachment on PEG-FITC and PEG-Maleimide-Coated Glass Substrates. Poly(D-lysine)-coated MatTek dishes were coated with 0.2 mg of NHS-PEG-FITC or thiol-reactive NHS-PEG-maleimide (NHS-PEG-MAL, MW = 3400, Nektar) and acetylated as described in section 2.3. To generate sulfhydryl groups for covalent coupling of mAb to NHS-PEG-MAL, 5 mg of anti-M13K07 mAb in 1 mL PBS-EDTA, pH = 7.4, was reacted with a 10-fold molar excess of 2-iminothiolane (Traut's reagent, Sigma) for 30 min at 25 °C. Excess Traut's reagent was removed by three centrifugation cycles of mAb/Traut's reagent on an Amicon-4 Ultra 100K MWCO spin column filtration device (Millipore) using PBS-EDTA as the rinse and

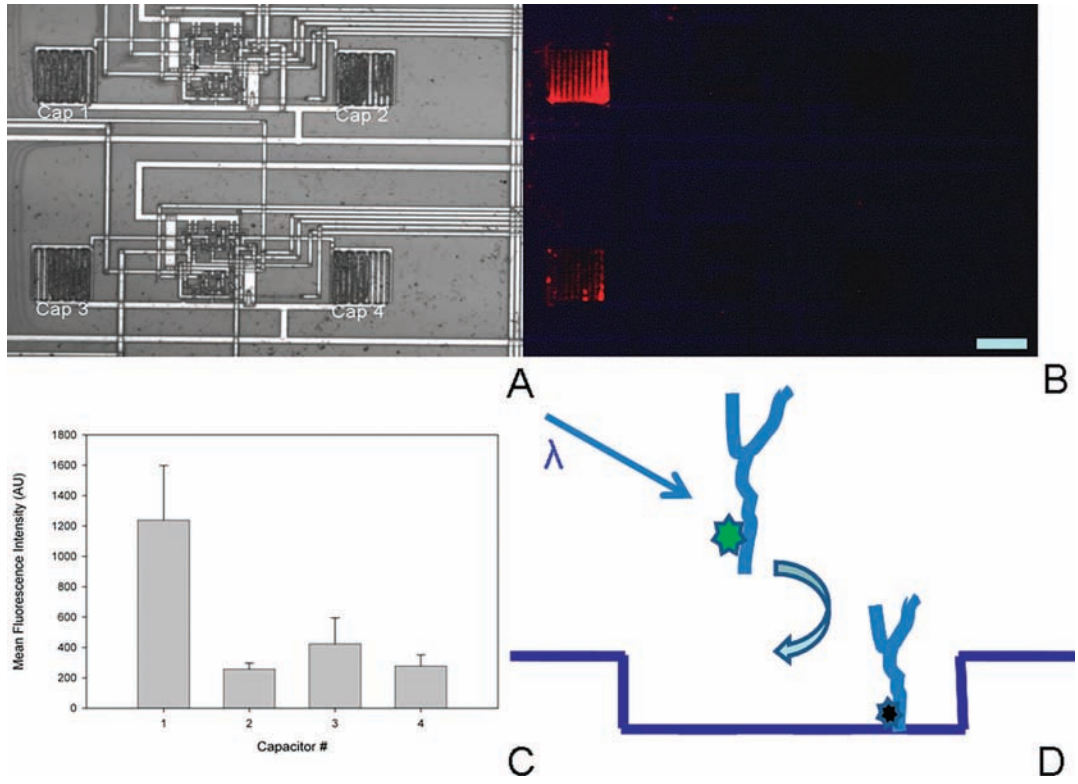

Figure 1. Light (A) and fluorescence (B) micrographs of a multiplexed capacitive biosensor photopatterned with anti-M13K07 monoclonal antibodies and isotype controls, with measured fluorescence intensities shown in (C). Parameters and reagents used for photoattachment using a confocal microscope: Cap 1, 30 mW, 50 bleach iterations, anti-M13K07 photopatterned; Cap 2, 30 mW, 50 bleach iterations, anti-Ms IgG photopatterned; Cap 3, 30 mW, 10 bleach iterations, anti-M13K07 photopatterned; Cap 4, no patterned antibody. (C) Fluorescence intensity measurements of Cy5-anti-M13K07-incubated sensors, reported as mean ± SD, $n = 3$. Bar = 10 μm.

resuspension buffer. For chemical cross-linking, 200 μg of mAb in 200 μL PBS-EDTA was pipetted onto the PEG-MAL surface and was reacted overnight at 4 °C. For photocrosslinking, 200 μg of purified mAb in a 200 μL solution of PBS-EDTA was pipetted on the PEG-FITC surface. The microwell of the dish was then photobleached using the X-Cite 120 light source (1.4 W) using a 2× objective for 10 min. Following both reactions, the dishes were rinsed 3× with PBS, saving the initial aspirate. Aspirate was collected from 20 MatTek dishes bearing either the PEG-FITC or PEG-MAL attachment linker. Protein concentration was determined using the Coomassie Plus assay (Pierce) according to manufacturer instructions.

3. RESULTS AND DISCUSSION

Our studies suggest that photobleaching can be used to pattern proteins and peptides on SiO_2, polyester, and glass surfaces. Photopatterning of anti-M13K07 mAb to capacitor surfaces was site-specific, with an achieved spatial resolution below 10 μm (Figure 1a,b). No signal was detected due to photopatterned IgG_1 control mAb capture of virus, or nonspecific binding of the virus itself, as indicated by mean fluorescence output (Figure 1c). In addition, no secondary antibody fluorescence was detected beyond the capacitor regions of the chip, indicating that diffusion of the bleached fluorophore did not interfere significantly with site-specific coupling, and that nonspecific adsorption was not significant. Specifically, the average fluorescence from 10 different noncapacitor regions of the chip was 237 ± 67, which was similar to control capacitor values (Figure 1c).

The fluorescence signal from the sandwich immunoassay generated from filament-coupled anti-M13K07 mAb using photoattachment chemistry was 2- to 3-fold higher than the signal generated by passively adsorbed antibodies (Figure 2). The enhanced signal could be due to either (a) an initially higher coupling efficiency using the photobleaching technique, and/or (b) greater preservation of bioactivity of photocoupled mAb. Although further studies would be required to differentiate between these two possibilities, we did observe that photocoupled antibodies appeared to be more tightly coupled, since successive washes of filament were associated with loss of passively adsorbed antibodies but with low loss of photocoupled antibody (data not shown).

Our studies also demonstrated that cell-adhesion peptides can be site-specifically coupled on tissue culture substratum (Figure 3). Irradiated PEG-FITC regions (Figure 3a) promoted fibroblast attachment similar in density and morphology observed on the native poly (D-lysine)-coated MatTek surface (Figure 3e). Nonirradiated PEG-FITC regions on the same were resistant to cell adhesion (Figure 3b). The lack of cell adhesion in nonirradiated regions was most likely due to the PEG coating on the surface which blocks adsorption of RGDS (Figure 3c), as well as the fibroblasts themselves (Figure 3f). The PEGylation of the surface was found to be important for controlling cell attachment, as acetylation of the surface alone was not sufficient (Figure 3d). Complete photobleaching of the entire PEG-FITC surface (from 1 to 3 h of continuous lamp illumination) did not result in cell attachment (Figure 3g,h). In a separate experiment, we demonstrated that attachment of 3T3 cells to PEG-RGDS was most likely due to specific peptide−integrin interactions, since competitive inhibition experiments (addition of 2 mM soluble RGDS peptide) reduced cell attachment by 82% (Supporting Information).

The mAb coupling efficiency of photoattachment and chemical crosslinking was compared and found to be similar. The efficiency of photocoupling was measured to be 3.3 pmol/cm^2. Thiol-maleimide crosslinking, a technique which has long been

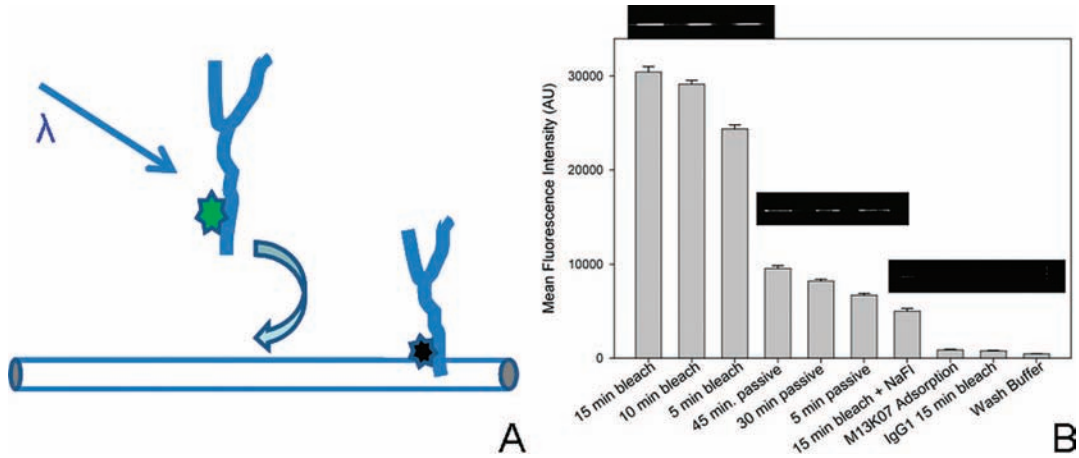

Figure 2. Schematic of a strategy for photocoupling of antibody to polyester filament (A) and resulting sandwich immunoassay Cy5-anti-M13K07 intensities (B). A representative filament is overlaid on the graph in (B).

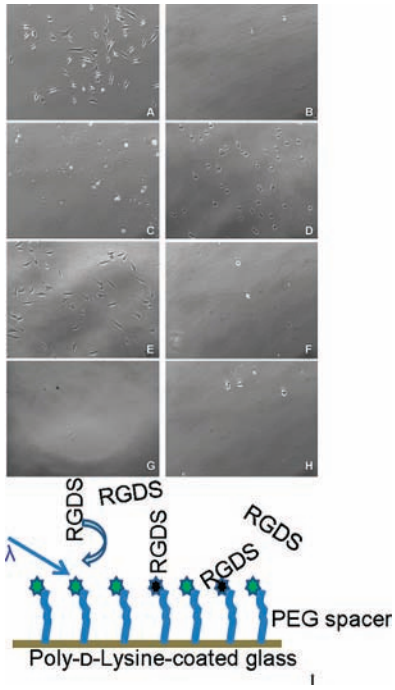

Figure 3. Representative micrographs of 3T3 fibroblast attachment on surface-engineered poly(D-lysine) MatTek dishes from three trials using PEG-FITC-based photoattachment diagrammed in (I). Experimental conditions for each substrate: (A) PEG-FITC and acetylation, RGDS photopatterned; (B) Same as in (A), but in an area where RGDS was not photopatterned; (C) PEG-FITC and acetylation, RGDS passively adsorbed; (D) No PEG-FITC, acetylation, RGDS passively adsorbed (cells are rounded); (E) No PEG-FITC, no RGDS (native surface); (F) PEG-FITC, no acetylation, no RGDS; (G) PEG-FITC and acetylation, bleached 1 h prior to cell adsorption, no RGDS; (H) PEG-FITC and acetylation, bleached 3 h. prior to cell adsorption, no RGDS. Cells in (A) and (E) showed similar viability of seeded cells as indicated by trypan blue exclusion (not shown). (50× magnification).

utilized for efficient, facile conjugation of proteins to material surfaces (*13*), resulted in a higher mAb coupling efficiency (4.2 pmol/cm^2). Although the chemical crosslinking technique was capable of immobilizing a higher quantity of mAb, further optimization of experimental conditions may produce higher yields for visible light photoconjugation, such as buffer strength, reaction volume, PEG molecular weight, and reagent concentrations. Furthermore, photopatterning offers control over site specificity of coupling, which in itself may warrant its future implementation.

The light patterning properties of the confocal microscope facilitated the efficient photoattachment of antibodies on the biosensor surface. With a fixed laser intensity (full output), the number of bleach iterations within the FRAP software module controlled the coupling efficiency of FITC-mAb. Furthermore, the ROI can be readily defined within the software to pattern microscale regions. The patterning of antibodies upon groups of four capacitors was achieved within 5 min, and real-time fluorescence intensity measurements within the software confirmed successful photobleaching. The confocal microscope should facilitate the implementation of photoattachment methods in various laboratories in biological and biomedical sciences, where they are readily available. Since these laboratories often do not have access to cleanroom facilities needed for photolithography, photoattachment chemistry may constitute a viable alternative to the in-house development of custom molecular and cellular arrays as diagnostic or biological study tools.

In addition to extending techniques related to the coupling of dye-conjugated biomolecules on surfaces, we also hypothesized that biomaterial substrates could be engineered to bear the photoreactive groups, thus obviating the need for bioconjugating proteins, a step which can often compromise native function. Poly(ethylene glycol) (PEG) has long been utilized for reducing protein adsorption to biomaterial surfaces, is biocompatible, and is amenable to the grafting of functional groups (*14*). NHS-PEG-FITC is a commercially available heterobifunctional reagent used to detect PEGylation efficiency in bioconjugate chemistry, and combines the properties of PEG with the bioconjugation moiety NHS (amine-reactive) for immobilization on a variety of substrates, as well as a FITC dye, to enable detection of the PEGylated species *in vitro* or *ex vivo*. We observed that pipetting an RGDS peptide solution over the PEG-FITC-functionalized glass substrate, followed by photobleaching of the dye groups, resulted in site-specific immobilization of the adhesion peptide, as indicated by fibroblast binding exclusively on regions of irradiation (Figure 3a). Therefore, the use of this reagent in the development of biosensor arrays affords the resistance of the coating to nonspecific adsorption of proteins.

Dye photobleaching generally involves the energy transfer from the dye in the excited state to molecular oxygen in the ground state (*15–17*). As a result of photobleaching, singlet molecular oxygen is produced, leaving the fluorophore with an unpaired electron. While the process of visible light coupling of dye-conjugated species has not been completely elucidated, it is possible that the unpaired electron on the dye serves as a binding site to an electron-rich substrate. Our data provide further evidence for the photobleached fluorophore as the

coupling moiety. When including 1 mg/mL sodium fluorescein (NaFl) as a free dye in the initial mAb coupling solution, we observed a decrease in fluorescence signal from the virus-associated Cy5 secondary antibody, indicating that the coupling technique was associated with fluorophore photobleaching (Figure 2b). In previous work, oxygen depletion in the coupling medium was associated with significantly lower photoattachment efficiency (*1*), which is consistent with our report that photobleaching chemistry is essential for the coupling reaction. Provided that photobleaching events drive the coupling of biomolecules onto the surfaces tested in this work, it is important to take necessary precautions when carrying out individual reactions. Samples were only exposed to ambient laboratory light for durations of <5 min, to minimize premature photobleaching due to the photolability of fluorescein.

This work expands upon previous approaches to achieve photopatterning of biomolecules, through adapting a confocal microscope to perform automated patterning of microscale regions, and by expanding the scope of surfaces which are candidate substrates for this technique. Future work will focus on the controlled orientation/deposition of cells on adhesion peptide-patterned surfaces. Such a feature would be useful in the development of arrays which incorporate cells as biosensors, or in the synthesis of 3-D tissue constructs, in which hierarchical organization of cells and proteins elicit specific cell functions (*18*). Our technique features the microscale resolution necessary to construct such devices, and nanoscale resolution is potentially achievable with this technique, when used in conjunction with techniques to overcome diffraction barriers, such as stimulated emission depletion fluorescence microscopy (STED) (*19, 20*). While fluorescein was used as the coupling moiety in this work, it has been demonstrated that photottachment strategies can be extended toward the patterning of multiple dye-labeled species, such as Alexa Fluor-labeled proteins (*1*).

4. CONCLUSION

Our studies have extended the utility of visible light photoattachment chemistry in creating biomolecular and/or cellular arrays in well-defined microscale regions on diverse substrates. The method is rapid and can be easily controlled on a spatial and temporal scale. Furthermore, protein activity is retained, and the high-efficiency conjugation of proteins using light patterning may facilitate the development of high-sensitivity screening platforms. Additionally, we have shown that a photoreactive substrate can be the mediator for photocoupling, eliminating the need for bioconjugation of species prior to patterning. In forthcoming applications which utilize cells as biosensors, this technique may be useful for controlling cell orientation and spreading. This rapid, flexible technique is readily accessible and can be implemented in a number of biomedical applications.

ACKNOWLEDGMENT

This work was supported in part by the National Institutes of Health (EB003516 (FRH), T32EY07135 (Jeff Schall, PI) (AJ)) and the Vanderbilt University Discovery Grant program. Confocal microscope-assisted patterning experiments were performed in part through the use of the VUMC Cell Imaging Shared Resource. We thank Ray Mernaugh for helpful discussions.

Supporting Information Available: Additonal information. This material is available free of charge via the Internet at http://pubs.acs.org.

LITERATURE CITED

(1) Holden, M. A., and Cremer, P. S. (2003) Light activated patterning of dye-labeled molecules on surfaces. *J. Am. Chem. Soc. 125*, 8074–5.
(2) Sumerel, J., Lewis, J., Doraiswamy, A., Deravi, L. F., Sewell, S. L., Gerdon, A. E., Wright, D. W., and Narayan, R. J. (2006) Piezoelectric ink jet processing of materials for medical and biological applications. *Biotechnol. J. 1*, 976–87.
(3) Stevens, M. M., and George, J. H. (2005) Exploring and engineering the cell surface interface. *Science 310*, 1135–8.
(4) Holden, M. A., Jung, S. Y., and Cremer, P. S. (1838) (2004) Patterning enzymes inside microfluidic channels via photoattachment chemistry. *Anal. Chem. 76*, 43.
(5) Blawas, A. S., and Reichert, W. M. (1998) Protein patterning. *Biomaterials 19*, 595–609.
(6) Clemence, J. F., Ranieri, J. P., Aebischer, P., and Sigrist, H. (1995) Photoimmobilization of a bioactive laminin fragment and pattern-guided selective neuronal cell attachment. *Bioconjugate Chem. 6*, 411–7.
(7) Balasubramanian, A., Bhuva, B., Mernaugh, R., and Haselton, F. R. (2005) Si-based sensor for virus detection. *IEEE Sens. J. 5*, 340–344.
(8) Stone, G. P., Lin, K. S., and Haselton, F. R. (2006) Adaptive virus detection using filament-coupled antibodies. *J. Biomed. Opt. 11*.
(9) Stone, G. P., Mernaugh, R., and Haselton, F. R. (2005) Virus detection using filament-coupled antibodies. *Biotechnol. Bioeng. 91*, 699–706.
(10) Stone, G. P., Wetzel, J. D., Russ, P. K., Dermody, T. S., and Haselton, F. R. (2006) Autonomous reovirus strain classification using filament-coupled antibodies. *Ann. Biomed. Eng. 34*, 1778–1785.
(11) DeLong, S. A., Gobin, A. S., and West, J. L. (2005) Covalent immobilization of RGDS on hydrogel surfaces to direct cell alignment and migration. *J. Controlled Release 109*, 139–48.
(12) Wu, Y. X., Masison, D. C., Eisenberg, E., and Greene, L. E. (2006) Application of photobleaching for measuring diffusion of prion proteins in cytosol of yeast cells. *Methods 39*, 43–49.
(13) Hermanson, G. T. (1996) *Bioconjugate Techniques*, Academic Press, San Diego.
(14) Tessmar, J. K., and Gopferich, A. M. (2007) Customized PEG-derived copolymers for tissue-engineering applications. *Macromol. Biosci. 7*, 23–39.
(15) Gaigalas, A. K., Wang, L., Cole, K. D., and Humphries, E. (2004) Photodegradation of fluorescein in solutions containing n-propyl gallate. *J. Phys. Chem. A 108*, 4378–4384.
(16) Song, L., Hennink, E. J., Young, I. T., and Tanke, H. J. (1995) Photobleaching kinetics of fluorescein in quantitative fluorescence microscopy. *Biophys. J. 68*, 2588–600.
(17) Song, L., Varma, C. A., Verhoeven, J. W., and Tanke, H. J. (1996) Influence of the triplet excited state on the photobleaching kinetics of fluorescein in microscopy. *Biophys. J. 70*, 2959–68.
(18) Albrecht, D. R., Underhill, G. H., Mendelson, A., and Bhatia, S. N. (2007) Multiphase electropatterning of cells and biomaterials. *Lab Chip 7*, 702–9.
(19) Willig, K. I., Harke, B., Medda, R., and Hell, S. W. (2007) STED microscopy with continuous wave beams. *Nat. Methods*.
(20) Willig, K. I., Kellner, R. R., Medda, R., Hein, B., Jakobs, S., and Hell, S. W. (2006) Nanoscale resolution in GFP-based microscopy. *Nat. Methods 3*, 721–3.

BC700406W

APRIL 2008
Volume 19, Number 4

© *Copyright 2008 by the American Chemical Society*

Bioconjugate Chemistry

COMMUNICATIONS

Enhanced Intracellular Delivery of Quantum Dot and Adenovirus Nanoparticles Triggered by Acidic pH via Surface Charge Reversal

Hyejung Mok, Ji Won Park, and Tae Gwan Park*

Department of Biological Sciences, Korea Advanced Institute of Science and Technology, Daejeon, 305-701, Korea. Received December 14, 2007; Revised Manuscript Received February 14, 2008

Quantum dot (QD) and adenovirus (ADV) nanoparticles were surface-modified with graft copolymers that exhibited a charge reversal behavior under acidic condition. Poly(L-lysine) (PLL) was grafted with multiple biotin-PEG chains (biotin-PEG-PLL graft copolymer), and the remaining primary amine groups in the PLL backbone were postmodified using citraconic anhydride, a pH-sensitive primary amine blocker, to generate carboxylate groups. The surfaces of streptavidin-conjugated QDs were modified with citraconylated biotin-PEG-PLL copolymer, producing net negatively charged QD nanoparticles. Under acidic conditions, citraconylated amide linkages were cleaved, resulting in the recovery of positively charged amine groups with subsequent alteration of surface charge values. Intracellular delivery of QD nanoparticles was greatly enhanced in an acidic pH condition due to the surface charge reversal. The surface of avidin-conjugated adenovirus (ADV-Avi) encoding an exogenous green fluorescent protein (GFP) gene was also modified in the same fashion. The expression extent of GFP was significantly increased at more acidic pH than pH 7.4. This study demonstrates that various nanosized drug carriers, imaging agents, and viruses could be surface-engineered to enhance their cellular uptake specifically at a low pH microenvironment like solid tumor tissue.

For the past decade, significant endeavors have been devoted to surface modification of various nanosized drug and imaging agent carriers such as iron oxide nanoparticles, quantum dots, liposomes, polymeric micelles, polymeric nanoparticles, and viruses to target them specifically to desired cells and tissues (*1*−*7*). In particular, targeted delivery systems for tumor cells are highly desirable to enhance therapeutic and diagnostic efficacy with reducing undesirable side effects. Targeting ligands including peptides, antibodies, carbohydrates, and aptamers, which specifically bind to the receptors overexpressed only in cancer cells, have been popularly tethered on the surface of nanocarriers to deliver them to the tumor tissue in a more specific manner. As alternative approaches, minute physiological changes in the environment of tumor tissues different from that of normal tissues have been utilized as triggering signals to nanocarriers for cancer treatment and tumor imaging (*8*−*10*). It is well-known that human and rodent solid tumor tissues exhibit a more acidic microenvironment than normal tissues, and their extracellular pH ranges from 5.8 to 7.4 (*11, 12*). Thus, a variety of pH-responsive nanoparticles were widely explored to increase the extent of cellular uptake only at the acidic tumor region. A wide array of pH-sensitive moieties, such as polyhistidine, β-amino esters, and sulfonamide, and acidic-cleavable linkages such as acetal, hydrazone, and orthoester have been employed in combination to produce multifunctional nanocar-

* Corresponding author. Tel: +82-42-869-2621; fax: +82-42-869-2610. E-mail address: tgpark@kaist.ac.kr.

10.1021/bc700464m CCC: $40.75 © 2008 American Chemical Society
Published on Web 03/26/2008

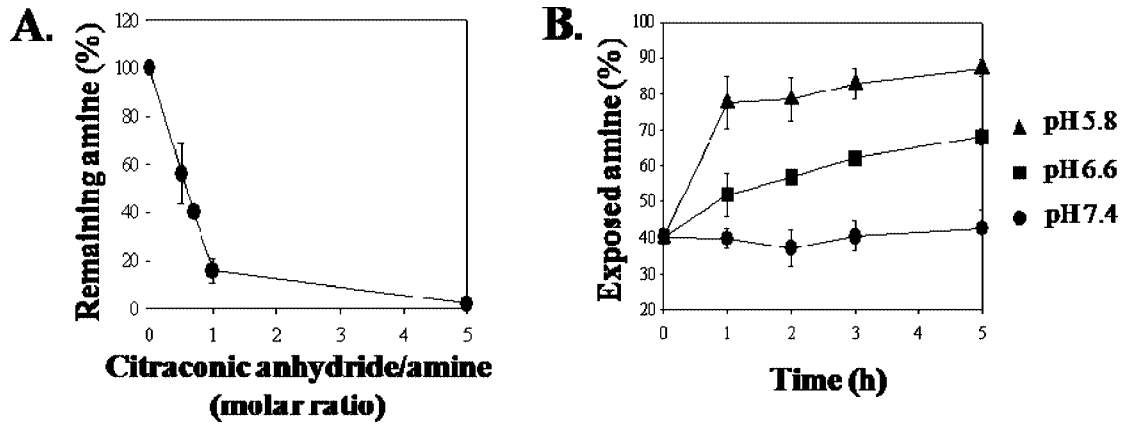

Figure 1. (A) The relative percent of primary amine after amine-blocking reaction by citraconic anhydride at various citraconic anhydride/amine molar ratios. (B) The relative percent of remaining amine group in the citraconylated biotin-PEG-PLL after incubation at pH 5.8 (triangle), 6.6 (square), and 7.4 (circle) at 37 °C as a function of incubation time. The error bars mean standard deviation.

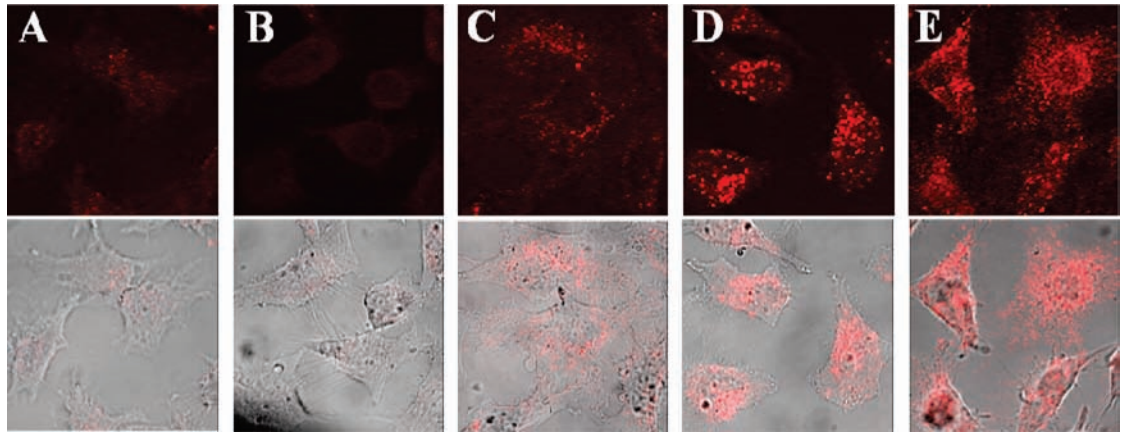

Figure 2. Confocal microscopy images of intracellular QD coated with citraconylated biotin-PEG-PLL and incubated for 3 h at (B) pH 7.4, (C) pH 6.6, and (D) pH 5.8 conditions for HeLa cells. The cells treated with (A) QD coated with as-prepared citraconylated biotin-PEG-PLL and (E) QD coated with noncitraconylated biotin-PEG-PLL were used as negative and positive controls, respectively.

riers that enabled the release of encapsulated or conjugated chemical and biological drugs in response to acidic pH (*13*−*16*). It was recently demonstrated that cationic diblock polymers containing primary amine groups, when conjugated with citraconic anhydride, showed charge reversal from negative to positive by cleavage of citraconic amide linkage (*16*). The charge reversal diblock copolymers were used as nanocontainers for releasing cationic enzymes only in acidic pH. In this communication, we demonstrated that QD nanoparticles surface-modified with amine-blocked biotin-PEG-grafted PLL copolymer by citraconylation could be delivered efficiently into cells under acidic condition via a surface charge reversal from negative to positive. ADV was also similarly modified to selectively enhance viral gene expression under the acidic condition.

A copolymer of biotin-poly(ethylene glycol) (PEG) grafted poly(L-lysine) (PLL) (biotin-PEG-PLL) was synthesized by reacting primary amine groups of PLL (average Mw: 1100, as determined from matrix-assisted laser desorption/ionization time-of flight (MALDI-TOF) mass spectroscopy, Supporting Information Figure S1) with a biotin-PEG-*N*-hydroxysuccinimide derivative (biotin-PEG-NHS). The resultant graft copolymer had ca. 2.5 biotinylated PEG chains per PLL backbone as characterized by ^{1}H NMR (Supporting Information Figure S2). The remaining primary amine groups of the PLL in the graft copolymer were further modified with a pH-specific amine blocker, citraconic anhydride. Citraconic anhydride has been known to be able to change the net charge of cationic polymers and peptides by replacing primary amine groups with carboxylate groups (*17*). After citraconylation reaction for 2 h at various molar ratios of citraconic anhydride/amine, the amount of remaining amine group in the PLL was measured by fluorescamine assay. As shown in Figure 1A, ∼60% of total amine groups in the biotin-PEG-PLL was modified at the citraconic anhydride/amine molar ratio of 0.7, suggesting that the net charge of biotin-PEG-PLL under that condition was slightly negative. The biotin-PEG-PLL copolymer with a citraconylation substitution degree of 60% was used for further study. To show the charge regeneration of primary amine groups in the citraconylated conjugate at different pH conditions, the amount of primary amine groups was quantitatively analyzed by fluorescamine assay after incubating at different pH conditions. Previously, it was reported that the amide bond formed by citraconylation reaction with primary amine group could be specifically cleaved in acidic pH due to a neighboring carboxylic acid group (*16, 17*). When the citraconylated conjugate was incubated at pH 5.8, 6.6, and 7.4, the relative amounts of exposed amine groups were 87.1 ± 2.4%, 68.1 ± 2.3%, and 42.7 ± 5.0% after 5 h incubation, respectively. The extent of regenerated amine group was significantly increased at pH 5.8 and 6.6 in a time-dependent manner, indicating that the net charge in the conjugate was recovered from negative to positive only in the acidic conditions.

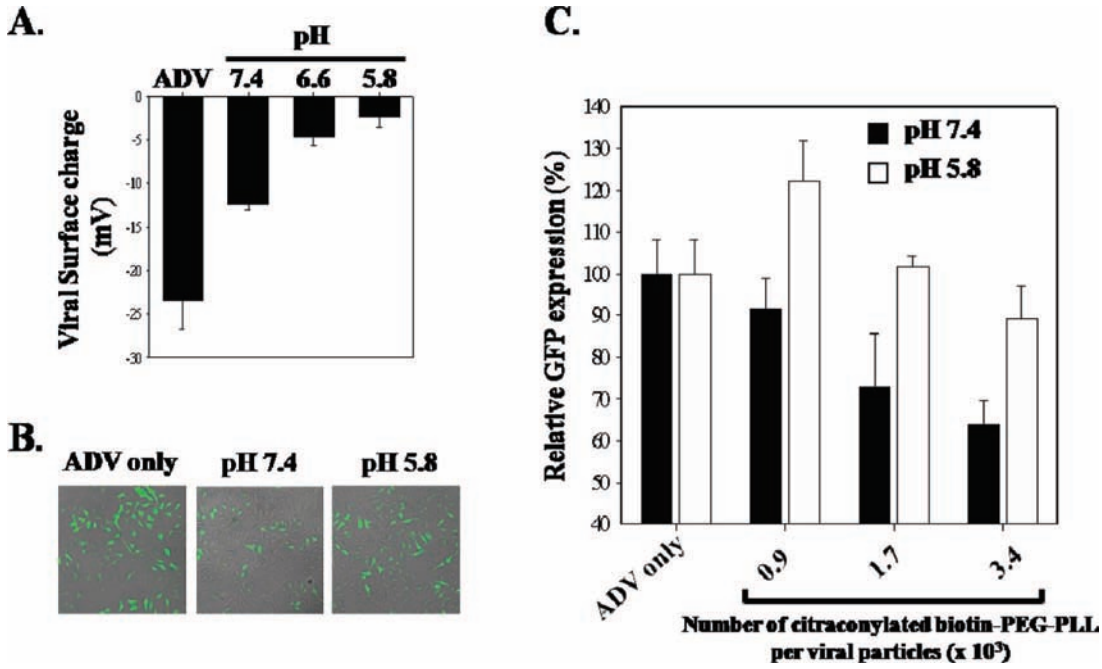

Figure 3. (A) Surface charge on ADV coated with citraconylated biotin-PEG-PLL incubated at pH 5.8, 6.6, and 7.4. (B) Confocal microscopy images of adenoviral gene, GFP expression for HeLa cells transfected with ADV coated with citraconylated biotin-PEG-PLL (3.4×10^3 per viral particles) after incubating at pH 5.8 and 7.4, respectively. (C) The extent of relative GFP expression (%) for HeLa cells transfected with ADV coated with various amounts of citraconylated biotin-PEG-PLL copolymer after incubating at pH 5.8 and 7.4. Naked ADV was used as a control in all experiments.

Scheme 1. (A) Synthesis of Citraconylated Biotin-PEG-PLL Copolymer and Its Charge Reversal at Acidic pH; (B) Surface Coating with Citraconylated Biotin-PEG-PLL onto Streptaividin-Quantum Dot and Avidin−Adenovirus Nanoparticles

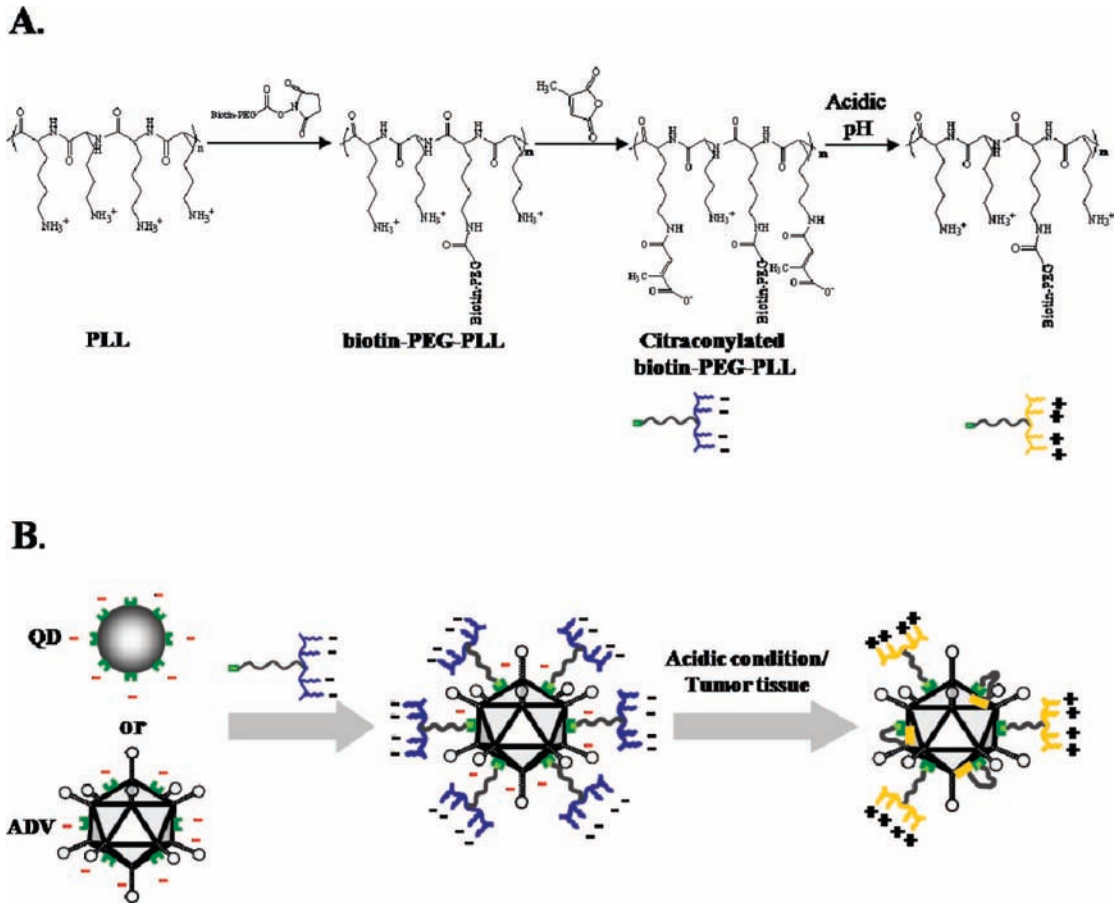

The resultant citraconylated biotin-PEG-PLL graft copolymer was immobilized onto the surface of streptavidin-conjugated QDs (QD-stp, 5−20 nm) via biotin−streptavidin interaction. Dynamic light scattering (DLS) measurement showed that QD-

stp and citraconylated biotin-PEG-PLL/QD-stp nanoparticles have hydrodynamic sizes of 12.0 ± 1.6 nm and 14.8 ± 5.8 nm, respectively. After incubating in buffer solutions of different pH values 5.8, 6.6, and 7.4 for 3 h, citraconylated biotin-PEG-PLL/QD-stp nanoparticles were treated to HeLa cells to show the intracellular uptake extent of QD. Cellular images visualized by confocal microscopy revealed that QD nanoparticles incubated at pH 5.8 and pH 6.6 were more significantly taken up by the cells than those at pH 7.4 (Figure 2). The enhanced intracellular uptake in the acidic condition was also analyzed using flow cytometry. As shown in Supporting Information Figure S3, a red fluorescent peak for QD in pH 5.8 was noticeably shifted to the right-hand side, compared to that at pH 7.4, suggesting that more efficient intracellular uptake occurred in the acidic condition. It is obvious that the net charge of the surface-anchored citraconylated conjugate was reversed from negative to positive, thereby facilitating nonspecific endocytic uptake of QD nanoparticles by increasing their charge interactions with the cell membrane. It was possible that some portion of the regenerated cationic PLL backbones was likely to be adsorbed onto the anionic surface of bare QD-stp nanoparticles via electrostatic interactions, resulting in the formation of multiple PEG loops as illustrated in Scheme 1 B.

ADV, a naturally evolved and well-defined nanoparticle, is approximately 60−90 nm in diameter. Although ADV shows high gene transfection efficiency in mammalian cells, its use as a gene carrier has been limited mainly due to nonspecific transfection and innate immune responses. To confer target-specific delivery capacity and reduced immune response, ADV was often PEGylated by tethering various targeting ligands to specific cells (*6*, *18*, *19*). In this study, surface charge reversal by citraconylated conjugate in response to acidic pH was also applied to ADV encoding for green fluorescent protein (GFP). To immobilize the citraconylated biotin-PEG-PLL copolymer onto the viral surface, avidin (avi) was preconjugated onto the ADV surface using the EDC/NHS reaction. The citraconylated biotin-PEG-PLL/ADV-avi nanoparticles were prepared via biotin−avidin interaction in a similar manner to QD-stp. Surface charge values after incubating at pH 5.8, 6.6, and 7.4 for 5 h were determined by a dynamic light scattering technique (Figure 3A). The surface charge value of naked ADV was about −20 mV at pH 7.4 due to the presence of anionic viral coat proteins (*4*). When citraconylated biotin-PEG-PLL/ADV-avi complex nanoparticles were incubated at pH 7.4, 6.6, and 5.8, the surface charge values became −12.3 ± 0.8, −4.7 ± 0.9, and −2.3 ± 1.2 mV, respectively. This suggests that the charge reversal on the surface of ADV occurred in response to acidic pH.

The GFP expression level of ADV was determined as a function of pH using confocal microscopy as shown in Figure 3B. The cells transfected with citraconylated biotin-PEG-PLL/ADV-avi nanoparticles at pH 7.4 showed significantly reduced extent of GFP gene expression, compared to those at pH 5.8. It is known that naked ADV nanoparticles were transported into cells via coxsackievirus−adenovirus receptor (CAR) mediated endocytosis (*19*, *20*). Surface-exposed fiber proteins on ADV were initially docked to the CAR on the cell membrane for cellular entry. After modifying the surface of ADV-avi with citraconylated biotin-PEG-PLL copolymers, the CAR-mediated mechanism would play a minor role in cellular uptake, because most of the fiber proteins on the surface were likely to be chemically conjugated with avidin and, more importantly, to be sterically inaccessible to the CAR by the presence of immobilized biotin-PEG-PLL copolymers. Thus, the citraconylated biotin-PEG-PLL/ADV-avi nanoparticles might be taken up by cells via a nonspecific endocytic pathway. The levels of GFP expression treated with ADV-avi coated with different amounts of citraconylated biotin-PEG-PLL were quantitatively analyzed at pH 7.4 and pH 5.8 using naked ADV as a control (GFP expression: 100%), as shown in Figure 3C. The relative extents of GFP expression for the cells transfected by ADV-avi coated with 0.9×10^3, 1.7×10^3, and 3.4×10^3 citraconylated biotin-PEG-PLL copolymers per viral particle were 122.2 ± 9.7%, 101.7 ± 2.5%, and 89.2 ± 7.8%, respectively, at pH 5.8, but they were 91.7 ± 7.2%, 72.8 ± 12.8%, and 63.8 ± 5.8% at pH 7.4 under the same condition. The results imply that the surface charge reversal of surface-engineered ADV nanoparticles, triggered by acidic pH condition, enhanced the extent of nonspecific cellular uptake and subsequently maintained the extent of viral gene expression to be similar to that of naked ADV. Since the surface charge value of fully regenerated biotin-PEG-PLL/ADV-avi nanoparticles at pH 5.8 was still negative at −2.3 ± 1.2 mV as shown in Figure 3A, it was postulated that the recovered cationic PLL chains were in part bound onto the anionic surface of ADV-avi by charge interactions, making PEG loops as shown in Scheme 1B. Although complete surface charge reversal (a net charge change from negative to positive) of citraconylated biotin-PEG-PLL/ADV-avi was not observed at acidic pH due to the rearrangement of PEG chains, a significant change in the surface charge value of ADV toward a positive direction could lead to enhanced cellular uptake and gene expression.

In conclusion, we demonstrated that QD and ADV nanoparticles immobilized by citraconylated biotin-PEG-PLL exhibited surface charge reversal at acidic pH. It was possible to deliver them into cells specifically under acidic conditions. The current targeting strategy is expected to have a wide range of applications for delivery of imaging and therapeutic agents to solid tumors that are known to have an acidic microenvironment.

ACKNOWLEDGMENT

This study was supported by grants from the National Research Laboratory project, the Ministry of Science and Technology, and the National Cancer Center, Republic of Korea (0620240-1).

Supporting Information Available: Detailed materials and methods. This material is available free of charge via the Internet at http://pubs.acs.org.

LITERATURE CITED

(1) Zhang, Y., Kohler, N., and Zhang, M. (2002) Surface modification of superparamagnetic magnetite nanoparticles and their intracellular uptake. *Biomaterials 23*, 1553–1561.

(2) Akerman, M. E., Chan, W. C., Laakkonen, P., Bhatia, S. N., and Ruoslahti, E. (2002) Nanocrystal targeting in vivo. *Proc. Natl. Acad. Sci. U.S.A. 99*, 12617–12621.

(3) Bae, K. H., Lee, Y., and Park, T. G. (2007) Oil-encapsulating PEO-PPO-PEO/PEG shell cross-linked nanocapsules for target-specific delivery of paclitaxel. *Biomacromolecules 8*, 650–656.

(4) Oh, I. K., Mok, H., and Park, T. G. (2006) Folate immobilized and PEGylated adenovirus for retargeting to tumor cells. *Bioconjugate Chem. 17*, 721–727.

(5) Farokhzad, O. C., Jon, S., Khademhosseini, A., Tran, T. N., Lavan, D. A., and Langer, R. (2004) Nanoparticle-aptamer bioconjugates: a new approach for targeting prostate cancer cells. *Cancer Res. 64*, 7668–7672.

(6) Oishi, M., Nagasaki, Y., Itaka, K., Nishiyama, N., and Kataoka, K. (2005) Lactosylated poly(ethylene glycol)-siRNA conjugate through acid-labile beta-thiopropionate linkage to construct pH-sensitive polyion complex micelles achieving enhanced gene silencing in hepatoma cells. *J. Am. Chem. Soc. 127*, 1624–1625.

(7) Bellocq, N. C., Pun, S. H., Jensen, G. S., and Davis, M. E. (2003) Transferrin-containing, cyclodextrin polymer-based par-

ticles for tumor-targeted gene delivery. *Bioconjugate Chem. 14*, 1122–32.

(8) Kong, G., Braun, R. D., and Dewhirst, M. W. (2000) Hyperthermia enables tumor-specific nanoparticle delivery: effect of particle size. *Cancer Res. 60*, 4440–4445.

(9) Krotz, F., de Wit, C., Sohn, H. Y., Zahler, S., Gloe, T., Pohl, U., and Plank, C. (2003) Magnetofection--a highly efficient tool for antisense oligonucleotide delivery in vitro and in vivo. *Mol. Ther. 7*, 700–710.

(10) Schmaljohann, D. (2006) Thermo- and pH-responsive polymers in drug delivery. *Adv. Drug Delivery Rev. 58*, 1655–1670.

(11) Tannock, I. F., and Rotin, D. (1989) Acid pH in tumors and its potential for therapeutic exploitation. *Cancer Res. 49*, 4373–4384.

(12) Newell, K., Franchi, A., Pouyssegur, J., and Tannock, I. (1993) Studies with glycolysis-deficient cells suggest that production of lactic acid is not the only cause of tumor acidity. *Proc. Natl. Acad. Sci. U.S.A. 90*, 1127–1131.

(13) Lee, E. S., Na, K., and Bae, Y. H. (2005) Super pH-sensitive multifunctional polymeric micelle. *Nano Lett. 5*, 325–329.

(14) Shim, W. S., Yoo, J. S., Bae, Y. H., and Lee, D. S. (2005) Novel injectable pH and temperature sensitive block copolymer hydrogel. *Biomacromolecules 6*, 2930–2934.

(15) Ulbrich, K., Etrych, T., Chytil, P., Jelinkova, M., and Rihova, B. (2003) HPMA copolymers with pH-controlled release of doxorubicin: in vitro cytotoxicity and in vivo antitumor activity. *J. Controlled Release 87*, 33–47.

(16) Lee, Y., Fukushima, S., Bae, Y., Hiki, S., Ishii, T., and Kataoka, K. (2007) A protein nanocarrier from charge-conversion polymer in response to endosomal pH. *J. Am. Chem. Soc. 129*, 5362–5363.

(17) Shetty, J. K., and Kinsella, J. E. (1980) Ready separation of proteins from nucleoprotein complexes by reversible modification of lysine residues. *Biochem. J. 191*, 269–272.

(18) Obenauer-Kutner, L. J., Ihnat, P. M., Yang, T. Y., Dovey-Hartman, B. J., Balu, A., Cullen, C., Bordens, R. W., and Grace, M. J. (2002) The use of field emission scanning electron microscopy to assess recombinant adenovirus stability. *Hum. Gene Ther. 13*, 1687–1696.

(19) Mok, H., Park, J. W., and Park, T. G. (2007) Microencapsulation of PEGylated adenovirus within PLGA microspheres for enhanced stability and gene transfection efficiency. *Pharm. Res. 24*, 2263–2269.

(20) Medina-Kauwe, L. K. (2003) Endocytosis of adenovirus and adenovirus capsid proteins. *Adv. Drug Delivery Rev. 55*, 1485–1496.

(21) Jeon, E., Kim, H-D, and Kim, J-S. (2003) Pluronic-grafted poly-(L)-lysine as a new synthetic gene carrier. *J. Biomed. Mater. Res., Part A 66*, 854–859.

(22) Duan, H., and Nie, S. (2007) Cell-penetrating quantum dots based on multivalent and endosome-disrupting surface coatings. *J. Am. Chem. Soc. 129*, 3333–3338.

(23) Murakami, P., and McCaman, M. T. (1999) Quantitation of adenovirus DNA and virus particles with the PicoGreen fluorescent Dye. *Anal. Biochem. 274*, 283–288.

(24) Maizel, J. V., Jr., White, D. O., and Scharff, M. D. (1968) The polypeptides of adenovirus. I. Evidence for multiple protein components in the virion and a comparison of types 2, 7A, and 12. *Virology 36*, 115–125.

(25) Park, J. W., Mok, H., and Park, T. G. (2008) Epidermal growth factor (EGF) receptor targeted delivery of PEGylated adenovirus. *Biochem. Biophys. Res. Commun. 366*, 769–774.

BC700464M

Characterization of Nanogap Chemical Reactivity Using Peptide-Capped Gold Nanoparticles and Electrical Detection

Lionel Marcon,[†,‡] Didier Stiévenard,[†] and Oleg Melnyk*[,‡]

Institut d'Electronique de Microélectronique et de Nanotechnologie, UMR CNRS 8520, Dpt ISEN, 41 Bd Vauban, 59046 Lille Cedex, France, and Institut de Biologie de Lille, UMR CNRS 8161, Universités de Lille 1 et 2, Institut Pasteur de Lille, IFR 142, 1 rue du Professeur Calmette, 59021 Lille Cedex, France. Received January 9, 2008; Revised Manuscript Received February 25, 2008

Nanogaps are usually combined with synthetic or biological molecules to produce nanodevices having novel properties. This combination is better realized by controlling the chemical properties of the nanogap. We show here that the presence of a specific chemical group inside nanogaps (30–90 nm) can be probed electrically using 10 nm gold nanoparticles derivatized by complementary functional groups. $100-10^4$-fold current increases were observed following the site-specific insertion of gold nanoparticles into the nanogap.

Nanofabrication techniques in semiconductor research have accelerated the interest in nanostructure materials. In particular, creating and using nanogaps between electrodes is the subject of intense research today. Nanogaps, which allow electrical contact to structures on the nanoscale, have applications ranging from dense microprocessor chips to biosensors. The structures involve many kinds of materials, from polymer to biological molecules, through the establishment of molecular assemblies based on the nanogap surface between metallic walls. The positioning of the synthetic or biological species inside the nanogap must be controlled to reach optimal electrical or detection properties. In this context, the chemical properties of the layer between the electrodes is of prime importance, since they will impose the imbibition of the nanogap and permit the formation of chemical bonds between the molecules of interest and the substrate (*1*).

Thin films can be characterized by a variety of physical or chemical methods. However, the characterization of the chemical properties of nanogaps is complicated because of the small size of the substrate delimited by the electrodes. Currently, some powerful techniques, like scanning electron microscopy (SEM), atomic force microscopy (AFM), and chemical force microscopy (CFM), allow the study of the structure or chemical properties of nanometer-sized surfaces but provide only limited information about their chemical nature. In this context, novel experimental tools are needed for probing rapidly the chemical reactivity of nanogaps.

We show here for the first time that a specific functional group in a 30–90 nm nanogap can be detected by combining peptide-capped gold nanoparticles and electrical detection. A semicarbazide layer and semicarbazone chemoselective ligation was used in this proof-of-concept study, which thus required the preparation of stable peptide-capped gold nanoparticles modified by aldehyde groups and control GNPs derivatized by amide groups. The chemoselective insertion of gold colloids into the nanogaps led to current increases from 2 to 4 orders of magnitude, in accord with the number of gold nanoparticles in the nanogaps detected by scanning electron microscopy.

The principle of the characterization method is described in Figure 1. The chip surface is incubated with aldehyde-modified GNPs (CHO-GNPs) or amide-modified GNPs ($CONH_2$-GNPs) as a control for the site-specific GNP insertion into the nanogap. The presence of semicarbazide groups between the electrodes allows the formation of a semicarbazone bond between semicarbazide groups of the substrate and aldehyde groups on the CHO-GNPs (*2*). The chemically driven insertion of GNPs into the nanogap is detected by measuring the current changes between the electrodes.

One of the key elements of the method is the design of CHO- and $CONH_2$-GNPs. Since their development more than 10 years ago (*3*), thiol-capped GNPs have been extensively studied in a broad range of structural, electronic, optical, and chemical aspects (*3–6*). The chemical modification of GNPs can be done using thiols or disulfides (*7*). These functionalities, which are compatible with a variety of chemical groups, react with gold substrates to form dense monolayers. In particular, cysteinyl-peptides can be used for the preparation of stable peptide-capped GNPs displaying appropriate functional groups at their periphery (*3*). This strategy was chosen here to prepare CHO- and $CONH_2$-GNPs as shown in Figure 2. Peptides **1** and **2** derived from the Ac-CYKLG sequence and modified at the C-terminus by an aldehyde or amide group, respectively, were synthesized using Fmoc/*t*Bu standard solid-phase peptide synthesis protocols (*8*) and a tartaramide linker (*9*). The α-oxo carboxamide group present at the C-terminus of peptide **1** is frequently used in bioconjugation chemistry (*10*). Its reactivity with semicarbazide-functionalized soluble or solid substrates has been documented in detail elsewhere (*11–15*). The thiol moiety of cysteine was protected by a *tert*-butyl sulfenyl group. Lys residue in position 3, which can bear a positive charge due to the side-chain amino group, was expected to facilitate the MALDI-TOF analysis of the peptides and the electrostatic repulsion of the peptide-capped GNPs.

The chemisorption of disulfides on gold leads to the formation of Au(I) thiolate species which are formed by oxidative addition of the S−S bond to the gold surface (*7*). Peptides **1** or **2** were thus reacted directly with 10 nm GNPs. Ligation of peptides **1** or **2** to the GNPs was monitored in real time by collecting UV–vis absorption spectra of the peptide−GNP mixture. The plasmon band of GNPs is indeed sensitive to the nanoparticle environment, and this property was exploited in various bioassays (*16–18*). The plasmon band of bare GNPs at 516.6 nm was shifted as expected to longer wavelengths in the

* Phone: 333 20 87 12 14, Fax: 333 20 87 12 35; oleg.melnyk@ibl.fr.
† UMR CNRS 8520.
‡ UMR CNRS 8161.

10.1021/bc8000084 CCC: $40.75 © 2008 American Chemical Society
Published on Web 03/19/2008

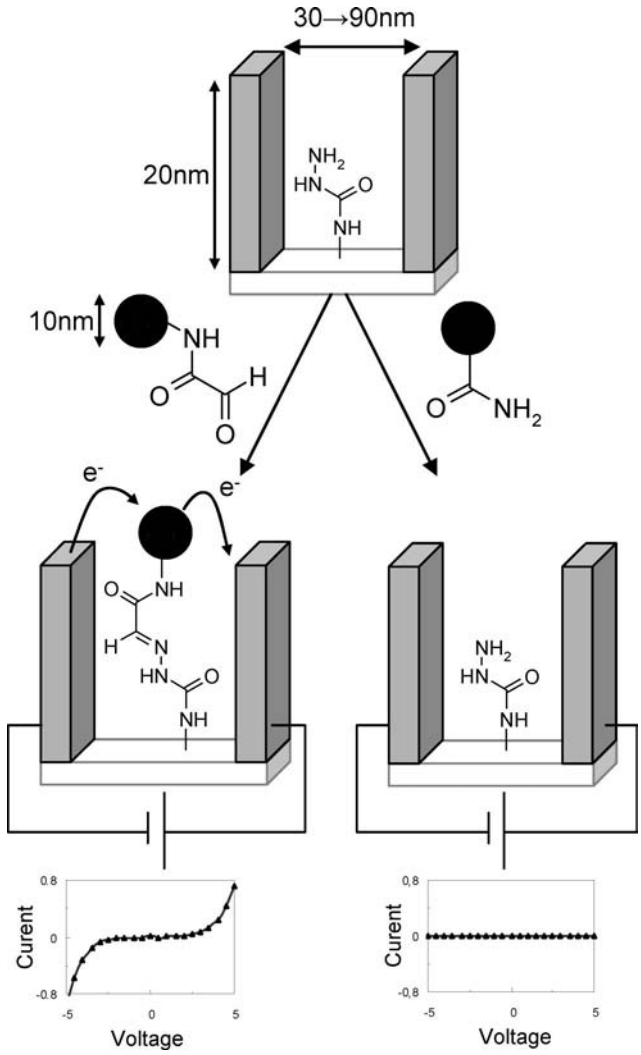

Figure 1. Principle of the characterization of the nanogap chemical reactivity using GNPs and electrical detection. The surface carrying the electrodes is modified by semicarbazide groups. The nanogap is then incubated with GNPs modified by complementary aldehyde groups (CHO-GNPs). Reaction between the GNPs and the surface between the electrodes leads to the site-specific insertion of CHO-GNPs into the nanogap, and thus to the increase of the nanogap conductance. GNPs modified by amide groups ($CONH_2$-GNPs) are used in the control experiment.

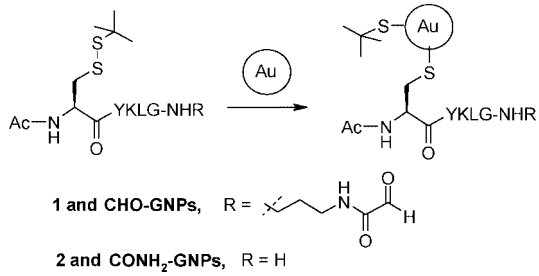

Figure 2. Synthesis of CHO- or $CONH_2$-GNPs by reaction of GNPs with peptides **1** or **2**, respectively.

presence of peptides **1** or **2** (Figure 3). The binding of both peptides to the GNPs occurred in less than 1 min at room temperature. After 3 min of reaction, bovine serum albumin (BSA) was added to the reaction medium to stabilize the suspension (*19*, *20*). The addition of BSA led to minor changes in the position of the plasmon band for both peptides and for the control experiment without peptide. The particles were finally purified by centrifugation and resuspension in PBS BSA

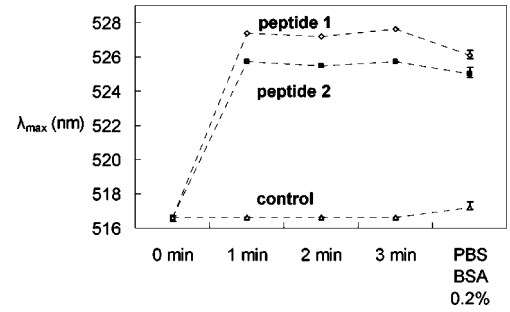

Figure 3. Wavelength of the plasmon absorption band of GNPs in the presence of CHO-peptide **1**, $CONH_2$-peptide **2**, or without peptide (control) as a function of the reaction time. First, 10 μL of 1 mg/mL peptide solution were mixed with 500 μL of the bare GNPs (5.2×10^{12} particles/mL). After 3 min, 75 μL of PBS BSA 0.2% buffer were added to stabilize the peptide-GNPs. pH of the bare GNPs was 7.9 for peptide **1** and 8.2 for peptide **2**, since aggregation of $CONH_2$-GNPs occurred at lower pH.

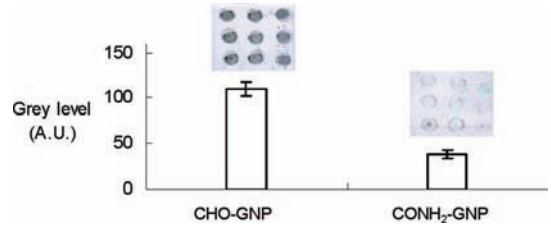

Figure 4. Grey level of the spots after incubation and enhancement of CHO- and $CONH_2$- suspensions. Inset: Gray-scale images quantified using *ImageJ* freeware (NIH, Bethesda, Maryland, USA). Drops of CHO- and $CONH_2$-GNPs suspensions (10 μL) were incubated onto semicarbazide microscope glass slides for 1 h at 37 °C. The silver enhancement with Ag^+/*p*-dihydroquinone was performed using a commercial kit (Silver Blue kit, Advanced Array Technology). Substrates were rinsed 5 min with blocking solution (block sol) and immersed 10 min at room temperature in the Ag^+/*p*-dihydroquinone solution (silver staining sol), and then washed with water, methanol, and dried. Slides were scanned with a HPScanJet 5300C scanner. Results are expressed as the mean of the gray level inside a spot minus the background around the spot ($n = 9$).

0.2% buffer. The final position of the absorption band of CHO- and $CONH_2$-GNPs after the washing steps was 526.1 and 525.0 nm, respectively. CHO- and $CONH_2$-GNPs were also analyzed by dynamic light scattering (DLS) to determine the size of the particles. The size of bare GNPs was 10.0 ± 1.4 nm, whereas the size of CHO- and $CONH_2$-GNPs was 12.4 ± 2.4 nm and 12.7 ± 2.2 nm, respectively. The DLS experiments confirmed that peptide capping of the GNPs occurred without aggregation. The CHO- and $CONH_2$-GNPs suspensions were found to be stable for at least one year when stored at +4 °C.

The reactivity of CHO-GNPs was studied by incubating a series of drops of the CHO- and $CONH_2$-GNPs suspensions with semicarbazide-functionalized microscope glass slides. Modification of microscope glass slides by a semicarbazide layer has been described in detail elsewhere (*21*). The surfaces were dried, washed, and the immobilized GNPs were detected by the immunogold silver staining enhancement technique (*22*, *23*). This method is based on the GNP-catalyzed reduction of silver ions by *p*-dihydroquinone. Precipitation of metallic silver on the GNPs leads to the formation of a silver layer whose gray level can be measured. The results of this experiment are shown in Figure 4. The signal displayed by CHO-GNPs was significantly higher (~3-fold) than those displayed by $CONH_2$-GNPs, showing a large impact of the α-oxo aldehyde group on GNP immobilization. These results, which are in accord with the GNP densities determined by SEM in the following experiment, show

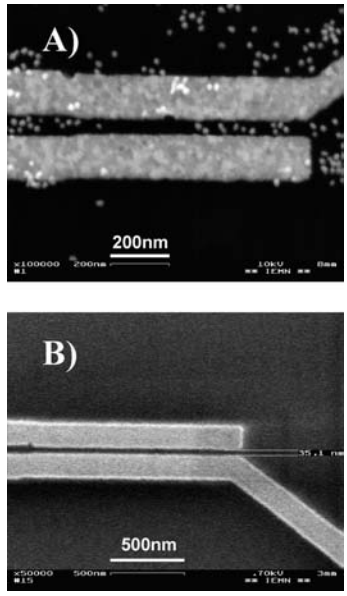

Figure 5. SEM images of the nanogaps after printing of CHO-GNPs (a) or $CONH_2$-GNPs (b). CHO-GNPs are clearly visible in the nanogap (Figure 5a). The scale of Figure 5b is larger to show the absence of $CONH_2$-GNPs on a large portion of the chip. Other images can be found in the Supporting Information. The nanoparticles were first printed and incubated on the nanoelectrodes. After washings with PBS containing 0.05% of Tween 20 (by vol), water, and ethanol, substrates were dried under a nitrogen stream and analyzed by SEM.

that CHO-GNPs were mainly immobilized through the formation of semicarbazone covalent bonds.

Next, gold nanoelectrodes were fabricated on a silicon substrate with gap dimensions varying from 30 to 90 nm and a thickness of 20 nm (15 nm Au on 5 nm Ti) as described elsewhere (*24*). The silicon chip was treated as before to coat the silicon oxide substrate by a semicarbazide layer. CHO- and $CONH_2$-GNPs were then printed onto the nanoelectrodes (19 nanoelectrodes for each GNP suspension) using a piezoelectric microarrayer (dispensed volume: 6 nL). The chips were incubated 6 h at 37 °C in a humid chamber to favor the formation of semicarbazone bonds between the CHO-GNPs and the semicarbazide surface. The chips were then washed and analyzed by SEM. The average GNP density in the area surrounding the nanoelectrodes was 150 ± 8 for CHO-GNPs and only 4 ± 2 particles/μm^2 for $CONH_2$-GNPs (images can be found in Supporting Information). The significant difference in GNP density is in agreement with the data of the silver precipitation experiment presented in Figure 4. In addition, Figure 5 shows that 120 ± 6 CHO-GNPs were present in the nanogaps, whereas no $CONH_2$-GNPs were seen between the electrodes. The chemoselective immobilization of CHO-GNPs in the nanogap shows the successful derivatization of the silicon oxide surface by a semicarbazide layer.

Moreover, we demonstrate here that the subsequent analysis of intensity–voltage $I(V)$ curves after printing of CHO- and $CONH_2$-GNPs yields valuable information regarding the presence of GNPs in the nanogap and thus its successful functionalization. Experimentally, the method is straightforward, requires no expensive techniques, and can be used for the quality control of chips. The *x, y* precision of the piezoelectric arrayer is high enough to allow the selective deposition of both GNP reagents on a subset of nanogaps whereas the other nanogaps remain unaltered and are available for other detection purposes.

The intensities measured at 5 V for CHO- and $CONH_2$-GNPs on bare or semicarbazide nanogaps were all below 10^{-13}A and exhibited a random shape associated with background noise. The printing of $CONH_2$-GNPs on semicarbazide chips led also to intensities lower than 10^{-13}A in agreement with the very low GNP densities observed by SEM. Interestingly, the printing of CHO-GNPs led to large current increments with factors between 2 and 4 orders of magnitude (Figure 6) for 10 of the 19 nanogaps. Those $I(V)$ curves are symmetric and exhibit a low conductivity gap around zero bias voltage. Such behavior suggests a Coulomb blockade, a process in which current is inhibited until electrons have enough energy to charge the GNPs. At low bias, the electrons do not have sufficient energy to overcome the Coulomb blockade. At high bias, the energy is sufficient for the electrons to tunnel from one electrode to another *via* the GNPs (*25, 26*). Independently of the exact conduction mechanism, $I(V)$ data confirm the presence of GNPs and thus the successful formation of the semicarbazide layer in the nanogap. The success of the method relies on the stability of the functional GNPs, their ability to react chemoselectively with the substrate, and importantly on the ease of removal of the GNPs that are only physisorbed on the surface during the washing steps.

In conclusion, we show for the first time the presence of a specific functional group in a nanogap by combining peptide-capped gold nanoparticles and electrical detection. Semicarbazide group was used in this proof-of-concept study, which thus required the preparation of stable peptide-capped gold nanoparticles modified by aldehyde groups and control GNPs derivatized by amide groups. The electrical measurements were in accord with SEM observations, mean GNP densities on the printed areas, and the number of GNPs trapped in the nanogaps.

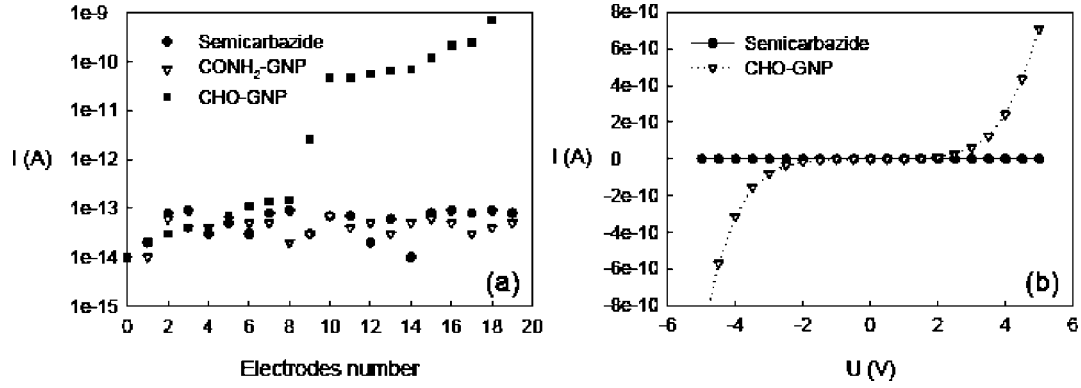

Figure 6. (a) Intensity at $V = 5$ V for 19 pairs of nanoelectrodes after semicarbazide functionalization (filled circles), incubation with $CONH_2$-GNP (open triangles), or incubation with CHO-GNP (filled squares). (b) Typical current–voltage curves before (filled circles) and after (open triangles) incubation with CHO-GNP. Measurements were performed in a nitrogen low-pressure chamber (0.2 mbar, H_2O and $O_2 < 0.1$ ppm) at room temperature with a pico-amperemeter HP4140B. The applied voltage ranged from −5 to +5 V with 500 mV steps. See also the legend of Figure 5 for other experimental details.

Interestingly, the nanoparticles could be precisely addressed on a subset of nanogaps for the quality control of the chip functionalization using a noncontact piezoelectric arrayer, whereas the other electrodes remained unchanged for other detection purposes. In principle, the method can be extended to other chemistries, since peptides are easy to synthesize and can be derivatized by various functional groups. The sequence of the peptide can also be easily adapted to match desired physicochemical properties.

ACKNOWLEDGMENT

This work was partly supported by the French Ministry of Research, grants from the EEC and from the Région Nord Pas-de-Calais. We also used the microarray platform facilities from the Institute of Biology (Lille, France).

Supporting Information Available: Synthetic protocols, RP-HPLC and MALDI-TOF analyses for peptides **1** and **2**. SEM images of CHO- or $CONH_2$-GNPs printed on semicarbazide functionalized chips. This material is available free of charge via the Internet at http://pubs.acs.org/BC.

LITERATURE CITED

(1) Brinkmann, M., Blossey, R., Marcon, L., Stievenard, D., Dufrene, Y. F., and Melnyk, O. (2006) Fluidics of a nanogap. *Langmuir 22*, 9784–9788.

(2) Olivier, C., Hot, D., Huot, L., Ollivier, N., El-Mahdi, O., Gouyette, C., Huynh-Dinh, T., Gras-Masse, H., Lemoine, Y., and Melnyk, O. (2003) α-oxo-semicarbazone peptide or oligodeoxynucleotide microarrays. *Bioconjugate Chem. 14*, 430–9.

(3) Wang, Z., Levy, R., Fernig, D. G., and Brust, M. (2005) The peptide route to multifunctional gold nanoparticles. *Bioconjugate Chem. 16*, 497–500.

(4) Hostetler, M. J., and Murray, R. W. (1997) Colloids and self-assembled monolayers, a review. *Curr. Opin. Colloid Interface Sci. 2*, 42–50.

(5) Templeton, A. C., Wuelfing, W. P., and Murray, R. W. (2000) Monolayer-protected cluster molecules. *Acc. Chem. Res. 33*, 27–36.

(6) Whetten, R. L., Shafigullin, M. N., Khoury, J. T., Schaaff, T. G., Vezmar, I., Alvarez, M. M., and Wilkinson, A. (1999) Crystal structures of molecular gold nanocrystal arrays. *Acc. Chem. Res. 32*, 397–406.

(7) Ulman, A. (1996) Formation and structure of self-assembled monolayers. *Chem. Rev. 96*, 1533–1554.

(8) Fields, G. B., and Noble, R. L. (1990) Solid phase peptide synthesis utilizing 9-fluorenylmethoxycarbonyl amino acids. *Int. J. Pept. Protein Res. 35*, 161–214.

(9) Melnyk, O., Duburcq, X., Olivier, C., Urbes, F., Auriault, C., and Gras-Masse, H. (2002) Peptide arrays for highly sensitive and specific antibody-binding fluorescence assays. *Bioconjugate Chem. 13*, 713–20.

(10) Melnyk, O., Fehrentz, J. A., Martinez, J., and Gras-Masse, H. (2000) Functionalization of peptides and proteins by aldehyde or keto groups. *Biopolymers 55*, 165–86.

(11) Duburcq, X., Olivier, C., Desmet, R., Halasa, M., Carion, O., Grandidier, B., Heim, T. M., Stievenard, D., Auriault, C., and Melnyk, O. (2004) Polypeptide semicarbazide glass slide microarrays: characterization and comparison with amine slides in serodetection studies. *Bioconjugate Chem. 15*, 317–25.

(12) Olivier, C., Hot, D., Huot, L., Ollivier, N., El-Mahdi, O., Gouyette, C., Huynh-Dinh, T., Gras-Masse, H., Lemoine, Y., and Melnyk, O. (2003) α-oxo semicarbazone peptide or oligodeoxynucleotide microarrays. *Bioconjugate Chem. 14*, 430–9.

(13) Blanchet, C., Joly, P., Granier, M., Lanneau, G. F., Cretin, M., Persin, M., Melnyk, O., and Durand, J.-O. (2003) Synthesis and chemical reactivity of semicarbazide-supported silicas. *Tetrahedron Lett. 44*, 4191–4194.

(14) Olivier, C., Perzyna, A., Coffinier, Y., Grandidier, B., Stievenard, D., Melnyk, O., and Durand, J.-O. (2006) Detecting the chemoselective ligation of peptides to silicon with the use of cobalt-carbonyl labels. *Langmuir 22*, 7059–7065.

(15) Joly, P., Ardès-Guisot, N., Kar, S., Granier, M., Durand, J.-O., and Melnyk, O. (2005) Hybrid bioorganic-inorganic materials prepared by site-specific ligation of peptides to functionalized polydisperse silica particules. *Eur. J. Org. Chem.* 2473–2480.

(16) Englebienne, P., Verhas, M., and Van Hoonacker, A. (2001) High-throughput screening using the surface plasmon resonance effect of colloidal gold nanoparticles. *Analyst 126*, 1645–1651.

(17) Ollivier, N., Olivier, C., Gouyette, C., Huynh-Dinh, T., Gras-Masse, H., and Melnyk, O. (2002) Synthesis of oligonucleotide-peptide conjugates using hydrazone chemical ligation. *Tetrahedron Lett. 43*, 997–999.

(18) Riboh, J. C., Haes, A. J., McFarland, A. D., Yonzon, C. R., and Van Duyne, R. P. (2003) A nanoscale optical biosensor: Real-time immu-noassay in physiological buffer enabled by improved nanoparticle adhesion. *J. Phys. Chem. B 107*, 1772–1780.

(19) Tkachenko, A. G., Xie, H., Coleman, D., Glomm, W., Ryan, J., Anderson, M. F., Franzen, S., and Feldheim, D. L. (2003) Multifunctional gold nanoparticle-peptide complexes for nuclear targeting. *J. Am. Chem. Soc. 125*, 4700–1.

(20) Xie, H., Tkachenko, A. G., Glomm, W. R., Ryan, J. A., Brennaman, M. K., Papanikolas, J. M., Franzen, S., and Feldheim, D. L. (2003) Critical flocculation concentrations, binding isotherms, and ligand exchange properties of peptide-modified gold nanoparticles studied by UV-visible, fluorescence, and time-correlated single photon counting spectroscopies. *Anal. Chem. 75*, 5797–805.

(21) Duburcq, X., Olivier, C., Desmet, R., Halasa, M., Carion, O., Grandidier, B., Heim, T., Stievenard, D., Auriault, C., and Melnyk, O. (2004) Polypeptide semicarbazide glass slide microarrays: characterization and comparison with amine slides in serodetection studies. *Bioconjugate Chem. 15*, 317–25.

(22) Hacker, G. W., and Danscher, G. (1994) Recent advances in immunogold-silver staining autometallography. *Cell Vis. (J. Anal. Morphol.) 1*, 102–109.

(23) Alexandre, I., Houbion, Y., Collet, J., Hamels, S., Demarteau, J., Gala, J. L., and Remacle, J. (2002) Compact disc with both numeric and genomic information as DNA microarray platform. *Biotechniques 33*, 435–6, 438–9.

(24) Haguet, V., Martin, D., Marcon, L., Heim, T., Stiévenard, D., Olivier, C., El-Mahdi, O., and Melnyk, O. (2004) Combined nanogap nanoparticles nanosensor for electrical detection of biomolecular interactions between polypeptides. *Appl. Phys. Lett. 84*, 1213–1215.

(25) Lindsay, S. (2005) Single-molecule electronic measurements with metal electrodes. *J. Chem. Educ. 82*, 727–733.

(26) Middleton, A. A., and Wingreen, N. S. (1993) Collective transport in arrays of small metallic dots. *Phys. Rev. Lett. 71*, 3198–3201.

BC8000084

ARTICLES

Multivalency of Sonic Hedgehog Conjugated to Linear Polymer Chains Modulates Protein Potency

Samuel T. Wall,[†,||] Krishanu Saha,[§] Randolph S. Ashton,[§] Kimberly R. Kam,[‡] David V. Schaffer,[†,§,||] and Kevin E. Healy*[,†,‡,||]

Department of Bioengineering, Department of Materials Science and Engineering, Department of Chemical Engineering, and UCSF/UCB Joint Graduate Group in Bioengineering, University of California, Berkeley, California. Received July 15, 2007; Revised Manuscript Received February 6, 2008

A potently active multivalent form of the protein Sonic hedgehog (Shh) was produced by bioconjugation of a modified recombinant form of Shh to the linear polymers poly(acrylic acid) (pAAc) and hyaluronic acid (HyA) via a two-step reaction exploiting carboimiide and maleimide chemistry. Efficiency of the conjugation was ~75% even at stoichiometric ratios of 30 Shh molecules per linear HyA chain (i.e., 30:1 Shh/HyA). Bioactivity of the conjugates was tested via a cellular assay across a range of stoichiometric ratios of Shh molecules to HyA linear chains, which was varied from 0.6:1 Shh/HyA to 22:1 Shh/HyA. Results indicate that low conjugation ratios decrease Shh bioactivity and high ratios increase this activity beyond the potency of monomeric Shh, with approximately equal activity between monomeric soluble Shh and conjugated Shh at 7:1 Shh/HyA. In addition, high-ratio constructs increased angiogenesis determined by the in vivo chick chorioallantoic membrane (CAM) assay. These results are captured by a kinetic model of multiple interactions between the Shh/HyA conjugates and cell surface receptors resulting in higher cell signaling at lower bulk Shh concentrations.

INTRODUCTION

The use of chemical tethers to create solid-phase forms of biologically active agents is a recurring theme across a wide range of medical and biological applications. Chemical tethers can be used to attach bioactive peptide sequences or proteins to surfaces (*1*), to impart bioactivity to porous (*2*) or hydrogel implants (*3, 4*), or in a wide-ranging number of drug delivery applications (*5*−*9*). However, solid-phase presentation can potentially alter the way that such bioactive molecules work in a biological setting; cells interacting with tethered forms of ligands can have altered protein internalization for signal pathway activation (*10*), limited access of the ligands to appropriate cell surface receptors (*11*), and perturbed thermodynamics of receptor−ligand binding due to steric or avidity effects (*12*−*14*). As the dynamics of most growth factor responses are studied as single soluble molecular forms, it is important to understand how tethering molecules affects their potency and influences their use in biomedical applications, particularly for molecules whose natural forms are biologically tethered due to interactions with the extracellular matrix or cell surface lipid bilayers.

In this work, we describe a system for the attachment of recombinant proteins with added cysteine residues to long-chain linear polymers containing free carboxylate groups, specifically the synthetic polymer poly(acrylic acid) (pAAc) and the biological polymer hyaluronic acid (HyA). This method, based on carbodiimide and maleimide chemistry, allowed for control of attachment stoichiometry of the large (~20 kDa) globular protein sonic hedgehog (Shh) to a long-chain linear polymer while maintaining protein activity. Progressively higher stoichiometric ratios of Shh to the linear polymer increased the potency of the protein by a factor of 10-fold over the soluble form as assessed by a cellular differentiation assay. In addition, the constructed multivalent proteins were tested for in vivo biological significance using an angiogenic assay utilizing the chick chorioallantoic membrane (CAM). In order to examine the mechanisms of increased activity of the multivalent form of the constructs, a kinetic model of the Shh pathway was developed to determine the likely effects of multiple binding events on the observed cellular response.

METHODS

Recombinant Shh and Bioconjugation Techniques. Using the cDNA of the N-terminal signaling domain of rat Shh (*15*), base pairs coding for an additional cysteine residue and a 6× His tag were added through PCR onto the c-terminus of the protein to allow for sulfhydryl-based reactions and protein purification, respectively. This tethering site was specifically chosen on the basis of studies demonstrating that this area of the protein is distant from its active site, and inert molecules attached there do not alter activity (*16*). In addition, two hydrophobic residues were added at the N-terminus to enhance the potency of the protein (*18*). The modified Shh PCR product was inserted into a pBAD-HisA (Invitrogen, Carlsbad, CA) plasmid, the resulting plasmid was confirmed by DNA sequenc-

* Correspondence to Professor Kevin E. Healy; University of California, Berkeley; 370 Hearst Memorial Mining Building, #1760; Berkeley, CA 94720-1760; E-mail:kehealy@berkeley.edu. Telephone: +510 643-3559. Fax:+(510) 642-5835.

† Department of Bioengineering.

‡ Department of Materials Science and Engineering.

§ Department of Chemical Engineering.

|| UCSF/UCB Joint Graduate Group in Bioengineering.

10.1021/bc700265k CCC: $40.75 © 2008 American Chemical Society
Published on Web 04/02/2008

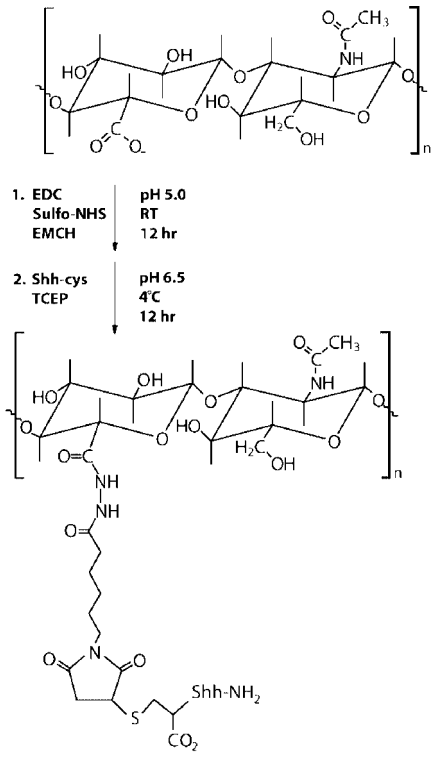

Figure 1. Bioconjugate scheme to graft recombinant Shh to the naturally derived polymer HyA (Shh-graft-HyA). A similar scheme utilizing the carboxylate groups on the polymer was used for the conjugation of the protein to synthetic high molecular weight poly(acrylic acid) (pAAc).

ing, and the protein expressed in BL21(DE3).pLys.E *E. coli* through arabinose induction . After induced protein expression, cells were lysed, and the resulting expressed Shh was purified using NiNTA (Qiagen, Valencia, CA) binding followed by imidazole elution. The purified protein was dialyzed into pH 7.4 PBS containing 10% glycerol, 2 mM EDTA, and 50 μM $ZnSO_4$.

Purified Shh was conjugated to linear polymers through a two-step reaction using carbodiimide chemistry at the carboxylate group of the polymer and a maleimide reaction at the protein C-terminal cysteine (Figure 1). The first step was the addition of [*N*-ϵ-maleimidocaproic acid] hydrazide (EMCH, Pierce Biotechnology, Rockford, IL) to the linear polymer to allow for the subsequent attachment of the protein. This nonimmunogenic hydrazide−maleimide hetereobifunctional cross-linker was added to the two linear polymers using the same general procedure, but with slightly different reaction conditions. For pAAc conjugates, 450 000 Da pAAc (Polysciences, Warrington, PA) at 2 mg/mL was reacted with 1-ethyl-3-[3-dimethylaminopropyl]carbodiimide hydrochloride (EDC) at 3.9 mg/ml, *N*-hydroxysulfosuccinimide (sulfo-NHS) at 1.1 mg/mL, and 0.5 mg/mL EMCH at room temperature for 2 h in pH 6.5 MES buffer as described for the attachment of small peptide sequences (*17*). For the activation of HyA, a method similar to that previously described for the attachment of hydrazides (*9*) was used with 10^6 Da MW HyA (Genzyme, Cambridge, MA). This was dissolved and reacted at 3 mg/mL with the same concentrations of EDC, sulfo-NHS, and EMCH used in the pAAc reaction overnight in 0.1 M MES buffer, pH 5.0. After the attachment of the EMCH, the resulting maleimide-activated linear polymers were separated from the unconjugated reagents through sequential dilution and centrifugation in 50 000 MW cutoff centrifuge filters (Pall Gellman).

The activated polymers were then reacted with the Shh in varying stoichiometric feed ratios to produce conjugates of varying molecular substitution. This reaction was performed at 4 °C overnight in 0.1 M MES buffer (pH 6.5) containing 50 μM Tris(2-carboxyethyl)phosphine hydrochloride (TCEP, Pierce Biotechnology, Rockford, IL) to keep the C-terminus Shh cysteine reduced for duration of the reaction. After the reaction, any remaining maleimide groups on the linear polymer were reduced by the addition of 0.5 mM dithiothreitol and incubation at 4 °C for 1 h.

All conjugation reactions were assayed by gel electrophoresis, comparing reaction solutions to an equal mass of unreacted Shh to visually inspect protein coupling efficiency. In addition, sets of triplicate Shh/HyA conjugation reactions at 20:1 and 10:1 molar feed ratios of Shh to HyA were dialyzed overnight in 0.1 MES buffer (pH 6.5) using Spectra/Por Float-A-Lyzer devices (Spectrum Laboratories, Rancho Dominguez, CA) to remove nonconjugated Shh. Protein concentrations in the dialyzed HyA-Shh solutions were then quantified using a microBCA assay (Pierce Biotechnology, Rockford, IL).

Bioactivity Assay. In order to test bioactivity, murine embryonic C3H10T1/2 cells (American Type Culture Collection, Manassas VA) were induced to differentiate into an osteogenic line by exposure to Shh as described elsewhere (*18, 19*). Briefly, the cells were plated at 5000 cells/well in 96 well plates in normal growth media (αMEM with 10% FBS). After 2 days, the medium was replaced with a low FBS (2%) media and supplemented with the proteins and/or conjugate reaction solutions. Test conditions included soluble Shh in the range of 1–100 nM, soluble Shh in the same range along with unconjugated HyA at 50 μ/mL, or the Shh/HyA conjugate in quantities such that the concentrations of Shh in the media solutions were also 1–100 nM. After incubation for an additional 3 days, the cells were washed and lysed, and the cell lysate was assayed for differentiation by measuring alkaline phosphatase (ALP) activity using the fluorescent probe 9-*H*-(1,3-dichloro-9,9-dimethylacridin-2-one-7-yl) phosphate (DDAO, Molecular Probes, Eugene OR). Unconjugated poly(acrylic acid) was shown to inhibit the differentiation of the cells, so bioactivity testing of these conjugates was not performed.

Angiogenesis Assay. As Shh is a known angiogenic agent (*20*), induced angiogenesis from soluble Shh and Shh/HyA conjugates was assayed using a CAM window assay. Fertile white leghorn eggs (Charles River, Franklin, CT) were incubated at 37 °C in a humidified environment until day 8, at which time 2 mL of albumin was removed from the blunt end of the egg, and a small 1 cm × 1 cm window was made in the shell on the opposite side. Sterile squares of filter paper loaded with sterile PBS, 0.1 μg of Shh, or 0.1 μg Shh of the 20:1 Shh/HyA feed ratio conjugate were placed directly on the developing CAM. This window was then sealed with parafilm and the eggs returned to the incubator. Angiogenesis around the test materials was microscopically evaluated 3 days later using an Olympus SZX7 stereoscope. High-resolution photomicrographs were taken using an attached QImaging Qfire camera. These images were analyzed using *ImageJ* software to quantify the number of blood vessels per unit length in a square perimeter surrounding the implants at distances of 0.1 and 0.25 cm away from its edge. Linear density measurements for each group were tested for statistical significance using a one-way ANOVA on both the 0.1 and 0.25 cm distance data, followed by pairwise Holm's *t* tests of the individual groups.

Molecular Modeling of Shh−HyA Conjugate Cell Signaling. We built upon binding and trafficking numerical models that describe expression of Gli transcriptional effectors in response to monomeric Shh (*21, 22*) and numerical kinetic models describing multivalent ligand–receptor binding (Figure S1, Supporting Information) (*23*). To develop the simplest model for the C3H10T1/2 bioactivity data in Figure 3, the following

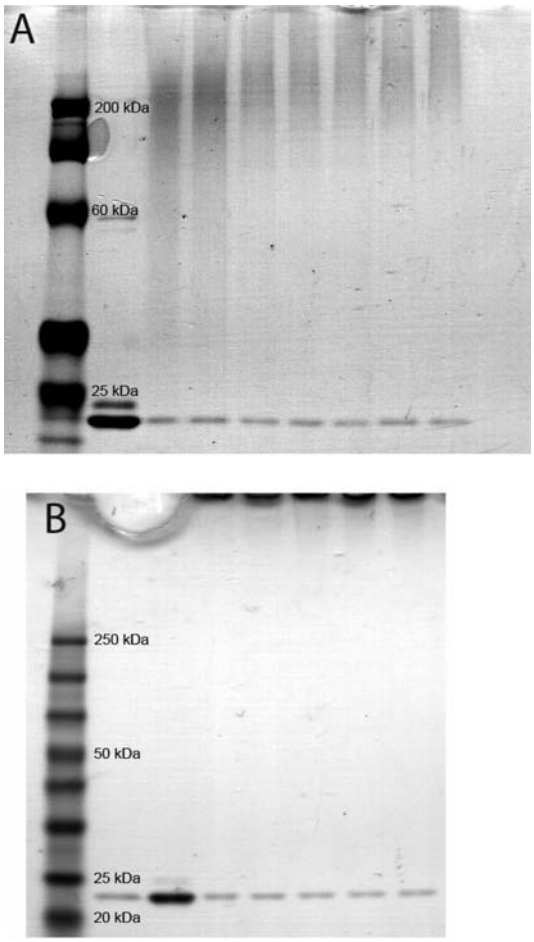

Figure 2. Gel electrophoresis of Shh and its conjugation products with pAAc (A) and HyA (B). In A, conjugates from 1:1 to 30:1 Shh/pAAc molar feed ratios appear as the loss of the Shh band and the appearance of a high molecular weight smear. In B, the large HyA conjugates are unable to enter the gel and are seen as bands residing at the top of the gel.

assumptions were invoked: Patched (Ptc) repression of Smoothened is not affected by the Ptc receptor aggregation; ligand-induced internalization rate is the same for all valencies; alkaline phosphatase activity is linearly proportional to Gli1 levels in a cell; and differentiation of a C3H10T1/2 cell does not change its responsiveness to Shh. Initial binding of the HyA−Shh conjugate was assumed to follow monomeric Shh-Ptc binding rates, but all other additional binding of Shh moieties from the conjugate to other Ptc receptors were assumed to occur at a higher rate. This assumption has been called the *equivalent site hypothesis* in that after initial binding, all subsequent sites on a multivalent conjugate for ligand binding are identical (*24*).

Model parameters were taken from literature (*21, 22*); however, a number of parameters were estimated directly from the bioactivity data in Figure 3. First, the monomeric Shh-Ptc binding constant k_{on}/k_{off} and the alkaline phosphatase activity/Gli1 expression ratio were estimated from the soluble Shh bioactivity curve. In addition, the multimeric Shh-Ptc binding constant was directly estimated from the 22:1 conjugate curve (see Table S1, Supporting Information). We also formulated an alternative model that incorporates steric hindrance of HyA chains as a simple reduction in conjugate binding affinity to Ptc. For the alternative model incorporating sterics, termed the "model with sterics", the multimeric Shh-Ptc binding constant

Table 1. Conjugation Ratios and Coupling Efficiencies Determined for Shh/HyA Reactions at 30:1 and 10:1 Molar Feed Ratios

	molar ratio of Shh/HyA		percent coupling	
feed ratio	30:1	10:1	30:1	10:1
trial 1	21.80	6.91	73.3%	69.8%
trial 2	22.58	6.65	76.0%	67.1%
trial 3	22.09	7.02	74.3%	70.8%
average	22.16	6.86	74.5%	69.2%
stdev	0.40	0.19	1.3%	1.9%

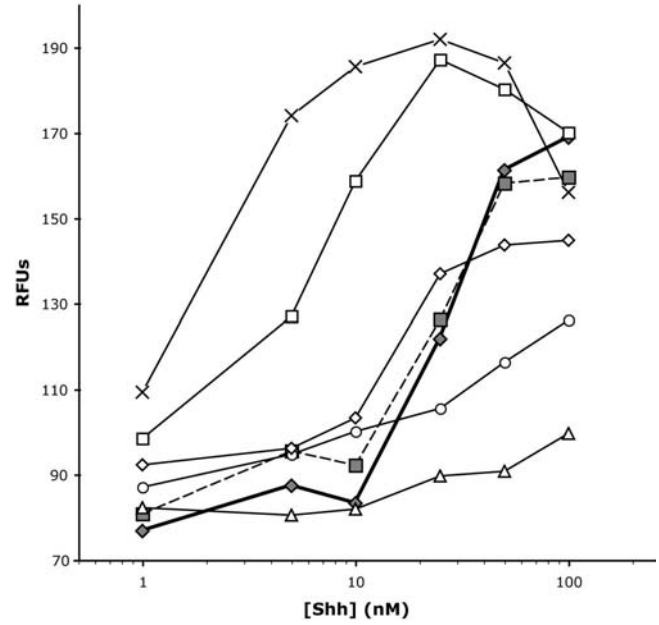

Figure 3. C3H10T1/2 bioactivity results against soluble Shh (♦, heavy line), soluble Shh with soluble HyA ■, dashed lines), and the Shh−HyA conjugates in stoichiometric ratios of 0.6:1 (△), 3.5:1 (○), 7:1 (◊), 14:1 (□), and 22:1 (×). Produced conjugates with Shh/HyA ratios of 0.6:1 and 3.5:1 have decreased efficacy on a unit basis of Shh compared to the freely soluble form, while 7:1–22:1 have increased bioactivity.

k_{on} for 0.6:1, 3.5:1, and 7:1 conjugation feed ratios was reduced 5.5-fold to match the experimental data from the 0.6:1 curve in Figure 3.

RESULTS

Chemical Conjugation. A recombinant rat Shh variant with a cysteine residue near the C-terminus was constructed, expressed, and purified via immobilized metal affinity chromatography. Conjugation of the recombinant protein was achieved on both pAAc and HyA with high efficiency. Using gel electophoresis, it was apparent that the reaction produced a decrease in the monomeric Shh band (Figure 2) and the appearance of a high molecular weight conjugate. For pAAc (Figure 2A) (MW = 450 000), this produced a smear through the gel with an increasing mass as the Shh conjugation molar feed ratio increased from 1:1 to 30:1. For HyA (MW = 10^6 Da), the high molecular weight conjugates did not penetrate deeply into the gel. By contrast, simply mixing the Shh with raw pAAc or HyA did not alter the Shh mobility in the gel (data not shown). Protein analysis of purified Shh/HyA reactions at 10:1 and 30:1 molar feed ratios performed in triplicate indicated that the reaction was reproducible with a high degree of efficiency at approximately 70−75% (Table 1). Molar feed ratios of 1:1, 5:1, 10:1, 20:1, and 30:1 produced Shh−HyA conjugates with molar substitution ratios of 0.6:1, 3.5:1, 7:1, 14:1, and 22:1, respectively.

C3H10T1/2 Cell Bioactivity Assay. Through the use of the murine embryonic cell line C3H10T1/2, conjugation of the Shh

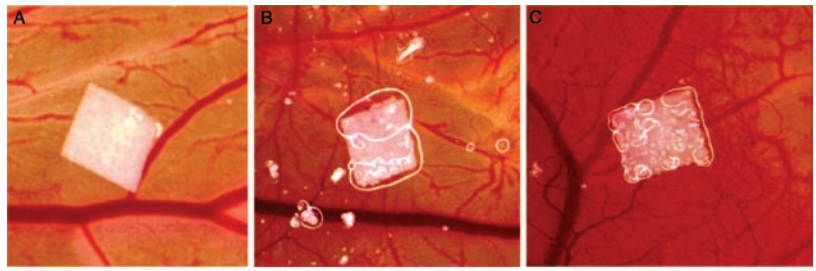

Figure 4. Panel of photomicrographs depicting CAM reactions to negative control samples (A), freely soluble Shh (B), and the 14:1 Shh/HyA multivalent form. Noted increased vessel density is apparent around the Shh sample as well as the conjugated form.

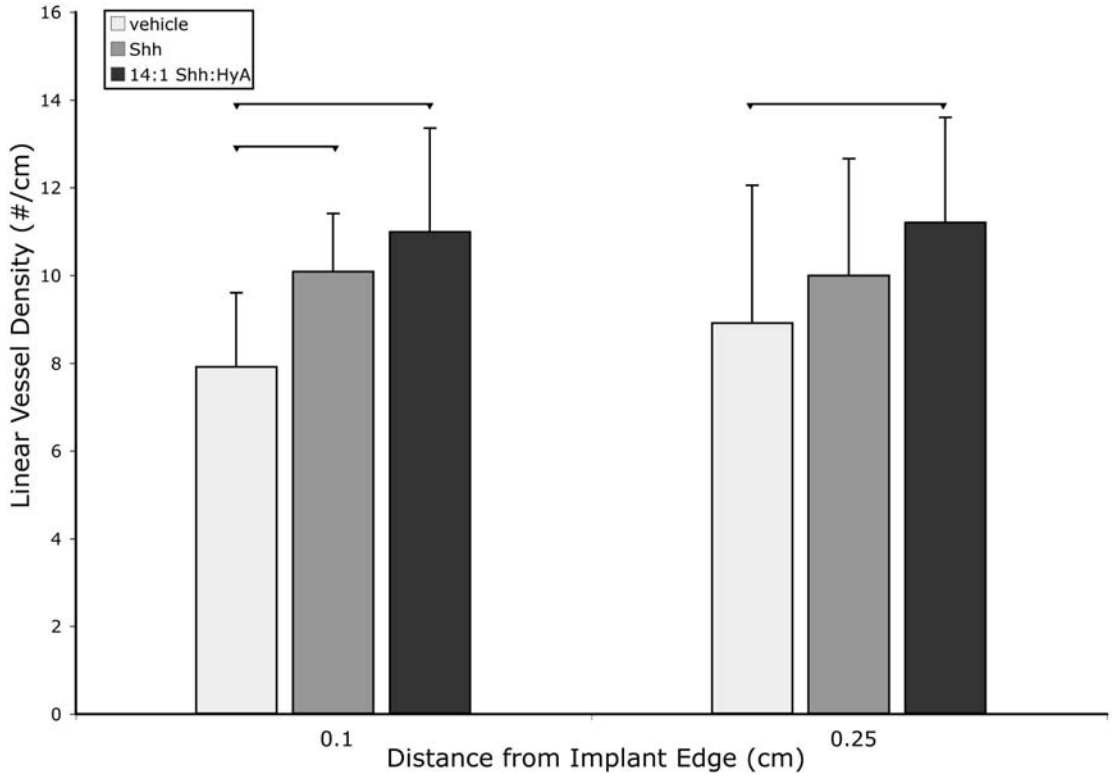

Figure 5. Quantitative results of angiogenesis in the CAM assay derived from photomicrograph image analysis. Increased vascular density is measured for both the soluble Shh and the Shh-*graft*-HyA in the 14:1 ratio. All three groups can be statistically separated at a distance of 0.1 cm from the edge of the implant, while at 0.25 cm, only the conjugated from is statistically different from the negative control.

was shown to dramatically alter the activity of the tethered protein when evaluated against actual Shh concentration in solution (Figure 3). Only HyA-conjugated Shh could be tested using this cell line, as pAAc inhibited the differentiation that soluble Shh induces in the cell line (data not shown). At low tethering (e.g., 3.5:1), the activity was decreased, with an estimated 10-fold increase in EC_{50} of the Shh in solution, presumably due to steric hindrances that the large linear polymer caused when attached. The activity increased back to normal when the conjugation ratio reached 7:1. Beyond this, activity of the tethered Shh was increased dramatically, with a 10-fold decrease in estimated EC_{50} values from the untethered Shh to the 22:1 construct.

CAM Angiogenesis Model. The CAM results indicated an increased potency for the conjugated Shh/HyA. Photographic analysis and quantification (Figures 4 and 5) revealed a statistically significant increase in vasculature around the Shh-loaded samples compared to the negative control within a close distance (0.1 cm) of the implant. While the Shh/HyA conjugated at a 14:1 ratio had an increased average vessel number over both the negative control and unconjugated Shh at 0.1 cm, it also had a longer-range persistent increase over the negative control at 0.25 cm. Although the soluble Shh also had an increased average vessel number over the negative control at this distance, this observation was not statistically significant.

Numerical Modeling of Multivalent Shh Bioactivity. We developed simple kinetic models of HyA−Shh conjugate binding, trafficking, and downstream signal activation. To focus on the effects of conjugate multivalency, a number of assumptions were invoked in the simplified models: Ptc receptor aggregation does not affect signal transduction; ligand internalization is not affected by valency; alkaline phosphatase activity is linearly proportional to Gli1 levels in a cell regardless of differentiation; and only two rates of conjugate binding occur—an initial binding of the conjugate and a higher binding rate for all additional Shh moieties from the conjugate to other Ptc receptors (see Supporting Information for model equations and parameters). With these assumptions, two types of models were developed, one incorporating steric hindrance of HyA chains as a simple reduction in conjugate binding affinity to Ptc, and one neglecting any influence of steric hindrance. These two models were termed “model with sterics” and “model without sterics”, respectively. Under these assumptions, modeling results indicated that increasing the conjugation ratio of Shh to its HyA carrier in the bioactivity assay should result in a progressive increase in cell signaling and decrease in the EC_{50}

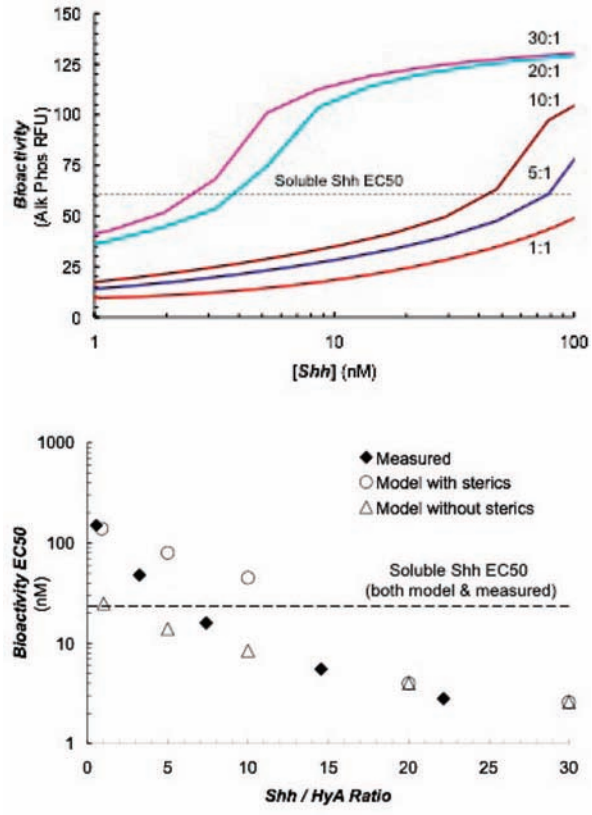

Figure 6. Numerical model results of Shh−HyA conjugate bioactivity in C3H10T1/2 cells. Activity as a function of Shh concentration for stoichiometric ratios 1:1–30:1 is shown on top for a model incorporating steric interaction (see text). A plot of EC_{50} versus substitution level for two types of models versus experimental results in Figure 3 is shown on the bottom. Both models capture the trend in EC_{50} with substitution ratio but fail to capture the increased amplitude of bioactivity for the 14:1 and 22:1 conjugates (see Figure 3).

(Figure 6). The estimated EC_{50} values from the experimental data were well-matched using both types of kinetic models at the tested conjugation ratios and with the aforementioned assumptions ($R^2 = 0.7$ for the model without sterics; $R^2 = 0.8$ for the model with sterics). For the model without sterics, EC_{50} values matched experimental results well at high conjugation ratios, but the modeling results overestimated the EC_{50} values for conjugation ratios 7:1 and lower (Figure 6). Results from the model with sterics can correct for this deviation (Figure 6); however, the fits at 3.5:1 and 7:1 conjugation ratios suggest that the exact mechanism of steric hindrance may vary from the one postulated in our model with sterics (see Discussion). Some features, such as the shape of the dose−response curve, as well as decreased peak location, were not as fit well using the developed model, as indicated by the comparison of Figures 3 and 6.

DISCUSSION

These results indicate that large proteins can be coupled to a linear polymer with high efficiency and controlled stoichiometry through the use of a heterobifunctional cross-linker under conditions that do not lead to loss of protein activity. On the contrary, coupling of a protein to a superstructure such as large linear polymer offers a method of modulating the activity of a protein by controlling its interaction with the cell. This method could be used to add multivalent protein functionality to both synthetic and biological polymers with equal efficiency. However, control of the reaction was much more difficult with the HyA than the pAAc. Conjugation to the pAAc was robust across a wide range of reaction pHs, concentrations, and times. On the other hand, adding the EMCH to the HyA required considerable optimization of the reaction conditions, as the reaction was much more sensitive to pH, concentrations, and time. High overall coupling efficiencies were observed only in the mildly acidic pH range 5.0–5.5 for the attachment of EMCH to HyA, which was consistent with the work of Pouyani et al. (*9*) and Vercruysse et al. (*25*). At neutral pH, although there are successful reports of EDC/sulfo-NHS mediated HyA bioconjugation (*26*, *27*) in these studies the overall conjugation was minimal. This may be due to hydrolysis of the maleimide rather than the lack of conjugation of the EMCH to the HyA chains, as the maleimide is susceptible to hydrolysis at pH > 6.5 and our scheme required long reaction times for the final protein attachment.

While the use of lower molecular weight HyA (∼250 kDa) in hydrazide mediated bioconjugation is observed in the literature (*28–30*), reporting better handling and more reproducible conjugation results, in our studies we chose to use high molecular weight HyA in order to maximize spacing and flexibility between conjugated protein molecules. We obtained reproducible results using this material, with repeated conjugation reactions producing nearly identical conjugation efficiencies and bioactivity curves. However, these results may be contributable to the reaction scheme used, for in our synthesis, the reaction was limited by the amount of protein added to the reaction. As only ∼1% of the available reaction sites on the HyA backbone are utilized on the highest conjugation ratio synthesized, if there is variability in the amount of EMCH substituted onto the backbone, this will be largely unnoticed as long as EMCH substitution rates exceed this small fraction of used sites.

The most striking result of our conjugation experiments was how the controlled attachment of Shh modulated protein activity as a function of valency. There are multiple possible mechanisms by which this increase in activity may result from tethering and include higher overall ligand affinity due to avidity effects, forced receptor multimerization, inhibition of receptor–ligand internalization, and changes to protein stability in solution. Such mechanisms have been previously identified and described for ligands such as DNA complexes (*6*, *7*), protein inhibitors (*8*, *12*), and growth factor pathways (*10*). We believe that similar mechanisms may be in action here, such as avidity effects from the interaction of multiple Shh molecules in the multivalent form with the Shh cell surface receptor Patched. Other mechanisms may be at play, as multimerization of Shh is known to change its short- and long-range activity in vivo (*31*), and internalization also plays a role in Shh activity (*32*, *33*).

Using novel numerical models, we attempted to elucidate the mechanism by which the bioactivity changes upon conjugation. In comparison to monomeric soluble Shh, multivalent Shh−HyA conjugates may have altered trafficking, binding, degradation, and signaling. Ordinary differential equations provide a convenient means to track the kinetics of each of these processes during Shh signal transduction. Both models—one incorporating sterics and one without sterics—can recapitulate the EC_{50} decrease with increasing valency (Figure 6). The poor fit at 3.5:1 and 7:1 conjugation ratios is likely due to the simple mechanism of steric hindrance that we incorporated into our model. In particular, steric hindrance effects on conjugate binding to Ptc is likely to change with conjugation ratio, since the average HyA chain length between Shh moieties that can shield Ptc reduces with increasing conjugation ratio. This effect has been described theoretically (*11*) and may be incorporated in future model development. A simpler model without internalization gave an even poorer fit with experiment, as did models that did not incorporate acceleration of binding after initial binding of

a multivalent conjugate, indicating the likely importance of these processes to the bioactivity of the conjugates (data not shown). Both models with and without sterics fail to describe the peak amplitude in bioactivity of the 14:1 and 22:1 conjugates (Figure 6). In our modeling results, we noticed that Ptc receptor aggregation levels have a biphasic relationship with increasing Shh concentration (data not shown): Ptc aggregation peaks at an intermediate Shh concentration much like the experimental results in Figure 3. The biphasic relationship, as described in the literature (*24*), occurs because, at high Shh concentrations, HyA−Shh conjugates compete with one another for available receptors and will be typically bound to fewer receptors, resulting in a lower avidity. Therefore, a peak in bioactivity as a function of Shh concentration could be due to Ptc receptor aggregation resulting in cooperativity in Ptc signal transduction. Future experimental work detailing Ptc cooperativity in Shh signal transduction is needed to justify future incorporation of such effects into our simple models. Also in future work, the equivalent site assumption could be relaxed to devise a binding relationship that scales with valency. Again, future experimental Ptc binding studies with conjugates of various valency may justify the incorporation of this effect into our simple models.

This work has significant implications for the fields of drug delivery and biomaterials. The surprising finding that the potency of Shh grafted onto a linear polymer is increased significantly over freely soluble Shh could be very useful in the design and administration of therapeutics as a means to increase potency. In addition, significant research effort is currently directed to impart bioactivity to materials for biological and biomedical applications, and the data and modeling presented provide insight into how the forced clustering of proteins on a surface or in a 3D matrix may alter the potency of the added protein or change the effectiveness of a peptide sequence. For example, linear polymers modified with bioactive agents have been incorporated into hydrogel networks to make bioactive semi-interpenetrating networks for tissue engineering applications (*34*, *35*). This research gives another form of modulation of added functionality in the solid state, as potency may be controllable by the both the amount of an agent added and its degree of substitution and spatial distribution.

ACKNOWLEDGMENT

This work was supported by LBNL LDRD 3668DS, by the Graduate Research and Education in Adaptive bio-Technology (GREAT) Training Program, UC Systemwide Biotechnology Research and Education Program 2005-280, and a Whitaker Foundation Graduate Fellowship.

Supporting Information Available: Details of the numerical kinetic model describing the signal pathway of Shh and the modifications to simulate the bioactivity effects of conjugated Shh are available. This material is available free of charge via the Internet at http://pubs.acs.org.

LITERATURE CITED

(1) Kuhl, P. R., and GriffithCima, L. G. (1996) Tethered epidermal growth factor as a paradigm for growth factor-induced stimulation from the solid phase. *Nat. Med. 2*, 1022–1027.

(2) Moon, J. J., Lee, S. H., and West, J. L. (2007) Synthetic biomimetic hydrogels incorporated with Ephrin-A1 for therapeutic angiogenesis. *Biomacromolecules 8*, 42–49.

(3) Seliktar, D., Zisch, A. H., Lutolf, M. P., Wrana, J. L., and Hubbell, J. A. (2004) MMP-2 sensitive, VEGF-bearing bioactive hydrogels for promotion of vascular healing. *J. Biomed. Mater. Res., Part A 68A*, 704–716.

(4) Zisch, A. H., Lutolf, M. P., Ehrbar, M., Raeber, G. P., Rizzi, S. C., Davies, N., Schmokel, H., Bezuidenhout, D., Djonov, V., Zilla, P., and Hubbell, J. A. (2003) Cell-demanded release of VEGF from synthetic, biointeractive cell-ingrowth matrices for vascularized tissue growth. *FASEB J. 17*, 2260.

(5) Ooya, T., and Yui, N. (2002) Multivalent interactions between biotin-polyrotaxane conjugates and streptavidin as a model of new targeting for transporters. *J. Controlled Release 80*, 219–228.

(6) Segura, T., and Shea, L. D. (2002) Surface-tethered DNA complexes for enhanced gene delivery. *Bioconjugate Chem. 13*, 621–629.

(7) Schaffer, D. V., and Lauffenburger, D. A. (1998) Optimization of cell surface binding enhances efficiency and specificity of molecular conjugate gene delivery. *J. Biol. Chem. 273*, 28004–28009.

(8) Thoma, G., Duthaler, R. O., Magnani, J. L., and Patton, J. T. (2001) Nanomolar E-selectin inhibitors: 700-fold potentiation of affinity by multivalent ligand presentation. *J. Am. Chem. Soc. 123*, 10113–10114.

(9) Pouyani, T., and Prestwich, G. D. (1994) Functionalized derivatives of hyaluronic-acid oligosaccharides - drug carriers and novel biomaterials. *Bioconjugate Chem. 5*, 339–347.

(10) York, S. J., Arneson, L. S., Gregory, W. T., Dahms, N. M., and Kornfeld, S. (1999) The rate of internalization of the mannose 6-phosphate/insulin-like growth factor II receptor is enhanced by multivalent ligand binding. *J. Biol. Chem. 274*, 1164–1171.

(11) Hlavacek, W. S., Posner, R. G., and Perelson, A. S. (1999) Steric effects on multivalent ligand-receptor binding: Exclusion of ligand sites by bound cell surface receptors. *Biophys. J. 76*, 3031–3043.

(12) Hubble, J. (1999) A model of multivalent ligand-receptor equilibria which explains the effect of multivalent binding inhibitors. *Mol. Immunol. 36*, 13–18.

(13) Muller, K. M., Arndt, K. M., and Pluckthun, A. (1998) Model and simulation of multivalent binding to fixed ligands. *Anal. Biochem. 261*, 149–158.

(14) Huskens, J., Mulder, A., Auletta, T., Nijhuis, C. A., Ludden, M. J. W., and Reinhoudt, D. N. (2004) A model for describing the thermodynamics of multivalent host-guest interactions at interfaces. *J. Am. Chem. Soc. 126*, 6784–6797.

(15) Lai, K., Kaspar, B. K., Gage, F. H., and Schaffer, D. V. (2003) Sonic hedgehog regulates adult neural progenitor proliferation in vitro and in vivo. *Nat. Neurosci. 6*, 21–27.

(16) Pepinsky, R. B., Rayhorn, P., Day, E. S., Dergay, A., Williams, K. P., Galdes, A., Taylor, F. R., Boriack-Sjodin, P. A., and Garber, E. A. (2000) Mapping Sonic hedgehog-receptor interactions by steric interference. *J. Biol. Chem. 275*, 10995–11001.

(17) Stile, R. A., and Healy, K. E. (2001) Thermo-responsive peptide-modified hydrogels for tissue regeneration. *Biomacromolecules 2*, 185–194.

(18) Taylor, F. R., Wen, D. Y., Garber, E. A., Carmillo, A. N., Baker, D. P., Arduini, R. M., Williams, K. P., Weinreb, P. H., Rayhorn, P., Hronowski, X. P., Whitty, A., Day, E. S., Boriack-Sjodin, A., Shapiro, R. I., Galdes, A., and Pepinsky, R. B. (2001) Enhanced potency of human sonic hedgehog by hydrophobic modification. *Biochemistry 40*, 4359–4371.

(19) Pepinsky, R. B., Zeng, C. H., Wen, D. Y., Rayhorn, P., Baker, D. P., Williams, K. P., Bixler, S. A., Ambrose, C. M., Garber, E. A., Miatkowski, K., Taylor, F. R., Wang, E. A., and Galdes, A. (1998) Identification of a palmitic acid-modified form of human Sonic hedgehog. *J. Biol. Chem. 273*, 14037–14045.

(20) Pola, R., Ling, L. E., Silver, M., Corbley, M. J., Kearney, M., Pepinsky, R. B., Shapiro, R., Taylor, F. R., Baker, D. P., Asahara, T., and Isner, J. M. (2001) The morphogen Sonic hedgehog is an indirect angiogenic agent upregulating two families of angiogenic growth factors. *Nat. Med. 7*, 706–711.

(21) Saha, K., and Schaffer, D. V. (2006) Signal dynamics in Sonic hedgehog tissue patterning. *Development 133*, 889–900.

(22) Lai, K., Robertson, M. J., and Schaffer, D. V. (2004) The Sonic hedgehog signaling system as a bistable genetic switch. *Biophys. J. 86*, 2748–2757.

(23) Perelson, A. S. (1981) Receptor clustering on a cell-surface 0.3. theory of receptor cross-linking by multivalent ligands - description by ligand states. *Math. Biosci. 53*, 1–39.

(24) Lauffenburger, D. A., and Linderman, J. J. (1993) Receptors: Models for Binding, Trafficking, and Signaling. Oxford University Press, New York.

(25) Vercruysse, K. P., Marecak, D. M., Marecek, J. F., and Prestwich, G. D. (1997) Synthesis and in vitro degradation of new polyvalent hydrazide cross-linked hydrogels of hyaluronic acid. *Bioconjugate Chem. 8*, 686–694.

(26) Bulpitt, P., and Aeschlimann, D. (1999) New strategy for chemical modification of hyaluronic acid: Preparation of functionalized derivatives and their use in the formation of novel biocompatible hydrogels. *J. Biomed. Mater. Res. 47*, 152–169.

(27) Stile, R. A., Barber, T. A., Castner, D. G., and Healy, K. E. (2002) Sequential robust design methodology and X-ray photoelectron spectroscopy to analyze the grafting of hyaluronic acid to glass substrates. *J. Biomed. Mater. Res. 61*, 391–398.

(28) Shu, X. Z., Liu, Y. C., Luo, Y., Roberts, M. C., and Prestwich, G. D. (2002) Disulfide cross-linked hyaluronan hydrogels. *Biomacromolecules 3*, 1304–1311.

(29) Luo, Y., Ziebell, M. R., and Prestwich, G. D. (2000) A hyaluronic acid-taxol antitumor bioconjugate targeted to cancer cells. *Biomacromolecules 1*, 208–218.

(30) Luo, Y., and Prestwich, G. D. (1999) Synthesis and selective cytotoxicity of a hyaluronic acid-antitumor bioconjugate. *Bioconjugate Chem. 10*, 755–763.

(31) Feng, J., White, B., Tyurina, O. V., Guner, B., Larson, T., Lee, H. Y., Karlstrom, R. O., and Kohtz, J. D. (2004) Synergistic and antagonistic roles of the Sonic hedgehog N- and C-terminal lipids. *Development 131*, 4357–4370.

(32) Torroja, C., Gorfinkiel, N., and Guerrero, I. (2004) Patched controls the Hedgehog gradient by endocytosis in a dynamin-dependent manner, but this internalization does not play a major role in signal transduction. *Development 131*, 2395–2408.

(33) Incardona, J. P., Lee, J. H., Robertson, C. P., Enga, K., Kapur, R. P., and Roelink, H. (2000) Receptor-mediated endocytosis of soluble and membrane-tethered Sonic hedgehog by Patched-1. *Proc. Natl. Acad. Sci. U.S.A. 97*, 12044–12049.

(34) Stile, R. A., Chung, E., Burghardt, W. R., and Healy, K. E. (2004) Poly(N-isopropylacrylamide)-based semi-interpenetrating polymer networks for tissue engineering applications. Effects of linear poly(acrylic acid) chains on rheology. *J. Biomater. Sci.-Polym. Ed. 15*, 865–878.

(35) Chung, E. H., Gilbert, M., Virdi, A. S., Sena, K., Sumner, D. R., and Healy, K. E. (2006) Biomimetic artificial ECMs stimulate bone regeneration. *J. Biomed. Mater. Res., Part A 79A*, 815–826.

BC700265K

Antibody−Dendrimer Conjugates: The Number, Not the Size of the Dendrimers, Determines the Immunoreactivity

C. Wängler, G. Moldenhauer, M. Eisenhut, U. Haberkorn, and W. Mier*

Universitaetsklinikum Heidelberg, Abteilung Nuklearmedizin, Germany. Received August 16, 2007; Revised Manuscript Received February 21, 2008

Radioimmunotherapy using antibodies with favorable tumor targeting properties and high binding affinity is increasingly applied in cancer therapy. The potential of this valuable cancer treatment modality could be further improved by increasing the specific activity of the labeled proteins. This can be done either by coupling a large number of chelators which leads to a decreased immunoreactivity or by conjugating a small number of multimeric chelators. In order to systematically investigate the influence of conjugations on immunoreactivity with respect to size and number of the conjugates, the anti-EGFR antibody hMAb425 was reacted with PAMAM dendrimers of different size containing up to 128 chelating agents per conjugation site. An improved dendrimer synthesis protocol was established to obtain compounds of high homogeneity suitable for the formation of defined protein conjugates. The quantitative derivatization of the PAMAM dendrimers with DOTA moieties and the characterization of the products by isotopic dilution titration using ^{111}In/^{nat}In are shown. The DOTA-containing dendrimers were conjugated with high efficiency to hMAb425 by applying Sulfo-SMCC as cross-linking agent and a 10- to 25-fold excess of the thiol-containing dendrimers. The determination of the immunoreactivities of the antibody−dendrimer conjugates by FACS analysis revealed a median retained immunoreactivity of 62.3% for 1.7 derivatization sites per antibody molecule, 55.4% for 2.8, 27.9% for 5.3, and 17.1% for 10.0 derivatization sites per antibody but no significant differences in immunoreactivity for different dendrimer sizes. These results show that the dendrimer size does not influence the immunoreactivity of the derivatized antibody significantly over a wide molecular weight range, whereas the number of derivatization sites has a crucial effect.

INTRODUCTION

Radioimmunotherapy is an expanding field in cancer therapy and shows very promising treatment results (*1–4*). However, the potential of this treatment modality has not yet been completely exploited. Besides heterogeneity in antigen expression, tumor load, perfusion defects, and tumor hypoxia, a further reason for this restraint resides in the low specific activity of the radiolabeled antibodies, which does not enable the delivery of optimal radioactive doses to tumor tissues and results in ineffective tumor treatment.

A solution for this problem is to introduce more than one radionuclide per protein to enhance the specific activity and by this the radioactive dose that can be applied to the tumor. However, it has been shown already that a few randomly distributed chelators or iodine atoms introduced into an IgG lead to a significant decrease of the immunoreactivity (*5, 6*). Consequently, an alternative method of introducing many chelators into an antibody molecule that does not lead to a drastic alteration of the properties of the protein is warranted. Recently, some studies about dendritic systems associated with antibodies were undertaken to solve this problem. The synthesized antibody−dendrimer conjugates showed preserved immunoreactivities of the antibodies and provided high specific activities (*7–10*).

In this study, we systematically investigated the influence of introduced dendritic structures with respect to size and the number of derivatization sites per protein. Using the anti-EGFR antibody hMAb425, we assessed the influence of DOTA-derivatized PAMAM dendrimers of various dendrimer generations and conjugation load on the immunoreactivity of antibodies. This study gives insights into a favorable derivatization pattern for antibody−PAMAM−dendrimer conjugates with a minimal loss of immunoreactivity, suited for improved radioimmunotherapy and diagnostic imaging.

EXPERIMENTAL PROCEDURES

General. All commercially available chemicals were of analytical grade and used without further purification. HPLC solvents containing TFA were prepared using 0.1% TFA (v/v).

The analytical HPLC system used was an Agilent 1100 system together with a Chromolith Performance (RP-18e, 100–4.6 mm, Merck, Germany) column. Semipreparative HPLC purifications were performed using a Gyncotech P-580 system (Germering, Germany) equipped with a variable SPD 6-A UV detector and a C-R5A integrator (both Shimadzu, Duisburg, Germany). The column applied for semipreparative purification was a Chromolith (RP-18e, 100–10 mm, Merck, Germany).

MALDI-TOF spectroscopy was performed using a Kratos Analytical Compact Maldi III system. ESI spectra were obtained using a Triple-Quadrupole-mass spectrometer TSQ 7000 (Thermo Fisher Scientific, Bremen). NMR spectra were taken using a Varian Mercury Plus 300 MHz and a Varian NMR System 500 MHz, respectively.

Thin layer chromatography was performed using Polygram SIL G/UV$_{254}$ TLC-plates (Macherey-Nagel, Düren, Germany). The PBS buffer consisted of 0.05 M phosphate, 0.15 M NaCl, at pH 7.2. Size-exclusion gel chromatography was carried out using NAP-5 columns (GE Healthcare Bio-Sciences AB, Uppsala, Sweden) and size-exclusion FPLC was performed on a Superdex 200 10/30 GL column (Amersham Biosciences AB, Uppsala, Sweden). ^{111}In was purchased from Perkin-Elmer (Rodgau, Germany).

* Universitaetsklinikum Heidelberg, Abteilung Nuklearmedizin, INF 400, Heidelberg, 69120, Germany. E-mail walter.mier@med.uni-heidelberg.de.

10.1021/bc700308q CCC: $40.75 © 2008 American Chemical Society
Published on Web 03/25/2008

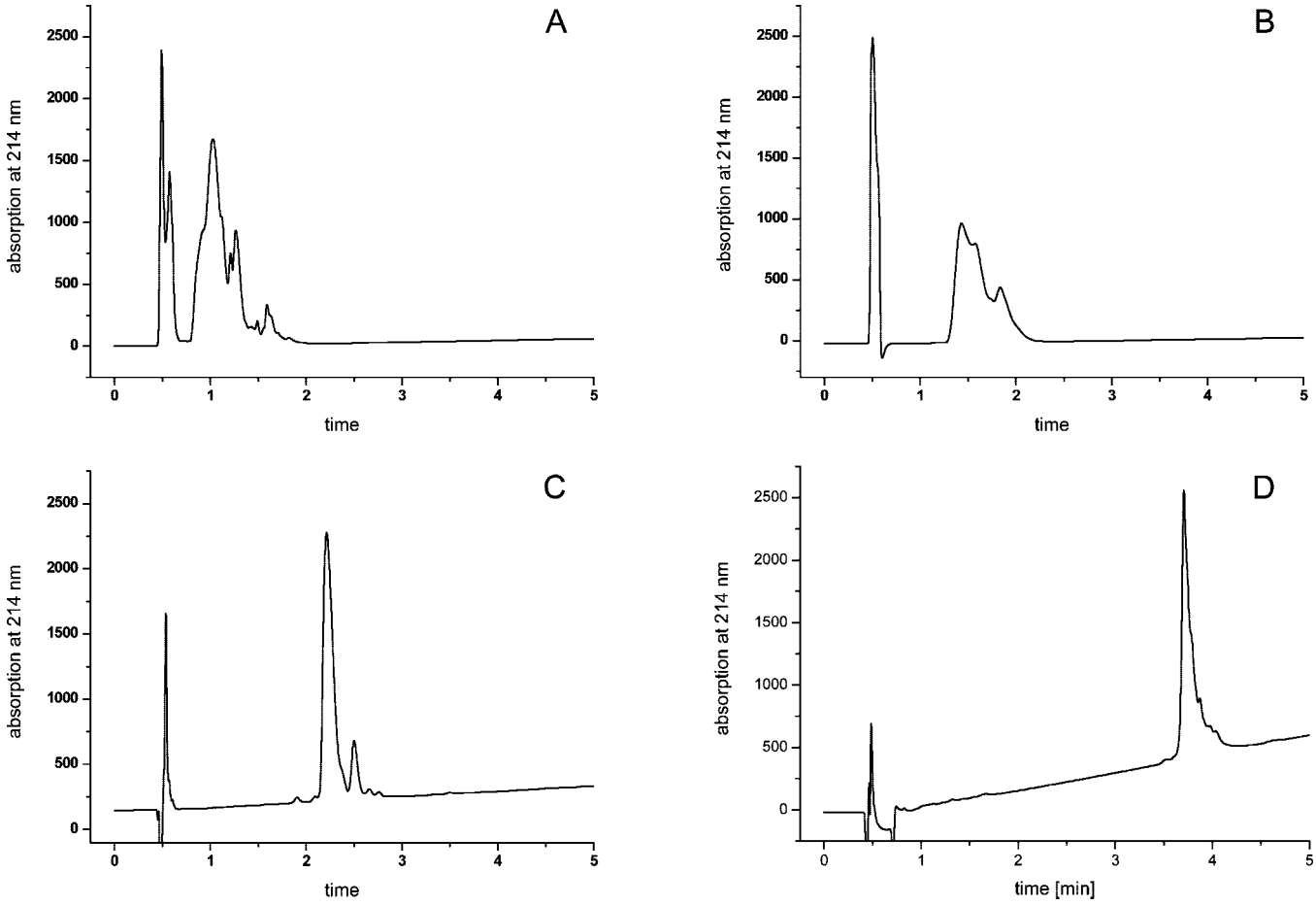

Figure 1. HPLC chromatograms of commercially available PAMAM dendrimers with 8 amino functions (A) and 16 amino functions (B). C and D show chromatograms of dendritic structures with 8 and 16 amino functions synthesized as described in the experimental procedures. Chromatograms were recorded at 214 nm and obtained using a Chromolith Performance column and a water/acetonitrile (+0.1% TFA (v/v)) gradient from 0% to 40% acetonitrile over 5 min in A and B. For C and D, a gradient from 20% to 45% acetonitrile over 5 min was used, as the compounds show a higher lipophilicity than the nonderivatized PAMAM dendrimers in A and B.

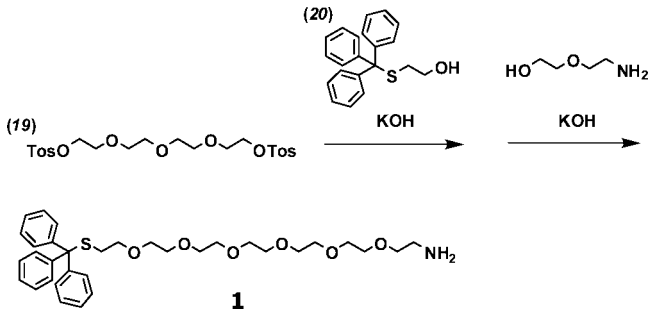

Figure 2. Synthesis scheme of the penta(ethylene glycol) linker.

Ellman′s Assay. A 2 mM solution of MESNA (sodium 2-mercaptoethanesulfonate) in PB (0.1 M, pH 8) was diluted to obtain solutions of the following concentrations: 125 μM, 64 μM, 32 μM, 16 μM, 8 μM, 4 μM, and 2 μM. To 1 mL of each of these solutions, 200 μL of a solution of Ellman′s reagent (5,5′-dithio-bis-(2-nitrobenzoic acid), 4 mg/mL in PB (0.1 M, pH 8)) was added and the absorption of the obtained mixtures was measured at 412 nm in a UV/vis spectrometer to give the calibration curve.

The thiol concentrations of the samples were determined analogously by adding 200 μL of the solution of Ellman′s reagent to 1 mL of sample in PB (0.1 M, pH 8) and by measuring the absorption at 412 nm.

The number of maleimides per dendrimer was determined by reacting it with an access of MESNA (5 equiv) and subsequent titration of free thiol with Ellman′s assay.

***S*-Trityl-mercaptoethyl-tetra(ethylene glycol)-tosylate.** To a solution of tetra(ethylene glycol)-bistosylate (22 g, 45 mmol), *S*-trityl-mercaptoethanol (10 g, 31 mmol), and TBAB (1.5 g, 4.5 mmol) in toluene (200 mL), powdered KOH (~3 g) was added. After two hours, the mixture was filtered and the resulting solution was evaporated. The remaining oil was purified via column chromatography on silica with *n*-hexane/acetone 2:1 as the eluent ($R_f = 0.4$). The product was obtained as a light yellow oil (11 g, 17 mmol, 55%).

***S*-Trityl-mercaptoethyl-penta(ethylene glycol)-ethylamine (G_0) (1).** To a solution of *S*-trityl-mercaptoethyl-tetra(ethylene glycol)-tosylate (28.5 g, 59 mmol), and 2-(2-aminoethoxy)ethanol (31 g, 296 mmol) in toluene (100 mL) and DMF (10 mL), powdered KOH (~5 g) was added. After five hours, the mixture was filtered and the resulting solution was evaporated. The remaining oil was purified via chromatography on silica with $CHCl_3$/ethanol 5:2 as the eluent ($R_f = 0.37$). The product was obtained as a yellow oil (15.5 g, 27 mmol, 45%).

Half-Generation PAMAM Dendrimers $G_{0.5}$ to $G_{6.5}$ (2, 4, 6, 8, 10, 12, and 14). A solution of the respective full-generation (G_X) dendrimer in methanol (20 mL) was added to methyl acrylate (200 equiv per amine function) and stirred for 3 to 31 days at room temperature. The volatile components were evaporated and the crude products were purified via chromatography on silica with *n*-hexane/acetone 4:5, ethanol/acetone

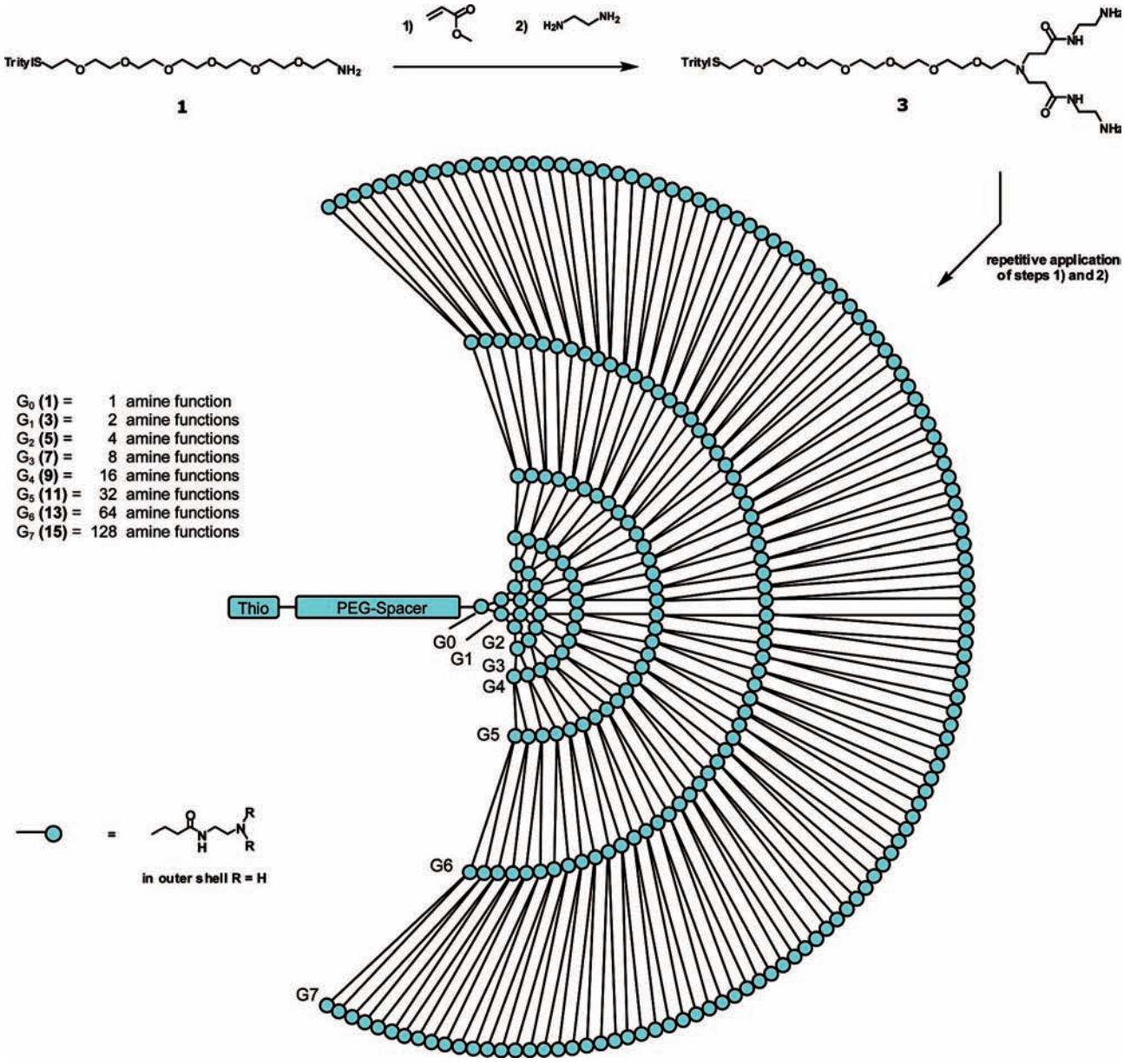

Figure 3. Synthesis scheme of the PAMAM dendrimers.

5:6, or 55% MeCN in water containing 0.1% TFA for smaller dendrimers and via semipreparative HPLC using a gradient of 0–100% MeCN + 0.1% TFA over 7 min as the eluent for larger dendrimers. The products were obtained as light yellow to orange oils in yields of 30% to 83%.

Full-Generation PAMAM Dendrimers G_1 to G_7 (3, 5, 7, 9, 11, 13, and 15). A solution of the respective half-generation dendrimer ($G_{X.5}$) in methanol (20 mL) was added dropwise to a cooled solution of ethylenediamine (400 equiv per methyl ester) over a half-hour and stirred for 5 to 41 days at 4 °C until the reaction was complete. Subsequently, the ethylenediamine was evaporated. In the case of smaller dendrimers, the products were found to be clean enough for further use. Larger dendrimers were purified using semipreparative HPLC using a gradient of 0–100% MeCN + 0.1% TFA over 7 min. The products were obtained as yellow to orange oils in yields of 70% to 99%.

G_0 to G_7 Maleimides (16, 19, 22, 25, 28, 31, 34, and 37). A solution of PyBOP (3.9 equiv per amine function of the respective dendrimer) and DIPEA (4 equiv per amine function) in DMF (300 μL) was added to maleimido caproic acid (4 equiv per amine function) and reacted for 2 min. Subsequently, this mixture was added to a solution of the respective full-generation dendrimer (G_X) (50 μmol) in DMF (200 μL). After one hour, 1 M NaOH (300 μL) and MeCN (1 mL) were added, and the volatile components were evaporated. After acidification with 1 M HCL (500 μL), the products were purified using semipreparative HPLC using a gradient of 0–100% MeCN + 0.1% TFA over 12 min. The products were isolated as colorless to brown oils in yields of 29% to 84% after lyophilization.

G_0 to G_7 *S*-trityl-Protected DOTA Dendrimers (17, 20, 23, 26, 29, 32, 35, and 38). To a solution of the respective maleimide-derivatized dendrimer (G_X maleimide) (10 μmol) in MeCN (200 μL) was added a solution of thiol-DOTA (4 equiv per maleimide) in 250 μL, and the mixture was reacted for 10 min. After acidification with 1 M HCL (200 μL), the products were purified using semipreparative HPLC using a gradient of 20–100% MeCN + 0.1% TFA over 8 min. The products were isolated as white to ocher solids in yields of 51% to 96% after lyophilization.

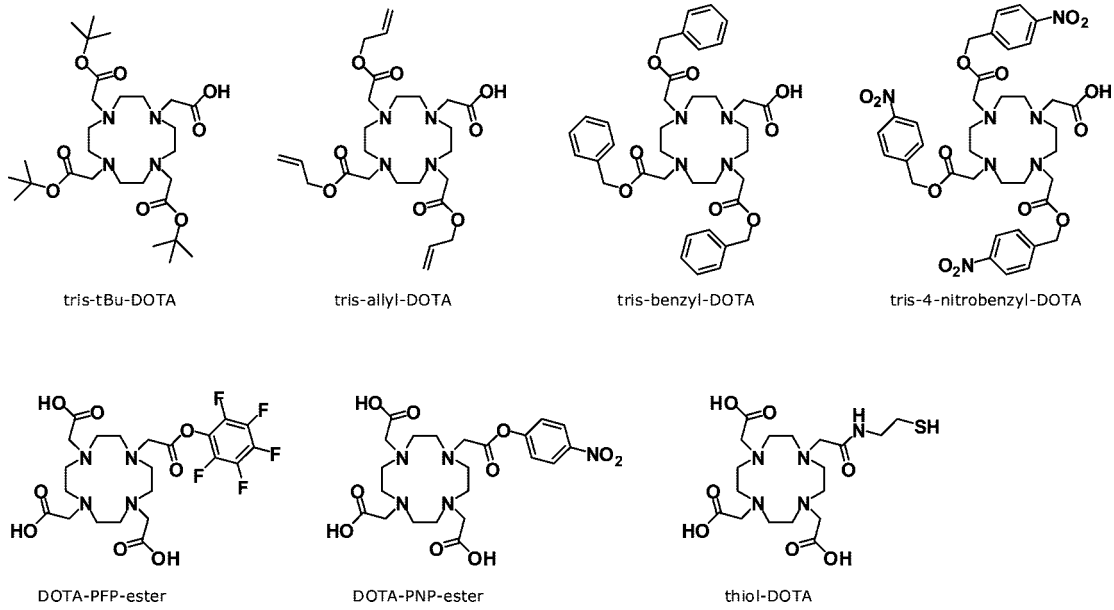

Figure 4. Structures of the studied DOTA-derivatives: tris-tBu-DOTA, tris-allyl-DOTA, tris-benzyl-DOTA, tris-4-nitrobenzyl-DOTA, DOTA−PFP−ester, DOTA–PNP−ester, and thiol-DOTA.

G_0 to G_7 Deprotected DOTA Dendrimers (18, 21, 24, 27, 30, 33, 36, and 39). The respective *S-trityl*-protected DOTA dendrimer (10 μmol) was dissolved in a mixture of TIS (200 μL) and TFA (2 mL) and reacted for 5 min. The volatile components were evaporated, and the products were purified using semipreparative HPLC using a gradient of 0–100% MeCN + 0.1% TFA over 7 min. The products were isolated as colorless oils or light ocher solids in yields of 58% to 98% after lyophilization.

Dervatization of hMAb425 with Sulfo-SMCC. A freshly prepared solution of Sulfo-SMCC (42 μg, 9.7×10^{-8} mol) in DMF/water 1:1 (10 μL) was added to a fresh solution of hMAb425 (2 mg, 1.39×10^{-8} mol) in 500 μL PBS. After one hour of incubation, the derivatized antibody was purified via size-exclusion chromatography using NAP-5 columns. The derivatized antibody was obtained in high yields (95–98%). The number of maleimide functions per antibody molecule was determined using MESNA and Ellman's assay and was found to be 1.7. The antibody derivatizations with more equivalents of Sulfo-SMCC were carried out according to this procedure.

hMAb425-DOTA$_X$-Dendrimers. To a solution of hMAb425, derivatized with Sulfo-SMCC (1.6 mg, 1.11×10^{-8} mol) in 500 μL PBS, was added a freshly prepared solution of the respective DOTA$_X$-dendrimer (25 equiv, 2.78×10^{-7} mol) in 100 μL PBS. The reaction was complete after 5 min and the products were analyzed using size-exclusion FPLC with PBS as the eluent (R_t between 13.7 and 16.1 min).

The conjugation of DOTA$_X$-dendrimers containing a lower number of equivalents of were carried out according to this procedure.

Immunoreactivities of the Antibody−Dendrimer Conjugates. *Cells.* The human colon adenocarcinoma cell line HT29 expressing considerable amounts of epidermal growth factor receptor was maintained in RPMI 1640 medium supplemented with 2 mM L-glutamine, 1 mM pyruvate, and 10% heat-inactivated fetal calf serum. Prior to use, cells were detached from the surface of the tissue culture flask by treatment with 0.25% trypsin plus 0.25% EDTA in PBS and counted.

Flow Cytometry. Serial dilutions of dendrimer-conjugated matuzumab were compared with unmodified matuzumab for binding to HT29 cells. For this, antibody dilutions ranging from 5 μg/mL to 1 ng/mL were prepared in FACS buffer (Dulbecco's PBS with 2% fetal calf serum and 0.1% sodium azide). Staining was performed in a 96-well microtiter plate (U-bottom). 100 μL/well antibody was mixed with 50 μL cell suspension containing 5×10^5 HT-29 cells and incubated for 1 h on ice. Cells were washed twice with FACS-buffer by centrifuging the plate and siphoning off the supernatant. Subsequently, 100 μL/well F(ab)′$_2$ goat-antihuman IgG (H+L)-FITC (Jackson ImmunoResearch, West Grove, PA) diluted 1:100 in FACS buffer was added as second-step reagent. The plate was incubated for 1 h on ice in the dark, and cells were washed again twice as above. Dead cells were discriminated by propidium iodide staining. Analysis was carried out on a FACScan cytometer (Becton Dickinson, Heidelberg, Germany) using the *CELLQUEST* software.

For each dendrimer conjugate as well as for unconjugated matuzumab, a binding curve was obtained by plotting the mean fluorescence intensity (MFI) versus the antibody concentration.

RESULTS AND DISCUSSION

Improvement of PAMAM Dendrimer Synthesis. Dendrimers have shown to be effective drug delivery vehicles for a variety of applications (*11–13*) and are also the basis for approved pharmaceuticals as, for example, for the diagnostic cardiac marker Stratus and the microbicide Vivagel. In general, a major advantage of dendrimers over polymers is their low dispersity. However, the homogeneity of commercially available dendrimers was found to be low (Figure 1A,B). Similar results have recently been described for commercially available PAMAM dendrimers which were analyzed with HPLC and MALDI-TOF spectrometry showing high polydispersities of the compounds (*14, 15*).

Therefore, these compounds were not chosen as building blocks for the syntheses of the DOTA-multimers. Attempts to synthesize PAMAM dendrimers according to literature methods (*16–18*) resulted in products with higher quality which, however, did not demonstrate sufficient homogeneity. Therefore, the synthesis protocols had to be improved.

The substantial modification was the strict limitation of the reaction temperatures to below 20 and 4 °C for the synthesis of half and full generations, respectively. Reactions conducted above the indicated temperatures led to highly fragmented products and a high amount of intramolecular ring formations, with the consequence of highly heterogeneous dendritic

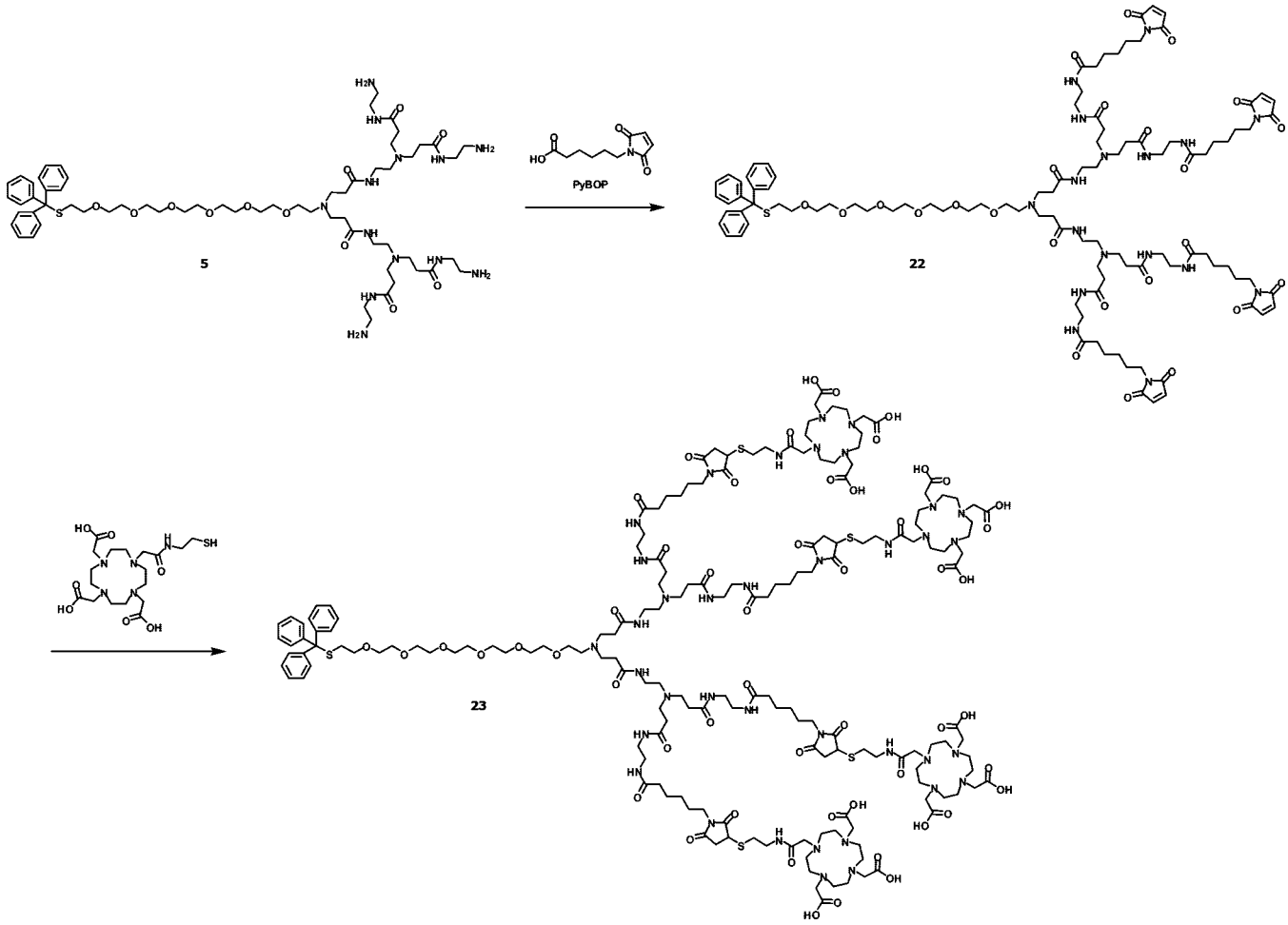

Figure 5. Synthesis scheme for the derivatization of the amino groups with maleimides and subsequently with thiol-DOTA as exemplified for the G_2 dendrimer (**5**).

Table 1. Characterization Results of the DOTA-Functionalized Dendrimers (n = 5 and 3 for the Determination of the Number of Maleimides and Functional Chelators, Respectively)

dendrimer generation (number of amino functions and chelators)/molecular weight	number of maleimides determined by mass spectrometry/ back-titration	number of functional chelators determined by mass spectrometry/ isotopic dilution titration
G_0 (1)/998 $^g/_{mol}$	1/–	1/–
G_1 (2)/1883 $^g/_{mol}$	2/–	2/–
G_2 (4)/3653 $^g/_{mol}$	4/–	4/–
G_3 (8)/7187 $^g/_{mol}$	8/–	8/9.9 ± 2.8
G_4 (16)/14261 $^g/_{mol}$	16/–	–/17.2 ± 0.4
G_5 (32)/28405 $^g/_{mol}$	–/33.1 ± 3.9	–/32.2 ± 0.3
G_6 (64)/55733 $^g/_{mol}$	–/62.9 ± 6.8	–/69.1 ± 6.7
G_7 (128)/112309 $^g/_{mol}$	–/120.2 ± 10.5	–/155.1 ± 33.7

structures and highly demanding purification steps. However, with the modifications of the synthesis protocol described, the dendrimers were obtained in good yields and purity (Figure 1C,D).

Table 2. Parameters of the Antibody−Sulfo-SMCC and −DOTA-Dendrimer Reactions

amount of Sulfo-SMCC applied relative to antibody	number of introduced maleimides per antibody	excess of $DOTA_X$-dendrimers applied relative to antibody
7 equiv	1.7	10 equiv
12 equiv	2.8	12.5 equiv
22 equiv	5.3	15 equiv
45 equiv	10.0	25 equiv

A penta(ethylene glycol) linker containing a thiol function was used as the starting structure element. This linker was introduced to enhance the accessibility of the reactive site of the dendritic system, thereby allowing the effective and selective introduction of the dendritic molecule into proteins or peptides. The linker system was synthesized starting from tetra(ethylene glycol)-bistosylate (*19*), *S*-trityl-mercaptoethanolamine (*20*) and 2-(2-amino-ethoxy)-ethanol as shown in Figure 2.

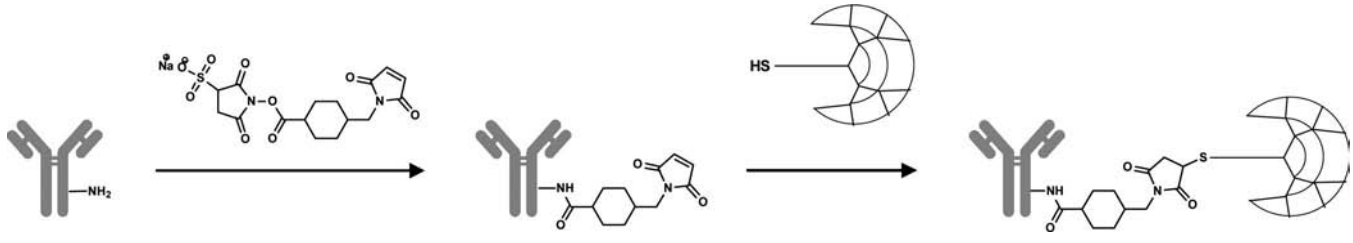

Figure 6. Schematic depiction of the conjugation of the DOTA-dendrimers to the antibody.

Table 3. Results of the Derivatization Reactions and Determination of the Immunoreactivities of the Antibody−Dendrimer Conjugates[a]

	immunoreactivity retained (number of dendrimers per antibody)			
antibody conjugate	1.7 maleimides per antibody	2.8 maleimides per antibody	5.3 maleimides per antibody	10.0 maleimides per antibody
hMAb425-DOTA$_1$	60.3% (0.4)	66.3% (0.5)	35.7% (1.0)	30.0% (1.9)
hMAb425-DOTA$_2$	68.4% (0.5)	64.3% (0.6)	31.3% (0.9)	24.4% (1.9)
hMAb425-DOTA$_4$	66.2% (0.5)	64.7% (0.6)	28.5% (1.1)	17.6% (2.1)
hMAb425-DOTA$_8$	57.8% (1.0)	55.3% (1.2)	26.7% (2.7)	13.0% (6.9)
hMAb425-DOTA$_{16}$	63.2% (0.8)	49.0% (1.5)	21.6% (2.5)	12.6% (5.8)
hMAb425-DOTA$_{32}$	60.6% (0.8)	40.8% (1.1)	27.9% (1.5)	14.2% (2.7)
hMAb425-DOTA$_{64}$	58.2% (1.7)	46.6% (2.6)	23.3% (3.6)	8.4% (7.3)
hMAb425-DOTA$_{128}$	63.9% (1.0)	56.1% (1.9)	28.5% (2.5)	16.4% (4.4)

[a] Immunoreactivities are given relative to the immunoreactivity of the underivatized antibody.

It represents the starting generation (G_0) of the dendrimer, as it shows no branching. Subsequently, the PAMAM dendrimers were grown on the terminal amino function of the linker by alternating reaction with methyl acrylate and ethylenediamine to give half ($G_{X.5}$) and full generations (G_{X+1}) of the dendrimer (Figure 3).

Using this method, we were able to synthesize PAMAM dendrimers of 1 to 128 amino functions on a penta(ethylene glycol) linker providing a thiol for selective coupling to a carrier protein. The dendrimers obtained were found to be of high homogeneity and are therefore suitable as building blocks for the synthesis of DOTA-multimers.

Formation of DOTA-Multimers. For the subsequent derivatization of the PAMAM dendrimer amino functions with DOTA, the following differently protected and activated DOTA-derivatives were studied with regard to their coupling yields and the homogeneity of the obtained products: tris-tBu-DOTA (*21*), DOTA−PFP−ester and DOTA–PNP−ester (*22*), tris-allyl-DOTA (*23*), tris-benzyl-DOTA (*24*), tris-4-nitrobenzyl-DOTA and thiol-DOTA (*25*) (Figure 4).

Tris-tBu-DOTA and tris-allyl-DOTA showed high coupling yields and very homogeneous coupling products. However, in both cases the deprotection resulted in mixtures that were difficult to purify. DOTA−PFP−ester, DOTA–PNP−ester, tris-benzyl-DOTA, and tris-4-nitrobenzyl-DOTA were found to react incompletely, thus producing inhomogeneous products even when applied in an excess of up to 5 equiv per amine function. This behavior was attributed to the relatively low reactivity of the active esters and the steric hindrance of tris-benzyl-DOTA and tris-4-nitrobenzyl-DOTA.

In contrast to the amide linked conjugates, the thiol-DOTA could be introduced quantitatively after preceding derivatization of the amino groups of the dendrimers with maleimido caproic acid (Figure 5).

Using these maleimide-bearing dendrimers, the DOTA-derivatized compounds were obtained in good yields and high purities. Furthermore, the coupling reaction was completed within a few minutes and did not require an additional deprotection step for the DOTA moieties.

The number of maleimides per dendritic structure was determined by reacting an aliquot of the maleimide-containing dendrimer with a 5-fold excess of MESNA (sodium 2-mercaptoethanesulfonate) for 5 min. The excess of thiol was subsequently quantified using the Ellman′s assay. The amount of reacted thiol corresponds to the amount of maleimides. Using this method, it could be shown that the reaction of the dendritic amines with maleimido caproic acid proceeded quantitatively (Table 1).

After the derivatization of the dendritic structures with thiol-DOTA, the number of functional chelators per dendrimer was determined by isotopic dilution titration (*22*) using a 10^{-10} mol/L solution of the respective dendrimer (relating to DOTA) and trace amounts of ^{111}In in the presence of a range of concentrations of ^{nat}In (10^{-5}, 10^{-6}, 7.5×10^{-7}, 5×10^{-7}, 2.5×10^{-7}, 10^{-7}, 7.5×10^{-8}, 5×10^{-8}, 2.5×10^{-8}, 10^{-8}, and 10^{-9} mol/mL) in sodium acetate buffer (0.4 M, pH 5). The complexation was stopped after 20 min at 60 °C by the addition of an excess of EDTA, and the amount of dendrimer-bound ^{111}In was determined by TLC. The results of the isotopic dilution titrations are shown in Table 1. Apparently, the number of functional chelators per dendrimer molecule provided a slight overestimation, which is possibly due to the formation of radiocolloids. However, the quantitative reaction of thiol-DOTA with the maleimide-containing dendrimers could be shown.

Using this technique, the amino functions of the PAMAM dendrimers were derivatized quantitatively with DOTA, yielding homogeneous products in good yields and short reaction times. Furthermore, additional deprotection steps were dispensable.

Conjugation of DOTA-Multimers to hMAb425. To determine the influence of the DOTA-containing structures on the immunoreactivity of an antibody, the dendrimers were conjugated to hMAb425. This humanized monoclonal antibody is directed against the EGF receptor and was recently investigated in clinical studies (*26–28*).

For the antibody derivatization, the protein was reacted with 7, 12, 22, or 45 equiv of the heterobifunctional cross-linker Sulfo-SMCC (sulfosuccinimidyl-4-(*N*-maleimidomethyl)-cyclohexane-1-carboxylate) for one hour and isolated using size-exclusion gel chromatography in high recovery rates of 95–98%. The antibody concentration in the obtained solution was determined using the Bradford Assay and the number of maleimides per antibody molecule was determined by back-titration with MESNA as described above and found to be 1.7, 2.8, 5.3, and 10.0 for an applied Sulfo-SMCC amount of 7, 12, 22, or 45 equiv, respectively.

The maleimide-derivatized antibodies were then reacted with the different DOTA-containing dendrimers for 5 min (Figure 6).

A summary of the reaction parameters of the antibody derivatization with Sulfo-SMCC and the following dendrimer conjugation is given in Table 2.

The number of dendritic structures per antibody was determined by ^{111}In-labeling of the DOTA-dendrimers and subsequent antibody conjugation as described above. The reaction mixtures were analyzed by size-exclusion FPLC and the amount of dendrimer conjugated was identified by determining the distribution of radioactivity between the protein and dendrimer fractions collected (results shown in Table 3).

The immunoreactivities of the antibody−dendrimer conjugates were determined by FACS analysis using HT29-cells. The immunoreactivities relative to the underivatized antibody were calculated from the corresponding IC_{50} values.

The results shown in Table 3 reveal that the dendrimer size does not influence the immunoreactivity of the derivatized antibody significantly. In contrast to this, the number of derivatization sites has a crucial effect.

These results show that the synthesis of antibody−dendrimer conjugates containing up to 128 chelating agents per binding site is feasible.

For comparison, a conjugate containing single DOTA moieties linked to the antibody hMAb425 was produced using *S*-2-(4-isothiocyanatobenzyl)-1,4,7,10-tetraazacyclododecane-tetraacetic acid (Macrocyclics Dallas, TX). This preparation contained approximately 5 DOTA molecules per antibody. The affinity measurement described in the experimental procedures showed that it retained 46.8% of its immunoreactivity.

The comprehensive study of the influence of the substitution pattern on the immunoreactivity revealed that the size of a conjugated dendritic structure does not significantly influence the immunoreactivity of antibodies over a wide molecular weight range, whereas the number of derivatization sites is the major factor that determines the binding affinity of the conjugates. Therefore, an antibody modification with dendritic structures should consist of a derivatization with few but large dendritic systems to obtain antibodies that result in a minor change of immunoreactivity. In this context, an antibody modification with less than 1.7 derivatization sites per antibody should lead to higher immunoreactivities of the conjugates than those shown above, though they would require a separation of the dendrimer-conjugated antibodies to attain high specific activities.

Additionally, a site-specific conjugation (*29*) of the dendritic structures to the constant region of the antibody might be used and allow a further improvement of the concept by less altered immunoreactivities of the antibody−dendrimer conjugates.

In these conjugates, only a minor fraction of the chelators in can be occupied by the radiometal and complexes formed with Ca(II), and other metal ions will be the predominant species in the circulation. It has to be investigated whether and to what extent large polar dendritic structures alter the pharmacokinetics and the specific accumulation of these antibody conjugates.

CONCLUSION

Several maleimide-reactive DOTA-containing PAMAM dendrimers of different sizes were synthesized for the introduction into antibodies and other macromolecules to enhance their specific activity for radioimmunotherapy and clinical diagnostics. For this purpose, the established synthesis protocols for PAMAM dendrimers were improved to obtain products of high homogeneity that are suited for further derivatization. For the subsequent coupling of DOTA moieties, a synthesis strategy was found that allows the quantitative derivatization of the PAMAM amino functions, making a deprotection of the DOTA moieties dispensable. The DOTA multimers were conjugated to the anti-EGFR-antibody hMAb425, the number of dendrimers per antibody molecule was determined, and immunoreactivity studies of the antibody−dendrimer conjugates were performed. These experiments showed that the dendrimer size over a wide range does not influence the immunoreactivity of the derivatized antibodies significantly, whereas the number of derivatization sites has a crucial effect.

LITERATURE CITED

(1) Leahy, M. F., Seymour, J. F., Hicks, R. J., and Turner, J. H. (2006) Multicenter phase II clinical study of iodine-131-Rituximab radioimmunotherapy in relapsed or refractory indolent non-hodgkin's lymphoma. *J. Clin. Oncol. 24*, 4418–4425.

(2) Gordon, L. I., Witzig, T., Molina, A., Czuczman, M., Emmanouilides, C., Joyce, R., Vo, K., Theuer, C., Pohlman, B., Bartlett, N., Wiseman, G., Darif, M., and White, C. (2004) Yttrium-90-labeled ibritumomab tiuxetan radioimmunotherapy produces high response rates and durable remissions in patients with previously treated B-cell lymphoma. *Clin. Lymphoma 5*, 98–101.

(3) Akabani, G., Reardon, D. A., Coleman, R. E., Wong, T. Z., Metzler, S. D., Bowsher, J. E., Barboriak, D. P., Provenzale, J. M., Greer, K. L., DeLong, D., Friedman, H. S., Friedman, A. H., Zhao, X. G., Pegram, C. N., McLendon, R. E., Bigner, D. D., and Zalutsky, M. R. (2005) Dosimetry and radiographic analysis of ^{131}I-labeled anti-tenascin 81C6 murine monoclonal antibody in newly diagnosed patients with malignant gliomas: A phase II study. *J. Nucl. Med. 46*, 1042–1051.

(4) Chen, Z. N., Mi, L., Xu, J., Song, F., Zhang, Q., Zhang, Z., Xing, J. L., Bian, H. J., Jiang, J. L., Wang, X. H., Shang, P., Qian, A. R., Zhang, S. H., Li, L., Li, Y., Feng, Q., Yu, X. L., Feng, Y., Yang, X. M., Tian, R., Wu, Z. B., Leng, N., Mo, T. S., Kuang, A. R., Tan, T. Z., Li, Y. C., Liang, D. R., Lu, W. S., Miao, J., Xu, G. H., Zhang, Z. H., Nan, K. J., Han, J., Liu, Q. G., Zhang, H. X., and Zhu, P. (2006) Targeting radioimmunotherapy of hepatocellular carcinoma with iodine (^{131}I) metuximab injection: clinical phase I/II trials. *Int. J. Radiat. Oncol. Biol. Phys. 65*, 435–44.

(5) Brechbiel, M. W., Gansow, O. A., Atcher, R. W., Schlom, J., Esteban, J., Simpson, D. E., and Colcher, D. (1986) Synthesis of 1-(*p*-isothiocyanatobenzyl) derivatives of DTPA and EDTA. Antibody labeling and tumor-imaging studies. *Inorg. Chem. 25*, 2112–2181.

(6) Nikula, T. K., Boccia, M., Curcio, M. J., Sgouros, G., Ma, Y., Finn, R. D., and Scheinberg, D. A. (1995) Impact of the high tyrosine fraction in complementary determining regions: measured and predicted effects of radioiododination on IgG immunoreactivity. *Mol. Immunol. 32*, 865–872.

(7) Thomas, T. P., Patri, A. K., Myc, A., Myaing, M. T., Ye, J. Y., and Norris, T. B., Jr. (2004) In vitro targeting of synthesized antibody-conjugated dendrimer nanoparticles. *Biomacromolecules 5*, 2269–2274.

(8) Kobayashi, H., Sato, N., Saga, T., Nakamoto, Y., Ishimori, T., Toyama, S., Togashi, K., Konishi, J., and Brechbiel, M. W. (2000) Monoclonal antibody-dendrimer conjugates enable radiolabeling of antibody with markedly high specific activity with minimal loss of immunoreactivity. *Eur. J. Nucl. Med. 27*, 1334–1339.

(9) Wu, G., Barth, R. F., Yang, W., Chatterjee, M., Tjarks, W., Ciesielski, M. J., and Fenstermaker, R. A. (2003) Site-specific conjugation of boron-containing dendrimers to anti-egf receptor monoclonal antibody cetuximab (IMC-C225) and its evaluation as a potential delivery agent for neutron capture therapy. *Bioconjugate Chem. 15*, 185–194.

(10) Wu, C., Brechbiel, M. W., Kozak, R. W., and Gansow, G. A. (1994) Metal-chelate-dendrimer-antibody constructs for use in radioimmunotherapy and imaging. *Bioorg. Med. Chem. Lett. 4*, 449–454.

(11) Wu, G., Barth, R. F., Yang, W., Kawabata, S., Zhang, L., and Green-Church, K. (2006) Targeted delivery of methotrexate to epidermal growth factor receptor-positive brain tumors by means of cetuximab (IMC-C225) dendrimer bioconjugates. *Mol. Cancer Ther. 5*, 52–59.

(12) Majoros, I. J., Myc, A., Thomas, T., and Mehta, C. B., Jr. (2006) PAMAM dendrimer-based multifunctional conjugate for cancer therapy: synthesis, characterization, and functionality. *Biomacromolecules 7*, 572–579.

(13) Padilla De Jesus, O. L., Ihre, H. R., Gagne, L., and Frechet, J. M., Jr. (2002) Polyester dendritic systems for drug delivery applications: in vitro and in vivo evaluation. *Bioconjugate Chem. 13*, 453–461.

(14) Islam, M. T., Shi, X., Balogh, L., and Baker, J. R., Jr. (2005) HPLC separation of different generations of poly(amidoamine) dendrimers modified with various terminal groups. *Anal. Chem. 77*, 2063–2070.

(15) Wang, X., Inapagolla, R., Kannan, S., Lieh-Lai, M., and Kannan, R. M. (2007) Synthesis, characterization, and in vitro activity of dendrimer-streptokinase conjugates. *Bioconjugate Chem. 18*, 791–799.

(16) Fréchet, J. M. J., Tomalia, D. A. (2002) *Dendrimers and other dendritic polymers.* (Scheirs, J. Ed.) pp 590–602, *Chapter 25*, Wiley, Chichester.

(17) Tomalia, D. A., Baker, H., Dewald, J., Hall, M., Kallos, G., Martin, S., Roeck, J., Ryder, J., and Smith, P. (1986) Dendritic

macromolecules: synthesis of starburst dendrimers. *Macromolecules 19*, 2466–2468.

(18) Peterson, J., Ebber, A., Allikmaa, V., and Lopp, M. (2001) Synthesis and cze analysis of PAMAM dendrimers with an ethylenediamine core. *Proc. Estonian Acad. Sci. Chem. 50*, 156–166.

(19) Maltese, M. (2001) Reductive demercuration in deprotection of trityl thioethers, trityl amines, and trityl ethers. *J. Org. Chem. 66*, 7615–7625.

(20) Chen, Y., and Baker, G. L. (1999) Synthesis and properties of ABA amphiphiles. *J. Org. Chem. 64*, 6870–6873.

(21) Heppeler, A., Froidevaux, S., Mäcke, H. R., Jermann, E., Béhé, M., Powell, P., and Hennig, M. (1999) Radiometal-labelled macrocyclic chelator-derivatised somatostatin analogue with superb tumour-targeting properties and potential for receptor-mediated internal radiotherapy. *Chem.—Eur. J. 5*, 1974–1981.

(22) Mier, W., Hoffend, J., Krämer, S., Schuhmacher, J., Hull, W. E., Eisenhut, M., and Haberkorn, U. (2005) Conjugation of DOTA using isolated phenolic active esters: the labeling and biodistribution of albumin as blood pool marker. *Bioconjugate Chem. 16*, 237–240.

(23) Wängler, B., Beck, C., Wagner-Utermann, U., Schirrmacher, E., Bauer, C., Rösch, F., Schirrmacher, R., and Eisenhut, M. (2006) Application of tris-allyl-DOTA in the preparation of DOTA-peptide conjugates. *Tetrahedron Lett. 47*, 5985–5988.

(24) Anelli, P. L., Lattuada, L., Gabellini, M., and Recanati, P. (2001) DOTA Tris(phenylmethyl) Ester: A new useful synthon for the synthesis of DOTA monoamides containing acid-labile bonds. *Bioconjugate Chem. 12*, 1081–1084.

(25) Mattila, K., Siltainsuu, J., Balaspiri, L., Ora, M., and Lönnberg, H. (2005) Derivatization of phosphopeptides with mercapto- and amino-functionalized conjugate groups by phosphate elimination and subsequent Michael addition. *Org. Biomol. Chem. 3*, 3039–3044.

(26) Seiden, M. V., Burris, H. A., Matulonis, U., Hall, J. B., Armstrong, D. K., Speyer, J., Weber, J. D. A., and Muggia, F. (2007) A phase II trial of EMD 72000 (matuzumab), a humanized anti-EGFR monoclonal antibody, in patients with platinum-resistant ovarian and primary peritoneal malignancies. *Gynecol. Oncol. 104*, 727–731.

(27) Kollmannsberger, C., Schittenhelm, M., Honecker, F., Tillner, J., Weber, D., Oechsle, K., Kanz, L., and Bokemeyer, C. (2006) A phase I study of the humanized monoclonal anti-epidermal growth factor receptor (EGFR) antibody EMD 72000 (matuzumab) in combination with paclitaxel in patients with EGFR-positive advanced non-small-cell lung cancer (NSCLC). *Ann. Oncol. 17*, 1007–1013.

(28) Graeven, U., Kremer, B., Südhoff, Th., Killing, B., Rojo, F., Weber, D., Tillner, J., Ünal, C., and Schmiegel, W. (2006) Phase I study of the humanised anti-EGFR monoclonal antibody matuzumab (EMD 72000) combined with gemcitabine in advanced pancreatic cancer. *Br. J. Cancer 94*, 1293–1299.

(29) Mindt, T. L., Jungi, V., Wyss, S., Friedli, A., Pla, G., Novak-Hofer, I., Grünberg, J., and Schibli, R. (2007) Modification of different igG1 antibodies via glutamine and lysine using bacterial and human tissue transglutaminase. *Bioconjugate Chem.* ASAP Article; DOI: 10.1021/bc700306n.

BC700308Q

Glycoside Esters of 5-Aminolevulinic Acid for Photodynamic Therapy of Cancer

Ramakrishnan Vallinayagam,[†,‡] Frédéric Schmitt,[†,§] Jérome Barge,[||] Georges Wagnieres,[||] Virginie Wenger,[‡] Reinhard Neier,[‡] and Lucienne Juillerat-Jeanneret*[,§]

Institute of Chemistry, Neuchâtel University, avenue de Bellevaux, P.O. Box 2, CH-2007 Neuchâtel, Switzerland, University Institute of Pathology, Centre Hospitalier Universitaire Vaudois (CHUV) and University of Lausanne (UNIL), Bugnon 25, CH-1011 Lausanne, Switzerland, and Swiss Federal Institute of Technology (EPFL), Laboratory of Photomedicine, EPFL, CH-1015 Lausanne, Switzerland. Received August 27, 2007; Revised Manuscript Received November 21, 2007

Aliphatic and ethylene glycol esters of 5-aminolevulinic acid (ALA) are very efficient precursors of the photosensitizer protoporphyrin IX (PpIX) for photodynamic therapy; however, they diffuse passively across the cell membrane and thus lack cell selectivity. We evaluated whether α-glucose, α-mannose, or β-galactose esters of ALA would present improved properties as precursors of PpIX. Esterification was performed either at the position O-1 or O-6 of the sugars with or without an ethylene glycol linker, and these glycoside esters of ALA were evaluated in human cells. The results demonstrated that glycoside esters of ALA are efficient precursors of PpIX in human cancer and angiogenic endothelial cells, comparable to free ALA, but not in normal human fibroblasts. PpIX production was confirmed by fluorescence microscopy and photodynamic treatment of cells. The O-1 or O-6 positions of functionalization and the nature of the sugar moiety did not influence PpIX production. The presence of the ethylene glycol linker generally resulted in decreased PpIX production. The uptake of these glycoside esters of ALA by cells was not decreased in the presence of high concentrations of the related sugars. Inhibitors of α-glucosidases or α-mannosidases did not decrease PpIX production. These results suggest the involvement of active non-glycoside-specific membrane transporter(s) for uptake and of esterases rather than glycosidases in the release of ALA from the glycoside esters of ALA.

INTRODUCTION

In recent years, fluorescent photodetection and photodynamic therapy (PDT) have received increasing attention as new approaches for the selective detection and treatment of cancer. These procedures involve the systemic or topical administration of agents leading to the accumulation of photosensitizers in the targeted tissues. Then, these photosensitizers are activated by light either to produce fluorescence, thus allowing detection of tumors, or to produce cytotoxic molecules, such as reactive oxygen species, which lead to tissue destruction by a multistep cascade. Photosensitizers can be prepared as already-light-reactive molecules, mostly as porphyrin or chlorin derivatives, or as precursor molecules able to generate the photosensitizing molecules inside the target cells using intracellular enzymatic pathways. One possibility is the production of the photosensitizer protoporphyrin IX (PpIX) from the precursor 5-aminolevulinic acid (ALA) (*1–4*). External addition of ALA, or its derivatives (*5–10*), results in enhanced synthesis of porphyrin by cells. In order to enter the cellular porphyrin biosynthetic pathways, precursor photosensitizers such as ALA must be internalized by target cells and processed to the photosensitizer PpIX. This processing depends on the presence in target cells of the necessary (1) receptor and transport systems, (2) enzymes able to release the active molecule ALA from its prodrug, and (3) enzymes able to perform the intracellular biosynthetic pathway to generate the photosensitizer PpIX (Scheme 1).

However, the selective accumulation of all photosensitizers, including ALA, in tumors is not discriminating enough, inducing damage to the surrounding tissue in PDT protocols and overall photosensitization. Thus, improvement in the selectivity of photosensitizers to tumor cells versus nontumoral cells is needed (*11, 12*). It has been previously shown in cancer that the angiogenic endothelial cells associated with cancer may also be valuable targets for photodynamic therapy, in addition to tumor cells themselves (*13–15*). Tumor-associated angiogenesis is presently under clinical evaluation also for new therapeutic approaches to cancer treatment other than PDT (*16–18*). It has also been shown that glycosylation pathways are deregulated in cancer and cancer cells, likely as a result of the increased metabolism and energy demand of actively metabolizing cells, such as cancer and proliferating endothelial cells (*19–22*). Thus, carbohydrates, including glucose, mannose, or galactose, may represent the means to selectively deliver therapeutic agents to cancer and cancer-associated cells, such as angiogenic endothelial cells, while sparing nontumoral cells such as fibroblasts.

We have previously shown that aliphatic and ethylene glycol esters of ALA increased PpIX production by cells; however, the kinetics of cell uptake suggested passive diffusion of these esters across the cell membrane and activation by cellular esterases, without cell selectivity (*8, 9*). We have also previously shown that amino acids and dipeptides coupled via a peptide bond to ALA were substrates for cellular peptidases, following their active transport across the cell membrane (*9, 10, 23*). Some selectivity for endothelial cells of peptide derivatives was obtained. To the best of our knowledge, no study has evaluated the cell uptake and efficacy of ALA conjugates of sugars, whereas in the context of photosensitizers for PDT, various

* Corresponding author. Dr. Lucienne Juillerat, PhD, PD, MER, University Institute of Pathology, rue du Bugnon 25, CH-1011 Lausanne, Switzerland. phone: +41 21 314 7173, fax: +41 21 314 7115, e-mail: lucienne.juillerat@chuv.ch.

[†] These two authors contributed equally to this work.

[‡] Neuchâtel University.

[§] CHUV and UNIL.

[||] EPFL.

10.1021/bc700324r CCC: $40.75 © 2008 American Chemical Society
Published on Web 03/15/2008

Scheme 1. Cellular Processing of the Glycoside−ALA Derivatives

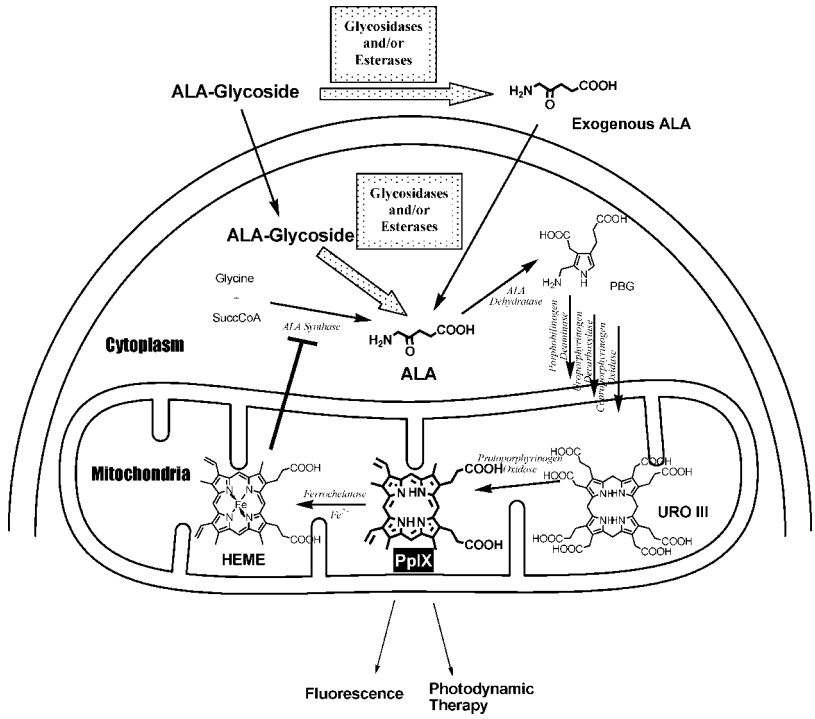

glycoside derivatives of porphyrins or chlorins have been synthesized in recent years demonstrating the potential for these derivatives to improve the transport of photosensitizers into cells (*24–31*). Therefore, in the present manuscript, our objectives were to prepare and evaluate glycoside esters of ALA in order to determine (i) if these conjugates are taken up by cells and are efficient precursors of PpIX in human tumor cells, angiogenic endothelial cells, and normal fibroblasts; (ii) if cellular enzymes, such as esterases or possibly glycosidases, can release ALA from these glycoside esters of ALA; (iii) if these conjugates display improved cell selectivity among tumor cells, endothelial cells, and fibroblasts; and (iv) if they can be used as precursors of photosensitizers for efficient PDT of cancer.

EXPERIMENTAL PROCEDURES

Chemistry. *General Methods.* Chemicals and solvents were purchased from Cambridge Isotope Laboratories, Fluka, Merck, and Acros and were of the highest purity available. They were used without further purification with the exception that solvents were distilled over drying agent when requested. D-(+)-Galactose, D-(+)-glucose, and D-(+)-mannose were from Fluka, Biochemika (≥99.5% purity); levulinic acid was from Acros, and 2,3,4,6-β-D-galactopyranosyl bromide was from Fluka. Lipase from *Candida antarctica* (LCA,Novozyme 435, 10 units/mg protein), proteinase from *Bacillus subtilis* (5 units per mg of protein) and porcine liver esterase (PLE, 24 units/mg protein) were from Sigma-Aldrich, and porcine pancreas lipase (PPL, 24 units/mg protein) was from Fluka.

Perkin-Elmer Spectrum One version B FT-IR was used for obtaining IR spectra with the resolution of 2 cm^{-1}. The solid and thick oily substances were analyzed by preparing KBr pellets. Liquid samples were analyzed as film (sandwich) by applying between two KBr plates. The absorption bands between 4000 and 400 cm^{-1} were measured. Software used was *Spectrum* v 5.0.1. The intensity of the spectrum was divided into five equal parts for the abbreviations vs (the maximum intensity), s (intense), m (medium intensity), w (weak), br (broad), and vw (very weak).

The NMR spectra were measured using a Variant Gemini XL-200 spectrometer at 298 K (^{1}H was measured at 200 Hz and ^{13}C at 50 Hz) or using a Bruker Avance-400 spectrometer at 298 K (^{1}H was measured at 400 Hz and ^{13}C was at 100 Hz). The internal standard for the spectra of ^{1}H was TMS ($\delta = 0.00$ ppm), $CHCl_3$ ($\delta = 7.26$ ppm), CH_3OH ($\delta = 3.31$ ppm), $(CH_3)_2SO$ ($\delta = 2.50$ ppm), or D_2O ($\delta = 4.79$ ppm). The internal standard for the spectra of ^{13}C was TMS ($\delta = 0.00$ ppm), $CHCl_3$ ($\delta = 77.16$ ppm), CH_3OH ($\delta = 49.00$ ppm), or $(CH_3)_2SO$ ($\delta = 39.52$ ppm). The ^{13}C spectra were measured by decoupling from ^{1}H. The chemical shift is given in ppm in the descending order and the coupling constant J in Hz. The multiplicity of signals were given abbreviations s (singlet), d (doublet), t (triplet), q (quartet), quint (quintet), dt (doublet of triplet), br (broad), and m (multiplet). The sign $\approx$ denotes for the average value of J varying from 0.2 to 0.4 Hz. The ratio of α to β is measured by area integration in the case of ^{1}H and by the intensity (height) of peak in the case of ^{13}C. All the products were measured for HETCOR (short-range), COSY, and DEPT 135 for the accurate interpretation of signals.

The mass spectra measurements for ESI (electrospray ionization) and for APCI (atmospheric pressure chemical ionization) were performed using a ThermoFinnigan LCQ (San Jose, California, USA), using the *Tune Plus* v 1.2 software. The values given are average masses of ion with precision in the range of ±0.1 values. The nature of the ion is written in parentheses together with the intensity. The high-resolution mass spectroscopy (HR-MS) was performed at the University of Fribourg (Switzerland) by Mr. F. Nydegger. The instrument used was a Brucker BioAPEX II daltonics using electrospray ionization (ESI).

*5-Bromo-4-oxo Methyl Pentanoate (**2**).* To a solution of levulinic acid **1** (100 g, 861 mmol, 1.0 equiv) in 860 mL methanol at 0 °C, bromine (44 mL, 861 mmol, 1.0 equiv) was added dropwise over 3 h. The addition of bromine was carried out in such a way that the reaction temperature never exceeded 30 °C. At the end of the addition, the solution was dark orange. The reaction mass was brought to room temperature and was kept stirring overnight at room temperature. The resultant

Scheme 2. Synthesis of Starting Materials[a]

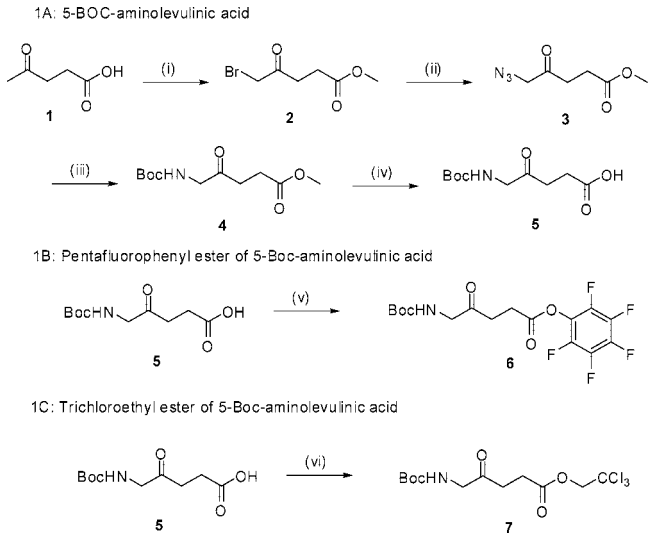

[a] Reagents and conditions: (i) Br_2, MeOH, reflux, 1.5 h; (ii) NaN_3, THF/H_2O, room temperature, 1 h; (iii) H_2/Pd, Boc_2O, room temperature, 12 h; (iv) porcine liver esterase (PLE), phosphate buffer pH 8.0, room temperature, 7 h; (v) C_6F_5OH, DCC, room temperature, 2 h; (vi) CCl_3CH_2OH, EDC, DMAP, room temperature, 3 h.

colorless solution was refluxed in MeOH for 1.5 h; then, solvent was evaporated. The yellow residue was dissolved in 400 mL of CH_2Cl_2 and extracted with 400 mL of H_2O. The organic phase was further extracted with 200 mL of a saturated solution of $NaHCO_3$, then with 3 × 200 mL of H_2O, dried over $MgSO_4$, filtered, and evaporated. The yellow residue (156 g) was subjected to fractional distillation by means of a Widmer column of 40 cm under reduced pressure (4×10^{-2} mbar), and fractions were collected according to changes of vapor temperature. One of the fractions contained 81 g of 5-bromo-4-oxo methyl pentanoate **2**, with 98% purity by ^{1}H NMR and with 45% yield. R_f (hexane/EtOAc 1:1): 0.50. Bp: ~80 °C at pressure = 0.045 mbar. n_D^{20}: 1.4820. IR (KBr): 3000m, 2953m, 2849w, 1734s, 1722s, 1439s, 1411s, 1359s, 1322m, 1207s, 1177s, 1079m, 1025m, 988m, 862w, 768vw, 694w, 595vw, 496vw, 464w. ^{1}H NMR (200 MHz, $CDCl_3$, 298 K): δ_H (ppm) = 3.95 (s, 2H, $H_2C(5)$); 3.67 (s, 3H, $H_3C(1^1)$; 2.95 (t, $^3J_{3-2} = 6.4$, 2H, $H_2C(3)$); 2.64 (t, $^3J_{2-3} = 6.4$, 2H, $H_2C(2)$). ^{13}C NMR (50 MHz, $CDCl_3$, 298 K): δ_C (ppm) = 201.3 (C(4)); 173.4 (C(1)); 52.6 ($C(1^1)$); 35.1 (C(3)); 34.7 (C(2)); 28.8 (C(5)). MS (ESI (+)): [M (^{79}Br) + Na]$^+$ = 231.1, [M (^{81}Br + Na]$^+$ = 233.0.

*5-Azido-4-oxo Methyl Pentanoate (**3**).* To a solution of NaN_3 (17.68 g, 272 mmol, 2 equiv) in 68 mL of deionized water at 0 °C, 70 mL of THF containing (28.43 g, 136 mmol, 1 equiv) was added dropwise. The yellow-colored reaction mass was brought to room temperature and stirred for a further 1 h. The resulting two phases were separated. The aqueous phase was extracted with 3 × 200 mL of EtOAc. The organic phases were combined and washed with 2 × 200 mL of H_2O, dried over $MgSO_4$, filtered, and evaporated. 22.05 g of 5-azido-4-oxo methyl pentanoate **3** was obtained with 95% yield as a yellow oil. R_f (hexane/EtOAc 2:1): 0.50; 0.33 (UV_{254} active, vanillin). IR (KBr): 3445w, 3366w, 3001m, 2956m, 2914m, 2850w, 2543vw, 2202m, 2106vs, 1732vs, 1619w, 1438s, 1417s, 1361s, 1280s, 1210s,1172s, 1096s, 1028m, 1008m, 988m, 921m, 885w, 843w, 799vw, 705vw, 607vw, 556m, 489vw. ^{1}H NMR (200 MHz, $CDCl_3$, 298 K): δ_H (ppm) = 4.03 (s, 2H, $H_2C(5)$); 3.69 (s, 3H, $H_3C(1^1)$; 2.76–2.72 (m, AA′ part of a system AA′BB′, 2H, $H_2C(3)$); 2.70–2.66 (m, BB′ part of a system AA′BB′, 2H, $H_2C(2)$). ^{13}C NMR (50 MHz, $CDCl_3$, 298 K): δ_C (ppm) = 202.9 (C(4)); 173.0 (C(1)); 57.3 (C(5); 51.9 ($C(1^1)$); 34.3 (C(3)); 27.4 (C(2)). MS (ESI(+)): *m*/*z* relative intensity [M + Na]$^+$ = 194.

*5-Boc-amino-4-oxo Methyl Pentanoate (**4**).* A solution of **3** (23 g, 134.37 mmol, 1 equiv) in 250 mL of EtOAc was charged in a hydrogenation autoclave reactor, followed by BOC anhydride (29.63 g, 135.76 mmol, 1.01 equiv) and by 5 g (4.7 mmol, 0.035 equiv) of 10% palladium on activated charcoal. The mass was subjected to hydrogenation in ambient temperature and to a pressure of 60 psi H_2 under mechanical agitation. After 24 h, the H_2 pressure was released and the reaction mass was filtered over celite, eluted with 3 × 25 mL of EtOAc, and the filtrate evaporated to obtain a yellow, oily mass. This yellow crude mass was purified by flash chromatography using a gradient eluent system from CH_2Cl_2/EtOAc 95:5 to CH_2Cl_2/EtOAc 85:15. A pure fraction of 5-Boc-amino-4-oxo methyl pentanoate **4** was obtained as a yellow oil (23.05 g, 70%). R_f (CH_2Cl_2/EtOAc 9:1): 0.25–0.30 (UV_{254} active, $KMnO_4$). IR (KBr): 3387s, 2979s, 2932s, 1735s, 1719s,1701s, 1697s, 1523s, 1518s, 1508s, 1500s, 1438s, 1412s, 1392s, 1252s, 1209s, 1165s, 1098m, 1060m, 1024m, 983m, 737m. ^{1}H NMR (400 MHz, $CDCl_3$, 298 K): δ_H (ppm) = 5.24 (sbr, 1H, NH); 4.03 (d, $^3J_{5\text{-}NH} = 3.6$ Hz, 2H, $H_2C(5)$); 3.64 (s, 3H, $H_3C(1^1)$; 2.71–2.68 (m, 2H, $H_2C(3)$); 2.63–2.59 (m, 2H, $H_2C(2)$); 1.40 (s, 9H, $H_3C(8^1,8^2,8^3)$. ^{13}C NMR (100 MHz, $CDCl_3$, 298 K): δ_C (ppm) = 204.5 (C(4)); 173.0 (C(1)); 155.7 (C(6)); 79.9 (C(7)); 52.0 ($C(1^1)$); 50.3 (C(5)); 34.4 (C(3)); 28.4 ($C(8^1,8^2,8^3)$); 27.6 (C(2)). MS (APCI (+)): *m*/*z* relative intensity (15, [M + Na]$^+$) = 269.1.

*5-Boc-amino-4-oxo Pentanoic Acid (**5**).* To 500 mL of phosphate buffer solution 0.1 M at pH 8, **4** (22.85 g, 93.2 mmol, 1 equiv) was added under agitation. Then, 300 mg of pig liver esterase (PLE, 24 units per mg of protein) were added under agitation. The pH of the reaction was maintained at pH 9 with 5 N NaOH. The reaction was followed by TLC (CH_2Cl_2/EtOAc 90:10) and was completed after 4 days. The reaction mixture was extracted with 3 × 200 mL of EtOAc; the aqueous phase was acidified to pH 2 with 6 N HCl, and extracted with 4 × 500 mL of EtOAc. The organic phases were combined and washed with 500 mL of saturated NaCl solution followed by 500 mL deionized water. The organic phase was dried over $MgSO_4$ and evaporated. A yellow crude solid product was obtained by trituration with ether at 0 °C. The white pure solid obtained was filtered and dried. Pure 5-Boc-amino-4-oxo pentanoic acid **5** was obtained as a white solid (13.7 g, 64%). R_f (EtOAc): 0.47 ($KMnO_4$, tailing). IR (KBr): 3379s, 2986mbr, 2919mbr, 2765w, 2692w, 2571w, 1707vs, 1686vs, 1506s, 1429s, 1407m, 1392m, 1383m, 1371m, 1363m, 1349m, 1295w, 1278m, 1240s, 1209s, 1170s, 1098w, 1065m, 1039vw, 1015m, 943m, 894m, 872m, 843vw, 803w, 787w, 759w, 741w, 653w, 575m. ^{1}H NMR (400 MHz, $CDCl_3$, 298 K): δ_H (ppm) = 11.30 (s, 1H, COOH); 5.35 (sbr, 1H, NH); 4.03 (d, $^3J_{5\text{-NH}} = 4.8$ Hz, 2H, $H_2C(5)$); 2.69–2.62 (m, 4H, $H_2C(2$ and $3)$); 1.40 (s, 9H, $H_3C(8^1,8^2,8^3)$. ^{13}C NMR (100 MHz, $CDCl_3$, 298 K): δ_C (ppm) = 204.5 (C(4)); 177.4 (C(1)); 156.0 (C(6)); 80.2 (C(7)); 50.3 (C(5)); 34.2 (C(3)); 28.4 ($C(8^1,8^2,8^3)$); 27.7 (C(2)). MS (APCI (−)): *m*/*z* relative intensity (95, [M − H]$^-$ = 230.1.

*Pentafluorophenyl Ester of 5-Boc-amino Levulinic Acid (**6**).* Under argon atmosphere, pentafluorophenol (2.7 g, 14.27 mmol, 1.1 equiv) was added to **5** (3 g, 12.97 mmol, 1 equiv) in 50 mL of CH_2Cl_2 at 0 °C, followed by 3 g of DCC (14.54 mmol, 1.12 equiv). The reaction was brought to room temperature and kept at room temperature overnight. The reaction mixture was filtered over celite and evaporated. The thick yellow, oily mass obtained was triturated with hexane to remove excess of pentafluorophenol. A white solid was obtained by filtration and dried to give 5.1 g of **6** (98%). R_f (CH_2Cl_2/EtOAc 95:5): 0.33 (UV_{254} active; $KMnO_4$). IR (KBr): 3009w, 2982w, 2948w, 2920w, 2669vw, 2458vw, 1798m, 1725s, 1694vs, 1656w, 1626w, 1527vs, 1518vs, 1468w, 1446w, 1426w, 1401w, 1392w, 1370m, 1359w, 1328w, 1271s, 1253m, 1235w, 1170m, 1146m,

Scheme 3. Synthesis of 6′-O-(ALA)-D-Glycosides[a]

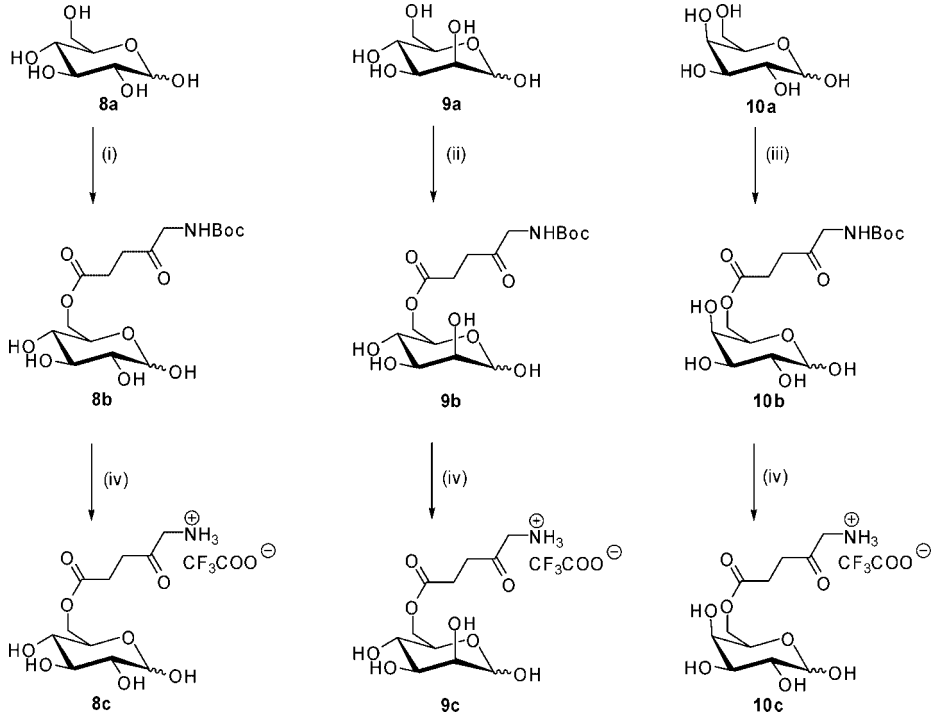

[a] Reagents and conditions: (i) **6**, subtilisin, 50 °C, 24 h; (ii) **6**, porcine pancreatic lipase (PPL), 50 °C, 48 h; (iii) **7**, porcine pancreatic lipase (PPL), 50 °C, 48 h; (iv) CF_3COOH, room temperature, 0.5 h.

Table 1. Chemical Structures and Anomeric Characteristics of the Glycoside Esters of ALA Prepared

Name and code	Structure	Ratio α/β	Overall Yield [%]	ORD $[\alpha]_D$
1-α-Glc-ALA (**8h**)	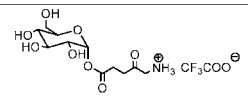	13 / 1	15	+128.1 (c=0.24)
1-α-Man-ALA (**9h**)	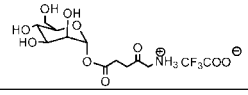	14 / 1	23.4	+228.7 (c=0.12)
1-β-Gal-ALA (**10i**)	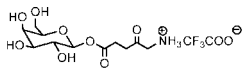	0.18 / 1	11.8	+40.9 (c=0.33)
6-α/β-Glc-ALA (**8c**)	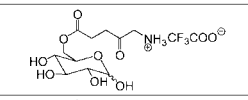	0.71 / 1	43.8	+24.2 (c=0.49)
6-α-Man-ALA (**9c**)	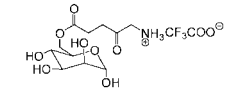	3.7 / 1	48.2	+14.4 (c=0.21)
6-β-Gal-ALA (**10c**)	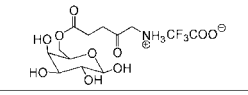	0.6 / 1	41.2	-48.5 (c=0.47)
1-α-Glc-EG-ALA (**8k**)	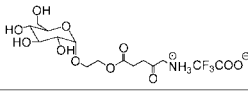	1 / 0	14.6	+246.1 (c=0.10)
1-α-Man-EG-ALA (**9k**)	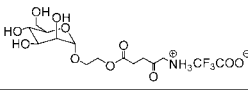	12.5 / 1	19.8	+85.7 (c=0.31)
1-β-Gal-EG-ALA (**10n**)	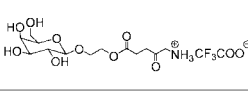	0 / 1	14.5	-55.9 (c=0.5)

1111s, 1042m, 1031m, 1007s, 989s, 977m, 895w, 864w, 828vw, 781vw, 751vw, 713vw, 666vw, 609w, 556w, 465vw. ^{1}H NMR (400 MHz, $CDCl_3$, 298 K): δ_H (ppm) = 5.25 (sbr, 1H, NH); 4.06 (d, $^3J_{5\text{-NH}} = 4.9$ Hz, 2H, $H_2C(5)$); 2.99 (t, $^3J_{2-3} = 6.5$ Hz, 2H, $H_2C(3)$); 2.87 (t, $^3J_{3-2} = 6.5$ Hz, 2H, $H_2C(2)$); 1.43 (s, 9H, $H_3C(8^a,8^b,8^c)$. ^{13}C NMR (100 MHz, $CDCl_3$, 298 K): δ_C (ppm) = 203.6 (C(4)); 168.8 (C(1)); 155.8 (C(6)); 142.4 (d × m, $^1J_{C-F}$ = 248 Hz, $C(1^2)$ or $C(1^3)$ or $C(1^4)$); 139.9 (d × m, $^1J_{C-F}$ = 244 Hz, $C(1^2)$ or $C(1^3)$ or $C(1^4)$); 137.5 (d × m, $^1J_{C-F} = 240$ Hz, $C(1^2)$ or $C(1^3)$ or $C(1^4)$); 125.0 ($C1^1$); 80.2 (C(7)); 50.3 (C(5)); 34.2 (C(3)); 28.4 ($C(8^1,8^2,8^3)$); 27.0 (C(2)). ^{19}F-NMR (188 MHz, $CDCl_3$, 298 K): δ_F (ppm) = −152.9 (m, 2F, (F-$C(1^2)$ and (F-$C(1^{2'})$); −158.2 (t, $^3J_{F-F} \approx 21.0$ Hz, 1F, (F-$C(1^4)$); −162.6 (m, 2F, (F-$C(1^3)$ and (F-$C(1^{3'})$). MS (APCI (−)): *m/z* relative intensity (95, $[M - H]^-$) = 230.1.

2,2,2-Trichloroethyl Ester of 5-Boc-amino Levulinic Acid (7). Under argon atmosphere, 2,2,2-trichloroethanol (1.267 g, 8.48 mmol, 2 equiv) was dissolved in 80 mL of CH_2Cl_2 at 0 °C, then DMAP (0.528 g, 4.32 mmol, 1 equiv) was added, followed by EDCI (0.912 g, 4.75 mmol, 1.1 equiv) and by **5** (1 g, 4.32 mmol, 1 equiv). The reaction was brought to room temperature and kept at room temperature overnight. The solvent was evaporated, and the reaction mass was dissolved in 100 mL of EtOAc and extracted with 200 mL of H_2O.The organic phase was washed with 170 mL of cold 1 N citric acid solution, followed by 200 mL of saturated $NaHCO_3$ solution and by 200 mL of saturated NaCl solution. The organic phase was dried over $MgSO_4$, and the solvent was evaporated. The remaining mass was purified by trituration with hexane to remove excess alcohol. A white solid was obtained by filtration and dried to afford 1.33 g of **7** (85%). R_f (hexane/EtOAc 7:3): 0.17 (UV_{254} active; $KMnO_4$). IR (KBr): 3361s, 3000w, 2981w, 2932w, 1759vs, 1721vs, 1688vs, 1528vs, 1477w, 1452w, 1408m, 1387m, 1369s, 1357m, 1333w, 1283vs, 1252m, 1195m, 1175s, 1156vs, 1134vs, 1084w, 1070w, 1043m, 1029w, 1006vw, 968w, 904w, 867vw, 831m, 797m, 768vw, 753vw, 716s, 681w, 654w, 584vw, 571w, 487vw, 465vw. ^{1}H NMR (400 MHz, $CDCl_3$, 298 K): δ_H (ppm) = 5.24 (sbr, 1H, NH); 4.70 (s, 2H, H_2C (1^1)); 4.04 (d, $^3J_{5\text{-NH}} = 5.0$ Hz, 2H, $H_2C(5)$); 2.77 (s, 4H, H_2C(2 and 3)); 1.41 (s, 9H, $H_3C(8^1,8^2,8^3)$). ^{13}C NMR (100 MHz, $CDCl_3$, 298 K): δ_C (ppm) = 204.0 (C(4)); 170.9 (C(1)); 155.7 (C(6)); 94.8 ($C(1^2)$); 80.0 (C(7)); 74.2 ($C(1^1)$); 50.3 (C(5)); 34.2 (C(3));

Scheme 4. Synthesis of 1′-*O*-(ALA)-D-Glycosides[a]

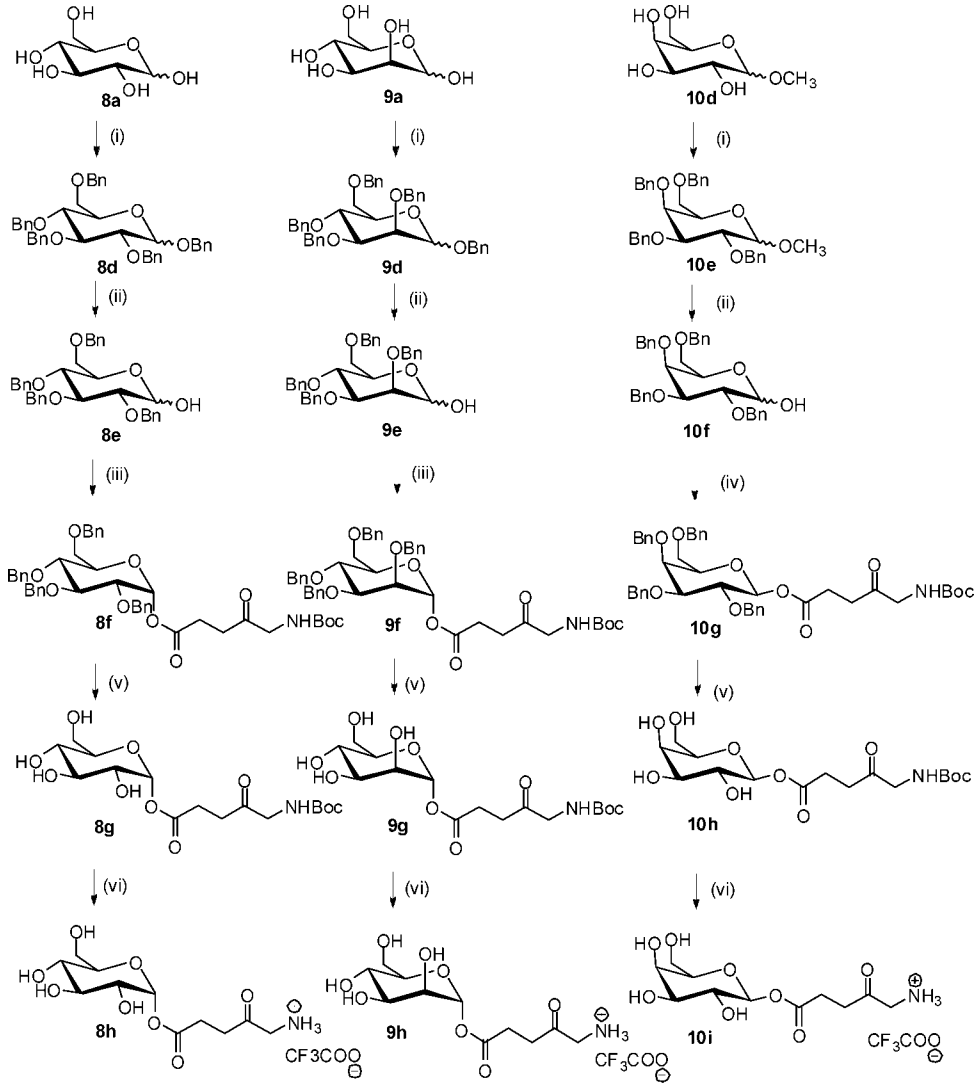

[a] Reagents and conditions: (i) NaH, BnBr, TBAI, room temperature, 8 h; (ii) 6 N HCl, CH_3COOH, 60 °C, 4 h; (iii) **5**, DCC, catalytic DMAP, 0 °C to room temperature, 5 h; (iv) **5**, EDCI, DMAP, 0 °C to room temperature, 7 h; (v) H_2/Pd, room temperature, 10 h; (vi) CF_3COOH, room temperature, 0.5 h.

28.4 (C(8^1,8^2,8^3)); 27.5 (C(2)). MS (APCI (+)): *m*/*z* relative intensity (95% intensity) $[M + H]^+ = 363.9$; (90% intensity) $[M + H]^+ = 362.0$; (32% intensity) $[M + H]^+ = 365.9$.

*6′-O-(5-Boc-amino levulinic acid)-α/β-D-glucose (**8b**).* Under argon atmosphere, to glucose **8a** (360.4 mg, 2 mmol, 1 equiv) dissolved in 10 mL of anhydrous pyridine were added subtilisin proteinase (1 g, 5 units per mg of protein; approximately 5 mmol, 2.5 equiv) and **6** (2.4 g, 6 mmol, 3 equiv). The reaction was heated to 50 °C, maintained at this temperature for 24 h, and followed by TLC (EtOAc/MeOH 1:1). The mixture was cooled to room temperature, and then the enzyme was filtered over a celite bed. The celite was washed with 3 × 10 mL of pyridine. Solvent was evaporated and the residue was purified using flash chromatography with gradient elution (CH_2Cl_2 100% to CH_2Cl_2/MeOH 85:15). The main fractions were concentrated and a purification was achieved by dissolution in 5 mL of CH_2Cl_2 and precipitation with 5 mL of hexane. **8b** was obtained as a white solid (375 mg, 48%). R_f (CH_2Cl_2/MeOH 85:15): 0.28; ($KMnO_4$). IR (KBr): 3411vs, 2979m, 2930m, 2509w, 1724vs, 1519s, 1424w, 1393m, 1368s, 1282m, 1254m, 1167vs, 1056s, 913w, 869w, 778w,734w, 640w, 560w. ^{1}H NMR (400 MHz, CD_3OD, 298 K): δ_H (ppm) = 5.10 (d, $^3J_{1'-2'}$ =3.7 Hz, 1H, HC(1′α)); 4.48 (d, $^3J_{1'-2'}$ =7.8 Hz, 1H, HC(1′β)); 4.38 (dd, $^3J_{5'-6'a} \approx 2.1$ Hz, $^3J_{6'a\text{ - }6'b}$ =11.8 Hz, 1H, HC(6′a β)); 4.32 (dd, $^3J_{5'-6'a} \approx 2.1$ Hz, $^3J_{6'a\text{-}6'b} = 11.8$ Hz,1H, HC(6′a α)); 4.21 (dd, $^3J_{5'-6'b} \approx 5.5$ Hz, $^3J_{6'a\text{ - }6'b} \approx 11.9$ Hz, 1H, HC(6′b α)); 4.16 (dd, $^3J_{5'-6'b} \approx 5.5$ Hz, $^3J_{6'a\text{-}6'b} \approx 11.8$ Hz, 1H, HC(6′b β)); 3.97–3.93 (m, 3H, $H_2C(5)$ and HC (5′α)); 3.67 (t, $^3J_{3'-4'} \approx 9.3$ Hz, $^3J_{3'-2'} = 9.3$ Hz, 1H, HC(3′α)); 3.46 (ddd, $^3J_{5'-6'a} \approx 2.1$ Hz, $^3J_{5'-6'b} \approx 5.5$ Hz, $^3J_{5'-4'} = 9.5$ Hz, 1H, HC(5′β)); 3.40–3.25 (m, 4H, HC(2′α), HC(3′β), HC(4′α), and HC(4′β)); 3.16 (dd, $^3J_{2'-1'} = 7.8$ Hz, $^3J_{2'\text{ - }3'} \approx 9.3$ Hz, 1H, HC(2′ β)); 2.75 (t, $^3J_{3-2} \approx 6.4$ Hz, 2H, $H_2C(3)$); 2.64 (t, $^3J_{2-3} \approx 6.4$ Hz, 2H, $H_2C(2)$); 1.43 (s, 9H, H_3C (8a, 8b, and 8c)); α/β ratio by ^{1}H NMR 1.25: 1. ^{13}C NMR (100 MHz, CD_3OD, 298 K): δ_C (ppm) = 207.0 (C(4)); 173.9 (C(1 α or β)); 173.8 (C(1 α or β)); 157.9 (C(6)); 97.7 (C(1′ β)); 93.5 (C(1′ α)); 80.5 (C(7)); 75.7 (C(2′ β)); 74.8 (C(5′ β)); 74.4(C(3′ α)); 77.4, 73.2, 71.4, 71.2 (C(2′ α), C(3′ β), C(4′ α) and C(4′ β)); 70.2 (C(5′ α)); 64.9 (C(6′ α)), 64.8 (C(6′ β)); 50.6 (C(5)); 34.7 (C(3)); 28.6 (C(8a, 8b, and 8c); 28.4 (C(2)). MS (ESI (+)): *m*/*z* relative intensity $[M + Na]^+ = 416.1$; $[M + H]^+ = 393.9$. HR-MS $[M + Na]^+ = 416.1524$ (calculated = 416.1533).

*6′-O-(5-Amino levulinic acid)-α/β-D-glucose (**8c**).* Trifluoroacetic acid (4.7 mL, 61 mmol, 50 equiv) was added dropwise to **8b** (480 mg, 1.22 mmol, 1 equiv) dissolved in 8 mL of

Scheme 5. Synthesis of 1-*O*-(ALA)-2-*O*-(Glycosyl) Ethylene Glycol[a]

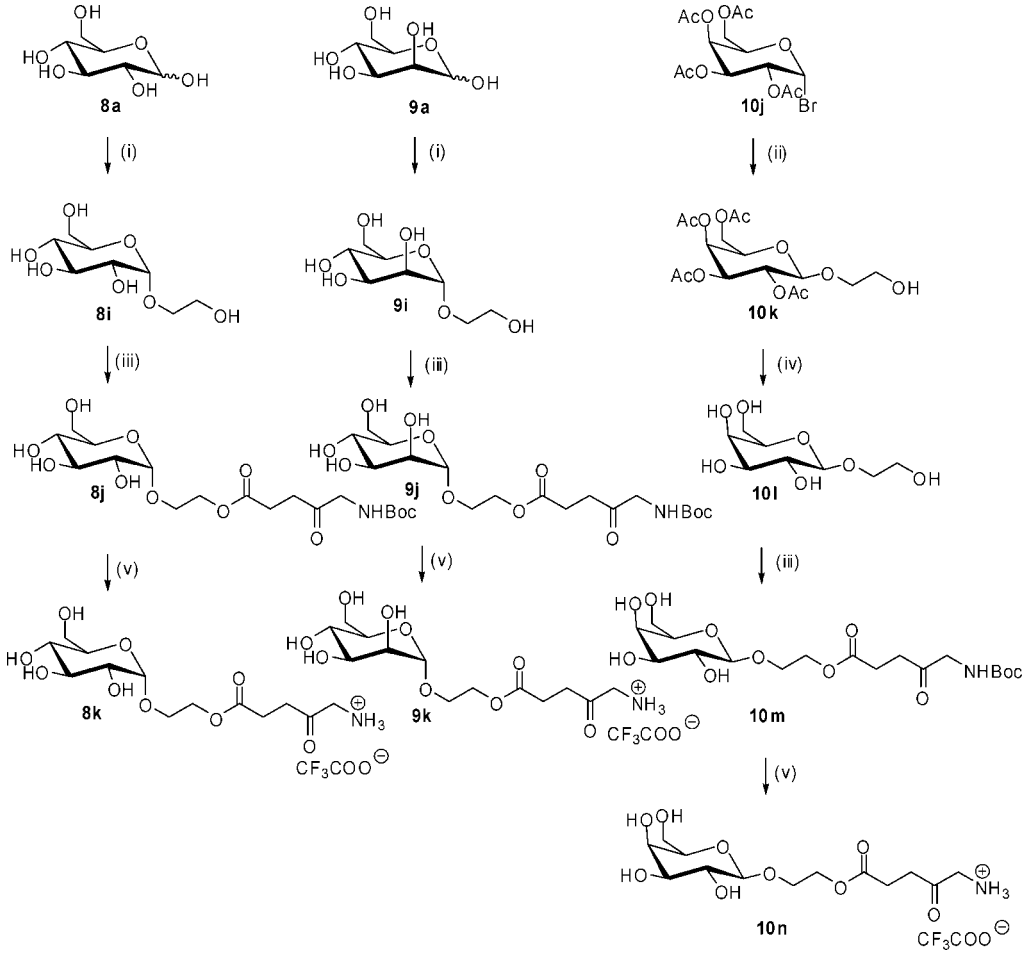

[a] Reagents and conditions: (i) ethylene glycol, Dowex 50WX 8-200, 70 °C, 72 h; (ii) ethylene glycol, Ag_2CO_3, room temperature, 4 h; (iii) **6**, lipase from *Candida antarctica* (LCA), 50 °C, 0.5 h; (iv) NaOMe, room temperature, 2 h; (v) CF_3COOH, room temperature, 0.5 h.

$CH_2Cl_2$and at −10 °C. The reaction was allowed to warm to room temperature and stirred for 1 h. When the deprotection of Boc was completed (controlled by the absence of Boc peak in ^1H NMR), CH_2Cl_2 and trifluoroacetic acid were evaporated. The product was triturated 3 times with dry ether and decanted. The solid product was dried under high vacuum, yielding **8c** as a highly hygroscopic white solid (457 mg, 92%). IR (KBr): 3388vs, 2923m, 1730vs, 1679vs, 1512w, 1429m, 1390m, 1317w, 1204vs, 1137vs, 1081m, 1056m, 913w, 839m, 800m, 772w, 723m, 632w, 597w. ^1H NMR (400 MHz, D_2O, 298 K): δ_H (ppm) = 5.21 (d, $^3J_{1'-2'}$ = 3.7 Hz, 1H, HC(1′α)); 4.65 (d, $^3J_{1'-2'}$ = 7.9 Hz, 1H, HC(1′β)); 4.41 (dd, $^3J_{5'-6'a}$ = 2.2 Hz, $^3J_{6'a\text{ - }6'b}$ = 12.2 Hz, 1H, HC(6′a α or β)); 4.37 (dd, $^3J_{5'-6'a} \approx$ 2.2 Hz, $^3J_{6'a\text{ - }6'b} \approx$ 12.2 Hz, 1H, HC(6′a α or β)); 4.34–4.25 (m, $^3J_{5'-6'b} \approx$ 5.3 Hz, $^3J_{6'a\text{ - }6'b} \approx$ 12.2 Hz, 2H, HC(6′b α and 6′b β)); 4.13 (s, 2H, $H_2C(5)$); 4.03–3.99 (m, 1H, HC(5′ α)); 3.71 (t, $^3J_{3'-4'}$ = 9.4 Hz, $^3J_{3'-2'}$ = 9.4 Hz, 1H, HC(3′ α)); 3.65 (ddd, $^3J_{5'-6'a} \approx$ 2.2 Hz, $^3J_{5'-6'b} \approx$ 5.3 Hz, $^3J_{5'-4'}$ = 9.5 Hz, 1H, HC(5′β)); 3.54 (dd, $^3J_{1'-2'}$ = 3.7 Hz, $^3J_{3'-2'}$ = 9.4 Hz, 1H, HC(2′ α)); 3.46 (m, $J_{3'-4'} \approx$ 9.4 Hz, $^3J_{3'-2'} \approx$ 9.4 Hz, $J_{5'-4'} \approx$ 9.4 Hz, 3H, HC(3′ β), HC(4′ α) and HC (4′ β)); 3.16 (dd, $^3J_{2'-1'} \approx$ 7.8 Hz, $^3J_{2'\text{ - }3'} \approx$ 9.4 Hz, 1H, HC(2′ β)); 2.75 (t, $^3J_{3-2}$ = 6.0 Hz, 2H, $H_2C(3)$); 2.64 (t, $^3J_{2-3} \approx$ 6.4, 2H, $H_2C(2)$); α/β ratio by ^1H NMR: 0.71: 1. ^{13}C NMR (100 MHz, D_2O, 298 K): δ_C (ppm) = 204.0 (C(4 α and β)); 174.6 (C(1 α or β)); 174.5 (C(1 α or β)); 116.7 (q, $^1J_{C-F}$ = 292.2, CF_3COO^-); 96.1 (C(1′ β)); 92.3 (C(1′ α)); 74.1 (C(2′ β)); 73.5 (C(5′ β)); 72.7(C(3′ α)); 75.6, 71.5, 69.7, 69.6 (C(2′ α), C(3′ β), C(4′ α) and C(4′ β)); 69.3 (C(5′ α)); 63.8(C(6′ α and 6′ β)); 47.2 (C(5)); 34.3(C(3)); 27.5 (C(2)). MS (ESI (+)): *m*/*z* relative intensity $[M - CF_3COO^-]^+$ = 293.9. HR-MS $[M - CF_3COO^-]^+$ = 294.1181 (calculated = 294.1189).

*6′-O-(5-Boc-amino levulinic acid)-α/β-D-mannose (**9b**).* To a solution of mannose **9a** (360.4 mg, 2 mmol, 1 equiv) in anhydrous pyridine (6 mL) under argon atmosphere, porcine pancreatic lipase (PPL) (650 mg, 24 units per mg of protein; approximately 15.6 mmol, 7.8 equiv) and **6** (1.6 g, 4 mmol, 2 equiv) were added. The reaction was heated to 50 °C and maintained at this temperature for approximately 48 h. The reaction was followed by TLC (EtOAc/MeOH 1:1). The reaction mass was cooled to room temperature and the enzyme was filtered over a celite bed; the celite was washed with 3 × 10 mL of pyridine. Pyridine was evaporated and the residue was extracted with 100 mL of toluene, then centrifuged to remove the unreacted **6** and pentafluorophenol. The settled mass was purified by flash chromatography using gradient elution. ($CH_2Cl_2$100% to CH_2Cl_2/MeOH 85:15). The main fractions were concentrated to give **9b** as a white solid (539 mg, 68.5%). R_f (CH_2Cl_2/MeOH 85:15): 0.24; ($KMnO_4$). IR (KBr): 3420vs, 2978m, 2931m, 2509w, 1717vs, 1520s, 1419w, 1393m, 1368s, 1283m, 1253m, 1167vs, 1059s, 868w, 806w, 781w, 674w, 600w, 499w. ^1H NMR (400 MHz, CD_3OD, 298 K): δ_H (ppm) = 5.10 (d, $^3J_{1'-2'} \approx$ 1.7 Hz, 1H, HC(1′ α)); 4.48 (d, $^3J_{1'-2'}$ = 1.0 Hz, 1H, HC(1′β)); 4.32 (dd, $^3J_{5'-6'a} \approx$ 2.1 Hz, $^3J_{6'a\text{ - }6'b}$ =11.8 Hz, 1H, HC(6′a α)); 4.25 (dd, $^3J_{5'-6'b} \approx$ 5.4 Hz, $^3J_{6'a\text{-}6'b}$ = 11.8 Hz, 1H, HC(6′b α)); 3.95–3.88 (m, 3H, $H_2C(5)$ and HC(5′ α)); 3.82 (dd, $^3J_{2'-1'}$ = 1.7 Hz, $^3J_{3'-2'}$ = 3.4 Hz, 1H, HC(2′ α)); 3.76 (dd, $^3J_{2'-3'} \approx$ 3.4 Hz, $^3J_{3'-4'} \approx$ 9.7 Hz, 1H, HC(3′ α));

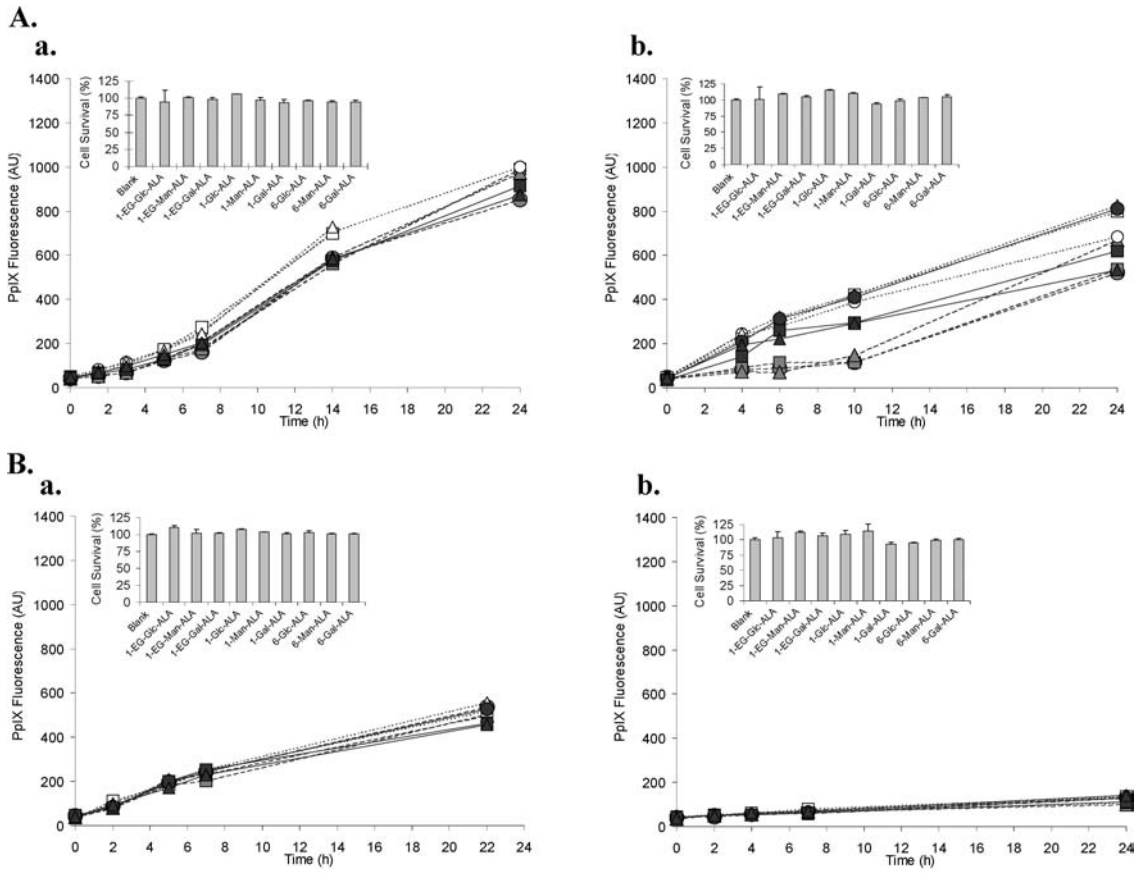

Figure 1. PpIX production by human cells from glycoside esters of ALA and cytotoxicity in the dark. Cells were exposed to 2 mM glycoside esters of ALA, and the increase of PpIX fluorescence was recorded for 24 h. Bars in the insert represent cell survival (%) at the end of experiment. 1-α-Glc-ALA **8h** (black circles); 1-α-Man-ALA **9h** (black squares); 1-*β*-Gal-ALA **10i** (black triangles); 6-α-Glc-ALA **8c** (white circles); 6-α-Man-ALA **9c** (white squares); 6-*β*-Gal-ALA **10c** (white triangles); 1-α-Glc-EG-ALA **8k** (gray circles); 1-α-Man-EG-ALA **9k** (gray squares); 1-*β*-Gal-EG-ALA **10n** (gray triangles). (A) Human colon SW480 (a) or lung A549 (b) carcinoma cells. (B) Human HCEC angiogenic endothelial cells (a) or human primary fibroblasts (VS59) (b).

3.57 (t, $^3J_{4'-3'} \approx 9.7$ Hz, $^3J_{4'-5'} \approx 9.7$ Hz, 1H, HC(4′ α)); 2.75–2.63 (m, 4H, $H_2C(3)$ and $H_2C(2)$); 1.42 (s, 9H, H_3C (8a, 8b, and 8c)); α/*β* ratio by ^{1}H NMR: 5.2:1. ^{13}C NMR (100 MHz, CD_3OD, 298 K): δ_C (ppm) = 207.0 (C(4)); 173.6 (C(1)); 157.4 (C(6)); 95.0 (C(1′ α)); 94.8 (C(1′ *β*)); 80.4 (C(7)); 71.8 (C(2′ α)); 71.5 (C(3′ α)); 70.6 (C(5′ α)); 68.0 C(4′ α)); 64.7 (C(6′ α)); 49.6 (C(5)); 34.5 (C(3)); 28.5 (C(8a, 8b, and 8c); 28.3 (C(2)). MS (ESI (+)): *m*/*z* relative intensity $[M + Na]^+ = 416.2$; $[M + H]^+ = 393.9$; $[M\text{-}t\text{Bu} + Na]^+ = 360.4$; $[M\text{-Boc} + Na]^+ = 316.1$; $[M\text{-Boc-}(CONH_2) + Na]^+ = 256.0$. HR-MS $[M + Na]^+ = 416.1523$ (calculated = 416.1533).

*6′-O-(5-Amino levulinic acid)-α/β-D-mannose (**9c**).* The deprotection of **9b** was realized with the same procedure as for **8c**, and it afforded **9c** with a good yield (91%). IR (KBr): 3388vs, 2928m, 1788w, 1731vs, 1678vs, 1517w, 1429m, 1391m, 1327w, 1204vs, 1138vs, 1068m, 913w, 839m, 800m, 776w, 723m, 598w, 520w, 500w. ^{1}H NMR (400 MHz, D_2O, 298 K): δ_H (ppm) = 5.06 (d, $^3J_{1'-2'} = 1.7$ Hz, 1H, HC(1′α)); 4.82 (d, $^3J_{1'-2'} = 1.0$ Hz, 1H, HC(1′ *β*)); 4.32–4.18 (m, 4H, $H_2C(6'\ \alpha)$ and $H_2C(6'\ \beta)$); 4.05 (s, 2H, $H_2C(5)$); 3.89 (ddd, $^3J_{5'-6'a} \approx 2.6$ Hz, $^3J_{5'-6'b} \approx 4.7$ Hz, $^3J_{5'-4'} = 9.9$ Hz, 1H, HC(5′ α)); 3.85 (dd, $^3J_{2'-1'} = 1.7$ Hz, $^3J_{3'-2'} \approx 3.4$ Hz, 1H, HC(2′ α)); 3.75 (dd, $^3J_{2'-3'a} \approx 3.4$ Hz, $^3J_{3'-4'} \approx 9.8$ Hz, 1H, HC(3′ α)); 3.60 (t, $^3J_{4'-3'} \approx 9.8$ Hz, $^3J_{4'-5'} = 9.8$ Hz, 1H, HC(4′ α)); 3.57–3.44 (m, 1H, HC(5′ *β*) and peaks due to ether solvent)); 2.85 (t, $^3J_{2-3} = 6.5$ Hz, 2H, $H_2C(3)$); 2.69 (t, $^3J_{3-2} = 6.5$ Hz, 2H, $H_2C(2)$); 1.07–1.15 (peaks due to ether solvent); α/*β* ratio by ^{1}H NMR: 3.67:1. ^{13}C NMR (100 MHz, D_2O, 298 K): δ_C (ppm) = 204.4 (C(4)); 174.9 (C(1α or *β*)); 174.8 (C(1α or *β*)); 163.5 (q, $^2J_{C-F}$ = 35.5, CF_3COO^-); 116.7 (q, $^1J_{C-F} \approx 291.0$, CF_3COO^-); 94.6 (C(1′ α)); 94.2 (C(1′ *β*)); 70.9, 70.4, 67.0 (C(2′ α), C(3′ α), and C(5′ α)); 73.8, 71.4, 66.7 (C(2′ *β*), C(3′ *β*), and C(5′ *β*)); 66.4 (C(4′ α and 4′ *β*)); 64.2 (C(6′ α and 6′ *β*)); 47.4 (C(5)); 34.6(C(3)); 27.7 (C(2)). HR-MS $[M - CF_3COO^-]^+ = 294.1184$ (calculated = 294.1189).

*6′-O-(5-Boc-amino levulinic acid)-α/β-D-galactose (**10b**).* To a solution of galactose **10a** (360.4 mg, 2 mmol, 1 equiv) in anhydrous pyridine (16 mL) under argon atmosphere, porcine pancreatic lipase (PPL) (1.9 g, 20 units per mg of protein; approximately 38 mmol, 19 equiv) and **7** (4.68 g, 12.8 mmol, 6.4 equiv) were added. The reaction was heated to 50 °C and maintained at this temperature for approximately 60 h. The reaction was controlled by TLC (EtOAc/MeOH 1:1). The mixture was cooled to room temperature and the enzyme was filtered over celite. The celite was eluted with 3 × 10 mL of pyridine. Solvent was evaporated and the residue was extracted with 100 mL of toluene, then centrifuged to remove the unreacted **7** and trichloroethanol. The solid pellet was purified by flash chromatography using gradient elution (CH_2Cl_2 100% to CH_2Cl_2/MeOH 85:15). The main fractions were concentrated and purified by dissolution in 8 mL of CH_2Cl_2 and precipitation in 8 mL of hexane. **10b** was obtained as white solid (348 mg, 44%). R_f (CH_2Cl_2/MeOH 85:15): 0.29 ($KMnO_4$). IR(KBr): 3414vs, 2981m, 2931m, 2347w, 1736vs, 1715vs, 1684vs, 1536s, 1416w, 1393w, 1368m, 1323w, 1301m, 1253m, 1200m, 1174s, 1149s, 1105m, 1091m, 1074s, 1030s, 997w, 921w, 859w, 800m, 692m, 645w, 568w, 468w. ^{1}H NMR (400 MHz, CD_3OD, 298

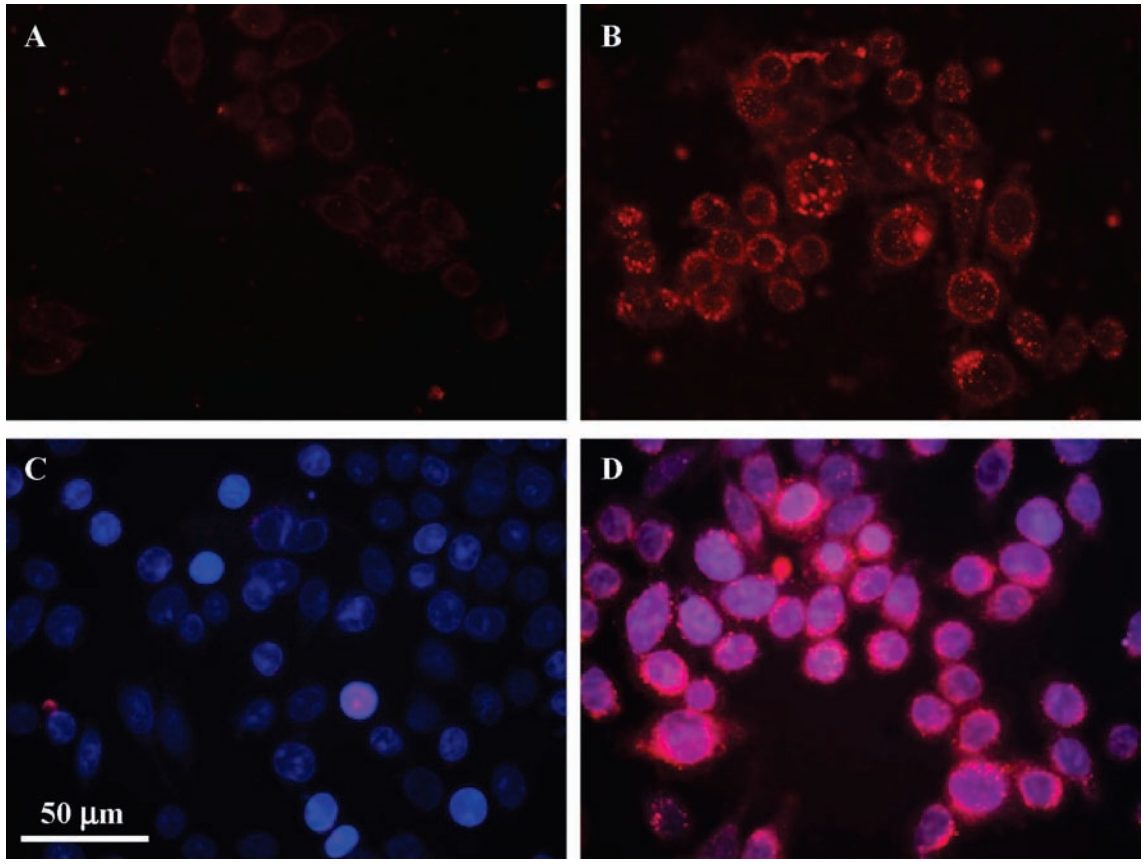

Figure 2. Fluorescence microscopy of SW480 colon cancer cells exposed to 1-α-Glc-ALA **8h**. SW480 colon cancer cells were grown on histological slides and incubated without (A (autofluorescence) and C) or with (B, 2 mM; and D, 4 mM) 1-α-Glc-ALA **8h** for 24 h in the dark, then either directly examined under a fluorescence microscope (A,B) or after DAPI coloration of the nuclei (C,D). Red fluorescence: PpIX. Blue fluorescence: DAPI.

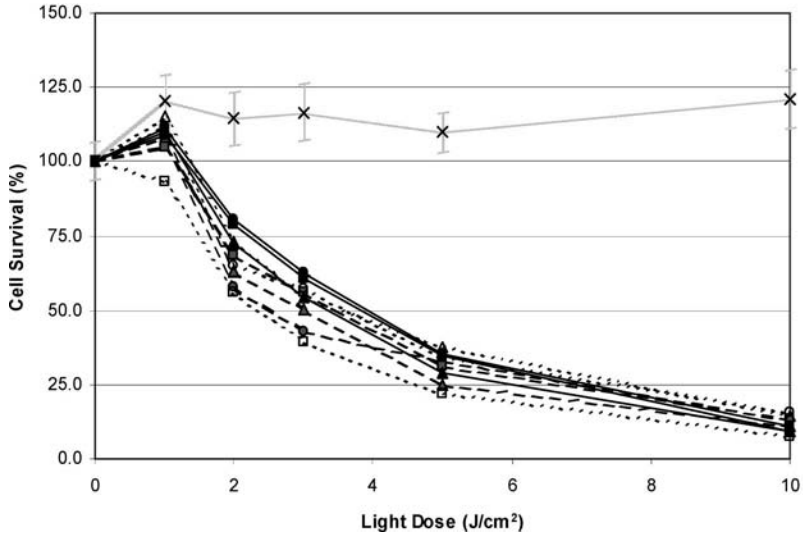

	DL_{50}[J/cm^2]
α-Glc-6-ALA **8c**	3.3
α-Man-6-ALA **9c**	2.4
β-Gal-6-ALA **10c**	3.6
α-Glc-1-ALA **8h**	3.8
α-Man-1-ALA **9h**	3.7
β-Gal-1-ALA **10i**	3.2
α-Glc-1-EG-ALA **8k**	2.6
α-Man-1-EG-ALA **9k**	3.3
β-Gal-1-EG-ALA **10n**	2.8
ALA	*2.5*

Figure 3. Photodynamic therapy of SW480 cells exposed to the glycoside esters of ALA. SW480 cells were exposed to 2 mM glycoside esters of ALA, ALA, or no compounds (control cells) during 24 h in the dark, then illuminated with a red laser ($\lambda = 635$ nm). The Alamar Blue assay was performed 24 h after the illumination, and the LD_{50} values (light dose necessary to inhibit 50% cell survival) were determined using medium effect algorithm. For the purpose of clarity, the standard deviations are not shown in the graph, but were always smaller that 10% of the value. 1-α-Glc-ALA **8h** (black circles); 1-α-Man-ALA **9h** (black squares); 1-β-Gal-ALA **10i** (black triangles); 6-α-Glc-ALA **8c** (white circles); 6-α-Man-ALA **9c** (white squares); 6-β-Gal-ALA **10c** (white triangles); 1-α-Glc-EG-ALA **8k** (gray circles); 1-α-Man-EG-ALA **9k** (gray squares); 1-β-Gal-EG-ALA **10n** (gray triangles); control cells (crosses).

K): δ_H (ppm) = 5.16 (d, $^3J_{1'-2'} = 3.5$ Hz, 1H, HC(1′ α)); 4.42 (d, $^3J_{1'-2'} = 7.2$ Hz, 1H, HC(1′β)); 4.26–4.16 (m, 5H, H_2C(6′ α and β) and HC(5′ α)); 3.95–3.93 (m, 3H, H_2C(5) and HC (4′α)); 3.86 (m, 1H, HC(3′ α)); 3.75 (dd, $^3J_{2'-1'} \approx 3.5$ Hz, $^3J_{3'-2'} = 9.8$ Hz, 1H, HC(2′ α)); 3.72–3.69 (m, 1H, HC(5′ β)); 3.47 (dd, $^3J_{2'-1'} \approx 7$ Hz, $^3J_{3'-2'} = 9.8$ Hz, 1H, HC(2′ β)); 2.77–2.63 (m, 4H, H_2C(3) and H_2C(2)); 1.43 (s, 9H, H_3C(8a, 8b, and 8c)); α/β ratio by ^{1}H NMR: 2.8:1. ^{13}C NMR (100 MHz, CD_3OD, 298 K): δ_C (ppm) = 207.2 (C(4)); 173.8 (C(1)); 158.0 (C(6)); 98.2 (C(1′ β)); 93.7 (C(1′ α)); 80.5 (C(7)); 70.6 (C(2′ α)); 70.5, 69.9 (C(3′ α) and C(4′ α)); 68.7 (C(5′ α)); 64.9 (C(6′ α)), 74.3, 73.4, 73.2, 64.6 (peaks due to β anomer); 50.5 (C(5)); 34.7

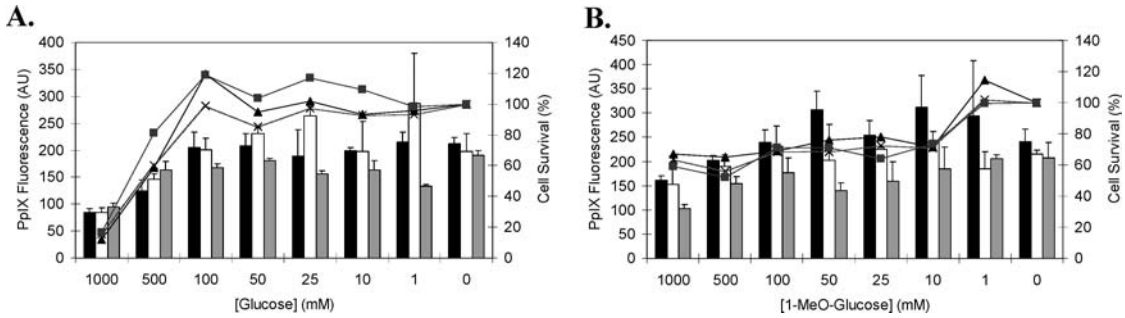

Figure 4. Competition of free glucose or 1-MeO-glucose with glucoside esters of ALA for PpIX production in SW480 cells. Production of PpIX by SW480 cells from glucoside esters of ALA (1 mM) in the presence of D-glucose (A) or 1-MeO-glucose (B) as competitive agents at the indicated concentrations. Bars represent PpIX production from 1-O-glucoside esters of ALA (black), 6-O-glucoside esters of ALA (white), and ethylene glycol glucoside esters of ALA (gray), and lines represent cell survival in the presence of competitive agent and 1-O-glucoside esters of ALA (triangles), 6-O-glucoside esters of ALA (crosses), or ethylene glycol glucoside esters of ALA (squares).

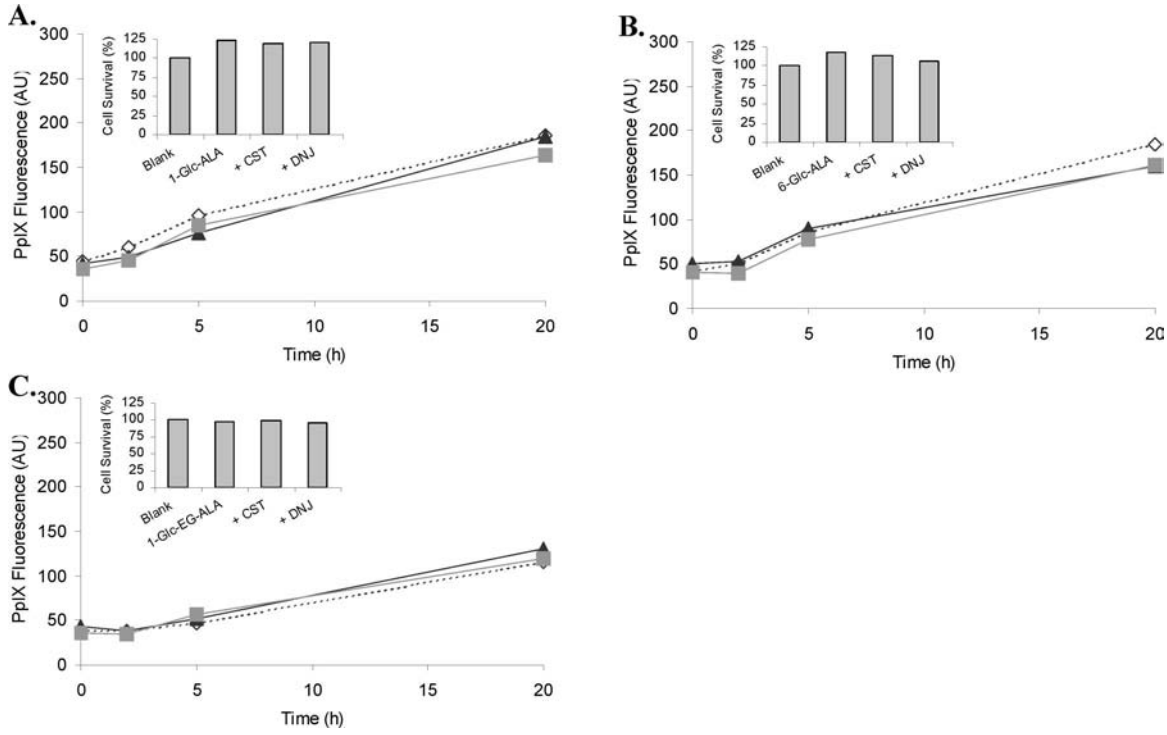

Figure 5. Inhibition of PpIX production in A549 cells by glucosidase inhibitors. Production of PpIX by A549 cells from (A) 1-α-Glc-ALA **8h**, (B) 6-α-Glc-ALA **8c**, and (C) 1-α-Glc-EG-ALA **8k** esters (2 mM) in the presence of 10 mM castanospermine (CST, A) or 1-deoxynojirimycin (DNJ). Lines represent PpIX production induced by glycoside-ALA esters without inhibitors (rhombuses) and with castanospermine (triangles), 1-deoxynojirimycin (squares), whereas bars in the insert represent cell survival (%) at the end of the experiment.

(C(3)); 28.6 (C(8a, 8b, and 8c); 28.4 (C(2)). HR-MS $[M + Na]^+$ = 416.1526 (calculated = 416.1533).

*6′-O-(5-Amino levulinic acid)-α/β-D-galactose (**10c**).* The deprotection of **10b** was realized with the same procedure as for **8c**, and it afforded **10c** with good yield (93%). IR (KBr): 3392vs, 2929m, 2027w, 1731vs, 1678vs, 1512w, 1430m, 1384m, 1317w, 1205vs, 1138vs, 1073m, 1038w, 917w, 872w, 839m, 800m, 723m, 598w, 520w, 500w. ^{1}H NMR (400 MHz, D_2O, 298 K): δ_H (ppm) = 5.23 (d, $^3J_{1'-2'}$ = 3.7 Hz, 1H, HC(1′α)); 4.55 (d, $^3J_{1'-2'}$ = 7.9 Hz, 1H, HC(1′ β)); 4.48–4.11 (m, 5H, H_2C(6′ α), H_2C(6′ β), and HC(5′ α); 4.10 (s, 2H, H_2C (5)); 3.97 (m, 1H, HC(3′ α)); 3.92 (dd, $^3J_{4'-5'}$ = 0.9 Hz, $^3J_{4'-3'}$ = 3.5 Hz, 1H, HC(4′ β)); 3.88 (ddd, $^3J_{5'-4'} \approx 0.9$ Hz, $^3J_{5'-6'a}$ = 4.3 Hz, $^3J_{5'-6'b}$ = 7.8 Hz, 1H, HC(5′ β)); 3.84–3.83 (m, 1H, HC(4′ α)); 3.80 (dd, $^3J_{2'-1'} \approx 3.7$ Hz, $^3J_{3'-2'}$ = 11 Hz, 1H, HC(2′ α)); 3.62 (dd, $^3J_{3'-4'}$ = 3.5 Hz, $^3J_{3'-2'} \approx 10$ Hz, 1H, HC (3′ β)); 3.55–3.48 (q, 2H, peaks due to ether solvent); 3.46 (dd, $^3J_{2'-1'}$ = 7.9 Hz, $^3J_{3'-2'}$ = 10 Hz, 1H, HC(2′ β)); 2.95 (t, $^3J_{2-3} \approx 6.5$ Hz, 2H, H_2C(3)); 2.72 (t, $^3J_{3-2} \approx 6.5$ Hz, 2H, H_2C(2)); 1.07–1.15 (peaks due to ether solvent); α/β ratio by ^{1}H NMR: 0.6:1. ^{13}C NMR (100 MHz, D_2O, 298 K): δ_C (ppm) = 204.4 (C(4)); 174.8 (C(1 α or β)); 174.7 (C(1 α or β)); 163.3 (q, $^2J_{C-F}$ = 35.0, CF_3COO^-); 116.6 (q, $^1J_{C-F} \approx 291.0$, CF_3COO^-); 96.8 (C(1′ β)); 92.7 (C(1′ α)); 72.9 (C(3′ β)); 72.7 (C(4′ β)); 72.0 (C(2′ β)); 69.6, 69.2, 69.0, 68.5, 68.4 (C(3′ α), C(5′ β), C(2′ α), C(5′ α) and C(4′ α)); 64.7, 64.5 (C(6′ α and 6′ β)); 47.4 (C(5)); 34.6(C(3)); 27.7 (C(2)). MS (ESI (+)): *m*/*z* relative intensity $[M - CF_3COO^-]^+$ = 294.0; $[M - CF_3COO^- + H]^+$= 295.0; $[M - CF_3COO^- - NH_3]^+$= 276.1. HR-MS $[M - CF_3COO^-]^+$ = 294.1181 (calculated = 294.1189).

*1,2,3,4,6-Penta-O-benzyl-α/β-D-glucose (**8d**).* To a solution of **8a** (541 mg, 3.0 mmol, 1 equiv) dissolved in anhydrous DMF (20 mL) at −20 °C under argon atmosphere, sodium hydride (730 mg, 30 mmol, 10 equiv, 2 equiv per −OH) was added in portions. The reaction was warmed to room temperature and stirred for 2 h. Then, the mixture was cooled to 5 °C, and tetrabutylammonium iodide (55.5 mg, 0.15 mmol, 0.05 equiv) and benzyl bromide (5.13 g, 3.6 mL, 30.0 mmol, 10 equiv, 2

equiv per −OH) were added dropwise. The reaction mixture was maintained at room temperature for 48 h, then cooled to 5 °C and quenched with MeOH (20 mL). The crude product was extracted with EtOAc (200 mL) and water (200 mL). The aqueous layer was extracted with EtOAc (3 × 200 mL) and the combined organic layers washed with brine (200 mL), dried over $MgSO_4$, and evaporated. The crude residue was purified by flash chromatography using gradient elution (hexane 100% to hexane/ether 80:20). The pure fractions were collected and concentrated to afford **8d** (1.4g, 74%). R_f (hexane/ether 80:20): 0.36 (UV_{254} active; $KMnO_4$). IR (KBr): 3435w, 3088w, 3064w, 3031m, 2914m, 2868m, 2809w, 1956w, 1874w, 1808w, 1636w, 1605w, 1587w, 1496m, 1453m, 1402w, 1363m, 1314w, 1277w, 1236w, 1215m, 1197w, 1157w, 1120s, 1074vs, 1041m, 1028s, 1002m, 949m, 909m, 831w, 753s, 736s, 698vs, 679w, 630w, 610w, 587w, 576w, 558w, 532w, 508w, 500w, 459w. ^{1}H NMR (400 MHz, $CDCl_3$, 298 K): δ_H (ppm) = 7.44–7.21 (m, 25H, H−Ar); 5.01 (d, $^2J_{1a\text{-}1a'}$ = 11.9 Hz, 1H, HC(1^a)); 4.99 (d, $^2J_{2a\text{-}2a'}$ = 10.9 Hz, 1H, HC(2^a)); 4.96 (d, $^2J_{3a\text{-}3a'}$= 10.9 Hz, 1H, HC(3^a)); 4.89 (d, $^3J_{1-2}$ = 3.6 Hz, 1H, HC(1 α)); 4.86 (d, $^2J_{4a\text{-}4a'}$ = 10.8 Hz, 1H, HC(4^a)); 4.82 (d, $^2J_{3a\text{-}3a'}$ = 10.9 Hz, 1H, HC($3^{a'}$)); 4.76 (d, $^2J_{2a\text{-}2a'}$ = 10.9 Hz, 1H, HC($2^{a'}$)); 4.71 (d, $^2J_{1a\text{-}1a'}$ ≈ 11.9 Hz, 1H, HC($1^{a'}$)); 4.67 (d, $^2J_{6a\text{-}6a'}$ = 12.2 Hz, 1H, HC(6^a)); 4.64 (d, $^2J_{6a\text{-}6a'}$ ≈ 12.2 Hz, 1H, HC($6^{a'}$); 4.61 (d, $^2J_{4a\text{-}4a'}$ ≈ 10.8 Hz, 1H, HC($4^{a'}$)); 4.55 (d, $^3J_{1-2}$ = 7.9 Hz, 1H, HC(1β)); 3.80 (dd, $^3J_{5-6}$ ≈ 2.0 Hz, $^3J_{6-6'}$ ≈ 11.0 Hz, 1H, HC(6 β)); 3.74 (dd, $^3J_{5-6a}$ ≈ 5.0 Hz, $^3J_{6-6'}$ = 11.8 Hz, 1H, HC(6′ β)); 3.73–3.50 (m, 4H, HC(2 β), HC(3 β), HC(4 β), and HC(5 β)); α/β ratio by ^{1}H NMR: could not be determined because of overlap of peaks. ^{13}C NMR (100 MHz, $CDCl_3$, 298 K): δ_C (ppm) = 138.8–137.2 ((C1^1), (C2^1), (C3^1), (C4^1), and (C6^1) of α and β); 128.4–127.5 ((C1^2, C1^3, C1^4, C2^2, C2^3, C2^4, C3^2, C3^3, C3^4, C4^2, C4^3, C4^4, C6^2, C6^3, C6^4) of α and β);102.6 (C(1 β)); 95.7 (C(1α)); 84.7, 82.3, 77.9, 74.9 (C(2 β), C(3 β), C(4 β), C(5 β)); 75.6, 75.0, 74.8, 73.5, 71.1 (C(1^a), C(2^a), C(3^a), C(4^a), C(6^a)); 68.9 (C(6 β)). MS (ESI (+)): *m/z* relative intensity $[M + Na]^+$ = 653.5.

*2,3,4,6-Tetra-O-benzyl-α/β-D-glucose (**8e**).* To **8d** (5.5 g, 8.72 mmol, 1 equiv) dissolved in acetic acid (110 mL), 6 N HCl (16.5 mL) was added, and the solution was heated to 60 °C. The reaction was monitored by TLC (hexane/EtOAc 8:2) and the starting material was totally consumed after 5 h. The mixture was diluted with water (400 mL) and extracted with CH_2Cl_2 (3 × 250 mL). The organic layer was washed with saturated $NaHCO_3$ aqueous solution (300 mL) and then with water (300 mL). The organic layer was dried over $MgSO_4$, concentrated, and the residue purified by flash chromatography to afford **8e** (2.74 g, 58%, major α anomer). R_f (CH_2Cl_2/EtOAc 9:1): 0.34 (UV_{254} active; $KMnO_4$). IR (KBr): 3435s, 3065w, 3031w, 2919m, 2863m, 1629m, 1497m, 1453s, 1400m, 1363m, 1327w, 1259w, 1209m, 1147vs, 1088vs, 1073vs, 1028vs, 1001m, 858w, 837w, 745vs, 696vs, 608w, 500w, 462w. ^{1}H NMR (400 MHz, $CDCl_3$, 298 K): δ_H (ppm) = 7.37–7.16 (m, 20H, H−Ar); 5.26 (d, $^3J_{1-2}$ = 3.5 Hz, 1H, HC(1α)); 4.99−4.50 (m, H_2CPh (α and β) and HC(1 β)); 4.07 (ddd, 1H, $^3J_{5'-6'a}$ ≈ 2.0 Hz, $^3J_{5'-6'b}$ ≈ 4.0 Hz, $^3J_{5'-4'}$ = 10.0 Hz, 1H, HC(5 α)); 4.00 (t, $^3J_{3-2}$ = 9.3 Hz, 1H, HC(3 α)); 3.75–3.65 (m, 8H, H_2C(6 α), H_2C(6 β), HC(4 α), HC(4 β)), HC(5 β), and HC(3 β)); 3.62 (dd, $^3J_{1-2}$ = 3.6 Hz, $^3J_{2-3}$ = 9.5 Hz, 1H, HC(2 α)); 3.43 (dd, $^3J_{1-2}$ = 7.7 Hz, $^3J_{2-3}$ = 9.5 Hz, 1H, HC(2 β)). α/β ratio by ^{1}H NMR could not be determined because of overlap of peaks (α anomer = major). ^{13}C NMR (100 MHz, $CDCl_3$, 298 K): δ_C (ppm) = 138.6–137.7 ((C2^1), (C3^1), (C4^1), and (C6^1) of α and β); 128.5–127.6 ((C2^2, C2^3, C2^4, C3^2, C3^3, C3^4, C4^2, C4^3, C4^4, C6^2, C6^3, C6^4) of α and β; 97.4 (C(1 β)); 91.3 (C(1 α)); 83.1 (C(2 β)); 81.7 (C(3 α)); 80.0 (C(2 α)); 70.3 (C(5 α)); 68.8 (C(6 β)); 68.50 (C(6 α)); 84.5, 77.7, 77.6, 74.7 (C(3 β), C(4 α), C(4 β), and C(5 β)); 75.7, 75.6, 75.0, 74.7, 73.5, 73.4, 73.2 (C(2^a), C(3^a), C(4^a), and C(6^a) of both α and β). MS (ESI (+)): *m/z* relative intensity $[M + Na]^+$ = 563.3.

*2′,3′,4′,6′-Tetra-O-benzyl-1′-O-(5-Boc-amino levulinic acid)-α-D-glucose (**8f**).* To **8e** (1.52 g, 2.8 mmol, 1 equiv) dissolved in CH_2Cl_2 (50 mL) at 0 °C under argon atmosphere, **5** (1.05 g, 4.54 mmol, 1.6 equiv), DCC (0.93 g, 4.5 mmol, 1.6 equiv), and DMAP (10 mg, 0.082 mmol, 0.03 equiv) were added. The reaction was warmed to room temperature, stirred for 5 h, and monitored by TLC (hexane/EtOAc 7:3). The mixture was filtered over celite and the filtrate concentrated. The residue was subjected to flash chromatography to afford **8f** (1.93 g, 81%). R_f (hexane/EtOAc 7:3): 0.19 (UV_{254} active; $KMnO_4$). ^{1}H NMR (400 MHz, $CDCl_3$, 298 K): δ_H (ppm) = 7.39–7.19 (*m*, 20H, H−Ar); 6.39 (d, $^3J_{1-2}$ = 3.5 Hz, 1H, HC(1′ α)); 5.68 (d, $^3J_{1-2}$ = 8.0 Hz, 1H, HC(1′β)); 5.30 (s, 1H, HN); 5.01 (d, $^2J_{2a\text{-}2a'}$ = 10.9 Hz, 1H, HC(2^a)); 4.90 (d, $^2J_{3a\text{-}3a'}$ = 10.7 Hz, 1H, HC(3^a)); 4.89 (d, $^2J_{2a\text{-}2a'}$ = 10.9 Hz, 1H, HC($2^{a'}$)); 4.72 (d, $^2J_{4a\text{-}4a'}$ = 11.5 Hz, 1H, HC(4^a)); 4.67 (d, $^2J_{4a\text{-}4a'}$ = 11.5 Hz, 1H, HC($4^{a'}$)); 4.65 (d, $^2J_{6a\text{-}6a'}$ = 12.1 Hz, 1H, HC(6^a)); 4.57 (d, $^2J_{3a\text{-}3a'}$ = 10.7 Hz, 1H, HC($3^{a'}$)); 4.52 (d, $^2J_{6a\text{-}6a'}$ = 12.1 Hz, 1H, HC($6^{a'}$) and other small peaks in this region due to H_2CPh of β anomer); 4.05 (d, $^3J_{5\text{-}NH}$ ≈ 4.0 Hz, 2H, H_2C(5)); 3.99 (t, $^3J_{3-2}$ = 9.3 Hz, 1H, HC(3′ α)); 3.93 (m, 1H, HC(5′ α)); 3.83–3.69 (m, 6H, HC(3′ β), HC(4′ α); HC(4′ β); HC(5′ β)); H_2C(6′ α); H_2C(6′ β); HC(2′ α)); 3.68–3.61 (m, 1H, HC(2′ β)); 2.76–2.67 (m, 4H, H_2C(3) and H_2C(2)); 1.49 (s, 9H, H_3C (8a, 8b, and 8c)); 3.53–3.42; α/β ratio by ^{1}H NMR: 6.9:1. ^{13}C NMR (100 MHz, $CDCl_3$, 298 K): δ_C (ppm) = 203.9 (C(4)); 171.0 (C(1)); 155.6 (C(6)); 138.5–137.5 ((C2^1), (C3^1), (C4^1), and (C6^1) of α and β); 128.4–127.6 ((C2^2, C2^3, C2^4, C3^2, C3^3, C3^4, C4^2, C4^3, C4^4, C6^2, C6^3, C6^4) of α and β); 94.3 (C(1′β)); 90.4 (C(1′ α)); 81.6 (C(3′ α)); 80.8 (C(2′ β)); 79.7 (C(7)); 78.7 (C(2′ α)); 72.8 (C(5′ α)); 68.0 (C(6′ α) and C(6′ β)); 84.7, 77.1, 76.8, 75.5 (C(3′ β), C(4′ α), C(4′ β), and C(5′ β)); 75.6, 75.2, 73.4, 73.1 (C(2^a), C(3^a), C(4^a), and C(6^a) of α anomer); 50.2 (C(5)); 34.1 (C(3)); 28.3 (C(8a, 8b, and 8c); 27.8 (C(2)); HR-MS $[M + Na]^+$ = 776.3407 (calculated = 776.3410).

*1′-O-(5-Boc-amino levulinic acid)-α-D-glucose (**8g**).* Under argon atmosphere, to **8f** (3 g, 3.98 mmol, 1 equiv) dissolved in CH_2Cl_2(100 mL), 50 mL of EtOH, and 10% Pd over activated carbon (4.234 g, 3.98 mmol, 1.0 equiv) were added. The reaction mass was agitated under H_2 for 12 h, and then the reaction mass was filtered over celite and the filtrate concentrated. The residue was subjected to flash chromatography to afford 1.513 g of pure **8g** which was further subjected to flash chromatography to afford only the α anomer of **8g** (50%). R_f (CH_2Cl_2/MeOH 8:2) = 0.37 ($KMnO_4$). IR (KBr): 3410vs, 2978m, 2925m, 1730vs, 1698vs, 1518m, 1393s, 1368s, 1254s, 1167vs, 1085s, 1049m, 1025m, 992m, 896w, 781w, 582vw, 464vw. ^{1}H NMR (400 MHz, $CDCl_3$ and CD_3OD, 298 K): δ_H (ppm) = 6.68 (sbr, NH); 6.08 (d, $^3J_{1'-2'}$ = 3.5 Hz, 1H, HC(1′α)); 5.45 (d, $^3J_{1'-2'}$ =8.0 Hz, 1H, HC(1′ β)); 3.93 (s, H_2C(5)); 3.78 (dd, $^3J_{6'a\text{-}5'}$ ≈ 2.5 Hz, $^3J_{6'a\text{-}6'b}$ ≈ 12.0 Hz 1H, HC(6′ α)); 3.73–3.61 (m, 3H, HC(6′b α), HC(5′ α), and HC(3′ α)); 3.55 (dd, $^3J_{1'-2'}$ ≈ 3.5 Hz, $^3J_{2'-3'}$ = 9.7 Hz, 1H, HC(2′ α)); 3.42 (t, $^3J_{3'-4'}$ ≈ 9.5 Hz, $^3J_{3'-4'}$ ≈ 9.5 Hz, 1H, HC(4′ α)); 2.81–2.68 (m, 4H, H_2C(3) and H_2C(2)); 1.43 (s, 9H, H_3C (8a, 8b, and 8c)); 5.23–4.81, 4.73–3.97, 1.39–1.23 (peaks due to impurity); α/β ratio by ^{1}H NMR: 7:1. ^{13}C NMR (100 MHz, $CDCl_3$and CD_3OD, 298 K): δ_C (ppm) = 206.8 (C(4)); 172.9 (C(1)); 157.9 (C(6)); 93.5 (C(1′ α)); 80.5 (C(7)); 71.8 (C(2′ α)); 75.4, 74.4, 70.5 ((C(3′ α)), C(4′ α), and (C(5′ α)); 61.9 (C(6′ α); 50.5 (C(5)); 34.7 (C(3)); 28.6 (C(8a, 8b, and 8c)); 28.5 (C(2)). MS (ESI (+)): *m/z* relative intensity $[M + Na]^+$ = 416.1. HR-MS $[M + Na]^+$ = 416.1529 (calculated = 416.1533).

*1′-O-(5-Amino levulinic acid)-α-D-glucose (**8h**).* To **8g** (1.24 g, 3.15 mmol, 1 equiv) dissolved in 50 mL of CH_2Cl_2 at −10 °C, trifluoroacetic acid (28.7 g, 19.3 mL, 252 mmol, 80 equiv) was added dropwise. The reaction mass was maintained at 0–5 °C for 1 h. When the deprotection of Boc was completed (controlled by the absence of Boc peak in ^{1}H NMR), CH_2Cl_2 and trifluoroacetic acid were evaporated. The product was triturated 3 times with dry ether and the ether solution was decanted. The solid product was purified by dissolution in 4 mL of MeOH and precipitation by 20 mL of ether. The mass was centrifuged and the solid dried, yielding 818 mg of **8h** as a highly hygroscopic white solid (73%). IR (KBr): 3379vs, 2929s, 2345vw, 1789s, 1734vs, 1678vs, 1516m, 1428s, 1384s, 1356m, 1204vs, 1190vs, 1139vs, 1083s, 1050s, 1029s, 992m, 957w, 905w, 839m, 801m, 775w, 723m, 598w, 552w, 521w, 464vw. ^{1}H NMR (400 MHz, D_2O, 298 K): δ_H (ppm) = 5.95 (d, $^3J_{1'-2'}$ = 3.5 Hz, 1H, HC(1′ α)); 5.38 (d, $^3J_{1'-2'}$ = 8.0 Hz, 1H, HC(1′*β*)); 3.97 (s, $H_2C(5)$); 3.66–3.50 (m, 5H, 2′α, 3′α, 5′α, 6′aα, and 6′bα); 3.33 (t, $^3J_{4'-3'} \approx 9.2$ Hz, $^3J_{4'-5'} \approx 9.2$ Hz 1H, HC(4′ α); 2.81–2.65 (m, 4H, $H_2C(3)$ and $H_2C(2)$); other small peaks due to *β* anomer and ether; α/*β* ratio by ^{1}H NMR: 13:1. ^{13}C NMR (100 MHz, D_2O, 298 K): δ_C (ppm) = 203.9 (C(4); 173.9 (C(1); 163.0 (q, $^2J_{C-F} \approx 36.0$, CF_3COO-); 116.4 (q, $^1J_{C-F} \approx 291.0$, CF_3COO-); 94.4 (C(1′ *β*)); 92.7 (C(1′ α)); 74.2 (C(5′ α)); 73.0 (C(3′ α)); 70.3 (C(2′ α)); 69.0 (C(4′ α)); 60.4 (C(6′ α)); 47.2 (C(5)); 34.3 (C(3)); 27.6 (C(2)) and other small peaks due to *β* anomer and ether. HR-MS [M − CF_3COO-]$^+$ = 294.11910 (calculated = 294.1189).

*1,2,3,4,6-Penta-O-benzyl-β-mannose (**9d**).* For the synthesis of **9d** starting from **9a**, the same procedure was followed as for **8d** (52%). R_f (hexane/ether 7:3): 0.21 (UV_{254} active; $KMnO_4$). ^{1}H NMR (400 MHz, $CDCl_3$, 298 K): δ_H (ppm) = 7.49–7.20 (m, 25H, H−Ar); 5.04 (d, $^2J_{1a-1a'}$ = 12.5 Hz, 1H, HC(1^a)); 5.03 (d, $^2J_{2a-2a'}$ = 12.0 Hz, 1H, HC(2^a)); 4.94 (d, $^2J_{3a-3a'}$ = 10.8 Hz, 1H, HC(3^a)); 4.92 (d, $^2J_{1a-1a'} \approx 11.9$ Hz, 1H, HC($1^{a'}$)); 4.69 (d, $^2J_{4a-4a'}$ = 12.1 Hz, 1H, HC(4^a)); 4.63 (d, $^2J_{2a-2a'} \approx 12.0$ Hz, 1H, HC($2^{a'}$)); 4.62 (d, $^2J_{4a-4a'}$ = 12.1 Hz, 1H, HC($4^{a'}$)); 4.57 (d, $^2J_{3a-3a'}$ = 10.8 Hz, 1H, HC($3^{a'}$)); 4.53 (d, $^2J_{6a-6a'}$ = 11.9 Hz, 1H, HC(6^a)); 4.46 (d, $^2J_{6a-6a'} \approx 11.9$ Hz, 1H, HC($6^{a'}$); 4.70–4.45 (m, 1H, HC(1 *β*)); 3.95–3.90 (m, 1H, HC(2 *β*)); 3.93 (t, $^3J_{3-4}$ = 9.8 Hz, $^3J_{4-5} \approx 9.8$ Hz, 1H, HC(4 *β*)); 3.87 (dd, $^3J_{5-6} \approx 2.0$ Hz, $^3J_{6-6'} \approx 11.0$ Hz, 1H, HC(6 *β*)); 3.81 (dd, $^3J_{5-6} \approx 6.0$ Hz, $^3J_{6-6'}$ = 11.0 Hz, 1H, HC(6′ *β*)); 3.52 (dd, $^3J_{2-3} \approx 3.0$ Hz, $^3J_{3-4} \approx 9.8$ Hz, 1H, HC(3 *β*)); 3.49 (ddd, $^3J_{5-6} \approx 2.0$ Hz, $^3J_{5-6'} \approx 6.0$ Hz, $^3J_{5-4} \approx 9.8$ Hz, 1H, HC(5 *β*)); α/*β* ratio by ^{1}H NMR: could not be determined because of peak overlap. ^{13}C NMR (100 MHz, $CDCl_3$, 298 K): δ_C (ppm) = 138.8–137.6 ((C1^1), (C2^1), (C3^1), (C4^1), and (C6^1) α and *β*); 128.4–127.5 ((C1^2, C1^3, C1^4, C2^2, C2^3, C2^4, C3^2, C3^3, C3^4, C4^2, C4^3, C4^4, C6^2, C6^3, C6^4) of α and *β*); 100.4 (C(1 *β*)); 82.5, 76.1, 75.1, 73.9 (C(2 *β*), C(3 *β*), C(4 *β*), C(5 *β*)); 75.2, 74.0, 73.6, 71.6, 70.9 (C(1^a), C(2^a), C(3^a), C(4^a), C(6^a)); 69.8 (C(6 *β*)). MS (ESI (+)): *m*/*z* relative intensity [M + Na]$^+$ = 653.6.

*2,3,4,6-Tetra-O-benzyl-α-D-mannose (**9e**).* For the synthesis of **9e** starting from **9d**, we followed the same procedure as we used for the synthesis of **8e** (major α anomer; 71%). R_f (hexane/EtOAc 6:4): 0.28 (UV_{254} active; $KMnO_4$). IR (KBr): 3400s, 3087m, 3063m, 3030s, 3006w, 2918s, 2866s, 1952vw, 1877vw, 1811vw, 1737w, 1605w, 1586vw, 1546vw, 1496s, 1453vs, 1393m, 1364s, 1265m, 1244m, 1208s, 1095vs, 1027vs, 910m, 843m, 820w, 797w, 736, 697, 607m, 528vw, 486vw, 464vw. ^{1}H NMR (400 MHz, $CDCl_3$, 298 K): δ_H (ppm) = 7.43–7.21 (m, 20H, H−Ar); 5.28 (d, $^3J_{1-2} \approx 2.0$ Hz, 1H, HC(1 α)); 4.93 (d, $^2J_{2a-2a'}$ = 10.9 Hz, 1H, HC(2^a)); 4.78 (d, $^2J_{3a-3a'}$ = 12.5 Hz, 1H, HC(3^a)); 4.74 (d, $^2J_{3a-3a'} \approx 12.5$ Hz, 1H, HC($3^{a'}$)); 4.67 (d, J_{1-2} = 1.1 Hz 1H, HC(1*β*)); 4.61 (d, $^2J_{4a-4a'}$ = 12.1 Hz, 1H, HC(4^a)); 4.59 (d, $^2J_{2a-2a'} \approx 10.9$ Hz, 1H, HC($2^{a'}$)); 4.58 (d, $^2J_{6a-6a'}$ = 11.5 Hz, 1H, HC(6^a)); 4.56 (d, $^2J_{4a-4a'}$ = 12.1 Hz, 1H, HC($4^{a'}$)); 4.55 (d, $^2J_{6a-6a'}$ = 11.5 Hz, 1H, HC($6^{a'}$); 4.13–4.08 (m, 1H, HC(5 α)); 4.02 (dd, $^3J_{2-3} \approx 3.0$ Hz, $^3J_{3-4} \approx 9.8$ Hz, 1H, HC(3 α)); 3.90 (t, $^3J_{3-4}$ = 9.8 Hz, $^3J_{4-5} \approx 9.8$ Hz, 1H, HC(4 α)); 3.83 (dd, $^3J_{1-2} \approx 2.0$ Hz, $^3J_{2-3} \approx 3.0$ Hz, 1H, HC(2 α)); 3.76 (dd, $^3J_{5-6} \approx 2.0$ Hz, $^3J_{6-6'} \approx$11.0 Hz, 1H, HC(6 α)); 3.71 (dd, $^3J_{5-6} \approx 6.5$ Hz, $^3J_{6-6'} \approx 11.0$ Hz, 1H, HC(6′ *β*)); 3.60 (dd, $^3J_{2-3} \approx 3.0$ Hz, $^3J_{3-4} \approx 9.8$ Hz, 1H, HC(3 *β*)); 4.65 (s, impurity); 4.19–4.13q, 2.08s, 1.3t (peaks due to EtOAc solvent); α/*β* ratio by ^{1}H NMR: could not be determined because of peak overlap. ^{13}C NMR (100 MHz, $CDCl_3$, 298 K): δ_C (ppm) = 138.5–137.9 ((C2^1), (C3^1), (C4^1), and (C6^1) α and *β*); 128.7–127.0 ((C2^2, C2^3, C2^4, C3^2, C3^3, C3^4, C4^2, C4^3, C4^4, C6^2, C6^3, C6^4) of α and *β*); 94.0 (C(1*β*)); 92.6(C(1α)); 83.0(C(3*β*)); 79.8(C(3α)); 75.3(C(4α)); 75.00(C(2α)); 71.3(C(5α)); 75.1, 73.3, 72.6, 72.1 ((C(2^a), C(3^a), C(4^a), C(6^a)); 69.7 (C(6α)); 171.3, 60.5, 21.0, 14.2 (peaks due to EtOAc). MS (ESI (+)): *m*/*z* relative intensity [M + Na]$^+$ = 563.3; [M + H]$^+$ = 541.1.

*2′,3′,4′,6′-Tetra-O-benzyl-1′-O-(5-Boc-amino levulinic acid)-α-D-mannose (**9f**).* For the synthesis of **9f** starting from **9e**, we followed the procedure that we used for the synthesis of **8f** (major α anomer; 82.2%). R_f (hexane/EtOAc 7:3): 0.15 (UV_{254} active; $KMnO_4$). ^{1}H NMR (400 MHz, $CDCl_3$, 298 K): δ_H (ppm) = 7.41–7.15 (m, 20H, H−Ar); 6.22 (d, $^3J_{1-2}$ = 1.9 Hz, 1H, HC(1′α)); 5.60 (m, 1H, HC(1′ *β*)); 5.18 (s, 1H, HN); 4.90 (d, $^2J_{2a-2a'}$ = 10.7 Hz, 1H, HC(2^a)); 4.78 (d, $^2J_{3a-3a'}$ = 12.3 Hz, 1H, HC(3^a)); 4.73 (d, $^2J_{3a-3a'}$ = 12.3 Hz, 1H, HC($3^{a'}$)); 4.67 (d, $^2J_{4a-4a'}$ = 12.1 Hz, 1H, HC(4^a)); 4.63 (d, $^2J_{6a-6a'}$ = 12.0 Hz, 1H, HC(6^a)); 4.59 (d, $^2J_{6a-6a'}$ = 12.0 Hz, 1H, HC($6^{a'}$); 4.55 (d, $^2J_{2a-2a'} \approx 10.7$ Hz, 1H, HC($2^{a'}$)); 4.54 (d, $^2J_{4a-4a'} \approx 12.1$ Hz, 1H, HC($4^{a'}$)); and other small peaks in this region due to H_2CPh of *β* anomer); 4.08 ((t, $^3J_{3-4}$ = 9.6 Hz, 1H, HC(4′ α)); 4.03 (d, $^3J_{5\text{-}NH}$ = 5.0 Hz, $H_2C(5)$); 3.87 (d, $^3J_{2-3} \approx 3$ Hz, $^3J_{3-4}$ = 9.4 Hz, 1H, HC(3′ α); 3.89–3.84 (m, 1H, HC(5′ α); 3.80–3.76 (m, 2H, HC(2′ α), and HC(6′ α); 2.79–2.57 (m, 4H, $H_2C(3)$ and $H_2C(2)$); 1.45 (s, 9H, H_3C (8a, 8b, and 8c)); 4.16–4.10q, 2.05s, 1.27t (peaks due to EtOAc solvent); α/*β* ratio by ^{1}H NMR: 5:1. ^{13}C NMR (100 MHz, $CDCl_3$, 298 K): δ_C (ppm) = 204.1 (C(4)); 171.1 (C(1 *β*)); 170.7 (C(1 α)); 155.7 (C(6)); 138.4–137.9 ((C2^1), (C3^1), (C4^1), and (C6^1) of α and *β*); 128.5–127.6 ((C2^2, C2^3, C2^4, C3^2, C3^3, C3^4, C4^2, C4^3, C4^4, C6^2, C6^3, C6^4) of α and *β*); 93.6 (C(1′ *β*)); 92.4 (C(1′α)); 80.0 (C(7)); 79.2 ((C(3′ α) or (C(5′ α)); 74.5 ((C(3′ α) or (C(5′ α)); 74.2 (C(4′ α)); 73.4 (C(2′ α)); 68.9 (C(6′ α)); 75.4, 73.5, 72.6, 72.1 (C(2^a), C(3^a), C(4^a), and C(6^a) of α anomer); 50.3 (C(5)); 34.2 (C(3)); 28.4 (C(8a, 8b, and 8c); 27.8 (C(2)). MS (ESI (+)): *m*/*z* relative intensity [M + Na]$^+$ = 776.3; HR-MS [M + Na]$^+$ = 776.3409 (calculated = 776.3410).

*1′-O-(5-Boc-amino levulinic acid)-α-D-mannose (**9g**).* For the synthesis of **9g** starting from **9f**, we followed the same procedure as we used for the synthesis of **8g** (major α anomer; 85.6%). R_f (CH_2Cl_2/MeOH 8:2) = 0.38 ($KMnO_4$). IR (KBr): 3435vs, 2992vw, 2978vw, 2950vw, 2933m, 2942vw, 2536w, 2495w, 1731vs, 1682vs, 1518vs, 1461vw, 1423w, 1408vw, 1392w, 1368s, 1349w, 1335vw, 1248s, 1183m, 1139s, 1116vw, 1097m, 1075w, 1055m, 1043m, 1025vw, 1014vw, 990m, 973s, 950vw, 899w, 870w, 828w, 815vw, 800m, 781vw, 767vw, 684vw, 667vw, 649vw, 585w, 566vw, 538w, 501vw, 460vw. ^{1}H NMR (400 MHz, $CDCl_3$ and CD_3OD, 298 K): δ_H (ppm) = 5.99 (d, $^3J_{1'-2'}$ = 1.7 Hz, 1H, HC(1′α)); 4.75 (d, $^3J_{1'-2'}$ = 1.6 Hz, 1H, HC(1′*β*)); 3.92 (s, $H_2C(5)$); 3.78 (dd, $^3J_{6'a-5'} \approx 2.5$ Hz, $^3J_{6'a-6'b} \approx 12.0$ Hz, 1H, HC(6′a α)); 3.76–3.60 (m, 5H, HC(6′b α), HC(5′α), (4′α), HC(3′α)) and HC(2′ α)); 2.81–2.63 (m, 4H, $H_2C(3)$ and $H_2C(2)$); 1.44 (s, 9H, H_3C (8a, 8b, and 8c)); α/*β* ratio by ^{1}H NMR: 8:1. ^{13}C NMR (100 MHz, $CDCl_3$ and CD_3OD, 298 K): δ_C (ppm) = 207.1 (C(4)); 172.3 (C(1)); 158.1 (C(6)); 101.0 (C(1′*β*); 95.3 (C(1′α)); 80.5 (C(7)); 76.6, 71.9,

70.6, 67.6 (C(2α), (C(3′α)), C(4′α) and (C(5′α)); 62.3 (C(6′α); 50.5 (C(5)); 34.7 (C(3)); 28.6 (C(8a, 8b, and 8c); 28.5 (C(2)). MS (ESI (+)): *m*/*z* relative intensity $[M + Na]^+ = 416.1$; $[M - H + H_2O]^- = 428.1$. HR-MS $[M + Na]^+ = 416.1524$ (calculated = 416.1533).

*1′-O-(5-Amino levulinic acid)-α-D-mannose (**9h**).* For the synthesis of **9h** starting from **9g**, we followed the same procedure as we used for the synthesis of **8h** (90%). IR (KBr): 3392vs, 2943w, 2527vw, 1731m, 1677vs, 1516vw, 1428m, 1203vs, 1137vs, 1068m, 960vw, 840w, 801m, 723m, 600vw, 518vw. ^{1}H NMR (400 MHz, D_2O, 298 K): δ_H (ppm) = 5.77 (d, $^3J_{1'-2'} = 1.8$ Hz, 1H, HC(1′α)); 4.66 (d, $^3J_{1'-2'} = 1.5$ Hz, 1H, HC(1′*β*)); 3.92 (s, $H_2C(5)$); 3.78 (dd, $^3J_{1'-2'} \approx 1.8$ Hz, $^3J_{2'-3'} = 3.3$ Hz, 1H, HC(2′α)); 3.71 (dd, $^3J_{1'-2'} \approx 1.8$ Hz, $^3J_{2'-3'} = 3.4$ Hz, 1H, HC(2′*β*)); 3.67–3.59 (m, 2H, HC(3α) and HC(6′a α)); 3.57–3.49 (m, 3H, HC(6′b α), HC(5′α), and HC(4′α)); 2.74 (t, $^3J_{2-3} \approx 6.5$ Hz, 2H, $H_2C(3)$); 2.57 (t, $^3J_{3-2} \approx 6.5$ Hz, 2H, $H_2C(2)$); 1.03–0.94 (peaks due to traces impurity); α/*β* ratio by ^{1}H NMR: 14:1. ^{13}C NMR (100 MHz, D_2O, 298 K): δ_C (ppm) = 203.9 (C(4)); 173.1 (C(1)); 162.7 (q, $^2J_{C-F} \approx 36.0$, CF_3COO-); 116.3 (q, $^1J_{C-F} \approx 290.0$, CF_3COO-); 99.6 (C(1′*β*)); 94.2 (C(1′α)); 69.1 (C(2′α)); 60.8(C(6′α)); 75.1, 70.4, 66.3 (C(3′α), C(5′α), and C(4′α)); 47.2 (C(5)); 34.3 (C(3)); 27.5 (C(2)). HR-MS $[M - CF_3COO-]^+ = 294.1184$ (calculated = 294.1189).

*α-Methyl-2,3,4,6-tetra-O-benzyl Galactoside (**10e**).* To α-methyl galactoside **10d** (2.5 g, 12.87 mmol, 1 equiv) dissolved in 140 mL of anhydrous DMF at −10 °C under argon atmosphere, sodium hydride (55% dispersion in mineral oil, 3.37 g, 77.2 mmol, 6 equiv, 1.5 equiv per −OH) was added in portions. The reaction mass was warmed to ambient temperature and stirred for 2 h, then the mass was cooled to 5 °C, tetrabutyl ammonium iodide (240 mg, 0.65 mmol, 0.05 equiv) and benzyl bromide (13.2 g, 9.2 mL, 77.2 mmol, 6 equiv, 1.5 equiv per −OH) were added dropwise. The reaction mass was maintained at room temperature for 24 h, then cooled to 5 °C and quenched with 40 mL of methanol. The crude product was extracted with 300 mL of EtOAc and 400 mL of water. The aqueous layer is extracted with 3 × 200 mL of EtOAc. The combined organic layers were washed with 300 mL of brine, dried over $MgSO_4$, and the solvent evaporated. The crude residue was subjected to flash chromatography (hexane/EtOAc 70:30). The pure fractions were collected and concentrated to afford **10e** (6.35 g, 89%). R_f (hexane/EtOAc 7:3): 0.33 (UV_{254} active; $KMnO_4$). IR (KBr): 3445w, 3087vw, 3063w, 3030m, 2917s, 2867m, 1951vw, 1874vw, 1809vw, 1736w, 1677w, 1606vw, 1586vw, 1496m, 1454s, 1351m, 1308vw, 1241w, 1194m, 1152vw, 1133w, 1099vs, 1051vs, 1028w, 911w, 839vw, 736vs, 697vs, 607w, 547w, 464vw. ^{1}H NMR (400 MHz, $CDCl_3$, 298 K): δ_H (ppm) = 7.38–7.19 (m, 25H, H−Ar); 4.94 (d, $^2J_{2a-2a'} = 11.5$ Hz, 1H, HC(2^a)); 4.82 (d, $^2J_{3a-3a'} = 11.7$ Hz, 1H, HC(3^a)); 4.79 (d, $^2J_{4a-4a'} = 11.6$ Hz, 1H, HC(4^a)); 4.70 (d, $^2J_{3a-3a'} \approx 11.7$ Hz, 1H, HC($3^{a'}$)); 4.68 (d, $^3J_{1-2} \approx 3.8$ Hz, 1H, HC(1α)); 4.65 (d, $^2J_{4a-4a'} \approx 11.61$ Hz, 1H, HC($4^{a'}$)); 4.56 (d, $^2J_{2a-2a'} = 11.5$ Hz, 1H, HC($2^{a'}$)); 4.45 (d, $^2J_{6a-6a'} = 11.8$ Hz, 1H, HC(6^a)); 4.36 (d, $^2J_{6a-6a'} = 11.8$ Hz, 1H, HC($6^{a'}$); 4.04 (dd, $^3J_{2-1} \approx 3.8$ Hz, $^3J_{2-3} \approx 10.0$ Hz, 1H, HC(2 α)); 4.03–3.92 (*m*, 2H, HC(3α) and HC(4 α)); 3.90 (t, $^3J_{5-6} \approx 6.4$ Hz, $^3J_{5-6'} \approx 6.4$ Hz, $^3J_{5-4} \approx 1.0$ Hz, 1H, HC(5 α)); 3.52 (d, $^2J_{5-6} = 6.4$ Hz, $^3J_{5-6'} = 6.4$ Hz, 2H, $H_2C(6\ \alpha)$); 3.34 (s, 3H, $H_3C(1^1)$; α/*β* ratio by ^{1}H NMR: only the α anomer. ^{13}C NMR (100 MHz, $CDCl_3$, 298 K): δ_C (ppm) = 138.7–137.9 (($C2^1$), ($C3^1$), ($C4^1$), and ($C6^1$)); 128.3–127.4 (($C2^2$, $C2^3$, $C2^4$, $C3^2$, $C3^3$, $C3^4$, $C4^2$, $C4^3$, $C4^4$, $C6^2$, $C6^3$, $C6^4$); 98.7 (C(1 α)); 79.0, 75.1 (C(3 α) and C(4 α)); 76.4 (C(2 α)); 69.1 (C(5 α); 69.0 (C(6 α)); 74.7, 73.5, 73.4, 73.2 (C(2^a), C(3^a), C(4^a), and C(6^a); 55.3 (C(1^1)). MS (ESI (+)): *m*/*z* relative intensity $[M + Na]^+ = 577.5$.

*2,3,4,6-Tetra-O-benzyl-α-galactose (**10f**).* To **10e** (4.7 g, 8.47 mmol, 1 equiv) dissolved in 100 mL of acetic acid, 15 mL of 6 N HCl were added, and the solution heated to 60 °C for 5–6 h, until the starting material disappeared by TLC (hexane/EtOAc 8:2). The mixture was diluted with 150 mL of water, extracted with 3 × 300 mL of CH_2Cl_2, and the organic layer washed with 250 mL of saturated $NaHCO_3$ and 250 mL of water. The organic layer was dried over $MgSO_4$, concentrated, and the residue was subjected to flash chromatography which afforded **10f** (2.1 g, major α anomer, 46%). R_f (hexane/EtOAc 7:3): 0.33 (UV_{254} active; $KMnO_4$). ^{1}H NMR (400 MHz, $CDCl_3$, 298 K): δ_H (ppm) = 7.49–7.23 (m, 20H, H−Ar); 5.37 (d, $^3J_{1-2} = 3.5$ Hz, 1H, HC(1α)); 5.03 (d, $^2J_{HC-HC} = 11.6$ Hz, H_2CPh); 5.02 (d, $^2J_{HC-HC} = 11.5$ Hz, H_2CPh); 4.89 (d, $^2J_{HC-HC} = 11.7$ Hz, H_2CPh); 4.88 (d, $^2J_{HC-HC} = 11.0$ Hz, H_2CPh); 4.87 (d, $^2J_{HC-HC} = 11.8$ Hz, H_2CPh); 4.83 (d, $^2J_{HC-HC} = 11.8$ Hz, H_2CPh); 4.81 (d, $^2J_{HC-HC} = 13.0$ Hz, H_2CPh); 4.78 (d, $^2J_{HC-HC} = 11.8$ Hz, H_2CPh); 4.72 (d, $^3J_{1-2} = 7.6$ Hz, 1H, HC(1*β*)); 4.68 (d, $^2J_{HC-HC} = 11.6$ Hz, H_2CPh); 4.66 (d, $^2J_{HC-HC} = 11.5$ Hz, H_2CPh); 4.56 (d, $^2J_{HC-HC} = 11.9$ Hz, H_2CPh); 4.54 (d, $^2J_{HC-HC} = 11.8$ Hz, H_2CPh); 4.47 (d, $^2J_{HC-HC} = 11.9$ Hz, H_2CPh); 4.46 (d, $^2J_{HC-HC} = 11.9$ Hz, H_2CPh); 4.26 (t, $^3J_{5-6a} = 6.3$ Hz, $^3J_{5-6b} = 6.3$ Hz, $^3J_{5-4} = 1.0$ Hz, 1H, HC(5α)); 4.12 (dd, $^3J_{1-2} \approx 3.6$ Hz, $^3J_{2-3} = 9.6$ Hz, 1H, HC(2α)); 3.87 (dd, $^3J_{1-2} = 7.6$ Hz, $^3J_{2-3} = 9.6$ Hz, 1H, HC(2*β*)); 4.08–3.51 (m, 9H, $H_2C(6\alpha)$, $H_2C(6\beta)$, HC(4α), HC(4*β*)), HC(5*β*), HC(3α)) and HC(3*β*); 2.13, 1.66, 1.43, 0.95 peaks due to traces of solvent and impurity; α/*β* ratio by ^{1}H NMR: 2.2:1. ^{13}C NMR (100 MHz, $CDCl_3$, 298 K): δ_C (ppm) = 138.6–137.7 (($C2^1$), ($C3^1$), ($C4^1$), and ($C6^1$) of α and *β*); 128.8–127.4 (($C2^2$, $C2^3$, $C2^4$, $C3^2$, $C3^3$, $C3^4$, $C4^2$, $C4^3$, $C4^4$, $C6^2$, $C6^3$, $C6^4$) of α and *β*; 98.3 (C(1*β*)); 92.3 (C(1α)); 79.2, 77.0, 75.3, 69.8 (C(2 α), (C(3 α), C(4 α), and C(5 α)); 82.6, 81.2, 74.1, 71.7 ((C(2 *β*)), C(3 *β*), C(4 *β*), and C(5 *β*)); 75.1, 73.9, 73.8, 73.4 (CH_2Ph of α anomer); 75.5, 75.0, 73.9, 73.4 (CH_2Ph of *β* anomer); 69.6 (C(6 α)); 69.4 (C(6 *β*)).

*2′,3′,4′,6′-Tetra-O-benzyl-1′-O-(5-Boc-amino levulinic acid)-β-D-galactose (**10g**).* Under argon atmosphere, to **10f** (1.98 g, 3.65 mmol, 1 equiv) with 70% of α anomer major dissolved in 80 mL of CH_2Cl_2 at 0 °C, DMAP (491 mg, 4.02 mmol, 1.1 equiv), EDCI (851 mg, 4.44 mmol, 1.21 equiv), and **5** (929 mg, 4.02 mmol, 1.1 equiv) were added. The reaction was warmed to room temperature, stirred for 7–8 h, and followed by TLC (hexane/EtOAc 7:3). When the reaction was complete, the mixture was concentrated and the residue was subjected to flash chromatography which afforded 10g (2.66 g, major *β* anomer; 96%). R_f (hexane/EtOAc 70:30): 0.15 (UV_{254} active; $KMnO_4$). ^{1}H NMR (400 MHz, $CDCl_3$, 298 K): δ_H (ppm) = 7.38–7.24 (m, 20H, H−Ar); 6.33 (d, $^3J_{1-2} = 3.5$ Hz, 1H, HC(1′α)); 5.57 (d, $^3J_{1-2} = 8.0$ Hz, 1H, HC(1′*β*)); 5.19 (s, 1H, HN); 4.93 (d, $^2J_{2a-2a'} = 11.5$ Hz, 1H, HC(2^a)); 4.83 (d, $^2J_{3a-3a'} = 11.3$ Hz, 1H, HC(3^a)); 4.81 (d, $^2J_{4a-4a'} = 11.7$ Hz, 1H, HC(4^a)); 4.75 (d, $^2J_{3a-3a'} = 11.3$ Hz, 1H, HC($3^{a'}$)); 4.74 (d, $^2J_{4a-4a'} \approx 11.7$ Hz, 1H, HC($4^{a'}$)); 4.61 (d, $^2J_{2a-2a'} = 11.5$ Hz, 1H, HC($2^{a'}$)); 4.43 (d, $^2J_{6a-6a'} = 11.7$ Hz, 1H, HC(6^a)); 4.38 (d, $^2J_{6a-6a'} = 11.7$ Hz, 1H, HC($6^{a'}$) and other small peaks in this region due to H_2CPh of α anomer); 4.00 (d, $^3J_{5\text{-}NH} \approx 4.7$ Hz, $H_2C(5)$); 3.95 (dd, $^3J_{2'-1'} = 8.0$ Hz, $^3J_{2'-3'} \approx 10.0$ Hz, 1H, HC(2′*β*)); 3.59 (dd, $^3J_{3'-4'} \approx 2.0$ Hz, $^3J_{3'-2'} \approx 10.0$ Hz, 1H, HC(3′*β*)); 3.68–3.51 (m, 3H, HC(4′*β*), HC(5′*β*)), and $H_2C(6'\beta)$; 2.70–2.58 (m, 4H, $H_2C(3)$ and $H_2C(2)$); 1.44 (s, 9H, H_3C (8^1, 8^2, and 8^3)); 4.13–4.08, 2.03, 1.25 (peaks due to EtOAc); α/*β* ratio by ^{1}H NMR: 0.15:1. ^{13}C NMR (100 MHz, $CDCl_3$, 298 K): δ_C (ppm) = 203.7 (C(4)); 171.0 (C(1)); 155.5 (C(6)); 138.3–137.6 (($C2^1$), ($C3^1$), ($C4^1$), and ($C6^1$) of α and *β*); 128.3–127.3 (($C2^2$, $C2^3$, $C2^4$, $C3^2$, $C3^3$, $C3^4$, $C4^2$, $C4^3$, $C4^4$, $C6^2$, $C6^3$, $C6^4$) of α and *β*); 94.5 (C(1′ *β*)); 91.1 (C(1′ α)); 82.2, 77.9, 74.0, 72.9 (C(2′ *β*), C(3′ *β*), C(4′ *β*), and C(5′ *β*)); 67.8 C(6′ *β*)); 75.2, 74.6, 73.4,

72.7 (C(2^a), C(3^a), C(4^a), and C(6^a)); 50.1 (C(5)); 33.8 (C(3)); 28.2 (C(8a, 8b, and 8c); 27.7 (C(2)). HR-MS $[M + Na]^+$ = 776.3406 (calculated = 776.3410).

*1′-O-(5-Boc-amino levulinic acid)-β-galactose (**10h**).* For the synthesis of **10h** starting from **10g**, we followed the same procedure as we used for the synthesis of **8g** (major β anomer; 74%). R_f (CH_2Cl_2/MeOH 8:2): = 0.21 ($KMnO_4$). IR (KBr): 3411vss, 29 77w, 2926m, 1732vs, 1695vs, 1520s, 1394vw, 1368s, 1336vw, 1253m, 1167s, 1073vs,1058w, 873vw, 782w, 767w, 686w, 538vw, 494vw. ^{1}H NMR (200 MHz, $CDCl_3$ and CD_3OD, 298 K): δ_H (ppm) = 6.12 (d, $^3J_{1'-2'}$ = 3.8 Hz, 1H, HC(1′α)); 5.42 (d, $^3J_{1'-2'}$ = 7.8 Hz, 1H, HC(1′β)); 3.93 (s, $H_2C(5)$); 3.88 (dd, $^3J_{4'-5'} \approx 0.8$ Hz, $^3J_{4'-3'}$ = 2.2 Hz, 1H, HC(4′β)); 3.84–3.58 (m, 4H, HC(2′β), HC(5′β), and $H_2C(6'\beta)$); 3.53 (dd, $^3J_{3'-4'} \approx 3.3$ Hz, $^3J_{3'-2'}$ = 10.0 Hz, 1H, HC(3′β)); 2.80–2.68 (m, 4H, $H_2C(3)$ and $H_2C(2)$); 1.44 (s, 9H, H_3C (8^1, 8^2, and 8^3)) (other peaks due to α anomer and ether solvent); α/β ratio by ^{1}H NMR: 0.07:1. ^{13}C NMR (50 MHz, $CDCl_3$ and CD_3OD, 298 K): δ_C (ppm) = 207.2 (C(4)); 173.2 (C(1)); 96.4 (C(1′β)); 80.6 (C(7)); 77.5 (C(5′β)); 74.7, 71.2, 70.0 (C(4′β), (C(2′β), and C(3′β)); 62.2 (C(6′β)); 50.7 (C(5)); 34.6 (C(3)); 28.7 (C(8^1, 8^2, and 8^3) and (C(2)). HR-MS $[M + Na]^+$ = 416.1526 (calculated = 416.1533).

*1′-O-(5-Amino levulinic acid)-β-galactose (**10i**).* For the synthesis of **10i** starting from **10h**, we followed the same procedure as we used for the synthesis of **8h** (40%). IR (KBr): 3378vs, 2933w, 1732vs, 1678vs, 1513m, 1428m, 1315w, 1204vs, 1136vs, 1071vs, 1021vw, 955vw, 892w, 839m, 800m, 781w, 723s, 704vw, 599vw, 530w. ^{1}H NMR (400 MHz, D_2O, 298 K): δ_H (ppm) = 5.99 (d, $^3J_{1'-2'}$ = 3.6 Hz, 1H, HC(1′α)); 5.36 (d, $^3J_{1'-2'}$ = 7.6 Hz, 1H, HC(1′β)); 3.99 (s, $H_2C(5)$); 3.82 (d, $^3J_{4'-3'}$ = 2.2 Hz, 1H, HC(4′β)); 3.67 (m, 1H, HC(5′β)); 3.60–3.59 (m, 4H, HC(2′β), HC(3′β), HC(6′a β), and HC(6′b β)); 2.82 (t, $^3J_{2-3} \approx 6.5$ Hz, 2H, $H_2C(3)$); 2.69 (t, $^3J_{3-2} \approx 6.0$ Hz, 2H, $H_2C(2)$); (other peaks due to α anomer and ether solvent); α/β ratio by ^{1}H NMR: 0.18:1. ^{13}C NMR (100 MHz, D_2O, 298 K): δ_C (ppm) = 204.0 (C(4)); 173.7 (C(1)); 163.3 (q, $^2J_{C-F}$ = 35.3, CF_3COO-); 116.6 (q, $^1J_{C-F}$ = 291.9, CF_3COO-); 95.0 (C(1′β)); 93.0 (C(1′α)); 76.5 (C(5′β)); 68.6(C(4′β)); 72.7, 69.6 (C(2′β) and C(3′β)); 61.1(C(6′β)); 47.3 (C(5)); 34.3 (C(3)); 27.2 (C(2)) and other peaks due to α anomer and ether solvent. MS (ESI (+)): *m*/*z* relative intensity $[M - CF_3COO-]^+$ = 294.1. HR-MS $[M - CF_3COO-]^+$ = 294.11869 (calculated = 294.1189).

*1-O-(α-D-Glucopyranosyl) Ethylene Glycol (**8i**).* Under argon atmosphere, to **8a** (5.7 g, 31.64 mmol, 1 equiv), ethylene glycol (40 g, 633 mmol, 20 equiv) and dried Dowex 50WX 8–200 resin (12 g) were added. The mixture was heated to 75 °C and stirred for 72 h. The resin was filtered over alumina sandwiched between celite and washed with ethylene glycol. Ethylene glycol was evaporated from the filtrate and the crude reaction mass was subjected to flash chromatography using gradient elution (CH_2Cl_2/MeOH 9:1 to CH_2Cl_2/MeOH 7:3) to afforded **8i** (2.57 g, major α anomer; 46%). R_f (CH_2Cl_2/MeOH 3:1) = 0.23 ($KMnO_4$). IR (KBr): 3369vs, 2927m, 2148vw, 1643w, 1415w, 1342w, 1261w, 1229w, 1151m, 1075w, 1028vs, 938w, 880w, 752vw, 702vw, 665vw, 604vw, 531vw, 496w, 458vw. ^{1}H NMR (400 MHz, D_2O, 298 K): δ_H (ppm) = 4.93 (d, $^3J_{1'-2'}$ = 3.7 Hz, 1H, HC (1′α)); 4.47 (d, $^3J_{1'-2'}$ = 7.9 Hz, 1H, HC(1′β)); 3.88–3.58 (m, 8H, H_2C (6′α), H_2C (1), $H_2C(2)$, HC (5′α), and HC (4′α); 3.54 (dd, $^3J_{2'-1'} \approx 3.7$ Hz, $^3J_{3'-2'}$ = 11 Hz, 1H, HC (2′α)); 3.39 (t, $^3J_{3'-4'}$ = 9.5 Hz, $^3J_{3'-2'}$ = 9.5 Hz, 1H, HC (3′α)); α/β ratio by ^{1}H NMR: 1:0.11. ^{13}C NMR (100 MHz, D_2O, 298 K): δ_C (ppm) = 105.0(C(1′β)); 100.9(C(1′α)); 74.1(C(2′α)); 72.2(C(3′α)); 75.7, 74.4, (C(4′α) and (C(5′α)); 71.6, 63.3, 63.2(C(1), C(2), and C(6′α)). MS (ESI (+)): *m*/*z* relative intensity [M with OH/OD + Na]$^+$ = 252.1. HR-MS $[M + Na]^+$ = 247.0783 (calculated = 247.0794).

*1-O-(5-Boc-amino levulinic acid)-2-O-(α-D-glucopyranosyl) Ethylene Glycol (**8j**).* Under argon atmosphere, to **8i** (225 mg, 1 mmol, 1 equiv) dissolved in 5 mL of anhydrous pyridine, 1.5 g of *Candida antarctica* lipase (LCA, Novozyme 435, 10 units per mg of protein; approximately 15 mmol, 15 equiv) and **6** (1.2 g, 3 mmol, 3 equiv) were added, the solution was heated to 50 °C for 30 min, and the reaction was followed by TLC (CH_2Cl_2/MeOH 3:1). The mass was cooled to room temperature and the enzyme was filtered over celite. Celite was washed with 3 × 10 mL of pyridine and solvent was evaporated. The residue was subjected to flash chromatography using gradient elution (CH_2Cl_2 100% to CH_2Cl_2/MeOH 85:15). The main fractions were concentrated to give **8j** as a white solid (210 mg, 48%). R_f (CH_2Cl_2/MeOH 85:15): 0.28 ($KMnO_4$). IR (KBr): 3395vs, 2977s, 2929s, 2355vw, 1728vs, 1709vs, 1517m, 1453vw, 1392vw, 1368m, 1285vw, 1254w, 1163s, 1076vw, 1024s, 887w, 782vw, 763vw, 703vw, 602vw, 562vw, 530vw, 500w. ^{1}H NMR (400 MHz, $CDCl_3$ and CD_3OD, 298 K): δ_H (ppm) = 4.82 (d, $^3J_{1'-2'}$ = 3.7 Hz, 1H, HC(1′α)); 4.32–4.24 (m, 3H, $H_2C(1)$ and HC(1′β)); 3.94 (s, 2H, $H_2C(1^5)$); 3.89 (ddd, $^3J_{1b\text{-}2a} \approx 3.3$ Hz, $^3J_{1a\text{-}2a} = 6.4$ Hz vicinal, $^3J_{2b\text{-}2a} = 11.5$ Hz geminal, 1H, HC(2a)); 3.79 (dd, $^3J_{5'-6'a} \approx 2.6$ Hz, $^3J_{6'a\text{-}6'b}$ = 11.9 Hz, 1H, HC(6′a α)); 3.71 (dd, $^3J_{5'-6'b} \approx 5.3$ Hz, $^3J_{6'a\text{-}6'b} \approx 11.9$ Hz, 1H, HC(6′b α)); 3.70–3.66 (m, 1H, HC (2b)); 3.63 (t, $^3J_{3'-4'} \approx 9.3$ Hz, $^3J_{3'-2'}$ = 9.3 Hz, 1H, HC(3′ α)); 3.58 (ddd, $^3J_{5'-6'a} \approx 2.7$ Hz, $^3J_{5'-6'b} \approx$ 5.0 Hz, $^3J_{5'-4'} \approx 9.9$ Hz, 1H, HC (5′ α)); 3.41 (dd, $^3J_{2'-1'}$ = 3.7 Hz, $^3J_{2'-3'}$ = 9.7 Hz, 1H, HC(2′ α)); 3.33 (t, $^3J_{3'-4'}$ = 9.2 Hz, $^3J_{4'-5'} \approx 9.3$ Hz, 1H, HC(4′ α)); 2.75 (t, $^3J_{1^3\text{-}1^2} \approx 6.5$ Hz, 2H, $H_2C(1^3)$); 2.64 (t, $^3J_{1^2\text{-}1^3} \approx 6.5$ Hz, 2H, $H_2C(1^2)$); 1.42 (s, 9H, H_3C (1^{8a}, 1^{8b}, and 1^{8c})); α/β ratio by ^{1}H NMR could not be determined because of overlap. ^{13}C NMR (100 MHz, $CDCl_3$ and CD_3OD, 298 K): δ_C (ppm) = 206.7 (C(1^4)); 173.6 (C(1^1)); 157.4 (C(1^6)); 103.7 ((C(1′ β) by DEPT); 99.5 (C(1′ α)); 80.4 (C(1^7)); 74.3(C(3′ α)); 72.8 (C(5′ α)); 72.6 (C(2′ α)); 70.8 (C(4′ α)); 66.3 (C(2)); 64.2(C(1)); 62.0 (C(6′ α)); 50.4 (C(1^5)); 34.6 (C(1^3)); 28.5 (C(1^{8a}, 1^{8b}, and 1^{8c}); 28.2 (C(1^2)). MS (ESI (+)): *m*/*z* relative intensity $[M + Na]^+$ = 460.2. HR-MS $[M + Na]^+$ = 460.1795 (calculated = 460.1795).

*1-O-(5-Amino levulinic acid)-2-O-(α-D-glucopyranosyl) Ethylene Glycol (**8k**).* To **8j** (220 mg, 0.50 mmol, 1 equiv) dissolved in 15 mL of CH_2Cl_2at −10 °C, trifluoroacetic acid (5.73 g, 3.85 mL, 50 mmol, 100 equiv) was added dropwise. The reaction was maintained at 0–5 °C for 1 h until the deprotection of Boc was complete (controlled by the absence of Boc peak in ^{1}H NMR). CH_2Cl_2 and trifluoroacetic acid were evaporated. The product was coevaporated 2 times with distilled ether, then triturated 3 times with dry ether and the ether solution was decanted. The solid product was purified by dissolution in 5 mL of MeOH and precipitation by 30 mL of ether. The mass was centrifuged and the solid dried to afford **8k** as a highly hygroscopic white solid (149 mg, 66%). IR (KBr): 3426vs, 2924m, 1789m, 1731m, 1679vs, 1521vw, 1399m, 1207vs, 1179vs, 1051w, 838w, 802w, 723m, 519vw, 501vw. ^{1}H NMR (400 MHz, D_2O, 298 K): δ_H (ppm) = 4.91 (d, $^3J_{1'-2'}$ = 3.7 Hz, 1H, HC(1′α)); 4.31–4.26 (m, 3H, $H_2C(1)$); 4.09 (s, 2H, $H_2C(1^5)$); 3.92–3.88 (m, 1H, HC(2a)); 3.80 (dd, $^3J_{5'-6'a} \approx 2.0$ Hz, $^3J_{6'a\text{-}6'b}$ = 12.1 Hz, 1H, HC(6′a α)); 3.72 (dd, $^3J_{5'-6'b} \approx 5.3$ Hz, $^3J_{6'a\text{-}6'b} \approx 12.2$ Hz, 1H, HC(6′b α)); 3.70–3.66 (m, 2H, HC (2b) and (5′ α)); 3.66 (t, $^3J_{3'-4'} \approx 9.5$ Hz, $^3J_{3'-2'}$ = 9.2 Hz, 1H, HC(3′ α)); 3.51 (dd, $^3J_{2'-1'}$ = 3.7 Hz, $^3J_{2'-3'}$ = 9.8 Hz, 1H, HC(2′ α)); 3.45–3.34 (m, 1H, HC(4′ α)); 2.89 (t, $^3J_{1^3\text{-}1^2} \approx 6.5$ Hz, 2H, $H_2C(1^3)$); 2.72 (t, $^3J_{1^2\text{-}1^3} \approx 6.5$ Hz, 2H, $H_2C(1^2)$); α/β ratio by ^{1}H NMR: only the α anomer. ^{13}C NMR (100 MHz, D_2O, 298 K): δ_C (ppm) = 204.0 (C(1^4)); 174.8 (C(1^3)); 163.1 (q, $^2J_{C-F}$ = 35.2, CF_3COO-); 116.5 (q, $^1J_{C-F} \approx 291.9$,

CF_3COO-); 98.5 (C(1′ α)); 73.1 (C(5′ α)); 72.0(C(3′ α)); 71.4 (C(2′ α)); 69.6 (C(4′ α)); 65.8 (C(2)); 64.4(C(1)); 60.6 (C(6′ α)); 47.1 (C(1^5)); 34.3 (C(1^3)); 27.5 (C(1^2)). MS (ESI (+)): *m/z* relative intensity $[M - CF_3COO^-]^+ = 340.1$; $[M - CF_3COO^- + H]^+ = 339.1$. HR-MS $[M - CF_3COO^-]^+ = 338.1441$ (calculated = 338.1451).

*1-O-(α-D-Mannopyranosyl) Ethylene Glycol (**9i**).* For the synthesis of **9i** using **9a** as starting material, we followed the same procedure as we used for the synthesis of **8i** (major α anomer; 63%). R_f (CH_2Cl_2/MeOH 3:1) = 0.28 ($KMnO_4$). ^1H NMR (400 MHz, D_2O, 298 K): δ_H (ppm) = 4.87 (d, $^3J_{1'-2'}$ = 1.7 Hz, 1H, HC(1′ α)); 4.68 (d, $^3J_{1'-2'}$ = 0.8 Hz, 1H, HC(1′β)); 3.96 (dd, $^3J_{2'-1'}$ = 1.7 Hz, $^3J_{3'-2'}$ = 3.4 Hz, 1H, HC(2′ α)); 3.87 (dd, $^3J_{6'a-5'} \approx 2.0$ Hz, $^3J_{6'a-6'b} = 11.4$ Hz, 1H, HC(6′ α a)); 3.84–3.71 (m, 5H, HC(6′ α b), $H_2C(2)$, HC(1a), and HC(3′ α); 3.65–3.57 (m, 3H, HC(5′α), HC(4′α), and HC(1b); α/β ratio by ^1H NMR: 8:1. ^{13}C NMR (100 MHz, D_2O, 298 K): δ_C (ppm) = 100.7(C(1′ β)); 100.6(C(1′ α)); 73.4(C(5′ α); 71.2((C(3′ α)); 70.7((C2′ α)); 69.2(C(1)); 67.5(C(4′ α); 61.7(C(6′ α)); 61.2 ((C(2)). MS (ESI (+)): *m/z* relative intensity [M with OH/OD + Na]$^+$ = 252.1; HR-MS $[M + Na]^+ = 247.0786$ (calculated = 247.0794).

*1-O-(5-Boc-amino levulinic acid)-2-O-(α-D-mannopyranosyl) Ethylene Glycol (**9j**).* Under argon atmosphere, to **9i** (540 mg, 2.4 mmol, 1 equiv) dissolved in 13 mL of anhydrous pyridine, 3.6 g of *Candida antarctica* lipase (LCA, Novozyme 435, 10 units per mg of protein; approximately 36 mmol, 15 equiv) and **6**(2.85 g, 7.18 mmol, 3 equiv) were added. The reaction was maintained at room temperature for 30 min and followed by TLC (CH_2Cl_2/MeOH 3:1). The mass was filtered over celite, celite was washed with 3 × 10 mL of pyridine, and solvent was evaporated. The residue was triturated with 2 × 50 mL of dry toluene/hexane (1:1), the upper clear supernatant layer was removed, and the solid sticky residue was subjected to flash chromatography using gradient elution (CH_2Cl_2 100% to CH_2Cl_2/MeOH 85:15). The main fractions were concentrated to give **9j** as a white solid (440 mg, 42%). R_f (CH_2Cl_2/MeOH 85:15): 0.20 ($KMnO_4$). IR (KBr): 3390vs, 2924vs, 1728vs, 1694vs, 1516m, 1384w, 1368m, 1252w, 1203w, 1175s, 1137s, 1063s, 977m, 915w, 878w, 804w, 723w, 680w, 579vw, 513vw. ^1H NMR (400 MHz, $CDCl_3$ and CD_3OD, 298 K): δ_H (ppm) = 4.78 (d, $^3J_{1'-2'}$ = 1.6 Hz, 1H, HC(1′α)); 4.26 (ddd, $^3J_{1a-2b} \approx 3.1$ Hz, $^3J_{1a-2a} \approx 6.3$ Hz vicinal, $^3J_{1a-1a'}$ = 11.9 Hz geminal, 1H, HC(1a)); 4.00 (ddd, $^3J_{1b-2a} \approx 3.1$ Hz, $^3J_{1b-2b}$ = 6.4 Hz vicinal, $^3J_{1b-1b'}$ = 11.9 Hz geminal, 1H, HC(1b)); 3.92 (s, 2H, $H_2C(1^5)$); 3.87 (ddd, $^3J_{1b-2a} \approx 3.1$ Hz, $^3J_{1a-2a} \approx 6.3$ Hz vicinal, $^3J_{2b-2a}$ = 11.5 Hz geminal, 1H, HC(2a)); 3.82 (dd, $^3J_{5'-6'a} \approx 2.5$ Hz, $^3J_{6'a-6'b}$ = 11.5 Hz, 1H, HC(6′a α)); 3.84–3.80 (m, 1H, HC(2′ α)); 3.75–3.60 (m, 1H, HC(2b)); 3.73 (dd, $^3J_{5'-6'b} \approx 5.3$ Hz, $^3J_{6'a-6'b} \approx 11.5$ Hz, 1H, HC(6′b α); 3.69 (dd, $^3J_{3'-2'} \approx 3.3$ Hz, $^3J_{3'-4'}$ = 9.2 Hz, 1H, HC(3′ α)); 3.63 (t, $^3J_{3'-4'}$ = 9.5 Hz, $^3J_{4'-5'} \approx 9.5$ Hz, 1H, HC(4′ α); 3.54 (ddd, $^3J_{5'-6'a} \approx 2.5$ Hz, $^3J_{5'-6'b} \approx 5.3$ Hz, $^3J_{5'-4'} \approx 9.3$ Hz, 1H, HC (5′ α)); 2.76 (t, $^3J_{1^3-1^2} \approx 6.5$ Hz, 2H, $H_2C(1^3)$); 2.62 (t, $^3J_{1^2-1^3} \approx 6.5$ Hz, 2H, $H_2C(1^2)$); 1.43 (s, 9H, H_3C (1^{8a}, 1^{8b}, and 1^{8c})); α/β ratio by ^1H NMR could not be determined because of overlap. ^{13}C NMR (100 MHz, $CDCl_3$ and CD_3OD, 298 K): δ_C (ppm) = 207.0 (C(1^4)); 173.8 (C(1^1)); 157.9 (C(1^6)); 101.4 ((C(1′β) by DEPT); 101.1 (C(1′ α)); 80.5 (C(1^7)); 74.1 (C(5′ α)); 72.1(C(3′ α)); 71.5 (C(2′ α)); 68.1 (C(4′ α)); 65.9 (C(2)); 64.4 (C(1)); 62.5 (C(6′ α)); 50.5 (C(1^5)); 34.7 (C(1^3)); 28.6 (C(1^{8a}, 1^{8b}, and 1^{8c}); 28.4 (C(1^2)). MS (ESI (+)): *m/z* relative intensity $[M + Na]^+ = 460.1$. HR-MS $[M + Na]^+ = 460.1790$ (calculated = 460.1795).

*1-O-(5-Amino levulinic acid)-2-O-(α-D-mannopyranosyl) Ethylene Glycol (**9k**).* For the synthesis of **9k** using **9j** as starting material, we used the same procedure as we used for the synthesis of **8k** (75%). IR (KBr): 3394s, 2929s, 1789s, 1732vs, 1678vs, 1516w, 1428vw, 1389vw, 1355vw, 1319vw, 1205vs, 1180vs, 1136vs, 1092w, 1064w, 975w, 884vw, 839m, 801m, 774w, 723m, 680w, 600vw, 519vw, 500w. ^1H NMR (400 MHz, D_2O, 298 K): δ_H (ppm) = 4.83 (d, $^3J_{1'-2'}$ = 1.7 Hz, 1H, HC(1′α)); 4.29 (ddd, $^3J_{1a-2b} \approx 2.7$ Hz, $^3J_{1a-2a} \approx 6.3$ Hz vicinal, $^3J_{1a-1a'}$ = 12.3 Hz geminal, 1H, HC(1a)); 4.22 (ddd, $^3J_{1b-2a} \approx 2.7$ Hz, $^3J_{1b-2b} \approx 6.3$ Hz vicinal, $^3J_{1b-1b'}$ = 12.3 Hz geminal, 1H, HC(1b)); 4.06 (s, 2H, $H_2C(1^5)$); 3.90–3.85 (m, 1H, HC(2a)); 3.88 (dd, $^3J_{1'-2'} \approx 1.7$ Hz, $^3J_{3'-2'}$ = 3.3 Hz, 1H, HC(2′ α)); 3.85–3.67 (m, 2H, HC(2b) and HC(6′b α); 3.82 (dd, $^3J_{5'-6'a} \approx 2.0$ Hz, $^3J_{6'a-6'b}$ = 11.6 Hz, 1H, HC(6′a α)); 3.71 (dd, $^3J_{3'-2'} \approx 3.7$ Hz, $^3J_{3'-4'}$ = 9.1 Hz, 1H, HC(3′ α)); 3.63 (m, 2H, HC (5′α) and HC(4′α); 2.87 (t, $^3J_{1^3-1^2} \approx 6.0$ Hz, 2H, $H_2C(1^3)$); 2.69 (t, $^3J_{1^2-1^3} \approx 6.0$ Hz, 2H, $H_2C(1^2)$); α/β ratio by ^1H NMR 12.5:1. ^{13}C NMR (100 MHz, D_2O, 298 K): δ_C (ppm) = 204.6 (C(1^4)); 175.5 (C(1^3)); 163.8 (q, $^2J_{C-F}$ = 36.2, CF_3COO^-); 117.3 (q, $^1J_{C-F} \approx 292$, CF_3COO^-); 100.9 ((C(1′β) by DEPT); 100.7 (C(1′ α)); 73.8 (C(5′ α)); 71.5 (C(3′ α)); 70.9 (C(2′ α)); 67.7 (C(4′ α)); 66.1 (C(2)); 65.0 (C(1)); 61.9 (C(6′ α)); 47.9 (C(1^5)); 35.2 (C(1^3)); 28.3 (C(1^2)). HR-MS $[M - CFCOO^-]^+ = 338.1440$ (calculated = 338.1451).

*1-O-(2′,3′,4′,6′-Tetraacetyl-β-D-galactopyranosyl) Ethylene Glycol (**10k**).* To ethylene glycol (13.14 g, 215 mmol, 22 equiv), 2,3,4,6-β-D-galactopyranosyl bromide **10j** (4 g, 9.73 mmol, 1 equiv) and silver carbonate (4.8 g, 17.4 mmol, 1.8 equiv) were added. The mixture was stirred until the CO_2 evolution ceased, then 50 mL of toluene was added, stirred, and precipitated silver salts were filtered. The filtrate separated into two layers; the ethylene glycol layer was repeatedly extracted with 3 × 50 mL of toluene. The combined toluene layers were evaporated under vacuum. The residue was crystallized with 10 mL of ether to give pure **10k** (2.66 g, 70%). Alternatively, the residue was also purified by flash chromatography (EtOAc/hexane 3:1). R_f (EtOAc/hexane 3:1) = 0.21 ($KMnO_4$). IR (KBr): 3580w, 3477vw, 2981vw, 2956vw, 2885vw, 1750vs, 1639vw, 1486vw, 1429w, 1368m, 1338vw, 1315w, 1254s, 1232s, 1219s, 1166vw, 1156w, 1128m, 1102vw, 1084w, 1067m, 1041s, 1022m, 969vw, 953w, 927w, 917vw, 899w, 875vw, 855w, 733w, 716w, 650vw, 629vw, 587w, 540w, 502vw, 493vw, 475vw. ^1H NMR (400 MHz, $CDCl_3$, 298 K): δ_H (ppm) = 5.29 (d, $^3J_{4'-3'}$ = 3.8 Hz, 1H, HC(4′ β); 5.10 (dd, $^3J_{2'-1'}$ = 8.0 Hz, $^3J_{2'-3'}$ = 10.4 Hz, 1H, HC(2′ β)); 4.94 (dd, $^3J_{3'-4'}$ = 3.4 Hz, $^3J_{3'-2'}$ = 10.4 Hz, 1H, HC(3′ β)); 4.44 (d, $^3J_{1'-2'}$ = 8.0 Hz, 1H, HC(1′ β); 4.05 (m, 2H, $H_2C(6')$); 3.89 (t, $^3J_{5'-6'a} \approx 6.6$ Hz, $^3J_{5'-6'b} \approx 6.6$ Hz, 1H, HC(5′)); 3.77 (ddd, $^3J_{1a-2b} \approx 4.0$ Hz, $^3J_{1a-2a} \approx 5.4$ Hz vicinal, $^3J_{1a-1b}$ = 11.0 Hz geminal, 1H, HC(1a)); 3.72 (ddd, $^3J_{1b-2a} \approx 3.5$ Hz, $^3J_{1b-2b} \approx 5.4$ Hz vicinal, $^3J_{1b-1a}$ = 11.0 Hz geminal, 1H, HC(1b)); 3.87 (m, 2H, $H_2C(2)$); 2.71 (d, $^3J_{2\text{-OH}} \approx 5.7$ Hz, 1H, OH); 2.06, 1.97, 1.96, 1.88 (4 × s, 12H, $H_3C(2')$, $H_3C(3')$, $H_3C(4')$, and $H_3C(6')$); α/β ratio by ^1H NMR only the β anomer. ^{13}C NMR (100 MHz, $CDCl_3$, 298 K): δ_C (ppm) = 170.3, 170.1, 169.9, 169.5 (C2′a), (C3′a), (C4′a), and (C6′a)); 101.7(C(1′ β)); 72.7((C(1)); 70.7, 70.6(C(5′) and C(3′)); 68.8(C2′); 66.9(C(4′); 61.7, 61.4 (C(6′) and (C(2)); 20.6, 20.5, 20.4 ((C2′b), (C3′b), (C4′b), and (C6′b)). MS (ESI (+)): *m/z* relative intensity $[M + Na]^+ = 415.1$.

*1-O-(β-D-galactopyranosyl) Ethylene Glycol (**10l**).* To **10k** (2.5 g, 6.37 mmol, 1 equiv) dissolved in 20 mL of MeOH, a 0.1 N sodium methoxide solution in MeOH (0.625 mL, 0.0625 mmol, 0.01 equiv) was added slowly at ambient temperature and maintained at ambient temperature for 2–3 h until the starting material was no longer detectable by TLC (CH_2Cl_2/MeOH 3:1). The reaction mass was then neutralized by adding dried Dowex resin, and filtered over basic alumina sandwiched between celite. The filtrate was concentrated and the residue was crystallized using ether as solvent to obtain **10l** (1.29 g,

90%). R_f (CH_2Cl_2/MeOH 3:1) = 0.24 ($KMnO_4$). IR (KBr): 3407vs, 3338vs, 2971vw, 2917m, 2893m, 2867m, 2657vw, 2157vw, 2041vw, 1635vw, 1471vw, 1482vw, 1457w, 1449w, 1406w, 1372w, 1343vw, 1288m, 1241w, 1225w, 1164m, 1146m, 1130m, 1118m, 1078vs, 1054w, 1031s, 1019s, 1000w, 945m, 907m, 889m, 835w, 780m, 706m, 632w, 604w, 548vw, 502w, 470vw. ^{1}H NMR (400 MHz, D_2O, 298 K): δ_H (ppm) = 4.43 (d, $^3J_{1'-2'}$ = 7.8 Hz, 1H, HC(1′β)); 4.05–3.98 (m, 1H, HC(1a); 3.93 (dd, 1H, HC(4′β); 3.83–3.73 (m, H_2C(6′), H_2C(2), and HC(1b); 3.71 ((dd, $^3J_{6'a-5'} \approx$ 4.2 Hz, $^3J_{5'-6'b}$ = 7.9 Hz, 1H, HC(5′β)); 3.67 (dd, $^3J_{3'-4'}$ = 3.4 Hz, $^3J_{3'-2'}$ = 9.9 Hz, 1H, HC(3′β)); 3.56 (dd, $^3J_{2'-1'}$ = 7.8 Hz, $^3J_{3'-2'}$ = 9.9 Hz, 1H, HC(2′β)); α/β ratio by ^{1}H NMR: only the β anomer. ^{13}C NMR (100 MHz, D_2O, 298 K): δ_C (ppm) = 103.4 (C(1′β)); 75.5 (C(5′β); 73.1((C(3′β)); 71.5 (C(1)); 71.2((C2′β)); 69.0(C(4′β); 61.4, 61.1 (C(6′β) and ((C(2)). MS (ESI (+)): *m/z* relative intensity [M with OH/OD + Na]$^+$ = 247.1. HR-MS [M + Na]$^+$ = 247.0783 (calculated = 247.0794).

*1-O-(5-Boc-aminolevulinic)-2-O-(β-D-galactopyranosyl)Ethylene Glycol (**10m**).* Under argon atmosphere, to **10l** (115 mg, 0.51 mmol, 1 equiv) dissolved in 3.5 mL of anhydrous pyridine, 1 g of *Candida antarctica* lipase (LCA, Novozyme 435, 10 units per mg of protein; approximately 10 mmol, 20 equiv) and **6** (1 g, 2.5 mmol, 5 equiv) were added. The reaction was maintained at ambient temperature for 10 min followed by TLC (CH_2Cl_2/MeOH 3:1). The mass was filtered over celite, celite washed with 3 × 10 mL of pyridine, and solvent was evaporated. The residue was triturated with 2 × 50 mL of dry toluene/hexane (1:1), the top clear layer was removed, and the sticky residue was subjected to flash chromatography using gradient elution (CH_2Cl_2 100% to CH_2Cl_2/MeOH 90:10). The main fractions were concentrated to give **10m** as a white solid (108 mg, 48%). R_f (CH_2Cl_2/MeOH 85:15): 0.23 ($KMnO_4$). IR (KBr): 3405vs, 2977m, 2930m, 1732vs, 1709vs, 1520m, 1393w, 1368m, 1286w, 1253w, 1165s, 1076s, 921w, 891w, 878w, 780m, 702w, 600vw, 548vw, 500vw. ^{1}H NMR (400 MHz, $CDCl_3$ and CD_3OD, 298 K): δ_H (ppm) = 4.25–4.22 (m, 3H, H_2C(1) and HC(1′β)); 4.03 (ddd, $^3J_{1b-2a} \approx$ 4.0 Hz, $^3J_{1a-2a} \approx$ 6.0 Hz vicinal, $^3J_{2b-2a}$ = 11.1 Hz geminal, 1H, HC(2a)); 3.91 (s, 2H, $H_2C(1^5)$); 3.82 (d, $^3J_{3'-4'} \approx$ 3.0 Hz, 1H, HC(4′ β); 3.79–3.65 (m, 3H, H_2C(6′) and HC(2b)); 3.56–3.47 (m, 2H, HC (5′β) and HC(2′β)); 3.45 (dd, $^3J_{3'-2'} \approx$ 3.0 Hz, $^3J_{3'-4'}$ = 9.2 Hz, 1H, HC(3′β)); 2.75 (t, $^3J_{1^3-1^2} \approx$ 6.5 Hz, 2H, $H_2C(1^3)$); 2.61 (t, $^3J_{1^2-1^3} \approx$ 6.5 Hz, 2H, $H_2C(1^2)$); 1.43 (s, 9H, H_3C (1^{8a}, 1^{8b}, and 1^{8c})); α/β ratio by ^{1}H NMR: only the β anomer. ^{13}C NMR (100 MHz, $CDCl_3$ and CD_3OD, 298 K): δ_C (ppm) = 205.9 ($C(1^4)$); 174.0 ($C(1^1)$); 157.0 ($C(1^6)$); 104.7 (C(1′β)); 80.0 ($C(1^7)$); 76.5 (C(5′β)); 74.6(C(3′β)); 72.2 (C(2′β)); 70.0 (C(4′β)); 68.2 (C(2)); 64.8 (C(1)); 62.3 (C(6′β)); 50.7 ($C(1^5)$); 34.8 ($C(1^3)$); 28.7 ($C(1^{8a}$, 1^{8b}, and 1^{8C}); 28.6 ($C(1^2)$). HR-MS [M + Na]$^+$ = 460.1791 (calculated = 460.1795).

*1-O-(5-Amino levulinic acid)-2-O-(β-D-galactopyranosyl) Ethylene Glycol (**10n**).* For the synthesis of **10n** using **10m** as starting material, we used the same procedure as we used for the synthesis of **8k** (57%). **IR** (KBr): 3407s, 2924s, 2854w, 1787s, 1733vs, 1677vs, 1513vw, 1431w, 1393w, 1205vs, 1182vs, 1135vs, 1078s, 1063w, 839m, 800m, 777w, 723m, 706w, 665vw, 598vw, 519vw. ^{1}H NMR (400 MHz, D_2O, 298 K): δ_H (ppm) = 4.43 (d, $^3J_{1'-2'}$ = 7.8 Hz, 1H, HC(1′β)); 4.31(t, $^3J_{1-2} \approx$ 4.5 Hz, H_2C(1)); 4.13 (s, 2H, $H_2C(1^5)$); 4.12–4.09 (m, 1H, HC(2a)); 3.92 (ddd, $^3J_{1b-2a} \approx$ 4.0 Hz, $^3J_{1a-2a} \approx$ 5.0 Hz vicinal, $^3J_{2b-2a}$ = 12 Hz geminal, 1H, HC(2b)); 3.91 (t, $^3J_{3'-4'} \approx$ 3.0 Hz, 1H, HC(4′ β)); 3.78–3.74 (m, 2H, H_2C(6′)); 3.69 (ddd, $^3J_{5'-4'} \approx$ 1.0 Hz, $^3J_{5'-6'a} \approx$ 3.5 Hz, $^3J_{5'-6'b} \approx$ overlap, 1H, HC (5′ β)); 3.65 (dd, $^3J_{3'-4'} \approx$ 3.5 Hz, $^3J_{3'-2'} \approx$ 10.0 Hz, 1H, HC(3′ β)); 3.51 (dd, $^3J_{2'-1'}$ = 7.8 Hz, $^3J_{2'-3'} \approx$ 10.0 Hz, 1H, HC(2′ β)); 2.93 (t, $^3J_{1^3-1^2} \approx$ 6.5 Hz, 2H, $H_2C(1^3)$); 2.75 (t, $^3J_{1^2-1^3} \approx$ 6.5 Hz, 2H, $H_2C(1^2)$); α/β ratio by ^{1}H NMR: only the β anomer. ^{13}C NMR (100 MHz, D_2O, 298 K): δ_C (ppm) = 204.4 ($C(1^4)$); 175.0 ($C(1^3)$); ~165 (CF_3COO^-); 115.3 (CF_3COO); 103.3 ((C(1′ β)); 75.5 (C(5′)); 73.0 (C(3′)); 71.0 (C(2′)); 68.9 (C(4′)); 68.0 (C(2)); 64.7 (C(1)); 61.3 (C(6′)); 47.4 ($C(1^5)$); 34.8 ($C(1^3)$); 27.8 ($C(1^2)$). MS (ESI (+)): *m/z* relative intensity [M − CF_3COO]$^+$ = 338.1. HR-MS [M − CF_3COO]$^+$ = 338.1445 (calculated = 338.1451).

Biology. *Cell Cultures.* Human carcinoma colon (HT-29, SW480), breast (MCF-7, T47D), and lung (A549) cells were obtained from the ATCC (American Tissue type Culture Collection, Manassas, VA, USA). Human HCEC endothelial cells were a kind gift of D. Stanimirovic, Ottawa, Canada, and human VS59, SS77, GE80 and GS78 primary fibroblasts were obtained from surgical biopsies using the explant technique (*32*), according to a protocol approved by the CHUV Ethics Committee and patients. All cells were routinely grown in DMEM medium containing 4.5 g/L glucose, 10% fetal calf serum (FCS), and antibiotics (all from Gibco, Basel, Switzerland).

Evaluation of PpIX Production from Glycoside Esters of ALA. The quantification of PpIX production in living cells loaded with photosensitizers was performed as previously described (*9*, *10*). Briefly, confluent cultures of cells in 48 well plates (Costar) were exposed at 37 °C to ALA conjugates in 4.5 g/L glucose DMEM medium without FCS and without phenol red (Gibco) in a thermostatted fluorescence microplate reader (Cytofluor, PerSeptive BioSystems), Fluorescence of samples was measured kinetically at excitation and emission wavenlengths specific for PpIX ($\lambda_{ex}/\lambda_{em}$ = 409 nm/645 nm, respectively), essentially as previously described (*9*, *10*). Alamar Blue reduction was used to quantify metabolically active cells. Briefly, 24 h after the addition of glycoside-ALA, the PpIX fluorescence in the cell layer was measured, then cells were exposed at 37 °C to Alamar Blue solution (10% final concentration, Serotec, Düsseldorf, Germany) added to the cell culture medium without medium change and fluorescence increase was recorded 2 h later in a fluorescence microplate reader (Cytofluor) at $\lambda_{ex}/\lambda_{em}$ = 530 nm/580 nm, respectively.

Fluorescence Microscopy. SW480 cells were grown on histological slides in complete medium until 25% confluent, then 1-α-Glc-ALA **8h** (2 mM or 4 mM) was added for a further incubation of 24 h. Slides were washed in PBS and either directly analyzed in PBS or incubated with the nuclear stain 4′,6′-diamidino-2-phenylindolylhydrochloride (DAPI, Roche Diagnostics, Mannheim, Germany, 1 μg/mL in PBS) for 10 min at 37 °C, washed with PBS, and examined under a fluorescence microscope in PBS (Axioplan2, Carl Zeiss, Feldbach, Switzerland) and filters set at 365 nm excitation light (BP 365/12, FT 395, LP 397) for DAPI and 535 nm excitation light (BP 510–560, FT 580, LP 590) for PpIX.

Photodynamic Therapy on Cells in Cultures. Confluent SW480 cells in 96 well plates (Costar) were incubated in complete medium with 2 mM of glycoside esters of ALA for 24 h in the dark. Culture medium was replaced by DMEM containing 5% FCS without phenol red (Gibco) and cells were illuminated with a laser at λ = 635 nm (laser diode Ceralas 635, Biolitec GmbH, Jena, Germany) and with a frontal diffuser (Medlight SA, Ecublens, Switzerland), at an irradiance of 17 mW/cm^2 and light doses ranging between 1 and 10 J/cm^2. Cell survival was assessed with Alamar Blue assay 24 h after the end of the irradiation. The LD_{50} (light dose necessary to induce 50% inhibition of cell growth) were determined after linearization using a medium effect algorithm as described (*12*).

Inhibition of PpIX Production in SW480 Cells by Free or 1-Methoxy Analogues of Sugars. SW480 human colon carcinoma cells were grown in 48 well plates (Costar) until 75% confluent. Medium was replaced by 4.5 g/L glucose DMEM

medium without FCS and without phenol red (Gibco) containing the competitive agent (D-glucose, D-mannose, D-galactose, 1-MeO-galactose (Sigma), 1-MeO-glucose, or 1-MeO-mannose (Fluka), 1–1000 mM) for 1 h at 37 °C. Then, glycoside esters of ALA were added at 1 mM final concentration and PpIX fluorescence of samples was measured in a fluorescence microplate reader (Cytofluor) after 24 h. Cell viability was measured using the Alamar Blue assay.

Inhibition of PpIX Production in A549 Cells by Specific Glycosidase Inhibitors. A549 human lung carcinoma cells were grown in 48 well plates (Costar) until 75% confluent. Medium was replaced by 4.5 g/L glucose DMEM medium without FCS and without phenol red (Gibco) containing the glycosidase inhibitors 1-deoxynojirimycin, 1-deoxymannojirimycin, and castanospermine (Tocris, Ellisville, MO, USA) at 0.5–10 mM. After 1 h at 37 °C, the glycoside esters of ALA were added at 1 mM final concentration and PpIX fluorescence of samples was measured in a fluorescence microplate reader (Cytofluor) after 24 h. Cell viability was measured using the Alamar Blue assay. The inhibitory effect of the inhibitors on glucosidase and mannosidase activities was controlled with their respective 4-methylumbelliferyl-glycoside substrates in intact living cells using methods adapted from previously described protocols for α-mannosidase activity in cell extracts and for peptidases activities in intact living cells (*23, 33*) (data not shown).

Calculations of Results. Each experiment was repeated in triplicate wells at least twice. Means and standard deviation were calculated.

RESULTS

Syntheses of the Glycoside Esters of ALA. Boc-protected 5-aminolevulinic acid (5-Boc-ALA) **5** or activated esters of 5-Boc-ALA **6** and **7** were used as starting material to synthesize glycoside esters of ALA, since preliminary results have shown that these protected derivatives of ALA not only facilitate the purification by column chromatography of the final products, but also improve the yield of ALA coupling to sugars. The syntheses of 5-Boc-ALA **5** in four steps from levulinic acid **1** and of activated pentafluorophenyl and trichloroethyl esters of 5-Boc-ALA, respectively, **6** and **7**, in one step from 5-Boc-ALA **5** are described in Scheme 2.

The synthesis of 6′-*O*-ALA conjugates of sugars **8c**, **9c**, and **10c** was performed according to Scheme 3. The regioselective synthesis of **8c**, **9c**, and **10c** was carried out by enzymatic transesterification of the activated esters **6** and **7** (*34, 35*). Proper combination of enzymes and the activated esters ensured regioselective esterification of sugars on the primary hydroxyl group. Deprotection of 6′-*O*-(Boc-ALA)-glycosides **8b**, **9b**, and **10b** yielded the 6′-*O*-(ALA)-α/*β*-D-Glc **8c**, 6′-*O*-(ALA)-α-D-Man **9c**, and 6′-*O*-(ALA)-*β*-D-Gal **10c** in good overall yield (>40%) and partial selectivity at the anomeric center (Table 1).

The synthesis of 1′-*O*-ALA conjugates of sugars **8h**, **9h**, and **10i** was performed according to Scheme 4. The regioselective synthesis of **8h**, **9h**, and **10i** was carried out using Boc-ALA **5** and benzyl protection/deprotection methodology. Sugars protected by benzyl groups on all the hydroxyl groups except on the anomeric hydroxyl group (C1) were synthesized according to published procedures (*36*). Then, the free hydroxyl group at C1 was esterified with 5-Boc-ALA **5** using catalytic DMAP and DCC coupling method to obtain the α anomer and using DMAP and EDCI coupling method to obtain the *β*-anomer (*37,38*). Then, the *O*-benzyl protecting groups of the sugars were deprotected using standard catalytic hydrogenation, followed by the removal of the Boc protecting group of ALA under standard acidic conditions to obtain 1′-*O*-(ALA)-α-D-Glc **8h**, 1′-*O*-(ALA)-α-D-Man **9h**, and 1′-*O*-(ALA)-*β*-D-Gal **10i** in modest overall yield (<20%) but in good purity at the anomeric center (Table 1).

The synthesis of 1-*O*-(ALA)-2-*O*-(glycosyl) ethylene glycol **8k**, **9k**, and **10n** (where ALA is linked to the glycosides via an ethylene glycol linker) (*38*) was performed according to Scheme 5. The syntheses of 1-*O*-(α-D-Glc) ethylene glycol **8i** and 1-*O*-(α-D-Man) ethylene glycol **9i** were carried out using standard Fischer glycosidation to get predominantly the α-anomers (*40–42*). The synthesis of 1-*O*-(*β*-D-Gal) ethylene glycol **10l** was carried out using standard Koenigs−Knorr synthesis (*43*) to get predominantly the *β*-anomer. The regioselective acylation of the 1-*O*-(glycosyl)-2-*O*-ethylene glycol **8i**, **9i**, and **10l** was carried out using the enzyme *Candida antarctica* lipase which acylates mainly at the glycol moiety (*44*). Following deprotection of the Boc protecting groups of the 1-*O*-(Boc-ALA)-2-*O*-(glycosyl) ethylene glycol **8j**, **9j**, and **10m**, 1-*O*-(ALA)-2-*O*-α-D-Glc ethylene glycol **8k**, 1-*O*-(ALA)-2-*O*-α-D-Man ethylene glycol **9k**, and 1-*O*-(ALA)-2-*O*-*β*-D-Gal ethylene glycol **10n**, respectively, were obtained in modest overall yield (<20%) but in good purity at the anomeric center (Table 1).

Evaluation of the Glycoside Esters of ALA in Cells. PpIX production induced from all the synthesized glycoside esters of ALA at increasing concentrations was evaluated (Supporting Information Figures S1, S2, and S3 for the 1-*O*-(ALA)-2-*O*-(glycosyl) ethylene glycol **8k**, **9k**, and **10n**, not shown for the other analogues) in human colon (HT-29, SW480), breast (MCF-7, T47D), or lung (A549) carcinoma cell lines, human HCEC endothelial cells, as a model for angiogenic endothelium, and in human normal fibroblasts (*32*) (VS59, SS77, GE80, or GS78) as models for non-tumor-associated cells. From these experiments, a 2 mM concentration was chosen for direct comparison between cells and between the glycoside esters of ALA. The time-dependent production of the fluorescent photosensitizer PpIX induced by the glycoside esters of ALA and ALA as a reference molecule was determined for 24 h of continuous exposure to the precursor. Cytotoxicity in the dark (no exposure to laser light) was evaluated 24 h after the addition of the prodrugs, using the Alamar Blue assay which evaluates biosynthetic activity in living cells (Figure 1, human colon SW480 and lung A549 tumor cells and nontumoral HCEC endothelial cells and VS59 fibroblasts, Supporting Information Figure S4 for the human breast T47D and colon HT-29 tumor cells). All human tumor cells and the HCEC endothelial cells synthesized PpIX from all derivatives at levels comparable to ALA (See Supporting Information Table S1), whereas human fibroblasts produced only very low levels of PpIX for all precursors, including free ALA. The nature of the sugar or the position of the substitution (positions O-1 or O-6) exerted only minor influence on cellular PpIX production, whereas the intercalation of an ethylene glycol linker generally resulted in a slower or decreased synthesis of PpIX by cells.

The SW480 human colon and A549 human lung carcinoma cells were chosen as model cells for further evaluations. In order to confirm intracellular localization of PpIX production, the specific fluorescence of PpIX was visualized by fluorescence microscopy in SW480 cells grown on histological slides and exposed for 24 h to 1-α-Glc-ALA **8h** (Figure 2). When exposed to a laser light of 635 nm wavelength which corresponds to the PpIX last Q-band of absorption, all glycoside esters of ALA were effective in inducing phototoxicity in SW480 cells which produce identical amounts of PpIX from all ALA conjugates of sugars (Figure 1), with an LD_{50} (light dose necessary to induce 50% inhibition of cell growth) between 2.3 and 4 J/cm^2 (Figure 3), comparable to ALA.

In order to define which part of the bioconjugate, either the glycoside or the ALA moieties, was responsible for cell uptake, we exposed SW480 cells to high concentrations of free glucose

or 1-*O*-methoxy glucose, and measured PpIX production (Figure 4 and Supporting Information Figure S5 for mannose and galactose evaluation). The presence of the competitive sugars did not affect the induced PpIX production by cells for all the glycoside esters of ALA. In order to determine whether esterase or glycosidase activities were responsible for the release of free ALA from the sugar, we inhibited cellular glucosidases with the specific α-glucosidase inhibitors castanospermine and 1-deoxynojirimycin (Figure 5), or the specific α-mannosidase inhibitor 1-deoxymannojirimycin (Supporting Information Figure S6), and measured PpIX production. No effects of these inhibitors were observed on PpIX production. When cells were exposed to the 4-methyl-umbellifery-α-glucose and 4-methyl-umbellifery-α-mannose substrates of α-glucosidases and α-mannosidases in the presence of these inhibitors, inhibition of these enzymatic activities was observed (results not shown).

DISCUSSION

In phototodynamic therapy, photosensitizers can be added topically, not only on the skin, but also in hollow organs such as the bladder or in the kystic structures of neoplasic and inflammatory diseases, or by painting the surface of the diseased areas, under the condition that the photosensitizers can be maintained long enough in this location. Applying photosensitizers systemically results in a bodywide distribution, unless the photosensitizers can be made cell-selective by preparing analogues of photosensitizers with a targeting moiety or incorporating photosensitizers into nano/microstructures such as particles or dendrimers (*11*). However, even under these conditions, the photosensitizer will mainly encounter the cells of the blood vessels and the circulating cells. In cancer, it is accepted that tumor cells and cells of the vascular wall, in particular, proliferating endothelial cells, express more transporters for nutrients, including carbohydrates, than quiescent cells. In this project, we focused more on the possibility to use a sugar prodrug of ALA as the precursor of the photosensitizer PpIX and/or as a means to enhance cell selectivity or cell uptake than on the mode of administration of photosensitizers, either topical or systemic.

In this manuscript, we report the first synthesis and characterization of anomerically pure ALA derivatives functionalized with hexose moieties. All the human carcinoma cells tested, from colon, breast, or lung origin, and the proliferating angiogenic HCEC endothelial cells synthesized PpIX from all conjugates prepared, at levels comparable to ALA, whereas human normal fibroblasts produced only very low levels of PpIX from all precursors. Therefore, the results presented here demonstrate that ALA conjugates of sugars are effective precursors of the photosensitizer PpIX and have the potential to be used in PDT protocols to treat tumor cells and the tumor-associated angiogenic endothelial cells while sparing nontumoral cells, such as fibroblasts. The nature of the sugar or the position of the substitution by ALA (positions O-1 or O-6) exerted only a minor influence, whereas the intercalation of an ethylene glycol linker generally resulted in a slower or decreased synthesis of PpIX. Using ethylene glycol linkers in glycoconjugated porphyrins, the length and nature of the linker was found to be an important factor for cellular uptake of porphyrin analogues by retinoblastoma cells (*25*). We had previously observed that ethylene glycol esters of ALA increased PpIX production by cells; however, the kinetics of cell uptake suggested free diffusion of these organic esters across the cell membrane (*9*). This information suggests that in the glycoside−ethylene glycol esters of ALA the ethylene glycol moiety, and its position between the sugar and ALA, is not determining for cell uptake of the conjugates.

Our approach did not allow us to distinguish whether these glycoside esters of ALA are transported intact inside cells, and then ALA is released intracellularly from these prodrugs acting as substrates for cellular glycosidases or esterases, or whether they are activated extracellularly, and then free ALA is transported inside cells. Competition studies with free or 1-*O*-methoxy analogues of the sugars had no effects on PpIX production. Moreover, similar levels of PpIX production by cells was observed between free ALA and the glycoside esters of ALA irrespective of the position of functionalization and the nature of the sugar. These observations strongly suggest an uptake mechanism able to recognize the ALA moiety rather than the sugar part of the conjugates. Inhibition studies with glycosidase inhibitors suggest the involvement of esterases rather than glycosidases in the release of ALA from the glycoside esters of ALA. This hypothesis is further supported by the slower production of PpIX induced by ethylene glycol ALA conjugates of sugar esters compared to the absence of the ethylene glycol linker. As we have previously shown that ALA−ethylene glycol esters are metabolized much more rapidly than ALA to PpIX, likely as the result of an increased passive diffusion of these esters across the cell membrane, compared to an active transport of ALA (*9*), we hypothesize that the initial activation of the glycoside−ethylene glycol esters of ALA prodrugs are enzymaticaly performed at the ethylene glycol−ALA bond and not at the glycoside−ethylene glycol bond. Such a hydrolytic step at the glycoside−ethylene glycol bond would have produced ethylene glycol−ALA esters, with a concomitant increased uptake and enhanced PpIX production by cells. It has also been shown by others that cancer cells are able to cleave ethylene glycol ether of sugars at the O-1 position from glycoconjugated porphyrins (*25*) or chlorins (*24*).

In conclusion, our ALA prodrugs may be precursors of the photosensitizer PpIX, but will not enhance cell selectivity; however, they may increase the residence time of the drugs at the surface of cells. Thus, these prodrugs may be more interesting for topical administration in conjunction with painting of the surface of diseased areas than for systemic administration. Glycoside esters of ALA are more efficient precursors of intracellular PpIX production in cancer cells or cancer-associated angiogenic endothelial cells than in normal human fibroblasts. As they are able to induce phototoxicity in the target cells when exposed to light, they can be effective in PDT of cancer. These prodrugs are more likely activated by esterases rather than by glycosidases and do not seem to use glycoside cell membrane transporters for cell uptake. The advantage of glycoside esters over esters of aliphatic alcohols resides in the release of an innocuous glycoside compared to a potentially toxic aliphatic alcohol following hydrolysis by esterases.

ACKNOWLEDGMENT

The authors want to thank S. Gerber-Lemaire, Y. Berger, C. Chapuis Bernasconi, and C. Kopp for helpful comments and technical assistance and the Swiss National Science Foundation (grants no 3152A0-102184, 205320-103518, and 205320-116556/1), Oncosuisse (grant no OCS-01308-02-2003), the République et Canton de Neuchâtel, and the Swiss Society for Multiple Sclerosis for financial support.

Supporting Information Available: Figures S1−S3 showing the dose–response curves of all cells to the 1-*O*-(ALA)-2-*O*-(glycosyl) ethylene glycol derivatives **8k**, **9k**, and **10n**; Figures S4, S5, and S6 describing the response of human breast T47D and colon HT-29 cells to all the compounds prepared, the effects of mannose and galactose analogues, and of the inhibitor of mannosidases on PpIX production by cells, respectively; and Table S1 showing the quantitative production of PpIX related to ALA. This material is available free of charge via the Internet at http://pubs.acs.org.

LITERATURE CITED

(1) He, D., Behar, S., Nomura, N., Sassa, S., and Lim, H. W. (1995) The effect of ALA and radiation on porphyrin/heme biosynthesis in endothelial cells. *Photochem. Photobiol. 61*, 656–661.

(2) Noodt, B. B., Berg, K., Stokke, T., Peng, Q., and Nesland, J. M. (1996) Apoptosis and necrosis induced with light and 5-aminolevulinic acid-derived protoporphyrin IX. *Br. J. Cancer 74*, 22–29.

(3) Peng, Q., Berg, K., Moan, J., Konghaug, M., and Nesland, J. M. (1997) 5-Aminolevulinic acid-based photodynamic therapy: principles and experimental research. *Photochem. Photobiol. 65*, 235–251.

(4) Wyld, L., Burn, J. L., Reed, M. W. R., and Brown, N. J. (1997) Factors affecting aminolevulinic acid-induced generation of protoporphyrin IX. *Br. J. Cancer 76*, 705–712.

(5) Casas, A., Perotti, C., Ortel, B., Di Venosa, G., Saccoliti, M., Battle, A., and Hasan, T. (2006) Tumor cell lines resistant to ALA-mediated photodynamic therapy and possible tools to target surviving cells. *Int. J. Oncol. 2*, 397–405.

(6) Casas, A., Battle, A. M. C., Butler, A. R., Robertson, D., Brown, E. H., MacRobert, A., and Riley, P. A. (1999) Comparative effects of ALA derivatives on protoporphyrin IX production in human and rat skin organ cultures. *Br. J. Cancer 80*, 1525–1532.

(7) Casas, A., and Battle, A. (2002) Rational design of 5-aminoleviulinic acid derivatives aimed at improved photodynamic therapy. *Curr. Med. Chem. 2*, 465–475.

(8) Uehlinger, P., Zellweger, M., Wagnières, G., Juillerat-Jeanneret, L., van den Bergh, H., and Lange, N. (2000) Aminolevulinic acid and its derivatives: physical chemical properties and protoporphyrin IX (PpIX) formation in cultured cells. *J. Photochem. Photobiol. B: Biol. 54*, 72–80.

(9) Berger, Y., Greppi, A., Siri, O., Neier, R., and Juillerat-Jeanneret, L. (2000) Ethylene glycol and amino acid derivatives of 5-aminolevulinic acid as new photosensitizing precursors of protoporphyrin IX in cells. *J. Med. Chem. 43*, 4738–4746.

(10) Berger, Y., Ingrassia, L., Neier, R., and Juillerat-Jeanneret, L. (2003) Evaluation of dipeptide-derivatives of 5-aminolevulinic acid as precursors for photosensitizers in photodynamic therapy. *Bioorg. Med. Chem. 11*, 1343–1351.

(11) Juillerat-Jeanneret, L. (2006) Drug targeting in cancer: targeting photosensitizers in photodynamic therapy. *Trends Cancer Res. 2*, 71–84.

(12) Schneider, R., Schmitt, F., Frochot, C., Fort, Y., Lourette, N., Guillemin, F., Müller, J. F., and Barberi-Heyob, M. (2005) Design, synthesis and biological evaluation of folic acid targeted tetraphenylporphyrin as novel photosensitizers for selective photodynamic therapy. *Bioorg. Med. Chem. 13*, 2799–2808.

(13) Gomer, C. J., Ferrario, A., Luna, M., Rucker, N., and Wong, S. (2006) Photodynamic therapy: combined modality approaches targeting the tumor microenvironment. *Lasers Surg. Med. 38*, 516–521.

(14) Busch, T. M. (2006) Local physiological changes during photodynamic therapy. *Lasers Surg. Med. 38*, 494–499.

(15) Chen, B., Pogue, B. W., Hoopes, P. J., and Hasan, T. (2006) Vascular and cellular targeting for photodynamic therapy. *Crit. Rev. Eukar. Gene Expression 16*, 279–305.

(16) Pandya, N. M., Dhalla, N. S., and Santani, D. D. (2006) Angiogenesis–a new target for future therapy. *Vasc. Pharmacol. 44*, 265–274.

(17) Kilarski, W. W., and Bikfalvi, A. (2007) Recent developments in tumor angiogenesis. *Curr. Pharm. Biotechnol. 8*, 3–9.

(18) Medina, M. A., Munoz-Ch Puli, R., and Quesada, A. R. (2007) Challenges of antiangiogenic cancer therapy: trials and errors, and renewed hope. *J. Cell. Mol. Med. 11*, 374–382.

(19) Jacob, G. S. (1995) Glycosylation in biology and medicine. *Curr. Opin. Struct. Biol. 5*, 605–611.

(20) Hakomori, S. (2002) Glycosylation defining cancer malignancy: new wine in an old bottle. *Proc. Nat. Acad. Sci. U.S.A. 99*, 10231–10233.

(21) Danguy, A., Camby, I., and Kiss, R. (2002) Galectins and cancer. *Biochim. Biophys. Acta 1572*, 285–293.

(22) Smith, T. A. (1999) Facilitative glucose transporter expression in human cancer tissue. *Br. J. Biomed. Sci. 56*, 285–292.

(23) Berger, Y., Chapuis Bernasconi, C., Schmitt, F., Neier, R., and Juillerat-Jeanneret, L. (2005) Determination of intracellular prolyl/glycyl-specific proteases in intact living human cells using protoporphyrin IX production as a reporter system. *Chem. Biol. 12*, 867–872.

(24) Laville, I., Figueiredo, T., Loock, B., Pigaglio, S., Maillard, P., Grierson, D. S., Carrez, D., Croisy, A., and Blais, J. (2003) Synthesis, cellular internalization and photodynamic activity of glucoconjugated derivatives of tri and tetra(meta-hydroxyphenyl)chlorins. *Bioorg. Med. Chem. 11*, 1643–1652.

(25) Laville, I., Pigaglio, S., Blais, J. C., Doz, F., Loock, B., Maillard, P., Grierson, D. S., and Blais, J. (2006) Photodynamic efficiency of diethylene glycol-linked glycoconjugated porphyrins in human retinoblastoma cells. *J. Med. Chem. 49*, 2558–2567.

(26) Di Stasio, B., Frochot, C., Dumas, D., Even, P., Zwier, J., Müller, A., Didelon, J., Guillemin, F., Viriot, M. L., and Barberi-Heyob, M. (2005) The 2-aminoglucosamide motif improves cellular uptake and photodynamic activity of tetraphenylporphyrin. *Eur. J. Med. Chem. 40*, 1111–1122.

(27) Carré, V., Gaud, O., Sylvain, I., Bourdon, O., Spiro, M., Blais, J., Granet, R., Krausz, P., and Guilloton, M. (1999) Fungicidal properties of meso-arylglycosylporphyrins: influence of sugar substituents on photoinduced damage in the yeast Saccharomyces cerevisiae. *J. Photochem. Photobiol. B: Biol. 48*, 57–62.

(28) Mikata, Y., Onchi, Y., Shibata, M., Kakuchi, T., Ono, H., Ogura, S., Okura, I., and Yano, S. (1998) Synthesis and phototoxic property of tetra- and octa-glycoconjugated tetraphenylchlorins. *Bioorg. Med. Chem. Lett. 8*, 3543–3548.

(29) Schell, C., and Hombrecher, H. K. (1999) Synthesis and investigation of glycosylated mono- and diarylporphyrins for photodynamic therapy. *Bioorg. Med. Chem. 7*, 1857–65.

(30) Sylvain, I., Zerrouki, R., Granet, R., Huang, Y. M., Lagorce, J. F., Guilloton, M., Blais, J. C., and Krausz, P. (2002) Synthesis and biological evaluation of thioglycosylated porphyrins for an application in photodynamic therapy. *Bioorg. Med. Chem. 10*, 57–69.

(31) Zheng, G., Graham, A., Shibata, M., Missert, J. R., Oseroff, A. R., Dougherty, T. J., and Pandrey, R. K. (2001) Synthesis of β-galactose-conjugated chlorins derived by enyne metathesis as galectin-specific photosensitizers for photodynamic therapy. *J. Org. Chem. 66*, 8709–8716.

(32) Poncet, S., Meyer, S., Richard, C., Aubert, J. D., and Juillerat-Jeanneret, L. (2005) The expression and function of the endothelin system in contractile properties of vaginal myofibroblasts of women with utero-vaginal prolapse. *Am. J. Obstet. Gynecol. 192*, 426–432.

(33) Fiaux, H., Popowycz, F., Favre, S., Schütz, C., Vogel, P., Gerber-Lemaire, S., and Juillerat-Jeanneret, L. (2005) Functionalized pyrrolidines inhibit α-mannosidase activity and growth of human glioblastoma and melanoma cells. *J. Med. Chem. 48*, 4237–4246.

(34) Therisod, M., and Klibanov, A. M. (1986) Facile enzymatic preparation of monoacylated sugars in pyridine. *J. Am. Chem. Soc. 108*, 5638–5640.

(35) Riva, S., Chopineau, J., Kieboom, A. P. G., and Klibanov, A. M. (1988) Protease-catalyzed regioselective esterification of sugars and related compounds in anhydrous dimethylformamide. *J. Am. Chem. Soc. 110*, 584–589.

(36) Decoster, E., Lacombe, J. M., Strebler, J. L., Ferrari, B., and Pavia, A. A. (1983) Another approach to the synthesis of benzyl derivatives of reducing monosaccharides. Study on the pyranose-furanose equilibrium using carbon-13 NMR. *J. Carbohydr. Chem. 2*, 329–341.

(37) Lubineau, A., Meyer, E., and Place, P. (1992) Synthesis of aryl D-gluco- and D-galacto-pyranosides and 1O-acyl-D-gluco- and -D-galacto-pyranoses exploiting the Mitsunobu reaction. Influence of the pKa of the acid on the stereoselectivity of the reaction. *Carbohydr. Res. 228*, 191–203.

(38) Bols, M., Hansen, H. C., and Smith, B. I. (1993) β-Selectivity of sterically hindered acyl chlorides in the acylation of 2,3,4,6-tetra-O-benzyl-α-D-glucopyranose. *Acta Chem. Scand. 47*, 532–534.

(39) Papot, S., Combaud, D., and Gesson, J. P. (1998) A new spacer group derived from arylmalonaldehydes for glucuronated prodrugs. *Bioorg. Med. Chem. Lett. 8*, 2545–2548.

(40) Helferich, B., and Muller, W. M. (1973) Synthesis of α-D-glycosides. *Chem. Ber. 106*, 715–716.

(41) Dotan, N., Arad, D., Frolow, F., and Freeman, A. (1999) Self-assembly of a tetrahedral lectin into predesigned diamond-like protein crystals. *Angew. Chem., Int. Ed. 38*, 2363–2366.

(42) Mowery, D. F. (1963) Methyl D-mannosides. The anomeric methyl D-mannofuranosides and -pyranosides by ion-exchange catalysis (Fischer method) and chromatography. *Meth. Carbohydr. Chem.* 328–331.

(43) Wulff, G., Roehle, G., and Krueger, W. (1970) Glycoside synthesis. I. New methods for preparation of glycosides. *Angew. Chem., Int. Ed. 9*, 455–456.

(44) Colombo, D., Ronchetti, F., Scala, A., Toma, L., Tokuda, H., and Nishino, H. (2003) Synthesis and anti-tumor-promoting activity of glycoglycerolipid analogues lacking the glycerol backbone. *Bioorg. Med. Chem. 11*, 909–912.

BC700324R

Characterization of Multilayered Nanoparticles Encapsulated in Yeast Cell Wall Particles for DNA Delivery

Ernesto R. Soto and Gary R. Ostroff*

Program in Molecular Medicine, University of Massachusetts Medical School, 373 Plantation Street, Worcester, Massachusetts 01605. Received August 28, 2007; Revised Manuscript Received January 22, 2008

Nonviral gene delivery technologies have been developed using layer-by-layer self-assembly of nanomaterials held together by electrostatic interactions in order to provide nanoparticulate materials that protect and deliver DNA to cells. Here we report a new DNA delivery technology based on the in situ layer-by-layer synthesis of DNA nanoparticles caged within hollow yeast cell wall particles (YCWP). YCWP provide protection and facilitate oral and systemic receptor-targeted delivery of DNA payloads to phagocytic cells. The nanoparticles inside YCWP consist of a core of tRNA/polyethylenimine (PEI) followed by a DNA layer that is finally coated with a protective outer layer of PEI. Using fluorescein and rhodamine labeling of tRNA, PEI, and DNA, the layer-by-layer formation of the nanoparticles was visualized by fluorescent microscopy and quantitated by fluorescence spectroscopy and flow cytometry. Optimal conditions (tRNA:YCWP, PEI:YCWP ratios and DNA load levels) to synthesize YCWP encapsulated nanoparticles were determined from these results. The high in vitro transfection efficiency of this encapsulated DNA delivery technology was demonstrated by the transfection of NIH3T3-D1 cells with YCWP-tRNA/PEI/gWizGFP/PEI formulations containing low amounts of the plasmid gWizGFP per particle to maximally express green fluorescent protein (GFP).

INTRODUCTION

An ideal DNA delivery system needs to meet three criteria: (1) it should protect DNA against nuclease degradation, (2) it should deliver the DNA through the plasma membrane and into the nucleus of target cells, and (3) it should have minimal detrimental effects (*1, 2*). Viral vectors are able to mediate efficient gene transfer with long-term gene expression but are limited by safety concerns of an acute immune response, immunogenicity, and insertional mutagenesis. Numerous strategies have been developed to accomplish nonviral mediated DNA delivery including, naked DNA, physical methods (gene gun (*3*), electroporation (*4*), hydrodynamic delivery (*5*), ultrasound (*6*)), chemical methods (liposomes, nanoparticles and microparticles composed of cationic lipids (*7*) and polymers *8, 9*), and DNA incorporation into cell ghosts, such as bacterial cells (*10*) and erythrocytes (*11, 12*). Although significant progress has been made in the development of nonviral gene delivery systems, the majority of the nonviral approaches remain significantly less efficient than viral vectors.

The formation of stable complexes between negatively charged genetic material and cationic polymers is the most commonly studied approach to develop nonviral delivery agents. The work of several groups has focused on synthesizing and characterizing a range of cationic polymers to provide the effective DNA condensation necessary to prevent degradation of the genetic material in negatively charged nanoparticles capable of DNA delivery into cells. Once inside the cells, these nanocomplexes should be capable of releasing DNA, and the toxicity of the free cationic polymer must be minimal. Polyethylenimine (PEI) has proven to be one of the best cationic polymers for nanocomplex formation with DNA and provides good transfection efficiencies; however, PEI is toxic to cells, thus limiting the concentration range that can be used (*1, 2, 13–15*). Ongoing work by many groups is seeking to identify cationic polymers with equal or better transfection efficiency as PEI but with reduced toxicity (*15–23*).

The layer-by-layer (LbL) self-assembly of materials held together by electrostatic interactions is a facile method for the fabrication of nanomaterials with potential applications in gene therapy (*1, 13, 14, 24, 25*). This has been demonstrated by LbL deposition of DNA and cationic polymers on different templates to fabricate colloidal particles (*14, 26–31*). For example, silica, polystyrene, or gold nanoparticles and biological materials have been used as templates in combination with different synthetic polymers and biopolymers. These multilayer coated particles have been studied as multifunctional carriers of biological materials, such as DNA and enzymes, by two different methods. One approach incorporated the delivery material as part of the multilayered structure (*14, 26*). A second method used removable cores to encapsulate the material inside the remaining hollow polyelectrolyte shell (*32*). Both methods require that efficient defoliation of the polyelectrolyte layers occurs within cells. The goal of producing delivery agents that are non-toxic, capable of efficiently protecting DNA, and undergoing defoliation to release DNA inside the cells has proven challenging, and an ideal gene delivery system remains elusive.

A new gene delivery system has been developed on the basis of the use of yeast cell wall particles (YCWP) (*33, 34*). YCWP are hollow and porous 2–4 μm microspheres prepared from Baker's yeast composed primarily of β-1,3-D-glucan and chitin, and in some forms, mannoproteins. This encapsulation system incorporates polyelectrolyte−DNA nanoparticles caged within the YCWP to provide for efficient intracellular DNA delivery and release and gene expression. Formation of the YCWP encapsulated polyelectrolyte nanoparticles follows a LbL approach, with the different components assembled through electrostatic interactions.

The advantages of the YCWP DNA delivery system include high DNA capacity, multiplexable DNA, protein, and siRNA delivery, oral bioavailability, β-1,3-D-glucan receptor targeting

* To whom correspondence should be addressed. Phone: 508-856-1530. Fax: 508-856-1617. E-mail: gary.ostroff@umassmed.edu.

10.1021/bc700329p CCC: $40.75 © 2008 American Chemical Society
Published on Web 04/01/2008

to macrophages and dendritic cells, and cell trafficking to the reticuloendothelial system and sites of pathology (*33–35*).

Characterization of LbL structures on planar 2D or 3D surfaces is possible by a variety of techniques (*36–39*), but most of these techniques are not amenable to characterize multilayered structures inside YCWP. The quantitative characterization of YCWP encapsulated polyelectrolyte nanoplex formation within YCWP was approached by selectively labeling each layer of the multilayered nanocomplex with fluorescent markers to optimize experimental conditions for preparation of these complexes inside YCWP. Evaluation of the different layers inside the YCWP was characterized by qualitative fluorescent microscopy and quantitative fluorescent spectroscopy and flow cytometry.

In this communication the LbL formation and characterization of nanoparticles synthesized inside YCWP is described leading to the optimization of this DNA delivery system for in vitro mammalian cell transfection.

EXPERIMENTAL PROCEDURES

Materials. Ribonucleic acid from Torula yeast, type VI, (tRNA); high molecular weight water-free branched PEI (25 kDa); DNA sodium salt from Salmon testes (DNA); and rhodamine B isothiocyanate were purchased from Sigma Aldrich (Allentown, PA) and used as received. 5-([4,6-Dichlorotriazin-2-yl]-amino)fluorescein monohydrochloride (DTAF) was purchased from Research Organics Inc. (Cleveland, OH). Solvents and buffer solutions were purchased from Sigma Aldrich or VWR and used without further purification.

Methods. *Rhodamine and Fluorescein Labeling of Nucleic Acids.* DNA or tRNA (10 mg) was dissolved in 10 mL of 5 mM EDTA. The material was sonicated until viscosity was lost, and 1.2 mL of 0.1 M carbonate buffer (pH 9.2) was added. DTAF or rhodamine at a concentration of 1 mg/mL in DMSO was added to the buffered DNA solution (10% v/v), and the solution was stirred at room temperature in the dark overnight. Tris buffer (2 mL, 1 M, pH 8.3) was added and the reaction mixture stirred for additional 15 min at room temperature to quench free fluorescent labeling reagent. Sodium chloride (1 mL of 1 M aqueous NaCl) and ethanol (30 mL) were added to the solution and incubated at −20 °C until a colored precipitate appeared. The precipitate was collected by centrifugation and washed with 70% ethanol until the supernatant was clear. The solid was dried and dissolved in water at a 10 mg/mL concentration and stored at 4 °C in the dark. The amount of fluorescent probe bound to each nucleic acid was determined spectrophotometrically by adsorption at 495 nm (DTAF) or 540 nm (rhodamine). The labeled DNA contains ∼2.3 ± 0.3% (w/w) of rhodamine and 5.9 ± 1.7% (w/w) of DTAF. tRNA was labeled with ∼0.15 ± 0.05% (w/w) of rhodamine and 0.6 ± 0.1% (w/w) of DTAF.

Rhodamine and Fluorescein Labeling of PEI. PEI was labeled following a similar procedure used for labeling of DNA and tRNA, with the following changes: PEI was dissolved in 5 mM EDTA at a concentration of 3 mg/mL. Rhodamine and DTAF were used at a concentration of 1 mg/mL in DMSO. After incubation with Tris buffer, 1 M NaCl was added (1 mL for each 10 mL of initial PEI solution). The product was purified by dialysis against water and lyophilized. Spectrophotometric characterization of the labeled PEI showed that the final product contains ∼3.1 ± 0.3% (w/w) of rhodamine and 5.7 ± 0.1% (w/w) of DTAF.

Preparation of YCWP (33). YCWP consist of two classes: glucan particles (GP) and glucan mannan particles (GMP). GP were prepared by suspending *Sacharomyces cerevisiae* (100 g of Fleishmans Bakers yeast, AB Mauri Food Inc., Chesterfield, MO) in 1 L of 1 M NaOH and heating to 80 °C for 1 h. The insoluble material containing the yeast cell walls was collected by centrifugation at 2000 × *g* for 10 min. This insoluble material was then suspended in 1 L of water, brought to pH 4–5 with HCl, and incubated at 55 °C for 1 h. The insoluble residue was again collected by centrifugation and washed once with 1 L of water, four times with 200 mL of isopropanol, and twice with 200 mL of acetone. The resulting slurry was placed in a glass tray and dried at room temperature to produce 12.4 g of a fine, slightly off-white powder.

GMP were prepared by suspending *S. cerevisiae* cell walls (75 g SAF-Mannan, SAF Agri, Milwaukee, WI) in 1 L of water, and the pH was adjusted to 12–12.5 with 1 M NaOH and heating to 60 °C for 1 h. The insoluble material containing the cell walls was recovered by centrifuging at 2000 × *g* for 10 min. This material was then suspended in 1 L of water, brought to pH 4–5 with HCl, and incubated at 55 °C for 1 h. The insoluble reside was recovered by centrifugation and washed once with 1 L of water, four times with 200 mL of dehydrated isopropanol, and twice with 200 mL of acetone. The resulting slurry was placed in a glass tray and dried at room temperature to produce 15.6 g of a fine, slightly off-white powder.

Preparation of GP and GMP Encapsulated Cationized Cores. Dry GP or GMP were mixed with a volume of the anionic core polymer tRNA (10 mg/mL in 50 mM Tris HCl pH 8, 2 mM EDTA, and 0.15 M NaCl (TEN)) to minimally hydrate the particles and incubated for 2 h to allow the particles to swell and adsorb the tRNA solution. Neutral PEI (2 mg/mL in TEN) was added in excess to form GP or GMP encapsulated tRNA polyplexes, and the particles were resuspended by homogenization or sonication. PEI adsorption and nanocomplex formation was allowed to proceed for at least 1 h. The suspension was centrifuged, and particles were resuspended in 70% ethanol to sterilize the particles and then washed three times in 0.9% saline, resuspended, counted with a hematocytomer, diluted to 1×10^8 particles/mL in 0.9% saline, and stored at −20 °C.

Preparation of GP or GMP Encapsulated Cores with DNA/PEI Coated Nanocomplexes. The binding of a DNA layer to the cationized nanoplexed cores inside GP or GMP was accomplished by preparing a suspension of GP or GMP encapsulated tRNA/PEI cores (1×10^8 particles/mL), DNA and saline solution (total volume = 75 μL). The suspension was incubated for 2 h to allow for DNA binding to the cationic nanoparticle surface, and neutral PEI (25 μL 0.01% w/v) in 0.9% saline was added to coat the DNA bound to the cationized nanoparticulate surface.

Fluorescence Assays. Fluorescence characterizations were carried out for each layer of the nanoplex delivery system by preparing YCWP samples containing one fluorescently labeled layer. The samples were prepared over a range of tRNA:YCWP and PEI:YCWP ratios and DNA concentrations to determine the optimal concentration for each layer. Fluorescence measurements were obtained with a Spectra Max Gemini XS plate reader (Molecular Devices, Union City, CA) using the SoftMax Pro v 5.0.1 software. Rhodamine fluorescence measurements were obtained at 573 nm after excitation at 540 nm, and the final fluorescence result was the average of nine measurements. The samples were mixed for 5 s before measurement. To avoid error introduced by light scattering produced by the particles, control measurements were obtained with a sample containing the same amount of particles/mL without any fluorescent compound. The final fluorescence results were corrected by subtracting the response for the control samples from the YCWP encapsulated fluorescent nanoplex samples. The amount of any particular fluorescent compound bound contained within the YCWP was determined from the fluorescence response using calibration

Table 1. Chemical Composition of YCWP (*42*)

composition	particle type	
	GP	GMP
glucan	80%	40%
mannan	<1%	40%
chitin	2–4%	2–4%

curves obtained by measuring the fluorescence of each rhodamine labeled material in solution over a linear response range.

Fluorescence Microscopy. An Arcturus fluorescence microscope was used to acquire fluorescent photomicrographs and to score transfection results for the Green Fluorescent Protein (GFP).

Flow Cytometry (FACS). FACS measurements were obtained with a Becton Dickinson FACSCalibur instrument (BD, Franklin Lakes, NJ). Samples were prepared for FACS analysis at a concentration of 2×10^6 particles/mL in PBS. Unmodified GP and GMP particles were used as negative controls, and GP particles chemically modified with rhodamine were used as the positive control. The particles were analyzed with an FL2 laser (570–610 nm) by collecting 20000 measurements. Gating and analysis was performed using FlowJo 6.4.2 software.

Transfection Experiments. YCWP-tRNA/PEI (10 μL, 1×10^8 particles/mL) suspensions were mixed with the indicated amount of gWizGFP plasmid DNA (Genlantis, San Diego, CA) over a concentration range of 0.01 to 0.1 μg/μL, and 0.9% saline solution was added to bring the total volume to 75 μL. DNA was bound to the YCWP-tRNA/PEI cationic nanoparticle surface for 2 h at room temperature. Then, 25 μL of 0.01% neutral PEI in 0.9% saline was added to coat the DNA surface for 20 min. Dulbecco's modified Eagle's medium (DMEM medium with 10% fetal calf serum, 1% penicillin-streptomycin, and 1% glutamine) was added and the final mixture transferred to 24-well plates containing $1-5 \times 10^5$ cells/well of the murine fibroblast cell line NIH3T3-D1 (*35, 40, 41*). The plates were incubated at 37 °C under 5% CO_2 overnight, the medium was changed, and the plates were incubated for an additional 16–24 h. After 40–48 h, the medium was removed, and the cells were washed once with phosphate buffer saline (PBS), fixed with 250 μL of 0.5% formalin in PBS, and scored for GFP expression by manual counting of the proportion of fluorescent cells following visualization with a fluorescence microscope.

Evaluation of YCWP and YCWP Encapsulated DNA Formulation Toxicity. YCWP-tRNA/PEI (10 μL, 1×10^8 particles/mL) suspensions were mixed with gWizGFP plasmid DNA and PEI following the transfection loading protocol. DMEM medium was added to the mixture and transferred to 24-well plates containing $1-5 \times 10^5$ NIH3T3-D1 cells/well. The plates were incubated at 37 °C under 5% CO_2 for 40–48 h. The medium was removed, and the cells were washed once with sterile PBS and treated with 0.5% trypsin-EDTA (Invitrogen, Carlsbad, CA; 20 μL of trypsin and 200 μL of PBS were added to each well). The contents of each well were collected by centrifugation (2500 rpm for 10 min), resuspended in 100 μL of 1:1 PBS−0.4% trypan blue (Mediatech, Herndon, VA), and counted using a hematocytometer to evaluate total cell number, and the viability was assessed by trypan blue exclusion.

RESULTS

YCWP are porous hollow 2–4 μm microspheres prepared from Baker's yeast composed primarily of β-1,3-D-glucan, mannoproteins, and chitin (Table 1). YCWP consist of two classes: GP and GMP. GP are composed primarily of β-1,3-D-glucan and low levels of chitin, whereas GMP contain both β-1,3-D-glucan and mannoproteins in the outer cell wall and low levels of chitin. Nanoparticulate cores composed of anionic and cationic polymers were constructed from tRNA and PEI within YCWP as described above (Figure 1a). These YCWP encapsulated cationic nanoparticulate cores were used to absorb DNA onto the cationized nanoparticulate surface and then coated with PEI to generate the YCWP DNA transfection formulations (Figure 1b).

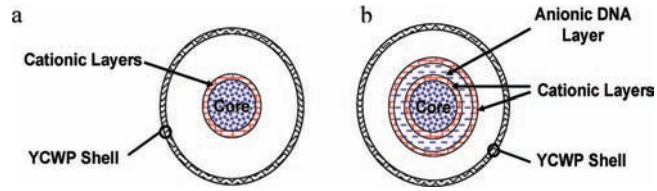

Figure 1. Schematic depiction of (a) nanoparticulate cores constructed within porous, hollow YCWP and (b) adsorption of DNA onto the YCWP encapsulated nanoparticulate core.

Table 2. Formulations Used To Evaluate tRNA Nanoplex Formation Inside YCWP

sample	Rho-tRNA:YCWP ratio (w/w)	PEI:YCWP ratio (w/w)	PEI:Rho-tRNA ratio (w/w)
1	0.01	4	400
2	0.025	4	160
3	0.05	1.32	26.4
4	0.05	4	80
5	0.05	13.2	264
6	0.075	4	53.3
7	0.1	1.32	13.2
8	0.1	4	40
9	0.1	13.2	132
10	0.25	4	16

Rhodamine labeled tRNA, DNA, or PEI were used to optimize the formation of each layer of the encapsulated nanoparticles. A calibration curve for each labeled compound was used to quantitate binding.

Optimization of the Synthesis of YCWP Encapsulated tRNA/PEI Nanoplex Cores by Fluorescent Component Analysis. The amount of fluorescent tRNA bound within the nanoplex cores inside 10^7 YCWP was evaluated at tRNA:YCWP ratios ranging from 0 to 0.25 as indicated in Table 2. Figure 2 shows the corresponding amount of tRNA in nanoplex cores that the fluorescence signal represents for each tRNA:particle ratio. The tRNA was efficiently incorporated into YCWP

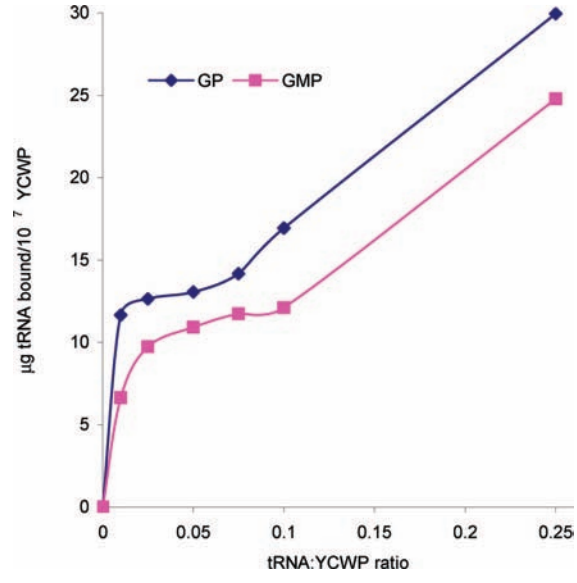

Figure 2. tRNA (μg) bound to YCWP encapsulated nanoplex cores as a function of tRNA:YCWP ratio.

Table 3. Formulation Conditions Used To Evaluate PEI Binding to tRNA Nanoplex Cores inside YCWP

sample	PEI:YCWP ratio (w/w)	PEI:Rho-tRNA ratio (w/w)
1	0.01	1
2	0.02	2
3	0.05	5
4	0.1	10
5	0.2	20
6	0.5	50
7	1	100
8	1.875	187.5
9	3.75	375

encapsulated nanoplexes over the tRNA:particle ratio tested. GP particles were capable of incorporating more tRNA in nanoplexes than GMP particles likely due to their larger hollow internal cavity.

The amount of fluorescent PEI incorporated into the tRNA nanoplex cores inside 10^7 YCWP was measured at a constant tRNA:YCWP ratio of 0.01 using the formulation ratios shown in Table 3. The results of these studies shown in Figure 3 indicate that PEI was efficiently incorporated into the tRNA nanoplex cores up to a PEI:YCWP ratio of 0.1 (w/w). More PEI was bound to GMP particles at all ratios tested, likely due to cationic PEI binding to negatively charged mannoproteins in the GMP wall.

Optimization of the Formation of DNA/PEI Complexes on YCWP Encapsulated tRNA/PEI Nanocomplex Cores by Fluorescence Analysis. Optimized YCWP formulations of YCWP-tRNA/PEI with a tRNA:YCWP ratio of 0.05 and a PEI:YP ratio of 4 were used as the starting material for the preparation of samples containing fluorescently labeled DNA. Rhodamine labeled DNA was added to this formulation over the range of 0−100 μg DNA/1 × 10^6 particles. PEI was then added at a PEI:DNA ratio of 2.5 to coat the DNA layer and prevent the DNA from washing off the tRNA/PEI cationic core surface. Figure 4 shows the amount of DNA bound for samples that were prepared with sonicated salmon sperm DNA (~5 kDa). DNA was effectively bound (80 ± 10%) over the range of DNA concentrations tested. In comparison, high molecular weight DNA (>40 kDa) was less effectively bound (40 ± 15%), suggesting that the porous YCWP hydrocolloid shell partially

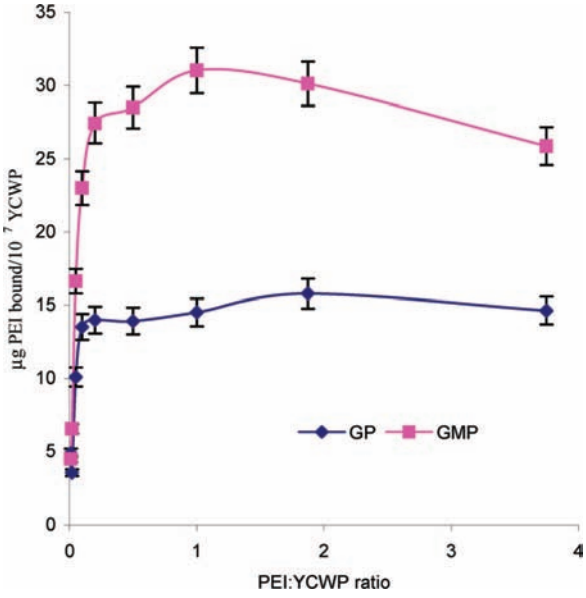

Figure 3. Fluorescent PEI (μg) bound to tRNA within YCWP to form nanoplex cores as a function of PEI loaded, at a constant tRNA:YCWP ratio of 0.01.

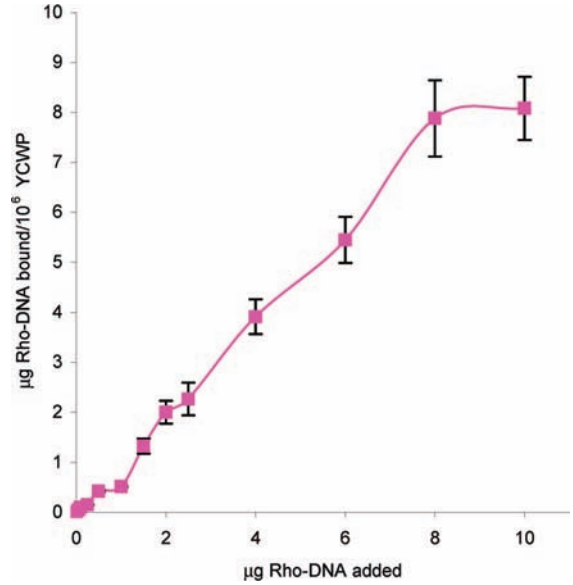

Figure 4. Amount of sonicated rhodamine-labeled salmon sperm DNA bound as a function of DNA concentration (μg of DNA/1 × 10^6 particles).

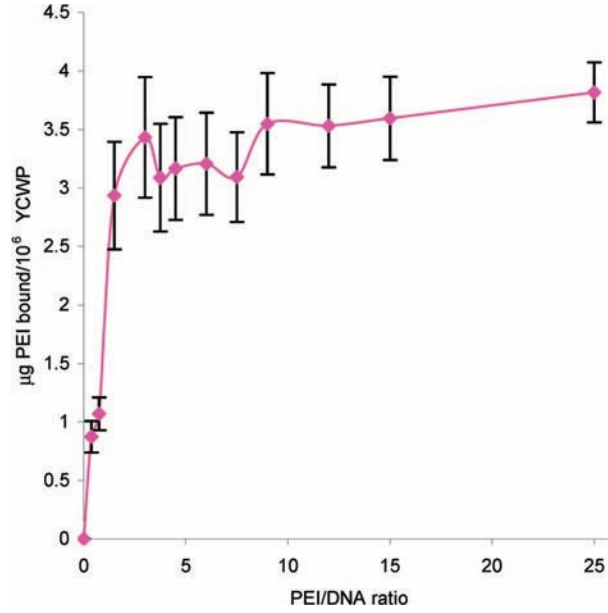

Figure 5. Amount of fluorescent PEI (μg) bound to YCWP-tRNA/PEI/DNA as a function of PEI loaded at a constant DNA load (10 μg of DNA) with a particle formulation of tRNA:YCWP ratio of 0.05 and PEI:YCWP ratio of 4 (w/w).

excludes the penetration of high molecular weight DNA molecules (data not shown). These results show the DNA binding capacity of plasmid sized DNA to be ~8 μg DNA/1 × 10^6 particles (~4 mg DNA/mg particles).

Optimization of the Final PEI Layer in the YCWP-tRNA/PEI/DNA/PEI Nanocomplex by Fluorescence Analysis. Coating of the DNA layer with a protective trapping polymer layer is important to stabilize the DNA and maximize transfection efficiency. The amount of fluorescent PEI bound to the DNA layer was measured at different DNA concentrations. It was determined that PEI adsorption reaches a maximum value at a PEI:DNA ratio higher than 3:1 (w/w) (Figure 5).

Flow Cytometry (FACS) and Fluorescence Microscopy. FACS measurements were obtained for different sets of titration experiments to quantitate tRNA, PEI, or DNA binding on a per

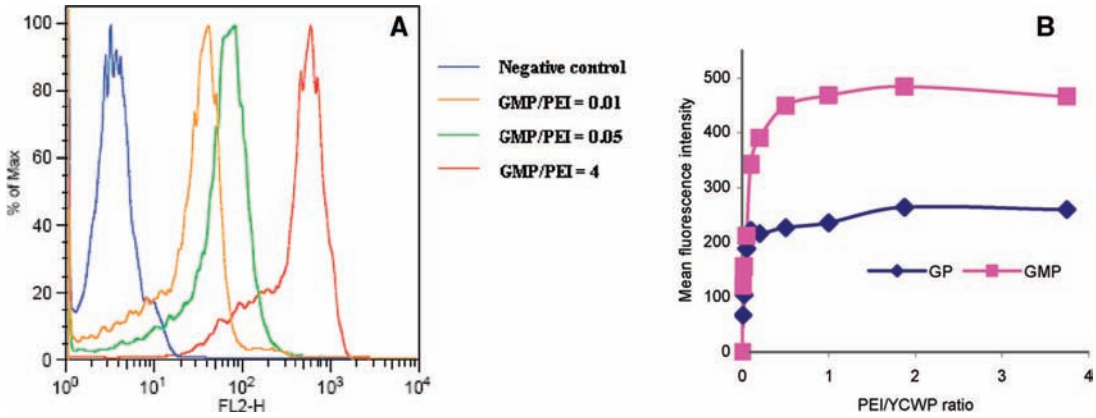

Figure 6. (A) FACS results showing the uniform increase of fluorescence from Rho-PEI bound to GMP-tRNA cores at different GMP:PEI ratios and (B) mean fluorescence intensity for Rho-PEI binding to both GP and GMP.

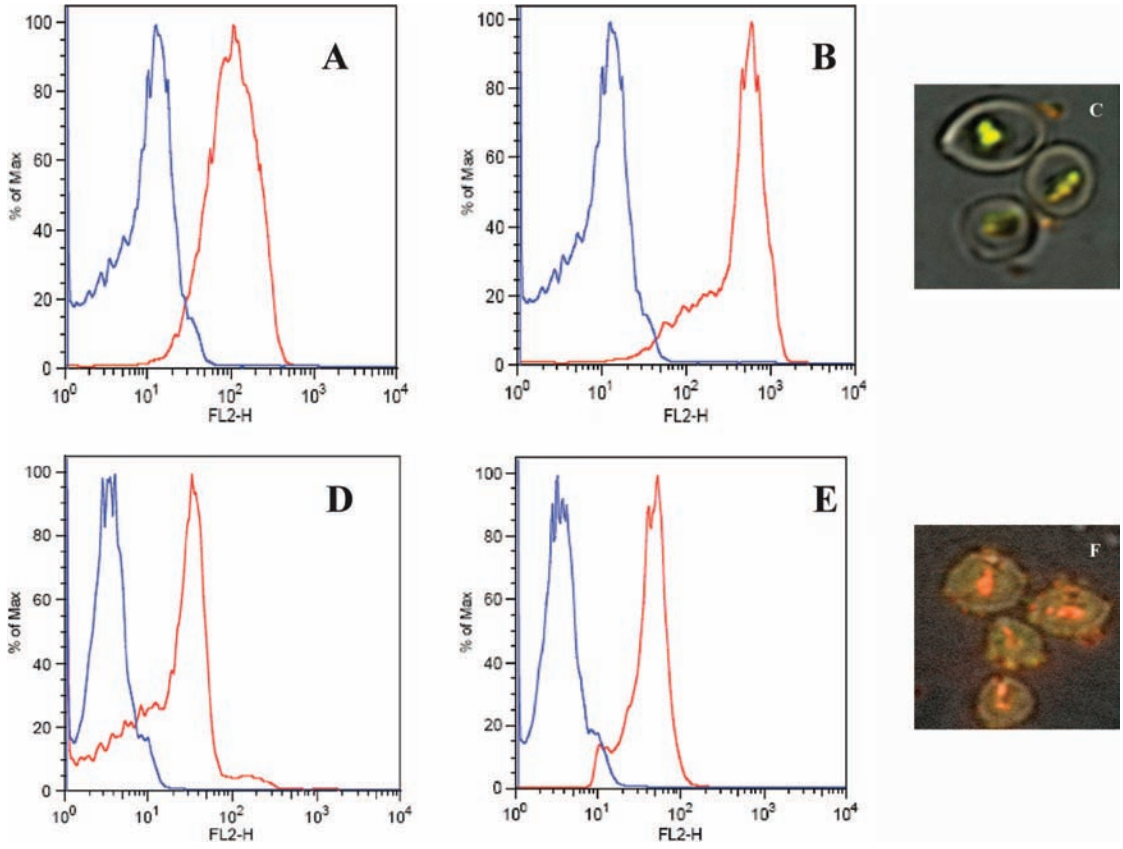

Figure 7. FACS results (blue lines indicate negative controls) and microscope images showing formation of nanoparticulate cores and adsorption of DNA/PEI complexes. (A) Rho-tRNA adsorbed into GMP at tRNA:GMP ratio of 0.1; (B) Rho-PEI bound to GMP-tRNA at a PEI:GMP ratio of 3.75; (C) overlay light/fluorescent microscopic image showing formation of nanoparticulate cores composed of DTAF-tRNA and Rho-PEI; (D) adsorption of 625 ng Rho-DNA to 10^6 GMP-tRNA/PEI particles; (E) adsorption of Rho-PEI to GMP-tRNA/PEI/DNA (25 μL of 0.01% Rho-PEI added to 500 ng of DNA); and (F) overlay light/fluorescent microscopic image of DNA/PEI nanocomplexes inside GMP showing Rho-DNA fluorescence.

particle basis and to assess the homogeneity of nanocomplex formation within YCWP. An example of this quantification is provided in Figure 6 for nanoparticle core formation. The FACS results (panel A) show that the fluorescence of Rhodamine labeled PEI bound to the GMP-tRNA core uniformly increases as the fluorescent PEI:GMP-tRNA ratio increases. In addition, a maximum fluorescence response of the same magnitude is observed for PEI:GMP or GP ratios greater than 1, confirming the bulk fluorescence measurements (panel B). Similar results were obtained for analysis of other layers (data not shown).

Figure 7 shows the maximum response for Rho-tRNA at GMP:tRNA ratio of 0.05 (panel A) and for Rho-PEI at a PEI:GMP ratio of 4 (panel B). Adsorption of both tRNA and PEI is further demonstrated by overlay fluorescent microscope images of particles containing nanoparticle cores labeled with two different fluorescent labels (Figure 7, panel C).

DNA binding to YCWP-tRNA/PEI nanocomplexes was evaluated on a per particle basis following fluorescent DNA binding by FACS. The FACS analysis (Figure 7, panel D) shows that >95% of the particles bind DNA. The formation of the final PEI layer of the YCWP-tRNA/PEI/DNA/PEI nanocomplexes was evaluated on a per particle basis following fluorescent PEI binding. The FACS analysis (Figure 7, panel E) shows that >85% of the particles bind PEI to levels detected by FACS analysis. Adsorption of both DNA and PEI on the nanoparticulate cores is shown by overlay fluorescent microscope images

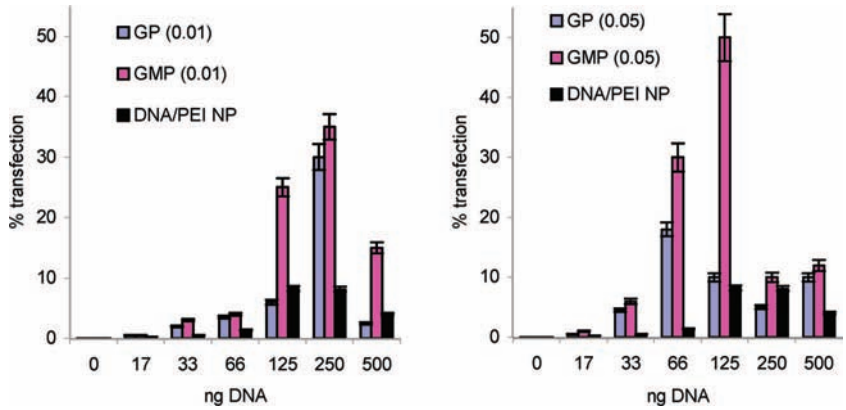

Figure 8. Transfection results for YCWP-tRNA/PEI particles with tRNA:YCWP ratios of 0.01 (left) and 0.05 (right) and a PEI:YCWP ratio of 4. Free DNA/PEI nanoparticles (NP) were used as control.

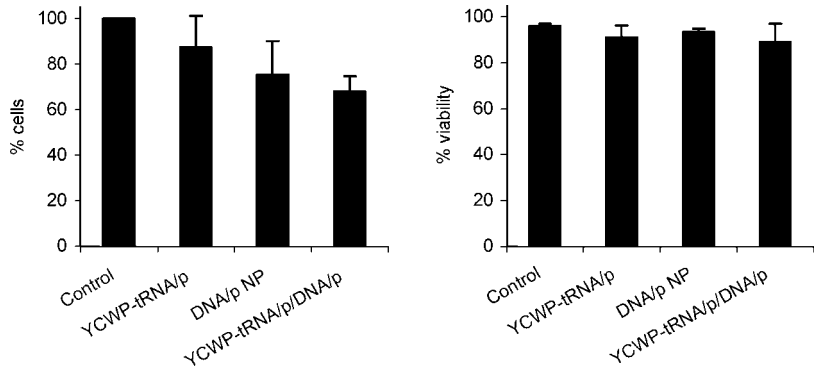

Figure 9. Toxicity of YCWP encapsulated cationic cores and YCWP encapsulated DNA formulations. Percentage of cells/well after 48 h of incubation normalized with respect to the control (left), and percentage of live cells/well after 48 h of incubation (right). Samples tested were saline control; YCWP encapsulated tRNA/PEI cationic cores; free DNA/PEI nanoparticles (NP); and YCWP-tRNA/PEI/DNA/PEI formulations used for transfection experiments.

with DNA and PEI labeled with two different colors (Figure 7, panel F), following a similar method to evaluate formation of the nanoparticulate tRNA/PEI core.

Transfection Results. Transfection experiments were carried out using NIH3T3-D1 cells. This cell line was derived from NIH3T3 by the integration of the dectin-1 gene to produce cells expressing the β-1,3-D-glucan receptor dectin-1 facilitating GP or GMP phagocytosis (*40, 41*). Several particle formulations using varied tRNA:YCWP ratios at a constant PEI:YCWP ratio of 4 were evaluated. Figure 8 shows the transfection results at different DNA loads for two formulations that consistently provided the highest transfection results.

YCWP Encapsulated Cationic Cores and YCWP Encapsulated DNA Formulation Toxicity. YCWP-tRNA/PEI cores and YCWP-tRNA/PEI/DNA/PEI formulations slow the growth rate of NIH3T3-D1 by ~20–30% compared to a saline control but have a negligible effect on cell viability (Figure 9). Free DNA/PEI nanocomplexes were evaluated as control showing an effect similar to that of the YCWP formulations. Excess PEI can be removed from YCWP-tRNA/PEI/DNA/PEI formulations by washing DNA/PEI layered preparations by centrifugation and resuspension in 0.9% saline to eliminate the growth inhibition (data not shown).

DISCUSSION

We have developed an efficient microparticle encapsulated nanoplex-based DNA delivery system through the solid-phase LbL synthesis of nanoparticles within carbohydrate microparticles YCWP. The advantages of the YCWP DNA delivery system include efficient DNA delivery, high capacity, multiplexable DNA, protein, and siRNA delivery, oral bioavailability, β-1,3-D-glucan receptor targeting to macrophages and dendritic cells, and cell trafficking to the reticuloendothelial system and sites of pathology (*33–35*).

YCWP are hollow and porous 2–4 μm microspheres prepared from Baker's yeast that have previously been demonstrated to serve as an antigen delivery system (*43*). The porous hydrocolloid shell is composed primarily of β-1,3-D-glucan, mannoproteins, and chitin and is typically <200 nm thick (Figure 1A) (*44*). YCWP consist of two classes; GP and GMP providing carbohydrate receptor-mediated targeting that facilitates oral uptake into gut associated macrophages and dendritic cells (*35*) and intracellular DNA delivery and gene expression in these cells (*34*). Formation of the polyelectrolyte nanocomplexes follows a LbL approach, with the different components assembled through electrostatic interactions (*45*).

The use of porous YCWP microcapsules as a carrier for transient gene expression therapy requires the formation of nanoparticulate cores within YCWP with the outmost layer being positively charged. This cationic layer can be used to electrostatically bind DNA to the positively charged core surface. The DNA is then coated with a second cationic polymer layer to protect the DNA.

An effective synthetic cationic polymer is PEI, a commercially available compound that has been used for gene delivery. PEI has a high positive charge that allows efficient condensation of anionic DNA. The presence of amines (only 15–20% are protonated at physiological pH) contributes to a proton−sponge mechanism, which is believed to mediate endosomal DNA release and be responsible for its high DNA transfection activity (*1, 9*). Other strategies previously reported to enhance transfection efficiency, used EndoPorter and hyalu-

ronic acid copolymers in the DNA layer to facilitate defoliation and endosomal DNA release, and Penetratin, a cationic peptide containing a nuclear localization signal to enhance DNA nuclear uptake (*34*).

To optimize the preparation of the nanocomplexes inside YCWP, we carried out a series of experiments to determine the conditions for maximal binding of each component in the encapsulated nanocomplexes. These studies used tRNA and PEI to form the nanoparticulate cores, DNA as the payload, and PEI to coat and protect the DNA payload caged inside the YCWP. Each of these polymers was fluorescently labeled with rhodamine, and fluorescence was used to quantify the binding of each layered component in the encapsulated nanocomplexes. Fluorescein labeled polymers were used to demonstrate colocalization of components in the encapsulated nanoplexes.

The first step was to characterize and optimize tRNA/PEI concentrations to maximize YCWP encapsulated nanocomplex core formation. In these experiments, YCWP encapsulated tRNA/PEI nanocomplexes were prepared at different PEI:tRNA ratios using rhodamine labeled tRNA. The fluorescence of YCWP encapsulated rhodamine labeled tRNA increased as a result of the formation of insoluble tRNA/PEI nanocomplexes within the YCWP. From these measurements it was determined that PEI:tRNA ratios of 5 or higher were necessary to optimally incorporate the tRNA into encapsulated nanocomplexes. At these ratios between 50 and 60% of the input tRNA was effectively encapsulated as nanoparticles in the YCWP. The results in Figure 2 show that it was possible to prepare YCWP encapsulated cationic nanocomplexes containing greater than 30 μg of tRNA nanoparticles per 200 μg of YCWP particles (1×10^8 particles).

To quantify PEI incorporation within the tRNA/PEI nanocomplexes inside YCWP, an optimal tRNA:YCWP ratio of 0.05 was chosen to prepare nanoplexed cores with different PEI:tRNA ratios. The results in Figure 3 show that the fluorescence of YCWP nanocomplexed cores prepared with labeled PEI reaches a saturation value at PEI:tRNA ratios as low as 5.

The use of FACS analysis allowed us to quantify tRNA and PEI binding on a per particle basis. The results for Rho-PEI incorporation in Figure 6 show a uniform increase in fluorescence with increasing Rho-PEI:YCWP-tRNA ratios demonstrating homogeneous nanocomplex formation within each YCWP. At a Rho-PEI:YCWP-tRNA ratio of 1 or higher the measured fluorescence reaches a constant value indicating the saturation value for PEI. These results support the experimental values for core formation determined from bulk fluorescence measurements (Figure 5).

The results from these studies allowed for the optimization of conditions to synthesize tRNA/PEI nanocomplex cores within YCWP to provide a sufficient cationic nanoparticle surface area for maximal DNA binding, while leaving enough space within the hollow YCWP for subsequent layers. Optimal conditions for nanoplex core formation required the use of tRNA:YCWP weight ratios between 0.01 and 0.05 and PEI:YCWP weight ratios higher than 0.5.

The next steps were to optimize DNA binding and PEI coating to form YCWP encapsulated tRNA/PEI/DNA/PEI multilayered nanocomplexes. It was observed that DNA must be used within an optimal concentration range to achieve high transfection efficiency, as high DNA levels did not necessarily translate to high transfection levels (*34*). It was also important to optimize the PEI formulation step to coat the DNA layer. PEI must completely coat the DNA layer to protect it from degradation before its release inside the cell. However, PEI is toxic, and its concentration should be minimized to reduce toxicity.

A YCWP-tRNA/PEI particle formulation with a tRNA:YCWP ratio of 0.05 and a PEI:YCWP ratio of 4 was used to quantify the amount of Rho-DNA that binds to the encapsulated nanoplex cores. It was found that Rho-DNA loosely binds to the cores and does not fully protect the DNA from enzymatic degradation as demonstrated by lower particle-associated fluorescence before PEI coating. Once PEI was used to coat the DNA layer, the percentage of DNA associated with the encapsulated cores increased to >80% (Figure 4) and the DNA was protected from enzymatic degradation ((*9,14*); data not shown). This high DNA load level of the YCWP DNA delivery system translates to the maximum delivery of $\sim 10^6$ plasmid molecules per YCWP.

A YCWP-tRNA/PEI particle formulation with a tRNA:YCWP ratio of 0.05, a PEI:YCWP ratio of 4, and a constant load of 10 μg of DNA/1×10^6 particles (DNA:YCWP ratio of 0.005**)** was used to quantify the amount of Rho-PEI coating of the encapsulated nanoplex cores loaded with a DNA payload. The results in Figure 5 show that PEI can be used at PEI:DNA ratios as low as 3:1 as the fluorescence response for Rhodamine-PEI trapped inside the particles reached a plateau at this PEI:DNA ratio. This PEI:DNA weight ratio of 3:1 is equivalent to an N/P ratio of $\sim$8. For 25 kDa branched PEI, a critical N/P ratio of 2.3:1 has been reported for formation of DNA/PEI nanoparticles (*46*), while N/P ratios of 6–8 are considered the minimum necessary for efficient DNA condensation and protection during DNA delivery to cells (*1*). Therefore, the required N/P ratio for DNA condensation within YCWP is found in the proper range reported by others for DNA/PEI nanoparticle formation.

The use of PEI as a nonviral cationic polymer is limited by its toxicity. The toxicity of PEI can be reduced by washing the PEI coated YCWP encapsulated nanoplexes to remove any unbound PEI. At a high particle:cell ratio of 10 particles:cell, unwashed YCWP encapsulated nanoplexes or DNA formulations slightly inhibit the growth rate of the cell line NIH3T3-D1 but do not induce cell death as evidenced by cell viabilities in excess of 90% (Figure 9). Several studies have identified other potentially useful cationic polymers as gene delivery vectors with the advantages of decreased toxicity and higher gene delivery efficiency than PEI. For example, toxicity of PEI can be significantly reduced by partial acetylation of amine groups (*18*) or polymers constructed from biodegradable ester units (*23*). The use of these other cationic polymers to form YCWP caged DNA nanocomplexes inside YCWP by an LbL approach is currently under investigation.

The impact of the optimization of the LbL assembly process of encapsulated DNA coated nanoplex cationic cores on transfection efficiency was assessed by YCWP mediated delivery of the plasmid gWizGFP to NIH3T3-D1 cells. The transfection results for particle formulations with two different tRNA:YP ratios and a constant PEI:YP ratio of 4 are shown in Figure 8. DNA delivered in the optimized YCWP delivery system efficiently transfects NIH3T3-D1; greater than 50% of cells are transfected by 125 ng DNA/5×10^5 cells when using a GMP formulation with a tRNA:GMP ratio of 0.05. Transfection efficiency of DNA/PEI nanocomplexes not trapped inside YCWP was negligible (<10%) at a DNA level of 125 ng/5×10^5 cells. In comparison, other groups have reported efficient in vitro transfection with unencapsulated DNA/PEI nanocomplexes using greater than 16-fold higher levels of plasmid DNA delivered/cell (*9, 47*).

The use of schizophyllan, a β-1,3-D-glucan polysaccharide to complex single stranded oligonucleotide sequences and serve as a targeting agent for DNA delivery, has been reported by Sakurai and colleagues (*48*). However, this DNA delivery strategy requires the synthesis of poly(dA) forming a hairpin

structure at both ends of the dsDNA and did not result in enhanced siRNA or DNA delivery compared to PEI polyplexes. Thus, the encapsulation of nanocomplexed DNA inside YCWP composed of β-1,3-D-glucan appears more important than β-1,3-D-glucan targeting of soluble or nanoparticulate DNA complexes to maximize DNA transfection.

CONCLUSIONS

Porous hollow YCWP have been shown to be an effective microparticulate delivery system to encapsulate DNA following LbL assembly of polymers by electrostatic interactions inside YCWP. Labeling of each layer with rhodamine allowed quantitative fluorescence analysis and optimization of LbL nanoplex synthesis within YCWP. The YCWP DNA delivery system efficiently delivered the plasmid, gWizGFP, and transfected NIH3T3-D1 cells. The advantages of the efficient YCWP DNA delivery system include high capacity, multiplexable DNA, protein, and siRNA delivery, oral bioavailability, β-1,3-D-glucan receptor targeting to macrophages and dendritic cells, and cell trafficking to the reticuloendothelial system and sites of pathology (*33–35*). Future communications will report on in vitro and in vivo YCWP-mediated DNA and siRNA delivery to macrophages, dendritic cells, tissues containing these cells.

ACKNOWLEDGMENT

The authors wish to thank Xiaoyun Huang and Marguerite Joly for technical assistance, Drs. Edward Ginns and Charles Specht (UMMS), and the UMMS FACS and Digital Imaging Core Facilities for assistance in microscopy. This work was supported in part by NIH 1R01NS054120-01, USIDNET, UMMS, and Commonwealth Medicine.

LITERATURE CITED

(1) Pack, D. W., Hoffman, A. S., Pun, S., and Stayton, P. S. (2005) Design and development of polymers for gene delivery. *Nat. Rev. Drug Discovery. 4*, 581–593.

(2) Rolland, A. (2006) Nuclear gene delivery: the Trojan horse approach. *Exp. Opin. Drug Delivery 3*, 1–10.

(3) Yang, N. S., Burkholder, J., Roberts, B., Martinell, B., and McCabe, D. (1990) *In vivo* and *in vitro* gene transfer to mammalian somatic cells by particle bombardment. *Proc. Natl. Acad. Sci. U.S.A. 87*, 9568–9572.

(4) Neumann, E., Schaefer-Ridder, M., Wang, Y., and Hofschneider, P. H. (1982) Gene transfer into mouse lyoma cells by electroporation in high electric fields. *EMBO J. 1*, 841–845.

(5) Liu, F., Song, Y., and Liu, D. (1999) Hydrodynamics-based transfection in animals by systemic administration of plasmid DNA. *Gene Ther. 6*, 1258–1266.

(6) Kim, H. J., Greenleaf, J. F., Kinnick, R. R., Bronk, J. T., and Bolander, M. (1996) Ultrasound-mediated transfection of mammalian cells. *Hum. Gene Ther. 7*, 1339–1346.

(7) Felgner, P. L., Gadek, T. R., Holm, M., Roman, R., Chan, H. W., Wenz, M., Northrop, J. P., Ringold, G. M., and Danielsen, M. (1987) Lipofection: a highly efficient, lipid-mediated DNA-transfection procedure. *Proc. Natl. Acad. Sci. U.S.A. 84*, 7413–7417.

(8) Wu, G. Y., and Wu, C. H. (1988) Receptor-mediated gene delivery and expression *in vivo*. *J. Biol. Chem. 263*, 14621–14624.

(9) Boussif, O., Lezoualc'h, F., Zanta, M. A., Mergny, M. D., Scherman, D., Demeneix, B., and Behr, J. P. (1995) A versatile vector for gene and oligonucleotide transfer into cells in culture and *in vivo*: polyethylenimine. *Proc. Natl. Acad. Sci. U.S.A. 92*, 7297–7301.

(10) Paukner, S., Kudela, P., Kohl, G., Schlapp, T., Friedrichs, S., and Lubitz, W. (2005) DNA-loaded bacterial ghosts efficiently mediate reporter gene transfer and expression in macrophages. *Mol. Ther. 11*, 215–223.

(11) Ihler, G. M., and Tsang, H. C. (1985) Erythrocyte carriers. *Crit. Rev. Ther. Drug Carrier Syst. 1*, 155–187.

(12) Byun, H. M., Suh, D., Yoon, H., Kim, J. M., Choi, H. G., Kim, W. K., Ko, J. J., and Oh, Y. K. (2004) Erythrocyte ghost-mediated gene delivery for prolonged and blood-targeted expression. *Gene Ther. 11*, 492–496.

(13) Sinha, R., Kim, G. J., Nie, S., and Shin, D. M. (2006) Nanotechnology in cancer therapeutics: bioconjugated nanoparticles for drug delivery. *Mol. Cancer Ther. 5*, 1909–1917.

(14) Reibetanz, U., Claus, C., Typlt, E., Hofmann, J., and Donath, E. (2006) Defoliation and plasmid delivery with layer-by-layer coated colloids. *Macromol. Biosci. 6*, 153–160.

(15) Thomas, M., Lu, J. J., Ge, Q., Zhang, C., Chen, J., and Klibanov, A. M. (2005) Full deacylation of polyethylenimine dramatically boosts its gene delivery efficiency and specificity to mouse lung. *Proc. Natl. Acad. Sci. U.S.A. 102*, 5679–5684.

(16) Forrest, M. L., Gabrielson, N., and Pack, D. W. (2005) Cyclodextrin - polyethylenimine conjugates for targeted in vitro gene delivery. *Biotechnol. Bioeng. 89*, 416–423.

(17) Thomas, M., and Klibanov, A. M. (2002) Enhancing polyethylenimine's delivery of plasmid DNA into mammalian cells. *Proc. Natl. Acad. Sci. U.S.A. 99*, 14640–14645.

(18) Gabrielson, N. P., and Pack, D. W. (2006) Acetylation of Polyethylenimine Enhances Gene Delivery via Weakened Polymer/DNA Interactions. *Biomacromolecules 7*, 2427–2435.

(19) Tang, G. P., Zeng, J. M., Gao, S. J., Ma, Y. X., Shi, L., Li, Y., Too, H.-P., and Wang, S. (2003) Polyethylene glycol modified polyethylenimine for improved CNS gene transfer: effects of PEGylation extent. *Biomaterials 24*, 2351–2362.

(20) Kloeckner, J., Bruzzano, S., Ogris, M., and Wagner, E. (2006) Gene Carriers Based on Hexanediol Diacrylate Linked Oligoethylenimine: Effect of Chemical Structure of Polymer on Biological Properties. *Bioconjugate Chem. 17*, 1339–1345.

(21) Kloeckner, J., Wagner, E., and Ogris, M. (2006) Degradable gene carriers based on oligomerized polyamines. *Eur. J. Pharm. Sci. 29*, 414–425.

(22) Green, J. J., Shi, J., Chiu, E., Leshchiner, E. S., Langer, R., and Anderson, D. G. (2006) Biodegradable Polymeric Vectors for Gene Delivery to Human Endothelial Cells. *Bioconjugate Chem. 17*, 1162–1169.

(23) Anderson, D. G., Akinc, A., Hossain, N., and Langer, R. (2005) Structure/property studies of polymeric gene delivery using a library of poly(β-amino esters). *Mol. Ther. 11*, 426–434.

(24) De Geest, B. G., Sanders, N. N., Sukhorukov, G. B., Demeester, J., and De Smedt, S. C. (2007) Release mechanisms for polyelectrolyte capsules. *Chem. Soc. Rev. 36*, 636–649.

(25) Meyer, M., and Wagner, E. (2006) Recent Developments in the Application of Plasmid DNA-Based Vectors and Small Interfering RNA Therapeutics for Cancer. *Hum. Gene Ther. 17*, 1062–1076.

(26) Fischlechner, M., Toellner, L., Messner, P., Grabherr, R., and Donath, E. (2006) Virus-engineered colloidal particles - a surface display system. *Angew. Chem., Int. Ed. 45*, 784–789.

(27) Zheng, M., and Huang, X. (2004) Nanoparticles Comprising a Mixed Monolayer for Specific Bindings with Biomolecules. *J. Am. Chem. Soc. 126*, 12047–12054.

(28) Amalvy, J. I., Unali, G.-F., Li, Y., Granger-Bevan, S., Armes, S. P., Binks, B. P., Rodrigues, J. A., and Whitby, C. P. (2004) Synthesis of Sterically Stabilized Polystyrene Latex Particles Using Cationic Block Copolymers and Macromonomers and Their Application as Stimulus-Responsive Particulate Emulsifiers for Oil-in-Water Emulsions. *Langmuir 20*, 4345–4354.

(29) Saxena, A., Mozumdar, S., and Johri, A. K. (2006) Ultra-low sized cross-linked polyvinylpyrrolidone nanoparticles as non-

viral vectors for in vivo gene delivery. *Biomaterials 27*, 5596–5602.
(30) Nie, Y., Zhang, Z.-R., and Duan, Y.-R. (2006) Combined use of polycationic peptide and biodegradable macromolecular polymer as a novel gene delivery system: a preliminary study. *Drug Deliv. 13*, 441–446.
(31) Zhu, J., Tang, A., Law, L. P., Feng, M., Ho, K. M., Lee, D. K. L., Harris, F. W., and Li, P. (2005) Amphiphilic Core-Shell Nanoparticles with Poly(ethylenimine) Shells as Potential Gene Delivery Carriers. *Bioconjugate Chem. 16*, 139–146.
(32) Dai, Z., Voigt, A., Leporatti, S., Donath, E., Dahne, L., and Mohwald, H. (2001) Layer-by-Layer Self-Assembly of Polyelectrolyte and Low Molecular Weight Species into Capsules. *Adv. Mater. 13*, 1339–1342.
(33) Ostroff, G. R. (2005) *U.S. Patent Application* 20050281781 *Publication* pp 45, U.S. Patent and Trademark Office, Alexandria, VA.
(34) Soto, E., and Ostroff, G. R. (2007) Oral Macrophage Mediated Gene Delivery System. *NSTI Nanotech 2007 Technical Proceedings 2*, 378–381.
(35) Hong, F., Yan, J., Baran, J. T., Allendorf, D. J., Hansen, R. D., Ostroff, G. R., Xing, P. X., Cheung, N.-K. V., and Ross, G. D. (2004) Mechanism by Which Orally Administered β-1,3-Glucans Enhance the Tumoricidal Activity of Antitumor Monoclonal Antibodies in Murine Tumor Models. *J. Immunol. 173*, 797–806.
(36) Jewell, C. M., Zhang, J., Fredin, N. J., Wolff, M. R., Hacker, T. A., and Lynn, D. M. (2006) Release of Plasmid DNA from Intravascular Stents Coated with Ultrathin Multilayered Polyelectrolyte Films. *Biomacromolecules. 7*, 2483–2491.
(37) Schoeler, B., Delorme, N., Doench, I., Sukhorukov, G. B., Fery, A., and Glinel, K. (2006) Polyelectrolyte Films Based on Polysaccharides of Different Conformations: Effects on Multilayer Structure and Mechanical Properties. *Biomacromolecules 7*, 2065–2071.
(38) Jessel, N., Oulad-Abdelghani, M., Meyer, F., Lavalle, P., Haikel, Y., Schaaf, P., and Voegel, J.-C. (2006) Multiple and time-scheduled in situ DNA delivery mediated by β-cyclodextrin embedded in a polyelectrolyte multilayer. *Proc. Natl. Acad. Sci. U.S.A. 103*, 8618–8621.
(39) Kulkarni, R. P., Wu, D. D., Davis, M. E., and Fraser, S. E. (2005) Quantitating intracellular transport of polyplexes by spatio-temporal image correlation spectroscopy. *Proc. Natl. Acad. Sci. U.S.A. 102*, 7523–7528.
(40) Marshall, A. S. J., Willment, J. A., Lin, H.-H., Williams, D. L., Gordon, S., and Brown, G. D. (2004) Identification and Characterization of a Novel Human Myeloid Inhibitory C-type Lectin-like Receptor (MICL) That Is Predominantly Expressed on Granulocytes and Monocytes. *J. Biol. Chem. 279*, 14792–14802.
(41) Willment, J. A., Gordon, S., and Brown, G. D. (2001) Characterization of the human β-glucan receptor and its alternatively spliced isoforms. *J. Biol. Chem. 276*, 43818–43823.
(42) Young, S., Ostroff, G. R., Zeidler-Erdely, P. C., Roberts, J. R., Antonini, J. M., and Castranova, V. (2007) A Comparison of the Pulmonary Inflammatory Potential of Different Components of Yeast Cell Wall. *J. Toxicol. Environ. Health, Part A 70*, 1116–1124.
(43) Ostroff G. R., Easson, D., Jr., and Jamas, S. A. (1991) A new beta glucan-based macrophage-targeted adjuvant. In *Polymeric drugs and drug delivery systems* (Dunn, R. L., and Ottenbrite, R. M., Eds.) Vol. 469, pp 52–59, American Chemical Society, Washington, DC.
(44) Klis, F. M., De Groot, P., and Hellingwerf, K. (2001) Molecular organization of the cell wall of Candida albicans. *Med. Mycol. 39*, 1–8.
(45) Decher, G. (1997) Fuzzy nanoassemblies: toward layered polymeric multicomposites. *Science 277*, 1232–1237.
(46) Bertschinger, M., Backliwal, G., Schertenleib, A., Jordan, M., Hacker, D. L., and Wurm, F. M. (2006) Disassembly of polyethylenimine-DNA particles in vitro: Implications for polyethylenimine-mediated DNA delivery. *J. Controlled Release 116*, 96–104.
(47) Pollard, H., Remy, J. S., Loussouarn, G., Demolombe, S., Behr, J. P., and Escande, D. (1998) Polyethylenimine but not cationic lipids promotes transgene delivery to the nucleus in mammalian cells. *J. Biol. Chem. 273*, 7507–7511.
(48) Anada, T., Karinaga, R., Koumoto, K., Mizu, M., Nagasaki, T., Kato, Y., Taira, K., Shinkai, S., and Sakurai, K. (2005) Linear double-stranded DNA that mimics an infective tail of virus genome to enhance transfection. *J. Controlled Release 108*, 529–539.

BC700329P

Novel Prodrugs of SN38 Using Multiarm Poly(ethylene glycol) Linkers

Hong Zhao,* Belen Rubio, Puja Sapra, Dechun Wu, Prasanna Reddy, Prakash Sai, Anthony Martinez, Ying Gao, Yoany Lozanguiez, Clifford Longley, Lee M. Greenberger, and Ivan D. Horak

Enzon Pharmaceuticals, Inc., 20 Kingsbridge Road, Piscataway, New Jersey 08854. Received August 31, 2007; Revised Manuscript Received January 30, 2008

CPT-11, also known as irinotecan, is a prodrug that is approved for the treatment of advanced colorectal cancer. The active metabolite of CPT-11, SN38 (7-ethyl-10-hydroxy-camptothecin), has 100- to 1000-fold more potent cytotoxic activity in tissue cell culture compared with CPT-11. However, parental administration of SN38 is not possible because of its inherently poor water solubility. It is reported here that a multiarm poly(ethylene glycol) (PEG) backbone linked to four SN38 molecules (PEG-SN38) has been successfully prepared with high drug loading and significantly improved water solubility (400- to 1000-fold increase). Three different protecting strategies have been developed in order to selectively acylate the 20-OH of SN38 to preserve its E-ring in the lactone form (the active form of SN38 with cytotoxic activities) while PEG is still attached. One chemical process has been optimized to make a large quantity of the PEG-SN38 conjugate with a high yield that can be readily adapted for scale-up production. The PEG-SN38 conjugates have shown excellent in vitro anticancer activity, with potency similar to that of native SN38, in a panel of cancer cell lines. The PEG-SN38 conjugates also have demonstrated superior anticancer activity in the MX-1 xenograft mice model compared with CPT-11. Among the four conjugates, PEG-Gly-(20)-SN38 (**23**) has been selected as the lead candidate for further preclinical development.

INTRODUCTION

Camptothecin and its analogues have potent cytotoxic activity in tumor cells grown in tissue culture and moderate anticancer efficacy in animal models. The compounds selectively inhibit topoisomerase I (TOP1) by trapping the enzyme during the cleavage of DNA (*1*), thereby prohibiting faithful cell division and protein production. This ultimately leads to cell death. Early clinical development of camptothecin carboxylate in the 1970s demonstrated that the compound had antitumor activity but also substantial toxicity (*2*). It was not until the discovery of more water-soluble derivatives of camptothecin that two TOP1 inhibitors (Hycamtin [topotecan] and Camptosar [CPT-11, irinotecan]) were approved as anticancer agents by the U.S. Food and Drug Administration (FDA) in 1997.

While CPT-11 has clinical utility, there are many limitations that suggest further improvement of the compound may be possible. One major limitation is that the active ingredient, SN38 (7-ethyl-10-camptothecin), which is produced by esterase-mediated hydrolysis of the solubilizing group on CPT-11 (the bispiperidine moiety), requires carboxylesterase-2. Although carboxylesterase-2 is present in abundance within the liver, its expression is far lower in the blood (*3, 4*). As a result, only 1−9% of an injected dose of CPT-11 is converted to SN38 (*3, 5, 6*) in humans (*6*). In addition, the lactone E-ring of CPT-11 (or SN38) can be readily converted to an open carboxylate form that is inactive against TOP1 (*6–8*) and binds tightly to human serum albumin. In particular, it is known that, 24 h after CPT-11 infusion in humans, approximately 25% and 55% of CPT-11 and SN38, respectively, are in the closed lactone form (*3*) compared with the total amount of CPT-11 and SN38. Hence, inhibition of the conversion to the inactive open carboxylate form of the molecule may have therapeutic benefit. Finally, while SN38 has 100- to 1000-fold more potent in vitro cytotoxic activity compared with CPT-11 (*3*), it has poor solubility in any pharmaceutically acceptable excipient and cannot be used for systemic applications (*9*).

One solution to alleviate the above-mentioned limitations is to PEGylate SN38. PEGylation is well-known for its capability to solubilize very insoluble small molecule compounds, prolong circulation time, and alter the biodistribution of parent drugs (*10*). In fact, we previously have shown that dramatic enhancement of circulating half-life, solubility, and in vivo efficacy of the native anticancer drug camptothecin was achieved utilizing a prodrug strategy in conjunction with the nonimmunogenic 40 kDa polymeric poly(ethylene glycol) (PEG) (*11*). The active lactone form of camptothecin was largely preserved during circulation due to the acylation through the 20-hydroxyl functional group where PEG was attached (*12*). The lactone stabilization was further proven in a separate study using different acylation agents with this 20-hydroxyl group (*13*). However, the PEG used in the camptothecin delivery was the bifunctional linear PEG that had only two active sites for drug conjugation. As a result, there was about 1.7% of camptothecin (CPT) by weight per PEG-CPT conjugate. Subsequently, a large amount of the compound was given to patients during clinical trials; most of the compound was inactive PEG polymer, which could be as high as 14 g of PEG per dose. Due to the high potency of SN38 and our enhanced ability to increase the loading of the drug onto PEG, it was reasoned that PEG-SN38 would overcome the limitations of CPT-11 or PEG-CPT. We report here the description of PEGylated SN38 derivatives that have remarkable efficacy in animal tumor models and have recently entered into phase I clinical trials.

CHEMISTRY

The most commonly used PEG is a linear polymer with either one or two functional groups at the two distal ends. Simple conjugation with such linear PEG will attach up to two drug molecules per PEG conjugate. To increase the payload, we previously developed methods by branching at the ends of PEG with trifunctional moieties such as aspartic acid and have successfully increased the loading of the water-soluble antican-

* Contact information: Telephone 732-980-4902, fax 732-885-2950, E-mail hong.zhao@enzon.com.

10.1021/bc700333s CCC: $40.75 © 2008 American Chemical Society
Published on Web 03/28/2008

Scheme 1

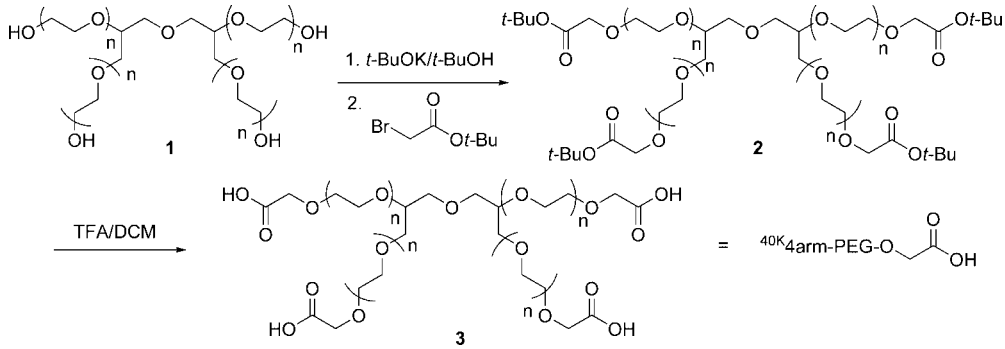

cer drug cytarabine (*14*). However, this approach involved multiple steps of preparation of both the branching small molecule part as well as the PEG linkers. In addition, the sites for drug molecule attachment were too close to each other in some cases, which caused steric hindrance among the functional groups and resulted in incomplete conjugation of drug molecules. When the two aromatic drug molecules were close to each other, the stacking phenomenon became another issue that could impact the solubility of the drug molecules. This could be a bigger concern in the case of the delivery of very insoluble drug molecules. Previously, Gopin and co-workers developed dendritic prodrugs for delivery of camptothecin (*15*). To increase the loading of water-insoluble cytotoxic compounds, we sought here to use the multiarm PEG as the carrier. The active sites at the end of each "arm" of multiarm PEG are far away from each other and behave independently. This property will help to eliminate the steric hindrance and stacking phenomenon when the drug molecules are too close to each other. It also will help the completion of the loading and improve the solubility of the loaded drug molecules. It has been demonstrated conclusively that substantial increments to the area under the drug concentration−time curve or circulation time can be achieved by PEG conjugation to small molecule drugs if the molecular weight of the PEG exceeds 20 000 Da (*10*). In this study, we chose to use 40 kDa four-arm-PEG-OH (**1**), which has an active group at the distal end of each arm. Upon full loading, this PEG can conjugate up to four SN38 molecules. To do so, we first converted compound **1** to four-arm-PEG-acid (**3**) using a previously reported method (*16*). Hence, **1** was first reacted with *t*-butyl bromoacetate in the presence of potassium *t*-butoxide to form the ester **2**, which was deprotected by trifluoroacetic acetic acid (TFA) to give the desired PEG acid **3** (Scheme 1).

SN38 (**4**) has two hydroxyl groups, i.e., 10-OH and 20-OH. Since the 10-OH group is more active, in order to selectively acylate the 20-OH of SN38, the 10-OH has to be protected first. We sought to use different amino acids as the linking moiety between the PEG and SN38. During the study, alanine (Ala), methionine (Met), sarcosine (Sar), and glycine (Gly) had been chosen as the linkers based on our previous research (*17*). To find the best protecting strategy, three different approaches were tried.

The first approach was the combination of acid-labile *t*-butylcarbonyl (Boc) group and base-labile 1,1-dioxobenzo[b]-thiophen-2-ylmethyloxycarbonyl (Bsmoc) group. The Bsmoc group developed by Carpino et al. (*18*) can be removed by treatment with a secondary amine via Michael addition that is conducted under extremely mild conditions. We used this protecting group in the past to synthesize and isolate moisture- and base-sensitive compounds such as 2′-paclitaxel glycinate (*19*). Thus, SN38 was first reacted with di-*t*-butyl dicarbonate to selectively protect the 10-OH with a Boc group to give compound **5** (Scheme 2), followed by reaction with Bsmoc-Ala to acylate the 20-OH to give compound **6**. One equivalent of 4-piperidinopiperidine was used to remove the Bsmoc group, and the resulting free amine was converted to HCl salt through an acid wash (**7**). It was found that the intermediate with a free amine group was not very stable and slowly converted into byproduct. Therefore, we had to make the HCl salt of this intermediate to avoid the free amine. A similar phenomenon has been disclosed by Liu and co-workers (*20*). Compound **7** was then coupled with four-arm-PEG acid (**3**) using *N*-ethyl-*N*′-(3-dimethylaminopropyl)carbodiimide hydrochloride (EDC) to give Boc-protected compound **8**. One final treatment with TFA yielded the final product PEG-Ala-(20)-SN38 (**9**). Another conjugate, PEG-Met-(20)-SN38 (**13**), was prepared in a similar fashion (Scheme 3).

In the second approach, Boc-protected compound **5** was reacted with Boc-Sar to give compound **14** (Scheme 4). TFA treatment removed both Boc groups on 10-OH and sarcosine to give **15** as the intermediate. At this time, the 10-OH was protected again through reaction with *tert*-butyldimethylsilyl chloride (TBDMS-Cl) to prevent side reactions in the following steps. The resulting molecule **16** was directly conjugated with **3** to give **17**, and the TBDMS protecting group was removed by TFA to give the final product PEG-Sar-(20)-SN38 (**18**). The problem for this approach was that intermediate **16** was not very stable either and slowly lost the silyl protecting group TBDMS during storage in refrigerator.

To resolve this stability issue, the more hindered *t*-butyldiphenylsilyl group (TBDPS) was used to protect the 10-OH directly in the third approach (Scheme 5). Thus, *t*-butyldiphenylsilyl chloride (TBDPS-Cl) reacted with SN38 selectively to give compound **19** in the first step. Subsequent acylation of 20-OH with Boc-Gly gave compound **20**. The Boc group can be removed by HCl in dioxane without affecting the TBDPS group. The resulting intermediate **21** was a very stable molecule even under elevated temperatures. This property ensured the possibility that key intermediate **21** could be scaled up to large quantities with high purity and stored either at room temperature or in the refrigerator for a prolonged period of time. The next conjugation with PEG acid (**3**) was done by using propane phosphonic acid anhydride (PPAC) as the coupling agent. The TBDPS group was finally removed with tetra-*n*-butylammonium fluoride (TBAF) to give pure conjugate **23**. This last approach has been successfully optimized and scaled up to hundreds of grams per batch on a repetitive base.

EXPERIMENTAL PROCEDURES

General Procedures. All reactions were run under an atmosphere of dry nitrogen or argon. Commercial reagents were used without further purification. All PEG compounds were dried under vacuum or by azeotropic distillation from toluene before use. ^{1}H and ^{13}C NMR spectra were obtained using a Varian Mercury 300 NMR spectrometer and deuterated chloroform and methanol as the solvents unless otherwise specified.

Scheme 2

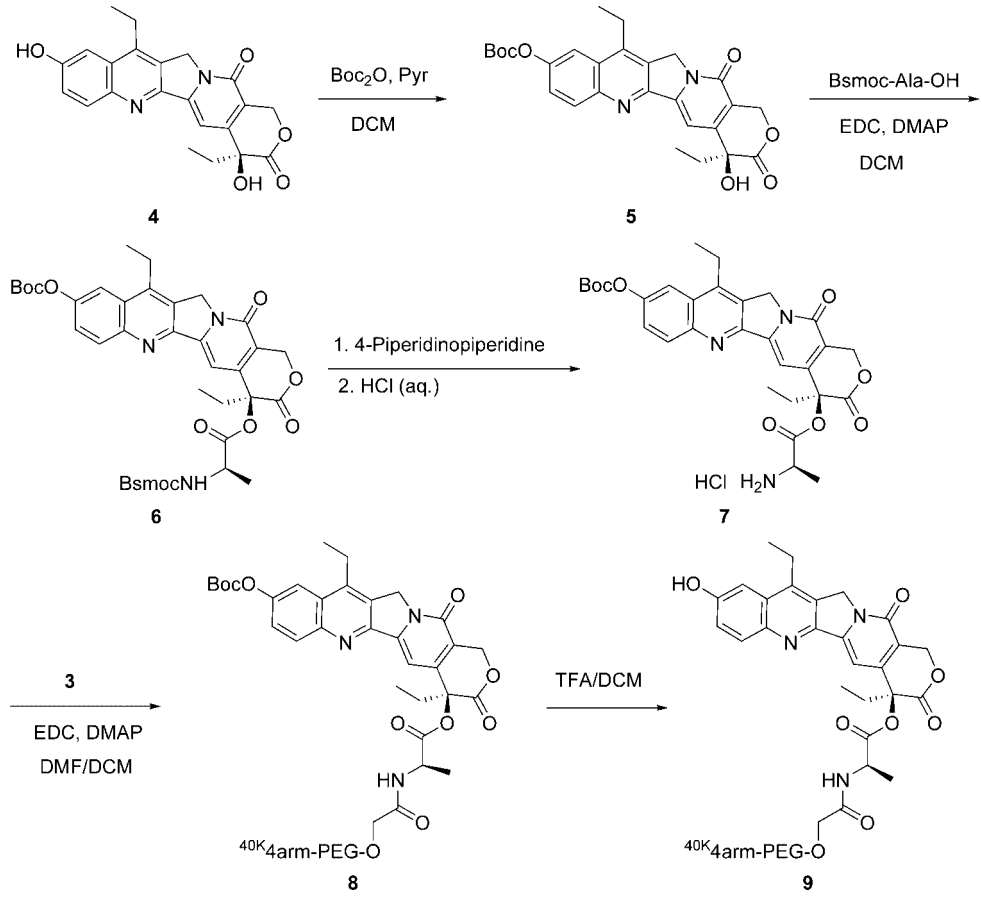

Chemical shifts (δ) are reported in ppm downfield from tetramethylsilane (TMS). Mass spectra (MS) were obtained by electrospray ionization (ESI).

HPLC Method. The reaction mixtures and the purity of intermediates and final products were monitored by a Beckman Coulter System Gold HPLC instrument. It employs a ZOBAX 300SB C8 reversed-phase column (150 × 4.6 mm) or a Phenomenex Jupiter 300A C18 reversed-phase column (150 × 4.6 mm) with a multiwavelength UV detector, using a gradient of 15–100% of acetonitrile in 0.05% TFA at a flow rate of 1 mL/min.

Compound 2. 40 kDa four-arm-PEG-OH (compound **1**, 12.5 g, 0.31 mmol) was azeotroped with 220 mL of toluene to remove 35 mL of toluene/water. The solution was cooled to 30 °C, and 1.0 M potassium *t*-butoxide in *t*-butanol (3.75 mL, 3.75 mmol) was added. The mixture was stirred at 30 °C for 30 min, and then *t*-butyl bromoacetate (0.975 g, 4.96 mmol) was added. The reaction was kept at 30 °C for 1 h and then was cooled to 25 °C. Ethyl ether (150 mL) was slowly added to precipitate the product. The crude product was filtered and washed with ethyl ether twice (2 × 125 mL). The resulting solids were dissolved in 50 mL of dichloromethane (DCM), precipitated with 350 mL of ethyl ether, filtered, and washed with ethyl ether (2 × 125 mL). The product was dried under vacuum at 40 °C to give compound **2** (12.25 g, 98% yield). ^{13}C NMR (75.4 MHz, $CDCl_3$): δ 27.71, 68.48–70.71 (PEG), 80.94, 168.97.

Compound 3. Compound **2** (12 g, 0.30 mmol) was dissolved in 120 mL of DCM, and then, 60 mL of TFA was added. The mixture was stirred at room temperature for 3 h, and then the solvent was removed under vacuum at 35 °C. The resulting oil was dissolved in 37.5 mL of DCM, and the crude product was precipitated with 375 mL of ethyl ether. After filtration, the resulting solids were dissolved in 30 mL of 0.5% $NaHCO_3$. The product was extracted with DCM (2 × 150 mL), and the combined organic layers were dried over $MgSO_4$. After filtration, the solvent was removed under vacuum at room temperature. The resulting residue was dissolved in 37.5 mL of DCM, and the product was precipitated with 300 mL of ethyl ether. The resulting solids were filtered, washed with ethyl ether (2 × 125 mL), and dried under vacuum at 40 °C to give compound **3** (10.75 g, 90% yield). ^{13}C NMR (75.4 MHz, $CDCl_3$): δ 67.93–71.6 (PEG), 170.83.

Compound 5. To a suspension of SN38 (compound **4**, 2.45 g, 6.25 mmol) in 250 mL of anhydrous DCM were added di-*tert*-butyl dicarbonate (1.764 g, 8.12 mmol) and anhydrous pyridine (15.2 mL, 185.5 mmol). The suspension was stirred overnight at room temperature. The hazy solution was filtered through celite, and the filtrate was washed with 0.5 N HCl (3 × 150 mL) and saturated $NaHCO_3$ (1 × 150 mL). The organic phase was dried over $MgSO_4$, filtered, and evaporated under vacuum at 30 °C. The resulting solids were dried under vacuum at 40 °C to give compound **5** (2.52 g, 82% yield). ^{1}H NMR (300 MHz, $CDCl_3$): δ 1.00 (3H, t, J = 7.3 Hz), 1.40 (3H, t, J = 7.7 Hz), 1.62 (9H, s), 1.81–1.97 (2H, m), 3.13 (2H, q, J = 7.7 Hz), 4.39 (1H, s, OH), 5.23 (2H, s), 5.29 (1H, d, J = 16.5 Hz), 5.73 (1H, d, J = 16.5 Hz), 7.63 (1H, dd, J = 2.6, 9.1 Hz), 7.69 (1H, s), 7.84 (1H, d, J = 2.2 Hz), 8.23 (1H, d, J = 9.1 Hz). ^{13}C NMR (75.4 MHz, $CDCl_3$): δ 7.90, 13.98, 23.17, 27.73, 31.62, 49.33, 66.18, 72.80, 84.26, 98.06, 113.88, 118.53, 124.98, 127.13, 127.19, 131.83, 145.15, 146.50, 147.00, 149.70, 150.02, 151.28, 151.60, 157.38, 173.53. HRMS (ESI) calcd for $C_{27}H_{28}N_2O_7$ $[M + H]^+$: 493.1975, found: 493.1969.

Compound 6. To a solution of compound **5** (0.85 g, 1.71 mmol) and Bsmoc-Ala-OH (0.68 g, 2.30 mmol) in 20 mL of anhydrous DCM at 0 °C were added EDC (0.51 g, 2.67 mmol) and 4-(dimethylamino)pyridine (DMAP, 65 mg, 0.53 mmol).

Scheme 3

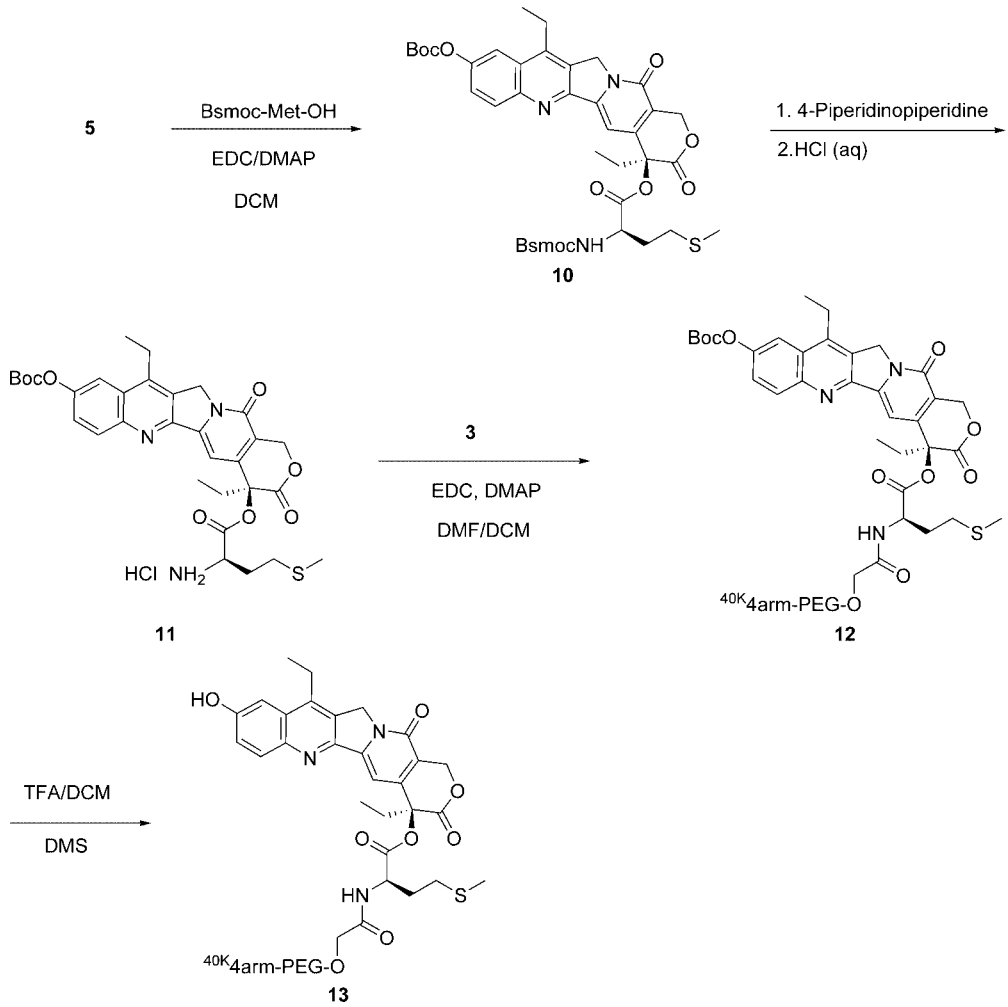

The mixture was stirred at 0 °C for 45 min and then warmed up to room temperature. When completion of the reaction was confirmed by HPLC, the reaction mixture was washed with 1% $NaHCO_3$ (2 × 50 mL), water (50 mL), and 0.1 N HCl (2 × 50 mL). The organic phase was dried over anhydrous $MgSO_4$, filtered, and evaporated under vacuum. The resulting solid was dried under vacuum at 40 °C to give compound **6** (1.28 g, 95% yield). ^{1}H NMR (300 MHz, $CDCl_3$): δ 0.90 (3H, t, J = 7.5 Hz), 1.37 (3H, t, J = 7.3 Hz), 1.56 (3H, d, J = 7.3 Hz), 1.61 (9H, s), 2.04–2.28 (2H, m), 3.13 (2H, q, J = 7.5 Hz), 4.51 (1H, quint, J = 7.2 Hz), 5.12–5.20 (2H, m), 5.23 (2H, s), 5.37 (1H, d, J = 17.0 Hz), 5.66 (1H, d, J = 17.0 Hz), 5.70 (1H, d, J = 7.0 Hz), 7.18 (1H, s), 7.21–7.78 (5H, m), 7.65 (1H, dd, J = 2.3, 9.1 Hz), 7.87 (1H, d, J = 2.3 Hz), 8.20 (1H, d, J = 9.4 Hz). ^{13}C NMR (75.4 MHz, $CDCl_3$): δ 7.53, 14.02, 17.94, 27.76, 31.7, 49.34, 49.96, 53.45, 56.66, 67.10, 76.64, 84.38, 95.90, 114.17, 120.01, 121.38, 125.14, 125.32, 127.08, 127.40, 130.33, 130.40, 130.45, 131.83, 133.60, 136.88, 139.08, 145.15, 145.35, 146.68, 147.17, 149.82, 151.33, 151.59, 154.78, 157.16, 166.83, 171.16. MS (ESI): 786.20 $[M + H]^+$. HRMS (ESI) calcd for $C_{40}H_{39}N_3O_{12}S$ $[M + H]^+$: 786.2333, found: 786.2321.

Compound 7. To a solution of compound **6** (4.2 g, 5.35 mmol) in 200 mL of anhydrous DCM was added 4-piperidinopiperidine (1.17 g, 6.96 mmol). The mixture was stirred at room temperature for 5 h and then washed with 0.1 N HCl (2 × 40 mL). The organic phase was dried over $MgSO_4$, filtered, and evaporated under vacuum to give compound **7** (2.8 g, 87% yield). ^{1}H NMR (300 MHz, CD_3OD): δ 1.08 (3H, t, J = 7.3 Hz), 1.37 (3H, t, J = 7.6 Hz), 1.58 (9H, s), 1.80 (3H, d, J = 7.0 Hz), 2.31 (2H, sept, J = 7.2 Hz), 3.18 (2H, q, J = 7.3 Hz), 4.41 (1H, q, J = 7.2 Hz), 5.25 (2H, s), 5.51 (1H, d, J = 17.0 Hz), 5.65 (1H, d, J = 17.0 Hz), 7.32 (1H, s), 7.65 (1H, dd, J = 2.3, 9.4 Hz), 7.95 (1H, d, J = 2.3 Hz), 8.14 (1H, d, J = 9.4 Hz). ^{13}C NMR (75.4 MHz, CD_3OD): δ 8.11, 14.27, 16.26, 23.90, 27.94, 32.12, 50.78, 67.86, 79.54, 85.11, 97.14, 115.80, 120.68, 126.66, 128.76, 129.26, 131.95, 146.74, 147.68, 147.82, 148.09, 151.37, 152.59, 152.90, 158.63, 168.30, 169.99. HRMS (ESI) calcd for $C_{30}H_{33}N_3O_8$ $[M + H]^+$: 564.2346, found: 564.2357.

Compound 8. To a solution of compound **7** (1.50 g, 2.5 mmol) and compound **3** (10.01 g, 0.25 mmol) in 100 mL of anhydrous DCM at 0 °C were added EDC (0.29 g, 1.5 mmol) and DMAP (0.30 g, 2.5 mmol). The mixture was stirred at 0 °C for 1 h and at room temperature overnight. The solvent was evaporated under vacuum. The residue was dissolved in 40 mL of DCM, and the crude product was precipitated with ethyl ether (300 mL). After filtration, the resulting solids were recrystallized with a mixture of dimethyl formamide/isopropyl alcohol (DMF/isopropyl alcohol [IPA], 60 mL /240 mL). Then, the solids were filtered, washed with ethyl ether (2 × 200 mL), and dried under vacuum at 40 °C to give compound **8** (8.5 g, 80% yield). ^{13}C NMR (75.4 MHz, $CDCl_3$) δ: 7.46, 13.87, 17.68, 23.04, 27.59, 31.53, 47.17, 49.13, 66.85, 69.67–70.88 (PEG), 84.11, 95.52, 113.83, 119.72, 124.85, 126.84, 127.14, 131.72, 145.05, 146.59, 146.97, 149.60, 151.09, 151.32, 156.92, 166.54, 169.29, 170.83.

Compound 9. Compound **8** (7.98 g, 0.19 mmol) was dissolved in 130 mL of 30% TFA in anhydrous DCM. The mixture was stirred for 3 h, and then the solvent was removed

Scheme 4

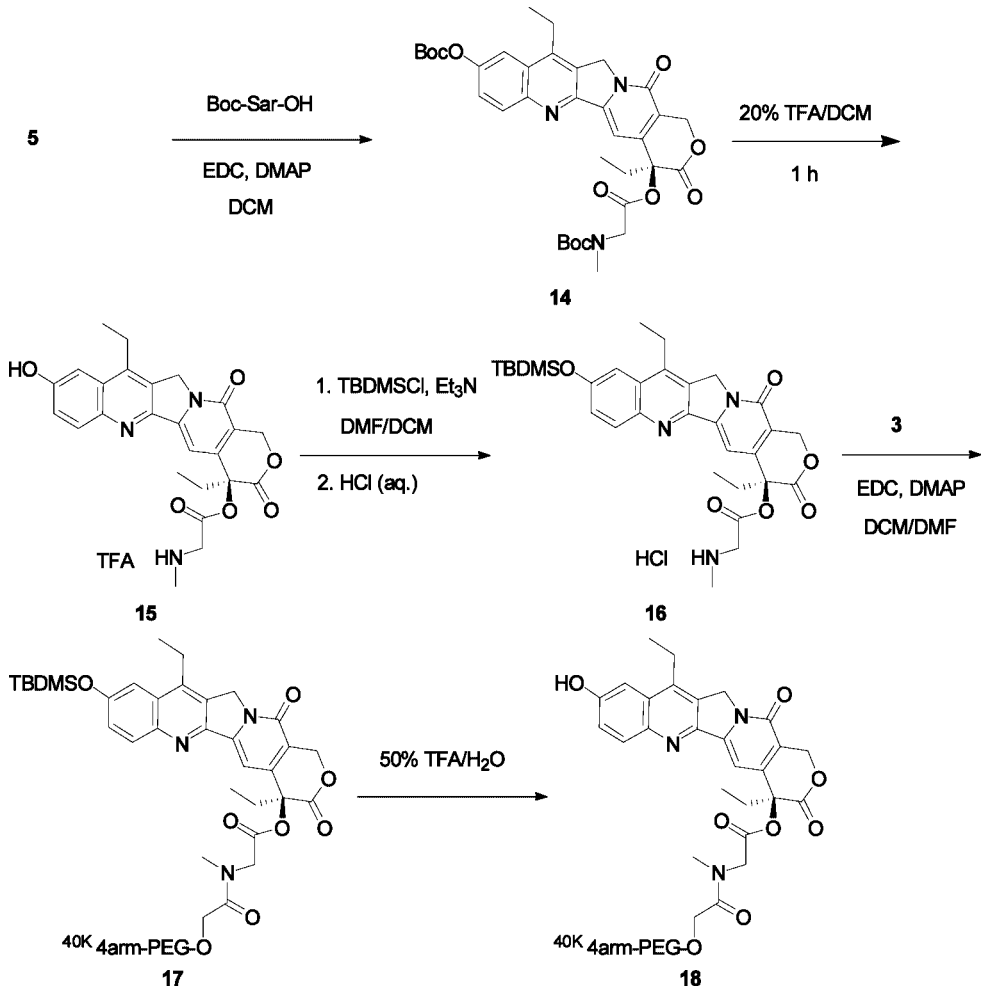

under vacuum at 35 °C. The residue was dissolved in 50 mL of DCM, and the crude product was precipitated with 350 mL of ethyl ether. After filtration, the resulting solids were recrystallized from a mixture of DMF/IPA (50 mL/200 mL). The solid was filtered, washed with ethyl ether (2 × 200 mL), and dried under vacuum to give compound **9** (6.7 g, 84% yield). ^{13}C NMR (75.4 MHz, $CDCl_3$): δ 7.46, 13.52, 17.78, 22.95, 31.53, 47.14, 49.14, 66.90, 69.57–71.15 (PEG), 78.08, 94.57, 105.10, 118.79, 122.47, 126.42, 128.26, 131.49, 143.00, 144.29, 145.03, 147.19, 148.36, 156.31, 157.00, 166.65, 169.30, 170.75.

Compound 10. To a solution of compound **5** (2.73 g, 5.53 mmol) and Bsmoc-Met-OH (3.19 g, 8.59 mmol) in 50 mL of anhydrous DCM at 0 °C were added EDC (1.64 g, 8.59 mmol) and DMAP (0.21 g, 1.72 mmol). The mixture was stirred at 0 °C for 45 min and at room temperature for 1 h. The reaction mixture was washed with 1% $NaHCO_3$ (2 × 100 mL), water (100 mL), and 0.1 N HCl (2 × 100 mL). The organic phase was dried over $MgSO_4$, filtered, and evaporated under vacuum. The resulting solids were dried under vacuum to give compound **10** (4.2 g, 88% yield). ^{1}H NMR (300 MHz, $CDCl_3$): δ 0.89 (3H, t, J = 7.3 Hz), 1.39 (3H, t, J = 7.7 Hz), 1.61 (9H, s), 2.03–2.15 (2H, m), 2.10 (3H, s), 2.19–2.31 (2H, m), 2.61 (2H, t, J = 7.0 Hz), 3.15 (2H, q, J = 7.5 Hz), 4.61 (1H, dt, J_d = 5.3 Hz, J_t = 7.9 Hz), 5.11–5.28 (4H, m), 5.39 (1 H, d, J = 17.1 Hz), 5.67 (1H, d, J = 17.1 Hz), 5.70 (1H, d, J = 7.0 Hz), 7.18 (1H, s), 7.23–7.68 (5H, m), 7.65 (1H, dd, J = 2.2, 9.2 Hz), 7.89 (1H, s), 8.21 (1H, d, J = 9.2 Hz). ^{13}C NMR (75.4 MHz, $CDCl_3$): δ 7.45, 13.92, 15.38, 23.12, 27.68, 29.65, 30.97, 31.57, 49.32, 53.54, 56.68, 66.99, 76.58, 84.28, 96.05, 114.09, 119.75, 121.17, 125.08, 125.27, 127.05, 130.15,130.29, 130.54, 131.65, 133.52, 136.69, 138.86, 145.10, 145.29, 146.55, 146.97, 149.69, 151.25, 151.39, 155.16, 157.08, 166.78, 170.33. HRMS (ESI) calcd for $C_{42}H_{43}N_3O_{12}S_2$ $[M + H]^+$: 846.2366, found: 846.2364.

Compound 11. To a solution of compound **10** (4.1 g, 4.85 mmol) in 200 mL anhydrous DCM was added 4-piperidinopiperidine (1.06 g, 6.31 mmol). The reaction mixture was stirred at room temperature for 5 h and then washed with 0.1 N HCl (2 × 40 mL). The organic phase was dried over $MgSO_4$, filtered, and evaporated under vacuum to give compound **11** (2.8 g, 88% yield). ^{1}H NMR (300 MHz, CD_3OD): δ 1.08 (3H, t, J = 7.3 Hz), 1.37 (3H, t, J = 7.6 Hz), 1.58 (9H, s), 2.19 (3H, s), 2.26–2.37 (3H, m), 2.51–2.58 (1H, m), 2.77 (2H, t, J = 7.3 Hz), 3.17 (2H, t, J = 7.5 Hz), 4.51 (1H, t, J = 6.4 Hz), 5.25 (2H, s), 5.52 (1H, d, J = 17.0 Hz), 5.66 (1H, d, J = 17.0 Hz), 7.35 (1H, s), 7.67 (1H, dd, J = 2.3, 9.1 Hz), 7.95 (1H, d, J = 2.3 Hz), 8.17 (1H, d, J = 9.1 Hz). ^{13}C NMR (75.4 MHz, CD_3OD): δ 8.15, 14.28, 15.13, 23.90, 27.94, 30.12, 30.84, 32.07, 50.83, 52.80, 67.92, 79.95, 85.14, 97.27, 115.78, 120.68, 126.66, 128.76, 129.25, 132.04, 146.58, 147.62, 147.85, 148.12, 151.36, 152.56, 152.90, 158.65, 168.24, 169.14. MS (ESI): 624.29 $[M + H]^+$. HRMS (ESI) calcd for $C_{32}H_{37}N_3O_8S$ $[M + H]^+$: 624.2380, found: 624.2381.

Compound 12. To a solution of compound **11** (1.48 g, 2.25 mmol) and compound **3** (9.0 g, 0.22 mmol) in 80 mL of anhydrous DCM at 0 °C were added EDC (0.26 g, 1.35 mmol) and DMAP (0.27 g, 2.25 mmol). The mixture was stirred at 0 °C for 1 h and at room temperature overnight. The reaction mixture was diluted with 70 mL of DCM and then extracted with 30 mL of 0.1 N HCl. The organic phase was dried over $MgSO_4$, filtered, and evaporated under vacuum. The residue was

Scheme 5

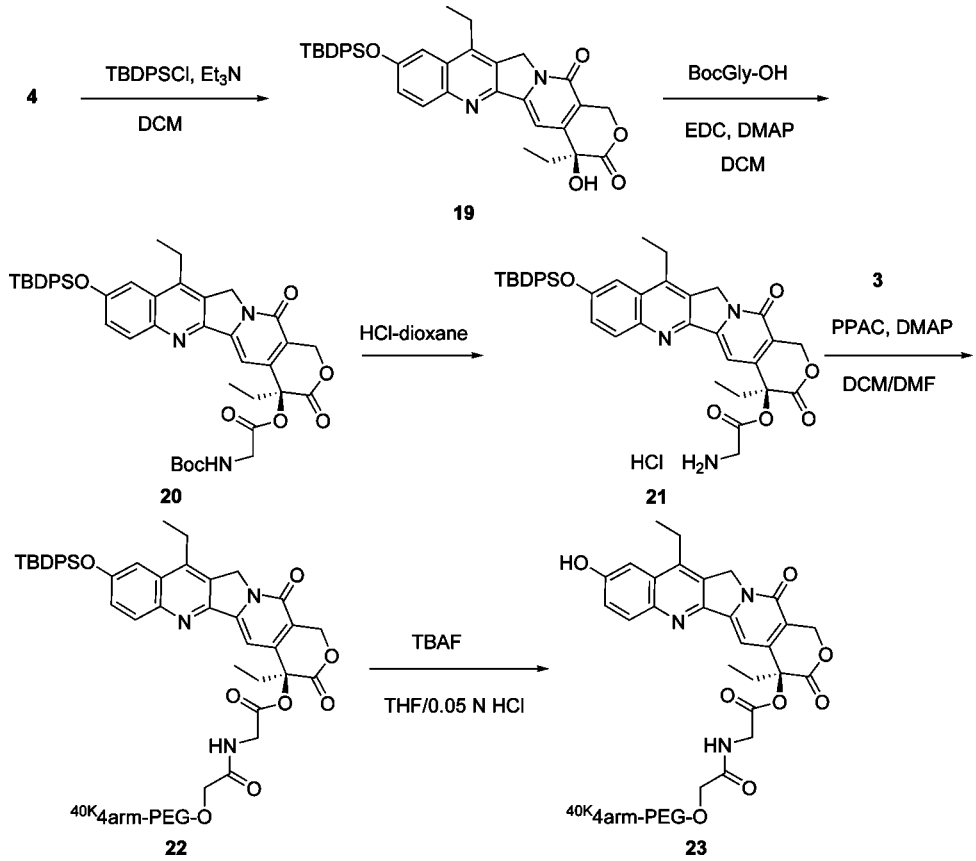

dissolved in 40 mL of DCM, and the crude product was precipitated with 300 mL of ethyl ether. After filtration, the resulting solids were recrystallized from a mixture of DMF/IPA (60 mL /240 mL). Then, the solid was filtered, washed with ethyl ether (2 × 200 mL), and dried under vacuum at 40 °C to give compound **12** (7.0 g, 74% yield). ^{13}C NMR (75.4 MHz, $CDCl_3$): δ 7.47, 13.85, 15.32, 23.06, 27.59, 29.62, 31.19, 31.53, 49.16, 50.68, 66.88, 69.93–70.97 (PEG), 78.10, 84.10, 95.53, 113.85, 119.66, 124.87, 126.81, 127.14, 131.68, 144.99, 146.62, 146.96, 149.58, 151.09, 151.24, 156.89, 166.49, 169.64, 169.82.

Compound 13. To a solution of 30% TFA in anhydrous DCM (100 mL) were added dimethyl sulfide (2.5 mL) and compound **12** (6.0 g, 0.14 mmol). The mixture was stirred for 3 h, and then the solvent was removed under vacuum at 35 °C. The residue was dissolved in 50 mL of DCM, and the crude product was precipitated with 350 mL of ether and filtered. The solids were recrystallized from a mixture of DMF/IPA (60/300 mL). Then, the solids were filtered, washed with ethyl ether (2 × 200 mL), and dried under vacuum to give compound **13** (5.1 g, 86% yield). ^{13}C NMR (75.4 MHz, $CDCl_3$): δ 7.49, 13.53, 15.35, 22.96, 29.65, 31.30, 31.56, 49.19, 50.71, 66.96, 69.58–71.02 (PEG), 78.11, 94.61, 105.12, 118.72, 122.46, 126.41, 128.27, 131.54, 142.94, 144.39, 144.96, 147.31, 148.37, 156.28, 157.01, 166.63, 169.74.

Compound 14. To a solution of Boc-Sar-OH (432 mg, 2.287 mmol) and compound **5** (750 mg, 1.52 mmol) in 75 mL of DCM at 0 °C were added EDC (837 mg, 0.686 mmol) and DMAP (432 mg, 2.287 mmol). The reaction mixture was stirred at 0 °C for 30 min and at room temperature for 1 h. The mixture was then washed with 0.5% $NaHCO_3$ (2 × 75 mL), water (2 × 75 mL), and 0.1 N HCl (75 mL). The organic layer was dried over $MgSO_4$ and filtered; the solvent was evaporated under vacuum and dried to give compound **14** (0.9 g, 89% yield). ^{1}H NMR (300 MHz, $CDCl_3$, rotamers, ratio 60:40): δ 1.05 (3H, t, J = 7.5 Hz), 1.39 (3H, t, J = 7.3 Hz), 1.43 (3.6H), 1.44 (5.4H, s), 1.62 (9H, s), 2.11–2.28 (2H, m), 2.95 (3H, s), 3.13–3.19 (2H, m), 4.05 (0.4H, d, J = 17.6 Hz), 4.13 (1.2H, s), 4.28 (0.4H, d, J = 17.6 Hz), 5.23 (0.8H, s), 5.24 (1.2H, s), 5.40 (1H, d, J = 17.2 Hz), 5.70 (1H, d, J = 17.2 Hz), 7.14 (0.6H, s), 7.32 (0.4H, s), 7.66 (1H, d, J = 9.2 Hz), 7.88 (0.4H, s), 7.89 (0.6H, s), 8.17 (0.6H, d, J = 9.2 Hz), 8.24 (0.4H, d, J = 9.2 Hz). ^{13}C NMR (75.4 MHz, $CDCl_3$): δ 7.68, 14.04, 23.25, 27.75, 28.31, 31.84, 35.42, 49.31, 50.27, 50.67, 66.99–70.97, 80.55, 84.40, 95.50, 96.47, 114.17, 119.80, 125.12, 126.98, 127.35, 131.59, 145.26, 145.58, 146.69, 147.09, 149.75, 151.33, 155.04, 157.13, 166.82, 168.81. HRMS (ESI) calcd for $C_{35}H_{41}N_3O_{10}$ $[M + H]^+$: 664.2870, found: 664.2877.

Compound 15. To a solution of compound **14** (0.9 g, 1.36 mmol) in 16 mL of DCM was added 4 mL of TFA. The reaction mixture was stirred at room temperature for 1 h, and then the solvent was evaporated under vacuum. The residue was dissolved in 10 mL of $CHCl_3$ and then precipitated by addition of ethyl ether. The product was filtered and dried to give compound **15** (0.7 g, 78% yield). ^{1}H NMR (300 MHz, CD_3OD): δ 1.08 (3H, t, J = 7.3 Hz), 1.34 (3H, t, J = 7.6 Hz), 2.16–2.34 (2H, m), 2.77 (3H, s), 3.08 (2H, q, J = 7.6 Hz), 4.31 (1H, d, J = 17.3 Hz), 4.40 (1H, d, J = 17.3 Hz), 5.20 (2H, s), 5.48 (1H, d, J = 16.7 Hz), 5.63 (1H, d, J = 17.0 Hz), 7.30 (1H, s), 7.37–7.42 (2H, m), 7.95 (1H, d, J = 9.1 Hz). ^{13}C NMR (75.4 MHz, CD_3OD): δ 8.07, 13.86, 23.81, 31.81, 33.55, 49.46, 50.79, 67.69, 79.86, 96.72, 105.93, 119.42, 124.01, 128.80, 130.02, 131.85, 145.00, 147.23, 148.59, 149.40, 158.61, 158.79, 167.04, 168.36. HRMS (ESI) calcd for $C_{25}H_{25}N_3O_6$ $[M + H]^+$: 464.1822, found: 464.1832.

Compound 16. To a solution of compound **15** (2.17 g, 3.75 mmol) in DMF/DCM (30 /200 mL) were added triethylamine (Et_3N, 2.4 mL, 17.40 mmol) and *t*-butyldimethylchlorosilane

(TBDMSCl, 2.04 g, 13.53 mmol). The reaction mixture was stirred at room temperature for 1 h. The organic layer was washed with 0.5% $NaHCO_3$, water, and 0.1 N HCl saturated with brine, and then dried over $MgSO_4$. After filtration and evaporation of the solvent under vacuum, the resulting oil was dissolved in DCM and precipitated by the addition of ethyl ether. The resulting solids were filtered to give compound **15** (2.00 g, 87% yield). ^{1}H NMR (300 MHz, CD_3OD): δ 0.23 (6H, s), 0.96 (9H, s), 0.98 (3H, t, J = 7.3 Hz), 1.30 (3H, t, J = 7.6 Hz), 2.13–2.18 (2H, m), 2.67 (3H, s), 3.11 (2H, q, J = 7.6 Hz), 4.10 (1H, d, J = 17.6 Hz), 4.22 (1H, d, J = 17.6 Hz), 5.23 (2H, s), 5.40 (1H, d, J = 16.7 Hz), 5.55 (1H, d, J = 16.7 Hz), 7.32 (1H, s), 7.38–7.43 (2H, m), 8.00 (1H, d, J = 9.1 Hz). ^{13}C NMR (75.4 MHz, CD_3OD): δ –4.14, 8.01, 14.10, 19.30, 23.98, 26.16, 31.78, 33.52, 49.46, 50.95, 67.66, 79.80, 97.41, 111.96, 119.99, 127.75, 129.28, 129.67, 131.57, 145.24, 146.86, 147.16, 148.02, 150.34, 156.69, 158.72, 167.02, 168.27. MS (ESI): 578.35 $[M + H]^+$. HRMS (ESI) calcd for $C_{31}H_{39}N_3O_6Si$ $[M + H]^+$: 578.2686, found: 578.2694.

Compound 17. To a solution of compound **3** (10 g, 0.25 mmol) in 150 mL of anhydrous DCM was added a solution of compound **16** (1.53 g, 2.5 mmol) in 20 mL of anhydrous DMF. The mixture was cooled to 0 °C. To this solution were added EDC (767 mg, 4 mmol) and DMAP (367 mg, 3 mmol). The reaction mixture was allowed to warm to room temperature slowly and stirred at room temperature overnight. The reaction mixture was then evaporated under vacuum, and the residue was dissolved in a minimum amount of DCM. After addition of ethyl ether, solid was formed and filtered under vacuum. The residue was dissolved in 30 mL of anhydrous acetonitrile (CH_3CN) and precipitated by addition of 600 mL IPA. The solids were filtered and washed with IPA and ethyl ether to give compound **17** (9.5 g, 89% yield). ^{13}C NMR (75.4 MHz, $CDCl_3$): δ –4.49, 7.29, 13.44, 18.02, 22.78, 25.38, 31.36, 34.90, 48.93, 66.68, 69.98–71.15 (PEG), 94.94, 109.97, 118.64, 125.45, 126.32, 127.66, 131.55, 143.08, 144.82, 146.83, 149.08, 154.53, 156.71, 166.72, 167.70, 169.24.

Compound 18. Compound **17** (7.8 g, 0.18 mmol) was dissolved in a 50% mixture of TFA in H_2O (200 mL). The reaction mixture was stirred at room temperature for 10 h. The mixture was then diluted with 100 mL of H_2O and extracted with DCM (2 × 300 mL). The combined organic phases were washed with H_2O (2 × 100 mL), dried over $MgSO_4$, filtered, and evaporated under vacuum. The residue was recrystallized with a mixture of DMF/IPA (100/400 mL). Then, the solids were filtered, washed with ethyl ether, and dried under vacuum at 40 °C to give compound **18** (6.8 g, 89% yield). ^{13}C NMR (75.4 MHz, $CDCl_3$): δ 7.51, 13.49, 22.89, 31.55, 35.18, 48.80, 49.11, 66.90, 69.57–71.13 (PEG), 78.08, 94.88, 105.00, 118.45, 122.45, 126.36, 128.14, 131.47, 142.79, 144.25, 145.09, 147.25, 148.37, 156.34, 156.96, 167.00, 167.86, 169.63.

Compound 19. To a suspension of compound **4** (2.0 g, 5.10 mmol) in 100 mL of anhydrous DCM were added Et_3N (3.2 mL, 22.93 mmol, 4.5 equiv) and *t*-butyldiphenylchlorosilane (TBDPSCl, 5.2 mL, 20.39 mmol). The reaction mixture was heated to reflux overnight and then was washed with 0.2 N HCl (2 × 50 mL), saturated $NaHCO_3$ (100 mL), and saturated NaCl (100 mL). The organic layer was dried over $MgSO_4$, filtered, and evaporated under vacuum. The residue was dissolved in DCM and precipitated by addition of hexane. The solids were filtered and dried under vacuum to give compound **19** (2.09 g, 65% yield). ^{1}H NMR (300 MHz, $CDCl_3$): δ 0.90 (3H, t, J = 7.6 Hz), 1.01 (3H, t, J = 7.3 Hz), 1.17 (9H, s), 1.83–1.92 (2H, m), 2.64 (2H, q, J = 6.9 Hz), 3.89 (1H, s), 5.11 (2H, s), 5.27 (1H, d, J = 16.1 Hz), 5.72 (1H, d, J = 16.4 Hz), 7.07 (2H, d, J = 2.63 Hz), 7.36–7.49 (7H, m), 7.58 (1H, s), 7.75–7.79 (4H, m), 8.05 (1H, d, J = 9.4 Hz). ^{13}C NMR (75.4 MHz, $CDCl_3$): δ 7.82, 13.28, 19.52, 22.86, 26.48, 31.52, 49.23, 66.25, 72.69, 97.25, 110.09, 117.57, 125.67, 126.57, 127.65, 127.81, 130.02, 131.69, 131.97, 135.26, 143.51, 145.05, 147.12, 149.55, 149.92, 154.73, 157.43, 173.72. HRMS (ESI) calcd for $C_{38}H_{38}N_2O_5Si$ $[M + H]^+$: 631.2628, found: 631.2622.

Compound 20. To a solution of compound **19** (3.78 g, 5.99 mmol) and Boc-Gly-OH (1.57 g, 8.99 mmol) in 100 mL of anhydrous DCM at 0 °C were added EDC (1.72 g, 8.99 mmol) and DMAP (329 mg, 2.69 mmol). The reaction mixture was stirred at 0 °C until HPLC showed complete disappearance of the starting material (approximately 2 h). The organic layer was washed with 0.5% $NaHCO_3$ (2 × 50 mL), water (1 × 50 mL), 0.1 N HCl (2 × 50 mL), and saturated NaCl (1 × 50 mL), and then dried over $MgSO_4$. After filtration, the solvent was evaporated under vacuum to give compound **20** (4.94 g, 100% yield). The solids were used in the next reaction without further purification. ^{1}H NMR (300 MHz, $CDCl_3$): δ 0.89 (3H, t, J = 7.6 Hz), 0.96 (3H, t, J = 7.5 Hz), 1.18 (9H, s), 1.40 (9H, s), 2.07–2.29 (3H, m), 2.64 (2H, q, J = 7.5 Hz), 4.01–4.22 (2H, m), 5.00 (1H, br s), 5.01 (2H, s), 5.37 (1H, d, J = 17.0 Hz), 5.66 (1H, d, J = 17.0 Hz), 7.08 (1H, d, J = 2.34 Hz), 7.16 (1H, s), 7.37–7.50 (7H, m), 7.77 (4H, d, J = 7.6 Hz), 8.05 (1H, d, J = 9.4 Hz). ^{13}C NMR (75.4 MHz, $CDCl_3$): δ 7.52, 13.30, 19.50, 22.86, 26.45, 28.21, 31.64, 42.28, 49.14, 67.00, 76.65, 79.96, 95.31, 110.13, 118.98, 125.75, 126.45, 127.68, 127.81, 130.03, 131.54, 131.92, 135.25, 143.65, 144.91, 145.19, 147.08, 149.27, 154.75, 155.14, 157.10, 166.98, 169.17. HRMS (ESI) calcd for $C_{45}H_{49}N_3O_8Si$ $[M + H]^+$: 788.3367, found: 788.3345.

Compound 21. To a solution of compound **20** (1 g, 1.27 mmol) in 5 mL anhydrous dioxane were added 5 mL of a 4 M solution of HCl in dioxane. The reaction mixture was stirred at room temperature until HPLC showed complete disappearance of the starting material (approximately 1 h). The reaction mixture was added to 50 mL of ethyl ether, and the resulting solid was filtered. After the solids were dissolved in 50 mL DCM and washed with brine, the pH was adjusted to 2.5 by addition of saturated $NaHCO_3$. The organic layer was dried over $MgSO_4$, filtered, and evaporated under vacuum. The residues were dissolved in 5 mL of DCM and precipitated by addition of 50 mL ethyl ether. Filtration afforded compound **21** (0.770 g, 84% yield). ^{1}H NMR (300 MHz, $CDCl_3$): δ 0.84 (3H, t, J = 7.6 Hz), 1.05 (3H, t, J = 7.3 Hz), 1.16 (9H, s), 2.15–2.30 (3H, m), 2.59 (2H, q, J = 7.6 Hz), 4.16 (1H, d, J = 17.9 Hz), 4.26 (1H, d, J = 17.9 Hz), 5.13 (2H, s), 5.46 (1H, d, J = 17.0 Hz), 5.60 (1H, d, J = 17.0 Hz), 7.11 (1H, d, J = 2.34 Hz), 7.30 (1H, s), 7.40–7.51 (6H, m), 7.56 (1H, dd, J = 2.34, 9.4 Hz), 7.77 (4H, dd, J = 7.6, 1.6 Hz), 7.98 (1H, d, J = 9.1 Hz). ^{13}C NMR (75.4 MHz, $CDCl_3$): δ 8.09, 13.72, 20.26, 23.61, 26.94, 31.83, 41.01, 50.71, 67.62, 79.51, 97.03, 111.65, 119.69, 127.13, 128.97, 128.99, 129.11, 131.43, 131.96, 133.00, 133.03,136.51, 145.62, 145.81, 147.24, 148.29, 150.58, 156.27, 158.68, 167.81, 168.34. MS (ESI): 688.40 $[M + H]^+$. HRMS (ESI) calcd for $C_{40}H_{41}N_3O_6Si$ $[M + H]^+$: 688.2843, found: 688.2844.

Compound 22. To a solution of compound **3** (1.4 g, 0.036 mmol) in 14 mL of anhydrous DCM were added compound **21** (0.207 g, 0.29 mmol), DMAP (0.175 g, 1.44 mmol), and PPAC (0.85 mL of a 50% solution in ethyl acetate, 1.44 mmol). The reaction mixture was stirred at room temperature overnight and then evaporated under vacuum. The resulting residue was dissolved in DCM, and the product was precipitated with ethyl ether and filtered. The residue was recrystallized with DMF/IPA to give compound **22** (1.25 g, 81% yield). ^{13}C NMR (75.4 MHz, $CDCl_3$): δ 7.45, 13.20, 19.39, 22.73, 26.42, 31.67, 40.21, 49.01, 66.83, 69.80–71.12 (PEG), 78.08, 95.16, 110.02, 118.83, 125.58, 126.40, 127.53, 127.73, 129.96, 131.49, 131.76, 131.82, 135.12, 143.51, 144.78, 145.13, 146.95, 149.21, 154.61, 156.92, 166.70, 168.46, 170.30.

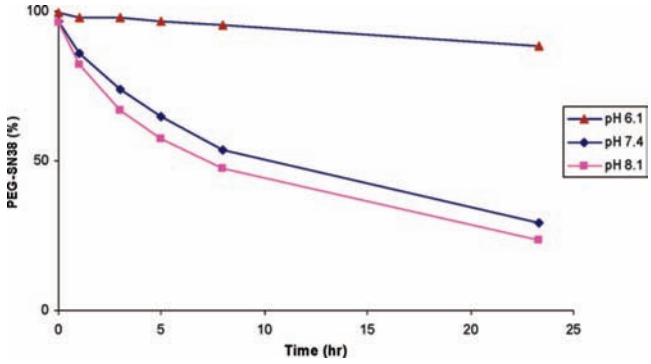

Figure 1. Stability of compound **23** in different pH conditions. Stability profile was determined using HPLC methods, by plotting the percentage of remaining compound **23** over a time course. The percentage was calculated on the basis of the ratio of the peak area of the analyte at 0, 1, 3, 5, 8, and 23 h vs the initial area peak. Each stability profile represents the average of two independent runs with the same sampling schedules. The standard deviation of each point is typically 2% or less.

Compound 23. Compound **22** (1.25 g, 0.029 mmol) was dissolved in a solution of TBAF (0.122 g, 0.46 mmol) in a 1:1 mixture of THF and 0.05 M HCl (12.5 mL). The reaction mixture was stirred at room temperature for 4 h and then extracted with DCM (2 × 30 mL). The combined organic phases were dried over $MgSO_4$, filtered, and evaporated under vacuum. The residue was dissolved in 7 mL of DMF and precipitated with 37 mL IPA. The solids were filtered and washed with IPA. Finally, the residue was dissolved in 2.5 mL of DCM and precipitated by the addition of 25 mL of ethyl ether. The solids were filtered and dried at 40 °C in vacuum oven overnight to give compound **23** (0.860 g, 71% yield). ^{13}C NMR (75.4 MHz, $CDCl_3$): δ 7.48, 13.52, 22.91, 31.67, 40.22, 49.12, 66.95, 69.70–70.87 (PEG), 78.14, 94.82, 105.03, 118.68, 122.54, 126.37, 128.20, 131.36, 142.92, 144.20, 144.98, 147.25, 148.29, 156.44, 156.98, 166.82, 168.49, 170.39.

Plasma Stability Study. PEG-SN38 conjugate (0.8 mg) was incubated with plasma (Biomeda, 1849 Bayshore Blvd., STE 200, Burlingame, CA 94010, 150 μL) at 37 °C for 0, 0.5, 2, 4, 6, 20, and 24 h. The mixtures were quenched with a 1:1 mixture of CH_3CN/MeOH (800 μL), vortexed for 1 min, and then filtered through a 0.2 μm filter membrane; 30 μL of the filtrate was analyzed by HPLC, measuring disappearance of the conjugates.

pH Stability Study. PEG-SN38 conjugate (10 mg/mL) was diluted into phosphate buffered saline adjusted to pH 6.1, 7.3, and 8.1 and incubated at 37 °C. Aliquots were removed at different time points and, after addition of an equal amount of DMSO, the samples were analyzed by HPLC, measuring disappearance of the conjugate. Stability profile graph was generated by plotting the percentage of remaining starting material over a time course (Figure 1). The percentage was calculated on the basis of the ratio of the peak area of the sample at 0, 1, 3, 5, 8, and 23 h vs the initial area peak. Each stability profile represents the average of two independent runs with the same sampling schedules. The standard deviation of each point is typically 2% or less.

In Vitro Cytotoxicity. All the cell lines were obtained from American type Culture Collection, Manassas, VA, and were grown in the listed medium: COLO 205 and OVCAR 3 (RPMI 1640 with 4.5 g/L glucose, 10 mM HEPES, 1 mM sodium pyruvate, 10% FBS); HT-29 (McCoy's 5a with 1.5 mM L-glutamine, 10% FBS) and A549 (Ham's F12K with 10% FBS). All cell lines were maintained at 37 °C (humidified, 5% CO_2). The medium was changed every 3 to 4 days and the cultures trypsinized and recultured when they reached 85% confluence. Media was obtained from Invitrogen corporation, CA. The in vitro cytotoxicity of PEG-SN38, SN38, and CPT-11 was determined using a cell proliferation (MTS) tetrazolium dye reduction assay. Briefly, adherent cells (10 000–20 000/well) were plated in 96-well plates and incubated overnight at 37 °C. The next morning, the cells were treated with serial dilutions of PEG-SN38, CPT-11, or SN38 dissolved in dimethyl sulfoxide (DMSO) and further incubated for 3–4 days at 37 °C. At the end of the incubation period, MTS dye was added, and formation of a colored product, formazan, was measured at 490 nm using a Spectramax 340PC reader (Molecular Devices, CA).

Table 1. Properties of PEG Conjugates

compound	% of loading	solubility (mg/mL)	$t_{1/2}$ (min)[b] human plasma	$t_{1/2}$ (min)[b] rat plasma
SN38		0.0072		
9	2.5	121 (3.0[a])	12.5	6.3
13	2.1	142 (2.9[a])	26.8	12.4
18	2.6	NA	19.0	10.5
23	3.7	180 (6.7[a])	12.3	3.5

[a] Equivalent to native SN38. [b] Based on the release of SN38.

In Vivo Efficacy Studies. Human mammary carcinoma (MX-1) tumor fragment were obtained from DTP, DCTD tumor repository, NCI, Bethesda, MD. Subcutaneous (s.c.) tumor xenograft models were established in the right axillary flank region of female nude mice (4–5 weeks) by injecting either human cancer cells or tumor fragments. MX-1 tumors were established by implanting a 4- to 5-mm^3 tissue fragment of MX-1 tumor collected from donor mice into the axillary flank of recipient nude mice.

RESULTS AND DISCUSSION

The objective of this study was to solubilize the insoluble anticancer molecule SN38, alter its pharmacokinetic profile, protect it in its active lactone form during transportation, and enhance its antitumor activity compared with CPT-11. To do so, we chose to use the four-arm-PEG to increase the loading of SN38 and developed highly efficient methods to make such PEG-SN38 conjugates. Three different protecting strategies had been tried, and four PEG-SN38 conjugates with different amino acid spacers were obtained successfully. The TBDPS-Boc protecting strategy (Scheme 5) had the advantage that every intermediate was stable; hence, they could be isolated, analyzed, and scaled up. The optimized method and process can be easily scaled up to multiple hundreds of grams with high quality and yield. Since the active ends of each PEG "arm" were far away from each other, they reacted independently with SN38 small molecule derivatives without steric hindrance compared with our previous branching approach. In addition, high water solubility of the PEG-SN38 conjugates was obtained by avoiding the stacking effect between lipophilic SN38 molecules. In the current approach, the loading by weight of SN38 could be as high as 3.7% compared with about 1.7% for PEG-CPT when linear bifunctional PEG was used.

As predicted, PEGylation has substantially increased the solubility of SN38, which is an insoluble molecule by itself (Table 1). The solubility of SN38 lactone in aqueous buffers published by Zhang et al. (*9*) is approximately 18 μM or 0.0072 mg/mL. All the PEG-SN38 conjugates have 120 to 180 mg/mL solubility in water, which is equivalent to as high as 6.7 mg/mL of SN38. This highly increased solubility makes it possible to systemically evaluate the therapeutic efficacy of SN38 in vivo.

The PEG conjugates were stable under neutral conditions in solution. Stability studies have demonstrated that PEG compounds release a minimum amount of free SN38 over 24 h at room temperature in clinically relevant solutions (Table 2). Since the linkage between the amino acid spacer and SN38 is an ester

Table 2. Stability at Room Temperature

compound	solution	time of detection (h)	released SN38 (%)
PEG-Ala-SN38 (**9**)	saline (0.9% NaCl)	0	0.1
		23	0.3
	water for injection	0	0.2
		24	1.6
PEG-Gly SN38 (**23**)	saline (0.9% NaCl)	0	0.09
		24	0.29
	water for injection	0	0
		24	0.29

Table 3. pH Stability Studies for Compound 23 at 37 °C

pH	6.1	7.4	8.1
$t_{½}$ (h)	256.7	14.3	12.2

Table 4. In Vitro Cytotoxicity of PEG Conjugates (IC_{50}, μM)

compound	COLO 205 (colorectal)	HT29 (colorectal)	OVCAR-3 (ovarian)	A549 (lung)
SN38 (**4**)	0.2 ± 0.2	0.1 ± 0.04	0.1 ± 0.02	1.0 ± 0.1
CPT-11	11 ± 1.4	27 ± 8.6	20 ± 7.1	67 ± 17
9	0.13 ± 0.022	0.21 ± 0.068	0.22 ± 0.01	3.9 ± 0.97
13	0.10 ± 0.024	0.21 ± 0.049	0.21 ± 0.047	2.1 ± 0.28
18	0.18 ± 0.013	0.34 ± 0.081	0.27 ± 0.11	5.1 ± 0.95
23	0.14 ± 0.032	0.52 ± 0.066	0.16 ± 0.032	3.1 ± 0.43

bond, it will hydrolyze and release the intact SN38 under basic conditions. As predicted, when treated with buffers, the releasing rate of SN38 increased as the pH was increased above 6.0 in phosphate buffer at 37 °C (Figure 1, Table 3). In the preclinical studies, the release of SN38 could be due to several mechanisms as previously proposed (*17*). The pH-dependent study clearly showed that SN38 could be release at pH 7.4 and 37 °C with a half-life of about 14 h (Table 3). However, the half-life for the same compound in rat plasma was around 12 min (Table 1), which indicates that enzymes play a role in the release. These enzymes could be either esterases or aminopeptidases (*17*, *21*). Enzymes that catalyze the hydrolysis of tertiary esters, although rare, have been previously reported in the literature (*21*).

All the PEG-SN38 conjugates were first tested for their in vitro anticancer activities in different cancer cell lines using a cell proliferation [MTS] tetrazolium dye reduction assay. Briefly, adherent cells (10 000–20 000 /well) were plated in 96-well plates and incubated overnight at 37 °C. The next morning, the cells were treated with serial dilutions of PEG-SN38, CPT-11, or SN38 dissolved in dimethyl sulfoxide (DMSO) and further incubated for 3–4 days at 37 °C. At the end of the incubation period, MTS dye was added and formation of a colored product, formazan, was measured at 490 nm using a Spectramax 340PC reader (Molecular Devices, CA.). All conjugates were found to be very potent against a panel of cell lines (Table 4). Sensitivity of cells to PEG-SN38 is in the order COLO 205 > HT29 = OVCAR-3 > A549. PEG-SN38 conjugates were equipotent to native SN38 and about 6.5- to 666-fold more potent than CPT-11.

One unique property of camptothecin and its analogues is that the E-ring has to be in the closed lactone form in order to have any anticancer activities (*3, 5, 6*). Our previous studies (*12, 13*) had proven that acylation through the 20-OH of camptothecin and its analogues will lock the E-ring in the active lactone form. Since PEG is attached to SN38 through the acylation at 20-OH position, all the PEG-SN38 conjugates will ensure the SN38 existing in its active form during circulation without any loss of activity. In comparison, the water-solubilizing bispiperidine group is attached to the 10-OH group of SN38 in CPT-11. As a result, about 75% of CPT-11 has the potential to lose its anticancer activity due to the lactone opening even before SN38 is released. The demonstrated potent in vitro anticancer activity of all PEG-SN38 conjugates further suggests that intact SN38 in its active closed lactone form was regenerated during the incubation with tumor cells.

Table 5. Maximum Tolerated Dose Results

conjugate	dose level (mg/kg)	survival/ total	comments[a]
9	5	4/4	
	10	4/4	
	20	4/4	
	40	0/4	1 found dead, 3 sacrificed due to body weight loss
23	5	4/4	
	10	4/4	
	20	4/4	
	40	3/4	1 sacrificed due to body weight loss

[a] Total of 4 mice per study group.

In order to conduct in vivo efficacy studies, the maximum tolerable doses (MTD) were first obtained in mice. Female naive athymic nude mice were injected intravenously with a single dose of PEG-SN38 ranging from 5 to 40 mg/kg. Mice were monitored daily for visible signs of toxicity and weighed biweekly. The MTD was defined as the highest dose at which no death occurred, and body weight loss was less than 20% of pretreatment animal weight (approximately 20 g). Two PEG conjugates were selected for this study. It was found that the MTD of PEG-Ala-SN38 (**9**) or PEG-Gly-SN38 (**23**) was between 20 and 40 mg/kg when injected intravenously as a single dose in nude mice (Table 5).

For in vivo efficacy studies, MX-1 tumors were established by implanting a 4–5 mm^3 tissue fragment of MX-1 tumor collected from donor mice into the right axillary flank of recipient nude mice. When tumors reached an average volume of 100 mm^3, mice were injected with either PEG-SN38 conjugates or CPT-11 as a single dose of 20 mg/kg or multiple 5 mg/kg doses (every 2 days [q2d] × 6). Mouse weight and tumor sizes were measured at the beginning of the study and twice weekly throughout the study. Mice were euthanized when individual tumor volumes reached 1670 mm^3, and all surviving mice were euthanized at 12 weeks. Treatment with either of the four conjugates as a single dose of 20 mg/kg or multiple doses of 5 mg/kg (q2d × 6) PEG-SN38 led to >99% tumor growth inhibition (TGI) and complete cures (no evidence of tumor upon visual external examination and palpation of injection site) of the animals up to 12 weeks after which the animals were humanely sacrificed (Figure 2, Tables 6 and 7). There was only one unexplained death, which occurred in the PEG-Ala-SN38 20-mg/kg group early within the study. At equivalent dose levels, treatment with CPT-11 caused a 26% and 44% TGI when given as a single dose or multiple injections, respectively.

There was no body weight loss in all the cured mice. The mice were followed up to 100 days, and no tumor was detected after animals were sacrificed. Therefore, all PEG-SN38 conjugates demonstrated excellent anticancer activities and warrant further preclinical development. They all were superior to CPT-11 since treatment with CPT-11 resulted in either no TGI (single dose) or partial TGI sustained for a short period of time (multiple-dose regimen). The much enhanced antitumor efficacy of the high molecular weight PEG-SN38 conjugates could be partially attributed to the improved biodistribution and passive tumor targeting effect due to the enhanced permeation and retention (EPR) effect (*22*). In conclusion, treatment with PEG-SN38 conjugates was significantly more effective than treatment with CPT-11 in the MX-1 preclinical xenograft model. Due to the excellent anticancer efficacy as well as straightforward chemistry with little or no inherent impurities generated during the transformations, compound **23** was selected as the lead

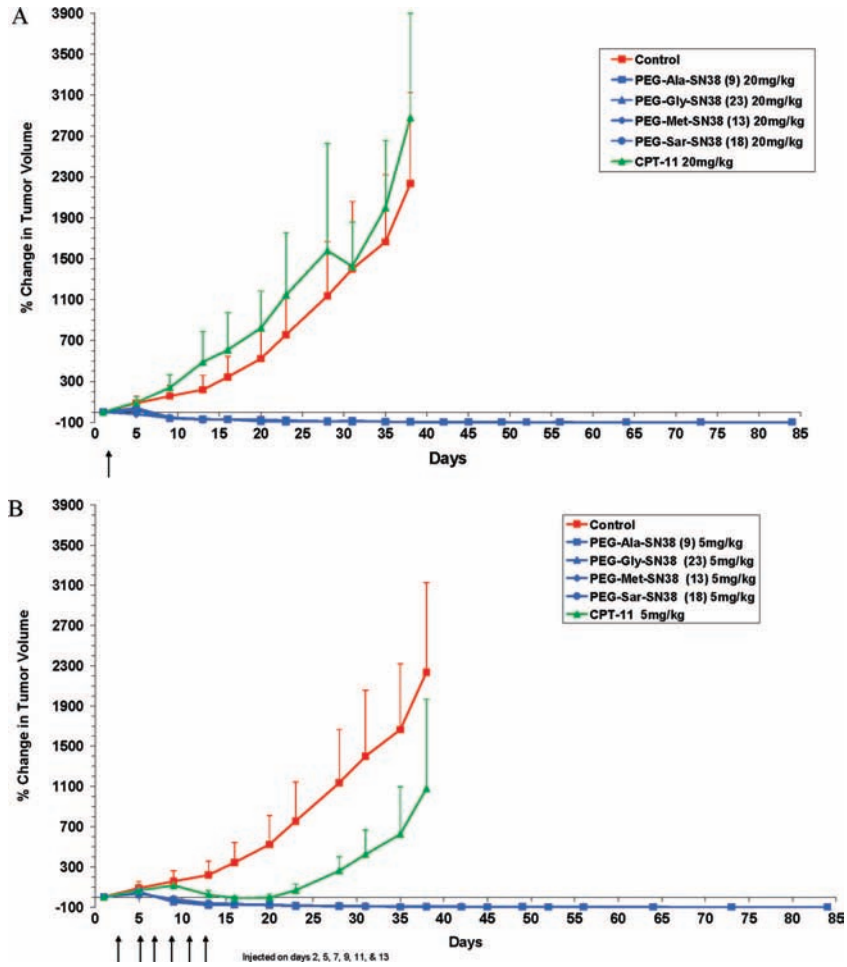

Figure 2. Therapeutic efficacy of PEG-SN38 conjugates in a xenograft model of breast cancer (MX-1). Female athymic nude mice (6 mice per group), were inoculated subcutaneously with 4- to 5-mm^3 tumor fragments of MX-1 breast tumors. When tumors reached an average volume of 100 mm^3, mice were injected with either PEG-SN38 conjugates or CPT-11 as a single dose of 20 mg/kg (panel A) or multiple 5-mg/kg doses (q2d × 6) (panel B). Data represent % change in tumor volume ± standard deviation.

Table 6. MX-1 (Breast) Xenograft Model (20 mg/kg single dose): Efficacy Comparison

compound	mean TV ± SD (mm^3)[a]	% change in TV ± SD[a]	TGI (%)[a]	Cures (%)[b]	T/C at 1000 mm^3 (%)
control	1136 ± 686	1399 ± 658	0	0	—
9	13 ± 9	−87 ± 11	99	83	1
13	8 ± 12	−95 ± 8	99	100	0
18	7 ± 10	−94 ± 10	99	100	0
23	7 ± 9	−94 ± 10	99	100	0
CPT-11	845 ± 50	1424 ± 432	26	0	122

[a] Mean tumor volume (TV), % change in TV, and % TGI data were taken at day 31. (By day 31, a significant percentage of control animals were euthanized due to excess tumor burden.) [b] % cures were taken at the termination of the study (12 weeks).

Table 7. MX-1 (breast) Xenograft Model (5 mg/kg q2d × 6): Efficacy Comparison

compound	mean TV ± SD (mm^3)[a]	% change in TV ± SD[a]	TGI (%)[a]	cures (%)[b]	T/C (%)
control	1136 ± 686	1399 ± 658	0	0	—
9	7 ± 10	−95 ± 8	99	100	0
13	4 ± 4	−96 ± 7	99	100	0
18	9 ± 10	−90 ± 13	99	100	0
23	12 ± 18	−91 ± 10	99	100	0
CPT-11	632 ± 698	423 ± 243	44	0	52

[a] Mean tumor TV, % change in TV, and % TGI data were taken at day 31. (By day 31, a significant percentage of control animals were euthanized due to excess tumor burden.) [b] % cures were taken at the termination of the study (12 weeks).

candidate for further preclinical development and has entered into phase I clinical trials.

CONCLUSION

PEGylation is well-known for its ability to improve pharmaceutical properties of small molecules and to enhance the efficacy due to the EPR effect. Using multiarm PEG linkers, we successfully developed several novel PEG-SN38 conjugates that have high drug loading and high water solubility. The chemistry for the conjugation of SN38 ensures that the anticancer molecule is locked into its active closed lactone form in the body until intact SN38 is released from the PEG conjugate. Of the three different protecting strategies used to make such PEG-SN38 conjugates, one process has been optimized and scaled up with high reproducibility and yields. The improved pharmacokinetic profile of SN38, especially the possible passive accumulation of PEG-SN38 conjugates at the solid tumor sites, resulted in much enhanced anticancer activity of SN38 in the MX-1 xenograft mice model compared with CPT-11. Compound **23** was selected as the lead candidate for further preclinical development. In vitro and in vivo activities of the lead compound have been reported in another communication (*23*).

ACKNOWLEDGMENT

We wish to thank Ms. Mary Mehlig and Ms. Jennifer Malaby for their in vitro and in vivo work, Mr. Syed Ali and Mr. Nish Sanghvi for their contribution in the scale up of PEG conjugate, Mr. Honghue Hsu, Ms. Michelle Boro, and Ms. Chia Chang for their analysis of PEG compounds, and Dr. Zhihua (John) Zhang for his helpful discussion.

Supporting Information Available: HPLC of compounds **9**, **13**, **18**, and **23** and pH stability studies for compound **23**. This material is available free of charge via the Internet at http://pubs.acs.org/BC.

LITERATURE CITED

(1) Pommier, Y. (2006) Topoisomerase I inhibitors: camptothecins and beyond. *Nat. Rev. Cancer 6*, 789–802.

(2) Gottlieb, J. A., Guarino, A. M., Call, J. B., Oliverio, V. T., and Block, J. B. (1970) Preliminary pharmacologic and clinical evaluation of camptothecin sodium (NSC-100880). *Cancer Chemother. Rep. 54*, 461–470.

(3) Chabot, G. G. (1997) Clinical pharmacokinetics of irinotecan. *Clin. Pharmacokinet. 33*, 245–259.

(4) Slatter, J. G., Su, P., Sams, J. P., Schaaf, L. J., and Wienkers, L. C. (1997) Bioactivation of the anticancer agent CPT-11 to SN-38 by human hepatic microsomal carboxylesterases and the *in vitro* assessment of potential drug interactions. *Drug Metab. Dispos. 25*, 1157–1164.

(5) Senter, P. D., Beam, K. S., Mixan, B., and Wahl, A. F. (2001) Identification and activities of human carboxylesterases for the activation of CPT-11, a clinically approved anticancer drug. *Bioconjugate Chem. 12*, 1074–1080.

(6) Slatter, J. G., Schaaf, L. J., Sams, J. P., Feenstra, K. L., Johnson, M. G., Bombardt, P. A., Cathcart, K. S., Verburg, M. T., Pearson, L. K., Compton, L. D., Miller, L. L., Baker, D. S., Pesheck, C. V., and Lord, R. S., 3rd. (2000) Pharmacokinetics, metabolism, and excretion of irinotecan (CPT-11) following i.v. infusion of [^{14}C]CPT-11 in cancer patients. *Drug Metab. Dispos. 28*, 423–433.

(7) Mathijssen, R. H. J., van Alphen, R. J., Verweij, J., Loos, W. J., Nooter, K., Stoter, G., and Sparreboom, A. (2001) Clinical pharmacokinetics and metabolism of irinotecan (CPT-11). *Clin. Cancer Res. 7*, 2182–2194.

(8) Smith, N. F., Figg, W. D., and Sparreboom, A. (2006) Pharmacogenetics of irinotecan metabolism and transport: an update. *Toxicol. In Vitro 20*, 163–175.

(9) Zhang, J., A., Xuan, T., Parmar, M., Ma, L., Ugwu, S., Ali, S., and Ahmad, I. (2004) Development and characterization of a novel liposome-based formulation of SN-38. *Int. J. Pharm. 270*, 93–107.

(10) Greenwald, R. B., and Zhao, H. (2007) Poly (ethylene glycol) prodrugs: altered pharmacokinetics and pharmacodynamics. *Prodrugs: Challenges and Rewards. Part 1* (Stella, V. J., Borchardt, R. T., Hageman, M. J., Oliyai, R., Maag, H. , and Tilley, J. W. , Eds.) pp 283−338, Chapter *2.3.1*, Springer, Boston.

(11) Greenwald, R. B., Choe, Y. H., McGuire, J., and Conover, C. D. (2003) Effective drug delivery by PEGylated drug conjugates. *Adv. Drug Delivery Rev. 55*, 217–250.

(12) Greenwald, R. B., Pendri, A., Conover, C., Gilbert, C., Yang, R., and Xia, J. (1996) Drug delivery systems. 2. Camptothecin 20-O-poly(ethylene glycol) ester transport forms. *J. Med. Chem. 39*, 1938–1940.

(13) Zhao, H., Lee, C., Sai, P., Choe, Y. H., Boro, M., Pendri, A., Guan, S., and Greenwald, R. B. (2000) 20-*O*-acylcamptothecin derivatives: evidence for lactone stabilization. *J. Org. Chem. 65*, 4601–4606.

(14) Choe, Y. H., Conover, C. D., Wu, D., Royzen, M., and Greenwald, R. B. (2002) Anticancer drug delivery systems: N4-acyl-poly(ethyleneglycol) prodrugs of ara-C. I. Efficacy in solid tumors. *J. Controlled Release 79*, 41–53.

(15) Gopin, A., Ebner, S., Attali, B., and Shabat, D. (2006) Enzymatic activation of second-generation dendritic prodrugs: conjugation of self-immolative dendrimers with poly(ethylene glycol) via click chemistry. *Bioconjugate Chem. 17*, 1432–1440.

(16) Greenwald, R. B., Gilbert, C. W., Pendri, A., Conover, C. D., Xia, J., and Martinez, A. (1996) Drug delivery systems: water soluble taxol 2′-poly(ethylene glycol) ester prodrugs-Design and *in vivo* effectiveness. *J. Med. Chem. 39*, 424–431.

(17) Conover, C. D., Greenwald, R. B., Pendri, A., and Shum, K. L. (1999) Camptothecin delivery systems: the utility of amino acid spacers for the conjugation to create prodrugs. *Anti-Cancer Drug Des. 14*, 499–506.

(18) Carpino, L. A., Philbin, M., Ismail, M., Truran, G. A., Mansour, E. M. E., Iguchi, S., Ionescu, D., El-Faham, A., Riemer, C., Warras, R., and Weiss, M. S. (1997) New family of base- and nucleophile-sensitive amino-protecting groups. A Michael-acceptor-based deblocking process. Practical utilization of the 1,1-dioxobenzo[*b*]thiophene- 2-ylmethylcarbonyl (Bsmoc) group. *J. Am. Chem. Soc. 119*, 9915–9916.

(19) Greenwald, R. B., Zhao, H., and Reddy, P. (2003) Synthesis, isolation, and characterization of 2′-paclitaxel glycinate: an application of the Bsmoc protecting group. *J. Org. Chem. 68*, 4894–4896.

(20) Liu, X., Zhang, J., Song, L., Lynn, B. C., and Burke, T. G. (2004) Degradation of camptothecin-20(*S*)-glycinate ester prodrug under physiological conditions. *J. Pharm. Biomed. Anal. 35*, 1113–1125.

(21) Yeo, S. H., Nihira, T., and Yamada, Y. (1998) Screening and identification of a novel lipase from Burkholderia sp. YY62 which hydrolyzes t-butyl esters effectively. *J. Gen. Appl. Microbiol. 44*, 147–152.

(22) Maeda, H., Wu, J., Sawa, T., Matsumura, Y., and Hori, K. (2000) Tumor vascular permeability and the EPR effect in macromolecular therapeutics: a review. *J. Controlled Release 65*, 271–284.

(23) Sapra, P., Zhao, H., Mehlig, M., Malaby, J., Kraft, P., Longley, C., Greenberger, L. M., and Horak, I. D. (2008) Novel delivery of SN38 markedly inhibits tumor growth in xenografts, including a CPT-11-refractory model. *Clin. Cancer Res. 14*, 1888−1896.

BC700333S

Display of a Peptide Mimotope on a Crystalline Bacterial Cell Surface Layer (S-layer) Lattice for Diagnosis of Epstein–Barr Virus Infection

Helga Tschiggerl,[†,‡] Joanne L. Casey,[§] Kathy Parisi,[§] Michael Foley,[§] and Uwe B. Sleytr*[,†]

Center for NanoBiotechnology, University of Natural Resources and Applied Life Sciences, Gregor-Mendel-Strasse 33, A-1180 Vienna, Austria, Nano-S Biotechnologie GmbH, Gregor-Mendel-Strasse 33, A-1180 Vienna, Austria, and AdAlta Pty Ltd, Department of Biochemistry, La Trobe University, VIC 3086, Australia. Received September 12, 2007; Revised Manuscript Received November 8, 2007

Fusion proteins based on the crystalline bacterial cell surface layer (S-layer) proteins SbpA from *Bacillus sphaericus* CCM 2177 and SbsB from *Geobacillus stearothermophilus* PV72/p2 and a peptide mimotope F1 that mimics an immunodominant epitope of Epstein–Barr virus (EBV) were designed and overexpressed in *Escherichia coli*. Constructs were designed such that the peptide mimotope was presented either at the C-terminus (SbpA/F1) or at the N-terminus (SbsB/F1) of the respective S-layer proteins. The resulting S-layer fusion proteins, SbpA/F1 and SbsB/F1, fully retained the intrinsic self-assembly capability of the S-layer moiety into monomolecular lattices. As determined by immunodot assays and ELISAs using monoclonal antibodies, the F1 mimotope was well-presented on the outer surface of the S-layer lattices and accessible for antibody binding. Further comparison of the two S-layer fusion proteins showed that the S-layer fusion protein SbpA/F1 had a higher antibody binding capacity than SbsB/F1 in aqueous solution and in immune sera, illustrating the importance of epitope orientation on the performance of solid-phase immunoassays. To assess the diagnostic values of S-layer mimotope fusion protein SbpA/F1, we screened a panel of 83 individual EBV IgM-positive, EBV negative, and potential cross-reactive sera for their reactivities. This resulted in 98.2% specificity and 89.3% sensitivity, and furthermore no cross-reactivity with related viral disease states including rheumatoid factor was observed. This study shows the potential of S-layer fusion proteins as a matrix for site-directed immobilization of small ligands in solid-phase immunoassays using EBV diagnostics as a model system.

INTRODUCTION

The use of peptide epitopes as diagnostic antigens in commercial diagnostics is a promising approach toward simpler and cheaper ELISA-based diagnostic assays. Diagnostic antigens may appear as complexes of more than one protein that are often highly glycosylated; therefore, it would be highly advantageous if, instead of the whole protein, one or more peptides mimicking diagnostically important epitope(s) could be used (*1*). Optimal presentation of peptide ligands is essential for the sensitivity of detection in solid-phase immuno-assays like ELISA. Peptides have to be immobilized in such a way that their three-dimensional structure, functionality, and binding sites are retained (*2*). Conventional immobilization procedures for small ligands used in ELISAs are based on covalent binding and adsorption/absorption of peptides on a solid surface. However, the accessibility of the peptide for capture of target antibodies has been recognized as the central problem of immobilized peptide ligands. For better exposition, spacer molecules, e.g., long alkyl chains, polyamino acids, or proteins, can be introduced, but common to all these spacers is nonspecific adsorption and overflexibility that may counteract the exposition of the ligands (*3, 4*). Furthermore, since the peptides are attached on the surface in random orientation, the signal-to-noise ratio can be high due to nonspecific binding (*5*).

The S-layer self-assembly systems introduce new possibilities for site-directed peptide epitope immobilization. As a novel approach, we have designed two chimeric proteins by fusing a peptide epitope to crystalline bacterial cell surface (S-layer) proteins. The suitability of S-layer protein lattices as matrices for the covalent immobilization of peptides has already been demonstrated for immunochemical-based assays such as ELISA (*6–9*). S-layers, in general, are monomolecular proteinaceous arrays that represent the outermost cell envelope component of many prokaryotic organisms (*10–14*). They are composed of identical (glycol) protein species that are aligned into 2D crystalline arrays. Isolated S-layer subunits usually have the intrinsic capability to self-assemble in suspension, on the air–liquid interface, on lipid films, or on solid supports (*12, 13, 15, 16*). By genetic engineering, discrete functions could be introduced into S-layer proteins (*17–26*). On the basis of the high density and regular display of the introduced functions, a broad spectrum of applications of S-layer fusion proteins is envisaged, particularly in the fields of biotechnology, molecular nanotechnology, and biomimetics (*14, 16, 27*). Regarding peptide epitope immobilization, the advantages offered by the S-layer self-assembly system are (i) the requirement of only a simple, one-step incubation process for site-directed immobilization without preceding surface activation of the support, (ii) the provision of a cushion to the peptide epitope through the S-layer moiety of the fusion protein preventing denaturation, and precluding a loss of detection sensitivity upon immobilization, (iii) the principle applicability of the "S-layer tag" to any peptide epitope, and (iv) the high flexibility for variation of peptide epitope groups within a single S-layer array by cocrystallization of different peptide epitope/S-layer fusion proteins.

* Corresponding author. Center for NanoBiotechnology, University of Natural Resources and Applied Life Sciences, Gregor-Mendel-Strasse 33, A-1180 Vienna, Austria. Tel: +43-1-47654 2201, Fax: +43-1-4789112, E-mail: uwe.sleytr@boku.ac.at.

[†] University of Natural Resources and Applied Life Sciences.

[‡] Nano-S Biotechnologie GmbH.

[§] AdAlta Pty Ltd.

10.1021/bc7003523 CCC: $40.75 © 2008 American Chemical Society
Published on Web 04/01/2008

In this study, the feasibility of fusing a peptide epitope to both the C-terminus and the N-terminus of an S-layer protein was investigated. For the setup of S-layer fusion proteins, two different types of proteins were used as S-layer protein moieties. The 200 amino acid deletion mutant of the 1268 amino acid S-layer protein SbpA of *Bacillus sphaericus* CCM 2177 (MW: 109.9 kDa) was chosen to fuse via its N-terminus toward the S-layer protein. This approach was based on previous structure–function studies revealing that the C-terminal deletion of SbpA resulted in a significant increase of the spatial accessibility of the C-terminus, while fully retaining the self-assembly capability of the proteins into a square (p4) S-layer lattice with a center-to-center spacing of the tetrameric morphological units of 13.1 nm (Figure 2A, inset) (*18*). An advantage of the SbpA system for nanobiotechnological applications is the dependence of its *in vitro* recrystallization on the presence of calcium ions, thus allowing control over lattice formation by varying the calcium ion concentration (*28*). Furthermore, the peptide epitope was attached to the N-terminus of mature full-length S-layer protein SbsB of *Geobacillus stearothermophilus* PV72/p2 (MW: 95.0 kDa). SbsB is generated from a 920 amino acid long preprotein by cleavage of a 31-aa signal sequence and assembles into an oblique (p1) lattice type with the lattice parameters $a = 10.4$ nm, $b = 7.9$ nm, and base angle $\gamma = 81°$ (Figure 2B, inset) (*29*). An understanding of the protein's structure–function relationship was gained in a preliminary study from the production and analysis of truncated forms, sequence analysis, and electron microscopy. The knowledge was used to select sequence positions for functional fusion (*24, 29, 30*).

As a peptide epitope fusion partner, we selected a 20 amino acid long peptide (F1) that mimics an immunodominant epitope of Epstein–Barr virus (EBV). In our previous study, we showed that the F1 mimotope can be used for the detection of IgM antibodies typically generated after infection with EBV. F1 was selected from a random peptide library displayed on phage by binding to the parent antibody thereby mimicking the three-dimensional conformational features of the epitope (*1*). The monoclonal antibody was generated by immunizing mice with crude EBV antigen. The exact antigen that the F1 peptide mimics is not known. In this study, we constructed S-layer/F1 peptide fusion proteins to investigate the presentation and orientation of the peptide mimotope within the S-layer lattice and have characterized the structure of the lattices. Following the successful proof of concept studies, this article deals with the investigation of the suitability of the system for diagnostic purposes. Therefore, we have also screened a panel of EBV clinical samples to evaluate the performance of the S-layer/F1 fusion proteins in diagnosis of Epstein–Barr virus infection.

EXPERIMENTAL PROCEDURES

Cloning of the Chimeric SbpA/F1 and SbsB/F1 Genes. Two constructs were synthesized with F1 peptide fused at the C-terminus (SbpA/F1) and F1 fused to the N-terminus (SbsB/F1) using pairs of complementary oligonucleotides. These were annealed to generate 10 amino acid inserts containing a $(gly)_4$ linker with the appropriate overhang for the ligation into restriction sites *Bam*HI-XhoI and NcoI-*Eco*RI (Table 1). For annealing, an equimolar mixture of one pair of phosphorylated oligonucleotides was heated to 98 °C for 2 min and cooled slowly to room temperature, allowing the complementary sequences to anneal. The two double-stranded inserts, SbpA/F1 and SbsB/F1, phosphorylated at both 5′-termini and, with the appropriate overhang at each end, were integrated into a pET28a (+) vector (Novagen), which contained the truncated S-layer protein gene $SbpA_{93–3204}$ with *Bam*HI-XhoI sites and $SbsB_{96–2760}$ with NcoI-*Eco*RI sites, respectively (*18*). Digestion of DNA with restriction endonucleases, separation of DNA fragments by agarose gel electrophoresis, ligation of DNA fragments, and transformation procedures were performed as described by Sambrook (*31*). DNA fragments were recovered from agarose gels by Qiaex II gel extraction kit (QIAgen). The constructs $SbpA_{93–3204}$/F1 and $SbsB_{96–2760}$/F1 were transformed into *E. coli* DH10b cells (Invitrogen) by electroporation.

Table 1. Amino Acid Sequence of F1 Mimotope Fused to the S-Layer Proteins[a]

peptide	amino acid sequence
F1	-YTDSSMAVTLMKFASNFLF-
oligonucleotide	**base sequence (5′−3′)**
Oligo_SbsB/NcoI	*CATG*TATACGGATAGCAGTATGGCTGTTAC TCTTATGAAGTTCGCTTCTAATTTTCTCT TTGGGGGGGGGGGG
Oligo_SbsB/*Eco*RI	*AATT*CCCCCCCCCCCCCCAAAGAGAAAATT AGAAGCGAACTTCATAAGAGTAACAGCC ATACTGCTATCCGTATA
Oligo_SbpA/*Bam*HI	*GATC*CGGGGGGGGGGGGGCGTATACGGAT AGCAGTATGGCTGTTACTCTTATGAAGTT CGCTTCTAATTTTCTCTTTTAAC
Oligo_SbpA/XhoI	*TCGA*GTTAAAAGAGAAAATTAGAAGCGAA CTTCATAAGAGTAACAGCCATACTGCT ATCCGTATACGCCCCCCCCCCCCG

[a] Base sequence of oligonucleotides used to generate the F1 encoding gene.

Overexpression and Purification of SbpA/F1 and SbsB/F1 Fusion Proteins. S-layer fusion proteins were overexpressed in *E. coli* BL21(DE3)star cells (Invitrogen) in a 4-l fermenter according to the pET System Manual (Novogen) and monitored by SDS-PAGE with Coomassie staining (*32*). For isolation of SbpA/F1 and SbsB/F1 proteins, the B-PER bacterial protein extraction reagent (Pierce) was used as an efficient method of extracting proteins from bacteria following the protocol provided by the manufacturer. The S-layer fusion proteins accumulated in the insoluble fraction and were extracted with 50 mM Tris-HCl/150 mM NaCl/5 M guanidine hydrochloride (GHCl) buffer pH 7.2. The suspension was then centrifuged at 36 000*g* for 30 min at 4 °C, and the supernatant containing the S-layer fusion protein was diluted 1:2 with 50 mM Tris-HCl buffer pH 7.2. The clear solution was subjected to permeation chromatography (GPC) using a Superdex 200 column (Pharmacia) equilibrated in 2.5 M GHCl in 50 mM Tris-HCl buffer pH 7.2. Fractions belonging to the peak corresponding to the expected molecular weight were pooled and dialyzed against four changes of MilliQ water for 18 h at 4 °C. Following dialysis, the protein solution was lyophilized and stored at –20 °C.

Self-Assembly and Recrystallization Properties of the S-Layer Fusion Proteins. In order to investigate the capability of the S-layer fusion protein, SbpA/F1 and SbsB/F1, to self-assemble in solution a series of refolding steps were carried out. Purified fusion proteins (3 mg) were dissolved in 1 mL of 5 M GHCl in 0.5 mM Tris-HCl, pH 7.2, and the solution was dialyzed against 10 mM $CaCl_2$ for 18 h at 4 °C with 5 buffer changes in the first 6 h. S-layer self-assembly products were adsorbed onto EM grids coated with pioloform and carbon. Negative staining was performed with uranylacetate (2% in distilled water, pH 4.3) for 2 min. Monomeric protein solutions of SbpA/F1 and SbsB/F1 were obtained after dialysis with 3 buffer changes of the GHCl extract against distilled water for 3 h at 4 °C and centrifugation of the dialysate at 16 000*g* for 5 min at 4 °C (AvantiJ-25, Beckman Coulter). Recrystallization of SbpA/F1 and SbsB/F1 monomers on 300 mesh copper grids, coated with pioloform and carbon, was investigated by transmission electron microscopy (*33*). For recrystallization on silicon wafers with a native silicon oxide layer (p-type, 100 orientation; 7 × 7 mm; IMEC) and polystyrene slides (Bilek), wafers and slides were washed with 70% ethanol immersed with 100 μL

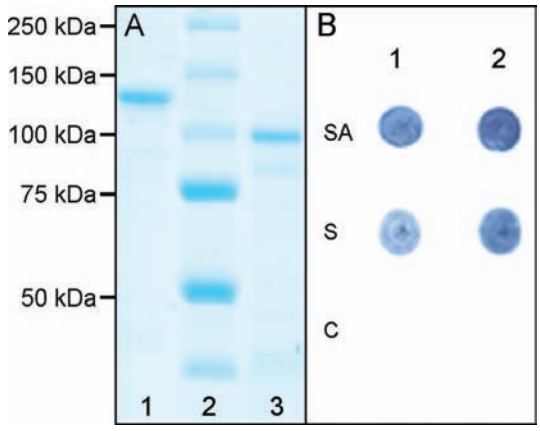

Figure 1. (A) SDS-PAGE analysis after Coomassie staining. Lane 1, purified SbpA/F1 fusion protein (MW: 112.4 kDa); lane 2, benchmark ladder (All blue, Biorad laboratories); lane 3, purified SbsB/F1 fusion protein (MW: 97.5 kDa). (B) Immunodot analysis of SbsB/F1 (1) and SbpA/F1 (2) of self-assembly products (SA), soluble S-layer fusion protein (S), and sole S-layer protein SbsB and SbpA, respectively, as control (C).

SbpA/F1 and SbsB/F1 (at 0.1 mg/mL) in 0.5 mM Tris-HCl/10 mM $CaCl_2$, pH 9.0, and incubated at 25 °C for 4 h. Atomic force microscopy (AFM) analysis was performed as described previously (*28*).

Immunodot Assays for Investigation of the Accessibility of Fused Mimotopes. To investigate the accessibility of the fused F1-domain in the water-soluble and recrystallized S-layer fusion proteins, 20 μL of SbpA/F1 and SbsB/F1 with an S-layer content of 1 mg/mL was dried onto a nitrocellulose membrane. After blocking with 2% Top Block (derivative of gelatine to block unspecific binding sites on surfaces, Fluka) in Tris-buffered saline (TBS) and incubation with 20 ng F1 monoclonal antibody (mAb) in 5 mL of TBS containing 2% Top Block with gentle agitation for 1 h at 25 °C, the membrane was washed three times with 0.5% Tween in TBS and subsequently incubated with an anti-Mouse IgG (whole molecule) alkaline phosphatase conjugate (antimouse AP, Sigma) diluted 1:5000 in blocking solution with gentle agitation for 1 h at 25 °C. After three further washing steps, detection was accomplished by treatment with 5-brom-4-chloro-3-indolyl phosphate and nitroblue tetrazolium chloride (BCIP/NBT, Roche).

Reactivity of F1 in SbpA/F1 and SbsB/F1 Fusions by ELISA. The presence of the F1 moiety in the S-layer fusion proteins was confirmed by performing ELISAs. S-layer fusion proteins (200 μL at 0.1 mg/mL) were coated onto microtiter plates (Greiner Bio-one) in 0.5 mM Tris-HCl/10 mM $CaCl_2$, pH 9.0, at 25 °C with gentle agitation for 4 h. For stabilization, the coated plates were incubated with a biomolecular stabilizator (StabilGuard, Surmodics) diluted 1:1 with phosphate buffered saline containing 0.1% Triton X-100 (PBS/Triton) for 4 h at 25 °C. Subsequently, the microtiter plates were dried overnight at 37 °C. For ELISA, the coated microtiter plates were blocked with 2% Top Block in PBS/Triton overnight at 4 °C. Subsequently, 100 μL per well of serial dilutions of anti-F1 antibody in PBS/Triton containing 2% Top Block (w/v) were added for 1 h with gentle agitation. The plates were washed three times with PBS/Triton and 110 μL per well antimouse peroxidase conjugate (Sigma) diluted 1: 2000 in PBS/Triton containing 2% Top Block was added and incubated as above. Subsequently, the plates were washed again as above, and the ELISA was developed with 3,3′,5,5′-tetramethylbenzidine substrate (TMB, Sigma). All samples were analyzed in duplicate, and wells coated with the wild-type S-layer protein SbpA without F1 peptide were used as controls.

Clinical Samples. Individual human serum samples were obtained from Queensland Medical Laboratory (Brisbane, Australia), and these had been previously tested with a commercial kit for EBV diagnosis. Samples ($n = 28$) defined as IgM positive were collected from individuals with recent or early-stage infectious mononucleosis. Negative sera ($n = 40$) were obtained from patients without EBV IgM or EBV IgG antibodies. Putative cross-reactive sera ($n = 15$) were also obtained that may cause false positive readings in EBV diagnostic tests; we analyzed 4 Parvovirus (Parvo), 2 Herpes Simplex virus (HSV), 3 cytomegalovirus (CMV), 3 Varicella Zoster (Zoster), and 2 Rheumatoid factor (RF) samples.

Screening of Clinical Samples by ELISA. Coated plates were blocked with 200 μL/well 2% BSA/PBS Tween 20 (0.1%) overnight at room temperature and washed twice with PBSTween to remove blocking agent. Serum samples were diluted 1/100 in fish gelatin diluent (PBS containing 2% fish gelatin [Sigma], 1% Tween-20, and 1% bovine serum albumin) and 100 μL applied to blocked wells in duplicate; the plate was incubated for 1 h shaking. Wells were washed 5 times with PBSTween, and 100 μL per well of sheep antihuman IgM conjugated to horse radish peroxidase (HRP, Chemicon) at 1/3500 dilution in fish gelatin diluent was added. After 1 h incubation and washing as above, bound IgM antibodies were detected with TMB substrate. All samples were analyzed in duplicate, and wells coated with the wild type S-layer protein SbpA without F1 peptide were used as controls.

RESULTS AND DISCUSSION

Cloning of the Chimeric S-Layer Fusion Proteins SbpA/F1 and SbsB/F1. Studies of the structure–function relationship of the S-layer proteins SbpA of *Bacillus sphaericus* CCM 2177 and SbsB *Geobacillus stearothermophilus* PV72/p2 were considered as presupposition for the construction of two novel S-layer fusion proteins, which retained assembly and recrystallization properties of the S-layer moiety, as well as the functionality of the fused peptide sequence (*17–26*). In attempt to optimize peptide presentation, a C-terminally truncated SbpA form and the full-length S-layer protein SbsB were selected as base forms for the construction of S-layer fusion proteins comprising the sequence of the 20-aa-long peptide F1 which mimics an immunodominant epitope of Epstein–Barr virus (EBV).

Two inserts encoding F1 peptide with overhangs of respective restriction sites were derived from alignment of two pairs of oligonucleotides. The inserts were ligated via the corresponding restriction sites into plasmid pET-28 (+)-$SbpA_{93-3204}$ and plasmid pET-28 (+)-$SbsB_{96-2760}$, containing the encoding sequence of the C-terminally truncated form of S-layer protein SbpA and the full-length S-layer protein SbsB, respectively. Sequence accuracy of the two S-layer mimotope fusion protein genes was proven by the sequencing service of Invitrogen.

Expression, Isolation, and Purification of the Chimeric S-Layer Fusion Proteins SbpA/F1 and SbsB/F1. The S-layer/F1 fusion proteins were overexpressed in *E. coli* BL21Star (DE3) cells harboring pET-28 (+)-$SbpA_{93-3204}$/F1 and pET-28 (+)-$SbsB_{96-2760}$/F1, respectively. For isolation of SbpA/F1 and SbsB/F1, the biomass harvested from a 3-l expression culture was treated with B-PER reagent. As previously observed for the sole recombinant S-layer proteins, the fusion proteins accumulated as inclusion bodies (*18*). SbpA/F1 and SbsB/F1 were extracted by treatment with 5 M GHCl (3 mL g^{-1} inclusion bodies) and finally enriched by GPC to high purity with overall yields of purified, monomeric protein chimera of 0.44 g (SbpA/F1) and 0.21 g (SbsB/F1) per liter of *E. coli* BL21Star(DE3) expression culture. The molecular masses of the purified chimeric proteins shown on SDS PAGE corresponded well to

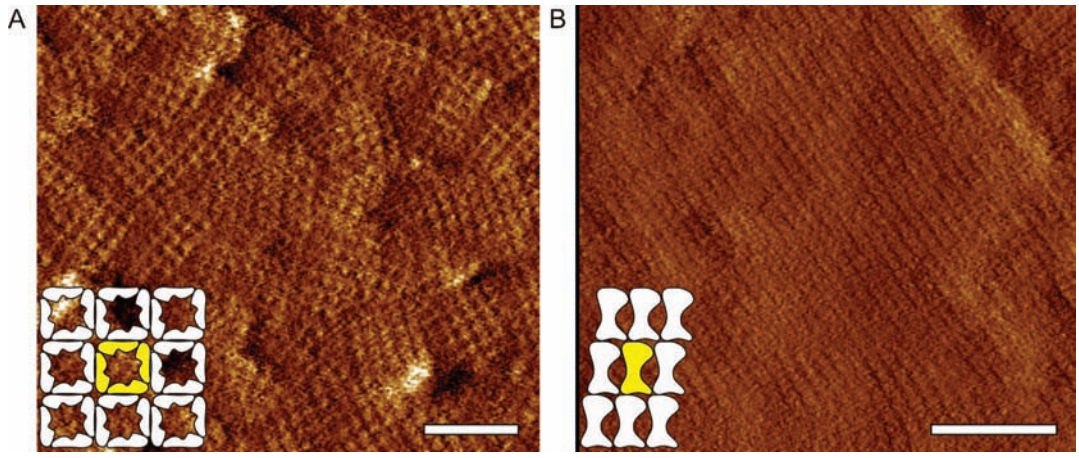

Figure 2. Atomic force microscopical images of the square lattice of SbpA/F1 (A) and the oblique lattice of SbsB/F1 (B) recrystallized on polystyrene slides. Bar, 100 nm.

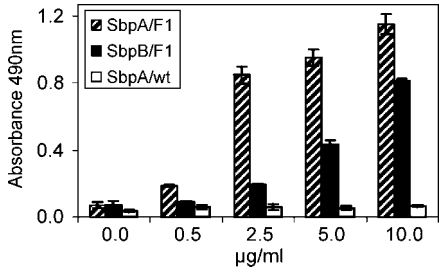

Figure 3. IgG binding capacity (F1 mAb offered: μg/mL) of S-layer mimotope fusion proteins SbpA/F1 and SbsB/F1 recrystallized on microtiter plates in comparison to wild-type S-layer protein SbpA.

the calculated molecular masses of 112.4 kDa (SbpA/F1) and 97.5 kDa (SbsB/F1) shown in Figure 2A.

Investigation of the Self-Assembly Properties of the S-Layer Fusion Proteins. Triggered by the S-layer moiety, the S-layer fusion proteins were capable of intrinsically self-assembling *in vitro* into flat sheets. The electron micrographs of negatively stained preparations clearly revealed the formation of S-layer self-assembly products of both S-layer fusion proteins in solution. The S-layer fusion protein SbpA/F1 exhibited the square lattice structure of native SbpA with a center-to-center spacing of tetrameric units of 13.1 nm (*12*). S-layer fusion protein SbsB/F1 showed the typical oblique lattice characteristic of native SbsB with the lattice parameters $a = 10.4$ nm, $b = 7.9$ nm, and base angle $\gamma = 81°$ (*13*) (electron micrographs not shown).

Investigations of Accessibility of Fused Mimotope Groups. Dot blot assays were performed to investigate the accessibility of the fused F1 for binding to IgG in monomeric and self-assembled S-layer fusion proteins. Immunodot experiments showed that the mimotope groups of the S-layer fusion proteins SbpA/F1 and SbsB/F1 were clearly accessible for IgG binding. According to the dots intensities, alignment of the mimotopes within the protein lattice resulted in better accessibility for IgG binding than when provided as monomeric S-layer fusion protein (Figure 1B).

Immobilization of the S-Layer Fusion Protein on Solid Supports. The capability of the two S-layer fusion proteins, SbpA/F1 and SbsB/F1, to recrystallize on solid supports was confirmed by AFM evidence. On silicon wafers (data not shown) as well as on polystyrene slides which present the material of ELISA wells, the S-layer fusion proteins exhibited the square (Figure 2A) and oblique (Figure 2B) lattice structures characteristic of native S-layer protein SbpA and SbsB, respectively. These microscopic analyses confirmed that the obtained S-layer fusion proteins can be considered model systems for the S-layer-based site-directed immobilization of small peptides used in diagnostics.

Investigation of the Reactivity of F1 in SbpA/F1 and SbsB/F1 Fusions by ELISA. Due to the specific physicochemical properties of the S-layer moieties (*18*), the S-layer fusion proteins were recrystallized onto microtiter wells, thereby exposing the F1 moiety at the C- or N-terminus in SbpA/F1 and SbsB/F1, respectively. The defined orientation of SbpA/F1 and SbsB/F1 was demonstrated via ELISA techniques that confirmed the ability of the F1 mimotope to bind parent F1 mAb in the formed monolayers (Figure 3). The S-layer fusion protein SbpA/F1 showed a better antibody binding capacity than S-layer fusion protein SbsB/F1 as shown by higher binding to the parent F1 mAb. The wild-type S-layer protein SbpA/wt chosen as the blank did not show any nonspecific binding of F1 mAb, giving a good signal-to-noise ratio (Figure 3).

We also compared SbpA/F1 and SbsB/F1 with a small set of EBV clinical samples. It was apparent in Figure 4A that F1 peptide when attached to SbpA was superior for recognizing IgM antibodies in the sera of patients with EBV. The better performance of the SbpA-based S-layer fusion protein was likely to be caused by the different molecular orientation of the mimotope F1 within the S-layer lattice. Fused via its N-terminus, the mimotope could fully deploy its functionality as IgM antibodies recognized this peptide conformation preferentially. The results obtained with the two different S-layer systems refer to different accessibilities of the functional groups within different S-layer lattices.

SbpA/F1 for Diagnosis of EBV. According to the data above, a more accurate assessment of the diagnostic value of the S-layer fusion protein rSbpA/F1 with a larger panel of positive, negative, and putative cross-reactive sera was performed. S-layer fusion protein SbpA/F1 was used in ELISAs as a solid phase for capture of IgM antibodies in clinical samples obtained from patients with EBV. To correct for background levels, the reactivity to SbpA/wt was also measured, and these values were subtracted from the SbpA/F1 readings. We analyzed 28 individual EBV samples and could identify IgM antibodies in 25 of these, resulting in 89.3% sensitivity (Figure 4B). Forty negative sera were analyzed and only 1 false positive was observed (98.2% specificity). In addition, very low reactivity was observed in 15 putative cross-reactive samples including rheumatoid factor, which is a common false positive in many commercial diagnostic tests (*1*).

These results were in good accordance with currently used commercially available assay systems based on the capture of IgM antibodies using complex EBV antigens (*34*). Due to the

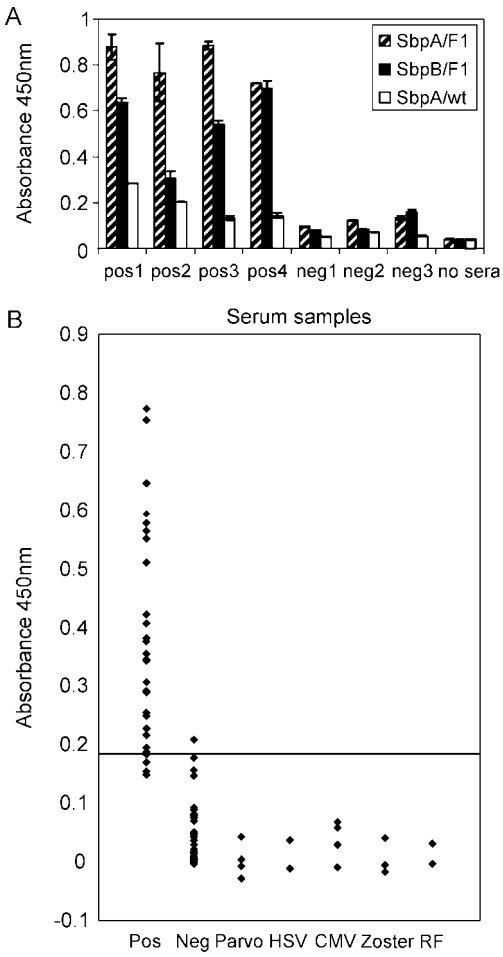

Figure 4. Screening of clinical samples using S-layer/F1 fusion proteins. (A) Detection of IgM antibodies in individual EBV-positive sera with SbpA/F1 and SbsB/F1 compared to wild-type SbpA/wt containing no F1 peptide, by ELISA. Mean values are plotted; error bars indicate the ranges of individual values. (B) ELISA showing the reactivity of SbpA/F1 fusion protein with EBV IgM positive ($n = 28$), negative ($n = 40$), and sera that could potentially be cross-reactive ($n = 15$): Parvovirus (Parvo, $n = 4$), Herpes Simplex virus (HSV, $n = 2$), cytomegalovirus (CMV, $n = 4$), Varicella Zoster (Zoster, $n = 3$), and Rheumatoid factor (RF, $n = 2$). Absorbencies for SbpA/F1 were subtracted from SbpA/wt readings and plotted. The cutoff level is defined as the mean of the negative population ($n = 40$) + 3 SD, shown as a horizontal line in the dot plot. The cutoff value for SbpA/F1 was 0.18.

high sensitivity and specificity of S-layer-based solid-phase immunoassays, S-layer proteins can be used as an immobilization matrix in ELISA-based diagnostics (*9*). Antibody capture with surface-displayed peptides is crucially affected by the accessibility of key residues of peptide ligands (*35*).The presentation of the small mimotope sequence within the S-layer lattice led to accurate accessibility and consequently reactivity of the displayed peptides. Furthermore, immobilization of peptides may cause partial denaturation at the site of adhesion to the support (*5*). It is conceivable that, with S-layer fusion proteins, the S-layer moiety acts as a cushion preventing denaturation of the mimotope upon immobilization.

CONCLUSION

The data presented here clearly demonstrate that S-layer-based self-assembly systems for functionalizing solid supports could have importance for the introduction of small peptide mimotopes in diagnostic assays. By exploiting the intrinsic self-assembly property of the S-layer protein moiety, the chimeric protein SbpA/F1 was used for spatial control over the display of the mimotope on planar surfaces. Linking the mimotope to the S-layer protein resulted in a biological function comparable to currently used commercially available assay systems using complex EBV antigens. This immobilization technology is applicable to any peptide and can be important for the development of novel diagnostic assays. Furthermore, this technology may facilitate the use of peptides as surrogate antigens in diagnostic assay.

ACKNOWLEDGMENT

We wish to thank Graham Street of Queensland Medical laboratory (Brisbane, Australia) for providing the clinical samples.

LITERATURE CITED

(1) Casey, J. L., Coley, A. M., Street, G., Parisi, K., Devine, P. L., and Foley, M. (2006) Peptide mimotopes selected from random peptide library for diagnosis of Epstein-Barr virus infection. *J. Clin. Microbiol. 44*, 764–771.

(2) Angenendt, P. (2005) Progress in protein and antibody microarray technology. *Drug Discovery Today 10*, 503–511.

(3) Hahn, R., Berger, E., Pflegerl, K., and Jungbauer, A. (2003) Directed immobilization of peptide ligands to accessible pore sites by conjugation with placeholder molecule. *Anal. Chem. 75*, 543–548.

(4) Hermanson, G. T., Mallia, A. K., and Smith, P. K. (1992) *Immobilization Affinity Ligand Techniques.* Academic Press Inc., San Diego, CA.

(5) Zhu, H., and Snyder, M. (2003) Protein chip technology. *Curr. Opin. Chem. Biol. 7*, 55–63.

(6) Breitwieser, A., Kupcu, S., Howorka, S., Weigert, S., Langer, C., Hoffmann-Sommergruber, K., Scheiner, O., Sleytr, U. B., and Sára, M. (1996) 2-D protein crystals as an immobilization matrix for producing reaction zones in dipstick-style immunoassays. *Biotechniques 21*, 918–925.

(7) Breitwieser, A., Mader, C., Schocher, I., Hoffmann-Sommergruber, K., Aberer, W., Scheiner, O., Sleytr, U. B., and Sára, M. (1998) A novel dipstick developed for rapid Bet v 1-specific IgE detection: recombinant allergen immobilized via a monoclonal antibody to crystalline bacterial cell-surface layers. *Allergy 53*, 786–793.

(8) Sleytr, U. B., and Sára, M. (1997) Bacterial and archaeal S-layer proteins: structure-function relationships and their biotechnological applications. *Trends Biotechnol. 15*, 20–26.

(9) Völkel, D., Zimmermann, K., Breitwieser, A., Sára, M., Pable, S., Glatzl, M., Scheiflinger, F., Schwarz, H. P., Sleytr, U. B., and Dorner, F. (2003) Immunochemical detection of prion protein on dipsticks prepared with crystalline bacterial cell-surface layers. *Transfusion 43*, 1677–1681.

(10) Sára, M., and Sleytr, U. B. (2000) S-Layer proteins. *J. Bacteriol. 182*, 859–68.

(11) Sleytr, U. B., and Beveridge, T. J. (1999) Bacterial S-layers. *Trends Microbiol. 7*, 253–260.

(12) Sleytr, U. B., Messner, P., Pum, D., and Sára, M. (1999) Crystalline bacterial cell surface layers (S-layers): from supramolecular cell structure to biomimetics and nanotechnology. *Angew. Chem., Int. Ed. 38*, 1034–1054.

(13) Sleytr, U. B., Sara, M., Pum, D., and Schuster, B. (2005) Crystalline bacterial cell surface layers (S-layers): a versatile self-assembly system, In *Supramolecular Polymers* (Ciferri, A., Ed.) pp 583–612, CRC Press LLC, Boca Raton, FL.

(14) Sleytr, U. B., Sára, M., Pum, D., and Schuster, B. (2002) Molecular nanotechnology and nanobiotechnology with two-dimensional protein crystals (S-layers), In *Nano-Surface Chemistry* (Rosoff, M., Ed.) pp 333–389, Marcel Dekker Inc., New York.

(15) Sleytr, U. B., Egelseer, E., Ilk, N., Pum, D., and Schuster, B. (2007) S-layers as a basic building block in a molecular construction kit. *FEBS J. 274*, 323–334.

(16) Sleytr, U. B., Huber, C., Ilk, N., Pum, D., Schuster, B., and Egelseer, E. (2007) S-layers as a tool kit for nanobiotechnological applications. *FEMS Microbiol. Lett. 267*, 131–144.

(17) Ilk, N., Küpcü, S., Moncayo, G., Klimt, S., Ecker, R. C., Hofer-Warbinek, R., Egelseer, E. M., Sleytr, U. B., and Sára, M. (2004) A functional chimaeric S-layer-enhanced green fluorescent protein to follow the uptake of S-layer-coated liposomes into eukaryotic cells. *Biochem. J. 379*, 441–448.

(18) Ilk, N., Völlenkle, C., Egelseer, E. M., Breitwieser, A., Sleytr, U. B., and Sára, M. (2002) Molecular characterization of the S-layer gene, sbpA, of *Bacillus sphaericus* CCM 2177 and production of a functional S-layer fusion protein with the ability to recrystallize in a defined orientation while presenting the fused allergen. *Appl. Environ. Microbiol. 68*, 3251–3260.

(19) Breitwieser, A., Egelseer, E. M., Moll, D., Ilk, N., Hotzy, C., Bohle, B., Ebner, C., Sleytr, U. B., and Sára, M. (2002) A recombinant bacterial cell surface (S-layer)-major birch pollen allergen-fusion protein (rSbsC/Bet v1) maintains the ability to self- assemble into regularly structured monomolecular lattices and the functionality of the allergen. *Protein Eng. 15*, 243–249.

(20) Pleschberger, M., Neubauer, A., Egelseer, E. M., Weigert, S., Lindner, B., Sleytr, U. B., Muyldermans, S., and Sára, M. (2003) Generation of a functional monomolecular protein lattice consisting of an s-layer fusion protein comprising the variable domain of a camel heavy chain antibody. *Bioconjugate Chem. 14*, 440–448.

(21) Pleschberger, M., Saerens, D., Weigert, S., Sleytr, U. B., Muyldermans, S., Sára, M., and Egelseer, E. M. (2004) An S-layer heavy chain camel antibody fusion protein for generation of a nanopatterned sensing layer to detect the prostate-specific antigen by surface plasmon resonance technology. *Bioconjugate Chem. 15*, 664–671.

(22) Völlenkle, C., Weigert, S., Ilk, N., Egelseer, E., Weber, V., Loth, F., Falkenhagen, D., Sleytr, U. B., and Sára, M. (2004) Construction of a functional S-layer fusion protein comprising an immunoglobulin G-binding domain for development of specific adsorbents for extracorporeal blood purification. *Appl. Environ. Microbiol. 70*, 1514–1521.

(23) Huber, C., Egelseer, E. M., Ilk, N., Sleytr, U. B., and Sára, M. (2006) S-layer-streptavidin fusion proteins and S-layer-specific heteropolysaccharides as part of a biomolecular construction kit for application in nanobiotechnology. *Microelectron. Eng. 83*, 1589–1593.

(24) Moll, D., Huber, C., Schlegel, B., Pum, D., Sleytr, U. B., and Sára, M. (2002) S-layer-streptavidin fusion proteins as template for nanopatterned molecular arrays. *Proc. Natl. Acad. Sci. U.S.A. 99*, 14646–14651.

(25) Schäffer, C., Novotny, R., Küpücü, S., Zayni, S., Scheberl, A., Friedman, J., Sleytr, U. B., and Messner, P. (2007) Novel types of biocataysts based on the S-layer self-assembly system from *Geobacillus stearothermophilus* NRS 2004/3a, exemplified with glucose-1-phosphate thymidylyltransferase RmlA: a nanobiotechnological approach. *Small 3*, 2–12.

(26) Tschiggerl, H., Breitwieser, A., de Roo, G., Verwoerd, T., Schäffer, C., and Sleytr, U. B. (2008) Exploitation of the S-layer self-assembly system for site directed immobilization of enzymes demonstrated for an extremophilic laminarinase from *Pyrococcus furiosus*. *J. Biotechnol. 133*, 403–441.

(27) Sára, M., Egelseer, E. M., Huber, C., Ilk, N., Pleschberger, M., Pum, D., and Sleytr, U. B. (2006) S-layer proteins: Potential application in nano(bio)technology, In *Microbial. Bionanotechnology: Biological Self-Assembly Systems and Biopolymer-Based Nanostructures*, pp 307–338, Horizon Bioscience Bernd Rehm Massey University, P. N. New Zealand.

(28) Györvary, E. S., Stein, O., Pum, D., and Sleytr, U. B. (2003) Self-assembly and recrystallization of bacterial S-layer proteins at silicon supports imaged in real time by atomic force microscopy. *J. Microsc. 212*, 300–306.

(29) Kuen, B., Koch, A., Asenbauer, E., Sára, M., and Lubitz, W. (1997) Molecular characterization of the *Bacillus stearothermophilus* PV72 S-layer gene sbsB induced by oxidative stress. *J. Bacteriol. 179*, 1664–1670.

(30) Howorka, S., Sára, M., Wang, Y., Kuen, B., Sleytr, U. B., Lubitz, W., and Bayley, H. (2000) Surface-accessible residues in the monomeric and assembled forms of a bacterial surface layer protein. *J. Biol. Chem. 275*, 37876–37886.

(31) Sambrook, J., Fritsch, E. F., and Maniatis, T. (1989) *Molecular Cloning. A Laboratory Manual*, 2nd ed., Cold Spring Harbor Labratory Press, Cold Spring Harbor, NY.

(32) Laemmli, U. K. (1970) Cleavage of structural proteins during the assembly of the head of bacteriophage T4. *Nature 227*, 680–685.

(33) Pum, D., Sára, M., and Sleytr, U. B. (1989) Structure, surface charge, and self-assembly of the S-layer lattice from *Bacillus coagulans* E38–66. *J. Bacteriol. 171*, 5296–5303.

(34) Svahn, A., Magnusson, M., Jägdahl, L., Schloss, L., Kahlmeter, G., and Linde, A. (1997) Evaluation of three commercial enzyme-linked Immunosorbent assays and two latex agglutination assays for diagnosis of primary Epstein-Barr virus infection. *J. Clin. Microbiol. 35*, 2728–2732.

(35) Andresen, H., Grötzinger, C., Zarse, K., Kreuzer, O. J., Ehrenreich-Förster, and Bier, F. K. (2006) Functional peptide microarrays for specific and sensitive antibody diagnostics. *Proteomics 6*, 1376–1384.

BC7003523

Unnatural Amino Acid Incorporation into Virus-Like Particles

Erica Strable,[†] Duane E. Prasuhn, Jr.,[†] Andrew K. Udit,[†] Steven Brown,[†] A. James Link,[‡] John T. Ngo,[‡] Gabriel Lander,[§] Joel Quispe,[§] Clinton S. Potter,[§] Bridget Carragher,[§] David A. Tirrell,[‡] and M. G. Finn*[,†]

Department of Chemistry and The Skaggs Institute of Chemical Biology, and National Resource for Automated Molecular Microscopy and Department of Cell Biology, The Scripps Research Institute, La Jolla, California 92037, and Division of Chemistry and Chemical Engineering, California Institute of Technology, Pasadena, California 91125. Received October 21, 2007; Revised Manuscript Received January 14, 2008

Virus-like particles composed of hepatitis B virus (HBV) or bacteriophage Qβ capsid proteins have been labeled with azide- or alkyne-containing unnatural amino acids by expression in a methionine auxotrophic strain of *E. coli*. The substitution does not affect the ability of the particles to self-assemble into icosahedral structures indistinguishable from native forms. The azide and alkyne groups were addressed by Cu(I)-catalyzed [3 + 2] cycloaddition: HBV particles were decomposed by the formation of more than 120 triazole linkages per capsid in a location-dependent manner, whereas Qβ suffered no such instability. The marriage of these well-known techniques of sense-codon reassignment and bioorthogonal chemical coupling provides the capability to construct polyvalent particles displaying a wide variety of functional groups with near-perfect control of spacing.

INTRODUCTION

A variety of strategies and expression systems have been employed to cotranslationally incorporate unnatural amino acids into proteins. The three most common approaches are the use of a nonsense or rare codon (*1–8*), the use of a larger (quadruplet) codon (*4, 9*), or the reassignment of a sense codon (*10–17*). In the last approach, codons for methionine (*11–15, 18, 19*), leucine (*20*), isoleucine (*21*), phenylalanine (*22*), tryptophan (*23, 24*), and proline (*25*) have been used for incorporation of unnatural amino acids. Here we employ this technique (*10, 16, 26*) to replace methionine with the unnatural amino acids azidohomoalanine (**1**, Figure 1) and homopropargyl glycine (**2**) for the first time in proteins that spontaneously assemble into virus-like particles in the host *E. coli* cell.

The incorporation of organic azides and terminal alkynes introduces highly energetic functional groups that are inert to biological molecules under physiological conditions. The azide group's "bio-orthogonality" has been particularly prized, due to its participation in the Staudinger reaction with phosphines (*27, 28*), cycloaddition with strained-ring alkynes (*27, 29–31*), and copper(I)-mediated cycloaddition with terminal alkynes (*32, 33*). We have developed the last of these into a robust tool for making connections with biological molecules (*34*) at reasonable concentrations (*35*). The process has been used by us and others for the selective modification of enzymes (*6, 36*), cells (*14, 15, 37*), virus particles (*7, 34, 35, 38, 39*), newly synthesized proteins (*40–43*), and tissue lysates (*44, 45*). The cotranslational incorporation of azides and alkynes into self-assembled virus-like particles enables their use in the chemoselective preparation of polyvalently labeled structures. In addition to providing near-perfect control over the positioning of desired groups on the virus surface, the genetic incorporation and subsequent chemical addressing of azides and alkynes allows the independent use of other bioconjugation techniques without protecting group manipulations or concerns about cross-reactivity.

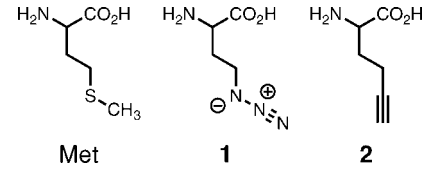

Figure 1. Methionine analogues **1** and **2** incorporated into virus-like capsids using codon reassignment.

The inner protein shell (core antigen) of hepatitis B virus is composed of either 180 (maximum diameter 318 Å) or 240 (maximum diameter 348 Å) copies of the coat protein (Figure 2) (*46, 47*). We will use the abbreviation HBV to refer to the latter structure, which is the predominant (*46*) particle used here; the designation HBcAg also appears in the literature. The native capsid protein is 183 amino acids in length; we employed the assembly domain composed of the first 149 amino acids (Cp149), which is largely α-helical and produces more than 95% of the 240-subunit particle. While a variety of recombinant protein expression systems have been used successfully to produce the HBV core antigen (*48, 49*), by far the most common has been *E. coli* (*50, 51*).

The *E. coli* bacteriophage Qβ is composed of 180 copies of the coat protein assembled into a $T = 3$ icosahedral virion (average diameter 270 Å, Figure 2) (*52, 53*), encapsidating a positive-sense RNA genome (*54*). The capsid protein is composed of 132 amino acids of mostly antiparallel β-sheet structure (*52, 55*). For a nonthermophile, the capsid is unusually stable toward extremes of pH, temperature, and chemical reagents, due to a combination of a large noncovalent contact area within capsid dimers. Furthermore, cysteine residues at positions 74 and 80, located at the five- and threefold axes of symmetry, respectively, form disulfide linkages to the corresponding residues of neighboring subunits. As a result, rings of five subunits are formed at the icosahedral fivefold symmetry axis, and rings of six protein subunits are formed around the threefold axis, with each protein dimer being linked to the capsid by four disulfide bonds. The coat protein of Qβ is tolerant of

* mgfinn@scripps.edu.
[†] Department of Chemistry and The Skaggs Institute of Chemical Biology,The Scripps Research Institute.
[‡] California Institute of Technology.
[§] National Resource for Automated Molecular Microscopy and Department of Cell Biology, The Scripps Research Institute.

10.1021/bc700390r CCC: $40.75 © 2008 American Chemical Society
Published on Web 03/05/2008

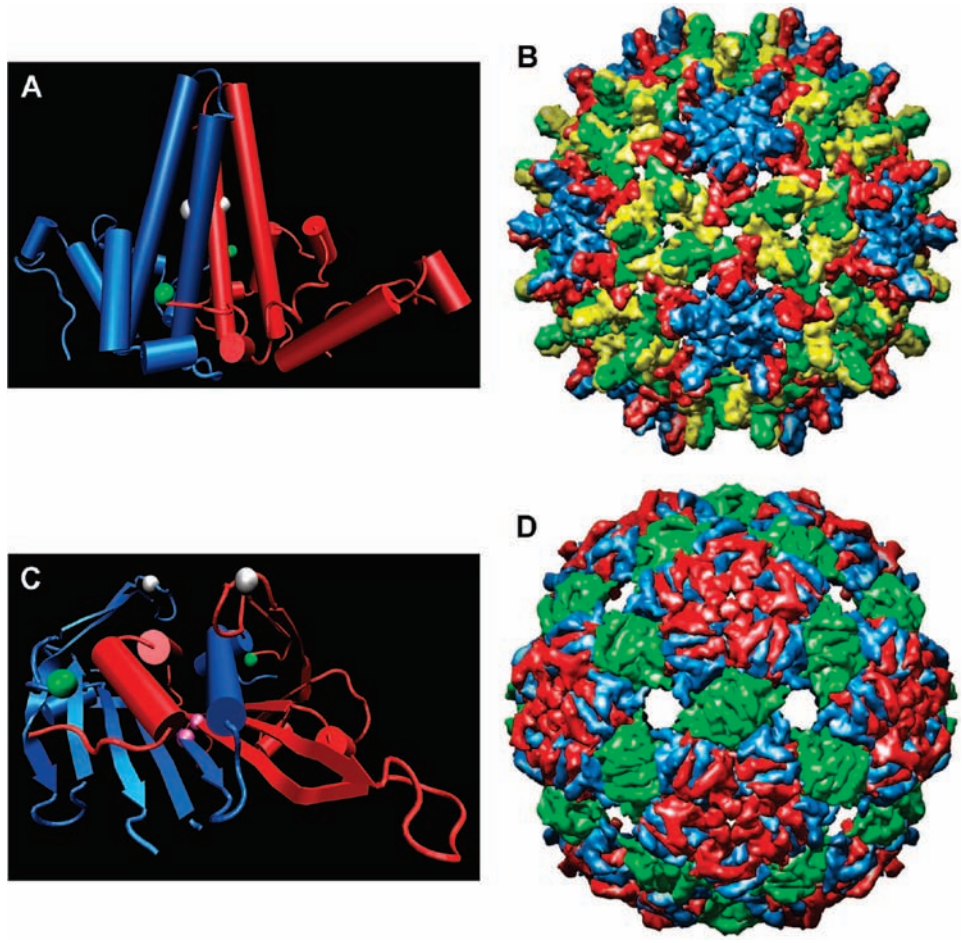

Figure 2. HBV and Qβ virus-like particles. (A) HBV dimer; (B) HBV virus-like particle; (C) Qβ dimer; (D) Qβ virus-like particle (*47*, *55*, *59*). Representations (A) and (C) look obliquely down onto the outside capsid surface, showing the 4-helix bundle for HBV and intertwined α-helix and loop segments over adjacent β-sheets for Qβ. The spheres mark the locations of methionine residues: green = *N*-termini, white = Met66 in HBV and K16 M in Qβ, purple = Qβ T93M.

genetic manipulation and can be recombinantly expressed in high yields (*56*–*58*), making it desirable for a variety of applications. All mention below of particles or virions refer to the noninfectious, self-assembled virus-like particles (VLPs) of either HBV or Qβ, encapsidating random cellular RNA.

RESULTS AND DISCUSSION

Unnatural Amino Acid Incorporation. We have incorporated the unnatural amino acids azidohomoalanine (**1**) and homopropargylglycine (**2**) into HBV and Qβ using reassignment of the methionine sense codon, which provides global replacement of all methionines with the unnatural amino acid. Thus, genetic engineering is usually required to place Met residues where the unnatural amino acids are desired. The presence of *N*-terminal methionine, required by the translational machinery, is variable for both HBV Cp149 and Qβ, as it is for many proteins expressed in *E. coli* (*60*). HBV contains one additional Met at position 66, situated halfway up the side of the four helix bundle and therefore accessible to solution-phase reactants (Figure 2A). The Qβ sequence has no other methionines, so mutants K16 M and T93 M were generated. The former places the new amino acid at the most exposed location of the capsid exterior, while the latter installs Met (or its surrogate) on the interior surface in a somewhat hindered position (Figure 2C).

For the efficient incorporation of unnatural amino acids, the protein must be expressed under tight inducible control. Native and mutant HBV and Qβ coat protein sequences were cloned into the pQE-60 plasmid (Qiagen) and the methionine auxotroph *E. coli* strain M15(pREP4)MA was used for expression. The transformed cells were grown in minimal media supplemented with all 20 naturally occurring amino acids. When the desired mass of cells was achieved, methionine was removed from the media by pelleting, washing, and resuspending the cells in minimal media containing all the natural amino acids except methionine. The cells were incubated at 37 °C for 30–60 min to allow the bacteria to deplete their intracellular stocks of methionine. Finally protein expression was initiated by distributing the cells in minimal media containing the 19 natural amino acids, 1 mM isopropyl-β-D-1-thiogalactopyranoside (IPTG), and 80 mg/L of racemic **1** or **2**.

A series of control experiments established that HBV or Qβ protein was produced only when the minimal media was supplemented by Met, **1**, or **2**, and only in the presence of IPTG. In media supplemented with **1** or **2**, the yield of isolated HBV or Qβ particles was approximately 20–60% of the amount of protein produced in normal media under the same induction by IPTG (Table 1), representing some of the highest yields of unnatural amino acid-containing proteins reported thus far (see Supporting Information).

HBV and Qβ VLPs containing **1** or **2** were indistinguishable in all physical characteristics from the analogous particles incorporating methionine (Figure 3). In each case, ultracentrifugation through sucrose gradients (not shown) and analysis on size-exclusion chromatography produced sharp virus bands at the same position as native capsids. Negative-stained transmission electron microscopy images of the particles

Table 1. Average Expression Levels of HBV and Qβ VLPs with Methionine, Azidohomoalanine (1), or Homopropargylglycine (2)

particle[a]	amino acid	yield (mg protein per g cells)	yield (mg protein per L culture)
HBV	Met	4–5 mg/g	80–100 mg/L
HBV(1M-N_3)$_{192}$(66M-N_3)$_{240}$	**1**	1–1.5 mg/g	20–30 mg/L
HBV(M66S)	Met	4–5 mg/g	80–100 mg/L
HBV(1M-N_3)$_{102}$(M66S)	**1**	2–3 mg/g	40–60 mg/L
Qβ	Met	3–4 mg/g	75–100 mg/L
Qβ(1M-N_3)$_{9-18}$	**1**	2–2.4 mg/g	50–60 mg/L
Qβ(K16M)	Met	3–4 mg/g	50–75 mg/L
Qβ(1M-N_3)$_{9-18}$(K16M-N_3)$_{180}$	**1**	1–2 mg/g	25–35 mg/L
Qβ(K16M-CCH)$_{90}$	**2**	2 mg/g	40 mg/L
Qβ(T93M)	Met	3–4 mg/g	50–75 mg/L
Qβ(1M-N_3)$_{9-18}$(T93M-N_3)$_{180}$	**1**	1–2 mg/g	25–35 mg/L

[a] Nomenclature: "HBV(1M-N_3)(66M-N_3)" denotes HBV particles with methionines at positions 1 and 66 (which happens to be the wild-type sequence) expressed in the presence of **1** to allow azide incorporation at those residues. Other particles are designated in analogous fashion, with "CCH" replacing "N_3" for those VLP's incorporating alkynyl amino acid **2**. Subscripts refer to the average number of unnatural amino acids incorporated at each position, as described in the text.

revealed homogeneous samples of icosahedral nonaggregated particles. (The HBV Cp149 particles containing **1** do not contain nucleic acid, and thus exhibit stain uptake with dark centers. Qβ particles are packed full of random cellular nucleic acid and have light centers in the negative stained images.) SDS-PAGE analyses revealed the same high purities of the capsids containing unnatural amino acids as those obtained with methionine. Last, the structures of both the HBV and Qβ virus-like particles with **1** were confirmed by cryo-electron microscopy image reconstruction. The electron density maps overlaid well with the published X-ray crystal structures for the native capsids.

The incorporation of **1** and **2** in place of methionine was confirmed by trypsin digestion and analysis of the resulting peptides using MALDI mass spectrometry, with the results summarized in Figure 4. Sequence coverage of the wild-type and **1**-labeled HBV Cp149 particle was nearly complete, with all but two residues included (Ile97, Arg98). Following normal expression in the presence of all 20 amino acids, Met was found at positions 1 and 66, the former in 70–90% of the protein, varying from batch to batch. The same result was observed when **1** was substituted for Met in the protocol described above, with **1** incorporated at the *N*-terminus in 70–90% of the protein produced, and completely (>95%) at position 66. The mutation M66S was also constructed, and found to contain the same 70–90% of **1** at the *N*-terminus when expressed with the unnatural amino acid.

Analysis of Qβ capsids required shorter trypsin digestion times to ensure limited proteolysis of the amino-terminal region. A coverage map that included all peptide fragments larger than three amino acids was obtained (Figure 4). Post-translational processing at the *N*-terminus was found to vary with the nature of the residue installed at that position. Under normal (Met-containing) expression, Met1 was never detected in either wild-type or mutant particles, showing that it was processed away during protein production (therefore, the amino acid numbering eliminates this residue). When **1** was substituted for Met in any form of the Qβ sequence, approximately 10% of the capsids were found to have the unnatural amino acid at the *N*-terminus. However, in approximately one of every five batches this level of incorporation spiked to as much as 90%. It was therefore necessary to analyze each preparation of Qβ capsids to determine the number of azide-containing residues available for conjugation. Incorporation of **1** at either of the internal positions tested (16 or 93) was uniformly excellent (>95%). The same type of analysis (not shown) revealed 50% incorporation of **2** into Qβ K16 M at position 16, with the remainder being Met. No homopropargyl glycine was detected at position 1.

Conjugation to Genetically Incorporated Azide and Alkyne Groups. Since the expression of HBV in the presence of **1** provided 70–90% incorporation at position 1 and complete incorporation at position 66, a maximum of approximately 410–460 azides per VLP should be available for conjugation. We employed these particles as reagents in the copper-catalyzed azide-alkyne cycloaddition (CuAAC) reaction, using CuOTf and accelerating ligand **4** under inert atmosphere as has been previously described (*61, 62*). The purified virus was pelleted out of solution, taken into an inert-atmosphere glovebox, and resuspended in degassed 0.1 M Tris buffer (pH 8.0) to prepare for reaction with fluorescein alkyne **3** under our standard conditions, as shown in Figure 5. After 16 h at room temperature, intact capsids could neither be detected by size-exclusion chromatography (Figure 6) nor recovered from sucrose gradients. However, gel electrophoresis (Figure 6) showed strong fluorescein labeling of the protein. Trypsin digestion and MALDI analysis in the manner described above revealed that approximately 50% of the sites at position 66 were labeled with fluorescein (equal intensities for the 56–81 fragment, m/z = 2919.3, and its labeled analogue with an increase in mass of 413 Da). Interestingly, fewer than 10% of the azide groups at position 1 were addressed.

HBV particles lacking incorporated azide groups were found to be stable toward the reaction conditions without coupling to fluorescein, ruling out nonspecific adsorption of the dye (Table 2, entry 1). All HBV particles were stable to the CuAAC reaction conditions (copper, ligand, buffer, and sample handling) and also toward extended incubation with fluorescein alkyne **3** in the absence of CuAAC catalyst. However, the particles did decompose when either ligand **4** or the previously used tris(triazolylmethyl)amine **5** was employed in the CuAAC process, showing that the nature of the ligand made no difference to particle stability. When the reaction time was varied, or the amount of catalyst was reduced, virus-like particles were recovered in yields inversely proportional to the amount of CuAAC reaction that had occurred. The use of rhodamine, biotin, or Gd(DOTA) reagents (**6**, **7**, or **8**) in place of fluorescein alkyne gave similar results. We therefore conclude that the decomposition of the particle was caused by the covalent attachment of these structures. We have previously observed other particles such as cowpea mosaic virus (CPMV) to be similarly sensitive to the covalent tethering of flat, hydrophobic species such ferrocene, tetramethylrhodamine, Fe(III) protoporphyrin IX, Ru(II) bipyridine complexes, and doxorubicin. However, the nature of the attached species varied somewhat in this case, and so it may well be that the triazole linkage, which is common to each of these examples, is responsible for the instability of the virus-like HBV particle. CPMV and Qβ have both been shown to be stable toward high levels of coverage by triazoles (*34, 35, 37, 38, 62*).

We attempted to strike a balance between covalent attachment and stability for HBV by varying the concentrations of CuOTf, ligand **4**, fluorescein-alkyne **3**, and protein. The use of 250 μM CuOTf with 500 μM ligand **4** slowed the reaction enough to allow the recovery of a maximum of 40% of the starting amount of capsids as intact icosahedra, bearing an average of 120 fluorescein molecules per capsid (Table 2, entry 2). The vast majority of these were attached to the M66 position and not to the *N*-terminal azidohomoalanine residue, as shown by trypsin digestion/MS. The loading value was determined by UV–vis absorbance spectroscopy of fluorescein (495 nm) in samples of purified labeled particles, with calibration using known samples under similar conditions (fluorescein in the presence of protein; protein concentrations determined by Lowry protein assay). It

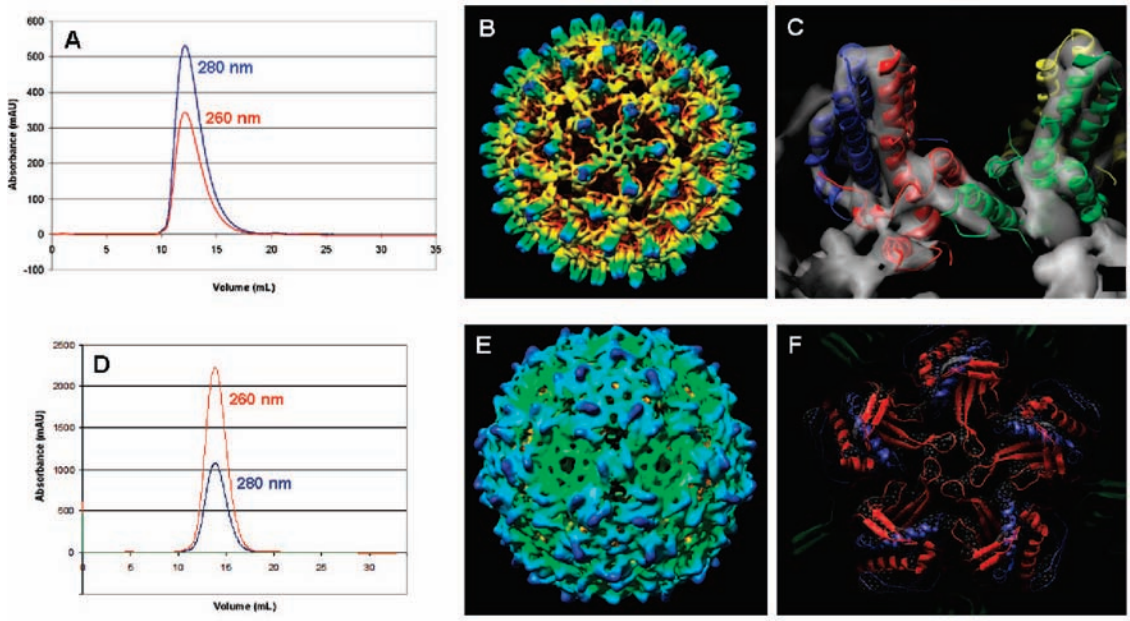

Figure 3. Characterization of the HBV (A-C) and Qβ (D-F) capsids containing **1**. (A and D) Size exclusion chromatography (Superose-6), with retention times matching those of intact native capsids. (B and E) Cryo-electron microscopy image reconstructions. (C and F) X-ray crystal structures docked into the cryo electron density maps. Characterization data for Qβ incorporating **2** may be found in Supporting Information.

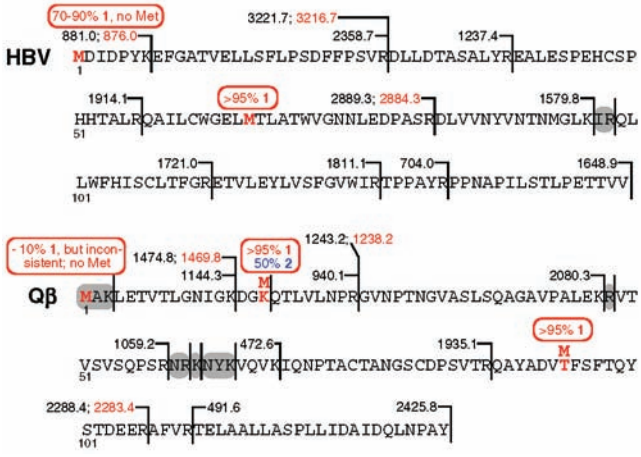

Figure 4. Summary of results from trypsin digestion and mass spectrometry of HBV and Qβ expressed with Met and **1** in locations marked in red. The detected fragments are indicated by the numerical values of *m*/*z* shown at the right of each; values in red are those with the unnatural amino acid incorporated. Many fused fragments (fragments derived from incomplete cleavage) were detected as well, giving rise to the same conclusions. The small peptides marked in gray were not detected. Conclusions about the level of incorporation of **1** at each indicated position are shown in the red ovals.

should also be noted that the attachment reaction was inhibited by the use of ligand **4** in greater than a 2:1 molar ratio with respect to Cu, consistent with previous observations (*61*), and that higher concentrations of Cu catalyst **4** gave rise to greater amounts of capsid decomposition as the number of reactions climbed above the 120-per-particle level.

The site of bioconjugation was moved from the spike to the "floor" of the HBV structure by mutation of M66 to serine. Expression of the M66S Cp149 mutant in the presence of azidohomoalanine **1** allowed the isolation of a particle having reactive azide only at the *N*-terminus (70–90% incorporation, Table 1). Reaction with fluorescein-alkyne **3** under the conditions shown in Figure 5 gave rise to the same approximate loading of 120 per particle, but isolated in significantly higher yield (60–70%, which represents the maximum possible recovery at this scale due to losses in sample handling from sucrose gradient purification; Table 2, entry 3). Since the HBV particle bearing azidohomoalanine at both positions 1 and 66 showed predominant labeling at the latter, we conclude that the more exposed position on the 4-helix bundle is both more reactive and more deleterious to capsid stability when labeled. Decomposition of the particle results in denaturation and precipitation, and thus removal of protein from the labeling reaction. The greater capsid stability in the M66S case may derive from the fact that the *N*-terminus, now the only site bearing azide groups, is relatively far from the interface between subunit dimers. Compounds attached by flexible linkers to M66, in contrast, are positioned to easily interact with the hydrophobic interior of each 4-helix bundle. The potential for small molecules to affect HBV capsid assembly and stability by binding at subunit interfaces has been previously illustrated for certain dihydropyrimidine derivatives (*63*, *64*).

Qβ proved to be much more amenable to CuAAC derivatization. Each of the few azide groups in the wild-type virus-like particle containing **1** at 5–10% of the *N*-terminal sites was addressed with alkyne reagent **4** (Table 2, entry 5). When **1** was additionally installed at each of the highly exposed K16 M positions, the particle was also completely labeled with fluorescein, causing no apparent decomposition (Table 2, entry 6). A rare sample in which azidohomoalanine was largely retained at the *N*-terminus, designated Qβ(1M-N_3)$_{160}$(K16M-N_3)$_{180}$, took on 306 $\pm$ 30 dyes under standard conditions, and 330 $\pm$ 20 dyes in the presence of higher concentrations of protein and catalyst, all with excellent particle yield and stability (Table 2, entry 7). Loading values were determined with calibrated measurements of fluorescein absorbance and protein concentration determined by a modified Lowry assay, since the Qβ VLP contains no tryptophan residues, making for poor UV–vis absorbance characteristics. The resulting particles and protein were characterized in the same manner as HBV above (see Figure 3 for size-exclusion chromatography and gel electrophoresis). Trypsin digestion and mass spectrometry confirmed the loading values by showing the expected peptide fragments (and only those fragments) to be increased by 413 Da.

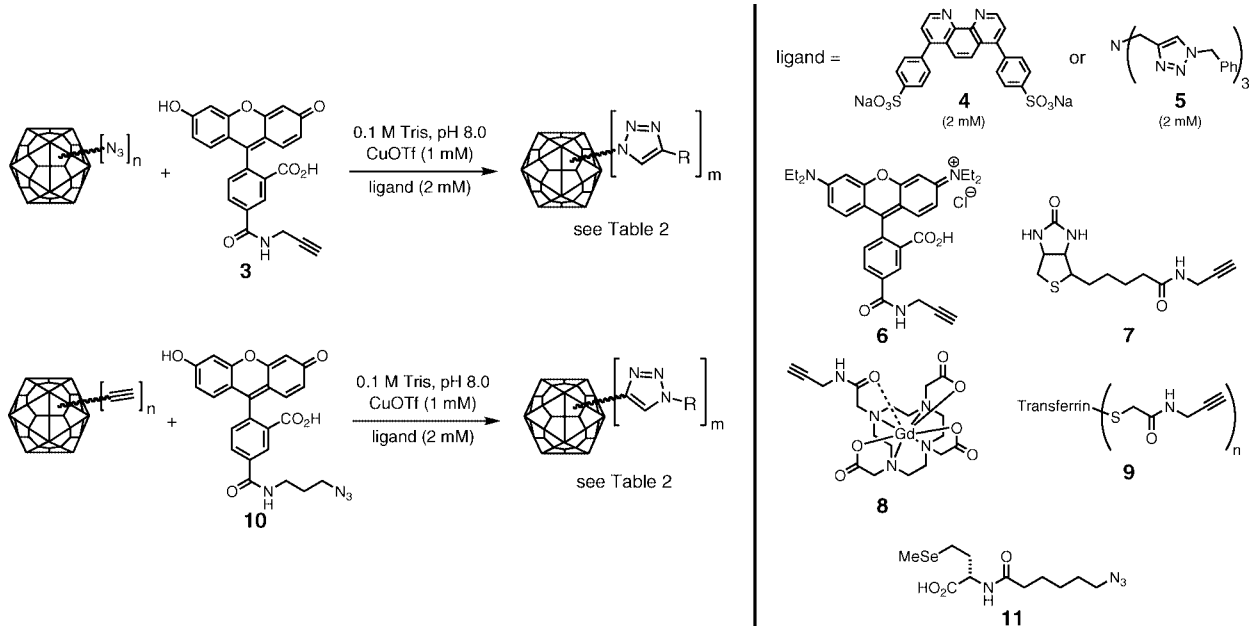

Figure 5. Copper-catalyzed azide-alkyne cycloaddition (CuAAC) reaction of virus-like particles with alkyne or azide derivatives.

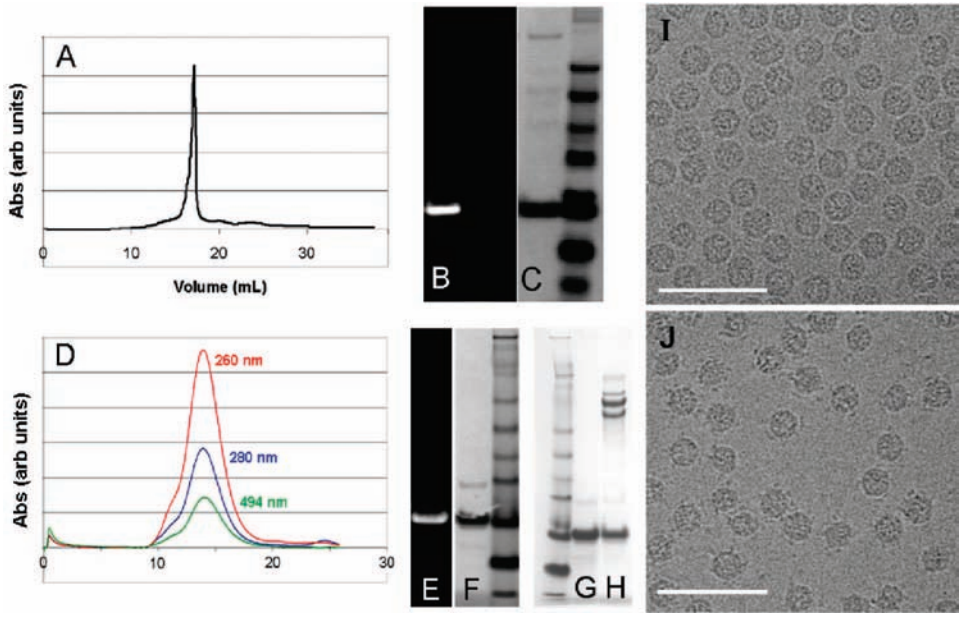

Figure 6. Characterization of virus-like capsids after CuAAC reactions: HBV = A−C; Qβ = D−H. (A) Size exclusion chromatography showing a peak with a retention volume of 18 mL corresponding to disassembled capsid. (B,C) SDS-PAGE of the Cp149 protein isolated from the reaction, visualized under ultraviolet illumination (B) and then with Coumassie staining (C). The right lane is a molecular weight ladder. (D) Size exclusion chromatography showing an elution volume of 14 mL, characteristic of intact Qβ capsids, and coelution of fluorescein with the protein showing covalent attachment. (E,F) SDS-PAGE of the Qβ protein showing fluorescein labeling as above. (G) Same as (F). (H) SDS-PAGE of purified Qβ-transferrin conjugate; the higher molecular weight bands are in the expected position for the Cp149-transferrin fusion, with multiple bands deriving from the somewhat impure nature of the starting transferrin sample. (I) Transmission electron microscopy (TEM) image of Qβ(1M-N_3)$_{9–18}$(K16M-N_3)$_{180}$. (J) TEM image of the same particle conjugated to transferrin-alkyne **9**, after purification. Note the appearance of spots surrounding most of the particles, due to the tethered 80 kD protein.

The accessibility of the K16M-N_3 insertion was further demonstrated by the chemoselective conjugation of a protein to the Qβ(1M-N_3)$_{9–18}$(K16M-N_3)$_{180}$ particle. Transferrin, an 80 kD iron transport protein, was derivatized with *N*-propargyl-bromoacetamide and purified to give **9** (Figure 5), in analogous fashion to a maleimide-alkyne derivative previously described (*35*). The CuAAC reaction of **9** with Qβ(1M-N_3)$_{9–18}$(K16M-N_3)$_{180}$ gave a particle bearing covalently attached transferrin, as shown by gel electrophoresis and TEM (Figure 6).

Qβ(1M-N_3)$_{9–18}$(T93M-N_3)$_{180}$, in which the nonterminal unnatural amino acid is on the interior surface of the capsid, was not nearly as reactive as the K16 M derivative (Table 2, entry 8). While all of the *N*-terminal residues were coupled to **3** under standard CuAAC conditions, only 30–40 dyes were attached to the particle in total, which means that only 20–30 of the 180 azide-labeled T93 M sites participated in the reaction. As before, yields of intact particles were good. The same result was observed when alkyne **8** was used. Position 93 has both a more congested protein environment than position 16, and may well be occluded by associated RNA packaged inside the particle, giving rise to sluggish reactivity.

Table 2. Results of CuAAC Reactions of VLP's Containing Unnatural Amino Acids, as Shown in Figure 5

entry	particle[a]	# incorporated per particle[b]	loading[c]	recovery[d]
1	HBV(66M)	none	0	60–70%
2	HBV(1M-N_3)$_{170–215}$(66M-N_3)$_{240}$	410–455	120 ± 15[e]	≤40%
3	HBV(1M-N_3)$_{170–215}$(M66S)	170–215	120 ± 25	60–70%
4	Qβ(K16M)	none	0	75–80%
5	Qβ(1M-N_3)$_{9–18}$	9–18	15 ± 3	80–85%
6	Qβ(1M-N_3)$_{9–18}$(K16M-N_3)$_{180}$	189–198	190 ± 20	75–80%
7	Qβ(1M-N_3)$_{160}$(K16M-N_3)$_{180}$	340	306 ± 30[f]	70–80%
8	Qβ(1M-N_3)$_{9–18}$(T93M-N_3)$_{180}$	189–198	35 ± 5	75–80%
9	Qβ(K16M-CCH)$_{90}$	90	50 ± 5	20%
10	Qβ(K16M-CCH)$_{90}$	90	85 ± 5[g]	75–80%

[a] See caption to Table 1 for nomenclature. [b] Total number of unnatural amino acids per particle, determined by trypsin digestion and mass spectrometry as described in the text. [c] The number of attached molecules (subscripts "m" in Figure 5). Unless otherwise indicated, the value was obtained from reaction with fluorescein reagents **3** or **10** and quantitation by calibrated UV–visible absorbance of the dye (average of at least three independent reactions). [d] Amount of purified intact capsids recovered from the reaction. [e] More than 90% of the attachments were made at position 66. [f] Under standard conditions; a loading of 330 ± 20 (75% recovery) was observed under the most forcing conditions tested. [g] Reaction with azide **11**, loading determined by quantitation of attached Se atoms by inductively coupled plasma optical emission spectroscopy.

Lastly, the alkyne-containing particle Qβ(K16M-CCH)$_{90}$ proved to be sensitive to the attachment of fluorescein azide **10** (Table 2, entry 9), giving rise to low recoveries of partially conjugated material. Note that azide **10**, and not alkyne **3**, induces instability in the resulting Qβ conjugate (each attached to unnatural amino acids installed at the same site). This is presumably a function of the longer tether between the reactive group and the fluorescein moiety in **10**, allowing the polycyclic aromatic structure to more easily interact with hydrophobic subunit interfaces in the particle. The use of selenomethionine derivative **11**, on the other hand, provided clean and complete triazole formation with no loss of particle integrity (Table 2, entry 10), showing again that triazole moieties are well tolerated by the Qβ capsid.

CONCLUSIONS

We describe here the first successful site-specific incorporation and subsequent reaction of unnatural amino acids into virus-like particles. The substitutions of azide- and alkyne-containing structures for methionine had no apparent effect on the ability of the resulting proteins to self-assemble into icosahedral capsids that are indistinguishable in structure from the native forms. Tight control over protein expression in methionine auxotrophic cells resulted in high yields of the assembled capsids. The degree of post-translational removal of unnatural amino acid introduced in position 1 in place of Met was variable, and was characterized by trypsin digestion and mass spectrometry analysis.

These novel capsids can be chemically addressed with perfect chemoselectivity by the CuAAC reaction. HBV was found to be sensitive to the coupling of molecules to the 4-helix-bundle spikes, while Qβ suffered from much fewer limitations in this regard. The low concentrations of azide and alkyne reagents required for coverage of most or all of the inserted azide and alkyne groups are made possible by the efficiency of the CuAAC process. Because the CuAAC reaction is insensitive to the substituents present on the azide and alkyne reactants and similarly unreactive with natural protein functional groups, the two-step process of genetically directed incorporation of azides or alkynes followed by CuAAC ligation provides a functional equivalent to the installation of almost any unnatural (triazole-linked) amino acid one can imagine.

EXPERIMENTAL PROCEDURES

CP149 HBV Plasmid Construction. A pET11c plasmid containing the Cp149 sequence was gratefully received from Prof. Adam Zlotnick of the Oklahoma University Health Sciences Center. In order to provide tight inducible control overexpression (pET11c was found to be constitutively expressed to an unacceptable degree), the HBV gene was amplified using the following primers: Cp149F 5′-AAG AAG GAG GAT ATA **GGT CTC AC** ATG GAC ATT GAC CCT-3′ and Cp149R 5′-TCG GGC TTT GTT AGC AGC CGG **AAG CTT** ATA CTA AAC AAC CGT-3′ The PCR product was sequentially digested with Hind III and Bsa I, and then ligated into pQE-60 plasmid (Qiagen) which had been sequentially digested with Hind III and Nco I. The resulting plasmid was transformed into competent M15MA cells harboring the pREP4 plasmid yielding the expression cells M15MA(pQE-60/HBV).

Site-Directed Mutagenesis of Cp149 HBV. Mutations were introduced into the coat protein of HBV by standard overlap PCR to remove the methionine at position 66 (M66S). The following general forward and reverse primers were used: Forward 5′-AGA ATT CAT TAA AGA GGA GAA ATT AAC-3′, Reverse 5′-CCA AGC TCA GCT AAT GCT TAT CCT-3′, M66SF 5′-GGA GAC TTA TCT ACT CTA GCT-3′, M66SR 5′-AGC TAG AGT AGA TAA GTC TCC-3′. The PCR products were sequentially digested with Hind III and NcoI and ligated into pQE-60 that had previously been digested with Hind III and Nco I. The resulting plasmids were transformed into competent M15MA cells yielding the following expression construct: M15MA(pQE-60/M66S HBV).

Insertion of the K16 M Qβ Coat Protein Gene into pQE-60. The coat protein gene for Qβ containing the point mutation K16 M was originally created in the pET-28b plasmid, which is not compatible with expression in M15 based Met auxotrophic *E. coli* cells. Therefore, the Qβ coat protein gene was amplified from the pET-28b plasmid using the following primers: QBF 5′-AAA GAG GAG AAA TTA AGG TCT CAC ATG GCA AAA TTA GAG ACT-3′ and QBR 5′-CCA AGC TCA GCT AAT T**AA GCT T**TA TTA ATA-3′ The PCR product was sequentially digested with Hind III and Bsa I. The digested PCR product was ligated into pQE-60 plasmid (Qiagen), which had been sequentially digested with Hind III and Nco I. The resulting plasmid was transformed into competent M15MA cells harboring the pREP4 plasmid yielding the expression cells M15MA(pQE-60/Qβ K16M).

Site-Directed Mutagenesis of K16 M Qβ. The following primers were used to introduce Met at position 93 (T93M), using standard overlap PCR as above: Forward 5′-AGA ATT CAT TAA AGA GGA GAA ATT AAC-3′, Reverse 5′-CCA AGC TCA GCT AAT GCT TAT CCT-3′, WTF 5′-GGA GAC TTA TCT ACT CTA GCT-3′, WTR 5′-AGC TAG AGT AGA TAA GTC TCC-3′. The PCR products were sequentially digested with Hind III and NcoI and ligated into pQE-60 that had previously been digested with Hind III and Nco I. The resulting plasmids were transformed into competent M15MA cells yielding the

following expression construct: M15MA(pQE-60/WT Qβ) and M15MA(pQE-60/T93 M Qβ).

Synthesis of Unnatural Amino Acids (1 and 2). Several short routes to azidohomoalanine (**1**) have been reported in the literature (*15*, *65–67*). We chose a simplified version of the method of Rappoport and co-workers (*68*), since the starting lactone is commercially available in racemic form at modest cost and an enantiospecific synthesis is not required because *E. coli* incorporates only the L-isomer during protein expression. α-Amino-γ-butyrolactone hydrobromide (5.02 g, 27.6 mmol) was refluxed in 1:1 HBr/glacial HOAc (250 mL) overnight (17–24 h). The HBr and acetic acid were then removed by rotary evaporation, yielding crude bromohomoalanine. The crude material was then dissolved in a solution of NaN_3 (9.00 g, 138 mmol) in water (125 mL) and refluxed again overnight. The solution was evaporated to dryness and the residual tan solid resuspended in a minimal volume of 0.1 M HCl. The acidic solution was passed through a column of Dowex 50WX4–100 ion-exchange resin, washing with water and eluting the product with 1 M NH_4OH. The collected fractions were evaporated to dryness, yielding an oil. Compound **1** was obtained as a tan solid (1.49 g, 10.3 mmol, 37%) upon resuspending in a minimal volume of water and lyophilizing. The purity of the solid was determined by NMR using pyridine as an internal standard and generally was >85% (overall yields 32–38%). ^{1}H NMR (D_2O, 200 MHz, $d_1 = 10$ s) δ 3.44 (t, 2H, $CHCH_2C\underline{H}_2N_3$), 3.07 (dd, 1H, $C\underline{H}CH_2CH_2N_3$), 1.58 (m, 2H, $CHC\underline{H}_2CH_2N_3$). Homopropargylglycine (**2**) was prepared as previously described (*10*).

Incorporation of 1 into HBV and Qβ. A single of colony of cells expressing the desired HBV or Qβ construct was used to inoculate 5 mL of SOB media containing carbenicillin (100 μg/mL) and kanamycin (50 μg/mL) and was grown overnight. The resulting culture was transferred into 500 mL of M9 minimal media supplemented with all 20 amino acids, carbenicillin (100 μg/mL), and kanamycin (100 μg/mL) and allowed to grow for 8 h. Aliquots (25 mL) of the resulting culture were transferred into each of 11 flasks containing 500 mL of fresh minimal media supplemented with all 20 amino acids, carbenicillin (100 μg/mL) and kanamycin (100 μg/mL) and allowed to grow overnight. In the morning the cells were pelleted and resuspended in 500 mL of fresh M9 minimal media supplemented with all of the natural amino acids minus methionine. The cells were agitated at 37 °C for 30–40 min, and then transferred into new flasks of M9 minimal media supplemented with all of the natural amino acids minus methionine, IPTG (1 mM), carbenicillin (100 μg/mL), kanamycin (100 μg/mL), and azidohomoalanine (80 mg of racemate). After 6 h at 37 °C, the cells were harvested and stored at −80 °C.

For each preparation, 30–60 g of cells were allowed to thaw at room temperature and were resuspended in 50 mL distilled water. Cold lysis buffer (200 mL, 50 mM HEPES pH 8.0, 500 mM NaCl, 0.1 mg/mL DNase1, and 0.1 mg/mL RNaseA) was added and the cells were subjected to three cycles of sonication (2 min sonication and 2 min rest per cycle). Lysozyme (1 mg per mL of lysis buffer) was added and the solution was stirred in the cold room for 1 h. Insoluble cell debris was removed by centrifugation at 10 000 rpm for 30 min in a JA-10 rotor (Beckman).

For HBV, ammonium sulfate was added to the supernatant to a final concentration of 40% of saturation, and allowed to stir at room temperature for 30 min. The precipitated HBV coat protein was separated by centrifugation (10 000 rpm, 30 min, JA-10 rotor), and then was resuspended in 0.1 M potassium phosphate buffer (50 mL, pH 7.0). Any remaining insoluble material was removed by centrifugation (10 000 rpm, 15 min, JA-17 rotor). Sodium chloride was added to a final concentration of 0.5 M and the HBV coat proteins were allowed to assemble overnight. The resulting assembled VLPs were separated from smaller proteins by ultrapelleting (42 000 rpm, 6 h, 4 °C, 50.2Ti rotor, L90K ultracentrifuge). The pelleted material was resuspended in 3–10 mL of 0.1 M potassium phosphate buffer (pH 7.0). Further purification was accomplished by the use of two successive sucrose gradient sedimentations (10–40% sucrose gradients in SW28 rotor at 28 000 rpm for 6 h at 4 °C.

For Qβ, PEG 8000 was added to the supernatant to a final concentration of 10% and the mixture was allowed to stir at room temperature for 30 min. The precipitated Qβ capsids were separated by centrifugation (10 000 rpm, 30 min, JA-10 rotor), and then resuspended in 0.1 M potassium phosphate buffer (50 mL, pH 7.0). Insoluble material was removed by centrifugation (10 000 rpm, 15 min, JA-17 rotor), and VLPs were isolated and purified as for HBV above, with final concentration by ultrapelleting.

Characterization of HBV and Qβ Particles. All protein preparations were analyzed by denaturing gel electrophoresis (4–12% NuPAGE Bis-Tris gel, Invitrogen) to estimate their purity; in all cases, the anticipated coat protein band constituted >95% of the intensity visualized by densitometry after Coomassie blue staining. HBV concentration was determined by absorbance at 280 nm, 1 mg/mL providing an absorbance value of 1.74. The concentrations of modified HBV and all Qβ particles were determined with the Modified Bradford Assay (Pierce, Inc.) and a BSA standard curve. Since HBV VLPs do not contain significant quantities of RNA, the ratio of absorbances at 260 nm vs 280 nm was 0.6–0.7. Qβ VLPs package random cellular nucleic acid, giving rise to A_{260}/A_{280} values of 1.8–1.9. The presence of individual, aggregated, and disassembled particles was determined by size-exclusion chromatography on a Superose 6 column using an Akta Explorer (GE Healthcare) fast protein liquid chromatography (FPLC) instrument. Transmission electron microscopy was performed by applying particles at a concentration of 0.2 mg/mL to a carbon-coated Formvar transmission electron grid. The grids were stained with 2% uranyl acetate, and visualized in a Phillips CM120 transmission electron microscope.

VLP samples were processed for determination of derivatization site(s) by MALDI mass spectrometry as follows. Samples (100 μL, 1–2 mg/mL protein) were mixed with 300 μL of 8 M urea and 30 μL of 1 M DTT, and incubated at 37 °C for 1 h to allow the protein to denature. Iodoacetamide (1 M, 50 μL) was added to cap any free cysteines and the sample was again incubated at 37 °C for 1 h. DTT (30 μL) was added to quench unreacted capping reagent, and the samples were diluted to a final volume of 1.9 mL using 25 mM ammonium bicarbonate (pH 8.0). Each sample was digested with 30 μg of either trypsin or Glu-C protease overnight at 37 °C. The samples were then concentrated to approximately 300 μL, and urea was removed with Zip-tips (Microcon) prior to MALDI analysis.

Cryoelectron Microscopy and Analysis. Samples were prepared for CryoEM analysis by preservation in vitreous ice via rapid-freeze plunging onto plasma cleaned Cflat carbon film grids using a Vitrobot (FEI Co). Data collection was performed on Tecnai F20 electron microscopes (FEI Co.) operating at 120 keV using a dose of $\sim 20e^-/Å^2$ and a nominal underfocus of 0.8 to 3 μm utilizing the Leginon data collection software (*69*). For the reconstructions, 735 micrographs of azidohomoalanine-incorporated HBV were collected at a nominal magnification of 80 000× at a pixel size of 0.14 nm at the specimen. 125 micrographs of azidohomoalanine-incorporated Qβ particles were collected at a nominal magnification of 50 000× at a pixel size of 0.23 nm at the specimen. All micrographs were collected on a 4000 × 4000 CCD camera (Gatan Inc.). CryoEM analysis of all other Qβ variants, including the transferrin-alkyne

conjugated particles, was performed under the same conditions as the azidohomoalanine-incorporated HBV particles.

The contrast transfer function (CTF) for each micrograph was estimated using the Automated CTF Estimation (ACE) package (*70*). 8906 HBV particles and 11 882 Qβ particles were extracted from the collected data at a box size of 304 × 304 pixels and 180 × 180 pixels, respectively. The HBV particles were binned by a factor of 2 for the reconstruction. Phase correction of the single particles and subsequent three-dimensional refinement was carried out with the EMAN software package (*71*). The amplitudes of the resulting refined structures were adjusted with the SPIDER software package (*72*). Resolution of the final HBV and Qβ densities were determined to be around 8 Å and 10 Å (respectively) according to 0.5 FSC criteria. Rigid-body docking of crystal structures into the reconstruction density and graphical representations were produced by the Chimera visualization software package (*73*, *74*).

Copper Catalyzed Azide-Alkyne Cycloaddition Reactions. Purified azide-containing HBV or Qβ particles were pelleted out of solution (42 000 rpm, 6 h), the supernatant was removed, and residual buffer was allowed to drain away from the pellet. The viral pellet was then taken into a nitrogen-filled glovebox (without exposure to vacuum) and resuspended in a minimal volume of degassed 0.1 M Tris at pH 8.0. A small aliquot of the virus solution was removed from the glovebox and used to determine virus concentration. A typical conjugation reaction employed a VLP concentration of 2 mg/mL in 0.1 M Tris (pH 8.0) in a round-bottomed 2 mL Eppendorf tube (rather than conical tubes that do not provide good mixing upon gentle agitation). Fluorescein alkyne **6** (final concentration 1 mM) was added, followed by a freshly prepared buffer solution of Cu(I) triflate and 2 equiv of ligand **4** or **5**. Final concentrations of Cu were either 100 μM or 250 μM for HBV, 500 μM or 1 mM for Qβ. The tube was sealed, placed in a secondary sealed container (usually a small round-bottomed flask), removed from the glovebox, and attached to a slow tumbler arm for agitation at room temperature for 16–18 h. After completion of the reaction, intact virus-like particles were separated from excess labeling reagent using a combination of 10–40% sucrose gradients (38 000 rpm, SW41 rotor, 4 h for HBV, 3 h for Qβ) and ultrapelleting.

ACKNOWLEDGMENT

This work was supported by the NIH (AI056013, RR021886, GM62523), the David & Lucille Packard Foundation Interdisciplinary Science Program, and the Canadian Institutes of Health Research (postdoctoral fellowship to A.K.U.).Cryo-electron microscopy was performed at the National Resource for Automated Molecular Microscopy which is supported by the NIH NCRR P41 program (RR17573).

Supporting Information Available: Details of protein expression, characterization of alkyne-labeled particles, and summary of previously reported yields of proteins incorporating unnatural amino acids. This material is available free of charge via the Internet at http://pubs.acs.org.

LITERATURE CITED

(1) Noren, C. J., Anthony-Cahill, S. J., Griffith, M. C., and Schultz, P. G. (1989) A general method for site-specific incorporation of unnatural amino acids into proteins. *Science 244*, 182–188.

(2) Cornish, V. W., Benson, D. R., Altenbach, C. A., Hideg, K., Hubbell, W. L., and Schultz, P. G. (1994) Site-specific incorporation of biophysical probes into proteins. *Proc. Natl. Acad. Sci. USA 91*, 2910–2914.

(3) Wang, L., Brock, A., Herberich, B., and Schultz, P. G. (2001) Expanding the genetic code of *Escherichia coli*. *Science 292*, 498–500.

(4) Anderson, J. C., and Schultz, P. G. (2003) Adaptation of an orthogonal archaeal leucyl-tRNA and synthetase pair for four-base, amber, and opal suppression. *Biochemistry 42*, 9598–9608.

(5) Chin, J. W., Cropp, T. A., Anderson, J. C., Mukherji, M., Zhang, Z., and Schultz, P. G. (2003) An expanded eukaryotic genetic code. *Science 301*, 964–967.

(6) Deiters, A., Cropp, T. A., Mukherji, M., Anderson, J. C., and Schultz Peter, G. (2003) Adding amino acids with novel reactivity to the genetic code of *Saccharomyces cerevisiae*. *J. Am. Chem. Soc. 125*, 11782–11783.

(7) Tian, F., Tsao, M.-L., and Schultz, P. G. (2004) A phage display system with unnatural amino acids. *J. Am. Chem. Soc. 125*, 15962–15963.

(8) Ryu, Y., and Schultz, P. G. (2006) Efficient incorporation of unnatural amino acids into proteins in *Escherichia coli*. *Nat. Methods 3*, 263–265.

(9) Anderson, J. C., Wu, N., Santoro, S. W., Lakshman, V., King, D. S., and Schultz, P. G. (2004) An expanded genetic code with a functional quadruplet codon. *Proc. Natl. Acad. Sci. USA 101*, 7566–7571.

(10) Van Hest, J. C. M., Kiick, K. L., and Tirrell, D. A. (2000) Efficient incorporation of unsaturated methionine analogues into proteins in vivo. *J. Am. Chem. Soc. 122*, 1282–1288.

(11) Kiick, K. L., and Tirrell David, A. (2000) Protein engineering by *in vivo*incorporation of non-natural amino acids: Control of incorporation of methioonine analogues by methionyl tRNA synthetase. *Tetrahedron 56*, 9487–9493.

(12) Kiick, K., L., Weberskirch, R., and Tirrell, D. A. (2001) Identification of an expanded set of translationally active methionine analogues in *Escherichia coli*. *FEBS Lett. 502*, 25–30.

(13) Kiick, K. L., Saxon, E., Tirrell, D. A., and Bertozzi, C. R. (2002) Incorporation of azides into recombinant proteins for chemoselective modification by the Staudinger ligation. *Proc. Natl. Acad. Sci. USA 99*, 19–24.

(14) Link, A. J., and Tirrell, D. A. (2003) Cell surface labeling of *Escherichia coli* via copper(I)-catalyzed [3 + 2] cycloaddition. *J. Am. Chem. Soc. 125*, 11164–11165.

(15) Link, A. J., Vink, M. K. S., and Tirrell, D. A. (2004) Presentation and detection of azide functionality in bacterial cell surface proteins. *J. Am. Chem. Soc. 126*, 10598–10602.

(16) Link, A. J., and Tirrell, D. A. (2005) Reassignment of sense codons *in vivo*. *Methods 36*, 291–298.

(17) Link, A. J., Vink, M. K. S., Agard, N. J., Prescher, J. A., Bertozzi, C. R., and Tirrell, D. A. (2006) Discovery of aminoacyl-tRNA synthetase activity through cell-surface display of non-canonical amino acids. *Proc. Natl. Acad. Sci. USA 103*, 10180–10185.

(18) van Hest, J. C. M., and Tirrell, D. A. (1998) Efficient introduction of alkene functionality into proteins *in vivo*. *FEBS Lett. 428*, 68–70.

(19) Kiick, K. L., Van Hest, J. C. M., and Tirrell, D. A. (2000) Expanding the scope of protein biosynthesis by altering the methionyl-tRNA synthetase activity of a bacterial expression host. *Angew. Chem., Int. Ed. 39*, 2148–2152.

(20) Tang, Y., and Tirrell, D. A. (2001) Biosynthesis of a highly stable coiled-coil protein containing hexafluoroleucine in an engineered bacterial host. *J. Am. Chem. Soc. 123*, 11089–11090.

(21) Wang, Q., Chan, T. R., Hilgraf, R., Fokin, V. V., Sharpless, K. B., and Finn, M. G. (2003) Bioconjugation by copper(I)-catalyzed azide-alkyne [3 + 2] cycloaddition. *J. Am. Chem. Soc. 125*, 3192–3193.

(22) Yoshikawa, E., Fournier, M. J., Mason, T. L., and Tirrell, D. A. (1994) Genetically Engineered fluoropolymers. Synthesis of repetitive polypeptides containing p-fluorophenylalanine residues. *Macromolecules 27*, 5471–5475.

(23) Budisa, N., Alefelder, S., Bae, J. H., Golbik, R., Minks, C., Huber, R., and Moroder, L. (2001) Proteins with β-(thienopyrrolyl)alanines as alternative chromophores and pharmaceutically active amino acids. *Protein Sci. 10*, 1281–1292.
(24) Bae, J. H., Alefelder, S., Kaiser, J. T., Friedrich, R., Moroder, L., and Budisa, N. (2001) Incorporation of β-seleno(3,2-b)pyrrolyl-alanine into proteins for phase determination in protein X-ray crystallography. *J. Mol. Biol. 309*, 925–936.
(25) Renner, C., Alefelder, S., Bae, J. H., Budisa, N., Huber, R., and Moroder, L. (2001) Fluoroprolines as tools for protein design and engineering. *Angew. Chem., Int. Ed. 40*, 923–925.
(26) Link, A. J., Mock, M. L., and Tirrell, D. A. (2003) Non-canonical amino acids in protein engineering. *Curr. Opin. Biotechnol. 14*, 603–609.
(27) Saxon, E., and Bertozzi Carolyn, R. (2000) Cell surface engineering by a modified Staudinger reaction. *Science 287*, 2007–2010.
(28) Vocadlo, D. J., and Bertozzi, C. R. (2004) A strategy for functional proteomic analysis of glycosidase activity from cell lysates. *Angew. Chem., Int. Ed. 43*, 5338–5342.
(29) Agard, N. J., Baskin, J. M., Prescher, J. A., Lo, A., and Bertozzi, C. R. (2006) A comparative study of bioorthogonal reactions with azides. *ACS Chem. Biol. 1*, 644–648.
(30) Mahal, L. K., Yarema, K. J., and Bertozzi Carolyn, R. (1997) Engineering chemical reactivity on cell surfaces through oligosaccharide biosynthesis. *Science 276*, 1125–1128.
(31) Agard, N. J., Prescher Jennifer, A., and Bertozzi Carolyn, R. (2004) A strain-promoted (3 + 2) azide-alkyne cycloaddition for covalent modification of biomolecules in living systems. *J. Am. Chem. Soc. 126*, 15046–15047.
(32) Rostovtsev, V. V., Green, L. G., Fokin, V. V., and Sharpless, K. B. (2002) A stepwise Huisgen cycloaddition process: Copper(I) catalyzed regioselective "ligation" of azides and terminal alkynes. *Angew. Chem., Int. Ed. 41*, 2596–2599.
(33) Tornøe, C. W., Christensen, C., and Meldal, M. (2002) Peptidotriazoles on solid phase: [1,2,3]-triazoles by regiospecific copper(I)-catalyzed 1,3-dipolar cycloadditions of terminal alkynes to azides. *J. Org. Chem. 67*, 3057–3062.
(34) Wang, Q., Chan, T. R., Hilgraf, R., Folkin, V. V., Sharpless, K. B., and Finn, M. G. (2003) Bioconjugation by copper(I)-catalyzed azide-alkyne (3 + 2) cycloaddition. *J. Am. Chem. Soc. 125*, 3192–3193.
(35) Sen Gupta, S., Kuzelka, J., Singh, P., Lewis, W. G., Manchester, M., and Finn, M. G. (2005) Accelerated bioorthogonal conjugation: a practical method for the ligation of diverse functional molecules to a polyvalent virus scaffold. *Bioconjugate Chem. 16*, 1572–1579.
(36) Deiters, A., Cropp, T. A., Summerer, D., Mukherji, M., and Schultz, P. G. (2004) Site-specific PEGylation of proteins containing unnatural amino acids. *Bioorg. Med. Chem. Lett. 14*, 5743–5745.
(37) Kaltgrad, E., Sen Gupta, S., Punna, S., Huang, C.-Y., Chang, A., Wong, C.-H., Finn, M. G., and Blixt, O. (2007) Anti-carbohydrate antibodies elicited by polyvalent display on a viral scaffold. *ChemBioChem 8*, 1455–1462.
(38) Prasuhn, J. D.E., Yeh, R. M., Obenaus, A., Manchester, M., and Finn, M. G. (2007) Viral MRI contrast agents: coordination of Gd by native virions and attachment of Gd complexes by azide-alkyne cycloaddition. *Chem. Commun. 12*, 1269–1271.
(39) Singh, P., Prasuhn, D. E. J., Yeh, R. M., Destito, G., Rae, C. S., Osborn, K., Finn, M. G., and Manchester, M. (2007) Bio-distribution, toxicity and pathology of cowpea mosaic virus nanoparticle in vivo. *J. Controlled Release 120*, 41–50.
(40) Beatty, K. E., Xie, F., Wang, Q., and Tirrell, D. A. (2005) Selective dye-labeling of newly synthesized proteins in bacterial cells. *J. Am. Chem. Soc. 127*, 14150–14151.
(41) Dieterich, D. C., Link, A. J., Graumann, J., Tirrell, D. A., and Schuman, E. M. (2006) Selective identification of newly synthesized proteins in mammalian cells using bioorthogonal noncanonical amino acid tagging (BONCAT). *Proc. Natl. Acad. Sci. USA 103*, 9482–9487.
(42) Beatty, K. E., Liu, J. C., Xie, F., Dieterich, D. C., Schuman, E. M., Wang, Q., and Tirrell David, A. (2006) Fluorescence visualization of newly synthesized proteins in mammalian cells. *Angew. Chem., Int. Ed. 45*, 7364–7367.
(43) Dieterich, D. C., Lee, J. J., Link, A. J., Graumann, J., Tirrell David, A., and Schuman, E. M. (2007) Labeling, detection, and identification of newly synthesized proteomes with bioorthogonal non-canonical amino acid tagging. *Nat. Prot. 2*, 532–540.
(44) Speers, A. E., and Cravatt, B. F. (2004) Profiling enzyme activities *in vivo* using click chemistry method. *Chem. Biol. 11*, 535–546.
(45) Speers, A. E., Adam, G. C., and Cravatt, B. F. (2003) Activity based protein profiling *in vivo* using a copper(I)-catalyzed azide-alkyne cycloaddition. *J. Am. Chem. Soc. 125*.
(46) Kenney, J. M., von Bonsdorff, C.-H., Nassal, M., and Fuller, S. D. (1995) Evolutionary conservation in the hepatitis B virus core structure: comparison of human and duck cores. *Structure 3*, 1009–1019.
(47) Wynne, S. A., Crowther, R. A., and Leslie, A. G. (1999) The crystal structure of human hepatitis B virus. *Mol. Cell 6*, 771–780.
(48) Hilditch, C. M., Rogers, L. J., and Bishop, D. H. L. (1990) Physicochemical analysis of the hepatitis B virus core antigen produced by a baculovirus expression vector. *J. Gen. Virol. 71*, 2755–2759.
(49) Allen, M., Bulte, J. W. M., Liepold, L., Basu, G., Zywicke, H. A., Frank, J. A., Young, M., and Douglas, T. (2005) Paramagnetic viral nanoparticles as potential high-relaxivity magnetic resonance contrast agents. *Magn. Res. Med. 54*, 807–812.
(50) Cohen, B. J., and Richmond, J. E. (1982) Electron microscopy of hepatitis B core antigen synthesized in *E. coli*. *Nature 296*, 677–678.
(51) Wingfield, P. T., Stahl, S. J., Williams, R. W., and Steven, A. C. (1995) Hepatitis core antigen produced in *Escherichia coli*: subunit composition, conformational analysis, andin vitro capsid assembly. *Biochemistry 34*, 4919–4932.
(52) Vallegaard, K., Fridborg, K., and Liljas, L. (1994) Crystallization and preliminary x-ray diffraction studies of the bacteriophage Qβ. *Acta Crystallogr., Sect. D: Biol. Cryst. D50*, 105–109.
(53) Tars, K., Bundule, M., Fridborg, K., and Liljas, L. (1997) The crystal structure of bacteriophage GA and a comparison of bacteriophages belonging to the major groups of *Escherichia coli* leviviruses. *J. Mol. Biol. 271*, 759–773.
(54) Overby, L. R., Barlow, G. H., Doi, R. H., Jacob, M., and Spiegelman, S. (1966) Comparison of two serologically distinct ribonucleic acid bacteriophages. *J. Bacteriol. 91*, 442–448.
(55) Golmohammadi, R., Fridborg, K., Bundule, M., Valegaard, K., and Liljas, L. (1996) The crystal structure of bacteriophage Qβ at 3.5 Å resolution. *Structure 4*, 543–554.
(56) Kozlovska, T. M., Cielens, I., Dreilinna, D., Dislers, A., Baumanis, V., Ose, V., and Pumpens, P. (1993) Recombinant RNA phage Qβ capsid particles synthesized and self-assembled in *Escherichia coli*. *Gene 137*, 133–137.
(57) Vasiljeva, I., Kozlovska, T., Cielens, I., Strelnikova, A., Kazaks, A., Ose, V., and Pumpens, P. (1998) Mosaic Qβ coats as a new presentation model. *FEBS Lett. 431*, 7–11.
(58) Freivalds, J., Dislers, A., Ose, V., Skrastina, D., Cielens, I., Pumpens, P., Sasnauskas, K., and Kazaks, A. (2006) Assembly of bacteriophage Qβ virus-like particles in yeast *Saccharomyces cerevisiae* and *Pichia pastoris*. *J. Biotechnol. 123*, 297–303.
(59) Shepherd, C. M., Borelli, I. A., Lander, G., Natarajan, P., Siddavanahalli, V., Bajaj, C., Johnson, J. E., Brooks, C. L., III, and Reddy, V. S. (2006) VIPERdb: a relational database for structural virology. *Nucleic Acids Res. 34*, D386–D389.
(60) Hirel, P.-H., Schmitter, J.-M., Dessen, P., Fayat, G., and Blanquet, S. (1989) Extent of *N*-terminal methionine excision from *Escherichia coli* proteins is governed by the side-chain length of the penultimate amino acid. *Proc. Natl. Acad. Sci. USA 86*, 8247–8251.

(61) Lewis, W. G., Magallon, F. G., Fokin, V. V., and Finn, M. G. (2004) Discovery and characterization of catalysts for azide-alkyne cycloaddition by fluorescence quenching. *J. Am. Chem. Soc. 126*, 9152–9153.

(62) Sen Gupta, S., Raja, K. S., Kaltgrad, E., Strable, E., and Finn, M. G. (2005) Virus-glycoploymer conjugates by copper(I)-catalysis of atom transfer radical polymerization and azide-alkyne cycloaddition. *Chem. Commun.* 4315–4317.

(63) Stray, S. J., Bourne, C. R., Punna, S., Lewis, W. G., Finn, M. G., and Zlotnick, A. (2005) A heteroaryldihydropyrimidine activates and can misdirect hepatitis B virus capsid assembly. *Proc. Natl. Acad. Sci. USA 102*, 8138–8143.

(64) Bourne, C. R., Finn, M. G., and Zlotnick, A. (2006) Global structural changes in hepatitis B virus capsids induced by the assembly effector HAP1. *J. Virol. 80*, 11055–11061.

(65) Mangold, J. B., Mischke, M. R., and LaVelle, J. M. (1989) Azidoalanine mutagenicity in *Salmonella*: Effect of homologation and α-methyl substitution. *Mut. Res. 308*, 33–42.

(66) Link, A. J., Vink, M. K. S., and Tirrell, D. A. (2007) Preparation of the functionalizable methionine surrogate azidohomoalanine *via* copper-catalyzed diazo transfer. *Nat. Protocols 2*, 1879–1883.

(67) Link, A. J., Vink, M. K. S., and Tirrell, D. A. (2007) Synthesis of the functionalizable methionine surrogate azidohomoalanine using Boc-homoserine as precursor. *Nat. Protocols 2*, 1884–1887.

(68) McLaughlin, M., Mohareb, R. M., and Rapoport, H. (2003) An efficient procedure for the preparation of 4-substituted 5-aminoimidazoles. *J. Org. Chem. 68*, 50–54.

(69) Suloway, C., Pulokas, J., Fellmann, D., Cheng, A., Guerra, F., Quispe, J., Stagg, S., Potter, C. S., and Carragher, B. (2005) Automated molecular microscopy: the new Leginon system. *J. Struct. Biol. 151*, 41–60.

(70) Mallick, S. P., Carragher, B., Potter, C. S., and Kriegman, D. J. (2005) ACE: automated CTF estimation. *Ultramicroscopy 104*, 8–29.

(71) Ludtke, S. J., Baldwin, P. R., and Chiu, W. (1999) EMAN: semiautomated software for high-resolution single-particle reconstructions. *J. Struct. Biol. 128*, 82–97.

(72) Frank, J., Radermacher, M., Penczek, P., Zhu, J., Li, Y., Ladjadj, M., and Leith, A. (1996) SPIDER and WEB: processing and visualization of images in 3D electron microscopy and related fields. *J. Struct. Biol. 116*, 190–199.

(73) Goddard, T. D., Huang, C. C., and Ferrin, T. E. (2005) Software extensions to UCSF Chimera for interactive visualization of large molecular assemblies. *Structure 13*, 473–482.

(74) Goddard, T. D., Huang, C. C., and Ferrin, T. E. (2007) Visualizing density maps with UCSF Chimera. *J. Struct. Biol. 157*, 281–287.

BC700390R

Enhanced Cell Penetration of Acid-Degradable Particles Functionalized with Cell-Penetrating Peptides

Jessica L. Cohen,[†] Adah Almutairi,[†] Joel A. Cohen,[†] Matt Bernstein,[‡] Steven L. Brody,[‡] Daniel P. Schuster,[‡] and Jean M. J. Fréchet*,[†]

College of Chemistry, University of California, Berkeley, California 94720-1460, and Washington University in St. Louis School of Medicine, St. Louis, Missouri. Received November 11, 2007; Revised Manuscript Received December 11, 2007

Biopharmaceuticals, such as proteins and DNA, have demonstrated their potential to prevent and cure diseases. The success of such therapeutic agents hinges upon their ability to cross complex barriers in the body and reach their target intact. In order to reap the full benefits of these therapeutic agents, a delivery vehicle capable of delivering cargo to all cell types, both phagocytic and non-phagocytic, is needed. This article presents the synthesis and evaluation of a microparticle delivery vehicle capable of cell penetration and sub-cellular triggered release of an encapsulated payload. pH-sensitive polyacrylamide particles functionalized with a polyarginine cell-penetrating peptide (CPP) were synthesized. The incorporation of a CPP into the microparticles led to efficient uptake by non-phagocytic cells in culture. In addition, the CPP-modified particles showed no cytotoxic effects at concentrations used in this study. The results suggest that these particles may provide a vehicle for the successful delivery of therapeutic agents to various cell types.

INTRODUCTION

In addition to small-molecule based drugs, biopharmaceuticals, such as proteins and DNA, have tremendous potential to prevent and cure diseases (*1–3*). Currently there are over 400 biotechnology medicines in development for the treatment of over 100 diseases, including medications to treat or help prevent multiple sclerosis, hepatitis, breast cancer, and diabetes (*4*). The widespread success of such therapeutic agents hinges upon their ability to cross complex barriers in the body and to reach their target intact. Exogenous therapeutic agents are notoriously unstable in the harsh *in vivo* environment due to proteolytic degradation, sequestration, and renal clearance. These factors limit their use as therapeutic agents. However, encapsulation strategies have successfully mitigated some of these stability and delivery issues by providing protection from physical and chemical damage (*5–11*). Recent advances in polymer synthesis have allowed formulations capable of encapsulation and controlled release of macromolecular therapeutic agents, thereby increasing their stability and ultimately their bioavailability (*12–15*). In addition, by incorporating certain ligands or compounds into the polymer backbone, it is possible to enhance delivery and targeting of the vehicle (*16, 17*). A recent delivery strategy involves the use of cell-penetrating peptides to enhance cellular uptake of cargo by non-phagocytic cells (*18*). Herein, we show the integration of ligands for cell penetration and sub-cellular triggered release in a single delivery vehicle.

Biodegradable polymers have been extensively investigated as potential carriers for biopharmaceuticals (*19–21*). Delivery of a therapeutic agent via encapsulation in particles incorporating programmed release mechanisms, such as acid-degradable crosslinks, allows for their controlled release at select targets, such as inflammatory tissues, tumors, and cells of the immune system. This selective delivery through triggered release mechanisms enables enhanced therapeutic efficiency, allowing lower doses of the therapeutic agent to be used, with less toxicity (*22–27*). Recently, we described the synthesis of polyacrylamide microparticles that incorporated acid-labile crosslinks into the polymer scaffold, as well as targeting groups on the surface (*28–31*). These acid-degradable particles were capable of encapsulating and delivering a protein antigen to phagocytic cells of the immune system, specifically macrophages and dendritic cells. These cell types specialize in taking up foreign matter and trafficking it to acidic sub-cellular lysosomal compartments. After the particles are phagocytosed in this manner, they degrade rapidly in the acidic lysosome, causing the protein payload to be released into the cytoplasm (*29, 30, 32*). This is hypothesized to occur through the destabilization of the lysosomal membrane as a result of the sudden increase in osmotic pressure, due to particle swelling and degradation (*33*).

The size of these particles (ranging from 200 nm to 1 μm in diameter) makes them well-suited for uptake by phagocytic cells, such as macrophages and dendritic cells. Thus, these particles have demonstrated great success at delivering a protected payload to cells of the immune system (*31, 34*). However, the majority of cells in the human body are non-phagocytic, meaning that they are not efficient at ingesting foreign matter and particulates. As a result, access to the lysosomal delivery pathway in non-phagocytic cells is limited, making it difficult to reap the full benefits of therapeutic delivery systems, such as the hydrogel system described above. Thus, one of the most important challenges facing the use of these particles to deliver therapeutic agents is overcoming their lack of uptake by non-phagocytic cells. This problem has motivated work toward making new delivery vehicles capable of encapsulation, cell membrane penetration, and programmed release. Our aim is to design a delivery vehicle that possesses these three properties. In order to create a universal delivery vehicle which would allow for the delivery of cargo to non-phagocytic cells, we have modified our existing delivery system for phagocytic cells by incorporating a cell-penetrating peptide into our pH-sensitive particles.

* Prof. Jean M. J. Fréchet, 718 Latimer Hall, University of California, Berkeley, Department of Chemistry, Berkeley, CA 94720-1460. E-mail: frechet@berkeley.edu. Tel: (510) 643-3077. Fax: (510) 643-3079.

[†] University of California.

[‡] Washington University in St. Louis School of Medicine.

10.1021/bc700414j CCC: $40.75 © 2008 American Chemical Society
Published on Web 03/05/2008

Cell membranes act as protective barriers for the cell, only allowing compounds within a narrow range of molecular size, polarity, and charge to enter. Overcoming the barrier of the cell membrane to deliver membrane-impermeable cargos often requires harsh methods such as electroporation or liposomal transfection. These methods are limited to *in vitro* applications and often cause unwanted cellular effects, such as high cytotoxicity (*35*). A more recently developed delivery strategy involves the use of cell-penetrating peptides. Cell-penetrating peptides (CPPs) are peptides with up to 30 amino acids with the ability to translocate across cell membranes of various cell types (*36*). CPPs have been used to deliver a range of cargos including proteins, DNA, antisense peptide nucleic acids, small-molecule drugs, liposomes, and nanoparticles into the cell both *in vitro* and *in vivo* (*37*) without disturbing the stability of the cell membrane and with low cytotoxic effects. CPPs offer several appealing properties as delivery agents including applicability to all cell types, no apparent size constraint of the cargo, and seemingly no immunogenic or inflammatory properties (*36*). CPPs consist of a diverse group of peptides derived from such sources as HIV-Tat, the third helix of the homeodomain of Antennapedia, VP22 herpes virus protein, and other synthetic peptides (*38*), including various arginine-rich sequences (*39–44*). One common feature among these CPPs is the high number of cationic residues, such as arginine. In one study, it was found that the HIV-Tat sequence could be replaced with a simple nonamer of arginine (*45*), suggesting that the guanidinium headgroup of arginine is the essential component of this sequence's ability to transport cargos into the cell (*41, 46, 47*). In addition to the guanidine headgroup, other factors such as the number of arginine residues (*47, 48*) and the length of the side chain (*41*) were found to be important factors in the control of translocation.

In this report, we describe the synthesis and evaluation of a new delivery vehicle for biopharmaceuticals. A cell-penetrating peptide (CPP) consisting of nine arginine residues was incorporated into acid-degradable polyacrylamide particles to enhance cellular uptake by non-phagocytic cells. Incorporation of the CPP was achieved by copolymerizing a functional monomer **2** with an acid-degradable crosslinker **1** and acrylamide (Scheme 1). The cell uptake of these modified particles in two epithelial cell lines was then investigated.

EXPERIMENTAL PROCEDURES

General Methods. All reagents were purchased from commercial sources and were used without further purification unless otherwise stated. The cell-penetrating peptide (acrylamide-Y-$(R)_9$-COOH) was purchased from Applied Peptech Suzhou. Acryloyl chloride was distilled prior to use. Triethylamine and tetrahydrofuran (THF) were dried by passing through two columns of neutral alumina within a commercial solvent purification apparatus. Combined organic layers after extractions were dried over $MgSO_4$, which was removed by filtration. Solvents were removed under reduced pressure using a rotary evaporator. Reactions requiring anhydrous conditions were performed in flame-dried vessels and under a positive pressure of dry nitrogen. ^{1}H NMR spectra were recorded at 300 or 400 MHz on a Bruker spectrometer. $CDCl_3$ was passed through a plug of basic alumina prior to recording NMR spectra of acid-sensitive samples. To prevent acid-catalyzed hydrolysis of acetal-containing compounds during chromatographic separation, 1% triethylamine was added to the solvents used for elution. Absorbance was measured using a microplate reader (Molecular Dynamics). Particles were imaged using a scanning electron microscope (S5000, Hitachi) after sputter-coating with a 35 Å platinum film.

Compound **1** was prepared following a literature procedure (*28*).

Scheme 1. Synthesis and Subsequent Degradation of CPP-Modified Microparticles

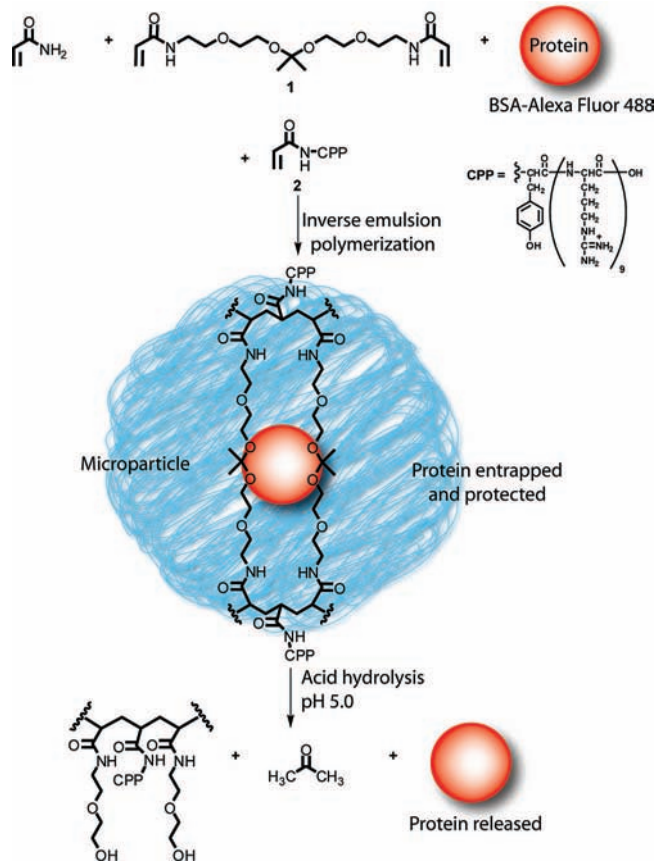

Synthesis of CPP-Modified Microparticles. Microparticles were prepared via an inverse emulsion free radical polymerization (*29, 30*). The organic phase consisted of 3% (w/v) of 3:1 (w/w) Span 80/Tween 80 in hexanes. The aqueous phase was prepared by dissolving cell-penetrating peptide monomer **2** (2.13 mg, 1.3×10^{-6} mol) in 250 μL of phosphate buffered saline (pH 8.0) containing 2 mg/mL BSA-Alexa Fluor 488 conjugate. The pH of this solution was adjusted by the addition of 0.1 M NaOH until the solution had a pH of approximately 8. Acrylamide (85 mg, 1.20 mmol) and acid-labile crosslinker **1** (37 mg, 0.10 mmol, 8 mol %) were dissolved in the aqueous phase. A 50% (w/v) ammonium persulfate solution (10 μL) was added to the aqueous phase. The aqueous phase was then combined with 2.5 mL of the organic phase. The emulsion was prepared by sonicating the solution in a water bath at rt for 30 cycles (ca. 1 s each) in rapid succession using a Branson 450 Sonifier with a ½ in flat tip, an output setting of 2, and a duty cycle of 40%. Polymerization was initiated by the addition of 20 μL of *N,N,N′,N′*-tetramethylethylenediamine (TMEDA) and continued for 10 min at room temperature with constant stirring. The particles were recovered by centrifugation at 1380*g* (rt) for 10 min using 5 μm PVDF spin filters (Ultrafree-CL Durapore, Millipore). The particles were washed with hexanes (2×2 mL) and acetone (3×2 mL), centrifuging after each wash. After collecting the particles, residual acetone was removed by drying under high vacuum overnight.

Non-degradable CPP-Modified Particles. Non-degradable particles were prepared following the method described above using *N,N′*-methylene-bis-acrylamide as the crosslinker. The aqueous phase consisted of acrylamide (103 mg, 1.45 mmol), *N,N′*-methylene-bis-acrylamide (19.0 mg, 0.12 mmol, 8 mol %), and cell-penetrating peptide (2.62 mg, 0.1 mol %) dissolved in 250 μL of phosphate buffered saline (pH 8.0) containing 2 mg/mL BSA-Alexa Fluor 488 conjugate.

Unmodified Microparticles. Unmodified degradable and non-degradable microparticles encapsulating BSA-Alexa Fluor 488 conjugate were prepared in a similar fashion as described above omitting monomer **2**. For the degradable particles, the aqueous phase consisted of acrylamide (87 mg, 1.22 mmol) and crosslinker **1** (38 mg, 0.11 mmol, 8 mol %) dissolved in 250 μL of phosphate buffered saline (pH 8.0) containing 2 mg/mL BSA-Alexa Fluor 488 conjugate. For the non-degradable particles, the monomer composition contained acrylamide (105 mg, 1.48 mmol) and *N*,*N*′-methylene-bis-acrylamide (20 mg, 0.13 mmol, 8 mol %) dissolved in 250 μL of phosphate buffered saline (pH 8.0) containing 2 mg/mL BSA-Alexa Fluor 488 conjugate. It was unnecessary to adjust the pH of the aqueous phase in these cases.

CPP Quantification. CPP quantification was performed using a Micro BCA Protein Assay Kit (Pierce Biotechnology, Rockford, IL). The particles were dispersed in 300 mM acetic acid buffer pH 5.0 at a concentration of 5 mg/mL and incubated at 37 °C overnight to degrade the particles. The solution was then analyzed for the concentration of peptide using the kit according to the manufacturer's instructions, and the fluorescence of the resulting solution was quantified on a microplate reader. A standard curve was prepared using known concentrations of peptide in acidic buffer (pH 5.0, 300 mM acetic acid).

Cell Culture. A lung epithelial cell line derived from transformed normal human airway epithelial cells (BEAS-2B, CRL-9609, American type Tissue Culture Collection, Manassas, VA) was used for the majority of cell-based studies. Confirmatory experiments were also conducted in an alternative epithelial cell line (HeLa, obtained from ATCC, catalog no. CCL-2). With both lines, cells were grown overnight to 50% confluence on four-well LabTek plastic chamber slides using Optimem (Invitrogen) media supplemented with 5% FBS and penicillin/streptomycin (approx 50 μg/mL final). Microparticles were added to the media when the cells were 50–60% confluent.

Cell Uptake Studies. Microparticles were sonicated for two 2 s pulses just prior to incubation with cells using concentrations ranging from 15 μg/mL to 500 μg/mL in a 500 μL volume. Cells were incubated with microparticles for 2 h then washed three times in PBS and allowed to incubate an additional 24 h (HeLa cells) or simply allowed to incubate for 2 or 24 h (BEAS-2B cells). At the end of the incubation period, cells were then fixed and imaged. All studies were conducted in duplicate using 2–3 different preparations of microparticles.

Confocal Microscopy. After incubation, chamber slides were washed with PBS and fixed in 4% paraformaldehyde for 15 min at rt. Following additional PBS washes, Alexa Fluor 568 conjugated phalloidin (1:80, Molecular Probes no. A12380) was added to each well and incubated 30 min at rt to label filamentous actin. Chambers were then removed from the slides, and slides were washed again in PBS with a final rinse in water. Following shaking to remove excess water, cells were covered with mounting media (Vectashield, Vector Laboratories, Burlingame, CA) containing 4′,6-diamidino-2-phenylindole (DAPI) to stain intracellular DNA, coverslipped, and sealed with Cytoseal-60. Cells were examined by indirect fluorescent microscopy using an Olympus BX51 and/or confocal microscopy using a Zeiss 510 LSM laser scanning fluorescent confocal microscope. Cells not treated with microparticles and a well with microparticles but no cells were also prepared to measure background fluorescence.

Cytotoxicity Assay. Possible cytotoxicity associated with cell microparticle uptake was assessed by measuring the release of lactic dehydrogenase (LDH) into cell media using a commercially available kit according to the manufacturer's instructions (Roche Laboratories). BEAS-2B cells were cultured in 100 mm dishes with DMEM/10% FBS to approximately 80% confluence. Cells were washed and then incubated for 24 h in fresh media containing 500 μg/mL non-degradable microparticles, 10 mM H_2O_2 (ensuring cell death, thereby serving as a positive control), or no treatment. Testing was done in duplicate. After incubation, media was recovered, centrifuged, and LDH concentrations were measured in 1 mL of supernatant.

RESULTS AND DISCUSSION

Preparation and Characterization of Microparticles Containing a Cell-Penetrating Peptide. The pH sensitivity of our microparticulate delivery system is imparted by an acetal-containing crosslinker **1** (Scheme 1). This dimethyl acetal crosslinker is relatively stable to hydrolysis under physiological conditions (pH 7.4) but degrades rapidly under the acidic conditions typically found in lysosomes (pH 5.0–5.5) (*28*). Incorporation of oligo(ethylene glycol) substituents enhances the solubility of the crosslinker in aqueous solution, an essential characteristic for the inverse emulsion polymerization technique used to prepare the particles. The inverse emulsion process allows for the encapsulation of hydrophilic molecules such as protein and DNA in the particles. Hydrolysis of crosslinker **1** produces acetone, a relatively nontoxic metabolic intermediate of fatty acid oxidation.

Particles containing a CPP were prepared using a 10 amino acid sequence that was modified on the N-terminus with an acrylamide group, **2** (Scheme 1). This acrylamide moiety enables the direct incorporation of the peptide into the particle during its preparation. The sequence selected for use in the particles was acrylamide-Y-$(R)_9$-COOH because nona-arginine has been shown to be the most effective cell-penetrating peptide known today that is composed of natural L-amino acid residues (*41, 49*). Nona-arginine (R_9) was shown to be 20-fold more efficient than HIV-$Tat_{49–57}$ at cellular uptake (*41*). A tyrosine residue was also incorporated into the peptide sequence to allow for radiolabeling of the peptide for future *in vivo* studies.

Microparticles encapsulating bovine serum albumin-Alexa Fluor 488 (BSA-Alexa Fluor 488), a model protein conjugated with a fluorescent tracer, and including CPP were successfully prepared and characterized to investigate the possibility of enhancing cellular uptake of the particles by non-phagocytic cells. The particles were prepared using an inverse emulsion polymerization technique similar to one described previously (*30*), forming protein-loaded polymer particles incorporating CPP. In this process, CPP and BSA-Alexa Fluor 488 conjugate were dissolved in an aqueous buffer along with acrylamide, acid-sensitive crosslinker **1**, and ammonium persulfate. The aqueous phase was then dispersed as droplets in an organic phase consisting of hexanes and a mixture of two surfactants. Free-radical polymerization was initiated by the addition of ammonium persulfate and TMEDA, resulting in cross-linked polymer particles decorated with cell-penetrating peptide throughout the particles but most importantly at the surface. A schematic representation of the synthesis and subsequent degradation of these particles is depicted in Scheme 1. Exposure of the cross-linked particles to an acidic environment leads to rapid hydrolysis of the acetal linkages. Degradation of the polymer particles thus results in the release of BSA-Alexa Fluor 488, acetone, and the CPP-containing polymer backbone.

The isolated particles analyzed in the dry state using scanning electron microscopy (Figure 1) had sizes ranging from 0.2 to 1 μm. Peptide incorporation was measured by degrading a sample of particles under acidic conditions and analyzing the concentration of peptide using a bicinchoninic acid (BCA) assay (*50*). Using this method, the peptide content in the particles was found to be 0.3% by mass.

Unmodified microparticles free of CPP were also prepared using the same inverse emulsion method but omitting monomer

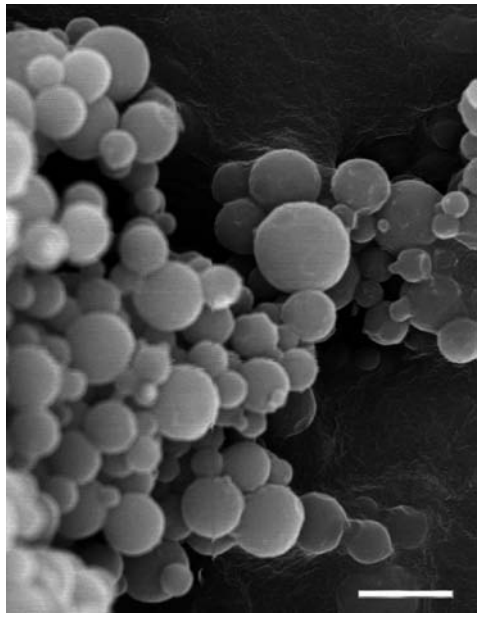

Figure 1. SEM image of CPP-modified microparticles. Scale bar = 1 μm.

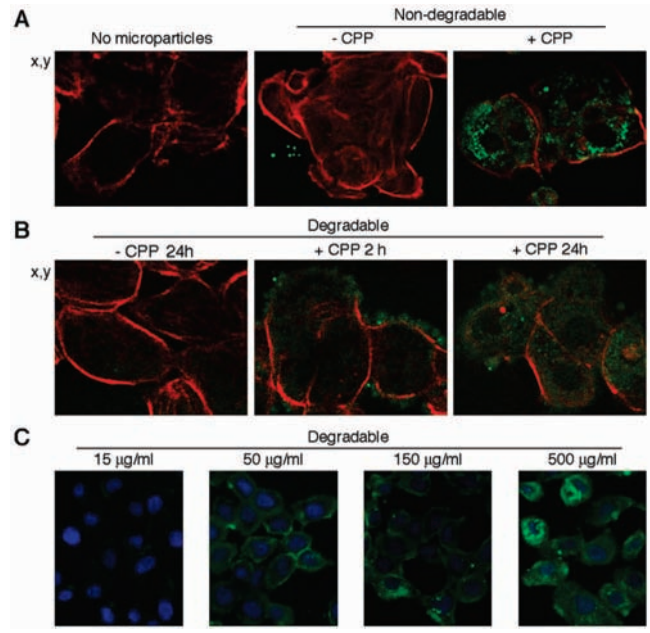

Figure 2. Representative confocal microscope images of BEAS-2B cells, taken at midcell level, 24 h after incubation with microparticles. Cell membranes and cytoskeleton are stained red by phalloidin. Panel A: The cellular accumulation of CPP-modified microparticles 500 μg/mL is markedly greater compared with cells incubated with particles without CPP modification. Panel B: A time dependency is seen when cells are incubated with microparticles at room temperature. At 2 h, most particles appear to be adherent on the cell surface. By 24 h, intracellular accumulation has increased markedly. Note also that the overall fluorescence appears to be more diffuse and less intense than with nondegradable particles. Panel C: Increasing fluorescence is seen intracellularly as microparticle concentration is increased in the medium.

2. These particles contain the same mole percent of cross-linking acetal as the functionalized particles described above. Non-degradable microparticles both with and without cell-penetrating peptide were also prepared as described above using *N*,*N*′-methylene-bis-acrylamide as the cross-linker instead of monomer **1**. SEM examination of these particles showed that they were similar in size and shape to the degradable CPP-modified particles (data not shown).

Cellular Uptake of CPP-Modified Microparticles by Non-Phagocytic Cells. The effect of the CPP modification of the microparticles on their interaction with BEAS-2B epithelial cells is shown in Figure 2. In the absence of microparticle incubation, cell membranes and elements of the intracellular Actin skeleton are clearly evident by phalloidin staining. As expected, no fluorescence from the Alexa Fluor 488 is seen, even at high magnification. When cells were incubated with unmodified non-degradable microparticles (panel A), midcell images obtained by confocal microscopy showed little fluorescence—only visible under high magnification—despite 24 h of incubation time. In contrast, the intracellular accumulation of CPP-modified non-degradable microparticles over the 24 h incubation period was readily evident.

Much research has been done to elucidate the mechanism by which cell-penetrating peptides mediate the transport of various cargoes across the cell membrane. The punctate appearance of microparticles within the cells shown in Figure 2 is consistent with endosomally mediated uptake. Studies by others suggest that uptake is facilitated by positively charged arginine residues (including those present in the CPP used in this study) forming bidentate hydrogen bonds with negatively charged phosphates, sulfates, and carboxylates on the cell surface (*49, 51*).

These results can be contrasted with those observed after cells were incubated with acid-degradable microparticles (panel B, Figure 2). In the absence of the CPP modification, only low levels of fluorescence were seen intracellularly, even after 24 h of incubation (again, most evident at high magnification). With CPP modification, however, high levels of fluorescence are obvious. After just 2 h incubation, microparticles are present both intracellularly as well as clustered on the cell surface. A similar pattern was seen when HeLa cells were incubated with acid-degradable CPP-modified microparticles (data not shown). This association with the cell membrane is probably due to the hydrogen bonding ability of the guanidine headgroup of arginine and the highly cationic nature of the cell-penetrating peptide. After 24 h incubation, the intracellular accumulation of the microparticles is even greater. Again, a similar phenomenon was observed when HeLa cells were incubated with these microparticles. Furthermore, in addition to a time dependency, the accumulation of the CPP-modified microparticles was also concentration-dependent (panel C, Figure 2).

Note, however, that the intensity of fluorescence is more diffuse and less intense than when cells were incubated with the non-degradable particles (compare panel B with panel A). We interpret this difference in appearance to be compatible with time-dependent intracellular microparticle degradation and release of the encapsulated protein. As mentioned above, acid-sensitive crosslinker **1** is chemically stable at pH 7.4, but rapidly hydrolyzes in the acidic environment (pH 5.0) of the lysosome. This hydrolysis is believed to result in an increase in osmotic pressure, leading to lysosomal disruption, thus providing delivery of the encapsulated cargo to the cytoplasm (*28–30*). These results are thus suggestive of release of the encapsulated BSA-Alexa Fluor 488 conjugate into the cytoplasm of the cell.

Importantly, there was no evidence of any cytotoxicity associated with intracellular accumulation of either degradable or non-degradable microparticles. Cells appeared viable with normal cell shape and morphology when viewed microscopically, and DAPI staining showed no evidence of nuclear fragmentation indicative of apoptosis. Furthermore, LDH concentrations in the media of cells incubated with non-degradable particles (with or without CPP modification) were $<$100 IU/mL. The LDH concentration in cells incubated without micro-

particles was also <100 IU/mL, whereas LDH levels were 4 times higher in cells treated with 10 mM H_2O_2 as a positive control.

CPP modification would be expected to be effective in any tissue. Thus, widespread intracellular accumulation of microparticles would be expected after intravenous administration *in vivo*. For some applications, this may be advantageous, but it is detrimental in others due to unwanted toxicities. It is possible that the microparticles could be further modified with highly specific tissue-targeting moieties that would result in reduced uptake in nontargeted tissues. However, with the lungs, a very attractive delivery strategy is to administer the microparticles intratracheally (e.g., as an aerosol). In this case, cellular uptake would likely remain confined to the lung epithelium, and indeed, it was for this reason that we chose a lung epithelial cell line as the primary target for these studies. Future studies will determine if CPP-modified microparticles will accumulate in lung epithelium after intratracheal delivery *in vivo*.

CONCLUSIONS

A microparticle delivery vehicle encapsulating a fluorescently labeled model protein and containing a cell-penetrating peptide was successfully prepared. *In vitro* studies demonstrated that this delivery vehicle is effective at promoting particle uptake in non-phagocytic epithelial cells. Thus, incorporation of a cell-penetrating peptide expands the potential applications of this delivery vehicle for use in non-phagocytic, as well as phagocytic, cell lines. In addition, by incorporating an acid-degradable crosslinker, the particles are capable of releasing the encapsulated payload upon uptake by these cells. Future studies will explore the feasibility of using these particles to deliver plasmid DNA, peptide nucleic acids, or small molecule therapeutic cargoes to lung epithelial cells to treat acute and chronic lung disease.

ACKNOWLEDGMENT

We thank the National Institutes of Health (PEN Grant 1 U01 HL080729-01) for funding of this research; additional NIH support (Grant RO1 EB005824) led to the development of the degradable carrier particles used in this study.

LITERATURE CITED

(1) Pack, D. W., Hoffman, A. S., Pun, S., and Stayton, P. S. (2005) Design and development of polymers for gene delivery. *Nat. Rev. Drug Discovery 4*, 581–593.
(2) Dembowsky, K., and Stadler, P. (2001) *Novel Therapeutic Proteins*, Wiley-VCH, New York.
(3) Carter, P. J. (2006) Potent antibody therapeutics by design. *Nat. Rev. Immun. 6*, 343–357.
(4) Walsh, G. (2005) Biopharmaceuticals: recent approvals and likely directions. *Trends Biotechnol. 23*, 553–558.
(5) Reis, C. P., Neufeld, R. J., Ribeiro, A. J., and Veiga, F. (2006) Nanoencapsulation I. Methods for preparation of drug-loaded polymeric nanoparticles. *Nanomedicine 2*, 8–21.
(6) Nishiyama, N., and Kataoka, K. (2006) Current state, achievements, and future prospects of polymeric micelles as nanocarriers for drug and gene delivery. *Pharmacol. Ther. 112*, 630–648.
(7) Goldberg, M., Langer, R., and Jia, X. (2007) Nanostructured materials for applications in drug delivery and tissue engineering. *J. Biomater. Sci., Polym. Ed. 18*, 241–268.
(8) Park, T. G., Jeong, J. H., and Kim, S. W. (2006) Current status of polymeric gene delivery systems. *Adv. Drug Delivery Rev. 58*, 467–486.
(9) Luo, D., and Saltzman, M. (2000) Synthetic DNA delivery systems. *Nat. Biotechnol. 18*, 33–37.
(10) Allen, T. M., and Cullis, P. R. (2004) Drug delivery systems: entering the mainstream. *Science 303*, 1818–1822.
(11) Rawat, M., Singh, D., Saraf, S., and Saraf, S. S. (2006) Nanocarriers: promising vehicles for bioactive drugs. *Biol. Pharm. Bull. 29*, 1790–1798.
(12) Vogelson, C. T. (2001) Advances in drug delivery systems. *Mod. Drug Discovery 4*, 49–50.
(13) Henry, C. M. (2002) Drug delivery. *Chem. Eng. News 80*, 39–47.
(14) Jin, S., and Ye, K. (2007) Nanoparticle-mediated drug delivery and gene therapy. *Biotechnol. Prog. 23*, 32–41.
(15) Pannier, A. K., and Shea, L. D. (2004) Controlled release systems for DNA delivery. *Mol. Ther. 10*, 19–26.
(16) Montet, X., Funovics, M., Montet-Abou, K., Weissleder, R., and Josephson, L. (2006) Multivalent effects of RGD peptides obtained by nanoparticle display. *J. Med. Chem. 49*, 6087–6093.
(17) Bae, Y., Jang, W., Nishiyama, N., Fukushima, S., and Kataoka, K. (2005) Multifunctional polymeric micelles with folate-mediated cancer cell targeting and pH triggered drug releasing properties for active intracellular drug delivery. *Mol. Biosyst. 1*, 242–250.
(18) Gupta, B., Levchenko, T. S., and Torchilin, V. P. (2005) Intracellular delivery of large molecules and small particles by cell-penetrating proteins and peptides. *Adv. Drug Delivery Rev. 57*, 637–651.
(19) Panyam, J., and Labhasetwar, V. (2003) Biodegradable nanoparticles for drug and gene delivery to cells and tissue. *Adv. Drug Delivery Rev. 55*, 329–347.
(20) Chasin, M., and Langer, R. Eds. (1990) *Biodegradable Polymers as Drug Delivery Systems*, CRC Press, New York.
(21) Amiji, M. (2004) *Polymeric Gene Delivery: Principles and Applications*, CRC Press, New York.
(22) Lynn, D. M., Amiji, M. M., and Langer, R. (2001) pH-Responsive polymer microspheres: rapid release of encapsulated material within the range of intracellular pH. *Angew. Chem., Int. Ed. 40*, 1707–1710.
(23) Haining, W. N., Anderson, D. G., Little, S. R., von Berwelt-Baildon, M. S., Cardoso, A. A., Alves, P., Kosmatopoulos, K., Nadler, L. M., Langer, R., and Kohane, D. S. (2004) pH-Triggered microparticles for peptide vaccination. *J. Immunol. 173*, 2578–2585.
(24) Little, S. R., Lynn, D. M., Ge, Q., Anderson, D. G., Puram, S. V., Chen, J., Eisen, H. N., and Langer, R. (2004) Poly-{beta} amino ester-containing microparticles enhance the activity of nonviral genetic vaccines. *Proc. Natl. Acad. Sci. U.S.A. 101*, 9534–9539.
(25) Khaja, S. D., Lee, S., and Murthy, N. (2007) Acid-degradable protein delivery vehicles based on metathesis chemistry. *Biomacromolecules 8*, 1391–1395.
(26) Lee, S., Yang, S. C., Heffernan, M. J., Taylor, W. R., and Murthy, N. (2007) Polyketal microparticles: a new delivery vehicle for superoxide dismutase. *Bioconjugate Chem. 18*, 4–7.
(27) Heffernan, M. J., and Murthy, N. (2005) Polyketal nanoparticles: a new pH-sensitive biodegradable drug delivery vehicle. *Bioconjugate Chem. 16*, 1340–1342.
(28) Kwon, Y. J., Standley, S. M., Goodwin, A. P., Gillies, E. R., and Fréchet, J. M. J. (2005) Directed antigen presentation using polymeric microparticulate carriers degradable at lysosomal pH for controlled immune response. *Mol. Pharm. 1*, 83–91.
(29) Murthy, N., Xu, M., Schuck, S., Kunisawa, J., Shastri, N., and Fréchet, J. M. J. (2003) A macromolecular delivery vehicle for protein-based vaccines: acid-degradable protein-loaded microgels. *Proc. Natl. Acad. Sci. U.S.A. 100*, 4995–5000.
(30) Standley, S. M., Kwon, Y. J., Murthy, N., Kunisawa, J., Shastri, N., Guillaudeu, S., Lau, L., and Fréchet, J. M. J. (2004) Acid-degradable particles for protein-based vaccines: enhanced survival rate for tumor challenged mice using ovalbumin model. *Bioconjugate Chem. 15*, 1281–1288.
(31) Standley, S. M., Mende, I., Goh, S. L., Kwon, Y. J., Beaudette, T. T., Engleman, E. G., and Fréchet, J. M. J. (2007) Incorporation of CpG oligonucleotide ligand into protein-loaded particle vaccines promotes antigen-specific CD8 T-cell immunity. *Bioconjugate Chem. 18*, 77–83.

(32) Murthy, N., Thng, Y. X., Schuck, S., Xu, M., and Fréchet, J. M. J. (2002) A novel strategy for encapsulation and release of proteins: hydrogels and microgels with acid-labile acetal crosslinkers. *J. Am. Chem. Soc. 124*, 12398–12399.

(33) Moore, M. W., Carbone, F. R., and Bevan, M. J. (1988) Introduction of soluble protein into the class I pathway of antigen processing and presentation. *Cell 54*, 777–785.

(34) Goh, S. L., Murthy, N., Xu, M., and Fréchet, J. M. J. (2004) Cross-linked microparticles as carriers for the delivery of plasmid DNA for vaccine development. *Bioconjugate Chem. 15*, 467–474.

(35) Webster, A., Compton, S. J., and Aylott, J. W. (2005) Optical calcium sensors: development of a generic method for their introduction to the cell using conjugated cell penetrating peptides. *The Analyst 130*, 163–170.

(36) Langel, U., and Lundberg, P. (2003) A brief introduction to cell-penetrating peptides. *J. Mol. Recognit. 16*, 227–233.

(37) Deitz, G. P., and Bahr, M. (2004) Delivery of bioactive molecules into the cell: the Trojan horse approach. *Mol. Cell. Neurosci. 27*, 85–131.

(38) Bhorade, R., Weissleder, R., Nakakoshi, T., Moore, A., and Tung, C. H. (2000) Macrocyclic chelators with paramagnetic cations are internalized into mammalian cells via a HIV-Tat derived membrane translocation peptide. *Bioconjugate Chem. 11*, 301–305.

(39) Futaki, S., Suzuki, T., Ohashi, W., Yagami, T., Tanaka, S., and Ueda, K. (2001) Arginine rich peptides. An abundant source of membrane-permeable peptides having potential as carriers for intracellular protein delivery. *J. Biol. Chem. 276*, 5836–5840.

(40) Futaki, S. (2005) Membrane-permeable arginine-rich peptides and the translocation mechanisms. *Adv. Drug Delivery Rev. 57*, 547–558.

(41) Wender, P. A., Mitchell, D. J., Pattabiraman, K., Pelkey, E. T., Steinman, L., and Rothbard, J. B. (2000) The design, synthesis, and evaluation of molecules that enable or enhance cellular uptake: peptoid molecular transporters. *Proc. Natl. Acad. Sci. U.S.A. 97*, 13003–13008.

(42) Melikov, K., and Chernomordik, L. V. (2005) Arginine-rich cell penetrating peptides: from endosomal uptake to nuclear delivery. *Cell. Mol. Life Sci. 62*, 2739–2749.

(43) Sheldon, K., Liu, D., Ferguson, J., and Gariepy, J. (1995) Loligomers: design of de novo peptide-based intracellular vehicles. *Proc. Natl. Acad. Sci. U.S.A. 92*, 2056–2060.

(44) Zhang, L., Torgerson, T. R., Liu, X. Y., Timmons, S., Colosia, A. D., Hawiger, J., and Tam, J. P. (1998) Preparation of functionally active cell-permeable peptides by single-step ligation of two peptide modules. *Proc. Natl. Acad. Sci. U.S.A. 95*, 9184–9189.

(45) Calnan, B. J., Tidor, B., Biancalana, S., Hudson, D., and Frankel, A. D. (1991) Arginine-mediated RNA recognition: the arginine fork. *Science 252*, 1167–1171.

(46) Rothbard, J. B., Garlington, S., Lin, Q., Kirschberg, T., Kreider, E., McGrane, P. L., Wender, P. A., and Khavari, P. A. (2000) Conjugation of arginine oligomers to cyclosporine A facilitates topical delivery and inhibition of inflammation. *Nat. Med. 6*, 1253–1257.

(47) Mitchell, D. J., Kim, D. T., Steinman, L., Fathman, C. G., and Rothbard, J. B. (2000) Polyarginine enters cells more efficiently than other polycationic homopolymers. *J. Peptide Res. 56*, 318–325.

(48) Suzuki, T., Futaki, S., Niwa, M., Tanaka, S., Ueda, K., and Sugiura, Y. (2002) Possible existence of common internalization mechanisms among arginine-rich peptides. *J. Biol. Chem. 277*, 2437–2443.

(49) Fuchs, S. M., and Raines, R. T. (2004) Pathway for polyarginine entry into mammalian cells. *Biochemistry 43*, 2438–2444.

(50) Smith, P. K., Krohn, R. I., Hermanson, G. T., Mallia, A. K., Gartner, F. H., Provenzano, M. D., Fujimoto, E. K., Goeke, N. M., Olson, B. J., and Klenk, D. C. (1985) Measuement of protein using bicinchoninic acid. *Anal. Biochem. 150*, 76–85.

(51) Rothbard, J. B., Jessop, T. C., and Wender, P. A. (2005) Adaptive translocation: the role of hydrogen bonding and membrane potential in the uptake of guanidinium-rich transporters in cells. *Adv. Drug Delivery Rev. 57*, 495–504.

BC700414J

Self-Assembled Cationic Nanogels for Intracellular Protein Delivery

Hirohito Ayame, Nobuyuki Morimoto, and Kazunari Akiyoshi*

Institute of Biomaterials and Bioengineering, Tokyo Medical and Dental University, 2-3-10 Kanda-Surugadai, Chiyoda-ku, Tokyo, 101-0062, Japan. Received November 20, 2007; Revised Manuscript Received February 8, 2008

An effective intracellular protein delivery system with self-assembled cationic nanogels is reported. Interaction of proteins with self-assembled nanogels of cationic cholesteryl group-bearing pullulans ($CHPNH_2$) was investigated by dynamic light scattering (DLS), transmission electron micrograph (TEM), fluorescence resonance energy transfer (FRET), and fluorescence correlation spectroscopy (FCS). The cationic nanogels strongly interacted with bovine serum albumin (BSA) and formed monodispersed nanoparticels (<50 nm). The complex more effectively internalized into HeLa cells than cationic liposomes and a protein transduction domain (PTD) based carrier even in the presence of serum. The higher efficiency of the nanogel carrier is probably due to the formation of colloidally stable nanoparticles with the protein. The enzymatic activity of β-galactosidase (β-Gal) was retained after internalization into cells. The nanogel carrier promoted nuclear delivery of a GFP-conjugated nuclear localization signal and Tat as a PTD (Tat-NLS-GFP). A blocking experiment with chemical inhibitors revealed the possible involvement of macropinocytosis in the uptake of the nanogel complex. After cellular uptake, the complex of the nanogel−protein was dissociated and the protein was released inside the cell. Such a self-assembled cationic nanogel system should create opportunities for novel applications of protein delivery.

INTRODUCTION

Intracellular delivery of exogenous proteins is a subject of great interest in bioscience and medical science. In particular, protein transduction domain (PTD) fusion proteins have been widely used in this field (*1, 2*). However, the synthesis and purification of PTD fusion proteins from bacteria are sometimes problematic due to low expression levels and aggregation of the fusion proteins in certain cases. Protein delivery can also be performed by a noncovalent method which uses a carrier, such as cationic liposomes (*3, 4*), polymer particles (*5, 6*), or PTD-based amphiphilic peptides (*7*). In the noncovalent method, existing recombinant proteins can be easily used by simply mixing the carrier and proteins. Although such carrier methods are convenient, the efficiency is not always high. One of the problems is colloidal instability of the complex between carrier and protein. The complex sometimes forms large aggregates. The control of the size of the complex is known to be the most important factor for effective intracellular protein delivery both *in vitro* and *iv vivo* (*8*). However, it is still difficult to control the size of the complex between carriers and proteins due to multiple point electrostatic interactions and hydrophobic interactions between them.

Nanosize hydrogels (nanogels), which are composed of nanoscale gel particles, have attracted growing interest with respect to their potential application in drug delivery systems (*9–15*). We have developed self-assembly methods for preparing physically cross-linked nanogels (<50 nm) through the controlled association of hydrophobically modified polymers in water (Figure 1) (*16–22*). In particular, cholesteryl group-bearing pullulan (CHP) forms nanoparticles by self-assembly in water (Rh = ∼15 nm). These particles behave like hydrated nanogels via cholesteryl nanodomains acting as physical cross-linking points (*16, 17*). CHP nanogels with such a nanosized hydrogel matrix form complex nanoparticles with various proteins (*18*). Since the nanogel network is comparable to that of proteins, the nanogel can hold a protein molecule in a segregated nanomatrix. The characteristic that each part of the nanogel network isolates protein molecules is advantageous in stabilizing proteins, because aggregation by protein–protein interactions can be prohibited. Therefore, the nanogels act as artificial chaperones, which both protect against the aggregation of denatured proteins and assist in the refolding of proteins (*19, 20*). These features allow the CHP nanogel to function as a protein carrier (*23–25*). Although CHP nanogels are useful as nanocarriers in drug delivery systems (DDS), intracellular uptake of the nanogel was relatively low due to the nonionic character of the polysaccharide pullulan. To achieve higher cellular uptake of the nanocarrier, we designed various cationic CHP derivatives, because in general cationic nanoparticles exhibit high cellular internalization efficiency. In this study, we focus attention on simple cationic nanogels, composed of an amphiphilic polysaccharide: ethylenediamine group functionalization of cholesteryl group-bearing pullulan ($CHPNH_2$) (Figure 1). At first, the interaction of proteins with self-assembled nanogels of $CHPNH_2$ was investigated in detail by various physicochemical techniques such as dynamic light scattering (DLS), transmission electron micrograph (TEM), and fluorescence resonance energy transfer (FRET) and by fluorescence correlation spectroscopy (FCS). It was show that the advantage of using nanogels as the protein carrier is the capacity to form a colloidally stable complex with proteins at the nanometer scale (<50 nm), which is a suitable size for effective intracellular uptake.

MATERIALS AND METHODS

Materials. FITC-labeled bovine serum albumin (FITC-BSA, 66 kDa), Rhodamine B isothiocyanate, and amiloride were purchased from Sigma-Aldrich (USA). A commercial protein carrier of cationic liposome (Pro-Ject) and a peptide-based carrier (Chariot) were purchased from Pierce (USA) and Active Motif (USA), respectively. Ikarugamycin and TokyoGreen-βGal were purchased from Biomol (USA) and Daiichi Pure Chemicals (Japan). Evoblue-BSA was synthesized with a protein-labeling kit according to the manufacturer's instructions (Olympus, Japan). Cell-counting kit-8 (CCK-8) was obtained from Dojindo

* akiyoshi.org@tmd.ac.jp.

10.1021/bc700422s CCC: $40.75 © 2008 American Chemical Society
Published on Web 03/13/2008

Laboratories (Japan). Tat-NLS-GFP (27 kDa) was a gift from Prof. T. Tsubata and Dr. K. Watanabe (Tokyo Medical and Dental University). β-Galactosidase (β-Gal, 540 kDa (tetramer)) and other reagents were purchased from Wako Pure Chemical Industries (Japan).

Synthesis of $CHPNH_2$ (7, 11, and 17 amino groups per 100 glucose units). Dried CHP (150 mg; 0.9 mmol equivalent of anhydrous glucoside units) was dissolved in 15 mL of DMSO, and 1,1-carbonyldiimidazole (25, 38, and 75 mg; 0.15, 0.23, and 0.46 mmol) was added to the mixture under dried nitrogen. After 4 h, ethylenediamine (100, 150, and 300 mg; 1.6, 2.5, and 5.0 mmol) was added to the mixture at room temperature. After being stirred for 24 h, the reaction mixture was dialyzed with the Spectra/Pore 6 dialysis bag (molecular weight cutoff 3500; Spectrum Laboratories, USA), using distilled water for 6 days at room temperature, and lyophilized. The degrees of substitution were determined by elemental analysis (CHN CORDER MT-5; Yanako Japan) ($CHPNH_2$(7): C, 40.9%; H, 6.75%; N, 1.22%. $CHPNH_2$(11): C, 42.1%; H, 6.82%; N, 1.67%. $CHPNH_2$(17): C, 40.0%; H, 6.94%; N, 2.44%).

Synthesis of $CHPNH_2$(17)-rhodamine ($CHPNH_2$(17)-Rh; 0.5 rhodamine groups per 100 glucose units). $CHPNH_2$(17) (100 mg; 0.6 mmol equiv of anhydrous glucoside units) was dissolved in phosphate-buffered saline (PBS: pH 7.4) at 2 mg/mL. Rhodamine B isothiocyanate (1.6 mg; 3.0 μmol) was added and the mixture was heated for 8 h at room temperature. The reaction mixture was dialyzed with the Spectra/Pore 6 dialysis bag by distilled water for 6 days at room temperature. The product was purified by size-exclusion chromatography on a Sephadex G-25. The degrees of substitution were determined by UV analysis using $\epsilon = 59\,000$ at 558 nm.

Preparation of $CHPNH_2$−Protein Complexes. $CHPNH_2$ (1–5 mg/mL) was suspended in PBS. The suspension was sonicated for 15 min with a sonicator probe and filtered through a Millipore filter (pore size 0.22 μm). $CHPNH_2$ nanogel solution and protein solution were mixed and kept at room temperature. An SLS experiment showed that the nanogels of both CHP and $CHPNH_2$ were constituted by approximately four CHP or $CHPNH_2$ macromolecules (*24*).

Fluorescence Resonance Energy Transfer (FRET). The rate of the binding of FITC-BSA to the $CHPNH_2$(17) nanogel was estimated by fluorescence resonance energy transfer (FRET). FRET was estimated by $CHPNH_2$(17)-Rh nanogels (10 nM) and FITC-BSA (10 nM) using an FP-6500 fluorescence spectrometer (JASCO, Japan). FITC-BSA-$CHPNH_2$ (17)-Rh nanogel complex was excited at 495 nm and the emission intensity was measured from 500 to 600 nm.

Fluorescence Correlation Spectroscopy (FCS). The binding constants of BSA with the nanogels were estimated by fluorescence correlation spectroscopy (FCS). FCS measurements were performed using an MF10S (Olympus, Japan). Various concentrations of the nanogel solutions were mixed with Evoblue-BSA (2.5 nM) solution. After the mixture was incubated for 1 h, the data were collected. All experiments were performed with an acquisition time of 15 s per measurement, and all measurements were repeated five times per sample. FCS data were analyzed with the MF10S software package. Binding constants were calculated from triplicate measurements with an Origin 7J (OriginLab) using the best fit.

$$K = \frac{1}{Kd} \quad Kd = \frac{[A][B]}{[AB]}$$

$$Y = \frac{Kd + [A] + [B] - \sqrt{(Kd + [A] + [B])^2 - 4[A][B]}}{2[A]}$$

Y: Evoblue-BSA and CHP or $CHPNH_2$ complexes degrees in the solution

[A]: Evoblue -BSA molar concentration

[B]: CHP or $CHPNH_2$ molar concentration of nanogel

Dynamic Light Scattering (DLS) and ζ-Potential Measurements. DLS and ζ-potential measurements were carried out with a Zetasizer Nano ZS instrument (Malvern Instruments, U.K.) equipped with a PELTIER temperature-control unit at 632.8 nm. The hydrodynamic radii of the nanogels (3 mg/mL) and nanogel (3 mg/mL)−protein (FITC-BSA, 0.52 mg/mL; FITC-β-Gal, 3.3 mg/mL) complex were determined with a Laplace inversion program (CONTIN). The ζ-potential measurements were performed using a capillary ζ-potential cell in automatic mode.

Transmission Electron Micrograph (TEM). TEM (H-600; Hitachi) observation was performed at an accelerating voltage of 100 V. Specimens were prepared by dropping 10 μL of a solution of $CHPNH_2$(17) (1 μM)−FITC-BSA (1 μM) complex on a grid and staining with 0.1% uranyl acetate.

Flow Cytometry. HeLa cells were cultured in Minimum Essential Medium (MEM) supplemented with 10% heat-inactivated fetal bovine serum (FBS). Cells were plated in a six-well culture dish at a density of 2.0×10^4 cells/well and cultured for 24 h at 37 °C in 5% CO_2. After the medium was removed, 1 mL of fresh MEM containing $CHPNH_2$ nanogel (10 nM)−FITC-BSA (10 nM) complex or $CHPNH_2$ nanogel (10 nM)−FITC-β-Gal (10 nM) was added and the cells were cultured at 37 °C in 5% CO_2. After incubation for periods of constant duration, cells were washed with medium, trypsinized, and suspended in stain buffer (BD PharMingen stain buffer, BD PharMingen USA). Flow cytometry was performed on a FACScalibur (BD Biosciences USA) with a 488 nm argon laser. The signal from the FL1 bandpass emission (530/30) was used for FITC.

The cellular uptake of $CHPNH_2$(17) nanogel (10 nM)−FITC-BSA (10 nM) complex was also examined by flow cytometry in NIH-3T3, cos-7, CHO-K1, and MC-3T3 cells. The cells were plated in a six-well culture dish at a density of 2.0×10^4 cells/well and cultured for 24 h at 37 °C in 5% humidified CO_2. After the medium was removed, 1 mL of fresh medium in the presence of serum containing $CHPNH_2$(17) nanogel (10 nM)−FITC-BSA (10 nM) complex was added. After incubation for periods of constant duration, cells were washed with medium, trypsinized, and suspended in stain buffer.

Cytotoxicity Assay. HeLa Cells were plated in a 96-well culture dish at a density of 1.0×10^3 cells/well and cultured for 24 h at 37 °C in 5% humidified CO_2. After the medium was removed, 50 μL of fresh MEM containing protein carriers ($CHPNH_2$ nanogel, peptide based carrier and cationic liposome) were added. Cells were cultured at 37 °C in 5% CO_2. After incubation for 4 h, the cells were washed with fresh medium. HeLa cells were cultured for 24 h, and cell counting kit-8 (CCK-8) solution (Dojindo Laboratories, Japan) was then added to the medium. After 2 h, the absorbance was measured at 450 nm using a microplate reader with a reference wavelength of 630 nm.

Confocal Laser Scanning Fluorescence Microscopy (CLSFM) of the Uptake of BSA into Cells. HeLa cells were plated in a glass-bottom dish (glass diameter 10 mm) at 1.0×10^4 cells/dish and cultured for 24 h at 37 °C in 5% humidified CO_2. After the culture medium was removed, 1 mL of $CHPNH_2$ nanogel (10 nM) complex solution with FITC-BSA (10 nM) was added to cells. After incubation for 4 h at 37 °C in 5% CO_2, the cells were washed with fresh medium and were observed by CLSFM (LSM510META, Carl Zeiss, German). In the case of the $CHPNH_2$(17)-Rh−FITC-BSA system, the cells were cultured for 2 or 18 h, and CLSFM observations were carried out with excitation by an argon laser (488 nm for FITC) and He−Ne laser (543 nm for rhodamine B). The emitted

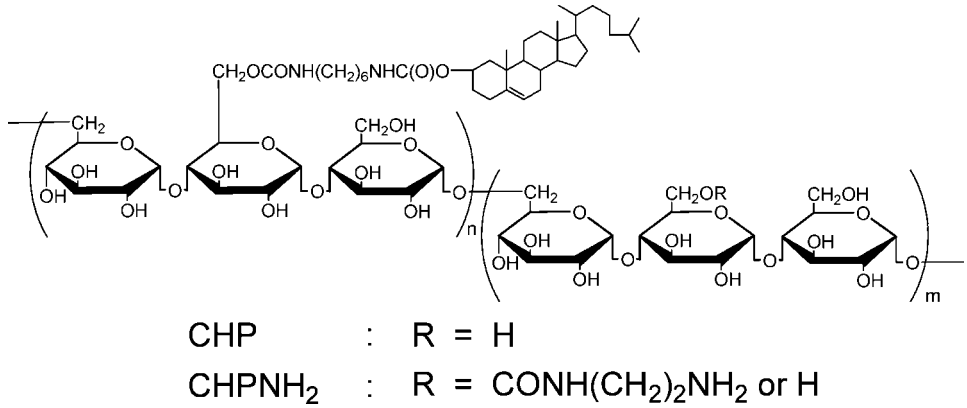

Figure 1. Chemical structure of cholesterol-bearing pullulan (CHP) and amino group-modified CHP ($CHPNH_2$) nanogels.

Table 1. Characteristics of CHP or $CHPNH_2$ Nanogels and Their Complexes with BSA

	CHP	$CHPNH_2$(7)	$CHPNH_2$(11)	$CHPNH_2$(17)
		Rh(nm)(PDI)		
nanogel	14.7 (0.110)	16.5 (0.200)	15.7 (0160)	13.8 (0.150)
BSA-complex	20.2 (0.144)	17.8 (0.140)	20.9 (0.202)	18.7 (0.138)
		ζ-Potential(mV)		
nanogel	-1.3 ± 0.4	$+3.0 \pm 0.4$	$+3.9 \pm 0.4$	$+7.7 \pm 0.1$
BSA-complex	-2.3 ± 0.4	$+2.2 \pm 0.2$	$+2.7 \pm 0.2$	$+6.4 \pm 0.5$
binding constant with BSA(M^{-1})	1.3 ($\pm$0.2) $\times 10^7$	1.3 ($\pm$0.7) $\times 10^7$	2.7 ($\pm$0.4) $\times 10^8$	5.3 ($\pm$1.1) $\times 10^8$

fluorescence was detected through a 503–530 nm bandpass filter and a 543 nm long-pass filter, respectively.

Intracellular Delivery of Protein Using Cationic Liposome. The tube dry film of cationic liposome in Pro-Ject Protein Transfection Reagent kit (Pro-Ject, PIERCE) was dissolved with 250 μL of chloroform and vortexed for 20 s. One experiment (six-well plate; 10 μL) of the cationic liposome was dispensed to tube and the solvent evaporated by placing the tube containing the cationic liposome under a laminar flow hood for 2 h at room temperature. FITC-BSA or FITC-β-Gal (100 μL; PBS solution) was added to the tube containing the dry film of cationic liposome and vortexed for 10–20 s, then incubated at room temperature for 5 min. In the experiment of flow cytometry, HeLa cells were cultured in MEM supplemented with 10% heat-inactivated FBS. Cells were plated in a six-well culture dish at a density of 2.0×10^4 cells/well and cultured for 24 h at 37 °C in 5% CO_2. After the medium was removed, 1 mL of fresh MEM containing cationic liposome−FITC-BSA (10 nM) or cationic liposome−FITC-β-Gal (10 nM) complex was added, and the cells were cultured at 37 °C in 5% CO_2. After incubation for periods of constant duration, cells were washed with medium, trypsinized, and suspended in stain buffer. Flow cytometry was performed on a FACScalibur with a 488 nm argon laser. The signal from the FL1 bandpass emission (530/30) was used for FITC. In CLSFM, HeLa cells were plated in a glass-bottom dish at 1.0×10^4 cells/dish and cultured for 24 h at 37 °C in 5% humidified CO_2. After the medium was removed, 1 mL of fresh MEM containing liposome−FITC-BSA (10 nM) complex or cationic liposome−FITC-β-Gal (10 nM) complex was added to cells. After incubation for 4 h at 37 °C in 5% CO_2, the cells were washed with fresh medium and were observed by CLSFM.

Intracellular Delivery of Protein Using Peptide-Based Carrier. The tube of Chariot Transfection Transduction Reagent kit (Chariot, ACTIVE MOTIF) was dissolved with 150 μL of H_2O. One experiment (six-well plate; 6 μL) of the peptide-based carrier was dispensed to tube. FITC-BSA or FITC-β-Gal (100 μL; PBS solution) was added to peptide-based carrier (6 μL in 100 μL; H_2O) and then incubated for 30 min at room temperature. In the flow cytometry case, HeLa cells were cultured in MEM supplemented with 10% heat-inactivated FBS. Cells were plated in a six-well culture dish at a density of 2.0×10^4 cells/well and cultured for 24 h at 37 °C in 5% CO_2. After the medium was removed, 600 μL of fresh MEM containing peptide-based carrier−FITC-BSA (17 nM) complex or peptide-based carrier−FITC-β-Gal (17 nM) was added and the cells were cultured at 37 °C for 1 h in 5% CO_2. After incubation, the cells were added to 1 mL of fresh medium and then were cultured for 3 h. After incubation for periods of constant duration, cells were washed with medium, trypsinized, and suspended in stain buffer. Flow cytometry was performed on a FACScalibur with a 488 nm argon laser. The signal from the FL1 bandpass emission (530/30) was used for FITC. In the CLSFM case, HeLa cells were plated in a glass-bottom dish at 1.0×10^4 cells/dish and cultured for 24 h at 37 °C in 5% humidified CO_2. After the medium was removed, 600 μL of fresh MEM containing peptide-based carrier−FITC-BSA (17 nM) complex or peptide-based carrier−FITC-β-Gal (17 nM) complex was added to cells. After incubation for 1 h at 37 °C in 5% CO_2, the cells were added to 1 mL of fresh medium and then were cultured for 3 h. After incubation for periods of constant duration, the cells were washed with fresh medium and were observed by CLSFM.

Intracellular Delivery of Enzyme β-Gal. The enzyme activity of β-Gal before and after complexation with nanogel was estimated by TokyoGreen-βGal as a substrate. The initial velocities of β-Gal (10 nM) in the absence and presence of $CHPNH_2$(17) nanogel (10 nM) after the addition of 30 μM of substrate TokyoGreen-βGal were estimated using an FP-6500 fluorescence spectrometer. The fluorescence of the TokyoGreen-βGal product by enzyme reaction was measured (ex. 490 nm, em. 510 nm). Initial velocity was estimated from the slope of the change of the intensity within 15 min.

In the experiment on the enzyme activity of β-Gal inside the cell, HeLa cells were plated in a glass-bottom dish at 1.0×10^4 cells/dish and cultured for 24 h at 37 °C in 5% humidified CO_2. After the culture medium was removed, 1 mL of $CHPNH_2$ complex solution with β-Gal (10 nM) was added to cells. After

incubation for 4 h at 37 °C in 5% CO_2, the cells were washed with fresh medium and then were cultured for 12 h. Tokyo-Green-βGal (10 μM) was added to the medium. After 30 min, CLSFM was observed with excitation by an argon laser (488 nm). The emitted fluorescence was detected through a 503–530 nm bandpass filter.

Inhibition of Specific Endocytotic Pathways. HeLa cells were plated in a six-well culture dish at a density of 2.0×10^4 cells/well and cultured for 24 h at 37 °C in 5% humidified CO_2. After the medium was removed, 1 mL of fresh MEM containing $CHPNH_2$ nanogel (10 nM)−FITC-BSA complex (10 nM) was added and incubated for 4 h at 4 or 37 °C in 5% CO_2. The cells were washed with fresh medium, trypsinized, and suspended in stain buffer. Flow cytometry was performed on a FACScalibur with a 488 nm argon laser. The signal from the FL1 bandpass emission (530/30) was used for FITC.

In an experiment using an endocytosis inhibitor, HeLa cells (2.0×10^4 cells/well) were pretreated with the clathrin-mediated endocytosis inhibitor, Ikarugamycin (IKA (0–5 μM)), or the macropinocytosis inhibitor, amiloride (0–100 μM), for 30 min at 37 °C in 5% CO_2 and then cultured with fresh medium containing $CHPNH_2(17)$ (10 nM)−FITC-BSA (10 nM) complexes with one of the inhibitors for 4 h at 37 °C in 5% CO_2. The cells were washed with fresh medium, trypsinized, and suspended in stain buffer. Flow cytometry was performed on a FACScalibur with a 488 nm argon laser. The signal from the FL1 bandpass emission (530/30) was used for FITC.

CLSFM Observation of Tat-NLS-GFP. HeLa cells were plated in a glass-bottom dish at 1.0×10^4 cells/dish and cultured for 24 h at 37 °C in 5% CO_2. After the culture medium was removed, 1 mL of $CHPNH_2$ complex solution with Tat-NLS-GFP (100 nM) was added to the cells for 4 h at 37 °C in 5% CO_2. The cells were washed with fresh medium and cultured for 24 h at 37 °C in 5% CO_2. After the addition of DAPI (300 nM), CLSFM was observed with excitation by an argon laser (488 nm for GFP) and a blue diode (405 nm for DAPI). The emitted fluorescence was detected through a 503–530 nm bandpass filter and a 420 nm long-pass filter, respectively.

RESULTS AND DISCUSSION

Interaction of the Cationic Nanogel with Proteins. We synthesized amino-fucntionalized CHP ($CHPNH_2$) by reacting CHP with ethylenediamine. The designation $CHPNH_2(17)$ means that 17 amino groups per 100 glucose units were introduced to a CHP macromolecule. Cationic derivatives of CHP also formed monodispersive nanogels (Rh = 14–17 nm) by DLS, similar to CHP (Table 1). Interaction between $CHPNH_2(17)$ nanogel and BSA as a model protein was estimated by fluorescence resonance energy transfer (FRET) and by fluorescence correlation spectroscopy (FCS). After FITC-labeled BSA (FITC-BSA) (10 nM) was added to rhodamine-labeled $CHPNH_2(17)$ nanogels (10 nM), FRET was effectively observable due to the complexation (Figure 2). The binding of FITC-BSA to the cationic nanogels was quite rapid ($t_{1/2}$< 5 min).

The binding constants of BSA (Evoblue-BSA (2.5 nM)) with nanogels were estimated on the basis of a molar concentration of BSA (mol/L) and a molar concentration of the CHP or $CHPNH_2$ nanogel (mol/L) by FCS (Figure 3). Even nonionic CHP nanogels strongly bound to BSA ($K = 1.3\ (\pm 0.2) \times 10^7\ M^{-1}$). We found the CHP nanogel trapped BSA in a hydrogel matrix and formed 1:1 complex nanoparticles, mainly by hydrophobic interaction (*17*). The $CHPNH_2(11)$ and $CHPNH_2(17)$ nanogels exhibited higher binding constants than the CHP nanogel (Table 1). This is due to both hydrophobic and electrostatic interactions between the cationic nanogels and anionic BSA (pI = 4.7). The $CHPNH_2$ nanogel−BSA complexes were slightly increased in size and still monodisperse

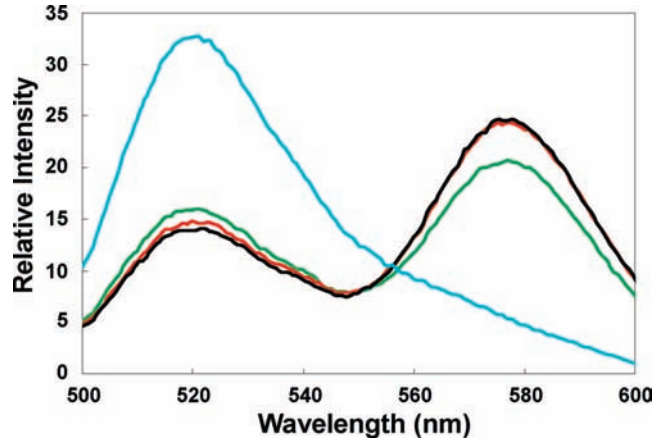

Figure 2. Emission spectra of FITC-BSA (blue line) and $CHPNH_2(17)$-Rh−FITC-BSA complex (ratio of BSA and nanogel = 1:1) after the formation of a complex at 1 (green line), 5 (red line), and 15 (black line) min, respectively. The concentrations of FITC-BSA and $CHPNH_2(17)$Rh nanogel were 10 nM.

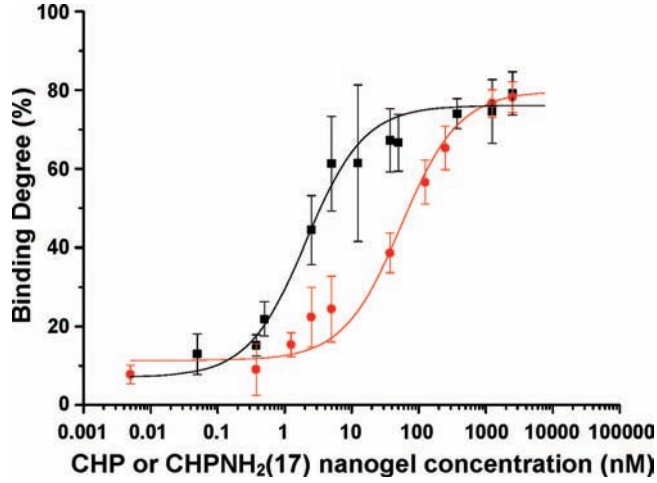

Figure 3. Binding curve between BSA and nanogels (CHP (circle) and $CHPNH_2(17)$ (square)) as estimated by FCS. Error bars represent the SD for three experiments performed in duplicate.

based on DLS (Table 1) and TEM observation (Figure 4). The zeta potentials were still positive after complexation. Colloidally stable cationic nanosized particles were formed after a simple mixing of the cationic nanogels and BSA. The self-assembled cationic nanogel is a unique macromolecular host for proteins. The nanogel structure, in which the network is comparable to the size of the protein, is suitable for effective protein trapping.

Interaction of Cationic Nanogel−Protein Complex with Cells. Protein delivery by $CHPNH_2$ nanogels to human cervical cancer (HeLa) cells was investigated. Complexes of nanogel−FITC-BSA were cultured with HeLa cells in MEM with 10% FBS. The fluorescence intensities of internalized FITC-BSA (10 nM) by $CHPNH_2$ nanogels (10 nM) were measured by flow cytometry. The time course of the cellular uptake of FITC-BSA with $CHPNH_2(17)$ nanogel was investigated. The uptake of FITC-BSA to cell increased over 6 h (Figure 5i). High cellular uptake was observed even in the case of a 1:1 molar mixture of FITC-BSA and $CHPNH_2$ nanogel (Figure 5ii). The uptake increased with an increase in the content of amino groups (Figure 5iii). The interaction of cationic nanogels with anionic domains on the cell surface due to various membrane proteoglycans may be an important factor in the cellular uptake of the nanogel complex. For example, Behr and co-workers demonstrated that, in the cellular uptake of cationic PEI/DNA complex,

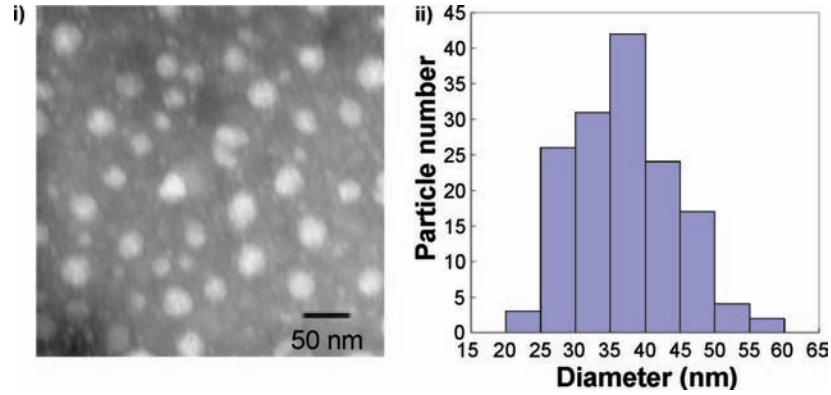

Figure 4. (i) TEM image (negative stain) of $CHPNH_2(17)$−FITC-BSA complex and (ii) particle size distribution determined from TEM images.

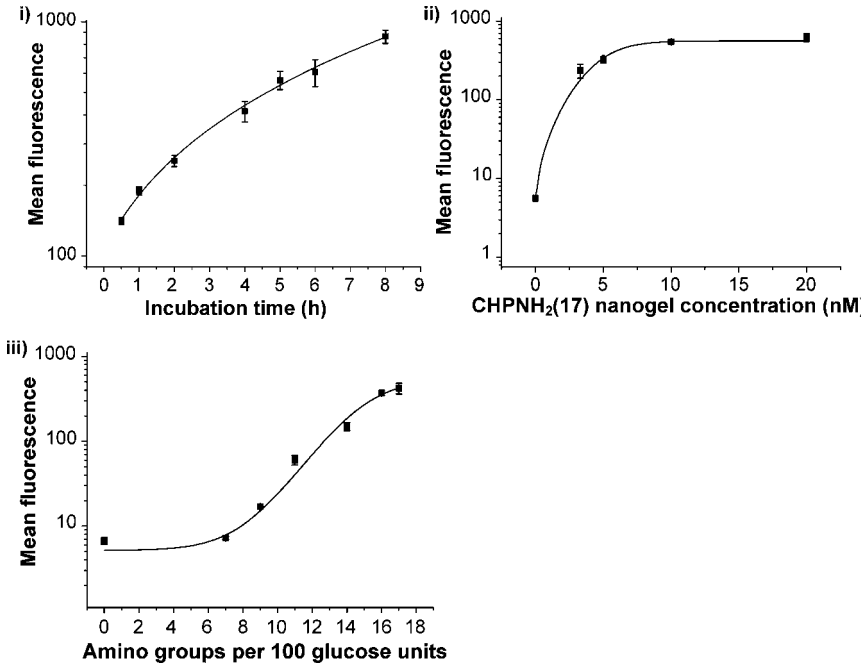

Figure 5. Cellular uptake of FITC-BSA (10 nM) by various cationic nanogels determined by flow cytometry. Error bars represent the SD for three experiments performed in duplicate. (i) Time course of the cellular uptake of FITC-BSA (10 nM) with $CHPNH_2(17)$ nanogel (10 nM) over 0.5, 1, 2, 4, and 6 h. (ii) Effect of molar complex formation $CHPNH_2$−FITC-BSA on cellular uptake. HeLa cells were cultured for 4 h in MEM containing FITC-BSA and $CHPNH_2$ nanogels (0, 3.3, 5.0, 10, and 20 nM) complexes. (iii) Effect of the degree of amino group substitution on cellular uptake. HeLa cells were cultured for 4 h in MEM containing CHP, $CHPNH_2(7)$, (9), (11), (14), (15), (16), and (17) (every nanogel concentration is 10 nM).

electrostatic interaction with anionic binding sites of syndecans (anionic heparan sulfate proteoglycans) play an important role (*27*).

We compared the efficiency of cellular uptake with those in other carrier systems such as cationic liposome and peptide-based carrier under the similar conditions. The mean fluorescence in the $CHPNH_2(17)$ nanogel system by flow cytometry was higher than that with cationic liposomes and a peptide-based carrier (Figure 6i). Images obtained by confocal laser scanning fluorescence microscopy (CLSFM) suggested that FITC-BSA was effectively internalized inside almost all of the cells by the nanogels (Figure 6ii−iv). Cell viability did not change even after incubation of the $CHPNH_2(17)$ nanogels (final concentration 10 or 100 nM) for 24 h though there was a slight toxicity in the case of both the cationic liposomes and peptide-based carrier (Supporting Information Figure S1) under the condition of cellular protein delivery.

We investigated protein delivery in various cell types such as CHO-K1 (chinese hamster ovary fibroblasts), cos-7 (african green monkey kidney fibroblasts), and NIH-3T3 (mouse embryonic fibroblasts) using three carrier systems. In all cell lines, effective cellular uptake of FITC-BSA by the nanogel $CHPNH_2(17)$ carrier was observed in comparison to the other carrier systems tested (Figure 7). This nanogel protein delivery system exhibited a general versatility for effective activity in a variety of cells.

The sizes of the cationic liposome−FITC BSA complex (Rh = 1490 nm) and peptide-based carrier (Rh = 750 nm) were larger than that of the $CHPNH_2(17)$ nanogel (Rh = 19 nm) as determined by DLS measurement. The size of the complex is an important factor in cellular uptake (*8*). A smaller carrier, comparable to the size of a virus, is effectively internalized into the cell. The higher efficiency of the nanogel carrier is probably due to the formation of nanoparticles of <50 nm in size even after complexation with proteins.

Intracellular Delivery of Enzyme β-Gal by Cationic Nanogel. The delivery and enzymaticactivity of β-Gal inside the cell were investigated. β-Gal (540 kDa (tetramer)) is a larger protein than BSA (66 kDa). The monodispersed nanoparticle was also formed after complexation of the

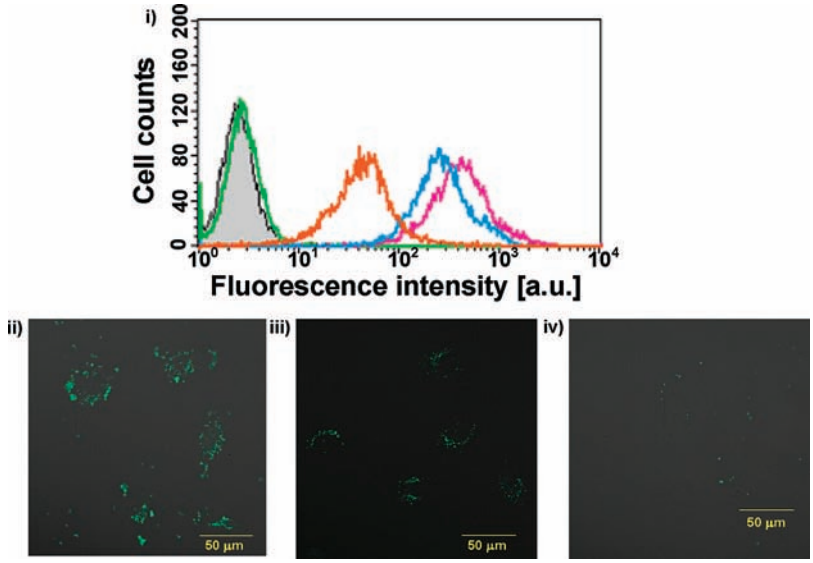

Figure 6. Uptake of FITC-BSA (10 nM) by HeLa cells after 4 h by various carriers. After being washed, HeLa cells were cultured for 4 h. (i) Flow cytometry data for cell only (black), FITC-BSA in the absence of carrier (green line), peptide-based carrier (orange line), cationic liposome (blue line), and $CHPNH_2$(17) nanogel (pink line). (ii−iv) CLSFM images of HeLa cells incubated with the carrier−protein complexes ((ii) $CHPNH_2$(17) nanogel, (iii) cationic liposome, and (iv) peptide based carrier).

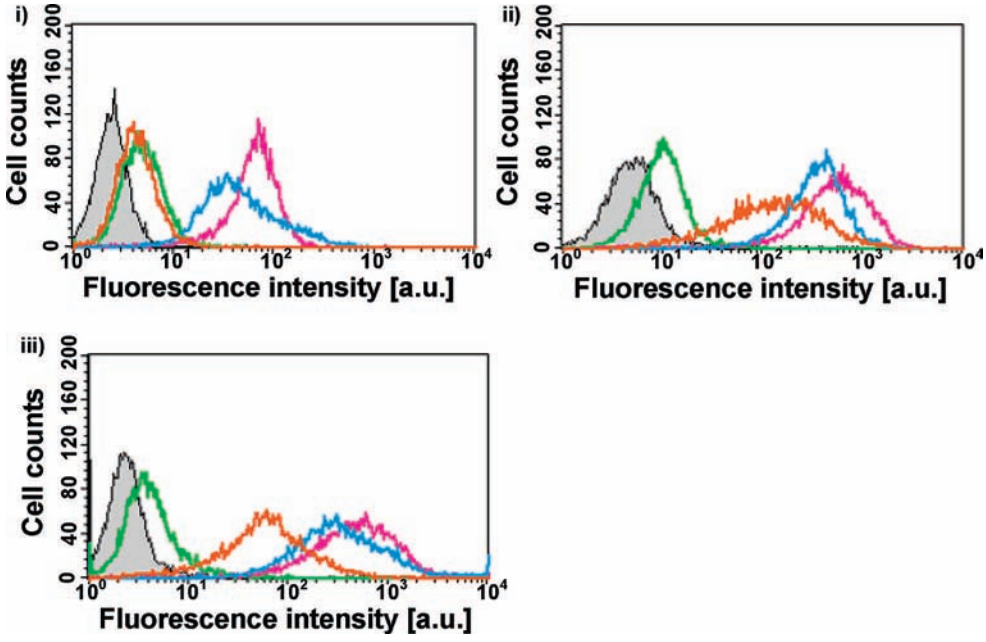

Figure 7. Flow cytometry data for uptake of FITC-BSA (10 nM) to (i) NIH-3T3, (ii) cos-7, and (iii) CHO-K1 cells after 4 h by various carriers. After being washed, HeLa cells were cultured for 4 h, cell only (black), FITC-BSA in the absence of carrier (green line), peptide-based carrier (orange line), cationic liposome (blue line), and $CHPNH_2$(17) nanogel (pink line).

$CHPNH_2$ nanogel with β-Gal (diameter 30 nm (PDI = 0.191)). The enzymatic activity *in vitro* (TokyoGreen-βGal as a substrate of β-Gal (*28*)) was retained after complexation ([initial velocity of $CHPNH_2$-β-Gal complex]/[initial velocity of β-Gal] was 0.95). The cellular uptake of FITC-β-Gal was investigated by CLSFM and flow cytometry. The nanogel carrier system was superior to the other carrier systems tested (Figure 8i). Cellular uptake was saturated at a 1:1 molar mixture of FITC-β-Gal (Figure 8ii).

The enzyme activity of β-Gal inside the cell was evaluated *in situ*on the basis of fluorescence of the reaction product of TokyoGreen-βGal (*28*). HeLa cells were incubated with nanogel−β-Gal complex for 4 h. After being washed, HeLa cells were cultured for 12 h, and the substrate was then added to the medium. The fluorescence spread uniformly throughout almost all of the cells by CLSFM (Figure 8iii). The enzyme may be delivered into the cytosol via endocytosis by nanogels. Another possibility is that the fluorescence product of TokyoGreen by enzyme reaction may escape from endosomes and spread into the cytosol. The enzyme activity of β-Gal was retained after $CHPNH_2$ nanogel-mediated intracellular delivery. The enzyme was found to be present in the native form inside the cells.

Uptake Mechanism of the Nanogel−Protein Complex. To obtain insight into the mechanism of the cellular internalization of the cationic nanogel, the following experiments were carried out. The cellular uptake of FITC-BSA by cationic nanogels decreased to 30%, based on the mean intensity of fluorescence at 4 °C compared to that at 37 °C by flow cytometry (Figure 9i). We next used chemical inhibitors to block specific endocytotic pathways,

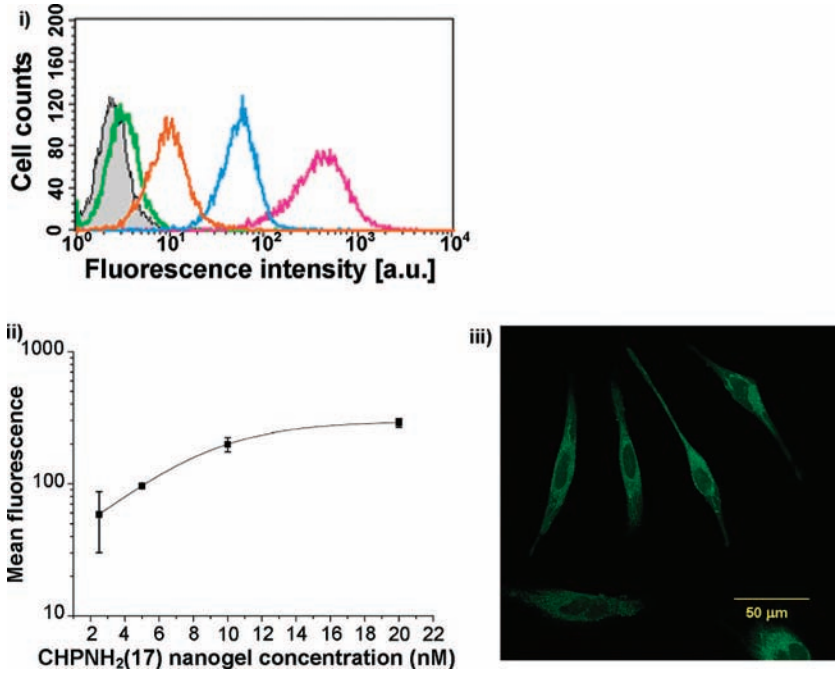

Figure 8. (i) Uptake of FITC-β-Gal (10 nM) by HeLa cells after 4 h by various carriers. After being washed, HeLa cells were cultured for 4 h. Flow cytometry data for cell only (black), FITC-BSA in the absence of carrier (green line), peptide-based carrier (orange line), cationic liposome (blue line), and $CHPNH_2$(17) nanogel (pink line). (ii) HeLa cells were cultured for 4 h in MEM containing FITC-β-Gal (10 nM) and $CHPNH_2$ nanogels (2.5, 5.0, 10, and 20 nM) complexes. Error bars represent the SD for three experiments performed in duplicate. (iii) The enzyme activity of β-Gal inside the cell was evaluated *in situ* by CLSFM. HeLa cells were incubated with $CHPNH_2$(17) nanogel (10 nM)−β-Gal (10 nM) complex for 4 h. After being washed, HeLa cells were cultured for 12 h, and the substrate was then added to the medium. The cells were observed by CLSFM.

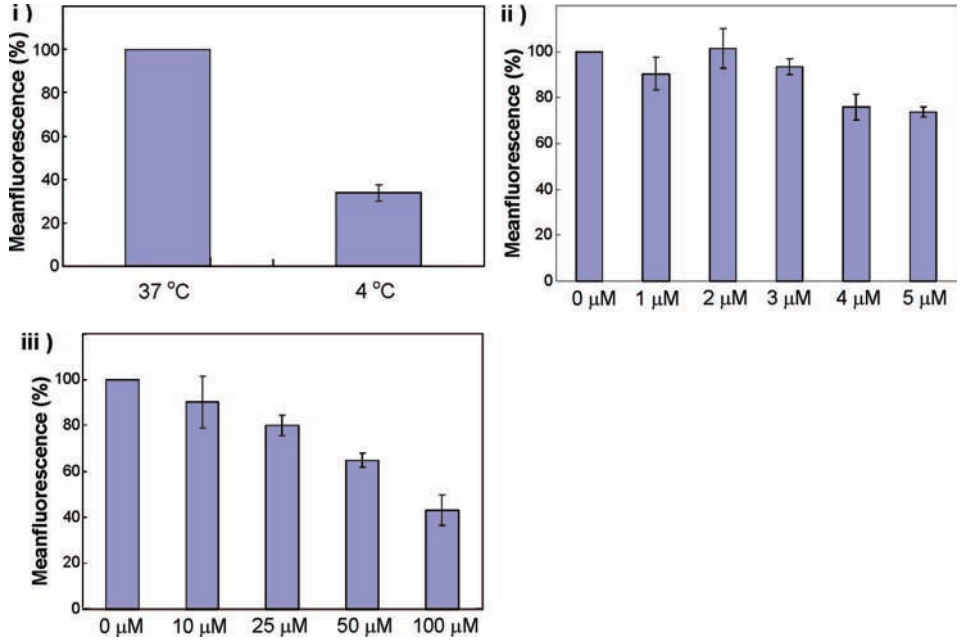

Figure 9. Inhibition of endocytosis prevents the formation of $CHPNH_2$(17) nanogel (10 nM)−FITC-BSA (10 nM) complexes. The mean fluorescence of cells was measured by flow cytometry and is represented as the percentage of that in untreated cells for 4 h at 37 °C: (i) low temperature (4 °C), (ii) clathrin-mediated endocytosis inhibitor, and (iii) macropinocytosis inhibitor. Error bars represent the SD for three experiments performed in duplicate.

such as clathrin-mediated endocytosis by Ikarugamycin (IKA) (*29*), which blocks the down-regulation of CD4 in response to phorbol myristate acetate and the macropinocytosis inhibitor amiloride, an inhibitor of the Na^+/H^+ exchange required for macropinocytosis (*30*). Cells were treated with these inhibitors before the addition of nanogel−FITC-BSA complex and then analyzed using flow cytometry. IKA inhibited the uptake of the complexes by 25% and amiloride inhibited uptake by up to 60% (Figure 9ii,iii). These results indicate the possible involvement of macropinocytosis in the uptake of the nanogel complex.

The fate of the complex of nanogel−BSA after uptake into the cell was investigated using different fluorescence probes between the nanogel (rhodamine-labeled $CHPNH_2$(17)) (red) and FITC-BSA (green) by CLSFM. After 2 h incubation, the complex had effectively internalized into the cell and most of the two fluorescences overlapped (yellow) (Figure 10i). This

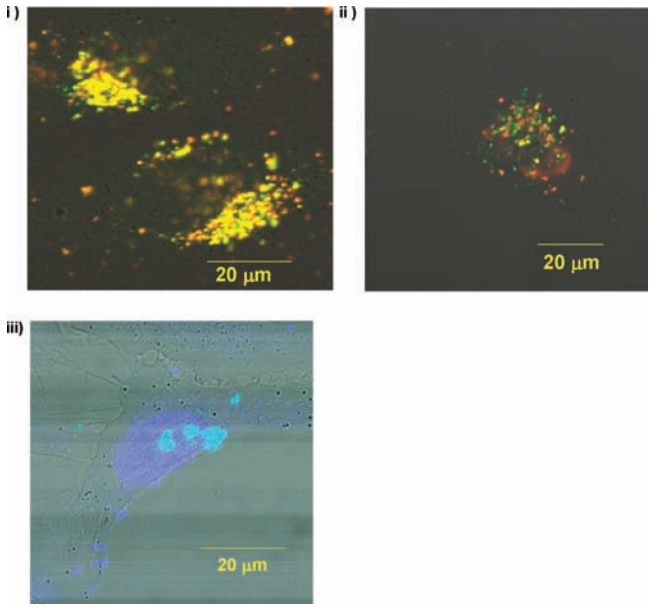

Figure 10. CLSFM images. (i,ii) HeLa cells were cultured with $CHPNH_2$Rh-FITC-BSA complexes (10 nM) (FITC-BSA (green), $CHPNH_2$(17)Rh (red), and overlay (yellow)) for 4 h. After being washed, HeLa cells were cultured for (i) 2 h and (ii) 18 h after washing. (iii) Intracellular localization of Tat-NLS-GFP (100 nM) by CHP-NH_2(17) nanogel (100 nM). The nuclei were stained with DAPI (blue).

means that FITC-BSA was internalized as a complex with the nanogel. After 18 h, however, the fluorescence of FITC-BSA (green) and rhodamine-labeled $CHPNH_2$ (red) were increased at different sites within the cell (Figure 10ii). This result suggests that the complex had become dissociated and the protein was released from the nanogels inside the cell including endosomes or cytosol. It may be possible that sorting of endosomes would give separate signals of BSA and nanogels. The ratio of BSA (green fluorecence) released from the nanogels was estimated to be approximately 20%, as shown in the Figure 10ii).

We previously reported that proteins encapsulated by CHP nanogel are released in the presence of an excess amount of other proteins without the disintegration of the nanogel. For example, chymotrypsin (Chy) entrapped in CHP nanogel was released in the presence of BSA (*31*). In an animal experiment, insulin entrapped in CHP nanogel was also released in a functional form in the bloodstream after intravenous injection (*23*). The main driving force of the binding of the protein with amphiphilic nanogel is hydrophobic interaction between the nanogel cholesterol groups and the hydrophobic domain of the protein. BSA probably expels Chy from the nanogel due to the more potent hydrophobicity property. Therefore, the encapsulated protein can be released by an exchange mechanism. The CHP nanogel is physically cross-linked with nanogels by self-assembly of the cholesterol group attached to pullulan. The dynamic property of the association of the cholesterol group enables encapsulation of the protein and also exchange of proteins.

In the intracellular uptake of the nanogel−protein complex, one of the explanations for the release of protein in the cell is the protein-exchange mechanism. The exchange reaction would effectively occur inside the cell, because the concentration of proteins in the cell is quite high. Another possibility is the disintegration of the nanogel inside the cell by cellular proteins or lipids or by enzyme degradation of polysaccharide. Finally, the cellular uptake of GFP-conjugated nuclear localization signal and Tat as a PTD (Tat-NLS-GFP) was investigated by flow cytometry and CLSFM. The results of flow cytometry showed the high cellular uptake of Tat-NLS-GFP by the nanogel delivery system, while Tat-NLSGFP was only slightly internalized into cells by itself because of the existence of PTD of Tat and an NLS amino sequence. After nanogel-mediated internalization, Tat-NLS-GFP was localized in the nuclei due to the effect of a nuclear localization signal by CLSFM (Figure 10iii). The results suggested that Tat-NLS-GFP was released from the nanogel and moved to the nucleus from the cytosol.

CONCLUSIONS

Cationic self-assembled nanogels strongly interacted with proteins such as bovine serum albumin (BSA) and β-Galactosidase (β-Gal), and formed a colloidally stable monodispersed nanoparticels (<50 nm). They have been demonstrated to be capable of effective transport of various proteins into various cells even in the presence of serum. The nanogel carrier complex was more effectively internalized into HeLa cells than cationic liposomes and protein transduction domain (PTD) based carrier system. The complex of the nanogel−protein was dissociated and the protein was released after internalization to the cell. The cationic nanogels system is useful as a carrier for intracellular protein delivery and as a tool in cell biology research.

The application of these nanogels to an antigen (oncoprotein) delivery system for high cellular and humoral immune responses is under investigation (*25*). It is possible to develop tailormade functional nanogels to create novel nanobiomaterials (nanogel engineering) through the self-assembly of functional associating polymers as the building blocks. For example, various stimuli-responsive nanogels can be obtained by the self-assembly of pH-responsive cholesteryl-bearing poly(amino acids) (*21*), thermoresponsive poly(*N*-isopropylacrylamide)-CHP (*22*), and photoresponsive spiropyrane-modified pullulan (*20*). This self-assembled nanogel should create new opportunities for protein delivery systems.

ACKNOWLEDGMENT

This work was supported by a Grant-in-Aid for Scientific Research from the Japanese government and CREST, JST. We thank Prof. T. Tsubata, Dr. K. Watanabe and Mr. Y. Kawaguchi (Tokyo Medical and Dental University) for the generous gift of Tat-NLS-GFP. We thank Prof. K. Tokunaga and Dr. H. Miyadera (Tokyo University) for using MF 10S. Pacific Edit reviewed the manuscript prior to submission.

Supporting Information Available: Additional figures as described in the text. This material is available free of charge via the Internet at http://pubs.acs.org.

LITERATURE CITED

(1) Wadia, J. S., Stan, R. V., and Dowdy, S. F. (2004) The TAT protein transduction domain (PTD) has been used to deliver a wide variety of biologically active cargo for the treatment of multiple preclinical. *Nat. Med. 10*, 310–315.

(2) Futaki, S. (2005) Membrane-permeable arginine-rich peptides and the translocation mechanisms. *Adv. Drug Delivery Rev. 57*, 547–558.

(3) Zelphati, O., Wang, Y., Kitada, S., Reed, J. C., Felgner, P. L., and Corbeil, J. (2001) Intracellular delivery of proteins with a new lipid-mediated delivery system. *J. Biol. Chem. 276*, 35103–35110.

(4) Dalkara, D., Zuber, G., and Behr, J. P. (2004) Intracytoplasmic delivery of anionic proteins. *Mol. Ther. 9*, 964–969.

(5) Majetei, N. V., and Kumar, R. (2000) Nano and microparticles as controlled drug delivery devices. *Pharm. Pharm. Sci. 3*, 234–258.

(6) Kwon, Y. J., Standley, S. M., Goh, S. L., and Frechet, M. J. (2005) Enhanced antigen presentation and immunostimulation of dendritic cells using acid-degradable cationic nanoparticles. *J. Controlled Release 105*, 199–212.

(7) Morris, M. C., Depollier, J., Mery, J., Heitz, F., and Divita, G. (2001) Enhanced antigen presentation and immunostimulation of dendritic cells using acid-degradable cationic nanoparticles. *Nat. Biotechnol. 19*, 1173–1176.

(8) Nakai, T., Kanamori, T., Sando, S., and Aoyama, Y. (2003) Remarkably size-regulated cell invasion by artificial viruses. saccharide-dependent self-aggregation of glycoviruses and its consequences in glycoviral gene delivery. *J. Am. Chem. Soc. 125*, 8465–8475.

(9) Vinogradov, S. V., Bronich, T. K., and Kabanov, A. V. (2002) Nanosized cationic hydrogels for drug delivery: preparation, properties and interactions with cells. *Adv. Drug Delivery Rev. 54*, 135–147.

(10) Nayak, S., and Lyon, L. A. (2005) Soft nanotechnology with soft nanoparticles. *Angew. Chem., Int Ed. 44*, 7686–7708.

(11) Kim, K., Lee, M., Park, H., Kim, J. H., Kim, S., Chung, H., Choi, K., Kim, I. S., Seong, B. L., and Kwon, I. C. (2006) Cell-permeable and biocompatible polymeric nanoparticles for apoptosis imaging. *J. Am. Chem. Soc. 128*, 3490–3491.

(12) Oh, J. K., Tang, C., Gao, H., Tsarevsky, N. V., and Matyjaszewski, K. (2006) Inverse miniemulsion ATRP: A new method for synthesis and functionalization of well-defined water-soluble/cross-linked polymeric particles. *J. Am. Chem. Soc. 128*, 5578–5584.

(13) Hayashi, H., Iijima, M., Kataoka, K., and Nagasaki, Y. (2004) pH-Sensitive nanogel possessing reactive PEG tethered chains on the surface. *Macromolecules 37*, 5389–5396.

(14) McAllister, K., Sazani, P., Adam, M., Cho, M. J., Rubinstein, M., Samulski, R. J., and DeSimone, J. M. (2002) Polymeric nanogels produced via inverse microemulsion polymerization as potential gene and antisense delivery agents. *J. Am. Chem. Soc. 124*, 15198–15207.

(15) Missirlis, D., Tirelli, N., and Hubbell, J. A. (2005) Amphiphilic hydrogel nanoparticles. preparation, characterization, and preliminary assessment as new colloidal drug carriers. *Langmuir 21*, 2605–2613.

(16) Akiyoshi, K., Deguchi, S., Moriguchi, N., Yamaguchi, S., and Sunamoto, J. M. (1993) Self-aggregates of hydrophobized polysaccharides in water. *Macromolecules 26*, 3062–3068.

(17) Akiyoshi, K., Deguchi, S., Tajima, T., Nishikawa, T., and Sunamoto, J. (1997) Microscopic structure and thermoresponsiveness of a hydrogel nanoparticle by self-assembly of a hydrophobized polysaccharide. *Macromolecules 30*, 857–861.

(18) Nishikawa, T., Akiyoshi, K., and Sunamoto, J. (1996) Macromolecular complexation between bovine serum albumin and the self-assembled hydrogel nanoparticle of hydrophobized polysaccharides. *J. Am. Chem. Soc. 118*, 6110–6115.

(19) Nomura, Y., Ikeda, M., Yamaguchi, N., Aoyama, Y., and Akiyoshi, K. (2003) Protein refolding assisted by self-assembled nanogels as novel artificial molecular chaperone. *FEBS Lett. 553*, 271–276.

(20) Hirakura, T., Nomura, Y., Aoyama, Y., and Akiyoshi, K. (2004) Photoresponsive nanogels formed by the self-assembly of spiropyrane-bearing pullulan that act as artificial molecular chaperones. *Biomacromolecules 5*, 1804–1809.

(21) Akiyoshi, K., Ueminami, A., Kurumada, S., and Nomura, Y. (2000) Self-association of cholesteryl-bearing poly(L-lysine) in water and control of its secondary structure by host-guest interaction with cyclodextrin. *Macromolecules 33*, 6752–6756.

(22) Morimoto, N., Winnik, F. M., and Akiyoshi, K. (2007) Botryoidal assembly of cholesteryl-pullulan/poly(*N*-isopropylacrylamide) nanogels. *Langmuir 23*, 217–223.

(23) Akiyoshi, K., Kobayashi, S., Shichibe, S., Mix, D., Baudys, M., Kim, S. W., and Sunamoto, J. (1998) Self-assembled hydrogel nanoparticle of cholesterol-bearing pullulan as a carrier of protein drugs: complexation and stabilization of insulin. *J. Controlled Release 54*, 313–320.

(24) Hasegawa, U., Nomura, S. M., Kaul, S. C., Hirano, T., and Akiyoshi, K. (2005) Nanogel-quantum dot hybrid nanoparticles for live cell imaging. *Biochem. Biophys. Res. Commun. 331*, 917–921.

(25) Ikuta, Y., Katayama, N., Wang, L., Okugawa, T., Takahashi, Y., Schmitt, M., Gu, X., Watanabe, M., Akiyoshi, K., Nakamura, H., Kuribayashi, K., Sunamoto, J., and Shiku, H. (2002) Presentation of a major histocompatibility complex class 1-binding peptide by monocyte-derived dendritic cells incorporating hydrophobized polysaccharide-truncated HER2 protein complex: implications for a polyvalent immuno-cell therapy. *Blood 99*, 3717–24.

(26) Kobayashi, T., Okamoto, N., Sawasaki, T., and Endo, Y. (2004) Presentation of a major histocompatibility complex class 1-binding peptide by monocyte-derived dendritic cells incorporating hydrophobized polysaccharide-truncated HER2 protein complex: implications for a polyvalent immuno-cell therapy. *Anal. Biochem. 332*, 58–66.

(27) Kopatz, I., Remy, J. S., and Behr, J. P. (2005) A model for non-viral gene delivery: through syndecan adhesion molecules and powered by actin. *J. Gene. Med. 6*, 769–776.

(28) Urano, Y., Kamiya, M., Kanda, K., Ueno, T., Hirose, K., and Nagano, T. (2005) Evolution of fluorescein as a platform for finely tunable fluorescence probes. *J. Am. Chem. Soc. 127*, 4888–4894.

(29) Luo, T., Fredericksen, B. L., Hasumi, K., Endo, A., and Garcia, J. V. (2001) Human Immunodeficiency virus type 1 nef-induced CD4 cell surface downregulation is inhibited by ikarugamycin. *J Virol. 75*, 2488–2492.

(30) West, M. A., Bretscher, M. S., and Watte, C. (1989) Distinct endocytotic pathways in epidermal growth factor-stimulated human carcinoma A431 cells. *J. Cell Biol. 109*, 2731–2739.

(31) Nishikawa, T., Akiyoshi, K., and Sunamoto, J. (1994) Supramolecular assembly between nanoparticles of hydrophobized polysaccharide and soluble protein complexation between the self-aggregate of cholesterol-bearing pullulan and α-chymotrypsin. *Macromolecules 27*, 7654–7659.

BC700422S

Amphiphilic Copolymer for Delivery of Xenobiotics: *In Vivo* Studies in a Freshwater Invertebrate, a Mesostominae Flatworm

Laetitia De Jong,[‡] Xavier Moreau,[‡] Alain Thiéry,[‡] Guilhem Godeau,[†,▽] Mark W. Grinstaff,[§] and Philippe Barthélémy*[,†,▽]

UMR-CNRS 6116, Institut Méditerranéen d'Ecologie et de Paléoécologie - IMEP (Biomarqueurs & Bioindicateurs Environnementaux), case 17, Université de Provence, 3 place Victor Hugo 13331 Marseille Cedex 3, France, INSERM U869, Bordeaux, F-33076, France, Université Victor Segalen Bordeaux 2, Bordeaux, F-33076, France, and Department of Biomedical Engineering, Metcalf Center for Science and Engineering, Boston University, Boston, Massachusetts 02215. Received November 21, 2007; Revised Manuscript Received February 1, 2008

The synthesis of an amphiphilic polymethacrylate copolymer containing cholesterol hydrophobic moieties and rhodamine as a fluorescent probe, the formation of microspheres, and the uptake of these microspheres in an invertebrate are reported. The cholesterol-derived methacryloyl monomer, which was prepared *via* a one-step synthesis, was copolymerized with methacrylic acid and methacryloxyethyl thiocarbamoyl rhodamine B in the presence of AIBN as initiator. The obtained dye-labeled copolymer was characterized by ^{1}H NMR and UV–vis spectroscopy. Fluorescence and TEM microscopies studies show that this amphiphilic copolymer aggregates to give microspheres with diameters ranging from 3 to 11 μm. The *in vivo* study in a freshwater invertebrate, a Mesostominae flatworm (Rhabdocoela, Thyphloplanidae), indicates that the microspheres enter the cells by endocytosis. The data collected demonstrate that the rhodamine B covalently attached to the amphiphilic copolymers is bioaccumulated without being translocated out of the cell by the multixenobiotic resistance (MXR) transporters. As the MXR system is similar to the multidrug resistance (MDR) first observed in tumor cell lines resistant to anticancer drugs, the present data confirm the significant role that amphiphilic copolymers can play in the ongoing development of drug delivery strategies to overcome multidrug resistance. These investigations illustrate a promising approach for the development of new medical and ecotoxicological tools that can deliver specific molecules within cells.

INTRODUCTION

Within the past four decades, there has been increased interest in the design of macromolecules for applications ranging from drug delivery (*1–3*) to biological imaging technologies (*4*). Polymer chemistry and engineering have had a direct impact on enhancing drug loading of therapeutic agents as well as creating stable biosensors for novel therapeutic (*5*) and diagnostic devices (*6*). With regard to polymeric microspheres, there are two broad categories: reservoir devices and polymer conjugates. The former involves carriers where a drug or a dye is physically incorporated into the polymeric matrix, whereas in the latter system, the drug is covalently linked to the polymer. Polymers under investigations include proteins, nucleic acids, and polysaccharides as well as synthetic polymers. Among the various options, the synthetic polymers, including polyanhydrides, polyesters, polyacrylic acids, polymethacrylates, and polyurethanes provide important avenues for research, primarily because of their ease of processing and the ability to control their chemical and physical properties. Synthetic polymers are also advantageous due to high physical stability, possibility of sustained drug release, and potential for functionalization.

In the polymer conjugates area, the bioactive molecule and/or the dye is covalently bound and transported to the tissues and cells. These macromolecular carriers should ideally be water-soluble, biocompatible, nontoxic, and nonimmunogenic (*7*), as well as degraded and/or eliminated from the organism (*8*). The biological rationale for the use of water-soluble copolymers as drug carriers is based on their unique biological behaviors in terms of pharmacokinetics properties and cellular uptake. It is well-known that high-molecular-weight polymers can accumulate in solid tumors due to the differences in the biochemical and physiological characteristics of healthy and malignant tissues (*9*). This feature termed "enhanced permeability and retention" (*10−12*) (EPR effect) was described by Maeda and his co-workers (*13*). The cellular uptake mechanism of a molecule is also known to depend on its molecular weight. Whereas most low-molecular-weight molecules penetrate into the cell *via* simple diffusion thought the cell membrane, macromolecules are taken up by the cell through endocytosis (*14*). During this step, a significant drop in the pH value takes place from the physiological values (7.2–7.4) in the extracellular space to pH 6.5–5.0 in the endosomes and finally to about pH 4.0 in primary and secondary lysosomes. Recently, Leroux and co-workers reported that synthetic polyanions derived from polycarboxylates can take advantage of this drop in pH to overcome the endosomal/lysosomal barrier and deliver macromolecular drugs (*15–17*). Moreover, it was reported that increasing the copolymer hydrophobicity by introducing hydrophobic monomers induced a destabilization of cell membranes facilitating the endosomal escape (*18*).

With the aim to further increase the hydrophobicity of polymethacrylate polyanions, an amphiphilic polymethacrylate copolymer has been synthesized. In this study, we have selected (i) the cholesterol as a highly hydrophobic species and (ii) rhodamine as a fluorescent marker as well as a substrate of the multixenobiotic resistance (MXR) pump transporter, which

* Corresponding author. Philippe.Barthelemy@bordeaux.inserm.fr.
[‡] UMR-CNRS 6116.
[†] INSERM U869.
[▽] Université Victor Segalen Bordeaux 2.
[§] Boston University.

10.1021/bc700425x CCC: $40.75 © 2008 American Chemical Society
Published on Web 03/15/2008

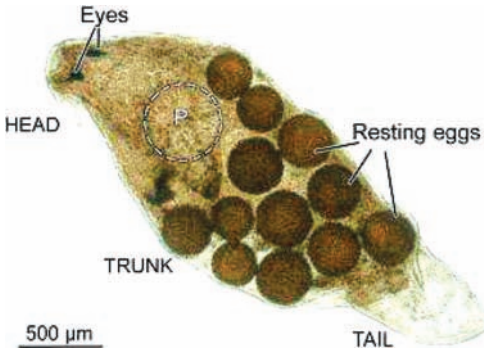

Figure 1. Photomicrography of a Mesostominae flatworm (Rhabdocoela, Thyphloplanidae). P: pharynx. Note the transparency of the organism.

removes xenobiotic molecules or drugs from the cell. These two functional monomers were prepared containing either cholesterol or rhodamine and copolymerized with methacrylate in the presence of AIBN to give the corresponding amphiphilic labeled copolymer. Based on the chemical features of this macromolecule (i) drug/dye polymer conjugate, (ii) amphipatic structure, (iii) pH-sensitive groups (carboxylates), we hypothesize that this carrier could play a significant role for drug delivery applications and/or imaging cells. A goal of this work is to investigate this new macromolecular carrier for *in vivo* delivery to a simple freshwater invertebrate: a Mesostominae flatworm (Platyhelminthes, Rhabdocoela, Thyphloplanidae) (Figure 1). Flatworms are acoelomata organisms, known as simplest triploblastic animals. They possess a simple body plan organization lacking respiratory and circulatory organs. The pharynx and epidermis are in contact with surrounding aquatic media. These flatworms also carry eggs within their body. The aquatic biota of these animals is convenient for copolymer incubation. Indeed, these organisms tolerate laboratory conditions of temperature, pH, and conductivity. Furthermore, their small size (between 2 mm to 3.5 mm long) and transparent soft body, devoid of cuticle, allows *in toto* epifluorescence microscopy observations. Aquatic invertebrates are also often used as environmental indicators for environmental risk assessment in the presence of xenobiotics such as pollutants (*19*). In general, the term xenobiotic is given to all chemicals, including drugs or pollutants that are foreign to the organism under investigation.

To study the *in vivo* uptake of the amphiphilic copolymer as well as its role in the delivery of a xenobiotic, we used the fluorescent marker, rhodamine B, covalently attached to the copolymer. Rhodamine B is a multixenobiotic resistance (MXR) pump transporter substrate; thus, animals were also incubated in a rhodamine B solution, with or without a MXR transporter inhibitor (verapamil). The MXR defense system, reported in many aquatic invertebrates, is thought to work in a similar manner to the multidrug resistance (MDR) P-glycoprotein (Pgp) observed in cancer cells (*20, 21*). It has been shown that MXR actively transports a variety of xenobiotics across the cell membrane (*22*).

In this paper, we describe a new amphiphilic copolymer labeled with rhodamine B, and report the results from *in vivo* studies in a freshwater invertebrate. The *in vivo* uptake of free rhodamine B and rhodamine B covalently attached to the amphiphilic copolymer carrier either in the presence or in the absence of the MXR inhibitor verapamil is discussed.

MATERIALS AND METHODS

Materials. *General Experiments and Analytical Conditions.* Unless noted otherwise, all starting materials were obtained from Aldrich, and were used without further purification; the solvents were redistilled on calcium chloride, calcium hydride, potassium hydroxide, or sodium according to the solvent used. All compounds were characterized using standard analytical and spectroscopic techniques such as ^{1}H spectroscopy (apparatus Bruker Avance DPX-300, ^{1}H at 300.13 MHz) and mass spectrometry (instrument JEOL SX 102, NBA matrix). The NMR chemical shifts are reported in ppm relative to tetramethylsilane using the deuterium signal of the solvent ($CDCl_3$, DMSO-d_6 or D_2O) as a heteronuclear reference for ^{1}H. The ^{1}H NMR coupling constants, *J*s, are reported in Hz. TEM microscopy experiments were performed on a Hitachi H 7650 (negative staining with ammonium molybdate 1% in water, Ni carbon-coated grids). Fluorescence microscopy experiments were realized on a Zeiss axiovert 200. UV spectroscopy measurements were carried out on a Lambda 25 (Perkin-Elmer, France) with Peltier temperature programmer PTP-6. Silica gel 60 (particle size 40–60 μm) was used for flash chromatography. Thin-layer chromatograms were performed with aluminum plates coated with silica gel 60 F_{254} (Merck). Varian silica gel reverse-phase C18 MEGA BE-C18, 2GM 12 mL, and Sephadex LH-20 (25–100 μm) were used for quantitative chromatography.

Synthesis. *N-(6-Cholesterylcarbonylaminohexyl)-2-methylacrylamide (Compound* **1***).* Triethylamine (0.6 mL, 4.03 mM, 2.1 equiv) was added under nitrogen dropwise to N-Boc-hexylammonium chloride (0.500 g, 1.94 mM, 1 equiv) in 50 mL of methylene chloride at 0 °C. Then, cholesterolchloroformiate (0.961 g, 2.14 mM, 1.1 equiv), dissolved in 20 mL of dry methylene chloride, was added to the reaction at 0 °C. The reaction mixture was stirred at 0 °C for 1 and 2 h at room temperature. The resulting mixture was washed 3 times with 20 mL of water and then dried over sodium sulfate. After removing the solvent, the crude material was dissolved in 20 mL of a 50/50 trifluoroacetic acid/dichloromethane mixture and stirred for 2 h. The solvent is removed under high vacuum. The trifloroacetate salt was suspended in DCM, and 0.5 mL of TEA was added to the reaction flask. Then, 0.1 mL of methacryloyl chloride was added to the solution at 0 °C. This solution was stirred for 1 h at 0 °C and 2 h at room temperature. Purification on a silica gel column (MeOH/DCM, 3/97) yielded 0.240 g of **1**. (Yield: 21%). ^{1}H NMR ($CDCl_3$) δ in ppm: 0.65–2.26 (m, skeleton of cholesterol, C*H*$_2$ decyl amine, C*H*$_3$ methacrylate), 3.2 (m, 4H, 2C*H*$_2$NH), 4.4 (m, 1H, *H*CO cholesterol), 4.6 (m, 1H, N*H*), 5.2 (s, 1H, C*H* methacryl), 5.3 (m, 1H, *CH* cholesterol), 5.6 (s, 1H, C*H* methacryl), 5.9 (m, 1H, N*H*). High resolution MS: $[M + H]^+$, theoritical $m/z = 597.4917$, observed $m/z = 597.5007$. Anal. Calcd. (M + 1/2 H_2O) C, 75.32%; H, 10.81%; N, 4.62%. Found C, 74.99%; H, 10.19%; N, 4.83%.

Copolymerization (Compound 2). *Copolymer* **2.** Compound **1** (0.02 g, 0.033 mM, 1 equiv), methacrylic acid (0.100 g, 1.15 mM, 35 equiv), methacryloxyethyl thiocarbamoyl rhodamine B (*N*-[9-(2-carboxy-x-methacryloxyethylthiocarbamoylphenyl)-6-diethylamino-3*H*-xanthen-3-ylidene]-*N*-ethylethanaminium chloride; PolyFluor 570) (0.005 g) and AIBN (0.005 g, 0.03 mM) were dissolved in 40 mL of dry methanol. The reaction mixture was heated under nitrogen for 24 h. Methanol was evaporated, and the resulting material was dissolved in a minimum amount of MeOH/DCM 50/50 and purified on Sephadex LH20. 43 mg of copolymer **2** was isolated. (conversion 81%). ^{1}H NMR (CD_3OD) δ in ppm (broad peaks): ^{1}H NMR ($CDCl_3$) δ in ppm: 0.65–2.26 (m, skeleton of cholesterol, C*H*$_2$ hexyl amine, C*H*$_2$ and C*H*$_3$ methacrylate, CH_2 and CH_3 of the rhodamine), 3.2 (m, C*H*$_2$NH), 4.1 (m, *H*CO cholesterol), 5.3 (m, *C*═*CH* cholesterol). Content % of each monomer was determined by measuring the integration between 0.65 and 2.26 ppm (cholesterol, CH_2 of hexyl amine, CH_2 and CH_3 of the rhodamine and polymer backbone), integration at 5.43 ppm (cholesterol *C*═CH)

Table 1. Experimental Design for *in Vivo* Uptake of the Rhodamine B (RhB) or of the Rhodamine B-Labeled Amphiphilic Copolymer (RhB-amphiphilic copolymer)

solutions of incubation	incubation period at 13 °C	incubation period at 4 °C
mineral water (control)	10 h	
RhB (5 μg.mL^{-1})	1 h 30, 4 h, 10 h	
Rh B (5 μg.mL^{-1}) + Verapamil (10 μM)	1 h 30, 4 h, 10 h	
RhB-amphiphilic copolymer (5 μg.mL^{-1})	1 h 30, 4 h, 10 h	10 h
RhB-amphiphilic copolymer (5 μg.mL^{-1}) + Verapamil (10 μM)	1 h 30, 4 h, 10 h	10 h

and at 7.83 ppm (corresponding to one aromatic rhodamine H), $x = 4\%$, $y = 95.6\%$, $z = 0.4\%$.

Transmission Electronic Microscopy (TEM). The copolymer was dispersed in either methanol or distilled water for TEM experiments. Typically, 1 mg of copolymer was dispersed in 1 mL of methanol. This solution was left for 3 h at RT prior to examination.

Fluorescence Microscopy. The samples were prepared by dispersing 5 mg of copolymer in 1 L of water. The pH of the solutions was adjusted by addition of either HCl (1 M) or NaOH (1 M). Prior to examination, these solutions were heated at 70 °C for 1 min and sonicated at RT for 5 min and left for 1 h at RT.

UV–vis Spectroscopy. UV–vis spectroscopy experiments were carried out on a Lambda 25 (Perkin-Elmer, France). The absorbance of the control samples containing free rhodamine was measured at 554 nm on aqueous solutions of free rhodamine at different concentrations (5×10^{-4} to 5×10^{-3} mg/mL. The UV–vis spectrum of the polymer was recorded on aqueous suspensions containing 0.1 mg/mL of polymer in water.

Material and Methods for *in Vivo* Studies. *Collection and Conservation of Biological Material.* Flatworms were collected in a temporary pound in the south of France with a hand net (125 μm mesh). Limnological parameters were the following: water temperature 15.3 °C; conductivity (C_{20}) 252 μS/cm; pH 7.02; dissolved oxygen 3 mg/L and 31% of saturation. Animals were brought back alive to the laboratory and maintained at 13 °C in a commercial mineral water (C_{20} = 200 μS/cm, pH 7.11). Water was refreshed daily and animals were fed every day with 1 mL of Teramin (Tetra Werke, Melle, Germany) dissolved in the commercial water (4 g/L).

Protocol for in Vivo Uptake of the Amphiphilic Copolymer. Solutions were prepared with the same mineral water used for the laboratory maintenance of flatworms. Flatworms were incubated in the dark either with rhodamine B alone (5 μg/mL) or with the rhodamine B-labeled amphiphilic copolymer (5 μg/mL). These experiments have been performed in the absence or in the presence of 10 μM of verapamil, a MXR transporter inhibitor. The temperature was 4 or 13 °C and pulse period 1 h 30, 4 h, or 10 h, followed by a 1 h chase period at room temperature to allow the expulsion of nonabsorbed material from the digestive tract. For each experimental condition, 5 flatworms were used. The experimental design is summarized in Table 1. Animals were then fixed in phosphate buffer containing paraformaldehyde 1% (PB-PFA 1%). After rinsing in phosphate buffer, animals were mounted in antifading medium (Gel/Mount, BiØmeda corp., Foster city, CA, USA) and observed under an epifluorescence microscope (Leica M1560).

Evidence of MXR Membrane Proteins in Flatworms. The presence and the density of MXR membrane proteins in flatworms were evaluated using a ELISA assay. A monoclonal primary antibody (mAb_1) raised against the human Pgp (C219 clone) was produced in mouse (Interchim, Montluçon, France). The C219 probe recognizes a sequence expressed by all MXR genes whose sequence is known, from bacteria to man (*23*). Fixed flatworms in PB-PFA 1% were weighted and then homogenized in Tris-HCl 0.05 M, pH 7.4, and centrifuged 20 min at 4 °C (14 000 *g*). The supernatant was discarded and membrane pellets were resuspended in PB (0.1 M, pH 7.2). The microplate wells were coated with 200 μL of this solution overnight at 4 °C (8 mg wet weight/well). Overnight coated wells were washed five times in 0.01% Triton X100-PB, then saturation was performed 1 h at 25 °C with BSA 0.1% diluted in 0.01% Triton X100-PB. Wells were incubated (1 h at 25 °C) with mAb_1 (1:10) and rinsed three times in 0.01% Triton X100-PB. Then, the wells were incubated in alkaline phosphatase-conjugated goat antimouse IgG (Ab_2, 1:1000) (Promega, Madison, WI, USA) in 0.01% Triton X100, 0.1% BSA in PB (1 h, at 25 °C). After five washes in 0.01% Triton X100-PB, the enzymatic reaction is initiated with the addition of 100 μL of *p*-nitrophenyl phosphate (p-NPP) dissolved in diethylethanolamine (Sigma, St Quentin-Fallavier, France). The optical density (OD_{405}), that reflects the membrane density in MXR-related proteins, was measured in triplicate at 10, 20, 30, and 40 min after the initiation with a microplate reader (ELX800 with KC4 software, Biotek Instrument) at 23 °C. The negative controls were done by incubating the mAb_1 and all the components except the membrane homogenates. The other controls consisted of (i) incubating all the components without the primary antibody for background studies, (ii) incubating Ab_2 alone, and, finally, (iii) incubating Ab_2 with 0.01% Triton X100 and 0.1% BSA in PB.

RESULTS AND DISCUSSION

The following three constituting monomeric building blocks were selected to prepare the amphiphilic copolymer: methacrylic acid (water-soluble part), methacryloyl cholesterol (hydrophobe), and methacrloyl rhodamine (fluorescent probe). Cholesterol was used as a hydrophobic moiety based on its known aggregation properties and its role in the lipid raft-mediated endocytosis (*24*). This natural lipid is also used in many cationic delivery systems including lipoplexes to both improve DNA delivery and increase the stability of formulations in the presence of serum (*25–27*). Recently, rhodamine was used as a probe to follow the release of a bioactive molecule entrapped in polymeric structures (*28*). This dye is also a known substrate of the multixenobiotic resistance (MXR) pump transporter, which removes xenobiotic molecules or drugs from the cell. Consequently, to easily follow the cellular uptake of our amphipatic copolymer structure, rhodamine was selected as a water-soluble model of a xenobiotic.

Synthesis. The amphiphilic copolymer was prepared as shown in Scheme 1. After synthesis of the cholesterol benzyloxycarbonyle (Boc) diamino derivative in basic conditions, this intermediate was treated with TFA in methylene chloride to afford the deprotected amine. A coupling reaction with methacryloyl chloride at 0 °C for 1 h and then at room temperature for 3 h yielded the expected methacryloyl cholesterol monomer **1**. The copolymerization reaction was followed by thin-layer chromatography (TLC) on silica gel (methanol/DCM 5/95). The free radical copolymerization (*29*) of the three methacryloyl monomers is facile. Specifically, the reaction mixture was heated under nitrogen for 24 h in the presence of AIBN and the resulting crude polymer purified on exclusion gel chromatography. Importantly, the synthetic strategy developed allows easy access in four steps to the cholesterol rhodamine labeled copolymer. The percentage of each monomer unit in the polymer ($x = 4.0\%$, $y = 95.6\%$, $z = 0.4\%$) was determined by measuring the integrations of CH_2 backbone and CH_2NH via ^1H NMR.

Physicochemical Studies. The UV–vis spectra of the copolymer labeled with rhodamine (Figure 2, blue) and the free rhodamine (Figure 2, red) in the region 500–600 nm are shown

Scheme 1[a]

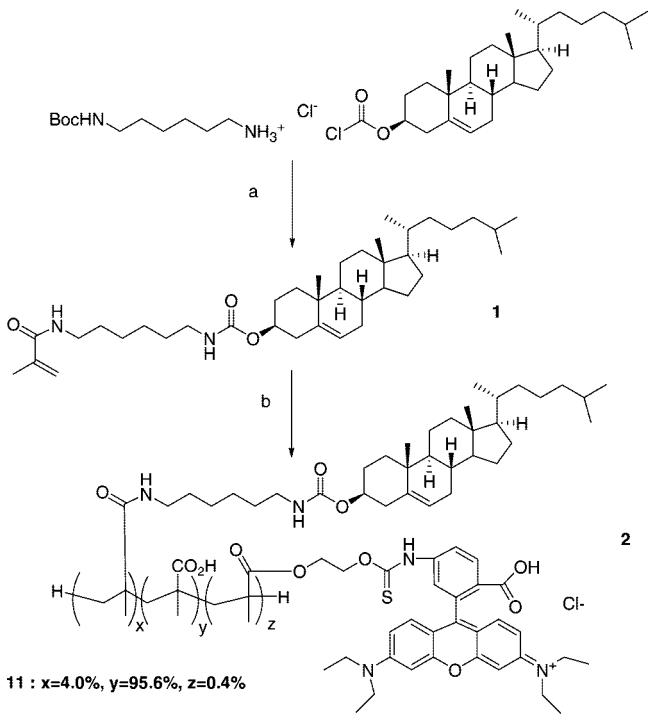

[a] (a) (1) TEA in DCM, 1 h 0 °C, then 2 h at RT. (2) TFA/DCM 50/50, 2 h at RT. (3) Methacryloyl chloride, TEA in DCM, 1 h 0 °C then 3 h at RT (yield: 21%). (b) AIBN, MeOH, reflux, 72 h, conversion: 81%.

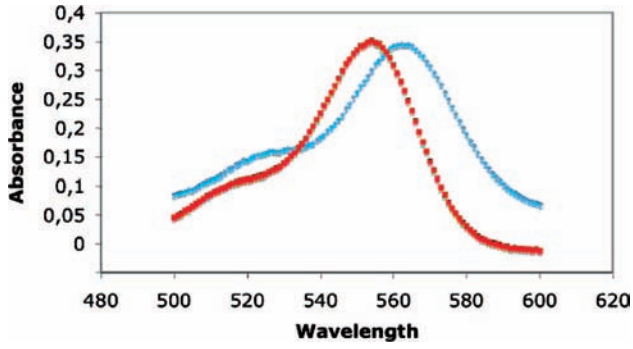

Figure 2. UV–vis spectra (absorbance vs wavelength in nm) of the copolymer labeled with rhodamine (blue) and the free rhodamine (red).

in Figure 2. The red shift observed for the labeled copolymer ($\lambda_{max} = 562$ nm) compared to free rhodamine in water ($\lambda_{max} = 554$ nm) can be attributed to the rhodamine being located in a more hydrophobic microenvironment of the copolymer structure and a resulting decrease in local polarity (*30*). The amount of rhodamine grafted to the polymeric structure was also determined by UV–vis spectroscopy. The absorbance measured at $\lambda_{max} = 562$ nm for a solution of the labeled copolymer at a concentration of 0.1 mg/mL corresponds to a concentration of rhodamine equivalent to 2×10^{-3} mg/mL (weight fraction of rhodamine = 2%). Note that a weight fraction of 2.% in rhodamine gives a mole fraction of 0.35%, similar to the value obtained from ^{1}H NMR analysis ($z = 0.4\%$).

As expected, the amphiphilic character of copolymer **2** tends to promote the formation of aggregates in both organic solutions and aqueous media. Amphiphilic copolymer (typical concentrations: 1 mg/mL) dissolved in methanol exhibits three populations of aggregates. The smallest particles are a few hundred nanometers in size, whereas the two other populations show hydrodynamic radii of a few micrometers and a few tens of micrometers, respectively.

Note that the formation of aggregates in both organic and aqueous solutions (water, methanol, DMF) prohibits the study of the isolated macromolecules. Consequently, despite numerous trials, including size exclusion chromatography (SEC) and dynamic light scattering (DLS) experiments, it was impossible to determine the average molecular weight of the copolymers, since the polymer exhibited an aggregated state even at low concentrations.

Microscopy Studies of the Aggregates. The size and morphology of the copolymer aggregates in solution were examined by fluorescence and electronic microscopies (TEM). As shown in Figure 3, the amphiphilic copolymer self-assembles in water to give large spherical aggregates with diameters of approximately 5 μm. These aggregates can be observed by using both light (Figure 3a) and fluorescence microscopies. The formation of aggregates was also confirmed by TEM (Figure 3b,c). At higher magnifications, TEM images (Figure 3c) show the presence of hollow microspheres similar to the ones reported by Caruso et al. (*31*). The folds and creases seen in the polymer microspheres are a result of evaporation of the solvent by air-drying. The size distribution of the objects obtained from TEM images reveals a relatively homogeneous population of microspheres with diameters ranging from 3 to 11 μm (Figure 4 blue). Note that the population of the microspheres observed by TEM (Figure 4 blue) is similar to the population of the same microspheres observed by *in vivo* by fluorescence microscopy (see the *in Vivo* Studies section) suggesting that the microspheres remain intact even after cellular uptake.

***In Vivo* Studies.** *Uptake of Rhodamine B.* The accumulation and efflux of model P-glycoprotein (Pgp) substrates such as fluorescent dyes (rhodamine B, rhodamine 123, etc.) is a method routinely used to follow the activity of the multixenobiotic resistance (MXR) defense mechanism in aquatic invertebrates (*32*), especially in the biomarker research field. Figure 5 presents the *in vivo* uptake of free rhodamine B by flatworms after 10 h of incubation at 13 °C either in the absence (Figure 5a) or in the presence (Figure 5b) of a MXR inhibitor, verapamil. The higher fluorescence intensity observed in the presence of verapamil indicates that, without verapamil, the molecules of rhodamine B inside the cells are actively expulsed *in vivo* by the MXR membrane efflux pump proteins.

To verify the presence of MXR transporters in these flatworms, an ELISA assay has been developed and performed. MXR transporters have been detected by the C219 antibody in membrane homogenates of flatworms. The optical density at 405 nm (OD_{405}) that reflects the membrane density in MXR-related proteins reaches 3.890 ± 0.005 for 8 mg wet weight of flatworms (Figure 6).

These results showing the absence of rhodamine B in flatworms in the absence of verapamil and presence of rhodamine B in flatworms in the presence of verapamil and the semiquantification of MXR-transporter membrane density demonstrate the presence of the MXR system in these Mesostominae flatworms. MXR genes have been highly conserved through the phylogenesis as demonstrated by their presence in microorganisms (*33*), plants (*34*), aquatic invertebrates (*35*), and vertebrates (*36*). In fact, the MXR system is similar to the multidrug resistance (MDR) first observed in tumor cell lines resistant to anticancer drugs (*20, 37–38*). One important mechanism of MDR involves the multidrug transporter, P-glycoprotein, which confers upon cells the ability to resist lethal doses of certain cytotoxic drugs by pumping them out of the cells, and thus reduce their cytotoxicity (*39–41*).

Uptake of Rhodamine B-Labeled Amphiphilic Copolymers. In light of the physicochemical properties of the copolymer and

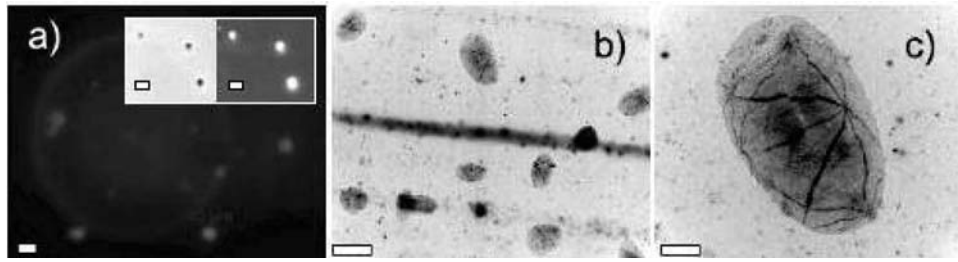

Figure 3. (a) Fluorescence microscopy image of copolymer aggregates in aqueous media at pH = 7.3 (concentrations = 5 mg/L, bar represents 10 μm). The insets left and right are light and fluorescence microscopy images of the same sample, respectively (bars represent 5 μm). (b,c) TEM images visualizing the polymer microspheres at different magnification (bars represent 10 and 2 μm for (b) and (c), respectively).

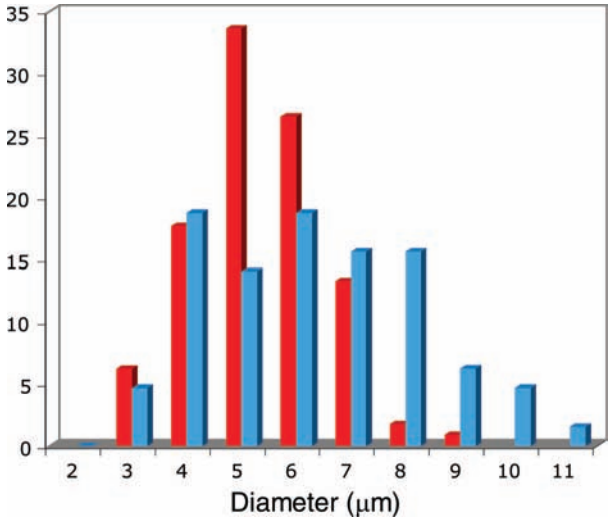

Figure 4. Size distributions of the microspheres (number of objects in percent vs size) obtained from (i) TEM images (blue) and (ii) fluorescence microscopy images (red) collected from the *in vivo* studies (copolymers in flatworm egg cells after 4 h incubation at 13 °C. See *in Vivo* Studies section for details).

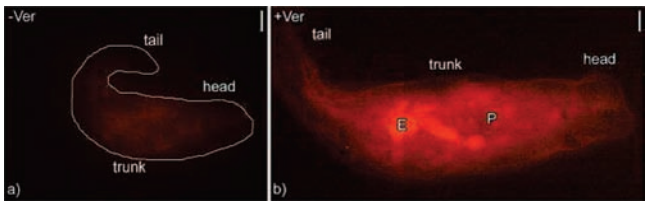

Figure 5. Uptake of rhodamine B by Mesostominae flatworms in the absence (a, −Ver) or in the presence (b, +Ver) of the MXR inhibitor verapamil after 10 h of incubation at 13 °C. Note the higher fluorescence intensity in (b) compared to (a). E: resting egg. P: pharynx. Bars = 200 μm.

the *in vivo* data collected with free rhodamine, we hypothesize that the amphiphilic macromolecule, which bears rhodamine B as a water-soluble model of xenobiotic, can be taken up by flatworms. In principle, the copolymer can be used as a carrier to improve the delivery of xenobiotics. In this context, two key issues must be addressed: (i) How is the copolymer taken up by the flatworms? (ii) Is the macromolecular carrier translocated out of the cells by the MXR system?

Endocytosis is a cellular uptake process that is coupled with temperature-dependent metabolic activities (*42*). To determine whether the rhodamine B-labeled amphiphilic copolymer is incorporated into the cells by endocytosis, the organisms were observed at two different temperatures, 13 and 4 °C, under an epifluorescence microscope. The lowest temperature corresponds to winter cold temperature tolerated by these organisms and the higher to spring water temperature of the temporary pond

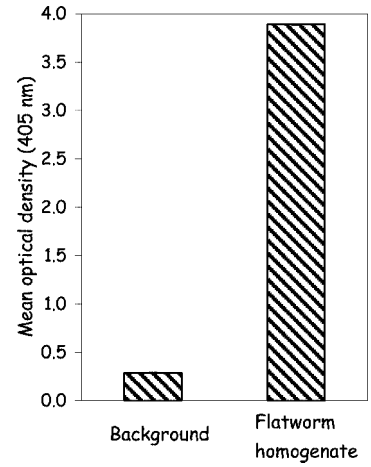

Figure 6. Optical density measured at 405 nm reflecting the density of MXR transporters in membrane homogenates of Mesostominae flatworms read at 40 min after the initiation.

where they live. A control sample showing flatworms by fluorescent microscopy is presented in Figure 7a.

For each experimental condition, rhodamine B-labeled amphiphilic copolymers are observed in flatworm cells by fluorescence microscopy. For a given incubation condition (same time and same temperature), no difference was noticed between samples treated with or without verapamil. At 13 °C, flatworms were exposed to rhodamine B-labeled amphiphilic copolymers for 1 h 30, 4 h, or 10 h. After 1 h 30 of exposure time, the labeled copolymer is observed in a few organelles, named rhabdites, which are located in some flatworm epidermal cells (Figure 7b). The rhabdite initially appears as a large Golgi saccule enclosed by an extensive system of microtubules. Golgi vesicles and vacuoles fuse with the limiting membrane of the rhabdite and contribute to enlarge this structure. Microtubules mediate movement of vesicles containing secretory material along the rhabdite length. Rhabdites are known to be acidophilic and contain predominantly proteins, which may be combined with a purine component and mucopolysaccharides (*43*, *44*). Rhabdite cells are parenchyma-derived cells that migrate into the epidermis. Once in the epidermis, the rhabdite cells become part of the epithelium. It has been proposed that most if not all of the epidermal cells originate from rhabdite cells or from other parenchyma-derived cells (*43*). After 4 h of incubation, the labeled copolymer is observed in several different cell types of the worm. For example, Figure 7c,d shows fluorescent objects within egg cells. The size distribution of the objects obtained from fluorescence microscopy images (Figure 7c,d) reveals a population of microspheres with a mean diameter of 4.25 ± 1.51 μm. Note that size distribution of the fluorescent objects observed *in vivo* (Figure 4, red graph) corresponds to the population of the microspheres obtained spontaneously with copolymer **2** (Figure 4, blue graph). Homogeneous dots in the

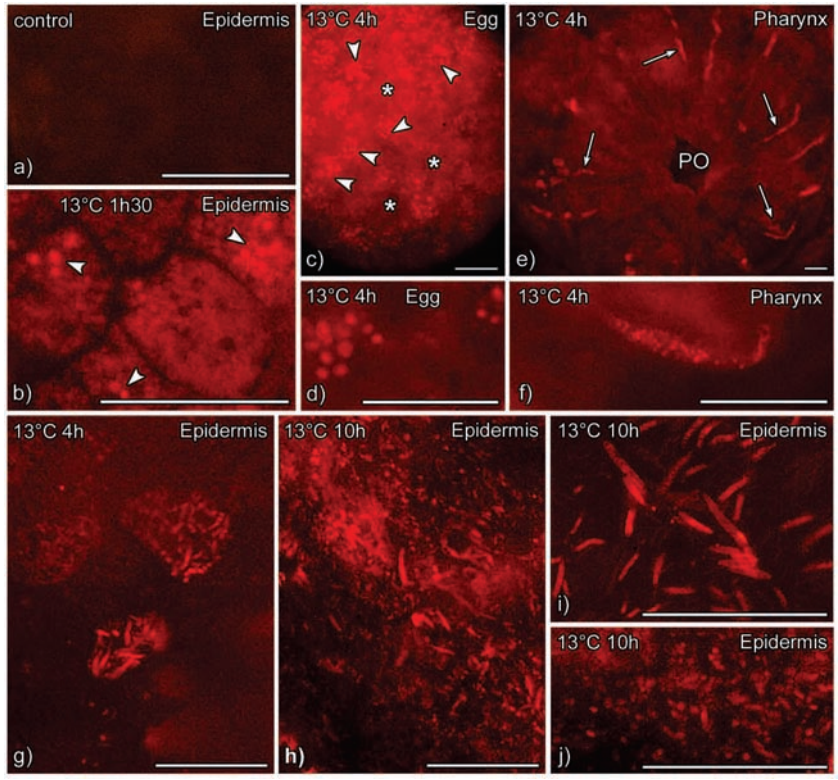

Figure 7. Fluorescence microscopy images showing the *in vivo* uptake of rhodamine B-labeled amphiphilic copolymers (5 μg/mL) by Mesostominae flatworms at 13 °C. (a) Control. (b) Arrowheads indicate a few labeled rhabdite. (c) Arrowheads indicate the uptake of the labeled copolymers into some cells in a resting egg; * indicates cells without labeling. (d) Detail of (c) showing labeled structures (mean diameter ± SEM = 4.25 ± 1.51 μm). (e) General view of the pharynx. Arrows indicate labeling into glandular cells. (f) Detail of a labeled pharyngeal glandular unit. (g−j) Uptake of the copolymers into rhabdite cells; note the increase of the uptake between 4 h (g) and 10 h (h); (i) longitudinal view of labeled rhabdites; (j) transverse view of labeled rhabdites. Bars = 50 μm.

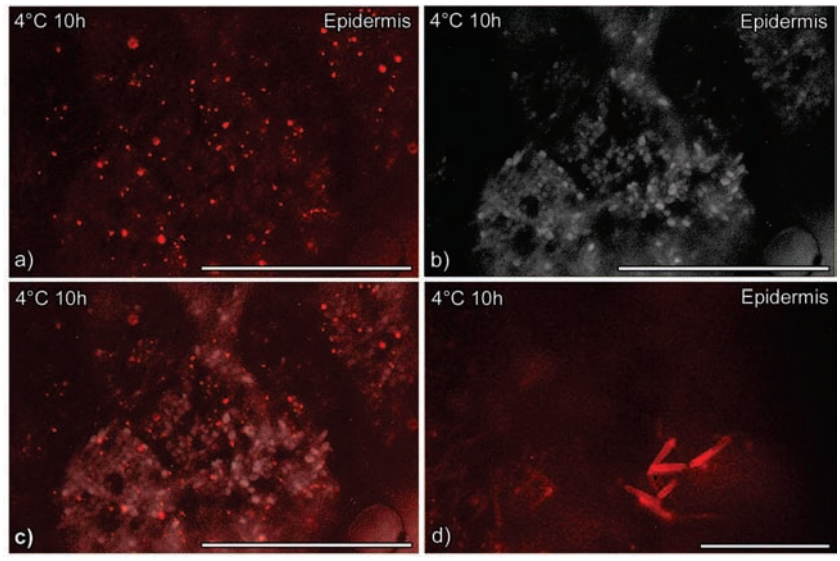

Figure 8. *In vivo* uptake of rhodamine B-labeled amphiphilic copolymers (5 μg.mL^{-1}) by Mesostominae flatworms at 4 °C. (a−c) Localization of rhodamine B-labeled amphiphilic copolymers in rhabdite cells: (a) Fluorescence view showing the localization of the labeled copolymer. (b) Autofluorescence view of (a) showing the localization of unlabeled rhabdites. (c) Merged image of (a) and (b). Note that the copolymers are located nearby the rhabdites. (d) View of a small cluster of labeled rhabdite. Note the scarcity of labeled rhabdites at 4 °C compared with their abundance at 13 °C (cf. Figure 7h). Bars = 50 μm.

pharyngeal glandular cells (Figure 7e,f) and numerous sticklike structures, which are typical mature rhabdites (Figure 7g), are also observed in the fluorescence microscopy images. After 10 h of exposure, numerous rhabdites are labeled (Figure 7h−j).

In the experiments performed at 4 °C for 10 h, labeled copolymers are observed near unlabeled rhabdites (Figure 8a−c). Some labeled rhabdites are also observed (Figure 8d). As the mean length of the rhabdites is 19.98 ± 3.52 and their mean diameter is 3.00 ± 0.80 μm, rhabdites are large enough to accumulate the amphiphilic copolymers. Furthermore, incorporation of the rhodamine B-labeled amphiphilic copolymers is time- and temperature-dependent. At 13 °C, the number of labeled rhabdites per surface unit is 1.83-fold higher at 10 h than at 4 h of incubation. For 10 h of

incubation, the number of labeled rhabdites per surface unit is 7.25-fold higher at 13 °C than at 4 °C. When flatworms were exposed to rhodamine B-labeled amphiphilic copolymers **2** for 10 h at 4 °C, the number of labeled rhabdites per surface unit represents only 13% of the maximum level measured after 10 h at 13 °C.

As has been recently reported by Suenaga et al. for a copolymer carrier featuring hydrophobic lauryloyl groups (*45*), cold temperature induces a remarkable decrease in the copolymer−rhodamine uptake, indicating that the polymer is internalized *via* an endocytosis mechanism. After a 10 h incubation at 4 °C, labeled copolymers observed near unlabeled rhabdites are probably endocytotic vesicles that are about to fuse with rhabdites (Figure 8a−c).

The following observations can be made from the above data: (i) Rhodamine B-labeled amphiphilic copolymers are *in vivo* uptaken *via* an endocytosis mechanism in the early phases of incubation in the invertebrate, and its localization is then observed in different cell types (pharyngeal glandular cells, resting egg cells, epidermis cells). (ii) After incorporation into epidermis cells, rhodamine B-labeled amphiphilic copolymers are concentrated in storage reserve structures, the rhabdites. This storage is observable after 4 h of incubation at 13 °C. The endocytotic pathways (receptors and membrane microdomains) responsible for the uptake of the amphiphilic copolymers need to be investigated further.

***In Vivo* Study Perspectives.** In an ecotoxicological study, Horvat et al. observed histological changes including a decrease in the number of rhabdites in the Platyhelminthe *Polycelis felina* (Daly.) after exposure to norflurazon herbicide (*46*). The *in vivo* uptake experiments described above show that the rhodamine B-labeled amphiphilic copolymer is taken up by the flatworm, enters the cells, and is accumulated in rhabdites. This pattern of amphiphilic copolymer uptake could be used as an ecotoxicological tool to measure cellular activity when animals are exposed to a xenobiotic(s). Moreover, the amphiphilic copolymer could be used as an *in vivo* carrier of specific molecules that could react with pollutants accumulated in cells and subsequently produce a detectable signal.

In the present study, we demonstrate that the bioaccumulation of the MXR substrate rhodamine B was dramatically increased when the rhodamine B was covalently attached to the amphiphilic copolymer and a resulting microsphere was formed. The translocation out of the cell by the MXR system is avoided in comparison to the free rhodamine. As the MXR system is similar to the MDR one, the *in vivo* uptake results strongly suggest that our amphiphilic copolymers can play a significant role in the field of carriers for drug delivery. This finding represents a potential therapeutic option that should be considered during the ongoing development of strategies to overcome multidrug resistance in cancer studies, as it was suggested for the treatment of human ovarian and endometrial cancers that express receptors for luteinizing hormone-releasing hormone with agents such as AN-152 bypassing their Pgp extrusion (*47*).

CONCLUSION

In this study, we have synthesized a new rhodamine-labeled amphiphilic copolymer featuring cholesterol moieties for *in vivo* delivery of xenobiotics and/or drugs. The amphiphilic copolymer structure was prepared from cholesterol-derived methacryloyl monomer, methacrylic acid, and methacryloxyethyl thiocarbamoyl rhodamine B. Fluorescence and TEM microscopies studies indicate that this amphiphilic copolymer aggregates to give microspheres. The *in vivo* experiments carried out on a simple triploblastic aquatic organism, a Mesostominae flatworm, clearly demonstrate that the copolymer/microsphere is bioaccumulated without being translocated out of the cell by the multixenobiotic resistance (MXR) transporters. Synthetic polyanions such as poly(methacrylic acid) are finding utility in enhancing the delivery of nucleic acids to cells, for example, as recently reported by Leroux and co-workers (*15*). Consequently, these and similar polyanionic polymers and copolymers are likely to be of further interest for the *in vitro* and *in vivo* delivery of oligonucleotides, small molecule drugs, and imaging agents. These investigations further support the synthesis and evaluation of new polyanion-based drug delivery vehicles and ecotoxicological tools.

ACKNOWLEDGMENT

The authors would like to thank Dr. Christophe Schatz and Pr. Sébastien Lecommandoux from the LCPO - ENSCPB of Bordeaux for kindly helping us with DLS and SEC experiments.

LITERATURE CITED

(1) Rigsdorf, H. (1975) Structure and properties of pharmacologically active polymers. *J. Polym. Sci. Polym. Symp. 51*, 135–153.
(2) Kopecek, J., and Rejmanová, P. (1983) Enzymatically degradable bonds in synthetic polymers, in Bruck S. D. (Ed.), *Controlled Drug Delivery*, pp 81–124, CRC Press, Boca Raton.
(3) Haag, R., and Kratz, F. (2006) Polymer therapeutics: concepts and applications. *Angew. Chem. Int. Ed. 118*, 1218–1237.
(4) Lin, Y., Weissleder, R., and Tung, C.-H. (2002) Novel near-infrared cyanine fluorochromes: synthesis, properties, and bioconjugation. *Bioconjugate Chem. 13*, 605–610.
(5) Bae, Y., Nishiyama, N., Fukushima, S., Koyama, H., Yasuhiro, M., and Kataoka, K. (2005) Preparation and biological characterization of polymeric micelle drug carriers with intracellular pH-triggered drug release property: tumor permeability, controlled subcellular drug distribution, and enhanced in vivo antitumor efficacy. *Bioconjugate Chem. 16*, 122–130.
(6) Ye, F., Ke, T., Jeong, E.-K., Wang, X., Sun, Y., Johnson, M., and Lu, Z.-R. (2006) Noninvasive visualization of in vivo drug delivery of poly(L-glutamic acid) using contrast-enhanced MRI. *Mol. Pharm. 3*, 507–515.
(7) Lu, Y., and Chen, S. C. (2004) Micro- and nano-fabrication of biodegradable polymers for drug delivery. *Adv. Drug Delivery Rev. 56*, 1621–1633.
(8) Godwin, A., Bolina, K., Clochard, M., Dinand, E., Rankin, S., Simic, S., and Brocchini, S. (2001) New strategies for polymer development in pharmaceutical science - a short review. *J. Pharm. Pharmacol. 53*, 1175–1184.
(9) Maeda, H. (2001) The enhanced permeability and retention (EPR) effect in tumor vasculature: the key role of tumor-selective macromolecular drug targeting. *Adv. Enzyme Regul. 41*, 189–207.
(10) Maeda, H., Wu, J., Sawa, T., Matsumura, Y., and Hori, K. (2000) Tumor vascular permeability and the EPR effect in macromolecular therapeutics: a review. *J. Controlled Release 65*, 271–284.
(11) Jain, R. K. (1987) Transport of molecules in the tumor interstitium: a review. *Cancer Res. 47*, 3039–3051.
(12) Jain, R. K. (1987) Transport of molecules across tumor vasculature. *Cancer Metastasis Rev. 6*, 559–593.
(13) Maeda, H., and Matsumura, Y. (1989) Tumoritropic and lymphotropic principles of macromolecular drugs. *Crit. Rev. Ther. Drug Carr. Syst. 6*, 193–210.
(14) Mukherjee, S., Ghosh, R. N., and Maxfield, F. R. (1997) Endocytosis. *Physiol. Rev. 77*, 759–803.
(15) Yessine, M.-A., Meier, C., Petereit, H.-U., and Leroux, J.-C. (2006) On the role of methacrylic acid copolymers in the intracellular delivery of antisense oligonucleotides. *Eur. J. Pharm. Biopharm. 63*, 1–10.
(16) Yessine, M.-A., and Leroux, J.-C. (2004) Membrane-destabilizing polyanions: interaction with lipid bilayers and endosomal escape of biomacromolecules. *Adv. Drug Delivery Rev. 56*, 999–102.

(17) Yessine, M.-A., Lafleur, M., Petereit, H.-U., Meier, C., and Leroux, J.-C. (2003) Characterization of the membrane destabilizing properties of different pH-sensitive methacrylic acid copolymers. *Biochim. Biophys. Acta 1613*, 28–38.
(18) Murthy, N., Robichaud, J. R., Tirell, D. A., Stayton, P. S., and Hoffman, A. S. (1999) The design and synthesis of polymers for eukaryotic membrane disruption. *J. Controlled Release 61*, 137–143.
(19) van den Brink, P. J., van Donk, E., Gylstra, R., Crum, S. J. H., and Brock, T. C. M. (1995) Effects of chronic low concentrations of the pesticides chlorpyrifos and atrazine in indoor freshwater microcosms. *Chemosphere 31*, 3181–3200.
(20) Kurelec, B., and Pivcevic, B. (1989) Distinct glutathione-dependant enzyme activities and a verapamil-sensitive binding of xenobiotics in a fresh-water mussel *Anodonta cygnea*. *Biochem. Biophys. Res. Commun. 164*, 934–940.
(21) Gottesman, M. M., and Pastan, I. (1993) Biochemistry of multidrug resistance mechanism in aquatic organism. *Aquat. Toxicol. 48*, 385–427.
(22) Bard, S. M. (2000) Multixenobiotic resistance as a cellular defense mechanism in aquatic organisms. *Aquat. Toxicol. 48*, 357–389.
(23) Endicott, J. A., and Ling, V. (1989) The biochemistry of P-glycoprotein-mediated multidrug resistance. *Annu. Rev. Biochem. 58*, 137–171.
(24) Foerg, C., Ziegler, U., Fernandez-Carneado, J., Giralt, E., Rennert, R., Beck-Sickinger, A. G., and Merkle, H. P. (2005) Decoding the entry of two novel cell-penetrating peptides in HeLa cells: lipid raft-mediated endocytosis and endosomal escape. *Biochemistry 44*, 72–81.
(25) El Ouahabi, A., Thiry, M., Pector, V., Fuks, R., Ruysschaert, J. M., and Vandenbranden, M. (1997) The role of endosome destabilizing activity in the gene transfer process mediated by cationic lipids. *FEBS Lett. 414*, 187–192.
(26) Bennett, M. J., Nantz, M. H., Balasubramaniam, R. P., Gruenert, D. C., and Malone, R. W. (1995) Cholesterol enhances cationic liposome-mediated DNA transfection of human respiratory epithelial cells. *Biosci. Rep. 15*, 47.
(27) Crook, K., Stevenson, B. J., Dubouchet, M., and Porteous, D. J. (1998) Inclusion of cholesterol in DOTAP transfection complexes increases the delivery of DNA to cells in vitro in the presence of serum. *Gene Ther. 5*, 137–143.
(28) Oh, J. K., Siegwart, D. J., Lee, H.-I., Sherwood, G., Peteanu, L., Hollinger, J. O., Kataoka, K., and Matyjaszewski, K. (2007) Biodegradable nanogels prepared by atom transfer radical polymerization as potential drug delivery carriers: synthesis, biodegradation, *in vitro* release, and bioconjugation. *J. Am. Chem. Soc. 129*, 5939–5945.
(29) Akashi, M., Beppu, k., Kikuchi, I., and Miyauchi, O. (1986) Synthesis and properties of hydrophilic copolymers containing 5-fluorouracil, thymine, or adenine. *Macromol. Sci.-Chem. 23*, 1233–1249.
(30) López Arbeloaa, T., López Arbeloaa, F., López Arbeloaa, I., Costelab, A., García-Morenob, I., Figuerab, J. M., Amat-Guerric, F., and Sastred, R. (1997) Photophysical and lasing properties of a new ester derivative of rhodamine 6G. *J. Lumin. 75*, 309–317.
(31) Caruso, F., Yang, W., Trau, D., and Renneberg, R. (2000) Microencapsulation of uncharged low molecular weight organic materials by polyelectrolyte multilayer self-assembly. *Langmuir 16*, 8932–8936.
(32) Žaja, R., Klobučar, G. I., Sauerborn Klobučar, R., Hackenberger, B. K., and Smital, T. (2006) Haemolymph as compartment for efficient and non-destructive determination of P-glycoprotein (Pgp) mediated MXR activity in bivalves. *Comp. Biochem. Physiol., Part C: Toxicol. Pharmacol. 143*, 103–12.
(33) Felmlee, T., Pellett, S., and Welch, R. A. (1985) Nucleotide sequence of an *Escherichia coli* chromosomal hemolysis. *J. Bacteriol. 163*, 94–105.
(34) Dudler, R., and Hertig, C. (1992) Structure of a mdr-like gene from *Arabidopsis thaliana*. *J. Biol. Chem. 267*, 5882–5888.
(35) Luedeking, A., and Koehler, A. (2004) Regulation of expression of multixenobiotic resistance (MXR) genes by environmental factors in the blue mussel *Mytilus edulis*. *Aquat. Toxicol. 69*, 1–10.
(36) Tutundjian, R., Cachot, J., Leboulenger, F., and Minier, C. (2002) Genetic and immunological characterization of a multixenobiotic resistance system in the turbot (*Scophthalmus maximus*). *Comp. Biochem. Physiol., Part B 132*, 463–471.
(37) Perez-Tomas, R. (2006) Multidrug resistance: retrospect and prospects in anti-cancer drug treatment. *Curr. Med. Chem. 13*, 1859–1876.
(38) Gottesman, M. M., and Pastan, I. (1993) Biochemistry of multidrug resistance mechanism in aquatic organism. *Aquat. Toxicol. 48*, 385–427.
(39) Endicott, J. A., and Ling, V. (1989) The biochemistry of P-glycoprotein-mediated multidrug resistance. *Annu. Rev. Biochem. 58*, 137–171.
(40) Juliano, R. L., and Ling, V. (1976) A surface glycoprotein modulating drug permeability in Chinese hamster ovary cell mutants. *Biochem. Biophys. Acta 455*, 152–62.
(41) Teodori, E., Dei, S., Martelli, C., Scapecchi, S., and Gualtieri, F. (2006) The functions and structure of ABC transporters: Implications for the design of new inhibitors of Pgp and MRP1 to control multidrug resistance (MDR). *Curr. Drug Targeting 7*, 893–909.
(42) Drin, G., Cottin, S., Blanc, E., and Rees, A. R. (2003) Studies on the internalization mechanism of cationic cell-penetrating peptides. *J. Biol. Chem. 278*, 31192–31201.
(43) Hay, E. D., and Coward, S. J. (1975) Fine structure studies of the Planarian, Dugesia. I. Nature of the "neoblast" and other cell types in noninjured worms. *J. Ultrastruct. Res. 50*, 1–21.
(44) Lentz, T. L. (1967) Rhabdite formation in Planaria: The role of microtubules. *J. Ultrastruct. Res. 17*, 114–126.
(45) Suenaga, M., Kaneko, Y., Kadokawa, J. C., Nishikawa, T., Mori, H., and Tabata, M. (2006) Amphiphilic poly(N-propargylamide) with galactose and lauryloyl groups: Synthesis and properties. *Macromol. Biosci. 6*, 1009–1018.
(46) Horvat, T., Kalafatić, M., Kopjar, N., and Kovačević, G. (2005) Toxicity testing of herbicide norflurazon on an aquatic bioindicator species - the planarian *Polycelis felina* (Daly). *Aquat. Toxicol. 73*, 342–352.
(47) Gunthert, A. R., Grundker, C., Bongertz, T., Schlott, T., Nagy, A., Schally, A. V., and Emons, G. (2004) Internalization of cytotoxic analog AN-152 of luteinizing hormone-releasing hormone induces apoptosis in human endometrial and ovarian cancer cell tines independent of multidrug resistance-1 (MDR-1) system. *Am. J. Obstet. Gynecol. 191*, 1164–1172.

BC700425X

Hemozymes Peroxidase Activity Of Artificial Hemoproteins Constructed From the *Streptomyces lividans* Xylanase A and Iron(III)-Carboxy-Substituted Porphyrins

Rémy Ricoux,[†] Roger Dubuc,[‡] Claude Dupont,[‡] Jean-Didier Marechal,[§] Aurore Martin,[†] Marion Sellier,[†] and Jean-Pierre Mahy*,[†]

Institut de Chimie Moléculaire et des Matériaux d'Orsay, UMR 8182 CNRS, Laboratoire de Chimie Bioorganique et Bioinorganique, Bât. 420, Université Paris XI, 91405 Orsay Cedex, France, Institut National de la Recherche Scientifique, INRS-Institut Armand-Frappier, 531 Boulevard des Prairies, Laval, Québec, H7V 1B7, Canada, and Unitat de Química Física, Departament de Química, Universitat Autònoma de Barcelona, Edifici C.n., 08193 Cerdonyola (Barcelona), Spain. Received November 28, 2007; Revised Manuscript Received January 19, 2008

To develop artificial hemoproteins that could lead to new selective oxidation biocatalysts, a strategy based on the insertion of various iron-porphyrin cofactors into Xylanase A (Xln10A) was chosen. This protein has a globally positive charge and a wide enough active site to accommodate metalloporphyrins that possess negatively charged substituents such as microperoxidase 8 (MP8), iron(III)-tetra-α_4-*ortho*-carboxyphenylporphyrin (Fe(T*o*CPP)), and iron(III)-tetra-*para*-carboxyphenylporphyrin (Fe(T*p*CPP)). Coordination chemistry of the iron atom and molecular modeling studies showed that only Fe(T*p*CPP) was able to insert deeply into Xln10A, with a K_D value of about 0.5 μM. Accordingly, Fe(T*p*CPP)-Xln10A bound only one imidazole molecule, whereas Fe(T*p*CPP) free in solution was able to bind two, and the UV–visible spectrum of the Fe(T*p*CPP)-Xln10A-imidazole complex suggested the binding of an amino acid of the protein on the iron atom, trans to the imidazole. Fe(T*p*CPP)-Xln10A was found to have peroxidase activity, as it was able to catalyze the oxidation of typical peroxidase cosubstrates such as guaiacol and *o*-dianisidine by H_2O_2. With these two cosubstrates, the K_M value measured with the Fe(T*p*CPP)-Xln10A complex was higher than those values observed with free Fe(T*p*CPP), probably because of the steric hindrance and the increased hydrophobicity caused by the protein around the iron atom of the porphyrin. The peroxidase activity was inhibited by imidazole, and a study of the pH dependence of the oxidation of *o*-dianisidine suggested that an amino acid with a pK_A of around 7.5 was participating in the catalysis. Finally, a very interesting protective effect against oxidative degradation of the porphyrin was provided by the protein.

Hemoproteins not only play a key role in the transport (hemoglobin) and storage (myoglobin) of dioxygen, the most abundant element of our environment, but some of them are also able to catalyze its activation (cytochromes P450) or to control the level of some of its reductive metabolites such as hydrogen peroxide (peroxidases, catalases). Using, respectively, dioxygen and hydrogen peroxide as oxidant, cytochromes P450 and peroxidases are able to catalyze, under biological conditions, the oxidation of numerous endogenous substrates including steroids, fatty acids, prostaglandins, and leukotrienes, as well as exogenous substrates such as drugs, insecticides, solvents, and hydrocarbons, even the most poorly reactive ones such as *n*-alkanes. Consequently, the design of artificial metalloenzymes that are able to efficiently catalyze oxidation reactions under mild conditions and with selectivities that are comparable to those exhibited by these enzymes is of great interest for the study and prediction of the oxidative metabolism of new biologically active molecules such as drugs. In addition, it represents a promising route to catalytic systems that can be used in organic synthesis for oxidation reactions that are important in industrial and fine chemistry, such as the stereoselective oxidation of alkanes and epoxidation of alkenes (*1*).

Considering the structure–activity relationships of hemoproteins, at least three structural elements have to be mimicked to design functional biomimetic systems (Figure 1): (i) the prosthetic group, a heme or iron(III)-protoporphyrin IX, which is responsible for electron transfer (peroxidases) (*2*) or oxene transfer reactions (cytochromes P450) (*1, 3*); (ii) the apoprotein which binds and site-isolates heme, preventing its aggregation and oxidative degradation, and its active-site amino acids, which not only provide a hydrophobic environment for the substrate and control its access to the heme (cytochromes P450), but also participate in some cases in catalysis (peroxidases) (*2*); (iii) the proximal axial ligand of the iron atom (histidine in peroxidases or cysteinate in cytochromes P450) which has a role in controlling the heme redox potential and the reactivity of the high-valent iron−oxo intermediates involved in their catalytic cycle (*4*).

In the past 10 years, several strategies have been reported for the design of artificial metalloproteins, either to increase or modify the reactivity of an already existing metalloprotein or to induce a new reactivity in a nonmetal protein. They include the introduction of metal binding sites in the active site of a protein by site-directed mutagenesis (*5–7*), the design of substrate binding cavities (*8–11*), chemical modification of prosthetic groups (*12–15*), and covalent attachment of metal cofactors (*16–20*). In particular, the covalent modification of proteins through the covalent binding of a metal cofactor to a cysteine residue is a powerful tool for the generation of new

* Corresponding author. Jean-Pierre Mahy, Institut de Chimie Moléculaire et des Matériaux d'Orsay, UMR 8182 CNRS, Laboratoire de Chimie Bioorganique et Bioinorganique, Bât. 420, Université Paris XI, 91405 Orsay Cedex, France, Fax: [33] 1 69 15 72 81, E-mail: jpmahy@icmo.u-psud.fr.

[†] UMR 8182 CNRS.

[‡] INRS-Institut Armand-Frappier.

[§] Universitat Autònoma de Barcelona.

10.1021/bc700435a CCC: $40.75 © 2008 American Chemical Society
Published on Web 03/07/2008

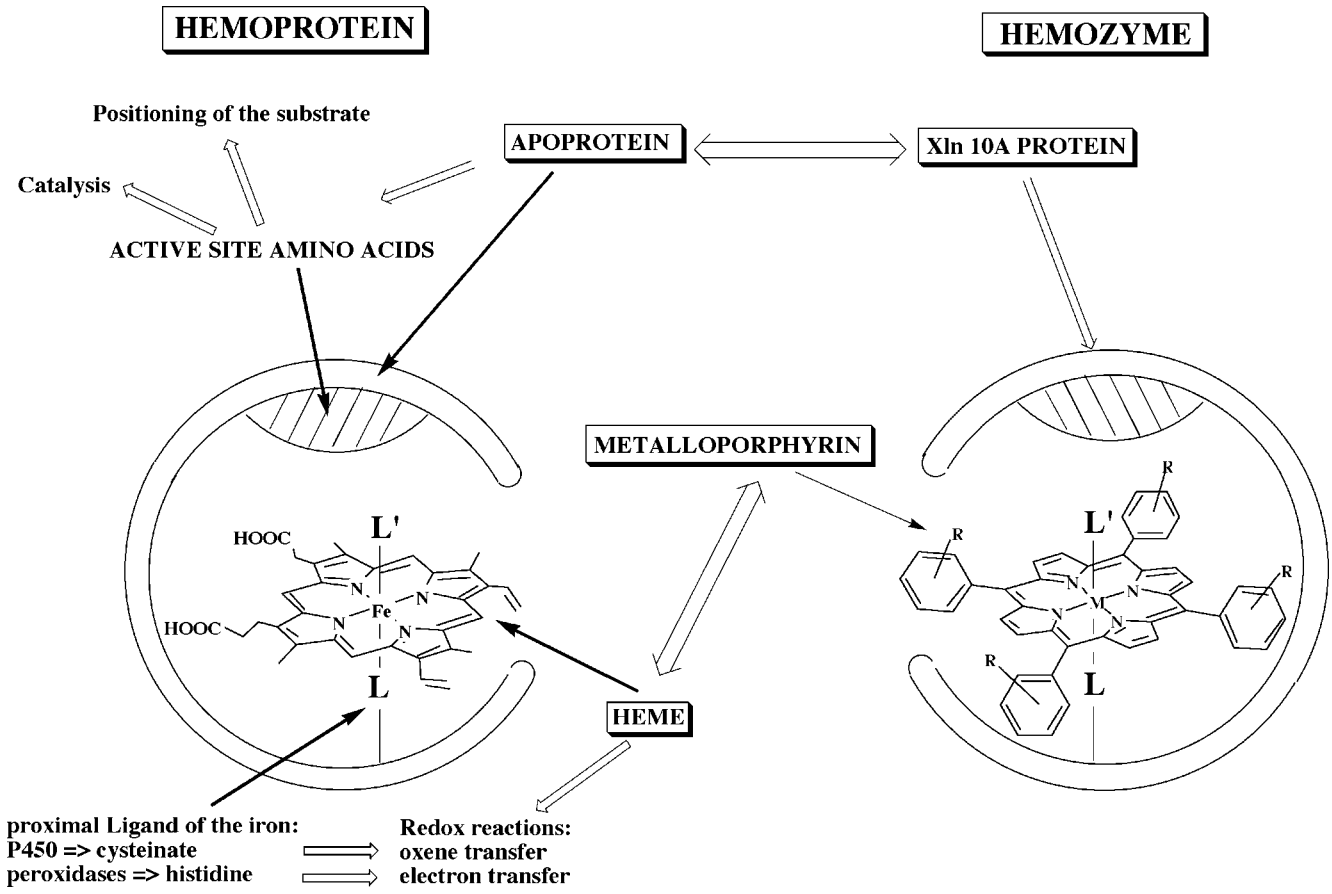

Figure 1. Schematic view of the structure of hemoproteins and their hybrid metalloporphyrin-Xln10A mimics: hemozymes.

metalloenzymes, although the efficiency of the modification is greatly dependent on the position and reactivity of the cysteinyl thiol functional group. However, on one hand, artificial hemoproteins with interesting peroxidase activities have also been obtained by the noncovalent association of a synthetic Fe(III)-$\alpha_3\beta$-tetra-*o*-carboxyphenylporphyrin (*21–25*) or microperoxidase 8 (MP8) (*26–29*) with monoclonal antibodies raised against these cofactors. The later MP8−antibody complexes were additionally shown to catalyze the stereoselective oxidation of sulfides by H_2O_2 (*29*). Furthermore, new artificial hemoproteins, also displaying interesting peroxidase activities, were obtained by insertion of modified hemes into mutated sperm whale myoglobin (*30–33*). Heat-resistant hemoproteins that are able to bind and release O_2 in an aqueous medium like hemoglobin and myoglobin were also obtained by incorporating Fe(II)-α_4-tetra-*o*-pivalamidophenylporphyrin into a thermoresistant xylanase (*34*, *35*) or into human serum albumin (HSA) (*36*). In order to generate new hemoproteins, we have thus chosen a simple strategy that involves the noncovalent incorporation of Fe(III)-α_4-tetra-*o*-carboxyphenylporphyrin (Fe(T*o*CPP)), Fe(III)-tetra-*p*-carboxyphenylporphyrin (Fe(T*p*CPP)), and MP8 (Scheme 1) into β-1,4-endoxylanase or xylanase A (Xln10A) from *Streptomyces lividans.*

Xylanase A hydrolyzes β-1,4 bonds in the main chain of xylan, the major component of hemi cellulose in the plant cell wall. In the pulp bleaching process, the enzymatic hydrolysis of xylan at high temperature has gained importance from an environmental point of view. Consequently, growing interest in xylanases that are able to work at high temperatures under extreme pH and ionic strength conditions has led to the discovery, cloning, and characterization of numerous enzymes, such as xylanase A from *Streptomyces lividans*, which shows optimal activity at 60 °C and pH 6. This enzyme is a 47 kDa protein which contains two domains: a 14 kDa C-terminal domain, named XBD, which belongs to the CBM13 family of carbohydrate binding modules for the binding of the substrate; and a 33 kDa N-terminal catalytic domain belonging to the GH10 family of glycosyl hydrolases. The three-dimensional structure of this domain has been elucidated and refined to a resolution of 1.2 A (*37*). It presents a standard $(\beta/\alpha)_8$ TIM-barrel fold that contains the two amino acids that are essential for catalysis, Glu 128 and Glu 236. The catalytic site globally appears as a crevice that is rich in positively charged amino acids. Thus, the porphyrins Fe(T*o*CPP), Fe(T*p*CPP), and MP8 were chosen because of the negative charges of their carboxylate substituents, which should be complementary to the positive character of the active site of Xln10A. Furthermore, these groups render the porphyrins more water-soluble.

Our results show that, among the three iron-porphyrins studied, Fe(T*p*CPP) is the porphyrin which inserts the best in Xln10A with a K_D value of 0.5 μM, and the corresponding Xln10A-Fe(T*p*CPP) complex shows an interesting peroxidase-like activity characterized by a k_{cat} value of 52 min^{-1} with *o*-dianisidine as cosubstrate. In the hybrid hemoprotein obtained, the Xln10A protein brings two interesting features that would be useful in its application as catalyst for selective oxidation reactions: first, it protects the porphyrin macrocycle from oxidative degradation, and second, it confers steric hindrance around the iron atom. In addition, pH dependence studies show that an amino acid side chain characterized by a pK_A value of about 7.5 could be participating in the catalysis.

EXPERIMENTAL SECTION

Preparation of Fe(III)-Porphyrins. *Purification of Microperoxidase 8.* Microperoxidase 8 (MP8) was prepared by sequential peptic and tryptic digestion of horse-heart cytochrome

Scheme 1. Structure and Nomenclature of the Porphyrins Discussed in This Paper

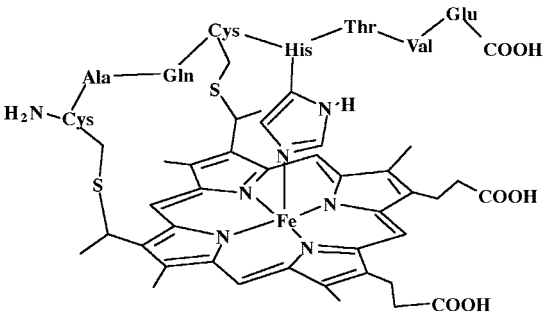

Microperoxidase 8 (MP8)

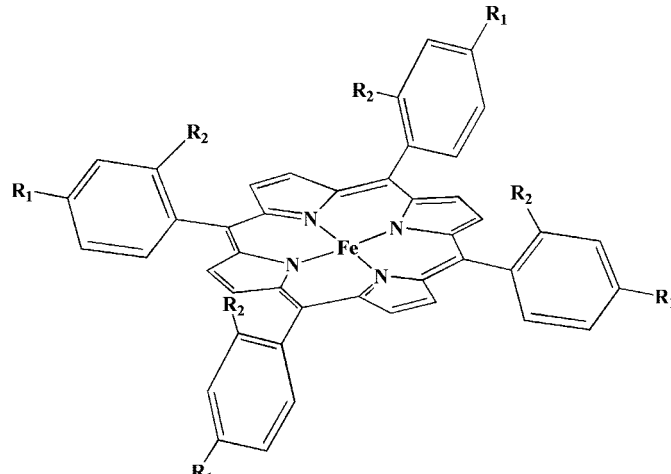

R_1 = COOH, R_2 = H — iron(III)-meso-tetrakis(para-carboxyphenyl)porphyrin Fe(TpCPP)

R_1 = H, R_2 = COOH — iron(III)-meso-tetrakis-α_4(ortho-carboxyphenyl)porphyrin α_4Fe(ToCPP)

c (Sigma) as previously described (*38*). The heme content was determined by the pyridine chromogen method (*38*). The purity of the sample was over 97% based on MALDI-TOF mass spectroscopy analysis.

Preparation of Fe(III)(ToCPP) and Fe(III)(TpCPP). The synthesis of the four atropoisomers of iron(III)-*meso-tetrakis*(*ortho*-carboxy-phenyl)porphyrin Fe(T*o*CPP) as well as that of iron(III)-*meso-tetrakis*(*para*-carboxy-phenyl)porphyrin Fe(T-*p*CPP) was carried out in three steps as described in a previous paper (*40*). The *ortho*-carboxymethyl- and *para*-carboxymethyl-substituted tetraaryl porphyrins were synthetized by reaction at room temperature of *ortho*- and *para*-carbomethoxybenzaldehyde, respectively, with pyrrole in CH_2Cl_2 in the presence of BF_3-etherate as a catalyst according to an already described procedure (*39, 40*). The atropoisomers of *meso-tetrakis*(*ortho*-carboxymethyl-phenyl)porphyrin (T*o*CMePP) were then separated on a silicagel column and have been identified, as was *meso-tetrakis*(*para*-carboxymethyl-phenyl)porphyrin (TpCMe-PP), by UV–visible absorption, ^{1}H NMR, and mass spectroscopies (*40*). The iron atom was inserted by reaction of (T*p*CMePP) and the isolated α_4-(T*o*CMePP) atropoisomer with $Fe(CO)_5$ in the presence of I_2 in toluene at room temperature to avoid isomerization (*41*). Finally, the *para*- and α_4-*ortho*-carboxy-substituted tetraarylporphyrin isomers were subsequently obtained by saponification of the methyl ester substituents in 2 M KOH in 80% EtOH at room temperature (*42*).

Production and Purification of Xylanase A (Xln10A). Seven-day-old cultures of *S. lividans* from Bennett-thiostrepton plates were used as the initial inoculum. The spores were scraped from the plates and inoculated into 12.5 mL minimal M14 medium (composition per liter: glucose, 10 g; K_2HPO_4, 5.0 g; $(NH_4)_2SO_4$, 1.4 g; KH_2PO_4, 1.0 g; $CaCl_2 \cdot 2H_2O$, 300 mg; $MgSO_4 \cdot 7H_2O$, 300 mg; $FeSO_4 \cdot H_2O$, 5.0 mg; $CoCl_2 \cdot 6H_2O$, 2.0 mg; $MnSO_4 \cdot H_2O$, 1.6 mg; $ZnSO_4 \cdot 7H_2O$, 1.4 mg; Tween 80, 2.0 mL; pH 7.4) and incubated for 18 h at 34 °C with agitation. Bacteria were recovered by centrifugation, used to inoculate 500 mL of the same medium, and allowed to grow for 72 h under the same conditions. Proteins contained in the supernatant of *S. lividans* culture were first concentrated by ultrafiltration with a 3 kDa cutoff membrane (Omega). The concentrated proteins were then loaded at 4 °C on a Sephacryl S100 beaded column (2.6 × 60 cm; Pharmacia) with 100 mM sodium phosphate pH 6.0, as the eluant. Purified Xln10A containing fractions were pooled, dialyzed, and freeze−dried.

Assay of Xylanase Activity. The glycosidic activity of Xln10A and of the Xln10A-Fe(TpCPP) complex enzyme was determined using a diffusion agar assay. 100 μL of a 1 μM enzyme solution in 50 mM PBS pH 7.5 were poured into 5 mm wells coated with RBB (Remazol-Brillant-Blue)-xylan and incubated at 37 °C for 2, 6, and 24 h. At each time, the diameter of the clearing zone around the well was measured and was indicative of the glycosidic activity.

Absorption Spectroscopy Measurements. Absorption spectra were recorded at 25 ± 0.1 °C, using an UVIKON 860 XL UV–visible spectrophotometer.

For the insertion of Fe(III)-porphyrins into Xln10A, a typical procedure was followed. The Xln10A-Fe-porphyrin complexes were prepared in 50 mM PBS, pH 7.5, by incubation for 2 h at 4 °C of 1.2 μM MP8, Fe(III)(T*o*CPP), or Fe(III)(T*p*CPP) with 1.8 μM Xln10A. The UV–visible characteristics of the Xln10A-Fe-porphyrin complexes obtained were recorded at 25 ± 0.1 °C and compared to those of the MP8, Fe(III)(T*o*CPP), and Fe(III)(T*p*CPP) recorded under the same conditions. In the case of Fe(III)(T*p*CPP), a titration with Xln10A was done as follows: 0.97 μM Fe(III)(T*p*CPP) in 50 mM PBS, pH 7.5, was incubated for 20 min with Xln10A at concentrations increasing from 0.05 to 4.96 μM and visible spectra were recorded between 350 and 650 nm. The absorbance at 412 nm was plotted against the Xln10A/Fe-porphyrin ratio, which allowed the determination of the Xln10A/Fe-porphyrin stoichiometry and the value of the dissociation constant (K_D).

For the reactions with imidazole, difference spectroscopy was used. The sample cuvette contained either 1.85 μM Fe-porphyrin or 1.85 μM Fe-porphyrin preincubated for 40 min at 4 °C with 1.85 μM Xln10A in 50 mM PBS, pH 7.5. The reference cuvette contained 50 mM PBS, pH 7.5. Equal increasing amounts of imidazole (2 M in the same buffer) were then added to both cuvettes, so as to obtain a final concentration ranging between 0.33 and 25 mM, and difference spectra were recorded between 350 and 650 nm.

In most cases, the spectral evolution observed involved the formation of well-defined isobestic points indicating the presence of two absorbing species. The reaction could then be represented by

$$PFe^{III} + nL \rightleftharpoons PFe^{III}(L)_n \quad (1)$$

P = MP8, T*o*CPP, T*p*CPP, Xln10A-MP8, Xln10A-T*o*CPP, Xln10A-T*p*CPP

L = imidazole

According to Brault and Rougee (*43*), it could then be analyzed by means of the standard equation

$$1/\Delta A = 1/\Delta A_\infty + K_D/\Delta A_\infty \times 1/[L]^n \quad (2)$$

where $\Delta A = A - A_0$, $\Delta A_\infty = A - A_\infty$, and A_0, A_∞, and A are the absorbances of the initial, final, and mixed species, respectively. The linearity of the graph representing $1/\Delta A$ as a function of $1/[L]^n$ was then assayed with $n = 1$ and $n = 2$, and K_D and A_∞ could be determined graphically. It is noteworthy that, when $n = 1$, $C_{50} = K_D$, whereas when $n = 2$, $C_{50} = K_D^{1/2}$, with C_{50} representing the concentration of ligand for which half of the starting Fe-porphyrin or Fe-porphyrin-Xln10A complex has been converted into porphyrin-Fe(L)$_n$ or Xln10A-porphyrin-Fe(L)$_n$.

Assay of Peroxidase Activity. To assay the peroxidase activity of Fe(T*p*CPP) and its complex with Xln10A, the oxidation of cosubstrates, namely, guaiacol, *o*-dianisidine and 2,6-dimethoxyphenol, by H_2O_2 was performed at 19 ± 0.1 °C in 50 mM PBS, pH 7.5. The absorbance was monitored for 6 min, respectively, at 490, 450, and 469 nm using an UVIKON 860 UV–visible spectrophotometer. The initial rates of oxidation were determined from the slope at the origin of the curve representing the variations of the absorbance at 490, 450, and 469 nm as a function of time, using respective ϵ values of 5500, 7500, and 27 500 M^{-1} cm^{-1} (*26*, *44*).

The influence of the H_2O_2 concentration on the oxidation of the cosubstrates was assayed. For this, guaiacol, *o*-dianisidine, and 2,6-dimethoxyphenol (1.2 mM) were oxidized by H_2O_2 at concentrations varying between 0.080 and 8 mM, in the presence of 1.2 μM Fe(T*p*CPP) or 1.2 μM Fe(T*p*CPP) preincubated for 2 h at 4 °C with 1.8 μM Xln10A as catalyst.

In a second set of experiments, the influence of the cosubstrate concentration on the rate of oxidation was assayed. The cosubstrates, at concentrations varying between 50 and 1200 μM, were oxidized by H_2O_2 2.4 mM in the presence of 1.2 μM Fe(T*p*CPP) or 1.2 μM Fe(T*p*CPP) preincubated for 2 h at 4 °C with 1.8 μM Xln10A as catalyst.

For the pH dependence studies, solutions of 1.2 μM Fe(T-*p*CPP) or 1.2 μM Fe(T*p*CPP) preincubated for 2 h at 4 °C with 1.8 μM Xln10A were prepared in 0.1 M citrate/phosphate buffer pH 4.1, 4.6, 5.0, 5.5, 6.0, 6.5, and 7.0, and in 0.1 M Tris−HCl buffer pH 7.3, 7.6, 7.9, and 9.1. 890 μM *o*-dianisidine was first added and the reaction was initiated by the addition of 320 μM H_2O_2. The absorbance was monitored at 450 nm as a function of time for 5 min, and the initial rate of oxidation was plotted as a function of the pH value.

The influence of imidazole on the kinetic parameters of the oxidation of *o*-dianisidine by H_2O_2 in the presence of 1.2 μM Fe(T*p*CPP) or 1.2 μM Xln10A-Fe(T*p*CPP) prepared as described above was examined as follows. The catalyst was further incubated for 2 h at 4 °C with imidazole at concentrations ranging between 0 and 50 mM. 890 μM *o*-dianisidine was then added, and the reaction was started by the addition of 320 μM H_2O_2. The initial rates of oxidation were then measured as described above.

Molecular Modeling. The atomic coordinates of Xln 10A were downloaded from the Protein Data Bank (*45*) (PDB code 1V0L) (*46*). The exploration of the protein cavity volumes and shapes were performed with CASTp (*47*) and Q-sitefinder (*48*) webserver.

The structures of the different *meso*-tetraphenyl-porphyrins have been generated using the *Chem3D* package (CambridgeSoft Corporation). A short minimization was performed on each compound using the MM2 force field (*49*) implemented in *Chem3D*. For the MP8 system, the environment of the heme has been generated from one of the crystal structures available of the human cytochrome C (PDB code 1CRI (*50*)). The minimization was followed by a short molecular dynamic run to better relax the system. All the volumes of the ligands have been calculated using the Connolly solvent excluded volume package included in *Chem3D*.

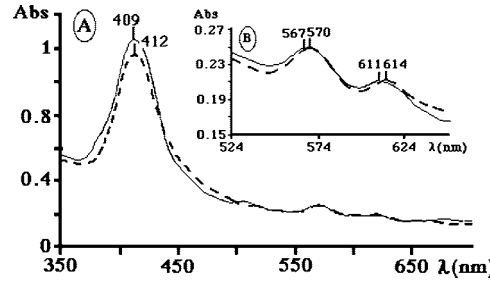

Figure 2. Incorporation of Fe(T*p*CPP) into Xln10A: (− − −) UV–visible spectrum of Fe(T*p*CPP), 1.2 μM in 50 mM PBS, pH 7.5; (—) UV–visible spectrum obtained after addition of 1.8 μM Xln10A corresponding to the Xln10A-Fe(T*p*CPP) complex. Inset: variations of the α,β bands under the same conditions.

Docking studies were performed using the GOLD v3 program (*51*) with the Chemscore (*52*) fitness function. The accessible docking space was defined as a 20 Å sphere around one of the residues at the core of the cleft. Fifty solutions were generated for each porphyrin macrocycle and ranked according to their Chemscore values. We selected this approach since it had been applied with success in predicting protein–ligand interactions for metal containing systems like cytochrome P450 (*53*). Since the ligand remains quite exposed to the solvent, a large number of low-energy solutions were analyzed in detail. Molecular graphics images were produced using the UCSF Chimera package from the Resource for Biocomputing, Visualization, and Informatics at the University of California, San Francisco (*54*).

RESULTS

Insertion of Fe(III)-Porphyrins into Xylanase A. The insertion of three Fe-porphyrins bearing negatively charged carboxylate substituents was examined by UV–visible spectroscopy as described in the experimental section. For this, 1.5 mol equiv of Xln10A was added to solutions of either microperoxidase 8 (MP8), Fe(T*p*CPP), or Fe(T*o*CPP), 1.2 μM in 50 mM PBS pH 7.5, a concentration for which no aggregation of the porphyrin complexes was observed. In the case of microperoxidase 8 (MP8), no significant change in its UV–visible spectrum was observed, except for a decrease in intensity of its Soret band at 397 nm (data not shown). This is characteristic of a simple hydrophobic interaction between MP8 and Xln10A with no amino acid side chain of the protein binding to the iron atom of MP8, leaving a vacant coordination site on the iron available for the binding of exogenous ligands and catalysis. Similarly, the addition of Xln10A to Fe(T*o*CPP) caused only a decrease of its Soret band at 396 nm (data not shown), showing that no amino acid side chain of Xln 10A was coordinating the iron atom in this complex either, leaving two vacant axial coordination positions on the iron atom.

Finally, the addition of 1.5 equiv Xln10A to Fe(T*p*CPP) 1.2 μM in 50 mM PBS, pH 7.5, was examined by UV–visible spectroscopy. The spectrum for Fe(T*p*CPP) before the addition of Xln10A (with maxima at 409, 567, and 611 nm) was characteristic of a high-spin pentacoordinate porphyrin-iron(III) species (Figure 2). A clear change in this spectrum was observed on addition of Xln10A, with one clear isosbestic point at 445 nm and two others, less clear, at around 575 and 612 nm, leading to a final spectrum with maxima at 412, 570, and 614 nm for the corresponding Xln10A-Fe-porphyrin complex. In addition,

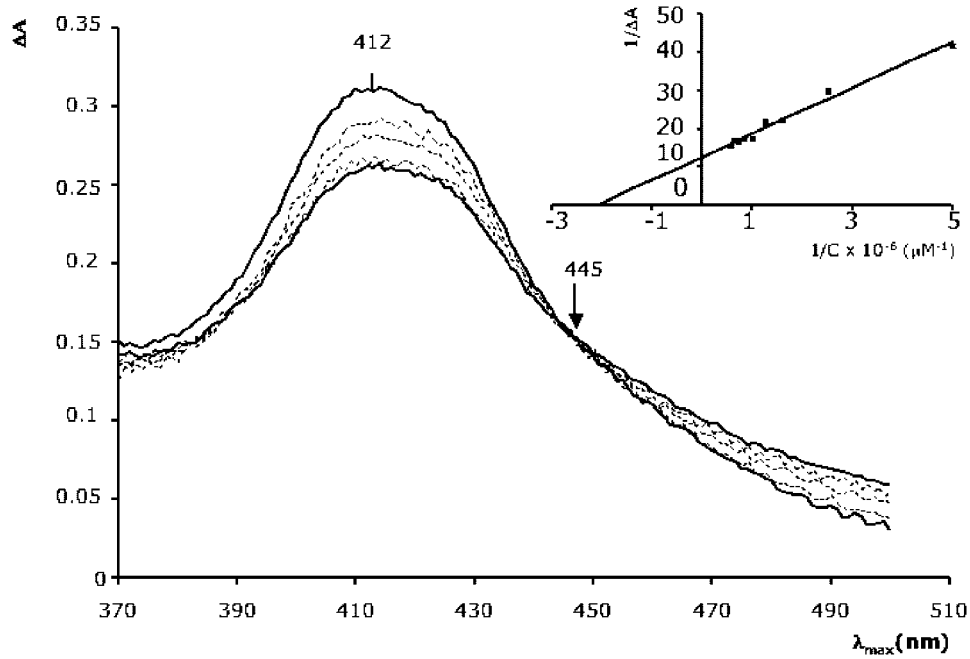

Figure 3. Titration of Fe(T*p*CPP) by Xln10A: evolution of the UV–visible spectrum of Fe(T*p*CPP), 0.97 μM in 50 mM PBS, pH 7.5, after addition of Xln10A at concentrations increasing from 0.05 μM to 4.96 μM. Inset: Double reciprocal plots of the absorbance at 412 nm versus the Xln10A/Fe-porphyrin ratio.

these changes in the UV–visible spectrum were independent of the pH, as similar variations in the spectra were recorded at pH 4.0, 5.1, 6, 6.6, 7.6, and 10.6 (data not shown). Since the final spectrum is also characteristic of a high-spin pentacoordinate iron(III)-porphyrin complex, this clearly indicates that the environment of the iron atom changes upon insertion of Fe(T*p*CPP) into Xln10A, which could be due to the binding of an amino acid side chain of Xln10A to the iron atom.

A titration of Fe(T*p*CPP), 0.97 μM in 50 mM PBS, pH 7.5, with Xln10A at concentrations increasing from 0.05 to 4.96 μM was performed (Figure 3). Double reciprocal plots of the absorbance at 412 nm versus the Xln10A/Fe-porphyrin ratio (Figure 3, inset) allowed us to determine a 1/1 Xln10A/Fe-porphyrin stoichiometry and a dissociation constant value K_D = 0.5 μM. This value was about 5-fold lower than those found for complexes of Fe(II)-2-[8-(2-methylimidazolyl)octanoyloxymethyl]-tetrakis-α_4-(*o*-pivalamidophenyl)porphyrin with xylanases from *Thermotoga maritima* (K_D = 2.2 μM) and *Dictioglomus thermophylum* (K_D = 2.9 μM) (*34, 35*) and was in agreement with a good affinity of Xln10A for Fe(T*p*CPP). This difference in affinity could be due to the rather flat shape of Fe(T*p*CPP) that better entered the cleft of Xln10A than the more bulky pivaloyl porphyrin did in the cleft of xylanases from *Thermotoga maritima* and *Dictioglomus thermophylum.*

Coordination of Imidazole on Fe(III)-Porphyrins and Their Complexes with Xylanase A. In order to evaluate the size of the cavity around the iron atom in the complexes of xylanase A with the three iron(III)-porphyrins, the coordination of imidazole on the iron atom was examined. To this effect, the progressive addition of imidazole (0–95 μM) to solutions of MP8, Fe(T*o*CPP), Fe(T*p*CPP), and the corresponding Fe-(porphyrin)-Xln 10A complexes, 1.85 μM in 50 mM PBS, pH 7.5, was analyzed by differential UV–visible spectroscopy as described in the Experimental Section. In all cases, the progressive appearance of a new spectrum, characteristic of an iron(III)-imidazole species, was observed (Table 1). The particular case of Fe(T*p*CPP) and Xln10A-Fe(T*p*CPP) is shown in Figure 4. In the case of Fe(T*p*CPP), a new spectrum with absorption maxima at 412, 545, and 581 nm and isobestic points at 402 and 439 nm is formed, whereas in the case of Xln10A-Fe(T*p*CPP), a new spectrum with absorption maxima at 415, 538, and 579 nm and isobestic points at 400 and 420 nm appears upon addition of imidazole. The inverse of the absorbance at the absorption maximum of the Fe-imidazole complex, $1/\Delta A_{\lambda max}$, was then plotted against the inverse of the concentration of imidazole added, 1/[ImH], and against the reverse of the square of the concentration of imidazole added, $1/[ImH]^2$, in order to determine whether one or two imidazoles were bound per iron atom and the corresponding K_D value, as described in the Experimental Section.

Table 1. Visible Characteristics, K_D and C_{50} Values of the Complexes of Fe(porphyrin) and Xln10A-Fe(porphyrin) with Imidazole in 50 mM PBS, pH 7.5, at 20 °C

Fe(porphyrin) or Xln10A+Fe(porphyrin)	number of imidazole ligands	λ_{max} (nm)	C_{50} (mM)	K_D
MP8	1	403	0.05	0.05 mM
Xln10A+MP8[a]	1	402	0.06	0.06 mM
Fe(T*o*CPP)	2	413	0.69	0.48 mM^2
Xln10A+Fe(T*o*CPP)[a]	2	412	0.67	0.49 mM^2
Fe(T*p*CPP)	2	415	3.4	11.6 mM^2
Xln10A-Fe(T*p*CPP)[b] complex	1	417	3.3	3.3 mM

[a] In these cases no complex coming from the insertion of MP8 or FeToCPP into the cleft of Xln10A was obtained. [b] Xln10A-Fe(T*p*CPP) was formed by insertion of FeTpCPP into the cleft of Xln10A.

With both MP8 and Xln10A-MP8, $1/\Delta A_{403}$ varied linearly as a function of 1/[ImH] and not as a function of $1/[ImH]^2$, which showed that only one imidazole was bound per iron atom in both cases. In addition, similar K_D values of 0.05 ± 0.01 and 0.06 ± 0.01 mM, respectively, were calculated for both complexes, which suggested that the xylanase protein had no effect on the binding of imidazole as a sixth ligand, trans to its histidine on the iron atom in microperoxidase 8. With both Fe(T*o*CPP) and Xln10A-Fe(T*o*CPP), $1/\Delta A_{413}$ varied linearly as a function of $1/[ImH]^2$ and not as a function of 1/[ImH], which showed that two imidazole ligands were bound per iron atom in both complexes. Here also, similar K_D values of 0.48 ± 0.01

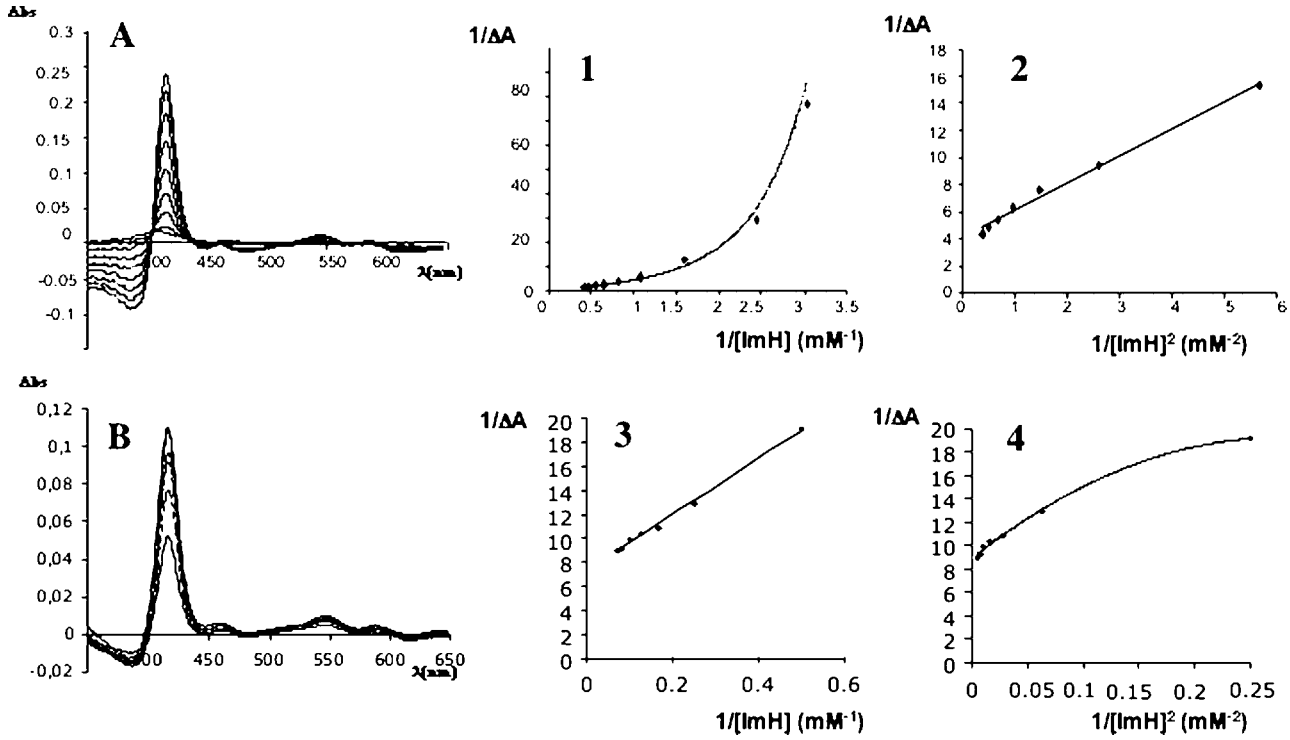

Figure 4. (A) Addition of imidazole to iron(III)-*meso*-tetrakis(*para*-carboxyphenyl)porphyrin (Fe(T*p*CPP)). Spectral evolution observed for the addition of 0 to 20 mM ImH to 1.85 μM Fe(T*p*CPP) in 50 mM PBS, pH 7.5, at 20 °C. Inset: corresponding values of $1/\Delta A_{412}$ plotted against 1/[ImH] (**1**) and 1/[ImH]^2 (**2**). (B) Addition of imidazole to the iron(III)-*meso*-tetrakis(*para*-carboxyphenyl)porphyrin Fe(T*p*CPP)-Xln10A complex. Spectral evolution observed for the addition of 0 to 20 mM ImH to 1.85 μM Fe(T*p*CPP)-Xln10A in 50 mM PBS, pH 7.5, at 20 °C. Inset: corresponding values of $1/\Delta A_{412}$ plotted against 1/[ImH] (**3**) and 1/[ImH]^2(**4**).

and 0.49 $\pm$ 0.01 mM^2, respectively, were calculated for both complexes, again suggesting that the xylanase protein had no effect on the binding of two imidazole ligands on the iron atom to give a hexacoordinate (T*o*CPP)Fe(ImH)$_2$ complex. In the case of Fe(T*p*CPP), $1/\Delta A_{413}$ varied linearly as a function of 1/[ImH]^2 (Figure 4), whereas in the case of Xln10A-Fe(T*p*CPP), $1/\Delta A_{413}$ varied linearly as a function of 1/[ImH] (Figure 4). This showed that, whereas free Fe(T*p*CPP) was able to bind two imidazole ligands as expected, Fe(T*p*CPP) incorporated into xylanase A was able to bind only one. It is thus likely that the xylanase protein brings steric hindrance around the plane of the porphyrin, leaving only one face accessible to ligands to coordinate to the iron atom.

Molecular Modeling. A series of molecular modeling studies have been carried out to address two major issues: (1) the characterization of the most probable binding site of the iron(III)-porphyrin complexes into the xylanase A structure and (2) the nature of the most stable binding modes of the Xln10A-iron(III)-porphyrin complexes when MP8, Fe(T*o*CPP), and Fe(T*p*CPP) are inserted into Xln10A.

The three iron(III)-porphyrin complexes discussed in this work have molecular structures substantially different from the natural substrate of Xln10A. Therefore, reasonable doubt exists as to whether the binding site of our porphyrin derivatives is the same as that of xylanes. We investigated this question by characterizing all possible accessible cavities of the Xln10A structure using a combination of different methods designed for this task. All the results agreed in predicting that the xylanase cleft is by far the largest accessible cavity. For example, the Q-sitefinder algorithm (*48*) showed that the cleft had a volume of 338 Å^3 (summing the volume of its different subpockets), while the three next cavities in size had volumes of 145, 100, and 98 Å^3, respectively. Since the porphyrin complexes are quite large (the approximated volume of the Fe(T*o*CPP) and Fe(T-*p*CPP) entities is around 600 Å^3), the Xln10A cleft appears as the most probable binding site for these compounds, though they are not expected to entirely fit into it.

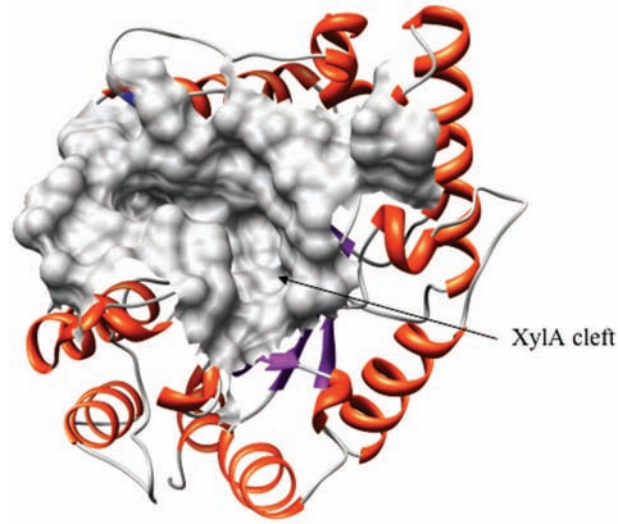

Figure 5. Upper view of the Xln10A cleft. Secondary structures of the protein are depicted in ribbon format. The solvent-accessible area of the cleft is shown in gray scale.

For MP8, not only its volume (approximately 1400 Å^3) but also its shape (mostly globular) suggests that its incorporation into this site is extremely poor. The optimized structure of the MP8 complex shows that this complex has a globular form, which suggests a very small complementarity of form with the narrow channel the cleft displays (Figure 5). This is in agreement with the experimental data that show that the activity of MP8 is not altered in solution in the presence of Xln10A.

On the contrary, the volumes of Fe(T*o*CPP) and Fe(T*p*CPP) (614 and 613 Å^3, respectively), as well as their planar shapes,

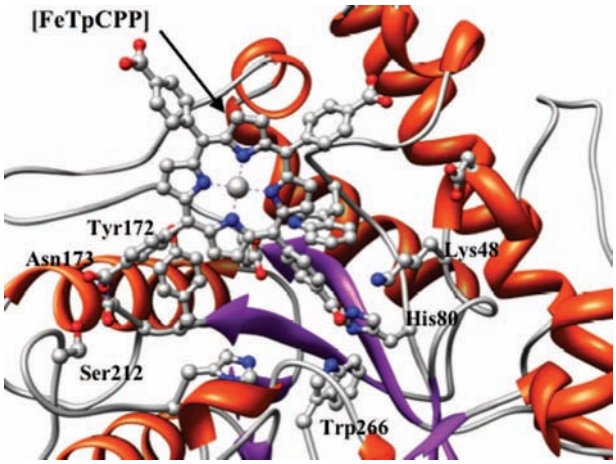

Figure 6. Best binding mode of the Fe(T*p*CPP)-Xln10A complex obtained using Gold with the Chemscore scoring function. The main interactions between the carboxylates of the Fe(T*p*CPP) and the polar patches {His80, Lys248, Trp266} (A) and {Ser212, Tyr172, Asn173} (B) are indicated.

suggest a substantial insertion of both iron(III)-porphyrin complexes into the cleft. To investigate the nature of the molecular complexes between these porphyrin derivatives and Xln10A, a series of molecular docking experiments were performed. From the 50 solutions obtained with the docking program Gold using the ChemScore scoring functions, striking differences in the structural properties of the predicted complexes were observed.

In general, all 50 solutions obtained from the docking of Fe(T*p*CPP) into Xln10A present a similar structural behavior. In low-energy solutions, two aromatic groups and part of the porphyrin ring are substantially anchored into the cleft. A strong hydrogen bonding network is observed between the carboxylates of two consecutive aromatic substituents of Fe(T*p*CPP) and the protein. One of the carboxylates interacts with a patch of three residues; two positive residues {His80, Lys48} and Trp266 and a second with another polar patch of three residues at the site opposite to the cleft {Ser212, Tyr172, Asn173} (Figure 6). It is noteworthy that a hydrogen bond is also frequently observed between a third carboxylate and Gln94: a residue that lies at the very surface of the protein (Figure 6). Finally, the general form of the Fe(T*p*CPP)-Xln10A complex shows the porphyrin tilted with respect to the average plane represented by the surface of the protein, and therefore, only one face of Fe(T*p*CPP) seems accessible to the solvent (Figure 7a).

The solutions obtained from the docking of Fe(T*o*CPP)-Xln10A complexes have a large structural variability, which depends mainly on which face of the porphyrin is occupied by the carboxylates. Although it is well-known that in *meso*-tetraphenyl-porphyrins the complete rotation of the phenyl is energetically demanding, our dockings have been performed allowing free rotation around the C_{meso}-phenyl bond in order to better explore of the conformational space. As a general feature, Fe(T*o*CPP)-Xln10A interactions are mainly based on hydrophobic contacts and have few hydrogen bond interations with the Xln10A cleft. In fact, Fe(T*o*CPP) appears to be unable to penetrate deeply into the cleft, and protein–ligand interactions mainly take place at the external part of the site (Figure 7b). At most, only one aromatic moiety fits into the cleft and most of the porphyrin remains exposed to the solvent. None of the low-energy Fe(T*o*CPP)-Xln10A complexes present an interaction of the carboxylates with the {His80, Lys48, Trp266} patch.

The comparison of calculated Fe(T*o*CPP)-Xln10A and Fe(T-*p*CPP)-Xln10A structures suggests that the carboxylates in the ortho position significantly alter the ability of the porphyrin to penetrate into the cleft, while on the contrary, the linear form of the para-substituted phenyls allows better penetration. This favors a strong polar interaction with the {His80, Lys48, Trp266} positive patch which lies slightly deeper into the cleft. This selectivity of Xln10A for the para- against the ortho-substituted porphyrin is confirmed by the computed binding energies with a significantly stronger predicted binding affinity for Fe(T*p*CPP) than Fe(T*o*CPP) (-28.8 and -24.4 kJ.mol^{-1} for best and average values of Fe(T*p*CPP) dockings and -23.8 and -18.8 kJ.mol^{-1} for best and average values of Fe(T*o*CPP) dockings, respectively).

Study of Peroxidase Activity of the Xln10A-Fe(TpCPP) Complex. *Oxidation of Various Peroxidase Cosubstrates.* Since the binding studies described above suggested that, among the assayed porphyrins, xylanase was able to influence only the accessibility of the iron of Fe(T*p*CPP), the complex associating Xln10A and Fe(T*p*CPP) appeared as the best candidate to lead to a selective catalyst for oxidation reactions. Consequently, the oxidation by H_2O_2 of several peroxidase cosubstrates, specifically two phenolic cosubstrates, guaiacol and 2,6-dimethoxyphenol, and a biaryl cosubstrate, *o*-dianisidine, was examined in the presence of Xln10A-Fe(T*p*CPP) as catalyst and compared to that catalyzed by free Fe(T*p*CPP).

The influence of the H_2O_2 concentration on the oxidation of the cosubstrates was first assayed. The rates of oxidation were measured as described in the Experimental Section, and the kinetic parameters were determined in each case from Lineweaver–Burk plots. The k_{cat} and K_M values calculated for the three substrates in the presence of Fe(T*p*CPP) and Xln10A-Fe(T*p*CPP) are reported in Table 2. The $K_M$value is higher in the case of the Xln10A-Fe(T*p*CPP) complex than for Fe(TpCPP) alone by factors of about 1.1, 1.6, and 5, respectively for guaiacol, 2,6-dimethoxypenol, and *o*-dianisidine. This showed that the affinity of H_2O_2 for the porphyrin was lower when it was incorporated into xylanase, which confirmed that access to the iron atom is restricted in the xylanase complex. With Xln10A-Fe(T*p*CPP) as catalyst, the k_{cat} value was lower for guaiacol and 2,6-dimethoxypenol, by factors of 3.1 and 1.6, respectively, whereas it was higher by a factor of 1.8 in the case of *o*-dianisidine. As a consequence, the catalytic efficiency k_{cat}/K_M was lower by a factor of 2.6, in the case of dimethoxyphenol, to 3.6, in the case of *o*-dianisidine, with Xln10A-Fe(T*p*CPP) when compared to Fe(T*p*CPP) alone as catalyst. This can probably be explained by the fact that guaiacol and 2,6-dimethoxyphenol are smaller hydrophobic substrates that can compete with H_2O_2 for the active site whereas *o*-dianisidine is a larger bicyclic compound, that hardly enters the porphyrin binding site in Xln10A.

However, the catalytic lifetime of Xln10A-Fe(TpCPP) is longer than that of Fe(T*p*CPP) alone, and when the plateau of catalytic activity is reached, more substrate has been oxidized, with all three substrates examined (data not shown). In addition, with higher concentrations of H_2O_2, the difference between the catalysts becomes more important. Typically, when *o*-dianisidine is oxidized under the conditions described above but with concentrations of H_2O_2 increasing from 80 to 640 μM, the concentration of *o*-dianisidine oxidized increases with the H_2O_2 concentration, from 18 to 37 μM with Xln10A-Fe(T*p*CPP) as catalyst (Figure 8) but decreases from 17 to 12 μM with Fe(TpCPP) as catalyst. This shows that xylanase has an important protecting effect toward oxidative degradations of the porphyrin.

The influence of the cosubstrate concentration on the rate of oxidation was then assayed in the cases of guaiacol and *o*-dianisidine. Table 3 shows the kinetic parameters that were determined in each case. In the case of *o*-dianisidine, the K_M value increases by a factor of 4 when Fe(T*p*CPP) is incorporated into xylanase, whereas at the same time, the k_{cat} value does not

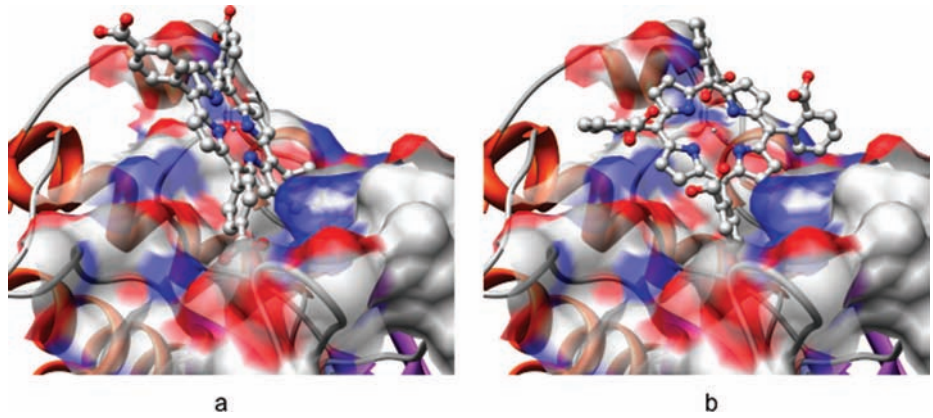

Figure 7. General view of the best binding mode predicted by Gold 3 with the Chemscore scoring function for Fe(T*p*CPP) (panel a) and Fe(T*o*CPP) (panel b).

Table 2. Comparison of Kinetic Parameters, Relative to H_2O_2, for the Oxidation of Various Reducing Cosubstrates by H_2O_2 Catalyzed by Fe(T*p*CPP) or Xln10A-Fe(T*p*CPP)

reducing cosubstrate	catalyst	K_M (mM)	k_{cat} (min^{-1})	k_{cat}/K_M (M^{-1} min^{-1})
guaiacol	Fe(T*p*CPP)	0.83	17.8	2.15×10^4
	Xln10A-Fe(T*p*CPP)	0.92	5.6	6.1×10^3
2,6-dimethoxyphenol	Fe(T*p*CPP)	0.28	9.3	3.43×10^4
	Xln10A-Fe(T*p*CPP)	0.45	6.1	2.16×10^4
o-dianisidine	Fe(T*p*CPP)	0.16	29.2	1.82×10^4
	Xln10A-Fe(T*p*CPP)	0.80	52.0	6.5×10^4

vary. Thus, the affinity for *o*-dianisidine decreases when Fe(T*p*CPP) is incorporated into xylanase, whereas the catalytic activity does not vary. In the case of guaiacol, on the contrary, the affinity increases, as shown by the K_M value which decreases from 0.44 to 0.24 mM, and the catalytic activity decreases as shown by the 11-fold decrease in the k_{cat} value, when Fe(T*p*CPP) is incorporated into xylanase. It is likely that *o*-dianisidine, which is a larger biaryl cosubstrate, does not enter easily inside the active site of xylanase, explaining the increase in K_M. However, the nature of the cosubstrate does not prevent H_2O_2 from interacting with the iron atom, leading to an unchanged catalysis. On the contrary, guaiacol, a smaller hydrophobic cosubstrate, enters the xylanase binding site more readily due to hydrophobic interactions, and K_M decreases. It also hinders the interaction of H_2O_2 with the iron atom causing a reduction in catalysis, and thus, k_{cat} decreases.

Influence of Imidazole on the Kinetic Parameters of the Oxidation of o-Dianisidine by H_2O_2. The influence of imidazole on the kinetic parameters of the oxidation of *o*-dianisidine by H_2O_2 in the presence of 1.2 μM Fe(T*p*CPP) or of 1.2 μM Xln10A-Fe(T*p*CPP) was examined. The catalyst was first incubated for 2 h at 4 °C with imidazole at concentrations ranging between 0 and 50 mM; then the *o*-dianisidine cosubstrate (890 μM) was added and the reaction was initiated by the addition of H_2O_2 (320 μM). The initial rates of oxidation were measured as described above. With both catalysts, the addition of imidazole caused an inhibition of the peroxidase activity. With Fe(T*p*CPP) as catalyst, the reaction is inhibited with an IC_{50} of about 11 mM, whereas with Xln10A-Fe(T*p*CPP), it is inhibited with an IC_{50} of about 25 mM.

pH Dependence Studies. To study the pH dependence of the peroxidase activity of Fe(T*p*CPP) and Xln10A-Fe(T*p*CPP), the oxidation of *o*-dianisidine by H_2O_2 was performed in the presence of these two catalysts at pHs ranging between 4.1 and 9.1, as described in the Experimental Section. Figure 9 shows that, in the case of Fe(T*p*CPP) alone, the rate of oxidation increases linearly with pH for pH values above 5. In the case of Xln10A-Fe(T*p*CPP), a sigmoid curve is found with an inflection point at about pH 7.5.

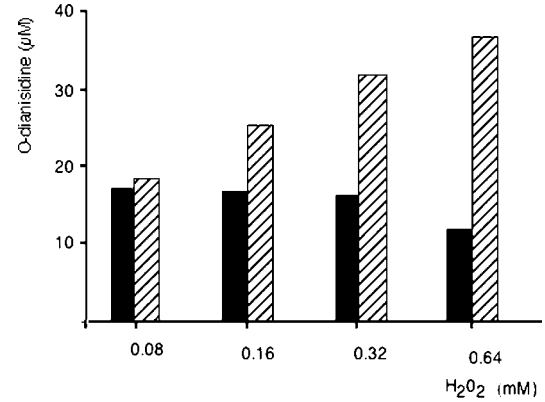

Figure 8. Variation of the concentration of *o*-dianisidine oxidized as a function of the concentration of H_2O_2. Concentration of *o*-dianisidine oxidized at the plateau, when 890 μM *o*-dianisidine is oxidized by H_2O_2 at concentrations increasing from 0.08 to 0.64 mM, with 1.2 μM Fe(T*p*CPP) or Xln10A-Fe(T*p*CPP) as catalyst, in 50 mM PBS, pH 7.5, at 20 °C.

Table 3. Comparison of Kinetic Parameters, Relative to the Reducing Cosubstrate, for the Oxidation of Guaiacol and *o*-Dianisidine by H_2O_2 Catalyzed by Fe(T*p*CPP) or Xln10A-Fe(T*p*CPP)

reducing cosubstrate	catalyst	K_M (mM)	k_{cat} (min^{-1})	k_{cat}/K_M (M^{-1} min^{-1})
guaiacol	Fe(T*p*CPP)	0.44	6.4	1.45×10^4
	Xln10A-Fe(T*p*CPP)	0.24	0.6	2.4×10^3
o-dianisidine	Fe(T*p*CPP)	0.23	17.5	7.5×10^4
	Xln10A-Fe(T*p*CPP)	0.80	17.6	2.2×10^4
2-methoxyphenol	wild type Mb (32)	54	168	3.1×10^3
2-methoxyphenol	RMb(H64D)-2 (32)	0.052	72	1.4×10^6
p-OH-phenyl propionic acid	wild type Mb (33)	72	60	8.4×10^2
p-OH-phenyl propionic acid	T67R/S92D Mb-H (33)	20	396	2.0×10^4

DISCUSSION

The insertion into Xln10A of three Fe-porphyrins which are water-soluble and bear negatively charged carboxylate substituents, microperoxidase 8 (MP8), Fe(III)-α_4-tetra-*o*-carboxyphenyl porphyrin Fe(T*o*CPP), and Fe(III)-tetra-*p*-carboxyphenylporphyrin Fe(T*p*CPP) (Figure 1), was studied in order to define a new hybrid hemoprotein that would have interesting properties as a catalyst for selective oxidation reactions. Our results clearly show that, among the three Fe-porphyrins studied,

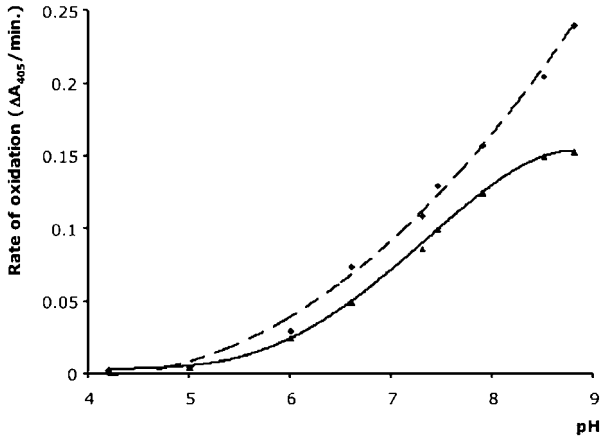

Figure 9. Influence of the pH on the peroxidase activity of Fe(T*p*CPP) and Fe(T*p*CPP)-Xln10A. Variation, as a function of the pH, of the initial rate of oxidation of 890 μM *o*-dianisidine by 320 μM H_2O_2 in the presence of 1.2 μM Fe(T*p*CPP) (- - -) or Fe(T*p*CPP)-Xln10A (—), in 0.1 M citrate/phosphate buffer pHs 4.1, 4.6, 5.0, 5.5, 6.0, 6.5, and 7.0, and in 0.1 M Tris−HCl buffer pHs 7.3, 7.6, 7.9, and 9.1.

only Fe(T*p*CPP) could lead to a new hemoprotein having such properties. First of all, UV–visible studies showed that most probably neither MP8 nor Fe(T*o*CPP) were inserted inside the cleft of Xln10A. Indeed, their titration by this protein did not lead to any significant change in their UV–visible spectrum, except a decrease in their Soret band which is characteristic of a nonspecific hydrophobic interaction between the protein and these two porphyrins, without any amino acid side chain coordinating to the iron atom. In agreement with this, similar results were observed when MP8 and Fe(T*o*CPP) were titrated by imidazole in the presence or absence of Xln10A. Both MP8 and MP8-Xln10A bound one imidazole ligand with a similar K_D value of about 0.05 mM, and both Fe(T*o*CPP) and Fe(T*o*CPP)-Xln10A bound two imidazole ligands with similar K_Ds of about 0.48 mM (Table 1). This showed that in both cases the Xln10A protein does not interact closely with the porphyrin macrocycle and does not prevent imidazole from binding on the iron atom. On the contrary, addition of Xln10A to Fe(T*p*CPP) led to a significant change in its UV–visible spectrum (Figure 2), with a 3 nm shift of its characteristic bands, which could be due to the binding of an amino acid side chain of Xln10A to the iron atom. A titration of Fe(T*p*CPP) by increasing amounts of Xln10A (Figure 3) clearly indicated a 1:1 Fe(T*p*CPP)/Xln10A stoichiometry and allowed a K_D of 0.5 μM to be measured for the obtained complex, that was close to the K_D values reported for complexes of Fe(II)-2-[8-(2-methylimidazolyl)octanoyloxymethyl]-tetrakis-α_4-(*o*-pivalamidophenyl)porphyrin with bacterial xylanases B (*34*, *35*). In addition, different results were observed when Fe(T*p*CPP) was titrated by imidazole in the presence or absence of Xln10A. Fe(T*p*CPP) bound two imidazole ligands with a K_D of 11.56 mM[2], whereas Fe(T*p*CPP)-Xln10A bound only one with a K_D of 3.3 mM (Table 1). This showed that the Xln10A protein interacted closely with the porphyrin macrocycle and brought steric hindrance around one face of the porphyrin, possibly with an amino acid side chain coordinating the iron atom, preventing imidazole from binding on this face.

Furthermore, these results were corroborated by molecular modeling studies that allowed a possible explanation of the difference in Xln10A-Fe-porphyrin interactions to be put forward. These analyses suggested that, in agreement with the UV–visible studies, both the large volume (V_{MP8} = 1400 Å^3 vs V_{cav} = 338 Å^3) and the globular shape of MP8 lead a very poor incorporation of MP8 into the quite narrow and elongated cleft of Xln10A. On the contrary, the volumes and shapes of Fe(T*o*CPP) and Fe(T*p*CPP) appeared reasonably close to those of the Xln10A cleft and suggested at least a partial insertion of both iron(III)-porphyrin complexes into it. A weak hydrophobic complementarity with the binding site of Xln10A was suggested for Fe(T*o*CPP) which bound perpendicularly to the surface of the protein with only one aromatic moiety inserted into the cleft and most of the porphyrin exposed to the solvent (Figure 7b). Therefore, both faces of Fe(T*o*CPP) seemed accessible to the solvent and could accommodate two axial imidazole ligands on its iron atom as showed by the absorption spectroscopy studies.

Finally, molecular modeling studies suggested that Fe(T*p*CPP) could be more deeply inserted into the Xln10A cleft, with two aromatic groups and part of the porphyrin ring anchored into the binding site (Figure 7a). A strong association was then observed, mainly due to a hydrogen-bonding network between the carboxylates of two consecutive aromatic substituents of Fe(T*p*CPP) and several side chains of protein residues. Indeed, from the docking experiments, it was predicted that the binding energies could be substantially stronger for Fe(T*p*CPP) than for Fe(T*o*CPP) by about 5 kJ.mol^{-1}. In the Fe(T*p*CPP)-Xln10A complex, the porphyrin is tilted with respect to the surface of the protein, and therefore, only one face of Fe(T*p*CPP) seems accessible to the solvent (Figure 7a) and this can explain why the binding of only one imidazole on the iron atom was observed in this complex.

In addition, the glycosidic activity of Xln10A and of the Xln10A-Fe(TpCPP) complex was determined using a diffusion agar assay as described in the Experimental Section. Thus, Xln10A and Xln10A-Fe(TpCPP), 1 μM in 50 mM PBS pH 7.5, were added to wells coated with RBB (Remazol-Brillant-Blue)-xylan and incubated at 37 °C for 2, 6, and 24 h. The glycosidic activity was then determined from the diameter of the clearing zone around the well that was due to the hydrolysis of xylan. Under those conditions, no clearing zones could be observed on RBB-xylan, in the presence of Xln10A-Fe(TpCPP) even after 24 h incubation, while Xln10A alone in PBS buffer showed increasing clearing zones with increasing incubation time. This clearly showed that the Xln10A-Fe(TpCPP) complex did not retain any glycosidic activity anymore. This constituted an additional strong argument proving that the Fe(TpCPP) molecule was competitively incorporated into the substrate binding cleft of the $(\beta/\alpha)_8$ TIM-barrel and affected the original enzymatic activity of the host xylanase.

The peroxidase activity of Fe(T*p*CPP)-Xln10A was then examined. This new hybrid hemoprotein was found able to catalyze the oxidation of several peroxidase cosubstrates, namely, guaiacol, 2,6-dimethoxyphenol, and *o*-dianisidine, with k_{cat} values between 3.4 and 52 min^{-1} and k_{cat}/K_M values between 6.1 × 10^3 and 6.5 × 10^4 M^{-1} min^{-1} (Table 2). These values are comparable to those already published for several Fe-porphyrin-antibody complexes (Table 3) that display k_{cat} values between 63 and 667 min^{-1} and k_{cat}/K_M between 3.7 × 10^3 and 2.9 × 10^5 M^{-1} min^{-1}, except for the 3A3-MP8 complex that displays higher k_{cat} (885 min^{-1}) and k_{cat}/K_M (2 × 10^6 M^{-1} min^{-1}) values (*26*). While the k_{cat} values remain comparable to those measured for the enzyme horseradish peroxidase (HRP) itself, the molar efficiency remains low when compared to that observed for this enzyme (k_{cat}/K_M = 6.1 × 10^8 M^{-1} min^{-1}) mainly because of the large difference in the affinity of the substrate, H_2O_2, which is much higher for HRP (K_M = 0.5 μM) (*59*) than for Fe(T*p*CPP)-Xln10A (K_M = 0.5–0.9 mM) (Table 4).

In order to examine the influence of the Xln10A protein on the catalytic activity of Fe(T*p*CPP), the kinetic parameters obtained for H_2O_2 in the presence of the three substrates with Fe(T*p*CPP)-Xln10A as catalyst have been compared with those obtained in the presence of Fe(T*p*CPP) alone as catalyst (Table 2). It appears that, in all the cases, the K_M values are higher with Fe(T*p*CPP)-Xln10A (K_M = 0.92, 0.45, and 0.80 mM) than

Table 4. Comparison of Kinetic Parameters for Oxidation of Various Cosubstrates by H_2O_2 Iron-Porphyrin-Protein Complexes[f]

complex (ref)	hapten[a]	substrate	k_{cat} (min^{-1})	$K_m(H_2O_2)$ (mM)	k_{cat}/K_m (M^{-1} min^{-1})
HRP (*59*)		leucomalachite green	306	0.0005	6.1×10^8
HRP (*60*)		*o*-dianisidine	700		
Fe^{III}(MPIX[b])7G12 (*55*)	N-CH_3-MPIX	*o*-dianisidine	394	24	1.6×10^4
		ABTS[e]	-	-	1.4×10^4
		pyrogallol	-	-	7.3×10^3
Fe^{III}(MPIX) (*55*)		*o*-dianisidine	166	43	3.8×10^3
Fe^{III}(MPIX)-9A5 (*56*)	N-CH_3-MPIX	pyrogallol	132	35	3.7×10^3
Fe^{III}(MPIX)-11D1 (*56*)	N-CH_2OH-MPIX	pyrogallol	86	13	6.6×10^3
Fe^{III}(MPIX) (*56*)		pyrogallol	21	100	2.4×10^2
Fe^{III}(T*p*CPP)[c]-13–1 L (*57*)	$TpCPPH_2$	pyrogallol	667	2.3	2.9×10^5
Fe(TMPyP)[f] (*58*)		pyrogallol	83		
Fe(TMPyP)-12E11G (*58*)	3MPy1C	pyrogallol	680	8.6	7.9×10^4
Fe^{III}(T*o*CPP)[d]-13G10 (*24*)	Fe(ToCPP)	ABTS	560	16	3.7×10^4
Fe^{III}(T*o*CPP)-14H7 (*21*)	Fe(ToCPP)	ABTS	63	9	7.1×10^3
Fe^{III}(T*o*CPP) (*21*)		ABTS	51	42	1.2×10^3
Fe(MPIX)-2B4 (*59*)	N-CH_3-MPIX	*o*-dianisidine	330	43	7.7×10^3
Fe(MPIX) (*59*)		*o*-dianisidine	77	25	3.1×10^3
MP8–3A3 (*26*)	MP8	*o*-dianisidine	885	0.45	2×10^6
MP8 (*26*)		*o*-dianisidine	590	0.4	1.45×10^6
Fe(T*p*CPP) (this work)		*o*-dianisidine	29.2	0.16	1.82×10^5
Xln10A-Fe(T*p*CPP) (this work)		*o*-dianisidine	52.0	0.80	6.5×10^4

[a] in the case of monoclonal antibodies. [b] MPIX, mesoporphyrin IX. [c] T*p*CPP, *meso*-tetrakis(*para*-carboxyphenyl)porphyrin. [d] T*o*CPP, *meso*-tetrakis(*ortho*-carboxyphenyl)porphyrin. [e] ABTS, 2,2-azinobis (3-ethylbenzothiazoline-6-sulfonic acid). [f] TMPyP, *meso*-tetrakis(4-methylpyridyl)porphyrin.

with Fe(TpCPP) alone (K_M = 0.83, 0.28, and 0.16 mM for guaiacol, 2,6-dimethoxyphenol, and *o*-dianisidine, respectively). It is likely that this is due both to the steric hindrance and to the increased hydrophobicity brought by the protein around the iron atom of the porphyrin. With Fe(TpCPP)-Xln10A, the k_{cat}value was lower than with Fe(TpCPP) alone in the case of guaiacol (5.6 and 17.8 min^{-1}, respectively) and 2,6-dimethoxyphenol (6.1 and 9.3 min^{-1}, respectively) but higher with *o*-dianisidine (52.0 and 29.2 min^{-1}, respectively). This could be explained by the fact that guaiacol and 2,6-dimethoxyphenol are smaller hydrophobic substrates that can compete with H_2O_2 for the active site whereas *o*-dianisidine is a larger bicyclic compound that hardly enters the porphyrin binding site in Xln10A.

The kinetic parameters for *o*-dianisidine and guaiacol have also been measured. They can be compared with the values reported for phenolic cosubstrates in the presence of myoglobin and new hemoproteins obtained by incorporation of modified hemes into recombinant myoglobin (Table 3). Both myoglobin and new myoglobin-derived hemoproteins lead to higher k_{cat} values (60–396 min^{-1}) (*32, 33*) than Xln10-Fe(TpCPP) with guaiacol (k_{cat} = 0.6 min^{-1}) and *o*-dianisidine (k_{cat} = 17.6 min^{-1}). Only one of the reported new hemoproteins, rMb(H64D)**2**, leads to a lower K_M value (K_M = 0.052 mM) (*32*) than Xln10-Fe(TpCPP) with guaiacol (K_M = 0.24 mM) and *o*-dianisidine (K_M = 0.80 mM). As a consequence, it also appears to be the more efficient catalyst, characterized by a k_{cat}/K_M value of 1.4 $\times$ 10^6 M^{-1} min^{-1} (*32*), whereas all the other myoglobin-derived hemoproteins display molar efficiencies that are in the same range as those displayed Xln10-Fe(TpCPP) (k_{cat}/K_M = 8.4 $\times$ 10^2 to 2.2 $\times$ 10^4 M^{-1} min^{-1}) (Table 3).

Oxidation of *o*-dianisidine by increasing amounts of H_2O_2, in the presence of either Xln10A-Fe(T*p*CPP) or Fe(T*p*CPP) alone as catalyst, led to a plateau value that was dependent upon the concentration of H_2O_2 that was used (Figure 8). This was due in both cases to a bleaching of the metalloporphyrin cofactor as was proven by two experimental observations: (i) UV–visible monitoring of the reaction showed a bleaching of the Soret band at, respectively, 409 nm for Fe(T*p*CPP) or 412 nm for Xln10A-Fe(T*p*CPP), (ii) further addition of the same amount of either H_2O_2 or *o*-dianisidine to the reaction mixture, once the plateau was reached, did not lead to any further oxidation of *o*-dianisidine. It is noteworthy, however, that another important advantage brought by the protein around the Fe-porphyrin cofactor could be shown: an important protecting effect toward oxidative degradation of the porphyrin. Indeed, with Xln10A-Fe(T*p*CPP) as catalyst, the reaction remains linear as a function of time for a longer time, and when the plateau is reached, more substrate is oxidized. Furthermore, as shown in the particular case of *o*-dianisidine (Figure 8), the concentration of cosubstrate oxidized increases with the H_2O_2 concentration over a wide range of concentrations (e.g., 80–640 μM), whereas under the same conditions, with Fe(T*p*CPP) as catalyst, the concentration of *o*-dianisidine oxidized significantly decreases.

When the effect of the addition of imidazole on the peroxidase activity was assayed, inhibition was observed with both Fe(T*p*CPP) and Fe(T*p*CPP)-Xln10A catalysts, with respective IC_{50} values of 11 and 25 mM. It is likely that this inhibition is due to the binding of imidazole ligands on the iron atom of Fe(T*p*CPP). With both Fe(T*p*CPP) and Xln10A-Fe(T*p*CPP), the IC_{50} value is larger than the C_{50} value for the binding of imidazole on the iron atom (C_{50} = 3.4 mM and 3.3 mM, respectively; Table 1), which could reflect competition between imidazole and the substrate to enter the active site as the basis of the inhibition.

Finally, a study of the catalytic activity as a function of pH showed that, whereas with Fe(T*p*CPP) alone the rate of oxidation of *o*-dianisidine by H_2O_2 increased linearly with pH for pH values above 5, a sigmoid curve with an inflection point at about pH 7.5 was found in the case of Xln10A-Fe(T*p*CPP). Since the solubility of Fe(TpCPP) decreases at lower pH values, and it cannot be ruled out that this could be involved in the decrease of peroxidase activity of the hemozyme at low pH. However, it is also likely that an amino acid side chain with a pK_A of about 7.5 could be participating in the catalysis. The amino acids located inside the binding pocket of Xln10A, that were both characterized by a pK_a value between 6 and 8 and close enough to the iron atom of the metalloporphyrin cofactor, were searched using molecular modeling. This allowed us to point out five amino acids that could possess those properties: Lys 48, Asp 50, His 80, Glu 128, and His 207 (Figure 10). Site-directed mutagenesis studies will be undertaken to examine which of them could be participating in catalysis.

CONCLUSION

The results described above show that the association of a synthetic iron(III)-tetra-*para*-carboxy-phenyl substituted porphyrin and a nonrelated protein xylanase A from *Streptomyces lividans*,

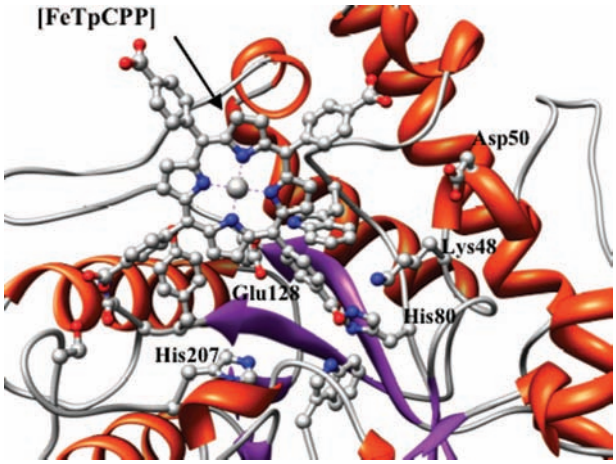

Figure 10. Amino acids located inside the binding pocket of Xln10A, that could be participating in the catalysis of the peroxidase reaction by the Xln10A-Fe(T*p*CCP) complex: Lys 48, Asp 50, His 80, Glu 128, and His 207.

leads to a new hybrid hemoprotein that displays interesting peroxidase activity. This new biocatalyst combines the advantages of both partners. First, Fe-tetraaryl-porphyrins are less sensible to oxidative degradations of meso bridges by oxidizing intermediates than natural hemes. The first positive effect of the protein is to increase this protection of the porphyrin ligand toward the highly reactive oxygenated species generated during the catalysis. Second, the protein also brings steric hindrance and an increased hydrophobic environment around the iron, two important characteristics that will be highly useful in the future for the catalysis of selective oxidation reactions. It may also be possible for the protein to bring amino acids that participate in the catalysis and in the binding of the iron. Preliminary molecular modeling experiments have already suggested a set of amino acids that could fill these functions. Further site-directed mutagenesis experiments are underway to confirm these results.

ACKNOWLEDGMENT

We thank the Ministère des Relations Internationales du Québec, the Consulat Général de France à Québec and the 61th Commission Permanente de Coopération Franco-Québecoise for a two-years collaboration grant between the team of Prof. J.-P Mahy (France) and that of Prof. C. Dupont (Quebec) that helped to develop this project.

LITERATURE CITED

(1) Mansuy, D., and Battioni, P. (1994) Cytochrome P450 model systems, in *MetaIloporphyrins in Catalytic Oxidations*, Sheldon, R. A., Ed., pp 99–132, Marcel Dekker, New York.

(2) Everse, J., Everse, K. E., and Grisham, M. B. (1991) *Peroxidases in Chemistry and Biology*, Vol *2*, CRC Press, Boca Raton.

(3) Ortiz de montellano, P. R. (1995) *Cytochrome P450: Structure, Mechanism and Biochemistry*, 2nd ed., Plenum Press, New York.

(4) Poulos, T. L. (1996) The role of proximal ligand in heme enzymes. *J. Biol. Inorg. Chem. 1*, 356–359.

(5) Sigman, J. A., Kwok, B. C., and Lu, Y. (2000) From myoglobin to heme-copper oxidase: design and engineering of a cub center into sperm whale myoglobin. *J. Am. Chem. Soc. 122*, 8192–8196.

(6) Braha, O., Walker, B., Cheley, S., Kasianowicz, J. J., Song, L., Gouaux, E., and Hagan, B. (1997) Designed protein pores as components for biosensors. *Chem. Biol. 4*, 497–505.

(7) Miyawaki, A., Llopis, J., Heim, R., McCaffery, J. M., Adams, J. A., Ikura, M., Tsien, and R. Y. (1997) Fluorescent indicators for Ca^{2+} based on green fluorescent proteins and calmodulin. *Nature 388*, 834–835.

(8) Pinto, A. L., Hellinga, H. W., and Caradonna, J. P. (1997) Construction of a catalytically active iron superoxide dismutase by rational protein design. *Proc. Natl. Acad. Sci. U.S.A. 94*, 5562–5567.

(9) Ozaki, S., Yang, H. J., Matsui, T., Goto, Y., and Watanabe, Y. (1999) Asymmetric oxidation catalyzed by myoglobin mutants. *Tetrahedron: Asymmetry 10*, 183–192.

(10) Hara, I., Ueno, T., Ozaki, S., Itoh, S., Lee, K., Ueyama, N., and Watanabe, Y. (2001) Oxidative modification of tryptophan 43 in the heme vicinity of the F43W/H64L myoglobin mutant. *J. Biol. Chem. 276*, 36067–36070.

(11) Kato, S., Yang, H. J., Ueno, T., Ozaki, S., Phillips, G. N., Fukuzumi, S., and Watanabe, Y. (2002) Asymmetric sulfoxidation and amine binding by H64D/V68A and H64D/V68S Mb: mechanistic insight into the chiral discrimination step. *J. Am. Chem. Soc. 124*, 8506–8507.

(12) Ozaki, S., and Ortiz de Montellano, P R. (1995) Molecular engineering of horseradish peroxidase: thioether sulfoxidation and styrene epoxidation by Phe-41 leucine and threonine mutants. *J. Am. Chem. Soc. 117*, 7056–7064.

(13) Neya, S., Funasaki, N., and Imai, K. (1988) Structure and function of the myoglobin containing octaethylhemin as a prosthetic group. *J. Biol. Chem. 263*, 8810–8815.

(14) Hayashi, T., Hitomi, Y., Ando, T., Mizutani, T., Hisaeda, Y., Kitagawa, S., and Ogoshi, H. (1999) Peroxidase activity of myoglobin is enhanced by chemical mutation of heme-propionates. *J. Am. Chem. Soc. 121*, 7747–7750.

(15) Hu, Y. Z., Tsukiji, S., Shinkai, S., Oishi, S., and Hamachi, I. (2000) Construction of artificial photosynthetic reaction centers on a protein surface: vectorial, multistep, and proton-coupled electron transfer for long-lived charge separation. *J. Am. Chem. Soc. 122*, 241–253.

(16) Monzani, E., Alzuet, G., Casella, L., Redaelli, C., Bassani, C., Sanangelantoni, A. M., Gullotti, M., Gioia, L. D., Santagostini, L., and Chillemi, F. (2000) Properties and reactivity of myoglobin reconstituted with chemically modified protohemin complexes. *Biochemistry 39*, 9571–9582.

(17) Davies, R. R., and Distefano, M. D. (1997) A semisynthetic metalloenzyme based on a protein cavity that catalyzes the enantioselective hydrolysis of ester and amide substrates. *J. Am. Chem. Soc. 119*, 11643–11652.

(18) Ma, S. K., and Lu, Y. (1999) Artificial metalloenzymes as asymetric catalysts. *J. Inorg. Biochem. 74*, 217.

(19) Ermacora, M. R., Delfino, J. M., Cuenoud, B., Schepartz, A., and Fox, R. O. (1992) Conformation-dependent cleavage of staphylococcal nuclease with a disulfide-linked iron chelate. *Proc. Natl. Acad. Sci. U.S.A. 89*, 6383–6387.

(20) Sigman, D. S., Bruice, T. W., Christopher, A. M., and Sutton, L. (1993) Targeted chemical nucleases. *Acc. Chem. Res. 26*, 98–104.

(21) Quilez, R., de Lauzon, S., Desfosses, B., Mansuy, D., and Mahy, J. P. (1996) Artificial peroxidase-like hemoproteins based on antibodies constructed from a specifically designed *ortho*-carboxy substituted tetraarylporphyrin hapten and exhibiting a high affinity for iron-porphyrins. *FEBS Lett. 395*, 73–76.

(22) Mahy, J. P., Desfosses, B., de Lauzon, S., Quilez, R., Desfosses, B., Lion, L., and Mansuy, D. (1998) Hemoabzymes Different strategies for obtaining artificial hemoproteins based on antibodies. *Appl. Biochem. Biotechnol. 75*, 103–127.

(23) de Lauzon, S., Quilez, R., Lion, L., Desfosses, B., Desfosses, B., Lee, I., Sari, M. A., Benkovic, S. J., Mansuy, D., and Mahy, J. P. (1998) Active site topology of artificial peroxidase-like hemoproteins based on antibodies constructed from a specifically designed *ortho*-carboxy-substituted tetraarylporphyrin. *Eur. J. Biochem. 257*, 121–130.

(24) de Lauzon, S., Desfosses, B., Mansuy, D., and Mahy, J. P. (1999) Studies of the reactivity of artificial peroxidase-like hemoproteins based on antibodies elicited against a specifically designed *ortho*-carboxy substituted tetraarylporphyrin. *FEBS Lett. 443*, 229–234.

(25) de Lauzon, S., Mansuy, D., and Mahy, J. P. (2002) Coordination chemistry of iron(III)-porphyrin-antibody complexes: influence on the peroxidase activity of the axial coordination of an imidazole on the iron atom. *Eur. J. Biochem. 269*, 1–11.

(26) Ricoux, R., Sauriat-Dorizon, H., Girgenti, E., Blanchard, D., and Mahy, J. P. (2002) Hemoabzymes: towards new biocatalysts for selective oxidations. *J. Immunol. Methods 269*, 39–57.

(27) Ricoux, R., Girgenti, E., Sauriat-Dorizon, H., Blanchard, D., and Mahy, J. P. (2002) Regioselective nitration of phenol induced by catalytic antibodies. *J. Protein Chem. 21*, 473–477.

(28) Ricoux, R., Girgenti, E., and Mahy, J. P. (2003) New biocatalysts mimicking oxidative hemoproteins: Hemoabzymes, in *Recent research Developments in Biochemistry*, Pandalai, S. G., Ed. Vol *4*, pp 757–778, Research Signpost, Kerala, India.

(29) Ricoux, R., Lukowska, E., Pezzotti, F., and Mahy, J. P. (2004) New activities of a catalytic antibody with a peroxidase activity: Formation of Fe(II)-RNO complexes and stereoselective oxidation of sulphides. *Eur. J. Biochem. 271*, 1277–1283.

(30) Roncone, R., Monzani, E., Murtas, M., Battaini, G., Pennati, A., Sanangelantoni, A. M., Zucotti, S., Bolognesi, M., and Casella, L. (2004) Engineering peroxidase activity in myoglobin: the haem cavity structure and peroxide activation in the T67R/S92D mutant and its derivative reconstituted with protohaemin-l-histidine. *Biochem. J. 377*, 717–24.

(31) Rone, R., Monzani, E., Nicolis, S., and Casella, L. (2004) Engineering and prosthetic-group modification of myoglobin: peroxidase activity, chemical stability and unfolding properties. *Eur. J. Inorg. Chem. 11*, 2203–2213.

(32) Sato, H., Hayashi, T., Ando, T., Hisaeda, Y., Ueno, T., and Watanabe, Y. (2004) Hybridization of modified-heme reconstitution and distal histidine mutation to functionalize sperm whale myoglobin. *J. Am. Chem. Soc. 126*, 436–437.

(33) Roncone, R,., Monzani, E., Labo, S., Sanangelantoni, A. M., and Casella, L. (2005) Catalytic activity, stability, unfolding, and degradation pathways of engineered and reconstituted myoglobins. *J. Biol. Inorg. Chem. 10*, 11–24.

(34) Komatsu, T., Ishihara, S., Tsuchida, E., Nishide, H., Morokuma, C., and Nakamura, S. (2003) Thermostable synthetic hemoproteins: thermophilic xylanases hybridized with dioxygen carrying meso-tetrakis(o-pivalamidophenyl)porphyrinatoiron(II) derivative. *Chem. Lett. 32*, 108–109.

(35) Komatsu, T., Ishihara, S., Tsuchida, E., Nishide, H., Morokuma, C., and Nakamura, S. (2005) Heat-resistant oxygen-carrying hemoproteins consist of recombinant xylanases and synthetic iron(II) porphyrin. *Biomacromolecules 6*, 1489–1494.

(36) Wang, R. M., Komatsu, T., Nakagawa, A., and Tsuchida, E. (2005) Human serum albumin bearing covalently attached iron(II) porphyrins as O2-coordination sites. *Bioconjugate Chem. 1*, 23–26.

(37) Ducros, V., Charnock, S. J., Derewenda, U., Derewenda, Z. S., Dauter, Z., Dupont, C., Shareck, F., Morosoli, R., Kluepfel, D., and Davies, J. G. (2000) Substrate specificity in glycoside hydrolase family 10. Structural and kinetic analysis of the Streptomyces lividans xylanase 10A. *J. Biol. Chem. 275*, 23020–23026.

(38) Aron, J., Baldwin, D. A., Marques, H., Pratt, J. M., and Adams, P. A. (1986) Hemes and hemoproteins 1: Preparation and analysis of heme containing octapeptide (Microperoxidase 8) and identification of the monomeric form in aqueous solution. *J. Inorg. Biochem. 27*, 227–243.

(39) de Lauzon, S., Quilez, R., Lion, L., Desfosses, B., Desfosses, B., Lee, I., Sari, M. A., Benkovic, S. J., Mansuy, D., and Mahy, J. P. (1998) Active site topology of artificial peroxidase-like hemoproteins based on antibodies constructed from a specifically designed *ortho*-carboxy-substituted tetraarylporphyrin. *Eur. J. Biochem. 257*, 121–130.

(40) Lindsey, J. S., and Wagner, R. W. (1989) Investigation of the synthesis of ortho-substituted tetraarylporphyrins. *J. Org. Chem. 54*, 828–836.

(41) Tsutsui, M., Ichikawa, M., Vohwinkel, F., and Suzuki, K. (1966) Unusual porphyrins. I. Preparation of chromium mesoporphyrin IX dimethyl ester. *J. Am. Chem. Soc. 88*, 854–855.

(42) Leondiadis, L., and Momenteau, M. (1989) 5,10,15,20-Tetrakis-(α,α,α,α-(*N*-ter-butyl-carbamoyl)phenyl)porphyrin: synthesis and redox properties of zinc(II) and copper(II) complexes. *J. Org. Chem. 54*, 6135–6138.

(43) Brault, D., and Rougee, M. (1974) Binding of imidazole and 2-methylimidazole by hemes in organic solvents. Evidence for five-coordination. *Biochem. Biophys. Res. Commun. 3*, 654–659.

(44) Heinfling, A., Martinez, M. J., Martinez, A. T., Bergbauer, M., and Szewzyk, U. (1998) Transformation of industrial dyes by manganese peroxidases from Bjerkandera adusta and Pleurotus eryngii in a manganese-independent reaction. *Appl. Environ. Microbiol. 64*, 2788–2793.

(45) Berman, H. M., Westbrook, J., Feng, Z., Gilliland, G., Bhat, T. N., Weissig, H., Shindyalov, I. N., and Bourne, P.E,. (2000) The protein data bank. *Nucleic Acids Res. 28*, 235–242.

(46) Gloster, T. M., Williams, S. J., Roberts, S., Tarling, C. A., Wicki, J., Withers, S. G., and Davies, G. J. (2004) Atomic resolution analyses of the binding of xylobiose-derived deoxynojirimycin and isofagomine to xylanase Xyn10A. *J. Chem. Soc., Chem. Commun. 16*, 1794–1795.

(47) Dundas, J., Ouyang, Z., Tseng, J., Binkowski, A., Turpaz, Y., and Liang, J. (2006) CASTp: computed atlas of surface topography of proteins with structural and topographical mapping of functionally annotated residues. *Nucleic Acids Res. 34*, W116–W118.

(48) Laurie, A. T. R., and Jackson, R. M. (2005) Q-SiteFinder: an energy-based method for the prediction of protein-ligand binding sites. *Bioinformatics 21*, 1908–1916.

(49) Allinger, N. L. (1977) MM2. A hydrocarbon force field utilizing V1 and V2 torsional terms. *J. Am. Chem. Soc. 99*, 8127–8134.

(50) Berghuis, A. M., Guillemette, J. G., McLendon, G., Sherman, F., Smith, M., and Brayer, G. D. (1994) The role of a conserved internal water molecule and its associated hydrogen bond network in cytochrome c. *J. Mol. Biol. 236*, 786–799.

(51) Verdonk, M. L., Cole, J. C., Hartshorn, M. J., Murray, C. W., and Taylor, R. D. (2003) Improved protein-ligand docking using GOLD. *Proteins 52*, 609–623.

(52) Eldridge, M. D., Murray, C. W., Auton, T. R., Paolini, G. V., and Mee, R. P. (1997) Empirical scoring functions: I. The development of a fast empirical scoring function to estimate the binding affinity of ligands in receptor complexes. *J. Comput.-Aided Mol. Des. 11*, 425–445.

(53) Maréchal, J. D., Yu, J., Brown, S., Kapelioukh, I., Rankin, E. M., Wolf, C. R., Roberts, G. C., Paine, M. J., and Sutcliffe, M. J. (2006) In silico and in vitro screening for inhibition of cytochrome P450 CYP3A4 by comedications commonly used by patients with cancer. *Drug Metab. Dispos. 34*, 534–538.

(54) Pettersen, E. F., Goddard, T. D., Huang, C. C., Couch, G. S., Greenblatt, D. M., Meng, E. C., and Ferrin, T. E. (2004) UCSF chimera - a visualization system for exploratory research and analysis. *J. Comput. Chem. 25*, 1605–1612.

(55) Cochran, A. G., and Schultz, P. G. (1990) Peroxidase activity of an antibody-heme complex. *J. Am. Chem. Soc. 112*, 9414–9415.

(56) Feng, Y., Liu, Z., Gao, G., Gao, S. J., Liu, X. Y., and Yang, T. S. (1995) Study of the abzyme with catalytic peroxidase activity. *Ann. N.Y. Acad. Sci. 750*, 271–276.

(57) Takagi, M., Khoda, K., Hamuro, T., Harada, A., Yamaguchi, H., Harada, A., Kamachi, M., and Imanaka, T. (1995) Thermostable peroxidase activity with a recombinant antibody L chain-porphyrin Fe(III) complex. *FEBS Lett. 375*, 273–276.

(58) Yamaguchi, H., Tsubouchi, K., Kawaguchi, K., Horita, E., and Harada, A. (2004) Peroxidase activity of cationic metalloporphyrin-antibody complexes. *Chem. Eur. J. 10*, 6179–6186.

(59) Kawamura-Konishi, Y., Asano, A., Yamasaki, M., Tashiro, H., and Suzuki, H. (1998) Peroxidase activity of an antibody-ferric porphyrin complex. *J. Mol. Catal. B: Enzym.* 4.

(60) Kuo, C-F., and Fridovich, I. (1988) Stimulation of the activity of horseradish peroxidase by nitrogenous compounds. *J. Biol. Chem. 363*, 3811–3817.

BC700435A

Fully Acid-Degradable Biocompatible Polyacetal Microparticles for Drug Delivery

Sergey E. Paramonov,† Eric M. Bachelder,† Tristan T. Beaudette, Stephany M. Standley, Cameron C. Lee, Jesse Dashe, and Jean M. J. Fréchet*

Department of Chemistry, University of California, Berkeley, California 94720-1460. Received December 4, 2007; Revised Manuscript Received February 22, 2008

A library of polyurethanes and polyureas with different hydrophobicities containing the same acid-degradable dimethyl ketal moiety embedded in the polymer main chain have been prepared. All polymers were synthesized using an AA-BB type step-growth polymerization by reaction of bis(*p*-nitrophenyl carbamate/carbonate) or diisocyanate monomers with an acid-degradable, ketal-containing diamine. These polymers were designed to hydrolyze at different rates in mildly acidic conditions as a function of their hydrophobicity to afford small molecules only with no polymeric byproduct. The library of polymers was screened for the formation of microparticles using a double emulsion technique. The microparticles that were obtained degraded significantly faster at acidic pH (5.0) than at physiological pH (7.4) with degradation kinetics related to the hydrophobicity of the starting polymer. In vitro studies demonstrated the ability of the FITC-BSA loaded microparticles to be phagocytosed by macrophages resulting in a 10-fold increase in the protein uptake compared to a free protein control; in addition, the microparticles were found to be nontoxic at the concentrations tested of up to 1 mg/mL. The ease of preparation of the polymers coupled with the ability to tune their hydrophobicity and the high acid sensitivity of the microparticles identify this new class of materials as promising candidates for the delivery of bioactive materials.

INTRODUCTION

Polymer based drug or vaccine delivery systems have attracted much attention due to their ability to perform multiple critical functions. These functions include delivering therapeutic or other bioactive agents to a specific site via a targeting mechanism, increasing the circulation times of drugs in the body, protecting drugs from degradation, or increasing the bioavailability of poorly soluble drugs. We are interested in developing polymer-based delivery vehicles that utilize a change in the pH of the medium to trigger the release of a payload, yet degrade fully into small molecules without leaving a polymeric residue. Several strategies have been utilized to prepare acid-degradable carriers including the use of pH responsive micelles (*1*), microparticles (*2–5*) and liposomes (*6–8*) that encapsulate the therapeutic molecules. In addition, covalent attachment of the drug to a polymer or dendrimer carrier through an acid-sensitive linkage has also been demonstrated (*9, 10*). In this way a therapeutic payload may be released (*11*) at a site utilizing the slightly acidic conditions found in inflamed tissue and tumors or in the endosomal/lysosomal compartments of cells.

However, it is important to consider the byproducts obtained in the degradation of a polymer carrier to ensure their complete clearance from the body. Many systems reported previously including poly(beta-amino) esters (*4, 12–14*), poly(ketal)s (*15*) and poly(acetal)s (*3, 16*) degrade significantly faster at the acidic pH of 5.0–6.0 than at the physiological pH of 7.4, but their degradation into small molecule products is either incomplete or only occurs within a time frame of days to weeks, which may in some instances reduce their applicability to practical systems.

We have explored a family of novel polymers that degrade only to small molecule products when subjected to the acidic conditions found in lysosomes (Figure 1). A highly reactive pH-sensitive diamine monomer was synthesized and allowed to react with a variety of bis(*p*-nitrophenyl carbamate/carbonate)s and diisocyanates (Figure 1a,b) to afford a family of acid-degradable polyureas and polyurethanes with various degrees of hydrophobicity (**17–24**) (Figure 1c). The polymers were further tested for their ability to encapsulate a water soluble protein via a double emulsion (water/oil/water) technique to afford pH-sensitive microparticles that can degradable in aqueous medium with appreciable kinetics (Figure 1d). The hydrophobicity of the polymer is an important parameter that affects both the microparticle preparation as well as the degradation kinetics. By employing an AA-BB type step growth polymerization in which AA is the acid-degradable diamine monomer and BB represents a variety of bis-electrophilic monomers with different hydrophobicities, we synthesized a library of polymers and identified those polymers that could both form suitable microparticles and degrade sufficiently fast to be used as delivery vehicles. The potential to use any of a wide variety of commercially available or easily synthesized bifunctional monomers to readily prepare polymers with variable physical properties further highlights the versatility of our approach.

The prepared microparticles were characterized by scanning electron microscopy (SEM) and dynamic light scattering (DLS) while their cellular uptake was visualized by laser confocal microscopy and analyzed by flow cytometry. The degradation of these microparticles over time in aqueous medium was monitored at pH 5.0 and 7.4 with several microparticles demonstrating both rapid degradation under acidic conditions and relative stability at physiological pH. Complete degradation into small molecule products (Figure

* Corresponding author. Fax: (510) 643-3079. E-mail: frechet@cchem.berkeley.edu.

† These authors made equal contributions to this work.

10.1021/bc7004472 CCC: $40.75 © 2008 American Chemical Society
Published on Web 03/29/2008

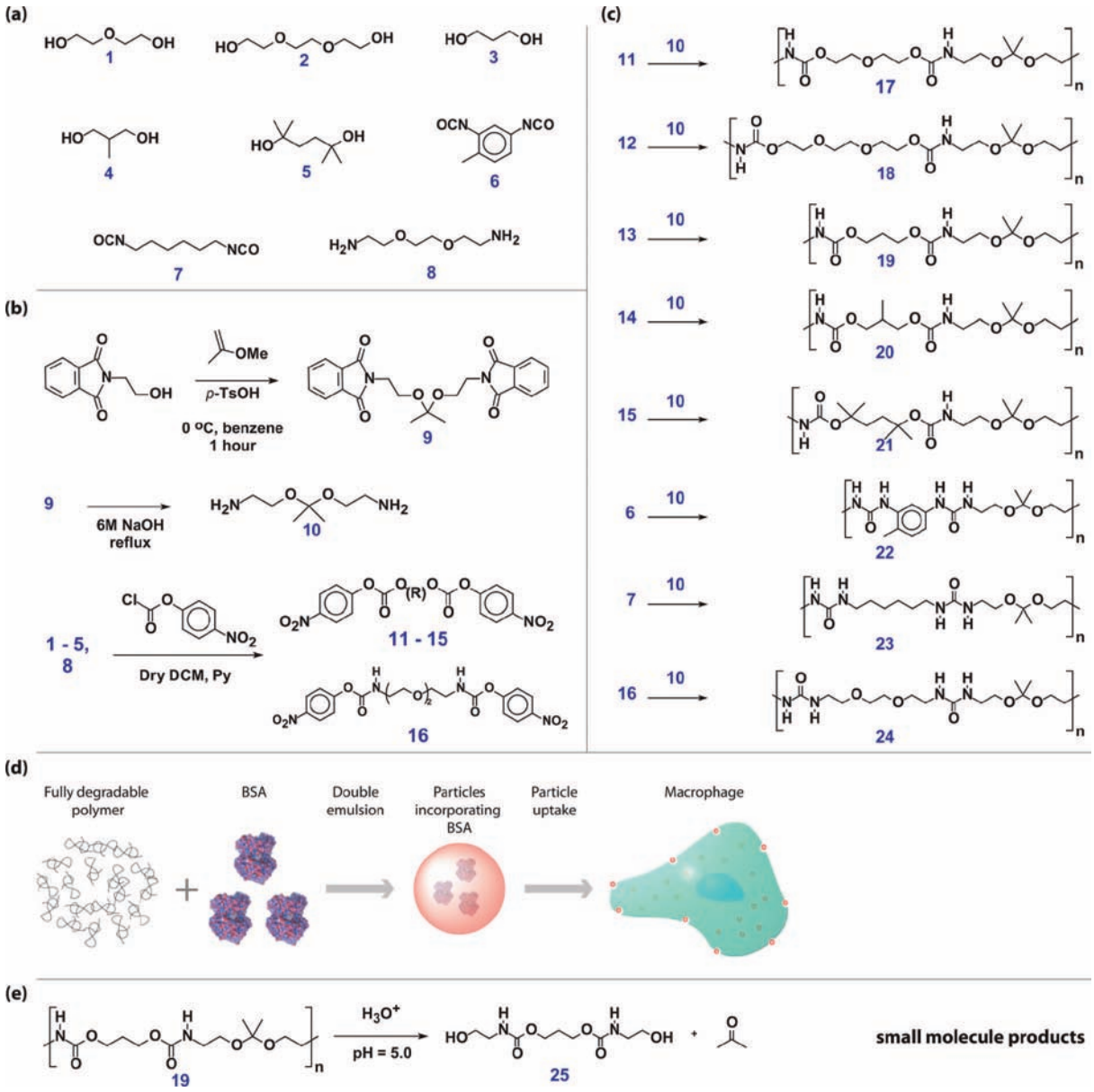

Figure 1. (a) Library of monomers used to produce acid-degradable polymers; (b) syntheses of acid-degradable diamine monomer **10** and activation of monomers **11**−**16**; (c) synthesis of acid-degradable polymers **17**−**24**; (d) schematic representation of encapsulation of FITC-BSA into acid-degradable microparticles and their subsequent uptake by macrophages; and (e) acid-catalyzed hydrolysis of the various polymers.

1e) was confirmed and cytotoxicity studies indicated no toxicity up to the highest concentration tested of 1 mg/mL.

EXPERIMENTAL SECTION

General Procedures and Materials. Reagents and materials were purchased from commercially available sources and were used without further purification unless otherwise noted. *p*-Toluenesulfonic acid was recrystallized from toluene. ^{1}H NMR spectra were recorded at 300 or 400 MHz, while ^{13}C spectra were recorded at 100 MHz. Reported chemical shifts (ppm) are relative to tetramethylsilane and coupling constants are reported in Hz. High resolution fast bombardment mass spectrometry (FAB-HRMS) analysis was performed at the UC Berkeley mass spectrometry facility. Elemental analyses were obtained from the UC Berkeley analytical facility. Size exclusion chromatography (SEC) experiments were performed on a Waters system with simultaneous analysis of UV absorbance and refractive index using 0.1 M LiBr solution in DMF. The SEC column (75 × 300 mm PLgel, 10^3 Å, 5 μm particle size) was calibrated using poly(methyl methacrylate) standards. Fourier transform infrared spectroscopy (FT-IR) was carried out on a Varian 3100 FT-IR spectrometer.

Synthesis of Compound 9. N-(2-hydroxyethyl)-phthalimide (20.29 g, 106 mmol, 1 equiv) was dissolved in 400 mL of dry benzene, residual water was removed by azeotropic distillation in a Dean–Stark distillation setup. The solution was cooled to 0 °C using an ice bath and 2-methoxy propene (10.15 mL, 106 mmol, 1 equiv) was carefully added to the solution along with *p*-toluenesulfonic acid (190 mg, 1 mmol). The reaction mixture was then stirred for an hour while keeping the temperature at 0 °C to avoid loss of the highly volatile 2-methoxy propene (bp: 34–36 °C). After one hour, the reaction mixture was heated to evaporate the solvent while additional amounts of dry benzene were added and subsequently evaporated over the course of 3 h. Finally, the reaction mixture was cooled to room temperature and triethylamine (TEA) (24 mL) was added to quench the reaction. To facilitate further purification, acetic anhydride (6 mL) was added to convert any unreacted alcohol groups into the corresponding acetate and the reaction mixture was allowed to stir overnight. The reaction mixture was then precipitated

by dropwise addition to a large excess of hexanes. The precipitated powder was collected and recrystallized twice from ethyl acetate. Yield: 55%. Spectroscopic characterization was consistent with that reported in the literature (*17*).

Synthesis of Compound 10. Compound **9** (17.03 g, 40.3 mmol) was deprotected in 6 M NaOH (100 mL) by heating the reaction mixture at reflux overnight. The product was extracted with $CHCl_3$/iPrOH (1/1) mixture three times and the fractions were combined and dried over anhydrous $MgSO_4$. The organic layer was filtered and evaporated *in vacuo*. The excess of iPrOH was removed by repeated azeotropic distillation with hexanes. Yield: 85%. IR (cm^{-1}): 3372 (br), 1568 (s), 1480 (s), 1380 (m). ^1H NMR (300 MHz, $CDCl_3$): ∂ 1.35 (s, 6H), 1.55 (s, ~4H), 2.82 (t, 4H, $J = 5.4$ Hz), 3.44 (t, 4H, 5.4 Hz). ^{13}C NMR (100 MHz, $CDCl_3$): ∂ 25.0, 42.1, 62.8, 99.7. Calcd: $[M + H]^+$ ($C_7H_{19}N_2O_2$) $m/z = 163.1447$. Found FAB-HRMS: $[M + H]^+ = 163.1446$. Anal. Calcd: C, 51.83; H, 11.18; N, 17.27. Found: C, 51.70; H, 11.24; N, 17.33.

Synthesis of Compounds 11–15. Compounds **11** and **12** were synthesized according to published procedures (*18*). Compounds **13**−**15** were synthesized according to the general procedure described below. Diol **3-5** (1.73 g, 19.3 mmol) was dried by azeotropic distillation with benzene and redissolved in 20 mL of dry CH_2Cl_2. Dry pyridine (9.3 mL, 115.7 mmol) was added and the reaction mixture was cooled to 0 °C. In a separate flask *p*-nitrophenolchloroformate (9.75 g, 48.4 mmol) was dissolved in dry CH_2Cl_2 (30 mL) and slowly added to the solution of diol under nitrogen atmosphere. The reaction mixture was allowed to stir overnight under N_2 while warming to room temperature. The crude reaction mixture was washed three times with NaH_2PO_4 (0.4 M, pH 4.6), the organic layer was dried over $MgSO_4$ and the solvent was removed under reduced pressure. The resulting solid was recrystallized three times from ethyl acetate.

Compound 13. Yield: 85%. IR (cm^{-1}): 1527 (s), 1594 (m), 1527 (m), 1760 (s), 2976 (w). ^1H NMR (400 MHz, $CDCl_3$): ∂ 2.23 (quintet, 2H, $J = 6$ Hz), 4.49 (t, 4H, $J = 6$ Hz), 7.39 (d, 4H, $J = 9.2$ Hz), 8.26 (d, 4H, $J = 9.2$ Hz). ^{13}C NMR (100 MHz, $CDCl_3$): ∂ 28.0, 65.7, 122.0, 125.6, 145.7, 152.6, 155.7. Calcd: $[M + Li]^+$ ($C_{17}H_{14}N_2O_{10}Li$) $m/z = 413.0808$. Found FAB-HRMS: $[M + Li]^+ = 413.0814$. Anal. Calcd: C, 50.25; H, 3.47; N, 6.89. Found: C, 50.46; H, 3.32; N, 6.77.

Compound 14. Yield: 79%. IR (cm^{-1}): 1530 (s), 1596 (m), 1618 (m), 1765 (s), 2958 (w). ^1H NMR (300 MHz, $CDCl_3$): ∂ 1.14 (d, 3H, $J = 7.2$ Hz), 2.37–2.48 (m, 1H), 4.31 (d, 4H, $J = 3$ Hz), 7.37 (d, 4H, $J = 9$ Hz), 8.25 (d, 4H, $J = 9$ Hz). ^{13}C NMR (100 MHz. $CDCl_3$) ∂ 13.4, 32.6, 70.1, 121.8, 128.4, 145.5, 152.5, 155.4. Calcd: $[M + H]^+$ ($C_{18}H_{17}N_2O_{10}$) $m/z = 421.0883$. Found FAB-HRMS: $[M + H]^+ = 421.0881$. Anal. Calcd: C, 51.43; H, 3.84; N, 6.66. Found: C, 51.22; H, 3.69; N, 6.53.

Compound 15. Yield: 82%. IR (cm^{-1}): 1529 (s), 1596 (m), 1618 (m), 1756 (s), 2979 (w). ^1H NMR (400 MHz, $CDCl_3$): ∂ 1.58 (s, 12H), 2.00 (s, 4H), 7.33 (d, 4H, $J = 9.2$ Hz), 8.20 (d, $J = 9.2$ Hz). ^{13}C NMR (100 MHz, $CDCl_3$): ∂ 25.8, 33.8, 86.0, 122.0, 125.1, 145.2, 150.4, 155.5. Calcd: $[M + Li]^+$ ($C_{22}H_{24}N_2O_{10}Li$) $m/z = 483.1591$. Found FAB-HRMS: $[M + Li]^+ = 483.1580$. Anal. Calcd: C, 55.46; H, 5.08; N, 5.88. Found: C, 55.79; H, 4.98; N, 5.77.

Synthesis of Compound 16. 2,2′-(Ethylenedioxy)bis(ethylamine) (1.00 g, 6.75 mmol) and pyridine (2.18 mL, 27.0 mmol) were dissolved in CH_2Cl_2 (250 mL); the reaction mixture was cooled to 0 °C and *p*-nitrophenyl chloroformate (5.44 g, 27.0 mmol) was added. The solution was warmed to RT while stirring for 24 h. The reaction mixture was then filtered and the solvent evaporated to afford a white solid. The crude product was dissolved in CH_2Cl_2 (150 mL) and washed with 1 M $NaHSO_4$ (3 × 30 mL). The organic layer was dried and the solvent was evaporated. The resulting solid was crystallized twice from CH_2Cl_2/hexanes providing **16** as a white solid in 68% yield. The ^1H NMR spectrum indicated that a 4:1 ratio of conformational isomers were present at RT. IR (cm^{-1}): 3329 (s), 1715 (s), 1539 (s). ^1H NMR (400 MHz, $CDCl_3$): ∂ 3.52 (dt, 3.2H, $J_1 = J_2 = 5$), 3.59 (dt, 0.8H, $J_1 = J_2 = 5$), 3.68 (t, 4H, $J = 5$), 3.71 (s, 4H), 5.68 (br, 1.6H), 5.90 (br, 0.2H), 6.35 (br, 0.2H), 7.30 (d, 4H, $J = 9$), 8.23 (d, 4H, $J = 9$). ^{13}C NMR (125 MHz, $CDCl_3$): ∂ 40.98, 69.54, 70.22, 121.88, 125.00, 144.60, 153.10, 155.77. FAB-MS *m/z*: $[M + H]^+$ 479. Anal. Calcd. for $C_{20}H_{22}N_4O_{10}$: C, 50.21; H, 4.64; N, 11.71. Found: C, 49.93; H, 4.59; N, 11.46.

Synthesis of Acid-Degradable Polyurethanes 17–21. Polymers **17**−**21** were synthesized according to the general procedure outlined below. Monomer **13** (1.962 mg, 4.68 mmol) was dissolved in dry CH_2Cl_2 (3 mL). Dry TEA (1 mL) was added to the solution. Compound **10** (759.8 mg, 4.68 mmol) dissolved in dry CH_2Cl_2 (3 mL) and dry TEA (1 mL) were mixed and the two solutions were combined and allowed to stir for 2 days while heated slightly. Over time the solutions became viscous indicating the formation of a polymer. The mixture was cooled to room temperature and the polymers were purified by dialysis against methanol containing 3% TEA using regenerated cellulose dialysis membranes with a nominal molecular weight cut off of 1500 Da.

Polymer 17. Yield: 50%. IR(cm^{-1}): 3334 (br), 1703 (s), 1536 (s), 1257 (s). ^1H NMR (400 MHz, DMSO-d_6): ∂ 1.23 (s, 6H), 3.06 (m, 4H), 3.34 (m, 4H), 3.51 (m, 8H), 4.02 (m, 4H), 7.16 (br, 2H). ^{13}C NMR (100 MHz, DMSO-d_6): ∂ 24.60, 40.55, 59.05, 63.07, 68.84, 69.65, 99.51, 156.19.

Polymer 18. Yield: 73%. IR(cm^{-1}): 3335 (br), 1707 (s), 1536 (s), 1257 (s), 1156 (s), 1057 (m). ^1H NMR (300 MHz, $CDCl_3$): ∂ 1.32 (s, 6H), 3.31 (m, 4H), 3.46 (t, 4H, $J = 5$), 3.68 (m, 8H), 5.34 (br, 2H). ^{13}C NMR (100 MHz, $CDCl_3$): ∂ 25.01, 41.30, 60.03, 64.08, 69.71, 100.40, 156.62.

Polymer 19. Yield: 65%. IR(cm^{-1}): 3328 (br), 1707 (s), 1532 (s), 1253 (s), 1154 (s), 1060 (m). ^1H NMR (400 MHz, $CDCl_3$): ∂ 1.34 (s, 6H), 1.93 (br, 2H), 3.31 (br, 4H), 3.46 (br, 4H), 4.13 (b, 4H), 5.51 (br, ~2H). ^{13}C NMR (100 MHz, $CDCl_3$): ∂ 24.7, 28.6, 59.7, 61.3, 100.1, 156.5.

Polymer 20. Yield: 70%. IR(cm^{-1}): 3344 (br), 1709 (s), 1532 (s), 1253 (s), 1156 (s), 1064 (m). ^1H NMR (400 MHz $CDCl_3$): ∂ 0.97 (br, 3H), 1.34 (s, 6H), 2.12 (br, 1H), 3.32 (br, 4H), 3.47 (br, 4H), 4.00 (br, 4H), 5.43 (br, ~2H). ^{13}C NMR (100 MHz, $CDCl_3$): ∂ 13.7, 24.8, 33.0, 41.7, 59.8, 66.2, 100.2, 156.6.

Polymer 21. Yield: 63%. IR(cm^{-1}): 3349 (br), 1704 (s), 1520 (s), 1261 (s), 1159 (s), 1067 (m). ^1H NMR (400 MHz, $CDCl_3$): ∂ 1.34 (s, 6H), 1.42 (s, 12H), 1.79 (s, 4H), 3.27 (br, 4H), 3.46 (br, 4H), 5.11 (br, ~2H). ^{13}C NMR (100 MHz, $CDCl_3$): ∂ 24.9, 26.4, 35.1, 40.7, 60.0, 80.9, 100.2, 155.8.

Synthesis of Acid-Degradable Polyureas 22–23. Compound **10** (0.102 g, 0.63 mmol) was dissolved in CH_2Cl_2 (5 mL). Triethylamine (9 μL, 0.06 mmol) and aqueous buffer (5 mL, 30 mM phosphate, pH 8) were added and the mixture was stirred rapidly to form an emulsion. A solution of freshly distilled diisocyanate **6** or **7** (105 μL, 0.65 mmol) in CH_2Cl_2 (5 mL) was then added in one portion to the stirred emulsion, and stirring was continued at RT for 16 h. The precipitated polymer was filtered, washed with CH_2Cl_2, and dried *in vacuo*. The polymers were obtained with yields of 80–90%.

Polymer 22. $^1H-^{13}C$ HMQC NMR was utilized to distinguish between NH and Ar−H residues. IR (cm^{-1}): 3331 (br), 2934, (s), 1644 (s), 1554 (s). ^1H NMR (400 MHz, DMSO-d_6): ∂ 1.30 (s, 6H), 1.9–2.2 (s, 3H), 3.21 (br, 4H), 3.41 (br, 4H), 6.03 (br, 1H), 6.5–6.7 (br, 1H), 6.85–7.0 (br, 1H), 7.10 (br, 1H), 7.64 (br, 1H), 7.69 (br, 1H), 8.44 (br, 1H). ^{13}C NMR (125 MHz,

DMSO-d_6): ∂ 17.24, 24.76, 24.79, 39.76, 39.92, 59.98, 99.63, 110.27, 111.65, 119.43, 129.95, 138.07, 138.46, 155.22, 155.34.

Polymer 23. Polymer **23** was sparingly soluble in typical laboratory solvents, which precluded ^{13}C NMR and SEC analyses. IR (cm^{-1}): 3335 (br), 2934 (s), 1624 (s), 1585 (s). ^{1}H NMR (500 MHz, DMSO-d_6): ∂ 1.1–1.4 (br, 14H), 2.9–3.2 (br, 8H), 3.3–3.4 (overlaps with water peak), 5.8–6.0 (br, 2H), 6.0–6.2 (br, 2H).

Synthesis of Acid-Degradable Polyurea 24. Compound **10** (0.108 g, 0.67 mmol) and triethylamine (186 μL, 1.33 mmol) were dissolved in CH_2Cl_2 (1.3 mL). To this solution was added solid **16** (0.318 g, 0.67 mmol) in one portion. After stirring overnight, the viscous yellow solution was added to an excess of 1:1 isopropanol/hexanes to yield the product as a pale yellow solid in 66% yield. IR (cm^{-1}): 3346 (br), 2869 (br), 1632 (s). ^{1}H NMR (400 MHz, DMSO-d_6): ∂ 1.25 (s, 6H), 3.15–3.2 (m, 8H), 3.25–3.4 (m, 8H), 3.50 (s, 4H), 5.98 (t, 2H, $J = 5$), 6.05 (t, 2H, $J = 5$). ^{13}C NMR (100 MHz, DMSO-d_6): ∂ 25.17, 39.65, 40.09, 60.42, 70.03, 70.61, 99.85, 158.53.

Production of BSA-Loaded Microparticles. Microparticles were made using a double emulsion water/oil/water (w/o/w) evaporation method similar to that described by Bilati et al. (*19*). Briefly, 5 mg of FITC - bovine serum albumin (FITC-BSA) was dissolved in phosphate buffered saline (PBS) (50 μL). In a separate container 200 mg of polymer was dissolved in 1 mL of dichloromethane and added to the FITC-BSA solution. The solution was then sonicated for fifteen seconds on ice at 30W with a Branson Sonifier 450 resulting in the formation of the primary emulsion. This emulsion was then added into a 2 mL 3% PVA/PBS pH 8.0 aqueous solution. The w/o/w solution was sonicated again for thirty seconds on ice at 30W to form a double emulsion. This emulsion was immediately poured into a 10 mL 0.3 wt % PBS/PVA solution and vigorously stirred magnetically for 4 h allowing the organic solvent to evaporate. After evaporation, the particles were washed five times using Spectrum Laboratories, Inc. (Rancho Dominguez, CA) tangential flow filters (TFF) with a surface area of 11 cm^2 and a pore size of 0.05 μm. To stabilize the suspensions of the particles, a 10 wt % solution of glucose in water was added as a cryoprotectant. The suspension of particles was then frozen and lyophilized.

The FITC-BSA encapsulation efficiency was determined by incubating the particles in pH 5 PBS for 3 days at 50 °C and quantifying the fluorescence of the released protein.

Microparticle Characterization and Degradation Study. Microparticles were characterized by scanning electron microscopy (SEM) using a Hitachi (Tokyo, Japan) S-5000 microscope. Size distribution of the particles was determined by dynamic light scattering (DLS) using a Malvern Instruments Nano ZS (Worcestershire, United Kingdom). After lyophilization, the particles were washed five times using TFF, and then 10 μL were dripped onto a silicon wafer. After drying 15 min the particles were sputter coated with platinum.

Degradation profiles of the particles were obtained at pH 7.4 and pH 5.0 by monitoring the production of acetone in the degrading samples via ^{1}H NMR as described previously (*17*). Briefly, 25 mg of the particle suspensions were placed in an NMR tube and 0.7 mL of the corresponding deuteriated PBS buffer was added. Tubes were sealed, incubated at 37 °C and analyzed by ^{1}H NMR at different time points. The release of acetone was measured as a ratio of the acetone peak integral to the integral of the internal standard peak (3-(trimethyl silyl) propionic-2,2,3,3,d_4 sodium salt). To obtain the total release of acetone 10 μL of concentrated deuteriated HCl was added to the NMR tube and the solutions incubated overnight.

Acid-Mediated Protein Release. To study acid-mediated protein release FITC-BSA loaded particles of polymer **19** were incubated in pH 5.0 and pH 7.4 buffer. Stock solutions of microparticles were maintained at 37 °C. Aliquots of 100 μL were taken at specific time points, centrifuged and the fluorescence of the supernatant solution was measured using Fluorolog, Instruments S.A., Inc. Measurements were taken until the fluorescence reached a maximum and further incubation did not result in a fluorescence increase. Reported fluorescence data were normalized to the maximum fluorescence values.

Microparticle Uptake by Macrophages. RAW 309 cells were obtained from ATCC (Manassas, VA) and grown according to ATCC directions. Microparticle uptake was investigated by fluorescently activated cell sorting (FACS) analysis with a four color Becton Dickinson (Franklin Lakes, NJ) FACS Calibur. Particles with encapsulated FITC-BSA were incubated with 200 000 cells/mL for up to 24 h. Particle uptake was measured by the mean fluorescent intensity (MFI). For each experiment, data was normalized with respect to the 24 h particle uptake. Free protein was used as a control. Macrophages incubated with particles for 6 and 24 h were imaged using laser confocal micrscopy. Cells were seeded onto a Laboratory Tek plastic slide in a 4-well cell culture plate at initial seeding density of 10 000 cells per well. After incubation, cells were washed 3 times with PBS buffer and fixed with 4% paraformaldehyde and their cytoskeleton was stained with Alexa Fluor 546 conjugated phalloidin. Vectashield mounting medium was added and the slides were sealed with Cytoseal-60. The prepared samples were then imaged on a LSM510 Meta laser confocal microscope (Carl Zeiss MicroImaging, Inc.).

Particle Cytotoxicity Studies. Particles were incubated with 10 000 RAW macrophages for 24 h. After 24 h particles were washed away with medium and cells were incubated in medium overnight. Cell viability was measured the following day with Promega's (Madison, Wisconsin) CellTiter 96AQ_{ueous}One Solution Cell Proliferation Assay MTS per the manufacturer's instructions. Cell viability was normalized to cells that were cultured without particles.

Degradation Byproducts. In order to show full degradation of the bulk polymer, the three different polymers were incubated with a 95% CD_3OD and 5% concentrated DCl in D_2O overnight. SEC was run on the different degraded polymers (Supporting Information, Figure 1) and their traces were compared to those of nondegraded polymer **19**. After incubating under the acidic conditions the polymers fully degraded into small molecules. In addition, a similar experiment was performed using deuteriated PBS buffer (pH 5.0) in order to assess the degradation of microparticles made of polymer **19** and **20**.

Degradation Byproducts Cytotoxicity. Polymer **19** was incubated in pH 5 buffer at 37 °C for three days. The resultant degraded material was then lyophilized and the toxicity of the degraded material was tested as described above for the particles.

Degradation Product of Polymer 19 (5% HCl in methanol). ^{1}H NMR (400 MHz, CD_3OD): ∂ 1.98 (t, 2H, $J = 4$ Hz), 3.25 (t, 4H, $J = 4$ Hz), 3.63 (t, 4H, $J = 4$ Hz), 4.14 (t, 4H, $J = 4$ Hz). ^{13}C NMR (100 MHz, CD_3OD): ∂ 28.4, 42.6, 60.5, 61.7, 157.9. Calcd: $[M + H]^+$ ($C_9H_{18}N_2O_6$) $m/z = 251$. Found LRMS: $[M + H]^+ = 251$.

Degradation Product of Polymer 19 (deuteriated PBS, pH 5.0). ^{1}H NMR (400 MHz, D_2O): ∂ 1.98 (t, 2H, $J = 4$ Hz), 3.21 (t, 4H, $J = 6$ Hz), 3.58 (t, 4H, $J = 6$ Hz), 4.10 (m, 4H). Calcd: $[M + H]^+$ ($C_9H_{18}N_2O_6$) $m/z = 251$. Found LRMS: $[M + H]^+ = 251$.

Degradation Product of Polymer 20 (5% HCl in methanol). ^{1}H NMR (400 MHz, CD_3OD): ∂ 0.97 (d, 3H, $J = 8$ Hz), 2.11 (m, 1H), 3.21 (t, 4H, $J = 4$ Hz), 3.57 (t, 4H, $J = 4$ Hz), 3.98 (d, 4H, $J = 8$ Hz). ^{13}C NMR (100 MHz, CD_3OD): ∂ 12.6, 33.1, 42.8, 60.5, 66.01, 157.8. Calcd: $[M + H]^+$ ($C_{10}H_{20}N_2O_6$) $m/z = 265$. Found LRMS: $[M + H]^+ = 265$.

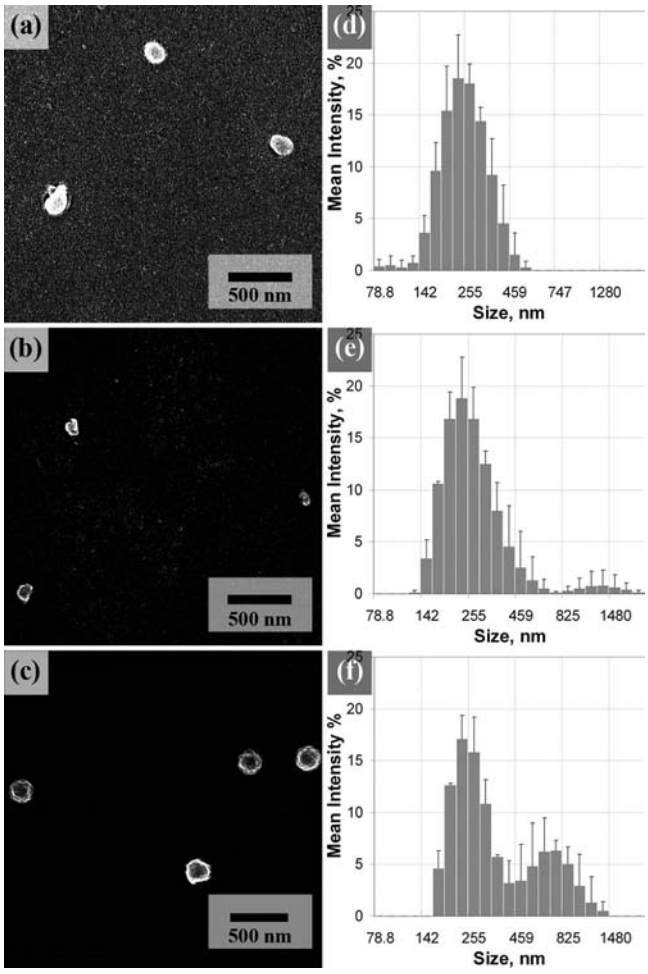

Figure 2. (a−c) SEM images of particles made from polymers **19**, **20**, and **21**; (d−f) particle size distribution as measured by dynamic light scattering (DLS). The particles obtained are individual particles several hundred nanometers in size, suitable for uptake by phagocytic cells.

Degradation Product of Polymer 20 (deuteriated PBS, pH 5.0). ^{1}H NMR (400 MHz, D_2O): ∂ 0.96 (d, 3H, $J = 7$ Hz), 2.18 (m, 1H), 3.25 (t, 4H, $J = 5$ Hz), 3.62 (t, 4H, $J = 5$ Hz), 4.03 (d, 4H, $J = 7$ Hz). Calcd: $[M + H]^+$ ($C_{10}H_{20}N_2O_6$) $m/z = 265$. Found LRMS: $[M + H]^+ = 265$.

Degradation Product of Polymer 21 (5% HCl in methanol). Spectroscopic characterization revealed a mixture of small molecule degradation products with the highest molecular mass of 339 as observed by mass spectrometric analysis.

RESULTS AND DISCUSSION

Design and Synthesis of Acid-Degradable Polymers. *Monomer Synthesis.* In order to prepare a library of acid-degradable polymers, several functional monomers were first synthesized. The key acid-degradable component was dimethyl ketal monomer **10**, which contains two amino groups for reaction with bis-electrophilic species. A similar dimethyl ketal we developed previously had a hydrolysis half-life of 6.8 h at pH 7.4, but its degradation half-life was only 1.5 min at pH 5.0, demonstrating its pH-dependent degradation kinetics (*20*).

Acid-degradable diamine **10** was synthesized in two steps (Figure 1b) following a modified literature procedure (*21*). Protected diamine **9** was prepared first by reacting N-(2-hydroxyethyl)-phthalimide with 2-methoxypropene. After 1 h of stirring at 0 °C the methanol byproduct was removed from the system by azeotropic distillation with benzene to shift the equilibrium toward product formation. Compound **9** was then deprotected under strongly basic conditions to afford acid-degradable monomer **10** in high yield.

Table 1. SEC data of Polymers 17−24[a]

	GPC			microparticle	protein loading,
polymer	M_n, kDa	M_w, kDa	PDI	size, nm	wt %
17	22	33	1.8	n/a	n/a
18	20	28	1.4	n/a	n/a
19	15	22	1.6	237±3	1.5
20	33	41	1.3	241±2	1.3
21	11	18	1.7	295±1	1.6
22	42	84	2.0	n/a	n/a
23		not soluble		n/a	n/a
24	17	40	2.4	n/a	n/a

[a] Average microparticle size is given as measured by dynamic light scattering.

Polyurethane synthesis required the activation of diols **1**−**5** using *p*-nitrophenyl chloroformate (Figure 1b) which afforded monomers **11**−**15** in good yields. Polyureas **22**, **23**, and **24** were synthesized using monomer **10** and either commercially available diisocyanates **6** and **7** or diisiocyanate derivative **16**, which was synthesized in one step as shown in Figure 1b.

Synthesis of Acid-Degradable Polymers. Five different polyurethanes **17**−**21** and one polyurea **24** were synthesized via the step-growth polymerization of acid-degradable monomer **10** and one of the six monomers **11**−**16** (Figure 1c). To prevent any deleterious acid-catalyzed hydrolysis, triethylamine was added to the polymerization reaction mixtures as well as to the methanol solution used during dialysis of the polymers (polymer **24** was isolated by precipitation from hexanes/isopropanol). To increase the molecular weight and yields of the polymers, the reaction mixtures were kept at elevated temperature, which increases the solubility of monomers and reduces the viscosity of the solution of growing polymer chains. Polyurethanes **22** and **23** were formed by interfacial polymerization of acid-degradable diamine **10** and monomers **6** and **7**, similar to a procedure reported elsewhere (*22*). The solution of diamine **10** at pH 8 was added to a rapidly stirred solution of the diisocyanate monomer **6** or **7** in dichloromethane which resulted in the precipitation of the polymers. The molecular weights and polydispersity index values (PDIs) shown in Table 1 are typical of polymers synthesized through such step-growth polymerizations (*23*).

Polymers **17**−**24** were designed with a flexible strategy whereby the key property of acid lability was provided by monomer **10** while the second monomer was tailored to control the hydrophobicity of the final polymer and hence its ability to be used in our water/oil/water double emulsion process to afford usable microparticles. Hydrophobicity is a key parameter that affects the solubility of the polymer in water, its degradation kinetics, and its ability to form stable microparticles. While more hydrophobic polymers require longer times to degrade (*24*), more hydrophilic ones may fail to form stable microparticles in aqueous solutions. Some of the polymers we prepared contained hydrophilic ethylene oxide units (**17**, **18**, **24**) whereas others contained hydrophobic aliphatic and aromatic chains of various lengths (**19**−**23**). The prepared polymers were designed to have different hydrophobicities and their ability to form acid-degradable microparticles was evaluated.

Polyureas **22**−**24** were found to be difficult to dissolve in water and were not easily dissolved in organic solvents. Unlike polyureas, polyurethanes **17**−**21** were easily dissolved in polar organic solvents such as DMSO and dichloromethane. Hydrophobic polyurethanes **19**−**21** were not soluble in water whereas more hydrophilic polymers **17** and **18** were slightly soluble. The difference in the solubility between polyurethanes and polyureas likely results from the stronger tendency of polyureas to associate via formation of interchain hydrogen bonds reducing

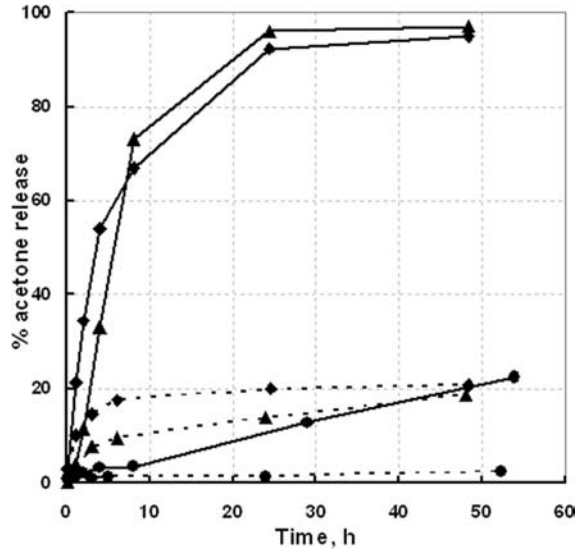

Figure 3. Degradation profiles of microparticles composed of polymers **19** (diamonds), **20** (triangles), and **21** (circles) as measured by release of acetone. Solid lines for degradation profiles at pH 5.0 and dotted lines for pH 7.4. Polymer **19** demonstrates the fastest degradation at pH 5. Polymer **21** shows the slowest degradation rate at the same pH due to its high hydrophobicity.

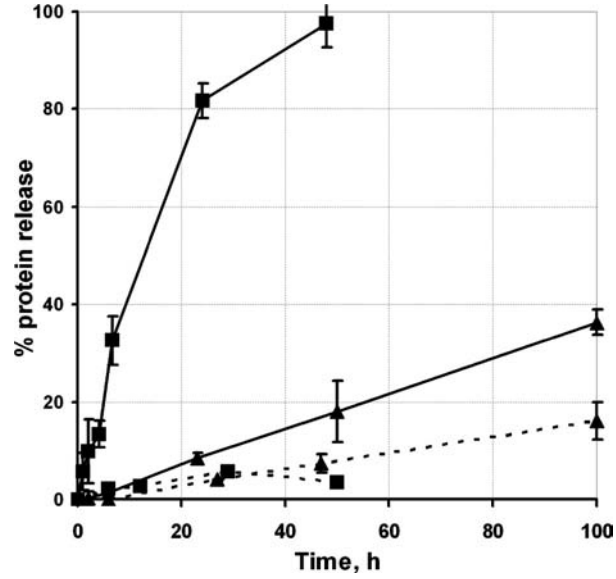

Figure 4. Acid mediated release of FITC-BSA from protein loaded microparticles of polymer **19** (squares) and**21** (triangles) at pH 5.0 (solid) and pH 7.4 (dashed). Release occurs much faster at acidic pH and the measured half-life is in good agreement with the half-life of polymer shell degradation measured in the acetone release experiment of Figure 3. Polymer **19** microparticles release the protein significantly faster than the polymer **21** microparticles.

the interactions of the polymer chains with water molecules. The solubility of the polymers in different solvents greatly affects their ability to form microparticles. For example the formation of microparticles from polyureas **22**−**24** proved to be very challenging due to their low solubility in dichloromethane. In contrast, polyurethanes **19**−**21** could be used to form stable microparticles while hydrophilic polyurethanes **17** and **18** produced unstable emulsions, most likely due to their excessive solubility in water.

Based on the ability to form microparticles, polyurethanes **19–21** were selected for further in depth studies, which included microparticle characterization by SEM and DLS, study of their pH sensitive degradation kinetics as well as model drug delivery studies *in vitro*.

Microparticle Preparation and Characterization. Microparticles were prepared using a double emulsion technique (*19*). A primary emulsion was formed by sonication of a solution of polyurethanes **19**−**21** in dichloromethane with an aqueous phase that contained FITC labeled bovine serum albumin (FITC-BSA). This emulsion was introduced into a second aqueous phase containing polyvinyl alcohol as an emulsion stabilizer. After rapidly stirring the emulsion for four hours the microparticles were isolated using tangential flow filtration (TFF) (*25*). Microparticles required the addition of a cryoprotectant to reduce their aggregation upon lyophilization and storage. It has been shown previously, that lyophilization can result in particle aggregation and that the addition of carbohydrates such as glucose, sucrose, or trehalose can help prevent this aggregation (*26*). Screening of several cryoprotectants showed that glucose was the most effective cryoprotectant to prevent aggregation of our microparticles prior to lyophilization. Particle yields after lyophilization ranged from 77 to 82% based on the polymer used, while protein loading efficiency ranged from 48 to 68% based on the starting mass of protein.

The microparticles were characterized by SEM and DLS (Figure 2a−f). In order to obtain satisfactory SEM images, microparticles were purified by removal of the cryoprotectant using TFF prior to sample preparation and were deposited onto silicon wafers at very dilute concentrations. According to SEM and DLS data, the prepared microparticles had average sizes of 230–300 nm (Figure 2, Table 1), which is a size range suitable for their uptake by phagocytic cells and for the passive targeting of macrophages and dendritic cells for *in vitro* and *in vivo* applications (*27–29*).

Acid-Mediated Microparticle Degradation. Microparticle degradation was studied at physiological pH (7.4) as well as lysosomal pH (5.0) (Figure 3). The degradation of the microparticles was monitored by ^{1}H NMR. Specifically, the appearance of acetone, the byproduct of acetal degradation, was measured over several days. All of the particles we synthesized degraded faster at pH 5.0 than at pH 7.4 while the degradation half-life of microparticles at pH 5.0 was highly dependent on the hydrophobicity of the starting polyurethane. Microparticles made from polyurethane **19**, the least hydrophobic polymer, had a degradation half-life of 3.4 h at pH 5.0 whereas microparticles made from polyurethane **20**, with an intermediate hydrophobicity, had a half-life of 5.9 h. Microparticles prepared with the most hydrophobic polyurethane **21** had the slowest rate of degradation with a half-life of more than 80 h under the conditions used for the measurement. Such a dependence of rate of degradation on the hydrophobicity of the polymer is no doubt related to the accessibility of the microparticle surface to hydronium ions. More hydrophobic surfaces are less accessible to hydronium ions and require longer times to fully degrade.

The varying degradation profiles of the prepared microparticles could be advantageous for a variety of applications in drug delivery that require different time frames for the release of a therapeutic agent. Moreover, using similar chemistry, a more extensive library of polyacetal polymers could be generated wherein the half-life of the polymer would be tuned by simply adjusting the hydrophobicity of the diol monomer or the acetal-containing monomer used in the polymerization.

As microparticles prepared from polyurethane **19** had the shortest degradation half-life, they were also characterized in terms of acid-mediated protein release with monitoring by fluorescence at both the physiological pH of 7.4 and at the lysosomal pH of 5.0 (Figure 4). As anticipated, protein release occurred much faster at acidic pH with more than 90% of the protein released after 40 h. The kinetics of protein release was similar to the kinetics of particle degradation with half-lives on

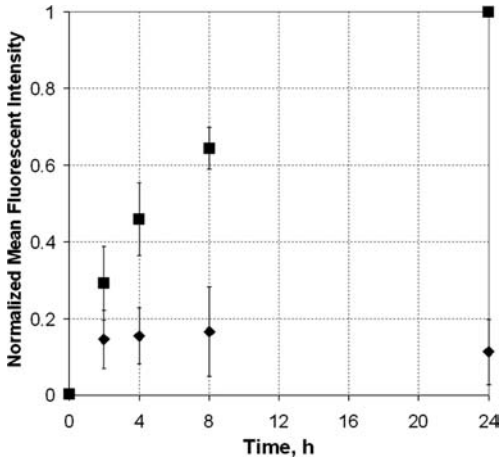

Figure 5. Normalized mean fluorescence intensity of macrophages incubated with FITC-BSA (solid diamonds) and FITC-BSA loaded microparticles (solid squares) at various time points as measured by flow cytometry. Incubation of cells with protein loaded microparticles results in a 10-fold increase in protein uptake after 24 h compared to free FITC-BSA.

the order of several hours (Figure 3). In contrast, microparticles prepared from polymer **21**, the slowest degrading polymer released the protein at a much slower rate than particles made from polymer **19** (Figure 4). Release of the protein from these microparticles occurred in an expected pH dependent manner with significantly faster release taking place at acidic pH (5.0). Due to their suitable polymer degradation profile and fast protein release kinetics polyurethane **19** microparticles were selected for use in subsequent *in vitro* experiments.

Microparticle Uptake by Macrophages. To show microparticle uptake in phagocytic cells, a murine macrophage cell line, RAW 309, was incubated with FITC-BSA containing microparticles for different time periods. Incubation with free FITC-BSA was used as a control experiment. Uptake of the protein was quantitatively measured by flow cytometry. The mean fluorescent intensity (MFI) of cells incubated for 2, 4, 8, and 24 h with microparticles is shown in Figure 5. In each experiment, the data was normalized to the fluorescence of the cell population that was incubated with microparticles for 24 h. Experimental data at each time point show that the macrophages took up statistically more FITC-BSA encapsulated in microparticles compared to free FITC-BSA only. After 24 h the microparticles encapsulating FITC-BSA showed a 10-fold higher uptake compared to the free protein control. These data are consistent with the findings of Solbrig et al. (*30*), who used double emulsion particles to increase the uptake of protein in bone marrow derived dendritic cells. More efficient uptake of the acid-degradable microparticles by phagocytic cells may lead to enhanced delivery of antigens to antigen presenting cells, such as macrophages or dendritic cells.

Uptake of the microparticles was also visualized directly by laser confocal microscopy. Macrophages were incubated with BSA loaded particles for 6 and 24 h. After the incubation period, cells were thoroughly washed with PBS buffer and their cytoskeleton was stained with Alexa Fluor 546 conjugated phalloidin. Figure 6 shows confocal microscopy images of macrophages incubated for 6 h (a−c) and 24 h (d−f). After 24 h the fluorescence in (d) appears more diffuse than observed in (a) and we speculate that this is related to the breakdown of the acid-degradable microparticles.

To study the toxicity of the particles, macrophages were incubated with varying concentrations of microparticles for 24 h. As seen in Figure 7, cell viability does not change significantly over the range of concentrations studied. Even at the highest concentration of microparticles we tested (1 mg/mL), the viability of the macrophages is similar to the untreated cells. Overall the toxicity of the microparticles appears to be comparable to that of the widely used poly(lactic-*co*-glycolic acid) (PLGA) (*32*). The negligible cytotoxicity of the particles is a favorable element when considering their further use in studies conducted both *in vitro* and *in vivo*.

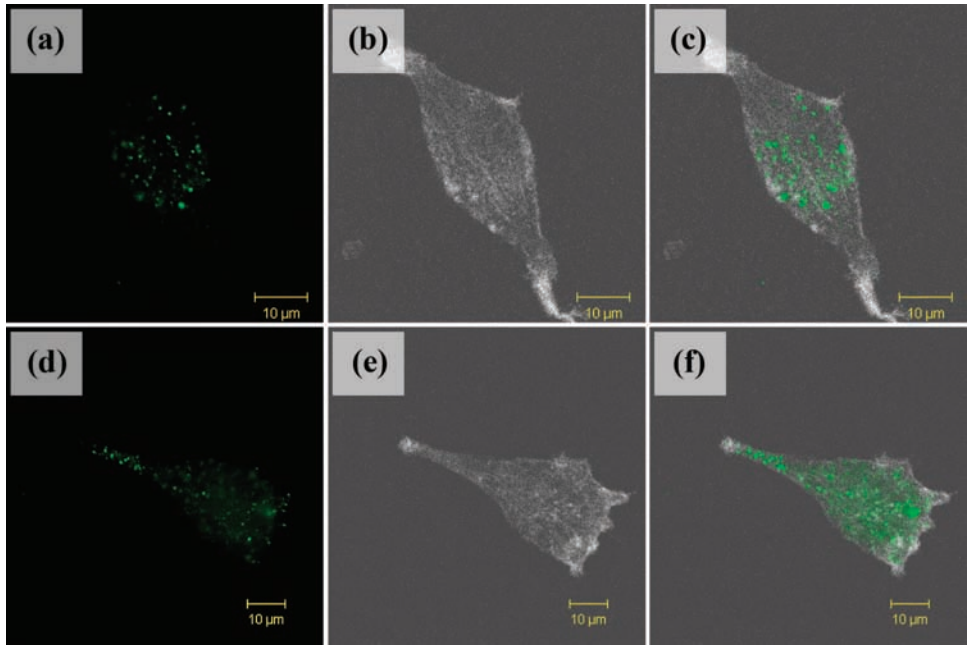

Figure 6. (a−c) Confocal microscopy image of a macrophage incubated with particles containing FITC-BSA for 6 h. (a) FITC-BSA; (b) F-Actin stained with Alexa Fluoro 546 conjugated phalloidin; (c) combined image of (a) and (b). (d−f) Confocal microscopy image of a macrophage incubated with particles containing FITC-BSA for 24 h. (d) FITC-BSA; (e) F-Actin stained with Alexa Fluoro 546 conjugated phalloidin; (f) combined image of (d) and (e). Fluorescence images (a) and (d) clearly demonstrate the uptake of the particles by microphages. FITC-induced fluorescence (d) appears to be more diffuse after 24 h likely due to the degradation of the particles in the lysosomes with concomitant release of FITC-BSA into the cytoplasm.

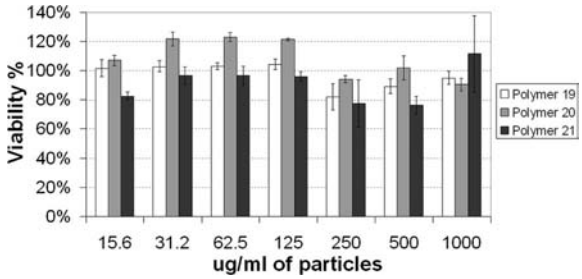

Figure 7. Toxicity of particles measured by incubation with macrophages for 24 h. The viability of cells incubated with particles was normalized to cells cultured without particles.

Degradation Products. As a preliminary step in the evaluation of the potential cytotoxicity of the newly synthesized polymers we explored whether or not large polymer fragments remain after degradation, as was the case with some of the earlier systems we have studied (*31*). Thus, the three polyurethanes **19**−**21** were degraded in the presence of deuteriated HCl and their degradation products were studied by NMR and mass spectrometry. In all cases the degradation products were low molecular weight products as expected from the acid catalyzed hydrolysis of the acetal moieties in the polymer backbone (Figure 1e). NMR spectra of the degradation products as well as mass spectrometry data and size exclusion chromatography (SEC) traces (Supporting Information, Figure 1) did not reveal the presence of residual high molecular weight polymers, which was supportive of complete degradation. Similar degradation experiments were performed for the faster degrading polymers **19** and **20** in deuteriated pH 5.0 PBS buffer to elucidate whether high molecular weight polymer fragments remained after the degradation in biologically relevant environments. NMR and mass-spectrometry data of the degradation products corresponded to expected low molecular weight byproduct confirming full degradation in the mildly acidic conditions. The absence of residual high molecular weight compounds should enable the fast elimination of byproduct from the body. In addition, we have found that the fully degraded byproducts of polymer **19** had no toxic effects on macrophages grown in culture (Supporting Information, Figure 2). These findings in which no significant toxicity is found for either the FITC-BSA loaded microparticles themselves (Figure 7) or their degradation products is encouraging as we prepare for testing of their use in formulated immunotherapeutic agents.

CONCLUSIONS

We have designed and synthesized a new class of fully acid-degradable polymers that degrade quickly in the mildly acidic environments similar to those found in endosomes and tumor tissues, but are more stable at the physiological pH of 7.4. The ease of preparation and the ability to tune polymer characteristics such as solubility and acid-sensitivity, identify this new class of polymers as promising materials for drug delivery. By screening a library of synthesized acid-degradable polymers we identified several polymers that possessed the necessary physical characteristics to form acid-degradable microparticles that can be dried to stable and redispersible powders when used with glucose as a cryoprotectant. A study of the hydrolysis of selected microparticles indicated that their degradation was complete leaving behind no high molecular weight byproduct. The particles were taken up by macrophages *in vitro* as confirmed by flow cytometry and confocal microscopy and facilitated a 10-fold increase in protein uptake compared to protein alone. The microparticles themselves were not toxic in the range of concentrations studied. In general, these acid-sensitive fully degradable polymers and corresponding microparticles may find use in the delivery of various therapeutic agent or vaccines (*11*, *33*), which makes them attractive targets for a number of medicinal targets.

ACKNOWLEDGMENT

We thank the National Institutes of Health (Grant RO1 EB005824) and the NIH Program of Excellence in Nanotechnology (1 U01 HL080729-01) for support of this fundamental work in the development of multipurpose therapeutic carriers.

Supporting Information Available: Additional data on cytotoxicity and cryoprotectants. This material is available free of charge via the Internet at http://pubs.acs.org.

LITERATURE CITED

(1) Gillies, E. R., Jonsson, T. B., and Fréchet, J. M. J. (2004) Stimuli-responsive supramolecular assemblies of linear-dendritic copolymers. *J. Am. Chem. Soc. 126*, 11936–11943.

(2) Lee, S., Yang, S. C., Heffernan, M. J., Taylor, W. R., and Murthy, N. (2007) Polyketal microparticles: a new delivery vehicle for superoxide dismutase. *Bioconjugate Chem. 18*, 4–7.

(3) Murthy, N., Thng, Y. X., Schuck, S., Xu, M. C., and Fréchet, J. M. J. (2002) A novel strategy for encapsulation and release of proteins: hydrogels and microgels with acid-labile acetal crosslinkers. *J. Am. Chem. Soc. 124*, 12398–12399.

(4) Lynn, D. M., Amiji, M., and Langer, R. (2001) pH-Responsive polymer microspheres: rapid release of encapsulated material within the range of intracellular pH. *Angew. Chem., Int. Ed. 40*, 1707–1710.

(5) Haining, W. N., Anderson, D. G., Little, S. R., von Berwelt-Baildon, M. S., Cardoso, A. A., Alves, P., Kosmatopoulos, K., Nadler, L. M., Langer, R., and Kohane, D. S. (2004) pH-triggered microparticles for peptide vaccination. *J. Immunol. 173*, 2578–2585.

(6) Huang, Z., Guo, X., Li, W., MacKay, A., and Szoka, J., F. C. (2006) Acid-triggered transformation of diortho ester phosphocholine liposome. *J. Am. Chem. Soc. 128*, 60–61.

(7) Roux, E., Francis, M., Winnik, F. M., and Leroux, J. (2002) Polymer based pH-sensitive carriers as a means to improve the cytoplasmic delivery of drugs. *Int. J. Pharm. 242*, 25–36.

(8) Couffin-Hoarau, A., and Leroux, J. (2004) Report on the use of poly(organophosphazenes) for the design of stimuli-responsive vesicles. *Biomacromolecules 5*, 2082–2087.

(9) Ulbrich, K., and Subr, V. (2004) Polymeric anticancer drugs with pH-controlled activation. *Adv. Drug. Delivery. Rev. 56*, 1023–1050.

(10) Hudecz, F., Clegg, J. A., Kajtar, J., Embleton, M. J., Szekerke, M., and Baldwin, R. W. (1992) Synthesis, conformation, biodistribution, and in vitro cytotoxicity of daunomycin-branched polypeptide conjugates. *Bioconjugate Chem. 3*, 49–57.

(11) Standley, S. M., Kwon, Y. J., Murthy, N., Kunisawa, J., Shastri, N., Guillaudeu, S. J., Lau, L., and Fréchet, J. M. J. (2004) Acid-degradable particles for protein-based vaccines: enhanced survival rate for tumor-challenged mice using ovalbumin model. *Bioconjugate Chem. 15*, 1281–1288.

(12) Shenoy, D., Fu, W., Li, J., Crasto, C., Jones, G., Dimarzio, C., Sridhar, S., and Amiji, M. (2006) Surface functionalization of gold nanoparticles using hetero-bifunctional poly(ethylene glycol) spacer for intracellular tracking and delivery. *Int. J. Nanomedicine 1*, 51–58.

(13) Shenoy, D., Little, S., Langer, R., and Amiji, M. (2005) Poly(ethylene oxide)-modified poly(beta-amino ester) nanoparticles as a pH-sensitive system for tumor-targeted delivery of hydrophobic drugs. 1. In vitro evaluations. *Mol. Pharm. 2*, 357–366.

(14) Shenoy, D., Little, S., Langer, R., and Amiji, M. (2005) Poly(ethylene oxide)-modified poly(beta-amino ester) nanopar-

ticles as a pH-sensitive system for tumor-targeted delivery of hydrophobic drugs: part 2. In vivo distribution and tumor localization studies. *Pharm. Res. 22*, 2107–2114.

(15) Heffernan, M. J., and Murthy, N. (2005) Polyketal nanoparticles: a new pH-sensitive biodegradable drug delivery vehicle. *Bioconjugate Chem. 16*, 1340–1342.

(16) Tomlinson, R., Klee, M., Garrett, S., Heller, J., Duncan, R., and Brocchini, S. (2002) Pendent chain functionalized polyacetals that display pH-dependent degradation: A platform for the development of novel polymer therapeutics. *Macromolecules 35*, 473–480.

(17) Jain, R., Standley, S. M., and Fréchet, J. M. J. (2007) Synthesis and degradation of pH-sensitive linear poly(amidoamine)s. *Macromolecules 40*, 452–457.

(18) Yeager, A. R., and Finney, N. S. (2004) The first direct evaluation of the two-active site mechanism for chitin synthase. *J. Org. Chem. 69*, 613–618.

(19) Bilati, U., Allemann, E., and Doelker, E. (2003) Sonication parameters for the preparation of biodegradable nanocapsules of controlled size by the double emulsion method. *Pharm. Dev. Technol. 8*, 1–9.

(20) Kwon, Y. J., Standley, S. M., Goodwin, A. P., Gillies, E. R., and Fréchet, J. M. J. (2005) Directed antigen presentation using polymeric microparticulate carriers degradable at lysosomal pH for controlled immune responses. *Mol. Pharm. 2*, 83–91.

(21) Sheppard, R. C., Goddard, P. (1993) Preparation and immunochemical use of polymers and polymer-peptide conjugates with cleavable crosslinkers. U.S. Patent 5,191,015.

(22) Nuyken, O., Stebani, J., and Lang, A. (1995) Synthesis and characterization of photopolymers with azo units. Interfacial polyaddition, photolysis, photodegradation. *Angew. Makromol. Chem. 226*, 143–160.

(23) Odian, G. G. (2004) *Step Polymerization. Principles of polymerization*, 4th ed., p 39, John Wiley & Sons, Inc., Hoboken.

(24) Khaja, S. D., Lee, S., and Murthy, N. (2007) Acid-degradable protein delivery vehicles based on metathesis chemistry. *Biomacromolecules 8*, 1391–1395.

(25) Dalwadi, G., Benson, H. A., and Chen, Y. (2005) Comparison of diafiltration and tangential flow filtration for purification of nanoparticle suspensions. *Pharm. Res. 22*, 2152–2162.

(26) Bozdag, S., Dillen, K., Vandervoort, J., and Ludwig, A. (2005) The effect of freeze-drying with different cryoprotectants and gamma-irradiation sterilization on the characteristics of ciprofloxacin HCl-loaded poly(D,L-lactide-glycolide) nanoparticles. *J. Pharm. Pharmacol. 57*, 699–707.

(27) Foged, C., Brodin, B., Frokjaer, S., and Sundblad, A. (2005) Particle size and surface charge affect particle uptake by human dendritic cells in an in vitro model. *Int. J. Pharm. 298*, 315–322.

(28) Hirota, K., Hasegawa, T., Hinata, H., Ito, F., Inagawa, H., Kochi, C., Soma, G., Makino, K., and Terada, H. (2007) Optimum conditions for efficient phagocytosis of rifampicin-loaded PLGA microspheres by alveolar macrophages. *J. Controlled Release 119*, 69–76.

(29) Xiang, S. D., Scholzen, A., Minigo, G., David, C., Apostolopoulos, V., Mottram, P. L., and Plebanski, M. (2006) Pathogen recognition and development of particulate vaccines: does size matter? *Methods 40*, 1–9.

(30) Solbrig, C. M., Saucier-Sawyer, J. K., Cody, V., Saltzman, W. M., and Hanlon, D. J. (2007) Polymer nanoparticles for immunotherapy from encapsulated tumor-associated antigens and whole tumor cells. *Mol. Pharm. 4*, 47–57.

(31) Murthy, N., Xu, M., Schuck, S., Kunisawa, J., Shastri, N., and Fréchet, J. M. J. (2003) A macromolecular delivery vehicle for protein-based vaccines: acid-degradable protein-loaded microgels. *Proc. Natl. Acad. Sci. U.S.A. 100*, 4995–5000.

(32) Little, S. R., Lynn, D. M., Puram, S. V., and Langer, R. (2005) Formulation and characterization of poly (beta amino ester) microparticles for genetic vaccine delivery. *J. Controlled Release 107*, 449–462.

(33) Goh, S. L., Murthy, N., Xu, M., and Fréchet, J. M. J. (2004) Crosslinked microparticles as carriers for the delivery of plasmid DNA for vaccine development. *Bioconjugate Chem. 15*, 467–474.

BC7004472

Application of an HIV gp41-Derived Peptide for Enhanced Intracellular Trafficking of Synthetic Gene and siRNA Delivery Vehicles

Ester J. Kwon, Jamie M. Bergen, and Suzie H. Pun*

Department of Bioengineering, University of Washington, 1705 NE Pacific Street, Seattle, Washington 98195. Received December 5, 2007; Revised Manuscript Received January 25, 2008

Endosomal release is an efficiency-limiting step for many nonviral gene delivery vehicles. In this work, nonviral gene delivery vehicles were modified with a membrane-lytic peptide taken from the endodomain of HIV gp41. Peptide was covalently linked to polyethylenimine (PEI) and the peptide-modified polymer was complexed with DNA. The resulting nanoparticles were shown to have similar physicochemical properties as complexes formed with unmodified PEI. The gp41-derived peptide demonstrated significant lytic activity both as free peptide and when conjugated to PEI. Significant increases in transgene expression were achieved in HeLa cells when compared to unmodified polyplexes at low polymer to DNA ratios. Additionally, peptide-modified polyplexes mediated significantly enhanced siRNA delivery compared to unmodified polyplexes. Despite increases in transgene expression and siRNA knockdown, there was no increase in internalization or binding of modified carriers as determined by flow cytometry. The hypothesis that the gp41-derived peptide increases the endosomal escape of vehicles is supported by confocal microscopy imaging of DNA distributions in transfected cells. This work demonstrates the use of a lytic peptide for improved trafficking of nonviral gene delivery vehicles.

INTRODUCTION

The development of safe and efficient gene delivery vehicles is necessary for clinical gene therapy. Synthetic vehicles offer potential advantages over viral-based vectors including safety and low immunogenicity, but transfection efficiencies from many of these systems remain suboptimal (*1, 2*). An effective nucleic acid delivery vehicle must mediate either cytoplasmic or nuclear delivery, depending on its therapeutic agent. Upon internalization, the majority of carriers accumulate within endocytic vesicles (*3*). Efficient release from these vehicles before lysosomal degradation has been shown to be a major barrier for many of these systems. Thus, it would be advantageous to develop methods to improve the endosomal release of new and existing vectors for future applications of nonviral gene delivery.

Polyethylenimine (PEI) has been used widely as a nonviral vector and is among the most efficient of cationic polymer delivery vehicles (*4*). The efficacies of PEI and other protonatable cationic polymers as gene delivery agents has been attributed to their buffering properties, which have been hypothesized to mediate endosomal escape via the proton sponge mechanism (*5, 6*). In brief, pH-sensitive polymers buffer endosomes during the natural acidification process, resulting in counterion and water accumulation in the vesicles, eventually leading to osmolysis. However, the buffering capacity of PEI is correlated to the amount of PEI that is present (*6, 7*). Purification of free PEI from polyplexes after formulation results in polyplexes with only a slight charge excess of PEI. These polyplexes are much less efficient at mediating gene transfer than unpurified polyplexes (*8, 9*). This has implications for *in vivo* delivery where unassociated polymer can be separated from DNA before endocytosis occurs. The development of agents that have more potent endosomal escape properties is therefore desirable.

* To whom correspondence should be addressed. Phone: (206) 685−3488. Fax: (206) 616−3928. E-mail: spun@u.washington.edu.

In an effort to develop more potent mediators of endosomal escape, research has looked to nature for inspiration. Peptides taken from the membrane-disrupting domains of proteins, such as melittin (*10*−*12*), Tat (*13*−*15*), and hemagglutinin (*16, 17*), have been incorporated into nonviral gene delivery vectors, as reviewed elsewhere (*18, 19*). In this paper, we report the application of a peptide from the endodomain of HIV gp41 envelope glycoprotein found to have lytic properties from a peptide screen recently reported in the literature (*20*). This sequence of HIV gp41, corresponding to residues 783−806 of gp160, has been shown to have high membrane association and the potential to form multimers (*21*). Peptides from this region of gp41 have been shown to adopt amphipathic α-helical structures and have the potential to form pores in membranes (*22, 23*). The goal of this work was to evaluate the lytic peptide from the endodomain of HIV gp41, HGP, as a mediator of enhanced intracellular trafficking of nonviral gene delivery vehicles. Our results demonstrate that modification of PEI with HGP increases transgene expression and siRNA knockdown, likely by increasing the efficiency of endosomal release.

METHODS

Synthesis of HGP-Modified PEI. C-terminal cysteine-terminated HGP peptide (LLGRRGWEVLKYWWNLLQY-WSQELC) was synthesized and HPLC purified by GenScript Corporation (Piscataway, NJ). Branched PEI with molecular weight 25 000 (Sigma, St. Louis, MO) was modified with succinimidyl 4-[*p*-maleimidophenyl]butyrate (SMPB) purchased from Pierce (Rockford, IL) at a molar excess of 5 according to manufacturer's protocol. SMPB-modified PEI was purified using a PD-10 column (GE Healthcare, Piscataway, NJ) and lyophilized. For peptide conjugation, SMPB-modified PEI was dissolved in DMF and reacted with 5 equiv HGP peptide in the presence of triethylamine (TEA) for 72 h. Unreacted peptide and TEA were removed by dialysis against a MWCO 10 000 membrane (Pierce) with water over 3 days. PEI concentration was determined by monitoring cuprammonium complexes formed by PEI and copper (II) acetate at 630 nm as described

10.1021/bc700448h CCC: $40.75 © 2008 American Chemical Society
Published on Web 04/01/2008

previously (*24*). HGP conjugation efficiency was determined by quantifying absorbance at 280 nm using UV/vis spectrophotometry.

Polyplex Formulation and Physicochemical Characterization. Polyplexes, complexes of polycations with nucleic acids, were formulated by adding equal volumes of polymer to nucleic acid at the desired charge ratio. The charge ratio is calculated on the basis of molar amount of polymer nitrogen to nucleic acid phosphate (N/P) ratio. Polyplexes were allowed to incubate for 10 min at room temperature to allow for complexation.

Complexation of DNA was monitored by agarose gel electrophoresis. Polyplexes were loaded on a 0.8% agarose gel containing 0.3 μg/mL ethidium bromide. Hydrodynamic size was measured in triplicate using a ZetaPALS zeta potential and particle size analyzer (Brookhaven Instruments Corp., Holtsville, NY) as described previously (*25*).

Dye Release Assay. Liposomes composed of L-α-phosphotidylcholine and cholesterol (Avanti Polar Lipids, Alabaster, AL) encapsulating 50 mM sulforhodamine B (Invitrogen, Carlsbad, CA) were prepared by extrusion through 100 nm polycarbonate membranes (Whatman, Florham Park, NJ) using the Avanti Mini-Extruder. Unencapsulated sulforhodamine B was removed by dialysis into 10 mM Tris pH 7.4, 20 mM NaCl, 0.1 mM EDTA.

Liposome lysis was monitored by dequenching of sulforhodamine B fluorescence upon release from liposomes. Fluorescence intensity was monitored using a Tecan Safire^2 microplate reader (Tecan Systems, Inc., San Jose, CA) by excitation at 565 nm and reading emission at 586 nm. Dye release was calculated as a percentage according to the equation

$$\% \text{ dye release} = \frac{F_m - F_0}{F_{100} - F_0} \times 100 \quad (1)$$

where F_m is the fluorescence value after 15 min of incubation with peptide or polyplex at 37 °C, F_0 is the fluorescence value of the initial liposome suspension, and F_{100} is the fluorescence value after incubation with a 0.05% Triton X-100 solution.

Cell Culture. HeLa cells purchased from ATCC (Manassas, VA) were cultured in complete growth medium (minimum essential medium with 10% fetal bovine serum and antibiotics). Cells were passaged every 2−3 days.

Plasmid Delivery to HeLa Cells, Evaluation of Transfection Efficiencies, and Cytotoxicity Assay. Transfection experiments were performed in triplicate. HeLa cells suspended in complete growth medium were seeded at 30 000 cells/well in 24-well plates and allowed to attach overnight. Polyplexes were formulated as described above using 1 μg of gWiz-Luciferase plasmid DNA (Aldevron, Fargo, ND) and then diluted in OptiMEM medium (Invitrogen). Cells were rinsed once with phosphate buffered saline, pH 7.4 (PBS), and incubated with polyplexes for 4 h at 37 °C in a 5% CO_2 atmosphere. Cells were rinsed with PBS and medium was replaced with fresh complete growth medium. Cells were returned to a 37 °C, 5% CO_2 atmosphere and luciferase expression was quantified after 48 h using a luciferase assay kit (Promega Corp., Madison, WI). Cells were washed with PBS, lysed with 200 μL of reagent lysis buffer (Promega Corp.), and frozen at −20 °C. 100 μL of luciferase substrate was added to 20 μL of lysate and luminescence was measured using a TECAN Safire^2 microplate reader. Luminescence was integrated for 1 s and recorded in relative light units (RLU). Luciferase activity is reported in luminescence normalized by protein content (RLU/mg), as measured by a BCA Protein Assay Kit (Pierce). Cytotoxity was measured by incubating polymer or polyplexes with HeLa cells as described above and adding the reagent 3-(4,5-dimethylthiazol-2-yl)-5-(3-carboxymethoxyphenyl)-2-(4-sulfophenyl)-2*H*-tetrazolium (MTS) (Promega Corp.) after 24 h. Cells were incubated in a 37 °C, 5% CO_2 atmosphere for 4 h and absorbance measurements of lysate at 490 nm were recorded.

siRNA Delivery to HeLa Cells and Expression Analysis by Quantitative PCR and GAPDH Activity Assay. siRNA targeting endogenous glyceraldehyde-3-phosphate dehydrogenase (siGAPDH) was purchased from Ambion (Silencer GAPDH siRNA; Austin, TX), and control siRNA targeting green fluorescent protein (siGFP) was synthesized by Dharmacon (Lafayette, CO) with the following sequence: 5′-GACGUAAACGGCCACAAGUUC-3′ (sense) and 5′-ACUUGUGGCCGUUUACGUCGC-3′ (antisense). HeLa cells were seeded on a 24-well plate as described for the plasmid transfection studies. For transfection, polyplexes were formulated by condensing either siGAPDH or siGFP with either PEI or PEI-HGP at an N/P ratio of 10 (60 pmol siRNA/well, triplicate samples). Polyplexes were diluted in 400 μL OptiMEM and incubated with cells for 5 h, after which the polyplex solution was removed and replaced with complete growth medium. 48 h after transfection, total RNA was isolated using an RNeasy Mini Kit (Qiagen, Valencia, CA). 500 ng of RNA from each sample was reverse-transcribed using Omniscript RT (Qiagen) and random hexamers as primers (Operon, Huntsville, AB). Quantitative PCR was performed using a model 7300 Real Time PCR system (Applied Biosystems, Foster City, CA) following universal thermal cycling parameters. GAPDH expression levels were determined in 20 μL reactions using TaqMan Universal PCR Master Mix (Applied Biosystems) and a TaqMan gene expression assay for human GAPDH, and were normalized by expression levels for β-actin (TaqMan gene expression assay for human ACTB). Relative GAPDH expression levels for each sample were determined on the basis of a comparison with untreated control samples, and were calculated by the $2^{-\Delta\Delta CT}$ method (*26*). To measure GAPDH activity, an identical transfection experiment was performed, and cell lysate was collected 48 h after transfection. GAPDH activity was measured in the lysate using the fluorescence-based KDalert GAPDH Assay Kit (Ambion). For each formulation, the degree of reduction in GAPDH activity mediated by siGAPDH was assessed by comparing GAPDH activity levels in siGAPDH- versus siGFP-treated samples.

Internalization and Binding Studies. Uptake and binding of PEI-HGP polyplexes relative to PEI polyplexes was investigated by flow cytometry. Nitro-2,1,3-benzoxadiazol-4-yl (NBD)-labeled oligonucleotides were prepared as described previously (*27*). HeLa cells were seeded at 300 000 cells/well in 6-well plates and allowed to attach overnight. One hour before transfection, cells were washed with PBS, supplemented with Gibco OptiMEM medium, and then equilibrated to either 37 or 4 °C. Polyplexes were formulated at an N/P ratio of 3 as described above using 4 μg of NBD-labeled oligo. Polyplex solution was added to cells and allowed to incubate for 3 h at either 37 or 4 °C. Cells were then washed twice with cold PBS, trypsinized, and resuspended in complete growth medium. Cell-associated fluorescence was quantified by flow cytometry using a BD FACScan (BD Biosciences, Franklin Lakes, NJ). Live cell populations were identified using forward and side-scattering profiles, and polyplex uptake was assessed by NBD fluorescence using *FlowJo* flow cytometry analysis software. Cell association was reported as mean fluorescence in relative fluorescence units (RFU).

Confocal Imaging. Confocal imaging was performed to determine the intracellular distribution of polyplexes. gWiz-Luciferase plasmid DNA was labeled with TOTO-3 (Invitrogen, Eugene, OR) at 1 dye per 100 base pairs and dialyzed into 10 mM Tris pH 7.4, 1 mM EDTA overnight at 4 °C. Glass coverslips were precoated with poly(L-lysine) in a 24-well plate

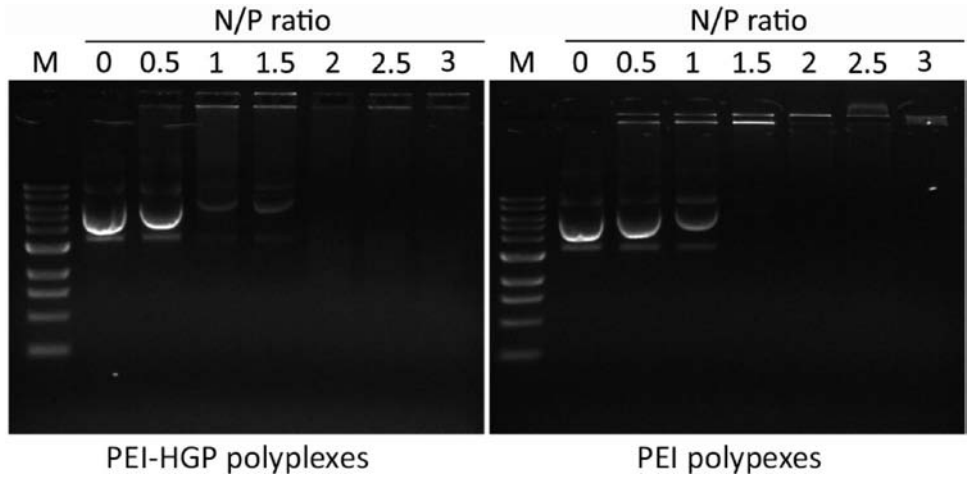

Figure 1. Gel retardation assay to monitor DNA complexation in PEI-HGP and PEI polyplexes at various N/P ratios. M: New England Biolabs 1kb ladder.

and HeLa cells were seeded at 75 000 cells/well in complete medium. 3 μg of TOTO-3 labeled DNA was complexed with PEI or PEI-HGP at N/P ratio 3 as described above and added to cells with 2 mg/mL Alexa Fluor 488-labeled dextran (MW 10 000, Invitrogen) for 1 or 3 h in a 37 °C, 5% CO_2 environment. Cells were then washed with PBS and Cell Scrub Buffer (Gene Therapy Systems, San Diego, CA), and then fixed for 7 min in 4% paraformaldehyde. Coverglasses were mounted onto a coverslip with Fluoromount-G (Southern Biotech, Birmingham, AL) and imaged with a Zeiss LSM 510 confocal microscope.

Chloroquine-Mediated Transfection Studies. HeLa cells were seeded at 120 000 cells/well in 6-well plates and allowed to attach overnight. Polyplexes were formulated at an N/P ratio of 3 as described above using 4 μg of pEGFP-C1 (Clontech Laboratories, Inc., Mountain View, CA) plasmid DNA that codes for the enhanced green fluorescent protein (EGFP) reporter. Polyplex was diluted in OptiMEM and added to cells. A 5 mM chloroquine stock solution was diluted to a final concentration of 0.1 mM and cells were allowed to incubate for 4 h in a 37 °C, 5% CO_2 atmosphere. Cells were rinsed with PBS and incubated for an additional 48 h in complete growth medium. Cells were imaged by brightfield and fluorescence microscopy. Transgene expression was quantified by EGFP fluorescence using flow cytometry as described above. EGFP expression is reported as the percent of EGFP positive cells.

Tail-Vein Injection. Female C57/Bl6 mice were purchased from Jackson Laboratory (Bar Harbor, ME). Polyplexes were formulated with 50 μg gWiz Luciferase plasmid DNA in 250 μL of 20 mM HEPES pH 7.4, 5% glucose. Polyplexes were delivered via tail-vein injections in 12−16 week old mice and lung tissue was excised 24 h after injection. Lungs were collected in reagent lysis buffer (Promega) supplemented with protease inhibitors (Roche) and underwent three freeze−thaw cycles. Tissue was mechanically homogenized using an IKA T8 Disperser (Wilmington, NC) and cell debris was spun down at 14 000 *g* for 15 min at 4 °C. Luciferase activity and protein content were measured as described above.

RESULTS

Synthesis of PEI-HGP and Polyplex Characterization. Moreno et al. recently screened 15 amino acid sequences from the HIV surface glycoprotein, gp41, in order to identify regions in the protein that interact with membranes. The sequence of HGP was chosen on the basis of its ability to mediate membrane rupture and is from the C-terminal tail region of HIV gp41 designated as the lentivirus peptide sequences (LLP-2/3) (*20*).

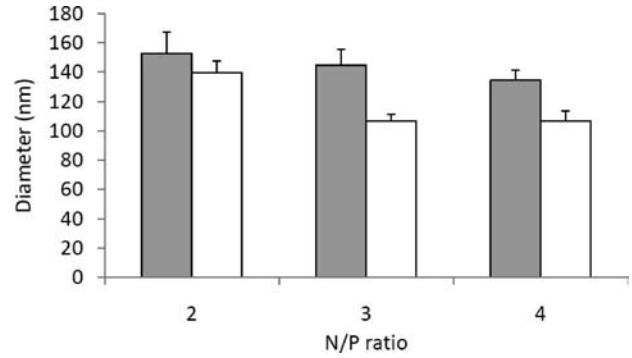

Figure 2. Hydrodynamic size of PEI-HGP (gray bars) and PEI (white bars) polyplexes were measured at N/P ratios 2, 3, and 4 using dynamic light scattering. Triplicate formulations were characterized at each charge ratio. Results are reported as mean diameter ± SD.

PEI-HGP was synthesized by conjugating a cysteine-terminated HGP to PEI with the heterobifunctional cross-linker SMPB. The concentration of peptide was determined by absorbance measurements at 280 nm and labeling efficiency was found to be 2−3 HGP per PEI on average.

Polyplexes with plasmid DNA were formed by addition of an equal volume of polymer to DNA followed by rapid mixing and incubation at room temperature for 10 min. Complex formation was examined by agarose gel electrophoresis (Figure 1). Uncomplexed DNA migrates into the gel, whereas complexed DNA is occluded and retained in the loading well. Uncomplexed gWiz-Luciferase plasmid is shown in lanes marked as N/P ratio 0. For both PEI and PEI-HGP, DNA is fully complexed at N/P ratio of 2. Therefore, HGP conjugation does not interfere with complex formation. This is expected, as the percentage of modification is low.

Hydrodynamic sizes of PEI and PEI-HGP polyplexes were measured using dynamic light scattering (DLS) in triplicate samples (Figure 2). For N/P ratios 2, 3, and 4, sizes of PEI-HGP polyplexes were 153 ± 14.7 nm, 144.8 ± 10.6 nm, and 134.4 ± 7.1 nm, respectively. Sizes of PEI polyplexes were 139.7 ± 7.7 nm, 106.7 ± 4.9 nm, and 107.0 ± 6.7 nm. PEI-HGP polyplexes are slightly larger in size.

Lytic Activity of HGP. The lytic activity of free HGP peptide and PEI-HGP polyplexes was determined by monitoring the release of sulforhodamine B dye from liposomes after incubation for 15 min at various peptide concentrations (*28*). Figure 3A shows that HGP displayed concentration-dependent lytic activity when incubated with liposomes. At a concentration of 0.63 μM,

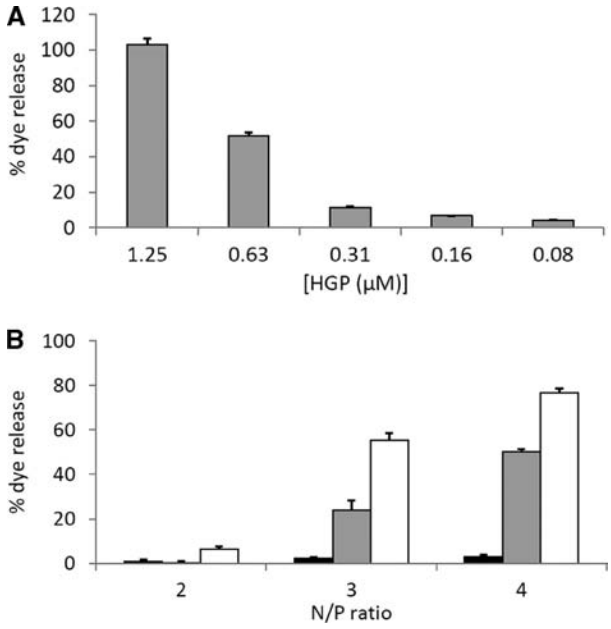

Figure 3. (A) Lytic activity of HGP was tested as free peptide using a fluorescence-based, liposomal leakage assay. (B) Lytic activities of HGP peptide (black bars), PEI polyplexes (gray bars), and PEI-HGP polyplexes (white bars) were compared. 100% dye release corresponded to fluorescence levels of liposomes treated with Triton X-100 surfactant for complete lysis. Results are reported as mean % dye release ± SD for triplicate samples.

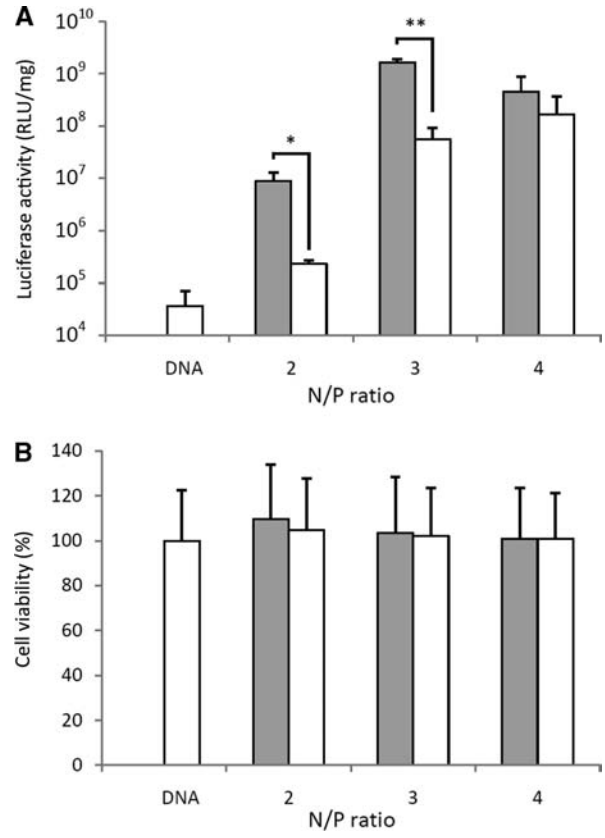

Figure 4. (A) Luciferase activity of PEI-HGP (gray bars) and PEI polyplexes (white bars) were compared in HeLa cells at N/P ratios 2, 3, and 4. (B) Cell viability of HeLa cells after transfection with PEI-HGP (gray bars) and PEI (white bars) polyplexes at N/P ratios 2, 3, and 4 as measured by MTS. Results are reported as mean RLU/mg ± SD for triplicate samples. (Student's *t*-test, $*p < 0.05$, $**p < 0.001$).

HGP was able to mediate approximately 50% dye release. The lytic activities of PEI and PEI-HGP polyplexes formulated at various N/P ratios were also evaluated (Figure 3B). The lytic activity of the equivalent amount of HGP incorporated in the PEI-HGP polyplexes was also determined for comparison. The concentrations of HGP peptide present in polyplex formulations of N/P ratios of 2, 3, and 4 were 0.13 μM, 0.19 μM, and 0.26 μM, respectively. Free peptides at these concentrations resulted in dye release percentages of 1.0%, 2.2%, and 3.0%. The dye release percentages for N/P ratios 2, 3, and 4 were 0.5%, 4.4%, and 50.3% for PEI and 6.5%, 55.3%, and 76.6% for PEI-HGP.

Evaluation of PEI-HGP for Plasmid DNA Delivery. Transfection efficiency of PEI and PEI-HGP polyplexes in HeLa cells as a function of N/P ratio was determined using the luciferase reporter gene system. PEI-HGP polyplexes showed increased expression profiles over unmodified polyplexes at N/P ratios of 2 and 3 (Figure 4A). At an N/P ratio of 2, transgene expression from PEI-HGP polyplexes ($8.9 \times 10^6 \pm 3.8 \times 10^6$ RLU/mg) was 38-fold higher than PEI polyplexes ($2.3 \times 10^5 \pm 4.0 \times 10^4$ RLU/mg) with a significance value of $p < 0.05$. At an N/P ratio of 3, transgene expression from PEI-HGP polyplexes ($1.7 \times 10^9 \pm 2.3 \times 10^8$ RLU/mg) was 30-fold higher than PEI polyplexes ($5.5 \times 10^7 \pm 3.7 \times 10^7$ RLU/mg) with a significance value of $p < 0.001$. At an N/P ratio of 4, transgene expression between PEI-HGP polyplexes ($4.5 \times 10^8 \pm 4.3 \times 10^8$ RLU/mg) was not statistically different than PEI polyplexes ($1.7 \times 10^8 \pm 2.0 \times 10^8$ RLU/mg). Increases in transfection efficiency at N/P ratios of 2 and 3 were confirmed in several separate experiments.

Cellular viability after transfection with PEI and PEI-HGP polyplexes was determined using an MTS assay and compared to untreated cells (Figure 4B). No toxicity was observed with these materials at N/P ratios 2, 3, and 4. At charge ratios greater than an N/P ratio of 15, the PEI-HGP polyplexes were more toxic than PEI polyplexes (data not shown).

Evaluation of PEI-HGP as an siRNA Carrier. The ability of HGP to enhance PEI-mediated siRNA delivery was evaluated in HeLa cells using siRNA targeting the endogenous GAPDH gene. While both PEI and PEI-HGP incorporating siGAPDH mediated significant GAPDH knockdown compared to identical polymer formulations incorporating siGFP, PEI-HGP was responsible for a significant enhancement in specific GAPDH knockdown activity compared to unmodified PEI ($53.4 \pm 2.2\%$ reduction in GAPDH expression for PEI vs $82.3 \pm 1.6\%$ reduction for PEI-HGP, $p < 0.001$) (Figure 5). In a similar experiment, cell lysates were collected and analyzed for GAPDH protein activity. Compared to the corresponding siGFP control, PEI/siGAPDH reduced GAPDH activity by $24.9 \pm 9.5\%$, while PEI-HGP/siGAPDH reduced GAPDH activity by $57.0 \pm 8.4\%$.

Binding and Internalization of PEI-HGP Polyplexes. Cellular binding and uptake of NBD-labeled PEI and PEI-HGP polyplexes was investigated using flow cytometry (Figure 6). Fluorescently labeled polyplexes were incubated with HeLa cells at 4 °C (for binding) and 37 °C (for binding and uptake) for three hours before analysis. At 4 °C, association of PEI polyplexes was greater than PEI-HGP polyplexes ($p < 0.005$). At 37 °C, there was no significant difference in total associated fluorescence between PEI and PEI-HGP polyplexes.

Confocal Imaging. In order to determine the intracellular distribution of carriers, PEI and PEI-HGP polyplexes containing TOTO-3-labeled plasmid DNA were incubated with cells for either 1 or 3 h, fixed, and imaged using confocal microscopy. Endosomes were labeled with Alexa488-dextran, a fluid-phase uptake marker. At 1 h, both PEI and PEI-hgp polyplexes exhibited punctate staining (data not shown). When PEI polyplexes were delivered for 3 h, DNA exhibited punctate intracellular staining that was colocalized with dextran (Figure

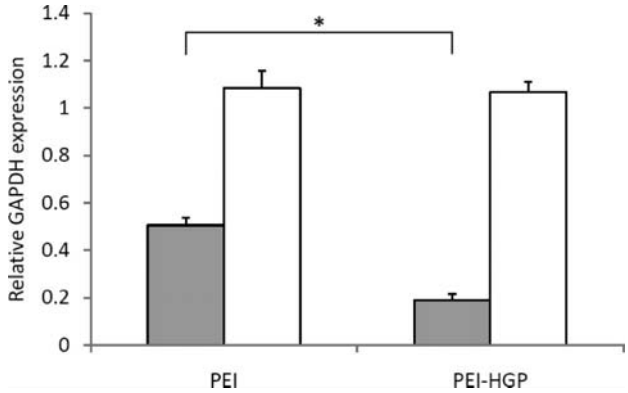

Figure 5. Quantification of GAPDH mRNA levels in HeLa cells following treatment with PEI or PEI-HGP polyplexes incorporating siRNA. Cells were transfected with polyplexes incorporating either siRNA against GAPDH (siGAPDH, gray bars) or siRNA against GFP (siGFP, white bars) as a negative control (N/P = 10). Total RNA was isolated 48 h after transfection, and relative GAPDH expression levels were measured by quantitative PCR. Values are normalized to an untreated control sample and are reported as the mean relative GAPDH expression ± SD for triplicate samples. (Student's *t* test, $*p < 0.001$).

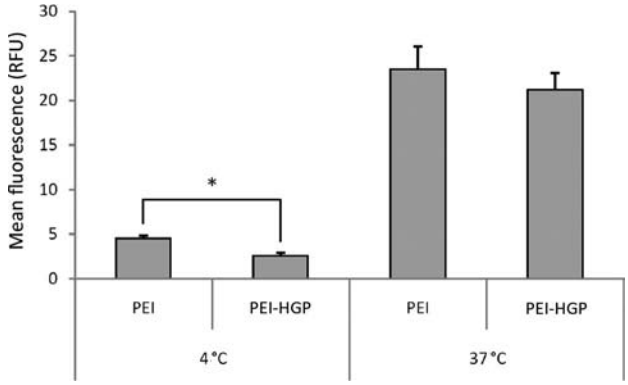

Figure 6. Binding and internalization of fluorescently labeled PEI and PEI-HGP polyplexes in HeLa cells. Cells were treated with polyplexes formulated at an N/P ratio 3 for 3 h at 4 °C (binding studies) and 37 °C (internalization studies) and analyzed by flow cytometry. Results are reported as mean fluorescence ± SD for triplicate samples. (Student's *t*-test, $*p < 0.005$).

7A). There were few examples of dextran staining that were not colocalized with DNA. When PEI-HGP polyplexes were delivered for 3 h, both punctate and diffuse DNA staining were observed (Figure 7B). Incidences of punctate DNA were colocalized with dextran, although there were examples of endocytic vesicles that were not colocalized with DNA. A substantial fraction (~30%) of cells had diffuse DNA fluorescence throughout the cells (white arrows).

Chloroquine-Mediated Transfection. In order to investigate the effects of HGP as a mediator of endosomal escape, PEI and PEI-HGP polyplex transfections were performed in the presence of chloroquine. Chloroquine is a small molecule buffering agent used to mediate endosomal escape of gene delivery vehicles (*29*−*31*). Polyplex transfections to HeLa cells were conducted in the presence of 100 μM chloroquine using an enhanced green fluorescent protein (EGFP) reporter gene. The percent of EGFP positive cells was measured by flow cytometry (Figure 8A). The percentage of EGFP positive cells after PEI-HGP transfection (20.1% ± 1.8%) was increased 16.1-fold when compared to PEI transfection (1.3% ± 0.3%, $p < 0.001$). Chloroquine increased the percentage of EGFP positive cells for both PEI and PEI-HGP; PEI transfection was increased 11.7-fold in the presence of chloroquine (14.6% ± 4.0%, $p < 0.01$), and PEI-HGP transfection was increased 3.8-fold in the presence of chloroquine (76.8% ± 3.7%, $p < 0.001$). Results from flow cytometry were verified by fluorescence microscopy (Figure 8B).

DISCUSSION

Escape from endocytic vesicles after internalization is necessary for efficient intracellular trafficking of nonviral gene therapy vehicles. For polyplex delivery, several strategies have been implemented to overcome this challenge, including pH-sensitive polymers (*32*), endosomal buffering polymers (*5*, *33*), and photosensitive systems (*34*). Membrane-interacting peptides, both natural and synthetic, have been utilized in gene delivery carriers (*15*, *35*, *36*). The use of these peptides has been shown to increase the efficiencies of delivery vehicles; however, delivery efficiencies from nonviral vectors remain suboptimal for most clinical gene therapy applications.

In this work, a lytic peptide was conjugated to a polymeric gene carrier and evaluated for its effect on gene and siRNA delivery. In a screen of HIV gp41 to identify peptides with potent lytic activity, the sequence of HGP was demonstrated to be the most lytic (*20*). Gp41, together with gp120, forms the monomer unit of the trimer HIV Env, the protein responsible for viral fusion of HIV. The sequence of HGP is from the lentiviral lytic peptide (LLP) domains 2 and 3 of the gp41 cytoplasmic tail. Another delivery system, MPG, is derived from the fusion domain of HIV gp41 and was shown to deliver oligonucleotides into the cytosol of 90% of cells in an endocytic independent pathway (*37*). However, peptides from the LLP regions of gp41 have not to our knowledge been applied in gene delivery systems.

In initial studies, the HGP peptide was compared with a recently identified peptide from adenovirus for relative lytic ability (*28*). A 10-fold higher concentration of peptide from adenovirus was needed to mediate 50% liposome disruption when compared to HGP (data not shown). Thus, we hypothesized that HGP may mediate efficient endosomal rupture at low peptide concentrations when incorporated in polycation delivery vectors.

PEI-HGP was synthesized by SMPB conjugation, and complete packaging of DNA at N/P ratio of 2 was confirmed by agarose gel electrophoresis. The same N/P ratio was needed to complex DNA with unmodified PEI (Figure 1), indicating that the ability for PEI to complex DNA is retained with peptide conjugation. This was expected, as the percentage of modified amines is very low (<0.5%). PEI-HGP polyplexes formed slightly larger polyplexes compared to PEI polyplexes (Figure 2). The difference in particle sizes of PEI-HGP polyplexes compared to PEI polyplexes is likely due to steric hindrance of peptides interfering with DNA complexation. Because polyplexes were of similar size, differences in transfection efficiencies between PEI-HGP and PEI polyplexes were most likely due to differences in the activity of HGP and not physical differences between polyplexes.

PEI and PEI-HGP polyplexes showed lytic activity that was dependent on the N/P ratio of formulation (Figure 3B). PEI-HGP polyplexes formulated at N/P ratios of 2, 3, and 4 used in the membrane lysis assay correspond to HGP concentrations of 0.13 μM, 0.19 μM, and 0.26 μM, respectively. PEI-HGP polyplexes showed increases in lytic activity over PEI polyplexes for each N/P ratio tested. The observed increase in lytic ability was much higher than what would be expected on the basis of the presence of HGP; free HGP at these low concentrations have minimal lytic activity (Figure 3A). The higher leakage values of PEI-HGP polyplexes when compared with HGP peptide at matched peptide concentrations may instead be attributed to increased local concentration of peptide tethered

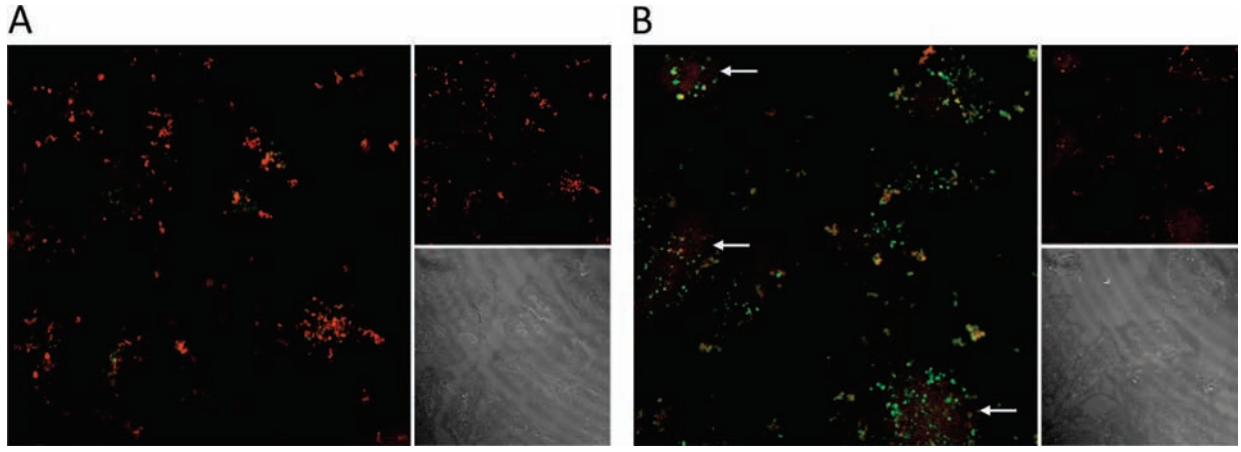

Figure 7. Confocal microscopy of HeLa cells incubated with PEI (A) and PEI-HGP (B) condensed TOTO-3 labeled gWiz-Luciferase DNA at N/P ratio 3. Vesicles are labeled with Alexa Fluor 488-labeled 10 000 Mw dextran. DNA/dextran (left panel), DNA (top right panel), and differential interference contrast (bottom right) images are shown. Arrows show cells exhibiting diffuse DNA fluorescence.

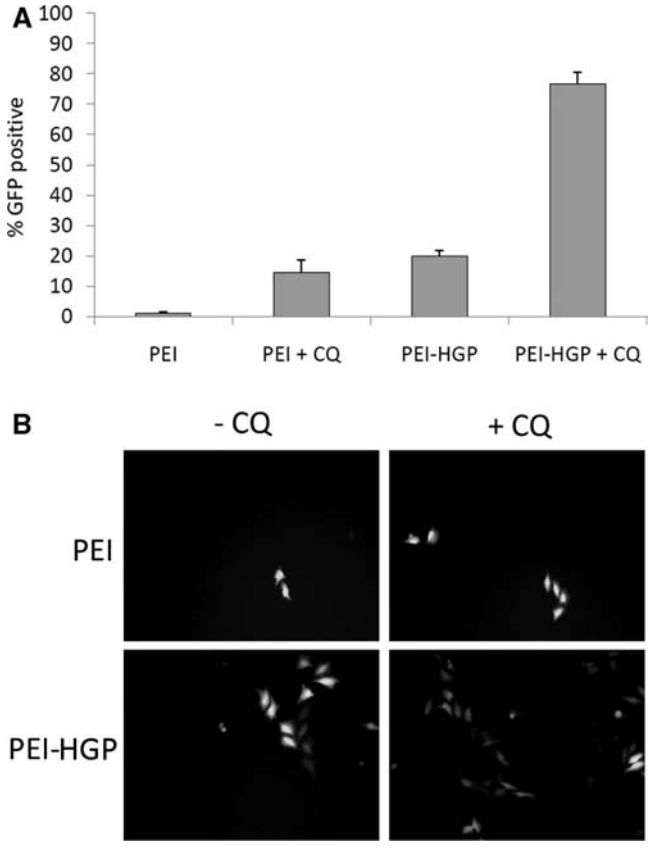

Figure 8. (A) Percentage of GFP positive HeLa cells after PEI or PEI-HGP polyplex transfection with and without chloroquine (CQ) with analysis by flow cytometry. (B) Fluorescence microscopy of representative EGFP-transfected cells.

to the polyplex surface. During membrane fusion, HIV gp41 has been shown to adopt a six-helix bundle configuration (*38*) and the endodomain of HIV gp41 has shown high potential to form multimers (*21*).

PEI-HGP was shown to be significantly more efficient than unmodified PEI for delivery of plasmids at low charge ratios (Figure 4A). Because polymer concentration (N/P ratio) also affects transfection efficiency, the polymer concentrations were carefully matched for PEI and PEI-HGP formulations by quantification of polymer concentration using copper (II) acetate and by gel retardation assay, which confirmed complete DNA condensation at similar charge ratios between the two formulations. At higher charge ratios, the difference between PEI-HGP and PEI transfection efficiency for plasmids is less significant, perhaps because the uncomplexed PEI polymer also exhibits membrane disruption ability (data not shown). Interestingly, siRNA delivery efficiency is enhanced by HGP at polymer charge ratios of 10 N/P, suggesting that the uncomplexed PEI polymer and HGP may act synergistically to increase siRNA availability in the cytoplasm (Figure 5).

In order to elucidate the mechanism for HGP-mediated increase in transfection, the efficiencies of polyplex binding, internalization, and endosomal release were investigated. The most likely route for the entry of PEI-HGP polyplexes is through endocytosis, which has been shown to be true for other endosomolytic peptide-modified delivery vehicles (*39*, *40*). Cellular internalization and binding was examined at 4 and 37 °C using flow cytometry (Figure 6). At 4 °C, a temperature at which endocytosis is inhibited (*41*), there is less cell-associated NBD fluorescence of PEI-HGP polyplexes than PEI polyplexes, indicating that there is less binding affinity of PEI-HGP polyplexes to the cellular membrane. Similar cell-associated NBD fluorescence of PEI-HGP polyplexes and PEI polyplexes at 37 °C suggests that the uptake efficiencies of PEI-HGP and PEI polyplexes are similar. Thus, the increase in transfection efficiency of PEI-HGP polyplexes is likely not due to more efficient uptake.

Confocal imaging is a technique that has been utilized to determine the intracellular distribution of nanoparticulate carriers (*3*). Cells incubated with PEI polyplexes showed punctate plasmid DNA staining that largely colocalized with endosomes, indicating that polyplexes were most likely trapped within endosomes (Figure 7A). Cells incubated with PEI-HGP polyplexes showed both punctate and diffuse plasmid DNA staining, which is markedly different than the staining observed with PEI polyplexes and indicative of endosomal release of vectors (Figure 7B). Increases in transgene expression mediated by HGP may therefore be explained by changes in intracellular trafficking, most likely escape from endocytic vesicles, since HGP modification of vehicles does not significantly alter uptake.

The HGP peptide is derived from the LLP-2 and -3 domains of gp41, which have previously been demonstrated to disrupt lipid membranes (*22*). These peptide regions have been shown to have amphipathic α-helical structure and are proposed to mediate membrane disruption by either spanning the membrane to form ion channels or by lying along the membrane surface (*22*). Formation of ion channels by viruses, called "viroporins", is a well-studied mechanism for membrane disruption based on a similar osmolytic mechanism to that proposed for PEI (*5*, *42*).

However, unlike PEI, membrane disruption by viroporins is not necessarily pH-sensitive. This raises the intriguing possibility that HGP may not only mediate enhanced endosomal release when coupled to PEI but may also change the release kinetics by relying on a critical peptide concentration in the endosomes instead of proton accumulation during endosomal maturation.

To further understand the intracellular trafficking pathway of PEI-HGP polyplexes, transfection studies were done in the presence of chloroquine. Chloroquine is a small molecule that is widely used to increase the transfection efficiency of gene delivery vehicles due to its ability to buffer endocytic compartments (*31*). In addition, chloroquine has been proposed to have auxiliary functions such as increasing the unpackaging of nucleic acids from their carriers and altering intracellular processing by changing the physical and biological characteristics of the released nucleic acids (*31*). When PEI and PEI-HGP polyplexes were coincubated with chloroquine, the transgene expression of both formulations was increased. These results indicate that HGP may be inadequate for complete release of carriers from endocytic vesicles or that the added increase in gene expression is due to the auxiliary functions of chloroquine. The observation that chloroquine increases the transgene expression of PEI-HGP polyplexes formulated at N/P ratio of 3 to greater than 75% of cells also implies that the vector can be further optimized to yield high transfection efficiencies. In addition, confocal microscopy images demonstrating the endosomal escape of PEI-HGP are supported by the observation that the effect of chloroquine on transgene expression is three times greater for PEI polyplexes over PEI-HGP polyplexes (Figure 7). Furthermore, the diffuse DNA staining observed in PEI-HGP transfected cells is also observed when PEI transfection was done in the presence of chloroquine (Supporting Information).

Pulmonary gene therapy has important applications such as cystic fibrosis and lung cancer. PEI has been one of the most effective cationic polymeric carriers used in lung gene therapy (*43*). When 50 μg of gWiz-Luciferase DNA condensed with PEI-HGP was injected into the tail vein of mice, statistically significant higher expression was found in the lung ($\sim$3-fold higher) compared to PEI (data not shown).

For the application of gene delivery *in vivo*, it is of particular importance to develop particles that can be efficient at low polymer to DNA ratios. PEI polyplex delivery has been shown to be quite efficient when there is excess PEI present; however, the removal of excess polymer results in polyplexes with N/P ratios between 2 and 3 (*8*). This has implications for *in vivo* delivery, as free polymer can be separated from complexes in the body. An additional benefit of achieving efficient transgene expression at low polymer to DNA ratios is improved cell viability, as increasing amounts of PEI can cause significant toxicity (*44*). We were therefore interested in increasing transgene expression at these low N/P ratios.

In conclusion, a lytic peptide conjugated to the cationic polymer PEI was able to significantly enhance plasmid delivery efficiency over unmodified PEI at N/P ratios of 2 and 3 in cultured cells and in the lung tissue of mice. In addition, PEI-HGP efficiently delivered siRNA to cultured cells. Investigation into the mechanism of HGP indicated that increases in delivery efficiency were not due to increases in uptake. Studies employing the small molecule chloroquine and confocal microscopy supported the hypothesis that increased transfection efficiency was most likely due to endosomal escape. The chloroquine-mediated increase of PEI-HGP polyplex transgene expression indicated that vehicle properties can be further optimized, perhaps by engineering materials that improve vector unpackaging or cytosolic trafficking. This work is applicable for the development of nonviral delivery vehicles that are biologically active for efficient nucleic acid transfer *in vivo*.

ACKNOWLEDGMENT

The authors thank Leonard Meuse for his assistance with tail-vein injections in *in vivo* transfection studies. This work was funded by the National Science Foundation (CBET 0448547), NIH/NINDS (5R21NS052030), and the National Hemophilia Foundation. Flow cytometry was conducted at the Cell Analysis Facility at the Immunology Department of the University of Washington. Confocal imaging was conducted at the Nanotech User Facility at the University of Washington. The Nanotech User Facility is a member of the National Nanotechnology Infrastructure Network (NNIN) which is supported by the National Science Foundation and the Center for Nanotechnology at the University of Washington.

Supporting Information Available: Confocal microscopy of PEI-HGP and PEI transfected cells in the presence of chloroquine. This material is available free of charge via the Internet at http://pubs.acs.org/BC.

LITERATURE CITED

(1) Pack, D. W., Hoffman, A. S., Pun, S., and Stayton, P. S. (2005) Design and development of polymers for gene delivery. *Nat. Rev. Drug Discovery 4*, 581–93.

(2) Demeneix, B., Hassani, Z., and Behr, J. P. (2004) Towards multifunctional synthetic vectors. *Curr. Gene Ther. 4*, 445–55.

(3) Akita, H., Ito, R., Khalil, I. A., Futaki, S., and Harashima, H. (2004) Quantitative three-dimensional analysis of the intracellular trafficking of plasmid DNA transfected by a nonviral gene delivery system using confocal laser scanning microscopy. *Mol. Ther. 9*, 443–51.

(4) Pollard, H., Remy, J. S., Loussouarn, G., Demolombe, S., Behr, J. P., and Escande, D. (1998) Polyethylenimine but not cationic lipids promotes transgene delivery to the nucleus in mammalian cells. *J. Biol. Chem. 273*, 7507–11.

(5) Sonawane, N. D., Szoka, F. C., Jr., and Verkman, A. S. (2003) Chloride accumulation and swelling in endosomes enhances DNA transfer by polyamine-DNA polyplexes. *J. Biol. Chem. 278*, 44826–31.

(6) Boussif, O., Lezoualc'h, F., Zanta, M. A., Mergny, M. D., Scherman, D., Demeneix, B., and Behr, J. P. (1995) A versatile vector for gene and oligonucleotide transfer into cells in culture and in vivo: polyethylenimine. *Proc. Natl. Acad. Sci. U.S.A. 92*, 7297–301.

(7) Florea, B. I., Meaney, C., Junginger, H. E., and Borchard, G. (2002) Transfection efficiency and toxicity of polyethylenimine in differentiated Calu-3 and nondifferentiated COS-1 cell cultures. *AAPS PharmSci 4*, E12.

(8) Boeckle, S., von Gersdorff, K., van der Piepen, S., Culms6ee, C., Wagner, E., and Ogris, M. (2004) Purification of polyethylenimine polyplexes highlights the role of free polycations in gene transfer. *J. Gene Med. 6*, 1102–11.

(9) Saul, J. M., Wang, C. H. K., Ng, C. P., and Pun, S. H. (2008) Multilayer nanocomplexes of polymer and DNA exhibit enhanced gene delivery. *Adv. Mater. 20*, 19–25.

(10) Boeckle, S., Fahrmeir, J., Roedl, W., Ogris, M., and Wagner, E. (2006) Melittin analogs with high lytic activity at endosomal pH enhance transfection with purified targeted PEI polyplexes. *J. Controlled Release 112*, 240–8.

(11) Chen, C. P., Kim, J. S., Steenblock, E., Liu, D., and Rice, K. G. (2006) Gene transfer with poly-melittin peptides. *Bioconjugate Chem. 17*, 1057–62.

(12) Ogris, M., Carlisle, R. C., Bettinger, T., and Seymour, L. W. (2001) Melittin enables efficient vesicular escape and enhanced nuclear access of nonviral gene delivery vectors. *J. Biol. Chem. 276*, 47550–5.

(13) Rudolph, C., Plank, C., Lausier, J., Schillinger, U., Muller, R. H., and Rosenecker, J. (2003) Oligomers of the arginine-rich

motif of the HIV-1 TAT protein are capable of transferring plasmid DNA into cells. *J. Biol. Chem. 278*, 11411–8.
(14) Brooks, H., Lebleu, B., and Vives, E. (2005) Tat peptide-mediated cellular delivery: back to basics. *Adv. Drug Delivery Rev. 57*, 559–77.
(15) Meade, B. R., and Dowdy, S. F. (2007) Exogenous siRNA delivery using peptide transduction domains/cell penetrating peptides. *Adv. Drug Delivery Rev. 59*, 134–40.
(16) Wagner, E., Plank, C., Zatloukal, K., Cotten, M., and Birnstiel, M. L. (1992) Influenza virus hemagglutinin HA-2 N-terminal fusogenic peptides augment gene transfer by transferrin-polylysine-DNA complexes: toward a synthetic virus-like gene-transfer vehicle. *Proc. Natl. Acad. Sci. U.S.A. 89*, 7934–8.
(17) Zhang, X., Collins, L., and Fabre, J. W. (2001) A powerful cooperative interaction between a fusogenic peptide and lipofectamine for the enhancement of receptor-targeted, non-viral gene delivery via integrin receptors. *J. Gene Med. 3*, 560–8.
(18) Bergen, J. M., and Pun, S. H. (2005) Peptide-enhanced nucleic acid delivery. *MRS Bull. 30*, 663–667.
(19) Martin, M. E., and Rice, K. G. (2007) Peptide-guided gene delivery. *AAPS J. 9*, E18–29.
(20) Moreno, M. R., Giudici, M., and Villalain, J. (2006) The membranotropic regions of the endo and ecto domains of HIV gp41 envelope glycoprotein. *Biochim. Biophys. Acta 1758*, 111–23.
(21) Chen, S. S., Lee, S. F., and Wang, C. T. (2001) Cellular membrane-binding ability of the C-terminal cytoplasmic domain of human immunodeficiency virus type 1 envelope transmembrane protein gp41. *J. Virol. 75*, 9925–38.
(22) Costin, J. M., Rausch, J. M., Garry, R. F., and Wimley, W. C. (2007) Viroporin potential of the lentivirus lytic peptide (LLP) domains of the HIV-1 gp41 protein. *Virol. J. 4*, 123.
(23) Srinivas, S. K., Srinivas, R. V., Anantharamaiah, G. M., Segrest, J. P., and Compans, R. W. (1992) Membrane interactions of synthetic peptides corresponding to amphipathic helical segments of the human immunodeficiency virus type-1 envelope glycoprotein. *J. Biol. Chem. 267*, 7121–7.
(24) von Harpe, A., Petersen, H., Li, Y., and Kissel, T. (2000) Characterization of commercially available and synthesized polyethylenimines for gene delivery. *J. Controlled Release 69*, 309–22.
(25) Park, I. K., Lasiene, J., Chou, S. H., Horner, P. J., and Pun, S. H. (2007) Neuron-specific delivery of nucleic acids mediated by Tet1-modified poly(ethylenimine). *J. Gene Med. 9*, 691–702.
(26) Livak, K. J., and Schmittgen, T. D. (2001) Analysis of relative gene expression data using real-time quantitative PCR and the 2(-Delta Delta C(T)) Method. *Methods 25*, 402–8.
(27) Bergen, J. M., Kwon, E. J., and Pun, S. H. (2008) Application of an environmentally-sensitive fluorophore for rapid analysis of the binding and internalization of gene carriers. *Bioconjugate Chem. 19*, 377–384.
(28) Wiethoff, C. M., Wodrich, H., Gerace, L., and Nemerow, G. R. (2005) Adenovirus protein VI mediates membrane disruption following capsid disassembly. *J. Virol. 79*, 1992–2000.
(29) Wagner, E., Zatloukal, K., Cotten, M., Kirlappos, H., Mechtler, K., Curiel, D. T., and Birnstiel, M. L. (1992) Coupling of adenovirus to transferrin-polylysine/DNA complexes greatly enhances receptor-mediated gene delivery and expression of transfected genes. *Proc. Natl. Acad. Sci. U.S.A. 89*, 6099–103.
(30) Erbacher, P., Roche, A. C., Monsigny, M., and Midoux, P. (1996) Putative role of chloroquine in gene transfer into a human hepatoma cell line by DNA/lactosylated polylysine complexes. *Exp. Cell Res. 225*, 186–94.
(31) Cheng, J., Zeidan, R., Mishra, S., Liu, A., Pun, S. H., Kulkarni, R. P., Jensen, G. S., Bellocq, N. C., and Davis, M. E. (2006) Structure-function correlation of chloroquine and analogues as transgene expression enhancers in nonviral gene delivery. *J. Med. Chem. 49*, 6522–31.
(32) Yessine, M. A., Dufresne, M. H., Meier, C., Petereit, H. U., and Leroux, J. C. (2007) Proton-actuated membrane-destabilizing polyion complex micelles. *Bioconjugate Chem. 18*, 1010–4.
(33) Oishi, M., Kataoka, K., and Nagasaki, Y. (2006) pH-responsive three-layered PEGylated polyplex micelle based on a lactosylated ABC triblock copolymer as a targetable and endosome-disruptive nonviral gene vector. *Bioconjugate Chem. 17*, 677–88.
(34) Nishiyama, N., Arnida, J. W. D., Date, K., Miyata, K., and Kataoka, K. (2006) Photochemical enhancement of transgene expression by polymeric micelles incorporating plasmid DNA and dendrimer-based photosensitizer. *J. Drug Target. 14*, 413–24.
(35) Cho, Y. W., Kim, J. D., and Park, K. (2003) Polycation gene delivery systems: escape from endosomes to cytosol. *J. Pharm. Pharmacol. 55*, 721–34.
(36) Li, W., Nicol, F., and Szoka, F. C., Jr (2004) GALA: a designed synthetic pH-responsive amphipathic peptide with applications in drug and gene delivery. *Adv. Drug Delivery Rev. 56*, 967–85.
(37) Morris, M. C., Vidal, P., Chaloin, L., Heitz, F., and Divita, G. (1997) A new peptide vector for efficient delivery of oligonucleotides into mammalian cells. *Nucleic Acids Res. 25*, 2730–6.
(38) Melikyan, G. B., Markosyan, R. M., Hemmati, H., Delmedico, M. K., Lambert, D. M., and Cohen, F. S. (2000) Evidence that the transition of HIV-1 gp41 into a six-helix bundle, not the bundle configuration, induces membrane fusion. *J. Cell Biol. 151*, 413–23.
(39) Vives, E. (2003) Cellular uptake [correction of utake] of the Tat peptide: an endocytosis mechanism following ionic interactions. *J. Mol. Recognit. 16*, 265–71.
(40) Lundberg, P., El-Andaloussi, S., Sutlu, T., Johansson, H., and Langel, U. (2007) Delivery of short interfering RNA using endosomolytic cell-penetrating peptides. *Faseb J. 21*, 2664–71.
(41) Lippincott-Schwartz, J., Roberts, T. H., and Hirschberg, K. (2000) Secretory protein trafficking and organelle dynamics in living cells. *Annu. Rev. Cell Dev. Biol. 16*, 557–89.
(42) Chernomordik, L., Chanturiya, A. N., Suss-Toby, E., Nora, E., and Zimmerberg, J. (1994) An amphipathic peptide from the C-terminal region of the human immunodeficiency virus envelope glycoprotein causes pore formation in membranes. *J. Virol. 68*, 7115–23.
(43) Densmore, C. L. (2006) Advances in noninvasive pulmonary gene therapy. *Curr. Drug Delivery 3*, 55–63.
(44) Fischer, D., Bieber, T., Li, Y., Elsasser, H. P., and Kissel, T. (1999) A novel non-viral vector for DNA delivery based on low molecular weight, branched polyethylenimine: effect of molecular weight on transfection efficiency and cytotoxicity. *Pharm. Res. 16*, 1273–9.

BC700448H

An ^{86}Y-Labeled Mirror-Image Oligonucleotide: Influence of Y-DOTA Isomers on the Biodistribution in Rats†

Joern Schlesinger,‡ Inge Koezle,‡ Ralf Bergmann,‡ Sergio Tamburini,§ Cristina Bolzati,§ Francesco Tisato,§ Bernhard Noll,‡ Sven Klussmann,|| Stefan Vonhoff,|| Frank Wuest,‡ Hans-Juergen Pietzsch,*,‡ and Joerg Steinbach‡

Institute of Radiopharmacy, Forschungszentrum Dresden-Rossendorf, Germany, ICIS−CNR, Corso Stati Uniti, 4, Padova, Italy, and NOXXON Pharma AG, Berlin, Germany. Received December 10, 2007; Revised Manuscript Received February 7, 2008

A mirror-image oligonucleotide (L-RNA) was radiolabeled with the positron emitting radionuclide ^{86}Y ($t_{1/2}$ = 14.7 h) via the bifunctional chelator approach. DOTA-modification of the L-RNA (sequence: 5′-aminohexyl UGA CUG ACU GAC-3′; MW 3975) was performed using (*S*)-*p*-SCN-Bn-DOTA. ^{86}Y radiolabeling of the DOTA-L-RNA produced more than one species as evidenced by HPLC radiometric detection. For the identification of the ^{86}Y-labeled L-RNA, the structural analogue nonradioactive precursor [Y((*S*)-*p*-NH$_2$-Bn-DOTA)]$^-$ was synthesized. Two coordination isomers were separated via HPLC adopting the square antiprismatic (SAP) and the twisted square antiprismatic (TSAP) geometry, respectively. Their stereochemical configuration in the solution state was assessed by NMR and circular dichroism spectroscopy. Both [Y((*S*)-*p*-NH$_2$-Bn-DOTA)]$^-$ isomers were converted into isothiocyanate derivatives [Y((*S*)-*p*-SCN-Bn-DOTA)]$^-$ and conjugated to the L-RNA. The identity of the [^{86}Y-DOTA]-L-RNA species was finally established by comparison of the radiometric (^{86}Y) and UV–visible chromatographic profiles. Biodistribution studies in Wistar rats showed minor changes in the biodistribution profile of the [^{86}Y((*S*)-*p*-NH$_2$-Bn-DOTA)]$^-$ complex isomers, while no significant differences were observed for the [^{86}Y-DOTA]-L-RNA isomers. High renal excretions were found for the [^{86}Y((*S*)-*p*-NH$_2$-Bn-DOTA)]$^-$ complex isomers as well as for the L-RNA isomers.

INTRODUCTION

The radiolabeling of oligonucleotides with radiometals (e.g. ^{68}Ga, ^{111}In, ^{99m}Tc, ^{86}Y) for *in vivo* imaging studies is usually performed via the bifunctional chelator (BFC)[1] approach (*1–4*). BFCs should form highly stable complexes with the radiometal while enabling facile conjugation of the radiometal complex to the biomolecule under mild conditions. A frequently utilized chelator for trivalent metals, such as In^{3+}, Ga^{3+}, Y^{3+}, and other ions of the lanthanide and actinide series, is 1,4,7,10-tetraazacyclododecane-*N*,*N*′,*N*″,*N*‴-tetraacetic acid (DOTA). DOTA is known to form thermodynamically stable complexes with lanthanides and yttrium isotopes, and the corresponding radiometal complex show in many cases high kinetic inertness *in vivo* (*5*). Examples of various DOTA derivatives used as BFCs are shown in Figure 1. The reactive functionality capable of being linked to the biomolecule can be introduced into the DOTA framework either at the ethylene bridge or via a chemical activation of a free carboxylic acid sidearm of DOTA.

The positron-emitting radionuclide ^{86}Y ($t_{1/2}$ = 14.7 h, β^+ = 33%, E_{avg} = 664 keV) is an attractive isotope for molecular imaging purposes. The extensive use of the high-energy electron-emitter ^{90}Y ($t_{1/2}$ = 64.06 h, β^- = 72%, $E_{\beta-}$ = 2.288 MeV), an excellent radionuclide for endoradiotherapy, makes the positron emitter ^{86}Y an ideal radionuclide for dosimetry assessment of ^{90}Y-labeled radiotherapeutics (*6*). ^{86}Y can be prepared on a small biomedical cyclotron employing the ^{86}Sr(p,n)^{86}Y nuclear reaction (*7*). The 14.7 h half-life of ^{86}Y allows PET studies of up to two days.

In the past decade, synthetic oligonucleotides have been suggested as molecular probes for the improved targeting of cancer using pretargeting methods (*8*, *9*). In this connection, Hnatowich and co-workers have previously shown that complementary phosphorodiamidate morpholino oligomers (MORF/cMORF) are useful molecular recognition systems for targeting prostate tumor in nude mice in combination with a monoclonal antibody (*10*). Another promising class of synthetic oligonucleotides consists of mirror-image oligonucleotides (L-ON) (*11*). L-ON are constructed of an L-configured ribose or deoxyribose. As shown previously, L-ON display an extraordinary high metabolic stability in the biological environment due to the high resistance to enzymatic degradation (*12*). To explore the potential of complementary L-ON as recognition systems for pretargeting, the present work deals with basic radiopharmaceutical chemistry

† Dedicated to Hartmut Spies in memoriam.

* Author to whom correspondence should be addressed: H.-J. Pietzsch, Institute of Radiopharmacy, Forschungszentrum Dresden-Rossendorf, PF 51 01 19, 01314 Dresden, Germany; h.j.pietzsch@fzd.de.

‡ Forschungszentrum Dresden-Rossendorf.

§ Corso Stati Uniti.

|| NOXXON Pharma AG.

[1] Abbreviations: BIRD, bilinear rotation decoupling; BFC, bifunctional chelator; COSY, correlation spectroscopy; DOTA, 1,4,7,10-tetraazacyclododecane-*N*,*N*′,*N*″,*N*‴-tetraacetic acid; DTPA, diethylenetriaminepentaacetic acid; ESI-MS, electrospray ionization-mass spectrometry; HMBC, heteronuclear multiple bond correlation; HMQC, heteronuclear multiple-quantum coherence experiment; HPLC, high pressure liquid chromatography; i.d., inner diameter; L-ON, mirror-image oligonucleotide; NMR, nuclear magnetic resonance; NOESY, nuclear overhause effect spectroscopy; p.i., post injection; PAGE, polyacrylamide gel electrophoresis; PET, positron emission tomography; R_f, retention factor; R_T, retention time; (*S*)-*p*-NH$_2$-Bn-DOTA, (*S*)-2-(4-aminobenzyl)-1,4,7,10-tetraazacyclododecane-*N*,*N*′,*N*″,*N*‴-tetraacetic acid; (*S*)-*p*-SCN-Bn-DOTA, (*S*)-2-(4-isothiocyanatobenzyl)-1,4,7,10-tetraazacyclododecane-*N*,*N*′,*N*″,*N*‴-tetraacetic acid; SAP, square antiprism; SDS, sodium dodecyl sulfate; SEC, size exclusion chromatography; SUV, standardized uptake value; TEAA, triethylammonium acetate; TLC, thin layer chromatography; TPPI, time-proportional phase incrementation; TSAP, twisted square antiprism.

10.1021/bc700453h CCC: $40.75 © 2008 American Chemical Society
Published on Web 03/18/2008

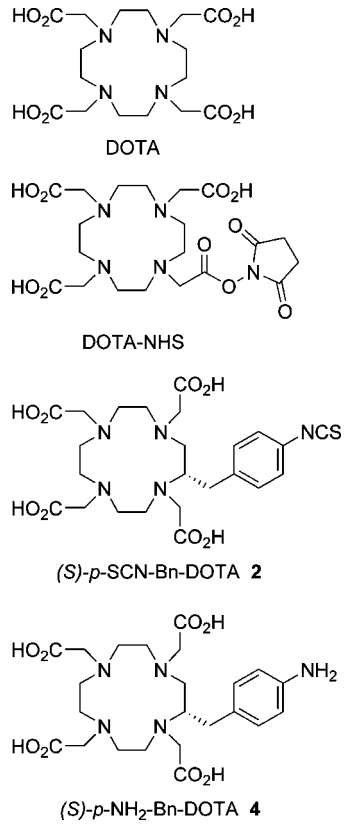

Figure 1. Bifunctional chelators based on the DOTA framework.

for labeling of an L-RNA as model system with the β^+-emitter ^{86}Y and subsequent radiopharmacological evaluation. An important criterion for the use of radiolabeled L-ON as molecular probes for *in vivo* imaging approaches is the radiochemical purity of the L-ON.

The purpose of this work was to characterize precisely different isomers formed during the complexation of a DOTA-functionalized L-RNA with Y(III). We report on the synthesis and NMR characterization of the nonradioactive [Y((*S*)-*p*-NH_2-Bn-DOTA)]$^-$ precursors isolated by HPLC and further analyzed by mass spectrometry, circular dichroism spectroscopy, and polarimetric measurements. The assessment of their solution structure allows one to determine the stereochemistry adopted by the pendant benzyl residue and to establish the identity with the compounds prepared at the "carrier-free" level with ^{86}Y. The isolated [^{86}Y((*S*)-*p*-NH_2-Bn-DOTA)]$^-$ isomers were further characterized by a comparative biodistribution study in Wistar rats and metabolite analysis. To draw conclusions to the observed [^{86}Y-DOTA]-L-RNA isomers, the amino groups of [Y(*p*-NH_2-Bn-DOTA)]$^-$ were transferred into isothiocyanate functionalities and the isomers were attached to the L-RNA. The coupling products were analyzed via HPLC and MALDI-TOF analysis. Finally, the biodistribution profiles of the [^{86}Y-DOTA]-L-RNA isomers were examined in rats, to characterize the influence of this chelate unit on the *in vivo* behavior of the L-RNA conjugate.

EXPERIMENTAL SECTION

Materials. L-RNA **1** [sequence: 5′-aminohexyl UGA CUG ACU GAC-3′, MW 3975] was obtained from NOXXON Pharma AG (Germany). (*S*)-*p*-SCN-Bn-DOTA **2** and (*S*)-*p*-NH_2-Bn-DOTA **4** were purchased from Macrocyclics (Dallas, TX, USA). ^{86}Y was purchased as [^{86}Y]YCl_3 in 0.04 M HCl (500 μL) from QSA Global GmbH (Germany).

Reactions and incubations were performed in 1.5 mL DNA low-binding tubes (Eppendorf, Germany) using a Thermomixer Comfort (Eppendorf, Germany). Lyophilization was carried out using an Alpha 2–4 LSC (Christ, Germany). L-RNA concentrations were determined via measurement of the UV absorbance at 260 nm using an Eppendorf (Germany) BIOPhotometer. Measurements of the pH-value in small volumes were performed using the pH sensor Biotrode (Metrohm, Germany).

Chromatographic Purifications and Analysis. HPLC purification and analysis were performed with a LaChrom Instrument (Hitachi-Merck, Germany) system, coupled with the radioisotope detector Gabi (Raytest, Germany). The used HPLC columns were as follows: (A) XTerra MS C_{18} column (Waters, USA) 3.0 × 50 mm i.d., 2.5 μm; (B) XTerra MS C_{18} column (Waters, USA) 4.6 × 50 mm i.d., 2.5 μm; (C) PLRP-S RP_{18} column (Varian Inc., USA) 4.6 × 250 mm i.d., 5 μm; (D) Aqua C_{18} column (Phenomenex, USA) 4.6 × 250 mm i.d., 5 μm; and (E) Aqua C_{18} column (Phenomenex, USA) 10 × 250 mm i.d., 5 μm. System A(I): flow 0.35 mL/min, gradient of acetonitrile (5% at 0 min, 13.5% at 18 min, 20.5% at 24 min, and 50% from 24 to 35 min) in 50 mM triethylammonium acetate (TEAA). System A(II): flow 0.35 mL/min and isocratic 5% acetonitrile in 0.1 M ammonium acetate. System A(III): flow 0.4 mL/min, gradient of acetonitrile (5% at 0 min, 7.3% at 35 min, and 50% from 36 to 40 min) in 50 mM ammonium acetate. System A(IV): flow 0.35 mL/min, linear gradient of acetonitrile (5% at 0 min, 29% at 25 min) in 50 mM NH_4OAc. System A(V): flow 0.3 mL/min and isocratic 2% acetonitrile. System B(I): flow 0.7 mL/min, gradient of acetonitrile (5% at 0 min, 7.7% from 41 to 44 min, 50% from 45 to 50 min) in 50 mM ammonium acetate. System B(II): flow 0.65 mL/min, gradient of acetonitrile (5% at 0 min, 50% from 20 to 25 min) in 0.1% TFA. System C(I): flow 1 mL/min, linear gradient of acetonitrile (5% at 0 min, 20% from 25 to 30 min) in 50 mM TEAA. System C(II): flow 1 mL/min, gradient of acetonitrile (5% at 0 min, 20% at 25 min, 40% at 30 min) in 50 mM TEAA. System C(III): flow 1 mL/min, linear gradient of acetonitrile (5% at 0 min, 11% at 25 min) in 50 mM TEAA. System D(I): flow 1 mL/min (E(I): flow 4 mL/min) and an isocratic elution with 5% acetonitrile in 50 mM triethylammonium hydrogencarbonate.

Mass Spectrometry. Mass spectra were recorded on a Quattro Ultima ESI-MS (Micromass, UK) and on a Daltonics Autoflex II TOF/TOF50 (Bruker, USA). The MALDI-TOF matrix, 3-hydroxypicolinic acid, was purchased from Aldrich (USA). The L-RNA probes were desalted for MALDI-TOF measurements using C_{18} purification tips (ZipTip, Millipore, USA) as described elsewhere (*13*).

NMR Studies. 1D and 2D spectra were recorded on an AMX300 spectrometer (Bruker, USA) equipped with direct and inverse broadband multinuclear probes and variable-temperature unit. ^{1}H and ^{13}C measurements were made at frequencies of 300.13 and 75.5 MHz, with complexes dissolved in D_2O and referenced using TSP as internal standard. The phase-sensitive COSY spectra were acquired using 2K data points in F2 and 512 increments in F1 dimensions and processed to a 2K × 1K matrix after apodalization with a QSine bell function in both dimensions. The phase-sensitive (TPPI) NOESY spectra were recorded at 25 °C using a mixing time (80 and 140 ms at 25 °C and 250 ms at 55 °C for Y**4b** and 110 ms at 25 °C for Y**4a**) measured using the standard inversion–recovery pulse sequence and processed as the COSY spectra. HMQC spectra were recorded using BIRD preparation period and 2K × 1K data points and processed using a square sine bell function in both dimensions. HMBC experiments were recorded using the pulse sequence inv4lplrnd of the Bruker software and acquired with 512 increments in the F1 dimension and 4K data points in the F2 dimension. Four dummy scans and 250 scans were used for spectral recording.

Circular Dichroism (CD) Spectroscopy and Polarimetric Measurements. CD measurements were carried out on a J-715 spectropolarimeter (Jasco GmbH, Germany) interfaced with a personal computer. The CD spectra were acquired and processed using the J-700 program for Windows. The experiments were carried out at room temperature using quartz cells (Hellma GmbH, Germany) with Suprasil windows and an optical path length of 0.02 cm. Spectra were recorded in the 190–300 nm wavelength range. The signal-to-noise ratio was improved by accumulating 8 scans. Polarimetric measurements were carried out on a 241 polarimeter (Perkin-Elmer LS, Finland) using an optical path length of 2 cm. Both CD and polarimetric measurements were performed using the deuterated aqueous solutions of Y**4a** and Y**4b** utilized for NMR studies.

[Y((*S*)-*p*-NH$_2$-Bn-DOTA)]$^-$. (*S*)-*p*-NH$_2$-Bn-DOTA **4** (25 mg, 40 μmol) in 1 mL ammonium acetate buffer (0.5 M, pH 6.8) was added to 87 μL of YCl_3 (0.5 M), and the mixture (pH 6.1) was incubated for 30 min at 90 °C. A solution of DTPA (300 μL, 30 mM, pH 6.0) was added, and the reaction mixture was incubated for 10 min at 40 °C to complex unreacted Y. The resulting isomers Y**4a** and Y**4b** were fractionized by HPLC system E(I), concentrated by evaporation, and lyophilized. For ESI-MS measurements, Y**4a** and Y**4b** were dissolved in acetonitrile and methanol (1:4 v/v) and the spectra were collected in the negative ion mode. ESI-MS: Y**4a**, *m/z* 594.2 $[M]^-$; Y**4b**, *m/z* 594.2 $[M]^-$. HPLC: A(V), R_T(Y**4a**) 2.1 min, R_T(Y**4b**) 2.5 min; A(II), R_T(Y**4a**) 4.4 min, R_T(Y**4b**) 6.5 min; C(III), R_T(Y**4a**), 13.7 min, R_T(Y**4b**) 15.0 min; D(I), R_T(Y**4a**) 12.9 min, R_T(Y**4b**) 20.3 min.

[Y((*S*)-*p*-SCN-Bn-DOTA)]$^-$. The [Y((*S*)-*p*-NH$_2$-Bn-DOTA)]$^-$ isomers Y**4a** and Y**4b** (8.3 mg, 14 μmol) in 1 mL water were added separately into 10 mL glass vials (Normag, Germany) equipped with a Teflon-coated magnetic stir bar and a rubber septum. CH_2Cl_2 (0.9 mL) and Cl_2CS (0.1 mL) were added, and the mixtures were stirred vigorously at room temperature. A ninhydrine test was performed to follow the reactions as described elsewhere (*14*). After 3 h, the water layers were removed carefully and the [Y((*S*)-*p*-SCN-Bn-DOTA)]$^-$ isomers Y**2a** and Y**2b** were transferred into new glass vials and washed twice with 1 mL CH_2Cl_2. Subsequently, the isomers were lyophilized and the compounds Y**2a** and Y**2b** were obtained as a pale yellow solid. The compounds Y**2a** and Y**2b** were dissolved in acetonitrile and water (1:4 v/v) and ESI-MS spectra of both isomers were collected in the positive ion mode. ESI-MS: Y**2a**, *m/z* 638.1 $[M + 2H]^+$; Y**2b**, *m/z* 638.1 $[M + 2H]^+$. HPLC: A(I), R_T(Y**2a**) 32.7 min, R_T(Y**2b**) 31.2 min, R_T(**2**) 26.5 min; B(II): R_T(Y**2a**) 13.8 min, R_T(Y**2b**) 12.8 min, R_T(**2**) 14.4 min.

[Y-DOTA]-Hexanol. (*S*)-*p*-SCN-Bn-DOTA **4** (8.0 mg, 11.5 μmol) was conjugated to 6-amino-1-hexanol (Fluka, USA) (10.4 mg, 88.8 μmol) in water (251 μL, pH 8.4) by incubation for 4 h at 40 °C. HPLC analysis indicated the complete consumption of the DOTA precursor **4**. Subsequently, 100 μL of the reaction mixture, 9.2 μL YCl_3 (0.5 M in 0.04 M HCl), and 200 μL ammonium acetate buffer (0.5 M) were incubated for 20 min at 90 °C and pH 5.8. Additionally, the [Y((*S*)-*p*-SCN-Bn-DOTA)]$^-$ isomers Y**2a** and Y**2b** (1.1 mg, 0.6 μmol) were conjugated separately to 6-amino-1-hexanol (2.4 mg, 0.6 μmol) by incubation in water for 1 h at 25 °C and pH 8.8. Product fractions of both reaction batches were separated via HPLC analyzed via ESI-MS. ESI-MS: Y**6a**, *m/z* 755.3 $[M + 2H]^+$; Y**6b**, *m/z* 755.4 $[M + 2H]^+$. HPLC: A(IV), R_T(Y**6a**) 16.3 min, R_T(Y**6b**) 17.0 min; C(II): R_T(Y**6a**) 26.0 min, R_T(Y**6b**) 26.8 min.

DOTA-L-RNA. (*S*)-*p*-SCN-Bn-DOTA **2** (6.3 mg, 9.0 μmol) was conjugated to L-RNA **1** (2.4 mg, 0.6 μmol) in 0.7 M sodium bicarbonate buffer (121 μL, pH 9.0) by incubation for 2 h at 40 °C. For the purification of DOTA-conjugate **3**, 300 μL ethanol (abs.) and 1100 μL 70% ethanol were added, and the mixture was centrifuged for 20 min at –10 °C and 14 000 rpm. The supernatant with unreacted (*S*)-*p*-SCN-Bn-DOTA **2**, and DOTA-thiourea **5** was removed and the pellet washed twice with 70% ethanol, centrifuged, and resuspended in 0.3 M sodium acetate for an additional precipitation with ethanol as described above. Subsequently, the pellet was resuspended in 100 μL water. DOTA-L-RNA **3** was purified via size exclusion chromatography (SEC) using a 25 × 490 mm column (P4 Biogel, Medium 90–180 μm, Bio-Rad Melville, USA) with 0.1 M ammonium acetate buffer (pH 7.0) as mobile phase at a flow rate of 17.5–18.4 mL/h. The UV absorbance was monitored at 260 nm. The identity of the DOTA-conjugate **3** was verified by mass spectrometry. Maldi-TOF: **3**, *m/z* 4521.4 $[M + H]^+$.

[Y-DOTA]-L-RNA. [Y((*S*)-*p*-SCN-Bn-DOTA)]$^-$ isomers Y**2a** and Y**2b** were conjugated separately to L-RNA **1** by incubation in borate buffer (12.5 mM, pH 9.6) for 3 h at 40 °C. Product fractions of both reaction batches were separated via HPLC and lyophilized. The separated HPLC fractions were analyzed via MALDI-TOF measurements. To confirm the identity of [^{86}Y-DOTA]-L-RNA isomers Y**3a** and Y**3b**, the DOTA-modified L-RNA **3** was radiolabeled with carrier-added ^{86}Y using a molar ratio of **3** to YCl_3 of 1:1. Both ^{86}Y-complex isomers [^{86}Y]**3a** and [^{86}Y]**3b** were analyzed by HPLC and Maldi-TOF. MALDI-TOF: Y**3a**, *m/z* 4613 $[M + 2H]^+$; Y**3b**, *m/z* 4612 $[M + 2H]^+$. HPLC: A(III), R_T(Y**3a**) 26.5 min, R_T(Y**3b**) 29.4 min, R_T([^{86}Y]**3a**) 26.8 min, R_T([^{86}Y]**3b**) 29.8 min.

[^{86}Y((*S*)-*p*-NH$_2$-Bn-DOTA)]$^-$. (*S*)-*p*-NH$_2$-Bn-DOTA **4** (66 μg, 0.1 μmol) in 450 μL ammonium acetate buffer (0.5 M, pH 7.0) was added to 100 μL of [^{86}Y]YCl_3 (21 MBq) and the mixture was incubated for 20 min at 90 °C. A solution of DTPA (10 μL, 30 mM, pH 6.0) was added, and the reaction mixture was incubated for 5 min at 40 °C to complex unreacted [^{86}Y]Y^{3+}. The [^{86}Y((*S*)-*p*-NH$_2$-Bn-DOTA)]$^-$ isomers [^{86}Y]**4a** and [^{86}Y]**4b** were separated by HPLC system A(II). Under these conditions, the [^{86}Y(DTPA)]$^{2-}$ complex eluted with the void volume from the column. HPLC fractions containing [^{86}Y]**4a** and [^{86}Y]**4b** were concentrated at 90 °C under a dinitrogen stream, and the residues were dissolved in saline.

HPLC fractions of the [^{86}Y((*S*)-*p*-NH$_2$-Bn-DOTA)]$^-$ isomers [^{86}Y]**4a** and [^{86}Y]**4b**, containing TEAA as ion pair reagent, was used for estimation of the partition coefficient. A saturated *n*-octanol/water system was prepared in 1.5 mL tubes containing 400 μL buffer (25 mM disodium hydrogen phosphate and 0.09 M sodium chloride (pH 7.4)) and 400 μL *n*-octanol. The isomers [^{86}Y]**4a** and [^{86}Y]**4b** (30 μL, app. 250 kBq) were added separately, and the solutions were shaken vigorously for 5 min and incubated on a wave mixer for 30 min. The organic and aqueous phases were separated by centrifugation for 5 min at 5000 rpm. Subsequently, 300 μL of the *n*-octanol layer was transferred into a new tube, and the phase boundary was removed carefully by adding 200 μL to the waste. Afterward, the water layer (300 μL, pH 7.0) was transferred into a separate tube. The radioactivity of the organic and aqueous phases was measured on the gamma counter in five experiments, and the average was calculated. The partition coefficient log $D_{7.0}$ was defined as the ratio of the amount of the radiotracer present in the organic layer to that present in the aqueous phase. Partition coefficient: log $D_{7.0}$ ([^{86}Y]**4a**), –2.0 ± 0.029; log $D_{7.0}$ ([^{86}Y]**4b**), −2.3 ± 0.032. HPLC: A(II), R_T([^{86}Y]**4a**) 5.0 min, R_T([^{86}Y]**4b**) 7.3 min; C(III): R_T([^{86}Y]**4a**) 14.4 min, R_T([^{86}Y]**4b**) 15.7 min.

[^{86}Y-DOTA]-L-RNA. Radiolabeling of the DOTA-modified L-RNA **3** (95–160 μg, 21–36 nmol) with [^{86}Y]YCl_3 was performed in 300–350 μL ammonium acetate buffer (0.5 M, pH 7.0). After the addition of 50–100 μL of [^{86}Y]YCl_3 (13–45 MBq), the mixture was incubated for 30–60 min at 90 °C. A solution of DTPA (10 μL, 30 mM, pH 6.0) was added, and the reaction mixture was incubated for 10 min at 40 °C to complex unreacted [^{86}Y]Y^{3+}. The HPLC separation of the isomers [^{86}Y]**3a** and [^{86}Y]**3b** were performed on system B(I). Under these conditions, the [^{86}Y(DTPA)]$^{2-}$ complex eluted with the void volume from the column. HPLC fractions containing the separated isomers [^{86}Y]**3a** and [^{86}Y]**3b** were concentrated in a stream of nitrogen at 40 °C for 10 min. HPLC: B(I), R_T([^{86}Y]**3a**) 29.7 min, R_T([^{86}Y]**3b**) 32.4 min; A(III), R_T([^{86}Y]**3a**) 27.5 min, R_T([^{86}Y]**3b**) 29.8 min.

Determination of the Time-Dependent Radiochemical Yield of [^{86}Y]3. The kinetics of ^{86}Y-complexation of L-RNA **3** was followed by SDS-PAGE. In four attempts, L-RNA **3** (100 μg, 22 nmol) and [^{86}Y]YCl_3 (50 μL, 12–45 MBq) was incubated in ammonium acetate buffer (0.5 M, 300 μL, pH 7.0) at 90 °C for 60 min. At specific time points (0, 3, 9, 12, 15, 20, 25, 30, 35, 40, 45, 50, 55, and 60 min), reaction aliquots (15 μL) were mixed with a solution of DTPA (10 μL, 15 mM, pH 6.0) and heated up to 40 °C for 10 min to complex free [^{86}Y]Y^{3+} as [^{86}Y(DTPA)]$^{2-}$ complex. SDS-PAGE was performed using a Multiphor II Electrophoresis (GE Healthcare, USA) system and SDS precast gels (GE Healthcare, USA), ExcelGel Gradient 8–18. A 10 bp DNA ladder (Invitrogen, USA) was applied as a molecular weight standard. After electrophoresis, the gel was exposed to a phosphor imaging plate for 2–4 min and scanned with a Fujix BAS 5000 (Fujifilm Europe, Germany). Subsequently, the gel was stained using ethidium bromide, and the DNA ladder was visualized and photographed under UV light. Radiochemical yields were calculated from the radioactivity area of the product peak related to the total radioactivity area using *Tina 2.09* software (Raytest, Germany).

Biodistribution. All animal experiments were performed in accordance with the German laws for the protection of animals and were approved by the regional council. The biodistribution profiles of the radiolabeled L-RNA isomers [^{86}Y]**3a** and [^{86}Y]**3b** and the [^{86}Y((*S*)-*p*-NH_2-Bn-DOTA)]$^-$ isomers [^{86}Y]**4a** and [^{86}Y]**4b** were studied in male Wistar rats (150 g body weight). For the time points 5 and 60 min, approximately 120 kBq aliquots of each compound were administered in 300 μL saline into the tail vein. For the longer examination period of 18 h, approximately 250 kBq aliquots of the L-RNA isomers [^{86}Y]**3a** and [^{86}Y]**3b** were administered. After the radiotracer application, four rats were anaesthetized for each radiotracer with ether at 5 min, 60 min, and 18 h, respectively. Blood was withdrawn by heart puncture, and the animals were euthanized. Organs and tissues were removed and weighed, and the radioactivity was measured in a calibrated well counter. The data were normalized to the amount of injected radioactivity and expressed as standardized uptake values (SUV). The SUV was calculated with following equation:

SUV = (organ activity/organ weight)/(total given activity/rat body weight)

The amount of radioactivity in urine was calculated as the total radioactivity of the injected dose subtracted by the values of all individual organs.

Metabolite Analysis. The *in vitro* stability analysis of the radiolabeled L-RNA [^{86}Y]**3b** was performed via HPLC as described in detail in the Supporting Information. The *ex vivo* autoradiography of the kidney sections containing the L-RNA [^{86}Y]**3b** was detailed in the Supporting Information.

[^{86}Y((S)-p-NH_2-Bn-DOTA)]$^-$. The [^{86}Y((*S*)-*p*-NH_2-Bn-DOTA)]$^-$ somers [^{86}Y]**4a** and [^{86}Y]**4b** (2.3 MBq) were injected separately and intravenously into male Wistar rats. After sacrificing the rats 60 min p.i., the bladders were removed. Urine samples were collected by puncture of the bladders and methanol was added to the sample in a ratio of 1:2. The mixtures were shaken vigorously and centrifuged for 10 min at 13 000 rpm. The supernatants were transferred into a new vial, and the solutions were concentrated at 65 °C in a stream of nitrogen. TLC analyses were performed on Merck (Germany) RP_{18} plates with system (I): 0.1 M ammonium acetate in 5% acetonitrile (pH 7.0) and with system (II): methanol and 10% ammonium acetate (9:1 v/v) as the running buffer. The dried TLC plates were exposed to phosphor imaging plates for 10 min. The plates were scanned and the rates of radioactivity were calculated as described above. HPLC analyses of the prepared urine samples ([^{86}Y]**4a**, 50 μL, 17 kBq; [^{86}Y]**4b**, 100 μL, 90 kBq) were performed on system C(II).

[^{86}Y-DOTA]-L-RNA. The radiolabeled L-RNA [^{86}Y]**3** (2.3 MBq) isomers was injected intravenously into a male Wistar rat. Arterial blood samples of the rat were collected after injection of the radiolabeled compounds after 1, 3, 5, and 10 min p.i. The plasma of the blood samples was separated by centrifugation for 10 min at 13 500 rpm and 23 °C. Subsequently, the plasma samples were diluted in buffer (25 mM disodium hydrogen phosphate and 0.09 M sodium chloride (pH 7.4)) in a ratio of 1:1 and applied on a 20% PAGE. The plasma fraction of the blood probes obtained after 20 min p.i. contained insufficient radioactivity (<10 cps) for a subsequent PAGE analysis.

After sacrificing the rat 60 min p.i., the bladder and the kidneys were removed. A urine sample was collected by puncture of the bladder. A volume of 500 μL of the urine sample was applied onto Microcon YM-10 centrifugal filter units (10 kDa MWCO, Millipore, USA) and centrifuged for 60 min at 13 500 rpm at RT to separate low molecular weight metabolites. The protein pellet in the sample reservoir was transferred into a new vial by an invert spin mode. The pellet was enzymatic digested with a solution A (10 mM Tris-HCl (pH 8.0), 100 mM NaCl, 25 mM EDTA, and 2.0 mg/mL Proteinase K (Serva, Germany)) at 65 °C for 20 min. Subsequently, the probe was mixed with phenol/chloroform (1:1 v/v) and centrifuged at 13 500 rpm for 10 min. The water phase was extracted with chloroform (1:1 v/v) and centrifuged as described above. The water phase and the YM-10 filtrate fraction were analyzed on HPLC system C(I) and via PAGE.

The rat kidneys were homogenized in solution A and digested at 65 °C for 20 min. The homogenates were extracted with phenol/chloroform (1:1 v/v) as described above and analyzed via PAGE with a native 20% polyacrylamide gel. A 10 bp DNA ladder (Fermentas, USA) was applied as a molecular weight marker. After electrophoresis, the gel was exposed to a phosphor imaging plate for 60 min and scanned with a Fujix BAS 5000 (Fuji Photo Film, Japan). Subsequently, the DNA ladder was stained using ethidium bromide, visualized, and photographed under UV light.

RESULTS AND DISCUSSION

DOTA-Modification of the 12mer L-RNA. The primary amine group of the 5′-hexylamine containing 12mer L-RNA **1** was used for modifications of **1** with a BFC. The coupling reaction between the L-RNA **1** and the DOTA derivative (*S*)-*p*-SCN-Bn-DOTA **2** accomplished in the formation of a selective thiourea bond **3** (see Figure 2). A 50-fold excess of **2** was required for quantitative reactions, since L-RNA **1** cannot be separated from DOTA-L-RNA **3** via size-exclusion chromatography (SEC).

It must be noted that isothiocyanates are easily hydrolyzed in aqueous alkaline solutions (*15*). As outlined in Figure 3,

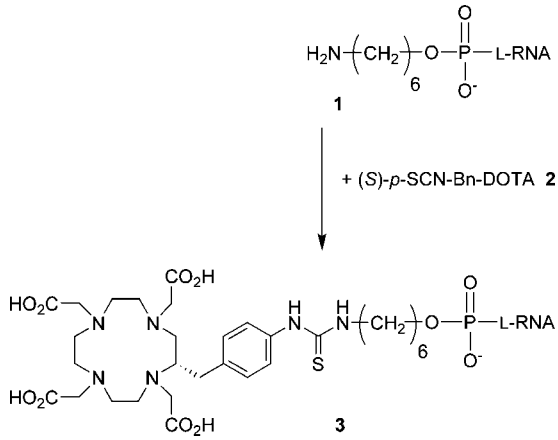

Figure 2. DOTA modification of the L-RNA **1** with (*S*)-*p*-SCN-Bn-DOTA **2** to DOTA-L-RNA **3**.

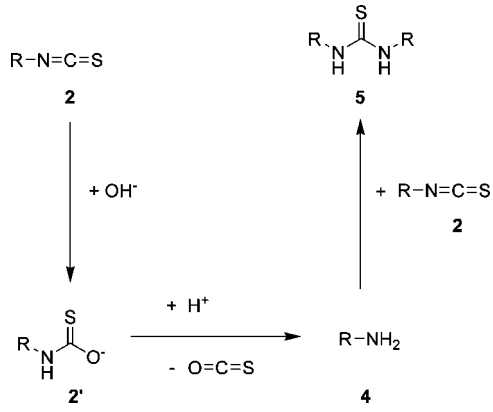

Figure 3. Hydrolysis of isothiocyanate **2** and proposed formation of symmetric thiourea **5**.

isothiocyanate **2** is hydrolyzed into primary amine **4** via the thiocarbamate **2′**, which subsequently reacts with an additional isothiocyanate **2** to afford symmetric thiourea **5**. The formation of symmetric DOTA-thiourea **5** was confirmed by ESI-MS analysis of SEC fractions containing **5**. SEC profiles of the reaction mixture and an ESI-MS spectrum of the DOTA-thiourea **5** are shown in the Supporting Information.

Complete separation of (*S*)-*p*-SCN-Bn-DOTA **2** and DOTA-thiourea **5** from the reaction batch was achieved through ethanol precipitation of DOTA-L-RNA **3** followed by SEC. Chemical purities of >95% for DOTA-L-RNA **3** were achieved as confirmed by HPLC chromatography. Only L-RNA **1** was detected as a minor (<5%) impurity.

Radiolabeling. DOTA-L-RNA **3** was used for radiolabeling with [^{86}Y]YCl_3. ^{86}Y-complexation kinetics of DOTA-conjugate **3** at 90 °C was monitored via PAGE as described in detail in the Supporting Information. The time-dependent radiochemical yields of [^{86}Y]**3** are shown in Figure 4. Compound [^{86}Y]**3** was obtained with the maximum radiochemical yield of 85 ± 2% already after 9 min. Less then 4% radioactivity was characterized as $[^{86}Y(DTPA)]^{2-}$ complex at the same time.

An important observation was made by analyzing the radiolabeled L-RNA [^{86}Y]**3** via ion-pair chromatography with a very shallow solvent gradient. Two isomers, [^{86}Y]**3a** and [^{86}Y]**3b**, could be observed in the radiometric profile with a difference in the retention times of 3 min. To verify the isomerization of the ^{86}Y-labeled L-RNA, the DOTA-conjugate **3** was radiolabeled with carrier added ^{86}Y, and the mixture was analyzed via HPLC. The ratio of the isomers [^{86}Y]**3a** and [^{86}Y]**3b** was found to be 1:2 in both the UV profile (Figure 5A) and the radiometric profile (Figure 5C).

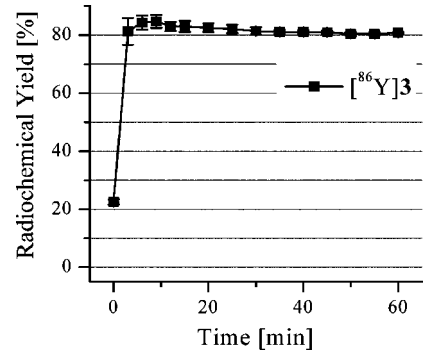

Figure 4. Kinetics of ^{86}Y-complexation of DOTA-L-RNA **3** expressed as % radiochemical yield as a function of time.

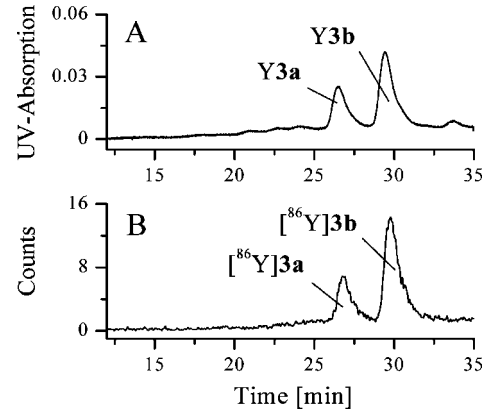

Figure 5. HPLC profiles of the L-RNA isomers: Analysis of the crude reaction mixture of [^{86}Y]**3** gave the same ratio of the isomers [^{86}Y]**3a** and [^{86}Y]**3b** (1:2) in both the UV profile (A) and the radiometric profile (B).

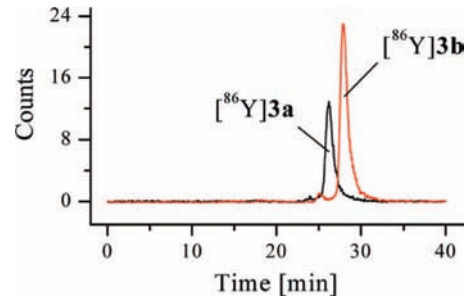

Figure 6. Overlay of the radiometric profiles of the separated HPLC fractions containing [^{86}Y]**3a** and [^{86}Y]**3b**.

The cumulative radiochemical yield of the isomer mixture [^{86}Y]**3** was determined separately by HPLC and PAGE analysis giving values of 73% and 85%, respectively. Conversely, thin layer chromatography did not give reproducible results. HPLC purification of the radiolabeled L-RNA [^{86}Y]**3** gave radiochemical purities of up to 98%. Effective specific activities of up to 0.15 MBq/μg were achieved as determined by HPLC. Hence, in a typical experiment starting from 24.1 MBq of [^{86}Y]YCl_3, 6 MBq of [^{86}Y-DOTA]-L-RNA [^{86}Y]**3** was obtained within 90 min. Additionally, the isomers [^{86}Y]**3a** and [^{86}Y]**3b** were separated via HPLC, and the obtained fractions were used for biodistribution studies in rats (see Figure 6).

Structure of LnDOTA$^-$ Complexes. The structure of $[Ln(DOTA)]^-$ complexes in solution have been examined extensively by NMR studies and are well-understood, as reviewed in ref (*16*). Briefly, the four nitrogen atoms of the azamacrocycle coordinate the metal from the upper side, while the four oxygen atoms of the pendant carboxylic acid arms coordinate the opposite bottom

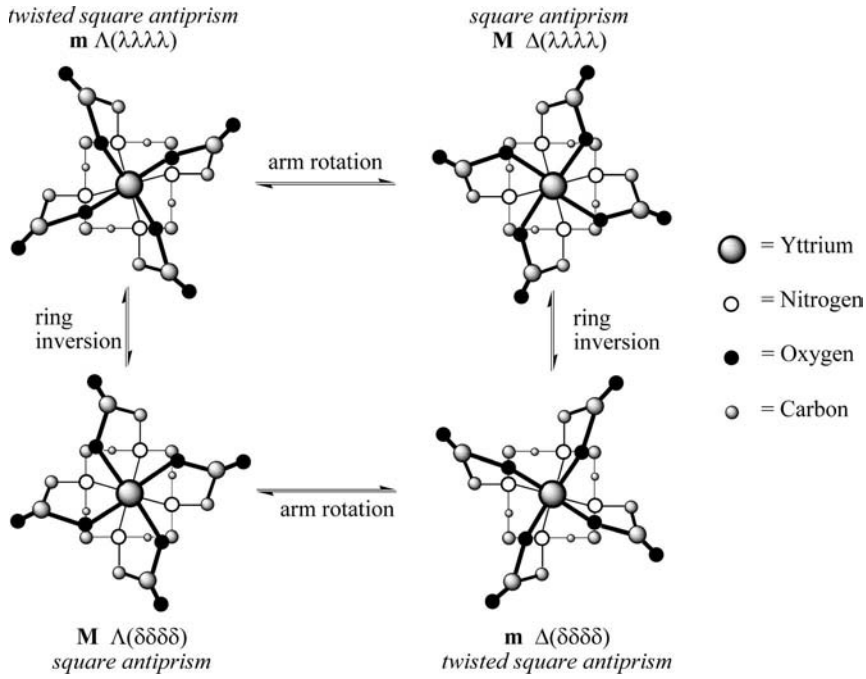

Figure 7. Interconversion pathways of the four possible stereoisomers of the [Y(DOTA)]$^-$ complex. The figure has been adapted from ref (*17*).

side. The coordination is usually completed by a capping water molecule inserted on the carboxylate face. These species adopt two coordination geometries: capped square antiprism (SAP or M; torsion angle ~39°) and capped twisted square antiprism (TSAP or m; torsion angle ~25°), which are related by elements of helicity of the carboxylate side arms (Δ or Λ) and flipping of the azamacrocycle (defined as either *δδδδ* or *λλλλ*), eventually resulting in formation of four stereoisomers related as two pairs of enantiomers designated as Δ(*λλλλ*) or Λ(*δδδδ*) (SAP type) and Δ(*δδδδ*) or Λ(*λλλλ*) (TSAP type) (see Figure 7). The SAP/TSAP ratio depends on the ionic radius of the lanthanide ion; the SAP geometry is preferred with larger ions (*17*). The trivalent yttrium ion has a large ionic radius (r_i = 1.075 Å for coordination number 9), thereby producing preferentially SAP isomers. The insertion of a substituent onto the carbon framework of the tetra-azamacrocycle introduces a new chiral center leading to the formation of additional stereoisomers. For steric reasons, such a side chain should adopt a pseudo equatorial conformation to avoid interactions with the macrocycle, thus "freezing-out" ring flip motion and locking the macrocycle ring into a (*δδδδ*) conformation (see Figure 8) (*18*).

Isomer Formation of the [Y((*S*)-*p*-NH$_2$-Bn-DOTA)]$^-$ Complex. After complexation of Y^{3+} with the (*S*)-*p*-NH$_2$-Bn-DOTA **4** chelator, two conformers could separated by ion pair chromatography (see Figure 10). HPLC analysis of the [Y((*S*)-*p*-NH$_2$-Bn-DOTA)]$^-$ isomers Y**4a** and Y**4b** was performed using ion pairing agents such as triethylammonium acetate (TEAA) or ammonium acetate. By analysis of the isomers Y**4a** and Y**4b** with HPLC system D(I), the retention times differ by 7.4 min. Without an ion pairing agent in the eluent, the retention times of the isomers Y**4a** and Y**4b** differ only by 0.44 min (system A(V)).

For both isomers Y**4a** and Y**4b**, the ratio of square antiprism (SAP) to twisted square antiprism (TSAP) was found to be 3:1. The thermal stability of the [Y((*S*)-*p*-NH$_2$-Bn-DOTA)]$^-$ isomers Y**4a** and Y**4b** were determined by separate incubation of Y**4a** and Y**4b** in water for seven days at 90 °C. No interconversions of the two isomers Y**4a** and Y**4b** were observed for this period by HPLC and NMR analysis.

NMR Spectra. The stereochemistry of the [Y((*S*)-*p*-NH$_2$-Bn-DOTA)]$^-$ isomer Y**4b** (peak 2 in Figure 10) was assessed through a battery of monodimensional and two-dimensional NMR spectra, taking into account that SAP geometry is usually adopted in DOTA-substituted metal complexes (*18, 19*). The diamagnetic nature of the Y(III) ion confines the proton signals of Y**4b** in a relatively narrow region compared to the usually large ppm window accessible in the case of paramagnetic lanthanide ions. In detail, Y**4b** dissolved in deuterated water exhibits four aromatic protons of the 4-amine-substituted benzyl residue (A_2B_2 system) at ca. 7.00 ppm and 25 aliphatic protons spread over the 3.70–2.10 ppm region as a series of overlapped multiplets. The unique methyne carbon C(4) (see Figure 11) is

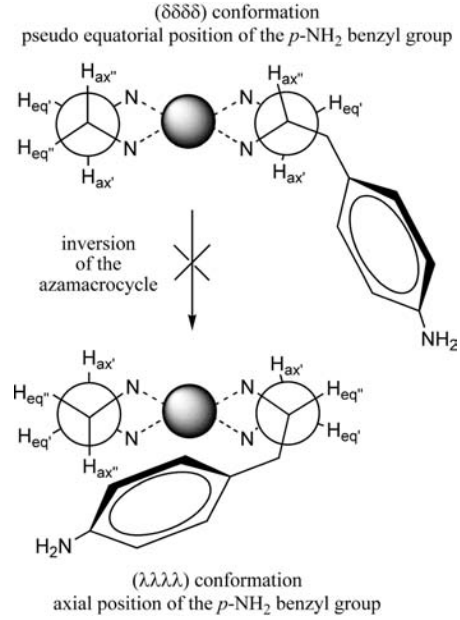

Figure 8. Newman projection of the [Y((*S*)-*p*-NH$_2$-Bn-DOTA)]$^-$ complex Y**4**. The figure has been adapted from ref (*18*). For steric reasons, the bulky *p*-NH$_2$ benzyl substituent looks the complex into a (*δδδδ*) conformation and inhibits the ring flip motion to the (*λλλλ*) conformation. As a result, only the Λ(*δδδδ*) SAP (M) and the Δ(*δδδδ*) TSAP (m) species are observed in solution as a pair of conformational isomers.

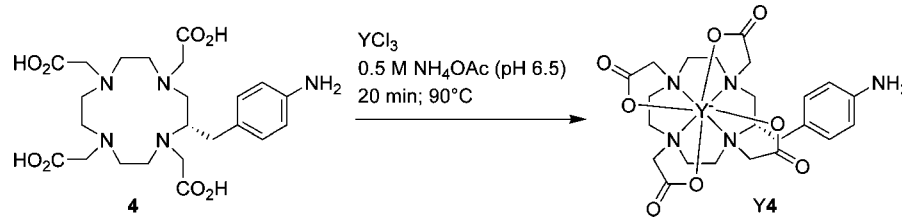

Figure 9. Complexation of Y^{3+} with the (*S*)-*p*-NH_2-Bn-DOTA **4** chelator.

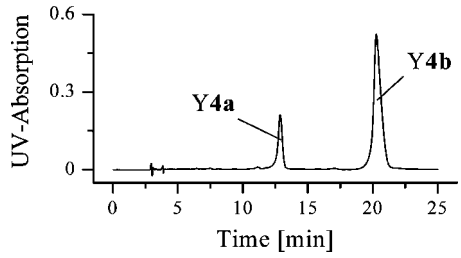

Figure 10. HPLC separation of the TSAP isomer Y**4a** and the SAP isomer Y**4b** of the [Y((*S*)-*p*-NH_2-Bn-DOTA)]$^-$ complex.

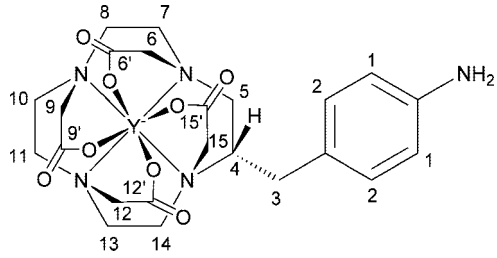

Figure 11. Proposed structure of the [Y((*S*)-*p*-NH_2-Bn-DOTA)]$^-$ isomer Y**4b**.

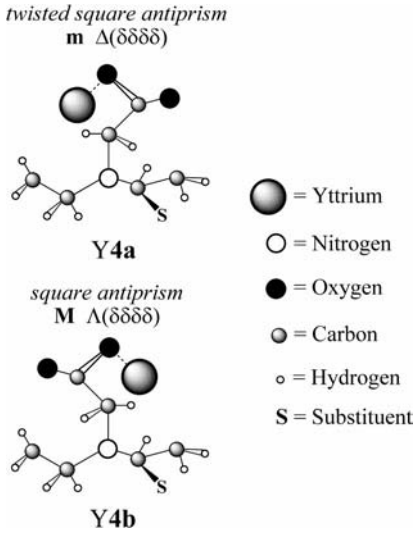

Figure 12. Structures of the [Y((*S*)-*p*-NH_2-Bn-DOTA)]$^-$ isomers Y**4a** and Y**4b** are represented schematically. The figure has been adapted from ref (*17*). Only the geometry around the N-CH_2-COO group next to the (*S*)-configured carbon atom bearing the *p*-NH_2 benzyl group **S** is given.

assigned by means of the $^{13}C\{^1H\}$ DEPT experiment at δ 66.68 ppm, and the corresponding methyne proton H(4) is found at δ 3.11 ppm according to the $^1H-^{13}C$ HMQC map correlation (Figure 13A). The $^1H-^1H$ COSY map indicates that H(4) is scalarly coupled with diastereotopic H(3) and H(5) methylene protons. The $^1H-^{13}C$ HMBC map shows the ^2J correlation of C(4) with H(3) and H(5) and the ^3J correlation with H(15) protons (Figure 13A). This acetate methylene is also correlated with the unique carbonyl (C(15′) at δ 180.41 ppm) slightly upfield shifted compared to the other three carbonyls (C(6′), C(9′), and C(12′), which fall at δ 180.59 ppm).

Moreover, the $^1H-^1H$ NOESY map shows the additional dipolar couplings of $H(5)_{eq}$ with aromatic H(2) and of H(4) with the unique acetate methylene group identified as H(15) (Figure 13B). The occurrence of the latter interaction establishes that methyne H(4) is axially positioned toward the N_4O_4-DOTA "sandwich" and that the bulkier benzyl residue is equatorially positioned away from the "sandwich". The pseudo equatorial position of the pendant group is in agreement with previous observations on similar DOTA-substituted Eu complexes (*18*). In addition, the aromatic H(2) protons display a distinctive coupling with $H(5)_{eq}$ (Figure 13B) along with the expected couplings with H(3) and H(4). According to these data, Y**4b** is assigned to be the SAP isomer $\Lambda(\delta\delta\delta\delta)\Lambda$ (see Figure 12).

The minor isomer Y**4a** (see Figure 12) shows broader ^1H and ^{13}C profiles which do not sharpen in the range 5−90 °C and, therefore, do not allow complete NMR characterization. The difficulty to obtain well-resolved spectra and the observation in the phase-sensitive $^1H-^1H$ NOESY map of wide areas of positive cross peaks in the methylene region suggest the occurrence of exchange processes in the NMR time scale. However, the retention of the pseudo equatorial conformation of the benzyl side chain allows the assignment of the minor isomer as the TSAP isomer $\Delta(\delta\delta\delta\delta)$.

In accordance with this assignment, both isomers rotate plane-polarized light to the identical direction (α(Y**4a**), +0.008; α(Y**4b**), +0.018) indicating the presence of the same chiral carbon in the tetra-aza backbone. On the contrary, circular dichroism spectroscopy shows absorptions in opposite directions in the far-UV region indicating change of helicity of the carboxylate groups (see Figure 14).

Radiolabeling and Estimation of the Partition Coefficient. The radiolabeling of (*S*)-*p*-NH_2-Bn-DOTA **2** with [^{86}Y]YCl_3 yielded two [^{86}Y((*S*)-*p*-NH_2-Bn-DOTA)] isomers [^{86}Y]**4a** and [^{86}Y]**4b** with a cumulative radiochemical yield of 99% as determined by HPLC. The complex isomers [^{86}Y]**4a** and [^{86}Y]**4b** were separated via HPLC, and the obtained fractions were used for biodistribution studies and metabolite analyses and for the estimation of the partition coefficient. The partition coefficient log $D_{7.0}$ was defined as the ratio of the amount of radiotracer present in the organic layer (*n*-octanol) to that present in the aqueous phase. The log $D_{7.0}$ values were determined in the presence of the ion pair reagent TEAA (log $D_{7.0}$ ([^{86}Y]**4a**) −2.0 ± 0.029; log $D_{7.0}$ ([^{86}Y]**4b**), −2.3 ± 0.032).

Isomerism of the [Y-DOTA]-L-RNA. To draw additional information from the isomeric forms of the chelate unit [Y((*S*)-*p*-NH_2-Bn-DOTA)]$^-$ Y**4**, both Y**4a** and Y**4b** isomers were attached separately to the L-RNA **1**. Thus, the amino group of the benzylamine residue in Y**4a** and Y**4b** was transferred into an isothiocyanate moiety by reaction of Y**4a** and Y**4b** with thiophosgene. The resulting [Y((*S*)-*p*-SCN-Bn-DOTA)]$^-$ complexes Y**2a** and Y**2b** were obtained quantitatively after 3 h, as confirmed by the ninhydrine test. After HPLC separation, both Y**2a** and Y**2b** were attached to the L-RNA **1** by incubation in

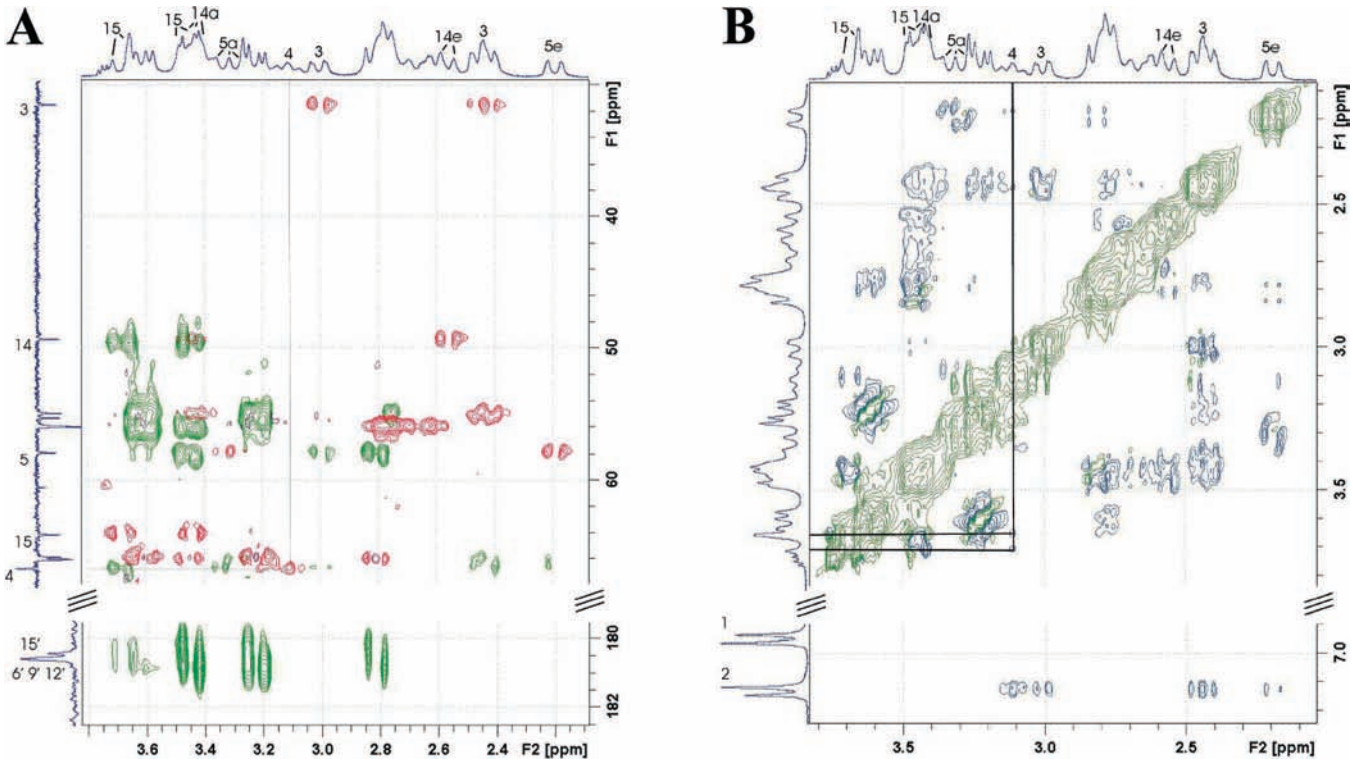

Figure 13. (A) Heterodinuclear $^{1}H-^{13}C$ HMQC (red) and HMBC (green) NMR maps of the Y**4b** isomer at 25 °C in D_2O (30–70 ppm of F1 projection: ^{13}C DEPT 135 spectrum). (B) NMR 2D NOESY map of the Y**4b** isomer at 25 °C in D_2O.

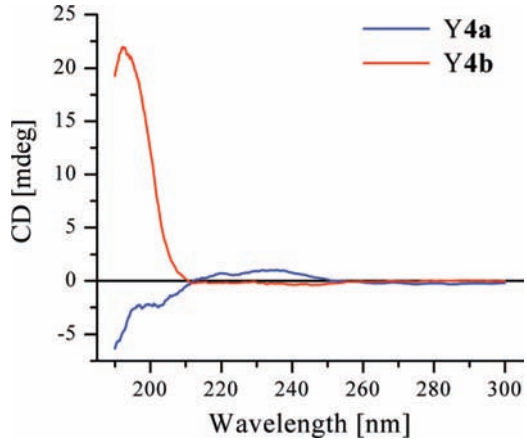

Figure 14. CD spectra of the [Y((*S*)-*p*-NH_2-Bn-DOTA)]$^-$ isomers Y**4a** and Y**4b**.

borate buffer (12.5 mM, pH 9.6) for 3 h at 40 °C. Product fractions of both reaction mixtures were separated via HPLC and lyophilized. The separated HPLC fractions containing the isomers Y**3a** and Y**3b** were analyzed via MALDI-TOF mass spectrometry and found the same mass (see Supporting Information). The identity of the [^{86}Y-DOTA]-L-RNA species was finally established by comparison of the radiometric (^{86}Y) and the UV–visible chromatographic profiles of the references Y**3a** and Y**3b**.

Biodistribution Studies. After HPLC separation (see Figure 6) the [^{86}Y-DOTA]-L-RNA isomers [^{86}Y]**3a**, [^{86}Y]**3b**, and the [^{86}Y((*S*)-*p*-NH_2-Bn-DOTA)]$^-$ isomers [^{86}Y]**4a**, [^{86}Y]**4b** were administered separately and intravenously to male Wistar rats. The biodistribution of the chelate units [^{86}Y]**4a** and [^{86}Y]**4b** were determined after 5 and 60 min. The biodistribution of the radiolabeled L-RNA isomers [^{86}Y]**3a** and [^{86}Y]**3b** were determined after 5 min, 60 min, and 18 h. The normalized concentrations of radioactivity expressed as SUV (standardized uptake values) in several organs are presented in Table 1.

Minor changes in the biodistribution profile of the complex isomers [^{86}Y]**4a** and [^{86}Y]**4b** were determined in the liver. The TSAP isomer [^{86}Y]**4a** indicate a higher liphophilicity (log $D_{7.0}$, -2.0 ± 0.03) and, as a result, a higher liver uptake after 5 min (1.7 ± 0.5) and 60 min (0.4 ± 0.1). In contrast, the SAP isomer showed a lower liphophilicity (log $D_{7.0}$, -2.3 ± 0.03) and a lower liver uptake after 5 min (0.5 ± 0.04) and 60 min (0.1 ± 0.04). The highest levels of radioactivity were determined after 60 min in the adrenals with SUV values of 4.1 ± 2.4 for the isomer [^{86}Y]**4a** and 2.6 ± 0.6 for the isomer [^{86}Y]**4b**. The SUV of the isomer [^{86}Y]**4a** in the kidneys reached 5.3 ± 1.3 after 5 min and decreased to 1.8 ± 0.19 after 60 min. For isomer [^{86}Y]**4b**, lower SUVs were observed in the kidneys with 4.4 ± 1.3 after 5 min and 1.1 ± 0.19 after 60 min. The SUVs in other organs were below 1.0 after 60 min for [^{86}Y]**4a** and [^{86}Y]**4b** in this study. A rapid clearance of the radioactivity was observed from blood, lungs, and liver for both compounds [^{86}Y]**4a** and [^{86}Y]**4b**. Very low SUVs were found in the brain for both compounds [^{86}Y]**4a** and [^{86}Y]**4b** after 60 min (0.09 ± 0.02 and 0.07 ± 0.02) suggesting that the negatively charged complexes are unable to cross the blood−brain barrier. The low uptake of radioactivity in the femur after 60 min (0.45 ± 0.28 and 0.32 ± 0.07) confirms the *in vivo* stability of the [^{86}Y((*S*)-*p*-NH_2-Bn-DOTA)]$^-$ isomers [^{86}Y]**4a** and [^{86}Y]**4b**, since free ^{86}Y accumulates in the bone (*20*).

No significant differences in the biodistribution were observed after 18 h for the radiolabeled L-RNA isomers [^{86}Y]**3a** and [^{86}Y]**3b**. The highest levels of radioactivity were measured in the kidneys and the adrenals. For both compounds, the SUVs of the kidneys slightly increased from 7.8 ± 1.0 ([^{86}Y]**3a**) and 8.8 ± 1.4 ([^{86}Y]**3b**), respectively, at 5 min to 9.8 ± 0.6 ([^{86}Y]**3a**) and 11 ± 2.0 ([^{86}Y]**3b**), respectively, at 18 h. Remarkably high SUVs (2.5 ± 0.4 and 2.0 ± 0.2) were also observed in the adrenal glands 18 h p.i. of the radiolabeled L-RNAs [^{86}Y]**3a** and [^{86}Y]**3b**. A rapid clearance of the radioactivity was observed

Table 1. Normalized Concentrations of Radioactivity in Selected Organs of Wistar Rats (Presented as SUV ± SD, $n = 4$)[a]

	5 min		60 min		5 min		60 min		18 h	
organ	[^{86}Y]**4a**	[^{86}Y]**4b**	[^{86}Y]**4a**	[^{86}Y]**4b**	[^{86}Y]**3a**	[^{86}Y]**3b**	[^{86}Y]**3a**	[^{86}Y]**3b**	[^{86}Y]**3a**	[^{86}Y]**3b**
blood	1.46 (0.18)	1.45 (0.13)	0.29 (0.14)	0.31 (0.08)	1.08 (0.12)	1.12 (0.20)	0.27 (0.05)	0.25 (0.07)	0.06 (0.01)	0.06 (0.01)
adrenal[b]	3.48 (0.97)	3.80 (1.32)	4.13 (2.40)	2.61 (0.59)	2.12 (0.27)	3.25 (0.46)	1.80 (0.08)	2.23 (0.24)	2.46 (0.38)	2.00 (0.20)
kidney[b]	5.34 (1.25)	4.40 (1.32)	1.81 (0.19)	1.14 (0.19)	7.78 (0.96)	8.75 (1.44)	7.09 (0.65)	6.63 (0.78)	9.81 (0.62)	11.16 (1.99)
muscle	0.57 (0.12)	0.56 (0.13)	0.29 (0.09)	0.27 (0.08)	0.46 (0.04)	0.45 (0.05)	0.16 (0.02)	0.23 (0.04)	0.21 (0.05)	0.19 (0.02)
heart	0.80 (0.09)	0.80 (0.14)	0.52 (0.32)	0.37 (0.12)	0.63 (0.02)	0.69 (0.04)	0.22 (0.01)	0.27 (0.03)	0.22 (0.01)	0.21 (0.01)
lung	1.29 (0.17)	1.27 (0.15)	0.52 (0.12)	0.68 (0.43)	1.05 (0.06)	1.06 (0.10)	0.33 (0.02)	0.39 (0.04)	0.25 (0.03)	0.23 (0.02)
liver	1.65 (0.45)	0.50 (0.04)	0.36 (0.10)	0.14 (0.04)	0.39 (0.03)	0.37 (0.05)	0.12 (0.01)	0.15 (0.02)	0.06 (0.01)	0.06 (0.01)
femur	0.78 (0.09)	0.77 (0.10)	0.45 (0.28)	0.32 (0.07)	0.99 (0.03)	0.79 (0.05)	0.55 (0.03)	0.41 (0.03)	0.34 (0.04)	0.31 (0.04)

[a] The SUVs were obtained after 5 and 60 min p.i. of [^{86}Y]**4a**, [^{86}Y]**4b**, [^{86}Y]**3a**, and [^{86}Y]**3b**. Additionally, the biodistribution of [^{86}Y]**3a** and [^{86}Y]**3b** were analyzed after 18 h p.i. [b] Designates the highest SUV.

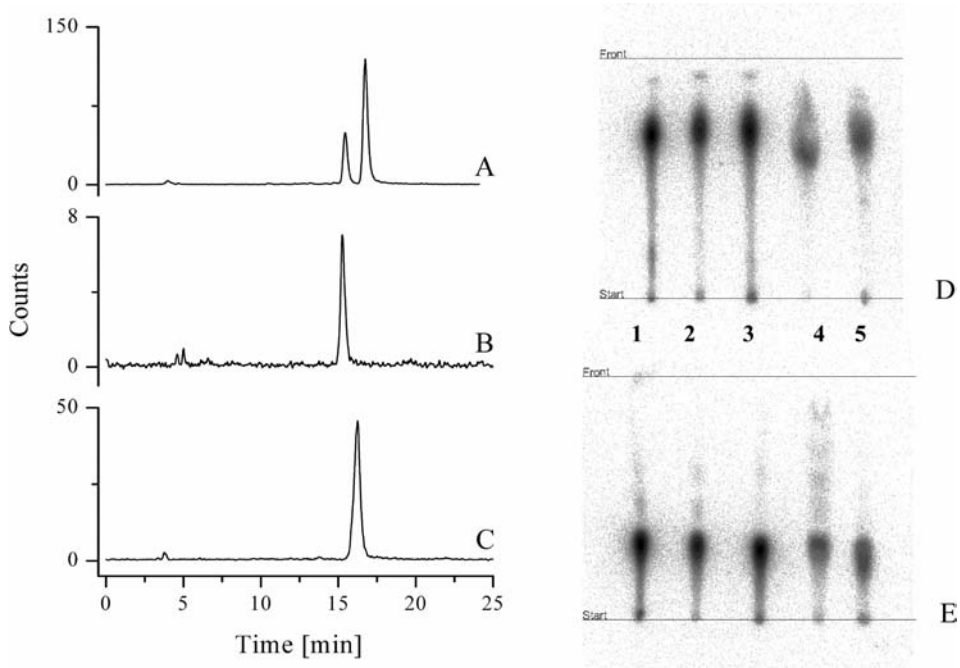

Figure 15. Radio-HPLC and radio-TLC chromatograms of the [^{86}Y((*S*)-*p*-NH$_2$-Bn-DOTA)]$^-$ isomers [^{86}Y]**4a** and [^{86}Y]**4b**: HPLC profiles of the reaction mixture (A) and urine samples from Wistar rats containing [^{86}Y]**4a** (B) and [^{86}Y]**4b** (C). Radio-TLC analyses of the urine samples with TLC systems I (D) and II (E). Applied samples in the lane: aliquot of the reaction mixture (1); HPLC fractions containing [^{86}Y]**4a** (2) and [^{86}Y]**4b** (3) as references; rat urine samples containing [^{86}Y]**4a** (4) and [^{86}Y]**4b** (5).

for [^{86}Y]**3a** and [^{86}Y]**3b** in the other organs with SUVs below 1.0 after 60 min and 18 h, respectively.

Metabolite Analysis. *[^{86}Y((S)-p-NH$_2$-Bn-DOTA)]$^-$ Isomers.* Metabolite analyses of urine samples containing the [^{86}Y((*S*)-*p*-NH$_2$-Bn-DOTA)]$^-$ isomers [^{86}Y]**4a** and [^{86}Y]**4b** were performed via radio-HPLC and radio-TLC. The results (see Figure 15) indicate that the isomers did not metabolize during the renal extraction in the urine. Due to the low resolution of TLC, equal R_f values were observed for the isomers [^{86}Y]**4a** and [^{86}Y]**4b** in both TLC systems (R_f, 0.23 (I); R_f, 0.71 (II)). The urine samples from Wistar rats containing [^{86}Y]**4a** and [^{86}Y]**4b** showed only minor changes of the R_f values ((I) R_f ([^{86}Y]**4a**), 0.26; R_f ([^{86}Y]**4b**), 0.27; (II) R_f ([^{86}Y]**4a**), 0.61; R_f ([^{86}Y]**4b**), 0.67). The observed differences could be explained by the inhomogeneous sample matrix, which might influence the chromatographic separation.

[^{86}Y-DOTA]-L-RNA Isomers. The *in vitro* stability of the radiolabeled L-RNA [^{86}Y]**3** isomer mixture was determined by incubation of [^{86}Y]**3** in whole rat blood for 12 h at 37 °C as described in the Supporting Information. No decomposition of [^{86}Y]**3** was observed for this period by analyzing via HPLC.

The high *in vivo* stability of the L-configured oligonucleotides (L-ON) was additionally confirmed by metabolite studies with the radiolabeled L-RNA [^{86}Y]**3b** isomer in Wistar rats. PAGE analysis of urine samples and kidney homogenates, obtained 60 min after administration of [^{86}Y]**3b**, showed no decomposition of the radiotracer for this period (see Figure 16).

The urine samples for the HPLC analysis were prepared via ultrafiltration with YM-10 filter units (10 kDa cutoff). Potential low molecular weight metabolites were separated by this method from the protein matrix. The remaining protein residue in the filter unit was enzymatically digested and the L-RNA fraction was extracted with phenol/chloroform. HPLC analysis of the YM-10 filtrate fraction (see Figure 17C) showed two metabolites M1 and M2 beside the intact compound [^{86}Y]**3b** in the radiometric profile. A comparison of the retention time of M2 and that of the potential metabolite [Y-DOTA]-hexanol Y**6b** of the L-RNA Y**3b** indicate that [^{86}Y]**3b** was cleaved at the phosphorus ester of the 5′-hexyl spacer with the subsequently release of [^{86}Y-DOTA]-hexanol [^{86}Y]**6b**. By analysis of the protein pellet fraction only, metabolite M1 was visible in HPLC (see Figure 17D). In all, over 85% of the radioactivity was eluted as intact [^{86}Y]**3b**.

***Ex Vivo* Autoradiography.** Recently, it has been shown that the kidneys are the primary site for the excretion of L-ON (*21*). As outlined in this report, the radioactivity of a radiolabeled [^{125}I]-L-RNA 25mer was found exclusively in the tubular structures of the renal cortex. In agreement with this observation, the autoradiogram obtained from kidney sections 60 min after injection of the radiolabeled L-RNA [^{86}Y]**3b** indicated the

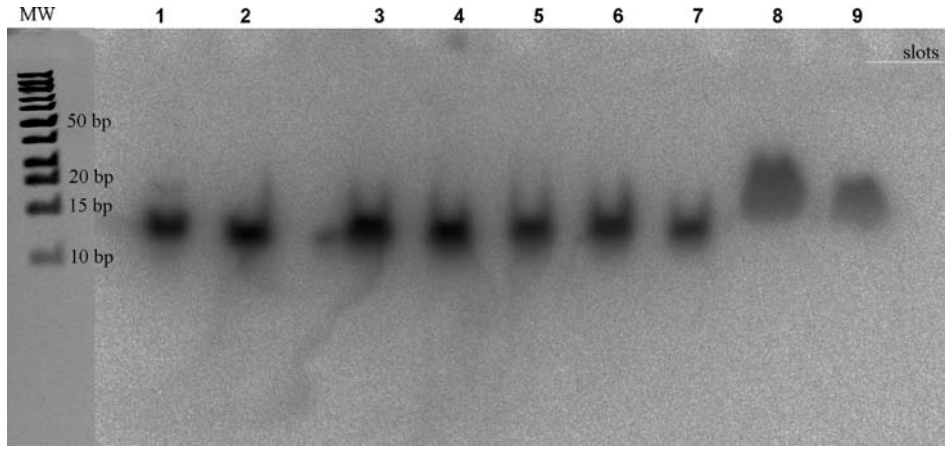

Figure 16. Image fusion of the autoradiogram of the exposed 20% polyacrylamide gel and the photographed 10 bp DNA ladder (MW) after staining with ethidium bromide. Applied samples in the lane: [^{86}Y]**3b** as reference (2); rat urine sample (5); YM-10 filtrate of rat urine sample (7); and rat kidney homogenate containing [^{86}Y]**3b** (9). The samples were obtained 60 min p.i. In the other lanes (1, 3, 4, 6, 8), the *in vivo* stability of a further ^{86}Y-labeled DOTA-12mer (lanes 1–4) was analyzed, which was published elsewhere (*4*). Variances in the running distance of the kidney homogenate samples could be explained by the inhomogeneous sample matrix, which might influence the electrophoretic separation.

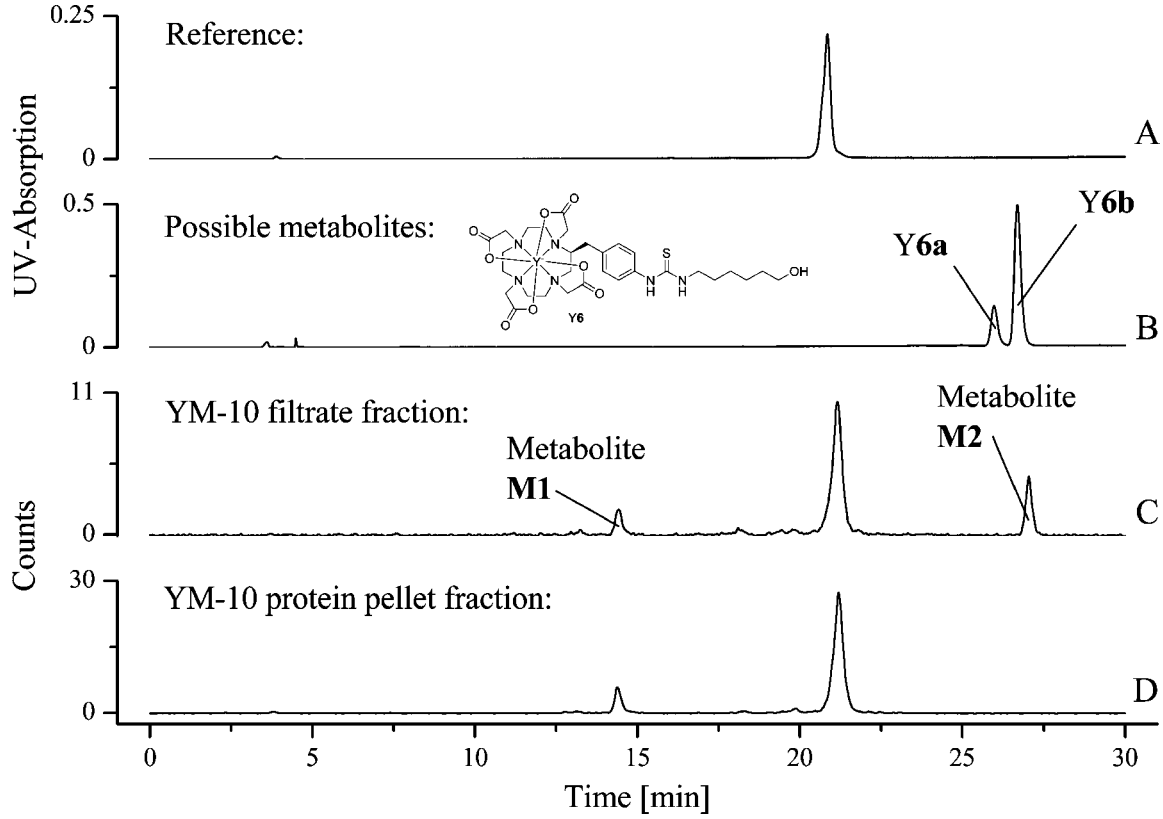

Figure 17. HPLC profiles of [Y-DOTA]-L-RNA Y**3b** as reference (A) and the [Y-DOTA]-hexanol isomers Y**6a** and Y**6b** as possible metabolites (B). Radio-HPLC profiles from rat urine samples collected 60 min p.i. of [^{86}Y]**3b**. (C) YM-10 filtrate fraction containing the low molecular weight metabolites M1 and M2. (D) Enzymatically digested protein pellet of the filter unit.

accumulation of the radioactivity in the renal cortex of the rats (see Figure 18). PAGE analysis of the kidney homogenates from these animals showed no decomposition of [^{86}Y]**3b** (see Figure 16).

CONCLUSIONS

In this study, we modified a mirror-image oligonucleotide (L-RNA **1**) via the bifunctional chelator approach with (*S*)-*p*-SCN-Bn-DOTA **2**. The ^{86}Y-labeling of the DOTA-conjugate **3** produced two isomer species [^{86}Y]**3a** and [^{86}Y]**3b** as evidenced by ion-pair chromatography with a very shallow solvent gradient. The isomerization of the conjugate [^{86}Y-DOTA]-L-RNA [^{86}Y]**3** was affected by different isomer structures of the ^{86}Y-DOTA complex. HPLC and NMR studies with the structural analogue nonradioactive precursor [Y((*S*)-*p*-NH_2-Bn-DOTA)]$^-$ Y**4** revealed that the complex Y**4** exists as two conformers, adopting the $\Lambda(\delta\delta\delta\delta)$ (SAP) (Y**4b**) and $\Delta(\delta\delta\delta\delta)$ (TSAP) (Y**4a**) configurations. The differences in the helicity of the carboxylate side arms (Λ or Δ) affected the lipophilicity of the conformers Y**4a** and Y**4b**. As a result, both isomers Y**4a** and Y**4b** differ not only in the retention time. At the tracer level, both ^{86}Y complex isomers [^{86}Y]**4a** and [^{86}Y]**4b** evidenced differences in the liver uptake in Wistar rats after 5 and 60 min. The TSAP isomer [^{86}Y]**4a** indicates a higher liphophilicity and

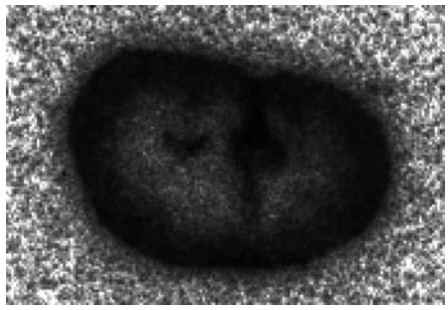

Figure 18. Autoradiogram obtained from a rat kidney sections 60 min after injection of [^{86}Y]**3b**.

a higher liver uptake. For this reason, it is important to characterize the influence of this chelate unit [^{86}Y]**4** on the *in vivo* behavior of the molecule to be labeled. Due to the high metabolic stability of the L-ON, the 12mer L-RNA **1** was a useful model for this investigation. Biodistribution studies with the L-RNA isomers [^{86}Y]**3a** and [^{86}Y]**3b** indicate no significant differences in the tissue and organ uptake of the rat up to 18 h. In conclusion, the 12mer L-RNA leveling the minor changes in the biodistribution profile of the [^{86}Y((*S*)-*p*-NH_2-Bn-DOTA)]$^-$ complex isomers [^{86}Y]**4a** and [^{86}Y]**4b** in rats. To confer this observation on other substances, like peptides or small organic molecules, further investigation are required.

HPLC analysis of rat urine samples containing [^{86}Y]**3b** suggested that the phosphorus ester of the 5′-hexyl spacer is a cleavage site in the radiolabeled L-RNA [^{86}Y]**3**. Besides that, more than 85% of [^{86}Y]**3b** was found intact in rat urine 60 min after injection. An additional metabolic stabilization of the L-RNA **1** can be achieved by a chemical modification of the linkage between the aminohexyl spacer and the L-ON. In conclusion, the high metabolic stability of the L-ON suggests the potential of this class of compounds as molecular probes for *in vivo* imaging applications.

ACKNOWLEDGMENT

This work was supported by the EU-FP6 integrated project BioCare contract no.: 505785. The authors thank Regina Herrlich for the performing the biodistribution and Mareike Barth for preparing the rat kidney autoradiograms. Furthermore, the authors thank Peggy Jaehrig for synthesis of several Y-DOTA chelates.

Supporting Information Available: ESI-MS spectra of the [Y((*S*)-*p*-NH_2-Bn-DOTA)]$^-$ isomers Y**4a**, Y**4b**; ESI-MS spectrum and SEC profiles of the formation of DOTA-thiourea **5**; MALDI-TOF spectra of Y**3a**, Y**3b**; *in vitro* stability data of [^{86}Y]**3**; metabolite analysis of [^{86}Y-DOTA]-L-RNA [^{86}Y]**3** from blood samples via PAGE. This material is available free of charge via the Internet at http://pubs.acs.org.

LITERATURE CITED

(1) Watanabe, N., Sawai, H., Endo, K., Shinozuka, K., Ozaki, H., Tanada, S., Murata, H., and Sasaki, Y. (1999) Labeling of phosphorothioate antisense oligonucleotides with yttrium-90. *Nucl. Med. Biol. 26*, 239–243.

(2) Liu, S., and Edwards, D. S. (2001) Bifunctional chelators for therapeutic lanthanide radiopharmaceuticals. *Bioconjugate Chem. 12*, 7–34.

(3) Roivainen, A., Tolvanen, T., Salomaki, S., Lendvai, G., Velikyan, I., Numminen, P., Valila, M., Sipila, H., Bergstrom, M., Harkonen, P., Lonnberg, H., and Langstrom, B. (2004) ^{68}Ga-labeled oligonucleotides for in vivo imaging with PET. *J. Nucl. Med. 45*, 347–355.

(4) Schlesinger, J., Bergmann, R., Klussmann, S., and Wuest, F. (2006) Synthesis and radiopharmacological characterisation of ^{86}Y and ^{68}Ga-Labelled L-RNA oligonucleotides as molecular probes for positron emission tomography (PET). *Lett. Drug Des. Discovery 3*, 330–335.

(5) Harrison, A., Walker, C. A., Parker, D., Jankowski, K. J., Cox, J. P., Craig, A. S., Sansom, J. M., Beeley, N. R., Boyce, R. A., Chaplin, L., et al. (1991) The in vivo release of ^{90}Y from cyclic and acyclic ligand-antibody conjugates. *Int. J. Rad. Appl. Instrum. B 18*, 469–476.

(6) Helisch, A., Forster, G. J., Reber, H., Buchholz, H. G., Arnold, R., Goke, B., Weber, M. M., Wiedenmann, B., Pauwels, S., Haus, U., Bouterfa, H., and Bartenstein, P. (2004) Pre-therapeutic dosimetry and biodistribution of ^{86}Y-DOTA-Phe1-Tyr3-octreotide versus ^{111}In-pentetreotide in patients with advanced neuroendocrine tumours. *Eur. J. Nucl. Med. Mol. Imaging 31*, 1386–1392.

(7) Yoo, J., Tang, L., Perkins, T. A., Rowland, D. J., Laforest, R., Lewis, J. S., and Welch, M. J. (2005) Preparation of high specific activity ^{86}Y using a small biomedical cyclotron. *Nucl. Med. Biol. 32*, 891–897.

(8) Liu, G., Mang'era, K., Liu, N., Gupta, S., Rusckowski, M., and Hnatowich, D. J. (2002) Tumor pretargeting in mice using ^{99m}Tc-labeled morpholino, a DNA analog. *J. Nucl. Med. 43*, 384–391.

(9) Rusckowski, M., Qu, T., Chang, F., and Hnatowich, D. J. (1997) Pretargeting using peptide nucleic acid. *Cancer 80*, 2699–2705.

(10) Liu, G., Dou, S., Pretorius, P. H., Liu, X., Rusckowski, M., and Hnatowich, D. J. (2008) Pretargeting CWR22 prostate tumor in mice with MORF-B72.3 antibody and radiolabeled cMORF. *Eur. J. Nucl. Med. Mol. Imaging 35*, 272–280.

(11) Urata, H., Ogura, E., Shinohara, K., Ueda, Y., and Akagi, M. (1992) Synthesis and properties of mirror-image DNA. *Nucleic Acids Res. 20*, 3325–3332.

(12) Klussmann, S., Nolte, A., Bald, R., Erdmann, V. A., and Furste, J. P. (1996) Mirror-image RNA that binds D-adenosine. *Nat. Biotechnol. 14*, 1112–1115.

(13) Ragas, J. A., Simmons, T. A., and Limbach, P. A. (2000) A comparative study on methods of optimal sample preparation for the analysis of oligonucleotides by matrix-assisted laser desorption/ionization mass spectrometry. *Analyst 125*, 575–581.

(14) Corson, D. T., and Meares, C. F. (2000) Efficient multigram synthesis of the bifunctional chelating agent (*S*)-1-*p*-isothiocyanatobenzyl-diethylenetriaminepentaacetic acid [correction of diethylenetetraminepentaacetic acid]. *Bioconjugate Chem. 11*, 292–299.

(15) Drobnica, L., Kristian, P., and Augustin, J. (1977) The Chemistry of the -NCS group, in *The Chemistry of Cyanates and their Thioderivatives. Part 2* (Patai, S., Ed.) pp 1119–1120, John Wiley & Sons, New York.

(16) Meyer, M., Dahaoui-Gindrey, V., Lecomte, C., and Guilard, L. (1998) Conformations and coordination schemes of carboxylate and carbamoyl derivatives of the tetraazamacrocycles cyclen and cyclam, and the relation to their protonation states. *Coordin. Chem. Rev. 180*, 1313–1405.

(17) Aime, S., Botta, M., Fasano, M., Marques, M. P. M., Geraldes, C. F. G. C., Pubanz, D., and Merbach, A. E. (1997) Conformational and coordination equilibria on DOTA complexes of lanthanide metal ions in aqueous solution studied by H-1-NMR spectroscopy. *Inorg. Chem. 36*, 2059–2068.

(18) Woods, M., Kovacs, Z., Kiraly, R., Brucher, E., Zhang, S., and Sherry, A. D. (2004) Solution dynamics and stability of lanthanide(III) (*S*)-2-(*p*-nitrobenzyl)DOTA complexes. *Inorg. Chem. 43*, 2845–2851.

(19) Corneillie, T. M., Fisher, A. J., and Meares, C. F. (2003) Crystal structures of two complexes of the rare-earth-DOTA-binding antibody 2D12.5: ligand generality from a chiral system. *J. Am. Chem. Soc. 125*, 15039–15048.

(20) Hnatowich, D. J., Chinol, M., Siebecker, D. A., Gionet, M., Griffin, T., Doherty, P. W., Hunter, R., and Kase, K. R. (1988) patient biodistribution of intraperitoneally administered yttrium-90-labeled antibody. *J. Nucl. Med. 29*, 1428–1435.

(21) Boisgard, R., Kuhnast, B., Vonhoff, S., Younes, C., Hinnen, F., Verbavatz, J. M., Rousseau, B., Furste, J. P., Wlotzka, B., Dolle, F., Klussmann, S., and Tavitian, B. (2005) In vivo biodistribution and pharmacokinetics of ^{18}F-labelled Spiegelmers: a new class of oligonucleotidic radiopharmaceuticals. *Eur. J. Nucl. Med. Mol. Imaging 32*, 470–477.

BC700453H

Preparation and in Vitro Evaluation of Novel Lipopeptide Transfection Agents for Efficient Gene Delivery

Tarwadi,[†] Jalal A. Jazayeri,[†] Richard J. Prankerd,[‡] and Colin W. Pouton*[,†]

Department of Pharmaceutical Biology and Department of Pharmaceutics, Victorian College of Pharmacy, Monash University, 381 Royal Parade, Parkville, Victoria 3052, Australia. Received December 14, 2007; Revised Manuscript Received February 1, 2008

Gene therapy by delivery of nonviral expression vectors is highly desirable, due to their safety, stability, and suitability for production as bulk pharmaceuticals. However, low transfection efficiency remains a limiting factor in application on nonviral gene delivery. Despite recent advances in the field, there are still major obstacles to overcome. In an attempt to construct more efficient nonviral gene delivery vectors, we have designed a series of novel lipopeptide transfection agents, consisting of an alkyl chain, one cysteine, 1 to 4 histidine and 1 to 3 lysine residues. The lipopeptides were designed to facilitate dimerization (by way of the cysteine residues), DNA binding at neutral pH (making use of charged lysine residues), and endosomal escape (by way of weakly basic histidine residues). DNA/lipopeptide complexes were evaluated for their biophysical properties and transfection efficiencies. The number and identity of amino acids incorporated in the lipopeptide construct affected their DNA/lipopeptide complex forming capacity. As the number of lysine residues in the lipopeptide increased, the DNA complexes formed became more stable, had higher zeta potential (particle surface charge), and produced smaller mean particle sizes (typically 110 nm at a charge ratio of 5.0 and 240 nm at a charge ratio of 1.0). The effect of inclusion of histidines in the lipopeptide moiety had the opposite effect on complex formation to lysine, but was necessary for high transfection efficiency. In vitro transfection studies in COS-7 cells revealed that the efficiency of gene delivery of the luciferase encoding plasmid, pCMV-Luc, mediated by all the lipopeptides, was much higher than poly(L-lysine) (PLL), which has no endosomal escape system, and in two cases was slightly higher than that of branched polyethylenimine (PEI). Lipopeptides with at least two lysine residues and at least one histidine residue produced spontaneous transfection complexes with plasmid DNA, indicating that endosomal escape was achieved by incorporation of histidine residues. These low molecular weight peptides can be readily synthesized and purified and offer new insights into the mechanism of action of transfection complexes.

INTRODUCTION

There are several strategies for mediating gene delivery to the nucleus of eukaryotic cells. One approach has been direct injection of naked DNA into a tissue. This has been attractive due to simplicity and lack of toxicity. However, the size and hydrophilic nature of DNA prevents it from being taken up by cells efficiently. Approximately 10^6 plasmid DNA are needed for a single cell transfection in vitro with less than 100 reaching the nucleus (*1*). This is due to several physical, chemical, and metabolic barriers in the cell interior, with the final obstacle being the nuclear membrane which, in the absence of cell division, is a major impediment to gene delivery. The DNA delivery system needs to prevent degradation and facilitate intracellular transport on its journey to the nucleus.

To achieve this target, several strategies are being exploited by researchers in the field of gene therapy. These include (i) physical methods, using mechanical or electrical forces, such as particle bombardment, gene guns, electroporation, microinjection, ultrasound, and hydrodynamic; (ii) chemical means (condensing DNA using cationic lipids or cationic polymers); and (iii) viral vectors (e.g., using adenoviruses). Viral vectors, although comparatively efficient, are considered to have safety problems associated with recombination events. Nonviral delivery vectors, on the other hand, are relatively inefficient in their current form and have not been successful for in vivo gene therapy. Nevertheless, they are attractive alternatives to viral and physical methods, because of their relative safety (for recent reviews, see refs *2*–*6*). Systematic efforts will be required to improve the efficiency of nonviral delivery before they can be used clinically.

Among the nonviral vehicles, cationic lipids have been explored most extensively, and many have been commercialized as in vitro transfection agents (*7*–*10*). Felgner and co-workers were the first to report a highly efficient lipid-mediated DNA-transfection agent using a synthetic cationic lipid, *N*-(1-(2,3-dioleyloxy)propyl]-*N*,*N*,*N*-trimethylammonium chloride (DOTMA) (*11*). They found that small unilamellar liposomes containing DOTMA interacted spontaneously with DNA to form lipid−DNA complexes. They also reported that, depending on the cell line used, DOTMA was 5- to 100-fold more efficient, compared to either the calcium phosphate or DEAE dextran transfection methods. In designing a cationic lipid as a transfection agent, they showed that the alkyl chain length and the number of double bonds could either increase or decrease the transfection efficiency (C14:0 > C18:1 > C16:0 > C18:0) (*7*).

Using a different set of cationic lipids, Wheeler et al. formulated a liposome composing of GAP-DLRIE; (±)-*N*-(3-aminopropyl)-*N*,*N*-dimethyl-2,3-bis-(dodecyloxy)-1-propanaminium bromide, and DOPE (dioleoylphosphatidyl-ethanolamine). This formulation enhanced chloramphenicol acetyl-transferase (CAT) expression in vivo by more than 100-fold (observed in mouse lung) (*12*). Recently, Slimani and co-workers reported

* Author for correspondence: Professor Colin W. Pouton, Department of Pharmaceutical Biology, Victorian College of Pharmacy, Monash University, 381 Royal Parade, Parkville, Victoria 3052, Australia. E-mail: colin.pouton@vcp.monash.edu.au, Tel: +613-99039562, Fax: +613-99039638.

[†] Department of Pharmaceutical Biology.

[‡] Department of Pharmaceutics.

10.1021/bc700463q CCC: $40.75 © 2008 American Chemical Society
Published on Web 03/12/2008

a ligand-bearing lipopeptide specifically targeting neurophilia fen-1 (NRPAL1) receptor, which is overexpressed by human breast cell lines (*13*). The lipopeptide was based on a palmitoyl fatty chain (C_{16}) linked to a sequence of seven amino acids (ATWLPPR). Upon transfection, they showed that the lipopeptide delivery of either a β-galactosidase reporter gene or a green fluorescence protein was selectively enhanced in NRPAL1 positive cells as compared to NRPAL1 negative cells.

The synthetic polycation polyethylenimine (PEI) has also been used widely in transfection studies, either alone (*14*) or by bonding to adenovirus particles (*15*) or to other viral protein and targeting devices (*16, 17*). However, although PEI and its derivatives have a prominent position in gene delivery research, due to their ability to facilitate endosomal escape which results in high transfection efficiency in vitro, the toxicity of PEI remains the drawback, especially for in vivo gene delivery applications (*14, 18*).

Low-molecular-weight cationic peptide-based nonviral vectors have considerable potential but are probably the least explored, whereas cationic polymers such as polyethylenimine (PEI) or poly(L-lysine) (PLL) have been investigated regularly (*19–25*). Recently, there have been several publications on peptide-based structures for delivery of DNA to mammalian cells (*8, 26–29*). Chen et al. reported that, in combination with cationic liposomes such as DOTAP, Lipofectin, Lipofectamine, and DOSPER branched copolymers of histidine and lysine were able to condense and enhance transfection efficiency in MDA-MB-435 cells (*30*). In addition, histidine-rich amphiphatic peptides were reported to transfect several cell lines with efficiencies comparable to those of DOTAP and PEI (*28*). Meanwhile, Lentz and co-workers reported the use of highly branched histidine−lysine peptides as carriers for small interfering RNA molecules (*29*). Arginine-rich peptides have also been exploited in nonviral gene transfer (*31, 32*). Arginine-rich peptides can facilitate the cellular uptake of macromolecules such as proteins, liposomes, and iron nanoparticles. They have also been shown to enhance DNA delivery by making use of protein transduction sequences, including hepta-arginine and $TAT_{47–57}$ (*31*).

A group led by Rice has been exploring the application of copolymers incorporating peptide sequences of cysteine, lysine, histidine, and tryptophan residues to mediate nonviral gene delivery (*33–35*). McKenzie et al. reported that a minimal repeating lysine chain of 18 residues, followed by tryptophan and an alkylated cysteine residue (AlKCMK$_{18}$, MW 2672 Da), formed small particles with DNA (~80 nm) and mediated efficient in vitro gene transfer to a level higher than that of PLL (MW of 1–4 kDa) (*34*). This group developed peptide-mediated gene delivery agents by inserting multiple cysteine residues into a short (dp 20) synthetic peptide (*33*). They found that the stability of cross-linked peptide DNA condensates increased in proportion to the number of cysteines incorporated into the peptide. They suggested that disulfide bond formation led to a decrease in particle size, relative to control peptide DNA condensates, and prevented dissociation of peptide DNA condensates (*33*). In addition, they demonstrated that substitution of His for Lys resulted in an optimal peptide of Cys-His-$(Lys)_6$-His-Cys, which provided a buffering condition capable of enhancing in vitro gene expression in the absence of chloroquine (*33*).

Despite recent advances in the design of nonviral gene delivery systems, transfection agents based on nonviral reagents are still very inefficient, particularly for in vivo gene delivery applications, where typically a very small proportion of cells are transfected. In this study, a series of lipopeptide transfection agents were designed and constructed. In addition to an investigation of transfection efficiency, these complexes were also evaluated in terms of their physical properties, since complex size and charge are known to influence processes involved in gene delivery. A better understanding of the physical properties of DNA complexes, in particular, the factors which promote DNA condensation, cellular uptake, and endosomal escape, will help design more efficient gene delivery vectors.

Table 1. Lipopeptide Structures and Their State of Ionization at pH 7.4

lipopeptide[a]	molecular weight (Da)[b]	charge[c]	purity %[d]
$LauCKH_2$-NH_2	761	1	>96
$LauCK_2H$-NH_2	696	2	>97
$PalCKH_2$-NH_2	761	1	>95
$PalCK_2H_2$-NH_2	889	2	>95
$PalCK_2H_3$-NH_2	1026	2	>95
$PalCK_2H_4$-NH_2	1163	2	>95
$PalCK_2H_5$-NH_2	1300	2	>95
$PalCK_3H_2$-NH_2	1017	3	>97
$PalCK_3H_3$-NH_2	1154	3	>95

[a] Lau: Lauryl; Pal: Palmitoyl. [b] Determined by mass spectrometry. [c] Determined as per number of protons. [d] The purity of the compounds was measured by HPLC using 218 nm UV absorption; SH was detected by Ellman's test.

EXPERIMENTAL PROCEDURES

Materials. The lipopeptides (Table 1) were synthesized by Auspep Pty. Ltd. (Parkville, Victoria, Australia). The purities of the compounds were examined by HPLC (Waters, USA) with nonspecific short-wavelength UV detection and found to be >95%. Their molecular weights were confirmed by mass spectrometry. The plasmid pCMV-Luc was a gift from Dr. David Melroy (University of Bath, UK) and the plasmid pCMV-β-gal stock solution (1 mg/mL in water) was obtained from Clontech (NSW, Australia). Lipofectamine was from Invitrogen (Melbourne, VIC, Australia); PLL (average M_w 15–30 kDa), branched PEI (average M_w 750 kDa), decamethonium (dication C_{10}), dodecyltrimethylammonium bromide (DDTAB), and hexadecyltrimethylammonium bromide (HDTAB) were from Sigma-Aldrich (Sydney, Australia). Dulbecco's Modified Eagle's Medium (DMEM) was from Invitrogen (Melbourne, VIC, Australia). All tissue culture flasks, including black polystyrene 96-well plates, were obtained from Corning Costar (Melbourne, VIC, Australia). All other chemicals were commercially obtained and were of analytical grade.

Design and Construction of Lipopeptides. The basic structure comprises an N-terminal alkylamide, one cysteine, 1 to 4 histidine and 1 to 3 lysine residues. The addition of each lysine provided a unit positive charge on the lipopeptide at neutral pH, which was able to interact with the negatively charged sugar–phosphate backbone of the DNA molecule. Histidine was included because its side hain is weakly basic and predominantly un-ionized at neutral pH, but is more highly protonated in the weakly acidic environment of the endosome. It was hypothesized that this phenomenon would facilitate release of the DNA−lipopeptide complex from the endosome. The number of lysine and histidine residues included in the lipopeptide was varied to explore the effect on transfection efficiency.

The inclusion of an alkyl amide chain, either lauryl (C_{12}) or palmitoyl (C_{16}), in the lipopeptide was intended to promote hydrophobic interactions to stabilize the lipopeptide−plasmid complex, subsequent to an initial ion interaction between primary amine and phosphate groups. To inform the choice of alkyl chain length, a range of dicationic molecules were investigated using the ethidium bromide exclusion assay (Table 2). The thiol-bearing cysteine residue was included with the intention of facilitating dimerization by disulfide formation on the DNA molecular template.

Plasmid DNA Isolation. The plasmid pCMV-Luc, a luciferase mammalian expression vector, was cultivated in *E. coli*,

Table 2. Structure of Molecules Used in DNA Condensation assays

	Structure of the molecules used in DNA condensation assays and their state of ionisation at pH 7.4	Ref
1	Decamethonium (dication C_{10}), molecular weight = 418.3, 2 N^+/molecule 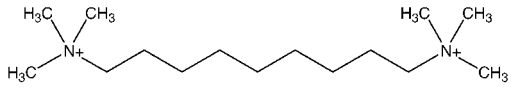	(*9, 50*)
2	Dodecyltrimethylammonium bromide (DDTAB), molecular weight = 308, 1 N^+/molecule 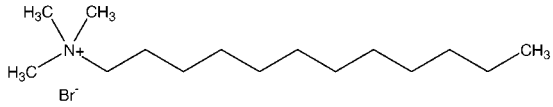	(*51*)
3	Hexadecyltrimethylammonium bromide (HDTAB), molecular weight = 364, 1 N^+/molecule 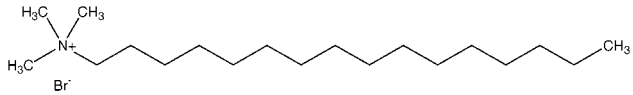	(*52*)
4	Poly-L-lysine (PLL), molecular weight of 1 L-lysine unit = 128 (1 N^+/unit) 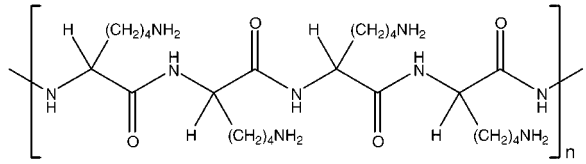	(*53-55*)

strain DH5-α, and isolated using a Qiagen Maxiprep kit (Qiagen Pty. Ltd., Clifton Hill, Victoria, Australia). The purity of each plasmid was checked electrophoretically on a 1% agarose gel. Their concentrations were determined from UV absorbance at 260 and 280 nm. Purified plasmids were resuspended in Milli-Q water (MQW) and frozen (−20 °C) until use.

Determination of Charge and N/P Ratios. The charge ratio (+/−) of DNA complexes refers to the number of positively charged (protonated) nitrogens provided by the transfection agent per negatively charged nucleotide unit. An average mass of 330 Da per nucleotide was used for the calculations. For example, to obtain a theoretical charge ratio of 1:1 between $PalCK_2H_2$ (889 Da, $2NH^+$/molecule) and DNA, 1 μg of DNA (3 nmol of nucleotide) was mixed with 1.3 μg of $PalCK_2H_2$ (1.5 nmol), since every molecule of $PalCK_2H_2$ generates 2 NH^+ groups. For the cationic polymer PEI, rather than using charge ratio, complexes were described in terms of the total nitrogen/phosphate (N/P) ratio.

DNA Condensation Assay. The ability of the lipopeptide constructs to condense DNA was evaluated using the ethidium bromide (EtBr) exclusion assay, as described by Murphy et al. (*36*). This assay was carried out in 96-well black plates; the fluorescence intensities were measured using a FluoStar OPTIMA plate reader (FluoStar OPTIMA, BMG Laboratory Technology, Sydney, NSW, Australia). A sample containing 5 μg plasmid DNA and an excess of EtBr (20 μL; 100 μg/mL) was used to calibrate the spectrofluorometer to 100% fluorescence intensity (λ_{ex} = 520 nm; λ_{em} = 610 nm). For the assays; 50 μL of 60 mM Tris HCl buffer (pH 7.4) was added to each well containing plasmid DNA. A series of charge ratios from 0 to 10 (or N/P ratios for PEI) of the DNA complexes were prepared. Milli-Q water was added to a total volume of 230 μL per well. The samples were left to stabilize at ambient temperature for 3 min after which 20 μL of EtBr solution was added. The 96-well plate was shaken orbitally for 30 s and the fluorescence intensity measured.

Gel Mobility Shift Assay. The formation of the DNA-transfection agent complex was studied using a gel mobility shift assay. A series of charge ratios from 0 to 5 (or N/P ratios for PEI) of the complexes were prepared in HEPES glucose buffer pH 7.4 (15 mM HEPES and 5.13% w/v glucose). Complexes of DNA (20 μg/mL) and transfection agent were incubated for 30 min at 37 °C. Subsequently, the samples (15 μL) were mixed with 3 μL of loading buffer and analyzed by 1% agarose gel electrophoresis. DNA bands were visualized by UV transillumination.

DNA−Lipopeptide Stability Assay. The susceptibility of the condensed DNA to enzymatic degradation was assessed by exposing the complex to nucleases (Turbo DNase, Ambion, Scoresby, VIC, Australia). The plasmid DNA sample (20 μg/mL) and the appropriate lipopeptide were diluted separately in HGB[1]pH 7.4 in a series of charge ratios from 0 to 5. The samples were then mixed and incubated in the presence of DNaseI (2U/μg DNA) on ice (4 °C) for 15 min prior to 1% agarose gel electrophoresis. DNA bands were visualized by UV transillumination.

[1]Abbreviations: HGB, HEPES glucose buffer; PBS, phosphate buffered saline, PEI, polyethylenimine; PLL, poly(L-lysine); EtBr, ethidium bromide; DOPE, (dioleoyl phosphatidyl-ethanolamine); DOTMA, *N*-[1-(2,3-dioleyloxy)propyl]-*N*,*N*,*N*-trimethylammonium chloride; DOTAP, *N*-[1-(2,3-dioleoyloxy)propyl]-*N*,*N*,*N*-trimethylammonium chloride.

Particle Sizing and Zeta Potential. The mean particle size and zeta potential (ζ) of each DNA−lipopeptide complex was determined with a Zetasizer Nano Series instrument (Malvern Instruments, Worcestershire, UK). Calibration of particle sizes was carried out with 60 nm ± 2.7 nm NIST/Nanosphere (Duke Scientific Corp. Palo Alto, CA, USA) standard polystyrene spheres. For calibration of zeta potential, the −50 mV ± 5 mV zeta potential standard was used. DNA−lipopeptide complexes were prepared in HEPES glucose buffer pH 7.4. The mean particle sizes were measured at 25 °C using 1.5 mL disposable cuvettes. Zeta potentials were determined at 25 °C using the folded capillary (Smoluchowski) cell (Malvern Instruments, Worcestershire, UK).

To study the physical stability of each DNA−lipopeptide complex, 40 μg of DNA (pCMV-Luc) was combined in a cuvette with each of $PalCK_2H_2$, $PalCK_2H_3$, $PalCK_3H_2$, or $PalCK_3H_3$ (at a charge ratio of 1.5), in a total of 500 μL of HEPES glucose buffer, pH 7.4. The mean particle size distributions were measured at 0.05, 0.5, 1, 2, 8, 30, 60, and 120 h after complex formation. The effect of DNA concentration on particle aggregation was studied at a fixed charge ratio of 1.5; DNA (2.5, 5, 10, 15, 20, or 40 μg) was diluted with 250 μL HGB pH 7.4 and then added dropwise into 250 μL HGB pH 7.4 containing the appropriate mass of $PalCK_3H_2$, $PalCK_3H_3$, PEI, or Lipofectamine to obtain DNA at a final concentration of 7.6, 15.2, 30.4, 45.6, 60.8, or 121.6 nM, respectively. The effect of increasing charge ratio on particle size and zeta potential was also studied. This was achieved by diluting 5 μg DNA in 250 μL of HGB pH 7.4 dropwise into 250 μL HGB pH 7.4 in a microtube containing the appropriate mass of $PalCK_2H$, $PalCK_2H_2$, $PalCK_3H_2$, or $PalCK_3H_3$ to obtain charge ratios of 0.5, 0.75, 1.0, 2.0, 3.0, 4.0, or 5.0, respectively.

Preparation of Lipopeptide/Plasmid DNA Complexes for Transfection. The plasmid pCMV-Luc (2 μg) was diluted in 12.5 μL HGB pH 7.4 and added to the lipopeptide solution (diluted in the 12.5 μL of the same buffer) in dropwise manner. Lipofectamine, PLL (MW 70–150 kDa) and branched PEI (MW 750 kDa) were used as positive controls.

In Vitro Transfection. COS-7 cells were cultured in DMEM media supplemented with 10% FCS, 100 units/mL penicillin, and 100 μg/mL streptomycin in a humidified incubator with 5% CO_2 at 37 °C. The day before transfection, cells were seeded at 5×10^4 cells/well in the 24-well plates. After reaching a confluency of ~60–70%, the cells were washed twice with PBS, and the medium replaced with Opti-MEM prior to addition of the DNA/lipopeptide complexes. After 24 h of incubation in Opti-MEM, cells were washed twice with PBS, then harvested by adding 115 μL/well of Reporter Lysis Buffer (Promega, NSW, Australia) and incubated for 15 min at room temperature. The cells were then scraped, collected, and centrifuged, and the supernatants were used for protein and luciferase assays.

Luciferase and Protein assays. After harvest, cells were centrifuged at 13 000 g for 2 min at 4 °C. The supernatant (50 μL) was used to measure luciferase activity using a luciferase detection kit (Promega, Annandale, NSW, Australia). Quantilum Recombinant Luciferase (QRL) (Promega, Annandale, NSW, Australia) was used as a standard for luciferase assays. Total protein concentrations were measured using the Bradford protein assay (Sigma Aldrich, Sydney, NSW, Australia). Bovine serum albumin (BSA; Sigma-Aldrich Sydney, NSW, Australia) was used as a standard for protein assays.

RESULTS

DNA Condensation Studies. The results of DNA condensation experiments showed that the alkyltrimethylammonium bromide with a C_{16} alkyl chain (HDTAB) condensed DNA as efficiently as PLL (Figures 1, 2A), whereas the C_{12} compound

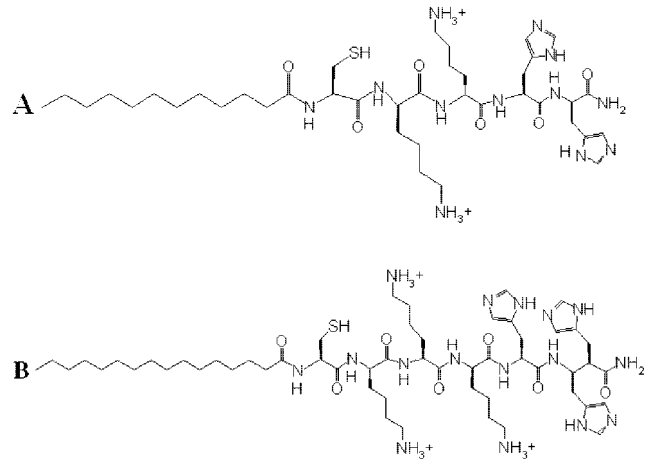

Figure 1. Representative structures of the lipopeptide-based transfection agents and their protonation at physiological pH 7.4: (A) Lauryl (C-12)-CK_2H_2 and (B) Palmitoyl (C-16)-CK_3H_3.

(DDTAB) and the decamethonium dication did not. Similarly, a lipopeptide bearing a palmitoyl (C_{16}) alkyl chain condensed DNA more efficiently than the corresponding lauryl (C_{12}) equivalent (Figure 2B). Lipopeptides with a single lysine residue, such as $PalCKH_2$, were weak condensers of DNA when compared to lipopeptides with two or three lysine residues (Figure 2C). The extent of DNA condensation by palmitoylated compounds with two lysine residues was a function of the number of histidine residues. At each charge ratio, the extent of ethidium exclusion decreased with increasing histidinyl chain length over the range 2–5 (Figure 2D).

Gel Mobility Shift Assay. Condensation of DNA with $PalCK_2H_2$ and $PalCK_2H_5$ caused retardation of DNA migration at charge ratios above 1 (Figure 3A,B). At a charge ratio of 0.5, migration was substantially retarded, though some DNA appeared to migrate into the gel from the $PalCK_2H_5$ complex, indicating less efficient condensation. Figure 3C shows that an N/P ratio of at least 1.5 was required to effect gel retardation by PEI. At charge ratios of 5.0 or above, the DNA-$PalCK_2H_2$ and DNA-$PalCK_2H_5$ complexes could not be detected on the agarose gel (Figure 3A,B). Similarly, DNA−PEI complexes, at an N/P ratio of 5 or above, were not identified on the gel (Figure 3C). This can be explained by the previous observation that more complete condensation at higher charge ratio prevents the binding of ethidium to the complex, as exemplified by the results of the ethidium exclusion experiments (Figure 2). The results of the gel-shift experiments suggest that immobilization of the complex occurred before the DNA was fully condensed.

Complex Stability in the Presence of DNase. The stability of lipopeptide−DNA complexes was evaluated in the presence of DNase to model the protection to enzymatic degradation resulting from condensation. Figure 4 shows a representative experiment using $PalCK_2H_2$ complexes. The results show that the majority of the mass of DNA in free solution was degraded after 30 min of incubation in the presence of DNase. At charge ratios greater than 1.0, the lipopeptide $PalCK_2H_2$ fully protected DNA from DNase degradation. The protection from nuclease degradation at this low charge ratio was superior to the protection given by cationic polymers and liposomes. This level of DNA protection by $PalCK_2H_2$ was also more pronounced than that offered by the cationic amphiphile guanidinocysteine *N*-decylamide (C_{10}-C^{G+}). The latter compound has been reported to protect DNA from serum degradation at a charge ratio of 3.0 (*37*), but as indicated by our ethidium exclusion studies (Figure 2), DNA condensation was less efficient than that achieved with $PalCK_2H_2$.

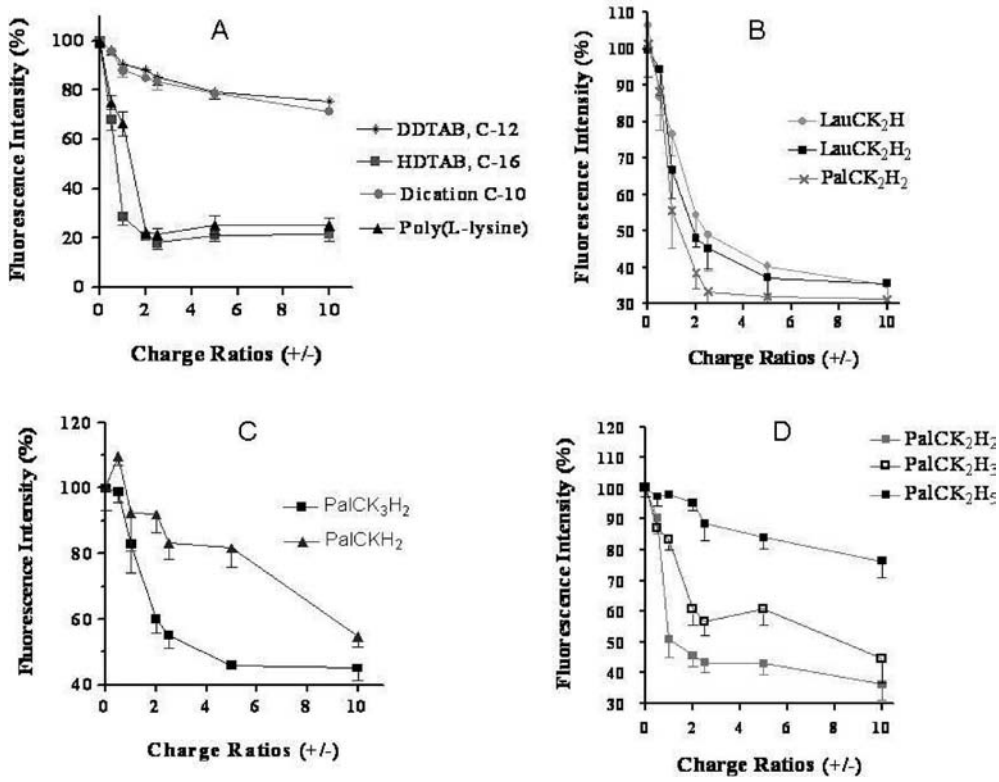

Figure 2. Condensation studies of DNA-transfection agents using ethidium bromide exclusion assay (measured at $\lambda_{ex} = 520$ nm and $\lambda_{em} = 610$ nm; FluoSTAR plate reader). Data are presented as mean ± SD ($n = 3$). (A) Comparison of alkyl chains, as the hydrophobic anchors, on ethidium exclusion during DNA condensation. (B) Effect of lauryl (C-12) and palmitoyl (C-16) chains on ethidium exclusion. (C) Effect of the number of lysine residues on ethidium exclusion by lipopeptides containing two histidine residues. (D) Effect of the number of histidine residues on the ability of lipopeptides with two lysine residues to condense DNA molecules.

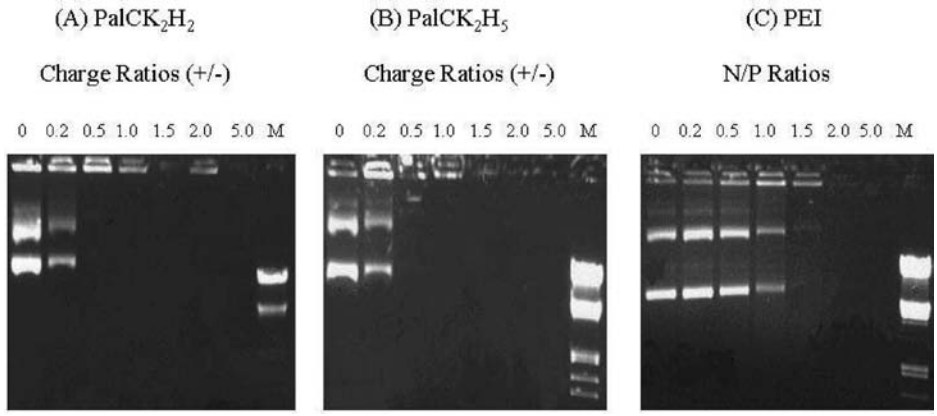

Figure 3. Gel mobility shift assays of DNA complexes formed by (A) $PalCK_2H_2$, (B) $PalCK_2H_5$, and (C) PEI. At a charge ratio of 1.0 or 1.5, both $PalCK_2H_2$ and $PalCK_2H_5$ effectively condensed the plasmid DNA to an extent analogous with condensation by PEI.

Physical stability of DNA−Lipopeptide Complexes. Particle size was determined over a 120 h period after formation of the complexes in HGB pH 7.4. This was of practical significance, particularly with regard to transfection studies, to ensure that the complexes did not aggregate during the period between formation and use, a common problem with polyelectrolyte complexes. Complexes formed at a charge ratio of 1.5, using 40 μg of DNA (243 nM) and the lipopeptides $PalCK_2H_2$, $PalCK_2H_3$, $PalCK_3H_2$, and $PalCK_3H_3$ in 500 μL HGB pH 7.4. These were completely stable for 1 h and had particle diameters in the range 250–300 nm. After longer time periods, some aggregation was evident with $PalCK_3H_2$ complexes (forming aggregates approximately twice the original diameter), but the other complexes remained unchanged for 60 h (Figure 5A). More aggregation was observed after 120 h, but $PalCK_3H_3$ complexes remained unchanged. A major advantage of the lipopeptides introduced in this study is their ability to form 200–300 nm complexes at relatively high DNA concentrations. Unlike complexes formed by Lipofectamine or PEI, the diameter of complexes of DNA with $PalCK_3H_2$ or $PalCK_3H_3$ was independent of DNA concentration over the range 10–120 μm (Figure 5B).

Mean Particle Size, Polydispersity Index, and Zeta Potential of Complexes. The mean particle size and zeta potential of complexes formed by DNA (15.2 nM) and lipopeptides (in 500 μL HGB pH 7.4) were examined as a function of increasing charge ratio (Figure 6A,B). As the charge ratios increased from 0.5 to 5.0, the mean particle sizes of the complexes formed with $PalCK_2H_2$, $PalCK_3H_2$, and $PalCK_3H_3$ decreased slightly (Figure 6A), from 230−260 nm down to

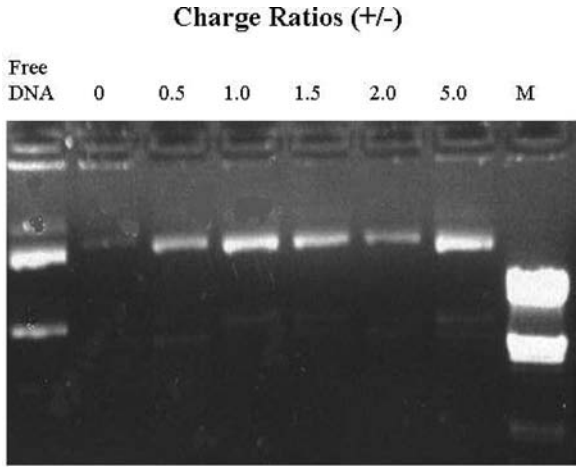

Figure 4. Stability of DNA-PalCK_2H_2 complexes against enzymatic degradation by DNase (Turbo DNase). In the absence of PalCK_2H_2 (a charge ratio = 0), the plasmid DNA was almost completely degraded. At a charge ratio of >1.0, the majority of the plasmid DNA remained intact after 30 min incubation with DNase at 4 °C.

110–150 nm at a charge ratio of 5.0 (Table 3). Complexes formed by PalCKH_2 were larger (Figure 2C), which may reflect a lower degree of DNA condensation by this lipopeptide, a hypothesis which is supported by the ethidium exclusion data. When PalCKH_2 was used to condense DNA the extent of ethidium exclusion was considerably lower than exclusion caused by K_2 or K_3 lipopeptides at the same charge ratio.

The zeta potential of complexes was a function of charge ratio and was similar for complexes formed by all lipopeptides. The zeta potential was negative at charge ratios below 1.0 and approached zero at a charge ratio of unity. When the charge ratio was increased above 1.0, the zeta potential became positive, reaching a maximum value of approximately +20 mV for charge ratios between 2.0 and 5.0 (Figure 6B).

Figure 7 shows typical values of the PDI, mean particle size, and zeta potential for 40 μg DNA complexed with (A) lipopeptide PalCK_2H_2, (B) PEI, and (C) Lipofectamine in HGB pH 7.4, at a charge ratio of 1.5 (N/P of 9.0 for PEI). For complexes of DNA−transfection agents shown, the PDI for the DNA−Lipofectamine complex was the highest (PDI = 1.0), indicating a wide size distribution. The Nanosizer data suggested that PEI and Lipofectamine complexes may have been multiphasic as well as polydisperse. DNA complexes formed by PalCK_2H_2 and other lipopeptides typically had more consistent particle size, narrower size distributions, and more precise zeta potentials than complexes formed with PEI or Lipofectamine.

For lipopeptides with the same number of histidine residues (2 or 3 histidines), we observed that, as the number of lysine residues in the lipopeptide increased, their mean particle sizes and polydispersities decreased (Tables 4 and 5). However, zeta potential was increased as the number of lysines was increased.

In Vitro Transfection Studies. The transfection efficiency of PalCK_2H_2 in Cos7 cells was found to be 80-fold greater than LauCK_2H_2 ($p < 0.001$) (Figure 8A), which correlated with its superior properties with respect to DNA condensation, complex stability, and resistance to nuclease digestion. PalCK_3H_2 was twice as effective as PalCK_3H_3 (Figure 8B). When the lipopeptides containing two histidine residues were compared, there were clear differences. The compound with one lysine residue was significantly less active than those with two or three lysine residues, which had similar activity (Figure 8C). For lipopeptides with three histidine residues, the K_3 lipopeptide was over twice as active as the K_2 lipopeptide (Figure 8D). When the best lipopeptides were compared with PEI and Lipofectamine,

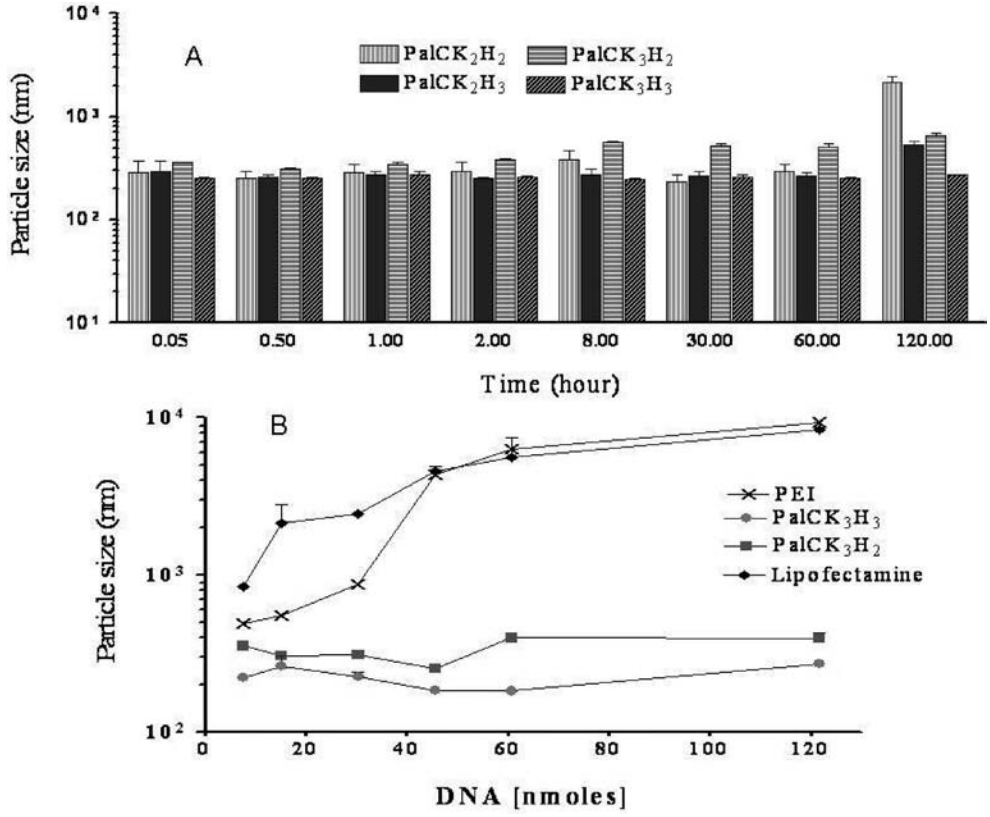

Figure 5. Physical stability of DNA complexes at a charge ratio of 1.5 formed in HEPES glucose buffer (HGB pH 7.4) at ambient temerapture: (A) Effect of storage time on mean particle size of complexes formed by four lipopeptides; (B) Effect of DNA concentration on mean particle size of complexes formed by lipopeptides, PEI, and Lipofectamine. Data are presented as mean ± SD ($n = 3$).

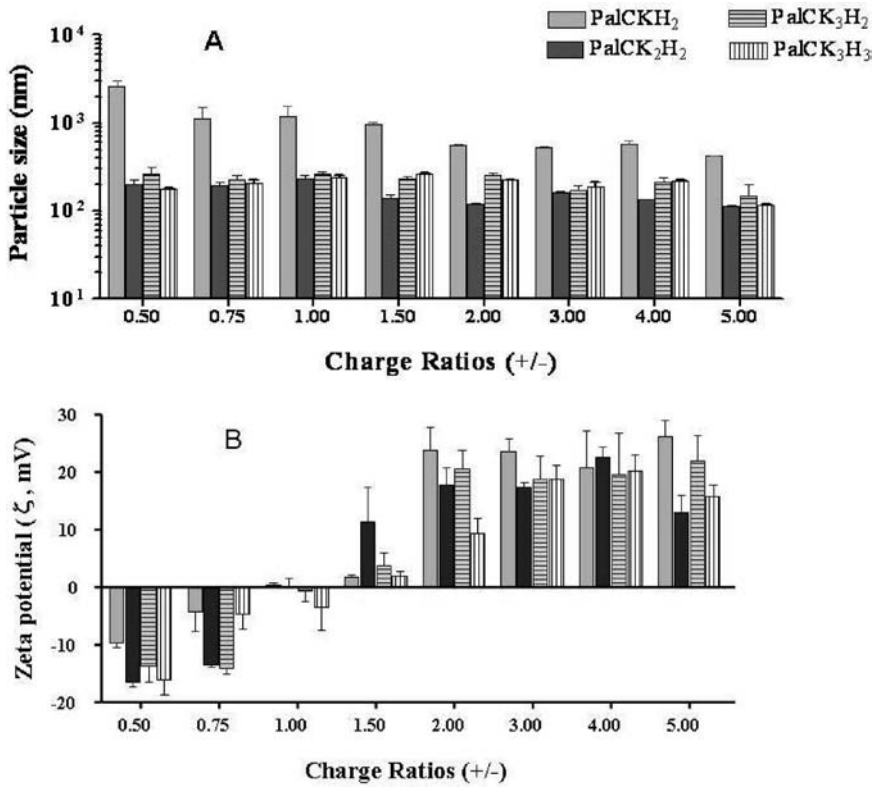

Figure 6. Effect of charge ratio on (A) mean particle size and (B) zeta potential of DNA−lipopeptide complexes formed in HGB at pH 7.4. Data are presented as mean ± SD ($n = 3$).

Table 3. Effect of Charge Ratio on Mean Particle Size of DNA−Lipopeptide Complexes

	charge ratio	
	particle size	
lipopeptide	0.5	5
$PalCK_2H_2$	229 ± 23 nm	112 ± 5 nm
$PalCK_3H_2$	256 ± 22 nm	146 ± 50 nm
$PalCK_3H_3$	240 ± 27 nm	117 ± 3 nm

activity was comparable, although generally Lipofectamine was a marginally better transfection agent in vitro (Figure 8E).

DISCUSSION

This project investigated the effect of lipopeptide composition (alkyl chain length, number of lysines, and histidines) on DNA complex formation and transfection efficiency, and compared these novel lipopeptides with PEI and Lipofectamine. DNA condensation studies indicated that the addition of an alkyl chain to the lipopeptide molecule promoted complexation, and that the palmitoyl peptides were more effective than the corresponding lauryl lipopeptides. We hypothesize that the presence of the alkyl chain promotes complex formation resulting from the increased entropy derived by loss of water structure around the alkyl chain, commonly called the hydrophobic effect. The longer hydrophobic palmitoyl (C_{16}) chain would be expected to promote a stronger hydrophobic interaction, and this results in more compact and stable particles that have improved transfection efficiency.

The lysine residues on the lipopeptides were included to provide a protonated amine group at neutral pH that effected condensation of plasmid DNA. The amino acid side chain of lysine has a $pK_a = 10.80$, and is therefore 99.96% ionized at pH 7.4, enabling ionic interaction with the negatively charged sugar–phosphate backbone of DNA. DNA condensation with lipopeptides such as $PalCK_2H_2$ took place efficiently, and zeta potential data suggested that the complex formed included all lysine residues in a one-to-one stoichiometric relationship with the nucleotides. At least two lysine residues were required for efficient condensation and good transfection efficiency. The advantage of including a third lysine residue was limited.

Histidine residues were included to provide a source of weakly basic groups. It was hypothesized that these residues would become protonated in the endosome, thereby promoting endosomal escape in a manner analogous to the mechanism by which PEI is thought to achieve transfection. This approach led to efficient DNA condensation and transfection by the compound $PalCK_2H_2$. Additional histidine residues might be expected to improve the efficiency of endosomal escape, but this strategy resulted in less efficient condensation, when compared to $PalCK_2H_2$ (Figure 2D). There was a clear rank order, $H_5 < H_4 < H_3 < H_2$, in condensation efficiency as determined by ethidium exclusion, for palmitoylated lipopeptides containing two lysine residues. The lipopeptide $PalCK_2H_4$, for example, with four histidine residues per lipopeptide, resulted in only 10% ethidium exclusion at a charge ratio of 2.0. In contrast the DNA−ethidium fluorescence intensities for $PalCK_2H_3$ and $PalCK_2H_2$ complexes, at the same charge ratio, were reduced to 40% and 55% of the initial value, respectively. We suggest that the reduction in efficiency of DNA condensation with increase in histidine chain length may be explained by steric hindrance or a decrease in the entropic driving force for complexation.

Cysteine was included in the design if the lipopeptides to promote complexation by formation of disulfide bonds in a manner analogous to the compounds described previously by Behr and colleagues (*36*). We hypothesized that, in the presence of the DNA template, the Cys-lipopeptide is likely to dimerize, leading to in situ formation of a transfection agent with a double alkyl chain. This is the main advantage of including cysteine in the lipopeptide structure, since most single alkyl chain

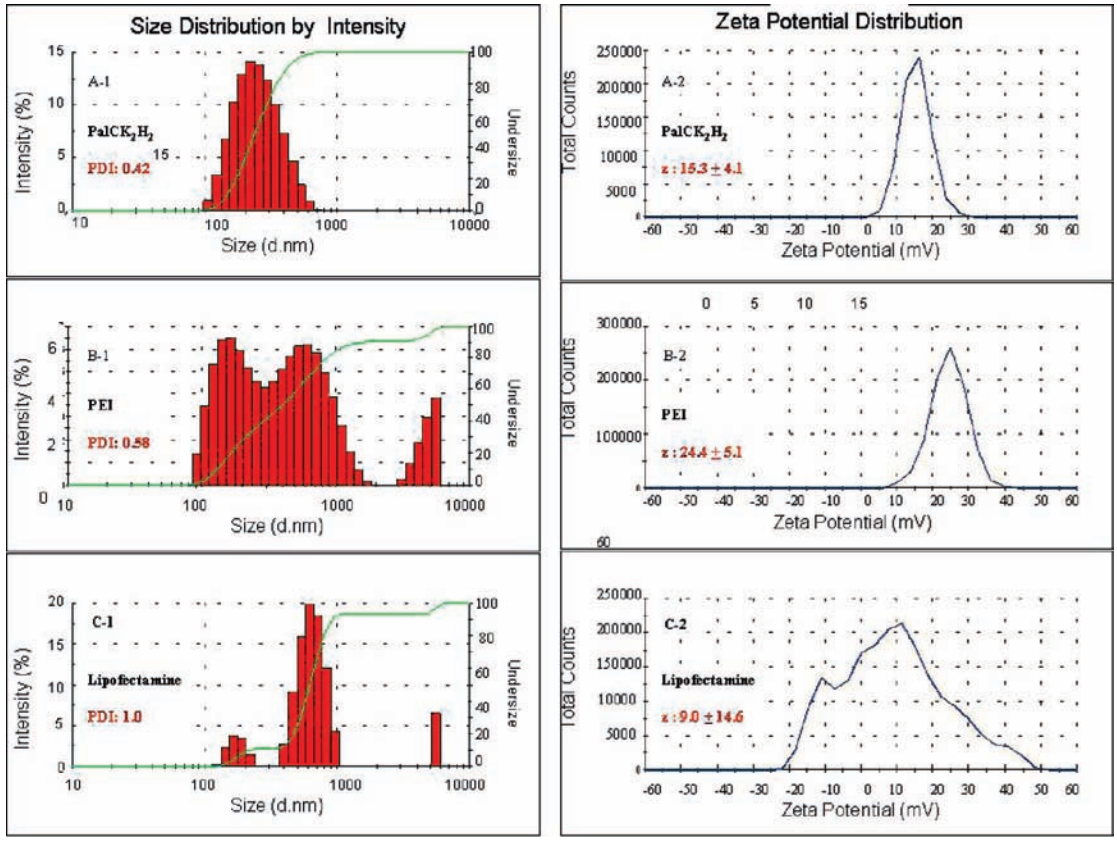

Figure 7. Typical size distributions and zeta potentials of DNA complexes formed at a charge ratio of 1.5 in HGB pH 7.4: with $PalCK_2H_2$ (A-1 and A-2), PEI (B-1 and B-2), and Lipofectamine (C-1 and C-2). The particle size data are expressed as a histogram showing the size distribution and as the cumulative % undersize, shown as the solid line plotted against particle size.

Table 4. Effect of Lipopeptide Structure on Mean Particle Sizes, Zeta Potential, and Polydispersity of DNA−Lipopeptide Complexes at a Charge Ratio of 1.5 in HGB pH 7.4[a]

lipopeptide	particle size (nm) (mean ± SD)	PDI (mean ± SD)	zeta potential (mV) (mean ± SD)
$PalCKH_2$	688 ± 28	0.77 ± 0.05	3.6 ± 1.7
$PalCK_2H_2$	240 ± 4.1	0.31 ± 0.03	13.2 ± 0.7
$PalCK_2H_3$	254 ± 6.2	0.35 ± 0.04	5.4 ± 0.3
$PalCK_3H_3$	247 ± 3.3	0.27 ± 0.001	6.3 ± 0.5

[a] Complexes were formed by diluting 40 μg DNA (~243 nM); data are represented as mean ± SD of triplicate measurements ($n = 3$).

Table 5. Effect of Coupling Histidine to $PalCK_2$ Lipopeptides on Mean Particle Size, Zeta Potential, and Polydispersity of DNA−Lipopeptide Complexes at a Charge Ratio of 1.5 in HGB pH 7.4[a]

lipopeptide	particle size (nm) mean ± SD	PDI mean ± SD	zeta potential (mV) mean ± SD
$PalCK_2H_2$	240 ± 4.1	0.31 ± 0.03	13.17 ± 0.74
$PalCK_2H_3$	254 ± 6.2	0.35 ± 0.04	5.44 ± 0.28
$PalCK_2H_4$	724 ± 317.0	0.67 ± 0.18	1.53 ± 0. 25
$PalCK_2H_5$	Sedimentation[b]	-	-

[a] Complexes were formed by diluting 40 μg DNA (~243 nM); data are presented as mean ± SD of triplicate measurements ($n = 3$). [b] The complex formed large aggregates that sedimented rapidly, therefore their mean particle sizes and other particle properties could not be determined with the Zetasizer Nano ZS.

transfection agents are (a) less efficient at condensing DNA and (b) generally regarded as toxic to cells (*38*). We have not established yet whether dimerization is indeed occurring after complexation, and this is the subject of further investigation in our laboratories.

In our studies, the mean diameters of the DNA−lipopeptide complexes were between 180 and 275 nm and 250–400 nm for DNA-$PalCK_3H_3$ and DNA-$PalCK_3H_2$, respectively. Particle mean size was approximately independent of DNA concentration, up to 120 nM. Typically, DNA complexes aggregate at high concentration. For example, Duguid et al. have reported that the diameter of DNA complexes formed at a charge ratio of 3.0 with synthetic cationic peptide analogues ($YKAK_nWK$) and the amphipathic peptide (GLFEALLELLESLWELLLEA) increased as DNA concentration increased (*39*). The lipopeptides described here are unlikely to bind more than one primary condensed DNA particle at once. This reduces the opportunity for particle cross-linking, which we suggest may explain the particle growth at high concentrations observed in this study with DNA−PEI or DNA−Lipofectamine complexes. The mean particle sizes of the DNA−PEI complexes were <500 nm at DNA concentrations of <10 nM, but complexes were 5–10 μm in diameter at concentrations of 60–120 nM. Similarly complexes of DNA−Lipofectamine resulted in a substantial particle aggregation (~8 μm) at high DNA concentration (~120 nM) (Figure 5B). Many DNA complexes are unstable over short periods of time. For example, Park et al. observed that complexes formed by 2 μg of DNA with linear or branched PEI (N/P = 10 in 1.2 mL PBS pH 7.2) increased in particle size when the complexes were incubated for longer than 10 min (*40*). The lipopeptides described here appear to form stable complexes even at high DNA concentrations, which we believe will be important for gene delivery in vivo.

The mean particle size and zeta potential of complexes were examined as a function of increasing charge ratio. In general terms, mean particle diameter decreased as charge ratio increased. In the case of complexes formed by the compound $PalCKH_2$, which only has one lysine residue, the mean particle

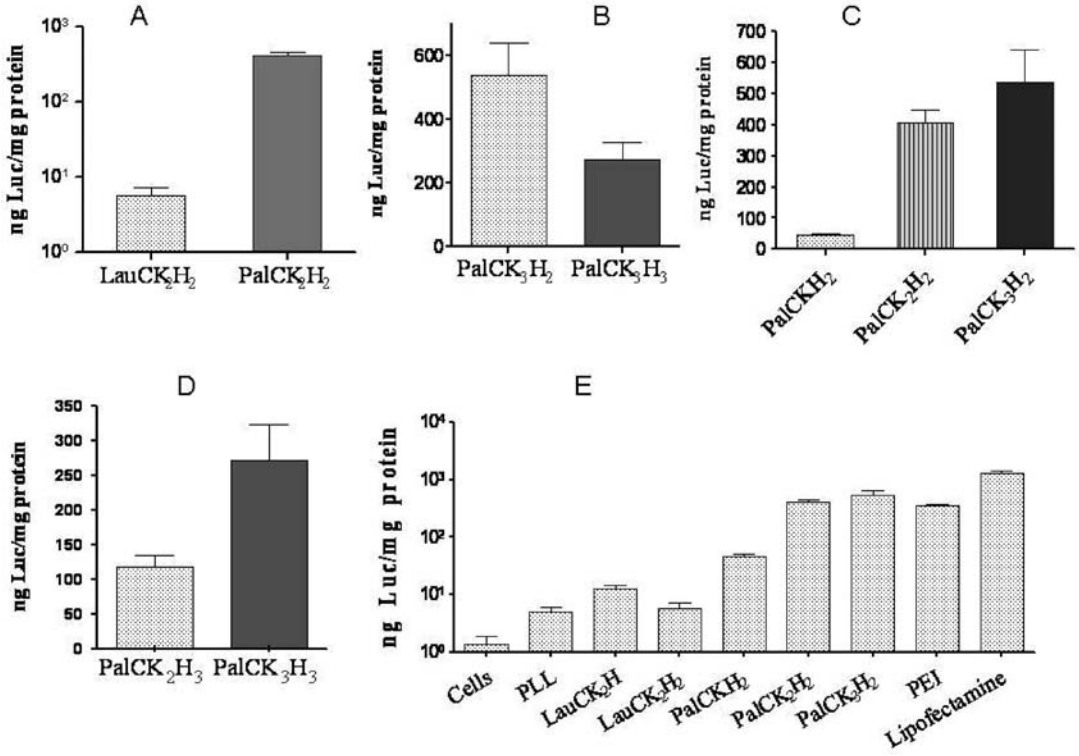

Figure 8. Transfection studies of DNA−lipopeptide complexes and DNA−Lipofectamine complexes at charge ratio of 1.5 in COS7 cells.The PEI complexes were formed at an N/P ratio of 9. Data are presented as mean ± SD for triplicate determinations ($n = 3$). Effect of (A) alkyl chains, lauryl, and palmitoyl on transfection efficiency; (B) the number of lysine residues in lipopeptides with two histidine residues; (C) the number of lysine residues in lipopeptides with three histidine residues; (D) the number of histidine residues in lipopeptides with three lysine residues. (E) The transfection efficiency of selected lipopeptide constructs compared to commercially available transfection agents (PLL, PEI, and Lipofectamine).

size decreased markedly from 1186 ± 375 nm at a charge ratio of 1.0 to 423 ± 5 nm at a charge ratio of 5.0. Particle sizes were smaller for complexes formed by $PalCK_2H_n$ lipopeptides, but they still decreased as charge ratio increased. These data were consistent with previous publications (*33, 41*). As the charge ratio increased from 0.5 to 5.0, the zeta potential of the complexes changed from a negative value (−16 ± 5 mV) to a positive value (approximately 20 ± 3 mV) (Figure 6B). No further increase in the zeta potentials of the complexes were observed when the charge ratio was increased above 2.5. This may indicate that much of the additional lipopeptide was in a free state when charge ratio exceeded this value. At a charge ratio of 1.0, the zeta potential was close to zero, which indicated that all or most of the lipopeptide was engaged in binding DNA. These observations were in agreement with another report which noted that the zeta potential of DNA complexes became positive at a charge ratio of >1.5 (*13*).

It is generally accepted that complexes of DNA and transfection agents are heterogeneous in particle size. As shown in Figure 7, at a charge ratio of 1.5 (N/P of 9.0 for PEI), the zeta potentials of $PalCK_2H_2$, PEI, and Lipofectamine complexes were positive: 15.3 ± 4.1 mV, 24.4 ± 5.1 mV, and 9.0 ± 14.6 mV, respectively. It was interesting to note that complexes which had a high polydispersity, such as Lipofectamine complexes, typically had a higher standard deviation for the estimated zeta potential, a further reflection of increased heterogeneity. We also observed that, at a charge ratio of 1.5, the zeta potential for some DNA−Lipofectamine complexes were negative, indicating that some of the transfection agent was not involved in binding DNA. This is in agreement with Slimani et al., who reported that the zeta potentials for complexes of DNA with liposomes (DMHAPC-Chol/DOPE (1:1) changed from negative to positive at a charge ratio of 1.5–2.0 (*13*). Gilot et al. also reported that the zeta potentials of complexes of DNA-cationic lipid GB12 (glycine betaine 12) were still negative at a charge ratio of 1.45 (*42*). These data show that the complexes produced with $PalCK_2H_2$ were less heterogeneous than complexes formed with two standard transfection agents, PEI and Lipofectamine. This is an important result in the search for better transfection agents.

The effect of extra lysine residues on the mean particle sizes, zeta potentials, and polydispersities of DNA complexes was to induce formation of more condensed DNA−lipopeptide complexes, though the $PalCK_2$ series compounds compared well with $PalCK_3$ series compounds. Increasing the number of histidine residues led to an increase in the mean particle size of DNA complexes and corresponding increases in polydispersity. Thus, although longer histidine chain length may have been advantageous for endosomal escape, any advantage was abrogated by less efficient DNA condensation, or additional aggregation of primary complexes. The compound $PalCK_2H_5$ resulted in substantial aggregation and sedimentation of DNA complexes. This may have been due to the hydrophobic nature of the imidazole side chain, rendering it less water-soluble compared to the effects of the lysine side chain. These observations were supported by the data obtained using the EtBr exclusion assay, when addition of more lysine in the lipopeptide constructs resulted in lower fluorescence intensity (more condensed particles), while addition of histidine residues had the opposite effect (Figure 2).

Experiments were conducted in order to determine the relative transfection efficiencies of the constructs. Several groups have reported that histidine-rich peptides have enhanced transgene expression (*43–46*), and it was our intention to exploit this property. However, our results suggest that there is an optimum histidine chain length for $PalCK_nH_m$ compounds, for efficient DNA condensation while retaining disruptive activity to the endosome. The sequence order of histidine residues in the

lipopeptide may also affect transfection efficiency, and this merits further study. We used linear clusters of K and H, i.e., K−K−K−H−H−H rather than alternating lysyl-histidinyl chains (H−K−H−K−H−K). Chen et al. reported that an alternating copolymer of histidine and lysine (with several variations of H−K, such as the (13mer)-[K−H−K−H−K−H−K−G−K−H−K−H−K−H−K], significantly enhanced the transfection efficiency of cationic liposomes up to 10-fold (*30*). The copolymer of H−K alone did not facilitate gene expression, suggesting that complexation may not have been efficient in the absence of the liposomes.

Midoux and co-workers reported that the transfection efficiency of a histidine-substituted (PLL) was much greater than unmodified PLL (*47*). This transfection efficiency was even higher than unmodified PLL complexes used in conjunction with chloroquine treatment. In the case of these graft copolymer DNA condensing agents, gene expression improved markedly at a low level of histidine substitution and only improved slightly with additional histidine substitution. It can therefore be concluded that those histidine residues whose side chains become protonated at pH ∼6.0 (endosome vesicle) contribute favorably to transfection by endosomal disruption, but that DNA condensation must also be efficient to gain maximum benefit. For this reason, addition of histidine residues does not always enhance overall transfection efficiency (*25, 47–49*).

The data presented in this study provide insights into new synthetic transfection agents that have several advantages for nonviral gene delivery. They are chromatographically purifiable, relatively low molecular weight compounds, which lack the inevitable heterogeneity of polymeric transfection agents, and therefore have advantages in terms of pharmaceutical analysis and characterization. Complexes formed with DNA are less sensitive to DNA concentration because they are unlikely to cross-link two or more primary particles. Although the in vitro transfection efficiencies of the lipopeptides reported here were lower than Lipofectamine, the transfection efficiencies of two of the lipopeptide constructs ($PalCK_2H_2$ and $PalCK_3H_2$) were much higher than PLL and somewhat higher than PEI (Figure 8E). It is likely that, by varying the ratio of histidine (H) and lysine (K) residues, as well as optimizing the sequence order and position of H−K, the transfection efficiency of the lipopeptide constructs might be significantly improved further. However, it should also be recognized that in vitro transfection is a poor indicator of activity in vivo, and high in vitro activity is often explained by sedimentation of large DNA complexes onto the cell surface during the transfection period (typically 4 h). In contrast, in vivo applications require complexes to be small and stable to promote improved biodistribution. The lipopeptides introduced here have the potential to improve gene delivery in vivo by producing stable complexes with DNA, and further investigation of their properties is warranted.

ACKNOWLEDGMENT

We wish to thank Dr. Ben Boyd for his assistance with the use of the Zetasizer Nano ZS. A scholarship for Tarwadi was provided by the Australian Government overseas aid program (AusAID).

LITERATURE CITED

(1) Tachibana, R., Harashima, H., Ide, N., Ukitsu, S., Ohta, Y., Suzuki, N., Kikuchi, H., Shinohara, Y., and Kiwada, H. (2002) Quantitative analysis of correlation between number of nuclear plasmids and gene expression activity after transfection with cationic liposomes. *Pharm. Res. 19*, 377–81.

(2) Glover, D. J., Lipps, H. J., and Jans, D. A. (2005) Towards safe, non-viral therapeutic gene expression in humans. *Nat. Rev. Genet. 6*, 299–310.

(3) Wasungu, L., and Hoekstra, D. (2006) Cationic lipids, lipoplexes and intracellular delivery of genes. *J. Controlled Release 116*, 255–64.

(4) Rettig, G., and Rice, K. (2007) Non-viral gene delivery: from the needle to the nucleus. *Expert Opin. Biol. Ther. 7*, 799–808.

(5) Zuhorn, I. S., Engberts, J. B., and Hoekstra, D. (2007) Gene delivery by cationic lipid vectors: overcoming cellular barriers. *Eur. Biophys. J. 36*, 349–62.

(6) Wiethoff, C. M., and Middaugh, C. R. (2003) Barriers to nonviral gene delivery. *J. Pharm. Sci. 92*, 203–17.

(7) Felgner, J. H., Kumar, R., Sridhar, C. N., Wheeler, C. J., Tsai, Y. J., Border, R., Ramsey, P., Martin, M., and Felgner, P. L. (1994) Enhanced gene delivery and mechanism studies with a novel series of cationic lipid formulations. *J. Biol. Chem. 269*, 2550–61.

(8) Zabner, J., Cheng, S. H., Meeker, D., Launspach, J., Balfour, R., Perricone, M. A., Morris, J. E., Marshall, J., Fasbender, A., Smith, A. E., and Welsh, M. J. (1997) Comparison of DNA-lipid complexes and DNA alone for gene transfer to cystic fibrosis airway epithelia in vivo. *J. Clin. Invest. 100*, 1529–37.

(9) Lee, R. J., and Huang, L. (1996) Folate-targeted, anionic liposome-entrapped polylysine-condensed DNA for tumor cell-specific gene transfer. *J. Biol. Chem. 271*, 8481–7.

(10) Lee, R. J., and Huang, L. (1997) Lipidic vector systems for gene transfer. *Crit. Rev. Ther. Drug Carrier Syst. 14*, 173–206.

(11) Felgner, P. L., Gadek, T. R., Holm, M., Roman, R., Chan, H. W., Wenz, M., Northrop, J. P., Ringold, G. M., and Danielsen, M. (1987) Lipofection: a highly efficient, lipid-mediated DNA-transfection procedure. *Proc. Natl. Acad. Sci. U.S.A. 84*, 7413–7.

(12) Wheeler, C. J., Felgner, P. L., Tsai, Y. J., Marshall, J., Sukhu, L., Doh, S. G., Hartikka, J., Nietupski, J., Manthorpe, M., Nichols, M., Plewe, M., Liang, X., Norman, J., Smith, A., and Cheng, S. H. (1996) A novel cationic lipid greatly enhances plasmid DNA delivery and expression in mouse lung. *Proc. Natl. Acad. Sci. U.S.A. 93*, 11454–9.

(13) Slimani, H., Guenin, E., Briane, D., Coudert, R., Charnaux, N., Starzec, A., Vassy, R., Lecouvey, M., Perret, Y. G., and Cao, A. (2006) Lipopeptide-based liposomes for DNA delivery into cells expressing neuropilin-1. *J. Drug Targeting 14*, 694–706.

(14) Moghimi, S. M., Symonds, P., Murray, J. C., Hunter, A. C., Debska, G., and Szewczyk, A. (2005) A two-stage poly(ethylenimine)-mediated cytotoxicity: implications for gene transfer/therapy. *Mol. Ther. 11*, 990–5.

(15) Baker, A., Saltik, M., Lehrmann, H., Killisch, I., Mautner, V., Lamm, G., Christofori, G., and Cotten, M. (1997) Polyethylenimine (PEI) is a simple, inexpensive and effective reagent for condensing and linking plasmid DNA to adenovirus for gene delivery. *Gene Ther. 4*, 773–82.

(16) Cogoni, C., and Macino, G. (1999) Gene silencing in *Neurospora crassa* requires a protein homologous to RNA-dependent RNA polymerase. *Nature 399*, 166–9.

(17) Cogoni, C., and Macino, G. (1999) Posttranscriptional gene silencing in *Neurospora* by a RecQ DNA helicase. *Science 286*, 2342–4.

(18) Neu, M., Fischer, D., and Kissel, T. (2005) Recent advances in rational gene transfer vector design based on poly(ethylene imine) and its derivatives. *J. Gene Med. 7*, 992–1009.

(19) Godbey, W. T., Wu, K. K., and Mikos, A. G. (1999) Tracking the intracellular path of poly(ethylenimine)/DNA complexes for gene delivery. *Proc. Natl. Acad. Sci. U.S.A. 96*, 5177–81.

(20) Godbey, W. T., Wu, K. K., and Mikos, A. G. (1999) Poly(ethylenimine) and its role in gene delivery. *J. Controlled Release 60*, 149–60.

(21) Wu, G. Y., and Wu, C. H. (1987) Receptor-mediated in vitro gene transformation by a soluble DNA carrier system. *J. Biol. Chem. 262*, 4429–4432.

(22) Hasida, M., Takemura, S., Nishikawa, M. A., and Takakura. (1998) Targeted delivery of plasmid DNA complexed with galactosylated poly(L-lysine). *J Controlled Release 53*, 301–310.

(23) Boussif, O., Lezoualc'h, F., Zanta, M. A., Mergny, M. D., Scherman, D., Demeneix, B., and Behr, J. P. (1995) A versatile vector for gene and oligonucleotide transfer into cells in culture and in vivo: polyethylenimine. *Proc. Natl. Acad. Sci. U.S.A. 92*, 7297–301.

(24) Pollard, H., Remy, J. S., Loussouarn, G., Demolombe, S., Behr, J. P., and Escande, D. (1998) Polyethylenimine but not cationic lipids promotes transgene delivery to the nucleus in mammalian cells. *J. Biol. Chem. 273*, 7507–11.

(25) Midoux, P., Mendes, C., Legrand, A., Raimond, J., Mayer, R., Monsigny, M., and Roche, A. C. (1993) Specific gene transfer mediated by lactosylated poly-L-lysine into hepatoma cells. *Nucleic Acids Res. 21*, 871–8.

(26) Vogt, T. C. B., and Bechinger, B. (1999) The interaction of histidine-containing amphipathic helical peptide antibiotics with lipid bilayers. *J. Biol. Chem. 274* (21), 29115–29121.

(27) Read, M. L., Singh, S., Ahmed, Z., Stevenson, M., Briggs, S. S., and Oupicky, D. (2005) A versatile reducible polycation-based system for efficient delivery of a broad range of nucleic acids. *Nucleic Acids Res. 33*, e86.

(28) Kichler, A., Leborgne, C., Marz, J., Danos, O., and Bechinger, B. (2003) Histidine-rich amphipathic peptide antibiotics promote efficient delivery of DNA into mammalian cells. *Proc. Natl. Acad. Sci. U.S.A. 100*, 1564–8.

(29) Lentz, K., Anchordoquy, T., and CS, L. (2006) Rationale for the selection of an aerosol delivery system for gene delivery. *J. Aerosol Med. 19* (3), 372.

(30) Chen, Q. R., Zhang, L., Stass, S. A., and Mixson, A. J. (2001) Branched co-polymers of histidine and lysine are efficient carriers of plasmids. *Nucleic Acids Res. 29*, 1334–40.

(31) Siprashvili, Z., Scholl, F. A., Oliver, S. F., Adams, A., Contag, C. H., Wender, P. A., and and Khavari, P. A. (2003) Gene transfer via reversible plasmid condensation with cysteine-flanked, internally spaced arginine-rich peptides. *Hum. Gene Ther. 14*, 1225–33.

(32) Lee, C. H., Woo, J. H., Cho, K. K., Kang, S. H., Kang, S. K., and Choi, Y. J. (2007) Expression and characterization of human growth hormone-Fc fusion proteins for transcytosis induction. *Biotechnol. Appl. Biochem. 46*, 211–7.

(33) McKenzie, D. L., Kwok, K. Y., and Rice, K. G. (2000) A potent new class of reductively activated peptide gene delivery agents. *J. Biol. Chem. 275*, 9970–7.

(34) McKenzie, D. L., Collard, W. T., and Rice, K. G. (1999) Comparative gene transfer efficiency of low molecular weight polylysine DNA-condensing peptides. *J. Pept. Res. 54*, 311–8.

(35) Martin, M., and KG, R. (2007) Peptide-guided gene delivery. *AAPS J. 9* (1), E18–29.

(36) Murphy, J. E., Uno, T., Hamer, J. D., Cohen, F. E., Dwarki, V., and Zuckermann, R. N. (1998) A combinatorial approach to the discovery of efficient cationic peptoid reagents for gene delivery. *Proc. Natl. Acad. Sci. U.S.A. 95*, 1517–22.

(37) Blessing, T., Remy, J. S., and Behr, J. P. (1998) Monomolecular collapse of plasmid DNA into stable virus-like particles. *Proc. Natl. Acad. Sci. U.S.A. 95*, 1427–31.

(38) Pinnaduwage, P., Schmitt, L., and Huang, L. (1989) Use of a quaternary ammonium detergent in liposome mediated DNA transfection of mouse L-cells. *Biochim. Biophys. Acta 985*, 33–7.

(39) Duguid, J. G., Li, C., Shi, M., Logan, M. J., Alila, H., Rolland, A., Tomlinson, E., Sparrow, J. T., and Smith, L. C. (1998) A physicochemical approach for predicting the effectiveness of peptide-based gene delivery systems for use in plasmid-based gene therapy. *Biophys. J. 74*, 2802–14.

(40) Park, I. K., Lasiene, J., Chou, S. H., Horner, P. J., and Pun, S. H. (2007) Neuron-specific delivery of nucleic acids mediated by Tet1-modified poly(ethylenimine). *J. Gene Med. 9*, 691–702.

(41) Way, J. C., Lauder, S., Brunkhorst, B., Kong, S. M., Qi, A., Webster, G., Campbell, I., McKenzie, S., Lan, Y., Marelli, B., Nguyen, L. A., Degon, S., Lo, K. M., and Gillies, S. D. (2005) *Protein Eng. Des. Sel.* 111–8.

(42) Gilot, D., Miramon, M. L., Benvegnu, T., Ferrieres, V., Loreal, O., Guguen-Guillouzo, C., Plusquellec, D., and Loyer, P. (2002) Cationic lipids derived from glycine betaine promote efficient and non-toxic gene transfection in cultured hepatocytes. *J. Gene Med. 4*, 415–27.

(43) Gottschalk, S., Sparrow, J. T., Hauer, J., Mims, M. P., Leland, F. E., Woo, S. L., and Smith, L. C. (1996) A novel DNA-peptide complex for efficient gene transfer and expression in mammalian cells. *Gene Ther. 3*, 448–57.

(44) Niidome, T., and Huang, L. (2002) Gene therapy progress and prospects: nonviral vectors. *Gene Ther. 9*, 1647–1652.

(45) Plank, C., Oberhauser, B., Mechtler, K., Koch, C., and Wagner, E. (1994) The influence of endosome-disruptive peptides on gene transfer using synthetic virus-like gene transfer systems. *J. Biol. Chem. 269*, 12918–24.

(46) Wyman, T. B., Nicol, F., Zelphati, O., Scaria, P. V., Plank, C., and Szoka, F. C., Jr. (1997) Design, synthesis, and characterization of a cationic peptide that binds to nucleic acids and permeabilizes bilayers. *Biochemistry 36*, 3008–17.

(47) Midoux, P., and Monsigny, M. (1999) Efficient gene transfer by histidylated polylysine/pDNA complexes. *Bioconjugate Chem. 10*, 406–11.

(48) Midoux, P., Kichler, A., Boutin, V., Maurizot, J. C., and Monsigny, M. (1998) Membrane permeabilization and efficient gene transfer by a peptide containing several histidines. *Bioconjugate Chem. 9*, 260–7.

(49) Pack, D. W., Putnam, D., and Langer, R. (2000) Design of imidazole-containing endosomolytic biopolymers for gene delivery. *Biotechnol. Bioeng. 67*, 217–23.

(50) Van Rossum, J. M., and Ariens, E. J. (1956) Chemical structure and biological activity of decamethonium derivatives. *Acta Physiol. Pharmacol. Neerl. 5*, 261–2.

(51) Sidhu, J., Bloor, T. L., Couderc-Azouani, S., Penfold, J., Holzwarth, J. F., and Wyn-Jones, E. (2004) Interactions of poly(amidoamine) dendrimers with the surfactants SDS, DTAB, and C12EO6: an equilibrium and structural study using a SDS selective electrode, isothermal titration calorimetry, and small angle neutron scattering. *Langmuir 20*, 9320–8.

(52) Li, Z., Zhu, S., Gan, K., Zhang, Q., Zeng, Z., Zhou, Y., Liu, H., Xiong, W., Li, X., and Li, G. (2005) Poly-L-lysine-modified silica nanoparticles: a potential oral gene delivery system. *J. Nanosci. Nanotechnol. 5*, 1199–203.

(53) Ainola, M. M., Mandelin, J. A., Liljestrom, M. P., Li, T. F., Hukkanen, M. V., and Konttinen, Y. T. (2005) Pannus invasion and cartilage degradation in rheumatoid arthritis: involvement of MMP-3 and interleukin-1beta. *Clin. Exp. Rheumatol. 23*, 644–50.

(54) Mannisto, M., Vanderkerken, S., Toncheva, V., Elomaa, M., Ruponen, M., Schacht, E., and Urtti, A. (2002) Structure-activity relationships of poly(L-lysines): effects of pegylation and molecular shape on physicochemical and biological properties in gene delivery. *J. Controlled Release 83*, 169–82.

(55) Kwoh, D. Y., Coffin, C. C., Lollo, C. P., Jovenal, J., Banaszczyk, M. G., Mullen, P., Phillips, A., Amini, A., Fabrycki, J., Bartholomew, R. M., Brostoff, S. W., and Carlo, D. J. (1999) Stabilization of poly-L-lysine/DNA polyplexes for in vivo gene delivery to the liver. *Biochim. Biophys. Acta 1444*, 171–90.

BC700463Q

Radiosynthesis and Biodistribution of Cyclic RGD Peptides Conjugated with Novel [^{18}F]Fluorinated Aldehyde-Containing Prosthetic Groups

Matthias Glaser,[†] Matthew Morrison,[§] Magne Solbakken,[‡] Joseph Arukwe,[‡] Hege Karlsen,[‡] Unni Wiggen,[‡] Sue Champion,[§] Grete Mørk Kindberg,[‡] and Alan Cuthbertson*[,‡]

Hammersmith Imanet, Du Cane Road, London W12ONN, U.K., GE Healthcare MDx Discovery Research, Nycoveien 2, NO-0401 Oslo, Norway, and GE Healthcare MDx Discovery Research, The Grove Centre, White Lion Road, Amersham, U.K.
Received December 18, 2007; Revised Manuscript Received February 13, 2008

Achieving high-yielding, robust, and reproducible chemistry is a prerequisite for the ^{18}F-labeling of peptides for quantitative receptor imaging using positron emission tomography (PET). In this study, we extend the toolbox of oxime chemistry to include the novel prosthetic groups [^{18}F]-(2-{2-[2-(2-fluoroethoxy)ethoxy]ethoxy}ethoxy)-acetaldehyde, [^{18}F]**5**, and [^{18}F]-4-(3-fluoropropoxy)benzaldehyde, [^{18}F]**9**, in addition to the widely used 4-[^{18}F]fluorobenzaldehyde, [^{18}F]**12**. The three ^{18}F-aldehydes were conjugated to the same aminooxy-bearing RGD peptide and the effect of the prosthetic group on biodistribution and tumor uptake studied in mice. The peptide conjugate [^{18}F]**7** was found to possess superior *in vivo* pharmacokinetics with higher tumor to blood, tumor to liver, tumor to muscle, and tumor to lung ratios than either [^{18}F]**10** or [^{18}F]**13**. The radioactivity from the [^{18}F]**7** conjugate excreted more extensively through the kidney route with 79%id passing through the urine and bladder at the 2 h time point compared to around 55%id for the more hydrophobic conjugates [^{18}F]**10** and [^{18}F]**13**. The chemical nature of a prosthetic group can be employed to tailor the overall biodistribution profile of the radiotracer. In this example, the hydrophilic nature of the ethylene glycol containing prosthetic group [^{18}F]**5** clearly influences the overall excretion pattern for the RGD peptide conjugate.

INRODUCTION

Integrins are heterodimeric glycoproteins involved in cell−cell and cell−matrix interactions (*1*). One of the most important members of this receptor class is the $\alpha_v\beta_3$ integrin, which is involved in the process of tumor-induced angiogenesis (*2*). We have previously reported on [^{99m}Tc]-NC100692, an RGD-containing peptide which has demonstrated clinical utility for imaging of breast cancer (*3*). The peptide pharmacophore binds strongly to the integrin receptors expressed on proliferating endothelial cells, and the structure allows for attachment of a variety of imaging reporter groups with no significant loss in binding affinity (*4*). These peptides therefore represent a new class of RGD-containing probes for the imaging of angiogenesis (*5–8*).

Although there are many examples of molecular imaging agents based on single photon emission computed tomography (SPECT), positron emission tomography (PET) represents a superior modality with respect to resolution, sensitivity, and the ability to acquire quantitative information from the imaging data (*9*). In addition, the widespread availability of [^{18}F]fluoride, optimal half-life (110 min), and low positron energy (0.64 MeV) makes this isotope the first choice for PET imaging (*10–13*). Significant challenges, however, still need to be overcome before ^{18}F-labeled peptides can be routinely manufactured for broad clinical application. Generic radiolabeling strategies using prosthetic groups offer the advantage that a significant part of the radiochemical process can be standardized and applied to multiple products. The prosthetic group must be unreactive toward the various functional groups found in peptides, forming instead a stable bond in a site-specific manner. The aforementioned criteria are met by utilizing oxime bond formation between an ^{18}F-aldehyde and an aminooxy-modified peptide. This type of chemoselective ligation chemistry has been employed in the past by ourselves and others using 4-[^{18}F]fluorobenzaldehyde with acceptable yields being reported for a range of peptides (*14–18*). We have previously observed, however, that the hydrophobic nature of this prosthetic group has an effect on *in vivo* pharmacokinetics, often increasing excretion of the tracer through the hepatobiliary system. The aim of this work was to further extend the toolbox of available ^{18}F-aldehydes with the principle goal of improving the pharmacokinetic profile of our RGD tracer. To this end, we considered a design strategy utilizing a short poly(ethylene glycol) (PEG) spacer as an integral component of the prosthetic group. Short PEG spacers are known to increase hydrophilicity and have been shown to improve the biodistribution profile of tracers *in vivo* (*19, 20*). As predicted, the PEG-containing conjugate [^{18}F]**7** demonstrated superior *in vivo* performance as compared to the more hydrophobic tracers [^{18}F]**10** and [^{18}F]**13** in the Lewis Lung Carcinoma mouse model (LLC). Micro-PET imaging studies were performed to examine the potential of this novel conjugate for the imaging of angiogenesis in vivo.

MATERIALS AND METHODS/EXPERIMENTAL PROCEDURES

Chemicals and solvents used were all reagent grade and used without further purification. The RGD core peptide **6** was synthesized as previously described in the literature from key intermediate NC100717 (*4*). ^{1}H NMR spectra were run at 25 °C on a Varian Unity Inova 500 MHz spectrometer equipped with a 5 mm ^{1}H-broadband PFG indirect detection probe. Mass analyses were recorded on a LCQ quadrupole ion-trap mass spectrometer (Thermo Finnigan). All chemicals used in radiolabeling were anhydrous solvents purchased from Sigma-Aldrich (Gillingham, UK). HPLC solvents were obtained from Fisher

* Corresponding author. E-mail: alan.cuthbertson@ge.com, Tel: +47 23185761; Fax: +47 23186014.
[†] Hammersmith Imanet.
[‡] GE Healthcare MDx Discovery Research, Norway.
[§] GE Healthcare MDx Discovery Research, U.K.

10.1021/bc700472w CCC: $40.75 © 2008 American Chemical Society
Published on Web 03/15/2008

Scientific (Loughborough, UK). Fluorine-18 was produced by a Scanditronix MC 40 cyclotron using the $^{18}O(p,n)^{18}F$ reaction. Enriched [^{18}O]H_2O (10–30% ^{18}O) was irradiated by protons (19 MeV) with an integrated beam current of 5–10 μAh. The microwave oven was made in-house and consisted of a brass cavity [coaxial resonance system with apperture (1.3 cm) for microreaction vessels] and an external magnetron (Microtron 200, Electro-Medical Supplies Ltd., Wantage, England). The temperature was measured using an internal fiber-optic probe (FTP3–003H, system FT1310 by Takaoka Electric Ltd., Japan). The HPLC system was a Beckman System Gold instrument equipped with a gamma detector (Bioscan Flow-count). A Phenomenex Luna C18(2) column (50 × 4.6 mm, 3 μm; flow rate 1 mL/min) was used for analytical HPLC. The preparative HPLC system utilized the semipreparative column Phenomenex Luna C18(2), 250 × 10 mm, 5 μm, at a flow rate of 4 mL/min unless otherwise stated. The following mobile phase/gradient systems were used. Gradient 1: solvent A, water (0.1%) TFA; solvent B, acetonitrile (0.1% TFA); 1 min 10% B, 10–50% B in 20 min. Gradient 2: solvent A, water (0.5%) TFA; solvent B, acetonitrile (0.5% TFA); 1 min 10% B, 10–50% B over 20 min.

Synthesis of Compound 1 (Scheme 1). To a stirring suspension of sodium hydride (248 mg, 5.15 mmol in mineral oil) in THF (5 mL) was added through a syringe a solution of 2-{2-[2-(2-hydroxyethoxy)ethoxy]ethoxy}ethanol (1.00 g, 5.15 mmol) in THF (5 mL) at ambient temperature. After gas evolution had ceased, the mixture was stirred for 45 min giving a clear slightly yellow solution. Bromoacetaldehyde dimethyl acetal (8.70 g, 51.5 mmol) was then added with stirring for 24 h followed by 3 mL of ethyl acetate for a further 2 h. The mixture was poured into ether (100 mL) and extracted with 10% aqueous K_2CO_3 (30 mL) and brine (30 mL). The organic phase was dried over Na_2SO_4, filtered, and evaporated. Excess bromoacetaldehyde dimethyl acetal was removed from the mixture by distillation and the residual oil purified by flash chromatography using 100% ethyl acetate to afford the pure product (355 mg, 21%). ^{1}H NMR ($CDCl_3$): δ 4.52 (t, 1H, $^3J_{HH}$ = 5.2 Hz, OCH_2CH), 4.20–4.24 (m, 2H, $CH_3CO_2CH_2CH_2O$), 3.69–3.72 (m, 2H, $CH_3CO_2CH_2CH_2O$), 3.63–3.69 (m, 12H, OCH_2CH_2O), 3.54 (d, 2H, $^3J_{HH}$ = 5.2 Hz, OCH_2CH), 3.39 (s, 6H, CH_3O), 2.08 (s, 3H, CH_3CO_2).

Synthesis of Compound 2. A solution of 1 N NaOH in methanol (1 mL) was added to a stirring solution of acetic acid 2-(2-{2-[2-(2,2-dimethoxyethoxy)ethoxy]ethoxy}ethoxy)ethyl ester (110 mg, 0.34 mmol) in methanol (3 mL) at ambient temperature. The reaction was monitored by TLC ($CHCl_3$/MeOH, 9:1) and was found to be complete within 30 min. The solvent was evaporated and the residue purified by flash chromatography (silica, $CHCl_3$/MeOH, 9:1) to afford the product (73 mg, 76%) as a colorless oil. ^{1}H NMR ($CDCl_3$): δ 4.52 (t, 1H, $^3J_{HH}$ = 5.2 Hz, OCH_2CH), 3.71–3.75 (m, 2H, $HOCH_2CH_2O$), 3.63–3.70 (m, 12H, OCH_2CH_2O), 3.59–3.63 (m, 2H, $HOCH_2CH_2O$), 3.55 (d, 2H, $^3J_{HH}$ = 5.2 Hz, OCH_2CH), 3.40 (s, 6H, CH_3O), 2.94 (broad s, 1H, $HOCH_2CH_2O$).

Synthesis of Compound 3. To a solution of alcohol **2** (60 mg, 0.21 mmol) in THF (1 mL), triethylamine (59 μL, 0.42 mmol), and methanesulfonyl chloride (24 μL, 0.30 mmol) were added with stirring. The reaction was monitored by TLC (silica, $CHCl_3$/MeOH, 9:1). After 2 h, the precipitated triethylamine hydrochloride salt was filtered off. The solvent was evaporated and the product obtained as an oil (75 mg, 99%) following flash chromatography (silica, chloroform/methanol (9:1). ^{1}H NMR ($CDCl_3$): δ 4.52 (t, 1H, $^3J_{HH}$ = 5.2 Hz, OCH_2CH), 4.37–4.40 (m, 2H, $CH_3SO_3CH_2CH_2O$), 3.75–3.78 (m, 2H, $CH_3SO_3CH_2CH_2O$), 3.62–3.69 (m, 12H, OCH_2CH_2O), 3.54 (d, 2H, $^3J_{HH}$ = 5.2 Hz, OCH_2CH), 3.40 (s, 6H, CH_3O), 3.08 (s, 3H, $CH_3SO_3CH_2CH_2O$).

Synthesis of Protected Aldehyde [^{18}F]4. To a Wheaton vial (2 mL) charged with Kryptofix-222 (10 mg), potassium carbonate (1 mg dissolved in 50 μL water), and acetonitrile (0.8 mL), the fluorine-18 containing water (1 mL) was added. The solvent was removed by heating at 110 °C for 1 h under a stream of nitrogen. A 0.5 mL portion of anhydrous acetonitrile was added and immediately removed by evaporation. This step was repeated an additional two times, followed by addition of mesylate **3** (1.0 mg, 2.7 μmol) in anhydrous DMSO (0.2 mL). After heating by microwave (5 min, 160 °C, 150 → 50 W) the reaction mixture was analyzed by HPLC (gradient 1, t_R = 7.8 min). After diluting with water (0.4 mL), the solution was applied to a SepPak ^{t}C18-plus cartridge preconditioned with acetonitrile (5 mL) and water (20 mL). The cartridge was flushed with water (10 mL) and [^{18}F]**4** eluted using acetonitrile (0.5 mL). The solvent was evaporated under a stream of nitrogen at 80 °C.

Synthesis of Aldehyde [^{18}F]5. To the above product was added a mixture of 12 M HCl (34 μL, 0.41 mmol) and acetonitrile (34 μL) and the vial left at room temperature for 15 min. Complete deprotection of starting material was observed as evidenced by HPLC analysis.

Synthesis of Aminooxy−Peptide Precursor 6. To peptide precursor NC100717 (detailed synthesis described in ref (*4*)) (150 mg, 0.12 mmol) in DMF (5 mL) was added a solution of Boc-aminooxyacetic acid (34 mg, 0.18 mmol), 7-azabenzotriazol-1-yloxy-tris-(pyrrolidino)phosphonium hexafluorophosphate (PyAOP) (94 mg, 0.18 mmol), and *N*-methylmorpholine (NMM) (40 μL, 0.36 mmol) in DMF (3 mL) and the mixture left stirring for 12 h. Excess solvent was evaporated in vacuo and the crude product purified by preparative HPLC chromatography (Phenomenex Luna C18 column, 00G-4253-V0; solvents A = water/0.1% TFA and B = CH_3CN/0.1% TFA; gradient 10–50% B over 60 min; flow 50 mL/ min; detection at 254 nm), affording 97 mg (57%) of pure compound (analytical HPLC: Phenomenex Luna C18 column, 00G-4252-E0; solvents: A = water + 0.1% TFA and B = CH_3CN + 0.1% TFA, gradient 10–50% B over 20 min; flow 1.0 mL/min; t_R 19.4 min, detected at 214 and 254 nm). Further characterization was carried out by mass spectrometry, giving an *m*/*z* value for the desired product at [M − H^+] 1431.2.

Synthesis of Peptide Conjugate [^{18}F]7. To a small centrifuge vial (PP with screw cap, 1.5 mL) was added Boc-aminooxy RGD peptide precursor **6** (1 mg, 0.7 μmol) and 0.2 mL of a 95% TFA solution containing 5% water. After standing for 5 min at room temperature, the solvent was removed under a flow of nitrogen. To the vial containing [^{18}F]**5** were added 28% ammonium hydroxide (48 μL, 0.71 mmol) and 0.5 M sodium acetate buffer pH 4.0 (50 μL). This mixture was transferred into the vial containing the peptide and the solution incubated at 75 °C for 7 min. The reaction mixture was cooled in an ice bath, quenched with 0.2 mL HPLC mobile phase (20% acetonitrile/ water), characterized by analytical HPLC (gradient 2, t_R = 11.8 and 12.0 min), and isolated by preparative HPLC (gradient 2, t_R = 13.0 min). The peptide conjugate [^{18}F]**7** was formulated, following evaporation in vacuo of excess solvent at 40–50 °C, by addition of PBS buffer containing 10% ethanol.

Synthesis of Compound 8 (Scheme 2). To a solution of 4-(3-hydroxypropoxy)benzaldehyde (1.4 g, 8.0 mmol) in dichloromethane (10 mL) was added triethylamine (1.2 mL, 8.5 mmol) and mesyl chloride (0.62 mL, 8.0 mmol). After stirring for 1.5 h at room temperature, the reaction mixture was washed with water and dried over Na_2SO_4 to give 1.8 g of crude material (yellow oil). An aliquot of 290 mg was purified by reverse-phase chromatography (column Phenomenex Luna C18(2) 5 μm

Scheme 1. Preparation of [18F](2-{2-[2-(2-Fluoroethoxy)ethoxy]ethoxy}ethoxy)acetaldehyde [18F]5 and Conjugation Reaction Forming Labeled RGD Peptide [18F]7

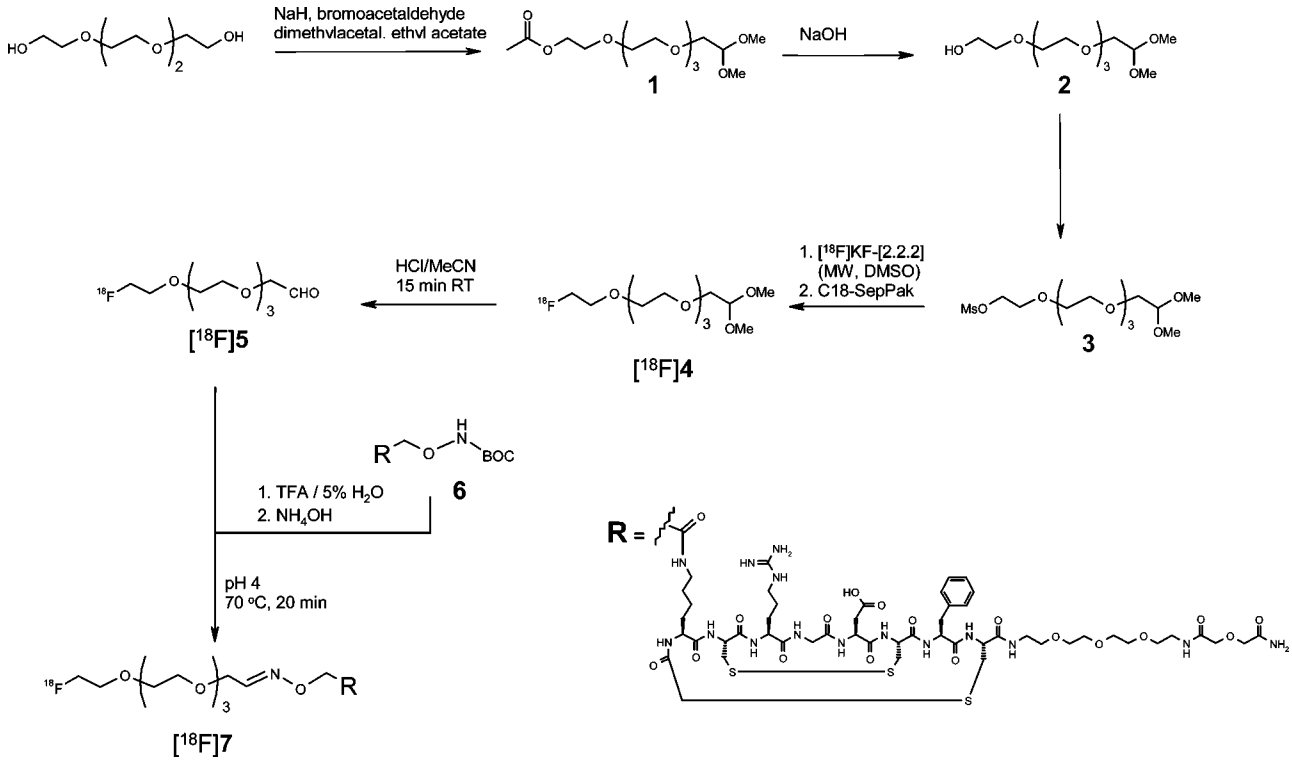

Table 1. Analytical and Isolated Radiochemical Yields of [18F]4

entry	solvent	temperature	reaction time	radiochemical yield, [18F]**4**
1	MeCN	80 °C	15 min	11%[b]
2	MeCN	80 °C	30 min	16%[b]
3	DMSO	80 °C	15 min	12%[b]
4	DMSO	80 °C	30 min	23%[b]
5[a]	MeCN	80 °C	30 min	18%[b]
6	DMSO	160 °C	5 min	60%[b] (33%)[c]
7	DMSO	160 °C[d]	5 min	97%[b] (62%)[c]

[a] [18F]TBAF vs [18F]KF-[2.2.2]. [b] Measured by HPLC. [c] Isolated and decay-corrected. [d] Microwave heating.

21.2 × 250 mm, solvents: A = water/0.1% TFA and B = acetonitrile/0.1% TFA; gradient 20–40% B over 60 min; flow 10.0 mL/ min). The structure was confirmed by NMR analysis. ^{1}H NMR [$CDCl_3$]: δ 2.279 (q, 2H, $MsOCH_2CH_2CH_2CH_2$, J = 6.0 Hz), 3.012 (s, 3H, CH_3); 4.190 (t, 2H, $MsOCH_2CH_2CH_2CH_2$, J = 5.9 Hz), 4.462 (t, 2H, $MsOCH_2CH_2CH_2CH_2$, J = 6.1 Hz), 7.010 (pd, 2H, aromatic, J = 8.8 Hz), 7.845 (pd, 2H, aromatic, J = 8.8 Hz); 9.895 (s, 1H, CHO).

Synthesis of Aldehyde [18F]9. A Wheaton vial (2 mL) was charged with tetrabutylammonium hydroxide solution (1.0 M in MeOH, 13.5 μL) and water (0.1 mL). After saturation with gaseous CO_2, acetonitrile (0.4 mL) and ^{18}F-containing water (178–485 MBq) were added. The water was removed azeotropically as described above, followed by addition of mesylate **8** (0.5 mg, 1.9 μmol) in anhydrous DMSO (0.2 mL). The mixture was heated in the microwave oven for 2 min at 110 °C. The product was identified by HPLC analysis (gradient 1, t_R = 16.1 min).

Synthesis of Peptide Conjugate [18F]10. Peptide **6** (4.0 mg, 2.8 μmol) was Boc-deprotected as described above and dissolved in 0.5 M ammonium acetate buffer pH 4.0 (0.1 mL). The reaction mixture containing [18F]**7** was added and the vial heated for 20 min at 70 °C. The coupling reaction was quenched by adding HPLC mobile phase (0.2 mL, 20% B). The labeled peptide [18F]**10** was identified by HPLC (gradient 1, t_R = 14.4 min), isolated by preparative HPLC (gradient 1, t_R = 15.4 min), and formulated by adding water (4 mL) followed by extraction using a SepPak C18-plus cartridge. The labeled peptide was eluted with ethanol (0.5 mL). After partial evaporation under a flow of nitrogen, the mixture was reconstituted with PBS.

Synthesis of Aldehyde [18F]12 (Scheme 3). To a Wheaton vial (2.0 mL) was added Kryptofix−222 (5 mg), potassium carbonate (1 mg in 50 μL water), acetonitrile (0.8 mL), and water containing [18F]fluoride. The water was removed azeotropically as described above. After addition of triflate **11** (0.5 mg, 1.6 μmol) in anhydrous DMSO, the vessel was heated for 15 min at 80 °C.

Synthesis of Peptide Conjugate [18F]13. Peptide **6** (2.3 mg, 1.6 μmol) was Boc-deprotected as described above, dissolved in 0.5 M ammonium acetate buffer pH 4.0 (0.2 mL), mixed with the solution containing [18F]**10**, and then heated to 70 °C for 10 min. [18F]**13** was identified by analytical HPLC (gradient

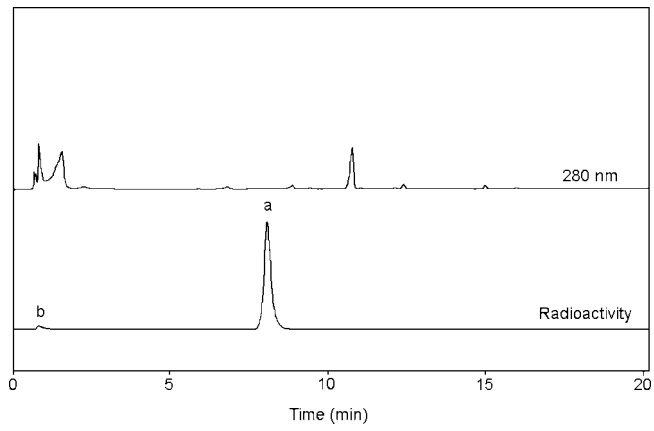

Figure 1. HPLC analysis of a reaction mixture containing diacetal peak (a) [18F]**4** and (b) polar radioactive byproduct (microwave heating at 160 °C for 5 min in DMSO).

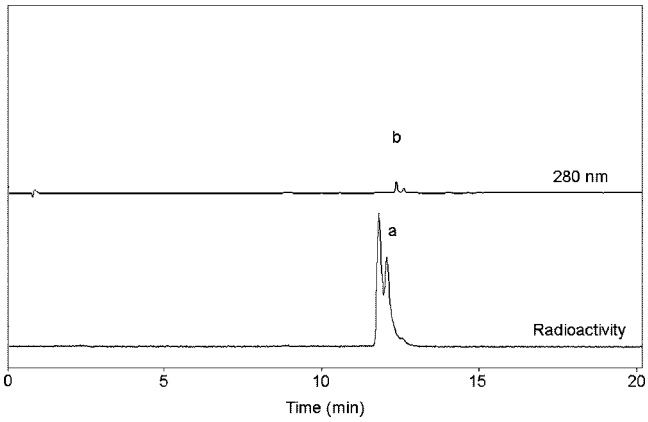

Figure 2. HPLC analysis of isolated labeled peptide (a) [^{18}F]**7** and (b) trace amounts of starting aminooxy peptide precursor.

Scheme 2. Preparation of [^{18}F]-4-(3-fluoropropoxy)benzaldehyde, [^{18}F]9, and Conjugation Reaction Forming Labeled RGD Peptide [^{18}F]10

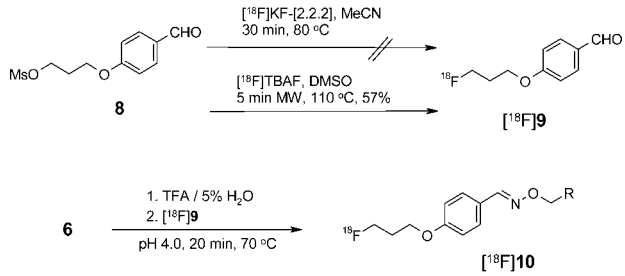

1, t_R = 13.7 min). After quenching with 0.1 mL HPLC mobile phase (20% acetonitrile/water), the product [^{18}F]**13** was isolated by preparative HPLC (gradient 1, t_R = 14.5 min) and formulated by SPE as described above.

The identities of all three ^{18}F-labeled peptide conjugates were confirmed by HPLC analysis in coelution experiments using authentic nonradioactive standards.

***In Vitro* Binding Assay.** Membranes from the human endothelial adenocarcinoma cell line EA-Hy926 were prepared and the K_d calculated for the purified membrane fraction. A competitive binding assay was then established to measure inhibition constants for each test substance without the need for labeling of the substance itself (*4*). ^{125}I-Echistatin was used as the labeled ligand and nonradioactive echistatin as a reference standard. A total of sixteen dilutions of test compound (either echistatin or test substance) were prepared and mixed with a combination of the radioactive tracer and membrane prior to incubation for 1 h at 37 °C. Following washing, the bound material was harvested on a filter using a Skatron microharvester. The filter spots were finally excised and counted in a Packard γ-counter. K_i values were calculated from the binding curves using *Prism* software.

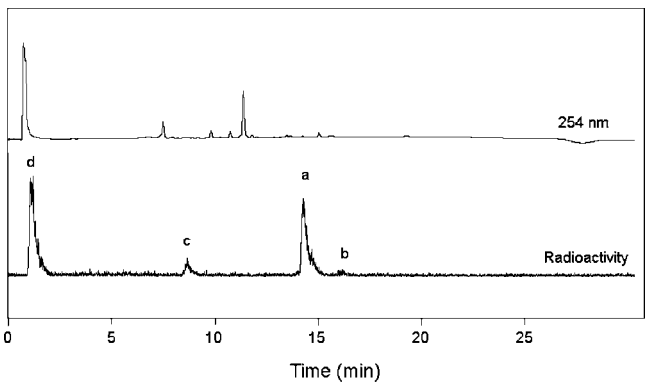

Figure 3. HPLC analysis of the one-pot peptide conjugation mixture: 5 min, 80 °C, pH 4.0, showing (a) the product [^{18}F]**10** (b) a trace of synthon [^{18}F]**9** (c) an unknown byproduct (d) [^{18}F]fluoride.

Scheme 3. Preparation of [^{18}F]-*p*-Fluorobenzaldehyde, [^{18}F]12, and Conjugation Reaction Forming Labeled RGD Peptide [^{18}F]13

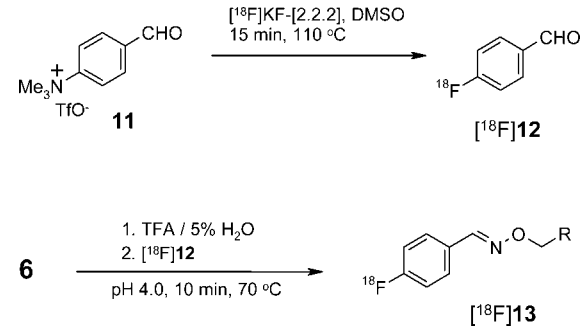

Table 2. Biodistribution of [^{18}F]7, [^{18}F]10, and [^{18}F]13 in the Mouse Lewis Lung Tumor Model[a]

biodistribution (%id/g)	[^{18}F]**7**	[^{18}F] **10**	[^{18}F]**13**
blood 5 min	9.73 (3.1)	7.30 (1.3)	8.70 (3.7)
blood 120 min	0.28 (0.1)	0.71 (0.2)	0.5 (0.2)
muscle 120 min	0.24 (0.1)	0.44 (0.1)	0.32 (0.2)
liver 120 min	1.13 (0.1)	3.28 (0.9)	2.98 (0.4)
lung 120 min	1.06 (0.15)	2.03 (0.4)	1.61 (0.4)
tumor 120 min	1.64 (0.1)	1.12 (0.3)	1.20 (0.3)
tumor: blood	5.9	1.6	2.2
tumor: lung	1.6	0.6	0.7
tumor: liver	1.5	0.3	0.4
tumor: muscle	6.9	2.6	3.7
% retained over 120 min	53	27	38
clearance (%id)			
urine 120 min	79 (3.6)	53 (2.7)	56 (1.1)
GI	5 (0.9)	23 (1.4)	21 (3.7)

[a] Summarized data at 5 and 120 min p.i. Average data (n > 3) of 2 independent experiments, presented as mean (SD).

Biodistribution Studies (LLC model). Lewis Lung carcinoma cells (LLC) (0.1 mL, 1 × 10^7 cells/ mL in medium) were injected subcutaneously into the right inner thigh of C57/BL6 mice (*ca.* 20 g; Charles River UK Ltd.). At 15 days following inoculation of the tumor cells, animals were divided into 3 groups (3 mice per group). Each mouse received 1.0 MBq of [^{18}F]**7**, [^{18}F]**10**, or [^{18}F]**13** as an intravenous bolus *via* the tail vein. Mice were sacrificed by cervical dislocation at 5, 60, and 120 min postinjection. Blood, tumor, and major organs were collected, weighed, and counted in a γ-counter (Wallac Wizard, Perkin-Elmer LAS (UK) Ltd.). The percentage of injected dose per gram (%id/g) or percentage of injected dose (%id) was determined for each sample.

The specificity of tumor uptake was determined by coinjecting an excess dose of nonradiolabeled RGD peptide with the [^{18}F]RGD peptide. Six LLC tumor-bearing mice were coinjected with 0.4 mg RGD peptide per kilogram of bodyweight, and the uptake of [^{18}F]RGD at 120 min postinjection in the blood, muscle, and tumor in these animals compared with that in control animals.

All animal experiments were approved by and carried out in compliance with the UK Home Office guidelines.

Imaging Studies. PET imaging was performed on a Micro-PET-P4 system (Siemens Inc., Knoxville, USA). Images were generated from three-dimensional sinogram data, rebinned to two-dimensional format by the FORE algorithm followed by

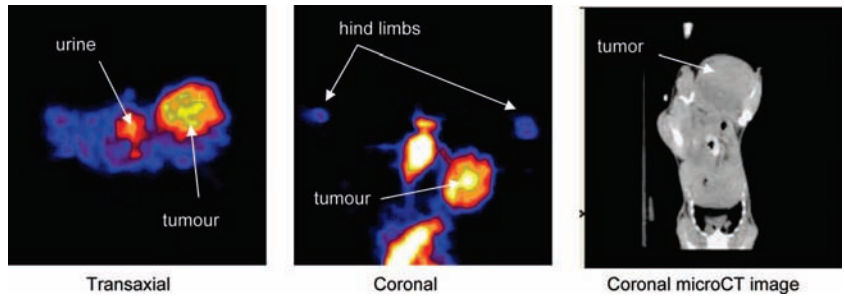

Figure 4. Transaxial and coronal MicroPET images of a mouse bearing a LLC tumor 2 h after tail vein injection of 8 MBq [18F]**7**. The animal was anaesthetized in the prone position using isoflurane.

two-dimensional filtered back-projection. For imaging studies, the animal model described above was used, followed by injection of 8.0 MBq of [18F]**7** as an intravenous bolus *via* the tail vein. Imaging was performed dynamically up to 120 min postinjection, with the animal anaesthetized in the prone position by inhaled isoflurane. Ten minutes prior to the beginning of the CT image, each mouse received an intravenous bolus of 0.1 mL Omnipaque (GE Healthcare, UK) in order to give improved tumor contrast. MicroCT imaging was performed using the microCAT II system (Siemens Inc., Knoxville, USA) with manufacturer recommended settings. MicroPET data were analyzed by using Amide software (http://amide.sourceforge.net).

RESULTS AND DISCUSSION

Radiosynthesis and Conjugation. Scheme 1 outlines the steps involved in the radiosynthesis of [18F]**5** and subsequent conjugation to the aminooxy-RGD precursor peptide **6**. Initial experiments to prepare the diacetal [18F]**4** using Kryptofix resulted in low labeling yields and so attempts were made to evaluate the effect of solvent and temperature on incorporation of [18F]fluoride. Changing the solvent from acetonitrile to dimethylsulfoxide did not significantly increase the yield at a reaction temperature of 80 °C (Table 1, entries 1 and 3). In addition, only modest improvement was observed with 30 min heating compared to 15 min (Table 1, entries 2 and 4) due to the rapid degradation of mesylate **3**. Although attempts at using the milder base [18F]TBAF (*21, 22*) gave no further improvement (Table 1, entry 5), increasing the temperature further to 160 °C for 5 min did favor the fluoridation reaction giving 60% radiochemical yield as evidenced by HPLC analysis (Table 1, entry 6). Optimal conditions were, however, established using microwave heating with near-quantitative incorporation of [18F]fluoride observed using an open vessel at 160 °C for 5 min (Table 1, entry 7). Figure 1 shows a typical HPLC analysis of the reaction mixture. Internal heating using microwaves gave better control of the [18F]fluoridation step and appeared to prevent side reactions. This result supports the growing evidence that microwave activation is often beneficial in PET radiochemistry (*23*).

The intermediate [18F]**4** was isolated by solid-phase extraction and following facile removal of the acetal groups aldehyde [18F]**5** was ready for conjugation with the aminooxy RGD peptide. Starting with 2 mg of peptide precursor, the desired compound [18F]**7** was obtained following preparative HPLC with a decay-corrected radiochemical conjugation yield of 24 ± 6% ($n = 10$) and a total radiochemical yield (decay-corrected referring to starting activity of [18F]fluoride) of 14 ± 6% ($n = 10$). Doubling the amount of precursor, however, to 4 mg increased the conjugation yield further to 51% with a total isolated yield of 38%. The analytical HPLC profile of the [18F]**7** revealed two peaks with identical retention times to the nonradioactive standard (Figure 2) formed by the isomerism of the oxime bond. The final product was formulated in PBS on a rotary evaporator with a recovery of 93 ± 7% ($n = 5$) in a total synthesis time of 3 h.

The radiosynthesis of aldehyde [18F]**9** was first attempted using the standard Kryptofix protocol in acetonitrile for 30 min at 80 °C as shown in Scheme 2. Surprisingly, only two byproducts with longer retention times were generated during the reaction as evidenced by HPLC analysis. In this case, the less basic [18F]TBAF system produced the desired aldehyde [18F]**9** in acceptable yields. Radiochemical yields could again be enhanced by microwave heating, the aldehyde [18F]**9** obtained in 57% yield after 5 min at 110 °C in DMSO, while with conventional heating, only 36% yield was obtained. In both experiments, the thermal lability of the mesylate **8** was found to be a limiting factor with complete decomposition occurring after 5 min. The Kryptofix/oxalate method, an alternative mild fluoridation approach, was tested under microwave conditions in DMSO (*24*). Although the mesylate precursor **8** appeared to have better stability, [18F]**9** was produced with a radiochemical yield of only 14% after 5 min heating at 110 °C. Optimal conditions were achieved with a combination of [18F]TBAF and microwave activation. [18F]**9** was isolated from the reaction mixture by solid-phase extraction with a radiochemical yield of 38% (decay corrected) and a radiochemical purity of 70%. Figure 3 shows the radio-HPLC of the conjugation step demonstrating that the aldehyde [18F]**9** was near-quantitatively consumed to give product [18F]**10**. Using the one-pot conjugation method, [18F]**10** was isolated following HPLC with an overall radiochemical yield of 14 ± 7% (decay-corrected, $n = 4$) and a radiochemical purity of 94%. The tracer was formulated by C18 SepPak extraction with a total synthesis time of 170 min.

[18F]**12** was obtained from 4-*N*,*N*,*N*-trimethylammonium benzaldehyde trifluoromethanesulfonate **11** following a literature method (*25*). On the basis of the labeling results for the fluoroaldehydes [18F]**5** and [18F]**9**, [18F]**12** was used in the conjugation step without isolation as shown in Scheme 3. The corresponding product [18F]**13** was obtained with a decay-corrected radiochemical yield of 23 ± 5% ($n = 3$) and a radiochemical purity of 96%. The radio-HPLC analysis of the reaction mixture after 10 min incubation indicated an almost quantitative coupling efficiency with only a trace of [18F]**12** remaining (5%).

***In Vitro* Affinity.** The competition binding assay (*4*) was established to measure the binding affinity for the integrin $\alpha_v\beta_3$ of the three conjugates. The nonradioactive compounds [19F]**7**, [19F]**10**, and [19F]**13** were found to compete with 125I-echistatin with K_i values calculated to be 2.3, 1.1, and 13.3 nM, respectively. In comparison, the α_v selective inhibitor cyclo(-Arg-Gly Asp-D-Phe-Lys-), a widely used RGD pharmacophore (*26*), had a K_i value in this assay of 27.8 nM. We would therefore suggest that differences observed in the biodistribution profiles

of the three conjugates could not be explained on the grounds of differences in the binding affinity for the integrin receptors *in vivo*.

Biodistribution and Imaging Studies. The conjugate [^{18}F]**7** demonstrated favorable biodistribution profile with good tumor uptake and retention at 120 min postinjection (1.64%id/g and 53%, respectively) as shown in Table 2. Additionally, due to the reduced background tissue uptake (e.g., in lung and liver) the ratios against tumor were improved with a tumor to blood ratio of ~6 and tumor to muscle ratio of ~7 at 120 min postinjection. The majority of the radioactivity was excreted via the urine, with 79%id in the urine and bladder 120 min postinjection. The localization of [^{18}F]**7** in LLC tumors as determined by MicroPET imaging is shown in Figure 4 alongside a microCT slice for anatomical reference. Representative transaxial and coronal images are shown from one mouse. There is clear visualization of the LLC tumor in the animal, along with clearance of [^{18}F]**7** through the bladder and gastrointestinal tract, which was consistent with the biodistribution data.

Although the blood kinetic profiles for [^{18}F]**13** and [^{18}F]**7** are similar, as summarized in Table 2, the increased lipophilicity of [^{18}F]**13** results in higher liver uptake compared to that of [^{18}F]**7** (data shown 120 min postinjection). Consequently, the amount of activity excreted via the liver into the gastrointestinal tract was around 21%id for [^{18}F]**13** compared to only 5%id for [^{18}F]**7**. Similarly, [^{18}F]**10** had significant gastrointestinal tract excretion (23%id) and lower urinary excretion (53%id).

Perhaps the most striking observation of the effect of the prosthetic group on biodistribution was seen on kidney excretion rates. In all, 79%id of [^{18}F]**7** activity passed into the urine and bladder and 5.4%id into the gastrointestinal (g.i.) tract at 2 h postinjection. This was compared to >20% g.i. excretion for both [^{18}F]**10** and [^{18}F]**13**.

In order to look at specificity, an *in vivo* blocking study with 10 μg excess unlabeled RGD peptide per animal resulted in a significantly reduced [^{18}F]**7** uptake in the tumor at 120 min postinjection. Tumor uptake was decreased from 1.48 ± 0.3%id/g to 0.76 ± 0.2%id/g ($p < 0.01$). Although this represents a 49% reduction of tumor uptake, further studies are needed with higher doses of nonradioactive peptide in order to achieve full blocking.

In summary, this work demonstrates that a rational approach to prosthetic group design can be successfully employed to optimize key *in vivo* characteristics of peptide-based tracers. Although localization of all three conjugates to the tumor was observed, [^{18}F]**7** possessed superior tumor to blood, lung, liver, and muscle ratios compared to the more hydrophobic conjugates [^{18}F]**10** and [^{18}F]**13**.

ACKNOWLEDGMENT

We would like to thank Colin Steel and the cyclotron operators of Hammersmith Imanet Ltd for providing us with fluorine-18.

Supporting Information Available: Supporting data for the synthesis of nonradioactive standards. This material is available free of charge via the Internet at http://pubs.acs.org.

LITERATURE CITED

(1) Cox, D., Aoki, T., Seki, J., Motoyama, Y., and Yoshida, K. (1994) The pharmacology of integrins. *Med. Res. Rev. 14*, 192–228.

(2) Eliceiri, B. P., and Cheresh, D. A. (1999) The role of alpha-(v) integrins during angiogenesis: insights into potential mechanisms of action and clinical development. *J. Clin. Invest. 103*, 1227–1230.

(3) Bach-Gansmo, T., Danielsson, R., Saracco, A., Wilczek, B., Bogsrud, T., Fangberget, A., Tangerud, Å., and Tobin, D. (2006) Integrin receptor imaging of breast cancer: A proof of concept study to evaluate ^{99m}Tc-NC100692. *J. Nucl. Med. 47*, 1434–1438.

(4) Indrevoll, B., Kindberg, G. M., Solbakken, M., Bjurgert, E., Johansen, J. H., Mendizabal, M., and Cuthbertson, A. (2006) NC100717; a versatile RGD scaffold for angiogenesis imaging. *Bioorg. Med. Chem. Lett. 16*, 6190–6193.

(5) Meyer, A., Auernheimer, A., Modlinger, A., and Kessler, H. (2006) Targeting RGD recognizing integrins: drug development, biomaterial research, tumor imaging and targeting. *Curr. Pharm. Des. 12*, 2723–2747.

(6) Haubner, R., Kuhnast, B., Mang, C., Weber, W. A., Kessler, H., Wester, H. J., and Schwaiger, M. (2004) [^{18}F]Galacto-RGD: Synthesis, radiolabeling, metabolic stability and radiation dose estimates. *Bioconjugate Chem. 15*, 61–69.

(7) Chen, X., Tohme, M., Park, R., Hou, Y., Bading, J. R., and Conti, P. (2004) Micro-PET Imaging of $\alpha_v\beta_3$-integrin expression with ^{18}F-labeled dimeric RGD peptide. *Mol. Imaging 3*, 96–104.

(8) Haubner, R., and Wester, H. J. (2004) Radiolabeled tracers for imaging of tumor angiogenesis and evaluation of anti-angiogenic therapies. *Curr. Pharm. Des. 10*, 1439–1455.

(9) Lundqvist, H., and Tolmachev, V. (2002) Targeting peptides and positron emission tomography. *Biopolymers (Pept. Sci.) 66*, 381–392.

(10) Adam, M. J., and Wilbur, D. S. (2005) Radiohalogens for imaging and therapy. *Chem. Soc. Rev. 34*, 153–63.

(11) Snyder, S., Kilbourn, M. R. (2003) Chemistry of Fluorine-18 Radiopharmaceuticals *Handbook of Radiopharmaceuticals, Radiochemistry and Applications* (Welch, M. J., Redvanly, C. S., Eds.) pp195–227, Chapter 6.

(12) Couturier, O., Luxen, A., Chatal, A., Vuillez, J. P., Rigo, P., and Hustinx, R. (2004) Fluorinated tracers for imaging cancer with positron emission tomography. *Eur. J. Nucl. Med. 31*, 1182–206.

(13) Glaser, M., Luthra, S. K., and Brady, F. (2003) Applications of positron-emitting halogens in PET oncology. *Int. J. Oncol. 22*, 253–67.

(14) Cuthbertson, A., Solbakken, M., Arukwe, J., Karlsen, H., Glaser, M. WO 2004/080492.

(15) Poethko, T., Schottelius, M., Thumshirn, G., Hersel, U., Herz, M., Henriksen, G., Kessler, H., Schwaiger, M., and Wester, H. J. (2004) Two-step methodology for high-yield routine radiohalogenation of peptides. *J. Nucl. Med. 45*, 892–902.

(16) Schottelius, M., Poethko, T., Herz, M., Reubi, J.-C., Kessler, H., Schwaiger, M., and Wester, H. J. (2004) First ^{18}F-labeled tracer suitable for routine clinical imaging of SST receptor-expressing tumors using positron emission tomography. *Clin. Cancer Res. 10*, 3593–606.

(17) Lee, Y. S., Jeong, J. M., Kim, H. W., Chang, Y. S., Ganasha, G. R., Suh, Y. G., Chi, D. Y., Kang, W. J., Kang, J. H., Lee, D. S., Chung, J. K., and Lee, M. C. (2005) An easy method for no-carrier-added ^{18}F-labeling of RGD peptide: Hydrazone formation between cRGDyK-HYNIC and 4-[^{18}F]fluorobenzaldehyde (FBA). *J. Labelled Compds. Radiopharm. 48*, S288.

(18) Bruus-Jensen, K., Poethko, T., Schottelius, M., Hauser, A., Schwaiger, M., and Wester, H. J. (2006) Chemoselective hydrazone formation between HYNIC-functionalized peptides and ^{18}F-fluorinated aldehydes. *Nucl. Med. Biol. 33*, 173–183.

(19) Zhang, W., Oya, S., Kung, M. P., Hou, C., Maier, D. L., and Kung, H. F. (2005) F-18 Polyethyleneglycol stilbenes as PET imaging agents targeting Aβ aggregates in the brain. *Nucl. Med. Biol. 32*, 799–809.

(20) Chen, X., Park, R., Hou, Y., Khankaldyyan, V., Gonzales-Gomez, I., Thome, M., Bading, J. R., Laug, W. E., and Conti, P. S. (2004) MicroPET imaging of brain tumor angiogenesis with ^{18}F-labeled PEGylated RGD peptide. *Eur. J. Nucl. Med. 31*, 1081–1089.

(21) Chi, S. Y., Kilbourn, M. R., Katzenellenbogen, J. A., and Welch, M. J. (1987) A rapid and efficient method for the fluoroalkylation of amines and amides. Development of a method suitable for incorporation of the short-lived positron emitting radionuclide fluorine-18. *J. Org. Chem. 52*, 658–664.

(22) Alauddin, M. M., Balatoni, J., and Gelovani, J. (2005) Synthesis of 3′-deoxy-3′-[^{18}F]fluoro-1-β-D-xylofuranosyluracil ([^{18}F]FMXU) for PET. *J. Labelled Compds. Radiopharm. 48*, 941–950.

(23) Stone-Elander, S., and Elander, N. (2002) Microwave applications in radiolabeling with short-lived positron-emitting radionuclides. *J. Labelled Compds. Radiopharm. 45*, 715–746.

(24) Hamacher, K. H. T., and Coenen, H. H. (2002) Electrochemical cell for separation of [^{18}F]fluoride from irradiated ^{18}O-water and subsequent no carrier added nucleophilic fluorination. *Appl. Radiat. Isot. 56*, 519–523.

(25) Haka, S. M., Kilbourn, M. R., Watkins, G. L., and Toorongian, S. A. (1989) Aryltrimethylammonium trifluoromethanesulfonates as precursors to aryl [^{18}F]fluorides: Improved synthesis of [^{18}F]GBR-13119. *J. Labelled Compds. Radiopharm. 27*, 823–833.

(26) Haubner, R., Wester, H. J., Weber, W. A., Mang, C., Ziegler, S. I., Goodman, S. L., Senekowitsch-Schmidtke, R., Kessle, H., and Schwaiger, M. (2001) Noninvasive imaging of $\alpha_v\beta_3$ intergrin expression using [^{18}F]-labeled RGD-containing glycopeptide and positron emission tomography. *Cancer Res. 61*, 1781–1785.

BC700472W

Preparation of Rh[16aneS$_4$-diol]^{211}At and Ir[16aneS$_4$-diol]^{211}At Complexes as Potential Precursors for Astatine Radiopharmaceuticals. Part I: Synthesis

Marek Pruszyński,*,† Aleksander Bilewicz,† and Michael R. Zalutsky‡

Department of Radiochemistry, Institute of Nuclear Chemistry and Technology, Dorodna 16, 03–195 Warszawa, Poland, and Department of Radiology, Duke University Medical Center, Durham, North Carolina 27710. Received November 8, 2007; Revised Manuscript Received February 1, 2008

The goal of this study was to evaluate a new approach that can be applied for labeling biomolecules with ^{211}At. Many astatine compounds that have been synthesized are unstable *in vivo*, providing motivation for seeking different ^{211}At labeling strategies. The approach evaluated in this study was to attach astatide anions to soft metal cations, which are also complexed by a bifunctional ligand. Ultimately, this complex could in principle be subsequently conjugated to a biomolecule with the proper selection of ligand functionality. We report here the attachment of ^{211}At$^-$ and *I$^-$ (*I = ^{131}I or ^{125}I) anions to the soft metal cations Rh(III) and Ir(III), which are complexed by the 1,5,9,13-tetrathiacyclohexadecane-3,11-diol (16aneS$_4$-diol) ligand. Radioactive *I$^-$ anions were used for preliminary studies directed at the optimization of reaction conditions and to provide a baseline for comparison of results with ^{211}At. Four complexes Rh[16aneS$_4$-diol]*I/^{211}At and Ir[16aneS$_4$-diol]*I/^{211}At were synthesized in high yield in a one-step procedure, and the products were characterized mainly by paper electrophoresis and reversed-phase HPLC. The influences of time and temperature of heating and concentrations of metal cations and sulfur ligand 16aneS$_4$-diol, as well as pH on the reaction yields were determined. Yields of about 80% were obtained when the quantities of Rh(III) or Ir(III) cations and 16aneS$_4$-diol ligand in the solutions were 62.5 nmol and 250 nmol, respectively, and the pH ranged 3.0–4.0. Syntheses required heating for 1–1.5 h at 75–80 °C. The influence of microwave heating on the time and completeness of the complexation reaction was evaluated and compared with the conventional method of heating in an oil bath. Microwave synthesis accelerates reactions significantly. With microwave heating, yields of about 75% for Rh[16aneS$_4$-diol]^{131}I and Ir[16aneS$_4$-diol]^{131}I complexes were obtained after only 20 min exposure of the reaction mixtures to microwave radiation. In conclusion, this study has shown that it is possible to attach an astatide anion to soft metal cations in a simple and fast one-step procedure, with high yields. These complexes will be evaluated as reagents for labeling biomolecules.

INTRODUCTION

In the field of targeted radiotherapy, the selection of radionuclide is related to the type of treated disease. Currently, many radionuclides are under intensive investigation for therapeutic applications, particularly the Auger emitter ^{67}Ga ($t_{1/2}$ = 3.3 d), ^{111}In ($t_{1/2}$ = 2.8 d), α-particle emitters ^{211}At ($t_{1/2}$ = 7.2 h), ^{212}Bi ($t_{1/2}$ = 1 h), ^{213}Bi ($t_{1/2}$ = 45.6 m), and β^--particle emitters ^{90}Y ($t_{1/2}$ = 64 h), ^{188}Re ($t_{1/2}$ = 16.7 h), and ^{177}Lu ($t_{1/2}$ = 6.7 d) (*1*). An important factor is the nature of the cytotoxic radionuclide, mainly its physical parameters such as half-life and the nature of its associated emissions. Solid tumors generally have been pursued with β^- emitters including ^{90}Y and ^{131}I, because their β^- particles have a tissue range of several millimeters. The effective tissue range of β^- particles is not optimal for treatment of tumors as small clusters of cells or single cells, and micrometastases, because much of the decay energy is deposited outside the boundary of the tumor. Treatment of these diseases might be more effective with α-emitters, which combine short-range and high linear energy transfer, a combination that results in the high relative biological effect and cytotoxicity (*2*). Thus, α particles are able to make double-strand breaks in DNA, lesions that have a relatively high probability of leading to a "kill effect" on tumor cells (*3*). The shorter path length (40–100 μm) of α particles also should help limit radiotoxicity to neighboring normal tissue. For these reasons; considerable effort has been placed recently on the development of the α-emitters ^{223}Ra ($t_{1/2}$ = 11.4 d), ^{225}Ac ($t_{1/2}$ = 10 d), generator-obtained ^{212}Bi, ^{213}Bi, as well as the cyclotron-produced ^{211}At. The latter may perhaps be the most promising candidate for targeted radiotherapy, because its 7.2 h half-life allows sufficient time for performing its transportation, synthetic chemistry and multistep labeling, quality control, and clinical application without the problematic characteristic of having relatively long-lived α-particle-emitting daughters. Besides, each event of astatine decay is accompanied by emission of high-energy α particles with average energy of 6.4 MeV, corresponding to a mean range in human tissue of 65 μm (*4*). Therefore, the ionization occurs within a small volume, and when astatine is localized within a tumor, the surrounding tissue will not suffer from its radiation. Additionally, its electron capture decay branch gives rise to Po K X-rays making ^{211}At easy to follow with standard nuclear detection devices including γ cameras for imaging (*5*). Dosimetry calculation and preclinical testing of compounds labeled with ^{211}At have indicated a significant therapeutic potential, at least in certain settings, relative to the use of radionuclides that emit particles with low linear energy transfer (*6–12*).

Because astatine is the heaviest member of the halogen group, it has generally been recognized as a nonmetal. It is also similar

* Marek Pruszyński, Institute of Nuclear Chemistry and Technology, Department of Radiochemistry, Dorodna 16, 03-195 Warszawa, Poland. E-mail: mprusz@ichtj.waw.pl; Tel.: (22) 504 12 52; Fax: (22) 811 15 32.

† Institute of Nuclear Chemistry and Technology.

‡ Duke University Medical Center.

10.1021/bc700413r CCC: $40.75 © 2008 American Chemical Society
Published on Web 03/14/2008

to iodine with regard to its biochemical properties. Thus, standard radioiodination protocols had been commonly adapted for preliminary ^{211}At labeling of biomolecules. Unfortunately, proteins labeled by direct electrophilic astatination were unstable due to rapid loss of ^{211}At in both *in vitro* and *in vivo* conditions (*13*). The reason was probably the unspecific binding of astatine to sulfur atoms in peptides instead of attaching to tyrosine residue, like in the case of radioiodine (*14*). This problem was circumvented later by using two-step procedures, where ^{211}At first was electrophilically incorporated into an aryl compound (e.g., benzoates) and, in the second step, coupled to a protein (*15–19*). Unfortunately, biomolecules labeled by this method have been found to not always be stable to *in vivo* deastatination (*20*). One of the reasons can be the nature of labeled carrier molecule, especially its rate and mode of metabolism (*21*), but this behavior also probably reflects the weaker aryl carbon−halogen bond for astatine when compared to that with iodine (bond strength for astatine is ∼49 kcal/mol and for iodine is ∼62 kcal/mol) (*22, 23*). This fact prompted investigations directed at identifying other labeling approaches that can yield rapid astatination and high stability. For example, the boron−astatine bond should be stronger than the carbon−astatine bond based on the general trend for boron−halogen bond energies (*24*). Therefore, boron cage moieties have been studied as pendant groups for radiolabeling proteins and peptides with radioiodine (*25, 26*) and with ^{211}At (*27, 28*). Studies with *nido*-carborane derivatives did not provide adequate stability of astatination of these compounds (*21*), whereas anionic monocarboranes were not reactive enough to be useful for radiohalogenation (*29*). However, recent experiments with *closo*-decaborate(2-) derivatives showed good stability and fast labeling of biomolecules with high yield (*30*), and studies on the optimization of the *closo*-decaborate(2-) conjugates for protein labeling are underway.

Herein, we have proposed an alternative method of labeling molecules with ^{211}At to solve stability problems of formed conjugates. Instead of using an electrophilic reaction, we decided to attach astatide anions to soft metal cations, which are also complexed by a bifunctional ligand. Ultimately, this complex could in principle be subsequently conjugated to a biomolecule with proper selection of ligand functionality. It can be expected that ^{211}At$^-$, similar to I$^-$ anions, should demonstrate soft ligand properties and form strong complexes with soft metal cations, like Hg(II), Pt(II), Rh(III), and Ir(III), according to the hard and soft acids and bases theory (HSAB) (*31*). On the basis of the generally observed trend that stability constant values for soft metal cation−halogen anion complexes increase in the halogen group, we can expect that a complex with astatide should be stronger than one with iodide. Previously, we reported that ^{211}At$^-$ formed strong complexes with Hg(II) cations, much stronger than I$^-$ (*32*). In the present paper, we describe the results of our studies on attaching ^{211}At$^-$ to complexes of Rh(III) or Ir(III) with the thioether ligand 1,5,9,13-tetrathiacyclohexadecane-3,11-diol (16aneS$_4$-diol). Rh(III) and Ir(III) cations were chosen because they are moderately soft metal cations, and we hypothesize that they will form strong bonds with the soft astatide anion. In addition, the very high kinetic inertness of low-spin Rh(III) and Ir(III) d^6 complexes is particularly well-suited to the formation of a stable conjugate. The 16aneS$_4$-diol ligand was selected for these initial model compound studies based on literature reports that it forms stable complexes with Rh(III) (*33*). Additionally, this macrocyclic tetra-thioether with diol functionality can be easily modified to create a bifunctional chelate ligand (*34*).

EXPERIMENTAL PROCEDURES

Reagents and Radioactivity. The macrocyclic crown thioether 1,5,9,13-tetrathiacyclohexadecane-3,11-diol (16aneS$_4$-diol) cis/trans mixture (Figure 1, panel A) was purchased from Aldrich Chemical Co. and used without further purification. Rhodium(III) nitrate hydrate $Rh(NO_3)_3 \cdot 3H_2O$ and iridium(III) chloride hydrate $IrCl_3 \cdot 3H_2O$ were obtained from Alfa Aesar, a Johnson Matthey Company. Solvents for HPLC analysis were obtained as HPLC grade and degassed before use by ultrasonification for 15–20 min. All other chemicals were of pure reagent grade and used as received unless otherwise specified. The ion exchange resins Dowex 1 × 8 and Dowex 50W × 8 of different mesh sizes were purchased at Sigma-Aldrich Company. The ^{131}I and ^{125}I in the form of Na*I (*I = ^{131}I or ^{125}I) in 0.1 M NaOH solution were supplied from Perkin-Elmer Life and Analytical Sciences (formerly NEN/Dupont, Billerica, MA) and from the Isotope Production Centre Polatom in Swierk (Poland) as high concentration/high specific activity radioiodide. ^{211}At was produced on the CS-30 cyclotron at the Duke University Medical Center. The targets were prepared from pure metallic bismuth and were irradiated with 28 MeV α particles using the ^{209}Bi(α,2n)^{211}At reaction. Separation of ^{211}At from the bismuth target was performed with a dry distillation method described in ref (*35*). Finally, the ^{211}At activity was washed out from the cooled trap by MeOH with Na_2SO_3 (10^{-4} M) addition to obtain ^{211}At in astatide form. All radioactive materials were handled according to approved protocols at the Institute of Nuclear Chemistry and Technology and at Duke University.

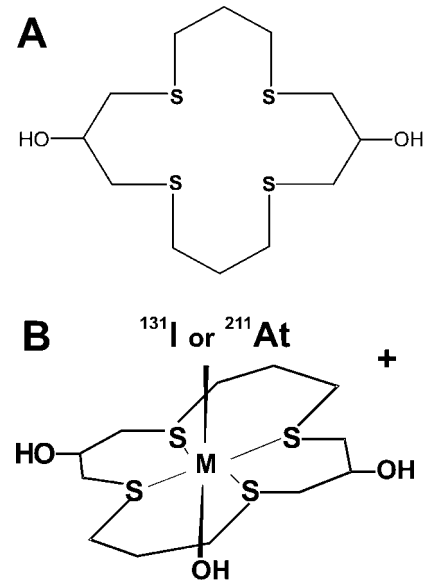

Figure 1. Structure of (A) macrocyclic thioether ligand 1,5,9,13-tetrathiacyclohexadecane-3,11-diol (16aneS$_4$-diol) and (B) cationic complexes *trans*-M[16aneS$_4$-diol]*I/^{211}At (M = Rh(III) or Ir(III)).

Measurements of ^{131}I, ^{125}I, and ^{211}At at Duke University were accomplished in a dose calibrator on a Capintec CRC-7 Radioisotope (Ramsey, NJ). The ^{133}Xe setting was used with a multiplication factor of 2.3, to count ^{211}At on that instrument. The ^{131}I radioactivity at the Institute of Nuclear Chemistry and Technology was measured in a NaI(Tl) well counter (Polon Alfa, Warszawa).

Preparation of Rh[16aneS$_4$-diol]*I/^{211}At and Ir[16aneS$_4$-diol]*I/^{211}At Complexes and Optimization of the Reaction Conditions. Rh[16aneS$_4$-diol]*I/^{211}At and Ir[16aneS$_4$-diol]*I/^{211}At complexes were prepared by addition 20 μL of *I$^-$ or ^{211}At$^-$ activity (6.5–70 MBq for *I and 4.5–30 MBq for ^{211}At) to the mixture of 125 μL Rh(III) or Ir(III) and 25 μL 16aneS$_4$-diol in water−ethanol solution. The quantities of metal cations and sulfur ligand were varied during the optimization reactions over the ranges 0.125–125 nmol and 18.75–250 nmol, respectively. After adjusting the pH to 4.0, by dropwise addition of

0.001–0.1 M HNO_3 or NaOH, the solutions were heated in sealed Eppendorf tubes or glass vials capped with Teflon-coated septa for about 2 h at 80 °C in an oil bath. Control experiments were also performed in which 125 μL of aqueous Rh(III) or Ir(III) solution was mixed with 25 μL of ethanol without sulfur ligand, and 20 μL of $*I^-$ or $^{211}At^-$ solution was added (blank 1). Blank 2 was prepared by mixing 125 μL of water without metal cation and 25 μL of 16aneS_4-diol ligand in ethanol and 20 μL of $*I^-$ or $^{211}At^-$. All control experiments were adjusted to pH 4.0 and heated under the same conditions as the main samples for the complexes. Solutions were analyzed mainly by paper electrophoresis and HPLC methods, but also by sorption on ion exchange resins.

The optimization of reaction conditions was focused on increasing the yield of synthesis, ideally, in a reaction time suitable for use with 7.2 h half-life ^{211}At. The influences of time and temperature of heating, concentrations of metal cations, sulfur ligand 16aneS_4-diol, and pH of the solutions on the reaction yields were determined. Optimization of each parameter was repeated 2 times for astatine complexes and 3 times for *I complexes in separate experiments. Each set of conditions during 1 experiment was replicated 2–3 times. First, optimization of reaction conditions was performed with *I radionuclides and later repeated with ^{211}At. The reaction volume in all cases was kept at 170 μL.

The formation of complexes was studied by heating solutions for different time periods (30–120 min) and over a wide range of temperatures (40–90 °C). For this experiment, the reaction mixtures contained 125 nmol of metal cation and 250 nmol of sulfur ligand, and the reaction was performed at pH 4.0.

The effect of metal cation concentration on complex formation yield was measured in solutions at pH 4.0 containing 250 nmol of sulfur ligand with the quantity of metal cation being varied from 0.125 to 125 nmol. Solutions were heated for 1–1.5 h at 75–80 °C. The influence of 16aneS_4-diol concentrations on reaction yield was evaluated by keeping the quantity of metal cation at 62.5 nmol, while varying the quantity of sulfur ligand in the range 18.75–250 nmol. The reactions were carried out at 75–80 °C for 1–1.5 h and at pH 4.0.

The effect of pH on the yield of the radiohalogenation reactions was also determined. For these studies, the reaction mixtures contained 62.5 nmol of metal cation and 250 nmol of 16aneS_4-diol. The pH was varied from 2 to 8.5 by addition of 0.001–0.1 M HNO_3 or NaOH, and the reaction mixtures were heated for 1–1.5 h at 75–80 °C. Buffers were not used to stabilize the pH, because studies in the literature indicating that several buffers (e.g., phosphate, carbonate) interfered with rhodium complexation (*33, 36*).

The influence of microwave heating on the yield of Rh[16aneS_4-diol]^{131}I and Ir[16aneS_4-diol]^{131}I complexes was determined under the best conditions found during the optimization experiments. The quantities of Rh(III) or Ir(III) cations and sulfur ligand in the solutions were kept at 125 nmol and 250 nmol, respectively, and the pH of the reaction mixture was between 3.0 and 4.0. A UniClever II microwave unit (Plazmatronika, Poland) was used for these studies. This device provides control of the processing time, radiation power, temperature, and pressure in a hermetically sealed autoclave. Prepared samples in glass vials were put into the UniClever apparatus, and microwave heating was performed for 5–35 min at 50% of power mode (corresponds to the 300 W absolute power). During this time, the temperature of the samples was maintained between 75 and 80 °C.

Radiochemical Analyses of Synthesized Complexes. The charge of the radioactive products was determined using paper electrophoresis and ion exchange methods. Electromigration was measured utilizing Sigma-Aldrich and Bio-Rad units on glass fiber Whatman Paper Chromedia GF83 (W. & R. Balston, Ltd., England) and cellulose fiber Whatman 3MM (Whatman International Ltd., England) at the potential gradient equal to 10 V/cm for 25–60 min. The electrolyte was 0.02 M phosphate buffer at pH 4.0 and 7.4. An aliquot of the radioactive reaction mixture was spotted on the center of paper strip, and the power supply was switched on. The distribution of radioactivity on the paper strips was measured by cutting the paper into 1 cm pieces and counting them in a NaI(Tl) well counter. Alternatively, a radiochromatographic strip scanner (BioScan System 200 Imaging Scanner) was utilized.

Dowex 1 × 8 and Dowex 50W × 8 ion exchange resins were rinsed with 250–500 mL 1 M $NaNO_3$ and then washed with deionized water. The resins were dried at 60–70 °C and stored in a desiccator. The distribution of radioactive compounds between the aqueous phase, and the ion exchange resin was analyzed by the batch method. Between 50 and 150 mg of ion exchange resin was added to Eppendorf tubes (two replicates for each sample during one experiment) containing 1.5 mL of 0.05 M $NaNO_3$ at pH 4.0 to which 5–20 μL of the radioactive compound was added. Tubes were shaken for 15–20 min, centrifuged, phases separated, and the radioactivity in the resin and solution counted on either a NaI(Tl) well-type counter or an automated gamma counter (1282 LKB Pharmacia, Turku, Finland).

Additionally, radiochemical identification of the reaction products was accomplished using reversed-phase HPLC with a Waters XTerra C18 column (5 μm, 250 × 4.5 mm) on a Beckman System Gold device equipped with both UV and radiometric (Gamma Detector 170) detectors. The gradient elution system utilized mobile phase A (deionized H_2O) and mobile phase B (100% acetonitrile) and flow rate of 1 mL/min, starting with 95% A/5% B for 5 min; then, the gradient was increased to 100% B over the next 30 min and then held at 100% B for 5 min, after which gradient parameters returned to the initial conditions during the next 5 min. The HPLC analysis took about 45 min. Both mobile phases contained 0.1% TFA.

RESULTS AND DISCUSSION

Astatine-211 is one of only a few α-emitters that have properties suitable for application to targeted radiotherapy of cancer, especially of micrometastatic disease, cancer resistant to other forms of radiation (e.g., melanoma), and ovarian carcinoma (*12, 37*). Although a large number of cancer cell selective monoclonal antibodies (mAbs) and other cancer cell targeting agents suitable for targeted radiotherapy have been developed, using them in the treatment of cancer is only possible when the radionuclide is stably coupled with the carrier molecule. In the case of highly toxic α-emitters, only conjugates that are stable toward *in vivo* release of the α-particle-emitting radionuclide can be used in targeted radiotherapy.

The stability of astatinated biomolecules has been a major impediment to the development of ^{211}At-labeled radiotherapeutics. Direct electrophilic astatination of proteins and peptides was unsuccessful. The yield of the reaction was low, and the labeled molecules were unstable to *in vivo* deastatination (*13*). More stable astatinated proteins have been prepared by acylation with a variety of astatobenzoic acid derivatives prepared from trialkylstannyl precursors (*15, 16*), but the problem with stability appeared when smaller, more rapidly metabolized molecules and mAb fragments (Fab′) were used (*20, 38*). The conjugates undergo rapidly deastatination, even with molecules for which *in vitro* studies indicated quite good stability in serum (*20*). Therefore, without a good chemical method of attaching ^{211}At to these potential cancer targeting agents that will provide high *in vivo* stability of formed conjugate, the application of this radionuclide in targeted radiotherapy will be limited.

The aim of this work was focused on finding a new stable labeled precursor for use in labeling of biomolecules with ^{211}At. The original idea is to attach astatide anions to soft metal cations, which are complexed by bifunctional ligand bearing a functionality that would facilitate attaching this complex to a biomolecule. We believe that the proposed combination of high kinetic inertness of Rh(III) and Ir(III) compounds with the formation of strong complexes between soft metal cations and soft anions will result in high stability of formed metal−astatide bond.

Results from literature studies show that the 16aneS$_4$-diol ligand reacts with $RhCl_3$ to form a cationic Rh[16aneS$_4$-diol]Cl$_2$ complex with a *trans*-Rh(III)Cl$_2$ core. In this complex, the sulfur donor atoms of the macrocyclic ligand occupy four equatorial positions, whereas the Cl^- anions are in the axial positions (*33*). Therefore, we hypothesized that analogous complexes could be formed in which one axial position is occupied by either the $*I^-$ or $^{211}At^-$ anion. It should be noted that in our studies we used $Rh(NO_3)_3$ for synthesis instead of $RhCl_3$, as was used previously (*33*). Therefore, due to the weak complexing properties of NO_3^- anions, we believe that the second axial position will be occupied by a OH^- group (Figure 1, panel B). We prepared the well-defined macroscopic nonradioactive Rh[16aneS$_4$-diol]Cl$_2$ complex according to a literature procedure (*33*). Following the same scheme, the Rh[16aneS$_4$-diol]I complex with cold iodine was prepared. The electrophoretic migration of the yellow Rh[16aneS$_4$-diol]Cl$_2$ complex was compared with the orange Rh[16aneS$_4$-diol]I complex and radioactive Rh[16aneS$_4$-diol]^{131}I. In all cases, the migration toward cathode was identical. Also, cospotting Rh[16aneS$_4$-diol]^{131}I with nonradioactive Rh[16aneS$_4$-diol]Cl$_2$ and Rh[16aneS$_4$-diol]I gave identical electrophoretic behavior. The properties of three complexes were also studied by reverse-phase HPLC using the gradient conditions mentioned above. The UV detection was performed at 275 nm for nonradioactive Rh[16aneS$_4$-diol]Cl$_2$ and Rh[16aneS$_4$-diol]I complexes, and the radioactive Rh[16aneS$_4$-diol]^{131}I complex was detected by the radiometric detector. The retention times for both nonradioactive Rh[16aneS$_4$-diol]Cl$_2$ and Rh[16aneS$_4$-diol]I complexes were identical and comparable to the radioactive Rh[16aneS$_4$-diol]^{131}I, with peaks appearing between 15 and 17 min. From these results, we assumed that the structures of cold Rh[16aneS$_4$-diol]I and radioactive Rh[16aneS$_4$-diol]^{131}I were identical to the structure of Rh[16aneS$_4$-diol]Cl$_2$ presented in ref (*33*).

Paper electrophoresis and ion exchange studies confirmed the predicted cationic character of the synthesized complexes. For example, the distribution of *I radioactivity on the paper strip for Rh[16aneS$_4$-diol]*I complex and control samples is presented in Figure 2. It is shown that, in the heated solution contained Rh(III) cations, sulfur ligand 16aneS$_4$-diol and $*I^-$, a cationic complex was formed, because most of the radioactivity (80–85%) migrated toward the cathode. During the electrophoretic studies, we also noticed that the percentage of radioactivity distributed on both fiber strips was similar; however, the migration of the complex on cellulose fiber was slower than on the glass one at the same applied voltage. In the case of Whatman GF83, migration of the cationic complex was 4.5–5.0 cm toward the cathode during 25 min, whereas for Whatman 3MM, fiber migration was 3.7–4.0 cm toward the cathode during 1 h. The last result is comparable to the migration reported for the cationic ^{105}Rh[16aneS$_4$-diol]Cl complex also on the cellulose fiber (Whatman #1) (*34*). The differences in migration range and time are probably due to different components and structures of both fibers. Nevertheless, the migration time did not influence the final results of the overall percentage distribution of radioactivity on the fibers, but for the electrophoretic studies, glass fiber was mainly used, because of the shorter analysis time, an advantage that was of particular importance for the characterization of the astatine complexes. The pH of the sodium phosphate buffer (4.0 or 7.4) used as the electrolyte did not influence the migration range and time for all four complexes, which were found to remain positively charged at the higher pH.

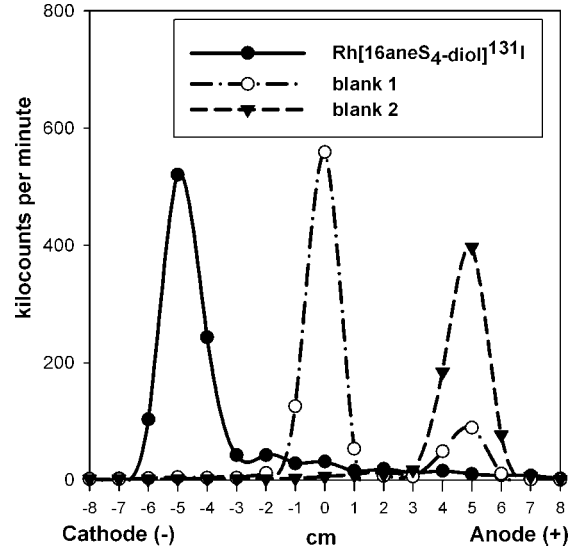

Figure 2. Electrophoretic analysis of heated mixtures: (Rh[16aneS$_4$-diol]*I) contained Rh(III) cations, 16aneS$_4$-diol ligand, and $*I^-$; blank 1 contained Rh(III) and $*I^-$ without sulfur ligand; blank 2 contained sulfur ligand and $*I^-$ without metal cations. Paper electrophoresis was performed on glass fiber Whatman Paper Chromedia GF83 using phosphate buffer (pH 4.0 or 7.4) at 10 V/cm for 25 min.

Confirmation that the synthesized complex Rh[16aneS$_4$-diol]*I has cationic character was also obtained from an experiment determining its adsorption on a cation exchange resin. In the case of the complex, most of the *I radioactivity was adsorbed on the cationic resin, with only 15–20% remaining in solution; this was nearly completely adsorbed on the anion exchange resin. This suggests that 15–20% of free iodide remains uncomplexed in solution at the end of the synthesis reaction.

Studies on control samples indicated that, in the heated solution of 16aneS$_4$-diol with $*I^-$ but without the metal cation (blank 2), all the radioactivity migrated toward the anode, consistent with uncomplexed iodide (Figure 2). This indicates that there are no interactions of the halogen anion with 16aneS$_4$-diol ligand in the absence of the metal. In the case of blank 1, where iodide was heated with Rh(III) cations in the absence of the 16aneS$_4$-diol ligand, most of the radioactivity stayed at the origin and only 10–35% moved toward the anode like iodide (Figure 2). Radioactivity from this compound also was not adsorbed on Dowex 50W × 8, but stayed in solution, even after a few hours of shaking. Only 10–35% was adsorbed on Dowex 1 × 8, suggesting the presence of uncomplexed iodide. We speculate that, in blank 1, the neutral species Rh(OH)$_2$*I was formed.

The results mentioned above were confirmed by reversed-phase HPLC as shown in Figure 3. If iodide was heated with the macrocyclic thioether ligand without metal cations (blank 2), only one peak was visible on the radiochromatogram (Figure 3, panel A) with a retention time of around 3.9 min. corresponding to an uncomplexed iodide standard. In the case of blank 1, where iodide was heated with Rh(III) cations in the absence of 16aneS$_4$-diol, two peaks were found with the retention times 3.9 and 5.4 min, corresponding to free iodide and probably neutral Rh(OH)$_2$*I, respectively (Figure 3, panel B). The synthesized cationic complex Rh[16aneS$_4$-diol]*I ap-

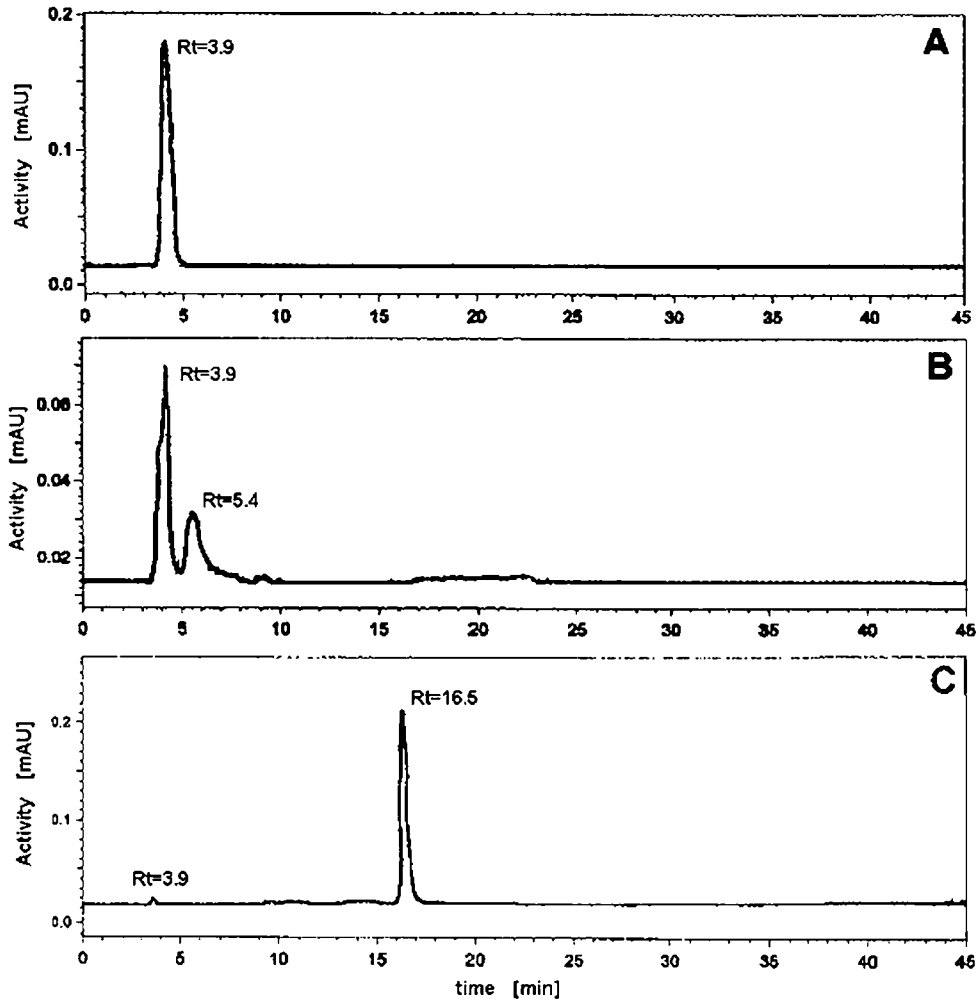

Figure 3. HPLC radiochromatograms of (A) control sample "blank 2"; (B) control sample "blank 1"; (C) sample containing cationic complex Rh[16aneS$_4$-diol]*I.

peared at 15–17 min when using the previously described gradient (Figure 3, panel C).

Although not shown, the results obtained by paper electrophoresis and reversed-phase HPLC methods for the other cationic complexes that were synthesized, Rh[16aneS$_4$-diol]^{211}At and Ir[16aneS$_4$-diol]*I/^{211}At, were quite similar to those described above for Rh[16aneS$_4$-diol]*I. Therefore, only the results for Rh[16aneS$_4$-diol]*I are shown as examples.

The synthesis of inert low-spin d^6 metal complexes often requires heating at high temperature and sometimes for extended time periods (*39*). Our studies also showed that temperature and time of heating are important parameters for high-yield synthesis of the desired complexes. The yield of Rh[16aneS$_4$-diol]*I synthesis was below 20% at 40 °C, even after 2 h of heating (Figure 4, panel A). Raising the temperature from 40 to 90 °C resulted in a sharply increased rate of reaction. The yield of Rh[16aneS$_4$-diol]*I complex formation was around 55–60% after 30 min of heating at 80–90 °C, and it was still increasing during the next 1.5 h, approaching a maximum value of about 90% at 2 h. The temperature-dependence studies for the Ir[16aneS$_4$-diol]*I complex were performed at 40, 60, and 80 °C (Figure 4, panel B). Generally, the obtained results were very similar to those for the Rh[16aneS$_4$-diol]*I complex. The yield of reaction was low at 40 °C and increased up to 87% after heating for 2 h at 80 °C. In the case of Rh[16aneS$_4$-diol]^{211}At and Ir[16aneS$_4$-diol]^{211}At, the effect of heating time on yield was evaluated only at 75–80 °C (Figure 4, panel C). The maximum reaction yield for both astatine complexes was about 80%, and could almost be achieved after 1.5 h of heating.

Microwave-assisted synthesis is commonly used in organic chemistry because it enhances chemical yields by reducing reaction times without causing major degradation or introducing undesired reactions. There are also few articles about preparation of transition metals coordination complexes using microwave techniques (*40*, *41*), including studies on Rh(III) complexes with bipyridine, cyclopentadiene, and pyridylazoresorcinol group ligands (*39*, *42*). This technique has been also applied to labeling biomolecules with short-lived radionuclides, which require procedures that afford the labeled product in a short reaction time. Therefore, it is used in the synthesis with ^{18}F (*43*, *44*), but also with other radiohalogens such as ^{123}I (*45*). Microwave heating may significantly accelerate the synthesis, especially of substitutionally inert second- and third-row transition metal coordination compounds (*40*). For example, the microwave synthesis of *cis*-[Rh(bpy)$_2$I$_2$][PF$_6$] (bpy = bipyridine) from RhCl$_3$ reduced the reaction time from 65 min to 12 min (*39*). In our studies, after 10 min of microwave heating, the yields for Rh[16aneS$_4$-diol]^{131}I and Ir[16aneS$_4$-diol]^{131}I complexes were 51% and 38%, respectively (Figure 5). During the next 10 min, the yields increased up to 75% and 73%, the level which was almost reached in conventional heating in the oil bath for 1.0 h at 75–80 °C. Finally, the yields obtained for Rh[16aneS$_4$-diol]^{131}I and Ir[16aneS$_4$-diol]^{131}I after 35 min of microwave heating were 90% and 83%, respectively. The temperatures of all samples exposed to microwave radiation were kept in the

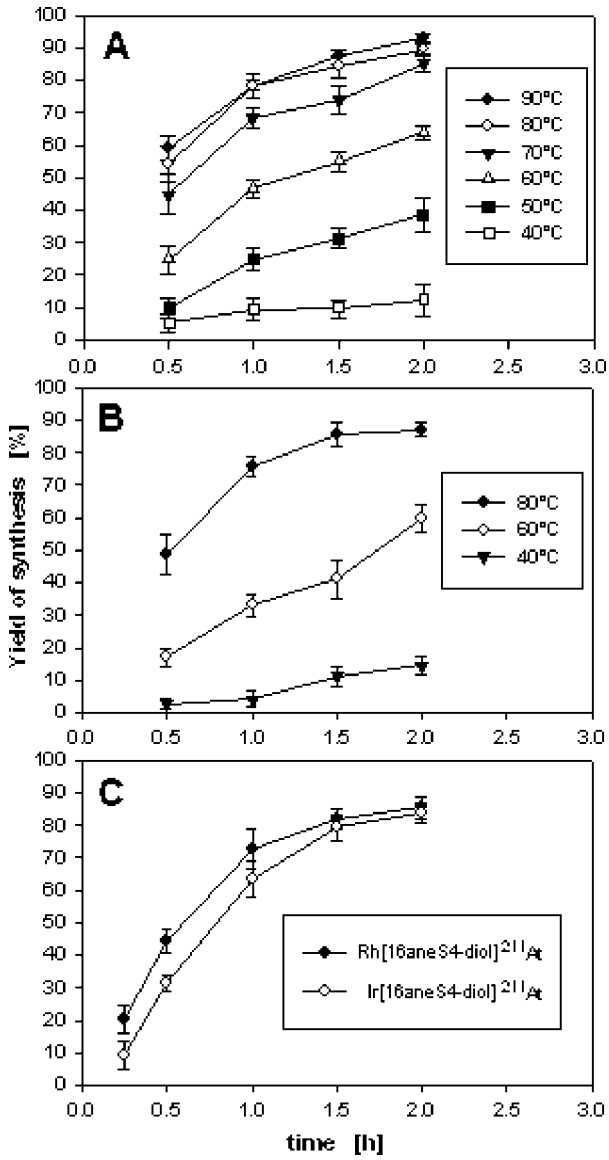

Figure 4. Influence of temperature and time of heating on the synthesis yield of complexes: (A) Rh[16aneS$_4$-diol]*I; (B) Ir[16aneS$_4$-diol]*I; (C) M[16aneS$_4$-diol]^{211}At (M = Rh(III) or Ir(III)).

range 75–80 °C by using only 50% of maximum during microwave irradiation.

Good synthesis yields of about 80% were obtained for Rh[16aneS$_4$-diol]*I/^{211}At and Ir[16aneS$_4$-diol]*I/^{211}At complexes from solutions containing 62.5 nmol of Rh(III) or Ir(III) cations, 250 nmol of 16aneS$_4$-diol ligand, and carrier-free radiohalogen. Decreasing the amount of metals cation in the reaction mixture resulted in a significant decrease in yield for all four complexes (Table 1). High complex formation yields were obtained even when the complexation reaction was performed under a 1:1 stoichiometry ratio of 16aneS$_4$-diol to Rh(III) or Ir(III) at pH 4.0 (n_M = 62.5 nmol). The yield was reduced when the ratio was less than 1:1 (Table 2).

The pH was an important parameter, which influenced the formation of all four complexes. The Rh[16aneS$_4$-diol]*I/^{211}At and Ir[16aneS$_4$-diol]*I/^{211}At yields were the highest in the range 3.0–4.0 and dramatically decreased with pH higher than 5.0, declining to 4.5 ± 0.4% and 12.4 ± 6.7% for *I and ^{211}At, respectively at pH 8.5 (Table 3). The reduction in complex formation probably was due to hydrolysis of the metal cations. During pH studies, we noticed that the decrease in yield for Rh[16aneS$_4$-diol]*I/^{211}At was greater than for Ir[16aneS$_4$-diol]*I/^{211}At. This is consistent with the hypothesis that this behavior reflects hydrolysis of the metal cation, because Ir(III) as a larger cation, which is below Rh(III) in the Periodic Table, should have a smaller affinity to hydrolysis reaction than Rh(III).

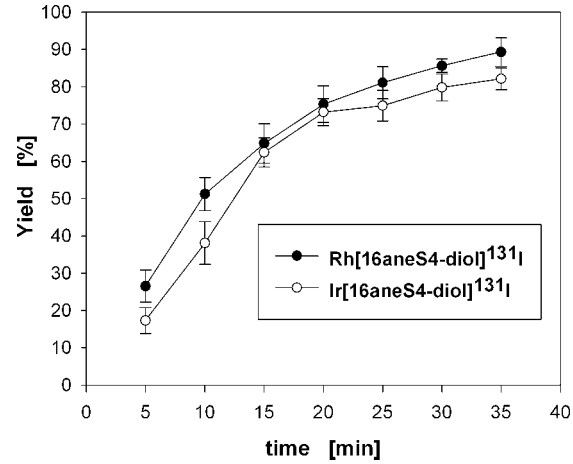

Figure 5. Yield of Rh[16aneS$_4$-diol]^{131}I and Ir[16aneS$_4$-diol]^{131}I complexes versus time of microwave exposition.

Table 1. Effect of Rh(III) and Ir(III) Concentration on the M[16aneS$_4$-diol]X (M = Rh(III) or Ir(III) and X = *I or ^{211}At) Complexes Yield at pH of ~4.0

	yield ± SD [%]			
quantity of metal n_M (nmol)	Rh[16aneS$_4$-diol]*I	Ir[16aneS$_4$-diol]*I	Rh[16aneS$_4$-diol]^{211}At	Ir[16aneS$_4$-diol]^{211}At
0.125	2.7 ± 1.5	1.8 ± 0.6	3.3 ± 2.6	4.6 ± 2.4
1.25	5.1 ± 2.0	7.4 ± 3.2	4.3 ± 2.4	5.5 ± 3.7
6.25	22.6 ± 5.6	19.3 ± 5.6	11.3 ± 5.5	9.4 ± 8.1
12.5	48.4 ± 3.9	50.5 ± 3.9	37.0 ± 6.0	33.1 ± 6.0
62.5	82.5 ± 4.8	79.2 ± 3.3	77.2 ± 8.2	73.3 ± 6.2
125.0	88.4 ± 3.3	85.8 ± 3.6	82.8 ± 4.6	81.3 ± 7.3

Table 2. Effect of 16aneS$_4$-diol Concentration on the M[16aneS$_4$-diol]X (M =Rh(III) or Ir(III) and X = *I or ^{211}At) Complexes Yield at pH of ~4.0

	yield ± SD [%]			
quantity of ligand n_{S4} (nmol)	Rh[16aneS$_4$-diol]*I	Ir[16aneS$_4$-diol]*I	Rh[16aneS$_4$-diol]^{211}At	Ir[16aneS$_4$-diol]^{211}At
18.75	2.1 ± 1.3	2.4 ± 1.8	3.1 ± 2.2	3.5 ± 2.6
25.0	7.4 ± 2.8	18.2 ± 1.3	9.5 ± 0.8	8.6 ± 4.5
62.5	43.8 ± 7.1	38.4 ± 1.3	48.7 ± 5.7	26.4 ± 7.6
125.0	73.8 ± 6.9	70.5 ± 3.1	69.6 ± 6.4	65.2 ± 8.7
187.5	79.4 ± 2.0	77.6 ± 2.8	76.5 ± 3.3	71.3 ± 6.5
250.0	82.1 ± 3.2	80.2 ± 2.5	78.3 ± 4.2	74.5 ± 2.8

Table 3. Yield of the M[16aneS$_4$-diol]X (M = Rh(III) or Ir(III) and X = *I or ^{211}At) Complexes Synthesis vs pH of Solution

	yield ± SD [%]			
pH	Rh[16aneS$_4$-diol]*I	Ir[16aneS$_4$-diol]*I	Rh[16aneS$_4$-diol]^{211}At	Ir[16aneS$_4$-diol]^{211}At
2.0	80.6 ± 3.2	74.7 ± 2.4	72.2 ± 8.1	68.9 ± 6.1
3.0	83.3 ± 2.9	76.5 ± 1.7	75.3 ± 4.5	74.8 ± 3.2
4.0	84.2 ± 4.3	80.2 ± 2.9	80.4 ± 4.2	75.1 ± 6.4
5.0	55.1 ± 9.4	65.7 ± 3.1	68.1 ± 3.6	69.0 ± 6.0
6.0	32.6 ± 8.2	62.4 ± 2.5	43.3 ± 3.4	58.4 ± 5.3
7.5	14.0 ± 7.7	27.3 ± 6.7	24.7 ± 5.2	35.0 ± 1.7
8.5	4.5 ± 0.4	-	12.4 ± 6.7	-

CONCLUSIONS

Our results demonstrate the feasibility of attaching ^{211}At$^-$ anions under mild conditions to moderately soft Rh(III) or Ir(III)

cations complexed by 16aneS$_4$-diol to form kinetically inert positively charged Rh[16aneS$_4$-diol]^{211}At and Ir[16aneS$_4$-diol]^{211}At complexes. The macrocyclic ligand 16aneS$_4$-diol with diol functionality was chosen for model studies, because it forms stable complex with Rh(III) and can be easily modified to provide a bifunctional chelate ligand. For further labeling studies with biomolecules, we will use a bifunctional sulfur ligand. A macrocyclic sulfur ligand with an additional carboxylic group as a functionality for attachment will probably be the best for conjugation with biomolecules. This type of ligand has been described previously. Li et al. (*34*) and Goswami et al. (*36*, *46*) utilized rhodium complexes with different bifunctional sulfur ligands and reported that the carboxylic group did not coordinate with the rhodium core in their complexes, even after heating at high temperatures for a long time. Therefore, we also do not expect the competition reaction and replacement of astatide or iodide in our complexes by the carboxylic group. However, this must be verified experimentally. The complexes labeled with ^{211}At, after appropriate purification, could be used in the future as the precursors for labeling of biomolecules such as monoclonal antibodies. Because the formation of Rh[16aneS$_4$-diol]^{211}At and Ir[16aneS$_4$-diol]^{211}At or complexes with similar bifunctional sulfur ligands requires heating at high temperatures, we anticipate the need for a two-step procedure for labeling biomolecules. First, the appropriate astatine complex should be synthesized and, after purification, conjugated at room temperature with the biomolecule via an appropriate functional group (e.g., carboxylic group mentioned above).

Studies with *I$^-$ anions were performed mainly for optimization of reaction conditions. In addition, results obtained during synthesis of Rh[16aneS$_4$-diol]*I and Ir[16aneS$_4$-diol]*I complexes, enable us to compare them with the results for ^{211}At complexes and make final conclusions. Generally, results obtained during optimization processes for all four complexes were comparable. However, we noticed that complexes with the Rh(III) cation core were formed with a few percent higher yield in comparison to complexes with the Ir(III) cation core. This situation was changed only when the effects of reaction pH were evaluated. Also, the yield for complexation with *I radionuclides was a few percent higher than for ^{211}At. Finally, we showed that microwave heating could significantly accelerate the reactions. Using microwaves, instead of conventional heating, reduced the time of reaction from 1−1.5 h to about 20–35 min with the approximate yield of 80%.

Preliminary stability studies of Rh[16aneS$_4$-diol]*I and Ir[16aneS$_4$-diol]*I complexes in PBS and human serum have been performed and gave promising results. Both iodine complexes were stable in PBS and human serum over 51 h incubation at 37 °C. The stability of Rh[16aneS$_4$-diol]^{211}At and Ir[16aneS$_4$-diol]^{211}At complexes was checked only in PBS solution. We did not observe any loss of astatine from the complexes after 6 h (almost one-half-life) incubation at 37 °C. Extended studies on the evaluation of the *in vitro* and *in vivo* stability of Rh[16aneS$_4$-diol]*I/^{211}At and Ir[16aneS$_4$-diol]*I/^{211}At complexes will be described in a subsequent publication.

ACKNOWLEDGMENT

This work was done under the N204 081 31/1939 and N204 143 32/3547 grants of Polish Ministry of Science and Higher Education. Part of the work was carried out in the frame of Marie Curie Action for the Transfer of Knowledge, contract no. MTKD-CT-2004-509224 with the European Commission and part was funded by Grant CA42324 from the National Institutes of Health of the United States. We gratefully acknowledge the Polish-US Fulbright Commission for enabling Marek Pruszyński to spend 5 months working at Duke University Medical Center, Durham, NC.

LITERATURE CITED

(1) Zalutsky, M. R. (2003) Radionuclide therapy. In *Radiochemistry and Radiopharmaceutical Chemistry in Life Sciences* (Rösch, F., Ed.) pp 315–348, Kluwer Academic Publishers, Dordrecht.

(2) Hall, E. J. (1988) *Radiobiology for the Radiologist* pp 161–177, Lippincott, Philadelphia.

(3) Ritter, M. A., Cleaver, J. W., and Tobias, C. A. (1977) High-LET radiations induce a large proportion of non-rejoining DNA breaks. *Nature 266*, 653–655.

(4) Lambrecht, R. M., and Mirzadeh, S. (1985) Cyclotron isotopes and radiopharmaceuticals-XXXV. Astatine-211. *Int. J. Appl. Radiat. Isot. 36*, 443–450.

(5) Turkington, T. G., Zalutsky, M. R., Jaszczak, R. J., Garg, P. K., Vaidyanathan, G., and Coleman, R. E. (1993) Measuring astatine-211 distributions with SPECT. *Phys. Med. Biol. 38*, 1121–1130.

(6) Vergote, I., Larsen, R. H., De Vos, L., Nesland, J. M., Bruland, Ø., Bjørgum, J., Alstad, J., Tropé, C., and Nustad, K. (1992) Therapeutic efficiacy of the α-emitter ^{211}At bound on microspheres compared with ^{90}Y and ^{32}P colloids in a murine intraperitoneal tumour model. *Gynecol. Oncol. 47*, 366–372.

(7) Strickland, D. K., Vaidyanathan, G., and Zalutsky, M. R. (1994) Cytotoxicity of α-particle emitting *m*-[^{211}At]astatobenzylguanidine on human neuroblastoma cells. *Cancer Res. 54*, 5414–5419.

(8) Larsen, R. H., Vaidyanathan, G., and Zalutsky, M. R. (1997) Cytotoxicity of α-particle emitting 5-[^{211}At]astato-2′-deoxyuridine in human cancer cells. *Int. J. Radiat. Biol. 72*, 79–90.

(9) Larsen, R. H., Murud, K. M., Akabani, G., Hoff, P., Bruland, Ø., and Zalutsky, M. R. (1999) At-211 and I-131-labeled bisphosphonates with high in vivo stability and bone accumulation. *J. Nucl. Med. 40*, 1197–1203.

(10) Andersson, H., Lindegren, S., Back, T., Jacobsson, L., Leser, G., and Horvath, G. (2000) Radioimmunotherapy of nude mice with intraperitoneally growing ovarian cancer xenograft utilizing ^{211}At-labelled monoclonal antibody MOv18. *Anticancer Res. 20*, 459–462.

(11) Humm, J. L., Roeske, J. C., Fisher, D. R., and Chen, G. T. Y. (1993) Microdosimetric concepts in radioimmunotherapy. *Med. Phys. 20*, 535–541.

(12) Zalutsky, M. R., and Bigner, D. D. (1996) Radioimmunotherapy with alpha-particle emitting radioimmunoconjugates. *Acta Oncol. 35*, 373–379.

(13) Vaughan, A. T. M., and Fremlin, J. H. (1978) Preparation of astatine labeled protein using an electrophilic reaction. *Int. J. Nucl. Med. Biol. 5*, 229–230.

(14) Visser, G. W. M., Diemer, E. L., and Kaspersen, F. M. (1981) The nature of the astatine-protein bond. *Int. J. Appl. Radiat. Isot. 32*, 905–912.

(15) Zalutsky, M. R., Stabin, M. G., Larsen, R. H., and Bigner, D. D. (1997) Tissue distribution and radiation dosimetry of astatine-211-labeled chimeric 81C6, an α-particle-emitting immunoconjugate. *Nucl. Med. Biol. 24*, 255–261.

(16) Yordanov, A. T., Garmestani, K., Zhang, M., Zhang, Z., Yao, Z., Phillips, K. E., Herring, B., Horak, E., Beitzel, M. P., Schwarz, U. P., Gansow, O. A., Plascjak, P. S., Eckelman, W. C., Waldmann, T. A., and Brechbiel, M. W. (2001) Preparation and in vivo evaluation of linkers for 211At labeling of humanized anti-Tac. *Nucl. Med. Biol. 28*, 845–856.

(17) Friedman, A. M., Zalutsky, M. R., Wung, W., Buckingham, F., Harper, P. V., Scherr, G. H., Wainer, B., Hunter, R. L., Appleman, E. H., Rothberg, R. M., Fitch, F. W., Stuart, F. P., and Simonian, S. J. (1977) Preparation and biologically stable and immunologically competent astatinated protein. *Int. J. Nucl. Med. Biol. 4*, 219–224.

(18) Vaughan, A. T. M. (1979) Labelling of proteins with ^{211}At using an Acylation Reaction. *Int. J. Appl. Radiat. Isot. 30*, 576–577.

(19) Zalutsky, M R., and Narula, A. S. (1988) Astatination of proteins using an *N*-succinimidyl tri-*n*-butylstannyl benzoate intermediate. *Appl. Radiat. Isot. 39*, 227–232.

(20) Hadley, S. W., Wilbur, D. S., Gray, M. A., and Atcher, R. W. (1991) Astatine-211 labeling of an antimelanoma antibody and its Fab fragment using *N*-succinimidyl *p*-[^{211}At]astatobenzoate: comparisons in vivo with the *p*-[^{125}I]iodobenzoyl conjugate. *Bioconjugate Chem. 2*, 171–179.

(21) Wilbur, D. S., Chyan, M. K., Hamlin, D. K., Kegley, B. B., Risler, R., Pathare, P. M., Quinn, J., Vessella, R. L., Foulon, C., Zalutsky, M. R., Wedge, T. J., and Hawthorne, M. F. (2004) Reagents for astatination of biomolecules: comparison of the in vivo distribution and stability of some radioiodinated/astatinated benzamidyl and *nido*-carboranyl compounds. *Bioconjugate Chem. 15*, 203–223.

(22) Berei, K., and Vasaros, L. (1981) *Organic Chemistry of Astatine*, Hungarian Academy of Sciences ReportKFKI-1981–10.

(23) Garg, P. K., John, C. S., and Zalutsky, M. R. (1995) Preparation and preliminary evaluation of 4-[^{211}At]astato-*N*-piperidinoethyl benzamide. *Nucl. Med. Biol. 22*, 467–473.

(24) Kerr, J. A. (1993) Strengths of Chemical Bonds. In *CRC Handbook of Chemistry and Physics* (Lide, D. R. Ed.) pp *9-123–9-145*, CRC Press, Boca Raton.

(25) Wilbur, D. S., Hamlin, D. K., and Srivastava, R. R. (1994) Radioiodinations of *nido*-carboranes. potential hydrophilic pendant groups for radiohalogenation of biological molecules. *J. Labelled Compd. Radiopharm. 35*, 199–201.

(26) Wilbur, D. S., Hamlin, D. K., Buhler, K. R., Srivastava, R. R., Suray, J. E., Daniel, J., and Vessella, R. L. (1995) Comparison of in vivo distribution of simple radioiodinated borane and carborane cage molecules. *Quat. J. Nucl. Med. 39*, 51–52.

(27) Orlova, A., Lebeda, O., Tolmachev, V., Sjöberg, S., Carlsson, J., and Lundqvist, H. (2000) Closo-dodecaborate(2-) anion as a prosthetic group for attachment of astatine to proteins. Aspects of the labelling chemistry with Chloramine-T. *J. Labelled Compd. Radiopharm. 43*, 251–260.

(28) Sjöström, A., Tolmachev, V., Lebeda, O., Koziorowski, J., Carlsson, J., and Lundqvist, H. (2003) Direct astatination of a tumour-binding protein, human epidermal growth factor, using nido-carborane as a prosthetic group. *J. Radioanal. Nucl. Chem. 256*, 191–197.

(29) Wilbur, D. S., Hamlin, D. K., Srivastava, R. R., and Chyan, M. K. (2004) Synthesis, radioiodination, and biodistribution of some nido- and closo-monocarbon carborane derivatives. *Nucl. Med. Biol. 31*, 523–530.

(30) Wilbur, D. S., Chyan, M. K., Hamlin, D. K., Vessella, R. L., Wedge, T. J., and Hawthorne, M. F. (2007) Reagents for astatination of biomolecules. 2. Conjugation of anionic boron cage pendant groups to a protein provides a method for direct labeling that is stable to in vivo deastatination. *Bioconjugate Chem. 18*, 1226–1240.

(31) Pearson, R. G. (1963) Hard and soft acids and bases. *J. Am. Chem. Soc. 85*, 3533–3543.

(32) Pruszyński, M., Bilewicz, A., Was, B., and Petelenz, B. (2006) Formation and stability of astatide-mercury complexes. *J. Radioanal. Nucl. Chem. 268*, 91–94.

(33) Venkatesh, M., Goswami, N., Volkert, W. A., Schlemper, E. O., Ketring, A. R., Barnes, C. L., and Jurisson, S. (1996) An Rh-105 complex of tetrathiacyclohexadecane diol with potential for formulating bifunctional chelates. *Nucl. Med. Biol. 23*, 33–40.

(34) Li, N., Struttman, M., Higginbotham, C., Grall, A. J., Skerlj, J. F., Vollano, J. F., Bridger, S. A., Ochrymowycz, L. A., Ketring, A. R., Abrams, M. J., and Volkert, W. A. (1997) Biodistribution of model ^{105}Rh-labeled tetradentate thiamacrocycles in rats. *Nucl. Med. Biol. 24*, 85–92.

(35) Koziorowski, J., Lebeda, O., and Weinreich, R. (1999) A cryotrap as flow reactor for synthesis of ^{211}At labeled compounds. *Appl. Radiat. Isot. 50*, 527–529.

(36) Goswami, N., Higginbotham, C., Volkert, W., Alberto, R., Nef, W., and Jurisson, S. (1999) Rhodium-105 tetrathioether complexes: radiochemistry and initial biological evaluation. *Nucl. Med. Biol. 26*, 951–957.

(37) Wilbur, D. S. (1991) Potential use of alpha emitting radionuclides in the treatment of cancer. *Antibody, Immunoconjugates, Radiopharm. 4*, 85–97.

(38) Garg, P. K., John, C. S., and Zalutsky, M. R. (1995) Preparation and preliminary evaluation of 4-[^{211}At]astato-*N*-piperidinoethyl benzamide. *Nucl. Med. Biol. 22*, 467–473.

(39) Amarante, D., Cherian, C., Emmel, C., Chen, H. Y., Dayal, S., Koshy, M., and Megehee, E. G. (2005) Improved synthetic routes to rhodium bipyridine complexes: comparison of microwave vs. conventional synthesis. *Inorg. Chim. Acta 358*, 2231–2238.

(40) Baghurst, D. R., Cooper, S. R., Greene, D. L., Mingos, D. M. P., and Reynolds, S. M. (1990) Application of microwave dielectric loss heating effects for the rapid and convenient synthesis of coordination compounds. *Polyhedron 9*, 893–895.

(41) Rau, S., Schäfer, B., Grüßing, A., Schebesta, S., Lamm, K., Vieth, J., Görls, H., Walther, D., Rudolph, M., Grummt, U. W., and Birkner, E. (2004) Efficient synthesis of ruthenium complexes of the type (R-bpy)$_2$RuCl$_2$ and [(R-bpy)$_2$Ru(L-L)]Cl$_2$ by microwave-activated reactions (R: H, Me, tert-But) (L-L: substituted bibenzimidazoles, bipyrimidine, and phenanthroline). *Inorg. Chim. Acta 357*, 4496–4503.

(42) Dedkov, Yu. M., Korsakova, N. V., and Radugina, O. G. (2000) Effect of microwave radiation on the complexation of rhodium(III) and iridium(IV) with reagents of the pyridylazoresorcinol group. *J. Anal. Chem. 55*, 1128–1131.

(43) Hwang, D. R., Moerlein, S. M., and Welch, M. J. (1989) Microwave-facilitated synthesis of [^{18}F]-Spiperone. *J. Labelled Compd. Radiopharm. 26*, 391.

(44) Lemaire, C., Cantineau, R., Christiaens, L., and Guillaume, M. (1989) Radiofluorination of Altanserine a potential serotonin receptor binding radiopharmaceutical for positron emission tomography. *J. Labelled Compd. Radiopharm. 36*, 336.

(45) Kumar, P., Wiebe, L. I., Asikoglu, M., Tandon, M., and McEwan, A. J. B. (2002) Microwave-assisted (radio)halogenation of nitroimidazole-based hypoxia markers. *Appl. Radiat. Isot. 57*, 697–703.

(46) Goswami, N., Alberto, R., Barnes, C. L., and Jurisson, S. (1997) Rhodium(III) complexes with acyclic tetrathioether ligands. Effects of back-bone chain length on the conformation of the Rh(III) complexes. *Inorg. Chem. 35*, 7546–7555.

BC700413R

Magnetic Proteinase K Reactor as a New Tool for Reproducible Limited Protein Digestion

Marcela Slováková,* Jean-Michel Peyrin,† Zuzana Bílková, Martina Juklíčková, Lenka Hernychová, and Jean-Louis Viovy

Laboratoire Physicochimie-Curie, Institut Curie, Paris Cedex 5, France, Unité de Virologie Immunologie Moléculaires, INRA, 78350 Jouy-en-Josas, France, Department of Biological and Biochemical Sciences, University of Pardubice, 53210 Pardubice, Czech Republic, and Institute of Molecular Pathology, University of Defence, Hradec Králové, Czech Republic. Received December 3, 2007; Revised Manuscript Received January 31, 2008

As an aid to differentiating between the prion proteins Prp^c and PrP^{Sc}, the preparation and use of immobilized Proteinase K (PK) is described. An accumulation of PrP^{Sc} in the central nervous system is the one of the causes of neurodegenerative disease. Current routine diagnosis is based on the postmortem detection of the distinct neuropathological lesion profiles of CNS and by the presence of the PK-resistant core of the prion protein isolated from brain lysates. An assay with PK immobilized to magnetic −COOH micro- and nanoparticles can offer a convenient as well as economic method. The individual immobilization steps were verified by measuring the ζ potential of the particles. The stability of the newly developed PK magnetic reactor, observed during kinetics measurements, was highly satisfactory. The calculated values of the apparent Michaelis constant (4.25 mM for native enzyme and 1.28 mM for immobilized enzyme) were determined from Lineweaver–Burk plots. Human growth hormone was digested using the newly prepared magnetic PK reactor and MALDI-TOF-MS analysis of the digests showed satisfactory efficiency. Controlled digestion of PrP^c from the Mov mouse cell line was demonstrated with Western blot detection.

INTRODUCTION

In general, proteolytic enzymes covalently bonded on solid carriers have a wide range of practical applications. Although their hydrolytic activity usually decreases slightly upon immobilization, they possess important advantages over dissolved enzymes, e.g., the possibility of recovery and reuse, simple operation, enhanced stability, and limited protease autolysis. The activity and stability of such biocatalysts after their immobilization depends on the type of carrier (biopolymer or synthetic, magnetic, size, porosity, etc.), the enzyme, and the immobilization method (*1*, *2*). The choice of matrix is a key factor in the operating range of the final application and degree of process automation (*3*, *4*).

The magnetic form of the particles provide the best simple, reproducible, and economic approaches, which enable a highly efficient and gentle separation, during either an immobilization procedure or biochemical applications (*2*), e.g., on-chip technology (*3*, *4*). Due to their small size (up to 1 μm in mean diameter), they offer a very large specific surface area. The specific surface area and size of the polymeric particles used in this research work (Ademtech, France) were within narrowly defined ranges. The composition of the particles is stable in solutions of widely ranging pH and at moderate salt concentrations. The surface charge density is negative at slightly basic pH, according to the manufacturer.

Proteinase K (PK) is a subtilisin family serine protease isolated from *Tritirachium album* Limber. This highly active extracellular alkaline serine endopeptidase was so named in the past because of its ability to digest native keratin (*5*–*7*). PK has an immense range of applications in pure and applied research. One of the fundamental fields of application of PK is its use together with a prion protein immunoblot for the detection of the pathological form of prion protein in various fluids and tissues. Other important applications of PK are in the scientific and biomedical fields: the removal of biomolecules, e.g., inhibitors, DNA molecules, highly resistant proteins, and glycoproteins, and so forth, from biological materials (*8*–*10*).

The main characteristics of PK have already been determined: molecular mass 28 930 (*11*), isoelectric point 8.9, optimal pH range for enzyme activity from 7.5 to 12 (*5*). Calcium ions are involved in this enzyme's activity, and additional calcium ions in solution are also required for the stability of the enzyme (*11*). This proteinase has unusual stability at low concentrations of SDS and urea. PK is primarily specific against aromatic or hydrophobic amino acid residues on the carboxyl side of the splitting point (*12*).

In this paper, we tested new magnetic carriers for utilization in a proteinase K reactor: 500A5 and 145TTa magnetic beads (styrenic copolymer with hydrophilic monomer, Ademtech, France), A120 magnetic alginate microparticles (Academy of Sciences, Czech Republic), Estapor magnetic latex microparticles (Merck, France). Along with optimizations of the grafting conditions, i.e., temperature, time, type and strength of buffer, the characterization of the enzyme reactor was a further aim of this work. The stability of the PK reactor was investigated in terms of multiple uses. The ζ potential and apparent Michaelis–Menten constant of the magnetic PK reactor were determined.

The newly prepared enzyme reactor was used for the proteolytic digestion of human growth hormone (HGH) (22 kDa) and PrP^c from the Mov mouse cell line. Mass spectrometry and

* Corresponding author. University of Pardubice, Department of Biological and Biochemical Sciences, Strossova 239, 53003 Pardubice, Czech Republic, Phone number +420 466 037 721. E-mail address Marcela.Slovakova@upce.cz.

† Present address: CNRS, Neurobiologie des Processus Adaptatifs, UMR7102 Boite 12, 9 quai saint Bernard, 75005 Paris.

10.1021/bc7004413 CCC: $40.75 © 2008 American Chemical Society
Published on Web 03/13/2008

Western blotting analysis were used to confirm digestion by the newly prepared enzyme reactor.

EXPERIMENTAL PROCEDURES

Chemicals. Proteinase K (E.C.3.4.21.64, lot 104K8622, 33 U/mg of solid protein), succinyl-Ala-Ala-Ala-*p*-nitroanilide (EC 257-823-5; substrate for PK), 1-ethyl-3-(3-dimethylaminopropyl)carbodiimide hydrochloride (EDAC), sodium azide, and the surfactants polyoxyethylsorbitane monolaurate (Tween 20), Triton X-405, and Triton X-100 were purchased from Sigma-Aldrich. The surfactant Pluronics F127 NF (PF 127) was purchased from the BASF Corporation (New Jersey, USA). The sodium salt of *N*-hydroxysulfosuccinimide and trifluoric acid were obtained from Fluka (Buchs, Switzerland). A Micro BCA Protein Assay Kit (Perbio Science, Pierce France) was used for complete protein determination. All other reagents, of analytical or electrophoresis quality, were obtained from international suppliers (Merck, Darmstadt, Germany; Bio/Rad, Hercules, CA, USA; Sigma, St. Louis, MO, USA). The mouse overexpressed PrP^c cells (Mov cell line) were lysated in a lysis buffer (0.5% sodium deoxycholate, 0.5% Triton X100, 50 mM Tris-HCl pH 7.4). The PK immobilized to Eupergit C was purchased from Sigma-Aldrich (USA).

Magnetic Carriers. The 500A5 (626 nm mean diameter) and 145TTa (980 nm mean diameter) magnetic latex beads used in this study were donated by Ademtech SA (Pessac, France), both functionalized with −COOH groups. The A120 magnetic alginate microparticles (−COOH) were donated by the Academy of Sciences (Czech Republic) (2–5 μm diameter). Magnetic latex microparticles (−COOH) were purchased from Estapor (Merck, France) (160 nm mean diameter). All stock solutions were stored in an aqueous suspension containing 0.09% NaN_3. Carriers were washed extensively with the enzyme buffer (10 mM phosphate buffer pH 7.3) before each use.

Equipment. A magnetic separator (Dynal, USA) was used for manipulations with the magnetic carriers. All microscopic observations were made using an inverted microscope (Zeiss Axiovert 100) with 10×, 5× (Zeiss), and 100× oil immersion (Olympus) objectives, and an intensified CCD camera (Lhesa, Cergy Pontoise, France). Spectrophotometers (Shimadzu Corporation, Japan, and NanoDrop, Nyxor Biotech, France) were used for measuring the optical density for catalytic activity quantification. A Voyager-DE STR MALDI-TOF spectrophotometer (Applied Biosystems, Germany) was utilized for mass spectrometry analysis.

Immobilization of PK (PK) on Magnetic Particles. Generally, 1 mg of magnetic particles (functionalized by –COOH) was washed with 10 mM of phosphate buffer (pH 7.3). Carboxyl groups were activated via the method developed by Staros et al. (*13*) using water-soluble carbodiimide EDAC [1-ethyl-3(3-dimethylaminopropyl) carbodiimide] at a concentration of 79 mM. Addition of *N*-hydroxysulfosuccinimide [sulfo-NHS], at a concentration of 12 mM, enhances the yield of amide bond formation (*14*). The chosen amount (from 1 to 4 mg) of PK was dissolved in 10 mM phosphate buffer (pH 7.3) with 5 mM $CaCl_2$; the total concentration of Ca^{2+} ions in the mixture was 1 mM according to (*11*). The immobilization time depends on the chosen temperature: at room temperature, the grafting reaction was maintained for 6 h; at 4 °C the reaction was maintained overnight. Blocking the unreacted activated sites on the particle surface was done with 100 mM Tris, 100 mM MES, and 52 mM EDAC at room temperature for 2 h. The PK reactor was washed and stored in 50 mM Tris/HCl buffer (pH 7.8) with 5 mM $CaCl_2$ and the addition of 0.02% sodium azide.

Immobilized PK Activity Assay. The specific enzyme activity was assayed using succinyl-Ala_3-*p*-nitroanilide as a substrate (*11, 15*). 1 I.U. of the activity is expressed as the amount of enzyme which can hydrolyze casein to produce the color equivalent to 1.0 μmol of tyrosine per minute at pH 7.5 and 37 °C (colored by the Folin-Cocteau reagent). The assays were routinely carried out at a substrate concentration of 1.05 mM and in 50 mM Tris/HCl buffer (pH 7.8) with 5 mM $CaCl_2$ (total volume 1 mL). Assay mixtures were composed of 50 mM Tris/HCl buffer (pH 8.0) $CaCl_2$ (5 mM), *N*-succinyl-Ala_3-*p*-nitroanilide (1.1 mM), and PK (immobilized or 2–10 μg/mL). The mixture was incubated for 15 min at room temperature. The reaction was terminated by adding 0.2 mL glacial acetic acid for the native enzyme or by the separation of the PK particles with a magnetic separator (Dynal, USA), and the optical density at 405 nm of free pNA was measured against the substrate solution as a reference. The final PK activity was estimated from the linear increase in optical density. Except for steps investigating thermal stability, all experiments were carried out at 25 °C.

Measurement of ζ Potential. A Zetasizer (Malvern Instrument, U.K.) was used in the ζ measurememt protocols. The ζ potential of the beads was measured in a phosphate buffer of strengths 10 and 100 mM and with pHs ranging from 3 to 11; the pH was adjusted with HCl and NaOH. The total volume for measurements was 1 mL, and the concentration of the beads was 3×10^{-3}%.

Determination of Apparent K_M and V_{max} for PK. The Michaelis–Menten kinetic parameters K_M and V_{max} for the hydrolytic reactions between succinyl-Ala-Ala-Ala-*p*-nitroanilide and PK were determined from Lineweaver–Burk (L-B) plots. All kinetic experiments were carried out in 50 mM Tris/HCl buffer (pH 7.8) at 25 °C (tempered solution). The concentration range of the substrate *N*-succinyl-Ala_3-*p*-nitroanilide was $(0.275-4.8) \times 10^{-3}$ mol/L.

Proteolysis of Proteins by Immobilized PK. The protein (human growth hormone, molecular size 22 kDa) was dissolved in 50 mM ammonium acetate (pH 7.8) and digested with soluble PK or an immobilized PK reactor in a microtube. Procedure: 100 μL of protein (1 mg/mL) was added to the appropriate amount of PK reactor (E:S 1:16), and digested over 4 h at room temperature with slow rotation.

Mass Spectrometry Analysis of Digested Protein by MALDI-TOF-MS. The digest of HGH was desalted using RP $ZipTip_{C18}$ (Millipore). 1 μL of each sample was applied to a MALDI plate and covered with 1 μL of 2,5-dihydroxybenzoic acid (DHB) (LaserBio Laboratories) as the matrix. For the matrix solution, DHB was dissolved in a solution containing 50% ACN and 0.3% trifluoracetic acid (Fluka Biochemika) to a DHB concentration of 50 mg/mL. The Voyager-DE STR MALDI-TOF mass spectrometer (Applied Biosystems) was used in all experiments. The MALDI-TOF measurements were carried out in positive ion reflectron mode with a mass range of m/z 110−2500. The list of detected monoisotopic masses (m/z) was used for protein identification with the PeptideMass tool of the ExPASy proteomic server (http://www.expasy.org/).

Digestion of Cell Lysate Overexpressing PrP^c. Mov cells are immortalized neuroglial cells isolated from mice expressing the ovine gene for PrP^c. Cells were grown as in (*16*). Once confluency was reached, cells were lysed in buffer (0.1% Triton X100, 0.1% sodium deoxycholate, 50 mM Tris, pH 7.2). Cell lysates were centrifuged for 2 min at 1000 *g* to remove cell debris, and stored at −20 °C until used. Cell lysates were then incubated with the proteinase K reactor for 2, 5, 10, 30, and 60 min at RT (0.7 μg of PK reactor for 100 μL of protein). Pefabloc SC (0.4 mM) was then added to stop the reaction, and proteins were precipitated with 4 volumes of cold methanol.

Western Blotting. Pellets were resuspended in sample buffer (50 mM Tris/HCl pH 7.8), boiled, subjected to 10% SDS/PAGE

Table 1. Influence of Temperature on Soluble PK assay with the Substrate *N*-Succinyl-Ala-Ala-Ala-p-NA (1.05 mM in volume 1 mL), Measured in 50 mM Tris/HCl, pH 7.8

temperature [°C]	PK amount [μg/mL]
25	4.84
37	5.16
50	4.88

Table 2. Influence of Buffering System on Soluble PK Assay with the Substrate *N*-Succinyl-Ala-Ala-Ala-p-NA (1.05 mM in volume 1 mL)

buffering solution	PK amount [μg/mL]
50 mM MES pH 6	1.83
10 mM sodium phosphate pH 7.3	1.9
50 mM TRIS/HCl pH 7.8	3.9

Table 3. Immobilization of PK to Microparticles 500A5 (Ademtech) in Various Buffering Solutions[a]

cross-linker	buffer, pH	conditions	amount of PK [μg/mg carrier]
EDAC, S-NHS	10 mM phosphate, pH 7.3	p6h,RT	9.92
EDAC, S-NHS	50 mM MES, pH 6	6 h,RT	4.81
EDAC, S-NHS	100 mM TRIS/HCl, pH 7.8	6 h,RT	3.29

[a] 10 mM sodium phosphate buffer at pH 7.3, 50 mM MES solution at pH 6.0, and 100 mM TRIS/HCl at pH 7.8, in the presence of 1 mM $CaCl_2$, 6 h at RT, slow rotation.

electrophoresis, and electrotransferred (1 h) onto nitrocellulose membranes. PrP^c was visualized with either ICSM18 or SAF 84.3 mAb overnight at 4 °C; both directed to the C-terminal half-of PrP^c. Western blots were developed by $AgNO_3$ (Amersham Pharmacia) in a darkroom.

RESULTS

Proteinase K Activity Assay. With regard to the proteinase K activity assay, we focused on common conditions for assays of the soluble enzyme to verify that these conditions are usable for the immobilized enzyme. Further, we wanted to verify that there is no change in the basic kinetic parameters of the enzyme assay.

To find the optimal conditions for the immobilized PK activity assay, various pH levels, buffering systems, and temperatures were examined for the soluble enzyme (Tables 1 and 2). The synthetic substrate *N*-succinyl-Ala-Ala-Ala-p-NA was used (*11*, *15*). The temperatures for both the soluble and immobilized enzyme were compared, and the results showed identical courses (data not shown). The activity was determined in three buffering solutions with differing pH levels (*5*, *11*).

Optimizations of PK Immobilization. Though commercial kits for binding proteins or enzymes to various carriers are now readily available, extensive optimizations are essential in testing newly developed carriers. Optimizations are needed to improve enzyme performance, for example, activity and stability.

Appropriate conditions for PK immobilization to 500A5 magnetic microparticles (Ademtech, France) were first proposed and subsequently optimized. The following paragraphs describe the experiments in which the composition of the immobilization mixture, addition of calcium ions, ionic strength in the mixture, temperature, and duration were examined.

Three buffers were tested for the immobilization procedure: 10 mM sodium phosphate buffer at pH 7.3, 50 mM MES at pH 6.0, and 50 mM MES at pH 7.3, all with 1 mM $CaCl_2$. The resulting enzyme activities suggested differences between the individual buffers during the grafting procedure (Table 3). The 10 mM phosphate buffer at pH 7.3 was determined to be the most suitable, then came 50 mM MES at pH 6.0 and pH 7.3.

Table 4. Monitoring Effects of Temperature and Reaction Time on Grafting Efficiency of PK to 500A5 (Ademtech)[a]

temperature	reaction time	amount of PK [μg/mg carrier]
4 °C	overnight	14.8
	6 h	5.5
RT	overnight	1.1
	6 h	10.1

[a] Immobilization occurred in 10 mM sodium phosphate buffer, pH 7.3, 6 h at RT, slow rotation.

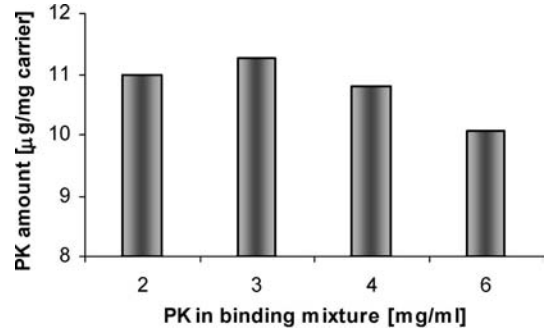

Figure 1. Binding efficiency of PK to 500A5 microparticles (Ademtech). Composition of the reaction mixture: 1 mg of magnetic particles, specified amount of PK, 79 mM EDAC, 12 mM S-NHS per 1 mg of the carrier, 6 h at RT, slow rotation.

One or two-step carbodiimide activations of −COOH particles using EDAC and/or S-NHS are known from the literature (*14*). In order to ensure the highest levels of PK reactor activity, both methods were tested (at pH 6.0). An immobilization protocol using only EDAC leads to a 24% lower enzyme activity (data not shown). It was proven that the combined use of EDAC and S-NHS activation is required for high PK reactor performance with 500A5 microparticles (Ademtech).

It was previously shown that the ratio of the protein and EDAC/S-NHS concentrations plays a role in the grafting efficiency and also in unwanted particle agglomeration (*17*). Increasing the concentration of EDAC/S-NHS produces a significant change in the charge of the beads, which then causes their repulsion or agglomeration. For these reasons, we looked for a compromise level of EDAC/S-NHS with a proven optimal ratio. A decrease in EDAC/S-NHS concentrations by half in the subsequent experiments using PK reactor prepared with 500A5 microparticles led to 30% lower levels of catalytic activity. The stability of the enzyme reactor was also dramatically lower.

In the next experiments, temperature and reaction time were altered; results of PK activity after immobilization are shown in Table 4.

The effect of the amount of PK per mg of particles added to the reaction volume was studied. Increasing quantities of PK added to 1 mg of 500A5 microparticles were incubated under fixed binding conditions: 6 h at room temperature. The enzyme activity was determined with the substrate succinyl-Ala_3-*p*-nitroanilide in 50 mM Tris/HCl at pH 7.8 with 5 mM $CaCl_2$. The highest activity was obtained using 3 mg of PK per mg of the carrier. Additional increases in initial PK concentration led to a decrease in final proteolytic activity (Figure 1).

Since calcium ions are involved in enzyme activity and are needed for enzyme stability (*11*), we studied the effect of Ca^{2+} on the covalent bond (Figure 2).

Zeta Potential Measurement. Zeta potential is a measure of the magnitude of the repulsion or attraction between particles. Its measurement provides detailed insight into the dispersion mechanism and is the key to electrostatic dispersion control. The most important factors that affects zeta potential are the pH and molar strength of the buffering solution used. Particles

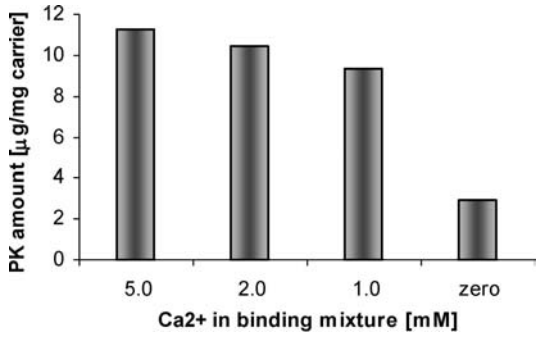

Figure 2. Effect of Ca^{2+} in binding solution on binding efficiency of PK reactor (500A5 microparticles).

Table 5. Zeta Potential Measurement for 500A5 particles (2%) in 10 mM and 100 mM Phosphate Buffer at pH 7.3 and Addition of 0.3% PF127 Surfactant

buffering	10 mM phosphate buffer pH 7.3	10 mM phosphate buffer pH 7.3 with 0.3% PF127	100 mM phosphate buffer pH 7.3
zeta potential value (mV)	−37.12	−23.1	−16.68

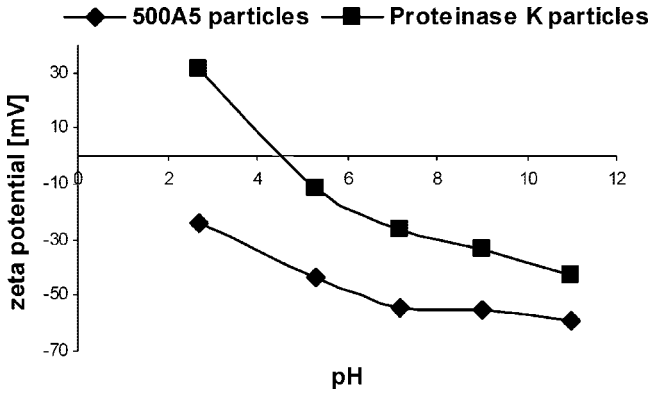

Figure 3. Zeta potential curves of magnetic 500A5 particles and of magnetic PK reactor (prepared with 500A5 particles) in 10 mM phosphate buffer at pH 7.3.

are considered to have a lower stability in the range −30 to 30 mV (*18*). By measuring the zeta potential (Table 5, Figure 3) of the 500A5 microparticles and preparing the PK reactor using the same particles, the optimal conditions were found to be as follows: 10 mM phosphate buffer at pH 7.3 with the addition of 0.3% PF127 surfactant. Under these conditions, the particles showed only a slight agglomeration, which affected neither the binding nor digestion processes.

The optimal conditions for the PK assay and for preparation of the PK reactor with 500A5 microparticles were used for other types of magnetic carriers and commercially available carriers in order to find the best working system.

In general, 1 mg of magnetic particles was activated by the above EDAC and S-NHS cross-linking two-step method at pH 7.3 and the immobilization procedure occurred at 4 °C overnight. Due to the different sizes and material compositions of the chosen microparticles, the obtained enzyme activities varied significantly (Table 6). The achieved activities of the PK reactors were also compared to a commercially available nonmagnetic PK reactor, consisting of PK bonded to Eupergit C macroporous acrylic beads (Sigma, USA). In comparison, the activity of the commercial nonmagnetic PK reactor only reached 6% of that of 500A5 particles (Ademtech).

Characteristics of PK Reactor. *Stability of PK Reactor.* Its storage and operational stabilities were analyzed. The activity remained the same as the initiatial value after 10 weeks. The catalytic activity per mg of carrier temporarily increased at the beginning of the observation period. One possible explanation is the conformation of the enzyme molecule was restored after the immobilization procedure (*3, 19*).

Operational Stability. By repeated use of the same aliquot at 25 °C with 1.05 mM substrate, up to 50% of the activity of the immobilized PK was maintained after 8 batches. In comparison, the reusability of the nonmagnetic commercially available PK reactor maintained 68% of its original activity after 8 repeats (data not shown).

Kinetic Constants. Enzyme reactor was characterized by measurement of Michaelis constant (K_M) which reflects the affinity between enzyme and substrate. The method used here was based on the frontal analysis of enzymatic reaction products, which was performed by the monitoring of the absorption at 405 nm of *p*-nitroaniline from the hydrolysis of succinyl-Ala-Ala-Ala-p-nitroanilide (*20*).

Our experimentally obtained data were processed in terms of Michaelis–Menten kinetics by the Lineweaver–Burk plots of v versus [S] as shown in Figure 4, where [S] is concentration and v the velocity of enzymatic reaction (*21*). Initial conditions of the reaction (ratio E:S, reaction volume) were chosen in agreement with Michelis−Menten kinetics. The apparent K_M of the PK reactor observed was 1.29 mM, and that of native PK 4.23 mM. The obtained K_M is influenced by the chemical composition of the carrier and by the microenvironment of the enzyme reactor from the bonded enzyme molecules, and is called apparent K_M (Figure 4). Maximum velocity V_i of the reaction catalyzed by the PK reactor was 0.36, which is 57% in comparison to native PK catalysis (value 0.63).

Application of Magnetic PK Reactor. *Digestion of Model Protein: Human Growth Hormone.* The efficiency of digestion was confirmed using a model protein human growth hormone (HGH) with a MW of 22 kDa by peptide mass fingerprinting. Proteolytic digestion was carried out in batch mode at room temperature for 15, 60, and 180 min and 24 h in 50 mM ammonium acetate (pH 7.8). The HGH was subsequently analyzed by Tricine/SDS PAGE (Figure 5) and Voyager-DE STR MALDI-TOF (Figure 6). The sequence coverage for the 15 min digestion of HGH, calculated from the list of obtained peptides, was 75%. It was proven that the proteolytic activity and specificity of PK were maintained after its immobilization to magnetic particles.

SDS PAGE and Western Blot of Digested PrP^c Peptides. Having shown that the PK reactor reproducibly digests a model protein, we thought to test its efficiency on a more complex medium such as a cell extract. We next digested proteins extracted from the immortalized Mov cell line overexpressing prion protein with the appropriate amount of the immobilized PK reactor (Figure 7). Our results showed a visible decay of the proteolysis-sensitive cellular prion protein with digestion time.

DISCUSSION

PK from *Tritirachium album* Limber (3.4.21.64) is reported as one of the most active serine proteases with a strong proteolytic activity on denatured proteins. The most interesting property of the enzyme is its capacity to degrade native proteins (*5*), which is commonly employed for differentiating between the physiological and pathological forms of prion protein (*22*).

This study reports the immobilization of PK on newly developed magnetic latex microparticles (Ademtech, France) and other chemically and structurally similar types of magnetic carriers. 500A5 microparticles were developed to have a reduced tendency to agglomerate and low levels of nonspecific sorption. Various conditions for coupling were utilized with the aim of

Table 6. Enzyme Activities of PK Magnetic Reactors Prepared with Carriers Differing in Polymer Coating and Size

label of carrier	material used (where known)	manufacturer	mean diameter (nm)	PK amount [μg/mg carrier] average from 3 immobilizations
500A5	magnetic, styrenic copolymer with hydrophilic monomer	Ademtech, Pessach, FR	626	12.09
145Tta	magnetic, styrenic copolymer with hydrophilic monomer	Ademtech, Pessach, FR	980	3.56
A120	magnetic, alginate	Academy of Sciences, CZ	2500	8.48
00–39	magnetic, latex	Estapor (Merck) FR	160	8.35
PK-reactor	acrylic, macro-porous	Sigma, USA	not shown	0.54

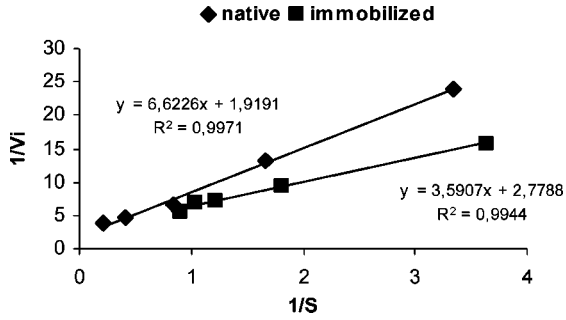

Figure 4. Lineweaver–Burk plots for native and immobilized PK using static method and succinyl-Ala-Ala-Ala-p-nitroanilide as substrate.

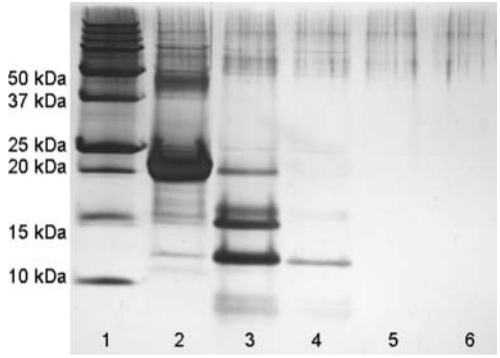

Figure 5. Tricine-SDS-PAGE analysis of digested HGH (PK reactor prepared with magnetic latex microparticles, Estapor). Positions: 1, molecular marker; 2, HGH; 3, HGH digested for 15 min; 4, HGH digested for 60 min; 5, HGH digested for 180 min; 6, HGH digested for 24 h. Conditions of electrophoresis: constant potential 30 V, current 0.03 A per gel for 30 min, then constant potential 100 V, current 0.03 A per gel for 60 min at 4 °C.

preparing a magnetic enzyme reactor with sufficient enzyme activity and stability.

From the surface chemistry, it is known that a pH slightly below the isoelectric point of the protein positively influences the grafting efficiency. The experimentally determined isoelectric point of PK was at the value 8.4 (data not shown), which is in general agreement with the value 8.9 in (*5*) and the theoretical value 8.25 from (*23*). At pH 7.3, the positively charged enzyme and negatively charged magnetic particles lead first to adsorption of the enzyme to the particle surface based on ionic forces and second to covalent linkage after carbodiimide activation in the immobilization procedure. By selecting a specific binding buffer, the subsequent adsorption of the enzyme molecules onto the particle surface potentiates a local amount of molecules in the immediate vicinity of the functional groups of the carrier, which enhances binding efficiency.

In the coupling reaction, N-substituted carbodiimide EDAC reacted with a carboxylic group of the 500A5 microparticles to form a highly reactive and short-lived acylisourea derivative. The activated species then reacted with the primary amines of the ligands to form a stable peptide bond. The binding efficiency was substantially increased by the presence of S-NHS as described in the paper by Staros (*24*). The two-step protocol at pH 7.3 in 10 mM phosphate buffer exhibited the highest binding yields and was chosen as optimal for further immobilizations (*25, 26*).

Temperature and reaction time have a considerable influence on the resulting enzyme reactor activity, especially with enzymes that have proteolytic and autolytic activities. Experiments with various immobilization procedures showed that using a low temperature of 4 °C with prolonged incubation overnight ensured a high binding efficiency of the enzyme reactor. The most possible explanation for the activity decrease after prolonged incubation overnight was autolytic activity (Table 4). If the immobilization was truncated from 6 to 2 h at room temperature, the resulting PK activity was very low and not sufficient for further applications.

To find a compromise between immobilization yield and catalytic activity, we optimized the amount of protein to 3 mg per mg of activated beads (500A5), corresponding to a reactor with high catalytic activity.

The X-ray structure study showed that two bound Ca^{2+} ions were required for the catalytic activity of PK (*11*). In the absence of Ca^{2+} ions, the catalytic activity of PK dropped to 20%, while the presence of Ca^{2+} slows down PK autolysis and also enhances thermal stability. In our experiments, increasing Ca^{2+} concentrations from 1 mM to 2.5 mM and 5 mM (the recommended concentration) only slightly increased the activity of the PK reactor (Figure 2). A Ca^{2+} increase to 5 mM negatively influenced the colloidal stability of the 500A5 microparticles. A total concentration of Ca^{2+} of 1 mM during the immobilization was considered to be sufficient.

Under all the studied and optimized conditions, this newly developed magnetic PK reactor prepared with 500A5 microparticles exhibited a more than sufficient storage and operational stability. These parameters are usually important for using an enzyme in routine laboratory work.

The "apparent" K_M of immobilized PK compared to the soluble enzyme exhibited a threeford higher affinity to the substrate. Such a decrease in the K_M values of immobilized enzymes has been recognized previously (*20, 27*), and has been ascribed to the presence of areas of increased substrate concentration around the particle due to electrostatic attraction or hydrophobic adsorption of the substrate to the solid. From a reaction rate point of view, the maximal velocity of substrate change was calculated as a change in optical density (formation of product) units per time unit. The lower rate of enzyme reaction with immobilized PK, shown by its maximum velocity V_i, can possibly be explained as due to limited diffusion of the substrate molecules to the surface of the particles and to the active sites of the immobilized enzyme.

The 500A5 microparticles exhibited slight bead agglomeration during manipulations, which may complicate reactor application and efficiency. The zeta potential measurement confirmed the necessity of adding the surfactant. The surfactant PF127 at concentration of 0.3% was considered optimal.

The magnetic PK reactor was applied in the proteolytic cleavage of high-molecular-weight substrates, the model substrate human growth hormone, and the cellular prion protein. Both HGH and PrP^c were digested by limited proteolysis, and

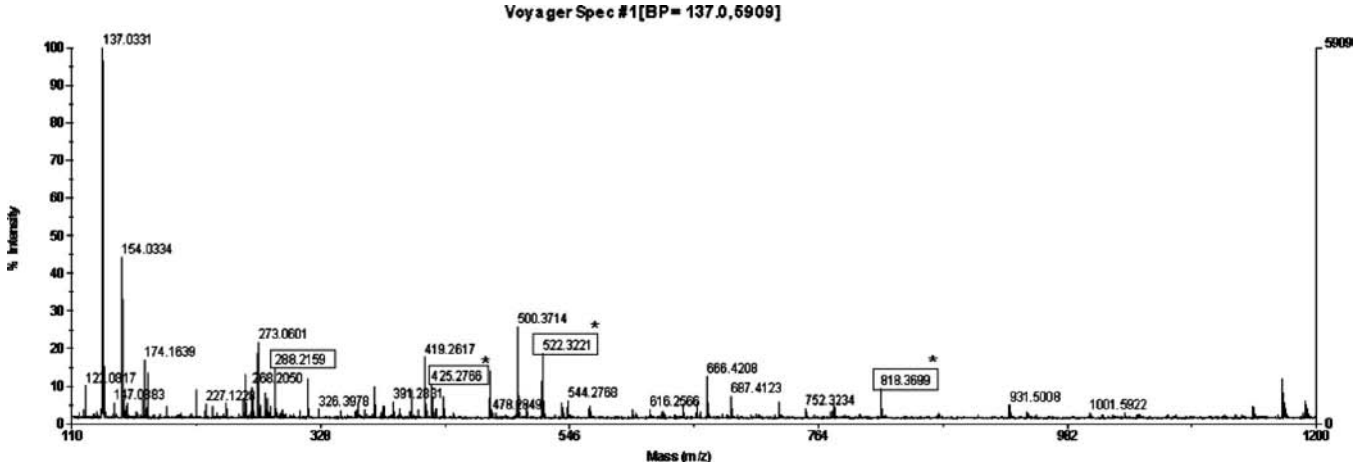

Figure 6. MALDI mass spectra of 15 min digested HGH by PK reactor (prepared with magnetic latex microparticles, Estapor). The framed masses correspond to identified peptides by the Expasy software (PeptideMass) with 0 or 1 (*) miscleavages. The nonframed masses arise from further miscleavages and contamination. Conditions of MS analysis: 1 μL of every digested sample was dried on MALDI-target before covering with 1 μL of DHB in ACN (50%) and TFA (0.3%) as the matrix ("dried droplet" technique). Calibration was performed with a standard peptide mixture with an *m*/*z* range of 800 to 3500 Da (LaserBio Laboratories, FR).

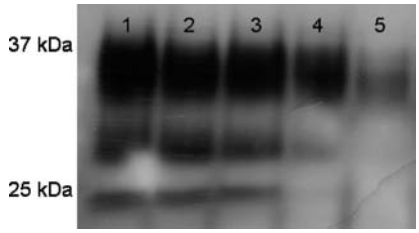

Figure 7. Western blotting of limited proteolysis of digested cellular prion protein (Mov cell line overexpressing ovine PrP^c). Samples were digested with PK reactor (0.7 μg, prepared with 500A5 microparticles, Ademtech) in 100 μL volume of cell lysate, precipitated with methanol, separated on 10% Tris/HCl gel, and blotted to nitrocellulose membrane with specific ICSM18 or SAF 84.3 mAb. Positions: 1, PrP^c digested for 2 min; 2, PrP^c digested for 5 min; 3, PrP^c digested for 10 min; 4, PrP^c digested for 30 min; and 5, PrP^c digested for 60 min.

mass spectrophotograms, electrophoreograms, and blots confirmed that the proteolysis system was working well. Through these experiments, we confirmed the PK magnetic reactor to be a useful tool for PrP digestion, with the use of a magnetic carrier being published for the first time.

CONCLUSION

This study describes (1) the methods used to optimize the PK grafting procedure, (2) the characterization and validation of the newly prepared magnetic enzyme reactor, and (3) the benefits of using immobilized PK in bioanalytical applications, and examples of those applications. We optimized a method for covalently bonding PK to a magnetic carrier with polymer coating and carboxylic derivatization. The carbodiimide chemistry used here to bind the enzyme to the new carrier gave the amide bonds excellent stability. The newly developed carrier prepared by the manufacturer Ademtech served as a good example of magnetic particles with a large range of possible uses. Furthermore, these optimized conditions, when applied to other magnetic nano and microparticles, showed high applicability and reusability. The results of this study also demonstrated that the storage conditions of the PK enzyme reactor are highly compatible with a laboratory routine. As examples of the simple handling of the magnetic PK reactor, the human growth hormone and mouse overexpressed PrP^c were digested and verified by the analytical methods MALDI-TOF-MS, PAGE, and Western Blot. This magnetic PK reactor can possibly be used for the digestion other resistant proteins with all features of covalently bonded enzymes.

ACKNOWLEDGMENT

We gratefully acknowledge the Ademtech Company, France, and Academy of Sciences, Czech Republic, for their donations of magnetic particle batches. This work was supported in part by Czech funding grant MSMT0021627502, the EU project "Neurotas" (contract no. 037953) and Czech Science Foundation 203/05/0241.

LITERATURE CITED

(1) Turkova, J. (1999) Oriented immobilization of biologically active proteins as a tool for revealing protein interactions and function. *J. Chromatogr., B: 722*, 11–31.
(2) Spanova, A., Rittich, B., Horak, D., Lenfeld, J., Prodelalova, J., Suvakova, J., and Strumcova, S. (2003) Immunomagnetic separation and detection of Salmonella cells using newly designed carriers. *J. Chromatogr., A: 1009* (1–2), 215–21.
(3) Bilkova, Z., Slovakova, M., Minc, N., Fuetterer, C., Cecal, R., Horak, D., Benes, M. J., Le Poitier, I., Krenkova, J., Przybylski, M., and Viovy, J. L. (2006) Functionalized magnetic micro- and nanoparticles: optimization and application to μ-chip trypsin digestion. *Electrophoresis 27*, 1811–1824.
(4) Slovakova, M., Minc, N., Bilkova, Z., Smadja, C., Faigle, W., Fütterer, C., Taverna, M., and Viovy, J. L. (2005) Use of self assembled magnetic beads for on-chip protein digestion. *Lab on Chip 5*, 935–942.
(5) Ebeling, W., Hennrich, N., Klockow, M., Metz, H., Orth, H. D., and Lang, H. (1974) PK from Tritirachium album Limber. *Eur. J. Biochem. 47* (1), 91–7.
(6) Pandhare, J., Dash, C., Rao, M., and Deshpande, V. (2003) Slow tight binding inhibition of PK by a proteinaceous inhibitor: conformational alterations responsible for conferring irreversibility to the enzyme-inhibitor complex. *J. Biol. Chem. 278* (49), 48735–48744.
(7) Betzel, C., Pal, G., and Saenger, W. (1988) Three-dimensional structure of PK at 0.15-nm resolution. *Eur. J. Biochem. 178*, 155–171.
(8) Horak, D., Rittich, B., Spanova, A., and Benes, M. J. (2005) Magnetic microparticulate carriers with immobilized selective ligands in DNA diagnostics. *Polymer 46*, 1245–1255.
(9) Daly, P., Corcoran, A., Mahon, B. P., and Doyle, S. (2002) High-sensitivity PCR detection of parvovirus B19 in plasma. *J. Clin. Mikrobiol. 40* (6), 1958–1962.

(10) Russo, G. L., Nisco, E. D., Fiore, G., Donato, P. D., d'Ischia, M., and Palub, A. (2003) Toxicity of melanin-free ink of Sepia officinalis to transformed cell lines: identification of the active factor as tyrosinase. *Biochem. Biophys. Res. Commun. 308,* 293–299.
(11) Bajorath, J., Hinrichs, W., and Saenger, W. (1988) The enzymatic activity of PK is controlled by calcium. *Eur. J. Biochem. 176* (2), 441–7.
(12) Morihara, K., and Tsuzuki, H. (1975) Specificity of PK from Tritirachium album Limber for synthetic peptides. *Agric. Biol. Chem. 39,* 1489–1492.
(13) Staros, J. V., Wright, R. W., and Swingle, D. M. (1986) Enhancement by N-hydroxysulfosuccinimide of water-soluble carbodiimide-mediated coupling reactions. *Anal. Biochem. 156,* 220–2.
(14) Hermanson, G. T. (1996) *Bioconjugate Techniques,* pp141, 156, 157, 159, 169–173, 470, 570–572, Academic Press, London.
(15) Peters, K., Pauli, D., Hache, H., Boteva, R. N., Genov, N. C., and Fittkau, S. (1989) Subtilisin DY–kinetics characterization and comparison with related proteinases. *Curr. Microbiol. 18,* 171–177.
(16) Cronier, S., Laude, H., and Peyrin, J. M. (2004) Prions can infect primary cultured neurons and astrocytes and promote neuronal cell death. *PNAS 101* (33), 12271–12276.
(17) Bilkova, Z., Castagne, A., Zanusso, G., Faronazzo, A., Monaco, S., Damoc, E., Przybylski, M., Benes, M., Lenfeld, J., Viovy, J. L., and Righetti, P. G. (2005) Immunoaffinity reactors for prion protein qualitative analysis. *Proteomics 5,* 639–647.
(18) Malvern instruments manual (2004).
(19) Bilkova, Z., Slovakova, M., Lycka, A., Horak, D., Lenfeld, J., Turkova, J., and Churacek, J. (2002) Oriented immobilisation of galactose oxidase to bead and magnetic bead cellulose and poly(HEMA-co-EDMA) and magnetic poly(HEMA-co-EDMA) microspheres. *J. Chromatogr., B: 770* (1–2), 25–34.
(20) Jiang, H., Zou, H., Wang, H., Ni, J., Zhang, Q., and Zhang, Y. (2000) On-line characterization of the activity and reaction kinetics of immobilized enzyme by high-performance frontal analysis. *J. Chromatogr., A: 903,* 77–84.
(21) Logan, S. R. (1998) *Physical Chemistry for the Biomedical Sciences,* Vol *77,* p 86, CRC Press, London.
(22) Prusiner, S. B. (1998) Prions. *Proc. Natl. Acad. Sci. U.S.A. 95,* 13363–13383.
(23) http://www.expasy.org/tools/pi_tool.html (accessed 11/20/2007.
(24) Staros, V. (1982) *N*-Hydroxysulfosuccinimide active esters bis(N-hydroxysulfosuccinimide) esters of two dicarboxylic acids are hydrophilic, membrane-impermeant, protein cross-linkers. *Biochemistry 21,* 3950–3955.
(25) Hermanson, G. T., Krishna, M. A., Smith, P. K. (1992) *Immobilized affinity ligand techniques,* pp 81–85, Academic Press, London.
(26) Cuatrecasas, P., Parikh, I. (1972) Adsorbents for affinity chromatography. Use of N-hydroxysuccinimide esters of agarose. *Biochemistry 11,* 2291–2298..
(27) Chibata, I., Tosa, T., Sato, T., and Mori, T. (1978) *Immobilized enzymes,* p 126, John Wiley & Sons, London.

BC7004413

TECHNICAL NOTES

Long Functionalized Poly(ethylene glycol)s of Defined Molecular Weight: Synthesis and Application in Solid-Phase Synthesis of Conjugates

Dan Niculescu-Duvaz, Jayne Getaz, and Caroline J. Springer*

Cancer Research UK Centre for Cancer Therapeutics, The Institute of Cancer Research, 15 Cotswold Road, Sutton, Surrey SM2 5NG, U.K. Received August 3, 2006; Revised Manuscript Received January 28, 2008

A concise synthesis of long-chain poly(ethylene glycol) (PEG) of defined molecular weight up to 29 ethyleneoxy units is described. These PEG diols were converted in a two-step synthesis into Fmoc-protected PEG amino acids, suitable as long linkers and compatible with solid-phase peptide synthesis. Long PEG chains (MW > 1000) can be readily synthesized with this method, which has the advantage of defined single molecular weight products over the comparable commercial polymers. The application of these PEG linkers to the synthesis of peptide−PEG−folate conjugates on a solid support was investigated. A method for the solid support synthesis of the targeting component of the conjugate, folic acid−cysteine, was developed, resulting in improved yields with respect to literature methods. The assembly of the peptide, PEG linker, and targeting group on solid support resulted in the synthesis of a conjugate of defined molecular weight and structure.

INTRODUCTION

Poly(ethylene glycol) is a biologically inert polymer that has been used extensively to alter the physiological properties of drugs, therapeutic proteins, liposomes, and polyplexes. Conjugation with PEG has been reported to confer a number of beneficial properties including increased solubility, reduced interaction with serum and complement proteins and a significantly increased half-life *in vivo* (*1*).

PEGylation can improve the performance and dosing frequency of peptides, proteins, antibodies, oligonucleotides and many small molecules by optimizing pharmacokinetics (PK), increasing bioavailability and decreasing immunogenicity. PEGylated therapeutic agents with clinical approval include liposomes, proteins, and aptamers (*2*, *3*).

In addition, PEG chains can act as spacers. In bioconjugation, the separation between components is often necessary to preserve the affinity and activity of each component of the conjugate. For example, polyplexes containing targeting ligands for specific tissues have been shown to retain better ligand–receptor binding affinity when separated by a PEG spacer (*4–6*). Labeling of peptides with fluorophores and biotin often includes a PEG chain to improve the activity/affinity of the reporter group (*7*).

The biological effects of PEG modification have been related to the molecular weight of the polyether used. In general, longer PEG chains are more efficient in improving the PK of conjugates and preserving the affinity of the targeting ligand for its receptor (*8*, *9*). PEG of higher molecular weight is obtained by relatively uncontrolled polymerization techniques, leading to polydispersity in the molecular weight of the product. Advances in anionic polymerization techniques have led to the synthesis of relatively well-defined monobenzylated PEG (*10*) and heterofunctional PEG (*11*) with polydispersity indexes equal or below 1.09. However, the products of polymerization show a range in molecular weights, even at low polydispersity indexes. An example of the MALDI mass spectrometry analysis of commercially available PEG is shown in Figure 1.

This heterogeneity in PEG molecular weight has an effect on the biological activity of the conjugates and compromises their characterization and quality control, which is important for clinical applications. Batch-to-batch variability could obscure the results and complicate investigations into the structure–activity relationship of these heterogeneous conjugates. The availability of intermediate and high molecular weight PEG of defined molecular weight (MW) is therefore highly desirable.

One method for obtaining longer PEG chains of defined MW is to synthesize them starting from commercially available shorter chains of defined length. A few reports have described synthetic routes to PEG of intermediate length (up to 24 units). Here, we describe a simple route to PEG up to 29 units, with potential to be extended to higher MW.

Another requirement for bioconjugation is that PEG chains need to be modified with functional groups that allow chemical coupling to biomolecules. The most common coupling strategies involve the formation of amide bonds (usually via activated esters of carboxylic acids) and thiol bonds (thioether or disulfide). One convenient functionalization of PEG is with an amino acid, which can be used in peptide synthesis on solid support, or it could be deprotected and coupled further to convert to a heterobifunctional linker. Here, we report a simple strategy for bifunctionalization of PEG diol to Fmoc-protected PEG amino acid.

The utility of these linkers is exemplified by the synthesis of a folate−PEG−amphipathic peptide conjugate on solid support. Amphipathic peptides have been used in nonviral gene therapy approaches with some success *in vitro* (*12*, *13*). These peptides are able to facilitate endosomal escape by destabilizing the endosomal membrane directly as a result of a change in

* Tel: +44 2087224214, Fax: +44 2087224046, E-mail: Caroline.Springer@icr.ac.uk.

10.1021/bc060242+ CCC: $40.75 © 2008 American Chemical Society
Published on Web 04/02/2008

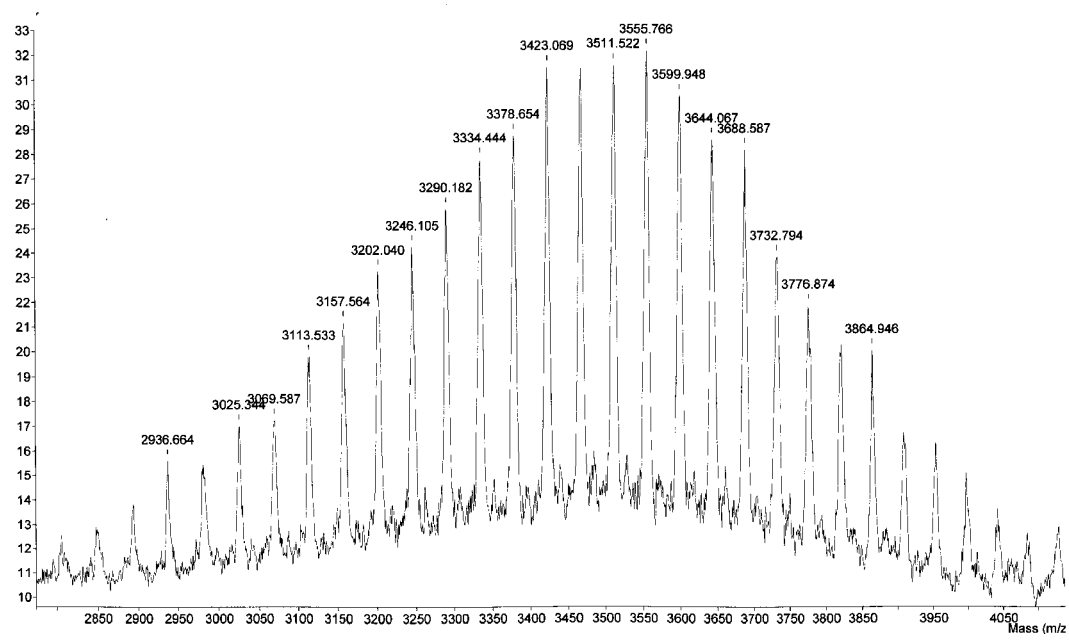

Figure 1. MALDI analysis of commercially available NHS-PEG3400-MAL. Polydispersity index 1.01.

conformation at the lower pH conditions within the endosomal compartment. Incorporation of such a peptide in a modular conjugate containing a PEG and a targeting ligand could lead to an effective nonviral gene vector for systemic application.

Folic acid is the small molecule ligand for the α-folate receptor, and is overexpressed in pituitary adenomas (*14*) and ovarian (*15*) cancers. Folic acid has been conjugated to drugs (*16*), macromolecules (*17*), liposomes (*5*) and polyplexes (*18*), in order to achieve specific targeting and enhanced uptake of conjugates in α-folate-expressing tumor cells. We have attached the folic acid to the amphiphatic peptide−PEG on solid support, and demonstrated the synthesis of a complex conjugate of defined structure on solid support. This conjugate is the prototype for potential modular nonviral vectors for gene delivery.

EXPERIMENTAL PROCEDURES

All starting materials, reagents, and solvents for reactions were reagent grade and used as purchased. Chromatography solvents were HPLC grade and were used without further purification. Reactions were monitored by thin layer chromatography (TLC) analysis using Merck silica gel 60 F-254 thin layer plates. LCMS analyses were performed on a Micromass LCT/Water's Alliance 2795 HPLC system with a Discovery 5 μm, C18, 50 mm × 4.6 mm i.d. column from Supelco at a temperature of 22 °C using the following solvent systems: solvent A, methanol; solvent B, 0.1% formic acid in water at a flow rate of 1 mL/min. Gradient starting with 10% A/90% B from 0 to 0.5 min, then 10% A/90% B to 90% A/10% B from 0.5 to 6.5 min and continuing at 90% A/10% B up to 10 min. From 10 to 10.5 min, the gradient reverted back to 10% A/90% B where the concentrations remained until 12 min. UV detection was at 254 nm and ionization was positive or negative ion electrospray. Molecular weight scan range is 50–1000. Samples were supplied as 1 mg/mL in DMSO or methanol with 3 μL injected on a partial loop fill. Preparative HPLC was carried out on an Agilent 1100 series system (Agilent Technologies, Wokingham, UK) using a Gemini C18 column (250 × 30.0 mm, 10 μm). Gradient (15 mL/min): 10% MeCN to 95% MeCN over 25 min, 5 min at 95% MeCN, 95% MeCN to 10% MeCN over 10 min. NMR spectra were recorded in DMSO-d_6 on a Bruker DPX 250 instrument operating at 250.13 MHz or on a Bruker Advance instrument 500 operating at 500.26 MHz. The signal of the deuterated solvent was used as internal reference; the chemical shifts are expressed in ppm (δ). MALDI analysis was carried out using either a Lasermat (Finnigan Mat, Hemel Hampstead, UK) or Dynamo system (Thermo Bioanalysis Ltd., Hemel Hampstead, UK). The samples were analyzed using a 0.4 μL matrix (5.1 mg α-cyano-4-hydroxy cinnamic acid in 100 μL TFA, 500 μL H_2O, and 500 μL MeCN).

1. Synthesis of Diols. *Preparation of BnO-PEG$_6$-OH (2). a. Using NaH.* A solution of hexa(ethylene glycol) (4.5 mL, 17.73 mmol) and NaH (60% in mineral oil) (0.85 g, 21.28 mmol) in dry THF (60 mL) was stirred under argon for 90 min. Benzyl bromide (2.1 mL, 17.73 mmol) was added dropwise, and the reaction was stirred at room temperature for 20 h. The reaction was quenched with H_2O, evaporated, extracted with EtOAc, and dried over $MgSO_4$. The residue was purified by column chromatography on silica (eluent EtOAc/hexane 5:1, then EtOAc) to afford the required product (2.37 g, 35%).

b. Using Ag$_2$O. Ag_2O (6.16 g, 26.60 mmol) and KI (1.18 g, 7.10 mmol) were suspended in dry DCM (150 mL) under argon. Hexa(ethylene glycol) (4.5 mL, 17.73 mmol) was added dropwise, followed by benzyl bromide (2.3 mL, 19.50 mmol) after 5 min. The reaction was stirred at room temperature for 2 h, then filtered through Celite. The filtrate was evaporated, extracted with AcOEt, and dried over $MgSO_4$. The residue was purified by column chromatography on silica (eluent EtOAc/acetone 4:1) to afford the required product (3.49 g, 53%). LC-MS (ES): 372 $[M + H]^+$, 395 $[M + Na]^+$. HPLC retention time (discovery column of LCMS): 5.59 min; the unsubstituted hexa(ethylene glycol) and disubstituted BnO-PEG$_6$-OBn have retention times of 3.10 and 7.05 min, and are present only in traces in the purified BnO-PEG$_6$-OH (**2**). ^{1}H NMR ($CDCl_3$): 7.35–7.34 (m, 5H, H_{arom}), 4.58 (s, 2H, PhCH_2), 3.73–3.60 (m, 25H, C$H_{2,PEG,}$ O*H*). ^{13}C NMR ($CDCl_3$): 138.32 (C_{arom}), 128.33 (CH_{arom}), 127.72 (CH_{arom}), 127.55 (CH_{arom}), 73.23 (PhCH_2), 72.58 (OCH_2CH_2OH), 70.64 ($CH_{2,PEG}$), 70.62 ($CH_{2,PEG}$), 70.60 ($CH_{2,PEG}$), 70.57 ($CH_{2,PEG}$), 70.54 ($CH_{2,PEG}$), 70.33 ($CH_{2,PEG}$), 69.47 ($CH_{2,PEG}$), 61.73 (CH_2OH).

Preparation of BnO-PEG$_{17}$-OBn (4). In a solution of BnO-PEG$_6$-OH (**2**) (2.97 g, 7.97 mmol) in dry THF (50 mL) under

argon, NaH (60% in mineral oil, 0.43 g, 10.63 mmol) was added and stirred at room temperature for 2 h. Penta(ethylene glycol) di(*p*-toluenesulfonate) (**3**) (0.9 mL, 1.99 mmol) was added and the reaction was refluxed for 20 h. A second portion of NaH (0.43 g, 10.63 mmol) was added and the reaction mixture was stirred for 1 h. A second portion of penta(ethylene glycol) di(*p*-toluenesulfonate) (0.9 mL, 1.99 mmol) was then added and the reaction was refluxed for a further 20 h. The reaction was quenched with H_2O, evaporated, extracted with EtOAc, and dried ($MgSO_4$). The residue was purified by precipitation from DCM with cold diethyl ether, to afford the required product (3.16 g, 84%). LC-MS (ES): 948 $[M + H]^+$, 474 $[M + 2H]^{2+}$. MALDI +ve ion mode: 968 $[M + Na]^+$, 984 $[M + K]^+$. ^{1}H NMR ($CDCl_3$): 7.35–7.34 (m, 10H, H_{arom}), 4.57 (s, 4H, PhCH_2), 3.66–3.64 (m, 68 H, C$H_{2,PEG}$). ^{13}C NMR ($CDCl_3$) 125 MHz: δ 128.30 (CH_{arom}), 127.67 (CH_{arom}), 127.52 (CH_{arom}), 73.17 (PhCH_2), 70.58 (C$H_{2,PEG}$), 70.54 (C$H_{2,PEG}$), 70.51 (C$H_{2,PEG}$).

*Preparation of PEG$_{17}$ Diol (**5**).* A solution of BnO-PEG$_{17}$-OBn (**4**) (3.16 g, 3.34 mmol) containing 10% Pd/C (0.07 g) in EtOH (60 mL) was stirred under hydrogen for 4 days. The reaction was filtered through Celite and the filtrate evaporated. The residue was purified by precipitation from DCM with cold diethyl ether, to afford the required product (2.48 g, 97%). LC-MS (ES): 767 $[M + H]^+$, 334 $[M + 2H]^{2+}$. ^{1}H NMR ($CDCl_3$) 500 MHz: δ 3.66–3.61 (m, 70 H, C$H_{2,PEG}$, O*H*). ^{13}C NMR ($CDCl_3$) 125 MHz: δ 72.46 (HOCH$_2$*C*H$_2$O), 70.43 (*C*H$_{2,PEG}$), 70.40 (*C*H$_{2,PEG}$), 70.19 (*C*H$_{2,PEG}$), 61.38 (HO*C*H$_2$CH$_2$O). Elemental analysis: ($C_{34}H_{70}O_{18}\cdot 0.5H_2O$): required C 52.63, H 9.22; found C 52.81, H 9.20.

*Preparation of BnO-PEG$_6$-OTos (**6**).* In a solution of BnO-PEG$_6$-OH (**2**) (2.00 g, 5.37 mmol) in dry DCM (100 mL), under argon, *p*-toluenesulfonyl chloride (1.54 g, 8.05 mmol), KI (0.36 g, 2.15 mmol), and Ag_2O (1.87 g, 8.05 mmol) were added. The reaction was stirred at reflux for 20 h under argon and protected from light. The mixture was filtered through Celite and the filtrate evaporated. The residue was purified by column chromatography on silica (eluent EtOAc) to afford the required product (2.60 g, 92%). LC-MS (ES): 526 $[M+H]^+$. ^{1}H NMR ($CDCl_3$): 7.81 (d, J = 8.50, 2H, CH_{arom}), 7.35–7.28 (m, 7H, CH_{arom}), 4.57 (s, 2H, PhCH_2), 3.70–3.58 (m, 24H, C$H_{2,PEG}$), 2.45 (s, 3H, CH_3). ^{13}C NMR ($CDCl_3$): 144.74 (C$_{arom}$), 138.33 (C$_{arom}$), 133.11 (C$_{arom}$), 129.80 (CH_{arom}), 128.32 (CH_{arom}), 127.94 (CH_{arom}), 127.69 (CH_{arom}), 127.54 (CH_{arom}), 73.20 (PhCH_2), 70.72 (C$H_{2,PEG}$), 70.64 (C$H_{2,PEG}$), 70.59 (C$H_{2,PEG}$), 70.55 (C$H_{2,PEG}$), 70.51 (CH_{2PEG}), 69.47 (OCH_2CH$_2$OTos), 68.65 (CH_2-OTos), 21.59 (CH_3).

*Preparation of BnO-PEG$_{29}$-OBn (**7**).* To a solution of PEG$_{17}$ diol (**5**) (0.50 g, 0.65 mmol) in dry THF (50 mL) under argon, NaH (0.52 g, 13.04 mmol) was added. The reaction was stirred under argon for 2 h at room temperature before a solution of BnO-PEG$_6$-OTos (**5**) (0.69 g, 1.3 mmol) in dry THF (5 mL) was added. The reaction was refluxed for 20 h. The reaction was quenched with H_2O, evaporated, extracted with EtOAc, and dried ($MgSO_4$). The residue was purified by precipitation from DCM with cold diethyl ether, to afford the required product (0.80 g, 83%). LC-MS (ES): 1476 $[M + H]^+$, 738 $[M + 2H]^{2+}$, 493 $[M + 3H]^{3+}$, MALDI +ve ion mode: 1495 $[M + Na]^+$. ^{1}H NMR ($CDCl_3$): δ 7.35–7.34 (m, 10H, H_{arom}), 4.57 (s, 4H, PhCH_2), 3.66–3.64 (m, 116 H, C$H_{2,PEG}$). ^{13}C NMR ($CDCl_3$): δ 128.28 (CH_{arom}), 127.64 (CH_{arom}), 127.50 (CH_{arom}), 73.16 (PhCH_2), 70.61 (C$H_{2,PEG}$), 70.56 (C$H_{2,PEG}$), 70.54 (C$H_{2,PEG}$).

*Preparation of PEG$_{29}$ Diol (**8**).* A solution of BnO-PEG$_{29}$-OBn (**7**) (0.60 g, 0.41 mmol) containing 10% Pd/C (0.01 g) in EtOH (10 mL) was stirred under hydrogen for 3 days. The reaction was filtered and the filtrate was evaporated. The residue was purified by precipitation from DCM with cold diethyl ether, to afford the required product (0.49 g, 93%). LC-MS (ES): 1296 $[M + H]^+$, 648 $[M + 2H]^{2+}$, 432 $[M + 3H]^{3+}$. MALDI +ve ion mode: 1318 $[M + Na]^+$. ^{1}H NMR ($CDCl_3$): δ 3.66–3.61 (m, 118 H, C$H_{2,PEG,}$ O*H*). ^{13}C NMR ($CDCl_3$): 72.52 (HOCH$_2$-*C*H$_2$O), 70.61 (*C*H$_{2,PEG}$), 70.57 (*C*H$_{2,PEG}$), 70.36 (*C*H$_{2,PEG}$), 61.71 (HO*C*H$_2$CH$_2$O). Elemental analysis ($C_{58}H_{118}O_{30}\cdot 0.5H_2O$): required C 53.40, H 9.19; found C 53.28, H 9.17.

2. Functionalization to Fmoc-Protected Amino Acid. *Preparation of PEG$_{17}$ Diacid (**9**).* Potassium *tert*-butoxide (2.93 g, 26.08 mmol) was added to a solution of PEG$_{17}$ diol (**5**) (1.00 g, 1.30 mmol) in *tert*-butanol (46 mL). The mixture was stirred at 50 °C under argon for 8 h, protected from light. Ethyl bromoacetate (2.9 mL, 26.08 mmol) was then added and a precipitate formed. The reaction was stirred for 24 h before being filtered and the filtrate evaporated. The residue was taken in 30 mL 1.0 M NaOH and stirred at room temperature for 8 h. The reaction was adjusted to pH 3 with 1.0 M HCl and extracted with chloroform. The organic layer was collected and dried with $MgSO_4$. The residue was purified by precipitation from DCM with cold diethyl ether, to afford the required product (0.91 g, 79%). LC-MS (ES): 883 $[M + H]^+$, 442 $[M + 2H]^{2+}$, 295 $[M + 3H]^{3+}$. MALDI +ve ion mode: 903 $[M + Na]^+$, 919 ($[M + K]^+$. ^{1}H NMR ($CDCl_3$): δ 4.08 (s, 4H, OCH_2COOH), 3.66–3.58 (m, 68 H, C$H_{2,PEG}$). ^{13}C NMR ($CDCl_3$): δ 172.00 (*C*O), 71.20 (*C*H$_{2,PEG}$), 70.64 (*C*H$_{2,PEG}$), 70.61 (*C*H$_{2,PEG}$), 70.54 (*C*H$_{2,PEG}$), 70.50 (*C*H$_{2,PEG}$), 70.46 (*C*H$_{2,PEG}$), 70.39 (*C*H$_{2,PEG}$), 68.81 (CO*C*H$_2$O).

*Preparation of PEG$_{29}$ Diacid (**10**).* The title compound was prepared starting from PEG$_{29}$ diol (**8**) (0.4 g, 0.31 mmol) using the same method as described for compound **9** (0.39 g, 88%). LC-MS (ES): 1412 $[M + H]^+$, 706 $[M + 2H]^{2+}$, 471 $[M + 3H]^{3+}$. MALDI +ve ion mode: 1433 $[M+Na]^+$. ^{1}H NMR ($CDCl_3$): δ 4.09 (s, 4H, OCH_2COOH), 3.60–3.58 (m, 116 H, C$H_{2,PEG}$). ^{13}C NMR ($CDCl_3$): δ 71.08 (C$H_{2,PEG}$), 70.61 (C$H_{2,PEG}$), 70.59 (C$H_{2,PEG}$), 70.54 (C$H_{2,PEG}$), 70.47 (C$H_{2,PEG}$), 70.44 (C$H_{2,PEG}$), 70.36 (C$H_{2,PEG}$), 68.86 (CO*C*H$_2$O).

*Preparation of Fmoc-PEG$_{17}$-COOH (**11**).* *N*-Hydroxysuccinimide (0.05 g, 0.45 mmol) was added to a solution of PEG$_{17}$ diacid (**9**) (0.40 g, 0.45 mmol) in dry DCM (40 mL) under argon. The reaction mixture was cooled in an ice bath, and a solution of DCC (0.09 g, 0.45 mmol) in dry DCM (5 mL) was added dropwise. The reaction was allowed to warm to room temperature and stirred for 4 h. A solution containing 1.0 equivalent of mono-Fmoc 1,3 diaminopropane hydrochloride (0.15 g, 0.45 mmol) in dry NMP (1 mL) was then added, followed by 4.0 equiv of triethylamine (0.3 mL, 1.81 mmol). The reaction was stirred at room temperature for 20 h before being evaporated. The residue was purified by preparative HPLC to afford the required product (0.12 g, 23%). LC-MS (ES): 1162 $[M + H]^+$, 581 $[M + 2H]^{2+}$. MALDI +ve ion mode: 1183 $[M + Na]^+$. HPLC retention time (min): 12.95. Purity by HPLC: 99%. ^{1}H NMR ($CDCl_3$): δ 7.75 (d, 2H, CH_{arom}, J = 7.45 Hz), 7.61 (d, 2H, CH_{arom}, J = 7.35 Hz), 7.39 (t, 2H, CH_{arom}, J = 7.45 Hz), 7.31 (t, 2H, CH_{arom}, J = 7.45 Hz), 5.79 (t, 2H, J = 6.35 Hz), 4.40 (d, 2H, FmocCH_2O, J = 7.25 Hz), 4.20 (t, 1H, FmocC*H*, J = 6.90 Hz), 4.14 (s, 2H, CH_2COOH), 4.00 (s, 2H, COCH_2O), 3.73–3.58 (m, 68H, C$H_{2,\ PEG}$), 3.35 (d, J = 6.20, 2H, CH_2NHCO), 3.21 (d, 2H, OCONHCH_2, J = 6.20), 1.69 (t, 2H, NHCH$_2$CH_2, J = 6.30 Hz). ^{13}C NMR ($CDCl_3$): δ 144.05 (C$_{arom}$), 141.29 (C$_{arom}$), 127.63 (CH_{arom}), 127.05 (CH_{arom}), 125.10 (CH_{arom}), 119.91 (CH_{arom}), 71.01 (C$H_{2,PEG}$), 70.93 (C$H_{2,PEG}$), 70.53 (C$H_{2,PEG}$), 70.46 (C$H_{2,PEG}$), 70.40 (C$H_{2,PEG}$), 70.29 (C$H_{2,PEG}$), 70.24 (C$H_{2,PEG}$), 70.13 (C$H_{2,PEG}$), 68.99 (CH_2CO), 66.35 (C$H_{2,Fmoc}$), 47.28 (CH_{Fmoc}), 37.72 (CH_2), 35.70 (CH_2), 29.71 (CH_2). Elemental analysis ($C_{52}H_{92}N_2O_{23}\cdot 2H_2O$): required C 56.17, H 8.08, N 2.34; found C 56.25, H 8.01, N 2.11.

*Preparation of Fmoc-PEG$_{29}$-COOH (**12**).* The title compound was prepared starting from PEG$_{29}$ diacid (**10**) (0.30 g, 0.21

mmol) using the same method as described for compound **11** (0.39 g, 88%). 0.13 g of required product was obtained. Yield: 35%. LC-MS (ES):1690 $[M + H]^+$, 845 $[M + 2H]^{2+}$, 564 $[M + 3H]^{3+}$. MALDI +ve ion mode: 1712 $[M + Na]^+$. HPLC retention time (min): 12.56. Purity by HPLC: 99%. ^{1}H NMR ($CDCl_3$): δ 7.84 (d, 2H, CH_{arom}, $J = 7.60$ Hz), 7.68 (d, 2H, CH_{arom}, $J = 7.25$ Hz), 7.51 (m, 1H, OCON*H*), 7.40 (t, 2H, CH_{arom}, $J = 7.40$ Hz), 7.32 (t, 2H, CH_{arom}, $J = 7.25$ Hz), 6.53 (m, 1 H, CH_2N*H*CO), 4.36 (d, 2H, FmocCH_2O, $J = 7.25$ Hz), 4.22 (t, 1H, FmocC*H*, $J = 6.77$ Hz), 4.10 (s, 2H, CH_2COOH), 3.92 (s, 2H, COCH_2O), 3.72–3.52 (m, 116H, C$H_{2,\ PEG}$), 3.32–3.28 (m, 2H, CH_2NHCO), 3.20–3.17 (m, 2H, OCONHCH_2), 1.70–1.67 (m, 2H, NHCH$_2$CH_2). ^{13}C NMR ($CDCl_3$): δ 170.68 (*C*$_{arom}$), 157.21 (*C*$_{arom}$), 145.07 (*C*H$_{arom}$), 142.00 (*C*H$_{arom}$), 128.38 (*C*H$_{arom}$), 127.82 (*C*H$_{arom}$), 125.94 (*C*H$_{arom}$), 120.68 (*C*H$_{arom}$), 71.66 (*C*H$_{2,PEG}$), 71.30 (*C*H$_{2,PEG}$), 71.13 (*C*H$_{2,PEG}$), 71.00 (*C*H$_{2,PEG}$), 70.94 (*C*H$_{2,PEG}$), 68.77 (*C*H$_2$CO), 66.62 (*C*H$_{2,Fmoc}$), 48.06 (*C*H$_{Fmoc}$), 38.64 (*C*H$_2$), 36.38 (*C*H$_2$), 29.71 (*C*H$_2$). Elemental analysis ($C_{80}H_{140}N_2O_{35}\cdot H_2O$): required C 56.26, H 8.38, N 1.64; found C 55.97, H 8.35, N 1.42.

3. Synthesis of the Peptide−PEG−Folate Conjugate. *Synthesis of Folic Acid-Cysteine Targeting Ligand (**13**).* A Glu(tBu)-Cys(Trt) dipeptide was synthesized on 0.65 g of Fmoc-Cys(Trt) HMP resin (loading capacity 0.58 mmol/g) using automated peptide synthesis. 4.0 equiv of Fmoc-Glu-O^{t}Bu (Bachem, UK) was utilized in each coupling step. The peptideo-resin was washed in DCM and MeOH and dried in a desiccator. Pteroic acid (0.10 g, 0.32 mmol) was taken up in dry DMF (3 mL) and dry DMSO (1.3 mL) and added to 0.19 g of peptideo-resin under argon. A 0.5 mM HOBt/HBTU solution in DMF (0.6 mL, 0.32 mmol) was added, followed by a 2.0 mM DIPEA solution in NMP (0.3 mL, 0.64 mmol). The reaction mixture was protected from light and shaken at room temperature for 24 h. The peptido-resin was filtered and washed in DMSO (4 mL) four times, DMSO/DMF 1:1 (4 mL) once, DMF (4 mL) once, and two alternating washes of DCM and MeOH (4 mL). The resin was then dried in a desiccator. 0.10 g of peptido-resin was cleaved using 3.0 mL cleavage mixture (0.75 g phenol, 0.5 mL thioanisole, 0.5 mL H_2O, 0.3 mL EDT, 10.0 mL TFA). The reaction was shaken at room temperature for 3 h. The filtrate was precipitated in cold diethyl ether and centrifuged to pellet. The pellet was washed in diethyl ether four times before drying in a desiccator 0.02 g of required product was obtained. Yield: 62% LC-MS (ES): 544 $[M + H]^+$. HPLC retention (min): 7.38. Purity by HPLC: 70%. ^{1}H NMR $(CD_3)_2SO$ 500 MHz: δ 8.66 (s, 1H, AromH$_1$), 8.21–8.17 (m, 2H, NH amide), 7.66 (d, 2H, $J = 8.50$, AromH$_4$), 7.33–7.23 (m, 3H, PhN*H*, N*H*$_2$), 6.64 (d, 2H, $J = 8.85$, AromH$_3$), 4.50 (s, 2H, H$_2$), 4.42–4.37 (m, 1H, H$_5$), 4.31–4.28 (m, 1H, H$_8$), 2.85–2.68 (2m, 2H, H$_9$), 2.31–2.19 (m, 2H, H$_7$), 2.09–1.86 (2m, 2H, H$_6$).

*Preparation of Amphipathic Peptide KKALLALALHHLAH-LALHLALALKKA (**14**) (**19**).* The peptide was synthesized using an ABI 433A peptide synthesizer (Applied Biosystems, California, USA) equipped with conductivity monitoring. The activation solution used in each coupling step contained HOBt/HBTU in DMF (0.5 mM) and DIPEA in NMP (2 mM). Each coupling step was carried out over approximately 4.5 min and was followed by a wash in NMP. Fmoc deprotection was carried out using 22% piperidine in DMF over 2 min and was followed by conductivity monitoring. This step was repeated up to 6 times. The peptide was synthesized on 149 mg of Fmoc-Ala HMP resin (loading capacity 0.7 mmol/g) using 10.0 equiv of amino acid in each coupling step. 462 mg of peptido-resin was obtained from the synthesis. Theoretical yield: 88%.

The peptide from 100 mg peptido-resin was cleaved using a cleavage mixture: 0.75 g crystalline phenol, 0.25 mL EDT, 0.50 mL thioanisole, 0.50 mL H_2O, and 10.00 mL TFA. Cleavage was carried out in an Isolute SPE single fritted reservoir (Argonaut Technologies Inc., Mid Glamorgan UK). The resin was filtered and the filtrate was collected and precipitated by adding cold diethyl ether. The precipitate was collected by centrifugation and washed with diethyl ether. The precipitate was dried in a desiccator.

The peptide was purified by semipreparative HPLC on a Jupiter C18 column (250 × 10 mm, 5 μm). A gradient was run at 3 mL/min from 95% H_2O (0.1% TFA), 5% MeCN (0.1% TFA) to 5% H_2O (0.1% TFA), 95% MeCN (0.1% TFA) over four column volumes. 38 mg of required product was obtained. Yield of purified peptide: 54%. MALDI +ve ion mode: 2779 $[M + H]^+$, 2801 $[M + Na]^+$. HPLC retention (min): 12.84. Purity by HPLC: 98%.

*Preparation of Amphipathic Peptide-PEG$_{17}$-NH-Fmoc (**15**).* 1.5 equiv each of FmocNHPEG$_{17}$-COOH (7 mg, 6.24 μmol) and HCTU (3 mg, 6.24 μmol) were taken up in dry NMP/DCM 9:1 (1 mL) and added to 25 mg amphipathic peptido-resin under argon. 3.0 equiv of DIPEA in NMP (2 mM) (0.01 mL, 12.0 μmol) were added and the reaction was shaken for 72 h. The reaction was filtered, rinsed in DMF, DCM, and MeOH, and dried in a desiccator. Cleavage was carried out as previously described. MALDI, +ve ion mode: 3923 $[M + H]^+$,3944 $[M + Na]^+$. HPLC retention (min): 13.47. Product in crude by HPLC: 66%.

*Preparation of Amphipathic Peptide-PEG$_{17}$-NH$_2$ (**16**).* 65 mg of amphipathic peptide-PEG$_{17}$-NHFmoc peptido-resin was taken up in 1.5 mL of 20% piperidine in DMF and shaken for 3 h. The reaction was filtered, rinsed in DMF, DCM, and MeOH, and dried in a desiccator. Cleavage was carried out as previously described. MALDI, +ve ion mode: 3700 $[M + H]^+$, 3722 $[M + Na]^+$. HPLC retention (min): 12.37.

*Preparation of Amphipathic Peptide-PEG$_{17}$-NH-Maleimide (**17**).* 10.0 equiv of 6-maleimidohexanoic acid *N*-hydroxysuccinimide ester (26 mg, 83.00 μmol) was taken up in dry DMF (2 mL) and added to 54 mg amphipathic peptide-PEG$_{17}$-NH$_2$ peptido-resin. The reaction was shaken for 72 h. The reaction was filtered, rinsed in DMF, DCM, and MeOH, and dried in a desiccator. Cleavage was carried out as previously described. MALDI, +ve ion mode: 3891 $[M + H]^+$, 3913 $[M + Na]^+$. HPLC retention (min): 12.62.

Preparation of Amphipathic Peptide-PEG$_{17}$-Folate Cysteine (*18*). 9 mg folate cysteine was taken up in dry DMF (1 mL) and added to 35 mg amphipathic peptide-PEG$_{17}$-maleimide peptido-resin under argon. The reaction was protected from light and shaken at room temperature for 72 h. The reaction was filtered, rinsed in DMSO, DMF, DCM, and MeOH, and dried in a desiccator. Cleavage was carried out as previously described. The crude product was purified by semipreparative HPLC on a Jupiter C18 column, followed by repeat purification on a Luna CN (250 × 6.4 mm, 5 μm) column. 1.2 mg of required product was obtained. Yield: 7% over four synthetic steps and two purification steps. HPLC retention time (standard conditions) (min): 10.90. HPLC retention time (Luna CN column, 250 × 4.60 mm, 5 μm, Phenomenex Ltd.) (min): 10.86. Purity by HPLC (standard conditions): 92%. MALDI: 4438 $[M + H]^+$.

RESULTS AND DISCUSSION

1. Synthesis of PEG17 and PEG29. The controlled synthesis of PEG is achieved by the Williamson ether formation; a suitably activated PEG chain is attacked by another PEG chain with a nucleophilic alkoxide ion. The use of protecting groups enables the controlled synthesis of extended PEG chains of defined MW.

Orthogonal protection with two different protecting groups has been used in the synthesis of smaller PEG oligomers (up to

Scheme 1. Synthesis of PEG_{17} and PEG_{29}

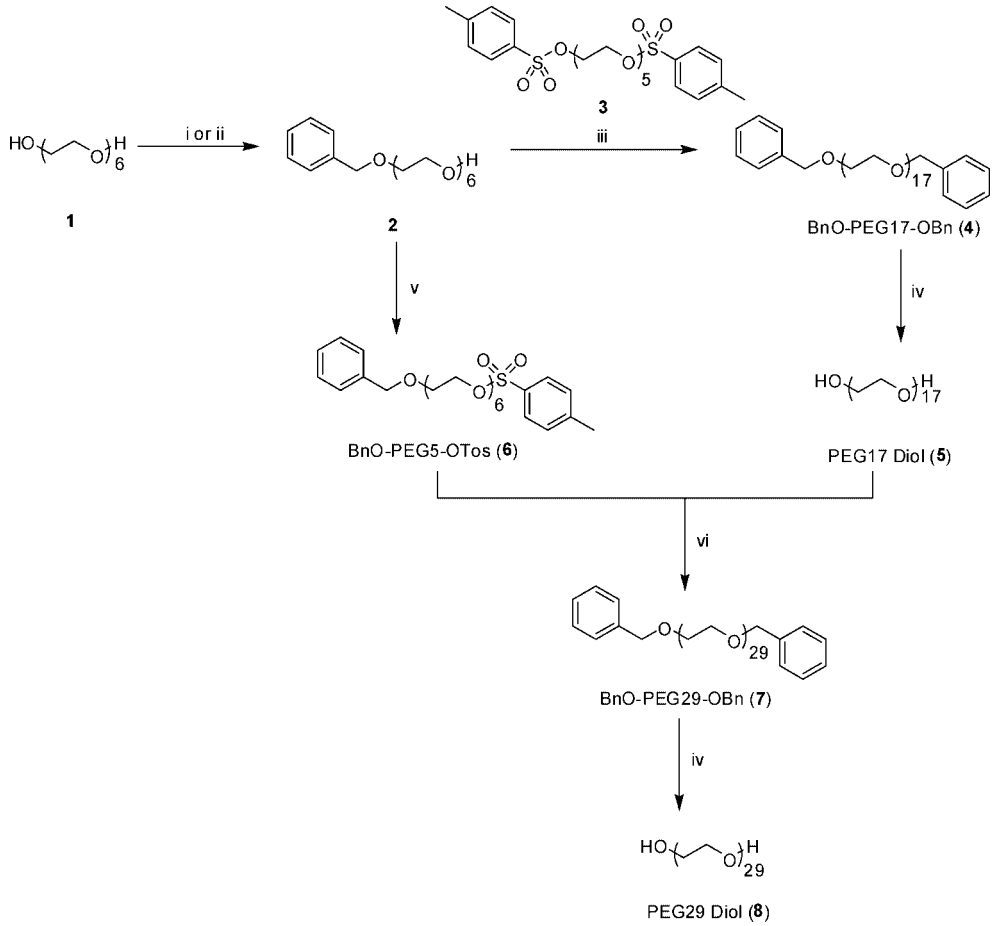

24 glycol units) (*20*, *21*). Our strategy is a quicker, more efficient route to PEG oligomers of defined MW, achieved through the simultaneous extension of both terminal hydroxyls of a PEG diol, using a single protecting group (Scheme 1). Similar approaches were investigated previously using monotritylated and ditosylated PEG oligomers (*22*, *23*). The oligomers synthesized were 12 and 16 units and synthesis was initiated with monoprotected ethylene and diethylene glycol.

Hexa(ethylene glycol) (**1**) and penta(ethylene glycol) ditosylate (**3**) were used as starting materials for the synthesis of PEG oligomers of 17 glycol units. Benzyl ether was chosen as the protecting group due to its stability under the basic conditions required to generate the alkoxide ion and ease of removal by hydrogenation.

The first step in this synthetic route required the generation of a monoprotected hexa(ethylene glycol) (**2**). The initial approach utilized sodium hydride to generate the alkoxide ion, followed by reaction with benzyl bromide. Monoprotection was achieved by carrying out the reaction in diluted solution. Yields from this approach were modest: at or below 35%.

An alternative approach to the monoprotection of diols involves the use of silver oxide. This method is milder, since there is no need for excess base to deprotonate the hydroxyl group, and it has been reported to result in monoprotection (*24*). The silver atom is hypothesized to act as a Lewis acid and complex with one hydroxyl group and the other terminal oxygen atom within a single PEG chain, which may make the proton that is not involved in the intramolecular bond more labile (*25*). Yields using this approach were improved to 52%.

The monoprotected hexa(ethylene glycol) (**2**) was reacted with ditosylated penta(ethylene glycol) (**3**) to afford **4**. An excess of sodium hydride was used to generate the monoprotected hexa(ethylene glycol) alkoxide, which was refluxed in dry THF in the presence of 2 equiv of penta(ethylene glycol) ditosylate. The reaction proceeded in good yield at 83%, with no contaminating monoprotected hexa(ethylene glycol) (**2**) as detected by HPLC. The product (**4**) was isolated by extraction and precipitation in cold ether and did not require purification by column chromatography, in contrast to the orthogonal protection approach (*21*). Hydrogenation of the product obtained proceeded quantitatively to yield the PEG_{17} diol (**5**) (Scheme 1).

The next step in PEG extension was the synthesis of PEG_{29} utilizing the PEG_{17} diol (**5**) and monoprotected hexa(ethylene glycol) tosylate (**6**). The monoprotected hexa(ethylene glycol) tosylate **6** was prepared from monobenzyl ether hexa(ethylene glycol) (**2**) using Ag_2O and tosyl chloride (*21*). The tosylate (**6**) (2 equiv) was reacted with the dialkoxide of PEG_{17} (**5**), to afford the dibenzylated PEG_{29} (**7**). Hydrogenation over palladium catalyst produced the PEG_{29} diol (**8**) (Scheme 1). The reaction proceeded in 70% yield over three steps from **5** to **8**. The product was isolated by precipitation from diethyl ether and did not require further purification. This novel approach has demonstrated a controlled, straightforward, and high-yielding synthesis of PEG chains of higher molecular weight in relatively few synthetic steps.

The MALDI analysis of the product showed a single peak (Figure 2A), unlike the distribution of molecular weights in commercial products (compare to Figure 1).

2. Functionalization of PEG17 and PEG29 as Fmoc-Protected Amino Acids. Methods to convert PEG diols to amino acids have been described (*26*, *27*). Here, we describe a short (two-step) synthetic approach to obtain a PEG amino acid directly in the Fmoc-protected form. This method generates the

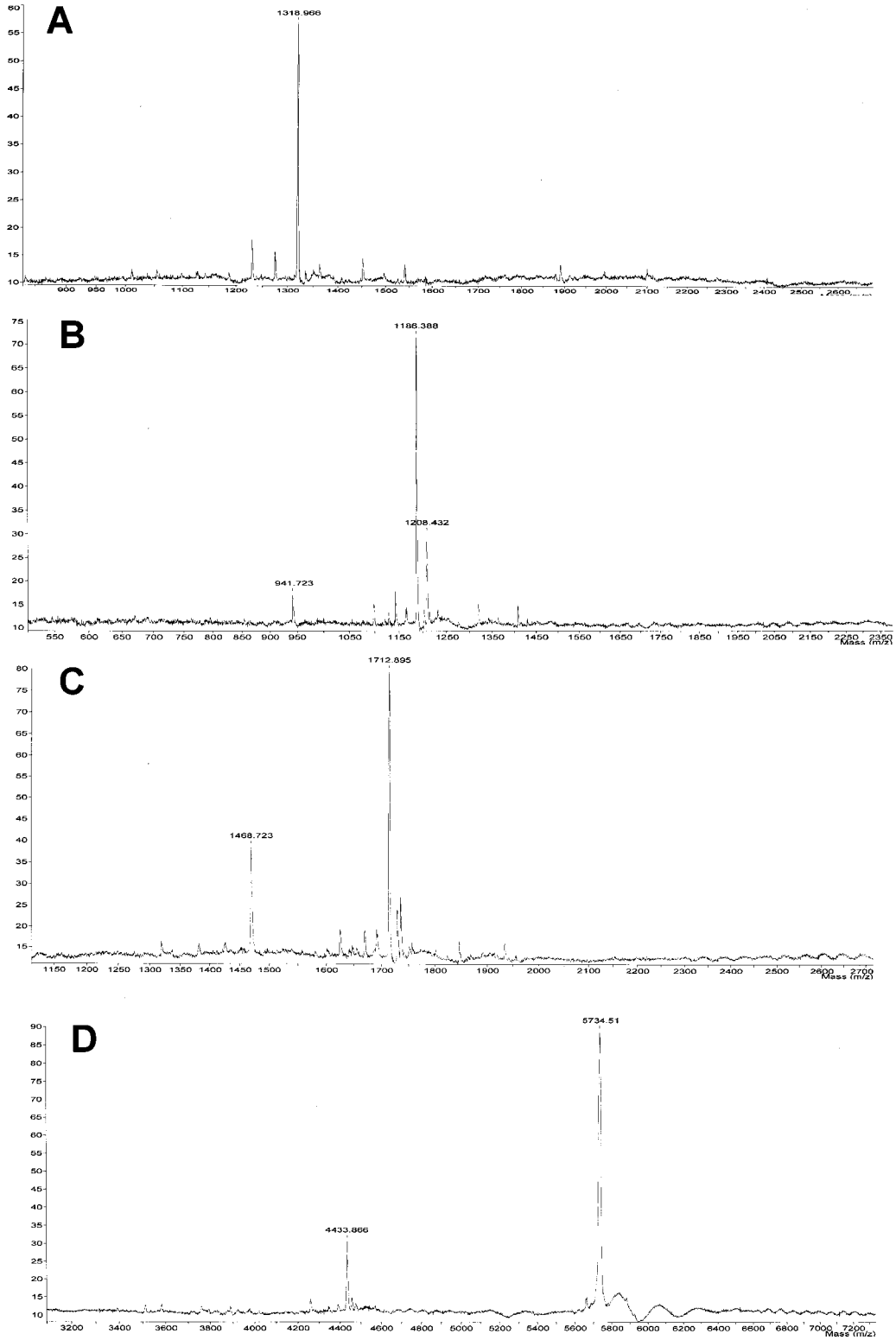

Figure 2. MALDI analysis. (A) PEG_{29} diol (**8**); (B) Fmoc-PEG_{17}-COOH (**11**); (C) Fmoc-PEG_{29}-COOH (**12**); (D) peptide-PEG_{17}-folate conjugate (**18**).

dicarboxylic acids of PEG (**9**) and (**10**), followed by the conversion of a single carboxyl group to mono-Fmoc 1,3 diamino propane to obtain the required mono-Fmoc PEG amino acids **11** and **12** (Scheme 2).

Veronese et al. synthesized a PEG carboxylic acid using ethyl bromoacetate and potassium *tert*-butoxide in *tert*-butanol, followed by the hydrolysis of the ethyl ester (*28*). This approach was successfully incorporated into the synthesis of the PEG diacids. The diacids were precipitation from DCM with diethyl ether, without need for further purification. Yields of up to 79% and 88% were obtained for PEG_{17} diacid (**9**) and PEG_{29} diacid (**10**), respectively.

The PEG diacids were coupled with 1 equiv of mono-Fmoc 1,3 diamino propane to obtain the required mono-Fmoc PEG amino acids **11** and **12** alongside the corresponding di-Fmoc amino modified PEG. Purification of this mixture was carried out using preparative HPLC on reverse-phase silica. Yields of the products were 23% and 35% for PEG_{17} amino acid (**11**)

Scheme 2. Synthesis of Fmoc-Protected PEG Amino Acids

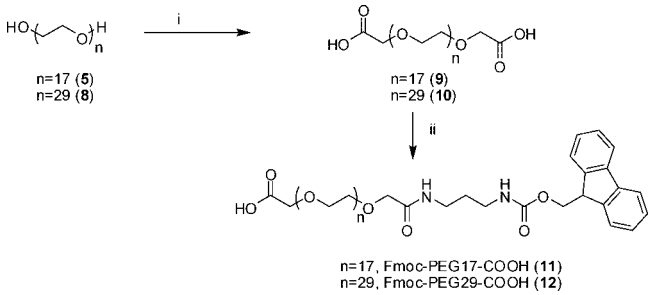

Scheme 3. Solid-Phase Synthesis of Folate−Cysteine Ligand

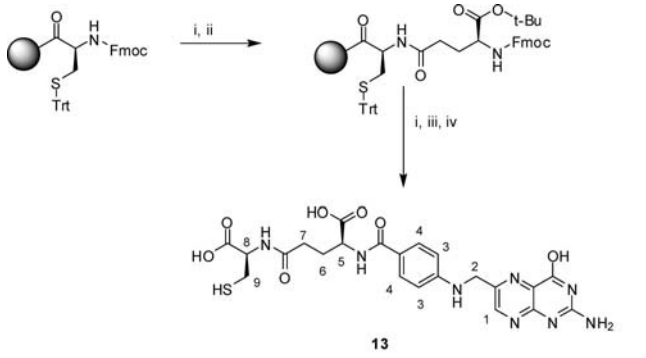

i. piperidine; ii. HOBt, HBTU, DIPEA, DMF, Fmoc-Glu(tBu)-OH; iii. HOBt, HBTU, DIPEA, DMF DMSO, pteroic acid; iv. TFA, phenol, thioanisole, H_2O, EDT.

and PEG_{29} amino acid (**12**), respectively. The MALDI analysis of **11** and **12** is shown in Figure 2B,C, respectively. The main peaks correspond to the product; the extra peaks at 942 (Figure 2B) and 1469 (Figure 2C) are due to the loss of Fmoc under the MALDI conditions.

3. Synthesis of the Peptide−PEG−folate Conjugate. The PEG_{17} amino acid (**11**) was used in the solid-phase synthesis of a conjugate comprising an amphiphatic peptide and a targeting moiety (folate) separated by the PEG_{17} linker. This conjugate is the prototype of a potential nonviral gene delivery vector, where the peptide achieves DNA condensation and endosomal escape, the folate is specifically targeting tumors overexpressing the α-folate receptor and contributes to conjugate internalization, and the PEG chain improves the PK properties of the conjugate and contributes to the DNA protection.

An amphiphatic histidine-rich peptide (KKALLALAL-HHLAHLALHLALALKKA) (**14**), reported to have high transfection efficiency (*19*), was chosen for the conjugate. The peptide was synthesized on solid support using Fmoc chemistry. A portion of the peptide was cleaved, purified, and analyzed; the bulk of the peptide was left on the resin and used for conjugate synthesis.

The folate−cysteine targeting ligand (**13**) was synthesized on a solid support. Advantages of this approach include higher purity of the final product and conjugation at only the preferred γ-carboxyl of the glutamic moiety, since suitable protected components such as Fmoc-Glu-O^{t}Bu are commercially available. Previous work by Zhang et al. described the synthesis of the folate−cysteine conjugate on a solid support utilizing the expensive N^{10}-trifluoroacetyl pteroic acid group, which improves the solubility of pteroic acid, but affords low yields due to its incomplete deprotection with base (*29*).

We carried out the solid-phase synthesis of folate−cysteine using the less expensive pteroic acid rather than its N^{10}-

Scheme 4. Synthesis of Peptide−PEG_{17}−Folate Conjugate

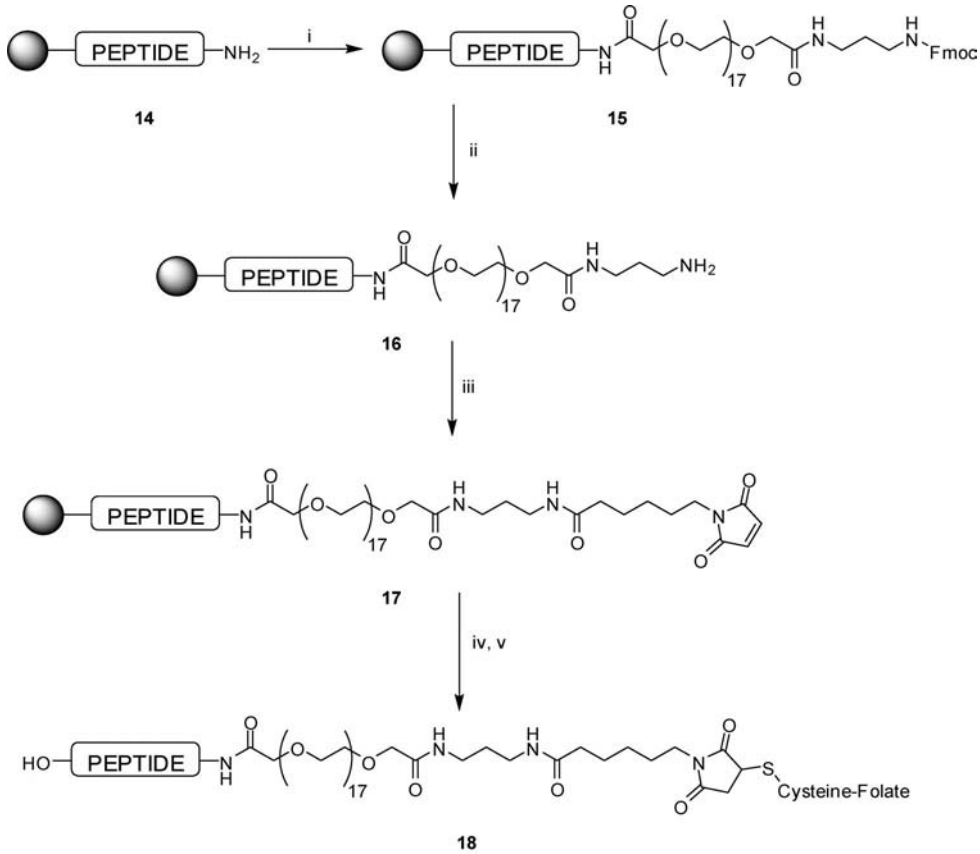

i. **11** (1.5 eq.), HCTU (1.5 eq.), DIPEA (3 eq.), DMF, 72 hours; ii. piperidine; iii. 6-maleimidohexanoic acid NHS ester, dry DMF, 24 hours; iv. **13**, DMF, 72 hours; v. TFA, phenol, thioanisole, H_2O, EDT.

trifluoroacetyl protected form. Synthesis of the Glu-Cys dipeptide was carried out using automated peptide synthesis. The final coupling of pteroic acid onto the dipeptide resin was carried out manually due to the low solubility of pteroic acid in NMP, which blocked the peptide synthesizer filters and prevented delivery to the reaction vessel. The manual coupling of pteroic acid utilized 3.0 equiv of pteroic acid in a mixture of DMF and DMSO and was carried out over 24 h. Despite the low solubility of pteroic acid, coupling to the dipeptide sequence proceeded efficiently and cleanly.

No coupling of the unprotected N^{10} amine of pteroic acid, leading to large multipteroate conjugates, was detected by MALDI analysis. This indicated that unprotected pteroic acid could be utilized in a viable route to the synthesis of folate−cysteine conjugates. This synthetic route is shown below in Scheme 3.

The yield obtained by using pteroic acid in the synthesis of the folate−cysteine conjugate was 64%, in comparison with yields of 38% obtained using the N^{10}-trifluoroacetyl pteroic acid as reported by Zhang et al. (*29*). Therefore, this approach was been shown to be a more efficient, less expensive synthesis of folate cysteine on a solid support.

The first step in the multicomponent vector assembly was the coupling of the FmocNH-PEG_{17}-COOH chain to the N-terminus of the resin-bound peptide. The coupling was carried out using the aminium-based coupling reagent HCTU. Optimization of the reaction conditions was required. The best conditions for coupling were found to be 1.5 equiv FmocNH-PEG_{17}-COOH, 1.5 equiv of HCTU, 3.0 equiv of DIPEA, dry DMF, 72 h. The conversion to the required product was 66%, as determined by HPLC analysis. Standard Fmoc deprotection conditions using 20% piperidine in DMF was quantitative and was followed by coupling to a commercially available NHS-activated ester of maleimide.

The success of this series of reactions validated the functionalization of PEG on solid support as an achievable step in the synthesis of multicomponent vectors. This approach is versatile and can be used to incorporate alternative coupling reagents. This could be of interest, as it has been reported that certain linkers such as maleimide can initiate linker-specific immune responses (*30*), and therefore, the ability to change the conjugation chemistry could be of benefit.

The maleimide functionalized peptide−PEG conjugate was coupled to the targeting ligand folate−cysteine. Folate−cysteine was dissolved in dry DMF, added to the peptido-resin and shaken for 72 h. The synthetic scheme demonstrating PEG and ligand coupling on solid support is shown in Scheme 4.

Coupling of folate−cysteine proceeded in good yield. Following cleavage from the resin, the multicomponent vector, amphipathic peptide-PEG_{17}-folate-cysteine, was purified twice by semipreparative HPLC. The first purification used a Jupiter C18 column; however, the required product was contaminated by a side product, amphipathic peptide−folate−cysteine, obtained due to the incomplete coupling of FmocNH-PEG_{17}-COOH. Therefore, the mixture obtained was further purified on a Luna CN column, which was able to separate the two products. The global yield of the complete vector was calculated from the amphipathic peptide resin over the four modification steps including FmocNH-PEG_{17}-COOH coupling, deprotection, 6-maleimidohexanoic acid NHS ester coupling, and folate−cysteine coupling and two purification steps. The yield of purified amphipathic peptide-PEG_{17}-folate-cysteine vector was 7%. This calculation is based on a theoretical amount of resin-bound peptide. The yield could be improved by acetylation of the unreacted resin-bound amphipathic peptide prior to Fmoc deprotection of the PEG oligomer. This would prevent the formation of the contaminating side product and reduce the number of purification steps required.

The MALDI analysis of the conjugate confirms the single molecular weight of the product (Figure 2D; the large peak at 5734 is the calibration standard).

SUMMARY AND CONCLUSION

An efficient synthetic route to long PEG oligomers was designed. This utilized only a benzyl ether protecting group which avoided the tedious purification and low overall yields of methods reported previously (*20*, *21*). The availability of starting materials longer than hexa(ethylene glycol) would make this route a practical method to obtain PEG of comparable length to polymeric commercial products, but with the added advantage of a single MW composition.

The functionalization as PEG amino acids suitable for solid-phase synthesis and heterobifunctional linkers was accomplished through the corresponding diacids and the coupling of a single equivalent of a monoprotected diamine. The preparation of two mono-Fmoc PEG amino acids of 17 and 29 units was achieved. This simple method also allows the rapid synthesis of a variety of PEG linkers. Using diamines with one amino group modified with other moieties instead of Fmoc (for example, biotin, maleimide, targeting ligands), the range of bifunctional PEG linkers can be greatly extended.

The application of these linkers was demonstrated by the synthesis of a complex conjugate on a solid support. An advantageous method for the solid support synthesis of the targeting component of the conjugate, folic acid−cysteine, was found, resulting in improved yields with respect to literature methods. The assembly of the peptide, PEG linker, and targeting group on a solid support was successful, resulting in a conjugate of defined molecular weight and structure. The successful synthesis of a complex multicomponent conjugate on a solid support demonstrates the power and versatility of this approach, and opens the way to the generation of a combinatorial library of peptide-PEG-targeting ligands with defined structure and molecular weight as potential nonviral vectors and conjugates for biological applications.

ACKNOWLEDGMENT

This work was supported by Cancer Research UK (CUK) grants number: C309/A2187, C107/A3096, and C1364/A3118 and the Institute of Cancer Research. We would like to acknowledge the Structural Chemistry Team: Amin Mirza and Meirion Richards for their support with MS and NMR analyses, and Jacky Metcalfe for support with peptide synthesis and MALDI analysis.

LITERATURE CITED

(1) Plank, C., Mechtler, K., Szoka, F. S. Jr., and Wagner, E. (1996) Activation of the complement system by synthetic DNA complexes: a potential barrier for intravenous gene delivery. *Hum. Gene Ther. 7*, 1437–1446.

(2) Harris, M., and Chess, R. (2003) Effect of pegylation on pharmaceuticals. *Nat. Rev. Drug Discovery 2*, 214–221.

(3) Ng, E., Shima, D., Calias, P., Cunningham, E., Guyer, D., and Adamis, A. (2006) Pegaptanib, a targeted anti-VEGF aptamer for ocular vascular disease. *Nat. Rev. Drug Discovery 5*, 123–132.

(4) Guo, W., and Lee, R. (1999) Receptor-targeted gene delivery via folate-conjugated polyethylenimine. *AAPS PharmSci. 1*, E19.

(5) Lee, R., and Low, P. (1994) Delivery of liposomes into cultured KB cells via folate receptor- mediated endocytosis. *J. Biol. Chem. 269*, 3198–3204.

(6) Leamon, C., Cooper, S., and Hardee, G. (2003) Folate-liposome-mediated antisense oligodeoxynucleotide targeting to

cancer cells: evaluation in vitro and in vivo. *Bioconjugate Chem. 14*, 738–747.
(7) Kumar, V., and Aldrich, J. (2003) A solid phase synthetic strategy for labelled peptides: Synthesis of a biotinylated derivative of the δ-opioid receptor antagonist TIPP (Tyr-Tic-Phe-Phe-OH). *Org. Lett. 5*, 613–616.
(8) Leamon, C., DePrince, R., and Hendren, R. (1999) Folate-mediated drug delivery: effect of alternative conjugation chemistry. *J. Drug Targeting 7*, 157–169.
(9) Petersen, H., Fechner, P. M., Martin, A. L., Kunath, K., Stolnik, S., Roberts, C. J., Fischer, D., Davies, M. C., and Kissel, T. (2002) Polyethylenimine-graft-poly(ethylene glycol) copolymers: influence of copolymer block structure on DNA complexation and biological activities as gene delivery system. *Bioconjugate Chem. 13*, 845–854.
(10) Reed, N. N., and Janda, K. D. (2000) A one-step synthesis of monoprotected polyethylene glycol ethers. *J. Org. Chem. 65*, 5843–5845.
(11) Nakamura, T., Nagasaki, Y., and Kataoka, K. (1998) Synthesis of heterobifunctional poly(ethylene glycol) with a reducing monosaccharide residue at one end. *Bioconjugate Chem. 9*, 300–303.
(12) Wyman, T. B., Nicol, F., Zelphati, O., Scaria, P. V., Plank, C., Francis, C., and Szoka, J. (1997) Design, synthesis, and characterization of a cationic peptide that binds to nucleic acids and permeabilizes bilayers. *Biochemistry 36*, 3008–3017.
(13) Rittner, K., Benavente, A., Bompard-Sorlet, A., Heitz, F., Divita, G., Brasseur, R., and Jacobs, E. (2002) New basic membrane-destabilizing peptides for plasmid-based gene delivery in vitro and in vivo. *Mol. Ther. 5*, 104–114.
(14) Evans, C.-O., Reddy, P., Brat, D. J., O'Neill, E. B., Craige, B., Stevens, V. L., and Oyesiku, N. M. (2003) Differential expression of folate receptor in pituitary adenomas. *Cancer Res.* 63.
(15) Toffoli, G., Cernigoi, C., Russo, A., Gallo, A., Bagnoli, M., and Boiocchi, M. (1997) Overexpression of folate binding protein in ovarian cancers. *Int. J. Cancer 74*, 193–198.
(16) Theti, D. S., Bavetsias, V., Skelton, L. A., Titley, J., Gibbs, D., Jansen, G., and Jackman, A. L. (2003) Selective delivery of CB300638, a cyclopenta[g]quinazoline-based thymidylate synthase inhibitor into human tumor cell lines overexpressing the α-isoform of the folate receptor. *Cancer Res. 63*, 3612–3618.
(17) Leamon, C. P., and Low, P. S. (1991) Delivery of macromolecules into living cells: A method that exploits folate receptor endocytosis. *Proc. Natl. Acad. Sci. U.S.A. 88*, 5572–5576.
(18) Mislick, K. A., Baldeschwieler, J. D., Kayyem, J. F., and Meade, T. J. (1995) Transfection of folate-polylysine DNA complexes: evidence for lysosomal delivery. *Bioconjugate Chem. 6*, 512–515.
(19) Kichler, A., Leborgne, C., Marz, J., Danos, O., and Bechinger, B. (2003) Histidine-rich amphipathic peptide antibiotics promote efficient delivery of DNA into mammalian cells. *Proc. Natl. Acad. Sci. U.S.A. 100*, 1564–1568.
(20) Burns, C. J., Field, L. D., Hashimoto, K., Petteys, B. J., Ridley, D. D., and Sandanayake, K.R.A.S. (1999) A convenient synthetic route to differentially functionalized long chain polyethylene glycols. *Synth. Commun. 29*, 2337–2347.
(21) Loiseau, F. A., Hii, K. K. M., and Hill, A. M. (2004) Multigram synthesis of well-defined extended bifunctional polyethylene glycol (PEG) chains. *J. Org. Chem. 69*, 639–647.
(22) Keegstra, E. M. D., Zwikker, J. W., Roest, M. R., and Jenneskens, L. W. (1992) A highly selective synthesis of monodisperse oligo(ethylene glycols). *J. Org. Chem. 57*, 6678–6680.
(23) Chen, Y., and Baker, G. L. (1999) Synthesis and properties of ABA amphiphiles. *J. Org. Chem. 64*, 6870–6873.
(24) Bouzide, A., and Sauve, G. (1997) Highly selective silver(I) oxide mediated monoprotection of symmetrical diols. *Tetrahedron Lett. 38*, 5945–5948.
(25) Bouzide, A., and Sauve, G. (2002) Silver(I) oxide mediated highly selective monotosylation of symmetrical diols. Application to the synthesis of polysubstituted cyclic ethers. *Org. Lett. 4*, 2329–2332.
(26) Svedhem, S., Hollander, C., Shi, J., Konradsson, P., Liedberg, B., and Svensson, S. (2001) Synthesis of a series of oligo(ethylene glycol)-terminated alkanethiol amides designed to address structure and stability of biosensing interfaces. *J. Org. Chem. 66*, 4494–4503.
(27) Shiyama, T., Minoru, F., Yamazaki, A., Terada, T., and Tanaka, A. (2004) Design and synthesis of novel hydrophilic spacers for the reduction of nonspecific binding proteins on affinity resins. *Bioorg. Med. Chem. 12*, 2831–2841.
(28) Veronese, F. M., Caliceti, P., Pastorino, A., Schiavon, O., Sartore, L., Banci, L., and Scolaro, L. M. (1989) Preparation, physico-chemical and pharmacokinetic characterisation of monomethyoxypoly(ethylene glycol)-derivatized superoxide dismutase. *J. Controlled Release 10*, 145–154.
(29) Zhang, Y., Guo, L., Roeske, R. W., Antony, A. C., and Jayaram, H. N. (2004) Pteroyl--glutamate-cysteine synthesis and its application in folate receptor-mediated cancer cell targeting using folate-tethered liposomes. *Anal. Biochem. 332*, 168–177.
(30) Boeckler, C., Frisch, B., Muller, S., and Schuber, F. (1996) Immunogenicity of new heterobifunctional cross-linking reagents used in the conjugation of synthetic peptides to liposomes. *J. Immunol. Methods 191*, 1–10.

BC060242+

MAY 2008
Volume 19, Number 5

© *Copyright 2008 by the American Chemical Society*

Bioconjugate Chemistry

COMMUNICATIONS

A Novel Near-Infrared Indocyanine Dye−Polyethylenimine Conjugate Allows DNA Delivery Imaging *in Vivo*

Andrea Masotti,*[,†,‡] Paola Vicennati,[†,‡] Federico Boschi,[§] Laura Calderan,[§] Andrea Sbarbati,[§] and Giancarlo Ortaggi[‡]

Chemistry Department, SAPIENZA Università di Roma, P.le Aldo Moro 5, 00185 Rome, Italy, and Department of Morphological-Biomedical Sciences, Section of Anatomy and Histology, University of Verona, Strada Le Grazie 8, 37134 Verona, Italy. Received September 14, 2007; Revised Manuscript Received February 27, 2008

Near-infrared (NIR) fluorescence light has been applied to monitor several biological events *in vivo* since it penetrates tissues more efficiently than visible light. Dyes exhibiting NIR fluorescence and having large Stokes shift are key elements for this promising optical imaging technology. Here, we report the synthesis of a novel conjugate between a near-infrared indocyanine dye and an organic polyamine polymer (polyethylenimine, PEI) (**IR820-PEI**) with high chemical stability and good optical properties. **IR820-PEI** absorbs at 665 nm, emits at 780 nm, and displays a large Stokes shift (115 nm). Moreover, the reported conjugate is able to bind DNA, and the delivery process can be monitored *in vivo* with noninvasive optical imaging techniques. These characteristics make **IR820-PEI** one of the most effective and versatile indocyanine dye polymeric-conjugate reported so far.

Near-infrared (NIR)-absorbing dyes represent an intriguing avenue for extracting biological information from living subjects since they can be monitored with safe, noninvasive optical imaging/contrasting techniques (*1–7*). Optical imaging represents a rapidly expanding field, with direct applications in pharmacology, molecular and cellular biology, and diagnostics. More sensitive optical sensors and new, powerful probes such as semiconductor nanocrystals (*8–11*), fluorescent proteins (*12, 13*), or NIR fluorescent molecules (*14–16*) have been synthesized and studied in the past few years.

While light in the visible range is routinely used for intravital microscopy, imaging of deeper tissues (>500 μm to cm) requires the use of near-infrared light, as hemoglobin and water, the major absorbers of visible and infrared light, respectively, have their lowest absorption coefficient in the NIR region (650−900 nm). The advantages of imaging in the NIR region (700−1100 nm) are numerous: the absence or significant reduction of background absorption, fluorescence, and light scattering along with high sensitivity, the availability of low-cost sources of irradiation (but no radiation is necessary for acquisition), and the versatility of different reporter probes. Numerous long-wavelength fluorophores belonging to the BODIPY (*17*), rhodamine (*18, 19*), and oxazine (*20*) have been used, but only cyanine dyes (*21–23*) have been reported to display large molar extinction coefficients, moderate-to-high fluorescence quantum yields, and a broad wavelength tunability (*24–26*).

* Andrea Masotti, Chemistry Department − SAPIENZA Università di Roma, 00185 Rome, Italy. Tel: (+39) 06 4991 3341; Fax: (+39) 06 490631; E-mail: andrea.masotti@uniroma1.it.
† These two authors equally contributed to the work.
‡ SAPIENZA Università di Roma.
§ University of Verona.

10.1021/bc700356f CCC: $40.75 © 2008 American Chemical Society
Published on Web 04/23/2008

Scheme 1[a]

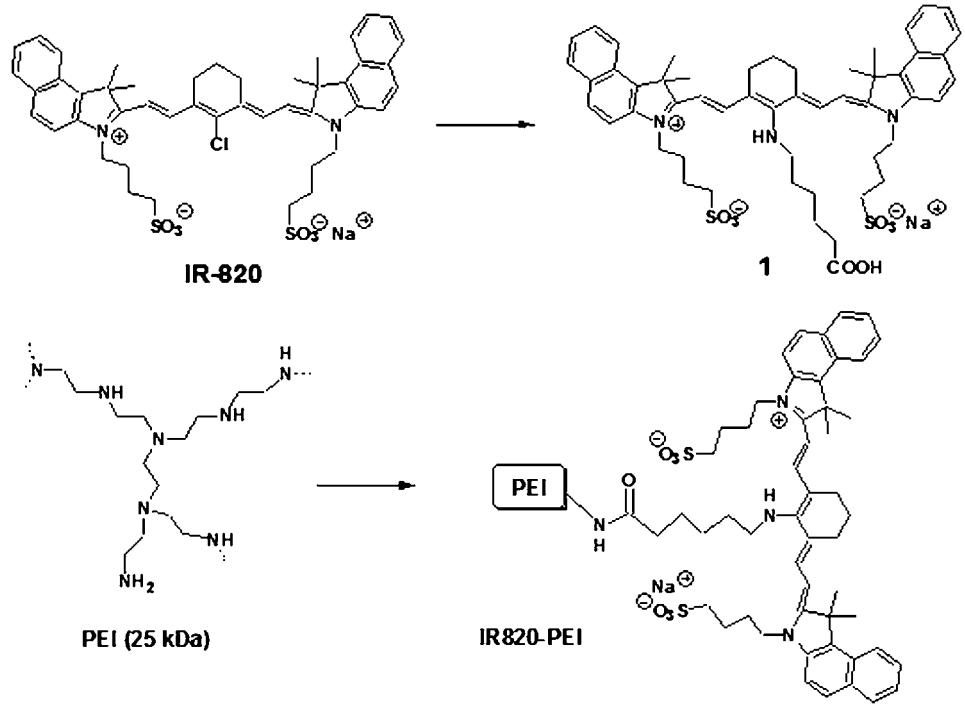

[a] Synthesis of **1**: DMF, TEA, $H_2N(CH_2)_5COOH$, 85 °C 3 h. Synthesis of **IR820-PEI**: DMF, EDC·HCl, **1**, rt 18 h.

Heptamethine dyes with a rigid chloro-cyclohexenyl ring in their moiety have increased photostability and a better fluorescence quantum yield, and also provide a useful reactive site for further chemical substitution (*27*, *28*). However, reactions replacing the central chlorine atom, with phenol (*26*) or thiophenol (*29*) have led to chemically unstable probes (*30*). Only heptamethine cyanine dyes containing C−N bonds were reported to display large Stokes shifts (around 100−140 nm) and considerably stronger fluorescence that might be attributed to an excited-state intramolecular charge transfer (ICT) between the donor and acceptor in the same dyes (*31*).

Recently, we reported an *in vitro* study focusing on polyethylenimine (PEI) and PEI derivatives able to form complexes (polyplexes) with DNA and to deliver (or transfect) it to cells (*32*). This polyamine polymer having a high cationic charge-density potential is able to establish electrostatic interactions with DNA and compact it efficiently and has been employed as a versatile vector for several biomedical applications (i.e., gene therapy) (*33*). Once penetrated into cells, PEI destabilizes the endosomal membrane due to the protonation of its numerous amino groups ("proton sponge" effect). The influx of protons and counterions into endosomes leads to membrane lysis and to the release of their internal contents (DNA). The conjugation of PEI with an NIR dye is aimed at obtaining a multifunctional delivery vector whose localization can be monitored *in vivo* with noninvasive techniques and that may serve to identify potential transfection sites and assess its efficiency to deliver DNA.

To obtain an NIR−PEI conjugate, we chose the recently reported indocyanine **IR-820** (See Scheme 1) among the heptametine NIR dyes, since its heterocyclic nitrogen atoms bear two alkyl-sulfonate groups that improve photostability and provide a sphere of solvation in water preventing this dye from aggregation.

Attempts to directly replace the *meso*-chlorine atom of **IR-820** with an amino group of PEI were unsuccessful. We hypothesized that the close proximity between the dye and the hindered polymeric structure could prevent this substitution. Thus, we replaced the *meso*-chlorine atom with a less-hindered carboxy-terminal amino linker (6-aminohexanoic acid), obtaining an intermediate (**1**) suitable for further conjugations (Scheme 1).

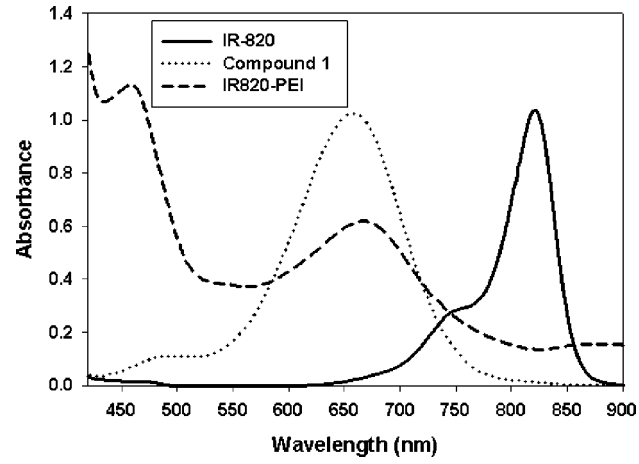

Figure 1. Visible/NIR absorption spectra of **IR-820** (solid line), **1** (dotted line), and **IR820-PEI** dyes (dashed line) in MeOH (0.1 mM, 25 °C).

The successful conjugation of **1** with PEI allowed us to obtain a near-infrared dye−polymer conjugate (**IR820-PEI**) highly soluble in water.

IR820-PEI absorbs at 665 nm (Figure 1) and emits at 780 nm displaying a large Stokes shift (115 nm) (Figure 2). These characteristics make this system more suitable for use as fluorescence probes than do common cyanine dyes.

To investigate the feasibility of employing **IR820-PEI** as a vector able to bind and deliver DNA, agarose gel retardation assays (Figure 3) were performed. **IR820-PEI** is able to bind DNA similarly to PEI itself, while intermediate **1**, being negatively charged, has no effect, as expected. These results confirm that, when PEI is derivatized at a small percentage of substitution, it substantially retains all the physicochemical and acid−base properties of the starting polymer (*32*).

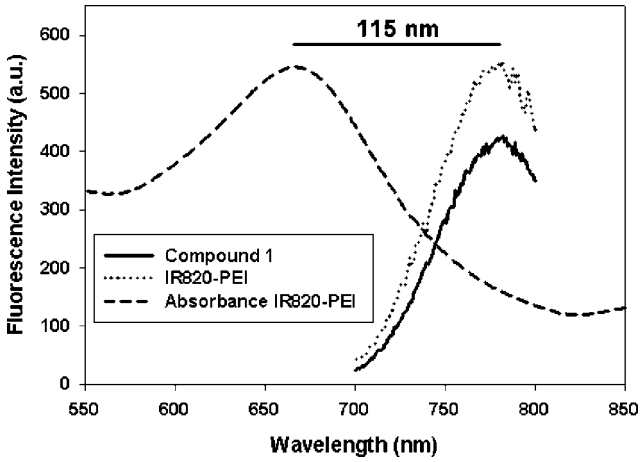

Figure 2. Emission spectra of **1** (solid line) and **IR820-PEI** (dotted line) dyes in MeOH (0.1 mM, 25 °C). The absorption spectrum (arbitrary unit) of **IR820-PEI** is also reported for comparison.

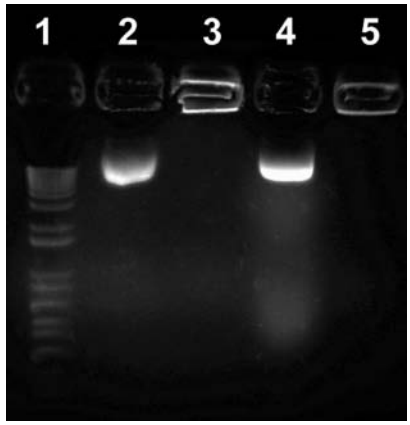

Figure 3. Gel retardation assay (agarose 1%) of **IR820-PEI**/DNA (lane 5) compared to **PEI**/DNA (lane 3) and **1**/DNA (lane 4). DNA ladder (lane 1) and reference β-Gal pDNA (lane 2) are also reported.

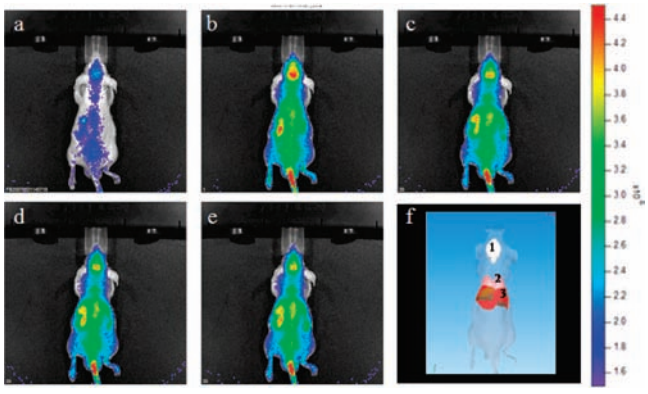

Figure 4. Optical images of a nude mouse with 2 mg/mL tail vein injection of **IR820-PEI**: preinjection (a), and after 1 min (b), 1 h (c), 2 h (d), and 3 h (e) from the injection. 3D reconstruction of mouse body and the organs of interest (f): 1, brain; 2, lungs; and 3, liver. Color bar on the right side indicates the signal efficiency of the fluorescence emission coming out from the animal.

The properties of the novel NIR system **IR820-PEI** and its ability to deliver DNA *in vivo* (**IR820-PEI**/DNA) were assessed using a VivoVision Systems, IVIS 200 Series Imaging System (Xenogen Corporation, Alameda, CA, USA). Figure 4 shows the optical images of a nude mouse before (Figure 4a) and after 1 min (Figure 4b), 1 h (Figure 4c), 2 h (Figure 4d), and 3 h from the injection of **IR820-PEI** (Figure 4e). Figure 4f shows

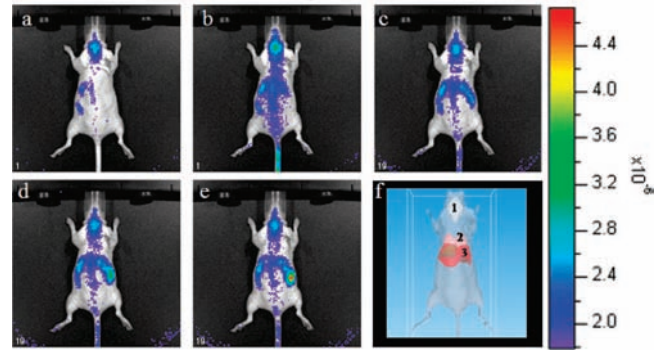

Figure 5. Optical images of a nude mouse with 2 mg/mL tail vein injection of **IR820-PEI-DNA**: preinjection (a), and after 1 min (b), 1 h (c), 2 h (d), and 3 h (e) from the injection. 3D reconstruction of mouse body and the organs of interest (f): 1, brain; 2, lungs; and 3, liver. Color bar on the right side indicates the signal efficiency of the fluorescence emission coming out from the animal.

the 3D reconstruction of the mouse body and the organs of interest (1, brain; 2, lungs; 3, liver). After i.v. injection of **IR820-PEI**, a signal enhancement localized in the regions corresponding to the brain and liver was observed. CCD camera collects light coming out from the skin of the animal without any *a priori* information regarding the deepness of the sources. However, excitation and emission photons employed in our experimental sessions have a mean path before absorption of 1−2 cm, and this property depends on the optical characteristic of tissues themselves. Thus, since the light can pass up to 2 cm through the animal body, sources located up to 2 cm below the skin can be visualized. However, in order to unambiguously localize the fluorescent dye accumulated in specific anatomical districts, a much more detailed study should be taken into account.

Figure 5 shows the optical images of a nude mouse before (Figure 5a) and after 1 min (Figure 5b), 1 h (Figure 5c), 2 h (Figure 5d), and 3 h from the injection of **IR820-PEI**/DNA (Figure 5e). Figure 5f shows the 3D reconstruction of the mouse body and the organs of interest (1, brain; 2, lungs; 3, liver). Also, in this case, after the i.v. injection of the **IR820-PEI**/DNA, optical images shown signal enhancement, in the region corresponding to the brain, lungs, and liver.

Optical imaging data suggest that, after intravenous tail vein injection of **IR820-PEI** or **IR820-PEI**/DNA, a predominant hepatic accumulation occurs. This effect is most likely due to a nonspecific electrostatic interaction between **IR820-PEI** (or **IR820-PEI**/DNA) conjugate and the negatively charged plasmatic membranes of capillary endothelial cells (i.e., sulfated proteoglycans, glycosylaminoglycans, etc.) that may explain the initial NIR dye biodistribution thought brain and lungs (the first highly vascularized organ encountered by NIR dyes after intravenous tail vein injection and in which blood flow is slower due to the capillary circulation). After 1 h, the two NIR systems began to accumulate in the liver, a typical store organ, and after 3 h, the signal intensity increased. The signal is clearly visible even after 24 h from the injection (see Figure 1S in Supporting Information). The reported distribution observed for **IR820-PEI** and **IR820-PEI**/DNA is in good agreement with published works on other systems like NIR-nanoparticles (*34*–*36*) and NIR-nanoprobes (*37*).

However, the fluorescence signal acquired by the optical imaging device might be due both to **IR820-PEI**/DNA complex and to unbound **IR820-PEI**. So, to discriminate between the contributions of these two species, we assessed the ability of **IR820-PEI** to bind a fluorescent oligonucleotide (randomized sequence) 5′-labeled with a Cy5.5 fluorochrome (**Cy5.5-ODN**) (Figure 6). This modified oligonucleotide emits in the red region

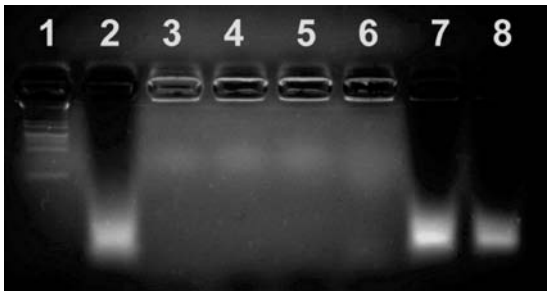

Figure 6. Gel retardation assay (agarose 4%) of **IR820-PEI** complexed with 0.3 (lane 3), 0.6 (lane 4), 1 (lane 5), 1.5 (lane 6), 2.5 (lane 7), and 3 nmol (lane 8) of **Cy5.5-ODN**. DNA ladder (lane 1) and reference **Cy5.5-ODN** (1 nmol) are also reported.

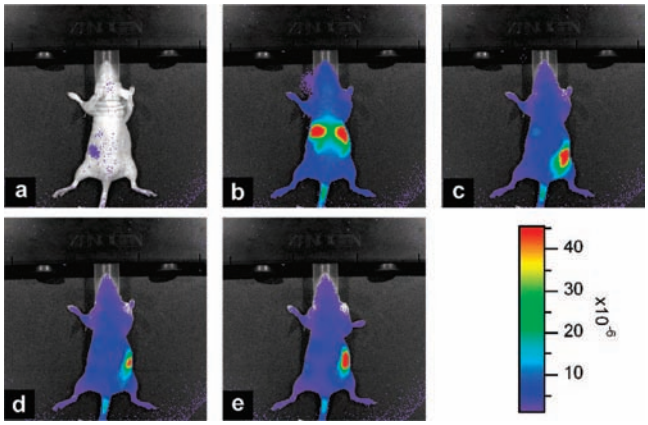

Figure 7. Optical images of a nude mouse with 2 mg/mL tail vein injection of **PEI/IR820-DNA**: pre injection (a), and after 4 min (b), 1 h (c), 2 h (d), and 3 h (e) from the injection. Color bar on the right side indicates the signal efficiency of the fluorescence emission coming out from the animal.

and not in the near-infrared region (like **IR820-PEI)**. For this reason, a differential localization of the cDNA and the delivery vector is possible through a sequential acquisition of the fluorescence emission first in the red then in the NIR region. Unfortunately, even if a partial accumulation of **IR820-PEI/Cy5.5-ODN** was observed in the liver, a spurious fluorescence emission coming out from the food ingested by the animal before the experiment was observed (see Figure 2S in Supporting Information). However, even if this experiment is neither significant nor conclusive, DNA accumulation in the liver is reported, and the region concerned is the same as that involved when using the **PEI-IR820**/(unlabeled)DNA complex.

Therefore, in order to overcome this problem and clearly see the localization of DNA (and not that of the delivery vector), we repeated the acquisition injecting a calf thymus DNA labeled with the same NIR dye used for **IR820-PEI** (indicated as **IR820-DNA**) (see Supporting Information) complexed with a solution of unlabeled **PEI**. In this way, it was possible to follow the fluorescence in the NIR region of the **PEI/IR820-DNA** complex and to obtain indications, at least in the initial stages, on DNA localization. DNA accumulated in the liver analogously to **IR820-PEI**/DNA (Figure 7). These results indicate, at least in a first approximation, that DNA is transported and/or delivered *in vivo* in the same regions, but additional assays are required to investigate the effective transfection *in vivo* of this novel synthesized system.

Liver uptake or nonselective accumulation into undesired organs is an obvious problem that should be taken into account, in the near future, for the development of efficient tumor-targeting therapies.

In conclusion, **IR820-PEI** is one of the most attractive near-infrared indocyanine dye−polymer conjugate molecules that should be further investigated for its potential use as a multifunctional system for targeted gene delivery by conjugation with selected molecules (i.e., folic acid, folate−PEG, etc.) or specific antibodies.

ACKNOWLEDGMENT

Authors thank Prof. M. Barteri and Dr. R. De Carolis for helpful discussions and MIUR (Ministero dell'Università e della Ricerca) (PRIN 2005 - prot. 2005039758) for financing.

Supporting Information Available: Materials and Methods section. This information is available free of charge via the Internet at http://pubs.acs.org.

LITERATURE CITED

(1) Daehne, S., Resch-Genger, U., and Wolfbeis, O. S. (1998) *Near-Infrared Dyes for High Technology Applications*; (Daehne, S., Resch-Genger, U., and Wolfbeis, O. S. Eds.)NATO ASI Series, 3. High Technology, Vol. 52, Kluwer Academic, Dordrecht.
(2) Fabian, J., Nakazumi, H., and Matsuoka, M. (1992) Near-infrared absorbing dyes. *Chem. Rev. 92*, 1197–1226.
(3) Mishra, A., Behera, R. K., Behera, P. K., Mishra, B. B., and Behera, G. B. (2000) Cyanines during the 1990s: A review. *Chem. Rev. 100*, 1973–2012.
(4) Law, K.-Y. (1993) Organic photoconductive materials: recent trends and developments. *Chem. Rev. 93*, 449–486.
(5) Zhao, W., and Carreira, E. M. (2005) Conformationally restricted aza-bodipy: a highly fluorescent, stable, near-infrared-absorbing dye. *Angew. Chem., Int. Ed. 44*, 1677–1679.
(6) Zhang, Z., and Achilefu, S. (2004) Synthesis and evaluation of polyhydroxylated near-infrared carbocyanine molecular probes. *Org. Lett. 6*, 2067–2070.
(7) Casalboni, M., De Matteis, F., Prosposito, P., Quatela, A., and Sarcinelli, F. (2003) Fluorescence efficiency of four infrared polymethine dyes. *Chem. Phys. Lett. 373*, 372–375.
(8) Michalet, X., Pinaud, F. F., Bentolila, L. A., Tsay, J. M., Doose, S., Li, J. J., Sundaresan, G., Wu, A. M., Gambhir, S. S., and Weiss, S. (2005) Quantum dots for live cells, in vivo imaging, and diagnostics. *Science 307*, 538–544.
(9) Dubertret, B., Skourides, P., Noriis, D. J., Noireaux, V., Brivanlou, A. H., and Libchader, A. (2002) In vivo imaging of quantum dots encapsulated in phospholipid micelles. *Science 298*, 1759–1762.
(10) So, M. K., Xu, C., Loening, A. M., Gambhir, S. S., and Rao, J. (2006) Self-illuminating quantum dot conjugates for in vivo imaging. *Nat. Biotechnol. 24*, 339–343.
(11) Ballou, B., Lagerholm, B. C., Ernst, L. A., Bruchez, M. P., and Waggoner, A. S. (2004) Noninvasive imaging of quantum dots in mice. *Bioconjugate Chem 15*, 79–86.
(12) Bhaumik, S., and Gambhir, S. S. (2002) Optical imaging of Renilla luciferase reporter gene expression in living mice. *Proc. Natl. Acad. Sci. U.S.A. 99*, 377–382.
(13) Contag, C. H., and Bachmann, M. H. (2002) Advances in in vivo bioluminescence imaging of gene expression. *Annu. Rev. Biomed. Eng. 4*, 235–260.
(14) Cheng, Z., Levi, J., Xiong, Z., Gheysens, O., Keren, S., Chen, X., and Gambhir, S. S. (2006) Near-infrared fluorescent deoxyglucose analogue for tumor optical imaging in cell culture and living mice. *Bioconjugate Chem. 17*, 662–669.
(15) Weissleder, R., Tung, C. H., Mahmood, U., and Bogdanov, A. (1999) In vivo imaging of tumors with protease-activated near-infrared fluorescent probes. *Nat. Biotechnol. 17*, 375–378.
(16) Becker, A., Hessenius, C., Licha, K., Ebert, B., Sukowski, U., Semmler, W., Wiedenmann, B., and Grötzinger, C. (2001) Receptor-targeted optical imaging of tumors with near-infrared fluorescent ligands. *Nat. Biotechnol. 19*, 327–331.

(17) Zhao, W., and Carreira, E. M. (2006) Conformationally restricted aza-BODIPY: Highly fluorescent, stable near-infrared absorbing dyes. *Chem.—Eur. J. 12*, 7254–7263.

(18) Liu, J., Diwu, Z., Leung, W.-Y., Lu, Y., Patch, B., and Haugland, R. P. (2003) Rational design and synthesis of a novel class of highly fluorescent rhodamine dyes that have strong absorption at long wavelengths. *Tetrahedron Lett. 44*, 4355–4359.

(19) Bandichhor, R., Petrescu, A. D., Vespa, A., Kier, A. B., Schroeder, F., and Burgess, K. (2006) Synthesis of a new water-soluble rhodamine derivative and application to protein labeling and intracellular imaging. *Bioconjugate Chem. 17*, 1219–1225.

(20) Jose, J., and Burgess, K. (2006) Benzophenoxazine-based fluorescent dyes for labeling biomolecules. *Tetrahedron 62*, 11021–11037.

(21) Lin, Y., Weissleder, R., and Tung, C.-H. (2002) Novel near-infrared cyanine fluorochromes: synthesis, properties, and bioconjugation. *Bioconjugate Chem. 13*, 605–610.

(22) Mader, O., Reiner, K., Egelhaaf, H.-J., Fischer, R., and Brock, R. (2004) Structure property analysis of pentamethine indocyanine dyes: identification of a new dye for life science applications. *Bioconjugate Chem. 15*, 70–78.

(23) Hilderbrand, S. A., Kelly, K. A., Weissleder, R., and Tung, C.- H. (2005) Monofunctional near-infrared fluorochromes for imaging applications. *Bioconjugate Chem. 16*, 1275–1281.

(24) Patonay, G., Salon, J., Sowell, J., and Strekowski, L. (2004) Noncovalent labeling of biomolecules with red and near-infrared dyes. *Molecules 9*, 40–49.

(25) Tung, C.-H. (2004) Fluorescent peptide probes for in vivo diagnostic imaging. *Biopolymers 76*, 391–403, and references cited therein.

(26) Zaheer, A., Lenkinski, R. E., Mahmood, A., Jones, A. G., Cantley, L. C., and Frangioni, J. V. (2001) In vivo near-infrared fluorescence imaging of osteoblastic activity. *Nat. Biotechnol. 12*, 1148–1154.

(27) Zhang, Z., Achilefu, and S. (2004) Synthesis and evaluation of polyhydroxylated near-infrared carbocyanine molecular probes. *Org. Lett. 6*, 2067–2070.

(28) Strekowski, L., Lipowska, M., and Patonay, G. (1992) Substitution reactions of a nucleofugal group in heptamethine cyanine dyes. Synthesis of an isothiocyanato derivative for labeling of proteins with a near-infrared chromophore. *J. Org. Chem. 57*, 4578–4580.

(29) Gallaher, D. L., and Johnson, M. E. (1999) Development of near-infrared fluorophoric labels for the determination of fatty acids separated by capillary electrophoresis with diode laser induced fluorescence detection. *Analyst 124*, 1541–1546.

(30) Narayanan, N., and Patonay, G. (1995) A new method for the synthesis of heptamethine cyanine dyes: synthesis of new near-infrared fluorescent labels. *J. Org. Chem. 60*, 2391–2395.

(31) Peng, X., Song, F., Lu, E., Wang, Y., Zhou, W., Fan, J., and Gao, Y. (2005) Heptamethine cyanine dyes with a large stokes shift and strong fluorescence: a paradigm for excited-state intramolecular charge transfer. *J. Am. Chem. Soc. 127*, 4170–4171.

(32) Masotti, A., Moretti, F., Mancini, F., Russo, G., Di Lauro, N., Checchia, P., Marianecci, C., Carafa, M., Santucci, E., and Ortaggi, G. (2007) Physicochemical and biological study of selected hydrophobic polyethylenimine-based polycationic liposomes and their complexes with DNA. *Bioorg. Med. Chem. 15*, 1504–15.

(33) Boussif, O., Lezoualc'h, F., Zanta, M. A., Mergny, M. D., Scherman, D., Demeneix, B., and Behr, J.-P. (1995) A versatile vector for gene and oligo nucleotide transfer into cells in culture and in vivo: polyethylenimine. *Proc. Natl. Acad. Sci. U.S.A. 92*, 7297–7301.

(34) Campbell, R. B., Fukumura, D., Brown, E. B., Mazzola, L. M., Izumi, Y., Jain, R. K., Torchilin, V. P., and Munn, L. L. (2002) Cationic charge determines the distribution of liposomes between the vascular and extravascular compartments of tumors. *Cancer Res. 62*, 6831–6836.

(35) Levchenko, T. S., Rammohan, R., Lukyanov, A. N., Whiteman, K. R., and Torchilin, V. P. (2002) Liposome clearance in mice: the effect of a separate and combined presence of surface charge and polymer coating. *Int. J. Pharm. 240*, 95–102.

(36) Thurston, G., McLean, J. W., Rizen, M., Baluk, P., Haskell, A., Murphy, T. J., Hanahan, D., and McDonald, D. M. (1998) Cationic liposomes target angiogenic endothelial cells in tumors and chronic inflammation in mice. *J. Clin. Invest. 101*, 1401–1413.

(37) Le Masne de Chermont, Q., Chanéac, C., Seguin, J., Pellé, F., Maîtrejean, S., Jolivet, J. P., Gourier, D., Bessodes, M., and Scherman, D. (2007) Nanoprobes with near-infrared persistent luminescence for in vivo imaging. *Proc. Natl. Acad. Sci. U.S.A. 104*, 9266–9271.

BC700356F

MBC94, a Conjugable Ligand for Cannabinoid CB_2 Receptor Imaging

Mingfeng Bai,[†] Michelle Sexton,[‡] Nephi Stella,[‡] and Darryl J. Bornhop*,[†]

Department of Chemistry, Vanderbilt University, VU Station B 351822, Nashville, Tennessee 37235-1822, and Department of Pharmacology, Psychiatry and Behavioral Sciences, Health Sciences Center, BB-1538c, University of Washington, Seattle, Washington 98195-7280. Received November 15, 2007; Revised Manuscript Received March 7, 2008

Cannabinoid CB_2 receptor is a particularly attractive target for noninvasive imaging of neuroinflammation and monitoring of therapeutic efficacy. Its expression is low to undetectable in healthy brain and induced in resident microglial cells (the macrophage of the brain) after cerebral ischemia, injury, and in neuroinflammatory disease. Additionally, immune cells migrating across the blood−brain barrier typically express CB_2 receptors, which adds to the expression pool of this target and provides a reliable indicator of inflammation in the brain. Here, we synthesized a novel conjugable CB_2 receptor ligand, mbc94, which has a terminal amino group that allows for facile conjugation to imaging moieties. A near-infrared (NIR) dye labeled mbc94, NIRmbc94, was developed for CB_2 targeted imaging. Preliminary evidence, including *in vitro* fluorescence imaging and a competition study, showed that NIRmbc94 specifically labeled CB_2-expressing cells.

Two cannabinoid receptors, CB_1 and CB_2, have been identified at the molecular level (*1*, *2*). They are G protein-coupled receptors that share an overall 44% amino acid homology and a 68% amino acid homology within their transmembrane domains (*1*). CB_1 receptors are abundantly expressed by neurons, whereas CB_2 receptors are abundantly expressed by immune cells (*3*, *4*).

The high level of CB_2 receptor expression in immune cells and much lower expression in other cell types, particularly in the CNS, makes this receptor an attractive target for imaging and monitoring of therapy (*3*, *4*) for neurological diseases. Specifically, CB_2 receptor expression is high in spleen, tonsils, and thymus and low—or even undetectable—in brain, thyroid, retina, placenta, skeletal muscle, kidney, liver, adrenal gland, heart, prostate, and ovary (*4*). This expression profile provides great opportunities for imaging with low background. Furthermore, CB_2 receptor expression is highly plastic and may be induced under specific disease conditions, for example, in tumor cells (*5*) and CNS-resident microglia. Accordingly, CB_2 receptor has become a predominant target for drug development aimed at treating pain (*6*, *7*), chronic inflammation (*8*), osteoporosis (*9*), malignant gliomas (*10*), tumors of immune origin (*11*), and immunological disorders (*12*,*13*), and thus developing a tool that allows for its precise mapping in tissue is essential.

Together with the characterization of the CB_2 receptor, a considerable effort has been made to develop CB_2 receptor−ligands. The term cannabinoid was first used to describe terpenophenolic compounds in *Cannabis sativa* L., among which (-)-trans-Δ^9-tetrahydrocanabinol (Δ^9-THC) is the main bioactive constituent (*14*). Many anti-inflammatory effects of Δ^9-THC have been described, including inhibition of tumor necrosis factor-α, interleukin-2, nitric oxide, and arachidonic acid production from macrophages and T cells (*8*, *15*).

CB_2 receptor ligands can be divided into three main groups: plant-derived, endogenous, and synthetic. The best-known plant-derived cannabinoid is Δ^9- THC, but cannabinol and cannabidiol also induce profound biological effects (*16*). Two endocannabinoids, arachidonoylethanolamide (anandamide) and 2-arachidonoyl glycerol (2-AG), have been identified (Figure 1) (*17*). Both molecules have greater affinity at CB_1 than CB_2 receptors (*18*). 2-AG acts as a full agonist at CB_1 and CB_2 receptor, and anandamide acts as a partial agonist (showing mixed agonist−antagonist properties) toward these receptors (*19*). Many synthetic cannabinoid receptor ligands have been developed, including HU-210, CP55940, WIN55212−2, SR141617A, AM630, and SR144528 (Figure 2). HU-210, CP55940, and WIN55212−2 are cannabinoid receptor agonists with no or marginal CB_1/CB_2 selectivity (*18*). AM630 and SR144528 are both selective CB_2 receptor ligands and behave as inverse agonists rather than "silent" or "neutral" antagonists. The CB_2/CB_1 affinity ratio is less for AM630 (CB_2/CB_1 affinity = 165) than for SR144528 (CB_2/CB_1 affinity > 700) (*18*). Accordingly, SR144528 has been widely used as a pharmacological tool to determine CB_2 receptor-mediated effects (*18*). However, the use of SR144528 for CB_2 receptor-targeted imaging has never been tested directly, since SR144528 is not conjugable. In other words, signaling moieties, such as fluorescent dyes, lanthanide chelates, and nanoparticles, cannot be easily coupled to SR144528. Thus, to further study CB_2 receptor and diseases associated with an increase in the expression of this receptor, development of a conjugable SR144528 analogue constitutes an essential step. Here, we synthesized such a conjugable SR144528

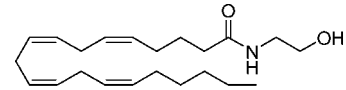

Anandamide

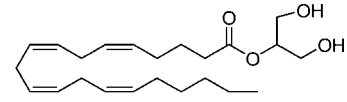

2-Arachidonyl-glycerol (2-AG)

Figure 1. Structures of endogenous CB_2 receptor ligands.

* Corresponding author. VU Station B 351822, 7300 Stevenson Center, Nashville, TN 37235-1822 Tel.: 615.322.4226. Fax: 615.343.1234. E-mail: Darryl.Bornhop@Vanderbilt.Edu.

[†] Vanderbilt University.

[‡] University of Washington.

10.1021/bc700419e CCC: $40.75 © 2008 American Chemical Society
Published on Web 04/30/2008

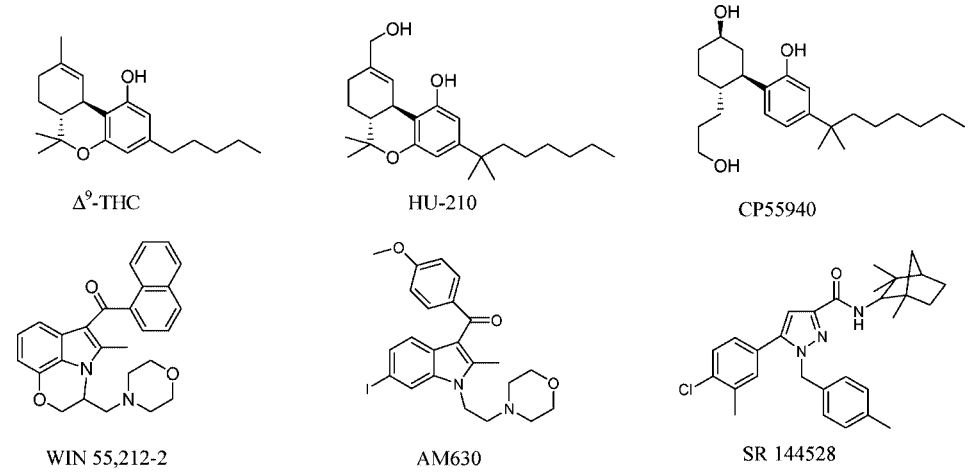

Figure 2. Structures of plant-derived and synthetic CB_2 receptor ligands.

Scheme 1. Synthesis of mbc94

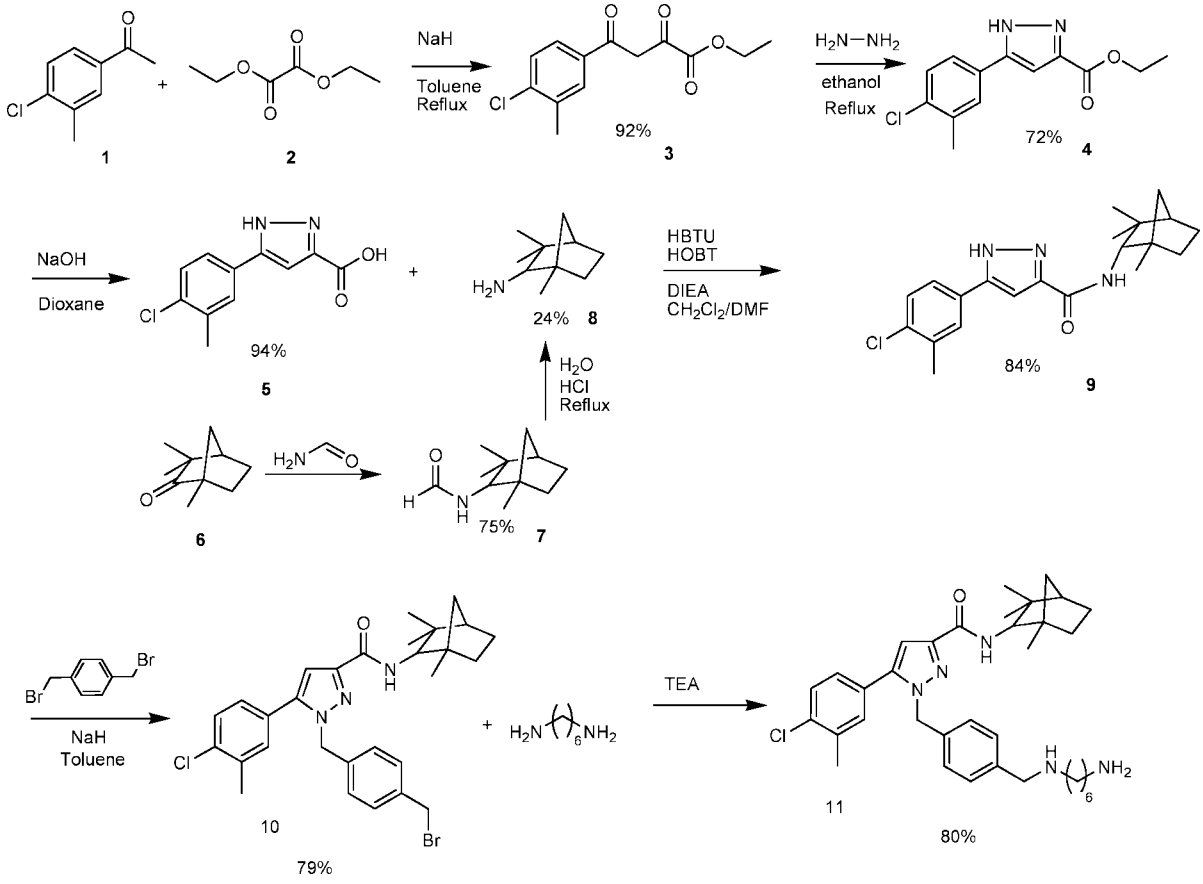

analogue, mbc94. To our knowledge, this is the only fully conjugable CB_2 receptor ligand in existence. It has a terminal amino group allowing easy conjugation to other molecules, including imaging moieties that can provide opportunities for CB_2 receptor-targeted imaging. A near-infrared (NIR) dye, IRDye 800CW NHS ester, was selected to label mbc94 for optical imaging. The resulting imaging agent, NIRmbc94, was used to label CB_2-expressing cells. Preliminary fluorescence imaging of live cells and competition study showed that indeed NIRmbc94 specifically labeled CB_2-expressing cells.

The synthetic pathway of the conjugable SR 144528 analogue, mbc94, is shown in Scheme 1. Compound **3** was prepared from 4′-chloro-3′methylacetophenone and diethyl oxalate as previously described (*20*). Formation of pyrazoles **4** and **5** was achieved by following literature procedures (*21*). Fenchylamine **8** was prepared by converting fenchone to a formamide **7**, followed by hydrolysis of the amide bond as previously described (*22*). Compound **9** was prepared using thionyl chloride before, but the yield was relatively low (70%) (*21*). We synthesized **9** by regular peptide coupling using 2-(1*H*-benzotriazole-1-yl)-1,1,3,3-tetramethyl uronium hexafluorophosphate (HBTU), and the yield was improved to 84%. The following N-alkylation with α,α-dibromo-*p*-xylene produced **10**, and another N-alkylation with 1,6-hexane diamine yielded the conjugable CB_2 receptor ligand, mbc94.

The use of NIR (650−900 nm) light has gained increasingly wide acceptance in molecular imaging during recent years (*23*)

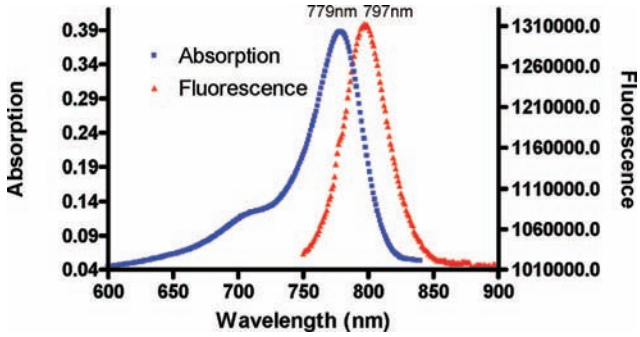

Figure 3. NIRmbc94 absorption and fluorescence in water.

in part because tissues are relatively transparent in this region of the electromagnetic spectrum, with hemoglobin, water, and lipids exhibiting low absorption coefficients (*24*). Therefore, we labeled mbc94 with a NIR dye, IRDye 800CW NHS ester, for NIR optical imaging. The reaction was monitored by analytical HPLC at 780 nm and the product, IRDye 800CW-mbc94 (NIRmbc94), was purified using a semipreparative HPLC and characterized by NMR and mass spectrometry. The absorption and emission spectra were then taken (Figure 3). NIRmbc94 has maximum absorption at 779 nm and emission at 797 nm (water), allowing deep tissue emission for enhanced *in vivo* imaging.

To test whether NIRmbc94 reliably binds to the CB_2 receptor, we already had in place a system wherein the receptor was both absent and present. Specifically, the highly malignant mouse astrocytoma cell line, DBT, lacks the targeted receptor (wild-type), and we generated a clone that stably expresses our target, 2D4DBT. First, we demonstrated that NIRmbc94 gave a significant signal ($S/N = 1.6$), whereas the "free" dye (IRDye 800CW acid) does not produce significant fluorescence, as illustrated by microscopy in the NIR (thus indicating a lack of nonspecific binding due to the dye: Figure 4). Next, as a preliminary indicator of specific targeting of our receptor, both wild-type cells and 2D4 clones were incubated 5 μM concentration of NIRmbc94. Figure 5B,E shows that the fluorescence signal is relatively low in wild-type DBT cells compared to the clone (A,D).

A competition study gave further evidence for specific binding of NIRmbc94 to CB_2 receptors. Specifically, in a preliminary competitive binding experiment, the fluorescence signal was significantly reduced when 100 nM SR144528 was added to compete with 5 μM NIRmbc94 at the receptor site. The lack of fluorescence is due to the higher-affinity unlabeled ligand, SR144528 (*25*), occupying the receptor site and thus inhibiting binding by NIRmbc94. This preliminary pharmacological characterization is typical, and the data indicate that we have indeed labeled our target of interest. More detailed pharmacological and biological characterization, including binding affinity (K_d) and reliable measurement of receptor expression (B_{max}) are in order and forthcoming.

In conclusion, we developed a conjugable CB_2 receptor ligand, mbc94, which has a terminal amino group, making it universally conjugable. An NIR dye-labeled mbc94, NIRmbc94, specifically labeled CB_2-expressing DBT cells, whereas the same cells incubated with same concentration of free NIR dye did not show any significant signal. In addition, the reduced fluorescence signal was observed from non-CB_2expressing wild-type DBT cells incubated with NIRmbc94 compared to CB_2-expressing DBT cells incubated with the same concentration of NIRmbc94. Finally, the specific binding of NIRmbc94 to CB_2 receptors was confirmed by *in vitro* competition study. A preliminary competition study in which cells were coincubated with NIRmbc94 and SR144528 showed signal reduction compared to cells incubated with NIRmbc94 only. Overall, mbc94 constitutes a promising conjugable CB_2 receptor ligand. NIRmbc94 specifically binds to CB_2 receptors and can potentially be used to image CB_2-expressing cells *in vivo*, including immune and cancer cells.

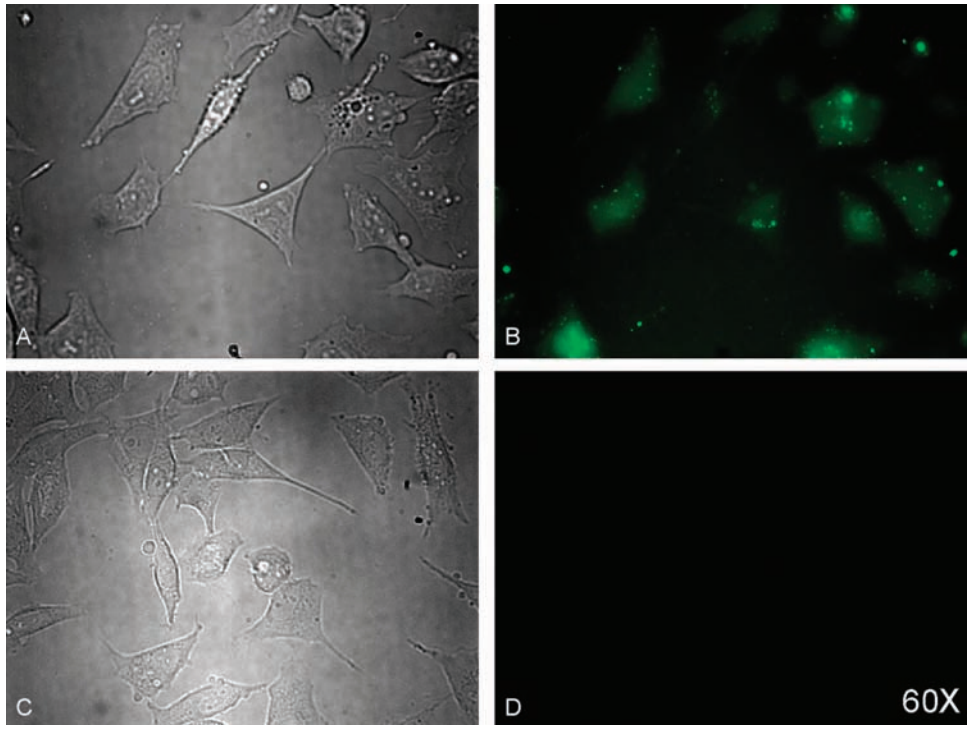

Figure 4. Fluorescence imaging of DBT cells incubated with NIRmbc94 or free NIR dye: (A) phase contrast microscopy of cells dosed with NIRmbc94; (B) fluorescence imaging of cells dosed with 5 μM NIRmbc94; (C) phase contrast microscopy of cells dosed with free NIR dye; (D) fluorescence imaging of cells dosed with 5 μM free NIR dye (control).

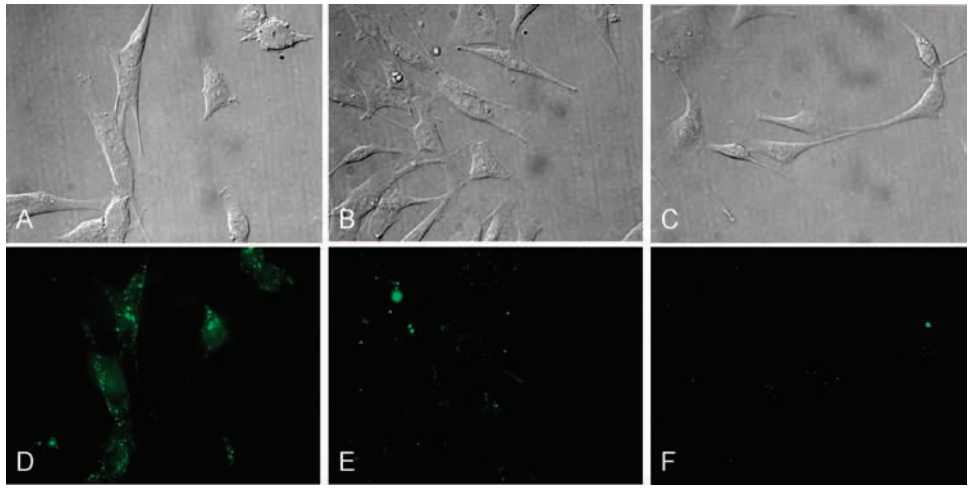

Figure 5. Fluorescence imaging of 2D4 (CB_2 expressing) and wild-type (WT, non-CB_2 expressing) DBT cells: (A) phase contrast microscopy of 2D4 DBT cells dosed with 5 μM NIRmbc94; (B) phase contrast microscopy of WT DBT cells dosed with 5 μM NIRmbc94; (C) phase contrast microscopy of 2D4 DBT cells dosed with 5 μM NIRmbc94 and 100 nM SR144528; (D) fluorescence imaging of 2D4 DBT cells dosed with 5 μM NIRmbc94; (E) fluorescence imaging of WT DBT cells dosed with 5 μM NIRmbc94; (F) fluorescence imaging of 2D4 DBT cells dosed with 5 μM NIRmbc94 and 100 nM SR144528.

Scheme 2. Synthesis of NIRmbc94

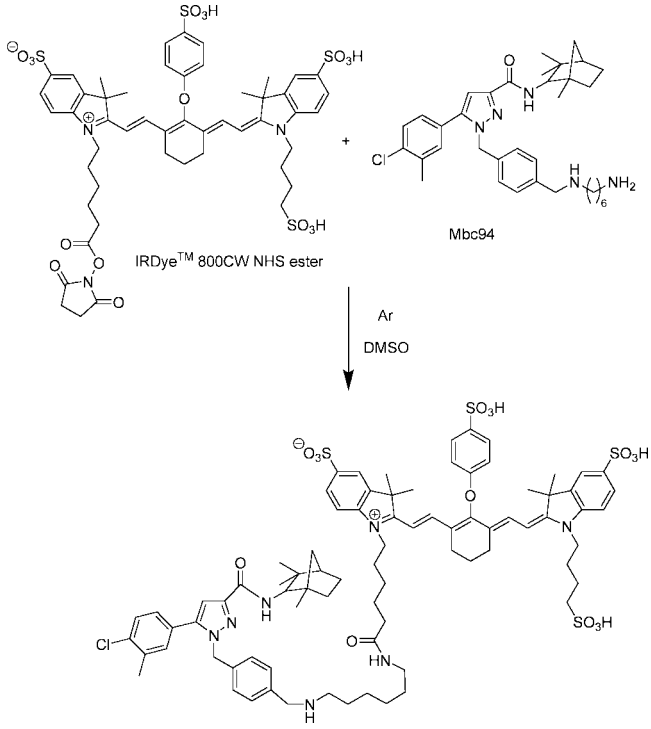

ACKNOWLEDGMENT

We thank Eiron Cudaback at the University of Washington for generating and providing CB_2-expressing (2D4 cells) and wild-type DBT cells. We also thank Department of Defense (grant # W81XWH-04-1-0432 to D.B.) and NIDA (grant # DA014486 to N.S.) for providing funding for this work.

Supporting Information Available: Details of experimental section. This material is available free of charge via the Internet at http://pubs.acs.org.

LITERATURE CITED

(1) Munro, S., Thomas, K. L., and Abushaar, M. (1993) Molecular characterization of a peripheral receptor for cannabinoids. *Nature 365*, 61–65.

(2) Matsuda, L. A., Lolait, S. J., Brownstein, M. J., Young, A. C., and Bonner, T. I. (1990) Structure of a cannabinoid receptor and functional expression of the cloned cDNA. *Nature 346*, 561–564.

(3) Pertwee, R. G. (1997) Pharmacology of cannabinoid CB_1 and CB_2 receptors. *Pharmacol. Ther. 74*, 129–180.

(4) Galiegue, S., Mary, S., Marchand, J., Dussossoy, D., Carriere, D., Carayon, P., Bouaboula, M., Shire, D., Lefur, G., and Casellas, P. (1995) Expression of central and peripheral cannabinoid receptors in human immune tissues and leukocyte subpopulations. *Eur. J. Biochem. 232*, 54–61.

(5) Fernandez-Ruiz, J., Romero, J., Velasco, G., Tolon, R. M., Ramos, J. A., and Guzman, M. (2007) Cannabinoid CB_2 receptor: a new target for controlling neural cell survival? *Trends Pharmacol. Sci. 28*, 39–45.

(6) Malan, T. P., Ibrahim, M. M., Lai, J., Vanderah, T. W., Makriyannis, A., and Porreca, F. (2003) CB_2 cannabinoid receptor agonists: pain relief without psychoactive effects? *Curr. Opin. Pharmacol. 3*, 62–67.

(7) Malan, T. P., Ibrahim, M. M., Deng, H. F., Liu, Q., Mata, H. P., Vanderah, T., Porreca, F., and Makriyannis, A. (2001) CB_2 cannabinoid receptor-mediated peripheral antinociception. *Pain 93*, 239–245.

(8) Iwamura, H., Suzuki, H., Ueda, Y., Kaya, T., and Inaba, T. (2001) In vitro and in vivo pharmacological characterization of JTE907, a novel selective ligand for cannabinoid CB_2 receptor. *J. Pharmacol. Exp. Ther. 296*, 420–425.

(9) Karsak, M., Ofek, O., Fogel, M., Wright, K., Tam, J., Gabet, Y., Birenboim, R., Attar-Namdar, M., Muller, R., Cohen-Solal, M., de Vernejoul, M., Shohami, E., Mechoulam, R., Zimmer, A., and Bab, I. (2004) The cannabinoid CB_2 receptor: A potential target for the diagnosis and treatment of osteoporosis. *J. Bone Miner. Res. 19*, S383–S383.

(10) Sanchez, C., de Ceballos, M. L., del Pulgar, T. G., Rueda, D., Corbacho, C., Velasco, G., Galve-Roperh, I., Huffman, J. W., Cajal, S. R. Y., and Guzman, M. (2001) Inhibition of glioma growth in vivo by selective activation of the CB_2 cannabinoid receptor. *Cancer Res. 61*, 5784–5789.

(11) McKallip, R. J., Lombard, C., Fisher, M., Martin, B. R., Ryu, S. H., Grant, S., Nagarkatti, P. S., and Nagarkatti, M. (2002) Targeting CB_2 cannabinoid receptors as a novel therapy to treat malignant lymphoblastic disease. *Blood 100*, 627–634.

(12) Walter, L., and Stella, N. (2004) Cannabinoids and neuroinflammation. *Br. J. Pharmacol. 141*, 775–785.

(13) Pertwee, R. G. (2002) Cannabinoids and multiple sclerosis. *Pharmacol. Therapeut. 95*, 165–174.

(14) Gaoni, Y., and Mechoulam, R. (1964) Isolation, structure, and partial synthesis of an active constituent of hashish. *J. Am. Chem. Soc. 86*, 1646–1647.

(15) Witting, A., and Stella, N. (2004) Cannabinoid signaling in glial cells in health and disease. *Curr. Neuropharmacol. 2*, 115–124.

(16) Mackie, K., and Stella, N. (2006) Cannabinoid receptors and endocannabinoids: Evidence for new players. *AAPS J. 8*, E298–E306.

(17) Piomelli, D. (2005) The endocannabinoid system: a drug discovery perspective. *Curr. Opin. Invest. Drugs 6*, 672–679.

(18) Pertwee, R. G., and Ross, R. A. (2002) Cannabinoid receptors and their ligands. *Prostaglandins, Leukotrienes Essent. Fatty Acids 66*, 101–121.

(19) Oka, S., Ikeda, S., Kishimoto, S., Gokoh, M., Yanagimoto, S., Waku, K., and Sugiura, T. (2004) 2-Arachidonoylglycerol, an endogenous cannabinoid receptor ligand, induces the migration of EoL-1 human eosinophilic leukemia cells and human peripheral blood eosinophils. *J. Leukocyte Biol. 76*, 1002–1009.

(20) Roy, A. K., and Batra, S. (2003) Facile Baylis-Hillman reaction of substituted 3-isoxazolecarbaldehydes: The impact of a proximal heteroatom within a heterocycle on the acceleration of the reaction. *Synthesis-Stuttgart* 2325–2330.

(21) Seltzman, H. H., Foster, M. C., Wyrick, C. D., Burgess, J. P., and Carroll, F. I. (2005) Tritiation of the cannabinoid receptor antagonist SR144528 involving lithium aluminum tritide reduction; assessment of the kinetic isotope effect by H-3-NMR. *J. Labelled Compds. Radiopharm. 48*, 589–596.

(22) Suchocki, J. A., May, E. L., Martin, T. J., George, C., and Martin, B. R. (1991) Synthesis of 2-exo-mecamylamine and 2-endo-mecamylamine analogs - structure-activity-relationships for nicotinic antagonism in the central-nervous-system. *J. Med. Chem. 34*, 1003–1010.

(23) Weissleder, R. (2001) A clearer vision for in vivo imaging. *Nat. Biotechnol. 19*, 316–317.

(24) Shah, K., and Weissleder, R. (2005) Molecular optical imaging: applications leading to the development of present day therapeutics. *Am. Soc. Exp. NeuroTherapeutics 2*, 215–225.

(25) Rinaldi-Carmona, M., Barth, F., Millan, J., Derocq, J. M., Casellas, P., Congy, C., Oustric, D., Sarran, M., Bouaboula, M., Calandra, B., Portier, M., Shire, D., Breliere, J. C., and Le Fur, G. (1998) SR 144528, the first potent and selective antagonist of the CB_2 cannabinoid receptor. *J. Pharmacol. Exp. Therapeut. 284*, 644–650.

BC700419E

ARTICLES

High-Throughput Method for Ranking the Affinity of Peptide Ligands Selected from Phage Display Libraries

A. González-Techera,[†] M. Umpiérrez-Failache,[†] S. Cardozo,[†] G. Obal,[‡] O. Pritsch,[‡,§] J. A. Last,[||] S. J. Gee,[⊥] B. D. Hammock,[⊥] and G. González-Sapienza*,[†]

Cátedra de Inmunología, Facultad de Química, Instituto de Higiene, and Departamento de Inmunobiología, Facultad de Medicina, UDELAR, Montevideo, Uruguay, Institut Pasteur de Montevideo, Uruguay, and Pulmonary/Critical Care Medicine, School of Medicine, and Department of Entomology and Cancer Research Center, University of California, Davis, California.
Received July 23, 2007; Revised Manuscript Received February 18, 2008

The use of phage display peptide libraries allows rapid isolation of peptide ligands for any target selector molecule. However, due to differences in peptide expression and the heterogeneity of the phage preparations, there is no easy way to compare the binding properties of the selected clones, which operates as a major "bottleneck" of the technology. Here, we present the development of a new type of library that allows rapid comparison of the relative affinity of the selected peptides in a high-throughput screening format. As a model system, a phage display peptide library constructed on a phagemid vector that contains the bacterial alkaline phosphatase gene (BAP) was selected with an antiherbicide antibody. Due to the intrinsic switching capacity of the library, the selected peptides were transferred "en masse" from the phage coat protein to BAP. This was coupled to an optimized affinity ELISA where normalized amounts of the peptide−BAP fusion allow direct comparison of the binding properties of hundreds of peptide ligands. The system was validated by plasmon surface resonance experiments using synthetic peptides, showing that the method discriminates among the affinities of the peptides within 3 orders of magnitude. In addition, the peptide−BAP protein can find direct application as a tracer reagent.

INTRODUCTION

The development of phage-displayed peptide libraries (*1*) allows millions of peptides to be screened, simultaneously, for binding to a target of interest. In these libraries, any one bacteriophage displays a distinctive peptide sequence typically fused to either the pIII or pVIII viral coat protein. The peptide sequence can be encoded in the phage DNA, or most commonly in a phagemid system, consisting of a vector that codes for the peptide−viral coat protein fusion, and utilizes a "helper phage" to allow recombinant phage production. Since even a single peptide−target binding event can be detected and amplified, the technique has the potential to discover peptides that specifically bind to almost any target. For this reason, the technology has been applied in many fields (*2*–*5*).

Typically, the outcome of the selection procedure (panning) is analyzed by the so-called phage ELISA, but this test does not provide any information other than a negative/positive binding result. Further evaluation of positive clones requires DNA sequencing of the encoded peptide and the preparation of the encoded sequences as synthetic peptides, which must then be individually analyzed by competitive ELISA or surface plasmon resonance experiments in order to identify the peptide sequences that bind with the highest affinities. For most purposes, not only the specificity, but very importantly, the affinity of the selected peptides is a major issue. This approach is a time-consuming and costly step that constitutes a major bottleneck for the technique, because it restricts the number of clones that can be assayed, and thereby contributes to the loss of low-abundancy but valuable clones.

In order to overcome these limitations, several works have been published in which model peptides selected from a phage library are transferred by different strategies to a partner molecule (i.e., maltose binding protein, bacterial alkaline phosphatase, etc.) to analyze the reactivity of the peptide out of the context of the phage particle (*6*−*9*). Due to its enzymatic activity and good expression in bacteria, BAP has been one of the most studied scaffolds. In this regard, Han et al. (*9*) devised a convenient method for the transference of the selected peptides to a highly active form of BAP using a ligation-independent cloning protocol, but the information provided by their procedure was only in terms of positive or negative binding. Other authors worked to obtain additional information on the peptide reactivity, particularly with regard to their relative affinity for the selector molecule (*6*, *8*), but their approaches required one by one processing of the peptide−BAP candidates. Indeed, these methods require the purification of the peptide−BAP protein for each individual clone, followed by adjustment of the BAP activity of each clone in order to assay comparative amounts of individual peptides, which greatly restricts the number of clones that can be examined.

* Corresponding author. Av. A. Navarro 3051, piso 2, 11600 Montevideo, Uruguay; ggonzal@fq.edu.uy; tel (5982) 4874334.
[†] Facultad de Química, UDELAR.
[‡] Institut Pasteur de Montevideo.
[§] Facultad de Medicina, UDELAR.
[||] School of Medicine, University of California, Davis.
[⊥] Department of Entomology and Cancer Research Center, University of California, Davis.

10.1021/bc700279y CCC: $40.75 © 2008 American Chemical Society
Published on Web 04/05/2008

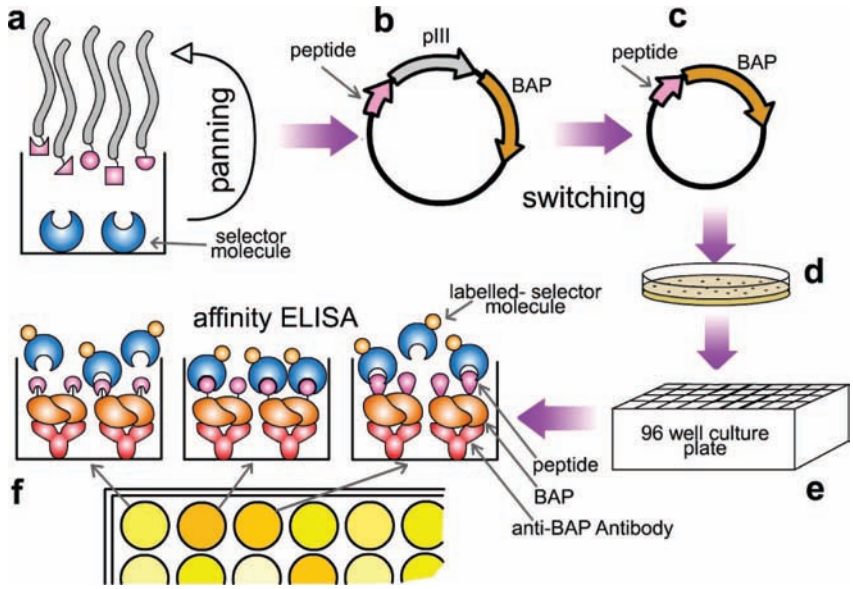

Figure 1. Schematic representation of the use of phage/mBAP switch libraries for the selection and high-throughput affinity evaluation of peptides. (a) The phage display paptide library containing the pAFF/mBAP vector is panned using standard protocols. (b) After 3–4 rounds of panning, the final phage output is amplified in *E. coli,* and the phagemid DNA is purified and digested with SpeI to delete pIII gene. (c) The digested pooled vectors are religated and used to transform *E. coli* to create a sublibrary of peptide−BAP fusion proteins. (d) The cells are plated and blue colonies (indicating BAP activity on the BCIP substrate) are individually transferred to 96-well block culture. (e) After overnight growth, the plates are centrifuged, the cell pellets are lysed with B-PER (Pierce), and the supernatants are analyzed by affinity ELISA. (f) Equal amounts of each peptide−mBAP protein are retained in the wells of a microtiter plate by capturing saturating concentrations of the cell lysates on wells coated with an anti-BAP antibody, and the fusion peptides are probed with the same concentration of the selector molecule (optionally labeled with biotin or a fluorescent tracer). Under these conditions, the readout of each well (amount of bound detector molecule) correlates with the affinity of the peptide under study.

To date, no practical procedure for high-throughput assessment of the relative affinities of the peptides selected from phage display libraries has been reported. Here, we present a novel method devised to solve the critical steps that limit this analysis. For this, we constructed a new type of phage display library with the intrinsic capacity of being easily "switched" into peptide−mBAP expression libraries. In this way, after initial selection of the phage library (usually three to four rounds of panning) the pool of selected phagemids is digested to remove the gene encoding the viral coat protein pIII, which allows fusion of the encoded peptides to the N-terminus of a highly active mutant bacterial alkaline phosphatase (mBAP). This switching process is coupled to a fast normalized selection procedure that does not require purification of the recombinant peptide−BAP fusions, and allows simultaneous direct investigation of hundreds of peptide candidates in terms of relative affinities and binding characteristics to the selector molecule. By this means, even if they are underrepresented, the most valuable peptide ligands can be rapidly identified. The method was developed and validated using a monoclonal antibody against the herbicide molinate as a model-selector molecule. In addition to providing information about the relative binding strengths of the peptides, the method yields ligand−enzyme recombinant proteins that can be used as tracer bioconjugates in different applications.

EXPERIMENTAL PROCEDURES

Cells and Plasmids. Vector pAFF2 (*10*) and *E. coli* cell strains ARI292 and ARI236 were kindly provided by Dr Peter Schatz; Affymax Research Institute, Palo Alto, CA. Vector pUY10 was a gift from Dr. Magela Laviña, Facultad de Ciencias, Montevideo, Uruguay. *E. coli* strain LMG194 (*11*), a strain derived from *E. coli* KS272 (*12*), a negative mutant for alkaline phosphatase, was a gift from Dr. Carina Gaggero, IIBCE, Montevideo, Uruguay.

Construction of pAFF/mBAP Phagemid Vector. Plasmid pUY10 encoding wild type BAP was used as template for PCR amplification using primers (5′-TC*AGTCGAC*ACTAGTGCT-GCTCAGGGCGATAT TACT-3′) and (5′-CAG*AAGCTT*T-TATTAGTGATGGTGATGGTGATGTTTCAGCC CCAGA-GCGGCTTTCATGGTGT- 3′). *Sal*I and *Hin*dIII restriction sites (italics) were introduced for cloning, as well as a SpeI site (underlined) at the 5′ end of the BAP gene to allow later elimination of pIII phage coat protein gene. After PCR amplification using *pfu* DNA polymerase (Stratagene), the BAP product was digested with *Sal*I and *Hin*dIII (New England Biolabs), and cloned into the arabinose regulatable phagemid vector pAFF2. Quickchange Site-Directed Mutagenesis Kit (Stratagene) was used both for removing a BstXI restriction site within BAP, as well as for introduction of a Asp101→Ser mutation in the BAP gene cloned in pAFF2. This amino acid change has been reported to possess enhanced BAP catalytic activity (mBAP) (*13*). The obtained phagemid was named pAFF/mBAP (Figure 2).

Cloning of a Model Peptide on pAFF/mBAP and Transference of the Peptide from pIII to mBAP. pAFF/mBAP vector was digested with BstXI restriction enzyme (New England Biolabs). The digested vector was mixed with two "half sites" adaptor oligonucleotides, ON-28 and ON-29, and the long DNA oligo coding for the cyclic peptide CAREGYPARYC, which binds to EB7 mAb (*14*) followed by a SpeI site (Figure **2**). The three oligonucleotides and the vector were annealed and later ligated with T4 DNA ligase (Invitrogen) using standard DNA procedures. ARI 236 competent cells were transformed with the ligation mix. Transformed cells were plated on LB agar ampicillin plates. DNA sequencing of clones confirmed the correct cloning of the model peptide fused to pIII phage coat protein. One of these clones was grown and a miniprep DNA extraction (Qiagen) was performed. Phagemid DNA was then digested with SpeI (New England Biolabs) restriction enzyme, removing pIII gene. Digestion was run on an agarose gel, and the band corresponding to the phagemid without the pIII gene was purified using QIAGEN Quiaquick gel extraction

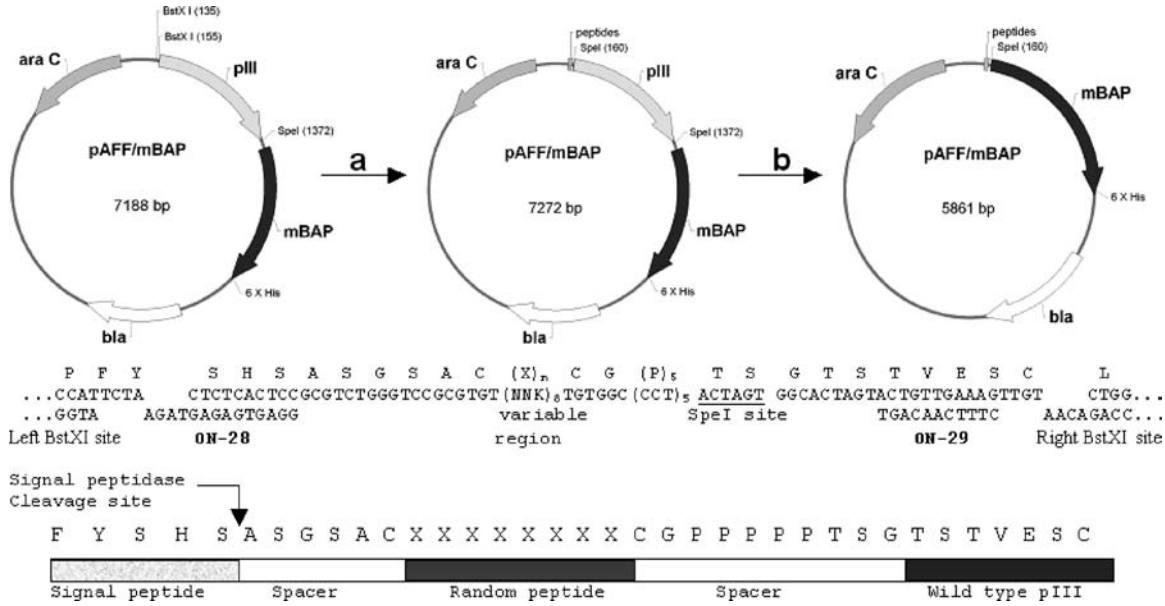

Figure 2. Representation of pAFF/mBAP vector, cloning of oligonucleotides in frame with pIII gene, and transfer of peptides from pIII to mBAP. pAFF/mBAP vector map: araC, arabinose represor gene; pIII, pIII phage coat protein gene; mBAP, mutated form of BAP gene with increased k_{cat}; bla, β-lactamase gene. (a) Library construction; the two BstXI restriction sites are used for cloning of the oligonucleotides encoding the peptides, as shown at the bottom. ON-28 and ON-29 adaptor oligonucleotides are used to form the cohesive termini required for ligation (bottom). The amino acid sequence of the assembled library is also shown at the bottom. (b) Library switching; SpeI digestion and ligation is used to switch from peptide−pIII to peptide−BAP expression. The SpeI restriction site required for this "switch" is shown underlined in the oligonucleotide sequence.

kit and ligated as described above. ARI 236 competent cells were transformed with the ligation mix. A direct screening for successful fusion of peptides−mBAP was performed by plating the transformed cells in LB plates with ampicillin (100 μg/mL), 0.2% arabinose, and BCIP (5-bromo, 4-chloro, 3-indolylphosphate (Pierce) at 40 μg/mL). After overnight incubation of the plates at 37 °C, bacterial colonies expressing peptide−BAP fusions could be clearly distinguished from colonies that were BAP by simply checking for blue colonies.

Capture of CAREGYPARYC-mBAP in ELISA Plate Wells. ARI 236 cells expressing the model fusion CAREGYPARYC-mBAP were cultured for 6 h at 37 °C after inducing with 0.2% arabinose. Cells were then pelleted by centrifugation (in aliquots of 1 mL) and the pellets were frozen at –80 °C. The cell pellet was lysed with 300 μL of B-PER reagent (Pierce) plus 1/25 volume of Complete EDTA-FREE Protease Inhibitor Cocktail (Roche Diagnostics, GmbH). Cell lysates were centrifuged and the supernatants were transferred to low-binding, nontreated, polystyrene plates (100 μL lysate + 100 uL AP wash buffer (50 mM Tris−Hcl pH = 8; 150 mM NaCl; 0.05% Tween-20)) and serial dilutions (twofold) were then performed in AP wash buffer. Dilutions were transferred to a 96-well microtiter plate (Nunc-Immuno Plate Maxi-Sorp) precoated with anti-BAP monoclonal antibody (mAb) (Sigma) at 1.25 μg/mL of IgG1 in 1× PBS (phosphate-buffered saline), polyclonal anti-BAP antibody (Polysciences, Inc.) at 2.5 μg/mL of total IgG in PBS 1×, both of them preblocked with BSA 1%. These serial dilutions were also transferred to a microtiter plate coated with Ni-NTA (Qiagen) and blocked with 1% bovine serum albumin (Sigma) in PBS buffer. Wells were washed 5 times with AP wash buffer and mBAP activity was detected by adding PNPP (*p*-nitrophenyl phosphate at 1 mg/mL) substrate (Pierce) in 50 mM Tris pH = 10, 200 mM NaCl, 1 mM $MgCl_2$. Plates were read at 405 nm in a microtiter plate reader (Multiskan MS, Labsystems).

Peptide Library Construction on pAFF-mBAP and Panning Procedure. A peptide phage library was constructed on pAFF/mBAP vector and harvested as described by Cwirla et al. (*15*). Library diversity was estimated to be around 2×10^8 independent clones. This library was panned against an antimolinate (herbicide) (*16*) mAb 14D7. Microtiter plates (Nunc-Immuno Plate Maxi-Sorp) were coated with mAb 14D7 at 5 μg/mL in PBS by incubating overnight at 4 °C (100 μL per well). Blocking was performed by completely filling the wells with 1% BSA in PBS and incubating at 37 °C for 1 h. After blocking, each well was washed 5 times with PBS−0.5% Tween-20 (PBST) and peptide library in PBS 1×−BSA1% was added to 6 precoated wells (approximately a total of 10^{11} phage particles). The plate was incubated for 2 h at 4 °C; wells were washed 10 times with cold PBST to remove unbound phages. Bound phages were eluted by adding 100 μL per well of elution buffer (0.1 N glycine, pH = 2.2 adjusted with HCl) and incubating at room temperature for 10 min. Neutralization of pH was done by adding 35 μL of 2 M Tris (pH unadjusted). The eluted phage (300 μL) were added to 10 mL of log-phase *E. coli* ARI 292 cells and amplified in LB media containing 0.25% K_2HPO_4, 0.1% $MgSO_4$, 0.1% glucose, and 100 μg/mL ampicillin to an OD_{600} = 0.4. Helper phage M13KO7 at a multiplicity of infection 10:1 was added. After a period of 30 min at 37 °C without shaking, arabinose and kanamycin were added at a final concentration of 0.02% and 40 μg/mL, respectively, and the cultures incubated overnight at 37 °C with vigorous shaking. This panning protocol was then repeated twice, and after three rounds of panning, individual amplified

Table 1. Peptide Sequences of Clones Isolated in the Third Round of Panning with mAb 14D7[a]

clone	peptide sequence
clone 8	C K G L H M W F N C
clone 4	C A **N P W L** L **K Y** C
clones 1, 9, 10	C N **N P W L** A **K Y** C
clones 2, 5	C A A M **G G W** S **K** C
clones 6, 7	C A G F **G G W** A **K** C
clone 3	C H L L **G G W** A **K** C

[a] Peptides are grouped on the basis of their consensus sequence; conserved amino acids are shown in bold.

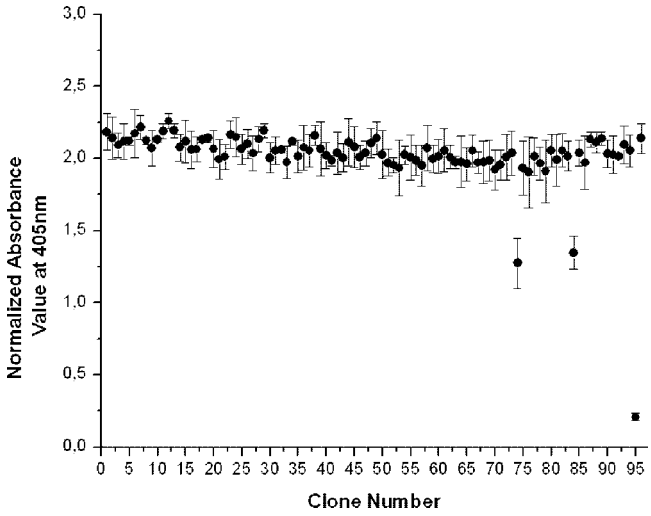

Figure 3. Comparative captured BAP activity of different peptide−mBAP fusion clones. Cell lysates from peptide−mBAP fusion expressing clones were used to saturate the binding capacity of microtiter plate wells coated with anti-BAP polyclonal antibodies. The retained BAP activity was detected with PNPP substrate, under conditions of initial velocity. Each value represents the average of three independent experiments (starting from the culture). The readout of replicates was normalized as described in the Methods section. Clone 95 corresponds to a negative control clone (LMG194 cells transformed with pAFF2 vector).

phage clones were tested for their ability to bind 14D7 coated wells. Phage ELISAs were performed as reported before (*5*).

High-Throughput Screening of the Peptide-mBAP Sublibrary Enriched in Clones Specific for mAb 14D7. ARI 292 cells were infected with approximately 5×10^7 phage particles from the third output of panning and grown in LB−ampicillin as described. Phagemid DNA was obtained using the Qiagen miniprep kit (Qiagen). The encoded peptides were fused to mBAP by switching with SpeI as described above. Competent LMG194 was transformed with the ligation mix and plated as described above. Blue colonies were individually inoculated in 0.5 mL of LB−ampicillin with 0.1% glucose in wells of a 2 mL 96-well block (Qiagen). The plate was sealed with airpore tapesheets (Qiagen) and grown with shaking at 37 °C. The next day, 80 μL of glycerol were added, and the block was frozen at –80 °C (master plate).

Replicates of this plate were established by touching the surface of the master plate frozen cultures with a multichannel micropipette using sterile tips. The tips were then used to inoculate 1 mL cultures of LB−ampicillin, 0.1% glucose, that were grown at 37 °C in a 96-well block. The next day, 5 μL was used to inoculate wells of a fresh block containing 1 mL of LB−ampicillin and 0.2% arabinose. The block plate was incubated for 6 h at 37 °C with vigorous shaking and was then centrifuged for 30 min at 1200 $\times$ *g* at 4 °C. The supernatant was discarded, and the pelleted cells were frozen at –80 °C. Each cell pellet was lysed with 300 μl of B-PER reagent (Pierce) plus 1/25 volume of Complete EDTA-FREE Protease Inhibitor Cocktail (Roche Diagnostics, GmbH) by gently pipetting up and down and using a multichannel micropipette. Cell lysates were centrifuged as previously, and 100 μL of each clone supernatant were transferred with a multichannel micropipette to each of two ELISA plates precoated with polyclonal anti-BAP antibody, and preblocked with 1% BSA. After 1 h incubation, one of the plates was washed 10 times with AP wash buffer, followed by addition of 100 μL of PNPP in substrate buffer (50 mM Tris, 200 mM NaCl, 1 mM $MgCl_2$, pH 10), and the reaction was incubated at 37 °C. The plate was read at 405 nm in a microtiter plate reader (Multiskan MS, Labsystems). The second plate was washed with PBS, 0.05% Tween 20 (PBST), and probed with 100 μL of biotinylated mAb 14D7 (0.6 μg/mL) in PBST for 1 h at room temperature. After washing, streptavidin−peroxidase (Roche Diagnostics) conjugate was added (1:1000 dilution) and incubation was continued for 30 min at room temperature. The plate was washed with PBST, and 100 μL of the peroxidase substrate (0.4 mL of a 6 mg/mL DMSO solution of 3,3′,5,5′-tetramethylbenzidine (TMB) and 0.1 mL of 1% H_20_2 in water in a total of 25 mL of 0.1 M citrate acetate buffer, pH 5.5) was dispensed into each well. The enzymatic reaction was stopped by the addition of 50 μL of 2 M H_2SO_4, and the absorbance was read at 450 nm. Three replicates were prepared in this way to perform three independent experiments for plates A and B. Values obtained for clone number 1 were used as an internal control for normalization of the ELISA values.

Affinity Measurement by Surface Plasmon Resonance. Interaction analyses were performed using a Biacore 3000 optical biosensor equipped with research-grade CM5 sensor chips (Biacore AB, Uppsala, Sweden). Data were collected at the highest collection rate, with the biosensor instrument thermostatted to 25 °C. HBS-P (10 mM Hepes, 0.15 M NaCl, 0.005% P20 surfactant, pH 7.4) running buffer, amine coupling reagents (*N*-ethyl-(3- dimethylaminopropyl) carbodiimide (EDC), *N*-hydroxysuccinimide (NHS), and ethanolamine HCl) were purchased from Biacore AB. mAb14D7 was immobilized on a CM5 sensor chip using standard amine-coupling chemistry. The carboxymethyl dextran surface was activated with a 7 min injection of a 1:1 ratio of 0.4 M EDC/0.1 M NHS. The antibody was coupled to the surface with a 7 min injection of 14D7 mAb diluted in 10 mM sodium acetate (pH = 5.0). Remaining activated groups were blocked with a 7 min injection of 1 M ethanolamine (pH = 8.5). The immobilization procedure was performed at 25 °C and a 14D7 surface density of approximately 12 000 RU was obtained. Peptides were assayed on the sensor chip in the 20 nM to 100 μM range.

Purification of Peptide−mBAP. Selected clones expressing different fusions were grown expressing the recombinant protein. Recombinant proteins were purified by standard Ni-NTA agarose (Qiagen) following manufacturers' instructions. An aliquot of the purified proteins was run on a 12% SDS-PAGE and stained with Coomasie blue.

Competitive Molinate Standard Curves Performed with Peptide−mBAP as Tracers. Nunc Maxisorp ELISA plates were coated with 0.6 ug/mL of 14D7 mAb and blocked as described above. After that, a fixed amount of peptide−mBAP previously assessed by checkerboard titration was mixed with different amounts of molinate and transferred to the 14D7 mAb coated wells, to allow competition for binding to the antibody. After 1 h incubation, plates were washed with AP Wash buffer and PNPP substrate was added. Plates were read as described above.

RESULTS

Overall View of the Concept of Phage/mBAP Switch Libraries and Vector Construction. The basic principles underlying the use of phage/mBAP switch libraries for the selection and evaluation of peptides are schematized in Figure 1. As shown in the figure, the system relies on two critical steps: first, it must allow massive transfer of the individual peptides selected on the phages to create a large peptide−mBAP library. Second, the peptide−mBAP expression library must be easily examined for the desired binding properties of the peptides. The developments required to accomplish these two aims are described in the following sections.

Vector Construction. Vector pAFF/mBAP (Figure 2), which contains a truncated version of the mutated *E. coli* BAP, was

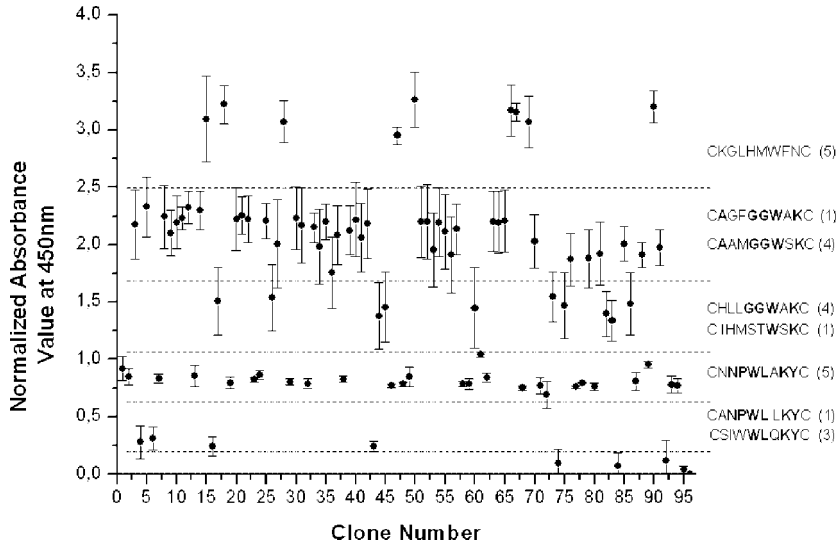

Figure 4. Affinity ELISA performed on the peptide−BAP fusion proteins probed with mAb 14D7. Saturating amounts of peptide−BAP fusion proteins captured on anti-BAP polyclonal antibody-coated wells were reacted with the same low amount of biotinylated mAb 14D7, and developed with streptavidin−horseradish peroxidase conjugate. According to the readouts, the peptides were divided into five groups (dotted lines). The sequences of five representative clones of each group are shown on the right side (consensus residues in bold), with their frequency indicated in parentheses. Each value represents the average of three independent experiments, each of them starting from a new culture from the "master plate". The readout of replicates was normalized as described in the Methods section. Clone 95 corresponds to a negative control clone (LMG194 cells transformed with pAFF2 vector).

Table 2. Kinetic Parameters of the Peptide−Antibody Interaction Measured by Surface Plasmon Resonance

peptide sequence	k_{on} (M^{-1} s^{-1})	k_{off} (s^{-1})	K_d (M)
CKGLHMWFNC	$3.1 \pm 0.1 \times 10^5$	$1.6 \pm 0.1 \times 10^{-2}$	$5.1 \pm 0.1 \times 10^{-8}$
CAAMGGWSKC	$8.3 \pm 0.1 \times 10^3$	$7.3 \pm 0.1 \times 10^{-3}$	$8.8 \pm 0.2 \times 10^{-7}$
CHLLGGWAKC	$2.8 \pm 0.1 \times 10^4$	$6.4 \pm 0.1 \times 10^{-2}$	$2.3 \pm 0.1 \times 10^{-6}$
CNNPWLAKYC	–	–	1×10^{-4} [a]

[a] No binding was observed for this peptide at the highest concentration (100 μM) assayed, indicating that its K_d is higher than 10^{-4} M, the detection limit of the Biacore 3000 instrument.

constructed as described in the Methods section. A shortened version of BAP (lacking residues 1–10) was used because it has been reported to be more resistant to proteolysis (*17*) with no loss of catalytic activity (*18*). A 6 × His tag was appended to its C-terminus to facilitate the purification of the recombinant protein. The vector contains two noncomplementary BstXI sites that are used to insert the random oligonucleotide sequences encoding the peptides. Oligonucleotide cloning introduces an additional SpeI site that allows later switching of peptide fusions from pIII to BAP.

Switch from pIII to m-BAP Using a Model Peptide. The system was initially explored using the model cyclic peptide CAREGYPARYC, which binds to mAb EB7 (*14*). The DNA sequence encoding for the peptide was cloned in frame with pIII in the pAFF-mBAP vector. Later, this construct was digested with SpeI (Figure 2), then ligated and used for transformation of *E. coli* ARI236. Peptides correctly fused to mBAP could be identified as blue colonies on LB ampicillin agar plates after addition of arabinose and the chromogenic substrate for alkaline phosphatase, BCIP (Figure 1d). Although the cells used for transformation (ARI236) have the wild-type alkaline phosphatase gene in their chromosome, streaking of this strain in control plates produced white colonies suggesting that endogenous expression of alkaline phosphatase is negligible. Fusion of peptides to mBAP through SpeI switching proved to be highly efficient, as nearly 99% of the colonies were positive by the BCIP assay.

Analysis of Peptide−mBAP Expression and Immobilization in ELISA Plate Wells. The expression of the peptide−mBAP fusion was studied using cell cultures of ARI 236 expressing the CAREGYPARYC−mBAP protein. After 6 h induction with arabinose, the expression of the recombinant peptide−BAP protein was analyzed by Western blot. The immunoreactivity of the peptide was easily detectable with mAb EB7 (*14*) and comparable to that of BAP with the anti-BAP antibody (Supporting Information, Figure A). Since BAP spontaneously forms dimers by self-association, two copies of the peptide are expected to be displayed when the enzyme is used as scaffold. Further analysis of the CAREGYPARYC−mBAP expression was tested by growing the clone in 1 mL cultures in 96-well culture blocks (supplementary methods). The cell pellet was lysed with B-PER reagent, and the supernatant was incubated into microtiter wells precoated with different antibodies or Ni-NTA. Saturation was directly examined by measuring BAP activity (Supporting Information, Figure B). The best capture efficiency was obtained with polyclonal anti-BAP antibodies. The supernatant could be diluted over 100 times without significant change in signal, showing that the amount of recombinant CAREGYPARYC−mBAP obtained from 1 mL culture was in large excess of the amount required to saturate the wells. This result proved to be valid for other peptide sequences as shown in the following section. The endogenous alkaline phosphatase activity, although detectable, was negligible and about 500-fold less than that of the recombinant protein. Nevertheless, to rule out any possible interference of this activity, we adopted the strain LMG194 for all of the following expression experiments. This strain is mutant for alkaline phosphatase, and also for the catabolic arabinose genes, and hence induction of gene expression can be done without arabinose being consumed by *E. coli*.

Panning a Library Constructed in pAFF-mBAP, Output Diversity and Switch of Selected Peptides from pIII to mBAP. A library coding for 8-mer cyclic peptides with an estimated diversity of 2×10^8 independent clones was constructed on phagemid pAFF-mBAP. As model selector molecule we used mAb 14D7 (Figure 1a), which is specific for the herbicide molinate, and is the basis for a competitive assay for this herbicide (*16*). Since competitive elution with the analyte would not warrant elution of the highest-affinity clones, we used acid conditions in order to ensure that all low- and high-affinity

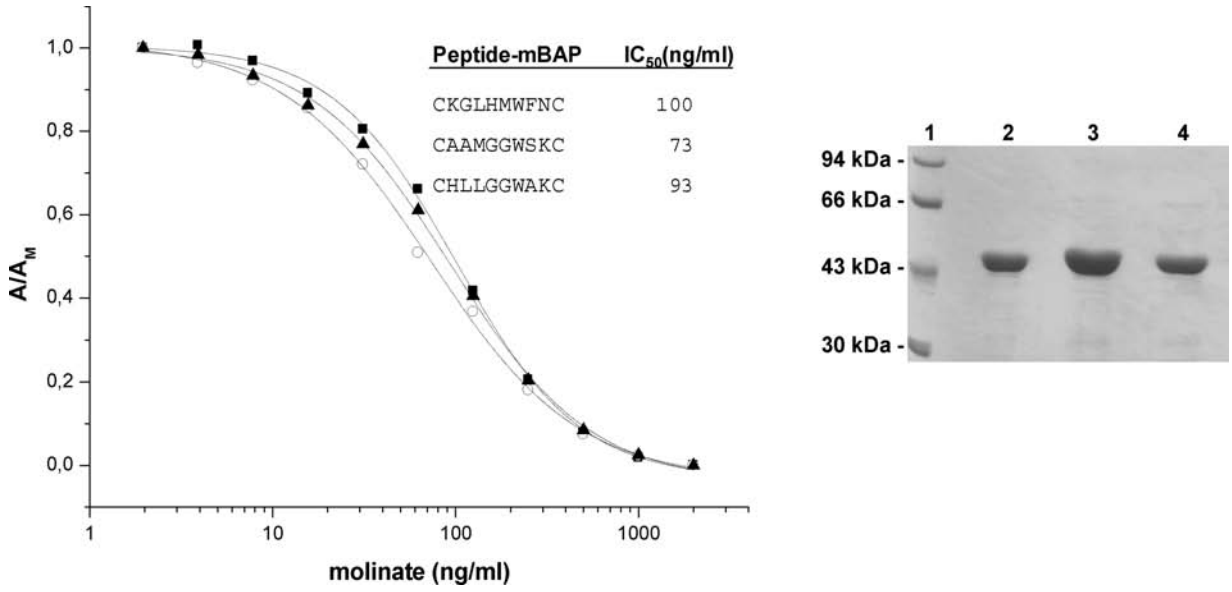

Figure 5. Purified peptide−mBAPs used as tracers in molinate competitive standard curves. Left panel: Peptides belonging to three groups with different affinities for mAb 14D7 (used for coating in the ELISA wells) were used as tracers to obtain competitive molinate standard curves. The peptide sequences and the corresponding amounts of molinate necessary to produce a 50% loss in signal (IC_{50}) are shown in the insert. Right panel: SDS-PAGE Coomassie blue stained: lane (1) molecular weight marker, (2) commercial affinity purified native BAP (Sigma), (3) Ni-NTA-agarose purified CAAMGGWSKC-mBAP, (4) Ni-NTA-agarose purified CHLLGGWAKC-mBAP.

clones were selected. After three rounds of panning, individual phage clones were tested for binding to the antibody by ELISA on plates coated with either mAb 14D7 or BSA (negative control). Ten out of ten clones examined were specific for the antibody, and six different sequences were identified (Table 1). Thus, at this point of the selection process most clones were specific and diverse, which was very convenient for the purpose of developing a method for ranking the affinities of a high number of clones. DNA from this pool of phage was "switched" with SpeI as described in the methods section (Figure 1b,c) and electroporated into LMG194. Blue colonies were picked from an arabinose-BCIP plate (Figure 1d) and were used to inoculate the "master plate" described in the Methods section.

High-Throughput Screening of the Relative Affinities of mAb 14D7 Specific Peptides. As mentioned before, the intrinsic affinity of the peptides for the selector molecule can not be estimated by phage ELISA (*6*). To overcome this limitation, we devised a method that rapidly normalizes the amount of peptide ligand to be tested by capturing saturating amounts of peptide−mBAP fusion on each of the microtiter wells to be analyzed. The method was applied to screen the third output of the panning experiment. Individual clones expressing peptide−mBAP fusions were picked from the "master plate", grown, and later lysed in 96-well square culture plates as described in the Methods section. Cell lysates were transferred to two identical plates coated with polyclonal anti-BAP antibody. One of the plates was used to verify that the same molar amount of each peptide−mBAP fusion (same BAP activity under conditions of initial velocity) was retained in each well, Figure 3. This was valid for all but two of the clones examined, clones 74 and 84. Once it was verified that the same amount of the peptides were retained in each well, mAb 14D7 (0.6 μg/mL) was used to examine the reactivity of the peptides. Under these conditions, the signal of each well is expected to be proportional to the affinity of the peptide for the antibody (Figure 1f). On the basis of the ELISA signal, the clones were grouped in five categories (Figure 4). Excellent reproducibility was attained for individual clones analyzed in three independent experiments. Sequence analysis of five clones from each category revealed peptide sequences characteristic of each group, supporting the assumption that the method sorts the peptides according to their reactivity with the antibody. Notice that, in none of the cases, was a peptide sequence belonging to a particular affinity group found in another group. To confirm this, four representative peptides belonging to each of the different affinity groups were synthesized (including disulfide formation). Binding of the soluble peptides to mAb 14D7 was studied using surface plasmon resonance. The results confirmed that the method properly sorts the peptides in a range of up to 3 orders of magnitude as shown in Table 2. Peptide CNNPW-LAKYC, which was the most abundant after selection, exhibited immeasurable interaction on the Biacore chip, showing that the avidity effect due to the two peptide copies expressed in the peptide−mBAP protein may be the cause of the moderate binding observed in the affinity ELISA. In spite of its low affinity for the antibody, this peptide was most probably preferentially selected due to a favorable expression in *E. coli*, which resulted in an over-representation of this phage clone in the amplified phage stock. This may also promote a multivalent display of the peptide in the phage particle reinforcing the avidity of the interaction with the antibody. Supporting that, experimental evidence of the preferential expression of this peptide was obtained during the preparation of the recombinant peptide−mBAP fusion proteins (not shown).

Finally, notice that, in addition to favor the selection of the desired peptides, the method produces peptide−mBAP fusions that have the potential of being used directly as probe or tracer reagents in different applications. Supporting that, the peptide−mBAP fusions of three of the peptides selected here could be used to set up sensitive competitive assays for molinate as shown in Figure 5. Similar IC_{50} values were obtained with the three peptide−mBAP tracers, and these values were similar to that obtained for the competitive assay set up using the chemically synthesized hapten (*16*) (69 ng/mL).

DISCUSSION

In the past decades, phage display has been consolidated as a reliable and rapid technology for the identification of bioactive peptides and antibody fragments selected from high-diversity libraries. For most purposes, not only the specificity, but very importantly, the affinity of the selected peptides is a major issue.

This is particularly true for bioactive peptides that must show agonist or antagonist activity at the low concentration reached at the place of action. For this reason, the affinity of the peptides obtained after the initial selection from fully random peptide libraries is often improved through the construction of a secondary phage display library (mutagenesis library). In the mutagenesis libraries, the consensus residues of the initial phage pool are over-represented to favor the optimization of their flanking residues along the selection process (*10, 19*). In both cases (random and mutagenesis libraries), the outcome of the panning experiments should be easily examined to identify the higher-affinity clones. However, the identification of high-affinity binders among the pool of selected phage-borne peptides is not an easy task, and there is currently no systematic, yet practical, method to do this.

To deal with this problem, several alternative methods have been developed to facilitate the evaluation of the specificity and relative affinity of the isolated peptides; some of these methods use BAP as a partner fusion protein to study the peptide out of the context of the phage (*69*), but they are not compatible with high-throughput analysis. Here, we present a simpler method for the generation of large collections of clones expressing peptide−BAP fusions, coupled with a new method for rapid and simultaneous evaluation of the relative affinity of a large numbers of clones. In this method (affinity ELISA), the BAP activity works as an internal control to verify that equal amounts of peptides are assayed in each well of the affinity ELISA. Notice that the use of a much simpler affinity ELISA based on the capture of the phage particle bearing the peptide with an antiphage antibody would not produce reliable results due to the differential expression of individual peptides, which, as discussed above, would affect the average copy number of the displayed peptides.

The method showed excellent reproducibility and allowed us to sort the peptides within a wide range of affinities (up to 3 orders of magnitude) as shown by surface plasmon resonance analysis. Although we cannot rule out that, depending on their sequences, the peptides may show occasional interactions with the fusion partner that affect their binding to the target, in the four cases examined here there was a complete agreement between the affinity ELISA and the surface plasmon resonance analysis. By modification of the affinity ELISA conditions, it may be possible to shift this range to the target affinity (i.e., using stringent washing, lower amount of selector molecule, lowering the incubation time with the substrate, etc.). Interestingly, the highest-affinity clone (CKGLHMWFNC) which happened to be a low-abundance clone (about one in ten in the third output) could be easily spotted. This shows the potential of the method as a tool to identify valuable clones that are underrepresented in the selected phage pool. These "rare" nonconsensus fitting and low-frequency clones would be probably lost by the standard procedure of DNA sequencing and chemical peptide synthesis based on consensus or single sequences.

An additional benefit of the method is that the selected peptides can be directly produced as recombinant peptide–protein fusions. In our model, the recombinant peptide is linked to a high-turnover mutated form of BAP, in a fixed stoichiometric relationship, constituting a highly defined bioconjugate reagent that can be promptly used, for instance, as an immunoassay reagent. The applications of the concept of switch phage libraries can be extended to fusion partners others than BAP. In principle, any gene that is properly expressed in the periplasmic compartment of *E. coli* could be used to substitute the BAP gene in the pAFF/mBAP-PhoA vector, allowing the creation of sublibraries carrying the desired gene. This may include a different tracer activity such as firefly luciferase or green fluorescent protein to monitor intracellular binding of the peptides, or intein genes, that may help to produce the free recombinant peptide.

ACKNOWLEDGMENT

This work was supported in part by National Institute of Health, Fogarty International Center Grant (TW05718); Dirección de Innovación Ciencia y Tecnología, Uruguay (PDT54-41); the National Institute of Environmental Health Sciences (Superfund Basic Research program P42 ES04699, Center P30 ES05707).

Supporting Information Available: Reactivity of the recombinant peptide−mBAP fusion protein with antipeptide antibody (EB7 mAb); capture of CAREGYPARYC−mBAP fusion on ELISA plates using different coating reagents. This material is available free of charge via the Internet at http://pubs.acs.org/BC.

LITERATURE CITED

(1) Smith, G. P. (1985) Filamentous fusion phage: novel expression vectors that display cloned antigens on the virion surface. *Science 228*, 1315–1317.

(2) Szardenings, M. (2003) Phage display of random peptide libraries: applications, limits, and potential. *J. Recept. Signal Transduction Res. 23*, 307–349.

(3) Weber, P. C., Pantoliano, M. W., and Thompson, L. D. (1992) Crystal structure and ligand-binding studies of a screened peptide complexed with streptavidin. *Biochemistry 31*, 9350–9354.

(4) Oldenburg, K. R., Loganathan, D., Goldstein, I. J., Schultz, P. G., and Gallop, M. A. (1992) Peptide ligands for a sugar-binding protein isolated from a random peptide library. *Proc. Natl. Acad. Sci. U.S.A. 89*, 5393–5397.

(5) Cardozo, S., Gonzalez-Techera, A., Last, J. A., Hammock, B. D., Kramer, K., and Gonzalez-Sapienza, G. G. (2005) Analyte peptidomimetics selected from phage display peptide libraries: a systematic strategy for the development of environmental immunoassays. *Environ. Sci. Technol. 39*, 4234–4241.

(6) Wright, R. M., Dudas, D., Gavin, B., Dottavio, D., Hexham, J. M., and Lake, P. (2001) A high-capacity alkaline phosphatase reporter system for the rapid analysis of specificity and relative affinity of peptides from phage-display libraries. *J. Immunol. Methods 253*, 223–232.

(7) Zwick, M. B., Bonnycastle, L. L., Noren, K. A., Venturini, S., Leong, E., Barbas, C. F., 3rd, Noren, C. J., and Scott, J. K. (1998) The maltose-binding protein as a scaffold for monovalent display of peptides derived from phage libraries. *Anal. Biochem. 264*, 87–97.

(8) Huang, X., Zhang, X. E., Zhou, Y. F., Zhang, Z. P., and Cass, A. E. (2007) Construction of a high sensitive Escherichia coli alkaline phosphatase reporter system for screening affinity peptides. *J. Biochem. Biophys. Methods 70*, 435–439.

(9) Han, Z., Karatan, E., Scholle, M. D., McCafferty, J., and Kay, B. K. (2004) Accelerated screening of phage-display output with alkaline phosphatase fusions. *Comb. Chem. High Throughput Screen. 7*, 55–62.

(10) Martens, C. L., Cwirla, S. E., Lee, R. Y., Whitehorn, E., Chen, E. Y., Bakker, A., Martin, E. L., Wagstrom, C., Gopalan, P., Smith, C. W., et al. (1995) Peptides which bind to E-selectin and block neutrophil adhesion. *J. Biol. Chem. 270*, 21129–21136.

(11) Guzman, L. M., Belin, D., Carson, M. J., and Beckwith, J. (1995) Tight regulation, modulation, and high-level expression by vectors containing the arabinose PBAD promoter. *J. Bacteriol. 177*, 4121–4130.

(12) Strauch, K. L., and Beckwith, J. (1988) An Escherichia coli mutation preventing degradation of abnormal periplasmic proteins. *Proc. Natl. Acad. Sci. U.S.A. 85*, 1576–1580.

(13) Mandecki, W., Shallcross, M. A., Sowadski, J., and Tomazic-Allen, S. (1991) Mutagenesis of conserved residues within the active site of *Escherichia coli* alkaline phosphatase yields enzymes with increased kcat. *Protein Eng. 4*, 801–804.

(14) Gonzalez-Sapienza, G., and Cachau, R. E. (2003) Identification of critical residues of an immunodominant region of Echinococcus granulosus antigen B. *J. Biol. Chem. 278*, 20179–20184.

(15) Cwirla, S. E., Peters, E. A., Barrett, R. W., and Dower, W. J. (1990) Peptides on phage: a vast library of peptides for identifying ligands. *Proc. Natl. Acad. Sci. U.S.A. 87*, 6378–6382.

(16) Rufo, C., Hammock, B. D., Gee, S. J., Last, J. A., and Gonzalez-Sapienza, G. (2004) Robust and sensitive monoclonal enzyme-linked immunosorbent assay for the herbicide molinate. *J. Agric. Food. Chem. 52*, 182–187.

(17) Nakata, A., Shinagawa, H., Rothman, F. G. (1987) *Phosphate Methods*, Torriani, Ed., p 139, American Society, Washington, DC.

(18) Hoffman, C. S., and Wright, A. (1985) Fusions of secreted proteins to alkaline phosphatase: an approach for studying protein secretion. *Proc. Natl. Acad. Sci. U.S.A. 82*, 5107–5111.

(19) Wrighton, N. C., Farrell, F. X., Chang, R., Kashyap, A. K., Barbone, F. P., Mulcahy, L. S., Johnson, D. L., Barrett, R. W., Jolliffe, L. K., and Dower, W. J. (1996) Small peptides as potent mimetics of the protein hormone erythropoietin. *Science 273*, 458–464.

BC700279Y

Synthesis and Evaluation of a Novel Fluorescent Photoprobe for Imaging Matrix Metalloproteinases

Andreas Faust,*[,†,‡,§] Bianca Waschkau,[†,§] Jens Waldeck,[†] Carsten Höltke,[†,‡] Hans-Jörg Breyholz,[‡] Stefan Wagner,[‡] Klaus Kopka,[‡] Walter Heindel,[†] Michael Schäfers,[‡,||] and Christoph Bremer[†,||]

Department of Clinical Radiology and Department of Nuclear Medicine, University Hospital Münster, Albert-Schweitzer-Str. 33, 48149 Münster, Germany, and Interdisciplinary Center for Clinical Research (IZKF Münster), Domagkstr. 3, University of Münster, 48149 Münster, Germany. Received November 5, 2007; Revised Manuscript Received February 1, 2008

The measurement of matrix metalloproteinase (MMP) activity in diseases like inflammation, oncogenesis, or atherosclerosis in vivo is highly desirable. Fine-tuned pyrimidine-2,4,6-triones (barbiturates) offer nonpeptidyl lead structures for developing imaging agents for specifically visualization of activated MMPs in vivo. The aim of this study was to modify a C-5-disubstituted barbiturate and thus design a highly affine, nonpeptidic, optical MMP inhibitor (MMPI)-ligand for imaging of activated MMPs in vivo. A convergent 10 step synthesis was developed, starting with a malonic ester and (4-bromophenoxy)benzene to generate 5-bromo-pyrimidine-2,4,6-trione as the key intermediate. To minimize the interactions between activated MMPs and the dye of the conjugate **6**, a PEGylated piperazine derivative was used as a spacer and an azide as a protected amino function. After linking both building blocks, reducing the azide (*Staudinger* reaction) and labeling with Cy 5.5, we obtained the nonhydroxamate MMP inhibitor **6** with high affinity (IC_{50}-value: 48 nM for MMP-2) measured in a fluorogenic assay using commercially available MMP-substrates and the purified enzyme. Zymography revealed an efficient blocking of enzyme activity of purified MMP-2 and MMP-9 and of MMP-containing cell supernatants (HT-1080), (A-673) using the PEGylated barbiturate **5**. Fluorescence microscopy studies using a highly (A-673) and a moderate (HT-1080) MMP-2 secreting cell line showed efficient binding of the Cy 5.5 labeled tracer **6** to the MMP-2 positive cells while MMP-2 negative cells (MCF-7) did not bind. Therefore, this new barbiturate-based MMP-probe has a high affinity and specificity toward MMP-2 and -9 and is thus a promising candidate for sensitive MMP detection in vivo.

INTRODUCTION

Molecular imaging of locally upregulated and activated matrix metalloproteinases (MMPs) in vivo is a clinical challenge. MMPs are zinc- and calcium-dependent endopeptidases and represent a subfamily of the metzincin superfamily. They are able to degrade all protein components of the extracellular matrix (ECM) with overlapping substrate specificities (*1–3*).

To date more than 20 human MMPs have been characterized. Based on their specificity the MMPs are classified into collagenases, gelatinases, stromelysins, and matrilysins. Another subclass of the MMPs is represented by the membrane-type MMPs (MT-MMPs) (*4, 5*). An increased MMP expression is associated with pathophysiological processes including the progression of cancer, cardiovascular diseases such as atherosclerosis, and inflammation (*6–13*).

Recently, the pyrimidine-2,4,6-triones (or barbiturates) were identified as nonhydroxamate MMP inhibitors that exhibit specific activities for a subgroup of secreted MMPs comprising the gelatinases A (MMP-2) and B (MMP-9), neutrophil collagenase (MMP-8), the membrane bound MMPs, MT-1-MMP (MMP-14), and MT-3-MMP (MMP-16) (*14*). Barbiturates are, therefore, promising candidates for molecular imaging of MMP activity. The enolic tautomer of the pyrimidine-2,4,6-triones binds to the zinc active site (*15, 16*). Recently, C-5-disubstituted pyrimidine-2,4,6-triones were exploited as a new class of potential MMP inhibiting radiotracers with improved MMP binding potency (*17, 18*).

Fluorochrome-based molecular tracers have been shown to allow highly sensitive visualization of molecular targets. Moreover, optical technologies are inexpensive and free of ionizing radiation and isotope decay as well as applicable to tomographic (e.g., fluorescence mediated tomography, FMT) and surface-weighted (e.g., fluorescence reflectance imaging, FRI) imaging techniques.

In this study the synthesis of a barbiturate-based MMP-2 and MMP-9 ligand is described. A poly(ethylene glycol) (PEG) spacer group containing the amino functionality was inserted to enable labeling with fluorescent dyes without changing the MMP binding pharmacophor. The conjugation of the fluorescent dye Cy 5.5 was accomplished by forming an amide bond under standard conditions. Enzyme activity assays and cell binding studies in vitro confirmed a high binding affinity of the probe to the target.

EXPERIMENTAL PROCEDURES

Materials and Methods. All chemicals, reagents, and solvents for the synthesis of the compounds were analytical grade and purchased from commercial sources. For the labeling procedure DNA-grade dimethylformamide was used. Melting points (uncorrected) were determined on a Stuart Scientific SMP3 capillary melting point apparatus. ^{1}H NMR and ^{13}C NMR spectra were recorded on a Bruker ARX 300 (Bruker BioSpin GmbH, Rheinstetten, Germany). Mass spectrometry was per-

* To whom correspondence should be addressed. Address: Department of Clinical Radiology, Albert-Schweitzer-Str. 33, University Hospital Münster, 48149 Münster, Germany. E-mail: faustan@uni-muenster.de. Tel.: +49-251-8347362. Fax: +49-251-8347363.

† Department of Clinical Radiology, University Hospital Münster.

‡ Department of Nuclear Medicine, University Hospital Münster.

§ These authors contributed equally to this work.

|| Interdisciplinary Center for Clinical Research.

10.1021/bc700409j CCC: $40.75 © 2008 American Chemical Society
Published on Web 04/09/2008

formed using a QUATTRO LCZ (Waters Micromass, Manchester, U.K.) spectrometer with a nanospray capillary inlet.

Synthetic Organic Chemistry. *N-Boc-Piperazine.* A solution of piperazine (27.60 g, 320 mmol) in 450 mL of dichloromethane was cooled to 0 °C. Di-*tert*-butyl dicarbonate (34.96 g, 160 mmol) in 150 mL of dichloromethane was added dropwise. The resulting mixture was stirred for 2 h at 0 °C and then at ambient temperature for 22 h. The precipitate was filtered off, and the filtrate was concentrated in vacuo. The crude product was dissolved in water (300 mL) and extracted with diethyl ether (3 × 200 mL). The organic layer was dried over magnesium sulfate and concentrated to give a colorless solid. Yield: 20.27 g (109 mmol, 68%). Mp: 72–73 °C. ^{1}H NMR ($CDCl_3$, 300 MHz): δ (ppm) = 1.46 (s, 9H, C(CH_3)$_3$), 1.85 (s, 1H, N*H*), 2.79–2.83 (m, 4H, NH(CH_2)$_2$), 3.37–3.41 (m, 4H, (CO)N(CH_2)$_2$). ^{13}C NMR ($CDCl_3$, 75 MHz): δ (ppm) = 28.3 (C(*C*H$_3$)$_3$), 45.8 (NHCH$_2$), 51.1 (CO)N(*C*H$_2$)$_2$), 79.4 (*C*(CH$_3$)$_3$), 154.7 (N(*C*O)O). MS (ES+) *m*/*e* = 209.1 (M + Na)$^+$, 187.1 (M + H)$^+$.

Tetraethyleneglycol Dimethanesulfonate. Methanesulfonyl chloride (317 mL, 470 g, 4.1 mol) was added dropwise over a period of 4 h to a solution of tetraethylene glycol (347 mL, 388 g, 2 mol) in dichloromethane (1.8 L) and triethyl amine (570 mL, 415 g, 4.1 mol) at 0 °C. The mixture was stirred at ambient temperature for an additional 16 h, and the resulting precipitate was filtered off. Concentration of the filtrate yielded an orange oil, which was used without further purification. Yield: 596 g (1.7 mol, 85%). ^{1}H NMR ($CDCl_3$, 300 MHz): δ (ppm) = 3.08 (s, 6H, SO$_3$C*H*$_3$), 3.65–3.68 (m, 8H, OC*H*$_2$C*H*$_2$O), 3.76–3.78 (m, 4H, SO$_3$CH$_2$C*H*$_2$), 4.37–4.40 (m, 4H, SO$_3$C*H*$_2$CH$_2$). ^{13}C NMR ($CDCl_3$, 75 MHz): δ (ppm) = 37.6 (SO$_3$*C*H$_3$), 68.9 (SO$_3$*C*H$_2$CH$_2$), 69.2 (SO$_3$CH$_2$*C*H$_2$), 70.4, 70.5 (OCH$_2$*C*H$_2$O). MS (ES+) *m*/*e* = 373.1 (M + Na)$^+$, 351.1 (M + H)$^+$.

*2-(2-(2-(2-Azidoethoxy)ethoxy)ethoxy)ethyl Methanesulfonate (**1**).* To a solution of tetraethyleneglycol dimethanesulfonate (83.4 g, 272 mmol) in dimethyl formamide (600 mL) was added sodium azide (10.6 g, 163 mmol), and the reaction mixture was stirred at 120 °C for 5 h. Most of the dimethyl formamide was removed in vacuo. The crude product was dissolved in ethyl acetate (400 mL) and washed with water (5 × 200 mL) and brine (200 mL) and dried over magnesium sulfate. After removing the solvent the resulting oil was chromatographed on a silica gel column (cyclohexane/EtOAc 2/1 to 1/1) to give a pale yellow oil. Yield: 17.2 g (58 mmol, 36%). ^{1}H NMR ($CDCl_3$, 300 MHz): δ (ppm) = 3.08 (s, 3H, SO$_3$C*H*$_3$), 3.64–3.69 and 3.76–3.79 (m, 14H, OC*H*$_2$C*H*$_2$O and OC*H*$_2$C*H*$_2$N$_3$), 4.37–4.40 (m, 2H, SO$_3$C*H*$_2$CH$_2$). ^{13}C NMR ($CDCl_3$, 75 MHz): δ (ppm) = 37.6 (SO$_3$*C*H$_3$), 51.0 (*C*H$_2$N$_3$), 68.8 (SO$_3$*C*H$_2$CH$_2$), 69.3 (SO$_3$CH$_2$*C*H$_2$), 69.9, 70.4, 70.5 (OCH$_2$*C*H$_2$O). MS (ES+) *m*/*e* = 319.1 (M + Na)$^+$, 297.1 (M + H)$^+$.

tert-Butyl-4-(2-(2-(2-(2-azidoethoxy)ethoxy)ethoxy)ethyl)piperazine-1-carboxylate. A solution of **1** (12.44 g, 41.8 mmol), *N*-Boc-piperazine (9.34 g, 50.2 mmol), and triethyl amine (8.3 g, 11.5 mL, 82 mmol) in acetonitrile (150 mL) was heated to reflux for 24 h. After removing the solvent the crude product was purified by column chromatography on silica gel (cyclohexane/EtOAc 1:2) to give a pale yellow oil. Yield: 9.76 g (25.2 mmol, 60%). ^{1}H NMR ($CDCl_3$, 300 MHz): δ (ppm) = 1.45 (s, 9H, C(CH_3)$_3$), 2.44 (t, 4H, (CO)NCH$_2$C*H*$_2$N, ^3J = 5.1 Hz), 2.59 (t, 2H, NCH$_2$CH$_2$NC*H*$_2$, ^3J = 6 Hz), 3.38 (t, 2H, C*H*$_2$N$_3$, ^3J = 5.4 Hz), 3.43 (t, 4H, (CO)NC*H*$_2$, ^3J = 5.1 Hz), 3.60–3.69 (m, 12H, OC*H*$_2$C*H*$_2$O). ^{13}C NMR ($CDCl_3$, 75 MHz): δ (ppm) = 28.3 (*C*(CH$_3$)$_3$), 43.7 ((CO)N*C*H$_2$), 50.6 (*C*H$_2$N$_3$), 53.2 (NCH$_2$CH$_2$NCH$_2$), 57.7 (NCH$_2$*C*H$_2$NCH$_2$), 68.8, 69.9, 70.3, 70.5 (OCH$_2$*C*H$_2$O). MS (ES+) *m*/*e* = 388.3 (M + H)$^+$.

*1-(2-(2-(2-(2-Azidoethoxy)ethoxy)ethoxy)ethyl)piperazine TFA Salt (**2**).* Trifluoroacetic acid (12 mL) was added to a solution of the Boc-protected PEGylated piperazine (3.64 g, 9.4 mmol) in dichloromethane (12 mL) and stirred for 2 h. The solvent was removed and the crude product chromatographed on a silica gel column (EtOAc/MeOH 9/1 to 4/1) to give a yellow sticky oil. Yield: 2.6 g (6.7 mmol, 71%). ^{1}H NMR ($CDCl_3$, 300 MHz): δ (ppm) = 3.38 (t, 2H, C*H*$_2$N$_3$, ^3J = 5.4 Hz), 3.62–3.91 (m, 22H, piperazine-C*H*$_2$ and OC*H*$_2$C*H*$_2$O), 9.81 (bs, 2H, $^+$NH$_2$). ^{13}C NMR ($CDCl_3$, 75 MHz): δ (ppm) = 42.3 (NH$_2$*C*H$_2$), 50.4 (*C*H$_2$N$_3$), 52.3 (NCH$_2$CH$_2$NCH$_2$), 58.5 (NCH$_2$*C*H$_2$NCH$_2$), 65.7, 69.9, 70.3, 70.4, 70.6 (OCH$_2$*C*H$_2$O). MS (ES+) *m*/*e* = 288.2 (M + H)$^+$.

*5-(4-Phenoxyphenyl)pyrimidine-2,4,6-trione (**3**).* A mixture of palladium acetate (135 mg, 0.6 mmol), copper difluoride (60 mg, 0.6 mmol), tri-*tert*-butyl phosphine (90% grade, 220 μL, 0.8 mmol), sodium *tert*-butoxide (6.98 g, 73 mmol), and tetrahydrofurane (30 mL) was prepared. 4-Bromophenyl phenylether (10.5 mL, 60 mmol) and diisopropyl malonate (14.4 mL, 76 mmol) were added consecutively. The clear solution was heated to reflux for 15 h. The resultant suspension was diluted with cyclohexane (30 mL), and 3 M HCl (7.5 mL, 22.5 mmol) was added. The mixture was filtered through Celite, and the filter pad was washed with cyclohexane/THF (1/1, 100 mL). After removing the solvent, the residue was dissolved in diethyl ether, washed with 3 M HCl (3 × 25 mL), 1 M NaHCO$_3$ (2 × 25 mL), and brine, dried over magnesium sulfate, and concentrated under reduced pressure yielding a yellow oil. Urea (6.41 g, 107 mmol) and isopropanol (130 mL) were added. The mixture was heated to 80 °C, and a 1 M solution of potassium *tert*-butoxide in THF (152 mL, 152 mmol) was added slowly over 3 h while distilling off approximately 70 mL of solvent and maintaining a reflux temperature between 75 and 85 °C. After the addition was complete the mixture was heated to reflux for an additional 16 h. Following cooling to ambient temperature concentrated HCl (15 mL) and water (35 mL) were slowly added and the mixture was stirred for 10 min. The solution was concentrated under reduced pressure to remove the organic solvents. The resulting aqueous mixture was diluted with water (100 mL), and the precipitate was filtered off. The off-white solid was dissolved in ethyl acetate (70 mL), heated to reflux for a few minutes, and after cooling to ambient temperature cyclohexane (35 mL) was slowly added. The precipitate was filtered off, washed with cyclohexane/EtOAc (1/1, 100 mL), and dried in vacuo to give an off-white solid. Yield: 4.2 g (12.3 mmol, 21%). ^{1}H NMR (DMSO-d_6, 300 MHz): δ (ppm) = 4.87 (s, 1H, C*H*), 6.91–7.49 (m, 9H, Ph*H*), 11.41 (bs, 2H, (CO)N*H*). ^{13}C NMR (d_6-DMSO, 75 MHz): δ (ppm) = 60.6 (barbituric-*C*H), 118.9, 123.6, 123.7, 130.4, 131.0 (Ph*C*H), 131.3 (q-Ph*C*CH), 157.1, 157.3 (q-Ph*C*O), 155.4 (NH*C*ONH), 172.8 (NH*C*OCH). MS (ES+) *m*/*e* = 319.1 (M + Na)$^+$.

*5-(4-(2-(2-(2-(2-Azidoethoxy)ethoxy)ethoxy)ethyl)piperazin-1-yl)-5-(4-phenoxyphenyl)-pyrimidine-2,4,6-trione (**4**).* A solution of **3** (3.9 g, 11.5 mmol) in dimethyl formamide (15 mL) was cooled to 0 °C, and a solution of *N*-bromosuccinimide (2.1 g, 11.5 mmol) in 10 mL of dimethyl formamide was added over 20 min while maintaining the temperature of the reaction mixture below 10 °C. After stirring for 20 min, **2** (4.6 g, 11.5 mmol) and potassium carbonate (3.22 g, 23 mmol) were added, and the mixture was stirred for 1 h at 0 °C followed by stirring for 20 h at ambient temperature. After removing the solvent, the crude product was dissolved in toluene (25 mL) and heated to reflux for a few minutes. After cooling to ambient temperature, diethyl ether (10 mL) was added dropwise and the resulting suspension was stored overnight at –20 °C. The precipitate was filtered off, washed with diethyl ether, and dried in vacuo giving a white powder. Yield: 2.9 g (4.9 mmol, 43%).

Table 1. MMP Inhibition Potencies of the Barbiturates for MMP-2 and -9 Expressed in IC_{50} Values

	IC_{50}[a] [nM]			
compound	MMP-2	MMP-9	$_c\log D$[b]	$_c\log P$[b]
4	24 ± 8	68 ± 10	1,84	2.15 ± 0.85
5	27 ± 3	138 ± 19	−0.34	1.29 ± 0.85
6	48 ± 5	n.d.[d]	n.d.[c]	n.d.[c]

[a] Values are the mean ± SD of three assays. [b] log *D* and log *P* values calculated by ACD/LogD Suite at physiological pH. [c] Could not be calculated by ACD/LogD Suite. [d] Not determined.

Table 2. Oligonucleotides Used as Primers

oligonucleotides	5′ → 3′ sequence
MMP-2-for	CAAAAACAAGAAGACATACATCTT
MMP-2-rev	GCTTCCAAACTTCACGCTC
MMP-9-for	TGGGGGGCAACTCGGC
MMP-9-for	GGAATGATCTAAGCCCAG
β-Actin-for	AAAGACCTGTACGCCAACAC
β-Actin-rev	GTCATACTCCTGCTTGCTGAT

Scheme 1. Synthesis of the PEG Spacer 2

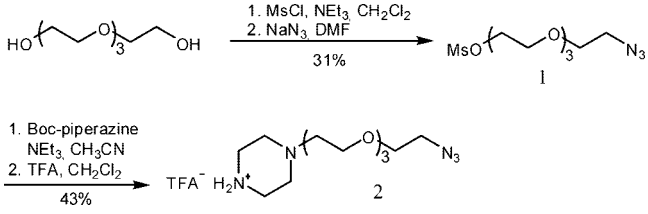

Mp: 139 °C. ^{1}H NMR (DMSO-d_6, 300 MHz): δ (ppm) = 2.41–2.50 (m, 10H, piperazine-*H*, $NCH_2CH_2NCH_2$), 3.36 (t, 2H, CH_2N_3, ^3J = 5.4 Hz), 3.44–3.59 (m, 12H, OCH_2CH_2O), 6.92–7.42 (m, 9H, Ph*H*), 11.57 (bs, 1H, N*H*). ^{13}C NMR (DMSO-d_6, 75 MHz): δ (ppm) = 47.3 (q-$CNCH_2$), 49.9 ($CH_2CH_2NCH_2$), 53.7 (CH_2N_3), 57.1 ($CH_2CH_2NCH_2$), 68.2, 69.2, 69.6, 69.7, 69.8 (OCH_2CH_2O), 73.8 (q-*C*$(CO)_2$), 118.0, 118.2, 118.5, 119.2 (Ph*C*H), 124.0 (q-Ph*C*), 127.7, 129.9, 130.1, 130.6 (Ph*C*H), 149.6 (NH*C*ONH), 156.9, 157.3 (q-Ph*C*O), 170.1 (*C*ONH). HRMS (ES+, $C_{28}H_{35}N_7O_7H$): calcd, 582.2761; found, 582.2760.

*5-(4-(2-(2-(2-(2-Aminoethoxy)ethoxy)ethoxy)ethyl)piperazin-1-yl)-5-(4-phenoxyphenyl)-pyrimidine-2,4,6-trione (**5**).* Triphenylphosphine (560 mg, 2.5 mmol) was added to a solution of **4** (1.16 g, 2 mmol) in tetrahydrofurane (50 mL), and the reaction mixture was stirred for 16 h at ambient temperature. Then water (0.1 mL) was added, and the mixture was stirred for 3 h. The solvent was removed under reduced pressure, and the residue was chromatographed on a silia gel column (EtOAc/MeOH 2/1 + 2% TEA) to give a colorless foam (R_f = 0.2). Yield: 785 mg (1.41 mmol, 71%). Mp: 50 °C. ^{1}H NMR ($CDCl_3$, 300 MHz): δ (ppm) = 2.57–2.81 (m, 10H, piperazine-*H*,$(CH_2)_2NCH_2$), 3.33 (bs, 2H, CH_2NH_2), 3.59–4.04 (m, 16H, OCH_2CH_2O, NH_2), 6.90–7.35 (m, 9H, Ph-*H*). ^{13}C NMR ($CDCl_3$, 75 MHz): δ (ppm) = 40.5 (CH_2NH_2), 45.6 (q-$CNCH_2$), 46.9 ($CH_2CH_2NCH_2$), 58.8 ($CH_2CH_2NCH_2$), 66.4, 69.4, 70.3, 70.9 (OCH_2CH_2O), 72.1 ($CH_2CH_2NH_2$), 74.0 (q-*C*$(CO)_2$), 118.5, 119.1 (Ph*C*H), 123.6 (q-Ph*C*), 129.7, 130.3, 131.2 (Ph*C*H), 149.7 (NH*C*ONH), 156.8, 157.3 (q-Ph*C*O), 170.3 (*C*ONH). HRMS (ES+, $C_{28}H_{37}N_5O_7H$): calcd, 556.2766; found, 556.2766.

Fluorochrome Conjugation. The amino-functionalized derivative **5** (1.0 mg, 1.7 μmol) was dissolved in 400 μL dry dimethylformamide including 10 μL triethylamine. To this solution was added Cy 5.5 NHS ester (Amersham Bioscience; 1 mg, 0.9 μmol). The reaction mixture was vortexed for 2 h at room temperature in the dark. Purification of the Cy 5.5-labeled derivative **6** was performed by gradient HPLC using a Knauer system with two K-1800 pumps, an S-2500 UV detector, and a RP-HPLC Nucleosil 100-5 C18 column (250 mm × 4.6 mm). Eluent A: water (0.1% TFA). Eluent B: acetonitrile (0.1% TFA). Gradient from 99% A to 40% A over 23 min at a flow rate of 5 mL/min, detection at λ = 254 nm. The appropriate fractions (t_R = 16.5 min) were collected, lyophilized, redissolved in PBS, and finally stored at –20 °C. The average content of **6** was 0.8 ± 0.2 μmol/mL (≈ 65%) as determined by fluorometer measurements with λ_{abs} = 678 nm and ε_{678} = 250 000 M^{-1} cm^{-1}. MS (ES−): *m*/*e* = 483.6 (100%), 484.0, 484.3, 484.6, 485.0 $[M]^{3-}$; 725.8, 726.3, 726.7, 727.4 $[M + H]^{2-}$.

In Vitro Enzyme Inhibition Assays. The synthetic broad-spectrum fluorogenic substrate (7-methoxycoumarin-4-yl) acetyl pro-Leu-Gly-Leu-(3-(2,4-dinitrophenyl)-L-2,3-diamino-propionyl)-Ala-Arg-NH_2 (R & D Systems, Minneapolis, U.S.A.) was used to measure MMP-2 and MMP-9 activities as described previously (*19*). The inhibition of human active MMP-2 and MMP-9 by the barbiturates **4** and **5** and the conjugate **6** was measured by preincubating MMP-2 (2 nM) or MMP-9 (2 nM) and inhibitor compounds at varying concentrations (10 pM –1 mM) in 50 mM Tris·HCl, pH 7.5, containing 0.2 M NaCl, 5 mM $CaCl_2$, 20 μM $ZnSO_4$, and 0.05% Brij 35 at 37 °C for 30 min. An aliquot of substrate (10 μL of a 50 μM solution) was then added to 90 μL of the preincubated MMP/inhibitor mixture, and the activity was determined at 37 °C by following product release per time. The fluorescence changes were monitored using a Fusion Universal Microplate Analyzer (Packard Bioscience, Massachusetts, U.S.A.) with excitation and emission wavelengths set to 330 and 390 nm, respectively. Reaction rates were measured from the initial 10 min of the reaction profile where product release was linear with time and plotted as a function of inhibitor dose. From the resulting inhibition curves, the IC_{50} value for each inhibitor was calculated by nonlinear regression analysis, performed using the Grace 5.1.8 software (Linux).

Cell Cultures. Three human carcinoma cell lines, purchased from ATCC (Manassas, VA, U.S.A.), were cultivated in the following media: fibrosarcoma HT-1080 (CCL-121) and adenocarcinoma MCF-7 (HTB-22) in RPMI-1640, and rhabdomyosarcoma A-673 (CRL-1598) in DMEM. Media (Invitrogen Corporation, San Diego, CA) were supplemented with 10% fetal calf serum (FCS), 1% penicillin and streptomycin (Biochrom AG, Berlin, Germany), 2 mM L-glutamine (Gibco BRL), and 13.5 mM sodiumbicarbonate when using A-673 cells. Cells were grown routinely in T75 flasks, incubated at 37 °C in a 5% CO_2 humidified air atmosphere until the cultures were confluent (80–100%); medium was changed every 3−4 days. The amount of vital cells was determined by trypan blue staining (Sigma-Aldrich Chemie GmbH, Munich, Germany). A total of 10^7 cells were washed three times in serum-free medium and incubated in freshly FCS-free medium for a further 24 h. For gelatine zymography and Western blotting the supernatant was collected and stored at –20 °C. For RNA isolation, adherent cells were washed with phosphate-buffered saline (PBS), treated with 0.5% trypsin, and harvested by centrifugation (5 min, 1400 × *g*).

RNA Isolation and cDNA Synthesis. Total RNA was isolated from harvested cells (see above) using the peqGOLD Total RNA Kit (PeqLab Biotechnology GmbH, Erlangen, Germany) according to the manufacture's instructions. To remove possible genomic DNA contaminations a DNase I digestion reaction mix, consisting of OBI DNase I Digestion Buffer and RNase-free DNase I (20 units/μL), was added directly to the surface of the HiBind spin column. Total RNA was eluted with RNase-free water and stored at –86 °C until use.

RNA concentrations and its purity were measured with the Quant-iT RNA Assay Kit (Invitrogen, Karlsruhe, Germany).

Scheme 2. Synthesis of the Barbiturate Precursor 5

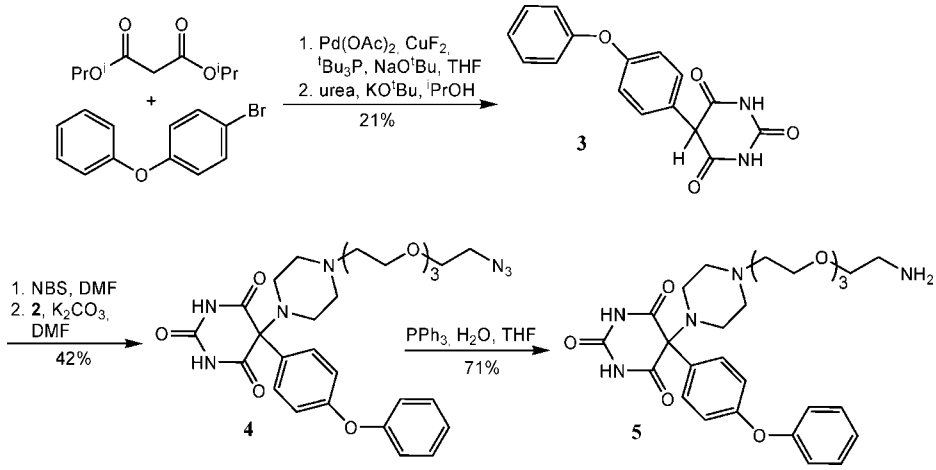

Scheme 3. Labeling of the Precursor 5 with the Cyanine Dye Cy5.5

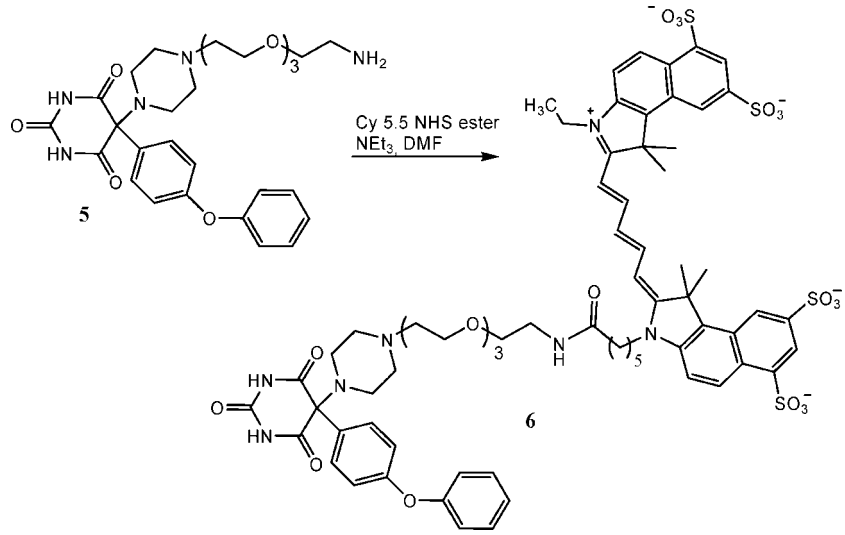

Prior to the reverse transcription reaction, total RNA was denatured at 65 °C for 10 min and subsequently placed on ice. Reverse transcription of RNA was performed using the RevertAid First Strand cDNA Synthesis Kit (MBI Fermentas, St. Leon-Roth) in a 20 μL reaction volume, consisting of 1 μg of total RNA, 5× reaction buffer, 1 mM of each nucleotide triphosphate, 20 units of RiboLock Ribonuclease Inhibitor, and 1 μL of random Hexamer (0.2 μg/μL). After incubation at 25 °C for 5 min, 200 units of RevertAid M-MuLV Reverse Transcriptase were added, and the reaction mixture was incubated according to the supplier's instructions. Synthesized cDNA was stored at –20 °C until use.

PCR Conditions. Polymerase chain reaction (PCR) reactions were performed in a total volume of 25 μL, containing 0.2 mM of each nucleotide triphosphate, 1× PCR-buffer, 50 μM of each primer (see Table 2), 1 mM $MgCl_2$, 1 unit of Taq DNA polymerase (PeqLab Biotechnologie GmbH, Erlangen, Germany), and 1 μL of synthesized cDNA. Thermal cycling conditions comprised an initial degradation step (94 °C, 3 min) and 35 cycles at 94 °C for 30 s, 60 °C for 20 s, and 72 °C for 30 s, followed by a final elongation step (72 °C, 1 min) in an Eppendorf Mastercycler EP Gradient (Eppendorf AG, Hamburg, Germany). PCR products were separated by agarose gel electrophoresis (2%) (Biozym Diagnostik GmbH, Oldendorf,

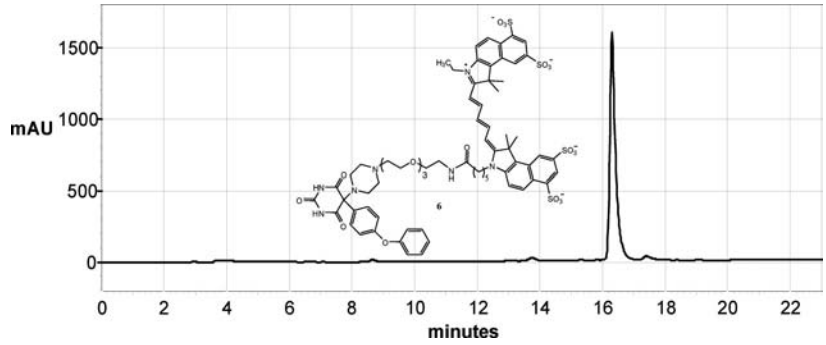

Figure 1. HPLC chromatogram of the purified conjugate **6** (UV-trace).

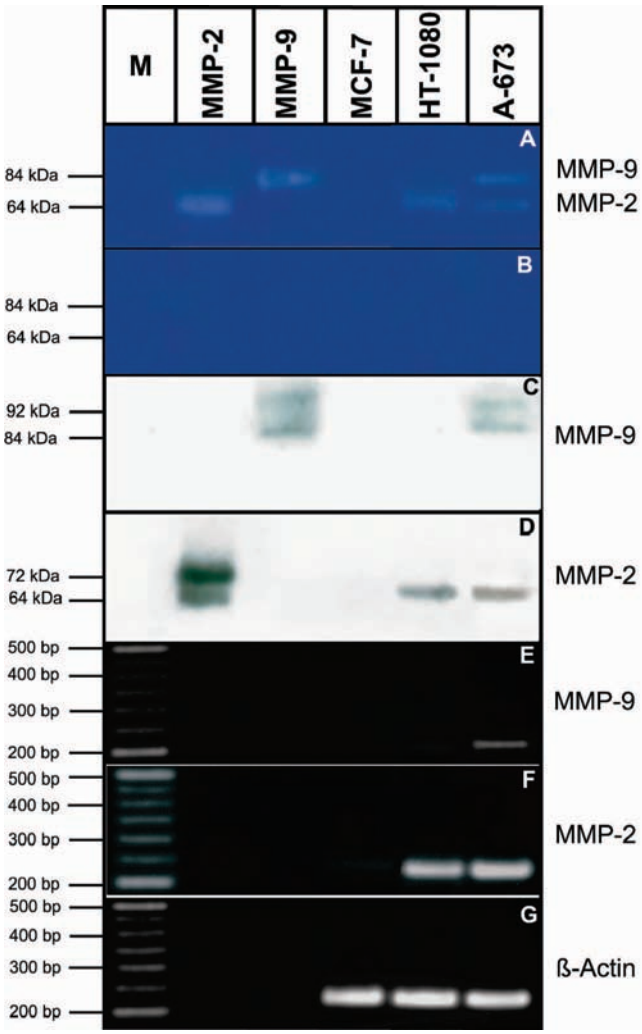

Figure 2. MMP-2 and -9 expression, secretion, and activity tests. Gelatinolytic activity of cell extracts was determined by zymography (A). Inhibition of the gelatinolytic activity with **5** (B). Western blot analysis of cell supernatants to detect pro-MMP-2, MMP-2 (C), pro-MMP-9, and MMP-9 (D). Semiquantitative PCR analysis was performed with the primer pairs listed in Table 2, specific for MMP-9 (E), MMP-2 (F), or β-Actin (G).

Germany). Fragment sizes were determined using the 50-bp DNA ladder standard (MBI Ferments, St. Leon-Rot, Germany).

Gelatine Zymography. Gelatine zymography was performed as described previously with minor modifications (*20*). Twenty microliters of FCS-free cell supernatant from 1×10^7 cells were mixed with (4×) SDS sample buffer without reducing agent and separated in a sodium dodecyl sulfate (SDS)−polyacrylamide electrophoretic gel (PAGE) (0.75 mm comb, 4 °C, 150 V). The 7% separating SDS gel contained 0.6 g/L gelatine to detect latent and activated forms of gelatinases. Following electrophoresis, the gel was washed twice in 2.5% Triton X-100 for 30 min at room temperature with shaking to remove residual SDS. Subsequently, zymograms were developed by incubation overnight at 37 °C with gentle shaking in collagenases buffer (50 mM Tris-HCl pH 7.8, 10 mM $CaCl_2$) and afterward stained/destained with 1% Coomassie Brillant Blue G-250 dissolved in 10% ethanol and 5% acetic acid at room temperature for 120 min. Active MMP-2 from human fibroblasts and MMP-9 from human recombinant NSO cells (Sigma-Aldrich Chemie GmbH, Munich, Germany) were used as a gelatinase control. Gelatinolytic/proteolytic activity was visible as clear bands (zones of gelatine degradation) against a dark blue background of stained gelatine.

Western Blot Analysis. Total protein was separated in nonreducing SDS-PAGE electrophoresis using separating gels with 10% and stacking gels with 4.5% polyacrylamide. Lanes were loaded with 20 μL of FCS-free cell supernatant and mixed with (6×) SDS buffer. After electrophoresis (4 °C, 100 V), proteins were transferred to PVDF membranes (Millipore Corporation, Bedford, MA) via electroblotting (4 °C, 60 V). Blots were blocked in tris-buffered saline-NaCl, pH 7.4, containing 1% bovine serum albumin, 0.5% milk powder (Carl Roth GmbH & Co KG, Karlsruhe, Germany), and 0.1% Tween 20, washed, and incubated at 37 °C for 120 min with 1:500 diluted primary polyclonal antibody against MMP-2 (Cell Signaling, New England Biolabs GmbH, Frankfurt a. M., Germany), which detects full length proenzyme (72 kDa) and cleaved active enzyme (64 kDa). Subsequently, blots were washed three times in tris-buffered saline, pH 7.4, containing 0.5% milk powder and 0.1% Tween 20 and incubated with 1:1000 diluted peroxidase-conjugated goat antirabbit IgG antibody (Vector, Burlingame, U.S.A.). Following three washing steps, peroxidase activity was revealed using ECL chemiluminescence (Amersham, Buckinghamshire, U.K.) according to the manufacturer's instructions to visualize signals. MMP-2 from human fibroblasts (Sigma-Aldrich Chemie GmbH, Munich, Germany) was used as a positive control.

In Vitro Cell Assays. The cell-based binding assay was performed in U-shaped polypropylene 24-well plates (Nunc); each well was seeded with 2.5×10^4 cells and grown in 1 mL of medium to confluence. Briefly, after washing the wells with PBS, 150 μL of preincubation buffer (50 mM Tris-HCl, 10 mM $CaCl_2$, 62 mM $ZnSO_4$, pH 7.4), with or without predosing using 50 μM **5**, was added to each well and incubated for 30 min at 37 °C. Following incubation, the preincubation buffer was replaced by binding buffer (50 mM Tris-HCl, 10 mM $CaCl_2$, 30 mM $ZnSO_4$, pH 7.4) containing 2 nmol of **6**. After an incubation time of 120 min at 37 °C, cells were washed with PBS, and subsequently 300 μL of medium/trypan blue solution (2:1 (v/v); Sigma-Aldrich Chemie GmbH, Munich, Germany) was added. Cells could be directly visualized by fluorescence microscopy (Nikon TE 2000-S, Tokyo, Japan) which was equipped with a mercury vapor lamp, 620/775 nm (excitation/emission) filters (AHF Analysentechnik AG, Tübingen, Germany), and a Nikon DXM1200F camera using the NIS-Elements BR 2.30 sofware (Nikon, Tokyo, Japan).

RESULTS AND DISCUSSION

As MMPs are involved in the regulation of the tumor microenvironment and expressed and activated in many types of human cancers, this distinct enzyme class appears to be a molecular target for imaging of cancer in vivo (*8*). The selective targeting of MMP-2, -9, and -14 may help to visualize tumor angiogenesis. These three MMPs are most consistently detected in malignant tissues in which they are associated with tumor aggressiveness, metastatic potential, and poor prognosis (*9*, *21*). Increased levels of activated MMPs in inflammatory, malignant, and degenerative diseases have been attributed to increased cytokine and growth-factor-stimulated gene transcription, enhanced zymogen activation, and an imbalance in the MMP: TIMP ratio, which can be used as a "noninvasive" diagnostic test for bilharzial bladder cancer (*22*, *23*).

The objective of this work was the modification of an existing lead structure (barbiturate) with a fluorescent dye, to allow near-infrared detection of the target enzymes. Taking into account the size of the dye molecule compared to that of the parent inhibitor, we have chosen a short PEG spacer to distance the dye from the MMP-binding site and preserve the desired binding affinity for gelatinases as outlined in Table 1. Furthermore, optical imaging techniques allow the detection of molecules in

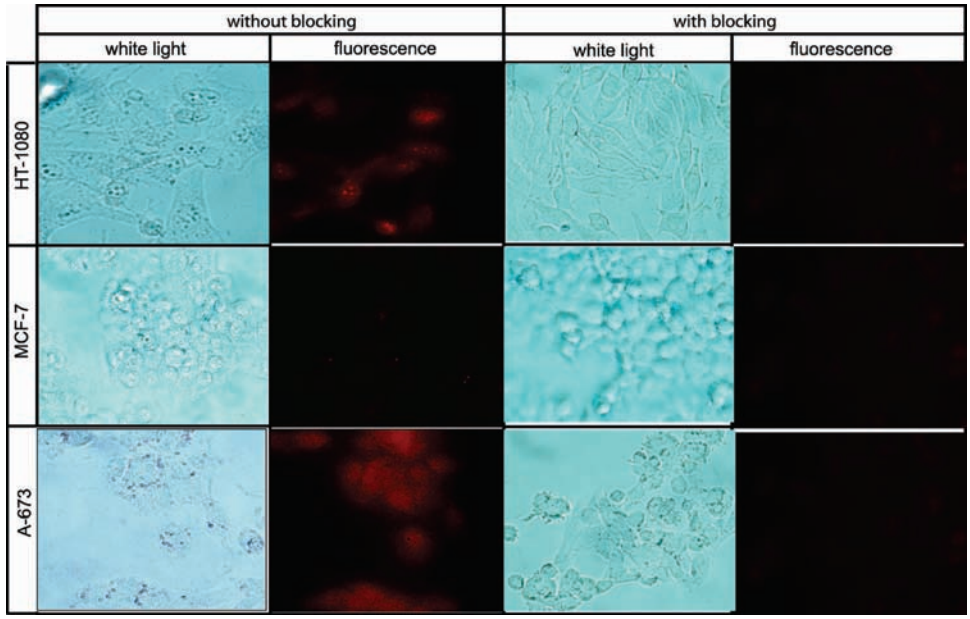

Figure 3. Fluorescence microscopy of the in vitro cellular assay of HT-1080, MCF-7, and A-673 cells, in the presence or absence of protease inhibitor **5** (50 μM) incubated with the Cy 5.5 labeled ligand **6** (2 nmol).

picomolar (10^{-12} M) concentrations, which is comparable to conventional scintigraphic imaging techniques. As well as high signal-to-noise ratios (SNRs), imaging in the near-infrared spectrum (λ = 650−950 nm) shows very efficient tissue penetration as the absorption by water and hemoglobin is relatively low ("diagnostic window") (*24*, *25*).

Chemistry. The PEGylated piperazine derivative **2** was prepared as illustrated in Scheme 1. Mesylation of tetraethylene glycol and subsequent mono-substitution with sodium azide on a large scale gave the PEGylated azide derivative **1** in a satisfactory yield. Nucleophilic substitution of the mesyl moiety with Boc-protected piperazine and subsequent deprotection with trifluoroacetic acid yielded the desired piperazine derivative **2** (*26*). To synthesize the barbiturate **3** (Scheme 2), in the first steps a Pd-catalyzed C−C bond formation followed by a condensation with urea was used (*27*). After bromination with *N*-bromo succinimide in DMF we linked the barbiturate with the PEGylated piperazine derivative **2** to get the PEGylated barbiturate **4**. For labeling with the NHS-ester of the commercially available cyanine dye Cy 5.5 it was necessary to reduce the azide function by a *Staudinger* reaction to get the precursor **5** in good yields.

Fluorochrome Conjugation. The amino functionalized compound **5** was used for the conjugation of Cy 5.5. The reaction was carried out in dry DMF with triethyl amine as the base (Scheme 3). The conjugate **6** was purified by reversed phase HPLC on an analytical column by collection of the appropriate fractions. After lyophilization and redissolving in PBS the sample showed a purity of >98% (HPLC) (Figure 1). The labeled ligand was verified by mass spectrometry with a triple negative charged ion emerging at 100% intensity. With a molecular mass of 1.45 kD the resulting probe belongs to the small molecule tracers. Moreover, the tracer's excitation and emission spectra were identical to that of the Cy 5.5 dye (Ex, 678 nm; Em, 692 nm).

In Vitro Enzyme Studies. The inhibition potencies of the barbiturates **4** and **5** and the conjugate **6** were measured for MMP-2 and MMP-9 using fluorogenic in vitro assays. The resulting MMP inhibitions were determined as IC_{50} values and calculated from a nonlinear regression fit of the concentration-dependent reaction rates. Both PEGylated barbiturates (MMP-2 and -9) and the conjugate **6** (MMP-2) show binding in the nanomolar range (Table 1), and these results were confirmed by zymography assays showing the potency of the labeled barbiturate **6** (Figure 2).

MMP-2 and -9 Transcription, Translation, and Activity Tests. For the biological characterization of **6** in vitro experiments on different cell lines were performed with respect to target expression on the genomic, proteomic, and functional level. To determine whether the chosen cell lines express and synthesize functional MMP-2 and -9, a semi-quantitative PCR analysis, Western blots, and zymography were performed. In the PCR analysis, MMP-2 and MMP-9 mRNA expression of the three human carcinoma cell lines were normalized by using the house keeping gene β-Actin. Whereas the rhabdomyosarcoma cell line A-673 expressed both MMPs, the fibrosarcoma cell line (HT-1080) only transcribed MMP-2 and the MCF-7 produced neither MMP-2 nor MMP-9 mRNA at detectable levels (Figure 2 E−G). The expression of both enzymes on the protein level was assessed by Western blotting with polyclonal antibodies against MMP-2 and MMP-9. These antibodies recognize the latent and active MMP forms and, therefore, reflect the cell lines via de novo synthesis levels of both enzymes (Figure 2 C,D). Similarly to the PCR results, Western blot analysis demonstrated that the human carcinoma cell line MCF-7 did not secrete MMP-2 and MMP-9 at detectable levels. However, activated MMP-2 (64 kDa) was secreted by HT-1080 and A-673 cells, respectively. Furthermore, in the A-673 supernatant pro-MMP-9 (92 kDa) and the active MMP-9 form (84 kDa) could be detected. Positive controls, that is, purified enzymes, give also clear signals as shown in Figure 2 C,D. The zymography perfectly corresponds to the results obtained by semiquantitative PCR and Western blot analysis. Gelatinolytic bands were visible for the cell lines HT-1080 and A-673, which secret active MMP-2 (62 kDa) with nearly similar levels. In addition to MMP-2 activity, MMP-9 (72 kDa) gelatinase activity was only detectable in the rhabdomyosarcoma cell line A-673. No gelatinase activity could be shown for the cell line MCF-7 (Figure 2 A). Incubation of the zymogram with the nonlabeled barbiturate **5** (100 μM) inhibited the MMP-2 and MMP-9 gelatinolytic activity,

completely confirming efficient binding of the probe precursor **5** (Figure 2 B). Zymographical analysis corroborated the former analysis and revealed the barbiturate **6** as a potential MMP-2 and -9 inhibitor. Therefore we used the Cy 5.5-labeled barbiturate in an in vitro cell binding assay in order to support these findings.

In Vitro Cellular Assay. Functionally active MMP-2 and MMP-9 ligands should bind to secreted MMP-2 and/or MMP-9 of monolayer cells. Indeed, a strong fluorescence signal was obtained from the surface of A-673 cells, which were shown to secret both MMP-2 and MMP-9 (Figure 3). The HT-1080 monolayer fluorescence was less powerful compared to that of A-673, and MCF-7 cells again failed to show the corresponding MMP activities. Predosing experiments using 50 μM of the unlabeled barbiturate **5** successfully blocked the binding of the Cy 5.5-labeled ligand **6** (Figure 3). In every case the cell integrity and viability were confirmed by a trypan blue test.

The aim of this work was to develop a nonpeptide MMPI with high MMP binding potency which is applicable for optical imaging of MMP-2 and -9. We have chosen a barbiturate as the lead structure and developed a route for the synthesis of an amino-PEG-derivatized compound which can be used for the conjugation of common amino-reactive fluorescent markers such as Cy 5.5. Thus, we obtained a near-infrared fluorescent photoprobe for the imaging of MMP-2 and -9. Applying semiquantitative PCR, Western blot analysis, and zymograms we checked not only the cells' transcriptional and translational levels but also their secretion levels and the functionality of the secreted MMPs. Taking this into account, the unlabeled barbiturate **5** blocked both MMP-2 and MMP-9 activities. Additional binding studies in vitro proved the inhibition capacities of the precursor **5** and revealed the specific binding capacities of the Cy 5.5-labeled ligand **6**. Thus, MMP-2 and -9 imaging with the fluorescent labeled probe **6** is feasible and should be applicable to imaging modalities to monitor activiated MMP-2 and -9 associated disease processes such as invasion, metastasis, and angiogenesis in cancer in vivo.

ACKNOWLEDGMENT

This work was supported by the Deutsche Forschungsgemeinschaft (SFB 656 project A4) and European Community (IP 6th framework; Grant LSHG-CT-2003-503259 (Mol. Img) and MoldDiag-Paca LSHB- CT-2006-018771). Thanks are due to Susanne Greese, Wiebke Gottschlich, Ulla Römer, Sandra Schröer, and Ingrid Otto-Valk for technical assistance, Prof. Dr. H. Luftmann at the Organic Chemistry Department of the WWU Münster for mass spectrometry, and Dr. Marilyn Law for reading the manuscript.

LITERATURE CITED

(1) Skiles, J. W., Gonnella, N. C., and Jeng, A. Y. (2004) The design, structure, and clinical update of small molecular weight matrix metalloproteinase inhibitors. *Curr. Med. Chem. 11*, 2911–2977.

(2) Tayebjee, M. H., Lip, G. Y. H., and MacFadyen, R. J. (2005) Matrix metalloproteinases in coronary artery disease: clinical and therapeutic implications and pathological significance. *Curr. Med. Chem. 12*, 917–925.

(3) Beaudeux, J. L., Giral, P., Bruckert, E., Foglietti, M. J., and Chapman, M. J. (2004) Matrix metalloproteinases, inflammation and atherosclerosis: therapeutic perspectives. *Clin. Chem. Lab. Med. 42*, 121–131.

(4) Overall, C. M., and López-Otín, C. (2002) Strategies for MMP inhibition in cancer: innovations for the post-trial era. *Nat. Rev. Cancer 2*, 657–672.

(5) Tayebjee, M. H., Lip, G. Y., and MacFadyen, R. J. (2005) Matrix metalloproteinases in coronary artery disease: clinical and therapeutic implications and pathological significance. *Curr. Med. Chem. 12*, 917–925.

(6) Folgueras, A. R., Pendas, A. M., Sanchez, L. M., and Lóez-Otín, C. (2004) Matrix metalloproteinases in cancer: from new functions to improved inhibition strategies. *Int. J. Dev. Biol. 48*, 411–424.

(7) Stamenkovic, I. (2003) Extracellular matrix remodelling: the role of matrix metalloproteinases. *J. Pathol. 200*, 448–464.

(8) Vihinen, P., Ala-aho, R., and Kahari, V. M. (2005) Matrix metalloproteinases as therapeutic targets in cancer. *Curr. Cancer Drug Targets 5*, 203–220.

(9) Egeblad, M., and Werb, Z. (2002) New functions for the matrix metalloproteinases in cancer progression. *Nat. Rev. Cancer 2*, 161–174.

(10) Heeneman, S., Cleutjens, J. P., Faber, B. C., Creemers, E. E., van Suylen, R-J., Lutgens, E., Cleutjens, K. B., and Daemen, M. J. (2003) The dynamic extracellular matrix: intervention strategies during heart failure and atherosclerosis. *J. Pathol. 200*, 516–525.

(11) Galis, Z. S., and Khatri, J. J. (2002) Matrix metalloproteinases in vascular remodeling and atherogenesis: the good, the bad, and the ugly. *Circ. Res. 90*, 251–262.

(12) Galis, Z. S. (2004) Vulnerable plaque: the devil is in the details. *Circulation 110*, 244–246.

(13) Newby, A. C. (2005) Dual role of matrix metalloproteinases (matrixins) in intimal thickening and atherosclerotic plaque rupture. *Physiol. Rev. 85*, 1–31.

(14) Grams, F., Brandstetter, H., D'Alo, S., Geppert, D., Krell, H. W., Leinert, H., Livi, V., Menta, E., Oliva, A., and Zimmermann, G. (2001) Pyrimidine-2,4,6-triones: a new effective and selective class of matrix metalloproteinase Inhibitors. *Biol. Chem. 382*, 1277–1285.

(15) Brandstetter, H., Grams, F., Glitz, D., Lang, A., Huber, R., Bode, W., Krell, H. W., and Engh, R. A. (2001) The 1.8-Å crystal structure of a matrix metalloproteinase-8 barbiturate inhibitor complex reveals a peviously unobserved mechanism for collagenase substrate recognition. *J. Biol. Chem. 276*, 17405–17412.

(16) Dunten, P., Kammlott, U., Crowther, R., Levin, W., Foley, L. H., Wang, P., and Palermo, R. (2001) X-ray structure of a novel matrix metalloproteinase inhibitor complexed to stromelysin. *Protein Sci. 10*, 923–926.

(17) Breyholz, H. J., Schäfers, M., Wagner, S., Höltke, C., Faust, A., Rabeneck, H., Levkau, B., Schober, O., and Kopka, K. (2005) C-5-disubstituted barbiturates as potential molecular probes for non-invasive MMP imaging. *J. Med. Chem. 48*, 3400–3409.

(18) Wagner, S., Breyholz, H. J., Faust, A., Höltke, C., Levkau, B., Schober, O., Schäfers, M., and Kopka, K. (2006) Molecular imaging of matrix metalloproteinases *in vivo* using small molecule inhibitors for SPECT and PET. *Curr. Med. Chem. 13*, 2819–38.

(19) Huang, W., Meng, Q., Suzuki, K., Nagase, H., and Brew, K. (1997) Mutational study of the amino-terminal domain of human tissue inhibitor of metalloproteinasees 1 (TIMP-1) locates an inhibitory region for matrix metalloproteinases. *J. Biol. Chem. 272*, 22086–22091.

(20) Heussen, C., and Dowdle, E. B. (1980) Electrophoretic analysis of plasminogen activators in polyacrylamide gels containing sodium dodecyl sulfate and copolymerized substrates. *Anal. Biochem. 102*, 196–202.

(21) Fingleton, B. (2003) Matrix metalloproteinase inhibitors for cancer therapy: the current situation and future prospects. *Expert Opin. Ther. Targets 7*, 385–397.

(22) George, S. J. (2000) Therapeutic potential of matrix metalloproteinase inhibitors in atherosclerosis. *Exp. Opin. Invest. Drugs 9*, 993–1007.

(23) Eissa, S., Ali-Labib, R., Swellam, M., Bassiony, M., Tash, F., and El-Zayat, T. M. (2007) Noninvasive Diagnosis of Bladder Cancer by Detection of Matrix Metalloproteinases (MMP-2 and

MMP-9) and Their Inhibitor (TIMP-2) in Urine. *Eur. Urol. 52*, 1388–1397.
(24) Bremer, C., Ntziachristos, V., Weitkamp, B., Theilmeier, G., Heindel, W., and Weissleder, R. (2005) Optical imaging of spontaneous breast tumors using protease sensing 'smart' optical probes. *Invest. Radiol. 40*, 321–327.
(25) Ntziachristos, V., Bremer, C., Graves, E. E., Ripoll, J., and Weissleder, R. (2002) In vivo tomographic imaging of near-infrared fluorescent probes. *Mol. Imaging 1*, 82–88.
(26) Tahtaoui, C., Parrot, I., Klotz, P., Guillier, F., Galzi, J. L., Hibert, M., and Ilien, B. (2004) Fluorescent pirenzepine derivatives as potential bitopic ligands of the human M1 muscarinic receptor. *J. Med. Chem. 47*, 4300–4315.
(27) Hutchings, S., Liu, W., and Radinov, R. (2006) *Heterocycles 67*, 763–768.

BC700409J

Factors Determining the Efficacy of Nuclear Delivery of Antisense Oligonucleotides by Gold Nanoparticles

Yanli Liu and Stefan Franzen*

Department of Chemistry, North Carolina State University, Raleigh, North Carolina 27695. Received November 16, 2007; Revised Manuscript Received February 19, 2008

The present study investigates the applicability of nanoparticle delivery vectors for two-stage targeting that involves both cell entry by endocytosis and nuclear targeting using viral peptide signals. A nanoparticle vector consists of four components: a carrier nanoparticle, a stabilizer, targeting peptides, and a therapeutic cargo. Extensive study of bovine serum albumin (BSA)-peptide stabilized nanoparticle conjugates demonstrated limitations of these systems due to colloidal instability when oligonucleotides and multiple peptides were attached to the BSA protein. We found that the widely used protein streptavidin (SA) was an appropriate alternative to BSA for cell-targeting experiments. Targeting peptides and gene splicing oligonucleotides were attached to SA-nanoparticles using biotin labels. The present study uses a gene-splicing assay as a test for oligonucleotide delivery to the cell nucleus. Successful modification of gene splicing by an antisense oligonucleotide indicates that the latter must have crossed the plasma membrane, entered the nucleus, found the target sequence in the newly transcribed pre-mRNA, and hybridized to it in the spliceosome strongly enough to displace the splicing factors designed to interact with the target sequence. Targeting nanoparticles that carry gene-splicing oligonucleotides were compared with a control experiment that used lipofectamine (LF). While enhanced activity was observed in the control experiment, in the presence of LF, no gene splicing was observed for the nanoparticle targeting vectors without LF. We conclude that sequestration of cargo from the harsh conditions of the endosome is a desirable strategy for cell-targeting nanoparticles.

INTRODUCTION

A variety of approaches are available that aim to improve the efficacy of oligonucleotide delivery. One of the most common strategies for delivery of oligonucleotides to cells is to complex the nucleic acid with cationic polymers (*1, 2*) and lipids (*3*). Because of the cytotoxicity and associated problems, strategies based on complexation with cationic polymers and lipids have been primarily used for *in vitro* studies. Another approach for nucleic acid delivery is the use of viral vectors, which are adept in cell entry and cell targeting (*4, 5*). Viral vectors are widely used in gene therapies, and there has been limited application to the delivery of short oligonucleotides for antisense therapy. Moreover, viral vectors have the drawback of potential infectivity and immunogenicity. The use of a nanoparticle-based delivery vector for nuclear targeting is inspired by the cell-targeting experiments that demonstrate the use of viral targeting peptides to facilitate internalization of nanoparticles in cells and including transport into cell nuclei. In theory, such targeting vectors have the advantage of safety and simplicity.

This study investigates the applicability of nanoparticle delivery vectors for two-stage targeting that involves both entry by endocytosis and nuclear targeting using viral peptide signals. A nanoparticle vector consists of four components: a carrier nanoparticle, a stabilizer, targeting peptides, and a therapeutic cargo. Figure 1 illustrates the construction of a nanoparticle-based delivery vector that has a stabilizer and carrier protein, targeting peptide, and oligonucleotide payload. Combining both targeting and functional modification of gene expression into one targeting nanoparticle is challenging. The first challenge is to prepare and characterize the nanoparticle-based delivery vectors, which requires the assembly of the various components onto a single nanoparticle without compromising functionality of any component in the system. A second challenge is to maintain the colloidal stability of nanoparticle.

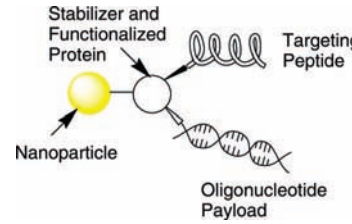

Figure 1. Illustration of a nanoparticle-based delivery vector.

The ease of synthesis and functionalization, unique optical properties, and biocompatibility of gold nanoparticles (Au-NPs) are advantages in intracellular diagnostic applications (*6–8*). These properties have recently sparked great interest in gold nanoparticles as a scaffold for cell-targeting studies (*9–12*). However, the large polarizability of Au-NPs decreases their colloidal stability (*13, 14*). Direct functionalization of stable Au-NPs by nucleic acids has provided stable formulations (*8, 15–17*), but functionalization by peptides has only been successful for a few sequences (*18*). For many years, protein stabilizers such as bovine serum albumin (BSA) have been used to improve the stability of citrate-stabilized Au-NPs as well as providing a protein layer that can be used to attach targeting peptides to the surface (*13, 19, 20*). The steric stabilization of proteins such as BSA is a key aspect of their application. Citrate-coated Au-NPs rapidly aggregate and precipitate at their isoelectric point. However, using ζ-potential measurements we have determined that BSA-stabilized Au-NPs are stable at their isoelectric point

* Corresponding author: Stefan Franzen, Department of Chemistry, North Carolina State University, Raleigh, NC 27695-8204. E-mail: Stefan_Franzen@ncsu.edu, Phone: (919)-515-8915, Fax: (919)-515-8920.

10.1021/bc700421u CCC: $40.75 © 2008 American Chemical Society
Published on Web 04/05/2008

and the pI of both Au-NPs and BSA is nearly the same, pI ~ 4.6 (*14*). Both BSA and Au-NPs are negatively charged at neutral pH, which provides electrostatic stabilization in addition to the steric stabilization. However, BSA-coated nanoparticles will aggregate when the BSA is cross-linked to basic peptides that increase the pI of the bioconjugate to a range that was not stable under physiological conditions (pH 7.4). The combination of peptides and oligonucleotides presents a further problem for colloidal stability BSA conjugates with nanoparticles. Streptavidin (SA) was identified as an appropriate alternative bioconjugation protein for cell-targeting experiments. SA is a tetrameric protein from *Streptomyces avidinii* that has strong biological and noncovalent affinity with the vitamin biotin ($K_d = 10^{-15}$ M) (*21*). SA can be easily attached to colloidal gold and streptavidin-conjugated Au-NPs of different sizes are readily available. Using this approach, we tested whether Au-NPs can both target a cell using peptide signals and carry an antisense cargo to the nucleus.

Virus-mimetic targeting peptides provide one method of cellular and nuclear targeting that can be applied to Au-NP conjugates. For example, the combination of two short peptides adapted from adenoviruses can promote receptor-mediated endocytosis (RME) via the coxsackie-adenoviral receptor (CAR) or the CD46 receptor and nuclear targeting via a nuclear localization signal (NLS) peptide that interacts with importin α/β and promotes transit through the nuclear pore complex (*19*). The sequences were derived from the full-length adenoviral fiber peptide, which has the ability to target CAR, CD46, and the importins (*22, 23*). Nanoparticles solubilized by BSA conjugates carrying peptides singly and in combination were used to show that a full-length peptide containing both CAR and CD46 was less effective for nuclear targeting than two shorter peptides that contained the same sequence information (*19*). The Arg-Gly-Asp (RGD) motif, naturally found in a number of proteins including laminin and fibronectin, has been used to target several cell lines (*24, 25*). RGD interacts with several surface receptors, most prominently the CD51 family. HeLa cells strongly express the CD51 receptor at a level of ~200 000 antibody binding receptors per cell (*26*). The most commonly used NLS peptide, the SV40 large T-antigen-derived NLS (PKKKRKV), can facilitate nuclear uptake of non-nuclear proteins with a molecular weight up to 465 kDa (*27*). Peptides can have more than one function, permitting cargo such as DNA (*28*) or Au-NPs (*20*) to be transported to the nucleus. While these methods have application for large cargo such as genes or nanoparticles, the use of targeting methods to transport smaller antisense oligonucleotides has been less well explored.

Antisense oligonucleotides have attracted attention as promising therapeutic agents (*29–31*). Applications of antisense oligonucleotides include both down-regulation of gene expression (*32–35*) and modulation of gene splicing (*29–31*). Antisense oligonucleotides are short sequence of nucleotides (DNA, RNA, or a chemical anologue) typically with 25 or fewer bases, which are designed to be complementary to a specific type of mRNA or precursor mRNAs (pre-mRNAs). The use of native RNA oligonucleotides in therapy has been limited because they are easily degraded by nucleases. Modified oligonucleotides such as 2′-*O*-methylphosphonate, phosphorothioate, morpholino (*36*), and peptide nucleic acid (PNA) (*37*) have shown resistance to nuclease degradation (*29, 38*). Antisense therapy is limited by the low intrinsic ability of oligonucleotides to target cells.

The present study uses a gene splicing assay (*39*) as a test for oligonucleotide delivery to the cell nucleus. Successful modification of gene splicing by an antisense oligonucleotide indicates that the latter must have crossed the plasma membrane, entered the nucleus, found the target sequence in the newly transcribed pre-mRNA, and hybridized to it in the spliceosome strongly enough to displace the splicing factors designed to interact with the target sequence. Moreover, a new product alternatively spliced mRNA is generated, which can be easily detected on a low background. Thus, apart from potential clinical applications, modification of splicing can be used as a positive readout assay to determine whether functional oligonucleotides have been delivered to the splicing machinery within the cell nucleus. In this model system, HeLa cells are stably transfected with a recombinant plasmid (pLuc/705) carrying the luciferase gene interrupted by a mutated human β-globin intron 2 (IVS2–705). The mutation in the intron causes aberrant splicing of luciferase pre-mRNA, preventing translation of luciferase (Luc), unless corrected by the presence of an antisense oligonucleotide targeted to the splice site. The splice correction assay therefore measures the ability of antisense oligonucleotides to correct splicing of an aberrant intron inserted into the Luciferase gene.

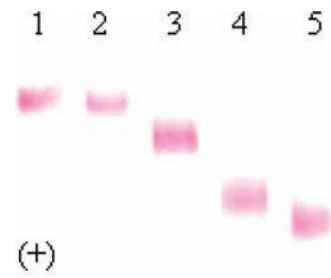

Figure 2. 1% Agarose gel electrophoresis of ON705-SA-Au-NPs. Lane 1: SA-Au-NPs with added ratio of SA/Au-NP of 500:1. Lanes 2–5: ON705-SA-Au-NPs with increasing ratios of ON705 to Au-NP of 100, 200, 300, and 500, respectively.

By using this positive readout assay, we have examined whether the presence of the nanoparticles (Au-NPs and quantum dots) and peptides affect the ability of oligonucleotides to interact with their nucleic acid target. These studies provide new insights into the possibilities and limitations of the biological applications of multifunctional nanoparticles.

RESULTS

Assembly and Characterization of the Particles Containing Peptides and/or Oligonucleotides. Agarose gel electrophoresis (1%) was used to confirm the binding of SA to Au-NPs and the binding of peptides and RNA oligonucleotides (ON705) to SA-Au-NPs. Citrate-coated Au-NPs tend to aggregate in the running condition of gel electrophoresis due to the high ionic concentration of the running buffer. The migration of the Au-NPs as shown in lane 1 of Figure 2 indicated that SA stabilized the particles and the charge/mass ratio of the particles was changed. Thus, it was confirmed that SA was bound to the Au-NPs. The gel shifts between lane 1 and lanes 2–5, respectively, confirmed the binding of biotin-labeled ON705 to SA-coated Au-NPs. The charge/mass ratio of the particles increased as more biotin-labeled ON705 was attached to particles. Saturation of biotin-labeled ON705 on SA-Au-NP occurred at a molar ratio of biotin-labeled ON705 to gold of roughly 500:1. Similarly, the distance difference of band migrations revealed in Figure 2 confirmed the binding of peptide large T to Au-NPs as well as the formation of mixed monolayer of peptides and oligonucleotides on SA-Au-NPs with different molar ratio of peptide to oligonucleotides.

Dynamic light scattering (DLS) also qualitatively confirmed the binding of SA and ON705 to Au-NPs. These data showed an increase in the hydrodynamic diameter (nm), which is expected following the binding of SA/oligonucleotides/(SA + peptide)-SA to citrate-coated Au-NPs (Table 3). These results also confirmed that the size of the nanoparticle conjugates was

compatible with the nuclear pore complex (<40 nm) (*40*). Fluorescence spectroscopy was employed to determine the surface coverage of SA and thiolated-oligonucleotides on Au-NP (*15*), and it was found that the surface coverage for SA was 14 ± 2 pmol/cm^2 and for thiolated-oligonucleotides was 26 ± 3 pmol/cm^2.

Once the ON705-SA-Au-NPs were prepared and characterized by UV–vis spectroscopy, gel electrophoresis, DLS, and fluorescence microscopy, they were tested in cell growth medium. One concern with the present formulation is that ON705 could dissociate from Au-NP surfaces once the ON705-SA-gold vectors were incubated with LF in a cell medium, which contains various proteins and high concentrations of salts. In order to test whether such dissociation occurs, gel electrophoresis was performed on two samples: the ON705-SA-Au-NPs and the incubation mixture of LF and ON705-SA-Au-NPs with Opti-MEM supplemented with 10% FBS. The band shift was observed for both samples (data not shown), confirming that ON705 was bound to the Au-NPs and did not dissociate from the nanoparticle surfaces.

Colloidal Stability of Nanoparticle Formulations. The colloidal stability of Au-NP formulations is sensitive to the ionic strength of the solution. An increase in ionic strength compresses the ionic double layer and thereby reduces the electrostatic repulsion between particles. When van der Waals attraction due to Au-NP polarizability outweighs electrostatic and steric repulsion, the Au-NPs aggregate. To determine the stability of the Au-NPs afforded by the combination of the stabilizer protein (SA), targeting peptides and oligonucleotides, a critical coagulation concentration (CCC) assay was conducted at various stages of the formulation of the targeting nanoparticles. In this assay, concentrated NaCl was added to a given Au-NP preparation in aliquots until precipitation was observed. Citrate-stabilized Au-NPs have a CCC of 50 mM NaCl. Cell media contains approximately 150 mM NaCl. Consequently, citrate-stabilized Au-NPs form a precipitate immediately upon the addition of Au-NPs into cell media. This can be easily observed in a phenol-free DMEM medium by a color change from red to blue. On the other hand, the formulations using SA as a stabilizer and for conjugation were all observed to be stable in cell media. It was found that SA-Au-NPs were stable in solutions containing up to 800 mM NaCl. ON705-SA-Au-NPs were stable in solutions up to 1 M NaCl. On the other hand, thiolated ON705-Au-NPs were stable in solutions up to 500 mM NaCl. The stability of (ON705 + peptide)-Au-NPs varied as different types of peptides were used. All the formulations of (ON705 + peptides)-Au-NPs that were studied in cell culture were stable in up to 300 nM NaCl solution.

Antisense Activity of Au-NP Conjugates Examined by the Luciferase Assay System. The antisense activity of Au-NPs loaded with ON705 oligonucleotides was studied using pLuc 705 HeLa cells. The Luc expression assay provides a means to quantitatively study the delivery of antisense agents for the alteration of gene splicing (*18*). By performing a Luc assay with Au-NPs carrying only ON705 oligonucleotides, which were transfected with LF, it was found that the oligonucleotides were able to reach the nucleus and interact with mRNA in the splicesome to correct the splice defect.

The expression of Luc was measured for increasing concentrations of ON705 both conjugated to Au-NPs and as a free oligonucleotide at a constant LF concentration (8 μg/200 μL). LF concentration is reported as it is measured in terms of the mass per well. Figure 3 shows that the Luc level reached a maximum at 0.3 μM of ON705 and then decreased to near-background levels at 1.0 μM in agreement with a previous report (*18*). This phenomenon has been explained as the dependence of the charge ratio of oligonucleotide to cationic lipid. At 8 μg of LF, the optimum value was 0.3 μM. Excess oligonucleotide results in a decrease in Luc expression because the LF complex is not able to neutralize the negative charge as effectively (*39*).

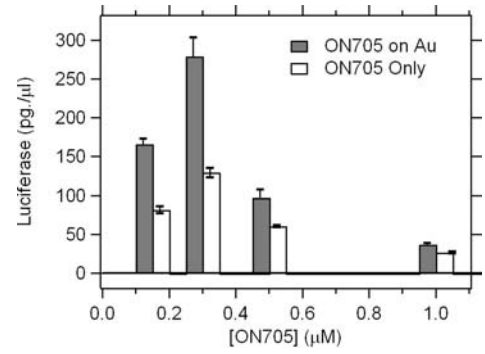

Figure 3. Relative antisense as a function of the concentration of ON705-gold and ON705 only with 8 μg of LF/ 200 μL solution in pLuc 705 HeLa cells. The maximum in activity reproduces previous studies of the concentration dependence of ON705 activity.

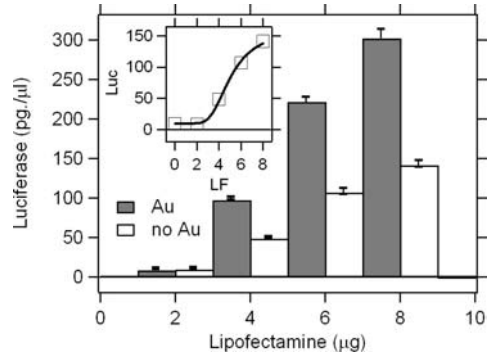

Figure 4. Relative antisense activity of ON705-Au-NPs and ON705 RNA only with a fixed concentration of ON705 (0.3 μM) in pLuc 705 HeLa cells as a function of the LF concentration. Comparisons were using 2, 4, 5, and 8 μg of LF per well volume of 200 μL. The inset shows the ON705 only data fit to a sigmoidal function.

Fixed concentrations of both ON705 and nanoparticles with increasing concentrations of LF were tested to study the dependence of antisense activity on LF concentration. The antisense activity increased in proportion to the LF concentration from 2 μg to 8 μg LF per well volume of 200 μL. In the experiment shown in Figure 4, the presence of Au-NPs was also compared without the addition of targeting peptides. In this experiment, it was found that Luc expression increased as LF concentration increased in an approximately sigmoidal fashion that can be modeled in terms of the equilibrium interaction between LF and ON705. Both Figures 3 and 4 show that Au-NPs facilitate the uptake of ON705 by a factor of 2 under all conditions where Luc protein is measured above the background level.

Relative Antisense Activity of Au-NPs Modified with Both Peptides and Oligonucleotides. Six formulations of targeting peptides using single- and double-labeled Au-NPs with virus peptides were prepared using the conjugation chemistry described above. The peptide sequences are given in Table 1 and the formulations are illustrated in Figure 5. The formulations were tested using the Luc expression assay. The data showed that, under the current experimental conditions, peptides did not enhance the nuclear targeting of oligonucleotides modified with Au-NPs in the absence of LF (Figure 6). Formulation 1 was the positive control consisting of 0.3 μM ON705 with LF. Control experiments performed with SA-modified ON705 and peptide at the same concentration (0.3 μM ON705) did not show any difference in the level of Luc expression compared to free

Table 1. Targeting Peptides of Viral Origin for Conjugation to SA-Stabilized Au Nanoparticles[a]

#	sequence (NH_2-)*	origin	ref
1	-FNPVYPYEDESKKKKKKGG-	adenoviral RME (CAR)	(*42*)
2	-AKRARLSTSFGGG-	adenoviral NLS (CD46)	(*51*)
3	-GFMDGRGGKKKKKKG-	integrin binding domain (IBD)	(*52*)

[a] All peptides have a fluorescence label at N-terminal and biotin nova tag at C-terminal.

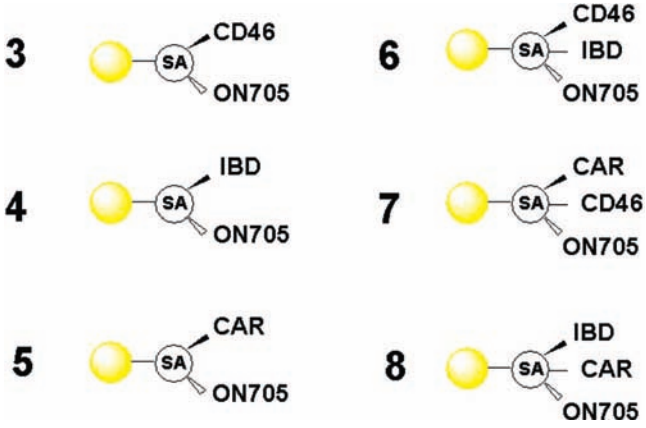

Figure 5. Representative nanoparticle formulations including one targeting peptide and an oligonucleotide payload. The stabilizer protein is streptavidin. The numbers correspond to the formulations in Figures 5 and 6.

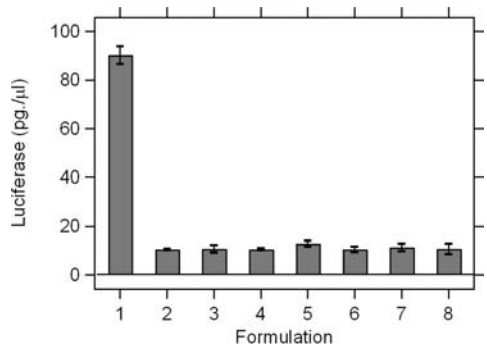

Figure 6. Relative antisense activity of Au-NPs modified with peptide and ON705 in the absence of LF detected as Luc expression. Formulation 1 was the positive control, consisting of free ON705 + LF. Formulation 2 was a negative control consisting of ON705 without LF. Formulations 3–8 are described in Figure 4. Concentrations of ON705, peptides, SA, and Au-NPs were 0.3 μM, 0.3 μM, 0.15 μM, and 6 nM, respectively.

ON705 (data not shown). Figure 6 shows that Luc was produced at the level of 90 pg/μL. Formulation 2 consisted of the same 0.3 μM ON705, but without any LF. The Luc produced in these cells was decreased 9-fold to 10 pg/μL. None of the preparations 3–8 using Au-NPs with targeting peptides and same total concentration of ON705 produced any Luc above the background level.

However, the same formulations of Au-NPs did target the nucleus of cells in the presence of LF as shown in Figure 7. Formulation 1 was the same positive control used in Figure 6 (also Formulation 1). Formulation 2 consisted of an LF-only experiment. The level of Luc expression in this experiment was 10 pg/μL, which is the same level of expression observed in the ON705-only experiment (formulation 2 in Figure 6). Formulations 3–8 showed an increase in Luc expression by a factor of 2, which is also the level of increase seen in the ON705-Au-NP experiments shown in Figures 3 and 4.

Relative Antisense Activity of QD Formulations. SA-modified QDs were coupled with peptides and ON705 to target

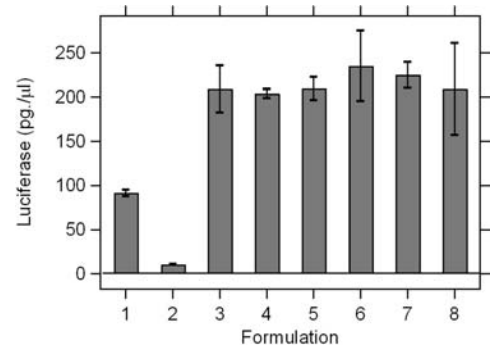

Figure 7. Relative antisense activity of Au-NPs modified with peptide and ON705 in the presence of LF detected as Luc expression. Formulation 1 was positive control, free ON705+ LF. Formulation 2 was a negative control consisting of LF without ON705. Formulations 3–8 are described in Figure 4 except that they each were combined with LF. Concentrations of ON705, peptides, SA, and Au-NPs were 0.3 μM, 0.3 μM, 0.15 μM, and 6 nM, respectively.

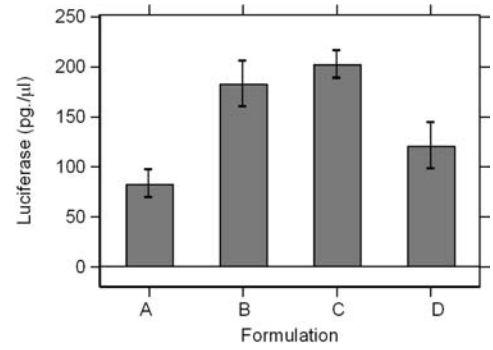

Figure 8. Comparison of relative antisense activity of Au-NPs with two different linkers and QDs in the presence of LF. Formulations correspond to the designations in Table 4.

Table 2. Oligonucleotides used for conjugation to SA-Stabilized Au-NPs, Citrate-Stabilized Au-NPs, and QDs

name	sequence (5′−3′)
ON705	CCU CUU ACC UCA GUU ACA
Thiol-ON705	Thiol MC6-D CCU CUU ACC UCA GUU ACA
Biotin-ON705	Bio PEG CCU CUU ACC UCA GUU ACA

Table 3. Dynamic Light Scattering (DLS) of 10 nm Diameter Gold Particles Modified with the Indicated Molecules

monolayer	hydrodynamic diameter (nm)
citrate	10.4 ± 0.5
SA	18.4 ± 0.9
(ON705 + peptides)-SA	20.0 ± 1.5
ON705-SH	20.3 ± 1.8

Table 4. Chemical Linkers Used to Test the Bioavailability of the ON705 Peptide and Effect of Nanoparticle Composition

sample	chemical linker used	nanoparticle employed	formulation
A	none	none	ON705
B	biotin	Au-NP	ON705-SA-Au-NP
C	thiol (-SH)	Au-NP	ON705-SH-Au-NP
D	biotin	QD	ON705-SA-QD

nucleus of the cells and correct aberrant pre-mRNA splicing. Similar results were obtained as those reported above using Au-NPs. The comparison given in Figure 8 shows that, although the QD (shown as formulation D in Figure 8 and Table 4) shows uptake in the presence of LF, it does not give greater uptake than Au-NPs. QDs did boost the Luc expression level in the presence of LF relative to ON705 alone. However, in the case

of QDs, the increase was approximately 50% rather than a factor of 2 (formulations A and D in Figure 8). Finally, as observed with Au-NPs, none of the 5 peptides tested enhanced the nuclear uptake of the Au-NPs in the absence of LF (data not shown).

Comparison of Bioavailability of Thiolated ON705 with Biotinylated ON705. A study of the relationships between the bioavailability of ON705 on two types of Au-NPs was made. The comparison in Figure 8 is shown in formulations B (biotinylated) and C (thiolated) as given in Table 4. Although the ON705 only Au-NP was taken up in the presence of LF, extensive experimentation using thiolated targeting peptides resulted in failure to create a stable formulation that combined targeting peptides and ON705.

DISCUSSION

In this study, we have employed a splice variant of the β-thalessemia intron as an assay for evaluating functional cellular uptake and nuclear targeting of the oligonucleotides conjugated to an Au-NP and QDs. The splice variant assay is specific for quantifying the uptake of multifunctional nanoparticles into the nucleus and for functional interaction with the spliceosome. A positive readout in the Luc assay provides information on the expression of Luc in an assay that involves tens of thousands of cells ($\sim 10^5$ cells per well of a 24-well plate). The results of this study indicate that the pLuc 705 reporter gene-splicing assay is an excellent method for a comparative study of antisense applications specific to nuclear targeting.

The Luc assay revealed that the antisense oligonucleotide ON705 was available to hybridize with pre-mRNA and functioned as a gene-splicing modifier according to its design. The studies showed that the availability of ON705 for gene splicing was not strongly dependent on the kind of chemical linker used or the presence of targeting peptides. Moreover, it was found that ON705 had a 2-fold increase in gene splicing efficiency when tethered to a Au-NP in the presence of LF. In the absence of LF, there was no increase in gene splicing above background. One possible explanation for the increased gene splicing efficiency is that the local density of ON705 attached to Au-NPs was significantly increased compared to free oligonucleotides in the cell media. The experiments were carried out at the ON705 concentration of maximum effective action (Figure 3) so that it is not possible for a minority population of free ON705 to give a signal that would compete with the population bound to nanoparticles (*39*). The fact that the assays showed enhanced expression of Luc in the presence of LF demonstrates that neither the preparation nor the colloidal stability of the nanoparticles is responsible for the lack of Luc expression.

The role of LF is well-known for transfection of genes, antisense oligonucleotides, and RNA interference applications. Commercially available Lipofectamine 2000 (LF) is a proprietary cationic lipid basically consisting of a positively charged headgroup and hydrocarbon chains. The positive charge interacts with the phosphate backbone of the nucleic acid and the negatively charged cell membrane, allowing the fusion of the liposome/nucleic acid with the cell membrane, forming a membrane-bound vesicle. After endocytosis, the complex escapes the endosomal/lysosome pathway, diffuses through the cytoplasm, and enters the nucleus of the cell. The use of gold nanoparticles as an aid to LF was not contemplated in this study, but was observed in the control experiments.

The results obtained here can be compared to cell-targeting studies for gene therapy and delivery of proteins. Nuclear targeting has been demonstrated using SA functionalized with targeting peptides attached to biotinylated DNA. Addition of the NLS peptide increased both nuclear uptake and expression of DNA after microinjection into the cytosol of HeLa cells (*41*). A 21-residue peptide carrier, Pep-1, has been used for protein (*42*) and quantum dot (*43*) internationalization. The peptide consists of a hydrophobic tryptophan-rich domain for efficient cell membrane translocation and the hydrophilic lysine-rich domain derived from the SV-40-T antigen NLS to facilitate solubility and nuclear targeting. The Pep-1 has been shown to be extremely efficient in the targeting of proteins into cells independent of endocytosis (*42*). Pep-1 is an example of a peptide transduction domain (PTD), which is sequence of cationic amino acids that interact with the cell membrane to facilitate entry via a route that is not believed to involve RME. Cationic peptides also have a known function in a manner that may have similarity to LF. However, PTDs in combination with Au-NPs have not yielded promising results. One reason for the lack of success with PTDs may be that cationic peptides tend to increase the pI of carrier proteins such as BSA and thereby reduce the colloidal stability of the nanoparticle.

The observations reported here indicate that nanoparticle integrity is compromised at some point during uptake in the cell. In the absence of LF, this could occur during receptor binding, endocytosis, escape from endosome/lysosome, cytosolic trafficking, or nuclear localization of nanoparticle vectors. Given that cellular internalization and nuclear targeting have been observed in independent experiments (*19*, *20*), it is unlikely that there is a problem with interaction with cell receptors. On the other hand, the nanoparticles could be endocytosed and then trapped in endosomes/lysosomes. The results here suggest multiple pathways could be involved in the process of cellular internalization and targeting (*44*, *45*). The degree to which each pathway contributes to the overall uptake and intracellular distribution depends on a variety of factors, including the structure of the peptide itself, peptide exposure, the loading density of peptide signal on the particle surface (*46*, *47*), the structure of the chemical linkage between the peptides, oligonucleotides, and nanoparticles, as well as the cell type.

CONCLUSION

The results obtained indicate that antisense oligonucleotides bound to nanoparticles are bioavailable to interact with pre-mRNA in the nucleus of the cells only under certain conditions. In the presence of LF, Au-NPs enhance the delivery efficiency of the antisense oligonucleotide ON705 compared to the control. However, the intrinsic targeting ability of the oligonucleotides attached to Au-NPs was not improved by the conjugation of targeting peptides that facilitate endocytosis or uptake. The results indicate that a strategy based on surface attachment of oligonucleotides or other therapeutic cargo has the potential for loss or degradation of the of the oligonucleotide cargo in cell-targeting experiments. Transit through endosomes results in the exposure of surface-attached molecules to harsh conditions that may compromise their efficacy in cell-targeting experiments. For this reason, sequestration of cargo inside a cage (*48–50*) may provide a mode-effective method for delivering cargo to cells.

MATERIALS AND METHODS

Nanoparticles and Targeting Peptide Preparations. Citrate-coated Au-NPs (10 and 20 nm in diameter) were purchased from Ted Pella. Streptavidin (SA) coated nanocrystals (CdSe/ZnS), QD605, were purchased from Quantum Dot Corporation. Streptavidin (SA) was purchased from Pierce. Texas Red-labeled streptavidin was purchased from Biomeda Corporation. Tris−HCl prepacked PAGE gels, native sample buffer, and biosafe Coomassie G250 stain were purchased from Bio-Rad. Agarose DNA grade, tris-boric acid-EDTA (TBE) 5× buffer, tris−glycine 10× buffer, and 20× saline−sodium citrate solution were purchased from Fisher Scientific. Dulbecco's modified Eagle's medium

(DMEM), fetal bovine serum (FBS), and Dulbecco's phosphate-buffered saline (DPBS) were purchased from BioWhittaker. Opti-MEM reduced serum medium and Lipofectamine (LF) were purchased from Invitrogen. pLuc 705 HeLa cells were a gift from R Kole at Lingberger Comprehensive Cancer Center at University of North Carolina at Chapel Hill. The Luciferase Reporter Assay kit was purchased from Applied Biosystem International (ABI, Foster City, CA).

The peptide sequences investigated in this work (Table 1) were synthesized by The University of North Carolina Peptide Synthesis Facility, purified by HPLC, and supplied in lyophilized form. The oligonucleotides were custom-ordered from MWG-Biotech (Ebersberg, Germany) or Integrated DNA Technologies (IDT, Coralville IA). The ON705 sequence was ordered as a free 18-mer RNA, a 5′-thiolated RNA, or a biotinylated and pegylated RNA (Table 2).

All UV–vis absorption measurements were acquired on a Hewlett-Packard 8453 Chemstation Photo Diode Array Spectrophotometer with attached Chemstation software.

Fluorescence intensity data were obtained using a Perkin-Elmer luminescence spectrometer LS50B or a BioTek FL-600 plate reader. Dynamic light scattering (DLS) measurements were obtained on a Malvern Zetasizer 1000.

Preparation of Streptavidin (SA) Coated Au-NPs. One milligram SA was dissolved in 1 mL of 10 mM phosphate-buffered saline (PBS) to produce a 16.7 μM SA stock solution. 140 μL of the above solution was added into 500 μL of 9.5 nM citrate-capped Au-NPs (10 nm in diameter), producing a molar ratio of SA to Au-NP of 500:1. The mixture was vortexed and then incubated at room temperature for at least half an hour. The excess SA was removed by centrifugation at 13 000 rpm for 20 min. The pellet was resuspended in 500 μL of PBS buffer.

Determination of Surface Coverage of Streptavidin (SA) on Au-NPs. In order to obtain the binding isotherm of Texas Red labeled streptavidin (TR-SA) on Au-NP surfaces, different surface coverages of SA on Au-NPs were prepared. For example, 10 nm Au-NPs (500 μL of 9.5 nM) were mixed with 63 μL of TR-SA solution (18.9 μM in PBS), producing a molar ratio Au/TR-SA of 1:250. After stirring for 30 min, those sols were centrifuged at 13 000 rpm for 15 min. Supernatants containing unbound proteins were carefully removed from the pellets, followed by washing the sediments with 200 μL of phosphate buffer two more times. All the supernatants for each sample were collected and then diluted to 1 mL. A standard curve was created by measuring the fluorescence intensities of TR-SA solutions ranging from 0.078 μM to 10 μM in 10 mM phosphate buffer (pH 7.4) and was used to determine the concentration of unbound TR-SA in the supernatant solution. The amount of TR-SA molecules bound on the nanoparticle surface was calculated by subtracting free TR-SA from the total amount of TR-SA added initially. The ratio TR-SA/AuNP was determined by measurement of the Au-NP concentration using the extinction coefficient of $\epsilon = 5 \times 10^8\ M^{-1}\ cm^{-1}$ to calculate the concentration.

Preparation of Peptide-Modified QDs. The peptides were incubated with SA-modified QDs (~10–15 nm in diameter) at a molar ratio of 10:1 to 20:1 in phosphate buffer saline (PBS) with 20 min of reaction time. The incorporation of biotinylated peptides onto the SA-QD conjugates under these conditions is best probed by gel electrophoresis, where the ratio of peptide/QDs spans from 1:1 to 50:1.

Preparation of ON705-SA-Au-NPs. The oligonucleotide ON705 was incubated with 1 mL of SA-coated Au-NPs (10 nm in diameter) at molar ratio of 75:1 in PBS. After 45 min, the mixture was centrifuged at 13 000 rpm for 20 min, and the pellet was washed 2 more times with PBS. The resulting nanoparticles were resuspended in 1 mL of PBS.

Preparation of (ON705 + peptides)-SA-Au-NPs. The peptides were mixed with ON705 in either a 1:1 or 2:1 molar ratio before mixing with 1 mL of Au-NPs (10 nm in diameter). The mixtures were incubated at room temperature for 1 h and purified by centrifugation (2×, 13 000 rpm for 20 min). The modified nanoparticles were resuspended in 1 mL of PBS buffer.

Preparation of ON705-Thiol (S)-Au-NPs. Oligonucleotide-modified Au-NP conjugates were prepared as previously described with a few modifications (*8*, *15*). Briefly, 50 μL of a 47.5 μM of oligonucleotide solution was added to 500 μL of 10 nm diameter Au-NPs (9.5 nM). The molar ratio of the final concentration of oligonucleotides to colloid was 400:1. The samples were placed into a water bath at 37 °C for 8 h, after which the solution was gradually brought to 0.1 M NaCl/10 mM Na phosphate pH 7.4. The samples were left in the solution for an additional 16 h at 37 °C. Then, samples were centrifuged at 13 500 rpm for 15 min three times, with 2× wash using 500 μL of 0.1 M NaCl/10 mM Na phosphate pH 7.4 in between to remove excess oligonucleotides. The final pellet was resuspended in 500 μL of 10 mM Na phosphate. Since a small amount of Au-NPs was discarded with the supernatant in the washing procedure, the corresponding nanoparticle concentration was determined by UV–visible absorption spectroscopy.

Determination of Surface Coverage of Oligonucleotides on Particle Surface. The quantification method to determine the surface coverage of oligonucleotides on the nanoparticle surface was mainly based on the literature procedure (*15*). Briefly, mercaptoethanol (ME) was added (final concentration 14 mM) to Au-NPs (20 nm in diameter) modified with fluorescein-labeled oligonucleotides in 10 mM phosphate, 0.1 M NaCl, pH 7.4. After 15 h incubation at room temperature with intermittent shaking, the solutions containing displaced oligonucleotides were separated from the gold by centrifugation at 10 500 rpm for 15 min three times, with 2× wash using 200 μL of 10 mM Na phosphate pH 7.4 in between in order to collect all free fluorescein−oligonucleotides. Standard linear calibration curves were prepared with known concentrations of fluorescein−oligonucleotides using identical buffer and ME concentrations. The fluorescence intensities were converted to molar concentrations of fluorescein−oligonucleotides by interpolation from a standard curve.

Determination of Critical Coagulation Concentrations (CCC). To determine the critical coagulation concentration (CCC) of SA, peptides, and oligonucleotides modified Au-NPs, a series of Eppendorf centrifuge tubes containing 500 μL of identical concentrations of Au-NPs (1.16 nM for 20 nm diameter and 9.4 nM for 10 nM) were prepared. Increasing volumes of a 1.7 M NaCl stock solution were added to each sample with the final salt concentration ranging from 20 mM to 1 M. The tubes were vortexed and then allowed to incubate for at least 3 h. Aggregation was assessed by monitoring changes in the characteristic Au-NP plasmon frequency. The threshold NaCl salt concentration in the gold sol, which caused the rapid aggregation of the particles, is determined as the CCC.

Nanoparticle Transfection with pLuc HeLa Cells. The experimental protocols were similar to those previously described (*18*). Briefly, The pLuc HeLa cells were cultured in Dulbecco's modified Eagle's medium (DMEM) supplemented with 10% fetal bovine serum (FBS) at 37 °C in a humidified atmosphere with 5% CO_2. HeLa 705 cells were grown in 24-well flasks to 95% confluency. The cells were washed twice with Dulbecco's phosphate-buffered saline (DPBS). The control experiments were performed with (1) mock transfected pLuc 705 cells, i.e., cells were incubated with media only or media containing LF; (2) free oligonucleotides in the absence of LF; (3) free oligonucleotides in the presence of LF. Au-NPs modified with ON705 were purified in order to remove excess ON705.

The nanoparticles incubated with cells were tested in two conditions as well: with or without the presence of LF.

The samples were mixed in Opti-MEM reduced serum media. For example, a 0.1 mL aliquot of an oligonucleotide at a given concentration (0.3 μM) in Opti-MEM was mixed with 8 μg of Lipofectamine to make a total volume of 200 μL. After being mixed, the preparation was left at room temperature for 15 min, followed by dilution to 1.0 mL with Opti-MEM. The cells were incubated at 37 °C for 4 or 5 h. The final concentrations for all oligonucleotides with or without nanoparticles were 0.15 μM. Subsequently, the media was replaced with DMEM containing 10% FBS. After an additional 18 h, the Luc reporter assay was performed following manufacturer's protocol (ABI). All experiments were done in triplicate.

ACKNOWLEDGMENT

We thank R. Kole for the gift of the Luc HeLa cell line that contains the Luc gene with a β-thalessemia intron. We acknowledge support from NIH grant CA098194.

LITERATURE CITED

(1) Hughes, J. A., Aronsohn, A. I., Avrutskaya, A. V., and Juliano, R. L. (1996) Evaluation of adjuvants that enhance the effectiveness of antisense oligodeoxynucleotides. *Pharm. Res. 13*, 404–410.

(2) Boussif, O., Lezoualch, F., Zanta, M. A., Mergny, M. D., Scherman, D., Demeneix, B., and Behr, J. P. (1995) A versatile vector for gene and oligonucleotide transfer into cells in culture and in-vivo - polyethylenimine. *Proc. Natl. Acad. Sci. U.S.A. 92*, 7297–7301.

(3) Bennett, C. F., Chiang, M. Y., Chan, H. D., Shoemaker, J. E. E., and Mirabelli, C. K. (1992) Cationic lipids enhance cellular uptake and activity of phosphorothioate antisense oligonucleotides. *Mol. Pharm. 41*, 1023–1033.

(4) Curiel, D. T., Agarwal, S., Wagner, E., and Cotten, M. (1991) Adenovirus enhancement of transferrin polylysine-mediated gene delivery. *Proc. Natl. Acad. Sci. U.S.A. 88*, 8850–8854.

(5) Rosenfeld, M. A., Siegfried, W., Yoshimura, K., Yoneyama, K., Fukayama, M., Stier, L. E., Paakko, P. K., Gilardi, P., Stratfordperricaudet, L. D., Perricaudet, M., Jallat, S., Pavirani, A., Lecocq, J. P., and Crystal, R. G. (1991) Adenovirus-mediated transfer of a recombinant α-L-antitrypsin gene to the lung epithelium in vivo. *Science 252*, 431–434.

(6) Liu, Y. L., Shipton, M. K., Ryan, J., Kaufman, E. D., Franzen, S., and Feldheim, D. L. (2007) Synthesis, stability, and cellular internalization of gold nanoparticles containing mixed peptide-poly(ethylene glycol) monolayers. *Anal. Chem. 79*, 2221–2229.

(7) Agbasi-Porter, C., Ryman-Rasmussen, J., Franzen, S., and Feldheim, D. (2006) Transcription inhibition using oligonucleotide-modified gold nanoparticles. *Bioconjugate Chem. 17*, 1178–1183.

(8) Pena, S. R. N., Raina, S., Goodrich, G. P., Fedoroff, N. V., and Keating, C. D. (2002) Hybridization and enzymatic extension of Au nanoparticle-bound oligonucleotides. *J. Am. Chem. Soc. 124*, 7314–7323.

(9) Rosi, N. L., Giljohann, D. A., Thaxton, C. S., Lytton-Jean, A. K. R., Han, M. S., and Mirkin, C. A. (2006) Oligonucleotide-modified gold nanoparticles for intracellular gene regulation. *Science 312*, 1027–1030.

(10) Kogan, M. J., Olmedo, I., Hosta, L., Guerrero, A. R., Cruz, L. J., and Albericio, F. (2007) Peptides and metallic nanoparticles for biomedical applications. *Nanomedicine 2*, 287–306.

(11) Oyelere, A. K., Chen, P. C., Huang, X. H., El-Sayed, I. H., and El-Sayed, M. A. (2007) Peptide-conjugated gold nanorods for nuclear targeting. *Bioconjugate Chem. 18*, 1490–1497.

(12) Fortina, P., Kricka, L. J., Graves, D. J., Park, J., Hyslop, T., Tam, F., Halas, N., Surrey, S., and Waldman, S. A. (2007) Applications of nanoparticles to diagnostics and therapeutics in colorectal cancer. *Trends Biotechnol. 25*, 145–152.

(13) Xie, H., Tkachenko, A. G., Glomm, W. R., Ryan, J. A., Brennaman, M. K., Papanikolas, J. M., Franzen, S., and Feldheim, D. L. (2003) Critical flocculation concentrations, binding isotherms, and ligand exchange properties of peptide-modified gold nanoparticles studied by UV-visible, fluorescence, and time-correlated single photon counting spectroscopies. *Anal. Chem. 75*, 5797–5805.

(14) Kaufman, E. D., Belyea, J., Johnson, M. C., Nicholson, Z. M., Ricks, J. L., Shah, P. K., Bayless, M., Pettersson, T., Feldoto, Z., Blomberg, E., Claesson, P., and Franzen, S. (2007) Probing protein adsorption onto mercaptoundecanoic acid stabilized gold nanoparticles and surfaces by quartz crystal microbalance and zeta-potential measurements. *Langmuir 23*, 6053–6062.

(15) Demers, L. M., Mirkin, C. A., Mucic, R. C., Reynolds, R. A., Letsinger, R. L., Elghanian, R., and Viswanadham, G. (2000) A fluorescence-based method for determining the surface coverage and hybridization efficiency of thiol-capped oligonucleotides bound to gold thin films and nanoparticles. *Anal. Chem. 72*, 5535–5541.

(16) Murphy, D., Redmond, G., de la Torre, B. G., and Eritja, R. (2004) Hybridization and melting Behavior of peptide nucleic acid (PNA) oligonucleotide chimeras conjugated to gold nanoparticles. *Helv. Chim. Acta 87*, 2727–2734.

(17) Nitin, N., Javier, D. J., and Richards-Kortum, R. (2007) Oligonucleotide-coated metallic nanoparticles as a flexible platform for molecular Imaging agents. *Bioconjugate Chem. 18*, 2090–2096.

(18) Levy, R., Thanh, N. T. K., Doty, R. C., Hussain, I., Nichols, R. J., Schiffrin, D. J., Brust, M., and Fernig, D. G. (2004) Rational and combinatorial design of peptide capping ligands for gold nanoparticles. *J. Am. Chem. Soc. 126*, 10076–10084.

(19) Tkachenko, A. G., Xie, H., Coleman, D., Glomm, W., Ryan, J., Anderson, M. F., Franzen, S., and Feldheim, D. L. (2003) Multifunctional gold nanoparticle-peptide complexes for nuclear targeting. *J. Am. Chem. Soc. 125*, 4700–4701.

(20) Tkachenko, A. G., Xie, H., Liu, Y. L., Coleman, D., Ryan, J., Glomm, W. R., Shipton, M. K., Franzen, S., and Feldheim, D. L. (2004) Cellular trajectories of peptide-modified gold particle complexes: Comparison of nuclear localization signals and peptide transduction domains. *Bioconjugate Chem. 15*, 482–490.

(21) Weber, P. C., Ohlendorf, D. H., Wendoloski, J. J., and Salemme, F. R. (1989) Structural origins of high-affinity biotin binding to streptavidin. *Science 243*, 85–88.

(22) Moritz, S., Colin, M., Keller, M., Klonjkowski, B., Capeau, J., Coutelle, C., Chroboczek, J., and Brahimi-Horn, M. C. (2003) Gene transfer by adenovirus-mimetic peptides in the presence of a cationic lipid and/or adenovirus. Analysis of the contribution of the viral and nonviral components. *Arch. Virol. 148*, 1–18.

(23) Cusack, S. (2005) Adenovirus complex structures. *Curr. Opin. Struct. Biol. 15*, 237–243.

(24) Okada, Y., Okada, N., Mizuguchi, H., Hayakawa, T., Nakagawa, S., and Mayumi, T. (2005) Transcriptional targeting of RGD fiber-mutant adenovirus vectors can improve the safety of suicide gene therapy for murine melanoma. *Cancer Gene Ther. 12*, 608–616.

(25) Eto, Y., Gao, J. Q., Sekiguchi, F., Kurachi, S., Katayama, K., Maeda, M., Kawasaki, K., Mizuguchi, H., Hayakawa, T., Tsutsumi, Y., Mayumi, T., and Nakagawa, S. (2005) PEGylated adenovirus vectors containing RGD peptides on the tip of PEG show high transduction efficiency and antibody evasion ability. *J. Gene Med. 7*, 604–612.

(26) Smith, R. A., and Giorgio, T. D. (2004) Quantitation and kinetics of CD51 surface receptor expression: Implications for targeted delivery. *Ann. Biomed. Eng. 32*, 635–644.

(27) Lanford, R. E., Kanda, P., and Kennedy, R. C. (1986) Induction of nuclear transport with a synthetic peptide homologous to the Sv40 T-antigen transport signal. *Cell 46*, 575–582.

(28) Zanta, M. A., Belguise-Valladier, P., and Behr, J. P. (1999) Gene delivery: A single nuclear localization signal peptide is

sufficient to carry DNA to the cell nucleus. *Proc. Natl. Acad. Sci. U.S.A. 96*, 91–96.
(29) Sazani, P., and Kole, R. (2003) Therapeutic potential of antisense oligonucleotides as modulators of alternative splicing. *J. Clin. Invest. 112*, 481–486.
(30) Kole, R., and Sazani, P. (2001) Antisense effects in the cell nucleus: Modification of splicing. *Curr. Opin. Mol. Ther. 3*, 229–234.
(31) Sierakowska, H., Gorman, L., Kang, S. H., and Kole, R. (2000) Antisense oligonucleotides and RNAs as modulators of pre-mRNA splicing. *Antisense Technol. Part A 2000* 506–521.
(32) Chan, J. H. P., Lim, S. H., and Wong, W. S. F. (2006) Antisense oligonucleotides: From design to therapeutic application. *Clin. Exp. Pharmacol. Physiol. 33*, 533–540.
(33) Yu, A. M. (2007) Small interfering RNA in drug metabolism and transport. *Curr. Drug Metabol. 8*, 700–708.
(34) Goodchild, J. (2004) Oligonucleotide therapeutics: 25 years agrowing. *Curr. Opin. Mol. Ther. 6*, 120–128.
(35) Crooke, S. T. (2004) Progress in antisense technology. *Ann. Rev. Med. 55*, 61–95.
(36) Gebski, B. L., Mann, C. J., Fletcher, S., and Wilton, S. D. (2003) Morpholino antisense oligonucleotides for inducing exon skipping. *J. Gene Med. 5*, S10–S10.
(37) Braasch, D. A., and Corey, D. R. (2002) Novel antisense and peptide nucleic acid strategies for controlling gene expression. *Biochemistry 41*, 4503–4510.
(38) Sazani, P., Kang, S. H., Maier, M. A., Wei, C. F., Dillman, J., Summerton, J., Manoharan, M., and Kole, R. (2001) Nuclear antisense effects of neutral, anionic and cationic oligonucleotide analogs. *Nucleic Acids Res. 29*, 3965–3974.
(39) Kang, S. H., Cho, M. J., and Kole, R. (1998) Up-regulation of luciferase gene expression with antisense oligonucleotides: Implications and applications in functional assay developments. *Biochemistry 37*, 6235–6239.
(40) Pante, N., and Kann, M. (2000) The functional diameter of the nuclear pore complex has been severely underestimated. *Mol. Biol. Cell 11*, 151A–152A.
(41) Ludtke, J. J., Zhang, G. F., Sebestyen, M. G., and Wolff, J. A. (1999) A nuclear localization signal can enhance both the nuclear transport and expression of 1 kb DNA. *J. Cell Sci. 112*, 2033–2041.
(42) Zhang, F., Andreassen, P., Fender, P., Geissler, E., Hernandez, J. F., and Chroboczek, J. (1999) A transfecting peptide derived from adenovirus fiber protein. *Gene Ther. 6*, 171–181.
(43) Rozenzhak, S. M., Kadakia, M. P., Caserta, T. M., Westbrook, T. R., Stone, M. O., and Naik, R. R. (2005) Cellular internalization and targeting of semiconductor quantum dots. *Chem. Commun.* 2217–2219.
(44) Richard, J. P., Melikov, K., Vives, E., Ramos, C., Verbeure, B., Gait, M. J., Chernomordik, L. V., and Lebleu, B. (2003) Cell-penetrating peptides - A reevaluation of the mechanism of cellular uptake. *J. Biol. Chem. 278*, 585–590.
(45) Lundberg, M., Wikstrom, S., and Johansson, M. (2003) Cell surface adherence and endocytosis of protein transduction domains. *Mol. Ther. 8*, 143–150.
(46) Gestwicki, J. E., Cairo, C. W., Strong, L. E., Oetjen, K. A., and Kiessling, L. L. (2002) Influencing receptor-ligand binding mechanisms with multivalent ligand architecture. *J. Am. Chem. Soc. 124*, 14922–14933.
(47) Warnement, M. R., Faley, S. L., Wikswo, J. P., and Rosenthal, S. J. (2006) Quantum dot probes for monitoring dynamic cellular response: Reporters of T cell activation. *IEEE Trans. Nanobiosci. 5*, 268–272.
(48) Loo, L., Guenther, R. H., Basnayake, V. R., Lommel, S. A., and Franzen, S. (2006) Controlled encapsidation of gold nanoparticles by a viral protein shell. *J. Am. Chem. Soc. 128*, 4502–4503.
(49) Loo, L., Guenther, R. H., Lommel, S. A., and Franzen, S. (2007) Encapsidation of nanoparticies by Red Clover Necrotic Mosaic Virus. *J. Am. Chem. Soc. 129*, 11111–11117.
(50) Loo, L., Guenther, R. H., Lommel, S. A., and Franzen, S. (2008) Infusion of dye molecules into Red clover necrotic mosaic virus. *Chem. Commun.* 88–90.
(51) Feldherr, C. M., and Akin, D. (1999) Signal-mediated nuclear transport in the amoeba. *J. Cell Sci. 112*, 2043–2048.
(52) Colin, M., Maurice, M., Trugnan, G., Kornprobst, M., Harbottle, R. P., Knight, A., Cooper, R. G., Miller, A. D., Capeau, J., Coutelle, C., and Brahimi-Horn, M. C. (2000) Cell delivery, intracellular trafficking and expression of an integrin-mediated gene transfer vector in tracheal epithelial cells. *Gene Ther. 7*, 139–152.

BC700421U

Cellular siRNA Delivery Mediated by a Cell-Permeant RNA-Binding Protein and Photoinduced RNA Interference

Tamaki Endoh, Masahiko Sisido, and Takashi Ohtsuki*

Department of Bioscience and Biotechnology, Okayama University, 3-1-1 Tsushimanaka, Okayama 700-8530, Japan. Received January 14, 2008; Revised Manuscript Received March 21, 2008

HIV-1 TAT peptide, which is a cell-penetrating peptide (CPP), was fused to the U1A RNA-binding domain (TatU1A) to generate a sequence-specific siRNA delivery system for mammalian cells. The siRNA contained a short 5′-extension that is specifically recognized by the U1A RNA-binding domain (*U1A*siRNA). Specific binding of TatU1A to the *U1A*siRNA was confirmed using a gel mobility shift assay. The *U1A*siRNA was internalized by cells only when it was preincubated with TatU1A before addition to the cells. Although most of the internalized siRNA seemed to be entrapped in endocytic compartments, efficient redistribution of the entrapped siRNAs was achieved by photostimulation of a fluorophore attached to TatU1A. Once in the cytoplasm, the siRNA induced RNAi-mediated gene silencing. We refer to this delivery strategy as CLIP-RNAi. CLIP-RNAi is a promising strategy for RNAi experiments and for pinpoint RNAi therapy.

INTRODUCTION

RNA interference (RNAi), discovered in *Caenorhabditis elegans*, is a phenomenon in which gene expression is down-regulated by a double-stranded RNA containing a sequence homologous to a specific gene (*1*). In mammals, the introduction of short double-stranded RNAs, termed small interfering RNAs (siRNAs) or short hairpin RNAs (shRNAs), into the cytoplasm can silence genes (*2–4*). RNAi-mediated gene silencing is now an essential method for analyzing protein function and an attractive therapeutic tool for interfering with the expression of undesirable genes such as oncogenes and viral genes. Experimental techniques to introduce siRNAs or shRNAs into mammalian cells usually involve either direct delivery of RNA or introduction of a gene encoding an shRNA (*5*). In therapeutic use, the latter strategy could cause undesirable gene recombination. Thus, an efficient and safe method for direct RNA delivery is essential for RNAi therapy.

Recently, cell-penetrating peptides (CPPs), such as partial sequences of the HIV-1 TAT protein and the *Drosophila* Antennapedia homeodomain, have been used to deliver fused or conjugated macromolecules into cells (*6–9*). CPPs enable the delivery of biologically active molecules into mammalian cells with high efficiency and low toxicity (*10, 11*).

To deliver siRNAs, several groups have covalently linked CPPs to siRNAs by introducing an amino or thiol group at one terminus of the siRNA (*12–14*). However, siRNAs can be introduced into mammalian cells by noncovalent, electrostatic conjugation to CPPs (*15–17*), a method which is much easier than covalent linking. One possible drawback of the noncovalent conjugation strategy is that the carrier molecule has no sequence specificity for the RNA. A nonspecific carrier could internalize naturally occurring extracellular RNAs (*18*, *19*) into cells, which may cause unexpected results. Thus, a cell-penetrating peptide or protein that noncovalently binds a specific RNA sequence is needed.

The U1 small nuclear ribonucleoprotein A (U1A) has a relatively small RNA binding domain (RBD) of 98 amino acids at its N-terminus. The U1A RBD recognizes a short RNA sequence with high specificity and affinity (*20, 21*). In this study, we genetically fused the U1A RBD to the HIV-1 TAT peptide (-YGRKKRRQRRR-), a well-characterized CPP. As a cargo partner, we prepared siRNAs bearing a short sequence that binds to the U1A RBD (*U1A* RNA sequence) and examined the specific binding of the fused protein (TatU1A) to the cargo RNA and internalization of the complex. We also examined the photoinduced release of RNA from endosomes, since internalized TatU1A/RNA complexes were entrapped in the endosomes. We refer to this delivery system as CLIP-RNAi (CPP-linked RBP-mediated RNA internalization and photo-induced RNAi).

EXPERIMENTAL SECTION

Plasmid Construction. Coding sequences for the TAT peptide and U1A RBD (amino acids 2 to 98) (*22*) (TatU1A) fusion construct were prepared by PCR ligation using two-step PCR. For the first PCR, the U1A RBD was amplified from human cDNA (Ambion Inc.) using the following primers: 5′-GGCAGTTCCCGAGACCC-3′ and 5′-GCGCTCGAGT-TATTTCATCTTGGCAATGATA-3′ (3XhoU1A). Double-stranded DNA encoding the Tat peptide was prepared by primer extension using the following primers: 5′-CATCATCACAG-CAGCGGCTACGGCCGCAAGAAACGCCGCCAGCGCCG-TCGCGGCTACCCA-3′ and 5′-CGGGTCTCGGGAACTGCG-CCGCTAGCGTAATCCGGAACATCGTATGGGTAGCCGCG-ACGGC-3′. For the second PCR, the first PCR product and primer extension product were ligated by PCR using 5′-GGCGCCATGGGCAGCCATCATCATCATCATCACAGCA-GCGGCTACGGC-3′ and 3XhoU1A as primers. The coding sequence of TatU1A was cloned into the *Nco* I−*Xho* I site of pET-28b to construct the expression vector pET-TatU1A.

Expression vectors for U1A RBD only [U1A(-Tat)] and TatU1A bearing a C-terminal Cys (TatU1A-C) were constructed from pET-TatU1A using the QuickChange Site-Directed Mutagenesis Kit (Stratagene). Mutagenesis was performed using two sets of primers: 5′-CACAGCAGCGGCTACGGCTAC-CCATACGATGTTCC-3′ and 5′-GGAACATCGTATGGG-TAGCCGTAGCCGCTGCTGTG-3′ for preparation of the U1A(-Tat) expression vector, and 5′-CAGATATCATTGCC-AAGATGAAAGGATCCTGCTAACTCGAGCACCACC-3′ and 5′-GGTGGTGCTCGAGTTAGCAGGATCCTTTCATCTTGG-

* To whom correspondence should be addressed. Tel: 81-86-251-8220; Fax: 81-86-251-8219; E-mail: ohtsuk@cc.okayama-u.ac.jp.

10.1021/bc800020n CCC: $40.75 © 2008 American Chemical Society
Published on Web 04/29/2008

CAATGATATCTG-3′ for preparation of the TatU1A-C expression vector. Underlined regions are inserted sequences encoding Gly-Ser-Cys residues just upstream of the stop codon.

The coding sequence for destabilized EGFP (dEGFP) (*23*) was prepared by PCR ligation. For the first PCR, EGFP was amplified from pEGFP-N3 (Clontech) using the following primers: 5′-CGCGCTAGCACCATGGTGAGCAAGGGCGAG-3′ (5pcDNAeGFP) and 5′-CTTGTACAGCTCGTCCATG-3′. Double-stranded DNA encoding the mutated degradation domain of mouse ornithine decarboxylase was prepared by primer extension using the following primers: 5′-CATGGACGAGCTGTACAAGAAGCTTAGCCATGGCTTCCCGCCGGCGGTGGCGGCGCAGGATGATGGCACGCTGCCCATGTC-3′ and 5′-CACATTGATCCTAGCAGAAGCACAGGCTGCAGGGTGACGGTCCATCCCGCTCTCCTGGGCACAAGACATGGGCAGCGTGCC-3′. For the second PCR, the first PCR product and primer extension product were ligated by PCR using the 5pcDNAeGFP and 5′-CGCCTCGAGTTACACATTGATCCTAGCAGAAG-3′ primers. The coding sequence of dEGFP was cloned into the *Nhe* I−*Xho* I site of pcDNA5/FRT (Invitrogen) to construct the expression vector pcDNA/FRT-dEGFP.

All coding sequences were confirmed by sequencing analysis using an ABI PRISM 310 genetic analyzer.

Preparation and Fluorescent Labeling of Proteins. *E. coli* strain BL21 (DE3) was transformed with pET-28b-derived expression vectors harboring TatU1A, U1A(-Tat), and TatU1A-C with N-terminal His-tags. The transformed cells were cultured, harvested by centrifugation, and then lysed by sonication and fractionated as described (24) with slight modifications. Buffer A [50 mM HEPES-KOH (pH 7.5), 150 mM $(NH_4)_2SO_4$, 7 mM $MgCl_2$, 20% glycerol, 7 mM β-mercaptoethanol, and 100 μM phenylmethylsulfonyl fluoride] was used to resuspend the cells, Buffer B [50 mM HEPES-KOH (pH 7.5), 1 M NH_4Cl, 40 mM imidazole, 20% glycerol, and 5 mM β-mercaptoethanol] was used to wash the Ni-NTA column, and Buffer C [50 mM HEPES-KOH (pH 7.5), 100 mM $(NH_4)_2SO_4$, 150 mM imidazole, 20% glycerol, and 5 mM β-mercaptoethanol] was used to elute the His-tagged protein. Purified proteins were then dialyzed against T buffer [20 mM HEPES-KOH (pH 7.4), 115 mM NaCl, 5.4 mM KCl, 1.8 mM $CaCl_2$, 0.8 mM $MgCl_2$, and 13.8 mM glucose] using Slide-A-Lyzer (Pierce).

To label TatU1A-C with Alexa Fluor 546, we mixed eluted TatU1A-C with 100 μM Alexa Fluor 546 C5 maleimide (Molecular Probes) in Buffer C and incubated the mixture at room temperature for 2 h. The Alexa-modified TatU1A-C (TatU1A-Alexa) was purified in a Centri-Sep spin column (Princeton Separations) equilibrated with T buffer.

Concentrations of all recombinant proteins were quantified using a Protein Assay Kit (Bio-Rad).

Preparation and Fluorescent Labeling of RNAs. All RNAs used in this study were purchased from Japan Bio Services Co., Ltd. In order to construct an siRNA-type cargo RNA, antisense and *U1A*-fused sense strands were dissolved in distilled water at final concentrations of 20 μM, and were then annealed by incubation at 90 °C for 1 min followed by a 60 min incubation at 37 °C. Hybridization was confirmed by polyacrylamide gel mobility shift assays. shRNA-type cargo RNA was annealed by incubation at 90 °C for 1 min followed by slow cooling (1 °C/min) to 30 °C to enhance intramolecular annealing. RNAs that targeted dEGFP mRNA (the coding region 274−292 relative to the first nucleotide of the start codon), luciferase mRNA (1188−1206), and epidermal growth factor receptor (EGFR) mRNA (2121−2139) are referred to as siGFP (or shGFP), siLuc (or shLuc), and shEGFR, respectively.

RNA was labeled with Cy3 or fluorescein using a LabelIT siRNA Tracker Intracellular Localization Kit (Mirus). To adjust

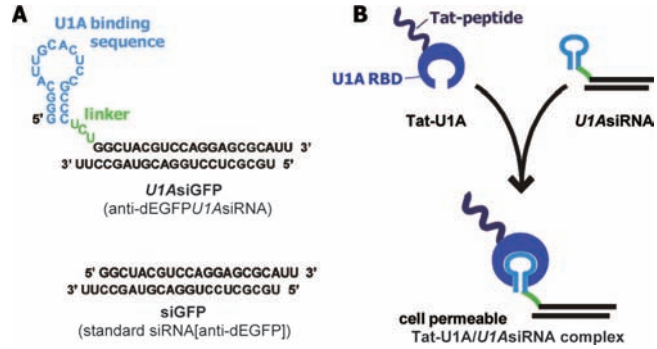

Figure 1. Construction of cell-permeable TatU1A/*U1A*siRNA complexes. (A) Sequences of the 5′-extended *U1A*siRNA and standard siRNA. The U1A-binding sequence and following UCU linker sequence were added to the 5′ end of the sense strand (upper). (B) TatU1A specifically bound to the 5′-extended U1A binding sequence, forming the cell permeable TatU1A/*U1A*siRNA complex.

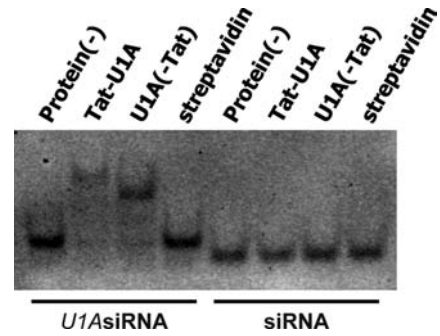

Figure 2. Specific interaction between TatU1A and *U1A*siRNA detected by gel mobility shift assays. Complex formation was initiated by mixing 500 nM siRNA with 1 μM of the indicated proteins, and 20 μL of the mixtures were loaded on the gel.

the RNA/fluorophore molar ratio of labeled siRNA and *U1A*-fused siRNA, only the antisense strand was labeled and the labeled antisense strand was mixed with the sense strand or the *U1A*-fused sense strand before the annealing procedure. Annealing using the labeled strand was performed by incubation of 20 μM each of the sense and antisense RNAs at 65 °C for 3 min followed by a 60 min incubation at 37 °C.

Gel Mobility Shift Assay. Purified proteins (1 μM) were mixed with 500 nM *U1A*siRNA or standard siRNA in T buffer. Streptavidin was purchased from Amresco (US) and used as a negative control protein. After a 10 min incubation at 37 °C, protein−RNA mixtures were analyzed in 6% native polyacrylamide gels with Gel-Shift buffer (50 mM Tris-HCl [pH 6.8], 10 mM $Mg(OAc)_2$, 65 mM NH_4OAc, 1 mM EDTA) at 4 °C. The gel was stained with ethidium bromide to detect RNAs.

Cell Culture and Construction of a Cell Line Expressing Destabilized EGFP. Chinese hamster ovary (CHO) cells (Invitrogen Flp-In-CHO cell line) were cultured at 37 °C under 5% CO_2 in Ham's F-12 medium supplemented with 10% fetal bovine serum (FBS). The human epidermoid carcinoma cell line A431 was kindly provided by Professor Seno (Okayama University) and cultured in Dulbecco's modified Eagle's medium (DMEM) supplemented with 10% FBS. Both media contained 100 units/mL penicillin and 100 μg/mL streptomycin. pcDNA/FRT-dEGFP was cotransfected with pOG-44 (Invitrogen) into Flp-In-CHO cells using the Effectene Transfection Reagent (Qiagen) and cultured in medium containing 500 μg/mL hygromycin B in order to construct a cell line stably expressing dEGFP (dEGFP-CHO).

RNA Delivery and Photoaccelerated Endosomal Escape. For RNA delivery experiments, a carrier protein (TatU1A or TatU1A-Alexa) and cargo RNA were mixed in 50 μL of

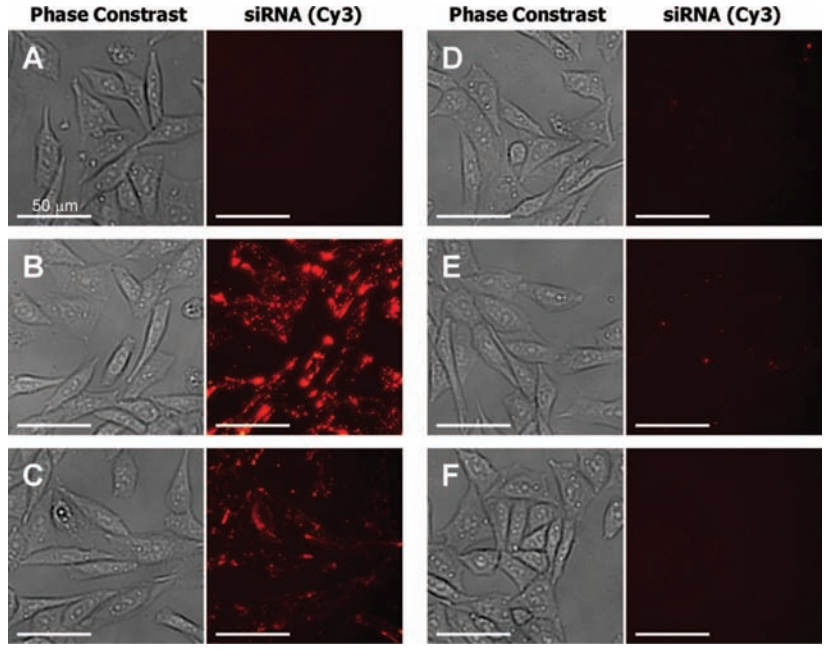

Figure 3. Cy3-*U1A*siRNA internalization into CHO cells mediated by TatU1A. Cellular images were obtained after incubation in the presence of TatU1A only (A), TatU1A and Cy3-*U1A*siRNA (B), TatU1A and Cy3-siRNA (C), Cy3-*U1A*siRNA only (D), U1A(-Tat) and Cy3-*U1A*siRNA (E), or T-buffer (F). Concentrations of RNA and protein were 200 nM and 1 μM, respectively. The cells were treated with RNase A to remove extracellularly bound RNAs before imaging. Scale bars = 50 μm. Fluorescence images were obtained with an excitation wavelength of 530−550 nm.

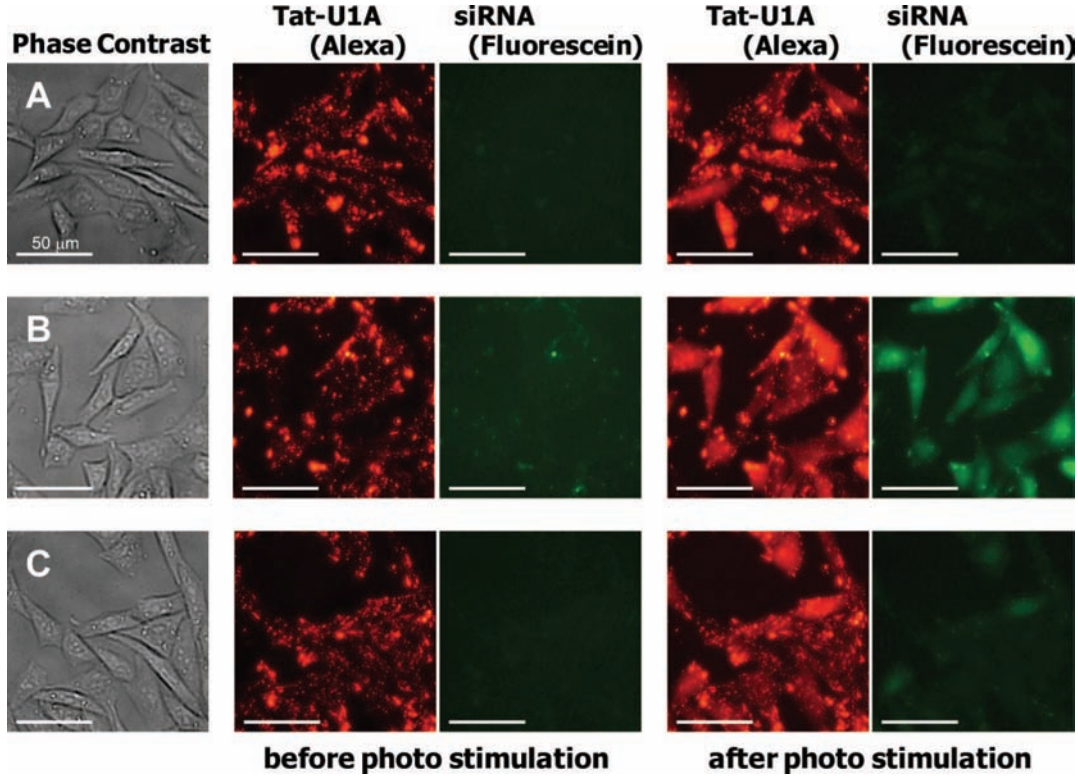

Figure 4. Photoinduced release of TatU1A-Alexa/Flc-*U1A*siRNA from endocytic compartments. TatU1A-Alexa only (A), TatU1A-Alexa and Flc-*U1A*siRNA (B), or TatU1A-Alexa and Flc-siRNA (C) were mixed to induce complex formation, added to CHO cells, and then incubated as described in the Materials and Methods section. Images were obtained before a 10 s light stimulation at 540 ± 10 nm and at 2 min after photostimulation. The excitation wavelengths were 530−550 nm for Alexa Fluor 546 and 460−495 nm for fluorescein.

T buffer at the indicated concentrations, and incubated at 37 °C for 10 min. Cells grown to 70% confluence in 96-well culture plates were then overlaid with the mixture. After a 3 h incubation at 37 °C in T buffer, cells were treated twice with culture medium containing 34 μg/mL RNase A for a total of 1 h at 37 °C to remove RNAs adhering to the extracellular surface of the cells. Cells were then washed with T buffer, and fluorescence images were obtained using a fluorescence microscope (IX51/IX2-FL-1/MP5Mc/OL-2, Olympus, Japan). In order to induce photoaccelerated endosomal escape of the internalized complex, cells were irradiated at 540 ± 10 nm for the indicated lengths of time with a 100 W halogen lamp (Olympus USH-1030L) passed through the 40× or 4× objective lens.

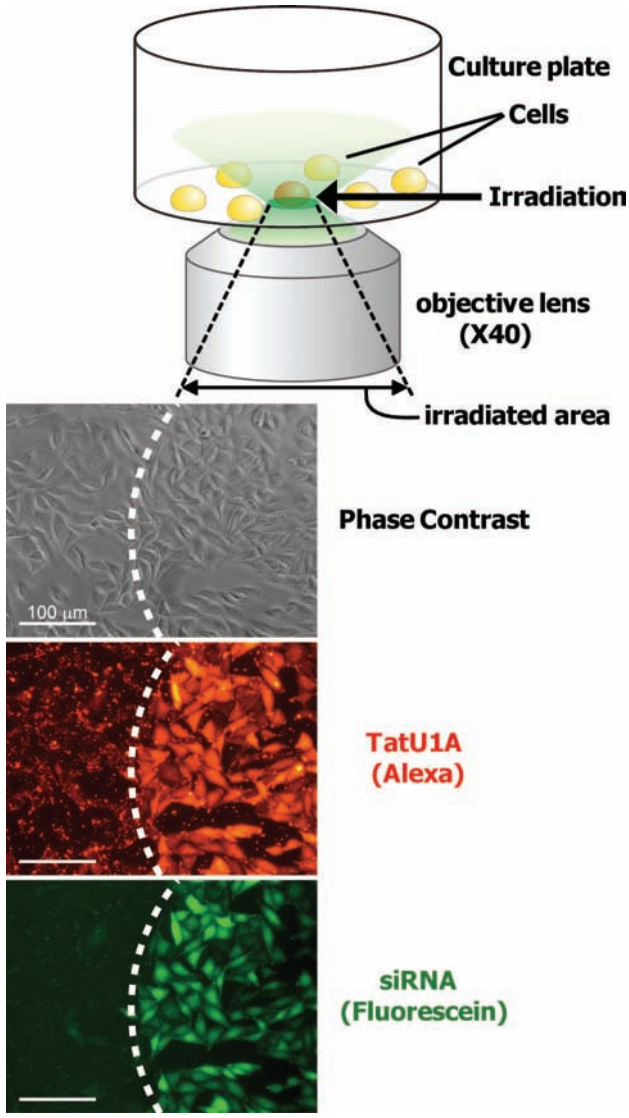

Figure 5. Region-specific photostimulation of cells. TatU1A-Alexa and Flc-*U1A*siRNA were mixed for complex formation, added to CHO cells, and incubated, as described in the Materials and Methods section. Images were obtained at 2 min after a 10 s light stimulation at 540 ± 10 nm. The excitation wavelengths were 530−550 nm for Alexa Fluor 546 and 460−495 nm for fluorescein. The irradiated area is to the right of the dotted line.

Induction of RNAi-Mediated EGFP Silencing. One day prior to RNA delivery, dEGFP-CHO cells were plated in a 96-well culture plate at a density of 2×10^4 cells per well. *U1A*-fused siRNA or shRNA was delivered into the cells using TatU1A-Alexa, and photoaccelerated endosomal escape was induced as described above. The cells were cultured at 37 °C. At 24 h after light stimulation, the culture medium was replaced with T buffer followed by two washes. The fluorescence intensity of adhering dEGFP-CHO cells was directly quantified by FLUOstar OPTIMA (BMG Labtech, Germany) using a 480 nm excitation and 540 nm emission filter set. The fluorescence intensity values were normalized by subtracting the values of the wells containing no cells. Cellular fluorescence images were subsequently obtained using a fluorescence microscope.

Induction of RNAi-Mediated Epidermal Growth Factor Receptor (EGFR) Silencing. One day prior to RNA delivery, A431 cells were plated in a 96-well culture plate at a density of 1×10^4 cells per well. *U1A*-fused shRNA was delivered to the cells using TatU1A-Alexa and photoaccelerated endosomal escape was induced as described above. The cells were cultured at 37 °C. At 72 h after light stimulation, cells were incubated with the Alexa488/EGF complex (Molecular Probes) (5 μg/mL) in medium for 30 min at 37 °C. The cells were then washed with T buffer, and fluorescence images were obtained.

Cell Viability Assay. In order to determine the effect of RNA delivery and light stimulation on cell viability, cell proliferation and cytotoxicity were evaluated using the Cell Counting Kit-8 (Dojindo, Japan) and a Cytotoxicity Detection Kit (LDH) (Roche, Switzerland), respectively. At 22 h after light stimulation, as described above, the culture medium was replaced with a medium containing 10 μL/well of cell counting kit substrate. The absorbance at 450 nm of each well was measured after a 2 h incubation at 37 °C. Simultaneously, an aliquot of medium was removed and mixed with the cytotoxicity detection substrate according to the manufacturer's protocol, and the absorbance at 490 nm was measured. The absorbances at 450 and 490 nm were measured using a FLUOstar OPTIMA instrument, and the values were normalized by subtracting the values measured in wells containing no cells. In the case of the cell proliferation assay, the values for cells incubated with T buffer without carrier protein and cargo RNA were considered to represent 100% proliferation. In the case of the cytotoxicity assay, the values for cells that were incubated with medium containing 0.2% NP-40 were considered to represent 100% cytotoxicity.

RESULTS AND DISCUSSION

Specific Interaction Between TatU1A and *U1A*siGFP. We hypothesized that TatU1A binding to a *U1A*-fused cargo RNA (Figure 1) would generate a cell-permeable complex that delivers the RNA to cells. We confirmed the specific interaction between TatU1A and *U1A*siGFP (Figure 1A) using a gel mobility shift assay (Figure 2). Shifted bands were present in the *U1A*siGFP and TatU1A or U1A(-Tat) preparations, but not in the control mixture of *U1A*siGFP and streptavidin. An siGFP lacking the *U1A* sequence did not exhibit a mobility shift in the presence of the U1A protein (Figure 2). These results demonstrate a specific interaction between the U1A RBD and *U1A* RNA and the formation of a TatU1A/*U1A*siGFP complex. When an excess of TatU1A was incubated with the *U1A*siGFP (2.5 μM TatU1A and 500 nM *U1A*siGFP), the U1A(-Tat)/*U1A*siGFP complex was observed as a very broad, faint band and no free *U1A*siRNA was detected (Supporting Information Figure 1). Furthermore, the siGFP band was also faint in the presence of excess TatU1A, but not in the presence of excess U1A(-Tat) (Supporting Information Figure 1). These results indicate that TatU1A selectively bound to *U1A*siGFP, but that nonspecific RNA binding also occurred, most likely due to electrostatic interactions between the polycationic Tat-peptide and polyanionic RNA.

siRNA Delivery into Mammalian Cells Using TatU1A as Carrier. Cy3-labeled *U1A*siGFP (Cy3-*U1A*siGFP) was prepared to examine whether siRNAs can be delivered to cells after forming a specific complex with TatU1A. Using a gel mobility shift assay, we confirmed that the Cy3 label does not affect *U1A*siGFP binding to TatU1A (data not shown). No Cy3 fluorescence was observed in CHO cells treated with *U1A*siGFP/TatU1A obtained by incubating 200 nM Cy3-*U1A*siGFP with 200 nM or 400 nM TatU1A (Supporting Information Figure 2). A 5× molar excess of TatU1A (1 μM) in complex formation was required to generate detectable fluorescence in cells. As shown in Figure 3, strong fluorescence was observed in cells treated with TatU1A/Cy3-*U1A*siGFP (Figure 3B), but no fluorescence was observed in cells treated with U1A(-Tat)/Cy3-*U1A*siGFP or Cy3-*U1A*siGFP alone (Figure 3D,E). Since both TatU1A and U1A(-Tat) form a protein−*U1A*siGFP complex, as shown in Figure 2, the results of Figure 3B,E indicate that cellular internalization of *U1A*siGFP was mediated by the

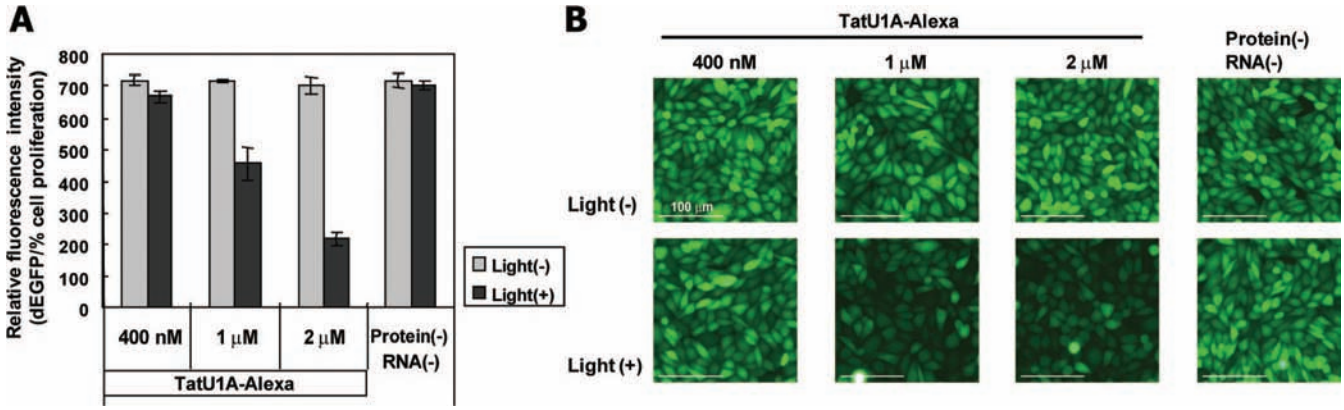

Figure 6. dEGFP silencing after siRNA redistribution mediated by light stimulation. *U1A*siGFP (200 nM) was mixed with TatU1A-Alexa for complex formation, added to dEGFP-CHO cells, and incubated as described in the Materials and Methods section. The relative fluorescence intensity (A) and fluorescent images (B) were evaluated after a 24 h incubation following a 60 s light stimulation or no stimulation. Irradiation was performed at 540 ± 10 nm for 60 s through a 4x objective lens. In (A), the fluorescence intensity was normalized by cell proliferation, estimated using a Cell Counting Kit-8. The dEGFP intensity in (A) is the mean ± standard deviation of three independent measurements.

Tat−peptide. Unexpectedly, weak fluorescent signals were also observed in cells treated with TatU1A/Cy3-siGFP (Figure 3C), indicating that a small amount of Cy3-siGFP entered the cells, potentially as a result of nonspecific interactions between Cy3-siGFP and TatU1A, as shown in Supporting Information Figure 1. Thus, *U1A*siGFP was selectively delivered to cells by TatU1A, probably because of the synergistic effect of two types of RNA−protein interactions: specific interactions between the *U1A* sequence and the U1A RBD and nonspecific interactions between the Tat−peptide and RNAs.

Release of siRNA from Endocytic Compartments by Photostimulation of TatU1A-Alexa. The internalized Cy3-*U1A*siGFP exhibited a punctuate cytoplasmic distribution (Figure 3B). This distribution indicated that Cy3-*U1A*siGFP was localized in endocytic compartments, as demonstrated by colocalization with LysoTracker Green (Molecular Probe), which labels lysosomes and other types of acidic compartments (Supporting Information Figure 3). Several groups have previously reported that Tat-peptide-mediated cellular internalization occurs through an endocytotic pathway by macropinocytosis (*25*). The transfer of Tat-peptide-conjugated macromolecular cargos from endocytic compartments to the cytosol is thus a critical step in activating the cargo's function in cells. Chloroquine and influenza-virus-derived hemagglutinin peptide (HA2) have been used to destabilize the endosomal membrane and enhance delivery of entrapped Tat-peptide-conjugated macromolecules to the cytosol (*25–27*). Recently, as an alternative strategy, two groups reported the efficient release of fluorescently labeled CPP or CPP-fused proteins from the endosome using photostimulation of the fluorophores (*28, 29*). This is a very attractive strategy because controlled light stimulation would enable region-specific delivery of cargo molecules.

We prepared TatU1A-Alexa bearing an Alexa Fluor 546 fluorophore to confirm whether the release of TatU1A-Alexa from endosomes could be induced by light stimulation. Since TatU1A-C contains a Cys residue only at the C-terminus, Alexa Fluor 546 C_5 maleimide reacts specifically with the C terminus. We confirmed that TatU1A-Alexa binds to *U1A*-fused cargo RNA using a gel mobility shift assay (data not shown). We also prepared fluorescein-modified siRNAs (Flc-*U1A*siGFP and Flc-siGFP) to examine whether the entrapped siRNA could be released into the cytoplasm following TatU1A-Alexa-mediated internalization. Fluorescent signals were monitored after incubation of CHO cells with TatU1A-Alexa/Flc-*U1A*siGFP complexes, TatU1A-Alexa/Flc-siGFP complexes, or TatU1A-Alexa alone (Figure 4). Prior to light stimulation, TatU1A-Alexa (red images) exhibited a punctuate distribution (Figures 4A−C) similar to that of Cy3-*U1A*siGFP (Figure 3B). The Flc-*U1A*siGFP signal (green) was very weak compared to the Cy3-*U1A*siGFP signal. The low pH in the endosomes diminishes the fluorescence, because fluorescein is pH-sensitive (*30*).

Next, we irradiated the cells at 540 ± 10 nm for 10 s using a 40× objective lens. In this procedure, the light from a 100 W halogen lamp was reduced to 12% of the total output using a neutral-density filter (Olympus 32-ND12) to avoid damaging the fluorophores and cells. Following this photostimulation, TatU1A-Alexa was widespread throughout the cytosol (Figures 4A−C). A widespread fluorescein signal was also observed in cells which were incubated with TatU1A-Alexa/Flc-*U1A*siGFP complexes (Figure 4B). The RNA released from endosomes by light stimulation was localized to the cytosol and nucleus as shown in Supporting Information Figure 4. The green fluorescence signal indicates that Flc-*U1A*siGFP but not TatU1A-Alexa is released from the endosome, because green fluorescence was not observed in cells treated only with TatU1A-Alexa (Figure 4A). The fluorescein signal from the Flc-*U1A*siGFP intensified after photostimulation (Figure 4B), reflecting the higher pH of the cytoplasm relative to the endosomes. In cells treated with TatU1A-Alexa/Flc-siGFP, the dispersed fluorescein signal was much weaker than in those treated with TatU1A-Alexa/Flc-*U1A*siGFP (Figure 4C), indicating that complex formation and uptake was enhanced in the latter. Figure 5 shows the region-specific redistribution of Flc-*U1A*siGFP. Green fluorescence in the cytoplasm was observed only in the irradiated area. These results indicate that *U1A*siGFP was delivered to CHO cells by the TatU1A protein and released into the cytoplasm by photostimulation of the Alexa 546 fluorophore. Although the mechanism of the cytosolic redistribution of TatU1A-Alexa is not well understood, reactive oxygen species generated by photostimulation may damage the membranes of endosomal compartments (*28, 29*). Several groups have used photostimulation of photosensitizers to produce reactive singlet oxygen and to induce the cytosolic redistribution of macro-biomolecules entrapped in the endocytic compartment (*31, 32*).

dEGFP Silencing Mediated by *U1A*-Fused Interfering RNA. In order to examine whether the redistributed cargo RNA can induce RNAi-mediated gene silencing, dEGFP-CHO cells were treated with complexes generated using 200 nM *U1A*siGFP and various concentrations of TatU1A-Alexa (Figure 6). Cells in the wells of a 96-well plate were then irradiated at 540 ± 10 nm for 60 s through a 4× objective lens. For irradiation through the 4× objective lens, we removed the neutral-density filter and extended the irradiation time because the light intensity is considerably weaker than that transmitted through the 40×

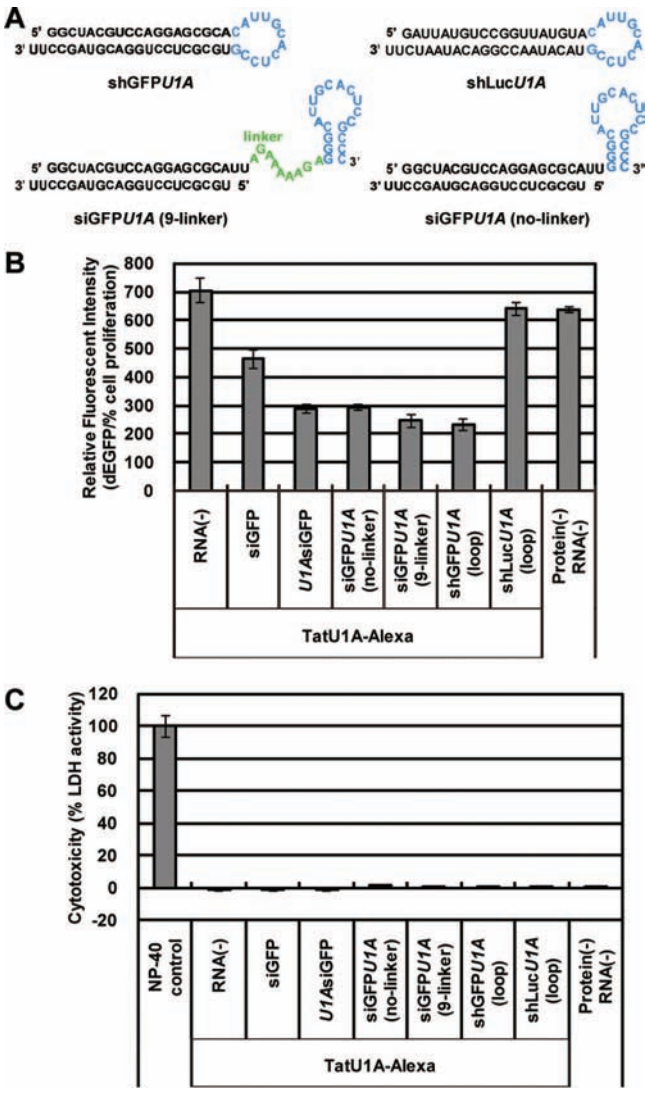

Figure 7. dEGFP silencing using *U1A*-fused RNAs. (A) Sequences of *U1A*-fused cargo RNA variants. RNA delivery to dEGFP-CHO cells was performed using complexes formed from incubating 2 μM TatU1A-Alexa and 200 nM cargo RNA. Cargo RNAs internalized with TatU1A-Alexa were redistributed into the cytosol using an 80 s photostimulation at 540 $\pm$ 10 nm through a 4$\times$ objective lens. Fluorescence intensity (B) and cytotoxicity (C) were evaluated at 24 h post-photostimulation. In (B), fluorescence intensity was normalized by cell proliferation, estimated using a Cell Counting Kit-8. The values in B and C are the mean $\pm$ standard deviation of three independent measurements.

objective lens. The dEGFP intensity was unchanged in cells treated with the TatU1A-Alexa/*U1A*siGFP complex, compared to cells treated with T buffer only, but decreased following irradiation of TatU1A-Alexa/*U1A*siGFP treated cells (Figure 6). We also confirmed the reduction in the mRNA level by RT-PCR (data not shown). These results indicate that the photostimulation-induced redistribution of *U1A*siGFP resulted in RNAi-mediated dEGFP silencing, and that the *U1A*-fused siGFP retains silencing activity. These results suggest that the internalized TatU1A-Alexa/*U1A*siGFP complex could not mediate gene silencing without light stimulation due to endosome trapping. In the subsequent RNAi experiments, we used a TatU1A-Alexa concentration of 2 μM, to increase the level of gene silencing (Figure 6).

We prepared various cargo RNA constructs (Figure 7A) in order to improve the RNAi efficiency. For siRNA type variants, the *U1A* sequence was linked to the 3′ terminus of the sense strand directly [siGFP*U1A*(no-linker)] or through a 9-mer linker [siGFP*U1A*(9-linker)]. For the shRNA-type variant, a minimum

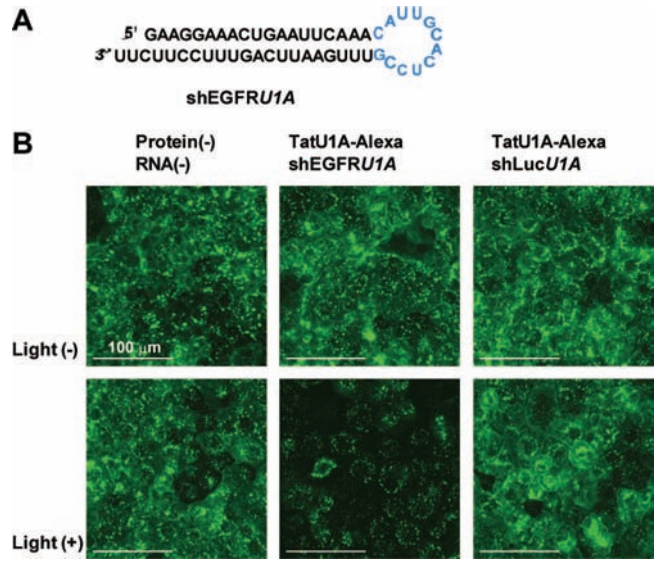

Figure 8. EGFR silencing in A431 cells. (A) Sequence of shRNA-type cargo RNA targeted EGFR. (B) A431 cells were incubated with a mixture of 2 μM TatU1A-Alexa and 200 nM cargo RNA. Cells were stained with an Alexa488/EGF complex (Molecular Probes) after 72 h of culture after a 60 s light stimulation through a 4$\times$ objective lens. Fluorescence images were obtained at an excitation wavelength of 460 to 495 nm.

U1A sequence was inserted in the loop region, which connects the sense and antisense strands (shGFP*U1A*). All the variants and standard siRNA (siGFP) were incubated with 2 μM TatU1A-Alexa for complex formation. Cells were treated with the complexes and siRNAs were redistributed using an 80 s light stimulation through a 4$\times$ objective lens. All the variants containing the *U1A* sequence induced dEGFP silencing, with the highest RNAi efficiency being induced by shGFP*U1A* (Figure 7B). The efficiency of dEGFP silencing by the standard siGFP was considerably weaker than the other variants, indicating that TatU1A-Alexa selectively delivers the *U1A* containing cargo RNAs. The shLuc*U1A*, an shRNA-type cargo RNA targeted to the luciferase gene, did not change the dEGFP intensity in cells, suggesting that there were no nonspecific effects resulting from treatment with the RNA (Figure 7B).

In order to compare the RNAi efficiency of this method with common transfection, cells were transfected with siGFP and siLuc using the TransIT-TKO transfection reagent (Mirus) according to the manufacturer's protocol (Supporting Information Figure 5). Our method, using 200 nM *U1A*siGFP, induced dEGFP silencing as effectively as TransIT-TKO mediated transfection with 10 nM siGFP (a concentration of approximately 10 nM is recommended in the manufacturer's protocol) (Figure 7B and Supporting Information Figure 5A), and the cytotoxicity associated with our method was considerably lower than that observed with transfection (Figure 7C and Supporting Information Figure 5B).

We estimated the effects of RNA concentration and photoirradiation time on dEGFP silencing (Supporting Information Figure 6). First, 2 μM TatU1A-Alexa was used to complex with various concentrations of shGFP*U1A*, and the cells were then incubated with the complexes and a 60 s light stimulation was then used to redistribute the RNA to the cytoplasm. On the basis of the results of this experiment, we used 200 nM RNA in the subsequent RNAi experiments. Cells were treated with complexes formed from 200 nM shGFP*U1A* and 2 μM TatU1A-Alexa and the length of photostimulation was varied. Longer irradiation times induced more efficient dEGFP silencing, and the effect was saturated at irradiation times longer than 60 s (Supporting Information Figure 6B). When cells were irradiated

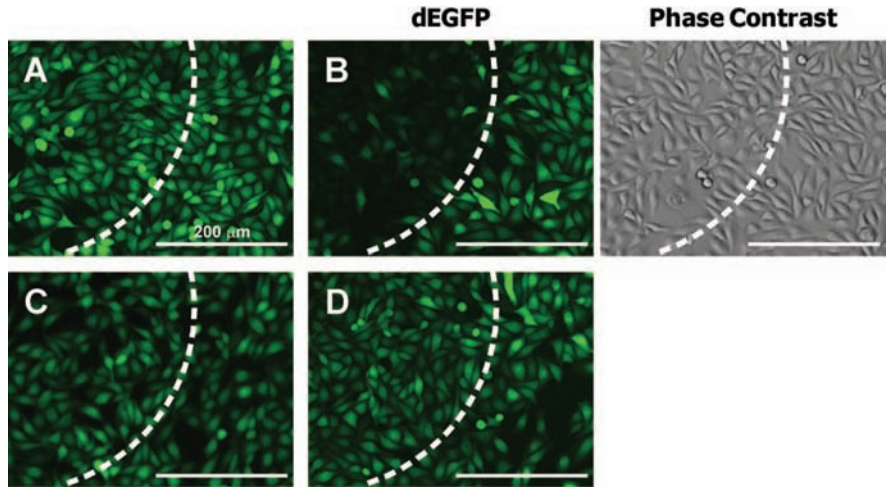

Figure 9. Region-specific silencing of the dEGFP gene. CHO cells expressing dEGFP were incubated with TatU1A-Alexa only (A), TatU1A-Alexa and shGFP*U1A* (B), TatU1A-Alexa and shLuc*U1A* (C), or TatU1A-Alexa and siGFP (D), and stimulated with light at 540 ± 10 nm as described in the Materials and Methods section. dEGFP fluorescence images of the photoirradiated area were obtained 20 h after photostimulation. In panel (B), a phase contrast image is shown below the fluorescence image. The irradiated area is to the left side of the dotted line.

for 120 s, cell proliferation was reduced to less than 80% (Supporting Information Figure 6C). Although prolonged irradiation damaged the cells, cellular damage was minimal with irradiation times of 60 s or less (Supporting Information Figure 6C), indicating that the silencing activity could be efficiently and safely regulated by photostimulation.

EGFR Silencing Mediated by shEGFR*U1A*. We prepared an shRNA-type *U1A*-fused cargo RNA, shEGFR*U1A* (Figure 8A), to reduce endogenous EGFR expression. EGFR is overexpressed in many tumors, and is a convenient target for cancer therapy. We selected the A431 cell line as a model of EGFR-overexpressing carcinoma cells. A431 cells were treated with complexes formed from 2 μM TatU1A-Alexa and 200 nM shEGFR*U1A*, and then irradiated with light at 540 ± 10 nm for 60 s through a 4× objective lens. Photostimulation of the cells reduced the Alexa488 fluorescence, which is proportional to the amount of EGF bound to EGFR (Figure 8B). Neither the cells without light stimulation nor the cells incubated with TatU1A-Alexa and shLuc*U1A* (nonspecific cargo RNA) reduced the fluorescent signal compared to control cells incubated with T buffer only. These results indicate that TatU1A-mediated RNA delivery and photoaccelerated endosomal escape was correlated with silencing of the endogeneous EGFR gene.

Region-Specific Gene Silencing Mediated by CLIP-RNAi. shGFP*U1A* and control RNAs (shLuc*U1A* and standard siGFP) were delivered to dEGFP-CHO cells using 2 μM TatU1A-Alexa for complex formation. TatU1A-Alexa only was used as a negative control. After a 4 h incubation, the cells were photostimulated for 5 s through the 40× objective lens, using a neutral-density filter to reduced the light intensity to 12%. Figure 9 shows the dEGFP fluorescence in the irradiated area at 20 h after photostimulation. The cells treated with TatU1A-Alexa and shGFP*U1A* exhibited a decrease in dEGFP only within the irradiated area (Figure 9B). In contrast, control cells treated with TatU1A-Alexa alone (Figure 9A), TatU1A-Alexa and shLuc*U1A* (Figure 9C), or TatU1A-Alexa and siGFP (Figure 9D) did not induce a decrease in dEGFP irrespective of photostimulation. These results indicate that RNA is only released from endosomes in areas of photostimulation and that RNAi is thus restricted to the irradiated areas.

CONCLUSIONS

We have demonstrated the efficient and selective delivery of an siRNA into mammalian cells mediated by TatU1A. Although several studies have induced RNAi in mammalian cells using CPPs, the release of siRNAs from the endosome is a rate-limiting step in activating RNAi. We achieved the cytosolic redistribution of cargo RNA using TatU1A-Alexa and controlled light stimulation. The method demonstrated here is a simple strategy to deliver any shRNA or siRNA bearing a short extension with a specific recognition sequence. In addition, the light stimulation strategy (CLIP-RNAi) enables the implementation of regionally and temporally controlled RNAi.

ACKNOWLEDGMENT

We thank H. Sakakoshi (Okayama Univ.) for his help with RNA purification, K. Kishimoto (Okayama Univ.) for his help with plasmid construction, Prof. M. Seno (Okayama Univ.) for the material, and Dr. J. Futami for Hoechst33342. This work was supported by a grant from the New Energy and Industrial Technology Development Organization (NEDO) (05A02707a).

Supporting Information Available: Supplementary figures. This material is available free of charge via the Internet at http://pubs.acs.org.

LITERATURE CITED

(1) Fire, A., Xu, S., Montgomery, M. K., Kostas, S. A., Driver, S. E., and Mello, C. C. (1998) Potent and specific genetic interference by double-stranded RNA in *Caenorhabditis elegans*. *Nature 391*, 806–11.

(2) Elbashir, S. M., Harborth, J., Lendeckel, W., Yalcin, A., Weber, K., and Tuschl, T. (2001) Duplexes of 21-nucleotide RNAs mediate RNA interference in cultured mammalian cells. *Nature 411*, 494–8.

(3) Caplen, N. J., Parrish, S., Imani, F., Fire, A., and Morgan, R. A. (2001) Specific inhibition of gene expression by small double-stranded RNAs in invertebrate and vertebrate systems. *Proc. Natl. Acad. Sci. U.S.A. 98*, 9742–7.

(4) Paddison, P. J., Caudy, A. A., and Hannon, G. J. (2002) Stable suppression of gene expression by RNAi in mammalian cells. *Proc. Natl. Acad. Sci. U.S.A. 99*, 1443–8.

(5) Li, C. X., Parker, A., Menocal, E., Xiang, S., Borodyansky, L., and Fruehauf, J. H. (2006) Delivery of RNA interference. *Cell Cycle 5*, 2103–9.

(6) Wadia, J. S., and Dowdy, S. F. (2002) Protein transduction technology. *Curr. Opin. Biotechnol. 13*, 52–6.

(7) Joliot, A., and Prochiantz, A. (2004) Transduction peptides: from technology to physiology. *Nat. Cell Biol. 6*, 189–96.
(8) Murriel, C. L., and Dowdy, S. F. (2006) Influence of protein transduction domains on intracellular delivery of macromolecules. *Expert Opin. Drug Delivery 3*, 739–46.
(9) Futaki, S. (2006) Oligoarginine vectors for intracellular delivery: design and cellular-uptake mechanisms. *Biopolymers 84* 241–9.
(10) Schwarze, S. R., Ho, A., Vocero-Akbani, A., and Dowdy, S. F. (1999) In vivo protein transduction: delivery of a biologically active protein into the mouse. *Science 285*, 1569–72.
(11) Del Gaizo, V., and Payne, R. M. (2003) A novel TAT-mitochondrial signal sequence fusion protein is processed, stays in mitochondria, and crosses the placenta. *Mol. Ther. 7*, 720–30.
(12) Muratovska, A., and Eccles, M. R. (2004) Conjugate for efficient delivery of short interfering RNA (siRNA) into mammalian cells. *FEBS Lett. 558*, 63–68.
(13) Chiu, Y. L., Ali, A., Chu, C. Y., Cao, H., and Rana, T. M. (2004) Visualizing a correlation between siRNA localization, cellular uptake, and RNAi in living cells. *Chem. Biol. 11*, 1165–75.
(14) Turner, J. J., Jones, S., Fabani, M. M., Ivanova, G., Arzumanov, A. A., and Gait, M. J. (2007) RNA targeting with peptide conjugates of oligonucleotides, siRNA and PNA. *Blood Cells Mol. Dis. 38*, 1–7.
(15) Simeoni, F., Morris, M. C., Heitz, F., and Divita, G. (2003) Insight into the mechanism of the peptide-based gene delivery system MPG: implications for delivery of siRNA into mammalian cells. *Nucleic Acids Res. 31*, 2717–24.
(16) Veldhoen, S., Laufer, S. D., Trampe, A., and Restle, T. (2006) Cellular delivery of small interfering RNA by a non-covalently attached cell-penetrating peptide: quantitative analysis of uptake and biological effect. *Nucleic Acids Res. 34*, 6561–73.
(17) Lundberg, P., El-Andaloussi, S., Sutlu, T., Johansson, H., and Langel, U. (2007) Delivery of short interfering RNA using endosomolytic cell-penetrating peptides. *FASEB J 21*, 2664–71.
(18) Kannemeier, C., Shibamiya, A., Nakazawa, F., Trusheim, H., Ruppert, C., Markart, P., Song, Y., Tzima, E., Kennerknecht, E., Niepmann, M., von Bruehl, M. L., Sedding, D., Massberg, S., Gunther, A., Engelmann, B., and Preissner, K. T. (2007) Extracellular RNA constitutes a natural procoagulant cofactor in blood coagulation. *Proc. Natl. Acad. Sci. U.S.A. 104*, 6388–93.
(19) Zhou, H., Xu, W., Qian, H., Yin, Q., Zhu, W., and Yan, Y. (2008) Circulating RNA as a novel tumor marker: An in vitro study of the origins and characteristics of extracellular RNA. *Cancer Lett 259*, 50–60.
(20) Oubridge, C., Ito, N., Evans, P. R., Teo, C. H., and Nagai, K. (1994) Crystal structure at 1.92 A resolution of the RNA-binding domain of the U1A spliceosomal protein complexed with an RNA hairpin. *Nature 372*, 432–8.
(21) Hall, K. B., and Stump, W. T. (1992) Interaction of N-terminal domain of U1A protein with an RNA stem/loop. *Nucleic Acids Res. 20*, 4283–90.
(22) Nagai, K., Oubridge, C., Jessen, T. H., Li, J., and Evans, P. R. (1990) Crystal structure of the RNA-binding domain of the U1 small nuclear ribonucleoprotein A. *Nature 348*, 515–20.
(23) Li, X., Zhao, X., Fang, Y., Jiang, X., Duong, T., Fan, C., Huang, C. C., and Kain, S. R. (1998) Generation of destabilized green fluorescent protein as a transcription reporter. *J. Biol. Chem. 273*, 34970–5.
(24) Ohtsuki, T., Watanabe, Y., Takemoto, C., Kawai, G., Ueda, T., Kita, K., Kojima, S., Kaziro, Y., Nyborg, J., and Watanabe, K. (2001) An "elongated" translation elongation factor Tu for truncated tRNAs in nematode mitochondria. *J. Biol. Chem. 276*, 21571–7.
(25) Wadia, J. S., Stan, R. V., and Dowdy, S. F. (2004) Transducible TAT-HA fusogenic peptide enhances escape of TAT-fusion proteins after lipid raft macropinocytosis. *Nat. Med. 10*, 310–5.
(26) Abes, S., Williams, D., Prevot, P., Thierry, A., Gait, M. J., and Lebleu, B. (2006) Endosome trapping limits the efficiency of splicing correction by PNA-oligolysine conjugates. *J. Controlled Release 110*, 595–604.
(27) Michiue, H., Tomizawa, K., Wei, F. Y., Matsushita, M., Lu, Y. F., Ichikawa, T., Tamiya, T., Date, I., and Matsui, H. (2005) The NH2 terminus of influenza virus hemagglutinin-2 subunit peptides enhances the antitumor potency of polyarginine-mediated p53 protein transduction. *J. Biol. Chem. 280*, 8285–9.
(28) Maiolo, J. R., 3rd, Ottinger, E. A., and Ferrer, M. (2004) Specific redistribution of cell-penetrating peptides from endosomes to the cytoplasm and nucleus upon laser illumination. *J. Am. Chem. Soc. 126*, 15376–7.
(29) Matsushita, M., Noguchi, H., Lu, Y. F., Tomizawa, K., Michiue, H., Li, S. T., Hirose, K., Bonner-Weir, S., and Matsui, H. (2004) Photo-acceleration of protein release from endosome in the protein transduction system. *FEBS Lett. 572*, 221–6.
(30) Klonis, N., and Sawyer, W. H. (1996) Spectral properties of the prototropic forms of fluorescein in aqueous solution. *J. Fluoresc. 6*, 147–157.
(31) Hogset, A., Prasmickaite, L., Selbo, P. K., Hellum, M., Engesaeter, B. O., Bonsted, A., and Berg, K. (2004) Photochemical internalisation in drug and gene delivery. *Adv. Drug Delivery Rev. 56*, 95–115.
(32) Oliveira, S., Fretz, M. M., Hogset, A., Storm, G., and Schiffelers, R. M. (2007) Photochemical internalization enhances silencing of epidermal growth factor receptor through improved endosomal escape of siRNA. *Biochim. Biophys. Acta 1768*, 1211–7.

BC800020N

Biocompatible and Biodegradable Polymersome Encapsulated Hemoglobin: A Potential Oxygen Carrier

Shahid Rameez, Houssam Alosta, and Andre F. Palmer*

Department of Chemical and Biomolecular Engineering, The Ohio State University 231A Koffolt Laboratories, 140 West 19th Avenue, Columbus, Ohio 43210. Received December 14, 2007; Revised Manuscript Received March 18, 2008

This work describes the development of polymersome-encapsulated hemoglobin (PEH) self-assembled from biodegradable and biocompatible amphiphilic diblock copolymers composed of poly(ethylene oxide) (PEO), poly(caprolactone) (PCL), and poly(lactide) (PLA). In the amphiphilic diblock, PEO functions as the hydrophilic block, while either PCL or PLA can function as the hydrophobic block. PEO, PCL, and PLA are biocompatible polymers, while the last two polymers are biodegradable. PEH dispersions were prepared by extrusion through 100 nm pore radii polycarbonate membranes. In this work, the encapsulation efficiency of human and bovine hemoglobin (hHb and bHb) in polymersomes was adjusted by varying the initial concentration of Hb. This approach yielded Hb loading capacities that were comparable to values in the literature that supported the successful resuscitation of hamsters experiencing hemorrhagic shock (*1*). Moreover, the Hb loading capacities of PEHs in this study can also be tailored simply by controlling the diblock copolymer concentration. In this study, typical Hb/diblock copolymer weight ratios ranged 1.2−1.5, with initial Hb concentrations less than 100 mg/mL. The size distribution, Hb encapsulation efficiency, oxygen affinity (P_{50}), cooperativity coefficient (n), and methemoglobin (metHb) level of these novel PEH dispersions were consistent with values required for efficient oxygen delivery in the systemic circulation (*2*−*5*). Taken together, our results demonstrate the development of novel PEH dispersions that are both biocompatible and biodegradable. These novel dispersions show very good promise as therapeutic oxygen carriers.

INTRODUCTION

Liposome-encapsulated hemoglobin (LEHb) comprises one subset of cellular Hb-based O_2 carriers (HBOCs). The architecture of these particles consists of a purified and concentrated Hb solution that is encapsulated inside the aqueous core of the liposome. Lipids are for the most part biocompatible. This property has motivated the development of liposomes as drug and protein carriers (*3*, *5*, *6*). Liposomes lack controlled release mechanisms and have several other pharmacokinetic limitations (e.g., limited half-life in the circulation) which minimize the effective delivery of therapeutic molecules (*7*). In order to mimic the carbohydrate coat on cell membranes and thus prolong the circulatory half-life of liposomes, biocompatible poly(ethylene glycol) (PEG) was attached to a small fraction (5−10 mol %) of the lipid headgroups on LEHb particles. This resulted in increased circulatory half-life of LEHb particles, due to decreased recognition by the reticuloendothelial system (RES). However, the beneficial effects gained by the prolonged circulation time of PEGylated LEHb is attenuated by significant particle accumulation in the liver and spleen. Splenic sequestration of LEHb particles saturates the RES, thereby limiting the effectiveness of the body's natural defense system against foreign bodies . To counteract these effects, we propose to use vesicles composed of amphiphilic diblock copolymers, instead of lipids, that have the ability to degrade once sequestered in the spleen. Biocompatible diblock copolymers that consist of a PEO block plus a degradable block, such as PEO-poly(lactic acid) (PEO-PLA) or PEO-poly(caprolactone) (PEO-PCL), are promising candidates for the preparation of polymer vesicles that have the native ability to evade the RES and degrade once sequestered in the spleen or liver (*8*−*10*).

Self-assembled polymer vesicles composed of diblock copolymer amphiphiles where one block is hydrophilic and the other block is hydrophobic are called polymersomes (*4*). These vesicles are synthetic in nature. The amphiphilic diblocks are similar in structure to lipids, but possess much larger molecular weights (*4*). In aqueous solution, the diblocks form an arrangement where the hydrophobic blocks tend to associate with each other to minimize direct exposure to water, whereas the more hydrophilic blocks face inner and outer hydrating solutions and thereby form the two interfaces of a typical bilayer membrane (*11*). Polymersomes are composed of synthetic polymers of molecular weights more typical of polypeptides (order of 10 kDa), whereas lipids possess molecular weights less than 1 kDa (*4*). Lipid membranes appear conducive to various cellular processes (endocytosis, cell division, receptor clustering, etc.) because of the flexibility afforded by the low molecular weight lipids, which made them an attractive candidate for an oxygen carrier over the last few decades. Polymersomes can be prepared from diblock copolymers by the same techniques used to prepare liposomes such as rehydration, sonication, and extrusion, which can generate unilamellar micrometer-sized vesicles as well as monodisperse submicrometer-sized vesicles (*12*).

Diblock copolymers consisting of poly(ethylene glycol-*b*-lactide) (PEG-PLA) or poly(ethylene glycol-*b*-caprolactone) (PEG-PCL) have been used to prepare controlled release polymer vesicles (*13*). One study (*13*) demonstrated the encapsulation of anticancer agents in polymersomes and their ability to release drug to cancer cells. Another study demonstrated degradable polymersomes being used in the growth arrest and shrinkage of rapidly growing tumors (*14*). In addition, polymersome-encapsulated paclitaxel has exhibited slow, steady release of the anticancer drug paclitaxel in human breast cancer cells. Paclitaxel−polymersomes have exhibited desirable restrained release profile and long-term stability.The formulations

* Corresponding author. E-mail: palmer.351@osu.edu.

10.1021/bc700465v CCC: $40.75 © 2008 American Chemical Society
Published on Web 04/29/2008

Table 1. Number-Averaged Molecular Weight (M_n), PEG Length, Hydrophilic Mass Faction ($f_{hydrophilic}$), and Hydrophobic Membrane Thickness (d) of the Biodegradable and Biocompatible Diblock Copolymers Used in This Study

diblock copolymer	M_n (kDa)	PEG length (kDa)	$f_{hydrophilic}$	d (nm)
PEO-b-PCL-1	1.65	0.55	0.33	~8
PEO-b-PCL-2	15	5	0.33	~18
PEO-b-PLA-1	10	5	0.33	~17
PEO-b-PLA-2	2.45	0.55	0.25	~8

also showed comparable activity to the drug alone in inhibiting the growth of MCF-7 human breast cancer cells (*15*).

Polymersomes made from either PEG-PLA or PEG-PCL form stable vesicles (*16*). Dynamic light scattering provides an accurate measurement of the vesicle size distribution. Periodic measurements over a period of time has shown that PEO-PBD polymersomes are stable whereas vesicles made with degradable copolymer PEO-PLA disassemble over a period of days at room temperature (*16*).

By changing the copolymer composition, especially the molecular weight and type of hydrophobic block, the release of encapsulated material from polymersomes can be adjusted accordingly (*17*). Biodegradable polymersomes also have the potential to be targeted to specific sites in the body, as has been shown by the specific interaction of antihuman serum albumin conjugated polymersomes with a human serum albumin coated sensor surface (*17*).

In this work, we prepare biodegradable and biocompatible polymersomes encapsulating Hb and show that they are promising candidates for hemoglobin-based oxygen carriers (HBOCs). To our knowledge, this is the first study that explores the possibility of employing biodegradable and biocompatible polymersomes to be used as HBOCs.

EXPERIMENTAL PROCEDURES

Materials. Four biodegradable and biocompatible diblock copolymers composed of poly(ethylene oxide-*b*-ϵ-caprolactone) and poly(ethylene oxide-*b*-lactide) (both DL and L forms) were used in this study. Two of these diblocks were composed of poly(ethylene oxide-*b*-caprolactone), and two were composed of poly(ethylene oxide-*b*-lactide). The diblock copolymers were purchased from Polymer Source Inc. (Dorval QC, Canada). For convenience, PEH composed of poly(ethylene oxide-*b*-ϵ-caprolactone) and poly(ethylene oxide-*b*-lactic acid) will be referred to as PEO-b-PCL-1, PEO-b-PCL-2, PEO-b-PLA-1, and PEO-b-PLA-2 (Table 1). Likewise, their corresponding controls (i.e., empty polymersomes) will be referred to as PEO-b-PCL-1 (control), PEO-b-PCL 2 (control), PEO-b-PLA-1 (control), and PEO-b-PLA-2 (control) (Table 1).

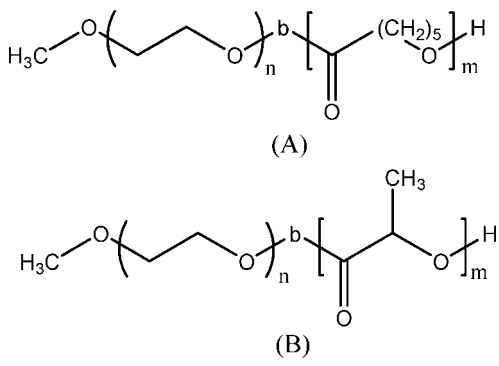

Figure 1. Chemical structure of (A) poly(ethylene oxide-*b*-ϵ-caprolactone) and (B) poly(ethylene oxide-*b*-lactide). The block inside the parentheses is hydrophilic (PEO), while the block inside the square bracket is hydrophobic (PCL or PLA).

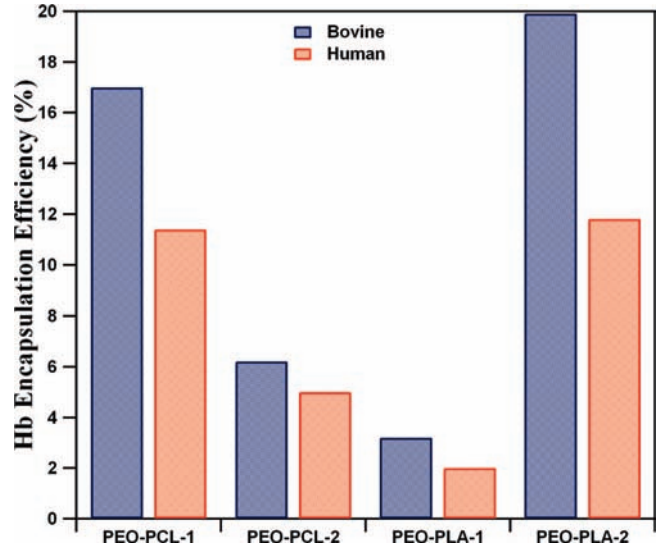

Figure 2. Comparison of Hb encapsulation efficiency in PEH dispersions extruded through 200 nm diameter polycarbonate membranes using different sources of Hb.

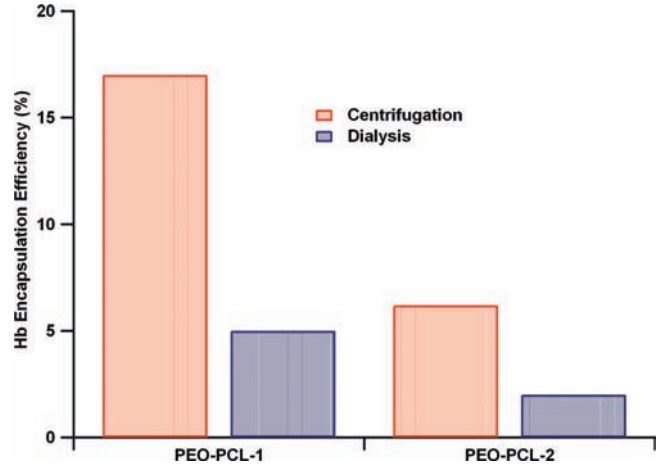

Figure 3. Comparison of bHb encapsulation efficiency in PEH dispersions extruded through 200 nm diameter polycarbonate membranes determined via the centrifugation and dialysis methods.

The chemical structures of PEO-b-PCL and PEO-b-PLA are shown in Figure 1, and the structural properties of the four diblock copolymers are summarized in Table 1.

Extraction and Purification of bHb and hHb from RBCs. Sterile bovine red blood cells (bRBCs) were purchased from QUAD 5 (Ryegate, MT), while human red blood cells (hRBCs) were obtained from the American Red Cross (Columbus, OH). Both bRBCs and hRBCs were initially prepared in the same manner for filtration. RBCs were harvested by centrifugation for 15 min at 4500 rpm and 4 °C. Collected cells were washed three times with a 0.9% (w/v) saline solution. The washed cells were then lysed on ice with 15 mOsM phosphate buffer solution (pH 7.2) for 1 h. The lysate was passed through a glass wool filter three times, then filtered through a paper filter to remove the majority of cell debris.

The filtrate was then passed through a four stage hollow fiber setup ranging from 0.2 μm to 50 kDa in molecular weight cutoff (MWCO). The Hb retentate from the 50 kDa MWCO filter was used for the experiments in this study. This method was used to both purify and concentrate the Hb used in this study.

Assay of Hb Solution. SDS-PAGE was used to determine the purity of fractionated Hb. The purity of Hb bands in each lane of the SDS-PAGE gel was assessed from the relative band

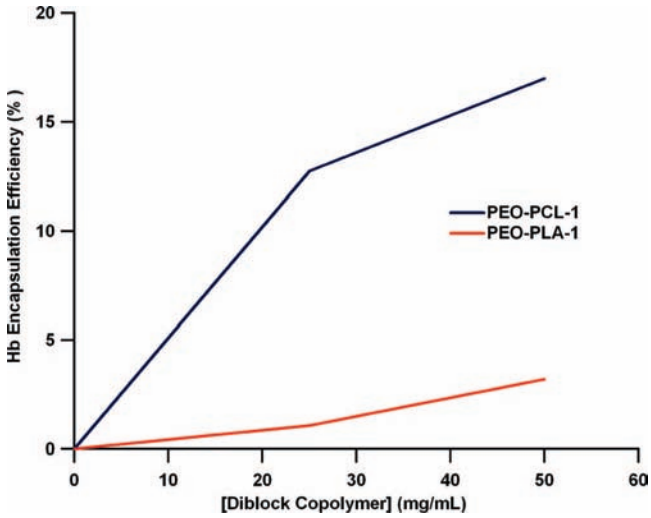

Figure 4. Effect of diblock copolymer concentration on bHb encapsulation efficiency in PEH dispersions extruded through 200 nm diameter polycarbonate membranes.

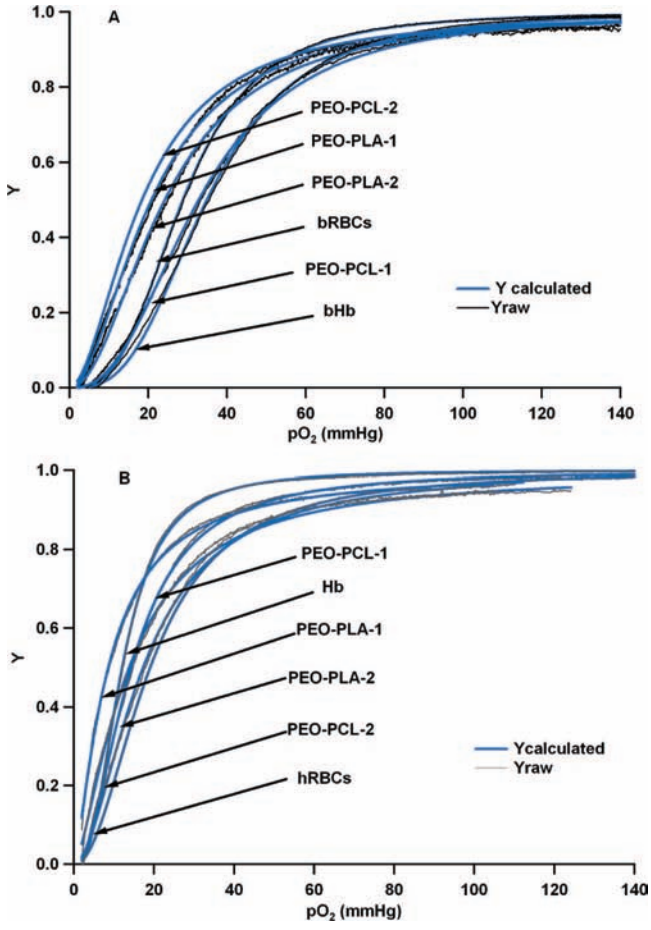

Figure 5. Oxygen equilibrium curves of PEH dispersions extruded through 200 nm diameter polycarbonate membranes comprising (A) bHb and (B) hHb. Here, *Y* is the fraction of Hb saturated with oxygen and pO_2 is the partial pressure of oxygen.

intensities using the *Quantity One 1-D* analysis software (Bio-Rad Laboratories, Hercules CA).

bHb with 97% purity and hHb with 96% purity were used to prepare PEHs. The freshly prepared Hb was buffer-exchanged with phosphate buffered saline (PBS) (pH 7.3). The metHb levels of the Hb solutions used in this study were always less than 3%.

PEH Preparation. 50 mg of diblock copolymer dried into a thin film was mixed with 1 mL of purified Hb in PBS at pH 7.3 as the extrusion buffer, in order to mimic the salinity and pH of blood plasma. The mixture was hydrated for at least 1 h.

To increase the efficiency of Hb entrapment in higher molecular weight copolymers, the copolymer/Hb mixture was subjected to 3 to 5 freeze/thaw cycles by alternatively placing the vials in a dry ice bath and warm water bath. After full hydration, the sample was extruded 20 times through 200 nm diameter polycarbonate membranes (Avanti Polar Lipids Alabaster, AL). Empty polymersomes were prepared in the same manner and used in the study as controls. Instead of hydrating with Hb solution, PBS was used as the hydration buffer. Both PEH and controls were used in the study immediately after preparation.

Dialysis and centrifugation methods were used to separate unencapsulated Hb from PEH particles. In the dialysis method, extruded PEH samples were dialyzed overnight using 300 kDa MWCO dialysis bags (Spectrum Laboratories Inc. Fort Lauderdale, FL) in PBS at 2−3 °C at a 1:1000 v/v dialyzed sample/PBS ratio in order to remove unencapsulated Hb. In the centrifugation method, extruded PEH samples were centrifuged at 14 000 rpm for 60 min. The supernatant containing unencapsulated Hb was discarded, while the PEH pellet was resuspended in PBS. This process was repeated 3 times until a clear supernatant was obtained.

PEH Size Distribution. An Eclipse asymmetric flow field flow fractionator (AFFFF) (Wyatt Technology Corp., Santa Barbara, CA) coupled in series to an 18-angle Dawn Heleos multiangle static light scattering (MASLS) photometer (Wyatt Technology Corp., Santa Barbara, CA) was used to measure the size distribution of PEHs and controls. The MASLS photometer was equipped with a 50 mW GaAs linearly polarized laser operating at a laser wavelength of 658 nm. *ASTRA* software (Wyatt Technology Corp., Santa Barbara, CA) was used to analyze the light scattering spectra and calculate the particle size distribution of the particle dispersions.

Hb Encapsulation Efficiency and Methemoglobin Level. In order to measure the Hb encapsulation efficiency and encapsulated methemoglobin (metHb) level, centrifuged PEHs were first lysed using 0.2% Triton X-100 (Sigma-Aldrich, St. Louis, MO) in PBS. The encapsulation efficiency was calculated using the following equation:

$$\text{Hb Encapsulating Efficiency (\%)} = \left[1 - \frac{V_1C_1 - V_2C_2}{V_1C_1}\right] \times 100 \quad (1)$$

where V_1 = Initial volume of unencapsulated Hb and PEH particles (mL);

C_1 = Initial concentration of Hb (mg/mL);

V_2 = Volume of PEH particles obtained after centrifugation (mL);

C_2 = Concentration of encapsulated Hb obtained after lysing PEHs (mg/mL).

The metHb levels of Hb encapsulated inside PEH particles were assayed via UV−vis spectroscopy (Thermo Electron Corp. Madison, USA) using the cyanomethemoglobin method detailed elsewhere (*2*−*5*, *7*, *18*). The absorbance of Hb extracted from lysed PEH dispersions was measured at 630 nm (L_1) against a blank reference (deionized water). Three drops of a 1:1 potassium cyanide solution made from equal parts of 10% KCN and 50 mM phosphate buffer were added to the lysed PEH samples. This converted methemoglobin to cyanomethemoglobin, which does not absorb at 630 nm. After 2 min, the

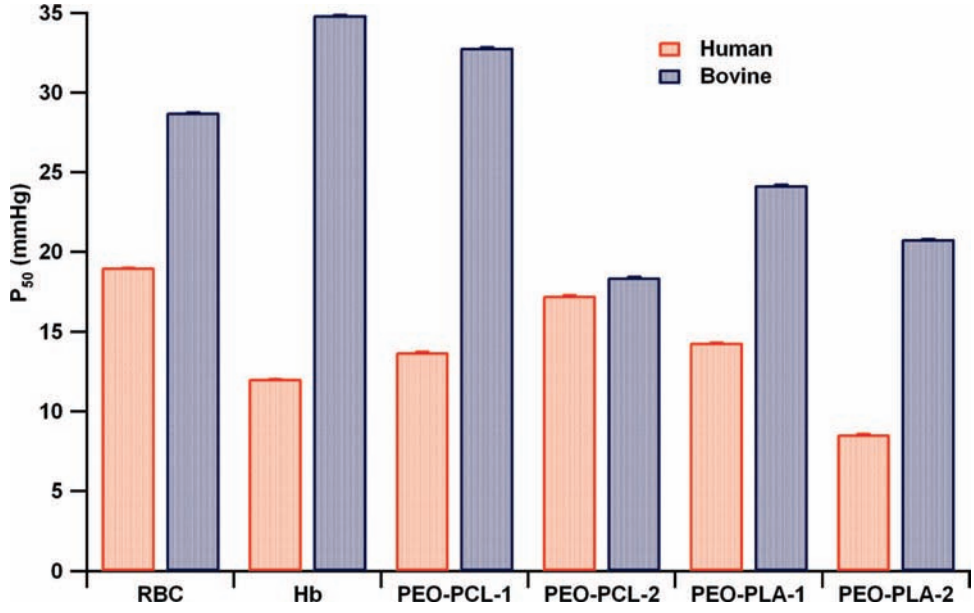

Figure 6. Oxygen affinity (P_{50}) of PEHs extruded through 200 nm diameter polycarbonate membranes.

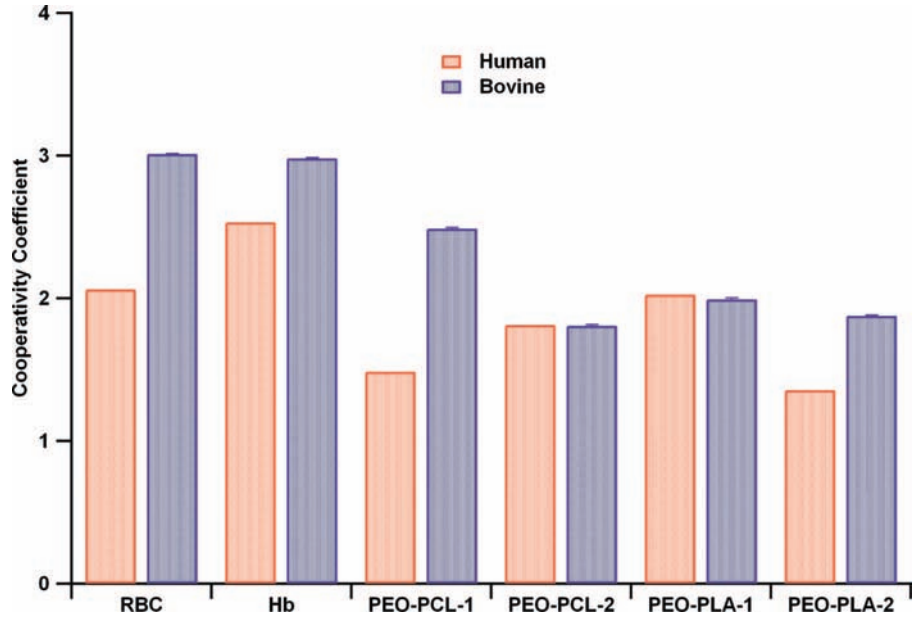

Figure 7. Cooperativity coefficient of PEHs extruded through 200 nm diameter polycarbonate membranes.

absorbance was read at 630 nm (L_2) against a blank reference. The concentration of metHb was determined as follows:

$$[\text{MetHb}]_{\text{mM}} = \frac{L_1 - L_2}{E} D_1 \qquad (2)$$

where $E = 3.7$ (cm $\times$ mM)$^{-1}$ is the extinction coefficient of metHb at 630 nm. The metHb level (%) is then expressed as follows:

$$[\text{MetHb}](\%) = \frac{[\text{MetHb}]_{\text{mM}}}{[\text{MetHb}]_{\text{mM}} + [\text{tHb}]_{\text{mM}}} \times 100 \qquad (3)$$

To determine the concentration of Hb, 3 drops of 20% potassium ferricyanide $K_3(Fe(CN)_6)$ was added to 3 mL samples diluted appropriately (D_2). The solution was allowed to react for 2 min before 3 drops of 10% KCN was added. The absorbance was then measured at 540 nm (L_3). The concentration of Hb was determined as follows:

$$[\text{tHb}]_{\text{mM}} = \frac{L_3}{E} D_2 \qquad (4)$$

where $E = 11.0$ (cm $\times$ mM)$^{-1}$ is the extinction coefficient for metHb at 540 nm.

Oxygen Equilibrium Binding Properties. The oxygen equilibrium binding curves of PEH dispersions were measured using a Hemox-Analyzer (TCS Scientific Corp. New Hope, PA) at physiological temperature (37 °C) (*4*, *7*, *18*) Briefly, 1 mL of PEH dispersion was added to a mixture containing 4 mL Hemox buffer, 20 μL of Additive-A, and 10 μL of antifoaming agent (TCS Scientific Corporation). The PEH dispersion was allowed to saturate to a pO_2 of 145 $\pm$ 2 mmHg using compressed air. The PEH dispersion was given extra time to saturate since oxygen takes a longer time to diffuse across the PEH membrane. After that, the gas stream was switched to pure N_2 to deoxygenate the PEH dispersion. The absorbances of oxy- and deoxy-Hb in solution were recorded as a function of pO_2 via dual wavelength spectroscopy. A six-parameter (A_0, A_∞, A_1, A_2, A_3, A_4) Adair model (5) and a four-parameter (A_0, A_∞, P_{50}, n) Hill model (6) were used to fit the oxygen equilibrium curves of PEH dispersions in order to regress the Adair parameters, as

Table 2. Mean Diameter, PEG Length, P_{50}, Cooperativity Coefficient (n), Encapsulated MetHb Level and Membrane Thickness (d) of LEHs, PEG-LEHs, LEAcHbs, Polymerized Hemoglobin, and PEHs

mean diameter (nm)	PEG length (kDa)	P_{50} (mmHg)	n	d (nm)	metHb level (%)	ref
			PEG-LEH			
230	0.55	33.2	2.2	3−4	<5	(*7*)
250	2	25.1	2.5	3−4	<5	
			LEAcHb			
272	2	28.5	2.1	3−4	<1	(*3*)
281	2	27.5	2.3	3−4	7.4	
			PEH			
200	12.6	22.2	2.4	35	<1	(*4*)
200	2.3	28.1	2.1	12−13	<1	
			LEH			
238	none	31.0	2.4	3−4	1.6	(*6*)
260	none	22.4	2.1	3−4	9.9	
			polymerized hemoglobin			
20:1[a]		20	1.5		8	(*24*)
40:1[a]		13	1.4		28	(*24*)
			PEH (this work)			
200	0.55	20.81	1.8	7.5	<5	
200	5	24.2	1.9	17.5	<5	

[a] Molar ratio of glutaraldehyde-Hb.

well as the P_{50} and cooperativity coefficient (n). In these equations, A_0 and A_∞ represent the absorbance at 0 mmHg and full saturation, respectively.

$$Y = \frac{\text{Abs} - A_0}{A_\infty - A_0} = \frac{A_1 \cdot pO_2 + 2A_2 \cdot pO_2^2 + 3A_3 \cdot pO_2^3 + 4A_4 \cdot pO_2^4}{4\left(1 + A_1 \cdot pO_2 + A_2 \cdot pO_2^2 + A_3 \cdot pO_2^3 + A_4 \cdot pO_2^4\right)} \quad (5)$$

$$Y = \frac{\text{Abs} - A_0}{A_\infty - A_0} = \frac{pO_2^n}{pO_2^n + P_{50}^n} \quad (6)$$

RESULTS AND DISCUSSION

Hb Encapsulation Efficiency. Figure 2 shows the encapsulation efficiency of PEHs extruded in PBS (pH 7.3). The Hb encapsulation efficiency was calculated using the centrifugation method. PBS was chosen as the extrusion buffer, since it produces monodisperse suspensions (*6*). Figure 2 shows that, as the molecular weight of the PEO block of the copolymer increases, the Hb encapsulation efficiency decreases. This observation is expected, since as the PEO chain lengths of the outer leaflets of polymersomes become larger, less volume in the core will be available for Hb encapsulation. We did not observe any effect on Hb encapsulation efficiency with a change in the chemical nature of the hydrophobic block (PLA or PCL). However, in all cases, the percentage of Hb encapsulation was generally low.

Moreover, Figure 2 shows that Hb encapsulation was more efficient with copolymers possessing lower molecular weight hydrophobic blocks. This is probably due to the relatively thin membrane of these polymersomes, which results in the availability of more internal core volume for Hb encapsulation. However, the use of PEH with higher molecular weight PEO does offer advantages in suppressing nonspecific protein interactions with the polymersome surface (*8*). This, in turn, influences the release properties of the polymersomes and will lead to more efficient removal of these particles from the body by the mononuclear phagocytic system.

Figure 3 compares the Hb encapsulation efficiency measured via centrifugation and dialysis methods. The PEHs used for the comparison were composed of different chain lengths of the same type of hydrophobic blocks (PEO-b-PCL-1 and PEO-b-PCL-2). The calculated Hb encapsulation efficiencies from the centrifugation method were higher than those of the dialysis method for both types of PEH dispersions. This may be due to the effect of dialysis on the hydrophilic outer and inner shell of PEHs, which swells during the dialysis process. This in turn results in the release of Hb, and hence reduces the observed Hb encapsulation efficiency. This observation is corroborated by the fact that the volume of packed PEH particles after dialysis was always greater than the initial packed volume of PEH particles before dialysis.

Figure 4 shows the effect of total polymer concentration on encapsulation of Hb in PEHs composed of two different types of hydrophobic blocks (PCL and PLA). The results show that encapsulation of Hb increased with increasing total polymer concentration. Therefore, by adjusting the diblock copolymer concentration, more or less polymersomes will be formed, and hence Hb encapsulation can be tailored accordingly.

It has been shown that the circulation half-life and *in vivo* stability of polymersomes surpass those of liposomes (*10*). The circulation half-lives of 100 nm diameter polymersomes with PEG brushes ranging from 1200 to 3680 Da and hydrophobic core thickness ranging from 9.6 to 14.8 nm were shown to be 10−20 h longer compared to PEG-liposomes with similar sizes (*10*). The hydrated PEO blocks obscures the hydrophobic core from the RES, which leads to the dependence of circulatory half-life of polymersomes on the molecular weight of PEO rather on the hydrophobic core thickness. Previous studies have also shown that the *in vivo* clearance mechanism of polymersomes appears to be similar to that of PEG-liposomes (*10*). This is achieved through opsonizing plasma protein deposition onto the membrane, which mediates clearance by the phagocytes of the liver and spleen (*10*).

In these experiments, the Hb/polymer weight ratio ranged between 1.2 to 1.5. These results are in the same range as those found in the literature. For example, Sakai et al. (*19*) obtained Hb/lipid weight ratios of ∼1.61, while that Takeoka et al. (*20*) obtained ratios near 1.7. However, our initial Hb concentration (70−80 mg/mL) was always less than the initial Hb concentrations used in their studies (>100 mg/mL) (*19*). Hence, it is possible for us to realize higher weight ratios.

The appropriate Hb concentration that is required for effective physiological oxygen delivery to tissues has recently been debated (*21*). For example, an Hb vesicle suspension containing 16 g/dL of Hb suspended to a volume fraction of 40% (v/v) yields an oxygen-carrying capacity that is comparable to that of blood (*21*). Therefore, our results suggest that the Hb/polymer weight ratio can be modified by simply varying the molecular weight of the diblock copolymer used in the formulation.

Oxygen Binding Properties. Equilibrium oxygen binding curves of PEH dispersions extruded through 200 nm pore diameter membranes are shown in Figure 5. All measured oxygen dissociation curves showed full saturation with O_2 at high pO_2s. While saturating the samples, it was observed that PEH dispersions took longer to saturate versus bovine and human RBCs. The membrane thickness of PEHs is greater than that of human and bovine RBCs. The increased membrane thickness results in the reduced permeability of oxygen across the PEH membrane. The oxygen binding properties of Hb were not compromised by encapsulation as is evident from the sigmoidal shape of the oxygen binding curves exhibited by all PEH dispersions. A decrease in the rate of PEH oxygen unloading or uptake is expected, because oxygen will take a longer time to diffuse across the PEH membrane.

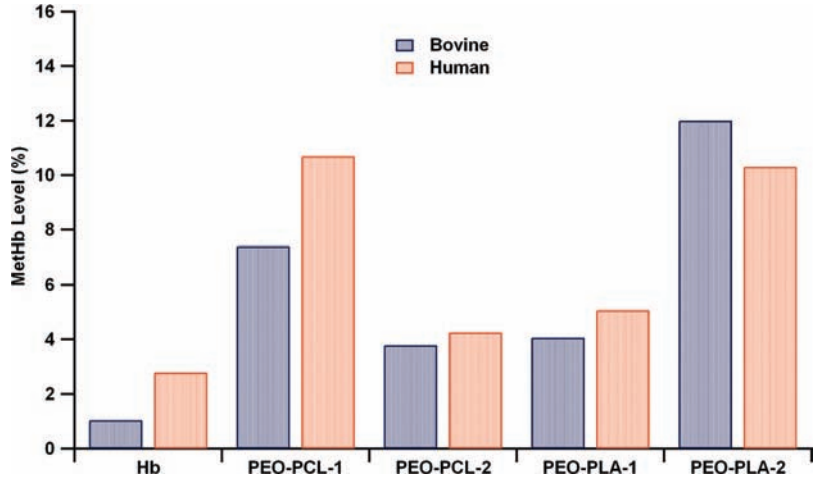

Figure 8. MetHb level of PEHs extruded through 200 nm diameter polycarbonate membranes.

Table 3. Phase Transition Temperatures Where T_m (°C) Is Melting Temperature and T_c (°C) is Crystallization Temperature

sample	T_m (°C)	T_c (°C)
PEO-PCL	52.4	18
PEO-PLA	48.1	-

The oxygen affinity (P_{50}) and cooperativity coefficient (n) of PEH dispersions are shown in Figures 6 and 7, respectively. The P_{50} and cooperativity coefficient were regressed from the oxygen equilibrium data using the Hill equation (eq 6). The P_{50} and n of all PEH dispersions vary depending upon the number-averaged molecular weight of the diblock copolymer. The variation in P_{50} for bHb was more significant than that of hHb. The P_{50} values for PEHs encapsulating hHb were generally low, in the range 8−18 mmHg, which makes them suitable for the oxygenation of ischemic tissues (*1*).

The cooperativity coefficient of Hb is a gauge of the ability of Hb to change from a low-affinity to a high-affinity state depending on the surrounding oxygen concentration. All PEH dispersions exhibited $n \approx 2$ for hHb and $n > 2$ for bHb, suggesting that all PEH dispersions display reasonable cooperativity with respect to oxygen binding and release. Table 2 compares the oxygen binding properties for select PEH dispersions and other encapsulated Hb dispersions. These results clearly show that oxygen binding properties of PEH dispersions are comparable to those of other Hb encapsulated systems (*3*−*5*).

Encapsulated MetHb Level. The metHb levels of PEH dispersions are shown in Figure 8. The metHb levels of the stock bHb solution and hHb were 1−1.5% and 2.5−3%, respectively. The metHb level of PEHs composed of lower molecular weight copolymers (PEO-b-PCL-1 and PEO-b-PLA-2) was higher than that of PEHs composed of higher molecular weight copolymers (PEO-b-PCL-2 and PEO-b-PLA-1).The increase in metHb level is primarily attributed to the rigorous preparation procedure of the PEHs and their high phase transition temperatures (Table 3), which are in the range 30−55 °C. However, the effect of higher phase transition temperatures decreased with increase in the molecular weight of the copolymer. This may be attributed to the fact that higher molecular weight copolymers produced polymersomes with thicker membranes, which maintained the oxidation state of the heme. Due to this, the increase in metHb level of Hb in higher molecular weight polymers was less significant than that of low molecular weight polymersomes.

In addition, the presence of chloride ions in the extrusion buffer was found to enhance Hb oxidation (*7*). However, the effect of Cl^- ions in this study was less significant that the effect

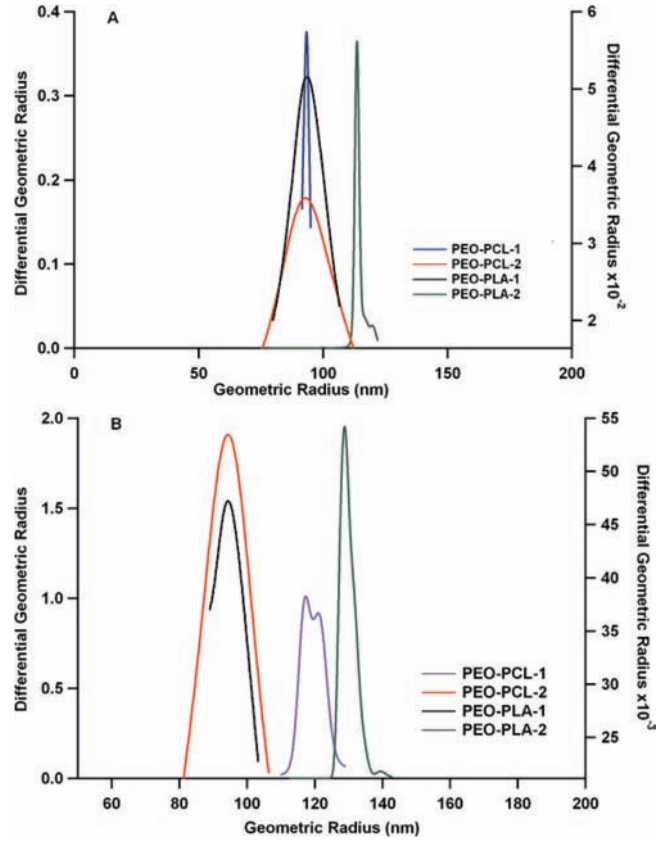

Figure 9. Size distribution of (A) empty polymersomes and (B) PEHs extruded through 200 nm diameter polycarbonate membranes.

of the vigorous preparation conditions, since the metHb levels of PEHs like PEO-b-PCL-2 and PEO-b-PLA-1 were comparable to the metHb levels of stock bHb and hHb solutions (<5%).

Also, unlike others (*22*), no reductants and catalases were used in this study to suppress Hb oxidation. However, the coencapsulation of low concentrations of reductants and catalases can be easily incorporated in order to further suppress Hb oxidation if desired. Unlike liposomes (*7*), the bilayer of polymersomes did not enhance Hb oxidation. Hb oxidation in LEAcHbs and nonmodified LEHs is mainly due to phospholipid peroxidation, which is not the case with polymersomes. Thus, encapsulation of Hb into polymersomes did not induce metHb formation. This is one important aspect that favors PEH as a potential cellular HBOC, since Hb oxidation reduces the amount of oxygen that is available for oxygen transport.

Size Distribution and Average Radii. The differential size distributions of empty polymersomes and PEHs extruded through 200 nm pore diameter membranes are shown in Figure 9, panels A and B, respectively. All polymersomes have monodisperse size distributions with an approximate distribution width of 20 nm and are generally Gaussian in shape . The average size of PEHs is greater than that of empty polymersomes, which may be due to swelling of polymersomes on encapsulating Hb.

According to previous studies (*16*, *23*), the average molecular shape is most simply a reflection of the hydrophilic fraction, *f*. To generate polymersomes in water, the value of *f* should be $\sim 35 \pm 10\%$; values of $f < 50\%$ presumably reflects the ability of hydration to balance a disproportionately large hydrophobic fraction (*16*, *23*). Hydrophilic fractions greater than 45% can be expected to form micelles (*16*), whereas molecules with $f <$ 25% can be expected to form inverted microstructures (*16*). Copolymers with molecular weight ranging 2000−20 000 Da have been observed to follow these packing rules and yield polymersomes when the *f* requirement is satisfied (*8*). The scaling of copolymer membrane thickness with copolymer molecular weight has been experimentally verified and confirmed by a novel coarse-grained molecular dynamics simulation that yielded the following expression:

$$d \approx \mathrm{MW}_\mathrm{h}^b \quad (b \cong 0.55) \tag{7}$$

where d = thickness of polymersome membrane;

$\mathrm{MW_h}$ = molecular weight of hydrophobic block.

This property of polymersome membranes thus presents a novel opportunity to study membrane properties as a function of membrane thickness *d* (*8*, *9*). The mean diameter of PEHs used in this study was calculated with eq 7 and shown in Table 2.

CONCLUSIONS

This study investigated the use of biodegradable and biocompatible diblock copolymers for the preparation of Hb-encapsulated polymersomes. Our results showed that the Hb encapsulation efficiency decreased with an increase in the molecular weight of the PEO block of the copolymer. However, changing the chemical nature of the hydrophobic block (PLA or PCL) did not result in any observable effect on Hb encapsulation efficiency. In addition, our results showed that Hb encapsulation increased with increasing total copolymer concentration. Thus, by adjusting the diblock copolymer concentration, Hb encapsulation can be tailored accordingly. The Hb/polymer weight ratio can also be modified in order to make the oxygen carrying capacity of PEHs comparable to that of blood.

Hb encapsulation did not affect oxygen binding properties of Hb, as is evident from the sigmoidal shape of the oxygen binding curves. In addition, the P_{50}s for PEHs encapsulating hHb were low, which makes them suitable for oxygenating ischemic tissues. All PEH dispersions showed reasonable cooperativity with respect to oxygen binding and release. Moreover, encapsulation of Hb inside polymersomes did not induce metHb formation. All polymersome dispersions exhibited monodisperse size distributions with an approximate distribution width of 20 nm. Taken together, all of our observations favor the use of PEHs as potential cellular HBOCs.

ACKNOWLEDGMENT

This work was supported by the National Institutes of Health grants R01HL078840 and R01DK070862 to A.F.P.

LITERATURE CITED

(1) Sakai, H., Cabrales, P., Tsai, A. G., Tsuchida, E., and Intaglietta, M. (2005) Oxygen release from low and normal P_{50} Hb vesicles in transiently occluded arterioles of the hamster window model. *Am. J. Physiol. Heart Circ. Physiol. 288*, H2897–2903.

(2) Dimino, M. L., and Palmer, A. F. (2007) High O_2 affinity hemoglobin-based oxygen carriers synthesized via polymerization of hemoglobin with ring-opened 2-chloroethyl-β-D-ructopyranoside and 1-*o*-octyl-β-D-glucopyranoside. *Biotechnol. Bioeng. 97*, 462–472.

(3) Li, S., Nickels, J., and Palmer, A. F. (2005) Liposome-encapsulated actin-hemoglobin (LEAcHb) artificial blood substitutes. *Biomaterials 26*, 3759–3769.

(4) Arifin, D. R., and Palmer, A. F. (2005) Polymersome encapsulated hemoglobin: a novel type of oxygen carrier. *Biomacromolecules 6*, 2172–2181.

(5) Arifin, D. R., and Palmer, A. F. (2005) Stability of liposome encapsulated hemoglobin dispersions. *Artif. Cells, Blood Substitutes, Biotechnol. 33*, 113–136.

(6) Arifin, D. R., and Palmer, A. F. (2003) Determination of size distribution and encapsulation efficiency of liposome-encapsulated hemoglobin blood substitutes using asymmetric flow field-flow fractionation coupled with multi-angle static light scattering. *Biotechnol. Prog. 19*, 1798–1811.

(7) Arifin, D. R., and Palmer, A. F. (2005) Physical properties and stability mechanisms of poly(ethylene glycol) conjugated liposome encapsulated hemoglobin dispersions. *Artif. Cells, Blood Substitues, Biotechnol. 33*, 137–162.

(8) Discher, D. E., and Ahmed, F. (2006) Polymersomes. *Annu. Rev. Biomed. Eng. 8*, 323–341.

(9) Discher, D. E., Ortiz, V., Srinivas, G., Klein, M. L., Kim, Y., Christian, D., Cai, S., Photos, P., and Ahmed, F. (2007) Emerging applications of polymersomes in delivery: From molecular dynamics to shrinkage of tumors. *Prog. Polym. Sci. 32*, 838–857.

(10) Photos, P. J., Bacakova, L., Discher, B., Bates, F. S., and Discher, D. E. (2003) Polymer vesicles in vivo: correlations with PEG molecular weight. *J. Controlled Release 90*, 323–334.

(11) Ahmed, F., Photos, P. J., and Discher, D. E. (2006) Polymersomes as viral capsid mimics. *Drug Dev. Res. 67*, 4–14.

(12) Lee, J. C. M., Bermudez, H., Discher, B. M., Sheehan, M. A., Won, Y.-Y., Bates, F. S., and Discher, D. E. (2001) Preparation, stability, and in vitro performance of vesicles made with diblock copolymers. *Biotechnol. Bioeng. 73*, 135–145.

(13) Ahmed, F., and Discher, D. E. (2004) Self-porating polymersomes of PEG-PLA and PEG-PCL: hydrolysis-triggered controlled release vesicles. *J. Controlled Release 96*, 37–53.

(14) Ahmed, F., Pakunlu, R. I., Srinivas, G., Brannan, A., Bates, F., Klein, M. L., Minko, T., and Discher, D. E. (2006) Shrinkage of a rapidly growing tumor by drug-loaded polymersomes: pH-triggered release through copolymer degradation. *Mol. Pharmaceutics 3*, 340–350.

(15) Li, S., Byrne, B., Welsh, J., and Palmer, A. F. (2007) Self-assembled poly(butadiene)-*b*-poly(ethylene oxide) polymersomes as paclitaxel carriers. *Biotechnol. Prog. 23*, 278–285.

(16) Discher, D. E., and Kamien, R. D. (2004) Self-assembly: Towards precision micelles. *Nature 430*, 519–520.

(17) Meng, F., Engbers, G. H. M., and Feijen, J. (2005) Biodegradable polymersomes as a basis for artificial cells: encapsulation, release and targeting. *J. Controlled Release 101*, 187–198.

(18) Dimino, M. L., and Palmer, A. F. (2007) Purification of bovine hemoglobin via fast performance liquid chromatography. *J. Chromatogr., B 856*, 353–7.

(19) Sakai, H., Hamada, K., Takeoka, S., Nishide, H., and Tsuchida, E. (1996) Physical properties of hemoglobin vesicles as red cell substitutes. *Biotechnol. Prog. 12*, 119–125.

(20) Takeoka, S., Ohgushi, T., Terase, K., Ohmori, T., and Tsuchida, E. (1996) Layer-controlled hemoglobin vesicles by interaction of hemoglobin with a phospholipid assembly. *Langmuir 12*, 1755–1759.

(21) Sakai, H., Sato, A., Takeoka, S., and Tsuchida, E. (2007) Rheological properties of hemoglobin vesicles (artificial oxygen carriers) suspended in a series of plasma-substitute solutions. *Langmuir 23*, 8121–8128.

(22) Atoji, T., Aihara, M., Sakai, H., Tsuchida, E., and Takeoka, S. (2006) Hemoglobin vesicles containing methemoglobin and tyrosine to suppress methemoglobin formation in vitro and in vivo. *Bioconjugate Chem. 17*, 1241–1245.

(23) Srinivas, G., Discher, D. E., and Klein, M. L. (2004) Self-assembly and properties of diblock copolymers by coarse-grain molecular dynamics. *Nat. Mater. 3*, 638–644.

(24) Eike, J. H., and Palmer, A. F. (2004) Effect of glutaraldehyde concentration on the physical properties of polymerized hemoglobin-based oxygen carriers. *Biotechnol. Prog. 20*, 1225–1232.

BC700465V

Zinc(II)-Coordinated Oligotyrosine: A New Class of Cell Penetrating Peptide

James R. Johnson, Hua Jiang, and Bradley D. Smith*

Department of Chemistry and Biochemistry, University of Notre Dame, Notre Dame, Indiana 46556 USA. Received December 16, 2007; Revised Manuscript Received January 20, 2008

A new series of cell penetrating peptides (CPPs) are described. The peptides are oligomers of Tyr-ZnDPA, a tyrosine derivative with an appended 2,2′-dipicolylamine unit that forms a very stable coordination complex with a zinc (II) cation. This in turn allows reversible association with a chelating oxyanion such as a carboxylate or phosphate derivative. The peptide oligomers $(Tyr\text{-}ZnDPA)_n$ where $n = 1, 2, 4, 8$, are highly water soluble, but upon association with fatty acids or phospholipids they partition into an organic octanol phase. Furthermore, a fluorescent, fluorescein-labeled version of the octamer, $(Tyr\text{-}ZnDPA)_8$-Fl, can enter living mammalian cells via endocytosis and a biotin derivative can deliver fluorescein-labeled streptavidin. Fluorescence microscopy and flow cytometry experiments show that cell uptake is diminished by conditions that inhibit endocytosis. Additionally, uptake of $(Tyr\text{-}ZnDPA)_8$-Fl is greater than fluorescein labeled octaarginine (Arg_8-Fl) in all cell lines tested (CHO, COS-7, HeLa). Another difference with Arg_8-Fl is that cell uptake of $(Tyr\text{-}ZnDPA)_8$-Fl does not require the presence of heparan sulfate proteoglycans on the cell surface. This difference may eventually be of practical value because drug delivery systems that employ alternative endocytic mechanisms may be optimal for different cell lines or they may deliver selectively to different organelles within a cell.

INTRODUCTION

Spontaneous diffusion of charged or high molecular weight compounds across the cell plasma membrane is kinetically unfavored which means that many potential drugs and diagnostic reagents are ineffective because they cannot reach their intracellular targets. To overcome this transport barrier, a range of cell delivery systems have been proposed and investigated, including cell surface receptors, synthetic transporters, nanotubes, and nanoparticles (*1–4*). In the mid 1960s Ryser and Hancock discovered that cationic peptides can promote the entry of macromolecules into living cells (*5–7*), and peptide mediated delivery has subsequently been applied to a wide variety of molecular cargo (*8*). Most designs of cell penetrating peptides (CPPs) are based on a membrane translocation sequence (sometimes referred to as a protein transduction sequence) that is within the larger structure of a larger transport-active protein like HIV-Tat or the *Drosophila antennapedia* homeodomain (*9, 10*). In other cases, the peptide designs are *de novo* (*11*). Usually, CPPs enter living cells via endocytosis; however, some appear to directly translocate across the plasma membrane in an energy-independent manner (*12*). The transported cargo includes biologically active proteins, DNA, liposomes, fluorescent dyes, and nanoparticles (*13–17*), and delivery success has even been achieved in vivo (*18, 19*). Often the peptide is covalently linked to the cargo (*20*), and in some cases the linker is cleavable (*21*). There are CPPs that associate noncovalently with the cargo (*22, 23*), and also CCPs that are activated by protease cleavage of an inhibitory segment (*24*).

We have designed a novel oligomeric CPP that requires metal cations for cell delivery activity. The peptide monomer is $(Tyr\text{-}ZnDPA)_1$ a tyrosine derivative with an appended 2,2′-dipicolylamine unit that forms a stable coordination complex with a zinc (II) cation (Scheme 1) (*25*). Previously, we have shown that this water soluble, zinc-coordinated monomer can associate with a chelating oxyanion such as a carboxylate or phosphate derivative. The resulting ternary complex is net neutral and if the oxyanion is sufficiently lipophilic, it can partition from water into vesicles. Here, we describe the anion binding and membrane partitioning properties of a various oligomers of $(Tyr\text{-}ZnDPA)_n$, where $n = 1, 2, 4, 8$ (Scheme 2). These peptide oligomers are also highly water soluble, but upon association with fatty acids or phospholipids they migrate into an organic octanol phase. Furthermore, we find that fluorescently labeled versions of these peptides can enter cells via endocytosis and that a biotin derivative of these peptides can deliver fluorescently labeled streptavidin. The results of this work raise the idea of a cell delivery system that is activated by increased local concentrations of zinc (*26*), and thus may be useful for selective delivery to zinc-rich tissues or to tissues upon stimulated zinc efflux from cells (*27, 28*).

Scheme 1. Association of $(Tyr\text{-}ZnDPA)_1$ with Carboxylate

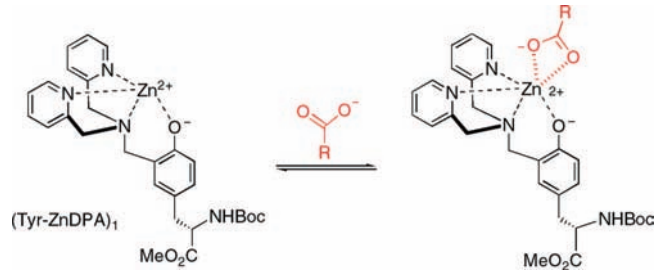

EXPERIMENTAL PROCEDURES

Synthesis. See Supporting Information.

Water/Organic Partitioning. (*1*) $(Tyr\text{-}ZnDPA)_n$ and sodium hydroxide were dissolved in water to give a 10 mM stock solution in each case. Lauric acid was dissolved in octanol to give 10 mM stock solution (*2*). To a 2 mL glass vial was added water (0.5 mL), octanol (0.5 mL), and an aqueous solution of $(Tyr\text{-}ZnDPA)_n$ (5 μL). For experiments with lauric acid, a solution of lauric acid (6 μL, 1.2 molar equiv per Zn) was added

* Fax: (+1) 574-631-6652, E-mail: smith.115@nd.edu.

10.1021/bc700466z CCC: $40.75 © 2008 American Chemical Society
Published on Web 04/10/2008

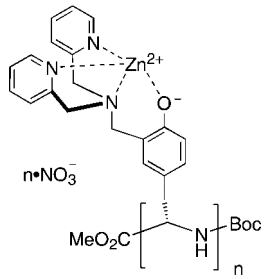

n=1, (Tyr-ZnDPA)$_1$
n=2, (Tyr-ZnDPA)$_2$
n=4, (Tyr-ZnDPA)$_4$
n=8, (Tyr-ZnDPA)$_8$

followed by a solution of sodium hydroxide (6 μL, 1.2 molar equiv). The mixed solution was shaken for 30 s and centrifuged. Spectrometric measurements were made with 100 μL aliquots from each layer. The aqueous phase was diluted with 0.1 mL octanol and 0.6 mL methanol. The octanol phase was diluted with 0.1 mL water and 0.6 mL methanol (*3*). The partitioning protocol for (Tyr-ZnDPA)$_n$-Fl is similar to above procedure. Since (Tyr-ZnDPA)$_1$-Fl is soluble in octanol rather than in water, no partition experiment was done in this case. The stock solution of (Tyr-ZnDPA)$_2$-Fl was 0.5 mM in a mixture of water and methanol (9:1). The stock solutions of (Tyr-ZnDPA)$_4$-Fl and (Tyr-ZnDPA)$_8$-Fl were 1 mM in water.

Eukaryotic Cell Culture. CHO, PGSA, PGSD, COS-7, and HeLa cells were cultured according to ATCC protocols. All cell lines were cultured in T75 cell culture flasks with vented caps and incubated at 37 °C in a humidified 5% CO_2 atmosphere. For fluorescence microscopy, cells were plated out on 8-well microscope chambered slides and allowed to grow to approximately 80% confluence. Upon treatment and incubation with CPPs, cells were rinsed 3 times with phenol free Dublecco's Minimum Essential Medium (DMEM) containing 2 mM L-glutamine, glucose, and supplemented with 10% fetal bovine serum. For flow cytometry all cell cultures were grown in 6-well cell culture plates to approximately 80% confluence. In preparation for flow cytometry cells were rinsed with phosphate buffered saline solution and then trypsinized for 10 min to remove externally bound peptide and to detach cells from the surface of well plates. Upon trypsinization, cells were resuspended in phenol-free DMEM. For both flow cytometry and fluorescence microscopy cells were analyzed in phenol-free DMEM.

Cell Toxicity. Cell toxicity was assessed via MTT assay using the Vybrant MTT Cell Proliferation Assay Kit (Invitrogen, V-13154). A 200 μL mixture of cells (approximately 5×10^4 cells/mL) in growth media were dispensed into each well of a 96-well plate and allowed to grow to 80% confluence. An aliquot of 1 mM (Tyr-ZnDPA)$_8$ in 50:50 water/methanol was administered to the first well in each treatment and subsequent wells were given a serial 2-fold dilution. The cells were allowed to incubate for 6 h at 37 °C, then the growth medium was removed and replaced with 100 μL of growth media supplemented with [3-(4,5-dimethylthiazol-2-yl)-2,5-diphenyltetrazolium bromide] (MTT) at a concentration of 1.2 mM. The cells were incubated at 37 °C for 4 h then treated with 100 μL of an SDS-HCl solution to kill the cells, and dissolve the formazan product. The SDS-HCl solution was prepared by adding 10 mL of 0.01 M HCl to 1 g of SDS. The SDS-HCl/cell solution was then incubated for 12 h at 37 °C, after which the absorbance of each well was read at 570 nm. In order to determine the viability in each sample the following equation was used:

$$\text{Cell Viability} = (\text{Abs} - \text{Abs}_{\text{Neg}})/(\text{Abs}_{\text{Con}} - \text{Abs}_{\text{Neg}})$$

where Abs is the absorbance of the test well, Abs_{Neg} is the absorbance of the negative control (no cells added to the well)

Scheme 2. Schematic View of (Tyr-ZnDPA)$_n$ and Association with Carboxylates

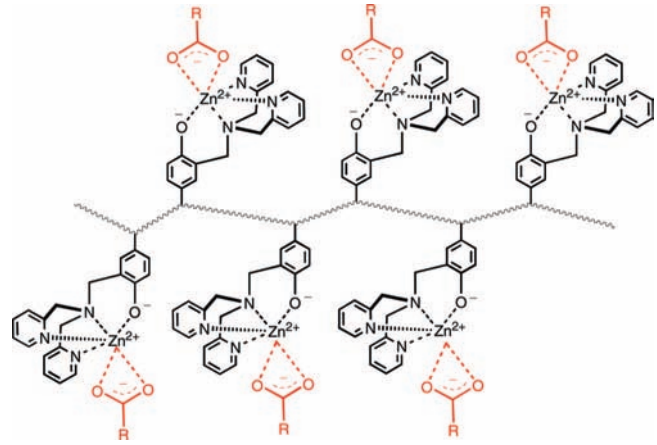

and Abs_{Con} is the absorbance of wells in which cells were not treated with (Tyr-ZnDPA)$_8$.

Fluorescence Microscopy. Fluorescence microscopy was conducted on a Nikon Eclipse TE-2000 U epifluorescence microscope equipped with blue field (Exciter: D360/40×, Dichroic: 400DCLP, Emitter: 460/50m), green field (Exciter: D360/40×, Dichroic: 400DCLP, Emitter: HQ535/50m), red field (Exciter: HQ545/30×, Dichroic: Q570LP, Emitter: HQ610/75m) filters, and far red (Exciter: HQ620/60X, Dichroic: 660LP, Emitter: HQ700/75m) filters. Images were acquired using a Photometrics 512-B black and white digital camera and appropriate field colors were added using Metamorph Software V6.2.

Flow Cytometry. Flow cytometry was conducted on a Beckman Coulter MPL 500 flow cytometer, and data was manipulated using the instrument's MPL and CXP software packages. After incubation, the cell cultures were prepared for flow cytometry analysis by removing the cell growth media, rinsing with PBS buffer, and treating with trypsin. This served to detach the cells from the culture wells and to degrade any remaining fluorescent peptide on the outside of the cells. Cell populations that were not pretreated in this manner exhibited greater fluorescence intensity due to externally bound peptide. Analysis was conducted for a minimum of 10 000 counting events.

Endocytosis Inhibition. For inhibition of endocytosis, cells were incubated at 4 °C for 15 min, treated with 10 μM (Tyr-ZnDPA)$_8$-Fl in growth media, and incubated for another 3 h at 4 °C. Cells were then prepared for analysis as previously described. For ATP depletion, cells were preincubated in growth media supplemented with 0.1% NaN_3 and 50 mM deoxyglucose for 1 h, then treated with 10 μM (Tyr-ZnDPA)$_8$-Fl and incubated for 3 h. For specific endocytosis mechanisms, cells were treated with chlorpromazine (30 μM), 400 mM sucrose, nystatin (25 μg/mL), amiloride (3 mM), or wortmannin (10 μM) for 1 h prior to administration of (Tyr-ZnDPA)$_8$-Fl in growth media. After a 3 h incubation, cells were prepared for flow cytometry analysis.

RESULTS

Synthesis. The doubly protected amino acid (Tyr-DPA)$_1$ was prepared in one step and large scale using cheap starting materials. The oligomeric series (Tyr-DPA)$_n$, where $n = 1$, 2, 4, 8 was subsequently constructed in high yields (≥80% for each step) using solution-state amide coupling chemistry with EDC/HOBt as the activating agent. Chromatographic purification was greatly facilitated by using silica gel and an admixture of acetonitrile/ammonium hydroxide as the eluent. The pure

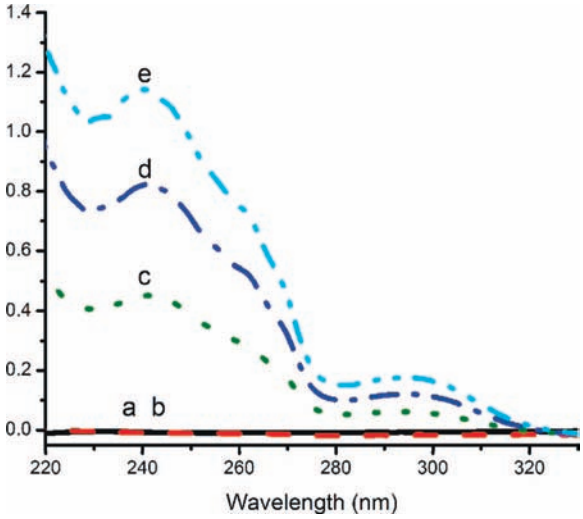

Figure 1. Absorption spectra of octanol phase after partitioning of (Tyr-ZnDPA)$_8$ (10 μM) between water and octanol with various molar equivalents of sodium laurate per Zn(II); (a) 0 equiv, (b) 0.5 equiv, (c) 0.75 equiv, (d) 1 equiv, (e) 1.5 equiv.

(Tyr-DPA)$_n$ peptides were converted into zinc(II) complexes, (Tyr-ZnDPA)$_n$, by simply stirring with a stoichiometric amount of $Zn(NO_3)_2$. To make the fluorescent conjugates, (Tyr-ZnDPA)$_n$-Fl, the amine versions of (Tyr-DPA)$_n$ were linked to FITC via an aminohexanioic acid chain, and the pure peptides converted into zinc(II) complexes. Fluorescein labeled octa(arginine), (Arg_8-Fl) was prepared by reported methods (*29*).

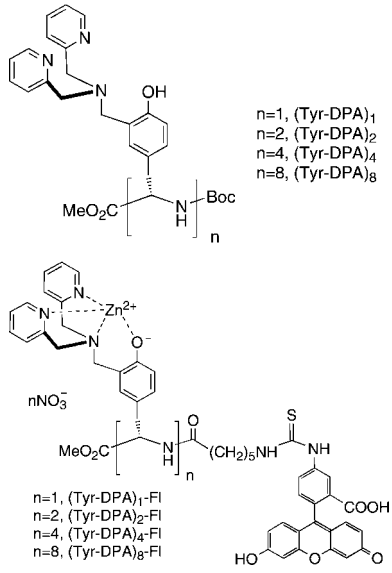

Liquid Water/Organic Partitioning Studies. The partitioning of unlabeled peptides (Tyr-ZnDPA)$_n$ between water and octanol is easily monitored by the UV absorption of the aromatic groups at 240 and 300 nm. In all cases, the zinc-coordinated oligomers are highly water-soluble and they reside completely in the aqueous phase. However, the presence of sodium laurate ($\geq$1.5 mol equiv per zinc cation) induces complete migration of each oligomer into the octanol phase. As shown in Figure 1, the presence of 0.5 mol equiv of sodium laurate is able to move significant amounts of the longest oligomer, (Tyr-ZnDPA)$_8$ into the octanol, but complete partitioning requires 1.5 mol equiv of laurate.

Similar phase transfer results were obtained with the fluorescein conjugated oligomers (Tyr-ZnDPA)$_n$-Fl. In this case, the yellow color of fluorescein tag can be monitored by the naked eye, and as shown in Figure 2, the sodium laurate promotes complete partitioning of (Tyr-ZnDPA)$_8$-Fl into the octanol layer. In Figure 3 is a comparison of the (Tyr-ZnDPA)$_8$-Fl partitioning induced by sodium laurate and the anionic phospholipid 1-palmitoyl-2-oleoylphosphatidylglycerol (POPG). In both cases, there is extensive peptide migration into the organic phase but the process is achieved more slightly readily with the POPG, reflecting its comparatively greater lipophilicity and higher affinity for the zinc cations in the peptide. The same (Tyr-ZnDPA)$_8$-Fl partitioning results were obtained with the anionic phospholipids 1-palmitoyl-2-oleoylphosphatidic acid (POPA) and 1-palmitoyl-2-oleoylphosphatidylserine (POPS), whereas no partitioning into the organic layer was induced by the presence of POPC (see Supporting Information).

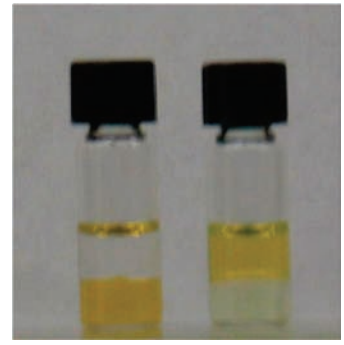

Figure 2. Partitioning of (Tyr-ZnDPA)$_8$-Fl (1 μM) between water and octanol: (left) with no sodium laurate present the peptide is completely in the lower aqueous phase. (right) the presence of 1.5 mol equiv of sodium laurate per Zn(II) induces complete migration into the upper octanol phase.

Octanol partitioning was also used to evaluate the affinity of (Tyr-ZnDPA)$_8$-Fl for the multianionic polysaccharide heparin (sodium salt from porcine intestinal mucosa, average molecular weight 3000 g/mol). In this case, the heparin was used as a water-soluble inhibitor of laurate induced transfer of (Tyr-ZnDPA)$_8$-Fl into the organic phase. As shown in Figure 4, peptide partitioning into octanol was prevented when the level of heparin in the aqueous phase was above 60 μg/mL. We infer that the multianionic heparin has a strong affinity for (Tyr-ZnDPA)$_8$-Fl and the ternary complex is not lipophilic.

Penetration of Fluorescent (Tyr-ZnDPA)$_n$ into Living Cells. The fluorescent peptides (Tyr-ZnDPA)$_n$-Fl were administered to a variety of eukaryotic mammalian cell lines (CHO, COS-7, HeLa) and examined for cellular uptake using fluorescence microscopy. Figure 5 shows fluorescent micrographs of CHO and COS-7 cells that have been incubated with (Tyr-ZnDPA)$_8$-Fl (10 μM) in serum supplemented growth media for 3 h at 37 °C. Binding of the (Tyr-ZnDPA)$_8$-Fl to the exterior of the cell was observed as early as 15 min after treatment and likely occurs immediately after administration of the compound to the cell culture. Within 1 h the fluorescence was confined to punctuate compartments within the cell. The presence of serum or growth media did not appear to inhibit uptake; however, administration of these peptides to cells in phosphate buffered saline caused precipitation, and diminished cell uptake as judged by fewer fluorescent endosomal compartments.

The amount of cell uptake of (Tyr-ZnDPA)$_n$-Fl was quantified by flow cytometry. The flow cytometry histograms in Figure 6 show that the order of uptake in HeLa cells is (Tyr-ZnDPA)$_8$-Fl > (Tyr-ZnDPA)$_4$-Fl > (Tyr-ZnDPA)$_2$-Fl. No uptake or cell surface binding was observed with (Tyr-ZnDPA)$_1$-Fl. Thus, cell adhesion and uptake increases substantially with the length and multivalency of the peptide. The uptake of (Tyr-ZnDPA)$_8$-Fl and Arg_8-Fl in different cell lines was compared by flow cytometry (see Supporting Information). With HeLa cells the

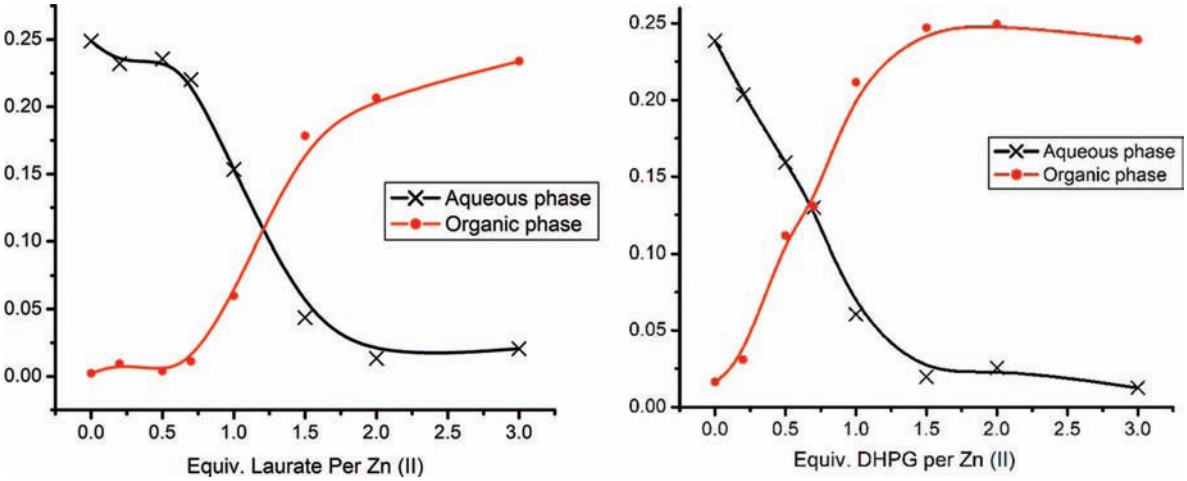

Figure 3. Amount of (Tyr-ZnDPA)$_8$-Fl (1 μM) (reflected by absorbance at 500 nm) in aqueous and organic phase after partitioning between water and octanol in the presence of: (left) various molar equivalents of sodium laurate per Zn(II); (right) various molar equivalents of POPG per Zn(II).

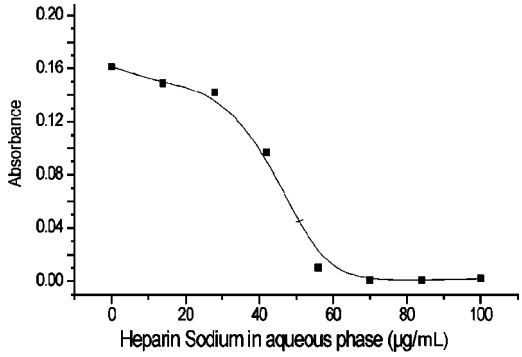

Figure 4. Amount of (Tyr-ZnDPA)$_8$-Fl (1 μM) in the organic phase (reflected by absorbance at 500 nm) for a two phase aqueous/octanol mixture that also contains sodium laurate (two molar equivalents of per Zn(II)) and various amounts of heparin sodium in the aqueous phase.

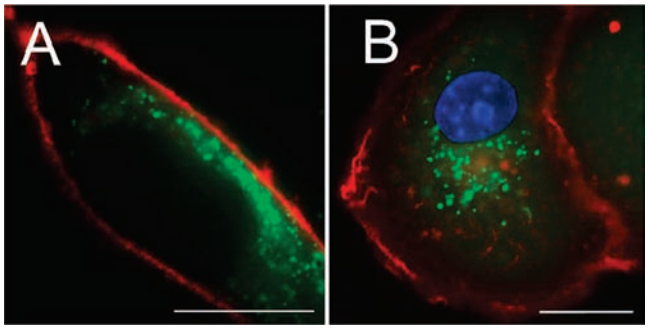

Figure 5. Panel A, a single CHO cell showing uptake of (Tyr-ZnDPA)$_8$-Fl (green). The plasma membrane is costained with FM 4–64 (1 μM) (red). Panel B, a single COS-7 cell showing uptake of (Tyr-ZnDPA)$_8$-Fl (10 μM) (green). The cellular membranes are costained with FM 4–64 (1 μM) (red) and the nucleus is costained with Hochest 33342 (1 μM) (blue). The bars denote a distance of 20 μm.

uptake of (Tyr-ZnDPA)$_8$-Fl was slightly greater, but with CHO and COS-7 cells the uptake was quite superior.

The toxicity of (Tyr-ZnDPA)$_8$ was determined by measuring cell viability using a standard MTT assay. The viability of CHO cells was unaffected by (Tyr-ZnDPA)$_8$ concentrations up to 40 μM, whereas the COS-7 cells were slightly effected with an approximate LD_{50} of 60 μM. With both cell lines there was little, if any measurable toxicity at the concentrations used in this study (10 μM).

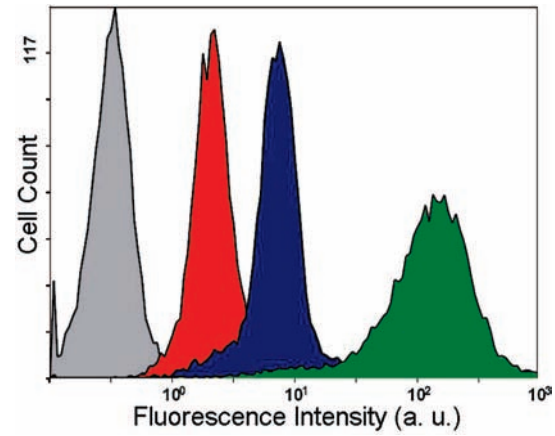

Figure 6. Overlay of flow cytometry histograms showing cellular uptake of the zinc tyrosine oligomers (10 μM) in HeLa cells. Histograms are as follows: gray, untreated cells; red, cells treated with of (Tyr-ZnDPA)$_2$-Fl; blue, cells treated with (Tyr-ZnDPA)$_4$-Fl; green, cells treated with (Tyr-ZnDPA)$_8$-Fl.

Table 1. Percent Cellular Uptake of (Tyr-ZnDPA)$_8$-Fl in the Presence of a Given Inhibitor As Quantified by Flow Cytometry[a]

		cell line		
compound	inhibits	COS-7	CHO	HeLa
4 °C incubation	endocytosis	0	0	0
NaN_3/DOG	endocytosis	0	0	0
Chlorpromazine	endocytosis[b]	6	13	50
Sucrose	endocytosis[b]	6	13	2
Nystatin	endocytosis[c]	60	40	80
Amiloride	pinocytosis	100	100	100
Wortmannin	pinocytosis	100	100	100

[a] Values are compared to uptake in the absence of inhibitor. [b] Clathrin-mediated endocytosis. [c] Caveolin-mediated endocytosis.

To determine how much of the cell uptake was due to endocytosis, the cell incubations were repeated under various conditions that inhibit endocytic processes (Table 1). The first method involved incubation of cell cultures at low temperature. Fluorescence microscopy and flow cytometry showed that incubation at 4 °C greatly inhibited the uptake of (Tyr-ZnDPA)$_8$-Fl. In addition, there was no entry into cells whose ATP levels were depleted of by preincubation with growth media supplemented with 0.1% NaN_3 and 50 mM deoxyglucose (DOG). These results indicate that cellular uptake occurs via one or more endocytosis mechanisms.

Table 2. Percent Uptake of Arg_8-Fl and $(Tyr\text{-}ZnDPA)_8$-Fl into PGSA and PGSD Cells Compared to Uptake into CHO Cells

peptide (10 μM)	PGSA	PGSD	CHO
Arg_8-Fl	<5	90	100
$(Tyr\text{-}ZnDPA)_8$-Fl	100	160	100

Additional mechanistic insight was gained by treating the cells with compounds that inhibit specific endocytosis processes. Separate samples of cells were each pretreated with an inhibitor prior to addition of $(Tyr\text{-}ZnDPA)_8$-Fl. Chlorpromazine and sucrose are known to be inhibitors of clathrin-mediated endocytosis while nystatin inhibits caveolin-mediated mechanisms (*30*). Cells were also treated with amiloride and wortmannin which inhibit pinocytosis. The amount of cell uptake was determined using flow cytometry and as summarized in Table 1, the inhibition varied with cell-type. The most effective inhibitors were chloropromazine and sucrose; whereas, amiloride and wortmannin were ineffective. Taken together the data in Table 1 indicates that $(Tyr\text{-}ZnDPA)_8$-Fl enters cells primarily by clathrin-mediated endocytosis.

There is strong evidence that oligo(arginine) internalization requires the presence of cell surface heparan sulfate proteoglycans (*30*). Since the phase transfer studies demonstrated that $(Tyr\text{-}ZnDPA)_8$-Fl also associates with the heavily sulfonated, heparin, we investigated if cell internalization was mediated by heparan sulfate proteoglycans. Our study compared the uptake into native CHO cells with entry into cells that were deficient in certain types of proteoglycans; that is, the PGSA 745 and PGSD 677 strains of CHO cells. PGSA cells do not have glycosaminoglycans because they are deficient in xylosyltransferase, which catalyzes attachment of the first sugar in glycosaminoglycan synthesis. Similarly, PGSD cells are deficient in both N-acetylglucosaminyltransferase and glucuronyltransferase activities and do not produce heparan sulfate, but they do produce chondroitin sulfate (*31, 32*). Separate samples of each cell type were treated with Arg_8-Fl and $(Tyr\text{-}ZnDPA)_8$-Fl (10 μM) and analyzed by both fluorescence microscopy and flow cytometry (Table 2). The decreased uptake of Arg_8-Fl was consistent with literature expectations. In contrast, the uptake of $(Tyr\text{-}ZnDPA)_8$-Fl into PGSA and PGSD cells was the same as native CHO cells (see Supporting Information). It appears that the presence of heparan sulfate proteoglycans on the cell surface is not necessary for uptake of $(Tyr\text{-}ZnDPA)_8$-Fl.

Streptavidin Delivery into Living Cells. Delivery of the versatile and multivalent protein, streptavidin into living cells is an important technical goal because it can be used to cotransport biotinylated cargo or target biotinylated intracellular targets. Previous studies have used Tat-streptavidin fusion protein (*33*), biotinylated antibody (*34*), biotinylated steroid (*35*), and biotinylated carbon nanotube (*36*). We prepared some zinc tyrosine-biotin conjugates and evaluate their abilities to noncovalently bind and transport the tetrameric streptavidin (molecular weight 64 kD) into living cells. Two groups of peptide-biotin conjugates were prepared. Direct attachment of the biotin to the N-terminal of the zinc tyrosine oligomers gave the series $(Tyr\text{-}ZnDPA)_n$-Biotin, whereas a longer spacer was attached to the C-terminal to make the series, $(Tyr\text{-}ZnDPA)_n$-TEO-Biotin.

These biotin conjugates were mixed separately with FITC labeled streptavidin and administered to living cells. There was no uptake of FITC-streptavidin when it was mixed with the $(Tyr\text{-}ZnDPA)_n$-Biotin, but cell delivery was achieved when the FITC-streptavidin was mixed with $(Tyr\text{-}ZnDPA)_n$-TEO-Biotin. Typical results with $(Tyr\text{-}ZnDPA)_8$-TEO-Biotin are shown in Figure 7. The fluorescence emission of the transported FITC-streptavidin appeared in the same types of endosomal compartments as the $(Tyr\text{-}ZnDPA)_n$-Fl series. A stoichiometry study indicated that FITC-streptavidin uptake increased until the $(Tyr\text{-}ZnDPA)_8$-TEO-Biotin: FITC-streptavidin ratio reached 4:1 and then remained constant for higher values.

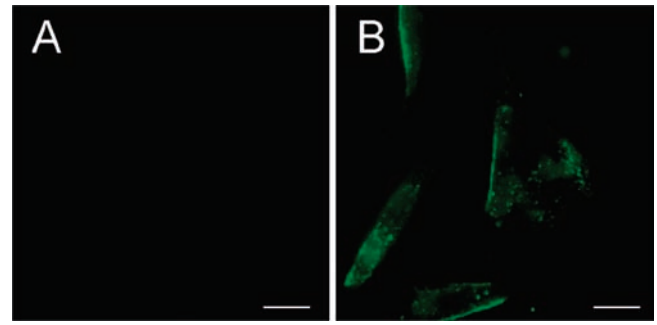

Figure 7. Fluorescence microscopy images of COS-7 cells treated with FITC-streptavidin (panel A) or $(Tyr\text{-}ZnDPA)_8$-TEO-Biotin complexed with FITC-streptavidin (panel B). The complexes were formed prior to cell treatment and complexes were administered at a concentration of 250 nM streptavidin.

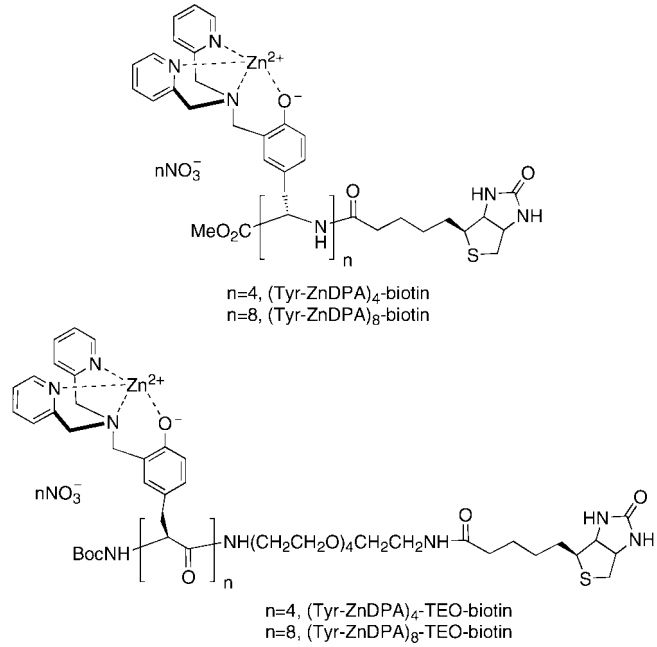

DISCUSSION

Cellular uptake of the $(Tyr\text{-}ZnDPA)_n$ peptides into living cells increases with peptide length and higher order multivalency. The biotin conjugate $(Tyr\text{-}ZnDPA)_8$-TEO-Biotin is able to promote internalization of the fluorescently labeled protein, streptavdin. In contrast, the biotin conjugate $(Tyr\text{-}ZnDPA)_8$-Biotin with a shorter linker is ineffective. The shorter linker may not allow the biotin group to reach the binding pocket of the streptavidin, or alternatively, the large streptavidin protein may prevent the peptide from achieving favorable interactions with the cell surface target (*37*). In any case, linker length is important for effective streptavidin delivery.

Uptake of the fluorescent octamer $(Tyr\text{-}ZnDPA)_8$-Fl is greater than the analogous Arg_8-Fl in all cell lines tested. Another striking difference with Arg_8-Fl is that cell uptake of $(Tyr\text{-}ZnDPA)_8$-Fl does not require the presence of heparan sulfate proteoglycans on the cell surface. It appears that the $(Tyr\text{-}ZnDPA)_n$ peptides target other markers on the cell surface, perhaps anionic phospholipids, negatively charged proteins (*38*), or cell surface carbohydrates (*39*). Our water/organic partitioning studies show that the $(Tyr\text{-}ZnDPA)_n$ peptides associate with anionic phospholipids and fatty acids to form lipophilic complexes that partition into organic phases. However, the cell entry

mechanism is primarily clathrin-mediated endocytosis and not passive diffusion through the plasma membrane. It appears that the $(Tyr\text{-}ZnDPA)_n$ peptides bind to the membrane surface and trigger an endocytosis event (*40*), or they may internalized by the routine membrane recycling mechanisms of the cell (*41–43*). While further studies are needed to fully elucidate the uptake mechanism(s) used by the $(Tyr\text{-}ZnDPA)_n$ peptides, the data in hand suggest that it differs to oligo(arginine) internalization. The distinction may eventually be of practical value because drug delivery systems that employ alternative endocytic mechanisms may be optimal for different cell lines or they may deliver selectively to different organelles within a cell (*44–46*).

The fluorescence microscopy data indicate that the transported peptides (or cotransported streptavidin) remain localized within endosomal compartments of the living cells. Therefore to effectively reach the cell cytosol it will be necessary to trigger endosomal release using an adjuvant (*47*, *48*). We plan to determine if these multivalent $(Tyr\text{-}ZnDPA)_n$ peptides can form noncovalent complexes with anionic cargo such as oligonucleotides and deliver them into cells. Another idea is to conjugate a $(Tyr\text{-}ZnDPA)_n$ peptide to a hydrophobic tryptophan-rich sequence and produce a zinc-dependent mimic of the noncovalent protein carrier Pep-1 (*49*). It may even be possible to create triggered cell delivery devices that can be activated by increases in local concentrations of zinc (II) cation.

ACKNOWLEDGMENT

This work was supported by the NIH and the Notre Dame CEST. We warmly thank Dr. W. Matthew Leevy for advice and assistance.

Supporting Information Available: Synthetic procedures and flow cytometry histograms. This material is available free of charge via the Internet at http://pubs.acs.org.

LITERATURE CITED

(1) Dunehoo, A. L., Anderson, M., Sumit, M., Kobayashi, N., Berkland, C., and Siahaan, T. J. (2006) Cell adhesion molecules for targeted drug delivery. *J. Pharm. Sci. 95*, 1856–1871.

(2) Janot, V., and Regen, S. L. (2005) A needle-and-thread approach to bilayer transport: Permeation of a molecular umbrella-oligonucleotide conjugate across a phospholipid membrane. *J. Am. Chem. Soc. 127*, 22–23.

(3) Kam, N. W., Jessop, T. W., Wender, P. A., and Dai, H. (2004) Nanotube molecular transporters: Internalization of carbon nanotube-protein conjugates into mammalian cells. *J. Am. Chem. Soc. 126*, 6850–6851.

(4) Kohane, D. S. (2007) Microparticles and nanoparticles for drug delivery. *Biotechnol. Bioeng. 96*, 203–209.

(5) Ryser, H. J., and Hancock, R. (1965) Histones and basic polyamino acids stimulate the uptake of albumin by tumor cells in culture. *Science 150*, 501–503.

(6) Ryser, H. J. (1967) Uptake of protein by mammalian cells: an underdeveloped area. The penetration of foreign proteins into mammalian cells can be measured and their functions explored. *Science 159*, 390–396.

(7) Ryser, H. J. (1968) A membrane effect of basic polymers dependent on molecular size. *Nature 215*, 934–936.

(8) Wigstaff, K. M., and Jans, D. A. (2006) Protein transduction: Cell penetrating peptides and their therapeutic applications. *Curr. Med. Chem. 13*, 1371–1387.

(9) Torchilin, V. P., Levchenko, T. S., Rammohan, R., Volodina, N., Papahadjopoulos-Sternberg, G., and D'Souza, G. G. (2003) Cell transfection *in vitro* and *in vivo* with nontoxic tat peptide-liposome-DNA complexes. *Proc. Natl. Acad. Sci. U.S.A. 100*, 1972–1977.

(10) Pietersz, G. A., Li, W., and Apostolopoulos, V. (2001) A 16-mer peptide (RQIKIWFQNRRMKWKK) from Antennapedia preferentially targets the Class I pathway. *Vaccine 9*, 1397–405.

(11) Temsamani, J., and Vidal, P. (2004) The use of cell-penetrating peptides for drug delivery. *Drug Discovery Today 9*, 1012–1019.

(12) Futaki, S. (2002) Arginine-rich peptides: Potential for intracellular delivery of macromolecule and the mystery of the translocation mechanism. *Int. J. Pharm. 245*, 1–7.

(13) Lu, J., Higashimoto, Y., Appella, E., and Celis, E. (2004) Multiepitope trojan antigen peptide vaccines for the induction of antitumor CTL and Th immune responses. *J. Immunol. 172*, 4575–4582.

(14) Rudolph, C., Plank, C., Lausier, J., Schillinger, U., Muller, R. H., and Rosenecker, J. (2003) Oligomers of the Arginine-rich Motif of the HIV-1 TAT protein are capable of transferring plasmid DNA into cells. *J. Biol. Chem. 278*, 11411–11418.

(15) Torchilin, V. P., Rammohan, R., Wiessig, V., and Levachenko, T. S. (2001) Tat peptide on the surface of liposomes affords their efficient intracellular delivery even at low temperature and in the presence of metabolic inhibitors. *Proc. Natl. Acad. Sci. U.S.A. 98*, 8786–8791.

(16) Bullok, K. E., Gammon, S. T., Violini, S., Prantner, A. M., Villalobos, V. M., Sharma, V., and Piwnica-Worms, D. (2006) Permeation peptide conjugates for in vivo molecular imaging applications. *Mol. Imag. 5*, 1–15.

(17) Josephson, L., Tung, C. H., Moore, A., and Weisselader, R. (2004) High-efficiency intracellular magnetic labeling with novel superparamagnetic-Tat peptide conjugates. *Bioconjugate Chem. 10*, 186–191.

(18) Mi, Z., Mai, J., Lu, X., and Robbins, P. D. (2000) Characterization of a class of cationic peptides able to facilitate efficient protein transduction *in Vitro* and *in Vivo*. *J. Mol. Therapy 2*, 339–347.

(19) Schwarze, S. R., Ho, A., Vocero-Akbani, A., and Dowdy, S. F. (1999) In vivo protein transduction: Delivery of a biologically active protein into the mouse. *Science 285*, 1569–1572.

(20) Venkatesan, N., and Kim, B. H. (2006) Peptide conjugates of oligonucleotides: Synthesis and applications. *Chem. Rev. 106*, 3712–3761.

(21) Vocero-Akani, A., Heyden, N., Lissy, N., Ratner, L., and Dowdy, R. (1999) S. Killing HIV-infected cells by transduction with an HIV protease activated caspase-3 protein. *Nat. Med. 5*, 29–33.

(22) Gros, E., Deshayes, S., Morris, M. C., Aldrian-Herrada, G., Depollier, J., Heitz, F., and Divita, G. (2006) A non-covalent peptide-based strategy for protein and peptide nucleic acid transduction. *Biochim. Biophys. Acta - Biomembranes 1758*, 384–393.

(23) Myrberg, H., Lindgren, M., and Langel, U. (2007) Protein delivery by the cell-penetrating peptide YTA2. *Bioconjugate Chem. 18*, 170–174.

(24) Jiang, T., Olson, E. S., Nguyen, Q. T., Roy, M., Jennings, P. A., and Tsien, R. Y. (2004) Tumor imaging by means of proteolytic activation of cell-penetrating peptides. *Proc. Natl. Acad. Sci. U.S.A. 101*, 17867–17872.

(25) Jiang, H., O'Neil, E. J., DiVittorio, K. M., and Smith, B. D. (2005) Anion-mediated phase transfer of Zinc(II)-coordinated tyrosine derivitives. *Org. Lett. 7*, 3013–3017.

(26) Füssl, A., Schleinfenbaum, A., Göritz, M., Riddell, A., Schultz, C., and Krämer, R. (2006) Cellular uptake of PNA-terpyridine conjugates and its enhancement by Zn^{2+} ions. *J. Am. Chem. Soc. 128*, 5986–5987.

(27) Qian, W., Gee, K. R., and Kennedy, R. (2003) Imaging of Zn^{2+} release from pancreatic beta-cells at the level of single excytotic events. *Anal. Chem. 75*, 3468–3475.

(28) Liuzzi, J. P., and Cousins, R. J. (2004) Mammalian zinc transporters. *Annu. Rev. Nutr*. 24151–24172.

(29) Wender, P. A., Rothbard, J. B., Jessop, T. C., Kreider, E. L., and Wylie, B. L. (2004) Oligocarbamate molecular transporters: Design, synthesis, and biological evaluaion of a new class of transporters for drug delivery. *J. Am. Chem. Soc. 124*, 13382–13383.

(30) Richard, J. P., Melikov, K., Brooks, H., Prevot, P., Lebleu, B., and Chernomordik, L. P. (2005) Cellular uptake of unconjugated TAT peptide involves clathrin-dependent endocytosis and heparan sulfate receptors. *J. Biol. Chem. 280*, 15300–15306.

(31) Esko, J. D., Stewart, T. E., and Taylor, W. H. (1985) Animal cell mutants defective in glycosaminoglycan biosynthesis. *Proc. Natl. Acad. Sci. U.S.A. 82*, 3197–3201.

(32) Esko, J. D., Rostand, K. S., and Weinke, J. L. (1988) Tumor formation dependent on proteoglycan biosynthesis. *Science 241*, 1092–1096.

(33) Albarran, B., To, R., and Stayton, P. R. (2005) A Tat-streptavidin fusion protein directs uptake of biotinylated cargo into mammalian cells. *Protein Eng. Des. Sel. 18*, 147–152.

(34) Lackey, C. A., Press, O. W., Hoffman, A. S., and Stayton, P. S. (2002) A biomimetic pH-responsive polymer directs endosomal release and intracellular delivery of an endocytosed antibody complex. *Bioconjugate Chem. 13*, 996–1001.

(35) Hussey, S. L., and Peterson, B. S. (2002) Efficient delivery of streptavidin to mammalian cells: Clathrin-mediated endocytosis regulated by a synthetic ligand. *J. Am. Chem. Soc. 124*, 6265–6273.

(36) Kam, N. W., Jessop, T. C., Wender, P. A., and Dai, H. (2004) Nanotube molecular transporters: Internalization of carbon nanotube-protein conjugates into mammalian cells. *J. Am. Chem. Soc. 126*, 6850–6851.

(37) Hussey, S. L., and Peterson, B. R. (2002) Efficient delivery of streptavidin to mammalian cells: Clathrin-mediated endocytosis regulated by a synthetic ligand. *J. Am. Chem. Soc. 124*, 6265–6273.

(38) Nisole, S., Krust, B., Callebaut, C., Guichard, G., Muller, S., Briand, J. P., and Hovanessian, A. G. (1999) The anti-HIV pseudopeptide HB-19 forms a complex with the cell-surface-expressed nucleolin independent of heparan sulfate proteoglycans. *J. Biol. Chem. 274*, 27875–27884.

(39) Fukuda, M. (1994) Cell surface carbohydrates: Cell-type specific expression. *Molecular Glycobiology* (Fukuda, M. and Hindsgaul, O. Eds.) pp. 1–52, Oxford University Press, New York.

(40) Fischer, P. M. (2007) Cellular uptake mechanisms and potential therapeutic utility of peptidic cell delivery vectors: Progress 2001−2006. *Med. Res. Rev. 27*, 755–795.

(41) Brooks, H., Lebleu, B., and Vives, E. (2005) Tat peptide-mediated cellular Delivery: Back to basics. *Adv. Drug Delivery Rev. 57*, 559–577.

(42) Kilic, G., Doctor, R. B., and Fitz, J. G. (2001) Insulin stimulates membrane conductance in a liver cell line: Evidence for insertion of ion channels through a phosphoinositide 3-kinase-dependent mechanism. *J. Biol. Chem. 276*, 26762–26768.

(43) Neuhaus, E. M., and Soldati, T. (2000) A myosin I is involved in membrane recycling from early endosomes. *J. Cell Biol. 150*, 1013–1026.

(44) Bareford, L. M., and Swaan, P. W. (2007) Endocytic mechanisms for targeted drug delivery. *Adv. Drug Delivery Rev. 59*, 748–758.

(45) Medina-Kauwe, L. K. (2007) Alternative endocytic mechanism exploited by pathogens: New avenues for therapeutic delivery? *Adv. Drug Delvery Rev. 59*, 798–809.

(46) Tarrago-Trani, M. T., and Storrie, B. (2007) Alternative routes for drug delivery to the cell interior: Pathways to the Golgi apparatus and endoplasmic reticulum. *Adv. Drug Delivery Rev. 59*, 782–797.

(47) Vogel, K., Wang, S., Lee, R. J., Chmielewski, J., and Low, P. S. (1996) Peptide mediated Release of folate-targeted liposome contents from endosomal compartments. *J. Am. Chem. Soc. 118*, 1581–1586.

(48) Rozema, D. B., Ekena, K., Lewis, D. L., Loomis, A. G., and Wolff, J. A. (2003) Endosomolysis by masking of a membrane-active agent (EMMA) for cytoplasmic release of macromolecules. *Bioconjugate Chem. 14*, 51–57.

(49) Morris, M. C., Depollier, J., Mery, J., Heitz, F. C., and Divita, G. (2001) A peptide carrier for the delivery of biologically active protens into mammalian cells. *Nat. Biotechnol. 19*, 1173–1176.

BC700466Z

Preparation of pH-Sensitive Poly(glycidol) Derivatives with Varying Hydrophobicities: Their Ability to Sensitize Stable Liposomes to pH

Naoki Sakaguchi, Chie Kojima, Atsushi Harada, and Kenji Kono*

Department of Applied Chemistry, Graduate School of Engineering, Osaka Prefecture University, 1-1 Gakuen-cho, Sakai, Osaka 599-8531, Japan. Received December 19, 2007; Revised Manuscript Received February 16, 2008

We have previously shown that modification with succinylated poly(glycidol) (SucPG) provides stable egg yolk phosphatidylcholine (EYPC) liposomes with pH-sensitive fusogenic property. Toward production of efficient pH-sensitive liposomes, in this study, we newly prepared three carboxylated poly(glycidol) derivatives with varying hydrophobicities by reacting poly(glycidol) with glutaric anhydride, 3-methylglutaric anhydride, and 1,2-cyclohexanedicarboxylic anhydride, respectively, designated as GluPG, MGluPG, and CHexPG. Correlation between side-chain structures of these polymers and their respective abilities to sensitize stable liposomes to pH was investigated. These polymers are soluble in water at neutral pH but became water-insoluble in weakly acidic conditions. The pH at which the polymer precipitated was higher in the order SucPG < GluPG < MGluPG < CHexPG, which is consistent with the number of carbon atoms of these polymers' side chains. Although CHexPG destabilized EYPC liposomes even at neutral pH, attachment of other polymers provided pH-sensitive properties to the liposomes. The liposomes bearing polymers with higher hydrophobicity exhibited more intense responses, such as content release and membrane fusion, at mildly acidic pH and achieved more efficient cytoplasmic delivery of membrane-impermeable dye molecules. As a result, modification with appropriate hydrophobicity, MGluPG, produced highly potent pH-sensitive liposomes, which might be useful for efficient cytoplasmic delivery of bioactive molecules, such as proteins and genes.

INTRODUCTION

Recent advances in protein and nucleic acid based therapies, such as immunotherapy and gene therapy, require efficient delivery systems of such labile bioactive molecules into the cytoplasm of target cells. In general, these molecules are not able to permeate a cellular membrane, although their site for action exists inside a cell, such as the nucleus. Therefore, it is necessary to use carrier systems that deliver these molecules into the cytoplasmic space of the target cell. Although various systems have been attempted for application to cytoplasmic delivery, pH-sensitive liposomes are a promising system. pH-sensitive liposomes are stable at physiological pH, but become destabilized and/or fusogenic under mildly acidic conditions. In general, a main pathway for cellular internalization of liposomes is shown to be endocytosis. Therefore, after being taken up by a cell, liposomes are trapped in endosomes and are eventually degraded in lysosome. Because the endosome has a weakly acidic environment, pH-sensitive liposomes induce destabilization of endosomes and/or fusion with endosomes, resulting in the release of encapsulated materials into the cytosol.

To date, various approaches to the production of pH-sensitive liposomes have been attempted. For example, pH-sensitive amphiphiles, such as oleic acid (*1*) and cholesteryl hemisuccinate (*2*), have been mixed with non-bilayer-forming phospholipid dioleoylphosphatidylethanolamine to yield pH-sensitive liposomes. In this case, pH-sensitive amphiphiles act as a pH-sensitive stabilizer, which stabilizes unstable liposomes only when they are negatively charged. However, the lipid molecules used for this type of pH-sensitive liposome have a strong tendency to form a hexagonal II structure; consequently, these liposomes are readily destabilized (*3*).

Another efficient method for pH-sensitization of liposomes is modification of stable liposomes with pH-sensitive membrane-active molecules. Various kinds of fusion peptides derived from viral fusogenic proteins and their analogues have been used as liposomal membranes. Synthetic polymers with carboxyl groups have also been used to sensitize liposomes to pH (*4, 5*). In comparison to peptide-based pH-sensitizers, synthetic polymers might be advantageous because of their simplicity of preparation and low immunogenicity.

Tirrell and co-workers have demonstrated that some poly(alkylacrylic acid)s interact with phospholipid membranes in a pH-dependent manner (*4, 6*). In particular, poly(2-ethylacrylic acid) exhibits a strong interaction with phospholipid membranes at mildly acidic pH: it permeabilizes and, at sufficiently high concentration, solubilizes them by micelle formation (*7*−*9*). In addition, they showed that attachment of this polymer onto the liposome surface gave pH-sensitive content release properties (*10*). Hoffman et al. further derivatized poly(2-ethacrylic acid) and obtained poly(2-propylacrylic acid), which exhibited even higher membranelytic activity than poly(2-ethylacrylic acid) (*11*−*13*).

In a previous study, we developed succinylated poly(glycidol), named SucPG, for sensitization of liposomes (Figure 1) (*13, 14*). This polymer has a backbone that resembles that of poly(ethylene glycol) (PEG) and carboxyl groups on the side chains, which control interaction of the polymer backbone with lipid membranes in a pH-dependent manner. We have shown that modification with SucPG gave stable phosphatidylcholine liposome pH-sensitive properties. The SucPG-modified liposomes are stable at neutral pH but exhibit considerable destabilization under mildly acidic conditions. In contrast to poly(2-ethacrylic acid), which induced destabilization by solubilizing liposomal lipid molecules upon protonation of its pendant carboxyl groups, SucPG caused fusion of liposomes

* Corresponding author. Kenji Kono; Department of Applied Chemistry, Graduate School of Engineering, Osaka Prefecture University, 1-1 Gakuen-cho, Sakai, Osaka 599-8531, Japan; Tel: +81-722-54-9330; Fax: +81-722-54-9330; E-mail kono@chem.osakafu-u.ac.jp.

10.1021/bc7004736 CCC: $40.75 © 2008 American Chemical Society
Published on Web 04/18/2008

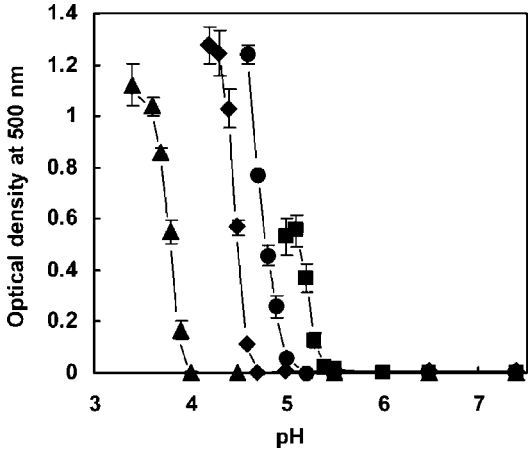

Figure 1. Optical densities at 500 nm for solutions of SucPG (▲), GluPG (◆), MGluPG (●), and CHexPG (■) dissolved in 30 mM sodium acetate and 120 mM NaCl at various pHs (0.25 mg/mL) at 25 °C. Each point is the mean ± SD ($n = 3$).

in the same situation (*8*, *13*). Because the fusion ability of liposomes is useful for cytoplasmic delivery of membrane-impermeable molecules, such as proteins and oligonucleotides, the fusogenic properties of the SucPG are of great importance. In fact, SucPG-modified liposomes were shown to deliver calcein into the cytosol through fusion with endosome/lysosome membranes (*14*). Fusion capabilities of SucPG-modified liposomes were used to increase the transfection activities of various lipoplexes: complexation of the SucPG-modified liposomes with lipoplexes generates efficient gene vectors (*15*, *16*).

Although the mechanism of destabilization of liposome membranes mediated by SucPG has not been clarified, it might be assumed that hydrophobic interaction of its backbone with the lipid membrane and hydrogen bond formation between the polymer carboxyl groups and phosphate groups of the phospholipid membrane are responsible for inducing fusion (*13*). Therefore, one strategy for production of polymers with high fusogenic activity might be synthesis of poly(glycidol) with carboxyl groups and enhanced hydrophobic characteristics. For this study, we prepared poly(glycidol) derivatives with various side chains having carboxyl groups with different chemical structures (Scheme 1). Correlation between hydrophobicity of the side chains of poly(glycidol) derivatives and their membrane active properties was investigated. The ability of these poly(glycidol) derivatives to provide pH-sensitive properties to stable liposomes has been described.

MATERIALS AND METHODS

Materials. Egg yolk phosphatidylcholine (EYPC) were kindly donated by Nippon Oil and Fats Co. (Tokyo, Japan). Pyrene, pyranine, and Triton X-100 was obtained from Tokyo Kasei Kogyo (Tokyo, Japan). *p*-Xylene-bis-pyridinium bromide (DPX) was from Molecular Probes (Oregon, USA).

N-(7-Nitrobenz-2-oxa-1,3-diazol-4-yl)dioleoylphosphatidylethanolamine (NBD-PE) and Lissamine rhodamine B-sulfonyl phosphatidylethanolamine (Rh-PE) were purchased from Avanti Polar Lipids (Birmingham, AL, USA). 1-Aminodecane was purchased from Nakalai Tesque (Kyoto, Japan). Glutaric anhydride and 1,2-cyclohexanedicarboxylic anhydride were from Tokyo Kasei Kogyo (Tokyo, Japan). 3-Methylglutaric anhydride was from Aldrich (Milwaukee, WI). 1-Ethyl-3-(3-dimethylaminopropyl) carbodiimide (EDC) was from Dojindo (Kumamoto, Japan).Triton X-100 was obtained from Tokyo Kasei Kogyo (Tokyo, Japan). Two kinds of poly(glycidol) [PG-1: number average molecular weight (Mn) 82 000, weight average molecular weight (Mw) 13 000; PG-2: Mn 8700, Mw 16 100] were prepared as previously reported (*13*, *14*). Succinylated poly(glycidol) (SucPG) was prepared using PG-1 as previously reported (*13*).

Synthesis of Poly(glycidol) Derivatives. Glutarylated poly(glycidol) (GluPG) was prepared by reaction of poly(glycidol) with glutaryl anhydride. Poly(glycidol) (PG-1) (2.0 g) was dissolved in *N*,*N*-dimethylformamide (19 mL) and 3.0 equiv of glutaryl anhydride (9.2 g) was added to the solution. The mixed solution was kept at 80 °C for 6 h with stirring. Then, the reaction mixture was evaporated and dialyzed against water for 7 days. The product was recovered by freeze−drying. 3-Methylglutarylated poly(glycidol) (MGluPG) and 2-carboxy-cyclohexanoylated poly(glycidol) (CHexPG) were prepared by the same procedure by the reaction of poly(glycidol) (PG-2) with 3-methylglutaric anhydride and 1,2-cyclohexanedicarboxylic anhydride, respectively. As anchor moieties for fixation of poly(glycidol) derivatives onto liposome membranes, 1-aminodecane was combined with carboxyl groups of these poly(glycidol) derivatives. Each polymer was dissolved in water around pH 5, and 1-aminodecane (0.15 equiv to carboxyl group of polymer) was reacted to carboxyl groups of the polymer using 1-ethyl-3-(3-dimethylaminopropyl)carbodiimide (0.2 equiv to carboxyl group of polymers) at 4 °C for two days with stirring. The resultant polymers were purified by washing with chloroform and subsequent dialysis in water.

Precipitation pH. Precipitation pHs of polymers were determined by measuring the optical density of aqueous polymer solutions (0.25 mg/mL) at various pH. Polymers were dissolved in 2.0 mL of acetate buffer (30 mM sodium acetate, 120 mM NaCl) adjusted to various pH. After 5 min incubation at 25 °C, optical densities (OD) of the polymer solutions at 500 nm were measured by using a spectrophotometer (Jasco V-520). Precipitation pH were determined by optical density−pH profile as the pH at which OD drastically rose.

Preparation of Pyranine-Loaded Liposomes. To a dry, thin membrane of EYPC (7 mg) was added 500 μL of pyranine solution containing 35 mM pyranine, 50 mM DPX, and 25 mM MES of pH 7.4, and the mixture was sonicated for 2 min using a bath-type sonicator. The liposome suspension was further hydrated by freeze and thaw, and extruded through a polycarbonate membrane with a pore size of 50 nm. The liposome suspension was applied to a G75 column to remove free pyranine from the pyranine-loaded liposomes.

Modification of Liposomes with Polymers. Liposome suspensions were obtained by the above procedure. To a liposome suspension (lipid concentration 17.5 mM) in the 25 mM MES and 125 mM NaCl buffer was added polymer solution (final concentration 10 mg/mL), and the mixture was incubated 60 min at room temperature. Liposomes were purified by gel filtering with a G75 column to separate excess polymer and nonencapsulated pyranine in the case of pyranine containing polymer-modified liposome.

Release of Pyranine from Liposome. Release of pyranine from liposome was measured as previously reported (*17*). Pyranine fluorescence was quenched by DPX inside of the liposomes, but this molecule exhibits intense fluorescence when released from the liposome (*17*). To a suspension of pyranine-loaded liposomes (lipid concentration 2.0×10^{-5} M) in the 25 mM MES and 125 mM NaCl buffer of varying pHs was added varying amounts of the polymer dissolved in the same buffer. Pyranine fluorescence at 512 nm with excitation at 416 nm was monitored by using a spectrofluorometer (Jasco FP-6500). 100% release was achieved by adding Triton X-100 (final concentration 0.1%) to the liposome suspension.

Fusion Assay. Fusion between bare EYPC liposomes and polymer-modified liposomes was detected by measuring reso-

Scheme 1. Synthetic Route for Various Poly(glycidol) Derivatives[a]

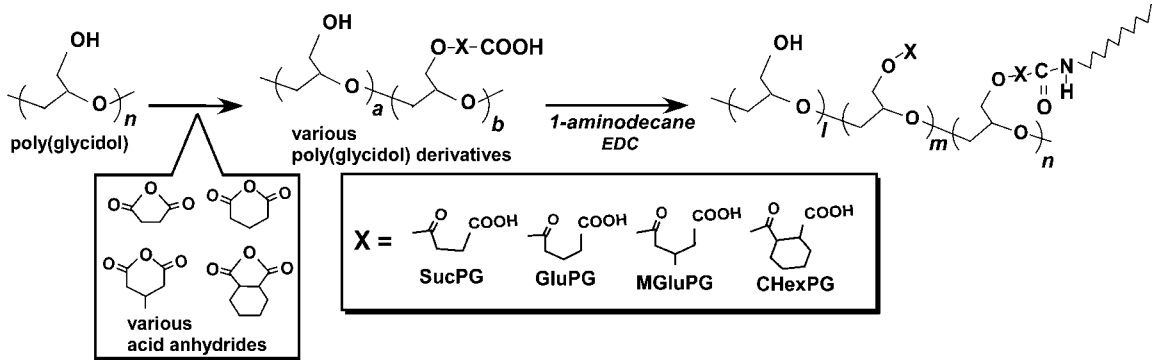

[a] EDC represents 1-ethyl-3-(3-dimethylaminopropyl) carbodiimide.

nance energy transfer between NBD-PE and Rh-PE (*15*, *19*). Polymer-modified liposomes containing NBD-PE and Rh-PE were prepared via the above method using the membrane composed of EYPC, NBD-PE, Rh-PE (98.8:0.6:0.6, mol/mol/mol), and varying amounts of the polymers. The labeled liposomes (final concentration of lipid 0.125 M) were mixed with fluorescent probe-free EYPC liposomes (final concentration of lipid 0.25 M) in 25 mM MES, and 125 mM NaCl solution of varying pHs and fluorescence intensities NBD-PE and Rh-PE followed. Their fusion was followed by monitoring the fluorescence intensity ratio of NBD-PE to Rh-PE (*R*). The excitation wavelength of NBD-PE was 450 nm, and monitoring wavelengths for NBD-PE and Rh-PE were 520 and 580 nm, respectively. Percentage increase in *R* was defined as

Percentage increase in

$$R = (R_t - R_0)/(R_{100} - R_0) \times 100 \quad (1)$$

where R_0 and R_t represent the initial and intermediary *R* values. R_{100} is the *R* of the labeled liposomes when the liposomes fused completely. The fluorescent lipid-labeled liposomes and the unlabeled liposomes were dissolved in methanol, dried by evaporation, and resuspended in MES buffer. The *R* value of the suspension was taken as R_{100} (*15*).

Pyrene Fluorescence. A known amount of pyrene in acetone solution was added to an empty flask, and acetone was removed under vacuum. Polymer (0.2 mg/mL) in the 25 mM MES and 125 mM NaCl buffer solutions of varying pHs were added the flask, yielding 1 μM concentration of pyrene. The sample solution was stirred overnight at room temperature, and emission spectra with excitation at 337 nm were recorded. The fluorescence intensity ratio of the first band at 373 nm to the third band at 384 nm (I_1/I_3) was analyzed as a function of pH of the solution.

Interaction of Liposomes with Cells. Polymer-modified liposomes containing calcein were prepared via the above procedure using an aqueous calcein solution (63 mM, pH 7.4) instead of an aqueous pyranine solution. HeLa cells (1.0×10^5) were seeded on glass-bottomed culture dishes and incubated in 10% FCS/DMEM overnight. The cells were washed with PBS and reincubated with fresh medium with 10% FCS (0.5 mL). Then, liposomes in the 20 mM Hepes and 130 mM NaCl suspension (0.5 mL) were added to the dishes (final concentration of liposomal lipid: 0.5 mM), and the cells were incubated for 4 h. For the incubation in the presence of NH_4Cl, cells were preincubated in 10% FCS/DMEM containing NH_4Cl (20 mM) for 1 h before the addition of liposome suspension. After the incubation with the liposomes, the cells were washed with PBS and were observed using a fluorescence microscope (BX51WI Olympus). In addition, cells were incubated for another 2 h in 10% FCS/DMEM with or without NH_4Cl (20 mM) and were observed using a fluorescence microscope.

RESULT AND DISCUSSION

Properties of Poly(glycidol) Derivatives. For a previous study, we developed SucPG, which generates fusogenic activity under weakly acidic conditions and is useful to produce pH-sensitive liposomes that destabilize at mildly acidic pH (*13*). In fact, we observed that SucPG-modified liposomes delivered membrane-impermeable fluorescent dye calcein efficiently into the cytosol through fusion with endosomal/lysosomal membranes (*14*). For the present study, we attempted to develop new polymers with even higher pH-responsive properties than SucPG. We postulated that both a PEG-like structure of the backbone and carboxyl groups on the side chains are important for their pH-dependent fusogenic activity (*13*). Therefore, an increase in the side chains hydrophobicity is expected to strengthen their interaction with the lipid membranes, thereby producing polymers with a high ability to destabilize lipid membranes in a pH-dependent manner.

Three kinds of polyglycidol derivatives with more hydrophobic side chains than those of SucPG were designed (Scheme 1). We synthesized them using the reaction of poly(glycidol) with various acid anhydrides according to Scheme 1. Compositions of these polymers were estimated using ^{1}H NMR and are listed in Table 1. For all polymers, only a small percentage of unreacted glycidol units around 2.0−3.8% remained on the polymer backbone after the reaction of poly(glycidol) with acid anhydrides, indicating that these reactions were very efficient; fundamentally, every repeating unit possesses a carboxyl group in the resultant polymers. We observed that ester bonds of these polymers were essentially not hydrolyzed during dialysis against distilled water for several days, indicating their high stability in water.

Many studies have shown that hydrophobic moieties, such as stearyl groups and cholesteryl groups, were incorporated into polymer chains to act as an anchor for their fixation to liposome membranes (*22*−*24*). We showed that attachment of 1-aminodecane to about 8 unit % of a SucPG chain is sufficient to fix the polymer chain onto an EYPC liposome membrane (*13*). On the basis of a previous study (*13*), we combined decylamine to about 10 unit % of the polymer chains in the present study using a condensing agent, EDC (Scheme 1). As shown in Table 1, decyl chains were attached to around 10 unit % of the polymer chains for all poly(glycidol) derivatives.

We first investigated the pH sensitivity of the poly(glycidol) derivatives because these polymers contain many carboxyl groups. Acid−base titration of these polymers was performed to estimate the pK_a values. As presented in Table 2, SucPG, GluPG, and MGluPG had almost equal pK_a values around 6.2−6.4, although CHexPG showed a somewhat higher pK_a

Table 1. Compositions of Various Poly(glycidol) Derivatives[a]

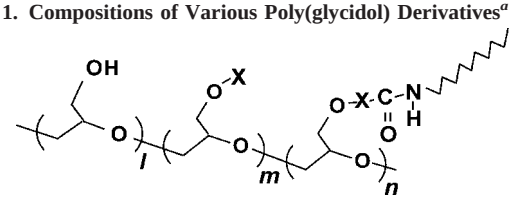

polymer	*l* (mol %)	*m* (mol %)	*n* (mol %)
SucPG	2.4	97.6	–
GluPG	2.0	98.0	–
MGluPG	3.8	96.2	–
CHexPG	2.3	97.7	–
SucPG-C_{10}	3.0	85.7	11.3
GluPG-C_{10}	3.7	83.8	12.5
MGluPG-C_{10}	5.6	86.6	7.8
CHexPG-C_{10}	3.2	85.7	11.1

[a] Estimated by ^{1}H NMR. SucPG-C_{10}, GluPG-C_{10}, MGluPG-C_{10}, and CHexPG-C_{10} are anchor-carrying types of corresponding poly(glycidol) derivatives.

Table 2. pK_a and Precipitation pH of Various Poly(glycidol) Derivatives

polymer	pK_a	precipitation pH	α at precipitation pH
SucPG	6.2	4.0	0.93
GluPG	6.4	4.7	0.95
MGluPG	6.3	5.0	0.93
CHexPG	7.0	5.4	0.99

value of 7.0. Hydrophobicity of side groups and conformation of polyelectrolytes are known to affect the dielectric constant around charged groups, thereby imparting different ionization characteristics (*25*−*27*). Because CHexPG has highly hydrophobic side groups, hydrophobic interactions among these side groups might engender a compact conformation, which enhances charge−charge interactions, resulting in suppression of dissociation of carboxyl groups (*27*).

Hydrophobicity of carboxylated polymers affects their precipitation behaviors (*28*). For that reason, we estimated the pH at which the polymers precipitate using the following optical densities (ODs) of these polymer solutions as the pH of the solution was decreased (Figure 1). These polymers were soluble in water at neutral pH; their solutions were transparent. However, the polymer solutions suddenly became turbid at a specific pH, which was defined as the precipitation pH. The precipitation pH thresholds for these poly(glycidol) derivatives were estimated as listed in Table 2. Apparently, the precipitation pH shifted to higher pH values as the number of carbon atoms in the side chains of the polymers increased. This result indicates that the precipitation pH increases with increasing hydrophobicity of the polymer side groups and is consistent with previous observation for methacrylic acid copolymers with varying hydrophobicities (*28*). Acid−base titration for these polymers indicated that the degree of protonation for their carboxyl groups was at pH 0.93−0.99 of the precipitation pH: most carboxyl groups must be protonated to elicit precipitation of these polymers.

Hydrophobicity of the polymers was further investigated using fluorescence of pyrene. An emission intensity ratio of the first (373 nm) to the third (384 nm) peaks of pyrene, I_1/I_3, is known to be sensitive to the microenvironmental polarity surrounding the pyrene molecule (*19*). Consequently, this ratio has been widely used to estimate the hydrophobic nature of polymers (*20, 21*). Figure 2 depicts the I_1/I_3 ratio of pyrene fluorescence in the buffer dissolving various polymers as a function of pH. In buffers dissolving SucPG and GluPG, the I_1/I_3 ratios of pyrene were appropriately 1.8 at any pH and were the same as the ratio in the buffer without polymers. This result suggests that these polymers formed no domains with a hydrophobic nature, even

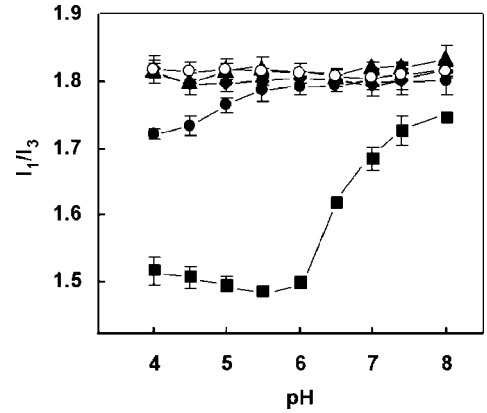

Figure 2. I_1/I_3 of pyrene fluorescence in MES 25 mM and NaCl 125 mM solution with SucPG (▲), GluPG (◆), MGluPG (●), and CHexPG (■), and without polymer (○). Concentration of polymers and pyrene were 0.2 mg/mL and 1 μM, respectively. I_1/I_3 was defined as the fluorescence intensity ratio of the first band at 373 nm to the third band at 384 nm.

after protonation of most carboxyl groups of the polymer chain. The presence of MGluPG affected the I_1/I_3 ratio, which tends to decrease below pH 5.5, indicating that this polymer formed domains with a hydrophobic nature. A more significant decrease in the I_1/I_3 ratio was shown by the presence of CHexPG, which caused a marked decrease in the ratio below pH 8.0. This polymer formed hydrophobic domains, even at physiological pH.

Interaction of Poly(glycidol) Derivatives with Lipid Membrane. We investigated the ability of these polymers to interact with liposomal membranes. The poly(glycidol) derivatives were added to liposomes encapsulating both pyranine and its fluorescence quencher DPX suspended in the buffer of varying pHs; leakage of pyranine from the liposomes was monitored by following pyranine fluorescence. Figure 3A,B depicts the time course and pH dependence of the pyranine release from the liposomes induced by the polymers. Although CHexPG induced a marked release at pH 6.5, other polymers exhibited no ability to induce a release of pyranine at any pH, indicating that SucPG, GluPG, and MGluPG have very weak or no ability to destabilize liposomal membrane.

In contrast, when their counterparts with anchor moieties, namely, SucPG-C10, GluPG-C10, MGluPG-C10, and CHexPG-C10, were added to the pyranine-loaded liposomes, an intensive release of the contents was observed for all polymers (Figure 3C,D). Considering that most of these polymers without anchors failed to induce content release, even at acidic pH, these polymers are necessarily associated with the liposome membranes before their protonation to induce content release from the liposomes. Because their backbone with PEG-like structure can form hydrogen bonding with carboxyl groups, both the polymer backbone and side-chain carboxyl groups might not efficiently interact with liposomal membranes when the polymer chains are dissolved in solution. However, when bound onto the liposome membrane, these polymers might strongly interact with the liposome membrane through hydrogen bonding between the side-chain carboxyl groups and the phosphate groups of the liposomal lipid and hydrophobic interaction between the polymer backbone and the lipid membrane, generating structural defects in the liposome membrane (*13*).

As shown in Figure 2D, the pH region in which the content release was triggered increased in the order of SucPG-C_{10}, GluPG-C_{10}, MGluPG-C_{10}, and CHexPG-C_{10}. Apparently, the polymers with higher hydrophobicity trigger the release at higher pH. Actually, CHexPG caused the release, even at neutral pH, whereas other polymers induced the release below pH 6.5 or 6,

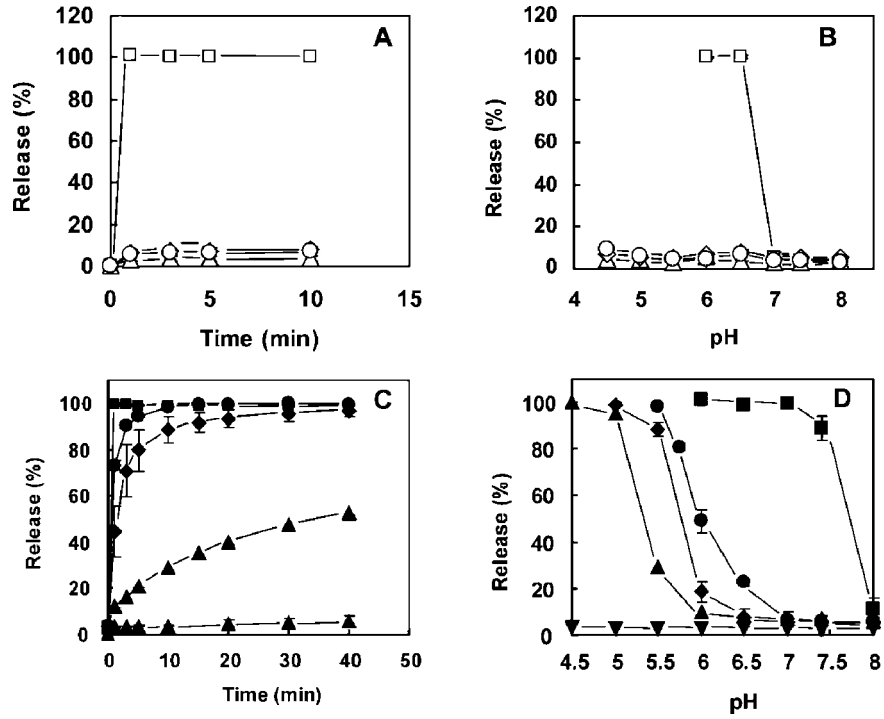

Figure 3. Pyranine release from egg yolk phosphatidylcholine liposomes induced by various poly(glycidol) derivatives. Time course at pH 6.5 (A) and pH dependence (B) of pyranine release induced by SucPG (△), GluPG (◇), MGluPG (○), and CHexPG (□). Time course at pH 6.5 (C) and pH dependence (D) of pyranine release induced by SucPG-C_{10} (▲), GluPG-C_{10} (◆), MGluPG-C_{10} (●), and CHexPG-C_{10} (■), and without polymer (▼). Measurements were performed in MES 25 mM and NaCl 125 mM solution at 25 °C. Percent release of pyranine after 10 min incubation was shown (B,D). Polymer and lipid concentrations were 0.1 mg/mL and 2.0×10^{-5} M, respectively. Each point is the mean ± SD ($n = 3$).

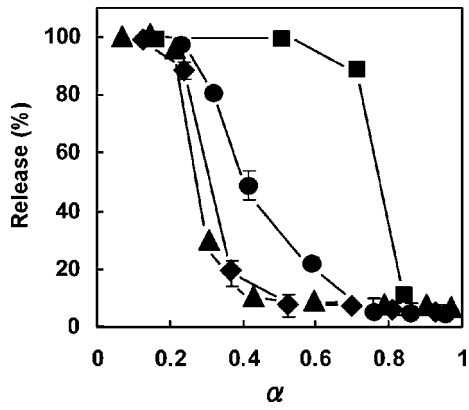

Figure 4. Correlation between dissociation degree (α) of polymers and their induced content release of liposomes. Percent release of pyranine after 10 min incubation with SucPG-C_{10} (▲), GluPG-C_{10} (◆), MGluPG-C_{10} (●), and CHexPG-C_{10} (■) was plotted against α of polymer.

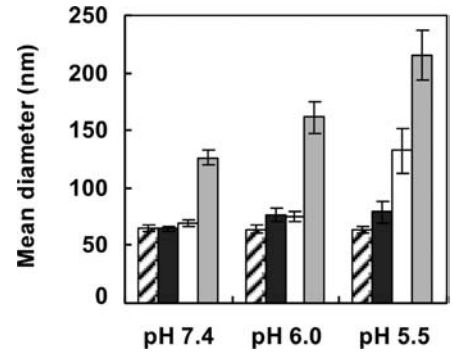

Figure 5. Mean diameters of egg yolk phosphatidylcholine liposomes after overnight incubation with SucPG-C_{10} (closed bars), MGluPG-C_{10} (open bars), and CHexPG-C_{10} (gray bars) at varying pHs. Mean diameters of the same liposomes after overnight incubation without polymer were also shown (diagonal bars). Measurements were performed in MES 25 mM and NaCl 125 mM solution at 25 °C. Polymer and lipid concentrations were 0.83 mg/mL and 1.7×10^{-4} M, respectively. Each point is the mean ± SD ($n = 3$).

which corresponds to the pH of endosome. In addition, their ability to destabilize the liposome membrane in the neutral and weakly acidic region increased with increasing hydrophobicity of the polymer side chains.

Because these polymers acquire the ability to destabilize the liposome membrane upon protonation of carboxyl groups on the side chains, we examined the correlation between the protonation degree and their membrane-destabilizing ability. Figure 4 depicts the percent release induced by the polymer as a function of dissociation degree α of the polymers evaluated using acid−base titration. Highly hydrophobic CHexPG can acquire the ability to induce the content release when only about 25% of carboxylate anions are protonated. In contrast, hydrophilic SucPG cannot induce the release until about 70−80% of carboxylate anions lose their negative charges by protonation. Indeed, dissociation of carboxyl groups might be affected in the peripheral region of the liposome. Therefore, the result indicated that polymers with higher hydrophobicity acquire membrane-destabilizing activity on a state with a lesser degree of protonation.

Interaction of the polymers with the liposomes was also investigated through inspection of the liposome size change. The EYPC liposomes with 60 nm diameter were incubated with SucPG-C_{10}, MGluPG-C_{10}, or CHexPG-C_{10} at varying pH overnight; their diameters were evaluated using DLS (Figure 5). The liposome size only slightly changed after incubation with SucPG-C_{10}, even at pH 5.5. Similarly, the liposome size was not affected when incubated with MGluPG-C_{10} at pH 7.4 and 6.0, but incubation at pH 5.5 caused an increase in diameter. Interaction with this polymer might induce destabilization of the liposome membrane, engendering their aggregation. Ag-

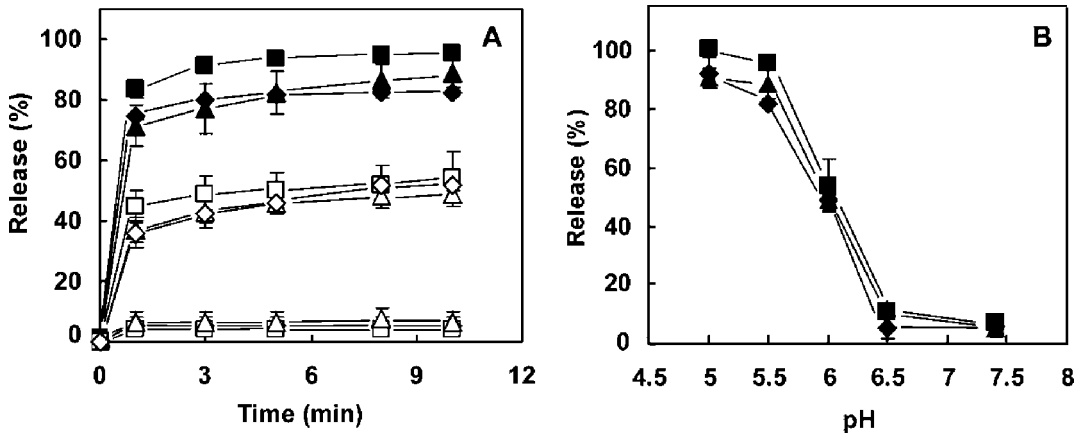

Figure 6. Pyranine release behaviors of egg yolk phosphatidylcholine liposomes modified with SucPG-C_{10} (triangles), GluPG-C_{10} (diamonds), and MGluPG-C_{10} (squares). (A) Time course at pHs 7.4 (open symbols), 6.0 (gray symbols), and 5.5 (closed symbols). (B) Percent release of pyranine from the polymer-modified liposomes after 10 min incubation as a function of pH. Lipid concentrations were 2.0×10^{-5} M. Each point is the mean ± SD ($n = 3$).

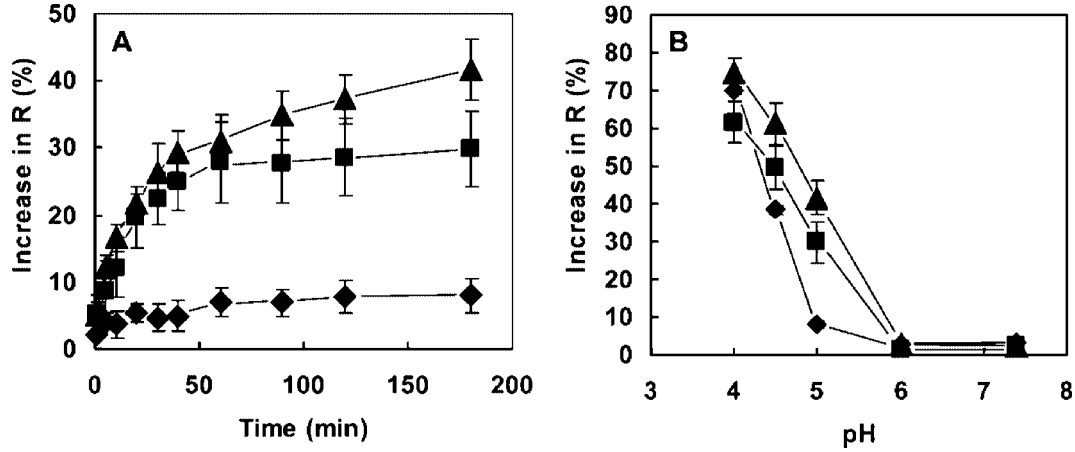

Figure 7. pH-sensitive fusogenic properties of polymer-modified liposomes. Time course at pH 5.0 (A) and pH dependence of percent increase in *R* values after mixing of fluorescent lipid-labeled liposomes modified with SucPG (◆), GluPG (■), and MGluPG (▲) after 3 h incubation at varying pHs. Measurements were performed in 25 mM MES and 125 mM NaCl at 37 °C. Each point is the mean ± SD ($n = 3$).

gregation of liposomes became more intensive when incubated with CHexPG-C_{10}. Indeed, polymer-induced aggregation was enhanced with decreasing pH, but this polymer exhibited the ability to induce liposome aggregation, even at neutral pH.

Preparation of pH-Sensitive Liposomes with Poly(glycidol) Derivatives. Results of a previous study showed that modification of liposomes with pH-sensitive polymers is an efficient means to prepare pH-sensitive liposomes (*10, 13, 24, 29*). Especially, modification with SucPG provided pH-sensitive fusion ability, which is useful for cytoplasmic delivery of membrane-impermeable molecules (*14*). Therefore, we next examined the ability of poly(glycidol) derivatives to render stable EYPC liposomes pH-sensitive. For this purpose, polymers are necessary to exhibit activity only under mildly acidic conditions. However, CHexPG exhibits membrane-destabilizing activity even at neutral pH; we examined three poly(glycidol) derivatives aside from CHexPG.

The liposomes were incubated with varying amounts of the polymers for varying periods and the liposomes were separated from the free polymers using gel filtration to achieve modification of EYPC liposomes with the polymers. Comparison of their content release performance revealed that incubation of liposomes (17.5 mM) in more than 2 mg/mL of the polymer solutions (pH 7.4) for more than 60 min yielded the highest performance (Supporting Information Figure S1). In addition, the zeta potential of these polymer-modified liposomes with the highest performance showed a constant value of about −31 mV (Supporting Information Figure S1). These results indicate that the polymer chains were fully incorporated into the liposome surface by incubation under these conditions. On the basis of these results, we prepared EYPC liposomes modified with the poly(glycidol) derivatives by incubating the liposomes in 10 mg/mL of the polymer solutions for 1 h, with subsequent gel filtration.

Figure 6 depicts pH-sensitive content release behaviors of liposomes modified with the SucPG-C_{10}, GluPG-C_{10}, and MGluPG-C_{10}. All liposomes retained pyranine at pH 7.4, indicating that they are stable at physiological pH. However, these liposomes enhanced their content release below pH 6.0; almost complete release was achieved at pH 5.5. This result demonstrates that these liposomes were able to destabilize the inside of early and late endosomes, which have respective environments with pH 6.5−6.0 and pH 6.0−5.0 (*30*). As portrayed in Figure 6, all liposomes exhibited a similar pH response. This observation differs greatly from the case of content release induced by addition of these polymers into the liposome suspensions, in which MGluPG-C_{10}, GluPG-C_{10}, and SucPG-C_{10}, respectively, exhibited content release enhancement around 6.5, 6.0, and 5.5 (Figure 3D). Apparently, the content release was enhanced in a higher pH region for the polymers attached to the liposomes than for the free polymers. Protonation of carboxylate anions of these polymers might be enhanced in

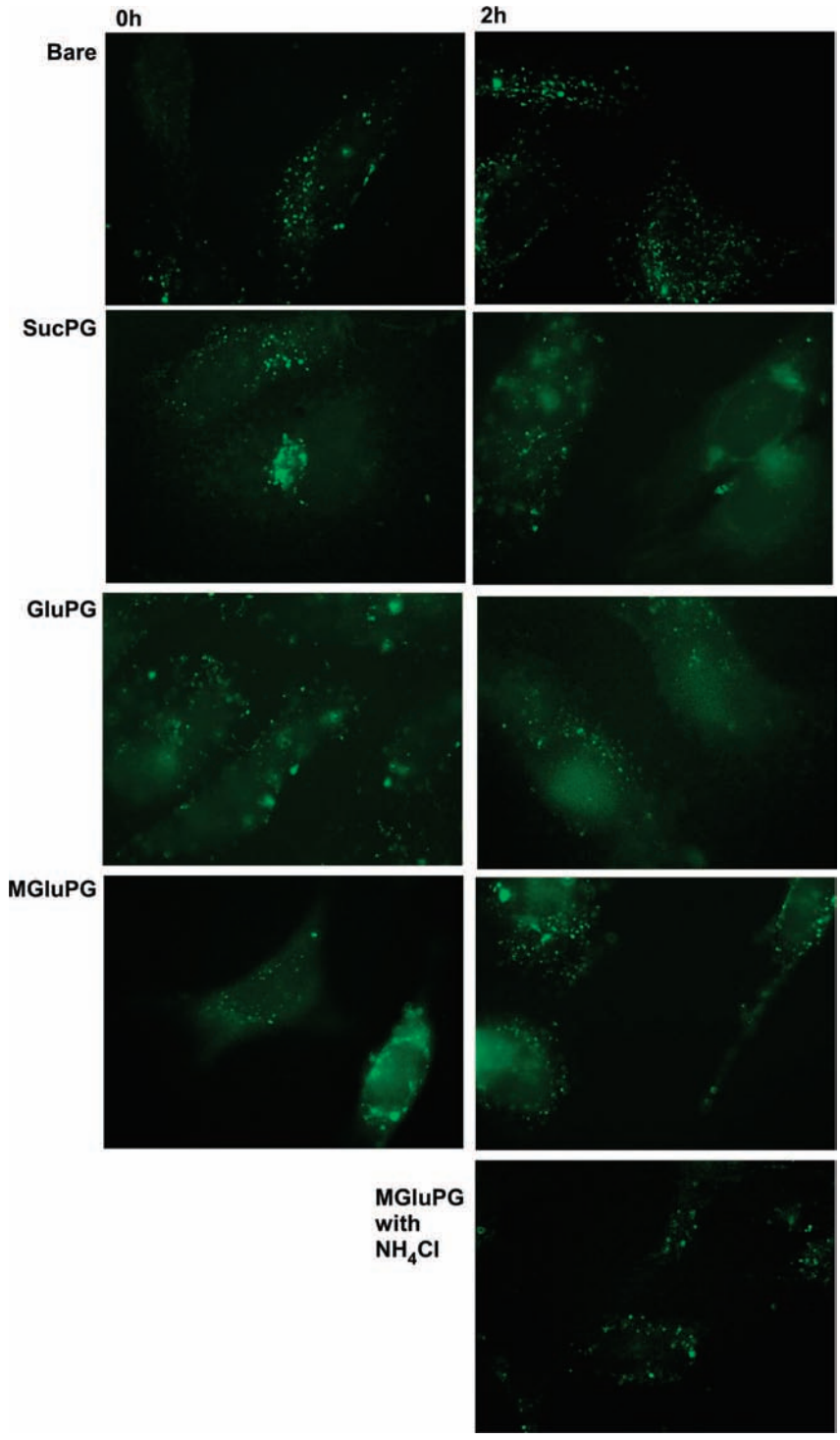

Figure 8. Fluorescence micrographs of HeLa cells treated with calcein-loaded liposomes modified with varying polymers or without polymer modification. The cells were incubated with liposomes for 4 h at 37 C° and were washed with PBS. Then, the cells were observed just after washing (left column) or after additional incubation in DMEM with 10% FCS at 37 C° for 2 h (right column) using a fluorescence microscope. Cells treated with liposomes in the presence of NH_4Cl were also shown.

the peripheral region of the liposome membrane, which is an environment with lower polarity than the aqueous medium. Therefore, the difference in hydrophobicity of these polymers' side chains might not reflect the pH region, where their protonation took place.

We also examined the pH response of these polymer-modified liposomes with respect to fusion ability. For this purpose, we prepared polymer-modified EYPC liposomes containing NBD-PE and Rh-PE, which have been used widely to detect fusion of liposomes (*18*). Fusion of the labeled liposomes with unlabeled liposomes causes dilution of these fluorescent lipids in the membrane. Therefore, their fusion results in decreased resonance energy transfer efficiency between these fluorescent lipids. In addition, previous results have shown that the fluorescence intensity ratio of NBD-PE to Rh-PE (*R*) is useful to monitor liposome fusion (*14, 15*).

Polymer-modified liposomes with the fluorescent lipids were mixed with the unlabeled EYPC liposomes and the fluorescence intensity ratio of NBD-PE to Rh-PE (*R*) for the mixed liposome suspension was calculated (Figure 7). Figure 7A depicts the

percentage increase in the *R*-value (see the Materials and Methods section) for the liposome suspensions at pH 5.0. The liposomes modified with SucPG exhibited a slight increase in the *R*-value, suggesting that this polymer increases the fusion ability of the liposome only slightly at pH 5.0. However, the liposomes modified with GluPG showed a marked increase in the *R*-value with time; the MGluPG-modified liposomes exhibited an even more significant increase in *R*, indicating that these polymers have a higher ability to render the stable liposomes fusogenic than SucPG. Their ability is influenced by differences of side-chain structures.

Figure 7B portrays the percent increase in the *R*-value after 3 h incubation for polymer-modified liposomes and plain liposomes. Irrespective of the polymer, these liposomes displayed no change in *R*-value at pH 7.4−6.0, but the *R*-values increased below pH 6.0, which indicates that these liposomes became fusogenic in the mildly acidic environment. Their fusion ability varies depending on the polymer attached to liposomes around pH 5.0. However, a further decrease in the ambient pH strengthened their fusion ability, and these polymer-modified liposomes acquired similar and strong fusion ability around pH 4.5−4.0. Actually, SucPG has fewer hydrophobic side chains than other polymers. For that reason, this polymer, with many charged groups, might not strongly destabilize the lipid membrane to cause liposome fusion. In contrast, GluPG and MGluPG, which possess hydrophobic side chains, might destabilize the liposome membrane even through their side chains are partly charged. Therefore, MGluPG, of which side chains are most hydrophobic among these polymers, produced liposomes with the highest fusion capability.

Interaction of Polymer-Modified Liposomes with Cells. Finally, we estimated their potential as a cytplasmic delivery vehicle for membrane-impermeabile molecules. For this purpose, we loaded calcein, which is a water-soluble fluorescent dye, in the polymer-modified EYPC liposomes. It is well-known that fluorescence of calcein is strongly quenched when encapsulated in the liposome at a high concentration, but becomes highly fluorescent once released from the liposome (*31*). Therefore, intracellular localization of calcein molecules released from the liposomes can be estimated from their fluorescence.

We incubated HeLa cells with the calcein-loaded liposomes for 4 h and washed them with PBS. Then, the treated cells were observed using a fluorescence microscope just after washing or after additional incubation in the medium for 2 h. As is seen in Figure 8, the cells treated with the calcein-loaded bare liposome displayed punctuate fluorescence. Considering that the liposomes were generally taken up by a cell via endocytosis, it is highly likely that calcein molecules were still trapped in endosome and/or lysosome (*14, 32*). In contrast, the cells treated with the calcein-loaded, polymer-modified liposomes showed diffused fluorescence, indicating that calcein molecules existed in cytoplasm. Because these liposomes have the ability to destabilize and fuse with lipid membranes under a weakly acidic environment, it is likely that calcein molecules were released from endosome or lysosome into cytoplasm.

On the basis of the comparison of calcein fluorescence observed in the liposome-treated cells, it seems that the ability of cytoplamic calcein delivery may differ among these polymer-modified liposomes. Punctuate fluorescence was mainly observed in the cells just after the incubation with SucPG-C_{10}-modified liposome, though additional 2 h incubation caused diffused fluorescence in the cell. In contrast, intensive diffused fluorescence was observed in the cells treated with MGluPG-C_{10}-modified liposomes, indicating that these polymers might possess a stronger ability to destabilize endosomal and lysosomal membranes than SucPG-C_{10}. In addition, when the treatment with the MGluPG-C_{10}-modified liposomes was performed in the presence of ammonium chloride, which is known to inhibit acidification of endosome and lysosome, punctuate fluorescence appeared in the cells, suggesting that acidification of these intracellular organelles is necessary for the transfer of calcein molecules into cytosol. These results demonstrate that modification of stable liposomes with fusogenic polymers, which strongly destabilize lipid membranes at weakly acidic pH, can produce pH-sensitive liposomes that achieve efficient cytoplasmic delivery of membrane-impermeable molecules.

CONCLUSION

We have previously used SucPG for pH sensitization of stable liposomes. In this study, we newly synthesized three pH-sensitive poly(glycidol) derivatives with side chains of varying hydrophobicities, GluPG, MGluPG, and CHexPG, and investigated a correlation between their side-chain structure and their ability to render stable liposomes pH-sensitive. Their ability for pH sensitization of liposomes was enhanced with increasing side-chain hydrophobicity. In particular, MGluPG, which possesses side chains with appropriate hydrophobicity, produced highly pH-sensitive liposomes that undergo content release and membrane fusion at mildly acidic pH, which corresponds to endosomal and lysosomal pH. Such properties of the liposomes are important for efficient cytoplasmic delivery of membrane-impermeable molecules because destabilization and fusion with endosome and/or lysosome membranes improves the transfer of liposomal contents to cytosol. In fact, MGluPG-modified liposomes encapsulating calcein efficiently delivered their contents into the cytosol of a cell. Considering their application into body, the increased hydrophobicity of the polymer may affect biodistribution of the liposomes. However, further incorporation of poly(ethylene glycol) grafts to the liposomes might cover the liposome surface and produce liposomes with high pH sensitivity and long circulating properties. Information obtained from this study is expected to be useful for development of highly efficient pH-sensitive liposomes and related vehicles for efficient cytoplasmic delivery of bioactive molecules, such as proteins and genes.

ACKNOWLEDGMENT

This work was supported in part by a Grant-in-Aid for Research on Nanotechnical Medicine from the Ministry of Health, Labor and Welfare of Japan and by a Grant-in-aid for Scientific Research from the Ministry of Education, Science, Sports, and Culture in Japan.

Supporting Information Available: Release of pyranine from SucPG-modified liposomes prepared by incubation of the liposomes with SucPG for varying periods. Release of pyranine from SucPG-modified liposomes prepared by incubation of liposomes with SucPG at varying concentrations. Zeta potentials of SucPG-modified liposomes prepared by incubation of liposomes with SucPG at varying concentrations for 1 h. This material is available free of charge via the Internet at http://pubs.acs.org.

LITERATURE CITED

(1) Liu, D., and Huang, L. (1990) pH-Sensitive, plasma-stable liposomes with relatively prolonged residence in circulation. *Biochim. Biophys. Acta 1022*, 348–354.

(2) Ellens, H., Bentz, J., and Szoka, F. C. (1984) pH-Induced destabilization of phosphatidylethanolamine-containing liposomes: role of bilayer contact. *Biochemistry 23*, 1532–1538.

(3) Webb, M. S., Hui, S. W., and Steponkus, P. L. (1993) Dehydration-induced lamellar-to-hexagonal-II phase transitions

in DOPE/DOPC mixtures. *Biochim. Biophys. Acta 1145*, 93–104.
(4) Seki, K., and Tirrell, D. A. (1984) pH-Dependent complexation of poly(acrylic acid) derivatives with phospholipid vesicle membrane. *Macromolecules 17*, 1692–1698.
(5) Zignani, M., Drummond, D. C., Meyer, O., Hong, K., and Leroux, J. C. (2000) In vitro characterization of a novel polymeric-based pH-sensitive liposome system. *Biochim. Biophys. Acta 1463*, 383–394.
(6) Fujiwara, M., Grubbs, R. H., and Baldeschwieler, J. D. (1997) Characterization of pH-dependent poly(acrylic acid) complexation with phospholipid vesicles. *J. Colloid Interface Sci. 185*, 210–216.
(7) Borden, K., Eum, K., Langley, K., Tan, J., Tirrell, D., and Voycheck, C. (1988) pH-dependent vesicle-to-micelle transition in an aqueous mixture of dipalmitoylphosphatidylcholine and a hydrophobic polyelectrolyte. *Macromolecules 21*, 2649–2651.
(8) Thomas, J. L., and Tirrell, D. A. (1992) Polyelectrolyte-sensitized phospholipid vesicles. *Acc. Chem. Res. 25*, 336–342.
(9) Tirrell, D., Takigawa, D., and Seki, K. (1985) pH Sensitization of phospholipid vesicles via complexation with synthetic poly(carboxylic acid)s. *Ann. N.Y. Acad. Sci. 446*, 237–248.
(10) Maeda, M., Kumano, A., and Tirrell, D. (1988) H+-Induced release of contents of phosphatidylcholine vesicles bearing surface-bound polyelectrolyte chains. *J. Am. Chem. Soc. 110*, 7455–7459.
(11) Murthy, N., Robichaud, J. R., Tirrell, D. A., Stayton, P. S., and Hoffman, A. S. (1999) The design and synthesis of polymers for eukaryotic membrane disruption. *J. Controlled Release 61*, 137–143.
(12) Lackey, C. A., Murthy, N., Press, O. W., Tirrell, D. A., Hoffman, A. S., and Stayton, P. S. (1999) Hemolytic activity of pH-responsive polymer-streptavidin bioconjugates. *Bioconjugate Chem. 10*, 401–405.
(13) Kono, K., Zenitani, K., and Takagishi, T. (1994) Novel pH-sensitive liposomes: liposomes bearing a poly(ethylene glycol) derivative with carboxyl groups. *Biochim. Biophys. Acta 1193*, 1–9.
(14) Kono, K., Igawa, T., and Takagishi, T. (1997) Cytoplasmic delivery of calcein mediated by liposomes modified with a pH-sensitive poly(ethylene glycol) derivative. *Biochim. Biophys. Acta 1325*, 143–154.
(15) Kono, K., Torikoshi, Y., Mitsutomi, M., Itoh, T., Emi, N., Yanagie, H., and Takagishi, T. (2001) Novel gene delivery systems: complexes of fusogenic polymer-modified liposomes and lipoplexes. *Gene Ther. 8*, 5–12.
(16) Sakaguchi, N., Kojima, C., Harada, A., Koiwai, K., Shimizu, K., Emi, N., and Kono, K. (2006) Enhancement of transfection activity of lipoplexes by complexation with transferrin-bearing fusogenic polymer-modified liposomes. *Int. J. Pharm. 325*, 186–190.
(17) Daleke, D. L., Hong, K., and Papahadjopoulos, D. (1990) Endocytosis of liposomes by macrophages: binding, acidification and leakage of liposomes monitored by a new fluorescence assay. *Biochim. Biophys. Acta 1024*, 352–366.
(18) Struck, D. K., Hoekstra, D., and Pagano, R. E. (1981) Use of resonance energy transfer to monitor membrane fusion. *Biochemistry 20*, 4093–4099.
(19) Kalyanasundaram, K., and Thomas, J. K. (1977) Environmental effects on vibronic band intensities in pyrene monomer fluorescence and their application in studies of micellar systems. *J. Am. Chem. Soc. 99*, 2039–2044.
(20) Schild, H. G., and Tirrell, D. A. (1991) Microheterogeneous solutions of amphiphilic copolymers of N-isopropylacrylamide. An investigation via fluorescence methods. *Langmuir 7*, 1319–1324.
(21) Tamano, K., Imae, T., Yusa, S., and Shimada, Y. (2005) Structure-selective dye uptake into an aggregate of a copolymer with linear polyelectrolyte block and hydrophobic block carrying pepdant dendritic moiety in water. *J. Phys. Chem. B 109*, 1226–1230.
(22) Kono, K., Hayashi, H., and Takagishi, T. (1994) Temperature-sensitive liposomes: liposomes bearing poly(N-isopropylacrylamide). *J. Controlled Release 30*, 69–75.
(23) Ringsdorf, H., Venzmer, J., and Winnik, F. M. (1991) Interaction of hydrophobically-modified poly-N-isopropylacrylamides with model membranes-or playing a molecular accordion. *Angew. Chem., Int. Ed. Engl. 30*, 315–318.
(24) Meyer, O., Papahadjopoulos, D., and Leroux, J. C. (1998) Copolymers of N-isopropylacrylamide can trigger pH sensitivity to stable liposomes. *FEBS Lett. 421*, 61–64.
(25) Yessine, M. A., and Leroux, J. C. (2004) Membrane-destabilizing polyanions: interaction with lpid bilayers and endosomal escape of miomacromolecules. *Adv. Drug Delivery Rev. 56*, 999–1021.
(26) Nylund, R. E., and Miller, W. G. (1965) Synthesis and potentiometric titration of random copolymers of L-leucine and L-glutamic acid. *J. Am. Chem. Soc. 87*, 3537–3553.
(27) Thomas, J. L., You, H., and Tirrell, D. A. (1995) Tuning the response of a pH-sensitive membrane switch. *J. Am. Chem. Soc. 117*, 2949–2950.
(28) Yassine, M. A., Lafleur, M., Meier, C., Petereit, H. U., and Leroux, J. C. (2003) Characterization of the membrane-destabilizing properties of different pH-sensitive methacylic acid copolymers. *Biochim. Biophys. Acta 1613*, 28–38.
(29) Kitano, H., Akatsuka, Y., and Ise, N. (1991) pH-Responsive liposomes which contain amphiphiles prepared by using lipophilic radical initiator. *Macromolecules 24*, 42–46.
(30) Mukherjee, S., Ghosh, R. N., and Maxfield, F. R. (1997) Endocytosis. *Physiol. Rev. 77*, 759–803.
(31) Allen, T. M. (1983) Calcein as a tool in liposome methodology. *Liposome Technology. Volume 3: Targeted drug delivery and biological interaction* (Gregoriadis, G. , Eds.) pp 177−182, CRC Press, Boca Raton, FL.
(32) Connor, J., and Huang, L. (1985) Efficient cytoplasmic delivery of a fluorescent dye by pH-sensitive immunoliposomes. *J. Cell Biol. 101*, 582–589.

BC7004736

Direct Site-Specific Labeling of the Cys-Tag Moiety in scVEGF with Technetium 99m

Zoia Levashova,[†] Marina Backer,[‡] Joseph M. Backer,[‡] and Francis G. Blankenberg*[,†]

Department of Radiology/MIPS, Stanford University School of Medicine, Stanford, California 94305, and Sibtech, Inc., Brookfield, Connecticut 06804. Received December 27, 2007; Revised Manuscript Received March 12, 2008

Angiogenesis is a fundamental feature of tumor development, and therefore, the tracers for molecular imaging of specific angiogenic biomarkers are expected to be useful for diagnostics, patient monitoring, and drug development. We have created a new class of imaging agents based on the most important mediator of angiogenesis, vascular endothelial growth factor (VEGF). Our latest version is a single-chain (sc) VEGF protein containing an N-terminal Cys-tag designed for site-specific modification with a variety of imaging and therapeutic moieties. We have recently found that the Cys-tag itself can form a stable chelate with ^{99m}Tc using tin-tricine as an exchange reagent. This self-chelation approach yields a highly stable and fully functional form of radiolabeled scVEGF that can be used as a SPECT tracer for tumor angiogenesis. Also of note is that directly labeled scVEGF has less than one-half the nonspecific renal uptake of ^{99m}Tc-HYNIC-scVEGF. The simple production of scVEGF for direct chelation of ^{99m}Tc makes it a promising molecular imaging agent for the oncology clinic.

INTRODUCTION

Angiogenesis is a fundamental feature of tumor growth, and the onset and/or presence of angiogenesis could be used for diagnostic purposes. On the other hand, since angiogenesis is critical for tumor growth, it is a target of massive drug development efforts. Current antiangiogenic drugs given in combination with chemotherapy or radiotherapy provide positive clinical effects in subsets of patients (*1*−*3*). As antiangiogenic treatments are quite expensive and are not without serious side effects (*4, 5*), there is a great desire for better diagnostic tools to guide the development as well as the efficient and safe use of these new drugs in cancer patients. In particular, clinical development of antiangiogenic drugs and combination therapeutic regimens need imaging tracers that can follow therapeutic targets in angiogenic vasculature (see refs (*6*−*8*) for review). Among such imaging targets, receptors for vascular endothelial growth factor (VEGF) are particularly attractive for several reasons. First, VEGF is the most important regulator of angiogenesis. Its signaling pathway, initiated by binding of VEGF to its cognate receptors VEGFR-1 and VEGFR-2, is the primary target of most anti- and pro-angiogenic therapeutic agents (*9*−*12*). Second, the receptors for VEGF, and most notably, VEGFR-2 (KDR/Flk-1), are selectively overexpressed by the endothelial cells of angiogenic tumor vessels (*9, 13*), providing an opportunity for enhanced tracer accumulation. Finally, VEGF receptors are in direct contact with the microcirculation of a tumor and are also internalized upon VEGF binding, allowing for receptor-mediated accumulation and trapping of VEGF-based imaging agents within target tissue.

To enable VEGF receptor imaging, we have recently developed a novel class of VEGF-based imaging agents (*14*−*17*). We have taken the $VEGF_{121}$ isoform of VEGF-A as the framework with which to engineer a single-chain (sc) fusion VEGF protein containing an N-terminal Cys-tag (*17*). Cys-tag is an α-helical 15-aa long N-terminal fragment of human ribonuclease I, in which arginine in position 4 is substituted for cysteine, providing a unique site for conjugation of a wide variety of payloads to Cys-tagged targeting proteins (*15, 16, 18*−*22*). For imaging in different modalities, we have site-specifically derivatized scVEGF with fluorescent dyes for near-infrared fluorescent (NIRF) imaging and with radionuclide chelators for positron emission tomography (PET) with ^{64}Cu and single photon emission computed tomography (SPECT) with ^{99m}Tc (*17*). Experiments with scVEGF-based tracers revealed VEGF receptor-mediated selective accumulation of such tracers by endothelial cells in tumor and surrounding host vasculature (*17*). Importantly, endogenous VEGF did not prevent enhanced uptake of the tracers in these compartments (*17*).

Although scVEGF-based targeted tracers displayed favorable imaging properties and relatively low uptake in nontargeted organs, we were concerned that making chelator/protein conjugates requires additional production steps that would present a separate set of obstacles for clinical tracer development.

Over the years, several groups reported that proteins engineered to have an additional cysteine with a free thiol group might be directly radiolabeled with ^{99m}Tc (*23*−*25*). Therefore, we tested whether Cys-tag in scVEGF can be directly radiolabeled with ^{99m}Tc and whether it would lead to a tracer with favorable imaging, biodistribution, and stability profile. We report here that direct labeling of scVEGF with ^{99m}Tc is a highly efficient process, providing a stable tracer with good imaging characteristics and a great reduction in nonspecific uptake, most notably in the kidney, as compared with HYNIC-labeled scVEGF. We expect that the simplicity of direct radiolabeling of the Cys-tag would be beneficial for the development of scVEGF and other protein-based SPECT tracers.

EXPERIMENTAL PROCEDURES

Production of Cys-Tagged scVEGF. The construction, expression, and purification of Cys-tagged scVEGF have been described recently (*17, 19, 22*). The protein was refolded in red-ox buffer containing glutathione, and therefore, in the final preparation of scVEGF the C4 thiol group in the Cys-tag was "protected" in a mixed disulfide bond with glutathione. Prior

* Corresponding author. Francis G. Blankenberg, M.D., 725 Welch Road, Room #1673, Stanford, CA 94304-1601. E-mail: blankenb@stanford.edu. Phone number: 650-497-8601. Fax number: 650-497-8745.

[†] Stanford University School of Medicine.

[‡] Sibtech, Inc.; jbacker@sibtech.com.

10.1021/bc7004818 CCC: $40.75 © 2008 American Chemical Society
Published on Web 04/12/2008

to radiolabeling, the C4 thiol group in scVEGF was "deprotected" by incubating scVEGF with equimolar amounts of DTT at 25 °C for 20 min in 0.1 M Tris−HCl pH 8.0 (*17*). Free SH groups were detected and quantitated by reaction with *N*-(1-pyrene)-maleimide as previously described elsewhere (*26*).

scVEGF Direct Radiolabeling with ^{99m}Tc. Deprotected scVEGF was radiolabeled, using [^{99m}Tc]-tricine as a precursor complex (*27*). Briefly, lyophilized tin-tricine reagent was reconstituted with 0.25 mL of degassed saline to give a final $SnCl_2 \cdot 2H_2O$ concentration of 3 mg/mL and a final tricine concentration of 100 mg/mL (pH 7.1). 2.5−5.0 μL tin-tricine was mixed with 30−50 μg of deprotected scVEGF and 10−20 mCi of ^{99m}Tc-pertechnetate in a final volume of 50−100 μL. After 30 min of incubation at 37 °C, radiolabeled protein, named scVEGF/Tc, was purified by gel-filtration on PD-10 Sephadex-25 columns. Specific activities ranged from 130 to 200 μCi/μg protein. Radiopurity was determined by ITLC using PBS as a solvent, and we observed ^{99m}Tc batch-dependent variations in the range 90−95%. The impurities were migrating with the front and appeared to arise from small and variable amounts of colloidal forms of ^{99m}Tc that were coeluted with scVEGF/Tc from PD-10 column.

Animals and Tumor Models. 5−6 week old female BALB/c mice were purchased from Charles River Laboratories (Wilmington, MA). 4T1*luc* cells were implanted into the left axillary fat pad, 10^4 cells per mouse. The protocol for the animal studies was approved by the Stanford University Institutional Animal Care and Use Committee.

Stability of scVEGF/Tc in Vitro and in Vivo. Testing was done as described in Backer et al. (*17*) for scVEGF labeled with ^{64}Cu. Briefly, Balb/c mice ($n = 3$) were injected i.v. with scVEGF/Tc (90 μCi/0.5 μg per mouse) and sacrificed 2 min later. Blood was collected and clarified by centrifugation. Plasma samples were incubated at 37 °C. After 15, 30, and 60 min of incubation, 1 μL plasma aliquots were analyzed by ITLC for a rough estimation of protein-bound radioactivity. Stability of scVEGF/Tc was tested by incubation of the probe in PBS at room temperature or at 95 °C with consequent analysis by ITLC and SDS-PAGE.

Structural and functional integrity of scVEGF/Tc recovered from blood was tested by its ability to bind to soluble VEGFR-2 receptor KDR-Fc (R&D Systems, Minneapolis, MN) immobilized on Protein A Sepharose as described previously (*17*). Briefly, Balb/c mice ($n = 3$) were injected via tail vein with scVEGF/Tc (1.2 mCi, 11 μg protein). At 3, 15, and 45 min after injection of tracer, blood samples were collected via supraorbital bleed, placed in citrate buffer, and clarified by centrifugation. Plasma aliquots containing equal amounts of radioactivity were mixed with Protein A Sepharose, either empty or loaded with KDR-Fc. After 1 h binding at 4 °C, Sepharose beads were spun down, extensively washed with RIPA buffer, separated by reducing SDS-PAGE on 10% gel, and analyzed by Western blotting with VEGF-specific mouse monoclonal antibody (BD Biosciences Pharmingen, San Jose, CA).

Scatchard Analysis of scVEGF/Tc Binding to Cellular VEGFR-2. Binding analysis was performed as described elsewhere for scVEGF-PEG-DOTA conjugate radiolabeled with ^{64}Cu (*17*). Briefly, 293/KDR cells overexpressing VEGFR-2 grown on 12-well plates were shifted to serum-free medium at room temperature for 45 min. Varying amounts of scVEGF/Tc were added to cells in triplicate wells for 90 min, followed by two PBS and one high-salt (0.5 M NaCl in PBS) wash. Cells were lyzed in 1% Triton X-100 containing buffer and assayed for ^{99m}Tc activity in a scintillation well counter (140 keV level, 20% window). Nonspecific binding was determined for the same amounts of scVEGF/Tc supplemented with 100-fold molar excess of nonradiolabeled scVEGF.

Blood Clearance and Biodistribution Studies. For blood clearance and biodistribution studies, 0.1−0.15 mCi of scVEGF/Tc per mouse ($n = 4$) was injected via the tail vein, and serial ~50 μL blood samples were taken via supraorbital sinus at various time points after injection. Tissue samples taken 1 and 3 h after injection were counted in a gamma counter along with three samples of standard activity (1/100 of injected dose). Results were calculated as the average of the percentage of injected dose (ID) or %ID per gram (g) of tissue ± 1 standard deviation of the mean.

A-SPECT-Imaging and Autoradiography. For SPECT imaging, 1.2 mCi of scVEGF/Tc per mouse ($n = 4$) was injected via tail vein. SPECT images were obtained 1 h after injection with the following parameters: 360° rotation, 64 steps, 30 s per step, 0.5 mm pinhole aperture, a 64 × 64 image matrix, and a 2.7 cm FOV using a small animal SPECT imaging gamma camera (A-SPECT, LumaGEM, Gamma Medica, Los Angeles). For autoradiography, tumors and pectoralis muscle from the healthy chest side were snap-frozen immediately after imaging, cryosectioned (60 μm thickness), and exposed to a phosphor storage screen for 16 h. The phosphor screen images were read out with a laser digitizer at a resolution of 50 μm per pixel. ROI analysis of radiotracer activity was performed using *ImageQuant TL* software. The maximal cts/pixel of the rim and the average cts/pixel of the center of the tumor were normalized to corresponding contralateral pectoral muscle uptake (minimum cts/pixel).

Tumor uptake analysis was performed using parametric 3-D regions of interest (ROI), interactively placed and sized, but geometric as described previously (*28*). ROIs of the rim, center, and contralateral axillary soft tissue (BKG) were drawn. The sum of the total number of counts adjusted for volume of the rim (upper 95th percentile) and soft tissue BKG (lower fifth percentile) was tabulated from the histograms of the rim and contralateral soft tissue ROI, respectively, for each tumor-bearing animal. The sums from the 34th and 68th percentiles (central portion of histogram) determined from the ROIs of the center of each tumor were also tabulated. The uptake of the rim and center of each tumor was then divided by the contralateral soft tissue uptake and presented as ratios of rim/BKG and center/BKG, respectively.

RESULTS

Direct Radiolabeling of Cys-Tagged scVEGF with ^{99m}Tc. scVEGF is functionally active single chain version of VEGF consisting of two 3−112 amino acid fragments of human $VEGF_{121}$ genetically fused head-to-tail and expressed with N-terminal Cys-tag for site-specific modification (*17*). Since scVEGF was refolded in the red-ox buffer containing glutathione, the thiol group in Cys-tag was "protected" in mixed disulfide bond with glutathione (*17*), and therefore, it was deprotected by incubation with equimolar amounts of DTT. This was immediately followed by radiolabeling with ^{99m}Tc using tin-tricine as a precursor complex. We found that the specific activity of a typical scVEGF/Tc preparation ranged from 130 to 200 μCi/μg protein, which compared favorably to the values obtained from the radiolabeling of scVEGF-HYNIC conjugates with ^{99m}Tc.

Activity and Stability of scVEGF/Tc. We then evaluated whether scVEGF/Tc retained its native affinity for the VEGFR-2 receptor using a radioligand binding assay performed with 293/KDR cells; a cell line that constitutively overexpresses VEGFR-2 (*29*). Scatchard analyses ($n = 3$) revealed a disassociation constant (K_d) of 1.28 ± 0.12 nM. The measured affinity of scVEGF/Tc for VEGFR-2 was similar to the K_d values reported previously for the scVEGF-PEG-DOTA/^{64}Cu complex (*17*) and iodinated $VEGF_{165}$ (*30*). We then tested the stability of scVEGF/Tc with several assays as outlined below.

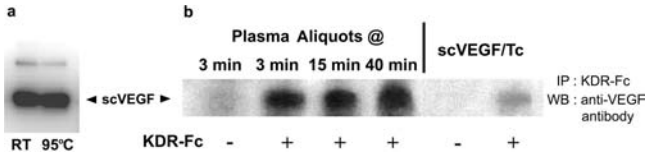

Figure 1. scVEGF/Tc stability in plasma. (A) scVEGF/Tc withstands nonreducing SDS-PAGE conditions even after a short incubation at 95 °C. Autoradiograph of nonreducing SDS-PAGE gel with scVEGF/Tc incubated at room temperature (RT) for 5 h or at 95 °C for 7 min; (B) scVEGF/Tc retains the ability to interact with soluble receptor after at least 40 min in the circulation. Western blot analysis of the SDS-PAGE gel with scVEGF/Tc was collected with KDR-Fc from blood volumes containing similar amounts of radioactivity. Free scVEGF/Tc at the indicated concentrations was similarly collected with KDR-Fc. (See Materials and Methods for experimental details.)

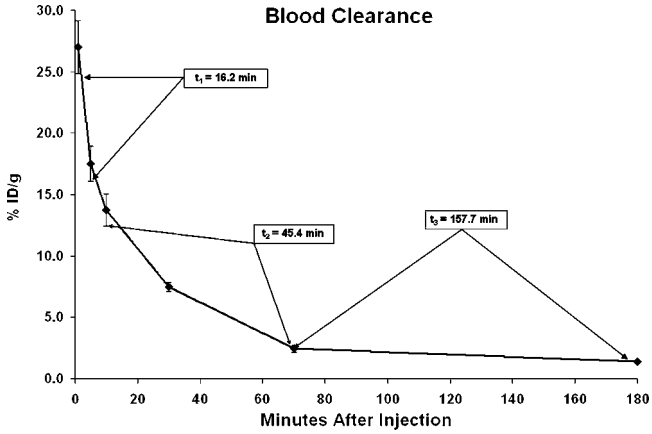

Figure 2. Blood Clearance of scVEGF/Tc. scVEGF/Tc was injected via the tail vein, 0.15 mCi per mouse ($n = 4$), and serial ~50 μL blood samples were taken via supraorbital bleed at various time points after injection. Results were calculated as the average of the percentage of injected dose (ID) per gram (g) of tissue ± standard deviation of the mean. t = half-life (in minutes). %ID/g = percent of injected dose per gram of blood.

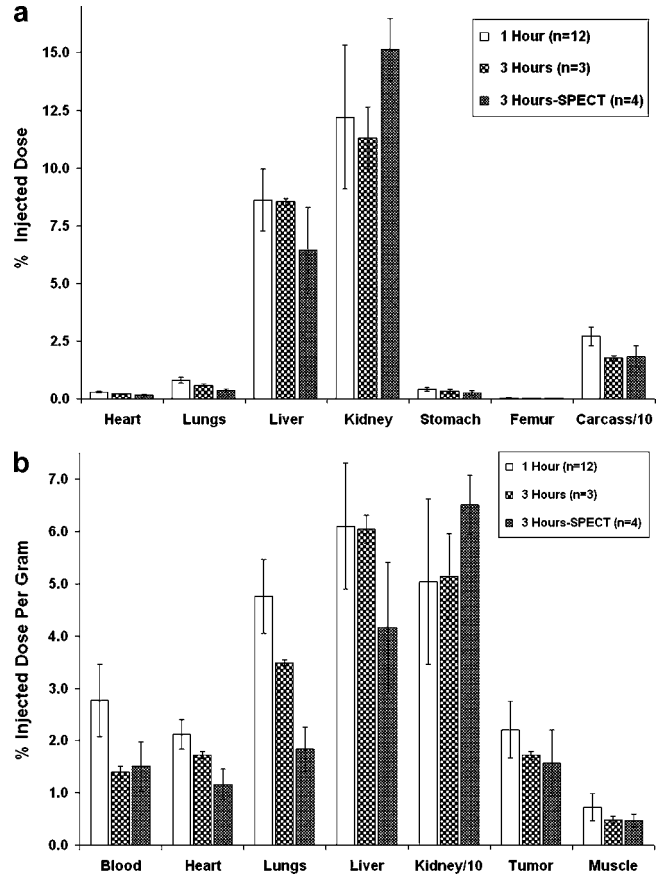

Figure 3. Biodistribution assay at 1 and 3 h after Injection of Tracer. scVEGF/Tc was injected as described in the legend to Figure 2. Biodistribution analysis was done 1 and 3 h postinjection. Three Hours-SPECT, mice received a 10-fold increased dose of tracer (1.2 mCi of radioactivity) and underwent SPECT imaging before sacrifice at 3 h. Standard deviations of the mean values are shown.

Table 1. Average Uptakes (%ID/g @ 1 h) of scVEGF-Based SPECT Tracers

tracer	kidney (%ID/g)	liver (%ID/g)
scVEGF/Tc ($n = 12$)	50.4 ± 15.8	6.1 ± 1.2
scVEGF-HYNIC/^{99m}Tc (*17*) ($n = 12$)	117.1 ± 14.0	5.9 ± 3.0
scVEGF-PEG-DOTA/^{99m}Tc (*17*) ($n = 4$)	28.0 ± 3.3	4.6 ± 1.0

The stability of scVEGF/Tc was initially tested in PBS at room temperature, and ITLC analysis indicated that over 90% of radioactivity remained bound to protein for at least 5 h. Then, we performed a 5 min incubation on an additional set of samples at 95 °C and found that at least 50% of radioactivity comigrated with scVEGF on the nonreducing SDS-PAGE gel (Figure 1a). scVEGF/Tc stability in the circulation of normal Balb/c mice was also tested. Since stability of scVEGF/Tc in vivo is dependent on the dissociation of ^{99m}Tc from protein as well as the integrity of scVEGF itself, we tested both using approaches described previously for scVEGF-HYNIC/^{99m}Tc and scVEGF-PEG-DOTA/^{64}Cu complexes (*17*). Citrated plasma was first obtained at 3, 15, and 40 min postinjection of tracer, and scVEGF/Tc complexes were then precipitated from the plasma aliquots containing the same amounts of radioactivity with a soluble form of VEGFR-2 receptor, KDR-Fc. Since binding to KDR-Fc requires structural integrity of scVEGF, we reasoned that this procedure should only select functionally active scVEGF/Tc complexes. Western blot analysis of the samples revealed that similar amounts of scVEGF were collected from each plasma sample, indicating that circulating scVEGF/Tc remained stable and capable of being a VEGF receptor for at least 40 min (Figure 1b). In this respect, the stability of scVEGF/Tc was similar to that reported for scVEGF-HYNIC/^{99m}Tc.

Blood Clearance and Biodistribution of scVEGF/Tc. scVEGF/Tc cleared rapidly from the circulation, with >95% tracer cleared within 1 h (Figure 2) after tail vein injection of tracer. The clearance rate could be best characterized by three separate exponential decay functions consisting of a rapid component in the first 10−15 min followed by a slower intermediate (20−70 min) and a prolonged terminal (80−180 min) component. The decrease in heart and lung uptake (Figure 3) paralleled the decrease in blood activity, while the tracer uptake of the remaining organs was essentially unchanged between 1 and 3 h. As summarized in Table 1, uptake in kidney obtained with scVEGF/Tc tracer was approximately one-half that seen with scVEGF-HYNIC/^{99m}Tc (*17*). We also prepared scVEGF-PEG-DOTA/^{99m}Tc tracer, based on previously described scVEGF-PEG-DOTA conjugate that proved to be efficient in decreasing nonspecific renal uptake (*17*) and found that pegylated tracer displayed kidney uptake only marginally below that of scVEGF/Tc (Table 1). Interestingly, the tumor uptake of scVEGF/Tc ranged from 1.7 to 2.5%ID/g with a relatively constant ratio of tumor/muscle uptake of 3.1 to 3.5 at 1 and 3 h, respectively.

A-SPECT-imaging and Autoradiographic Studies with scVEGF/Tc. SPECT imaging revealed marked tumor uptake as compared with soft tissue (Figure 4) in a fashion similar to our previously described forms of radiolabeled scVEGF (*14, 16, 17*). The uptake of tracer was particularly high in the tumor

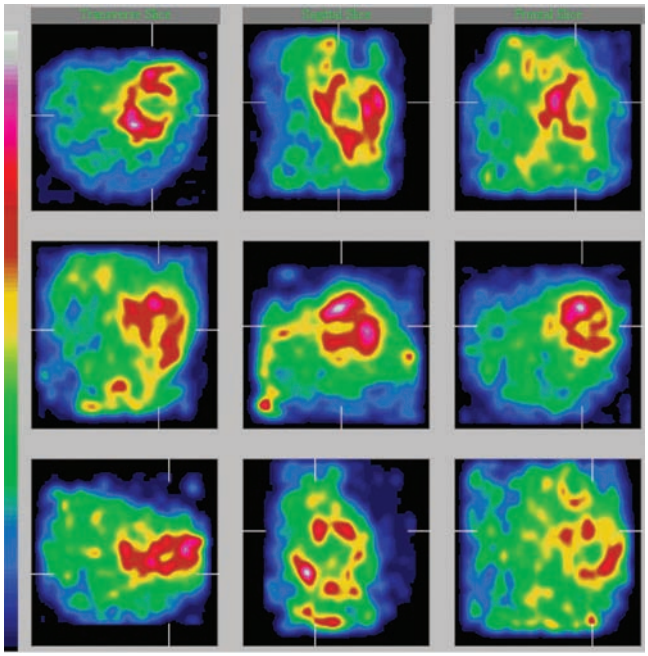

Figure 4. SPECT imaging with scVEGF/Tc. Representative transverse, sagittal, and frontal images of three 4T1 tumor-bearing mice are shown. Note the intense rim uptake of tracer at the tumor periphery that at ROI analysis was 7 to 10 times greater than soft tissue uptake of the contralateral axilla (see Figure 5). The central portions of tumor also had 3- to 4-fold greater uptake of tracer as compared with soft tissue background. Tumors weighed between 0.3 and 0.5 g (8 to 10 mm in diameter).

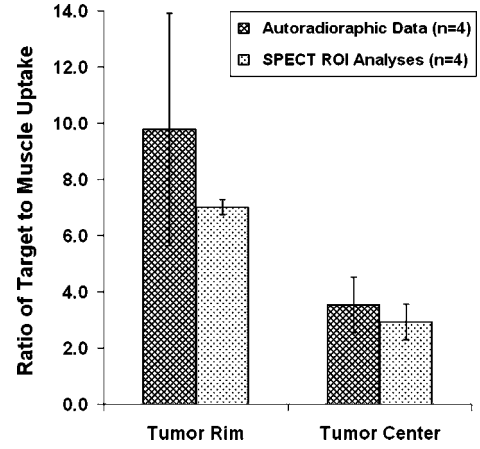

Figure 5. ROI analysis of SPECT and autoradiographic data. Multiple three-dimensional ROIs were placed on the rim and central portions of tumor from each animal that underwent SPECT imaging. Soft tissue background uptake was taken from an ROI placed in the contralateral axilla (muscle) expressed as unity. A similar type of ROI analysis was performed of histologic sections of these same tumors seen with autoradiography. The contralateral pectoralis major muscle was used for the calculation of the soft tissue background uptake of tracer. Standard deviation of mean values for the angiogenic rim and central portions of tumor are shown for both SPECT and autoradiographic ROI analyses.

periphery, in the so-called "angiogenic rim", where VEGF receptors are usually expressed at high levels. In addition, histological examination of tumor sections revealed visibly functional tumor tissue in the central portions of tumor, thereby excluding the possibility that low tracer uptake in these areas might be due to necrosis. ROI analyses of tumor and its margins seen at SPECT imaging demonstrated a rim uptake 7 to 10 times greater than muscle as well as a central tumor to muscle uptake ratio of 3 to 4 (Figure 5). Similar ratios were observed with autoradiography.

DISCUSSION

We report here that the Cys-tag in scVEGF can be directly radiolabeled with ^{99m}Tc in a site-specific fashion, yielding a tracer suitable for SPECT imaging. Over the years, several groups reported that proteins engineered to have an additional cysteine with a free thiol group could be directly labeled with ^{99m}Tc (although with different exchange agents such as tin-glucoheptonate) without modifying the protein with chelators such as HYNIC, DTPA, or DOTA (*23*−*25*). As these investigators found, the preparation of a tracer via direct site-specific radiolabeling is far less complicated than a two-step process that requires the synthesis of protein/chelator conjugate prior to radiolabeling. Direct site-specific radiolabeling of scVEGF produces a tracer with a high specific activity, high in vivo stability, rapid blood clearance, and favorable imaging characteristics similar to those of previously described scVEGF-HYNIC/^{99m}Tc (*17*). Furthermore, given the simplicity and short production time of directly labeled scVEGF, we suggest that the Cys-tag might be suitable for direct radiolabeling with ^{94}Tc for PET imaging at facilities equipped with on-site cyclotrons ($t_{1/2}$ of ^{94}Tc = 52.5 min). Unexpectedly, scVEGF/Tc displayed a superior biodistribution, with an approximately 2-fold decrease in kidney uptake of tracer, as compared to scVEGF-HYNIC/^{99m}Tc. This of course is a distinct advantage with respect to the further development of scVEGF as a new radiopharmaceutical for SPECT imaging.

In addition to the simplicity in preparation, scVEGF/Tc has several other potential advantages over several VEGF-based tracers tested by other groups for the imaging of VEGF receptors in ischemic and tumor angiogenic vasculature in humans, mice, and rabbits (*31*−*38*). These tracers were prepared by random ^{123}I-iodination of $VEGF_{121}$ and $VEGF_{165}$ (*31*−*34*), by random conjugation of ^{64}Cu chelator to a wild-type and mutant $VEGF_{121}$ (*35, 36*), by site-specific conjugation of ^{111}I chelator to Cys-116 in $VEGF_{121}$ (*37*), and by constructing transferrin-$VEGF_{165}$ fusion protein for exchange loading with ^{111}I (*38*). As our scVEGF/Tc, other tracers selectively accumulated in the areas of angiogenic vasculature with tumor uptake in the range from 1% to 7%ID/g (*31*−*34*) and reaching 15%ID/g for very small tumors (*36*). As expected, the random modification of VEGF resulted in nonuniform preparations of tracers with a significant decrease in functional activity (see, for example, refs ,*36*), as compared with unmodified protein. The decreased functional activity of radiolabeled VEGF means the loss of the ability to selectively bind to and specifically image VEGF receptors, which compromises the whole idea of molecular targeted imaging. Of note, we have previously used random modification of scVEGF with biotin to create an inactive protein control to study the specificity of scVEGF binding in vivo (*17*). Another concern with all but one (*37*) of the previously described VEGF-based tracers is the high liver uptake of these constructs (more than 30%ID/g in refs (*37, 38*) and more than 15% in refs *35, 36*).

In summary, we have found that the Cys-tag of scVEGF can be used to site-specifically attach ^{99m}Tc without the need for a bifunctional chelator such as HYNIC. The labeling process is both fast and efficient and has no demonstrable effect on the native binding affinity of scVEGF to VEGFR-2. The tracer also is stable in vivo with rapid blood clearance and has half the renal uptake of ^{99m}Tc-HYNIC-scVEGF. scVEGF/Tc also displays excellent SPECT imaging characteristics and is able to define both central tumor uptake and its angiogenic rim in a fashion similar to that observed at autoradiography. The ease of labeling and the simplicity of production make scVEGF/Tc

a promising tracer for the oncology clinic in the near future. Furthermore, considering that direct radiolabeling described here depends on Cys-tag, rather than on the nature of Cys-tagged protein, we expect that this strategy might be used as a standardized approach to the development of protein-based SPECT tracers.

LITERATURE CITED

(1) Kerbel, R., and Folkman, J. (2002) Clinical translation of angiogenesis inhibitors. *Nat. Rev. Cancer 2*, 727–39.

(2) Gille, J. (2006) Antiangiogenic cancer therapies get their act together: current developments and future prospects of growth factor- and growth factor receptor-targeted approaches. *Exp. Dermatol. 15*, 175–186.

(3) Gwyther, S. J., and Schwartz, L. H. (2007) How to assess anti-tumour efficacy by imaging techniques. *Eur. J. Cancer*. [Online early access]. Published online Nov 38, 2007.

(4) Izzedine, H., Rixe, O., Billemont, B., Baumelou, A., and Deray, G. (2007) Angiogenesis inhibitor therapies: focus on kidney toxicity and hypertension. *Am. J. Kidney Dis. 50*, 203–218.

(5) Cabebe, E., and Wakelee, H. (2007) Role of anti-angiogenesis agents in treating NSCLC: focus on bevacizumab and VEGFR tyrosine kinase inhibitors. *Curr. Treat. Options Oncol. 8*, 15–27.

(6) Haubner, R., and Wester, H. J. (2004) Radiolabeled tracers for imaging of tumor angiogenesis and evaluation of anti-angiogenic therapies. *Curr. Pharm. Design 10*, 1439–1455.

(7) Miller, J. C., Pien, H. H., Sahani, D., Sorensen, A. G., and Thrall, J. H. (2005) Imaging angiogenesis: applications and potential for drug development. *J. Natl.Cancer Inst. 97*, 172–87.

(8) Cai, W., Rao, J., Gambhir, S. S., and Chen, X. (2006) How molecular imaging is speeding up antiangiogenic drug development. *Mol Cancer Ther. 5*, 2624–33.

(9) Shibuya, M. (2006) Vascular endothelial growth factor receptor-1 (VEGFR-1/Flt-1): a dual regulator for angiogenesis. *Angiogenesis 9*, 225–230.

(10) Carmeliet, P. (2005) Angiogenesis in life, disease and medicine. *Nature 438*, 932–936.

(11) Rahimi, N. (2006) VEGFR-1 and VEGFR-2: two non-identical twins with a unique physiognomy. *Front. Biosci. 11*, 818–829.

(12) Ribatti, D., Nico, B., Crivellato, E., Roccaro, A. M., and Vacca, A. (2007) The history of the angiogenic switch concept. *Leukemia 21*, 44–52.

(13) Walsh, D. A. (2007) Pathophysiologic mechanisms of angiogenesis. *Adv. Clin. Chem. 44*, 187–221.

(14) Blankenberg, F. G., Mandl, S., Cao, Y. A., O'Connell-Rodwell, C., Contag, C., Mari, C., Gaynutdinov, T. I., Vanderheyden, J. L., Backer, M. V., and Backer, J. M. (2004) Tumor imaging using a standardized radiolabeled adapter protein docked to vascular endothelial growth factor. *J. Nucl. Med. 45*, 1373–1380.

(15) Backer, M. V., Gaynutdinov, T. I., Patel, V., Bandyopadhyaya, A. K., Thirumamagal, B. T., Tjarks, W., Barth, R. F., Claffey, K., and Backer, J. M. (2005) Vascular endothelial growth factor selectively targets boronated dendrimers to tumor vasculature. *Mol. Cancer Ther. 4*, 1423–1429.

(16) Blankenberg, F. G., Backer, M. V., Levashova, Z., Patel, V., and Backer, J. M. (2006) In vivo tumor angiogenesis imaging with site-specific labeled 99mTc-HYNIC-VEGF. *Eur. J. Nuclear Med. Mol. Imag. 33*, 841–848.

(17) Backer, M. V., Levashova, Z., Patel, V., Jehning, B. T., Claffey, K., Blankenberg, F. G., and Backer, J. M. (2007) Molecular imaging of VEGF receptors in angiogenic vasculature with single-chain VEGF driven probes. *Nat. Med. 13*, 504–509.

(18) Thirumamagal, B. T. S., Zhao, X. B., Bandyopadhyaya, A. K., Narayanasamy, S., Johnsamuel, J., Tiwari, R., Golightly, D. W., Patel, V., Jehning, B. T., Backer, M. V., Barth, R. F., Lee, R. J., Backer, J. M., and Tjarks, W. (2006) Receptor-targeted liposomal delivery of boron-containing cholesterol mimics for boron neutron capture therapy (BNCT). *Bioconjugate Chem. 17*, 1141–1150.

(19) Backer, M. V., Patel, V., Jehning, B. T., Claffey, K., and Backer, J. M. (2006) Surface immobilization of active vascular endothelial growth factor via a cysteine-containing tag. *Biomaterials 27*, 5452–5458.

(20) Backer, M., Patel, V., Jehning, B., and Backer, J. M. (2006) Self-assembled "dock and lock" system for linking payloads to targeting proteins. *Bioconjugate Chem. 17*, 912–919.

(21) Backer, M. V., Patel, V., Jehning, B. T., Claffey, K., Karginov, V. A., and Backer, J. M. (2007) Inhibition of anthrax protective antigen outside and inside the cell. *Antimicrob. Agents Chemother. 51*, 245–251.

(22) Backer, M. V., Levashova, Z., Levenson, R., Blankenberg, F. G., and Backer, J. M. (2008) Cysteine-Containing Fusion Tag for Site-Specific Conjugation of Therapeutic and Imaging Agents to Targeting Proteins. In *Methods in Molecular Medicine, Peptide-Based Drug Design* (Otros, L., Ed.) The Humana Press Inc., Totowa, NJ (In press).

(23) George, A. J., Jamar, F., Tai, M. S., Heelan, B. T., Adams, G. P., McCartney, J. E., Houston, L. L., Weiner, L. M., Oppermann, H., and Peters, A. M. (1995) Radiometal labeling of recombinant proteins by a genetically engineered minimal chelation site: technetium-99m coordination by single-chain Fv antibody fusion proteins through a C-terminal cysteinyl. *Proc. Natl. Acad. Sci. U.S.A. 92*, 8358–8362.

(24) Bogdanov, A., Jr., Simonova, M., and Weissleder, R. (1998) Design of metal-binding green fluorescent protein variants. *Biochim. Biophys. Acta 1397*, 56–64.

(25) Tait, J. F., Brown, D. S., Gibson, D. F., Blankenberg, F. G., and Strauss, H. W. (2000) Development and characterization of annexin V mutants with endogenous chelation sites for ^{99m}Tc. *Bioconjugate Chem. 11*, 918–925.

(26) Backer, M. V., Gaynutdinov, T. I., Gorshkova, I. I., Crouch, R. J., Hu, T., Aloise, R., Arab, M., Przekop, K., and Backer, J. M. (2003) Humanized docking system for assembly of targeting drug delivery complexes. *J. Controlled Release 89*, 499–511.

(27) Larsen, S. K., Solomon, H. F., Caldwell, G., and Abrams, M. J. (1995) [99mTc]tricine: a useful precursor complex for the radiolabeling of hydrazinonicotinate protein conjugates. *Bioconjugate Chem. 6*, 635–638.

(28) Tang, X. N., Wang, Q., Koike, M. A., Cheng, D., Goris, M. L., Blankenberg, F. G., and Yenari, M. A. (2007) Monitoring the protective effects of minocycline treatment with radiolabeled annexin V in an experimental model of focal cerebral ischemia. *J. Nucl. Med. 48*, 1822–1828.

(29) Backer, M. V., and Backer, J. M. (2001) Targeting endothelial cells overexpressing VEGFR-2: selective toxicity of Shiga-like toxin-VEGF fusion proteins. *Bioconjugate Chem. 12*, 1066–73.

(30) Backer, M. V., and Backer, J. M. (2001) Functionally active VEGF fusion proteins. *Protein Expr. Purif. 23*, 1–7.

(31) Li, S., Peck-Radosavljevic, M., Koller, E., Koller, F., Kaserer, K., Kreil, A., Kapiotis, S., Hamwi, A., Weich, H. A., Valent, P., Angelberger, P., Dudczak, R., and Virgolini, I. (2001) Characterization of (123) I-vascular endothelial growth factor-binding sites expressed on human tumour cells: possible implication for tumour scintigraphy. *Int. J. Cancer. 91*, 789–796.

(32) Li, S., Peck-Radosavljevic, M., Kienast, O., Preitfellner, J., Hamilton, G., Kurtaran, A., Pirich, C., Angelberger, P., and Dudczak, R. (2003) Imaging gastrointestinal tumours using vascular endothelial growth factor-165 (VEGF165) receptor scintigraphy. *Ann. Oncol. 14*, 1274–1277.

(33) Li, S., Peck-Radosavljevic, M., Kienast, O., Preitfellner, J., Havlik, E., Schima, W., Traub-Weidinger, T., Graf, S., Beheshti, M., Schmid, M., Angelberger, P., and Dudczak, R. (2004) Iodine-123-vascular endothelial growth factor-165 (123I-VEGF165). Biodistribution, safety and radiation dosimetry in patients with pancreatic carcinoma. *Q. J. Nucl. Med. Mol. Imaging 48*, 198–206.

(34) Cornelissen, B., Oltenfreiter, R., Kersemans, Staelens, L., Frankenne, F., Foidart, J.-M., and Slegers, G. (2005) In vitro and in vivo evaluation of [^{123}I]-VEGF$_{165}$ as a potential tumor marker. *Nucl. Med. Biol. 32*, 431–436.

(35) Cai, W., Chen, K., Mohamedali, K. A., Cao, Q., Gambhir, S. S., Rosenblum, M. G., and Chen, X. (2006) PET of vascular endothelial growth factor receptor expression. *J. Nucl. Med. 47*, 2048–2056.

(36) Wang, H., Cai, W., Chen, K., Li, Z. B., Kashefi, A., He, L., and Chen, X. (2007) A new PET tracer specific for vascular endothelial growth factor receptor 2. *Eur. J. Nucl. Med. Mol. Imaging 34*, 2001–10.

(37) Lu, E., Wagner, W. R., Schellenberger, U., Abraham, J. A., Klibanov, A. L., Woulfe, S. R., Csikari, M. M., Fischer, D., Schreiner, G. F., Brandenburger, G. H., and Villanueva, F. S. (2003) Targeted in vivo labeling of receptors for vascular endothelial growth factor: approach to identification of ischemic tissue. *Circulation 108*, 97–103.

(38) Chan, C., Sandhu, J., Guha, A., Scollard, D. A., Wang, J., Chen, P., Bai, K., Lee, L., and Reilly, R. M. (2005) A human transferrin-vascular endothelial growth factor (hnTf-VEGF) fusion protein containing an integrated binding site for (111) In for imaging tumor angiogenesis. *J. Nucl. Med. 46*, 1745–1752.

BC7004818

Evaluation of Cationic Assemblies Constructed with Amino Acid Based Lipids for Plasmid DNA Delivery

Yosuke Obata, Daisuke Suzuki, and Shinji Takeoka*

Department of Life Science and Medical Bioscience, Graduate School of Advanced Science and Engineering, Waseda University, Tokyo 169-8555, Japan. Received November 13, 2007; Revised Manuscript Received February 13, 2008

We synthesized cationic lipids bearing lysine, histidine, or arginine as a cationic headgroup for use in gene transfer studies. The cationic assemblies formed from lysine- or arginine-type lipids gave unilamellar vesicles (∼100 nm diameter), whereas the morphology of the histidine-type lipids was tube-like. The competences of the cationic assemblies were sufficient to form lipoplexes, and the resulting lipoplexes were evaluated in terms of gene expression efficiencies with COS-7 cells. The lysine- or arginine-type lipids exhibited higher gene expression efficiencies than that of Lipofectamine2000, a conventional transgenic reagent, indicating that stable lipoplexes could be prepared between spherical cationic assemblies and plasmid DNA. The gene expression efficiency in relation to the cationic headgroup of the lipids was as follows: lysine ≥ arginine > histidine. In addition, gene expression efficiency was enhanced by decreasing the length of the alkyl chain of the hydrophobic moiety. Unlike Lipofectamine2000, no reduction in transfection efficiency in the presence of fetal bovine serum was observed for the lipoplexes formed using synthetic cationic lipids. Moreover, the synthetic cationic lipids revealed remarkably low cytotoxicity compared with Lipofectamine2000. In conclusion, cationic assemblies formed from 1,5-ditetradecyl-*N*-lysyl-L-glutamate or 1,5-ditetradecyl-*N*-arginyl-L-glutamate can be used as an effective plasmid DNA delivery system.

INTRODUCTION

Gene therapy has become an important alternative approach for the treatment of diseases that until recently were considered incurable. Viral vectors such as adenovirus vectors, adeno-associated virus vectors, or retrovirus vectors have been utilized in clinical trials. However, some side effects including immunoresponse and infection have been reported (*1*). Therefore, the development of nonviral vectors for practical gene therapy is keenly awaited.

Nonviral vectors constructed using synthetic polymers or amphiphiles have been explored for the delivery of nucleic acid to living cells. However, nonviral vectors constructed from cationic polymers such as poly(L-lysine) (PLL) (*2–4*), polyethyleneimine (PEI), (*5–8*) or chitosan (*9–11*) generally exhibit quite low expression efficiencies in comparison to viral vectors. Moreover, cationic polymers usually display high levels of cytotoxicity as a result of their slow rate of degradation in transfected cells, resulting in long-term stress. To reduce the problem of toxicity, cationic amphiphiles have been utilized as an alternative to cationic polymers. Lipoplexes are generally formed by electrostatic complexation between negatively charged nucleic acids and positively charged liposomes. Both preclinical and clinical studies (Phase I and II) have shown lipoplexes to be a less toxic delivery system than those composed of cationic polymers (*12–15*). However, despite these promising developments the expression level of current cationic lipid-based transgenic regents, such as LipofectaminePlus, is several thousand-fold lower than that of adenovirus vectors (*16, 17*).

To enhance gene expression efficiency, various cationic liposomes have been utilized to investigate the mechanism of intracellular delivery of nucleic acids to the cytoplasm or nucleus (*18–20*). When lipoplexes are taken up by the target cell, membrane fusion occurs between the cationic liposomal components and the endosomal membrane of early endosomes (pH 6.0–6.5), leading to the release of nucleic acids into cytoplasm. The released nucleic acids generally accumulate in the nucleus (*21*). Critical factors for intracellular delivery of nucleic acids include the size of the lipoplex, the ratio of lipid to nucleic acid, morphology of the lipoplex, and liposome composition. Generally, the cationic liposomes must be less than about 100 nm in diameter for efficient uptake into cells. The lipid-to-nucleic acid ratio is estimated from the ratio of the nitrogen groups of the cationic compound to the phosphate groups of the nucleic acid (N/P ratio). An appropriate N/P ratio is dependent on the headgroup structure of the cationic lipids. Dioleoylphosphatidylethanolamine (DOPE) has been utilized as a helper lipid of the liposomal membrane because it alters the assembling state of the cationic lipids due to the bilayer-to-hexagonal phase transition of DOPE triggered by lowering pH (*22–24*). However, DOPE-containing liposomes cannot be used in the presence of serum proteins, which reduce their fusogenic potential (*25*). Moreover, Bhattacharya et al. focused on a spacer between the headgroup of cholesterol-based gemini lipids to reduce the influences of serum proteins on lipoplex (*26–28*). Cationic lipids are generally composed of a cationic headgroup and a hydrophobic moiety such as a hydrocarbon chain (*29–32*) or cholesterol derivative (*26, 33*). The hydrophobic moiety is linked to the lipid backbone by an amide, ester, or ether bond. Spermine or spermidine has been widely utilized as the headgroup to condense nucleic acid. The representative components are 2,3-dioleyloxy-*N*-[2(sperminecarboxamide)ethyl]-*N*,*N*-dimethyl-1-propanaminium-trifluoroacetate (DOSPA) and dioctadecylamidoglycyl spermine (DOGS). The high level of cytotoxicity of these compounds was confirmed by experiments using Lipofectamine2000 reagent containing DOSPA. Kim et al. recently reported a cationic lipid having an aspartate backbone and a lysine headgroup that gave an efficient gene expression efficiency and reduced cytotoxicity (*34*). Subsequently, they reported in the following study that the glutamate

* Corresponding author. Phone: +813-5286-3217. Fax: +813-5286-3217. E-mail: takeoka@waseda.jp.

10.1021/bc700416u CCC: $40.75 © 2008 American Chemical Society
Published on Web 04/23/2008

Scheme 1. Synthesis of Amino Acid Based Cationic Lipids Bearing Lysine, Histidine, or Arginine as a Cationic Head Group

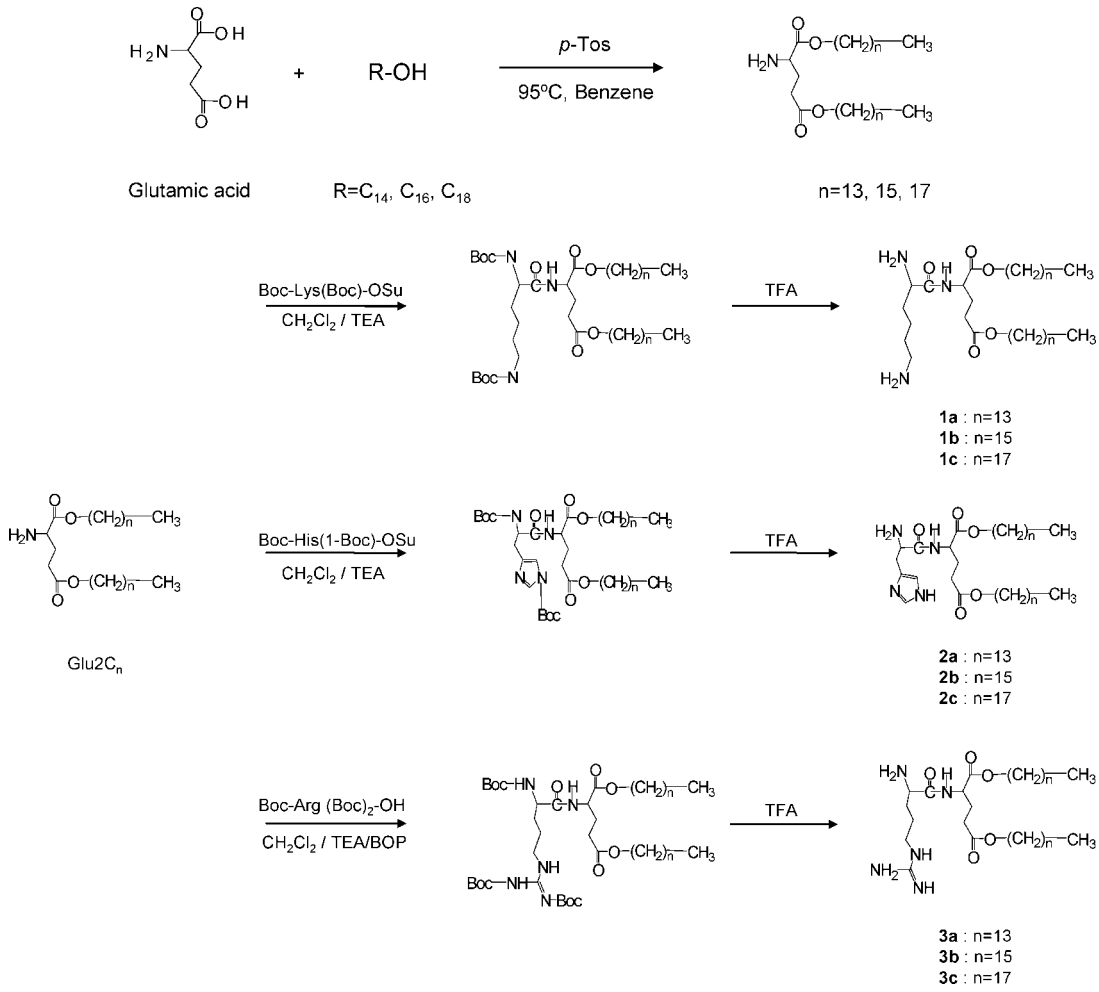

backbone had a higher potency to transfer nucleic acid than the aspartate backbone (*35*). We have also demonstrated the utilities of the lipids having a glutamate backbone and investigated their potential as a liposomal gene delivery system (*36, 37*).

In this study, we focus on the cationic lipid-based nucleic acid carriers without using phospholipid. We synthesized a series of cationic lipids having a glutamate backbone and a cationic amino acid such as lysine, histidine, or arginine as the headgroup. Assemblies of these compounds were then investigated in terms of morphology, complexation profiles with plasmid DNA (pDNA), and the dispersion state of the resulting lipoplexes by altering the cationic headgroup and length of the alkyl chains of the cationic lipids. Lipoplexes containing pDNA-encoding luciferase were constructed with a series of amino acid based lipids and various lipid-to-pDNA ratios. Cytotoxicities of these pDNA carriers were then compared with conventional Lipofectamine2000. The appropriate structure of the cationic lipid was soaked.

MATERIALS AND METHODS

Materials. The following reagents were purchased from Kanto Chemical Inc. (Tokyo, Japan): L-glutamic acid, *p*-toluenesulfonic acid monohydrate (*p*-Tos), benzotriazol-1-yloxytris(dimethylamino)phosphonium hexafluorophosphate (BOP), tetradecyl alcohol, hexadecyl alcohol, or octadecyl alcohol. N_α,N_ϵ-Di-*tert*-butoxycarbonyl-L-lysine hydroxysuccinimide ester (Boc-Lys(Boc)-OSu), N_α,N_ϵ-di-*tert*-butoxycarbonyl-L-histidine hydroxysuccinimide ester (Boc-His(1-Boc)-OSu), and N_α,N_δ,N_ω-tri-*tert*-butoxycarbonyl-L-arginine (Boc-Arg(Boc)$_2$-OH) were purchased from Kokusan Chemical (Tokyo, Japan). All organic reagents employed in the synthesis of the amino acid based cationic lipids were obtained from Kanto Chemical.

Synthesis of Amino Acid Based Cationic Lipids. a (1,5-ditetradecyl-L-glutamate), **b** (1,5-dihexadecyl-L-glutamate), and **c** (1,5-dioctadecyl-L-glutamate) were synthesized as a hydrophobic moiety, and then they were conjugated to the cationic head-groups such as lysine, histidine, and arginine as shown in Scheme 1. The syntheses of the cationic lipids and their characterization are shown in Supporting Information.

Preparation of Cationic Assemblies Formed from the Synthetic Lipids. The lyophilized lipid powder (10 mg) was hydrated in deionized water (1 mL) for 2 h and extruded with a LIPEX EXTRUDER (Northern Lipids Inc.; Vancouver, Canada) with membrane filters (cellulose acetate filters with pore sizes of 3.00, 0.80, 0.65, 0.45, 0.22, 0.10 μm, Millipore Inc., Bedford, MA) at 60 °C. The cationic assemblies were prepared from the lysine- (**1a**−**1c**), histidine- (**2a**−**2c**), or arginine- (**3a**−**3c**) type lipids. The lipid concentration of the cationic assemblies was determined by estimating the lipid weight after the freeze-drying the cationic assembling dispersion.

Microscopic Observation of the Cationic Assemblies. The cationic assemblies were observed by transmission electron microscopy (TEM). A drop of the sample dispersion was placed on a 100 mesh copper grid, and then the excess dispersion was removed with a filter paper. A drop of 2% phosphotungstic acid solution (pH 7.4) was added to the grid and then dried for 12 h in a desiccator. The morphology of the cationic assemblies was observed by TEM (JM-1011, JEOL).

Preparation of Lipoplexes. The cationic assemblies were mixed with a phRL-TK plasmid vector (4045 bp, HSV promoter; Promega, Madison, WI) encoding renilla luciferase. The mixed solutions were gently agitated and incubated at room temperature for 15 min. The solutions were then diluted with an appropriate amount of Dulbecco's modified Eagle's medium (DMEM) with or without fetal bovine serum (FBS) for analyzing the gene transferring efficiency. Lipofectamine2000 (Invitrogen, Carlsbad, CA) was used for gene transfer studies according to the manufacturer's guidelines.

Measurement of Size Distribution and Zeta-Potential of the Lipoplexes. The dispersion of the cationic assemblies (150 nmol as lipid concentration) was diluted with distilled water (1 mL). The mean particle diameter was then measured using a dynamic light scattering spectrophotometer (N4 PLUS Submicron Particle Size Analyzer; Beckman-Coulter Inc., Fullerton, FL). The zeta-potential of the lipoplexes dispersed in distilled water was measured with a Zetasizer (Zetasizer4; Malvern, UK). The lipoplex dispersed in water (15 μmol as lipid concentration, 1 mL) was loaded in the capillary cell mounted on the apparatus and measured three times at 37 °C.

Gel Retardation Assay of the Lipoplexes. The lipoplexes prepared by varying the lipid-to-pDNA ratio were applied to a 1% seaplaque GTG agarose gel (Takara Bio. Inc., Otsu, Japan) in 1% Tris−acetate−EDTA (Invitrogen). After electrophoresis for 30 min, the agarose gel was rinsed in an ethidium bromide (EtBr) solution for 10 min. The gel was then rinsed in distilled water for 15 min and visualized on a UV transilluminator (GelDoc XR system; Bio-Rad, Hercules, CA).

Measurement of Gene Expression Efficiency of the Lipoplexes by COS-7 Cells. COS-7 cells (transformed African green monkey kidney fibroblast cells) were utilized for evaluating the gene expression efficiency of various lipoplexes. The COS-7 cells (1×10^4 cells) were seeded on 96-well plates and incubated at 37 °C under 5% CO_2 for 12 h. The COS-7 cells were cultured with DMEM containing 10% FBS. The medium in the cell culture dishes was changed to a fresh medium (100 μL) in the presence of lipoplexes containing 2 μg/mL of pDNA as a final concentration. After incubation at 37 °C for 24 h, the cells were washed twice with an ice-cold PBS solution and then lysed with a lysis buffer from the luciferase assay kit (Promega, Madison, WI). The luciferase activity in a 10 μL aliquot of the cell lysate was measured with a Microlumat Plus (EG&G Berthold, BadWilbad, Germany). The protein concentration of each well lysate was determined by a standard protein assay (Bio-Rad Protein Assay; Bio-Rad). The luciferase activity in each sample was normalized to the relative light unit (RLU) per microgram of protein.

Calorimetric Analysis of the Cationic Assemblies. A gel-to-lipid crystalline phase transition temperature (T_c) of the cationic assemblies from the synthetic amino acid based cationic lipids was investigated using a differential scanning calorimeter (DSC). The dispersion containing 40 μmol lipids of cationic assemblies was added to a silver pan and sealed. A reference pan was mounted with 30 μL of distilled water. The sample pan and the reference pan were placed in a DSC cell compartment (Differential Scanning Colorimeter Q2000; TA Instruments, Newcastle, DE). The measurement was usually started from 0 °C, and the temperature was raised at a rate of 2 °C/min up to 80 °C. The transition temperature was estimated from the DSC curve.

Fusion Assay of the Cationic Assemblies with Model Membrane. The membrane fusion between the cationic assemblies and liposomes with biomembrane-mimicking lipid composition was investigated to explore the gene transfer mechanism of the prepared lipoplexes by using a fluorescence resonance energy transfer (FRET) assay. The model liposomes constructed with DOPC/DOPE/DOPS/cholesterol (45:20:20:15, wt %) were labeled with *N*-(7-nitrobenz-2-oxa-1,3-diazol-4-yl)-phosphatidylethanolamine (NBD-PE) and rhodamine-phosphatidylethanolamine (Rho-PE), of which concentrations were 1 mol %. For the fusion assay, 500 μL of the labeled liposomes (500 μM as lipid concentration) was added to 500 μL of the prepared lipoplexes (500 μM as lipid concentration). The mixed solution was then incubated at 37 °C for an appropriate period of time. Fluorescence intensity was recorded using an excitation wavelength of 460 nm and an emission wavelength of 525 nm. The time course of the lipid mixing percentage between the model membrane and the cationic assemblies was determined using the following equation:

$$\text{Lipid Mixing \%} = ((F_t - F_0)/(F_{TX} - F_0)) \times 100$$

where F_t is the fluorescence intensity at an appropriate time, F_0 is the fluorescence intensity just after dilution with distilled water, and F_{TX} is the fluorescence intensity after the addition of Triton X-100 to solubilize the liposomes.

Table 1. Size Distribution of Cationic Assemblies Constructed with the Cationic Lipids after Extrusion

lipid composition	particle size (nm)
1a	89 ± 37
1b	38 ± 31
1c	116 ± 54
2b	93 ± 34
2c	97 ± 37
3a	90 ± 32
3b	93 ± 34
3c	92 ± 40

Cytotoxicity of the Lipoplexes. The cytotoxicity of the lipoplexes constructed with the cationic assemblies and pDNA was investigated with COS-7 cells. The COS-7 cells (1×10^4 cells) were seeded on a 96-well plate and incubated at 37 °C under 5% CO_2 for 12 h. The COS-7 cells were cultured with DMEM containing 10% FBS. The medium in the cell culture dish was changed to a fresh medium (100 μL) containing an appropriate concentration of the lipoplexes diluted with a medium containing 10% FBS. After incubation at 37 °C for 24 h, the medium was changed to a medium (110 μL) containing a tetrazolium salt (WST-1) and incubated for 30 min. Formazan (absorbance at 540 nm) is then produced by succinate−tetrazolium reductase in living cells. The absorbance at 540 nm was monitored using a microplate reader (Perkin-Elmer Japan Co. Ltd., Tokyo, Japan).

RESULTS

Synthesis of the Amino Acid Based Cationic Lipids. We synthesized a series of amino acid based cationic lipids that were expected to display gene transferring capacity by utilizing the headgroup amino acid (lysine, histidine, or arginine) as shown in Scheme 1. Two long-chain alcohol molecules of varying chain length were esterified to the carboxyl groups of glutamic acid (**a**−**c**). The yield of **a**−**c** after recrystallization was high (i.e., >70%). Protected amino acid reagents, such as Boc-Lys(Boc)-OSu, Boc-His(1-Boc)-OSu, or Boc-Arg(Boc)$_2$-OH, were reacted with the amino group of **a**−**c** via an amide linkage. Deprotection with trifluoroacetic acid led to the formation of the amino acid based cationic lipids. Thus, we succeeded in devising an efficient synthetic route to generate cationic lipids using a minimal number of steps, followed by recrystallization to give a cost-effective purification method.

Cationic Assembling Structures. The cationic assemblies formed from the synthetic amino acid based cationic lipids were prepared by an extrusion method (Table 1) and were observed using TEM (Figure 1). In addition, we confirmed that the

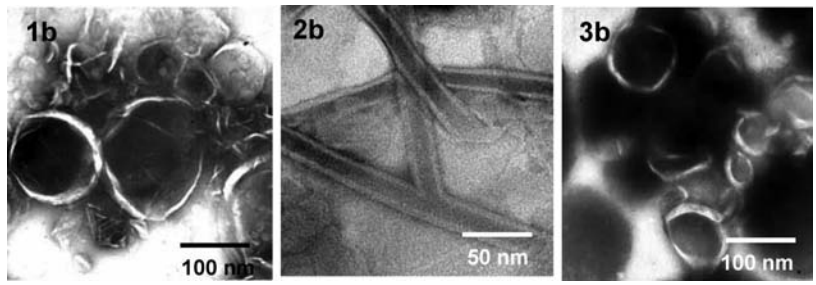

Figure 1. Transmission electron microscopic images of the cationic assemblies constructed with (a) **1b**, (b) **2b**, or (c) **3b** lipid, stained with 2% sodium phosphotungstic acid.

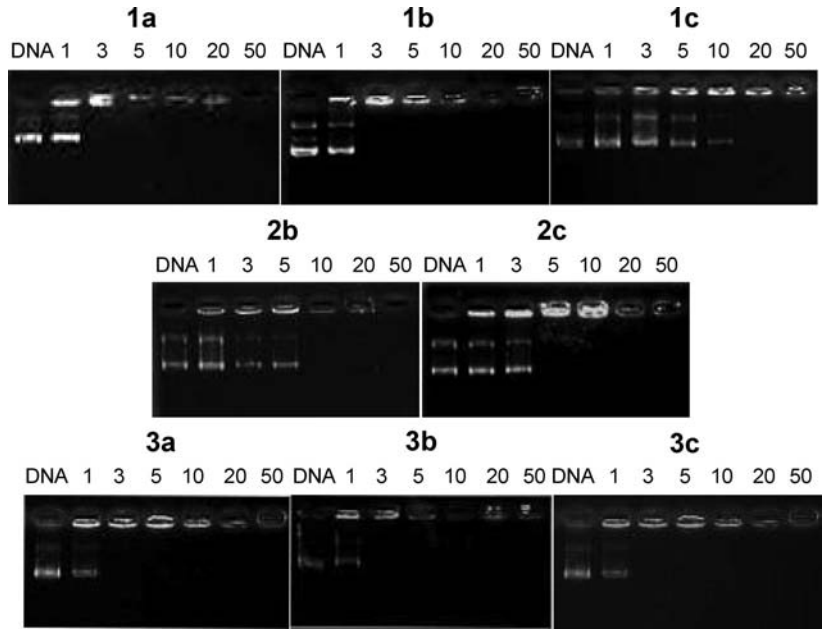

Figure 2. Gel retardation of lipoplexes constructed with cationic assemblies and pDNA with various lipid-to-pDNA ratios (w/w).

structure of the cationic assemblies was influenced by the headgroup of the lipids. Assemblies prepared from the lysine-(**1a**−**1b**) or arginine-type lipid (**3a**−**3c**) formed unilamellar vesicles with a diameter of approximately 100 nm by DLS measurements but more than 100 nm in size for the cationic assembly of **1c**. By contrast, morphology of the histidine-type lipids (**2b**, **2c**) was tube-like. The histidine-type lipid **2a** aggregated when dispersed in distilled water and could not permeate through a membrane filter of pore size 3 μm. No further characterization of **2a** was performed in this study. Moreover, morphologies of the unilamellar vesicles formed from lysine-, arginine-, or histidine-type lipids were less influenced by variations in the length of alkyl chains.

Lipoplex Formation of the Cationic Assemblies with pDNA. We analyzed lipoplex formation between the cationic assemblies by varying the lipid-to-pDNA ratio and pDNA using agarose gel retardation assays (Figure 2). The abilities of all the cationic assemblies were enough to form lipoplexes. Excess pDNA was barely detectable using a lipid-to-pDNA ratio of 3 in the cationic assemblies of **1a**, **1b**, and **3a–3c**. For **1c**, **2b**, and **2c**, the lipid-to-pDNA ratios had to be increased to 20, 10, and 10, respectively. Having prepared the lipoplexes, spontaneous pDNA released into the solution was scarcely detectable even after several hours.

In particular, we investigated the lipoplexes composed of **1a** and **3a** with respect to size distribution and zeta-potential (Figure 3). The apparent size of the lipoplex composed of **1a** and pDNA continuously increased with increasing lipid-to-pDNA ratios from 1 to 5. However, any further increase in the lipid-to-pDNA ratio resulted in a reduction in the size of lipoplex. The 90 nm unilamellar vesicles of **1a** increased in size to 390 nm lipoplexes at a lipid-to-pDNA of 10. The zeta-potential of the lipoplex composed of **1a** dramatically increased as the lipid-to-pDNA ratio was raised from 1 to 3. However, additional increases in the lipid-to-pDNA ratio from 3 to 50 resulted only in a gradual rise in zeta-potential, reaching a maximum of around +40 mV. The size of the lipoplexes composed of **3a** also increased as the lipid-to-pDNA ratio was raised to 5, although the zeta-potential was constant (+25 mV) at ratios greater than 5.

Luciferase Activity of the Cationic Assemblies. We evaluated the gene transferring efficiency of lipoplexes composed of the synthetic lipids using COS-7 cells (Figure 4). Lipoplexes composed of each cationic assembly and luciferase-encoding pDNA were prepared by varying the lipid-to-pDNA ratio with fixing the pDNA concentration of 2 μg/mL. The lipoplexes were then transfected into COS-7 cells. For the lysine-type lipids, gene expression efficiency exhibited a maximum value at a **1a**-to-pDNA ratio of 10, which was 2.2-fold higher compared with that for Lipofectamine2000 reagent in the absence of FBS (Figure 4A). The gene expression level after transfection with **1a**, **1b**, and **1c** tended to increase with shorter alkyl chains. The gene transferring efficiency with **1c** was the lowest of the three lysine-type lipids. In addition, gene expression efficiency with Lipofectamine2000 was considerably reduced in the presence of FBS (Figure 4B). By contrast, gene expression levels determined using lipoplexes formed from **1a**−**1c** displayed

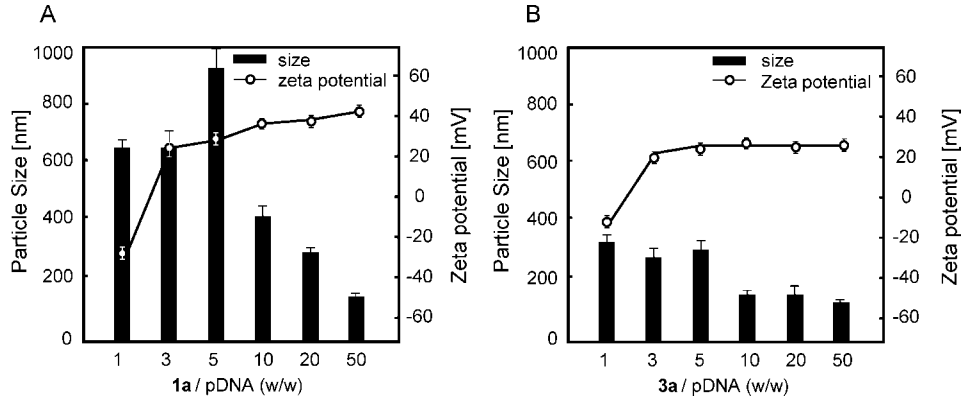

Figure 3. Size distribution and zeta-potential of the lipoplex constructed with (A) **1a** or (B) **3a** lipid. The lipoplexes were dispersed in distilled water at 37 °C.

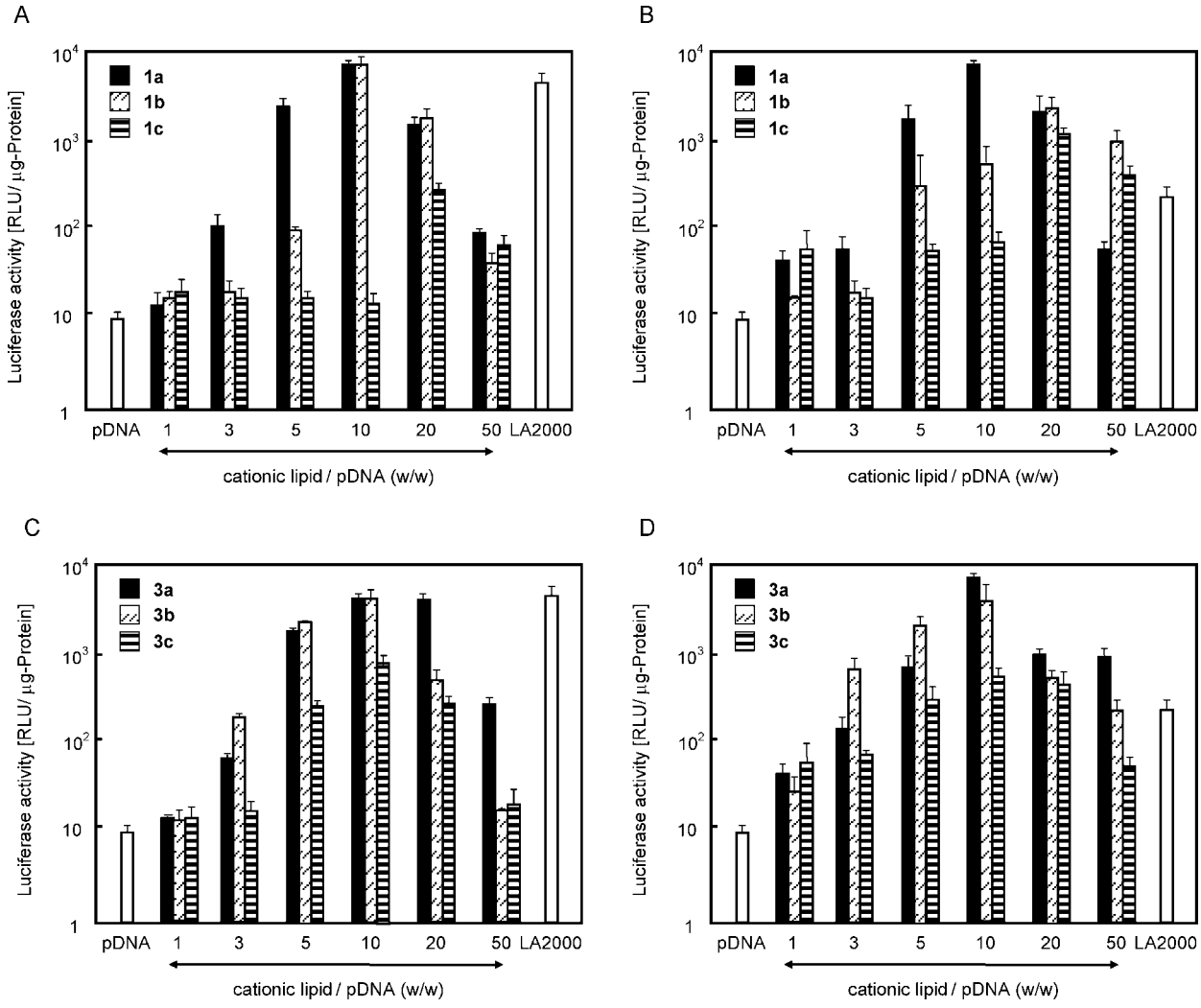

Figure 4. Luciferase activity of COS-7 cells transfected with the lipoplexes. The luciferase activities varied according to the lysine-type lipid-to-pDNA ratio in the (A) absence or (B) presence of fetal bovine serum. The luciferase activity with the lipoplexes varied according to the arginine-type lipid-to-pDNA ratio in the (C) absence or (D) presence of fetal bovine serum.

no significant difference in the presence/absence of FBS. Consequently, in the presence of FBS the expression level of **1a** at a lipid-to-pDNA ratio of 10 was 12-fold higher than that observed using lipofectamine2000.

In addition, we investigated the gene transferring efficiencies of cationic assemblies prepared from the other cationic lipids having a histidine or an arginine as the cationic headgroup. Cationic assemblies formed from histidine-type lipids **2b** or **2c** did not give detectable levels (ca. 200 RLU at all lipid-to-pDNA ratios) of gene expression. The gene expression efficiencies for the arginine-type lipids were as high as those obtained for the lysine-type lipids. The arginine-type **3a**−**3c** also showed a maximum gene expression efficiency at a lipid-to-pDNA ratio of 10 (Figure 4C). Furthermore, the gene expression efficiency for **3a**−**3c** increased as the length of the alkyl chain was reduced. In addition, the gene expression efficiency with the arginine-type lipids was not significantly affected by the presence of FBS (Figure 4D).

A

Compounds	1a	1b	1c	3a	3b	3c
Transition temp. (°C)	26.3	43.3	53.2	24.7	42.5	52.7

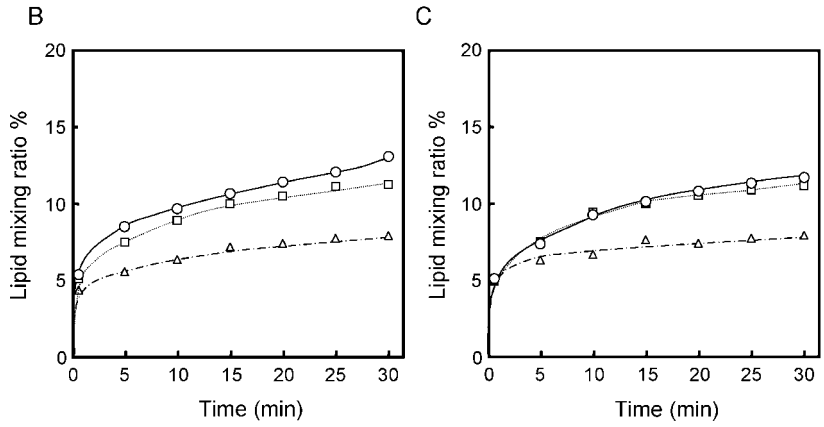

Figure 5. Fusogenic potential of cationic assemblies formed from the synthetic lipids. (A) A transition temperature of cationic assemblies by DSC analysis. (B) Fusogenic potential between the cationic assemblies from **1a** (circle), **1b** (square), or **1c** (triangle) and biomembrane mimicking liposome at 37 °C. (C) Fusogenic potential between the cationic assemblies from **3a** (circle), **3b** (square), and **3c** (triangle).

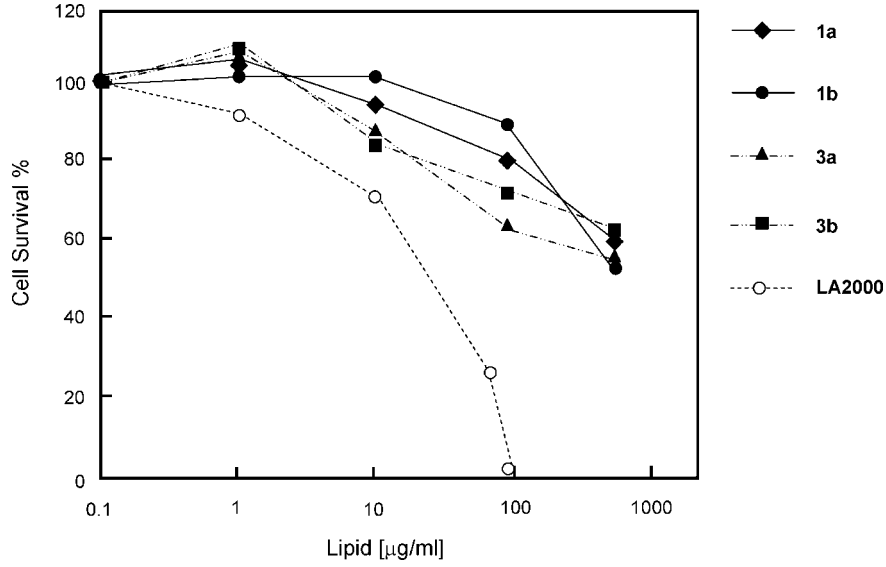

Figure 6. Cytotoxicity of COS-7 cells transfected with lipoplexes constructed using synthetic cationic lipids and pDNA compared with lipofectamine2000 reagent. Lipoplexes were added to COS-7 cells and incubated for 24 h. Cytotoxicity was estimated using the WST assay.

Effect of the Hydrophobic Moiety of the Cationic Assemblies on Fusogenic Potential to a Biomembrane. The fusogenic potential of the cationic assemblies to biomembrane mimicking liposomes was investigated (Figure 5). We confirmed that the difference in the fusogenic potential of the prepared cationic assemblies was based on fluidity. The transition temperatures of the lysine-type lipids **1a**, **1b**, and **1c** were 26.3, 43.3, and 53.2 °C, respectively (Figure 5A). For the arginine-type lipids **3a**, **3b**, and **3c**, the transition temperatures were 24.7, 42.5, and 52.7 °C, respectively. Similar analyses of **2b** and **2c** were conducted to obtain the transition temperatures of 34.4 and 42.3 °C, respectively. Our results indicate that the transition temperature of the cationic assemblies increased with increasing alkyl chain length. Thus, the hydrophobic moiety appears to have a direct effect on fusogenic potential. There was no significant difference in transition temperature between the lysine-type and the arginine-type series of lipids having the same alkyl chain length. Among the lysine-type lipids, **1a** exhibited the highest fusogenic potential (Figure 5B). The fusogenic ratio of **1a** gradually increased and reached about 13% after incubation for 30 min at 37 °C. **1b** showed a slightly lower fusogenic potential than **1a**. However, the fusogenic potential of **1c** was significantly diminished compared to those of **1a** and **1b**. A similar trend was also observed for the arginine-type lipids (Figure 5C). The fusogenic potentials of **3a** and **3b** were almost the same, whereas that of **3c** was significantly lower. The fusogenic potentials of the lysine-type lipids were slightly higher than those of the arginine-type lipids. Our data would highlight the influence of the hydrophobic moiety on fusogenic potential.

Cytotoxicities of the Lipoplexes. We investigated the cytotoxicities of the lipoplexes constructed with the various synthetic cationic lipids (Figure 6). All cationic lipids were revealed to have low toxicity. Lipoplex composed of lipofectamine2000 reagent at a lipid-to-pDNA ratio of 3 was toxic to around 100% of COS-7 cells at a lipid concentration of 100 μg/mL. By contrast, lipoplexes constructed of the cationic assemblies of **1a**, **1b**, **3a**, or **3c** exhibited significantly lower toxicities. For example, more than half of the cells seeded on a

culture dish survived even in the presence of 1 mg/mL lipid concentration of lipoplex (i.e., ~50 times higher lipid concentration compared to the experiment using Lipofectamine2000).

DISCUSSION

Our objective in this study was to develop cationic lipids with a high gene transferring efficiency that could be readily and inexpensively synthesized. We analyzed amino acid based cationic lipids and tested their ability to form lipoplex. Initially, we focused on the molecular assemblies formed from synthetic cationic lipids. The lysine- or arginine-type lipids formed unilamellar vesicles, whereas the histidine-type lipid formed a tube-like structure. These results indicate that the overall architecture of the assemblies is largely determined by the nature of the hydrophilic headgroup. It was reported that assemblies formed from amino acid based lipids with an asymmetric carbon can adopt various structures such as a tube, fiber, or ribbon (*38, 39*). Here, we confirmed that the synthetic amino acid based lipids with two asymmetric carbon atoms would be expected to take various assembling structures. After extrusion, the histidine-type lipid initially formed a vesicular structure that was observed by TEM (data not shown). However, the ratio of tube-like assemblies gradually increased over a period of a week during storage at 4 °C. If the transition temperature is exceeded during the extrusion procedure, a rearrangement of lipid molecules into unstable bilayer vesicles might occur. Subsequent incubation at low temperatures will then cause the vesicles to gradually aggregate and fuse into a more stable state, that is, in this case a tube-like structure (*40*). Therefore, we conclude that **2a**, **2b**, and **2c** cannot form stable vesicle dispersions because of an unfavorable balance of hydrophilic and hydrophobic characteristics and the particular structure of the histidine moiety.

All the cationic assemblies were confirmed to form lipoplexes with pDNA from a gel retardation assay. When the lipid-to-pDNA ratio was >3, no excess pDNA was detected for **1a**, **1b**, **3a**, and **3b** (the estimated N/P ratio of 2.7). Because the unilamellar vesicles comprise both an outer and an inner layer, the more accurate N/P ratio is about 1.4 if there were no change of inner- and outer-lipid composition after lipoplex formation. Therefore, a proportion of the amino groups of the outer layer of the liposome do not have access to the phosphate groups of the pDNA. When **1c** was utilized as a component of the cationic assembly, more lipids were required to form lipoplexes. Indeed, the size of cationic assembly of **1c** was large in comparison to that of **1a** or **1b**. If **1c** would take a unilamellar structure, the portion of the amino groups of the vesicle, which can access pDNA, should be equal to those of **1a** and **1b**. However, more **1c** lipid was required to form a lipoplex with the pDNA. Therefore, we regarded the cationic assemblies of **1c** as multilamellar structures. Therefore, we defined the cationic assemblies as multilamellar structures. Cationic assemblies from the histidine-type lipids formed a stable complex with the pDNA at a lipid-to-pDNA ratio of 10 (N/P = 8). More histidine-type lipid based cationic assemblies were required to form lipoplex than the lysine- or arginine-type lipids. On the basis of pK_a values of the different amino groups, electrostatic interaction of the tertiary amino group of histidine will be much weaker than that of the primary amino group of lysine or arginine. Thus, we might anticipate that the competence of the histidine-type lipids to form lipoplexes will be relatively low. Indeed, this conclusion is further supported by previous studies using cationic amino-acid derivatives derived from tryptophan-type lipids, which exhibited low levels of gene expression in transfection experiments (*41*). Moreover, tube-like assemblies might be unable to form a lipoplex with pDNA. No further analysis of the histidine type-lipids was performed in this study. Therefore, our analysis shows that assemblies with a lysine or arginine headgroup are the most appropriate to form lipoplexes.

The maximum values of gene expression efficiency for **1a**−**1c** and **3a**−**3c** were obtained at a lipid-to-pDNA ratio of 10. The zeta-potential of lipoplexes exhibiting the highest level of gene expression was about +38 mV for **1a** and +22 mV for **3a** at a lipid-to-pDNA ratio of 10. Under the transfection conditions used in this study, the amino groups of the lysine or arginine moieties would be fully protonated. Therefore, the difference in zeta-potential between the lipoplexes of **1a** and those of **3a** must be caused by variation in the length of the alkyl side chains of the cationic amino acids. The amino group of lysine has a higher zeta-potential than that of arginine because it is located at the terminus of a relatively long side chain.

Comparison of gene transfer efficiency with respect to the headgroup of the cationic lipids is as follows: lysine ≥ arginine > histidine. Thus, both lysine and arginine form appropriate headgroups to bind pDNA and display a high affinity for the cell membrane. Although the lipoplex formation using histidine-type lipids was confirmed by gel retardation, the level of gene expression was quite low. This low level of gene expression might be due to poor cellular uptake of the tube-like assemblies, which were several micrometers in length and 10 nm in diameter. Furthermore, after endocytosis the electrostatic interaction between the tertiary amino group of the histidine and the phosphate group of pDNA is presumably very weak in the acidic environment of the endosome. Thus, delivery of pDNA into the nucleus will be very inefficient.

In our study, uniform vesicles from **1a**−**1c** or **3a**−**3c** having a glutamate backbone showed high levels of gene transfer efficiency. Kim et al. reported lysine-type lipid derivatives (*O*,*O*′-dimyristyl-*N*-lysyl aspartate (DMKD) and *O*,*O*′-dimyristyl-*N*-lysyl glutamate (DMKE)) (*34, 35*), and DMKD showed a maximum gene expression at a lipid-to-pDNA ratio of 5. We traced their experiments using the same aspartic acid derivatives and clarified that the lipid assemblies formed a mixture of ribbon-like and vesicular structures (data not shown). So far, there has been no definite to instruct a difference in molecular assembly between the glutamate- and aspartate-based lipids. From this comparison, we adopted the glutamate backbone rather than the aspartate backbone. The cationic liposomes composed of cholesterol and DMKE or **1a** were also evaluated in vivo to indicate the usefulness of the glutamate backbone (*35*).

The gene expression efficiencies of our cationic lipids were also dependent on the length of the alkyl chain. Order of gene expression efficiency in terms of the number of carbon atoms in the alkyl chain was as follows: 14 > 16 > 18. The gene expression efficiency of a lipoplex is generally known to be dependent on the T_c of the cationic lipid (*42, 43*). Two independent studies involving a series of cationic lipids of different alkyl chain lengths showed the expression efficiency to be: $C_{14} > C_{oleyl} > C_{18} > C_{16} > C_{12}$ by Felgner et al. (*44*) or $C_{14} > C_{oleyl} > C_{16} > C_{18}$ by Floch et al. (*45, 46*). However, because lipoplexes utilize helper lipids, such as DOPE or cholesterol, the fluidity of the liposomal membrane is not solely dependent on the fluidity of the pure cationic lipids. Lipid membranes of high fluidity tend to promote fusion with a biological membrane, leading to high gene expression efficiency (*18, 42, 43*). Thus, we also analyzed the fusogenic potential of the cationic assemblies using a model membrane that mimics a biomembrane. The fusogenic potentials of the lipoplexes from **1c** (T_c, 53.2 °C) or **3c** (T_c, 52.7 °C) with low fluidity were quite low, resulting in quite low gene expression efficiency in comparison with that of **1a** (T_c, 26.3 °C) or **3a** (T_c, 24.7 °C) of high fluidity. In our study, cationic assemblies with high fluidity led to high gene expression.

A low level of gene expression efficiency in the presence of FBS has been a major barrier to the medical application of gene therapy (*25*). In general, the phospholipid molecules in the liposomal membrane are thought to be removed by high density lipoproteins (HDL) in serum (*47*). This would result in poor fusogenic ability to the biological membrane in the presence of FBS, leading to low gene expression efficiency, particularly when DOPE was utilized as a liposomal component. In our study, the reduction in gene expression with DOPE-containing transgenic reagents was also confirmed in the presence of FBS. However, cationic assemblies formed from the synthetic lipids under optimal conditions displayed no reduction in gene expression efficiency in the presence of FBS. This observation suggests that the amino acid based cationic lipids are not influenced by FBS. Thus, we succeeded in constructing cationic carriers based on non-DOPE.

The cytotoxicity of the lipoplexes was evaluated using COS-7 cells. Compared with conventional Lipofectamine2000, cytotoxicity of the lipoplexes constructed with the synthetic amino acid based cationic lipids was very low. Toxicity of the conventional reagent is probably related to the presence of multivalent cationic compounds such as DOGS or DOSPA. Specifically, after dissociation of the pDNA the multivalent cationic compounds aggregate with various intracellular organelles, leading to cell death. By contrast, amino acid based cationic lipids are easily dissociated and metabolized. Furthermore, the ester bond in the linker region of the amino acid based cationic lipids is readily hydrolyzed in the cell, thereby lowering their cytotoxicity (*48*).

In conclusion, we constructed pDNA carriers with synthetic amino acid based cationic lipids. In particular, cationic lipids having lysine or arginine as a headgroup and two C_{14} alkyl chains as hydrophobic moieties were shown to display a high level of gene transfer efficiency equal to that of standard Lipofectamine2000 in the absence of FBS. Additionally, in the presence of FBS, our pDNA carriers provided much higher efficiency than that of Lipofectamine2000. Moreover, the cytotoxicity of our cationic lipids was only one-fifth that of Lipofectamine2000. Thus, results from our in vitro experiments show that lipoplexes formed from these amino acid based cationic lipids are promising candidates for further investigations in vivo. We are currently constructing cationic lipids focusing on the moiety between the lysine headgroup and the hydrophobic moiety to enhance gene expression.

ACKNOWLEDGMENT

The author thanks Oxygenix Corp. and LocomoGene Corp. for useful discussion about the evaluation for the nucleic acid carriers. This work was supported by GCOE program "Practical Chemical Wisdom" from MEXT, Japan.

Supporting Information Available: ^{1}H NMR spectrums and characterizations of the synthetic amino acid based lipids. This information is available free of charge via the Internet at http://pubs.acs.org.

LITERATURE CITED

(1) Raper, S. E., Yudkoff, M., Chirmule, N., Gao, G. P., Nunes, F., Haskal, Z. J., Furth, E. E., Propert, K. J., Robinson, M. B., Magosin, S., Simoes, H., Speicher, L., Hughes, J., Tazelaar, J., Wivel, N. A., Wilson, J. M., and Batshaw, M. L. (2002) A pilot study of in vivo liver-directed gene transfer with an adenoviral vector in partial ornithine transcarbamylase deficiency. *Hum. Gene Ther. 13*, 163–175.

(2) Itaka, K., Yamauchi, A., Harada, K., Nakamura, H., Kawaguchi, H., and Kataoka, K. (2003) Polyion complex micelles from plasmid DNA and poly(ethyleneglycol)-poly(L-lysine) block copolymer as serum-tolerable polyplex system: Physicochemical properties of micelles relevant to gene transfection efficiency. *Biomaterials 24*, 4495–4506.

(3) Okuda, T., Kidoaki, S., Ohsaki, M., Koyama, Y., Yoshikawa, K., Niidome, T., and Aoyagi, H. (2003) Time-dependent complex formation of dendritic poly (L-lysine) with plasmid DNA and correlation with in vitro transfection efficiencies. *Org. Biomol. Chem. 1*, 1270–1273.

(4) Yamagata, M., Kawano, T., Shiba, K., Mori, T., Katayama, Y., and Niidome, T. (2007) Structural advantage of dendritic poly(L-lysine) for gene delivery into cells. *Bioorg. Med. Chem. 15*, 526–32.

(5) Gebhart, C. L., Sriadibhatla, S., Vinogradov, S., Lemieux, P., Alakhov, V., and Kabanov, A. V. (2002) Design and formulation of polyplexes based on pluronic-polyethyleneimine conjugates for gene transfer. *Bioconjugate Chem. 13*, 937–944.

(6) Banerjee, P., Weissleder, R., and Bogdanov, A., Jr. (2006) Linear polyethyleneimine grafted to a hyperbranched poly(ethylene glycol)-like core: A copolymer for gene delivery. *Bioconjugate Chem. 17*, 125–131.

(7) Goula, D., Remy, J. S., Erbacher, P., Wasowicz, M., Levi, G., Abdallah, B., and Demeneix, B. A. (1998) Size, diffusibility and transfection performance of linear PEI/DNA complexes in the mouse central nervous system. *Gene Ther. 5*, 712–717.

(8) Takeuchi, Y., Kurohane, K., Ichikawa, K., Yonezawa, S., Ori, H., Koishi, T., Nango, M., and Oku, N. (2003) Polycation liposome enhances the endocytic uptake of photosensitizer into cells in the presence of serum. *Bioconjugate Chem. 14*, 790–796.

(9) Wong, K., Sun, G., Zhang, X. Q., Dai, H., Liu, Y., He, C. B., and Leong, K. W. (2006) PEI-g-chitosan, a novel gene delivery system with transfection efficiency comparable to polyethylenimine in vitro and after liver administration in vivo. *Bioconjugate Chem. 17*, 152–158.

(10) Chan, P., Kurisawa, M., Chung, J. E., and Yang, Y. Y. (2007) Synthesis and characterization of chitosan-g-poly(ethylene glycol)-folate as a non-viral carrier for tumor-targeted gene delivery. *Biomaterials 28*, 540–549.

(11) Lavertu, M., Méthot, S., Tran-Khanh, N., and Buschmann, M. D. (2007) High efficiency gene transfer using chitosan/DNA nanoparticles with specific combinations of molecular weight and degree of deacetylation. *Biomaterials 27*, 4815–4824.

(12) Cullis, P. R., Wheeler, J. J., Palmer, L., Ossanlou, M., MacLachlan, I., Graham, R. W., Zhang, Y. P., Hope, M. J., and Scherrer, P. (1999) Stabilized plasmid-lipid particles: Construction and characterization. *Gene Ther. 6*, 271–281.

(13) Wheeler, C. J., Felgner, P. L., and Tsai, Y. J. (1996) A novel cationic lipid greatly enhances plasmid DNA delivery and expression in mouse lung. *Proc. Natl. Acad. Sci. U.S.A. 93*, 11454–11459.

(14) Dass, C. R., and Burton, M. A. (2002) A model for evaluating selective delivery of plasmid DNA to tumors via the vasculature. *Cancer Biother. Radiopharm. 17*, 501–505.

(15) Dass, C. R. (2004) Lipoplex-mediated delivery of nucleic acids: Factors affecting in vivo transfection. *J. Mol. Med. 82*, 579–591.

(16) Tachibana, R., Harashima, H., Shinohara, Y., and Kiwada, H. (2001) Quantitative studies on the nuclear transport of plasmid DNA and gene expression employing nonviral vectors. *Adv. Drug Delivery Rev. 52*, 219–226.

(17) Hama, S., Akita, H., Ito, H., Mizuguchi, R., and Hayakawa, H. (2006) Quantitative comparison of intracellular trafficking and nuclear transcription between adenoviral and lipoplex systems. *Mol. Ther. 13*, 786–794.

(18) Nakanishi, M., and Noguchi, A. (2001) Confocal and probe microscopy to study gene transfection mediated by cationic liposomes with a cationic cholesterol derivative. *Adv. Drug Delivery Rev. 52*, 197–207.

(19) Lechardeur, D., and Lukacs, G. L. (2002) Intracellular barriers to non-viral gene transfer. *Curr. Gene Ther. 2*, 183–194.

(20) Zuhorn, I. S., and Hoekstra, D. (2002) On the mechanism of cationic amphiphile-mediated transfection. To fuse or not to fuse: Is that the question? *J. Membr. Biol. 189*, 167–179.
(21) Xu, Y., and Szoka, F. C. (1996) Mechanism of DNA release from cationic liposome/DNA complexes used in cell transfection. *Biochemistry 35*, 5616–5623.
(22) Ishida, T., Kirchmeier, M. J., Moase, E. H., Zalipsky, S., and Allen, T. M. (2001) Targeted delivery and triggered release of liposomal doxorubicin enhanced cytotoxicity against human B lymphoma cells. *Biochim. Biophys. Acta 1515*, 144–158.
(23) Ellens, H., Bentz, J., and Szoka, F. C. (1984) pH-Induced destabilization of phosphatidylethanolamine-containing liposomes, Roles of Bilayer Contact. *Biochemistry 23*, 1532–1538.
(24) Wheeler, J. J., Palmer, L., Ossanlou, M., MacLachlan, I., Graham, R. W., Zhang, Y. P., Hope, M. J., Scherrer, P., and Cullis, P. R. (1999) Stabilized plasmid-lipid particles: construction and characterization. *Gene Ther. 6*, 271–281.
(25) Bailey, A. L., and Cullis, P. R. (1997) Membrane fusion with cationic liposomes: Effects of target membrane lipid composition. *Biochemistry 36*, 1628–34.
(26) Bhattacharya, S., and Dileep, P. V. (1999) Synthesis of novel cationic lipids with oxyethylene spacers at the linkages between hydrocarbon chains and pseudoglyceryl backbone. *Tetrahedron Lett. 40*, 8167–8171.
(27) Bajaj, A., Kondaiah, P., and Bhattacharya, S. (2007) Synthesis and gene transfer activities of novel serum compatible cholesterol-based gemini lipids possessing oxyethylene-type Spacers. *J. Med. Chem. 50*, 2432–2442.
(28) Bajaj, A., Kondaiah, P., and Bhattacharya, S. (2007) Synthesis and gene transfer activities of novel serum compatible cholesterol-based Gemini lipids possessing oxyethylene-type spacers. *Bioconjugate Chem. 18*, 1537–1546.
(29) Gaucheron, J., Santaella, C., and Vierling, P. (2001) Highly fluorinated lipospermines for gene transfer: Synthesis and evaluation of their in vitro transfection efficiency. *Bioconjugate Chem. 12*, 114–128.
(30) Sen, J., and Chaudhuri, A. (2005) Design, syntheses, and transfection biology of novel non-cholesterol-based guanidinylated cationic lipids. *J. Med. Chem. 48*, 812–820.
(31) Choi, J. S., Lee, E. J., Jang, H. S., and Park, J. S. (2001) New cationic liposomes for gene transfer into mammalian cells with high efficiency and low toxicity. *Bioconjugate Chem. 12*, 108–113.
(32) Hasegawa, S., Hirashima, N., and Nakanishi, M. (2001) Microtubule involvement in the intracellular dynamics for gene transfection mediated by cationic liposomes. *Gene Ther. 8*, 1669–1673.
(33) Bajaj, A., Paul, B., Indi, S. S., Kondaiah, P., and Bhattacharya, S. (2007) Effect of the Hydrocarbon Chain and Polymethylene Spacer Lengths on Gene Transfection Efficacies of Gemini Lipids Based on Aromatic Backbone. *Bioconjugate Chem. 18*, 2144–2158.
(34) Kim, H. S., Moon, J., Kim, K. S., Choi, M. M., Lee, J. E., Heo, Y., Cho, D. H., Jang, D. O., and Park, Y. S. (2004) Gene-transferring efficiencies of novel diamino catonic lipids with varied hydrocarbon chain. *Bioconjugate Chem. 15*, 1095–1101.
(35) Kim, H. S., Song, I. H., Kim, J. C., Kim, E. J., Jang, D. O., and Park, Y. S. (2006) In vitro and in vivo gene-transferring characteristics of novel cationic lipids, DMKD O, O′-dimyristyl-N-lysyl aspartate) and DMKE (O, O′-dimyristyl-N-lysyl glutamate. *J. Controlled Release 115*, 234–241.
(36) Okamura, Y., Maekawa, I., Teramura, Y., Maruyama, H., Handa, M., Ikeda, Y., and Takeoka, S. (2005) Hemostatic effects of phospholipid vesicles carrying fibrinogen γ-chain dodecapeptide in vitro and in vivo. *Bioconjugate Chem. 16*, 1589–1596.
(37) Takeoka, S. (2005) Production of artificial blood using molecular assembling science. *Artif. Blood 13*, 136–147.
(38) Shimizu, T. (2003) Bottom-up synthesis and norphological control of high-axial-ratio nanostructures through molecular self-assembly. *Polym. J. 35*, 1–22.
(39) Yamada, N., Ariga, K., Naito, M., Matsubara, K., and Koyama, E. (1998) Regulation of β-sheet structures within amyloid-like β-sheet assemblage from tripeptide derivatives. *J. Am. Chem. Soc. 120*, 12192–12199.
(40) Lauf, U., Fahr, A., Westesen, K., and Ulrich, A. S. (2004) Novel lipid nanotubes in dispersions of DMPC. *ChemPhysChem 5*, 1246–1249.
(41) Heyes, J. A., Duvaz, D. N., Cooper, R. G., and Springer, C. J. (2002) Synthesis of novel cationic lipids: Effect of structural modification on the efficacy of gene transfer. *J. Med. Chem. 45*, 99–114.
(42) Rädler, J. O., Koltover, I., Salditt, T., and Safinya, C. R. (1997) Structure of DNA-cationic liposome complexes: DNA intercalation in multi-lamellar membranes in distinct interhelical packing regimes. *Science 275*, 810–814.
(43) Zantl, R., Baicu, L., Artzner, F., Sprenger, I., Rapp, G., and Rädler, J. O. (1999) Thermotropic phase behavior of cationic lipid-DNA complexes compared to binary lipid mixtures. *J. Phys. Chem. B 103*, 10300–10310.
(44) Felgner, P. L., Gadek, T. R., Holm, M., Roman, R., Chan, H. W., Wenz, M., Northrop, J. P., Ringold, G. M., and Danielsen, M. (1987) Lipofectin: a highly efficient, lipid-mediated DNA transfection procedure. *Proc. Natl. Acad. Sci. U.S.A. 84*, 7413–7417.
(45) Floch, V., Audrezet, M. P., Guillaume, C., Gobin, E., Bolch, G. L., Clement, J. C., Yaouanc, J. J., Abbayes, H. D., Mercier, B., Leroy, J. P., Abgrall, J. F., and Ferec, C. (1998) Transgene expression kinetics after transition with cationic phosphonolipids in hematopoietic nonadherent cells. *Biochim. Biophys. Acta 1371*, 53–70.
(46) Floch, V., Loisel, S., Guenin, E., Herve, A. C., Clement, J. C., Yaouanc, J. J., Abbayes, H. D., and Ferec, C. (2000) Cation substitution in cationic phosphonolipids: A new concept to improve transfection activity and decrease cellular toxicity. *J. Med. Chem. 43*, 4617–4628.
(47) Allen, T. M., and Cleland, L. G. (1980) Serum-induced leakage of liposome contents. *Biochim. Biophys. Acta 597*, 418–426.
(48) Leventis, R., and Silvirus, J. R. (1990) Interactions of mammalian cells with lipid dispersion containing metabolizable cationic amphiphiles. *Biochim. Biophys. Acta 1023*, 124–132.

BC700416U

End Modification of a Linear DNA Duplex Enhances NER-Mediated Excision of an Internal Pt(II)-Lesion

Tracey McGregor Mason,[†] Michael B. Smeaton,[†] Joyce C. Y. Cheung, Les A. Hanakahi, and Paul S. Miller*

Department of Biochemistry and Molecular Biology, Johns Hopkins Bloomberg School of Public Health, Johns Hopkins University, 615 North Wolfe Street, Baltimore, Maryland 21205. Received November 27, 2007; Revised Manuscript Received February 11, 2008

The study of DNA repair has been facilitated by the development of extract-based *in vitro* assay systems and the use of synthetic DNA duplexes that contain site-specific lesions as repair substrates. Unfortunately, exposed DNA termini can be a liability when working in crude cell extracts because they are targets for DNA end-modifying enzymes and binding sites for proteins that recognize DNA termini. In particular, the double-strand break repair protein Ku is an abundant DNA end-binding protein that has been shown to interfere with nucleotide excision repair (NER) *in vitro*. To facilitate the investigation of NER in whole-cell extracts, we explored ways of modifying the exposed ends of synthetic repair substrates to prevent Ku binding and improve *in vitro* NER efficiency. Replacement of six contiguous phosphodiester linkages at the 3′-ends of the duplex repair substrate with nuclease-resistant nonionic methylphosphonate linkages resulted in a 280-fold decrease in binding affinity between Ku and the modified duplex. These results are consistent with the published crystal structure of a Ku/DNA complex [Walker et al. (2001) *Nature 412*, 607−614] and show that the 3′-terminal phosphodiester linkages of linear DNA duplexes are important determinants in DNA end-binding by Ku. Using HeLa whole-cell extracts and a 149-base pair DNA duplex repair substrate, we tested the effects of modification of exposed DNA termini on NER-mediated *in vitro* excision of a 1,3-GTG-Pt(II) intrastrand cross-link. Methylphosphonate modification at the 3′-ends of the repair substrate resulted in a 1.6-fold increase in excision. Derivatization of the 5′-ends of the duplex with biotin and subsequent conjugation with streptavidin to block Ku binding resulted in a 2.3-fold increase excision. By combining these modifications, we were able to effectively reduce Ku-derived interference of NER excision *in vitro* and observed a 4.4-fold increase in platinum lesion excision. These modifications are easy to incorporate into synthetic oligonucleotides and may find general utility whenever synthetic linear duplex DNAs are used as substrates to investigate DNA repair in whole-cell extracts.

INTRODUCTION

Studies of DNA repair often use damaged plasmid DNA or lesion-containing, double-stranded, linear DNA duplexes as repair substrates. Plasmid DNA is problematic as a substrate for *in vitro* repair studies because the size of the substrate makes it difficult to characterize and quantify the repair process. Unlike plasmid DNA, synthetic linear duplexes that contain site-specific lesions are readily synthesized and can be labeled in a variety of ways for high-sensitivity detection of repair activity. Such synthetic linear DNA duplexes provide convenient and easily manipulatable substrates for carrying out detailed studies of DNA repair. For example, linear DNA duplexes of ∼150 bp in length that contain a 1,3-diammineplatinum(II) intrastrand cross-link have been instrumental in the study of nucleotide excision repair (NER) in whole-cell extracts derived from Chinese hamster ovary (CHO) and human (HeLa) cell lines (*1*, *2*). Similar synthetic DNA duplexes have been employed in the study of psoralen interstrand cross-link repair in whole-cell extracts and in fully reconstituted reactions using purified repair proteins (*3*–*6*).

A potential problem with using linear duplexes in repair studies is the presence of exposed DNA termini, which are targets for DNA end-modifying enzymes, such as nucleases or phosphatases, and binding sites for proteins that recognize DNA ends. In particular, proteins involved in the recognition and repair of DNA double-strand breaks (DSB) have been shown to bind at exposed DNA termini of synthetic duplexes (*7*). The DSB repair protein Ku70/80 (Ku), which participates in both DSB repair and in immunoglobulin gene recombination, is a DNA end-binding protein that is abundant in whole-cell extracts (*8*–*12*). Previous studies have suggested that Ku not only binds DNA ends, but once bound can translocate along the DNA duplex. This makes it possible for several Ku molecules to occupy a single linear duplex and to potentially interfere with damage recognition or processing (*13*).

In this article, we present strategies that can improve efficiency in extract-based DNA repair assay systems by preventing recognition of DNA termini by end-binding and -modifying factors. Introduction of nuclease-resistant, nonionic methylphosphonate linkages at the 3′-termini of the duplexes significantly reduces Ku binding. Derivatization of the 5′-ends of the duplex with biotin and subsequent conjugation with streptavidin is known to block binding of Ku to linear DNA duplexes (*14*). We have found that, in combination, these two modifications significantly enhance NER-mediated excision of an internal 1,3-Pt(II) intrastrand cross-link from a 149 bp linear duplex when incubated with a HeLa whole cell extract.

EXPERIMENTAL PROCEDURES

Protected deoxyribonucleoside 3′-*O*-phosphoramidites, 5′-biotin phosphoramidite, and oligonucleotide synthesis reagents

* Correspondence should be addressed to Paul S. Miller, Department of Biochemistry and Molecular Biology, Johns Hopkins Bloomberg School of Public Health, 615 North Wolfe Street, Baltimore, MD 21205. E-mail: pmiller@jhsph.edu, Phone: (410)-955-3489, Fax: (410)-955-2926.

[†] These authors contributed equally to this work.

10.1021/bc7004363 CCC: $40.75 © 2008 American Chemical Society
Published on Web 05/01/2008

Table 1. Linear DNA Duplex Sequences

Duplex	Sequence[a]
1	5'-GTTTTTAGTTTTATGTTCTAGA 3'-CAAAAATCAAAATACAAGATCT-biotin
2	5'-G***TTTTT***AGTTTTATGTTCTAGA 3'-CAAAAATCAAAATACAAGATCT-biotin
3	5'-GTTTTTAGTTTTATGTTCTAGA 3'-C***AAAAAT***CAAAATACAAGATCT-biotin
4	5'-TGCATCCTAACGTTAGGTCTC-**B-C-X-D-E**-ACTGCCAAGTCTGAGTACTTGACTC 3'- CGTAGGATTGCAATCCAGAGGACTG-**B-C-X-D-E--**TTCAGACTCATGAACTGAGCC
5	5'-TG***CATCC***TAACGTTAGGTCTC-**B-C-X-D-E**-ACTGCCAAGTCTGAGTACTTGACTC 3'- CGTAGGATTGCAATCCAGAGGACTG-**B-C-X-D-E--**TTCAGACTCATGA***ACTGA***GCC
6	5'-TGCATCCTAACGTTAGGTCTC-**B-C-X-D-E**-ACTGCCAAGTCTGAGTAC***TTGACT***C 3'- C***GTAGGA***TTGCAATCCAGAGGACTG-**B-C-X-D-E--**TTCAGACTCATGAA*CTGA*GCC
B	5′-CTGACTCAGGTGAAGCTTCAAGCCT 3'- AGTCCACTTCGAAGTTCGGAGAAG
C	5′-CTTCCTTAATCCGGAGACTTGAAAA 3'- GAATTAGGCCTCTGAAC
X	Pt 5'- CTTCGTGTCCCTC 3'-TTTTGAAGCACAGG
D	5′- ACGACCTGCAGTCTATA 3′-GAGTGCTGGACGTCAGATATGTCCT
E	5′-CAGGATGTCAAGTCTAGACACTTC 3′- ACAGTTCAGATCTGTGAAGTGACGG

[a] Methylphosphonate internucleotide linkages are located on the 3′-side of the nucleosides shown in bold italics. G indicates a platinated G residue. The component duplexes that were used to form the full-length duplexes are separated by dashes.

were purchased from Glen Research, Inc. Protected deoxyribonucleoside-3′-*O*-methylphosphonamidites were a product of JBL, Inc. *Cis*-diamminedichloroplatinum (II) was purchased from Sigma-Aldrich, Inc. Polynucleotide kinase and T_4 DNA ligase were obtained from New England Biolabs, Inc. Reactions employing these enzymes were carried out in buffer supplied by the manufacturer. High performance liquid chromatography (HPLC) was performed on a Varian instrument using a 0.4 × 25 cm Dionex strong anion exchange (SAX) column. MALDI-TOF mass spectra were obtained on an Applied Biosystems Voyager mass spectrometer at the AB Mass Spectrometry/Proteomics Facility, Johns Hopkins School of Medicine, with support from a National Center for Research Resources shared instrumentation grant 1S10-RR14702. Talon metal affinity resin beads were purchased from BD Biosciences, Inc., and the Hi-trap heparin and Hi-trap Q columns were obtained from General Electric Health Sciences, Inc. Coomassie Fluor Orange was a product of Molecular Probes, Inc. Surface plasmon resonance experiments were performed on a BIACORE 3000 instrument. Streptavidin-coated sensor chips (Sensor Chip SA) and Surfactant P20 were purchased from Biacore, Inc. Phosphorimage screens were read on a Typhoon 9200 phosphorimager.

Oligonucleotide Synthesis. The sequences of the oligodeoxyribonucleotides used in these studies are shown in Table 1. The oligonucleotides and biotin-conjugated oligonucleotides were synthesized on controlled pore glass (CPG) supports by standard phosphoramidite chemistry using an Applied Biosystems model 392 or model 3400 DNA/RNA synthesizer. Phosphoramidite concentrations were 0.15 M; coupling times were 120 s; and the activator was 5-ethylthiotetrazole. In the case of the methylphosphonate-derivatized oligonucleotides, the standard oxidizing agent was replaced with a solution containing 1.27 g iodine, 12.5 mL 2,6-lutidine, and 100 μL water in 37.5 mL tetrahydrofuran, and standard Cap B reagent was replaced with a solution containing 1.25 g of 4-*N*,*N*′-dimethylaminopyridine in 50 mL of anhydrous pyridine. The DNA synthesizer was programmed to remove the 5′-terminal dimethoxytrityl group after the final coupling step. The oligonucleotides were cleaved from their CPG supports and deprotected by treating the support with 400 μL of 95% ethanol/concentrated ammonium hydroxide (1:3 v/v) at 55 °C for 3.5 h. In the case of the methylphosphonate-derivatized oligonucleotides, a two-step deprotection procedure was used. The CPG support was first treated with 95% ethanol/concentrated ammonium hydroxide (1:3 v/v) for 2.5 h at room temperature. The supernatant was removed from the support and evaporated. The residue was treated with a solution containing 22.5 μL 95% ethanol, 22.5 μL acetonitrile, and 50 μL ethylenediamine for 6 h at room temperature. The solution was cooled to 4 °C and neutralized with 600 μL of ice-cold 2 N hydrochloric acid. The oligonucleotide was then desalted on a C-18 SEP PAK cartridge (Waters, Inc.) or C-18 Clarity column (Phenomenex, Inc.) and eluted from the column with 50% aqueous acetonitrile. Oligonucleotides 30 nucleotides in length or shorter were purified by SAX HPLC using a 30 min linear gradient of 0−0.5 M sodium chloride at a flow rate of 1 mL/min. Longer oligonucleotides were purified on 20 cm × 20 cm × 0.75 mm 20% polyacrylamide gels containing 7 M urea in a TBE running buffer that consisted of 89 mM Tris, 89 mM boric acid, and 2 mM ethylenediaminetetraacetic acid, pH 8.0. The oligonucleotides were located on the gel by UV shadowing and extracted from the gel by incubating the gel overnight at 37 °C in a buffer containing 20% acetonitrile in 0.1 M ammonium acetate, pH 6.2. The gel-purified oligonucleotides were desalted on C-18 cartridges as described above and their compositions were confirmed by MALDI-TOF mass spectrometry.

Platinated oligonucleotide X (upper strand of duplex **X**) was prepared by incubating 26.5 nmol of the oligonucleotide in a solution containing 36 μM (54 nmol) *cis*-diamminedichloroplatinum (II) in 1.5 mL of Tris-EDTA buffer at 37 °C for 16 h. The reaction mixture was desalted using a SEP PAK cartridge and the platinated oligonucleotide, whose retention time is less than that of the nonplatinated oligomer, was purified by SAX HPLC using a linear gradient of 0.0−0.5 M sodium chloride in

buffer containing 20% acetonitrile in 50 mM Tris, pH 7.8. The purified oligonucleotide was desalted on a SEP PAK cartridge and its composition was confirmed by MALDI-TOF mass spectrometry, *m*/*z* calcd 4078.64, *m*/*z* found 4079.36.

Preparation of Oligonucleotide Duplexes. Duplexes **1**−**3** were prepared by annealing their component oligonucleotides in a buffer containing 70 mM Tris, pH 7.5, 10 mM magnesium chloride, and 5 mM dithiothreitol. The 149-mer duplexes **4**−**6** were prepared by ligation of their component duplexes following a procedure described by Huang et al. (*1*) The upper, platinated strand of duplex **X** (10 pmol) was first phosphorylated with [γ-^{32}P] ATP (6000 Ci/mmol) using T4 polynucleotide kinase. After excess ATP was removed using a G-10 spin column, the phosphorylated duplex was annealed to 15 pmol of its phosphorylated complementary strand to form duplex **X**. This duplex was then mixed with 15 pmol each of the appropriate phosphorylated component duplexes in 1X ligase buffer (New England Biolabs, Inc.) supplemented with 1 mM ATP incubated with 1000 units of T4 DNA ligase for 30 min at room temperature followed by overnight incubation at 16 °C. The reaction mixture was concentrated to <5 μL; dissolved in 25 μL of 80% formamide, containing 0.05% xylene cyanol and 0.05% bromophenol blue; and electrophoresced on a 6% denaturing polyacrylamide gel. Products were located by autoradiography of the wet gel. The slowest migrating band was excised, and the duplex was extracted from the gel by incubating the gel slice overnight at 37 °C in 1 mL of buffer containing 20% acetonitrile in 0.1 M ammonium acetate, pH 6.2. The buffer containing the 149-mer was lyophilized to 200 μL; the DNA was precipitated by addition of ethanol and 20 μg of oyster glycogen; and the resulting pellet was washed with 70% ethanol. The duplex was then dissolved in a buffer containing 100 mM KCl in Tris-EDTA buffer and annealed by heating at 90 °C for 5 min followed by slow cooling to <30 °C. Duplexes containing biotin as well as their control, phosphodiester-ended duplexes were incubated with streptavidin (Invitrogen) at a ratio of 1 μg streptavidin per 20 fmol of substrate for a minimum of overnight at 4 °C. Solutions of each duplex were stored at 4 °C and used before significant decay of the ^{32}P had occurred.

Cell Culture. HeLa cells (Biovest International Inc., National Cell Culture Center) were grown in suspension at (2.5−5) × 10^5 cells/mL in Jolick's MEM, 5% newborn calf serum, 100 units/mL penicillin, and 100 μg/mL streptomycin (PenStrep). Adherent CHO AA8 cells (a gift from Dr. Michael Seidman) were grown to large scale using a 10-layer CellSTACK culture chamber (Corning) to yield ~10^9 cells. Ku 80 deficient XR-V15B cells (obtained from ATCC) were grown in minimal essential medium, alpha modification, 10% FBS, and PenStrep in T-175 flasks.

Preparation of HeLa Whole-Cell Extracts. Large-scale preparations (~10^9 cells) of whole cell extracts from HeLa and CHO AA8 cells for the NER experiments were prepared as described by Manley et al. (*15*) using helpful procedural information described by Wood et al. (*16*) and by Reardon and Sancar (*17*). Nucleotide excision repair competent extracts were obtained when the cells were harvested in log phase growth. Protease inhibitors were added during the extract preparation to a final concentration of 1 mM phenylmethylsulfonyl fluoride (PMSF), 10 μg/mL aprotinin, 5 μg/mL leupeptin, and 100 μg/mL soybean trypsin inhibitor. Protein concentrations were determined using a BCA protein assay kit (Pierce Chemical Co.) and the extracts were stored at −80 °C in buffer containing 25 mM HEPES, pH 7.9, 100 mM potassium chloride, 12 mM magnesium chloride, 0.5 mM EDTA, 2 mM dithiothreitol, and 12.5% glycerol (v/v). A mini-NER whole cell extract method (*18*) was used to prepare and concentrate NER active extracts from ~5 × 10^7 XR-V15B cells.

Preparation of Ku70/80. Baculovirus expression vectors for Ku 70, pBacKu70, and Ku 80, pBac-his$_6$Ku80 were prepared as described in (*12*). Human Ku70 cDNA was amplified by PCR with primers 5′-d-GATCAAGGAGATACATATGTCAGGGTG GGAG-3′ and 5′-d-GCACTAGTTCAGTCCTGGAAGTG-3′ and TOPO cloned into pCR 8/GW/TOPO (Invitrogen) to produce pENTKu70, which was recombined into pDEST8 (Invitrogen) to produce pBacKu70. Human Ku80 cDNA (a generous gift from M. Lieber) was amplified with primers 5′-d-GGGGA-CAAGTTTGTACAAAAAAGCAGGCTCTTAAGAAGG AG-ATATACCATG-3′ and 5′-d-GGGGACCACTTTGTACAA-GAAAGCTGGGTCCTATATCATGTCCAATAAATC-3′, which include *att* sites for recombination into pDONR221 (Invitrogen). The N-terminal 5 amino acids were restored by site-directed mutagenesis (Stratagene) to generate pREhis$_6$Ku80, which was recombined into pDEST8 to create pBac-his$_6$Ku80. Baculoviruses for independent expression of Ku70 and his$_6$Ku80 were generated using the Bac-to-Bac Baculovirus Expression system (Invitrogen) according to manufacturer's instructions.

One liter of Sf-21 insect cells (10^6 cells/mL) was coinfected with Ku70 virus (MOI 10) and his$_6$Ku80 virus (MOI 5) for 4 days. Cells were harvested by centrifugation at 1000*g* for 15 min at 4 °C and the pellets were stored at −80 °C. Cells were resuspended in Buffer L, which contained 50 mM Tris pH 7.5, 0.3 M sodium chloride, 0.4 M ammonium acetate, 10% glycerol, 2 mM β-mercaptoethanol, and 0.1 M phenylmethylsulfonyl fluoride supplemented with 0.2% NP-40 and 20 mM imidazole; lysed by 30 strokes in a Dounce homogenizer with a loose-fitting pestle, and the lysate sonicated and cleared by centrifugation at 10 000*g* for 10 min at 4 °C. Cleared lysates were bound in batch to Talon metal affinity resin beads for 1 h at 4 °C. The beads were washed in Buffer L containing 20 mM imidazole, packed into a column, and fractions were eluted with Buffer L containing 0.5 M imidazole. Peak fractions were dialyzed against Buffer A, which contained 50 mM Tris pH 7.5, 50 mM sodium chloride, 1 mM dithiothreitol, and 1 mM sodium metabisulfite (NaMBS) supplemented with 5% glycerol; loaded onto a 5 mL Hi-trap heparin column; and eluted with a 0.05−1 M gradient of sodium chloride. Peak fractions were dialyzed against Buffer A containing 5% glycerol; loaded onto a 1 mL Hi-trap Q column; and eluted with a 0.05−1 M gradient of sodium chloride. Peak fractions were dialyzed into Buffer A containing 0.5 mM EDTA and 10% glycerol and stored at −80 °C.

Surface Plasmon Resonance Binding Experiments. Binding experiments were carried out in running buffer containing 84 mM potassium monohydrogen phosphate, pH 7.0, 10 mM sodium bicarbonate, 1 mM magnesium sulfate, 4 mM potassium chloride, 1% glycerol, 2 mM dithiothreitol, 0.5 mM EDTA, and 0.005% Surfactant P20 (Biacore, Inc.) at 25 °C. Biotinylated duplexes **1**−**3** were each immobilized on the surface of a streptavidin-coated sensor chip. The amount of DNA added was such that the level of Ku bound corresponded to 75−150 response units. Ku70/his$_6$-Ku80 was then diluted into the running buffer at final concentrations of 1, 5, 10, 25, 50, or 100 nM; and the solutions were injected onto the DNA surface at a flow rate of 90 μL/min. The second lowest and second highest concentrations were injected in duplicate with each kinetic run. Ku was allowed to first pass through a control cell with a naked streptavidin surface, followed by the experimental cell immobilized with the desired DNA−substrate. The association phase lasted 45 s with a dissociation phase of 1800 s or longer in which only running buffer was flowed over the surface. The chip was regenerated with a 1 min injection of 0.005% SDS at 30 μL/min. Kinetic data were obtained by fitting the sensograms to a 1:1 Langmiur binding model using the Biacore BiaEvaluation software (version 4.1). Apparent association, K_A,

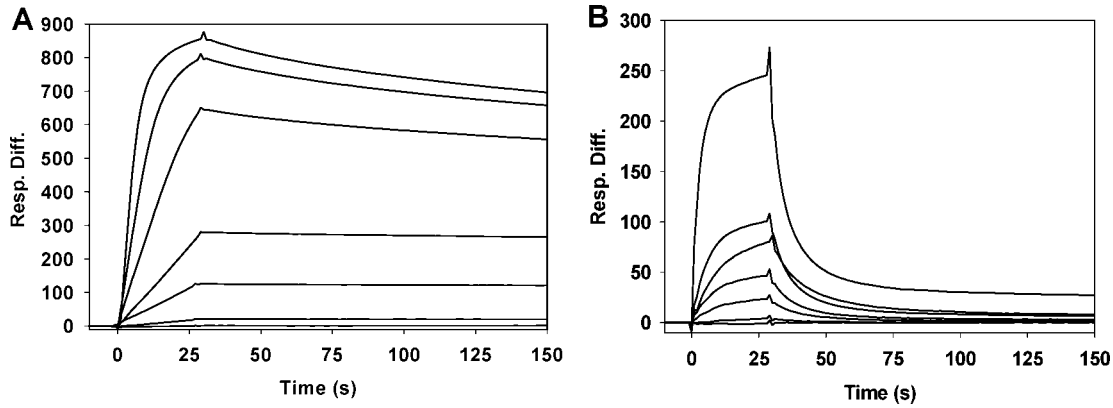

Figure 1. Effects of increasing Ku concentration, 0, 1, 5, 10, 25, 50, and 100 nM, on the rates of formation and dissociation of complexes formed with (A) duplex **1** and (B) duplex **3** as measured by surface plasmon resonance.

and dissociation, K_D, constants were then calculated from the observed rates of association, k_a, and dissociation, k_d.

Excision Assay in Whole-Cell Extract. Excision reactions were carried out as previously described (*1, 17*) with minor modifications. The reactions were performed in silanized Eppendorf tubes in 25 μL of a buffer containing 25 mM HEPES, pH 7.9, 4.4 mM magnesium chloride, 0.1 mM EDTA, 1 mM dithiothreitol, 70 mM potassium chloride, 4 mM ATP, 200 μg/mL bovine serum albumin, 2.5% glycerol, 40 ng of pGEM3Z plasmid DNA, and 5−10 μL (75−150 μg) of HeLa whole-cell extract or 2.5 μL (~50 μg) of AA8 or XR-V15B extract. Where indicated, recombinant Ku protein was added to a final concentration of 16 nM. The solution was held on ice for 10 min. The reactions were then initiated by addition of 10 fmol of ^{32}P-labeled substrate followed by incubation at 30 °C for 1 h. The reactions were stopped by incubating with 10 μg of proteinase K in the presence of 0.3% SDS for 15 min at 37 °C, diluted with water to a volume of 200 μL, and then extracted once with phenol/chloroform/isoamyl alcohol (25:24:1 v/v) using phase lock gel tubes (Eppendorf) followed by extraction with chloroform/isoamyl alcohol (24:1). The DNA was precipitated by addition of 2.5 volumes of absolute ethanol, 0.12 M sodium acetate, and 20 μg of oyster glycogen in a silanized Eppendorf tube. The precipitate was washed with 70% ethanol and dissolved in 10 μL of loading buffer. Samples were electrophoresced on a prerun (1.5 h) 20 cm × 45 cm × 0.4 mm 10% denaturing polyacrylamide sequencing gel at 1800 V until the bromophenol blue dye was 12 cm from the bottom of the gel. The gel was fixed in a solution containing 5% methanol, 5% acetic acid, and 90% water for 5 min; dried on a gel dryer; and exposed to a phosphorimager screen overnight. The intensity of the excision products was quantified and normalized to the total signal in the lane using *Image Quant 5.2* software. Quantification of the level of excision products was done on samples in which saturation of the signal had not been reached.

RESULTS AND DISCUSSION

Interaction of Methylphosphonate-Modified Oligonucleotide Duplexes with Ku70/80. The ends of linear DNA duplexes are potential binding sites for DNA end-binding proteins such as Ku. A recent crystal structure of the complex formed between Ku and the end of a 14-bp DNA duplex (*19*) showed that a limited number of contacts are made between the protein and the sugar−phosphate backbone of the duplex, whereas no contacts were observed between either subunit of the protein and the bases of the duplex. Of these, four ionic contacts are made between arginine residues 258, 403, and 404 of Ku70 and the first, second, and third internucleotide phosphates from the 3′-end of the duplex. The third, fourth, and fifth internucleotide phosphates from the 5′-end of the duplex make nonionic contacts with serine 78, asparagine 275, and glutamine 278, respectively, of Ku70 and the fourth internucleotide phosphate from the 5′-end makes an ionic contact with arginine 431 of Ku80. It appeared likely that disruption of these contacts, especially the ionic contacts, could attenuate binding of Ku to DNA. To test this hypothesis, we prepared oligonucleotide duplexes in which the negatively charged internucleotide phosphate linkages at the 3′- or 5′-ends of the duplex were replaced with nonionic methylphosphonate groups and examined the interactions of these methylphosphonate-modified duplexes with purified recombinant Ku using surface plasmon resonance (SPR). Because methylphosphonate linkages are completely resistant to hydrolysis by exo- and endonucleases, their presence at the ends of the duplex would also be expected to protect the duplex from exonucleolytic digestion when incubated in cellular extracts.

We prepared a series of methylphosphonate-modified oligodeoxyribonucleotide duplexes, whose sequences are shown in Table 1. Duplexes **1**−**3** are 22 bp in length, a size that is sufficient to accommodate a single Ku heterodimer (*20, 21*). One end of each duplex contains a 5′-biotin moiety. Duplex **2** has a tract of five contiguous methylphosphonate linkages one nucleotide in from the 5′-teminus of the nonbiotinylated end, and duplex **3** has six contiguous methylphosphonate linkages starting at the 3′-terminus of the nonbiotinylated end. Introduction of methylphosphonate linkages on one strand at the ends of the duplex results in a small decrease (~5 °C) in the thermal stability of the duplex as measured by UV melting experiments (data not shown).

The effects of methylphosphonate modification on the interactions of Ku with the linear DNA duplexes were determined using surface plasmon resonance to measure the kinetics of binding between Ku and the 22-bp duplexes, **1**−**3**. Streptavidin-coated SPR sensor chips were conjugated with the biotin-modified duplexes. The rate of association was determined by flowing increasing concentrations of Ku over the chip and measuring the response relative to a control channel that lacked the duplex. The rate of dissociation was then measured by flowing buffer that lacked Ku over the chip. Sensograms for unmodified duplex **1** and modified duplex **3** obtained at different concentrations of Ku are shown in Figure 1. Because these duplexes can only accommodate a single Ku heterodimer, rate constants for the association and dissociation steps were determined by fitting the data from the sensograms to a 1:1 Langmiur binding model (*21, 22*). The results are presented in Table 2.

Ku rapidly associates with unmodified duplex **1**, and the resulting complex shows a relatively slow rate of dissociation. The apparent

Table 2. Ku Binding Parameters Derived from SPR Experiments

duplex	k_a (M^{-1} s^{-1})	k_d (s^{-1})	K_D (nM)	K_A (M^{-1})	χ^2
1	2.3×10^6	1.5×10^{-3}	0.65	1538×10^6	564
2	1.4×10^6	4.3×10^{-3}	3.1	323×10^6	346
3	0.11×10^6	20×10^{-3}	182	5×10^6	50

dissociation constant, K_D, of the complex, 0.65 nM, calculated from these measured rate constants is similar to that previously reported for the complex formed between Ku and a 22-bp DNA duplex, 0.16 nM (*21*). Introduction of methylphosphonate linkages at the 5′-end of duplex **2** decreases the association rate by a factor of 1.6 and increases the dissociation rate by a factor of 2.9. The calculated K_D consequently increases by a factor of 4.8. A more significant effect is seen when methylphosphonate linkages are introduced at the 3′-end of duplex **3**. In this case, the association rate decreases by a factor of 20.9 while the dissociation rate increases by a factor of 13.3 resulting in a K_D that is 280 times greater than that of the complex formed by Ku and unmodified duplex **1**.

As described above, the crystal structure of a Ku/DNA duplex identifies contacts between amino acid residues of Ku70 and the phosphodiester linkages at positions 3, 4, and 5 of the strand at the 5′-end and positions 1, 2, and 3 of the strand at the 3′-end. Because methylphosphonate internucleotide linkages lack the negative charge found in natural phosphodiester linkages, they cannot bind through ionic interactions with positively charged side chains of amino acids such as arginine. In addition, the methyl group of the methylphosphonate linkage, whose size is slightly greater than that of the nonbridging phosphodiester oxygen it replaces, could provide steric hindrance to side-chain binding and/or interfere with hydrogen bonding interactions. Replacement of the phosphodiester groups at the end of the duplex with methylphosphonate linkages could therefore interfere with the initial interactions necessary for Ku to gain access to the DNA end and thus reduce overall binding affinity.

Placement of methylphosphonate linkages on the 3′- or 5′-end of the duplex affects Ku binding in different ways. The presence of 3′-methylphosphonate linkages, as in duplex **3**, results in an almost 300-fold decrease in the apparent binding affinity of the methylphosphonate-modified duplex compared to that of unmodified duplex **1**. On the other hand, placing the methylphosphonate linkages on the 5′-end of the duplex, as in duplex **2**, results in only a 4.8-fold decrease in binding affinity. This difference may reflect the greater number of ionic contacts, four, that are made between arginines 258, 403, and 404 of the 70S subunit and the phosphates at the 3′-end of the duplex versus the single ionic contact between arginine 431 of the 80S subunit and the phosphate at the 5′-end of the duplex. When methylphosphonate linkages are placed on both the 3′- and 5′-ends of the duplex, the binding affinity (K_D 69 nM) is approximately 2.6 times higher than that seen for duplex **3** (data not shown). Possibly, the presence of the methylphosphonate linkages on both strands of the duplex causes fraying or distortion of the ends, which enables Ku to bind.

Effects of Terminal Modifications on NER-Mediated Excision. Linear DNA duplexes that contain a platinum(II) 1,3, -GNG- type intrastrand cross-link are excellent substrates for nucleotide excision repair-mediated processing in HeLa cell extracts (*2*). We examined the ability of HeLa whole cell extracts to process platinum lesions in 149-bp duplexes that terminated with phosphodiester linkages (duplex **4**) or with methylphosphonate linkages on either the 5′- (duplex **5**) or 3′- (duplex **6**) ends of the duplex. The platinated -GTG- lesion was located on one strand in the middle of the duplex and the duplex carried a ^{32}P label, which was positioned on the platinated strand at the junction of the **C** and **X** duplexes. These labeled, 149-bp duplexes were prepared by ligating shorter, component duplexes using T_4 DNA ligase and purified by electrophoresis on denaturing polyacrylamide gels.

As shown in Figure 2A, lane 1, incubation of unmodified duplex **4** with the HeLa extract produced a series of oligonucleotides 26−30 nucleotides in length. These oligonucleotides result from dual incisions made by the NER endonucleases XPF and XPG on the 5′- and 3′-sides, respectively, of the strand carrying the platinum intrastrand cross-link. Identical dual incisions were observed when methylphosphonate-derivatized duplexes **5**, lane 2, or **6**, lane 3, were incubated with the HeLa whole-cell extract, although the intensities of the excised oligonucleotides varied significantly from those derived from duplex **4**.

The excision experiments for each duplex were run in triplicate and the intensities of the excision products relative to the total amount of duplex loaded on the gel were quantified by phosphorimaging. It should be noted that excision efficiency is dependent upon the amount of extract used and, equally important, upon the activity of the extract. We have found, not unexpectedly, that the inherent repair activity of a particular extract varies from preparation to preparation. For this reason, we have used the same extract preparation for a single set of experiments and within that set have compared the excision efficiencies of the modified duplexes to that of an unmodified control duplex. This procedure controls for the inherent differences in repair activity when different preparations of extract are used.

As shown in Figure 2B, a significant increase, approximately 60%, in the amount of excision products was observed for 3′-methylphosphonate-derivatized duplex **6** relative to unmodified duplex **4**. This result is consistent with the reduced binding of Ku to the ends of this modified duplex. In contrast, the duplex containing 5′-methylphosphonates, **5**, did not show an increased level of excision products. This result is not entirely unexpected if one considers the amount of Ku protein present in the extracts. On the basis of the amount of Ku found in HeLa cells (*23*), we estimate that the concentration of Ku in the excision reaction is approximately 70 nM, which is 175-fold greater than the duplex concentration (0.4 nM). In the case of duplex **6**, the Ku concentration is less than the expected dissociation constant (182 nM) of the Ku/**6** complex calculated from the SPR data. Consequently, Ku would not be expected to bind to duplex **6** to any significant extent under the conditions of the excision experiment. On the other hand, the concentration of Ku is significantly higher than the expected K_D (3.1 nM) of the Ku/**5** complex. Under these conditions, Ku would be expected to be able to bind and interfere with excision.

The binding experiments described in the previous section showed that 3′-terminal methylphosphonate linkages significantly impair the ability of Ku to bind to the ends of linear DNA duplexes. These results together with the results from excision experiments with 3′-methylphosphonate-derivatized duplex **6** suggested that interference with Ku binding to linear substrates might allow more efficient excision of the platinated oligonucleotide. To test this, we prepared a biotinylated derivative of duplex **4**, **biotin-4**, in which biotins were attached to both 5′-ends of the duplex. Conjugation of biotinylated ends of the duplex with streptavidin creates a linear duplex that can no longer bind Ku (*14*). As shown in Figure 2C, incubation of duplex **4**, lane 1, or duplex **biotin-4**, lane 2, in the HeLa whole-cell extract in the presence of streptavidin produced the expected excision products. However, in agreement with the results obtained with duplex **6**, the excision reaction proceeded approximately 2.3 times more efficiently when access to the

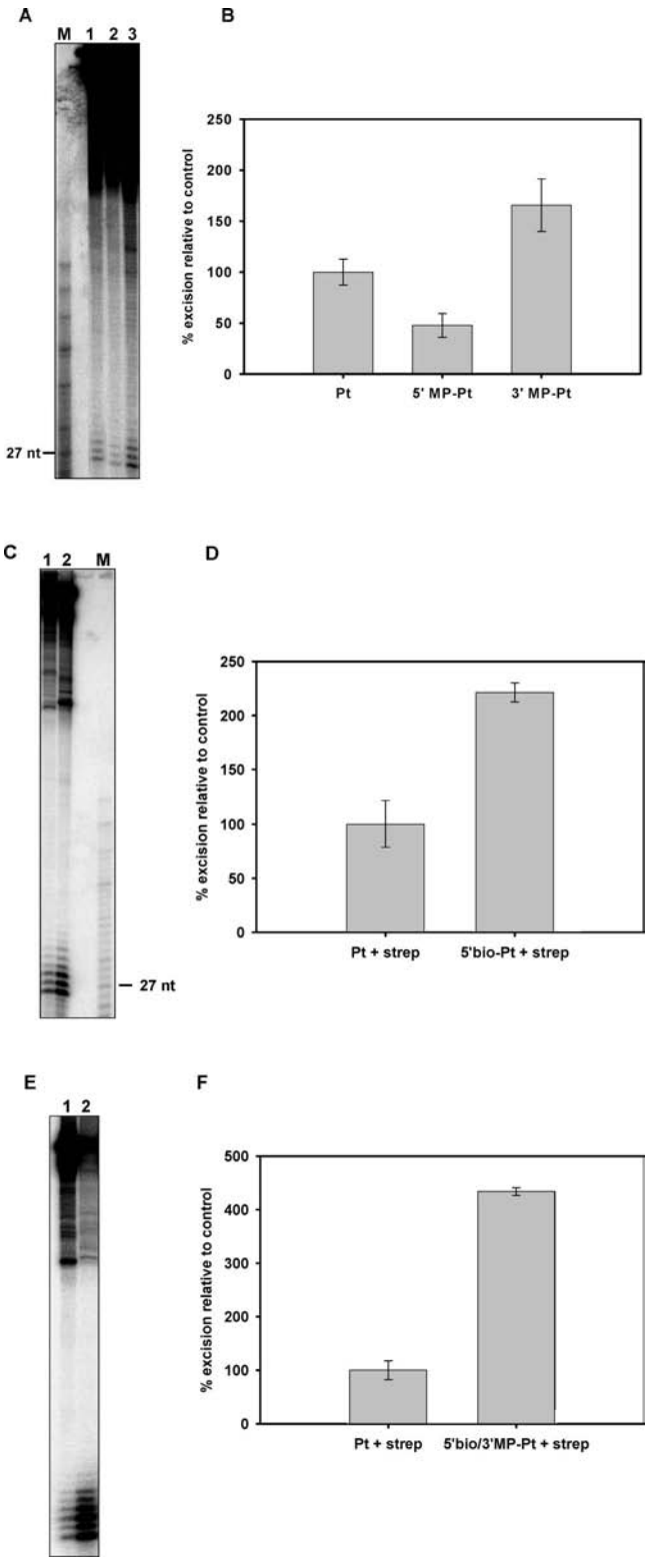

Figure 2. Effect of end-modification on NER-mediated excision. Duplexes were each incubated with HeLa whole-cell extract for 60 min at 30 °C and the products analyzed by denaturing PAGE as described in the Experimental Procedures. Molecular weight markers are shown in lane M. The excision products are 26−30 nucleotides in length. Excision products were quantified from three independent experiments and were plotted as the percentage of the excision products derived from an unmodified control duplex. Error bars represent the standard error from the mean. (A,B) NER-mediated excision on duplex **4** (lane 1) (Pt), **5** (lane 2) (5′-MP-Pt), or **6** (lane 3) (3′-MP-Pt). (C,D) NER-mediated excision on duplex **4** (lane 1) (Pt + strep) or the 5′-biotinylated derivative of duplex **4** (**biotin-4**, lane 2) (5′-bio-Pt + strep) in the presence of streptavidin. (E,F) NER-mediated excision on duplex **4** (lane 1) (Pt + strep) or duplex **biotin-6** (lane 2) (5′-bio/3′-MP-Pt + strep) in the presence of streptavidin.

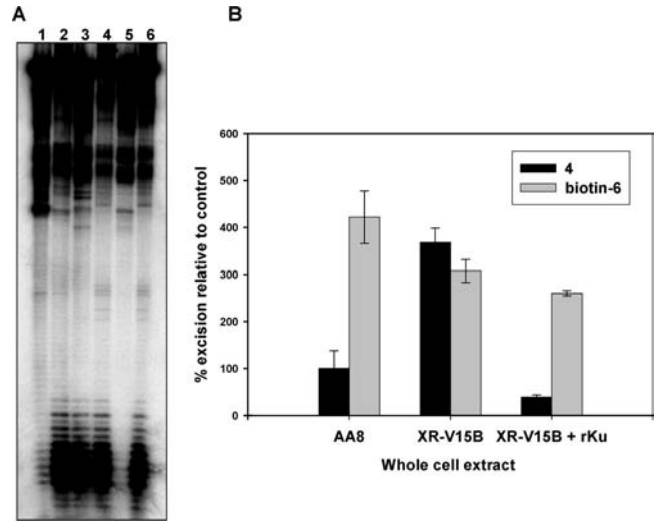

Figure 3. Blocking the ends of linear duplexes increases NER-mediated excision activity in CHO extracts through inhibition of Ku binding. (A) Duplex **4** (lanes 1, 3, and 5) or duplex **biotin-6** (lanes 2, 4, and 6) were each incubated in the presence of streptavidin in whole-cell extracts derived from CHO wild-type AA8 (lanes 1 and 2) or Ku80-deficient XR-V15B (lanes 3 and 4) cells, or in XR-V15B extract that had been supplemented with recombinant Ku (rKu) protein (lanes 5 and 6). (B) Quantification of excision products from three or four independent experiments. The levels of excision products were normalized to the total counts in the lane and plotted as the percentage of the excision products derived from control duplex **4** when incubated in wild-type AA8 extract. Error bars represent the standard error from the mean.

exposed DNA termini was prevented by the conjugating streptavidin to **biotin-4** (Figure 2D).

An even greater increase in NER excision efficiency was seen when both 5′-ends of duplex **6**, which contains six 3′-methylphosphonate linkages, were derivatized with biotin (**biotin-6**). As shown in Figure 2E, excision products identical to those of unmodified duplex **4**, lane 1, are produced when **biotin-6**, lane 2, is incubated with HeLa whole-cell extract in the presence of streptavidin. However, the efficiency of excision is 4.4 times greater for **biotin-6** compared to that of duplex **4** (see Figure 2F). It appears that the combination of the two modifications, 5′-biotin/streptavidin and 3′-methylphosphonate linkages, acts in a synergistic manner to enhance overall NER excision without affecting the nature of the products that are formed. Thus, on average, the incision efficiency increased from ∼4% for the unmodified duplex, **4**, to ∼16% for the modified duplex, **biotin-6**. This synergy may result from the effects of both modifications on Ku binding (and possibly other end binding proteins in the extract) and the ability of the 3′-methylphosphonate linkages to protect the substrate from degradation by 3′-exonucleases.

Further evidence that Ku is responsible for reduced NER excision activity was obtained from the following experiments. Unmodified duplex **4** or 5′-biotinylated duplex **6** (**biotin-6**) were each incubated in whole-cell extracts prepared from a wild-type Chinese hamster ovary (CHO) cell line, AA8, or in extracts derived from a CHO cell line deficient in Ku80, XR-V15B. As shown in Figure 3A and B, the efficiency of excision for duplex **biotin-6**, lane 2, was approximately 4.2 times that of unmodified duplex **4**, lane 1, a result that is comparable to that seen in the HeLa whole-cell extract. In contrast to this result, similar excision efficiencies were seen when duplex **4**, lane 3, or duplex **biotin-6**, lane 4, were incubated in an extract prepared from a Ku80-deficient cell line, XR-V15B. This mutant contains an internal deletion of amino acids 372−417 which results in loss of function. When this mutant extract is supplemented with

recombinant Ku, the difference in excision efficiencies between duplex **4**, lane 5, and duplex **biotin-6**, lane 6, is restored to that seen in the wild-type cell extract. These results further demonstrate that Ku inhibits the NER-mediated excision reaction and that 5′-biotin-streptavidin/3′-methylphosphonate modifications protect the substrate from this inhibition by blocking Ku end-binding.

CONCLUSIONS

Synthetic linear DNA duplexes that contain site-specific lesions are useful substrates for studying DNA repair processes in whole-cell extracts. The ends of these synthetic repair substrates, however, can serve as recognition sites for end-binding and end-modifying proteins. Because end-binding by these proteins may affect lesion recognition or processing in whole-cell extracts, use of synthetic repair substrates may be accompanied by reduced efficiency or low signal-to-noise. Our results show that Ku uses the phosphodiester linkages at the 3′-termini of linear DNA duplexes as an important determinant in DNA end-binding and that replacement of these linkages with nonionic methylphosphonate linkages significantly reduced the ability of Ku to bind to modified duplexes. Conjugation of streptavidin to the 5′-biotinylated ends of the repair substrate sterically blocks binding by Ku and, presumably, other end-binding proteins. Incorporation of both these modifications into a linear duplex repair substrate significantly increased the efficiency of NER-mediated excision in whole-cell extracts. This approach may find general utility in the study of DNA repair processes in extract-based assays.

ACKNOWLEDGMENT

The authors wish to thank Drs. Joyce Reardon and Aziz Sancar for providing guidance in preparing HeLa whole-cell extracts; Ms. Maggie Wear for assisting in the preparation of the methylphosphonate-modified oligonucleotides; and Dr. Terry Brown for allowing us to use his Typhoon phosphorimager. This research was supported by grants form the National Cancer Institute, CA CA082785, (P.S.M.) and the National Institutes of Health, GM070639 (L.A.H.). T.M.M. was supported by a Ruth L. Kirchstein National Research Service Award (CA108326).

LITERATURE CITED

(1) Huang, J. C., Zamble, D. B., Reardon, J. T., Lippard, S. J., and Sancar, A. (1994) HMG-domain proteins specifically inhibit the repair of the major DNA adduct of the anticancer drug cisplatin by human excision nuclease. *Proc. Natl. Acad. Sci. U.S.A. 91*, 10394–8.

(2) Zamble, D. B., Mu, D., Reardon, J. T., Sancar, A., and Lippard, S. J. (1996) Repair of cisplain-DNA adducts by the mammalian excision nuclease. *Biochemistry 35*, 10004–10013.

(3) Kumaresan, K. R., Hang, B., and Lambert, M. W. (1995) Human endonucleolytic incision of DNA 3′ and 5′ to a site-directed psoralen monoadduct and interstrand cross-link. *J. Biol. Chem. 270*, 30709–16.

(4) Bessho, T., Mu, D., and Sancar, A. (1997) Initiation of DNA interstrand cross-link repair in humans: The nucleotide excision repair system makes dual incisions 5′ to the cross-linked base and removes a 22- to 28-nucleotide-long damage-free strand. *Mol. Cell Biol. 17*, 6822–30.

(5) Kuraoka, I., Robertz, W. R., Ariza, R. R., Biggerstaff, M., Essigmann, J. M., and Wood, R. D. (2000) Repair of an interstrand DNA cross-link initiated by ERCC1-XPF repair/recombination nuclease. *J. Biol. Chem. 275*, 26632–26636.

(6) Mu, D., Bessho, T., Nechev, L. V., Chen, D. J., Harris, T. M., Hearst, J. E., and Sancar, A. (2000) DNA interstrand cross-links induce futile repair synthesis in mammalian cell extracts. *Mol. Cell Biol. 20*, 2446–54.

(7) Kysela, B., Doherty, A. J., Chovanec, M., Stiff, T., Ameer-Beg, S. M., Vojnovic, B., Girard, P. M., and Jeggo, P. A. (2003) Ku stimulation of DNA ligase IV-dependent ligation requires inward movement along the DNA molecule. *J. Biol. Chem. 278*, 22466–74.

(8) Jackson, S. P., and Jeggo, P. A. (1995) DNA double-strand break repair and V(D)J recombination: Involvement of DNA-PK. *Trends Biochem. Sci. 20*, 412–5.

(9) Jeggo, P. A., Taccioli, G. E., and Jackson, S. P. (1995) Menage a trois: Double strand break repair, V(D)J recombination and DNA-PK. *Bioessays 17*, 949–57.

(10) Lieber, M. (1996) Immunoglobulin diversity: Rearranging by cutting and repairing. *Curr. Biol. 6*, 134–6.

(11) Collis, S. J., DeWeese, T. L., Jeggo, P. A., and Parker, A. R. (2005) The life and death of DNA-PK. *Oncogene 24*, 949–61.

(12) Cheung, J. C. Y., Salerno, B., Hanakahi, L. A. Evidence for an inositol hexakisphosphate-dependent role for Ku in mammalian NHEJ that is independent of its role in the DNA-dependent protein kinase *J. Biol. Chem.* submitted.

(13) Calsou, P., Frit, P., and Salles, B. (1996) Double strand breaks in DNA inhibit nucleotide excision repair in vitro. *J. Biol. Chem. 271*, 27601–7.

(14) Yoo, S., Kimzey, A., and Dynan, W. S. (1999) Photocross-linking of an oriented DNA repair complex. Ku bound at a single DNA end. *J. Biol. Chem. 274*, 20034–20039.

(15) Manley, J. L., Fire, A., Cano, A., Sharp, P. A., and Gefter, M. L. (1980) DNA-dependent transcription of adenovirus genes in a soluble whole-cell extract. *Proc. Natl. Acad. Sci. U.S.A. 77*, 3855–9.

(16) Wood, R. D., Biggerstaff, M., and Shivji, M. K. K. (1995) Detection and measurement of nucleotide excision repair synthesis by mammalian cell extracts *in vitro*. *Methods 7*, 163–175.

(17) Reardon, J. T., and Sancar, A. (2006) Purification and characterization of *E. coli* and human nucleotide excision repair enzyme systems. *Methods Enzymol. 408*, 189–213.

(18) Smeaton, M. B., Miller, P. S., Ketner, G., and Hanakahi, L. A. (2007) Small-scale extracts for the study of nucleotide excision repair and non-homologous end joining. *Nucleic Acids Res. 35*, e152.

(19) Walker, J. R., Corpina, R. A., and Goldberg, J. (2001) Structure of the Ku heterodimer bound to DNA and its implications for double-strand break repair. *Nature 412*, 607–14.

(20) Falzon, M., Fewell, J. W., and Kuff, E. L. (1993) Ebp-80, a transcription factor closely resembling the human autoantigen Ku, recognizes single- to double-strand transitions in DNA. *J. Biol. Chem. 268*, 10546–52.

(21) Ma, Y., and Lieber, M. R. (2001) DNA length-dependent cooperative interactions in the binding of Ku to DNA. *Biochemistry 40*, 9638–46.

(22) Taghva, A., Ma, Y., and Lieber, M. R. (2002) Analysis of the kinetic and equilibrium binding of Ku protein to DNA. *J. Theor. Biol. 214*, 85–97.

(23) Mimori, T., Hardin, J. A., and Steitz, J. A. (1986) Characterization of the DNA-binding protein antigen Ku recognized by autoantibodies from patients with rheumatic disorders. *J. Biol. Chem. 261*, 2274–2278.

BC7004363

Protein Conjugation with Amphiphilic Block Copolymers for Enhanced Cellular Delivery

Xiang Yi,[†] Elena Batrakova,[†] William A. Banks,[‡] Serguei Vinogradov,[†] and Alexander V. Kabanov*[,†,§]

Department of Pharmaceutical Sciences and Center for Drug Delivery and Nanomedicine, College of Pharmacy, University of Nebraska Medical Center (UNMC), Omaha, Nebraska 68198-5830, Geriatric Research Education and Clinical Center, Veterans Affairs Medical Center and Saint Louis School of Medicine, Department of Internal Medicine, Division of Geriatrics, St. Louis, Missouri 63106, and Faculty of Chemistry, M.V. Lomonosov Moscow State University, 119899 Moscow, Russia. Received November 30, 2007; Revised Manuscript Received March 18, 2008

Modification of a model protein, horseradish peroxidase (HRP), with amphiphilic block copolymer poly(ethylene oxide)-*b*-poly(propylene oxide)-*b*-poly(ethylene oxide) (Pluronic), was previously shown to enhance the transport of this protein across the blood−brain barrier *in vivo* and brain microvessel endothelial cells *in vitro*. This work develops procedures for synthesis and characterization of HRP with Pluronic copolymers, having different lengths of poly(ethylene oxide) (PEO) and poly(propylene oxide) (PPO) blocks. Four monoamine Pluronic derivatives (L81, P85, L121, P123) were synthesized and successfully conjugated to a model protein, HRP, *via* biodegradable or nondegradable linkers (dithiobis(succinimidyl propionate) (DSP), dimethyl 3,3′-dithiobispropionimidate (DTBP), and disuccinimidyl propionate (DSS)). The conjugation was confirmed by HRP amino group titration, matrix-assisted laser desorption/ionization-time of flight spectroscopy, and cation-exchange chromatography. HRP conjugates containing an average of one to two Pluronic moieties and retaining in most cases over 70% of the activity were synthesized. Increased cellular uptake of these conjugates was demonstrated using the Mardin-Derby canine kidney cell line and primary bovine brain microvessel endothelial cells. The optimal modifications included Pluronic L81 and P85. These copolymers have shorter PPO chains compared to Pluronic P123 and L121, which were less efficient. There was little if any dependence of the uptake on the length of the hydrophilic PEO block for the optimal modifications. The proposed modifications may be used to increase cellular uptake of other proteins.

INTRODUCTION

Use of proteins as therapeutic agents in many cases is hindered by an inability of protein molecules to cross cell membranes and physiological barriers, such as the blood−brain barrier (BBB) (*1*, *2*). To address this limitation, we have proposed to covalently modify proteins with amphiphilic groups, in particular, triblock copolymers, poly(ethylene oxide)-*b*-poly(propylene oxide)-*b*-poly(ethylene oxide) (PEO-PPO-PEO), also known as Pluronic or poloxamers (*3*). Using *in vitro* and *in vivo* models, we have shown that a model protein, horseradish peroxidase (HRP), modified with Pluronic P85 (P85) *via* a degradable disulfide linker can cross the BBB and accumulate in the brain (*4*). Pluronic P85 alone is readily transported into cells *via* caveolae-mediated endocytosis (paper in preparation). Evidently, it also can serve as a synthetic transduction modulator that facilitates cell transport of a protein as large as HRP. The transport efficiency of protein−Pluronic conjugates should strongly depend on the lengths of Pluronic hydrophobic (PPO) and hydrophilic (PEO) blocks (*5*) . Therefore, to develop optimal protein modifications one needs to establish robust procedures for (i) protein conjugation with the block copolymers with different lengths of PPO and PEO blocks and (ii) characterization of these conjugates. This work uses HRP as a model protein for conjugation with the block copolymers that differ in the (1) lengths of PPO block (L81 and P85 vs L121, and P123) and (2) overall hydrophobicity (L81 and L121 vs P85 and P123). The conjugates were synthesized by attaching one end of a Pluronic molecule to HRP amino groups via either degradable (disulfide) or nondegradable linkers. The products are characterized by amino group titration and matrix-assisted laser desorption/ionization-time of flight (MALDI-TOF) spectroscopy. The uptake of the conjugates in the Mardin-Derby canine kidney (MDCK) cell line and primary bovine brain microvessel endothelial cells (BBMEC) is characterized to establish the most promising modifications. On the basis of these studies, L81 and P85 were identified as the best copolymers to enhance cell uptake of HRP.

EXPERIMENTAL PROCEDURES

Materials and Devices. HRP type VI-A, MW 43 kDa, 4-methoxyltrityl chloride (MTr-Cl), 1,1′- carbonyldiimidazole (CDI), 1,2-ethylenediamine (EDA), 2,4,6-trinitrobenzenesulfonic acid (TNBS), ninhydrin, hydrindantin, 2-methyoxy ethanol, trifluoroacetic acid (TFA), triethylamine, anhydrous acetonitrile, anhydrous pyridine, methanol, dichloromethane, toluene, acetone, ethanol, and dimethylformamide were purchased from Sigma-Aldrich Co. (St. Louis, MO). Pluronic block copolymers, L81 (lot no. WSOO-25087), P85 (lot no. WPOP-587A), L121 (lot no. WPAC-550B), and P123 (lot no. WPIV-612B) were kindly provided by BASF Corp. (Paris-pany, NJ). Their characteristics are summarized in Table 1. Dithiobis(succinimidyl propionate) (DSP), dimethyl 3,3′-dithiobispropionimidate (DTBP), and disuccinimidyl propionate (DSS) were from Pierce Biotech Co. (Rockford, IL). Sephadex LH-20 gel and Illustra

* Correspondence to Alexander V. Kabanov, Center for Drug Delivery and Nanomedicine, 985830 Nebraska Medical Center, Omaha, NE 68198-5830. Tel: (402) 559-9364; Fax (402) 559-9365; akabanov@unmc.edu.
[†] UNMC.
[‡] Veterans Affairs Medical Center and Saint Louis School of Medicine.
[§] M.V. Lomonosov Moscow State University.

10.1021/bc700443k CCC: $40.75 © 2008 American Chemical Society
Published on Web 04/16/2008

Table 1. Structure and Properties of Pluronic Copolymers

Pluronic	structure	MW	HLB[a]	CMC (%)[b]
L81	$EO_3-PO_{43}-EO_3$	2750	2	0.006
P85	$EO_{26}-PO_{40}-EO_{26}$	4600	16	0.03
L121	$EO_5-PO_{68}-EO_5$	4400	1	0.0004
P123	$EO_{19}-PO_{69}-EO_{19}$	5750	8	0.0025

[a] Hydrophilic−lipophilic balance (HLB). [b] Critical micelle concentration (CMC) in aqueous solution values at 37 °C as determined using pyrene probe.

NAP-25 columns were from Amersham Biosciences (Pittsburgh, PA). Toyopearl MD-G SP column (10 mm ID × 6.8 cm) was from Tosoh Co. (Japan). Amicon ultra-15 centrifugal filter, MWCO 30K, membrane NMWL was from Millipore Co. (Billerica, MA). Spectro/Por membrane (MWCO 2000) was from Spectrum Laboratory Inc. (New Brunswick, NJ). Flexible thin-layer chromatography (TLC) plates were from Whatman Ltd. (Mobile, AL).

Monoamine P85 Derivative. To produce monoamine P85, first, the hydroxyl group at one end of the P85 chain was protected by MTr-Cl. Second, the hydroxyl group at the other end was activated using CDI and then reacted with EDA (Scheme 1) (*6*). The monoamine P85 was obtained after deprotecting the hydroxyl group in the presence of TFA. In detail, 3 g of P85 (MW 4600) was dried overnight *in vacuo* at 50 °C and then dissolved in 15 mL of anhydrous pyridine. One molar equivalent of MTr-Cl (200 mg) was dissolved in 10 mL of anhydrous pyridine and added to the P85 solution. The reaction was allowed to proceed for 3 h at 25 °C and then stopped by adding 1 mL of methanol. The pyridine was removed *in vacuo* by coevaporation with 3 × 15 mL of toluene. The mono-MTr-P85 was isolated from nonreacted copolymer and bis-MTr-P85 by adsorption chromatography on Silicagel column (3 × 20 cm) using stepwise gradient elution of 200 mL of dichloromethane containing 2%, 5%, and 10% methanol. Fractions containing bis-substituted MTr-Pluronic eluted first ($R_f = 0.8$), followed by monosubstituted MTr-Pluronic ($R_f = 0.6$) and free Pluronic ($R_f = 0.4$). The products were then analyzed by TLC in dichloromethane/MeOH, 9:1, and detected in TFA vapors (a test for MTr-group). The collected mono-MTr-P85 was dried by coevaporation with 2 × 15 mL of anhydrous acetonitrile *in vacuo* and then reacted with 5-fold molar excess of CDI (530 mg) in 10 mL of anhydrous acetonitrile. After incubation for 2 h at 25 °C, the reaction mixture was treated with 0.2 mL of water for 20 min to neutralize the nonreacted CDI, and then added to an excess of EDA in 20 mL of ethanol upon stirring. The mixture was kept overnight at 25 °C and then diluted by 50 mL of water and dialyzed for 18 h using a membrane with MWCO 2000 kDa against 20% aqueous ethanol (2 × 2 L) to remove small molecular mass reagents including EDA. After the dialysis, the polymer was concentrated *in vacuo*, coevaporated twice with methanol (10 mL), and redissolved in 50 mL of 2% TFA in dichloromethane. After incubation for 1 h at 25 °C, the bright yellow solution was concentrated *in vacuo* and neutralized by 5 mL of 10% triethylamine in methanol. The resulting monoamine P85 was isolated by gel filtration on a Sephadex LH-20 column (2.5 × 30 cm) and analyzed by TLC in dichloromethane/MeOH, 9:1. The monoamine P85 develops a blue color after spraying with 1% ninhydrine solution in ethanol (a test for an amino group).

Monoamine L81, L121, and P123 Derivatives. The monoamine derivatives of L81, L121, and P123 were synthesized using a modified procedure. In particular, to remove excess of EDA, modified L121 and P123 were dialyzed against 30−40% aqueous ethanol using a membrane with MWCO 2000 kDa. L81 was dialyzed against 30% aqueous ethanol using a membrane with MWCO 1000 kDa.

Amino Group Determination by Ninhydrin Assay. The stock solution of ninhydrin was prepared by adding 1.03 g of ninhydrin, 0.18 g of hydrindantin, 12.8 mL of 4 N sodium acetate buffer (pH5.5) to 38.5 mL of methylcelosolve. For the standard calibration curve, 0.5 mL of glycine (10^{-4} to 10^{-5} M) in acetate buffer (pH 5.5) was mixed with 0.25 mL the ninhydrin solution. The mixture was heated at 100 °C for 15 min and supplemented with 0.75 mL 50% aqueous ethanol. The absorbance was measured at 570 nm.

Conjugation of HRP with Monoamine Pluronic. Monoamine P85 (200 mg) in 0.5 mL of methanol was mixed with DSP (105 mg, 6-fold molar excess) solution in 0.5 mL of DMF stored over molecular sieves (4 Å). The mixture was supplemented with 0.1 mL sodium borate buffer (0.1 M, pH 8) and incubated for 30 min at 25 °C. Excess of DSP was removed by gel filtration on a Sephadex LH-20 column (2.5 × 30 cm) in methanol, and the solvent was removed *in vacuo*. Activated copolymer was dissolved in 1 mL 20% aqueous ethanol and mixed with HRP (16 mg) in 0.5 mL of 0.1 M sodium borate (pH 8). The homogeneous reaction mixture was incubated overnight at 4 °C. The activated monoamine L81, L121, or P123 (200 mg) was dissolved in 1 mL of 30−40% aqueous ethanol and reacted with HRP in 0.5 mL of 0.1 M sodium borate (pH 8). Modifications of HRP with monoamine P85 *via* DSS and DTBP were carried out using a similar procedure. DTBP was directly dissolved in 0.5 mL of sodium borate buffer (0.1 M, pH 8) and reacted with monoamine P85 in 0.5 mL of 20% aqueous ethanol.

Purification of HRP−Pluronic Conjugates. The conjugates were precipitated in cold acetone to remove the excess of nonreacted copolymers. Briefly, about 1 mL of the above reaction mixtures was added dropwise to 25 mL of cold acetone upon stirring. After incubating for 1 h at 4 °C, the brown precipitate containing HRP conjugates was collected at 3000 rpm for 10 min at 4 °C, washed by cold ethanol (2 × 10 mL), and dried *in vacuo*. Alternatively, the conjugates were washed with 20% aqueous ethanol and separated using Amicon ultra-15 centrifuge filter (MWCO 30 kDa) at 3800 rpm at 4 °C for 15 min. The extent of separation of nonreacted copolymers was assayed by TLC on silica gel plates in dichloromethane/methanol, 9:1. In this system, copolymers migrated ($R_f = 0.4$), while the conjugate was immobile. If free copolymer was detected, the purification procedure was repeated. To separate unmodified HRP, the conjugates were further purified on Toyopearl SP cation exchange column (1 cm × 6.8 cm) equilibrated with 10 mM CH_3COONa/10 mM NaCl/5% EtOH, pH 4.1, in the gradient of 0.2 M NaCl in 10 mM CH_3COONa/5% EtOH, pH 4.1. The final conjugates were desalted in Amicon ultra-15 centrifuge tube (MWCO 30 kDa) and freeze-dried.

MALDI-TOF spectra. Mass values of HRP−Pluronic conjugates were determined using a Voyager-DE Pro STR MALDI-TOF mass spectrometer (Applied Biosystems/MDS SCIEX, Foster City, CA). Samples were prepared by (1) plate coating with 0.5 μL saturated sinapinic acid in 50% acetonitrile with 0.1% TFA; (2) depositing 0.5 μL solution of HRP−Pluronic conjugates in water (10^{-5} M); and, finally, (3) coating with 0.5 μL saturated sinapinic acid in 50% acetonitrile with 0.1% TFA. External calibration was performed using bovine serum albumin (Applied Biosystems, Foster City, CA). Mass spectra were recorded with the laser intensity set between 5000 to 10 000 au Typically, three acquisitions (100 shots each) were pulled together for each sample.

Enzymatic Activity of HRP−Pluronic Conjugates. *o*-Phenylenediamine was used to measure the HRP enzymatic activity as described earlier (*7*). Briefly, 1 to 20 ng/mL HRP−Pluronic conjugates were mixed with 20 μL of a fresh *o*-phenylenediamine solution (0.05 mg/mL) in citrate buffer (0.1 M, pH 5.0)

Scheme 1. Synthesis of Monoamine Pluronic

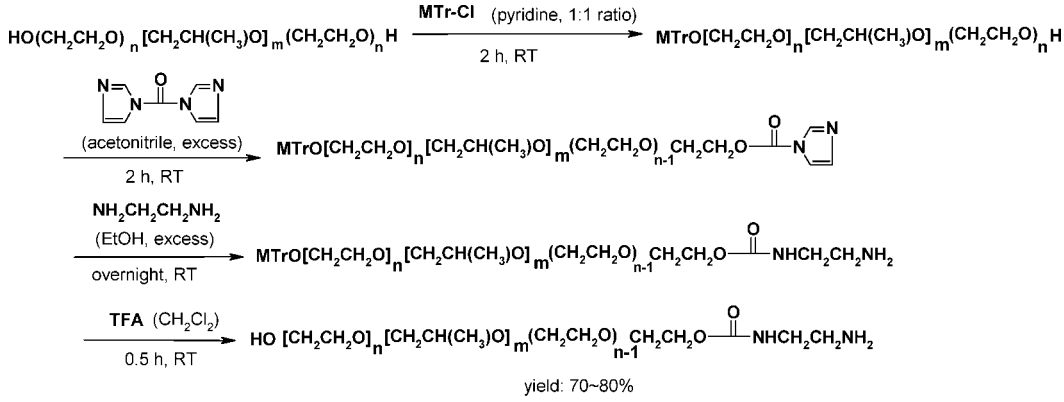

containing 0.01% Triton X-100, 0.1 g/mL BSA, and 0.2% H_2O_2. The reaction mixture was added to 96-well plates to a final volume of 200 μL in citrate buffer (0.1 M, pH 5.0). After incubating at 37 °C for 5 min, the reaction was stopped by adding 20 μL of a 0.5% Na_2SO_3 solution in 2 N H_2SO_4, and the absorbance was measured at 490 nm in the microplate reader Multiskan MCC/340 (Fisher Scientific, Pittsburgh, PA).

Degree of Modification by TNBS Assay. Ten microliter aliquots of HRP−Pluronic conjugate solutions (protein concentration 0.1−0.6 mg/mL) were mixed with 10 μL of TNBS solution (1.7 mM) in 80 μL of sodium borate buffer (0.1 M, pH 9.5) and incubated at 37 °C for 2 h. The absorbance was measured at 405 nm using the microplate reader. The protein content was measured using a BCA kit from Pierce (Rockford, IL). The degree of modification (average number of amino groups modified) was calculated according to the equation

$$S(\text{modification degree}) = 7 \times \frac{A_{\text{native}}/C_{\text{native}} - A_{\text{modified}}/C_{\text{modified}}}{A_{\text{native}}/C_{\text{native}}}$$

where A_{native} and A_{modified} were the absorbences and C_{native} and C_{modified} the concentrations of native and modified HRP, respectively. The total number of primary amino groups including lysine residues and terminal amine group in HRP is 7.

Cells. MDCK cells (from ATCC, CCL-34) were seeded in 24-well plates at a density of 50 000 cells/well in Dulbecco's Modified Eagle Medium (DMEM) (Invitrogen, Carlsbad, California, cat no 41500−034) supplemented with 0.5% penicillin/streptomycin and 10% fetal bovine serum (Invitrogen, Carlsbad, California). The cells were cultured at 37 °C with 95% humidity and 5% CO_2, and grown for two days until 80−90% confluence. BBMEC were isolated from the gray matter of the bovine cerebral cortex by enzymatic digestion followed by subsequent centrifugations (*8*). Cells were seeded onto collagen-coated, fibronectin-treated 24-well plate at a density of 50 000 cells/well and grown to confluence (typically 10−12 days) in a culture media consisting of 45% minimum essential medium (MEM), 45% Ham's F-12 nutrient mix (Gibco, Life Tech., Grand Island, NY), 10 mM HEPES, pH 7.4, 13 mM sodium bicarbonate, heparin, gentamicin, amphotericin B (Sigma), and 10% horse serum.

Cellular Uptake. MDCK cell and BBMEC monolayers in 24-well plates were washed twice in assay buffer containing 122 mM NaCl, 25 mM $NaHCO_3$, 10 mM glucose, 3 mM KCl, 1.2 mM $MgSO_4$, 0.4 mM K_2HPO_4, 1.4 mM $CaCl_2$, and 10 mM HEPES. Cells were exposed to unmodified or modified HRP in assay buffer for various time intervals at 37 °C, then washed with cold phosphate-buffered saline five times and lysed in 1% Triton X-100. No cellular toxicity was observed during treatment. Aliquots of cell lysates (20 μL) were taken for HRP activity determination as described above. Separate calibration curves were used for unmodified or modified HRP. The amounts of cell-associated HRP were normalized for the cell protein as determined by Pierce BCA.

RESULTS AND DISCUSSION

Synthesis of Pluronic Monoamine Derivatives. A general procedure for introduction of amino group in Pluronic is presented in Scheme 1. Good separation of monosubstituted MTr-Pluronic from bis-substituted and free Pluronic was achieved using a silicagel column for each copolymer used (L81, P85, L121, and P123). The purity of the fractions was assessed by TLC. For all polymers, the monosubstituted MTr-Pluronic exhibited $R_f = 0.6$, the bis-substituted MTr-Pluronic $R_f = 0.8$, and free Pluronic $R_f = 0.4$. Fractions containing the monosubstituted MTr-Pluronic were collected, and these fractions did not contain bis-substituted MTr-Pluronic or free Pluronic. Subsequent transformation of the end-protected MTr-Pluronic to the amino derivatives using CDI and EDA proceeds in mild conditions and is well-established for conjugation of poly(ethylene glycol) to amino groups of peptides (*9*). The reaction yields were from 70% to 80% by weight. The modification degrees (number of amino groups per copolymer molecule) were 0.96 (L81), 0.74 (P85), 0.74 (L121), and 0.81 (P123) as determined by ninhydrin assay. No trace of EDA was detected by TLC. The NMR spectra, before and after modification, show no change in $-CH_2CH_2O-$ and $-CH_2CH(CH_3)O-$ signals, suggesting that the copolymer backbone remained intact (data not shown).

Synthesis and Purification of HRP−P85 Conjugates. Three types of homobifunctional cross-linking reagents, DSP, DSS, and DTBP, were used to conjugate HRP and monoamine P85 (Scheme 2). Two reagents, DSP and DTBP, contain disulfide bond and are degradable in the reducing environments, such as intracellular glutathione (*10*). In contrast, DSS produces a stable nondegradable link. The water-insoluble DSP and DSS were reacted with monoamine P85 derivatives in DMF/methanol, while DTBP was reacted in water. After purification, the activated P85 derivatives were conjugated to HRP in 20% aqueous ethanol. The resulting conjugates were purified, first, by acetone precipitation or filtration and, second, by cation exchange chromatography. In the case of DSP-activated P85 derivative, the reaction yield depended on pH, with pH 8.0 being optimal (Figure 1). Similar results were obtained for DSS-activated P85 (data not shown). However, DTBP-activated P85 was more stable at higher pH and, therefore, produced high yield of the protein conjugate at pH 8.0 and 9.0.

Table 2 summarizes the characteristics of the HRP−Pluronic conjugates obtained with different reagents and modification conditions. The residual enzymatic activity of HRP−P85

Scheme 2. Conjugation of HRP with Monoamine P85 through Biodegradable Linkers DSP, DTBP and Nondegradable Linker DSS

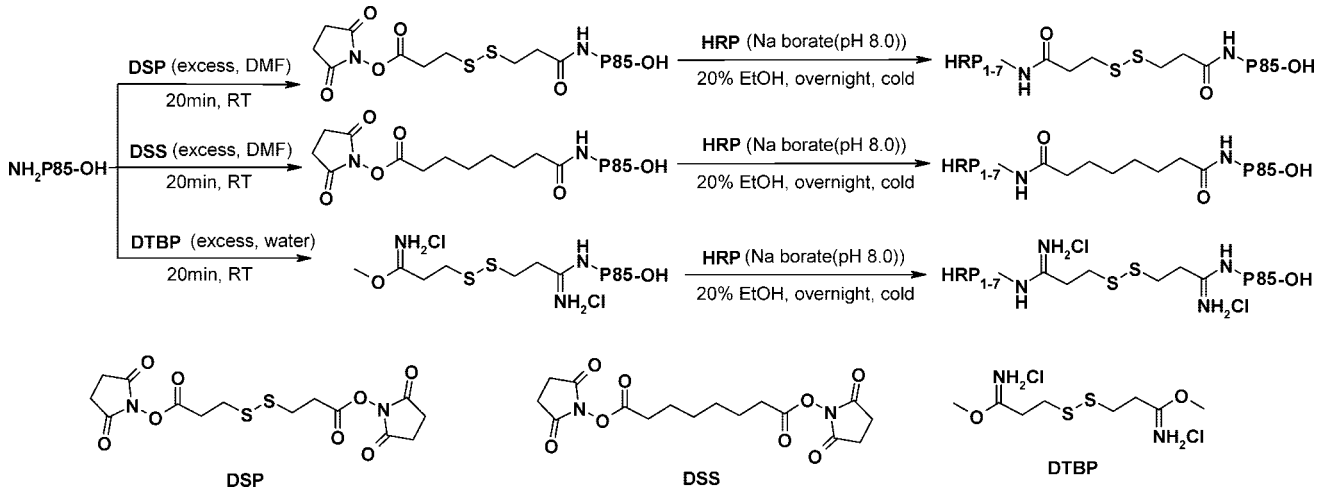

conjugates was relatively higher for DSP and DSS-linked conjugates (70% to 85% of initial HRP), but somewhat lower for DTBP-linked conjugates (56%). The average modifications degrees of HRP-P85 as determined by TNBS titration assay were from ca. 1 to 2. However, MALDI-TOF revealed that the conjugates contained a mixture of unmodified HRP and HRP−P85 conjugates with 1, 2, and 3 P85 chains attached (Figure 2a). The presence of the free P85 in these conjugates depended on the purification procedure. No free copolymer was detected for HRP−P85 precipitated by acetone, while the filtration could not separate the free copolymer completely.

Conjugation of HRP with Monoamine L81, L121, and P123. The reaction conditions were modified for conjugation of HRP with L81, L121, and P123, which are more hydrophobic compared to P85. In these cases, the DSP-activated copolymers were conjugated to the protein in aqueous ethanol (30% to 40%

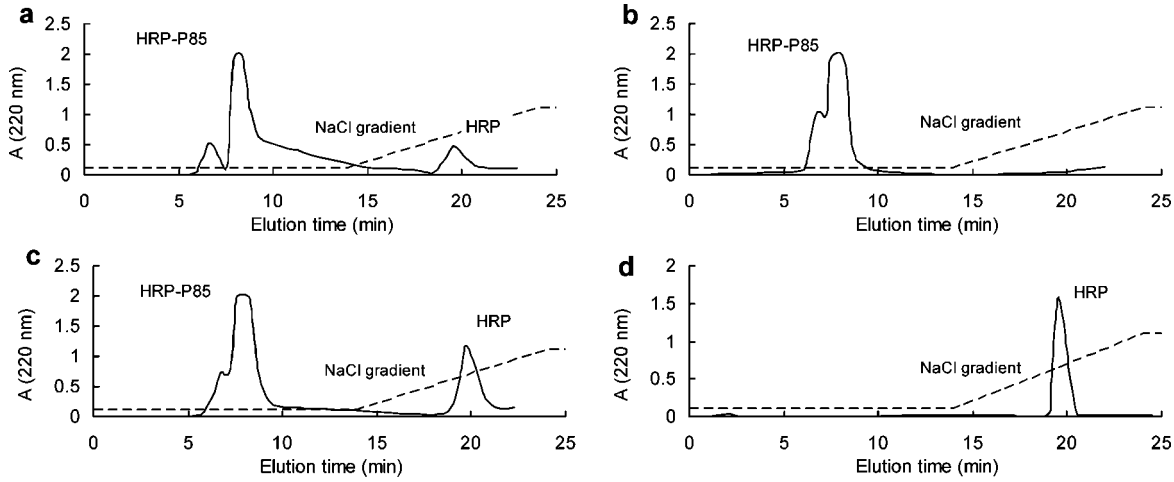

Figure 1. Chromatographic profiles of HRP−P85 conjugates obtained using DSP at different pH: (a) 7.4, (b) 8.0, (c) 9.0, and (d) unmodified HRP. Chromatography conditions: Toyopearl MD-G SP column (10 mm i.d. × 6.8 cm) in NaCl salt gradient (0.01−0.2 M) (pH 4.3, elution rate 1 mL/min, detection at 220 nm).

Table 2. Characteristics of HRP−Pluronic Conjugates

Pluronic	linker	Pluronic/HRP molar ratio during the reaction	reaction conditions time/ temperature/pH[a]	purification method[b]	modification degree[c]	residual activity[d]
P85	DSP	120	24 h/4 °C/pH8.0	F	1.3	85
P85	DSP	240	24 h/4 °C/pH8.0	A	1.39	ND
P85	DSP	240	36 h/4 °C/pH8.0	A	1.41	ND
P85	DSP	120	24 h/4 °C/pH8.0	A	1.03	70
P85	DTBP	120	24 h/4 °C/pH9.0	A	1.59	56
P85	DSS	120	24 h/4 °C/pH8.0	F	1.88	ND
L81	DSP	180	24 h/4 °C/pH8.0	F	2.55	96
L81	DSP	120	24 h/4 °C/pH8.0	A	0.95	81
P123	DSP	120	3 h/25 °C/pH8.0	F	1.80	85
P123	DSP	120	24 h/4 °C/pH8.0	A	1.26	ND
L121	DSP	120	3 h/25 °C/pH8.0	F	0.23	92
L121	DSP	120	24 h/4 °C/pH8.0	A	1.50	65

[a] Last stage of conjugation of HRP with activated derivative. [b] The excess of Pluronic was removed by acetone precipitation (A) or filtration of the conjugate in the aqueous ethanol solution (F). [c] Number of copolymer chains per HRP as determined by TNBS titration of amino groups. [d] Residual activity was determined by *o*-phenylenediamine reaction and calculated on the basis of the percentage of the activity of the native HRP.

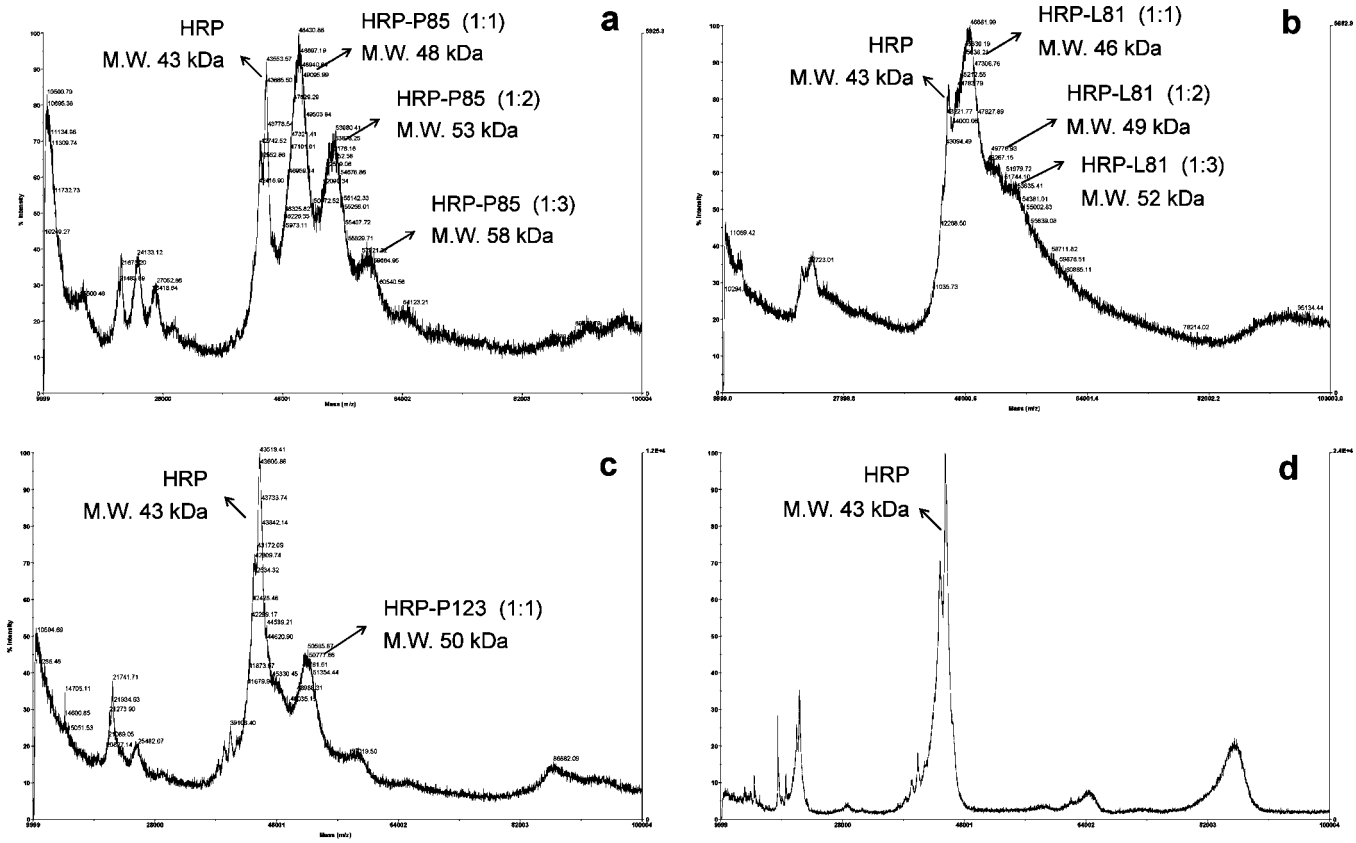

Figure 2. Mass spectra of HRP−Pluronic conjugates obtained by MALDI-TOF: (a) HRP−P85; (b) HRP−L81; (c) HRP−P123; and (d) unmodified HRP. (a) HRP−P85 MW 48 kDa (1:1), 53 kDa (1:2), and 58 kDa (1:3); (b) HRP−P81 MW 46 kDa (1:1), 49 kDa (1:2), and 52 kDa (1:3); (c) HRP−P123 MW 50 kDa (1:1); (d) HRP MW 43 kDa.

v/v) mixtures to decrease hydrophobic association between the PPO chains. Furthermore, especially in the case of the most hydrophobic L121, the modification degrees considerably increased when the conjugation was carried out at lower temperature and for longer exposure time (Table 2). The PPO segment exhibits a lower critical solution temperature (LCST), and therefore, the decrease of the temperature (4 °C) favors disaggregation of Pluronic molecules (*11*). Notably, the excess of L81, L121, and P123 was completely removed during purification of the conjugates in cold acetone but not by the filtration (data not shown). Furthermore, even for the samples with the lower modification degrees, there was poor separation between the conjugates and unmodified HRP. However, the unmodified protein was observed along with various HRP−L81 and HRP−P123 conjugates in the mass spectra (Figure 2b,c). Obviously, separation of free HRP from the conjugates on a cation exchange column was only partial, as the mass spectra demonstrated. A possible reason was that under the separation conditions the modified HRP formed aggregates that also entrapped unmodified HRP and were eluted within the column elution volume. Increasing the ethanol content in the elution buffer from the original 5% to 20% could be a future solution to dissociate the aggregates and enhance the separation. HRP−L121 conjugates were not detectable in MALDI-TOF, possibly due to high hydrophobicity of such conjugates (data not shown in the figure). The remaining activity of HRP after conjugation was high (81% to 96% of initial HRP), except for the HRP−L121 conjugate with higher modification degree, which was purified by precipitation in acetone (65%) (Table 2). Altogether, the procedures described in most cases resulted in HPR−Pluronic conjugates with relatively high yield, purity, and enzymatic activity.

Cellular Uptake of HPR−Pluronic Conjugates. The uptake of unmodified HRP in both MDCK cells (Figure 3) and BBMEC

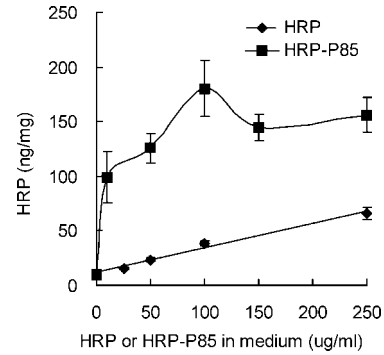

Figure 3. Uptake of HRP and HRP−P85 conjugate with DSP link in MDCK cells at 60 min as a function of the enzyme concentration in cell culture medium. The amount of HRP is normalized for the total cellular protein (ng/mg). Data were obtained in quadruplicate and presented as means ± SEM.

(data not shown) increased almost linearly as the protein concentration increased up to ca. 250 μg/mL. This behavior is characteristic of fluid-phase endocytosis (*12*). Contrary to that, the cellular uptake of HRP−P85 was bimodal, with an initial sharp increase in uptake at 10 μg/mL followed by a slower increase up to 250 μg/mL. This suggests a different mechanism for the uptake of the modified protein and may indicate adsorption endocytosis (*13*). Clearly, the uptake was greatly increased after the modification, possibly due to binding of hydrophobic PPO chains with the cell membranes. (Notably, the studies presented in this work report the total uptake, which combines membrane binding and internalization components. A detailed characterization of the uptake mechanisms will be reported separately.)

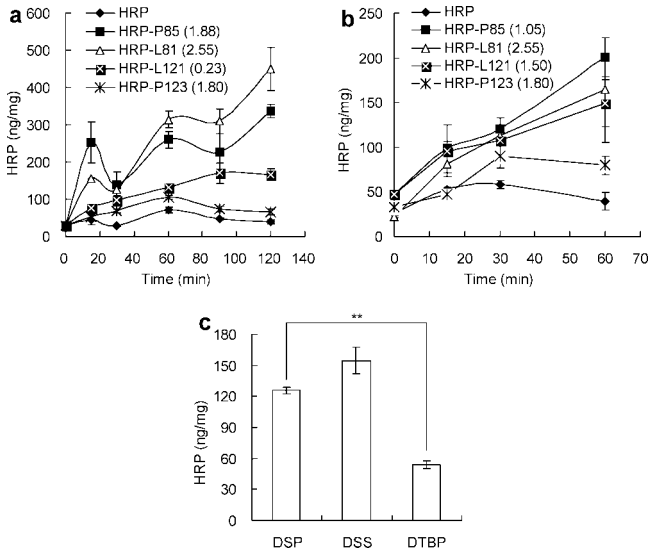

Figure 4. Uptake of HRP−Pluronic conjugates in (a,c) MDCK cells and (b) BBMEC monolayers. The conjugates were prepared using (a,b) DSP or (c) different cross-linkers as shown in the figure. The modification degree of the conjugates was indicated in the brackets. Data were obtained in quadruplicate and presented as means ± SEM. Statistical analysis was done using the Student *t* test. The symbol ** indicates statistical significance ($p < 0.01$).

Further, 50 μg/mL was selected as the concentration for the comparison of the unmodified and different conjugated HRP. In both cell models, there was a considerable increase (4- to 5-fold) in the uptake of HRP−P85 and HRP−L81 conjugates compared to the unmodified HRP (Figure 4a,b). Furthermore, the HRP−L121 conjugate also exhibited significant uptake increase, especially in the BBMEC monolayers. The least efficient uptake was observed in the case of HRP−P123. Evidently, the length of the hydrophobic PPO block is an important factor for the membrane binding and/or cell internalization of HRP conjugates. P85 and L81 contained about 40 propylene oxide units, whereas L121 and P123 contained about 70 propylene oxide units (Table 1). Therefore, the copolymers with shorter PPO chains overall appeared to be more efficient than those with longer PPO chains. This may be due to the anchoring of long PPO chains in the membranes that can prevent internalization of the corresponding conjugates in the cells. Notably, in the case of the free Pluronic the cellular uptake was also less efficient for the copolymers with longer PPO chains compared to the copolymers with shorter PPO chains because of strong binding of long PPO chains in the membranes (*5*). No aggregates were observed for all of the four conjugates in the concentration that were used in cellular experimentation when detecting in the sedimentation experiment (data not shown). Obviously, during the cellular uptake the conjugates were exposed to the membrane in the unimer form. It is also interesting that the length of the PEO chain had little if any effect on the uptake of the HRP−P85 and HRP−L81 conjugates having the same size of the PPO chains. At the same time, one may expect that the length of PEO chain could have a significant effect on the pharmacokinetics and distribution of the modified protein in the body (*14*). This will be examined for these conjugates in subsequent studies. Finally, in MDCK cells there was no difference in the uptake of HRP−P85 conjugates with degradable DSP and nondegradable DSS linkers (Figure 4c). However, the HRP−P85 conjugate with degradable positively charged DTBP linker was taken up much less efficiently than the conjugate with the degradable uncharged DSP linker. Since it is well-known that cationic compounds are generally transported more efficiently into cells, the reason for the decreased uptake of HRP−P85 conjugate with DTBP linker may be, for example, modification of different lysine amines in HRP compared to other conjugates. The differences in localization of the P85 chain in the HRP molecule may have a profound effect on the conjugate's transport characteristics due to the effects of the neighboring amino acids.

In summary, we have generated four monoamine Pluronic derivatives and successfully conjugated them to a model protein, HRP, *via* biodegradable or nondegradable linkers. The formation of covalent conjugates was demonstrated qualitatively by mass spectroscopy and quantitatively by TNBS assay. The purification procedures have been established. Using these methods, we obtained HRP conjugates containing an average of ca. 1 to 2 Pluronic moieties per protein molecule and retaining in most cases over 70% of the activity of the native HRP. The increased cellular uptake of the conjugates was demonstrated using MDCK cells and BBMEC monolayers. As a result of these modifications, a very hydrophilic protein, HRP, more efficiently bound with these cells than the unmodified analogue. The optimal polymers for modifications included P85 and L81. Between these two conjugates, there was little if any dependence of the uptake on the length of the hydrophilic PEO block of Pluronic, suggesting that its hydrophobic PPO block plays a decisive role in the conjugate interactions with cells. The results of this work will facilitate development of a novel method for the cellular delivery of proteins (*4*).

ACKNOWLEDGMENT

This study was supported by National Institute of Health RO1 NS051334. We also gratefully acknowledge the UNMC Mass Spectrometry and Proteomics Core Facility for assistance in MALDI-TOF experiments and Dr. Xiaobin Zhang (UNMC) for assistance in BBMEC isolation and culture.

LITERATURE CITED

(1) Abbott, N. J., Ronnback, L., and Hansson, E. (2006) Astrocyte-endothelial interactions at the blood-brain barrier. *Nat. Rev. Neurosci. 7*, 41–53.

(2) Begley, D. J. (2004) Delivery of therapeutic agents to the central nervous system: the problems and the possibilities. *Pharmacol. Ther. 104*, 29–45.

(3) Kabanov, A. V., and Alakhov, V. Y. (2002) Pluronic block copolymers in drug delivery: from micellar nanocontainers to biological response modifiers. *Crit. Rev. Ther. Drug Carrier Syst. 19*, 1–72.

(4) Batrakova, E. V., Vinogradov, S. V., Robinson, S. M., Niehoff, M. L., Banks, W. A., and Kabanov, A. V. (2005) Polypeptide point modifications with fatty acid and amphiphilic block copolymers for enhanced brain delivery. *Bioconjugate Chem. 16*, 793–802.

(5) Batrakova, E. V., Li, S., Alakhov, V. Y., Miller, D. W., and Kabanov, A. V. (2003) Optimal structure requirements for pluronic block copolymers in modifying P-glycoprotein drug efflux transporter activity in bovine brain microvessel endothelial cells. *J. Pharmacol. Exp. Ther. 304*, 845–54.

(6) Vinogradov, S. V., Bronich, T. K., and Kabanov, A. V. (1998) Self-assembly of polyamine-poly(ethylene glycol) copolymers with phosphorothioate oligonucleotides. *Bioconjugate Chem. 9*, 805–12.

(7) Slepnev, V. I., Phalente, L., Labrousse, H., Melik-Nubarov, N. S., Mayau, V., Goud, B., Buttin, G., and Kabanov, A. V. (1995) Fatty acid acylated peroxidase as a model for the study of interactions of hydrophobically-modified proteins with mammalian cells. *Bioconjugate Chem. 6*, 608–15.

(8) Miller, D. W., Audus, K. L., and Borchardt, R. T. (1992) Application of cultured endothelial cells of the brain microvasculature in the study of the blood-brain barrier. *Methods Cell Sci. 14*, 217–224.

(9) Beauchamp, C. O., Gonias, S. L., Menapace, D. P., and Pizzo, S. V. (1983) A new procedure for the synthesis of polyethylene glycol-protein adducts; effects on function, receptor recognition, and clearance of superoxide dismutase, lactoferrin, and alpha 2-macroglobulin. *Anal. Biochem. 131*, 25–33.

(10) Colcher, D., Pavlinkova, G., Beresford, G., Booth, B. J., Choudhury, A., and Batra, S. K. (1998) Pharmacokinetics and biodistribution of genetically-engineered antibodies. *Q. J. Nucl. Med. 42*, 225–41.

(11) Liang, X., Guo, C., Ma, J., Wang, J., Chen, S., and Liu, H. (2007) Temperature-dependent aggregation and disaggregation of poly(ethylene oxide)-poly(propylene oxide)-poly(ethylene oxide) block copolymer in aqueous solution. *J. Phys. Chem. B 111*, 13217–13220.

(12) Steinman, R. M., and Cohn, Z. A. (1972) The interaction of particulate horseradish peroxidase (HRP)-anti HRP immune complexes with mouse peritoneal macrophages in vitro. *J. Cell Biol. 55*, 616–34.

(13) Raub, T. J., and Audus, K. L. (1990) Adsorptive endocytosis and membrane recycling by cultured primary bovine brain microvessel endothelial cell monolayers. *J. Cell Sci. (Pt 1) 97*, 127–38.

(14) Katre, N. V. (1993) The conjugation of proteins with polyethylene glycol and other polymers: Altering properties of proteins to enhance their therapeutic potential. *Adv. Drug Delivery Rev. 10*, 91–114.

BC700443K

In Vitro Cytotoxicity, Chemotactic Effect, and Cellular Uptake of Branched Polypeptides with Poly[L-Lys] Backbone by J774 Murine Macrophage Cell Line

Rita Szabó,[†] Gábor Mezö,[†] Éva Pállinger,[‡] Péter Kovács,[§] László Köhidai,[§] Szilvia Bösze,[†] and Ferenc Hudecz*[,†,||]

Research Group of Peptide Chemistry at Eötvös L. University, Hungarian Academy of Sciences, Budapest 112, POB 32, H-1518 Hungary, Research Group for Inflammation Biology and Immunogenomics of Hungarian Academy of Scineces and Semmelweis University, H-1085, Budapest, Hungary, Department of Genetics, Cell and Immunobiology, Semmelweis University, H-1085, Budapest, Hungary, and Department of Organic Chemistry, Eötvös L. University, Budapest 112, POB 32, H-1518 Hungary. Received December 10, 2007; Revised Manuscript Received February 26, 2008

Branched polypeptides with polylysine backbone are promising candidates for selective delivery of drugs, epitopes. or reporter molecules. We reported earlier that polylysine-based polypeptides with polyanionic character were internalized by murine bone marrow derived macrophages via class A scavenger receptor. In the present studies, our investigations were extended to seven polypeptides with different amino acid composition and charge properties. We report on our findings on the concentration-dependent influence of these compounds on survival and chemotaxis of the murine macrophage-like cell line J774 and internalization properties of the polypeptides by J774 cells. Our observations indicate that the polypeptides regardless of their charge properties were essentially nontoxic and did not alter significantly the chemotaxis of J774 cells; therefore, the polypeptides suit the requirements for nontoxic and "neutral" carrier molecules. We also demonstrated that the polypeptides were internalized efficiently by J774 cells, depending on their chemical structure and charge properties. Using the scavenger receptor–ligand fucoidan as inhibitor, we established that the scavenger receptor played a role–in accordance with findings on murine bone marrow derived macrophages in the internalization only of the polyanionic polypeptides.

INTRODUCTION

Most of the compounds recently applied therapeutically for tumors and infectious diseases are small molecules that enter the cells via diffusion. Coupling of drugs to macromolecular carriers would not only improve their solubility but also could decrease side effects and offers a new possibility of cell- or tissue-specific introduction (*1*). The conjugation of these agents alters the mechanism of their internalization, because the larger conjugates cannot penetrate the cell membrane by diffusion but are internalized by a more specific active transport mechanism, e.g., macropinocytosis or receptor-mediated endocytosis, depending on the properties of the carrier (*2*, *3*). Synthetic polymers have been widely used as carriers of bioactive compounds, epitopes, or reporter molecules. Most of the polymeric carriers like the nonbiodegradable HPMA (*N*-(2-hydroxypropyl)methacrylamide copolymer) (*4*, *5*) and DIVEMA (divinyl ether−maleic anhydride copolymer) (*6*) or biodegradable polymeric carriers like poly(α-amino acids), poly[Lys], poly[Glu], or poly[Tyr]) (*7*–*9*), do not possess a specific targeting moiety. In our laboratory, several groups of poly(L-lysine)-based branched polypeptides were developed and applied as macromolecular carriers of drugs and epitopes (*3*). The first group of the polymeric polypeptides studied in the present work can be described with the general formula of poly[Lys(X_i)][1]; X_iK, possesses a single amino acid coupled to the ϵ-amino groups of the lysine residues. The other group of polypeptides, poly[Lys(DL-Ala_m)] (*10*), contain a short oligo[DL-alanine] side chain or an additional amino acid coupled to the α-amino group of the terminal alanines with the general formula poly[Lys(X_i-DL-Ala_m)], XAK, where $i \cong 1$ and $m \cong 4$ (*11*). *In vitro* and *in vivo* physiological properties of poly[L-lysine]-based polymeric polypeptides like *in vitro* and *in vivo* cytotoxicity (*12*, *13*), biodistribution (*14*, *15*), blood clearance (*13*), immunogenicity (*16*), and immunomodulatory effect (*17*, *18*); chemotaxis (*19*) and class-A scavenger receptor (SR-A)-mediated cellular uptake have been investigated systematically over the past few years (*20*). Physicochemical properties of the polypeptides as interaction with phosphoplipid bilayers were also examined recently (*21*, *22*). Our previous data confirmed that amino acid composition and length of the side chains and charge of the terminal amino acid greatly influence the biological properties of the polypeptides and their drug conjugates, e.g., with daunomycin (*23*, *24*) and methotrexate (*25*). We have also demonstrated that polylysine-based polypeptides with polyanionic character (SuccEAK and

* Corresponding author. Ferenc Hudecz, Ph.D., D.Sc., Research Group of Peptide Chemistry, Hungarian Academy of Sciences, Eötvös L. University, Budapest 112, POB 32, H-1518 Hungary. Fax: 36-1-372-2620, Tel: 36-1-372 2828, E-mail: fhudecz@elte.hu.

[†] Research Group of Peptide Chemistry at Eötvös L. University.

[‡] Research Group for Inflammation Biology and Immunogenomics of Hungarian Academy of Scineces and Semmelweis University.

[§] Department of Genetics, Cell and Immunobiology, Semmelweis University.

[||] Department of Organic Chemistry, Eötvös L. University.

[1] Abbreviations: Abbreviations of amino acids and their derivatives follow the revised recommendation of the IUPAC-IUB Committee on Biochemical Nomenclature entitled "Nomenclature and Symbolism for Amino Acids and Peptides" (recommendations of 1983). Nomenclature of branched chain polypeptides is used in accordance with the recommended nomenclature of graft polypeptides (*26*). For the sake of brevity codes of branched chain polypeptides were constructed by us using the one-letter codes of amino acids. All amino acids are L configuration unless otherwise stated. The other abbreviations in this paper are the following: Pcp, pentachlorophenyl; HOBt, 1-hydroxybezotriazole; DMSO, dimethyl sulfoxide; DMF, *N*,*N*-dimethyl-formamide; TEA, triethylamine; PBS, phosphate-buffered saline; Ac, acetyl; Succ, succinyl; Mal, maleyl; CF, 5(6)-carboxyfluorescein.

10.1021/bc7004544 CCC: $40.75 © 2008 American Chemical Society
Published on Web 04/23/2008

MalEAK) enter murine bone marrow derived macrophages via SR-A-mediated endocytosis, and not only the charge density but also the chemical structure of the anionic end group have an influence on the efficacy of the internalization (*20*). In this article, we describe our findings on the effect of seven structurally related polypeptides with different characteristics according to their amino acid composition and charge properties on survival and chemotaxis of the J774 murine macrophage cell line. In order to determine the correlation between efficient cellular uptake and chemical structure of polypeptide carriers, we investigated the internalization of the polypeptides in several aspects. In order to find the carrier that can be most efficiently internalized by macrophages, we carried out the comparative study of the polypeptides with different charge properties on the macrophage cell line J774. We also wanted to clarify whether the scavenger receptor is involved in the uptake of the polyanionic polypeptides, using the scavenger receptor–ligand fucoidan as inhibitor. Our results indicate that the polypeptides elicited only moderate toxicity on J774 cells except the control polypeptide poly(L-lysine). They did not alter significantly the chemotaxis of the cells either. We demonstrated that the polypeptides were internalized efficiently by J774 cells depending on their chemical structure and charge properties. Taken together, the polypeptides suit the requirements for nontoxic and nonchemotactic macromolecular carriers. We established that the scavenger receptor played a role only in the internalization of two polyanionic polypeptides, poly[Lys(Succ-$Glu_{1.0}$-DL-$Ala_{3.8}$)], SuccEAK, and poly[Lys(Mal-$Glu_{1.0}$-DL-$Ala_{3.8}$)], MalEAK; thus, these polypeptides can be promising candidates as macromolecular carriers in drug conjugates applied for cell-specific delivery into macrophages.

MATERIALS AND METHODS

Reagents. Amino acids used for this study, HCl, acetic anhydride, succinic anhydride, and DMF were purchased from REANAL (Budapest, Hungary). Pentachlorophenol, 1-hydroxybenzotriazole, triethylamine, and DMSO were from Fluka (Buchs, Switzerland). Acetonitrile was from Merck (Darmstadt, Germany). Fucoidan from *Fucus vesiculosus* and 5(6)-carboxyfluorescein succinimide ester were obtained from Sigma-Aldrich Hungary Ltd. (Budapest, Hungary).

Synthesis of Poly[Lys(X_i)], X_iK and Poly[Lys(X_i-DL-Ala_m)], XAK-Type Polypeptides. Poly[Lys(X_i)] (X_iK) where X = Pro and XAK-type polypeptides where X = Ser or Glu were prepared according to Mezö et al. (*27*). Briefly, poly[Lys(DL-Ala_m)], AK, was synthesized by grafting short oligomeric DL-Ala chains to the $^{\epsilon}NH_2$ group of lysine residues using *N*-carboxy-DL-Ala-anhydride. Polymerization was continued at room temperature for 2 days. Terminal amino acids (X) were coupled to the $^{\alpha}NH_2$ groups of the terminal amino acid of the oligoalanine chains, where X = Glu or Ser. In the case of X_iK polypeptides, terminal amino acid was coupled to the $^{\epsilon}NH_2$-groups of polylysine as Z-X-OPcp, where X = Pro. The coupling reaction was carried out by *in situ* active ester method using an equivalent amount of 1-hydroxybenzotriazole (HOBt) dissolved in DMF as activating reagent (*28*). The polypeptides were purified by dialysis against distilled water for two days using a Visking tube (cutoff = 10000 Da) and isolated by freeze-drying.

Synthesis of Polyanionic Derivatives of Poly[Lys(Glu_i-DL-Ala_m)], (EAK). Synthesis of polypeptides of polyanionic character was performed via modification of EAK polypeptide as described previously (*20*, *29*). Briefly, acetylation was carried out in DMF/water = 9:1 solvent mixture using 5 equiv freshly prepared imidazolyl acetate (*30*). Succinylation and maleylation were performed in 0.1 M carbonate buffer (pH 9.2) using 0.022 g (0.22 mmol) succinic anhydride or 0.02 g (0.2 mmol) maleic anhydride dissolved in DMSO (c = 100 mg/mL). The reaction was continued for 4 h at RT, followed by dialysis against distilled water for 2 days and then freeze−drying.

Amino Acid Analysis. Amino acid composition of the polymeric polypeptides was determined by amino acid analysis using a Beckman 6300 analyzer (Fullerton, USA) after hydrolysis in 6 M HCl in sealed and evacuated tubes at 105 °C for 24 h.

Labeling of Polymeric Polypeptides with 5(6)-Carboxyfluorescein. Ten milligrams (6×10^{-7} to 1.9×10^{-7} mol) polypeptides was dissolved in 2 mL sodium carbonate buffer (0.1 M; pH 9.4). 5(6)-Carboxyfluorescein succinimide ester was dissolved in DMF (c = 10 mg/mL, 0.21 mM) and was added to the polypeptide solution in 20 μL aliquots. The reaction was continued for 1 h at room temperature with continuous stirring. The product was purified by gel filtration on a PD10 column filled with Sephadex G25 using distilled water as eluent. The samples were then freeze-dried, and they were resolved in PBS (0.1 M, pH 7.4) before use. Carboxyfluorescein content of the samples was determined by RP-HPLC as described earlier (*20*).

Cell Culturing. J774 murine macrophage cell line of Balb/c origin was maintained in RPMI 1640 medium containing 10% FCS, 2 mM L-glutamine, and 0.16 mg/mL streptomycin at 37 °C in 5% CO_2 atmosphere. Cells were harvested in the logarithmic phase of growth.

Cytotoxicity of the Polypeptides on J774 Cells. Cells were divided into 96 well tissue-culture plates in 200 μL culture medium (RPMI 1640, 10% FCS, 2 mM L-glutamine, and 0.16 mg/mL streptomycin) with initial cell number of 10^5 cells/well. The polypeptides were dissolved in fresh culture medium and were added to the cells at final concentrations of 0.2, 2.0, 20, and 200 μg/mL. After 1 and 24 h incubation at 37 °C, cell viability was determined by MTT assay using 0.37 mg/mL final concentration of MTT (3-(4,5-dimethylthiazol-2-yl)-2,5-diphenyltetrazolium bromide) in each well. After 3 h incubation, the absorbance was measured with an ELISA reader (Labsystems MS Reader) at 540 and 620 nm as reference wavelengths. Statistical analysis of data was performed by ANOVA of *Origin 7.5*.

Chemotaxis of J774 Cells. Chemotactic ability of compounds was analyzed in a 96 well NeuroProbe chamber (96 well Boyden chamber) in the 0.02–20 μg/mL concentration range. A polycarbonate filter with 5 μm pore diameter was placed between the inner chambers containing the polypeptide solution and the outer chambers, in which J774 cells were placed (10^5 cells/well). The chamber was incubated at 37 °C for 3 h. The amount of the viable cells was determined by MTT assay using 24 h incubation with MTT. Statistical analysis was performed by ANOVA of *Origin 7.5*.

Uptake of Polypeptides by Nonattached Cells. Cells were plated on 24 well tissue culture plate (10^5 cells/well) 24 h prior to the experiment. Cells were incubated with 5(6)-CF-labeled polypeptides at 0.02, 0.2, 2, and 20 μg/mL for 60 min concentration or at 20 μg/mL for 1, 15, 30, 45, and 60 min. Extracellular fluorescence was quenched using 0.5% (m/V) trypane blue solution. Cells were washed twice with PBS (0.1 M; pH 7.4) then fixed with 4% (m/V) formaldehyde dissolved in PBS (0.1 M; pH 7.4). Change of fluorescence of the cells was determined by flow cytometry (FACSCalibur, Becton Dickinson, or BD LSR II) measuring 5000 or 10 000 cells. Data were analyzed with *CellQuest Pro* or *FACS DiVa* software. The mean fluorescence of untreated control cells was subtracted from the mean fluorescence of treated samples under all assay conditions applied. Statistical analysis of data was performed using Student's t test at the 95% confidence level.

Uptake of Polypeptides by Adherent Cells. Cells were plated into 24 well tissue culture plate (10^5 cells/well) 24 h

Table 1. Characteristics of Polylysine-Based Branched Chain Polymeric Polypeptides with Poly[Lys(X_i-DL-Ala_m)] Formula

		amino acid composition[b]					
polypeptide	code[a]	Lys	Ala (*m*)	X (*i*)	DP_n[c]	M_w[d] ± 5%	CF [%][e]
poly[Lys]	–	1.00	–	–	130	16700	–
poly[Lys(Pro_i)]	P_iK	1.00	–	0.95	90	24800	18.6
poly[Lys(DL-Ala_m)]	AK	1.00	3.80	–	60	23800	1.55
poly[Lys(Ser_i-DL-Ala_m)]	SAK	1.00	3.80	0.90	60	27400	2.4
poly[Lys(Glu_i-DL-Ala_m)]	EAK	1.00	3.80	1.00	60	31600	1.4
poly[Lys(Ac-Glu_i-DL-Ala_m)]	AcEAK	1.00	3.80	1.00	60	34500	2.6
poly[Lys(Succ-Glu_i-DL-Ala_m)]	SuccEAK	1.00	3.80	1.00	60	37900	1.6
poly[Lys(Succ-Glu_i-DL-Ala_m)]	MalEAK	1.00	3.80	1.00	60	37800	0.72

[a] Code of branched chain polymeric polypeptides, based on one-letter symbol of amino acids. K represents lysine, A represents alanine, and X is a proteinogenic amino acid in the side chain; *m* characterizes the average length of the oligo-DL-alanine side chains ($m \cong 4$), whereas *i* describes the average degree of substitution of amino acid X ($i \cong 1$) (*26*). [b] Amino acid composition was determined by amino acid analysis after hydrolysis in 6 M HCl at 105 °C for 24 h. [c] Average degree of polymerization determined by sedimentation equilibrium measurements. [d] Average molecular mass of polymers; calculated from the average degree of polymerization (DP_n) of poly[Lys] and of the side chain composition. [e] Average degree of substitution for 5(6)-carboxyfluorescein (CF) was determined by reverse-phase HPLC after hydrolysis of the samples in 6 M HCl at 105 °C for 24 h.

before treating with the polypeptides. Before the addition of CF-labeled polypeptides, cells were washed with serum-free medium and then incubated with the solution of the CF-labeled polypeptides in serum-free RPMI 1640 for 1 h at 37 or 4 °C. In case of inhibition, cells were pretreated with fucoidan dissolved in RPMI 1640 at 20 μg/mL concentration for 30 min. The presence of the inhibitor was maintained throughout the experiment (*30*). After 1 h incubation with the polypeptides at $c = 20$ μg/mL, cells were washed twice with RPMI. Cells were washed 2 times with PBS (0.1 M; pH 7.4) and then fixed with 4% (m/V) formaldehyde/PBS (0.1 M; pH 7.4). Cells were examined by flow cytometry (FACSCalibur and LSR II, Becton Dickinson). Data were recorded measuring 5000–10 000 cells, and fluorescence mean values were calculated. Statistical analysis of data was performed using Student's *t* test at the 95% confidence level.

Study of Uptake by Confocal Microscopy. For the microscopic studies, cells were mounted onto microscopic coverslips and placed into a 24 well tissue culture plate and allowed to attach for 24 h. Cells were treated with the CF-labeled polypeptides in serum-free RPMI 1640 medium for 1 h. Then, cells were fixed with 4% (m/V) formaldehyde/PBS (0.1 M; pH 7.4) and the coverslips were placed onto microscopic slides. The mounted cells were analyzed in a BIO RAD MRC 1024 confocal scanning laser microscope equipped with a krypton/argon mixed-gas laser as a light source. Excitation was carried out at $\lambda = 480$ nm.

RESULTS

Branched Chain Polypeptides. Branched polypeptides with the general formula poly[Lys(X_i)] or poly[Lys(X_i-DL-Ala_m)], ($m \cong 4$, $i \cong 1$) were used for these studies. Poly[Lys($Pro_{0.95}$)] (P_iK) and poly[Lys(DL-$Ala_{3.8}$)] (AK) and XAK type polypeptide poly[Lys($Ser_{0.9}$-DL-$Ala_{3.8}$)] (SAK) possessed polycationic character. Poly[Lys($Glu_{1.0}$-DL-$Ala_{3.8}$)] (EAK), an amphoteric polypeptide carrying free α-amino and γ-carboxyl groups, and its three polyanionic derivatives, in which the $^{\alpha}NH_2$ groups of the terminal glutamic acid residues were modified by acetyl, succinyl, and maleyl groups, were also examined. The three polyanionic polypeptides possess slightly different charge properties. Poly[Lys(Ac-$Glu_{1.0}$-DL-$Ala_{3.8}$)] (AcEAK) carries one negative charge per monomer unit, whereas poly[Lys(Succ-$Glu_{1.0}$-DL-$Ala_{3.8}$)] (SuccEAK) and (poly[Lys-(Mal-$Glu_{1.0}$-DL-$Ala_{3.8}$)] (MalEAK) polypeptides contain two negative charges in their each monomer unit. The polypeptides were characterized with their amino acid composition and their relative average molar mass, determined by sedimentation equilibrium analysis. Chemical characteristics of the polypeptides are shown in Table 1.

Cytotoxicity of Polylysine-Based Polypeptides on J774 Cells. Cytotoxicity of the polypeptides was tested on J774 cells at the concentration range 0.2−200 μg/mL by MTT assay using polylysine as a control. Time dependence of the cytotoxic effect was also examined. Results are expressed as a percentage of optical density measured in the case of the untreated cells. Cytotoxicity proved to be dependent on the charge of the *N*-terminal amino acid of the side chains and on the distance of the charged group from the polylysine backbone. We found that after a 1 h incubation only the control polypeptide (poly[Lys]) was toxic (cytotoxicity = 88 ± 0.14% at 200 μg/mL, $LC_{50} = 65.7$ μg/mL). After the 24 h treatment, two other polycationic polypeptides like poly[Lys($Pro_{0.95}$)] (P_iK) (cytotoxicity = 54.6 ± 12% at $c = 200$ μg/mL, $LC_{50} = 153.65$ μg/mL), poly[Lys($Ser_{0.9}$-DL-$Ala_{3.8}$)] (SAK) (cytotoxicity = 15.2 ± 9% at $c = 200$ μg/mL) and also polyanionic poly[Lys(Succ-$Glu_{1.0}$-DL-$Ala_{3.8}$)] (SuccEAK) exhibited a moderate cytotoxicity (38.4 ± 1.4% at $c = 200$ μg/mL) at the highest concentration studied (Figure 1).

Chemotaxis of J774 Cells. Chemotaxis of the polypeptides was studied using a 96 well NeuroProbe chamber at 0.02, 0.2, 2.0, and 20 μg/mL concentration. The amount of the viable migrated cells was determined by MTT assay. Two polycationic polypeptides, poly[Lys($Pro_{0.95}$)] (P_iK) and poly[Lys($Ser_{0.9}$-DL-$Ala_{3.8}$)] (SAK) induced a slight but significant chemotactic response on J774 cells, in both in an optimal concentration, which is characteristic of each polypeptide. Poly[Lys($Pro_{0.95}$)] (P_iK) elicited a repellent effect at $c = 20$ μg/mL, whereas SAK proved to be slightly chemoattractant at $c = 0.2$ μg/mL and 2.0 μg/mL (Table 2).

Uptake of Carboxyfluorescein-Labeled Polypeptides by J774 Cells. The internalization properties of polylysine-based polypeptides were studied on J774 cells under different conditions. The influence of polypeptide concentration, incubation time, and temperature was investigated on the uptake of CF-labeled polypeptides. We also studied the involvement of the scavenger receptor in the internalization process in inhibition assays.

Uptake of the Polypeptides by Nonattached Cells. The uptake of the polypeptides by nonattached J774 cells was examined using flow cytometry and confocal microscopy as well. The polycationic polypeptide (poly[Lys($Pro_{0.95}$)] (P_iK) possessing short side chains was taken up already at 2 μg/mL concentration. The uptake of poly[Lys($Ser_{0.9}$-DL-$Ala_{3.8}$)] (SAK) with polycationic character was significant only at the highest concentration studied, whereas the presence of amphoteric EAK (poly[Lys-($Glu_{1.0}$-DL-$Ala_{3.8}$)]) was not detectable in the cells. The polycationic AK (poly[Lys(DL-$Ala_{3.8}$)]) and P_iK ((poly[Lys($Pro_{0.95}$)]) were taken up the most efficiently. As poly[Lys(DL-$Ala_{3.8}$)] (AK)

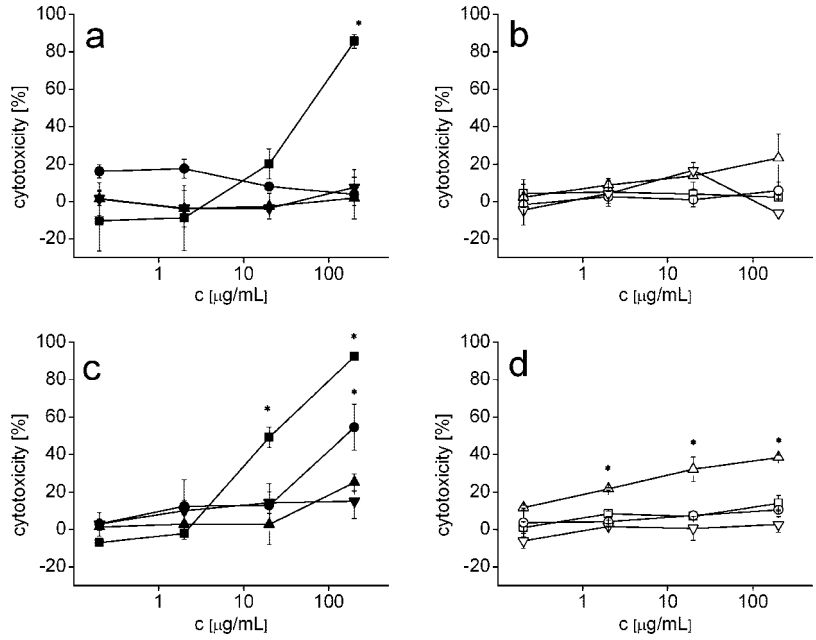

Figure 1. The effect of the branched CF polypeptides on the viability of J774 cells. Graphs a and b represent the 1 h treatment; c and d represent the 24 h treatment. Diagrams represent the average cytotoxicity of the polypeptides as a percentage of untreated control ± SD. Poly[L-Lys] ($\bar{DP}_n$ = 130, $\bar{M}_w$ = 16 800) was used as control. Statistical analysis of data was performed by Student's *t* test. (a) Polycationic polypeptides (■ poly[Lys], ● P_iK, ▲ AK, ▼ SAK); (b) amphoteric (□ EAK) and polyanionic polypeptides (O AcEAK, Δ SuccEAK, ∇ MalEAK).

Table 2. Chemotactic Effect of Polylysine Based Polypeptides on J774 Cells[a]

concn [μg/mL]	P_iK	AK	SAK	EAK	AcEAK	SuccEAK	MalEAK
0.02	108 ± 5	106 ± 1	131 ± 27	104 ± 4	101 ± 8	116 ± 7	82 ± 11
0.2	95 ± 1	98 ± 1	*113 ± 6	110 ± 4	101 ± 1	105 ± 6	85 ± 8
2	91 ± 8	101 ± 6	*115 ± 2	114 ± 9	109 ± 11	105 ± 9	105 ± 11
20	*86 ± 4	104 ± 15	118 ± 9	102 ± 4	99 ± 5	97 ± 15	85 ± 18

[a] Chemotactic ability of the cells was analyzed in a 96 well NeuroProbe chamber. The number of migrated cells was determined by MTT assay. Chemotactic index was expressed as percentage of control ± SD. Data represent the mean of 8 parallels. Statistical analysis of data was performed by one-way ANOVA of *Origin5* (*$p < 0.05$).

was one of the polypeptides that could be detected the best in the cells, time dependence of the uptake of this polypeptide was also examined by confocal microscopy (Figure 2). In the microscopic images, the binding of the CF-labeled AK (poly[Lys-(DL-$Ala_{3.8}$)]) polypeptide to the cell surface could be observed even after 1 min incubation. The vesicles containing the labeled polypeptide appear within the cells after 30 min incubation, and the number of the vesicles increased after 60 min incubation time (Figure 2).

Uptake of the Polypeptides by Adherent Cells. The rate of the uptake was influenced by the charge and the polypeptide concentration. Uptake of polycationic polypeptides and poly[Lys-(Succ-$Glu_{1.0}$-DL-$Ala_{3.8}$)] (SuccEAK) was dependent on the polypeptide concentration, whereas SAK (poly[Lys($Ser_{0.9}$-DL-$Ala_{3.8}$)]), EAK (poly[Lys($Glu_{1.0}$-DL-$Ala_{3.8}$)]), and AcEAK (poly-[Lys(Ac-$Glu_{1.0}$-DL-$Ala_{3.8}$)]) were ingested only at the highest concentration applied (c = 20 μg/mL) (Figure 3). The kinetics of the uptake was examined by flow cytometry after 0, 5, 15, 30, 45, and 60 min incubation with the polypeptides. The internalization of the polyanionic polypeptides by J774 cells was in direct proportion to the incubation period, except (poly[Lys($Pro_{0.95}$)] (P_iK), where the kinetics of the uptake was exponential, and we could observe a saturation kinetics in the case of poly[Lys($Ser_{0.9}$-DL-$Ala_{3.8}$)] (SAK) polypeptide (Figure 4). An increased uptake of the polycationic AK, poly[Lys(DL-$Ala_{3.8}$)], the polyanionic SuccEAK (poly[Lys(Succ-$Glu_{1.0}$-DL-$Ala_{3.8}$)]), and MalEAK (poly[Lys(Mal-$Glu_{1.0}$-DL-$Ala_{3.8}$)]) could be observed after attachment of the cells to the surface (Figure 5). Images taken by confocal microscopy also confirmed that CF-SuccEAK, poly[Lys(Succ-$Glu_{1.0}$-DL-$Ala_{3.8}$)] was ingested by the adherent cells at a higher level compared to nonadherent cells (Figure 5). By contrast, polycationic polypeptides like P_iK poly[Lys($Pro_{0.95}$)]), SAK (poly[Lys($Ser_{0.9}$-DL-$Ala_{3.8}$)]), AK (poly-[Lys(DL-$Ala_{3.8}$)]) were ingested at a higher level by the nonadherent J774 cells (Figure 6). The uptake of the polypeptides proved to be dependent also on temperature. By analyzing data obtained for two different temperatures, we detected a significant decrease in the internalization at 4 °C compared to 37 °C (Figure 7).

Effect of SR-Antagonist Fucoidan on the Uptake of the Polypeptides. We examined the role of the scavenger receptor in the internalization of the polypeptides; therefore, the uptake was inhibited with a SR ligand, the sulfated polysaccharide fucoidan. We found that 30 min pretreatment ($c_{fucoidan}$ = 20 μg/mL) significantly inhibited the uptake of polyanionic polypeptides, SuccEAK (poly[Lys(Succ-$Glu_{1.0}$-DL-$Ala_{3.8}$)]) and MalEAK (poly[Lys(Mal-$Glu_{1.0}$-DL-$Ala_{3.8}$)]) but did not alter the uptake of polyanionic AcEAK (poly[Lys(Ac-$Glu_{1.0}$-DL-$Ala_{3.8}$)]) and polycationic AK (poly[Lys(DL-$Ala_{3.8}$)]). These results indicate that scavenger receptors play a role in the internalization of the two polyanionic polypeptides that possess two negative charges per monomer unit (Figure 8).

DISCUSSION

Recently, studies on cell-specific introduction of drugs is one of the most actively developing areas of drug delivery research. Numerous antitumor and antiparasitic agents as methotrexate or anthracyclines entering the cell membrane by diffusion are toxic not only to the target cells but also to the other cell types

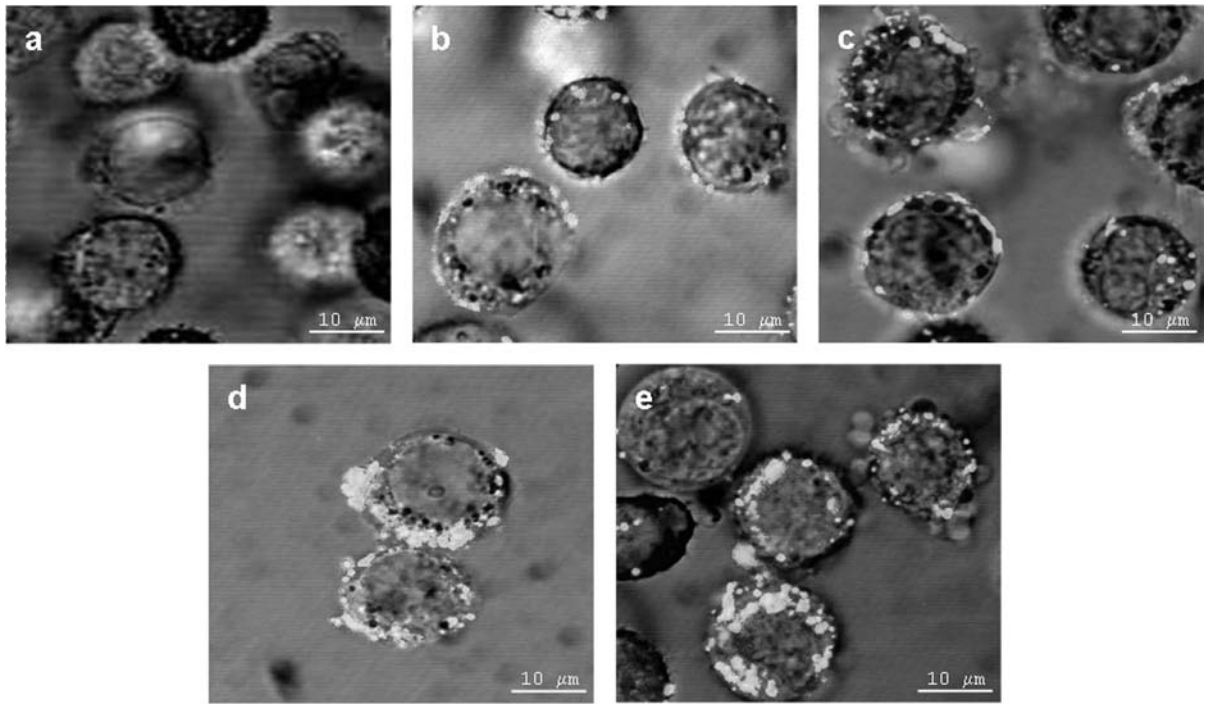

Figure 2. Time dependence of the endocytosis of CF-poly[Lys(DL-$Ala_{3,8}$)] (AK) polypeptide by nonattached J774 cells. The cells were analyzed by confocal microscopy (λ_{ex} = 488 nm): (a) untreated control, (b) CF-AK 1 min, (c) CF-AK 15 min, (d) CF-AK 30 min, (e) CF-AK 60 min.

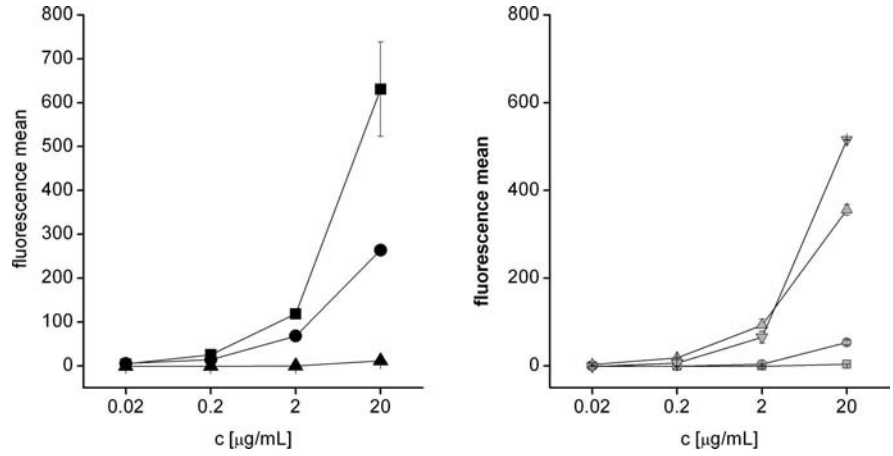

Figure 3. Concentration dependence of the uptake of the CF-polypeptides by J774 cells after 60 min incubation with the polypeptides. Symbols represent the average of mean fluorescence values of a representative experiment of two independent assays ± SD after subtracting the control. (a) Polycationic polypeptides (■ P_iK, ● AK, ▲ SAK); (b) amphoteric (□ EAK) and polyanionic polypeptides (○ AcEAK, Δ SuccEAK, ∇ MalEAK).

of the organism (*31*). On the other hand, small hydrophilic molecules like peptides, oligonucleotides, and small proteins with low membrane permeability cannot reach the site of action (*32*). These problems can be solved by applying macromolecular carriers that can decrease the toxicity and improve the specificity of drugs or can deliver hydrophilic compounds through the cell membrane. The use of macromolecular carriers can also break multidrug resistance (*33*) and enhance the immunogenicity of the original compound (*34*). There are some important requirements for the ideal macromolecular carrier. It must not be toxic or immunogenic; it should possess reactive groups that can be modified by a simple chemical reaction; the carrier has to retain its specificity after conjugation and must not alter the efficacy of the active compound coupled to it (*35*).

J774 cells have been used for several cell physiological studies related to macrophages. Their inflammatory response (*36*), signal transduction (*37*), killing activity, and phagocytosis (*37–39*) and chemotactic activity (*40*) have been investigated in detail. Claus et al. characterized the activity of their endosomal enzymes (*41*). Maturation of phagosomes (*42*) and the effect of antimycobacterial agents (*43*) were also studied on *Mycobacterium*-infected J774 cells. J774 cells were used for modeling macrophages in several investigations on cell-specific delivery of active compounds via scavenger receptors (*44–46*).

The aim of our studies was to examine the effect of a group of systematically developed chemically related polypeptides on the macrophage like cell line J774. Our previous studies indicated that the chemical structure of the polypeptides, especially the charge and length of the side chains, influenced markedly the biological effects and physicochemical characteristics of the polypeptides (*12, 17*). Our present results show that charge and structure of the side chains both have a marked influence on *in vitro* toxicity and uptake of polylysine based

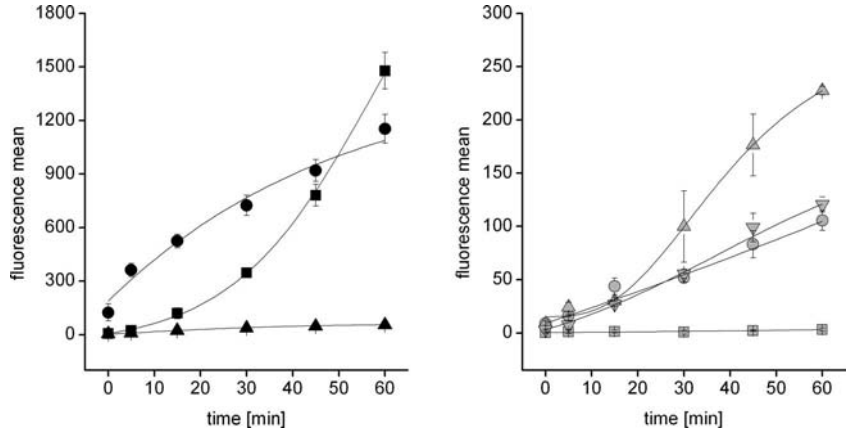

Figure 4. Time dependence of the endocytosis of polypeptides at $c = 20\ \mu$g/mL. Symbols represent the average of mean fluorescence values of a representative experiment of three independent assays ± SD after subtracting the control. (a) Polycationic polypeptides (■ P_iK, ● AK, ▲ SAK); (b) amphoteric (□ EAK) and polyanionic polypeptides (○ AcEAK, Δ SuccEAK, ∇ MalEAK).

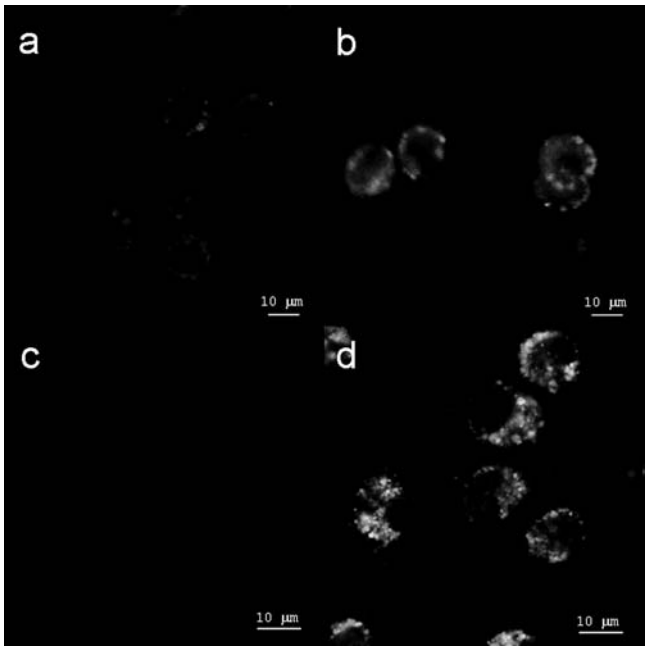

Figure 5. Internalization of CF-poly[Lys(Succ-$Glu_{1.0}$-DL-$Ala_{3.8}$)] (CF-SuccEAK) polypeptide at $c = 20\ \mu$g/mL by nonadherent (a) untreated, (b) CF-SuccEAK treated, and adherent (c) untreated, (d) CF-SuccEAK treated J774 cells at 60 min. Cells were analyzed by confocal microscopy with $\lambda_{ex} = 488$ nm.

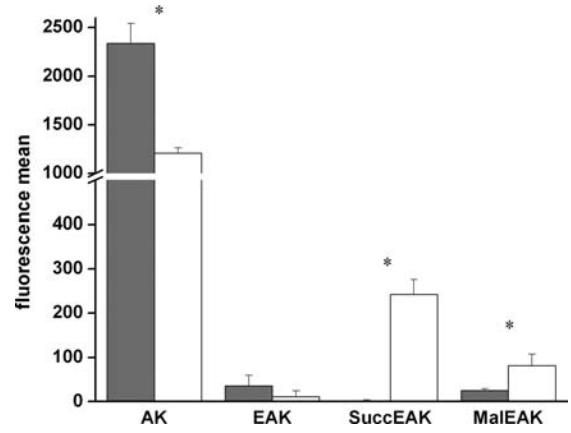

Figure 6. Uptake of polypeptides by nonattached and adherent J774 cells. Columns represent the average of mean fluorescence values of a representative of two independent assays ± SD after subtracting the control. ■ nonattached cells; □ adherent cells. Statistical analysis of data was performed by Student's *t* test; $*p < 0.05$.

polypeptides, whereas the structure of the terminal amino acid derivative could determine the chemotactic character of the molecule.

We determined the cytotoxicity of the branched-chain polypeptides after 1 and 24 h. We found that the branched chain polypeptides elicited moderate cytotoxicity at the highest concentration in contrast with control poly[Lys] containing free ε-amino groups that induced a marked cell death after 1 and 24 h incubation as well. We also observed a difference between the polyanionic polypeptides. AcEAK (poly[Lys(Ac-$Glu_{1.0}$-DL-$Ala_{3.8}$)]) and MalEAK poly[Lys(Mal-$Glu_{1.0}$-DL-$Ala_{3.8}$)] elicited a markedly lower toxicity on J774 cells than SuccEAK poly-[Lys(Succ-$Glu_{0.9}$-DL-$Ala_{3.8}$)]. Taken together, cytotoxicity of the polypeptides proved to be dependent on the charge of the *N*-terminal amino acid of the side chains, and in the case of polyanionic polypeptides, on the structure of the anionic end group.

Various molecules like bacterial peptides (e.g., fMLF) (*47*), chemokines, nucleotides (ADP), and molecules of the complement system (C5a) (*40*) can activate the chemotaxis of monocytes and macrophage-like cells. We would apply carriers that are able to elicit a chemotactic response and draw the cells to the target cell population, but these molecules usually induce an immune response as well. To avoid immunogenicity, it is advisable to choose a neutral carrier that does not induce chemotaxis but rather contains a nonchemotactic targeting moiety. Our previous studies on *Tetrahymena pyriformis* (*19*) demonstrated that the character of the terminal amino acid of the branches determined the chemotactic activity of the model organism. Compared to *Tetrahymena*, chemotactic activity of J774 cells was markedly lower. In summary, the polypeptides did not influence significantly the chemotaxis of the J774 cells, so they can be applied as neutral, nonchemotactic macromolecular carriers of drug targeting with respect to chemotactic drug targeting, a special type of drug delivery described recently (*48*).

Results of the internalization studies obtained by flow cytometry and confocal laser scanning microscopy illustrated that J774 cells ingested polypeptides depending on the polypeptide concentration, the incubation time, and the temperature. The charge of the side chains influenced markedly the rate and kinetics of the uptake. We observed a difference between the polypeptide internalization of nonadherent and adherent cells. Floating J774 cells internalized polycationic polypeptides more effectively than polyanionic ones, whereas the uptake of polyanionic polypeptides was significantly increased by the adherent cells. As adherent cells express certain receptors that

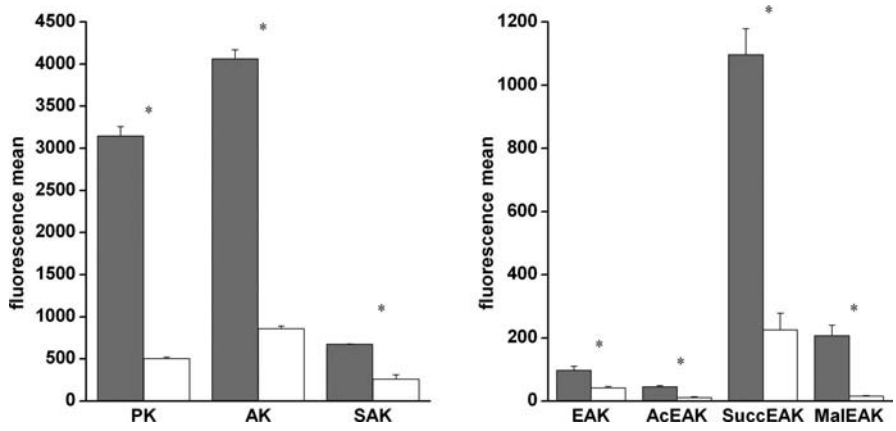

Figure 7. Uptake of polypeptides at 4 and 37 °C at $c = 20$ μg/mL after 1 h. Columns represent the average of mean fluorescence values of a representative experiment of two independent assays ± SD after subtracting the control. ■ 37 °C; □ 4 °C. Statistical analysis of data was performed by Student's *t* test; *$p < 0.05$.

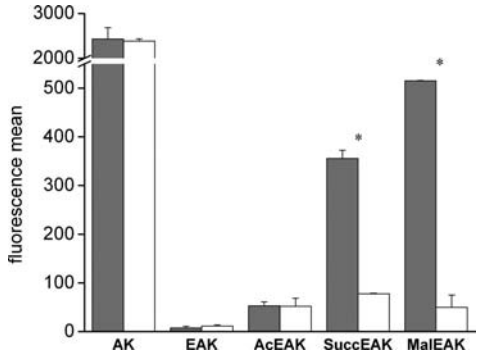

Figure 8. Uptake of the polypeptides in the presence of SR ligand fucoidan applied as inhibitor. Columns represent the average of mean fluorescence values of a representative experiment of two independent assays ± SD after subtracting the control. ■, Uptake of the polypeptides ($c = 20$ μg/mL) without pretreatment; □, uptake of polypeptide after pretreatment with fucoidan ($c = 20$ μg/mL). Statistical analysis of data was performed by Student's *t* test; *$p < 0.05$.

play a role in the internalization process (e.g., scavenger receptors) to a greater extent than nonadherent cells (*49*), the more effective uptake of polyanionic polypeptides (SuccEAK and MalEAK) imply a receptor-dependent uptake mechanism. Examination of the internalization by confocal microscopy seems to confirm that uptake of the polypeptides occurs by endocytosis: the polypeptides were ingested by the cells in vesicles can be observed in the microscopic images well.

In order to clarify whether a scavenger receptor is involved in the internalization of the polypeptides, we carried out inhibition experiments using a class A scavenger receptor ligand, the sulfated polysaccharide fucoidan as inhibitor (*30*). We observed that pretreatment with fucoidan reduced the uptake of both polyanionic polypeptides that possessed two anionic groups per monomer unit, but the internalization of AcEAK bearing only one negatively charged group on each monomer, and polycationic AK used as negative control was taken up at the same level after the inhibition. We can presume that the charge density (e.g., the number of negative charges per unit in the polyanionic polypeptides) influences the internalization of the polypeptides. These observations indicate that MalEAK and SuccEAK are taken up by J774 cells via scavenger receptor but AcEAK could be recognized by the same receptor with a much lower affinity, or AcEAK and polycationic polypeptides as well are ingested by a different process.

In conclusion, on the basis of results presented and discussed above we could select an appropriate polypeptide with the chemical characteristics that are essential for intracellular delivery. These polypeptides are essentially nontoxic, neutral macromolecular carriers for drugs that are to be introduced to specific cell types. We can presume that polyanionic polypeptides will be able to transport the drugs coupled to them into the macrophage cells via scavenger receptor. On the other hand, by further investigation of the polycationic polypeptides we can find an application that requires a non-cell-specific but effective delivery of reporter molecules, nucleotides, or small proteins into the cell.

ACKNOWLEDGMENT

This work was supported by Öveges József Programme (OMFB-00180/2007), GVOP-3.2.1-2004-04-0352/3.0 and GVOP-3.2.1-2004-04-0005/3.0 from National Office for Research and Technology, Hungary. The authors thank Dr. Hedvig Medzyhradszky-Schweiger for the amino acid analyses.

LITERATURE CITED

(1) Duncan, R., Gac-Breton, S., Keane, R., Musila, R., Sat, Y. N., Satchi, R., and Searle, F. (2001) Polymer-drug conjugates, PDEPT and PELT: basic principles for design and transfer from the laboratory to clinic. *J. Controlled Release 74*, 135–146.

(2) Abraham, R., Singh, N., Mukhopadhyay, A., Basu, S. K., Baal, V., and Rath, S. (1995) Modulation of immunogenicity and antigenicity of proteins by maleylation to target scavenger receptors on macrophages. *J. Immunol. 154*, 1–8.

(3) Hudecz, F., Reményi, J., Szabŏ, R., Kŏczán, Gy., Mezõ, G., Kovács, P., and Gaál, D. (2003) Drug targeting by macromolecules without recognition unit? *J. Mol. Recognit. 16*, 288–298.

(4) Duncan, R., Kopečkova-Rejmanova, P., Strohalm, J., Hume, I., Cable, H. C., Pohl, J., Lloyd, J. B., and Kopecek, J. (1987) Anticancer agents coupled to N-(2-hydroxypropyl)methacrylamide copolymers. I. Evaluation of daunomycin and puromycin conjugates in vitro. *Br. J. Cancer 55*, 165–74.

(5) Jensen, K. D., Nori, A., Tijerina, M., Kopečkova, P., and Kopeček, J. (2003) Cytoplasmic delivery and nuclear targeting of synthetic macromolecules. *J. Controlled Release 87*, 89–105.

(6) Przybylski, M., Zaharko, D. S., Chirigos, M. A., Adamson, R. H., Schultz, R. M., and Ringsdorf, H. (1978) DIVEMA-methotrexate: immune-adjuvant role of polymeric carriers linked to antitumor agents. *Cancer Treat. Rep. 62*, 1837–43.

(7) Ward, C. M., Read, M. L., and Seymour, L. W. (2001) Systemic circulation of poly(L-lysine)/DNA vectors is influenced by polycation molecular weight and type of DNA: differential circulation in mice and rats and the implications for human gene therapy. *Blood 97*, 2221–2229.

(8) Li, C. (2002) Poly(L-glutamic acid) - anticancer drug conjugates. *Adv. Drug Delivery Rev. 54*, 695–713.

(9) Bourke, S. L., and Kohn, J. (2003) Polymers derived from the amino acid L-tyrosine: polycarbonates, polyarylates and copolymers with poly(ethylene glycol). *Adv. Drug Delivery Rev. 55*, 447–466.
(10) Mezö, G., Kajtár, J., Hudecz, F., and Szekerke, M. (1993) Carrier design: conformational studies of amino acid (X) and oligopeptide (X-DL-Ala$_m$) substituted poly (L-lysine). *Biopolymers 33*, 873–85.
(11) Mezö, G., Kajtár, J., Nagy, I. B., Szekerke, M., and Hudecz, F. (1997) Carrier design: synthesis and conformational studies of poly(L-lysine) based branched polypeptides with hydroxyl groups in the side chains. *Biopolymers 42*, 713–730.
(12) Hudecz, F. (1995) Design of synthetic branched-chain polypeptides as carriers for bioactive molecules. *Anti-Cancer Drugs 6*, 171–193.
(13) Hudecz, F., Pimm, M. V., Rajnavölgyi, É., Mezö, G., Fabra, A., Gaál, D., Kovács, A. L., Horváth, A., and Szekerke, M. (1999) Carrier design: new generation of polycationic branched polypeptides containing OH groups with prolonged blood survival and diminished *in vitro* cytotoxicity. *Bioconjugate Chem. 10*, 781–790.
(14) Clegg, J. A., Hudecz, F., Mezö, G., Pimm, M. V., Szekerke, M., and Baldwin, R. W. (1990) Carrier design: biodistribution of branched chain polypeptides with poly(L-lysine) backbone. *Bioconjugate Chem. 2*, 425–430.
(15) Pimm, M. V., Gribben, S. J., Bogdán, K., and Hudecz, F. (1995) The effect of charge on the biodistribution in mice of branched polipeptides with poly(L-lysine) backbone labelled with ^{125}I, ^{111}In or ^{51}Cr. *J. Controlled Release 37*, 161–17.
(16) Rajnavölgyi, É., Hudecz, F., Mezö, G., Szekerke, M., and Gergely, J. (1986) Isotype distribution and fine specificity of the antibody response of inbred mouse strains of four compounds belonging to of a new group of synthetic branched polypeptides. *Mol. Immunol. 23*, 27–37.
(17) Mezö, G., Hudecz, F., Kajtár, J., Szókán, Gy., and Szekerke, M. (1989) The influence of the side-chain sequence on the structure-activity correlations of immunomodulatory branched polypeptides. Synthesis and conformational analysis of new model polypeptides. *Biopolymers 28*, 1801–1826.
(18) Gaál, D., Hudecz, F., and Szekerke, M. (1984) Immunomodulatory effect of synthetic branched polypeptides I. *J. Biol. Response Modif. 3*, 174–84.
(19) Szabó, R., Köhidai, L., Mezö, G., and Hudecz, F. (2002) Effect of the polylysine based polymeric polypeptides on the growth and chemotaxis of Tetrahymena pyriformis. *J. Bioact. Compat. Polym. 17*, 399–415.
(20) Szabó, R., Peiser, L., Plüddemann, A., Bösze, Sz., Heinsbroek, S., Gordon, S., and Hudecz, F. (2005) Uptake of branched polypeptides with poly[L-Lys] backbone by bone-marrow culture-derived murine macrophages: the role of the class A scavenger receptor. *Bioconjugate Chem. 16*, 1442–1450.
(21) Nagy, I. B., Hudecz, F., Alsina, M. A., and Reig, F. (2003) Physicochemical characterization of branched chain polymeric polypeptide carriers based on a poly-lysine backbone. *Biopolymers 70*, 323–335.
(22) Szabó, R., Hudecz, F., and Reig, F. (2003) Interfacial interactions between poly[L-lysine]-based branched polypeptides and phospholipid model membranes. *J. Colloid Interface Sci. 267*, 18–24.
(23) Reményi, J., Balázs, B., Tóth, S., Falus, A., Tóth, G., and Hudecz, F. (2003) Isomer-dependent daunomycin release and in vitro antitumour effect of cis-aconityl-daunomycin. *Biochem. Biophys. Res. Commun. 303*, 556–561.
(24) Reményi, J., Csík, G., Kovács, P., Reig, F., and Hudecz, F. (2006) The effect of the structure of branched polypeptide carrier on intracellular delivery of daunomycin. *Biochem. Biophys. Acta 1758*, 280–289.
(25) Kóczán, G., Ghoose, A. C., Mookerjee, A., and Hudecz, F. (2002) Methotrexate conjugate with branched polypeptide influences *Leishmania donovani* infection *in vitro* and in experimental animals. *Bioconjugate Chem. 13*, 518–524.
(26) IUPAC-IUB Commision on biochemical nomenclature. (1984) *Eur. J. Biochem. 138*, 9–37.
(27) Mezö, G., Hudecz, F., Kajtár, J., Szókán, Gy., and Szekerke, M. (1989) The influence of the side-chain sequence on the structure-activity correlations of immunomodulatory branched polypeptides. Synthesis and conformational analysis of new model polypeptides. *Biopolymers 28*, 1801–26.
(28) Mezö, G., Votavova, H., Hudecz, F., Kajtár, J., Sponar, J., and Szekerke, M. (1988) Conformation of branched polypeptides: The influence of DL-alanine oligomer spacers in the side chains. *Collect. Czech. Chem. Commun. 53*, 2843–2853.
(29) Mezö, G., Mezõ, I., Pimm, M. V., Kajtár, J., Seprödi, J., Teplán, I., Kovács, M., Vincze, B., Pályi, I., Idei, M., Szekerke, M., and Hudecz, F. (1996) Synthesis, conformation and hormone-related in vitro antitumor activity of a gonadotropin-releasing hormone antagonist-branched polypeptide conjugate. *Bioconjugate Chem. 7*, 642–650.
(30) Peiser, L., Makepeace, K., Plüddemann, A., Savino, S., Wright, J. C., Pizza, M., Rappuoli, R., Moxon, E. R., and Gordon, S. (2006) Identification of neisseria meningitidis nonlipopolysaccharide ligands for class A macrophage scavenger receptor by using a novel assay. *Infect. Immun. 74*, 5191–5199.
(31) Petrak, K. (2005) Essential properties of drug-targeting delivery systems. *Drug Discovery Today 10*, 1667–1673.
(32) Tung, C.-H., and Weissleder, R. (2003) Arginine containing peptides as delivery vectors. *Adv. Drug Delivery Rev. 55*, 281–294.
(33) Mukhopadhyay, A., Mukhopadhyay, B., and Basu, S. K. (1995) Circumvention of multidrug resistance in neoplastic cells through scavenger receptor mediated drug delivery. *FEBS Lett. 376*, 95–98.
(34) Hilbert, Á., Hudecz, F., Mezö, G., Mucsi, I., Kajtár, J., Kurucz, I., Gergely, J., and Rajnavölgyi, É. (1994) The influence of branched polypeptide carriers on the immunogenicity of predicted epitopes of HSV-1 glycoprotein D. *Scand. J. Immunol. 40*, 609–617.
(35) Takaura, Y., and Hashida, M. (1995) Macromolecular drug carrier systems in cancer chemotherapy: mavromolecular prodrugs. *Clin. Rev. Oncol. 18*, 207–231.
(36) Sautebin, L., Ianaro, A., Rombolà, L., Ialenti, A., Sala, A., and Di Rosa, M. (1999) Cyclooxygenase-2-dwpwndent generation of 8-epiprostaglandin F2a by lipopolysaccharide-activated J774 macrophages. *Inflamm. Res. 48*, 503–508.
(37) Kügler, S., Schüller, S., and Goebel, W. (1997) Involvement of MAP-kinases and -phosphatases in uptake and intracellular replication of Lysteria monocytogenes in J774 macrophage cells. *FEMS Mocrobiol. Lett. 157*, 131–136.
(38) Ralph, P., and Nakoinz, I. (1975) Phagocytosis and cytolysis by a macrophage tumour and its cloned cell line. *Nature (London) 257*, 393–394.
(39) Liang-Takasaki, C.-J., Mäkelä, P. H., and Leive, L. (1982) Phagocytosis of bacteria by macrophages: changing the carbohydrate of lipopolysaccharide alters interaction with complement and macrophages. *J. Immunol. 128*, 1229–1235.
(40) McCloskey, M. A., Fan, Y., and Luther, S. (1999) Chemotaxis of rat mast cells toward adenine nucleotides. *J. Immunol. 163*, 970–977.
(41) Claus, V., Jahraus, A., Tjelle, T., Berg, T., Kirschkei, H., Faulstich, H., and Griffiths, G. (1998) Lysosomal Enzyme Trafficking between Phagosomes, Endosomes, and Lysosomes in J774 Macrophages. *J. Biol. Chem. 273*, 9842–9851.
(42) Hostetter, J., Steadham, E., Haynes, J., Bailey, T., and Cheville, N. (2003) Phagosomal maturation and intracellular survival Mycobacterium avium subspecies paratuberculosis in J774 cells. *CIMID 26*, 269–283.
(43) Wright, E. L., Quenelle, D. C., Suling, W. J., and Barrow, W. W. (1996) Use of mono Mac 6 human monocytic cell line and J774 murine macrophage cell line in parallel antimycobacterial drug studies. *Antimicrob. Agents Chemother. 40*, 2206–2208.
(44) Mukhopadhyay, A., Mukhopadhyay, B., Srivastava, R. K., and Basu, S. K. (1992) Scavenger-receptor mediated delivery of

daunomycin elicits selective toxicity towards neoplastic cells of macrophage lineage. *Biochem. J. 284*, 237–241.

(45) Brasseur, N., Langlois, R., La Madeleine, C., Ouellet, R., and van Lier, J. E. (1999) Receptor-mediated targeting of phtalocyanines to macrophages via covalent coupling to native or maleylated bovine serum albumin. *Photochem. Photobiol. 69*, 345–352.

(46) Prasad, V., Hashim, S., Mukhopadhyay, A., Basu, S. K., and Roy, R. P. (1999) Oligonucleotides tethered to a short polyguanylic acid stretch are targeted to macrophages: Enhanced antiviral activity of a vesicular stomatitis virus-specific antisense oligonucleotide. *Antimicrob. Agents Chemother. 43*, 2689–2696.

(47) Heit, B., Tavener, S., Raharjo, E., and Kubes, P. (2002) An intracellular signaling hierarchy determines direction of migration in opposing chemotactic gradients. *J. Cell. Biol. 159*, 91–102.

(48) Mezö, G., Láng, O., Jakab, A., Bai, K. B., Szabó, I., Schlosser, G., Láng, J., Köhidai, L., and Hudecz, F. (2006) Synthesis of oligotuftsin-based branched oligopeptide conjugates for chemotactic drug targeting. *J. Pept. Sci. 12*, 328–336.

(49) de Villiers, W. J., Fraser, I. P., and Gordon, S. (1994) Cytokine and growth factor regulation of macrophage scavenger receptor expression and function. *Immunol. Lett. 43*, 73–79.

BC7004544

Synthesis and Screening of a Library of Re/Tc-Based Amyloid Probes Derived from β-Breaker Peptides

Karin A. Stephenson,[†] Leslie C. Reid,[†] Jon Zubieta,[‡] John W. Babich,[§] Mei-Ping Kung,[⊥] Hank F. Kung,[⊥] and John F. Valliant*,[†]

Departments of Chemistry and Medical Physics & Applied Radiation Sciences, McMaster University, Hamilton, ON, Canada, L8S 4M1, Department of Chemistry, Syracuse University, Syracuse, New York 13244-4100, Molecular Insight Pharmaceuticals Inc., Cambridge, Massachusetts 02142, and Department of Radiology, University of Pennsylvania, Philadelphia, Pennsylvania 19104. Received January 2, 2008; Revised Manuscript Received February 13, 2008

Through the development and application of a unique approach for producing Re-metallopeptides, a new class of peptide-derived probes that are designed to target β-amyloid plaques was developed. Derivatives of a class of β-breaker peptides having the core sequence lvffa or affvl (lower case letters represent D-amino acids) and the single amino acid chelate quinoline (SAACQ) ligand which can bind Re and ^{99m}Tc were prepared on an automated peptide synthesizer. Both monomeric and dimeric peptides were synthesized in modest to good yields where in select examples a biotin-containing amino acid derivative was included to act as a linker point for further conjugation to carrier proteins. The Re complexes for all reported peptides were prepared similarly and screened for their ability to inhibit fibrillogenesis. Two of the reported compounds showed excellent inhibitory properties (**8a**: 40 ± 5% amyloid formation versus control; **16**: 40 ± 4%) and warrant further investigation. For one of these leads, the ^{99m}Tc analogue was synthesized and the product showed high stability toward histidine and cysteine challenges, making it a viable candidate for *in vivo* biodistribution studies.

INTRODUCTION

Alzheimer's disease (AD) is a progressive neurodegenerative affliction that involves the formation of plaques and neurofibrillary tangles, which ultimately lead to neuronal death in both the hippocampus and frontal cortex (*1, 2*). Senile plaques can occupy up to 15% of the brain volume in some advanced AD patients and are composed primarily of β-amyloid peptides ($A\beta^{1-40,42,43}$) (*1, 3*). Amyloid peptides are naturally occurring entities, but in AD patients, the peptides form plaques in the brain: a process that stems from a change in the mechanism of cleavage of the amyloid precursor protein (*1, 4, 5*). The formation of senile plaques has been correlated with the progression of the disease and has therefore emerged as a promising target for the treatment of AD (*1, 6, 7*).

There has been a major effort put into developing radioimaging agents that allow for serial monitoring of the progression of AD and for assessing the impact of therapy. ^{18}F-deoxyglucose (FDG) is used to diagnose the early onset of disease by visualizing reduced metabolism of glucose associated with cell death in the brains of AD patients (*2*). Unfortunately, FDG is not able to specifically identify β-amyloid plaques; therefore, to better characterize changes in plaque load, work in the field has been geared toward developing plaque-targeting PET and SPECT agents (*8*−*12*).

Maggio and co-workers reported that $A\beta^{1-40}$ labeled with ^{125}I rapidly deposits on β-amyloid plaques in isolated tissue. Not surprisingly, the labeled peptide showed particularly poor brain uptake *in vivo* (*13*). However, conjugation of an $A\beta^{1-40}$-biotin derivative to a streptavidin-tagged monoclonal antibody (mAb) for the human insulin receptor markedly improved transport across the BBB (*14, 15*). Uptake of the mAb-^{125}I-biotin-$A\beta^{1-40}$ conjugate in rhesus monkey brains was observed using autoradiography.

Structure−activity relationships (SARs) have shown that fragments of the full $A\beta^{1-40}$ peptide can exhibit binding to plaques and inhibition of β-amyloid fibrillogenesis (*4, 16*−*21*). β-sheet breaker peptides having as few as four amino acids (LVFF) have been able to significantly inhibit fibril formation (*22*). The key hydrophobic motif, LVFF, which is common to most AD β-sheet breaker peptides, binds amyloid plaques and can prevent soluble Aβ peptides from forming structured aggregates (*4, 16*−*19*). Given that strategies for enabling peptides to cross the BBB exist, radiotracers based on β-breaker peptides would offer a new means for imaging β-amyloid plaques and for assessing therapies aimed at solubilizing plaques.

The traditional approach for developing ^{99m}Tc-labeled probes of this type would involve appending a technetium chelator to the N-terminus of a core β-breaker peptide sequence. After isolation, attempts would be made to prepare the rhenium complex of the product, which would serve as a reference standard for the ^{99m}Tc analogue and as a compound to test the ability of the metallopeptide derivative to bind plaques and/or inhibit amyloid fibrillogenesis. This linear discovery approach is time-consuming with respect to isolating and fully characterizing the Re complexes and identifying the optimal sequence for the vector and site of derivatization on the peptide backbone.

We report here a new approach in which an organometallic complex of an amino acid analogue is used to insert the metal into various positions in lvffa and affvl sequences. A synthetic methodology was developed such that multivalent (i.e., dimeric) peptides could be prepared and biotin incorporated into the backbone of the peptide as a linker site for conjugation to carrier proteins. The ability of the Re complexes to prevent fibril

* To whom correspondence should be addressed. Tel: 905-525-9140, ext. 22840. FAX: 905-522-2509. E-mail: valliant@mcmaster.ca.
[†] McMaster University.
[‡] Syracuse University.
[§] Molecular Insight Pharmaceuticals Inc.
[⊥] University of Pennsylvania.

10.1021/bc800001g CCC: $40.75 © 2008 American Chemical Society
Published on Web 04/12/2008

formation was subsequently determined *in vitro* in order to identify lead compounds for further testing.

EXPERIMENTAL PROCEDURES

Instrumentation. All peptides were prepared on an Advanced ChemTech 348Ω peptide synthesizer using a 40-well reaction vessel. Peptides were analyzed by electrospray mass spectrometry using a Micromass Quattro Ultima instrument in positive ion mode. Samples were dissolved in 50% CH_3CN /H_2O prior to analysis. FTIR spectra were acquired on a Bio-Rad FTS-40 FTIR spectrometer.

Analytical HPLC was performed using a Varian Pro Star model 330 PDA detector, model 230 solvent delivery system, and a C-18 Microsorb column (4.6 × 250 mm, 300 Å−5 μm). Semipreparative HPLC was carried out using a Varian Pro Star HPLC fitted with a model 320 UV detector, a model 215 solvent delivery system, and a C-18 Microsorb column (10 × 250 mm, 300 Å−5 μm). Peptides (**1**−**16**) were analyzed using a gradient of 5% to 100% CH_3CN containing 0.1% TFA over 40 min at flow rate of 1.0 mL min^{-1}. All runs were monitored at λ = 254 and 214 nm. For the reactions involving ^{99m}Tc, HPLC experiments were performed on a Varian Prostar model 230 HPLC instrument coupled to a Bio-Rad IN/US γ-detector using a Varian Nucleosil (L × ID = 250 × 4.6 mm) analytical column (300 Å − 5 μm, RP-C18). The mobile phase for the analysis of $[Tc(CO)_3(H_2O)_3]^+$ consisted of solvent A, triethylammonium phosphate buffer (pH = 2−2.5); solvent B, CH_3OH. Gradient: 0−3 min, 100% A; 3−6 min, 100% A to 75% A; 6−9 min, 75% A to 67% A; 9−20 min, 67% A to 0% A; 20−22 min, 0% A; 22−25 min, 0% A to 100% A; 25−30 min, 100% A. For the labeled peptide, the elution conditions were 5−100% CH_3CN containing 0.1% TFA over 30 min at flow rate of 1.0 mL min^{-1}.

Materials and Methods. Unless otherwise stated, all reagents and solvents were ACS grade or higher and used without further purification from commercial suppliers. Polystyrene-based N-α-9-fluorenylmethoxycarbonyl (Fmoc)-glycine loaded Wang resin (0.82 mmol g^{-1}, 1% divinylbenzene, 200−400 mesh) was obtained from NovaBiochem Inc. Fmoc-protected amino acids were purchased from NovaBiochem Inc., Bachem Inc., and Advanced ChemTech Inc. Peptides were prepared on an Advanced Chemtech 348 synthesizer. The $A\beta^{1-40}$ was purchased from rPeptide (cat# A-1001-1, lot# 3120440A).

Caution: ^{99m}Tc is radioactive and should only be handled in an appropriately equipped and licensed facility.

Solid-Phase Peptide Synthesis. Fmoc-glycine loaded Wang resin (0.82 mmol/g; 100 mg/well) was added to 16 wells in the reaction block, washed with DMF (2 mL/well), and shaken at 600 rpm for 1 min. The wells were then filtered and the resin washed with THF (2 mL/well) three times, shaking at 600 rpm for 1 min and draining for 90 s per wash. The same washing was repeated two additional times with DMF to complete the general wash cycle. This general wash cycle was used between every deprotection and coupling step.

Fmoc deprotection was accomplished by adding a 20% v/v piperidine−DMF solution (2 mL/well) and shaking for 5 min at 600 rpm. After draining the reaction wells, the deprotection procedure was repeated this time with shaking for 10 min. The deprotected resin-bound amino acid was then washed with the general wash cycle. For amino acid coupling reactions, standard methods involving HBTU were employed. The linear peptides were prepared by adding DMF (200 μL) to the active vessels followed by a 4-fold excess of the appropriate protected amino acid as a 0.5 M solution in DMF. Four equivalents of HBTU as a 0.5 M solution in DMF was then added, followed by an 8-fold excess of DIPEA as 2.0 M solution in DMF. The reaction vessel was subsequently shaken for 80 min at 600 rpm. Following filtration, the resin was washed as described above and the cycles repeated to prepare peptides **1**−**8a**.

The branched peptides were prepared using the same HBTU coupling strategy described above. At the point of branching, Fmoc-D-Lys(Mtt)-OH was introduced into the peptide where, prior to Mtt deprotection, THF (2 mL) was added to the appropriate reaction wells and the suspension shaken at 600 rpm for 4 min. After filtration, the THF wash was repeated twice to ensure that no residual DMF was present. The Mtt group (Mtt = 4-methyltrityl) was selectively removed by the manual addition of 2 mL of a freshly prepared cocktail of 1% TFA and 3% TIS in DCM (v/v/v), followed by shaking for 15 min at 600 rpm. After filtration, the procedure was repeated, this time shaking for 30 min. The resin was then tested for complete deprotection by adding a small amount of resin to a 1:1 (v/v) solution of TFA and DCM. When the resin did not turn yellow, Mtt deprotection was assumed to be complete, and the next amino acid was added in 8-fold excess. Eight equivalents of HBTU as a 0.5 M solution in DMF and a 16-fold excess of DIPEA as a 1.0 M solution in DMF were added and the mixture shaken at 600 rpm for 80 min, then filtered. The same conditions were used to add each subsequent amino acid in compounds **9**−**16**.

At the end of the synthesis, resin-bound peptides were removed from the reaction block and transferred to 20 mL glass vials. EDT (2%), water (2%), and TIS (2%) in TFA (v/v/v/v) cooled to 0 °C were added to the resin samples and the vials shaken at 400 rpm for 90 min at room temperature. The reaction vessels were subsequently filtered into cold diethyl ether and the heterogeneous mixtures centrifuged at 3000 rpm and −5 °C for 10 min. The resultant pellets were washed with cold diethyl ether (3 × 25 mL), dissolved in distilled−deionized water, and lyophilized to yield white solids for the peptides containing the free ligand and pink solids if rhenium was present (Table 1).

Preparation of $[^{99m}Tc(CO)_3(OH_2)_3]^+$. A 10 mL penicillin vial fitted with a rubber septum and containing $K_2[BH_3{\cdot}CO_2]$, (8.5 mg, 63 μmol), $Na_2B_4O_7{\cdot}10H_2O$ (2.9 mg, 8.0 μmol), Na/K-tartrate (15.0 mg, 53 μmol), and Na_2CO_3 (4.0 mg, 38 μmol) was flushed with N_2(g) for 15 min. $^{99m}TcO_4^-$ (370 MBq) in 500 μL of saline was added by syringe, and the solution heated at 95 °C for 30 min. After cooling in an ice bath, the solution was neutralized by the addition of 12 M HCl. Gradient HPLC was performed to assess purity and yield.

Radiolabeling of Compound **7.** Compound **7** (1.0 mg, 0.71 μmol) in 200 μL of distilled−deionized water and 300 μL of CH_3CN was added via a syringe to the solution containing $[^{99m}Tc(CO)_3(OH_2)_3]^+$ (346 MBq) and the mixture heated to 55 °C for 3 h. The reaction mixture was subsequently loaded onto a solid-phase extraction cartridge (Waters, C_{18}), which had been conditioned with absolute ethanol (10 mL), CH_3CN (10 mL), 1:1 CH_3CN /10 mM HCl (10 mL), and 10 mM HCl (10 mL) prior to use. Small (1 mL) fractions were collected from the following gradient elution protocol: 10 mM HCl (7 × 1 mL), 1:4 CH_3CN/10 mM HCl (2 × 1 mL), 1:1 CH_3CN/10 mM HCl (2 × 1 mL), 4:1 CH_3CN/10 mM HCl (2 × 1 mL), and finally CH_3CN (5 × 1 mL). Compound **8b** eluted in fractions 11 and 12, which were concentrated to 200 μL, and the product was isolated by HPLC. The radiochemical yield of **8b** was 25%, and the radiochemical purity was >98%.

Ligand Challenge Experiments. Two vials each containing 3.7−7.4 MBq of purified **8b** in distilled−deionized water (100 μL) were incubated separately with 500 μL of solutions containing cysteine (0.010 M in 100 mM sodium phosphate buffer, pH = 7.2) and histidine (0.010 M in 100 mM sodium

Table 1. Numbering Scheme, Isolated Yield, and Characterization Data for Compounds 1−16[a,b]

compound no.	peptide sequence	yield (%)	HPLC t_R (min.)	MS (*m/z*)	IR υ [M(CO)] (cm^{-1})
1	SAACQ-lvffag	36	20.3	1063	–
2	ReSAACQ-lvffag	63	22.3	1335	2031, 1915
3	k(N$^{\epsilon}$Biotin)-SAACQ-lvffag	73	20.3	1419	–
4	k(N$^{\epsilon}$Biotin)-ReSAACQ-lvffag	48	22.1	1688	2031, 1918
5	SAACQ-affvlg	66	21.0	1064	–
6	ReSAACQ-affvlg	26	22.9	1333	2031, 1915
7	k(N$^{\epsilon}$Biotin)-SAACQ-affvlg	60	20.6	1418	–
8a	k(N$^{\epsilon}$Biotin)-ReSAACQ-affvlg	72	22.7	1688	2032, 1929
9	lvffa-SAACQ-k(N$^{\epsilon}$affvl)g	62	21.7	1770	–
10	lvffa-ReSAACQ-k(N$^{\epsilon}$affvl)g	20	23.8	2041	2032, 1927
11	lvffa-SAACQ-k(N$^{\epsilon}$affvl)k(N$^{\epsilon}$Biotin)g	31	21.0	2126[b]	–
12	lvffa-ReSAACQ-k(N$^{\epsilon}$affvl)k(N$^{\epsilon}$Biotin)g	37	22.7	2394[b]	2032, 1925
13	affvl-SAACQ-k(N$^{\epsilon}$lvffa)g	38	22.0	1770	–
14	affvl-ReSAACQ-k(N$^{\epsilon}$lvffa)g	37	24.0	2041[b]	2031, 1918
15	affvl-SAACQ-k(N$^{\epsilon}$lvffa)k(N$^{\epsilon}$Biotin)g	57	21.6	2124[b]	–
16	affvl-ReSAACQ-k(N$^{\epsilon}$lvffa)k(N$^{\epsilon}$Biotin)g	16	23.2	2395[b]	2031, 1923

[a] Peptides containing a single targeting sequence are written with the N-terminal group on the left. For the dimeric peptides, the first sequence is written with the N-terminus on the left, while the second group is written beginning with the amino acid attached to lysine at the branching point. [b] Indicates peak in the MS appears as m/2 and m/3 in positive ion mode.

Table 2. Percentage of Amyloid Fibrils Formed after Incubation of Aβ^{1-40} with the Re-Containing Peptides at 37 °C for 5 Days

compound no.	sequence	% amyloid
	DMSO control	100
2	ReSAACQ-lvffag	48 ± 4
4	k(N$^{\epsilon}$Biotin)-ReSAACQ-lvffag	43 ± 2
6	ReSAACQ-affvlg	47 ± 7
8a	k(N$^{\epsilon}$Biotin)-ReSAACQ-affvlg	40 ± 5
10	lvffa-ReSAACQ-k(N$^{\epsilon}$affvl)g	69 ± 4
12	lvffa-ReSAACQ-k(N$^{\epsilon}$affvl)k(N$^{\epsilon}$Biotin)g	55 ± 5
14	affvl-ReSAACQ-k(N$^{\epsilon}$lvffa)g	58 ± 4
16	affvl-ReSAACQ-k(N$^{\epsilon}$lvffa)k(N$^{\epsilon}$Biotin)g	40 ± 4

phosphate buffer, pH = 7.2). The reaction mixtures were heated to 37 °C for 24 h after which aliquots were taken and analyzed by HPLC.

In Vitro Screening. Aβ^{1-40} (0.5 mg, rPeptide) was initially dissolved in 100 μL of 0.1% TFA and then 250 μL of 10 mM EDTA added (solution A). The presence of premature fibril formation was checked routinely by taking an aliquot of the solution (10 μL) and adding it to 500 μL of 2 μM Thioflavin T (ThT). The fluorescence was then measured at excitation and emission wavelengths of 440 and 485 nm, respectively, using 10 nm band-pass filters. After ensuring that no fibrils were present, an additional 250 μL of 20 mM sodium phosphate buffer (pH 7.4)/10 mM EDTA was added to solution A to form the Aβ^{1-40} stock solution (solution B). Rhenium-labeled peptides (**2**, **4**, **6**, **8a**, **10**, **12**, **14**, and **16**) were then dissolved in DMSO and diluted with 20 mM sodium phosphate buffer (pH 7.4) so that the final DMSO concentration was 25%. The required volume of rhenium peptide solution was then added to 40 μL of the Aβ^{1-40} stock solution (solution B) so that there was a 1:1 molar ratio of Aβ^{1-40} peptide and the desired rhenium peptide. The resulting solutions were then incubated for 5 days at 37 °C in duplicate. Following incubation, 40 μL of each solution was added to 500 μL of 2 μM ThT and fluorescence measured using a PerkinElmer LS55 luminescence spectrometer (10 nm slit widths). The percentage of amyloid (Table 2) was then calculated by dividing the fluorescence measurements by those found for the control consisting of 25% DMSO in 20 mM sodium phosphate buffer (pH 7.4)/10 mM EDTA and 40 μL of the Aβ^{1-40} stock solution (solution B).

RESULTS

The target peptides were prepared containing the single amino acid chelate−quinoline (SAACQ) ligand, which is an amino acid analogue that is capable of binding Tc and Re. The reported compounds were derived from the targeting sequence lvffa and the reverse sequence affvl, which are both reported to bind to β-amyloid plaques. The library consisted of 16 unique compounds, half of which possess a single targeting vector (Figure 1), while the remainder possess two targeting sequences (Figure 2). Biotin was introduced into select peptides to provide a convenient means to conjugate the peptides to vectors that facilitate crossing the BBB. For compounds **1**−**8a**, biotin and the SAACQ ligand were incorporated adjacent to the N-terminus of each peptide, as this site is known to tolerate introduction of large groups without affecting binding (*4*, *16*−*19*), while for compounds **9**−**16**, they were incorporated adjacent to the terminus that is distant to the two targeting sequences.

Peptides **1**−**16** (Table 1) were prepared in parallel on an automated 348 ACT synthesizer using a 40-well reaction block using all D-amino acids. Starting with Fmoc-glycine loaded Wang resin, peptides **1**−**8a**, which contain a single targeting sequence, were synthesized using standard Fmoc/HBTU peptide coupling and deprotection strategies (Scheme 1). In cases where biotin was introduced into the peptides, Fmoc-D-Lys(N$^{\epsilon}$-Biotin)-OH was added to the N-terminal amino acid again using standard coupling procedures.

Preparation of peptides containing two targeting sequences was accomplished using Fmoc-D-Lys(N$^{\epsilon}$-Mtt)-OH (Mtt = 4-methyltrityl) as a bridging site (Scheme 2). Mtt was selectively removed during peptide synthesis using a solution of 1% TFA and 3% TIS in DCM (v/v/v). The time required for complete deprotection was monitored by adding a small amount of resin to a 1:1 (v/v) solution of TFA and DCM. In the case where a yellow color appeared, which suggested the presence of Mtt, the reaction was allowed to continue (*23*, *24*). Following complete Mtt deprotection, the Fmoc group was then removed using 20% piperidine/DMF and the two targeting sequences built up simultaneously using an 8-fold excess of the appropriate Fmoc-protected amino acid derivatives per coupling step.

Conjugates **1**−**16** were cleaved from the solid support using a standard cleavage cocktail, precipitated from cold diethyl ether and collected by centrifugation (−5 °C, 10 min, 3000 rpm). Peptides were washed three times with cold diethyl ether, dissolved in water, and lyophilized to yield white solids. HPLC and mass spectrometry analysis confirmed the purity and molecular weight of the peptides (Table 1).

***In Vitro* Screening—Thioflavin T Inhibition Assay.** The Re-containing peptides **2**, **4**, **6**, **8a**, **10**, **12**, **14**, and **16** were incubated with the native peptide Aβ^{1-40} in a 1:1 ratio (10 μM) at 37 °C for 5 days in parallel with controls containing no competitor and 25% DMSO. It was found that 25% DMSO was required

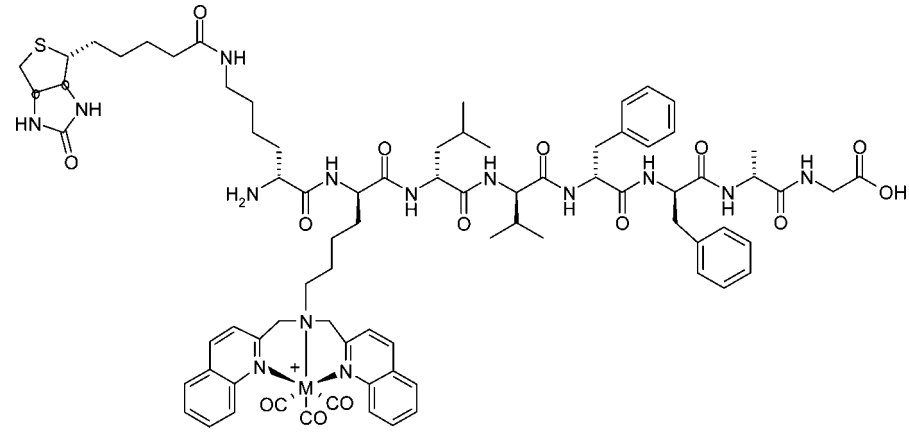

Figure 1. General structure for agents containing a single targeting sequence and biotin (k(N$^{\epsilon}$Biotin)-ReSAACQ-lvffag).

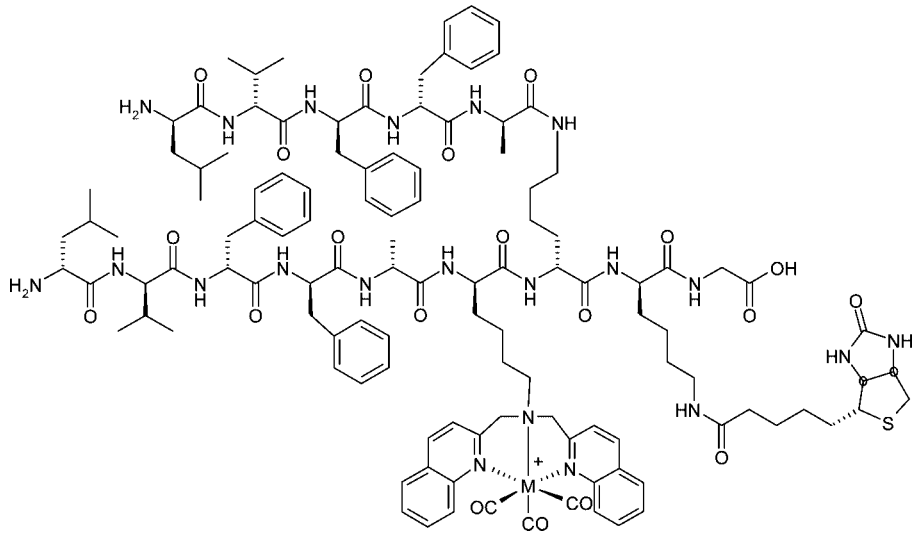

Figure 2. General structure for agents containing two identical targeting sequences and biotin (lvffa-ReSAACQ-k(N$^{\epsilon}$affvl)k(N$^{\epsilon}$Biotin)g).

in order to solubilize the peptide conjugates at the required concentration. Consequently, this solvent composition was used as the reference solution to calculate the percentage of amyloid. CH_3CN was initially considered, but test experiments demonstrated that the presence of this solvent increased the formation of fibrils when compared to controls. Following incubation with the peptides, 40 μL aliquots of each mixture were added to 500 μL of 2 μM ThT (giving a final DMSO content that was less than 2%) and the fluorescence intensity measured at excitation and emission wavelengths of 440 and 485 nm, respectively. The percentages of amyloid present (Table 2) were found by dividing the fluorescence intensities observed in the presence and absence of the competitor. Therefore, 100% amyloid would indicate that the peptide was unable to inhibit the formation of fibrils and would correspond to the largest fluorescence intensity.

Technetium Labeling. To demonstrate that sufficient quantities of the radiolabeled peptides could be produced for *in vivo* imaging studies, compound **7** in a mixture of water and CH_3CN was added to a solution containing $[^{99m}Tc(CO)_3(OH_2)_3]^+$ and the mixture heated at 55 °C for 3 h (Scheme 3). The labeled product **8b** was isolated by solid-phase extraction followed by semipreparative HPLC in 25% radiochemical yield in greater than 98% radiochemical purity. The retention time of **8b** in the γ-HPLC matched that for the Re reference standard **8a**, which was detected by UV (Figure 3).

Cysteine and histidine challenge studies were performed to test the robustness of the metal complex. A large excess of each amino acid was added to solutions of **8b** and the mixtures heated at 37 °C for 24 h. The ^{99m}Tc complex showed only very minor signs of degradation (less than 2%) in either test (Figure 4).

DISCUSSION

β-breaker peptides are under investigation as an experimental therapeutic strategy for reducing amyloid plaque loads. Radioactive analogues labeled with ^{99m}Tc would afford the opportunity to study the distribution of variants of this class of compounds *in vivo*, and if they are capable of targeting amyloid plaques, the tracers could also be used to assess the impact of other emerging plaque-reducing treatment strategies. The advantages to using ^{99m}Tc over other isotopes are that it is widely available at a low cost and the vast majority of hospitals have the capacity to image Tc labeled compounds.

Our group recently described a new and robust method for derivatizing peptides with a chelating system (referred to as the single amino acid chelate quinoline or SAACQ) that is capable of binding ^{99m}Tc. The approach is flexible in that the chelate, which is derived from lysine, can be introduced at any position within the backbone of the peptide. A further advantage is that the chelate forms a robust metal complex with rhenium, which can also be incorporated into peptides. As a result, it is conceivable that libraries of all manners of chelate−peptide conjugates and the nonradioactive Re analogues of the target ^{99m}Tc complexes can be prepared in parallel. This would make it possible to screen an exact and nonradioactive replica of any peptide-targeted agent *in vitro* prior to undertaking an evaluation of the ^{99m}Tc analogue *in vivo*.

Scheme 1. Synthesis of Single Vector Peptides (3, 4) Containing Biotin

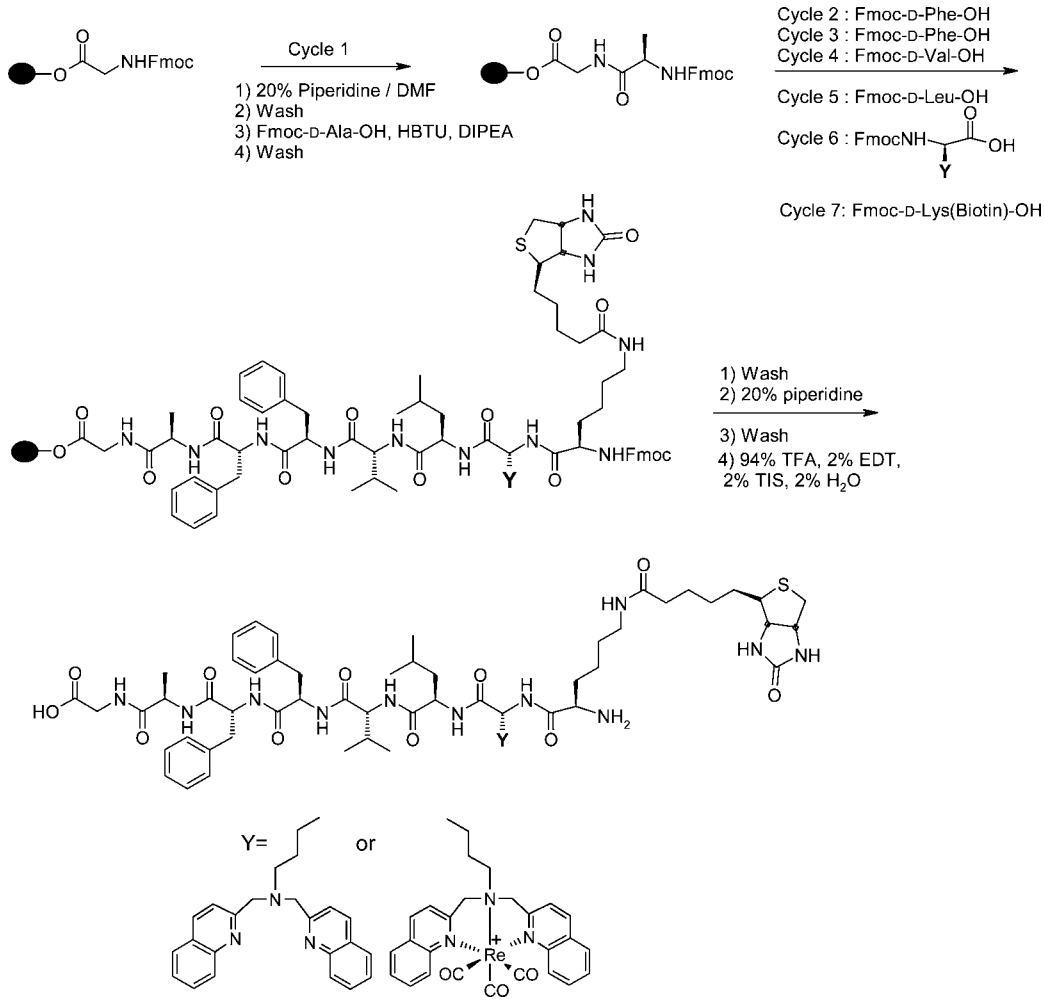

The peptide conjugates **1**−**16** were successfully prepared in parallel using standard peptide coupling strategies on an automated synthesizer. The peptides were constructed from an Fmoc-glycine loaded Wang resin using D-amino acids, which were employed to avoid future issues of premature degradation of the targeting agent *in vivo*. Peptides **1**−**8a** were prepared with a single copy of the lvffa or affvl sequences, while compounds **9**−**16** contained two copies. The introduction of the two vectors was made possible through the incorporation of Fmoc-D-Lys(Mtt)-OH, which provided a branching point. The preparation of multivalent peptides containing a single chelate group in the backbone of the probe as opposed to conjugated to the N-terminus or a pendent lysine is not commonly observed in radiopharmaceutical chemistry because the appropriately functionalized chelates have not been available until recently. For the bivalent peptides presented here, two identical targeting sequences were used. However, it is easy to see how two unique vectors could be introduced by removing the Mtt group after the first peptide has been synthesized. This type of approach could be used to incorporate a second sequence to improve affinity for the target or to alter the pharmacokinetics.

All peptide conjugates (**1**−**16**) were cleaved using a standard cleavage cocktail, and the conjugates were isolated in modest to good yields (Table 2) as white solids if they contained SAACQ and as pink solids if they contained Re. HPLC analysis indicated that both monomers and dimers containing SAACQ were prepared such that they did not require further purification. Analogues prepared with ReSAACQ were isolated in greater than 90% purity whereupon HPLC was used to increase this value to 99%. Despite the structural complexity of peptides, particularly compounds **9**−**16**, it was possible to prepare multimilligram quantities (greater than 50 mg) of each of the products. The ability to scale up reactions, which can be readily accomplished using the reported approach, is an important consideration for compounds that are going to move on to preclinical and clinical evaluation.

Peptide conjugates **2**, **4**, **6**, **8a**, **10**, **12**, **14**, and **16** were tested for their ability to inhibit fibrillogenesis using a standard assay for determining the ability of compounds, particularly peptides, to bind to β-amyloid plaques (*4*, *17*, *20*, *25*). Thioflavin T (ThT) is a dye used to stain amyloid fibrils found in the brains of AD patients postmortem (*26*). When ThT binds to plaques, there is a unique red shift in its absorption spectrum, which is distinct from the unbound dye. The unbound dye has excitation and emission maxima of 385 and 445 nm, which shift to 450 and 485 nm, respectively, upon binding (*17*, *27*). As a result, the formation of ordered $A\beta^{1-40}$ fibrils can be quantitated *in vitro* by measuring the increase in fluorescence intensity at the different wavelengths (*20*, *28*, *29*). β-breaker peptides have been evaluated using this technique and demonstrated good inhibition of ThT binding (*16*, *19*, *20*, *25*, *28*, *29*).

In order to solubilize the hydrophobic peptides, 25% DMSO was required, which was not problematic, as control experiments using 0%, 5%, and 25% DMSO did not show significant differences in the extent of fibril formation. All peptides studied demonstrated some inhibition of fibrillogenesis where somewhat surprisingly the peptides containing one copy of the targeting sequence were generally more effective than the dimers with the exception of compound **16**. In general, the peptides showed inhibition numbers that were as good as if not superior to the

Scheme 2. Synthesis of Peptides (11, 12) Containing Two Targeting Sequences and Biotin

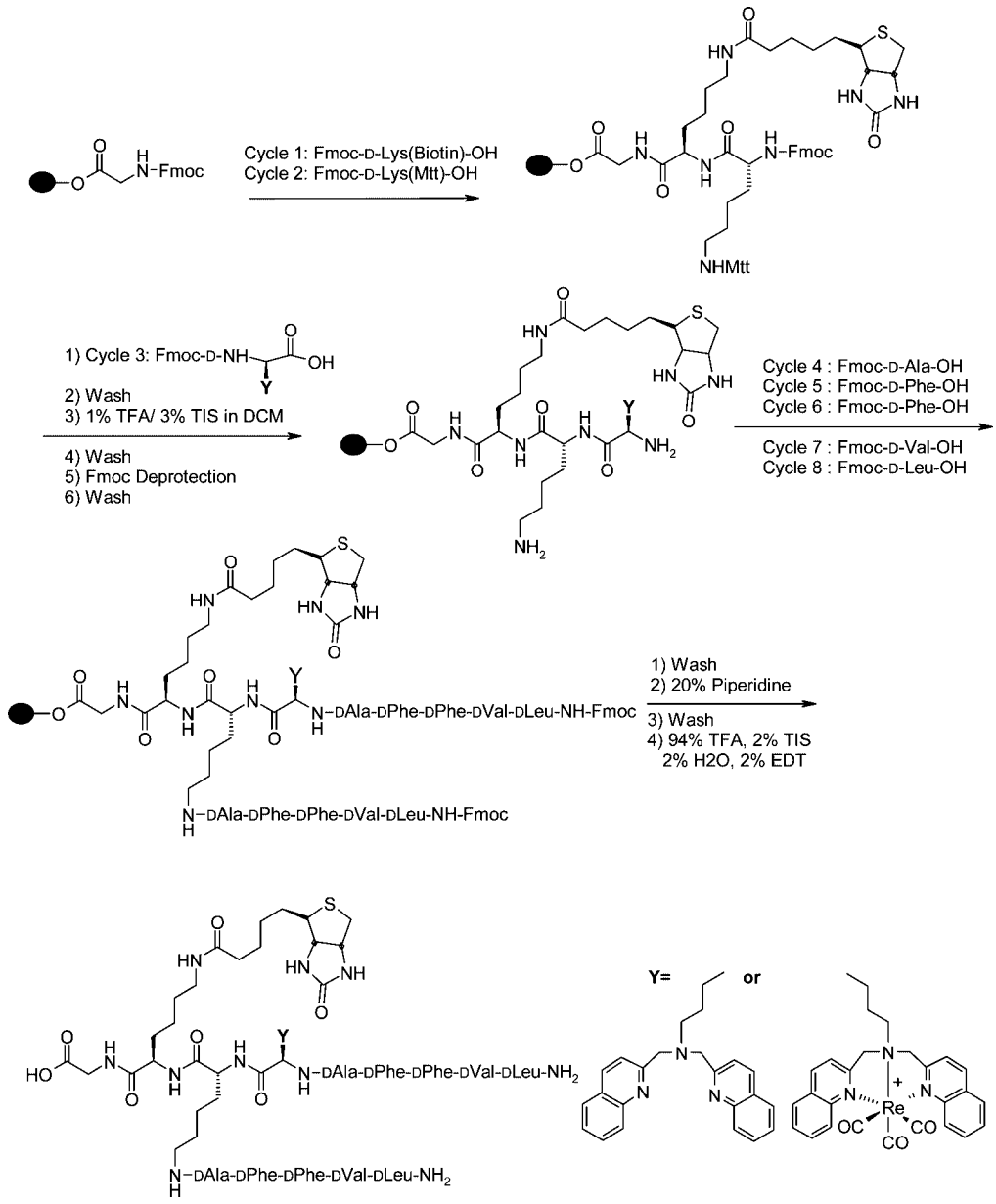

values reported for the parent peptides. For example, Soto and co-workers found lvffa had 89 ± 2.7% amyloid when present in a 10-fold excess compared to Aβ^{1-40}, while Zhang et al. prepared the D-analogue of klvff and reported the extent of amyloid formation as 76% (*17*). The rhenium analogue Re-SAACQ-lvffag was more potent and showed 48 ± 4% inhibition when used in a 1:1 ratio with Aβ^{1-40}. These results indicate that the presence of the metal complex and/or biotin derivative did not have a detrimental impact on the ability of the peptide to bind to amyloid. The most promising agents for further evaluation are compounds **8a** and **16**, both of which contain biotin as a site for further derivatization.

The next phase of the work was to demonstrate that the ^{99m}Tc analogues could be prepared and that the products are sufficiently robust to screen *in vivo*. Compound **7** was selected as a model compound and labeled using $[^{99m}Tc(CO)_3(OH_2)_3]^+$, which can be readily prepared in high yield using an instant kit (*30*−*34*). The labeled product, k(N$^{\epsilon}$Biotin)-^{99m}TcSAACQ-lvffag (**8b**) was isolated by solid-phase extraction and HPLC purification. The latter technique was employed to remove any unlabeled ligand, thus affording the product in high effective specific activity. Analytical HPLC in fact indicated that the reaction was quantitative; however, the isolated radiochemical yield after semipreparative HPLC was greatly reduced largely due to absorption of the labeled peptide on the column. Nevertheless, the desired product was isolated in high radiochemical purity (greater than 98%), and its retention time matched that of the Re analogue. Ligand challenge studies on the product showed no significant signs of degradation (Figure 4), which is consistent with the d^6 electronic configuration of the octahedral metal complex.

CONCLUSIONS

An amino acid derived chelating system for ^{99m}Tc and Re was used to create a small library of β-breaker peptide derivatives. The Re complexes, which were synthesized in parallel with the free ligands, were tested for their ability to inhibit fibrillogenesis, and two promising leads were identified. The ^{99m}Tc analogue of one of these was isolated in modest yield but exquisite purity, and it was resistant to ligand challenge against both histidine and cysteine. Amyloid plaques are associated with a number of diseases beyond simply AD,

Scheme 3. Labeling of Compound 7 with ^{99m}Tc

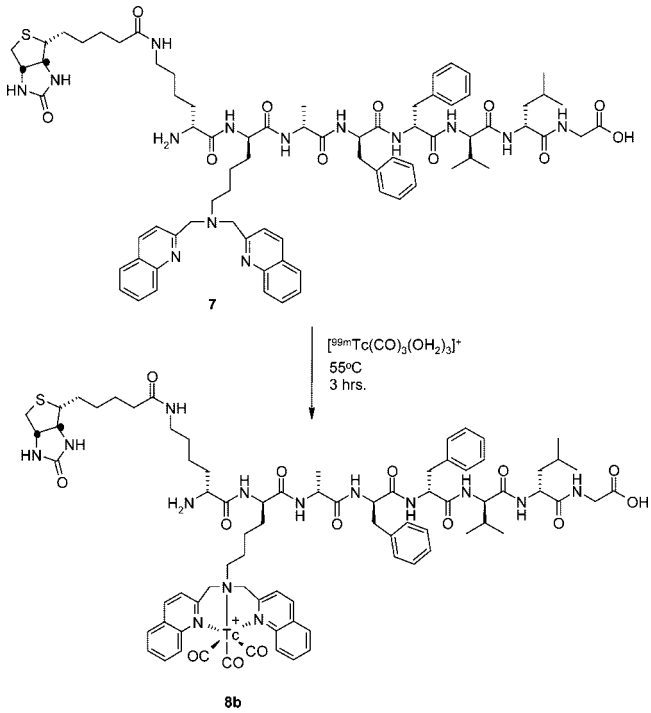

consequently molecular imaging probes for this particular target like those reported here could have significant utility in both clinical applications and in supporting early trials involving emerging therapeutics. Furthermore, the results presented demonstrate that the ReSAACQ system can be used to efficiently generate multiple Re-metallopeptides in parallel, which can be screened directly to identify lead agents in a time and resource efficient manner.

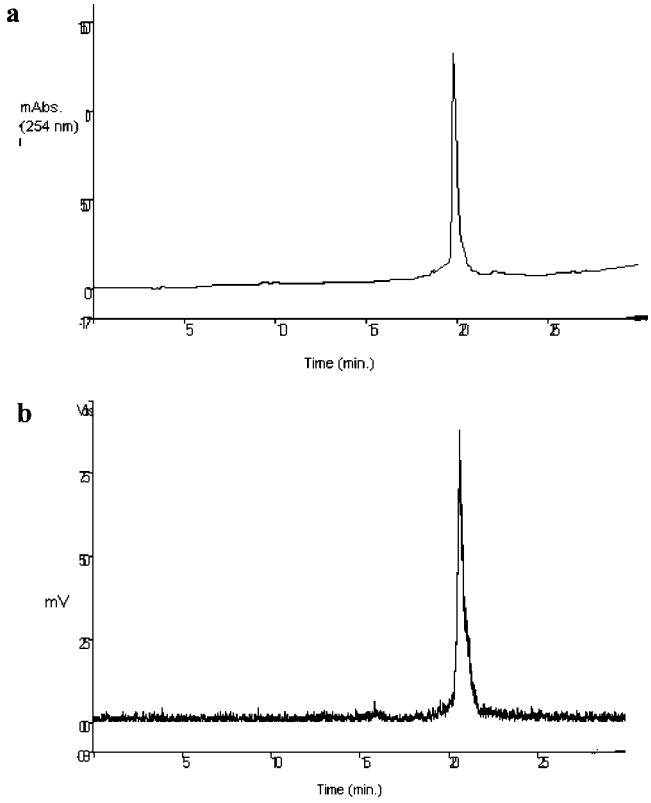

Figure 3. (a) UV-HPLC chromatogram of **8a** (R_t = 19.7 min) and (b) γ-HPLC chromatogram of purified **8b** (R_t = 20.4 min).

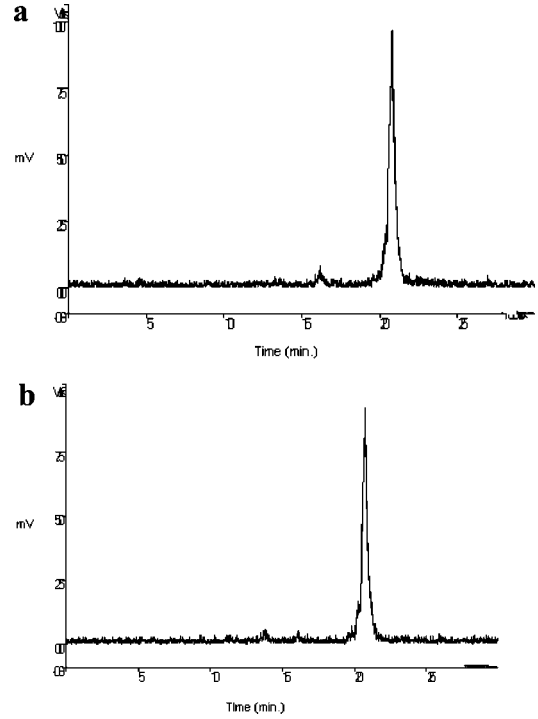

Figure 4. γ-HPLC radiochromatograms of samples from the histidine (a) and cysteine (b) challenge experiments involving **8b** (R_t = 20.6 min) after 24 h at 37 °C.

ACKNOWLEDGMENT

We would like to acknowledge funding from the Ontario Research and Development Challenge Fund (ORDCF) and The National Sciences and Engineering Research Council (NSERC) of Canada for a Scholarship for K.A.S.

Supporting Information Available: Structures of the ligands; HPLC, IR, and ESMS data. This material is available free of charge via the Internet at http://pubs.acs.org.

LITERATURE CITED

(1) Bachurin, S. O. (2002) Medicinal chemistry approaches for the treatment and prevention of Alzheimer's disease. *Med. Res. Rev. 23*, 48–88.

(2) Mattson, M. P. (2004) Pathways towards and away from Alzheimer's disease. *Nature 430*, 631–639.

(3) Kurihara, A., and Pardridge, W. M. (2000) Aβ^{1-40} peptide radiopharmaceuticals for biotin amyloid imaging: ^{111}In chelation, conjugation to poly(ethylene glycol)-biotin linkers, and autoradiography with Alzheimer's disease brain sections. *Bioconjugate Chem. 11*, 380–386.

(4) Soto, C. (1999) Plaque busters: strategies to inhibit amyloid formation in Alzheimer's disease. *Mol. Med. Today 5*, 343–350.

(5) Geula, C., Wu, C. K., Saroff, D., Lorenzo, A., Yuan, M., and Yankner, B. A. (1998) Aging renders the brain vulnerable to amyloid β-protein neurotoxicity. *Nat. Med. 4*, 827–831.

(6) Hardy, J., and Selkoe, D. J. (2002) The amyloid hypothesis of Alzheimer's disease: progress and problems on the road to therapeutics. *Science 297*, 353–356.

(7) Pitschke, M., Prior, R., Haupt, M., and Riesner, D. (1998) Detection of single amyloid β-protein aggregates in the cerebrospinal fluid of Alzheimer's patients by fluorescence correlation spectroscopy. *Nat. Med. 4*, 832–834.

(8) Verhoeff, N. P., Wilson, A. A., Takeshita, S., Trop, L., Hussey, D., Singh, K., Kung, H. F., Kung, M.-P., and Houle, S. (2004) In vivo imaging of Alzheimer disease β-amyloid with [11C]SB-13 PET. *Am. J. Geriatr. Psychiatry 12*, 584–595.

(9) Klunk, W. E., Engler, H., Nordberg, A., Wang, Y., Blomqvist, G., Holt, D. P., Bergstrom, M., Savitcheva, I., Huang, G.-f., Estrada, S., Ausen, B., Debnath, M. L., Barletta, J., Price, J. C., Sandell, J., Lopresti, B. J., Wall, A., Koivisto, P., Antoni, G., Mathis, C. A., and Langstrom, B. (2004) Imaging brain amyloid in Alzheimer's disease with Pittsburgh Compound-B. *Ann. Neurol. 55*, 306–319.

(10) Qu, W., Kung, M.-P., Hou, C., Oya, S., and Kung, H. F. (2007) Quick assembly of 1,4-diphenyltriazoles as probes targeting β-amyloid aggregates in Alzheimer's disease. *J. Med. Chem. 50*, 3380–3387.

(11) Qu, W., Kung, M.-P., Hou, C., Benedum, T. E., and Kung, H. F. (2007) Novel styrylpyridines as probes for SPECT imaging of amyloid plaques. *J. Med. Chem. 50*, 2157–2165.

(12) Chandra, R., Oya, S., Kung, M.-P., Hou, C., Jin, L.-W., and Kung, H. F. (2007) New diphenylacetylenes as probes for positron emission tomographic imaging of amyloid plaques. *J. Med. Chem. 50*, 2415–2423.

(13) Maggio, J. E., Stimson, E. R., Ghilardi, J. R., Allen, C. J., Dahl, C. E., Whitcomb, D. C., Vigna, S. R., Vinters, H. V., Labenski, M. E., and Mantyh, P. W. (1992) Reversible in vitro growth of Alzheimer disease β-amyloid plaques by deposition of labeled amyloid peptide. *Proc. Natl. Acad. Sci. U.S.A. 89*, 5462–5466.

(14) Wu, D., Yang, J., and Pardridge, W. M. (1997) Drug targeting of a peptide radiopharmaceutical through the primate blood-brain barrier in vivo with a monoclonal antibody to the human insulin receptor. *J. Clin. Invest. 100*, 1804–1812.

(15) Saito, Y., Buciak, J., Yang, J., and Pardridge, W. M. (1995) Vector-mediated delivery of 125 I-labeled β-amyloid peptide $A\beta^{1-40}$ through the blood-brain barrier and binding to Alzheimer disease amyloid of the $A\beta^{1-40}$/vector complex. *Proc. Natl. Acad. Sci. U.S.A. 92*, 10227–10231.

(16) Chalifour, R. J., McLaughlin, R. W., Lavoie, L., Morissette, C., Tremblay, N., Boule, M., Sarazin, D. S., Lacombe, D., Tremblay, P., and Gervais, F. (2003) Stereoselective interactions of peptide inhibitors with the β-amyloid peptide. *J. Biol. Chem. 278*, 34874–34881.

(17) Zhang, G., Leibowitz, M. J., Sinko, P. J., and Stein, S. (2003) Multiple-peptide conjugates for binding β-amyloid plaques of Alzheimer's disease. *Bioconjugate Chem. 14*, 86–92.

(18) Gazit, E. (2002) Mechanistic studies of the process of amyloid fibrils formation by the use of peptide fragments and analogues: implications for the design of fibrillization inhibitors. *Curr. Med. Chem. 9*, 1725–1735.

(19) Gordon, D. J., Sciarretta, K. L., and Meredith, S. C. (2001) Inhibition of 102-amyloid(40) fibrillogenesis and disassembly of β-amyloid(40) fibrils by short β-amyloid congeners containing N-methyl amino acids at alternate residues. *Biochemistry 40*, 8237–8245.

(20) Soto, C., Kindy, M. S., Baumann, M., and Frangione, B. (1996) Inhibition of Alzheimer's amyloidosis by peptides that prevent β-sheet conformation. *Biochem. Biophys. Res. Commun. 226*, 672–680.

(21) Soto, C., Sigurdsson, E. M., Morelli, L., Kumar, R. A., Castano, E. M., and Frangione, B. (1998) β-Sheet breaker peptides inhibit fibrillogenesis in a rat brain model of amyloidosis: Implications for Alzheimer's therapy. *Nat. Med. 4*, 822–826.

(22) Findeis, M. A., Musso, G. M., Arico-Muendel, C. C., Benjamin, H. W., Hundal, A. M., Lee, J.-J., Chin, J., Kelley, M., Wakefield, J., Hayward, N. J., and Molineaux, S. M. (1999) Modified-peptide inhibitors of amyloid β-peptide polymerization. *Biochemistry 38*, 6791–6800.

(23) Chan, W. C., and White, P. D. (2000) *FMOC Solid-Phase Peptide Synthesis, A Practical Approach*, Oxford University Press, New York.

(24) Li, D., and Elbert, D. L. (2002) The kinetics of the removal of the N-methyltrityl (mtt) group during synthesis of branched peptides. *J. Pept. Res. 60*, 300–303.

(25) Poduslo, J. F., Curran, G. L., Kumar, A., Frangione, B., and Soto, C. (1999) Beta-sheet breaker peptide inhibitor of Alzheimer's amyloidogenesis with increased blood-brain barrier permeability and resistance to proteolytic degradation in plasma. *J. Neurobiol. 39*, 371–382.

(26) Mathis, C. A., Wang, Y., and Klunk, W. E. (2004) Imaging β-amyloid plaques and neurofibrillary tangles in the aging human brain. *Curr. Pharm. Des. 10*, 1469–1492.

(27) LeVine, H. I. (1993) Thioflavine T interaction with synthetic Alzheimer's disease β-amyloid peptides: Detection of amyloid aggregation in solution. *Protein Sci. 2*, 404–410.

(28) Adessi, C., Frossard, M.-J., Boissard, C., Fraga, S., Bieler, S., Ruckle, T., Vilbois, F., Robinson, S. M., Mutter, M., Banks, W. A., and Soto, C. (2003) Pharmacological profiles of peptide drug candidates for the treatment of Alzheimer's disease. *J. Biol. Chem. 278*, 13905–13911.

(29) Hetenyi, C., Kortvelyesi, T., and Penke, B. (2002) Mapping of possible binding sequences of two β-sheet breaker peptides on β-amyloid peptide of Alzheimer's disease. *Bioorg. Med. Chem. 10*, 1587–1593.

(30) Egli, A., Alberto, R., Tannahill, L., Schibli, R., Abram, U., Schaffland, A., Waibel, R., Tourwe, D., Jeannin, L., Iterbeke, K., and Schubiger, P. A. (1999) Organometallic ^{99m}Tc-aquaion labels peptide to an unprecedented high specific activity. *J. Nucl. Med. 40*, 1913–1917.

(31) Alberto, R., Schibli, R., Egli, A., Schubiger, A. P., Abram, U., and Kaden, T. A. (1998) A novel organometallic aqua complex of technetium for the labeling of biomolecules: synthesis of $[^{99m}Tc(OH_2)_3(CO)_3]^+$ from $[^{99m}TcO_4]^-$ in aqueous solution and its reaction with a bifunctional ligand. *J. Am. Chem. Soc. 120*, 7987–7988.

(32) Alberto, R., Schibli, R., Waibel, R., Abram, U., and Schubiger, A. P. (1999) Basic aqueous chemistry of $[M(OH_2)_3(CO)_3]^+$ (M=Re, Tc) directed towards radiopharmaceutical application. *Coord. Chem. Rev. 190−192*, 901–919.

(33) Alberto, R., Ortner, K., Wheatley, N., Schibli, R., and Schubiger, A. P. (2001) Synthesis and properties of boranocarbonate: a convenient in situ CO source for the aqueous preparation of $[^{99m}Tc(OH_2)_3(CO)_3]^+$. *J. Am. Chem. Soc. 123*, 3135–3136.

(34) Jaouen, G., Top, S., Vessieres, A., and Alberto, R. (2000) New paradigms for synthetic pathways inspired by bioorganometallic chemistry. *J. Organomet. Chem. 600*, 23–26.

BC800001G

Synthesis and Proteomic Activity Evaluation of a new Isotope-Coded Affinity Tagging (ICAT) Reagent

Annalisa Guaragna,* Angela Amoresano, Vittoria Pinto, Gianluca Monti, Guido Mastrobuoni, Gennaro Marino, and Giovanni Palumbo

Dipartimento di Chimica Organica e Biochimica Università di Napoli Federico II Via Cinthia, 4 I-80126 Napoli, Italy. Received January 9, 2008; Revised Manuscript Received March 4, 2008

During recent years, quantitative proteome profiling has taken advantage of incorporating the traditional stable isotope dilution analysis into global scale or discovery-based proteomic experiments that use mass spectrometers as detectors to allow the pairwise study of differently expressed proteins. Quantitative protein analysis by means of the isotope-coded affinity tag (ICAT) method and tandem mass spectrometry (MS) enables the pairwise comparison of protein expression levels in biological samples. Herein, a modified ICAT reagent, named BAA-ICAT (*beta-alanine-arm*-ICAT) in which the polyether linker is replaced by a more water-soluble polyamide one, was investigated.

INTRODUCTION

Biological sciences are currently experiencing a sort of paradoxical situation in which the protein sequence, the corresponding coding gene, its chromosomic localization, or even the regulation mechanisms may have been elucidated but the biological role of the protein in the cell is still completely obscure. The static nature of the genome, in fact, cannot be compared to the dynamic properties of the proteome; protein expression profiles change several times during the cell cycle and are heavily affected by a number of intra- and extracellular stimuli (temperature, stress, apoptotic signals, etc.) (*1–6*). Moreover, the occurrence of alternative splicing and post-translational modifications led to a complete rethinking of the old paradigm "one gene−one protein". The key to understanding proteins and their behavior in biological systems lies in dramatically improving the analysis of the proteome. However, several classes of proteins, in particular, low-abundance proteins, remain difficult to characterize using standard proteomics techniques.

The driving technology nowadays supporting proteomic investigations is usually mass spectrometry (*7*); often the interest is not only in the identification of a peptide, but also in its quantification. To permit a global characterization of the proteome with more rapid and more detailed investigation, a great deal of intellectual effort has been focused on developing innovative methods (*8, 9*), including staining of proteins separated by two-dimensional polyacrylamide gel electrophoresis (2D-PAGE) (*10*) and their quantitation by fluorescence intensity measurement (*11*) and heavy-isotope-coded affinity tags (ICAT) (*12, 13*). The latter holds several advantages over the gel-based protein quantifications in terms of convenience, reduction in process time, accuracy, and throughput. The ICAT strategy is based on the utilization of isotopically labeled chemical probes (ICAT, Figure 1) which interact with a specific set of proteins and allow the identification of proteins and a quantitative comparison of protein abundances between complex proteomes. ICAT reagent comprises three functional elements:

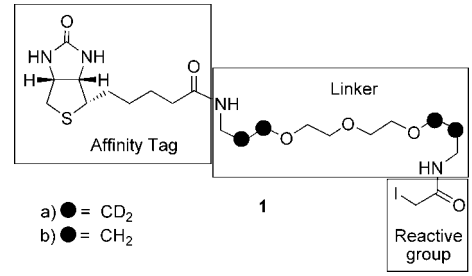

Figure 1. ICAT reagent in "heavy" (1a) or "light" (1b) form.

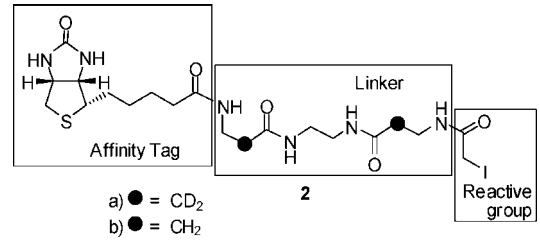

Figure 2. β-alanine-arm-ICAT (BAA-ICAT) structure.

(a) a specific reactive group able to covalently bind a nucleophile active site (e.g., primary alkyl iodide for covalent bond to SH groups of peptide cysteine residues); (b) an ethylene glycol linker that occurs in a "heavy" (see 1a) or "light" (see 1b) form and provides the basis for accurate quantification by MS spectrometry; (c) a biotin group that enables the isolation of the tagged peptides from complex peptide mixtures via avidin affinity chromatography.

This approach makes use of the principle of isotope dilution for analysis. For the quantitative analysis, two proteomes in two different states (e.g., normal and disease state) are labeled with the "light" (nondeuterated) and "heavy" (deuterated) ICAT reagent, respectively. For the quantitative comparison between two proteomes in two different states (e.g., normal and disease state), the "light" (nondeuterated) ICAT reagent is used to covalently tag proteins of one proteome and the "heavy" (deuterated) ICAT reagent is used to covalently tag proteins of a second proteome. The two proteomes are then combined for quantitative analysis. Analysis often involves further steps such

* To whom correspondence should be addressed. Dipartimento di Chimica Organica e Biochimica Università di Napoli Federico II Via Cinthia, 4 I-80126 Napoli, Italy; Phone (+39) 081 674 118. Fax: (+39) 081 674 119. E-mail: guaragna@unina.it.

10.1021/bc800010b CCC: $40.75 © 2008 American Chemical Society
Published on Web 04/12/2008

Scheme 1. Synthesis of β-Alanine-Arm-ICAT (BAA-ICAT) Reagents

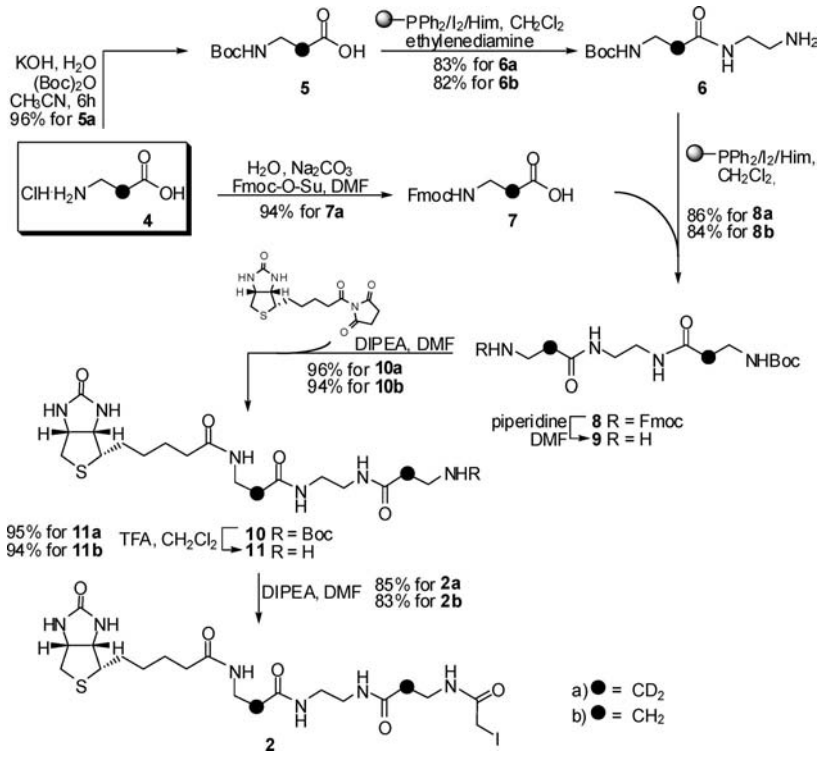

as digestion of the mixture with a protease (e.g., trypsin), isolation of the ICAT-labeled peptides by affinity purification on avidin, and analysis of the isolated labeled peptide mixture by liquid chromatography–mass spectrometry (LC/MS). Prior mixing of proteins that have been labeled with either "light" or "heavy" ICAT reagents eliminates many of the potential experimental errors associated with postlabeling analysis. ICAT analysis profiles the relative amounts of cysteine-containing peptides derived from tryptic digests of protein extracts, leading to a deeper analysis of a proteome. A nice feature of the ICAT approach is that the in vitro incorporation of a stable isotope into one of the two samples being compared obviates the need to analyze by mass spectrometry the control and experimental samples separately.

Recently, the newest ICAT reagent (Applied Biosystems) has been introduced. This reagent has a thiol-specific reactive group adjacent to an alkyl linker, which contains either nine [^{12}C] or nine [^{13}C] atoms—thus resulting in a mass difference of 9 Da between the control and the corresponding experimental version of the same tryptic peptide (*14*). Compared with the first-generation ICAT reagent, the new cleavable reagent resulted in improved sequence information and gave higher-confidence quantitation in a single experiment. The alkyl linker in the ICAT reagent is connected to a (cleavable) biotin group which allows rapid affinity isolation of cysteine-containing tryptic peptides. Incorporation of ^{13}C into the ICAT heavy reagent molecule promotes coelution of the heavy and light isotopes in reversed-phase chromatography, thereby increasing accuracy of quantification measurements by mass spectrometry. In spite of the intriguing features of the above reagent, the high synthetic cost somewhat reduces its wide applicability.

In this context, a new ICAT reagent, namely, *beta-alanine-arm*-ICAT (BAA-ICAT), has been designed (Figure 2) by a straightforward and convenient synthetic procedure, which keeps most of the advantages from the last ICAT versions (such as high accuracy in analysis and similar chromatographic behavior of the light and heavy forms).

EXPERIMENTAL PROCEDURES

General Methods and Materials. All reagents were used as purchased without further purification except for iodoacetic anhydride purified by recrystallization (petroleum ether/ethyl ether, 7:3). All moisture-sensitive reactions were carried out under a positive pressure of N_2 using oven-dried glassware. Anhydrous DMF was distilled from BaO; anhydrous DCM was distilled from P_2O_5. Triphenylphosphine polymer-bound was purchased from Fluka Chemical Co. and dried under high

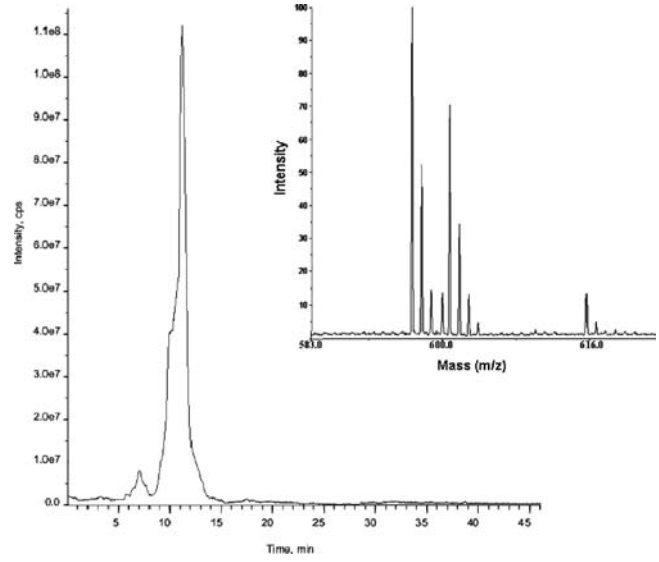

Figure 3. Total ion current chromatogram of the ES/MS analysis carried out on an equimolar mixture of light and heavy BAA-ICAT. Inset: Electrospray mass spectrum of HPLC eluting fraction. The molecular ions are indicated.

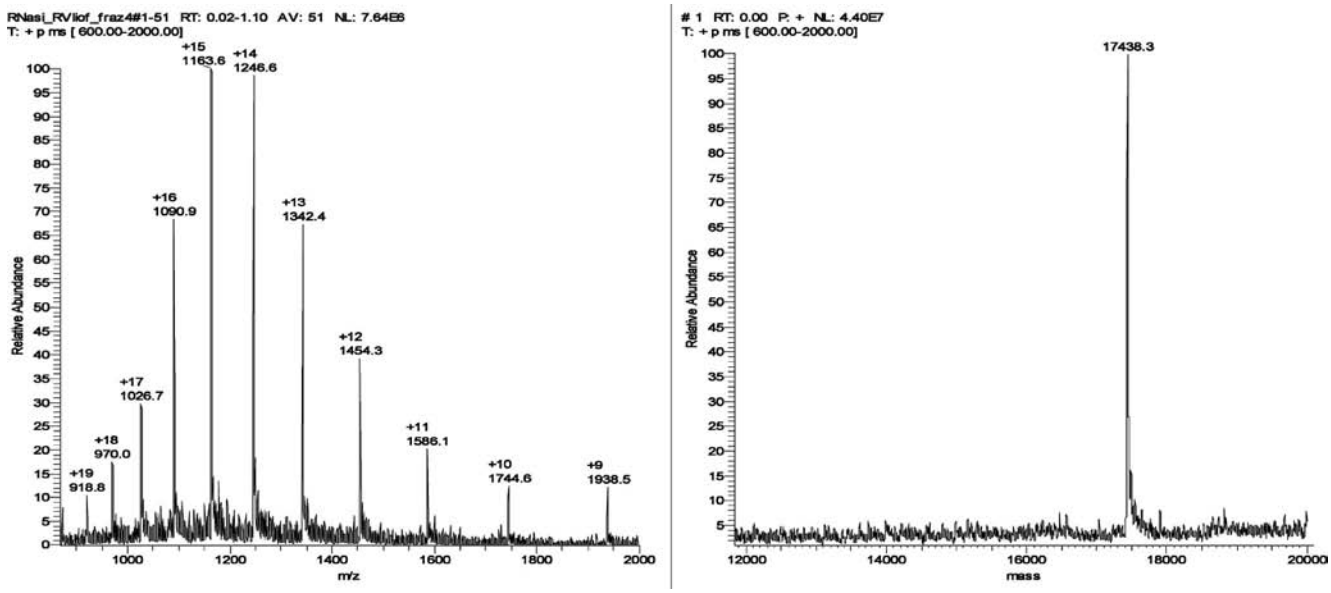

Figure 4. Electrospray analysis of BAA-ICAT labelled RNAase. (left) multicharged spectrum. (right) multicharged spectrum deconvolution. The absence of molecular weights different from 17438.3 shows specific and complete labeling of SH residues.

Table 1. MALDIMS and ESMSMS Analysis of the Tryptic Peptides Modified by BAA-ICAT Labeling

$[M + H]^+$, *m/z*	sequence[a]	peptide
1002.5	NVA*C*K	62–66
1327.0	YPN*C*AYK	92–98
1482.2	STMSITD*C*R	77–85
3340.5	*C*KPVNTFVHESLADVQAV*C*SQK	40–61
3636.0	HIIVA*C*EGNPYVPVHFDASV	105–124
3109.0	NGQTN*C*YQSYSTMSITD*C*R	67–85
2776.8	QHMDSSTSAASSSNY*C*NQMMK	11–31

[a] Modified cysteine residues were inferred by ESMSMS analysis.

vacuum at 70 °C. Thin layer chromatography (TLC) was performed using Silica Gel 60 F254, Merck plates; visualization was achieved by inspection under UV light or with ninhydrin spray. Silica gel column chromatography was performed using Merck Kieselgel 60 (70–230 mesh). Melting points were measured with a capillary apparatus and are uncorrected. ^{1}H and ^{13}C NMR spectra were recorded with the following instruments: Varian Gemini 200, Varian Gemini 300 MHz, and Bruker DRX (400 MHz) spectrometers. ESI-MS: Waters Micromass ZQ were recorded in positive mode. HRMS-EI: Micromass Q-TOF micro.

Heavy and Light BAA-ICAT Synthesis and Characterization. *Preparation of 2,2-^{2}H-β-alanine (**4a**).* A magnetically stirred solution of pure 2,2-^{2}H-*N*-Boc-3-amino-proprionitrile (prepared according to ref (*15*)) (2.5 g, 14.5 mmol) in dioxane (20 mL) and conc aq hydrogen chloride (20 mL) was heated under reflux for 8 h. After cooling, to the solution aq $NaHCO_3$ until pH ∼ 8 (50 mL) was added and extracted with Et_2O (3 × 50 mL). The organic layer was then washed with water until neutral, dried (Na_2SO_4), and evaporated under reduced pressure to afford pure **4a** as a crystalline white solid (1.2 g, yield 93%): mp 122.2–124.4 °C. ^{1}H NMR (200 MHz, D_2O): δ 3.28 (bs, 2H, CH_2N). ^{13}C NMR (50 MHz, D_2O): ppm 34.5 (CD_2), 37.4, 179.3. ESI-MS: *m/z* = 150.04 $[M + Na]^+$. HRMS: calcd for $C_3H_6D_2ClNO_2$ 127.0369, found 127.0375.

*Compound **6a.*** To a magnetically stirred suspension of dry polystyryl diphenyl phosphine (2.0 g, ∼6.2 phosphine units) in anhydrous CH_2Cl_2 (15 mL) at room temperature, a solution of I_2 (1.57 g, 6.2 mmol) in the same solvent (20 mL) was added dropwise in the dark and under dry nitrogen atmosphere. After 15 min, imidazole (1.68 g, 24.8 mmol) and solid dideuterated 2,2-^{2}H-*N*-Boc-β-alanine (**5a**) (1.0 g, 5.2 mmol, prepared using standard conditions) were added in one portion to the suspension. The reaction was kept at room temperature for 3 h (TLC monitoring: $CHCl_3/CH_3OH$, 8:2) until all the starting amino acid was completely consumed. Then, ethylenediamine (5.2 mL, 78.0 mmol) was added in one portion to the mixture. After 1 h, the reaction mixture was filtered through a glass sintered funnel and washed with CH_2Cl_2. The filtrate was treated with a 5 N solution of $Na_2O_3S_2$ (20 mL) and the organic layer washed with brine until neutral. The combined water layers were re-extracted several times with a mixture of CH_2Cl_2/MeOH (95:5). The organic layers were dried (Na_2SO_4) and evaporated under reduced pressure to afford the pure dideuterated **6a** (83% yield): oil. ^{1}H NMR (400 MHz, $CDCl_3$): δ 1.43 (s, 9H, Boc-CH_3), 2.80 (bs, 2H, CH_2N), 3.20–3.45 (m, 4H, 2 × CH_2N), 4.06 (bs, 2H, NH_2), 5.50 (bs, 1H, NH), 7.04 (bs, 1H, NH). ^{13}C NMR (100 MHz, $CDCl_3$): ppm 28.3, 36.1 (CD_2), 36.6, 41.0, 41.7, 79.1, 156.2, 172.1. ESI-MS: *m/z* 234.20 $[M + H]^+$. HRMS: calcd for $C_{10}H_{19}D_2N_3O_3$ 233.1708, found 233.1702.

*Compound **6b.*** Prepared under the same conditions reported above starting from a commercial sample of **5b** and ethylenediamine. (82% yield): mp 140.5–142.6 °C. ^{1}H NMR (200 MHz, $CDCl_3$): δ 1.38 (s, 9H, Boc-CH_3), 1.62 (bs, 2H, NH_2), 2.32 (t, *J* = 6.8 Hz, 2H, CH_2CO), 2.76 (t, *J* = 6.8 Hz, 2H, CH_2N), 3.20–3.42 (m, 4H, 2 × CH_2N), 5.52 (bs, 1H, NH), 6.78 (bs, 1H, NH). ^{13}C NMR (50 MHz, $CDCl_3$): ppm 28.2, 36.2, 36.7, 41.2, 41.9, 79.2, 156.2, 171.9. ESI-MS: *m/z* 232.19 $[M + H]^+$. HRMS: calcd for $C_{10}H_{21}O_3N_3$ 231.1583, found 231.1590.

*Compound **8a.*** To a magnetically stirred suspension of dry polystyryl diphenyl phosphine (1.2 g, ∼3.8 phosphine units) in anhydrous CH_2Cl_2 (10 mL) at r.t., a solution of I_2 (0.96 g, 3.8 mmol) in the same solvent (15 mL) was added dropwise in the dark and under dry nitrogen atmosphere. After 15 min, imidazole (1.0 g, 15.2 mmol) and **7a** (1.0 g, 3.2 mmol, prepared using standard conditions) were added in one portion to the suspension. The reaction was kept at room temperature for 3 h (TLC monitoring: $CHCl_3/CH_3OH$, 8:2) until all the starting amino acid was completely consumed. Then, **6a** (0.67 g, 3.5 mmol) was added in one portion to the mixture. After 12 h, the reaction mixture was filtered through a glass sintered funnel and washed with a mixture of CH_2Cl_2/MeOH (95:5). The filtrate was treated with a 5 N solution of $Na_2O_3S_2$ (20 mL) and the organic layer washed with brine until neutral. The organic layers dried (Na_2SO_4)

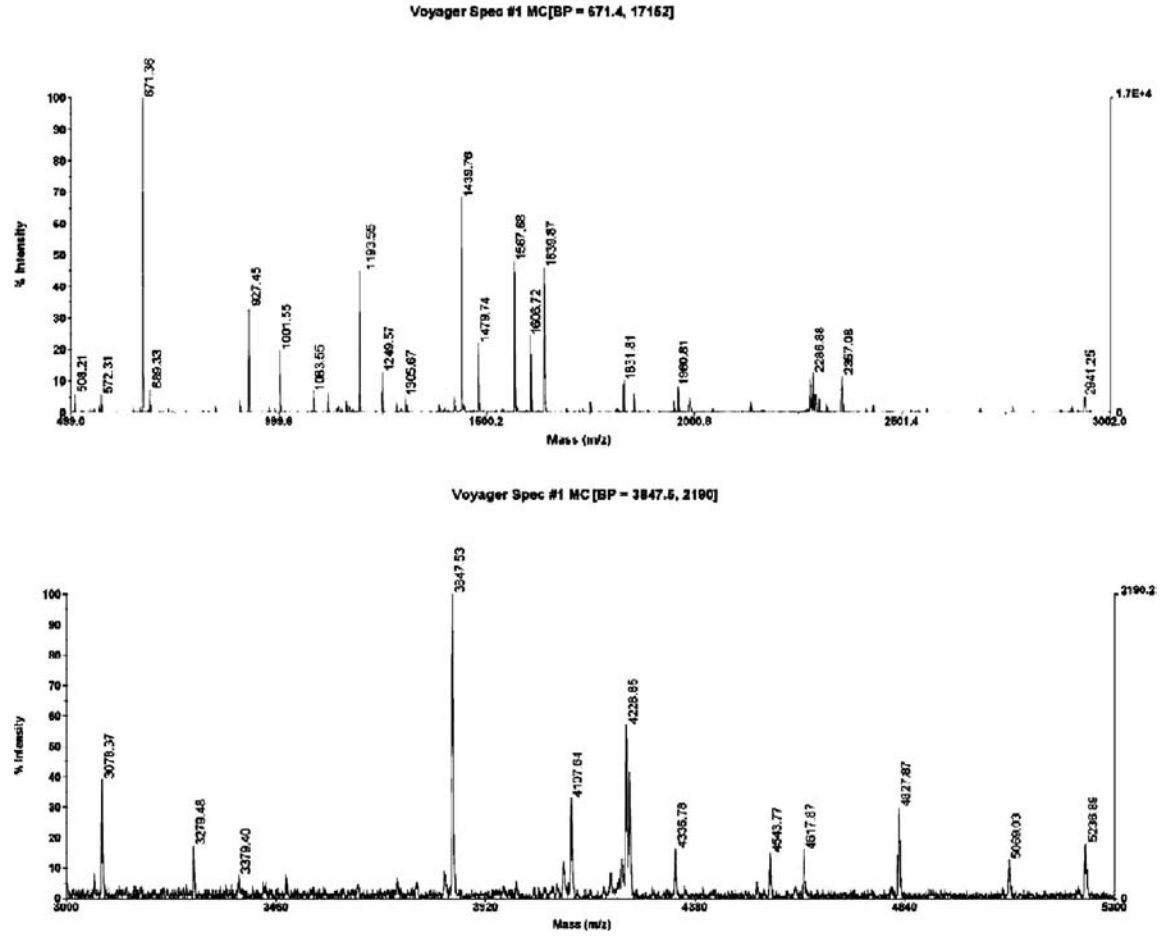

Figure 5. MALDIMS spectrum of triptic BSA digest modified with BAA-ICAT.

and evaporated under reduced pressure afforded a crude product which was purified by crystallization (from EtOAc) giving the pure dideuterated **8a** (1.5 g, 86% yield): mp 137.2–138.7 °C. ^{1}H NMR (200 MHz, $CDCl_3$): δ 1.38 (s, 9H; Boc-CH_3), 2.78 (t, J = 6.8 Hz, 2H; CH_2N), 2.90–3.00 (m, 2H; CH_2N), 3.01–3.18 (m, 1H, Fmoc-CH), 4.24–4.42 (m, 6H; 2 × CH_2N, Fmoc-CH_2), 4.10 (bt, 1H; NH), 5.34 (bs, 1H; NH), 6.65 (bs, 1H; NH), 7.22–7.43 (m, 4H; arom-H), 7.56 (d, J = 7.3 Hz, 2H; arom-H), 7.76 (d, J = 7.0 Hz, 2H; arom-H). ^{13}C NMR (50 MHz, $CDCl_3$): ppm 28.2, 35.8 (CD_2 weak multiplet), 36.7 (CD_2 weak multiplet), 38.6, 39.5, 40.2, 40.7, 77.6, 79.1, 109.7, 120.0, 121.4, 127.2, 128.9, 137.4, 139.4 (12 C), 155.4, 157.2, 170.5, 171.5. ESI-MS: m/z 529.32 $[M + H]^+$. HRMS: calcd for $C_{28}H_{32}D_4O_6N_4$ 528.2886, found 528.2895.

*Compound **8b.*** Prepared under the same conditions reported above starting from **6b** and a commercial sample of **7b**. (84% yield), mp 130.5–132.3 °C. ^{1}H NMR (200 MHz, $CDCl_3$): δ 1.38 (s, 9H; Boc-CH_3), 2.09–2.23 (m, 4H, 2 × CH_2CO), 2.80 (t, J = 6.8 Hz, 2H; CH_2N), 2.89–3.00 (m, 2H; CH_2N), 3.02–3.16 (m, 1H, Fmoc-CH), 4.22–4.40 (m, 6H; 2 × CH_2N, Fmoc-CH_2), 4.11 (bt, 1H; NH), 5.33 (bs, 1H; NH), 6.64 (bs, 1H; NH), 7.21–7.44 (m, 4H; arom-H), 7.57 (d, J = 7.3 Hz, 2H; arom-H), 7.77 (d, J = 7.0 Hz, 2H; arom-H). ^{13}C NMR (50 MHz, DMSO-d_6): ppm 28.3, 35.6, 36.9, 38.7, 39.4, 40.4, 40.5, 77.5, 79.0, 109.9, 120.2, 121.5, 127.5, 128.8, 137.5, 139.6 (12 C), 155.4, 157.2, 170.4, 171.5. ESI-MS: m/z 525.29 $[M + H]^+$. HRMS: calcd for $C_{28}H_{36}N_4O_6$ 524.2635, found 524.2630.

*Compound **9a.*** To a solution 5% piperidine solution in *N*,*N*-dimethylformamide (DMF) (15 mL) **8a** (1.4 g, 2.6 mmol) is added at room temperature. After 2 h, the solvent was evaporated under reduced pressure to afford a crude product which was purified by silica gel column chromatography ($CHCl_3$/CH_3OH, 8:2) to give the pure **9a** (0.77 g, 95% yield): mp 129.4–131.0 °C. ^{1}H NMR (200 MHz, $CDCl_3$): δ 1.43 (s, 9H; Boc-CH_3), 1.78 (bs, 2H; NH_2), 3.10 (s, 2H; CH_2N), 3.38–3.44 (m, 6H; 3 × CH_2N), 5.45 (bt, J = 5.6 Hz, 1H; NH), 6.78 (bs, 1H; NH), 7.50 (bs, 1H; NH). ^{13}C NMR (50 MHz, $CDCl_3$): ppm 28.4, 36.6 (CD_2 weak multiplet), 37.7 (CD_2 weak multiplet), 39.3, 40.1, 79.4, 156.0, 172.2, 173.5. ESI-MS: m/z 329.34 $[M + Na]^+$. HRMS: calcd for $C_{13}H_{22}D_4O_4N_4$ 306.2205, found 306.2213.

*Compound **9b.*** Prepared under the same conditions reported above starting from **8b**. (96% yield), mp 127.8–129.3 °C. ^{1}H NMR (200 MHz, $CDCl_3$): δ 1.40 (s, 9H, Boc-CH_3), 1.80 (bs, 2H; NH_2), 2.14–2.40 (m, 4H; 2 × CH_2CO), 2.90–3.13 (m, 2H; CH_2N), 3.38–3.45 (m, 6H; 3 × CH_2N), 5.45 (bt, J = 6.0 Hz, 1H; NH), 6.78 (bs, 1H; NH), 7.70 (bs, 1H; NH). ^{13}C NMR (50 MHz, $CDCl_3$): ppm 28.2, 36.3, 37.9, 39.2, 39.9, 79.3, 156.1, 172.1, 173.3. ESI-MS: m/z 325.25 $[M + Na]^+$. HRMS: calcd for $C_{13}H_{26}O_4N_4$ 302.1954, found 302.1949.

*Compound **10a.*** To a magnetically stirred solution of biotin succinimidyl ester (0.70 g, 2.3 mmol) in anhydrous DMF (5 mL) at room temperature and under nitrogen atmosphere, *N*,*N*-diisopropylethylamine (0.39 mL, 0.05 mmol) and **9a** (15 mg, 0.05 mmol) were added. After 5 h (TLC: $CHCl_3$/MeOH, 8:2), the solvent was removed under reduced pressure to afford a crude product which was purified by crystallization (from $CHCl_3$) giving the pure **10a** (1.2 g, 96% yield). mp 230.0 °C dec. ^{1}H NMR (200 MHz, CD_3OD): δ 1.44 (s, 9H; Boc-CH_3), 1.52–1.79 (m, 6H; 3 × CH_2), 2.18 (t, J = 7.3 Hz, 2H; CH_2CO), 2.71 (d, J = 12.7 Hz, 1H; CH_aS), 2.92 (dd, J = 4.8 Hz, J = 12.7 Hz, 1H; CH_bS), 3.20–3.25 (m,

Table 2. MALDIMS Analysis of BAA-ICAT Identified BSA Peptides

$[M + H]^+$, *m/z*				$[M + H]^+$, *m/z*			
observed	calculated	peptide	number of Cys residue	observed	calculated	peptide	number of Cys residue
508.21	508.25	205–208	0	1960.81	1960.66	475–483	2
572.31	572.36	195–198	0	1988.81	1988.65	436–444	2
649.30	649.33	181–185	0	2044.95	2045.03	144–159	0
665.34	665.38	132–136	0	2113.92	2113.76	276–285	2
689.39	689.37	212–217	0	2135.94	2135.91	445–458	1
817.45	817.49	428–435	0	2135.94	2135.92	485–499	1
847.46	847.50	218–224	0	2279.13	2279.11	459–474	1
906.44	906.47	181–187	0	2285.88	2285.75	52–64	2
927.45	927.49	137–143	0	2292.01	2292.00	484–499	1
990.53	990.36	484–487	1	2300.98	2300.68	82–93	2
1001.55	1001.59	209–217	0	2300.98	2301.08	317–335	0
1014.57	1014.62	525–533	0	2319.02	2319.31	205–224	0
1078.53	2424.21	2–10	0	2319.02	2319.00	505–520	1
1083.55	1083.60	137–144	0	2355.07	2355.17	188–204	1
1117.50	1117.43	199–204	1	2355.07	2354.94	274–285	2
1142.67	1142.71	524–533	0	2431.05	2431.05	115–131	1
1163.58	1163.63	42–51	0	2559.14	2559.14	115–132	1
1169.57	1169.50	174–180	1	2688.22	2688.24	505–523	1
1193.55	1193.60	1–10	0	2766.21	2766.22	378–396	1
1249.57	1249.62	11–20	0	2816.28	2816.33	505–524	1
1283.67	1283.71	337–347	0	2882.24	2882.28	485–504	1
1305.67	1305.72	378–388	0	2903.35	2903.34	21–41	1
1308.64	1308.73	534–544	0	2909.24	2909.27	500–520	1
1309.64	1309.56	459–465	1	2940.26	2939.98	82–98	2
1386.68	1386.62	197–204	1	2940.26	2940.30	389–409	1
1399.62	1399.69	545–556	0	2952.22	2952.25	94–114	1
1439.76	1439.81	336–347	0	3077.40	3077.41	115–136	1
1445.70	1445.55	99–106	1	3278.48	3278.51	500–523	1
1445.70	1445.76	133–143	0	3406.60	3406.60	500–524	1
1479.74	1479.52	389–396	1	3430.40	3430.36	42–64	1
1479.74	1479.80	397–409	0	3481.38	3481.18	243–261	3
1567.68	1567.74	323–335	0	3845.53	3845.40	240–261	3
1573.80	1573.85	132–143	0	3985.76	3985.88	115–143	1
1606.72	1606.67	199–208	1	4105.60	4105.55	436–458	3
1639.87	1639.94	413–427	0	4226.86	4227.00	378–409	1
1692.85	1692.94	225–239	0	4233.71	4233.64	475–499	3
1723.76	1723.84	323–336	0	4333.70	4333.83	286–316	2
1731.78	1731.84	144–156	0	4512.74	4512.66	351–377	3
1750.88	1750.97	218–232	0	4615.94	4615.86	233–261	3
1830.81	1830.77	65–76	1	4824.88	4824.88	348–377	3
1854.76	1854.72	262–273	1	5067.03	5067.17	286–322	2
1950.94	1950.90	459–471	1	5233.90	5233.91	82–114	3

1H; CHS), 3.25–3.37 (m, 6H; 3 × CH_2N), 3.46 (bs, 2H; CH_2N), 4.30 (dd, $J = 4.8$ Hz, $J = 7.8$ Hz, 1H; CHN), 4.49 (dd, $J = 4.8$ Hz, $J = 7.8$ Hz, 1H; CHN). ^{13}C NMR (75 MHz, CD_3OD): ppm 27.2, 28.3, 29.8, 30.0, 33.2, 37.0 (CD_2 weak multiplet), 37.2, 37.3 (CD_2 weak multiplet), 38.7, 40.1, 40.6, 41.3, 57.2, 61.9, 63.6, 79.9, 156.5, 163.3, 172.5, 172.6, 176.3. ESI-MS: *m/z* 533.36 $[M + H]^+$. HRMS: calcd for $C_{23}H_{36}D_4N_6O_6S$ 532.2981, found 532.2987.

*Compound **10b.*** Prepared under the same conditions reported above starting from biotin succinimidyl ester and **9b**. (94% yield), mp 220.4 °C dec. ^1H NMR (200 MHz, CD_3OD): δ 1.43 (s, 9H, Boc-CH_3), 1.53–1.78 (m, 6H; 3 × CH_2), 2.20 (t, $J = 7.3$ Hz, 2H; CH_2CO), 2.34 (t, $J = 6.7$ Hz, 2H; CH_2CO), 2.38 (t, $J = 6.8$ Hz, 2H; CH_2CO), 2.70 (d, $J = 12.7$ Hz, 1H; CH_aS), 2.93 (dd, $J = 4.8$ Hz, $J = 12.7$ Hz, 1H; CH_bS), 3.18–3.23 (m, 1H; CHS), 3.24–3.37 (m, 6H; 3 × CH_2N), 3.45 (dt, $J = 2.7$ Hz, $J = 6.8$ Hz, 2H; CH_2N), 4.30 (dd, $J = 4.8$ Hz, $J = 8.0$ Hz, 1H; CH_aN), 4.49 (dd, $J = 4.8$ Hz, $J = 7.8$ Hz, 1H; CH_bN). ^{13}C NMR (75 MHz, CD_3OD): ppm 27.1, 28.3, 29.6, 30.2, 33.3, 37.2, 37.3, 37.4, 38.6, 40.2, 40.7, 41.4, 57.3, 61.8, 63.7, 79.8, 156.4, 163.2, 172.4, 172.5, 176.4. ESI-MS: *m/z* 529.36 $[M + H]^+$. HRMS: calcd for $C_{23}H_{40}N_6O_6S$ 528.2730, found 528.2738.

*Compound **11a.*** To a magnetically stirred solution of **10a** (1.1 g, 2.0 mmol) in CH_2Cl_2 (15 mL), at room temperature, TFA was added (7.5 mL). After 1 h (TLC: $CHCl_3$/MeOH 8:2), the solvent was removed under reduced pressure to afford a crude product which was purified by crystallization (from Et_2O) to give the pure **11a** (0.85 g, 95% yield): mp 119.0–120.2 °C dec. ^1H NMR (400 MHz, CD_3OD): δ 1.52–1.78 (m, 6H; 3 × CH_2), 2.20 (t, $J = 7.3$ Hz, 2H; CH_2CO), 2.70 (d, $J = 12.7$ Hz, 1H; CH_aS), 2.93 (dd, $J = 4.8$ Hz, $J = 12.7$ Hz, 1H; CH_bS), 3.16–3.22 (m, 1H; CHS), 3.25–3.36 (m, 6H; 3 × CH_2N), 3.43 (bs, 2H; CH_2N), 4.30 (dd, $J = 4.4$ Hz, $J = 7.8$ Hz, 1H; CHN), 4.48 (dd, $J = 4.3$ Hz, $J = 7.8$ Hz, 1H; CHN). ^{13}C NMR (75 MHz, CD_3OD): ppm 27.1, 29.7, 30.1, 33.1, 37.1 (CD_2 weak multiplet), 37.3, 37.4 (CD_2 weak multiplet), 37.5, 40.1, 40.5, 41.2, 57.3, 61.8, 63.5, 163.3, 172.4, 172.6, 176.4. ESI-MS: *m/z* 433.30 $[M + H]^+$. HRMS: calcd for $C_{18}H_{28}D_4N_6O_4S$ 432.2457, found 432.2452.

*Compound **11b.*** Prepared under the same conditions reported above starting from **10b**. (94% yield), mp 116.8–118.0 °C. ^1H NMR (400 MHz, CD_3OD): δ 1.52–1.78 (m, 6H; 3 × CH_2), 2.20 (t, $J = 7.3$ Hz, 2H; CH_2CO), 2.38 (t, $J = 6.8$ Hz, 2H; CH_2CO), 2.58 (t, $J = 6.4$ Hz, 2H; CH_2CO), 2.70 (d, $J = 12.7$ Hz, 1H; CH_aS), 2.93 (dd, $J = 4.8$ Hz, $J = 12.7$ Hz, 1H; CH_bS), 3.16–3.22 (m, 1H; CHS), 3.25–3.36 (m, 6H; 3 × CH_2N), 3.43 (dt, $J = 6.8$ Hz, $J = 2.7$ Hz, 2H; CH_2N), 4.30 (dd, $J = 4.4$ Hz, $J = 7.8$ Hz, 1H; CHN), 4.48 (dd, $J = 4.4$ Hz, $J = 7.8$ Hz, 1H; CHN). ^{13}C NMR (75 MHz, CD_3OD): ppm 27.2, 29.8, 30.0, 33.3, 37.0, 37.2, 37.3, 37.5, 40.0, 40.7, 41.4, 57.1, 61.7, 63.6,

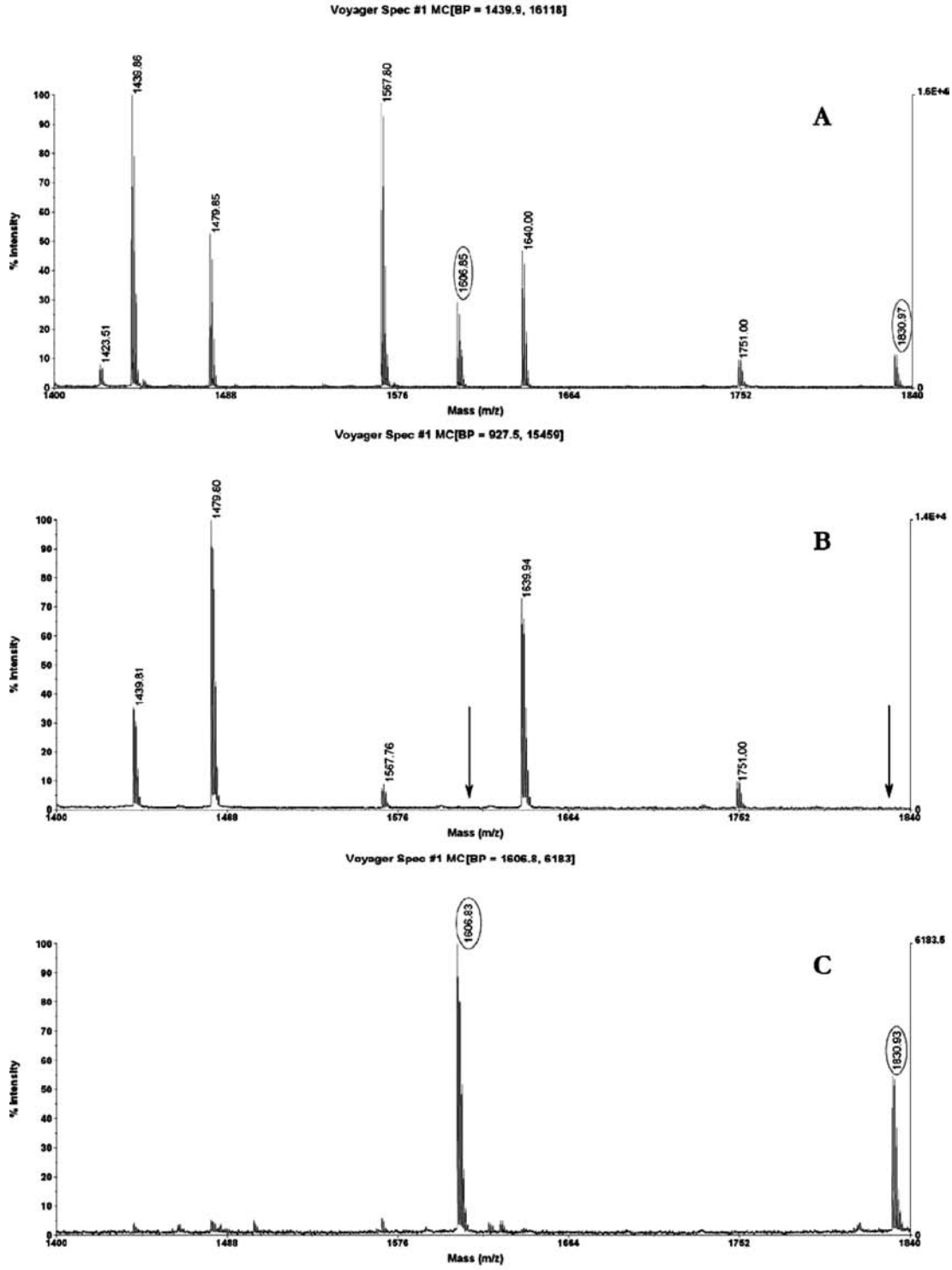

Figure 6. MALDIMS spectrum of BSA digest before (panel A) and after (panel C) affinity purification step. The MALDIMS spectrum of the supernatant after the purification step is showm in panel B. Modified peptides are indicated by a circle. The arrows indicate the disappearance of modified peptide after the affinity chromatography step.

163.3, 172.5, 172.6, 176.3. ESI-MS: *m/z* 429.25 $[M + H]^+$. HRMS: calcd for $C_{18}H_{32}N_6O_4S$ 428.2206, found 428.2210.

Compound ***2a.*** To a magnetically stirred solution of **11a** (0.80 g, 1.8 mmol) in anhydrous DMF (5 mL) at room temperature and under nitrogen atmosphere *N*,*N*-diisopropylethylamine (0.64 mL, 3.7 mmol) and iodoacetic anhydride (1.3 g, 3.7 mmol) were added. After 3 h (TLC: $CHCl_3$/MeOH = 8:2), the solvent was removed under reduced pressure to afford a crude product which was purified by crystallization (from $Et_2O/CHCl_3$) giving the pure **2a** (0.95 g, 85% yield): mp 210.3 °C dec. ^{1}H NMR (200 MHz, D_2O): δ 1.25–1.63 (m, 6H; 3 × CH_2), 2.10 (t, J = 7.2 Hz, 2H; CH_2CO), 2.65 (d, J = 13.0 Hz, 1H; CH_aS), 2.75 (dd, J = 4.7 Hz, J = 13.0 Hz, 1H; CH_bS), 3.15–3.22 (m, 7H; CHS, 3 × CH_2N), 3.31 (d, J = 9.4 Hz, 2H; CH_2N), 3.60 (s, 2H; CH_2I), 4.28 (dd, J = 4.4 Hz, J = 7.6 Hz, 1H; CHN), 4.48 (dd, J = 4.7 Hz, J = 7.6 Hz, 1H; CHN). ^{13}C NMR (75 MHz, D_2O): ppm 8.1, 27.3, 29.6, 30.2, 33.2, 37.3 (weak multiplet), 37.4, 37.5 (weak multiplet), 38.3, 40.1, 40.6, 41.5, 57.4, 61.7, 63.6, 163.3, 172.5, 172.7, 172.9, 176.3. ESI-MS: *m/z* 601.20 $[M + H]^+$,

Table 3. MALDIMS Analysis of Labeled Tryptic Protein Mixture

$[M + H]^+$, *m/z*				
observed	calculated	protein	peptide	numbers of cys residue
1017.44	1017.38	α-lactalbumine	59–62	1
1030.51	1030.51	lysozyme	14–21	0
1045.54	1045.53	lysozyme	117–125	0
1121.47	1121.40	α-lactalbumine	6–10	1
1150.62	1150.61	RNAase	1–10	0
1200.65	1200.65	α-lactalbumine	99–108	0
1390.76	1390.76	anhydrase	76–88	0
1404.54	1404.47	lysozyme	62–68	1
1428.64	1428.64	lysozyme	34–45	0
1460.65	1460.59	lysozyme	6–14	1
1491.67	1491.62	α-lactalbumine	6–13	1
1581.81	1581.81	anhydrase	113–125	0
1669.94	1669.94	α-lactalbumine	95–108	0
1675.79	1675.79	lysozyme	98–112	0
1709.82	1709.91	anhydrase	112–125	0
1720.76	1720.73	α-lactalbumine	1–10	1
1736.72	1736.70	lysozyme	22–33	1
1744.78	1744.74	lysozyme	115–125	1
1753.83	1753.83	lysozyme	46–61	0
1803.90	1803.89	lysozyme	97–112	0
1848.83	1847.83	α-lactalbumine	6–16	1
1902.75	1902.73	lysozyme	62–73	1
1915.78	1915.75	RNAase	86–98	1
2091.31	2090.95	α-lactalbumine	1–13	1
2140.98	2140.91	anhydrase	9–26	0
2198.21	2198.21	anhydrase	36–56	0
2253.15	2253.15	anhydrase	126–147	0
2354.29	2355.31	anhydrase	36–57	0
2510.11	2510.15	anhydrase	58–79	0
2559.47	2559.07	RNAase	86–104	1
2635.56	2635.16	RNAase	105–124	1
2715.87	2715.07	α-lactalbumine	109–123	1
2776.40	2776.00	RNAase	11–31	1
2852.47	2852.47	anhydrase	226–250	0
3108.87	3108.07	RNAase	67–85	2
3146.73	3146.33	lysozyme	22–45	1
3277.89	3278.49	RNAase	99–124	1
3339.17	3339.37	RNAase	40–61	2
3470.17	3470.62	anhydrase	58–88	0
3611.30	3610.50	RNAase	38–61	2
3742.62	3741.42	lysozyme	74–96	3
3779.91	3779.51	RNAase	2–31	1
3870.71	3869.51	lysozyme	74–97	3
4072.13	4072.13	anhydrase	111–147	0
4092.62	4091.42	RNAase	62–85	3
4918.98	4917.48	α-lactalbumine	63–93	3
5006.00	5004.81	RNAase	67–98	3
5051.32	5050.12	RNAase	34–66	3
5122.64	5122.24	α-lactalbumine	17–58	1

623.16 $[M + Na]^+$. HRMS: calcd for $C_{20}H_{29}D_4IN_6O_5S$ 600.1529, found 600.1533.

*Compound **2b.*** Prepared under the same conditions reported above starting from **11b**. (83% yield): mp 210.7 °C dec. ^1H NMR (200 MHz, D_2O): δ 1.25–1.63 (m, 6H; 3 × CH_2), 2.10 (t, J = 7.2 Hz, 2H; CH_2CO), 2.31 (t, J = 6.5 Hz, 4H; 2 × CH_2CO), 2.65 (d, J = 13.0 Hz, 1H; CH_aS), 2.75 (dd, J = 4.7 Hz, J = 13.0 Hz, 1H; CH_bS), 3.15–3.22 (m, 7H; CHS, 3 × CH_2N), 3.25–3.35 (m, 2H; CH_2N), 3.60 (s, 2H; CH_2I), 4.28 (dd, J = 4.4 Hz, J = 7.6 Hz, 1H; CHN), 4.48 (dd, J = 4.7 Hz, J = 7.6 Hz, 1H; CHN). ^{13}C NMR (75 MHz, D_2O): ppm 8.3, 27.1, 29.8, 30.0, 33.0, 37.2, 37.3, 37.4, 38.5, 40.1, 40.8, 41.5, 57.3, 61.8, 63.6, 163.3, 172.5, 172.6, 172.8, 176.4. ESI-MS: *m/z* 597.15 $[M + H]^+$, 619.12 $[M + Na]^+$. HRMS: calcd for $C_{20}H_{33}IN_6O_5S$ 596.1278, found 596.1283.

Proteomic Activity evaluation. *Materials and methods.* Carbonic anhydrase, lysozime, alpha lactalbumine, RNase A, trypsin, EDTA, iodoacetamide and *tert*-butylphosphine were purchased from Sigma and tris(hydroxymethyl)-aminoethane from Fluka. Prepacked PD-10 gel filtration cartridges were from Pharmacia. Prepacked Sep pak C18 cartridges were purchased from Waters. DHB and α-cyano-hydroxycinnamic acid were purchased from Sigma. C18 reverse phase HPLC *narrow bore* (250 × 2.1 mm, 5 μm) was from Phenomenex. Guanidinium chloride and resin conjugated with avidin was from Pierce. All other reagents and solvents were of the highest purity available from Carlo Erba.

Proteins from Pseudoalteromonas haloplanktis TAC 125. The sample of liquid culture of *P. haloplanktis* was centrifuged and the supernatant recovered. The low molecular weight fraction was then eliminated by gel filtration on PD10 columns. The purification was performed as described above in this section, but the temperature was kept at 2.0 °C to minimize proteolytic activity of proteases. The protein containing fractions were then pooled, lyophilized and stored at –20 °C till to the analysis.

Enzymatic hydrolyses. Protein solution was digested with Trypsin in 50 mm ammonium bicarbonate buffer, pH = 8.0, at 37 °C overnight, using a 1:50 w:w enzyme-to-substrate ratio. Peptide mixtures were either directly analyzed by MALDI mass spectrometry or submitted to LC-MS analysis.

MALDI MS Analyses. MALDI-TOF mass spectra were recorded using an Applied Biosystem Voyager DE-PRO instrument. A mixture of analyte and matrix solution (α-cyano-hydroxycinnamic acid 10 mg/mL in 66% acetonitrile, 0.1% TFA, in MilliQ water) was applied to the metallic sample plate and dried down at room temperature. Mass calibration was performed using external peptide standards. Raw data were analyzed using the computer software provided by the manufacturer and reported as monoisotopic masses.

Liquid Chromatography-Electrospray Tandem Mass Spectrometry (LC/ES/MS/MS). Tryptic peptide mixtures obtained from *in situ* digestions as previously described were also analyzed by "on-line" LC/ES/MS/MS using an LCQ ion trap instrument (Finnigan Corp., San José, CA). Proteolytic digests were fractionated on a HP 1100 HPLC apparatus (Hewlett-Packard, Palo Alto, CA) using a narrow-bore Phenomenex Jupiter C18 column (250 × 2.1 mm, 300 Å) (Torrance, CA) with 0.05% TFA, 5% formic acid in H_2O (solvent A), and 0.05% TFA, 5% formic acid in acetonitrile (solvent B) by means of a linear gradient from 5% to 70% solvent B in 65 min at a flow rate of 0.2 mL/min. The effluent was directly inserted into the ion source through the electrospray probe, and both ES/MS and ES/MS/MS spectra were acquired throughout the entire analysis by using the software provided with the instrument.

BAA-ICAT Derivatization. S−S bridge reduction was carried out in denaturing buffer (guanidinium chloride 6 m, Tris/HCl 300 mm, EDTA 5 mm, pH = 8.3) using 100:1 TBP/cysteine molar ratio, under nitrogen for 30 min at 37 °C. Reduced samples were derivatized with BAA-ICAT using 10:1 reactive/cysteine molar ratio under nitrogen for 2 h, at 25 °C in the dark. The sample was purified by gel filtration on a PD10 column in 10 mM AMBIC pH = 8.0. After trypsin digestion, derivatized peptides were purified by an affinity chromatography step using avidin agarose resin. The coupling step was performed in phosphate buffer 0.1 M, NaCl 0.15 m, pH = 7.2, for 2 h at room temperature under stirring. The biotinylated peptides were eluted by using a solution containing acetonitrile 50%, H_2O 50%, TFA 0.5%.

RESULTS AND DISCUSSION

Synthesis of ICAT Reagent Analogue. As a part of our ongoing program directed toward the achievement of new reagents for protein expression analysis, here we describe the synthesis and applications of a novel type of isotope-coded affinity tags (ICAT) reagents **2a** and **2b**, respectively, in "heavy" and "light" form, in which the polyether linker is replaced by

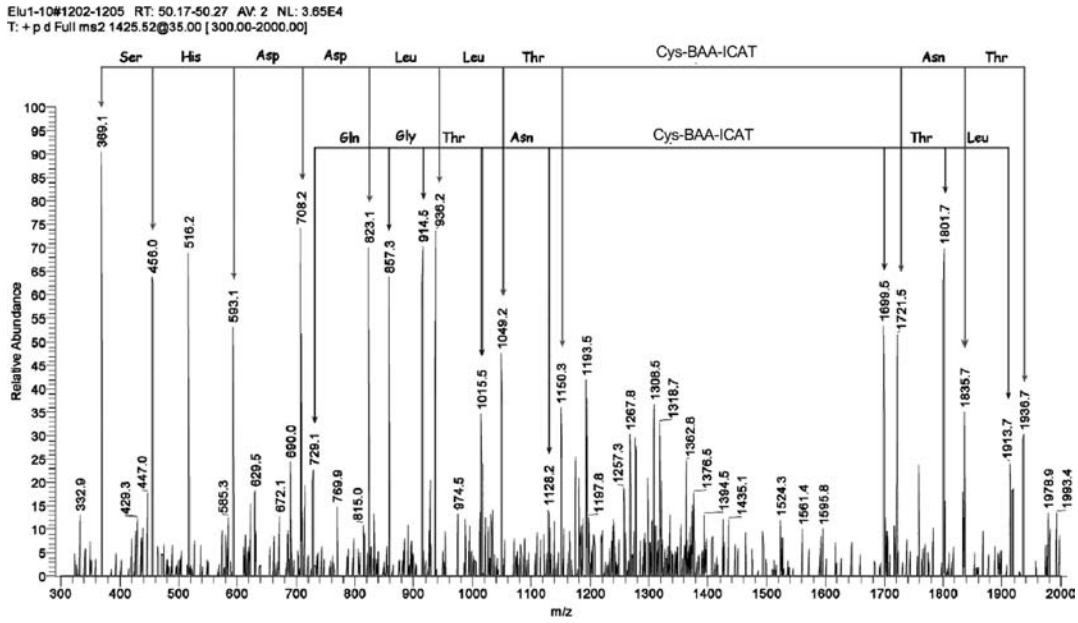

Figure 7. MSMS spectrum of the precursor ion at *m*/*z* 1425.6. Proper annotation of the fragmentations are indicated.

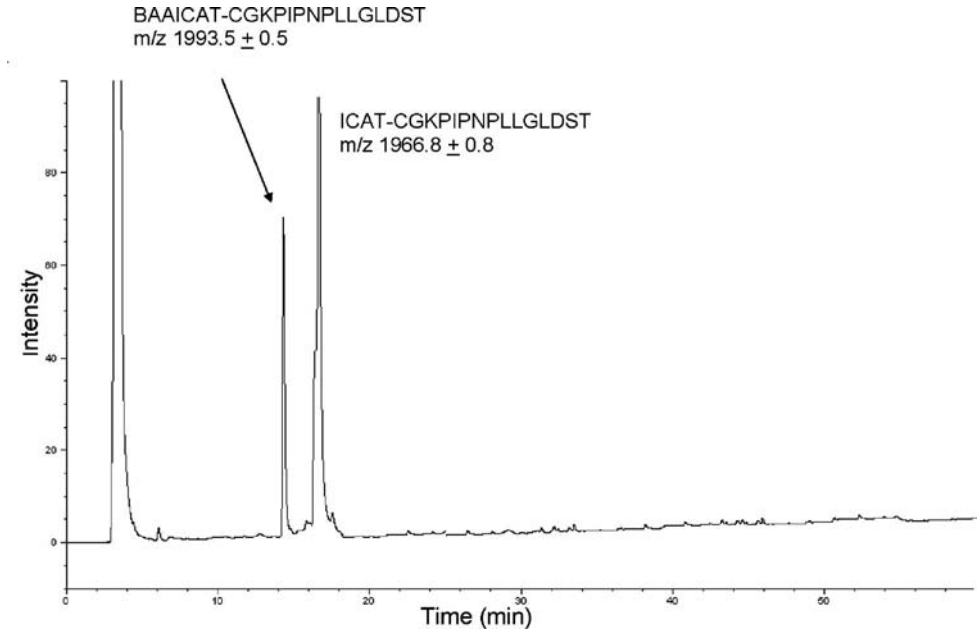

Figure 8. Total ion current profile of peptide mixture constituted of BAA-ICAT (*m*/*z* 1993.5 ± 0.5) and ICAT (*m*/*z* 1966.8 ± 0.8) derivatives.

a more water-soluble polyamide one. We introduce the acronym *beta-alanine-arm*-ICAT (BAA-ICAT) to indicate this novel reagent.

Our strategy is essentially based on the following: (i) preparation of "light" and "heavy" linkers by reaction of ethylenediamine with β-alanine and 2,2-dideuterated β-alanine, respectively; (ii) coupling reaction of activated biotin with the prepared linkers; (iii) addition of the reactive iodoacetyl group to the free amino function of biotinylated linkers.

The first step of our synthesis relies on the preparation of a linker which consists of two β-Ala units bridged by an ethylenediamine spacer. The linker was prepared in both light (d_0) and heavy (d_4) forms; the former was prepared starting from commercially available β-alanine; conversely, the latter (d_4) was obtained using a 2,2-dideuterated-β-alanine specially prepared by a suitably modified α-amino acid homologation procedure (*15*).

Our first attempts in using a free diamine linker failed due to the formation of a bis-biotinylated compound. To ensure monobiotinylation during the coupling reaction with biotin, a large molar excess of diamine linker was used. Unfortunately, the excess of unreacted linker, being quite polar, is difficult to recover from the reaction mixture and results in a significant loss of the diamine. To overcome these problems, we planned to prepare an orthogonally protected diamine linker like **8** (Scheme 1).

The synthesis of the heavy linker was then accomplished as follows. Deuterium-labeled units **5a** (2,2-^{2}H-*N*-Boc-β-alanine) and **7a** (2,2-^{2}H-*N*-Fmoc-β-alanine) were prepared in four steps (starting from commercially available α-glycine) by a suitably modified α-amino acid homologation procedure we have recently reported (*15*). The key step of our methodology is the deuterium incorporation by means of sodium borodeuteride ($NaBD_4$) during the reduction of the α-amino acid carboxylic

function, which enables us to obtain the final compound **4a** with 98% isotopic purity. The protection of the NH_2 functionality with a Boc or Fmoc group, respectively, led to heavy **5a** and **7a**. Carboxylic acid function activation of **5a**, for the amide bond formation, was accomplished by means of the *in situ* formed acyl iodide using a suspension of triphenylphosphine polymer-bound/iodine complex (polystyryl diphenyl iodophosphonium iodide) (*15, 16*) in anhydrous dichloromethane (Scheme 1).

After some minutes, ethylene diamine was added to the suspension affording the amide **6a** in 83% yield. The triphenylphosphine polymer-bound/halogen complex is a Lewis acid and a dehydrating agent widely employed in miscellaneous reactions with low environmental impact (*17*). In fact, it avoids contamination from byproducts and use of non-environmentally friendly solvents in the purification processes. Indeed, under our conditions the phosphine oxide that is linked to the polymeric matrix and imidazolium salt are the only byproducts of the reaction and can thus be easily separated by simple filtration.

The free amine **6a** was then coupled with 2,2-^{2}H-*N*-Fmoc-β-alanine **7a** using the same carboxylic acid activation procedure, so far described, leading to **8a**. Once more, no further purification was necessary; a simple filtration of the suspension allowed us to obtain the pure orthogonally protected diamine linker **8a** in 86% yield. Finally, selective removal of Fmoc protection with piperidine afforded amine **9a** in almost quantitative yield.

The light linker **9b** (d_0) was synthetized using the same synthetic protocol starting from the commercially available *N*-Boc-β-alanine (**5b**) and *N*-Fmoc-β-alanine (**7b**).

Linkers **9a**,**b** were then separately coupled to biotin in the activated form biotin succinimidyl ester in anhydrous dimethylformamide (DMF), in the presence of *N*,*N*′-diisopropylethylamine (DIPEA), to smoothly give **10a**,**b** in 96% and 94% yields, respectively. *N*-Boc protecting group removal, by treatment with TFA, led to biotinylated (d_4)-linker monoamine **11a** and to its analogue in the light form **11b**, which were finally treated with iodoacetic anhydride affording the (heavy) ICAT reagent analogue **2a** in 85% yield and the (light) reagent **2b** in 83% yield.

Specific Proteomic Activity Evaluation. The first step was based on the mass spectral analysis of light and heavy form of the reagent. Equimolar amounts of reagents (1 nmol) were mixed and submitted to LCMS analysis. As shown in Figure 3, a single peak could be observed in the TIC profile. The ESMS spectrum showed the occurrence of two signals at *m*/*z* 597.5 and 601.2 corresponding to the light and heavy forms of BAA-ICAT, respectively, thus indicating the coelution of the reagents. The mass difference within the heavy BAA-ICAT reagent (4 Da) reliably allows a good separation between the molecular ions. The light and heavy molecules are chemically identical; the isotope effect leading to the separation of the species in reversed-phase chromatography seems to be removed. The coelution of the isotopes could probably be attributed to a reduced number of deuterium atoms and to the different chemical nature (polyamide) of the BAA-ICAT. This represents an advantage of this new reagent with respect to commercial ICAT. In fact, in order to solve the isotope effect which complicated quantitation analysis, cleavable ICAT reagents were proposed (*14, 18, 19*). Moreover, the ESMS analysis revealed that the preparation of the d_4 analogue was almost homogeneous. Indeed, only 10% of the d_3 form can be detected on the basis of the isotope distribution of compound **2a** (Figure 3, inset).

In a proof of principle, the novel reagent **2a** was tested by using RNase A as the standard protein. An aliquot of protein was reduced and the eight cysteine residue modified with **2a** as previously described (*20*). The protein was purified by reverse-phase HPLC and directly analyzed by ESMS. Figure 4 shows the corresponding ES spectra transformed on a real mass scale. The analysis of the modified protein sample showed the presence of a major component whose molecular weight was measured as 17438.3 $\pm$ 0.6 Da. This value was attributed to the protein carrying eight modifying groups.

The identification of the modification sites was accomplished by employing the MALDI mapping procedure. Thus, a labeled protein sample was submitted to trypsin digestion and the resulting peptide mixture directly analyzed by MALDIMS.

Table 1 shows the mass signals recorded in the spectra that were assigned to the corresponding peptides within the enzyme sequence on the basis of their mass value and trypsin specificity, taking into account a mass increment of 468.1 Da due to the labeling moiety. The MALDI mass spectrum showed the occurrence of a series of signals attributed to the peptide fragments containing cysteine residues completely modified by the reagent. The peptide mixtures were then purified by affinity chromatography and the resulting mixture analyzed by MALDIMS, thus revealing the absence of signals corresponding to the unmodified peptides.

The fine localization of the modifying group was achieved by LCMSMS analysis of the modified peptide mixture, and the ESMSMS results are summarized in Table 1.

Similar results were obtained when the labeling procedure was carried out on bovine serum albumin, a model protein containing 35 cysteine residues. Figure 5 showed the direct MALDIMS analysis carried out on the peptide mixture. All the assignments were manually performed on the basis of the theoretical mass values of the tryptic peptides within BSA sequence and on the basis of mass increment of 468.1 Da due to the BAA-ICAT moiety. A total sequence coverage of 88% was observed by MALDIMS spectral analysis, leading to the identification of 30 BAA-ICAT modified cysteines (on a total of 35) as summarized in Table 2. No peptides carrying unmodified cysteine residues were detected.

After the affinity purification, only biotinylated species were recovered, indicating the disappearance of the unmodified peptides. As an example, Figure 6 shows an enlargement of the MALDIMS spectrum before (panel A) and after (panel C) the affinity purification step. The yield of the purification step is illustrated in panel B. The MALDIMS spectrum in fact showed the disappearance of modified Cys-containing peptides. The same analysis performed using the ICAT kit from Applied Biosystem gave similar results, allowing the identification of peptides containing 28 biotinylated cysteine residues.

Finally, a mixture of equimolar amount of four proteins (lysozyme, α-lactalbumin, RNaseA, and carbonic anhydrase) was submitted to the proposed strategy, thus leading to the enrichment and fine characterization of the labeled peptides as summarized in Table 3. As a whole, the mass spectra analyses allowed the identification of peptides containing 21 on 24 modified cysteine residues present in the protein mixture tested.

To verify the feasibility of the proposed labeling reactive, the optimized protocol was then applied on the protein sample from *Pseudoalteromonas haloplanktis* as described above. Our group has a long-standing tradition in the study of this antarctic bacterium (*21, 22*) Thus, a proteomic study could by useful in highlighting the molecular processes of this psicrophilic organism. The peptide mixture was directly analyzed by RP-HPLC/ESI-MSMS.

Here, we report preliminary results on the selective labeling of cysteine residues of the soluble secreted proteins of this bacterium. A direct database search was not possible because the *P. haloplanktis* genome is still not available on the Internet. In fact, only recently (*23*) has the genome of the latter been deciphered, but not yet annotated. However, manual interpreta-

tion of the MSMS spectra allowed us to obtain ten internal sequences of cysteine-containing peptides labeled with reagent **2a**.

As an example, we report the spectrum, properly annotated (Figure 7) and obtained by MSMS analysis performed on the precursor ion at *m*/*z* 1425.6. Manual interpretation of the tandem MS spectra led to the internal sequence SHDDLLTCNTGN showing the occurrence of a Cys residue modified with a **2a** moiety. Optimization of labeling conditions and the identification of labeled bacterial proteins by homology search are still in progress.

The labeling strategy has been tuned by using the light form of the reagent. The rational behind the choice of this reagent is its higher water solubility, thus avoiding complications arising from solubility in aqueous buffer with respect to the already proposed ICAT reagents. As an example, two aliquots of a standard Cys-containing peptide (CGKPIPNPLLGLDST, MW 1524.8) were derivatized with standard light ICAT and BAA-ICAT, respectively, and submitted to LCMS analysis. As shown in the Figure 8, a lower retention time was observed for the BAA-ICAT modified peptide (ESMS analysis: *m*/*z* 1993.5, mass shift, 468.1 Da) with respect to the peptide derivatized with ICAT reagent (ESMS analysis: *m*/*z* 1966.8, mass shift, 442.2 Da), thus indicating reduced hydrophobicity for the BAAA-ICAT with respect to the commercial ICAT.

Moreover, the synthesis has been accomplished in a few steps and in reasonable overall yield. The new residues in the sequence were shown to be stable and easily identifiable under general conditions for tandem mass spectrometric sequencing.

As further application, it would be possible to address the problem of quantification, due to the availability of the heavy form of BAA-ICAT. Quantitation analysis could be performed basically following the strategy outlined by Gygi et al. (*12*) The peptides could be quantified by measuring, in the mixture, the relative signal intensities for pairs of peptide−ions of identical sequence differentially labeled with light or heavy BAA-ICAT.

ACKNOWLEDGMENT

^{1}H and ^{13}C NMR spectra, MALDI-TOF mass spectra were performed at Centro Interdipartimentale di Metodologie Chimico-Fisiche (CIMCF), Universita‘ di Napoli Federico II.

Supporting Information Available: Experimental data and selected copies of ^{1}H NMR spectra. This information is available free of charge via the Internet at http://pubs.acs.org.

LITERATURE CITED

(1) Godovac-Zimmermann, J., and Brown, L. R. (2001) Perspectives for mass spectrometry and functional proteomics. *Mass Spectrom. Rev. 20*, 1–57.

(2) Patterson, S. D., and Aebersold, R. H. (2003) Proteomics: the first decade and beyond. *Nat. Genet. (Suppl.) 33*, 311–323.

(3) Zhu, H., Bilgin, M., and Snyder, M. (2003) Proteomics. *Annu. Rev. Biochem. 72*, 783–812.

(4) Tyers, M., and Mann, M. (2003) From genomics to proteomics. *Nature 422*, 193–197.

(5) Kirkpatrick, D. S., Gerber, S. A., and Gygi, S. P. (2005) The absolute quantification strategy: a general procedure for the quantification of proteins and post-translational modifications. *Methods 35*, 265–73.

(6) Vosseller, K., Hansen, K. C., Chalkley, R. J., Trinidad, J. C., Wells, L., Hart, G. W., and Burlingame, A. L. (2005) Quantitative analysis of both protein expression and serine/threonine post-translational modifications through stable isotope labeling with dithiothreitol. *Proteomics 5*, 388–398.

(7) Ferguson, P. L., and Smith, R. D. (2003) Proteome analysis by mass spectrometry. *Annu. Rev. Biophys. Biomol. Struct. 32*, 399–424.

(8) Cravatt, B. F., and Sorensen, E. J. (2000) Chemical strategies for the global analysis of protein function. *Curr. Opin. Chem. Biol. 4*, 663–668.

(9) Adam, G. C., Sorensen, E. J., and Cravatt, B. F. (2002) Chemical strategies for functional proteomics. *Mol. Cell. Proteomics 1*, 781–790.

(10) Gygi, S. P., Corthals, G. L., Zhang, Y., and Aebersold, R. (2000) Evaluation of two-dimensional gel electrophoresis based proteome analysis technology. *Proc. Natl. Acad. Sci. U.S.A. 97*, 9390–9395.

(11) Yan, Y., and Marriott, G. (2003) Analysis of protein interactions using fluorescence technologies. *Curr. Opin. Chem. Biol. 7*, 635–640.

(12) Gygi, S. P., Rist, B., Gerber, S. A., Turecek, F., Gelb, M. H., and Aebersold, R. (1999) Quantitative analysis of complex protein mixtures using isotope-coded affinity tags. *Nat. Biotechnol. 17*, 994–999.

(13) Gygi, S. P., Rist, B., Griffin, T. J., Eng, J., and Aebersold, R. (2002) Proteome analysis of low-abundance proteins using multidimensional chromatography and isotope-coded affinity tags. *J. Proteome Res. 1*, 47–54.

(14) Yi, E. C., Li, X. J, Cooke, K., Lee, H., Raught, B., Page, A., Aneliunas, V., Hieter, P., Goodlett, D. R., and Aebersold, R. (2005) Increased quantitative proteome coverage with (13)C/(12)C-based, acid-cleavable isotope-coded affinity tag reagent and modified data acquisition scheme. *Proteomics 5*, 380–387.

(15) Guaragna, A., Pedatella, S., Pinto, V., and Palumbo, G. (2006) Synthesis of *C*-protected 2,2-dideutero β^3-amino acids. *Synthesis* 4013–4016.

(16) Guaragna, A., De Nisco, M., Pedatella, S., Pinto, V., and Palumbo, G. (2006) An expeditious procedure for the synthesis of isotopically labelled fatty acids: preparation of 2,2-d2-nonadecanoic acid. *J. Labelled Compd. Radiopharm. 49*, 675–682.

(17) Pedatella, S., Guaragna, A., D’Alonzo, D., De Nisco, M., and Palumbo, G. (2006) Triphenylphosphine polymer-bound/iodine complex: a suitable reagent for preparation of *O*-isopropylidene sugar derivatives. *Synthesis* 305–308.

(18) Fauq, A. H., Kache, R., Khan, M. A., and Vega, I. E. (2006) Synthesis of acid-cleavable light isotope-coded affinity tags (ICAT-L) for potential use in proteomic expression profiling analysis. *Bioconjugate Chem. 17*, 248–254.

(19) Yu, L. R., Conrads, T. P., Uo, T., Issaq, H. J., Morrison, R. S., and Veenstra, T. D. (2004) Evaluation of the acid-cleavable isotope-coded affinity tag reagents: application to camptothecin-treated cortical neurons. *J. Proteome Res. 3*, 469–477.

(20) Nitti, G., Orru′, S., Bloch, C., Mohry, L., Marino, G., and Pucci, P. (1995) Amino acid sequence and disulfide bridge pattern of three [gamma]-thionins from *Sorghum bicolor*. *Eur. J. Biochem. 228*, 250–256.

(21) Birolo, L., Tutino, M. L., Fontanella, B., Gerday, C., Mainolfi, K., Pascarella, S., Sannia, G., Vinci, F., and Marino, G. (2000) Aspartate aminotransferase from the Antarctic bacterium *Pseudoalteromonas haloplanktis* TAC 125. Cloning, expression, properties, and molecular modelling. *Eur. J. Biochem. 267*, 2790–2802.

(22) Kivelä, H. M., Madonna, S., Krupovìc, M., Tutino, M. L., and Bamford, J. K. (2008) Genetics for *Pseudoalteromonas* provides tools to manipulate marine bacterial virus PM2. *J. Bacteriol. 190*, 1298–1307.

(23) Médigue, C., Krin, E., Pascal, G., Barbe, V., Bernsel, A., Bertin, P. N., Cheung, F., Cruveiller, S., D’Amico, S., Duilio, A., Fang, G., Feller, G., Ho, C., Mangenot, S., Marino, G., Nilsson, J., Parrilli, E., Rocha, E. P., Rouy, Z., Sekowska, A., Tutino, M. L., Vallenet, D., von Heijne, G., and Danchin, A. (2005) Coping with cold: the genome of the versatile marine Antarctica bacterium *Pseudoalteromonas haloplanktis* TAC125. *Genome Res. 15*, 1325–1335.

BC800010B

New 9- or 10-Dentate Luminescent Lanthanide Chelates

Pinghua Ge[†] and Paul R. Selvin*[,†,‡]

Department of Physics and Center for Biophysics and Computational Biology, University of Illinois, Urbana, Illinois 61801.
Received January 22, 2008; Revised Manuscript Received March 5, 2008

Polyaminocarboxylate-based luminescent lanthanide complexes have unusual emission properties, including millisecond excited-state lifetimes and sharply spiked spectra compared to common organic fluorophores. There are three distinct sections in the structure of the luminescent lanthanide chelates: a polyaminocarboxylate backbone to bind the lanthanide ions tightly, an antenna molecule to sensitize the emission of lanthanide ions, and a reactive group to attach to biomolecules. We have previously reported the modifications on the chelates, on the antenna molecules (commonly cs124), and on the reactive sites. In searching for stronger binding chelates and better protection from solvent hydration, here we report the modification of the coordination number of the chelates. A series of 9- and 10-dentate chelates were synthesized. Among them, the 1-oxa-4,7-diazacyclononane (N_2O)-containing chelate provides the best protection to the lanthanide ions from solvent molecule attack, and forms the most stable lanthanide coordination compounds. The TTHA-based chelate provides moderately good protection to the lanthanide ions.

INTRODUCTION

Luminescence resonance energy transfer (LRET) is a modification of the widely used technique of fluorescence resonance energy transfer (FRET) and can be used to accurately determine the distance between two sites bearing an energy transfer donor and an energy acceptor in a biomolecule (*1, 2*). In LRET, the energy transfer donor is a luminescent lanthanide atom and the acceptor is a conventional (organic) fluorophore. The lanthanide energy transfer donor typically involves a chelate to bind and protect the lanthanide from solvent quenching effects, a covalently attached organic chromophore to act as an antenna to absorb excitation light and transfer the energy to lanthanide ions, and a covalently attached reactive site to attach to biomolecules (see structure **I**, DTPA-cs124-maleimide, as an example).

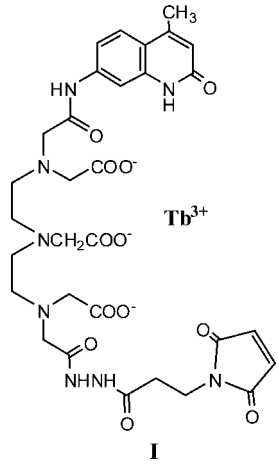

I

The fundamental advantages of LRET arise because the donor emission is long-lived with millisecond lifetime and is sharply spiked (peaks of a few nanometer widths) (*1*), has a high quantum yield (*3*), and is unpolarized (*4*). This enables temporal and spectral discrimination against the acceptor (a conventional fluorophore), which has nanosecond-lifetime and is broadly spread in wavelength (*1*).

We have published a number of papers on LRET (partially reviewed in *1, 5*), showing its advantages in model systems such as DNA oligomers (*6, 7*) and the ability to measure distance changes of an angstrom reliably even on large protein complexes such as actomyosin (*8, 9*) and in ion channels in living cells (*10–12*). Other researchers have successfully used the technique on DNA−protein complexes (*13–15*), actomyosin (*16*), protein−protein interactions in cells (*17, 18*), and detection of binding of many different biomolecules (*2, 19*).

The current DTPA (diethylenetriaminepentaacetic acid)-based chelates (**I**) works moderately well with both terbium and europium. The disadvantage of such chelates is that they are 8-dentate chelates; therefore, one or more water molecules can bind to lanthanide ions when these chelates coordinate to lanthanide ions (*20*). Because of the hydration on the lanthanide ions, the lifetime is relatively shortened by the solvent quenching effect. Also, the relatively low stability constant or fast dissociation and trans-metalation kinetics limits their application in the physiological environment. On the other hand, here we show that two different chelates, TTHA (triethylenetetraamine-hexanoic acid) and a chelate made from diazacrown ethers, have more than 8 coordination numbers, minimizing the hydration to the lanthanide.

TTHA-based lanthanide chelate is a 10-dentate ligand and has shown no hydration to lanthanide ions when coordinated (*21*). Although TTHA-based lanthanide chelates with coumarin derivatives as sensitizers (which works for Eu^{3+} only) have been reported (*13*), no TTHA-based amine reactive or thiol reactive lanthanide probes with cs124 as sensitizer (which works with both Tb^{3+} and Eu^{3+}) have been synthesized. Here, we report the syntheses of TTHA-based thiol reactive chelates.

The class of macrocycles known as crown ethers has been widely studied since their metal ion-coordinating capabilities were first reported by Pedersen (*22*). Derivations of the crown ether include the replacement of one or more of the ring's oxygen atoms with nitrogen atoms, resulting in azacrown ethers,

* To whom correspondence should be addressed at Dept. of Physics, 1110 W. Green St., Univ. of Illinois, Urbana, IL 61801, (217) 244-3371(tel); (217) 244-7559 (fax); selvin@uiuc.edu.

[†] Department of Physics.

[‡] Center for Biophysics and Computational Biology.

10.1021/bc800030z CCC: $40.75 © 2008 American Chemical Society
Published on Web 04/29/2008

and/or the attachment of one or more side arms to the ring to form a so-called lariat or armed crown ether. There are numerous publications on the metal-complexing properties of diazacrown ethers containing side chains attached to the nitrogen atoms of the macrocycle (*23*). We have synthesized a new type of lanthanide chelate derived from diazacrown ethers. Our chelates contain two ethyliminodiacetic acid side chains and have increased ability to bind lanthanide ions to better protect the lanthanide ions from solvent hydration (see structure **II**) and from other potential chelators such as ATP and EDTA.

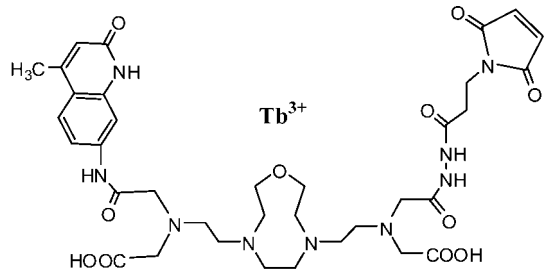

II

EXPERIMENTAL METHODS

Chemicals and Materials. The following were purchased from Sigma-Aldrich: triethylenetetraminehexaacetic acid (TTHA), 7-amino-4-methyl-2-(1*H*)-quinolinone (carbostyril 124, cs124), isobutyl chloroformate, anhydrous dimethyl sulfoxide (DMSO, in sure seal bottle), and triethylamine (for reaction). DMSO and triethylamine were dried over activated molecular sieves before use. 1,7-Diaza-12-crown-4 (N_2O_2) was purchased from Acros Organics. Triethylenetetramine hexaacetic acid dianhydride (caTTHA) (*24*), 1-oxa-4,7-diazacyclononane (N_2O) (*25*), and *N*,*N*-bis[(*tert*-butoxycarbonyl)methyl]-2-bromoethylamine (*26*) were synthesized according to published methods. Glacial acetic acid, methanol, and triethylamine (for making TEAA buffer) were purchased from Fisher Scientific. β-Maleimidopropionic acid hydrazide.TFA (EMPH·TFA) was purchased from Molecular Biosciences (Boulder, CO). (*R*)-2-Amino-2-carboxyethylmethanethiosulfonate (Cys-MTS) was purchased from Toronto Research Chemicals, Inc. (North York, Ontario, Canada). Ubiquitin was a gift from Invitrogen Inc. (Madison, WI). Distilled and deionized (18 MΩ cm^{-1}) water was used throughout. All glassware was washed with a mixed acid solution and thoroughly rinsed with deionized, distilled water. All plastic labware was purchased from Biorad (metal-free). All chemicals were of the purest grade available.

Purification. Most commonly, reverse-phase high-performance liquid chromatography was performed at room temperature on a Waters model 600 system with a Dynamax 60 Å C_{18} column (10 or 25 mm i.d. $\times$ 250 mm) using a linear gradient (solvent A = 0.1 M triethylammonium acetate, pH 6.5; solvent B = methanol/or acetonitrile).

Spectroscopy. Time-resolved and gated luminescence measurements were made on a laboratory-built spectrometer described previously, employing a 5 ns excitation pulse at 337 nm followed by time-resolved detection of lanthanide emission (*27*). The number of waters in the primary coordination sphere of the lanthanide was determined via the method of Horrocks and Sudnick (*28*): # of waters = $q(\tau_{H2O}^{-1} - \tau_{D2O}^{-1})$, ($q = 1.05$ for Eu, 4.2 for Tb).

Synthesis (Charts 1, *2*). *N_2O-Tetracarboxylic Acid.* 1-Oxa-4,7-diazacyclononane (N_2O) (100 mg, 0.77 mmol) and *N*,*N*-bis[(*tert*-butoxycarbonyl)methyl]-2-bromoethylamine (550 mg, 1.56 mmol) were dissolved in 5 mL of CH_3CN. 10 mL of phosphate buffer (2 M, pH 8.0) was added to the mixture. The solution was stirred at room temperature for 36 h. Ethyl acetate (10 mL) was added to the mixture. The aqueous solution was separated and extracted with ethyl acetate 2 $\times$ 5 mL. The combined organic layer was washed with water 3 $\times$ 5 mL. The organic layer was dried over anhydrous Na_2SO_4. The solvent was removed under reduced pressure to afford a colorless oil (458 mg, 89% yield. MS: 673, M + 1, FAB). The product was used for the next step without further purification.

200 mg (0.30 mmol) of the above-prepared material was dissolved in 6 M HCl/MeOH solution (5 mL). The mixture was stirred at room temperature for 2 h. Ether was added to the mixture. White precipitate was formed. The white precipitate was collected by filtration and dried (114 mg, 73% yield. MS: 447, M − 1, ESI).

N_2O_2-tetracarboxylic acid was also synthesized with the same method in similar yield and confirmed by mass spectrometry (MS: 491, M − 1, ESI).

General Procedure for Syntheses of N_2O- and N_2O_2-Based Lanthanide Chelates. 1 equiv of N_2O-tetracarboxylic acid was dissolved in a mixture of DMSO and 7 equiv of Et_3N under N_2. 2.2 equiv of isobutyl chloroformate was added and stirred at room temperature for 1.5 h. 0.7 equiv of cs124 dissolved in DMSO was added slowly to the above solution with vigorous stirring. The reaction was stirred at room temperature for 2 h. The solution was saved for the following steps.

If non-thiol-reactive chelates were to be synthesized, the above solution was quenched by addition of acetic acid and 0.1 M TEAA buffer (pH 6.5). The products were purified by reverse-phase HPLC with a linear gradient (typically 20−40% CH_3CN/TEAA pH 6.5 over 40 min). The yield varies from ~35% to ~50% as judged from the HPLC profiles (Table 1).

If the thiol-reactive forms of chelates were to be synthesized, the above solution was transferred to a DMSO solution containing 1.3 equiv of EMPH·TFA (or Cys-MTS) rapidly under N_2. The reaction was stirred at room temperature for 1 h. Acetic acid and 0.1 M TEAA (pH 6.5) buffer were added to quench the reaction. The product was purified by reverse-phase HPLC with a linear gradient (typically 20−40% CH_3CN/TEAA pH 6.5 over 40 min). The yield varies from ~20% to ~30% as judged from the HPLC profiles (Table 1).

General Procedure for Syntheses of TTHA-Based Lanthanide Chelates. Triethylenetetramine hexaacetic acid dianhydride (caTTHA) (1 equiv) was dissolved in a mixture of DMSO and 5 equiv of Et_3N under N_2. 0.7 equiv of cs124 dissolved in DMSO was added slowly to the above solution with vigorous stirring. The reaction was stirred at room temperature for 2 h. 1.3 equiv of thiol-reactive reagents (EMPH·TFA or Cys-MTS) dissolved in DMSO was added to the above solution. The reaction was stirred for 1 h at room temperature. Acetic acid and 0.1 M TEAA (pH 6.5) were added to quench the reaction. The product was purified by reverse-phase HPLC with a linear gradient (typically 30−50% MeOH/TEAA pH 6.5 over 40 min). The yield varies from ~20% to 50% as judged from the HPLC profiles (Table 1).

Addition of Metals. $TbCl_3$ or $EuCl_3$ was added to the chelate in a 1:1.2 molar ratio at usually >0.5 mM concentration at pH 6.5−7.5, usually in 0.1 M TEAA, pH 6.5 buffer, and allowed to stand for 30 min at room temperature before use.

Coupling to Biomolecules. Similar labeling conditions for conjugation to muscle proteins (*29*, *30*) were employed. The procedure for labeling Shaker K^+ ion channels in *Xenopus* oocytes has also been published (*10*, *11*). The thiol-reactive chelates were coupled to Ubiquitin (an 8.9 kDa protein containing a single cysteine) at a typical ratio of 10:1 with a protein concentration of ~15 μM. The coupling reaction was carried out at 4 °C overnight in 20 mM HEPES, pH 7.4, 5 mM $MgCl_2$. The excess lanthanide chelates were removed either by

Chart 1

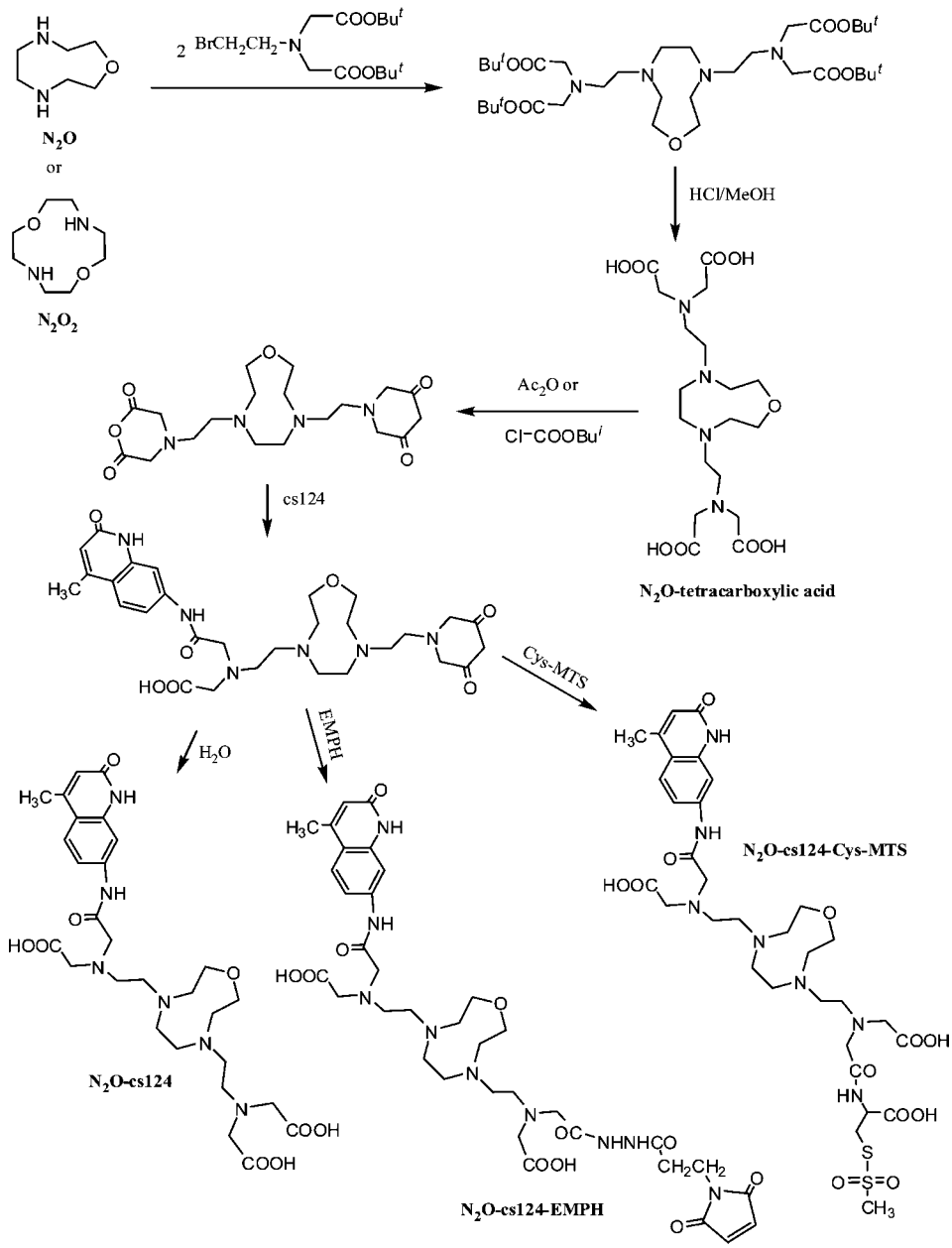

passing the reaction mixture through a Sephadex G-50 size exclusion column or by dialyzing the reaction mixture through Pierce Slide-A-Lyzer Dialysis Cassette.

RESULTS AND DISCUSSION

Syntheses. DTPA-based lanthanide chelates can be readily prepared by reacting commercially available DTPA dianhydride (caDTPA) with 1 equiv of cs124 and 1 equiv of thiol-reactive reagents. The same principle can apply to the new chelate syntheses. The synthesis of the dianhydride form of TTHA has been reported (*24*). TTHA dianhydride was reacted with 1 equiv of cs124 first, followed by addition of 1 equiv of thiol-reactive reagents to form TTHA-cs124-EMPH or TTHA-cs124-Cys-MTS in good yield. 1-Oxa-4,7-diazacyclononane (N_2O) and 1,7-diaza-12-crown-4 (N_2O_2) were reacted with 2 equiv of *N*,*N*-bis[(*tert*-butoxycarbonyl)methyl]-2-bromoethylamine. The resulting tetra-*tert*-butylcarboxylates were then hydrolyzed with HCl in methanol to yield the free acid form of N_2O-tetracarboxylic acid and N_2O_2-tetracarboxylic acid. The two tetracarboxylic acid compounds could react with either acetic anhydride or isobutyl chloroformate to form dianhydride intermediates. These dianhydride intermediates can be either isolated or used for the next step without isolation. Following the sequence by reacting with cs124 first and then thiol-reactive reagents, the lanthanide chelates with N_2O and N_2O_2 in the middle of their backbones were synthesized in satisfy yield.

All of the lanthanide chelates were purified by reverse-phase HPLC and identified by mass spectroscopy, UV−vis, and lanthanide luminescence properties.

Photophysical Properties of the Lanthanide Complexes with the New Chelates. The Tb^{3+} and Eu^{3+} emission spectra are shown in Figure 1. All of the Tb^{3+} and Eu^{3+} complexes exhibit their characteristic sharply spiked asymmetric emission spectra with their most intense luminescent transitions centered at 546 nm ($^5D_4 \rightarrow {}^7F_5$) for Tb^{3+} and 614 nm ($^5D_0 \rightarrow {}^7F_2$). Table 2 lists the excited-state lifetimes of Tb^{3+} and Eu^{3+} measured for their complexes with the new chelates. Table 3 lists the excited-state lifetimes of Tb^{3+} and Eu^{3+} measured for their complexes with the new thiol-reactive chelates labeled to proteins (Ubiquitin, and *Xenopus* oocytes) or glutathione.

Chart 2

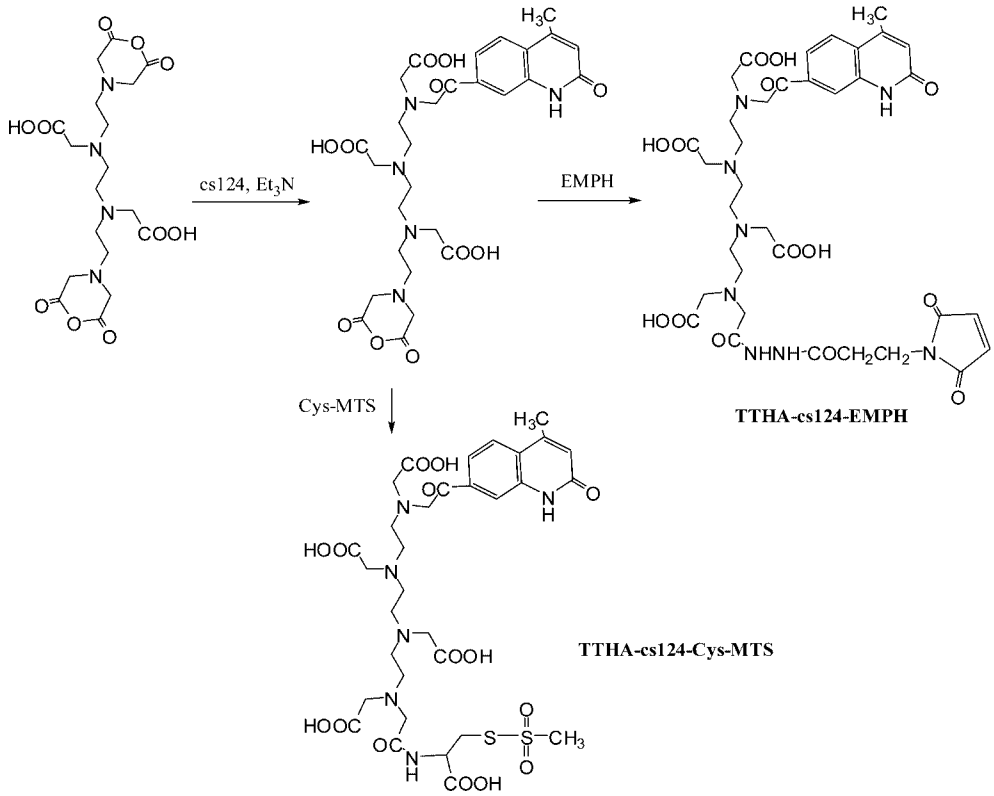

Table 1. Synthesized New Lanthanide Chelates

thiol-reactive chelates	linear gradients	retention time (min)	yield (%)	MS M − 1, ESI⁻
N_2O-cs124	20−40% ACN/TEAA	12	35	603
N_2O_2-cs124	20−40% ACN/TEAA	13	50	647
N_2O-cs124-EMPH	20−40% ACN/TEAA	19	20	768
N_2O-cs124-Cys-MTS	20−40% ACN/TEAA	17	30	784
TTHA-cs124-EMPH	30−50% MeOH/TEAA	22	20	814
TTHA-cs124-Cys-MTS	30−50% MeOH/TEAA	16	30	830

Generally, the Tb^{3+} and Eu^{3+} complexes of these chelates have comparable emission brightness to that of the benchmark chelate, DTPA-cs124. For all (except N_2O_2-cs124) of the non-thiol-reactive chelates, their lanthanide emission intensities are at least 10% higher than that of the reference complex. One apparent reason behind the results is that these chelates are either 9- or 10-dentate chelates. DTPA-cs124 is an 8-dentate chelate. When it coordinates to lanthanide ions, a water molecule is also coordinated to the lanthanide ions in the inner coordination sphere (*20*). The hydration of lanthanide ions is the main source of quenching of lanthanide emission. In contrast, the newly synthesized 9- or 10-dentate chelates can provide enough coordination sites for lanthanide ions that few water molecules can compete to coordinate to lanthanide ions. Therefore, the quenching effect from hydration of lanthanide ions is eliminated. This assumption that little or no water molecules in the lanthanide inner coordination spheres of these new chelate complexes is evident from their corresponding lifetime measurements, as all of these chelates exhibit significantly longer lifetimes than that of DTPA-cs124. Using the Horrocks and Sudnick empirical equation, the number of waters in the primary coordination sphere of Tb^{3+} and Eu^{3+} is found as follows: N_2O-cs124 (0.02, 0.29), N_2O_2-cs124 (0.22, Tb^{3+} only), TTHA-cs124 (0.2, 0.3) (*21*). These data clearly indicate that the new chelates provide better protection to the lanthanide ions from solvent solvation, and limit the accessibility of water molecules to the metal center. Especially for N_2O-cs124, no water molecules coordinate when it binds to Tb^{3+}. Therefore, the new 9- or 10-dentate chelates can shield the lanthanide ions from solvent attack. However, other factors will also contribute to the relative intensity changes. For N_2O_2-cs124, its Tb^{3+} emission intensity is only about 20% that of DTPA-cs124, while its Eu^{3+} emission is undetectable at 1 μM concentration. Yet, its lifetime for Tb^{3+} is significantly longer than that of the reference complex. The calculated number of water molecules coordinated to Tb^{3+} is only 0.22. The facts are that its emission intensity is concentration-dependent and its lifetime is concentration-independent. These observations indicate that the binding stability constant

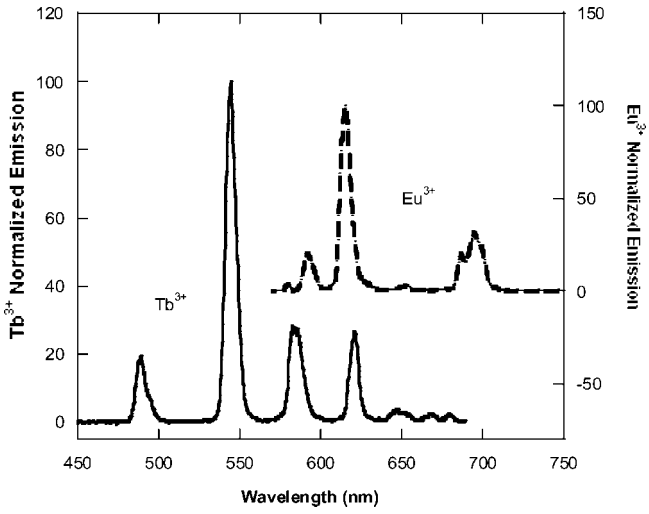

Figure 1. Normalized Tb^{3+} and Eu^{3+} emission spectra of N_2O-cs124 in 0.1 M TEAA pH 6.5 at a concentration of 1 μM. Tb^{3+} and Eu^{3+} display their characteristic sharply spiked spectra. Pulsed excitation was at 40 Hz, 3.5 μJ/pulse for Eu^{3+}, 3.0 μJ/pulse for Tb^{3+}; integration times are 1 s for $Tb^{3+}$and 5 s for Eu^{3+}.

Table 2. Photophysics Data of the New 9- And 10-Dentate Chelates[a]

metal	chelates	τH_2O	τD_2O	$\tau H_2O/\tau D_2O$	no of waters	relative brightness
Tb^{3+}	DTPA-cs124	1.55	2.63	0.59	1.1 (*21*)	1
	N_2O-cs124	1.89	1.91	0.99	0.02	1.3
	N_2O_2-cs124	2.50	2.88	0.87	0.22	0.2
	N_2O-cs124-EMPH	1.93 (81%) 0.72 (19%)				0.4
	N_2O-cs124-Cys-MTS	1.97 (82%) 1.21 (18%)				0.2
	TTHA-cs124	2.10	2.37	0.89	0.2	1.1 (*21*)
	TTHA-cs124	2.10	2.31	0.91	0.19	0.31[b]
	TTHA-cs124-8-me	2.27				0.33
	TTHA-cs124-EMPH	1.97 (31%) 0.81 (69%)				0.73
	TTHA-cs124-Cys-MTS	2.07 (93%) 0.24 (7%)				1.3
Eu^{3+}	DTPA-cs124	0.62	2.42	0.26	1.26 (*21*)	1
	N_2O-cs124	1.0	1.39	0.72	0.29	1.22
	N_2O_2-cs124					N/A[c]
	N_2O-cs124-EMPH	1.03 (41%) 0.60 (22%) 0.04 (37%)				0.3
	TTHA-cs124	1.19	1.79	0.66	0.3 (*21*)	2.7
	TTHA-cs124	1.16				1.45[b]
	TTHA-cs124-8-me	1.15				2.37
	TTHA-cs124-EMPH	1.25				0.89
	TTHA-cs124-Cys-MTS	1.20				0.69

[a] All emissions are measured at 1 μM lanthanide concentration with a slight excess of chelate. [b] From this work. [c] Concentration-dependent. At 1 μM, no emission detected.

Table 3. Lifetimes of Tb^{3+} and Eu^{3+} Complexes of Thiol-Reactive 9-, 10-Dentate Chelates Labeled to Proteins or Glutathione

metal	chelate	protein	lifetimes (ms)
Tb^{3+}	N_2O-cs124-EMPH	Shaker K^+ channels in oocyte cells[a]	1.34 (75%); 0.22 (25%)
		Ubiquitin	1.74 (82%); 0.29 (18%)
	TTHA-cs124-EMPH	Shaker K^+ channels in oocyte cells[a]	1.84 (86%); 0.32 (14%)
		Ubiquitin	1.94 (74%); 0.49 (26%)
		Glutathione	1.89
	TTHA-cs124-Cys-MTS	Ubiquitin	1.92 (63%); 0.33 (37%)
Eu^{3+}	TTHA-cs124-EMPH	Shaker K^+ channels in oocyte cells[a]	0.69 (43%); 0.21 (57%)
		Glutathione	1.04

[a] Details of ion channel expression can be found in [Posson (2005) *Nature 436*, 848−851].

of N_2O_2-cs124 to lanthanide ions is relatively small. There is an equilibrium between lanthanide ion bound and unbound N_2O_2-cs124 in solution. Such results were also observed for TETA-cs124 (1,4,8,11-tetraazacyclotetradecane-1,4,8,11-tetraacetic acid, TETA) (*21*). After converting to the thiol-reactive form, there is a tendency for the emission intensity to decrease.

The 8-methyl cs124 derivative (cs124-8-me) sensitized TTHA chelate (TTHA-cs124-8-me) was also synthesized. It has a slightly increased lifetime compared to TTHA-cs124 (2.27 ms vs 2.14 ms). This is consistent with the observation of blocked back energy transfer from lanthanide emission to antenna molecule by the 8-methyl group observed for DTPA chelate (*5*). Its Tb^{3+} emission intensity is only about 30% that of the corresponding reference complex, as is the TTHA-cs124 chelate which was made in this work. The hypothesis for this intensity decrease is that Tb^{3+} remains 9-coordinated in TTHA-cs124-8-me and TTHA-cs124. The TTHA chelates provide 10-coordinate sites. The terminal carboxylate arm with sensitizer has to compete with other free carboxylic acid arms to coordinate to the lanthanide center, resulting in an equilibrium between bound and nonbound forms of the carboxylate arms coordinating to the metal center. The case where the cs124 is not bound to the lanthanide probably will not sensitize the emission of terbium because the antenna molecule is far away from metal center. On the basis of the fact that the intensity of TTHA chelates is only about 30% that of the reference complex, it is reasonable to assume that the equilibrium is in favor of the nonbound form, probably due to the spatial hindrance and overall charges of the antenna molecule. At ~pH 7, the side arms in TTHA are deprotonated as carboxylates. When neutral antenna molecule (cs124 or cs124-8-me) attached to form an amide bond, the −1 charge from the carboxylate sidearm will be gone. Hence, the coordination capability of the carbonyl oxygen atom from the amide bond will change. However, we reported that the intensity of TTHA-cs124 is 110% that of the reference complex in our previous work (*21*). We believe that this is because the structures of the two TTHA-cs124 chelates are slightly different. In the present work, we converted TTHA into its dianhydride form first, and then reacted TTHA dianhydride with cs124 and derivatives. By doing this, the antenna molecule is exclusively at the terminals of the TTHA backbone chain. In our previous work, the free acid form of TTHA was activated by reacting with isobutyl chloroformate first, followed by reacting with cs124 in a one-pot reaction. All of the carboxylic acid groups in TTHA could be activated, and hence a mixture is formed with the antenna molecule in both the middle and terminals of the TTHA backbone chain. If the antenna molecule is in the middle of the TTHA backbone chain, it probably will coordinate to the lanthanide center, because after the TTHA backbone chain coordinates to lanthanide, it will bring the carboxylate arm with the antenna molecule very close to the metal center. In contrast, the carboxylate arm with the antenna molecule at the terminals of TTHA backbone chain will have greater freedom to move around.

The Eu^{3+} emission intensity of TTHA-cs124 chelates is significantly increased compared the reference complex. The Eu-TTHA-cs124-8-me emission intensity is 237% that of reference, and the Eu-TTHA-cs124 emission intensity is 145% that of reference. The increased emission intensity is a good indication that the coordination number of Eu^{3+} has increased to 10. It is demonstrated that the $^5D_0 \rightarrow {}^7F_2$ emission intensity increase of Eu^{3+} is linearly proportional to the average coordination number of nitrates to Eu^{3+}, regardless of solvents (*20*). In a 0.047 M Eu^{3+} DMF solution, the intensity increases 1.8× per coordination number increase. Although different coordination chelates were used, the further intensity increase

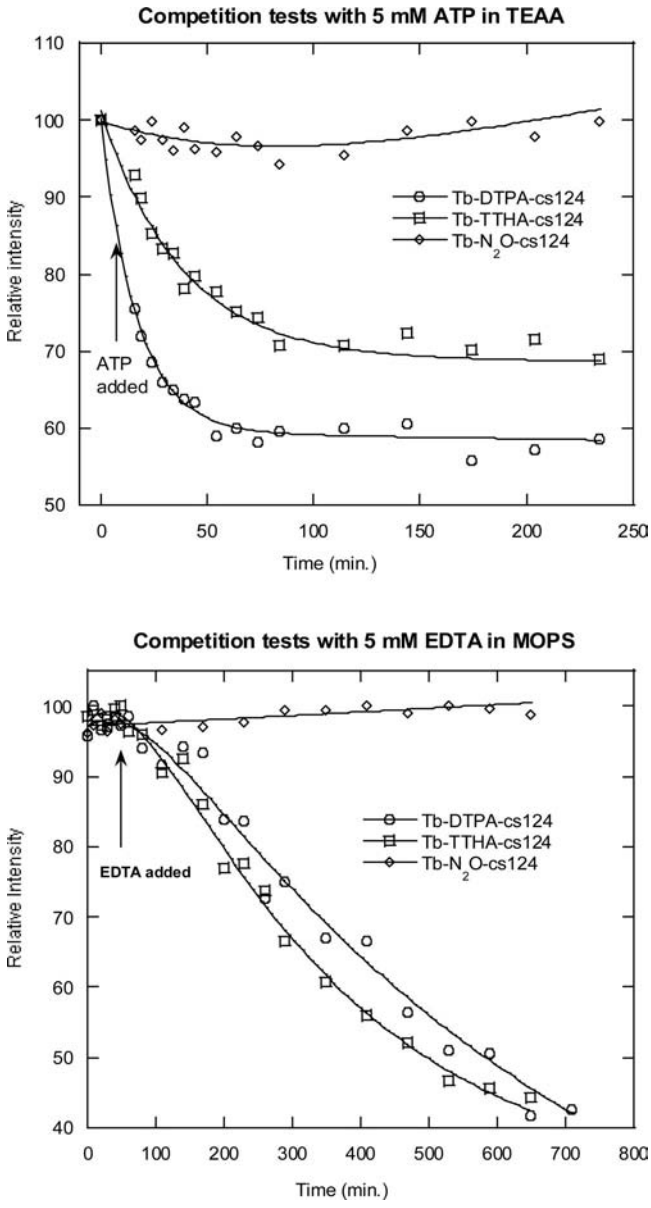

Figure 2. Relative Tb^{3+} emission intensity over time in the presence of EDTA or ATP of chelates of DTPA-cs124, TTHA-cs124, and N_2O-cs124.

of TTHA-cs124-8-me from TTHA-cs124 is probably due to the blocking of energy back transfer effect by the 8-methyl substitute.

To compare the stability of the lanthanide complexes of the new chelates, the Tb^{3+} emission intensity was measured over time in the presence of ATP or EDTA for the nonreactive chelates of DTPA-cs124, TTHA-cs124, and N_2O-cs124 (Figure 2). In the presence of 5 mM of EDTA, the Tb^{3+} emission intensity for both of TTHA-cs124 and DTPA-cs124 decreases to ~50% of the initial intensity in ~8−9 h. In the presence of 5 mM of ATP, the Tb^{3+} emission intensity of DTPA-cs124 decreases to ~60% of its initial intensity in ~50 min after addition of ATP. After this period of time, no further significant intensity decrease was observed, suggesting that equilibrium has been achieved. The Tb^{3+} emission intensity of TTHA-cs124 decreases to ~70% of its initial intensity in ~70 min after addition of ATP, indicating that equilibrium is also achieved at this point. In both cases, the Tb^{3+} emission intensity of N_2O-cs124 virtually does not change. These results suggest that the macrocycle-containing lanthanide chelate, N_2O-cs124, is a much stronger lanthanide binding chelate than the linear DTPA-cs124 and TTHA-cs124 chelates, and its lanthanide complexes are much more stable under physiological conditions.

The thiol-reactive chelates are selectively reacted with Ubiquitin, Shaker potassium ion channel expressed in oocyte, and glutathione. Generally, after labeling to proteins, the luminescent lanthanide emission exhibits a biexponential lifetime decay fit with the majority a long-lifetime component (usually >70%) and the rest a short-lifetime component (<30%). It is interesting to note that, after reacting with glutathione, the originally biexponential thiol-reactive chelates become single-exponential.

CONCLUSIONS

As part of the project to modify the luminescent lanthanide chelate backbone structures to provide stronger and better hydration protection chelates, new 9- and 10-dentate lanthanide chelates have been synthesized. The syntheses of these chelates are straightforward, relatively simple, and in good yields, especially for TTHA-based chelates. The principle for the synthesis is to prepare a backbone precursor similar to DTPA dianhydride. The dianhydride functional groups allow an antenna molecule and a reactive group to attach to the backbone molecule separately. The new chelates provide better protection to lanthanide ions from solvent hydration, as evidenced from their longer lifetimes and relatively higher emission intensity. The 1-oxa-4,7-diazacyclononane (N_2O)-containing chelates provide the best protection to the lanthanide ions from solvent molecule attack. Its Tb^{3+} complex is the most stable complex and does not undergo dissociation in the presence of other competing chelates at relatively high concentration. The TTHA-based chelates provide moderately good protection to the lanthanide ions.

ACKNOWLEDGMENT

This work is supported by NIH grants AR44420 and GM074770. We thank Dr. Kurt Vogel from Invitrogen Inc. for the generous gift of Ubiquitin protein. The labeling experiments to oocytes expressing Shaker ion channels were done by Dr. David Posson. The mass spectrometry was obtained by the Mass Spectrometry Center, University of Illinois at Urbana−Champaign.

LITERATURE CITED

(1) Selvin, P. R. (2002) Principles and biophysical applications of luminescent lanthanide probes. *Annu. Rev. Biophys. Biomol. Struct. 31*, 275–302.
(2) Mathis, G. (1993) Rare earth cryptates and homogeneous fluoroimmunoassays with human sera. *Clin. Chem. 39*, 1953–1959.
(3) Xiao, M., and Selvin, P. R. (2001) Quantum yields of luminescent lanthanide chelates and far-red dyes measured by resonance energy transfer. *J. Am. Chem. Soc. 123*, 7067–7073.
(4) Reifenberger, J., Snyder, G. E., Baym, G. A., and Selvin, P. R. (2003) Emission polarization properties of europium and terbium chelates. *J. Phys. Chem B 107*, 12862–12873.
(5) Reifenberger, J. G., Ge, P. and Selvin, P. R. (2005) *Progress in Lanthanides as Luminescent Probes*, Springer, Berlin.
(6) Selvin, P. R., and Hearst, J. E. (1994) Luminescence energy transfer using a terbium chelate: Improvements on fluorescence energy transfer. *Proc. Natl. Acad. Sci. U.S.A. 91*, 10024–10028.
(7) Selvin, P. R., Rana, T. M., and Hearst, J. E. (1994) Luminescence resonance energy transfer. *J. Am. Chem. Soc. 116*, 6029–6030.
(8) Xiao, M., Reifenberger, J. G., Wells, A. L., Baldacchino, C., Chen, L. Q., Ge, P., Sweeney, H. L., and Selvin, P. R. (2003) An actin-dependent conformational change in myosin. *Nat. Struct. Biol. 10*, 402–8.

(9) Xiao, M., Li, H., Snyder, G. E., Cooke, R., G. Yount, R., and Selvin, P. R. (1998) Conformational changes between the active-site and regulatory light chain of myosin as determined by luminescence resonance energy transfer: The effect of nucleotides and actin. *Proc. Natl. Acad. Sci. U.S.A. 95*, 15309–15314.

(10) Cha, A., Snyder, G. E., Selvin, P. R., and Bezanilla, F. (1999) Atomic scale movement of the voltage sensing region in a potassium channel measured via spectroscopy. *Nature 402*, 809–813.

(11) Posson, D. J., Ge, P., Miller, C., Bezanilla, F., and Selvin, P. R. (2005) Small vertical movement of a K^+ channel voltage-sensor measured with luminescence energy transfer. *Nature 436*, 848–851.

(12) Richardson, J., Blunck, R., Ge, P., Selvin, P. R., Bezanilla, F., Papazian, D., and Correa, A. M. (2006) Common topology of prokaryotic voltage-gated ion channels in the lipid bilayer. *Proc. Natl. Acad. Sci. U.S.A. 103*, 15865–15870.

(13) Heyduk, E., Heyduk, T., Claus, P., and Wisniewski, J. R. (1997) Conformational changes of DNA induced by binding of chironomus high mobility group protein 1a (cHMG1a). *J. Biol. Chem. 272*, 19763–19770.

(14) Heyduk, E., and Heyduk, T. (1999) Architecture of a complex between the sigma70 subunit of Escherichia coli RNA polymerase and the nontemplate strand oligonucleotide. Luminescence resonance energy transfer study. *J. Biol. Chem. 274*, 3315–22.

(15) Callaci, S., Heyduk, E., and Heyduk, T. (1999) Core RNA polymerase from *E. coli* induces a major change in the domain arrangement of the sigma 70 subunit. *Mol. Cell 3*, 229–238.

(16) Xu, J., and Root, D. D. (1998) Domain motion between the regulatory light chain and the nucleotide site in skeletal myosin. *J. Struct. Biol. 123*, 150–61.

(17) Root, D. D. (1997) *In situ* molecular association of dystrophin with Actin revealed by sensitized emission immuno-resonance energy transfer. *Proc. Natl. Acad. Sci. U.S.A. 94*, 5685–5690.

(18) Vazquez-Ibar, J. L., Weinglass, A. B., and Kaback, H. R. (2002) Engineering a terbium-binding site into an integral membrane protein for luminescence energy transfer. *Proc. Natl. Acad. Sci. U.S.A. 99*, 3487–3492.

(19) Mathis, G. (1995) Probing molecular interactions with homogeneous techniques based on rare earth cryptates and fluorescence energy transfer. *Clin. Chem. 41*, 1391–1397.

(20) Bunzli, J.-C. G. (1989) Luminescent Probes, in *Lanthanide Probes in Life, Chemical and Earth Sciences, Theory and Practice* (Bunzli, J.-C. G., and Choppin, G. R., Eds.) pp 219−293, Elsevier, New York.

(21) Li, M., and Selvin, P. R. (1995) Luminescent lanthanide polyaminocarboxylate chelates: the effect of chelate structure. *J. Am. Chem. Soc. 117*, 8132–8138.

(22) Pedersen, C. J. (1967) Cyclic polyethers and their complexes with metal salts. *J. Am. Chem. Soc. 89*, 7017.

(23) Gorden, A. E. V., Xu, J., and Raymond, K. N. (2003) Rational design of sequestering agents for plutonium and other actinides. *Chem. Rev. 103*, 4207–4282.

(24) Zitha-Bovens, E., Muller, R. N., Laurent, S., Elst, L. V., Geraldes, C. F. G. C., van Bekkum, H., and Peters, J. A. (2005) Structure and dynamics of lanthanide complexes of triethylenetetramine-N,N,N′,N″,N‴,N‴-hexaacetic acid (H6ttha) and of diamides H4ttha(NHR) derived from H6ttha as studied by NMR, NMRD, and EPR. *Helv. Chim. Acta 88*, 618–632.

(25) Qian, L., Sun, Z., and Bowman-James, K. (1996) Synthesis of polyaza macrocyclic ligands. *Supermol. Chem. 6*, 313–325.

(26) Williams, M. A., and Rapoport, H. (1993) Synthesis of enantiomerically pure diethylenetriaminepentaacetic acid analogues. L-Phenylalanine as the educt for substitution at the central acetic acid. *J. Org. Chem. 58*, 1151–1158.

(27) Xiao, M., and Selvin, P. R. (1999) An improved instrument for measuring time-resolved lanthanide emission and resonance energy transfer. *Rev. Sci. Instrum. 70*, 3877–3881.

(28) Horrocks, W. D., Jr., and Sudnick, D. R. (1979) Lanthanide ion probes of structure in biology. Laser-induced luminescence decay constants provide a direct measure of the number of metal-coordinated water molecules. *J. Am. Chem. Soc. 101*, 334–350.

(29) Burmeister-Getz, E., Cooke, R., and Selvin, P. R. (1998) Luminescence resonance energy transfer measurements in myosin. *Biophys. J. 75*, 2451–2458.

(30) Chen, J., and Selvin, P. R. (1999) Thiol-reactive luminescent lanthanide chelates. *Bioconjugate Chem. 10*, 311–315.

BC800030Z

CORRECTIONS

Volume 19, Number 3, 2008.

Guy Patchornik

Purification of His-tagged Proteins with [Desthiobiotin-BSA-EDTA] Conjugates Exhibiting Resistance to EDTA

The author regrets an error in the Methods section. On page 675, under General Purification Protocol for His6-Tagged Proteins Utilizing DB-BSA-EDTA Conjugates, the text "Step IV. Elution: The His-tagged protein was eluted from the pellet into 50–100 μL of 50 mM imidazole and 100 mM Tris pH 7 within 5–10 min" should read "Step IV. Elution: The His-tagged protein was eluted from the pellet into 50–100 μL of 50 mM imidazole and 50 mM Tris pH 8 within 5–10 min".

BC800123J

10.1021/bc800123j
Published on Web 05/01/2008

JUNE 2008
Volume 19, Number 6

© *Copyright 2008 by the American Chemical Society*

Bioconjugate Chemistry

COMMUNICATIONS

Increasing Solubility of Proteins and Peptides by Site-Specific Modification with Betaine

Junpeng Xiao, Alex Burn, and Thomas J. Tolbert*

Department of Chemistry and Interdisciplinary Biochemistry Graduate Program, Indiana University, Bloomington, Indiana 47405. Received February 15, 2008; Revised Manuscript Received May 1, 2008

Proteins and peptides with low solubility and which aggregate are often encountered in biochemical studies and in pharmaceutical applications of polypeptides. Here, we report a new strategy to improve solubility and prevent aggregation of polypeptides using site-specific modification with the small molecule betaine, which contains a quaternary ammonium moiety. Betaine was site-selectively attached to the N-termini of two aggregation-prone polypeptide models, the bacterial enzyme xanthine-guanine phosphoribosyltransferase (CG-GPRT) and the HIV entry inhibitor peptide CG-T20, utilizing native chemical ligation. N-terminal cysteines for the betaine ligation reactions were generated from His-tagged fusion proteins using TEV protease cleavage. Ligation of the betaine thioester (**1**) to the N-terminal cysteine-containing polypeptide models proceeded in high yield, though denaturing conditions were required for CG-T20 due to the hydrophobic nature of this peptide. CD spectroscopy and GPRT activity assays indicate that the betaine modification of CG-GPRT and CG-T20 does not significantly affect structure or activity of the polypeptides. Solubility and turbidity measurements of betaine-modified and unmodified polypeptides demonstrate that betaine modification can greatly increase solubility. Finally, it is shown that betaine-modified CG-T20 acts as an inhibitor of the aggregation of unmodified CG-T20.

Polypeptides with low solubility and high tendency for aggregation have caused many problems in academic and industrial research for several reasons. First, many types of biochemical and biophysical studies, especially structural analyses, are hampered by low solubility. In particular, high-resolution structural studies using NMR spectroscopy and X-ray crystallography usually require millimolar concentrations of protein or peptide samples (*1, 2*), but many proteins and peptides aggregate at millimolar concentrations. In addition, low solubility and aggregation are significant problems in the development of pharmacologically active proteins and peptides. Many bioactive proteins and peptides are abandoned during drug discovery due to low solubility and high tendency for aggregation, although they have good therapeutic potential (*3, 4*). Furthermore, many neurodegenerative diseases such as Alzheimer's, Parkinson's, and prion diseases are characterized by formation of protein or peptide aggregates in brain tissue (*5–8*). Because of this, blocking protein or peptide aggregation is an important therapeutic strategy to counter neurodegenerative diseases.

To overcome problems with polypeptide solubility and aggregation, different strategies have been investigated. Fusion of the target polypeptides to a solubilizing protein fusion partner (*9–13*) such as maltose-binding protein (MBP) (*10, 11*), glutathione S-transferase (GST) (*12*), and green fluorescent

* To whom correspondence should be addressed. Thomas J. Tolbert, Department of Chemistry, 800 E. Kirkwood Ave., Indiana University, Bloomington, IN 47405. E-mail: tolbert@indiana.edu. Tel: 812-856-1887. Fax: 812-855-8300.

10.1021/bc800063k CCC: $40.75 © 2008 American Chemical Society
Published on Web 05/23/2008

Scheme 1. Synthesis of Betaine Thioester (1)

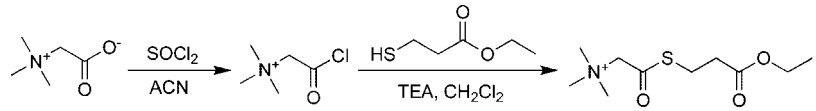

1

protein (GFP) (*13*) have been utilized to increase the solubility of polypeptides. Glycosylation with hydrophilic carbohydrates (*14*) and PEGylation with water-soluble poly(ethylene glycol) (PEG) chains (*15–17*) have also been used to improve the solubility of polypeptides. However, these strategies require introduction of large molecules onto proteins and peptides, which may perturb their structure and function. To overcome this issue, addition of short solubility enhancement peptide tags, which usually contain 5−10 positively charged amino acids, to the N- or C-terminus of proteins and peptides has been reported (*18, 19*). These peptide tags are relatively small for large proteins, but for peptides and small proteins they can be a significant fraction of those polypeptides' molecular weight. Introduction of such peptide tags during solid-phase peptide synthesis adds additional coupling steps that can reduce yields, and introduction of polylysine or polyarginine tags during protein expression may lead to proteolytic complications. Because of these factors, low molecular weight solubility enhancement tags that can be introduced after recombinant protein expression or peptide synthesis would be useful.

Here, we report a new strategy to incorporate a betaine moiety as a small solubility enhancement tag onto the N-terminus of polypeptides utilizing native chemical ligation/expressed protein ligation. The betaine moiety is a small molecule that contains a positively charged quaternary ammonium group with the molecular weight of only 100. We were initially investigating incorporation of the betaine moiety onto the N-terminus of polypeptides as a mass tag. During our investigation, we noticed an interesting side effect of this modification, that betaine-modified polypeptides are more soluble in aqueous solution. To investigate this effect further, we site-specifically modified two aggregation-prone model polypeptides, the 153-residue enzyme xanthine-guanine phosphoribosyltransferase (GPRT) and the 38-residue peptide CG-T20 with the betaine moiety. GPRT is a hydrophobic protein that usually forms a tetramer in its native state (*20, 21*). It is stable in solution at neutral pH, but aggregates and precipitates when the pH is below 6. CG-T20 is a slightly modified version of the HIV entry inhibitor peptide T20 (also called Fuzeon, Enfuvirtide, or DP-178) with a CysGly addition to the N-terminus (*2, 22*). It is also a hydrophobic peptide that exhibits solubility problems at neutral and acidic pH. Thus, both GPRT and CG-T20 are good models to investigate the effect of betaine modification on solubility and aggregation.

The strategy that we utilized for the site-specific modification of polypeptides involves generating an N-terminal cysteine by tobacco etch virus NIa protease (TEV protease) cleavage and then ligating a betaine thioester (**1**) (Scheme 1) onto the N-terminal cysteine by native chemical ligation/expressed protein ligation (Figure 1). Native chemical ligation was first introduced by Kent and co-workers for chemical synthesis of polypeptides (*23*). It is a chemoselective ligation between an N-terminal cysteine and a thioester to form a native peptide bond. In this reaction, only the N-terminal cysteine reacts, all other internal cysteines are unreactive, and so it is chemoselective for N-terminal cysteines. This reaction has been extended to expressed polypeptides by Muir and others for protein modification (*24, 25*). Utilization of this reaction enables site-specific N-terminal modification of our model polypeptides with the betaine moiety.

Generation of N-terminal cysteines for native chemical ligation has been accomplished using TEV protease to cleave N-terminally His-tagged fusion proteins (*26, 27*). A fusion protein of His-CG-GPRT, which contains the TEV protease cleavable sequence, was produced to generate CG-GPRT as described previously (Figure 1a) (*26*). Expression of a TEV-cleavable form of CG-T20 was somewhat more complicated due to the hydrophobic nature of this peptide. The first attempt to express CG-T20 fused with a His-tagged GPRT carrier protein containing a TEV protease cleavable linker was unsuccessful because the fusion protein was expressed as inclusion bodies and could not be resolubilized (*27*). Next, we decided to fuse small ubiquitin-related modifier (SUMO) to the N-terminus of CG-T20 with a TEV protease cleavable linker between SUMO and CG-T20, because of SUMO's ability to enhance protein expression and solubility (*28–30*). Overexpression of SUMO-CG-T20 fusion protein still resulted in inclusion bodies, due to

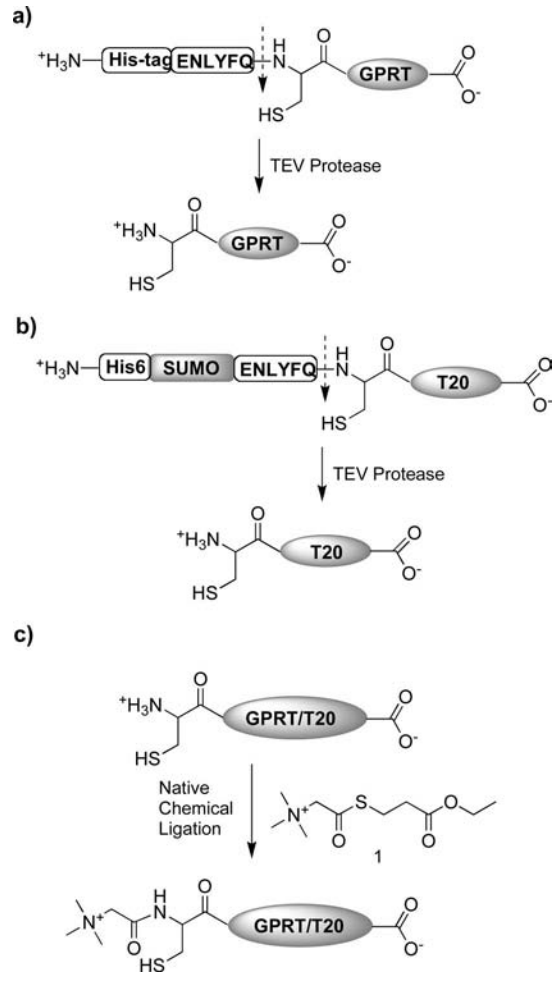

Figure 1. The strategies for site-specific modification of CG-GPRT and CG-T20 with betaine. (a) TEV protease cleavage of the His-CG-GPRT fusion protein to give the N-terminal cysteine-containing GPRT (CG-GPRT). (b) TEV protease cleavage of the SUMO-CG-T20 fusion protein to give the N-terminal cysteine-containing T20 (CG-T20). (c) Ligation of betaine thioester to the N-terminal cysteine of CG-GPRT or CG-T20 to give the betaine-CG-GPRT conjugate or the betaine-CG-T20 conjugate.

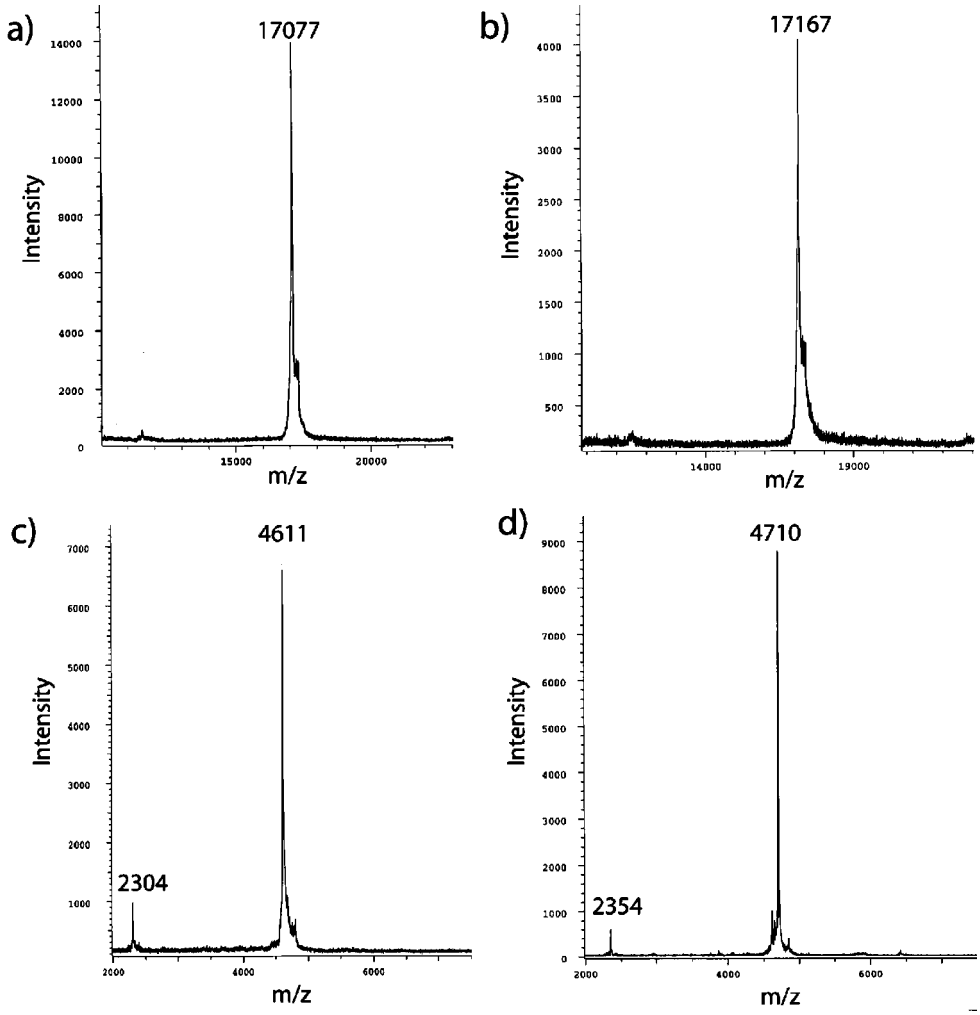

Figure 2. MALDI-TOF mass spectra of (a) CG-GPRT, calcd 17074, found 17077; (b) betaine-CG-GPRT conjugate, calcd 17174, found 17167; (c) CG-T20, calcd 4611, found 4611; (d) betaine-CG-T20 conjugate, calcd 4711, found 4710.

the insolubility of the CG-T20 peptide. However, after purification by Ni^{2+}-NTA affinity chromatography under denaturing conditions, the purified SUMO-CG-T20 was refolded to afford the soluble SUMO-CG-T20 fusion protein.

N-terminal cysteine-containing CG-GPRT and CG-T20 were prepared by TEV protease cleavage for 24 h followed by purification by reverse-phase HPLC and lyophilization to give white powders. The production of cleaved CG-GPRT and CG-T20 was confirmed by MALDI-TOF mass spectrometry (Figure 2a,c). A two-step cleavage/labeling reaction procedure (*26*) was used to ligate the betaine thioester onto the N-terminal cysteine of CG-GPRT. The ligation gave a high yield of betaine-CG-GPRT conjugate (>95%) after 24 h incubation as observed by MALDI-TOF mass spectrometry (Figure 2b). Although the cleavage of SUMO-CG-T20 was conducted under native conditions, the ligation of CG-T20 with the betaine thioester was conducted under denaturing conditions (7 M guanidine hydrochloride) because of the insolubility of the CG-T20 in native conditions. This ligation gave a high yield of betaine-CG-T20 conjugate (>95%) after 24 h incubation as observed by MALDI-TOF mass spectrometry (Figure 2d). Both the betaine-CG-GPRT conjugate and betaine-CG-T20 conjugate were purified by reverse-phase HPLC and lyophilized to give white powders.

The effects of betaine modification on the structure and function of CG-GPRT and CG-T20 were assessed by far-UV circular dichroism (CD) spectroscopy and enzyme assays. Betaine modification had little or no effect on the CD spectra of CG-GPRT and CG-T20, indicating that betaine modification on the N-terminus of these polypeptides did not alter their structures appreciably (see Supporting Information). GPRT activity assays also showed that betaine modification had little effect on the specific activity of CG-GPRT compared to betaine-modified CG-GPRT (14.90 μmol/min per mg vs 14.16 μmol/min per mg, respectively; see Supporting Information). Overall, these results indicate that addition of a betaine moiety does not significantly affect the structure and function of these polypeptides.

To investigate the effect of betaine modification on aggregation and solubility, the turbidity and percent solubility of CG-GPRT and betaine-CG-GPRT conjugate at different pH values were determined using standard procedures for determining protein solubility and aggregration (Figure 3a,b, square and circle symbols) (*18*, *31*–*33*). The proteins were dissolved to 1 mg/mL concentration in 100 mM sodium phosphate buffer pH 9 followed by pH adjustment to 5, 6, and 7 with 1 M HCl. After 24 h incubation at 4 °C, the turbidity at 400 nm was measured to determine the insoluble aggregates. Then, the precipitate was removed by centrifugation and the concentrations of the supernatants were determined by UV absorbance at 280 nm (*31*–*33*). The percent solubility was determined by comparing the concentration of the supernatant to the initial concentration. As anticipated, both the CG-GPRT and the betaine-CG-GPRT conjugate aggregated and precipitated under acidic conditions after incubation for 24 h. The turbidity of the protein solution was increased for both the CG-GPRT and the betaine-CG-GPRT conjugate as the pH of the solution became more

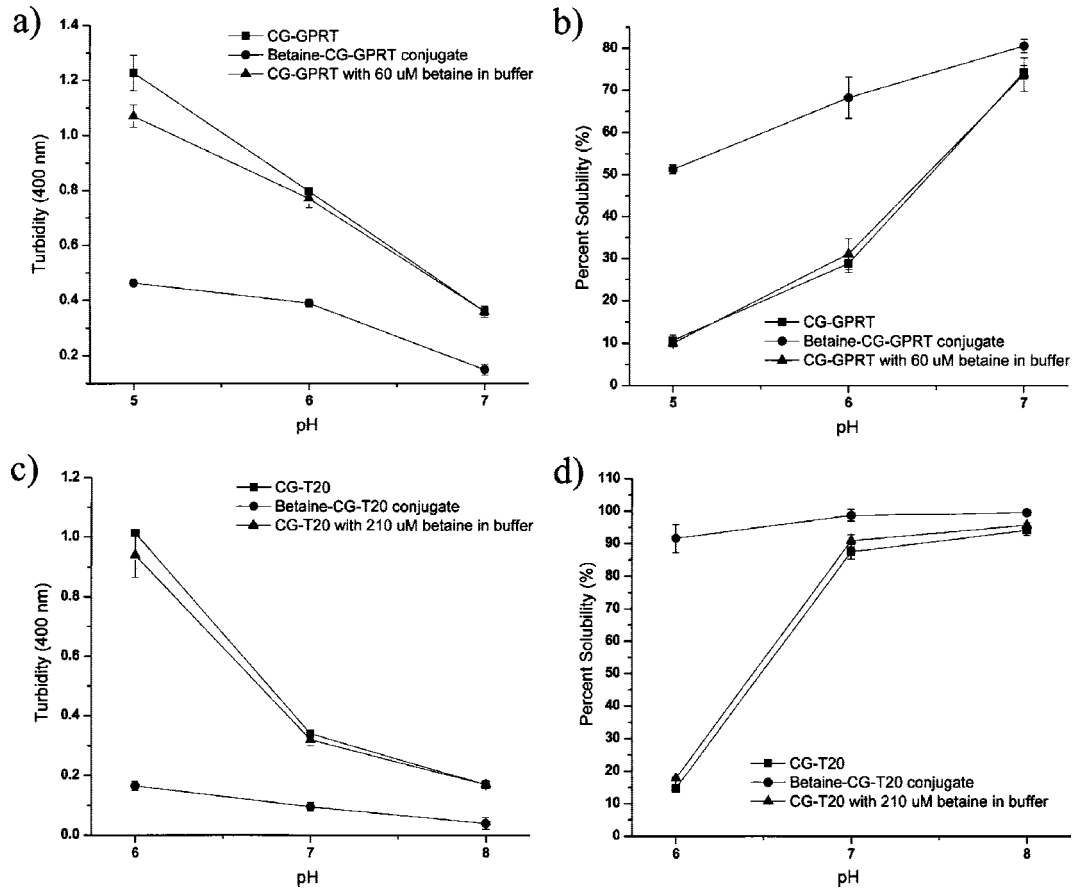

Figure 3. Effects of betaine modification on turbidity and solubility of CG-GPRT and CG-T20. (a) Turbidity (at 400 nm) of CG-GPRT in phosphate buffer (square), betaine-CG-GPRT conjugate in phosphate buffer (circle), and CG-GPRT with 60 μM betaine in phosphate buffer (triangle) at pH 5, 6, and 7. (b) Percent solubility of CG-GPRT in phosphate buffer (square), betaine-CG-GPRT conjugate in phosphate buffer (circle), and CG-GPRT with 60 μM betaine in phosphate buffer (triangle) at pH 5, 6, and 7. (c) Turbidity (at 400 nm) of CG-T20 in phosphate buffer (square), betaine-CG-T20 conjugate in phosphate buffer (circle), and CG-T20 with 210 μM betaine in phosphate buffer (triangle) at pH 6, 7, and 8. (d) Percent solubility of CG-T20 in phosphate buffer (square), betaine-CG-T20 conjugate in phosphate buffer (circle), and CG-T20 with 210 μM betaine in phosphate buffer (triangle) at pH 6, 7, and 8. The concentration of all proteins and peptides are 1 mg/mL.

acidic (Figure 3a). However, at all pHs, the turbidity of the betaine-CG-GPRT conjugate was lower than that of CG-GPRT, especially at lower pH. These results indicate that the betaine-modified CG-GPRT forms a smaller amount of insoluble aggregates than unmodified CG-GPRT under the same conditions. It is possible that some soluble aggregates may have been present in the solution that would not be detected by the turbidity assay, but it is clear from the turbidity data that betaine modification decreases the formation of insoluble aggregates. The solubility of both proteins decreased as the pH of the solution was decreased (Figure 3b), and the solubility of the betaine-CG-GPRT conjugate was higher than that of the CG-GPRT at all pHs, with the difference being greater at lower pH. The consistency between the turbidity results and percent solubility results suggests that the protein concentration changes after incubation are due to protein aggregation and precipitation and not other factors that could cause protein loss such as surface absorbance or loss during centrifugation. Thus, all of these results indicate that the betaine-modified CG-GPRT protein has less aggregation propensity and better solubility than unmodified CG-GPRT protein, especially at acidic pH. As a control, the turbidity and percent solubility of a 1 mg/mL sample of CG-GPRT with the presence of 60 μM betaine (the same concentration of free betaine as there was conjugated betaine in the 1 mg/mL of betaine-CG-GPRT conjugate experiment) were also determined at pH 5, 6, and 7 (Figure 3a,b, triangle symbol). With the presence of free betaine, both the turbidity and the percent solubility of CG-GPRT were almost the same as those of CG-GPRT in the experiment without betaine at all (Figure 3a,b). This suggests that the reduced aggregation and increased solubility of the betaine-CG-GPRT protein were actually caused by the covalent attachment of betaine onto the protein, not caused by the introduction of the betaine moiety into the protein solution.

Next, we also performed the same aggregation, solubility, and control experiments for the CG-T20 peptide and betaine-CG-T20 conjugate at pH 6, 7, and 8. The turbidity and percent solubility measurements gave similar but more pronounced results than the CG-GPRT protein experiments (Figure 3c,d). At pH 7 and 8, over 85% of the CG-T20 and almost 100% of the betaine-CG-T20 conjugate were soluble in solution, which indicated that there was little or no protein loss during the incubation and centrifugation. When the pH was dropped down to 6, most of the CG-T20 (about 85%) aggregated and precipitated. However, about 92% of the betaine-CG-T20 conjugate was still soluble. The turbidity measurements were consistent with the results obtained in the solubility measurements. In the free betaine control experiment, as we observed with CG-GPRT, the present of free betaine in the solution did not change the turbidity and solubility of CG-T20 much (Figure 3c,d). All these results indicate that the covalent betaine modification can reduce the aggregation propensity and increase the solubility of both the CG-GPRT protein and the CG-T20 peptide, especially at acidic pH.

As described above, betaine modification of our aggregation-prone model protein and peptide reduces aggregation

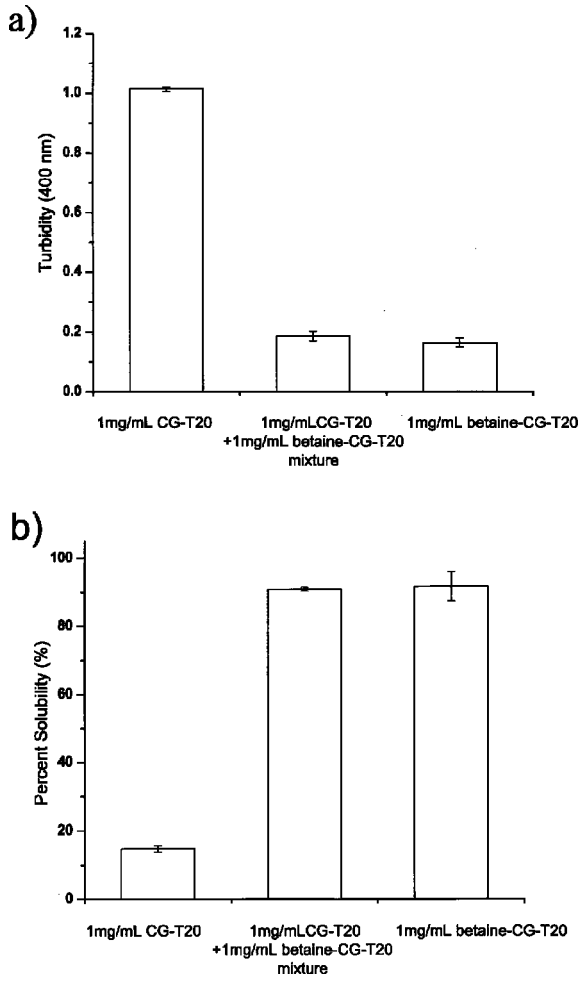

Figure 4. Betaine-CG-T20 conjugate inhibits the aggregation of CG-T20. (a) Turbidity (at 400 nm) of CG-T20 (1 mg/mL), mixture of CG-T20 (1 mg/mL) and betaine-CG-T20 conjugate (1 mg/mL), and betaine-CG-T20 conjugate (1 mg/mL) at pH 6. (b) Percent solubility of CG-T20 (1 mg/mL), mixture of CG-T20 (1 mg/mL) and betaine-CG-T20 conjugate (1 mg/mL), and betaine-CG-T20 conjugate (1 mg/mL) at pH 6.

and increases solubility of the modified polypeptides. To investigate further as to whether the betaine-modified polypeptides can inhibit the aggregation of unmodified polypeptides, an aggregation inhibition assay was performed with CG-T20. In this assay, a mixture of 1 mg of unmodified CG-T20 and 1 mg betaine-modified CG-T20 was dissolved in 1 mL 100 mM sodium phosphate buffer pH 9 followed by pH adjustment with 1 M HCl. After 24 h incubation at 4 °C, the turbidity and percent solubility were determined. Because the largest differences in turbidity and solubility were observed between CG-T20 and the betaine-CG-T20 conjugate at pH 6, the turbidity and percent solubility were measured at pH 6 (Figure 4). Although there was a total of 2 mg/mL of CG-T20 species in the solution, the turbidity of this mixture (0.187) was almost same as that of the betaine-CG-T20 conjugate (0.165) (Figure 4a). The percent solubility of this CG-T20 and betaine-CG-T20 mixture (90.8%) was also as high as that of the betaine-CG-T20 conjugate (91.6%) (Figure 4b). These results indicate that the betaine-modified CG-T20 can not only prevent the aggregation of itself, but it can also inhibit the aggregation of unmodified CG-T20.

In conclusion, we have investigated the effect of site-specific betaine modification on the aggregation and solubility of polypeptides, using the enzyme CG-GPRT and the HIV entry inhibitor peptide CG-T20 as models. The site-specific modification was achieved by native chemical ligation between a betaine thioester and TEV protease generated N-terminal cysteines on CG-GPRT and CG-T20. As demonstrated here, the betaine modification can reduce the aggregation propensity and increase the solubility of both the CG-GPRT protein and the CG-T20 peptide without significantly affecting their structures and functions. Compared to the unmodified polypeptides, betaine modification increased the solubility of CG-GPRT approximately 4.8-fold at pH 5, and the solubility of CG-T20 was increased 6.2-fold at pH 6 (Figure 3). This compares favorably with solubility increases that have been reported for polyarginine and polylysine tags of five and six residues (*18*), but with a much smaller molecular weight 100 betaine modification achieving similar solubility enhancements. In addition, our investigation demonstrated that the betaine-CG-T20 conjugate is able to function as an inhibitor of the aggregation of unmodified CG-T20. Thus, the betaine modification strategy presented here may prove useful for alleviating aggregation and solubility problems of many hydrophobic proteins and peptides to facilitate biochemical, structural, and pharmaceutical studies.

ACKNOWLEDGMENT

This project was supported by Indiana University. We thank Jonathan A. Karty and Angela M. Hansen for assistance in mass spectrometry and Brian S. Hamilton for assistance in circular dichroism measurement.

Supporting Information Available: Experimental procedures; ^{1}H NMR spectra, ^{13}C NMR spectra and HR-ESI-MS spectra of betaine thioester (1); MALDI-TOF spectra and CD spectra of CG-GPRT, betaine-CG-GPRT conjugate, CG-T20 and betaine-CG-T20 conjugate This material is available free of charge via the Internet at http://pubs.acs.org.

LITERATURE CITED

(1) Yee, A., Pardee, K., Christendat, D., Savchenko, A., Edwards, A. M., and Arrowsmith, C. H. (2003) Structural proteomics: Toward high-throughput structural biology as a tool in functional genomics. *Acc. Chem. Res. 36*, 183–189.
(2) Biron, Z., Khare, S., Quadt, S. R., Hayek, Y., Naider, F., and Anglister, J. (2005) The 2F5 epitope is helical in the HIV-1 entry inhibitor T-20. *Biochemistry 44*, 13602–13611.
(3) Chi, E. Y., Krishnan, S., Randolph, T. W., and Carpenter, J. F. (2003) Physical stability of proteins in aqueous solution: Mechanism and driving forces in nonnative protein aggregation. *Pharm. Res. 20*, 1325–1336.
(4) Fowler, S. B., Poon, S., Muff, R., Chiti, F., Dobson, C. M., and Zurdo, J. (2005) Rational design of aggregation-resistant bioactive peptides: Reengineering human calcitonin. *Proc. Natl. Acad. Sci. U.S.A. 102*, 10105–10110.
(5) Taylor, J. P., Hardy, J., and Fischbeck, K. H. (2002) Toxic proteins in neurodegenerative disease. *Science 296*, 1991–1995.
(6) Ross, C. A., and Poirier, M. A. (2004) Protein aggregation and neurodegenerative disease. *Nat. Med. 10*, S10–17.
(7) Fink, A. L. (2006) The aggregation and fibrillation of α-synuclein. *Acc. Chem. Res. 39*, 628–634.
(8) Haass, C., and Selkoe, D. J. (2007) Soluble protein oligomers in neurodegeneration: lessons from the Alzheimer's amyloid *β*-peptides. *Nat. Rev. Mol. Cell. Biol. 8*, 101–112.
(9) Samuelsson, E., Moks, T., Nilsson, B., and Uhlen, M. (1994) Enhanced in vitro refolding of insulin-like growth factor I using a solubilizing fusion partner. *Biochemistry 33*, 4207–4211.
(10) Kapust, R. B., and Waugh, D. S. (1999) *Escherichia coli* maltose-binding protein is uncommonly effective at promoting the solubility of polypeptides to which it is fused. *Protein Sci. 8*, 1668–1674.

(11) Kataeva, I., Chang, J., Xu, H., Luan, C-H., Zhou, J., Uversky, V. N., Lin, D., Horanyi, P., Liu, Z. J., Ljungdahl, L. G., Rose, J., Luo, M., and Wang, B-C. (2005) Improving solubility of *Shewanella oneidensis* MR-1 and *Clostridium thermocellum* JW-20 proteins expressed into *Esherichia coli*. *J. Proteome Res. 4*, 1942–1951.

(12) Luo, Y., Huang, X., and Mckeehan, W. L. (2007) High yield, purity and activity of soluble recombinant Bacteroides thetaiotaomicron GST-heparinase I from *Escherichia coli*. *Arch. Biochem. Biophys. 460*, 17–24.

(13) Loose, C. R., Langer, R. S., and Stephanopoulos, G. N. (2007) Optimization of protein fusion partner length for maximizing in vitro translation of peptides. *Biotechnol. Prog. 23*, 444–451.

(14) Sinclair, A. M., and Elliott, S. (2005) Glycoengineering: The effect of glycosylation on the properties of therapeutic proteins. *J. Pharm. Sci. 94*, 1626–1635.

(15) Pomroy, N. C., and Deber, C. M. (1999) Conjugation of polyethylene glycol via a disulfide bond confers water solubility upon a peptide model of a protein transmembrane segment. *Anal. Biochem. 275*, 224–230.

(16) Basu, A., Yang, K., Wang, M., Liu, S., Chintala, R., Palm, T., Zhao, H., Peng, P., Wu, D., Zhang, Z., Hua, J., Hsieh, M-C., Zhou, J., Petti, G., Li, X., Janjua, A., Mendez, M., Liu, J., Longley, C., Zhang, Z., Mehlig, M., Borowski, V., Viswanathan, M., and Filpula, D. (2006) Structure-function engineering of interferon-β-1b for improving stability, solubility, potency, immunogenicity, and pharmacokinetic properties by site-selective mono-PEGylation. *Bioconjugate Chem. 17*, 618–630.

(17) Marsac, Y., Cramer, J., Olschewski, D., Alexandrov, K., and Becker, C. F. (2006) Site-specific attachment of polyethylene glycol-like oligomers to proteins and peptides. *Bioconjugate Chem. 17*, 1492–1498.

(18) Kato, A., Maki, K., Ebina, T., Kuwajima, K., Soda, K., and Kuroda, Y. (2007) Mutational analysis of protein solubility enhancement using short peptide tags. *Biopolymers 85*, 12–18.

(19) Johnson, E. C., Malito, E., Shen, Y., Rich, D., Tang, W-J., and Kent, S. B. (2007) Modular total chemical synthesis of a human immunodeficiency virus type 1 protease. *J. Am. Chem. Soc. 129*, 11480–11490.

(20) Holden, J. A., and Kelley, W. N. (1978) Human hypoxanthine-guanine phosphoribosyltransferase evidence for tetrameric structure. *J. Biol. Chem. 253*, 4459–4463.

(21) Vos, S., de Jersey, J., and Martin, J. L. (1997) Crystal structure of *Escherichia coli* xanthine phosphoribosyltransferase. *Biochemistry 36*, 4125–4134.

(22) Krambovitis, E., Porichis, F., and Spandidos, D. A. (2005) HIV entry inhibitors: a new gnenration of antiretroviral drugs. *Acta. Pharmacol. Sin. 26*, 1165–1173.

(23) Dawson, P. E., Muir, T. W., Clark-Lewis, I., and Kent, S. B. H. (1994) Synthesis of proteins by native chemical ligation. *Science 266*, 776–779.

(24) Muir, T. W., Sondhi, D., and Cole, P. A. (1998) Expressed protein ligation: A general method for protein engineering. *Proc. Natl. Acad. Sci. U.S.A. 95*, 6705–6710.

(25) Erlanson, D. A., Chytil, M., and Verdine, G. L. (1996) The leucine zipper domain controls the orientation of AP-1 in the NFAT•AP-1•DNA complex. *Chem. Biol. 3*, 981–991.

(26) Tolbert, T. J., and Wong, C-H. (2002) New methods for proteomic research: Preparation of proteins with N-terminal cysteines for labeling and conjugation. *Angew. Chem., Int. Ed. 41*, 2171–2174.

(27) Tolbert, T. J., Franke, D., and Wong, C-H. (2005) A new strategy for glycoprotein synthesis: Ligation of synthetic glycopeptides with truncated proteins expressed in *E. coli* as TEV protease cleavable fusion protein. *Bioorg. Med. Chem. 13*, 909–915.

(28) Marblestone, J. G., Edavettal, S. C., Lim, Y., Lim, P., Zuo, X., and Butt, T. R. (2006) Comparison of SUMO fusion technology with traditional gene fusion systems: enhanced expression and solubility with SUMO. *Protein Sci. 15*, 182–189.

(29) Zuo, X., Li, S., Hall, J., Mattern, M. R., Tran, H., Shoo, J., Tan, R., Weiss, S. R., and Butt, T. R. (2005) Enhanced expression and purification of membrane proteins by SUMO fusion in *Escherichia coli*. *J. Struct. Funct. Genom. 6*, 103–111.

(30) Butt, T. R., Edavettal, S. C., Hall, J. P., and Mattern, M. R. (2005) SUMO fusion technology for difficult-to-express proteins. *Protein Expr. Purif. 43*, 1–9.

(31) Janciauskiene, S., García de Frutos, P., Carlemalm, E., Dahlbäck, B., and Eriksson, S. (1995) Inhibition of Alzheimer β-peptide fibril formation by serum amyloid P component. *J. Biol. Chem. 270*, 26041–26044.

(32) Jarrett, J. T., and Lansbury, P. T., Jr. (1992) Amyloid fibril formation requires a chemically discriminating nucleation event: Studies of an amyloidogenic sequence from the bacterial protein OsmB. *Biochemistry 31*, 12345–12352.

(33) Jarrett, J. T., Berger, E. P., and Lansbury, P. T., Jr. (1993) The carboxy terminus of β amyloid protein is critical for the seeding of amyloid formation: implications for the pathogenesis of Alzheimer's disease. *Biochemistry 32*, 4693–4697.

BC800063K

A Collagen-Binding Mimetic of Neural Cell Adhesion Molecule

Hiroko Miyazaki,[†] Koichi Kato,[†] Yuji Teramura,[‡] and Hiroo Iwata*[,†]

Department of Reparative Materials, Institute for Frontier Medical Sciences and Department of Polymer Chemistry, Graduate School of Engineering, Kyoto University, Kyoto, Japan. Received December 18, 2007; Revised Manuscript Received April 13, 2008

A chimeric protein consisting of a cell-adhesive peptide derived from a neural cell adhesion molecule and a collagen-binding domain was synthesized using recombinant DNA technology. Here, we demonstrate that the chimeric protein binds to type I collagen and promotes the adhesion and neurite extension of hippocampus neurons. These results suggest that the chimeric protein has potential to provide microenvironments for neurons to adhere and survive in collagen-based matrices for use in cell-based therapies for central nervous disorders.

INTRODUCTION

Stem cell-based therapy is recognized as a potential therapeutic strategy for neurodegenerative diseases (*1, 2*). However, the low level of cell survival following transplantation is the major problem associated with current techniques (*3*). Cell death after transplantation is attributed in part to anoikis-induced apoptosis caused by the destruction of cell−substrate and cell−cell interactions upon cell preparation (*4*). Other factors include inflammatory reactions caused by activated microglia infiltrating into injection sites (*5*).

To overcome these adverse effects, we are involved in the development of collagen-based biodegradable matrices that act as temporal barriers against the infiltration of inflammatory cells and, at the same time, initially provide substrates for neuronal cell adhesion mediated by cell adhesion molecules. To date, several research groups utilized collagen matrices (*6–9*) to provide favorable microenvironments for the proliferation and controlled differentiation of neural stem/progenitor cells. However, current technologies have simply used collagen matrices as physical carriers without expectation for adhesion signaling in neural cells.

Our approach is to design collagen matrices containing a peptide sequence that facilitates neural cell adhesion molecule (NCAM)-mediated signaling in neurons. To efficiently incorporate the peptide into the collagen matrix, a chimeric protein consisting of a NCAM-related peptide and the A3 domain of the von Willebrand factor (vWF) was synthesized by means of recombinant DNA technology. Since the vWF A3 domain has an affinity for type I collagen (*10*), the chimeric protein is expected to specifically bind to collagen matrices, displaying the peptide toward neurons.

As a NCAM-related peptide, we chose a 12 amino acid residue peptide (GRILARGEINFK), termed P2, derived from NCAM (*11–13*). NCAM is abundantly expressed on neurons and their progenitors, and plays a pivotal role in neuronal development, synaptic plasticity, and regeneration (*14, 15*). NCAM belongs to the immunoglobulin (Ig) superfamily, and its extracellular domain is composed of N-terminal five Ig-like modules with two consecutive fibronectin type III modules. The double-reciprocal, homophilic interactions of NCAMs activate intracellular signaling pathways in neurons, leading to neurite outgrowth. The P2 peptide sequence contained in the second Ig (IgII) module was identified as a binding site for the first Ig (IgI) module and interestingly shown to act as an agonist for NCAM, promoting neuronal differentiation and survival (*11–13*).

In this communication, we describe the preparation and characterization of a chimeric protein that consists of the P2 peptide and the collagen-binding A3 domain of vWF (P2-vWFCBD). The affinity of P2-vWFCBD to type I collagen was studied by surface plasmon resonance (SPR) analysis. The feasibility of P2-vWFCBD for the promotion of neuronal adhesion and its outgrowth on collagen was examined using the primary culture of hippocampus neurons.

EXPERIMENTAL PROCEDURES

Chimeric Gene Construct. The cDNA (cDNA) encoding the human vWF A3 domain [189 amino acids (aa)] (*10*) was generated by polymerase chain reaction (PCR) using human pancreas cDNA library as a template. The PCR primers were designed to introduce an EcoR I restriction site at the 5′ end (CGAATTCGACTGCAGCCAGCCCCTGGAC) and an Xho I restriction site at the 3′ end (for P2-containing protein: GCTCGAGCTTGAAGTTGATTTCCCCGCGGGCCAGGATCCTGCCAGAGCACAGTTTGTGGAGGAAGG; for control protein: GCTCGAGAGAGCACAGTTTGTGGAGGAAGG). The underlined sequences encode P2 peptide. The chimeric cDNA was digested with EcoR I and Xho I and ligated to pET32a (Novagen) that had been linearized by digestion with the same enzymes. As shown in Figure 1, the EcoR I−Xho I site in pET32a was located downstream of hydrophilic thioredoxin tag (Trx-tag; 105 aa), N-terminal hexahistidine tag (His-tag), and S-peptide tag (S-tag; 15 aa); and upstream of C-terminal His-tag. A thrombin cleavage site (LVPAGS) was inserted between the N-terminal His-tag and S-tag. The plasmids, pET32-P2-vWFCBD and pET32-vWFCBD, were amplified in *E. coli* strain DH5α. The correctness of the plasmids was verified by sequencing.

Protein Expression and Purification. *E. coli* strain BL21-(DE3)pLysS (Novagen) was transformed with pET32-P2-vWFCBD and pET32-vWFCBD. Chimeric and control proteins were expressed using the Overnight Express Autoinduction System (Novagen). Proteins expressed as soluble forms were purified over His Trap HP column (Amersham). The proteins were then digested with thrombin (50 unit per mg protein) to remove the Trx-tag and N-terminal His-tag followed by

* Corresponding author. Hiroo Iwata, Department of Reparative Materials, Institute for Frontier Medical Sciences, Kyoto University, 53 Kawahara-cho, Shogoin, Sakyo-ku, Kyoto 606-8507, Japan; Phone +81-75-751-4119; Fax +81-75-751-4646; E-mail iwata@frontier.kyoto-u.ac.jp.

[†] Institute for Frontier Medical Sciences.

[‡] Graduate School of Engineering.

10.1021/bc700470v CCC: $40.75 © 2008 American Chemical Society
Published on Web 05/14/2008

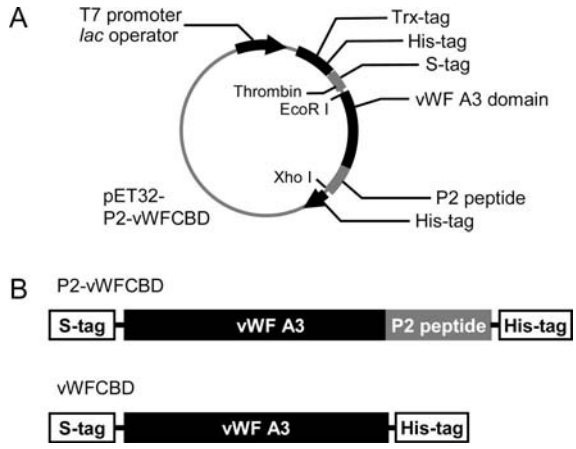

Figure 1. (A) A construct for the expression of P2-vWFCBD. The construct of control vWFCBD had a similar structure but was deficient in the oligonucleotide sequence for P2. (B) Domain structure of P2-vWFCBD and vWFCBD obtained by digesting the expressed proteins with thrombin.

purification using S-tag Purification Kit (Novagen). The purity and molecular size of the proteins were analyzed by sodium dodecylsulfate−polyacrylamide gel electrophoresis (SDS-PAGE). Protein identity was assessed by Western blot using antibody against hexahistidine tag (Abcam Ltd., Cambridge, UK) and horseradish peroxidase-linked secondary antibody against mouse immunoglobulin G (GE Healthcare UK Ltd., Buckinghamshire, UK).

SPR Analysis. The self-assembled monolayer of 11-mercaptoundecanoic acid was formed on the glass plate having a 49-nm-thick gold layer, as reported before (*16*). The glass plate was mounted to an SPR sensor equipped with a flow cell (*16*). The light reflectance was continuously monitored at a constant incident angle 0.5° smaller than the angle for the occurrence of SPR during the following procedures. Type I collagen (Sigma) was dissolved in 0.1 M acetic acid buffer (pH 4.6) to a concentration of 0.1 mg/mL, and the solution was circulated to adsorb collagen onto the monolayer. After washing with acetic acid buffer and phosphate buffered saline (PBS), PBS containing 1 mg/mL bovine serum albumin (BSA; Sigma) was circulated to block the nonspecific adsorption of proteins. Then, the solution of P2-vWFCBD or vWFCBD in PBS (20 μg/mL) was circulated to bind these proteins to collagen. Finally, the light reflectance was converted to the resonance angular shift. All measurements were carried out at 37 °C.

Circular Dichroism (CD) Spectroscopy. CD spectra of P2-vWFCBD and vWFCBD were recorded using JASCO J-805 spectropolarimeter. P2-vWFCBD and vWFCBD were dissolved in Dulbecco's PBS (pH 7.4) to a mean residue concentration of 757 and 930 μM, respectively. Spectra were acquired in a 0.5 cm path length cell at a response time of 0.5 s, a bandwidth of 1 nm, a scan speed of 100 nm/min, and 20 °C with an accumulation of eight scans.

Cell Isolation. The hippocampus was isolated from fetus of Wistar rats (E18) and dissociated into single neurons by trypsin digestion (*17*). Animal experiments were conducted according to the guidelines of the Animal Experimentation Committee of the Institute. Neurons were suspended in Neurobasal medium (Gibco) containing 2% B27 supplement (Gibco), 100 U/mL penicillin, and 100 μg/mL streptomycin, and used immediately for cell culture assays.

Cell Culture. A two-well culture slide coated with type I collagen (BioCoat, BD Biosciences) was blocked with BSA. Then, the solution of P2-vWFCBD and vWFCBD (3.0 μM) were added to the wells and incubated at 37 °C for 3 h to allow the binding of these proteins to collagen. After washing the slide with PBS, hippocampus neurons were seeded at a density of 10 000 cells/cm^2 and incubated at 37 °C under 5% CO_2 atmosphere. In some wells, a synthetic peptide GRILARGEINFK (Invitrogen) was added to a final concentration of 7.2 μM. After 3-day culture, cells were fixed with paraformaldehyde, and cell membranes were permeabilized with TritonX-100. Then, cells were immunocytochemically stained using an

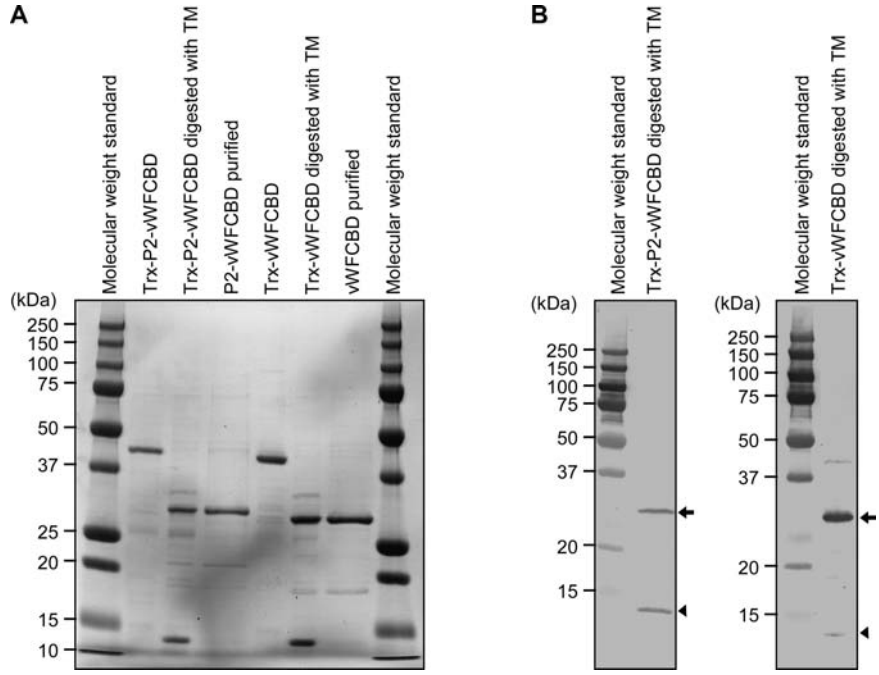

Figure 2. The result of (A) SDS-PAGE and (B) Western blot. (A) Proteins were electrophoresed in 12.5% polyacrylamide gel and visualized by Coomassie brilliant blue staining. (B) Proteins were blotted to PVDF membranes and probed using primary antibody against His-tag and horseradish peroxidase-linked secondary antibody against immunoglobulin G. Protein bands were visualized using Immunostaining HRP-1000 (Konica Minolta MG, Tokyo, Japan). Arrows and arrowheads indicate bands for, respectively, vWFCBD-containing polypeptides and Trx-tag containing fragments. TM: thrombin.

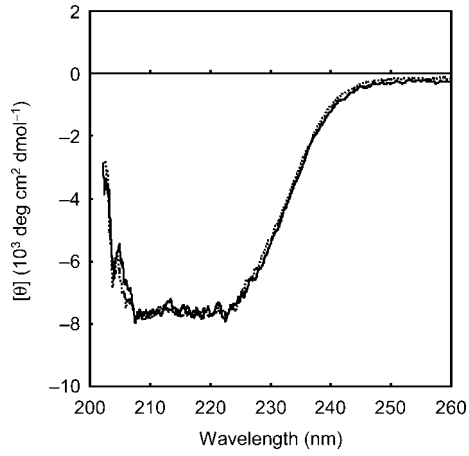

Figure 3. Far-UV CD spectra of (solid line) P2-vWFCBD and (dashed line) vWFCBD at 20 °C. Mean residue molar ellipticity [θ] is shown as a function of wavelength.

antibody to class III β-tubulin (Covance, NJ) and a fluorescently labeled secondary antibody. Cells were observed with an Olympus IX71 fluorescent microscope. The number of adhered cells was determined on four different fluorescent images and averaged.

RESULTS

Characterization of Proteins. As shown in Figure 2A, single bands were visualized by the SDS-PAGE analysis of proteins expressed in *E. coli* and purified by nickel chelate chromatography before thrombin digestion (Trx-P2-vWFCBD and Trx-vWFCBD). These bands split into two bands 26−27 kDa and 13 kDa by thrombin digestion. The former bands correspond to P2-vWFCBD and vWFCBD, whereas the latter to the segments containing the Trx-tag and the N-terminal His-tag. Further purification using the S-tag resulted in single bands corresponding to P2-vWFCBD and vWFCBD. Molecular weights estimated from the mobility of these bands are 27 kDa for P2-vWFCBD and 26 kDa for vWFCBD, in accordance with those expected from amino acid compositions. Figure 2B shows the results of Western blotting performed for Trx-P2-vWFCBD and Trx-vWFCBD after digestion with thrombin. In both cases, two protein bands were visualized at the positions of 26−27 kDa and 13 kDa, similar to the results of SDS-PAGE for corresponding samples (Figure 2A).

As shown in Figure 3, the CD spectra of P2-vWFCBD and vWFCBD are characteristic of α-helical and β-sheet secondary structure with minima at 208 and 222 nm both for α-helix and at 216 nm for β-sheet, although signal-to-noise ratios are small due to the relatively low concentration of proteins.

Binding to Collagen. The affinity of P2-vWFCBD and vWFCBD for collagen was studied by SPR analysis. As shown in Figure 4, the sensorgrams indicate the adsorption of collagen onto the carboxylic acid-terminated alkanethiol monolayer and also BSA to the surface with preadsorbed collagen. The subsequent circulation of P2-vWFCBD (Figure 4A) or vWFCBD (Figure 4B) resulted in the shift of the resonance angle, indicating the binding of these proteins. The presence of polypeptide segments containing the Trx-tag and N-terminal His-tag (proteins before thrombin digestion) hindered the binding of these proteins to collagen, even though CD spectra for these proteins obviously exhibited α-helical and β-sheet secondary structure (data not shown). The surface density of P2-vWFCBD and vWFCBD was estimated to be approximately 0.1 μg/cm^2 when adsorbed from 20 μg/mL solution, under the assumption that no replacement takes place with preadsorbed BSA and the unit angle shift corresponds to 0.5 μg/cm^2 (*18*). It was found that SPR sensorgrams decayed with time in washout phases of collagen, BSA, and fusion proteins. The gradual decrease in the resonance angles may be attributed to the intermolecular association of collagen initiated in neutral buffer solution at 37 °C. This makes it impossible to precisely determine the affinity constants for the binding of P2-vWFCBD and vWFCBD with collagen.

Adhesion of Neurons and Neurite Outgrowth. P2-vWFCBD and vWFCBD were bound to collagen-coated glass substrates. Hippocampus neurons were cultured on these surfaces for 3 days. It is obvious that cells adhered to and extended neurites on the collagen-coated surface with P2-vWFCBD (Figure 5A). In marked contrast, a small number of neurons were adhered to the collagen with vWFCBD during the entire culture periods, with poor neurite outgrowth (Figure 5B). This result is similar to our observation on untreated collagen (data not shown). These results suggest that the surface-bound P2 peptide has promotive effects on the adhesion of neurons and neurite outgrowth. The addition of soluble P2 peptide to the medium resulted in the inhibition of cell adhesion and neurite outgrowth on the surface with P2-vWFCBD (Figure 5C), indicating that the promotive effects of P2-vWFCBD involve the interaction of surface-bound P2 peptide with cell surface NCAM. The removal of the Trx-tag and the N-terminal His-tag by thrombin digestion was crucial for the adhesion of neurons and neurite outgrowth (data not shown), presumably due to the effect that the bulky segments hindered the binding

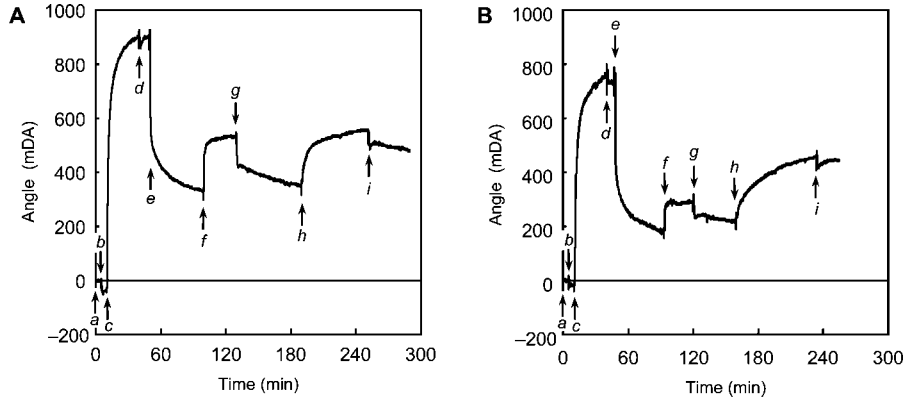

Figure 4. Representative SPR sensorgram recorded for the sequential adsorption of collagen and BSA onto the glass surface with a self-assembled monolayer of COOH-terminated alkanethiol, and the subsequent binding of (A) P2-vWFCBD and (B) vWFCBD. Proteins and buffers circulated: (a) PBS (pH 7.4), (b) sodium acetate buffer (pH 4.6), (c) 0.1 mg/mL collagen in sodium acetate buffer (pH 4.6), (d) sodium acetate buffer (pH 4.6), (e) PBS (pH 7.4), (f) 1 mg/mL BSA in PBS (pH 7.4), (g) PBS (pH 7.4), (h) 20 μg/mL P2-vWFCBD or vWFCBD in PBS (pH 7.4), and (i) PBS (pH 7.4). Measurements were carried out at 37 °C.

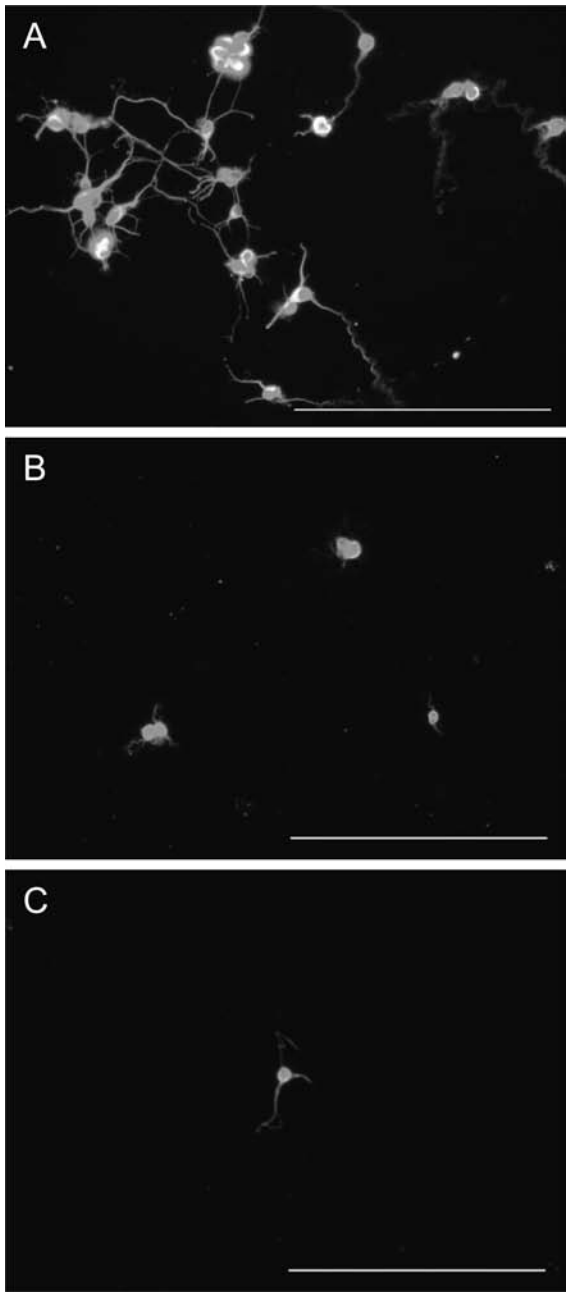

Figure 5. Fluorescent microphotographs of hippocampus neurons cultured for 3 days on the collagen-coated glass surface with (A) P2-vWFCBD and (B) vWFCBD. (C) Neurons were cultured on the collagen-coated surface with P2-vWFCBD in the presence of soluble P2 peptide. Cells were visualized by immunofluorescent staining using antibody against class III β-tubulin. Scale bar: 200 μm.

of vWFCBD to collagen and/or P2 to NCAM. Figure 6 shows the quantitative data obtained from the adhesion assay. It is seen that the number of adhered cells was much larger on the collagen-coated surface with P2-vWFCBD than on that with vWFCBD. In addition, soluble P2 significantly reduces the number of cells adhering to the collagen-coated surface with P2-vWFCBD.

DISCUSSION

The incorporation of protein-based components or the related small peptides have potential for designing collagen-based biomaterials capable of directly regulating neuronal adhesion and neurite outgrowth. Our previous study (*19*) revealed that the vWFCBD-containing chimeric protein enables us to densely

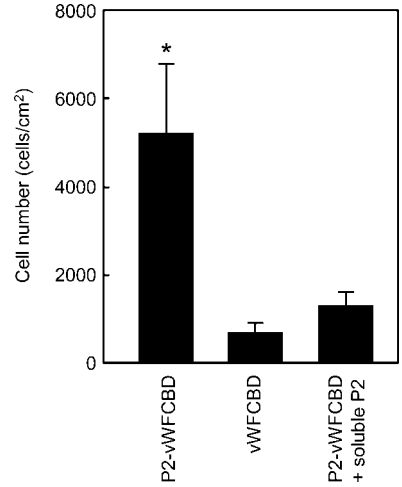

Figure 6. The number of neurons adhered to the collagen-coated glass surface with P2-vWFCBD and vWFCBD. The data are also shown for cells cultured on collagen with P2-vWFCBD in the presence of soluble P2 peptide. Cell numbers were determined 3 day after seeding. Error bars represent standard error of the mean ($n = 4$). *Statistically significant compared to the other two conditions ($p < 0.05$, Student's *t* test).

display the functional fusion partner on collagen fibrils. This strategy based on specific molecular recognition is also adapted in the present study. The chimeric protein containing a terminal anchoring domain can be immobilized onto substrates in the proper orientation by simple procedures under physiological conditions (*20*). These features form a marked contrast to covalent immobilization achieved by chemical reactions.

It was reported that the A3 domain of vWF has an affinity for type I collagen (*10*) with an association constant of the order of 10^8 M^{-1} (*21*). It was revealed from our SPR analysis that P2-vWFCBD and vWFCBD bind to collagen, suggesting the minor effect of additional sequences such as N-terminal S-tag and C-terminal His-tag. Furthermore, the binding is not affected by fusing the 12-aa residue P2 peptide at the C-terminus. In addition, the CD spectra shown in Figure 3 are in accordance with that previously reported for the recombinant A3 domain (*22*), suggesting the high conformational integrity of our proteins. To improve much more the structural stability of chimeric proteins, it is interesting to use collagen-binding peptides of shorter length, for instance, a 10-aa sequence within the D2 domain of vWF (*23*) and a 35-aa sequence in bone sialoprotein (*24*).

The results of cell culture demonstrate that the adhesion of neurons was promoted because of the P2 peptide displayed on the collagen substrate that is originally inert for neurons. It is known that the double-reciprocal binding of IgI and IgII modules of NCAMs promotes cell−cell adhesion and activates intracellular signaling pathways (*15*). Therefore, we expect that the P2-vWFCBD/collagen composite mimics the surface of neurons interacting with adjacent cells through NCAM−NCAM homophilic binding. P2 is a small peptide contained as a consecutive sequence of the FG loop in the NCAM IgII module (*13*). Our data suggest that the fusion with vWFCBD and the His-tag has minor effects on the function of the small P2 peptide.

In summary, we have reported here the synthesis of the collagen binding mimetic of NCAM, P2-vWFCBD, that mediates adhesion of neurons to a collagen matrix. The experimental data indicate that the P2-vWFCBD binds to collagen through vWFCBD, while the P2 peptide facilitates adhesion of neurons through interaction with NCAM. These findings suggest that P2-vWFCBD has the potential to provide favorable microenvironments for neurons to adhere and survive in collagen-based

matrices. Although this paper focuses on the utilization of the chimeric protein for controlling neuronal behaviors, the CBD-mediated modification of collagen will find a broad range of applications by appropriately selecting fusion partners.

ACKNOWLEDGMENT

This work was supported by Kobe Cluster, the Knowledge-Based Cluster Creation Project, and Grants-in-Aid for Scientific Research (No. 19659364), MEXT.

LITERATURE CITED

(1) Björklund, A., and Lindvall, O. (2000) Cell replacement therapies for central nervous system disorders. *Nat. Neurosci. 3*, 537–544.

(2) Goldman, S. (2005) Stem and progenitor cell-based therapy of the human central nervous system. *Nat. Biotechnol. 23*, 862–871.

(3) Takahashi, J. (2007) Stem cell therapy for Parkinson's disease. *Expert Rev. Neurother. 7*, 667–675.

(4) Marchionini, D. M., Collier, T. J., Camargo, M., McGuire, S., Pitzer, M., and Sortwell, C. E. (2003) Interference with anoikis-induced cell death of dopamine neurons: implications for augmenting embryonic graft survival in a rat model of Parkinson's disease. *J. Comp. Neurol. 464*, 172–179.

(5) Tambur, A. R. (2004) Transplantation immunology and the central nervous system. *Neurol. Res. 26*, 243–255.

(6) O'Connor, S. M., Stenger, D. A., Shaffer, K. M., Maric, D., Barker, J. L., and Ma, W. (2000) Primary neural precursor cell expansion, differentiation and cytosolic Ca^{2+} response in three-dimensional collagen gel. *J. Neurosci. Methods 102*, 187–195.

(7) Chen, S. S., Revoltella, R. P., Papini, S., Michelini, M., Fitzgerald, W., Zimmerberg, J., and Margolis, L. (2003) Multilineage differentiation of rhesus monkey embryonic stem cells in three-dimensional culture systems. *Stem Cells 21*, 281–295.

(8) Itoh, T., Satou, T., Dote, K., Hashimoto, S., and Ito, H. (2005) Effect of basic fibroblast growth factor on cultured rat neural stem cell in three-dimensional collagen gel. *Neurol. Res. 27*, 429–432.

(9) Brannvall, K., Bergman, K., Wallenquist, U., Svahn, S., Bowden, T., Hilborn, J., and Forsberg-Nilsson, K. (2007) Enhanced neuronal differentiation in a three-dimensional collagen-hyaluronan matrix. *J. Neurosci. Res. 85*, 2138–2146.

(10) Huizinga, E. G., Martijn van der Plas, R., Kroon, J., Sixma, J. J., and Gros, P. (1997) Crystal structure of the A3 domain of human von Willebrand factor: implications for collagen binding. *Structure 5*, 1147–1156.

(11) Li, S., Kolkova, K., Rudenko, O., Soroka, V., Poulsen, F. M., Bock, E., and Berezin, V. (2005) Triple effect of mimetic peptides interfering with neural cell adhesion molecule homophilic cis interactions. *Biochemistry 44*, 5034–5040.

(12) Pedersen, M. V., Køhler, L. B., Ditlevsen, D. K., Li, S., Berezin, V., and Bock, E. (2004) Neuritogenic and survival-promoting effects of the P2 peptide derived from a homophilic binding site in the neural cell adhesion molecule. *J. Neurosci. Res. 75*, 55–65.

(13) Soroka, V, Kiryushko, D., Novitskaya, V., Rønn, L. C. B., Poulsen, F. M., Holm, A., Bock, E., and Berezin, V. (2002) Induction of neuronal differentiation by a peptide corresponding to the homophilic binding site of the second Ig module of the neural cell adhesion molecule. *J. Biol. Chem. 277*, 24676–24683.

(14) Jørgensen, O. S., and Bock, E. (1974) Brain specific synaptosomal membrane proteins demonstrated by crossed immunoelectrophoresis. *J. Neurochem. 23*, 879–880.

(15) Kiselyov, V. V., Soroka, V., Berezin, V., and Bock, E. (2005) Structural biology of NCAM homophilic binding and activation of FGFR. *J. Neurochem. 94*, 1169–1179.

(16) Hirata, I., Hioki, Y., Toda, M., Kitazawa, T., Murakami, Y., Kitano, E., Kitamura, H., Ikada, Y., and Iwata, H. (2003) Deposition of complement protein C3b on mixed self-assembled monolayers carrying surface hydroxyl and methyl groups studied by surface plasmon resonance. *J. Biomed. Mater. Res., Part A 66*, 669–676.

(17) Kudoh, S. N., Kiyosue, K., and Taguchi, T. (2002) A synaptic potentiation by a protein factor distinct from those induced by neurotrophins. *Int. J. Dev. Neurosci. 20*, 55–62.

(18) Knoll, W. (1991) Polymer thin films and interfaces characterized with evanescent light. *Makromol. Chem. 192*, 2827–2856.

(19) Kato, K., Sato, H., and Iwata, H. (2007) Ultrastructural study on the specific binding of genetically engineered epidermal growth factor to type I collagen fibrils. *Bioconjugate Chem. 18*, 2137–2143.

(20) Nakaji-Hirabayashi, T., Kato, K., Arima, Y., and Iwata, H. (2007) Oriented immobilization of epidermal growth factor onto culture substrates for the selective expansion of neural stem cells. *Biomaterials 28*, 3517–3529.

(21) Romijn, R. A., Westein, E., Bouma, B., Schiphorst, M. E., Sixma, J. J., Lenting, P. J., and Huizinga, E. G. (2003) Mapping the collagen-binding site in the von Willebrand factor-A3 domain. *J. Biol. Chem. 278*, 15035–15039.

(22) Auton, M., Cruz, M. A., and Moake, J. (2007) Conformational stability and domain unfolding of the von Willebrand factor A domains. *J. Mol. Biol. 366*, 986–1000.

(23) Tuan, T. L., Cheung, D. T., Wu, L. T., Yee, A., Gabriel, S., Han, B., Morton, L., Nimni, M. E., and Hall, F. L. (1996) Engineering, expression and renaturation of targeted TGF-beta fusion proteins. *Connect. Tiss. Res. 34*, 1–9.

(24) Tye, C. E., Hunter, G. K., and Goldberg, H. A. (2005) Identification of the type I collagen-binding domain of bone sialoprotein and characterization of the mechanism of interaction. *J. Biol. Chem. 280*, 13487–13492.

BC700470V

Strategy for Efficient Site-Specific FRET-Dye Labeling of Ubiquitin

Michael Wen-Pin Kao,[§,†] Li-Ling Yang,[§,‡] Jacky Chih-Kai Lin,[†] Tsong-Shin Lim,[||] Wunshain Fann,*[,‡] and Rita P.-Y. Chen*[,†]

Institute of Biological Chemistry, Academia Sinica, Taipei 115, Institute of Atomic and Molecular Sciences, Academia Sinica, Taipei 106, and Department of Physics, Tunghai University, Taichung 407, Taiwan, R. O. C. Received December 27, 2007; Revised Manuscript Received May 1, 2008

To study conformational changes within a single protein molecule, sp-FRET (single pair fluorescence resonance energy transfer) is an important technique to provide distance information. However, incorporating donor and acceptor dyes into the same protein molecule is not an easy task. Here, we report a strategy for the efficient double-labeling of a protein on a solid support. An ubiquitin mutant with two Cys mutations, one with high solvent accessibility and the other with low solvent accessibility, was constructed. The protein was bound to magnetic beads and reacted with the dyes. The first dye reacted with the side-chain of the Cys with the high solvent accessibility and the second with the other Cys under partially denaturing conditions. Using this method, we can easily label two dyes in a site-specific way on ubiquitin with a satisfied yield. The labeling sites for donor and acceptor dyes can be easily swapped.

As a spectroscopic ruler, the FRET (fluorescence resonance energy transfer) technique can provide invaluable information on structural dynamics and has been widely used in studying protein−protein interactions using donor and acceptor dyes attached to different protein molecules (*1, 2*). To study conformational changes within a single molecule, two dyes have to be added to the same molecule, which is a challenge in the case of proteins (*3, 4*). Cysteine (Cys) is the most common residue used for labeling due to its unique functional group. Labeling a short peptide with two dyes is straightforward and can be achieved by synthesizing the peptide chemically and adding the dye during the procedure (*5*). In contrast, labeling a protein with two different dyes is more difficult. Small labeled proteins can be obtained by chemical ligation of a short labeled segment to the rest of the protein (*6*). For big proteins, one method is to mix the protein with both dyes and purify the double-labeled protein from unlabeled protein, donor-labeled protein (labeled at either one or two sites), and acceptor-labeled protein (labeled at either one or two sites) (*7–9*). Another more popular method for protein labeling is to add one dye first, then react the labeled protein with the second dye. (*10, 15*) This method has been used to double-label the cold shock protein (Csp) with Alexa-488 and Alexa-594 (*13, 14, 16*) and chymotrypsin inhibitor 2 (CI2) and acyl-CoA binding protein (ACBP) with Alexa-532 and Alexa-647 (*15*). One disadvantage of this method is that protein labeled at a single site with the first dye must be separated from the unlabeled protein and protein labeled at both sites with the first dye. To avoid the formation of the two sites-labeled protein, a substoichiometric quantity of the first dye is usually used, which makes the coupling yield low. However, it cannot control the position where the first dye is added. Hong and Maret (*17*) labeled metallothionein in a more specific way. The donor dye, Alexa-488, was added to the N-terminal amino group of metallothionein and the acceptor dye, Alexa-546, was reacted with the Cys residue in the linker region of the protein. Ha et al. (*18*) also used this method to label the Cys residue and N-terminus of Staphylococcal nuclease with TMR and Cy5, respectively.

Here, we report a strategy for the efficient double-labeling of a protein on a solid support (Scheme 1). The choice of labeling sites is the most critical point in making the labeling more site-specific. Because the yield of the labeling reaction depends on the degree of exposure of the sulfhydryl group of the Cys residue to the environment, we can easily add the first dye to a more exposed Cys, then add the second to a less exposed Cys with the aid of denaturant.

Haas and co-workers (*11*) measured the reactivity of six Cys in adenylate kinase by determining the rate constants for the reaction of the six single-Cys mutants with 5,5′-dithiobis(2-nitrobenzoic acid), then chose one highly reactive cysteine and one less reactive cysteine as the labeling sites. Based on the measured reactivity, they showed that the reactivity of reaction sites could be predicted using a computer program (*19*). Here, we chose the 76 amino acid protein, ubiquitin, which has no cysteine residues, as our target and used commercial software to predict the side-chain solvent accessibility of different sites after mutation to Cys. We aimed to add one Cys in the N-terminal region and one in the C-terminal region. One ubiquitin mutant with a single Cys insertion between Met1 and Gln2, named m[C]q, was predicted, using *Discovery Studio* software (version 1.7, Accelrys, USA), to have a higher solvent accessibility. Its side-chain solvent accessible surface was predicted as 56.1 ± 8.7 Å and the percentage of residue solvent accessibility as 46.5 ± 7.3% based on 20 energy-minimized structures. A Ser65 → Cys mutant, named S65C, had a predicted side-chain solvent accessible surface of 28.0 ± 7.0 Å and a percentage of residue solvent accessibility of 21.0 ± 5.4%.

Another important feature of our strategy is the use of magnetic beads, which can tolerate high concentrations of denaturants, such as 6 M GdnHCl and 8 M urea. The advantages of carrying out the reaction on a solid support include the

* To whom correspondence could be addressed. Rita P.-Y. Chen, Institute of Biological Chemistry, Academia Sinica, No. 128, Sec. 2, Academia Rd, Nankang, Taipei, 115, Taiwan; Tel. +886-2-2785-5696, Fax +886-2-2788-9759, E-mail: pyc@gate.sinica.edu.tw. Wunshain Fann, Institute of Atomic and Molecular Sciences, Academia Sinica, No. 1, Sec. 4, Roosevelt Rd, Taipei, 10617, Taiwan; Tel. +886-2-23668237, E-mail: fann@gate.sinica.edu.tw.

§ These authors made an equal contribution.

† Institute of Biological Chemistry, Academia Sinica.

‡ Institute of Atomic and Molecular Sciences, Academia Sinica.

|| Tunghai University.

10.1021/bc700480j CCC: $40.75 © 2008 American Chemical Society
Published on Web 05/29/2008

Scheme 1. Design of Labeling Strategy

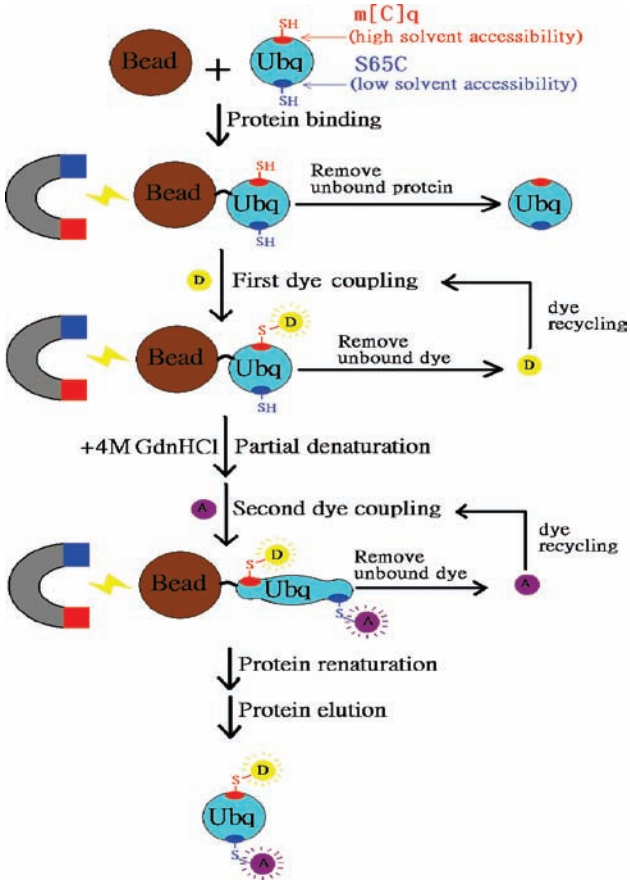

following: (1) avoiding disulfide bond formation in the protein; (2) easy removal of free dye after reaction for reuse, thus saving on cost; and (3) avoiding protein aggregation under partially denaturing conditions. A 6-His tail was added to the end of ubiquitin for bead binding. For the dye pair, we selected Alexa Fluor 488 and Alexa Fluor 594 as our donor and acceptor dyes, respectively.

The mutant proteins m[C]q and S65C were expressed separately. As predicted, m[C]q was easily labeled with dye. Met1 in m[C]q was found to be removed by cell proteases, but its removal did not affect the reactivity of Cys2 with reagent. The dye coupling reaction was almost complete within two hours (Figure 1A). In contrast, S65C could not be labeled without the aid of denaturant (Figure 1B). When 4 M GdnHCl was added to the reaction mixture, the coupling yield of S65C was ≥76%.

A mutant for double-labeling needs one Cys with high solvent accessibility and one with low solvent accessibility. These two sites with different reactivities were therefore selected as our labeling sites. The double mutant protein, named m[C]q/S65C, was constructed and expressed and showed the same structure and structural stability as wild-type ubiquitin using circular dichroism spectroscopy and nuclear magnetic resonance (see Supporting Information).

Importantly, our method can also be used to easily swap the dye labeling positions. When Alexa-488 was added first and Alexa-594 second to m[C]q/S65C, a double-labeled protein with the donor dye at the N-terminal end and the acceptor dye at the C-terminal end, denoted A488-m[C]q/S65C-A594, was obtained. The emission spectra of A488-m[C]q/S65C-A594 showed acceptor emission due to energy transfer when the donor was excited (Figure 2A). When the labels were swapped and Alexa-594 added to m[C]q/S65C before Alexa-488, the protein A594-m[C]q/S65C-A488 was obtained. The excitation spectra of

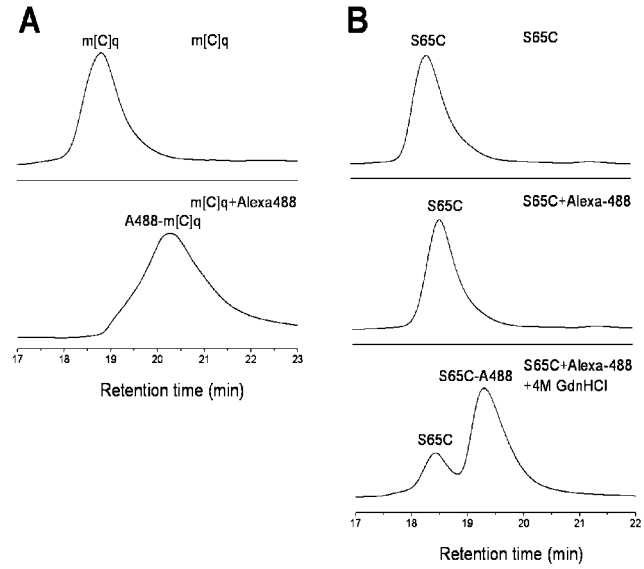

Figure 1. HPLC profiles of the dye coupling reactions of the proteins m[C]q (A) and S65C (B). The samples were analyzed by HPLC on a Vydac C18 column and the proteins detected by their absorbance at 220 nm. The proteins were resolved using a 30 min gradient of acetonitrile (15% for 5 min; 15−27% for 5 min; 27−35% for 20 min) in 0.1% trifluoroacetic acid.

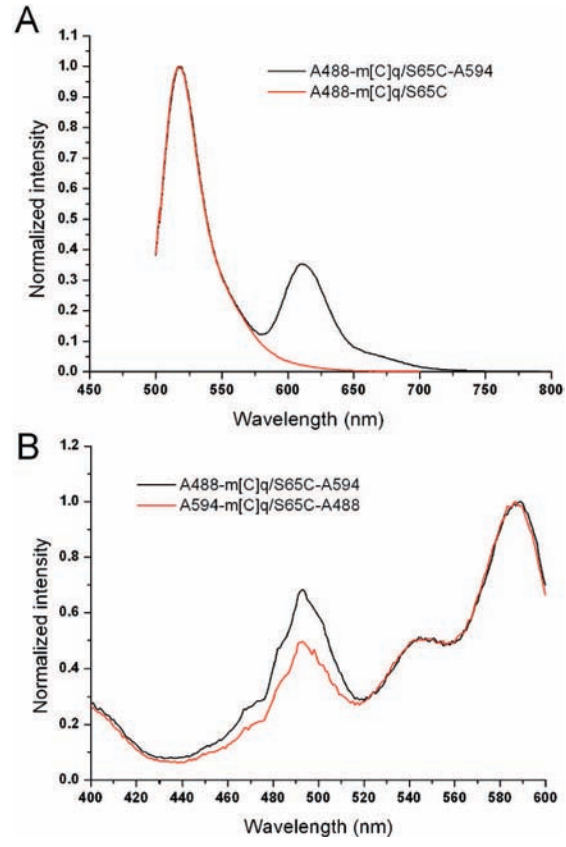

Figure 2. (A) Fluorescence emission scan of A488-m[C]q/S65C-A594 and A488-m[C]q/S65C. The excitation wavelength is 493 nm. (B) Fluorescence−excitation scan of A488-m[C]q/S65C-A594 and A594-m[C]q/S65C-A488. The emission wavelength is 620 nm. Samples were dissolved in distilled water with 0.1% Tween-20 and 5 mM DABCO (1,4-diazabicyclo[2.2.2]octane).

A488-m[C]q/S65C-A594 and A594-m[C]q/S65C-A488 were compared in Figure 2B. From the comparison of the spectra, different contributions of the donor dye in the acceptor

fluorescence suggested that the dye-labeling position can affect the efficiency of energy transfer. In protein-labeling studies, heterogeneity of the donor and acceptor labeling sites can only be ignored if each dye does not interact with the surface of the protein and is able to rotate freely or if the interaction does not interfere with the photophysics of the fluorophores and the stability of the protein. Using the normal Cys-labeling strategy, site-specific labeling is not easy to achieve, but our strategy makes this possible and can also be used to make the reversely labeled protein for comparison.

ACKNOWLEDGMENT

This work was supported by an Academia Sinica program project (AS-94-TP-A01). We are grateful for the technical support of Dr. Huei-Chun Chang of the Biophysical Instrumentation Laboratory in the Institute of Biological Chemistry. We thank Dr. Kay-Hooi Khoo and Ms. Chi-Chi Chou for the mass analysis. Proteomic mass spectrometry analyses were performed by the Core Facilities for Proteomics Research located at the Institute of Biological Chemistry, Academia Sinica, supported by a National Science Council grant (NSC 95-3112-B-001-014) and the Academia Sinica. The NMR spectra were obtained at the High-Field Nuclear Magnetic Resonance Center (HF-NMRC) supported by the National Research Program for Genomic Medicine.

Supporting Information Available: Methods for protein expression, dye labeling, and computer calculation; circular dichroism spectra of ubiquitin, m[C]q/S65C, A488-m[C]q/S65C and A488-m[C]q/S65C-A594 (Figure S1); denaturation curves of ubiquitin, m[C]q/S65C, A488-m[C]q/S65C and A488-m[C]q/S65C-A594 (Figure S2); TOCSY spectra of ubiquitin and m[C]q/S65C (Figure S3); kinetic trace of A488-m[C]q/S65C-A594 during refolding (Figure S4); mass results of m[C]q/S65C, A488-m[C]q/S65C, and A488-m[C]q/S65C-A594 after trypsin digestion (Figure S5); electrophoresis images of ubiquitin and its mutants with and without dye-labeling (Figure S6). This material is available free of charge via the Internet at http://pubs.acs.org.

LITERATURE CITED

(1) Weiss, S. (2000) Measuring conformational dynamics of biomolecules by single molecule fluorescence spectroscopy. *Nat. Struct. Biol. 7*, 724–729.

(2) Selvin, P. R. (2000) The renaissance of fluorescence resonance energy transfer. *Nat. Struct. Biol. 7*, 730–734.

(3) Kapanidis, A. N., and Weiss, S. (2002) Fluorescent probes and bioconjugation chemistries for single-molecule fluorescence analysis of biomolecules. *J. Chem. Phys. 117*, 10953–10964.

(4) Heyes, C. D., Kobitski, A. Y., Amirgoulova, E. V., and Nienhaus, G. U. (2004) Biocompatible surfaces for specific tethering of individual protein molecules. *J. Phys. Chem. B 108*, 13387–13394.

(5) Schuler, B., Lipman, E. A., Steinbach, P. J., Kumke, M., and Eaton, W. A. (2005) Polyproline and the "spectroscopic ruler" revisited with single-molecule fluorescence. *Proc. Natl. Acad. Sci. U.S.A. 102*, 2754–2759.

(6) Deniz, A. A., Laurence, T. A., Beligere, G. S., Dahan, M., Martin, A. B., Chemla, D. S., Dawson, P. E., Schultz, P. G., and Weiss, S. (2000) Single-molecule protein folding: diffusion fluorescence resonance energy transfer studies of the denaturation of chymotrypsin inhibitor 2. *Proc. Natl. Acad. Sci. U.S.A. 97*, 5179–5184.

(7) Margittai, M., Widengren, J., Schweinberger, E., Schroder, G. F., Felekyan, S., Haustein, E., Konig, M., Fasshauer, D., Grubmuller, H., Jahn, R., and Seidel, C. A. M. (2003) Single-molecule fluorescence resonance energy transfer reveals a dynamic equilibrium between closed and open conformations of syntaxin 1. *Proc. Natl. Acad. Sci. U.S.A. 100*, 15516–15521.

(8) Kuzmenkina, E. V., Heyes, C. D., and Nienhaus, G. U. (2005) Single-molecule Forster resonance energy transfer study of protein dynamics under denaturing conditions. *Proc. Natl. Acad. Sci. U.S.A. 102*, 15471–15476.

(9) Kuzmenkina, E. V., Heyes, C. D., and Nienhaus, G. U. (2006) Single-molecule FRET study of denaturant induced unfolding of RNase H. *J. Mol. Biol. 357*, 313–324.

(10) Rhoades, E., Gussakovsky, E., and Haran, G. (2003) Watching proteins fold one molecule at a time. *Proc. Natl. Acad. Sci. U.S.A. 100*, 3197–3202.

(11) Ratner, V., Kahana, E., Eichler, M., and Haas, E. (2002) A general strategy for site-specific double labeling of globular proteins for kinetic FRET studies. *Bioconjugate Chem. 13*, 1163–1170.

(12) Ratner, V., Sinev, M., and Haas, E. (2000) Determination of intramolecular distance distribution during protein folding on the millisecond timescale. *J. Mol. Biol. 299*, 1363–1371.

(13) Lipman, E. A., Schuler, B., Bakajin, O., and Eaton, W. A. (2003) Single-molecule measurement of protein folding kinetics. *Science 301*, 1233–1235.

(14) Schuler, B., Lipman, E. A., and Eaton, W. A. (2002) Probing the free-energy surface for protein folding with single-molecule fluorescence spectroscopy. *Nature 419*, 743–747.

(15) Laurence, T. A., Kong, X., Jager, M., and Weiss, S. (2005) Probing structural heterogeneities and fluctuations of nucleic acids and denatured proteins. *Proc. Natl. Acad. Sci. U.S.A. 102*, 17348–17353.

(16) Rhoades, E., Cohen, M., Schuler, B., and Haran, G. (2004) Two-state folding observed in individual protein molecules. *J. Am. Chem. Soc. 126*, 14686–14687.

(17) Hong, S. H., and Maret, W. (2003) A fluorescence resonance energy transfer sensor for the beta-domain of metallothionein. *Proc. Natl. Acad. Sci. U.S.A. 100*, 2255–2260.

(18) Ha, T., Ting, A. Y., Liang, J., Caldwell, W. B., Deniz, A. A., Chemla, D. S., Schultz, P. G., and Weiss, S. (1999) Single-molecule fluorescence spectroscopy of enzyme conformational dynamics and cleavage mechanism. *Proc. Natl. Acad. Sci. U.S.A. 96*, 893–898.

(19) Jacob, M. H., Amir, D., Ratner, V., Gussakowsky, E., and Haas, E. (2005) Predicting reactivities of protein surface cysteines as part of a strategy for selective multiple labeling. *Biochemistry 44*, 13664–13672.

BC700480J

Site-Specific Modification of *Candida antarctica* Lipase B via Residue-Specific Incorporation of a Non-Canonical Amino Acid

Sanne Schoffelen, Mark H. L. Lambermon, Mark B. van Eldijk, and Jan C. M. van Hest*

Department of Bioorganic Chemistry, Institute for Molecules and Materials, Radboud University Nijmegen, The Netherlands.
Received January 15, 2008; Revised Manuscript Received April 13, 2008

In order to modify proteins in a controlled way, new functionalities need to be introduced in a defined manner. One way to accomplish this is by the incorporation of a non-natural amino acid of which the side chain can selectively be reacted to other molecules. We have investigated whether the relatively simple method of residue-specific replacement of methionine by azidohomoalanine can be used to achieve monofunctionalization of the model enzyme *Candida antarctica* lipase B. A protein variant was engineered with one additional methionine residue. Due to the high hydrophobicity and low abundance of methionine, this was the only residue out of five that was exposed to the solvent. The use of the Cu^{I}-catalyzed [3 + 2] cycloaddition under native conditions resulted in a monofunctionalized enzyme which retained hydrolytic activity. The strategy can be considered a convenient tool to modify proteins at a single position as long as one solvent-exposed methionine is available.

The introduction of novel functionalities into proteins has been extensively studied in recent decades. Chromophores, polymers, and polypeptides have been coupled to proteins to study or manipulate their function (*1, 2*). In most of these cases, the side chain functionalities of the amino acids cysteine and lysine were targeted for conjugation reactions because of the reactivity of the free thiol and amine moieties, respectively (*3–5*). However, cysteines are often involved in disulfide bonds that occur inside proteins. Breakage of these bonds can easily lead to loss of structural integrity and, hence, function. Lysine residues are positively charged, predominantly located at the protein surface, and relatively abundant. As a consequence, it is very likely that multiple functional handles are introduced when this residue is targeted for modification (*6*). Since the properties of the bioconjugates thus generated are influenced by the degree and site of modification, it is highly desirable to introduce new functional groups in a more defined manner (*7, 8*).

One approach to achieve this involves the modification of proteinogenic amino acids of which only some residues are exposed to the solvent. As an example, Francis et al. have shown that tyrosine can be functionalized using π-allylpalladium complexes (*9*). Only 4 tyrosines are present in their model protein chymotrypsinogen (245 amino acids in total). Two residues are surface-accessible and were therefore selectively modified. This strategy is somewhat limited, since most hydrophobic amino acids have no suitable reactivity in the side chain. One way to overcome this limitation is by replacing natural amino acids with non-canonical analogues with similar structure. This replacement can be performed in a residue-specific manner using auxotrophic bacterial strains. The bacteria, being unable to produce one of the natural amino acids, incorporates the supplied non-canonical analogue at each position in the protein where normally the natural amino acid would be present (*10*). In this way, there are still multiple reactive handles introduced. Non-natural amino acids can also be introduced in a site-directed way via in vivo techniques such as the amber suppressor method (*11–13*). One of the drawbacks of the latter method is that it involves complicated and time-consuming molecular biology procedures.

We hypothesized that, as an alternative to tyrosine, methionine would be a good candidate for monofunctionalization of proteins. It is one of the least abundant amino acids in proteins and is among the most hydrophobic residues. Except for the N-terminal residue, it is expected to be predominantly buried inside proteins (*14, 15*). The methyl thioether is not very reactive, but it has been shown that the non-natural amino acid azidohomoalanine can efficiently replace methionine when a methionine auxotrophic *E. coli* strain is used for protein production (*16*). Upon introduction of the azide moiety, it is possible to apply the bioorthogonal Cu^{I}-catalyzed [3 + 2] cycloaddition (*17*), which has been shown before to work very well for protein modification (*18–21*).

Although the replacement of methionine by reactive analogues has been well-established, it has not been investigated whether the limited availability of this residue can be used to control the number of conjugation sites. Previously, recombinant proteins were chemoselectively modified by replacing methionine with azidohomoalanine, followed by the Staudinger ligation under denaturing conditions (*22*). The presence of eight azides led to the formation of at least five different ligation products in a reduced environment. The use of native conditions during the ligation reaction is expected to limit the labeling to solvent-exposed azide residues only.

In order to study whether this relatively simple method can be used to site-specifically functionalize proteins, we have investigated the model enzyme *Candida antarctica* lipase B (CalB). The protein variant that was used contains five methionine residues, four of which are buried inside the protein. We show that replacing methionine **1** with azidohomoalanine **2** (Scheme 1) leads to the introduction of only one accessible azide for reaction with alkynes via the Cu^{I}-catalyzed [3 + 2] cycloaddition, also known as the click reaction. Thus, a residue-specific substitution leads effectively to an enzyme which can be functionalized at a single defined position. Importantly, we found that the enzyme remains active after non-natural amino acid incorporation and click chemistry.

CalB (EC 3.1.1.3) is widely used in organic synthesis as a biocatalyst with broad substrate specificity. The enzyme main-

* Correspondence author. Jan C. M van Hest, Department of Bioorganic Chemistry, Radboud University Nijmegen, Heyendaalseweg 135, 6525 AJ Nijmegen, The Netherlands. Phone: +31 24 3653204, Fax: +31 24 3653393, E-mail: j.vanhest@science.ru.nl.

10.1021/bc800019v CCC: $40.75 © 2008 American Chemical Society
Published on Web 05/08/2008

Scheme 1. Non-Canonical Amino Acid Azidohomoalanine 2 as a Structural Analogue of Methionine 1

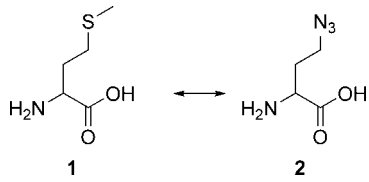

tains its activity in organic solvents and is used for various applications such as amidation reactions, dynamic kinetic resolution, esterification, and ring-opening polymerization (*23, 24*). The processed protein consists of 317 amino acids and has a molecular weight of 33 kDa. We cloned the gene encoding this polypeptide in an expression plasmid containing an N-terminal periplasmic localization signal and a C-terminal histidine tag (*25*). As a consequence of the cloning strategy we used, our CalB gene encoded 5 methionine residues, whereas wild-type CalB contains 4. The extra residue was the first amino acid after cleavage of the periplasmic localization peptide (Figure 1).

Protein synthesis was induced in methionine auxotrophic *E. coli* bacteria. Residue-specific incorporation of **2** was achieved using the method described elsewhere (*16*). The mass of CalB containing azidohomoalanine (AHA-CalB) had to be 25 Da less than the mass of CalB with methionine residues (Met-CalB), i.e., 5 Da for each methionine−azidohomoalanine replacement. This mass difference was detected by ESI-TOF mass spectrometry (Figure 2). Additional peaks appeared as well, with a mass difference of 63 Da between adjacent peaks. This is due to the presence of traces of Cu ions most probably coordinated to the histidine tag.

To investigate whether the azide moieties in the protein were reactive toward alkynes, AHA-CalB was incubated with alkyne-functionalized dansyl **3** (20 equiv) in the presence of 1 mM $CuSO_4$, sodium ascorbate, and bathophenanthroline ligand **4** (all 30 equiv). The reaction was allowed to proceed overnight at room temperature in phosphate buffer (pH 7.0). Met-CalB was used as a negative control. Protein samples were dialyzed against buffer to remove unreacted dansyl and click reagents. Proteins were separated by electrophoresis, and labeling was verified by

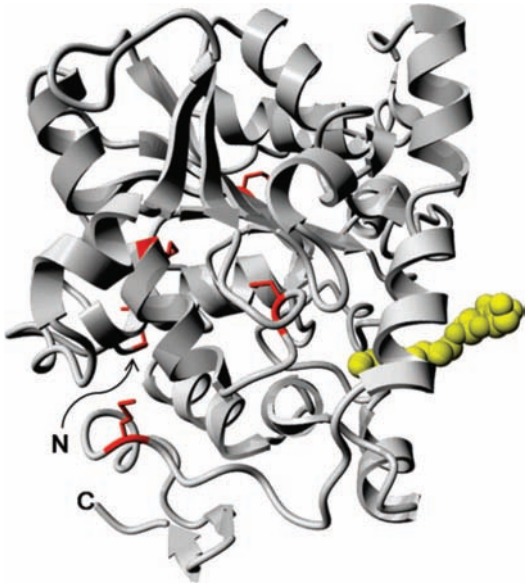

Figure 1. Structure of mature CalB with methionine residues shown in red and a substrate (yellow) positioned near the active site. The N and C termini are indicated as well. The conformation was derived from the PDB file '1tca' with addition of a methionine and a glycine to the N-terminus.

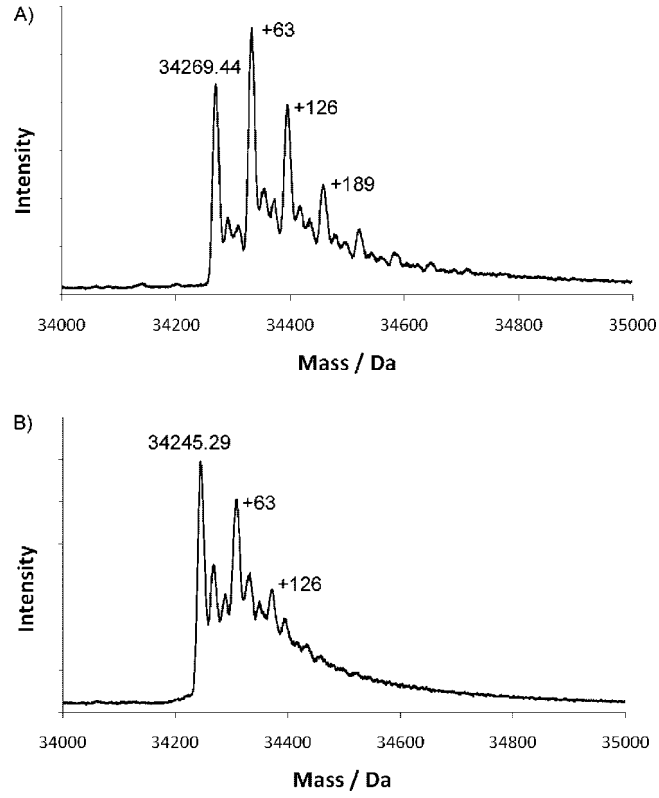

Figure 2. ESI-TOF mass spectra of (A) Met-CalB and (B) AHA-CalB. Upon deconvolution, peaks corresponding to the calculated masses (34 269.72 Da for Met-CalB and 34 244.93 Da for AHA-CalB) were detected.

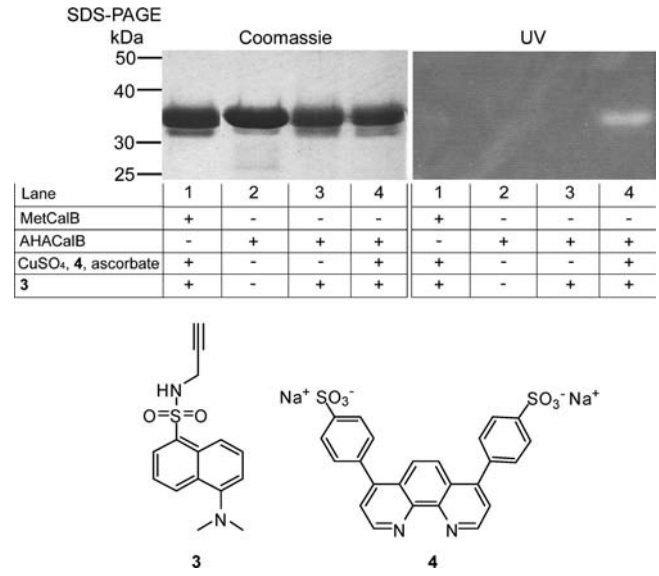

Figure 3. Labeling of AHA-CalB with alkynyl−dansyl **3** in the presence of $CuSO_4$, ascorbate, and bathophenantroline ligand **4**. Reactions were analyzed by SDS-PAGE, with gels stained with Coomassie after fluorescence visualization by UV.

visualizing the fluorescent bioconjugate by UV (Figure 3). Only AHA-CalB treated with Cu catalyst and **3** turned out to be specifically labeled.

To identify which of the azides were reactive toward the alkyne-functionalized dansyl, reacted and nonreacted AHA-CalB and Met-CalB samples were treated with trypsin, and digests were analyzed by MALDI-TOF mass spectrometry. As expected, fragments containing methionine in Met-CalB proved to be five units lower in mass in the AHA-CalB sample, due to

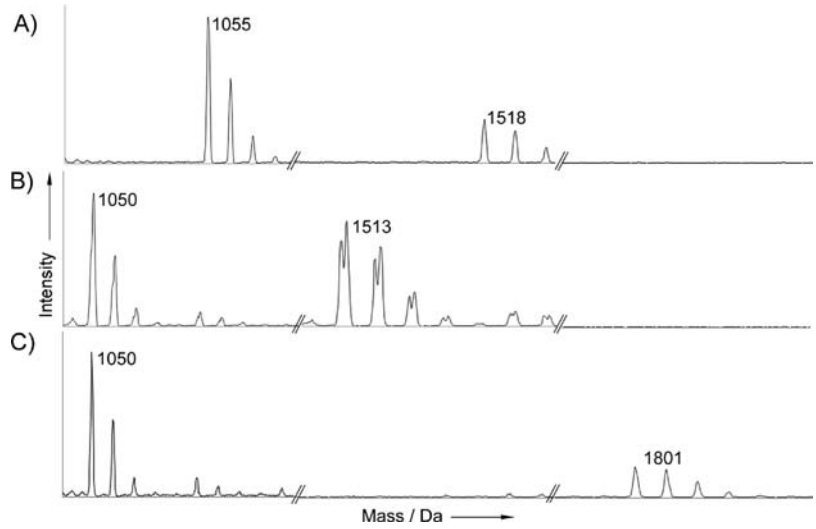

Figure 4. MALDI-TOF spectra of two tryptic fragments derived from (A) Met-CalB incubated with dansyl, (B) AHA-CalB, and (C) AHA-CalB reacted with dansyl. The peak at 1055/1050 Da comes from the peptide fragment with residue numbers 130−138. The peak at 1518/1513 Da originates from the N-terminal peptide fragment (residue numbers 1−15) to which alkynyl−dansyl can be linked. Attachment of dansyl causes a mass shift of 288 Da, leading to a peak at 1801 Da.

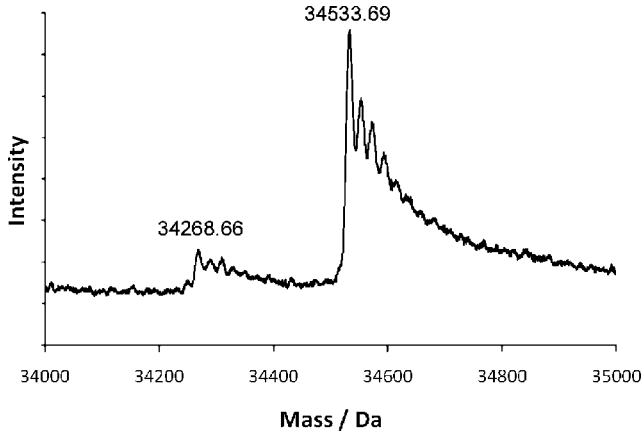

Figure 5. ESI-TOF mass spectrum of AHA-CalB reacted with dansyl. One dansyl was attached to AHA-CalB resulting in addition of 288 Da to the AHA-CalB mass of 34 245 Da. As expected, the nonreactive fraction of Met-CalB was detected at 34 269 Da.

the presence of azidohomoalanine (Figure 4). For example, the peptide fragment of residues 130−138 containing methionine at residue number 131 (1055 Da) was detected as a fragment of 1050 Da in the tryptic digest of unreacted AHA-CalB. The same fragment was present in the digest of dansyl-reacted AHA-CalB, indicating that no dansyl had been attached to this azide moiety. By contrast, a mass shift of 288 Da (corresponding to the weight of dansyl) was detected for the peptide fragment of residues 1−15 containing an azide at residue position 1. It was therefore concluded that this azide, being located at the N-terminus of the processed protein, was accessible for ligation reactions. It was observed that the labeling with dansyl was quantitative, as no residual signal at 1513 Da was detected. Finally, these data show that, as expected, there is a small fraction of methionine present in AHA-CalB (see small peaks at 1055 and 1518 Da in Figure 4B,C). The degree of azidohomoalanine incorporation was shown to be 90%.

The addition of dansyl to AHA-CalB was further analyzed by ESI-TOF mass spectrometry. Only one dansyl molecule was found to be attached to the protein, giving the expected mass of 34 533 Da (Figure 5). The fraction of CalB which contained methionine instead of azidohomoalanine was detected as a residual peak at 34 269 Da.

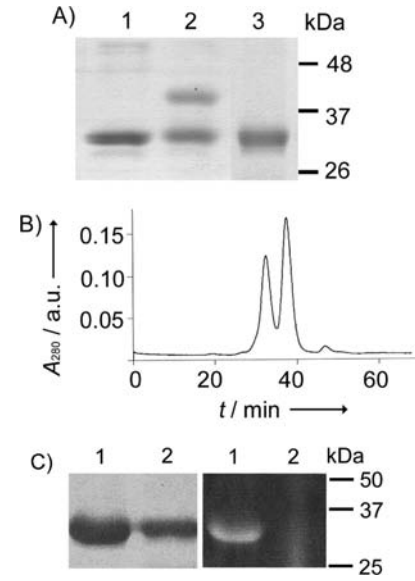

Figure 6. Labeling of AHA-CalB and AHA-CalB(M > G) with PEG5000 and alkynyl−dansyl **3**. (A) PEGylation reactions, analyzed by SDS-PAGE using Coomassie staining: 1, Met-CalB; 2, AHA-CalB; 3, AHA-CalB(M > G). (B) Separation of PEGylated AHA-CalB from nonreacted CalB by size-exclusion chromatography. (C) Click reactions with alkynyl−dansyl, analyzed by SDS-PAGE, and visualized by UV prior to Coomassie staining: 1, AHA-CalB; 2, AHA-CalB(M > G).

Subsequently, alkyne-functionalized PEG(5000) was coupled to AHA-CalB. After removal of the excess PEG(5000) by clicking to azide-functionalized resin (*26*), attachment of the polymer to CalB was analyzed by gel electrophoresis (Figure 6A). A single band shift was detected between 37 and 48 kDa. Nonfunctionalized CalB was separated from the PEGylated fraction by size-exclusion chromatography (Figure 6B). The chromatogram showed two peaks indicating that only one derivative had been produced.

The N-terminal methionine codon was replaced by glycine, indicated as AHA-CalB(M > G). Upon reaction with alkynyl-PEG(5000), no pegylation was observed by gel electrophoresis. Moreover, labeling of AHA-CalB(M > G) with alkynyl−dansyl did not result in a fluorescent band on SDS-PAGE gel (Figure

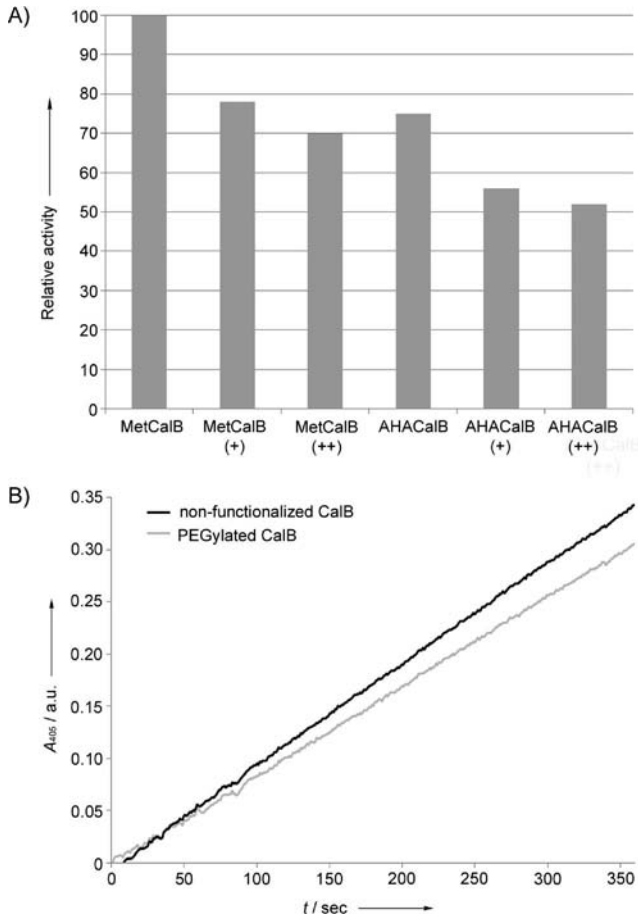

Figure 7. (A) Hydrolytic activity of Met-CalB and AHA-CalB, and the influence of click reagents. Formation of *para*-nitrophenol was monitored by detecting absorbance at 405 nm. (+) = after incubation with $CuSO_4$, ascorbate, and ligand **4**; (++) = after incubation with $CuSO_4$, ascorbate, ligand **4**, and alkynyl−dansyl **3**. (B) Comparison of the hydrolytic activity of PEGylated CalB and the nonfunctionalized fraction. The latter sample consists of a small fraction of Met-CalB together with nonlabeled AHA-CalB.

6C). This confirms that, of all five azides introduced in nonmutated AHA-CalB, only the N-terminal one was accessible for clicking.

The enzymatic activity of different CalB variants was analyzed by hydrolysis of *para*-nitrophenyl butyrate. Formation of *para*-nitrophenol by Met-CalB and AHA-CalB was monitored by measuring absorbance at 405 nm. Upon introduction of azidohomoalanine, hydrolytic activity was retained for 75% (Figure 7A). Additionally, we investigated the effect of the click reaction on enzymatic activity. Met-CalB and AHA-CalB were incubated in the presence of click reagents, with or without alkynyl−dansyl. Subsequent measurements showed that the reagents had some negative effect on the activities of both Met-CalB and AHA-CalB. As shown in Figure 7A, the activity of Met-CalB was decreased to 70%. The activity of AHA-CalB was reduced to 52% after incubation with dansyl and click reagents, which is 69% of the activity of nontreated AHA-CalB.

Additionally, the enzymatic activities of both the PEG-CalB conjugate and the nonpegylated CalB fraction were monitored after size-exclusion chromatography. Comparing the fractions, which were derived from the same click reaction mixture, revealed that there was hardly any loss of activity due to attachment of the polymer itself (Figure 7B).

To conclude, we have developed a convenient method to modify CalB protein in a site-directed way. An azide-bearing methionine analogue was introduced to act as functional handle. Subsequently, other molecules were covalently linked via the highly selective Cu^I-catalyzed click reaction. Although multiple azides were introduced, only one moiety appeared to be reactive under native conditions, as the other residues were buried inside the protein. The method seems to be a good substitute for the less-straightforward amber suppressor strategy.

Our method can be considered a versatile tool to modify proteins in a site-specific way, as long as one solvent-accessible methionine residue is present. In many cases, it will be the N-terminal methionine that is available. It should be noted, however, that the N-terminal methionine or its analogue can be cleaved off during post-translational processing (*27*). If no other methionine is accessible, a novel residue can be introduced via a single mutagenesis step. Therefore, the method is not restricted to N-terminal labeling. It can also be used to modify other regions of the protein surface with absolute control over the site of modification.

After the entire modification procedure, catalytic activity was partially retained. Part of the hydrolytic activity was lost due to the incorporation of the non-proteinogenic amino acid and the use of $CuSO_4$, ascorbate and ligand. Application of a copper-free click reaction such as the Staudinger ligation, the strain-promoted [3 + 2] azide-alkyne cycloaddition, or the reaction between azides and oxanorbornadienes may lead to less loss in activity (*22*, *28*, *29*). As reported elsewhere, the modification strategy has been successfully applied to immobilize CalB on polymersomes (*30*).

ACKNOWLEDGMENT

The authors thank A. J. Dirks for preparing the alkyne-functionalized PEG5000, and R. Brinkhuis and J. Opsteen for providing the alkynyl−dansyl and azide resin, respectively. We thank E. Akpa for providing the CalB gene and P. van Galen and H. op den Camp for help with mass spectrometry analysis. H. Venselaar is thanked for providing the picture of our CalB protein containing the extra methionine and glycine at the N-terminus.

Supporting Information Available: Materials, CalB plasmid cloning, synthesis of azidohomoalanine and alkynyl-PEG(5000), protein production, click reaction conditions, and characterization procedures including enzyme activity assay, SDS-PAGE, MALDI, and ESI-TOF analysis. This material is available free of charge via the Internet at http://pubs.acs.org.

LITERATURE CITED

(1) Pasut, G., and Veronese, F. M. (2006) PEGylation of proteins as tailored chemistry for optimized bioconjugates. *Polymer Therapeutics I: Polymers as Drugs, Conjugates and Gene Delivery Systems 192*, 95–134.

(2) Federico, R., Cona, A., Caliceti, P., and Veronese, F. M. (2006) Histaminase PEGylation: Preparation and characterization of a new bioconjugate for therapeutic application. *J. Controlled Release 115*, 168–174.

(3) Dirks, A. J., van Berkel, S. S., Hatzakis, N. S., Opsteen, J. A., van Delft, F. L., Cornelissen, J. J. L. M., Rowan, A. E., van Hest, J. C. M., Rutjes, F. P. J. T., and Nolte, R. J. M. (2005) Preparation of biohybrid amphiphiles via the copper catalysed Huisgen [3 + 2] dipolar cycloaddition reaction. *Chem. Commun.* 4172–4174.

(4) Blank, K., Morfill, J., and Gaub, H. E. (2006) Site-specific immobilization of genetically engineered variants of *Candida antarctica* lipase B. *ChemBioChem 7*, 1349–1351.

(5) Veronese, F. M., Sacca, B., de Laureto, P. P., Sergi, M., Caliceti, P., Schiavon, O., and Orsolini, P. (2001) New PEGs for peptide and protein modification, suitable for identification of the PEGylation site. *Bioconjugate Chem. 12*, 62–70.

(6) Wang, Y., Youngster, S., Grace, M., Bausch, J., Bordens, R., and Wyss, D. F. (2002) Structural and biological characterization of pegylated recombinant interferon alpha-2b and its therapeutic implications. *Adv. Drug Delivery Rev. 54*, 547–570.

(7) Thordarson, P., Le Droumaguet, B., and Velonia, K. (2006) Well-defined protein-polymer conjugates-synthesis and potential applications. *Appl. Microbiol. Biotechnol. 73*, 243–254.

(8) Heredia, K. L., Bontempo, D., Ly, T., Byers, T. J., Halstenberg, S., and Maynard, H. D. (2005) In situ preparation of protein - "Smart" polymer conjugates with retention of bioactivity. *J. Am. Chem. Soc. 127*, 16955–16960.

(9) Tilley, S. D., and Francis, M. B. (2006) Tyrosine-selective protein alkylation using pi-allylpalladium complexes. *J. Am. Chem. Soc. 128*, 1080–1081.

(10) van Hest, J. C. M., Kiick, K. L., and Tirrell, D. A. (2002) Efficient incorporation of unsaturated methionine analogues into proteins in vivo. *J. Am. Chem. Soc. 122*, 1282–1288.

(11) Wang, L., and Schultz, P. G. (2005) Expanding the genetic code. *Angew. Chem., Int. Ed. 44*, 34–66.

(12) Deiters, A., Cropp, T. A., Summerer, D., Mukherji, M., and Schultz, P. G. (2004) Site-specific PEGylation of proteins containing unnatural amino acids. *Bioorg. Med. Chem. Lett. 14*, 5743–5745.

(13) Kodama, K., Fukuzawa, S., Nakayama, H., Kigawa, T., Sakamoto, K., Yabuki, T., Matsuda, N., Shirouzu, M., Takio, K., Tachibana, K., and Yokoyama, S. (2006) Regioselective carbon-carbon bond formation in proteins with palladium catalysis; New protein chemistry by organometallic chemistry. *ChemBioChem 7*, 134–139.

(14) Janin, J., and Wodak, S. (1978) Conformation of amino acid side-chains in proteins. *J. Mol. Biol. 125*, 357–386.

(15) Cornette, J. L., Cease, K. B., Margalit, H., Spouge, J. L., Berzofsky, J. A., and DeLisi, C. (1987) Hydrophobicity scales and computational techniques for detecting amphipathic structures in proteins. *J. Mol. Biol. 195*, 659–685.

(16) Link, A. J., and Tirrell, D. A. (2005) Reassignment of sense codons in vivo. *Methods 36*, 291–298.

(17) Rostovtsev, V. V., Green, L. G., Fokin, V. V., and Sharpless, K. B. (2002) A stepwise Huisgen cycloaddition process: Copper(I)-catalyzed regioselective "ligation" of azides and terminal alkynes. *Angew. Chem., Int. Ed. 41*, 2596–2599.

(18) Gupta, S. S., Kuzelka, J., Singh, P., Lewis, W. G., Manchester, M., and Finn, M. G. (2005) Accelerated bioorthogonal conjugation: A practical method for the Ligation of diverse functional molecules to a polyvalent virus scaffold. *Bioconjugate Chem. 16*, 1572–1579.

(19) Beatty, K. E., Xie, F., Wang, Q., and Tirrell, D. A. (2005) Selective dye-labeling of newly synthesized proteins in bacterial cells. *J. Am. Chem. Soc. 127*, 14150–14151.

(20) Iida, S., Asakura, N., Tabata, K., Okura, I., and Kamachi, T. (2006) Incorporation of unnatural amino acids into cytochrome c3 and specific viologen binding to the unnatural amino acid. *ChemBioChem 7*, 1853–1855.

(21) van Kasteren, S. I., Kramer, H. B., Jensen, H. H., Campbell, S. J., Kirkpatrick, J., Oldham, N. J., Anthony, D. C., and Davis, B. G. (2007) Expanding the diversity of chemical protein modification allows post-translational mimicry. *Nature 446*, 1105–1109.

(22) Kiick, K. L., Saxon, E., Tirrell, D. A., and Bertozzi, C. R. (2002) Incorporation of azides into recombinant proteins for chemoselective modification by the Staudinger ligation. *Proc. Natl. Acad. Sci. U.S.A. 99*, 19–24.

(23) Gotor-Fernandez, V., Busto, E., and Gotor, V. (2006) *Candida antarctica* lipase B: An ideal biocatalyst for the preparation of nitrogenated organic compounds. *Adv. Synth. Catal. 348*, 797–812.

(24) Peeters, J., Palmans, A. R. A., Veld, M., Scheijen, F., Heise, A., and Meijer, E. W. (2004) Cascade synthesis of chiral block copolymers combining lipase catalyzed ring opening polymerization and atom transfer radical polymerization. *Biomacromolecules 5*, 1862–1868.

(25) Blank, K., Morfill, J., Gumpp, H., and Gaub, H. E. (2006) Functional expression of *Candida antarctica* lipase B in *Escherichia coli*. *J. Biotechnol. 125*, 474–483.

(26) Opsteen, J. A., and van Hest, J. C. M. (2005) Modular synthesis of block copolymers via cycloaddition of terminal azide and alkyne functionalized polymers. *ChemComm 1*, 57–59.

(27) Wang, A., Winblade Nairn, N., Johnson, R. S., Tirrell, D. A., and Grabstein, K. (2008) Processing of N-terminal unnatural amino acids in recombinant human interferon-β in *Escherichia coli*. *ChemBioChem 9*, 324–330.

(28) Agard, N. J, Prescher, J. A., and Bertozzi, C. R. (2004) A strain-promoted [3 + 2] azide-alkyne cycloaddition for covalent modification of blomolecules in living systems. *J. Am. Chem. Soc. 126*, 15046–15047.

(29) van Berkel, S. S., Dirks, A. J., Debets, M. F., van Delft, F. L., Cornelissen, J. J. L. M., Nolte, R. J. M., and Rutjes, F. P. J. T. (2007) Metal-free triazole formation as a tool for bioconjugation. *ChemBioChem 8*, 1504–1508.

(30) van Dongen, S. F. M., Nallani, M., Schoffelen, S., Cornelissen, J. L. M., Nolte, R. J. M., and van Hest, J. C. M. (2008) A block copolymer for functionalisation of polymersome surfaces. *Macromol. Rapid Commun. 29*, 321–325.

BC800019V

A DNA Duplex-Based, Tailor-Made Fluorescent Sensor for Porphyrin Derivatives

Kazuhisa Fujimoto,* Yu Muto, and Masahiko Inouye*

Graduate School of Pharmaceutical Sciences, University of Toyama, Sugitani 2630, Toyama 930-0194, Japan. Received April 1, 2008; Revised Manuscript Received April 16, 2008

We synthesized a DNA-based fluorescent sensor, tailored to the recognition and signaling for hydrophobic guest molecules. The sensor molecule is made of three functional moieties, per-*O*-methylated *β*-cyclodextrin (per-Me-*β*-CD), DNA, and pyrene as guest-binding, dimerizing, and signaling ones, respectively. Addition of a porphyrin derivative as a hydrophobic guest molecule induced emission switching of the sensor molecule from monomer to excimer due to the DNA hybridization promoted by the host−guest binding.

In host−guest chemistry, most of host molecules have been developed according to preorganization concepts in order to selectively recognize target molecules (*1*, *2*) since the breakthrough of crown ethers by Pedersen (*3*). The preorganization approach, however, demands many designing and synthetic efforts, so that it hardly supplies a series of host molecules with generality and versatility for various biologically important species. In proteins, innumerable combinations of amino acid residues in the primary sequences realize these aspects for recognizing substrates with a specific manner. If we can apply the combination of functional components, as seen in proteins, for designing artificial host molecules, such a design technique will shed fresh light on host−guest chemistry. Recently, we reported a new type of molecular design for host molecules working in water, inspired by the structural motif of antibodies (*4*). The designed host molecules consist of two monomers, each of which possesses three functional regions for guest-binding (recognition units), dimerizing (cDNAs), and signaling (fluorophores). In that study, crown ether and pyrene were used as the guest-binding and signaling sites, respectively, for targeting metal cations. A cooperative binding of the two crown ethers for metal cations promotes the hybridization of the cDNAs to induce a monomer−excimer emission switching from the pyrene fluorophores. This tailormade design method allows a variety of recognition units to be introduced at the ends of DNAs homogeneously or heterogeneously. Here, to demonstrate the generality and versatility of our method, we newly developed a fluorescent sensor **1** (**1a** + **1b**) for porphyrin derivatives on the basis of the design technique mentioned above.

We chose per-*O*-methylated *β*-cyclodextrin (per-Me-*β*-CD) as a recognition moiety in the new fluorescent sensor because

* E-mail: fujimoto@pha.u-toyama.ac.jp (K.F.); inouye@pha.u-toyama.ac.jp (M.I.).

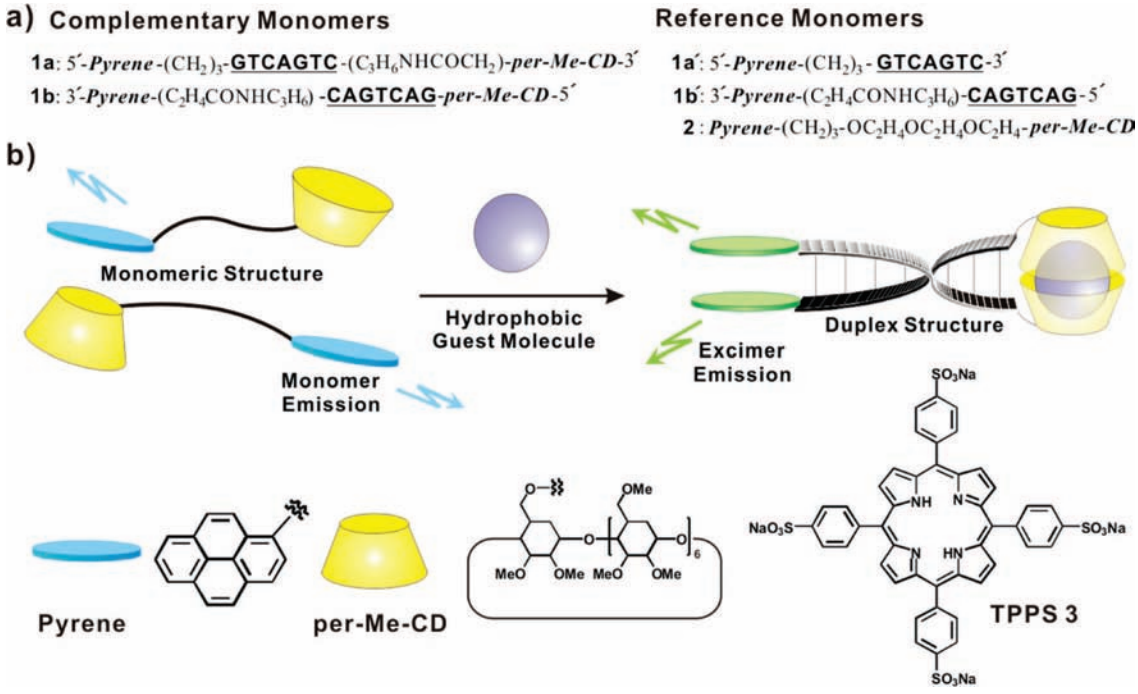

Figure 1. (a) Chemical structures of **1** (**1a** + **1b**), **1′** (**1a′** + **1b′**), and **2**. (b) A schematic representation of a duplex-based fluorescent sensor **1** with monomer−excimer switching in the presence of TPPS **3** as a guest molecule.

10.1021/bc800133e CCC: $40.75 © 2008 American Chemical Society
Published on Web 05/09/2008

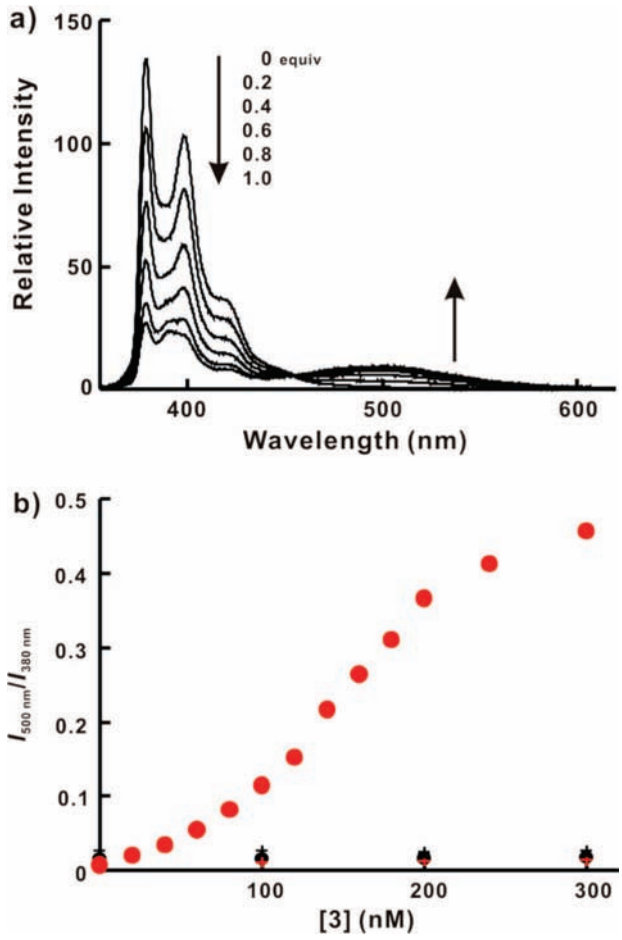

Figure 2. (a) Fluorescence titration spectra of **1** ([**1a**] = [**1b**] = 200 nM; [Tris-HCl], 20 mM, at pH 8.0) on titration with **3** (0−1 equiv) at 25 °C. Excitation wavelength was 350 nm. (b) Plots of the intensity ratio ($I_{500\ nm}/I_{380\ nm}$) against the concentration of **3** ([Host], 200 nM; [Tris-HCl], 20 mM, at pH 8.0) °C. Red circle, **1a**/**1b**; black circle, **1a**/**1b′**; black plus, **1a′**/**1b**; and red plus, **1a′**/**1b′**.

Scheme 1

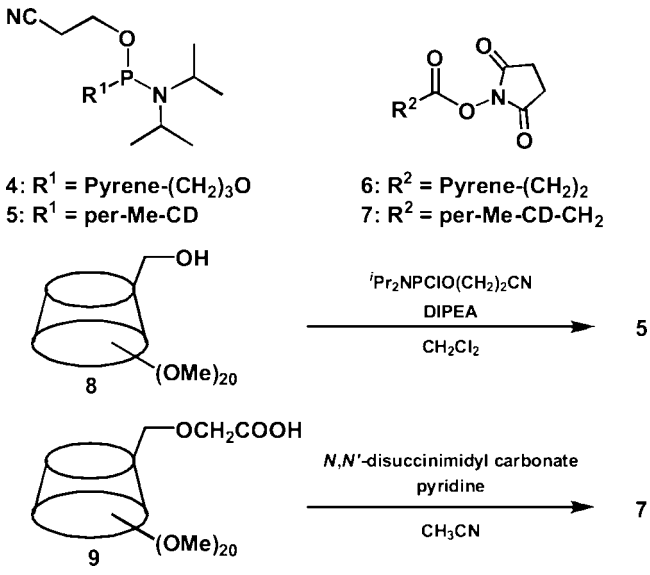

the skeleton had been reported to strongly recognize porphyrin derivatives such as TPPS **3** in a 2:1 binding manner by Kano et al. (Figure 1) (*5*). Furthermore, per-Me-*β*-CD shows good solubility in water as compared to native *β*-CD, so that it should contribute to improve the water solubilities of **1a** and **1b** as well as the DNA moieties do. As shown in Figure 1b, when the per-Me-*β*-CD moieties capture **3** in a 2:1 binding manner accompanying the duplex formation of the DNA ones, emission switching will occur from the pyrene monomer to excimer. The two monomers **1a** and **1b** comprising complementary 7-mer DNAs were synthesized according to the procedure published previously (*4*). In the DNA moieties of these monomers, **1a** was functionalized with the pyrene-modified phosphoramidite **4** (*6*) and the CD-attached succinimidyl ester **7** at 5′ and 3′ ends, respectively, while **1b** was linked with **5** and **6** in the style opposite that of **1a**. The syntheses of the pyrene derivatives **4** and **6** have been reported in our previous paper (*6*). The CD derivatives **5** and **7** were newly synthesized from mono-6-hydroxy permethylated *β*-cyclodextrin **8** (*7*) and 6^{I}-*O*-carboxymethyl-2^{I-VII},3^{I-VII},6^{II-VII}-eicosa-*O*-methyl-cyclomaltoheptaose **9** (*8*), respectively (Scheme 1). The following reference monomers were prepared for using in control experiments: both **1a′** and **1b′** lack the per-Me-*β*-CD moiety (*4*), and **2** possesses an oxy-ethylene spacer instead of DNA (Figure 1a).

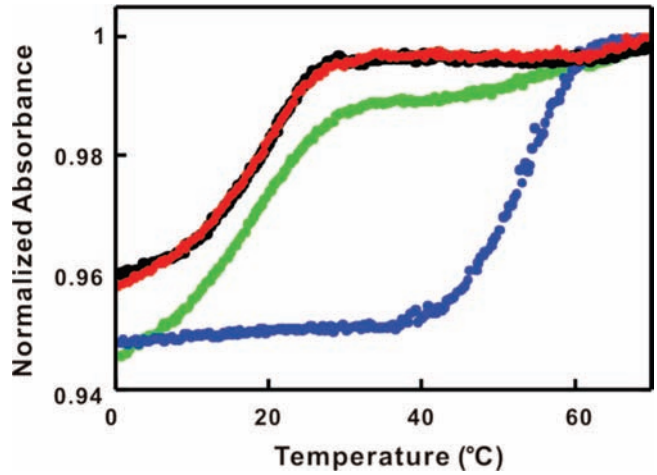

Figure 3. Normalized melting curves at 260 nm. Melting curves were normalized with the division by the each absorbance at 60 °C. The solution for the measurements contained **1** or **1′** (duplex, 2.5 *μ*M) and 20 mM Tris-HCl (pH 8.0) in the presence or absence of **3** (2.5 *μ*M). Blue, **1**+**3**; green, **1**; red, **1′**+**3**; black, **1′**.

To explore the sensing ability of **1** for the porphyrin **3**, fluorescence titration experiments were carried out in an aqueous buffer solution (Figure 2a). As **3** was continuously added to the solution of **1a**/**1b** ([**1a**] = [**1b**] = 200 nM), the monomer emission intensity ($I_{380\ nm}$) decreased while the excimer emission one ($I_{500\ nm}$) increased; the spectral change was completed in the presence of 1.5 equiv of **3** against **1a** or **1b**. In this spectral change, the isoemissive point was observed at 448 nm, which indicates the presence of only two types of fluorescent species in the solution, the single-stranded **1a** (and **1b**) and the associated form. For certifying the 2:1 binding manner of the CD moieties to **3**, control experiments were performed by use of the following combinations **1a**/**1b′**, **1a′**/**1b**, and **1a′**/**1b′**, in which **1a′** and **1b′** lack the CD moieties. The ratio of the emission intensities ($I_{500\ nm}/I_{380\ nm}$) was plotted against the concentration of **3**, and we observed no meaningful changes for the three combinations (Figure 2b). The only combination of **1a**/**1b** showed a significant change in the intensity ratio, meaning that a set of per-Me-*β*-CDs is indispensable for the binding. Therefore, the emission switching is likely to be responsible for the duplex formation between **1a** and **1b** by the addition of **3**. To demonstrate this, melting temperatures (T_m) and CD spectra were measured for **1** and **1′** in the absence and presence of **3**. Figure 3 shows melting curves at 260 nm, normalized with the division by the each absorbance at 60 °C. The T_m value of **1** in the presence of **3** extensively increased up to 53 °C compared with 19 °C for **1** itself, while the value of **1′** hardly changed in the

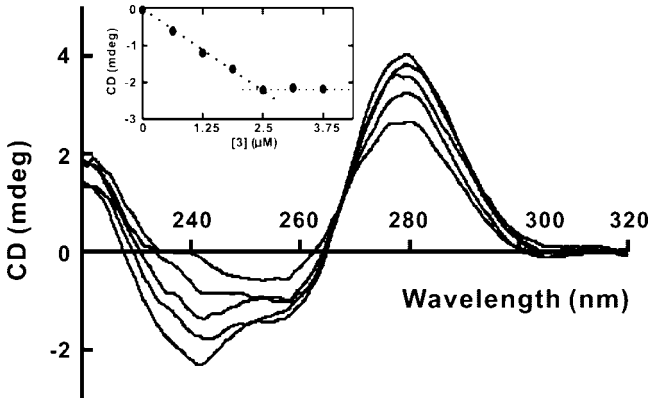

Figure 4. CD titration spectra of **1** (duplex, 2.5 μM; [Tris-HCl], 20 mM, at pH 8.0) on titration with **3** (0−1 equiv). Inset: plots of the CD intensities at 240 nm against the concentration of **3**.

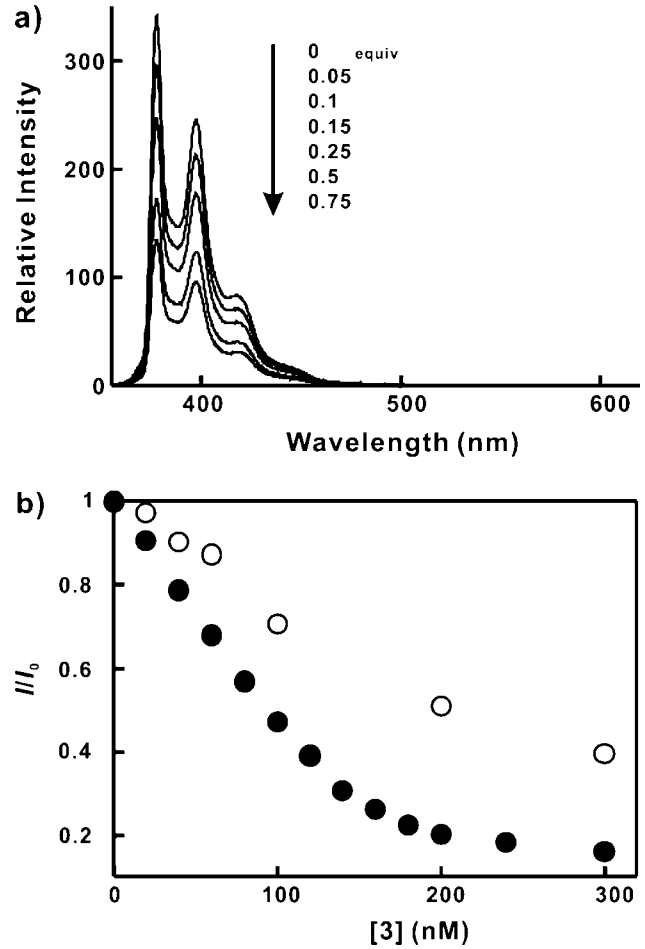

Figure 5. (a) Fluorescence titration spectra of **2** ([**2**] = 400 nM; [Tris-HCl], 20 mM, at pH 8.0) on titration with **3** (0−0.75 equiv). Excitation wavelength was 350 nm. (b) Plots of the monomer emission intensities (I/I_0) at 380 nm against the concentration of **3**. Closed circle, **1** (duplex, 200 nM); open circle, **2** ([**2**] = 400 nM).

presence of **3** (19 °C). The Cotton effects in the DNA-absorptive region of **1** were enhanced by the consecutive addition of **3** (Figure 4). When the CD intensity of **1** at 240 nm was plotted against the concentration of **3**, the intensity change was saturated in the presence of 1 equiv of **3** (Figure 4, inset). The CD titration almost accords with the fluorescent one performed under the more diluted condition in Figure 2. These findings indicate the duplex formation-driven emission switching of **1** in the presence of **3**.

Since per-Me-β-CD itself can bind to TPPS **3** in a 2:1 binding manner, even a fluorescent sensor lacking in DNA moieties may detect **3** by emission switching. Therefore, an additional control experiment was carried out with **2** (Supporting Information Scheme S1) possessing an oxy-ethylene spacer instead of a DNA moiety. The fluorescent titration of **2** is shown in Figure 5a under the same conditions as mentioned in Figure 2 except for [**2**] = 400 nM. When **3** was added to the solution of **2**, the monomer emission was decreased, whereas the corresponding excimer emission never rose. Another emissive band scarcely appeared around 650 nm from the porphyrin core of **3**. These spectral changes might be due to a fluorescence resonance energy transfer (FRET) (*9*) from the pyrene fluorophores to **3** because the monomer emissive region of the pyrenes overlaps with the Soret band of **3**. After the excitation energy of the pyrene monomer had been transferred to **3**, most of the energy might be consumed in nonradiative processes. The rigid duplex moiety in **1** is likely necessary for inhibiting the energy transfer from the pyrene to the bound porphyrin. Next, to display the contribution of the DNA moieties of **1** for binding to **3**, each of the monomer intensities (I/I_0) at 380 nm of **1** and **2** was plotted against the concentration of **3** (Figure 5b). The intensity change of **1** is almost saturated at [**3**] = 200 nM, while that of **2** continues at the concentration of 300 nM. From this comparison between **1** and **2**, the DNA moieties in **1** were found to partially contribute the binding to **3**.

In conclusion, we have developed a new class of fluorescent sensor for hydrophobic target molecules. This DNA-based, tailormade fluorescent sensor could recognize TPPS in a 2:1 binding manner at the per-Me-β-CD moieties, detecting it by monomer−excimer emission switching. We are now introducing new recognition units such as native β-CD into DNA backbones in order to target various biologically important species and to display the practicability of our design technique.

Supporting Information Available: All experimental procedures. This material is available free of charge via the Internet at http://pubs.acs.org.

LITERATURE CITED

(1) Atwood, J. L., Davies, J. E., MacNicol, D., and Vögtle, F., Eds. (1996) *Comprehensive Supramolecular Chemistry*, Vols *1* and *9*, Elsevier, Oxford.

(2) Dodziuk, H. (2001) *Introduction to Supramolecular Chemistry*, Kluwer Academic Publishers, Dordrecht.

(3) Pedersen, C. J. (1988) The discovery of crown ethers. *Angew. Chem., Int. Ed. 27*, 1021–1027.

(4) Fujimoto, K., Muto, Y., and Inouye, M. (2005) A general and versatile molecular design for host molecules working in water: a duplex-based potassium sensor consisting of three functional regions. *Chem. Commun.* 4780–4782.

(5) Kano, K., Nishiyabu, R., Asada, T., and Kuroda, Y. (2002) Static and dynamic behavior of 2:1 inclusion complexes of cyclodextrins and charged porphyrins in aqueous organic media. *J. Am. Chem. Soc. 124*, 9937–9944.

(6) Fujimoto, K., Shimizu, H., and Inouye, M. (2004) Unambiguous detection of target DNAs by excimer–monomer switching molecular beacons. *J. Org. Chem. 69*, 3271–3275.

(7) Chen, Z., Bradshaw, J. S., and Lee, M. L. (1996) A convenient synthesis of mono-6-hydroxy permethylated β-cyclodextrin via tert-butyldimethylsilylation. *Tetrahedron Lett. 37*, 6831–6834.

(8) Tisse, S., Peulon-Agasse, V., Oulyadi, H., Marsais, F., and Combret, J. C. (2003) Selective access and full characterization of mono-acidic permethylated β-cyclodextrin derivatives and their methyl esters. *Tetrahedron: Asymmetry 14*, 2259–2266.

(9) Stryer, L. (1978) Fluorescence energy-transfer as a spectroscopic ruler. *Annu. Rev. Biochem. 47*, 819–846.

BC800133E

ARTICLES

Multimodal Silica-Shelled Quantum Dots: Direct Intracellular Delivery, Photosensitization, Toxic, and Microcirculation Effects

Rumiana Bakalova,*,† Zhivko Zhelev,† Ichio Aoki,† Kazuto Masamoto,† Milka Mileva,‡ Takayuki Obata,† Makoto Higuchi,† Veselina Gadjeva,§ and Iwao Kanno†

Molecular Imaging Center, National Institute of Radiological Sciences (NIRS), 4-9-1 Anagawa, Chiba 263-8555, Japan, Department of Medical Physics and Biophysics, Medical University, Sofia, Bulgaria, and Department of Chemistry and Biochemistry, Medical Faculty, Thracian University, Stara Zagora, Bulgaria. Received November 28, 2007; Revised Manuscript Received March 13, 2008

In the present study, we describe a multimodal QD probe with combined fluorescent and paramagnetic properties, based on silica-shelled single QD micelles with incorporated paramagnetic substances [tris(2,2,6,6-tetramethyl-3,5-heptanedionate)/gadolinium] into the micelle and/or silica coat. The probe was characterized with high photoluminescence quantum yield and good positive MRI contrast, low cytotoxicity, and easy intracellular delivery in viable cells. The intravenous administration of the probe in experimental animals did not affect significantly the physiological parameters and microcirculation (e.g., heart rate, blood pressure, diameter and shape of blood vessels), which makes it appropriate for tracing of blood circulation and *in vivo* multimodal imaging using fluorescent confocal microscopy, two-photon microscopy, and MRI.

INTRODUCTION

The careful design of the architecture of water-soluble QDs enables the creation of nanobioprobes that are compatible with several imaging techniques, so-called multimodal imaging. This opens the door to the existing prospect of simultaneous imaging of QD probes by a variety of techniques including optical imaging, magnetic resonance imaging (MRI), positron emission tomography (PET), computed tomography (CT), and X-ray imaging.

In particular, by fabricating QD probes that exhibit both fluorescent and paramagnetic properties, optical imaging and MRI can be used in a complementary fashion. This is a powerful combination, as the MRI offers an ability to follow the distribution of molecules *in vivo* or provide an anatomical reference, whereas the optical imaging can be applied to obtain detailed information at subcellular levels. The potential applications include monitoring tissue implants and studying the real-time dynamics of tumor metastases and biochemical mediators that might be responsible for many diseases.

The use of a single multimodal probe with two or more imaging techniques has several advantages. The conventional (nonmultimodal) probes, used in PET, MRI, or optical imaging, have different structures and properties, which determine their different target affinity and pharmacodynamics in the organism. Often, the target can be detected by several imaging techniques using several imaging probes with different properties and pharmacodynamics, so the results cannot be easily compared and verified. The researchers and clinicians are faced with the dilemma of which technique to choose and which data to accept as true. The use of a single multimodal probe with two or more imaging techniques minimizes the artifacts and enables a precise comparative analysis of the images, obtained by different techniques.

The existing prospect of using QDs as multimodal imaging probes attracts the interest of researchers in many different scientific fields, and the number of publications on the topic has increased exponentially in recent years (*1*−*21*). However, so far, the results are preliminary and interpretations are still speculative, especially in terms of *in vivo* deep-tissue imaging.

Perhaps the most attractive for development of multimodal imaging probes (optical and paramagnetic) are silica-shelled QDs. The silica is a bioinert material. The silica shell enables incorporation of a large amount of contrast substances inside the silica sphere (e.g., CdSe, CdTe, CdS, InAs, or InP QDs and Fe_2O_3, Fe_3O_4, $CoFe_2O_4$, $MnFe_2O_4$, FePt, or $CoPt_3$ paramagnetic nanoparticles; fluorescent/paramagnetic heterodimers, such as Fe_3O_4-Au, CoPt-Au, FePt-Ag, Fe_3O_4-Au-PbSe, γ-Fe_2O_3-CdS, FePt-CdS, Co/CdS core/shell, Co/CdSe core/shell, CdSe/Zn_{1-x}-Mn_xS; QDs and paramagnetic fatty acids) (*3*, *7*, *13*, *15*, *16*). In addition, paramagnetic substances (e.g., chelators for gadolinium, manganese, etc.) could also be attached on the surface of silica-coated QDs (*5*, *15*, *18*−*20*). The high fluorescent contrast (as a result of high quantum yield of QDs) and the high paramagnetic contrast (as a result of incorporation of a large amount of paramagnetic substances in the small volume of the silica sphere) enable development of a probe that could be detected *in vivo* in a single manner, simultaneously using optical imaging and MRI. In that case, even single cells and molecular targets could be visualized.

* Rumiana Bakalova, PhD, Department of Biophysics, Molecular Imaging Center, National Institute of Radiological Sciences (NIRS), 4-9-1 Anagawa, Chiba 263-8555, Japan. Tel.: +81-43-206-4067. Fax: +81-43-206-3276 . E-mail: bakalova@nirs.go.jp.

† NIRS.

‡ Medical University, Sofia, Bulgaria.

§ Thracian University.

10.1021/bc700431c CCC: $40.75 © 2008 American Chemical Society
Published on Web 05/22/2008

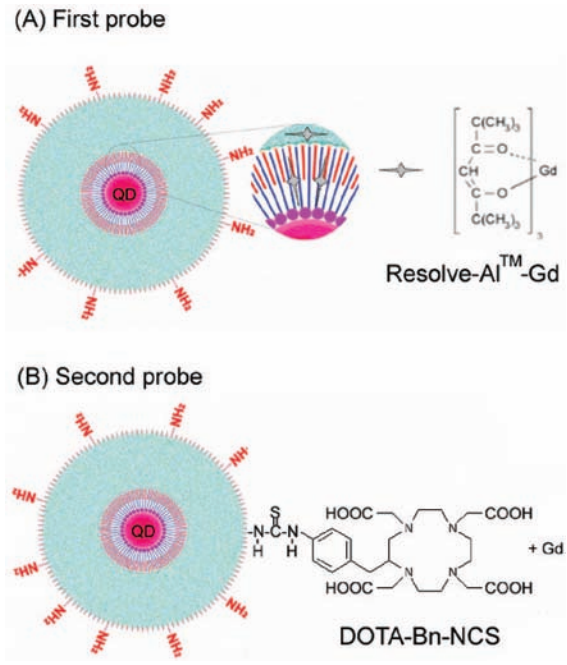

Figure 1. Structure of multimodal silica-shelled QD probes. In the first probe (A), the gadolinium complex is incorporated into the silica coat and/or hydrophobic micelle around the QD. In the second probe (B), the gadolinium complex is conjugated on the surface of silica sphere.

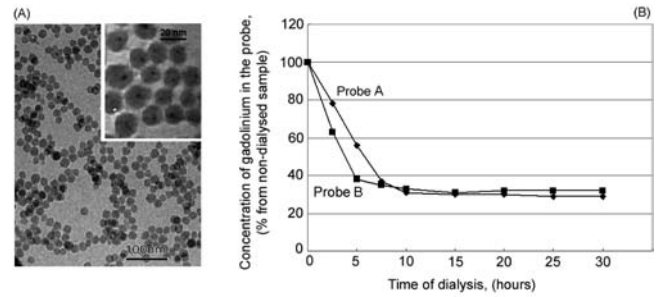

(C) Spectral characteristics of probes (A) and (B).

Spectral characteristic	Probe (A)	Probe (B)
PL QY (%)		
- in distilled water	~35-50	~35-50
- in 10 mM PBS, pH 7.4	~30-45	~32-48
- in 20 mM Tris-HCl, pH 7.4	~27-45	~25-45
T_1 (ms)	264.2 +/- 5.6	281.0 +/- 19.2
T_2 (ms)	80.0 +/- 0.8	142.5 +/- 2.8

Figure 2. (A) Transmission electron micrographs of silica-shelled QD micelles. (B) Retention of gadolinium complex in the silica sphere (probe A) or on the surface of the silica sphere (probe B) after purification via dialysis. (C) Fluorescent and paramagnetic characteristics of probes A and B. The probes were purified using 48 h dialysis. Longitudinal relaxation time (T_1) and transverse relaxation time (T_2) were calculated at equal concentrations of both probes (corresponding to 500 nM QDs). The QD concentration was calculated from the absorbance spectra of multimodal silica-shelled QDs, using the equation of Yu et al. (*38*). The MRI measurements were performed in a 4.7 T magnet (General Electric, CT) interfaced to a Bruker Avance console (Bruker Medical GmbH, Germany). A 30 mm diameter Litz coil (Doty Scientific Inc., SC, USA) was used for measurement of the samples. The sample temperature was maintained at room temperature (~22−24 °C). The measurements were performed in the following order: T_1-weighted imaging using conventional spin−echo (SE) sequence; multiecho SE imaging for T_2 calculations; and inversion−recovery SE imaging for T_1 calculations. For calculation of photoluminescence quantum yield (PL QY), the spectrally integrated emission of particle dispersion in different aqueous solutions (distilled water, PBS, or Tris buffer) was compared with the emission of an ethanol solution of rhodamine 6G (Fluka) of identical optical density (<0.015) at the excitation wavelength 365 nm.

The present study accents the biocompatibility of multimodal QD probes based on silica-shelled single QD micelles with incorporated gadolinium complexes into the micelle and/or silica coat. We tried to clarify the applicability of this probe for blood vessel tracing in the brain, estimating its effect on the major physiological characteristics (such as blood pressure, heart rate, and brain microcirculation) after *in vivo* intravenous (i.v.) administration.

EXPERIMENTAL PROCEDURES

Synthesis and Characterization of Multimodal QDs. Two multimodal QD-based probes were synthesized (Figure 1). The synthesis of the first probe (Figure 1A) was performed as it was described in our previous manuscripts (*21*). The synthesis of the second probe (Figure 1B) was performed according to refs 22, 23 (with slight modifications) (*22*, *23*) Briefly, the gadolinium complex *S*-2-(4-isothiocyanatobenzyl)-1,4,7,10-tetraazacyclododecane tetraacetic acid/gadolinium (DOTA-Bn-NCS/gadolinium) was mixed with amino-functionalized QDs (400:1, mol/mol) in 10 mM PBS (pH 8.0). After 1 h incubation at room temperature, the conjugate was purified using dialysis, as described in our previous manuscript (*21*). DOTA-Bn-NCS/gadolinium complex was purchased from Macrocyclics Co. (USA). The same molar ratio gadolinium complex/QD = 400:1 was used in the synthesis of the first probe. After purification, the gadolinium concentration in the respective probe was measured using ^{1}H-MRI as described below. The structure and size of nanoparticles were characterized by TEM and DLS. Their spectral characteristics were measured using fluorescent spectroscopy, absorbance spectroscopy, and MRI.

Cell Cultures. HeLa cells were cultured in Minimum Essential Medium (MEM, GIBCO, Invitrogen, USA), supplemented with 10% inactivated FBS (Sanko, Japan). A-549 cells, derived from human lung cancer, Jurkat and K-562 cell lines, derived from human acute lymphoblastic leukemia or chronic myeloid leukemia, respectively, were cultured in RPMI-1640 medium (GIBCO, Invitrogen, USA), supplemented with 10% inactivated FBS (Sanko, Japan), 100 U/mL penicillin (GIBCO, Invitrogen, USA), and 100 μg/mL streptomycin (GIBCO, Invitrogen, USA). One day before the treatment with QDs, the cells (1×10^5 cells/mL) were dispensed in 100 μL aliquots in 96-well plates and cultured overnight in medium without FBS and antibiotics, in humidified atmosphere (5% CO_2, 37 °C).

Intracellular Delivery of Multimodal QDs (MRI Measurements and Data Analysis). The MRI measurements were performed in a 4.7 T magnet (General Electric, CT) or a 7.0 T magnet (Kobelco, Japan) interfaced to a Bruker Avance console (Bruker Medical GmbH, Germany). A 30 mm diameter Litz coil (Doty Scientific Inc., SC, USA) or 70 mm diameter volume coil (Bruker) was used for measurement of the samples. The details are indicated in the figure captions. The PCR tubes were mounted on a plastic holder for 4.7 T or on a 70 mm diameter volume coil for 7.0 T and set in the center of the coil. The sample temperature was maintained at room temperature (approximately 22−24 °C). The measurements were performed in the following order: T_1 weighted imaging, using conventional spin−echo (SE) sequence; multiecho SE imaging for T_2 calculations; and inversion−recovery SE imaging for T_1 calculations.

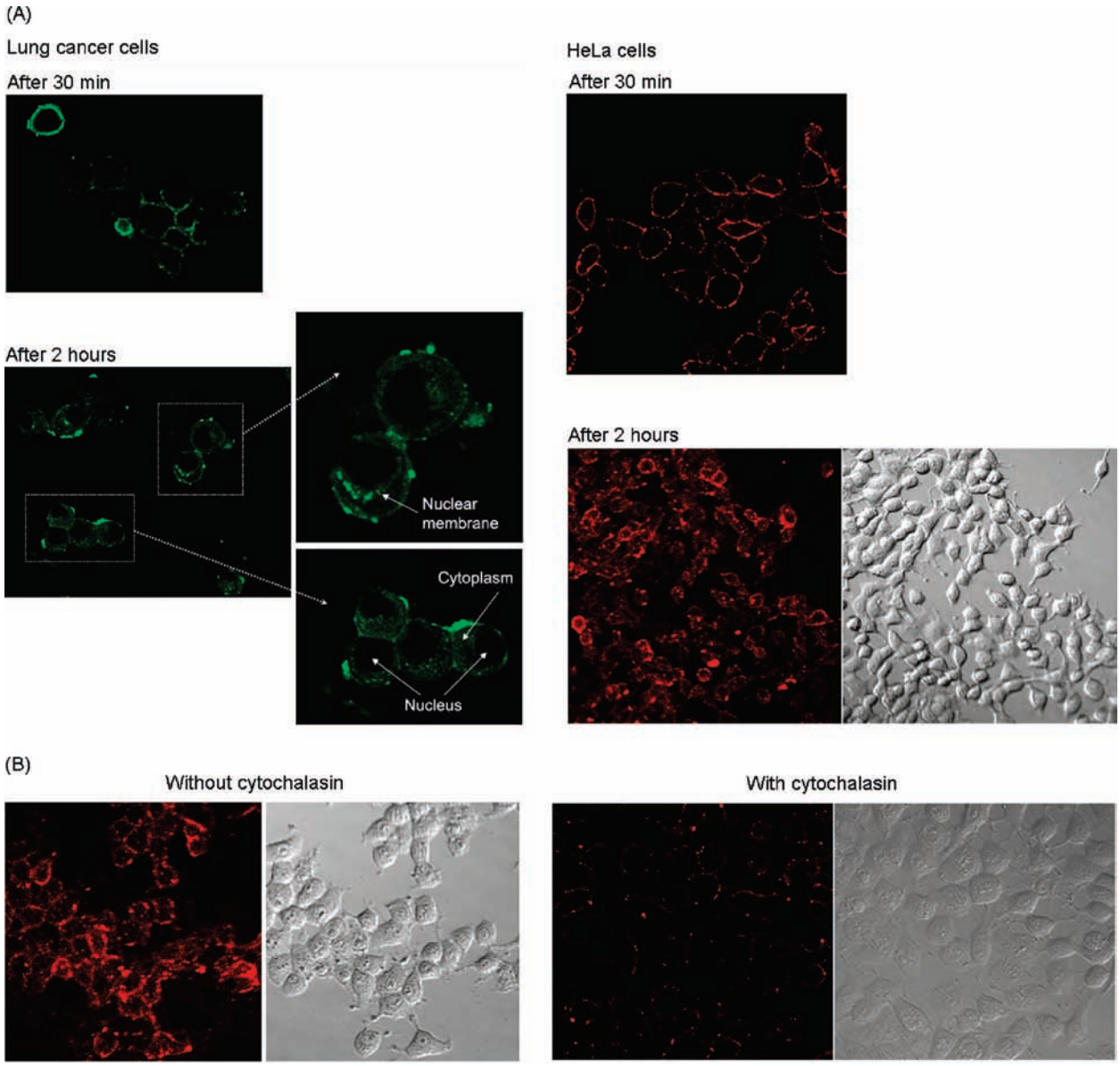

Figure 3. (A) Fluorescent confocal images of the intracellular delivery of multimodal silica-shelled QD probe in living cultured cells. The cells, dispensed in 96-well glass plates, were incubated with the probe (approximately 500 nM of QDs) within 30 min or 2 h in humidified atmosphere (5% CO_2, 37 °C), in the dark. After incubation, the cells were washed three times with PBS and subjected to fluorescent confocal microscopy. (B) Fluorescent confocal images of intracellular delivery of the QD probe in living cells in the absence and in the presence of cytochalasin (5 μg/mL). The cells were incubated with the probe within 2 h in humidified atmosphere (in the dark), washed three times with PBS, and subjected to fluorescence confocal microscopy. In both cases, the images were obtained using an Olympus FV1000 microscope (excitation wavelength, 488 nm; emission filters, 535 nm for lung cancer cells, 615 nm for HeLa cells; differential interference contrast; section scanning).

T_1 weighted imaging: Two dimensional (2D), multislice, T_1 weighted images were obtained using a conventional SE sequence with the following parameters: Pulse repetition time (TR) = 177 or 400 ms, echo time (TE) = 6.65 ms, matrix size = 64 × 64, slice orientation = horizontal, field of view (FOV) = 6.4 × 3.2 mm^2, slice thickness (ST) = 3 mm, and number of acquisitions (NA) = 1.

Multiecho imaging: 2D multislice multiecho imaging were performed to generate T_2 maps with the following parameters: TR = 6000 ms, TE = 6.65, 13.3, 19.95, 26.6, 33.25, 39.9, 46.55, 53.2, 59.85, 66.5, 73.15, 79.8, 86.45, 93.1, 99.75, and 106.4 ms, number of echoes = 16, matrix size = 64 × 64, slice orientation = horizontal, FOV = 6.4 × 3.2 mm^2, ST = 3 mm, and NA = 1.

Inversion−recovery: 2D multislice inversion−recovery MRIs were obtained using a spin−echo acquisition for T_1 map calculation with the following parameters: TR = 6000 ms, TE = 6.65 ms, inversion time = 6.45, 400, 800, 1200, 1600, 2000, 3000, 4000 ms, matrix size = 64 × 64, slice orientation = horizontal, FOV = 6.4 × 3.2 mm^2, ST = 3 mm, and NA = 1.

Quantitative T_1 maps were calculated by a nonlinear least-squares fitting using inversion−recovery MRIs. In addition, quantitative T_2 maps were calculated by a nonlinear least-squares fitting using multiecho imaging. All calculations and analyses were performed using *MRVision* image analysis software (version 1.5.8, MRVision Co., MA) on Solaris (Sun Microsystems, Inc., CA) and Macintosh (Mac OS X, version 10.4, Apple Computer, CA). All data are presented as mean ± SD.

Intracellular Delivery of Multimodal QDs (Fluorescent Confocal Microscopy). 10 μL of QD probe (50 pmol) was incubated with 90 μL cancer cells (containing 1 × 10^5 cells) in medium, within 30 min or 2 h, in a humidified atmosphere. The cell suspension was washed twice by PBS and analyzed by fluorescence confocal microscopy for intracellular delivery

of QDs. An Olympus FV1000 microscope was used in the analysis (excitation wavelength, 488 nm; emission filters, 535 or 615 nm; differential interference contrast; section scanning).

Photosensitization. The cells (90 μL, 2×10^5 cells/mL) were incubated with QDs (50 pmol in 10 μL) in medium,within 24 h, in humidified atmosphere (5% CO_2, 37 °C). The cells were washed twice with fresh medium and subjected to irradiation with laser or UV mercury lamp.

The laser irradiation of the cell suspension was carried out continuously on a confocal microscope for 30 min, changing the plane of irradiation in the well area (96-well plate). The cells were washed twice with PBS, and cell viability was detected using flow cytometry.

The UV irradiation was carried out under the experimental scheme mentioned below, to ensure irradiation with low-intensity UV light without significant heating of the sample and side effects: mercury lamp → UV-filter (UTF-34U, Sigma-Koki) (to restrict the light under 340 nm) → quartz platform → plates with cell suspension. The samples were placed in a fixed position relative to the camera to ensure equal spatial distribution of the energy during irradiation. The irradiation was carried out with the following regime: 10 min irradiation followed by 10 min break, repeated for a total duration of 30 min. Time-dependent monitoring of the level and spatial distribution of the energy during UV irradiation was carried out and was found to be relatively constant during the experiment. The temperature of the sample was also monitored over time and was found to vary in the interval 22−28 °C. After irradiation, the cells were washed twice by PBS, and the cell viability was detected by flow cytometry.

In both cases, the control samples contained QD nontreated cells.

Cytotoxicity Test (Flow Cytometry). The cells (2×10^5 cells/mL) were incubated with QDs (500 nM; $\lambda_{em} = 525$ nm−green fluorescence) in medium, within 24 h, in a humidified atmosphere (5% CO_2, 37 °C), and after that washed twice by PBS. The dead cells were labeled by propidium iodide (PI), and cell viability was analyzed by flow cytometry (flow cytometer Beckman Coulter-Epics XL). The flow cytometer was operated in accordance with the manufacturer's recommendations after fine adjustments for optimization. The forward- and site-scatter parameters were adjusted to accommodate the inclusion of both live and dead cells within the acquisition data with quadrant markers drawn to distinguish PI labeled dead cells (red fluorescence) from PI nonlabeled viable cells. The control sample contained QD nontreated cells. The viability of QD treated cells was calculated as the percentage from viability of nontreated (control) cells. No cells were excluded from the analysis and ∼5000 cells were counted for each sample. The data were collected and analyzed using *XL System II* software.

Pharmacodynamics. Mice (ICR, ∼20−25 g) were injected intravenously through the tail vain with 50 pmol (in 100 μL, a single injection) multimodal silica-shelled QDs. Serial sacrifices were carried out at the sixth and 24th hour after the injection. Several organs (brain, spleen, liver, lung, kidneys) were isolated, homogenized, and analyzed for QD amount, using NMR spectroscopy.

Two-Photon Imaging of Brain Circulation *in Vivo*. The animal (Sprague−Dawley rats, $n = 4$, ∼340 g) was anesthetized with isoflurane (4% for induction, 2% for surgery, and 1.4% during the measurements). The tracheal intubation was performed, and the femoral vein was catheterized for drug administration. The skull over the somatosensory cortex (3 mm × 3 mm) was removed, and the dura was kept intact. The body temperature was maintained (37 °C), and the systemic arterial blood pressure was periodically monitored from the tail artery. The heartbeat and end tidal gas levels were continuously monitored. To visualize brain microcirculation, 5% FITC−Dextran (70 kDa) was intravenously (i.v.) injected (0.3 mL/h), and excited with 900 nm pulse-laser (Maitai HP, Spectral Physics) under a microscope (SP5, Leica) equipped with a 10× objective lens (0.30 numerical aperture). The vessel diameter was then determined by measuring the width of the vessel image projected across the 15 *z*-images (up to ∼0.3 mm from the cortical surface) in each vessel segment. All measured parameters were considered as controls under the conditions mentioned above. After the stoppage of FITC−Dextran infusion, FITC−Dextran was partially washed from the brain circulation by short i.v. infusion of saline solution. Then, QD was injected (single injection, 0.3 mL of 0.5 μM QD concentration) into the rat, and all parameters were measured as described above.

RESULTS AND DISCUSSION

Structure and Characterization of Multimodal Silica-Shelled QDs. Our multimodal QD probe was composed of single QD micelles incorporated in small silica spheres (15−20 nm in diameter) and amphiphilic gadolinium complex [tris(2,2,6,6-tetramethyl-3,5-heptanedionate)/gadolinium, trivial name Resolve Al−Gd] incorporated into the micelle part and/or silica coat (Figure 1A). For comparison, we used a second probe, consisting of QDs conjugated with DOTA-Bn-NCS/gadolinium (Figure 1B).

In the first probe, the micelle around the QD allows an incorporation of strongly hydrophobic paramagnetic substances in the silica sphere. The hydrophobic micelle isolates QD nanocrystal from the polar molecules, penetrating from the environment in the silica sphere, and maintains the fluorescent properties. At the same time, the paramagnetic molecules, incorporated in the silica coat or micelle, are accessible to the water, which is beneficial for ^{1}H MRI contrast agents and, in particular, for gadolinium ions. The surface of the silica sphere was amino-functionalized and ready for bioconjugation. At acidic pH (3.0), the probe (A) had a surface potential of +31 mV (detected by zeta-potential titration), which decreased to −37 mV at pH 10.0. At physiological pH (7.4), the zeta potential was +6.9 mV.

Both probes consist of a single QD per one silica sphere (Figure 2A), which allows normalization of their concentrations to the QD concentration in moles and facilitates the dose-dependent analyses in life science research. Both probes strongly retain about 25−30% of the gadolinium complex added initially to the reaction mixture (Figure 2B). The concentration of the gadolinium complex decreased during purification by dialysis up to 10 h. After this time, there were no changes (Figure 2B), which was an indication for a retention of the complex in the silica coat or on the surface of the silica sphere.

The close distance between QDs and paramagnetic substances (especially paramagnetic nanoparticles) results in a decrease of their fluorescent and paramagnetic characteristics in comparison with the isolated materials (*13, 15*). In the present study, we compared the spectral properties of both multimodal probes, described above (Figure 2C). In probe A, gadolinium ions are in close proximity to QD (Figure 1A), and in probe B, gadolinium ions are far from QD (Figure 1B). The fluorescence quantum yield (QY) of both probes was ∼35−50% in aqueous solution (depending on QD size). It was ∼1.4 times lower than the QY of QDs in organic solvent and the same as the QY of silica-shelled QDs without gadolinium. The incorporation of gadolinium ions into the silica sphere also did not affect the profile of the absorbance and fluorescent spectra of silica-shelled QDs, as well as their paramagnetic characteristics. After purification, T_1 (longitudinal relaxation time) and T_2 (transverse relaxation time) of probe (A) were shorter than T_1 and T_2 of probe (B) (Figure 2C). We calculated that the numbers of

(A) T_1 weighted images

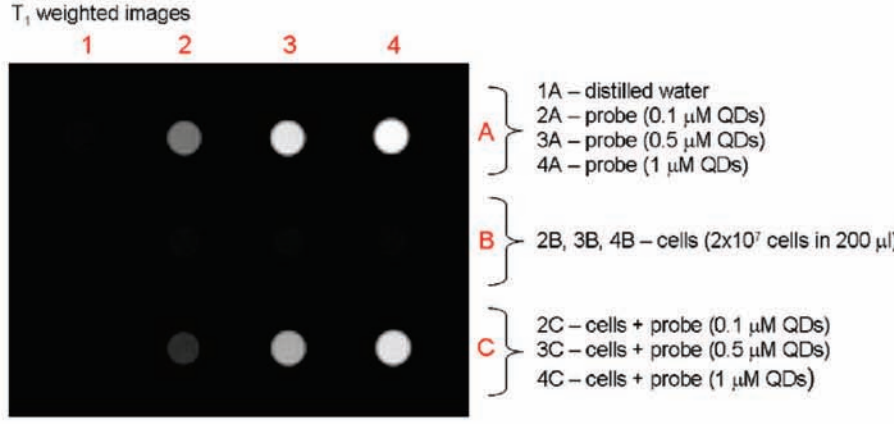

T_1 quantitative (ms)

	2	3	4
A (probe)	606.7 +/- 5.5	220.9 +/- 1.9	114.8 +/- 1.5
C (probe + cells)	1243.6 +/- 9.3	358.8 +/- 4.9	186.6 +/- 1.7

Distilled water: T_1 = 3030.9 +/- 20.6 ms. Cells only: T_1 = 3017.6 +/- 26.3 ms.

(B) T_2 weighted images

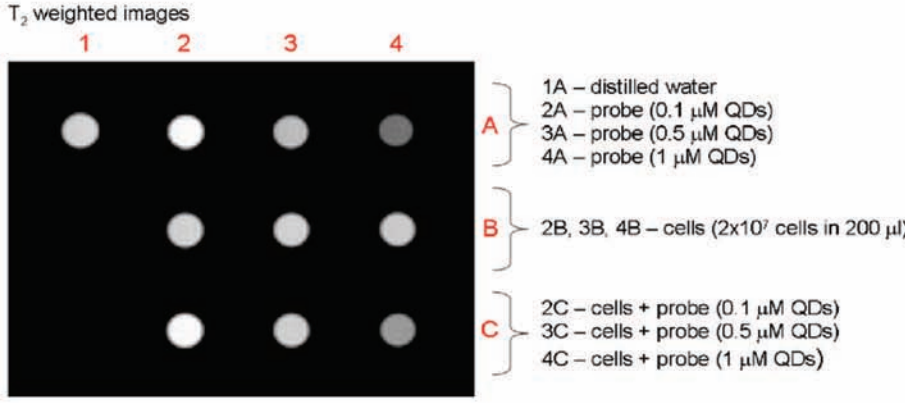

T_2 quantitative (ms)

	2	3	4
A (probe)	261.8 +/- 3.3	138.0 +/- 1.6	81.3 +/- 0.8
C (probe + cells)	304.7 +/- 3.3	176.8 +/- 1.9	114.9 +/- 1.0

Distilled water: T_2 = 440.0 +/- 9.4 ms. Cells only: T_2 = 368.0 +/- 7.0 ms.

Figure 4. T_1- and T_2-weighted images and quantitative values of samples, containing probe only (A2−A4), cells only (B2−B4), or cells incubated with probe (C2−C4). Incubation conditions: Lung cancer cells (2×10^7) were dispensed in plates, containing 20 mL cultured medium. The probe was added to the plates in different concentrations (1 μM, 0.5 μM, or 0.1 μM QDs, respectively). The incubation was carried out during 2 h in humidified atmosphere (5% CO_2, 37 °C). The cells were collected by centrifugation, washed three times by PBS (containing 1% Trypsin), and finally resuspended in 200 μL PBS. All samples were treated in the same manner. The concentration of the probe in moles was approximate. It was calculated from the absorbance spectra of QD incorporated into the silica spheres, using the equation of Yu et al. (*38*). The MRI measurements were performed in a 7.0 T magnet (Kobelco, Japan) interfaced to a Bruker Avance console (Bruker Medical GmbH, Germany). A 70 mm diameter volume coil (Bruker) was used for measurement of the samples. The sample temperature was maintained at room temperature (~22−24 °C). The measurements were performed as follows: T_1-weighted imaging using conventional spin−echo (SE) sequence and inversion−recovery SE imaging for T_1 calculations. The multiecho SE imaging was measured for T_2-weighted imaging and T_2 calculations.

chelating molecules attached on or incorporated in one silica sphere were approximately same (Gd/QD ~ 18:1 and ~17.6:1, mol/mol, for probe A and probe B, respectively). This indicates that the incorporation of gadolinium in close proximity to QD

Table 1. Cytotoxicity and Photosensitization of Multimodal Silica-Shelled QDs

treatment	HeLa cells[a]	A549 cells[a]	Jurkat cells[a]	K562 cells[a]
+ 500 nM QDs	98 +/− 6	95 +/− 9	97 +/− 7	101 +/− 5
+ Laser irradiation	96 +/− 8	97 +/− 9	98 +/− 5	98 +/− 8
+ 500 nM QDs + Laser irradiation	95 +/− 4	98 +/− 10	96 +/− 6	96 +/− 8
+ UV irradiation	87 +/− 4	89 +/− 5	91 +/− 5	89 +/− 6
+ 500 nM QDs + UV irradiation	85 +/− 7	84 +/− 8	88 +/− 3	87 +/− 6

[a] Cell viability (% from control). The control samples contain nontreated cells. The results are mean +/− SD from four independent experiments.

does not significantly affect its paramagnetic properties, presumably because of the isolation of both materials from the hydrophobic micelle.

All experiments on viable cells and animals were performed using probe A only.

Direct Intracellular Delivery of Multimodal Silica-Shelled QDs. Figure 3A represents fluorescent images of HeLa and lung cancer cells, labeled with probe A. The amino-functionalized (and positively charged) probe possessed an easy and comparatively fast intracellular delivery without transfection techniques. It was found that the probe penetrates through the cytoplasmic membrane via an endocytotic mechanism. The cytochalasin (an inhibitor of endocytosis) suppressed its intracellular delivery (Figure 3B). The probe was localized into the cytoplasm, uniformly distributed. A concentration of the probe in close proximity to the nuclear membrane was detected, which indicates an interaction with some intracellular compartments. No fluorescence was detected in the nucleus within 4 h incubation.

The facilitated permeability of silica-shelled QDs allows their application in the detection of intracellular targets (antigens, membrane compartments, subcellular organelles, etc.) in viable cells without transfection techniques. Currently, QDs are applied predominantly for labeling of cell surface antigens *in vitro* and *in vivo* or for extra- and intracellular labeling of fixed cells. Their application for labeling of intracellular components in viable cells requires transfection techniques for penetration through plasmatic membrane. The already published data indicate that QDs could be delivered in viable mammalian cells via four different mechanisms: nonspecific endocytosis/pinocytosis facilitated by polycationic transfectants (as lipofectamine); microinjection; electroporation; and peptide-induced transport (*24*−*28*). It is widely accepted that the transfection techniques maintain the risk of artifacts, some of them are toxic, and they have to be replaced with direct approaches for intracellular delivery of QDs. We observed that an appropriate polymer coating of QDs (such as positively charged silica) could facilitate their direct intracellular delivery and random distribution into the cells (*29*), which was also reported by other authors (*30*).

If the cells were washed several times with phosphate-buffered saline, concentrated, and subjected to MRI, a high MRI contrast was observed on the T_1- and T_2-weighted images (Figures 4). The T_1 and T_2 values allow calculation of the approximated absolute amount of multimodal QDs delivered into the cells, using two independent calibration curves. The calibration curve represents the relationship between the pure probe in known concentrations and T_1 or T_2 values, respectively. It was found that approximately 58−75% of the probe was delivered into the cells and/or bound on the cell surface.

Cytotoxicity, Photosensitization, and Pharmacodynamics. All experiments with cultured cells were provided in medium without FBS. The cell viability of A459, Jurkat, K562, and HeLa cells was ∼100% after 24 h incubation with QDs in 500 nM concentration (Table 1). The nanoparticles (500 nM) were also nontoxic under continuous UV or laser irradiation of the cell suspension after preliminary incubation with QDs for 24 h. The cell viability did not change within 30 min of continuous laser irradiation of QD-treated and QD-nontreated (control) cells. Under UV irradiation, the viability of QD-treated and QD-nontreated (control) cells decreased slightly (∼10%) in comparison with nonirradiated cells, as a result of nonspecific effects of UV light on cell viability (Table 1).

Several groups have demonstrated photosensitization of living cells using CdSe or CdTe core QDs (*31*−*35*). However, the overcoating (inorganic or organic) usually suppresses or eliminates the photosensitization effect (*31, 32, 35*).

Regarding cytotoxicity of nanoparticles, it is necessary to note that this parameter is usually clarified on cancer cells that are inherently resistant to many external agents. The data on normal cells are scanty. Currently, there are insufficient data on the metabolism of QDs in live organisms, and it is not clear what will happen if the nanoparticles are accumulated in different organs for a long time. Their excretion through kidneys avoiding any long-term accumulation and metabolism in the liver, bone marrow, or other organs seems to be the best possibility. Choi and colleagues have demonstrated that a hydrodynamic diameter of <5.5 nm of organic-coated QDs results in rapid and efficient renal filtration and urinary excretion from the body. Increasing the diameter by >15 nm usually prevents renal excretion and increases the blood half-life by about 300 times and the whole body half-life by about 700 times (*36*). The authors also have reported that the purely cationic charge is associated with an increase in hydrodynamic diameter of the QDs after incubation with serum.

Our pharmacodynamic study shows that nonPEGylated silica-shelled QDs persist in the blood circulation within an hour after i.v. injection in mice (half-life ∼20 min). Six hours after the injection, a comparatively large amount of QDs were detected in spleen, a very low amount in liver and kidney, and none in lung and brain (data are not shown). A similar result was obtained 24 h after the injection. Recently, Yang and colleagues reported that QDs (commercial Qtracker 705) are accumulated predominantly in spleen, liver, and kidney after i.v. injection in mice, and they do not metabolize within 28 h (*36*).

Effects on Physiological Characteristics and Brain Circulation. The intravenous application of the probe in rat did not affect significantly the physiological parameters, e.g., hart rate, blood pressure, and microcirculation (Figure 5). The multimodal QDs (300 μL of 1 μM stock solution) were injected into the femoral vain. Ten minutes after the injection, the heart rate increased slightly with subsequent normalization to the baseline level within 40 min. The blood pressure was stable within 20 min after the injection and decreased about 10% after 80 min (Table 2). The brain vasculature was visualized in the somatosensory cortex using two-photon microscopy, and the fluorescence was detected up to a 200 μm depth (Figure 5). The probe did not affect the diameter and structure of the blood vessels, which makes it an appropriate tracer for brain vasculature in the study of brain phenomena, e.g., visualization of neuron/astrocyte/blood vessel structure and investigation of neurovascular coupling.

In conclusion, the described strategy of the design of multimodal QDs allows the development of probes with high fluorescent and paramagnetic contrast characteristics and comparatively soft effects on cell homeostasis and animal physiology. The described QD probe is appropriate for *in vitro* and *in vivo* tracing of cells and blood vessels, simultaneously using fluorescent microscopy and MRI. After conjugation with appropriate ligands, the probe could be applied for target-selective molecular imaging *in vitro* and *in vivo*. The easy intracellular

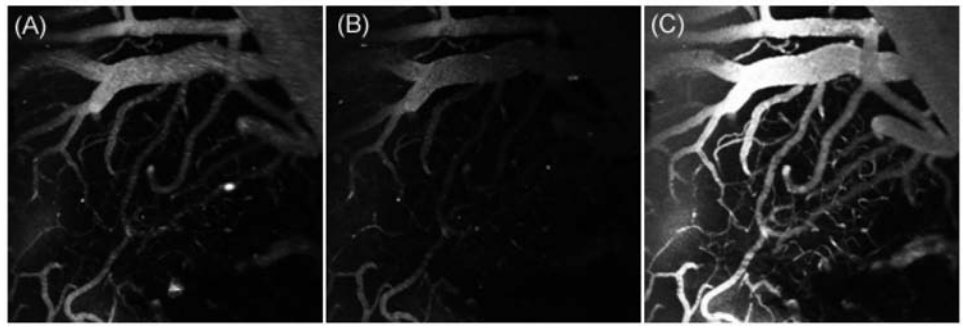

Figure 5. Two-photon images of brain circulation before and after i.v. injection of multimodal silica-shelled QDs in rat. In the images: (A) FITC−Dextran (0.5 mL of 5 μM concentration) was injected in ~340 g rat, and the image was obtained after 20 min at $\lambda_{ex} = 900$ nm and $\lambda_{em} = 525$ nm. (B) FITC−Dextran was washed from the brain vasculature by i.v. infusion of saline solution, and the image was obtained at $\lambda_{ex} = 900$ nm and $\lambda_{em} = 525$ nm. (C) QDs (0.3 mL of 1 μM QD concentration) were injected in the same rat. The image was obtained after 20 min at $\lambda_{ex} = 900$ nm and $\lambda_{em} = 560$ nm. Representative images from three independent experiments are shown in the figure.

Table 2. Physiological Characteristics before and After i.v. Injection of Silica-Shelled QDs in Experimental Animals under Anesthesia[a]

parameter	before	~20 min after i.v. injection
blood pressure, (mmHg)	95.3 +/− 7.8	93.5 +/− 16.2
heart rate, (BPM)	304 +/− 62	348 +/− 43
blood vessel diameter		
arteries, (μm)	26 +/− 8	constant
veins, (μm)	43 +/− 20	constant

[a] $n = 3$ (n = number of rats in the group); QD concentration = 80 pmol (in 300 L).

delivery of these silica-shelled QDs allows avoidance of conventional transfectants that are inherently toxic.

ACKNOWLEDGMENT

The technical assistance of Misao Yoneyama and Jeff Kershaw (NIRS, Chiba, Japan) in MRI measurements and data analysis is gratefully acknowledged. The animal experiments were approved by the Animal Care and Use Committee of NIRS-Chiba.

LITERATURE CITED

(1) Alivisatos, A. P., Gu, W., and Larabell, C. Quantum dots as cellular probes. *Annu. Rev. Biomed. Eng. 7*, 55–76.

(2) Redl, F. X., Cho, K.-S., Murray, C. B., and O'Brien, S. (2003) Three-dimensional binary superlattices of magnetic nanocrystals and semiconductor quantum dots. *Nature 423*, 968–971.

(3) Wang, D. S., He, J. B., Rosenzweig, N., and Rosenzweig, Z. (2004) Superparamagnetic Fe_2O_3 Beads-CdSe/ZnS quantum dots core-shell nanocomposite particles for cell separation. *Nano Lett. 4*, 409–413.

(4) Gu, H., Zheng, R., Zhang, X., and Xu, B. (2004) Facile one-pot synthesis of bifunctional heterodimers of nanoparticles: a conjugate of quantum dot and magnetic nanoparticles. *J. Am. Chem. Soc. 126*, 5664–5665.

(5) Michalet, X., Pinaud, F. F., Bentolila, L. A., Tsay, J. M., Doose, S., Li, J. J., Sundaresan, G., Wu, A. M., Gambhir, S. S., and Weiss, S. (2005) Quantum dots for live cells, in vivo imaging, and diagnostics. *Science 307*, 538–544.

(6) Santra, S., Yang, H., Holloway, P. H., Stanley, J. T., and Mericle, R. A. (2005) Synthesis of water-dispersible fluorescent, radio-opaque, and paramagnetic CdS:Mn/ZnS quantum dots: a multifunctional probe for bioimaging. *J. Am. Chem. Soc. 127*, 1656–1657.

(7) Yi, D. K., Selvan, S. T., Lee, S. S., Papaefthymiou, G. C., Kundaliya, D., and Ying, J. Y. (2005) Silica-coated nanocomposites of magnetic nanoparticles and quantum dots. *J. Am. Chem. Soc. 127*, 4990–4991.

(8) Know, K.-W., and Shim, M. (2005) γ-Fe_2O_3/II-VI sulfide nanocrystal heterojunctions. *J. Am. Chem. Soc. 127*, 10269–10275.

(9) Pellegrino, T., Kudera, S., Liedl, T., Javier, A. M., Manna, L., and Parak, W. J. (2005) On the development of colloidal nanoparticles towards multifunctional structures and their possible use for biological applications. *Small 1*, 48–63.

(10) Kim, H., Achermann, M., Balet, L. P., Hollingsworth, J. A., and Klimov, V. I. (2005) Synthesis and characterization of Co/CdSe core/shell nanocomposites: bifunctional magnetic-optical nanocrystals. *J. Am. Chem. Soc. 127*, 544–546.

(11) Know, K.-W., Lee, B. H., and Shim, M. (2006) Structural evolution in metal oxide/semiconductor colloidal nanocrystal heterostructures. *Chem. Mater. 18*, 6357–6363.

(12) Pellegrino, T., Fiore, A., Carlino, E., Giannini, C., Cozzoli, P. D., Ciccarella, G., Respaud, M., Palmirotta, L., Cingolani, R., and Manna, L. (2006) Heterodimers based on CoPt3-Au nanocrystals with tunable domain size. *J. Am. Chem. Soc. 128*, 6680–6698.

(13) Cozzoli, P. D., Pellegrino, T., and Manna, L. (2006) Synthesis, properties and perspectives of hybrid nanocrystal structures. *Chem. Soc. Rev. 35*, 1195–1208.

(14) Mulder, W. J. M., Koole, R., Brandwijk, R. J., Storm, G., Chin, P. T. K., Strijkers, G. J., Donega, C. M., Nicolay, K., and Griffioen, A. W. (2006) Quantum dots with a paramagnetic coating as a bimodal molecular imaging probe. *Nano Lett. 6*, 1–6.

(15) Selvan, S. T., Patra, P. K., Ang, C. Y., and Ying, J. Y. (2007) Synthesis of silica-coated semiconductor and magnetic quantum dots and their use in the imaging of live cells. *Angew. Chem., Int. Ed. 46*, 1–6.

(16) Wang, S., Jarrett, B. R., Kauzlarich, S. M., and Louie, A. Y. (2007) Core/shell quantum dots with high relaxivity and photoluminescence for multimodality imaging. *J. Am. Chem. Soc. 129*, 3848–3856.

(17) Prinzen, L., Miserus, R.-J., Dirksen, A., Hackeng, T. M., Deckers, N., Bitsch, N. J., Megens, R. T. A., Douma, K., Heemskerk, J. W., Kooi, E., Frederik, P. M., Slaaf, D. W., Zandvoort, M., and Reutelingsperger, C. P. M. (2007) Optical and magnetic resonance imaging of cell death and platelet activation using annexin a5-functionalized quantum dots. *Nano Lett. 7*, 93–100.

(18) Oostendorp, M., Douma, K., Stelt, B. J., Hackeng, T. M., Dirksen, A., Van Zandvoort, M. A., Post, M. J., and Backes, W. H. (2007) Feasibility of cNGR labeled paramagnetic quantum dots for molecular MRI and two-photon laser scanning microscopy of neovascularization. *Proc. Int. Soc. Magn. Reson. Med. 15*, 1164.

(19) Grant, S. C., Zheng, T., Marshall, G. P., Yang, H., Dutta, D., Cornnell, H., Santra, S., Holloway, P. H., Moudgil, B. M., Scott, E. W., Laywell, E. D., Walter, G. A., Edison, A. S., Steindler, D. A., and Weiss, M. D. (2006) MR microscopy of multipotent

astrocytic stem cells labeled with multimodal QDots applied to a neonatal murine model of hypoxic ischemic encephalopathy. *Proc. Int. Soc. Magn. Reson. Med. 14*, 1990.

(20) Bakalova, R., Zhelev, Z., Aoki, I., and Kanno, I. (2007) Designing quantum dot probes. *Nat. Photonics 1*, 487–489.

(21) Bakalova, R., Zhelev, Z., Aoki, I., Ohba, H., Imai, Y., and Kanno, I. (2006) Silica-shelled single quantum dot micelles as imaging probes with dual or multimodality. *Anal. Chem. 78*, 5925–5932.

(22) Bryant, L. H., Brechbiel, M. W., Wu, C., Bulte, J. W. M., Herynek, V., and Frank, J. A. (1999) Synthesis and relaxometry of high-generation (*G*=5, 7, 9, and 10) PAMAM dendrimer-DOTA-gadolinium chelates. *J. Magn. Res. Imaging 9*, 348–352.

(23) Wu, C., Brechbiel, M. W., Kozak, E. W., and Gansow, O. A. (1994) Metal-chelate-dendrimer-antibody constructs for use in radioimmunotherapy and imaging. *Bioorg. Med. Chem. Lett. 4*, 449–454.

(24) Dubertret, B., Skourides, P., Norris, D. J., Noireaux, V., and Libchaber, A. (2002) In vivo imaging of quantum dots encapsulated in phospholipids micelles. *Science 298*, 1759–1762.

(25) Matteakis, L. C., Dias, J. M., Choi, Y. J., Gong, J., Bruches, M. P., Liu, J., and Wang, E. (2004) Optical coding of mammalian cells using semiconductor quantum dots. *Anal. Biochem. 327*, 200–208.

(26) Jaiswal, J. K., Mattoussi, H., Mauro, J. M., and Simon, S. M. (2003) Long-term multiple color imaging of live cells using quantum dot bioconjugates. *Nat. Biotechnol. 21*, 47–51.

(27) Chen, F., and Gerion, D. (2004) CdSe/ZnS nanocrystal-peptide conjugates for long-term, nontoxic imaging and nuclear targeting in living cells. *Nano Lett. 4*, 1827–1832.

(28) Derfus, A. M., Chan, W. C. W., and Bhatia, S. N. (2004) Intracellular delivery of quantum dots for live cell labeling and organelle tracking. *Adv. Mater. 16*, 961–966.

(29) Zhelev, Z., Ohba, H., and Bakalova, R. (2006) Single quantum dot-micelles coated with silica shell as potentially non-cytotoxic fluorescent cell tracers. *J. Am. Chem. Soc. 128*, 6324–6325.

(30) Duan, H., and Nie, S. (2007) Cell-penetrating quantum dots based on multivalent and endosome-disrupting surface coatings. *J. Am. Chem. Soc. 129*, 3333–3338.

(31) Defrus, A. M., Chan, W. C. W., and Bhatia, S. N. (2004) Probing the cytotoxicity of quantum dots. *Nano Lett. 4*, 11–18.

(32) Bakalova, R., Ohba, H., Zhelev, Z., Nagase, T., Jose, R., Ishikawa, M., and Baba, Y. (2004) Quantum dot anti-CD conjugates: Are they potential photosensitizers or potentiators of classical photosensitizing agents in photodynamic therapy of cancer? *Nano Lett. 4*, 1567–1573.

(33) Bakalova, R., Ohba, H., Zhelev, Z., Ishikawa, M., and Baba, Y. (2004) Quantum dots as photosensitizers? *Nat. Biotechnol. 22*, 1361–1362.

(34) Cho, S. J., Maysinger, D., Jain, M., Roder, B., Hackbarth, S., and Winnik, F. M. (2007) Long-term exposure to CdTe quantum dots causes functional impairments in live cells. *Langmuir 23*, 1974–1980.

(35) Hardman, R. (2006) A toxicologic review of quantum dots: toxicity depends on physicochemical and environmental factors. *Environ. Health Perspect. 114*, 165–172.

(36) Choi, H. S., Liu, W., Misra, P., Tanaka, E., Zimmer, J. P., Ipe, B. I., Bawendi, M. G., and Frangioni, J. V. (2007) Renal clearance of quantum dots. *Nat. Biotechnol. 25*, 1165–1170.

(37) Yang, R. S. H., Chang, L. W., Wu, J.-P., Tsai, M.-H., Wang, H.-J., Kuo, Y.-C., yeh, T.-K., Yang, C. S., and Lin, P. (2007) Persistent tissue kinetics and redistribution of nanoparticles, quantum dot 705, in mice: ICP-MS quantitative assessment. *Environ. Health Perspect. 115*, 1339–1343.

(38) Yu, W. W., Qu, L., Guo, W., and Peng, X. (2003) Experimental determination of the extinction coefficient of CdTe, CdSe, and CdS nanocrystals. *Chem. Mater. 15*, 2854–2860.

BC700431C

Synthesis and Biological Characterization of Novel 2-Quinolinecarboxamide Ligands of the Peripheral Benzodiazepine Receptors Bearing Technetium-99m or Rhenium

Andrea Cappelli,*[,†] Alessandra Mancini,[†] Francesco Sudati,[‡] Salvatore Valenti,[†] Maurizio Anzini,[†] Sara Belloli,[‡] Rosa Maria Moresco,[‡] Mario Matarrese,[‡] Mauro Vaghi,[‡] Andrea Fabro,[‡] Ferruccio Fazio,[‡] and Salvatore Vomero[†]

Dipartimento Farmaco Chimico Tecnologico and European Research Centre for Drug Discovery and Development, Università degli Studi di Siena, Via A. Moro, 53100 Siena, Italy, and Istituto di Bioimmagini e Fisiologia Molecolare, CNR, Università di Milano/Bicocca, Istituto H. S. Raffaele, Via Olgettina 60, 20132 Milano, Italy. Received November 29, 2007; Revised Manuscript Received April 16, 2008

Potential receptor imaging agents based on Tc-99m for the in vivo visualization of the peripheral benzodiazepine receptor (PBR) have been designed on the basis of the information provided by the previously published structure−affinity relationship studies, which suggested the existence of tolerance to voluminous substituents in the receptor area interacting with 3-position of the quinoline nucleus of 2-quinolinecarboxamides **5**. In the first step of the investigation, the stereoelectronic features of the above-indicated receptor area were also probed by means of 4-phenyl-3-[(1-piperazinyl)methyl]-2-quinolinecarboxamide derivatives bearing different substituents on the terminal piperazine nitrogen atom (compounds **6a**−**f**). The structure−affinity relationship data confirmed the existence of a tolerance to bulky lipophilic substituents and stimulated the design of bifunctional ligands based on the 4-phenyl-3-[(1-piperazinyl)methyl]-2-quinolinecarboxamide moiety (compounds **6h,j,k,m**). The submicromolar PBR affinity of rhenium complexes **6j,m** suggests that the presence of their metal−ligand moieties with encaged rhenium is fairly compatible with the interaction with the PBR binding site. Thus, in order to obtain information on the in vivo behavior of these bifunctional ligands, ^{99m}Tc-labeled compounds **6h,k** were synthesized and evaluated in preliminary biodistribution and single photon emission tomography (SPET) studies. The results suggest that both tracers do not present a clear preferential distribution in tissues rich in PBR, probably because of their molecular dimensions, which may hamper both the intracellular diffusion toward PBR and the interaction with the binding site.

INTRODUCTION

The peripheral benzodiazepine receptor (PBR) is a 169-amino acid protein (18 kDa) with five trans-membrane domains localized on the mitochondrial outer membrane (*1–3*). PBR is functionally linked to the voltage-dependent anion channel (VDAC) and to the adenine nucleotide translocase (ANT) and might be implicated in the regulation of the opening of the mitochondrial permeability transition pore (MPTP). This receptor is highly expressed in steroidogenic tissues such as adrenal gland, but also in kidney, heart, testis, and at a lower level in the brain parenchyma, ependyma, choroid plexus, and olfactory neurons. Moreover, PBR is overexpressed in a variety of tumors (e.g., certain brain tumors, ovarian cancer, liver tumors, breast carcinoma, colorectal cancer, etc.) and its expression appears to be related to the degree of tumor malignancy (*4–11*). In addition, PBR is overexpressed on activated microglial cells localized in lesioned brain areas of patients with neurodegenerative or neuroinflammatory diseases like Alzheimer's disease, and Huntington's disease or multiple sclerosis (*12–14*).

PK11195 (**1**, Figure 1) is an isoquinolinecarboxamide derivative, which was both found to bind the PBR with nanomolar affinity and is the most widely used pharmacological tool for the study of the expression and the function of PBR. Carbon-11 labeled compound **1** was used for the in vivo imaging of microglial/macrophage activation present in different brain disorders including tumors by means of positron emission tomography (PET) (*15–19*). In addition, a potential role for compound **1** and more in general for PBR in the in vivo monitoring of macrophage infiltration in respiratory disorders has been recently proposed (*20–22*). These results have stimulated the research and development of a large number of potential PET radiotracers based on PBR ligands in different

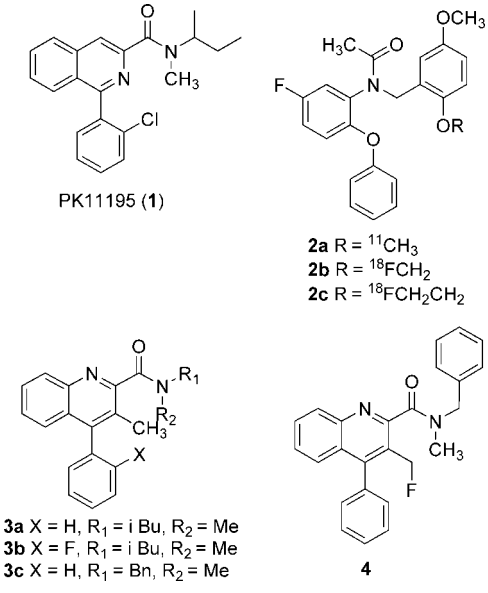

Figure 1. Structures of PBR ligands **1**−**4**.

* Corresponding author. Tel.: +39 0577 234320; fax: +39 0577 234333; e-mail: cappelli@unisi.it.
† Università degli Studi di Siena.
‡ Università di Milano/Bicocca.

10.1021/bc700437g CCC: $40.75 © 2008 American Chemical Society
Published on Web 05/30/2008

laboratories all over the world (for a recent review, see ref (*23*)). Among the most significant, labeled DAA1106 (**2a**: R = $^{11}CH_3$), and its fluoromethyl (**2b**: R = $^{18}FCH_2$) and fluoroethyl (**2c**: R = $^{18}FCH_2CH_2$) derivatives were described and [^{18}F]-FEDAA1106 (**2c**) was proposed as a useful PET ligand for PBR which is currently used for the PBR imaging in human brain (*24*).

Potent 2-quinolinecarboxamide PBR ligands **3a**−**c** were ^{11}C-labeled and the biodistribution studies suggested that these compounds are promising PET tracers for the in vivo imaging of PBR (*25*–*27*). Their evaluation in an excitotoxic model of Huntington's disease in rats showed that benzyl derivative **3c** can be considered an interesting candidate for the in vivo PET monitoring of neurodegenerative processes (*28*). Moreover, compound **3c** served as a lead in the design of fluoroderivative **4**, which shows subnanomolar PBR affinity, and was therefore considered for labeling with C-11 and F-18. The results obtained with ^{11}C-labeled **4** in ex vivo biodistribution, inhibition, and small animal YAP-(S)PET studies are very promising (*29*), and the ^{18}F-labeling of **4** is now in progress.

Nevertheless, C-11 and F-18 labeling shows some limitations, since the production of these radioisotopes requires the use of an on-site cyclotron, an apparatus that is not always present in all nuclear medicine centers. On the other hand, technetium-99m is the ideal diagnostic single-photon radionuclide with a 6 h half-life, 140 keV γ-radiation, no particulate radiation, and ready availability in all nuclear medicine centers by means of transportable ^{99}Mo/^{99m}Tc generators (*30*, *31*). These advantages explain the general use of Tc-99m-labeled compounds in routine clinical practice and, at the same time, stimulate the design and synthesis of new PBR ligands labeled with Tc-99m.

The preparation of a receptor−ligand bearing Tc-99m is a difficult undertaking because the compound must satisfy a series of physicochemical requirements in order to reach and interact selectively with the target receptor. For instance, passive transport through biological membranes can be achieved only for complexes having a neutral charge and a suitable lipophilic feature. Furthermore, the molecular shape of the receptor imaging agent has to fit the binding site of the target receptor to allow the establishment of a strong and selective interaction (*32*).

In the design of the receptor imaging agents based on Tc-99m, two main strategies have been developed in recent years (*32*–*34*). The bifunctional chelate approach is based on the conjugation of the bioactive group (receptor−ligand moiety, RLM) to a metal complex through a suitable linkage. Thus, the "bifunctional ligand" can be designed as the result of the combination of a strong chelating group for the radionuclide (metal−ligand moiety, MLM) with the RLM by means of a suitable linker connecting these two molecular portions. After the radionuclide has been coordinated by the chelating system, the resulting conjugate shows RLM as an appended side chain.

The design of new receptor imaging agents based on Tc-99m for the in vivo visualization of the PBR could rely on the information provided by the previously published structure−affinity relationship studies, which suggested the presence of tolerance to voluminous substituents in the receptor area interacting with 3-position of the quinoline nucleus of 2-quinolinecarboxamides **5** (*35*, *36*).

Therefore, bifunctional ligands **6** (Figure 2) could be envisioned to interact with a sufficient potency with PBR given that the binding site would be capable of accommodating the MLM with the encaged radionuclide. In the first step of the investigation, the stereoelectronic features of the above-indicated receptor area was explored by means of probes **6a**−**f** and unlabeled compounds **6j,m** bearing rhenium in their MLM. Rhenium is an excellent model for the radioactive Tc-99m because it forms

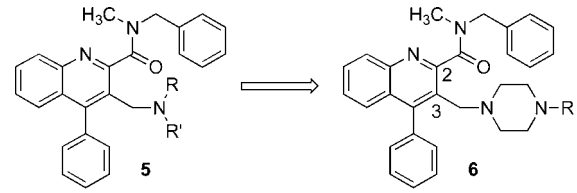

Figure 2. Design of PBR ligands **6**.

equally stable complexes showing lipophilicity and square pyramidal structures very similar to those formed by technetium. In the second phase, potential receptor imaging agents **6h,k** bearing Tc-99m were synthesized and evaluated in preliminary ex-vivo biodistribution and single photon emission tomography (SPET) studies.

EXPERIMENTAL PROCEDURES

Chemistry. All chemicals used were of reagent grade. Yields refer to purified products and are not optimized. Melting points were determined in open capillaries on a Gallenkamp apparatus and are uncorrected. Microanalyses were carried out by means of a Perkin-Elmer 240C or a Perkin-Elmer Series II CHNS/O Analyzer 2400. Merck silica gel 60 (230−400 mesh) was used for column chromatography. Merck TLC plates, silica gel 60 F_{254}, were used for TLC. ^{1}H NMR spectra were recorded with a Bruker AC 200 or a Bruker DRX 400 AVANCE spectrometer in the indicated solvents (TMS as internal standard); the values of the chemical shifts are expressed in ppm and the coupling constants (*J*) in Hz. Mass spectra were recorded on either a Varian Saturn 3 spectrometer or a ThermoFinnigan LCQ-Deca.

***N*-Benzyl-*N*-methyl-4-phenyl-3-[(piperazin-1-yl)methyl]-2-quinolinecarboxamide (6a).** A mixture of **7** (1.2 g, 3.0 mmol) in ethanol (40 mL) with piperazine (0.78 g, 9.0 mmol) was refluxed for 20 min under nitrogen. The solvent was removed under reduced pressure and the resulting residue was diluted with $CHCl_3$. The organic layer was washed with water, dried over sodium sulfate, and evaporated under reduced pressure. The resulting dark residue was purified by flash chromatography with ethyl acetate−TEA−methanol (6:3:1) as the eluent to give **6a** (0.81 g, yield 60%) as a light brown glassy solid. Since the amide nitrogen of this compound bears two different substituents, the ^{1}H NMR spectrum shows the presence of two different rotamers in equilibrium. For the sake of simplification, the integral intensities have not been given. ^{1}H NMR (200 MHz, $CDCl_3$): 2.16 (m), 2.30 (m), 2.50 (m), 2.80 (m), 2.96 (s), 3.03 (s), 3.58 (br s), 4.38 (br s), 4.80 (s), 7.21−7.74 (m), 8.03 (d, J = 8.4), 8.11 (d, J = 8.3). MS(ESI): m/z 451 ($M+H^+$). Anal. ($C_{29}H_{30}N_4O\cdot H_2O$) C, H, N.

1,4-Bis-[[2-[(*N*-benzylmethylamino)carbonyl]-4-phenylquinolin-3-yl]methyl]piperazine (6b). This compound was obtained from the flash chromatography purification of compound **6a** as a less polar fraction [dichloromethane−ethyl acetate (7:3) as the eluent]. Compound **6b** was obtained as a white solid (0.30 g, yield 25%, mp 290−293 °C dec.). Since the amide nitrogen of this compound bears two different substituents, the ^{1}H NMR spectrum shows the presence of different rotamers in equilibrium. For the sake of simplification the integral intensities have not been given. ^{1}H NMR (200 MHz, $CDCl_3$): 2.12 (br s), 2.80 (s), 2.85 (s), 2.89 (s), 2.93 (s), 3.47 (br s), 3.58 (br s), 4.22 (br s), 4.67 (s), 4.73 (s), 7.21−7.70 (m), 7.98−8.12 (m). MS(ESI): m/z 815 ($M+H^+$). Anal. ($C_{54}H_{50}N_6O_2\cdot H_2O$) C, H, N.

3-[[4-(Anilinocarbonyl)piperazin-1-yl]methyl]-*N*-benzyl-*N*-methyl-4-phenyl-2-quinolinecarboxamide (6c). To a solution of **6a** (0.10 g, 0.22 mmol) in $CHCl_3$ (6 mL) cooled at 0−5 °C, a solution of phenylisocyanate (24 μL, 0.22 mmol) in $CHCl_3$ (2 mL) was slowly added. The reaction mixture was stirred for 1 h at room temperature, washed with water, dried over sodium

sulfate, and evaporated under reduced pressure. The residue was purified by flash chromatography with dichloromethane-ethyl acetate (7:3) as the eluent to give **6c** (0.082 g, yield 65%) as a pale yellow glassy solid. Since the amide nitrogen of this compound bears two different substituents, the ^{1}H NMR spectrum shows the presence of two different rotamers in equilibrium. For the sake of simplification, the integral intensities have not been given. ^{1}H NMR (200 MHz, $CDCl_3$): 2.14 (m), 2.28 (m), 2.94 (s), 3.00 (m), 3.35 (m), 3.55 (br s), 4.35 (br s), 4.77 (s), 6.62 (s), 6.90 (m), 7.12−7.71 (m), 8.03 (d, J = 8.3), 8.10 (d, J = 8.4). MS(ESI): m/z 570 ($M+H^+$). Anal. ($C_{36}H_{35}N_5O_2\cdot 0.5H_2O$) C, H, N.

***N*-Benzyl-3-[[4-[2-(1,3-dioxo-2,3-dihydro-1*H*-isoindol-2-yl)ethyl]piperazin-1-yl]methyl]-*N*-methyl-4-phenyl-2-quinolinecarboxamide (6d).** A mixture of **6a** (0.13 g, 0.29 mmol) in DMF (20 mL) with N-(2-bromoethyl)phthalimide (0.11 g, 0.43 mmol) and Na_2CO_3 (0.31 g, 2.9 mmol) was heated at 120 °C for 2 h. The solvent was removed under reduced pressure and the resulting residue was diluted with ethyl acetate. The organic layer was washed with water, dried over sodium sulfate, and evaporated under reduced pressure. The residue was purified by flash chromatography with ethyl acetate as the eluent to give **6d** (0.043 g, yield 24%) as a pale yellow glassy solid. Since the amide nitrogen of this compound bears two different substituents, the ^{1}H NMR spectrum shows the presence of two different rotamers in equilibrium. For the sake of simplification, the integral intensities have not been given. ^{1}H NMR (200 MHz, $CDCl_3$): 2.02−2.45 (m), 2.62 (t, J = 6.5), 2.94 (s), 3.01 (s), 3.40−3.87 (m), 4.36 (s), 4.78 (s), 7.18−7.85 (m), 8.02 (d, J = 8.3), 8.10 (d, J = 8.3). MS(ESI): m/z 624 ($M+H^+$). Anal. ($C_{39}H_{37}N_5O_3\cdot 0.67H_2O$) C, H, N.

***N*-Benzyl-3-[[4-[3-(1,3-dioxo-2,3-dihydro-1*H*-isoindol-2-yl)propyl]piperazin-1-yl]methyl]-*N*-methyl-4-phenyl-2-quinolinecarboxamide (6e).** A mixture of **6a** (0.15 g, 0.33 mmol) in ethanol (20 mL) with *N*-(3-bromopropyl)phthalimide (0.13 g, 0.49 mmol) and Na_2CO_3 (0.35 g, 3.3 mmol) was refluxed for 12 h. The solvent was removed under reduced pressure and the resulting residue was diluted with ethyl acetate. The organic layer was washed with water, dried over sodium sulfate, and evaporated under reduced pressure. Purification of the residue by flash chromatography with ethyl acetate as the eluent gave **6e** as a pale yellow oil, which crystallized on standing (0.10 g, yield 47%, mp 177−179 °C). Since the amide nitrogen of this compound bears two different substituents, the ^{1}H NMR spectrum shows the presence of two different rotamers in equilibrium. For the sake of simplification, the integral intensities have not been given. ^{1}H NMR (200 MHz, $CDCl_3$): 1.72−2.38 (m), 2.90 (s), 2.98 (s), 3.43 (br s), 3.71 (m), 4.32 (br s), 4.75 (s), 7.20−7.76 (m), 8.01 (d, J = 8.3), 8.09 (d, J = 8.4). MS(ESI): m/z 638 ($M+H^+$). Anal. ($C_{40}H_{39}N_5O_3$) C, H, N.

***N*-Benzyl-3-[[4-[4-(1,3-dioxo-2,3-dihydro-1*H*-isoindol-2-yl)butyl]piperazin-1-yl]methyl]-*N*-methyl-4-phenyl-2-quinolinecarboxamide (6f).** The title compound was prepared from **6a** (0.15 g, 0.33 mmol), *N*-(4-bromobutyl)phthalimide (0.14 g, 0.50 mmol), and Na_2CO_3 (0.35 g, 3.3 mmol) following the procedure described for **6e**, and was purified by flash chromatography with ethyl acetate as the eluent to obtain **6f** (0.087 g, yield 40%) as a pale yellow oil. Since the amide nitrogen of this compound bears two different substituents, the ^{1}H NMR spectrum shows the presence of two different rotamers in equilibrium. For the sake of simplification, the integral intensities have not been given. ^{1}H NMR (200 MHz, $CDCl_3$): 1.31−1.68 (m) 1.90−2.43 (m), 2.93 (s), 3.01 (s), 3.42−3.71 (m), 4.34 (br s), 4.78 (s), 7.18−7.82 (m), 8.02 (d, J = 8.5), 8.09 (d, J = 8.3). MS(ESI): m/z 652 ($M+H^+$). Anal. ($C_{41}H_{41}N_5O_3\cdot C_4H_8O_2\cdot 0.67CH_2Cl_2$) C, H, N.

***N*-Benzyl-3-[[4-[*N*-[(benzoylthio)acetyl]glycylglycylglicyl]-piperazin-1-yl]methyl]-*N*-methyl-4-phenyl-2quinolinecarboxamide (6g).** A mixture of **8** (*37–39*) (0.12 g, 0.23 mmol) in acetonitrile (20 mL) with **6a** (0.10 g, 0.22 mmol) was stirred at room temperature for 2 h under nitrogen. The reaction mixture was then poured into ice−water and the precipitate was extracted with ethyl acetate. The organic layer was dried over sodium sulfate and concentrated under reduced pressure. The resulting brown foam was purified by flash chromatography with ethyl acetate−methanol (85:15) as the eluent to give amide derivative **6g** (0.12 g, yield 68%) as a light brown foam. Since the amide nitrogen of this compound bears two different substituents, the ^{1}H NMR spectrum shows the presence of two different rotamers in equilibrium. For the sake of simplification, the integral intensities have not been given. ^{1}H NMR (200 MHz, $CDCl_3$): 2.11 (m), 2.31 (m), 2.80 (m), 2.95 (s), 3.02 (s), 3.12 (m), 3.26 (m), 3.47 (m), 3.59 (m), 3.78 (s), 3.84 (d, J = 4.0), 3.98 (m), 4.36 (s), 4.77 (s), 6.80−7.07 (m), 7.19 (m), 7.33−7.73 (m), 7.92 (m), 8.03 (d, J = 8.3), 8.12 (d, J = 8.4). MS(ESI): m/z 822 ($M+Na^+$). Anal. ($C_{44}H_{45}N_7O_6S\cdot 1.5H_2O$) C, H, N.

***N*-[3-[4-[[2-[(*N*-benzylmethylamino)carbonyl]-4-phenylquinolin-3-yl]methyl]piperazin-1-yl]propyl]-*N*-[[[2-[(triphenylmethyl)thio]ethyl]amino]carbonylmethyl]-*S*-(triphenylmethyl)-2-aminoethanethiol (6i).** A mixture of **6a** (0.19 g, 0.42 mmol), **9** (*40–42*) (0.32 g, 0.42 mmol), Na_2CO_3 (0.22 g, 2.1 mmol), and NaI (0.08 g, 0.53 mmol) in dry CH_3CN was refluxed for 9 h under nitrogen. The reaction mixture was cooled to room temperature and the solid was filtered off. The filtrate was evaporated under reduced pressure and the residue was purified by flash chromatography with ethyl acetate−TEA (95:5) as the eluent to give **6i** (0.36 g, yield 73%) as a light brown foam. Since the amide nitrogen of this compound bears two different substituents, the ^{1}H NMR spectrum shows the presence of two different rotamers in equilibrium. For the sake of simplification, the integral intensities have not been given. ^{1}H NMR (200 MHz, $CDCl_3$): 1.45 (m), 1.93−2.35 (m), 2.80−3.02 (m), 3.59 (br s), 4.35 (br s), 4.79 (s), 7.05−7.72 (m), 8.05 (d, J = 8.4), 8.13 (d, J = 8.4). MS(ESI): m/z 1169.6 ($M+H^+$). Anal. ($C_{76}H_{76}N_6O_2S_2\cdot 2H_2O$) C, H, N.

[*N*-[3-[4-[[2-[(*N*-benzylmethylamino)carbonyl]-4-phenylquinolin-3-yl]methyl]piperazin-1-yl]propyl]-*N*-[[(2-mercaptoethyl)-amino]carbonylmethyl]-2-aminoethanethiolato]rhenium(V) Oxide (6j). Compound **6i** (0.16 g, 0.14 mmol) was dissolved into boiling ethanol (10 mL) under nitrogen. To this a solution of $SnCl_2$ (0.04 g, 0.18 mmol in 0.85 mL of 0.05 N HCl) was added, followed immediately by a solution of $NaReO_4$ (0.05 g, 0.18 mmol in 0.85 mL of 0.05 N HCl). The resulting mixture was refluxed for 26 h. Subsequently, the addition of the same amounts of $SnCl_2$ and $NaReO_4$ was repeated twice and the reaction mixture was refluxed for additional 26 h, diluted with acetonitrile, and filtered. The filtrate was evaporated under reduced pressure and the resulting brown residue was partitioned between a saturated $NaHCO_3$ solution and chloroform. The organic layer was dried over sodium sulfate and evaporated under reduced pressure. The resulting residue was purified by flash chromatography with ethyl acetate−TEA (95:5) as the eluent to give **6j** (0.061 g, yield 49%) as a pink glassy solid. Since the amide nitrogen of this compound bears two different substituents, the ^{1}H NMR spectrum shows the presence of two different rotamers in equilibrium. For the sake of simplification, the integral intensities have not been given. ^{1}H NMR (400 MHz, $CDCl_3$): 0.91 (m), 1.07−1.37 (m), 1.55−2.40 (m), 2.81 (m), 2.90 (s), 2.94 (s), 2.99 (s), 3.02 (s), 3.16−3.36 (m), 3.55 (m), 3.88 (m), 4.04 (m), 4.36 (br s), 4.59 (m), 4.78 (s), 7.22−7.71 (m), 8.02 (d, J = 7.8), 8.10 (d, J = 8.1). MS(ESI): m/z 885 ($M+H^+$). Anal. ($C_{38}H_{45}N_6O_3ReS_2\cdot C_4H_8O_2$) C, H, N.

***N*-[[4-[[2-[(*N*-benzylmethylamino)carbonyl]-4-phenylquinolin-3-yl]methyl]piperazin-1-yl]carbonylmethyl]-*N*-[[[2-[(triphenylmethyl)thio]ethyl]amino]carbonylmethyl]-*S*-(triphenylmethyl)-2-aminoethanethiol (6l).** To a solution of **10** (*43*) (0.23 g, 0.31 mmol) with **6a** (0.18 g, 0.40 mmol) in dry CH_2Cl_2 (15 mL) cooled at 0−5 °C, HOBt (0.19 g, 1.4 mmol) was added. The resulting mixture was stirred at 0−5 °C for 30 min and a solution of EDCI (0.35 g, 1.8 mmol) in dry CH_2Cl_2 (7 mL) was added. The reaction mixture was stirred at room temperature for 18 h and washed in sequence with 1 M HCl, a saturated solution of $NaHCO_3$ and H_2O, dried over sodium sulfate, and evaporated under reduced pressure. The residue was purified by chromatography with ethyl acetate−petroleum ether (7:3) as the eluent to give **6l** (0.17 g, yield 47%) as a white foam. Since the amide nitrogen of this compound bears two different substituents, the ^{1}H NMR spectrum shows the presence of two different rotamers in equilibrium. For the sake of simplification, the integral intensities have not been given. ^{1}H NMR (200 MHz, $CDCl_3$): 2.03− 2.37 (m), 2.57−2.69 (m) 2.91−3.17 (m), 3.39 (br s), 3.60 (br s), 4.35 (br s), 4.77 (s), 7.07−7.72 (m), 8.04 (d, J = 8.3), 8.12 (d, J = 8.3). MS(ESI): m/z 1169.7 ($M+H^+$). Anal. ($C_{75}H_{72}N_6O_3S_2 \cdot 2H_2O$) C, H, N.

[*N*-[[4-[[2-[(*N*-benzylmethylamino)carbonyl]-4-phenylquinolin-3-yl]methyl]piperazin-1-yl]carbonylmethyl]-*N*-[[(2-mercaptoethyl)amino]carbonylmethyl]-2-aminoethanethiolato]rhenium(V) Oxide (6m). Compound **6l** (0.16 g, 0.14 mmol) was dissolved into boiling ethanol (15 mL) under nitrogen. To this a solution of $SnCl_2$ (0.04 g, 0.18 mmol in 0.85 mL of 0.05 N HCl) was added, followed immediately by a solution of $NaReO_4$ (0.05 g, 0.18 mmol in 0.85 mL of 0.05 N HCl). The resulting mixture was refluxed for 17 h. Subsequently, the addition of the same amounts of $SnCl_2$ and $NaReO_4$ was repeated once and the reaction mixture was refluxed for additional 24 h, diluted with acetonitrile, and filtered. The filtrate was evaporated under reduced pressure and the resulting brown residue was partitioned between a saturated $NaHCO_3$ solution and chloroform. The organic layer was dried over sodium sulfate and evaporated under reduced pressure. The resulting residue was purified by flash chromatography with ethyl acetate−TEA (85:15) as the eluent to give **6m** (0.012 g, yield 10%) as pink glassy solid. Since the amide nitrogen of this compound bears two different substituents, the ^{1}H NMR spectrum shows the presence of two different rotamers in equilibrium. For the sake of simplification, the integral intensities have not been given. ^{1}H NMR (200 MHz, $CDCl_3$): 0.87 (m), 1.10−1.36 (m), 1.45−1.63 (m), 1.95−2.40 (m), 2.56−3.80 (m), 4.09−4.38 (m), 4.55−4.83 (m), 7.24−7.67 (m), 8.04 (d, J = 8.5), 8.11 (d, J = 8.3). MS(ESI): m/z 885 ($M+H^+$). Anal. ($C_{37}H_{41}N_6O_4ReS_2$) C, H, N.

Radiosynthesis. Negatively charged complex **6h** was prepared by means of the conventional $SnCl_2$ radiolabeling procedure. Briefly, to 0.3 mg of the ligand in 0.30 mL of CH_3CN and 150 μL of 1 M Na_2CO_3 was added 0.50 mg of $SnCl_2 \times 2H_2O$ dissolved in 200 μL of 0.01 N HCl containing 20 mCi of $Na^{99m}TcO_4$. The mixture was heated at 100 °C for 15 min and the radioligand was recovered by solid-phase extraction (SPE) on a preactivated Sep-Pak C-18 cartridge (Millipore). The Sep-Pak was washed with water (10 mL) and eluted with ethanol (2.0 mL). The eluate was concentrated under a nitrogen stream. The residue was dissolved into saline and the resulting solution was sterilized through a sterile 0.22 μm filter (Gelman Acrodisc).

High-performance liquid chromatography (HPLC) was performed with AKTA basic gradient system (GE Health Care) and relative variable-wavelength UV detector in series with radiochemical Bioscan Flow Count detector.

The quality control assays of the unlabeled reference standard **6g** and final radioligand **6h** were performed on a reverse-phase analytical HPLC Chromolith C-18; (100 × 4.6 mm) with the following solvent systems: A, 0.1% TFA in water; B, CH_3CN. Gradient: 0−1 min 100% A, 1−16 min 100% B; 16 min 0% B; 16−20 min 100% B. In the analysis of the ^{99m}Tc labeled compound **6h**, unlabeled reference standard **6g** was used for comparison (Figure 3).

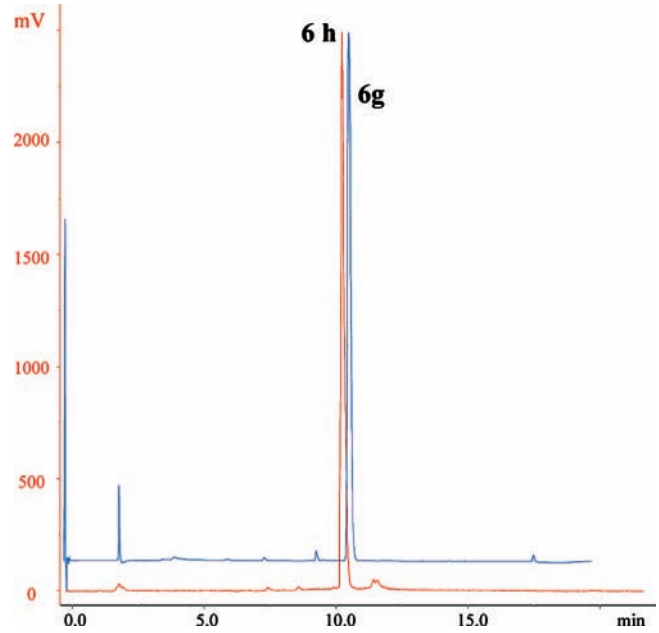

Figure 3. Radiochemical purity of radioligand **6h** (RT = 10.22) in comparison with unlabeled reference standard **6g** (RT = 10.45).

Neutral technetium complex **6k** was prepared by thiol group deprotection and labeling by means of glucoheptonate (GH) as the transfer ligand. Briefly, 0.5 mg of ligand was deprotected in 2.5 mL of EtOH with 0.5 mL of acetone and 0.4 mL of 0.5 N HCl by heating at 100 °C for 15 min. To the deprotected ligand solution was added 0.5 mL of glucoheptonate kit previously labeled with 150−200 mCi of $Na^{99m}TcO_4$, and the reaction mixture was heated at 100 °C for 15 min. The radioligand was recovered by solid-phase extraction (SPE) on preactivated Sep-Pak C-18 cartridge (Millipore). The Sep-Pak was washed with ammonium acetate 0.1 M (5 mL) before eluting with ethanol (2 mL). The eluate was concentrated under a nitrogen stream. The residue was dissolved into saline and the resulting solution was sterilized through a sterile 0.22 μm filter (Gelman Acrodisc).

HPLC was performed with the same system as above. Quality control evaluation of the unlabeled reference standard **6j**, ^{99m}Tc-GH, and final radioligand was performed on a reverse-phase analytical HPLC Alltech C-8 (250 × 4.6 mm, 5 μm) with the following solvent systems: A, 0.1 M ammonium acetate; B, CH_3CN. Gradient: 0−1 min 5% B; 1−16 min 100% B; 16−19 min 100% B; 19 min 5% B; 19−25 min 5% B (Figure 4).

Instant thin-layer chromatography on silica gel (ITLC-SG, Gelman Sciences) was performed by using different mobile phases. Acetone was used to determine ^{99m}Tc-GH (R_f = 0) and the amount of free $^{99m}TcO_4$ (R_f = 1); 50% acetonitrile-water; for ^{99m}Tc colloid (R_f = 0).

In Vitro Binding Assays. Male Sprague−Dawley CD rats (Charles River Italia, Calco, CO, Italy) with body masses of 200−250 g were used. Rats were acclimatized to the new housing conditions for at least one week. They were housed six per cage under an artificial 12-h-light, 12-h-dark cycle at a constant temperature of 22 ± 2 °C and a relative humidity of 65%. They had free access to water and standard laboratory food at all times. Animal care and handling throughout the

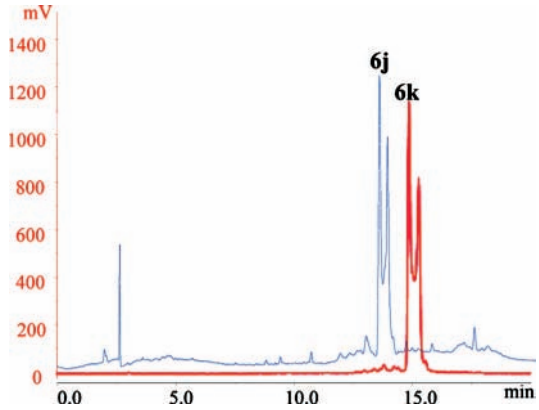

Figure 4. Radiochemical purity of radioligand **6k** (RT = 14.96−15.34) in comparison with unlabeled reference standard **6j** (RT = 14.3). Compounds **6j,k** are resolved into the corresponding rotamers.

experimental procedures were in accordance with the European Communities Council Directive of 24 November 1986 (86/609/EEC).

Rats were sacrificed by decapitation and their brains were rapidly dissected into the various areas which were stored at −80 °C until the day of the assay. The binding assays were performed as described in the literature (*44*). The cerebral cortex was subsequently thawed and then homogenized in 50 volumes of ice-cold Dulbecco's phosphate-buffered saline (PBS) pH 7.4 at 4 °C with a Polytron PT 10 disrupter (setting 5 for 20 s). The homogenate was centrifuged at 40 000*g* and 4 °C for 30 min and the resulting pellet was resuspended in the same volume of fresh buffer and recentrifuged. The new pellet was resuspended in 10 volumes of the incubation buffer (PBS) and used for the binding assay.

[^{3}H]PK11195 binding was measured in a final volume of 500 μL, consisting of 50 μL of membrane suspension (0.15−0.20 mg of protein), 50 μL of [^{3}H]PK11195 (s.a. 85.5 Ci/mmol, New England Nuclear; final assay concentration of 1 nM), 5 μL of drug solution or solvent, 395 μL of PBS. The binding reaction was performed at 25 °C for 90 min and began with the addition of membranes. The incubation was terminated by rapid filtration through glass-fiber filters (Whatman GF/B) which had been presoaked with 0.3% polyethyleneimine and placed in a cell harvester filtration manifold (Brandel). The filters were washed five times with 4 mL of ice-cold PBS, after which filter-bound radioactivity was quantified by liquid scintillation spectrometry. Nonspecific binding was defined as binding in the presence of 10 μM of unlabeled PK11195 (Sigma). Specific binding was determined by subtracting the nonspecific from the total binding and was about 80% of the total binding. The concentration of the test compounds that inhibited [^{3}H]ligand binding by 50% (IC_{50}) was determined by means of Jandel Sigmaplot (*45*) program with 6 to 10 concentrations of the displacers, each performed in triplicate.

Kinetic Experiments. Animals. Male CD-1 mice (35−40 g; Charles River, Italy) were used for biodistribution, small-animal SPET imaging, and inhibition studies. Animal experiments were approved by the Ethical Committee for animal care of the San Raffaele Hospital and carried out in agreement with the Italian and EEC recommendations for the care and use of laboratory animals.

Biodistribution. All animal group (n = 3) received an intraperitoneal injection of 0.74−0.92 MBq (20−25 μCi) of [^{99m}Tc]**6h** or [^{99m}Tc]**6k**. The mice were killed by cervical dislocation at 30, 60, and 240 min after intraperitoneal injection of the radiotracer in 200 μL saline vehicle. Blood samples were collected by cardiac puncture. The tissue samples were weighed and their radioactivity was determined in an automated γ-counter

Scheme 1[a]

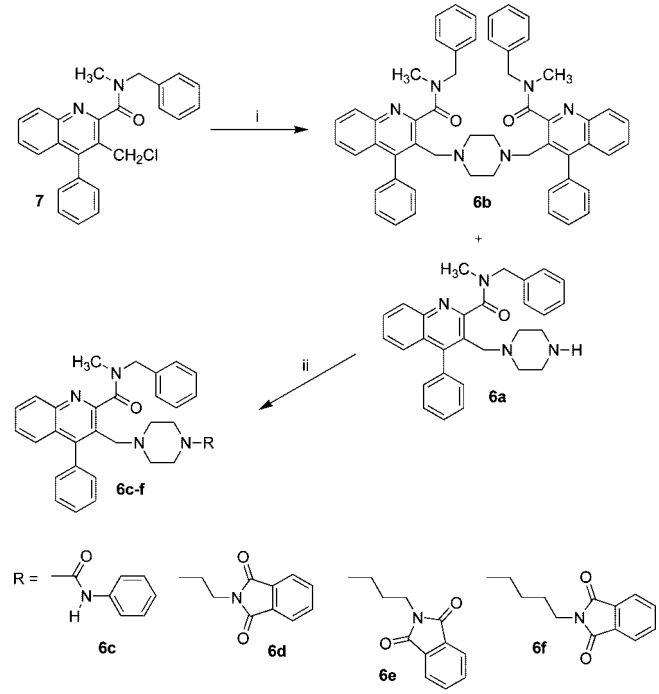

[a] Reagents: (i) piperazine, EtOH; (ii) phenylisocianate, $CHCl_3$ or N-(2-bromoethyl)phthalimide, Na_2CO_3, DMF or N-(3-bromopropyl)-phthalimide, Na_2CO_3, EtOH or N-(4-bromobutyl)phthalimide, Na_2CO_3, EtOH.

(1282 Compugamma CS; Pharmacia/LKB Nuclear Inc.) and expressed as the percentage of injected dose per gram of tissue (%ID/g).

Small Animal YAP-(S)PET Studies. The kinetics of biodistribution was further explored at later times using a dedicated small animal SPET scanner YAP-(S)PET II (ISE, Pisa, Italy). This small animal tomography is able to perform both PET and SPET modalities. It is made up of four detector heads composed each of a 4 × 4 cm^2 of $YAlO_3$:Ce (YAP:Ce) matrix of 27 × 27 elements, 1.5 × 1.5 × 20 mm^3 each, directly coupled to a PS-PMT (Hamamatsu R2486). The four modules are positioned on a rotating gantry; the opposite detectors are in time coincidence when used in SPET mode. For both PET and SPET modalities, the system operates in 3-D data acquisition mode with an axial field of view (FOV) of 4 cm and a transaxial FOV diameter of 4 cm, providing a set of 27 slices of 1.5 mm thickness. The switching to the SPET modality is made by replacing the tungsten septum (used in PET for shielding the scintillators from the background outside the FOV) with a high-resolution parallel hole, lead collimator (0.6 mm, 0.15 mm septum) in front of each crystal. The default acquisition energy window is 50−850 keV.

Compounds [^{99m}Tc]**6h** and [^{99m}Tc]**6k** were intravenously administered in two CD-1 mice. The animals were scanned in SPET modality at 1, 6, and 24 h after the injection of 3.26 and 2.61 mCi (120.6 and 96.6 MBq), respectively. Each mouse was anesthetized with 1.7% tribromoethanol solution (10 μL/g of weight, i.p.) before scanning and positioned supine on the tomograph bed, with the thorax centered in the FOV. The study was achieved acquiring two bed positions in 1 h approximately. Furthermore, a 30 min brain acquisition was performed 6 h after the injection for compound [^{99m}Tc]**6h** and 1 h after the injection for compound [^{99m}Tc]**6k**. 3D data were reconstructed by the EM (Expectation Maximization) algorithm (*46*).

Inhibition Studies. The specificity of [^{99m}Tc]**6k** uptake was studied in mice pretreated with PK11195 (5 mg/kg, dissolved

Scheme 2[a]

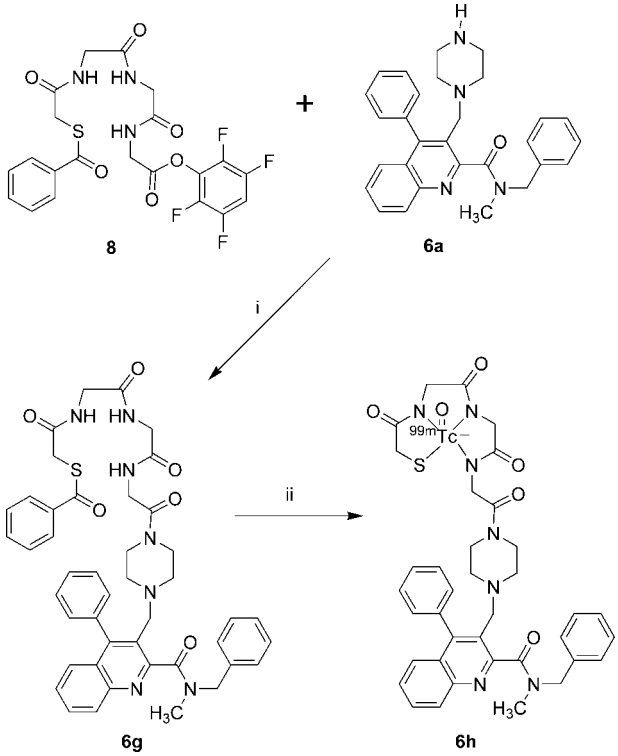

[a] Reagents: (i) CH_3CN; (ii) $Na^{99m}TcO_4$, $SnCl_2 \times 2H_2O$, 0.01 N HCl, Na_2CO_3, CH_3CN.

Scheme 3[a]

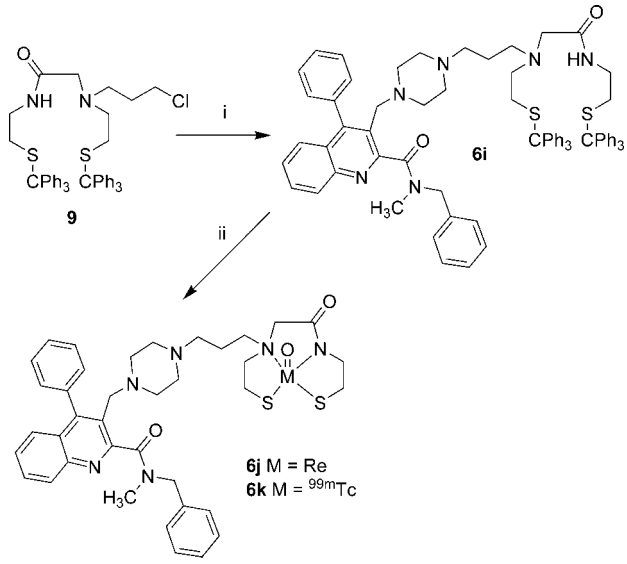

[a] Reagents: (i) **6a**, NaI, Na_2CO_3, CH_3CN; (ii) for compound **6j**: $NaReO_4$, $SnCl_2 \times 2H_2O$, 0.05 N HCl, EtOH; for compound **6k**: 0.5 N HCl, EtOH, CH_3COCH_3, GH kit labelled with $Na^{99m}TcO_4$.

into DMSO−EtOH 1:1, i.p., $n = 3$) or with a vehicle (i.p., $n = 3$) injected 60 min before the radioligand administration. The inhibitory effect of unlabeled PK11195 was evaluated 4 h after the tracer injection on the basis of our previous experience and was compared to the preinjection of the vehicle. After this time, the mice were sacrificed by cervical dislocation and processed as described above for the biodistribution to obtain the %ID/g for peripheral tissues derived from vehicle or PK11195 injected mice.

Scheme 4[a]

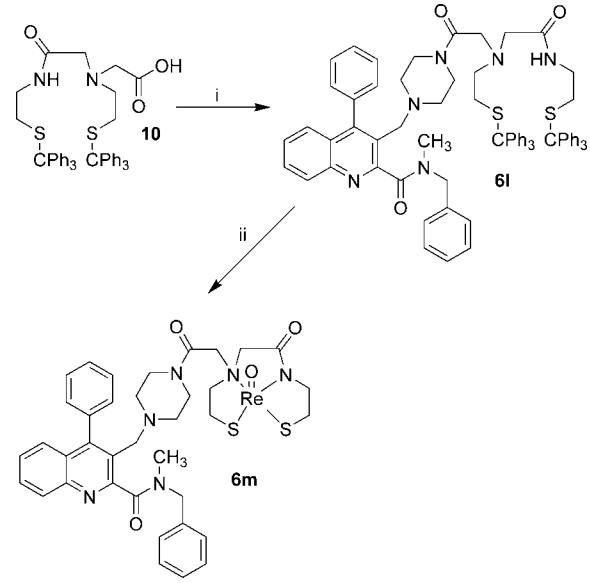

[a] Reagents: (i) **6a**, HOBt, EDCI, CH_2Cl_2; (ii) $NaReO_4$, $SnCl_2 \times 2H_2O$, 0.05 N HCl, EtOH.

Table 1. PBR Binding Affinities of Compounds 3c, 5a,b, and 6a−g,j,m

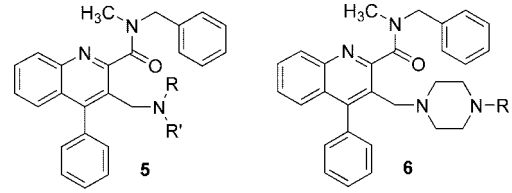

compd	R	R′	IC_{50} (nM) ± SEM[a]
3c			2.1−4.6[b]
5a	C_2H_5	C_2H_5	12[b]
5b	$CH_2C_6H_5$	C_2H_5	13[b]
6a	H		301 ± 29
6b	See Scheme 1		70 ± 8.5
6c	CONH-C_6H_5		24 ± 2.6
6d	CH_2CH_2-phthalimido		37 ± 3.3
6e	$CH_2CH_2CH_2$-phthalimido		22 ± 1.9
6f	$CH_2CH_2CH_2CH_2$-phthalimido		36 ± 2.8
6g	$(COCH_2NH)_3COCH_2SCOC_6H_5$		209 ± 26
6h	see Scheme 2		NT[c]
6i	see Scheme 3		NT[c]
6j	see Scheme 3 (M = Re)		127 ± 15
6k	see Scheme 3 (M = Tc-99m)		NT[c]
6l	see Scheme 4		NT[c]
6m	see Scheme 4		187 ± 19
1			2.5 ± 0.4

[a] Each value is the mean ± SEM of 3 determinations and represents the concentration giving half the maximum inhibition of [^{3}H]**1** (final concentration 1 nM) specific binding to rat cortical membranes. [b] See ref 36. [c] NT: not tested.

RESULTS

Chemistry. The PBR probes **6a−f** were synthesized from the previously described chloromethyl derivative **7** (*36*) as depicted in Scheme 1.

Reaction of **7** with a large excess of piperazine gave piperazinyl derivative **6a** along with a small amount of double alkylation product **6b**, which was separated by flash chromatography. Phenylurea derivative **6c** was prepared by reaction of **6a** with phenylisocyanate, while phthalimidoalkyl derivatives **6d−f** were synthesized by alkylation of **6a** with the appropriate *N*-(bromoalkyl)phthalimides in the presence of sodium carbonate as the base.

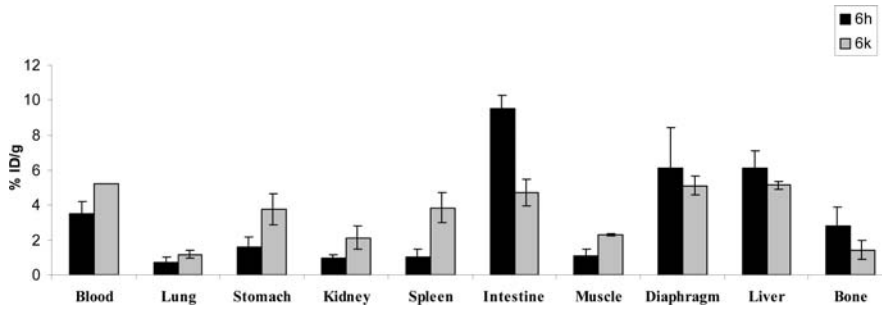

Figure 5. Comparison of tissue distribution of **6h,k** in CD-1 mouse 60 min after the radiotracer injection. The column where the error is not indicated was obtained with two mice.

Table 2. Tissue Distribution of [^{99m}Tc]6h in CD-1 Mouse[a]

tissue	30 min	60 min	240 min
blood	1.65[b]	3.52 ± 0.67	0.23[b]
lung	0.46 ± 0.12	0.71 ± 0.29	0.69[b]
diaphragm	7.26 ± 0.60	6.11 ± 2.31	4.20 ± 1.67
liver	4.84 ± 0.78	6.12 ± 0.94	2.62 ± 1.35
intestine	0.52 ± 0.21	9.52 ± 0.76	3.87 ± 1.47
stomach	0.53 ± 0.10	1.57 ± 0.6	0.41 ± 0.24
spleen	0.69 ± 0.44	1.02 ± 0.44	0.49 ± 0.13
kidney	0.49 ± 0.11	0.93 ± 0.22	0.40 ± 0.25
muscle	0.61 ± 0.21	1.08 ± 0.38	0.71 ± 0.20
bone	1.43 ± 0.53	2.82 ± 1.09	0.61[b]

[a] Radioactivity concentration is expressed as % of injected dose per gram of tissue (%ID/g). Values are expressed as mean ± SD of three rats for each time point. [b] The corresponding values were obtained with two mice.

Table 3. Tissue Distribution of [^{99m}Tc]6k in CD-1 Mouse[a]

tissue	30 min	60 min	240 min
blood	1.08 ± 0.40	5.25[b]	4.44 ± 1.37
lung	1.19 ± 0.24	1.16 ± 0.23	1.05 ± 0.26
diaphragm	4.74 ± 1.3	5.12 ± 0.55	7.92 ± 1.35
liver	3.48 ± 1.65	5.14 ± 0.20	4.80 ± 0.45
intestine	2.26 ± 0.83	4.71 ± 0.77	3.06 ± 1.35
stomach	1.72 ± 0.57	3.77 ± 0.90	2.13 ± 0.32
spleen	2.07 ± 1.32	3.85 ± 0.88	3.43 ± 0.72
kidney	1.28[b]	2.13 ± 0.69	1.50 ± 0.10
muscle	1.04 ± 0.75	2.28 ± 0.01	0.89 ± 0.21
bone	1.18 ± 0.32	1.43 ± 0.53	1.56 ± 0.22

[a] Radioactivity concentration is expressed as % of injected dose per gram of tissue (%ID/g). Values are expressed as mean ± SD of three rats for each time point. [b] The corresponding values were obtained with two mice.

Compound **6g** was obtained by conjugation of **6a** with *S*-benzoylmercaptoacetylglycylglycylglycine (*S*-Bz-MAG$_3$, Scheme 2) via activated ester **8** (*37–39*). Negatively charged complex **6h** was prepared by means of conventional radiolabeling procedure with ^{99m}Tc (see Experimental Procedures).

Cross-coupling reaction of synthon **9** (*40–42*) with piperazinylderivative **6a** provided **6i** (Scheme 3), which underwent rhenium incorporation with sodium perrhenate under reductive conditions ($SnCl_2$) in ethanol to give the neutral complex **6j**. On the other hand, neutral technetium complex **6k** was prepared by employing glucoheptonate (GH) as the transfer ligand (see Experimental Procedures).

Finally, neutral rhenium complex **6m** (showing the N_2S_2 MLM of **6j** and the carbonylmethyl spacer of **6 h**) was prepared as shown in Scheme 4. Acid **10** was synthesized as described in the literature (*43*) and conjugated with the piperazinyl derivative **6a** in the presence of HOBt and EDCI to afford **6l**. Neutral complex **6m** was obtained in low yield from **6l** by means of the procedure shown above.

Binding Studies. Compounds **6a−g,j,m** were tested for their potential activity in inhibiting the specific binding of [^{3}H]**1** to rat cortical membrane in comparison with reference compound **1**. The results of the binding studies are shown in Table 1, along with the previously published PBR affinities of 2-quinolinecarboxamide derivatives **5a,b** that are included for comparison.

The structure−affinity relationship (SAFIR) analysis of the compounds designed to probe the receptor tolerance to bulky substituent shows that the introduction of the piperazine substituent of compound **6a** produces a significant decrease in PBR affinity. The comparison between this result and that obtained with previously published *N*,*N*-diethylderivative **5a** suggests that the affinity decrease can be attributed to the presence of the second basic nitrogen atom (the terminal piperazine nitrogen), which confers to compound **6a** hydrophilic characters inappropriate for the interaction with the PBR binding site. This assumption is supported by the affinity shown by phenylurea derivative **6c**, which shows an IC_{50} value similar to that shown by compounds **5a,b**.

Interestingly, the replacement of the −CONHPh group of phenylurea derivative **6c** with a phthalimidoethyl one of **6d** appears to be well-tolerated by the PBR binding site. Furthermore, the nanomolar PBR affinity shown by **6d** appears to be stable to the elongation of the spacer between the terminal piperazine nitrogen and the phthalimide moiety up to three methylene unities (compound **6e**) or four methylene unities (**6f**). These results, taken together with the nanomolar affinity shown by the symmetrically substituted piperazine derivative **6b**, demonstrate that the PBR binding site is capable of accommodating a large variety of molecules based on the 4-phenylquinolin-2-carboxamide scaffold. Thus, the results of the first phase of the investigation confirmed the PBR tolerance to bulky substituents and gave impulse to the development of the second phase.

In the design of the receptor imaging agents based on Tc-99m, the physicochemical characteristics of the final complex were taken into consideration. Thus, neutral **6j,k,m** and negatively charged **6h** complexes were prepared in order to evaluate the difference in the biological properties. Protected precursor **6g** and cold neutral rhenium complexes **6j,m** were studied in the same binding system described for the other ligands belonging to the same class. The submicromolar PBR affinity shown by **6j,m** (IC_{50} values of 127 and 187 nM, respectively) suggests that their MLMs with encaged rhenium interact with PBR binding site less effectively than the phthalimido probe of compounds **6d−f** (IC_{50} values 22−37 nM). However, the reasonable affinity of rhenium complexes **6j,m** and the fact that rhenium has been described to show virtually identical structural properties in its complexes compared to technetium (*31*) motivated the evaluation of technetium-99m labeled complexes **6h,k** in order to obtain information on the in vivo behavior of these bifunctional ligands.

KINETIC STUDIES

Biodistribution. Exvivo biodistribution studies in mice indicate that, after intraperitoneal injection, radiotracer

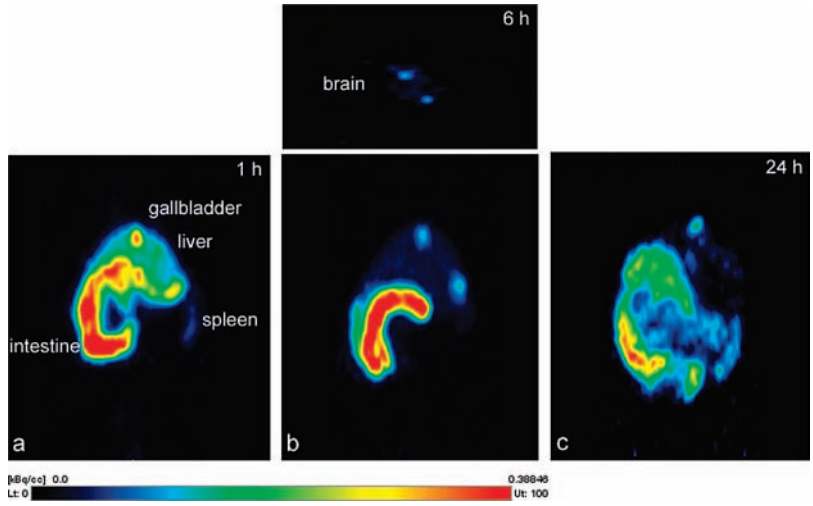

Figure 6. YAP-(S)PET II images of [^{99m}Tc]**6h** distribution in one CD-1 mouse at 1 (a), 6 (b), and 24 h (c) after the i.v. injection of 3.26 mCi of the radiotracer. (a) 1 h. Transaxial view of 3D-rendering reconstruction of whole body acquisition (two beds in present count modality). (b) 6 h. Top, transaxial view of 3D-rendering reconstruction of brain (one bed in present time modality); bottom, transaxial view of 3D-rendering reconstruction of whole body acquisition (two beds in present count modality). (c) 24 h. Transaxial view of 3D-rendering reconstruction of whole body acquisition (two beds in present count modality).

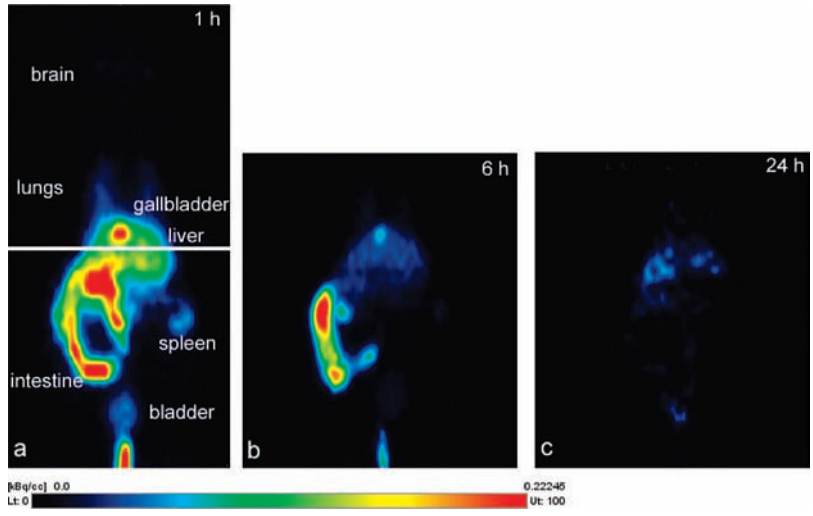

Figure 7. YAP-(S)PET II images of [^{99m}Tc]**6k** distribution in one CD-1 mouse acquired at several time points after the i.v. injection of 2.61 mCi of the radioligand. (a) 1 h. Top, transaxial view of 3D-rendering reconstruction of brain and thorax (one bed in present time modality); bottom, transaxial view of 3D-rendering reconstruction of the abdomen (one bed in present time modality). (b) 6 h. Transaxial view of 3D-rendering reconstruction of whole body acquisition (two beds in present count modality). (c) 24 h. Transaxial view of 3D-rendering reconstruction of whole body acquisition (two beds in present count modality).

[^{99m}Tc]**6h** and [^{99m}Tc]**6k** preferentially accumulate in liver, intestine, and stomach. Similar results are described in the literature for the biodistribution of somatostatin analogue RC-160 labeled with ^{188}Re- or ^{99m}Tc-MAG$_3$ (*39*). However, differently from the negatively charged complex **6h**, neutral **6k** accumulates also in two organs expressing PBR-like spleen and kidney (Figure 5, Tables 2 and 3) although radioactivity was lower than that measured in blood. Maximum levels of radioactivity were observed 60 min after injection of both tracers.

SPET Studies. SPET biodistribution profiles of **6h** and **6k** are shown in Figures 6 and 7. One hour after injection, radioactivity preferentially accumulated in the liver, gallbladder, small intestine, urinary bladder, and spleen, although this last organ was better visualized in the animal injected with neutral complex **6k** (Figure 7). At this time, accumulation of radioactivity was observed in the stomach of the animal injected with **6h** and a small signal of uptake appeared in the lung of the animal injected with **6k**. Six hours after the injection of both radiotracers, the majority of the activity shifted to the first portion of the small intestine especially in the case of compound **6h**. Finally after 24 h, radioactivity was still present in the liver and intestine for **6h** and in liver and urinary bladder for **6k**. For both compounds, we failed to observe a significant radioactivity accumulation in the heart and brain.

Inhibition Studies. The specificity of [^{99m}Tc]**6k** in vivo binding to PBR was evaluated in mice pretreated with PK11195 (5 mg/kg, i.p., $n = 3$) or with the vehicle (i.p., $n = 3$), 1 h before the radioligand administration. The results of the inhibition experiments 4 h after [^{99m}Tc]**6k** injection are shown in Figure 8.

The only significant effect of PK11195 preadministration was observed in the lung, while no significant effects were observed in the remaining tissues.

DISCUSSION AND CONCLUSIONS

The exploration of the PBR binding site by means of 3-substituted-2-quinolinecarboxamide derivatives **6a**−**f** con-

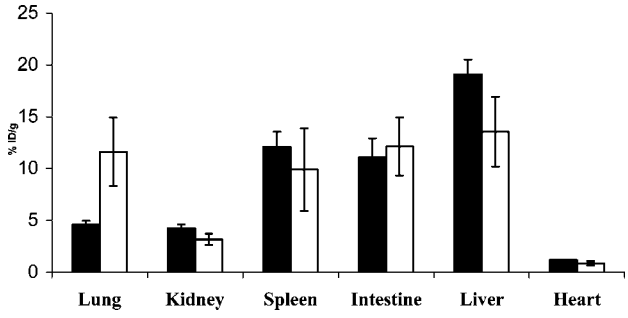

Figure 8. Effect of PK11195 pretreatment on [^{99m}Tc]**6k** radioactivity uptake in peripheral tissues of mice measured 4 h after [^{99m}Tc]**6k** injection. The radioactivity concentration is expressed as % of the injected dose per gram of tissue (%ID/g); 5 mg/kg of PK11195 (pretreated, black) or vehicle (basal, white) were administered 1 h before [^{99m}Tc]**6k** injection.

firmed the existence of a tolerance to bulky lipophilic substituents and stimulated the design and synthesis of bifunctional ligands **6h,j,k,m**. The submicromolar PBR affinity shown by cold rhenium complexes **6j,m** encouraged the preparation of technetium-99m labeled compounds **6h,k** and their evaluation in ex vivo biodistribution and in small animal SPET studies. The results obtained indicate that both tracers do not present a clear preferential distribution in high PBR expressing tissues. In fact, none of them was taken up by the heart, and only neutral complex **6k** displayed activity in spleen, kidney, and lung. In addition, these levels were lower or comparable to those observed in blood and **6k** uptake appeared to be inhibited by unlabeled PK11195 only in lung. A possible explanation is the high molecular weight of these tracers that may hamper transmembrane diffusion and the reaching of the intracellular target receptor. However, compounds **6h,k** show very similar shapes and dimensions (i.e., MW is ca. 800), but different properties in both the spacer and the MLM. In particular, compound **6h** shows the contemporary presence of a negative charge in the MLM and a basic nitrogen atom in the piperazine moiety. The protonation in the physiological environment is likely to produces a zwitterionic character in this MAG_3 derivative that is not present in **6k** and may play a significant role in the membrane passage and, as a consequence, in the biodistribution features. Therefore, **6h** can be ultimately considered a negative control capable of highlighting the relatively favorable properties of **6k.** On the basis of the above results, we believe that negatively charged complex **6h** has inadequate kinetic properties to be further explored as a PBR ligand, while additional experiments on selected animal models are required to establish the potential usefulness in tumor imaging or in the monitoring of lung inflammation of neutral complex **6k** based on the MLM present in technepine, fluoratec, and other interesting tracers (*32, 41, 42*).

ACKNOWLEDGMENT

The authors are grateful to Prof. Stefania D'Agata D'Ottavi for the careful reading of the manuscript and to Prof. Giovanni Biggio and Prof. Alessandra Concas for the binding studies performed on compounds **6a**−**g,j,m**. This work was financially supported by Ministero dell'Università e della Ricerca - PRIN (Programmi di ricerca di Rilevante Interesse Nazionale) and by EMIL (European Molecular Imaging Laboratory), Sixth European Program, Project No: LSHC-CT-2004-503569.

Supporting Information Available: Analytical data for compounds **6a**−**g,i,j,l,m**. This material is available free of charge via the Internet at http://pubs.acs.org.

LITERATURE CITED

(1) Papadopoulos, V., Baraldi, M., Guilarte, T. R., Knudsen, T. B., Lacapère, J.-J., Lindemann, P., Norenberg, M. D., Nutt, D., Weizman, A., Zhang, M.-R., and Gavish, M. (2006) Translocator protein (18 kDa): new nomenclature for the peripheral-type benzodiazepine receptor based on its structure and molecular function. *Trends Pharmacol. Sci. 27*, 402–409.

(2) Gavish, M., Katz, Y., Bar-Ami, S., and Weizman, R. (1992) Biochemical, physiological, and pathological aspects of the peripheral benzodiazepine receptor. *J. Neurochem. 58*, 1589–1601.

(3) Beurdeley-Thomas, A., Miccoli, L., Oudard, S., Dutrillaux, B., and Poupon, M. F. (2000) The peripheral benzodiazepine receptors: a review. *J. Neurooncol. 46*, 45–56.

(4) Starosta-Rubinstein, S., Ciliax, B. J., Penney, J. B., McKeever, P., and Young, A. B. (1987) Imaging of a glioma using peripheral benzodiazepine receptor ligands. *Proc. Natl. Acad. Sci. U.S.A. 84*, 891–895.

(5) Black, K. L., Ikezaki, K., and Toga, A. W. (1989) Imaging of brain tumors using peripheral benzodiazepine receptor ligands. *J. Neurosurg. 71*, 113–118.

(6) Black, K. L., Ikezaki, K., Santori, E., Becker, D. P., and Vinters, H. V. (1990) Specific high-affinity binding of peripheral benzodiazepine receptor ligands to brain tumors in rat and man. *Cancer 65*, 93–97.

(7) Miettinen, H., Kononen, J., Haapasalo, H., Helen, P., Sallinen, P., Harjuntausta, T., Helin, H., and Alho, H. (1995) Expression of peripheral-type benzodiazepine receptor and diazepam binding inhibitor in human astrocytomas: relationship to cell proliferation. *Cancer Res. 55*, 2691–2695.

(8) Batra, S., and Iosif, C. S. (1998) Elevated concentrations of mitochondrial peripheral benzodiazepine receptors in ovarian tumors. *Int. J. Oncol. 12*, 1295–1298.

(9) Venturini, I., Alho, H., Podkletnova, I., Corsi, L., Rybnikova, E., Pellicci, R., Baraldi, M., Pelto-Huikko, M., Helen, P., and Zeneroli, M. L. (1999) Increased expression of peripheral benzodiazepine receptors and diazepam binding inhibitor in human tumors sited in the liver. *Life Sci. 65*, 2223–2231.

(10) Hardwick, M., Fertikh, D., Culty, M., Li, H., Vidic, B., and Papadopoulos, V. (1999) Peripheral-type benzodiazepine receptor (PBR) in human breast cancer: correlation of breast cancer cell agressive phenotype with PBR expression, nuclear localization, and PBR-mediated cell proliferation and nuclear transport of cholesterol. *Cancer Res. 59*, 831–842.

(11) Maaser, K., Grabowski, P., Sutter, A. P., Hopfner, M., Foss, H. D., Stein, H., Berger, G., Gavish, M., Zeitz, M., and Scherubl, H. (2002) Overexpression of the peripheral benzodiazepine receptor is a relevant prognostic factor in stage III colorectal cancer. *Clin. Cancer Res. 8*, 3205–3209.

(12) Diorio, D., Welner, S. A., Butterworth, R. F., Meaney, M. J., and Suranyi-Cadotte, B. E. (1991) Peripheral benzodiazepine binding sites in Alzheimer's disease frontal and temporal cortex. *Neurobiol. Aging 12*, 255–258.

(13) Vowinckel, E., Reutens, D., Becher, B., Verge, G., Evans, A., Owens, T., and Antel, J. P. (1997) PK11195 binding to the peripheral benzodiazepine receptor as a marker of microglia activation in multiple sclerosis and experimental autoimmune encephalomyelitis. *J. Neurosci. Res. 50*, 345–353.

(14) Schoemaker, H., Morelli, M., and Deshmukh, P. (1982) [^{3}H]Ro 5−4864 benzodiazepine binding in the kainate lesioned striatum and Huntington's diseased basal ganglia. *Brain Res. 248*, 396–401.

(15) Pike, V. W., Halldin, C., Crouzel, C., Barrè, L., Nutt, D. J., Osman, S., Shah, F., Turton, D. R., and Waters, S. L. (1993) Radioligands for PET studies of central benzodiazepine receptors and PK (peripheral benzodiazepine) binding sites - Current status. *Nucl. Med. Biol. 20*, 503–525.

(16) Junck, L., Olson, J. M., Ciliax, B. J., Koeppe, R. A., Watkins, G. L., Jewett, D. M., McKeever, P. E., Wieland, D. M., Kilbourn, M. R., Starosta-Rubinstein, S., Mancini, W. R., Kuhl, D. E.,

Greenberg, H. S., and Youngf, A. B. (1989) PET imaging of human gliomas with ligands for the peripheral benzodiazepine binding site. *Ann. Neurol. 26*, 752–758.

(17) Pappata, S., Cornu, P., Samson, Y., Prenant, C., Benavides, J., Scatton, B., Crouzel, C., Hauw, J. J., and Syrota, A. (1991) PET study of carbon-11-PK 11195 binding to peripheral type benzodiazepine sites in glioblastoma: a case report. *J. Nucl. Med. 32*, 1608–1610.

(18) Junck, L., Jewett, D.M., Kilbourn, M. R., Young, A. B., and Kuhl, D. E. (1990) PET imaging of cerebral infarcts using a ligand for the peripheral benzodiazepine binding site. *Neurology 40* (1), 265.

(19) Charbonneau, P., Syrota, A., Crouzel, C., Valois, J. M., Prenant, C., and Crouzel, M. (1986) Peripheral-type benzodiazepine receptors in the living heart characterized by positron emission tomography. *Circulation 73*, 476–483.

(20) Hardwick, M. J., Chen, M. K., Baidoo, K., Pomper, M. G., and Guilarte, T. R. (2005) In vivo imaging of peripheral benzodiazepine receptors in mouse lungs: a biomarker of inflammation. *Mol. Imaging 4*, 432–438.

(21) Audi, S. H., Dawson, C. A., Ahlf, S. B., and Roerig, D. L. (2002) Lung tissue mitochondrial benzodiazepine receptors increase in a model of pulmonary inflammation. *Lung 180*, 241–250.

(22) Jones, H. A., Valind, S. O., Clark, I. C., Bolden, G. E., Krausz, T., Schofield, J. B., Boobis, A. R., and Haslett, C. (2002) Kinetics of lung macrophages monitored in vivo following particulate challenge in rabbits. *Toxicol. Appl. Pharmacol. 183*, 46–54.

(23) Venneti, S., Lopresti, B. J., and Wiley, C. A. (2006) The peripheral benzodiazepine receptor (translocator protein 18 kDa) in microglia: from pathology to imaging. *Prog. Neurobiol. 80*, 308–322.

(24) Zhang, M. R., Maeda, J., Ogawa, M., Noguchi, J., Ito, T., Yoshida, Y., Okauchi, T., Obayashi, S., Suhara, T., and Suzuki, K. (2004) Development of a new radioligand, N-(5fluoro-2-phenoxyphenyl)-N-(2-[^{18}F]fluoroethyl-5-methoxybenzyl)acetamide, for PET imaging of peripheral benzodiazepine receptor in primate brain. *J. Med. Chem. 47*, 2228–2235.

(25) Matarrese, M., Moresco, R. M., Cappelli, A., Anzini, M., Vomero, S., Simonelli, P., Verza, E., Magni, F., Sudati, F., Soloviev, D., Todde, S., Carpinelli, A., Galli Kienle, M., and Fazio, F. (2001) Labeling and evaluation of N-[11C]methylated quinoline-2-carboxamides as potential radioligands for visualization of peripheral benzodiazepine receptors. *J. Med. Chem. 44*, 579–585.

(26) Matarrese, M., Soloviev, D., Cappelli, A., Todde, S., Moresco, R. M., Anzini, M., Vomero, S., Sudati, F., Carpinelli, A., Perugini, F., Galli Kienle, M., and Fazio, F. (1999) Synthesis of the novel [^{11}C]-labelled quinoline carboxamides: analogues of PK-11195 as putative radioligands for PET studies of peripheral type benzodiazepine receptors. *J. Labelled Cpd. Radiopharm. 42*, S397−S399.

(27) Cappelli, A., Anzini, M., Vomero, S., De Benedetti, P. G., Menziani, M. C., Giorgi, G., and Manzoni, C. (1997) Mapping the peripheral benzodiazepine receptor binding site by conformationally restrained derivatives of 1-(2-chlorophenyl)-N-methyl-N-(1-methylpropyl)-3-isoquinolinecarboxamide (PK11195). *J. Med. Chem. 40*, 2910–2921.

(28) Belloli, S., Moresco, R. M., Matarrese, M., Biella, G., Sanvito, F., Simonelli, P., Turolla, E., Olivieri, S., Popoli, P., Cappelli, A., Vomero, S., Galli-Kienle, M., and Fazio, F. (2004) Evaluation of three quinoline-2-carboxamide derivatives as potential radioligands for the in vivo PET imaging of neurodegeneration. *Neurochem. Int. 44*, 433–440.

(29) Cappelli, A., Matarrese, M., Moresco, R. M., Valenti, S., Anzini, M., Vomero, S., Turolla, E., Belloli, S., Simonelli, P., Filannino, M. A., Lecchi, M., and Fazio, F. (2006) Synthesis, labeling, and biological evaluation of halogenated quinoline-2-carboxamides as potential radioligands for visualization of peripheral benzodiazepine receptors. *Bioorg. Med. Chem. 14*, 4055–4066.

(30) Schwochau, K. (2000) *Technetium. Chemistry and radiopharmaceutical applications*; Wiley-VCH, Weinheim, Germany.

(31) Fritzberg, A. R., Abrams, P. G., Beaumier, P. L., Kasina, S., Morgan, A. C., Rao, T. N., Sanderson, J. A., Srinivasan, A., Wilbur, D. S., and Vanderheyden, J. L. (1988) Specific and stable labeling of antibodies with technetium-99m with a diamide dithiolate chelating agent. *Proc. Natl. Acad. Sci. U.S.A. 85*, 4025–4029.

(32) Hom, R. K., and Katzenellenbogen, J. A. (1997) Technetium-99m-labeled receptor-specific small-molecule radiopharmaceuticals: recent developments and encouraging results. *Nucl. Med. Biol. 24*, 485–498.

(33) Jurisson, S. S., and Lydon, J. D. (1999) Potential technetium small molecule radiopharmaceuticals. *Chem. Rev. 99*, 2205–2215.

(34) Chi, D. Y., Neil, J. P., Anderson, C. J., Welch, M. J., and Katzenellenbogen, J. A. (1994) Homodimeric and heterodimeric bis(aminothiol) oxometal complexes with rhenium(V) and technetium(V). Control of heterodimeric complex formation and an approach to metal complexes that mimic steroid hormones. *J. Med. Chem. 37*, 928–937.

(35) Anzini, M., Cappelli, A., Vomero, S., Seeber, M., Menziani, M. C., Langer, T., Hagen, B., Manzoni, C., and Bourguignon, J. J. (2001) Mapping and fitting the peripheral benzodiazepine receptor binding site by carboxamide derivatives. Comparison of different approaches to quantitative ligand-receptor interaction modeling. *J. Med. Chem. 44*, 1134–1150.

(36) Cappelli, A., Pericot Mohr, G., Gallelli, A., Giuliani, G., Anzini, M., Vomero, S., Fresta, M., Porcu, P., Maciocco, E., Concas, A., Biggio, G., and Donati, A. (2003) Structure-activity relationships in carboxamide derivatives based on the targeted delivery of radionuclides and boron atoms by means of peripheral benzodiazepine receptor ligands. *J. Med. Chem. 46*, 3568–3571.

(37) Fritzberg, A. R., Kasina, S., Vanderheyden, J. L., and Srinivasan, A. (1988) Metal-radionuclide-labeled proteins and glycoproteins and their preparation for diagnosis and therapyEur. Pat. Appl. EP284071A2 CA 111:53446.

(38) Grummon, G., Rajagopalan, R., Palenik, G. J., Kaziol, A. E., and Nosco, D. L. (1995) Synthesis, characterization and crystal structures of technetium (V)-oxo complexes useful in nuclear medicine. 1. Complexes of mercaptoacetylglycylglycylglycine (MAG_3) and its methyl ester derivative (MAG_3OMe). *Inorg. Chem. 34*, 1764–1772.

(39) Guhlke, S., Schaffland, A., Zamora, P. O., Sartor, J., Diekmann, D., Bender, H., Knapp, F. F., and Biersack, H. J. (1998) 188Re- and 99m Tc-MAG3 as prosthetic groups for labeling amines and peptides: approaches with pre- and postconjugate labeling. *Nuc. Med. Biol. 25*, 621–631.

(40) O'Neil, J. P., Wilson, S. R., and Katzenellenbogen, J. A. (1994) Preparation and structural characterization of monoamine-monoamide bis(thiol) oxo complexes of technetium (V) and rhenium (V). *Inorg. Chem. 33*, 319–323.

(41) Meltzer, P. C., Blundell, P., Jones, A. G., Mahmood, A., Garada, B., Zimmerman, R. E., Davison, A., Holman, B. L., and Madras, B. K. (1997) A technetium-99m SPECT imaging agent which targets the dopamine transporter in primate brain. *J. Med. Chem. 40*, 1835–1844.

(42) Meltzer, P. C., Blundell, P., Zona, T., Yang, L., Huang, H., Bonab, A. A., Livini, E., Fischman, A., and Madras, B. K. (2003) A second-generation 99m technetium single photon emission computed tomography agent that provides in vivo images of the dopamine transporter in primate brain. *J. Med. Chem. 46*, 3483–3496.

(43) Li, G., Ma, B., Missert, J. R., Grossman, Z. D., and Pandey, R. K. (1999) Synthesis of N_2S_2 conjugates of the highly specific mitochondrial diazepam binding inhibitor (DBI) receptor complexes. *Heterocycles 51*, 2855–2860.

(44) Trapani, G., Laquintana, V., Denora, N., Trapani, A., Lepedota, A., Latrofa, A., Franco, M., Serra, M., Pisu, M. G., Floris, I., Sanna, E., Biggio, G., and Liso, G. (2005) Structure-

activity relationships and effects on neuroactive steroid synthesis in a series of 2-phenylimidazo[1,2-a]pyridineacetamide peripheral benzodiazepine receptor ligands. *J. Med. Chem. 48*292–305.

(45) Sigma Plot, Jandel Scientific Graphing Software for Windows, San Raphael, CA, USA, 1995.

(46) Motta, A., Damiani, C., Del Guerra, A., Di Domenico, G., and Zavattini, G. (2002) Use of a fast EM algorithm for 3D image reconstruction with the YAP-PET tomograph. *Comput. Med. Imaging Graphics 26*, 293–302.

BC700437G

How Changes in the Sequence of the Peptide CLPFFD-NH_2 Can Modify the Conjugation and Stability of Gold Nanoparticles and Their Affinity for β-Amyloid Fibrils

Ivonne Olmedo,[⊥,†] Eyleen Araya,[⊥,†,‡] Fausto Sanz,[‡] Elias Medina,[†] Jordi Arbiol,[§] Pedro Toledo,[||] Alejandro Álvarez-Lueje,[†] Ernest Giralt,[#] and Marcelo J. Kogan*[,†]

Departamento de Química Farmacológica y Toxicológica, Facultad de Ciencias Químicas y Farmacéuticas, Universidad de Chile, Olivos 1007, Independencia, and Centro para la Investigación Interdisciplinaria Avanzada en Ciencias de Materiales, Santiago Chile, Department of Physical Chemistry, University of Barcelona, IBEC and CIBER-BB, Marti i Franques 1-13 E-08028 Barcelona, and TEM-MAT, Serveis Cientificotècnics, Universitat de Barcelona, Lluís Solé i Sabarís 1-3, E-08028 Barcelona, Spain, Chemical Engineering Department, Surface Analysis Laboratory (ASIF), University of Concepción, PO Box 160-C, Correo 3, Concepción, Chile, Institute for Research in Biomedicine, Barcelona Science Park, Baldiri Reixach 10, E-08028 Barcelona, Spain, and Departament de Química Orgànica, Universitat de Barcelona, Martí i Franquès, E-08028, Barcelona, Spain. Received October 20, 2007; Revised Manuscript Received March 31, 2008

In a previous work, we studied the interaction of β-amyloid fibrils (Aβ) with gold nanoparticles (AuNP) conjugated with the peptide CLPFFD-NH_2. Here, we studied the effect of changing the residue sequence of the peptide CLPFFD-NH_2 on the efficiency of conjugation to AuNP, the stability of the conjugates, and the affinity of the conjugates to the Aβ fibrils. We conjugated the AuNP with CLPFFD-NH_2 isomeric peptides (CDLPFF-NH_2 and CLPDFF-NH_2) and characterized the resulting conjugates with different techniques including UV−Vis, TEM, EELS, XPS, analysis of amino acids, agarose gel electrophoresis, and CD. In addition, we determined the proportion of AuNP bonded to the Aβ fibrils by ICP-MS. AuNP-CLPFFD-NH_2 was the most stable of the conjugates and presented more affinity for Aβ fibrils with respect to the other conjugates and bare AuNP. These findings help to better understand the way peptide sequences affect conjugation and stability of AuNP and their interaction with Aβ fibrils. The peptide sequence, the steric effects, and the charge and disposition of hydrophilic and hydrophobic residues are crucial parameters when considering the design of AuNP peptide conjugates for biomedical applications.

INTRODUCTION

Present-day nanomedicine exploits carefully a broad variety of structured nanoparticles. These nanoparticles may serve as diagnostic and therapeutic antiviral, antitumor, or anticancer agents (*1*, *2*). Metallic nanoparticles (NP) can be made so as to respond resonantly to a time-varying magnetic field, with advantageous results related to the transference of energy to the NP. For example, the particles can be made to heat up, leading to its use as a hyperthermia agent, by delivering toxic amounts of thermal energy to targeted bodies such as tumors. The NP can also act as enhanced chemotherapy and radiotherapy agents, where a moderate degree of tissue warming results in more effective destruction of malignant cells. Local heat delivered by NP selectively attached to a target can be used as *molecular surgery* to safely remove toxic and clogging aggregates. Recently, we applied this principle to protein aggregates, concretely to the protein Aβ, involved in Alzheimer's disease (*3*). We redissolved Aβ deposits remotely by using the local heat dissipated by gold nanoparticles (AuNP) conjugated to the peptide CLPFFD-NH_2. The resulting conjugate was selectively attached to the aggregates of Aβ, and then the system was irradiated with low gigahertz electromagnetic fields.

The determinant success in therapeutic and diagnostic use of NP is the ability to deliver them to the desired target. In this sense, NP can be coated with biological molecules to make them recognize the biological target. From the point of view of molecular recognition, peptides have a number of properties participating in ligand−receptor and protein−protein molecular interactions (*4*). For instance, peptides are involved in molecular recognition of antibodies, which is relevant in the field of clinical diagnosis of infectious diseases (*5*) and in the design of new drugs and vaccines (*6*).

Capping AuNP with peptides could increase stability and biocompatibility; however, recently one of the main concerns has become how peptides interact and pack on a NP surface and how the anchorage to the AuNP surface affects molecular recognition of the biological target and the stability of the AuNP (*1*). Thiol-based organic stabilizers have been widely used as capping agents to stabilize AuNP (*7*–*12*). In particular, Levy et al. have developed a family of peptides called CALNN that increases the stability of AuNP (*13*). In our case, the amphipathic peptide CLPFFD-NH_2 also has a cysteine residue (C) which contains a thiol group allowing a strong interaction with the gold surface. This interaction may be additive to that of the N-terminal primary amine, since amino groups are also known to have a strong interaction with gold surfaces (*14*). Moreover, it has been shown by Bellino et al. (*15*) that the presence of the C residue and a positively charged ammonium group in the vicinity of the thiol significantly accelerates the adsorption kinetics of thiols onto citrate-stabilized AuNP. Bare AuNPs are stabilized by citrate anions, which are common electrostatic

* Corresponding author. Marcelo J. Kogan. Phone: 5629782897, Fax: 5629782988, e-mail: mkogan@ciq.uchile.cl.

[⊥] These authors contributed equally to this work.

[†] Universidad de Chile.

[‡] Department of Physical Chemistry, University of Barcelona.

[§] Serveis Cientificotècnics, Universitat de Barcelona.

[||] University of Concepción.

[#] Institute for Research in Biomedicine, Barcelona and Department de Química Orgànica, Universitat de Barcelona.

10.1021/bc800016y CCC: $40.75 © 2008 American Chemical Society
Published on Web 05/30/2008

stabilizing agents, because the particles are typically synthesized through a citric acid reduction reaction (*13*). Electrostatic stabilization arises from mutual repulsion between neighboring AuNPs resulting from the negative surface charges of the citrate layer. Peptide CLPFFD-NH_2 is bound spontaneously to the AuNP replacing the citrate coating on the AuNP by forming stable Au−S bonds, as seen in the case of other peptides as CALNN (*13*).

In order to direct the AuNP to the toxic Aβ fibrils, in a previous work we conjugated AuNP to the peptide CLPFFD-NH_2, forming the AuNP-CLPFFD-NH_2 conjugate, which selectively attaches to the Aβ fibrils (*3*). This peptide is a fragment corresponding to the physiological molecule Aβ (1−42) and recognizes a particular (hydrophobic) domain of the β-sheet structure (the sequence ^{17}LVF^{20}F which is one of the hydrophobic cores of the native protein Aβ). In that work, we demonstrated that CLPFFD-NH_2 increases the affinity of AuNP for Aβ. The CLPFFD-NH_2 peptide contains at the C-terminal extreme an Asp residue (D) that confers primary amphipathicity to the molecule (i.e., in the C-terminal end of the sequence there is a polar charged residue, and following the sequence there are preponderantly hydrophobic residues), and increases the solubility of the peptide molecule. The presence of the residues Leu (L), Phe (F), and Phe (F), also present in the native sequence, confers to the molecule the ability to recognize the aggregates of Aβ (*16*).

The aim of this work is to explore the effect of changing the residue sequence of CLPFFD-NH_2 on the AuNP peptide conjugation, stability, and affinity to Aβ fibrils. The purpose is to modify the distances between the AuNP surface and the position of the negatively charged hydrophilic residue at pH 7.4 (i.e., the D residue).

EXPERIMENTAL PROCEDURES

Synthesis of AuNP. Citrate-coated AuNPs (12.5 ± 1.7 nm) were prepared by citrate reduction of $HAuCl_4$. An aqueous solution of $HAuCl_4$ (100 mL, 1 mM) was refluxed for 5−10 min, and a warm (50−60 °C) aqueous solution of sodium citrate (10 mL, 38.8 mM) was added quickly. Reflux was continued for another 30 min until a deep red solution appeared. The solution was filtered through 0.45 μm Millipore syringe filters to remove any precipitate, the pH was adjusted to 7.4 using dilute NaOH solution, and the filtrate was stored at 4 °C. AuNP were observed by transmission electronic microscopy (TEM) using a JEOL JEM-1010 microscope. The specimen was prepared by dropping AuNP on Formvar carbon-coated copper microgrids and letting them dry.

Peptide Synthesis. CLPFFD-NH_2, CDLPFF-NH_2, and CLPDFF-NH_2 were synthesized following fluorenylmethyloxycarbonyl (Fmoc) strategy and solid-phase synthesis. Fmoc-protected amino acids were purchased from Novabiochem (Laufelfingen, Switzerland) and Perseptive Biosystems (Framingham, Massachusetts). *O*-(Benzotriazol-1-yl)-*N*,*N*,*N*′,*N*′-tetramethyluronium tetrafluoroborate (TBTU), Fmoc-AM handle, and resin MBHA were also obtained from Novabiochem. Chemical reagents *N*,*N*′-diisopropylcarbodiimide (DIPCI), 1-hydroxy-1*H*-Benzotriazole (HOBt), triethylsilane, and dimethylaminopyridine (DMAP) were from Fluka (Buchs, Switzerland). Manual synthesis including the following steps: (i) resin washing with DMF (5 × 30 s); (ii) Fmoc removal with 20% piperidine/DMF (1 × 1 min + 2 × 7 min); (iii) washing with DMF (5 × 30 s), (iv) washing with DMF (5 × 30 s) and CH_2Cl_2 (5 × 30 s); (v) Kaiser's test (with a peptide−resin sample); (vi) DMF washing (5 × 30 s). Cleavage of the peptide was carried out by acidolysis with trifluoroacetic acid (TFA) using triethylsilane and water as scavengers (94:3:3, v/v/v) for 60−90 min. TFA was removed with N_2 stream and the oily residue precipitated with dry *tert*-butyl ether. Peptide crude was recovered by centrifugation and decantation of the *tert*-butyl ether phase. The solid was redissolved in 10% acetic acid (AcH) and lyophilized. The peptide was analyzed by RP-HPLC [Waters 996 photodiode array detector (λ = 443 nm) equipped with a Waters 2695 separation module (Milford, MA), a Symmetry column (C18, 5 μm, 4.6 × 150 mm), and Millennium software; flow rate = 1 mL/min, gradient = 5−100% B over 15 min (A = 0.045% TFA in H_2O, and B = 0.036% TFA in acetonitrile)]. The peptide was purified by semipreparative RP-HPLC [Waters 2487 Dual Absorbance Detector equipped with a Waters 2700 Sample Manager, a Waters 600 Controller, a Waters Fraction Collector, a Symmetry column (C18, 5 μm, 30 × 100 mm), and Millennium software]. The peptide was finally characterized by amino acid analysis with a Beckman 6300 analyzer and by MALDI-TOF with a Bruker model Biflex III. Amino acid analysis of CLPFFD-NH_2: Asp 1.0 (1), Pro 0.97 (1), Leu 1.0 (1), Phe 2.03 (2) and mass spectrometry MALDI-TOF: CLPFFD-NH_2, $[M+H^+]$=740 and $[M+Na^+]$=762. Stock solutions of the peptides were prepared by dissolution in water. The pH was adjusted to 7.4 using concentrated NaOH, and the resulting 1.3 mM solution was filtered using 0.2 μm PVDF filters and kept as aliquots at −80 °C. An amino acid analysis (Alta Biosciences, Birmingham, U.K.) indicates a final concentration of 1.28 mM after filtering.

Conjugation of Peptides to AuNP. CLPFFD-NH_2, CLPDFF-NH_2, and CDLPFF-NH_2 capped AuNPs were prepared by mixing 5 nM AuNP and peptide stock solution in a volume ratio of 10 to 1. The conjugation was made in the presence of peptide excess in order to ensure full conversion of the AuNP and, consequently, homogeneous conjugation. The AuNP were afterward purified first in a 450 nm filter and then by dialysis (during three days in a membrane Spectra/Por MWCO 6−8000 against 1.2 mM sodium citrate and the solution was changed 6 times) to eliminate the excess of peptide. UV−Vis absorption spectra were recorded at room temperature with a Unicam UV/vis spectrophotometer (UV3). In order to check the absence of nonconjugated peptide, 3 mL of the conjugated solution were centrifuged at 13 500 rpm for 30 min (AuNP peptide sediments) and the supernatant was evaporated to dryness and an analysis of amino acids was carried out. On the other hand, the absence of free peptide both in the supernatant and in the NP pellet (the conjugated AuNP) was also checked by HPLC ES-MS. Separately, the NP pellet and the residue of the supernatant (after the draining) were suspended in 300 μL of 1% TFA and filtered through a 220 nm filter. In any case, the presence of the peptide was detected.

XPS. X-ray photoelectron spectroscopy (XPS) experiments were performed in a PHI 5500 Multitechnique System (from Physical Electronics) with a monochromatic X-ray source (Al Kα line of 1486.6 eV energy and 350 W), placed perpendicular to the analyzer axis and calibrated using the $3d_{5/2}$ line of Ag with a full width at half-maximum (fwhm) of 0.8 eV. The analyzed area was a circle of 0.8 mm diameter, and the selected resolution for the spectra was 187.5 eV of pass energy and 0.8 eV/step for the general spectra and 23.5 eV of pass energy and 0.1 eV/step for the spectra of the different elements. Some measurements were done after some cleaning by sputtering the surface with an Ar^+ ion source (4 keV energy). All measurements were made in an ultrahigh-vacuum chamber pressure between 5×10^{-9} and 2×10^{-8} Torr.

EELS. Electron energy loss spectra (EELS) were obtained in a Gatan Image Filter (GIF 2000) coupled to the JEOL 2010F microscope, with an energy resolution of 1.2 eV.

Estimation of the Number of Peptide Molecules per AuNP. The amount of peptide molecule per NP was estimated by analysis of amino acids and absorption spectrophotometry.

The concentration of AuNP in the solutions was obtained taking into account the molar coefficient of extinction of the 12 nm diameter ($5.7 \times 10^7\ M^{-1}\ cm^{-1}$) AuNP and an analysis of amino acids of the pellet obtained after centrifugation of the conjugates at 13500 rpm for 30 min (in such conditions the NP sediment). The number of peptide molecules per AuNP was obtained by dividing the number of peptide molecules per mL of solution by the number of particles per mL of solution. This ratio was obtained in triplicate in three independent synthesis and conjugation.

Zeta Potential. The zeta potential (Zeta sizer 3000, Malvern Instruments, UK) measurements of the 12 nm diameter AuNP consisted of five repeats of each AuNP solution. The AuNP in 1.2 mM citrate solution were adjusted to pH 7.4 with a 0.1 M buffer phosphate solution, and a final buffer concentration of 10 mM. Because the zeta potential measurements were performed in an aqueous solution, the Smolouchowski approximation was used to calculate the zeta potential from measured electrophoretic mobility.

Electrophoresis. Submarine gel electrophoresis of the AuNP-peptide conjugates was performed in 1.5% agarose gels (Molecular Biology grade, Roche) using as a running 10 mM phosphate buffer in 1.2 mM sodium citrate. The field strength was held constant at 120 V and the current was 97 mA. 50 μL of AuNP solutions were mixed with 50 μL of 1:9 glycerol/buffer solution and loaded in the gels.

Stability of AuNP and Their Conjugates. (a) Characterization of NP aggregation by UV−visible Spectrometry. UV−Vis absorption spectra were recorded at room temperature with a Unicam UV/Vis spectrophotometer (UV3). The aggregation parameter (AP) was defined as follows: $AP = (A - A_0)/A_0$, where A is the integrated absorbance between 600 and 700 nm and A_0 is the integrated absorbance between 600 and 700 nm of the dispersed solution.

(b) Dialysis against water. Ten mL of the colloidal solutions of AuNP were dialyzed in 2 L of water (during 1 day in a membrane Spectra/Por MWCO 6−8000 against water, and the water was changed at 1 h and 3 h).

(c) Stability in running agarose electrophoresis with buffer solutions. 500 μL of each solution were mixed with 500 μL of phosphate buffer and the aggregation parameter (AP) was determined by UV−vis spectrophotometry.

(d) Stability in artificial cerebrospinal fluid buffer (ACSF): 124 mM NaCl, KCl 5 mM, NaH_2PO_4 1.25 mM, $MgCl_2$ 2 mM, $CaCl_2$ 2 mM, $NaHCO_3$ 26 mM, dextrose 10 mM (see ref (*17*)). 50 μL of each 5 nM colloidal solution was mixed with 950 μL of ACSF buffer and the aggregation parameter (AP) was determined by UV−Vis spectrophotometry.

(e) Stability in rat serum. 50 μL of each 5 nM colloidal solution were mixed with 950 μL of serum and the aggregation parameter (AP) was determined by UV−Vis spectrophotometry. For spectrophotometric measurement, a blank with 50 μL of citrate and 950 μL of serum was used. Serum was obtained from blood collected from Sprague−Dawley male rats (200−300 g). The blood was centrifuged (at room temperature) at 3000 rpm and supernatant liquid was collected.

Circular Dichroism (CD). 150 μL of 40 nM colloidal solution was mixed with 50 μL of phosphate buffer saline and 86 μL of trifluoroethanol (TFE) were added. Circular dichroism spectra were recorded with a Jasco J700 spectropolarimeter (Great Dumnow, UK), at a spectral bandwidth of 1 nm, with a time constant of 4 s (scan speed 10 nm/min) and a step resolution of 0.2 nm. Each spectrum was the result of three accumulations and were measured at 25 °C. A blank spectrum of 150 μL of 1.2 mM citrate, 50 μL of phosphate buffer saline and 86 μL of TFE was subtracted from each conjugate spectrum. Mean residue ellipticity, $[\theta]_{MR}$, is given in units by $deg \cdot cm^2 \cdot dmol^{-1}$.

Interaction with Amyloid Fibrils. (a) Preparation of Aβ_{1-42} solution. Aβ_{1-42} was purchased from Peptide Institute, Inc. (Japan). Water−peptide aliquots were lyophilized again in glass vials and stored at −20 °C until used. A variant of Zagorski's protocol was followed in order to obtain a homogeneous Aβ_{1-42} solution free from aggregates (*18*). Summarizing, in the same vial where it was lyophilized, Aβ_{1-42} was treated with TFA in order to eliminate any pre-existing aggregates. TFA was then evaporated under a stream of nitrogen. To thoroughly remove TFA, 1,1,1,3,3,3-hexafluoro-2-propanol was added and evaporated under a nitrogen stream. This last step was repeated three times and the sample was finally left overnight in a desiccator. The desiccated aliquot was carefully and completely resuspended in 18 μL of 10 mM NaOH per each 100 μL of final sample. Finally, 10 μL of 200 mM phosphate buffer and water was added to complete 100 μL (200 μL of the sample was prepared). All solutions are cleaned of small particles by filtration through a 0.20 μm pore size filter (Millipore). At the end of the process, Aβ_{1-42} was at a concentration of 40 μM. The solution was divided into four aliquots of 50 μL each and incubated at 37 °C for 4 h with mechanical shaking.

(b) Interaction of the samples with AuNP and the conjugates. 150 μL of 1 nM AuNP-CLPFFD-NH_2, AuNP-CDLPFF-NH_2, or AuNP-CLPDFF-NH_2 were added to the Aβ_{1-42} solutions and the samples were incubated for 44 additional h at 37 °C with mechanical shaking (nonmature fibrils: i.e. the 2 day old samples) or for 164 additional h at 37 °C with mechanical shaking (mature Aβ precipitated fibrils: i.e., the 7 day old samples). For TEM observations, aliquots of 1 μL of the preparations were diluted in cold (4 °C) with 20 mM PBS buffer (pH 7.4) to a final peptide concentration of 1 μM. Then, the samples were adsorbed for 1 min onto glow discharged carbon-coated colloidal films on 200 mesh copper grids. The TEM grids were then blotted and washed in Milli-Q water before negative staining with 2% uranyl acetate for visualization by TEM (JEOL JEM-1010).

(c) Quantification of gold in fibrils and supernatants. In order to separate the free and bound nanoparticles a centrifugation at 5000 rpm during 5 min was carried out. The pellet was washed with 20 mM phosphate buffer, and the first and the second supernatant were mixed. The concentration of proteins in the total supernatant was determined following the Bradford protocol. The content of gold in both pellet and supernatant was analyzed by ICP-MS after lyophilization.

(d) Determination of gold content in pellets and supernatant. The determinations were carried out in triplicate. The ICP multielement standard was obtained from high purity standards (QCS-26). Samples were digested by using a Millestone MLS-1200 Mega plus EM-45 microwave oven and following USEPA Method IO-3.1. Basically, this consists of extraction of the elements using 10 mL of a nitric acid−hydrogen peroxide (10:1) solution. After the digestion process, gold was determined directly by ICP-MS (Fisons VG-PlasmaQuad) in each fraction. The values obtained in μg/L were expressed in μg in the pellets and supernatants, and finally the ratio between gold in the supernatant (free AuNP) and in the pellet-bound AuNP were calculated. The contents of protein in the pellets of all the samples and in all the supernatants were similar, indicating that the presence of nanoparticles does not affect the fibril formation. In addition to quantify the amount of Aβ fibrils formed in the presence of the AuNPs, thioflavine T assays were performed observing that quantity of Aβ fibrils in the samples of 2 and 7 days (AuNP + fibrils, AuNP-CLPFFD-NH_2 + fibrils, AuNP-CDLPFF-NH_2 + fibrils, and AuNP-CLPDFF-NH_2 + fibrils)

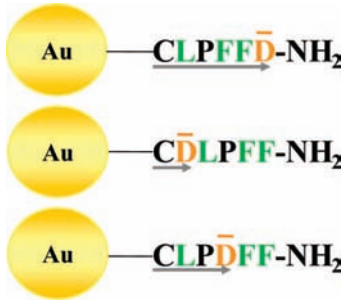

Figure 1. Schematic representation of the peptides conjugated to AuNP at physiological pH 7.4 (The calculated isoelectric point, using the software *Insight II*, of the free peptides is approximately 5.6). In orange is represented the D residues which have a formal negative charge at this pH. In green are represented the hydrophobic residues (LFF). Note that in AuNP-CLPFFD-NH_2 and in AuNP-CDLPFF-NH_2 the hydrophobic residues LFF are uninterrupted by the hydrophilic residue D, which would allow an optimal interaction with the Aβ fibrils. On the other hand, in AuNP-CLPDFF-NH_2 the hydrophobic residues LFF are interrupted by the hydrophilic D. The gray arrows show schematically the distance between the gold surface and the D residue assuming an extended peptide conformation.

were similar, indicating that AuNP does not interfere in the process of Aβ aggregation (data not shown).

RESULTS AND DISCUSSION

Rational Design of the Isomers of CLPFFD-NH_2 for Conjugation with AuNP. For pharmaceutical application of a conjugate AuNP−peptide, it is important to take into account the colloidal stability and the recognition ability of the conjugate AuNP−peptide to the desired target, in this case to the Aβ fibrils. To maintain colloidal stability, it is important that the charge of the AuNP be exposed to the bulk solution to form the double layer that stabilizes the colloid. On the other hand, for recognition purposes it is important that the hydrophobic residues on the conjugate be exposed, in this case L, F, and F residues, to the Aβ fibrils. We chose two isomers of peptide CLPFFD-NH_2, i.e., peptide CDLPFF-NH_2 and peptide CLPDFF-NH_2. When the peptide adopts an extended conformation, the D residue localizes away from the gold surface in the case of CLPFFD-NH_2, while in the case of AuNP-CDLPFF-NH_2, it is near the AuNP surface (Figure 1). In the case of CLPDFF-NH_2, an intermediate situation occurs. In conjugates AuNP–peptide, the stability of the colloid will be modulated by the exposition of the charge to form the double layer and the steric repulsion produced by the peptide capping. On the other hand, the affinity of the conjugates for Aβ fibrils will be modulated by the peptide structure and the exposition of the hydrophobic residues L, F, and F to Aβ fibrils in the cases of CLPFFD-NH_2 and CDLPFF-NH_2, in contrast to CLPDFF-$NH_2$where the L, F, and F residue sequence is interrupted by the hydrophilic charged residue D.

Synthesis and Characterization of AuNP−Peptide Conjugates. AuNP of 12.5 ± 1.7 nm in diameter (Figure 2) were synthesized by reduction of $HAuCl_4$ with sodium citrate in accord with a previous work (*13*).

The AuNP−peptide conjugates were prepared by mixing the colloidal AuNP solution with an excess of peptide to obtain a completely functionalized AuNP surface. The conjugates were exhaustively characterized by using UV−Vis spectrophotometry, EELS, XPS, amino acid analysis, gel electrophoresis, and CD. The peptides were synthesized following a solid-phase synthesis and Fmoc/tbu strategy (*19*). Several dialyses were then performed over three days in order to purge the remaining nonconjugated peptide. Figure 3 shows UV−Vis spectra of the bare AuNP and peptide conjugated to AuNP. The characteristic shift of the surface plasmon resonance band from 519 to 527 nm was observed in the conjugates.

EELS and XPS techniques were used to prove the presence of S−Au bonds on the surface. EELS spectra in the region between 50 and 240 eV were obtained on the AuNP surface from the different samples in order to evaluate the presence of sulfur, and ensure in this way the functionalization of the AuNP with the different peptides (Figure 4A). In Figure 4B, we show a detail of the electron energy loss near edge spectra (ELNES) at the S $L_{2,3}$ edge (165 eV), showing that the edge shape dramatically changes when obtaining the spectrum of the bare AuNP with regard to the peptide-functionalized AuNP. All sample spectra show the typical S $L_{2,3}$-edge slope characteristic of the peptide functionalization (Figure 4B). The spectra obtained on the surface of AuNP in samples AuNP-CLPFFD-NH_2 (red-line spectrum), AuNP-CDLPFF-NH_2 (green-line spectrum), and AuNP-CLPDFF-NH_2 (blue-line) present a clear edge at 165 eV, which is indicative of the presence of sulfur bonded atoms ($L_{2,3}$-edge). This last result corroborates the presence of S atoms at the Au surface, and consequently, the presence of S bonded atoms would imply the functionalization of the AuNP with the peptides in all the samples studied.

Further characterization of the colloids by XPS was performed. In Supporting Information Figure S1, we present survey spectra for four samples taken under similar conditions. In AuNP−peptide conjugates, the expected peaks from S 2p, S 2s, and Au 4f core levels were detected. High-resolution data have also been recorded in the S 2p, S 2s, and Au 4f, spectral regions (Supporting Information Figures S2, S3, and S4). The S 2p signal consists of a broad band with a maximum at 162.2 eV that corresponds to the chemisorptions of sulfur grafted onto gold (*20–23*). A similar trend is also observed with the S 2s photoelectron peak (see Supporting Information Table T1). This peak is a particularly good parameter since it is a singlet, thus making the interpretation straightforward. The S 2s photoelectron binding energy (BE) from bulk peptide with the free thiol and AuNP peptide thiolate are found at 228.2 and 227.3, respectively (Supporting Information Table 1). Similar behavior was reported by Bensebaa et al. (*24*). The accuracy of these BE values is estimated to be ±0.2 eV at the worst. In the case of bare AuNP and capped AuNP, the signal corresponding to Au $4f_{7/2}$ is positioned at 84.2 eV (see Supporting Information Figure S4). The fact that the measured Au $4f_{7/2}$ photoelectron BE is not detected by the sulfur chemisorption is probably because the peak separation is too small. The same result was obtained in capped AuNP with alkanethiolates (*24*).

The number of peptides per AuNP was calculated by dividing the quantity of grafted peptide (obtained by analysis of amino acids of the AuNP pellet) by the amount of AuNP in solution, which was photometrically determined (see Experimental Section). The degree of conjugation follows the order AuNP-CLPFFD-NH_2 > AuNP-CLPDFF-NH_2 > AuNP-CDLPFF-NH_2 (460 ± 30, 420 ± 10, and 203 ± 5 peptide molecules per AuNP). Assuming that (i) the surface of a 12.5 nm in diameter AuNP is 490 nm^2, (ii) the projection of a cylindrical peptide molecule (with cylindrical base) resting along its base on the gold surface in an extended conformation is 0.6 nm^2 (estimated by molecular modeling with the program *Insight II*), and (iii) a hexagonal close-packed lattice in which the maximum number of molecule not exceeding the packing density of 74% is 609 molecules, we conclude that our peptide molecules (for instance, only 460 in the case of AuNP-CLPFFD-NH_2) are not forming a compact self-assembled monolayer (SAM).

Effect of the Residue Sequence in the Stability of the AuNP−Peptide Conjugates. CLPFFD-NH_2, CDLPFF-NH_2, and CLPDFF-NH_2 are more stable than bare AuNP. At 4 °C, AuNP-CLPFFD-NH_2 and AuNP-CLPDFF-NH_2 do not aggregate at pH = 7.4 (in buffer phosphate 10 mM) for one year, but AuNP-CDLPFF-NH_2 and bare AuNP do (see Supporting

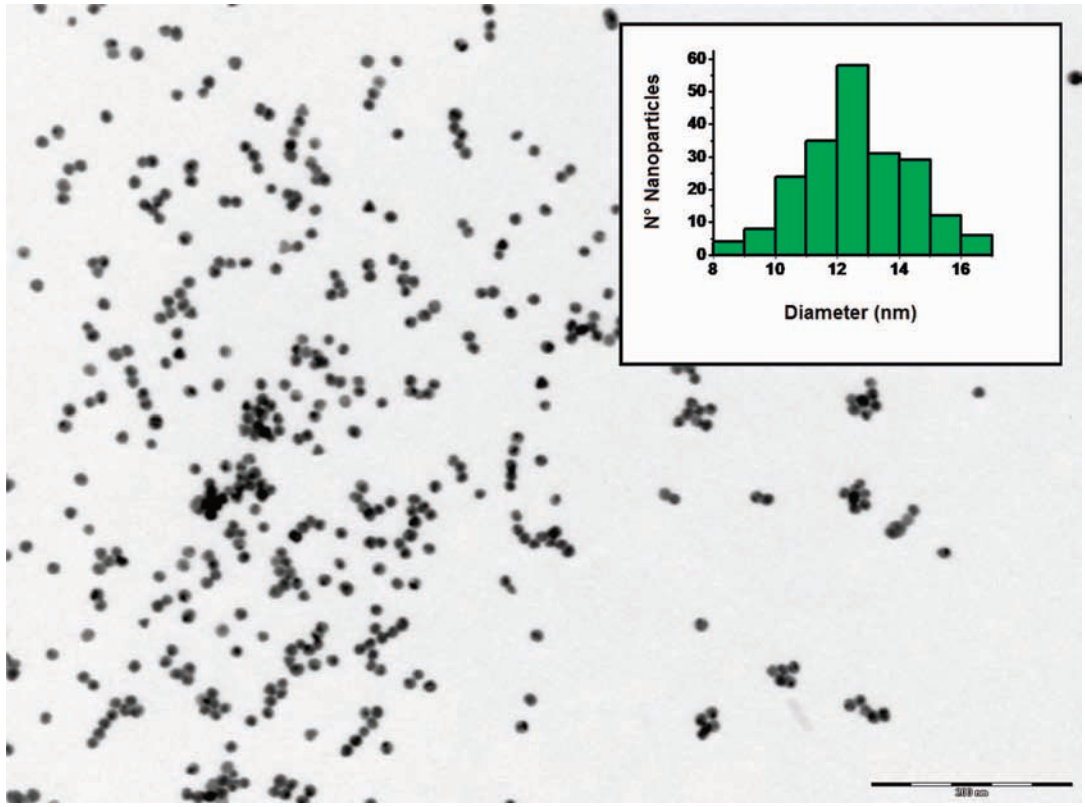

Figure 2. TEM micrograph of AuNP. The insert shows the distribution diameter of the AuNP.

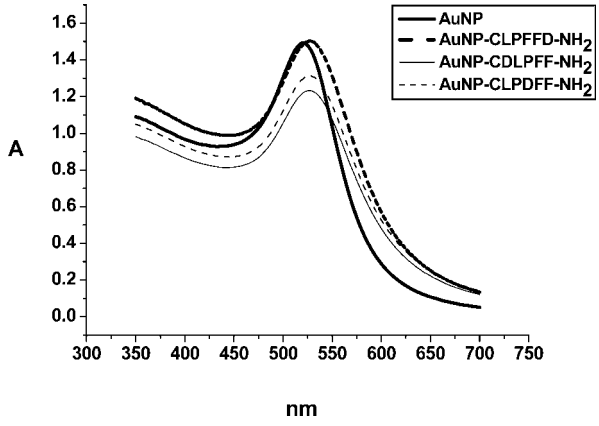

Figure 3. UV−vis spectra of bare AuNP and peptide-capped AuNP.

Information Figure S5). Peptide stabilization of AuNP is a documented phenomenon (*1*), although the effect of the peptide sequence in the stability has been documented for only the peptide CALNN (*13*).

In order to evaluate the stability of the AuNP−peptide conjugates, we measured the UV−Vis spectra for different conditions and determined the AP, in the way defined by Levy et al. (ref (*13*); see Experimental Section). The stability of the AuNP and their conjugates was studied both after fast freezing/defreezing (Figure 5A) and after fast freezing/freeze-drying and reconstitution in water (Figure 5B). AuNP-CLPFFD-NH_2 and AuNP-CLPDFF-NH_2 were more stable than AuNP-CDLPFF-NH_2 and bare AuNP in both conditions (Figure 5A,B). These results also reveal higher exposition of the hydrophobic residues F and F to the solvent (10 mM phosphate buffer, pH 7.4 in 1.2 mM sodium citrate) in the case of AuNP-CDLPFF-NH_2 than in the cases AuNP-CLPFFD-NH_2 and AuNP-CLPDFF-NH_2, a direct consequence of having the F groups in the conjugate AuNP-CDLPFF-NH_2 located far from the influence of the charged aspartic group. Thus, after freezing, the hydrophobic groups of AuNP-CDLPFF-NH_2 particles freely interact through van der Waals interactions (excluding water) producing aggregation and subsequent colloid flocculation.

In colloids there are several interactions that determine the stability. The combination of van der Waals attractive forces and steric forces form the basis for the theory of steric stabilization. Fine particles tend to attract each other due to van der Waals attractive forces that can be neutralized through the addition of charge and/or grafting molecules onto the nanoparticle surface. In the first case, stabilization occurs due to electrostatic repulsion, while in the second case, stabilization occurs due to steric repulsive forces (*25*). Here, we report on two parameters related to the nanoparticle charge, the zeta potential and migration in an electrophoresis gel.

Effect of the Residue Sequence on the Charge of the AuNP−peptide Conjugate. The classical Derjaguin-Landau-Verwey-Overbeekn (DLVO) theory has been widely employed in colloid science for understanding colloidal interaction in liquids (*26–28*). The salient feature of the theory indicates that a colloidal system remains stable if repulsion forces dominate particle interactions over attractive van der Waals forces. However, when attractive forces dominate, then colloidal particles cluster together forming flocculates and aggregates. The origin of stabilizing repulsion forces may be Coulombic, entropic arising from the confinement of thermally mobile surface groups, or a combination. Higher (absolute) values of zeta potentials yield stronger Coulombic repulsion between the particles, thus diminishing the impact of the van der Waals force attractions. Table 1 summarizes the zeta potentials corresponding to bare AuNP and AuNP−peptide conjugates. In general, AuNP−peptide conjugates present lower zeta potential (absolute) values than bare AuNP. We attribute this to the replacement of ion citrates (ion citrates have three dissociated negatively charged carboxylic groups at pH 7.4) with peptide molecules (which bear one formal negative charge at pH 7.4). For instance,

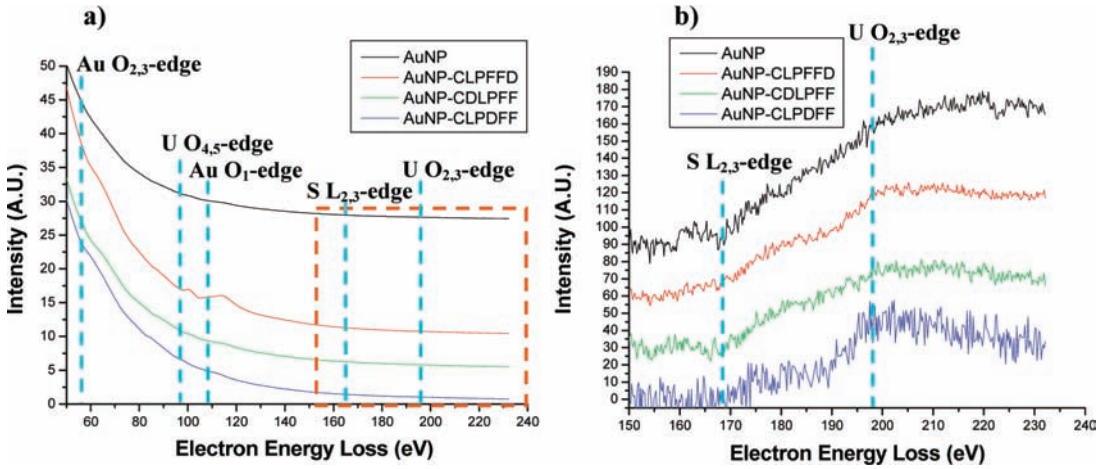

Figure 4. (A) EELS spectra obtained on the surface of 12.5 nm sized AuNP, nonfunctionalized (black line), and functionalized with different peptides (red, blue, and green spectra). (B) Detail of the S $L_{2,3}$ ELNES spectra obtained from the spectra showed in a. Au $O_{2,3}$-edge 54 eV; Au O_1-edge 83 eV; U $O_{4,5}$-edge 96 eV; U $O_{2,3}$-edge 195 eV; S $L_{2,3}$-edge 165 eV.

Table 1. Zeta Potential of Bare and AuNP−peptide Conjugates at pH 7.4 (10 mM phosphate buffer pH 7.4, in 1.2 mM citrate)[a]

colloid	zeta potential mV (std. dev. in mV)
AuNP	−54.3 (2.9)
AuNP-CLPFFD-NH_2	−43.7 (1.5)
AuNP-CDLPFF-NH_2	−34.9 (0.6)
AuNP-CLPDFF-NH_2	−42.8 (1.0)

[a] Low std dev in all cases suggests homogeneous zeta potential distribution and thus capping degree.

the replacement of one peptide molecule with one citrate ion will reduce the total negative charge of the AuNP in two units. However, the diminution of the charge density is not always accompanied by an increase in the peptide grafting density. Remarkably, in the case of AuNP-CDLPFF-NH_2 in which the quantity of peptide molecules covering the surface is lower with respect to the other isomers (203 versus approximately 400 in the other two cases), the zeta potential is lower than that for the other conjugates. In this case, the presence of a carboxylate group belonging to the D residue situated near the surface, seems to induce the exclusion of more molecules of adsorbed citrate (due to the repulsive interaction between D residues and citrate carboxylates) with respect to the other conjugates.

Zeta potential values explain the higher stability of AuNP-CLPFFD-NH_2 and AuNP-CLPDFF-NH_2 with respect to AuNP-CDLPFF-NH_2. Even though in general AuNP−peptides present lower zeta potential values (absolute) with respect to bare AuNPs, the first are more stable than the latter possibly due to the steric stabilization produced by the peptide molecules.

Colloid stability of AuNP−peptide conjugates is enhanced by entropic repulsive interactions of the protruding peptide groups on the particles in water; these groups should not be considered as fixed or rigid, but rather as a superficial layer of flexible segments that expand or collapse on the surface. In this way, van der Waals attractive forces can be neutralized thorough the chemisorption of peptide molecules on the colloid surface and stabilization occurs due to steric repulsive forces as was described for other molecules adsorbed on nanoparticle (*25*, *29*). So, the experimental stability order AuNP-CLPFFD-NH_2 > AuNP-CLPDFF-NH_2 > AuNP-CDLPFF-NH_2 > AuNP would correspond with peptide functionalization that is AuNP-CLPFFD-NH_2 > AuNP-CLPDFF-NH_2 > AuNP-CDLPFF-NH_2 and bare AuNP.

We also ran an electrophoresis agarose gel in phosphate buffer at pH 7.4 (10 mM) (the same conditions under which we studied the interaction with Aβ fibrils; see below). In such conditions the electrophoretic relative mobilities of the nanoparticles follow the order AuNP-CLPFFD-NH_2 ≅ AuNP-CLPDFF-NH_2 > AuNP-CDLPFF-NH_2 > bare AuNP (Figure 6). It is important to mention that bare AuNP presented aggregation in the running conditions in contrast with the AuNP−peptide conjugates. Other works in the literature show that bare AuNP does migrate in agarose gel; however, it does when stabilized with phosphines, compounds which are different from the citrate used here (*30*). On the other hand, the lower mobility of AuNP-CDLPFF-NH_2 with respect to the other conjugates we attribute to the lower resulting surface charge produced by the exclusion of citrate molecules from the surfaces (see previous section). In the case of bare AuNP, particles aggregate (in Figure 6 see the dark coloration corresponding to AuNP in the sample loading position) no matter their high zeta potential (Table 1). This reason is unclear to us; undesired interaction of the citrate ions with the buffer (during the running) in not discarded at this point.

From a pharmaceutical point of view, it is important to determine the stability of AuNP in the absence of citrate, simply because this salt is not present in biological medium. Here, we study the stability of the conjugates and bare AuNP after deprivation of the citrate ion in the media.

Stability of AuNP and Their Conjugates after Citrate Ion Deprivation. The citrate ions play an important role in the stability of the AuNP colloids; however, the interaction of these ions with the gold surface is weak. In the conjugation process of the peptides containing thiols, there is a replacement of citrate ions by peptide molecules forming a stable binding. However, the replacement is not complete because the AuNPs are not capped with a compact SAM; thus on the surface of the AuNP, there are citrate ions and peptide molecules that together contribute to form the stabilizing double layer. To evaluate the stability of AuNP and AuNP−peptide conjugates after citrate ion deprivation, we performed a dialysis against water for 24 h. This deprivation is caused by desorption due to the diffusion process of citrate ions outside the membrane dialysis to equilibrate the chemical potential of AuNP that to the solution. We choose this way to eliminate the citrate in order to avoid centrifugation and reconstitution in a buffer media because a certain degree of aggregation could occur after centrifugation.

After deprivation of the citrate ions, the system reaches thermodynamic equilibrium concentrations inside and outside the membrane; the AP for the AuNP and AuNP−peptide was determined by spectrophotometry after 24 h of dialysis against water. AuNP were unstable (AP = 3.40 ± 0.97) which could be attributed to desorption of weakly interacting adsorbed citrate

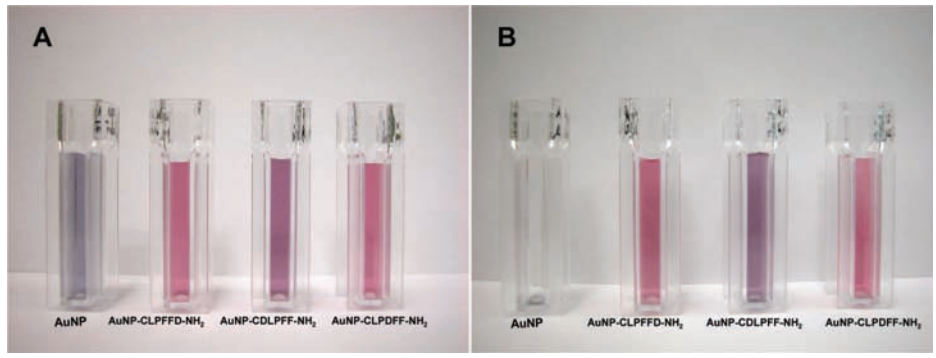

Figure 5. Photographies of colloidal solutions of bare AuNP and conjugated AuNP after: (A) freezing and defreezing and reconstitution in water (AP: 0.09 ± 0.03 for AuNP-CLPFFD-NH_2 and 0.06 ± 0.01 of AuNP-CLPDFF-NH_2, 0.45 ± 0.06 for AuNP-CDLPFF-NH_2, and 5.37 ± 0.24 for bare AuNP). (B) After freezing and freeze-drying the colloidal solutions and reconstitution in water (AP: 0.10 ± 0.05 for AuNP-CLPFFD-NH_2 and 0.14 ± 0.16 for AuNP-CLPDFF-NH_2, 0.35 ± 0.13, for AuNP-CDLPFF-NH_2 and for bare AuNP the AP could not be determined because the sample was totally precipitated).

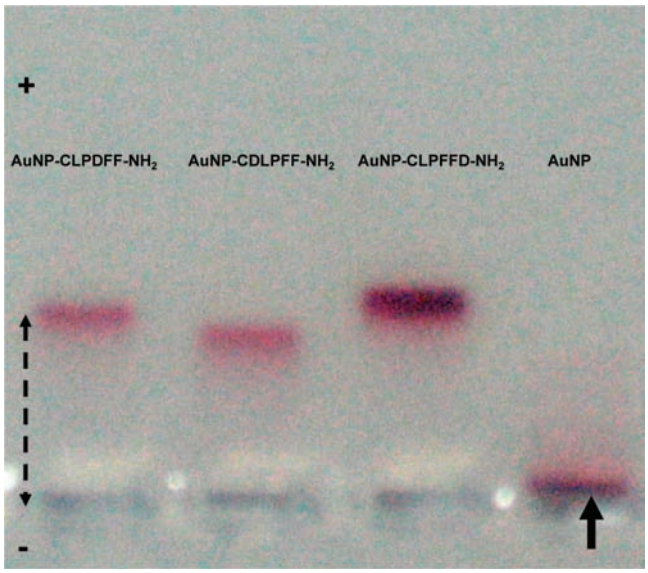

Figure 6. Electrophoresis of AuNP and AuNP−peptide conjugates in agarose gel. Run was performed in 10 mM phosphate buffer pH 7.4 in 1.2 mM citrate at 120 V for 8 min. The arrow indicates the loading sample position of AuNP. The dotted arrow indicates a real distance of 1.5 cm.

ions, which in turn leads to flocculation. AuNP-CDLPFF-NH_2 was also unstable, turning the determination of AP impossible. In contrast, AuNP-CLPFFD-NH_2 and AuNP-CLPDFF-NH_2 (AP = 0.15 ± 0.01 and 0.73 ± 0.01, respectively) were more stable than AuNP and AuNP-CDLPFF-NH_2. The higher stability of AuNP-CLPFFD-NH_2 and AuNP-CLPDFF-NH_2 with respect to AuNP-CDLPFF-NH_2 could be attributed to the higher degree of stable functionalization confered to the AuNP surface, which protects the conjugate against citrate deprivation. Exposition of carboxylic groups belonging to the D residues increases repulsion between the nanoparticles ensuring colloidal stability. In contrast, in AuNP-CDLPFF-NH_2, the degree of functionalization is low, thus leading to low protection against citrate deprivation; as a result, aggregation inevitably occurs due mainly to interaction of hydrophobic groups to exclude water.

The stability of nanoparticles in biological fluids is an important issue for its practical application. We studied the stability of the nanoparticles in less artificial conditions, as in the case of ACSF, a typical buffer used for neurophysiological studies (*17*), and in rat serum.

Stability of AuNP and Their Conjugates in a Medium that Mimics Cerebrospinal Fluid. We determined the AP of bare and capped AuNPs incubated for 48 h, at 4 °C. 5 nM AuNPs were diluted in AuNP/ACSF buffer (1:20). Figure 7 shows that only AuNP-CLPFFD-NH_2 were stable (AP = 0.05 ± 0.01) in ACSF, while the other conjugates and bare AuNP were unstable in such conditions (AP could not be determined due to precipitation).

Stability of AuNP and Their Conjugates in Rat Serum. The AP of bare and capped AuNP was determined in rat serum. The nanoparticle samples were diluted in serum in a 1:20 ratio (nanoparticle/serum) and UV−Vis spectra were obtained (Supporting Information S6). After 48 h, all the samples were stable. It should be noted that a bathochromic shift in all cases was observed before starting incubation (t = 0 h). This shift and stability of all samples could be attributed to nanoparticle capping with serum proteins that stabilizes the colloidal particles.

The secondary structure that adopts the peptide molecules onto the AuNP surface is related to both process, the grafting and the interaction of the anchored peptide molecules with amyloid aggregates. We carried out CD spectra of the conjugates in order to obtain information about the influence of the sequence on the structure of the peptides conjugated to AuNP.

CD Spectra of Conjugates AuNP−Peptide. In an attempt to characterize the possible differences in the secondary structures of the different peptides attached to the surface of AuNP, we have recorded the CD spectra of the conjugates. In the case of CDLPFF, this measurement was not possible due to the weak contribution of peptide yielded by the low degree of AuNP functionalization. On the contrary, Figure 8 shows the CD spectra of AuNP-CLPFFD-NH_2 and AuNP-CLPDFF-NH_2. In the first conjugate, a β structure is present, while a disordered structure is found in the second conjugate. In accordance with our CD experiments, a *hypothetical* model is proposed (Figure 9) that allows visualization of how CLPFFD-NH_2 is grafted on the AuNP surface, allowing the accommodation of a higher number of peptide molecules in relation to the isomer CLPDFF-NH_2. In the case of the peptide CLPFFD-NH_2, which presents primary amphipathicity (*31*), the hydrophilic head (D) is far from the surface and the peptide tends to adopt an extended β conformation. The molecules are orthogonally oriented to the AuNP surface, exposing the D and avoiding the interaction between the gold surface and the terminal amide. This behavior was recently proposed by Pomerantz et al. for the deposit of amphiphilic β-peptides onto gold surfaces (*32*). In the case of peptide CLPDFF-NH_2, in which the primary amphipathicity is not well-defined because the D group is intercalated in the sequence between the hydrophobic residues, the peptide molecules adopt a disordered structure and fewer molecules could be accommodated onto the gold surface. In this case, the terminal amide group could be in contact with the gold surface as proposed for non-amphipathic structures (*32*).

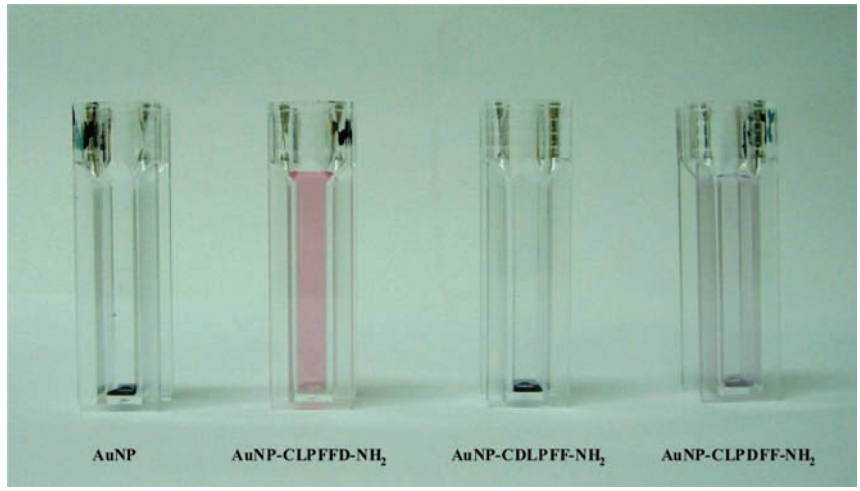

Figure 7. Photographs of colloidal solutions of bare AuNP and conjugated AuNP after incubation in ACSF for 48 h at 4 °C (AP, 0.05 ± 0.01 for AuNP-CLPFFD-NH_2; for bare AuNP and other conjugates, the AP could not be determined because the sample was totally precipitated).

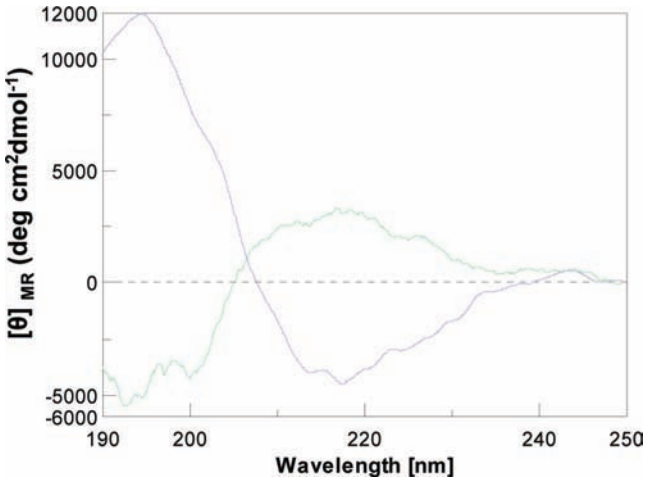

Figure 8. Far-UV CD spectra of AuNP-CLPFFD-NH_2 (blue) and AuNP-CLPDFF-NH_2(green) at pH = 7.4.

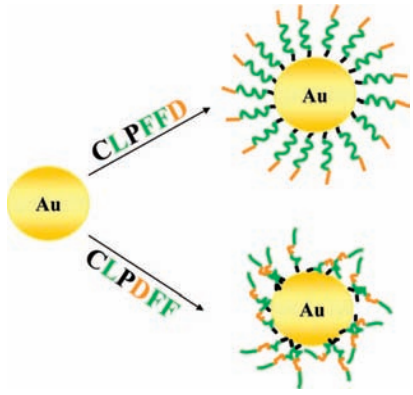

Figure 9. Hypothetical cartoon based on CD results. The hydrophobic groups are represented in green and the hydrophilic groups in orange. In the case of AuNP-CLPFFD-NH_2, the peptide is oriented orthogonally to the gold surface adopting a β secondary structure, while in AuNP-CLPDFF-NH_2, the peptide is in a disordered structure. Note that in the first the degree of functionalization and exposition of D is higher than in the case of AuNP-CLPDFF-NH_2. The scale of the molecules is not in proportion with the nanoparticles.

Interaction of AuNP and AuNP−Peptide Conjugates with Aβ Fibrils. To determine the affinity of AuNP−peptide conjugates for Aβ fibrils, we incubated Aβ with AuNP and their conjugates, for 2 days to form immature fibrils and for 7 days

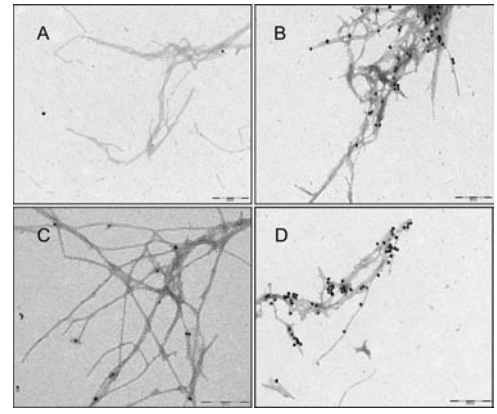

Figure 10. TEM micrograph of 7 day old amyloid fibrils stained with uranil acetate incubated with (A) AuNP, (B) AuNP-CLPFFD-NH_2, (C) AuNP-CDLPFF-NH_2, and (D) AuNP-CLPDFF-NH_2. Bars represent 200 nm.

to form mature fibrils. In both cases of samples, bare AuNP showed by TEM low degree of interaction with the fibril while the three AuNP−peptide conjugates showed a higher degree of interaction (Figure 10). This result could be explained by the presence of hydrophobic groups L, F, and F present in the peptides that which are able to recognize the hydrophobic nucleus in Aβ.

To quantitatively evaluate the affinity or adhesion of each conjugate to the Aβ fibril, we centrifuged the corresponding sample at 2300 *g* for 5 min; under such conditions, the unbound free AuNP remained suspended but the Aβ fibrils bound to AuNP did precipitate forming a pellet. The gold content both in the pellets and in the supernatants was determined by ICP-MS. Gold content ratios between that in the supernatant (unbound free AuNP) and that in the pellet (AuNP attached to the fibrils) are summarized in Table 2. The conjugate AuNP-CLPFFD-NH_2 adheres better to Aβ fibrils than the other conjugates. According to CD results, this peptide adopts a β secondary structure, which could favor the interaction of the residues L F F with Aβ fibrils. In addition, the presence of D groups at the C-terminal position produces the repulsion needed to maintain the peptide chain separation, avoiding self-aggregation between the peptide molecules conjugated to the AuNP. Thus, the adhesive interaction between the conjugate and the Aβ fibril becomes possible. Moreover, the stability of this conjugate in ACSF

Table 2. Proportion of Unbound Gold (AuNP in the supernatant) and Gold Bound to the Aβ fibrils (AuNP in the pellet)[a]

	ratio of gold (supernatant/pellet) (2 d)	ratio of gold (supernatant/pellet) (7 d)
AuNP + Fibrils	6.50 ± 0.05	0.21 ± 0.05
AuNP-CLPFFD +Fibrils	1.50 ± 0.01	0.03 ± 0.02
AuNP-CDLPFF + Fibrils	3.51 ± 0.03	0.11 ± 0.02
AuNP-CLPDFF + Fibrils	3.03 ± 0.03	0.12 ± 0.05

[a] The pellet was washed with 10 mM phosphate buffer pH 7.4 in 1.2 mM citrate and centrifuged (both supernatants were mixed). The pellets and the suppernatants were lyophilized. The gold content in the pellets and in the supernatants was determined by ICP-MS.

and serum is a very important factor in future biomedical applications.

Several conclusions can be drawn from this set of experiments. The peptide sequence influences the degree of conjugation, the stability, and the interaction of AuNP−peptide conjugates. In our opinion, there are two critical factors to be considered: the position of the negative charge and the capacity to adopt a secondary structure. The position of the negative charge could be related with the colloidal stability. In the case of AuNP-CLPFFD-NH_2, the D residues could be located in a more external position contributing to repulsion between particles increasing the colloidal stability. On the other hand, CLPFFD-NH_2 anchored to the AuNP adopts a β secondary structure increasing the ability to interact with Aβ. Following the hypothetical model proposed in Figure 9, the higher number of peptide molecules are accommodated on the surface producing steric hindrance which contribute to colloidal stability. In contrast in the isomer CLPDFF-NH_2, the peptide adopts a more disordered structure avoiding the accommodation of molecules, reducing the degree of functionalization, the stability, and the affinity for Aβ.

The results obtained here provide a first answer to the important concern of the way bioactive peptides could allocate once they are anchored to AuNP surface and the way conjugates could interact with the biological target. However, to determine the conformation of a peptide molecule on the AuNP surface, further experiments are now in progress in our laboratory. Due to the importance that AuNP have in therapy and diagnosis, it is very helpful to understand the parameters governing the stability and interaction with the therapeutic target.

ACKNOWLEDGMENT

We acknowledge Elisenda Coll of Servei Cientific-Tecnics (Universitat de Barcelona) for assistance in TEM observations. This work was supported by FONDECYT 1061142, FONDAP 11980002 (17 07 0002), and AECI A/5987/06. E.G. thanks MCYT-FEDER (Nanobiomed-CONSOLIDER, BIO 2005-00295 and NAN 2004-09159-C04-02).

Supporting Information Available: Additional data as described in the text. This material is available free of charge via the Internet at http://pubs.acs.org.

LITERATURE CITED

(1) Kogan, M. J., Olmedo, I., Hosta, L., Guerrero, A. R., Cruz, L. J., and Albericio, F. (2007) Peptides and metallic nanoparticles for biomedical applications. *Nanomedicine 2*, 287–306.

(2) De la Fuente, J., and Berry, C. C. (2005) Tat peptide as an efficient molecule to translocate gold nanoparticles into the cell nucleus. *Bioconjugate Chem. 16*, 1176–1180.

(3) Kogan, M. J., Bastus, N. G., Amigo, R., Grillo-Bosch, D., and Araya, E. (2006) Nanoparticle-mediated local and remote manipulation of protein aggregation. *Nano Lett. 6*, 110–115.

(4) Efremov, R. G., Chugunov, A. O., Pyrkov, T. V., Priestle, J. P., Arseniev, A. S., and Jacoby, E. (2007) Molecular lipophilicity in protein modeling and drug design. *Curr. Med. Chem. 14*, 393–415.

(5) Naz, R. K., and Dabir, P. (2007) Peptide vaccines against cancer, infectious diseases, and conception. *Front. Biosci 12*, 1833–1844.

(6) Cruz, L. J., Iglesias, E., Aguilar, J. C., Cabrales, A., Reyes, O., and Andreu, D. (2004) Different immune response of mice immunized with conjugates containing multiple copies of either consensus or mixotope versions of the V3 loop peptide from human immunodeficiency virus type. *Bioconjugate Chem. 15*, 1110–1117.

(7) Hostetler, M. J., and Murray, R. W. (1997) Colloids and self-assembled monolayers. *Curr. Opin. Colloid Interface Sci. 2*, 42–50.

(8) Templeton, A. C., Wuelfing, M. P., and Murray, R. W. (2000) Monolayer-protected cluster molecules. *Acc. Chem. Res. 33*, 27–36.

(9) Whetten, R. L., Shafigullin, M. N., Khoury, J. T., Schaaff, T. G., Vezmar, I., Alvarez, M. M., and Wilkinson, A. (1999) Crystal structures of molecular gold nanocrystal arrays. *Acc. Chem. Res. 32*, 397–406.

(10) Brust, M., and Kiely, C. J. (2002) Some recent advances in nanostructure preparation from gold and silver particles: A short topical review. *Colloids Surf., A 202*, 175–186.

(11) Brust, M., and Kiely, C. J. (2004) Monolayer Protected Clusters of Gold and Silver. *Colloids and colloid assemblies* (Caruso, F., Ed.) pp 96−119, Wiley-VCH, Weinheim.

(12) Daniel, M. C., and Astruc, D. (2004) Gold nanoparticles: assembly, supramolecular chemistry, quantum-size related properties, and applications towards biology, catalysis and nanotechnology. *Chem. Rev. 104*, 293–346.

(13) Levy, R., Thanh, N. T. K., Doty, R. C., Nichols, R. J., Schiffrin, D. J., Brust, M., and Fernig, D. G. (2004) Rational and combinatorial design of peptide as capping ligands for gold nanoparticles. *J. Am. Chem. Soc. 126*, 10076–10084.

(14) Zhang, J., Chi, Q., Nielsen, J. U., Friis, E. P., Andersen, J. E. T., and Ulstrup, J. (2000) Two-dimensional cysteine and cystine cluster networks on Au(111) disclosed by voltammetry and in situ scanning tunneling microscopy. *Langmuir 16*, 7229–7237.

(15) Bellino, M. G., Calvo, E. J., and Gordillo, G. (2004) Adsorption kinetics of charged thiols on gold nanoparticles. *Phys. Chem. Chem. Phys. 6*, 424–428.

(16) Soto, C., Kindy, M. S., Baumann, M., and Frangione, B. (1996) Inhibition of Alzheimer's amyloidosis by peptides that prevent beta-sheet conformation. *Biochem. Biophys. Res. Commun. 226*, 672–680.

(17) Rozas, C., Frank, H., Heynen, A. J., Morales, B., Bear, M. F., and Kirkwood, A. (2001) Developmental inhibitory gate controls the relay of activity to the superficial layers of the visual cortex. *J. Neurosci. 21*, 6791–6801.

(18) Zagorski, M. G., Yang, J., Shao, H. Y., Ma, K., Zeng, H., and Hong, A. (1999) Methodological and chemical factors affecting Aβ amyloidogenicity. *Method Enzymol. 309*, 189–204.

(19) Dörner, B., Ostresh, J. M., Houghten, R. A., Frank, R., Tiepold, A., Fox, J. E., Bray, A. M., Ede, N. J., James, I. W., Wickham, G. (2000) Manual multiple synthesis methods, 1. Simultaneous multiple peptide synthesis - the T-bag method. *Fmoc Solid Phase Peptide Synthesis - A Practical Approach* (Chan, W. C., and White, P. D., Eds.) pp 303−327, Oxford University Press, Oxford.

(20) Brust, M., Walker, M., Bethell, D., Schiffrin, D. J., and Whyman, R. J. (1994) Synthesis of thiol-derivatized gold nanoparticles in a 2-phase liquid system. *Chem. Soc.: Chem. Commun. 7*, 801–802.

(21) Leff, D. V., Ohara, P. C., Heath, J. R., and Gelbart, W. M. (1995) Thermodynamic control of gold nanocrystal size: experiment and theory. *J. Phys. Chem. 99*, 7036–7041.

(22) Badia, A., Singh, S., Demers, L., Cuccia, L., Brown, G. R., and Lennox, R. B. (1996) Self-assembled monolayers on gold nanoparticles. *Chem. Eur. J. 2*, 359–363.

(23) Bishop, A. R., and Nuzzo, R. G. (1996) Self-assembled monolayers: Recent developments and applications. *Curr. Opin. Colloid Interface Sci. 1*, 127–136.

(24) Bensebaa, F., Zhou, Y., Deslandes, Y., Kruus, E, and Ellis, T. H. (1998) XPS study of metal-sulfur bonds in metal-alkanethiolate materials. *Surf. Sci. 405*, L472–L476.

(25) Zaman, A. A. (2000) Effect of polyethylene oxide on the viscosity of dispersion of charged silica particles: interplay between rheology, adsorption, and surface charge. *Colloid Polym. Sci. 278*, 1187–1197.

(26) Hunter, R. J. (1995) *Foundations of Colloid Science.* Oxford Sci. Pub, Clarendon Press, Oxford, U.K.

(27) Verwey, E. J. W., Overbeek, J. Th. G. (1999) *Theory of the Stability of Lyophobic Colloids*, Dover, Mineola, NY.

(28) Lee, K., Sathyagal, A. N., and McCormick, A. V. (1998) A closer look at an aggregation model of the Stöber process. *Colloids Surf., A 144*, 115–125.

(29) Ishikawa, Y., and Katoh, Y., OhshimaH. (2005) Colloidal stability of aqueous polymeric dispersions: Effect of pH and salt concentration. *Colloids Surf., B 42*, 53–58.

(30) Sandstrom, P., and Akerman, B. (2004) Electrophoretic properties of DNA-modified colloidal gold nanoparticles. *Langmuir 20*, 4182–4186.

(31) Fernandez-Carneado, J., Kogan, M. J., Pujals, S., and Giralt, E. (2004) Amphipathic peptides and drug delivery. *Biopolymers 76*, 196–203.

(32) Pomerantz, W. C., Cadwell, K. D., Hsu, Y-J., Gellman, S. H., and Abbott, N. L. (2007) Sequence dependent behavior of amphiphilic β-peptides on gold surfaces. *Chem. Mater. 19*, 4436–4441.

BC800016Y

Polyketal Copolymers: A New Acid-Sensitive Delivery Vehicle for Treating Acute Inflammatory Diseases

Stephen C. Yang,[†] Mahesh Bhide,[‡] Ian N. Crispe,[‡] Robert H. Pierce,[‡,#] and Niren Murthy*[,†]

Wallace H. Coulter Department of Biomedical Engineering and Parker H. Petit Institute for Bioengineering and Bioscience, Georgia Institute of Technology, Atlanta, Georgia 30332, and David H. Smith Center for Vaccine Biology and Immunology and the Department of Pathology, University of Rochester, Rochester, New York 14627. Received November 30, 2007; Revised Manuscript Received April 8, 2008

Acute inflammatory diseases are a major cause of death in the world, and effective treatments are greatly needed. Macrophages play a central role in causing acute inflammatory diseases, and there is currently great interest in developing drug delivery vehicles that can target therapeutics to macrophages. Microparticles formulated from aliphatic polyketals have great potential to enhance the treatment of acute inflammatory diseases, due to their ability to passively target therapeutics to macrophages, their acid sensitivity, and their biocompatible degradation products. However, existing aliphatic polyketals are unsuitable for treating acute inflammatory diseases because they require weeks to hydrolyze, and strategies for accelerating their hydrolysis kinetics are greatly needed. In this report, we demonstrate that the hydrolysis kinetics of aliphatic polyketals can be accelerated by increasing their hydrophilic/hydrophobic balance. Aliphatic polyketals of varying hydrophobicity were synthesized, via the acetal exchange reaction, and their hydrolysis kinetics were investigated at the pH values of 4.5 and 7.4. A polyketal termed PK3 was developed, which had the hydrolysis kinetics suitable for treating acute inflammatory diseases. PK3 has a hydrolysis half-life of 2 days at pH 4.5, but requires several weeks to hydrolyze at pH 7.4. Microparticles were formulated with PK3, which encapsulated the anti-inflammatory drug, imatinib. *In vivo* experiments demonstrated that PK3 microparticles were able to significantly improve the efficacy of imatinib in treating acute liver failure. We anticipate that aliphatic polyketals will have numerous applications for the treatment of acute inflammatory diseases, given their pH sensitivity, tunable hydrolysis kinetics, and biocompatible degradation products.

INTRODUCTION

Acute inflammatory diseases such as acute lung injury and acute liver failure cause millions of deaths each year, and effective treatments are greatly needed (*1, 2*). Pro-inflammatory cytokines secreted by macrophages play a central role in mediating acute inflammatory diseases, and drug delivery vehicles that can target therapeutics to macrophages have great clinical potential (*3*). A key drug delivery requirement for the treatment of many acute inflammatory diseases is fast release of drugs to diseased organs, within several hours. This is because, at the time of patient diagnosis, significant tissue damage has already occurred, and organ function is rapidly deteriorating (*4*). It has been challenging to develop clinically acceptable drug delivery vehicles that can target therapeutics to macrophages and release them rapidly. Liposomes are a potential delivery vehicle for treating acute inflammatory diseases, due to their ability to target macrophages (*5*). However, their serum instability and poor storage properties have slowed their progress in clinical trials. Microparticles, based on biodegradable polymers, also have potential to enhance the treatment of acute inflammatory diseases. Microparticles can be freeze-dried, have an excellent shelf life, and can also passively target therapeutics to macrophages (*6, 7*). However, currently used biomaterials for drug delivery are predominantly based on polyesters, which are potentially problematic for treating acute inflammatory diseases because of their slow hydrolysis kinetics and acidic degradation products, which themselves frequently cause inflammation (*8, 9*).

Microparticles formulated from polyketals are a new drug delivery vehicle, which degrade into neutral compounds comprising acetone and diols, and should therefore avoid the inflammatory problems associated with polyester-based materials (*9–13*). At present, only two polyketals have been synthesized for drug delivery, poly(1,4-phenyleneacetone dimethylene ketal) (PPADK) and poly(cyclohexane-1,4-diyl acetone dimethylene ketal) (PCADK) (*12, 13*). PPADK has excellent hydrolysis kinetics for treating acute inflammatory diseases, having a half-life of 35 h at pH 5.0, but degrades into benzene dimethanol, a compound with potential toxicity, due to its aromatic ring. PCADK is an aliphatic polyketal, which degrades into acetone and 1,4-cyclohexanedimethanol, both of which have excellent biocompatibility. However, PCADK has a hydrolysis half-life of 24 days at pH 4.5, which is too slow for applications involving the treatment of acute inflammatory diseases, and therefore strategies that can accelerate its hydrolysis kinetics are greatly needed.

In this report, we demonstrate that the hydrolysis kinetics of PCADK derived aliphatic polyketals can be accelerated by increasing their hydrophilic/hydrophobic balance. Using this principle, we were able to generate a polyketal copolymer, termed PK3, which had a hydrolysis half-life of 2 days at pH 4.5 but several weeks at pH 7.4. Microparticles formulated from PK3 should be suitable for treating acute inflammatory diseases because they should hydrolyze and release therapeutics rapidly in the phagolysosomes of macrophages, but remain stable at

* Corresponding author. Telephone 404-385-5145, fax 404-894-4243, e mail: niren.murthy@bme.gatech.edu.

[†] Georgia Institute of Technology.

[‡] University of Rochester.

[#] Present address: Department of Experimental Pathology and Pharmacology, Schering-Plough Biopharma, Palo Alto, CA 94304.

10.1021/bc700442g CCC: $40.75 © 2008 American Chemical Society
Published on Web 05/24/2008

Scheme 1. PK3, a New Biomaterial for Treating Acute Inflammatory Diseases[a]

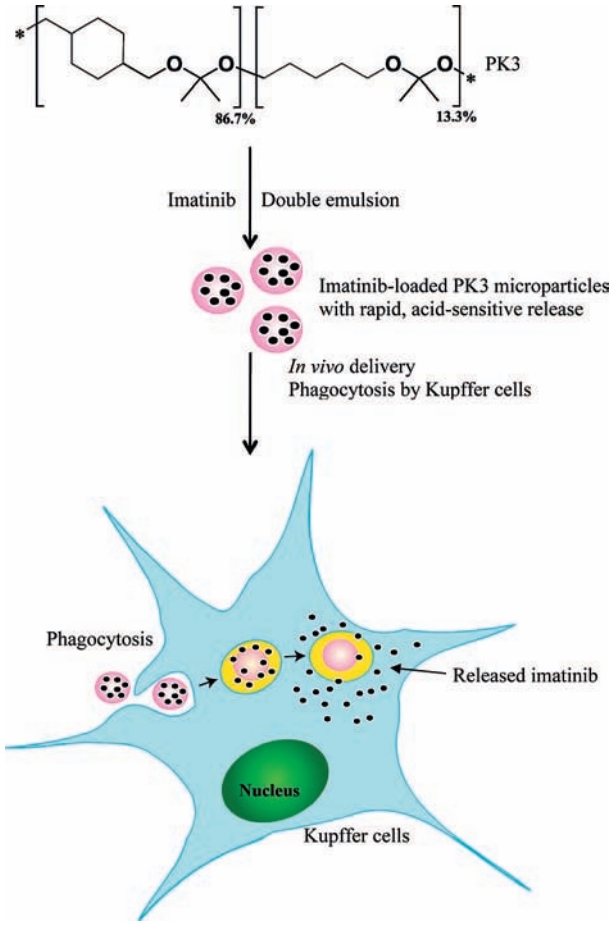

[a] PK3 is a new polyketal copolymer, which hydrolyzes rapidly at the acidic pH of the macrophage phagosome. PK3 is designed to deliver therapeutics to liver macrophages and enhance the treatment of acute liver failure. PK3 microparticles were capable of enhancing the delivery of imatinib in mice suffering from acute liver failure.

physiological pH. PK3 was used to generate microparticles 1−3 μm in size, which encapsulated the NF_KB inhibitor imatinib, using a solvent evaporation procedure. The therapeutic efficacy of these PK3-imatinib microparticles was investigated in mice, using a Concavalin A (Con A) model of acute liver failure (Scheme 1). The results from these experiments demonstrate that imatinib-loaded PK3 microparticles significantly enhanced the therapeutic efficacy of imatinib, presumably due to their accumulation in liver macrophages (Kupffer cells). Based on these results, we anticipate that aliphatic copolyketals will have numerous applications for the treatment of acute inflammatory diseases.

EXPERIMENTAL SECTION

Materials. All chemicals were purchased from Sigma-Aldrich (St. Louis, MO) and were used as received unless otherwise specified. Benzene and 2,2-dimethoxypropane were purified by distillation. Imatinib was a gift from Novartis.

Animals. Male C57/BL6 mice were purchased from Jackson Laboratory (Bar Harbor, ME). All animal experiments were approved by the Institutional Animal Care and Use Committee (IACUC) of the University of Rochester Medical Center.

Synthesis of Polyketal Copolymers. Polyketal copolymers were synthesized in a 25 mL two-necked flask, connected to a short-path distilling head. The diols, 1,4-cyclohexanedimethanol (1.04 g, 7.25 mmol) and 1,4-butanediol, 1,5-pentanediol, 1,6-hexanediol, or 1,8-octanediol, were dissolved in 20 mL of distilled benzene and kept at 100 °C. Recrystallized *p*-toluenesulfonic acid (5.5 mg, 0.029 mmol) was dissolved in ethyl acetate (500 μL) and added to the benzene solution. The ethyl acetate was distilled off, and the polymerization reaction was initiated by the addition of 2,2-dimethoxypropane (equimolar to the two diols combined). Additional doses of 2,2-dimethoxypropane (500 μL) and benzene (2 mL) were subsequently added to the reaction, every hour for six hours, via a metering funnel, to compensate for 2,2-dimethoxypropane and benzene that had distilled off. After 24 h, the reaction was stopped with triethylamine (100 μL). The copolymers were isolated by precipitation into cold hexanes and analyzed by ^{1}H NMR and GPC. In general, the resulting polymers had number average molecular weights between 2000 to 3000 Da. Table 1 lists the compositions and molecular weights of the polyketal copolymers synthesized. ^{1}H NMR spectra were obtained from a Varian Mercury VX 400 MHz NMR spectrometer (Palo Alto, CA) using $CDCl_3$ as the solvent. PK1 ^{1}H NMR (400 MHz, $CDCl_3$, δ): 3.4−3.18 (m, 4H, CH_2), 1.66 (s, 1.9H, CH), 1.85−0.93 (m, 8H, CH_2), and 1.32 (s, 6H, CH_3). PK2 ^{1}H NMR (400 MHz, $CDCl_3$, δ): 3.4−3.18 (m, 4H, CH_2), 1.66 (s, 1.8H, CH), 1.85−0.93 (m. 8H, CH_2), and 1.32 (s, 6H, CH_3). PK3 ^{1}H NMR (400 MHz, $CDCl_3$, δ): 3.4−3.18 (m, 4H, CH_2), 1.64 (s, 1.7H, CH), 1.85−0.93 (m, 8.2H, CH_2), and 1.32 (s, 6H, CH_3). PK4 ^{1}H NMR (400 MHz, $CDCl_3$, δ): 3.4−3.18 (m, 4H, CH_2), 1.68 (s, 2H, CH), 1.85−0.93 (m, 8H, CH_2), and 1.32 (s, 6H, CH_3). PK5 ^{1}H NMR (400 MHz, $CDCl_3$, δ): 3.4−3.18 (m, 4H, CH_2), 1.67 (s, 1.8H, CH), 1.85−0.93 (m, 8H, CH_2), and 1.32 (s, 6H, CH_3). PK6 ^{1}H NMR (400 MHz, $CDCl_3$, δ): 3.4−3.18 (m, 4H, CH_2), 1.68 (s, 1.8H, CH), 1.85−0.93 (m, 8H, CH_2), and 1.32 (s, 6H, CH_3).

Gel Permeation Chromatography. The molecular weights of the polyketal copolymers were determined by gel permeation chromatography (GPC) using a Shimadzu system (Kyoto, Japan) equipped with a UV detector. Tetrahydrofuran was used as the mobile phase at a flow rate of 1 mL/min. Polystyrene standards (peak M_w = 1060, 2970, and 10680) from Polymer Laboratories (Amherst, MA) were used to establish a molecular weight calibration curve.

Hydrolysis of Polyketal Copolymers. The hydrolysis of the polyketal copolymers was measured according to the procedures of Lee et al. (*13*). Briefly, polymer samples (20 mg) were placed in buffered water (1 mL) at the pH values of 4.5 (100 mM AcOH) and 7.4 (100 mM Na_2HPO_4) at 37 °C. The polymer samples were mixed by gentle shaking and, at specific time points, were extracted into $CDCl_3$ (1 mL). The $CDCl_3$ phase was isolated and analyzed by ^{1}H NMR, to determine the percent hydrolysis.

Release Kinetics of Rhodamine B from PK3 Microparticles. Rhodamine B was encapsulated in PK3 microparticles using single emulsion procedures. Rhodamine B-loaded PK3 microparticles (10 mg) were suspended in pH 4.5 and pH 7.4 buffer solutions (10 mL). The suspensions were kept at 37 °C under gentle shaking. At specific time points, the suspensions (100 μL) were centrifuged at 10 000*g* for 2 min to remove unhydrolyzed particles. The supernatant (3 μL) was then diluted in pH 7.4 buffer (3 mL), which was then analyzed by a Shimadzu spectrofluorophotometer (Kyoto, Japan) to quantify the relative concentration of rhodamine B released form the PK3 microparticles (excitation wavelength = 556 nm, emission wavelength = 573 nm).

Formulation of Imatinib-Loaded PK3 Microparticles. Imatinib-loaded microparticles were formulated from PK3 using a modified water/oil/water emulsion method. Briefly, PK3 (100 mg) was dissolved in dichloromethane (1 mL), and in a separate vial imatinib (40 mg) was dissolved in deionized water (400

Table 1. Compositions and Molecular Weight of Polyketal Copolymers Synthesized

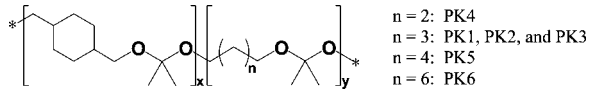

	polymer composition			
polymer ID	monomer diol A (*x*)	monomer diol B (*y*)	M_n	PDI[a]
PK1	1,4-cyclohexanedimethanol (98.03%)	1,5-pentanediol (1.93%)	2149	1.742
PK2	1,4-cyclohexanedimethanol (92.46%)	1,5-pentanediol (7.56%)	2530	1.629
PK3	1,4-cyclohexanedimethanol (86.70%)	1,5-pentanediol (13.30%)	2596	1.432
PK4	1,4-cyclohexanedimethanol (96.75%)	1,4-butanediol (3.25%)	2637	1.553
PK5	1,4-cyclohexanedimethanol (85.32%)	1,6-hexanediol (14.68%)	2122	1.538
PK6	1,4-cyclohexanedimethanol (87.31%)	1,8-octanediol (12.69%)	2181	1.786

[a] PDI: polydispersity index, calculated as the weight average molecular weight (M_w) divided by the number average molecular weight (M_n).

Table 2. Hydrolysis Half-Lives of Polyketal Copolymers at pH 4.5 and pH 7.4, at 37 °C

	polymer composition						
PK ID	diol A	percent diol A	diol B	percent diol B	half-life at pH 4.5	estimated half-life at pH 7.4	log *P* of diol B[a]
PK4	1,4-cyclohexane dimethanol	96.75%	1,4-butanediol	3.25%	1.0 day	54 days	−0.83
PK3		86.70%	1,5-pentanediol	13.30%	1.8 days	39 days	0.27
PK5		85.32%	1,6-hexanediol	14.68%	4.4 days	53 days	0.76
PK6		87.31%	1,8-octanediol	12.69%	18.6 days	360 days	1.75

[a] log *P* is the logarithm of the water/octanol partition coefficient; the log *P* data were obtained from the Syracuse Research Corporation's PhysProp Database.

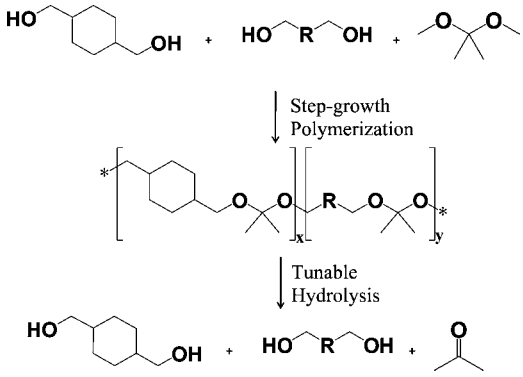

Figure 1. Synthesis of polyketal copolymers from 1,4-cyclohexanedimethanol, a second diol, and 2,2-dimethoxypropane. Hydrolysis kinetics of polyketals can be controlled by manipulating the hydrophilicity of the polyketals through copolymerizing 1,4-cyclohexandimethanol with a more hydrophilic diol.

μL). The aqueous solution of imatinib was mixed with the PK3 solution, and sonicated for 60 s (Misonix Incorporated, Farmigdale, NY). The sonicated mixture was then immersed in liquid nitrogen for 15 s, and a 5% w/w PVA solution (pH 7.45, 12 mL) was added to it. This mixture was homogenized for 120 s with a Powergen 500 homogenizer (Fisher Scientific, Waltham, MA), and then transferred to a beaker containing 1% w/w PVA (pH 7.4, 40 mL). This solution was stirred for 3 h with a magnetic stir bar to evaporate the organic solvent. The particles were isolated by centrifuging at 10 000*g* for 15 min, washed twice with PBS buffer (15 mL), and freeze-dried.

Scanning Electron Microscopy (SEM). SEM images were taken to analyze the morphology of the polyketal microparticles. Briefly, SEM samples were prepared by attaching lyophilized particles onto 12.7 mm diameter aluminum sample mounting stubs (Electron Microscopy Sciences, Hatifield, PA), using conductive double-sided carbon discs (SPI Supplies, West Chester, PA). The samples were coated with a gold sputter coater (International Scientific Instruments, Prahran, Australia) for 2 min under an argon atmosphere. The SEM samples were subsequently analyzed using a Hitachi S-800 scanning electron microscope (Tokyo, Japan).

Determination of Imatinib Loading in PK3 Microparticles. The loading of imatinib in PK3 microparticles was determined by UV spectrometry. A UV calibration curve for imatinib was established at 268 nm, with a Shimadzu UV-1700 spectrometer (Kyoto, Japan) in pH 7.4 buffer. Imatinib-loaded PK3 particles were dissolved in a small amount of methylene chloride, and the imatinib was extracted into pH 7.4 buffer (100 mM Na_2HPO_4). The absorbance of both the aqueous and organic phases was measured to verify that all the imatinib was partitioned into the aqueous phase. The concentration of imatinib loaded into the PK3 microparticles was determined against the established calibration curve as mentioned above.

Treatment of Acute Liver Failure in Mice with Imatinib-Loaded PK3 Microparticles. Male C57/BL6 mice, 6−8 weeks old, were used in these studies. Appropriate doses of imatinib-PK3 particles (containing between 5 μg/kg to 500 μg/kg of imatinib), or an equal quantity of free imatinib, was suspended/dissolved in PBS (200 μL) and was injected intravenously using a 26 G5/8 sterilized needle. One hour later, Con A (15 mg/kg), dissolved in PBS (200 μL), was injected into the intraperitoneal cavity using a 26 G5/8 sterilized needle. Between 4 and 8 mice were used per experimental group. The mice were euthanized 8 h after the Con A injection, by cervical dislocation. Blood was then withdrawn from the heart using a 26 G5/8 sterilized needle, and kept at 4 °C overnight. The serum was isolated by centrifuging at 600*g* for 10 min and sent to the core facility at the University of Rochester for measurement of ALT levels.

RESULTS AND DISCUSSION

There is currently great interest in developing microparticle-based delivery vehicles that have the biocompatibility and hydrolysis kinetics needed to treat acute inflammatory diseases. Microparticles formulated from the aliphatic polyketal PCADK have excellent biocompatibility and degrade under the acidic conditions of the phagolysosome. However, the slow hydrolysis kinetics of PCADK make it unsuitable for treating acute inflammatory diseases, and therefore strategies for accelerating its hydrolysis kinetics are greatly needed. We previously hypothesized that the slow hydrolysis kinetics of PCADK was due to its hydrophobicity, making the diffusion of water into the polymer matrix the rate-limiting step in ketal hydrolysis (*13*). This hypothesis was based on the fact that the hydrolysis half-

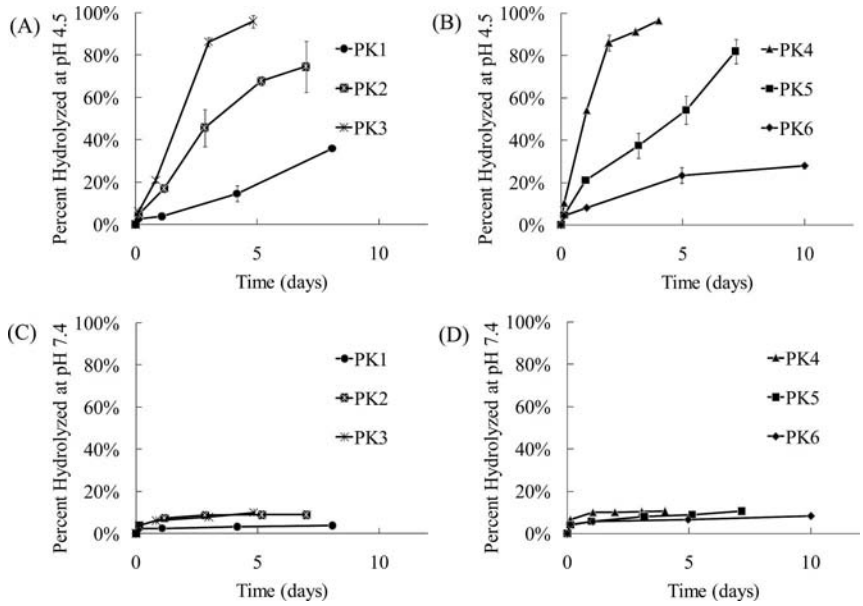

Figure 2. Hydrolysis kinetics of polyketals can be tuned by copolymerization. (A) Hydrolysis profiles of PK1, PK2, and PK3 at pH 4.5; (B) hydrolysis profiles of PK4, PK5, and PK6 at pH 4.5; (C) hydrolysis profiles of PK1, PK2, and PK3 at pH 7.4; and (D) hydrolysis profiles of PK4, PK5, and PK6 at pH 7.4. Data are presented as mean ± standard deviation. All experiments were conducted in triplicate at 37 °C.

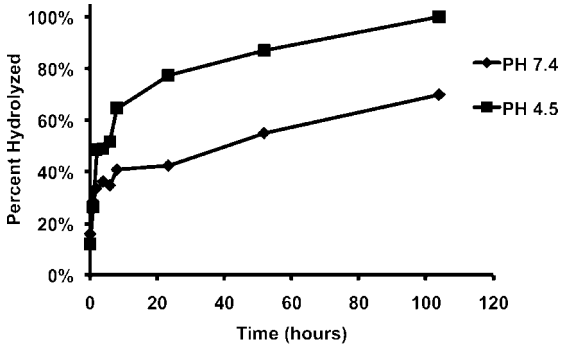

Figure 3. Release kinetics of rhodamine B encapsulated in PK3 microparticles.

life of a water-soluble dimethylacetone-based ketal is only 2 min at pH 5.0, which is 3 to 4 orders of magnitude faster than the hydrolysis of the ketal linkages in PCADK (*14*). Additionally, the hydrolysis kinetics of other water-insoluble polymers, such as polyanhydrides, also scale with their hydrophobicity (*10*). In this report, the role of hydrophobicity in governing the hydrolysis kinetics of polyketals was investigated. This was accomplished by synthesizing polyketal copolymers of varying hydrophobicity and measuring their hydrolysis kinetics.

Six polyketal copolymers were synthesized in this report (PK1−PK6, Table 1), by copolymerizing 1,4-cyclohexanedimethanol with 1,4-butanediol, 1,5-pentanediol, 1,6-hexanediol, or 1,8-octanediol. The hydrophobicity of these diols is different from that of 1,4-cyclohexanedimethanol (log $P = 1.46$, where $P =$ water/octanol partition coefficient), as evidenced by their respective log P values (Table 2). The synthesis of all the polyketal copolymers reported in this study was accomplished using the acetal exchange reaction, and was performed on a multigram scale with yields of 50−60% (Figure 1). In general, the introduction of additional diols other than 1,4-cyclohexanedimethanol did not cause any synthetic complications, and procedures developed for the synthesis of PCADK were suitable for the synthesis of all the copolymers. Importantly, all the polyketal copolymers reported in Table 1 were solid, and therefore have the potential for formulation into microparticles.

The hydrolysis kinetics of PK1 to PK6 were measured at the pH values of 4.5 and 7.4 to determine their behavior in the acidic environment of phagolysosomes and in the blood. Figure 2 demonstrates that all the polyketal copolymers (PK1−PK6) undergo acid-catalyzed hydrolysis, and that their hydrolysis kinetics scale with their hydrophilicity. PK1, PK2, and PK3 are copolymers synthesized from 1,4-cyclohexanedimethanol and 1,5-pentanediol. Their hydrophilicity scales with the amount of 1,5-pentanediol incorporated into the copolymer. This is due to the large difference in hydrophilicity between 1,5-pentanediol and 1,4-cyclohexanedimethanol, as evidenced by their respective log P values of 0.27 and 1.46. Figure 2A demonstrates that 1,5-pentanediol significantly accelerates the pH 4.5 hydrolysis kinetics of 1,4-cyclohexanedimethanol-based polyketals. For example, the hydrolysis half-life of PCADK, a homopolyketal synthesized from 1,4-cyclohexanedimethanol, is 24 days at pH 4.5 (*13*). On the other hand, PK3, a copolymer that incorporates 13 mol % 1,5-pentanediol and 87 mol % 1,4-cyclohexanedimethanol, had a hydrolysis half-life of only 2 days at pH 4.5. Similarly, PK2, another PCADK-derived copolymer, incorporating 7.5 mol % of 1,5-pentanediol, had a hydrolysis half-life of 3 days at pH 4.5, which is faster than PCADK but slower than PK3. PK1, the third copolymer derived from PCADK, incorporating 2 mol % 1,5-pentanediol, was only 30% hydrolyzed after 10 days at pH 4.5, which was expected based on its low incorporation of 1,5-pentanediol[1].

To determine if diols other than 1,5-pentanediol could similarly influence the hydrolysis kinetics of PCADK-derived copolymers, the hydrolysis kinetics of PK4, PK5, and PK6 were also investigated. These polyketals are PCADK-derived copolymers synthesized from 1,4-cyclohexanedimethanol and either 1,4-butanediol, 1,6-hexanediol, or 1,8-octanediol. Figure 2B,D and Table 2 demonstrate that this set of copolymers also has an inverse relationship between hydrophobicity and hydrolysis kinetics. For example, PK4, a copolymer synthesized from 1,4-cyclohexanedimethanol and 1,4-butanediol, has the

[1] Similar copolymers with higher incorporation of 1,5-pentanediol were also generated; however, those copolymers were viscous liquids, which are not suitable for formulation into microparticles for drug delivery. Therefore, we only focused our hydrolysis analysis on the solid polyketal copolymers, PK1, PK2, and PK3.

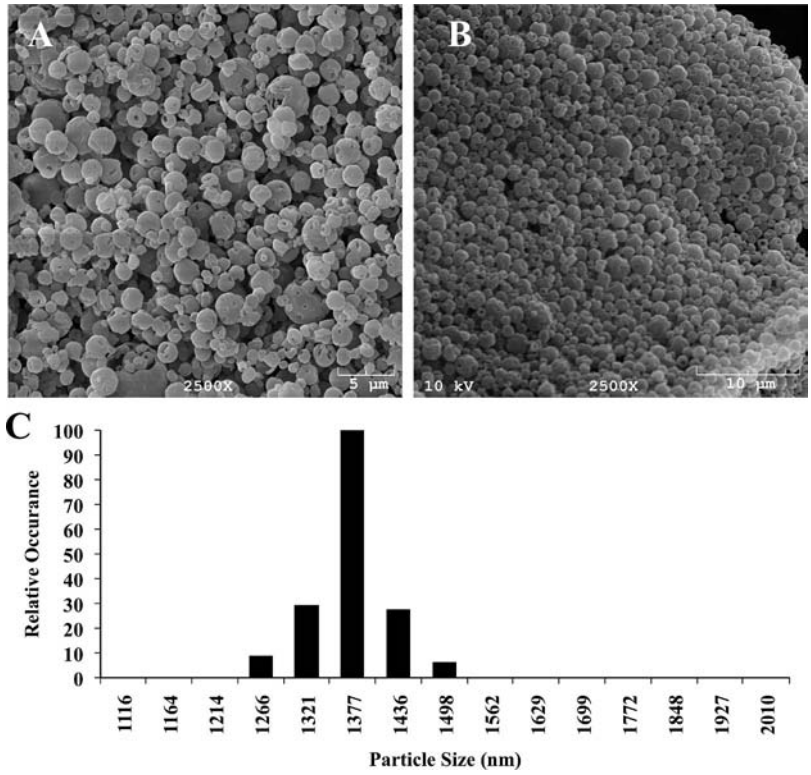

Figure 4. SEM images of particles formulated with PK3. (A) SEM image of empty particles formulated via double emulsion. (B) SEM images of imatinib-loaded PK3 microparticles formulated via double emulsion. (C) Size distribution of imatinib-loaded PK3 microparticles as determined by dynamic light scattering (DLS).

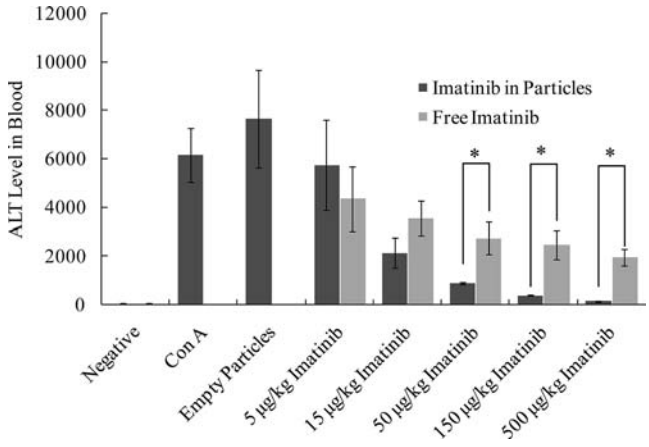

Figure 5. PK3 microparticles improve the efficacy of imatinib in treating acute liver failure in mice. Mice were injected intravenously with either imatinib or imatinib in PK3 microparticles, acute liver failure was then induced by intraperitoneal injection of Con A (15 mg/kg). Eight hours later, ALT levels in the blood were analyzed. * indicates statistical significance (Student's t test, $P > 0.05$, $n = 4$ to 8).

fastest hydrolysis kinetics of all the copolyketals, with a hydrolysis half-life of 1 day at pH 4.5. This is predicted based on the more hydrophilic nature of 1,4-butanediol in comparison to the other diols. On the other hand, PK6, a copolymer composed of 1,4-cyclohexanedimethanol and 1,8-octanediol, had a pH 4.5 hydrolysis half-life of 18.6 days. In summary, these data demonstrate that the hydrolysis kinetics of polyketals can be tuned by varying their hydrophilicity and further support the hypothesis that diffusion of water into the polyketals is the rate-determining step governing their hydrolysis. Importantly, the hydrolysis kinetics of all the polyketal copolymers, PK 1−6, were pH-sensitive; in general, they hydrolyzed at least 1 order of magnitude faster at pH 4.5 than at pH 7.4.

We chose PK3 for further investigation as a drug carrier for the treatment of acute inflammatory diseases because of its suitable hydrolysis kinetics and biocompatible degradation products. The copolymer PK4 has faster hydrolysis kinetics than PK3; however, it degrades into 1,4-butanediol, which is converted into γ-hydroxybutyrate *in vivo*, and subsequently causes toxicity to the central nervous system (*15*). Microparticles were formulated from PK3, using a solvent evaporation procedure. Figure 4A demonstrates that the size range of PK3 microparticles is between 1 and 5 μm, which is suitable for phagocytosis by macrophages.

In order to determine whether or not PK3 microparticles would have suitable drug-release kinetics for treating acute inflammatory diseases, a release study was conducted on PK3 microparticles which encapsulated the fluorescent dye, rhodamine B. Figure 3 demonstrates that the release half-life of rhodamine B from PK3 microparticles is approximately 6 h at pH 4.5 and 40 h at pH 7.4, which is suitable for treating acute liver failure. The drug-release kinetics of PK3 microparticles is 20 times faster than that of PCADK microparticles, which had a release half-life of 5 days at pH 4.5 and over 15 days at pH 7.4 (data not shown).

PK3 microparticles were used to enhance the delivery of imatinib in treating acute liver failure. Imatinib is a kinase inhibitor that inhibits NF-κB activation and has great potential for treating acute inflammatory diseases (*16, 17*). The activation of NF-κB in macrophages leads to the production of cytokines and reactive oxygen species, the central causes of tissue damage during acute inflammatory diseases. Although imatinib has shown promise for treating acute inflammatory diseases in mouse models, there are also numerous side effects associated with imatinib, including heart failure and hepatic toxicity (*18, 19*). PK3 microparticles should enhance the efficacy of imatinib by targeting it to macrophages, thereby increasing its concentration at the target site, and also by reducing the toxic side effects of

imatinib on the heart and liver. Imatinib was encapsulated into PK3 microparticles through double emulsion procedures. These macroparticles were approximately 1.5 μm in size on average, as determined by SEM and DLS, which is suitable for delivering drugs to phagocytic cells such as Kupffer cells (Figure 4B,C). The loading of imatinib in PK3 microparticles was determined to be 0.90 $\pm$ 0.10 μg imatinib per 1 mg of particles ($n = 3$), suggesting that the encapsulation efficiency of imatinib in PK3 microparticles was approximately 0.32%.

The ability of PK3 microparticles to enhance the delivery of imatinib was investigated in mice suffering from Con A-induced acute liver failure. Mice were injected with either imatinib in solution (0.1 μg to 10 μg of imatinib dissolved in 200 μL of saline) or an equivalent amount of imatinib loaded in PK3 microparticles (0.11 mg to 11 mg of imatinib-loaded PK3 microparticles suspended in 200 μL of saline). Acute liver failure was subsequently induced by an intraperitoneal injection of Con A. The severity of liver injury in these mice was determined by measuring the alanine aminotransaminase (ALT) level in their blood, which is a clinical surrogate marker for hepatocyte injury. Figure 5 demonstrates that PK3 microparticles enhanced the treatment efficacy of imatinib in preventing Con A-induced liver damage. For example, a dose of 500 μg/kg of free imatinib resulted in an ALT value of approximately 2000 U, whereas 500 μg/kg of imatinib encapsulated in PK3 microparticles reduced the ALT values to baseline levels of only 50 U. The therapeutic efficacy of 15 μg/kg of imatinib loaded in PK3 microparticles was similar to that of 500 μg/kg of free imatinib. These experiments demonstrate that imatinib-loaded PK3 microparticles significantly enhanced the therapeutic efficacy of imatinib, presumably due to their accumulation in liver macrophages. No noticeable toxicity was observed by injection of empty PK3 microparticles (11 mg suspended in 200 μL of saline), as shown in Figure 5.

CONCLUSIONS

In this report, we demonstrate that the hydrolysis rates of polyketals can be tuned by varying their hydrophilicity. Using this strategy, an aliphatic polyketal copolymer, PK3, was identified, which had a hydrolysis half-life of 2 days at pH 4.5, but was stable for several weeks at pH 7.4. Microparticles were formulated from PK3, which encapsulated the kinase inhibitor, imatinib, and these PK3 microparticles significantly improved the efficacy of imatinib in treating Con A-induced liver damage *in vivo*. Based on these findings, we anticipate numerous applications of copolymers of polyketals for treating acute inflammatory diseases, given their pH sensitivity, rapid and tunable hydrolysis kinetics, and biocompatible degradation products.

ACKNOWLEDGMENT

This work was funded in part by the Georgia Tech/Emory Center for the Engineering of Living Tissues (funded by NSF-EEC-9731643), NSF-BES-0546962 CAREER AWARD, NIH UO1 HL80711-01, NIH R21 EB006418, R01AI064463, and J&J/GT Health Care Innovation Seed Grant Proposal. S. C. Yang is supported by an NSF IGERT Fellowship.

LITERATURE CITED

(1) Angus, D. C., Linde-Zwirble, W. T., Lidicker, J., Clermont, G., Carcillo, J., and Pinsky, M. R. (2001) Epidemiology of severe sepsis in the United States: Analysis of incidence, outcome, and associated costs of care. *Crit. Care Med. 29*, 1303–1310.

(2) Hudson, L. D., and Steinberg, K. P. (1999) Epidemiology of acute lung injury and ARDS. *Chest 116*, 74S–a-82.

(3) Goodman, R. B., Pugin, J., Lee, J. S., and Matthay, M. A. (2003) Cytokine-mediated inflammation in acute lung injury. *Cytokine Growth Factor Rev. 14*, 523–535.

(4) O'Grady, J. G., and Schalm, S. W. (1993) Acute liver failure: Redefining the syndromes. *Lancet 342*, 273.

(5) Higuchi, Y., Kawakami, S., Yamashita, F., and Hashida, M. (2007) The potential role of fucosylated cationic liposome/NFκB decoy complexes in the treatment of cytokine-related liver disease. *Biomaterials 28*, 532–539.

(6) Wullaert, A., van Loo, G., Heyninck, K., and BeyaertR. (2007) Hepatic tumor necrosis factor signaling and nuclear factor-κB: Effects on liver homeostasis and beyond. *Endocr. Rev. 2006*, 0031.

(7) Zender, L., Hutker, S., Liedtke, C., Tillmann, H. L., Zender, S., Mundt, B., Waltemathe, M., Gosling, T., Flemming, P., Malek, N. P., Trautwein, C., Manns, M. P., Kuhnel, F., and Kubicka, S. (2003) Caspase 8 small interfering RNA prevents acute liver failure in mice. *Proc. Natl. Acad. Sci. U.S.A. 100*, 7797–7802.

(8) Anderson, J. M., and Shive, M. S. (1997) Biodegradation and biocompatibility of PLA and PLGA microspheres. *Adv. Drug Delivery Rev. 28*, 5.

(9) Fu, K., Pack, D. W., Klibanov, A. M., and Langer, R. (2000) Visual evidence of acidic environment within degrading poly-(lactic-co-glycolic acid) (PLGA) microspheres. *Pharm. Res. 17*, 100.

(10) Gopferich, A., and Tessmar, J. (2002) Polyanhydride degradation and erosion. *Adv. Drug Delivery Rev. 54*, 911.

(11) Kumar, N., Langer, R. S., and Domb, A. J. (2002) Polyanhydrides: an overview. *Adv. Drug Delivery Rev. 54*, 889.

(12) Heffernan, M. J., and Murthy, N. (2005) Polyketal nanoparticles: a new pH-sensitive biodegradable drug delivery vehicle. *Bioconjugate Chem. 16*, 1340.

(13) Lee, S., Yang, S. C., Heffernan, M. J., Taylor, W. R., and Murthy, N. (2007) Polyketal microparticles: a new delivery vehicle for superoxide dismutase. *Bioconjugate Chem. 18*, 4–7.

(14) Kwon, Y. J., Standley, S. M., Goodwin, A. P., Gillies, E. R., and Frechet, J. M. J. (2005) Directed antigen presentation using polymeric microparticulate carriers degradable at lysosomal pH for controlled immune responses. *Mol. Pharmaceutics 2*, 83–91.

(15) Zvosec, D. L., Smith, S. W., McCutcheon, J. R., Spillane, J., Hall, B. J., and Peacock, E. A. (2001) Adverse events, including death, associated with the use of 1,4-butanediol. *N. Engl. J. Med. 344*, 87–94.

(16) Deininger, M. W. N., and Druker, B. J. (2003) Specific targeted therapy of chronic myelogenous leukemia with imatinib. *Pharmacol. Rev. 55*, 401–423.

(17) Wolf, A. M., Wolf, D., Rumpold, H., Ludwiczek, S., Enrich, B., Gastl, G., Weiss, G., and Tilg, H. (2005) The kinase inhibitor imatinib mesylate inhibits TNF-α production in vitro and prevents TNF-dependent acute hepatic inflammation. *Proc. Natl. Acad. Sci. U.S.A. 102*, 13622–13627.

(18) Kerkela, R., Grazette, L., Yacobi, R., Iliescu, C., Patten, R., Beahm, C., Walters, B., Shevtsov, S., Pesant, S., Clubb, F. J., Rosenzweig, A., Salomon, R. N., Van Etten, R. A., Alroy, J., Durand, J.-B., and Force, T. (2006) Cardiotoxicity of the cancer therapeutic agent imatinib mesylate. *Nat. Med. 12*, 908–916.

(19) Yeon Hee, P., Hae Jeong, P., Bong-Seog, K., Eunyoung, H., Kyung Hee, J., Seo Hyun, Y., Sung Vin, Y., and Joo-Ho, C. (2006) BNP as a marker of the heart failure in the treatment of imatinib mesylate. *Cancer Lett. 243*, 16–22.

BC700442G

^{99m}Tc-Labeled Bombesin(7−14)NH_2 with Favorable Properties for SPECT Imaging of Colon Cancer

Jiyun Shi,[†] Bing Jia,[†] Zhaofei Liu,[†] Zhi Yang,[‡] Zilin Yu,[†] Kai Chen,[§] Xiaoyuan Chen,[§] Shuang Liu,*[,||] and Fan Wang*[,†]

Medical Isotopes Research Center, Peking University, Beijing 100083, China, Department of Nuclear Medicine, Peking University Oncology School, Beijing 100036, China, Molecular Imaging Program at Stanford (MIPS), Department of Radiology, Stanford University School of Medicine, California 94305, and School of Health Sciences, Purdue University, Indiana 47907.
Received December 18, 2007; Revised Manuscript Received April 5, 2008

In this report, we present the synthesis and evaluation of the ^{99m}Tc-labeled β-Ala-BN(7−14)NH_2 (ABN = β-Ala-Gln-Trp-Ala-Val-Gly-His-Leu-Met-NH_2) as a new radiotracer for tumor imaging in the BALB/c nude mice bearing HT-29 human colon cancer xenografts. The gastrin releasing peptide receptor binding affinity of ABN and HYNIC-ABN (6-hydrazinonicotinamide) was assessed via a competitive displacement of ^{125}I-[Tyr4]BBN bound to the PC-3 human prostate carcinoma cells. The IC_{50} values were calculated to be 24 ± 2 nM and 38 ± 1 nM for ABN and HYNIC-ABN, respectively. HYNIC is the bifunctional coupling agent for ^{99m}Tc-labeling, while tricine and TPPTS (trisodium triphenylphosphine-3,3′,3″-trisulfonate) are used as coligands to prepare the ternary ligand complex [^{99m}Tc(HYNIC-ABN)(tricine)(TPPTS)] in very high yield and high specific activity. Because of its high hydrophilicity (log $P = -2.39 \pm 0.06$), [^{99m}Tc(HYNIC-ABN)(tricine)(TPPS)] was excreted mainly through the renal route with little radioactivity accumulation in the liver, lungs, stomach, and gastrointestinal tract. The tumor uptake at 30 min postinjection (p.i.) was 1.59 ± 0.23%ID/g with a steady tumor washout over the 4 h study period. As a result, it had the best *T*/*B* ratios in the blood (2.37 ± 0.68), liver (1.69 ± 0.41), and muscle (11.17 ± 3.32) at 1 h p.i. Most of the injected radioactivity was found in the urine sample at 1 h p.i., and there was no intact [^{99m}Tc(HYNIC-ABN)(tricine)(TPPTS)] detectable in the urine, kidney, and liver samples. Its metabolic instability may contribute to its rapid clearance from the liver, lungs, and stomach. Despite the steady radioactivity washout, the tumors could be clearly visualized in planar images of the BALB/c nude mice bearing the HT-29 human colon xenografts at 1 and 4 h p.i. The favorable excretion kinetics from the liver, lungs, stomach, and gastrointestinal tract makes [^{99m}Tc(HYNIC-ABN)(tricine)(TPPTS)] a promising SPECT radiotracer for imaging colon cancer.

INTRODUCTION

Colon cancer is the second leading cause of cancer-related deaths. It is estimated that about 130 000 men and women will develop colon cancer and more than 50 000 will die from it each year in the United States (American Cancer Society: http://www.cancer.org). The lifetime risk for individuals to develop colon cancer is ∼6%, but it may increase to 18% among individuals who have a relative (parent, sibling, or child) with colon cancer. Therefore, accurate early detection is highly desirable so that various therapeutic regimens can be given before the primary tumors become widespread.

Bombesin (BN) is a small peptide containing 14 amino acids (Glu-Gln-Arg-Leu-Gly-Asn-Gln-Trp-Ala-Val-Gly-His-Leu-Met-NH_2). It was originally isolated from the skin of amphibian *Bombina orientalis* (*1*, *2*). The BN-like peptides have very high binding affinity for the gastrin-releasing peptide (GRP) receptor (*3*–*5*), and produce a wide range of biological responses in peripheral tissues as well as in the central nervous system, including stimulation of gastrointestinal hormone release, exocrine secretion, and maintenance of circadian rhythms. In addition, it has been established that the GRP/BN peptides promote proliferation in cancer cells. The overexpression of GRP receptor (GRPR) has been demonstrated in a large number of tumors, including prostate, breast, colon, and small cell lung cancer (*6*–*13*). The distribution of BN-like peptides and the expression of their receptors have been reviewed (*3*, *4*). Because of its highly restricted overexpression on tumor cells, the GRPR is emerging as an attractive target for both cancer therapy and early detection (*3*, *4*, *14*–*17*).

BN(7−14)NH_2 is the peptide sequence responsible for specific binding of the GRPRs overexpressed on tumor cells. Most of the radiolabeled BN-like peptides are based on or contain the BN(7−14)NH_2 peptide sequence. These radiolabeled BN-like peptides were designed as tumor-specific radiotracers for early diagnosis or systemic radiotherapy of the GRPR-positive tumors, and have been reviewed extensively (*14*–*17*). The radionuclides include ^{111}In (*18*–*20*), ^{177}Lu (*21*–*23*), ^{68}Ga (*24*), ^{64}Cu (*25*–*32*), ^{188}Re (*33*), and ^{99m}Tc (*34*–*47*). While ^{68}Ga and ^{64}Cu are particularly useful for imaging tumors by positron emission tomography (PET), ^{99m}Tc is the radionuclide of choice for tumor imaging by single photon computed tomography (SPECT) due to its excellent nuclear properties ($t_{1/2}$ = 6 h and single photon emission at 140 keV), rich and diverse coordination chemistry, easy availability at low cost, and high specific activity (*48*–*50*).

* To whom correspondence should be addressed. Dr. Shuang Liu, School of Health Sciences, Purdue University, 550 Stadium Mall Drive, West Lafayette, IN 47907. Phone: 765-494-0236, Fax: 765-496-3367, Email: lius@pharmacy.purdue.edu; or Dr. Fan Wang, Medical Isotopes Research Center, Peking University, 38# Xueyuan Road, Beijing 100083, China. Phone and Fax: 86-10-82801145, Email: wangfan@bjmu.edu.cn.

[†] Peking University.

[‡] Peking University Oncology School.

[§] Stanford University School of Medicine.

[||] Purdue University.

10.1021/bc700471z CCC: $40.75 © 2008 American Chemical Society
Published on Web 05/21/2008

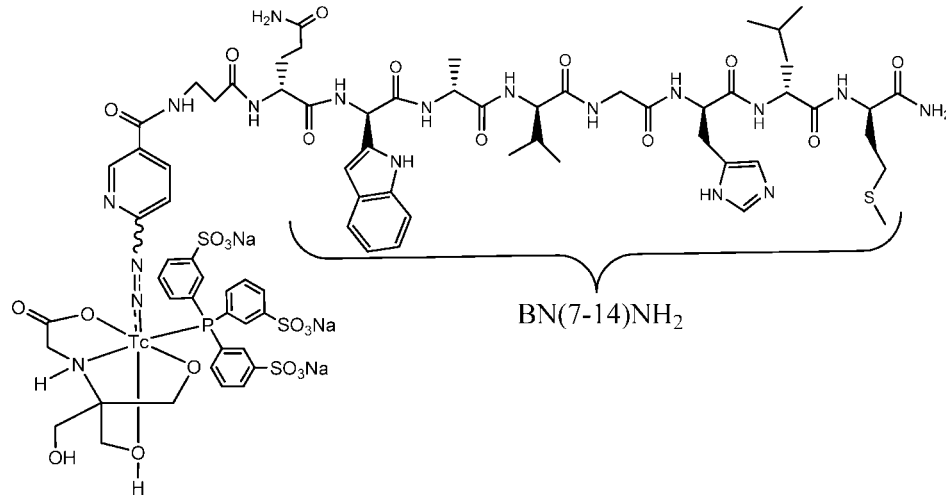

Figure 1. Structure of the ternary ligand complex [^{99m}Tc(HYNIC-ABN)(tricine)(TPPTS)].

In this study, we used β-Ala-BN(7−14)NH_2 (Figure 1: ABN in short) as the biomolecule for tumor targeting and 6-hydrazinonicotinic acid (HYNIC) as the bifunctional coupling agent (BFC) for the ^{99m}Tc-labeling. Since HYNIC is monodentate in the ^{99m}Tc-HYNIC core, tricine and TPPTS (trisodium triphenylphosphine-3,3′,3″-trisulfonate) are used as coligands to prepare the complex [^{99m}Tc(HYNIC-ABN)(tricine)(TPPTS)] (Figure 1). This ternary ligand system (HYNIC, tricine, and TPPTS) has been successfully used for the ^{99m}Tc-labeling of small biomolecules, including chemotactic peptides (*51*) and LTB_4 receptor antagonists (*52, 53*) for imaging infection and inflammation, integrin $\alpha_v\beta_3$ antagonists for imaging tumor angiogenesis (*54–58*), and GPIIb/IIIa receptor antagonists for imaging deep vein thrombosis (*59*). The BALB/c nude mice bearing HT-29 human colon cancer xenografts were used for both biodistribution and imaging studies. Normal BALB/c nude mice were used for metabolism study. The main objective is to evaluate [^{99m}Tc(HYNIC-ABN)(tricine)(TPPTS)] as a potential new radiotracer for SPECT imaging of colon cancer.

EXPERIMENTAL SECTION

Materials. Tricine and TPPTS were purchased from Sigma/Aldrich (St. Louis, MO), and were used without further purification. The peptide conjugate, HYNIC-β-Ala-BN(7−14)NH_2 (HYNIC-ABN), was obtained from CS Bio Co. (Menlo Park, CA). Na$^{99m}TcO_4$ was obtained from a commercial ^{99}Mo/^{99m}Tc generator **(**Beijing Atom High Tech Co. Ltd., Beijing, China). ^{125}I-[Tyr4]BBN was obtained from Perkin-Elmer Life and Analytical Sciences (North Billarica, MA).

Methods. The radio-HPLC method used a HP Hewlett Packard Series 1100 HPLC system equipped with a Radioflow Detector LB509 and a reversed-phase Zorbax SB-C18 column (4.6 mm × 250 mm, 5 μm). The flow rate was 1.0 mL/min. The mobile phase was isocratic with 90% solvent A (0.01 M phosphate buffer, pH = 6.0) and 10% solvent B (acetonitrile) at 0−5 min, followed by a gradient mobile phase going from 10% solvent B at 5 min to 50% solvent B at 20 min, then to 80% solvent B at 22 min, and back to baseline 10% solvent B at 25 min. The ITLC method used Gelman Sciences silica-gel paper strips and a 1:1 mixture of acetone and saline as eluant. The ^{99m}Tc complexes migrated to the solvent front while $^{99m}TcO_4^-$ and [^{99m}Tc]colloid remained at origin.

Synthesis of [^{99m}Tc(HYNIC-ABN)(tricine)(TPPTS)]. To a clean 5 cc vial were added 100 μL of the HYNIC-ABN solution (100 μg/mL in H_2O), 100 μL of tricine solution (100 mg/mL in 25 mM succinate buffer, pH 5.0), 20 μL of $SnCl_2$ solution (3.0 mg/mL in 0.1 N HCl), and 100 μL of Na$^{99m}TcO_4$ (370 MBq) in saline. The reaction mixture was kept at room temperature for 10 min. To the reaction mixture above was added 120 μL of the TPPTS solution (50 mg/mL in 25 mM succinate buffer, pH 5.0). The vial containing the reaction mixture was sealed, cramped, and heated at 100 °C for 30 min. After cooling to room temperature, a sample of the resulting solution was analyzed by ITLC and radio-HPLC.

Dose Preparation for Animal Studies. [^{99m}Tc(HYNIC-ABN)(tricine)(TPPTS)] was purified using a Sep-Pak C-18 cartridge (Waters, MA) before being used for animal studies. The Sep-Pak C-18 cartridge was activated with ethanol (10 mL) and was washed with water (10 mL). After the radiotracer was loaded, the Sep-Pak C-18 cartridge was washed with saline (10 mL) to remove the unlabeled ^{99m}Tc and excess coligands. The radiotracer was eluted with 80% ethanol (0.4 mL). Doses for animal studies were prepared by dissolving the Sep-Pak purified radiotracer in saline to give a concentration of 150 μCi/mL for biodistribution study, 4.0 mCi/mL for the metabolism study, and 2.0 mCi/mL for the planar imaging study.

Partition Coefficient. The partition coefficient was determined using the following procedure: [^{99m}Tc(HYNIC-ABN)-(tricine)(TPPTS)] was prepared and purified using the Sep-Pak C-18 cartridge. Volatiles in the mobile phase were completely removed under vacuum. The residue was dissolved in a mixture of equal volume (0.5 mL/0.5 mL) *n*-octanol and 25 mM phosphate buffer (pH = 7.4). After vortexing for 2 min, samples in triplicate were obtained from *n*-octanol and aqueous layers and were counted in a γ-counter (Wallac 1470−002, Perkin-Elmer, Finland). The log *P* value is reported as an average of three different measurements.

***In Vitro* Cell-Binding Assay.** *In vitro* GRPR binding affinity and specificity of ABN and HYNIC-ABN were assessed via a competitive displacement assay with ^{125}I-[Tyr4]BBN as the radioligand. Experiments were performed using the GRPR-positive PC-3 prostate carcinoma cells according to the literature method (*32*). The 50% inhibitory concentration (IC_{50}) values were calculated by fitting the data with nonlinear regression using *GraphPad Prism 4.0* (GraphPad Software, San Diego, CA). Experiments were performed twice with triplicate samples. IC_{50} values are reported as an average of these samples plus the standard deviation.

Internalization Kinetics. The internalization assay was performed according to the literature method (*37, 47*) with slight modification. Briefly, the HT-29 cells were incubated in the 24-well plates in quadruplicate with [^{99m}Tc(HYNIC-ABN)(tricine)(TPPTS)] (∼0.1 μCi/well) for 2 h at 4 °C, and then were washed with ice-cold PBS to remove the unbound radioactivity.

After washing, the cells were incubated in the prewarmed culture medium at 37 °C for 0, 5, 15, 30, 60, and 120 min for internalization. The cell-surface bound radiotracer was removed by acid wash (50 mM glycine−HCl/100 mM NaCl, pH 2.8). Subsequently, the cells were solubilized by incubation with 2 M NaOH at 37 °C, and the resulting solution in each well was harvested to determine the internalized radioactivity in a γ-counter (Wallac 1470−002, Perkin-Elmer, Finland). The results were expressed as a percentage of the total radioactivity (surface-bound plus internalized). The same experiment was performed twice with quadruplicate samples.

Efflux Kinetics. The HT-29 cells cultured in 24-well plates were incubated at 37 °C with [^{99m}Tc(HYNIC-ABN)(tricine)-(TPPTS)] (~0.1 μCi/well) for 1 h to allow maximal internalization. The cells were washed three times with ice-cold PBS to remove the unbound radioactivity, then were incubated in the prewarmed culture medium at 37 °C for a specific period of time (0, 15, 30, 60, 120, and 240 min). At the specified time point, the cell-surface bound radioactivity was removed by acid wash (50 mM glycine−HCl/100 mM NaCl, pH 2.8). Subsequently, the cells were solubilized by incubation with 2 M NaOH at 37 °C, and the resulting solution in each well was harvested to determine the internalized radioactivity in a γ-counter (Wallac 1470−002, Perkin-Elmer, Finland). Data are expressed as the percentage of maximal intracellular radioactivity. The same experiment was performed twice with quadruplicate samples.

Animal Model. All animal experiments were performed in accordance with guidelines of Peking University Health Science Center Animal Care and Use Committee. The HT-29 human colon cancer cells were obtained from Professor Xiaoyan Qiu, Peking University Health Science Center, and were maintained at 37 °C and 5% CO_2 in Dulbecco's modified Eagle's medium (DMEM) containing 10% fetal bovine serum (FBS). Female BALB/c nude mice (4−5 weeks of age) were purchased from the Department of Experimental Animal, Peking University Health Science Center. The HT-29 cells (5×10^6) were implanted subcutaneously into the right upper flanks of nude mice. When tumors reached ~0.8 cm in mean diameter, the tumor-bearing mice were used for biodistribution and imaging studies. Sixteen tumor-bearing mice were randomly divided into four groups, each of which had four animals. Each tumor-bearing mouse was administered intravenously with [^{99m}Tc-(HYNIC-ABN)(tricine)(TPPTS)] (~15 μCi) dissolved in 0.1 mL of saline via the tail vein. Animals were anesthetized with intraperitoneal injection of sodium pentobarbital at a dose of 45.0 mg/kg, and were sacrificed by cervical dislocation at 0.5, 1, 2, and 4 h postinjection (p.i.). Blood was withdrawn from the eye through a capillary tube. Organs of interest (tumor, heart, liver, spleen, kidney, lung, stomach, intestine, and muscle) were harvested, washed with saline, dried with absorbent tissues, weighed, and measured for radioactivity in a γ-counter (Wallac 1470−002, Perkin-Elmer, Finland). The organ uptake was calculated as a percentage of the injected dose per gram of tissue mass (%ID/g). The biodistribution data and *T*/*B* ratios were reported as an average plus the standard deviation based on the results from four animals at each time point.

Metabolism. The metabolic stability of [^{99m}Tc(HYNIC-ABN)(tricine)(TPPTS)] was evaluated using two normal BALB/c nude mice. Each mouse was administered via tail vein the radiotracer (~800 μCi) dissolved in 0.2 mL saline. The urine samples were collected at 1 h p.i. by manual void, and were mixed with an equal volume of saline. The mixture was centrifuged at 8000 rpm for 5 min. The supernatant was collected and filtered through a 0.22 μm Millex-LG syringe-driven filter unit to remove the precipitate and large proteins. The filtrate was analyzed by radio-HPLC. Both the liver and kidney simples were also harvested at 1 h p.i., and were pulped.

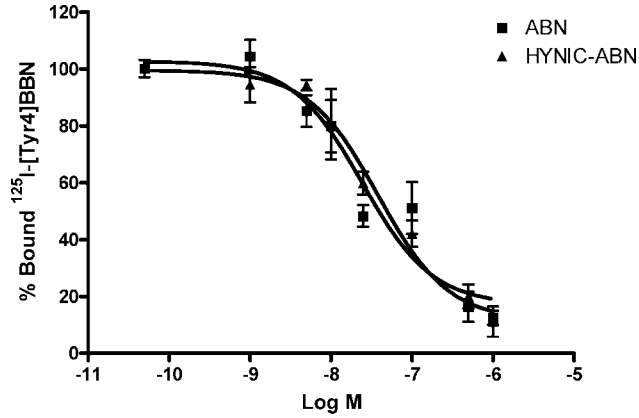

Figure 2. Displacement curves of ^{125}I-[Tyr4]BBN bound to the GRPR-positive PC-3 human prostate carcinoma cells by ABN and HYNIC-ABN. The IC_{50} values were calculated to be 24 ± 2 and 38 ± 1 nM for ABN and HYNIC-ABN, respectively.

The homogenates were mixed with an equal volume of saline, separately. The resulting mixture was vortexed for 5−10 min. After centrifuging at 8000 rpm for 5 min, the supernatant was collected and passed through a 0.22 μm Millex-LG syringe-driven filter unit to remove any precipitate and particles. The filtrate was then analyzed by radio-HPLC.

Scintigraphic Imaging. The imaging study was performed using the female BALB/c nude mice bearing the HT-29 human colon cancer xenografts. Animals were anesthetized with intraperitoneal injection of sodium pentobarbital at a dose of 45.0 mg/kg. Each tumor-bearing mouse was administered intravenously with [^{99m}Tc(HYNIC-ABN)(tricine)(TPPTS)] (~400 μCi) in 0.2 mL saline via tail vein. Animals were placed prone on a two-head γ-camera (SIEMENS, E. CAM) equipped with a parallel-hole, low-energy, and high-resolution collimator. Posterior images were acquired 1 and 4 h p.i. The imaging data were stored digitally in a 128 × 128 matrix. The acquisition count limits were set at 200 K. In the blocking experiment, each tumor-bearing mouse was administered intravenously with excess HYNIC-ABN (300 μg dissolved in 0.1 mL of saline) 30 min prior to administration of [^{99m}Tc(HYNIC-ABN)(tricine)(TPPTS)]. The posterior images were acquired 1 h p.i. using the same procedure above. After completion of imaging, animals were sacrificed by cervical dislocation.

RESULTS

GRP Receptor Binding Affinity of ABN and HYNIC-ABN. The *in vitro* GRPR binding affinities and specificities of ABN and HYNIC-ABN were assessed via a competitive displacement assay using ^{125}I-[Tyr4]BBN as the radioligand. It was found that ABN and HYNIC-ABN were able to compete with ^{125}I-[Tyr4]BBN bound to PC-3 prostate carcinoma cells (Figure 2). The IC_{50} values were 24 ± 2 nM and 38 ± 1 nM for ABN and HYNIC-ABN, respectively. The attachment of HYNIC group seems to slightly reduce the GRPR binding affinity of ABN, but this difference may not be significant within the error of this assay.

Radiochemistry. [^{99m}Tc(HYNIC-ABN)(tricine)(TPPTS)] was prepared in two steps. First, HYNIC-ABN reacted with $Na^{99m}TcO_4$ in the presence of excess tricine and $SnCl_2$ to form the intermediate [^{99m}Tc(HYNIC-ABN)(tricine)$_2$], which was then allowed to react with TPPTS to form the ternary ligand complex [^{99m}Tc(HYNIC-ABN)(tricine)(TPPTS)]. The specific activity was ~1200 mCi/μmol. The radiochemical purity was >95% after Sep-Pak purification. [^{99m}Tc(HYNIC-ABN)(tricine)(TPPTS)] was analyzed using a reversed-phase HPLC method. A radio-HPLC chromatogram is shown in the top panel

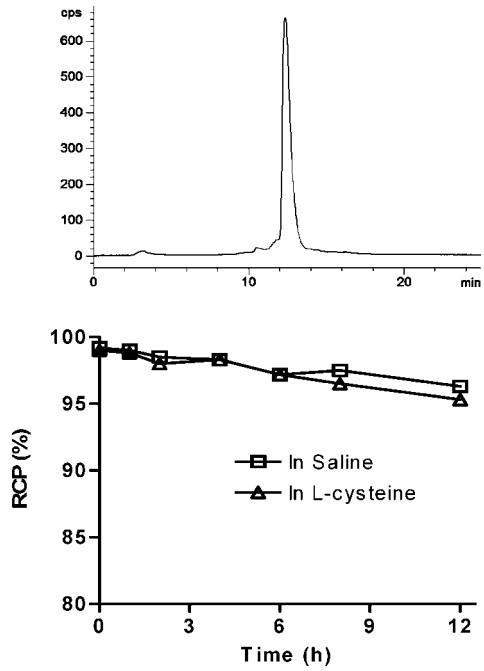

Figure 3. A typical radio-HPLC chromatogram (top) and solution stability data (bottom) for [^{99m}Tc(HYNIC-ABN)(tricine)(TPPTS)] in saline and in the presence of excess cysteine (1 mg/mL, pH = 7.4).

of Figure 3. The HPLC retention time was 12.2 min for [^{99m}Tc(HYNIC-ABN)(tricine)(TPPTS)]. The partition coefficient was determined in an equal volume mixture of *n*-octanol and 25 mM phosphate buffer (pH = 7.4). The log *P* value was -2.39 ± 0.06. The solution stability of [^{99m}Tc(HYNIC-ABN)(tricine)(TPPTS)] was monitored by radio-HPLC in saline and in the presence of excess cysteine (1.0 mg/mL, pH = 7.4). The solution stability data of [^{99m}Tc(HYNIC-ABN)(tricine)(TPPTS)] is shown in the bottom panel of Figure 3. It is quite clear that [^{99m}Tc(HYNIC-ABN)(tricine)(TPPTS)] is able to maintain its stability over 12 h in saline and in the presence of excess cysteine.

Internalization and Efflux Kinetics. The internalization and efflux kinetics of [^{99m}Tc(HYNIC-ABN)(tricine)(TPPTS)] is shown in Figure 4. The rate of internalization was time and temperature dependent. At 4 °C, the receptor binding took place, but there was no internalization (<1%). At 37 °C, there was a rapid internalization with 35 ± 2% of the cell-associated radioactivity being internalized at 5 min postincubation (Figure 4, left). The maximum was reached with 68 ± 5% of the internalized radioactivity at 30 min postincubation. In spite of the fast internalization, there was no significant retention of radioactivity inside tumor cells since the internalized radioactivity was quickly released. After 15 min incubation at 37 °C, 49 ± 3% of the internalized radioactivity remained. Only ~20% of the internalized radioactivity remained after 1 h (Figure 4, right).

Biodistribution Characteristics. The biodistribution study was performed using the BALB/c nude mice bearing HT-29 human colon cancer xenografts. The selected biodistribution data and T/B ratios for [^{99m}Tc(HYNIC-ABN)(tricine)(TPPTS)] are summarized in Figure 5. In general, [^{99m}Tc(HYNIC-ABN)(tricine)(TPPTS)] had a rapid clearance, predominantly through the renal route. Most of the injected dose was in the urinary system by 1 h p.i. with little radioactivity accumulation in the blood (0.50 ± 0.15%ID/g), liver (0.68 ± 0.16%ID/g), muscle (0.14 ± 0.04%ID/g), and gastrointestinal tract (0.63 ± 0.21%ID/g) at 1 h p.i. The tumor uptake was the highest (1.59 ± 0.23%ID/g) at 30 min p.i., with a steady decrease over the 4 h study period. [^{99m}Tc(HYNIC-ABN)(tricine)(TPPTS)] had the best *T*/*B* ratios for blood (2.37 ± 0.68), liver (1.69 ± 0.41), and muscle (11.17 ± 3.32) at 1 h p.i.

Imaging Studies. Figure 6 illustrates representative planar images of the tumor-bearing mice administered with ~400 μCi of [^{99m}Tc(HYNIC-ABN)(tricine)(TPPTS)] at 1 h p.i. (left) and 4 h p.i. (middle), as well as in the presence of excess HYNIC-ABN (right) at 1 h p.i. Arrows indicate the presence of the tumor (T) and kidneys (K). The HT-29 tumor is clearly visualized at 1 h p.i. with excellent tumor-to-background contrast. At 1 h p.i., the "hottest" spots are tumor, kidneys, and bladder. By 4 h p.i., the radioactivity in the chest region almost completely disappears while the tumor is still clearly seen. These data are consistent with those obtained from the *ex vivo* biodistribution study (Figure 5).

The blocking experiment by preinjecting or coinjecting a known receptor−ligand is often used to demonstrate the tumor specificity of the target-specific radiotracers. In this study, we used HYNIC-ABN as the blocking agent. Preinjection of excess HYNIC-ABN result in a significant reduction in the tumor uptake of [^{99m}Tc(HYNIC-ABN)(tricine)(TPPTS)] (Figure 6, right), indicating that its tumor localization is at least partially GRPR-mediated. There is also a significant reduction in radiotracer accumulation in several noncancerous organs, such as liver, stomach, intestine, and kidneys, due to the blockage of GRPRs in these organs (*1*, *3*, *4*).

Metabolic Properties. Metabolism study was performed using normal BALB/c mice by analyzing the samples from urine, kidney, and liver. Figure 7 shows typical radio-HPLC chromatograms of [^{99m}Tc(HYNIC-ABN)(tricine)(TPPTS)] in the kit matrix before injection (A), in the urine (B), in the kidney (C), and in the liver (D). [^{99m}Tc(HYNIC-ABN)(tricine)(TPPTS)] was completely metabolized in urine, kidney, and liver samples at 1 h p.i. The majority of the injected radioactivity was found in the urine sample at 1 h p.i. Compared with urine sample, the radioactivity level was almost undetectable in the liver and kidney samples.

DISCUSSION

Since colon cancer occurs in the torso area, it is necessary for the radiotracer to have a minimal radioactivity accumulation in the liver, lungs, stomach and gastrointestinal tract. There are several factors influencing the radiotracer excretion kinetics. These include the molecular charge, solution stability, lipophilicity and metabolic stability of the radiotracer. For the last several years, intensive efforts have been made to optimize the radiotracer pharmacokinetics by using different ^{99m}Tc cores (*34*, *36*, *37*, *41*, *44*, *46*), BFCs (*34*, *39*, *44*), and linker groups (*36*, *39*). It was reported that the linker groups, such as β-Ala-β-Ala or 3,6-dioxa-8-aminooctanoic acid, had a significant impact on tumor uptake, excretion kinetics, and metabolic stability of the ^{99m}Tc-labeled BN(7−14)NH_2 (*36*). A major disadvantage of using the ^{99m}Tc$(CO)_3^+$ core for the ^{99m}Tc-labeling of BN(7−14)NH_2 derivatives is that the radiotracer often has high uptake in the liver and intestine (*36*). Recently, NOTA and DOTA were used as BFCs for preparation of the ^{64}Cu-labeled BN-like peptides (*25*–*29*). Results from biodistribution and microPET imaging studies show that the ^{64}Cu-labeled NOTA-BN conjugates have very little accumulation in the liver, lungs, stomach, and intestine (*29*). The BFCs and radiometal chelates can be used to improve the radiotracer clearance from the noncancerous organs.

In this study, we used HYNIC as the BFC and tricine/TPPTS as coligands to prepare [^{99m}Tc(HYNIC-ABN)(tricine)(TPPTS)]. We found that [^{99m}Tc(HYNIC-ABN)(tricine)(TPPTS)] was excreted rapidly via the renal route with very little radioactivity accumulation in the blood, liver, muscle, and gastrointestinal

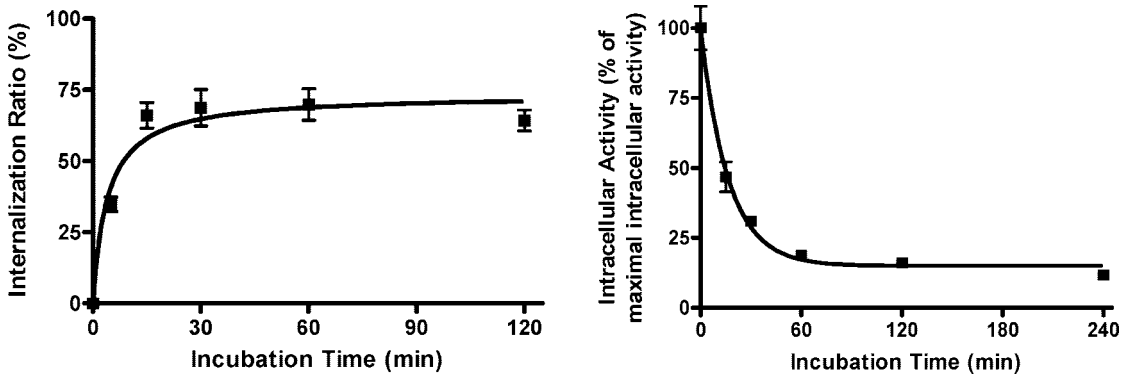

Figure 4. Internalization (left) and efflux (right) kinetics of [^{99m}Tc(HYNIC-ABN)(tricine)(TPPTS)].

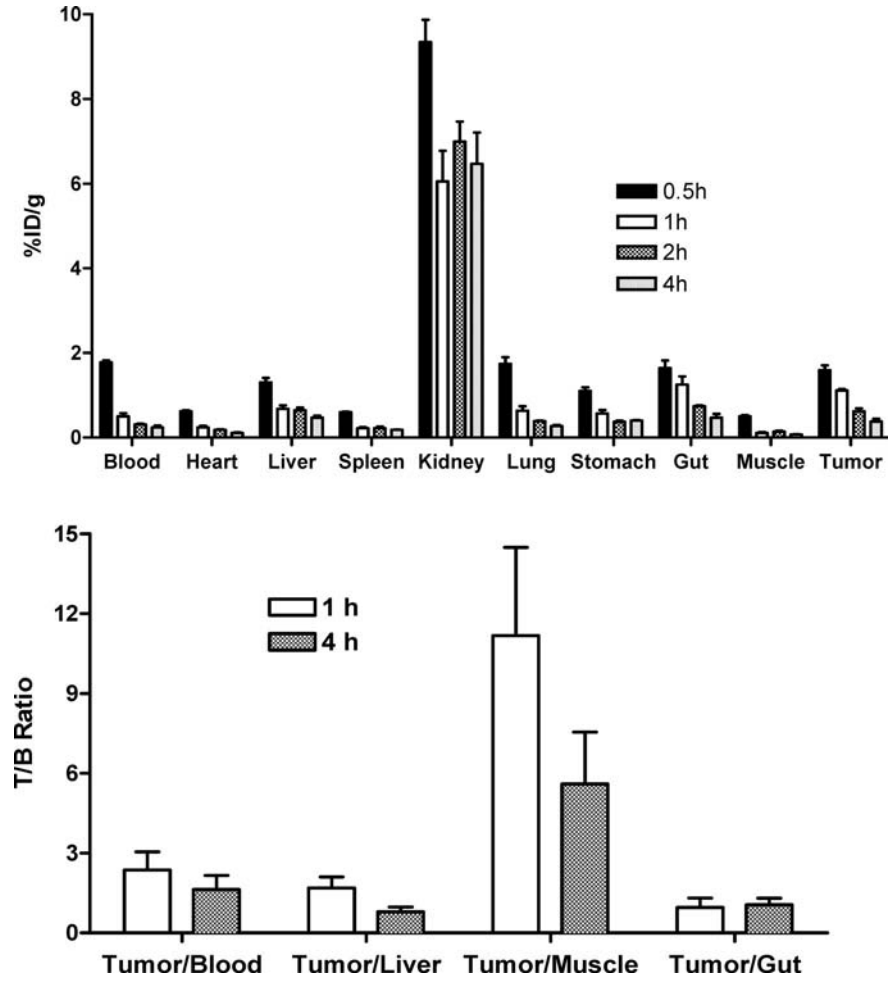

Figure 5. Organ uptake (top) and *T*/*B* ratios (bottom) for [^{99m}Tc(HYNIC-ABN)(tricine)(TPPTS)] in BALB/c nude mice bearing the HT-29 human colon cancer xenografts. Each data point represents an average of biodistribution data in four animals.

tract at >1 h p.i. (Figure 5). The tumor uptake was the highest (1.59 ± 0.23%ID/g) at 30 min p.i. with a steady decrease over the 4 h study period. This radiotracer had the best *T*/*B* ratios in the blood (2.37 ± 0.68), liver (1.69 ± 0.41), and muscle (11.17 ± 3.32) at 1 h p.i. The rapid tumor washout is also seen in images of the tumor-bearing mice (Figure 6), which is consistent with the rapid efflux kinetics of [^{99m}Tc(HYNIC-ABN)(tricine)(TPPTS)] (Figure 4). Similar tumor washout was also reported for the ^{99m}Tc(CO)$_3$-labeled BN(7−14)NH$_2$ derivatives (*36*, *37*). Results from the blocking experiment show that the tumor uptake of [^{99m}Tc(HYNIC-ABN)(tricine)(TPPTS)] is at least partially GRPR-mediated. The radiotracer uptake decreased in the liver, stomach, and intestine in the presence of excess HYNIC-ABN, which strongly suggests that the GRPRs are also expressed in these organs. Compared with the ^{99m}Tc(CO)$_3$-labeled His-linker-BN(7−14)NH$_2$ (linker = β-Ala-β-Ala or 3,6-dioxa-8-aminooctanoic acid) (*36*), [^{99m}Tc(HYNIC-ABN)(tricine)(TPPTS)] has the advantage with respect to its rapid clearance from blood, liver, muscle, and gastrointestinal tract.

The solution stability data shows that [^{99m}Tc(HYNIC-ABN)(tricine)(TPPTS)] is stable for >12 h in the presence of excess cysteine (Figure 3). However, results from the metabolism study indicate that [^{99m}Tc(HYNIC-ABN)(tricine)(TPPTS)] is completely metabolized at 1 h p.i. in the urine, kidney, and liver samples, probably due to rapid enzymatic degradation. Earlier studies showed that BN-like peptides could be easily metabolized by the neutral endopeptidase E.C.3.4.24.11 and the

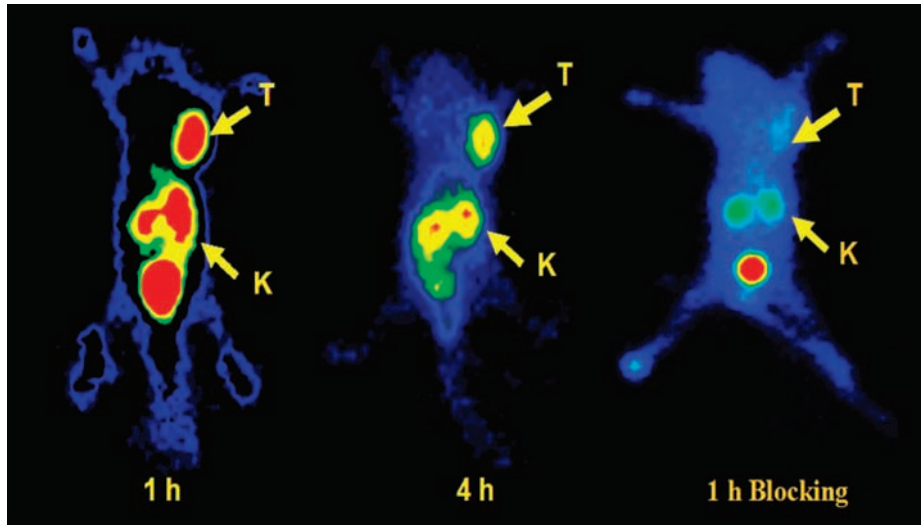

Figure 6. Static planar images of the tumor-bearing mice administered with ~400 μCi of [^{99m}Tc(HYNIC-ABN)(tricine)(TPPTS)] at 1 h p.i. (left) and 4 h p.i. (middle), as well as in the presence of excess HYNIC-ABN (right). Arrows indicate the presence of the tumor (T) and kidneys (K).

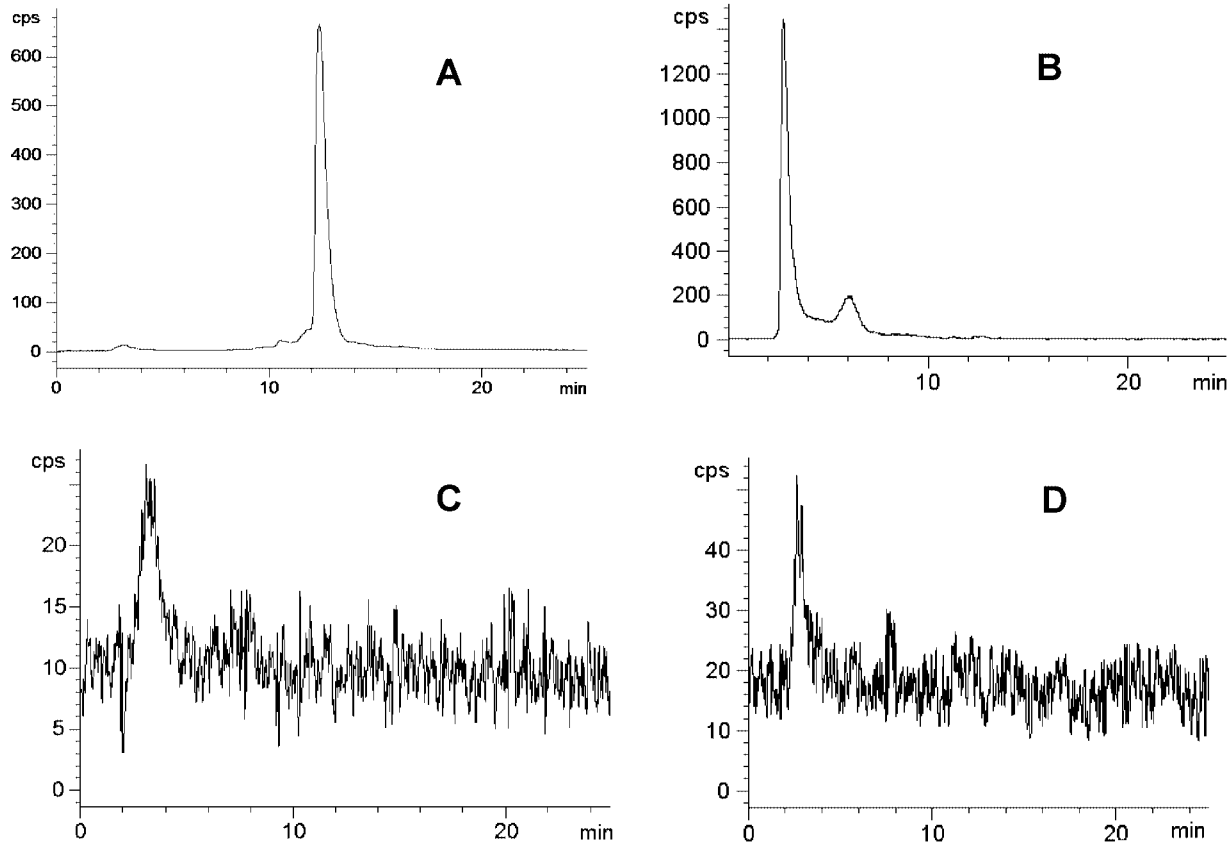

Figure 7. Radio-HPLC chromatograms of [^{99m}Tc(HYNIC-ABN)(tricine)(TPPTS)] in the kit matrix before injection (A), in the urine (B), in the liver (C), and in the kidney (D) at 1 h p.i.

angiotensin-converting enzyme (*60–62*). This metabolic instability may contribute, in part, to the rapid washout of [^{99m}Tc(HYNIC-ABN)(tricine)(TPPTS)] from tumor and noncancerous organs, such as the liver, lungs, muscle, stomach, and gastrointestinal tract.

The GRPR binding affinities of ABN and HYNIC-ABN are very similar to those reported for DOTA-linker-bombesin(7−14) (linker = triglycine, glycine-serine-glycine, or glycine-serine-serine) (*27*) and those reported for the $Re(CO)_3$ complexes of His-linker-BN(7−14)NH_2 (linker = β-Ala-β-Ala or 3,6-dioxa-8-aminooctanoic acid) (*36*). However, the tumor uptake of [^{99m}Tc(HYNIC-ABN)(tricine)(TPPTS)] in HT-29 colon cancer is not as high as the values reported for the ^{64}Cu-labeled DOTA-linker-bombesin(7−14) conjugates (linker = triglycine, glycine-serine-glycine, or glycine-serine-serine) in the PC-3 prostate cancer (*27*). There are two main reasons for the low tumor uptake of [^{99m}Tc(HYNIC-ABN)(tricine)(TPPTS)] reported in this study. The expression level of GRPRs on HT-29 cells may not be as high as that on PC-3 prostate cancer cells. The attachment of the ^{99m}Tc chelate (^{99m}Tc, HYNIC, tricine and TPPTS) may significantly reduce the GRPR binding affinity of [^{99m}Tc(HYNIC-ABN)(tricine)(TPPTS)], which seems to be supported by the fact that the IC_{50} value of ABN (24 ± 2 nM) is slightly lower than that of HYNIC-ABN (38 ± 1 nM). It

must be emphasized that the difference in the tumor-bearing mice (BALB/c versus SCID) may also contribute to the variation of tumor uptake and excretion kinetics of the radiotracer. Therefore, caution must be taken when comparing the biodistribution data obtained by two different research laboratories using two different tumor-bearing animal models.

CONCLUSION

The ternary ligand system (HYNIC, tricine, and TPPTS) has been successfully used for ^{99m}Tc-labeling of β-Ala-BN(7−14)NH_2. [^{99m}Tc(HYNIC-ABN)(tricine)(TPPTS)] can be prepared in high yield and high specific activity. Because of its hydrophilicity (log $P = -2.39 \pm 0.06$), [^{99m}Tc(HYNIC-ABN)(tricine)(TPPS)] is excreted mainly via the renal route with little radioactivity accumulation in the liver, lungs, stomach, and gastrointestinal tract. Its metabolic instability may contribute, in part, to its rapid clearance from the tumor and nontumor organs, such as the blood, liver, lungs, and stomach. As a result, it has the best *T*/*B* ratios in the blood, liver, and muscle at 1 h p.i. The tumor can be clearly visualized as early as 30−60 min p.i. by planar imaging of the BALB/c nude mice bearing the HT-29 human colon xenografts. The combination of relatively high tumor uptake with its extremely favorable pharmacokinetics makes [^{99m}Tc(HYNIC-ABN)(tricine)(TPPTS)] a promising SPECT radiotracer for imaging colon cancer.

ACKNOWLEDGMENT

Authors would like to thank Professor Xiaoyan Qiu, Peking University Health Science Center, for providing the HT-29 human colon cancer cells, and Huiyun Zhao, Peking University Medical Isotopes Research Center, for technical support. This work is supported, in part, by research grants: Z00004105040311 and D0206001041991 (F.W.) from the Beijing Science and Technology Program, 30640067(F.W.) from the NSF, 1R01 CA115883-01A2 (S.L.) from the National Cancer Institute (NCI), and BCTR0503947 (S.L.) from the Susan G. Komen Breast Cancer Foundation.

LITERATURE CITED

(1) Erspamer, V., Erpamer, G. F., and Inselvini, M. (1970) Some pharmacological actions of alytesin and bombesin. *J. Pharm. Pharmacol. 22*, 875–876.

(2) Prasad, S., Mathur, A., Gupta, N., Jaggi, M., and Singh, A. T. (2007) Bombesin analogs containing α-amino-isobutyric acid with potent anticancer activity. *J. Pept. Sci. 13*, 54–62.

(3) Ohki-Hamazaki, H., Iwabuchi, M., and Maekawa, F. (2005) Development and function of bombesin-like peptides and their receptors. *Int. J. Dev. Biol. 49*, 293–300.

(4) Patel, O., Shulkes, A., and Baldwin, G. S. (2006) Gastrin-releasing peptide and cancer. *Biochim. Biophys. Acta 1766*, 23–41.

(5) Nakagawa, T., Hocart, S. J., Schumann, M., Tapia, J. A., Mantey, S. A., Coy, D. H., Tokita, K., Katsuno, T., and Jensen, R. T. (2005) Identification of key amino acids in the gastrin-releasing peptide receptor (GRPR) responsible for high affinity binding of gastrin-releasing peptide (GRP). *Biochem. Pharmacol. 69*, 579–593.

(6) Moody, T. W., Carney, D. N., Cuttitta, F., Quattrocchi, K., and Minna, J. D. (1985) High affinity receptors for bombesin/GRP-like peptides on human small cell lung cancer. *Life Sci. 37*, 105–113.

(7) Radulovic, S. S., Milovanovic, S. R., Cai, R. Z., and Schally, A. V. (1992) The binding of bombesin and somatostatin and their analogs to human colon cancers. *Proc. Soc. Exp. Biol. Med. 200*, 394–401.

(8) Carroll, R. E., Matkowskyj, K. A., Chakrabarti, S., McDonald, T. J., and Benya, R. V. (1999) Aberrant expression of gastrin-releasing peptide and its receptor by well-differentiated colon cancers in humans. *Am. J. Physiol. 276*, G655–G665.

(9) Saurin, J. C., Nemoz-Gaillard, E., Sordat, B., Cuber, J. C., Coy, D. H., Abello, J., and Chayvialle, J. A. (1999) Bombesin stimulates adhesion, spreading, lamellipodia formation, and proliferation in the human colon carcinoma Isreco1 cell line[1]. *Cancer Res. 59*, 962–967.

(10) Carroll, R. E., Ostrovskiy, D., Lee, S., Danilkovich, A., and Benya, R. V. (2000) Characterization of gastrin-releasing peptide and its receptor aberrantly expressed by human colon cancer cell lines. *Mol. Pharmacol. 58*, 601–607.

(11) Saurin, J. C., Fallavier, M., Sordat, B., Gevrey, J. C., Chayvialle, J. A., and Abello, J. (2002) Bombesin stimulates invasion and migration of isreco1 colon carcinoma cells in a Rho-dependent manner. *Cancer Res. 62*, 4829–4835.

(12) Cassano, G., Resta, N., Gasparre, G., Lippe, C., and Guanti, G. (2001) The proliferative response of HT-29 human colon adenocarcinoma cells to bombesin-like peptides. *Cancer Lett. 172*, 151–157.

(13) Varvarigou, A., Bouziotis, P., Zikos, C., Scopinaro, F., and De Vincentis, G. (2004) Gastrin-releasing peptide (GRP) analogues for cancer imaging. *Cancer Biother. Radiopharm. 19*, 219–229.

(14) Reubi, J. C. (2003) Peptide receptors as molecular targets for cancer diagnosis and therapy. *Endocr. Rev. 24*, 389–427.

(15) Jong, M., Kwekkeboom, D., Valkema, R., and Krenning, E. P. (2003) Radiolabelled peptides for tumour therapy: Current status and future directions. *Eur. J. Nucl. Med. 30*, 463–469.

(16) Van de Wiele, C., Dumont, F., van Belle, S., Slegers, G., Peers, S. H., and Dierckx, R. A. (2001) Is there a role for agonist gastrin-releasing peptide receptor radioligands in tumour imaging? *Nucl. Med. Commun. 22*, 5–15.

(17) Hoffman, T. J., Quinn, T. P., and Volkert, W. A. (2001) Radiometallated receptor-avid peptide conjugates for specific in vivo targeting of cancer cells. *Nucl. Med. Biol. 28*, 527–539.

(18) Breeman, W. A., De Jong, M., Bernard, B. F., Kwekkeboom, D. J., Srinivasan, A., van der Pluijm, M. E., Hofland, L. J., Visser, T. J., and Krenning, E. P. (1999) Pre-clinical evaluation of [^{111}In-DTPA-Pro[1], Tyr[4]] bombesin, a new radioligand for bombesin-receptor scintigraphy. *Int. J. Cancer. 83*, 657–663.

(19) Zhang, H. W., Chen, J. H., Waldherr, C., Hinni, K., Waser, B., Reubi, J. C., and Maecke, H. R. (2004) Synthesis and evaluation of bombesin derivatives on the basis of pan-bombesin peptides labeled with indium-111, lutetium-177, and yttrium-90 for targeting bombesin receptor-expressing tumors. *Cancer Res. 64*, 6707–6715.

(20) Hoffman, T. J., Gali, H., Smith, C. J., Sieckman, G. L., Hayes, D. L., Owen, N. K., and Volkert, W. A. (2003) Novel series of ^{111}In labeled bombesin analogs as potential radiopharmaceuticals for specific targeting of gastrin-releasing peptide receptors expressed on human prostate cancer cells. *J. Nucl. Med. 44*, 823–831.

(21) Smith, C. J., Gali, H., Sieckman, G. L., Hayes, D. L., Owen, N. K., Mazuru, D. G., Volkert, W. A., and Hoffman, T. J. (2003) Radiochemical investigations of ^{177}Lu-DOTA-8-Aoc-BBN[7−14]NH_2: an in vitro/in vivo assessment of the targeting ability of this new radiopharmaceutical for PC-3 human prostate cancer cells. *Nucl. Med. Biol. 30*, 101–109.

(22) Hu, F., Cutler, C. S., Hoffman, T., Sieckman, G., Volkert, W. A., and Jurisson, S. S. (2002) Pm-149 DOTA bombesin analogs for potential radiotherapy in vivo comparison with Sm-153 and Lu-177 labeled DO3A-amide-βAla-BBN(7−14)NH_2. *Nucl. Med. Biol. 29*, 423–430.

(23) Waser, B., Eltschinger, V., Linder, K., Nunn, A., and Reubi, J. C. (2007) Selective in vitro targeting of GRP and NMB receptors in human tumours with the new bombesin tracer ^{177}Lu-AMBA. *Eur. J. Nucl. Med. Mol. Imaging 34*, 95–100.

(24) Schuhmacher, J., Zhang, H., Doll, J., Mäcke, H. R., Matys, R., Hauser, H., Henze, M., Haberkorn, U., and Eisenhut, M.

(2005) GRP receptor-targeted PET of a rat pancreas carcinoma xenograft in nude mice with a ^{68}Ga-labeled bombesin(6−14) analog. *J. Nucl. Med. 46*, 691–699.

(25) Biddlecombe, G. B., Rogers, B. E., de Visser, M., Parry, J. J., de Jong, M., Erion, J. L., and Lewis, J. S. (2007) Molecular imaging of gastrin-releasing peptide receptor-positive tumors in mice using ^{64}Cu- and ^{86}Y-DOTA-(Pro^1, Tyr^4)-Bombesin(1−14). *Bioconjugate Chem. 18*, 724–730.

(26) Parry, J. J., Andrews, R., and Rogers, B. E. (2007) MicroPET imaging of breast cancer using radiolabeled bombesin analogs targeting the gastrin-releasing peptide receptor. *Breast Cancer Res. Treat. 101*, 175–183.

(27) Parry, J. J., Kelly, T. S., Andrews, J., and Rogers, B. E. (2007) in vitro and in vivo evaluation of ^{64}Cu-labeled DOTA-Linker-Bombesin(7−14) analogues containing different amino acid linker moiety. *Bioconjugate Chem. 18*, 1110–1117.

(28) Garrison, J. C., Rold, T. L., Sieckman, G. L., Figueroa, S. D., Volkert, W. A., Jurisson, S. S., and Hoffman, T. J. (2007) In vivo evaluation and small-animal PET/CT of a prostate cancer mouse model using ^{64}Cu Bombesin analogs: side-by-side comparison of the CB-TE2A and DOTA chelation systems. *J. Nucl. Med. 48*, 1327–1337.

(29) Prasanphanich, A. F., Nanda, P. K., Rold, T. L., Ma, L., Lewis, M. J., Garrison, J. C., Hoffman, T. J., Sieckman, G. L., Figueroa, S. D., and Smith, C. J. (2007) [^{64}Cu-NOTA-8-Aoc-BBN(7−14)NH_2] targeting vector for positron-emission tomography imaging of gastrin-releasing peptide receptor-expressing tissues. *Proc. Natl. Acad. Sci. U.S.A. 104*, 12462–12467.

(30) Yang, Y., Zhang, X., Xiong, Z., and Chen, X. (2006) Comparative in vitro and in vivo evaluation of two ^{64}Cu-labeled bombesin analogs in a mouse model of human prostate adenocarcinoma. *Nucl. Med. Biol. 33*, 371–380.

(31) Rogers, B. E., Bigott, H. M., McCarthy, D. W., Manna, D. D., Kim, J., Sharp, T. L., and Welch, M. J. (2003) MicroPET Imaging of a gastrin-releasing peptide receptor-positive tumor in a mouse model of human prostate cancer using a ^{64}Cu-labeled bombesin analogue. *Bioconjugate Chem. 14*, 756–763.

(32) Chen, X., Park, R., Hou, Y., Tohme, M., Shahinian, A. H., Bading, J. R., and Conti, P. S. (2004) MicroPET and autoradiographic imaging of GRP receptor expression with ^{64}Cu-DOTA-[Lys^3]bombesin in human prostate adenocarcinoma xenografts. *J. Nucl. Med. 45*, 1390–1397.

(33) Smith, C. J., Sieckman, G. L., Owen, N. K., Hayes, D. L., Mazuru, D. G., Volkert, W. A., and Hoffman, T. J. (2003) Radiochemical investigation of [^{188}Re(H_2O)$(CO)_3$-diaminopropionic acid-SSS-bombesin(7−14)NH_2]: syntheses, radiolabeling and in vitro/in vivo GRP receptor targeting studies. *Anticancer Res. 23*, 63–70.

(34) Karra, S. R., Schibli, R., Gali, H., Katti, K. V., Hoffman, T. J., Higginbotham, C., Sieckman, G. L., and Volkert, W. A. (1999) ^{99m}Tc-labeling and in vivo studies of a bombesin analogue with a novel water-soluble dithiadiphosphine-based bifunctional chelating agent. *Bioconjugate Chem. 10*, 254–260.

(35) Van de Wiele, C., Dumont, F., Broecke, V. R., Oosterlinck, W., Cocquyt, V., Serreyn, R., Peers, S., Thornback, J., Slegers, G., and Dierckx, R. A. (2000) Technetium-99m RP527, a GRP analogue for visualisation of GRP receptor-expressing malignancies: a feasibility study. *Eur. J. Nucl. Med. 27*, 1694–1699.

(36) Garayoa, E. G., Rüegg, D., Bläuenstein, P., Zwimpfer, M., Khan, I. U., Maes, V., Blanc, A., Beck-Sickinger, A. G., Tourwé, D. A., and Schubiger, P. A. (2007) Chemical and biological characterization of new Re$(CO)_3$/[^{99m}Tc]$(CO)_3$ bombesin analogues. *Nucl. Med. Biol. 34*, 17–28.

(37) La Bella, R., Garayoa, E. G., Bähler, M., Bläuenstein, P., Schibli, R., Conrath, P., Tourwé, D., and Schubiger, P. A. (2002) A ^{99m}Tc(I)-postlabeled high affinity bombesin analogue as a potential tumor imaging agent. *Bioconjugate Chem. 13*, 599–604.

(38) Scopinaro, F., Varvarigou, A., Ussof, W., De Vincentis, G., Sourlingas, T. G., Evangelatos, G. P., Datsteris, J., and Archimandritis, S. C. (2002) Technetium labeled bombesin like peptide: preliminary report on breast cancer uptake in patients. *Cancer Biother. Radiopharm. 17*, 327–335.

(39) Smith, C. J., Gali, H., Sieckman, G. L., Higginbotham, C., Volkert, W. A., and Hoffman, T. J. (2003) Radiochemical investigations of ^{99m}Tc-N_3S-X-BBN[7−14]NH_2: an in vitro/in vivo structure-activity relationship study where X = 0-, 3-, 5-, 8-, and 11-carbon tethering moieties. *Bioconjugate Chem. 14*, 93–102.

(40) Scopinaro, F., De Vincentis, G., Varvarigou, A. D., Laurenti, C., Iori, F., Remediani, S., Chiarini, S., and Stella, S. (2003) ^{99m}Tc-bombesin detects prostate cancer and invasion of pelvic lymph nodes. *Eur. J. Nucl. Med. Mol. Imaging 30*, 1378–1382.

(41) Nock, B., Nikolopoulou, A., Chiotellis, E., Loudos, G., Maintas, D., Reubi, J. C., and Maina, T. (2003) [^{99m}Tc]Demobesin 1, a novel potent bombesin analogue for GRP receptor-targeted tumour imaging. *Eur. J. Nucl. Med. Mol. Imaging 30*, 247–258.

(42) Scopinaro, F., De Vincentis, G.e., and Corazziari, E.,. (2004) Detection of colon cancer with ^{99m}Tc-labeled bombesin derivative (^{99m}Tc-leu13-BN1). *Cancer Bioth. Radiopharm. 19*, 245–252.

(43) Nock, B. A., Nikolopoulou, A., Galanis, A., Cordopatis, P., Waser, B., Reubi, J. C., and Maina, T. (2005) Potent bombesin-like peptides for GRP-receptor targeting of tumors with ^{99m}Tc: A preclinical study. *J. Med. Chem. 48*, 100–110.

(44) Faintuch, B. L., Santos, S. R., Souza, A. L. F. M., Hoffman, T. J., Greeley, M., and Smith, C. J. (2005) ^{99m}Tc-HYNIC-bombesin(7−14)NH_2: radiochemical evaluation with co-ligands EDDA (EDDA = Ethylenediamine-N,N′-diacetic acid), tricine, and nicotinic acid. *Synth. React. Inorg. Met.-Org. Chem. 35*, 43–51.

(45) Lin, K. S., Luu, A., Baidoo, K. E., Hossein, H. G., Chen, M-K., Brenneman, K., Pili, R., Pomper, M., Carducci, M. A., and Wagner, H. N., Jr. (2005) A new high affinity technetium-99m-bombesin analogue with low abdominal accumulation. *Bioconjugate Chem. 16*, 43–50.

(46) Kunstler, J-U., Veerendra, B., Figueroa, S. D., Sieckman, G. L., Rold, T. L., Hoffman, T. J., Smith, C. J., and Pietzsch, H. J. (2007) Organometallic ^{99m}Tc(III) '4 + 1′ bombesin(7−14) conjugates: synthesis, radiolabeling, and in vitro/in vivo studies. *Bioconjugate Chem. 18*, 1651–1661.

(47) Guillermina, F-F., Consuelo, A. de M., Jeanette, R-C., Martha, P-L., and María, T. R-I. (2006) Preparation and evaluation of ^{99m}Tc-EDDA/HYNIC-[Lys^3]-bombesin for imaging gastrin-releasing peptide receptor-positive tumours. *Nucl. Med. Commun. 27*, 371–376.

(48) Liu, S., Edwards, D. S., and Barrett, J. A. (1997) ^{99m}Tc-labeling of highly potent small peptides. *Bioconjugate Chem. 8*, 621–636.

(49) Liu, S., and Edwards, D. S. (1999) ^{99m}Tc-labeled small peptides as diagnostic radiopharmaceuticals. *Chem. Rev. 99*, 2235–2268.

(50) Liu, S. (2004) The role of coordination chemistry in development of target-specific radiopharmaceuticals. *Chem. Soc. Rev. 33*, 1–18.

(51) Edwards, D. S., Liu, S., Ziegler, M. C., Harris, A. R., Crocker, A. C., Heminway, S. J., and Barrett, J. A. (1999) RP463: A stabilized technetium-99m complex of a hydrazino nicotinamide conjugated chemotactic peptide for infection imaging. *Bioconjugate Chem. 10*, 884–891.

(52) Brouwers, A. H., Laverman, P., Boerman, O. C., Oyen, W. J. G., Barrett, J. A., Harris, T. D., Edwards, D. S., and Corstens, F. H. M. (2000) A ^{99}Tc^m-labeled leukotriene B4 receptor antagonist for scintigraphic detection of infection in rabbits. *Nucl. Med. Commun. 21*, 1043–1051.

(53) Liu, S., Harris, A. R., Ziegler, M. C., Edwards, D. S., and Williams, N. E. (2002) ^{99m}Tc-labeling of a hydrazinonictotinamide-conjugated LTB_4 receptor antagonist useful for imaging infection and inflammation. *Bioconjugate Chem. 13*, 881–886.

(54) Liu, S., Edwards, D. S., Ziegler, M. C., Harris, A. R., Hemingway, S. J., and Barrett, J. A. (2001) ^{99m}Tc-Labeling of a hydrazinonictotinamide-conjugated vitronectin receptor antagonist useful for imaging tumors. *Bioconjugate Chem. 12*, 624–629.

(55) Liu, S., Hsieh, W., Kim, Y. S., and Mohammed, S. I. (2005) Effect of coligands on biodistribution characteristics of ternary ligand ^{99m}Tc complexes of a HYNIC-conjugated cyclic RGDfK dimer. *Bioconjugate Chem. 16*, 1580–1588.

(56) Liu, S., He, Z., Hsieh, W. Y., Kim, Y. S., and Jiang, Y. (2006) Impact of PKM linkers on biodistribution characteristics of the ^{99m}Tc-labeled cyclic RGDfK dimer. *Bioconjugate Chem. 17*, 1499–1507.

(57) Jia, B., Shi, J., Yang, Z., Xu, B., Liu, Z., Zhao, H., Liu, S., and Wang, F. (2006) ^{99m}Tc-labeled cyclic RGDfK dimer: initial evaluation for SPECT imaging of glioma integrin $\alpha_v\beta_3$ expression. *Bioconjugate Chem. 17*, 1069–1076.

(58) Liu, S., Hsieh, W., Jiang, Y., Kim, Y. S., Sreerama, S. G., Chen, X., Jia, B., and Wang, F. (2007) Evaluation of a ^{99m}Tc-labeled cyclic RGD tetramer for non-invasive imaging integrin $\alpha_v\beta_3$-positive breast cancer. *Bioconjugate Chem. 18*, 438–446.

(59) Edwards, D. S., Liu, S., Barrett, J. A., Harris, A. R., Looby, R. J., Ziegler, M. C., Heminway, S. J., and Carroll, T. R. (1997) New and versatile ternary ligand system for technetium radiopharmaceuticals: water soluble phosphines and tricine as coligands in labeling a hydrazinonicotinamide-modified cyclic glycoprotein IIb/IIIa receptor antagonist with ^{99m}Tc. *Bioconjugate Chem. 8*, 146–154.

(60) Grady, E. F., Slice, L. W., Brant, W. O., Walsh, J. H., Payan, D. G., and Bunnett, N. W. (1995) Direct observation of endocytosis of gastrin releasing peptide and its receptor. *J. Biol. Chem. 270*, 4603–4611.

(61) Slice, L. W., Yee, H. F., Jr., and Walsh, J. H. (1998) Visualization of internalization and recycling of the gastrin releasing peptide receptor-green fluorescent protein chimera expressed in epithelial cells. *Receptors Channels 6*, 201–212.

(62) Coy, D. H., Mungan, Z., Rossowski, W. J., Cheng, B. L., Lin, J. T., Mrozinski, J. E., Jr., and Jensen, R. T. (1992) Development of a potent bombesin receptor antagonist with prolonged in vivo inhibitory activity on bombesin-stimulated amylase and protein release in the rat. *Peptides 13*, 775–781.

BC700471Z

Bioconjugated Quantum Rods as Targeted Probes for Efficient Transmigration Across an in Vitro Blood−Brain Barrier

Gaixia Xu,[†,§] Ken-Tye Yong,[†] Indrajit Roy,[†] Supriya D. Mahajan,[‡] Hong Ding,[†] Stanley A. Schwartz,[‡] and Paras N. Prasad*[,†]

Institute For Lasers, Photonics And Biophotonics, The State University of New York, Buffalo, New York 14260-3000, Department of Medicine, Division of Allergy, Immunology, and Rheumatology, Buffalo General Hospital, Buffalo, New York 14203 and Institute of Optoelectronics, ShenZhen University, China, 518060. Received December 21, 2007; Revised Manuscript Received March 25, 2008

We report here, what we believe to be the first time, the successful transport of bioconjugated quantum rods (QRs) across an in vitro blood−brain barrier (BBB) model via a receptor-mediated transport, as well as the use of QR multiplexing technique to compare simultaneously the transmigration efficiency of different biomolecules across the BBB. The migration rate of bioconjugated QRs crossing the in vitro BBB was found to be concentration- and time-dependent. This work illustrates a nanoparticle-based platform that will not only allow a direct visualization of the transmigration ability of various kinds of biomolecules across the BBB, but also facilitate the development of novel diagnostic and therapeutic nanoprobes for early diagnosis and therapy of various disorders of the brain following systemic administration.

INTRODUCTION

The blood−brain barrier (BBB) is a dynamic interface between the body and the brain, which is actively engaged in regulatory functions of the central nervous system (CNS), in addition to its primary role of protecting the brain from harmful substances and fluctuations in blood (*1–3*). Brain microvascular endothelial cells (BMVECs) composing the BBB are underlined by a continuous basement membrane, reinforced by pericytes and astrocytic endfeet, and are connected with adjacent endothelial cells (*4–9*). Owing to the presence of continuous strands of tight junctions between adjacent lateral endothelial membranes, the BBB is almost completely sealed, and therefore, it strictly limits the entrance of systemically circulating endogenous and exogenous compounds into the CNS (*3, 10, 11*). Thus, while the BBB constitutes a natural defense mechanism that safeguards the brain against the invasion of various circulating toxins and infected cells, it also offers a significant impediment toward the delivery of various diagnostic and therapeutic agents in the brain via the systemic route (*4, 12*). Therefore, targeted delivery across the BBB is one of the most challenging fields of research dealing with the treatment of various neurological disorders (*13, 14*).[1]

In general, transport mechanisms across the BBB can be broadly divided into three types, namely, passive, carrier-mediated, and vesicular transport (*6*). For example, lipid-soluble, nonpolar substances can enter the brain by passive diffusion across the BBB. On the other hand, polar substances and small peptides can be transported across the endothelium by carrier-mediated influx. Lastly, the vesicular transport is by either receptor-mediated or absorptive-mediated transcytosis via cationic proteins. However, to date, there are still many unknown and undiscovered parameters that are affecting the permeability of the BBB (*10, 15*). Thus, it is of great importance to systematically investigate the molecular composition, structure, and transport kinetics of the BBB under a variety of conditions in order to comprehend the underlying mechanisms of BBB permeability, which will help us to devise novel strategies for enhanced delivery of various neuropharmaceuticals into the brain.

Currently, nanotechnology is being investigated for overcoming the limited penetration of drugs through the BBB, which is an extremely important and evolving area in CNS pharmacology (*16–20*). To date, various types of nanoparticles and liposomes have been synthesized and used as drug carriers or contrast agents for targeted drug delivery and diagnosis of brain tumors across the BBB (*17, 21–24*). It is generally understood that drug-loaded nanoparticles can cross over the BBB as an intact entity, which will then release the drugs within the CNS. Though few liposomal and polymeric nanoparticles have been used for targeted delivery across the BBB, there have been no reports of using high-quality quantum dots (QDs) or quantum rods (QRs) as targeted probes to monitor the transmigration of specific molecules through BBB. The use of QD/QRs as luminescence probes for numerous biological and biomedical applications has become an area of intense research focus over the past few years (*25–28*). They offer several advantages over organic dyes, including increased brightness, stability against photobleaching, excitation within a broad spectral range, and a tunable and narrow emission spectrum. The QD/QR surface can be functionalized with a variety of biomolecules and have shown the potential to dramatically outperform conventional organic dyes in imaging of cellular and subcellular structures and in a variety of bioassays (*29–31*). Recently, targeted QD/QR-based probes have been modified to carry therapeutic molecules such as anticancer drugs and short interfering (si) RNA (*32, 33*).

Recently, our group has shown that the QR/QD bioconjugates can serve as targeted optical probes for two-photon fluorescence imaging of cancer cells (*34, 35*). Here, we further extended the application of QR bioconjugates as efficient targeted probes for

* Corresponding author. E-mail: pnprasad@buffalo.edu.
[†] The State University of New York.
[‡] Buffalo General Hospital.
[§] ShenZhen University.

[1]Abbreviations: CNS, central nervous system; BBB, blood−brain barrier; QD, quantum dot; QR, qauntum rod; Tf, transferrin; TfR, transferrin receptor; aC4, anti-Claudin 4; BMVECs, brain microvascular endothelial cells; NHAs, normal human astrocytes.

10.1021/bc700477u CCC: $40.75 © 2008 American Chemical Society
Published on Web 05/13/2008

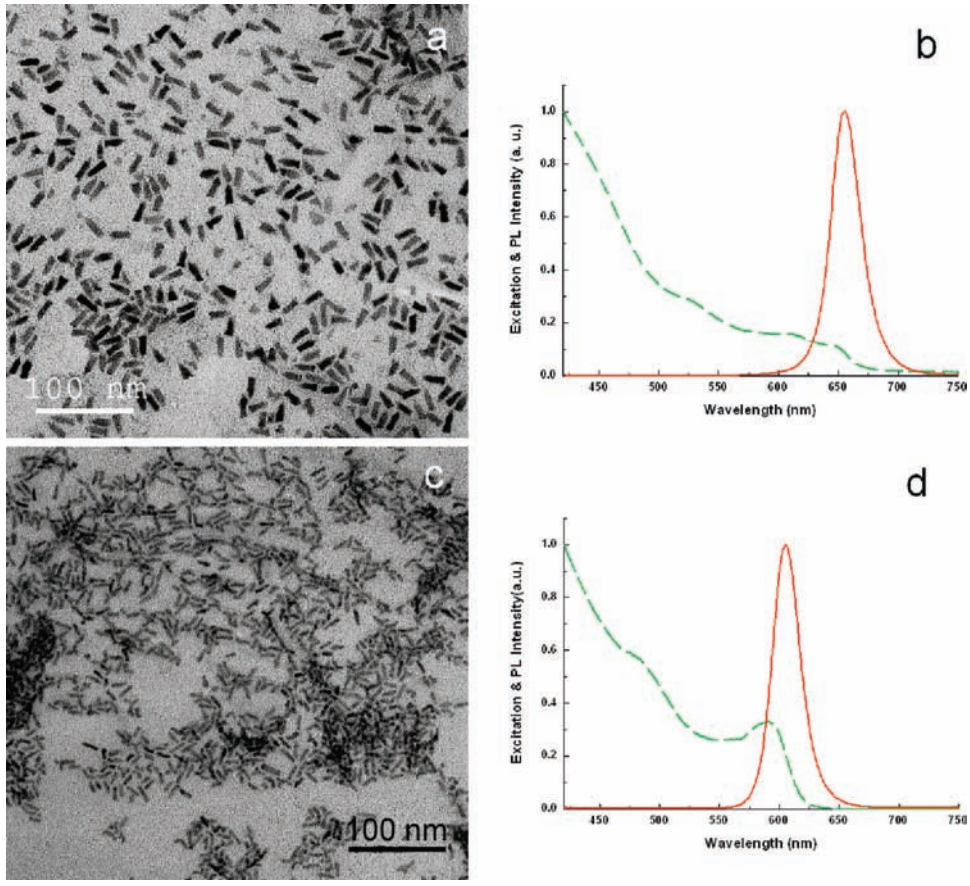

Figure 1. TEM images of CdSe/CdS/ZnS QRs cast from aqueous dispersions (a,c). The red- (a) and orange- (b) emitting QRs have average lengths of 26 and 14 nm and diameters of 6.5 and 4 nm, respectively. UV−vis−NIR absorption (green) and PL emission (red) spectra of monodispersed red- (b) and orange- (d) emitting CdSe/CdS/ZnS QRs.

transmigration across the BBB. A validated endothelial and astrocytic coculture BBB model was used to examine the transmigration of QR bioconjugates across the BBB (*36–38*). It is known that the transferrin receptor (TfR) is a kind of specific BBB transporter that allows selected biomolecules to move across the BBB (*39*). Transferrin (Tf)-conjugated QRs were synthesized and used for transport across the in vitro BBB model via a receptor-mediated transport mechanism. It was found that the migration rate of Tf-conjugated QRs crossing the in vitro BBB is concentration- and time-dependent. Further, another tight-junction protein Claudin-4 was used concurrently to validate the multiplex imaging technique and also to evaluate quasi-quantitatively the comparative transmigration efficiency and specificity of Tf and anti-Claudin 4 antibody (aC4), by conjugating them with red and orange emitting QRs, respectively. The results showed higher transmigration efficiency of Tf-conjugated QRs over the aC4-conjugated ones across the BBB. To the best of our knowledge, this is the first time that the QR multiplexing technique is employed to compare the targeting efficiency of different specific molecules across the BBB. These results illustrate a nanoparticle-based platform that will not only allow a direct visualization and quantification of the transmigration ability of various kinds of biomolecules across the BBB, but also facilitate the development of novel diagnostic and therapeutic nanoprobes for early diagnosis and therapy of various disorders of the brain following systemic administration.

RESULTS AND DISCUSSION

Figure 1a,c shows TEM images of red- and orange-emitting CdSe/CdS/ZnS QRs cast from aqueous media, respectively. The red- and orange-emitting QRs have lengths of 26 and 14 nm, and diameters of 6.5 and 4 nm, respectively. The absorption and PL spectra of the red and orange QRs are also shown in Figure 1b,d, respectively. Absorption spectra of the QRs show the expected structure with absorption onsets of 615 and 589 nm for red- and orange-emitting QRs, respectively. The PL spectra of the red- and the orange-emitting monodispersed QRs show band edge emission at 658 and 608 nm. Thus, we refer to the red- and orange-emitting QRs as 658 nm QRs and 608 nm QRs, respectively. These stored QRs can be directly used for cell staining without any sign of quenching effects. The photoluminescence quantum yields (QY) of 608 and 658 nm

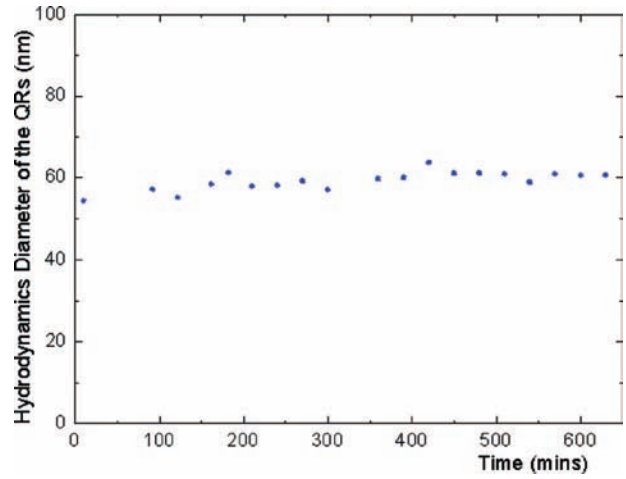

Figure 2. Time-dependent hydrodynamic diameter of lysine coated QRs dispersed in PBS buffer.

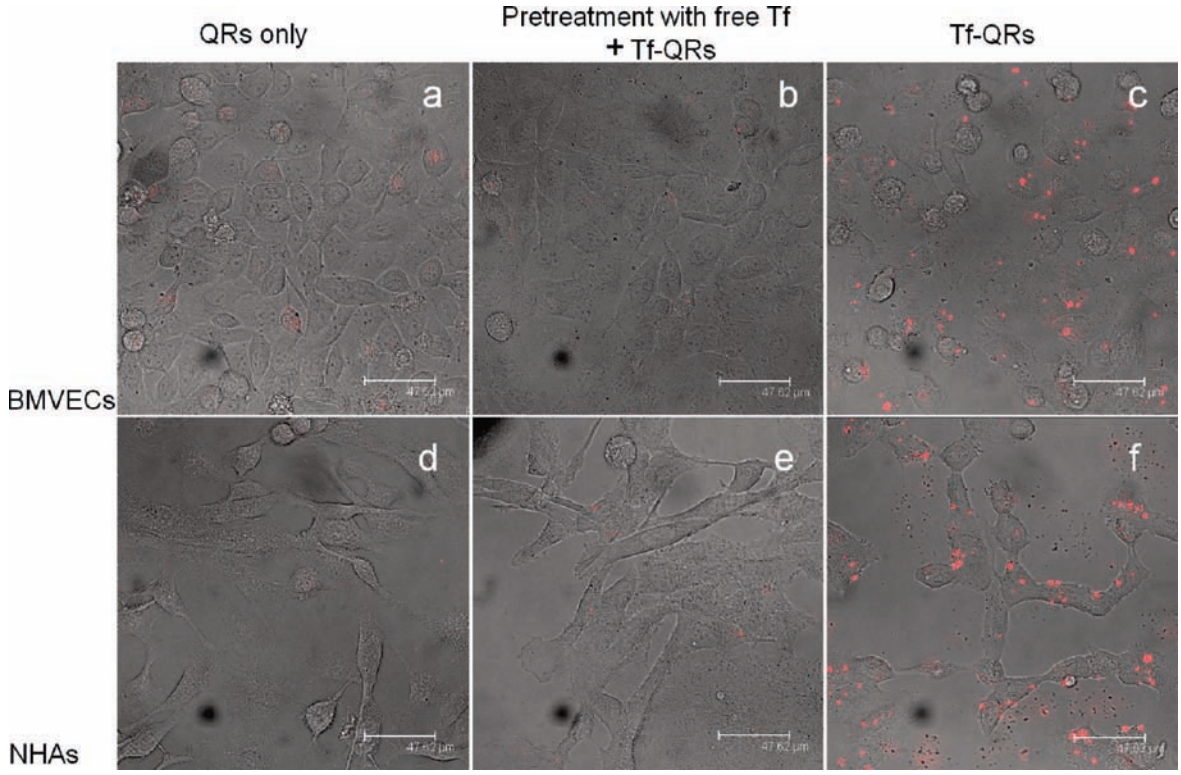

Figure 3. Confocal microscopic images of BMVEC and NHA cells, treated with (a,d) lysine-coated CdSe/CdS/ZnS QRs. (c,f) Tf-conjugated CdSe/CdS/ZnS QRs. Cells in (b) and (e) were saturated with free Tf for 2 h, before treatment with QR-Tf. Confocal microscopy images were obtained with laser excitation at 405 nm.

QRs are estimated to be 30% and 50%, respectively, which are sufficiently high for bioimaging.

In this study, dynamic light scattering (DLS) was also used to determine the colloidal stability of the QRs dispersed in PBS (pH = 7.4). The time-dependent profile of the effective diameter of the QRs is shown in Figure 2. Over the time range from 0 to 600 min, the effective diameter varies by less than 10%, suggesting that their colloidal stability is not affected under physiological pH. It is worth mentioning that the size of the QRs is ~26 nm in length and ~6.5 nm in width and their total hydrodynamic size is further increased by the MUA and lysine coating. Therefore, light scattering data show a total hydrodynamic diameter of ~60 nm. The light scattering analysis assumes that particles are spherical. Thus, the actual sizes determined by light scattering in our case cannot be taken literally. Therefore, we want to stress that the light scattering technique used here is solely to prove the nonaggregation of the QRs under physiological conditions.

To employ QRs as an efficient targeted contrast agent for traversing the BBB, the QRs must be conjugated with specific biorecognition molecules. To date, it is well-known that the transferrin receptor (TfR) is highly localized on the endothelial surfaces of the brain. TfR will generally trigger the receptor-mediated transport across the BBB because it undergoes trancytosis through the BBB. Thus, transferrin (Tf), an iron-transporting protein, was chosen as one of the specific ligands for facilitating transport across the BBB.

Prior to pursuing the in vitro BBB model studies, primary human BMVEC and normal human astrocyte (NHA) cells were individually studied to confirm the selective uptake of the Tf-QR biocojugates. Figure 3c,f represents confocal images showing robust staining of BMVEC and NHA cells, respectively, following treatment with Tf-QRs conjugates. Minimal uptake was observed with unconjugated QRs (Figure 3a,d). This result suggests that the Tf-conjugated QRs are transported within BMVEC and NHA cells through the transferrin receptor-mediated endocytosis pathway. To further confirm the targeted delivery of QR-Tf bioconjugates is receptor-mediated, the BMVEC and NHA were presaturated with free Tf in order to block the available Tf receptors on the cell surface. The results indicated significant reduction in the uptake of QR-Tf bioconjugates (Figure 3b,e), suggesting the specific nature of the uptake (*34*, *35*). In addition to these experiments, we have also performed local spectral analysis in order to quantify the cellular uptake of the nanoparticles in the various conditions given above. The local spectra were plotted as an average of spectral intensity obtained from different random points within the confocal fluorescence images. Figure 4 shows that the fluorescence signal obtained from the cells (both BMVECs and NHAs)

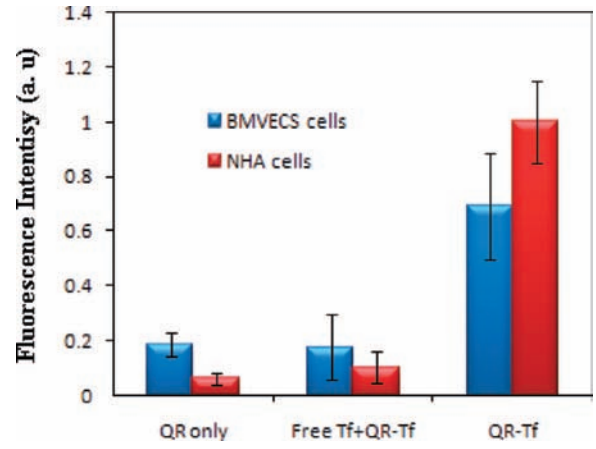

Figure 4. Fluorescence signal distribution collected from BMVEC and NHA cells following treatment with non-bioconjugated (QR only) and bioconjugated (QR-Tf) QRs. The effect of saturating cells with free Tf prior to treatment with QR-Tf is also represented. The error bars represent the range that was obtained for each point from a total of four points.

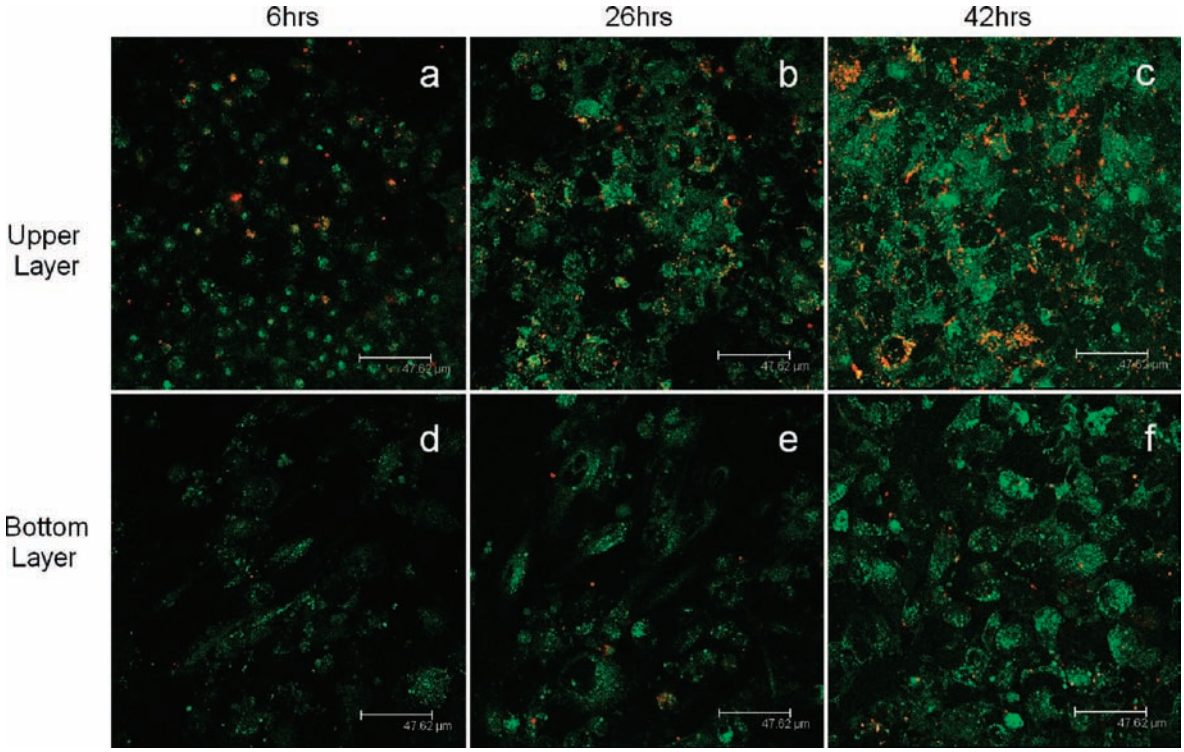

Figure 5. Confocal microscopic image of upper and bottom layer of BBB model treated with Tf-conjugated red QRs. In all cases, green represents emission the autofluorescence and red represents emission from 658 nm QRs.

following treatment with the QR-Tf bioconjugates is significantly higher than that obtained from cells treated with nonbioconjugated QRs and QR-Tf bioconjugates following presaturation with free Tfs. This result presents a semiquantitative estimation that reflects the superiority of the receptor-mediated cellular uptake over passive uptake.

On the basis of the successful in vitro experiment on the individual cell lines, we hypothesized that these bioconjugates could be used as efficient targeted probes for crossing the BBB. In this work, the bioconjugates were used to study the transmigration activity across an in vitro BBB model, which is established using primary human BMVEC and NHA cells. A schematic drawing of the BBB model is presented in the Supporting Information (Scheme 1). This in vitro BBB model consists of two-compartment wells in a culture plate. After formation of the model, Tf-QR bioconjugates were introduced into the upper chamber (blood end of the model) and incubated for different time points and bioconjugate concentrations. Next, the media from upper and bottom (brain end of the model) chambers were separately collected and the photoluminescence (PL) of the media was measured using a spectrofluorimeter in order to estimate the transmigration rate of the bioconjugates across the BBB. Confocal imaging technique was used to study and examine the BMVEC-PET-NHA cell layers (both upper and bottom sides) labeled with the QR bioconjugates.

Figure 5 shows the confocal images of upper and lower sides of the BBB model incubated with the Tf-QR bioconjugates at 6, 26, and 42 h, respectively. The autofluorescence signal (green) from the cells was used as the background for comparison. The upper panel shows confocal images of the BMVEC layer and the bottom panel is for the NHA layer. As shown in Figure 5, the uptake of Tf-QRs in both upper and bottom cell layers increases with the incubation time. This suggests that the migration of the Tf-QR conjugates is driven by both receptor mediated and kinetic processes.

To confirm the receptor-mediated uptake process, control experiments were performed using unconjugated QRs incubated with the BBB model. After 26 h, the upper and bottom layers were carefully rinsed with PBS solution and examined under a confocal microscope. As expected, minimal uptake was observed in the BBB model treated with unconjugated QRs upon comparison to the Tf-QRs (Supporting Information, Figure S1).

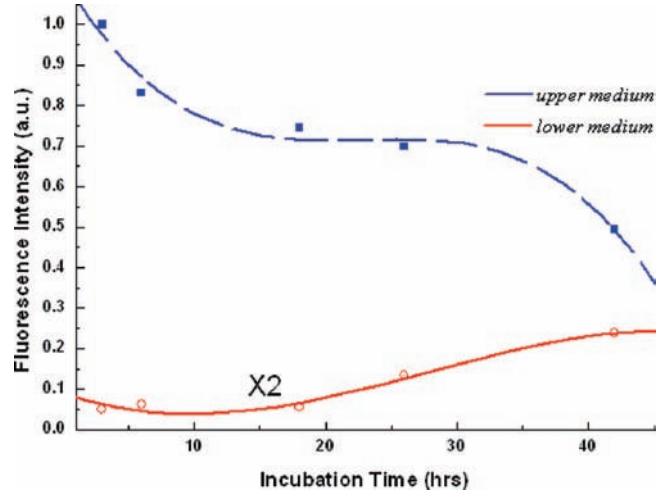

Figure 6. Relationship between fluorescence intensity changes of medium and the incubation time.

To further probe efficiency of permeability of Tf-QRs across the BBB, the PL intensities of the media from the upper and bottom chambers of the BBB model were systematically measured as a function of treatment time and analyzed. Figure 6 shows the band edge emission of the Tf-QRs in the upper and bottom chambers of the BBB model treated for various incubation times. Although there is clear time dependence, the upper medium retains more than 70% of their initial PL intensity, even at 26 h. Over the time range of 26 to 42 h, the PL intensity varies by more than 30%. This suggests that there is a critical period for significant passage of Tf-QRs through the BBB that is greater than 26 h.

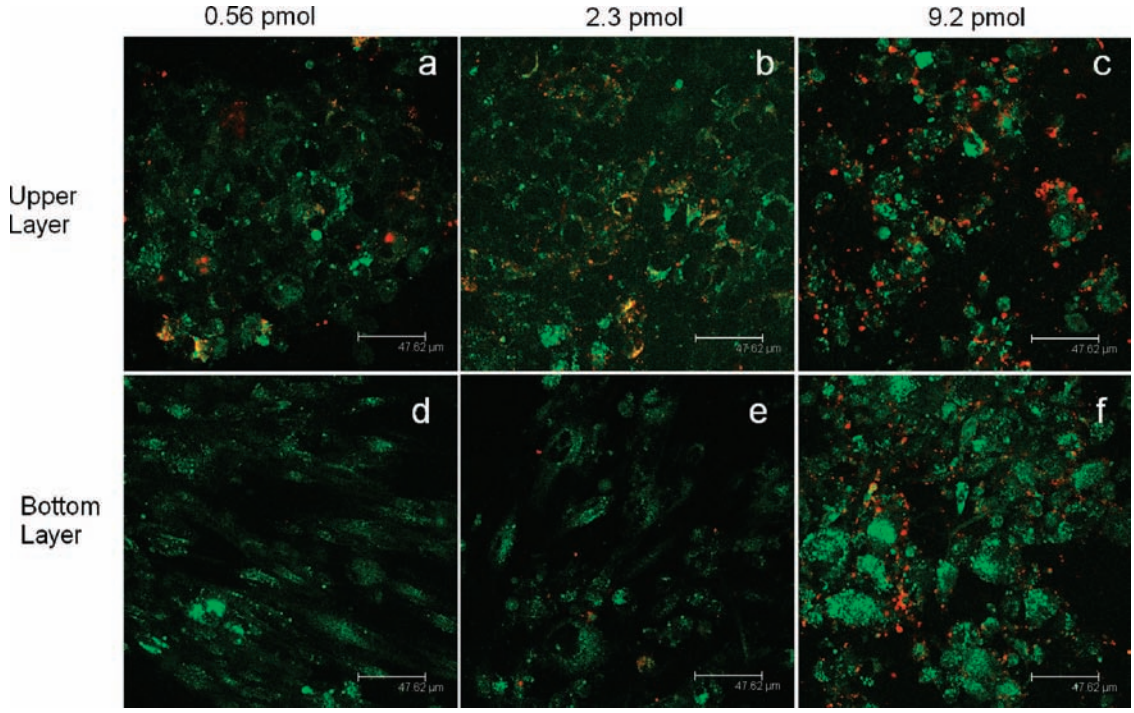

Figure 7. Confocal microscopic image of upper and bottom layers of the BBB model treated with ~0.56, 2.3, and 9.2 pmol of Tf-conjugated red QRs. In all cases, green represents emission of the autofluorescence and red represents emission from 658 nm Tf-QRs.

To better understand the effects of amount of Tf-QR bioconjugates on the permeability and transport kinetics across the in vitro BBB model, three different concentrations of Tf-QRs were used. Figure 7 presents the confocal images of the upper and lower sides of the BBB model incubated with ~0.56, 2.3, and 9.2 pmol of Tf-QRs at 26 h. From the confocal microscopy analysis, we find that the quantities of Tf-QRs labeled on both BMVEC (upper) and NHA (lower) cell layers increase with the increment of the Tf-QR concentration. However, when the Tf-QR concentration exceeded 9.2 pmol, a large amount of morphologically damaged cells was observed, suggesting that this concentration is the maximum tolerated dose prior to the onset of cytotoxicity.

In addition to conjugation of Tf, we have also conjugated aC4 with QRs for evaluating the specificity of different targeting molecules for BMVECs and NHAs. To compare the targeting specificity of aC4 and Tf on the cells, a multiplexed imaging technique was used by employing two different colors of QRs. More specifically, the 608 nm QRs were conjugated with aC4 and the 658 nm QRs were conjugated with Tf for specific targeting to Claudin 4 and transferrin receptors, respectively, on the BBB (and its constituent cells). Figure S2 (Supporting Information) shows confocal images of BMVEC and NHA cells colabeled with 4.0 pmol aC4-QRs (608 nm) and 0.46 pmol Tf-QRs (658 nm). Although the aC4-QRs (608 nm) is added about in a concentration 8.7 times than that for Tf-QRs (658 nm), the uptake of the 658 nm QR bioconjugates is slightly higher than that for the 608 nm QRs, as seen from the localized spectral analysis. The uptake concentration of Tf-QR bioconjugates was estimated to be twice the amount of aC4-QRs for both BMVEC and NHA cells (see Supporting Information Table S1). This experiment clearly demonstrates the Claudin 4 antigen also mediates targeting on BMVEC and NHA cells, but the targeting efficiency is significantly lower than that using the transferrin receptor.

The same formulation was further employed to compare the transmigration efficiency of aC4 and Tf for the in vitro BBB model. Figure 8 shows confocal images and spectra of the upper and bottom cell layers of the intact BBB model, again demonstrating superior staining/transmigration of the Tf-QRs (658 nm) over the aC4-QRs (608 nm). Local spectral analysis of the overall labeling of bioconjugates on the cells confirms that the fluorescence signal from the Tf-QR (658 nm) bioconjugates is more intense than that from the aC4-QR (608 nm) bioconjugates. Here, it was found that the uptake concentration of Tf-QR bioconjugates was three times the concentration of aC4-QRs at the bottom layer (see Supporting Information Table S1). From these results, it appears that it is more efficient to use the Tf-conjugated QRs for transport across the BBB, which agrees with the fact that the transferrin receptors are overexpressed in the BBB cells. Therefore, upon comparing the targeting molecules used in this work, Tf has higher affinity for individual cells lines composing the BBB and better transmigration efficiency across the in vitro BBB model. In comparison the aC4-QRs (608 nm), although can be targeted to the individual cells, are less suited as a nanocarrier to pass through the BBB owing to their lower tansmigration ability. This multiplexing technique can provide a novel nanophotonic method to screen a number of potential ligands for targeted delivery of diagnostics and therapeutics across the BBB, which will shorten the research cycle of CNS drug discovery and screening.

Besides using the QRs as biomarkers, we have also systematically investigated their cyctotoxicity effects on the BMVEC and NHA cell lines. Figure S3 (Supporting Information) shows the in vitro cytotoxicity effects of lysine-coated QRs, Tf-QRs, and aC4-QRs on the BMVEC and NHA cell lines. All the bioconjugates maintained greater than 80% cell viability, even at particle concentration as high as 7.9 pmol. This indicates that such bioconjugates can be used as efficient nanoprobes at noncytotoxic dosages.

In conclusion, we have used photostable, water-dispersible lysine-coated CdSe/CdS/ZnS QRs as efficient targeted probes for monitoring transport across an in vitro BBB model. The lysine-coated QRs can be readily conjugated with Tf and aC4 for specific targeting of the BBB cells. The receptor-mediated uptake of Tf-QR bioconjugates into the BMVEC and the NHA cells was confirmed by presaturating the cells with free Tf,

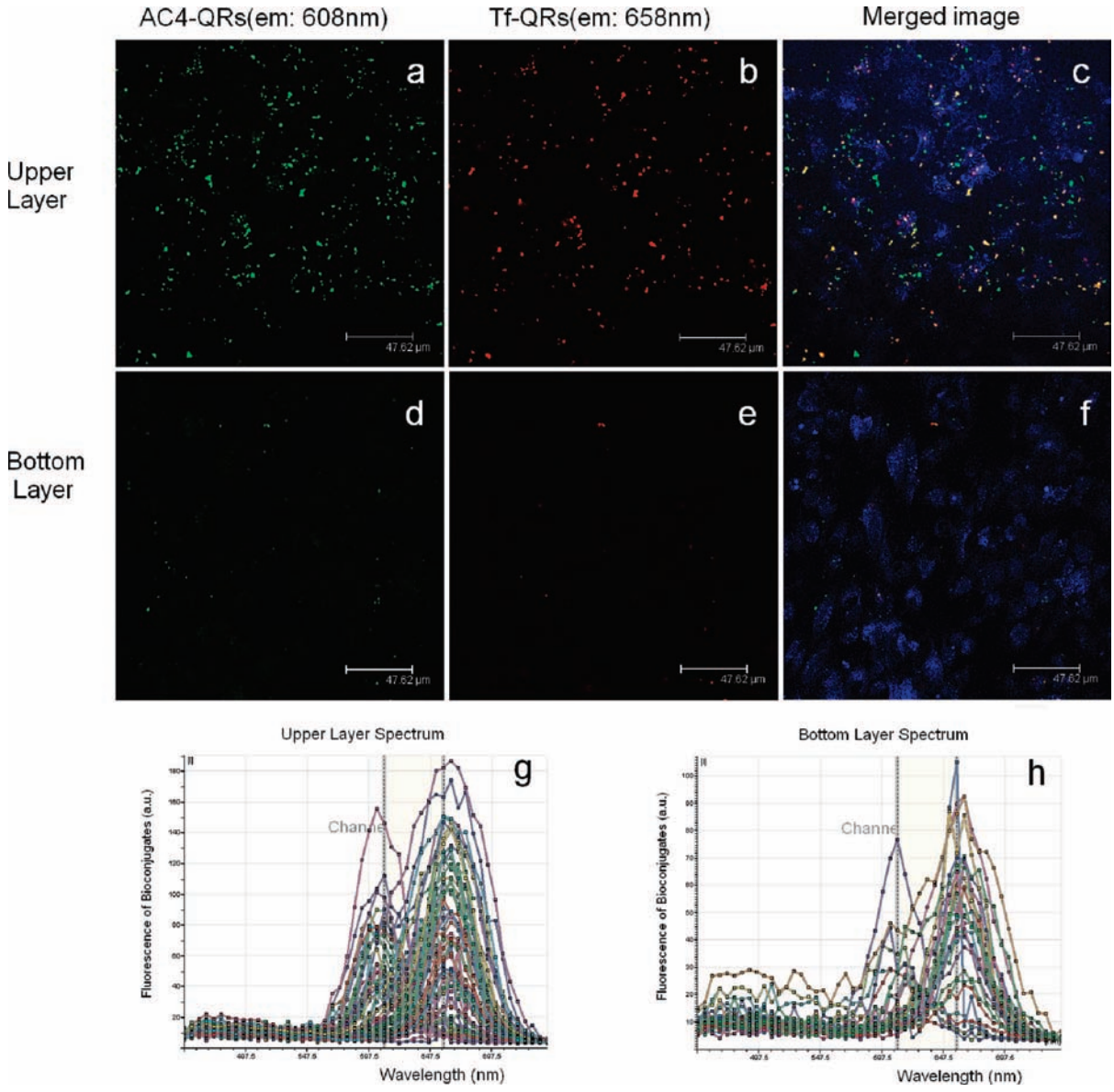

Figure 8. Confocal microscopic images and the local spectra of upper and bottom layer of the BBB model treated with multiplexed bioconjugates. The BBB model was treated with both aC4-conjugated 608 nm QRs and Tf-conjugated 658 nm QRs for 26 h incubation. In all cases, blue represents emission of the autofluorescence, green represents emission from 608 nm QRs, and red represents emission from 658 nm QRs. Confocal microscopy images were obtained with laser excitation at 405 nm. Scale bar: 47.62 μm.

thereby drastically lowering the uptake of the Tf-QR bioconjugates. This work demonstrates a nanoparticle-based platform that will not only allow a direct visualization of the transmigration ability of various kinds of biomolecules across the BBB, but also facilitate the development of novel diagnostic and therapeutic nanoprobes for early diagnosis and therapy of various disorders of the brain, following systemic administration. QRs, owing to their high surface area, can be coincorporated with other diagnostic and therapeutic molecules for targeted therapy of CNS disorders. Development of such multifunctional QRs with combined diagnostic, targeting, and therapeutic molecules are in progress.

ACKNOWLEDGMENT

This study was supported by grants from the NCI RO1CA119397 and the John R. Oishei Foundation. Support from the Center of Excellence in Bioinformatics and Life Sciences at the University at Buffalo is also acknowledged.

Supporting Information Available: Description of the materials, experimental methods, supplementary figures and table. This material is available free of charge via the Internet at http://pubs.acs.org.

LITERATURE CITED

(1) Dallasta, L. M. (1999) Blood-brain barrier tight junction disruption in human immunodeficiency virus-1 encephalitis. *Am. J. Pathol. 155*, 1915–1927.

(2) Ge, S., Song, L., and Pachter, J. S. (2005) Where is the blood-brain barrier. . .really? *J. Neurosci. Res. 79*, 421–427.

(3) Wolburg, H., and Lippoldt, A. (2002) Tight junctions of the blood-brain barrier: development, composition and regulation. *Vasc. Pharmacol. 38*, 323–337.

(4) Abbott, N. J. (2004) Prediction of blood-brain barrier permeation in drug discovery from in vivo, in vitro and in silico models. *Drug Discovery Today: Technol. 1*, 407–416.

(5) Abbott, N. J. (2005) Dynamics of CNS barriers: evolution, differentiation and modulation. *Cell. Mol. Neurobiol. 25*, 5–23.

(6) Abbott, N. J., Lars, R., and Elisabeth, H. (2006) Astrocyte-endothelial interactions at the blood-brain barrier. *Nat. Rev. Neurosci. 7*, 41–53.

(7) Begley, D. J., and Brightman, M. W. (2003) Structural and functional aspects of the blood-brain barrier. *Prog. Drug Res. 61*, 40–78.
(8) Cornell-Bell, A. H., Finkbeiner, S. M., Cooper, M. S., and Smith, S. J. (1990) Glutamate induces calcium waves in cultured astrocytes: long-range glial signalling. *Science 247*, 470–473.
(9) Schroeter, M. L. (1999) Astrocytes enhance radical defence in capillary endothelial cells constituting the blood-brain barrier. *FEBS Lett. 449*, 241–244.
(10) Gloor, S. M., Wachtel, M., Bolliger, M. F., Ishihara, H., Landmann, R., and Frei, K. (2001) Molecular and cellular permeability control at the blood-brain barrier. *Brain Res. Rev. 36*, 258–264.
(11) Huber, J. D., Egleton, R. D., and Davis, T. P. (2001) Molecular physiology and pathophysiology of tight junctions in the blood-brain barrier. *Trends Neurosci. 24*, 719–725.
(12) Teichberg, V. I. (2007) From the liver to the brain across the blood-brain barrier. *Proc. Natl. Acad. Sci. U.S.A. 104*, 7315–7316.
(13) Pardridge, W. M. (2002) Drug and gene targeting to the brain with molecular trojan horses. *Nat. Rev. Drug Discovery 1*, 131–139.
(14) Pardridge, W. M. (2003) Blood-brain barrier drug targeting: the future of brain drug development. *Mol. Interv. 3*, 90–105.
(15) Abbott, N. J. (2002) Astrocyte-endothelial interactions and blood-brain barrier permeability. *J. Anat. 200*, 629–638.
(16) Emerich, D. F., and Thanos, C. G. (2007) Targeted nanoparticle-based drug delivery and diagnosis. *J. Drug Targeting 15*, 163–183.
(17) Tiwari, S. B., and Amiji, M. M. (2006) A review of nanocarrier-based CNS delivery systems. *Curr. Drug Delivery 3*, 219–232.
(18) Verma, B.J. S. a. I. M. (2007) Targeted delivery of proteins across the blood brain barrier. *Proc. Natl Acad. Sci. U.S.A. 104*, 7594–7599.
(19) Yang, C. S., Chang, C. H., Tsai, P. J., Chen, W. Y., Tseng, F. G., and Lo, L. W. (2004) Nanoparticle-based in vivo investigation on blood-brain barrier permeability following ischemia and reperfusion. *Anal. Chem. 76*, 4465–4471.
(20) Yesim, A., Yemisci, M., Andrieux, K., Gursoy, R. N., Alonso, M. J., Fernandez-Megia, E., Novoa-Carballal, R., Quinoa, E., Riguera, R., Sargon, M. F., Celik, H. H., Demir, A. S., Hincal, A. A., Dalkara, T., Capan, Y., and Couvreur, P. (2005) Development and brain delivery of chitosan-PEG nanoparticles functionalized with the monoclonal antibody OX26. *Bioconjugate Chem. 16*, 1503–1511.
(21) Costantino, L., Gandolfi, F., Bossy-Nobs, L., Tosi, G., Gurny, R., Rivasi, F., Angela Vandelli, M., and Forni, F. (2006) Nanoparticulate drug carriers based on hybrid poly(D,L-lactide-co-glycolide)-dendron structures. *Biomaterials 27*, 4635–4645.
(22) Vinogradov, S. V., Batrakova, E. V., and Kabanov, A. V. (2004) Nanogels for oligonucleotide delivery to the brain. *Bioconjugate Chem. 15*, 50–60.
(23) Zhu, J., Tang, A., Law, L. P., Feng, M., Ho, K. M., Lee, D. K. L., Harris, F. W., and Li, P. (2005) Amphiphilic core-shell nanoparticles with poly(ethylenimine) shells as potential gene delivery carriers. *Bioconjugate Chem. 16*, 139–146.
(24) Pardridge, W. M. (2007) Drug targeting to the Brain. *Pharm. Res. 24*, 1733–1744.
(25) Bruchez, M., Jr., Moronne, M., Gin, P., Weiss, S., and Alivisatos, A. P. (1998) Semiconductor nanocrystals as fluorescent biological labels. *Science 281*, 2013–2016.
(26) Chan, W. C., and nbsp, W, and Nie, S. (1998) Quantum dot bioconjugates for ultrasensitive nonisotopic detection. *Science 281*, 2016–2018.
(27) Peng, X., Manna, L., Yang, W., Wickham, J., Scher, E., Kadavanich, A., and Alivisatos, A. P. (2000) Shape control of CdSe nanocrystals. *Nature 404*, 59–61.
(28) Peng, Z. A., and Peng, X. (2002) Nearly monodisperse and shape-controlled CdSe nanocrystals via alternative routes: nucleation and growth. *J. Am. Chem. Soc. 124*, 3343–3353.
(29) Fu, A., Gu, W., Boussert, B., Koski, K., Gerion, D., Manna, L., LeGros, M., Larabell, C. A., and Alivisatos, A. P. (2007) Semiconductor quantum rods as single molecule fluorescent biological labels. *Nano Lett. 7*, 179–182.
(30) Medintz, I. L., Uyeda, H. T., Goldman, E. R., and Mattoussi, H. (2005) Quantum dot bioconjugates for imaging, labelling and sensing. *Nat. Mater. 4*, 435–446.
(31) Michalet, X., Pinaud, F. F., Bentolila, L. A., Tsay, J. M., Doose, S., Li, J. J., Sundaresan, G., Wu, A. M., Gambhir, S. S., and Weiss, S. (2005) Quantum dots for live cells, in vivo imaging, and diagnostics. *Science 307*, 538–544.
(32) Bagalkot, V., Zhang, L., Levy-Nissenbaum, E., Jon, S., Kantoff, P. W., Langer, R., and Farokhzad, O. C. (2007) Quantum dot-aptamer conjugates for synchronous cancer imaging, therapy, and sensing of drug delivery based on bi-fluorescence resonance energy transfer. *Nano Lett. 7*, 3065–3070.
(33) Derfus, A. M., Chen, A. A., Min, D. H., Ruoslahti, E., and Bhatia, S. N. (2007) Targeted quantum dot conjugates for siRNA delivery. *Bioconjugate Chem. 18*, 1391–1396.
(34) Qian, J., Yong, K. T., Roy, I., Ohulchanskyy, T. Y., Bergey, E. J., Lee, H. H., Tramposch, K. M., He, S., Maitra, A., and Prasad, P. N. (2007) Imaging pancreatic cancer using surface-functionalized quantum dots. *J. Phys. Chem. B 111*, 6969–6972.
(35) Yong, K. T., Qian, J., Roy, I., Lee, H. H., Bergey, E. J., Tramposch, K. M., He, S., Swihart, M. T., Maitra, A., and Prasad, P. N. (2007) Quantum rod bioconjugates as targeted probes for confocal and two-photon fluorescence imaging of cancer cells. *Nano Lett. 7*, 761–765.
(36) Duport, S. (1998) An in vitro blood-brain barrier model: cocultures between endothelial cells and organotypic brain slice cultures. *Proc. Natl Acad. Sci. U.S.A. 95*, 1840–1845.
(37) Mahajan, S., Schwartz, S. A., Sykes, D., Chawda, R., Aalinkeel, R., and Nair, M. P. N. (2004) Effect of HIV peptides on trans-endothelial migration of dendritic cells across the blood brain barrier. *12th International Congress of Immunology and 4th Annual Conference of FOCIS* 153–159.
(38) Persidsky, Y., and Gendelman, H. E. (1997) Development of laboratory and animal model systems for HIV-1 encephalitis and its associated dementia. *J. Leukocyte Biol. 62*, 100–106.
(39) Sun, H., Li, H., and Sadler, P. J. (1999) Transferrin as a metal ion mediator. *Chem. Rev. 99*, 2817–2842.

BC700477U

Synthesis and Evaluation of Near-Infrared (NIR) Dye−Herceptin Conjugates as Photoacoustic Computed Tomography (PCT) Probes for HER2 Expression in Breast Cancer

Sibaprasad Bhattacharyya,*,† Shuyan Wang,† Daniel Reinecke,‡ William Kiser, Jr.,§ Robert A. Kruger,‡ and Timothy R. DeGrado*,†

Department of Radiology, Imaging Science Division, Indiana University-School of Medicine, Indianapolis, Indiana, OptoSonics Inc., Indianapolis, Indiana, and Pennsylvania State University, University Park, Pennsylvania. Received December 31, 2007; Revised Manuscript Received March 18, 2008

We are evaluating PCT imaging in conjunction with NIR dye labeled Herceptin antibody for noninvasive assessment of HER2 expression in tumors. Herceptin was labeled with Alexa Fluor-750 amine reactive dye for characterization of photoacoustic and fluorescence signals. Measurements were performed in solution and after incubation in cultured cell lines that were positive or negative in expression of HER2. The dye to antibody ratio was controlled to achieve a broad range of degree of labeling (DOL = 2 to 15). Photoacoustic signal intensity of Herceptin−dye conjugates in solution increased with increases over the entire DOL range studied. In contrast, fluorescence exhibited significant quenching for higher DOL. In vitro PCT imaging of the labeled HER2 (+) and HER2 (−) cells revealed the targeting specificity of the NIR dye labeled Herceptin. In HER2 (+) cells lines, photoacoustic signal intensity gradually increased with increasing DOL and with increasing number of cells. These results demonstrate that PCT-based measurement of HER2 receptor binding using NIR dye labeled Herceptin is feasible. The absence of a quenching effect with increased DOL advantages this method over traditional methods based on fluorescence measurement.

INTRODUCTION

Recently, there has been growing interest in photoacoustic computed tomography (PCT) imaging (*1–8*). It is a noninvasive imaging modality capable for obtaining both structural and functional information in biological tissues. In PCT, short pulses of stimulating radiation (e.g., laser or radiowaves) are differentially absorbed in tissue, resulting in subsequent thermal expansion and ultrasonic emission. The ultrasonic signals are measured by use of wide-band ultrasonic transducers. Photoacoustic signals thus obtained are free from the deleterious effects of optical scattering in biological tissue. The imaging depth in tissue exceeds standard optical imaging techniques, and systems can be designed to achieve excellent spatial resolution throughout a 3-D volume. Over the last ten years, the technology has advanced from relative obscurity to demonstration levels for a variety of applications including breast imaging and animal brain imaging (*9, 10*). A natural extension of imaging the intrinsic optical contrast of tissue is to demonstrate the ability of photoacoustic imaging to detect contrast agents based on optically absorbing dyes that exhibit well-defined absorption peaks in the near-infrared (NIR). The ultimate goal of this work is to develop a NIR dye based, target-specific contrast agent that can be used as a PCT probe for cancer imaging.

The HER2 gene is among those most frequently altered in human cancer (*11, 12*). HER2 encodes a 185 KDa protein that resides on the surface of the cell and has receptor tyrosine kinase activity. The receptor, which is a member of the EGFR family, is expressed on the cell membrane of a variety of epithelial cell types, and through the binding of specific factors, regulates aspects of cell growth and division. The level of gene amplification is correlated with protein expression (*13, 14*). While HER2 is expressed in normal cells and several types of cancers, it is of particular interest in breast cancer (*15*). It has elevated levels in 25−30% of breast cancers, and is linked to unfavorable prognosis, shorter relapse time, and low survival rate (*11*). A breakthrough in the treatment of metastatic breast cancer occurred with the FDA approval of Herceptin (Genentech, South San Francisco, CA) in 1998. Herceptin is a humanized antibody that has a high binding affinity to the HER2 cell surface receptor. Binding of Herceptin to HER2 prevents the binding of the growth factors to the receptor, resulting in tumor growth inhibition. Herceptin is an excellent candidate for the development of a photoacoustic molecular probe because of its clinical relevance, and because there is currently no imaging methodology available for clinicians to image HER2 binding in humans (*16, 17*). However, the low HER2 receptor density limits the concentration of bound molecular probe, requiring a highly sensitive imaging system for detection. A second complication is the difficulty of identifying a suitable contrast agent for the monoclonal antibody.

NIR dyes of labeled Herceptin molecular probe may increase the localized optical absorption at their point of localization in tissue. When NIR dyes absorb light energy, electrons within the molecules jump to excited states and then promptly dissipate this energy in two prominent ways. A nonradiative pathway produces heat and subsequent thermal expansion in tissue, giving rise to the photoacoustic signal. The second path is a radiative (emission) pathway, known as fluorescence (*18*). Simple energy conservation considerations suggest that what is not released as heat must be released as light (fluorescence): the more fluorescent the sample, the smaller the photoacoustic waveform (*19*).

* Corresponding author. Prof. Timothy R. DeGrado, Radiology, Brigham and Women Hospital, Harvard Medical School, Boston, MA; e-mail tdegrado@partners.org.

† Indiana University-School of Medicine.

‡ OptoSonics Inc.

§ Pennsylvania State University.

10.1021/bc700482u CCC: $40.75 © 2008 American Chemical Society
Published on Web 05/28/2008

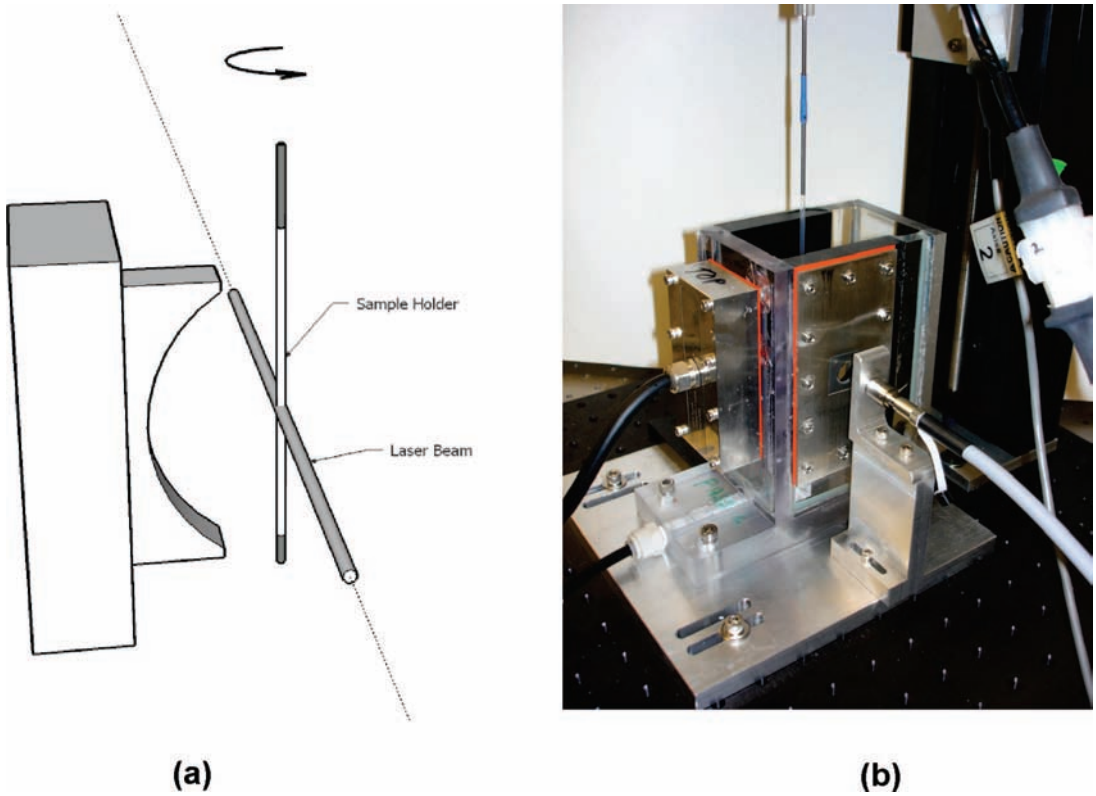

Figure 1. (a) Schematic diagram of PCT measurement of the probe in solution. (b) Instrument for PCT imaging of the probe in solution.

The fraction of the absorbed light energy that is reradiated as fluorescence is termed fluorescence quantum yield (QY). Often the fluorescence QY for NIR fluorescing dyes is very low, especially in the near-infrared. For example, the fluorescence QY for cyanine dyes that fluoresce within the optical imaging window is typically 10−15% (*20*). The remaining 85−90% of the absorbed energy is available for the photoacoustic waveform. If we increase the number of dye molecules per antibody (generally known as degree of labeling, DOL) to greater than 3, the fluorescence QY of the attached dye molecule will decrease further because of its self-quenching behavior in the excited state (*21*, *22*).

As Herceptin is a large molecule (185 KDa), it was anticipated that cell uptake would not be affected significantly if it is conjugated with several dye molecules. The NIR dyes with very low fluorescence QY appeared to be a good choice for PCT. By labeling Herceptin with several NIR dye molecules, a large NIR absorption may be achieved with less fluorescence. Thus, we hypothesized that NIR dye labeled Herceptin would be a suitable probe to detect breast cancer by PCT. Herein, we report the preparation and evaluation of Herceptin−dye conjugates with a broad range of DOLs as PCT probes for HER2 expressing breast cancer.

MATERIALS AND METHODS

Reagents. The amine-reactive dyes Alexa Fluor 750 (AF750) and AF647 were obtained as a dry powder from Invitrogen. One milligram of the dye was dissolved in 200 μL of anhydrous DMSO (Sigma St. Louis. MO) under reduced light conditions and stored at −80 °C. Herceptin antibody was obtained from Genentech (South San Francisco, CA).

Preparation of Herceptin−Dye Conjugates. All steps were performed under reduced light conditions. Covalent conjugation reactions contained 5 mg/mL Herceptin and various molar ratios of AF750 in 0.1 M bicarbonate buffer, pH 8.5. Reaction volume was ∼200 μL. Conjugation was initiated by addition of AF-750, followed by agitation (without frothing) for 2 h at RT. Dye-labeled Herceptin was purified by size-exclusion chromatography in Sephadex G-25 using (0.1 M) bicarbonate buffer as eluent. Purity of the probe was checked by discontinuous phase gel electrophoresis technique using a solution of free dye as standard. The degree of labeling (DOL) and the concentration of the conjugated Herceptin (mg/mL) were estimated using the extinction coefficients of Herceptin (ϵ_{280nm} = 225 000 M^{-1} cm^{-1}) and AF750 (ϵ_{749nm} = 240 000 M^{-1} cm^{-1}) in 0.1 M bicarbonate buffer, with correction for the 4.0% measured absorbance at 280 nm due to AF750:

$$\mathrm{DOL} = (\mathrm{Abs}_{749nm}/\epsilon_{749nm})/[(\mathrm{Abs}_{280nm} - 0.04 \times \mathrm{Abs}_{749nm})/\epsilon_{280nm}]$$

$$\text{Herceptin conc. (mg/mL)} = [(\mathrm{Abs}_{280nm} - 0.04 \times \mathrm{Abs}_{749nm})/\epsilon_{280nm}] \times \mathrm{MW}_{\mathrm{Herceptin}} \times \text{dilution factor} \quad (1)$$

Herceptin−AF647 conjugates were prepared in a similar way. DOL and concentration of conjugated Herceptin were estimated using the extinction coefficient of AF647 (ϵ_{650nm} = 239 000 M^{-1} cm^{-1}) in 0.1 M bicarbonate buffer, with correction for the 3.0% measured absorbance at 280 nm due to AF647.

$$\mathrm{DOL} = (\mathrm{Abs}_{650nm}/\epsilon_{650nm})/[(\mathrm{Abs}_{280nm} - 0.04 \times \mathrm{Abs}_{650nm})/\epsilon_{280nm}]$$

$$\text{Herceptin conc. (mg/mL)} = [(\mathrm{Abs}_{280nm} - 0.04 \times \mathrm{Abs}_{650nm})/\epsilon_{280nm}] \times \mathrm{MW}_{\mathrm{Herceptin}} \times \text{dilution factor} \quad (2)$$

Instrumentation for Probe Imaging in Solution. A protocol was developed to image AF-750 dye and dye−herceptin conjugates in solution. The imaging system was the Photoacoustic Spectrometry System (PASS) developed by OptoSonics, Indianapolis. Figure 1 shows the schematic diagram and imaging setup for the PASS system. The transducer array (custom 5.0 MHz, 128-element, Imasonic, France) was oriented vertically. The sample solution was held within a thin-walled FEP tube (Zeus, South Carolina, ID = 2.2 mm), and placed vertically in front of the array. The optical fiber was mounted so that

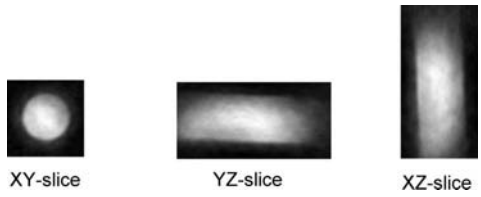

Figure 2. Representative PCT images of the Herceptin−AF750 conjugate in solution.

excitation light entered the side of the tank through a transparent glass window and hit the sample tube. The fiber output was first collimated with a lens and then reduced in intensity with a 12% neutral density (ND) filter thereby delivering a fluence of 6.2 mJ/cm^2 to the sample, which is about an order of magnitude greater than the fluence used typically in our fluorescence imaging device. Mylar film (0.0021/2 aluminized PET, >99% reflectance) was placed in front of the array to protect it from scattered light. The imaging tank was filled with water to provide an acoustic path. The imaging field of view (FOV) was roughly a cube with side length of 6 mm.

The first step in the reconstruction process is to compute the first temporal derivatives of the incident pressure waveforms $p_{\mathbf{r}}(t)$ from each of the 128 signals $p'_{\mathbf{r}}(t)$ recorded with the linear array. In practice, we do not measure $p_{\mathbf{r}}(t)$ directly, because the impulse response of the transducers used to record the thermoacoustic pressure was not a delta function. What we measure instead is $p_{\mathbf{r}}(t)$:

$$p'_{\mathbf{r}}(t) = p_{\mathbf{r}}(t) * i_{\mathbf{r}}(t) \tag{3}$$

where $i_{\mathbf{r}}(t)$ is the impulse response of the transducer at position $\mathbf{r}$ and * denotes convolution. We then compute $[\partial p_{\mathbf{r}}(t)]/\partial t$ in a single *filtering* step:

$$\frac{\partial p_{\mathbf{r}}(t)}{\partial t} \approx \mathrm{IFFT}\left[\frac{j\omega P'_{\mathbf{r}}(\omega)}{I_{\mathbf{r}}(\omega)}\right]\left[\frac{1+\cos\left(\frac{\pi\omega}{\omega_C}\right)}{2}\right] \tag{4}$$

where $I_{\mathbf{r}}(\omega)$ and $P'_{\mathbf{r}}(\omega)$ are the Fourier transforms of the transducer impulse responses and signals recorded by each transducer element, respectively, and $\mathbf{r}$ denotes the spatial locations at which each of the 128 pressure signals were recorded. The apodizing function $[1 + \cos(\pi\omega/\omega_C)]/2$ was used to bandwidth limit the signal to ω_c; in this case, $\omega_c = 8$ MHz. The last step in the reconstruction process is to back-project each of the $[\partial p_{\mathbf{r}}(t)]/\partial t$ computed using eq 4 over circular paths of radii $\tau_{\mathbf{r}}(x,y.z)*v_s$, where $\tau_{\mathbf{r}}(x,y.z)$ are the transit times for acoustic waves to travel from each volume element $(x,y.z)$ to each detector location $\mathbf{r}$, and v_s is the velocity of sound.

Dual-wavelength subtraction was used to remove reconstruction artifacts. Data were acquired at 32 evenly spaced angles by rotating the sample tube. Images were obtained at each angle at 745 and 810 nm. Four laser (Vibrant NIR OPOTEK, www.optek.com) pulses were averaged together at each wavelength to reduce the noise. A custom-designed laser output monitor used a reflective window to extract a small percentage of the laser light for measurement with an integrating sphere and photodiode. This allowed compensation for the variation of the laser output with wavelength and number of pulses. The image at 810 nm was subtracted from the 745 image with an experimentally determined scaling factor (k) based on measurements of the photoacoustic contrast of the DMSO buffer and the plastic holder at each wavelength. For these experiments, k was fixed to a value of 1.4, at which nearly all of the extraneous signals were removed as verified by analysis of the weighted PCT difference image in the absence of labeled cells. *In vivo* measurements would require a different scaling factor to account for the presence of hemoglobin. The measured resolution of the system was about 0.18 mm, significantly lower resolution than the reconstruction voxel size of 0.05 mm. For this reason, adjacent slices of the reconstructed image were averaged together before making quantitative measurements. A region-of-interest (ROI) tool was used to select a region in the center of the tube of the subtracted *XY*-slice image (Figure 2) and record the average and standard deviation values. Sample optical densities measured before and after the photoacoustic experiments were found to be the same, indicating that no photobleaching had occurred during photoexcitation.

Instrumentation for Cell Measurements. Figure 3 shows the imaging tank for the PCT-LIN system. The linear transducer array was mounted below the bottom of the clear PVC sample holder and oriented vertically upward. The optical fiber was mounted to the top of the sample holder assembly to deliver the laser directly down through the sample. The fiber output was first collimated and reduced in intensity with a 12% ND filter before reaching the sample. Mylar film in front of the array protected it from the direct beam. The sample holder assembly was positioned so the tip of the holder was at the region of greatest sensitivity, approximately 2 cm from the array face, as shown in Figure 3. The tank was filled with water to a level just below the sample holder. Figure 4 shows a detail of the sample holder assembly. The clear PVC sample holder had a thickness of approximately 0.02 in at the tip. It had a low optical absorption and gave a minimal photoacoustic signal in the NIR wavelengths. The diameter of the tip was less than 2 mm and the available sample volume was 100−150 μL. Figure 4a shows the exploded view of the assembly. The sample holder was suspended in the assembly so that no structural pieces were within the imaging field of view. The sample holder was conical and self-centering in the bottom aperture of the assembly. The cylindrical section was placed in the assembly after the sample holder and locked with a set screw to fix the holder in place.

We investigated two different techniques to resolve the signal of interest from the competing signals from artifacts and background sources. The first was dual-wavelength subtraction as previously described. The second was blank subtraction, whereby the sample holder was emptied, filled with buffer, imaged again, and the resultant image subtracted from the cell-filled image. In principle, the blank subtraction yielded a subtraction with somewhat higher signal, but it was sensitive to repositioning errors. In practice, we obtained the most robust results using the dual-wavelength technique.

Relative Quantum Yields (rQY). Relative fluorescence quantum yields (rQY-fl) or fluorescence per fluorophore of each dye−antibody conjugate were determined in comparison to that of the corresponding free dye, which was assumed to be 1. Fluorescence emission spectra were obtained from the samples of matched absorbance at the excitation wavelength (710 nm), and the integrated signals were normalized to that of the free dye to calculate rQY-fl. Absorbance was measured with an independent laboratory UV−vis spectrophotometer (Varian Cary 50, Palo Alto, CA). Fluorescence was measured with a Cary-Eclipse fluorimeter for AF750 conjugates.

In a similar way, the relative photoacoustic quantum yields (rQY-PA) or acoustic signal intensity per dye of each conjugate were determined by PASS in comparison to that of the corresponding free dye, which was assumed to be 1. Acoustic signals were obtained from the samples of matched absorbance at the excitation wavelength (745 nm for AF-750 conjugates) using photoacoustic instruments developed by OptoSonics Inc. Signals thus obtained were normalized to that of the free dye to calculate relative photoacoustic QY.

Fluorescence Measurement by Flow Cytometry. Fluorescence of the labeled HER2(+) cells was measured by flow

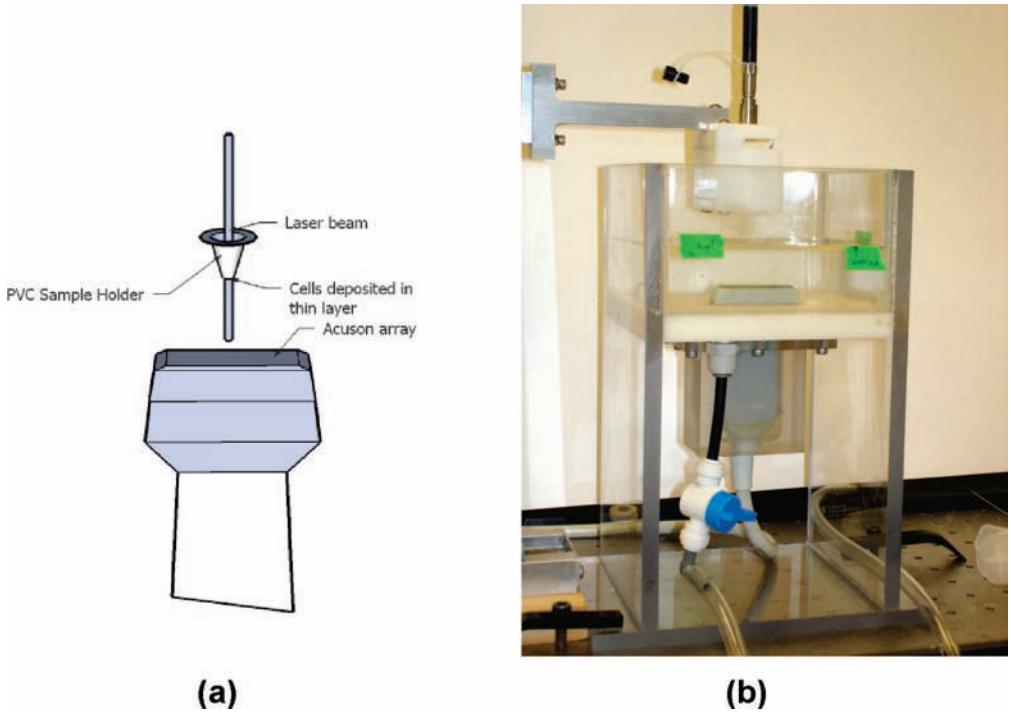

Figure 3. (a) Schematic diagram for PCT imaging of cells. (b) Instrument for PCT cell imaging.

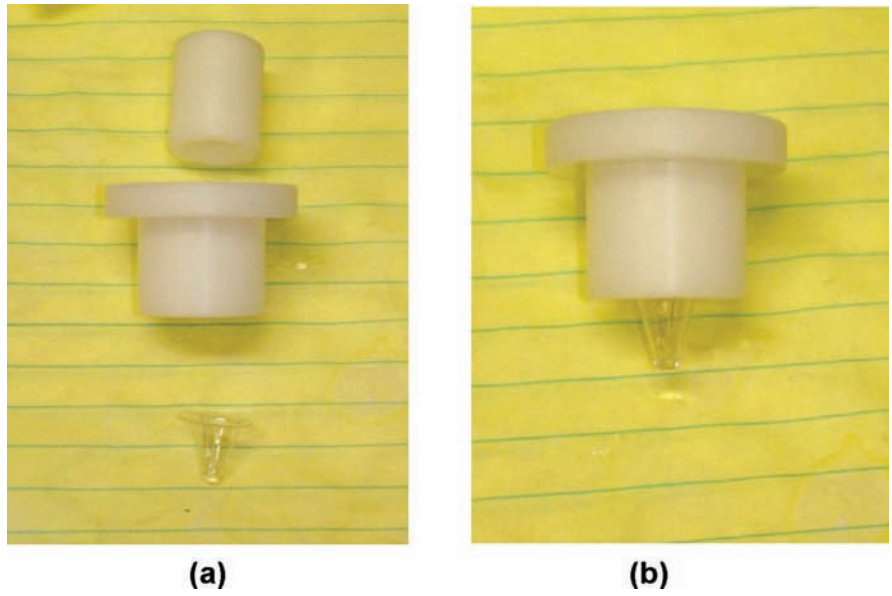

Figure 4. Sample holder assemblies for cell imaging.

cytometry. A direct comparison of fluorescence and photoacoustic signal could not be made using AF750-labeled Herceptin because the flow cytometer (FACS Calibur) could not operate at wavelengths exceeding 635 nm. For this reason, Herceptin was conjugated with AF647 dye in equivalent labeling conditions to those used for AF750. Approximately 0.5×10^6 breast cancer cells were incubated with ~50 μg probe (Herceptin-AF647) at 37 °C for 1.5 h. After labeling, cells were washed out three times by PBS, then the labeled cells were suspended in ~500 μL of PBS for flow cytometry measurements. Three measurements were made at each DOL. Suspension of corresponding unlabeled cells was used as control.

Cell-Binding Measurements by PCT. Both HER2 positive (MCF-7 and BT-474) and HER2 negative (MCF-7-PC-DMA and MDA-MB-231) cell lines were utilized for binding of the dye−Herceptin conjugates following standard cell culture protocols. Cells were maintained at 37 °C and 5% CO_2 in a humidified atmosphere. Approximately 0.5×10^6 breast cancer cells were incubated with ~50 μg probe (Herceptin-AF 750) at 37 °C for 1.5 h. After labeling, cells were washed out three times by PBS, then the labeled cells were suspended in PBS. Cells were counted in a Beckman Coulter cell counting machine before transferring to the sample holder. Finally, the cells were pelleted to the bottom of the sample holder by centrifugation.

For the AF-750−Herceptin-labeled cells, a 0.1 M solution of sodium bicarbonate in 25% DMSO was used. The labeled cells were transferred to the PCT sample holder so that the entire population could be contained in 100 μL of appropriate buffer. The sample was then centrifuged at 4000 rpm for 10 min. The cells formed a small layer at the tip of the holder. The sample holder was carefully placed in the assembly using the provided tool and one side of the holder was marked to designate this

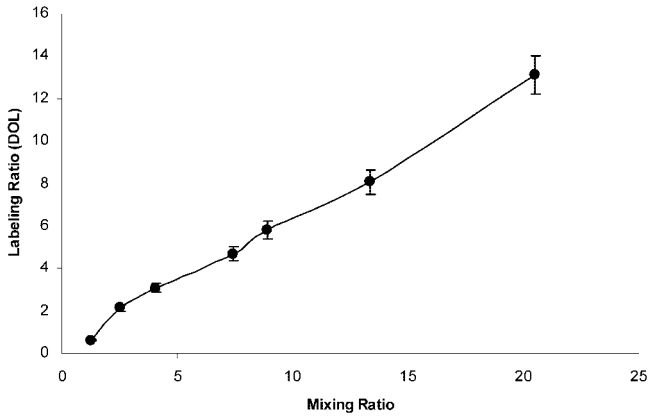

Figure 5. The dye (AF750) to protein (Herceptin) molar labeling ratio was measured at various dyes to protein molar mixing ratios.

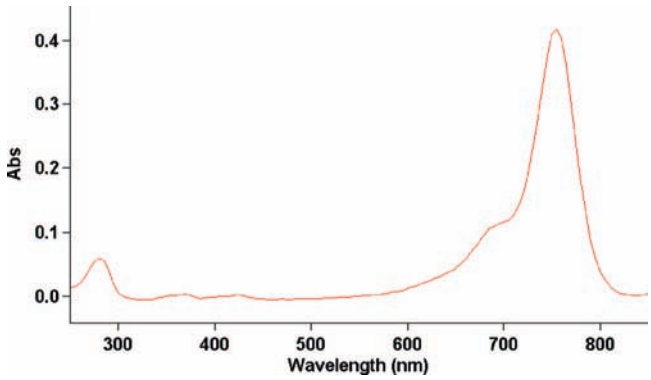

Figure 6. Representative UV−vis spectrum of Herceptin−AF750 conjugate (DOL 7) in 0.1 M bicarbonate buffer.

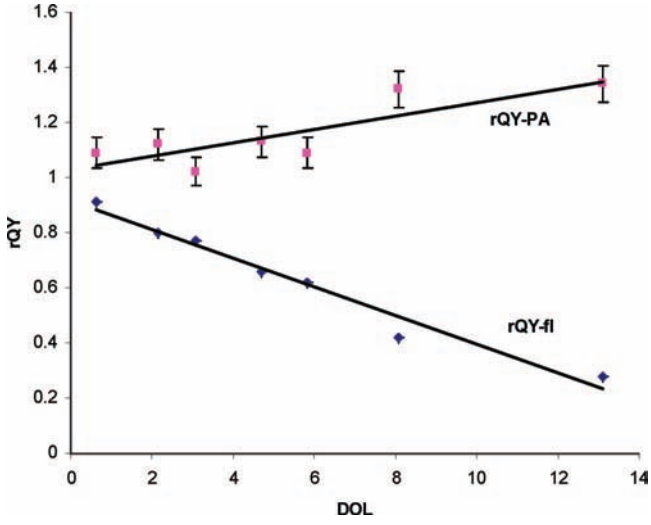

Figure 7. Per dye photoacoustic and per dye fluorescence signal intensity comparison with increase in DOL of Herceptin−AF750 conjugates.

orientation as 6 o'clock. The cylinder was inserted and locked in place. It was then placed in the imaging tank and rotated to align the index marks.

Images were acquired for the sample at 745 and 810 nm with 32 laser pulses per image. Then the 810 nm image was subtracted from the 745 nm image with an experimentally determined scaling factor (*k*) based on the varying absorption of the DMSO buffer (about 1.2 for PVC in 25% DMSO buffer). Nearly all of the extraneous signals were removed. The holder assembly was removed carefully by loosening the screw and

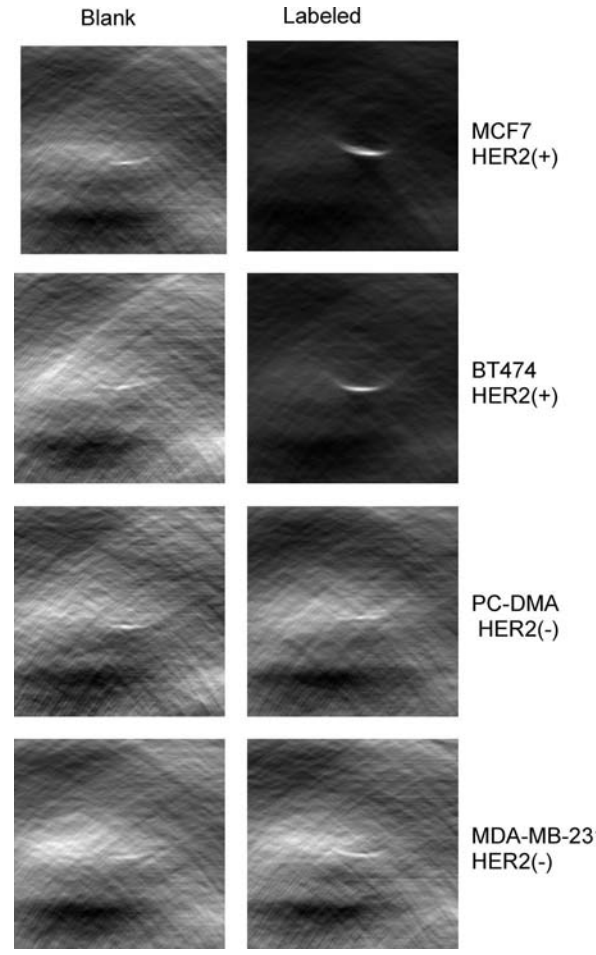

Figure 8. PCT images of HER2 positive and HER2 negative cell lines.

rotating the sample holder by 90° (3 o'clock) and two more images were obtained and subtracted as before. The same procedure was followed for the orientations at 180° (12 o'clock) and 270° (9 o'clock) from the initial position. We found no significant evidence of photobleaching of the sample for these 4 orientations. The ROI tool was used to take a small, thin ROI at the tip of the holder that corresponded to the layer of cells and the maximum value of photoacoustic intensities were measured. All 4 measurements from the different orientations were averaged together.

RESULTS AND DISCUSSION

After reactions of AF-750 or AF-647 with Herceptin, the products were isolated by gel filtration to a purity ≥98%. Increasing the dye to Herceptin molar ratio in the conjugation reaction over the range 2−21:1 resulted in increasing actual dye to antibody ratios, or degree of labeling (DOL), of 1−13:1 (Figure 5). A representative UV−vis spectrum of Herceptin−dye conjugate is shown in Figure 6.

In solution imaging of the probe, 25% DMSO in bicarbonate buffer was used to minimize the microbubble formation. Dye absorption maxima were at 745 nm, so the image obtained at this wavelength was due to dye and background (sample holder, microbubbles, etc.). At 810 nm, dye absorption was negligible; images obtained at this wavelength were indicative of the background. Corrected images of dye absorption were obtained by subtracting 810 nm image from the corresponding 745 nm images. For both solution and cell-binding measurements, the lambda subtraction technique worked effectively to eliminate background variation including microbubbles from the image.

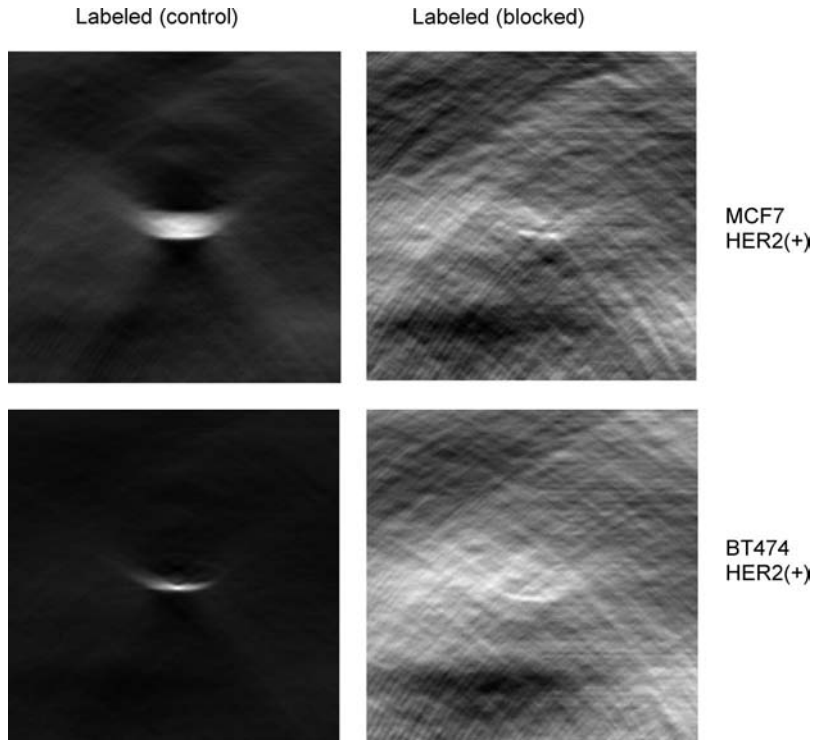

Figure 9. PCT images of unblocked and blocked HER2(+) cells.

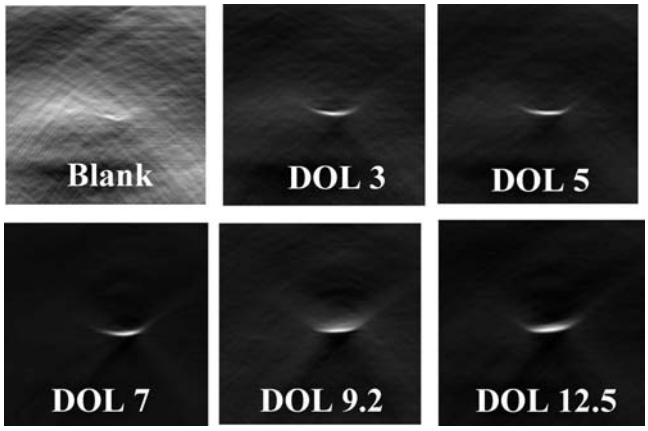

Figure 10. Representative PCT images of MCF7 HER2 positive cell lines at different DOL at constant no. of cells (0.2×10^6).

In cell-binding measurements, cells were packed to form a thin layer at the bottom of the sample holder by centrifuging using a hanging bucket rotor. Loose packing produced low-quality images. The sample holder could accommodate up to 0.3 million cells at the bottom to form a uniform layer. If the number exceeded 0.3 million, the layer became thicker, and the acoustic signal did not scale with the number of cells.

rQY-fl vs rQY-PA of AF750−Herceptin Conjugates. As the DOL increased, the fluorescence of any single fluorophore decreased when compared with free AF750 in solution. Comparative measurement between free Alexa Fluor dye molecules and Herceptin−Alexa Fluor conjugates in solution showed that with increasing DOL from 1 to 13, fluorescence intensity per dye (rQY-fl) gradually decreased (up to ~70%). Measurement of corresponding photoacoustic signal intensity (rQY-PA) per dye produced meaningful results. Though the data showed considerable noise, we observed that rQY-PA was gradually increased (up to ~25%) with increase in DOL (Figure 7). It is suggested that increased heat generated due to fluorescence quenching is the source of increased photoacoustic signal intensity per dye molecule.

Receptor Specificity of the Probe by PCT. HER2 positive (BT-474 and MCF-7) and HER2 negative (MCF-7-PC-DMA and MDA-MB-231) cell lines were incubated with Herceptin−dye conjugates (DOL 5). Approximately 0.2×10^6 cells of each cell line were used for cell imaging by PCT. In addition, blank samples, for which cells were not exposed to the probe, were imaged.

Figure 8 shows representative images of blank and labeled cell lines. Only HER2 positive cell lines gave high-intensity acoustic images. Signal intensity of HER2 negative cell lines was similar to that of corresponding unlabeled cells.

In a blocking experiment, HER2 positive (BT-474 and MCF-7) cells were at first incubated with unlabeled Herceptin for 1 h at 37 °C, then equal amount of Herceptin−dye conjugate (DOL 5) was added and incubated again for another 1.5 h.

PCT image intensities (Figure 9) showed that unlabeled Herceptin blocked >95% of the Herceptin−dye conjugate binding to the HER2 positive cells, demonstrating the specificity of labeled Herceptin binding to HER2. (Figure 10).

PCT Imaging of HER2 Positive Cells. In order to evaluate NIR dye labeled Herceptin as a PCT probe, HER2 positive cell lines were incubated with Herceptin−dye conjugates having different DOL, followed by PCT imaging. Equal numbers of cells (0.2×10^6) were used to determine the variation of acoustic signal intensity with increase in DOL of the probe. In Figure 10, cell imaging of MCF7 cells is shown. After subtraction of the PCT intensity corresponding to a sample with no probe (blank), signal intensity increased with increasing DOL (Figure 11). In contrast to this finding, fluorescence signal intensity from cells generally decreases for DOL greater than 3 (*21–23*). There was a slight upward exponential trend of the intensity vs DOL plots (Figure 11), indicating the tendency toward an increase in photoacoustic signal intensity per dye (Figure 7) as DOL is increased. The results also indicate that cell uptake of the probe does not appear to suffer from saturation effects at the HER2 receptors.

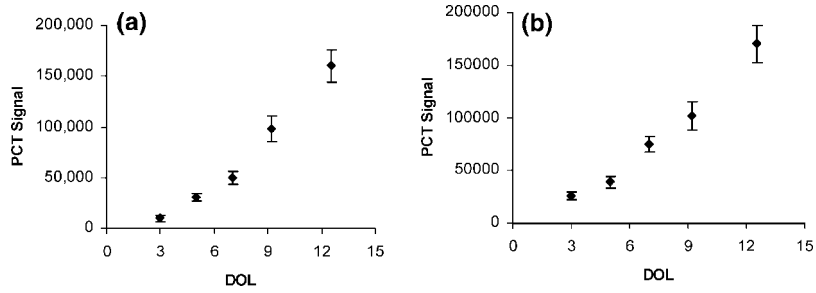

Figure 11. DOL vs peak photoacoustic signal intensity (arb. unit) of PCT images obtained by using ROI tool. Plot (a) is for MCF7 and plot (b) is for BT474 cell lines labeled with Herceptin−AF750 conjugates.

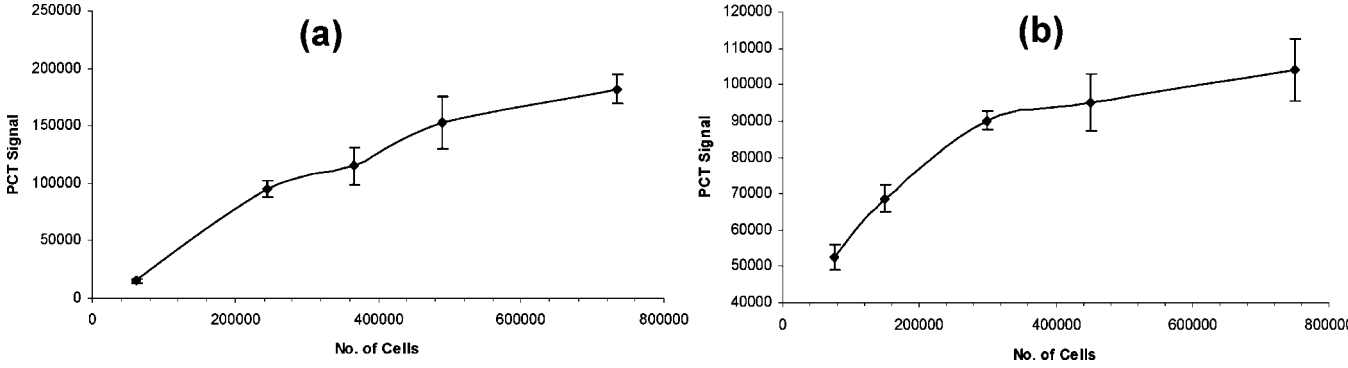

Figure 12. Change of PCT signal intensity with no. of cells at constant DOL: plot (a) BT474 HER2(+), DOL 6 (b) MCF7 HER2(+), DOL 4.5, and plot.

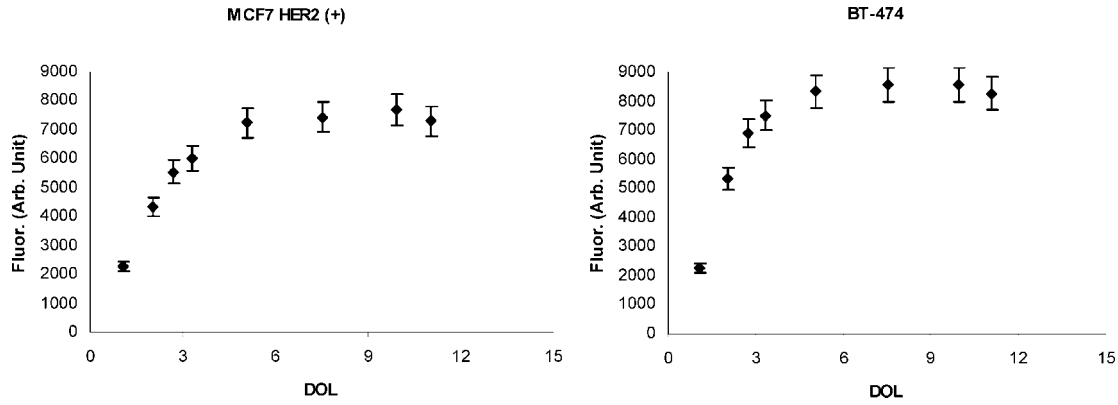

Figure 13. Fluorescence vs DOL of HER(+) cells labeled with Herceptin−AF647 conjugates obtained by flow cytometry.

Acoustic signal intensity was also varied with number of cells per sample while keeping DOL constant. The acoustic signal gradually increased with the number of cells up to of 0.3 million (Figure 12). Because of the narrow sample holder tip, when the number of cells exceeded 0.3 million, the cell layer became substantially thicker. The resultant signal plateaued because the layer was no longer contained within a thickness equivalent to the spatial resolution of the PCT system, i.e., 0.2 mm. This was verified by analyzing the apparent thickness of the PCT image of the cells. Experiments in the two HER2 positive cell lines yielded similar results.

The uncertainties of the PCT signals shown in Figures 11 and 12 were derived from four measurements made at different orientations for each sample. The signal was clearly dependent on the orientation the holder. For example, orientations at 6 and 12 o'clock gave similar PCT signal values, as did 3 and 9 o'clock orientations, but the two groups were distinct. The dependence on orientation was a function of the position relative to the linear array. For larger number of cells in the tube (Figure 12), the distinction of PCT signal between two groups became larger because the cells were less uniformly deposited on the bottom. We could typically see the layer creeping up one side of the tube as the number of cells increased. Our solution to this problem was to measure at four orientations and average the measurements.

Fluorescence and PCT Signal vs DOL of HER2(+) Cells. In order to compare PCT signal with fluorescence signal of the cells labeled by Herceptin−dye conjugates, we performed flow cytometry experiments to determine the fluorescence intensity per labeled cell. Because the flow cytometer (FACS Calibur) could not excite beyond 635 nm, AF647 was substituted for AF750 as labeling dye. AF647 and AF750 are almost equivalent in terms of their molecular weight and molar extinction coefficient. The flow cytometry data (Figure 13) for both cell lines indicated that fluorescence signal intensity reached a plateau higher DOL values, whereas PCT signal intensity (Figure 11) increased with DOL over the entire DOL range.

CONCLUSION

From this *in vitro* study, we have successfully demonstrated potential for NIR dye labeled Herceptin to be used as a PCT

probe for breast cancer. A large PCT signal with respect to control (cells with no probe) was obtained by labeling Herceptin with several dye molecules per molecule of protein. Unlike fluorescence, the photoacoustic signal gradually increased with increasing DOL of the dye. Moreover, it was shown that cellular binding to HER2 positive cell lines was maintained with increase in DOL of the dye over the range of 2 to 13. *In vivo* and *in vitro* studies with different low-fluorescence QY dyes are underway. It is believed that this labeling and detection scheme will be applicable to a broad class of biomolecules.

Before this technique can be translated to clinical applications, we will have to deal with two issues: obtaining sufficient SNR at depths of 2−3 cm in the breast, and accounting for hemodynamic variation within tumors. Phantom experiments suggest that we can detect dye concentrations in the 50−100 nM range at a depth of 30 mm. The confounding issues of hemodynamic variability can be mitigated to a large degree by choosing a differential pair of wavelengths that are 20−40 nm apart and straddle the falling edge of the dye absorption curve. In this case, the differential dye signal is maximized, while the differential hemoglobin signal is minimized. Work is ongoing to quantify these properties in greater detail.

ACKNOWLEDGMENT

Authors are thankful to Dr. Kathy D. Miller for providing breast cancer cell lines. This work is supported by National Institutes of Health: R01-CA108620 and R44-CA114839.

LITERATURE CITED

(1) Kiser, Jr.,W. L., Reinecke, D., DeGrado, T., Bhattacharyya, S., and Kruger, R. A. (2007) Photoacoustic molecular imaging. *Proc. SPIE 6437*, 21–27.

(2) Bhattacharyya, S., Wang, S., Reinecke, D., Jr., Kruger, R. A., and DeGrado, T. R. (2007)Evaluation of NIR-dye labeled herceptin as a thermoacoustic computed tomography (TCT) probe for HER-2 expression in breast cancer. AMI/SMI Meeting, Providence, RI (Abstract).

(3) Kaufmann, B. A., and Lindner, J. R. (2007) Molecular imaging with targeted contrast ultrasound. *Curr. Opin. Biotechnol. 18*, 11–16.

(4) Song, K. H., Stoica, G., and Wang, L. H. V. (2006) In-vivo three dimensional photoacoustic imaging of blood vessels in tissue. *Opt. Lett. 23*, 648–650.

(5) Klibanov, A. L. (2005) Ligand-carrying gas-filled microbubbles: ultrasound contrast agents for targeted molecular imaging. *Bioconjugate Chem. 16*, 9–17.

(6) Bloch, S. H., Dayton, P. A., and Ferrara, K. W. (2004) Targeted imaging using ultrasound contrast agents. progress and opportunities for clinical and research applications. *IEEE Eng. Med. Biol. Mag. 23*, 18–29.

(7) Oraesky, A., Karabutov, A., Solomatin, V. S., Savateeva, E. V., Andreev, V. G., Gatalica, Z., Singh, H., and Fleming, R. Y. D. (2001) Laser optoacoustic imaging of breast cancer in vivo. *Proc. SPIE 4256*, 12–22.

(8) Kruger, R. A., Jr., Reinecke, D. R., Kruger, G. A., and Eisenhart, R. L. (1999) Thermoacoustic computed tomography of the breast at 434 MHz. *Proc. IEEE, MTT-S:* 591–594.

(9) Xu, Y., and Wang, L. H. (2006) Rhesus monkey brain imaging through intact skull with thermoacoustic tomography. *IEEE Transactions on Ultrasonics Ferroelectrics and Frequency Control 53* (3), 542–548.

(10) Wang, X., Xie, X., Ku, G., Stoica, G., and Wang, L. H. (2006) Non invasive imaging of hemoglobin concentration and oxygenation in the rat brain using high-resolution photoacoustic tomography. *J. Biomed. Opt. 11* (2), 024015.

(11) Wang, S. C., Zhang, L., Hortobagyi, G. N., and Hung, M. C. (2001) Targeting Her-2: recent developments and future directions for breast cancer patients. *Sem. Oncol. 28* (6), 21–29, Suppl 18 (December).

(12) Hynes, N. E., and Stern, D. F. (1994) The biology of erB-2/neu/Her-2 and its role in cancer. *Biochim. Biophys. Acta 1198*, 165–184.

(13) Slamon, D. J., Clark, G. M., Wong, S. G., Levin, W. J., Ullrich, A., and McGuire, W. L. (1987) Human breast cancer: correlation of relapse and survival with amplification of Her2/neu oncogene. *Science 235*, 177–182.

(14) Venter, D. J., Tuzi, N. L., Kumar, S., and Gullick, W. J. (1987) Overexpression of the c-erbB-2 oncoprotein in human breast carcinomas; immunohistological assessment correlates with gene amplification. *Lancet 2*, 69–72.

(15) Yarden, Y. (2001) Biology of Her2 and its importance in breast cancer. *Oncology 61*, 1–13.

(16) Nelson, N. J. (2000) Experts debate value of Her2 testing methods. *J. Natl. Cancer Inst. 92* (4), 16.

(17) Van de Vijver, M. (2002) Emerging technologies for Her2 testing. *Oncology 63*, 33–38.

(18) Kohen, E., Santus, R., and Hirschberg, J. G. (2002) *Fluorescence Probes in Oncology*, Chapter 2, Imperial College Press, London.

(19) Kurian, E., Prendergast, F. G., and Small, J. R. (1997) Photoacoustic analysis of proteins: volumetric signals and fluorescence quantum yields. *Biophys. J. 73*, 466–476.

(20) Licha, K., Riefke, B., Ebert, B., and Grontzinger, C. (2002) Cyanine dyes as contrast agents in biomedical optical imaging. *Acta Radio. 9*, S320–S322.

(21) Steinberg, T. H., Nyhus, J. K., Aggeler, B., Leong, L., and Greenfield, L. (2006)Functional Labeling of in vivo Imaging Optical Probes. Poster presentation at Society of Molecular Imaging annual meeting, Hawaii.

(22) Berlier, J. E., Rothe, A., Buller, G., Bradford, J., Gray, D. R., Filanoski, B. J., Telford, W. G., Yue, S., Liu, J., Cheung, C. Y., Chang, W., Hirsch, J. D., Beechem, J. M., and Haugland, R. P. (2003) Quantitative comparison of long-wavelength alexa fluor dyes to cy dyes: fluorescence of the dyes and their bioconjugates. *J. Histochem. Cytochem. 51* (12), 1699–1712.

(23) Ohnishi, S., Lomnes, S. J., Laurance, R. G., Gogbashian, A., Mariani, G., and Frangioni, J. V. (2005) Organic alternative to quantum dots for intraoperative near-infrared fluorescent sentinel lymph node mapping. *Mol. Imaging 4* (3), 172–181.

BC700482U

Functionalized Thermoresponsive Micelles Self-Assembled from Biotin-PEG-*b*-P(NIPAAm-*co*-HMAAm)-*b*-PMMA for Tumor Cell Target

Cheng Cheng, Hua Wei, Jing-Ling Zhu, Cong Chang, Han Cheng, Cao Li, Si-Xue Cheng, Xian-Zheng Zhang,* and Ren-Xi Zhuo

Key Laboratory of Biomedical Polymers of Ministry of Education and Department of Chemistry, Wuhan University, Wuhan 430072, China. Received January 4, 2008; Revised Manuscript Received March 30, 2008

Novel micelles, comprising hydrophilic PEG shells, hydrophobic PMMA cores, and thermosensitive P(NIPAAm-*co*-HMAAm) segments were self-assembled from the biotin-PEG-*b*-P(NIPAAm-*co*-HMAAm)-*b*-PMMA triblock copolymer. The thermosensitive micelles exhibited superior stability and showed thermotriggered drug release behavior upon temperature alterations. The fluorescence spectroscopy and confocal microscopy studies confirmed that the self-assembled biotinylated micelles can be specifically and efficiently bonded to cancer cells with the administration of biotin−transferrin, suggesting that the multifunctional micelles have great potential as drug carriers for tumor targeting chemotherapy.

INTRODUCTION

Traditional cancer chemotherapy relies on the premise that rapidly proliferating cancer cells are more likely to be killed by anticancer drugs. However, the nonspecific actions of the anticancer agents lead to systemic toxicity, causing undesirable severe side effects such as damage to liver, kidney, hair loss, and bone marrow (*1*). To reduce the side effects and to increase the local drug concentration at the targeting site, biotin−avidin systems (BAS) have been introduced to drug delivery systems to realize pretargeting in tumor chemotherapy (*2, 3*). Due to the considerable binding affinity between biotin and avidin, BAS can serve as a universal linkage between biotinylated polymeric drug carriers and other proteins. In the pretargeting approach, the biotinylated therapeutic carrier is administered after an appropriate delay, followed by the administration of active targeting ligands, such as avidin-conjugated monoclonal antibodies (*4*).

In the past decade, amphiphilic block copolymers have been extensively investigated with respect to fundamental research as well as biomedical applications (*5–14*). The unique character of the amphiphilic block copolymers enables them to self-assemble in an aqueous solution to form micelles (*15–20*). Due to the small size and the hydrophilic surface, polymeric micelles are not easily recognized and captured by the reticuloendothelial systems (RES) (*21, 22*). Accordingly, the polymeric micelles have a relatively long circulation time after intravenous administration and, as a result, they enrich in tumor tissues due to the enhanced permeation and retention effect (EPR effect) (*23*). Very recently, intelligent polymeric materials have been developed to be drug carriers for controlled release, such as stimuli-responsive polymeric micelles (*24–27*) and bioactive site-specific targeting carriers (*4, 28*). To date, as far as we know, very few studies deal with multifunctional drug carriers especially self-assembled polymeric micelles with both environmental sensitivity and specific targeting function (*29, 30*).

In this study, we designed and prepared a new type of multifunctional micelle as the drug carrier which not only has thermosensitivity, but also can be functionalized with a variety of ligands. The micelles were self-assembled by biotinylated amphiphilic biotin−poly(ethylene glycol)-*block*-poly(*N*-isopropylacrylamide-*co*-*N*-hydroxylmethylacrylamide)-*block*-poly(methyl methacrylate) (biotin-PEG-*b*- P(NIPAAm-*co*-HMAAm)-*b*-PMMA) triblock copolymer. The self-assembly and thermally induced change of the triblock copolymer micelle are schematically illustrated in Scheme 1. In the triblock copolymer, the PEG block was introduced as a hydrophilic segment due to its good biocompatibility and ability to stabilize the micelles and to protect them from being cleared up by the RES (*31*). Since the PEG shell was hydrophilic regardless of the temperature, the micelles self-assembled from the triblock copolymer would be more stable in water due to the fact that the PEG shell would prevent the aggregation of conventional PNIPAAm-based micelles once reaching the temperature above the LCST (*20, 32, 33*). Besides, the flexible PEG spacer offered an optimized accessibility for ligands (*28*). The PMMA block was used as a hydrophobic segment. The purpose to incorporate the poly(*N*-isopropylacrylamide-*co*-*N*-hydroxylmethylacrylamide) block was to endow the copolymer with thermosensitivity. Poly(*N*-isopropylacrylamide) (PNIPAAm) is known for exhibiting a reversible thermoresponsive phase transition in an aqueous solution at around 32 °C, termed lower critical solution temperature (LCST). However, such a LCST is not always favorable for biomedical applications since the physiologic temperature is around 37 °C. Herein, the hydrophilic *N*-hydroxylmethylacrylamide (HMAAm) was employed to adjust the LCST of the copolymer, since HMAAm is more hydrophilic, and an increase in its content would lead to a higher LCST. The

Scheme 1. Schematic Illustration of the Thermally Induced Structure Change of Micelles Self-Assembled from the Triblock Copolymer in an Aqueous Solution

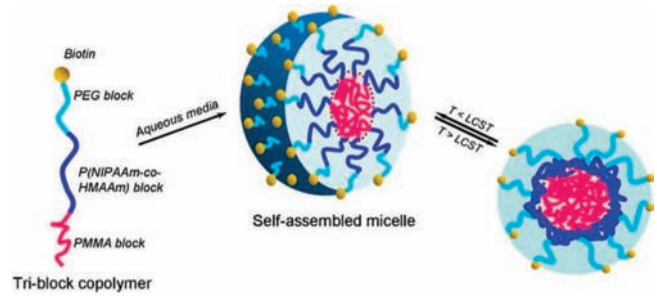

* Corresponding author. Tel./fax: +86 27 68754509. E-mail address: xz-zhang@whu.edu.cn (X. Zhang).

10.1021/bc8000062 CCC: $40.75 © 2008 American Chemical Society
Published on Web 05/14/2008

P(NIPAAm-*co*-HMAAm) block was hydrophilic when the temperature was lower than the LCST, and became hydrophobic when the temperature was higher than the LCST.

Furthermore, the biotin molecule was introduced to the micelle drug delivery system and BAS can be further used as reagents for pretargeting method in chemotherapy to increase the local concentration of drug at the target site resulting from the fact that active recognizing ligands can be incorporated into the drug delivery system through biotin−avidin interactions. In the pretargeting approach, the biotinylated drug carrier is administered after an appropriate delay, following the recognizing ligands conjugated with avidin, instead of coupling with them directly which may cause the denaturation of these ligands during the synthesis process in organic solvent. In addition, the delay allows for the antibody to localize and concentrate in the specific tissues, and then the thermoresponsive drug carrier can perform the controlled thermotriggered release by changing the environmental temperature.

MATERIALS AND METHODS

Materials. *N*-Isopropylacrylamide (NIPAAm), 3-mercaptopropionic acid (MPA), and 2-amino-ethanethiol hydrochloride (AET·HCl) purchased from Acros were used as received. Rhodamine B, *N*-hydroxymethylacrylamide (HMAAm), *N*-hydroxysuccinimide (NHS), and dicyclohexylcarbodiimide (DCC) were obtained from Tianjin Chemical Reagent Co. (Tianjin, China) and used as received. Biotin, dithiobis (succinimidyl propionate) (DSP), and fluorescein isothiocyanate-labeled avidin (FITC-avidin) were purchased from Pierce, and used as received. 1,1-Carbonyldiimidazole (CDI) and biotinylated transferrin (biotin-trasferrin) obtained from Sigma-Aldrich were used as received. *N*,*N*′-Dimethylformamide (DMF), methyl methacrylate (MMA), tetrahydrofuran (THF), and 1,4-dioxane obtained from Shanghai Chemical Reagent Co. were used after distillation. Diamine poly(ethylene glycol) (H_2N-PEG-NH_2) with a molecular weight of 3000 g/mol (in THF) and 4,4′-azobis-4-cyanovaleric acid (ACVA) were purchased from Fluka and used as received. Dithiothreitol (DTT) was obtained from Shanghai BoAo Biotechnical Co. Ltd. and used as received. *N*,*N*′-Azobisisobutyronitrile (AIBN) provided by Shanghai Chemical Reagent Co. (Shanghai, China) was used after recrystallization from 95% ethanol. MTX was kindly gifted by SuRi Biochem Co. Ltd. (Suzhou, China). All other reagents and solvents were used without further purification.

Preparation of Biotin-PEG-*b*-P(NIPAAm-*co*-HMAAm)-*b*-PMMA. Amino-terminated biotinylated poly(ethylene glycol) (biotin-PEG-NH_2) was synthesized according to the literature (*24*). Biotin-PEG-NH_2 (1.77×10^{-4} mol) was dissolved in 3 mL DMSO. DSP (8.85×10^{-5} mol) in 3 mL of DMF was then added to the reaction flask to obtain biotin−PEG dimer and biotin−PEG was connected by disulfide bonds. The reaction mixture was stirred for 24 h at room temperature. The dimer was reduced by adding DTT (2.66×10^{-4} mol) to the reaction mixture and the reaction was carried out at room temperature for 24 h to obtain sulfhydryl-terminated biotinylated PEG (biotin-PEG-SH).

Carboxyl-terminated biotin-PEG-*b*-P(NIPAAm-*co*-HMAAm) block was synthesized by copolymerizing NIPAAm and HMAAm (the molar ratio of NIPAAm and HMAAm is 10:1) by using ACVA as an initiator (*30, 31*) and biotin-PEG-SH as a macromolecular chain transfer reagent. Amino-terminated PMMA (PMMA-NH_2) was prepared by radical polymerization by using AET·HCl as a chain transfer agent. MMA (4.8×10^{-2} mol), AET·HCl (1.92×10^{-3} mol), and AIBN (2.4×10^{-4} mol) were dissolved in 20 mL DMF. The solution was degassed by bubbling with nitrogen for 30 min. Polymerization was carried out at 60 °C for 6 h. After reaction, the product was purified by repeated precipitation in water, and then the product was dried in vacuum.

The resulting carboxyl-terminated biotin-PEG-*b*-P(NIPAAm-*co*-HMAAm) (0.10 g), PMMA-NH_2 (0.10 g), and NHS (4.0×10^{-5} mol) were dissolved in 4 mL dioxane. DCC (4.0×10^{-5} mol) in 1 mL dioxane was added dropwise to the solution under nitrogen atmosphere. After 24 h reaction at room temperature, the product was precipitated in excess diethyl ether and dried in vacuum after filtration.

GPC Measurements. Number-average molecular weight (M_n) of PMMA-NH_2, biotin-PEG-*b*-P(NIPAAm-*co*-HMAAm)-COOH, and biotin-PEG-*b*-P(NIPAAm -*co*-HMAAm)-*b*-PMMA were determined by gel permeation chromatographic (GPC) system equipped with a Waters 2690D separations module and a Waters 2410 refractive index detector. THF was used as the eluent at a flow rate of 0.3 mL/min. Waters millennium module software was used to calculate molecular weight on the basis of a universal calibration curve generated by polystyrene standard with narrow molecular weight distribution.

Optical Absorption Measurements. Optical absorbance of the biotin-PEG-*b*-P(NIPAAm-*co*-HMAAm)-COOH and biotin-PEG-*b*-P(NIPAAm-*co*- HMAAm)-*b*-PMMA copolymer aqueous solution (600 mg/L) at various temperatures was measured at 542 nm with a Lambda Bio40 UV−vis spectrometer (Perkin-Elmer). Sample cell was thermostatted in a refrigerated circulator bath at a predefined temperature prior to measurements. The LCST of the polymer solution was defined as the temperature producing a half-increase of the total increase in optical absorbance.

In Vitro Cytotoxicity Study. For each well in a 96-well plate, 200 μL of human vein endothelial cell line (ECV304) in RPMI1640, with a concentration of 2.5×10^5 cells/mL, was added. After incubation for 24 h in incubator (37 °C, 5% CO_2), The culture medium was changed to 200 μL of RPMI1640 containing biotin-PEG-*b*-P(NIPAAm-*co*-HMAAm)-*b*-PMMA copolymer with a particular concentration and the mixture was further incubated for 48 h. Then, RPMI1640 with polymer was replaced by fresh RPMI1640 and 20 μL of MTT solution (5 mg/mL) and was added to the ECV304. After incubation for 4 h, 200 μL of DMSO was added and shaken at room temperature. The optical density (OD) was measured at 570 nm with a Microplate Reader (model 550).

Micelle Formation. Membrane-dialysis method was used to prepare micelles through self-assembly of biotin-PEG-*b*-P(NIPAAm-*co*-HMAAm)-*b*-PMMA copolymer. In brief, the triblock copolymer (10 mg) was dissolved in 2 mL DMF. The solution was put into a dialysis tube (molecular weight cutoff: 8000−10 000 g/mol) and subjected to dialysis against 1000 mL distilled water for 24 h, then lyophilized before further examinations.

FT-IR and ^{1}H NMR Characterizations. FT-IR spectra were recorded on an AVATAR 360 spectrometer. Samples were pressed into potassium bromide (KBr) pellets. ^{1}H NMR spectra were recorded on a Mercury VX-300 spectrometer at 300 Hz using $CDCl_3$ and D_2O as the solvents.

Fluorescence Measurements. Fluorescence spectra were recorded on a LS55 luminescence spectrometer (Perkin-Elmer) and pyrene was used as a hydrophobic fluorescent probe (*20*). Aliquots of pyrene solutions (6×10^{-6} M in acetone,1 mL) were added to containers, and the acetone was allowed to evaporate. Ten-milliliter aqueous polymer solutions at different concentrations were then added to the containers containing the pyrene residue. It should be noted that all the aqueous sample solutions contained excess pyrene residue at the same concentration of 6×10^{-7} M. The solutions were kept at room temperature for 24 h to reach the solubilization equilibrium of

pyrene in the aqueous phase. Excitation was carried out at 340 nm, and emission spectra were recorded ranging from 350 to 600 nm. Both excitation and emission bandwidths were 10 nm. From the pyrene emission spectra, the intensities (peak height) of I_{373nm} were analyzed as a function of the polymer concentration.

Transmission Electron Microscopy (TEM). A drop of micelle suspension stained by a drop of 1% (w/v) phosphotungstic acid was placed on a copper grid with Formvar film and dried before observation on a JEM-100CXa transmission electron microscope (TEM) at an acceleration voltage of 80 kV.

Size Distribution Measurements. The size distribution of micelles was determined by a Nano Series Nano-ZS (MALVERN Instrument) zetasizer. The micelle aqueous solution (100 mg/L) was passed through a 0.45 μm pore-sized syringe filter and kept in the thermostat of the apparatus at 37 °C (±0.05 °C) for 20 min to reach the equilibrium prior to the measurements.

Drug Loading and In Vitro Drug Release. Biotin-PEG-*b*-P(NIPAAm-*co*- HMAAm)-*b*-PMMA triblock copolymer (10 mg) and MTX (5 mg) were dissolved in 2 mL DMF. The solution was put into a dialysis tube and subjected to dialysis against 1000 mL distilled water at 25 °C for 24 h. To determine the EE, the drug-loaded micelles solution was lyophilized, and then dissolved in DMF and analyzed by UV absorbance at 303 nm.

After dialysis, the dialysis tube was directly immersed into 400 mL distilled water. Aliquots of 4 mL were withdrawn from the solution periodically. The volume of solution was held constant by adding 4 mL distilled water after each sampling. The amount of MTX released from micelles was measured at different temperatures using UV absorbance at 303 nm.

Fluorescence Dye Loading. Biotin-PEG-*b*-P(NIPAAm-*co*-HMAAm)-*b*-PMMA triblock copolymer (10 mg) and rhodamine B (5 mg) were dissolved in 2 mL DMF. The solution was put into a dialysis tube and subjected to dialysis against 1000 mL distilled water at 25 °C for 24 h. Then, the dye-loaded micelles were lyophilized before further measurements.

Cell Uptake Study. The dye-loaded freeze-dried micelles (200 μg) and FITC-avidin 100 μg were dissolved in 1.0 mL 0.01 M phosphate buffer saline (PBS, pH 7.4), respectively. Then the two solutions were mixed and shaken at room temperature for 30 min. The solution was centrifuged (10 000−12 000 r/min) for 15 min, and then the sediment was washed with cold PBS three times, and suspended again in 2.0 mL PBS as the FITC-labeled micelle samples. HeLa, A549, and ECV304 cells were seeded into a 24-well plate (1×10^5 cells/well) containing 1 mL of DMEM media to grow to ~70% confluence after 24 h incubation. 100 μL biotin−transferrin (200 μg/mL) was then added in each well and incubated with cells for 2 h at 37 °C. After the incubation, the medium was removed and cells were washed with cold PBS three times. Then, 1 mL DEME medium containing 100 μL FITC-avidin-rhodamine B loaded micelle complex was added in each well and incubated with cells for another 2 h at 37 °C. After that, medium was again removed and cells were washed with cold PBS three times. In addition, another plate of HeLa sample was administrated without the biotin−transferrin step for comparison. Finally, 1 mL of DMSO was added in each well to lyse cells. Fluorescence emission intensities of FITC at 490 nm and rhodamine B at 570 nm (LS55 luminescence spectrometer, Perkin-Elmer) provided means for the measurement of internalized FITC and rhodamine B levels.

Confocal Microscopy Observation. Cells were seeded into specific confocal investigation plates containing 1 mL DMEM media (1×10^5 cells/plate). Then the samples were treated in the same way of fluorescent spectroscopy analysis. The fluorescent images of cells were analyzed using laser scanning confocal microscopy (Leica TCS SP2AOBS, Germany).

Scheme 2. Synthesis of Biotin-PEG-*b*-P(NIPAAm-*co*-HMAAm)-*b*-PMMA Triblock Copolymer

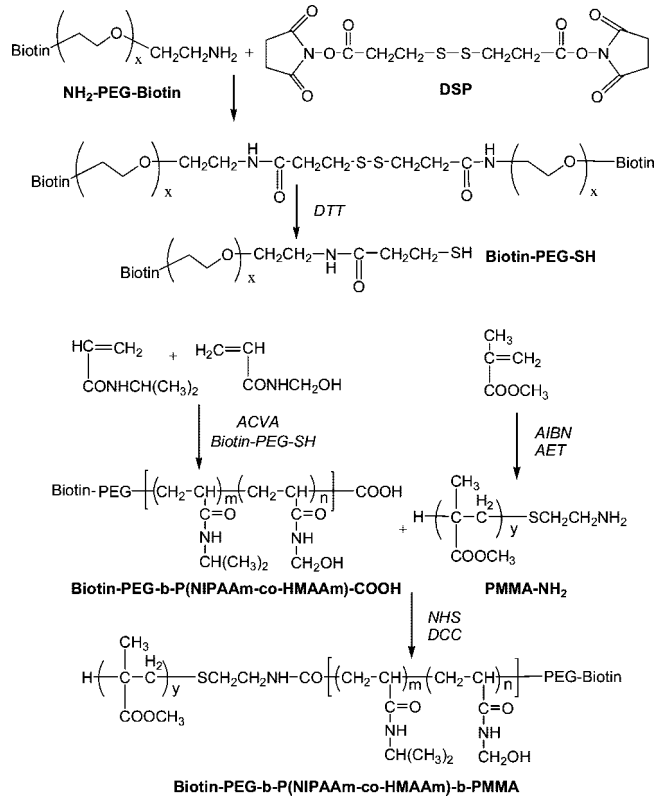

Table 1. GPC Data of Biotin-PEG-*b*-P(NIPAAm-*co*-HMAAm)-COOH, PMMA-NH_2, and Biotin-PEG-*b*-P(NIPAAm-*co*-HMAAm)-*b*-PMMA

sample	M_n	M_w/M_n
biotin-PEG-*b*-P(NIPAAm-*co*-HMAAm)-COOH	11 032	1.6
PMMA-NH_2	5 473	1.7
biotin-PEG-*b*-P(NIPAAm-*co*-HMAAm)-*b*-PMMA	15 484	1.8

RESULTS AND DISCUSSION

Synthesis of Biotin-PEG-*b*-P(NIPAAm-*co*-HMAAm)-*b*-PMMA. Carboxyl-terminated biotin-PEG-*b*-P(NIPAAm-*co*-HMAAm) block (biotin-PEG-*b*-P(NIPAAm-*co*-HMAAm)-COOH) was synthesized by copolymerizing NIPAAm and HMAAm by using ACVA as an initiator and biotin-PEG-SH as a macromolecular chain transfer reagent. And amino-terminated PMMA (PMMA-NH_2) was prepared by radical polymerization by using AET·HCl as a chain transfer agent. Finally, the triblock copolymers of biotin-PEG-*b*-P(NIPAAm-*co*-HMAAm)-*b*-PMMA were obtained by a condensation reaction between the carboxylic end groups of biotin-PEG-*b*-P(NIPAAm-*co*-HMAAm) and amino end groups of PMMA. The detailed synthesis procedure is illustrated in Scheme 2. The block coupling was confirmed by molecular weights determined by GPC (Table 1) and ^{1}H NMR spectrum of biotin-PEG-*b*-P(NIPAAm-*co*-HMAAm)-*b*-PMMA in $CDCl_3$ (Figure 4a), which reveals the presence of signals from PEG, P(NIPAAm-*co*-HMAAm), and PMMA blocks.

In addition, it can be seen from Figure 1 that the LCSTs of biotin-PEG-*b*-P(NIPAAm-*co*-HMAAm)-COOH and biotin-PEG-*b*-P(NIPAAm- *co*-HMAAm)-*b*-PMMA were determined to be 43.1 and 40.8 °C, respectively.

Cytotoxicity Study. Cytotoxicity study was performed to evaluate the cytotoxicity of the biotinylated triblock copolymer.

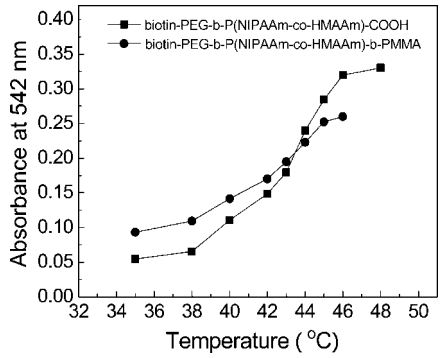

Figure 1. Optical absorbance of biotin-PEG-*b*-P(NIPAAm-*co*-HMAAm)-COOH and biotin-PEG-*b*-P(NIPAAm-*co*-HMAAm)-*b*-PMMA triblock copolymer in aqueous solutions/suspensions at various temperatures. (Polymer concentration was 600 mg/L).

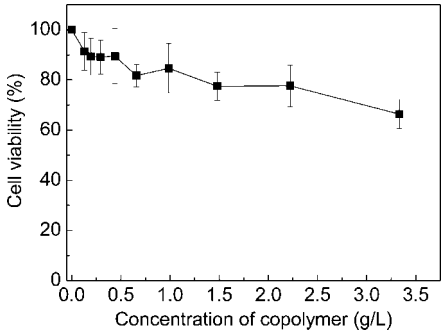

Figure 2. Cytotoxicity study of biotin-PEG-*b*-P(NIPAAm-*co*-HMAAm)-*b*-PMMA triblock copolymer.

The effect of the polymer concentration on the proliferation of human vein endothelial cells (ECV304) was studied and it can be seen from Figure 2 that the cell viability was above 60% even when the copolymer concentration was as high as 3.3 g/L, suggesting that the copolymer exhibits no apparent cytotoxicity.

Micelle Formation. The structures of biotin-PEG-*b*-P(NIPAAm-*co*- HMAAm)-COOH, PMMA-NH_2, biotin-PEG-*b*-P(NIPAAm-*co*-HMAAm)-*b*-PMMA block copolymer, and the resulting micelles were characterized by FT-IR. As exhibited in the FT-IR spectra, the absorbance of amide carbonyl groups in P(NIPAAm-*co*-HMAAm) occurs at 1650 cm^{-1}, and bending frequency of amide N−H appears at 1550 cm^{-1} (Figure 3a). Stretch vibration for C═O in ester in PMMA-NH_2 appears at 1730 cm^{-1} (Figure 3b). All the peaks mentioned above can be seen from the spectrum of biotin-PEG-*b*-P(NIPAAm-*co*-HMAAm)-*b*-PMMA polymer (Figure 3c), which supports the formation of the triblock copolymers. Furthermore, it has been found that the absorbance of C═O in the ester segments is quite weak in the spectrum of biotin-PEG-*b*-P(NIPAAm-*co*-HMAAm)-*b*-PMMA micelles (Figure 3d), as compared with that in the spectrum of copolymer. However, the typical peaks at 1550 and 1650 cm^{-1} from the P(NIPAAm-*co*-HMAAm) segment in the spectrum of micelle (Figure 3d) are as strong as those in the spectrum of biotin-PEG-*b*-P(NIPAAm-*co*-HMAAm)-COOH regardless of the formation of micelles (Figure 3a). According to our previous study (*33*), the reason is that block copolymers form core−shell micellar structure with completely isolated hydrophobic inner cores and hydrophilic outer shells. Consequently, the peak for stretch vibration of C═O in the ester segments of micelles is apparently weakened.

^{1}H NMR analyses can provide another insight into the self-assembly process since aggregation may result in a decreased mobility of the core-forming block and a resultant suppression of the NMR signal intensities. The blocks in amphiphilic biotin-PEG-*b*-P(NIPAAm-*co*-HMAAm)-*b*-PMMA possess disparate solubilities in selective solvents. Consequently, the NMR signals originating from all three blocks can be recorded when using $CDCl_3$. In contrast, the use of water as NMR solvent results in insufficient mobility and a suppression of the signals pertinent to PMMA block. In fact, as shown in Figure 4b, the use of water results in the total absence of characteristic NMR signals originating from PMMA block. This result indicates the formation of the well-defined core−shell structure of the block copolymer in aqueous solution, which exhibits a shell of biotin-PEG-*b*-P(NIPAAm-*co*-HMAAm) and a core of PMMA.

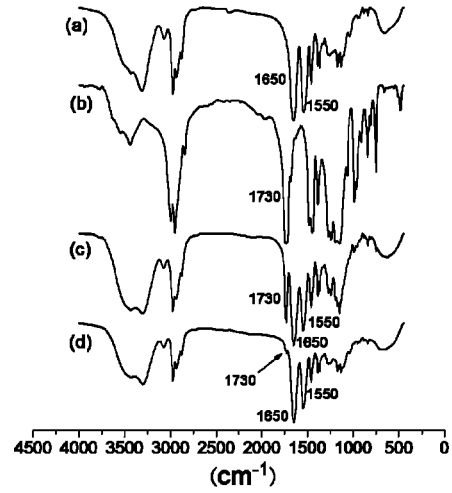

Figure 3. FT-IR spectra of (a) biotin-PEG-*b*-P(NIPAAm-*co*-HMAAm)-COOH; (b) PMMA-NH_2; (c) biotin-PEG-*b*-P(NIPAAm-*co*-HMAAm)-*b*-PMMA block copolymer; and (d) biotin-PEG-*b*-P(NIPAAm-*co*-HMAAm)-*b*-PMMA micelles.

The formation of micelles from the triblock copolymers was also verified by a fluorescence probe technique using pyrene. In the emission spectra (Figure 5a), fluorescence intensity increases with increasing copolymer concentration, due to the fact that pyrene in water has a very small absorption, which increases when it is transferred into a hydrophobic environment. This effect also supports the proposed micelle formation. From the plot of fluorescence intensity versus polymer concentration (Figure 5b), fluorescence intensity is essentially constant at low concentration. Above a certain concentration, intensity increases dramatically, indicating formation of micelles and the transfer of pyrene into the hydrophobic core of the micelles. This concentration can be defined as the critical micellar concentration (cmc). The cmc value of the triblock copolymer obtained in this study is a low concentration of 8.5 mg/L, implying that the micelles could be used in very dilute aqueous media such as body fluids.

In a word, the results of fluorescence are in good agreement with those of FT-IR and ^{1}H NMR. From these results, we conclude that the triblock copolymers do form micelles in the aqueous media, which further conforms that the triblock copolymer was successfully synthesized because a physical mixture of the three polymers would lead to the separation in water.

Characterization of Polymeric Particles. As can be visualized by transmission electron microscopy (TEM) (Figure 6a), the self-assembled micelles are well-dispersed as individual particles with a regularly spherical shape. As shown in Figure 6b, the micelles exhibited a narrow size distribution with an average diameter of 195 nm (PDI 0.115). Compared with the size determined by the particle-size analyzer, the particle size observed by TEM is smaller. The variation in particle size measured by TEM and particle-size analyzer is attributed to the fact that dynamic light scattering (DLS) measurement of

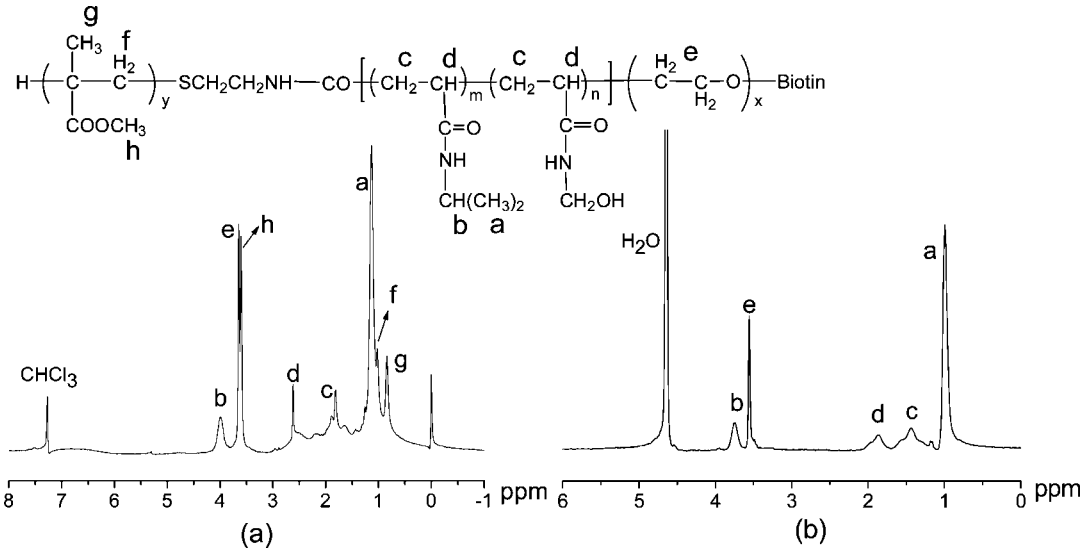

Figure 4. [1]HNMR spectra of biotin-PEG-*b*-P(NIPAAm-*co*-HMAAm)-*b*-PMMA in (a) $CDCl_3$ and (b) D_2O, respectively.

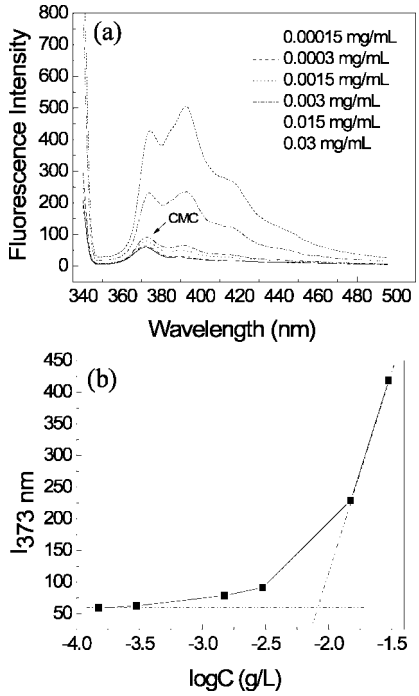

Figure 5. (a) Fluorescence emission spectra of pyrene with increasing concentration of biotin-PEG-*b*-P(NIPAAm-*co*-HMAAm)-*b*-PMMA; (b) the intensity of I_{373} nm in the emission spectra as a function of logarithm of copolymer concentration.

the particle-size analyzer gives the hydrodynamic diameter rather than the actual diameter of the dried particles. Similar discrepancy in size was also reported in the literature (*34*, *37*, *38*). In order to provide direct evidence of the stability of the micelles formed by the triblock copolymers, we kept the micelles aqueous solution for 40 days at room temperature. No obvious change in the morphology of the micelles was observed after 40 days (Figure 6c), indicating the micelles have superior stability in aqueous solution at room temperature. Consistent with the TEM observation, it was found that the size (average diameter 186 nm) and the size distribution (PDI 0.070) were very similar to that obtained 40 days before (Figure 6d). This suggests that the superior stability of the micelles would be favorable for the practical biomedical applications.

In Vitro Drug Release. The thermotriggered drug release behavior of the biotin-PEG-*b*-P(NIPAAm-*co*-HMAAm)-*b*-PMMA micelles was also investigated in this study. Methotrexate (MTX), a poorly water-soluble anticancer drug, was loaded in the micelles by the membrane-dialysis method at room temperature with entrapment efficiency (EE) of around 10%. The in vitro drug release property of the biotin-PEG-*b*-P(NIPAAm-*co*-HMAAm)-*b*-PMMA micelles was evaluated at temperatures below (37 °C) and above (43 °C) the LCST of biotin-PEG-*b*-P(NIPAAm-*co*-HMAAm)-*b*-PMMA micelle. The drug release profiles show drastic changes with temperature alterations as presented in Figure 7. Compared with the release at 37 °C, the drug release is accelerated dramatically at 43 °C due to the temperature-induced structural changes of the micelles. When the temperature increased above the LCST, the P(NIPAAm-*co*-HMAAm) segment becomes hydrophobic, which makes the hydrophilic shell of the micelle structure become thinner. As a result, the drug diffuses out quickly and about 92% of the drug is released from the micelles during 96 h at 43 °C.

Cell Uptake Study. Cervical cancer HeLa cells have been extensively characterized for intracellular delivery through receptor-mediated endocytosis using the iron-carrying protein transferrin for targeting (*39–41*). In the two-step pretargeting protocol, we used HeLa cells to study the intracellular uptake of the triblock copolymer micelles in vitro. Rhodamine B, a versatile fluorescence dye, was initially entrapped in the micelles during the dialysis at room temperature as a probe. FITC-labeled avidin was then associated with the rhodamine B loaded biotinylated micelles. Then after the preincubation of biotin−transferrin and HeLa cells, FITC-avidin-rhodamine B loaded micelle complex was infused to "chase" biotin−transferrin through the biotin−avidin interaction. Based on the fluorescence emission intensities of rhodamine B at 570 nm and FITC at 490 nm, the cell uptake of the FITC-avidin-rhodamine B loaded micelle was calculated as follows (*42*):

Uptake = [(concentration of the dye internalized into cells in each well)/(concentration of the dye added in each well)] × 100%

Human lung cancer cells (A549) and vein endothelial cells (ECV304) with the same administration procedure as well as the HeLa samples free of the preincubating with biotinylated transferrin were also studied for comparison. The cell uptake calculated by both fluorescence probes is presented in Figure 8. Based on the fluorescence probe of FITC, with the presence of biotin−transferrin, cell uptake values are 30.6% for HeLa, 9.4% for A549, and 8.7% for ECV304, respectively. On the

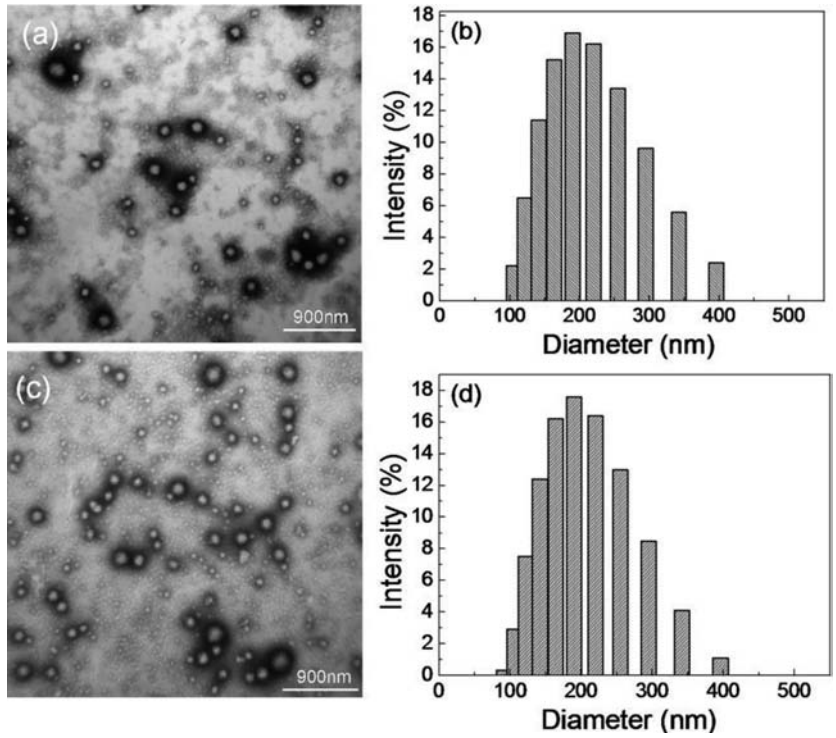

Figure 6. (a) TEM image and (b) size distribution of biotin-PEG-*b*-P(NIPAAm-*co*-HMAAm)-*b*-PMMA micelles; (c) TEM image and (d) size distribution of biotin-PEG-*b*-P(NIPAAm-*co*-HMAAm)-*b*-PMMA micelles self-assembled in an aqueous medium after 40 days.

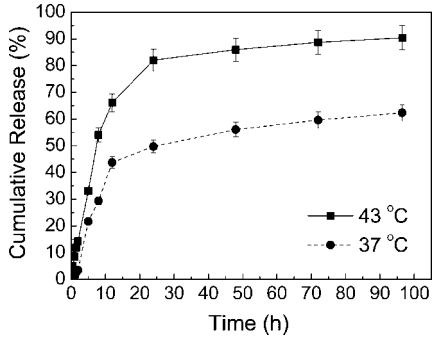

Figure 7. Drug release from the thermoresponsive biotin-PEG-*b*-P(NIPAAm-*co*-HMAAm)-*b*-PMMA micelles loaded with MTX at different temperatures (37 and 43 °C).

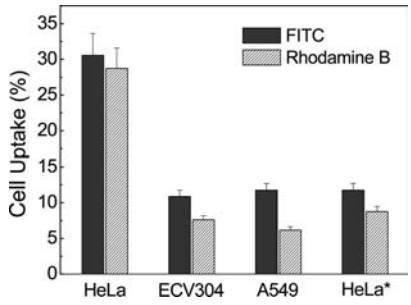

Figure 8. The rate of double fluorescence probes labeled triblock copolymer micelle drug carriers uptaken by different cells at 37 °C. HeLa* means Hela cells without the biotin-transferrin preincubating was used as the control.

contrary, in the absence of biotin−transferrin, the HeLa cell uptake is merely around 9.4%. And the above four results calculated from rhodamine B are 28.7%, 6.1%, 4.9%, 7.0%, respectively. These results were in close accord with that of the other fluorescence probe.

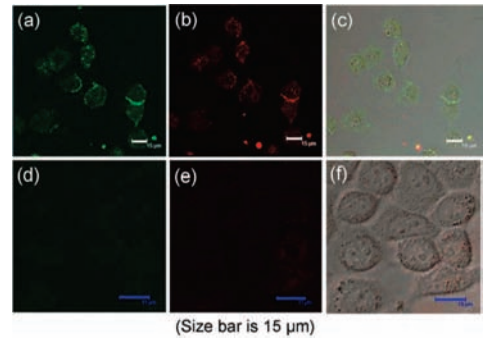

Figure 9. Confocal microscopy images of HeLa cells with pretargeting treatment incubated with FITC-avidin and rhodamine B loaded micelles under different observation conditions (a−c). Confocal microscopy images of HeLa cells without pretargeting treatment incubated with FITC-avidin and Rhodamine B loaded micelles under different observation conditions (d−f). The green fluorescence in images (a) and (d) represent the existence of FITC (FITC labeled avidin), and the red fluorescence in images (b) and (e) represent the existence of rhodamine B (rhodamine B loaded biotinylated micelle). (c) and (f) are the coalescent of bright-field and double fluorescence images, and the yellow fluorescence in them indicate the coexistence of green (FITC) and red fluorescence (rhodamine B).

Confocal Microscopy Observation. The internalization of the triblock copolymer micelles into HeLa cells was also visualized by confocal microscopy. After 2 h incubation with FITC-avidin-rhodamine B loaded micelle complex at 37 °C, HeLa cells pretreated with biotin−transferrin (Figure 9a,b,c) show remarkably more intense fluorescence in both cell membrane and cell cytoplasm than those free of biotin−transferrin pretreatment (Figure 9d,e,f), confirming the facilitation of the cell binding and internalization for the pretagerting approach. In the confocal images, the green fluorescence belongs to FITC (FITC labeled avidin), while the red fluorescence belongs to rhodamine B (rhodamine B loaded biotinylated micelle). Furthermore, the yellow fluorescence in Figure 9c shows the coexistence of green (FITC) and red fluorescence (rhodamine

B) indicating the intracellular delivery of dye (as poorly soluble drug model) by triblock copolymer micelles as well as the biotin molecule does exist in the copolymer since the micelle conjugate with FITC labeled avidin through the action of biotin. In addition, the confocal microscopy investigations of A549 and ECV304 are in a similar situation to Figure 9d,e,f. Overall, the qualitative results from double-fluorescence probe microscopy studies are in good agreement with the quantitative results obtained from fluorescence spectroscopy, substantiating the involvement of transferrin-mediated internalization in the cellular uptake of triblock copolymer micellar drug carrier.

CONCLUSIONS

In summary, novel micelles, comprising hydrophilic PEG shells, hydrophobic PMMA cores, and thermosensitive P(NIPAAm-*co*-HMAAm) segments were self-assembled from the biotin-PEG-*b*-P(NIPAAm-*co*-HMAAm)-*b*-PMMA triblock copolymer. The TEM observation and size distribution analysis illustrated the superior stability of the thermosensitive micelles. The polymeric micelles showed a thermotriggered drug release behavior upon temperature alterations ascribed to the thermoinduced structural change of the micellar structure. The pretargeting delivery property of the triblock copolymer micelles was investigated by fluorescence spectroscopy as well as confocal microscopy, and the results confirmed that the self-assembled micelles can be specifically and efficiently bonded to cancer cells with the administration of biotin−transferrin, suggesting that the multifunctional micelles have great potential as drug carriers for the tumor targeting chemotherapy.

ACKNOWLEDGMENT

This work was supported by National Natural Science Foundation of China (50633020) and National Key Basic Research Program of China (2005CB623903).

LITERATURE CITED

(1) Jaracz, S., Chen, J., Kuznetsova, V. L., and Ojima, I. (2005) Recent advances in tumor-targeting anticancer drug conjugates. *Bioorgan. Med. Chem. 13*, 5043–54.

(2) Ouchi, T., Yamabe, E., Hara, K., Hirai, M., and Ohya, Y. (2004) Design of attachment type of drug delivery system by complex formation of avidin with biotinyl drug model and biotinyl saccharide. *J. Controlled Release 94*, 281–91.

(3) Hong, C. Y., and Pan, C. Y. (2006) Direct synthesis of biotinylated stimuli-responsive polymer and diblock copolymer by RAFT polymerization using biotinylated trithiocarbonate as RAFT agent. *Macromolecules 39*, 3517–24.

(4) Nobs, L., Buchegger, F., Gurny, R., and Allemann, E. (2006) Biodegradable nanoparticles for direct or two-step tumor immunotargeting. *Bioconjugate Chem. 17*, 139–45.

(5) O'Reilly, R. K., Joralemon, M. J., Wooley, K. L., and Hawker, C. J. (2005) Functionalization of micelles and shell cross-linked nanoparticles using click chemistry. *Chem. Mater. 17*, 5976–88.

(6) O'Reilly, R. K., Hawker, C. J., and Wooley, K. L. (2006) Cross-linked block copolymer micelles: functional nanostructures of great potential and versatility. *Chem. Soc. Rev. 35*, 1068–83.

(7) Webber, G. B., Wanless, E. J., Armes, S. P., Tang, Y. Q., Li, Y. T., and Biggs, S. (2004) Nano-anemones: stimulus-responsive copolymer-micelle surfaces. *Adv. Mater. 16*, 1794–8.

(8) Liu, F. T., and Liu, G. J. (2001) Poly(solketal methacrylate)-block- poly(2-cinnamnoyloxyethyl methacrylate)-block-poly(allyl methacrylate): synthesis and micelle formation. *Macromolecules 34*, 1302–7.

(9) Brigger, I., Dubernet, C., and Couvreur, P. (2002) Nanoparticles in cancer therapy and diagnosis. *Adv. Drug Delivery Rev. 54*, 631–51.

(10) Rosler, A., Vandermeulen, G. W. M., and Klok, H. A. (2001) Advanced drug delivery devices via self-assembly of amphiphilic block copolymers. *Adv. Drug Delivery Rev. 53*, 95–108.

(11) Allen, C., Maysinger, D., and Eisenberg, A. (1999) Nano-engineering block copolymer aggregates for drug delivery. *Colloids Surf., B 16*, 3–27.

(12) Kwon, G. S. (2003) Polymeric micelles for delivery of poorly water-soluble compounds. *Crit. Rev. Ther. Drug Carrier Syst. 20*, 357–403.

(13) Li, J., Li, X., Ni, X., and Leong, K. W. (2003) Synthesis and characterization of new biodegradable amphiphilic poly(ethylene oxide)-*b*-poly[(R)-3-hydroxybutyrate]-*b*-poly(ethylene oxide) triblock copolymers. *Macromolecules 36*, 2661–7.

(14) Liu, K. L., Goh, S. H., and Li, J. (2008) Controlled synthesis and characterizations of amphiphilic poly[(R,S)-3-hydroxybutyrate]-poly(ethylene glycol)-poly[(R,S)-3-hydroxybuty rate] triblock copolymers. *Polymer 49*, 732–41.

(15) Li, J., Ni, X., Li, X., Tan, N. K., Lim, C. T., Ramakrishna, S., and Leong, K. W. (2005) Micellization phenomena of biodegradable amphiphilic triblock copolymers consisting of poly(β-hydroxyalkanoic acid) and poly(ethylene oxide). *Langmuir 21*, 8681–5.

(16) Li, X., Mya, K. Y., Ni, X., He, C., Leong, K. W., and Li, J. (2006) Dynamic and static light scattering studies on self-aggregation behavior of biodegradable amphiphilic poly(ethylene oxide)-poly[(R)-3-hydroxybutyrate]-poly(ethylene oxide) triblock copolymers in aqueous solution. *J. Phys. Chem. B 110*, 5920–6.

(17) Cammas-Marion, S., Okano, T., and Kataoka, K. (1999) Functional and site-specific macromolecular micelles as high potential drug carriers. *Colloids Surf., B 16*, 207–15.

(18) Chen, X. R., Ding, X. B., and Zheng, Z. H. (2005) Intelligent crew-cut aggregates formed by thermosensitive block copolymers and their multiple morphologies. *Macromol. Biosci. 5*, 157–63.

(19) Zhang, J. X., Qiu, L. Y., Jin, Y., and Zhu, K. J. (2005) Physicochemical characterization of polymeric micelles constructed from novel amphiphilic polyphosphazene with poly(*N*-isopropylacrylamide) and ethyl 4-aminobenzoate as side groups. *Colloids Surf., B 43*, 123–30.

(20) Chung, J. E., Yokoyama, M., Aoyagi, T., Sakurai, Y., and Okano, T. (1999) Thermo-responsive drug delivery from polymeric micelles constructed using block copolymers of poly(*N*-isopropylacrylamide) and poly(butylmethacrylate). *J. Controlled Release 62*, 115–27.

(21) Jones, M. C., and Leroux, J. C. (1999) Polymeric micelles-a new generation of colloidal drug carriers. *Eur. J. Pharmaceut. Biopharmaceut. 48*, 101–11.

(22) Kataoka, K., Harada, A., and Nagasaki, Y. (2001) Block copolymer micelles for drug delivery: design, characterization and biological significance. *Adv. Drug Delivery Rev. 47*, 113–31.

(23) Maeda, H., Wu, J., Sawa, T., Matsumura, Y., and Hori, K. (2000) Tumor vascular permeability and the EPR effect in macromolecular therapeutics: a review. *J. Controlled Release 65*, 271–84.

(24) Liu, X. M., Pramoda, K., Yang, Y. Y., Chow, S. Y., and He, C. B. (2004) Cholesteryl-grafted functional amphiphilic poly(*N*-isopropylacrylamide-co-*N*-hydroxylmethylacrylamide): synthesis, temperature sensitivity, self-assembly and encapsulation of a hydrophobic agent. *Biomaterials 5*, 2619–28.

(25) Gillies, E. R., Jonsson, T. B., and Frechet, J. M. J. (2004) Stimuli-responsive supramolecular assemblies of linear-dendritic copolymers. *J. Am. Chem. Soc. 126*, 11936–43.

(26) Hay, D. N. T., Rickert, P. G., Seifert, S., and Firestone, M. A. (2004) Thermoresponsive nanostructures by self-assembly of a poly(*N*-isopropylacrylamide)-lipid conjugate. *J. Am. Chem. Soc. 126*, 2290–1.

(27) Topp, M. D. C., Dijkstra, P. J., Talsma, H., and Feijen, J. (1997) Thermosensitive micelle-forming block copolymers of poly(ethylene glycol) and poly(*N*-isopropylacrylamide). *Macromolecules 30*, 8518–20.

(28) Gref, R., Couvreur, P., Barratt, G., and Mysiakine, E. (2003) Surface-engineered nanoparticles for multiple ligand coupling. *Biomaterials 24*, 4529–37.

(29) Lee, E. S., Na, K., and Bae, Y. H. (2005) Super pH-sensitive multifunctional polymeric micelle. *Nano Lett. 5*, 325–9.

(30) Sawant, R. M., Hurley, J. P., Salmaso, S., Kale, A., Tolcheva, E., Levchenko, T. S., and Torchilin, V. P. (2006) "SMART" drug delivery systems: double-targeted pH-responsive pharmaceutical nanocarriers. *Bioconjugate Chem. 17*, 943–9.

(31) Tan, J. F., Ravi, P., Too, H. P., Hatton, T. A., and Tam, K. C. (2005) Association behavior of biotinylated and non-biotinylated poly(ethylene oxide)-b-poly(2-(diethylamino)ethyl methacrylate). *Biomacromolecules 6*, 498–506.

(32) Li, Y. Y., Zhang, X. Z., Kim, G. C., Cheng, H., Cheng, S. X., and Zhuo, R. X. (2006) Thermosensitive Y-shaped micelles of poly(oleic acid-Y-*N*-isopropylacrylamide) for drug delivery. *Small 2*, 917–23.

(33) Wei, H., Zhang, X. Z., Zhou, Y., Cheng, S. X., and Zhuo, R. X. (2006) Self-assembled thermoresponsive micelles of poly(N-isopropylacrylamide-b-methyl methacrylate. *Biomaterials 27*, 2028–34.

(34) Li, Y. Y., Zhang, X. Z., Zhu, J. L., Cheng, H., Cheng, S. X., and Zhuo, R. X. (2007) Self-assembled, thermoresponsive micelles based on triblock PMMA-b-PNIPAAm-b-PMMA copolymer for drug delivery. *Nanotechnology* 18 Art. No. 215605.

(35) Chen, G., and Hoffman, A. S. (1995) Graft copolymers that exhibit temperature-induced phase transitions over a wide range of pH. *Nature 373*, 49–52.

(36) Wei, H., Zhang, X. Z., Cheng, C., Cheng, S. X., and Zhuo, R. X. (2007) Self-assembled, thermosensitive micelles of a star block copolymer based on PMMA and PNIPAAm for controlled drug delivery. *Biomaterials 28*, 99–107.

(37) Morita, T., Horikiri, Y., Suzuki, T., and Yoshino, T. (2001) Preparation of gelatin microparticles by co-lyophilization with poly(ethylene glycol): characterization and application to entrapment into biodegradable microspheres. *Int. J. Pharm. 219*, 127–37.

(38) Ye, Q., Zhang, Z. C., Jia, H. T., He, W. D., and Ge, X. W. (2002) Formation of monodisperse polyacrylamide particles by radiation-induced dispersion polymerization: Particle size and size distribution. *J. Colloid Interface Sci. 253*, 279–84.

(39) Chan, W. C., and Nie, S. (1998) Quantum dot bioconjugates for ultrasensitive nonisotopic detection. *Science 281*, 2016–2018.

(40) Das, M., Mardyani, S., Chan, W. C. W., and Kumacheva, E. (2006) Biofunctionalized pH-responsive microgels for cancer cell targeting: rational design. *Adv. Mater. 18*, 80–3.

(41) Zhang, H., Mardyani, S., and Chan, W. C. W. (2006) Design of biocompatible chitosan microgels for targeted pH-mediated intracellular release of cancer therapeutics. *Biomacromolecules 7*, 1568–72.

(42) Xiong, X. B., Mahmud, A., Uludag, H., and Lavasanifar, A. (2007) Conjugation of arginine-glycine-aspartic acid peptides to poly(ethylene oxide)-b-poly(epsilon-caprolactone) micelles for enhanced intracellular drug delivery to metastatic tumor cells. *Biomacromolecules 8*, 874–84.

BC8000062

Synthesis and Application of [^{18}F]FDG-Maleimidehexyloxime ([^{18}F]FDG-MHO): A [^{18}F]FDG-Based Prosthetic Group for the Chemoselective ^{18}F-Labeling of Peptides and Proteins†

Frank Wuest,* Mathias Berndt, Ralf Bergmann, Joerg van den Hoff, and Jens Pietzsch

Research Center Dresden-Rossendorf, Institute for Radiopharmacy, PF 510 119, D-01314 Dresden, Germany. Received January 9, 2008; Revised Manuscript Received February 25, 2008

2-[^{18}F]Fluoro-2-deoxy-D-glucose ([^{18}F]FDG) as the most important PET radiotracer is available in almost every PET center. However, there are only very few examples using [^{18}F]FDG as a building block for the synthesis of ^{18}F-labeled compounds. The present study describes the use of [^{18}F]FDG as a building block for the synthesis of ^{18}F-labeled peptides and proteins. [^{18}F]FDG was converted into [^{18}F]FDG-maleimidehexyloxime ([^{18}F]FDG-MHO), a novel [^{18}F]FDG-based prosthetic group for the mild and thiol group-specific ^{18}F labeling of peptides and proteins. The reaction was performed at 100 °C for 15 min in a sealed vial containing [^{18}F]FDG and *N*-(6-aminoxy-hexyl)maleimide in 80% ethanol. [^{18}F]FDG-MHO was obtained in 45−69% radiochemical yield (based upon [^{18}F]FDG) after HPLC purification in a total synthesis time of 45 min. Chemoselecetive conjugation of [^{18}F]FDG-MHO to thiol groups was investigated by the reaction with the tripeptide glutathione (GSH) and the single cysteine containing protein annexin A5 (anxA5). Radiolabeled annexin A5 ([^{18}F]FDG-MHO-anxA5) was obtained in 43−58% radiochemical yield (based upon [^{18}F]FDG-MHO, $n = 6$), and [^{18}F]FDG-MHO-anxA5 was used for a pilot small animal PET study to assess in vivo biodistribution and kinetics in a HT-29 murine xenograft model.

INTRODUCTION

Compounds labeled with short-lived positron-emitting radionuclides have extensively been utilized to target selective physiological and biochemical processes at the molecular and cellular level in vivo by means of positron emission tomography (PET) as the most advanced noninvasive imaging methodology. Besides numerous small molecular weight compounds, in recent years several radiolabeled molecules such as peptides, proteins, and aptamers have been proposed as highly target-specific PET imaging probes. In this context, various radiolabeled peptides and proteins, including antibodies and antibody fragments, have been used in nuclear medicine for imaging of tumors and inflammatory processes.

Within the spectrum of available positron emitters, fluorine-18 (^{18}F) is a particularly attractive radionuclide due to its favorable nuclear and chemical properties. ^{18}F can be produced in high amounts via several nuclear reactions in particle accelerators (cyclotrons) at high specific radioactivity. The low positron energy of 0.64 MeV results in low radiation doses and short tissue range, and the relatively long 109.7 min half-life allows complex and multistep radiosyntheses and scanning protocols extending 4 to 6 h. However, radiochemistry with ^{18}F focused on peptide and protein labeling also implies specific challenges. Thus, direct incorporation of ^{18}F at high specific radioactivity as [^{18}F]fluoride into peptides and proteins is hampered due to the harsh reaction conditions occurring during [^{18}F]fluoride labeling reactions. In order to circumvent this obstacle, peptide and protein labeling with ^{18}F is usually carried out by means of prosthetic groups, also referred to as bifunctional labeling agents (*1–6*). This approach involves ^{18}F incorporation into a small organic molecule capable of being linked to peptides, proteins, antibodies, and oligonucleotides under mild conditions. Such linkage of ^{18}F-labeled prosthetic groups can be accomplished via acylation (*6–18*), amidation (*19*), imidation (*20*), alkylation (*19–32*), photochemical conjugation (*6, 33–35*), and oxime (*36, 37*) or hydrazone formation (*38, 39*). Every linking method has its own advantage and limitations. Depending on the conjugation mechanism and the multitude of functional groups abundant in proteins (e.g., lysine residues), the chemoselective and regioselective introduction of the radiolabel into a defined position represents a special challenge. Moreover, the laborious, time-consuming, and multistep synthesis of most ^{18}F-labeled prosthetic groups represents another drawback, which has limited the availability and applicability of prosthetic groups in routine ^{18}F-labeling reactions.

As a consequence, the routine ^{18}F labeling of molecules like peptides and proteins should preferentially involve simple and efficient radiolabeling methods based on readily available prosthetic groups while allowing the chemo- and regioselective introduction of the radiolabel.

2-[^{18}F]Fluoro-2-deoxy-D-glucose ([^{18}F]FDG) is the most important radiotracer for PET imaging in nuclear medicine. Its highly efficient radiosynthesis makes this radiotracer available in almost every PET center worldwide. However, despite the convenient automated synthesis and almost unlimited availability of [^{18}F]FDG there are only very few examples using [^{18}F]FDG and peracetylated [^{18}F]FDG (1,3,4,6-tetra-*O*-acetyl-2-[^{18}F]fluoro-2-deoxyglucose) as building blocks for the radiosynthesis of ^{18}F-labeled compounds (Figure 1).

One of the first reports dealing with [^{18}F]FDG as ^{18}F building block was written by Borman et al. on the synthesis of β-*O*-D-galactopyranosyl-(1,4′)-2′-[^{18}F]fluoro-2′-deoxy-D-glucopyra-

† A part of this report has been presented at the 53rd annual meeting of the Society of Nuclear Medicine, San Diego 2006, June 3−7, and has been published in abstract form: M. Berndt, C. Hultsch, R. Bergmann, J. Pietzsch, and F. Wuest. A novel role for [^{18}F]FDG: Synthesis and application of a [^{18}F]FDG-based prosthetic group for peptide and protein labeling. *J. Nucl. Med.* **2006**, *47*, 83.

* Address for correspondence: Frank Wuest, Institute of Radiopharmacy, Research Center Dresden-Rossendorf, P.O.-Box 51 01 19, 01314 Dresden, Germany. (f.wuest@fzd.de.)

10.1021/bc8000112 CCC: $40.75 © 2008 American Chemical Society
Published on Web 05/16/2008

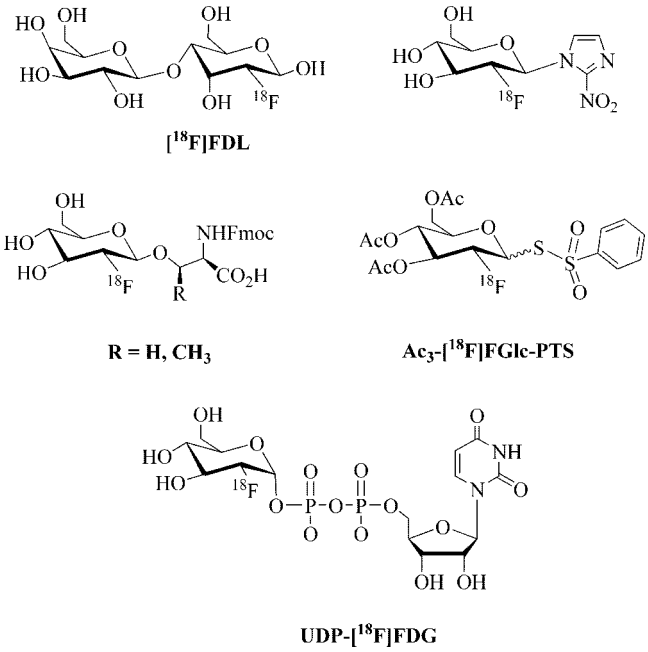

Figure 1. Structures of ^{18}F-labeled radiotracers synthesized starting from [^{18}F]FDG or peracetylated [^{18}F]FDG.

nose (2′-[^{18}F]fluoro-deoxylactose, [^{18}F]FDL) using an enzymatic reaction starting from [^{18}F]FDG (*40*). Although the obtained radiochemical yield was quite low (3.4% decay-corrected, starting from [^{18}F]FDG), the authors could perform preliminary biological evaluation of [^{18}F]FDL involving biodistribution studies in mice. Starting from peracetylated [^{18}F]FDG as ^{18}F building block, Patt and co-workers developed a FDG-based radiotracer for imaging hypoxia (*41*). HPLC-purified peracetylated [^{18}F]FDG was treated with 2-nitroimidazole in the presence of $Hg(CN)_2$ as a source for cyanide anion and the Lewis acid $SnCl_4$ to give a glucose-coupled 2-nitroimidazole intermediate. After removal of the acetyl protecting groups of the intermediate applying reaction conditions similar to the [^{18}F]FDG production method, the desired [^{18}F]FDG-coupled 2-nitroimidazole could be isolated and used in subsequent biological studies.

The use of peracetylated [^{18}F]FDG as building block in the radiosynthesis of ^{18}F-glycosylated amino acids serine and threonine has been reported by Prante et al. (*42, 43*). The authors describe two different reaction pathways involving either the reaction of an intermediate glucopyranosyl bromide with Fmoc-Ser-OH or Z-Ser-OBn in the presence of AgOTf or direct conversion of peracetylated [^{18}FDG] with Fmoc-protected serine or threonine in the presence of Lewis acid BF_3 into glycosylated amino acids. The glycosylation reaction involving a glucopyranosyl bromide intermediate according to a Koenigs-Knorr reaction afforded radiochemical yields of 67%, whereas the BF_3-mediated method provided significantly lower radiochemical yields of 27% suggesting the suitability of Koenig-Knorr reaction conditions for ^{18}F-glycosylation of protected bioactive peptides.

Another reaction with peracetylated [^{18}F]FDG was described by the same author aiming at the enzymatic synthesis of uridine-5′-diphospho-2-deoxy-2-[^{18}F]fluoro-α-D-glucopyranose (UDP-[^{18}F]FDG) (*44*). Starting from peracetylated [^{18}F]FDG, a MacDonald synthesis was used to prepare [^{18}F]FDG-1-phosphate which was successfully subjected to an enzymatic reaction to prepare UDP-[^{18}F]FDG. This method is also discussed as a highly selective and mild ^{18}F-labeling method for glycosylated biomolecules.

Very recently, 3,4,5-tri-*O*-acetyl-2-[^{18}F]fluoro-2-deoxy-D-glucopyranosyl 1-phenylthiosulfonate (Ac_3-[^{18}F]FGLc-PTS) was reported as a novel thiol-reactive reagent for the chemoselective ^{18}F-glycosylation of peptides (*45*). Ac_3-[^{18}F]FGLc-PTS was prepared in three steps in radiochemical yield of 33%. The feasibility of using Ac_3-[^{18}F]FGLc-PTS as a thiol-reactive agent was demonstrated through chemoselective bioconjugation to a cycteine-containing model pentapeptide and to the integrin $\alpha_V\beta_3$-affine peptide c(RGDfC). Both peptides could be labeled in conjugation yields greater than 90%.

The present study aims at the use of [^{18}F]FDG as a ^{18}F building block for the convenient synthesis of a thiol-reactive prosthetic group for the chemoselective conjugation to cysteine-containing peptides and proteins. In recent years, several maleimide-functionalized prosthetic groups have been shown to be especially suitable as chemoselective agents for the site-specific ^{18}F labeling of cysteine-containing peptides under mild reaction conditions (*19–22, 32, 46*).

Herein, we report on the use of [^{18}F]FDG as a suitable building block for the synthesis of ^{18}F-labeled peptides and proteins. The presented approach involves the design and synthesis of [^{18}F]FDG-maleimidehexyloxime ([^{18}F]FDG-MHO) as a novel [^{18}F]FDG-based prosthetic group for the mild and thiol group-specific ^{18}F labeling of peptides and proteins. The feasibility of [^{18}F]FDG-MHO as thiol group-reactive prosthetic group was assessed through the reaction with cycteine-containing tripeptide glutathione and with single thiol group-containing protein annexin A5 (anxA5). The present work is concluded with a pilot small animal PET study to assess biodistribution and kinetics of chemoselectively radiolabeled anxA5 in a human colorectal adenocarcinoma (HT-29) murine xenograft model in vivo.

EXPERIMENTAL METHODS

General. All commercial reagents and solvents were used without further purification unless otherwise specified. Nuclear magnetic resonance spectra were recorded on a Varian Unity 300 MHz spectrometer. ^{1}H and ^{19}F chemical shifts were given in ppm and were referenced with the residual solvent resonances relative to tetramethylsilane (TMS). Mass spectra were obtained on a Quattro/LC mass spectrometer (MICROMASS) by electrospray ionization. Thin-layer chromatography (TLC) was performed on Merck silica gel F-254 aluminum plates, with visualization under UV (254 nm).

[^{18}F]FDG was prepared according to refs (*47, 48*). HPLC analyses were carried out with a SUPELCOSIL LC-18S column (4.6 × 250 mm, 5 mm) using isocratic elution with CH_3CN/0.1 M ammonium formate (30/70) gradient pump L2500 (Merck, Hitachi) with a flow rate of 1 mL/min. The products were monitored by an UV detector L4500 (Merck, Hitachi) at 254 nm and by γ-detection with a scintillation detector GABI (X-RAYTEST). Semipreparative HPLC was performed with a Merck LiChroCart 250−10 column at a flow rate 4 mL/min. Solvent A: CH_3CN; solvent B: 0.1 M ammonium formate. The following gradient was used: 0 min 15% A, 20 min 70% A, 30 min 70% A. Radio-TLC analyses of glutathione coupling with [^{18}F]FDG-MHO was performed on Merck RP18 F-254 aluminum plates. Radio-sodium dodecyl sulfate polyacrylamide gel electrophoresis (SDS-PAGE) was performed according to published literature procedure (*32*). Aminooxy-maleimide hydrochloride **1** (*32*) and [^{18}F]FDG (*47, 48*) were prepared according to literature.

2-Fluoro-3,4,5,6-tetrahydroxyhexanal-*O*-[3-(2,5-dioxo-2,5-dihydropyrrol-1-yl)hexyl]oxime (FDG-MHO). 2-Fluorodeoxyglucose (50 mg, 275 μmol) and aminooxymaleimide × HCl **1** (69 mg, 277 μmol) were dissolved in 5 mL of EtOH/H_2O (4:1) and the resulting solution was refluxed for 1 h. The mixture was concentrated under reduced pressure. After the addition of water (50 mL), the mixture was passed through a C18 SepPak

cartridge. The cartridge was washed with water (10 mL) and the product was eluted with EtOH (2 mL). The solvent was evaporated to give 77 mg (75%) of the desired compound FDG-MHO as a colorless glass. ^{1}H NMR (400 MHz, CD_3OD) δ 7.48 (dd, 1H, J_{H-F} = 7.5 Hz, J_{H-H} = 6.1 Hz; =NHOR), 6.79 (s, 2H, CH=CH), 5.03 (dt, 1H, J_{H-F} = 48.4 Hz, J_{H-H} = 7.5 Hz; CH-F), 4.08 (dd, 1H, J = 7.1 Hz, J = 1.6 Hz), 4.05 (t, 2H, J = 6.6 Hz; =NO−CH_2), 3.77 (dd, 1H, J = 11.2 Hz, J = 3.4 Hz), 3.69 (m, 1H), 3.58−3.66 (m, 2H), 3.48 (t, J = 7.1 Hz, 2H; CH_2-maleimide), 1.53−1.67 (m, 4H, CH_2), 1.26−1.42 (m, 4H, CH_2). ^{13}C NMR (100 MHz, CD_3OD) δ 26.1, 27.3, 28.6, 29.3, 38.5, 62.5, 71.2 (d, J_{C-F} = 7.9 Hz), 71.7, 72.5, 91.4 (d, J_{C-F} = 169.9 Hz), 134.2, 145.8 (d, J_{C-F} = 23.7 Hz), 172.7. ^{19}F-NMR (376 MHz, CD_3OD) δ −61.67 (ddd, J = 45.8 Hz, J = 12.2 Hz, J = 6.1 Hz), LR-MS (ESI, positive): m/z 377.4 $[M+H]^+$, 399.3 $[M+Na]^+$.

2-[^{18}F]Fluoro-3,4,5,6-tetrahydroxyhexanal-*O*-[3-(2,5-dioxo-2,5-dihydropyrrol-1-yl)hexyl]oxime ([^{18}F]FDG-MHO). [^{18}F]-FDG solution in saline (1 mL, 400−700 MBq) was added to vial containing aminooxymaleimide hydrochloride **1** (5 mg, 13.3 μmol) in EtOH (4 mL). The vial was sealed and heated at 100 °C for 15 min. After evaporation of the solvent and addition of water (20 mL), the mixture was passed through a SepPak cartridge. The crude prudct was eluted with acetonitrile (1 mL) and subjected to semipreparative HPLC for purification. The peak eluting at 18−19 min was collected, diluted with water (20 mL), and passed through a SepPak cartridge. Elution with EtOH (1 mL) gave the desired product in high radiochemical purity (>95%). In a typical experiment, starting from 420 MBq of [^{18}F]FDG, 135 MBq of [^{18}F]FDG-MHO (42% radiochemical yield based upon [^{18}F]FDG) could be obtained within 45 min.

Radiolabeling of Gluthathione with [^{18}F]FDG-MHO. [^{18}F]FDG-MHO in ethanol (25 μL, 8 MBq) was added to 900 μL of glutathione solutions (1.0 mg/mL up to 10 ng/mL) in phosphate-buffer (pH = 7.2) and incubated at room temperature. The progress of the reaction was monitored by radio-TLC after 10 min. Radio-TLC: R_f = 0.8, CH_3CN/water (80/20).

Radiolabeling of anxA5 with [^{18}F]FDG-MHO. [^{18}F]FDG-MHO in ethanol (25 μL, 18−20 MBq) was added to 100 μL of anxA5 solution (1.0 mg/mL recombinant AnxA5 (kind gift from Dr. Nediljko Budisa), isolated from *Escherichia coli* B834 (DE3), transformed with plasmid pASET-pp4, as described by Burger et al. (*49*)) in 0.05 mol/L Tris-HCl (pH 7.4) and incubated for 30 min at room temperature. The reaction mixture was applied to size exclusion chromatography (Äkta Prime plus, HiTrap Desalting column 5 mL) and eluted with phosphate-buffered saline (pH 7.2; 0.5 mL/min). The collected high molecular weight fractions were combined to give 6−8 MBq (44−58%, decay-corrected, based upon [^{18}F]FDG-MHO) of radiolabeled anxA5. Radiochemical purity radiolabeled anxA5 was greater 95% as determined by radio-sodium dodecyl sulfate polyacrylamide gel electrophoresis (SDS-PAGE). The isolated product was directly used for small animal PET imaging studies.

Small Animal PET Imaging of ^{18}F-labeled anxA5. Dynamic small animal PET studies were performed with a dedicated PET scanner for small animals (microPET P4, Siemens Preclinical Solutions, Knoxville, TN, USA). For imaging studies, mice were anesthetized with a desflurane 10% oxygen/40% air mixture and catheters with hypodermic needle were placed into a tail vein. The animals were then positioned and immobilized prone with their medial axis parallel to the axial axis of the scanner on a heated bed. In a typical experiment, 1 MBq of [^{18}F]FDG-MHO-anxA5 was administered in a total volume of 0.5 mL over 1 min using a programmable syringe pump 30 s after start of the PET data acquisition. Dynamic PET scanning was carried out for 14 400 s (4 h), using the following time intervals (frames) for sinogram generation: 15 × 10 s, 5 × 30 s, 5 × 60 s, 4 × 300 s, and 21 × 600 s. The PET data were reconstructed using a 3D OSEM MAP iteration algorithm provided by the PET scanner producer. The image data were evaluated with the program ROVER (ABX GmbH, Radeberg, Germany) to get 3D regions of interest (ROI) of tissues of interest. The time activity concentration curves and the activity amounts were further processed using software written in the R language (R Development Core Team: R: A Language and Environment for Statistical Computing, http://www.R-project.org, R Foundation for Statistical Computing, Vienna, Austria (2007). ISBN 3−900051−07−0.).

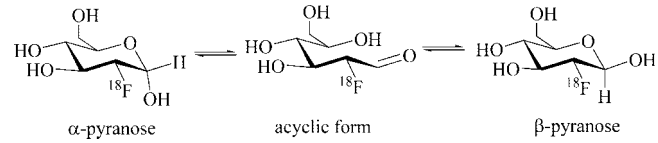

Figure 2. Proposed mutarotation of glucose analogue [^{18}F]FDG via an acyclic form.

RESULTS AND DISCUSSION

[^{18}]FDG as the most important PET radiotracer for in vivo imaging of glycolysis in nuclear medicine has found multiple applications in the fields of oncology, neurology, and cardiology. In aqueous solutions, [^{18}F]FDG consists of a mixture of α/β anomers. The process behind the equilibration between the α anomer and the β anomer is known as mutarotation. Mechanistically, the isomerization must proceed with ring opening via a small concentration of the acyclic form (Figure 2). To the best of our knowledge, however, the exact amount of each isomeric form of [^{18}F]FDG in aqueous solution is still not known yet.

In the case of D-glucose, in aqueous solution at room temperature the amounts of the α and β anomers were determined to be 38% and 62%, respectively. The amount of the acyclic form is reported to be as little as 0.003% (*50*).

A comparable situation should be expected for the glucose analogue [^{18}F]FDG. Although presumably available in only very small amounts, in principle the open chain aldehyde form of [^{18}F]FDG should allow chemoselective aldehyde group-based reactions. A very prominent and chemoselective reaction represents the aminooxy−aldehyde coupling reaction to yield the corresponding oxime. Recently, the chemoselective oxime formation was shown to be a promising and versatile approach for both the convenient synthesis of ^{18}F-labeled prosthetic groups (*20, 32*) and the direct ^{18}F-labeling of aminooxy group-functionalized peptides (*36*) with readily available 4-[^{18}F]fluorobenzaldehyde.

Likewise, chemoselective reaction between the acyclic aldehyde form of [^{18}F]FDG with aminooxy group-containing compound **1** should lead to the corresponding oxime derivative [^{18}F]FDG-MHO. However, in the case of hexoses as aldehyde components in the aminooxy−aldehyde coupling reaction the formation of isomeric products must be considered. Hence, Ramsay et al. observed the formation of three isomeric products with identical molecular mass when they investigated the reaction of *O*-(4-(nitrobenzyl)-hydroxylamine with glucose at pH 4 (*51*). The observed isomers were proposed to be a mixture of *E*- and *Z*- acyclic oximes and α- and β-cyclic products (pyranoses and furanoses, respectively.). Accordingly, chemoselective condensation between the hexose FDG and aminooxy-functionalized maleimide **1** should also lead to a mixture of isomers as shown in Figure 3.

Synthesis of the Reference Compound FDG-MHO. Reference compound FDG-MHO was prepared by heating equimolar amounts of [^{19}]FDG and aminooxy compound **1** in EtOH/H_2O (4:1) for two hours. After solid-phase extraction using a C18

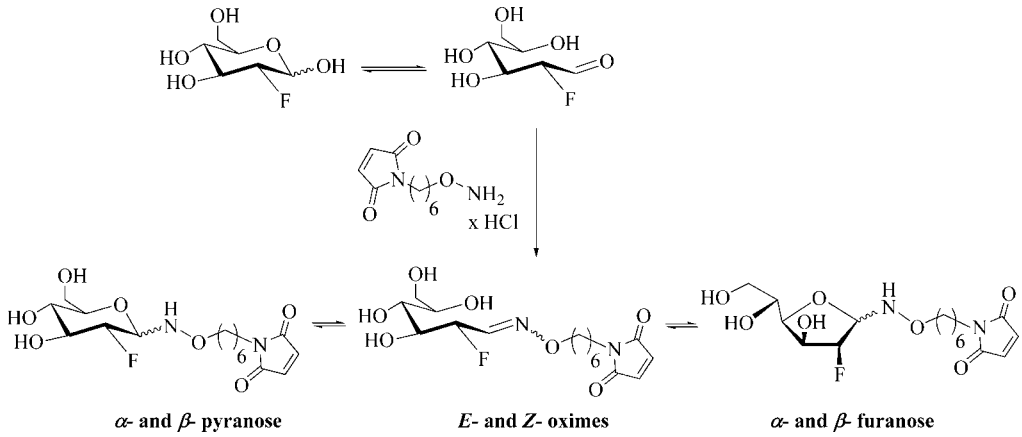

Figure 3. Proposed isomer formation through aminooxy−aldehyde coupling reaction involving FDG.

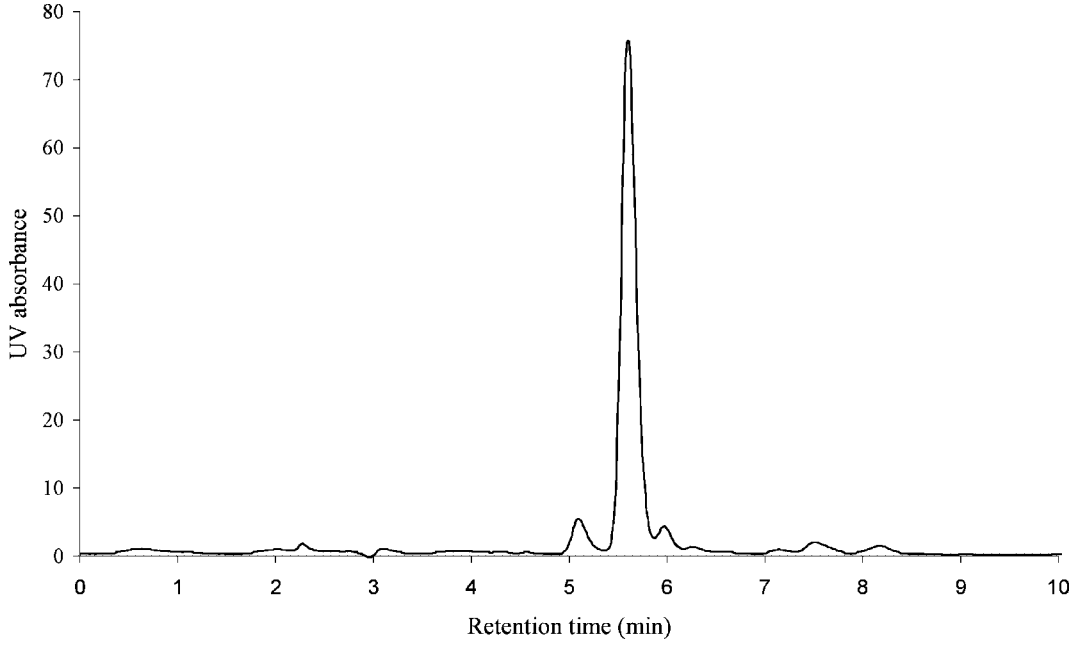

Figure 4. HPLC analysis of isolated product of the aminooxy−aldehyde coupling reaction with FDG.

SepPak cartridge and evaporation of the solvent, the desired reference compound FDG-MHO was obtained as a glass in 79% yield. HPLC analysis of the product indicated, however, the formation of several compounds consisting of a major product (>90%, t_R = 5.6 min) accompanied by at least two smaller peaks at retention times of 5.1 and 6.0 min, respectively (Figure 4).

The three peaks were collected and subjected to mass spectrometric analysis (ESI, positive). The peaks at 5.1 and 5.6 min showed identical mass peaks of *m*/*z* 377.4 ([M+H]$^+$) and *m*/*z* 399.35 ([M+Na]$^+$), respectively, suggesting the formation of at least two isomers. The formation of isomers during the aminooxy−aldehyde conjugation reaction between the hexose FDG and aminooxy compound **1** in aqueous media is in accordance with the report by Ramsay et al. (*51*). However, NMR analysis of the isolated reaction product in CD_3OD shows only one distinct compound. In the ^{1}H NMR spectra, the observed characteristic doublet−doublet coupling pattern (J_{H-F} = 7.5 Hz, J_{H-H} = 6.1 Hz) at 7.48 ppm correlates with one proton as expected for an oxime proton (=N*H*−OR). No signals were found which would refer to the formation of related pyranose or furanose isomers as depicted in Figure 3. It is known from the literature that oxime protons of *E*- and *Z*-isomers show characteristic chemical shift differences, being, e.g., 7.56 ppm for the *E*-isomer and 6.95 ppm for the *Z*-isomer (*52*). The observed more downfield shifted signal at 7.48 ppm would agree with an *E*-isomer oxime proton. Consequently, we conclude that the product possesses an open-chain *E*-oxime structure.

Radiosynthesis of [^{18}F]FDG-MHO. The radiosynthesis of [^{18}F]FDG-MHO is given in Figure 5.

The reaction is based on treatment of a [^{18}F]FDG solution, which was prepared according to the well-established [^{18}F]FDG synthesis (*47*, *48*), with aminooxy-functionalized compound **1**. Notably, the used [^{18}F]FDG solution contains substantial amounts of D-glucose (50−70 μg per milliliter [^{18}F]FDG solution) as typically formed during the [^{18}F]FDG production process starting from mannose triflate and subsequent basic hydrolysis. Therefore, formation of the corresponding glucose product must be considered. The formation of the glucose product was confirmed through LC-MS (ESI, positive) analysis of the collected mass peak (*m*/*z* 375.2 [M+H]$^+$, *m*/*z* 397.4 [M+Na]$^+$) in the semipreparative HPLC (t_R = 19−21 min). To avoid complete consumption of the amino-oxy labeling precursor by the reaction with glucose, the amount of labeling precursor has to be sufficiently high to give the desired [^{18}F]FDG-MHO compound in satisfactory radiochemical yields. Thus, best results were obtained when at least 10 mg (40 μmol) of compound **1** per milliliter [^{18}F]FDG solution was used. The

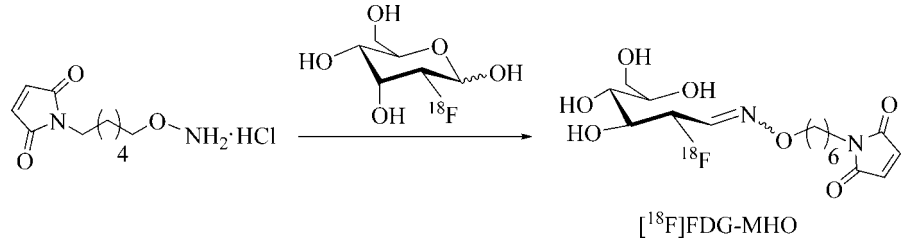

Figure 5. Radiosynthesis of [^{18}F]FDG-MHO.

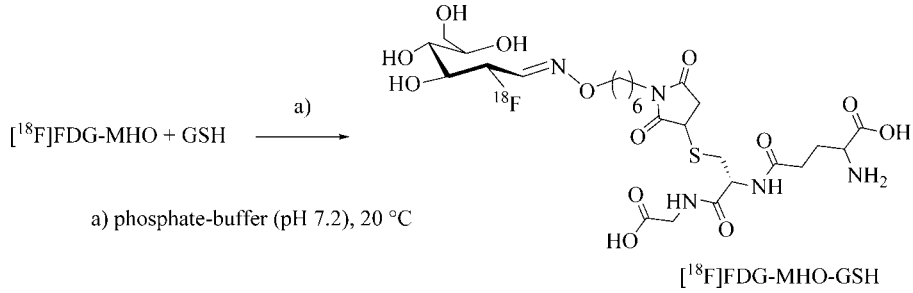

Figure 6. Radiolabeling of GSH with [^{18}F]FDG-MHO.

Table 1. Radiolabeling of GSH with [^{18}F]FDG-MHO

GSH concentration	1 mg/mL	100 μg/mL	10 μg/mL	1 μg/mL	100 ng/mL	10 ng/mL	1 ng/mL
% Product	>95	>95	>95	>95	92	47	38

reaction proceeded best in 80% ethanol as the solvent at 100 °C for 15 min. After semipreparative HPLC purification desired [^{18}F]FDG-MHO could be isolated in 45−69% radiochemical yield based upon [^{18}F]FDG (decay-corrected) within 45 min in high radiochemical purity (greater than 95%).

The obtained radiochemical yield of 45−69% for [^{18}F]FDG-MHO is comparable with related maleimide-containing ^{18}F prosthetic groups such as *N*-{4-[(4-[^{18}F]fluorobenzylidene)-aminooxy]butyl}maleimide (*20*), [^{18}F]FBAM (*32*), [^{18}F]FPyME (*21*), and [^{18}F]FBEM (*46*). However, the facile availability of [^{18}F]FDG as the labeling precursor in the coupling reaction circumvents the laborious preparation of ^{18}F-labeled precursors such as 4-[^{18}F]fluorobenzaldehyde, [^{18}F]fluoropyridine derivatives, or [^{18}F]SFB as intermediates required for the synthesis of *N*-{4-[(4-[^{18}F]Fluorobenzylidene)aminooxy]butyl}maleimide, [^{18}F]FBAM, [^{18}F]FPyME, and [^{18}F]FBEM, respectively. Thus, the simple single step reaction sequence starting from easily available [^{18}F]FDG make the synthesis of [^{18}F]FDG-MHO a very attractive alternative to previously published maleimide-containing ^{18}F prosthetic groups.

Radiolabeling of Glutathione (GSH). Various thiol-reactive agents containing a maleimide group have successfully been used for the chemoselective modification of peptides and proteins. Thiol-specific Michael reaction of maleimide-containing prosthetic groups provides high chemoselectivity when compared with amine and carboxylate-reactive labeling agents. The labeling properties of the bifunctional labeling agent [^{18}F]FDG-MHO for chemoselective conjugation toward thiol groups was exemplified by the reaction with the cysteine-containing tripeptide glutathione (GSH) and the single thiol group-containing protein anxA5 (Figure 6).

The ^{18}F-labeling reaction was performed at room temperature for 10 min in a phosphate buffer solution (pH 7.2) containing various GSH concentrations ranging from 1 ng/mL to 1.0 mg/mL. Conversion of [^{18}F]FDG-MHO into conjugate [^{18}F]FDG-MHO-GSH was monitored by radio-TLC analysis as previously reported (*32*). The conversion refers to as the percentage of radioactivity area of coupling product [^{18}F]FDG-MHO-GSH relative to the total radioactivity area. The results are summarized in Table 1.

More than 95% of the labeling reagent [^{18}F]FDG-MHO was converted into the corresponding GSH conjugate at GSH concentrations ranging from 1.0 mg/mL to 1 μg/mL after 10 min at room temperature. At lower GSH concentrations of 100, 10, and 1 ng/mL, the conversions were still good to moderate, being 92%, 47%, and 38%, respectively. The dependency of the radiochemical yield upon the peptide concentration has also been reported in previous publications describing the ^{18}F-labeling of peptides via prosthetic group labeling strategies (*13*). The labeling efficiency of [^{18}F]FDG-MHO toward GSH in this work is superior to recently reported results in the literature involving maleimide-containing prosthetic groups for ^{18}F-labelings, especially at very low GSH concentrations (*20, 32*). The determined radiochemical yields of 92% and 47% at 100 ng/mL and 10 ng/mL for [^{18}F]FDG-MHO are significantly higher compared to the 20% and 5% radiochemical yield observed at similar GSH concentrations of 100 and 10 ng/mL in the case of the prosthetic group [^{18}F]FBAM (*32*). Thus, the obtained excellent radiochemical yields even at very low GSH concentrations after 10 min at room temperature make the bifunctional labeling agent [^{18}F]FDG-MHO an excellent ^{18}F prosthetic group for the efficient labeling of thiol groups under mild reaction conditions compatible with peptides and proteins.

Radiolabeling of Annexin A5 (anxA5). The feasibility of [^{18}F]FDG-MHO as a thiol-reactive bifunctional labeling agent was further assessed by using the single thiol group-containing protein annexin A5 (anxA5) as a model. The mature human anxA5 is a 36 kDa, 319 amino acid protein which belongs to a family of calcium-dependent phospholipid-binding interfacial membrane proteins.

In the past decade, anxA5 binding has become one of the standard procedures to measure apoptosis in histopathology (*55*). Moreover, an increasing number of reports deal with radiolabeled anxA5 as molecular probes for imaging apoptosis in vivo (*56*). In this line, ^{99m}Tc-, ^{68}Ga-, ^{18}F-, ^{123}I-, and ^{124}I-labeled annexin derivatives have been prepared and studied. In the case

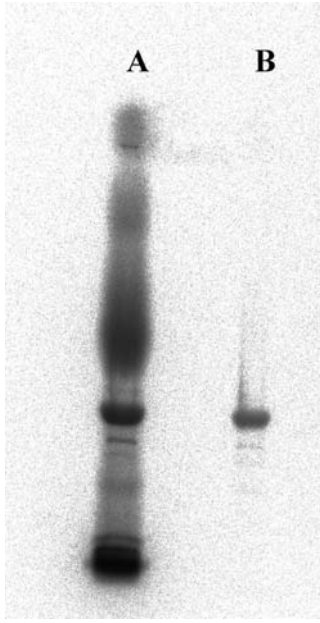

Figure 7. Representative radio-SDS-PAGE pattern of the reaction mixture (A) and the purified ^{18}F-labeled anxA5 (B). The figure shows radioactivity distribution as determined by radioluminography using a BAS 5000 scanner (Fujix, Japan). The radioluminograms were analyzed with the AIDA software package (Raytest GmbH, Germany).

of ^{18}F-labeled anxA5 derivatives, all described radiosyntheses were based on the reaction of anxA5 with the amine-group reactive prosthetic group [^{18}F]SFB (*57–61*). Consequently, incorporation of the ^{18}F label was achieved via nonchemoselective, random [^{18}F]fluorobenzoylation of variations of the total 22 lysine residues or the chemically accessible N-terminus of anxA5. On the other hand, mature anxA5 contains only one chemically accessible cysteine residue at position 315 (position 316, often cited in the literature, refers to the unprocessed precursor). Therefore, anxA5 should prove a suitable model for the chemoselective ^{18}F radiolabeling of proteins possessing one single cysteine residue. Radiolabeling of anxA5 with the thiol-group reactive agent [^{18}F]FDG-MHO is expected not to lead to adverse modification of anxA5. Moreover, modification of the cysteine residue in anxA5 should not alter the biological activity and functionality of the protein. This assumption is supported by recent data from the patent literature reporting the same binding affinity of anxA5 or annexin conjugates for phosphatidylserine-containing membranes when cysteine 315 is deleted or replaced with serine or other non-sulfur-containing amino acids (*62, 63*).

The radiolabeling of anxA5 was performed through chemoselective alkylation of the cysteine residue in anxA5 with maleimide [^{18}F]FDG-MHO. Treatment of anxA5 (100 μg, 2.8 nmol) in Tris buffer (pH = 7.4) with [^{18}F]FDG-MHO and subsequent size-exclusion chromatography afforded 43−58% (decay-corrected, based upon [^{18}F]FDG-MHO, n = 6) of [^{18}F]FDG-MHO-anxA5 within 60 min. Considering the low anxA5 concentration used (2.25 μM) and the presence of a single cysteine residue as the sole potential reaction site, the radiochemical yield is remarkably good. The high efficiency of the chemoselective introduction of the ^{18}F label via maleimide-containing prosthetic group [^{18}F]FDG-MHO into anxA5 is further confirmed when comparing the obtained 43−58% radiochemical yields with the reported yields of [^{18}F]SFB-based anxA5 derivatives. Thus, conjugation reaction with [^{18}F]SFB using a comparable amount of anxA5 (100 μg) gave only a 10% radiochemical yield based upon [^{18}F]SFB (*58*). Higher radiochemical yields of up to 70% for the conjugation step were only achievable when fairly high protein concentrations of up to 6 mg/mL were used (*57, 60, 61*). Moreover, conjugation reaction of anxA5 with [^{18}F]SFB can rely on the availability of 22 lysine residues and the N-terminus in the protein as potential reaction sites. This leads to a highly random [^{18}F]fluorobenzoylation of the available primary amines abundant in anxA5, thus avoiding a regioselective and chemoselective introduction of the ^{18}F label as in the case of [^{18}F]FDG-MHO-anxA5. Moreover, in some instances the use of the amine-reactive agent [^{18}F]SFB for protein labeling can fail completely. As an example, steric hindrance of the *N*-terminal region of apoB-100 due to oxidative modification of apoB-100 by myeloperoxidase or hypochlorous acid prevents radiolabeling with the acylation agent [^{18}F]SFB (*32*).

Starting from 20 MBq of [^{18}F]FDG-MHO, the effective specific activity of purified ^{18}F-labeled anxA5 was calculated to be 2−4 GBq/μmol at the end of synthesis (related to anxA5, M_r = 36 000 Da). Purification of the reaction mixture by size-exclusion chromatography gave radiochemically pure [^{18}F]FDG-MHO-anxA5, which could be completely separated from unreacted [^{18}F]FDG-MHO and other radioactive byproduct not further identified. The quality of purified [^{18}F]FDG-MHO-anxA5 was suitable to be used directly for subsequent small animal PET studies. Radiolabeling and purification of radiolabeled anxA5 was monitored by radio-SDS-PAGE. Figure 7 shows representative radio-SDS-PAGE patterns of the reaction mixture (lane A) and purified ^{18}F-labeled anxA5 fraction (lane B).

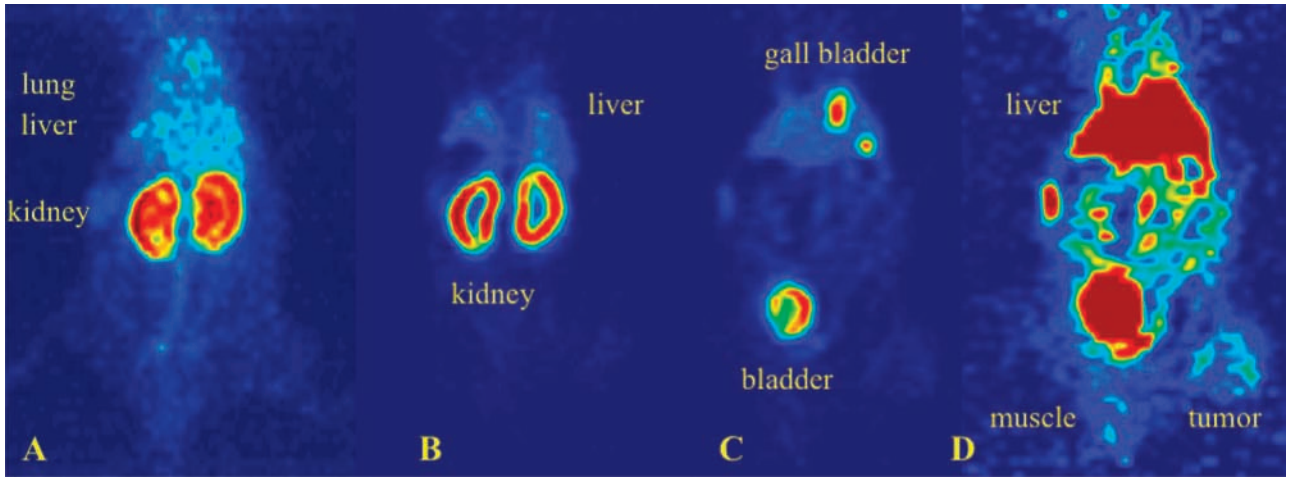

Figure 8. Small animal PET images of [^{18}F]FDG-MHO-anxA5 at 2 min (A) and 4 h (B,C,D) after tracer application. (B) Coronal section on the level of kidneys. (C) Coronal section on the level of xenographted tumor. (D) Coronal section as (C) but expanded scale intensity.

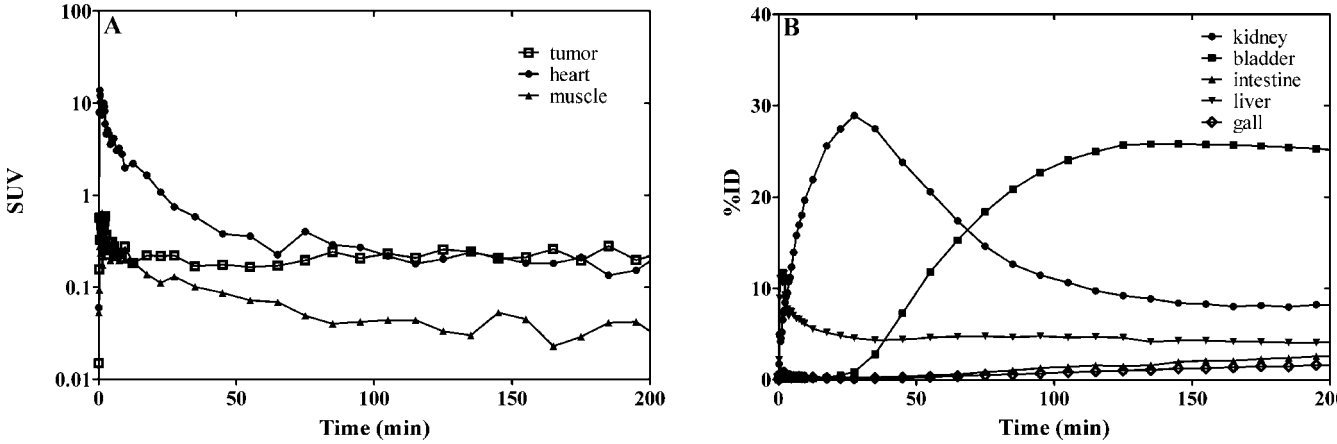

Figure 9. Representative time−activity curves from one animal after single intravenous application of [^{18}F]FDG-MHO-anxA5. (A) Time−activity concentration (SUV) curves of the heart, tumor, and muscle (note the semilogarithmic scale). (B) Time−activity (%ID) curves of liver, intestine, gall bladder, kidney, and urinary bladder.

Small Animal PET Imaging of [^{18}F]FDG-MHO-anxA5. Biodistribution and kinetics of [^{18}F]FDG-MHO-anxA5 was evaluated in a pilot small animal PET study in a human colorectal adenocarcinoma (HT-29) murine xenograft model. The murine xenograft model was not treated with an apoptosis inducing agent. Figure 8 shows small animal PET images at 2 min and 4 h after injection of [^{18}F]FDG-MHO-anxA5.

Figure 9 depicts representative time−activity curves for heart (blood pool), tumor, and muscle (A), liver, intestine, gall bladder, kidney, and urinary bladder (B).

After intravenous application of [^{18}F]FDG-MHO-anxA5, the radiotracer was rapidly distributed in the blood pool. [^{18}F]FDG-MHO-anxA5 showed a blood clearance with a mean half-life of 6.5 min, which is slower in comparison to the 2.6 min half-life as determined for [^{18}F]fluorobenzoylated anxA5 (R. Bergmann et al., unpublished results). Thus, chemoselective labeling of the cysteine residue in anxA5 with [^{18}F]FDG-MHO leads to a ^{18}F-labeled anxA5 derivative with a longer residence time in the blood pool resulting in a better availability of the radiotracer for in vivo imaging of apoptosis.

Radiolabeled anxA5 was mainly accumulated in the kidney cortex, reaching 8.2%ID at 200 min p.i. The high activity accumulation in the renal excretory system is consistent with reports in the literature using ^{18}F-labeled anxA5 derivatives in normal rats (*59*, *61*). At the same time point, approximately 4%ID of the injected activity was found in the liver. A part of activity was eliminated into the bile (1.6%ID at 200 min p.i.) and intestine (2.6%ID at 200 min p.i.). The activity in the xenografted tumor increased over the time reaching a tumor-to-muscle ratio of about 3 at 200 min p.i. Therefore, although the absolute activity in the HT-29 tumor was relatively low (SUV = 0.12) the tumor could be clearly delineated in the PET images (Figure 9).

CONCLUSION

We have developed a novel thiol-reactive prosthetic group ([^{18}F]FDG-MHO) based upon the readily available PET radiotracer [^{18}F]FDG. The straightforward access to [^{18}F]FDG makes this procedure especially attractive, e.g., for research groups without a complete PET facility. The novel prosthetic group was used for the chemoselective ^{18}F-labeling of glutathione as a thiol-containing model peptide and single cysteine residue containing anxA5 as a model protein. The use of [^{18}F]FDG-MHO as thiol group reactive prosthetic group allows the exclusive labeling of cysteine 315 in anxA5 while providing excellent radiochemical yields for the conjugation step even at very low protein concentration. Moreover, [^{18}F]FDG-MHO-anxA5 represents the first example of a defined, chemoselectively ^{18}F-labeled annexin derivative.

Taken together, the ease of preparation and the excellent yields of the conjugation step with cysteine residues make [^{18}F]FDG-MHO a very interesting and promising novel prosthetic group for chemoselective ^{18}F labeling of thiol group-containing peptides and proteins.

ACKNOWLEDGMENT

The authors wish to thank S. Preusche for radionuclide production, T. Krauss for technical assistance, K. Schumann, D. Pfitzmann, and R. Herrlich for assistance in animal experiments. We are grateful to Dr. N. Budisa, Max Planck Institute of Biochemistry, Molecular Biotechnology, for the kind gift of recombinant Annexin A5. The project was partly supported by the EU project BioCare No. 505785 and by a grant from the Deutsche Forschungsgemeinschaft (DFG; grant no. PI304/1-1).

LITERATURE CITED

(1) Wester, H. J., and Schottelius, M. (2007) Fluorine-18 labeling of peptides and proteins. *Ernst Schering Res. Found. Workshop 62*, 79–111.
(2) Okarvi, S. M. (2001) Recent progress in fluorine-18 labelled peptide radiopharmaceuticals. *Eur. J. Nucl. Med. 28*, 929–938.
(3) Wuest, F. (2005) Aspects of positron emission tomography radiochemistry as relevant for food chemistry. *Amino Acids 29*, 323–339.
(4) Wilbur, D. S. (1992) Radiohalogenation of proteins: an overview of radionuclides, labeling methods, and reagents for conjugate labeling. *Bioconjugate Chem. 3*, 433–470.
(5) Kilbourn, M. R., Dence, C. S., Welch, M. J., and Mathias, C. J. (1987) Fluorine-18 labeling of proteins. *J. Nucl. Med. 28*, 462–470.
(6) Wester, H. J., Hamacher, K., and Stöcklin, G. (1996) A comparative study of N.C.A. fluorine-18 labeling of proteins via acylation and photochemical conjugation. *Nucl. Med. Biol. 23*, 365–372.
(7) Müller-Platz, C. M., Kloster, G., Legler, G., and StöckIin, G. (1982) 18F-Fluoroacetate: An agent for introducing n.c.a. fluorine-18 into urokinase without loss of biological activity. *J. Label. Compd. Radiopharm. 19*, 1645.
(8) Guhlke, S., Coenen, H. H., and Stöcklin, G. (1994) Fluoroacylation agents based on small n.c.a. [^{18P}F]fluorocarboxylic acids. *Appl. Radiat. Isot. 45*, 715–727.
(9) Hostetler, E. D., Edwards, W. B., Anderson, C. J., and Welch, M. J. (1999) Synthesis of 4-[18F]fluorobenzoyl octreotide and

biodistribution in tumour-bearing Lewis rats. *J. Label. Compd. Radiopharm. 42*, S720−S722.

(10) Vaidyanathan, G., and Zalutsky, M. R. (1992) Labeling proteins with fluorine-18 using N-succinimidyl 4-[18F]fluorobenzoate. *Int. J. Rad. Appl. Instrum. B 19*, 275–281.

(11) Vaidyanathan, G., and Zalutsky, M. R. (1994) Improved synthesis of N-succinimidyl 4-[18F]fluorobenzoate and its application to the labeling of a monoclonal antibody fragment. *Bioconjugate Chem. 5*, 352–356.

(12) Page, R. L., Garg, P. K., Vaidyanathan, G., and Zalutsky, M. R. (1994) Preclinical evaluation and PET imaging of 18F-labeled Mel-14 F(ab′)2 fragment in normal dogs. *Nucl. Med. Biol. 21*, 911–919.

(13) Wuest, F., Hultsch, C., Bergmann, R., Johannsen, B., and Henle, T. (2003) Radiolabelling of isopeptide N-ϵ-(γ-glutamyl)-L-lysine by conjugation with N-succinimidyl-4-[18F]fluorobenzoate. *Appl. Radiat. Isot. 59*, 43–48.

(14) Garg, P. K., Garg, S., and Zalutsky, M. R. (1991) Fluorine-18 labeling of monoclonal antibodies and fragments with preservation of immunoreactivity. *Bioconjugate Chem. 2*, 44–49.

(15) Herman, L. W., Fischman, A. J., Tompkins, R. G., Hanson, R. N., Byon, C., Strauss, H. W., and Elmaleh, D. R. (1994) The use of pentafluorophenyl derivatives for the 18F labelling of proteins. *Nucl. Med. Biol. 21*, 1005–1010.

(16) Lang, L., and Eckelman, W. C. (1994) One-step synthesis of 18F labelled [18F]-N-succinimidyl 4-(fluoromethyl)benzoate for protein labelling. *Appl. Radiat. Isot. 45*, 1155–1163.

(17) Lang, L., and Eckelman, W. C. (1997) Labeling Proteins at high specific activity using N-succinimidyl 4-[18F](fluoromethyl) benzoate. *Appl. Radiat. Isot. 48*, 169–173.

(18) Shai, Y., Kenneth, L. K., Channing, M. A., Dunn, B. B., Lesniak, M. A., Eastman, R. C., Finn, R. D., Roth, J., and Jacobson, K. A. (1989) 18F-labelled insulin: a prosthetic group methodology for incorporation of a positron emitter into peptides and proteins. *Biochemistry 28*, 4801–4806.

(19) Shiue, C. Y., Wolf, A. P., and Heinfeld, J. F. (1989) Synthesis of 18F-labelled N-(p-[18F]fluorophenyl)maleimide and its derivatives for labelling monoclonal antibody with 18F. *J. Label. Compd. Radiopharm. 26*, 287–289.

(20) Toyokuni, T., Walsh, J. C., Dominguez, A., Phelps, M. E., Barrio, J. R., Gambhir, S. S., and Satyamurthy, N. (2003) Synthesis of a new heterobifunctional linker, N-[4-(Aminooxy-)butyl]maleimide, for facile access to a thiol-reactive F-18-Labeling agent. *Bioconjugate Chem. 14*, 1253–1259.

(21) de Bruin, B., Kuhnast, B., Hinnen, F., Yaouancq, L., Amessou, M., Johannes, L., Samson, A., Boisgard, R., Tavitian, B., and Dolle, F. (2005) 1-[3-(2-[F-18]fluoropyridin-3-yloxy)propyl]pyrrole-2,5-dione: Design, synthesis, and radiosynthesis of a new[F-18]fluoropyridine-based maleimide reagent for the labeling of peptides and proteins. *Bioconjugate Chem. 16*, 406–420.

(22) Dolle, F., Hinnen, F. B. L., Boisgard, R., Sanson, A., F., R.-M., and Tavitian, B. (2003) Radiosynthesis of a [18F]fluoropyridine-based maleimide reagent for protein labelling. *J. Label. Compd. Radiopharm. 46*, S15.

(23) Kilbourn, M. R., Dence, C. S., Welch, M. J., and Mathias, C. J. (1987) F-18 labeling of proteins. *J. Nucl. Med. 28*, 462–470.

(24) Dence, C. S., McCarthy, T. J., and Welch, M. J. (1993) Improved synthesis of [18F]4-fluorophenacyl bromide: the use of polymer supported perbromide. *Appl. Radiat. Isot. 44*, 981–983.

(25) Dolle, F., Hinnen, F., Vaufrey, F., Tavitian, B., and Crouzel, C. (1997) A general method for labeling oligodeoxynucleotides with F-18 for in vivo PET imaging. *J. Label. Compd. Radiopharm. 39*, 319–330.

(26) Kuhnast, B., Dolle, F., Vaufrey, F., Hinnen, F., Crouzel, C., and Tavitian, B. (2000) Fluorine-18 labeling of oligonucleotides bearing chemically-modified ribose-phosphate backbones. *J. Label. Compd. Radiopharm. 43*, 837–848.

(27) Kuhnast, B., Dolle, F., and Tavitian, B. (2002) Fluorine-18 labeling of peptide nucleic acids. Journal. *J. Label. Compd. Radiopharm. 45*, 1–11.

(28) Kuhnast, B., de Bruin, A., Hinnen, F., Tavitian, B., and Dolle, F. (2004) Design and synthesis of a new [F-18]fluoropyridine-based haloacetamide reagent for the labeling of oligonucleotides: 2-bromo-N-[3-(2-[F-18]fluoropyridin-3-yloxy)propyl]acetamide. *Bioconjugate Chem. 15*, 617–627.

(29) Kuhnast, B., Dolle, F., Terrazzino, S., Rousseau, B., Loc'h, C., Vaufrey, F., Hinnen, F., Doignon, I., Pillon, F., David, C., Crouzel, C., and Tavitian, B. (2000) General method to label antisense oligonucleotides with radioactive halogens for pharmacological and imaging studies. *Bioconjugate Chem. 11*, 627–636.

(30) Kuhnast, B., Hinnen, F., Boisgard, R., Tavitian, B., and Dolle, F. (2003) Fluorine-18 labelling of oligonucleotides: Prosthetic labelling at the 5 ′-end using the N-(4-[F-18[fluorobenzyl)-2-bromoacetamide reagent. *J. Label. Compd. Radiopharm. 46*, 1093–1103.

(31) Kuhnast, B., Klussmann, S., Hinnen, F., Boisgard, R., Rousseau, B., Furste, J. P., Tavitian, B., and Dolle, F. (2004) Fluorine-18-and iodine-125-labelling of spiegelmers. *J. Label. Compd. Radiopharm. 46*, 1205–1219.

(32) Berndt, M., Pietzsch, J., and Wuest, F. (2007) Labeling of low-density lipoproteins using the 18F-labeled thiol-reactive reagent N-[6-(4-[18F]fluorobenzylidene)aminooxyhexyl]maleimide. *Nucl. Med. Biol. 34*, 5–15.

(33) Hashizume, K., Hashimoto, N., and Miyake, Y. (1995) Synthesis of positron labelled photoactive compounds: 18F labelled aryl azides for positron labelling of biochemical molecules. *J. Org. Chem. 60*, 6680–6681.

(34) Lange, C. W., VanBrocklin, H. F., and Taylor, S. E. (2002) Photoconjugation of 3-azido-5-nitrobenzyl-[18F]fluoride to an oligonucleotide aptamer. *J. Label. Compd. Radiopharm. 45*, 257–268.

(35) Patt, J., and Patt, M. (2002) Reaction of [18F]4-fluorobenzenediazonium cations with cystein or cycteinyl group: Preparation of 18F-labeled S-aryl-cysteine and a radiolabeled peptide. *J. Label. Compd. Radiopharm. 45*, 1229–1238.

(36) Poethko, T., Schottelius, M., Thumshirn, G., Hersel, U., Herz, M., Henriksen, G., Kessler, H., Schwaiger, M., and Wester, H. J. (2004) Two-step methodology for high-yield routine radiohalogenation of peptides: (18)F-labeled RGD and octreotide analogs. *J. Nucl. Med. 45*, 892–902.

(37) Hultsch, C., Berndt, M., Bergmann, R., and Wuest, F. (2007) Radiolabeling of multimeric neurotensin(8−13) analogs with the short-lived positron emitter fluorine-18. *Appl. Radiat. Isot. 65*, 818–826.

(38) Lee, Y. S., Jeong, J. M., Kim, H. W., Chang, Y. S., KimY. J., Hong, M. K., Rai, G. B., Chi, D. Y., Kang, W. J., Kang, J. H., Lee, D. S., Chung, J. K., Lee, M. C., and Suh, Y. G. (2006) An improved method of 18F peptide labeling: hydrazone formation with HYNIC-conjugated c(RGDyK). *Nucl. Med. Biol. 33*, 677–683.

(39) Chang, Y. S., Jeong, J. M., Lee, Y. S., Kim, H. W., Rai, G. B., Lee, S. J., Lee, D. S., Chung, J. K., and Lee, M. C. (2005) Preparation of 18F-human serum albumin: a simple and efficient protein labeling method with 18F using a hydrazone-formation method. *Bioconjugate Chem. 16*, 1329–1333.

(40) Bormans, G., and Verbruggen, A. (2001) Enzymatic synthesis and biodistribution in mice of β-O-D-galactopyranosyl-(1,4′)-2′-[18F]fluoro-2′-deoxy-D-glucopyranose (2′-[18F]fluorodeoxylactose]. *J. Label. Compd. Radiopharm. 44*, 417–423.

(41) Patt, M., Sorger, D., Scheunemann, M., and Stöcklin, G. (2002) Adduct of 2-[18F]FDG and 2-nitroimidazole as a putative radiotracer for the detection of hypoxia with PET: synthesis, in vitro- and in vivo-characterization. *Appl. Radiat. Isot. 57*, 705–712.

(42) Marschauer, S., Pischetsrieder, M., Kuwert, T., and Prante, O. (2005) Utility of 1,3,4,6-tetra-O-acetyl-2-deoxy-2-[18F]fluoro-

glucopyranoside for no-carrier-added 18F-glycosylation of amino acids. *J. Label. Compd. Radiopharm. 48*, 701–719.

(43) Marschauer, S., Kuwert, T., and Prante, O. (2006) 18F-glycosylation using Koenigs-Knorr conditions: a comparative study. *J. Label. Compd. Radiopharm. 49*, 101–108.

(44) Prante, O., Hamacher, K., and Coenen, H. H. (2007) Chemoenzymatic n.c.a synthesis of the coenzyme UDP-2-deoxy-2-[18F]fluoro-α-D-glucopyranose as substrate of glycosyltransferases. *J. Label. Compd. Radiopharm. 50*, 55–63.

(45) Prante, O., Einsiedel, J., Haubner, R., Gmeiner, P., Wester, H. J., Kuwert, T., and Maschauer, S. (2007) 3,4,6-Tri-O-acetyl-2-deoxy-2-[18F]fluoroglucopyranosyl phenylthiosulfonate: a thiol-reactive agent for the chemoselective 18F-glycosylation of peptides. *Bioconjugate Chem. 18*, 254–262.

(46) Cai, W., Zhang, X., Wu, Y., and Chen, X. (2006) A thiol-reactive 18F-labeling agent, N-[2-(4−18F-fluorobenzamido)ethyl]maleimide, and synthesis of RGD peptide-based tracer for PET imaging of $\alpha_v\beta_3$ integrin expression. *J. Nucl. Med. 47*, 1172–1180.

(47) Hamacher, K., Coenen, H. H., and Stöcklin, G. (1986) Efficient stereospecific synthesis of no-carrier-added 2-[18F]-fluoro-2-deoxy-D-glucose using aminopolyether supported nucleophilic substitution. *J. Nucl. Med. 27*, 235–238.

(48) Füchtner, F., Steinbach, J., Mäding, P., and Johannsen, B. (1996) Basic hydrolysis of 2-[18F]fluoro-1,3,4,6-tetra-O-acetyl-D-glucose in the preparation of 2-[^{18}F]fluoro-2-deoxy-D-glucose. *Appl. Radiat. Isot. 47*, 61–66.

(49) Burger, A., Berendes, R., Voges, D., Huber, R., and Demange, P. (1993) A rapid and efficient purification method for recombinant annexin V for biophysical studies. *FEBS Lett. 329*, 25–28.

(50) Meier, H. J., and Ullrich, V. (1995) Grundlagen der organischen Chemie für Biowissenschaftler. G. Fischer Verlag, 1. Aufl.

(51) Ramsay, S. L., Freeman, C., Grace, P. B., Redmond, J. W., and MacLeod, J. K. (2001) Mild tagging procedures for the structural analysis of glycans. *Carbohydr. Res. 333*, 59–71.

(52) Karabatsos, G. J., and Hsi, N. (1967) Structural studies by nuclear magnetic resonance-XI: conformations and configurations of oxime *O*-methyl ethers. *Tetrahedron 23*, 1079–1095.

(53) Funakoshi, T., Heimark, R. L., Hendrickson, L. E., McMullen, B. A., and Fujikawa, K. (1987) Human placental antico-agulant protein: isolation and characterization. *Biochemistry 26*, 5572–5578.

(54) Thiagarajan, P., and Benedict, C. R. (1997) Inhibition of arterial thrombosis by recombinant annexin V in a rabbit carotid artery injury model. *Circulation 96*, 2339–2347.

(55) Stadelmann, C., and Lassmann, H. (2000) Detection of apoptosis in tissue sections. *Cell Tissue Res. 301*, 19–31.

(56) Boersma, H. H., KietselaerB. L., Stolk, L. M., Bennaghmouch, A., Hofstra, L., Narula, J., Heidendal, G. A., and Reutelingsperger, C. P. (2005) Past, present, and future of annexin A5: from protein discovery to clinical applications. *J. Nucl. Med. 46*, 2035–2050.

(57) Zijlstra, S., Gunawan, J., and Burchert, W. (2003) Synthesis and evaluation of a 18F-labelled recombinant AnxA5 derivative, for identification and quantification of apoptotic cells with PET. *Appl. Radiat. Isot. 58*, 201–207.

(58) Murakami, Y., Takamatsu, H., Taki, J., Tatsumi, M., Noda, A., Ichise, R., Tait, J. F., and Nishimura, S. (2004) 18F-labelled annexin V: a PET tracer for apoptosis imaging. *Eur. J. Nucl. Med. Mol. Imaging 31*, 469–474.

(59) Yagle, K. J., Eary, J. F., Tait, J. F., Grierson, J. R., Link, J. M., Lewellen, B., Gibson, D. F., and Krohn, K. A. (2005) Evaluation of 18F-annexin V as a PET imaging agent in an animal model of apoptosis. *J. Nucl. Med. 46*, 658–666.

(60) Toretsky, J., Levenson, A., Weinberg, I. N., Tait, J. F., Uren, A., and Mease, R. C. (2004) Preparation of F-18 labeled annexin V: a potential PET radiopharmaceutical for imaging cell death. *Nucl. Med. Biol. 31*, 747–752.

(61) Grierson, J. R., Yagle, K. J., Eary, J. F., Tait, J. F., Gibson, D. F., Lewellen, B., Link, J. M., and Krohn, K. A. (2004) Production of [F-18]fluoroannexin for imaging apoptosis with PET. *Bioconjugate Chem. 15*, 373–379.

(62) Reutelingsperger, C. P. M., Moonen, P., and Vermaire, A. (2007) Annexin derivatives suitable for pretargeting in therapy and diagnosis. WO/2007/069895.

(63) Tait, J. F., and Brown, D. S. (2000) Annexin derivatives with endogenous chelation sites. WO/2000/073332.

BC8000112

NanoFerrite Particle Based Radioimmunonanoparticles: Binding Affinity and In Vivo Pharmacokinetics

A. Natarajan,*[,†] C. Gruettner,[‡] R. Ivkov,[§] G. L. DeNardo,[†] G. Mirick,[†] A. Yuan,[†] A. Foreman,[§] and S. J. DeNardo[†]

School of Medicine, University of California Davis, Sacramento, California, Micromod Partikeltechnologie, GmbH, Rostock-Warnemuende, Germany, and Triton BioSystems, Inc., Chelmsford, Massachusetts. Received January 11, 2008; Revised Manuscript Received May 2, 2008

Dextran and PEG-coated iron oxide nanoparticles (NP), when suitably modified to enable conjugation with molecular targeting agents, provide opportunities to target cancer cells. Monoclonal antibodies, scFv, and peptides conjugated to 20 nm NP have been reported to target cancer for imaging and alternating magnetic field (AMF) therapy. The physical characteristics of NPs can affect their in vivo performance. Surface morphology, surface charge density, and particle size are considered important factors that determine pharmacokinetics, toxicity, and biodistribution. New NanoFerrite (NF) particles having improved specific AMF absorption rates and diameters of 30 and 100 nm were studied to evaluate the variation in their in vitro and in vivo characteristics in comparison to the previously studied 20 nm superparamagnetic iron oxide (SPIO) NP. SPIO NP 20 nm and NF NP 30 and 100 nm were conjugated to ^{111}In-DOTA-ChL6, a radioimmunoconjugate. Radioimmunoconjugates were conjugated to NPs using 25 μg of RIC/mg of NP by carbodiimide chemistry. The radioimmunonanoparticles (RINP) were purified and characterized by PAGE, cellulose acetate electrophoresis (CAE), live cell binding assays, and pharmacokinetics in athymic mice bearing human breast cancer (HBT 3477) xenografts. RINP (2.2 mg) were injected iv and whole body; blood and tissue data were collected at 4, 24, and 48 h. The preparations used for animal study were >90% monomeric by PAGE and CAE. The immunoreactivity of the RINP was 40−60% compared to ^{111}In-ChL6. Specific activities of the doses were 20−25 μCi/2.2 mg and 6−11 μg of mAb/2.2 mg of NP. Mean tumor uptakes (% ID/g ± SD) of each SPIO 20 nm, NF 30 nm, and 100 nm RINP at 48 h were 9.00 ± 0.8 (20 nm), 3.0 ± 0.3 (30 nm), and 4.5 ± 0.8 (100 nm), respectively; the ranges of tissue uptakes were liver (16−32 ± 1−8), kidney (7.0−15 ± 1), spleen (8−17 ± 3−8), lymph nodes 5−6 ± 1−2), and lung (2.0−4 ± 0.1−2). In conclusion, this study demonstrated that 100 nm NF NP could be conjugated to ^{111}In-mAb so that the resulting RINP had characteristics suitable for AMF therapy. Although 100 nm RINP targeted tumor less than 20 nm SPIO RINP, their heating capacity is typically 6 times greater, suggesting the 100 nm NF RINP could still deliver better therapy with AMF.

INTRODUCTION

Dextran and PEG-coated magnetic iron oxide nanoparticles linked to a fluorescent or radiolabeled molecular targeting agent have been used to (a) deliver heat selectively at the microenvironment of tumors with external AMF, (b) construct the multiple mono- or bispecific targeting units, and (c) image and trace the NP kinetics in vivo (*1*–*5*). Systemic delivery of nanoparticles specifically to cancer tissues in concentrations sufficient to achieve a therapeutic thermal dose induced by external alternating magnetic field has also been demonstrated to be predicted by calculated heat dosimetry (*5*, *6*). This can allow specific heating of cancer tissues using RINP by AMF, providing a promising treatment modality (*7*). Radioactivity quantitation should provide sufficient concentration of the particles retained in the tumor tissue relative to nearby normal tissues, and the characteristic specific AMF absorption rates (SAR) of the particles, to allow calculations of selective heat generation in tumor with moderate AMF amplitudes.

Exposure of tissue to alternating magnetic fields results in the deposition of heat through the induction of eddy currents in tissues that is dependent upon the field frequency, amplitude, duration of exposure, and area of exposed tissue (*5*). This induced heating can be controlled and minimized through judicious selection of AMF parameters and, when combined with appropriately targeted particles, can lead to successful therapy. Thus, successful therapy requires that an appropriate combination of AMF parameters be directed to tumor tissue containing a sufficiently high concentration of particles capable of producing therapeutic heat at the chosen AMF amplitudes, and minimizing both AMF exposure and particle concentrations in nearby surrounding tissues. In this manner, cytotoxic heat can be deposited specifically into the tumor microenvironment while simultaneously minimizing the nonspecific heating of surrounding healthy tissues.

The elevation of tissue temperature to between 40 and 45 °C is often called hyperthermia (*8*). There is a clear rationale for using hyperthermia in cancer treatment because hyperthermia is known to cause direct cytotoxicity and because it also acts as a radiation and chemo sensitizer (*8*). However, there is generally no intrinsic difference between hyperthermia sensitivity of normal and tumor cells, except for hematological malignancies (*9*). On the other hand, selective tumor cell kill can be achieved in vivo in this range because of characteristic differences between normal and tumor physiology. The architecture and vasculature in solid tumors is chaotic, producing

* Corresponding author. Arutselvan Natarajan, Ph.D., Radiodiagnosis & Therapy, Molecular Cancer Institute, 1508 Alhambra Blvd., Room 3100, Sacramento, CA 95816. Phone: 916-734-3787. Fax: 916-703-5014. E-mail: arutselvan.natarajan@ucdmc.ucdavis.edu.

† School of Medicine, University of California Davis, Sacramento, California, USA.

‡ Micromod Partikeltechnologie, GmbH, Rostock-Warnemuende, Germany.

§ Triton BioSystems, Inc., Chelmsford, Massachusetts, USA.

10.1021/bc800015n CCC: $40.75 © 2008 American Chemical Society
Published on Web 06/03/2008

hypoxic and low-pH [2−4] conditions that sensitize cells to thermal damage.

The effect of hyperthermia depends upon the achieved temperature and time of exposure. At temperatures above 42.5−43 °C, the exposure time can be halved with each 1 °C temperature increase to give an equivalent cell kill (*9, 10*). Hyperthermia inhibits cellular repair of sublethal radiation damage and also induces increasing radiosensitivity due to tumor reoxygenation. Despite the beneficial attributes of hyperthermia for cancer treatment, its clinical application has been limited because of a general inability to (a) deliver sufficient heat selectively to the tumor tissue and (b) accurately predict or measure heat dose deposited in the tumor (*8–10*).

Tumor-targeted heat therapy using the combination of NP and AMF has the potential to overcome both these limitations. In a previous study, 20 nm dextran matrix nanoparticles containing superparamagnetic iron oxide were linked to breast cancer targeting chimeric L6 (ChL6) monoclonal antibody (bioprobe), demonstrating the feasibility of delivering thermoablation to cancer cells (*5*). More key to clinical application of NP/AMF therapy, the demonstration of heat thermal dosimetry was predictive of tumor response and minimal normal tissue toxicity (*7*).

In order to further raise the therapeutic index of tumor response without normal tissue toxicity, an increased heat dose is needed. The heat dose (J/g of tumor tissue) can be increased by a combination of increased particle concentration in the tumor and/or increased heat output of the particles. The latter can be achieved only with higher SAR particles, because increasing heat from the particles by using higher AMF amplitudes or duration of exposure increases the potential for nonspecific heating (*5, 7, 11*).

New NF particles with high specific AMF absorption rates were synthesized by high-pressure homogenization according to a core−shell method, having a range of sizes 20−100 nm (*12*). Selected NF particles 30 and 100 nm were synthesized and characterized for the present study; measured specific absorption rates (SAR) demonstrated 7−10× higher SAR at various AMF amplitudes and 150 kHz over 20 nm SPIO particles (*12*). The NF particles possess an iron oxide core (density >5 g/cm^3) (10−60 nm) that is surrounded by a dextran shell. The iron content of the particles is >50% w/w, and they are separable with a permanent magnet. The dextran shell was further modified by cross-linking and addition of carboxyl-terminated PEG (PEG-COOH) for antibody conjugation (*12*).

By contrast, the previously described 20 nm SPIO particles are produced by the precipitation of ferric and ferrous chlorides in the presence of dextran (*13–15*). These particles consist of <40% w/w iron in a dextran matrix that is not cross-linked. Separation can be achieved only with the use of a high gradient magnetic field; thus, they are not separable with a permanent magnet. SAR values produced by these particles have been measured to range 27−105 W per gram of iron (*12*), several times lower than that observed with the NF particles.

Because of the significantly different physical and magnetic characteristics exhibited by the NF and SPIO particles, the potential utility of NF-based RINPs for cancer therapy must be validated with a study of their in vivo performance after conjugation with a monoclonal antibody (ChL6). This report describes the development of ^{111}In-ChL6 linked to various NPs: 20 nm SPIO, 30 nm NF, and 100 nm NF to produce RINP. Mean RINP diameter and size distributions were measured by photon correlation spectroscopy. In vitro and in vivo targeting and pharmacokinetics (PK) of the RINPs were characterized. The in vivo tumor targeting and in vitro SAR data were compared for the various RINPs to predict thermal dose deliverable at the cancer tissues by various AMF amplitudes (at 150 kHz) to enhance further development of optimal particles for future NP-AMF thermal therapy.

EXPERIMENTAL PROCEDURES

Materials. Carrier-free ^{111}In (MDS Nordion, Ontario, Canada) was purchased as $^{111}InCl_3$ in 0.05 M HCl. Chimeric L6 (ChL6), human-mouse monoclonal antibody chimera (Bristol-Myers Squibb Pharmaceutical Research Institute, Seattle, WA), reacts with an integral membrane glycoprotein highly expressed on human breast, colon, ovary, and lung carcinomas (*16, 17*). ChL6 was specified as greater than 95% pure monomeric IgG by polyacrylamide gel electrophoresis (PAGE). High gradient magnetic field (HGMF) columns and separator, Nanomag-D-SPIO 20 nm (product #79−56−201), and COOH-functionalized dextran and poly(ethylene glycol) (PEG) coated NF particles of 30 nm (84−56−301) and 100 nm (84−56−102) in suspension (15−25 mg/ml) were obtained from micromod Partikeltechnologie, GmbH (Rostock, Germany). MES (2-(4-morpholino) ethanesulfonic acid), EDC (1-ethyl-3-(3-dimethylaminopropyl)-carbodiimide HCl), NHS (*N*-hydroxysuccinimide), glycine, and PBS were purchased from Sigma Chemical Co., St. Louis, MO. EDC activated NPs were purified by membrane dialyzer 3400 kDa cutoff (Pierce, Rockford, IL) dialysis bags. *S*-2-(4-Isothiocyanatobenzyl)-1,4,7,10-tetraazacyclododecane-*N*,*N*′,*N*″,*N*‴-tetraacetic acid (DOTA-Bz-SCN) was purchased from Macrocyclics (Dallas, TX).

Preparation of SPIO and NanoFerrite particles (NF). SPIO particles were prepared by the precipitation of ferric and ferrous chlorides in the presence of dextran (*13, 14*). NF particles (International and European patents WO 2005006356, WO 20050271745, and DE 10331439) were synthesized by high-pressure homogenization by the core−shell method (*12*). Briefly, a monodisperse aqueous iron oxide suspension (25 mg/mL) was homogenized with an excess of dextran at pressures above 500 bar and at temperatures above 70 °C, for 30 min. NF particles with iron content 45% (w/w) were obtained after magnetic sedimentation in a crystallization disk at an NdFeB permanent magnet and washing with deionized water. The NF particles were cross-linked by a modified Josephson method (*18*) with a mixture of poly(ethylene glycol) diglycidyl ether and epichlorohydrin at pH 11−12 for 24 h at room temperature. After magnetic separation, particles were washed with deionized water, and NF particle suspension with an iron concentration of 20−25 mg/mL was obtained. The particles were functionalized with amino groups by shaking with ammonia at room temperature for 24 h. The amine-functionalized NF particles were further washed three times with deionized water by magnetic separation and filtered through 0.22 mm Millex-GP filters (Millipore). These NF particles were further modified by EDC and poly(ethylene glycol) 600 diacid using MES buffer (pH 6.3) and incubated for 2 h at room temperature for COOH functionalization. The narrow size distributions of the NF particles obtained were in two diameter ranges 20−40 and 80−100 nm (*12*).

Preparation of Radioimmunoconjugate (RIC). The immunoconjugate (DOTA-Bz-ChL6) was prepared by the previously described method (*19*), with slight modifications. Conjugation was carried out with final concentrations of 0.15 mM ChL6 (20 mg/mL) and 2.0 mM DOTA-Bz-SCN mixed in 0.1 M tetramethylammonium phosphate, pH 9, at 37 °C with 2 h incubation. The DOTA-Bz-ChL6 conjugate was purified by G50 molecular sieving chromatography and transferred to 0.1 M ammonium acetate, pH 5.3. The RIC preparation was carried out using ^{111}In chloride in 0.05 M HCl (0.2 GBq) buffered in 0.1 M ammonium acetate at pH 5.3, and DOTA-Bz-ChL6 (2.5

mg) added. The solution was incubated for 30 min at 37 °C, and then 0.1 M sodium ethylene diamine tetraacetate (EDTA) (Fisher Scientific, Pittsburgh, PA) was added to a final concentration of 10 mM to scavenge nonspecifically bound ^{111}In. ^{111}In-DOTA-Bz-ChL6 was purified from ^{111}In-EDTA by molecular sieving chromatography.

The reaction mixture of RIC was purified by a molecular sieving (Penefsky) column. Purity was estimated by HPLC (Beckman Coulter System Gold 128, Fullerton, CA) with a radioactive detector (Raytest USA, Wilmington, NC) using an SEC 3000 column (GE Health care) eluted at 1 mL per minute by phosphate buffer solution. The yield and quality assurance (QA) of the RIC were evaluated by HPLC and cellulose acetate electrophoresis (CAE) strips (Gelman Sciences Inc., Ann Arbour, MI) performed on 0.05 M sodium barbital buffer at pH 8.6. The RIC bands on CAE strips and TLC plates were exposed on phosphor imager plates and scanned by Fuji Film imager (BAS 1800 II). The data were converted to digital peaks by Fuji film MultiGaugeV2.1 software.

Preparation of RINP. Three lots of nanoparticles, 20 nm SPIO and 30 and 100 nm NF (*12*), were used for the conjugation of RIC in in vitro targeting effect and in vivo mouse studies. ^{111}In-DOTA-Bz-ChL6 was conjugated with the nanoparticles via amide linkage to the carboxyl (COOH) terminated coating to prepare the ^{111}In-ChL6 NP. For each of the preparations, 6 mg of EDC and 12 mg of NHS in 0.5 mL of 0.5 M MES buffer were mixed with 5 mL of 10 mg/mL of NP. This suspension was incubated for 1 h at RT with continuous mixing, then placed into 3400 MWCO dialysis bags, and dialyzed against 4 L of saline for 1 h. ^{111}In-DOTA-Bz-ChL6 (0.5 mCi/0.2 mg/0.2 mL of PBS) suspended in 0.3 mL of 0.1 M MES buffer was mixed with the activated SPIO and NF particle suspension and incubated for 1 h at RT with continuous mixing (20−25 μg ^{111}In-ChL6/mg of NP). The preparations of 20 nm SPIO and 30 nm NF particles conjugated ^{111}In-DOTA-Bz-ChL6-NP, 2 mL, were again placed into dialysis bags (3400 MWCO) (3 mL), and dialyzed against 4 L of saline at RT for 1 h. The 100 nm BNF particles were purified by magnetic separation. The RINP products were mixed with 20 mL of 25 mM glycine in PBS at RT (15 min), and then purified by high grade magnetic field (HGMF) column (20 and 30 nm) and magnetic separator (100 nm) using PBS to remove the nonbound ^{111}In-DOTA-Bz-ChL6. Non-immunoreactive RINP (negative control) was prepared by a similar method, except the RIC used for conjugation to NP was non-immunoreactive.

The final suspensions that were collected from the magnetic column or separator with PBS wash after removing from the magnetic field were brown and yielded 3−5 μg of ^{111}In-ChL6/mg with specific activities of 6−10 μCi/mg of RINP. The concentration of the particles was estimated by UV/vis spectrophotometry at a wavelength of 492 nm using unconjugated beads as a reference, and protein concentration was estimated at a wavelength of 280 nm and also calculated from decay-corrected radioactivity. 2 μL aliquots of final products were applied to multiple CAE strips for electrophoresis of 11 and 45 min.

Preparation of Nontargeted Radionanoparticles (RNP). The nontargeted RNP (negative control) was prepared by conjugation of radiolabeled ^{111}In-DOTA-Bz-NH_2 to COOH functionalized 20 nm NP via amide linkage according to published procedure (*20*). Briefly, the ^{111}In-DOTA-Bz-NH_2 (1.5×10^{16} molecules; 5 mCi/20 μg) diluted in 0.5 mL of 0.1 mM MES buffer was mixed to a carbodiimide-activated NP suspension, and incubated for 2 h at room temperature with continuous mixing (reaction ratio was 6×10^{14} molecules of DOTA/mg of NP). The radiolabeled ^{111}In-DOTA-Bz-NP was purified by a 3400 MW cutoff dialysis membrane against 4 L of saline at RT for 1 h. After 1 h, the dialyzed product was quenched with glycine (25 mM) for 15 min to terminate the remaining active sites on the particle surface. This suspension was further purified by high gradient magnetic field column using saline as both washing and final eluent buffer. The specific activity of the RNP was 10−15 μCi/mg of RNP.

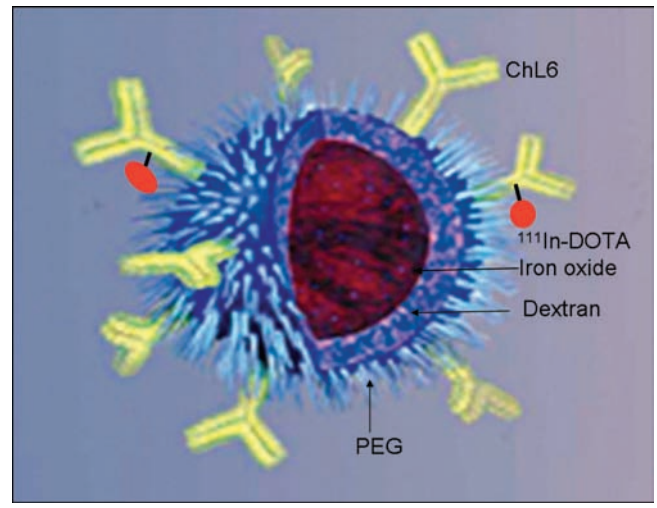

Figure 1. Simple diagram of a BNF-type particle coated with PEG to link ^{111}In-ChL6 to construct RINP. The particle core (reddish-brown sphere in center) is iron oxide.

In Vitro Cell Binding Assay of RINP. Purified RINP of each lot was evaluated by in vitro immunoreactivity as % of RINP bound to HBT 3477 cells. Relative immunoreactivity was established by comparing with reference ^{111}In-ChL6 alone used in these studies (*21*). The ^{111}In-DOTA-ChL6, RINP, and viable cells (2×10^7 cells/mL) were diluted to the desired concentrations in phosphate buffered saline (pH 7) to find the maximal binding percentage corresponding to the reported method (*22*). ^{111}In-DOTA-ChL6 (10 ng) and RINP of each (50 μl, 0.04 mg/mL) were added to triplicate tubes. One million cells (50 μL) were added to the triplicates, vortexed, and incubated for 1 h at room temperature. The cells were pelleted by centrifugation at $300 \times g$ for 10 min, and the supernatant and cells were counted. The percentage bound was calculated as follows: [cell bound cpm/(cell cpm + supernatant cpm)] × 100.

RINP Size Measurement. RINP size was measured by dynamic light scattering (photon correlation spectroscopy) using a Zetasizer 3000 (Malvern Instruments Ltd., UK) after suspensions had undergone 0.45 m filtration. This instrument uses a 5 mW He Ne laser (633 nm) and measures particle sizes from 2 to 3000 nm. Fluctuations in the intensity of scattered light (at 90° to the incident) are analyzed through the use of autocorrelation functions.

Animal Studies. Female (7−9 week old) athymic Balb/c nu/nu mice (Harlan Sprague−Dawley, Inc., Frederick, MD) were maintained according to University of California animal care guidelines on a normal diet ad libitum and under pathogen-free conditions. HBT 3477 cells were harvested in log phase; 3.0×10^6 cells were injected subcutaneously on both sides of the abdomen of mice for the PK study. Five groups of mice with 9 animals per group and 2 HBT3477 tumors per mouse were used for the PK study, and 3 mice with bilateral HBT3477 were used for WBAR study. RNP negative control (group 1) and non-immunoreactive RINP (group 2) were studied at 24 and 48 h; and 20, 30, and 100 RINP experimental groups (groups 3−5) were studied at 4, 24, and 48 h time points. All mice studies were initiated 2 to 4 weeks after implantation when the tumor volume was 100−350 mm^3. PK and WBAR studies were performed using RINP doses of 20−25 μCi per mg of RINP,

Table 1. Specification of RINP[a]

NP size (nm)	initial NP (mg)	[Fe]/[NP] mg/mg	RINP yield (mg)	[RIC] μg/mg of NP	SA μCi/mg of RINP	QA		
						CAE 45′ %	PAGE %	RIR %
20	50	0.46	26	5	8	95	90	79
30	50	0.63	26	4	7	75	85	57
100	50	0.6	35	3	6	90	90	60

[a] SA: specific activity. RIR: relative immunoreactivity.

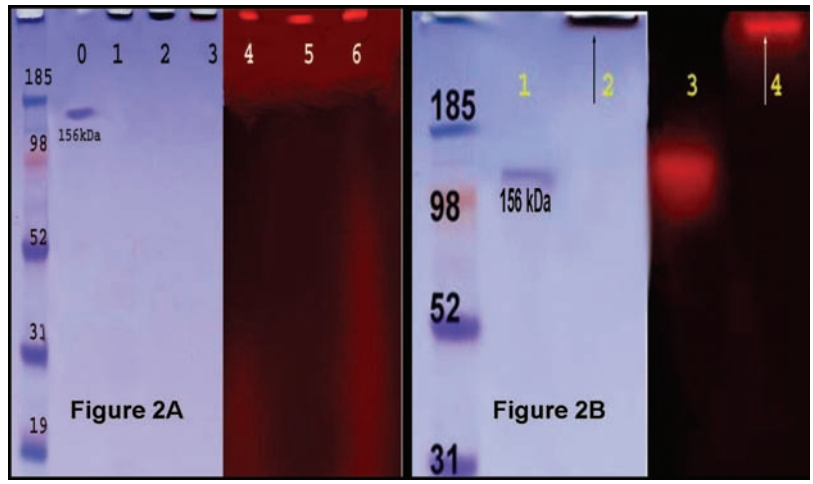

Figure 2. RINP on 4−12% SDS−PAGE spectrum. Left: CB stained for protein detection. Right: same PAGE scanned on Fuji phosphor Imager for radioactivity detection. (A) RINP (20, 30, and 100 nm) on 4−12% SDS−PAGE spectrum: lane 0, ^{111}In-DOTA-Bz-ChL6; lanes 1−3, RINP (20, 30, and 100 nm)—brown band at origin, no unconjugated ^{111}In-ChL6 observed; lanes 4−6: radioactivity bands at origin correspond to RINP (20, 30, and 100 nm). (B) Lane 1, ^{111}In-DOTA-Bz-ChL6; lane 2, RINP (100 nm)—brown band at origin; lane 3, ^{111}In-DOTA-Bz-ChL6; and lane 4, radioactivity band at origin corresponds to RINP.

injected iv into a lateral tail vein with an additional 50 μg ChL6 (cold) in 200 μL saline.

Whole Body Autoradiography (WBAR). WBAR was conducted as previously described (*23, 24*). 24 h after tail vein injection of 50 μg/50 μCi/200 μL/5 mg of RINP, mice were anesthetized using an intravenous injection of 50 mg/mL of 100 μL aqueous solutions of sodium pentobarbital, then flash-frozen in a hexane/dry ice bath. The frozen mice were embedded in 4% carboxymethylcellulose and sagittal sections were generated with a Leica Polycut at −20 °C. Sections of 50 μm thickness were obtained to show tumors, spleen, kidney, liver, and the midline of the vertebral column. Radiographs of the sections were prepared by exposing the sections to X-ray film (Kodak BioMax MS, Rochester, NY).

Pharmacokinetic Study. RINP doses were injected iv in 200−250 μL saline. In the pharmacokinetic studies, whole body activity was measured in a dose calibrator (CRC-12, Capintech, Inc., Pittsburgh, PA) immediately, and again at 1, 4, 24, and 48 h; and values were expressed as %ID. Blood activity, expressed as %ID/mL, was determined by counting 2 μL blood samples, collected at 5 min and 1, 4, 24, and 48 h after injection in a gamma well counter (Pharmacia LKB, Piscataway, NJ) calibrated using ^{111}In standards in the appropriate sample configuration and volumes. The mice were sacrificed and organs and tissue samples collected. Activity, expressed as %ID/g, was measured in a gamma well counter in a manner similar to that used for blood activity (*25*). Specific activity and dose used for animal study was 20−25 μCi/5−10 μg of mAb/2.2 mg RINP or non-immunoreactive RINP.

RESULTS

Preparation, Characterization, and Quality Assurance of RIC, RNP, and Various RINP. Figure 1 shows a simple schematic diagram of a representative NF-type RINP. Table 1 indicates the specification of various sizes of RINP. The purified

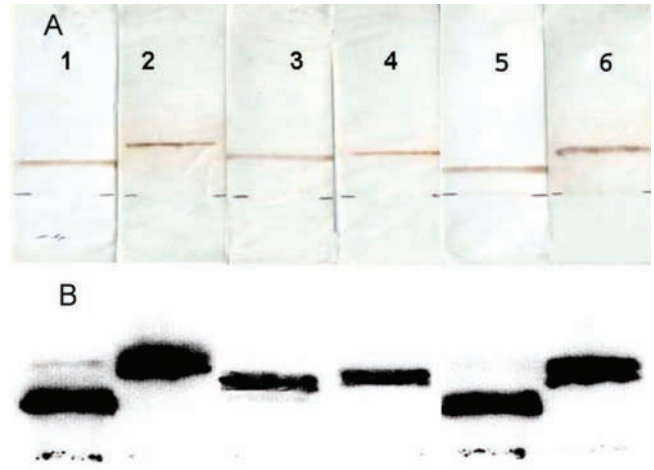

Figure 3. CAE characterization of RINPs.^{111}In-ChL6 modified NPs of 20 nm (lanes 1,2), 30 nm (lanes 3,4), and 100 nm (lanes 5,6) were tested on CAE strips, using pH 8.5 buffer, 300 V, at 11 min (lanes 1, 3, and 5) and 45 min (lanes 2, 4, and 6) time points. (A) RINPs tested on CAE strips were scanned by laser scanner (brown bands correspond to iron oxide of NPs visible at different distance from the origin (2 cm above from bottom of the strip). (B) The same CAE strips were scanned on Fuji Imager to analyze the migration pattern of RINPs by size and charge effect traced by radioactivity. The migration distances of each lot of NPs have identical distance by radioactivity and band stain. RINP preparations were greater than 95% pure. The purity of the RINP on CAE 11 min and 45 min showed greater than 90% monomeric product. RINP preparation does not contain aggregated particles or free ^{111}In-ChL6 molecules.

RIC molecule of ^{111}In-DOTA-Bz-ChL6 was evaluated by CAE, HPLC, and PAGE prior to conjugation to NP. The specific activity of the RIC was 0.5 μCi/μg with greater than 95% monomeric by HPLC, CAE, and PAGE (Figure 2A, lane 0, and Figure 2B, lanes 1 and 3). The absolute binding of RIC in the

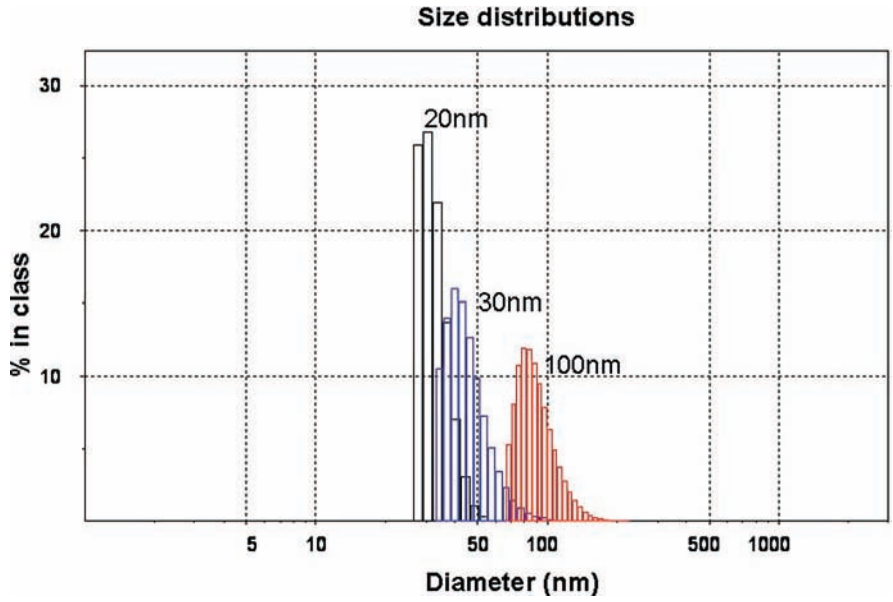

Figure 4. RINP size distributions were measured by photon correlation spectroscopy (Zetasizer 3000, Malvern Instruments, Ltd.).

live cell assay was >70% and equal to 100% compared to ^{125}I-ChL6 as reference standard. The RIC used for non-immunoreactive RINP (20 nm) was 4% compared to ^{125}I-ChL6 as reference standard. Using carbodiimide chemistry, RINP products were prepared by conjugation of ^{111}In-DOTA-Bz-ChL6 to COOH functionalized NP of 20, 30, and 100 nm particles; and the amounts of ^{111}In-ChL6 linked to NPs were 5, 4, and 3 (μg/mg), respectively. In the case of non-immunoreactive RINP, the ^{111}In-ChL6 (non-immunoreactivity) was linked to 20 nm NP with 6 μg/mg of NP. Similarly, particles without targeting molecules, such as nontargeting 20 nm NP (RNP), were prepared for the negative control (10 μCi/mg) using ^{111}In-DOTA-Bz-NH_2 and 20 nm NP.

All of the RINPs were greater than 90% monomeric by PAGE (Figure 2A,B) and CAE (Figure 3). Each purified RINP was a dark brown, homogeneous suspension and remained at the origin of PAGE. The RINPs (20, 30, and 100 nm) shown in Figure 2A, by Coomassie in lanes 1−3 and radioactivity in lanes 4−6, did not migrate due to the high molecular weight. However, no unbound ChL6 or ^{111}In-DOTA-ChL6 was observed, corresponding to the control protein in Figure 2A lane 0 and Figure 2B lane 1 or control radiolabeled ChL6 in lane 3. Figure 3 shows the evaluation of the RINP mobility by CAE at 11 min (lanes 1, 3, and 5) and 45 min (lanes 2, 4, and 6). These preparations are >90% monomeric with no aggregation or unbound free ChL6. The specific activity of the final purified RINP was 6−8 μCi/3−5 μg of ^{111}In-ChL6/mg of NP. The concentration of ^{111}In-ChL6 conjugated to NP was estimated by decay-corrected specific activity of the RINP, and the ^{111}In-ChL6 conjugated to each NP was as 6−10 molecules per bead.

Using photon correlation spectroscopy, the sizes of the RINPs were (Figure 4) distributed to narrow diameter ranges 20−30, 30−40, and 70−100 nm. RINP sizes did not change compared to NP size prior to conjugation with ^{111}In-mAb (*12*). Thus, RIC conjugation on NP did not influence or alter the initial particle diameters.

In Vitro Cell Binding Assay. The radioimmunoassay (RIA) of RIC and RINP was tested using HBT 3477 human breast cancer cells. Relative immunoreactivity of the RINP showed 57−79% compared to control RIC tested on HBT 3477 (Table 1).

WBAR and PK in Mice. The WBAR obtained from a mouse sacrificed 24 h after injection of the 100 nm RINP showed that the particles were able to target tumor in vivo (Figure 5). Blood and body clearances of the RINP (Figures 6 and 7) and mean RINP concentrations (%ID/g) in lung, kidney, and lymph node (Figure 8) were similar to ^{111}In-ChL6-NP as previously reported (*7*). In vivo tumor targeting of RINPs were compared with RNP (without the targeting mAb molecules) and non-immunoreactive RINP (20 nm). Figure 8 shows that mean concentrations of RINP of each preparation in tumor in the PK study were between 4 and 9% ID/g over 2 days. RNP 20 nm NP with no targeting molecules and non-immunoreactive RINP (20 nm) were used as a negative control and demonstrated (Figure 8) tumor

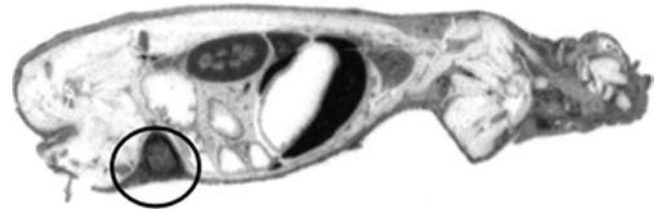

Figure 5. Sagittal section of the WBAR image obtained from euthanized mice 24 h after tail vain injection of ^{111}In-ChL6-NP (100 nm BNF). The HBT3477 tumor (human breast cancer) bearing nude mice received 50 μCi/5 mg of RINP dose. Accumulations of RINPs are mostly in kidney, liver, and tumor (circle).

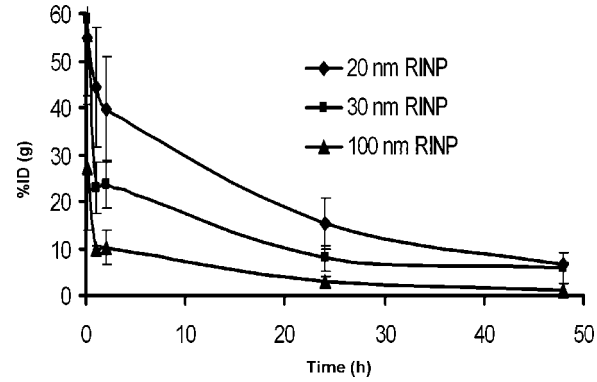

Figure 6. Pharmacokinetic study of RINPs in mice with HBT3477 human breast cancer xenografts (nine animals per group; three groups total). Three RINP blood clearances were compared at various time points: 5 min, and 1, 2, 4, 24, and 48 h.

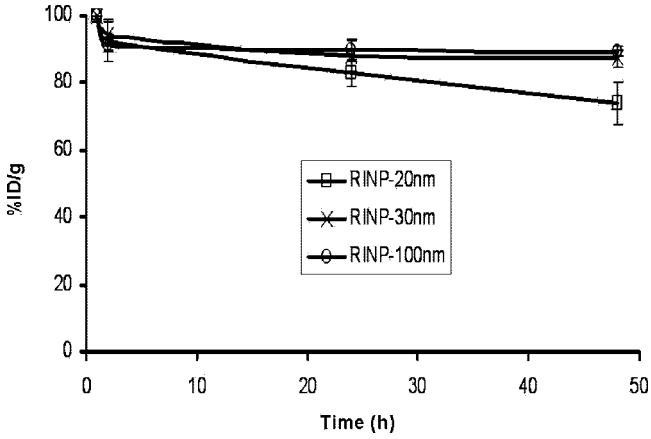

Figure 7. The pharmacokinetic study of three RINPs (20, 30, and 100 nm) in mice with HBT3477 human breast cancer xenograft. Body clearances were compared at various time points of 2, 4, 24, and 48 h. (Nine animals per group; total five groups were used; non-immunoreactive RINP (20 nm) and RNP (20 nm) negative control groups were not represented in these data.)

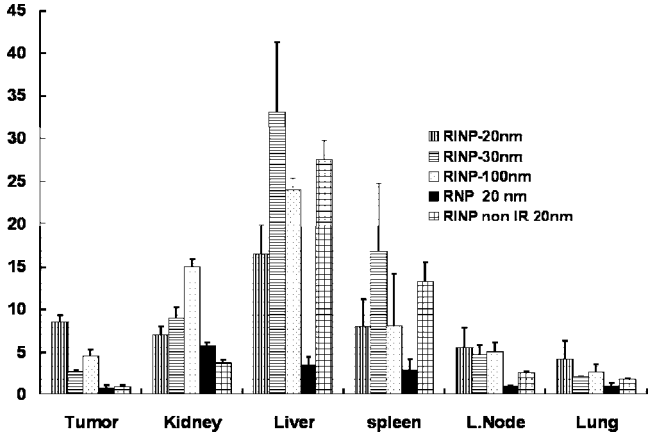

Figure 8. Pharmacokinetic biodistribution of the RINPs (20, 30, and 100 nm size), negative controls of RNP (20 nm) NP without targeting molecules, and RINP (20 nm) non-immunoreactive were measured as %ID/g in various organs after 48 h injection. The difference between targeted (RINP) and nontargeted particles (RNP) and non-immunoreactive RINP (*5*) should be noted. The mean ± SD (error bars) were calculated based on three animals ($n = 3$) in each study group. IR = immunoreactive.

accumulation of less than 0.5% ID/g. The differences in tumor uptake observed between the targeted and nontargeted NPs were substantial. The 20 nm RINP tumor uptake was consistent with previous observations (*5, 7*). Both 30 nm and 100 nm BNF particles demonstrated a lower tumor uptake than SPIOs, with little difference between the two.

DISCUSSION

Focused hyperthermia (FH) can be achieved at selective cancer tissues by ligand directed magnetic nanoparticles using AMF to activate NP to deliver heat (*26*). This treatment modality is more advantageous than other thermotherapies, because heat is induced locally by external AMF application through activation of cancer-targeted nanoparticles which are preferentially retained in the microenvironment of the tumor tissues at higher concentrations than in the immediately surrounding normal tissues (*27, 28*). In this approach, the AMF is preferentially directed to the regions containing cancer (*11*), and the field amplitude can be adjusted to provide NP heat lethal only at the cancer tissues while minimizing the heat deposited elsewhere, thus sparing the surrounding normal tissues. To enhance the FH, high SAR NF-type particles were developed (*12*). Two sizes of these NF-type particles were evaluated in this study to characterize their in vivo performance in comparison with a previously used 20 nm SPIO particle. Future selection of a preferred RINP will be based on two criteria: (1) concentration of the particles targeted at the tumor; and (2) particle SAR heat after AMF activation.

Table 2. SAR Values for BNF- and SPIO-type Particles As Reported in Ref (*12*)

nanoparticle type (diameter)	SAR[a] (W/g iron)			
	29 kA/m	58 kA/m	86 kA/m	104 kA/m
20 nm SPIO	27	66	76	105
30 nm BNF	90	253	380	438
100 nm BNF	140	437	528	642

[a] SAR values measured for different mean diameter NPs as a function of the amplitude of the AMF.

Three types of RINP were created using the 20 nm (SPIO) and 30 and 100 nm (NF) particles linked to ^{111}In-ChL6 to target breast cancer in mice. In our previous study, we demonstrated that RINPs based on 20 nm SPIO particles were successfully utilized for thermal therapy in a mouse model (*7*). However, the SPIO particle SAR value was not sufficient to induce enough heat to eradicate the cancer completely with modest amplitudes of AMF at a frequency of 150 kHz.

In this study, we have compared 30 and 100 nm RINP from NF particles with previously tested 20 nm SPIO RINP. All of these preparations had a high purity and excellent immunoreactivity and were similar to the preparation used in the earlier therapy studies. The in vivo PK and WBAR study showed that 100 nm RINP accumulation in tumor was 50% that of 20 nm SPIO RINP. However, the SAR value of 100 nm particles has been measured to be up to 6 times higher (Table 2) than that of 20 nm SPIO particles. Therefore, the calculated net heat induction for any specific AMF in cancer tissue by 100 nm RINP is expected to be 3 times higher than that produced by 20 nm RINP (SPIO).

Important characteristics of magnetic NP for FH applications are narrow particle size distribution and high SAR values providing substantial heat at lower AMF (*29*). In general, RINP accumulation at the tumor tissues depends on the RINP affinity, the presence of abundant cancer cell targets for the molecules linked to NP, circulation half-time, and tumor vessel permeability. The NP of SPIO and NF preparations were different in surface morphology, physical characteristics (density), surface charge, PEG concentration, and functional modification, which may affect the PK. The cellular and tissue uptake was affected by several characteristics of the nanoparticles, e.g., particle size, coatings, and charge, as demonstrated by Wu et al. (*30*). In another study, surface properties had a larger impact on cellular uptake of SPIO particles rather than particle size (*31*). In our study, ^{111}In-DOTA conjugated RNP (negative control) showed less than 5% uptake in liver and spleen compared to RINPs, which showed above 10% as shown in Figure 8. This may be due to increased anionic charge of the RNP. However, this was not the focus of this study. NP design and chemical conjugation were optimized in such a way that RINP preparations were fully functional to target the antigen both in vitro and in vivo. The particles were also coated with PEG molecules to increase plasma half-time and decrease uptake in normal tissues. The present study clearly confirms that the NF-based 100 nm RINP are able to penetrate the tumor vessels sufficiently well for moderate tumor accumulation (see Figures 5 and 8). In conclusion, we have created RINP

of varying sizes using SPIO and NF NP to target breast cancer for focused hyperthermia. Analytical methods have been developed to characterize the RINP. Radiotracer was utilized on NP to establish RINP targeting in the tumor, to predict thermal dose in the tumor, and to quantify RINP tissue biodistributions. Although 100 nm NF RINP targeted tumor less than 20 nm SPIO RINP, because their heating capacity was 6 times higher, 100 nm BNF RINP should provide 3 times greater heat dose in tumor with AMF activation. A complete characterization of the physical and magnetic properties of these particles and how these are affected by the chemical modifications of the surface coatings is underway.

ACKNOWLEDGMENT

This work was supported by U.S. Army Medical and Material Command under Contract Number W81XWH-04-C-0142 and National Cancer Institute NCI grant PO1-CA47829.

LITERATURE CITED

(1) Ito, A., Honda, H., and Kobayashi, T. (2006) Cancer immunotherapy based on intracellular hyperthermia using magnetite nanoparticles: a novel concept of "heat-controlled necrosis" with heat shock protein expression. *Cancer Immunol. Immunother. 55*, 320–328.

(2) Gref, R., Couvreur, P., Barratt, G., and Mysiakine, E. (2003) Surface-engineered nanoparticles for multiple ligand coupling. *Biomaterials 24*, 4529–4537.

(3) Rudershaun, R., Gruttner, C., Frank, M., Teller, J., and Westphal, F. (2002) Multifunctional superparamagnectic nanoparticles for life science applications. *Eur. Cells Mater. 3*, 81–83.

(4) Jordan, A., Hauff-maeir, Q., Wust, P., and Johannsen, M. (2006) Nanoparticles for Thermotherapy, in *Nanaomaterials for Cancer Therapy* (Kumar, C. S. S. R., Ed.) pp 242−258, Chapter 8, WILEY-VCH, Weinheim.

(5) DeNardo, S. J., DeNardo, G. L., Miers, L. A., Natarajan, A., Foreman, A. R., Gruettner, C., Adamson, G. N., and Ivkov, R. (2005) Development of tumor targeting bioprobes (^{111}In-chimeric L6 monoclonal antibody nanoparticles) for alternating magnetic field cancer therapy. *Clin. Cancer Res. 11*, 7087s–7092s.

(6) Ito, A., Tanaka, K., Honda, H., Abe, S., Yamaguchi, H., and Kobayashi, T. (2003) Complete regression of mouse mammary carcinoma with a size greater than 15 mm by frequent repeated hyperthermia using magnetite nanoparticles. *J Biosci. Bioeng. 96*, 364–369.

(7) DeNardo, S. J., DeNardo, G. L., Natarajan, A., Miers, L. A., Foreman, A. R., Gruettner, C., Adamson, G. N., and Ivkov, R. (2007) Thermal dosimetry predictive of efficacy of ^{111}In-ChL6 nanoparticle AMF-induced thermoablative therapy for human breast cancer in mice. *J. Nucl. Med. 48*, 437–444.

(8) Dewhirst, M. W., Jones, E., Samulski, T., Vujaskovic, Z., Li, C., and Prosnitz, L. (2003) Hyperthermia, in *Cancer Medicine* (Kufe, D., Pollock, R., Weichselbaum, R., Bast, R., Gansler, T., Holland, J., and Frei, E., Eds.) 6th ed., pp 623−636, BC Decker, Inc., Hamilton, Ontario.

(9) Van der, Z. J. (2002) Heating the patient: a promising approach? *Ann. Oncol. 13*, 1173–1184.

(10) Dewhirst, M. W., Viglianti, B. L., Lora-Michiels, M., Hanson, M. W., and Hoopes, P. J. (2003) Basic principles of thermal dosimetry and thermal thresholds for tissue damage from hyperthermia. *Int. J. Hyperthermia 19*, 267–294.

(11) Ivkov, R., DeNardo, S. J., Daum, W., Foreman, A., Goldstein, R., and DeNardo, G. L. (2005) Application of high amplitude alternating magnetic fields for heat induction of nanoparticles localized in cancer. *Clin. Cancer Res. 11*, 7093s–7103s.

(12) Gruttner, C., Muller, K., Teller, J., Westphal, F., Foreman, A., and Ivkov, R. (2007) Synthesis and antibody conjugation of magnetic nanoparticles with improved specific power absorption rates for alternating magnetic field cancer therapy. *J. Magn. Magn. Mater. 311*, 181–186.

(13) Grüttner, C., Teller, J., Schütt, W., Westphal, F., Schümichen, C., and Paulke, B. R. (1997) in *Scientific and Clinical Applications of Magnetic Carriers* (Häfeli, U. O., Schütt, W., Teller, J., and Zborowski, M., Eds.) pp 53, Plenum Press, New York.

(14) Rudershausen, S., Gruttner, C., Frank, M., Teller, J., and Westphal, F. (2002) Multifunctional superparamagnetic nanoparticles for life science applications. *Eur. Cells Mater. 3*, 81–83.

(15) Schütt, W., Grüttner, C., Teller, J., Westphal, F., Häfeli, U. O., Paulke, B. R., Goetz, P., Rutz, W., Putzar, H., Dunkelmann, S., Finck, W., and Schümichen, C. (1997) The concept of magneto-radionuclide-therapy. *Jpn. J. Electrophor. 47*, 173–179.

(16) Liu, A. Y., Robinson, R. R., Hellstrom, K. E., Murray, E. D. J., Chang, C. P., and Hellstrom, I. (1987) Chimeric mouse-human IgG1 antibody that can mediate lysis of cancer cells. *Proc. Natl. Acad. Sci. U.S.A. 84*, 3439–3443.

(17) Hellstrom, I., Horn, D., Linsley, P., Brown, J. P., Brankovan, V., and Hellstrom, K. E. (1986) Monoclonal antibodies raised against human lung carcinomas. *Cancer Res. 46*, 3917–3923.

(18) Josephson, L., Tung, C. H., Moore, A., and Weissleder, R. (1999) High-efficiency intracellular magnetic labeling with novel superparamagnetic-Tat peptide conjugates. *Bioconjugate Chem. 10*, 186–191.

(19) McCall, M. J., Diril, H., and Meares, C. F. (1990) Simplified method for conjugating macrocyclic bifunctional chelating agents to antibodies via 2-iminothiolane. *Bioconjugate Chem. 1*, 222–226.

(20) Natarajan, A., Xiong, C. Y., Gruettner, C., DeNardo, G. L., and DeNardo, S. J. (2008) Development of multivalent radioimmunonanoparticles for cancer imaging and therapy. *Cancer Biother. Radiopharm. 23*, 82–91.

(21) Kukis, D. L., DeNardo, G. L., DeNardo, S. J., Mirick, G. R., Miers, L. A., Greiner, D. P., and Meares, C. F. (1995) Effect of the extent of chelate substitution on the immunoreactivity and biodistribution of 2IT-BAT-Lym-1 immunoconjugates. *Cancer Res. 55*, 878–884.

(22) Winthrop, M. D., DeNardo, S. J., Albrecht, H., Mirick, G. R., Kroger, L. A., Lamborn, K. R., Venclovas, C., Colvin, M. E., Burke, P. A., and DeNardo, G. L. (2003) Selection and characterization of Anti-MUC-1 scFvs intended for targeted therapy. *Clin. Cancer Res. 9*, 3845s–3853s.

(23) Fand, I., and McNally, W. P. (1981) The technique of whole-body autoradiography, in *Current Trends in Morphological Techniques* (Johnson, J. E., Ed.) 1st ed., pp 1−28, CRC Press, Boca Raton, FL.

(24) DeNardo, G. L., Kroger, L. A., DeNardo, S. J., Miers, L. A., Salako, Q., Kukis, D. L., Fand, I., Shen, S., Renn, O., and Meares, C. F. (1994) Comparative toxicity studies of yttrium-90 MX-DTPA and 2-IT-BAD conjugated monoclonal antibody (BrE-3). *Cancer 73*, 1012–1022.

(25) DeNardo, S. J., Burke, P. A., Leigh, B. R., O'Donnell, R. T., Miers, L. A., Kroger, L. A., Goodman, S. L., Matzku, S., Jonczyk, A., Lamborn, K. R., and DeNardo, G. L. (2000) Neovascular targeting with cyclic RGD peptide (cRGDf-ACHA) to enhance delivery of radioimmunotherapy. *Cancer Biother. Radiopharm. 15*, 71–79.

(26) Hilger, I., Hiergeist, R., Hergt, R., Winnefeld, K., Schubert, H., and Kaiser, W. A. (2002) Thermal ablation of tumors using magnetic nanoparticles: an in vivo feasibility study. *Invest. Radiol. 37*, 580–586.

(27) Wust, P., Gneveckow, U., Johannsen, M., Bohmer, D., Henkel, T., Kahmann, F., Sehouli, J., Felix, R., Ricke, J., and Jordan, A. (2006) Magnetic nanoparticles for interstitial thermotherapy−feasibility, tolerance and achieved temperatures. *Int. J. Hypertherm. 22*, 673–685.

(28) Jordan, A., Scholz, R., Maier-Hauff, K., van Landeghem, F. K., Waldoefner, N., Teichgraeber, U., Pinkernelle, J., Bruhn,

H., Neumann, F., Thiesen, B., von, D. A., and Felix, R. (2006) The effect of thermotherapy using magnetic nanoparticles on rat malignant glioma. *J. Neurooncol. 78*, 7–14.

(29) Kim, D. H., Lee, S. H., Im, K. H., Kim, K. N., Kim, K. M., Shim, I. B., Lee, M. H., and Lee, Y. K. (2006) Surface-modified magnetite nanoparticles for hyperthermia: Preparation, characterization, and cytotoxicity studies. *Curr. Appl. Phys. 6*, e242–e246.

(30) Wu, Y. J., Muldoon., L. L., Varallyay, C., Markwardt, S., Jones, R. E., and Neuwelt, E. A. (2007) In vivo leukocyte labeling with intravenous ferumoxides/protamine sulfate complex and in vitro characterization for cellular magnetic resonance imaging. *Am. J. Physiol. Cell Physiol. 293*, C1698–C1708.

(31) Metz, S., Bonaterra, G., Rudelius, M., Settles, M., Rummeny, E. J., and Daldrup-Link, H. E. (2004) Capacity of human monocytes to phagocytose approved iron oxide MR contrast agents in vitro. *Eur. Radiol. 14*, 1851–1858.

BC800015N

A Reduction-Triggered Fluorescence Probe for Sensing Nucleic Acids

Hiroshi Abe,*[,†] Jin Wang,[†] Kazuhiro Furukawa,[†,‡] Kazuma Oki,[‡] Miwako Uda,[†,‡] Satoshi Tsuneda,[‡] and Yoshihiro Ito*[,†]

Nano Medical Engineering Laboratory, Discovery Research Institute, RIKEN, 2-1, Hirosawa, Wako-Shi, Saitama, 351-0198 Japan, Department of Life Science and Medical Bio-Science, Waseda University, 3-4-1 Ohkubo, Shinjuku-ku, Tokyo 169-8555, Japan. Received January 12, 2008; Revised Manuscript Received March 31, 2008

We have developed a reduction-triggered fluorescence probe with a new fluorogenic compound derivatized from Rhodamine for sensing oligonucleotides. The chemistry to activate the compound involves the reaction between the azide group of rhodamine derivatives and the reducing reagents, with the fluorescence signal appearing after reduction of the azide group. The signal/background ratio of this fluorogenic compound reached 2100-fold enhancement in fluorescence intensity. Dithio-1,4-threitol or triphenylphosphine as reducing reagents were successfully utilized for this chemistry to be introduced into the DNA probe. The genetic detection requires that two strands of DNA bind onto target oligonucleotides, one probe carrying a reducible fluorogenic compound while the other carries the reducing reagents. The reaction proceeds automatically without any enzymes or reagents under biological conditions to produce a fluorescence signal within 10−20 min in the presence of target DNA or RNA. In addition, the probe was very stable under biological conditions, even such extreme conditions as pH 5 solution, pH 10 solution, or high temperature (90 °C) with no undesirable background signal. The probes were successfully applied to the detection of oligonucleotides at the single nucleotide level in solution and endogenous RNA in bacterial cells.

INTRODUCTION

Fluorescent-labeled oligonucleotides are becoming important tools for detecting oligonucleotide sequences (*1, 2*). A possible application is the detection of RNA species in cells by in situ hybridization (*3–5*). However, standard fluorescent probes require careful handling to avoid nonspecific signals. Fluorogenic probes with a fluorescence on/off mechanism have been developed to avoid this problem (*6–13*). Some of these probes have been applied to the detection of RNA in cells (*14–17*). Examples are molecular beacon (MB) (*15, 16*) or target-assisted chemical ligation (*14, 18*). Target-dependent fluorescence enhancement of these methods is based on the resonance energy transfer (RET) mechanism, for which a pair of quencher and fluorescence dyes is normally used. However, higher sensitivity for the detection method is still required to monitor gene expression in cells. Recently, various fluorogenic compounds have been developed for the detection of small biological substances (*19–23*). For example, diaminofluorescein when used for the detection of nitric oxide (NO) reacts with NO to yield a fluorescent compound through triazole formation (*21*). The boronate fluorescein derivative for detection of hydrogen peroxide (H_2O_2) reacts with H_2O_2 to yield a fluorescent form through cleavage of the carbon−boron bond (*20*). In these examples, detection is triggered by a chemical reaction accompanied by transformation of the chemical structure of the fluorogenic compound. Fluorescence modulation is caused by photoinduced electron transfer or absorption change. The signal/background (*S*/*B*) ratio of this type of molecule could exceed that of the RET mechanism (*24*). However, there are few reports that describe chemical reaction-triggered fluorogenic molecules for oligonucleotide sensing, although this method offers high sensitivity (*25*). Here, we report a reduction-triggered fluorescence (RETF) probe that shows a high *S*/*B* ratio for sensing oligonucleotides (Figure 1). A new fluorescence molecule, rhodamine azide, that we designed and synthesized is activated only by a specific reducing reagent on the oligonucleotide target and is very stable under biological conditions, showing little background fluorescence. The probe was applied to the sensing of nucleic acids in vitro and of endogenous RNA in bacterial cells.

EXPERIMENTAL PROCEDURES

t-Boc-Rhodamine 110 Azide (2). t-Boc-Rhodamine 110 (48.0 mg, 0.112 mmol) was dissolved in CH_3CN (8 mL) and CH_2Cl_2 (4 mL) under Ar (g). TFA (12.4 μL, 0.167 mmol) was added, followed by addition of isopentyl nitrite (17.8 μL, 0.134 mmol) at 0 °C. After stirring for 2 h at 0 °C, sodium azide (15.0 mg, 0.223 mmol) was added to the resulting solution, followed by stirring for 1 h at ambient temperature. The reaction was quenched with saturated aqueous $NaHCO_3$. The aqueous layer was extracted with AcOEt (×2), and the combined organic layers were dried over Na_2SO_4, concentrated, and subjected to flash column chromatography (silica gel, 6:1 hexane/EtOAc) to give azide-Rhodamine 110-t-Boc (**2**) as a pale yellow crystalline solid (36.5 mg, 80.0 μmol, 71%). ^{1}H NMR (400 MHz, $CDCl_3$) δ 1.53 (9H, s), 6.61 (1H, brs), 6.68 (1H, d, J = 3.2 Hz), 6.71 (1H, d, J = 3.2 Hz), 6.77 (1H, d, J = 8.5 Hz), 6.87 (1H, dd, J = 2.2 Hz, 8.8 Hz), 6.93 (1H, d, J = 1.9 Hz), 7.12 (1H, brd, J = 7.3 Hz), 7.56 (1H, brs), 7.62 (1H, dt, J = 1.0 Hz, 7.5 Hz), 7.66 (1H, dt, J = 1.2 Hz, 7.6 Hz), 8.02 (1H, brd, J = 7.3 Hz). ^{13}C NMR (100 MHz, $CDCl_3$) δ 28.36, 81.25, 82.19, 105.97, 107.21, 112.87, 114.26, 114.74, 115.59, 123.70, 125.07, 126.22, 128.45, 129.43, 129.78, 135.04, 140.56, 142.37, 151.47, 152.08, 152.95, 169.13. QSTAR (Applied Biosystems/MDS SCIEX) (ESI): [MH+] $C_{25}H_{21}N_4O_5$: calculated 457.1512, found 457.1509.

* Corresponding author. Hiroshi Abe or Yoshihiro Ito. E-mail: h-abe@riken.jp or y-ito@riken.jp. Nano Medical Engineering Laboratory, Discovery Research Institute, RIKEN 2-1, Hirosawa, Wako-Shi, Saitama, 351-0198 Japan. TEL: +81-(0)48-467-9303, FAX: +81-(0)48-467-2827.

† RIKEN.

‡ Waseda University.

10.1021/bc800014d CCC: $40.75 © 2008 American Chemical Society
Published on Web 05/14/2008

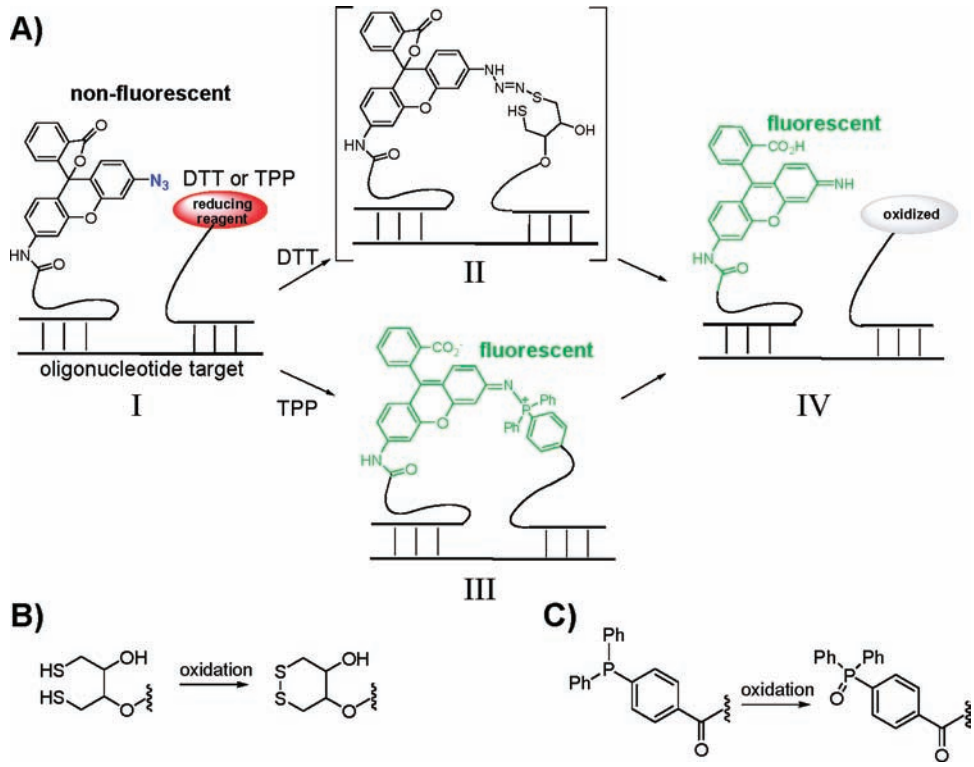

Figure 1. Fluorescence emission of an RETF probe by reducing reagents. (A) Reduction of azide on rhodamine by DTT or TPP as reducing reagents. (B) Oxidation of DTT. (C) Oxidation of TPP.

Rhodamine 110-Azide (3). Azide-Rhodamine 110-t-Boc (**2**) (30.8 mg, 67.5 μmol) was dissolved in 4.0 M HCl solution in dioxane (3 mL). The resulting solution was stirred at ambient temperature for 3 h. Solvent was removed under reduced pressure, and the residue was purified by TLC plate (9:1 $CHCl_3$/MeOH). Azide-Rhodamine 110 (**3**) was isolated as a pale pink crystalline solid (23.8 mg, 66.8 μmol, 99%). ^{1}H NMR (400 MHz, $CDCl_3$) δ 3.92 (2H, s), 6.36 (1H, dd, J = 2.4 Hz, 8.5 Hz), 6.52 (1H, d, J = 2.2 Hz), 6.55 (1H, d, J = 8.5 Hz), 6.67 (1H, dd, J = 2.2 Hz, 8.5 Hz), 6.74 (1H, d, J = 8.5 Hz), 6.92 (1H, d, J = 2.2 Hz), 7.16 (1H, d, J = 7.6 Hz), 7.61 (1H, dt, J = 1.0 Hz, 7.3 Hz), 7.66 (1H, dt, J = 1.2 Hz, 7.5 Hz), 8.01 (1H, d, J = 7.6 Hz). ^{13}C NMR (100 MHz, $CDCl_3$) δ 82.82, 101.15, 106.95, 108.15, 111.67, 114.39, 115.82, 123.63, 124.80, 126.54, 128.93, 129.38, 129.48, 134.73, 142.03, 148.62, 151.97, 152.11, 152.73, 169.06. QSTAR (Applied Biosystems/MDS SCIEX) (ESI): [MH+] $C_{20}H_{13}N_4O_3$: calculated 357.0988, found 357.0988.

Bromoacetylamide-Rhodamine 110-Azide (4). Azide-Rhodamine 110 (**3**) (17.9 mg, 50.2 μmol) was dissolved in $CHCl_3$ (4 mL). Anhydrous potassium bicarbonate (138.2 mg, 1.0 mmol) was added. The reaction mixture was cooled to 0 °C, followed by addition of bromoacetyl bromide (43.7 μL, 0.50 mmol). The resulting solution was stirred at ambient temperature for 12 h, and the reaction was quenched with saturated aqueous Na_2CO_3. The aqueous layer was extracted with $CHCl_3$ (×2), and the combined organic layers were dried over Na_2SO_4, concentrated, and subjected to flash column chromatography (silica gel, 3:1 hexane/EtOAc) to give bromoacetylamide-Rhodamine 110-azide (**4**) (22.6 mg, 47.4 mmol, 94%) as a pale yellow crystalline solid. ^{1}H NMR (400 MHz, CDCl3) δ 4.03 (2H, s), 6.71 (1H, dd, J = 2.2 Hz, 8.6 Hz), 6.75 (1H, d, J = 8.5 Hz), 6.79 (1H, d, J = 8.6 Hz), 6.95 (1H, d, J = 2.2 Hz), 7.05 (1H, dd, J = 2.2 Hz, 8.8 Hz), 7.13 (1H, brd, J = 7.6 Hz), 7.64 (1H, dt, J = 1.0 Hz, 7.6 Hz), 7.68 (1H, dt, J = 1.2 Hz, 7.6 Hz), 7.74 (1H, d, J = 1.9 Hz), 8.04 (1H, brd, J = 6.8 Hz), 8.33 (1H, brs). ^{13}C NMR (100 MHz, $CDCl_3$) δ 29.21, 81.89, 107.11, 107.82, 114.86, 115.15, 115.43, 123.57, 125.03, 125.87, 128.38, 129.26, 129.82, 135.12, 138.86, 142.46, 151.09, 151.77, 152.68, 163.60, 169.11. QSTAR (Applied Biosystems/MDS SCIEX) (ESI): [MH+] $C_{22}H_{14}BrN_4O_4$: calculated 477.0198, found 477.0196.

t-Boc-Rhodamine 110-Triphenylphosphine-aza-ylide (5a). t-Boc-rhodamine 110 azide (**2**) (13.4 mg, 29.4 μmol) was dissolved in anhydrous THF (1.1 mL). Triphenylphosphine (9.1 mg, 34.7 μmol) was added. After 2 h reaction, solvent was removed under reduced pressure, and the residue was purified by PLC plate (1:1 hexane/AcOEt). t-Boc-rhodamine 110-triphenylphosphine-aza-ylide (20.3 mg, 29.4 mmol, quantative) was obtained as a red crystalline solid. ^{1}H NMR (400 MHz, CDCl3) δ 1.50 (9H, dd, J = 3.8 Hz, 5.3 Hz), 6.34 (1H, m), 6.47 (1H, m), 6.56 (1H, m), 6.64 (1H, m), 6.73 (1H, m), 6.81 (1H, m), 7.13 (1H, m), 7.47 (6H, m), 7.54 (4H, m), 7.60 (1H, m), 7.66 (3H, m), 7.73 (3H, m), 7.97 (1H, m). QSTAR (Applied Biosystems/MDS SCIEX) (ESI): [MH+] 691.2362, found 691.2374.

Reaction of Compound 2 with DTT. t-Boc-rhodamine 110 azide (**2**) (0.37 mg, 0.8 μmol) was dissolved in methanol (2.0 mL). Dithiothreitol (30.6 mg, μmmol) was added. The reaction was monitored by fluorescence and UV spectra. The maximum wavelength of fluorescent emission was observed at 525 nm. Mass spectrometry analysis showed that the product was rhodamine amine (**1**). ([MH+] $C_{25}H_{23}N_2O_5$: 431.161, MALDI-TOF MS found: 431.167).

Reaction of Compound 2 with TPP. t-Boc-rhodamine 110 azide (**2**) (11.1 mg, 24.3 μmol) was dissolved in anhydrous THF (2.43 mL). Triphenylphosphine (7.0 mg, 30.5 μmol) was added. The reaction was monitored by fluorescence and UV spectra (fluorescence measurements were conducted by diluting 1.5 μL reaction mixture with 1500 μL methanol. Absorption measurements were conducted by diluting 4.0 μL reaction mixture with 196 μL methanol.). As showed in Figure 5A, the maximum wavelength of fluorescent emission was observed at 550 nm 10 min later. After 1 h reaction, the fluorescent emission at 550 nm was saturated and no additional fluorescent emission was

observed. Mass spectrometry analysis showed that the product was aza-ylide (**5a**). ([MH+] $C_{43}H_{36}N_2O_5P$: 691.236, MALDI-TOF MS found: 691.304).

Synthesis of Unmodified Oligonucleotides. All oligonucleotides were synthesized on a 0.2 μmol scale on a DNA synthesizer (H-8-SE; Gene World) using standard phosphoroamidite coupling chemistry. Deprotection and cleavage from the CPG support was carried out by incubation in concentrated ammonia for 4 h at 55 °C. Following deprotection, the oligonucleotides were purified by reverse-phase column chromatography (MicroPure II column; Biosearch Technologies), and quantitated by UV absorbance using the nearest-neighbor approximation to calculate molar absorptivities.

3′-Rhodamine-Azide-Conjugated Oligonucleotide (probe 1). The bromoacetyl group of the rhodamine-azide (**4**) was reacted with the phosphorothioate group on the ODNs. For 3′ phosphorothioate sequences, the 3′-phosphate CPG was sulfurized by the sulfurizing reagent (Glen Research) after the first nucleotide was added. 75 nmol of the 3′-phosphorothioate oligonucleotide in 50 μL of 400 mM triethylammonium bicarbonate buffer were shaken for 5 h at room temperature with 750 nmol of rhodamine-azide (**4**) in 200 μL of dimethylformamide. The reacted products were collected by ethanol precipitation. Next, the products were purified by reverse-phase HPLC (0−80% acetonitrile/50 mM triethylammonium acetate gradient). The probe structure was confirmed by ESI-TOF mass spectrometry. 5′-GCCGGCGG-Rh-azide-3′: calculated mass, $C_{104}H_{126}N_{33}O_{51}P_9$ 2942.5; found 2942.5.

5′-Dithiothreitol (DTT)-Linked Oligonucleotide (probe 2). Dithiol phosphoroamidite (DTPA; Glen Research) was used to prepare 5′-DTT-modified oligonucleotide. Deprotection and cleavage from the CPG support was carried out by the standard method. Following deprotection, the oligonucleotide was purified by reverse-phase column chromatography and quantitated by UV absorbance. To cleave the disulfide bond, 10 nmol of purified oligonucleotide was treated with 250 μL of 100 mM TCEP in phosphate buffer (pH 6.0). The reacted products were collected by ethanol precipitation, and then preserved in 100 μM DTT solution. The probe structure was confirmed by MALDI-TOF mass spectrometry. 5′-DTT-TGTGGGCA-3′: calculated mass, $C_{83}H_{108}N_{32}O_{51}P_8S_2$ 2980.4; found 2979.7.

5′ Triphenylphosphine (TPP)-Linked Oligonucleotide (probe 3). Carboxy-triphenylphosphine (TPP) NHS ester was reacted with 5′-amino-modified oligonucleotide. 5′-amino-modifier C6 (Glen Research) was used to prepare 5′-amino-modified oligonucleotide. 50 nmol of the 5′-amino-modified oligonucleotide in 135 μL of 93 mM sodium tetraborate (pH 8.5) was shaken for 5 h at room temperature with 2 μmol of TPP NHS ester in 115 μL of dimethylformamide. The reacted products were collected by ethanol precipitation. Next, the collected products were purified by reverse-phase HPLC (0−50% acetonitrile/50 mM triethylammonium acetate gradient). The probe structure was confirmed by ESI-TOF mass spectrometry. 5′-TPP-TGTGGGCA-3′: calculated mass, $C_{104}H_{126}N_{33}O_{51}P_9$ 2931.6; found 2932.6. A peak corresponding to the oxidized product (+O) was also seen and presumed to arise from oxidation during purification.

Fluorescence Measurement. Reactions on the DNA template were performed in 1.2 mL of tris-borate buffer (70 mM, pH 8.0) containing 10 mM $MgCl_2$ with target DNA (500 nM), probe 1 (500 nM), and probe 2 (1 μM) or probe 3 (500 nM) at 25 °C. In the case of probe 2, DTT (100 μM) was added to the reaction mixture. The increase of fluorescence intensity produced by reduction of rhodamine-azide on probe 1 was continuously monitored at time intervals. Reactions were observed by fluorescence spectrometry (FP-6500; JASCO). Fluorescence spectra were measured under the following conditions: excitation, 490 nm. For the time course of the azide reduction, the fluorescence intensity was measured for 0.5 s at 1 min intervals: excitation, 490 nm; emission, 550 nm (TPP) or 530 nm (DTT).

Imaging of RNA in Fixed *E. coli* Cells. *Escherichia coli* K12 (NBRC 3301) was grown aerobically on a rotary shaker in Luria−Bertani broth (WAKO) at 30 °C for 20 h. The cells were centrifuged and were fixed with 4% paraformaldehyde−PBS solution for 2 h before being washed with PBS and resuspended in PBS/ethanol (1:1; vol/vol). Fixed cells were stored at −20 °C. Oligonucleotide probes were targeted to nucleotides 968−997 in 23S rRNA of *E. coli* K12 since Fuchs et al. described the accessibility of this site was superior to other sites (*26*). Both rhodamine-azide probe (5′-CTGGCGGTCTGGGTT-Rh-azide-3′) and triphenylphosphine probe (5′-TPP-GTTTCCCTCT-TCACG-3′) were 15 nt in length. After attaching fixed *E. coli* on the glass slide, 9 μL of hybridization buffer (20 mM Tris−HCl pH 7.2, 0.9 M NaCl, 0.1% SDS, 440 nM rhodamine-azide probe, 440 nM triphenylphosphine probe, and 0.025% PEG6000) were applied to each well. After incubation at 37 °C for 30 min, hybridization buffer was briefly removed with distilled water without the conventional washing step, air-dried, and mounted in Slow Fadeβ Gold antifade reagent (Invitrogen). Fluorescence images were obtained through a fluorescence microscope (Carl Zeiss Axioskop 2 Plus) with mercury lamp, using digital camera (Carl Zeiss AxioCam HRm) and imaging software (Carl Zeiss *AxioVision 3.0*). Microscope settings were as follows: ex. 480/40 band-pass filter; ex. 510 nm with long-pass filters, exposure time 2 s.

RESULTS

Principle of Fluorescence Emission of the RETF Probe. The RETF probe consists of two separated DNA strands, with one probe having a reducible fluorogenic compound, while the other probe has reducing reagents. The chemistry of the RETF probe involves reaction between the azide group of nonfluorescent rhodamine derivatives and reducing reagents on an oligonucleotide template (Figure 1A). This reaction proceeds only in the presence of complementary oligonucleotide templates. After reduction of the azide group (**I**), the rhodamine derivative with the aza-ylide group (**III**) or the amino group (**IV**) emits fluorescence. Dithiothreitol (DTT) or triphenylphosphine (TPP) can be used as reducing reagent for this chemistry. DTT directly reduces the an azide group (**I**) to an amino group (**IV**) with the formation of a disulfide bond (Figure 1B). The Staudinger reaction using TPP as a reducing reagent produces an aza-ylide (**III**), which hydrolyzes to give a primary amine (**IV**) and the corresponding phosphorus compound (Figure 1C). This reaction works orthogonally in biological conditions or even in cells.

Synthesis of Rhodamine Azide. The synthesis of rhodamine azide derivatives (**4**) is shown in Scheme 1. The previously reported mono-Boc-rhodamine 110 (**1**) (*27*) was transformed to the diazo derivative by treatment with $NaNO_2$, and the diazo group was replaced with an azide group by the addition of NaN_3 to the reaction mixture. Treatment with trifluoroacetic acid to remove the Boc group of compound **2** did not give the desired product **3** because of damage to the azide group. The Boc group was successfully deprotected by treatment with 4 M HCl/dioxane solution, followed by introduction of the bromoacetyl group by treatment with bromoacetyl bromide and sodium bicarbonate to give the desired compound **4**. Compound **4** was introduced into the DNA probe.

Reaction of Rhodamine Azide (2) with Reducing Reagents. Rhodamine azide **2** showed no absorbance at wavelengths longer than 310 nm in methanol, but the corresponding rhodamine amine **1** showed a maximum absorption at 490 nm. When a high concentration of DTT or TPP was added to a solution of

Scheme 1[a]

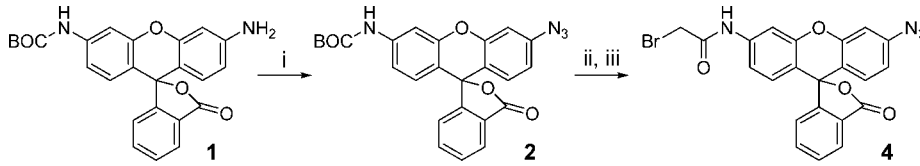

[a] (i) Isopentyl nitrite, TFA, CH_3CN/CH_2Cl_2, 0 °C, 2 h, then NaN_3, CH_3CN/CH_2Cl_2, rt, 1 h, 70%; (ii) 4.0 M HCl in dioxane, rt, 3 h, compound **3**: 99%; (iii) bromoacetyl bromide, $NaHCO_3$, $CHCl_3$, rt, 12 h, 94%.

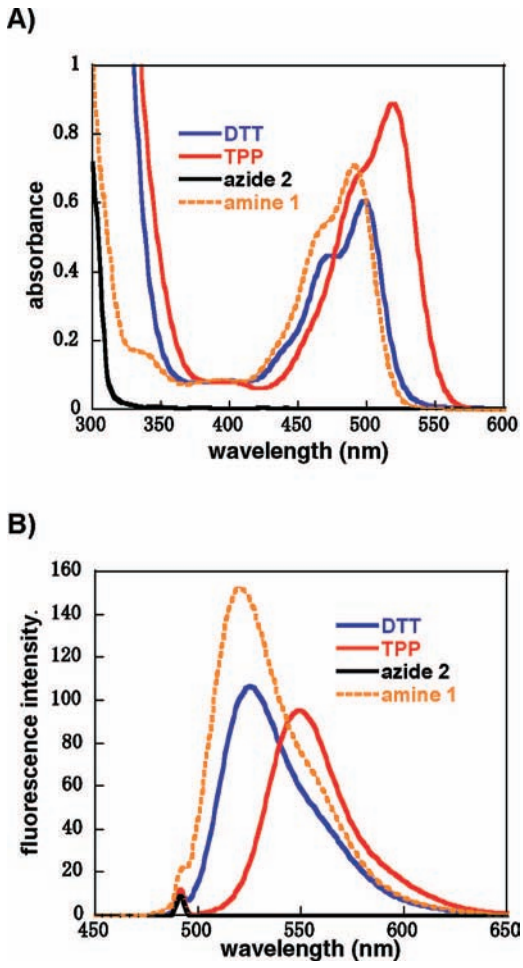

Figure 2. (A) Absorption spectra of 200 μM azide 2 after treatment with DTT (blue solid line) or TPP (red solid line), azide 2 (black solid line) without any treatment, or amine 1 (orange broken line) in methanol. (B) Fluorescent emission spectra with excitation at 490 nm of 10 μM azide 2 by treatment with DTT (blue solid line) or TPP (red solid line), azide 2 (black solid line) without any treatment, or amine 1 (orange broken line) in methanol.

azide **2**, a peak having a maximum at 495 or 518 nm increased, respectively, resulting from reduction of the azide group (Figure 2A). The fluorescence properties of rhodamine derivatives were also examined. No significant fluorescence with excitation at 490 nm was observed for azide **4**. On the other hand, rhodamine amine **1** showed strong fluorescence emission at around 520 nm. After the addition of DTT or TPP to the solution of azide **4**, a strong emission appeared around 520 or 550 nm, respectively, where the emission was enhanced almost 2100-fold (Figure 2B). We isolated these products and analyzed the structures by NMR spectroscopy and mass spectrometry. The product resulting from the DTT treatment was amine **1**. In contrast, TPP treatment gave aza-ylide **5a** (Scheme 1). It seems that not **5a** but **5b** with longer π-conjugation in the equilibrium structures emits fluorescence at 550 nm. Thus, we conclude that both reducing reagents can transform rhodamine azide into a

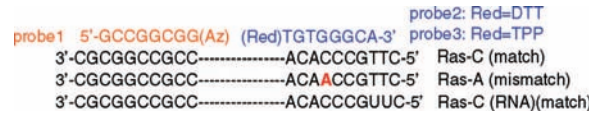

Figure 3. Probe 1 is an 8-mer ODN modified with rhodamine azide **4** (Az) at the 3′-terminal. Probes 2 and 3 are 8-mer ODNs modified with DTT or TPP as reducing reagents (Red) at the 5′-terminal. The DNA targets are 20-mer ODNs with a fully matched sequence (Ras-C) and a one-base mismatched sequence (Ras-A). Ras-C (RNA) is the fully matched RNA target.

fluorescent form by intermolecular reaction at the small compound level.

Design of the RETF Probe. To test the utility of the RETF system for fluorescence-based oligonucleotide detection, we designed three new DNA probes (Figure 3). Probe 1 was modified at the 3′-terminal with rhodamine azide **4**, where the bromoacetyl group of **4** was reacted with the phosphorothioate group at the 3′-end of the DNA probe. Probe 2 was modified at the 5′-terminal with DTT using commercially available phosphoramidite reagents. Probe 3 was modified at the 5′-terminal with 2′-carboxytriphenylphosphine (TPP), which was conjugated with the 5′-amino linker of the DNA probe through amide bond formation. Two DNA templates originating from the human Ras gene sequence, which is known as an oncogene, were designed containing Ras-C with a full match sequence and Ras-A with a one-base mismatch, respectively (Figure 3). Ras-C (RNA) was also designed, corresponding to the Ras-C DNA strand.

Reaction of the RETF Probe. An important issue for the detector probe is that it shows neither background fluorescence nor a false signal under biological conditions, in order to achieve a high *S*/*B* ratio. The probe should be very stable in any biological conditions. To determine the stability of the RETF probe, we treated the probe under various extreme conditions and checked the resulting signal. As a consequence, it was found that probe 1 with rhodamine azide was fully stable under acidic or basic conditions at pH 5−10 and under light irradiation at 490 nm, and at a high temperature of 90 °C for at least 10 min, as indicated by the lack of increase in fluorescence (Figures 4 and 5). However, when a high concentration of tris(2-carboxyethyl)phosphine (TCEP) was added to a solution of probe 1, a strong fluorescence signal appeared as the result of reduction of rhodamine azide on probe 1. Thus, we conclude that probe 1 with rhodamine azide was fully stable under various biological conditions to show no undesired fluorescence signal and was responsive to only the specific reducing reagents.

Next, we tested whether the RETF probe can detect target DNA or RNA sequences to produce a fluorescence signal (Figure 5). When 500 nM probe 1 and 1 μM probe 2 were incubated in pH 8.0 tris-borate buffer, the fluorescence signal at 530 nm increased in the presence of a target Ras-C over 60 min by reduction of the azide group to the amino group of probe 1, and no significant increase in fluorescence was observed in the absence of Ras-C (Figure 5A). When 500 nM probe 1 and 500 nM probe 3 were incubated in buffer, the increase in fluorescence at 550 nm was monitored. Probe 3 reacted with probe 1 in the presence of target Ras-C much faster than did

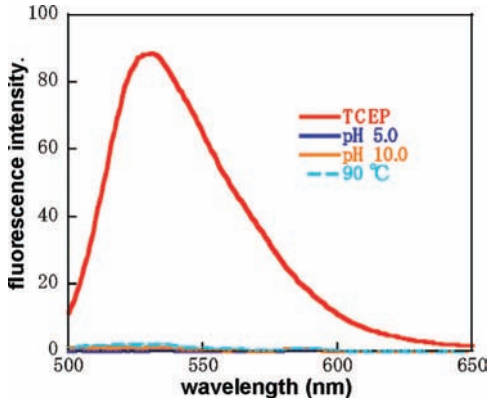

Figure 4. Stability of probe 1 under various conditions. The stability of the rhodamine-azide probe (probe 1) was tested at pH 5.0, 10.0, and high-temperature (90 °C) conditions. Probe 1 was incubated at pH 5.0 (blue solid line) or 10.0 (orange solid line) tris-borate buffer for 30 min at room temperature or in pH 8.0 tris-borate buffer for 10 min at 90 °C (light blue broken line). No significant fluorescence with excitation of 490 nm was observed in these conditions by comparison with the spectra after the treatment of TCEP (red solid line).

probe 2, and the signal at 550 nm reached the saturation phase within 20 min (Figure 5A). The signal did not increase in the absence of Ras-C over 30 min, even under continuous light irradiation at 490 nm.

The ability to achieve single base discrimination is important for diagnostic applications. The reaction of probe 1 with probe 3 in the presence of one-base-mismatched target Ras-A was carried out and showed good single base mismatch discrimination, dropping in initial rate by 18.8-fold, compared with fully matched Ras-C (Figure 5B).

RNA is an important target for detection, especially for imaging cellular RNA. However, because RNA−DNA duplexes form a different helical structure from DNA−DNA duplexes, there is no guarantee that such a chemical reaction on the template would proceed in the same way when detecting RNA as happened with DNA. Thus, we prepared an RNA target, Ras-C (RNA), and compared the reaction rates with the corresponding DNA target, Ras-C. When Ras-C (RNA) was targeted, almost identical time-course spectra as for Ras-C (DNA) were obtained from both probe 2 and probe 3 (Figure 5C). The fluorescence signal at 550 nm from the reaction of probe 1 and probe 2 with Ras-C (RNA) reached the saturation phase in 20 min, similar to the Ras-C, DNA target. Thus, the RETF probe seems to be capable of detecting both DNA and RNA targets.

Figure 6A shows the time-dependent fluorescence intensities at 530 and 550 nm in the reaction of probe 1 and probe 3 in the presence of the Ras-C template over 600 min. The signal at 550 nm quickly increased in the initial stage and slightly dropped after 30 min, but the signal at 530 nm continuously increased over the 600 min. The maximum wavelength in the fluorescence spectra shifted from 550 to 530 nm (Figure 6B). HPLC (Figure 7A,B) and MALDI-TOF mass analysis (Supporting Information Figure S1) showed that 67% of probe 1 had reacted with probe 3 after 10 min to give the corresponding ligated product with an aza-ylide bond (**III**) (peak 2: 52%) and reduced probe 1 with an amino group (**IV**) (peak 3: 15%) (Figures 1 and 7A). After 24 h, the aza-ylide peak completely disappeared and the product with an amino group was obtained in 86% yield (peak 1, Figure 7B). In contrast, reaction with probe 2 (DTT) showed only reduced product in 36% yield after 2 h (Figure 7C). Thus, we conclude that, in the reaction of probe 1 and probe 3, the increase in fluorescence at 530 nm indicates the formation of reduced probe 1 with the amino group of rhodamine (**IV**) from the hydrolysis of the aza-ylide product (**III**) (*28*). In contrast, probe

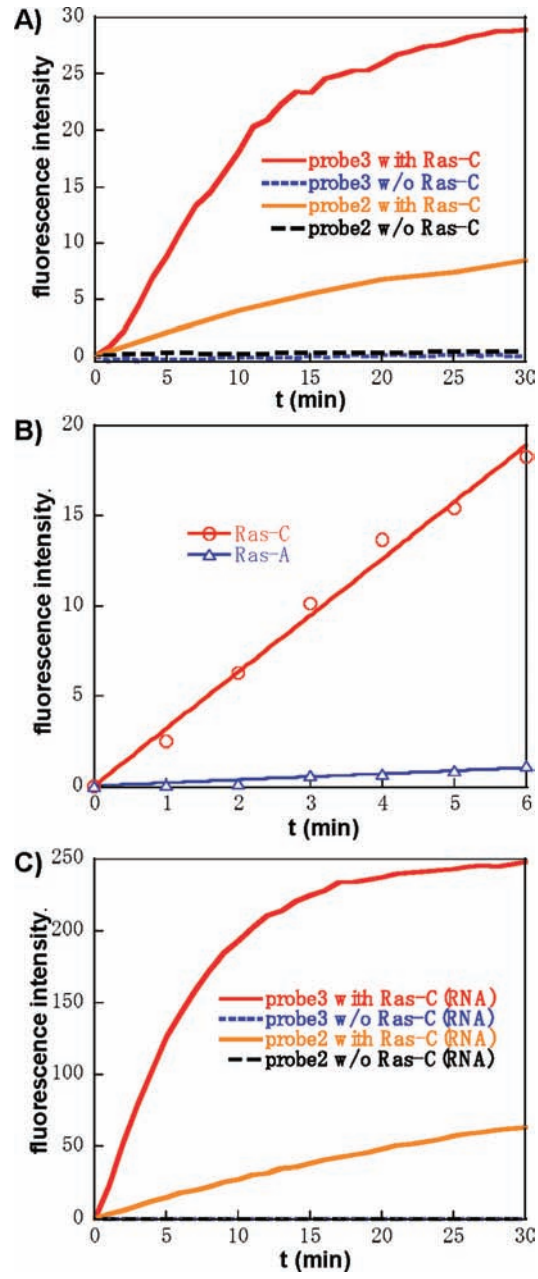

Figure 5. (A) Time course of the fluorescence intensity in the reaction of probe 1 with probe 2 or probe 3. Fluorescence emission at 530 nm (probe 2) or 550 nm (probe 3), respectively, was monitored by excitation at 490 nm. The reactions were carried out under the following conditions in pH 8.0 tris-borate buffer containing 10 mM $MgCl_2$, 1 μM probe 2, 100 μM DTT, and 500 nM probe 1 with (orange solid line) or without (black broken line) Ras-C, or 500 nM probe 3 and 500 nM probe 1 with (red solid line) or without (blue broken line) Ras-C. (B) The time course of the fluorescence intensity in the reaction of probe 1 with probe 3 in the presence of Ras-C (match; circle) or Ras-A (mismatch; triangle). The reaction conditions were the same as above. (C) Time course of the fluorescence intensity in the reaction of probe 1 with probe 2 or probe 3 with RNA target. The reactions were carried out with 500 nM probe 1 with (orange solid line) or without (black broken line) Ras-C (RNA), or 500 nM probe 3 and 500 nM probe 1 with (red solid line) or without (blue broken line).

2 directly reduces the azide group of probe 1 to the corresponding amine (**IV**).

Imaging of RNA in Bacterial Cells. Fluorescence in situ hybridization (FISH) is becoming broadly adopted by microbiologists because of the existence of a growing database of rRNA (rRNA) sequences. However, the standard fluorescent probes require a careful washing step in the protocol to remove

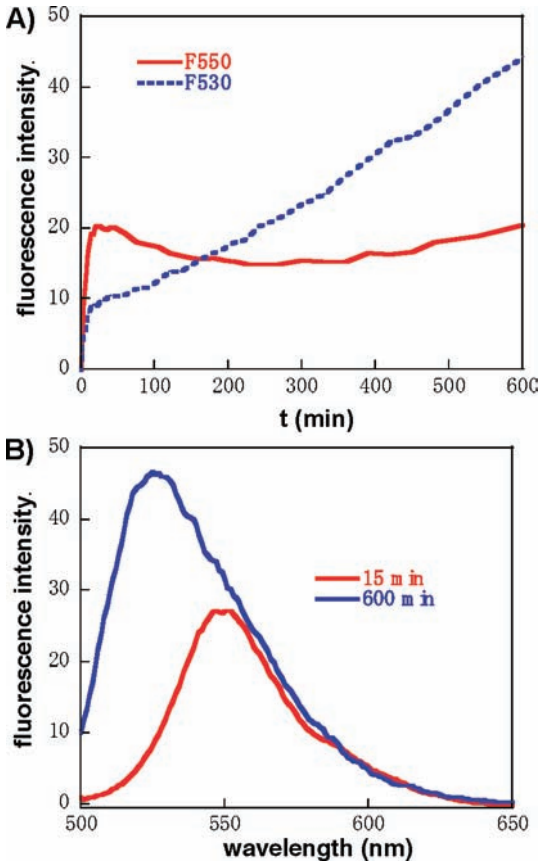

Figure 6. (A) Time course of the fluorescence intensity in the reaction between 500 nM probe 1 and 500 nM probe 3 in the presence of 500 nM Ras-C. Emissions at 550 nm (red solid line) and 530 nm (blue broken line) were monitored simultaneously. (B) Fluorescence spectra were measured after 15 min (red solid line) and 600 min (blue solid line) incubation with probes 1 and 3 in the presence of Ras-C. The maximum wavelength in the fluorescence spectra shifted from 550 to 530 nm.

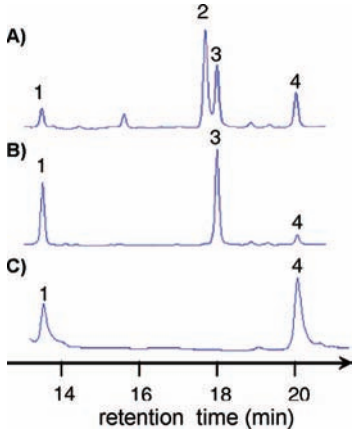

Figure 7. HPLC analysis of the reaction mixture. (A) 10 min reaction with probe 3, (B) 24 h reaction with probe 3, (C) 2 h reaction with probe 2. Peak 1, reduced probe 1 with amino group; Peak 2, ligated product with aza-ylide bond; Peak 3, oxidized probe 3; Peak 4, probe 1 with azide group. Each peak was analyzed by mass spectrometry.

nonspecific signals. Here, we tested a nonwashing protocol for detection of 23S rRNA in the *Escherichia coli* K12 strain (NBRC3301) by use of an RETF probe. Probes were designed for targeting sequence 968−997 on 23S rRNA, which is known to be accessible by the standard FISH probe (*26*). The rhodamine azide probe and the TPP probe with matched sequence are both

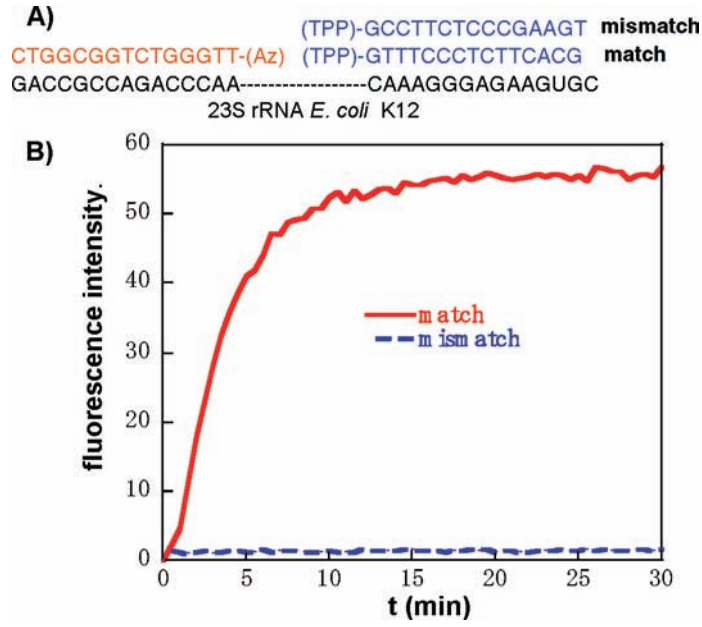

Figure 8. (A) Probe sequences for 23S rRNA of *E. coli* K12. Designed 15-mer probes are a rhodamine-azide probe with fully matched sequence, TPP probe with fully matched sequence, and TPP probe with mismatched sequence. (B) Time course of the fluorescence intensity in the reaction between 500 nM rhodamine-azide probe and 500 nM matched TPP probe or mismatched TPP probe in the presence of 500 nM target DNA. Reaction was monitored by excitation at 490 nm and emission at 550 nm.

15 bases long (Figure 8A). The TPP probe with mismatched sequence was tested as a control. Before imaging experiments, probes were tested in in vitro experiments to target corresponding DNA sequences (Figure 8B). The matched probe pair produced a strong fluorescent signal and completed the reaction within 10 min, and no significant signal was observed from a mismatched probe pair (Figure 8B).

We then proceeded to test the probes in bacterial cells. Cells were fixed with paraformaldehyde according to literature methods and were incubated with probes at 37 °C for 30 min. Cell mixtures were directly spotted on a slide glass without a washing step and observed using a microscope. Figure 9A−D show fluorescence images and bright-field transmission images of cells. A strong fluorescent signal was observed in the case of the matched probe pair (Figure 9A), but no signal was observed from the mismatched probe pair (Figure 9B). The data show that the RETF probe can be used to detect specific RNA sequences in structured biological targets in cells. This suggests the possibility of their general use in identifying bacterial pathogens by their rRNAs.

DISCUSSION

Many fluorogenic probes for sensing oligonucleotides have been developed, such as MBs (*6*, *16*) and quenched autoligation (QUAL) probes (*14*, *18*, *29*). These probes produce a fluorescent signal based on the RET mechanism, for which a pair of quencher and fluorescence dyes is normally used. The quenching efficiency reaches a maximum of 98%, if the position of a pair of dyes is carefully optimized (*24*). The corresponding *S*/*B* ratio is 50:1. In contrast, rhodamine azide of the RETF probe emits by an absorption change triggered by a chemical reaction. The *S*/*B* ratio reaches 2100:1 (Figure 2). This property is clearly helpful for sensing. Another issue for an MB is that protein binds to the beacon to yield a false fluorescent signal (*30*). QUAL probes also have the potential to yield false fluorescent signals through automatic hydrolysis of the quencher. A novel

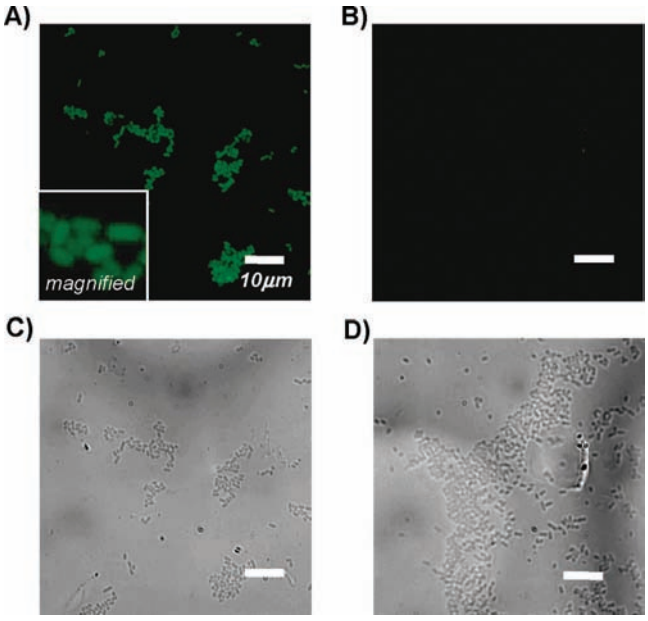

Figure 9. Imaging of 23S rRNA in fixed *E. coli* K12 (NBRC3301). Pictures showed a specific signal with a matched probe pair and little or no signal with a mismatched pair. Microscope settings were as follows: excitation, 480/40 band-pass filter; emission, 510 nm with long-pass filters; exposure time, 2 s. (A) Rhodamine-azide probe/matched TPP probe. (B) Rhodamine-azide probe/mismatched TPP probe. (C) Bright-field picture under the conditions of (A). (D) Bright-field picture under the conditions of (B).

fluorogenic system has been reported, that is, nucleic acid-triggered fluorescent probe activation by the Staudinger reaction, and showed that the fluorescence signal emerged subsequent to cleavage of the ester bond, which produces the possibility of yielding background fluorescence by automatic or enzymatic hydrolysis of the ester bond (*25*). The method has not been applied to the detection of cellular RNAs. On the other hand, the RETF probe accepts not only TPP in the Staudinger reaction, but also other reducing reagents, such as DTT, for reduction of the azide group to switch the fluorescence on and has no hydrolysis problems, which results in minimization of background fluorescence. In addition, as shown in Figure 4, the RETF probe has proven to be fully stable under various conditions such as pH 5−10, light irradiation at 490 nm, and high temperature of 90 °C. This result implies that the RETF probe operates under wide biological conditions without producing an undesirable false fluorescence signal. An issue of our method to be solved is oxidative deactivation of the reducing reagent on the probe in solution, although that does not produce a false signal. We showed one example of a single base discrimination study. The discrimination ability depends on the identity of the mutation and its nearest neighbors, as well as the length of the probe. Therefore, the probe should be carefully designed in each case to achieve single nucleotide resolution.

We carefully analyzed the reaction mechanism between rhodamine azide and reducing reagents. The DTT probe directly reduces rhodamine azide on the probe to fluorescent rhodamine amine (Figure 1). On the other hand, the reaction of the TPP probe initially produces a fluorescent ligation product with an aza-ylide bond, then gives a fluorescent product with rhodamine amine through hydrolysis of the aza-ylide bond (Figure 1). The key finding here is that the rhodamine aza-ylide derivative is fluorescent. This mechanism was supported by several experimental results. In a small compound, rhodamine azide **2** is directly reduced to amine **1** by DTT. The rhodamine aza-ylide derivative **5b** was isolated from the reaction of **2** with TPP (Scheme 2). Aza-ylide **5b** with open lactone form was stable in methanol and showed fluorescence emission at 550 nm, as opposed to amine **2**, which emits fluorescence at 520 nm (Figure 2). Interestingly, when the trialkylphosphine TCEP was employed as a reducing reagent, rhodamine azide **2** was directly reduced to amine **2** without formation of the aza-ylide product in methanol (Figure 4). This result suggests that TPP as a triarylphosphine can stabilize the aza-ylide intermediate because of the presence of long π-conjugation. The reaction of the rhodamine azide probe with the reducing probe on the DNA template proceeded in a similar manner as the reaction of rhodamine azide **2** in the small compound. The existence of a ligated product with an aza-ylide linkage was verified by HPLC and mass spectrometric analysis shown in Figure 7 and Supporting Information Figure S1. Further spectroscopic analysis clearly indicates hydrolysis of the aza-ylide bond in solution with increasing emission signal at 530 nm resulting from the formation of the amino rhodamine probe (Figure 6).

Fluorescence activation by reduction of the azide group of rhodamine is a new molecular mechanism as a fluorogenic compound. After reduction of the azide group, the rhodamine derivative opens the lactone ring to form a carboxylate and emits fluorescence. The reaction of the TPP probe is complete within 10−15 min with both DNA and RNA targets. The reaction speed is faster than other DNA-templated chemical reactions that are able to produce fluorescence. As we have shown, the method was successfully applied to visualization of 28S rRNA in *E. coli* by a nonwashing protocol with probes. It could be applied to detect RNA species in living cells. Future work will be aimed at making new azide fluorescent compounds for multiple color detection and sensing RNA species in living cells.

CONCLUSION

We developed a reduction-triggered fluorescence (RETF) probe for sensing oligonucleotides. The chemistry involves the reaction between the azide group of rhodamine derivatives and reducing reagents on a DNA template. A new fluorogenic compound, rhodamine azide **4**, was designed and synthesized for this chemistry. After reduction of the azide group to the amino group, the rhodamine derivative emits fluorescence. DTT, TPP, or other reducing reagents can be used for this chemistry. Reaction of the RETF probe proceeded without any enzymes or reagents, and offered a high signal and very low background fluorescence under biological conditions. We successfully applied the probe to detection of oligonucleotides in solution and endogenous RNA in bacterial cells.

Scheme 2

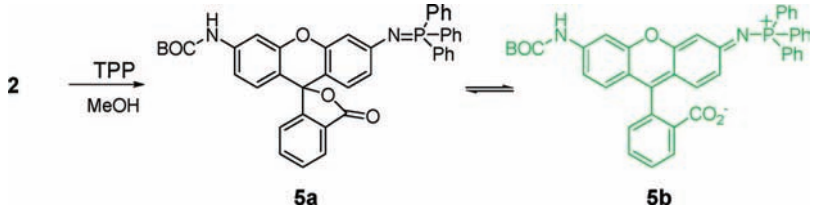

ACKNOWLEDGMENT

H. A. was supported financially by the Riken Directors' Fund, MEXT (Ministry of Education, Culture, Sports, Science and Technology of Japan) and NEDO (New Energy and Industrial Technology Development Organization of Japan). This work was also supported by Grant-in-Aid for Scientific Research on Priority Areas "Lifesurveyor" from MEXT.

Supporting Information Available: MALDI-TOF mass analysis of products in the reaction of RETF probe, and ^{1}H-NMR and ^{13}C-NMR data. This material is available free of charge via the Internet at http://pubs.acs.org.

LITERATURE CITED

(1) DeLong, E. F., Wickham, G. S., and Pace, N. R. (1989) Phylogenetic stains: ribosomal RNA-based probes for the identification of single cells. *Science 243*, 1360–1363.

(2) Levsky, J. M., and Singer, R. H. (2003) Fluorescence in situ hybridization: past, present and future. *J. Cell Sci. 116*, 2833–2838.

(3) Amann, R., Fuchs, B. M., and Behrens, S. (2001) The identification of microorganisms by fluorescence in situ hybridisation. *Curr. Opin. Biotechnol. 12*, 231–236.

(4) Moter, A., and Gobel, U. B. (2000) Fluorescence in situ hybridization (FISH) for direct visualization of microorganisms. *J. Microbiol. Methods 41*, 85–112.

(5) Levsky, J. M., Shenoy, S. M., Pezo, R. C., and Singer, R. H. (2002) Single-cell gene expression profiling. *Science 297*, 836–840.

(6) Tyagi, S., and Kramer, F. R. (1996) Molecular beacons: probes that fluoresce upon hybridization. *Nat. Biotechnol. 14*, 303–308.

(7) Sando, S., and Kool, E. T. (2002) Quencher as leaving group: efficient detection of DNA-joining reactions. *J. Am. Chem. Soc. 124*, 2096–2097.

(8) Okamoto, A., Tanaka, K., Fukuta, T., and Saito, I. (2003) Design of base-discriminating fluorescent nucleoside and its application to t/c SNP typing. *J. Am. Chem. Soc. 125*, 9296–9297.

(9) Babendure, J. R., Adams, S. R., and Tsien, R. Y. (2003) Aptamers switch on fluorescence of triphenylmethane dyes. *J. Am. Chem. Soc. 125*, 14716–14717.

(10) Kolpashchikov, D. M. (2006) A binary DNA probe for highly specific nucleic Acid recognition. *J. Am. Chem. Soc. 128*, 10625–10628.

(11) Ha, T., Enderle, T., Ogletree, D. F., Chemla, D. S., Selvin, P. R., and Weiss, S. (1996) Probing the interaction between two single molecules: Fluorescence resonance energy transfer between a single donor and a single acceptor. *Proc. Natl. Acad. Sci. U.S.A. 93*, 6264–6268.

(12) Piatek, A. S., Tyagi, S., Pol, A. C., Telenti, A., Miller, L. P., Kramer, F. R., and Alland, D. (1998) Molecular beacon sequence analysis for detecting drug resistance in Mycobacterium tuberculosis. *Nat. Biotechnol. 16*, 359–363.

(13) Sando, S., and Kool, E. T. (2002) Imaging of RNA in bacteria with self-ligating quenched probes. *J. Am. Chem. Soc. 124*, 9686–9687.

(14) Abe, H., and Kool, E. T. (2006) Flow cytometric detection of specific RNAs in native human cells with quenched autoligating FRET probes. *Proc. Natl. Acad. Sci. U.S.A. 103*, 263–268.

(15) Sokol, D. L., Zhang, X., Lu, P., and Gewirtz, A. M. (1998) Real time detection of DNA.RNA hybridization in living cells. *Proc. Natl. Acad. Sci. U.S.A. 95*, 11538–11543.

(16) Bratu, D. P., Cha, B.-j., Mhlanga, M. M., Kramer, F. R., and Tyagi, S. (2003) Visualizing the distribution and transport of mRNAs in living cells. *Proc. Natl. Acad. Sci. U.S.A. 100*, 13308–13313.

(17) Tsuji, A., Koshimoto, H., Sato, Y., Hirano, M., Sei-Iida, Y., Kondo, S., and Ishibashi, K. (2000) Direct observation of specific messenger RNA in a single living cell under a fluorescence microscope. *Biophys. J. 78*, 3260–3274.

(18) Sando, S., Abe, H., and Kool, E. T. (2004) Quenched autoligating DNAs: multicolor identification of nucleic acids at single nucleotide resolution. *J. Am. Chem. Soc. 126*, 1081–1087.

(19) Maeda, H., Fukuyasu, Y., Yoshida, S., Fukuda, M., Saeki, K., Matsuno, H., Yamauchi, Y., Yoshida, K., Hirata, K., and Miyamoto, K. (2004) Fluorescent probes for hydrogen peroxide based on a non-oxidative mechanism. *Angew. Chem., Int. Ed. Eng. 43*, 2389–2391.

(20) Miller, E. W., Tulyathan, O., Isacoff, E. Y., and Chang, C. J. (2007) Molecular imaging of hydrogen peroxide produced for cell signaling. *Nat. Chem. Biol. 3*, 263–267.

(21) Kojima, H., Nakatsubo, N., Kikuchi, K., Kawahara, S., Kirino, Y., Nagoshi, H., Hirata, Y., and Nagano, T. (1998) Detection and imaging of nitric oxide with novel fluorescent indicators: Diaminofluoresceins. *Anal. Chem. 70*, 2446–2453.

(22) Dale, T. J., and Rebek, J., Jr (2006) Fluorescent sensors for organophosphorus nerve agent mimics. *J. Am. Chem. Soc. 128*, 4500–4501.

(23) Lemieux, G. A., de Graffenried, C. L., and Bertozzi, C. R. (2003) A fluorogenic dye activated by the Staudinger ligation. *J. Am. Chem. Soc. 125*, 4708–4709.

(24) Marras, S. A., Kramer, F. R., and Tyagi, S. (2002) Efficiencies of fluorescence resonance energy transfer and contact-mediated quenching in oligonucleotide probes. *Nucleic Acids Res. 30*, e122.

(25) Cai, J., Li, X., Yue, X., and Taylor, J. S. (2004) Nucleic acid-triggered fluorescent probe activation by the Staudinger reaction. *J. Am. Chem. Soc. 126*, 16324–16325.

(26) Fuchs, B. M., Syutsubo, K., Ludwig, W., and Amann, R. (2001) In situ accessibility of Escherichia coli 23S rRNA to fluorescently labeled oligonucleotide probes. *Appl. Environ. Microbiol. 67*, 961–968.

(27) Lavis, L. D., Chao, T. Y., and Raines, R. T. (2006) Fluorogenic label for biomolecular imaging. *ACS Chem. Biol. 1*, 252–260.

(28) Sakurai, K., Snyder, T. M., and Liu, D. R. (2005) DNA-templated functional group transformations enable sequence-programmed synthesis using small-molecule reagents. *J. Am. Chem. Soc. 127*, 1660–1661.

(29) Silverman, A. P., and Kool, E. T. (2006) Detecting RNA and DNA with templated chemical reactions. *Chem. Rev. 106*, 3775–3789.

(30) Molenaar, C., Marras, S. A., Slats, J. C., Truffert, J. C., Lemaitre, M., Raap, A. K., Dirks, R. W., Tanke, H. J., Dirks, R. W., Molenaar, C., and Tanke, H. J. (2001) Linear 2′ O-Methyl RNA probes for the visualization of RNA in living cells. *Nucleic Acids Res. 29*, E89.

BC800014D

SUPPORTING INFORMATION

A reduction-triggered fluorescence probe for sensing nucleic acids

Hiroshi Abe, Jin Wang, Kazuhiro Furukawa, Kazuma Oki, Miwako Uda, Satoshi Tsuneda and Yoshihiro Ito**

Nano Medical Engineering Laboratory Discovery Research Institute, RIKEN 2-1, Hirosawa, Wako-Shi, Saitama, 351-0198 Japan.

Department of Chemical Engineering, Waseda University, 3-4-1 Ohkubo, Shinjuku-ku, Tokyo 169-8555, Japan

h-abe@riken and y-ito@riken.jp

CONTENTS:

Figure S1 MALDI–TOF mass analysis of products in the reaction of RETF probe

^{1}H-NMR and ^{13}C-NMR

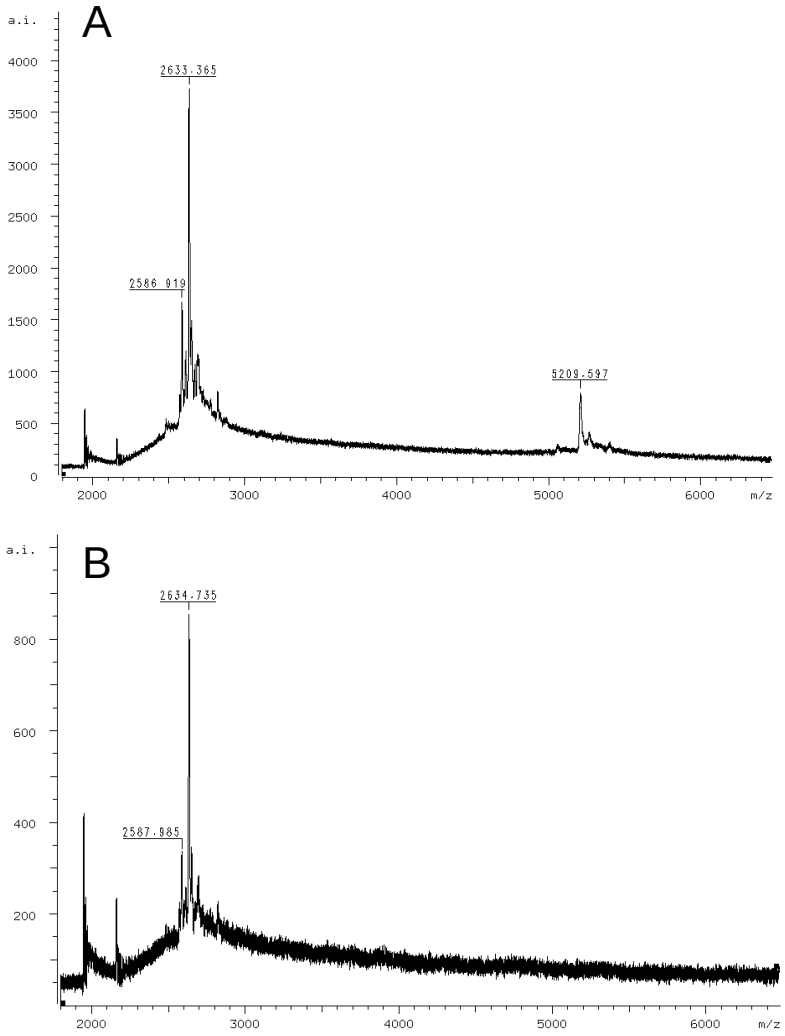

Figure S1. MALDI–TOF mass analysis of products in the reaction of RETF probe

MALDI–TOF spectra of the reaction products between probe 1 and probe 3 after 10 min (A) or 24 hours (B). The peak derived from the ligated product was found only at 10 min (calculated mass, $C_{183}H_{212}N_{59}O_{92}P_{15}S$ 5204.0; found 5209.6).

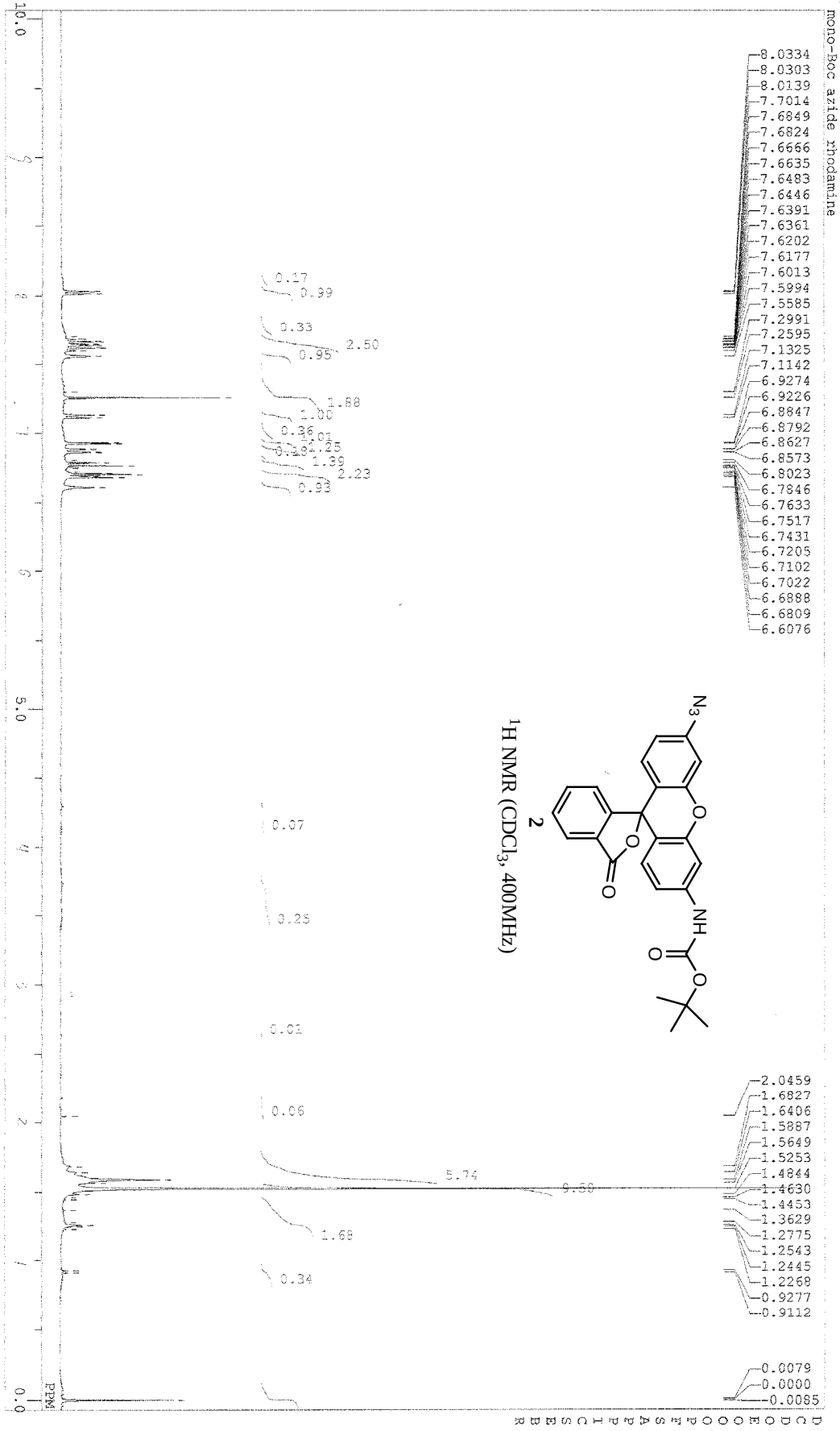
C:\Winnmr98\COMMON\mono-Boc azide rhodamine.als
mono-Boc azide rhodamine
8.0334
8.0303
8.0139
7.7014
7.6849
7.6824
7.6666
7.6635
7.6483
7.6446
7.6391
7.6361
7.6202
7.6177
7.6013
7.5994
7.5585
7.2991
7.2595
7.1325
7.1142
6.9274
6.9226
6.8847
6.8792
6.8627
6.8573
6.8023
6.7846
6.7633
6.7517
6.7431
6.7205
6.7102
6.7022
6.6888
6.6809
6.6076
0.17
0.99
0.33
2.50
0.95
1.88
1.00
0.36
1.01
1.25
1.39
2.23
0.93
0.07
0.25
0.01
0.06
5.74
9.50
1.68
0.34
2.0459
1.6827
1.6406
1.5887
1.5649
1.5253
1.4844
1.4630
1.4453
1.3629
1.2775
1.2543
1.2445
1.2268
0.9277
0.9112
0.0079
0.0000
-0.0085
PPM
10.0
5.0
0.0
N3
O
O
O
NH
O
O
2
1H NMR (CDCl3, 400MHz)

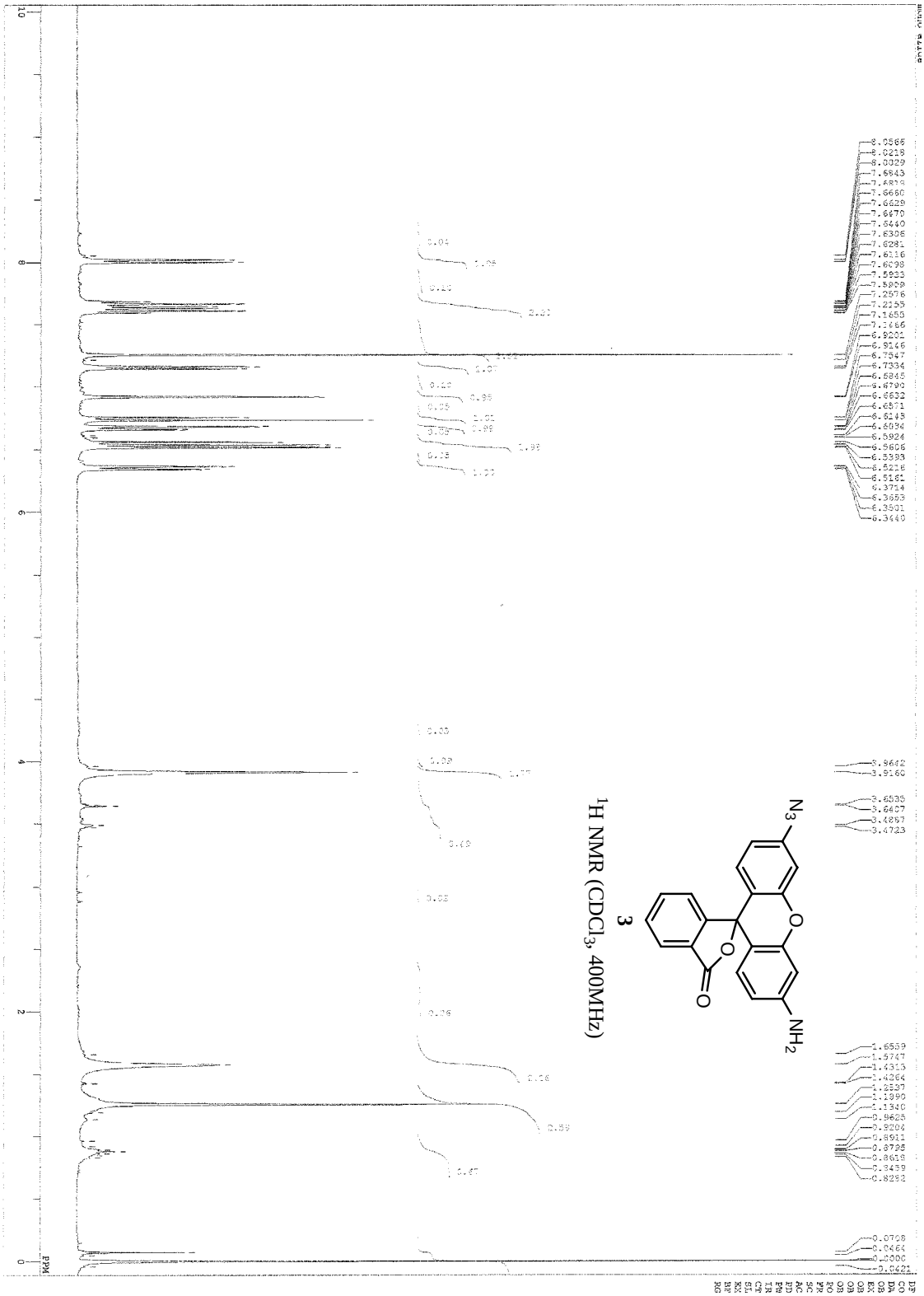

3

^{1}H NMR ($CDCl_3$, 400MHz)

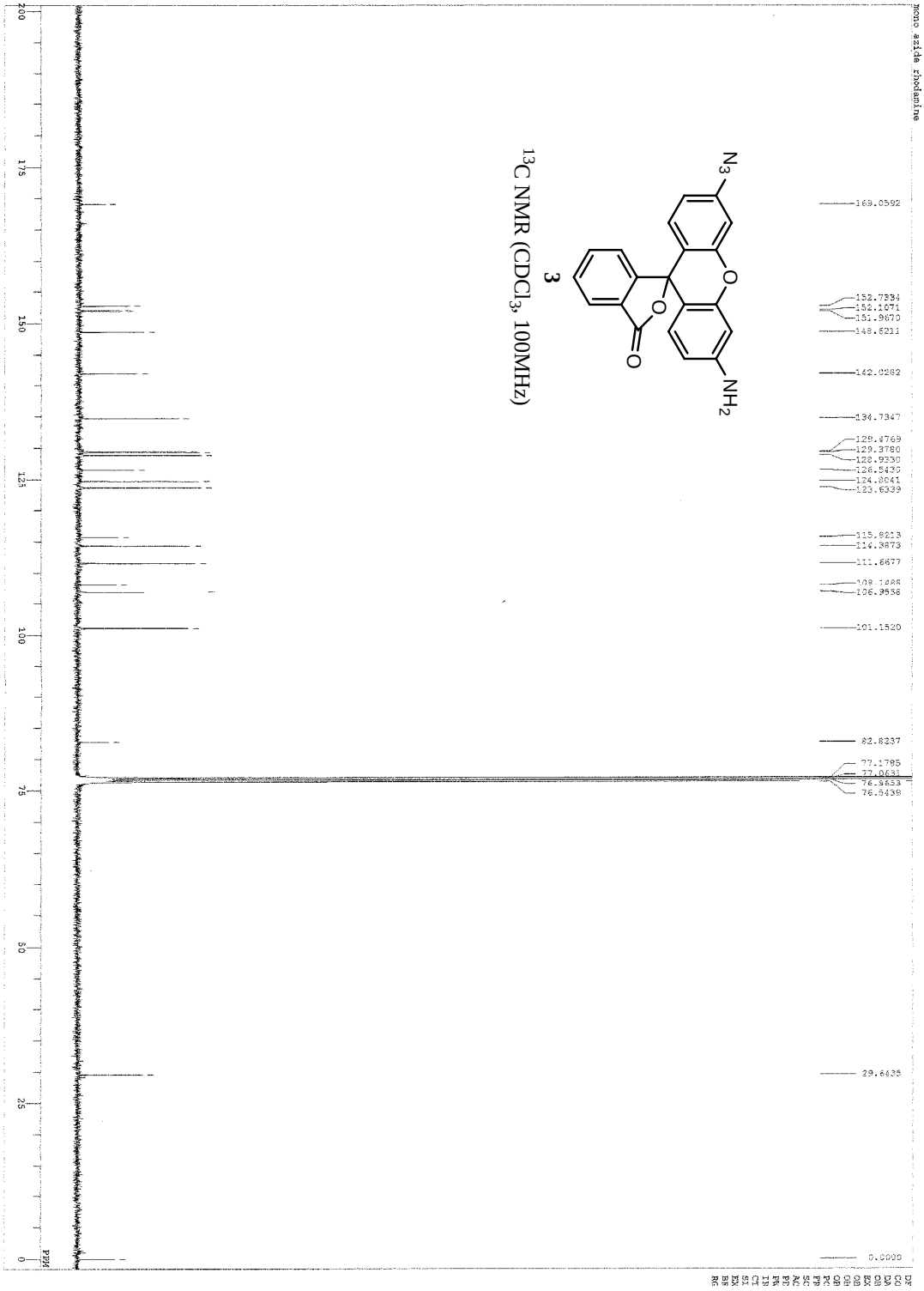

3

^{13}C NMR ($CDCl_3$, 100MHz)

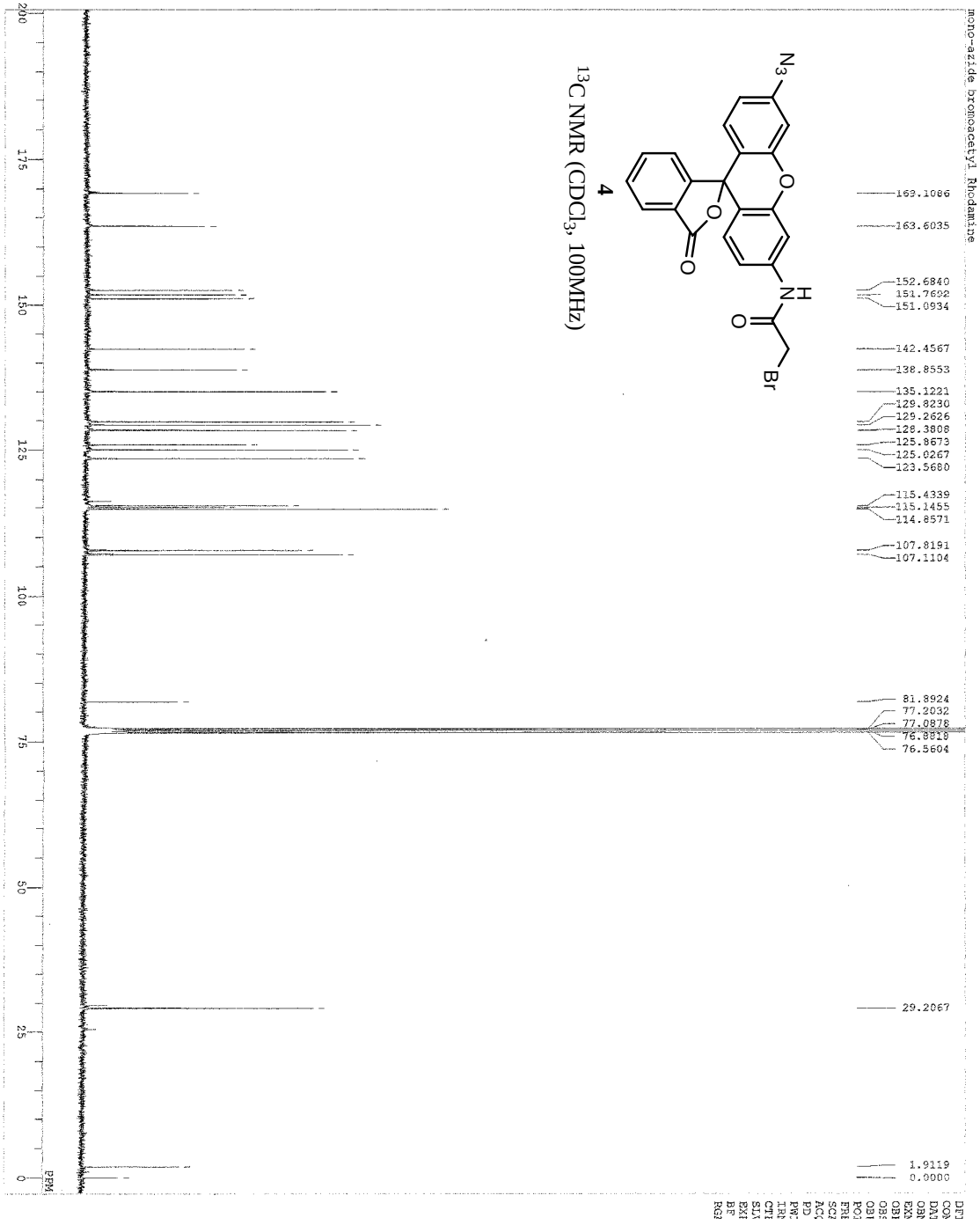

4

^{13}C NMR ($CDCl_3$, 100MHz)

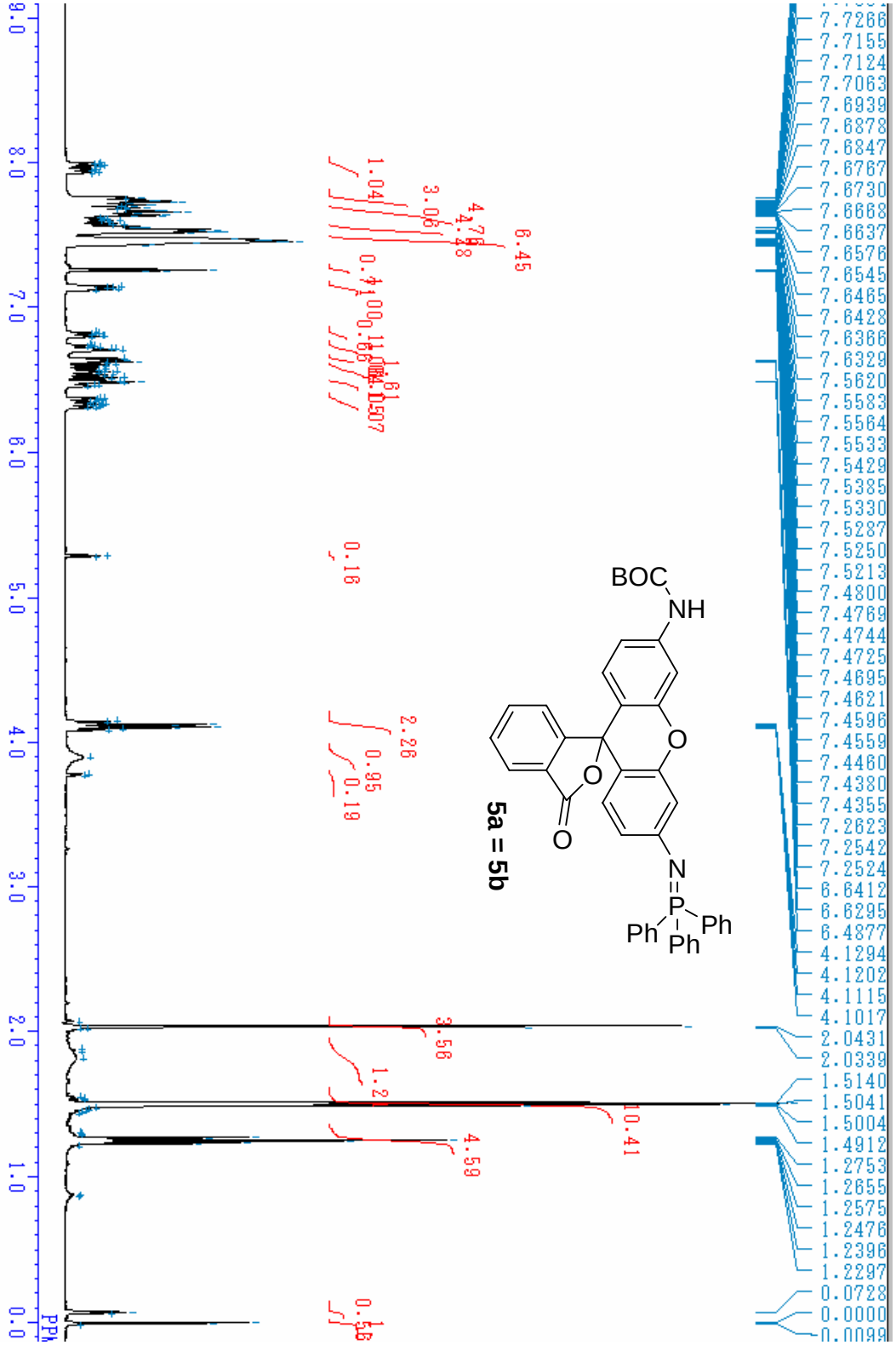
BOC
NH
O
O
O
N
P
Ph
Ph
Ph
5a = 5b

Development of a Thyroid Hormone Receptor Targeting Conjugate

Jianfei Zheng, Atsushi Hashimoto,[†] Marc Putnam,[‡] Katherine Miller, and John T. Koh*

Department of Chemistry and Biochemistry, University of Delaware, Newark, Delaware 19716. Received January 24, 2008; Revised Manuscript Received March 14, 2008

Molecular conjugates of hormone receptor−ligands with molecular probes or functional domains are finding diverse applications in chemical biology. Whereas many examples of hormone conjugates that target steroid hormone receptors have been reported, practical ligand conjugates that target the nuclear thyroid hormone receptor (TRβ) are lacking. TR-targeting conjugate scaffolds based on the ligands GC-1 and NH-2 and the natural ligand triiodothyronine (T3) were synthesized and evaluated in vitro and in cellular assays. Whereas the T3 or GC-1 based conjugates did not bind TRβ with high affinity, the NH-2 inspired fluorescein-conjugate JZ01 showed low nanomolar affinity for TRβ and could be used as a nonradiometric probe for ligand binding. A related analogue JZ07 was a potent TR antagonist that is 13-fold selective for TRβ over TRα. JZ01 localizes in the nuclei of TRβ expressing cells and may serve as a prototype for other TR-targeting conjugates.

INTRODUCTION

Advances in chemical biology have led to many important new applications of hormone conjugates as tools to probe nuclear receptor biology. The high affinity and specificity of small-molecule hormones can be used to selectively direct new bimolecular functions to the sites of nuclear hormone receptors (NHR) action. Notable examples include testosterone-based PROTAC conjugates that can down-regulate AR stability by recruiting ubiqitin ligases (*1, 2*), or peptoid activation domain conjugates of dexamethasone that can be used to activate transcription from GR (glucocorticoid receptor) independent of its normal coactivator proteins (*3*). Other examples include fluorescent NHR agonists or ligand−fluorophore conjugates that have been used as nonradiometric methods for detecting NHR binding (*4*). Yet another new and exciting discovery in this area is hormone conjugates that selectively regulate non-nuclear hormone actions by limiting cellular penetration and localization (*5*).

The development of hormone conjugates for NHRs is not always straightforward, as NHR agonist ligands are generally completely encapsulated by the protein in their bound forms. Many NHR antagonist have been shown to have molecular appendages or "extensions" that displace the active conformation of helix-12, an essential element of the coactivator binding site (*6–9*). In some cases, these appendages extend to the receptor surface providing a potential handle for generating new hormone conjugates. Structure−activity relationship studies revealed that the design of such molecular extensions is more complicated than simply introducing steric bulk at an appropriate site on the ligand, as subtle structural modifications to these extensions can have a substantial effect on ligand activity (*10–12*). Therefore, a priori, it is not obvious how to modify an agonist structure in a manner that would allow reporter groups or functional domains to be presented from the receptor surface while maintaining high-affinity binding.

The thyroid hormone receptors are important regulators of genes involved in metabolic regulation and homeostasis, as well as critical events in development (*13*). Mutations of TRβ have been implicated in RTH (resistance to thyroid hormone) as well as certain forms of cancer (*14–17*). New molecular probes of thyroid hormone action may help understand the molecular roles of TR in normal development and in these TR-associated disease states. Examples of thyroxine−fluorophore conjugates have been reported that change properties upon binding antithyroxine (T4) antibodies or detergent; however, no TR-targeting conjugates have been developed that effectively target the nuclear thyroid hormone receptor (TR) (*18, 19*).

Recently, several TR antagonists and partial agonists prompted us to investigate the development of TR-targeting hormone conjugates. Of the recently described antagonists, the compound NH-3 and the closely related agonist NH-2 (Figure 1) were of particular interest because the 5′-arylethynyl appendages could be expected to point toward helix-12 and have demonstrated subnanomolar affinity for TRβ (*11*). Although NH-2 is reported to be a TR agonist, the additional *n*-pentyl substitution of NH-2 could be envisioned to access the protein surface from the ligand binding site of TR through displacement of helix-12 or from repositioning of helix-11 as has been observed in some TR−ligand cocrystal structures (*20*). Scaffold I was therefore proposed as a conjugate scaffold for presentation of molecular probes from TR (Figure 1). To evaluate the properties of scaffold I as a means to synthesize TR-targeting conjugates, we generated the fluorescein conjugated probe JZ01 and evaluated its ability to bind to TRβ.

EXPERIMENTAL PROCEDURES

Synthesis of JZ01 and JZ07 5-(2,6-dimethyl-4-(triisopropylsilyloxy)benzyl)-3-isopropyl-2-(methoxymethoxy)benzaldehyde (2). Compound **1**was made as previously described (*21*). To a solution of **1** (2.3 g, 4.9 mmol) in a 2:1 (v/v) mixture of anhydrous THF and hexane (48 mL) at −78 °C under N_2 was added 5.4 mL 2 M *n*-BuLi solution in anhydrous hexane (10.8 mmol). The solution was allowed to warm to room temperature and stirred for 2 h before DMF (1.15 mL, 14.7 mmol) was added dropwise to the stirring solution. After an hour, the solution was poured over 1 N cold HCl solution (100 mL) and the mixture was extracted with ethyl acetate (2 × 50 mL). The organic extracts were washed with water (20 mL) and brine (20 mL), dried over

[†] Current address: Mitsubishi Pharma Corporation, 2-2-6, Nihonbashi-Honcho, Chuo-ku, Tokyo 103-8405, Japan.

[‡] Current Address: Hercules Incorporated, Wilmington, Delaware 19808.

10.1021/bc8000326 CCC: $40.75 © 2008 American Chemical Society
Published on Web 05/29/2008

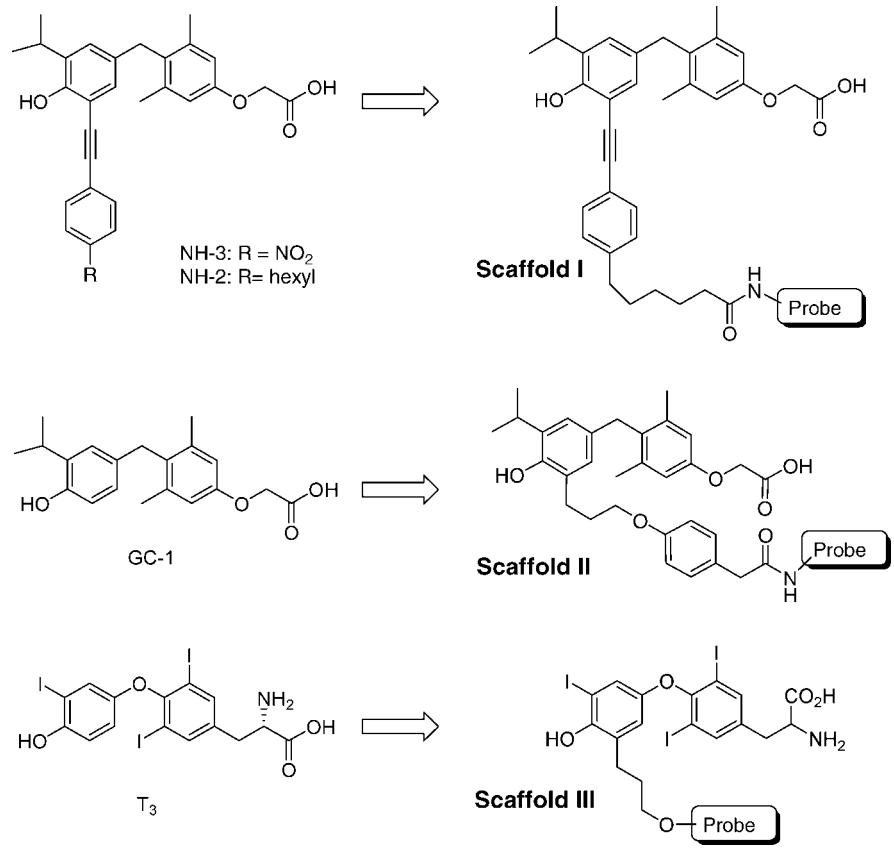

Figure 1. Thyroid hormone, T3, and the synthetic thyroid hormone analogues, GC-1 and NH-2/NH-3 and proposed TR-targeting conjugate scaffolds.

MgSO4, filtered, and evaporated under reduced pressure. The resulting crude product was purified by flash column chromatography on silica gel (1:10 ethyl acetate/hexane) to give compound **2** (1.68 g, 3.37 mmol, 69%). ^{1}H NMR (400 MHz, $CDCl_3$) δ 10.22 (s, 1H), 7.34 (d, J = 1.6 Hz, 1H), 7.13 (d, J = 1.6 Hz, 1H), 6.63 (s, 2H), 5.02 (s, 2H), 3.96 (s, 2H), 3.58 (s, 3H), 3.32 (heptet, J = 6.8 Hz, 1H), 2.16 (s, 6H), 1.27 (heptet, J = 6.8 Hz, 3H), 1.15−1.11 (m, 24H). ^{13}C NMR (100 MHz, $CDCl_3$) δ 191.09, 155.65, 154.22, 142.80, 138.03, 137.13, 132.24, 129.42, 128.76, 125.96, 119.68, 101.74, 57.76, 33.77, 26.18, 23.49, 20.37, 18.00, 12.54. HRMS (CI) calculated for $[C_{30}H_{46}O_4Si + H]^+$ 499.3244, found 499.3209.

(4-(3-ethynyl-5-isopropyl-4-(methoxymethoxy)benzyl)-3,5-dimethylphenoxy)triisopropylsilane (3). To a solution of diisopropylamine (0.46 g, 4.5 mmol) in anhydrous THF (10 mL) at −78 °C was added 1.8 mL 2.0 M solution of *n*-BuLi in anhydrous hexane (3.6 mmol). The solution was allowed to warm up to 0 °C and stirred for 30 min before it was cooled to −78 °C. Then 1.8 mL 2.0 M solution of TMS−diazomethane in anhydrous hexane was added dropwise to the solution at −78 °C and the solution was stirred for 30 min. To the reaction solution at −78 °C, **2** (1.5 g, 3.0 mmol) in 10 mL anhydrous THF was added dropwise and the solution was stirred at −78 °C for 1 h. Then the solution was allowed to reflux for 2.5 h, cooled to room temperature, and poured over ice−water. The mixture was extracted with ethyl acetate (2 × 50 mL), and organic extracts were washed with water (20 mL) and brine solution (20 mL), dried over $MgSO_4$, and evaporated under reduced pressure. The resulting residue was purified by flash column chromatography on silica gel (1:10 ethyl acetate/hexane) to give **3** (0.9 g, 1.8 mmol, 60%). ^{1}H NMR (400 MHz, $CDCl_3$) δ 6.90 (d, J = 2 Hz, 1H), 6.86 (d, J = 2 Hz, 1H), 6.60 (s, 2H), 5.17 (s, 2H), 3.88 (s, 2H), 3.60 (s, 3H), 3.36 (heptet, J = 6.8 Hz, 1H), 3.17 (s, 1H), 2.15 (s, 6H), 1.25 (heptet, J = 6.8 Hz, 3H), 1.23−1.10 (m, 24H). ^{13}C NMR (100 MHz, $CDCl_3$) δ 154.50, 154.07, 141.95, 138.13, 136.06, 130.52, 128.99, 127.04, 119.55, 115.39, 99.89, 81.21, 80.55, 57.55, 33.65, 26.34, 23.34, 20.36, 18.00, 12.71. HRMS (CI) calculated for $[C_{31}H_{46}O_4Si + H]^+$ 495.3294, found 495.3275.

Methyl 6-(4-((5-(2,6-dimethyl-4-(triisopropylsilyloxy)benzyl)-3-isopropyl-2-(methoxymethoxy)phenyl)ethynyl)phenyl)hexanoate (5). Compound **4** was prepared as previously described. CuI (17 mg, 0.086 mmol) and bis(triphenylphosphine)palladium(II) chloride (61 mg, 0.086 mmol) were added into a Schlenk flask, and the flask was vacuumed then backfilled with N_2 atmosphere 3 times. Compound **3** (850 mg, 1.72 mmol) and compound **4** (630 mg, 1.89 mmol) were dissolved in 20 mL distilled piperidine and the solution was added to the Schlenk flask. The reaction mixture was stirred overnight at 40 °C. The reaction mixture was poured over 100 mL cold 0.1 N HCl solution and extracted ethyl acetate (2 × 50 mL). The organic extracts were washed with water (30 mL) and brine solution (30 mL), dried over $MgSO_4$, and evaporated under reduced pressure. The resulting crude product was purified by flash column chromatography on silica gel (1:10 ethyl acetate/hexane) to give **5** (950 mg, 79%). ^{1}H NMR (400 MHz, $CDCl_3$) δ 7.39 (d, J = 8 Hz, 2H), 7.12 (d, J = 8 Hz, 2H), 6.89 (d, J = 0.8 Hz, 2H), 6.63 (s, 2H), 5.26 (s, 2H), 3.91 (s, 2H), 3.64 (s, 3H), 3.60 (s, 3H), 3.39 (heptet, J = 6.8 Hz, 1H), 2.60 (t, J = 7.6 Hz, 2H), 2.29 (t, J = 7.6 Hz, 2H), 2.17 (s, 6H), 1.64 (m, 4H), 1.34−1.23 (m, 5H), 1.16 (d, J = 7.2 Hz, 6H), 1.11 (d, J = 7.2 Hz, 18H). ^{13}C NMR (100 MHz, $CDCl_3$) δ 174.12, 154.07, 153.81, 142.93, 141.84, 138.18, 135.99, 131.38, 129.81, 129.20, 128.48, 126.40, 120.73, 119.59, 116.61, 99.78, 92.94, 86.39, 57.55, 51.47, 35.66, 33.97, 33.75, 30.87, 28.70, 26.43, 24.79, 23.40, 20.42, 18.04, 12.74. HRMS (ESI) calculated for $[C_{44}H_{62}O_5Si + Na]^+$ 721.4264, found 721.4231.

Methyl 6-(4-((5-(4-Hydroxy-2,6-dimethylbenzyl)-3-isopropyl-2-(methoxymethoxy) phenyl)ethynyl)phenyl)hexanoate (6). To a solution of compound **5** (140 mg, 0.2 mmol) in 2 mL THF was added 0.4 mL 1 M solution of Bu_4NF in THF (0.4 mmol). The solution was stirred for 30 min and poured over 0.1 N HCl (30 mL). The mixture was extracted with ethyl acetate (2 × 30 mL). The organic portions were combined, washed with water (15 mL) and brine solution (15 mL), dried over $MgSO_4$, and evaporated under reduced pressure. The resulting crude product was purified by flash column chromatography on silica gel (1:4 ethyl acetate/hexane) to yield **6** (96 mg, 88%). ^{1}H NMR (400 MHz, $CDCl_3$) δ 7.40 (d, J = 8.4 Hz, 2H), 7.12 (d, J = 8.4 Hz, 2H), 6.96 (d, J = 2 Hz, 1H), 6.86 (d, J = 2 Hz, 1H), 6.56 (s, 2H), 5.26 (s, 2H), 5.21 (s, 1H), 3.89 (s, 2H), 3.67 (s, 3H), 3.61 (s, 3H), 3.41 (heptet, J = 6.8 Hz, 1H), 2.60 (t, J = 8 Hz, 2H), 2.31 (t, J = 8 Hz, 2H), 2.17 (s, 6H), 1.64 (m, 4H), 1.35 (m, 2H), 1.17 (d, J = 6.8 Hz, 6H). ^{13}C NMR (100 MHz, $CDCl_3$) δ 174.49, 153.78 (*2*), 142.97, 141.87, 138.67, 136.01, 131.38, 129.54, 128.70, 128.47, 126.64, 120.61, 116.66, 114.90, 99.76, 93.03, 86.30, 57.60, 51.62, 35.63, 34.02, 33.76, 30.83, 28.68, 26.46, 24.77, 23.43, 20.40. HRMS (ESI) calculated for $[C_{35}H_{42}O_5 + Na]^+$ 565.2930, found 565.2946.

Methyl 6-(4-((5-(4-(2-*Tert*-butoxy-2-oxoethoxy)-2,6-dimethylbenzyl)-3-isopropyl-2-(methoxymethoxy)phenyl)ethynyl)phenyl)hexanoate (7). To the solution of **6** (49 mg, 0.09 mmol) and cesium carbonate (117 mg, 0.36 mmol) in 4 mL 1:1 (v/v) mixture of anhydrous THF and DMF was added *tert*-butylbromoacetate (0.029 mL, 0.18 mmol). The reaction mixture was allowed to stir for 6 h at room temperature, then poured over 15 mL of cold 0.1 N HCl and extracted with ethyl acetate (3 × 15 mL). The combined organic extracts were washed with water (10 mL) and brine solution (10 mL) and concentrated under reduced pressure to afford crude product, which was purified by flash column chromatography on silica gel (1:4 ethyl acetate/hexane) to yield **7** (54.1 mg, 92%). ^{1}H NMR (400 MHz, $CDCl_3$) δ 7.39 (d, J = 8 Hz, 2H), 7.12 (d, J = 8 Hz, 2H), 6.94 (d, J = 2 Hz, 1H), 6.85 (d, J = 2.4 Hz, 1H), 6.63 (s, 2H), 5.25 (s, 2H), 4.52 (s, 2H), 3.91 (s, 2H), 3.67 (s, 3H), 3.61 (s, 3H), 3.41 (heptet, J = 6.8 Hz, 1H), 2.61 (t, J = 7.6 Hz, 2H), 2.31 (t, J = 7.6 Hz, 2H), 2.21 (s, 6H), 1.68−1.61 (m, 4H), 1.49 (s, 9H), 1.35 (m, 2H), 1.17 (d, J = 7.2 Hz, 6H). ^{13}C NMR (100 MHz, $CDCl_3$) δ 174.19, 168.35, 156.03, 153.85, 142.95, 141.88, 138.48, 135.76, 131.37, 129.69, 129.56, 128.44, 126.57, 120.63, 116.64, 114.22, 99.76, 92.97, 86.27, 82.18, 65.74, 57.58, 51.51, 35.64, 33.98, 33.83, 30.04, 28.68, 28.06, 26.44, 24.76, 23.40, 20.59. HRMS (ESI) calculated for $[C_{41}H_{52}O_7 + Na]^+$ 679.3611, found 679.3644.

6-(4-((5-(4-(2-*Tert*-butoxy-2-oxoethoxy)-2,6-dimethylbenzyl)-3-isopropyl-2-(methoxymethoxy)phenyl)ethynyl)phenyl)hexanoic acid (8). To the solution of **7** (40 mg, 0.06 mmol) in 0.3 mL of THF was added 0.66 mL of 0.1 N LiOH solution over 2 h. The reaction mixture was stirred for 24 h, poured over 5 mL of cold 0.1 N HCl, and extracted with ethyl acetate (2 × 15 mL). The organic extracts were washed with water (2 × 10 mL) and brine solution (10 mL), dried over $MgSO_4$, and evaporated under reduced pressure. The resulting crude was purified by flash column chromatography on silica gel (1:2 ethyl acetate/hexane) to yield **8** (22.4 mg, 58%). ^{1}H NMR (400 MHz, $CDCl_3$) δ 7.39(d, J = 8.4 Hz, 2H), 7.12 (d, J = 8.4 Hz, 2H), 6.94 (d, J = 2 Hz, 1H), 6.85 (d, J = 2 Hz, 1H), 6.63 (s, 2H), 5.25 (s, 2H), 4.51 (s, 2H), 3.91 (s, 2H), 3.60 (s, 3H), 3.41 (heptet, J = 6.8 Hz, 1H), 2.61 (t, J = 7.6 Hz, 2H), 2.35 (t, J = 7.6 Hz, 2H), 2.21 (s, 6H), 1.69−1.61 (m, 4H), 1.49 (s, 9H), 1.39−1.37 (m, 2H), 1.80 (d, J = 6.8 Hz, 6H). ^{13}C NMR (100 MHz, $CDCl_3$) δ 179.53, 168.40, 156.03, 153.85, 142.90, 141.88, 138.48, 135.77, 131.39, 129.69, 129.58, 128.31, 126.58, 120.66, 116.65, 114.23, 99.76, 92.98, 86.29, 82.21, 65.75, 57.58, 35.63, 33.88, 33.84, 30.85, 28.62, 28.06, 26.44, 24.49, 23.41, 20.60. HRMS (ESI) calculated for $[C_{40}H_{50}O_7$+Na$]^+$ 665.3454, found 665.3436.

Perfluorophenyl 6-(4-((5-(4-(2-*Tert*-butoxy-2-oxoethoxy)-2,6-dimethylbenzyl)-3-isopropyl-2-(methoxymethoxy)phenyl)ethynyl)phenyl)hexanoate (9). To **8** (18 mg, 0.029 mmol) in anhydrous THF was added triethyl amine (0.0045 mL, 0.032 mmol) and then pentafluorophenyl trifluoroacetate (0.006 mL, 0.035 mmol). The solution was stirred for 30 min and diluted with 3 mL of ethyl acetate before pouring over cold 0.1 N HCl. The mixture was extracted with ethyl acetate (2 × 10 mL), washed with water (2 × 5 mL) and brine solution (5 mL), dried over $MgSO_4$, and concentrated under reduced pressure to yield **9** (22 mg, 94%) without further purification. ^{1}H NMR (400 MHz, $CDCl_3$) δ 7.41 (d, J = 8 Hz, 2H), 7.13 (d, J = 8.4 Hz, 2H), 6.94 (d, J = 2.4 Hz, 1H), 6.85 (d, J = 2.0 Hz, 1H), 6.63 (s, 2H), 5.25 (s, 2H), 4.51 (s, 2H), 3.91 (s, 2H), 3.61 (s, 3H), 3.41 (heptet, J = 6.8 Hz, 1H), 2.66 (m, 4H), 2.21 (s, 6H), 1.83−1.63 (m, 4H), 1.49−1.40 (m, 11H), 1.83 (d, J = 6.8 Hz, 6H). ^{13}C NMR (100 MHz, $CDCl_3$) δ 169.48, 168.43, 156.02, 153.85, 142.86, 141.89, 138.48, 135.78, 131.42, 131.34, 129.70, 129.57, 128.43, 126.61, 120.75, 116.62, 114.22, 99.76, 92.92, 86.33, 82.24, 65.73, 57. 58, 35.58, 33.83, 33.23, 30.71, 28.38, 28.05, 26.44, 24.60, 23.39, 20.58. HRMS (ESI) calculated for $[C_{46}H_{49}F_5O_7 + Na]^+$ 831.3296, found 831.3322.

***N*-Fluoresceinylmethyl 6-(4-((5-(4-(2-*Tert*-butoxy-2-oxoethoxy)-2,6-dimethylbenzyl)-3-isopropyl-2-(methoxymethoxy)-phenyl)ethynyl)phenyl)hexanamide (10).** To the solution of **9** (18.5 mg, 0.023 mmol) and 10 mg 5-(aminomethyl)fluorescein, hydrochloride (Invitrogen, catalog number A1353) in 1 mL of 1:1 (v/v) mixture of anhydrous THF and DMF was added TEA (6.8 μL, 0.048 mmol) and the solution was allowed to stir at room temperature for 2 h. The reaction mixture was pour over cold water (5 mL), extracted with ethyl acetate (2 × 10 mL), washed with brine solution (2 × 5 mL), dried over $MgSO_4$, and evaporated under reduced pressure. The resulting crude product was purified by column chromatography on silica gel (1:9 MeOH/CH_2Cl_2) to yield **10** (7.7 mg, 34%) and recovered 9.0 mg of **9** (49%). ^{1}H NMR (400 MHz, $CDCl_3$) δ 7.81 (s, 1H), 7.57 (d, J = 8 Hz, 1H), 7.26 (d, J = 8 Hz, 2H), 7.08−7.03 (m, 3H), 6.89 (d, J = 1.6 Hz, 1H), 6.72 (d, J = 2 Hz, 1H), 6.57−6.54 (m, 4H), 6.48−6.42 (m, 4H), 5.10 (s, 2H), 4.45 (s, 2H), 4.42 (s, 2H), 3.86 (s, 2H), 3.46 (s, 3H), 3.32 (heptet, J = 6.8 Hz, 1H), 2.53 (t, J = 6.4 Hz, 2H), 2.19 (t, J = 6.8 Hz, 2H), 2.10 (s, 6H), 1.62−1.54 (m, 4H), 1.37 (s, 9H), 1.37−1.30 (m, 2H), 1.07 (d, J = 6.8 Hz, 6H). HRMS (ESI) calculated for $[C_{73}H_{53}NO_6 + Na]^+$ 702.3771, found 702.3759.

***N*-Fluoresceinylmethyl 6-(4-((5-(4-(Carboxymethoxy)-2,6-dimethylbenzyl)-2-hydroxy-3-isopropylphenyl)ethynyl)phenyl)hexanamide (JZ01).** To the solution of **10** (3.8 mg, 0.0039 mmol) in 0.5 mL of THF was added 1 mL of 6 N HCl (aq). The reaction mixture was allowed to stir at 40 °C for 3 h and then extracted with ethyl acetate (3 × 5 mL). The organic extracts were washed with H_2O (2 mL) and brine solution (2 mL), dried over $MgSO_4$, and concentrated under reduced pressure. The resulting residue was purified by reverse-phase HPLC (Higgins, C8, 5 μm, 40−60% acetonitrile/water) to yield JZ01 (0.73 mg, 21%). Purity was assessed by HPLC (UV, 254 nm) to be >98%. ^{1}H NMR (400 MHz, $CDCl_3$) δ 7.85 (s, 1H), 7.51 (d, J = 7.6 Hz, 1H), 7.31 (d, J = 8 Hz, 2H), 7.12−7.03 (m, 3H), 6.83 (s, 1H), 7.73−7.20 (m, 2H), 7.57−7.55 (m, 5H), 6.45 (d, J = 8.8 Hz, 2H), 4.42 (s, 2H), 4.26 (s, 2H), 3.79 (s, 2H), 3.54 (s, 2H), 3.38 (heptet, J = 6.8 Hz, 1H), 2.54 (t, J = 7.6 Hz, 2H), 2.19 (t, J = 7.6 Hz, 2H), 2.10 (s, 6H), 1.63−1.52 (m, 4H), 1.31−1.25 (m, 2H), 1.02 (d, J = 6.4 Hz, 6H), HRMS (ESI) calculated for $[C_{55}H_{51}NO_{10} + H]^+$ 886.3591, found 886.3608.

(*Tert*-butyl-2-(4-(3-isopropyl-4-(methoxymethoxy)-5-((4-(6-oxo-6-(prop-2-ynylamino)hexyl)phenyl)ethynyl)benzyl)-3,5-dimethylphenoxy)acetate) (11). To a solution of 39.0 mg of **9** (0.048 mmol) and 26 mg of propargyl amine (0.48 mmol) in 0.9 mL of anhydrous THF was added a solution of 6 mg of TEA in 0.1 mL of anhydrous THF. After 30 min at ambient temperature, the solution was diluted with 15 mL of ethyl acetate and washed with 2 × 5 mL of 0.1 N HCl (aq) and 2 × 5 mL of brine, dried over Mg_2SO_4, and evaporated under reduced pressure. The residue was purified by flash column chromatography on silica gel (1:1 ethyl acetate/hexane) to yield 29.2 mg of **11** (89%). ^{1}H NMR (400 MHz, $CDCl_3$) δ 7.40 (d, J = 8.0 Hz, 2H), 7.11 (d, J = 8.0 Hz, 2H), 6.94 (d, J = 2.4 Hz, 1H), 6.85 (d, J = 2.0 Hz, 1H), 6.63 (s, 2H), 5.74 (s, 2H), 4.51 (s, 2H), 4.04−4.02 (m, 2H), 3.91 (s, 2H), 3.41 (heptet, J = 6.8 Hz, 1H), 2.60 (t, J = 7.6 Hz, 2H), 2.22−2.15 (m, 9H), 1.70−1.59 (m, 4H), 1.49 (s, 9H), 1.35−1.20 (m, 2H), 1.18 (d, J = 6.8 Hz, 6H). ^{13}C NMR (100 MHz, $CDCl_3$) δ 172.57, 168.37, 156.04, 153.84, 142.95, 141.89, 138.47, 135.77, 131.37, 129.70, 129.56, 128.45, 126.59, 120.63, 116.64, 114.24, 99.75, 92.98, 86.31, 82.19, 79.67, 71.53, 65.75, 57.57, 36.27, 35.63, 33.83, 30.87, 29.13, 28.74, 28.06, 26.44, 25.31, 23.40, 20.58. HRMS (ESI) calculated for $[C_{37}H_{41}NO_5+Na]^+$ 602.2882, found 602.2875.

(2-(4-(4-Hydroxy-3-isopropyl-5-((4-(6-oxo-6-(prop-2-ynylamino)hexyl)phenyl)ethynyl)benzyl)-3,5-dimethylphenoxy)-acetic acid) (JZ07). To a solution of 14.6 mg of **11** in 1 mL of THF was added 1 mL of 6 N HCl (aq) . The reaction mixture was stirred at 40 °C for 8 h. The reaction mixture was cooled, diluted with 15 mL ethyl acetate, washed with 3 × 5 mL H_2O (×3) and 5 mL of brine (×2), dried over Mg_2SO_4, and evaporated under reduced pressure. The resulting residue was purified by flash column chromatography on silica gel (1:15 MeOH/DCM) to yield 11.6 mg of JZ07 (95%). ^{1}H NMR (400 MHz, $CDCl_3$) δ 7.40 (dd, J = 7.6 Hz, 1.6 Hz, 2H), 7.12 (d, J = 8.4 Hz, 2H), 6.94 (d, J = 1.6 Hz, 1H), 6.69 (d, J = 1.6 Hz, 1H), 6.65 (s, 2H), 5.68 (bs, 1H), 4.66 (s, 2H), 4.05−4.03 (m, 2H), 3.88 (s, 2H), 3.26 (heptet, d, J = 6.8 Hz, 1H), 2.60 (t, d, J = 7.6 Hz, 2H), 2.23−2.14 (m, 9H), 1.69−1.61 (m, 4H), 1.36−1.30 (m, 2H), 1.22 (d, d, J = 7.2 Hz, 6H). ^{13}C NMR (100 MHz, $CDCl_3$) δ 172.95, 172.44, 155.51, 152.05, 143.43, 138.75, 134.12, 131.54, 131.36, 130.62, 128.57, 127.31, 127.01, 119.75, 114.18, 109.09, 96.05, 83.32, 79.44, 71.72, 64.91, 36.25, 35.60, 33.64, 30.77, 29.27, 28.64, 27.55, 25.30, 22.34, 20.55. HRMS (ESI) calculated for $[C_{37}H_{41}NO_5+Na]^+$ 602.2882, found 602.2875.

Plasmid Construction. Expression vectors pET15b-TRβ wild-type, F451Δ and C446Δ mutant was constructed by subcloning the wild-type and mutant sequences for thyroid hormone receptor into the BamH I and Nde I sites of pET15b (Novagen), using the cloning primers 5′-GGAAAATTCCATATGACCCCCAACAGTATGACAGAAAATGGC-3′ and 5′-CGCGGATCCCTAATCCTCGAACACTTCCAGGAACAAAGG-3′ (w.t.).

Protein Expression and Purification. Full-length histidine-tagged recombinant thyroid receptor protein was expressed in *E. coli* and purified by Ni-NTA affinity chromatography. Rosetta (DE3)pLysS cells (Novagen) were transformed with pET15b-TRβ (wt or mutant). The cells were grown at 18 °C in 500 mL Luria Broth containing 100 μg/mL ampicillin and 34 μg/mL chloramphenicol to an OD of 0.3, at which point protein expression was induced with 1 mM IPTG and continued for 20 h at 18 °C. The cells were harvested by centrifugation at 4000 *g* for 30 min at 4 °C and the cell pellet was immediately frozen at −80 °C. Cells were resuspended with 5 mL lysis buffer (50 mM Tris, pH 8.0, 300 mM NaCl, 12 mM 2-mercaptoethanol, 10% glycerol, and Roche complete EDTA free protease inhibitors) and sonicated on ice (15 s bursts, 4 times). The lysate was centrifuged for 10 min at 14 000 *g* (4 °C) and the soluble supernatant was loaded onto Ni-NTA resin (Qiagen) from which thyroid receptor was eluted with 250 mM imidazole. Protein concentration was determined by Bradford assay (BioRad) and purity was assessed by SDS-PAGE and Western blot with thyroid hormone receptor monoclonal antibody C3 (Covance). Yield was approximately 1 mg purified protein per liter of culture.

Binding Assay and Competition Assay. A 0.7 mM stock solution of JZ01 in DMSO was prepared, which was diluted with binding buffer containing 50 mM sodium phosphate, 150 mM NaCl, 1 mM DTT, 1 mM EDTA, 0.01% Nonidet P-40, and 10% glycerol (pH = 7.2) to obtain a 5.0 nM solution. Solutions of TRβ with different concentrations ranging from 1 μM to 0.3 nM were prepared with the same buffer. 90 μL aliquots of the TRβ solutions were mixed with 10 μL of 5.0 nM JZ01 solution in individual triplicate wells of a 96-well plate and incubated at room temperature for 1 h. Fluorescence polarization value (mP) was measured on Fusion plate reader (Perkin-Elmer, excitation = 485 nM, emission = 535 nM). As a control, solutions of ovalbumin with concentrations ranging from 1 μM to 1 nM were prepared, then mixed with the solution of JZ01 and measured with fluorescence polarization value similarly to TRβ. The probe JZ01 bound to TRβ with an apparent EC_{50} = 21.4 ± 5.6 nM and the dynamic range about 250 mP. Ovalbumin showed only a very small change of fluorescence polarization even at a high concentration of 1 μM. (Note: BSA should not be used as a control as it has known thyronine binding capacity).

The ligands T3 and GC-1 were evaluated for their ability to competitively displace the probe JZ01 from TRβ. A solution of TRβ (43 μL, 2.8 μM) was added to 6 mL of 0.1 nM probe JZ01 in the binding buffer containing 50 mM sodium phosphate, 150 mM NaCl, 1 mM DTT, 1 mM EDTA, 0.01% Nonidet P-40, and 10% glycerol (pH = 7.2) and aliquoted into individual wells of a 96-well plate (90 μL/well). The solutions were incubated at room temperature for 30 min before adding the solutions of ligands. The stock solutions of the ligands were diluted with the same buffer to achieve different concentrations ranging from 100 μM to 1 nM. Then 10 μL of the solutions of ligands were added to the wells containing 90 μL of solution of JZ01 and TRβ and incubated at room temperature for 1 h before taking the FP value. The assay was conducted in triplicate. The measured FP value (mP) was plotted against the concentration of the ligands. The IC_{50} values for T3 and GC-1 were determined to be 429.3 ± 249.2 nM and 214.23 ± 134.7 nM, respectively.

Cellular Reporter Gene Assays. Cellular reporter gene assays were performed as described previously (*22*). Briefly, HEK293 cells were transiently transfected (Calcium phosphate method) with pSG5-TRβ (or pSG5-TRα), DR4-tk-Luc (reporter), and pRL-CMV (control). Ligand-dependent transcription response was measured by dual-luciferase assay (Promega) following manufacturer's protocol. Under these assay conditions, T3 is slightly more potent in TRα (EC_{50} = 0.61 nM) than in TRβ (EC_{50} = 1.4 nM).

Cellular Localization Studies. Cellular localization studies were performed with NIH3T3 cells seeded at 45 000 cells per well in 24-well plates. Cells were transfected with pSG5-TRβ using Lipofectamine 2000 (Invitrogen) following the manufacturer's protocol. After 24 h, the cells were washed and treated with 50 nM of JZ01 in PBS buffer at 37 °C for 1 h. Direct DAPI treatment without fixation/permeabilization was achieved by treatment with 600 nM of DAPI (Invitrogen) at room temperature for 2 min followed by PBS wash (500 μL × 2). Fixation/permeabilization was performed by treatment with 4% formaldehyde in PBS at 37 °C for 15 min, washed 2× in PBS,

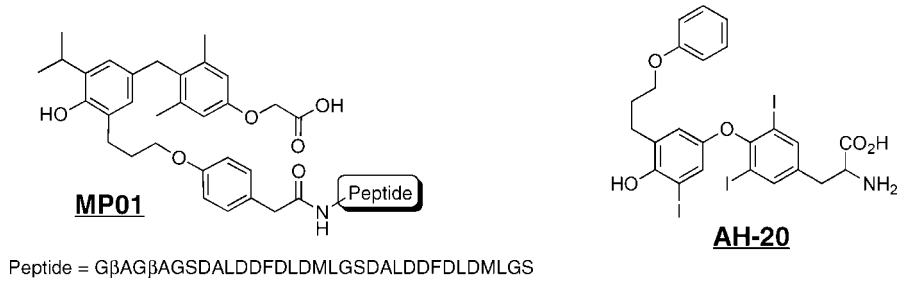

Figure 2. Structures of hormone conjugates MP01 and AH-20.

Scheme 1. Synthesis of Scaffold I Based Fluorescent Probe JZ01[a]

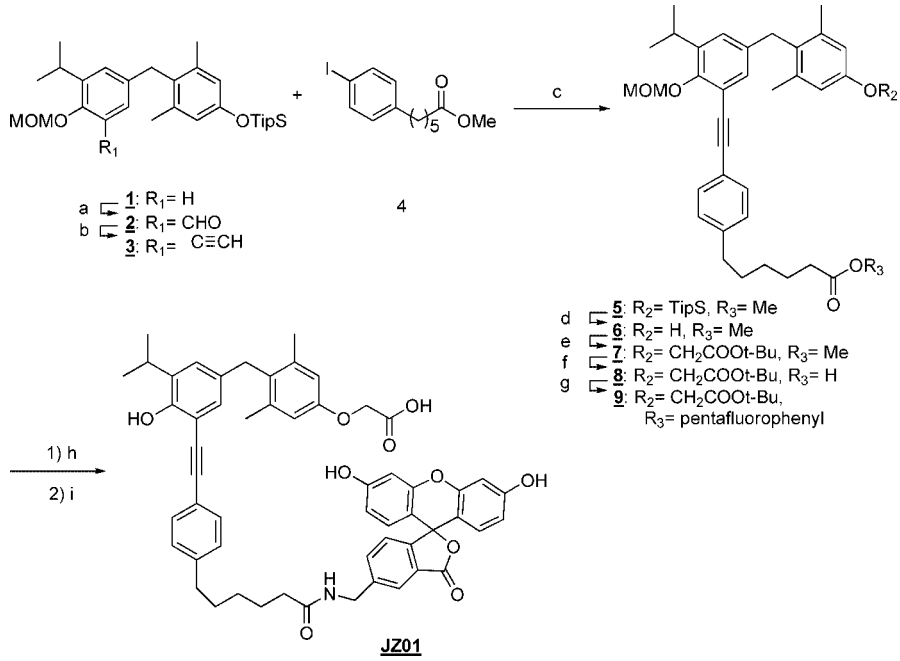

[a] (a) (1) n-BuLi,THF/Hexane, (2) DMF; (b) $TMSCLiN_2$, THF; (c) $(PPh_3)_2PdCl_2$, CuI, Piperidine; (d) TBAF,THF; (e) Cs_2CO_3, *tert*-butyl bromoacetate, DMF/THF; (f) LiOH, H_2O/THF; (g) pentafluorophenyl trifluoroacetate, TEA, THF, 0 °C−RT; (h) 5-(aminomethyl)fluorescein hydrochloride, TEA, THF/DMF; (i) 6 N HCl(aq)/THF, 40°C.

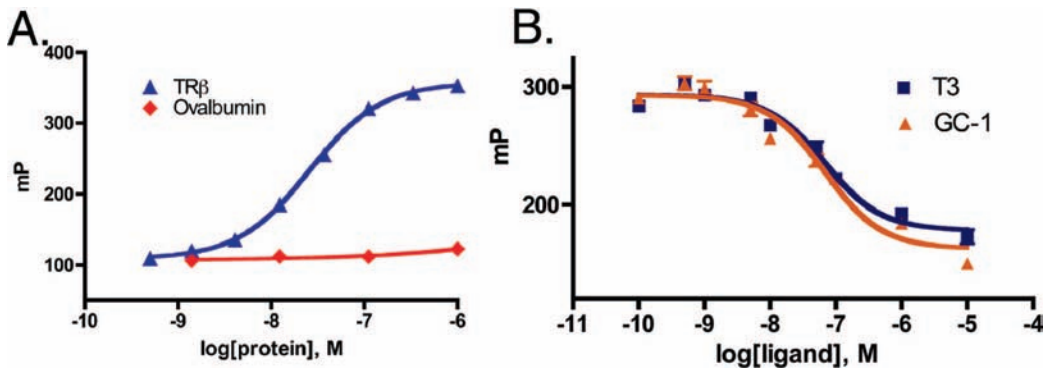

Figure 3. (A) Fluorescence polarization titration of JZ01 (0.5 nM) with TRβ (σ) and ovalbumin control (ϑ). (B) Competitive titration of JZ01 (0.1 nM) and TRβ (20 nM) with T3 (ν) and GC-1 (σ).

followed by treatment with 0.2% Triton X-100 in PBS for 10 min and 2× rinse with PBS. DAPI solution (600 nM in PBS) was then applied to the fixed/permeabilized cells, incubated for 2 min, and washed 2× in PBS according to the Invitrogen protocol.

RESULTS

In the course of developing JZ01, we developed two additional scaffolds having flexible tethers attached via the 5′-position of T3 and the halogen-free thyromimetic GC-1 (Figure 1, scaffolds II and III) (*21*). Model conjugate AH-20 based on the structure of T3 and the peptide conjugate MP01 based on GC-1 were also conjugated via the 5′-position but showed poor affinity by radioligand displacement assays (Figure 2; see Supporting Information). AH-20 showed no appreciable binding to TRβ wild-type below 1 μM, suggesting that the T3 core itself is not sufficient to provide high-affinity binding to TRβ when it has a flexible alkyl tether at the 5′-position. The GC-1 based

peptide conjugate, MP01, shows submicromolar binding to TRβ wild-type (K_i = 580 nM) but is over 2500× less potent than T3 or GC-1.

To further explore the properties of MP01, we evaluated its binding to truncated forms of the receptor TRβC446Δ and TRβF451Δ in radioligand displacement assays. These nonsense mutants completely lack the c-terminal helix-12 but have previously been shown to retain low nanomolar binding affinity for T3 (*23*, *24*). MP01 had modest but improved binding to the nonsense mutants TRβC446Δ, K_i = 73.8 nM (log K_i = 1.86 ± 2.37), and TRβF451Δ, K_i = 237 (log K_i = 2.37 ± 1.27 nM) (*25*). The improved affinities of MP01 for the these receptors lacking helix-12 imply that this scaffold forms unfavorable interactions with helix-12 in its bound conformation. Together, these examples further illustrate that the development of high-affinity scaffolds for TR targeting conjugates is nontrivial and often depends on subtle aspects of the ligand structure.

Synthesis of JZ01, a Fluorescent Conjugate Based on NH-2. The fluorescent probe, JZ01, was synthesized from the differentially protected bisphenol **1** by formylation of the methoxymethyl (MOM) protected phenol followed by Corey-Fuchs alkynylation. Sonogoshira coupling afforded the diarylalkyne **5** in good yield. Desilylation and alkylation of the triisopropyl silyl (TiPS) protected phenol followed by selective hydrolysis of the methyl ester afforded compound **8**, which served as the protected form of our scaffold. The scaffold **8** can be coupled to amine probes such as 5-(aminomethyl)fluorescein via the pentafluorophenyl ester. Deprotection with 6 N aqueous HCl in THF afforded the target fluorescent probe compound JZ01 (Scheme 1).

Fluorescence Polarization Assays with JZ01. The affinity of JZ01 for TRβ can be measured directly by fluoresence polarization (FP) assay (Figure 3A). The polarization of the fluorescent probe JZ01 (0.5 nM) was measured as a function of increasing concentration of full-length TRβ. A sigmoidal dose−response of the FP value (mP) was observed with TRβ but not with ovalbumin control. The titration curve showed that the probe JZ01 bound to TRβ with K_d = 21.4 ± 5.6 nM. These results suggest that the NH-2-inspired conjugate scaffold was a high-affinity probe for TRβ, that could accommodate even relatively bulky substitutions such as fluorescein. As a probe for binding the conjugate, JZ01 provided a relatively large dynamic range even at probe concentrations below 1 nM.

To further explore the utility of JZ01, we evaluated its ability to serve as a nonradiometric probe for TR binding of ligands through competition. Competition assays were conducted with the native TR ligand, T3, and GC-1 as the competing ligands. The measured FP value (mP) was plotted against the concentration of the competing ligands (Figure 3B). T3 and GC-1 have been reported to have similar potencies toward TRβ and were determined to have IC_{50} values of 152.9 ± 87 nM and 93.5 ± 26 nM (average of two determinations ± min/max), respectively, using fluorescence polarization. JZ01 provides a facile nonradiometric means to compare the potency of TRβ ligands by competition.

Subtype Selective Antagonist. The agonist and antagonist activities of JZ01 for TRα and TRβ were further determined by cellular reporter gene assays in HEK293 cells transiently transfected with pSG5TRα or pSG5TRβ and a DR4-luc reporter. JZ01 showed no detectable agonist activity at or below 250 nM (data not shown). JZ01 does have significant antagonist activity at 250 nM (38% reduction in activity) against 1 nM T3 in cells expressing TRβ but only slight antagonist activity (15% reduction) with 1 nM T3 in cells expressing TRα (Figure 4A). Concerns about potential fluorescein aggregation of JZ01 at high concentrations precluded us from establishing an accurate measure of its potency (IC_{50}).

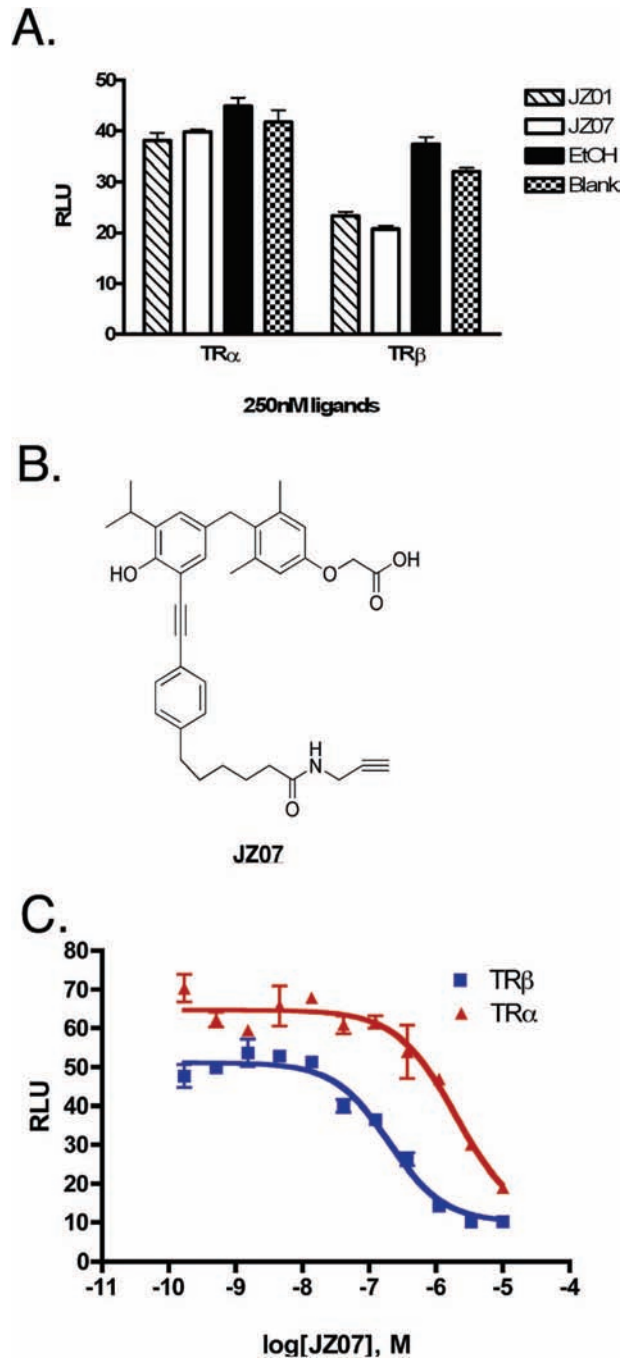

Figure 4. Antagonist activities of ligands in cellular luciferase reporter gene assays. (A) 250 nM ligands with 1 nM T3 andTRα or TRβ. (B) Structure of JZ07. (C) Cellular dose−response behavior of JZ07 vs 1 nM T3 and TRα (σ) or TRβ (ν).

To assess the generic subtype selectivity of Scaffold I, the analogue JZ07, having a propargyl group in place of the fluorescein of JZ01, was prepared by coupling propargyl amine to intermediate **9** (**11**, R_3═$NHCH_2CCH$) followed by deprotection (Figure 4B). The smaller propargyl amide can be used to assess the intrinsic selectivity of the scaffold in the absence of potential influence of the much larger fluorescein group of JZ01. JZ07 had nearly identical activity to JZ01 at 250 nM in antagonist assays with TRβ wt and T3 (Figure 4A). The analogue JZ07 showed no signs of cellular toxicity at concentrations up to 10 μM and is a full antagonist of TRα (IC_{50} = 2.83 ± 0.3 μM) and TRβ (IC_{50} = 221 ± 76 nM) (Figure 4C). This is in contrast to the parent compound NH-2 that was reported as a weak TRβ agonist (*26*). In addition to being more potent

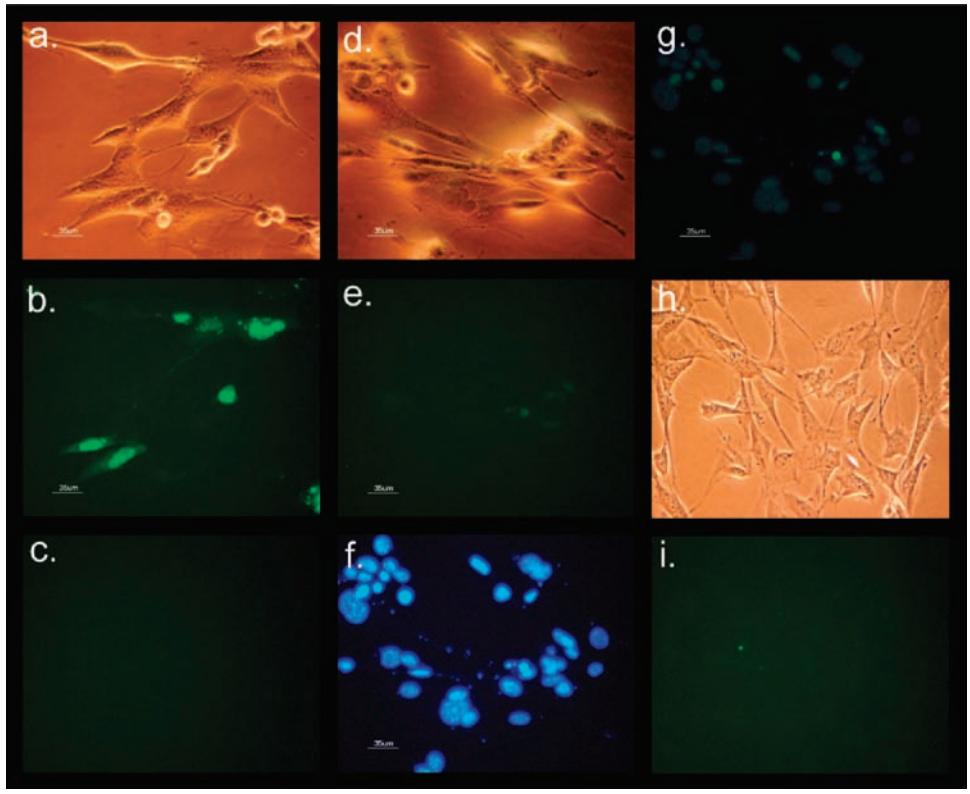

Figure 5. (a) 3T3 cells transfected with pSG5-TRβ with 50 nM of JZ01 and stained with DAPI; (b) cells from panel viewed under fluorescein filter (Nikon B-2E/C); (c) DAPI-stained pSG5-TRB transfected 3T3 cells view under fluorescein filter; (d) pSG5-TRB transfected 3T3 cells with 50 nM, fixed and DAPI-stained; (e) cells from panel d viewed under fluorescein filter; (f) cells from panel d observed under DAPI-filter; (g) merge of panels e and f; (h) 3T3 cells (no TRβ) with JZ01; (i) same as panel h observed under fluorescein filter.

than the structurally related nitro-substituted antagonist NH-3, the compound JZ07 is as subtype selective as the most selective TR antagonist reported to date ($IC_{50}\alpha/IC_{50}\beta = 12.8$) (*27–30*).

Subcellular localization of JZ01 was further examined in NIH3T3 cells treated with 50 nM JZ01 and visualized by fluorescence microscopy (Figure 5). Strong intracellular JZ01 fluorescence was visible only in NIH3T3 cells transfected with pSG5TRβ (compare Figure 5b and f). This cellular fluorescence is almost completely blocked by the addition of 500 nM T3, further supporting that staining is TR-specific (see Supporting Information). JZ01's localization was further demonstrated to be nuclear and coincident with DAPI nuclear stain. Whereas efficient DAPI staining requires first fixing the cells, the fixation process caused significant loss of the intracellular but noncovalently bound JZ01 (compare Figure 5b to e). Nonetheless, although the JZ01 fluorescence is diminished JZ01 is clearly coincident with the DAPI nuclear stain (Figure 5g). In the absence of transfected TRβ, JZ01 is more diffuse and less intense, suggesting that JZ01 is indeed binding TRβ in cells (Figure 5i).

DISCUSSION

Studies with the fluorescent probe JZ01 and antagonist JZ07 demonstrate that Scaffold I represents, to our knowledge, the first thyroid hormone conjugate capable of high-affinity binding of the nuclear thyroid hormone receptor TRβ. Conceptually similar molecular scaffolds based on the natural hormone T3 or the halogen-free thyromimetic GC-1 were not found to be as effective. The compound JZ01 can serve as an efficient probe for direct visualization of TRβ expression in cells and as a nonradiometric probe for ligand binding in vitro. The analogue JZ07 is a potent and highly β-subtype-selective TR antagonist. These findings suggest that scaffold I may be employed as a general scaffold for making β-selective TR-targeting hormone conjugates for a variety of applications in chemical biology.

ACKNOWLEDGMENT

We thank the National Institutes of Health DK054257 for support of this work. A.H. was supported by Mitsubishi Pharma Corp.

Supporting Information Available: Complete synthetic details for the preparation ad characterization of of MP01 and AH-20 along with additional cellular imaging methods are available. This material is available free of charge via the Internet at http://pubs.acs.org.

LITERATURE CITED

(1) Schneekloth, J. S., Fonseca, F. N., Koldobskiy, M., Mandal, A., Deshaies, R., Sakamoto, K., and Crews, C. M. (2004) Chemical genetic control of protein levels: Selective in vivo targeted degradation. *J. Am. Chem. Soc. 126*, 3748–3754.

(2) Sakamoto, K. M., Kim, K. B., Verma, R., Ransick, A., Stein, B., Crews, C. M., and Deshaies, R. J. (2003) Development of protacs to target cancer-promoting proteins for ubiquitination and degradation. *Mol. Cell. Proteomics 2*, 1350–1358.

(3) Liu, B., Alluri, P. G., Yu, P., and Kodadek, T. (2005) A potent transactivation domain mimic with activity in living cells. *J. Am. Chem. Soc. 127*, 8254–8255.

(4) Ohno, K., Fukushima, T., Santa, T., Waizumi, N., Tokuyama, H., Maeda, M., and Imai, K. (2002) Estrogen receptor binding assay method for endocrine disruptors using fluorescence polarization. *Anal. Chem. 74*, 4391–4396.

(5) Chambliss, K. I., Kumar, P., Yuhanna, I. S., Katzenellenbogen, B. S., Katzenellenbogen, J. A., Chieko, M., and Shaul, P. W. (2006) Estrogen dendrimer conjugate reveals that estrogen-

induced endothelial cell migration and proliferation are mediated by non-nuclear estrogen receptors that interact directly with G alpha i. *Circulation 114*, 157–157.
(6) Brzozowski, A. M., Pike, A. C., Dauter, Z., Hubbard, R. E., Bonn, T., Engstrom, O., Ohman, L., Greene, G. L., Gustafsson, J. A., and Carlquist, M. (1997) Molecular basis of agonism and antagonism in the oestrogen receptor. *Nature 389*, 753–758.
(7) Pike, A. C., Brzozowski, A. M., Hubbard, R. E., Bonn, T., Thorsell, A. G., Engstrom, O., Ljunggren, J., Gustafsson, J. A., and Carlquist, M. (1999) Structure of the ligand-binding domain of oestrogen receptor beta in the presence of a partial agonist and a full antagonist. *EMBO J. 18*, 4608–4618.
(8) Shiau, A. K., Barstad, D., Loria, P. M., Cheng, L., Kushner, P. J., Agard, D. A., and Greene, G. L. (1998) The structural basis of estrogen receptor/coactivator recognition and the antagonism of this interaction by tamoxifen. *Cell 95*, 927–937.
(9) Xu, H. E., Stanley, T. B., Montana, V. G., Lambert, M. H., Shearer, B. G., Cobb, J. E., McKee, D. D., Galardi, C. M., Plunket, K. D., Nolte, R. T., Parks, D. J., Moore, J. T., Kliewer, S. A., Willson, T. M., and Stimmel, J. B. (2002) Structural basis for antagonist-mediated recruitment of nuclear co-repressors by PPAR alpha. *Nature 415*, 813–817.
(10) Weatherman, R. V., Fletterick, R. J., and Scanlan, T. S. (1999) Nuclear-receptor ligands and ligand-binding domains. *Annu. Rev. Biochem. 68*, 559–581.
(11) Nguyen, N. H., Apriletti, J. W., Lima, S. T. C., Webb, P., Baxter, J. D., and Scanlan, T. S. (2002) Rational design and synthesis of a novel thyroid hormone antagonist that blocks coactivator recruitment. *J. Med. Chem. 45*, 3310–3320.
(12) Baxter, J. D., Goede, P., Apriletti, J. W., West, B. L., Feng, W. J., Mellstrom, K., Fletterick, R. J., Wagner, R. L., Kushner, P. J., Ribeiro, R. C. J., Webb, P., Scanlan, T. S., and Nilsson, S. (2002) Structure-based design and synthesis of a thyroid hormone receptor (TR) antagonist. *Endocrinology 143*, 517–524.
(13) Yen, P. M. (2001) Physiological and molecular basis of thyroid hormone action. *Physiol. Rev. 81*, 1097–1142.
(14) Yen, P. M., and Cheng, S. Y. (2003) Germline and somatic thyroid hormone receptor mutations in man. *J. Endocrinol. Invest. 26*, 780–787.
(15) Cheng, S. Y. (2003) Thyroid hormone mutations in cancer. *Mol. Cell. Endocrinol. 213*, 23–30.
(16) Hulbert, A. J. (2000) Thyroid hormones and their effects: a new perspective. *Biol. Rev. 75*, 519–631.
(17) Kopp, P., Kitajima, K., and Jameson, J. L. (1996) Syndrome of resistance to thyroid hormone: insights into thyroid hormone action. *Proc. Soc. Exp. Biol. Med. 211*, 49–61.
(18) Leeson, P. D., Emmett, J. C., Shah, V. P., Showell, G. A., Novelli, R., Prain, H. D., Benson, M. G., Ellis, D., Pearce, N. J., and Underwood, A. H. (1989) Selective thyromimetics-cardiac-sparing thyroid-hormone analogs containing 3′-arylmethyl substituents. *J. Med. Chem. 32*, 320–336.
(19) Yokoyama, N., Walker, G. N., Main, A. J., Stanton, J. L., Morrissey, M. M., Boehm, C., Engle, A., Neubert, A. D., Wasvary, J. M., Stephan, Z. F., and Steele, R. E. (1995) Synthesis and structure-activity-relationships of oxamic acid and acetic-acid derivatives related to L-thyronine. *J. Med. Chem. 38*, 695–707.
(20) Borngraeber, S., Budny, M. J., Chiellini, G., Cunha-Lima, S. T., Togashi, M., Webb, P., Baxter, J. D., Scanlan, T. S., and Fletterick, R. J. (2003) Ligand selectivity by seeking hydrophobicity in thyroid hormone receptor. *Proc. Natl. Acad. Sci. U.S.A. 100*, 15358–15363.
(21) Chiellini, G., Nguyen, N. H., Yoshihara, H. A. I., and Scanlan, T. S. (2000) Improved synthesis of the iodine-free thyromimetic GC-1. *Bioorg. Med. Chem. Lett. 10*, 2607–2611.
(22) Shi, Y., Ye, H., Link, K. H., Putnam, M. C., Hubner, I., Dowdel, S., and Koh, J. T. (2005) Mutant-selective thyromimetics for the chemical rescue of thyroid hormone mutants associated with resistance to thyroid hormone (RTH). *Biochem. J. 44*, 4612–4626.
(23) Miyoshi, Y., Nakamura, H., Sasaki, S., Tagami, T., Misaki, T., Konishi, J., and Nakao, K. (1995) Two consecutive nucleotide substitutions resulting in the T3 receptor beta gene resulting in an 11-amino acid truncation in a patient with generalized resistance to thyroid hormone. *Mol. Cell. Endocrinol. 114*, 9–17.
(24) Taniyama, M., Kusano, S., Miyoshi, Y., Nakamura, H., Kaihara, M., Tobe, T., Tomita, M., Katagiri, T., and Ban, Y. (1996) Mild resistance to thyroid hormone with a truncated thyroid hormone receptor beta. *Exp. Clin. Endocrinol. Diabetes 104*, 339–343.
(25) Note:. K_i determined by nonlinear regression of single run ± 95% confidence interval.
(26) Nguyen, N. H., Apriletti, J. W., Baxter, J. D., and Scanlan, T. S. (2005) Hammett analysis of selective thyroid hormone receptor modulators reveals structural and electronic requirements for hormone antagonists. *J. Am. Chem. Soc. 127*, 4599–4608.
(27) Malm, J., Gordon, S., Brandt, P., Carlsson, B., Agback, P., Saeidi, A. B., and Sandberg, J. (2007) Thyroid receptor ligands. *Bioorg. Med. Chem. 17*, 2018–2021.
(28) Dow, R. L., Schneider, S. R., Paight, E. S., Hank, R. F., Chiang, P., Cornelius, P., Lee, E., Newsome, W. P., Swick, A. G., Spitzer, J., Hargrove, D. M., Patterson, T. A., Pandit, J., Chrunyk, B. A., LeMotte, P. K., Danley, D. E., Rosner, M. H., Ammirati, M. J., Simons, S. P., Schulte, G. K., Tate, B. F., and DaSilva-Jardine, P. (2003) Discovery of a novel series of 6-azauracil-based thyroid hormone receptor ligands: Potent, TR beta subtype-selective thyromimetics. *Bioorg. Med. Chem. Lett. 13*, 379–382.
(29) Koehler, K., Gordon, S., Brandt, P., Carlsson, B., Backsbro-Saeidi, A., Apelqvist, T., Agback, P., Grover, G. J., Nelson, W., Grynfarb, M., Farnegardh, M., Rehnmark, S., and Malm, J. (2006) Thyroid receptor ligands. 6. A high affinity "direct antagonist" selective for the thyroid hormone receptor. *J. Med. Chem. 49*, 6635–6637.
(30) Komatsu, T., Hirano, T., Songkram, C., Kawachi, E., and Kagechika, H. (2007) Novel thyroid hormone receptor antagonists with an N-alkylated diphenylamine skeleton. *Bioorg. Med. Chem. 15*, 3115–3126.

BC8000326

One-Electron Oxidation of Condensed DNA Toroids: Injection-Site Dependent Charge (Radical Cation) Mobility

Prolay Das and Gary B. Schuster*

School of Chemistry and Biochemistry, Georgia Institute of Technology, Atlanta, Georgia 30332. Received January 26, 2008; Revised Manuscript Received March 18, 2008

DNA condensates were formed by treating linear pUC19 plasmids ligated to an AQ-containing oligomer with spermidine. The condensates are toroid-shaped objects having a radius of 70 to 100 nm. Irradiation of the condensates with UV light (absorbed by the anthraquinone) causes the one-electron oxidation of the DNA and concomitant reaction at GG steps of the oligomer. Analysis of the distance dependence of the reaction at guanine in these condensates reveals a dependency on the position of the AQ. This observation is attributed to a reduction in the rate for trapping of the radical cation in the relatively dehydrated interior of the condensate.

INTRODUCTION

A clear understanding of the mechanisms for oxidative damage to DNA is essential because these processes are considered to be responsible for mutations, aging, and some diseases (*1*). Extensive experimentation has shown that a radical cation (electron "hole") introduced into a duplex DNA oligomer in solution by one-electron oxidation will migrate long distances by hopping before being irreversibly trapped by reaction with water or molecular oxygen at a remote nucleobase (*2–5*). In this process, the radical cation is self-stabilized in a distortion of the DNA and its nearby solvent and counterion environment that spreads the charge over several bases (a polaron). Thermal activation (by phonons) causes the polaron to hop from one site to a neighboring site. Trapping of the radical cation occurs at the most reactive nucleobase, which is typically a guanine, G_n-site ($n = 2, 3$) or, in the absence of guanine, a thymine (*6, 7*). The site at which the radical cation is trapped is typically revealed by chemical or enzymatic treatment that results in strand cleavage at the damaged base (*8*).

Most reported studies of long-distance radical cation transfer in DNA have been carried out using short oligomers in solution (*9–12*). For example, the UV irradiation of an anthraquinone group (AQ) that is covalently linked to a 5′-terminus of a duplex DNA oligomer results in oxidative damage to remote bases. We recently reported the results from a set of experiments in which DNA from a linearized plasmid was ligated to an AQ-containing oligomer, formed into a condensate, and then irradiated (*13*). Condensates are nanometer-scale particles produced from extended DNA chains in the presence of multivalent cations such as spermine or spermidine (*14–19*). They are sometimes used as models for studying gene packing in viruses, bacteria, or eukaryotic cells. Our previous investigation showed that the charge migration effectiveness decreased in the condensate compared with that in a similar short oligomer in solution. This observation was attributed to a reduction in the formation of charge-transfer effective states in the condensate (*13*). In that study, by design, the AQ group was at a terminal position of the duplexes that comprise the condensate. Clearly, those are unique positions and the reactions of radical cations near those sites may not represent the properties of the majority of the nucleobases in the condensate. In the current study, we prepared condensates from an oligomer that is doubly ligated to two linearized pUC19 plasmids. This construction causes the AQ group to be in an interior position of the condensate. The pattern of oxidative damage in this system reveals a complex competition between charge hopping and charge trapping within the condensate.

EXPERIMENTAL PROCEDURES

Materials and Methods. The pUC19 plasmid, T4 DNA ligase, *Hin*dIII, *Eco*RI, PaeR7 I restriction endonucleases, and T4 polynucleotide kinase were purchased from New England Biolabs. [γ-^{32}P]ATP and nonradioactive ATP were purchased from Amersham Biosciences. Gel extraction kits were purchased from Qiagen. Gelase agarose gel-digesting preparation was obtained from Epicenter Biotechnologies, and spermidine hydrochloride was obtained from Aldrich. DNA oligomers and the uridine AQ were synthesized by standard procedures on an Expedite 8909 DNA synthesizer (*20*). The phosphorylation of the 5′-end of DNA2 was achieved in the DNA synthesizer with chemical phosphorylation reagent II, obtained from Glen Research (Sterling, VA). The oligonucleotides were purified by reverse-phase HPLC on a Hitachi (Tokyo) preparative HPLC system using a Dynamax C18 column. Purified oligomers were desalted with Sep-Pak columns and characterized by mass spectroscopy. UV melting and cooling curves were recorded on a Cary 1E spectrophotometer (Varian) equipped with a multicell block, temperature controller, and sample transport accessory. Buffer-exchanging spin columns, enzyme removal, and other spin columns are obtained from Millipore Corporation (Bedford, MA).

Restriction Digestion and Alkaline Phosphatase Treatment of Plasmid. A 2 μg sample of pUC19 plasmid was treated with 5 μL of *Hin*dIII restriction endonuclease in a microcentrifuge tube (total volume of 50 μL) containing 1 × *Hin*dIII buffer and incubated overnight at 37 °C. To this solution, 0.5 μL sample of shrimp alkaline phosphatase (SAP) was added at the same restriction buffer concentration. The reaction mixture was incubated at 37 °C for an additional 30 min, followed by heating at 65 °C for 15 min. The SAP-treated restriction digest was passed through a Micropure-EZ centrifugal filter device to eliminate the restriction enzyme and SAP. The restriction buffer was replaced with nanopure water by means of buffer-exchange spin columns. The linearized plasmid samples were precipitated with ethanol, washed twice with 80% ethanol, and air-dried. The SAP-treated linearized plasmid was resuspended in water, and its concentration was measured by UV−vis spectroscopy. The same procedure was carried out for restriction digestion of

10.1021/bc8000358 CCC: $40.75 © 2008 American Chemical Society
Published on Web 05/09/2008

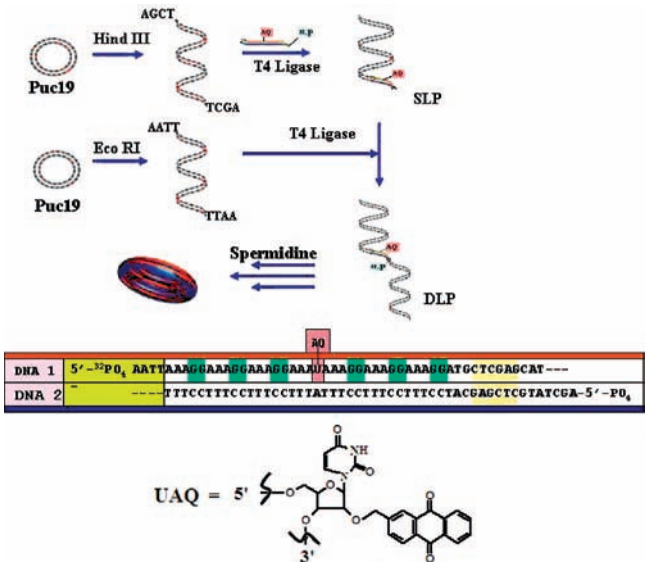

Figure 1. A schematic representation of the experimental design for the DNA constructs used in this work. pUC19 is cut with Hind III enzyme and ligated to the *Hind*III compatible ends of DNA1/ DNA2, to form SLP. Further ligation of SLP with *Eco*RI linearized pUC19 give DLP. Treatment of SLP and DLP with spermidine leads to toroid-shaped condensate formation, DNA1/DNA2 is a double-stranded DNA oligomer that has two cohesive ends; one of them is complementary to Hind III cut linearized pUC19 (shown as dark yellow) and the other complementary to *Eco*RI cut linearized pUC19. The oligomer duplex also has an AQ group linked covalently to a uridine (AQ, structure shown), a 5′-^{32}P radiolabel, and a palindromic sequence which is cut by Pae R7 I (shown as canary yellow).

pUC19 with *Eco*RI enzyme and SAP treatment. In all cases, analytical, nondenaturing, low-melting agarose gels were run to identify and compare the linearized plasmids from uncut relaxed and supercoiled plasmid and also to confirm inhibition of self-ligation by SAP. The single- (SLP) and double- (DLP) ligated plasmid condensates were treated with PaeR7 I restriction endonuclease after irradiation. The restriction digestions were carried out in the presence of NEB buffer 4 and were supplemented by 5 μg of bovine serum albumin and incubated at 37 °C for 1 h. The reaction mixtures were used without further purification for subsequent piperidine treatment.

Preparation of Radiolabeled DNA. The DNA1 oligomer (Figure 1) was radiolabeled with [γ-^{32}P] ATP and T4-polynucleotide kinase enzyme (PNK) and isolated by standard methods on a 20% denaturing polyacrylamide gel. The DNA was precipitated by addition of cold ethanol, vortexed, placed on dry ice, and then centrifuged. The DNA sample was washed twice with 80% ethanol and then air-dried. The air-dried DNA pellets were redissolved in water and passed through buffer-exchange spin columns to eliminate ammonium, magnesium, and acetate ions from the gel elution buffer.

Ligation of Plasmids with Radiolabeled Oligonucleotides. Equimolar concentrations (3 μM) of radiolabeled DNA1 and complementary sequence DNA2 were mixed in 10 mM sodium phosphate buffer at pH 7.0, annealed by heating for 10 min at 90 °C, and then cooled very slowly to room temperature. The oligomer was ligated to the Hind III linearized pUC19 plasmid (10:1 molar ratio) with T4 DNA ligase, 10 mM ATP in 1 × T4 ligase buffer at 16 °C overnight in a Neslab RTE-7 incubator (Newington, NH). The success of the ligation reaction was assessed by autoradiography on an analytical, nondenaturing low-melting agarose gel following standard procedures (*21*).

The DNA in the reaction mixture was washed with ethanol and mixed with nondenaturing dye containing bromophenol blue and xylene cyanol in water and glycerol (4:1). The ligated plasmid DNA band was isolated from a nondenaturing 1% preparative agarose gel in 1 × TAE buffer (Tris−acetate−EDTA) containing ethidium bromide for visualization. The gel pieces were collected in centrifuge tubes and heated at 65 °C for 10 min, followed by addition of 1 μL of 50 × reaction buffer of gelase agarose gel-digesting enzyme, per 50 μL of molten agarose. The solutions were incubated overnight after the addition of one unit of gelase enzyme per 200 mg of molten agarose. The gelase digestions were washed with ethanol and then passed through Qiagen nucleotide removal spin columns for elimination of the last traces of agarose.

The gel-extracted SLP was subjected to a second phase ligation by the addition of equimolar amounts of linearized pUC19 plasmid, cut with *Eco*RI restriction enzyme, in the presence of T4 DNA ligase and 10 mM ATP in 1 × T4-ligase buffer at 20 °C. Preparative agarose gel and gel extraction procedures, as above, were performed to obtain purified double-ligated plasmid (DLP).

Dynamic Light Scattering Study. A solution of doubly ligated plasmid containing the sandwiched oligomer duplex-DNA1/DNA2 (25 μg) was added to an equal volume of spermidine solutions (50−600 μM at increments of 50 uM). All experiments were performed in 10 mM sodium phosphate buffer (pH 7.2). All solutions were filtered through Amicon UltraFree MC centrifugal filters (diameter, 0.22 μm; Millipore) before introducing them into the light scattering instrument. After 5 min of gentle agitation, the samples were analyzed by dynamic light scattering using a Dynapro MS X dynamic light-scattering instrument (Proterion, Piscataway, NJ). Decondensation experiments were performed by addition of NaCl (final concentration 2 M) to the solutions containing the DNA and spermidine at appropriate concentrations.

Transmission Electron Microscope Studies. DNA condensates were prepared according to the standard procedure (*22*); doubly ligated plasmids were deposited on a carbon-coated copper grid (Ted Pella, Redding, CA) and allowed to settle for 10 min. The grids were stained by the direct addition of 5 μL of a 2% uranyl acetate solution, rinsed in 95% ethanol, and then air-dried. Images of the DNA condensates at room temperature were collected on film using a JEOL-100C transmission electron microscope at 100 000× magnification.

UV Irradiation and Strand-Cleavage Analysis. DNA solutions of the radiolabeled oligomer duplex, SLP and DLP were irradiated in microcentrifuge tubes (20 μL, 10 mM sodium phosphate buffer) containing varying concentrations of spermidine at ca. 30 °C in a Rayonet Photoreactor (Southern New England Ultraviolet, Barnsford, CT) equipped with 16 × 350 nm lamps. After irradiation, the samples were washed with ethanol, dried, and treated at 90 °C with 1 M piperidine for 30 min. The piperidine was evaporated, and the samples were dried and suspended in denaturing loading buffer and analyzed by electrophoresis on a 20% 19:1 acrylamide/bis-acrylamide containing 7 M urea Tris−borate−EDTA buffer. Cleavage sites were visualized by autoradiography and quantified by phosphorimagery.

RESULTS

Preparation of Internally Linked AQ-DNA. We constructed a linear DNA oligomer (DLP; see Figure 1) that is composed of an AQ-containing duplex oligomer (DNA1/DNA2) linked at both ends to linearized pUC19 plasmids. The duplex is formed from strands DNA1 and DNA2 and it has two cohesive ends. The 5′-end of DNA1 has a 5′-AATT-3′ overhang that is compatible with the EcoR1 restriction-cut ends of pUC19. This 5′-end also contains a [^{32}P]-radiolabeled phosphate group that will permit visualization of the experimental results by autoradiography. The 3′-end of DNA1 forms a four-base

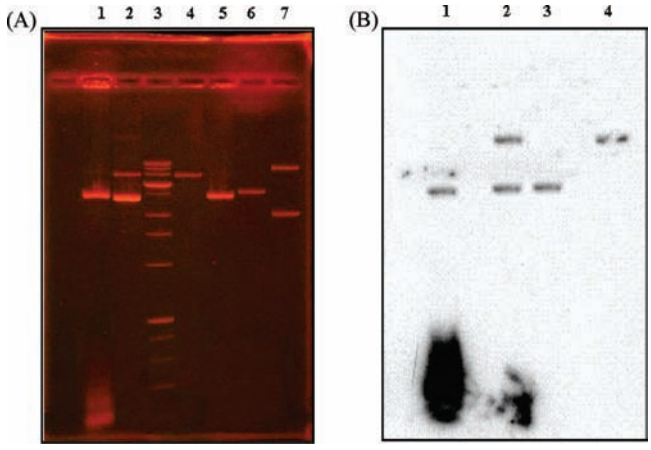

Figure 2. (A) Nondenaturing low melting agarose gel showing the Rf of DNA1/DNA2, SLP, and DLP. Lane 1: The reaction mixture from ligation of DNA1/DNA2 with Hind III cut linearized plasmid. Lane 2: The reaction mixture from ligation of gel-extracted SLP and *Eco*RI cut linearized pUC19. Lane 3: 1 Kb DNA ladder. Lane 4: The gel extracted DLP. Lane 5: The gel extracted SLP. Lane 6: pUC19 control, cut with Hind III restriction endonuclease. Lane 7: circular pUC19 in supercoiled and relaxed form. (B) Autoradiography of low-melting agarose gel showing DNA1/DNA2, DLP, and SLP. Lane 1: The reaction mixture from ligation of DNA1/DNA2 with Hind III cut linearized plasmid. Lane 2: The reaction mixture from ligation of SLP with *Eco*RI cut linearized plasmid. Lane 3: Isolated and purified SLP. Lane 4: Isolated and purified DLP.

recessed cohesive end in the DNA1/DNA2 duplex that is complementary to the overhang of a *Hin*dIII cut pUC19 plasmid. DNA1 also has an AQ group linked covalently to a uridine in a central location. In addition, the DNA1 strand contains six GG steps (three on each side of the AQ) that will serve as indicator sites for the reactions of the radical cation.

The DNA1/DNA2 duplex was prepared by following standard techniques that have been reported previously (*12*). The melting temperature (T_m) for this AQ-containing duplex is 68 °C, which is 3.5 °C higher than that of the corresponding duplex where the uridine-linked AQ has been replaced by a thymine. This indicates that the AQ group stabilizes the duplex oligomer, probably by intercalation (*20*).

DLP was prepared in two steps from DNA1/DNA2. In the first step, ligation of DNA1/DNA2 with *Hin*dIII linearized pUC19 gives SLP (see Figure 1). The *Hin*dIII cuts pUC19 at a unique position (base number 447) leaving two overhanging 5′-AGCT-3′ cohesive ends. This 2680 base pair linearized plasmid was treated with shrimp alkaline phosphatase (SAP) before reaction with DNA1/DNA2 to inhibit self-ligation. The T4 DNA ligase catalyzed reaction of DNA1/DNA2 with the *Hin*dIII cut plasmid gives the SLP construct in ca. 50% yield having an AQ group close to its terminus. SLP was purified by preparative agarose gel electrophoresis to remove unligated and self-ligated DNA1/DNA2 (see Figure 2). In the second step of formation of DLP, pUC19 linearized by reaction with EcoR1, which cuts the plasmid at the unique 5′-AATT-3′ sequence site (base number 396), was ligated (after treatment with SAP) to SLP to give DLP, which was further purified by gel electrophoresis. Thus formed, the DLP construct is a linear DNA polymer containing 5407 base pairs that has the DNA1/DNA2 AQ-containing oligomer in the central position between the two linearized pUC19 plasmids. Finally, it should be noted that the *Hin*dIII compatible end of DNA1/DNA2 contains a 5′-CTC-GAG-3′/3′-GAGCTC-5′ restriction site for PaeR7 endonuclease. This sequence does not occur in pUC19. This fact allows for the selective disassembly of the SLP and DLP constructs for analytical purposes after their irradiation.

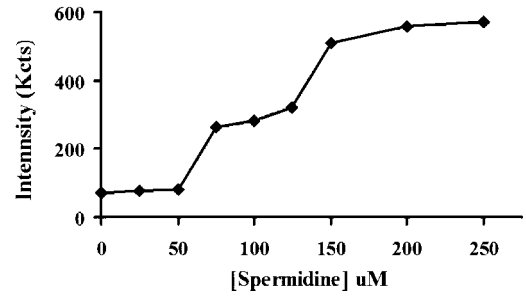

Figure 3. Dynamic light scattering experiment: Plot of the intensity of scattered light against the concentration of spermidine in DLP.

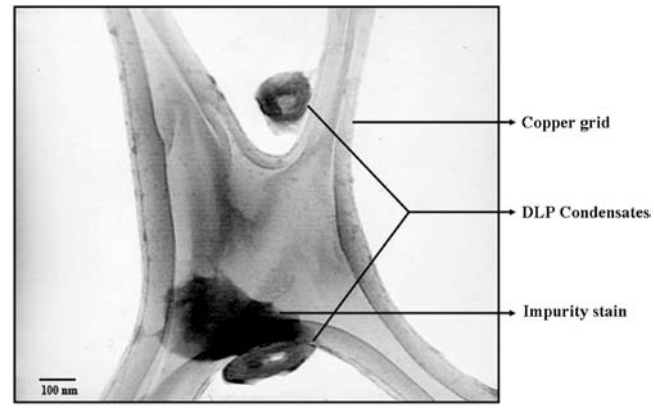

Figure 4. Transmission electron microscopic image of DNA condensate formed from DLP at pH = 7 with 100 μM spermidine in 1 × Tris−EDTA buffer. Scale indicates 100 nm. Images are taken at 100 000 magnification in a JEOL 100C TEM instrument.

Formation of DNA Condensates from DLP with Spermidine (DLP-Condensate). It is well-known that treatment of DNA with polycations such as spermidine can lead to the formation of condensate structures (*14*, *15*). We converted DLP to condensates in this way and characterized those structures by dynamic light scattering and by transmission electron microscopy.

Dynamic light scattering experiments were conducted to assess the effect of spermidine on SLP and DLP. Solutions of purified SLP and DLP oligomers were prepared with various concentrations of spermidine, and their hydrodynamic radii were measured by light scattering. In the absence of spermidine, solutions of SLP and DLP do not show meaningful scattering. The data for DLP are shown in Figure 3; the behavior of SLP (not shown) is essentially identical to that of DLP. With the addition of spermidine, the light scattering intensity of DLP solutions increases, indicating that particles are being formed and their hydrodynamic radii increase with the spermidine concentration. At spermidine concentrations between 25 and 50 μM, the light scattering intensity is low and derived particle radii ranges 40−50 nm. With an increase in spermidine concentration to the range between 75 and 125 μM, the light scattering intensity increases and then reaches a plateau, which indicates the formation of stable particles having calculated radii of 70 to 90 nm. We refer to these particles as DLP-condensates. At higher spermidine concentration, the light scattering experiment indicates the formation of larger aggregates that eventually precipitate from solution. As expected (*17*), the light scattering experiments show that condensate formation is reversed by the addition of NaCl (2 M) to the solution of DLP and spermidine. The formation of condensates by DLP with the spermidine concentration at 100 μM was confirmed by transmission electron microscopy (Figure 4), which reveals stable, toroid-like structures with radii of 80−100 nm.

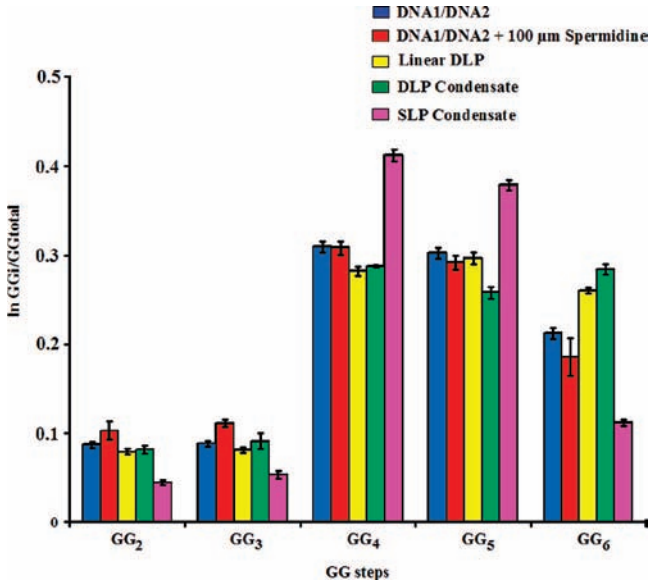

Figure 5. Normalized damage ratios for DNA1/DNA2, DLP, and SLP irradiated in the presence or absence of spermidine, as indicated. Each bar corresponds to a GG step. The AQ is between GG3 and GG4. Damage ratios for DNA1/DNA2 are after 45 min of irradiation and those for DLP and SLP are after 2 h of irradiation.

UV Irradiation of UAQ-DNA1/DNA2, SLP, and DLP. It is known that UV irradiation of an AQ that is covalently linked to duplex DNA at an internal position introduces a nucleobase radical cation and results in reaction far removed from the anthraquinone (*20*). Those reactions are routinely revealed as strand cleavage at remote GG sites by treatment of the irradiated sample with piperidine (*23*). We carried out experiments on DNA1/DNA2, SLP, SLP-condensate, DLP, and DLP-condensate to assess the effect of condensate formation on the migration and reaction of the radical cations introduced by UV irradiation of the covalently linked AQ group.

Solutions of DNA1/DNA2, DLP, and SLP, with and without spermidine, were irradiated with UV light to low conversion (single hit conditions) and then analyzed to assess the amount of reaction that occurred at each of the GG steps of the DNA1/DNA2 oligomer. Analysis by high-resolution PAGE requires the deconstruction of the ligated plasmid. This was accomplished by its treatment with endonuclease PaeR7 I and Sac I, which excises the oligomer portion from the plasmid−oligomer−plasmid system. These results are shown in the form of a histogram in Figure 5. Autoradiograms from the PAGE analyses of irradiated samples of SLP and DLP after deconstruction and treatment with piperidine are shown in Supporting Information (Figures S1 and S2).

These experiments show that UV irradiation and piperidine treatment of DNA1/DNA2, DLP, and SLP result in strand cleavage at GG steps on both the 3′ and 5′ sides of the AQ in each of the constructs both in the linear form and as the condensate. As has been previously observed, the efficiency of reaction to the 5′ side of the AQ is greater than to its 3′ side (*20*). This is true for DNA1/DNA2, as well as SLP and DLP. As expected, the efficiency of strand cleavage generally falls off the farther the GG step is located from the AQ. As a control experiment, solutions of DNA1/DNA2 containing spermidine were irradiated and analyzed. Piperidine treatment and PAGE analysis of the irradiated samples show (see Figure 5) that the presence of the spermidine (100 μM) does not affect the relative reactivity of the GG steps of the oligomer. In contrast, comparison of the results from irradiation of SLP without added spermidine to those containing 100 μM of spermidine reveals a strand cleavage pattern showing that condensate formation results in an increased distance dependence for reaction at GG steps; that is, GG damage decrease more sharply with distance from the AQ for SLP-condensate compared with DNA1/DNA2 and SLP. This finding is consistent with previous experiments in which the AQ group is at the terminal position of the DNA that forms the condensate (*13*).

Comparison of the relative reactivity of radical cations at the GG steps of DLP and DLP-condensate provides a remarkable finding. Unlike the case for SLP, condensate formation has little effect on the distance dependence of reaction for DLP (see Figure 5). A close look at the GG damage pattern for DLP-condensate (in the presence of 100 μM of spermidine) reveals that reactions at the guanines are essentially identical to those observed for linear DLP (no spermidine) and for DNA1/DNA2 with or without spermidine present. Evidently, the position of the AQ in the condensate has a powerful affect on the distance dependence of radical cation migration efficiency. When the AQ is at or near the end of the DNA strands that comprise the condensate, remote reaction of GG steps is inhibited, but when the AQ at the middle of the DNA stand, condensate formation has no measurable effect on the efficiency of remote reaction.

DISCUSSION

The one-electron oxidation of DNA generates a radical cation that migrates by a thermally activated hopping process requiring local structural distortion of DNA (*24*). These local structural distortions include the redistribution of surrounding water molecules and counterions, which are responsible for stabilizing the self-trapped radical cation (*25*). If the rate for hopping of the radical cation (k_{hop}) is greater than for its irreversible trapping (k_{trap}) at guanine-rich regions of the DNA, then the radical cation will be distributed approximately equally (thermodynamic control) to all equivalent sites. However, if the rate of trapping of the radical cation is greater than that for hopping, then the probability of reaction at remote sites typically falls off exponentially with distance (kinetic control) (*5*).

In an earlier report (*13*), we showed that when the AQ is located at a terminal position the efficiency of charge hopping decreases significantly when linear DNA is converted to a toroidal condensate by the addition of spermidine. In the present case, we find a similar result for SLP-condensate, which has the AQ group near the terminus of the DNA chain. However, no such effect is observed for DLP-condensate where the AQ group is in the center of a long DNA chain. Clearly, the efficiency of radical cation hopping is affected by an environmental change associated with condensate formation that is different near the ends of the chain than it is at the middle.

It is not possible to reach a unique explanation for this observation from these experiments because their outcome is determined by the ratio of the rates of hopping and trapping (*5*). That is, the observed effect might be a result of an increase in the magnitude of the rate of hopping near the center of the condensate, or it could be a result of the trapping rate becoming smaller (or some combination of these two effects). Nevertheless, valuable insight into the nature of radical cation migration and trapping in complex DNA structures results from these findings.

In SLP, where the AQ group is 22 base pairs from a terminus, the GG damage falls off normally with distance. Evidently, positioning the AQ group at an internal position near a terminus does not change the behavior compared with the case when the AQ is at the terminus, as it is in the previously reported example (*13*). Thus, the factors responsible for differentiation of the behavior of SLP and DLP-condensates cannot be directly tied to the specific nature of the chemical linkage of the AQ to the DNA strand.

It has been reported that the surface-to-surface spacing between adjacent DNA helices in condensed structures is ca.

1−2 water molecules in diameter (*26*). This indicates that the DNA molecules that comprise condensates are considerably dehydrated compared with DNA oligomers in solution. Thus, there is a relative absence of water in the interior of the DLP-condensate. Water and to a lesser extent O_2 are the reagents responsible for the trapping of the radical cation that leads eventually to strand cleavage. A lower concentration of these trapping reagents in the interior of the condensate would lead to a decrease in the rate of trapping of the migrating radical cation. As a result of this factor, the radical cations formed in dehydrated regions of the condensate would migrate with reduced distance dependence compared to those formed in well-hydrated regions. This explanation accounts for the findings with the DLP-condensate if it is assumed that the interior regions of the condensate are less hydrated, which seems reasonable. Interestingly, it has been suggested that the amazing resistance to radiation damage exhibited by the bacterium *Deinococcus radiodurans* is related to toroid-like structures found in its DNA that inhibit diffusion (*27*).

Alternatively, the reduced distance dependence observed for DLP-condensate might be caused by an increase in the rate of hopping, although this seems less likely. Multivalent cations such as spermidine not only cause condensation but also modify the local structure of the DNA (*28*). If these local structural changes are different in the interior of the condensate than near the terminus of a DNA chain, and if these changes accelerate the rate of radical cation hopping, then these factors could account for the difference we observe between SLP and DLP condensates. Although it seems less likely, this explanation can not be ruled out with the available data.

CONCLUSION

DNA condensates were formed from constructs created by ligating an AQ-containing oligomer to one or two linearized pUC19 plasmids. In the first case (SLP), the oligomer is near a terminal position of the DNA chain. In the second case (DLP), the oligomer is in the central position between two linearized plasmids. Both constructs are converted to condensates when they are treated with spermidine. The condensates were characterized by dynamic light scattering and TEM and found to be toroid-shaped objects having a radius of 70 to 100 nm. Irradiation of the condensates with UV light (absorbed by the AQ) causes the one-electron oxidation of the DNA resulting in the conversion of a nucleobase to its radical cation. The radical cation migrates along the DNA chain and is trapped at GG steps where it reacts irreversibly with H_2O or O_2. The site of reaction is revealed (after enzymatic deconstruction of the condensate) by autoradiography. Analysis of the distance dependence of radical cation migration in these condensates reveals a dependency on the position of the AQ. The radical cation migrates more efficiently in DLP-condensate than in SLP. This observation is attributed to a reduction in the rate for trapping of the radical cation in the relatively dehydrated interior of the DLP condensate compared with SLP. Alternatively, this effect could be due to a unique local structural change in the interior of the DLP condensate that increases the rate of radical cation hopping. These findings illuminate the challenge of extrapolating results obtained for linear DNA oligomers in solution to more complex DNA structures.

ACKNOWLEDGMENT

We thank Prof. Andrew Lyon (School of Chemistry and Biochemistry, Georgia Institute of Technology) for assistance with dynamic light scattering experiments; Dr. Sriram Kanvah for synthesizing the DNA oligomer strands. This work was supported by a grant from National Science Foundation and by the Vassar Woolley Foundation.

Supporting Information Available: Autoradiogram showing results from the irradiation of DNA1/DNA2, DLP and SLP and their condensates are shown in Figures S1 and S2.This material is available free of charge via the Internet at http://pubs.acs.org.

LITERATURE CITED

(1) Demple, B., and Harrison, L. (1994) Repair of oxidative damage to DNA: Enzymology and biology. *Annu. Rev. Biochem. 63*, 915–948.

(2) Gasper, S. M., and Schuster, G. B. (1997) Intramolecular photoinduced electron transfer to anthraquinones linked to duplex DNA: The effect of gaps and traps on long-range radical cation migration. *J. Am. Chem. Soc. 119*, 12762–12771.

(3) Nunez, M., Hall, D. B., and Barton, J. K. (1999) Long-range oxidative damage to DNA: Effects of distance and sequence. *Chem. Biol. 6*, 85–97.

(4) Schuster, G. B., and Landman, U. (2004) The mechanism of long-distance radical cation transport in duplex DNA: Ion-gated hopping of polaron-like distortions. *Top. Curr. Chem. 236*, 139–162.

(5) Liu, C.-S., Hernandez, R., and Schuster, G. B. (2004) Mechanism for radical cation transport in duplex DNA oligonucleotides. *J. Am. Chem. Soc. 126*, 2877–2884.

(6) Joseph, J., and Schuster, G. B. (2006) Emergent functionality of nucleobase radical cations in duplex DNA: Prediction of reactivity using qualitative potential energy landscapes. *J. Am. Chem. Soc. 128*, 6070–6074.

(7) Joy, A., Ghosh, A. K., and Schuster, G. B. (2006) One-electron oxidation of DNA oligomers that lack guanine: Reaction and strand cleavage at remote thymines by long-distance radical cation hopping. *J. Am. Chem. Soc. 128*, 5346–5347.

(8) Boone, E., and Schuster, G. B. (2002) Long-range oxidative damage in duplex DNA: the effect of bulged G in a G−C tract and tandem G/A mispairs. *Nucleic Acids Res. 30*, 830–837.

(9) Giese, B. (2000) Long-distance charge transport in DNA: The hopping mechanism. *Acc. Chem. Res. 33*, 631–636.

(10) Giese, B. (2002) Long-distance electron transfer through DNA. *Annu. Rev. Biochem. 71*, 51–70.

(11) Lewis, F. D., Liu, J., Weigel, W., Rettig, W., Kurnikov, I. V., and Beratan, D. N. (2002) Donor-bridge-acceptor energetics determine the distance dependence of electron tunneling in DNA. *Proc. Natl. Acad. Sci. U.S.A. 99*, 12536–12541.

(12) Liu, C. S., and Schuster, G. B. (2003) Base sequence effects in radical cation migration in duplex DNA: Support for the polaron-like hopping model. *J. Am. Chem. Soc. 125*, 6098–6102.

(13) Das, P., and Schuster, G. B. (2005) Effect of condensate formation on long-distance radical cation migration in DNA. *Proc. Natl. Acad. Sci. U.S.A. 102*, 4014227−14231.

(14) Bloomfield, V. A. (1996) DNA condensation. *Curr. Opin. Struct. Biol. 6*, 334–341.

(15) Bloomfield, V. A. (1997) DNA condensation by multivalent cations. *Biopolymers 44*, 269–282.

(16) Chattoraj, D. K., Gosule, L. C., and Schellman, J. A. (1978) DNA condensation with polyamines: II. Electron microscopic studies. *J. Mol. Biol. 121*, 327–337.

(17) Widom, J., and Baldwin, R. L. (1980) Cation-induced toroidal condensation of DNA: Studies with $Co^{3+}(NH_3)_6$. *J. Mol. Biol. 144*, 431–453.

(18) Koltover, I., Wager, K., and Safinya, C. R. (2000) DNA condensation in two dimensions. *Proc. Natl. Acad. Sci. U.S.A. 97*, 14046–14051.

(19) Gosule, L. C., and Schellman, J. A. (1976) Compact form of DNA induced by spermidine. *Nature 259*, 333–335.

(20) Ly, D., Sanii, L., and Schuster, G. B. (1999) Mechanism of charge transport in DNA: Internally-linked anthraquinone conjugates support phonon-assisted polaron hopping. *J. Am. Chem. Soc. 121*, 9400–9410.

(21) Robinson, D. H., and Lafleche, G. J. (2001) Nucleic acid electrophoresis in agarose gels. *Essential molecular biology: A practical approach. Volume 1*. (Brown, T. A., Ed.) pp. 94−111, Chapter 5, Oxford University Press, London.

(22) Conwell, C. C., Vilfran, I. D., and Hud, N. V. (2003) Controlling the size of nanoscale toroidal DNA condensates with static curvature and ionic strength. *Proc. Natl. Acad. Sci. U.S.A. 100*, 9296–9301.

(23) Ly, D., Kan, Y., Armitage, B., and Schuster, G. B. (1996) Cleavage of DNA by irradiation of substituted anthraquinones: Intercalation promotes electron transfer and efficient reaction at GG Steps. *J. Am. Chem. Soc. 118*, 8747–8748.

(24) Schuster, G. B. (2000) Long-range charge transfer in DNA: Transient structural distortions control the distance dependence. *Acc. Chem. Res. 33*, 253–260.

(25) Barnett, R. N., Cleveland, C. L., Joy, A., Landman, U., and Schuster, G. B. (2001) Charge migration in DNA: Ion-gated transport. *Science 294*, 5542567−571.

(26) Schellman, J. A., and Parthasarathy, N. (1984) X-ray diffraction studies on cation-collapsed DNA. *J. Mol. Biol. 175*, 313–329.

(27) Levin-Zaidman, S., Englander, J., Shimoni, E., Sharma, A. K., Minton, K. W., and Minsky, A. (2003) Ringlike structure of the *Deinococcus radiodurans* genome. A key to radioresistance? *Science 229*, 254–256.

(28) Levin-Zaidman, S., Reich, Z., Wachtel, E. J., and Minsky, A. (1996) Flow of structural information between four DNA conformational levels. *Biochemistry 35*, 2985–2991.

BC8000358

Conjugation to Hyperbranched Polyglycerols Improves RGD-Mediated Inhibition of Platelet Function in Vitro

J. G. Zhang,[†] O. B. Krajden,[†] R. K. Kainthan, J. N. Kizhakkedathu, I. Constantinescu, D. E. Brooks, and M. I. C. Gyongyossy-Issa*

Canadian Blood Services, Research & Development, Department of Pathology and Laboratory Medicine, at UBC Centre for Blood Research, 2350 Life Sciences Mall, Vancouver BC. Received January 30, 2008; Revised Manuscript Received March 10, 2008

RGD (arginine-glycine-aspartic acid) is a known peptide sequence that binds platelet integrin GPIIbIIIa and disrupts platelet−fibrinogen binding and platelet cross-linking during thrombosis. RGD peptides are unsuitable for clinical applications due to their high 50% inhibitory concentration (IC_{50}) and low in vivo residence times. We addressed these issues by conjugating RGD peptides to biocompatible macromolecular carriers: hyperbranched polyglycerols (HPG) via divinyl sulfone. The GPIIbIIIa binding activity of RGD was maintained after conjugation and the effectiveness of the HPG−RGD conjugate was dependent upon molecular weight and the number of RGD peptides attached to each HPG molecule. These polyvalent inhibitors of platelet aggregation decreased the IC_{50} of RGD in an inverse linear manner based on the number of RGD peptides per HPG. Since HPG−RGD conjugates do not cause platelet activation by degranulation and certain substitution ratios do not increase fibrinogen binding to resting platelets, HPG−RGD may serve as a model for a novel class of antithrombotics.

INTRODUCTION

Peptidomimetics are short amino acid sequences that have shape and hydropathic profiles that provide epitope behavior such that they can be selectively screened for ligand- or receptor-like activity to target specific binding sites. The prospect of deploying such polypeptides in a therapeutic setting presents a promising lead in rational drug design; for example, a peptidomimetic was used to induce apoptosis of malignant leukemic cells without affecting healthy tissue (*1*) or to inhibit thrombin (*2*). In addition, Arg-Gly-Asp (RGD)-coupled liposomes were used to target activated platelets as a method for vascular drug delivery (*3*).

The RGD peptide sequence is a motif found in fibronectin, vitronectin, osteopontin, collagens, thrombospondin, fibrinogen, and von Willebrand factor and can mediate integrin adhesion and cellular communication (*4*). The RGD motif disrupts platelet aggregation by binding to the platelet glycoprotein IIb/IIIa integrin receptor (GPIIbIIIa) to cause competitive exclusion of fibrinogen from its binding site (*5*); hence, RGD and RGD-containing conjugates are effective antithrombotics (*6*) as fibrinogen-mediated bridging and platelet aggregation are essential steps in primary hemostasis. The GPIIbIIIa−fibrinogen interaction is clinically relevant and a new generation of antithrombotics specifically targets this interaction (*7*). To this end, a number of laboratories have defined the pharmacophore of RGD (*8*), and explored a wide variety of chemical modifications on simple peptidomimetic structures designed to compete with fibrinogen, in order to improve either their binding affinity for GPIIbIIIa or their pharmacokinetic profile (*1, 6–10*). RGD, RGD variants, and RGD mimics have proven to be successful antithrombotics both in vitro and in vivo (*11, 12*).

In order to be clinically useful, a mimetic compound must evade rapid elimination from the host and demonstrate high efficacy at comparatively low doses. RGD, RGD variants, and RGD mimics suffer from limited in vivo retention due to their small size. A well-known solution to this problem is to couple such peptides to long-circulating materials. Studies have described the conjugation of RGD to albumins (*13*), to polyethylenimine−poly(ethylene glycol) (*14*), and to liposomes (*15*). Other macromolecules, such as hyperbranched polyglycerols (HPG), are also potentially viable choices as carriers.

HPG are water-soluble, biocompatible polyether polyols (*16, 17*) that can be synthesized in a controlled manner with predetermined molecular weights and narrow molecular weight distributions (*18*). Recently, some of us reported the synthesis of very high molecular weight HPGs (MW values up to 1.48×10^6) with low polydispersities (PDI): PDI $= M_w/M_n = 1.1-1.4$, where M_w and M_n are the weight-average and number-average molecular weights, respectively (*18*). These polymers show excellent biocompatibility properties both in vitro (*19*) and in vivo (*20*). The plasma circulation half-lives were found to depend on the molecular weight, and half-lives as high as 60 h were achieved for high molecular weight polymers (*20*). As the number of hydroxyl groups approximately equals the degree of polymerization, synthesis of higher molecular weight HPGs is a major development given the difficulty of synthesizing high molecular weight dendrimers. These materials have numerous applications in nanomedicine, and one such application is the use of HPGs as carriers of peptides for biomedical applications where multivalency/polyvalency can be exploited.

We now report the conjugation of RGD-containing peptides to hyperbranched polyglycerol (HPG), and the effects of these constructs on platelet aggregation. We conjugated HPGs of different molecular weights with peptides carrying the RGD motif (*21*) and examined the in vitro activity of the conjugates. We used the ability of the RGD-conjugated HPG to inhibit the GPIIbIIIa−fibrinogen receptor−ligand interactions to determine the suitability of HPG as a viable carrier in this setting. We compared the HPG−RGD conjugates to the unconjugated HPG and the free peptide for inhibition of fibrinogen binding to platelets as a prelude to disaggregation studies. We also

[†] J.G. Zhang and O.B. Krajden contributed equally to this work.

* Correspondence to Dr. Maria Gyongyossy-Issa, Canadian Blood Services, UBC Centre for Blood Research, 4th Floor, 2350 Health Sciences Mall, Vancouver, BC, V6T 1Z3, Canada. E-mail: maria.issa@blood.ca.

10.1021/bc8000408 CCC: $40.75 © 2008 American Chemical Society
Published on Web 05/14/2008

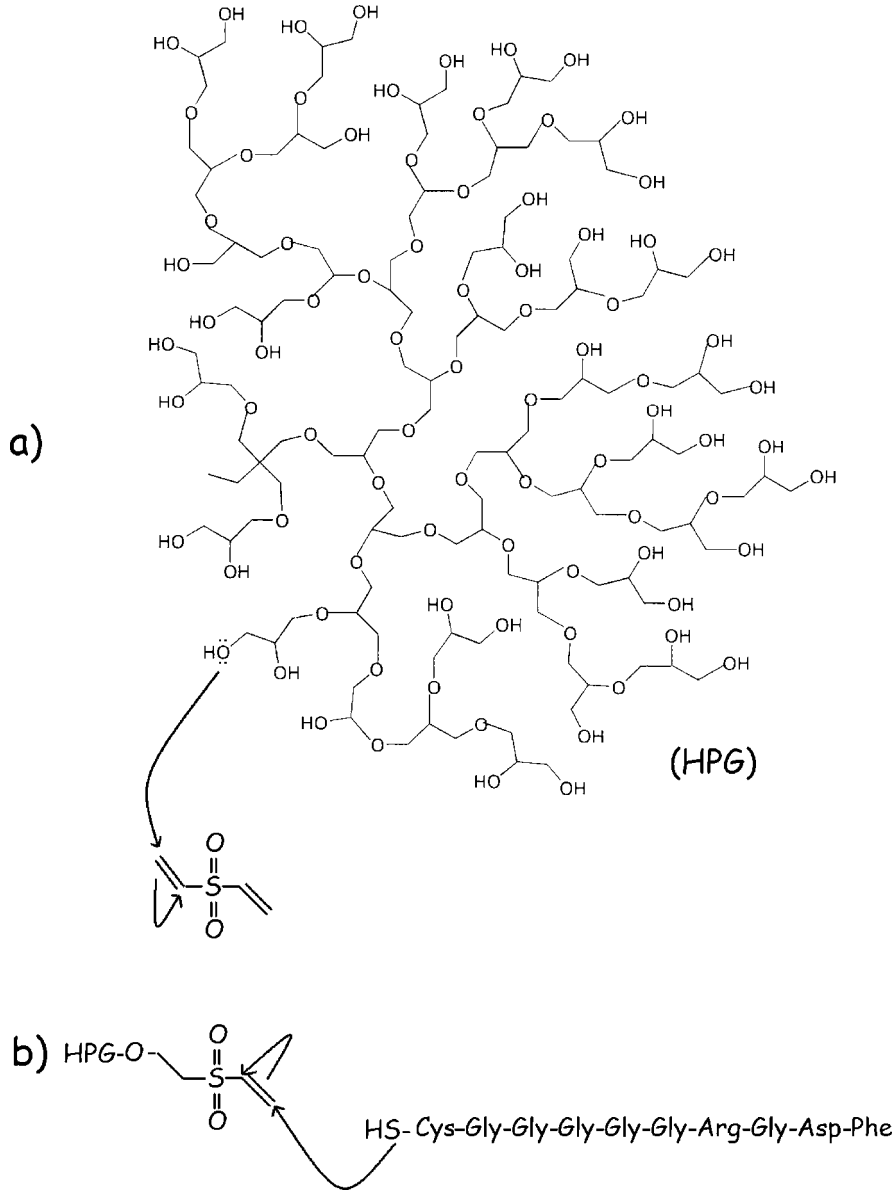

Figure 1. Functionalization of HPG and conjugation of peptides. (a) Functionalization of HPG hydroxyl groups with divinyl sulfone; (b) conjugation of peptides to functionalized HPG via cysteine side chains.

demonstrated RGD-dependent ligand-like association of the conjugates with the GPIIbIIIa receptor complex.

We found that both the HPG molecular weight at identical substitution levels and its level of substitution influence the subsequent function of such macromolecular constructs, and that certain combinations are suitable for inhibition of platelet−platelet binding and thus have antithrombotic potential.

EXPERIMENTAL PROCEDURES

Peptides and Proteins. The peptidomimetic CGGGGGRGDF, (MW = 882) was synthesized by the University of BC's Nucleic Acid and Peptide Synthesis unit to >90% purity as tested by HPLC. Lyophilized material was weighed and used to make standardized stock solutions.

Polyglycerols and Conjugation. Hyperbranched polyglycerols of molecular weights 3, 100, and 515 kDa were synthesized as described previously (*18*). The conjugation of the peptide to the HPG was achieved through cysteine coupling to vinyl sulfone functionalized polymers. A typical reaction procedure (HPG−RGD conjgate C-7) was as follows. Initially, the HPG-515 kDa polymer (100 mg) was dissolved in 3 mL dimethyl sulfoxide (DMSO) and up to 20% of the $n \sim 7000$ theoretical hydroxyl groups were deprotonated with 20 mg potassium hydride (30 wt % dispersion in mineral oil, Sigma-Aldrich, Canada). Divinyl sulfone (20 μL, corresponding to a polymer−peptide ratio of 1:1000) was added and stirred at 22 °C for 12 h. After the reaction, methanol was added and the reaction mixture was passed through an Amberlite IRC-150 cation exchange column (Sigma-Aldrich, Canada) to remove the potassium ions. The polymer was then precipitated in acetone and dried. For the peptide coupling, 5 mg vinyl sulfone functionalized polymer was dissolved in 2 mL DMSO (Sigma-Aldrich, Canada) and stirred with an excess amount of peptide (15 mg) for 2 days at 22 °C. The excess peptide was removed by dialysis (cellulose acetate membrane, MW cutoff 1000, Spectrum Laboratories Inc., USA) against HEPES buffered saline (HBS, 10 mM HEPES, 150 mM NaCl, pH 7.40) and the conjugate was collected by lyophilization (Figure 1). The other conjugates were synthesized using appropriate amounts (Table 1) of divinyl sulfone. For subsequent experiments, stock solutions were made from weighed, lyophilized material.

Table 1. Synthesis, Characterization, and Evaluation of RGD and RGD−HPG Conjugates

name	HPG platform MW	UV spec. RGD peptides per HPG	estimated resultant MW	IC_{50} (M)	[RGD] used to achieve IC_{50} (M)
RGDF	—	—	0.882 kDa	5.0×10^{-5}	5.0×10^{-5}
C-1	3 kDa	0.11	3.1 kDa	5.0×10^{-4}	5.5×10^{-5}
C-2	3 kDa	0.05	3.0 kDa	5.0×10^{-3}	2.5×10^{-4}
C-3	100 kDa	125	210 kDa	3.3×10^{-7}	4.1×10^{-5}
C-4	100 kDa	151	233 kDa	2.2×10^{-7}	3.3×10^{-5}
C-5	515 kDa	1.01×10^{3}	1410 kDa	1.2×10^{-8}	1.2×10^{-5}
C-6	515 kDa	1.42×10^{3}	1770 kDa	1.4×10^{-8}	2.0×10^{-5}
C-7	515 kDa	1.51×10^{3}	1850 kDa	1.2×10^{-8}	1.8×10^{-5}

Characterization of the HPG−RGD Conjugates. The HPG−RGD conjugates were characterized for substitution levels by UV absorption at 278 nm on an ND-1000 spectrophotometer (Nanodrop Technologies, USA). A calibration curve was made using standards made from the free peptide molecules at varying concentrations (1.0×10^{-7} M to 6.0×10^{-3} M). For each conjugate, solutions containing a range of concentrations were measured and related to the standard curve.

Preparation of Human Platelets. As approved by the CBS Ethics Board, samples of whole blood were drawn from healthy, consenting donors into 2.7−4.0 mL citrated tubes (BD, USA). Platelet-rich plasma (PRP) was extracted by centrifugation in a Beckman (CS-6R) benchtop centrifuge (Beckman Coulter, USA) of whole blood at 850 rpm ($r = 203.57$ mm) for 15 min. Platelet-rich plasma from a number of unrelated donors was evaluated on an Adiva 120 Hematology Analyzer (Bayer, Canada) and standardized to a concentration of 300×10^9 cells/L in HBS.

Effects of the Unconjugated HPG on Resting and Activated Platelets. First, we examined the effect of the various molecular weights of unconjugated HPG on resting and activated platelets. For resting platelets, 45 μL aliquots of HBS were mixed with 5 μL PRP and 5 μL of 3, 100, and 500 kDa HPG polymers at each of 1.0×10^{-3}, 1.3×10^{-7}, and 2.9×10^{-8} M concentrations and incubated for 40 min, and then 5 μL of human fibrinogen (Sigma-Aldrich, Canada), at 5 mg/mL dissolved in bicarbonate buffer (100 mM $NaHCO_3$, pH 8.30) was added and the incubation continued for 30 min before the addition of 5 μL 1.5 mg/mL fluorescein isothiocyanate (FITC)-conjugated monoclonal mouse antihuman fibrinogen IgG (Biocytex, France) and continued incubation in the dark for 30 min. Similarly, to assay the effect of unconjugated HPG on activated platelets, 5 μL 10 mM $MnCl_2$ to activate GPIIbIIIa (*22*) was included in the above assay.

Effects of the Conjugated HPG on Resting Platelets. Thereafter, we determined whether the conjugated HPGs were capable of activating resting platelets. For this, the fibrinogen−antifibrinogen detection system of the above assay was replaced by 5 μL 2 mg/mL of phycoeryhtrin (PE)-conjugated mouse antihuman CD62 IgG1 (Beckman-Coulter, Canada) to detect P-Selectin expression on the platelet surface.

Effects of the Conjugated HPG on Activated Platelets. Finally, we examined the effect of the RGD-conjugated HPGs first on resting platelets ability to bind fibrinogen, then on activated platelets using appropriate modifications of the above assay systems. Negative controls included incubating with mouse IgG-FITC of the same isotype, and/or omitting the conjugate, and/or omitting the addition of $MnCl_2$ to activate platelet GPIIbIIIa which allows for the detection of baseline binding to fibrinogen. Positive controls for platelet fibrinogen binding did not contain conjugates. After the incubations, the samples were diluted and fixed with 0.2% formolsaline (0.2% formaldehyde, 150 mM NaCl, pH 7.20) before being submitted for analysis on the FACS flow cytometer (BD, USA).

Enzyme Cleavage. RGD conjugated to the 3 kDa HPG was dissolved in HBS to a final concentration of 1 mM and treated with 1 mM Trypsin-TPCK (Sigma-Aldrich, Canada) for 15 min at 37 °C. Enzyme cleavage was stopped with the addition 2 mM soybean trypsin-inhibitor (SBTI, Sigma-Aldrich, Canada) for another 15 min. Controls included premixed and incubated trypsin-TPCK with SBTI added to platelets only, to peptides only, and to the RGD-conjugated HPG. Enzyme treatment was followed by flow cytometry as already described.

Microscopy. In a standard ELISA plate, PRP was incubated at 37 °C for 100 min with 10 μL 100 mM $MnCl_2$, and an amount of conjugate with a final conjugate concentration equal to the conjugate 50% inhibitory concentration (IC_{50}) and a final platelet concentration of 300×10^9 cells/L in a 200 μL volume. Negative controls consisted of platelets incubated alone, while positive controls included 10 μL 100 mM $MnCl_2$ as a platelet agonist. These samples were examined at 400× magnification on a Leica DMIL inverted microscope (Leica Microsystems, Germany) with 1-S55 filter. Pictures were taken with Micropublisher 3.3 Cooled RTV and the QCapture program (Q-Imaging, Canada).

Aggregometry. PRP (300×10^9 cells/L, final concentration) was incubated at 37 °C for 100 min with conjugates or unsubstituted HPG at a final concentration equal to the IC_{50} of that conjugate, in a total volume of 315 μL. The samples were loaded in the aggregometer (Chrono-Log, USA) and compared to a platelet-poor plasma derived from the same blood source, produced by high-speed centrifugation. To initiate aggregation, 25 μL of 100 mM $MnCl_2$ was added and the aggregation curve was recorded for 12 min.

RESULTS

Synthesis and Characterization of HPG−Peptide Conjugates. Peptides carrying the RGD motif were conjugated to HPGs of different molecular weights (Table 1). As the number of hydroxyl groups approximately equals the degree of polymerization a large number of peptide moieties can be coupled to the high molecular weight HPG which are thus ideal for realizing polyvalency. It is to be noted that the hydrodynamic radii of these branched molecules increase only marginally with molecular weights and are in the range 7−10 nm as described earlier (*18*). The extent of functionalization was kept below 20% of the total hydroxyl groups as highly deprotonated HPGs are insoluble in DMSO (*23*). The alkoxide groups were reacted with divinyl sulfone, and the resulting vinyl sulfone end groups were utilized to couple the cysteine-terminated peptides (Figure 1).

The presence phenylalanine residues allows for the quantitative determination of the degree of substitution of the peptide by UV spectrophotometry. The degrees of substitution were determined to be 0.05−0.1 for the 3 kDa conjugates, 125−150 for 100 kDa conjugates, and 1000−1500 for 515 kDa conjugates.

Effects of the Unconjugated HPG on Resting and Activated Platelets. Naked, unconjugated HPGs do not induce fibrinogen binding to platelets above normal levels (Figure 2), nor do they inhibit fibrinogen binding to either resting or activated platelets (Figure 2). Furthermore, the RGD peptides and conjugated HPGs did not cause any platelet activation as

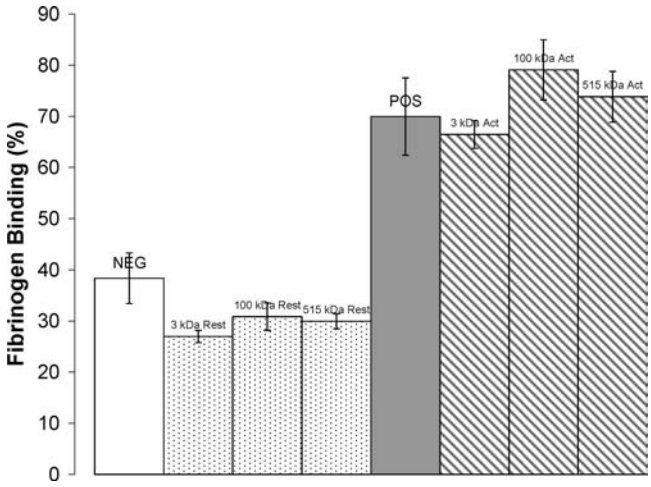

Figure 2. Evaluation of unconjugated HPGs. NEG (*1*): resting platelets; 3 kDa, 100 kDa, and 515 kDa rest. Dotted histograms: resting platelets incubated with 3, 100, and 515 kDa HPG, respectively. POS (filled histogram): Mn^{2+} activated platelets; 3 kDa, 100 kDa, and 515 kDa act. Striped histograms: Mn^{2+} activated platelets incubated with 3, 100, and 515 kDa HPG, respectively.

detected by degranulation and consequent CD62 surface expression above control levels.

Effects of the Conjugated HPG on Resting Platelets. Conjugated HPG increased fibrinogen binding to resting platelets in a size- and substitution-dependent manner. Free RGD peptide and smaller (3 kDa) conjugates did not increase the levels of fibrinogen bound to resting platelets; however, the larger conjugates (100 kDa and 515 kDa) significantly enhanced ($p < 0.05$) fibrinogen binding. This trend also applied to large conjugates in a substitution-dependent manner: platelet fibrinogen binding was increased significantly ($p < 0.05$) with increasing degrees of substitution by RGD peptides (Figure 3a). Tryptic removal of the RGD conjugated to the HPG confirmed that the inhibition of fibrinogen binding was RGD-dependent (Figure 3b).

Effects of the Conjugated HPG on Activated Platelets. Conjugated HPGs inhibition of fibrinogen binding to platelets is concentration-, size-, and substitution-dependent. This was true especially for the 100 kDa and 515 kDa conjugates (Figure 4). That this inhibition was specific and required the presence of the RGD motif was confirmed by the loss of function after enzymatic removal of the RGD (Figure 3b). Based on the titration curves, we derived IC_{50} values that are shown in Table 1. The relationship among HPG size, substitution, and resultant IC_{50} is summarized in Figure 5.

Macroscopic Platelet Aggregation. In general, both the free RGD peptides and the RGD-conjugated HPG inhibited agonist-induced, macroscopic platelet aggregation whether the aggregation was assessed visually via light microscopy or semiquantitated by lumiaggregometry (Table 1). We also found that HPG−RGD conjugates do not cause spontaneous aggregation of resting platelets as could have been suggested by the increased fibrinogen binding by platelets incubated with conjugates of high substitution (C-7).

DISCUSSION

The attachment of RGD peptides to HPG confers unique attributes to the resulting construct: the HPG gains specificity and thereby function; while the peptidomimetic gains polyvalency and thereby binding avidity.

Characterization. Peptide attachment increases the theoretical molecular weight of the HPG-conjugates depending on the number of available sites that can be functionalized on the

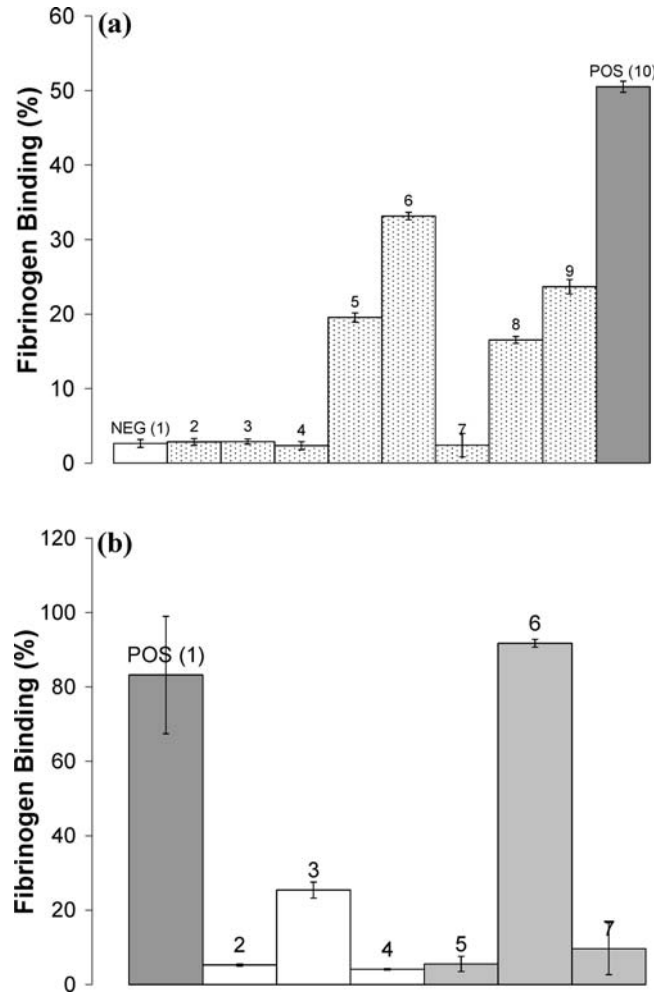

Figure 3. (a) Effect of HPG−RGD conjugates on fibrinogen binding by resting platelets. NEG (*1*): resting platelets. Dotted histograms: resting platelets incubated with RGD (*2*), C-1 (*3*), C-2 (*4*), C-3 (*5*), C-4 (*6*), C-5 (*7*), C-6 (*8*), C-7 (*9*) HPG−RGD conjugates at their respective IC_{50} concentrations; POS (*10*): Mn^{2+} activated platelets. (b) Trypsin proteolysis assay. Histogram POS (*1*): ADP activated platelets. Histogram 2: platelets incubated with RGD at IC_{50} and activated with ADP. Histogram 3: platelets incubated with tryptic digest of RGD peptides and activated with ADP. Histogram 4: platelets incubated with SBTI inhibited tryptic digest of RGD peptide and activated with ADP. Histogram 5: platelets incubated with C-1 HPG−RGD conjugate at IC_{50} and activated with ADP. Histogram 6: platelets incubated with tryptic digest of C-1 HPG−RGD conjugate and activated with ADP. Histogram 7: platelets incubated with SBTI inhibited tryptic digest of C-1 HPG−RGD conjugate peptide and activated with ADP.

surface of the HPG polymer. The branch density of the HPG varies directly with the molecular weight of the polymer while the Stokes' radius of the molecule remains relatively stable at about 7−10 nm for the 100 kDa and 515 kDa HPG molecules (*18*). The peptidomimetic is <1 nm in length, thus based on the level of substitution, peptide conjugation can approximately triple the theoretical MW of the 515 kDa HPG polymer to up to 1850 kDa for the HPG−RGD conjugate. Since attachment of the peptides is through divinyl sulfone, a reaction with limited yields, it is not surprising that the 3 kDa HPG (C-1 and C-2) carried few RGD peptides after conjugation. The achieved peptide density has steric implications for subsequent function due to its polyvalent binding to multiple GPIIbIIIa receptors on the platelet surface.

The design of the peptide included an N-terminal cystine for attachment and five glycine residues to facilitate the RGD motif's access to the GPIIbIIIa binding pocket (*5*). The RGDF sequence was considered by Foster et al. (*24*) to be the most

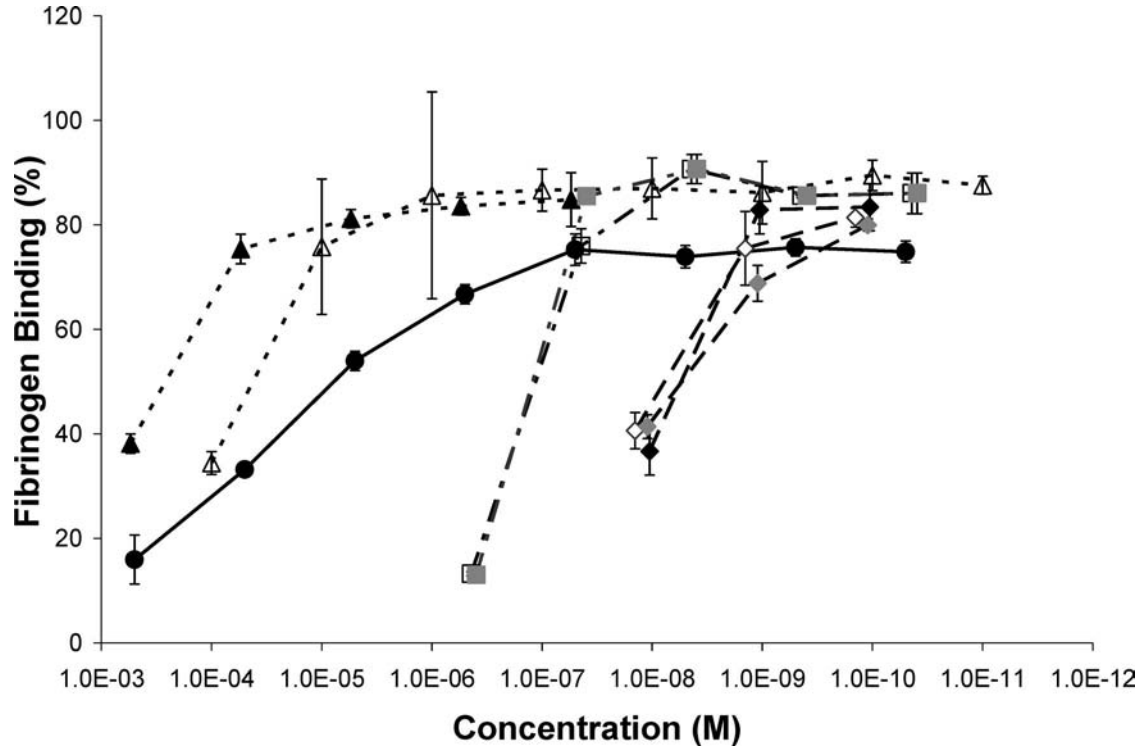

Figure 4. Inhibitory effects of HPG−RGD conjugates. Platelets are incubated with RGD or HPG conjugates and fibrinogen at varying concentrations and activated with Mn^{2+}. RGD, solid circle. 3 kDa HPG conjugates are marked with triangles and dotted lines: C-1, △; C-2, ▲. 100 kDa conjugates are marked with squares and dashed lines with dots in between: C-3, □; C-4, gray ■. 515 kDa conjugates are marked with diamonds and dashed lines: C-5, ◇; C-6, gray ◆; C-7, ◆.

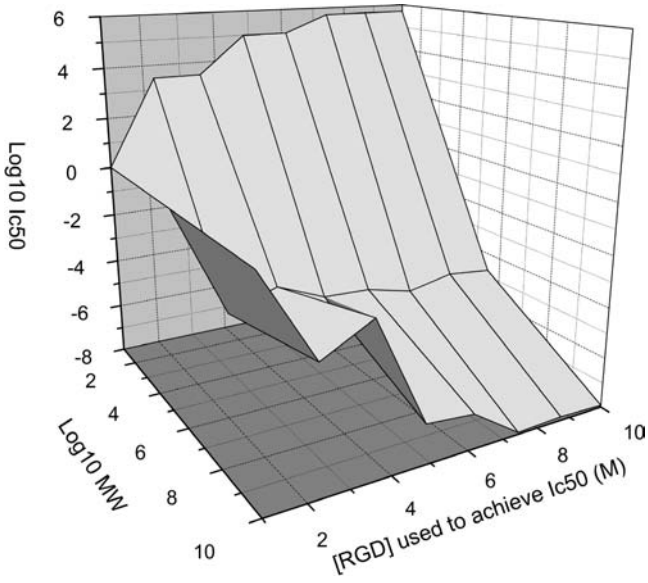

Figure 5. Relationships among IC_{50}, HPG polymer molecular weight and amount of RGD peptides conjugated to HPG. Parameters are plotted on logarithmic scales.

potent of the small RGD-peptidomimetics ($IC_{50} = 8 \times 10^{-3}$ M) and the phenylalanine was also useful for detection and UV tracking of the peptide (*24*).

Function. In order to evaluate whether RGD-conjugated HPGs have specific interactions with platelets, the naked, unconjugated HPGsb were examined first. Both the original studies (*19*, *20*) and the assays presented here involving either resting or activated platelets show no significant alterations of fibrinogen binding to platelets. Although plasma fibrinogen concentration, platelet surface GPIIbIIIa levels, and degree of preparation-induced platelet activation vary with the individual, similar IC_{50} values were obtained with the plasma and cells of all blood donors. Furthermore, neither the naked HPG nor the RGD-conjugated HPG caused platelet activation as defined by degranulation and CD62 expression. However, the RGD-conjugated HPG promoted some fibrinogen binding to resting platelets in a manner that could be related to both HPG molecular size and degree of RGD substitution: the more dense RGD brushes on HPG increased fibrinogen binding to platelets more so than diffuse RGD brushes. This can be attributed to cooperativity of GPIIbIIIa binding of RGD motifs such that RGD binding to a GPIIbIIIa receptor enhances the ability of other GPIIbIIIa molecules to bind fibrinogen (*25*, *26*).

The most important finding was that fibrinogen binding to activated platelets and subsequent platelet aggregate formation is inhibited by RGD-conjugated HPG in a manner related to HPG size (Figure 4) and to its degree of substitution (Figure 4). As the 3 kDa conjugates carried few RGD peptides, higher concentrations were needed to achieve the same degree of inhibition as obtained for free RGD peptides. However, both the 100 kDa and 515 kDa HPG conjugates carry 100−1500 RGD peptides, and thus they are able to reduce the IC_{50} of free RGD peptides by 2 to 3 orders of magnitude. Extrapolating from this data (Figure 5), it is possible to derive the substitution/MW relationship to achieve optimal platelet inhibition.

The large decrease of the IC_{50} and the corresponding increase of the HPG-conjugated RGD peptides' inhibitory effect may be a matter of kinetics. As a result of the polyvalent presentation of the RGD conjugated to HPG, the binding of RGD to platelet GPIIbIIIa is enhanced due to both a higher local concentration of RGD peptides and a slowed dissociation due to several concurrent dynamic associations of HPG−RGD with two or more GPIIbIIIa integrins. In addition, there is cooperativity among GPIIbIIIa receptors, such that a single bound RGD changes the GPIIbIIIa conformation to increase the likelihood of further ligand binding (*25*, *26*).

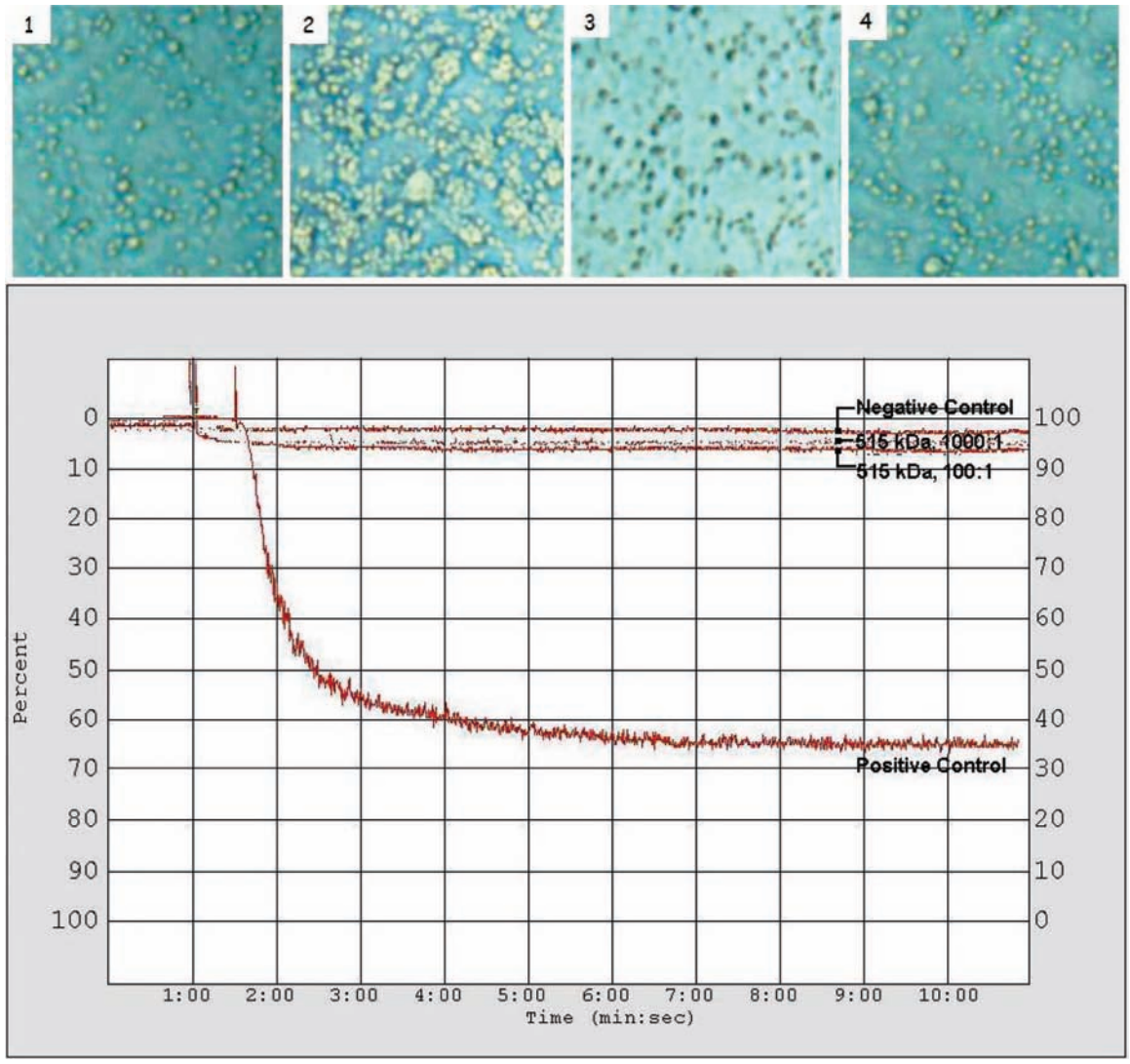

Figure 6. Light microscopy and aggregometry. Compound light microscopy 400×: panel 1, resting platelets; panel 2, Mn^{2+} activated platelets; panel 3, Mn^{2+} activated platelets incubated in C-5 HPG−RGD; panel 4, Mn^{2+} activated platelets incubated with C-7 HPG−RGD. Aggregometry graph: negative control, resting platelets; positive control, Mn^{2+} activated platelets; C-5 HPG−RGD, platelets incubated with RGD conjugate and activated with Mn^{2+}; C-7 HPG−RGD, platelets incubated with RGD conjugate and activated with Mn^{2+}.

It is known that free RGD peptides can activate the GPIIbIIIa receptors such that an increased number of the receptors are converted to the "open" configuration that is capable of binding fibrinogen (*25*, *26*). Thus, it is not unlikely that the HPG-carried RGD generate a similar activating effect. The increased fibrinogen binding seen on flow cytometry with resting platelets caused by high molecular weight, high-substitution HPG−RGD does not seem to cause spontaneous platelet aggregation macroscopically, as observed by light microscopy and lumiaggregometry. They do, however, still inhibit the macroscopic aggregation of Mn^{2+} activated platelets as detected both macroscopically (Figure 6; Table 2) and by flow cytometry (Figure 4).

Table 2. Light Microscopy of RGD−HPG Conjugates and Aggregation of Resting and Mn^{2+} Activated Platelets in the Presence of Free RGD Peptides and RGD−HPG Conjugates at Their Respective IC_{50} Values

	microscopy of visible aggregates		aggregometry
assay	resting platelets	Mn^{2+} activated platelets	% aggregation
negative control	−−	−−	1
positive control	+++++		70
RGDF	−−	−−	5
C-1	−−	−−	5
C-2	−−	−−	5
C-3	−−	−−	5
C-4	−−	−−	5
C-5	−−	−−	5
C-6	−−	−−	10
C-7	−−	−−	5

CONCLUSIONS

We have demonstrated that RGD-based peptidomimetics can be conjugated to HPG polymers of varying molecular weight via divinyl sulfone and still retain receptor binding activity. The inhibitory effects of the HPG conjugates vary directly with the size and degree of substitution by the RGD peptides. We were able to increase the platelet inhibitory function of RGD by 2 to 3 orders of magnitude through conjugation to a macromolecular carrier, thereby increasing its local concentration as well as decreasing its dissociation kinetics. In addition, we found that, at high levels of RGD substitution, HPG conjugates may enhance platelet−fibrinogen binding to a certain extent and yet not result in activation by degranulation. Only in extreme cases do platelets aggregate spontaneously at a microscopic level: the use of the higher molecular weight carriers with moderate levels of conjugated peptides, such as C-5 and C-6, are suitable for

the development of an antithrombotic drug. Further studies of RGD and other peptidomimetics and their enhanced effectiveness through conjugation to macromolecular carriers are being investigated.

ACKNOWLEDGMENT

Funding: M.I.G.'s grant from Canadian Blood Services, CIHR STPTS.We would like to acknowledge the UBC Center for Blood Research, the Canadian Heart and Stroke Foundation, and the Canadian Institutes of Health Research for their support of J.G.Z.'s graduate studentship. We would also like to thank Bayer-Canadian Blood Services and Natural Science and Engineering Research Council of Canada grants to D.E.B., who supported R.K.K. through the Bayer-Canadian Blood Services-Hema-Quebec Partnership Fund. Infrastructure facility is supported by Canada Foundation for Innovation, Michael Smith Foundation for Health Research and BC Knowledge Development Fund. J.N.K. acknowledges CBS/CIHR New Investigator award in Transfusion Science. This study was supported by MGI's Infrastructure grant from Canadian Blood Services. In addition, we would like to recognize the contributions of donors and volunteers without whom this project could not have come to fruition.

LITERATURE CITED

(1) Walensky, L. D., Kung, A. L., Esche, I., Malia, T. J., Barbuto, S., Wright, R. D., Wagner, G., Verdine, G. L., and Korsmeyer, S. J. (2004) Activation of apoptosis in vivo by a hydrocarbon-stapled BH3 helix. *Science 3*, 1466–1470.

(2) Hauptmann, J. (2002) Pharmacokinetics of an emerging new class of Anticoagulant/antithrombotic drugs. *Eur. J. Clin. Pharmacol. 57*, 751–758.

(3) Gupta, A. S., Huang, G., Lestini, B. J., Sagnella, S., Kottke-Marchant, K., and Marchant, R. E. (2005) RGD-modified liposomes targeted to activated platelets as a potential vascular drug delivery system. *J. Thromb. Haemostas. 93*, 106–114.

(4) Ruoslahti, E., and Pierschbacher, M. D. (1987) New perspectives in cell adhesion: RGD and integrins. *Science 238*, 491–497.

(5) Beer, J. H., Springer, K. T., and Coller, B. S. (1992) Immobilized Arg-Gly-Asp (RGD) peptides of varying lengths as structural probes of the platelet glycoprotein IIb/IIIa receptor. *Blood 79*, 117–128.

(6) Gould, R. (1994) The integrin αIIbβ3 as an antithrombotic. *Perspect. Drug Discovery Des. 1*, 537–548.

(7) Gabriel, H. M., and Oliveira, E. I. (2006) Role of abciximab in the treatment of coronary artery disease. *Exp. Opin. Biol. Ther. 6*, 935–46.

(8) Ojima, I., Chakravarty, S., and Dong, Q. (1995) Antithrombotic agents: from RGD to peptide mimetics. *Bioorg. Med. Chem. 3*, 337–360.

(9) Lee, I., and Marchant, R. E. (2003) Molecular interaction studies of hemostasis: fibrinogen ligand-human platelet receptor interactions. *Ultramicroscopy 97*, 341–352.

(10) Mousa, S. A., Bozarth, J. M., Naik, U. P., and Slee, A. (2001) Platelet GPIIb/IIIa binding characteristics of small molecule RGD mimetic: distinct binding profile for Roxifiban. *Br. J. Pharmacol. 133*, 331–336.

(11) Nicholson, N. S., Panzer-Knodle, S. G., Salyers, A. K., Taite, B. B., King, L. W., Miyano, M., Gorczynski, R. J., Williams, M. H., Zupec, M. E., and Tjoeng, F. S. (1991) In vitro and in vivo effects of a peptide mimetic (SC-47643) of RGD as an antiplatelet and antithrombotic agent. *Thromb Res. 62*, 567–78.

(12) Sheu, J. R., and Huang, T. F. (1994) Ex-vivo and in-vivo antithrombotic effect of triflavin, an RGD-containing peptide. *Pharm. Pharmacol. 46*, 58–62.

(13) Temming, K., Lacombe, M., Schaapveld, R. Q., Orfi, L., Kéri, G., Poelstra, K., Molema, G., and Kok, R. J. (2006) Rational design of RGD-albumin conjugates for targeted delivery of the VEGF-R kinase inhibitor PTK787 to angiogenic endothelium. *ChemMedChem 1*, 1200–1203.

(14) Kim, W. J., Yockman, J. W., Jeong, J. H., Christensen, L. V., Lee, M., Kim, Y. H., and Kim, S. W. (2005) Soluble Flt-1 gene delivery using PEI-g-PEG-RGD conjugate for anti-angiogenesis. *J. Controlled Release 106*, 224–234.

(15) Janssena, A. P. C. A., Schiffelersa, R. M., ten Hagenb, T. L. M., Koninga, G. A., Schraac, A. J., Kokc, R. J., Storm, G., and Molemac, G. (2003) Peptide-targeted PEG-liposomes in anti-angiogenic therapy. *Int. J. Pharm. 254*, 55–58.

(16) Sunder, A., Mulhaupt, R., and Frey, H. (2000) Hyperbranched polyether-polyols based on polyglycerol: polarity design by block copolymerization with propylene oxide. *Macromolecules 33*, 309–314.

(17) Sunder, A., Heinemann, J., and Frey, H. (2000) Controlling the growth of polymer trees: concepts and perspectives for hyperbranched polymers. *Chem.-Eur. J. 6*, 2499–2506.

(18) Kainthan, R. K., Mulawan, E. B., Hatzikiriakos, S. G., and Brooks, D. E. (2006) Synthesis, characterization, and viscoelastic properties of high molecular weight branched polyglycerols. *Macromolecules 39*, 7708–7717.

(19) Kainthan, R. K., Hester, S. R., Levin, E., Devine, D. V., and Brooks, D. E. (2007) In vitro biological evaluation of high molecular weight hyperbranched polyglycerols. *Biomaterials 28*, 4581–4590.

(20) Kainthan, R. K., and Brooks, D. E. (2007) In vivo biological evaluation of high molecular weight hyperbranched polyglycerols. *Biomaterials 28*, 4779–4787.

(21) Anderluh, M., Stefanic, C. J., Kikelj, P., Janes, D., Murn, D., Nadrah, J., Tominc, K., Addicks, M., Giannis, E., Stegnar, A., and Dolenc, M. (2005) Design and synthesis of novel platelet fibrinogen receptor antagonists with 2H-1,4-benzoxazine-3(4H)-one scaffold. A systematic study. *Eur. J. Med. Chem. 40*, 25–49.

(22) Walsh, G. M., Sheehan, D., Kinsella, A., Moran, N., and O'Neill, S. (2004) Redox modulation of integrin [correction of integin] alpha IIb beta 3 involves a novel allosteric regulation of its thiol isomerase activity. *Biochemistry 43*, 473–480.

(23) Knischka, R., Lutz, P. J., Sunder, A., Mülhaupt, R., and Frey, H. (2000) Functional poly(ethylene oxide) multiarm star polymers: Core-first synthesis using hyperbranched polyglycerol initiators. *Macromolecules 33*, 315–320.

(24) Foster, M. R., Hornby, E. J., Brown, S., Kitchin, J., Hann, M., and Ward, P. (1993) Improved potency and specificity of Arg-Gly-Asp (RGD) containing peptides as fibrinogen receptor blocking drugs. *Thromb. Res. 72*, 231–245.

(25) Bassler, N., Loeffler, C., Mangin, P., Yuan, Y., Schwartz, M., Hagemeyer, C. E., Eisenhardt, S. U., Ahrens, I., Bode, C., Jackson, S. P., and Peter, K. (2007) A mechanistic model for paradoxical platelet activation by ligand-mimetic alphaIIb beta3 (GPIIb/IIIa) antagonists. *Arterioscler. Thromb. Vasc. Biol. 27*, e9−e15.

(26) Dickfeld, T., Ruf, A., Pogatsa-Murray, G., Muller, I., Engelmann, B., Taubitz, W., Fischer, J., Meier, O., and Gawaz, M. (2001) Differential antiplatelet effects of various glycoprotein IIb-IIIa antagonists. *Thromb. Res. 101*, 53–64.

BC8000408

Oral Delivery of Peptide Drugs Using Nanoparticles Self-Assembled by Poly(γ-glutamic acid) and a Chitosan Derivative Functionalized by Trimethylation

Fwu-Long Mi,[†] Yong-Yi Wu,[‡] Yu-Hsin Lin,[‡,§] Kiran Sonaje,[‡] Yi-Cheng Ho,[†] Chiung-Tong Chen,[||] Jyuhn-Huarng Juang,[⊥] and Hsing-Wen Sung*[,‡]

Department of Biotechnology, Vanung University, Chungli, Taoyuan, Department of Chemical Engineering, National Tsing Hua University, Hsinchu, Taiwan, ROC, Department of Biological Science and Technology, China Medical University, Taichung, Division of Biotechnology and Pharmaceutical Research, National Health Research Institutes, Zhunan, Miaoli, and Division of Endocrinology and Metabolism, Chung Gung University and Memorial Hospital, Kweishan, Taoyuan, Taiwan, ROC. Received February 26, 2008; Revised Manuscript Received May 3, 2008

In the study, chitosan (CS) was conjugated with trimethyl groups for the synthesis of *N*-trimethyl chitosan (TMC) polymers with different degrees of quaternization. Nanoparticles (NPs) self-assembled by the synthesized TMC and poly(γ-glutamic acid) (γ-PGA, TMC/γ-PGA NPs) were prepared for oral delivery of insulin. The loading efficiency and loading content of insulin in TMC/γ-PGA NPs were 73.8 $\pm$ 2.9% and 23.5 $\pm$ 2.1%, respectively. TMC/γ-PGA NPs had superior stability in a broader pH range to CS/γ-PGA NPs; the *in vitro* release profiles of insulin from both test NPs were significantly affected by their stability at distinct pH environments. At pH 7.0, CS/γ-PGA NPs became disintegrated, resulting in a rapid release of insulin, which failed to provide an adequate retention of loaded insulin, while the cumulative amount of insulin released from TMC/γ-PGA NPs was significantly reduced. At pH 7.4, TMC/γ-PGA NPs were significantly swelled and a sustained release profile of insulin was observed. Confocal microscopy confirmed that TMC40/γ-PGA NPs opened the tight junctions of Caco-2 cells to allow the transport of insulin along the paracellular pathway. Transepithelial-electrical-resistance measurements and transport studies implied that CS/γ-PGA NPs can be effective as an insulin carrier only in a limited area of the intestinal lumen where the pH values are close to the pK_a of CS. In contrast, TMC40/γ-PGA NPs may be a suitable carrier for transmucosal delivery of insulin within the entire intestinal tract.

INTRODUCTION

The oral route is the most convenient and comfortable means of administering protein/peptide drugs such as insulin, because the pain caused by injection could be avoided, leading to a higher patient compliance (*1*, *2*). However, protein/peptide drugs are readily degraded by the low pH of gastric medium in the stomach. Additionally, different digestive enzymes in the stomach and small intestine may lead to degradation of protein/peptide drugs (*3*–*5*). Therefore, a pH-responsive drug delivery system that is stable in the gastrointestinal (GI) tract and can swell significantly or disintegrate and subsequently release the loaded drug when adhering and infiltrating into the mucus of the intestinal tract is desired.

Chitosan (CS) and poly(γ-glutamic acid) (γ-PGA) have been used for the purpose of gene or drug delivery (*6*–*11*). In our recent study, a nanoparticle (NP) system composed of CS and γ-PGA for oral delivery of insulin via the paracellular transport was developed (*12*, *13*). We found that the prepared NPs remained intact in the pH range 2.5−6.6; however, outside this range, they became unstable and disintegrated, thus limiting the efficacy of insulin delivery. It is known that the natural pH environment in the GI tract varies from acidic in the stomach to slightly alkaline in the small intestine (*14*). CS lacks the advantage of good solubility at neutral pH values. It aggregates in solutions at pH values above 6.5, and only protonated CS (i.e., in its uncoiled configuration) can trigger the opening of tight junctions, thereby facilitating the paracellular transport of hydrophilic compounds (*15*). To overcome these problems, CS was conjugated with trimethyl groups for the synthesis of *N*-trimethyl chitosan (TMC) polymers with different degrees of quaternization. The partially quaternized TMC, which shows higher aqueous solubility than CS in a much broader pH range (*15*), was used in this study to prepare NPs.

The synthesized TMC polymers were analyzed by the proton nuclear magnetic resonance (^{1}H NMR) and Fourier transformed infrared (FT-IR) spectroscopy. Preparation of NPs self-assembled by TMC and γ-PGA (TMC/γ-PGA NPs) was reported and their mean particle sizes as well as zeta potential values in response to simulated GI media were examined by dynamic light scattering. Molecular dynamic (MD) simulations were used to investigate the structural changes of the self-assembled TMC/γ-PGA complex at distinct pH environments. Evaluation of test NPs in enhancing the intestinal paracellular transport was investigated *in vitro* in Caco-2 cell monolayers. The change of transepithelial electrical resistance (TEER) for the tightness of cell monolayers was measured and the paracellular transport of insulin was visualized using confocal laser scanning microscopy (CLSM) and quantified by enzyme-linked immunosorbent

* Correspondence to Hsing-Wen Sung, PhD, Professor, Department of Chemical Engineering/Bioengineering Program, National Tsing Hua University, Hsinchu, Taiwan 30013. Phone: 886-3-574-2504, Fax: 886-3-572-6832. E-mail: hwsung@che.nthu.edu.tw.

[†] Vanung University.

[‡] National Tsing Hua University.

[§] China Medical University.

[||] National Health Research Institutes.

[⊥] Chung Gung University and Memorial Hospital.

10.1021/bc800076n CCC: $40.75 © 2008 American Chemical Society
Published on Web 06/03/2008

assay (ELISA). Additionally, the release profiles of insulin from test NPs were studied in simulated GI media.

MATERIALS AND METHODS

Synthesis and Characterization of TMC. CS (MW 60 kDa) with a degree of deacetylation of approximately 85% was acquired from Koyo Chemical Co. Ltd. (Japan). TMC55 with a degree of quaternization of about 55% was synthesized from CS using a two-step methylation procedure described by Sieval et al. (*16*). By varying the number of reaction steps and the amount of base used, TMC25 and TMC40 with degrees of quaternization of approximately 25% and 40%, respectively, were synthesized by a method reported by Polnok et al. (*17*). The obtained TMC was purified by dialysis against water for 3 days and then freeze-dried. The purified TMC was analyzed by ^{1}H NMR (Varian Unityionva 500 NMR Spectrometer, Missouri) and FT-IR (Perkin-Elmer Spectrum RX1 FT-IR System, Buckinghamshire, England). Degrees of quaternization of the synthesized TMC polymers were estimated using ^{1}H NMR spectra (*17*).

Preparation and Characterization of NPs. TMC/γ-PGA NPs were prepared using a simple ionic-gelation method under magnetic stirring at room temperature. In brief, an aqueous γ-PGA (Vedan, Taichung, Taiwan, MW 60 kDa, 1.0 mg/mL, 2 mL) was added by flush mixing with a pipet tip into an aqueous TMC [1.2 mg/mL, 10 mL, in deionized (DI) water, pH 6.0]. The self-assembled NPs were collected by centrifugation at 15 000 rpm for 50 min. Supernatants were discarded and NPs were resuspended in DI water for further studies. The mean particle sizes and zeta potential values of NPs were measured using a Zetasizer (3000HS, Malvern Instruments Ltd., Worcestershire, UK). The characteristics of NPs were investigated at distinct pH values (simulating the pH environments in the GI tract) (*18*–*20*).

MD Simulation of NPs at Distinct pH Environments. MD simulations were performed with the program NAMD (*21*) using parameters adapted from the CHARMM (*22*) force field. TMC and γ-PGA used in simulations were oligomers consisting of 10 monomers. The models were minimized to remove unfavorable contacts, brought to 310 K by velocity rescaling and equilibrated for 1 ns. Before any MD trajectory was run, 40 ps of energy minimization was performed to relax conformational and structural tensions. This minimum structure was the starting point for MD simulations. For this purpose, the molecule was embedded into a cubic simulation box of 80 Å. A cutoff distance of 12 Å was employed for the nonbonded and electrostatic interactions. The heating process was performed from 0 to 310 K through Langevin damping with a coefficient of 10 ps^{-1}. A time step of 2 fs was employed for rescaling the temperature. After 20 ps heating to 310 K, equilibration trajectories of 1 ns were recorded, which provided the data for the structural and thermodynamic evaluations. The equations of motion were integrated with the Shake algorithm with a time step of 1 fs. Figures displaying atomistic pictures of molecules were generated using VMD (*23*).

Preparation of Insulin-Containing NPs. A sample of 100 mg of insulin (from bovine pancreas, 27.4 IU/mg, Sigma-Aldrich, St. Louis, MO) was dissolved in 10 mL of 0.01 N HCl, and this solution was neutralized with 0.1 N NaOH (*24*). The insulin solution was then diluted with DI water to make a 3 mg/mL insulin stock solution. The insulin stock solution (1 mL) was premixed with an aqueous γ-PGA (3 mg/mL, 1 mL). Subsequently, $MgSO_4$ (6 mg/mL, 1 mL) was blended into the mixture and thoroughly stirred for 30 min. The mixed solution was added into an aqueous TMC (1.2 mg/mL, 10 mL) under magnetic stirring at room temperature as described before.

To determine their insulin loading content and loading efficiency, NPs were collected by centrifugation at 15 000 rpm, 4 °C for 50 min, and the insulin concentration in the supernatant was assayed by high-performance liquid chromatography (HPLC). The drug loading content and loading efficiency of NPs were determined as follows (*12*, *13*).

$$\text{Loading Content (\%)} = \frac{\text{total amount of insulin} - \text{free insulin}}{\text{weight of NPs}} \times 100\%$$

$$\text{Loading Efficiency (\%)} = \frac{\text{total amount of insulin} - \text{free insulin}}{\text{total amount of insulin}} \times 100\%$$

The release profiles of insulin from test NPs were investigated in distinct dissolution media (pH 2.5, 6.4, 7.0, and 7.4, simulating the pH environments in the GI tract) at 37 °C under agitation (100 rpm, DISTEK-2230A, North Brunswick, NJ). At particular time intervals, samples were taken out and centrifuged and supernatants were used for the HPLC analysis. The amount of insulin released was expressed as a percentage of the total insulin associated with NPs as calculated from the loading efficiency (*25*). The stability of the released insulin was determined by analyzing its conformation using an Aviv 202 spectropolarimeter (Aviv Associates, Lakewood, NJ) and comparing the spectrum with that of standard insulin (*26*).

TEER Measurements and Transport Studies. Caco-2 cell monolayers were cultured on the tissue-culture-treated polycarbonate filter (diameter 24.5 mm, growth area 4.7 cm^2) in Costar Transwell 6 wells/plates (Corning Costar Corp., NY) and were used for transport experiments approximately 21 days after seeding (TEER values in the range 600−800 Ω cm^2). Evaluation of test NPs (0.2 mg/mL, 1 mL) in enhancing the intestinal paracellular transport at pH 6.6, 7.0, and 7.4 (in the donor compartment; at pH 7.4 in the receiver compartment) was investigated in Caco-2 cell monolayers (*27*). The change of TEER for the tightness of cell monolayers was measured with a Millicell-Electrical Resistance System (Millipore Corp., Bedford, MA). Simultaneously, samples (50 μL) were collected from the receiver compartment at distinct time intervals and the insulin concentrations were measured using ELISA (bovine insulin kit, Mercodia AB, Uppsala, Sweden) (*28*). The transport of insulin through Caco-2 cell monolayers was expressed as the cumulative insulin transport (*29*).

Fluorescent NP Preparation and CLSM Visualization. Cy3-labeled insulin (Cy3-insulin) was synthesized by a method described in the literature (*30*). To remove the unconjugated Cy3, the synthesized Cy3-insulin was dialyzed in the dark against 5 L of 0.01 N HCl and replaced on a daily basis until no fluorescence was detected in the supernatant. The resultant Cy3-insulin was lyophilized in a freeze−dryer. Fluorescent NPs loaded with Cy3-insulin were then prepared for the CLSM study as per the procedure described above. The transport medium (pH 7.0) containing fluorescent NPs (0.2 mg/mL, 1 mL) was introduced into the donor compartment of Caco-2 cell monolayers, while the medium in the receiver compartment was maintained at pH 7.4 (*31*). After incubation for specific time intervals at 37 °C, test samples were aspirated. Cells were then washed twice with prewarmed phosphate buffered saline (PBS) before they were fixed in 3.7% paraformaldehyde (*32*). Subsequently, the fixed cells were examined under a CLSM (TCS SL, Leica, Germany).

Visualization of Opening Tight Junctions. Caco-2 cell monolayers were incubated with test NPs (0.2 mg/mL, 1 mL). After 120 min, the incubated NPs were removed and cells were fixed in 3.7% paraformaldehyde. Cells were washed three times with PBS and permeabilized with 0.2% Triton X-100 and RNase (100 μg/mL) for 15 min at 37 °C. The wash was repeated and cells were blocked with 5% normal goat serum (Jackson ImmunoResearch Laboratories, West Grove, PA) in PBS for

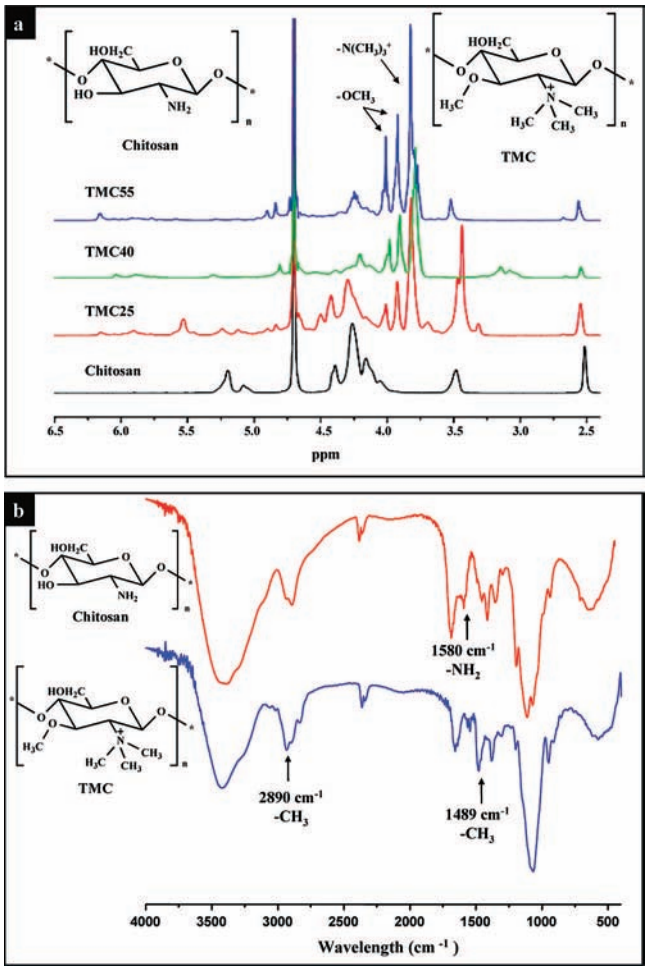

Figure 1. (a) ^{1}H NMR spectra of chitosan (CS) and *N*-trimethyl chitosan (TMC) polymers with different degrees of quaternization; (b) FT-IR spectra of CS and TMC40.

60 min at 37 °C. Subsequently, cells were treated with the rabbit anti-ZO-1 mAb (Zymed Laborates, San Francisco, CA) at 1:50 dilution for 60 min at 37 °C. After washing three times with PBS, cells were incubated in the Cy-5 conjugated goat antirabbit IgG at 1:100 dilution (Jackson ImmunoResearch Laboratories). Additionally, cells were costained to visualize nuclei by propidium iodide (PI, P4864, Sigma-Aldrich, St. Louis, MO). The stained cells were evenly mounted on slides and examined under a CLSM. Superimposed images were performed with LCS Lite software (version 2.0).

Statistical Analysis. Comparison between two groups was analyzed by the one-tailed Student's *t*-test and multiple group comparison was performed by one-way ANOVA followed by Fisher's LSD using statistical software (SPSS, Chicago, IL). All data are presented as a mean value with its standard deviation indicated (mean ± SD). Differences were considered to be statistically significant when p values were less than 0.05.

RESULTS AND DISCUSSION

Characterization of TMC. Figure 1a,b shows the ^{1}H NMR and FT-IR spectra of CS and the synthesized TMC, respectively. As shown in Figure 1a, TMC showed a new signal at 3.82 ppm [$-N(CH_3)_3^+$], while those observed at 3.82−4.04 ppm corresponded to $-OCH_3$ (*13*, *33*). In the FT-IR spectra, the intensity of the characteristic peak (2890 cm^{-1}, C−H stretch) increased and a new peak at 1489 cm^{-1} ($-CH_3$ antisym deformation) was observed on TMC, while the characteristic peak (1580 cm^{-1}) of $-NH_2$ on CS decreased (*33*). These results indicated that TMC was successfully synthesized. Degrees of quaternization of the synthesized TMC polymers, estimated from the obtained ^{1}H NMR spectra, were 24.8% (TMC25), 42.8% (TMC40), and 54.5% (TMC55), respectively.

Table 1. Mean Particle Sizes, Zeta Potential Values, and Polydispersity Indices of Nanoparticles (NPs) Self-Assembled by TMC Polymers with Different Degrees of Quaternization and γ-PGA (n = 5 batches)[a]

	mean particle size (nm)	zeta potential (mV)	polydispersity index
CS/γ-PGA NPs	104.1 ± 1.2	36.2 ± 2.5	0.11 ± 0.02
TMC25/γ-PGA NPs	101.3 ± 3.1	30.9 ± 2.1	0.13 ± 0.04
TMC40/γ-PGA NPs	106.3 ± 2.3	32.3 ± 2.1	0.15 ± 0.14
TMC55/γ-PGA NPs	114.6 ± 2.3	30.6 ± 3.8	0.12 ± 0.03

[a] TMC: *N*-trimethyl chitosan. CS: Chitosan. γ-PGA: Poly(γ-glutamic acid).

Preparation of NPs. In the study, NPs were self-assembled instantaneously upon addition of an aqueous γ-PGA into an aqueous TMC (with a TMC/γ-PGA weight ratio of 6:1) under magnetic stirring at room temperature. The amount of positively charged TMC significantly exceeded that of negatively charged γ-PGA; some of excessive TMC molecules were entangled onto the surfaces of NPs, thus displaying a positive surface charge (Table 1). The degree of quaternization on TMC had little effects on the mean particle size and zeta potential of NPs.

pH-Responsive Characteristics of NPs. The stomach pH is about 1.0−2.0 in the presence of food, while the fasting pH of the stomach is 2.5−3.7 (*18–20*). The pH values in the duodenum and the jejunum and proximal ileum are 6.0−6.6 and 6.6−7.0, respectively, while the mean pH in the distal ileum and in the body fluid at intercellular spaces between enterocytes is about 7.4 (*14*, *19*, *20*). Therefore, characterization of test NPs in response to distinct pH environments must be investigated.

Peppas et al. prepared poly(methacrylic acid-*g*-ethylene glycol) (PMAA-g-EG) NPs for oral administration of insulin (*24*, *34*, *35*). It was shown that the prepared NPs were pH-responsive and mucoadhesive. The results of TEER measurements and transport studies implied that PMAA-g-EG NPs were effective as a transmucosal carrier and able to open the tight junctions between Caco-2 cells.

In contrast to PMAA, TMC is a positively charged polymer and has been used as an intestinal permeation enhancer (*29*), and its mechanism of opening tight junctions is similar to that of protonated CS (*15*). Additionally, TMC showed no indication of epithelial damage or cytotoxicity (*15*). The mucoadhesive characteristics of the CS-coated NPs (FITC-labeled) in vivo were previously reported by our group (*36*). In this study, the FITC-labeled CS NPs were orally administered in a rat model and the intestinal segments were retrieved 3 h afterwards. It was found that the administered CS NPs were colocalized with ZO-1 proteins at the epithelial junctions. Also, it has been reported that TMC-containing formulations exceeded the potency of CS in mucoadhesion (*29*). The mucoadhesive properties of CS and TMC have also been reported in large animals such as pigs (*37*).

The basic concept of the study is that the orally administered NPs with excessive mucoadhesive TMC (*29*) on their surfaces may adhere and infiltrate into the mucus of the intestinal tract, and then mediate transiently opening the tight junctions between enterocytes (Figure 2). It is known that the tight junctions opened by absorption enhancers are less than 20 nm in width (*38–40*). Consequently, the NPs infiltrated into the mucus must become unstable (swelling or disintegration); thus, their loaded insulin can be released and permeated through the paracellular pathway to the bloodstream.

It is known that the pK_a values of CS (amine groups) and γ-PGA (carboxylic groups) are 6.5 and 2.9, respectively (*12*).

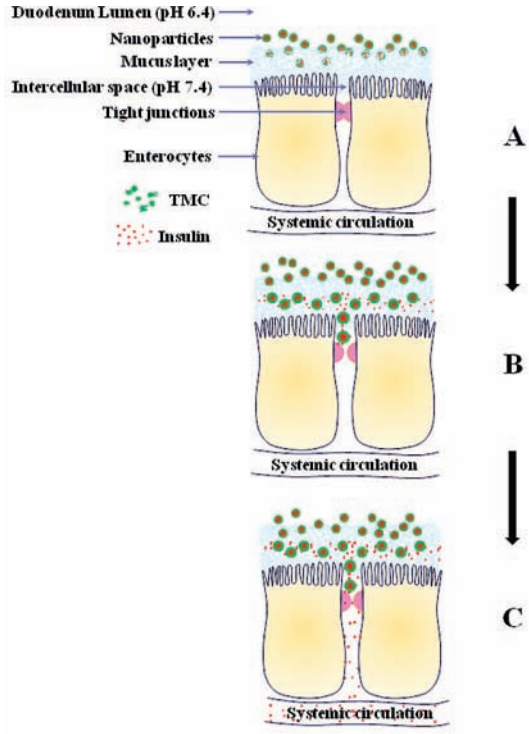

Figure 2. Schematic illustrations of the presumed mechanism of opening tight junctions by test nanoparticles and transporting of their encapsulated drug (using duodenum as an example).

In the study, NPs were prepared in DI water (pH 6.0). At pH 6.0, CS (TMC25) and γ-PGA were ionized. The ionized CS (TMC25) and γ-PGA could form polyelectrolyte complexes, which resulted in a matrix structure with a spherical shape. At pH 1.2−2.0, most carboxylic groups on γ-PGA were in the form of −COOH. Hence, there was little electrostatic interaction between CS (TMC25) and γ-PGA; thus, NPs became disintegrated (Table 2). Similarly, at pH values above 6.6, the free amine groups on CS (TMC25) were deprotonated, thus leading to the disintegration of NPs. This might limit the efficacy of drug delivery and absorption in the small intestine.

With increasing the degree of quaternization on TMC (TMC40 and TMC55), the stability of NPs in the pH range 6.6−7.4 increased significantly. However, the swelling of TMC55/γ-PGA NPs at pH 7.4 was minimal (due to the highly quaternized TMC55), which might limit the release of loaded drugs. In contrast, TMC40/γ-PGA NPs swelled significantly with increasing pH value (Figure 3). Therefore, TMC40/γ-PGA NPs were chosen to load insulin and used for the rest of the study. As shown in Table 2, TMC40/γ-PGA NPs still retained a positive surface charge with a zeta potential value of 17.3 mV at pH 7.4.

The results of MD simulations showed that the molecular chains of TMC40 (in blue) and γ-PGA (in red) in their self-assembled complex were tightly entangled to each other at pH 6.0 (Figure 4). The surface of the complex was dominated by TMC40 molecules. Relaxations of TMC40 and γ-PGA molecular chains at pH 2.5 (pH 7.4) resulted in a moderate (significant) swelling of the TMC40/γ-PGA complex, while its surface was still dominated by the positively charged TMC molecules, thus retaining a positive surface charge.

Table 2. Mean Particle Sizes, Zeta Potential Values, and Polydispersity Indices of Nanoparticles (NPs) Self-Assembled by TMC Polymers with Different Degrees of Quaternization and γ-PGA at Distinct pH Environments (n = 5 batches)[a]

	mean particle size (nm)	zeta potential (mV)	polydispersity index
	CS/γ-PGA NPs		
pH 1.2	N/A	N/A	1
pH 2.0	N/A	N/A	1
pH 2.5	113.3 ± 1.6	38.6 ± 0.8	0.14 ± 0.01
pH 6.0	104.1 ± 1.2	36.2 ± 2.5	0.11 ± 0.02
pH 6.6	245.6 ± 4.5	12.9 ± 0.4	0.17 ± 0.11
pH 7.0	N/A	N/A	1
pH 7.4	N/A	N/A	1
	TMC25/γ-PGA NPs		
pH 1.2	N/A	N/A	1
pH 2.0	N/A	N/A	1
pH 2.5	396.4 ± 4.7	32.1 ± 1.6	0.32 ± 0.11
pH 6.0	101.3 ± 3.1	30.9 ± 2.1	0.13 ± 0.04
pH 6.6	N/A	N/A	1
pH 7.0	N/A	N/A	1
pH 7.4	N/A	N/A	1
	TMC40/γ-PGA NPs		
pH 1.2	N/A	N/A	1
pH 2.0	N/A	N/A	1
pH 2.3	272.2 ± 2.3	38.6 ± 2.7	0.25 ± 0.23
pH 2.5	252.4 ± 3.5	35.4 ± 1.1	0.21 ± 0.04
pH 6.0	106.3 ± 2.3	32.3 ± 2.1	0.15 ± 0.14
pH 6.6	238.3 ± 3.1	24.3 ± 1.4	0.09 ± 0.03
pH 7.0	296.7 ± 4.7	20.4 ± 0.3	0.18 ± 0.11
pH 7.4	498.4 ± 6.8	17.3 ± 0.6	0.38 ± 0.21
	TMC55/γ-PGA NPs		
pH 1.2	N/A	N/A	1
pH 2.0	252.5 ± 4.1	35.6 ± 4.2	0.16 ± 0.08
pH 2.5	221.4 ± 3.5	32.5 ± 3.4	0.15 ± 0.02
pH 6.0	114.6 ± 2.3	30.6 ± 3.8	0.12 ± 0.03
pH 6.6	141.2 ± 1.6	24.8 ± 3.4	0.15 ± 0.02
pH 7.0	144.6 ± 4.8	20.4 ± 1.7	0.18 ± 0.14
pH 7.4	141.2 ± 0.9	18.9 ± 4.1	0.11 ± 0.11

[a] N/A: Precipitation of aggregates was observed; TMC: *N*-trimethyl chitosan; CS: chitosan; γ-PGA: Poly(γ-glutamic acid).

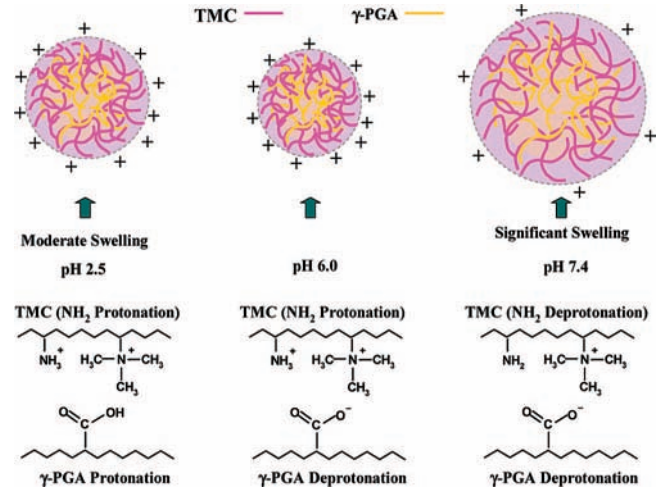

Figure 3. Schematic illustrations of the pH-responsive characteristics of TMC40/γ-PGA NPs at distinct pH environments. TMC: *N*-trimethyl chitosan. γ-PGA: poly(γ-glutamic acid).

Characteristics of Insulin-Containing NPs and Their Release Profiles. In the study, we found that the loading efficiency and loading content of insulin in TMC40/γ-PGA NPs were only 20.8 ± 1.9% and 4.2 ± 1.6% (n = 5 batches), respectively. To increase the amount of insulin loaded, Mg^{2+} was blended in the premixed aqueous insulin/γ-PGA in the

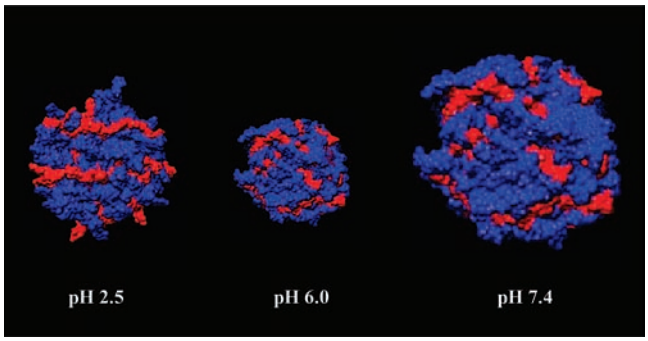

Figure 4. Structural changes of the self-assembled TMC40/γ-PGA complex at distinct pH environments obtained by molecular dynamic simulations. TMC: *N*-trimethyl chitosan (in blue). γ-PGA: poly(γ-glutamic acid) (in red).

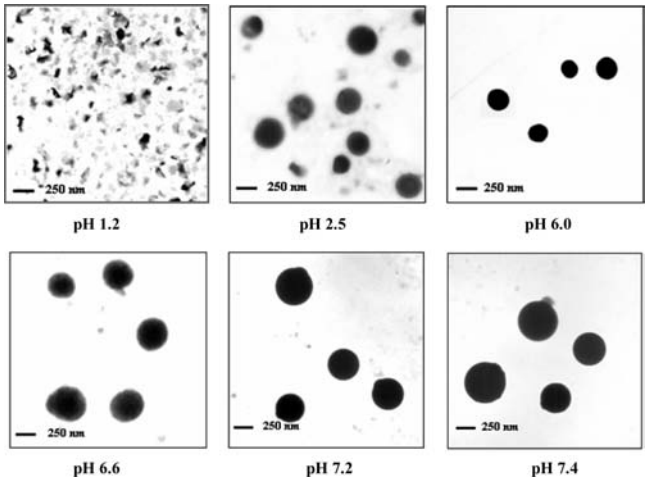

Figure 5. TEM micrographs of the insulin-containing TMC40/γ-PGA nanoparticles at distinct pH environments. TMC: *N*-trimethyl chitosan. γ-PGA: poly(γ-glutamic acid).

preparation of NPs. It was reported in our previous study that insulin could conjugate with γ-PGA via divalent metal ions such as Zn^{2+} (*13*, *36*), thus increasing the drug loading efficiency and loading content in NPs. In the present study, we found that the NPs prepared with Mg^{2+} had a better stability than their counterparts with Zn^{2+} (data not shown). Mg^{2+} is one of the most abundant ions present in living cells. It was reported that daily Mg^{2+} administration in diabetic patients improves insulin-mediated glucose uptake (*41*). In the presence of Mg^{2+}, the insulin loading efficiency (73.8 ± 2.9%) and loading content (23.5 ± 2.1%, $n = 5$ batches) in TMC40/γ-PGA NPs increased significantly.

The morphology, mean particle sizes, zeta potential values, and polydispersity indices of the insulin-containing TMC40/γ-PGA NPs at distinct pH values are shown in Figure 5 and Table 3, respectively. As shown, the pH-responsive characteristics of the insulin-containing TMC40/γ-PGA NPs were similar to their empty counterparts (Table 2).

Figure 6a shows the release profiles of insulin from the insulin-containing CS/γ-PGA and TMC40/γ-PGA NPs at pH 2.5, 6.4, 7.0, and 7.4, simulating the pH environments in the stomach before a meal (similar to the conventional injectable insulin therapy), the small intestine, and the body fluid at intercellular spaces between enterocytes, respectively. As mentioned already, the insulin-containing TMC40/γ-PGA NPs were prepared at pH 6.0, which was close to the pI of native insulin. It has been reported that at this pH value, insulin associated with CS/TPP NPs primarily through hydrophobic interactions and the associated insulin released rapidly and

Table 3. Mean Particle Sizes, Zeta Potential Values, and Polydispersity Indices of Insulin-Containing TMC40/γ-PGA Nanoparticles at Distinct pH Environments ($n = 5$ batches)[a]

	mean particle size (nm)	zeta potential (mV)	polydispersity index
pH 1.2	N/A	N/A	1
pH 2.0	N/A	N/A	1
pH 2.3	312.2 ± 2.2	36.6 ± 1.7	0.23± 0.21
pH 2.5	292.5 ± 2.5	32.1 ± 1.4	0.18± 0.13
pH 6.0	148.6 ± 2.1	30.1 ± 1.8	0.12± 0.01
pH 6.6	262.2 ± 3.2	25.5 ± 2.4	0.11± 0.15
pH 7.0	336.7 ± 2.3	18.4 ± 1.3	0.23± 0.13
pH 7.4	522.4 ± 5.9	14.2 ± 0.6	0.44± 0.36

[a] TMC: *N*-trimethyl chitosan. γ-PGA: Poly(γ-glutamic acid). N/A: Precipitation of aggregates was observed.

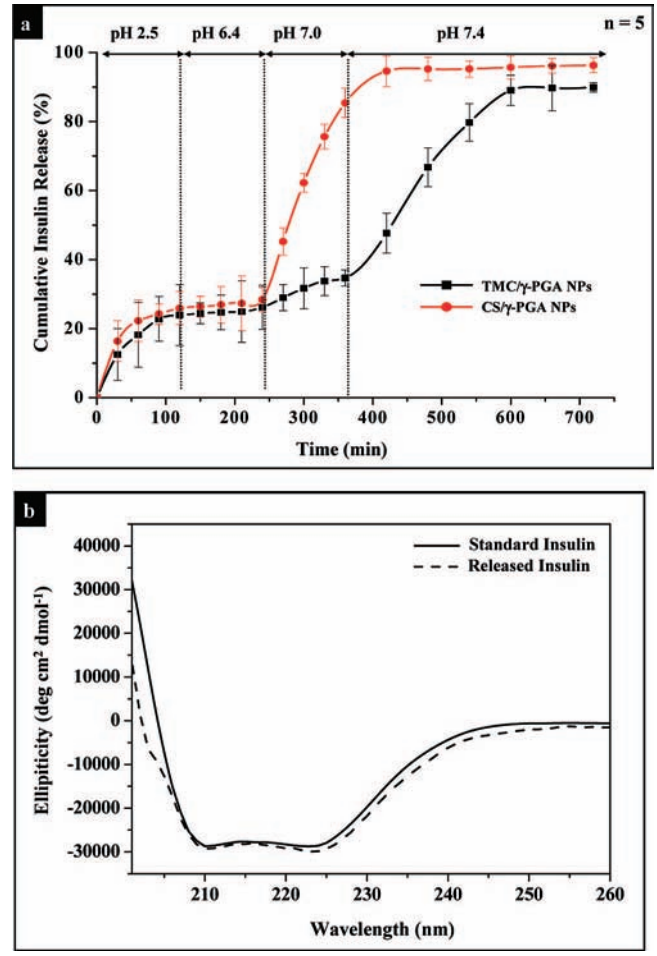

Figure 6. (a) Release profiles of insulin from CS/γ-PGA and TMC40/γ-PGA nanoparticles (NPs) at pH 2.5, 6.4, 7.0, and 7.4, simulating the pH environments in the fasting stomach, the small intestine, and the body fluid at intercellular spaces between enterocytes, respectively. (b) Circular dichroism spectra of the insulin released from test nanoparticles at pH 7.4 and the standard insulin. CS: chitosan. TMC: *N*-trimethyl chitosan. γ-PGA: poly(γ-glutamic acid).

completely in aqueous media at pH 2.0 to 7.4 (*25*). Therefore, the release of insulin from the prepared NPs should be mainly influenced by their pH-dependent swelling property.

At pH 2.5 (the stomach before meal) and 6.4 (the duodenum), the release profiles of insulin from both test NPs were similar. At pH 7.0 (the jejunum and the proximal ileum), CS/γ-PGA NPs became disintegrated (Table 2), resulting in a rapid release of insulin, which failed to provide an adequate retention of loaded insulin (approximately 85% of the loaded insulin was released). In contrast, for TMC/γ-PGA NPs, the cumulative amount of insulin released was significantly reduced to about

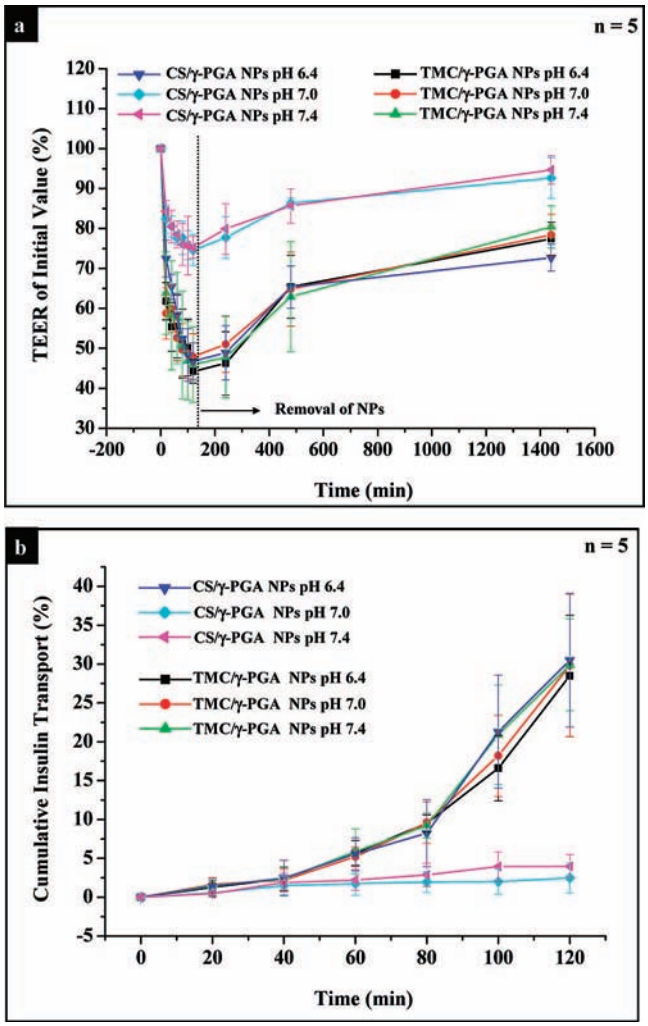

Figure 7. (a) Effects of CS/γ-PGA and TMC40/γ-PGA nanoparticles (NPs) on TEER values of Caco-2 cell monolayers at distinct pH values. (b) Cumulative amounts of insulin transported through Caco-2 cell monolayers incubated with test nanoparticles as a function of time at distinct pH values. CS: chitosan. TMC: *N*-trimethyl chitosan. γ-PGA: poly(γ-glutamic acid).

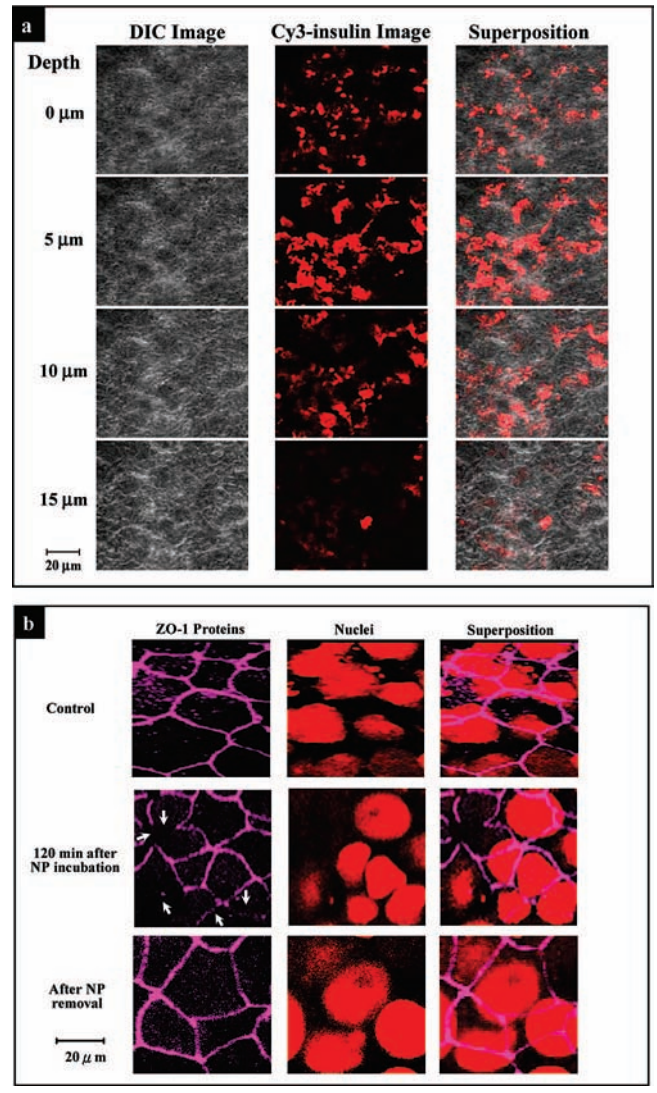

Figure 8. (a) DIC and fluorescence images (taken by an inverted confocal laser scanning microscope) of four optical sections (at different depths) of Caco-2 cell monolayers 120 min after incubation with the Cy3-insulin containing TMC40/γ-PGA NPs. (b) Fluorescence images of Caco-2 cell monolayers immunofluorescently stained for ZO-1 proteins after incubation with TMC40/γ-PGA NPs for 120 min. TMC: *N*-trimethyl chitosan. γ-PGA: poly(γ-glutamic acid).

30%, due to their comparative stability at pH 7.0. At pH 7.4 (the distal ileum and the body fluid at intercellular spaces), TMC/γ-PGA NPs were significantly swelled and a sustained release profile of insulin was observed. As indicated by the circular dichroism spectra (Figure 6b), no significant conformation change was observed for the insulin released from TMC/γ-PGA NPs at pH 7.4 as compared to the standard insulin.

TEER Measurements and Insulin Transport Studies. Effects of CS/γ-PGA and TMC40/γ-PGA NPs on the TEER and the amount of insulin transported across Caco-2 cell monolayers as a function of time at distinct intestinal pH environments are shown in Figure 7a,b. As shown, incubation of CS/γ-PGA NPs on the apical side of Caco-2 cell monolayers at pH 6.4 led to an immediate reduction in TEER and a significant amount of insulin transported. However, at pH 7.0 and 7.4, the reduction in TEER and the amount of insulin transported through Caco-2 cells were significantly limited. These results implied that CS/γ-PGA NPs can be effective as an insulin carrier only in a limited area of the intestinal lumen (the duodenum) where the pH values are close to the pK_a of CS.

In contrast, TMC40/γ-PGA NPs significantly decreased the TEER and increased the amount of insulin transported across Caco-2 cell monolayers at all test intestinal pH environments, indicating a specific interaction of the cationic NPs (Table 3) with components of the tight junctions at neutral pH values. These findings suggested that TMC40/γ-PGA NPs may be a suitable carrier for transmucosal delivery of protein/peptide drugs within the entire intestinal lumen (the duodenum, jejunum, and ileum). After removal of the incubated test particles, a gradual increase in TEER was observed, indicating that the effect of TMC40/γ-PGA NPs on the tight junction's regulation is transient and reversible.

CLSM Visualization. Figure 8a shows the differential interference contrast (DIC) and fluorescence images of 4 optical sections of Caco-2 cell monolayers 120 min after incubation with the Cy3-insulin-containing TMC40/γ-PGA NPs using CLSM. This noninvasive method allows for optical sectioning and imaging of the transport of insulin across Caco-2 cell monolayers, without disrupting their structure (*42*). As shown, fluorescent images were observed at intercellular spaces between adjacent cells, suggesting that TMC40/γ-PGA NPs opened the tight junctions of Caco-2 cells to allow the transport of insulin by passive diffusion along the paracellular pathway. These

findings confirmed the results observed in our TEER measurements and insulin-transport experiments (Figure 7a,b).

The opening of the tight junctions of cell monolayers by TMC40/γ-PGA NPs was shown in Figure 8b. As shown, the staining for ZO-1 tight junction proteins showed a continuous ring appearance between adjacent cells before incubation with test NPs (control). After incubation with test NPs, the staining for ZO-1 proteins appeared discontinuous (indicated by white arrows), indicating the opening of cell tight junctions. ZO-1 proteins are thought to be a linkage molecule between occludin and actin cytoskeleton and play important roles in the rearrangement of cell−cell contacts (*43*, *44*). After removal of NPs, the discontinuous staining for ZO-1 proteins appeared again, indicating the restoration of cell tight junctions.

CONCLUSIONS

A pH-responsive NP system self-assembled by TMC and γ-PGA for oral delivery of insulin was successfully prepared in the study. TEER experiments showed that TMC/γ-PGA NPs were able to open the tight junctions between Caco-2 cells, and their effect on the tight junction's integrity appeared to be reversible. CLSM confirmed that TMC/γ-PGA NPs opened the tight junctions of cell monolayers to allow the transport of insulin along the paracellular pathway at all test intestinal pH environments. These findings suggested that TMC40/γ-PGA NPs may be a suitable carrier for transmucosal delivery of protein/peptide drugs within the entire intestinal lumen.

ACKNOWLEDGMENT

This work was supported by a grant from the National Science Council (NSC 96-2120-M-007-004), Taiwan, Republic of China.

LITERATURE CITED

(1) Carino, G. P., and Mathiowitz, E. (1999) Oral insulin delivery. *Adv. Drug Delivery Rev. 35*, 249–257.

(2) Zambanini, A., Newson, R. B., Maisey, M., and Feher, M. D. (1999) Injection related anxiety in insulin-treated diabetes. *Diabetes Res. Clin. Pract. 46*, 239–246.

(3) Owens, D. R., Zinman, B., and Bolli, G. (2003) Alternative routes of insulin delivery. *Diabetes Med. 20*, 886–898.

(4) Khafagy, E. S., Morishita, M., Onuki, Y., and Takayama, K. (2007) Current challenges in non-invasive insulin delivery systems: A comparative review. *Adv. Drug Delivery Rev. 59*, 1521–1546.

(5) Binder, C., Lauritzen, T., Faber, O., and Pramming, S. (1984) Insulin pharmacokinetics. *Diabetes Care 7*, 188–199.

(6) Kim, T. H., Jiang, H. L., Jere, D., Park, I. K., Cho, M. H., Nah, J. W., Choi, Y. J., Akaike, T., and Cho, C. S. (2007) Chemical modification of chitosan as a gene carrier in vitro and in vivo. *Prog. Polym. Sci. 32*, 726–753.

(7) Kato, Y., Onishi, H., and Machida, Y. (2000) Evaluation of *N*-succinyl-chitosan as a systemic long-circulating polymer. *Biomaterials 21*, 1579–1585.

(8) Smoum, R., Rubinstein, A., and Srebnik, M. (2006) Chitosan-pentaglycine-phenylboronic acid conjugate: A potential colon-specific platform for calcitonin. *Bioconjugate Chem. 17*, 1000–1007.

(9) Wong, K., Sun, G., Zhang, X. Q., Dai, H., Liu, Y., He, C. B., and Leong, K. W. (2006) PEI-g-chitosan, a novel gene delivery system with transfection efficiency comparable to polyethylenimine in vitro and after liver administration in vivo. *Bioconjugate Chem. 17*, 152–158.

(10) Liang, H. F., Chen, S. C., Chen, M. C., Lee, P. W., Chen, C. T., and Sung, H. W. (2006) Paclitaxel-loaded poly(γ-glutamic acid)-poly(lactide) nanoparticles as a targeted drug delivery system against cultured HepG2 cells. *Bioconjugate Chem. 17*, 291–299.

(11) Loretz, B., Thaler, M., and Bernkop-Schnurch, A. (2007) Role of sulfhydryl groups in transfection? A case study with chitosan-NAC nanoparticles. *Bioconjugate Chem. 18*, 1028–1035.

(12) Lin, Y. H., Chung, C. K., Chen, C. T., Liang, H. F., Chen, S. C., and Sung, H. W. (2005) Preparation of nanoparticles composed of chitosan/poly-γ-glutamic acid and evaluation of their permeability through Caco-2 cells. *Biomacromolecules 6*, 104–1112.

(13) Lin, Y. H., Mi, F. L., Chen, C. T., Chang, W. C., Peng, S. F., Liang, H. F., and Sung, H. W. (2007) Preparation and characterization of nanoparticles shelled with chitosan for oral insulin delivery. *Biomacromolecules 8*, 146–152.

(14) Evans, D. F., Pye, G., Bramley, R., Clark, A. G., Dyson, T. J., and Hardcastle, J. D. (1988) Measurement of gastrointestinal pH profiles in normal ambulant human subjects. *Gut 29*, 1035–1041.

(15) Kotzé, A. F., Lueβen, H. L., de Leeuw, B. J., de Boer, B. G., Verhoef, J. C., and Junginger, H. E. (1998) Comparison of the effect of different chitosan salts and N-trimethyl chitosan chloride on the permeability of intestinal epithelial cells (Caco-2). *J. Controlled Release 51*, 35–46.

(16) Sieval, A. B., Thanou, M., Kotze, A. F., Verhoef, J. C., Brussee, J., and Junginger, H. E. (1998) Preparation and NMR characterization of highly substituted N-trimethyl chitosan chloride. *Carbohydr. Polym. 36*, 157–165.

(17) Polnok, A., Borchard, G., Verhoef, J. C., Sarisuta, N., Junginger, H. E., Borchard, G., Verhoef, J. C., Sarisuta, N., and Junginger, H. E. (2004) Influence of methylation process on the degree of quaternization of *N*-trimethylchitosan chloride. *Eur. J. Pharm. Biopharm. 57*, 77–83.

(18) Thouzeau, C., Peters, G., Le Bohec, C., and Le Maho, Y. (2004) Adjustments of gastric pH, motility and temperature during long-term preservation of stomach contents in free-ranging incubating king penguins. *J. Exp. Biol. 207*, 2715–2724.

(19) Eaimtrakarn, S., Itoh, Y., Kishimoto, J. I., Yoshikawa, Y., Shibata, N., and Takada, K. (2001) Retention and transit of intestinal mucoadhesive films in rat small intestine. *Int. J. Pharm. 224*, 61–67.

(20) Shargel, L. and Yu, A. (1999) *Applied Biopharmaceutics and Pharmacokinetics*, pp 99−128, 4th ed., McGraw-Hill, New York.

(21) Nelson, M., Humphrey, W., Gursoy, A., Dalke, A., Kalé, L., and Skeel, R. D. (1996) NAMD: A parallel object-oriented molecular dynamics program. *Int. J. Supercomput. Appl. High Perform. Comput. 10*, 251–256.

(22) Brooks, B. R., Bruccoleri, R. E., Olafson, B. D., States, D. J., Swaminathan, S., and Karplus, M. (1983) CHARMM: A program for macromolecular energy, minimization, and dynamics calculations. *J. Comput. Chem. 4*, 187–217.

(23) Humphrey, W., Dalke, A., and Schulten, K. (1996) VMD: Visual molecular dynamics. *J. Mol. Graph. 14*, 27–38.

(24) Kim, B., and Peppas, N. A. (2003) In vitro release behavior and stability of insulin in complexation hydrogels as oral drug delivery carriers. *Int. J. Pharm. 266*, 29–37.

(25) Ma, Z., Yeoh, H. H., and Lim, L. Y. (2002) Formulation pH modulates the interaction of insulin with chitosan nanoparticles. *J. Pharm. Sci. 91*, 1396–1404.

(26) Quaglia, F., De Rosa, G., Granata, E., Ungaro, F., Fattal, E., and La Rotonda, M. I. (2003) Feeding liquid, non-ionic surfactant and cyclodextrin affect the properties of insulin-loaded poly-(lactide-co-glycolide) microspheres prepared by spray-drying. *J. Controlled Release 86*, 267–278.

(27) He, X., Sugawara, M., Takekuma, Y., and Miyazaki, K. (2004) Absorption of ester prodrugs in Caco-2 and rat intestine models. *Antimicrob. Agents Chemother. 48*, 2604–2609.

(28) Yun, Z., Takagi, M., and Yoshida, T. (2003) Repeated addition of insulin for dynamic control of apoptosis in serum-free culture of Chinese hamster ovary cells. *J. Biosci. Bioeng. 96*, 59–64.

(29) Florea, B. I., Thanou, M., Junginger, H. E., and Borchard, G. (2006) Enhancement of bronchial octreotide absorption by chitosan and *N*-trimethyl chitosan shows linear in vitro/in vivo correlation. *J. Controlled Release 110*, 353–361.

(30) Zubtsov, D. A., Ivanov, S. M., Rubina, A. Y., Dementieva, E. I., Chechetkin, V. R., and Zasedatelev, A. S. (2006) Effect of mixing on reaction-diffusion kinetics for protein hydrogel-based microchips. *J. Biotechnol. 122*, 16–27.

(31) Ranaldi, G., Marigliano, I., Vespignani, I., Perozzi, G., and Sambuy, Y. (2002) The effect of chitosan and other polycations on tight junction permeability in the human intestinal Caco-2 cell line. *J. Nutrit. Biochem. 13*, 157–167.

(32) Ma, Z., and Lim, L. Y. (2003) Uptake of chitosan and associated insulin in Caco-2 cell monolayers: A comparison between chitosan molecules and chitosan nanoparticles. *Pharm. Res. 20*, 1812–1819.

(33) de Britto, D., and Assis, O. B. G. (2007) A novel method for obtaining a quaternary salt of chitosan. *Carbohydr. Polym. 69*, 305–310.

(34) Robinson, D. N., and Peppas, N. A. (2002) Preparation and characterization of pH-responsive poly(methacrylic acid-*g*-ethylene glycol) nanospheres. *Macromolecules 35*, 3668–3674.

(35) Ichikawa, H., and Peppas, N. A. (2003) Novel complexation hydrogels for oral peptide delivery: In vitro evaluation of their cytocompatibility and insulin-transport enhancing effects using Caco-2 cell monolayers. *J. Biomed. Mater. Res. 67*, 609–617.

(36) Lin, Y. H., Chen, C. T., Liang, H. F., Kulkarni, A. R., Lee, P. W., Chen, C. H., and Sung, H. W. (2007) Novel nanoparticles for oral insulin delivery via the paracellular pathway. *Nanotechnology 18*, 1–11.

(37) Thanou, M., Verhoef, J. C., Verheijden, J. H. M., and Junginger, H. E. (2001) Intestinal Absorption of Octreotide Using Trimethyl Chitosan Chloride: Studies in Pigs. *Pharm. Res. 18*, 823–828.

(38) Marttin, E., Verhoef, J. C., Spies, F., van der Meulen, J., Nagelkerke, J. F., Koerten, H. K., and Merkus, F. W. H. M. (1999) The effect of methylated β-cyclodextrins on the tight junctions of the rat nasal respiratory epithelium: Electron microscopic and confocal laser scanning microscopic visualization studies. *J. Controlled Release 57*, 205–213.

(39) Adamson, R. H., Lenz, J. F., Zhang, X., Adamson, G. N., Weinbaum, S., and Curry, F. E. (2004) Oncotic pressures opposing filtration across non-fenestrated rat microvessels. *J. Physiol. 557*, 889–907.

(40) Adson, A., Burton, P. S., Raub, T. J., Barsuhn, C. L., Audus, K. L., and Ho, N. F. H. (1995) Passive diffusion of weak organic electrolytes across Caco-2 cell monolayers: Uncoupling the contributions of hydrodynamic, transcellular, and paracellular barriers. *J. Pharm. Sci. 84*, 1197–1204.

(41) Barbagallo, M., Dominguez, L. J., Galioto, A., Ferlisi, A., Cani, C., Malfa, L., Pineo, A., Busardo, A., and Paolisso, G. (2003) Role of magnesium in insulin action, diabetes and cardiometabolic syndrome X. *Mol. Aspects Med. 24*, 39–52.

(42) Smith, J., Wood, E., and Dornish, M. (2004) Effect of chitosan on epithelial cell tight junctions. *Pharm. Res. 21*, 43–49.

(43) Ward, P. D., Tippin, T. K., and Thakker, D. R. (2000) Enhancing paracellular permeability by modulating epithelial tight junctions. *Pharm. Sci. Technol. Today 3*, 346–358.

(44) Smith, J. M., Dornish, M., and Wood, E. J. (2005) Involvement of protein kinase C in chitosan glutamate-mediated tight junction disruption. *Biomaterials 26*, 3269–3276.

BC800076N

Development of Novel ^{68}Ga- and ^{18}F-Labeled GnRH-I Analogues with High GnRHR-Targeting Efficiency

Margret Schottelius,* Sebastian Berger, Thorsten Poethko, Markus Schwaiger, and Hans-Jürgen Wester

Nuklearmedizinische Klinik and Poliklinik, Klinikum rechts der Isar, Technische Universität München, 81675 München, Germany. Received February 12, 2008; Revised Manuscript Received April 28, 2008

A large majority of tumors of the reproductive system express the gonadotropin releasing hormone receptor (GnRHR). Blockade and activation of this receptor with various antagonistic and agonistic analogues of native GnRH-I (pGlu^1-His^2-Trp^3-Ser^4-Tyr^5-Gly^6-Leu^7-Arg^8-Pro^9-Gly^{10}-NH$_2$), respectively, has shown efficient suppression of tumor growth. In this study, the GnRH-receptor system has been evaluated with respect to its suitability as a target for in vivo peptide receptor targeting using radiolabeled GnRH-analogues, and in parallel, new ^{18}F- and ^{68Ga}-labeled GnRH analogues have been developed. In vitro radioligand binding assays performed with various GnRHR-expressing human cell lines using [^{125}I]Triptorelin (D-Trp^6-GnRH-I) as the standard radioligand revealed a very low level of GnRH receptor expression on the cell surface. Generally, total cellular activity was very low (~3% of the applied activity), and only a small fraction (max. 40%) of cell-associated activity could be attributed to receptor-specific radioligand binding/internalization. However, substitution of fetal calf serum by NU serum in the culture medium led to increased and stable GnRHR-expression, especially in the ovarian cancer cell line EFO-27, thus allowing for a stable experimental setup for the evaluation of the new radiolabeled GnRH-I analogues. The new radiolabeled GnRH-I analogues developed in this study were all based on the D-Lys^6-GnRH-I-scaffold. For ^{68}Ga-labeling, the latter was coupled with DOTA at D-Lys^6. To allow ^{18}F-labeling via chemoselective oxime formation, D-Lys^6-GnRH-I was also conjugated with Ahx (aminohexanoic acid) or β-Ala, which in turn was coupled with Boc-aminooxyacetic acid. ^{18}F-labeling via oxime formation with 4-[^{18}F]fluorobenzaldehyde was performed using the Boc-protected precursors. Receptor affinities of [^{68}Ga]DOTA-GnRH-I, D-Lys^6-Ahx([^{18}F]FBOA)-GnRH-I, and D-Lys^6-βAla([^{18}F]FBOA)-GnRH-I (FBOA = fluorobenzyloxime acetyl) were determined using GnRHR-membrane preparations, and internalization efficiency of the new radioligands was determined in EFO-27 cells. Both quantities were highest for D-Lys^6-Ahx([^{18}F]FBOA)-GnRH-I ($IC_{50} = 0.50 \pm 0.08$ nM vs 0.13 ± 0.08 nM for Triptorelin; internalization: 86 ± 16% of the internal reference [^{125}I]Triptorelin), already substantially reduced in the case of the -βAla([^{18}F]FBOA)-derivative ($IC_{50} = 0.86 \pm 0.13$ nM; internalization: 42 ± 3% of [^{125}I]Triptorelin), while the [^{68}Ga]DOTA-analogue showed almost complete loss of binding affinity and ligand internalization ($IC_{50} = 13.3 \pm 1.0$ nM; internalization: 2.6 ± 1.0% of [^{125}I]Triptorelin). Generally, the lipophilic residue [^{18}F]FBOA is much better tolerated as a modification of the D-Lys^6-side chain, with receptor affinity of the respective analogues strongly depending upon spacer length between the D-Lys^6-side chain and the [^{18}F]FBOA-moiety. In summary, D-Lys^6(Ahx-[^{18}F]FBOA)-GnRH-I shows the highest potential for efficient GnRHR-targeting in vivo of the compounds investigated. Unfortunately, however, the very low cell surface expression of GnRH-receptors and thus very low radioligand uptake by GnRHR-positive tumor cells found in vitro was also confirmed by a preliminary biodistribution study in OVCAR-3 xenografted nude mice using the standard GnRHR radioligand [^{125}I]Triptorelin. Tumor uptake was lower than blood activity concentration at 1 h p.i. (0.49 ± 0.05 vs 0.96 ± 0.13 for tumor and blood, respectively). These data seriously challenge the suitability of the GnRHR-system as a suitable target for in vivo peptide receptor imaging using radiolabeled GnRH-I derivatives, despite the availability of high-affinity radiolabeled receptor−ligands such as D-Lys^6(Ahx-[^{18}F]FBOA)-GnRH-I.

INTRODUCTION

Neuropeptide receptors are overexpressed on a wide variety of human tumors. Due to their expression on the cell surface, they represent excellent molecular targets for radiolabeled neuropeptide analogues—their specific accumulation in receptor expressing tumors not only often allows high-contrast visualization of human malignancies, but also constitutes the basis for endoradiotherapeutic approaches. The somatostatin (sst) receptor system represents a prototype for successful peptide receptor targeting: the receptor, its function, and its expression pattern in normal and neoplastic tissues have been thoroughly investigated, and an increasing number of optimized receptor−ligands labeled with a variety of radionuclides are available for both diagnostic and therapeutic applications (*1–6*).

The success and increasing clinical impact of sst-targeting in nuclear oncology has prompted intensified research with respect to the identification of novel peptide receptors as potential candidates for in vivo tumor targeting (*7*, *8*), and novel and/or optimized radioligands are currently being developed for–among others–bombesin (*9*, *10*), cholecystokinin (*11*), and glucagon-like peptide-1 receptors (*12*), to mention only a few.

Another receptor, which represents an interesting novel target in this field, is the gonadotropin releasing hormone receptor (GnRHR), also known as luteinizing hormone releasing hormone receptor (LHRHR). Its two subtypes, GnRHR-I and GnRHR-II, have been shown to be strongly expressed on the majority

* To whom correspondence should be addressed. Margret Schottelius, Ph.D, Nuklearmedizinische Klinik and Poliklinik, Klinikum rechts der Isar, Technische Universität München, Ismaninger Strasse 22, D - 81675 München, Germany. Tel: # 49 89 4140 6492. Fax: # 49 89 4140 4897. E-mail: M.Schottelius@lrz.tum.de.

10.1021/bc800058k CCC: $40.75 © 2008 American Chemical Society
Published on Web 05/30/2008

of tumors of the human reproductive system, either one subtype exclusively or both together: 80% of endometrial, 78% of ovarian, 52% of mammary, and 86% of prostate cancers are GnRHR-positive (*13, 14*). Expression of GnRHRs has also been demonstrated in human tumor specimens and cancer cell lines originating from liver (*15*), lanrynx (*16*), pancreas (*17*), kidney (*18*), brain (*19*), blood cells (*20, 21*), and skin (*22, 23*).

The GnRH receptor system has been studied intensely as a target for peptidic drugs during the past decade. A broad palette of agonistic and antagonistic analogues derived from the native decapeptide ligand GnRH-I is clinically used for effective suppression of the pituitary−gonadal axis and consequently of the growth of hormone-dependent cancers (*24*). However, based on the finding that GnRH analogues also exert direct antiproliferative effects on GnRHR-expressing tumor cells (*13, 24*), cytotoxic analogues such as the 2-pyrrolidino-doxorubicin-coupled D-Lys^6-GnRH-derivative AN-207 have been developed and show high therapeutic efficiency in animal models (*21, 25–27*).

Despite the clinical success of the pharmacological application of GnRH-derivatives (*28*), the GnRHR-system has not been exploited as a target for scintigraphic imaging using radiolabeled ligands yet. To date, only one ^{99m}Tc-labeled GnRH-analogue is known which has been specifically developed as a potential SPECT tracer (*29*). Unfortunately, the introduction of the radiometal via backbone cyclization of the peptide was accompanied by a dramatic loss of binding affinity, hampering the applicability of this analogue as an in vivo imaging agent.

This study was therefore conducted to address two major open questions: First, is the GnRH-receptor system a suitable target for in vivo receptor imaging? And second, which structural prerequisites have to be met for the development of high-affinity radiolabeled GnRH analogues?

To address the first question, several human cancer cell lines, i.e., the ovarian cancer cell lines EFO-27 and SKOV-3, the breast cancer cell lines MDA-MB 231 and SKBR-3, as well as the prostate cancer cell lines LNCaP and DU-145, all know to express either GnRHR-I and/or GnRHR-II (*30–34*), were screened for GnRHR-expression using the standard radioligands [^{125}I]Triptorelin (pGlu-His-Trp-Ser-[^{125}I]Tyr-D-Trp-Leu-Arg-Pro-Gly-NH_2) for GnRHR-I (expressed on EFO-27, MDA-MB 231, SKBR-3, and LNCaP cells) or [^{125}I]D-Lys6-GnRH-II (pGlu-His-Trp-Ser-His-D-Lys-Trp-[^{125}I]Tyr-Pro-Gly-NH_2) or GnRHR-II (expressed on SKOV-3 and DU-145 cells), and the extent of receptor-specific ligand binding was determined. Furthermore, the dependence of specific radioligand binding, reflecting the level of receptor expression, on the medium supplement, which had been previously documented for DU-145 cells (*35*), was investigated for all six cell lines. The cells were grown in parallel both with fetal calf serum (FCS) or with Nu-Serum as serum supplements. Nu-Serum is a semisynthetic serum supplement containing, among other components, EGF, ECGS, insulin, human transferrin, triiodothyronine, progesterone, estradiol-17β, and testosterone, thus mimicking much more closely the physiological tumor cell growth conditions than FCS.

In parallel, new radiolabeled GnRH analogues were developed. Previous studies had demonstrated that both the N- and the C-terminus of GnRH-ligands are responsible for receptor binding, and that their amino acid sequences are responsible for the agonistic or antagonistic profile of the peptide (*36, 37*). The development of a multitude of highly potent GnRH-I analogues further yielded important structure−activity relationships: first, introduction of a D-amino acid in position 6 leads to a substantial stabilization of the peptide toward degradation in vivo and an increased receptor affinity, and second, the amino acid in position 6 shows remarkable tolerance toward even bulky chemical modifications, both in GnRH agonists and antagonists (*37–39*).

Since agonism is an important prerequisite for ligand internalization, ideally leading to high intracellular tracer accumulation and enhanced tumor to nontumor ratios in vivo, the GnRH-I-agonist D-Lys^6-GnRH-I (pGlu-His-Trp-Ser-Tyr-D-Lys-Leu-Arg-Pro-Gly-NH_2) was chosen as a scaffold for radioligand development. To investigate the flexibility of the ligand with respect to the type of moiety attached to D-Lys^6, two different synthetic approaches toward GnRH-I-analogues labeled with positron emitters were chosen: (A) the macrocyclic chelator DOTA (1,4,7,10-tetraazacyclododecane-*N′*,*N″*,*N‴*,*N⁗*-tetraacetic acid) was directly attached for ^{68}Ga-labeling; and (B) the structure of the high-affinity cytotoxic analogue AN-207 ((*25*); Figure 1) was used as a lead structure for the development of ^{18}F-labeled GnRH-I-derivatives. To investigate the impact of spacer length between the peptide core and the hydrophobic moiety ([^{18}F]FBOA (4-[^{18}F]fluorobenzyloxim acetyl-) in the case of the ^{18}F-analogues), two different spacers, aminohexanoic acid (Ahx) and β-alanine (β-Ala), were coupled to D-Lys^6 and further functionalized with (Boc)aminooxyacetic acid for chemoselective ^{18}F-labeling via oxime formation with 4-[^{18}F]fluorobenzaldehyde (*40*) (Figure 1).

The new radiolabeled compounds were evaluated in vitro, both using cell membranes to determine receptor affinity and using GnRH-I-expressing EFO-27 cells to assess internalization efficiency. In addition, an exemplary in vitro serum stability study was performed for D-Lys^6(Ahx-[^{18}F]FBOA)-GnRH-I.

Furthermore, a preliminary evaluation of the OVCAR-3 cell line as a transplantable xenograft model for in vivo GnRH-I-targeting was carried out using the reference ligand [^{125}I]Triptorelin.

MATERIALS AND METHODS

General Conditions. Most Fmoc (9-fluorenylmethoxycarbonyl-) amino acids, N-Boc-aminooxyacetic acid, and Rink amide resin (100−200 mesh) were purchased from Novabiochem (Merck Biosciences, Schwalbach, Germany). Boc-Pyr-OH (N-Boc-pyroglutamic acid) and Boc-β-Ala-OH were supplied by Bachem (Heidelberg, Germany). 6-Boc-Ahx-OSu was purchased from Fluka (Neu-Ulm, Germany). DOTA (1,4,7,10-tetraazacyclododecane-*N′*,*N″*,*N‴*,*N⁗*-tetraacetic acid) was obtained from Macrocyclics (Dallas, Texas, USA). Solvents and all other organic reagents and were purchased from Merck Eurolab (Darmstadt, Germany), Aldrich or Fluka (Neu-Ulm, Germany).

Solid-phase peptide synthesis was carried out manually using a flask shaker (St. John Associates Inc., USA).

Analytical RP-HPLC was performed on a Nucleosil 100 C18 (5 μm, 125 × 4.0 mm) column (CS Chromatographie Service, Langerwehe, Germany) using a Sykam gradient HPLC System (Sykam GmbH, Fürstenfeldbruck, Germany). The peptides were eluted applying different gradients of 0.1% (v/v) TFA (trifluoroacetic acid) in H_2O (solvent A) and 0.1% TFA (v/v) in acetonitrile (solvent B) at a constant flow of 1 mL/min (specific gradients are cited in the text). UV detection was performed at 220 nm using a 206 PHD UV−vis detector or an UVIS 200 photometer (Linear Instruments Corporation, Reno, NV).

Preparative RP-HPLC was performed on the same HPLC system using a YMC J'Sphere ODS-H80 (150 × 20 mm, S-4 μm, 8 nm) column (YMC Europe, Schermbeck, Germany) at a constant flow of 9 mL/min.

Both retention times t_R as well as the capacity factors K' are cited in the text. K' is calculated as follows:

$$K' = \frac{t_R - t_0}{t_0} \qquad t_R = \text{retention time}$$

$$t_0 = \frac{\text{dead volume of the column [mL]}}{\text{flow [mL} \times \text{min}^{-1}\text{]}}$$

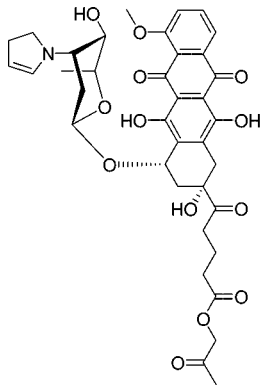

AN-207

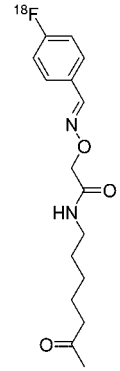

[^{18}F]FBOA-Ahx-

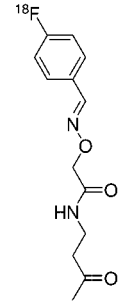

[^{18}F]FBOA-β-Ala-

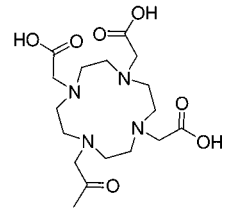

DOTA-

pGlu - His - Trp - Ser - Tyr - DLys - Leu - Arg - Pro - Gly-NH_2

D-Lys^6-GnRH-I

pGlu - His - Trp - Ser - Tyr - DTrp - Leu - Arg - Pro - Gly-NH_2

Triptorelin

pGlu - His - Trp - Ser - His - DLys - Trp - Tyr - Pro - Gly-NH_2

D-Lys^6-GnRH-II

Figure 1. Structures of some selected GnRHR-binding compounds and of the new radiolabeled GnRH-I analogues developed in this study. FBOA = fluorobenzyloxime acetyl, DOTA = 1,4,7,10-tetraazacyclododecane-*N′*,*N″*,*N‴*,*N⁗*-tetraacetic acid.

Mass spectra were recorded on the LC-MS system LCQ from Finnigan (Bremen, Germany) using the Hewlett-Packard series 1100 HPLC system.

Peptide Synthesis. *Triptorelin (D-Trp^6-GnRH-I).* Coupling of the first amino acid, Fmoc-Gly-OH, to the resin was performed as specified by the manufacturer. Briefly, the resin was allowed to preswell in NMP (*N*-methylpyrrolidon) for 30 min. Then, the *N*-terminal Fmoc-protecting group was cleaved off using 20% piperidine in DMF (dimethyl formamide). After thoroughly washing the resin with NMP, Fmoc-Gly-OH was coupled to the resin using HOBt (1-hydroxybenzotriazol) and TBTU (*O*-(1*H*-benzotriazol-1-yl)-*N*,*N*,*N′*,*N′*-tetramethyluronium-tetrafluoroborate) as coupling reagents and DIPEA (*N*-ethyl diisopropylamine) as a base. The subsequent assembly of the peptide sequence pGlu(Boc)-His(Trt)-Trp(Boc)-Ser(tBu)-Tyr(tBu)-D-Trp(Boc)-Leu-Arg(Pbf)-Pro- on the resin-bound amino acid was performed according to standard Fmoc-protocol. Cleavage from the resin was carried out using a mixture of 95% TFA, 2.5% water, and 2.5% triisobutylsilane (v/v/v). The fully deprotected crude peptide was precipitated using diethyl ether and dried. A small fraction of crude Triptorelin was then purified via preparative HPLC (22−37% B in 20 min). Triptorelin (40 mg) was obtained in a purity (220 nm) >98%. Triptorelin: HPLC (10 → 35% B in 20 min): t_R = 12.3 min; K' = 6.65. Calculated monoisotopic mass ($C_{64}H_{82}N_{18}O_{13}$): 1310.6. found: m/z = 1312.1 $[M+H]^+$, 1333.9 $[M+Na]^+$.

D-Lys^6-GnRH-I. D-Lys^6(Dde)-GnRH-I was synthesized via SPPS (solid phase peptide synthesis) in analogy to Triptorelin with the sole difference that Fmoc-D-Trp(Boc)-OH was replaced by Fmoc-D-Lys(Dde)-OH during SPPS. After cleavage from the resin, D-Lys^6(Dde)-GnRH-I was precipitated using diethyl ether, dried, and stored at −20 °C. For further derivatization, the Dde-protecting group in D-Lys^6(Dde)-GnRH-I was removed using 2% hydrazine hydrate (30%) in DMF. After 10 min, deprotected D-Lys^6-GnRH-I was precipitated using diethyl ether, washed with ether, and dried. The crude peptide was used for subsequent derivatizations without further purification. D-Lys^6-GnRH-I: HPLC (10 → 35% B in 20 min): t_R = 7.1 min; K' = 3.94. Calculated monoisotopic mass ($C_{59}H_{84}N_{18}O_{13}$): 1252.7. found: m/z = 1253.8 $[M+H]^+$, 1275.7 $[M+Na]^+$.

D-Lys^6-GnRH-II. The synthesis of D-Lys^6(Dde)-GnRH-II (pGlu-His-Trp-Ser-His-D-Lys-Trp-Tyr-Pro-Gly-NH_2) was carried out entirely in analogy to D-Lys^6(Dde)-GnRH-I. After Dde-deprotection, the crude peptide was purified via preparative RP-HPLC. D-Lys^6-GnRH-II: HPLC (15 → 45% B in 20 min): t_R = 9.0 min; K' = 4.86. Calculated monoisotopic mass ($C_{64}H_{78}N_{18}O_{13}$): 1306.6. found: m/z = 1307.9 $[M+H]^+$, 1330.0 $[M+Na]^+$.

D-Lys^6(DOTA)-GnRH-I. The macrocyclic chelator DOTA was coupled to the side chain of D-Lys^6 in D-Lys^6-GnRH-I according to a previously published protocol (*41*). Briefly, DOTA (2 equiv, 0.37 mmol) was preactivated with NHS (*N*-hydroxysuccinimide, 2.5 equiv), EDCI (1-ethyl-3-(3′-dimethylaminopropyl)-carbodiimide, 2.5 equiv) and DIPEA (5 equiv) in water for 30 min. Then, D-Lys^6-GnRH-I (1 equiv, 0.18 mmol) dissolved in DMF was slowly added under vigorous stirring. After 90 min, the solvents were evaporated in vacuo, the residue was resuspended in methanol, and the suspension was centrifuged. The super-

natant methanolic solution was concentrated in vacuo and added dropwise to an excess of diethyl ether. The precipitate (crude D-Lys^6(DOTA)-GnRH-I) was dried and subsequently purified using preparative HPLC (14−30% B in 20 min). D-Lys^6(DOTA)-GnRH-I (47 mg) was obtained in 16% yield and a purity (220 nm) of 97.6%. D-Lys^6(DOTA)-GnRH-I: HPLC (10 → 35% B in 20 min): $t_R = 10.9$ min; $K' = 5.19$. Calculated monoisotopic mass ($C_{75}H_{110}N_{22}O_{20}$): 1638.8. found: $m/z = 1640.0$ $[M+H]^+$, 821.1 $[(M+2H)/2]^{2+}$, 1662.0 $[M+Na]^+$, 1677.9 $[M+K]^+$.

D-Lys^6(Ahx-AOA(Boc))-GnRH-I. Coupling with Boc-Ahx-OH and Deprotection. Boc-Ahx-OSu (1.5 equiv, 0.52 mmol), HOBt (1.5 equiv, 0.52 mmol), and TBTU (1.5 equiv, 0.52 mmol) were dissolved in DMF; DIPEA (4 equiv, 2.08 mmol) was added, and the mixture was preactivated for 15 min. Then, this solution was added to a solution of D-Lys^6-GnRH-I (1 equiv, 0.35 mmol) in DMF. After 30 min of stirring at RT (room temperature), the crude product was precipitated using diethyl ether, washed, and dried (D-Lys^6(Ahx(Boc))-GnRH-I: HPLC (20 → 70% B in 15 min): $t_R = 10.3$ min; $K' = 4.35$). For Boc-deprotection, the dried residue was redissolved in a 1:1 mixture (v/v) of TFA and dichloromethane. Usually, deprotection was complete within 15 min. The deprotected peptide was then precipitated using diethyl ether, washed, and redissolved in water/MeOH for subsequent preparative HPLC purification (16−27% B in 20 min). D-Lys^6(Ahx)-GnRH-I: HPLC (20 → 70% B in 15 min): $t_R = 4.8$ min; $K' = 1.83$. Calculated monoisotopic mass ($C_{65}H_{95}N_{19}O_{14}$): 1365.6. found: $m/z = 1366.7$ $[M+H]^+$, 684.2 $[(M+2H)/2]^{2+}$, 1388.7 $[M+Na]^+$.

Coupling with N-(Boc)-Aminooxyacetic Acid. N-(Boc)-aminooxyacetic acid (AOA(Boc)) was coupled to D-Lys^6(Ahx)-GnRH-I under optimized coupling conditions (*42*). Briefly, AOA(Boc) (1.2 equiv, 0.030 mmol) was preactivated for 15 min with HOAt (1-hydroxy-7-azabenzotriazole, 1.2 equiv, 0.030 mmol), DIC (diisopropylcarbodiimide, 1.2 equiv, 0.030 mmol), and pyridine (2 equiv, 0.052 mmol) in DMF. This solution was added to a solution of D-Lys^6(Ahx)-GnRH-I (1 equiv, 0.026 mmol) in DMF. After stirring at RT for 35 min, the product peptide was precipitated using diethyl ether, washed, and isolated using preparative HPLC purification (24−52% B in 20 min). D-Lys^6(Ahx-AOA(Boc))-GnRH-I was obtained in 50% yield and a purity > 90%. D-Lys^6(Ahx-AOA(Boc))-GnRH-I: HPLC (20 → 70% B in 15 min): $t_R = 9.2$ min; $K' = 4.21$. Calculated monoisotopic mass ($C_{72}H_{106}N_{20}O_{18}$): 1538.5. found: $m/z = 1539.6$ $[M+H]^+$, 1439.7 $[M\text{-Boc}+H]^+$.

D-Lys^6(β-Ala-AOA(Boc))-GnRH-I. Coupling with Boc-β-Ala-OH and Deprotection. Coupling of Boc-β-Ala-OH to D-Lys^6-GnRH-I as well as subsequent Boc-deprotection were performed in analogy to the Ahx-analogue. After preparative HPLC purification (16−23% B in 20 min), D-Lys^6(β-Ala)-GnRH-I was obtained in 21% yield. D-Lys^6(β-Ala)-GnRH-I: HPLC (20 → 70% B in 15 min): $t_R = 2.8$ min; $K' = 0.58$. Calculated monoisotopic mass ($C_{62}H_{89}N_{19}O_{14}$): 1323.7. found: $m/z = 1324.8$ $[M+H]^+$, 1346.7 $[M+Na]^+$.

Coupling with N-(Boc)-Aminooxyacetic Acid. N-(Boc)-aminooxyacetic acid (AOA(Boc)) was coupled to D-Lys^6(β-Ala)-GnRH-I as described for the Ahx-derivative. After preparative HPLC purification (22−46% B in 20 min), D-Lys^6(β-Ala-AOA(Boc))-GnRH-I was obtained in 49% yield and a purity > 90%. D-Lys^6(β-Ala-AOA(Boc))-GnRH-I: HPLC (20 → 70% B in 15 min): $t_R = 8.5$ min; $K' = 3.73$. Calculated monoisotopic mass ($C_{69}H_{100}N_{20}O_{18}$): 1496.5. found: $m/z = 1497.6$ $[M+H]^+$, 1397.7 $[M\text{-Boc}+H]^+$.

Synthesis of the Reference Compounds. *D-Lys^6(Ga-DOTA)-GnRH-I.* D-Lys^6(DOTA)-GnRH-I was dissolved in 0.1 N NaOAc (pH = 4.5), and an equimolar amount of $GaNO_3$ was added. After heating to 90 °C for 30 min, the reaction mixture was cooled to RT, and D-Lys^6(Ga-DOTA)-GnRH-I was immediately purified using preparative HPLC (14−30% B in 20 min). The peptide was obtained in 97% purity (220 nm). D-Lys^6(Ga-DOTA)-GnRH-I: HPLC (10 → 35% B in 20 min): $t_R = 7.6$ min; $K' = 3.61$. Calculated monoisotopic mass ($C_{75}H_{108}N_{22}O_{20}Ga$): 1705.7. found: $m/z = 1705.9$ $[M]^+$, 854.0 $[(M+H)/2]^{2+}$, 570.2 $[(M+2H)/3]^{3+}$.

D-Lys^6(Ahx-FBOA)-GnRH-I and D-Lys^6(β-Ala-FBOA)-GnRH-I. Immediately prior to the reaction with 4-fluorobenzaldehyde, D-Lys^6(Ahx-AOA(Boc))GnRH-I and D-Lys^6(β-Ala-AOA(Boc))-GnRH-I were deprotected using a 1:1 mixture (v/v) of TFA and dichloromethane. After 15 min, the deprotected peptides were precipitated using diethyl ether, washed, and redissolved in water/MeOH. Then, an equimolar amount of 4-fluorobenzaldehyde was added. After 30 min at 60 °C, the respective coupling product was purified using RP-HPLC (D-Lys^6(Ahx-FBOA)GnRH-I: 20−66% B in 20 min, D-Lys^6(β-Ala-FBOA)-GnRH-I: 22−60% B in 20 min). The purity (220 nm) of both the Ahx- and β-Ala-reference compound was >98%. D-Lys^6(Ahx-FBOA)GnRH-I: HPLC (20 → 70% B in 15 min): $t_R = 10.3$ min; $K' = 4.84$. Calculated monoisotopic mass for D-Lys^6(Ahx-FBOA)GnRH-I ($C_{74}H_{101}N_{20}O_{16}F$): 1544.5. found: $m/z = 1545.9$ $[M+H]^+$, 773.9 $[(M+2H)/2]^{2+}$, 1567.7 $[M+Na]^+$. D-Lys^6(β-Ala-FBOA)GnRH-I: HPLC (20 → 70% B in 15 min): $t_R = 9.6$ min; $K' = 4.55$. Calculated monoisotopic mass for D-Lys^6(β-Ala-FBOA)GnRH-I ($C_{71}H_{95}N_{20}O_{16}F$): 1502.5. found: $m/z = 1503.8$ $[M+H]^+$, 752.8 $[(M+2H)/2]^{2+}$, 1525.5 $[M+Na]^+$.

Radiolabeling. *Instrumentation.* Radio-HPLC was performed on a Nucleosil 100 C18 (5 μm, 125 × 4.0 mm) column using a Sykam gradient system (Sykam GmbH, Fürstenfeldbruck, Germany) and an UVIS 200 photometer (Linear Instruments Corporation, Reno, NV). For radioactivity measurement, the outlet of the UV-photometer was connected to a Na(Tl) well-type scintillation counter Ace Mate 925-Scint (EG&G Ortec, München, Germany).

[^{125}I]Triptorelin and D-Lys^6-[^{125}I]GnRH-II. Iodogen Method. A solution of approx 200 μg of peptide in 200 μL of TRIS-HCl buffer (25 mM, 0.4 M NaCl, pH 7.5) was transferred to an Eppendorf tube coated with 50 μg of Iodogen (Pierce, Rockford, USA). After the addition of 5−20 μL (18.5−74 MBq) of n.c.a. [^{125}I]NaI in 0.05 M NaOH (Hartmann Analytic, Brauschweig, Germany), the cap was vortexed, and the labeling reaction was allowed to proceed for 15 min at RT. The peptide solution was then removed from the insoluble oxidizing agent, and the radiolabeled peptide was separated from unreacted precursor via RP-HPLC using an isocratic solvent mixture of 24% (D-Lys^6-[^{125}I]GnRH-II) or 32% ([^{125}I]Triptorelin) EtOH (0.5% AcOH) in water (0.5% AcOH). Radiochemical yields after purification ranged from 35% to 65%.

Chloramine T Method. Triptorelin (100 μg) was dissolved in 100 μL of TRIS-HCl buffer (25 mM, 0.4 M NaCl, pH 7.5). After addition of 10 μL (37 MBq) of n.c.a. [^{125}I]NaI in 0.05 M NaOH and 50 μL of a Chloramine T solution (1 mg/mL), the labeling reaction was allowed to proceed for 15 min at RT. Then, 10 μL of a $Na_2S_2O_5$ solution (1 mg/mL) and 120 μL of TRIS-HCl buffer were added, and [^{125}I]Triptorelin was purified via RP-HPLC as described above. Radiochemical yields after purification ranged from 79% to 87%.

For use in the in vitro experiments, the HPLC eluate was evaporated to dryness, and [^{125}I]Triptorelin was redissolved in RPMI-1640 medium containing 5% BSA (activity concentration of approx 100 000 cpm/10 μL). [^{125}I]Triptorelin: 32% EtOH isocratic: t_R (range) = 6.6−8.5 min; K' (range) = 3.77−4.83. [^{125}I]D-Lys^6-GnRH-II: 24% EtOH isocratic: t_R (range) = 7.7−9.5 min; K' (range) = 4.13−5.33.

D-Lys^6([^{68}Ga]DOTA)-GnRH-I. $^{68}GaCl_3$ was eluted with 0.1 N HCl from an in-house OBNINSK ^{68}Ge/^{68}Ga-generator (1.48 GBq; Chemotrade Chemiehandelsgesellschaft mbH, Leipzig,

Germany). To 1.3 mL of the generator eluate were added 150 μL of HEPES (2.5 M) and 7 μg (4.25 nmol) of D-Lys^6(DOTA)-GnRH-I in 7 μL of water, and the reaction mixture was heated to 95 °C for 20 min. After cooling to RT, the reaction mixture was diluted with 2 mL of water, and D-Lys^6([^{68}Ga]DOTA)-GnRH-I was immobilized on a Sep-Pak Plus C-18 cartridge (Waters, Eschborn, Germany), washed with 10 mL of water, and eluted with 2 mL of ethanol. The solvent was then evaporated in vacuo and the product was redissolved in RPMI-1640 medium (Biochrom, Berlin, Germany) containing 5% BSA (bovine serum albumin) and diluted to an activity concentration of approx 500 000 cpm/10 μL for use in internalization studies. Quality control was performed using a standard TLC system.

D-Lys^6(Ahx-[^{18}F]FBOA)-GnRH-I and D-Lys^6(β-Ala-[^{18}F]-FBOA)-GnRH-I. The synthesis of 4-[^{18}F]fluorobenzaldehyde from 4-formyl-*N*,*N*,*N*-trimethylanilinium triflate was performed as described previously (*40*). For peptide labeling, 10 μL of a 10 mM solution of D-Lys^6(Ahx/β-Ala-AOA(Boc))-GnRH-I in water was added to 20−40 μL of a freshly prepared methanolic 4-[^{18}F]fluorobenzaldehyde solution. Then, 1 μL of TFA was added. After 15 min at 75 °C and product isolation via RP-HPLC (15−50% B in 20 min, analytical column), both [^{18}F]FBOA-GnRH-I-analogues were obtained in radiochemical yields of 74−85% (based on 4-[^{18}F]fluorobenzaldehyde) and an overall synthesis time of approx 60 min. For use in in vitro studies, the HPLC eluate was evaporated to dryness, and the [^{18}F]FBOA-peptides were redissolved in RPMI-1640 medium containing 5% BSA (activity concentration of approx 250 000 cpm/10 μL). D-Lys^6(Ahx-[^{18}F]FBOA)GnRH-I: HPLC (15 → 50% B in 20 min): t_R = 16.7 min; K' = 9.14. D-Lys^6(β-Ala-[^{18}F]FBOA)GnRH-I: HPLC (15 → 50% B in 20 min): t_R = 15.2 min; K' = 8.77.

Lipophilicity. To a solution of approx 2 kBq of radiolabeled peptide in 500 μL of PBS (pH 7.4), 500 μL of octanol were added (n = 6). Vials were vortexed vigorously for 3 min. To achieve quantitative phase separation, the vials were centrifuged at 14 600 × g for 6 min in a Biofuge 15 (Heraeus Sepatech, Osterode, Germany). The activity concentrations in 100 μL samples of both the aequous and organic phases were measured in a γ-counter. Both the partition coefficient P_{ow}, which is defined as the molar concentration ratio of a single species A between octanol and water at equilibrium and log P_{ow}, which is an important parameter used to characterize lipophilicity of a compound (*43*), were calculated.

Cell Culture. The ovarian cancer cell line EFO-27 was purchased from DSMZ (Braunschweig, Germany). OVCAR-3 ovarian cancer cells were a kind gift from Dr. A. Krüger, Institute of experimental oncology, Klinikum rechts der Isar, TU München, Germany. The prostate cancer cell lines DU-145 and LNCaP as well as the breast cancer cell lines MDA-MB 231 and SKBR-3 were kindly supplied by the group of Prof. R. Senekowitsch-Schmidtke, Department of Nuclear Medicine, Klinikum rechts der Isar, TU München, Germany. All cell lines except SKBR-3 were grown in RPMI-1640 medium supplemented with either 10% FCS (fetal celf serum; Biochrom, Berlin, Germany) or 10% Nu-Serum (BD Bioscience, Heidelberg, Germany). SKBR-3 cells were grown in Gibco DMEM/Nutrition Mix F-12 with Glutamax-I (1:1) (invitrogen, Karlsruhe, Germany) supplemented with the same two sera mentioned above. Cultures were maintained at 37 °C in a 5% CO_2/humidified air atmosphere. For cell counting, a CASY1-TT cell counter and analyzer system (Schärfe System GmbH, Reutlingen, Germany) was used.

Determination of the Serum Dependence of [^{125}I]Triptorelin Binding. One day prior to the experiment, cells that had been grown in medium containing either FCS or Nu-Serum were harvested using Trypsin/EDTA (0.05% and 0.02%) in PBS, centrifuged, resuspended with culture medium, transferred into 24-well plates (1 mL/well), and placed in the incubator overnight.

On the day of the experiment (cell count: 160 000−220 000 cells/well), the culture medium was removed and the cells were washed once with 250 μL of medium (unsupplemented RPMI-1640) before being left to equilibrate in 190 μL of medium at 37 °C for a minimum of 15 min before the experiment. Then, 50 μL per well of medium containing 5% BSA (n = 3, control experiment, nca conditions) or of a 25 μM solution of Triptorelin in the same medium (n = 3, determination of nonspecific binding) were added. This was followed by the addition of ∼100 000 cpm [^{125}I]Triptorelin in 10 μL of medium (5% BSA). The cells were then incubated for 60 and 120 min, respectively, at 37 °C in a 5% CO_2/humidified air atmosphere. Incubation was terminated by removal of the incubation medium. Cells were thoroughly rinsed with 250 μL of fresh medium. The wash medium was combined with the supernatant of the previous step. This fraction represents the amount of free radioligand. To determine the amount of bound radioligand, cells were lysed by the addition of 300 μL of 1 N NaOH, transferred to vials, and combined with 250 μL of PBS used for rinsing the wells. Quantification of the amount of free and bound activity was performed in a γ-counter (Wallach, Turku, Finland).

Internalization Studies. In general, the internalization experiments were performed in strict analogy to the experiments described above. However, because all internalization experiments were performed as dual tracer experiments, cells were not only incubated with the reference [^{125}I]Triptorelin, but with a mixture of radioligands, i.e., of ∼100 000 cpm [^{125}I]Triptorelin and either ∼250 000 cpm of the respective [^{18}F]FBOA-GnRH-I-analogue or ∼500 000 cpm D-Lys^6([^{68}Ga]DOTA)-GnRH-I. After the addition of the radioligands, the cells were incubated for 10, 30, 60, and 120 min at 37 °C. After removal of the incubation medium and washing with medium, an additional acid wash step was performed to remove surface-bound (acid-releasable) radioactivity. Cells were incubated with 250 μL of ice cold acid wash buffer (0.02 M NaOAc buffered with AcOH to pH = 5), and after removal of the acid wash buffer, the cells were thoroughly rinsed with another 250 μL of ice cold acid wash buffer. Both acid wash fractions were combined. The internalized activity was released by incubation with 250 μL of 1 N NaOH as described above. Quantification of the amount of free, acid-releasable, and internalized activity was performed in a γ-counter.

Determination of IC_{50} Using Cell Membranes. Cell membrane preparations of cells expressing the human GnRHR were obtained from Chemicon International (Hampshire, UK). Assembly of the competition binding curves was performed in close analogy to the manufacturer's protocol. Briefly, solutions of unlabeled competitor (Triptorelin, D-Lys^6(Ga-DOTA)-GnRH-I, D-Lys^6(Ahx-FBOA)-GnRH-I, and D-Lys^6(β-Ala-FBOA)-GnRH-I; 20 μL, concentration range from $1\cdot10^{-11}$ to $1\cdot10^{-5}$ M, n = 3, per concentration and peptide) in binding buffer (50 mM HEPES, 5 mM $MgCl_2$, 1 mM $CaCl_2$, 0.2% BSA, buffered to pH 7.4 using 1 N NaOH) were pipetted into a 96-well plate. To each well, 20 μL of [^{125}I]Triptorelin in binding buffer (approx 100 000 cpm) was added. Then, 10 μg of cell membrane in 60 μL of binding buffer was added and incubated for 90 min at RT. The final radioligand concentration in the incubation mixture was 0.42 nM. Membranes were then aspired onto a glass fiber filtermat (Printed Filtermat B, Wallach, Turku, Finland), which had been preconditioned with 0.33% polyethylenimine for 30 min and then washed five times with 200 μL (per well) of wash buffer (50 mM HEPES, 500 mM NaCl, 0.1% BSA, buffered to pH 7.4 using 1 N NaOH), using a Mach II M Harvester 96 (Tomtec CE, Etten-Leur, The Netherlands).

Membranes were washed 15 times with 100 μL (per well) of wash buffer. The filtermat was then cut into squares containing the membrane from the respective wells, and membrane bound activity was counted in a γ-counter.

Serum Stability. To four 500 μL samples of freshly prepared human serum was added 50 μL of a solution containing 4.6 MBq of D-Lys^6(Ahx-[^{18}F]FBOA)GnRH-I in PBS (pH = 7.5). The mixtures were incubated in a 5% CO_2 environment at 37 °C. After 10, 30, 60, and 120 min, respectively, the samples were removed from the incubator and diluted with 10 mL of water. The solution was applied to a Sep-Pak Plus C-18 cartridge, and the eluate was collected (fraction I). Then, the cartridge was washed with 10 mL of water. The eluate was again collected (fraction II). After drying with 10 mL of air, the cartridge was eluted with 2 mL of 70% EtOH containing 1% (v/v) 0.1 N HCl (fraction III). The radioactivity in all eluates (fractions I−III) as well as the activity remaining bound to the cartridge material were counted in a Capintec. The activity collected in the EtOH-eluate was further analyzed via analytical RP-HPLC (5 → 90% B in 20 min).

Biodistribution Study. To establish tumor growth, OVCAR-3 cells were detached from the surface of the culture flasks using 1 mM EDTA in PBS, centrifuged, and resuspended in serum-free culture medium. Concentration of the cell suspension was $5 \cdot 10^6$ cells/100 μL medium. Nude mice (Swiss nu/nu, female, 6−8 weeks; Charles River, Sulzfeld, Germany) were injected with 100 μL of the cell suspension subcutaneously into the flank. Six weeks after tumor transplantation, all mice showed solid palpable tumor masses (tumor weight 0.15−0.8 g) and were used for the experiments.

For biodistribution studies, mice ($n = 3$) were intravenously injected with 0.37 MBq [^{125}I]Triptorelin in 100 μL PBS into the tail vein. To determine nonspecific tracer accumulation, 25 μg of unlabeled Triptorelin was coinjected ($n = 3$). At 60 min after radioligand injection, mice were sacrificed and dissected. The organs of interest were removed, weighed, and counted in a γ-counter (Wallach, Turku, Finland). Data are expressed as percent injected dose per gram tissue (%iD/g).

RESULTS

Peptide Synthesis. Triptorelin (pGlu-His-Trp-Ser-Tyr-D-Trp-Leu-Arg-Pro-Gly-NH_2), D-Lys^6-GnRH-I (pGlu-His-Trp-Ser-Tyr-D-Lys-Leu-Arg-Pro-Gly-NH_2) as well as D-Lys^6-GnRH-II (pGlu-His-Trp-Ser-His-D-Lys-Trp-Tyr-Pro-Gly-NH_2) were assembled on Rink Amide resin via a standard Fmoc-protocol. Cleavage from the resin was carried out using 95% trifluoroacetic acid (TFA), leading to concomitant side chain deprotection. Triptorelin and D-Lys^6-GnRH-II were then purified via preparative HPLC and were obtained in purities > 98% (220 nm).

D-Lys^6-GnRH-I was further derivatized on the Lys^6-side chain, either by direct coupling with unprotected DOTA (*41*) to yield D-Lys^6(DOTA)-GnRH-I or by coupling with different spacers (aminohexanoic acid (Ahx) or β-Ala), deprotection, and subsequent coupling with (Boc)aminooxyacetic acid ((Boc)Aoa) (Figure 1).

After workup and product isolation via preparative HPLC, D-Lys^6(DOTA)-GnRH-I was obtained in 16% yield. Due to impurities in the starting peptide and resulting formation of side products, necessitating an intermediate HPLC purification step, yields of D-Lys^6((Boc)Ahx)- and D-Lys^6((Boc)β-Ala)GnRH-I were also comparably low (approx 20%). The respective (Boc)Aoa-derivatives, however, were obtained in 50% yield after preparative HPLC isolation. Purities of these compounds were somewhat lower than for the other peptides synthesized in this study (90 vs >98%), which is occasioned by unavoidable cleavage of the Boc-protecting group from the Aoa-functionality during solvent evaporation after preparative HPLC, the 10% impurity consisting of the respective Ahx-Aoa- and β-Ala-Aoa-peptides. However, since the Aoa-deprotected peptides are the reactive species during ^{18}F-labeling and are in any case generated in situ during the labeling reaction, no attempt was made to further purify the seemingly impure D-Lys^6(Ahx-(Boc)Aoa)- and D-Lys^6(β-Ala-(Boc)Aoa)GnRH-I preparations, and they were used as such for the labeling reaction.

Radiolabeling. Radioiodination of Triptorelin and D-Lys^6-GnRH-II was initially carried out using the Iodogen method. However, under these conditions, radiochemical yields were comparably low (35−65% after HPLC purification) due to the formation of radiolabeled side products, and an optimized protocol based on a method described in the literature (*44*) was developed. Using chloramine T as an oxidant, the incorporation of radioiodide into the peptide was improved, and the formation of radioiodinated side products was successfully suppressed, leading to radiochemical yields of [^{125}I[Triptorelin of 82−89% after HPLC isolation. Because unreacted precursor was completely separated from both radioiodinated peptides, respectively, via HPLC, the specific activity of the radioiodinated compounds was assumed to be that of the radioiodide used for their preparation, i.e., 74 TBq/mmol.

^{18}F-labeling via oxime formation with 4-[^{18}F]fluorobenzaldehyde was performed in analogy to a previously published method (*40*), but with one major modification. Instead of first preparing and purifying the deprotected aminooxy-functionalized peptides and then using them for the labeling reaction, they were generated in situ from the protected (Boc)Aoa-precursors in the acidic (pH = 2) reaction milieu at 75 °C. Compared to the original labeling protocol, this necessitated a higher peptide concentration in the reaction mixture (2.5 vs 0.5 mM), since Boc-deprotection was not quantitative under the reaction conditions. However, D-Lys^6(Ahx-[^{18}F]FBOA)-GnRH-I and D-Lys^6(β-Ala-[^{18}F]FBOA)-GnRH-I were obtained in high yields (74−85% based on 4-[^{18}F]fluorobenzaldehyde) and high radiochemical purities (>99%) in an overall synthesis time of approx. 60 min (including RP-HPLC purification). Identity of the [^{18}F]FBOA-peptides was confirmed via coinjection with the ^{19}F-reference compounds (Figure 2). The variance in peak symmetry between the UV and the radiochromatogram, i.e., tailing of the activity peak, is due to suboptimal lead shielding of the detector.

^{68}Ga-labeling of D-Lys^6(DOTA)-GnRH-I was carried out according to a standard radiometalation strategy. After purification via a RP-18 cartridge, D-Lys^6([^{68}Ga]DOTA)-GnRH-I was obtained in 94% radiochemical yield and >99% radiochemical purity and a specific activity of 18.1 TBq/mmol.

Lipophilicity. For all radiolabeled peptides, the partition coefficient *P* between *n*-octanol and PBS (0.01 M, pH 7.4) and log *P* as a standard quantity to describe ligand lipophilicity (*43*) were determined. Lipophilicities of [^{125}I]Triptorelin and D-Lys^6-(Ahx-[^{18}F]FBOA)-GnRH-I were similar ([^{125}I]Triptorelin: log $P = -0.247 \pm 0.016$, D-Lys^6(Ahx-[^{18}F]FBOA)-GnRH-I: log $P = -0.395 \pm 0.016$), whereas it was lower in the case of D-Lys^6(β-Ala-[^{18}F]FBOA)-analogue due to the reduced length of the aliphatic chain compared to its Ahx-counterpart (log $P = -0.686 \pm 0.060$). With a log *P* of -3.703 ± 0.019, D-Lys^6([^{68}Ga]DOTA)-GnRH-I was the most hydrophilic of the compounds investigated.

In Vitro Studies. *Serum Dependence of [^{125}I]Triptorelin/D-Lys^6-[^{125}I]GnRH-II Binding.* All cell lines investigated (EFO-27, SKOV-3, LNCaP, DU-145, MDA-MB 231, SKBR-3) were cultured in parallel with different medium supplements, i.e., fetal calf serum (FCS) and Nu-Serum, a semisynthetic serum supplement. To evaluate the influence of culture conditions on GnRHR-expression, cells, that had been grown in the presence of the different serum supplements, were incubated with the

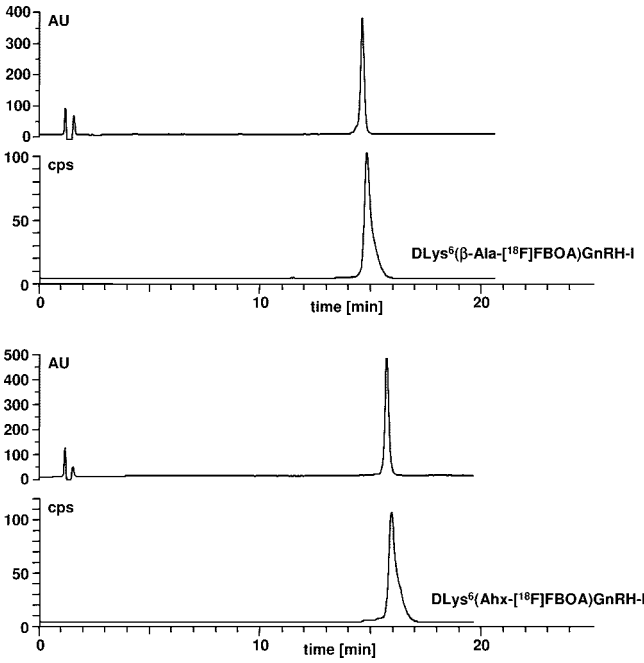

Figure 2. Analytical chromatograms of the coinjection of D-Lys^6(β-Ala-[^{18}F]FBOA)-GnRH-I (upper panel) and D-Lys^6(Ahx-[^{18}F]FBOA)-GnRH-I (lower panel) with their respective ^{19}F-analogues, i.e., D-Lys^6(β-Ala-FBOA)-GnRH-I and D-Lys^6(Ahx-FBOA)-GnRH-I. RP-HPLC was performed using a Nucleosil 100 C18 column and a gradient of 15 → 50% B in 20 min (A = 0.1% TFA, B = 0.1% TFA in acetonitrile).

respective standard radioligand for 60 and 120 min, and total as well as nonspecific radioligand uptake in the presence of an excess of cold competitor (5 μM) at the respective time point were determined. For EFO-27, LNCaP, MDA-MB 231, and SKBR-3 cells, which express the GnRH-I-receptor (*14*, *30*, *31*, *33*, *34*), [^{125}I]Triptorelin was used as the radioligand. The cell lines SKOV-3 and DU-145 have been shown to express the putative GnRH-II-receptor (*30, 32*), and thus the GnRH-II analogue D-Lys^6-[^{125}I]GnRH-II, was used as the radioligand to evaluate whether potential effects of the serum supplement on receptor expression could also be observed in the case of the receptor type II.

Data obtained for the cells grown with Nu-Serum and FCS are shown in Figure 3. Generally, cellular uptake of [^{125}I]Triptorelin or D-Lys^6-[^{125}I]GnRH-II was low (≤3.5% of total activity), and the extent of nonspecific binding was high (55−80% of total binding). This is reflected by the low percentage of specific ligand binding (in % of total binding) shown in Figure 3. However, substitution of FCS in the culture medium by Nu-Serum increased the fraction of specifically bound ligand in all cell lines and independently of the receptor subtype, indicating stronger GnRHR expression under these culture conditions. The observed increase in specific binding was highest (increase by a factor of ∼2) in EFO-27, LNCaP, and MDA-MB 231 cells. Of the cell lines investigated, EFO-27 cells showed the highest absolute radioligand uptake (3.01 ± 0.19% and 3.11 ± 0.18% of the applied activity after 60 and 120 min, respectively; LNCaP, 2.49 ± 0.15% and 2.55 ± 0.18%; MDA-MB, 1.53 ± 0.07% and 2.15 ± 0.18%), and thus EFO-27 cells cultured with Nu-Serum were chosen as the in vitro model for the evaluation of the new radioligands developed in this study.

Internalization Studies. Since high cellular uptake of radiolabeled peptide agonists greatly enhances the tumor to background ratio in peptide receptor imaging, the new ^{68}Ga- and ^{18}F-labeled GnRH-I analogues were also evaluated with respect to their internalization into EFO-27 cells. All studies were

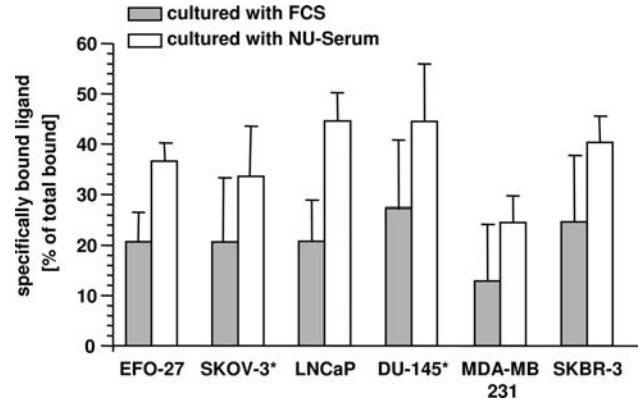

Figure 3. Dependence of radioligand uptake into different human GnRHR-positive cell lines on the serum supplement. Cells were grown using either fetal calf serum (FCS) or semisynthetic Nu-Serum for several weeks. They were then transferred into 24-well plates and incubated for 60 min with either the GnRHR-I ligand [^{125}I]Triptorelin or the GnRHR-II ligand [^{125}I]D-Lys^6-GnRH-II (GnRHR-II expressing cells are labeled with an asterisk (*)). Data are means of triplicate experiments (n = 3) and are given as specifically bound radioligand (= total − nonspecifically bound) in % of total binding. Nonspecific binding was determined in the presence of an excess (5 μM) of cold ligand.

performed in triplicate as dual tracer experiments with the respective ^{68}Ga- and ^{18}F-labeled peptides and [^{125}I]Triptorelin as an internal reference. This experimental setup assures comparability of the data obtained for the ^{68}Ga- and ^{18}F-labeled peptides, because the differences in specific activity between the radiometallated (c.a.) and radiofluorinated (n.c.a.) peptides are significant and may lead to large variations in cellular ligand uptake. However, uptake data for [^{125}I]Triptorelin in all experiments showed that the internalization of the reference peptide is unchanged by the different final peptide concentrations in the assay wells (1.8 nM for D-Lys^6([^{68}Ga]DOTA)-GnRH-I, subnanomolar for the ^{18}F-labeled peptides). Furthermore, performing the internalization studies as dual tracer experiments also allows elimination of systematic errors due to variable cell count or cell viability.

In the case of slowly internalizing receptors such as GnRHR (*45, 46*), it is of particular importance to be able to discriminate between internalized and receptor-bound radioligand. Thus, an acid wash was performed after the incubation step to release receptor-bound radioligand before lysis of the cells. Then, both acid-releasable (receptor-bound) and internalized activity were quantified.

Of the new compounds investigated, D-Lys^6(Ahx-[^{18}F]FBOA)-GnRH-I showed the highest internalization into EFO-27 cells. However, its cellular uptake was slightly lower than that of the reference [^{125}I]Triptorelin (85.8 ± 16.0% and 84.9 ± 5.6% of the internalization found for [^{125}I]Triptorelin in the same experiment at 60 and 120 min, respectively) (Table 1). The D-Lys^6(β-Ala-[^{18}F]FBOA)-analogue, however, showed less than half of the internalization found for [^{125}I]Triptorelin, and for D-Lys^6([^{68}Ga]DOTA)-GnRH-I almost no internalization was detected.

As already observed in the initial uptake studies (serum depencence of GnRHR-I expression), nonspecific receptor binding and internalization in the presence of an excess of unlabeled Triptorelin (5 μM) was high. For the two ^{18}F-labeled analogues, only approx 10% of the acid-releasable activity was specifically bound to the cell membrane at 60 min ([^{125}I]Triptorelin: 17%), and only 20−30% ([^{125}I]Triptorelin: 37%) of the internalized activity was found to be taken up specifically. In the case of D-Lys^6([^{68}Ga]DOTA)-GnRH-I, no specific receptor binding or internalization was observed.

Table 1. Internalization of the Different Radiolabeled GnRH-I-Analogues into GnRHR-Expressing EFO-27 Ovary Carcinoma Cells[a]

peptide	internalization [% of [^{125}I]Triptorelin]
[^{125}I]Triptorelin	100
D-Lys^6(Ahx-[^{18}F]FBOA)-GnRH-I	86 ± 16
D-Lys^6(β-Ala-[^{18}F]FBOA)-GnRH-I	42 ± 3
D-Lys^6([^{68}Ga]DOTA)-GnRH-I	2.6 ± 1.0

[a] Cells were coincubated with both the ^{18}F- or ^{68}Ga-labeled compound and the reference [^{125}I]Triptorelin for 60 min at 37° C (n = 3). Data are given in % of the internalization of the reference [^{125}I]Triptorelin in the same experiment and are means ± SD (triplicate determination).

Table 2. Binding Affinities of the Reference Triptorelin and the Three New GnRH-I-Analogues to the Human GnRHR[a]

peptide	IC_{50} [nM]
Triptorelin	0.13 ± 0.01
D-Lys^6(Ahx-FBOA)-GnRH-I	0.50 ± 0.08
D-Lys^6(β-Ala-FBOA)-GnRH-I	0.86 ± 0.13
D-Lys^6(Ga-DOTA)-GnRH-I	13.27 ± 1.01

[a] Competitive binding studies were performed using a membrane preparation of GnRHR-expressing cells (10 μg membrane/sample) with [^{125}I]Triptorelin as the radioligand (n = 3 for each peptide concentration). Experiments were carried out in triplicate. Data are means ± SD.

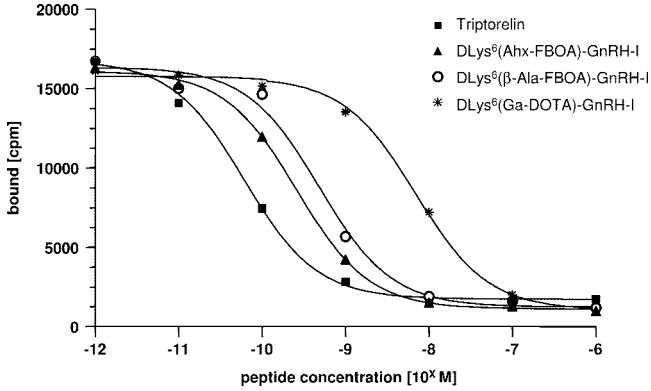

Figure 4. Exemplary IC_{50}-curves obtained for the different new GnRH-I analogues and the reference Triptorelin using GnRHR-membrane preparations (10 μg/well, n = 3; error bars are omitted for better clarity) and [^{125}I]Triptorelin as the radioligand. Data represent one of three separate determinations.

The internalization data for D-Lys^6(Ahx-[^{18}F]FBOA)-GnRH-I were also confirmed in the ovarian cancer cell line OVCAR-3, which in contrast to the EFO-27 cell line is a well-established tumor model and was chosen as a model for the potential future in vivo evaluation of the new GnRH-I analogues. In OVCAR-3 cells, D-Lys^6(Ahx-[^{18}F]FBOA)-GnRH-I showed 85.3 ± 15.8% and 89.1 ± 15.0% of the internalization of [^{125}I]Triptorelin at 60 and 120 min, respectively. In OVCAR-3 cells, however, the fraction of nonspecifically bound/internalized ligand (approx 90% in both cases) is even higher than in EFO-27 cells.

Determination of IC_{50}. The GnRH-receptor affinities of Triptorelin, D-Lys^6(Ahx-FBOA)-GnRH-I, D-Lys^6(β-Ala-FBOA)-GnRH-I, and D-Lys^6(Ga-DOTA)-GnRH-I were determined using a commercially available membrane preparation of GnRHR-I-expressing cells and [^{125}I]Triptorelin as the radioligand. Results are summarized in Table 2. While the Ga-DOTA-analogue shows a loss of binding affinity by a factor of ~100 compared to the reference Triptorelin, both FBOA-analogues display only slightly reduced receptor affinities, which are still in the subnanomolar range (Figure 4). The order of affinities, however, reflects the trend already observed for the internalization efficiencies of the respective GnRHR-ligands, i.e., Triptorelin > D-Lys^6(Ahx-FBOA)-GnRH-I > D-Lys^6(β-Ala-FBOA)-GnRH-I ≫ D-Lys^6(Ga-DOTA)-GnRH-I.

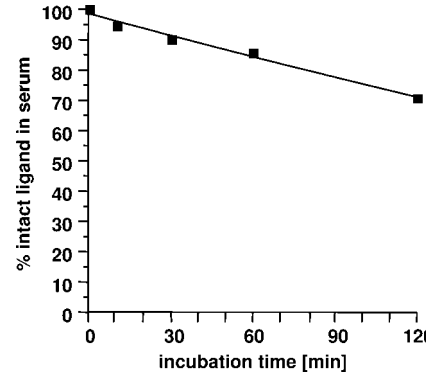

Figure 5. Stability of D-Lys^6(Ahx-[^{18}F]FBOA)-GnRH-I in human serum. Data represent the amount of intact tracer found in serum after incubation at 37 °C for 30 to 240 min. A one-phase exponential fit yielded a calculated serum half-life of 254 ± 18 min for D-Lys^6-(Ahx-[^{18}F]FBOA)-GnRH-I.

Table 3. Biodistribution of [^{125}I]Triptorelin in OVCAR-3 Tumor Bearing Nude Mice 60 min p.i. (n = 3)[a]

organ	activity accumulation [%iD/g]
blood	0.96 ± 0.13
heart	0.54 ± 0.01
lung	1.49 ± 0.28
liver	2.39 ± 1.03
intestine	13.56 ± 3.57
stomach	2.64 ± 0.64
kidney	2.82 ± 0.67
spleen	0.54 ± 0.10
pancreas	0.52 ± 0.10
muscle	0.22 ± 0.05
OVCAR-3 tumor	0.49 ± 0.05

[a] Data are given in % injected dose per gram tissue (%iD/g).

Serum Stability. The new GnRH-I-analogue with the highest receptor affinity and internalization efficiency, D-Lys^6(Ahx-[^{18}F]FBOA)-GnRH-I, was investigated with respect to its stability in human serum (Figure 5). The radiolabeled peptide was incubated with human serum for up to 120 min, followed by extraction of the radioactivity using a RP-18 cartridge. The cartridge eluate was analyzed using RP-HPLC.

Over time, an increasing amount of a hydrophilic metabolite with no retention on the RP-18-material of the extraction cartridge was formed (5.4%, 9.9%, 14.4%, and 29.3% of the total activity applied to the cartridge after 10, 30, 60, and 120 min incubation, respectively). This metabolite was always eluted in the washing step with water and was not further characterized. At all time points investigated, however, the activity immobilized on the cartridge (elution with a slightly acidified ethanolic solution) was analyzed using RP-HPLC and was found to consist exclusively of intact tracer. Formation of further metabolites was not observed.

The decrease of the amount of intact D-Lys^6(Ahx-[^{18}F]FBOA)-GnRH-I over time is illustrated in Figure 5. A one-phase exponential fit of the data yielded a serum half-life of 254 ± 18 min for this ligand.

In Vivo Biodistribution Study. To evaluate the potential of OVCAR-3 xenografts as an in vivo model for GnRHR-imaging, a preliminary biodistribution study for the reference ligand [^{125}I]Triptorelin was performed in OVCAR-3 tumor bearing nude mice. Data are summarized in Table 3.

The highest accumulation of [^{125}I]Triptorelin was observed in the organs of the gastrointestinal tract, probably due to a predominant hepatobiliary clearance of the tracer, and in the kidneys. Unfortunately, uptake of [^{125}I]Triptorelin in the

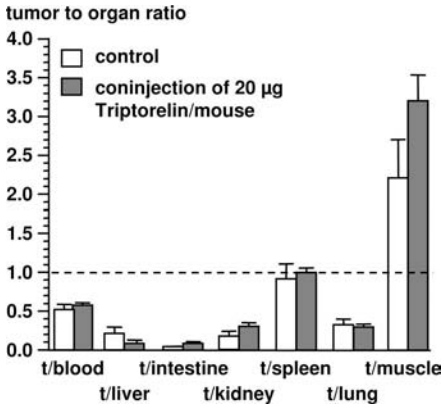

Figure 6. Tumor to organ ratios for [^{125}I]Triptorelin in OVCAR-3 tumor bearing nude mice at 60 min p.i.. White bars represent the control experiment (tracer only, $n = 3$); gray bars represent blocking conditions (coinjection of 20 μg Triptorelin, $n = 3$).

OVCAR-3 tumors was as low as nonspecific tracer accumulation in heart, spleen, and pancreas (~0.5%iD/g). This leads to very low tumor-to-organ ratios of 0.51, 0.21, 0.04, 0.17, and 2.22 for blood, liver, intestine, kidney, and muscle, respectively (Figure 6).

Furthermore, a blocking study was performed, in which 20 μg of unlabeled Triptorelin was coinjected. In this study, absolute tracer accumulation in all organs was approx threefold higher than observed in the control experiment (data not shown), which might be occasioned by a slowed tracer excretion due to some pharmacological effect caused by Triptorelin. However, tumor to organ ratios were nearly identical to those found in the control experiment (Figure 6), demonstrating that tracer accumulation in OVCAR-3 tumors is not receptor-mediated.

DISCUSSION

Due to their high incidence on human tumors of the reproductive system, GnRH-receptors have been successfully used for direct targeting with potent GnRH-analogues, leading to tumor growth suppression (*24*). However, to our knowledge only one attempt to exploit this receptor system as a target for in vivo peptide receptor imaging has been reported to date (*29*).

One possible reason for this circumstance is the fact that almost no data are available concerning the level of GnRH-receptor protein expression in human tumor cell lines, since for most studies investigating, e.g., GnRH receptor function transiently transfected cells are used (*45, 47*), and receptor expression in cancer cell lines or tumor specimens is almost exclusively determined using mRNA blotting techniques or hormonal response studies (*34*). For the evaluation of GnRH-radiotracers, however, receptor expression on the respective human tumor cell lines is a crucial quantity, because high cellular radioligand uptake and thus the possibility for high-contrast GnRHR-imaging depends on high intrinsic membrane presentation of the target receptor.

Furthermore, the capacity of the receptor to internalize the radioligand is helpful to achieve high activity accumulation in tumor tissue. Among all G-protein coupled receptors that have been cloned to date, the type I mammalian GnRHR is the only receptor fully lacking the C-terminal cytoplasmatic tail, which is highly important for effective receptor internalization (*45, 46*). Nevertheless, the human GnRHR-I is internalized (*45, 48*), albeit slowly. In a very recent study, it has been demonstrated that this internalization is constitutive and not–as previously assumed–agonist-induced, and also cannot be stimulated above constitutive level in the presence of various GnRH-analogues (*49*). In contrast, the type II mammalian and nonmammalian GnRHRs, which possess intracellular C-tails of varying length, are rapidly internalized (*45, 46*).

From this point of view, the type II GnRHR seems more suitable for targeting with radiolabeled GnRH-analogues than the type I receptor. However, it is still a matter of ongoing debate whether a functional human GnRHR-II exists at all. Some studies suggest GnRHR-II mediated actions of ant/agonistic GnRH-I or GnRH-II analogues on GnRHR-expressing cancer cells (*50, 51*), others indicate ligand-selective active conformations of GnRHR-I, explaining the different ligand-induced signaling observed for GnRH-I and -II analogues (*52*), and others demonstrate modulation of GnRHR-I function by expression of GnRHR-II gene fragments (*53*).

Therefore, the focus of this study was directed toward the evaluation of the GnRH-I receptor as a potential target for radiolabeled GnRH-I-analogues as well as the parallel development of high-affinity GnRH-I analogues labeled with positron-emitting radionuclides (^{18}F, ^{68}Ga) for potential use in GnRHR-imaging via PET.

First, several GnRHR-expressing cell lines derived from human ovarian (EFO-27, SKOV-3, OVCAR-3), breast (MDA-MB 231, SKBR-3), and prostate cancer specimens (LNCaP, DU-145) were screened for GnRHR-expression using a radioligand binding assay. While EFO-27, MDA-MB 231, SKBR-3, and LNCaP cells have been reported to express GnRHR-I only (*14, 30, 31, 33, 34*), OVCAR-3 cells express both the human type I and type II GnRHR (*30*), and DU-145 and SKOV-3 cells have been shown to express the type II GnRHR (*30, 32*). Although, based on the argumentation above, the focus of this study was the evaluation of the GnRH-I receptor as a potential target for peptide receptor imaging, the latter two cell lines were also included in this study and screened for GnRHR-II expression using the corresponding standard radioligand D-Lys^6-[^{125}I]GnRH-II. This allows comparison of two receptor subtypes, GnRHR-I and the putative GnRHR-II, with respect to the level of receptor expression and efficiency of radioligand uptake, and thus identification of the more suitable target receptor for the intended purpose.

Unfortunately, GnRHR-expression and thus radioligand uptake was low in all cell lines investigated ($\leq$3.5% of the applied activity after a 120 min incubation) and independent of the receptor subtype. Furthermore, the level of nonspecific binding, which was determined in the presence of an excess of unlabeled peptide (5 μM), was >55% for all cell lines. These data are consistent with a previous study, in which GnRHR-expression on different breast cancer cell line membranes was investigated using [^{125}I][D-Ala^6-N$_\alpha$MeLeu^7-Pro^9-NEt]-GnRH-I as the radioligand (*31*). Similar results were obtained using membranes of SKBR-3 and MDA-MB 231 cells: very low receptor binding (~1.5% of applied activity) and a high level ($\geq$50%) of nonspecific binding was found.

Another problem encountered during the in vitro studies presented here was that absolute radioligand uptake did not correlate with the cell count in the respective assay in most cases, indicating variable levels of receptor expression or receptor presentation on the cell surface (data not shown), even when cell culture conditions were kept constant for the different assays. However, reliability of the in vitro system can be partially improved by the choice of the appropriate serum supplement used for cell culture. Substituting fetal calf serum (FCS) by a semisynthetic serum supplement, Nu-Serum, leads to an increase in the fraction of specifically bound radioligand in all cell lines, independently of the GnRH receptor type investigated, indicating enhanced receptor expression under these conditions (Figure 3). This had already been documented previously for DU-145 cells (*35*), and seems, based on the data obtained in this study, a suitable means to enhance and stabilize

GnRHR-expression in cell culture, thus providing reliable in vitro systems for the evaluation of new radiolabeled GnRHR-ligands. In this study, EFO-27 cells were chosen as the optimal in vitro model due to their comparably high and constant receptor expression.

Generally, the low GnRH receptor protein expression, that has been observed in this study, is explainable by the results of recent studies elucidating the regulation of human GnRHR-expression. Obviously, a large proportion of the human GnRHR protein is inefficiently processed by the cell under physiological conditions and is retained at the site of production, the endoplasmatic reticulum, or an intracellular pool (*49*). This inefficient routing to the plasma membrane seems to be due to a high degree of protein misfolding which can be partly overcome by the action of so-called "pharmacoperones", small membrane-permeable antagonistic molecules that stabilize the correct receptor conformation and thus allow efficient routing to the plasma membrane (*54–56*). In contrast to the GnRHRs of other species, that show high plasma membrane expression, the human receptor seems to have specifically evolved by point mutation to be inefficiently folded and thus retained intracellularly. However, despite its very low membrane expression (approx 2000 receptors/cell in MCF7 and LNCaP cells (*56*)) signaling of the human GnRHR is very robust, suggesting that a proportion of the intracellular receptors might traffic to the cell surface during stimulation and thus providing a rationale for the successful application of GnRH-analogues for suppression of tumor growth (*24*).

In parallel to the evaluation of the different cell lines as potential in vitro models, three novel GnRH-I analogues were developed (Figure 1): D-Lys^6([^{68}Ga]DOTA)-GnRH-I, D-Lys^6(Ahx-[^{18}F]FBOA)-GnRH-I, and D-Lys^6(β-Ala-[^{18}F]FBOA)-GnRH-I.

While radiolabeling of the first was performed according to a standard protocol, the strategy for ^{18}F-labeling via oxime formation with 4-[^{18}F]fluorobenzaldehyde was modified as compared to a previous method (*40*). Instead of the deprotected aminooxy-functionalized peptides, their respective Boc-protected precursors, i.e., D-Lys^6(Ahx-(Boc)AoA)-GnRH-I and D-Lys^6(β-Ala-(Boc)AoA)-GnRH-I, were used for the labeling reaction. One substantial problem with using the deprotected peptides is the very high reactivity of the aminooxy group toward ketones and aldehydes of any kind, leading to the formation of unwanted conjugates with even traces of acetone or formaldehyde and softeners during workup or storage of the purified peptides. This problem can be avoided using the Boc-protected precursors. In this study, deprotection of the aminooxy group was carried out in situ during the labeling reaction, and the [^{18}F]FBOA-peptides were obtained in high radiochemical yields, identical to those obtained when the deprotected precursors were used (*40*). It is important to note, however, that a 5-fold higher peptide concentration was needed for efficient labeling as compared to deprotected aminooxy-peptides. However, this potential drawback is balanced by the much greater ease of peptide precursor preparation and handling as well as facilitated HPLC purification of the corresponding [^{18}F]FBOA-peptides due to a significantly lower fraction of unlabeled impurities in the case of the Boc-protected analogues.

In vitro evaluation of D-Lys^6([^{68}Ga]DOTA)-GnRH-I, D-Lys^6(Ahx-[^{18}F]FBOA)-GnRH-I, and D-Lys^6(β-Ala-[^{18}F]FBOA)-GnRH-I yielded unexpected results with respect to the sensitivity of the D-Lys^6-GnRH-I scaffold toward chemical modification of the D-Lys^6-side chain. While data from the literature had indicated that even very large molecules such as proteins (*37, 39*) could be conjugated to this position without significantly affecting receptor affinity, the modifications introduced in this study had substantial effects on receptor affinity and ligand internalization. Interestingly, introduction of a highly hydrophilic moiety, i.e., [^{68}Ga]DOTA, on the D-Lys^6-side chain led to a hundredfold decrease in receptor affinity compared to the reference peptide Triptorelin, while the effect of conjugation with the lipophilic residue [^{18}F]FBOA via different spacers (Ahx, β-Ala) was very small, i.e., a loss of binding affinity by a factor of 4 to 6 (Table 2). These data indicate first that only lipophilic modifications are well-tolerated in this position, and second that spacer length between the D-Lys^6-side chain and the lipophilic moiety has significant impact on the receptor affinity of D-Lys^6-modified GnRH-I analogues.

The receptor binding data obtained via membrane binding assays correlate well with the internalization data from studies using EFO-27 cells (Table 1). Receptor-mediated internalization of the [^{68}Ga]DOTA-analogue was negligible, corresponding to the very low receptor affinity of this compound, while cellular uptake of D-Lys^6(Ahx-[^{18}F]FBOA)-GnRH-I was close to that of the reference [^{125}I]Triptorelin, reflecting the similar receptor affinity of these radioligands.

Because D-Lys^6(Ahx-[^{18}F]FBOA)-GnRH-I showed the most promising in vitro profile of the new compounds evaluated, its in vitro stability in human serum was investigated in preparation for future in vivo evaluation. The calculated serum half-life of this compound is >4 h, indicating both sufficient stability of the peptide scaffold as well as of the oxime bond between the aminooxy-functionalized peptide and 4-[^{18}F]fluorobenzaldehyde and thus suitable stability for in vivo application for imaging purposes.

Another step toward the future in vivo evaluation of D-Lys^6(Ahx-[^{18}F]FBOA)-GnRH-I was the search for an appropriate in vivo tumor model. Because EFO-27 cells are not tumorigenic in mice, internalization of D-Lys^6(Ahx-[^{18}F]FBOA)-GnRH-I and of the standard ligand [^{125}I]Triptorelin were also investigated in OVCAR-3 cells, a well-established GnRHR-expressing transplantable tumor model. For both peptides, absolute radioligand uptake was identical to that observed in EFO-27 cells, and the difference in internalization efficiency between the two peptides was also identical in both cell lines, indicating the suitability of OVCAR-3 cells as a transplantable tumor model for the future in vivo evaluation of new radiolabeled GnRH-I analogues.

To confirm this, a preliminary biodistribution study was performed in OVCAR-3 tumor bearing nude mice. Because [^{125}I]Triptorelin has an even higher receptor affinity than D-Lys^6(Ahx-[^{18}F]FBOA)-GnRH-I and therefore can be viewed as a "gold standard"-GnRH-ligand, [^{125}I]Triptorelin was used as the radioligand for the evaluation of the OVCAR-3 tumor model. The comparably high lipophilicity of [^{125}I]Triptorelin leads to predominant hepatobiliary clearance of the radioligand, as illustrated by the very high uptake in intestine and also substantial hepatic accumulation (Table 3). Because the lipophilicity of D-Lys^6(Ahx-[^{18}F]FBOA)-GnRH-I is similar to that of [^{125}I]Triptorelin, the excretion patterns of both radioligands will probably be very similar. Consequently, a high extent of hepatobiliary excretion and thus high background activity can also be expected for the fluorinated peptide. Therefore, based on the experience from studies with different glycosylated somatostatin receptor−ligands, which have demonstrated that only ligands with a log $P < 1.6$ show a suitable excretion pattern for high-contrast peptide receptor imaging (*57, 58*), pharmacokinetic ligand optimization is warranted before performing in vivo studies with D-Lys^6(Ahx-[^{18}F]FBOA)-GnRH-I.

With respect to receptor-specific tracer accumulation, the biodistribution data of [^{125}I]Triptorelin (Table 3) parallel the in vitro data found for all GnRHR-expressing cell lines investigated in this study: the level of GnRHR-expression on the respective tumor cells seems to be very low. Tumor uptake of [^{125}I]Triptorelin was as low as nonspecific tracer accumulation in organs such as heart, spleen, and pancreas (~0.5%iD/g) and is even

lower than blood activity concentration at the same time point (0.96%iD/g at 60 min p.i.). A blocking study revealed the absence of receptor-mediated tumor accumulation (Figure 6). However, to confirm this observation and to be able to quantify GnRH-I-receptor expression in OVCAR-3 tumors more precisely, ex vivo GnRHR-autoradiography or immunohistochemistry after excision of the implanted tumor would be necessary.

Nevertheless, this observation seriously challenges the suitability of the GnRH receptor system as a target for peptide receptor imaging, since the obvious lack of receptor-mediated tracer accumulation will not allow high-contrast imaging and sensitive detection of GnRHR-positive lesions, even if overall tracer pharmacokinetics are substantially improved.

CONCLUSION

The in vitro evaluation of the three new radiolabeled GnRH-I analogues investigated in this study, D-Lys^6([^{68}Ga]DOTA)-GnRH-I, D-Lys^6(Ahx-[^{18}F]FBOA)-GnRH-I, and D-Lys^6(β-Ala-[^{18}F]FBOA)-GnRH-I, yielded interesting insights into the structural requirements for the development of high-affinity radiolabeled GnRH-I agonists. Obviously, in this study only the conjugation of lipophilic residues to the D-Lys^6-side chain is well-tolerated by the peptide scaffold without significant loss of binding affinity, and spacer length between the D-Lys^6-side chain and the hydrophobic moiety has substantial impact on the receptor affinity of the radioligand.

Of the new compounds investigated, D-Lys^6(Ahx-[^{18}F]FBOA)-GnRH-I shows the highest receptor affinity and internalization efficiency into GnRHR-expressing tumor cells, bearing the highest structural homology to a previously developed high-affinity cytotoxic GnRH-I analogue. D-Lys^6(Ahx-[^{18}F]FBOA)-GnRH-I illustrates again the versatility and ease of the newly developed ^{18}F-labeling method via chemoselective oxime formation with 4-[^{18}F]fluorobenzaldehyde, especially when the Boc-protected aminooxy-peptide is used as the labeling precursor, and represents the first radiolabeled GnRH-I analogue with suitable binding characteristics for efficient GnRHR-targeting.

Unfortunately, both the in vitro radioligand binding assays performed with various GnRHR-expressing human cancer cell lines as well as the initial in vivo biodistribution study carried out using OVCAR-3 tumor-bearing nude mice indicated a very low level of GnRHR expression on the cell surface. While this obviously does not seem to hamper application of nonradiolabeled GnRH-analogues for the effective suppression of tumor growth, as demonstrated in a variety of studies, it has a deleterious impact on the suitability of the GnRHR system as a suitable target for peptide receptor imaging using radiolabeled GnRH-analogues. In our opinion, GnRH receptors represent a highly interesting target for pharmacological interventions, but do not fulfill the prerequisites for successful peptide receptor imaging, even when suitable receptor−ligands as developed in this study are available.

ACKNOWLEDGMENT

This work was supported by a KKF (Kommission für Klinische Forschung am Klinikum rechts der Isar) grant (N^o 48-03) and by a MMW grant (Wissenschaftliches Herausgeberkollegium der Münchner Medizinischen Wochenschrift).

LITERATURE CITED

(1) Ginj, M., Chen, J., Walter, M. A., Eltschinger, V., Reubi, J. C., and Maecke, H. R. (2005) Preclinical evaluation of new and highly potent analogues of octreotide for predictive imaging and targeted radiotherapy. *Clin. Cancer Res. 11*, 1136–1145.

(2) Esser, J. P., Krenning, E. P., Teunissen, J. J., Kooij, P. P., van Gameren, A. L., Bakker, W. H., and Kwekkeboom, D. J. (2006) Comparison of [^{177}Lu-DOTA^0,Tyr^3]octreotate and [^{177}Lu-DOTA^0,Tyr^3]octreotide: which peptide is preferable for PRRT? *Eur. J. Nucl. Med. Mol. Imaging 33*, 1346–1351.

(3) Schottelius, M., Poethko, T., Herz, M., Reubi, J. C., Kessler, H., Schwaiger, M., and Wester, H. J. (2004) First ^{18}F-labeled tracer suitable for routine clinical imaging of sst receptor-expressing tumors using positron emission tomography. *Clin. Cancer Res. 10*, 3593–3606.

(4) Meisetschlager, G., Poethko, T., Stahl, A., Wolf, I., Scheidhauer, K., Schottelius, M., Herz, M., Wester, H. J., and Schwaiger, M. (2006) Gluc-Lys([^{18}F]FP)-TOCA PET in patients with SSTR-positive tumors: biodistribution and diagnostic evaluation compared with [^{111}In]DTPA-octreotide. *J. Nucl. Med. 47*, 566–573.

(5) Decristoforo, C., Mather, S. J., Cholewinski, W., Donnemiller, E., Riccabona, G., and Moncayo, R. (2000) ^{99m}Tc-EDDA/HYNIC-TOC: a new ^{99m}Tc-labelled radiopharma-ceutical for imaging somatostatin receptor-positive tumours; first clinical results and intra-patient comparison with ^{111}In-labelled octreotide derivatives. *Eur. J. Nucl. Med. 27*, 1318–1325.

(6) Forrer, F., Waldherr, C., Maecke, H. R., and Mueller-Brand, J. (2006) Targeted radionuclide therapy with ^{90}Y-DOTATOC in patients with neuroendocrine tumors. *Anticancer Res. 26*, 703–707.

(7) Reubi, J. C. (2003) Peptide receptors as molecular targets for cancer diagnosis and therapy. *Endocrine Rev. 24*, 389–427.

(8) Reubi, J. C., and Waser, B. (2003) Concomitant expression of several peptide receptors in neuroendocrine tumors: molecular basis for in vivo multireceptor tumour targeting. *Eur. J. Nucl. Med. Mol. Imaging 30*, 781–793.

(9) Zhang, H., Chen, J., Waldherr, C., Hinni, K., Waser, B., Reubi, J. C., and Maecke, H. R. (2004) Synthesis and evaluation of bombesin derivatives on the basis of pan-bombesin peptides labeled with indium-111, lutetium-177, and yttrium-90 for targeting bombesin receptor-expressing tumors. *Cancer Res. 64*, 6707–6715.

(10) Waser, B., Eltschinger, V., Linder, K., Nunn, A., and Reubi, J. C. (2007) Selective in vitro targeting of GRP and NMB receptors in human tumours with the new bombesin tracer ^{177}Lu-AMBA. *Eur. J. Nucl. Med. Mol. Imaging 34*, 95–100.

(11) Nock, B. A., Maina, T., Behe, M., Nikolopoulou, A., Gotthardt, M., Schmitt, J. S., Behr, T. M., and Macke, H. R. (2005) CCK-2/gastrin receptor-targeted tumor imaging with ^{99m}Tc-labeled minigastrin analogs. *J. Nucl. Med. 46*, 1727–1736.

(12) Wild, D., Béhé, M., Wicki, A., Storch, D., Waser, B., Gotthardt., M., Keil, B., Christofori, G., Reubi, J. C., and Mäcke, H. R. (2006) [Lys^{40}(Ahx-DTPA-^{111}In)NH$_2$]Exedin-4, a very promising ligand for glucagon-like peptide-1 (GLP-1) receptor targeting. *J. Nucl. Med. 47*, 2025–2033.

(13) Schally, A. V. (1999) Luteinizing hormone-releasing hormone analogs: their impact on the control of tumorigenesis. *Peptides 20*, 1247–1262.

(14) Halmos, G., Arencibia, J. M., Schally, A. V., Davis, R., and Bostwick, D. G. (2000) High Incidence of receptors for luteinizing hormone releasing hormone (LHRH) and LHRH receptor gene expression in human prostate cancers. *J. Urol. 163*, 623–629.

(15) Pati, D., and Habibi, H. R. (1995) Inhibition of human hepatocarcinoma cell proliferation by mammalian and fish gonadotropin-releasing hormones. *Endocrinology 136*, 75–84.

(16) Krebs, L. J., Wang, X., Nagy, A., Schally, A. V., Prasad, P. N., and Liebow, C. (2002) A conjugate of doxorubicin and an analog of Luteinizing Hormone-Releasing Hormone shows increased efficacy against oral and laryngeal cancers. *Oral Oncol. 38*, 657–663.

(17) Friess, H., Buchler, M., Kiesel, L., Kruger, M., and Beger, H. G. (1991) LH-RH receptors in the human pancreas. Basis for antihormonal treatment in ductal carcinoma of the pancreas. *Int. J. Pancreatol. 10*, 151–159.

(18) Sion-Vardi, N., Kaneti, J., Segal-Abramson, T., Giat, J., Levy, J., and Sharoni, Y. (1992) Gonadotropin-releasing hormone specific binding sites in normal and malignant renal tissue. *J. Urol. 148*, 1568–1570.

(19) van Groeninghen, J. C., Kiesel, L., Winkler, D., and Zwirner, M. (1998) Effects of luteinizing hormone-releasing hormone on nervous system tumours. *Lancet 352*, 372–373.

(20) Chen, A., Ganor, Y., Rahimipour, S., Ben-Aroya, N., Koch, Y., and Levite, M. (2002) The neuropeptides GnRH-II and GnRH-I are produced by human T cells and trigger laminin receptor gene expression, adhesion, chemotaxis and homing to specific organs. *Nat. Med. 8*, 1421–1426.

(21) Keller, G., Schally, A. V., Gaiser, T., Nagy, A., Baker, B., Halmos, G., and Engel, J. B. (2005) Receptors for luteinizing hormone releasing hormone (LHRH) expressed in human non-Hodgkin's lymphomas can be targeted for therapy with the cytotoxic LHRH analogue AN-207. *Eur. J. Cancer 41*, 2196–2202.

(22) Moretti, R. M., Montangnani-Marelli, M., van Groeninghen, J. C., and Limonta, P. (2002) Locally expressed GnRH receptors mediate the oncostatic and antimetastatic activity of GnRH agonists on melanoma cells. *J. Clin. Endocrin. Metab. 87*, 3791–3797.

(23) Keller, G., Schally, A. V., Gaiser, T., Nagy, A., Baker, B., Westphal, G., Halmos, G., and Engel, J. B. (2005) Human malignant melanomas express receptors for luteinizing hormone releasing hormone allowing targeted therapy with cytotoxic luteinizing hormone releasing hormone analogue. *Cancer Res. 65*, 5857–5863.

(24) Montagnani-Marelli, M., Moretti, R. M., Januszkiewicz-Caulier, J., Motta, M., and Limonta, P. (2006) Gonadotropin-releasing hormone (GnRH) receptors in tumors: a new rationale for the therapeutical application of GnRH analogs in cancer patients? *Curr. Cancer Drug Targets 6*, 257–269.

(25) Nagy, A., Schally, A. V., Armatis, P., Szepeshazi, K., Halmos, G., Kovacs, M., Zarandi, M., Groot, K., Miyazaki, M., Jungwirth, A., and Horvath, J. (1996) Cytotoxic analogs of luteinizing hormone-releasing hormone containing doxorubicin or 2-pyrrolinodoxorubicin, a derivative 500−1000 times more potent. *Proc. Natl. Acad. Sci. U.S.A. 93*, 7269–7273.

(26) Nagy, A., and Schally, A. V. (2005) Targeting of cytotoxic luteinizing hormone-releasing hormone analogs to breast, ovarian, endometrial, and prostate cancers. *Biol. Reprod. 73*, 851–859.

(27) Keller, G., Schally, A. V., Gaiser, T., Nagy, A., Baker, B., Halmos, G., and Engel, J. B. (2005) Receptors for luteinizing hormone releasing hormone expressed on human renal cell carcinomas can be used for targeted chemotherapy with cytotoxic luteinizing hormone releasing hormone analogues. *Clin. Cancer Res. 11*, 5549–5557.

(28) Harrison, G. S., Wiermann, M. E., Nett, T. M., and Glode, L. M. (2004) Gonadotropin-releasing hormone and its receptor in normal and malignant cells. *Endocrine-Related Cancer 11*, 725–748.

(29) Barda, Y., Cohen, N., Lev, V., Ben-Aroya, N., Koch, Y., Mishani, E., Fridkin, M., and Gilon, C. (2004) Backbone metal cyclization: novel ^{99m}Tc labeled GnRH analog as potential SPECT molecular imaging agent in cancer. *Nucl. Med. Biol. 31*, 921–933.

(30) Gründker, C., Schlotawa, L., Viereck, V., Eicke, N., Horst, A., Kairies, B., and Emons, G. (2004) Antiproliferative effects of the GnRH antagonist Cetrorelix and of GnRH-II on human endometrial and ovarian cancer cells are not mediated through the GnRH type I receptor. *Eur. J. Endocrinol. 151*, 141–149.

(31) Eidne, K. A., Flanagan, C. A., Harris, N. S., and Millar, R. P. (1987) Gonadotropin-releasing hormone (GnRH)-binding sites in human breast cancer cell lines and inhibitory effects of GnRH-Antagonists. *J. Clin. Endocrinol. Metab. 64*, 425–432.

(32) Enomoto, M., Endo, D., Kawashima, S., and Park, M. K. (2004) Human Type II GnRH receptor mediates effects of GnRH on cell proliferation. *Zool. Sci. 21*, 763–770.

(33) Bahk, J. Y., Hyun, J. S., Lee, H., Kim, M. O., Cho, G. J., Lee, B. H., and Choi, W. S. (1998) Expression of gonadotropin-releasing hormone (GnRH) and GnRH receptor mRNA in prostate cancer cells and effect of GnRH on the proliferation of prostate cancer cells. *Urol. Res. 26*, 259–264.

(34) Hapgood, J. P., Sadie, H., van Biljon, W., and Ronacher, K. (2005) Regulation of expression of gonadotrophin-releasing hormone receptor genes. *J. Neuroendocrinol. 17*, 619–638.

(35) Enomoto, M., Mori, T., and Park, M. K. (2002) Influence of serum supplements in culture medium on gonadotrolin-releasing hormone effects on colony formation. *Life Sci. 71*, 2153–2160.

(36) Söderhäll, J. A., Polymeropoulos, E. E., Paulini, K., Günther, E., and Kühne, R. (2005) Antagonist and agonist binding models of the human gonadotropin-releasing hormone receptor. *Biochem. Biophys. Res. Commun. 333*, 568–582.

(37) Beckers, T., Bernd, M., Kutscher, B., Kühne, R., Hoffmann, S., and Reissmann, T. (2001) Structure-Function Studies of linear and cyclized peptide antagonists of the GnRH receptor. *Biochem. Biophys. Res. Commun. 289*, 653–663.

(38) Letsch, M., Schally, A. V., Szepeshazi, K., Halmos, G., and Nagy, A. (2003) Preclinical evaluation of targeted cytotoxic luteinizing hormone releasing hormone analogue AN-152 in androgen-sensitive and insensitive prostate cancers. *Clin. Cancer Res. 9*, 4505–4513.

(39) Yang, W. H., Wieczorck, M., Allen, M. C., and Nett, T. M. (2003) Cytotoxic activity of gonadotropin-releasing hormone (GnRH)-pokeweed antiviral protein conjugates in cell lines expressing GnRH receptors. *Endocrinology 144*, 1456–1463.

(40) Poethko, T., Schottelius, M., Thumshirn, G., Hersel, U., Herz, M., Henriksen, G., Kessler, H., Schwaiger, M., and Wester, H. J. (2004) Two-step methodology for high-yield routine radiohalogenation of peptides: ^{18}F-labelled RGD- and octreotide analogs. *J. Nucl. Med. 45*, 892–902.

(41) Schottelius, M., Schwaiger, M., and Wester, H. J. (2003) Rapid and high-yield solution phase synthesis of DOTA-Tyr^3-octreotide and DOTA-Tyr^3-octreotate using unprotected DOTA. *Tetrahedron Lett. 44*, 2393–2396.

(42) Shin, I., and Park, K. (2003) Solution phase synthesis of aminooxy peptoids in the C to N and N to C directions. *Org. Lett. 4*, 869–872.

(43) Buchwald, P., and Bodor, N. (1998) Octanol-water partition of nonzwitterionic peptides: predictive power of a molecular size-based model. *Proteins: Struct., Funct. Genet. 30*, 86–99.

(44) Segal-Abramson, T., Kitroser, H., Levy, J., Schally, A. V., and Sharoni, Y. (1992) Direct effects of luteinizing hormone-releasing hormone agonists and antagonists on MCF-7 mammary cancer cells. *Proc. Natl. Acad. Sci. U.S.A. 89*, 2336–2339.

(45) Caunt, C. J., Finch, A. R., Sedgley, K. R., Oakley, L., Luttrell, L. M., and McArdle, C. A. (2006) Arrestin-mediated ERK activation by gonadotropin-releasing hormone receptors: receptor-specific activation mechanisms and compartmentalization. *J. Biol. Chem. 281*, 2701–2710.

(46) Millar, R. P., Lu, Z. L., Pawson, A. J., Flanagan, C. A., Morgan, K., and Maudsley, S. R. (2004) Gonadotropin-releasing hormone receptors. *Endocr. Rev. 25*, 235–275.

(47) Hislop, J. N., Madziva, M. T., Everest, H. M., Harding, T., Uney, J. B., Willars, G. B., Millar, R. P., Troskie, B. E., Davidson, J. S., and McArdle, C. A. (2000) Desensitization and internalization of human and xenopus gonadotropin-releasing hormone receptors expressed in alphaT4 pituitary cells using recombinant adenovirus. *Endocrinology 141*, 4564–4575.

(48) Vreci, M., Anderson, L., Hanyaloglu, A., McGregor, A. M., Groarke, A. D., Milligan, G., Taylor, P. L., and Eidne, K. A. (1998) Agonist-induced endocytosis and recycling of the gonadotropin-releasing hormone receptor: effect of beta-arrestin in internalization kinetics. *Mol. Endocrinol. 12*, 1818–1829.

(49) Pawson, A. J., Faccenda, E., Maudsley, S., Lu, Z. L., Naor, Z., and Millar, R. P. (2008) Mammalian type I Gonadotropin-releasing hormone receptors undergo slow, constitutive, agonist-independent internalization. *Endocrinology 149* (3), 1415–1422.

(50) Grundker, C., Schlotawa, L., Viereck, V., Eicke, N., Horst, A., Kairies, B., and Emons, G. (2004) Antiproliferative effects of the GnRH antagonist cetrorelix and of GnRH-II on human endometrial and ovarian cancer cells are not mediated through the GnRH type I receptor. *Eur. J. Endocrinol. 151*, 141–149.

(51) Fister, S., Gunthert, A. R., Emons, G., and Grundker, C. (2007) Gonadotropin-releasing hormone type II antagonists induce apoptotic cell death in human endometrial and ovarian cancer cells in vitro and in vivo. *Cancer Res. 67*, 1750–1756.

(52) Lu, Z. L., Gallagher, R., Sellar, R., Coetsee, M., and Millar, R. P. (2005) Mutations remote from the human gonadotropin-releasing hormone (GnRH) receptor-binding sites specifically increase binding affinity for GnRH II but not GnRH I: evidence for ligand-selective, receptor-active conformations. *J. Biol. Chem. 280*, 29796–29803.

(53) Pawson, A. J., Maudsley, S., Morgan, K., Davidson, L., Naor, Z., and Millar, R. P. (2005) Inhibition of human type I gonadotropin-releasing hormone receptor (GnRHR) function by expression of a human type II GnRHR gene fragment. *Endocrinology 146*, 2639–2649.

(54) Ulloa-Aguirre, A., Janovick, J. A., Brothers, S. P., and Conn, P. M. (2004) Pharmacologic rescue of conformationally-defective proteins: implications for the treatment of human disease. *Traffic 5*, 821–837.

(55) Janovick, J. A., Knollman, P. E., Brothers, S. P., Ayala-Yanez, R., Aziz, A. S., and Conn, P. M. (2006) Regulation of G protein-coupled receptor trafficking by inefficient plasma membrane expression: molecular basis of an evolved strategy. *J. Biol. Chem. 281*, 8417–8425.

(56) Sedgley, K. R., Finch, A. R., Caunt, C. J., McArdle, C. A. Intracellular gonadotropin-releasing hormone receptors in breast cancer and gonadotrope lineage cells, *J. Endocrinol. 191*, 625−636.

(57) Schottelius, M., Wester, H. J., Reubi, J. C., Senekowitsch-Schmidtke, R., and Schwaiger, M. (2002) Improvement of pharmacokinetics of radioiodinated Tyr^3-octreotide by conjugation with carbohydrates. *Bioconjugate Chem. 13*, 1021–1030.

(58) Wester, H. J., Schottelius, M., Poethko, T., Bruus-Jensen, K., and Schwaiger, M. (2004) Radiolabelled carbohydrated somatostatin analogs: a brief review of the current status. *Cancer Biother. Radiopharm. 19*, 231–244.

BC800058K

Minisequencing with Acyclonucleoside Triphosphates Tethered to Lanthanide(III) Chelates

Pia Ollikka, Alice Ylikoski, Annukka Kaatrasalo, Heli Harvala, Harri Hakala, and Jari Hovinen*

PerkinElmer Life and Analytical Sciences, Turku Site, POB 10, FI-20101 Turku, Finland. Received March 3, 2008; Revised Manuscript Received April 14, 2008

Four acyclic nucleoside triphosphates (derivatives of cytosine, thymine, 7-deazaadenine, and 7-deazaguanine) labeled with nonluminescent europium, terbium, dysprosium, and samarium chelates of 2,2′,2″,2‴-[[4-(4-isothiocyanatophenyl)ethyl]pyridine-2,6-diyl]bis(methylenenitrilo)]tetrakis(acetic acid) were applied to minisequencing using two mutations (Δ*F* 508 and 1717−1 G to A) of cystic fibrosis as a model system. When synthetic targets were used, all four alleles involved could be analyzed in a single reaction using four terminating substrates labeled with four different lanthanide(III) chelates and DELFIA technology for detection. Blood spot samples without DNA isolations were used for PCR amplification and genotyping the target mutations by minisequencing. The single- and dual-labeled minisequencing assays were robust, while the four-label assay still requires further optimization of the multiplexed PCR amplification.

INTRODUCTION

Over 15 years ago, a method called minisequencing was introduced for the detection of point mutations in DNA (*1, 2*). The method involves hybridization of a single-stranded target DNA with a primer that ends immediately before the site of mutation, and elongation of the chain with a single-labeled dideoxyribonucleoside 5′-triphosphate (ddNTP). Parallel runs with each of the four possible labeled nucleotides enable identification of the mutated base. Originally, only radioactive detection was employed (*2–6*). Later, the detection has been predominantly based on fluorescence, where the ddNTPs are labeled with dyes and the identification of the single nucleotide polymorphisms (SNPs) is based on the signal intensity of each dye-specific emission wavelength (*7–13*). Nowadays, SNPs can be genotyped using multiplex, four-color fluorescent minisequencing in a microarray format (*11, 12*). However, application of fluorescence techniques in SNP analysis suffers from low detection sensitivity and problems associated with the properties of the labeled triphosphates to act as good substrates for DNA polymerases. Furthermore, the organic fluorophores as labels have several drawbacks, such as Raman and Rayleigh scattering, short Stokes' shift, low water solubility, and concentration quenching. By contrast, the unique properties of lanthanide(III) chelates such as strong long-decay time luminescence make them ideal markers for numerous applications (*14–16*). Furthermore, the large Stokes' shift and very sharp emission bands enable the simultaneous use of four lanthanides (i.e., Eu, Tb, Sm, and Dy) in the analysis. Time-resolved fluorimetric assays based on lanthanide(III) chelates have found applications in diagnostics, research, and high-throughput screening. The heterogeneous DELFIA technique is applied especially in assays requiring exceptional sensitivity, robustness, and multilabel approach. Up to now, this technology has not been applied for sequencing, although each of four DNA bases could be analyzed with the four different lanthanide(III) ions commonly used in DELFIA based assays.

We report here the preparation of four different acyclonucleoside triphosphates labeled with different lanthanide(III) chelates. Also, their applicability in detection of mutations in a model system (cystic fibrosis mutations Δ*F* 508 and 1717−1 G to A) has been demonstrated.

* Dr. Jari Hovinen. Tel +358 2 2678 513; fax +358 2 2678 380; jari.hovinen@perkinelmer.com.

EXPERIMENTAL PROCEDURES

General. The PCR primers, minisequencing primers, and synthetic 5′-biotinylated targets for optimization of the minisequencing reactions (cystic fibrosis mutations Δ*F* 508 in exon 10 and 1717−1 G to A in exon 11 of CFTR gene) were purchased from Sigma-Genosys (HPLC purified). The sequences of synthetic targets and primers are shown in Table 1. HPLC purifications of the labeled acyclonucleoside triphosphates were performed using a Merck-Hitachi L-7100 instrument and a reversed-phase column (Termoquest Hypersil 4.6 μm). Mobile phase: Buffer A, 0.02 M triethylammonium acetate (pH 7.5); Buffer B, A in 50% (v/v) acetonitrile. Gradient: from 0 to 30 min from 10% to 45% B and from 30 to 35 min from 45% to 100% B. Flow rate was 1.0 mL min^{-1}. ESI-TOF mass spectra were recorded on an Applied Biosystems Mariner instrument. For PCR, DNA polymerase (DyNAzyme II), buffer solution, and $MgCl_2$ solution were purchased from Finnzymes, and dNTPs were from GE Healthcare. For minisequencing, DNA polymerase (AcycloPol), dilution buffer, unlabeled acycloterminators, streptavidin-coated microtiter plates, assay buffer, DELFIA Wash Solution, DELFIA Enhancement solution, DELFIA Enhancer, and lanthanide(III) chelates were from PerkinElmer Life and Analytical Sciences. Wallac DBS puncher, DELFIA Plateshake, Platewash, Plate Dispense, and Victor D Multilabel Counter were from PerkinElmer Life and Analytical Sciences. PCR and minisequencing reactions were performed on a GeneAmp 9700 Instrument (Applied Biosystems) and an IEMS incubator (Labsystems), respectively.

Synthesis of Labeled Acyclonucleoside Triphosphates (acycloNTP-Lns). The acycloterminators tethered to propargylamino group (1.0 nmol) (*17*) and 2,2′,2″,2‴-[[4-(4-isothiocyanatophenyl)ethyl]pyridine-2,6-diyl]bis(methylenenitrilo)]tetrakis(acetic acid) lanthanide(III) (*18*) (3.0 nmol) were dissolved in sterile water (40 μL). Pyridine (90 μL) and triethylamine (2 μL) were added, and the reaction was allowed to proceed overnight at ambient temperature. The products were isolated by precipitation with acetone (5 mL). The precipitate was dried,

10.1021/bc800081n CCC: $40.75 © 2008 American Chemical Society
Published on Web 05/28/2008

Table 1. Sequences of Synthetic Targets and Primers

CFTR mutation	oligonucleotide	wt/m	sequence in 5′ - 3′[a]
Δ*F* 508	PCR primer_forward	both	AAG CAC AGT GGA AGA ATT TC
Δ*F* 508	PCR primer_reverse	both	Biotin-CTC TTC TAG TTG GCA TGC T
Δ*F* 508	sequencing primer	both	GCA CCA TTA AAG AAA ATA TCA T
Δ*F* 508	synthetic target	wild type	Biotin-ATA GGA AAC ACC AAA GAT GAT ATT TTC TTT AAT GGT GCC AGG
Δ*F* 508	synthetic target	mutant	Biotin-ATA GGA AAC ACC AΔAT GAT ATT TTC TTT AAT GGT GCC AGG
1717−1 G to A	PCR primer_forward	both	GAG CAT ACT AAA AGT GAC TC
1717−1 G to A	PCR primer_reverse	both	Biotin-CAT GAA TGA CAT TTA CAG CAA
1717−1 G to A	sequencing primer	both	TCT AAT TTT CTA TTT TTG GTA ATA
1717−1 G to A	synthetic target	wild type	Biotin-CTT GGA GAT GTC CTA TTA CCA AAA ATA GAA AAT TAG AGA GTC
1717−1 G to A	synthetic target	mutant	Biotin-CTT GGA GAT GTC TTA TTA CCA AAA ATA GAA AAT TAG AGA GTC

[a] Δ indicates the trinucleotide deletion. Sequence complement to the sequencing primer underlined.

redissolved in sterile water (1 mL), purified on HPLC, and characterized by ESI-TOF MS. The following *acyclo*NTP-Lns were prepared:

*acyclo*GTP-Sm: ESI-TOF MS for $C_{36}H_{40}N_9O_{20}P_3SSm^-$ (M^-) calcd, 1195.05; obsd, 1195.10

*acyclo*GTP-Eu: ESI-TOF MS for $C_{36}H_{40}N_9O_{20}P_3SEu^-$ (M^-) calcd, 1196.05; obsd, 1195.13

*acyclo*GTP-Tb: ESI-TOF MS for $C_{36}H_{40}N_9O_{20}P_3STb^-$ (M^-) calcd, 1202.06; obsd, 1202.01

*acyclo*ATP-Tb: ESI-TOF MS for $C_{36}H_{40}N_9O_{19}P_3STb^-$ (M^-) calcd, 1186.06; obsd, 1186.12

*acyclo*ATP-Dy: ESI-TOF MS for $C_{36}H_{40}N_9O_{19}P_3SDy^-$ (M^-) calcd, 1191.07; obsd, 1191.11

*acyclo*UTP-Eu: ESI-TOF MS for $C_{34}H_{38}N_7O_{21}P_3SEu^-$ (M^-) calcd, 1158.03; obsd, 1158.12

*acyclo*UTP-Tb: ESI-TOF MS for $C_{34}H_{38}N_7O_{21}P_3STb^-$ (M^-) calcd, 1164.03; obsd, 1164.08

*acyclo*CTP-Eu: ESI-TOF MS for $C_{34}H_{39}N_8O_{20}P_3SEu^-$ (M^-) calcd, 1157.04; obsd, 1157.07

*acyclo*CTP-Tb: ESI-TOF MS for $C_{34}H_{39}N_8O_{20}P_3STb^-$ (M^-) calcd, 1163.05; obsd, 1162.91

PCR. For the analysis of the mutations, dried blood samples on a filter paper were used. From a dried blood spot sample, a 3.2 mm disk was punched directly into the PCR tube and 100 μL of master mix was added. The 100 μL amplification reactions contained 1× Dynazyme buffer, nucleotides (0.2 mM), $MgCl_2$ (2.5 mM), primers, and 1 U of Dynazyme II Polymerase enzyme. For single- and dual-label minisequencing assays, the PCR mixtures contained either Δ*F* 508 or 1717−1 G to A primer pairs. For four-label minisequencing, the PCR mixture contained all four PCR primers. The primer concentrations for Δ*F* 508 amplifications were 0.2 μM, while the primer concentrations for 1717−1 G to A amplification were 0.1 μM. In the positive control reactions, the blood disk was substituted with 200−300 ng of purified DNA. The negative control reaction contained only the reaction mixture. The PCR program used was the following: preheating to 95 °C followed by 30 cycles of 95 °C for 1 min, 56 °C for 1 min, and 72 °C for 1 min. When the amplification was completed, the PCR products were cooled to 4 °C and stored at −20 °C. Both the mutations in exons 10 and 11 were amplified using the same reaction conditions.

Minisequencing Reactions Using Synthetic Oligonucleotides. The minisequencing reaction was optimized using synthetic targets simulating the wild-type and mutated alleles of the exons 10 and 11. The biotinylated synthetic targets were allowed to bind to the streptavidin-coated wells (10^{11} target molecules per well in 50 μL of DELFIA Assay Buffer containing 1 M NaCl and 0.1% Tween 20) for 30 min with shaking at ambient temperature. Unbound targets were removed using DELFIA Wash Solution and Platewash (3 washings). The minisequencing reaction conditions were optimized as the function of concentration of reaction components (primers, acyclonucleotides, and enzyme), reaction time, reaction volume and temperature, and the focus was on the signal levels and specificity of the reaction. The minisequencing reaction was allowed to proceed in sealed plates with shaking for 20 min at 50 °C. The reactions contained 1 pmol of sequencing primers, 1−5 pmol of *acyclo*NTP-Lns, and 50 μL of reaction buffer. The optimized reaction buffer consisted of 10 mM Tris-HCl, pH 8.5, 50 mM NaCl, 50 μM EDTA, 7.5 mM $MgCl_2$, 0.1 mg/mL BSA, and 0.4 U/mL AcycloPol polymerase. When the reactions were completed, the wells were rinsed 6 times with DELFIA Wash Solution. Analyses of reactions were performed according to DELFIA protocol using Victor D Multilabel Counter. Shortly, lanthanide ions were released to solution using DELFIA Enhancement Solution (200 μL) and shaking for 25 min. In the case of Tb and Dy, additional incubation of 5 min after the addition of 50 μL DELFIA Enhancer was used. Luminescent chelates formed during this period of time were measured with Victor D Multilabel Counter.

Minisequencing of PCR Products. The minisequencing reaction optimized with synthetic oligonucleotides was tested with PCR products. The capture of the PCR product was performed in a total volume of 50 μL as described above. A 25 μL aliquot of PCR product together with 25 μL of DELFIA Assay Buffer containing 1 M NaCl and 0.1% Tween 20 was transferred and allowed to bind onto streptavidin-coated microtiter plates, and after the washing the products bound to the wells were denatured by shaking for 5 min in the presence of NaOH (10 mM) and EDTA (300 μM). The unbound single-stranded DNA and the denaturation solution were removed by washing three times. The minisequencing reaction was performed in 50 μL as described above. The control reactions were the following: positive PCR control containing purified DNA, negative PCR control containing only the PCR reaction mixture, and a positive minisequencing control containing 10^{11} molecules of the synthetic target. The negative minisequencing control was performed in the reaction buffer in the absence of the enzyme.

RESULTS

Synthesis of the Labeled Acyclonucleoside Triphosphates. The acycloterminators labeled with four different lanthanide(III) chelates were synthesized by allowing the acycloterminators tethered to propargylamino group to react with europium, terbium, samarium, and dysprosium chelates of the DELFIA DNA labeling chelate, 2,2′,2″,2‴-[[4-(4-isothiocyanatophenyl)-ethyl]pyridine-2,6-diyl]bis(methylenenitrilo)]tetrakis(acetic acid). After precipitation from acetone, the crude products were

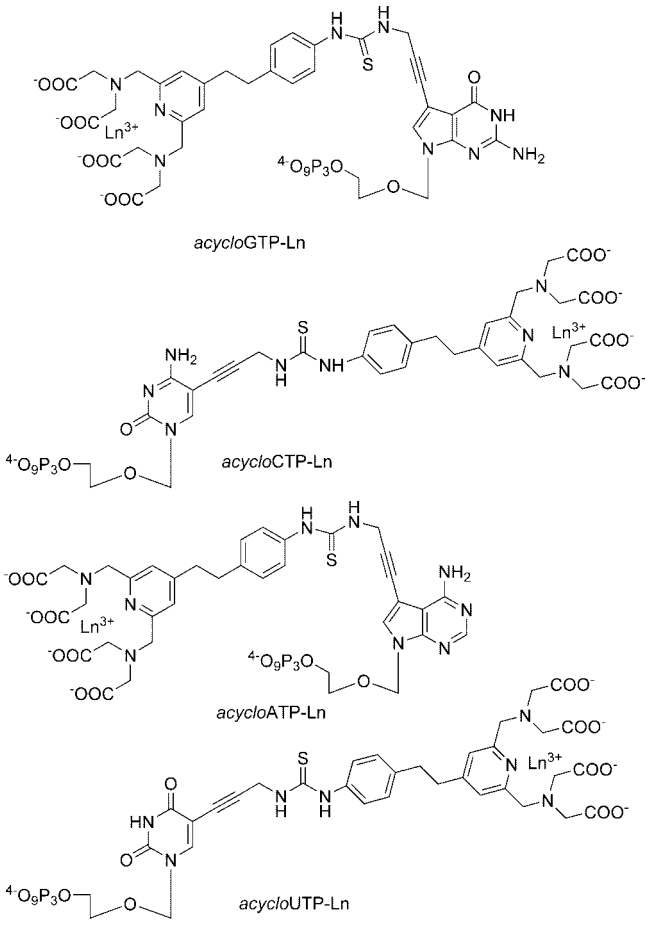

Figure 1. Structures of the acycloterminators labeled with lanthanide(III) chelates. Ln is Eu, Tb, Sm, and Dy.

redissolved in water and purified on HPLC. The labeled triphosphates were analyzed on mass spectrometry, and the observed molecular weights were in accordance with the proposed structures (Figure 1). Accordingly, in all the cases the ligand structure is the same, and each of the four nucleobases can be identified by using the specific signal derived from europium, samarium, terbium, and dysprosium.

Optimization of Minisequencing. The minisequencing reaction conditions were optimized using synthetic oligonucleotides as the function of reaction components, temperature, and time. For Δ*F* 508 mutation, the best results were obtained using a 22-base primer; the use of longer primers caused significant cross reactivity, and the shorter sequences, in turn, resulted in decrease of the specific signal. For 1717−1 G to A mutation, the primer did not have a significant effect on the signal-to-noise ratio, and a 24-mer primer was chosen. With respect to both mutations, 1 pmol of primer per well was enough, and the use of higher amounts did not give better results.

In single-label assays with synthetic oligonucleotides, one of the acyclonucleotides was labeled with europium (5 pmol per well) and the other three acyclonucleotides were unlabeled (5 pmol per well). In dual- and four-label assays, the suitability of each label to each nucleotide was investigated. In the dual-label assay for detection of Δ*F* 508 mutation, the best results were obtained using *acyclo*CTP-Eu and *acyclo*UTP-Tb, wherein *acyclo*ATP and *acyclo*GTP were unlabeled, and when each of which was 1 pmol per well. For detection of 1717−1 G to A mutation, in turn, the best results were obtained using *acyclo*GTP-Eu and *acyclo*ATP-Tb (1 pmol of each per well) and 5-fold excess of the unlabeled *acyclo*CTP and *acyclo*UTP. In four-label assays, where both of the mutations were analyzed from a single reaction, the following labels were chosen: *acyclo*CTP-Eu (5 pmol), *acyclo*UTP-Tb (1 pmol), *acyclo*GTP-Sm (5 pmol), and *acyclo*ATP-Dy (5 pmol). In all cases, the best results were obtained at 50 °C using a 20 min reaction time. The most suitable reaction volume was 50 μL.

Minisequencing of PCR Products. In the first set of experiments, PCR amplified products of 32 blood spots were analyzed using single-label assays. Only the mutant and wild-type alleles of Δ*F* 508 mutation were analyzed, each in their own reactions using *acyclo*CTP-Eu specific to the wild type-allele, and *acyclo*UTP-Eu specific to the mutant allele. The differentiation of wild-type, carrier, and mutant was based on the data obtained with the synthetic model developed above, and the result was calculated as a ratio of mutant *acyclo*UTP signal to wild-type *acyclo*CTP signal. Here, the UTP/CTP ratio for wild-type samples was below 1, for mutants over 5, and for carriers 1.5−2.5 (Figure 2). Accordingly, the single-label method allows us to detect all mutants, carriers, and wild-type samples from the blood spots.

In dual-label assays, both the wild-type and mutant alleles of the same target area were analyzed from a single reaction. Genotyping of Δ*F* 508 and 1717−1 G to A mutations from 16 blood spot samples was performed using two dual-label assays.

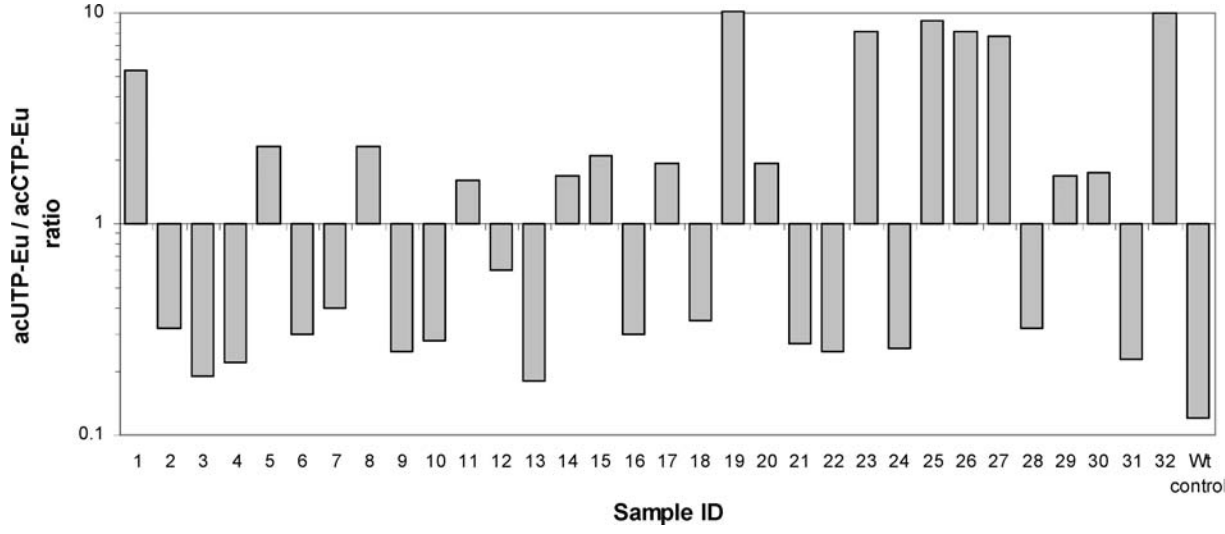

Figure 2. Minisequencing of blood disk samples with a single-label assay. The single-label assays utilized *acyclo*CTP-Eu for the detection of wild-type allele and *acyclo*UTP-Eu for the detection of mutant allele. The UTP/CTP ratio for wild-type, mutant, and carrier samples were below 1, over 5, and 1.5−2.5, respectively.

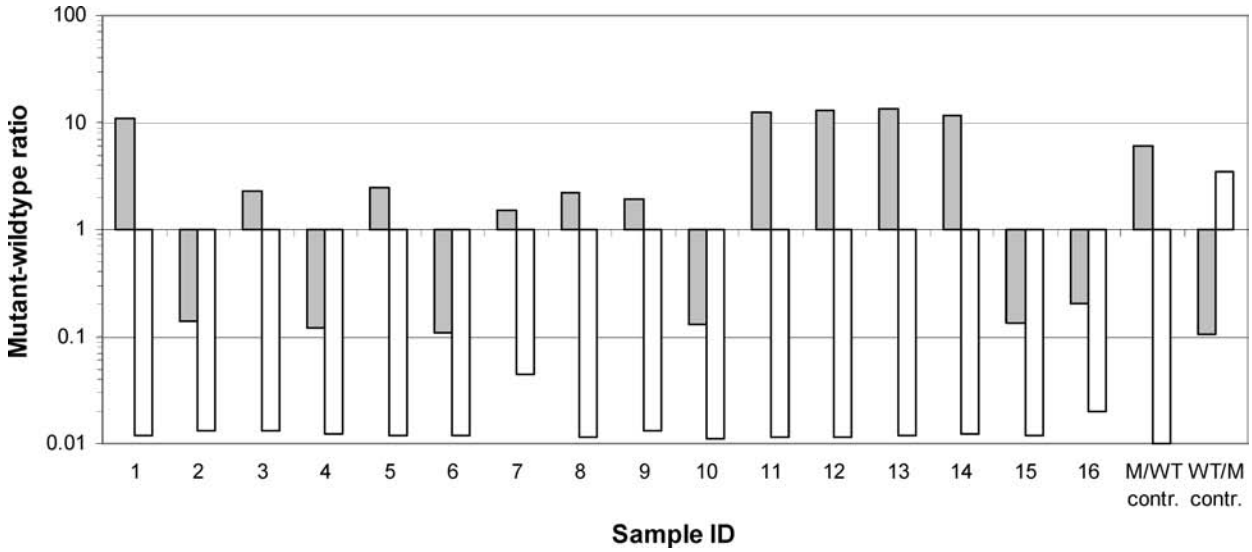

Figure 3. Minisequencing of blood disk samples with a dual-label assay. The dual-label assay for Δ*F* 508 utilized *acyclo*CTP-Eu for the detection of wild-type allele and *acyclo*UTP-Tb for the detection of mutant allele. The dual-label assay for 1717−1 G to A utilized *acyclo*GTP-Eu for the detection of wild-type allele and *acyclo*ATP-Tb for the detection of mutant allele. The control samples were mutant (M)/wild-type (WT) and wild-type (WT)/mutant (M) with respect to Δ*F* 508/1717−1 G to A. For the Δ*F* 508 assay (gray bars), the UTP/CTP ratios for wild-type, mutant, and carrier samples were below 1, over 5, and 1.5−2.5, respectively. For the 1717−1 G to A assay (white bars), the ATP/GTP ratios for wild type was below 0.1, for mutant over 1, and that for carrier was not determined due to lack of carrier samples.

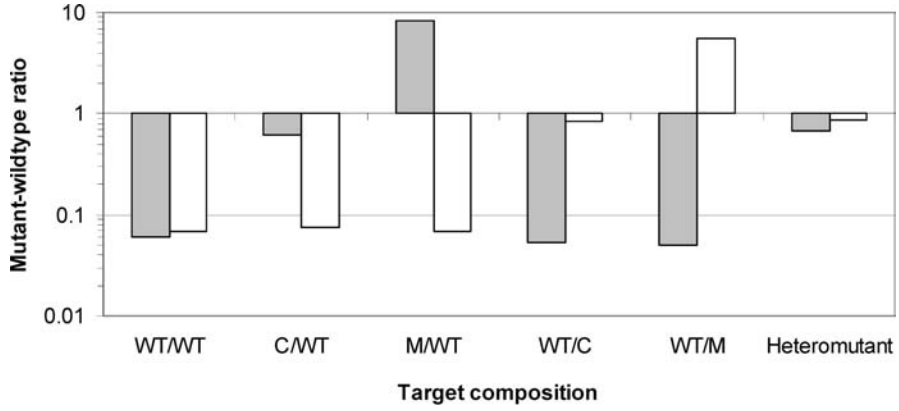

Figure 4. Minisequencing of synthetic DNA samples with a four-label assay. The four-label assay utilized *acyclo*CTP-Eu for wild type Δ*F* 508, *acyclo*UTP-Tb for mutant Δ*F* 508, *acyclo*GTP-Sm for wild-type 1717−1 G to A, and *acyclo*ATP-Dy for mutant 1717−1 G to A. *X*-axis shows the target composition in respect to Δ*F* 508/1717−1 G to A. WT, C, and M denote wild-type, carrier, and mutant, respectively. Gray bars show the Δ*F* 508 (UTP/CTP ratio) and white bars the 1717−1 G to A (ATP/GTP ratio) results. The mutant/wild-type signal ratio for wild type, mutant, and carrier samples was below 0.1, over 5, and 0.5−1, respectively.

The *acyclo*CTP-Eu/*acyclo*UTP-Tb pair and *acyclo*GTP-Eu/*acyclo*ATP-Tb pair was chosen for Δ*F* 508 and 1717−1 G to A mutations, respectively. GTP and ATP were specific nucleotides for wild-type and mutated sequences of the 1717−1 G to A mutation. The UTP/CTP ratio for Δ*F* 508 samples was comparable to the single-label assay (Figure 3). The ATP/GTP ratio in the 1717−1 G to A wild-type samples was always below 0.05 (mean of 16 samples 0.015) (Figure 3). Accordingly, the dual-label minisequencing reaction easily differentiates the wild-type and mutated sequences.

The four-label system was first tested with synthetic oligonucleotides. By mixing Δ*F* 508 and 1717−1 G to A target sequences, we could simulate the conditions in real patient samples. The concentration of oligonucleotide targets used (2×10^{11} molecules/well) was comparable to PCR product concentration used in earlier experiments. The Δ*F* 508 and 1717−1 G to A mutations were measured using *acyclo*CTP-Eu and *acyclo*UTP-Tb for wild-type and mutated Δ*F* 508, respectively, and *acyclo*GTP-Sm and *acyclo*ATP-Dy for the wild-type and mutated 1717−1 G to A, respectively. The four-label assay clearly discriminates the four different targets in the same reaction: UTP/CTP for wild-type, carrier, and mutated Δ*F* 508, and ATP/GTP for wild-type, carrier, and mutated 1717−1 G to A were clearly divided into three groups (Figure 4). For the four-label assay with synthetic targets, the mutant/wild-type signal ratio was below 0.1, 0.5−1, and over 5 for the wild-type, carrier, and mutant samples, respectively. Although the results with the synthetic targets were very promising, our four-label system could not discriminate PCR-amplified products from blood-spot samples.

DISCUSSION

To study the applicability of acyclonucleoside triphosphates labeled with lanthanide(III) chelates to minisequencing, we selected the major mutation Δ*F* 508 (frequency 66%) as well as the mutation 1717−1 G to A (frequency 0.6%), which is among the eight most common mutations of CF in the world. Δ*F* 508 is a three base deletion in the exon 10 of CFTR gene codon 508, while in 1717−1 G to A there is a single transversion of G to A in the position before exon 11. The three base deletion in Δ*F* 508 causes the loss of phenylalanine in CFTR protein,

and the transversion of G to A at position 1717 has an effect on breakdown of the mRNA produced by the gene.

We knew in advance that out of the 32 samples 7 were Δ*F* 508 mutant homozygotes, 9 were Δ*F* 508 heterozygote carriers, and the genotypes of the remaining 16 samples were unknown. By using the single-label assay, we could easily determine the genotype for Δ*F* 508 mutation for all 32 samples. The results of the known samples were in accordance with the previous information. However, since this approach requires the determination of each allele in separate reactions, it is time-consuming and requires significant amounts of rather expensive reagents.

In the dual-label assays, we could determine both wild-type and mutated alleles of each mutation in a single reaction. Accordingly, for determination of Δ*F* 508 and 1717−1 G to A mutations, only two reactions were needed. The results of the Δ*F* 508 analysis were in accordance with the results obtained in the single-label assays. All the samples were analyzed as 1717−1 G to A wild types. Although we did not know in advance any of the genotypes of 1717−1 G to A mutations, it is not likely that any of the samples were 1717−1 G to A carriers or mutants due to the extremely low abundance of that mutation (0.6% of population). Although we did not have blood spot samples of 1717−1 G to A carriers or mutants, the results obtained with synthetic mutated sequences show that the system is sensitive enough to analyze 1717−1 G to A mutations. Due to lack of carrier samples, we did not estimate the carrier ranges for 1717−1 G to A.

Although the four-label assay was sensitive enough to differentiate the synthetic targets, we were not able to perform the same assay with blood spot specimens. Since the minisequencing is working well with the synthetic targets, the problem with blood spot samples is, in all likelihood, derived from PCR amplification, which has been shown to be the bottleneck of minisequencing (*1*). For the four-label assay, we had to amplify the sequences of both the mutations in the same PCR reaction, i.e., there were two biotinylated and two nonbiotinylated primers in the same reaction. Accordingly, and in contrast to single- and dual-label assays, we had two different mutation sequences as well as two different pairs of PCR primers in a single well, which can bind to each other. Therefore, in order to use four-label assay for blood spot samples, optimization of multiplex-PCR amplification is required. Alternatively, a software program enabling data extraction should be developed.

The major goal of the present work was to develop a method based on minisequencing where we could determine the genotype of the patient two mutations in a single reaction using four different lanthanide-labeled nucleotides. Although this goal has not been reached yet, we have clearly demonstrated that the dual-label assay is well-suited for detection of Δ*F* 508 and 1717−1 G to A mutations involved in CF: the assay is simple, and the mutations can be determined directly from the products of PCR-amplified blood spot samples. The method is also suitable for detection of four alleles simultaneously.

LITERATURE CITED

(1) For a review, see (a) Syvänen, A.-C. (1999) From gels to chips: "minisequencing" primer extension for analysis of point mutations and single nucleotide polymorphism. *Hum. Mutat. 13*, 1–10.

(2) Syvänen, A.-C., Aalto-Setälä, K., Harju, L., Kontula, K., and Söderlund, H. (1990) A primer-guided nucleotide incorporation assay in the genotyping of aspartylglucosaminuria in Finland. *Genomics 12*, 590–595.

(3) Sokolov, B. P. (1990) Primer extension technique for the detection of single nucleotides in genomic DNA. *Nucleic Acids Res. 18*, 3671.

(4) Jalanko, A., Kere, J., Savilahti, E., Swartz, M., Syvänen, A.-C., Ranki, M., and Söderlund, H. (1992) Screening for defined cystic fibrosis mutations by solid-phase minisequencing. *Clin. Chem. 38*, 39–43.

(5) Ikonen, E., Manninen, T., Peltonen, L., and Syvänen, A.-C. (1992) Quantitative determination of rare mRNA species by PCR and solid-phase minisequencing. *PCR Methods Amplification 1*, 234–240.

(6) Ihalainen, J., Siitari, H., Laine, S., Syvänen, A.-C., and Palotie, A. (1994) Towards automatic detection of point mutations: use of scintillating microplates in solid−phase minisequencing. *Biotechniques 16*, 938–943.

(7) Chen, X., Zehnbauer, B., Gnirke, A., and Kwok, P. Y. (1997) Fluorescence energy transfer detection as a homogenous DNA diagnostic method. *Proc. Natl. Acad. Sci. U.S.A. 94*, 10756–10761.

(8) Shapero, M. H., Leuther, K. K., Nguyen, A., Scott, M., and Jones, K. W. (2001) SNP genotyping by multiplex solid-phase amplification and fluorescent minisequencing. *Genome Res. 11*, 1926–1934.

(9) Raitio, M., Lindroos, K., Laukkanen, M., Pastinen, T., Sistonen, P., Sajantila, A., and Syvänen, A.-C. (2001) Y-Chromosomal SNPs in Finno-Ugric-speaking population analyzed by minisequencing on microarrays. *Genome Res. 11*, 471–482.

(10) Brown, N. M., Bernacki, S., Pratt, V. M., and Stenzel, T. T. (2001) Fluorescent, multiplexed, automated, primer-extension assay for 3120 + 1 *G*=A and 1148 T mutations in cystic fibrosis. *Clin. Chem. 47*, 2053–2055.

(11) Lindroos, K., Liljedahl, U., Raitio, M., and Syvänen, A.-C. (2001) Minisequencing on oligonucleotide microarrays: comparison of immobilisation chemistries. *Nucleic Acids Res. 29*, e69.

(12) Lindroos, K., Sugurdsson, S., Johansson, K., Rönnblom, L., and Syvänen, A.-C. (2002) Multiplexing SNP genotyping in pooled DNA samples by a four-color microarray system. *Nucleic Acids Res. 30*, e70.

(13) Wang, W., Kham, S. K. Y., Yeo, G.-H., Quah, T.-C., and Chong, S. S. (2003) Multiplex minisequencing screen for common Southeast Asian and Indian β-thalassemia mutations. *Clin. Chem. 49*, 209–218.

(14) Hemmilä, I. (1991) *Applications of Fluorescence in Immunoassays*, Vol *117*, Chemical Analysis: A Series of Monographs on Analytical Chemistry and Its Applications, John Wiley & Sons, Inc. New York.

(15) Hemmilä, I., Dakubu, S., Mukkala, V.-M., Siitari, H., and Lövgren, T. (1984) Europium as a label in time-resolved immunofluorometric assays. *Anal. Biochem. 137*, 335–343.

(16) Hemmilä, I., and Mukkala, V.-M. (2001) Time-resolution in fluorometry technologies, labels, and applications. *Crit. Rev. Clin. Lab. Sci. 38*, 441–4519.

(17) Hobbs, F. W., Jr, and Trainor, G. L. Alkynylamino-nucleosides, U.S. Patent 5,151,507.

(18) Takalo, H., Mukkala, V.-M., Mikola, H., Liitti, P., and Hemmilä, I. (1994) Synthesis of europium(III) chelates suitable for labeling of bioactive molecules. *Bioconjugate Chem. 5*, 278–282.

BC800081N

Enhanced Loading Efficiency and Retention of ^{225}Ac in Rigid Liposomes for Potential Targeted Therapy of Micrometastases

Min-Yuan Chang,[†] Jonathan Seideman,[‡] and Stavroula Sofou*[,†]

Othmer-Jacobs Department of Chemical and Biological Engineering, Polytechnic University, 6 MetroTech Center, Brooklyn, New York 11201, and Molecular Pharmacology and Chemistry, Memorial Sloan-Kettering Cancer Center, 1275 York Ave, New York, New York 10021. Received November 29, 2007; Revised Manuscript Received April 22, 2008

Targeted α-particle emitters are promising therapeutics for micrometastatic disease. Actinium-225 has a 10-day half-life and generates a total of four α-particles per parent decay rendering ^{225}Ac an attractive candidate for α-therapy. For cancer cells with low surface expression levels of molecular targets, targeting strategies of ^{225}Ac using radiolabeled carriers of low specific radioactivities (such as antibodies) may not deliver enough α-particle emitters at the targeted cancer cells to result in killing. We previously proposed and showed using passive ^{225}Ac entrapment that liposomes can stably retain encapsulated ^{225}Ac for long time periods, and that antibody-conjugated liposomes (immunoliposomes) with encapsulated ^{225}Ac can specifically target and become internalized by cancer cells. However, to enable therapeutic use of ^{225}Ac-containing liposomes, high activities of ^{225}Ac need to be stably encapsulated into liposomes. In this study, various conditions for active loading of ^{225}Ac in preformed liposomes (ionophore-type, encapsulated buffer solution, and loading time) were evaluated, and liposomes with up to 73 ± 9% of the initial activity of ^{225}Ac (0.2−200 μCi) were developed. Retention of radioactive contents by liposomes was evaluated at 37 °C in phosphate buffer and in serum-supplemented media. The main fraction of released ^{225}Ac from liposomes occurs within the first two hours of incubation. Beyond this two hour point, the encapsulated radioactivity is released from liposomes slowly with an approximate half-life of the order of several days. In some cases, after 30 days, ^{225}Ac retention as high as 81 ± 7% of the initially encapsulated radioactivity was achieved. The ^{225}Ac loading protocol was also applied to immunoliposome loading without significant loss of targeting efficacy. Liposomes with surface-conjugated antibodies that are loaded with ^{225}Ac overcome the limitations of low specific activity for molecular carriers and are expected to be therapeutically useful against tumor cells having a low antigen density.

INTRODUCTION

α-Particle emitters hold great promise as therapeutics for micrometastatic disease. Because of their high-energy deposition of approximately 80 keV/μm and short range that is consistent with the dimensions of micrometastases (50 to 100 μm), α-particles, when specifically targeted to cancer cells, can combine high cell-killing efficacies with minimal normal-tissue irradiation. Cell survival studies have shown that as few as one to three tracks across the nucleus may result in cell death and is also independent of oxygenation state or cell-cycle during irradiation (*1*–*3*). Actinium-225 has a 10-day half-life and generates three α-particle emitting daughters (^{221}Fr ($t_{1/2}$ = 4.9 min), ^{217}At ($t_{1/2}$ = 32.3 ms), ^{213}Bi ($t_{1/2}$ = 45.59 min)), and a total of 4 α-particles per decay, that render ^{225}Ac an attractive candidate for α-therapy of micrometastatic disease.

For the particular case of cancer cells with low surface-expression levels of molecular targets (*4*), delivery of ^{225}Ac mediated by radiolabeled antibodies may not reach adequately high delivered activities at the targeted cancer cells. This is due to the generally low specific activity of radiolabeled antibodies with ^{225}Ac (*5*–*7*), with reported values to as high as 1 conjugated ^{225}Ac atom per 2300 antibodies (*8*). Tumor targeting liposomes with high activities of encapsulated ^{225}Ac could provide an alternative carrier for such cases where tumor localization also coincides with areas of usual liposome accumulation (liver, bone marrow) (*9*, *10*) or for targeting of micrometastatic clusters or single cancer cells that circulate in the bloodstream or reside in confined areas such as the peritoneal cavity. Liposomes are closed self-assembled structures of lipids, the nontoxic amphiphilic molecules of natural origin, and have been extensively studied for applications in drug delivery (*11*, *12*). Compared to using antibodies or other molecular carriers, liposomes have the substantial advantage of high drug-to-carrier (or ligand) ratios (*11*). In addition, the liposome surface can be used as a platform to conjugate targeting ligands resulting in ligand multivalency with possibly enhanced binding efficacies (*11*, *13*).

Liposomes have been previously considered for diagnostic and therapeutic delivery of radionuclides (*14*–*17*). We have previously investigated passive encapsulation of ^{225}Ac in liposomes as a means of retaining ^{225}Ac and its α-particle-emitting daughters within liposomes during delivery (*8*, *18*). We have shown that liposomes can stably retain encapsulated ^{225}Ac for 30 days. However, only passive radionuclide entrapment was used in these studies that resulted in low encapsulated activities. To enable the therapeutic use of ^{225}Ac, high activities of ^{225}Ac need to be encapsulated into liposomes.

In this study, PEGylated liposomes, composed of rigid membranes to enable long blood circulation times (*19*, *20*), were developed and characterized for size and stability. Different conditions (ionophore-type, encapsulated buffer solution, and loading time) were evaluated to maximize the yield of active loading of ^{225}Ac into preformed liposomes. Retention of encapsulated ^{225}Ac by liposomes was evaluated at 37 °C over

* Corresponding author. Stavroula Sofou, Ph.D., Polytechnic University, 6 MetroTech Center Brooklyn, NY 11201. Phone: 718 260 3863. Fax: 718 260 3125. E-mail: ssofou@poly.edu.

[†] Polytechnic University.

[‡] Memorial Sloan-Kettering Cancer Center.

10.1021/bc700440a CCC: $40.75 © 2008 American Chemical Society
Published on Web 05/28/2008

time in model conditions (phosphate buffer) and in serum-containing media.

For potential targeted α-particle therapy, liposomes conjugated to tumor targeting antibodies (immunoliposomes) were developed and their binding to cancer cells was evaluated *in vitro*. However, to efficiently load liposomes with ^{225}Ac, the suspension needs to be annealed to relatively high temperatures (at least 60 °C) to allow formation of a stable chelant between ^{225}Ac and the liposome-encapsulated DOTA[1] (*7*). In addition, elevated temperatures above the lipid membrane glass transition temperature (58 °C) are also required to increase the permeability of the liposomal membrane bilayer to the radionuclide−ionophore complexes (*21*). These relatively high temperatures may interfere either with the activity of liposome-conjugated antibodies or with the reactive groups on liposomes that will be used as linkers to antibodies at a following bioconjugation step. In our studies, maleimide-functionalized lipids are used presenting, therefore, a temperature limitation due to their potential hydrolysis (*22*). Consequently, the sequences of liposome immunolabeling and of liposome radionuclide loading were interchanged in order to determine the order that optimizes the development of immunolabeled liposomes combining maximum binding efficiency with maximum encapsulated ^{225}Ac activities.

MATERIALS AND METHODS

Reagents. 1,2-Dinonadecanoyl-*sn*-glycero-3-phosphocholine (DNPC), 1,2-distearoyl- *sn*-glycero-3-phosphoethanolamine-*N*-[methoxy(poly(ethylene glycol))-2000] (DSPE-PEG-2000), 1,2-distearoyl-*sn*-glycero-3-phosphoethanolamine-*N*-[maleimide-(poly(ethylene glycol))2000] (DSPE-PEG-Maleimide lipid), 1,2-dipalmitoyl-*sn*-glycero-3-phosphoethanolamine-*N*-(Lissamine Rhodamine B Sulfonyl) (rhodamine-lipid), were purchased from Avanti Polar Lipids (Alabaster, AL). Phosphate buffered saline (PBS), Sephadex G-50, Sepharose 4B, ascorbic acid, tetramethylammonium acetate, sucrose, diethylenetriaminepentaacetic acid (DTPA), calcium ionophore A23187, and 8-hydroxyquinoline (Oxine) were obtained from Sigma-Aldrich (Atlanta, GA). Ethylenediaminetetraacetic acid (EDTA), disodium salt, sodium hydroxide (NaOH), and HEPES were purchased from Fisher Scientific (Pittsburgh, PA). Hydrochloric acid (HCl) was purchased from Spectrum (New Brunswick, NJ). *p*-Isothiocyanatobenzyl-1,4,7,10-tetraazacyclododecane-1,4,7,10-tetraacetic acid (DOTA) was purchased from Macrocyclics (Dallas, TX). Actinium-225 was provided by Dr. George Sgouros and Dr. David Scheinberg. RPMI 1640 medium and fetal bovine serum (FBS) were purchased from Irvine Scientific (Santa Ana, CA). Cholesterol powder, Traut's Reagent, BSA Assay Kit, and Ellman's Assay Kit, were purchased from Pierce (Rockford, IL).

Liposome Preparation. Lipids in chloroform (DNPC (70 mol % of total lipid), DSPE-PEG-2000 (3 mol % of total lipid), cholesterol (30 mol % total lipid), rhodamine-lipid (1 mol % of total lipid), and DSPE-PEG-Maleimide lipid (2 mol % of total lipid for immunoliposomes)) were combined in a 25 mL round-bottom flask. Chloroform was evaporated in a Buchi rotavapor R-200 (Buchi, Flawil, Switzerland) for 10 min at 55 °C followed by evaporation under N_2 stream for 5 min. For liposomes to be loaded with ^{225}Ac, the dried lipid film was then hydrated in 1 mL acetate buffer (150 mM tetramethylammonium acetate, containing 5 mg/mL DOTA and 2.25 mg/mL ascorbic acid, pH 4.5) or 1 mL of citrate buffer (225 mM citrate buffer, containing 5 mg/mL DOTA and 2.25 mg/mL ascorbic acid, pH 4.0) for 2 h at 50 °C. The lipid suspension (10 mM lipid) was then extruded 21 times through 2 stacked polycarbonate filters of 200 nm pore diameter (Avestin Inc., Ottawa, Canada) followed by 21 times through 100 nm pore diameter. Extrusion was carried at 65 °C for DNPC liposomes in a water bath. After extrusion, exchange of the liposomes' surrounding buffer was performed by size exclusion chromatography (SEC) using a Sephadex G-50 column (11 cm length) eluted with isosmolar HEPES buffer (20 mM HEPES, 200 mM sucrose, pH 7.4). All solutions were chelexed before liposome and buffer preparation.

For liposome loading with the fluorophore calcein, the dried lipid film was hydrated in 1 mL of 1 mM calcein solution containing 2.5 mM HEPES, 75 mM NaCl, and 50 μM EDTA (pH 7.4) for 1 h at 50 °C. The lipid suspension (10 mM lipid) was then extruded 21 times as above, and unentrapped calcein was removed by SEC using a Sephadex G-50 column (11 cm length) eluted with isosmolar HEPES buffer.

Liposome Size Distribution Determination. Dynamic light scattering (DLS) of liposome suspensions was studied with an N4 plus autocorrelator (Beckman-Coulter, Fullerton, CA), equipped with a 632.8 nm He−Ne laser light source. Scattering was detected at 23.0°, 30.2°, 62.6°, and 90°, and particle size distributions at each angle were calculated from autocorrelation data analysis by CONTIN (*23*). The average liposome size was calculated to be the *y*-intercept at zero angle of the measured average particle size values versus $\sin^2(\theta)$ (*24*). All buffer solutions used were filtered with 0.22 μm filters just before liposome preparation. The collection times for the autocorrelation data were 1−10 min.

Differential Scanning Calorimetry. DSC scans of liposome suspensions (0.5 mL, 2.5 mM total lipid) in phosphate buffer (pH = 7.4) were performed using a VP-DSC Instrument (MicroCal, LLC, Northampton, MA) from 25 to 85 °C at a scan rate of 5 °C /h. The thermograph of the corresponding buffer was also acquired at identical conditions, and was subtracted from the excess heat capacity curves.

Liposome Loading with Actinium-225. Immediately before liposome active loading, ^{225}Ac (0.2−200 μCi) was dissolved in 30 μL HCl (3 mM) and was mixed with different ionophores: Oxine (3 μL of 11 mM oxine in ethanol with 97 μL of 20 mM sodium acetate) or A23187 (0.4 mg A23187 in 50 v/v water/ethanol). Then, the ionophore/radionuclide solution was incubated with liposomes (1 mL of 5 μmol total lipid/mL) in a dry bath at 65 °C. At different incubation times (15, 30, and 60 min), lipid samples were removed from the parent liposome suspension, and were mixed with DTPA (0.3 mM final concentration) after being cooled in ice-cold water for 5 min. Unentrapped ^{225}Ac was separated from liposomes by SEC using a Sephadex G-50 column (11 cm length, equilibrated and eluted with PBS, 1 mM EDTA, pH 7.4). Entrapment efficiency was calculated from the ratio of activities retained within the liposomes after SEC divided by the activities contained by the liposome suspension before SEC. Activities were measured 20 h later to allow for equilibrium to be reached before counting the γ-emissions of bismuth-213 (^{213}Bi) decay.

In these studies, the major upper temperature limitation is the preservation of the functionality of antibodies that are already conjugated via maleimide groups on the surface of liposomes, or of the maleimide groups if the bioconjugation reaction succeeds the liposome radiolabeling. Even if a different chemistry was used for antibody conjugation to liposomes, the liposome radiolabeling stage would still be restricted toward the upper temperature limit due to the potential thermal hydrolysis of phospholipids and PEGylated lipids comprising the liposome membranes that would not allow use of high temperatures (*25*).

In these studies, complexes of ^{225}Ac with the encapsulated chelant DOTA are potentially formed after diffusion of the

[1] *p*-Isothiocyanatobenzyl-1,4,7,10-tetraazacyclododecane-1,4,7,10-tetraacetic acid (DOTA).

^{225}Ac-ionophore complex from the solution across the bilayer membrane into the encapsulated aqueous core of liposomes during the loading period of liposomes. In order to evaluate the extent of formation of ^{225}Ac complexes with the chelant DOTA during the time period of liposome loading and to compare with the extent of formation of ^{225}Ac complexes with each ionophore, radioactivity was incubated separately with the chelant, and with each ionophore, and also with both the chelant and the ionophore in conditions identical to those of the encapsulated aqueous volume during liposome loading, and the extent of formation of each type of complex was assessed using cation exchange chromatography. The concentrations of ionophores in the incubation mixture were calculated to agree with the concentrations used for loading liposome suspensions in the presence of the acetate or of the citrate buffers that were encapsulated in liposomes (please see above paragraph). The mole ratio of DOTA to ionophores in the incubation mixture was calculated to be the same as during radionuclide loading of liposomes. For these calculations, since DOTA was passively encapsulated into liposomes, the maximum encapsulation efficiency of 5% of total volume, and initial DOTA used, was assumed (*26*). After a 15 min and 60 min incubation at 65 °C, each mixture was then passed through a cation exchange column (SP Sephadex C-25, Pharmacia Biotech, Sweden), equilibrated, and eluted with acetate or citrate buffer. The ion exchange group in the column is a sulfopropyl group that remains charged over the pH range of 4.0 to 13.0, therefore, maintaining high capacity to capture cations. This column was chosen to challenge the ^{225}Ac-ionophore complexes but not the ^{225}Ac-DOTA complexes. The eluted samples were allowed to reach equilibrium before γ-photon counting.

Measurement of Retention of Encapsulated Actinium-225 by Liposomes. The protocol to measure the retention of ^{225}Ac is described, in detail, elsewhere (*18*). Briefly, the γ-emissions (radioactivity equilibrium values) of ^{213}Bi were measured in liposome fractions, which were separated, at different times, from the parent liposome population and the free radionuclides by SEC (Sephadex G-50). The samples were counted using a Cobra γ-counter (Packard Instrument Co., Inc.). For monitoring ^{225}Ac, the window 150−600 keV was used, which includes the chief ^{213}Bi photopeak. Repeated measurements were performed on three different liposome preparations of each combination of ionophore and encapsulated acidic buffer. Retention of activity by liposomes was monitored for 30 days. This time period was chosen on basis of the focus of this work, which is to evaluate retention of radionuclide contents by the liposomal delivery carriers during circulation of the carriers in the body before their blood clearance and accumulation at particular tissues and their cellular uptake. In particular, the average blood circulation half-life of i.v. administered liposomes is 20 to 30 h in mice (*27*) and between 30 and 90 h in humans (*28*).

Liposome Immunolabeling. The protocol to immunolabel liposomes is described elsewhere (*29*). Briefly, Trastuzumab purified from Herceptin (Genentech, South San Francisco, CA) was activated with Traut's reagent (1 mL of 0.5 mg/mL antibody in PBS buffer (1 mM EDTA, pH 8) with 0.15 mg Traut's reagent for 1.5 h), was purified by a PD-10 column (Amersham Biosciences, Piscataway, NJ) eluted with PBS buffer (1 mM EDTA, pH 7.4), and was reacted with maleimide-lipids contained in liposomes (2 mol % of total lipid) in a nitrogen atmosphere for 40 min at room temperature (the ratio of liposomes to antibody was 0.5 mg activated antibody to 7.5 μmol lipids in a total volume of 1 mL). Unbound antibodies were separated from immunoliposomes by SEC using a Sepharose 4B column (11 cm length) eluted with PBS buffer (1 mM EDTA, pH 7.4). In purified immunoliposome suspensions, a protein assay was used to quantify the concentration of antibodies, and lipid concentration was determined by the fluorescence intensity of rhodamine-lipids contained in liposomes. Using the measured values of conjugated antibodies per lipid, the average number of antibodies per liposome was calculated (*29*) using for input values the mean size of liposomes (as measured by DLS) and the headgroup surface area per lipid (70 Å^2) (*26*).

Cell Line. The metastatic ovarian carcinoma cell line, SKOV3-NMP2 was derived from serial passage of the parental SKOV3 cell line in nude mice (*30*), and was propagated at 37 °C, in 5% CO_2 in RPMI 1640 media supplemented with 10% fetal bovine serum, 100 units/mL penicillin, and 100 μg/mL streptomycin. Cell concentration was determined by counting trypsinized cells with a hemocytometer.

Flow Cytometry. Immunoliposome binding was evaluated in the ovarian cancer SKOV3-NMP2 line for Trastuzumab-labeled liposomes. Cells were grown to confluency and were resuspended and adjusted to 5.6 million cells per milliliter in ice-cold FACS buffer (PBS with 1 mM EDTA, 0.5% BSA, and 0.02% sodium azide). Liposome suspensions (0.25 μmol lipid in 0.1 mL) were mixed with 180 μL of cell suspensions on ice. After incubation at 4 °C for variable times, samples were washed with ice-cold FACS buffer. Cell pellets were separated from the supernatant by centrifugation (three times) and were then resuspended in 400 μL of FACS buffer, and their fluorescence was measured by flow cytometry following the intensity of the liposome-encapsulated fluorescent calcein (FC 500 System, Beckman culture, Fullerton, CA).

Liposome Annealing before Immunolabeling. Maleimide-containing PEGylated liposomes were annealed at 65 °C in a dry bath for one hour. After annealing (that is required for the radionuclide loading and chelation), liposomes were allowed to cool in ice-cold water for 5 min before the liposome immunolabeling reaction with antibodies was initiated.

Liposome Immunolabeling before Annealing. After liposome immunolabeling as described above, immunoliposomes were annealed at 65 °C in a dry bath for one hour. After annealing (that is required for the radionuclide loading and chelation), liposomes were allowed to cool before evaluation of their binding efficacy to cells.

RESULTS

The size of PEGylated liposomes measured by DLS was 121 ± 6 nm in diameter.

Efficiency of Actinium-225 Loading in Preformed Liposomes. The optimal temperature range for chelation of ^{225}Ac to DOTA is reported between 55 and 60 °C (*7*). We chose to perform liposome loading and chelation of ^{225}Ac with the encapsulated DOTA at 65 °C to also ensure adequate permeability of the lipid bilayer membrane to the radionuclide−ionophore complex. The DSC thermogram of the lipid composition exhibits significant thermotropic responsiveness (greatest change in the heat capacity) at temperatures below 65 °C, indicating that the lipid membranes should be mostly in fluid phase at temperatures at or above 65 °C (Figure 1). Higher loading temperatures were not explored since they present an instability source for the structure and binding efficacy of conjugated antibodies on immunoliposomes (vide infra).

The loading efficiency of ^{225}Ac in PEGylated liposomes is shown in Figure 2A,B for liposomes with encapsulated acetate and citrate buffer, respectively, for two types of ionophores (Oxine and A23187) and with increasing loading times (15, 30, and 60 min). Liposomes encapsulating acetate buffer (Figure 2A) exhibited loading efficiencies that increase with increasing incubation time to similar extents for both ionophones studied: from 28 ± 7% to 63 ± 13% for oxine, and from 38 ± 3% to

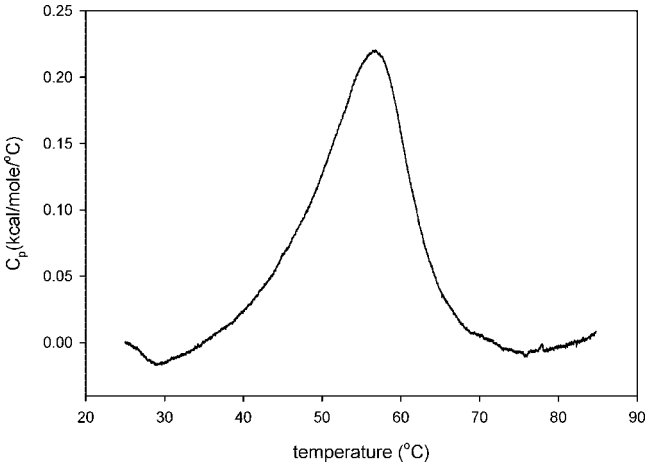

Figure 1. DSC thermogram of the PEGylated liposomes composed of DNPC lipids and cholesterol in phosphate buffer.

61 ± 18% for A23187. Longer loading times (1.5 h) did not result in a significant increase of loading yield and were, therefore, not explored systematically (data not shown). Liposomes encapsulating citrate buffer (Figure 2B) exhibited time-independent loading of ^{225}Ac that is, however, a strong function of the ionophore type. Oxine-mediated loading resulted in low radiation entrapment efficacies (average value: 15 ± 2%), and A23187-mediated loading resulted in significantly greater extents (62 ± 10%).

Studies of ^{225}Ac loading into liposomes in suspensions containing PBS buffer resulted in considerably lower loading yields than the yields in suspensions containing HEPES buffer which was, therefore, explored in this work.

The preferential formation of ^{225}Ac complexes with the chelant DOTA compared to ^{225}Ac complexes with each ionophore was evaluated in acetate and citrate buffer over time in conditions identical to liposome loading. In acetate buffer, in the presence of oxine, the extent of complex formation between ^{225}Ac and the chelant DOTA increases with time. The yield becomes 47% after 15 min, and after 60 min of incubation, all radiation is eluted from the cation exchange column, suggesting complete chelation of the radionuclide with DOTA (Figure A, Supporting Information). When both DOTA and the ionophore A23187 are present, 31% and 47% of the total radioactivity is in the form of ^{225}Ac-DOTA chelates after 15 and 60 min of incubation, respectively (Figure B, Supporting Information). The cation exchange column used in these studies was unable to challenge the complexes formed between ^{225}Ac and the citrate buffer, which seems to behave as a chelating agent for the radionuclide (*31*, *32*).

Efficiency of Actinium-225 Retention by Liposomes. After ^{225}Ac loading, the retention efficiency of ^{225}Ac by all PEGylated liposomes was studied and is shown in Figures 3 to 6 for liposome suspensions incubated at 37 °C in PBS and 10% serum-supplemented media over time. The main fraction of released ^{225}Ac from all liposomes occurs within the first two hours of incubation, and beyond this point, the retained radioactivity is stably carried by liposomes for approximately 30 days.

All liposome suspensions with encapsulated acetate buffer (Figures 3 and 4) exhibited more extensive release (within the first two hours of incubation) of radioactive contents compared to liposomes encapsulating citrate buffer (Figures 5 and 6). In particular, for oxine-mediated loading (Figure 3A,B,C), extensive content release was observed both in PBS and in serum supplemented media. Increase in loading time correlates with higher retention of radioactive contents by liposomes during the first two hours of incubation at 37 °C (Figure 3A,B,C). When A23187 was used to mediate active ^{225}Ac loading into liposomes with encapsulated acetate buffer (Figure 4A,B,C), radionuclide retention was independent of the loading time and decreased by approximately 50% within the first two hours of incubation in PBS and by approximately 64% in serum.

In liposomes encapsulating citrate buffer following oxine-mediated loading (Figure 5A,B,C), within the first two hours of incubation at 37 °C, liposomes exhibit higher content retention with increasing loading time, as is the case when acetate buffer and oxine are used (Figure 3A,B,C). Liposomes encapsulating citrate buffer that were loaded using A23187 exhibited the greatest content retention that increases with loading time (Figure 6A,B,C). In particular, these liposomes retained the encapsulated ^{225}Ac at levels that range from 54% to 81% (when liposomes were incubated in PBS) and from 35% to 56% when liposomes were incubated in serum-supplemented media. Actinium-225 was stably retained by these liposomes for a period of 20−30 days (Figure 6A,B,C).

For both types of encapsulated buffers used, A23187 always results in higher retention of radioactivity by liposomes compared to when oxine is used to load liposomes. With increasing incubation times, oxine-mediated loading results in radionuclide retention that approaches the retention exhibited by A23187-mediated loading. Only when A23187 is used in acetate buffer is the retention independent of loading time.

Cell Binding Specificity of Immunoliposomes. The conjugation reaction resulted in 68 ± 13 bound antibodies per liposome. Using flow cytometry, a significant shift in fluorescence counts was detected only when immunoliposomes were incubated with SKOV3-NMP2 cells with unblocked HER2/neu receptors (please see Supporting Information, Figure C).

Effect of Heating and Bioconjugation Sequence on the Cell Binding Efficacy of Immunoliposomes. The average ratios of conjugated antibodies per liposome were measured to be 14 ± 2 (or 15.6 ± 1.7 g of bound antibody per mole of lipid) when bioconjugation preceded the annealing at 65 °C for one hour, and 7 ± 1 (or 7.5 ± 0.2 g of bound antibody per mole of lipid) when annealing (of one hour) preceded the bioconjugation step.

It is shown in Figure 7 that when annealing of liposomes (that is required for loading of liposomes with ^{225}Ac) takes place after the bioconjugation reaction, immunoliposomes bind to cancer cells (bar indicated as b) with 80% of the maximum efficacy (bar indicated as c); this maximum value corresponds to immunoliposome binding when no additional annealing takes place. When annealing at 65 °C takes place before the bioconjugation reaction, then the specific binding of immunoliposomes to SKOV3-NMP2 cells decreases to 60% (bar indicated as a) of the maximum binding efficacy. Hydrolysis of the maleimide groups at the elevated annealing temperature before conjugation to antibodies could be a potential explanation for the decreased number of conjugated antibodies and, therefore, of cell specific binding of immunoliposomes (*22*). Antibody denaturation during annealing after liposome immunoconjugation could also play a role in decreasing immunoliposome binding. This relatively small decrease in binding efficacy seems disproportional to the decrease of liposome-bound antibodies. It has been shown that immunoliposome binding efficacy increases with higher surface densities of liposome-conjugated antibodies, but beyond some critical value of grafting densities, more surface-conjugated antibodies do not result in higher binding efficacies of immunoliposomes (*29*). If the initial grafting density corresponding to 68 ± 13 bound antibodies per liposome is beyond this critical value, then the small

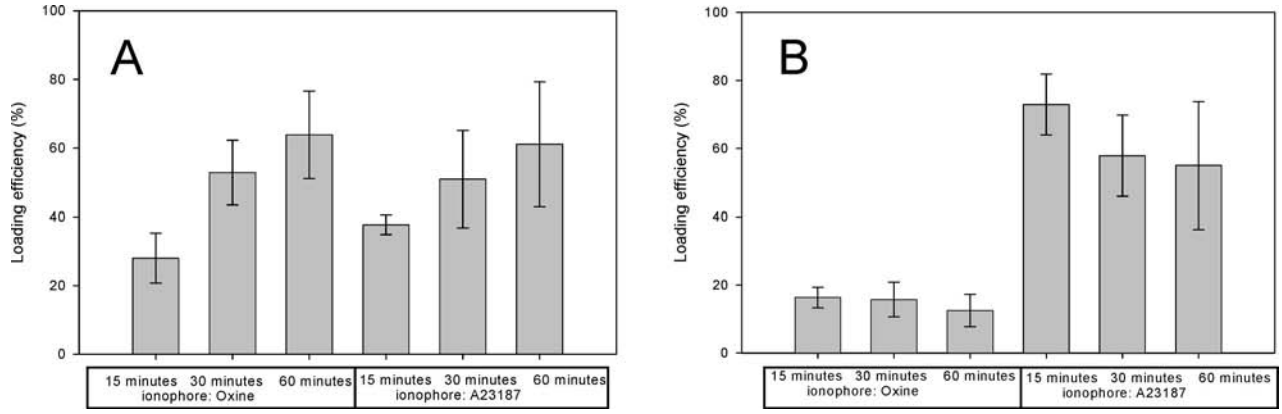

Figure 2. Loading efficiency of actinium-225 in preformed PEGylated liposomes with encapsulated (A) acetate buffer and (B) citrate buffer using oxine-ionophore and A23187-ionophore for different loading times. Error bars correspond to standard deviations of multiple measurements (of three liposome preparations).

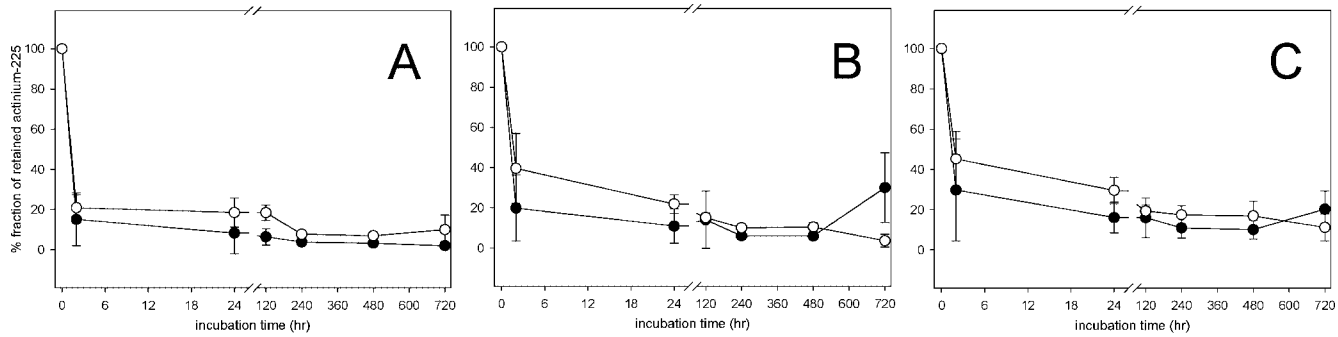

Figure 3. Retention of actinium-225 by PEGylated liposomes with encapsulated acetate buffer over time incubated at 37 °C in PBS (○) and in RPMI1640 with 10% FBS (●). Radionuclide loading was performed using oxine ionophore for different loading times: (A) 15 min, (B) 30 min, (C) 60 min. Error bars correspond to standard deviations of multiple measurements (of three liposome preparations).

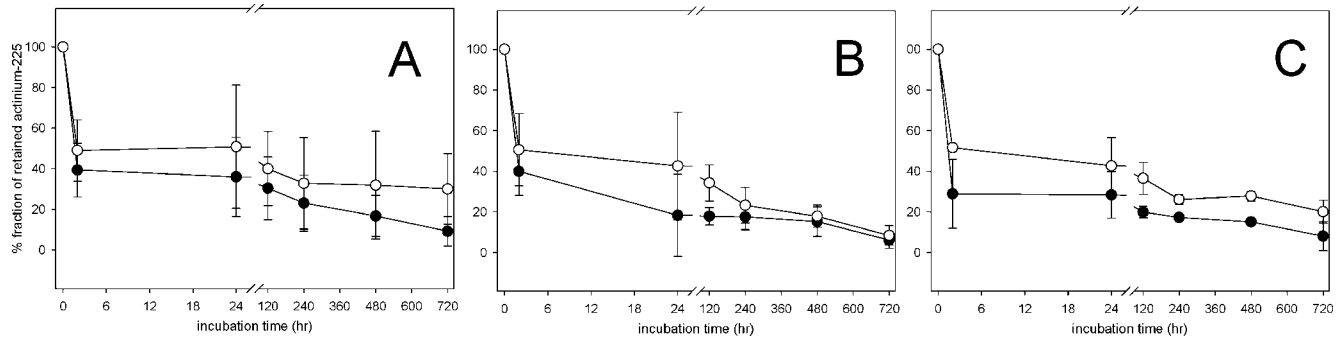

Figure 4. Retention of actinium-225 by PEGylated liposomes with encapsulated acetate buffer over time incubated at 37 °C in PBS (○) and in RPMI1640 with 10% FBS (●). Radionuclide loading was performed using A23187 ionophore for different loading times: (A) 15 min, (B) 30 min, (C) 60 min. Error bars correspond to standard deviations of multiple measurements (of three liposome preparations).

decrease in liposome binding at such significantly lower antibody densities could possibly be explained.

DISCUSSION

Actinium-225 is a promising α-particle generator for the therapy of micrometastatic cancer since it emits a total of four α-particles per parent decay. Liposomes have been studied for the delivery of ^{225}Ac and were shown to adequately retain the parent nuclide (*8, 18*). However, passive entrapment of radionuclides into liposomes will only yield approximately 5% loading of initially used radioactivity, rendering this approach economically unfeasible and producing radioactive liposomes with low specific activities. High encapsulated activities of ^{225}Ac by liposomes are required in order to enable consideration of these drug carriers for α-particle therapy of cancer. In this work, PEGylated liposomes composed of rigid membranes were developed to allow for long circulation times in the bloodstream with minimal release of encapsulated contents. Different conditions were evaluated for optimizing (1) the radionuclide loading into preformed liposomes, (2) the retention of radioactivity by these carriers over time, and (3) the binding efficacy of antibody-conjugated liposomes (immunoliposomes) for potential specific targeting of cancer cells.

In particular, two types of ionophores (oxine and A23187) and two different types of liposome-encapsulated buffers (citrate buffer and acetate buffer) were studied for variable loading intervals to encapsulate ^{225}Ac in PEGylated liposomes composed of DNPC and cholesterol. Oxine has previously been reported to facilitate transport of trivalent cations (indium-111 and gallium-67) through the lipid membrane of liposomes composed

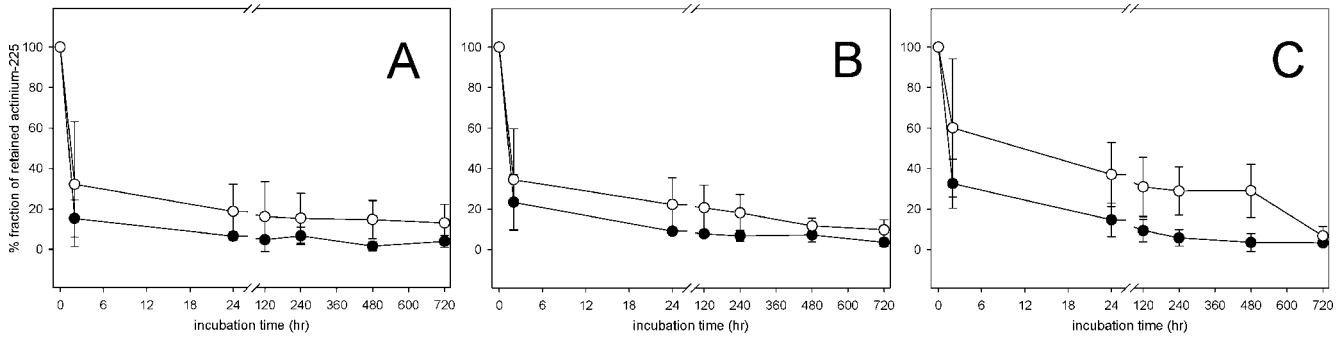

Figure 5. Retention of actinium-225 by PEGylated liposomes with encapsulated citrate buffer over time incubated at 37 °C in PBS (○) and in RPMI1640 with 10% FBS (●). Radionuclide loading was performed using oxine ionophore for different loading times: (A) 15 min, (B) 30 min, (C) 60 min. Error bars correspond to standard deviations of multiple measurements (of three liposome preparations).

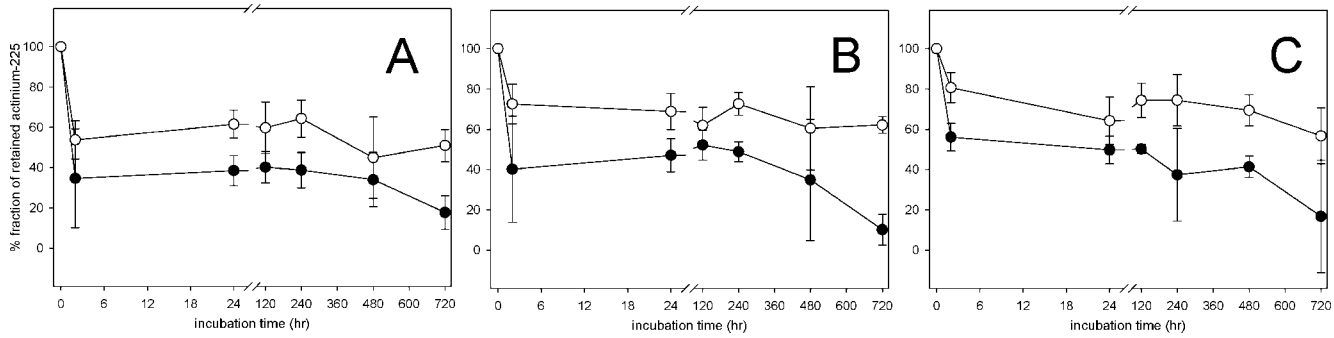

Figure 6. Retention of actinium-225 by PEGylated-liposomes with encapsulated citrate buffer over time incubated at 37 °C in PBS (○) and in RPMI1640 with 10% FBS (●). Radionuclide loading was performed using A23187 ionophore for different loading times: (A) 15 min, (B) 30 min, (C) 60 min. Error bars correspond to standard deviations of multiple measurements (of three liposome preparations).

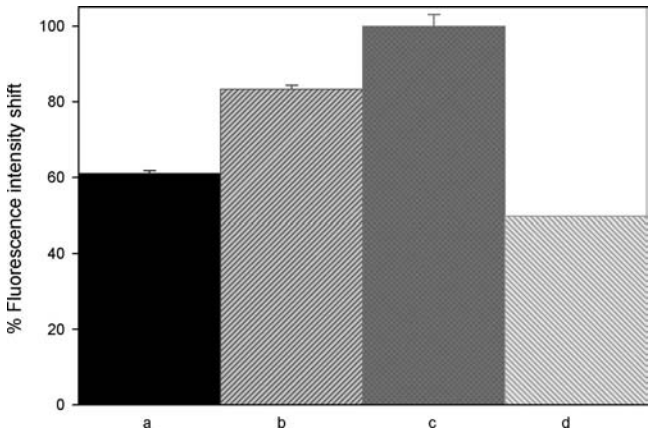

Figure 7. Effect of additional annealing on the binding of calcein-encapsulating anti-HER2/neu-labeled liposomes to SKOV3-NMP2 cells. Cell fluorescence due to liposomes bound to cells: (a) immunoliposomes were annealed before bioconjugation; (b) immunoliposomes were annealed after bioconjugation; (c) immunoliposomes were immunoconjugated without additional annealing; (d) fluorescence due to cells alone.

of high T_g lipids (*32*), and A23187 has been reported for the transport of divalent radium-223 and trivalent actinium-228 (*17*), and of indium-111 (*21*) through liposome membranes. In the present studies, both commercially available A23187 and oxine were evaluated in order to maximize the potential loading efficiency of actinium-225 in liposomes. A23187 and oxine are lipophilic molecules and act as ionophores by forming complexes with cations resulting in effective shielding (camouflage) of their charge. These complexes can diffuse across the hydrophobic region of the lipid bilayer membranes. It is possible that more than one molecule of A23187 or oxine forms a complex with the radionuclides (*21, 33, 34*). Complexes containing different numbers of ionophores per radionuclide will result in different configurations with variable diffusion rates across the lipid bilayer (*33*). Potentially different rates of diffusion across the bilayer could affect the yield of liposome loading with radionuclides. In addition, to effectively load liposomes, the complexes of the encapsulated chelant DOTA and the transported radionuclides should be more stable than the complexes of radionuclides with the ionophores used to facilitate the radionuclide transport across the liposome membrane. DOTA is described to form stable chelates with ^{225}Ac (*7*), and was therefore encapsulated into liposomes. The encapsulated buffers studied in this work (acetate and citrate) were chosen on the basis of literature reports (*7, 17*), and the pH of the aqueous liposome phase (4.0 to 4.5) was chosen to agree with typical reported conditions for optimal chelation of ^{225}Ac by DOTA (*7*) and to completely avoid potential hydrolysis of the ^{225}Ac cations. The absence of encapsulated chelators in liposomes is reported to not result in loading of liposomes with radionuclides (*33*). In our studies, the loading temperature was set above the T_g of the liposome membranes, evaluated by DSC, in order to increase the membrane fluidity, and, therefore, the permeability of the ionophore/radionuclide complex across the bilayer (*21*). In our studies, the optimal loading temperature was found to be 65 °C. At this temperature, significant membrane transport of the radionuclide/ionophore complexes is observed and chelation of actinium-225 by the encapsulated DOTA occurs with minimal thermal hydrolysis of the lipids comprising the membrane (*25*), and the conjugated antibodies or attached maleimide groups (*22*).

This study shows that ^{225}Ac is loaded to a higher yield in preformed liposomes and is more stably retained over time when the ionophore A23187 is used with liposomes encapsulating citrate buffer. We did not distinctly measure the transport rates across the lipid bilayer of each ionophore−radionuclide complex. However, the diffusion rates of both complexes of ^{225}Ac

with ionophores across the lipid bilayer should be comparable, since in liposomes encapsulating acetate buffer, the loading efficacies are identical for both ionophores over all time points studied. In liposomes containing citrate buffer, oxine resulted in extremely low and time-independent loading of ^{225}Ac. This result could potentially be attributed to slow kinetics of formation of the chelate between ^{225}Ac and the encapsulated DOTA in the presence of citrate buffer. Contrary to oxine, when A23187 delivers the radionuclide in the presence of both acetate and citrate buffers, the chelation reaction to DOTA seems to proceed faster.

All liposomes exhibited significant release of encapsulated contents mainly within the first two hours after the start of incubation into PBS and serum supplemented media at 37 °C. This behavior does not seem to depend on the specific ionophore/buffer combination used, and it is possibly due to the sudden temperature change of the lipid bilayer membranes when liposomes are introduced to 37 °C from room temperature. Heating of the liposomal membrane at temperatures close to the bilayer's transition temperature has been reported to increase the permeability of the bilayer that has been attributed to the presence of grain boundaries (due to lipid packing defects) that melt at these temperatures (*35*, *36*). The membrane of DNPC-cholesterol lipids contains 30 mol % cholesterol and is shown by the DSC thermogram (Figure 1). Cholesterol decreases the range of temperature response of the DNPC-based membrane from 72 °C ($=T_g$ of DNPC lipid) to lower values that extend to the vicinity of 37 °C. Therefore, a hypothesis of formation of transient local melted lipid domains within the lipid bilayer could explain the increased bilayer permeability at the onset of incubation of the liposome suspension from 25 to 37 °C. Alternatively, the initial increased release of contents could be due to differences in osmolarity between the encapsulated liposome contents and the surrounding environment.

Membrane permeability to radionuclides is expected to be a function of the size of radionuclide complex, and the complex's net charge or hydrophobicity. Free radionuclides are charged species and are expected to diffuse across the bilayer membrane very slowly over the period of several days due to the hydrophobic barrier presented by the lipid acyl chains (*37*). In addition, trivalent cations can electrostatically adsorb on the phosphatidyl choline headgroups of lipid membranes (*18*, *33*). It is expected that, for fluid membranes, the membrane permeability to ^{225}Ac-DOTA chelates should be lower than the membrane permeability to ^{225}Ac-ionophore complexes (*21*, *33*, *34*), since ionophores are lipophilic molecules that upon complexation may camouflage the radionuclide's charge, exhibiting increased membrane permeabilities. However, gel phase bilayer membranes, such as those used in the present studies, are expected to exhibit considerably lower diffusivities to all species. Our studies, after the first two hours of incubation at 37 °C, exhibit generally slow release of radioactive contents for 30 days. On the contrary, during the first part of incubation at 37 °C, the extent of formation of transient lipid packing discontinuities due to sudden melting of grain boundaries across the bilayer membrane can be potentially large and comparable to either complexed form of the radionuclide. Such transient structures should allow release of any form of complexed ^{225}Ac.

In the studies of content release from liposomes, the complexed form of the radionuclide (^{225}Ac-DOTA or ^{225}Ac-ionophore) that is released from liposomes was not directly identified. In parallel studies, however, the extent of formation of ^{225}Ac-DOTA chelants compared to ^{225}Ac-ionophore complexes was evaluated in conditions identical to those of the encapsulated aqueous volume during liposome loading. The species of radionuclide complexes were identified using a cation exchange column that selectively challenges the ^{225}Ac-ionophore complexes. Our findings suggest that, after 60 min of incubation in acetate buffer when both the chelant DOTA and the ionophore oxine are present, all of ^{225}Ac is in the form of ^{225}Ac-DOTA chelates. When A23187 is used, after 60 min of incubation (corresponding to 60 min of liposome loading) 47% of the total radioactivity is in the form of ^{225}Ac-DOTA chelates. These studies could be indicative of the complexed forms of the released radioactivity from liposomes during content retention studies. In the presence of citrate buffer, the cation exchange column that was used could not challenge the complexes formed with ^{225}Ac, probably due to the excess of citrate buffer that could be acting as a weak chelant to the radionuclide (*31*, *32*). Nevertheless, it is possible for the enhanced formation of ^{225}Ac-DOTA chelants versus ^{225}Ac-ionophore complexes with increasing incubation times that was observed in the case of acetate buffer to also occur in the case of citrate buffer, independently of the inability of the cation exchange column to selectively challenge and quantitate the different species of complexes.

We developed liposomes and showed that it is possible to achieve as high as 55−73% loading efficacies using PEGylated liposomes containing DNPC lipids and cholesterol. In some cases, after the first 24 h in serum-supplemented media at 37 °C, the remaining radioactivity (as high as 74% of the encapsulated ^{225}Ac for 55% loading yield) is stably retained by liposomes for several weeks. Thus, for 370 MBq (10 mCi) ^{225}Ac initial activity, and 41% ^{225}Ac overall loading/retention efficacy (the product of the aforementioned 55% loading yield and 74% retention), we can project that we can stably encapsulate three ^{225}Ac nuclides per every two liposomes (for 3.3×10^{13} liposomes, starting with 5 μmol lipid, with a mean diameter of 100 nm based on our protocols). Assuming an average number of 50 antibodies per liposome, then each immunoliposome construct results in 1 ^{225}Ac nuclide per 34 lipid-conjugated antibodies. Analogous to immunoreactivity of radiolabeled antibodies that can exceed 80−90% (*6*), immunoliposomes have significantly lower binding capacity (2−4.5%) (*8*, *29*). However, the drug-to-ligand ratios are significantly enhanced for immunoliposomes (1:34) compared to radiolabeled antibodies (1:2300). Although many other factors determine the actual delivered dose at the targeted cancer cells *in vivo*, high encapsulated activities by liposomes could potentially make feasible the α-particle therapy using ^{225}Ac delivered by liposomes. Specific targeting of ^{225}Ac can also be achieved using these liposomes, and as shown in this study, it is possible to develop such immunolabeled liposomes for the delivery of radionuclides while also retaining 80% of their binding efficacy to cancer cells.

Liposome biodistributions and pharmacokinetics commonly include significant uptake by the liver, spleen, and bone marrow. Minimization of toxicities using these delivery vehicles could be achieved by specifically targeting liposomes to cancer cells using surface conjugated antibodies or other targeting ligands forming immunoliposomes. Immunoliposomes can be used for the targeted therapy of circulating micrometastases or of single cancer cells, or for locoregional administration. Direct administration of immunoliposomes at the site where cancer cells reside could lead to faster binding to the target. This may allow for lower liposome doses to be administered, eventually resulting in lower localization at normal organs with lower toxicities.

Our studies on the stability of liposomes in serum-supplemented media could only be indicative of their stability in human blood. It is expected that in the bloodstream the presence of divalent cations and enzymes could contribute to additional liposome destabilization *in vivo* and could result in further release of radioactive contents. Additional studies *in vivo* for

the optimization of these liposome membranes regarding radionuclide retention are in progress.

Micrometastatic disease is still a treatment challenge. Depending on the disease localization throughout the body, targeted liposomes could be potentially used to carry ^{225}Ac which is a powerful α-particle generator. This work suggests that immunoliposomes bearing high specific activities of ^{225}Ac with adequate binding efficacy and specificity to cancer cells can be developed and may potentially be used for targeted α-particle therapy of micrometastatic cancer. *In vivo* evaluation of the stability and targeting specificity of these liposomes is necessary.

ACKNOWLEDGMENT

We thank Dr. George Sgouros at Johns Hopkins University for providing Actinium-225, Dr. David Scheinberg at Memorial Sloan-Kettering Cancer Center (MSKCC) for providing Actinium-225 and for use of his laboratory facilities, Dr. Michael McDevitt (MSKCC) for reading the manuscript and his suggestions, and Mr. Shrirang Karve (Polytechnic University) for assistance with the DSC studies. This study was supported by Polytechnic University and the Othmer Major Project Initiative.

Supporting Information Available: Evaluation of the extent of complex formation of ^{225}Ac with the chelant DOTA and the ionophores oxine and A23187 in conditions identical to those of the encapsulated aqueous volume during liposome loading. Demonstration of specific binding of anti-HER2/neu liposomes with cells. Effect of incubation time. This material is available free of charge via the Internet at http://pubs.acs.org

LITERATURE CITED

(1) Humm, J. L. (1987) A microdosimetric model of astatine-211 labeled antibodies for radioimmunotherapy. *Int. J. Radiat. Oncol. Biol. Phys. 13*, 1767–1773.

(2) Humm, J. L., and Chin, L. M. (1993) A model of cell inactivation by alpha-particle internal emitters. *Radiat. Res. 134*, 143–150.

(3) Macklis, R. M., Kinsey, B. M., Kassis, A. I., Ferrara, J. L., Archer, R. W., Hines, J. J., Coleman, C. N., Adelstein, S. J., and Burakoff, S. J. (1988) Radioimmunotherapy with alpha-particle-emitting immunoconjugates. *Science 240*, 1024–1026.

(4) McQuarrie, S. A., Mercer, J. R., Syme, A., Suresh, M. R., and Miller, G. G. (2005) Preliminary results of nanopharmaceuticals used in the radiotherapy of ovarian cancer. *J. Pharmaceut. Sci. 7*, 29–34.

(5) Ballangrud, G., Yang, W.-H., Palm, S., Enmon, R., Borchardt, P., Pellegrini, V., McDevitt, M., Scheinberg, D., and Sgouros, G. (2004) Alpha-particle emitting atomic generator (actinium-225)-labeled trastuzumab (herceptin) targeting of breast cancer spheroids: efficacy versus HER2/neu expression. *Clin. Cancer Res. 10*, 4489–4497.

(6) Borchardt, P., Yuan, R., Miederer, M., McDevitt, M., and Scheinberg, D. (2003) Targeted actinium-225 in vivo generators for therapy of ovarian cancer. *Cancer Res. 63*, 5084.

(7) McDevitt, M. R., Ma, D., Simon, J., Frank, R. K., Kiefer, G. E., and Scheinberg, D. A. (2002) Design and synthesis of actinium-225 radioimmunopharmaceuticals. *Appl. Radiat. Isot. 57*, 841–847.

(8) Sofou, S., Kappel, B. J., Jaggi, J. S., McDevitt, M. R., Scheinberg, D. A., and Sgouros, G. (2007) Enhanced retention of the alpha-particle-emitting daughters of actinium-225 by liposome carriers. *Bioconjugate Chem. 18*, 2061–2067.

(9) Emfietzoglou, D., Kostarelos, K., and Sgouros, G. (2001) An analytic dosimetry study for the use of radionuclide-liposome conjugates in internal radiotherapy. *J. Nucl. Med. 42*, 499–504.

(10) Syrigos, K. N., Vile, R. G., Peters, A. M., and Harrington, K. J. (2003) Biodistribution and pharmacokinetics of 111In-DTPA-labelled pegylated liposomes after intraperitoneal injection. *Acta Oncol. 42*, 147–153.

(11) Allen, T. M. (2002) Ligand-targeted therapeutics in anticancer therapy. *Nat. Cancer Rev. 2*, 750–763.

(12) Sofou, S. (2007) Surface-active liposomes for targeted cancer therapy. *Nanomedicine (London, U.K.) 2*, 711–724.

(13) Chiu, G. N. C., Edwards, L. A., Kapanen, A. I., Malinen, M. M., Dragowska, W. H., Warburton, C., Chikh, G. G., Fang, K. Y. Y., Tan, S., Sy, J., Tucker, C., Waterhouse, D. N., Klasa, R., and Bally, M. B. (2007) Modulation of cancer cell survival pathways using multivalent liposomal therapeutic antibody constructs. *Mol. Cancer Ther. 6*, 844–855.

(14) Emfietzoglou, D., Kostarelos, K., Papakostas, A., Yang, W. H., Ballangrud, A., Song, H., and Sgouros, G. (2005) Liposome-mediated radiotherapeutics within avascular tumor spheroids: comparative dosimetry study for various radionuclides, liposome systems, and a targeting antibody. *J. Nucl. Med. 46*, 89–97.

(15) Kostarelos, K., Emfietzoglou, D., Papakostas, A., W, H., Y., Ballangrud, A. M., and, and Sgouros, G. (2005) Engineering lipid vesicles of enhanced intratumoral transport capabilities: correlating liposome characteristics with penetration into human prostate tumor spheroids. *J. Liposome Res. 15*, 15–27.

(16) Zielhuis, S. W., Nijsen, J. F. W., Seppenwoodle, J. H., Zonnenberg, B. A., Bakker, C. J. G., Hennink, W. E., van Rijk, P. P., and van het Schip, A. D. (2005) Lanthanide bearing microparticulate systems for multi-modality imaging and targeted therapy of cancer. *Curr. Med. Chem.: AntiCancer Agents 5*, 303–313.

(17) Henriksen, G., Schoultz, B. W., Michaelsen, T. E., Bruland, O. S., and Larsen, R. H. (2004) Sterically stabilized liposomes as a carrier for alpha-emitting radium and actinium radionuclides. *Nucl. Med. Biol. 31*, 441–449.

(18) Sofou, S., Thomas, J. L., Lin, H.-Y., McDevitt, M. R., Scheinberg, D. A., and Sgouros, G. (2004) Engineered liposomes for potential α-particle therapy of metastatic cancer. *J. Nucl. Med. 45*, 253–260.

(19) Allen, C., Dos Santos, N., Gallagher, R., Chiu, G. N. C., Shu, Y., Li, W. M., Johnstone, S. A., Janoff, A. S., Mayer, L. D., Webb, M. S., and Bally, M. B. (2002) Controlling the physical behavior and biological performance of liposome formulations through use of surface grafted poly(ethylene glycol). *Bioscience Rep. 22*, 225–250.

(20) Gabizon, A., and Papahadjopoulos, D. (1988) Liposome formulations with prolonged circulation time in blood and enhanced uptake by tumors. *Proc. Natl. Acad. Sci. U.S.A. 85*, 6949–6953.

(21) Mauk, M., and Gamble, R. (1979) Preparation of lipid vesicles containing high levels of entrapped radioactive cations. *Anal. Biochem. 94*, 302–307.

(22) Gregory, J. (1955) The stability of n-ethylmaleimide and its reaction with sulfhydryl groups. *J. Am. Chem. Soc. 77*, 3922–3923.

(23) Provencher, S. W. (1982) A constrained regularization method for inverting data represented by linear algebraic or integral equations. *Comput. Phys. Commun. 27*, 213–227.

(24) Teraoka, I. (2002) *Polymer Solutions: An Introduction to Physical Properties*, John Wiley & Sons, New York.

(25) Torchilin, V., and Weissig, V. (2003) *Liposomes-A Practical Approach*, Oxford University Press, New York.

(26) Lasic, D. D. (1993) *Liposomes from Physics to Applications*, Elsevier, Amsterdam.

(27) Allen, T. M., Brandeis, E., Hansen, C. B., Kao, G. Y., and Zalipsky, S. (1995) A new strategy for attachment of antibodies to sterically stabilized liposomes resulting in efficient targeting to cancer cells. *Biochim. Biophys. Acta 1237*, 99–108.

(28) Gabizon, A., Shmeeda, H., and Barenholz, Y. (2003) Pharmacokinetics of pegylated liposomal Doxorubicin: review of animal and human studies. *Clin. Pharmacokinet. 42*, 419–436.

(29) Kirpotin, D. B., Park, J. W., Hong, S. K., Zalipsky, S., Li, W.-L., Carter, P., Benz, C. C., and Papahadjopoulos, D. (1997) Sterically stabilized anti-HER2 immunoliposomes: design and targeting to human breast cancer cells *in vitro*. *Biochemistry 36*, 66–75.

(30) Mujoo, K., Maneval, D. C., Anderson, S. C., and Gutterman, J. U. (1996) Adenoviral-mediated p53 tumor suppressor gene therapy of human ovarian carcinoma. *Oncogene 12*, 1617–1623.

(31) Duzgunes, D. (2003) Fluorescence assays for liposome fusion. *Methods Enzymol. 372*, 260–274.

(32) Hwang, K. J., Merriam, J. E., Beaumier, P. L., and Luk, K.-F. S. (1982) Encapsulation, with high efficiency, of radioactive metal ions in liposomes. *Biochim. Biophys. Acta 716*, 101–109.

(33) Hwang, K. (1978) Modes of interaction of (In3+)-8-hydroxyquinoline with membrane bilayer. *J. Nucl. Med. 19*, 1162–1170.

(34) Pfeiffer, D. R., Reed, P. W., and Lardy, H. A. (1974) Unltraviolet and fluorescent spectral properties of the divalent cation ionophore A23187 and its metal ion complexes. *Biochemistry 13*, 4007–4014.

(35) Clerc, S. G., and Thompson, T. E. (1995) Permeability of dimyristoyl phosphatidylcholine/dipalmitoyl phosphatidylcholine bilayer membranes with coexisting gel and liquid-crystalline phases. *Biophys. J. 68*, 2333–2341.

(36) Needham, D., and Dewhirst, M. W. (2001) The development and testing of a new temperature-sensitive drug delivery system for the treatment of solid tumors. *Adv. Drug Delivery Rev. 53*, 285–305.

(37) Cevc, G., and Marsh, D. (1987) *Phospholipid bilayers: physical principles and models*, Wiley-Interscience, New York.

BC700440A

Structure−Activity Investigation on the Gene Transfection Properties of Cardiolipin Mimicking Gemini Lipid Analogues

Avinash Bajaj,[†] Bishwajit Paul,[†] Paturu Kondaiah,[‡] and Santanu Bhattacharya*[,†,§]

Department of Organic Chemistry and Department of Molecular Reproduction, Development and Genetics, Indian Institute of Science, Bangalore 560 012, India, and Chemical Biology Unit of JNCASR, Bangalore 560 064, India. Received December 19, 2007; Revised Manuscript Received March 14, 2008

A structure−activity relationship has been explored on the gene transfection efficiencies of cardiolipin mimicking gemini lipid analogues upon variation of length and hydrophilicity of the spacer between the cationic ammonium headgroups and lipid hydrocarbon chain lengths. All the gemini lipids were found to be highly superior in gene transfer abilities as compared to their monomeric lipid and a related commercially available formulation. Pseudoglyceryl gemini lipids bearing an oxyethylene ($-CH_2-(CH_2-O-CH_2)_m-CH_2-$) spacer were found to be superior gene transfecting agents as compared to those bearing polymethylene ($-(CH_2)_m-$) spacers. The major characteristic feature of the present set of gemini lipids is their serum compatibility, which is most often the major hurdle in liposome-mediated gene delivery.

INTRODUCTION

Gene therapy refers to the introduction of foreign genes into cells with the aim of providing a therapeutic effect (*1*). Several strategies like suicide gene therapy (*2*), corrective gene therapy, and antisense oligonucleotide therapy (*3*) have been used under the umbrella of gene therapy. One of the major hurdles that must however, be overcome in order to succeed in gene therapy is the development of efficient gene delivery vehicles. Natural or engineered viruses are very competent vectors (*4*) toward this end. However, such biological materials have a high risk of being infectious or immunogenic as compared to their synthetic counterparts. This has imposed serious limits on their use. Unlike viral vectors, lipid−DNA complexes are easy to prepare, have no limit in the size of genes that can be delivered, and have low toxicity and significantly low immunogenicity (*5–10*). Various nonviral formulations have been developed with modification at the headgroup region, linker, and hydrophobic parts (*11–30*). We have shown that the use of an ether linkage leads to a significant increase in the transfection efficiency as compared to its ester- or urethane-based cholesterol lipid analogues (*31, 32*).

However, the rational search for new molecular entities for gene delivery continues. For instance, gemini surfactants, possessing two surfactant units covalently joined by a spacer, have been shown to possess unusual aggregation and biological properties (*21, 33–41*). Similarly, gemini lipids constitute a dimeric class of lipids, where two monomeric lipid molecules are joined together through a suitable spacer. The length and the nature of the spacer (e.g., flexibility, hydration, etc.) dramatically influence the aggregation properties of the resulting gemini lipids (*42, 43*). Since the spacer is in the dynamic interfacial region in vesicular aggregates, changes in the length and the nature of the spacer modulate the aggregation properties significantly (*44–46*).

Nature has always been instructive for molecular designers. Cardiolipin (glycerol-bridged phosphatidic acid) constitutes a class of complex phospholipids that occur in the heart and skeletal muscles (*47–49*). Taking the inspiration from the cardiolipins, we reported for the first time the synthesis and membrane-forming properties of pseudoglyceryl backbone based gemini cationic lipids with different spacers (*42, 43*). It was shown that the aggregation behavior, membrane organization, and lipid packing of gemini lipids strongly depend upon the length and the nature of the spacer (*50–52*). We have recently exploited cholesterol and aromatic-based gemini lipids for the delivery of the DNA into mammalian cells and this works efficiently even in the presence of serum; (*53*). These investigations reveal that the gene delivery activity is more efficient with gemini lipids and its efficiency strongly depends on the length and the nature of the spacer between the headgroups (*53–56*). Efficient transfection profiles of the above gemini lipids inspired us to examine the gene transfection properties of the gemini lipids based on the pseudoglyceryl backbone, although a corresponding monomeric lipid (DOTMA) is known to be a commercially available transfection reagent. The aggregation properties of gemini lipids had been reported already (*50, 51*), but there has been no attempt to examine the effect of the length and nature of the spacer on the gene transfection activity.

Toward this end, we have synthesized eight cationic gemini lipids possessing a polymethylene spacer and six additional cationic gemini lipids possessing an oxyethylene spacer between the cationic ammonium headgroups. Thus, we have varied the length and the nature of the spacer between the headgroups, from hydrophobic polymethylene [$-(CH_2)_m-$] to hydrophilic oxyethylene [$-CH_2-(CH_2-O-CH_2)_m-CH_2-$] units (Figure 1). In these two series, we have also examined the effect of variation of the chain length from tetradecyl (n-$C_{14}H_{29}$) to hexadecyl (n-$C_{16}H_{33}$) chains. Though synthetically more demanding, ether functionality was chosen to link the hydrocarbon chains with the pseudoglyceryl backbone to ensure long-term chemical stability of these lipids. We have investigated the transfection properties of all the cationic lipids in detail in HeLa cells both in the absence and in the presence of serum; and compared them

* Corresponding author. E-mail: sb@orgchem.iisc.ernet.in, Phone: (91)-80-2293-2664; Fax: (91)-80-2360-0529.

[†] Department of Organic Chemistry, Indian Institute of Science.

[‡] Department of Molecular Reproduction, Development and Genetics, Indian Institute of Science.

[§] Chemical Biology Unit of JNCASR.

10.1021/bc700474r CCC: $40.75 © 2008 American Chemical Society
Published on Web 05/29/2008

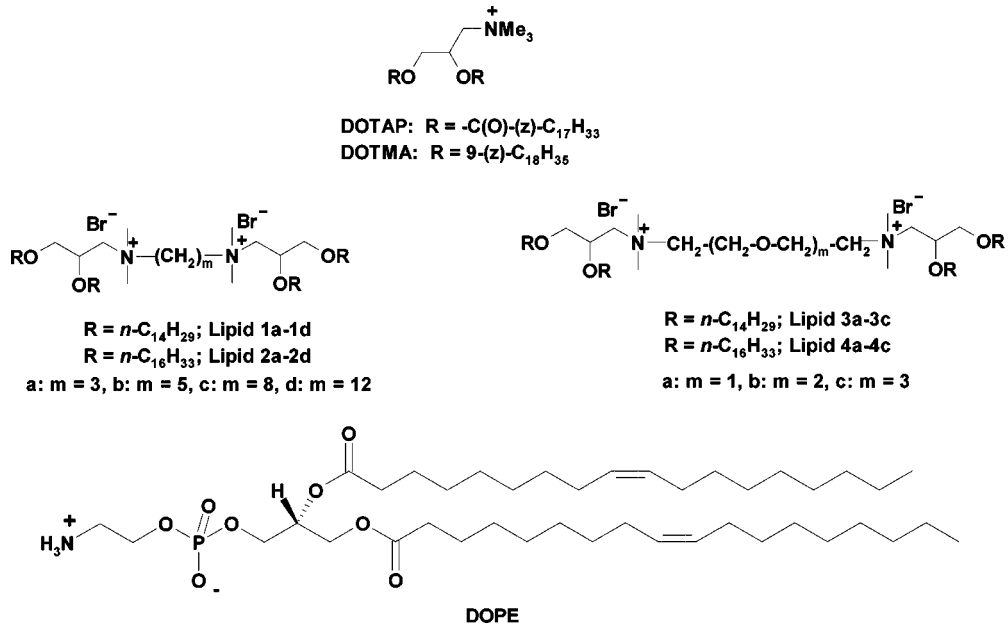

Figure 1. Molecular structures of gemini lipids synthesized and studied in this work, and the structures of DOTMA, DOTAP, and DOPE.

with that of Lipofectin, which is a commercially available 1:1 (w/w) liposomal formulation of DOTMA and DOPE.[1]

EXPERIMENTAL PROCEDURES

Materials and Methods. All reagents, solvents, and chemicals used in this study were of the highest purity available. The solvents were dried prior to use. Column chromatography was performed using 60−120 mesh silica gel. NMR spectra were recorded using a Jeol JNM λ-300 (300 MHz for ^{1}H) spectrometer. The chemical shifts (δ) are reported in ppm downfield from the internal standard: TMS, for ^{1}H NMR. Mass spectra were recorded on a Kratos PCKompact SEQ V1.2.2 MALDI-TOF spectrometer or on a MicroMass ESI-TOF spectrometer or Shimadzu table-top GC-MS or ESI-MS (HP1100LC-MSD). Infrared (IR) spectra were recorded on a Jasco FT-IR 410 spectrometer using KBr pellets or neat. Gemini lipids were synthesized and characterized fully by their ^{1}H NMR, mass spectra, and elemental analysis.

Synthesis. *2,3-Bis-hydroxy-1-benzyloxypropanol (**6**) (**43**).* 1,2-*O*-Isopropylidene glycerol **5** (10 g, 75.6 mmol) was mixed with powdered KOH (8.8 g, 156.6 mmol) in 45 mL of dry benzene. The solution first turned yellow and then rose red within 5 min. Benzyl chloride (19.8 g, 156.6 mmol) was added into the reaction mixture, and the resulting mixture was refluxed for 24 h. The water formed during the reaction was removed by Dean−Stark apparatus. The reaction mixture was allowed to cool down to room temperature, and it was then diluted further with benzene (100 mL) and washed successively with water (80 mL), 0.2 N HCl (50 mL), 3% $NaHCO_3$ (50 mL), and again with water. The benzene layer was separated by separatory funnel, and it was dried over anhydrous Na_2SO_4, and solvent was removed under reduced pressure. The crude product, 1,2-*O*-isopropylidene glycerol benzyl ether, was taken up in 100 mL of MeOH−H_2O (2:1), and *p*-TsOH (5.75 g, 30.3 mmol) was added into it and the mixture was stirred at room temperature for 5 h. The reaction mixture was neutralized with solid $NaHCO_3$. The mixture was filtered and washed with $CHCl_3$, and then the organic layer was evaporated under reduced pressure. The reaction mixture was dissolved in $CHCl_3$ (200 mL) and washed successively with saturated aqueous $NaHCO_3$ (100 mL), water (100 mL), and then saturated brine solution (100 mL). The organic layer was separated, dried over anhydrous Na_2SO_4, and the required compound (R_f∼0.8 at MeOH−$CHCl_3$ (2:98)) was purified by column chromatography over silica gel (60−120 mesh size) using MeOH/$CHCl_3$ (3:97). The isolated yield of **6** was 57%. FT-IR (neat): 3100−3650 cm^{-1} (OH str.). ^{1}H NMR ($CDCl_3$, 300 MHz) δ: 2.65 (br s, 2H, 2 × O*H*), 3.45−3.71 (m, 4H, 2 × CH_2O), 3.75−4.02 (m, 1H, OC*H*), 4.05 (s, 2H, OCH_2Ph), 7.35 (s, 5H, ArH). ESI-MS for $C_{10}H_{14}O_3$: calcd 182.22; found 205 [M + Na$^+$] (*43*).

*2,3-Bis(alkyloxy)-1-benzyloxypropanol (**7a**, **7b**).* A mixture of 2,3-bis-hydroxy-1-benzyloxypropanol, **6**, (16.48 mmol), powdered potassium hydroxide (3.8 g, 65.9 mmol), and appropriate long chain alkyl bromide (49.45 mmol) in dry benzene (50 mL) was refluxed for 24 h with continuous stirring. The water formed during the reaction was removed by using a Dean−Stark apparatus. The reaction mixture was cooled and diluted with ethyl acetate (100 mL), and it was washed successively with water (50 mL), 1 N HCl (50 mL), and 2.5% $NaHCO_3$ solution (50 mL) and again with water. The organic layer was dried over anhydrous Na_2SO_4. The product was purified by column chromatography over silica gel (60−120 mesh) using EtOAc/hexane (5:95). A viscous oily compound was isolated in 85−90% (9.2 g) yield.

*2,3-Bis(tetradecyloxy)-1-benzyloxypropanol (**7a**).* FT-IR (neat): 1115 cm^{-1} (asym. str. of C−O−C). ^{1}H NMR ($CDCl_3$, 300 MHz) δ: 0.78−0.83 (t, 6H, 2 × -CH_3, J = 6 Hz), 1.18 (br m, 44H, 2 × -(CH_2)$_{11}$-), 1.45−1.52 (m, 4H, 2 × -O−CH_2−CH_2), 3.33−3.55 (m, 9H, 4 × -OCH_2 and 1 × -OC*H*), 4.6 (s, 2H, -OCH_2−Ar), 7.21 (s, 5H, Ar*H*). ESI-MS for $C_{38}H_{70}O_3$: calcd 574.98; found 598 [M + Na$^+$].

[1]Abbreviations: DOPE, 1,2-dioleoyl-L-α-glycero-3-phosphatidylethanolamine; DOTMA, *N*-[1-(2,3-dioleyloxy)propane]-*N*,*N*,*N*-trimethylammonium chloride; DOTAP, *N*-[1-(2,3-dioleoyloxy)]-*N*,*N*,*N*-trimethylammonium propane chloride; MFI, mean fluorescence intensity; FACS, fluorescence-activated cell sorting; FBS, fetal bovine serum; DMEM, Dulbecco's Modified Eagle's Medium; MTT, 3-(4,5-dimethylthiazole-2-yl)-2,5-diphenyltetrazolium bromide; GFP, green fluorescence protein; TEM, transmission electron microscope; ESI-MS, electron spray ionization mass spectrometry; MALDI-TOF, matrix assisted laser desorption/ionization time-of-flight; N/P represents the charge ratio of lipid/DNA, where N denotes the charge on lipid because of ammonium headgroup and P represents the charge on DNA because of phosphate.

*2,3-Bis(hexadecyloxy)-1-benzyloxypropanol (**7b**).* FTIR (neat): 1115 cm^{-1} (asym. str. of C−O−C). ^1H NMR ($CDCl_3$, 300 MHz) δ: 0.90 (t, 6H, 2 × -C*H*$_3$), 1.10 (br s, 52H, 2 × -(C*H*$_2$)$_{13}$-), 1.50−1.80 (m, 4H, 2 × -OCH$_2$−C*H*$_2$), 3.40−3.75 (m, 9H, 4 × -OC*H*$_2$ and -OC*H*), 4.55 (s, 2H, -C*H*$_2$Ph), 7.27−7.34 (m, 5H, Ar*H*). ESI-MS for $C_{42}H_{78}O_3$: calcd 631.09; found 630 [M^+] (*43*).

*2,3-Bis(alkyloxy)propanol (**8a**, **8b**).* A solution of appropriate 2,3-bis(alkyloxy)-1-benzyloxypropanol (**7a**, **7b**) (12.94 mmol) in (1:1) mixture of methanol and ethyl acetate (50 mL) was hydrogenated using 10% Pd−C catalyst (0.2 g) for 24 h, at 40 Psi pressure, during which almost all the starting material was converted to the alcohol. Then, Pd−C was filtered off and the solvent was removed. The solid obtained was dissolved in hot ethyl acetate and kept at room temperature for recrystallization. The solid was filtered and washed with hexane. The resulting solid was recrystallized several times to get pure, white solid. The rest of the compound, which was in filtrate, was purified by column chromatography over silica with EtOAc/hexane (1:9) as the eluting solvent ($R_f \sim 0.4$ in EtOAc/hexane (1:9)). The overall yield after purification was 90−94%.

*2,3-Bis(tetradecyloxy)propanol (**8a**).* FT-IR (Nujol): 1115 cm^{-1} (asym. str. of C−O−C), 3471 cm^{-1} (O−H str.). ^1H NMR ($CDCl_3$, 300 MHz) δ: 0.83−0.87 (t, 6H, 2 × -C*H*$_3$, $J = 6$ Hz), 1.23 (br. m, 44H, 2× -(C*H*$_2$)$_{11}$-), 1.52 (m, 4H, 2 × -O−CH$_2$−C*H*$_2$), 3.39−3.68 (m, 9H, 4 × -OC*H*$_2$ and 1 × -OC*H*). ESI-MS for $C_{31}H_{64}O_3$: calcd 484.85; found 484 [M^+].

*2,3-Bis(hexadecyloxy)propanol (**8b**).* FT-IR (Nujol): 1115 cm^{-1} (asym. str. of C−O−C), 3471 cm^{-1} (O−H str.). ^1H NMR ($CDCl_3$, 300 MHz) δ: 0.89 (t, 6H, 2 × -C*H*$_3$), 1.15−1.40 (br. s, 52H, 2 × (C*H*$_2$)$_{13}$-), 1.50−1.80 (m, 4H, 2 × -OCH$_2$−C*H*$_2$), 3.40−3.75 (m, 9H, 4 × -OC*H*$_2$ and 1 × - OC*H*). ESI-MS for $C_{35}H_{72}O_3$: calcd 540.96; found 540 [M^+] (*43*).

*2,3-Bis(alkyloxy)propylbromide (**9a**, **9b**).* To a well-stirred solution of 2,3-bis(alkyloxy)propanol (**8a**, **8b**) (3.7 mmol) and CBr_4 (2.46 g, 7.4 mmol.) in dry CH_2Cl_2 (85 mL) at ∼15 °C, a solution of Ph_3P (1.47 g, 5.6 mmol.) in dry CH_2Cl_2 (7 mL) was added dropwise over a period of 30 min. The reaction mixture was stirred at room temperature for another 12 h until TLC showed the disappearance of the spot due to starting material. Dichloromethane was removed under vacuum and the residual mass was repeatedly extracted using hexane. The combined extract was evaporated to dryness. The required compound was purified by column chromatography over a silica gel (60−120 mesh) column using hexane and EtOAc mixture. The fraction, which was collected using EtOAc/hexane (1:50) on removal of organic solvent, afforded a viscous liquid in quantitative yield. It solidified on standing. The pure compound gave a spot with R_f value of 0.8 in EtOAc/hexane (1:4).

*2,3-Bis(tetradecyloxy)propylbromide (**9a**).* FT-IR (Nujol): 1121 cm^{-1} (asym. str. of C−O−C). ^1H NMR ($CDCl_3$ 300 MHz) δ: 0.86−0.90 (t, 6H, 2 × -C*H*$_3$, $J = 6$ Hz), 1.26 (br. m, 44H, 2 × -(C*H*$_2$)$_{11}$-), 1.51−1.58 (m, 4H, 2 × -OC*H*$_2$-CH$_2$), 3.43−3.58 (m, 9H, 3 × -OC*H*$_2$, 1 × -OC*H*, 1 × -C*H*$_2$Br). MALDI-TOF for $C_{31}H_{63}BrO_2$: calcd 547.75; found 546.5 [M^+].

*2,3-Bis(hexadecyloxy)propylbromide (**9b**).* FT-IR (Nujol): 1121 cm^{-1} (asym. str. of C−O−C). ^1H NMR ($CDCl_3$ 300 MHz) δ: 0.89 (t, 6H, 2 × -C*H*$_3$), 1.15−1.40 (br. s, 52H, 2 × -(C*H*$_2$)$_{13}$-), 1.54−1.8 (m, 4H, 2 × -OCH$_2$−C*H*$_2$), 3.33−3.50 (m, 9H, 3 × -OC*H*$_2$, 1 × -OCH, 1 × -OC*H*$_2$Br). MALDI-TOF for $C_{35}H_{71}BrO_2$: calcd 603.86; found 626.5 [M + Na]$^+$ (*43*).

*D,L-[1,2-Di-O-alkyloxy-3-(N,N′-dimethylamine)] Propane (**10a**, **10b**).* Dry NMe_2 gas was dissolved in anhydrous ethanol (5.0 mL) in a screw-top pressure tube at 0 °C, so that volume increased to 15 mL. To this solution, individual bromohydrin **9a** or **9b** (1.66 mmol) in dry ethanol (3.0 mL) was added (3.0 mL) at 0 °C. The tube was heated with stirring at 80 °C for 48 h. Solvent was removed to furnish a crude white mass, which was recrystallized several times from $CHCl_3$/acetone/EtOAc (1:10:1) mixture.

*D,L-[1,2-Di-O-tetradecyloxy-3-(N,N′-dimethylamine)] Propane (**10a**).* ^1H NMR ($CDCl_3$, 300 MHz) δ: 0.83−0.87 (t, 6H, 2 × -C*H*$_3$, $J = 6$ Hz), 1.23 (br m, 44H, 2 × -(C*H*$_2$)$_{11}$-), 1.54 (m, 4H, 2 × -OCH$_2$−C*H*$_2$), 2.24 (s, 6H, -N(C*H*$_3$)$_2$), 2.30−2.38 (m, 2H, -C*H*$_2$N), 3.38−3.60 (m, 7H, 3 × -OC*H*$_2$, 1 × -OC*H*). ESI-MS for $C_{33}H_{69}NO_2$: calcd 511.92; found 512.54 [M + H^+].

*D,L-[1,2-Di-O-hexadecyloxy-3-(N,N′-dimethylamine)] Propane (**10b**).* ^1H NMR ($CDCl_3$, 300 MHz) δ: 0.83−0.87 (t, 6H, 2 × -C*H*$_3$, $J = 6$ Hz), 1.26 (br m, 52H, 2 × -(C*H*$_2$)$_{11}$-), 1.54 (m, 4H, 2 × -OCH$_2$−C*H*$_2$), 2.28 (s, 6H, -N(C*H*$_3$)$_2$, 2.29−2.43 (m, 2H, -C*H*$_2$N), 3.38−3.58 (m, 7H, 3 × -OC*H*$_2$, 1 × -OC*H*). ESI-MS for $C_{37}H_{77}NO_2$: calcd 568.03; found 568.6 [M^+].

General Method for the Synthesis of Gemini Lipids. A solution of **10a** or **10b** (1.0 mmol) and appropriate dibromoalkane (0.33 mmol) in dry MeOH−EtOAc mixture was refluxed over a period of 48−96 h. It was cooled, and solvent was evaporated to give a crude solid. It was repeatedly washed with dry acetone to remove the traces of unreacted starting material and finally subjected to repeated crystallizations from a mixture of either acetone and methanol (∼9:1) or ethyl acetate and methanol (∼9:1). Repeated crystallizations afforded a white compound found to be pure by TLC, R_f ∼020−0.30 in $CHCl_3$/MeOH, 10:1 (yield 50−70%). All compounds were found to be hygroscopic, and a few of them also crystallized as hydrates despite prolonged drying under vacuum. They gave satisfactory ^1H NMR, ESI-MS, and elemental analysis.

Pertinent spectroscopic data are given below.

*Lipid **1a**: Propanediyl-α,ω-bis[D,L-N-(1,2-di-O-tetradecyl-3-propyl)-N,N-dimethylammonium bromide].* ^1H NMR ($CDCl_3$, 300 MHz) δ: 0.85 (t, 12H, 4 × -C*H*$_3$), 1.25−1.50 (br. s, 88H, 4 × -(C*H*$_2$)$_{11}$-), 1.55−1.80 (br. m, 8H, 4 × -O−CH$_2$−C*H*$_2$), 2.70−2.73 (br m, 2H, -N$^+$CH$_2$C*H*$_2$CH$_2$N$^+$-), 3.36−4.14 (m, 34H, 2 × -N$^+$(C*H*$_3$)$_2$, 6 × −O−C*H*$_2$−CH$_2$, 2 × −O−C*H*−CH$_2$, and 2 × -C*H*$_2$NC*H*$_2$-). ESI-MS for $C_{69}H_{144}N_2O_4Br_2$: calcd 1225.73; found 532.6 [M^{+2}/2], 1146.0 [M^{+2} + Br^-] Elemental analysis (%) for $C_{69}H_{144}N_2O_4Br_2$: calcd C 67.61, H 11.84, N 2.29; found C 67.34, H 11.65, N 2.37.

*Lipid **1b**: Pentanediyl-α,ω-bis[D,L-N-(1,2-di-O-tetradecyl-3-propyl)-N,N-dimethylammonium bromide].* ^1H NMR ($CDCl_3$, 300 MHz) δ: 0.85 (t, 12H, 4 × -C*H*$_3$), 1.25−1.50 (br m, 88H, 4 × -(C*H*$_2$)$_{11}$-), 1.51 (br m, 8H, 4 × -O−CH$_2$−C*H*$_2$), 1.98 (br m, 6H, -N$^+$CH$_2$C*H*$_2$C*H*$_2$C*H*$_2$CH$_2$N$^+$-), 3.36−4.0 (m, 34H, 2 × -N$^+$(C*H*$_3$)$_2$, 6 × -O−C*H*$_2$−CH$_2$, 2 × -O−C*H*−CH$_2$, and 2 × -C*H*$_2$NC*H*$_2$-). ESI-MS for $C_{71}H_{148}N_2O_4Br_2$: calcd 1253.78; found 546.62 [M^{+2}/2], 1174.1 [M^{+2} + Br^-]. Elemental analysis (%) for $C_{71}H_{148}N_2O_4Br_2$: calcd C 68.02, H 11.90, N 2.23; found C 67.99, H 11.65, N 2.66.

*Lipid **1c**: Octanediyl-α,ω-bis[D,L-N-(1,2-di-O-tetradecyl-3-propyl)-N,N-dimethylammonium bromide].* ^1H NMR ($CDCl_3$, 300 MHz) δ: 0.85 (t, 12H, 4 × -C*H*$_3$), 1.25−1.50 (br m, 100H, 4 × -(C*H*$_2$)$_{11}$- and -N$^+$CH$_2$(C*H*$_2$)$_6$CH$_2$N$^+$-), 1.55 (br m, 8H, 4 × -O−CH$_2$−C*H*$_2$), 3.33−4.03 (m, 34H, 2 × -N$^+$(C*H*$_3$)$_2$, 6 × -O−C*H*$_2$−CH$_2$, 2 × -O−C*H*−CH$_2$, and 2 × -C*H*$_2$NC*H*$_2$-). ESI-MS for $C_{74}H_{154}N_2O_4Br_2$: calcd 1295.86; found 567.7 [M^{+2}/2], 1216.1 [M^{+2} + Br^-]. Elemental analysis (%) for $C_{74}H_{154}N_2O_4Br_2 \cdot 2H_2O$: calcd C 66.73, H 11.97, N 2.10; found C 66.87, H 11.59, N 2.46.

*Lipid **1d**: Dodecanediyl-α,ω-bis[D,L-N-(1,2-di-O-tetradecyl-3-propyl)-N,N-dimethylammonium bromide].* ^1H NMR ($CDCl_3$, 300 MHz) δ: 0.85 (t, 12H, 4 × -C*H*$_3$), 1.25−1.50 (br m, 108H, 4 × -(C*H*$_2$)$_{11}$- and -N$^+$CH$_2$(C*H*$_2$)$_{10}$CH$_2$N$^+$-), 1.51 (br m, 8H, 2 × -OCH$_2$C*H*$_2$), 3.36−4.0 (m, 34H, 2 × -N$^+$(C*H*$_3$)$_2$, 6 × -OC*H*$_2$, 2 × -OC*H*, and −2 × -C*H*$_2$NC*H*$_2$-); ESI-MS for $C_{78}H_{162}N_2O_4Br_2$: calcd 1351.97; found 595.7 [M^{+2}/2], 1272.2 [M^{+2} +

Br^-]. Elemental analysis (%) for $C_{78}H_{162}N_2O_4Br_2$: calcd C 69.30, H 12.08, N 2.07; found C 69.17, H 11.69, N 2.43.

Lipid **2a***: Propanediyl-α,ω-bis[D,L-N-(1,2-di-O-hexadecyl-3-propyl)-N,N-dimethylammonium bromide].* ^{1}H NMR ($CDCl_3$, 300 MHz) δ: 0.83−0.87 (t, 12H, 4 × -CH_3), 1.25 (br s, 104H, 4 × -(CH_2)$_{13}$), 1.52 (br m, 8H, 4 × -OCH$_2$CH_2), 2.80−2.92 (br m, 2H, -N$^+$CH$_2$CH_2CH_2N$^+$-), 3.35−4.15 (m, 34H, 2 × -N$^+$(CH_3)$_2$, 6 × -O−CH_2−CH$_2$, 2 × -O−CH−CH$_2$, and 2 × -CH_2NCH_2-). ESI-MS for $C_{77}H_{160}N_2O_4Br_2$: calcd 1337.94; found 588.7 [M^{+2}/2], 1258.0 [M^{+2} + Br^-]. Elemental analysis (%) for $C_{77}H_{160}N_2O_4Br_2$: calcd C 69.12, H 12.05, N 2.09; found C 68.34, H 11.93, N 2.22.

Lipid **2b***: Pentanediyl-α,ω-bis[D,L-N-(1,2-di-O-hexadecyl-3-propyl)-N,N-dimethylammonium bromide].* ^{1}H NMR ($CDCl_3$, 300 MHz) δ: 0.85 (t, 12H, 4 × -CH_3), 1.25−1.50 (br m, 110H, 4 × -(CH_2)$_{13}$ and -N$^+$CH$_2$CH_2CH_2CH_2CH$_2$N$^+$-), 1.52 (br m, 8H, 4 × -OCH$_2$CH_2), 3.34−3.99 (m, 34H, 2 × -N$^+$(CH_3)$_2$, 6 × -O−CH_2−CH$_2$, 2 × -O−CH−CH$_2$, and 2 × -CH_2NCH_2-). ESI-MS for $C_{79}H_{164}N_2O_4Br_2$: calcd 1360.00; found 602.7 [M^{+2}/2], 1286.0 [M^{+2} + Br^-]. Elemental analysis (%) for $C_{79}H_{164}N_2O_4Br_2 \cdot H_2O$: calcd C 68.56, H 12.09, N 2.02; found C 68.76, H 11.79, N 2.31.

Lipid **2c***: Octanediyl-α,ω-bis[D,L-N-(1,2-di-O-hexadecyl-3-propyl)-N,N-dimethylammonium bromide].* ^{1}H NMR ($CDCl_3$, 300 MHz) δ: 0.85 (t, 12H, 4 × -CH_3), 1.25−1.50 (br m, 116H, 4 × -(CH_2)$_{13}$ and -N$^+$CH$_2$(CH_2)$_6$CH$_2$N$^+$-), 1.52 (br m, 8H, 4 × -O−CH$_2$−CH_2), 3.38−4.03 (m, 34H, 2 × -N$^+$(CH_3)$_2$, 6 × -O−CH_2−CH$_2$, 2 × -O−CH−CH$_2$, and 2 × -CH_2NCH_2-). ESI-MS for $C_{82}H_{172}N_2O_4Br_2$: calcd 1408.08; found: 623.7 [M^{+2}/2], 1328.2 [M^{+2} + Br^-]. Elemental analysis (%) for $C_{82}H_{172}N_2O_4Br_2 \cdot H_2O$: calcd C 68.97, H 12.28, N 1.96; found C 68.61, H 11.93, N 2.24.

Lipid **2d***: Dodecanediyl-α,ω-bis[D,L-N-(1,2-di-O-hexadecyl-3-propyl)-N,N-dimethylammonium bromide].* ^{1}H NMR ($CDCl_3$, 300 MHz) δ: 0.85 (t, 12H, 4 × -CH_3), 1.25−1.50 (br m, 124H, 4 × -(CH_2)$_{13}$ and -N$^+$CH$_2$(CH_2)$_{12}$CH$_2$N$^+$-), 1.52 (br m, 8H, 4 × -O−CH$_2$−CH_2), 3.36−4.06 (m, 34H, 2 × -N$^+$(CH_3)$_2$, 6 × -O−CH_2−CH$_2$, 2 × -O−CH−CH$_2$, and 2 × -CH_2NCH_2-). ESI-MS for $C_{86}H_{178}N_2O_4Br_2$: calcd 1464.19; found 651.7 [M^{+2}/2], 1384.3 [M^{+2} + Br^-]. Elemental analysis (%) for $C_{86}H_{178}N_2O_4Br_2 \cdot 2H_2O$: calcd C 68.85, H 12.23, N 1.87; found C 68.61, H 11.93, N 2.20.

Lipid **3a***: Bis[D,L-N-(1,2-di-O-tetradecyl-3-propyl)-N,N-dimethylammonium bromide] Diethyl Ether.* ^{1}H NMR ($CDCl_3$, 300 MHz) δ: 0.83−0.87 (t, 12H, 4 × CH_3), 1.23 (br s, 88H, 4 × (CH_2)$_{11}$), 1.52 (s, 8H, 4 × -O−CH_2−CH$_2$), 3.38−4.39 (m, 38H, 4 × -N−CH_3, 4 × -N−CH_2, 2 × -O−CH_2−CH, 2 × -O−CH−CH$_2$, 4 × -O−CH_2−CH$_2$, 2 × -O−CH_2−CH_2−N). ESI-MS for $C_{70}H_{146}N_2O_5Br_2$: calcd 1257.77; found 547.7 [M^{+2}/2], 1176.0 [M^{+2} + Br^-]. Elemental analysis (%) for $C_{70}H_{146}N_2O_5Br_2 \cdot 2H_2O$: calcd C 65.09, H 11.72, N 2.23; found C 65.40, H 11.46, N 2.21.

Lipid **3b**. *Bis[D,L-N-(1,2-di-O-tetradecyl-3-propyl)-N,N-dimethylammonium bromide] Diethoxyethane.* ^{1}H NMR ($CDCl_3$, 300 MHz) δ: 0.84 (t, 12H, 4 × CH_3), 1.23 (br s, 88H, 4 × (CH_2)$_{11}$), 1.51 (s, 8H, 4 × -O−CH_2−CH$_2$), 3.39−4.08 (m, 42H, 4 × -N−CH_3, 4 × -N−CH_2, 2 × -O−CH_2−CH, 2 × -O−CH−CH$_2$, 4 × -O−CH_2−CH$_2$, 2 × -O−CH_2−CH_2−N, -O−CH_2−CH_2−O-). ESI-MS for $C_{72}H_{150}N_2O_6Br_2$: calcd 1301.82; found 569.9 [M^{+2}/2], 1220.0 [M^{+2} + Br^-]. Elemental analysis (%) for $C_{72}H_{150}N_2O_6Br_2$: calcd C 66.53, H 11.63, N 2.16; found C 66.12, H 11.71, N 2.29.

Lipid **3c***: Bis[D,L-N-(1,2,-di-O-tetradecyl-3-propyl)-N,N-dimethylammonium bromide] Bis(ethoxyethyl)ether.* ^{1}H NMR ($CDCl_3$, 300 MHz) δ: 0.83 (t, 12H, 4 × CH_3), 1.23 (br s, 88H, 4 × (CH_2)$_{11}$), 1.52 (s, 8H, 4 × -O−CH$_2$−CH_2), 3.41−4.10 (m, 46H, 4 × -N−CH_3, 4 × -N−CH_2, 2 × -O−CH_2−CH, 2 × -O−CH−CH$_2$, 4 × -O−CH_2−CH$_2$, 2 × -O−CH_2−CH_2−N, 2 × -O−CH_2−CH_2−O-). ESI-MS for $C_{74}H_{154}N_2O_7Br_2$: calcd 1345.88; found 592.4 [M^{+2}/2], 1264.0 [M^{+2} + Br^-]. Elemental analysis (%) for $C_{74}H_{154}N_2O_7Br_2 \cdot H_2O$: calcd C 65.26, H 11.55, N 2.06; found C 65.16, H 11.42, N 2.19.

Lipid **4a***: Bis[D,L-N-(1,2,-di-O-hexadecyl-3-propyl)-N,N-dimethylammonium bromide] Diethyl Ether.* ^{1}H NMR ($CDCl_3$, 300 MHz) δ: 0.83−0.87 (t, 12H, 4 × CH_3), 1.23 (br s, 104H, 4 × (CH_2)$_{13}$), 1.52 (s, 8H, 4 × -O−CH$_2$−CH_2), 3.39−4.43 (m, 38H, 4 × -N−CH_3, 4 × -N−CH_2, 2 × -O−CH_2−CH, 2 × -O−CH−CH$_2$, 4 × -O−CH_2−CH$_2$, 2 × -O−CH_2−CH_2−N). ESI-MS for $C_{78}H_{162}Br_2N_2O_5$: calcd 1369.99; found 603.7 [M^{+2}/2]. Elemental analysis (%) for $C_{78}H_{162}Br_2N_2O_5$: calcd C 68.49, H 11.94, N 2.05; found C 68.6, H 12.01, N 2.20.

Lipid **4b***: Bis[D,L-N-(1,2,-di-O-hexadecyl-3-propyl)-N,N dimethylammoniumbromide] Diethoxyethane.* ^{1}H NMR ($CDCl_3$, 300 MHz) δ: 0.83−0.87 (t, 12H, 4 × CH_3), 1.23 (br s, 104H, 4 × (CH_2)$_{13}$), 1.41 (s, 8H, 4 × -O−CH_2−CH$_2$), 3.39−4.08 (m, 42H, 4 × -N−CH_3, 4 × -N−CH_2, 2 × -O−CH_2−CH, 2 × -O−CH−CH$_2$, 4 × -O−CH_2−CH$_2$, 2 × -O−CH_2−CH_2−N, -O−CH_2−CH_2−O-). ESI-MS for $C_{80}H_{166}$ $Br_2N_2O_6$: calcd 1414.04; found 1332.1 [M^{+2} + Br^-]. Elemental analysis (%) for $C_{80}H_{166}$ $Br_2N_2O_6 \cdot 3H_2O$: calcd C 65.54, H 11.83, N 1.91; found C 65.72, H 11.53, N 2.01.

Lipid **4c***: Bis[D,L-N-(1,2,-di-O-hexadecyl-3-propyl)-N,N-dimethylammonium bromide] bis(ethoxyethyl)ether.* ^{1}H NMR ($CDCl_3$, 300 MHz) δ: 0.83 (t, 12H, 4 × CH_3), 1.23 (br s, 104H, 4 × (CH_2)$_{13}$), 1.52 (s, 8H, 4 × -O−CH$_2$−CH_2), 3.35−4.02 (m, 46H, 4 × -N−CH_2, 2 × -O−CH_2−CH, 2 × -O−CH−CH$_2$, 4 × -O−CH_2−CH$_2$, 2 × -O−CH_2−CH_2−N, 2 × -O−CH_2−CH$_2$−O-). ESI-MS for $C_{82}H_{170}Br_2N_2O_7$: calcd 1458.09; found 1376.1 [M^{+2} + Br^-]. Elemental analysis (%) for $C_{82}H_{170}Br_2N_2O_7 \cdot 4H_2O$: calcd C 64.45, H 11.74, N 1.83; found C 64.27, H 11.45, N 2.06.

Liposome Preparation. Individual lipid or its mixture with DOPE in the desired mole ratio was dissolved in chloroform in autoclaved Wheaton glass vials. Thin films were made by evaporation of the organic solvent under a steady stream of dry nitrogen. Last traces of organic solvent were removed by keeping these films under vacuum overnight. Freshly autoclaved water (Milli-Q) was added to individual film such that the final concentration of the cationic lipid was 1 mM. The mixtures were kept for hydration at 4 °C for 10−12 h and were repeatedly freeze−thawed (ice-cold water to 70 °C) with intermittent vortexing to ensure hydration. Sonication of these suspensions for 15 min in a bath sonicator at 70 °C afforded closed cationic liposomes as evidenced from transmission electron microscopy. Liposomes were prepared and kept under sterile conditions. Formulations were stable and, if stored frozen, possessed long shelf-life.

Transmission Electron Microscopy. Freshly prepared aqueous suspensions of each cationic lipid (1 mM) or lipoplex were examined under transmission electron microscopy by negative staining using 1% uranyl acetate. A 10 μL sample of the suspension was loaded onto Formvar-coated, 400 mesh copper grids and allowed to remain for 1 min. Excess fluid was wicked off the grids by touching their edges to filter paper, and 10 μL of 1% uranyl acetate was applied on the same grid after which the excess stain was similarly wicked off. The grid was air-dried for 30 min, and the specimens were observed under TEM (JEOL 200-CX) operating at an acceleration voltage of 120 keV. Micrographs were recorded at a magnification of 5000−20 000×.

Plasmid DNA. pEGFP-c3 (Clontech, USA), which encodes for an enhanced green fluorescence protein (GFP) under a CMV promoter, was amplified in *Escherichia coli* (DH5α) and purified using Qiagen Midi Prep Plasmid Purification protocol (Qiagen, Germany). Purity of the plasmid was checked by electrophoresis

on 1.0% agarose gel. Concentration of the DNA was estimated spectroscopically by measuring the absorption at 260 nm and confirmed by gel electrophoresis. The plasmid preparations showing a value of $OD_{260}/OD_{280} > 1.8$ were used.

Cell Culture. Cells (HeLa) were cultured in Dulbecco's Modified Eagle's Medium (DMEM; Sigma) supplemented with 10% fetal bovine serum (FBS) in T25 culture flasks (Nunc, Denmark) and were incubated at 37 °C in a humidified atmosphere containing 5% CO_2. Cells were regularly passaged by trypsinization with 0.1% trypsin (EDTA 0.02%, dextrose 0.05%, and trypsin 0.1%) in PBS (pH 7.2).

Cytotoxicity. Toxicity of each cationic lipid formulation toward HeLa cells was determined using 3-(4,5-dimethylthiazole-2-yl)-2,5-diphenyltetrazolium bromide (MTT) reduction assay following literature procedures (*57, 58*). Cytotoxicity levels of the lipid formulations optimal for transfection experiments were found out under conditions exactly similar for transfection conditions. Nearly 12 000 cells/well were plated in 96 well plates. After 24 h, optimized lipid/DOPE formulations were complexed with 0.2 μg of the DNA at various N/P ratios for 30 min. DNA−lipid complexes were added to the cells in the absence of serum. After 6 h of incubation, lipoplexes were removed and 200 μL of media with 10% FBS was added. After 42 h, 20 μL of MTT solution was added and the cells were incubated further for 4 h. Blue formazan crystals were seen when checked under microscope. Media was removed and 200 μL of DMSO was added per well. The absorbance was measured using a microtiter plate reader. The % viability was then calculated as $[\{A_{590}(\text{treated cells}) - \text{background}]/[A_{590}(\text{untreated cells}) - \text{background}\}] \times 100$.

Transfection Procedure. All transfection experiments were carried out in HeLa Cells in antibiotic-free media unless specified otherwise. In a typical experiment, 24-well plates were seeded with 45 000 cells/well in antibiotic-free media 24 h before transfection such that they were at least ~70% confluent at the time of transfection. For transfection, lipid formulation and DNA were serially diluted separately in DMEM containing no serum to have the required working stocks. DNA was used at a concentration of 0.8 μg/well unless specified otherwise. The lipid and DNA were complexed in a volume of 200 μL by incubating the desired amount of lipid formulation and DNA together at room temperature for about 30 min. The lipid concentrations were varied so as to obtain the required lipid/DNA (N/P) charge ratios. Charge ratios here present the ratio of charge on cationic lipid (in mol) to nucleotide base molarity and were calculated by considering the average nucleotide mass of 330. After 30 min of complexation, 200 μL of media was added to the complexes (final DNA concentration = 12.12 μM). Old media was removed from the wells, cells were washed with DMEM, and lipid−DNA complexes in 200 μL media were added to the cells. The plates were then incubated for 6 h at 37 °C in a humidified atmosphere containing 5% CO_2. At the end of incubation period, media was removed and cells were washed with DMEM; 500 μL of DMEM containing 10% FBS was added per well. Plates were further incubated for a period of 42 h before checking for the reporter gene expression. GFP expression was examined by fluorescence microscopy and was quantified by flow cytometry analysis. Control transfections were performed in each case by using commercially available transfection reagent Lipofectin using standard conditions specified by the manufacturer. All the experiments were done in duplicate, and results presented are the average of at least two such independent experiments done on two different days.

For transfections in the presence of serum, lipid and DNA were separately diluted in serum-free media as already mentioned and the complexation was done in serum-free media (200 μL) for 30 min. The complex was then diluted to 400 μL with DMEM containing 20% FBS so as to achieve a final serum concentration of 10%. The cells were then incubated with this complex for 6 h. At the end of the incubation period, medium was removed and cells were washed with DMEM; 200 μL of DMEM containing 10% FBS was added per well.

Gel Retardation. To examine the complexation of DNA with cationic lipid suspensions at different lipid-DNA ratios, we prepared lipid−DNA complexes at different lipid−DNA charge ratios in an identical manner as was done with transfection experiments. After 30 min of incubation, these complexes were electrophoretically run on a 1.0% agarose gel. The uncomplexed DNA moved out of well, but the DNA that was complexed with lipid remained inside the well (*59*).

Flow Cytometry. The reporter gene expression was examined by fluorescence microscopy at regular intervals and was quantified 48 h post-transfection by flow cytometry. Percentages of transfected cells were obtained by determining the statistics of cells fluorescing above the control level whereas nontransfected cells were used as the control. Approximately 10 000 cells were analyzed to achieve the statistical data, which have been presented as the average of at least two independent measurements. For flow cytometry analysis, ~48 h post-transfection, old media was removed from the wells; cells were washed with PBS and trypsinized by adding 100 μL of 0.1% trypsin. To each well, 200 μL of PBS containing 20% FBS was added. Duplicate cultures were pooled and analyzed by flow cytometry immediately using a Becton and Dickinson flow cytometer equipped with a fixed laser source at 488 nm.

FACS Analysis. FACS data were analyzed by public domain *WinMDI* software to eliminate data from cell debris (particles smaller than cells), dead cells, and clumps of two or more cells. Subcellular debris and clumps can be distinguished from single cells by size (estimated by the intensity of low angle forward scatter). Dead cells have lower forward scatter and higher side scatter than living cells. The FACS scans had been configured to display the fluorescence signals only from those particles with a specified set of scatter properties, namely, living single cells. This is called a scatter-gated fluorescence analysis. Therefore, the data from dead cells had been eliminated by gating out brightly fluorescent cells.

Membrane Hydration Studies. Membrane hydration studies on lipid vesicles were performed using Paldan as a hydrated probe (*50*). All the fluorescence experiments were carried out on sonicated lipid suspensions using a lipid-to-probe ratio 1000:3. The width of excitation and emission slit was 5 nm. Generalized polarization of emission (GP) was calculated using the equation

$$GP_{em} = \frac{I_{440} - I_{490}}{I_{440} + I_{490}} \quad (1)$$

where I_{440} and I_{490} represent the fluorescent intensities at 440 and 490 nm. For the GP values reported herein, an excitation wavelength of 350 nm was used. The lower the GP value is, the higher the hydration (*50*). Therefore, we calculated the parameter called membrane hydration by inversing and normalizing the GP values such that the parameter values increase with increase in membrane hydration.

Differential Scanning Calorimetry. Multilamellar vesicles of 1 mM concentration were prepared in degassed water as mentioned above, and their thermotropic behavior was investigated by high-sensitivity differential scanning calorimetry using a CSC-4100 model, multicell differential scanning calorimeter (Calorimetric Science Corporation, Utah, USA). A baseline thermogram was obtained using degassed water (0.5 mL) in all the ampoules including the reference cell to normalize cell to cell differences. Samples were taken in the cells such that the differences in weight with the baseline experiment to the sample

Scheme 1[a]

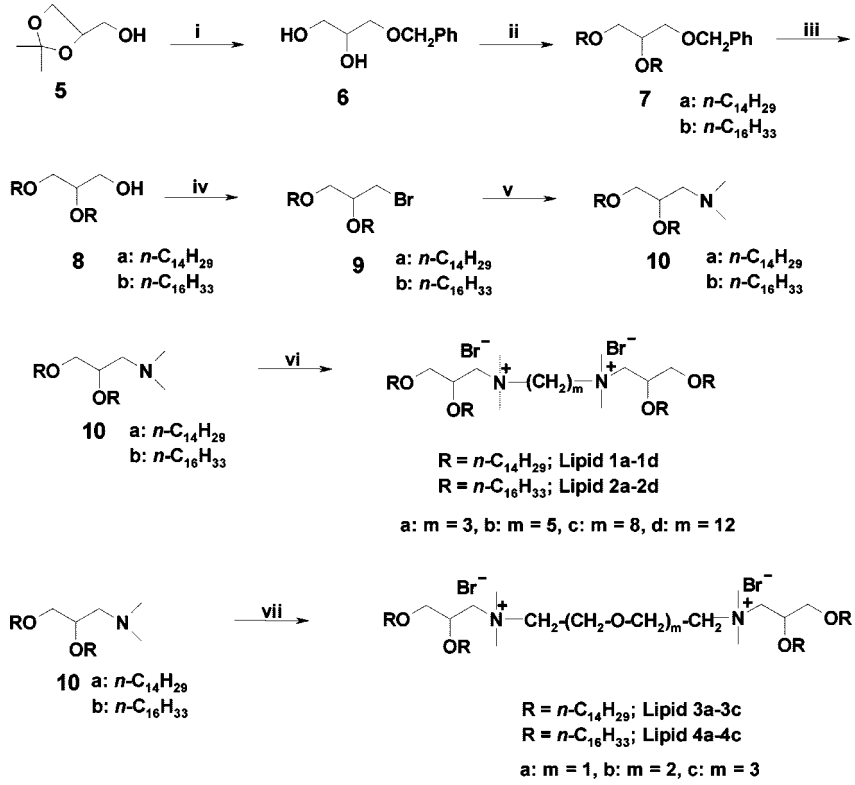

[a] Reagents and Conditions. (i) (a) KOH, $PhCH_2Cl$, benzene, reflux, 24 h; and (b) *p*-TsOH, MeOH−H_2O, rt, 5 h; overall 57% isolated yield. (ii) *n*-$C_{14}H_{29}Br$ or *n*-$C_{16}H_{33}Br$, KOH, benzene (Dean-Stark), reflux, 24 h, 85−90%; (iii) 10% Pd−C, H_2 (40 psi), MeOH−EtOAc (1:1), 24 h, 90−94%; (iv) CBr_4, Ph_3P, CH_2Cl_2, 10 °C (30 min), rt (12 h), quantitative yield; (v) Me_2NH (excess), MeOH−EtOAc, rt, 24 h, 95%; (vi) $Br(CH_2)_mBr$, MeOH−EtOAc (2:1), 80 °C, screw-top pressure tube, 48−96 h, 40−50%; (vii) $BrCH_2(CH_2OCH_2)_mCH_2Br$, MeOH−EtOAc (2:1), 80 °C, screw-top pressure tube, 48−96 h, 40−50%.

run were less than 0.001 g in the respective ampoules. The measurements were carried out in the temperature range 20−90 °C. The scan rate was 20 °C per hour for all the lipids. The thermograms for vesicular suspensions were obtained by subtracting the respective baseline thermogram from the sample thermogram using the software CpCalc provided by the manufacturer.

Ethidium Bromide Intercalation Assay (*60*). Fluorescence emission due to ethidium bromide (EB) at 590 nm was monitored in a Hitachi model F-4500 spectrofluorimeter (λ_{ex} = 526 nm with 10 nm slit widths for both excitation and emission). Typically, emission was measured for EB (25 μM) in 5 mM HEPES, 0.1 M NaCl, pH 7.4 buffer. To this, CT-DNA (40 μM) was added and again emission due to EB upon intercalative complexation with DNA was measured at 25 °C. Then, an aliquot of a given liposome (2 μM) was added into performed EB/CT−DNA complex in 5 mM HEPES (pH 7.4) buffer. This resulted in the fluorescence quenching due to displacement of EB molecules from intercalated sites caused due to distortion in the DNA double-helix upon addition of cationic lipid aggregates. Progressive addition of SDS (2 μM aliquot) to cationic lipid/DNA complex formed as described resulted in the release of DNA from cationic lipid/DNA complex. Due to release of DNA, EB gets reintercalated and fluorescence emission increases. If F_0 is the fluorescence intensity (FI) of unintercalated and F_{max} is the FI of fully intercalated EB, and F_x is the FI for a given concentration of liposome or SDS, then % FI = $(F_x - F_0)/(F_{max} - F_0)$.

RESULTS AND DISCUSSION

Chemistry. The pseudoglyceryl backbone, which is similar to the glycerol-based, naturally occurring phospholipids, was considered for the synthesis of new gemini cationic lipids. Fourteen gemini lipids differing in the hydrocarbon chains and the length and nature of the spacers between the cationic headgroups have been synthesized using previously reported procedures (*61*). First, the CH_2OH group of the primary building block, 1,2-isopropylidene glycerol **5**, was protected in the form of benzyl ether (Scheme 1). Then, the isopropylidene group was removed by treatment with *p*-TsOH in aqueous MeOH to obtain **6** in 57% isolated yield (Scheme 1). The diol **6** was fully alkylated using 3 equiv of *n*-tetradecyl bromide (*n*-$C_{14}H_{29}Br$) or *n*-hexadecyl bromide (*n*-$C_{16}H_{33}Br$) in the presence of KOH under reflux conditions to give **7a** or **7b** in 85−90% yields, which upon hydrogenolysis at 40 psi pressure in the presence of 10% Pd−C afforded **8a**/**8b** in quantitative yields. In a subsequent step, alcohols (**8a**, **8b**) were converted to the corresponding bromides (**9a**, **9b**) in quantitative yields by reaction with PPh_3/CBr_4 in dry dichloromethane. Bromides **9a**, **9b** were then reacted with Me_2NH in EtOAc−MeOH (1:1) mixture to give **10a** and **10b** in ∼95% yields. The gemini lipids have been synthesized from the precursor 1,2-di-*O*-tetradecyl-3-(dimethylamino)]propane (**10a**) or 1,2-di-*O*-hexadecyl-3-(dimethylamino)]propane (**10b**) by reacting it with corresponding α,ω-dibromoalkanes or α,ω-dibromoethoxyalkanes in pressure tube at 80 °C for 48−96 h. All the newly synthesized lipids including gemini lipids have been purified by repeated precipitation with mixtures of MeOH, EtOAc, and acetone. The resulting lipids were characterized by ^1H NMR, mass spectroscopy, and elemental analysis, and the spectral and analytical data were consistent with their assigned structures.

Aggregate Formation from Cationic Gemini Lipids and Mixed Liposome formation with DOPE. Liposomes could be conveniently prepared from each gemini lipid alone or with

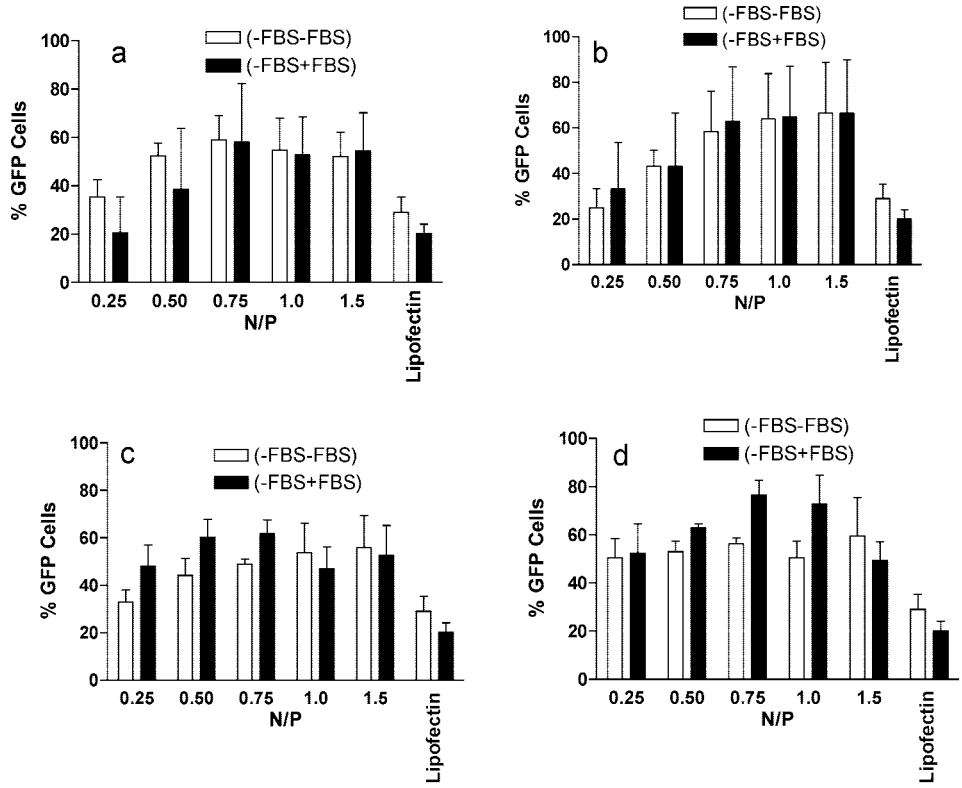

Figure 2. Transfection efficiencies of gemini lipids using optimized lipid/DOPE formulations at various N/P ratios in the absence (-FBS − FBS) and the presence (-FBS + FBS) of serum. (a) **1a**; (b) **1b**; (c) **1c**; (d) **1d**. Concentration of the DNA = 0.8 μg/well. Data expressed as number of GFP positive cells as obtained from flow cytometry analysis.

naturally occurring helper lipid 1,2-dioleoyl-L-α-glycero-3-phosphatidyl ethanolamine (DOPE) by first subjecting the films of lipid mixtures to hydration, repeated freeze−thaw cycles, followed by sonication at 70 °C for 15 min. All the lipid molecules mentioned here formed stable, optically clear suspensions in water. Gemini lipids with oxyethylene spacers have been found to get dispersed more easily than the lipids with polymethylene spacers. Generally, TEM examination of air-dried, aqueous suspensions revealed the existence of closed aggregate structures for all the gemini lipids (not shown) (*50, 51*). Vesicles were prepared under sterile conditions and were resonicated for 5 min at room temperature before transfection experiments. The vesicular suspensions were sufficiently stable, and no precipitation was observed within three months if stored at 4 °C.

Transfection Biology. *Optimization of Lipid/DOPE Ratio.* The neat lipid suspensions were found to show low transfection efficacies (not shown). Naturally occurring lipids such as DOPE has been known to increase the efficiency of transfection in lipid-mediated gene transfer applications (*62*) Accordingly gemini lipid/DOPE mixed lipid suspensions were examined for transfection. In order to determine the most effective formulation, transfections with identical lipid/DNA mole ratio (or N/P ratio) by variation of the mole ratios of gemini lipids in DOPE were done. To determine the optimized transfection efficiency, both the number of transfected cells and the mean fluorescence intensity were considered. The mean fluorescence intensities (MFI) defined for GFP-positive cells reveal that the level of GFP expression with a higher MFI value correlates positively with high GFP expression (*19*). These data were obtained from flow cytometric analysis. All the lipids except lipid **3c** showed maximum transfection efficiency at a lipid/DOPE mole ratio of 1:2, whereas the lipid/DOPE optimization ratio for lipid **3c** was found to be 1:3.

Optimization of Lipid/DNA Charge Ratio. The cationic liposomes of gemini lipids were prepared in an optimized lipid/DOPE mole ratio, and EGFP-c3 plasmid DNA was used as the reporter gene across the lipid/DNA charge ratios from 0.25:1 to 1.5:1. It should be noted that 1 mol of cationic gemini lipid possesses two units of charges. Therefore, the transfections were performed in lipid/DNA mole ratios from 0.125:1 to 0.75:1. Gemini lipids showed significantly enhanced transfection efficiency as compared to commercially available reagent, Lipofectin. Lipofectin is a monomeric lipid, structurally related to the present set of lipids, and is based on a 1:1(w/w) ratio of DOTMA/DOPE formulation. Among gemini lipids, transfection efficiency was found to be dependent upon the length and nature of the spacer between headgroups and also on the hydrocarbon chain lengths.

Polymethylene Spacer-Based Gemini Lipids. Among lipids **1a**−**1d**, lipid **1b** possessing a pentamethylene (-$(CH_2)_5$-) spacer was found to be the best transfecting agent, and with the further increase in the length of the spacer, the transfection efficiency decreased as shown in Figure 2. However, in the presence of serum, lipid **1d** possessing a longer spacer (-$(CH_2)_{12}$- showed enhanced transfection efficiency, transfecting nearly 70% of the cells. DOPE mixed lipid **1a**−**1d** formulations possessing *n*-$C_{14}H_{29}$ chains were found to be better transfecting agents than the lipid formulations **2a**−**2d** bearing *n*-$C_{16}H_{33}$ chains. Among lipids **2a**−**2d**, **2a** and **2b** were found to be better transfecting agents than other analogues as presented in Figure 3. However, the major drawback of gemini lipid **2a** formulation was its lack of compatibility with serum, as the transfection efficiency decreased drastically in the presence of 10% serum. In case of other lipid (**2b**−**2d**) formulations, there was little decrease in the transfection efficacies in the presence of 10% serum. Lipid **1a**−**1d** formulations showed maximum transfection efficiency at lipid/DNA charge ratio of 1.0 and transfection profiles

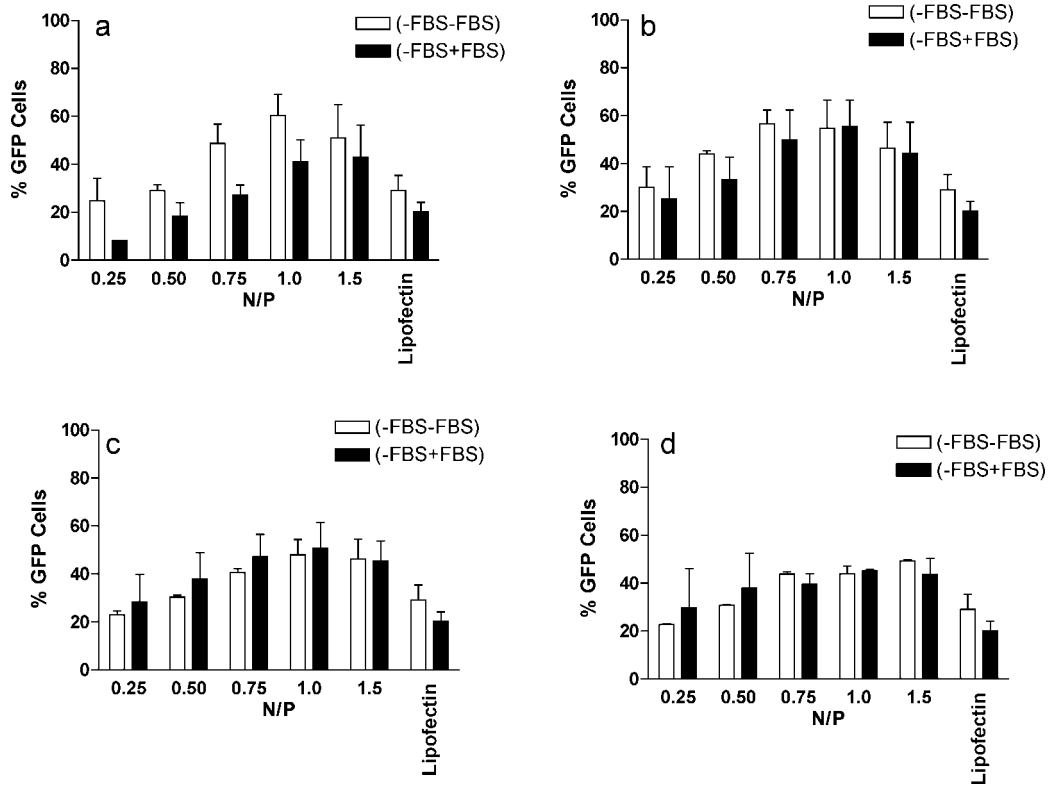

Figure 3. Transfection efficiencies of gemini lipids using optimized lipid/DOPE formulations at various N/P ratios in the absence (-FBS − FBS) and the presence (-FBS + FBS) of serum. (a) **2a**; (b) **2b**; (c) **2c**; (d) **2d**. Concentration of the DNA = 0.8 μg/well. Data expressed as number of GFP positive cells as obtained from flow cytometry analysis.

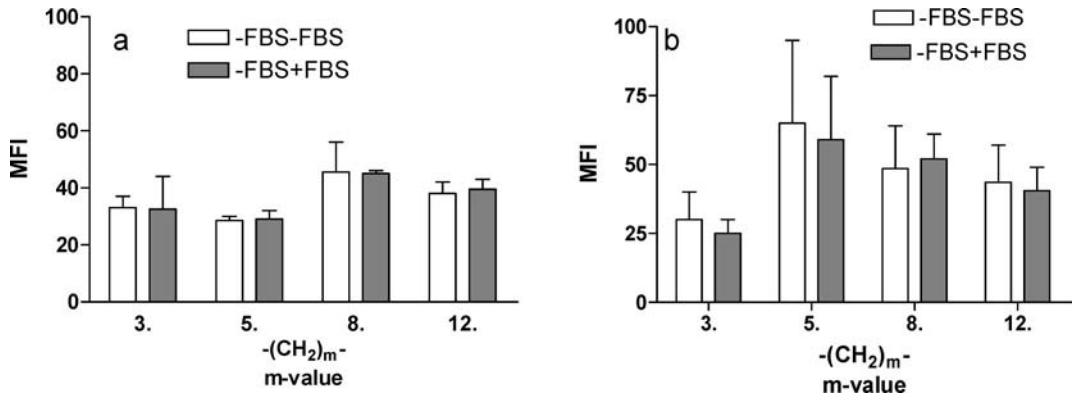

Figure 4. Effect of the length of the spacer on the MFI observed in the case of gemini lipid formulations in the absence (-FBS − FBS) and the presence (-FBS + FBS) of serum (a) *n*-$C_{14}H_{29}$ based gemini lipids (b) *n*-$C_{16}H_{33}$ based gemini lipids. Concentration of the DNA = 0.8 μg/well. Data expressed as MFI as obtained from flow cytometry analysis.

followed a bell-shaped graph. With lipid **2a**−**2d** formulations, maximum transfection efficiencies were achieved at the lipid/DNA charge ratio of 1.5. Comparative transfection profiles showed that the gemini lipids bearing *n*-$C_{14}H_{29}$ chains were better transfecting agents as compared to the lipids bearing *n*-$C_{16}H_{33}$ chains and the optimized length of the spacer was -$(CH_2)_5$- toward this end.

Mean fluorescence intensities (MFI) observed from the FACS scans after the transfection with gemini lipid formulations in the absence and presence of serum is shown in Figure 4. MFI provides an estimate of the average amount of protein expressed inside the transfected cells, which also indirectly indicates the amount of the DNA delivered inside the cells. MFI results suggest that the amount of the DNA delivered by gemini lipid **1a**−**1d** formulations was comparatively less than that in case of **2a**−**2d**. Gemini lipid **2b** formulation possessing *n*-$C_{16}H_{33}$ chains and a -$(CH_2)_5$- spacer showed maximum MFI. With an increase in the length of the spacer in the gemini lipid, the MFI decreased. As mentioned earlier, the gemini lipid **1b** possessing *n*-$C_{14}H_{29}$ chains with a -$(CH_2)_5$- spacer showed maximum transfection activity in terms of the number of cells, but the MFI observed here was nearly half that of lipid **2b/DOPE** formulation. These results suggest that the lipid **1b/DOPE** formulation transfects the maximum number of cells, whereas lipid **2b/DOPE** transfects maximum amount of the DNA into the cells among the polymethylene spacer-based gemini lipids.

Oxyethylene Spacer-Based Gemini Lipids. Transfection efficacy of oxyethylene spacer based gemini lipids are shown in Figures 5–8. In the absence of serum, DOPE-containing lipid (**3a**−**3c**) formulations were found to be as effective as Lipofectin in terms of the number of transfected cells (Figure 5), whereas to our great surprise, in the presence of 10% serum, the transfection efficacy of gemini lipids (**3a**−**3c**) increased dramatically. Lipid **3a-DOPE** formulation was able to transfect

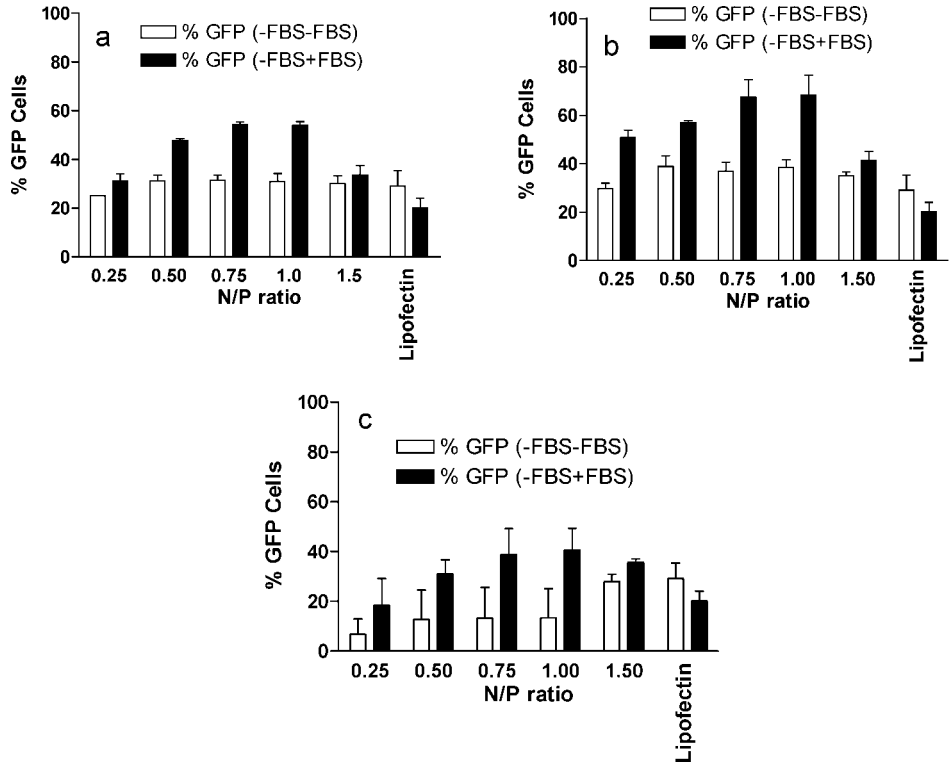

Figure 5. Transfection efficiencies of gemini lipids using optimized lipid/DOPE formulations at various N/P ratios in the absence (-FBS − FBS) and the presence (-FBS + FBS) of serum. (a) **3a**; (b) **3b**; (c) **3c**. Concentration of the DNA = 0.8 μg/well. Data expressed as number of GFP-positive cells as obtained from flow cytometry analysis.

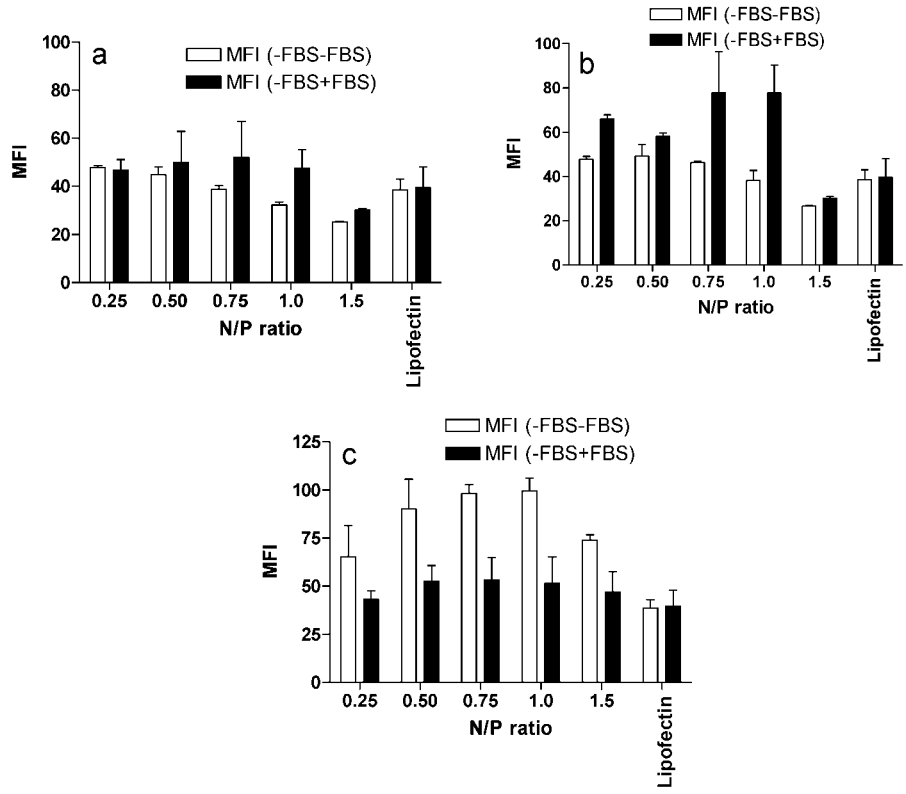

Figure 6. Transfection efficiencies of gemini lipids using optimized lipid/DOPE formulations at various N/P ratios in the absence (-FBS − FBS) and the presence (-FBS + FBS) of serum. (a) **3a**; (b) **3b**; (c) **3c**. Concentration of the DNA = 0.8 μg/well. Data expressed as MFI as obtained from flow cytometry analysis.

nearly 45% of cells as compared to ∼15% transfection efficacy of Lipofectin in presence of 10% serum conditions. More than 60% of the cells transfected in the case of lipid **3b** formulation in the presence of serum as compared to ∼40% without serum. Lipid **3c-DOPE** formulation was found to be less efficient in gene delivery both in the absence and in the presence of serum conditions. MFI observed from flow cytometric analysis for transfections by gemini lipids **3a**−**3c** are shown in Figure 6. In

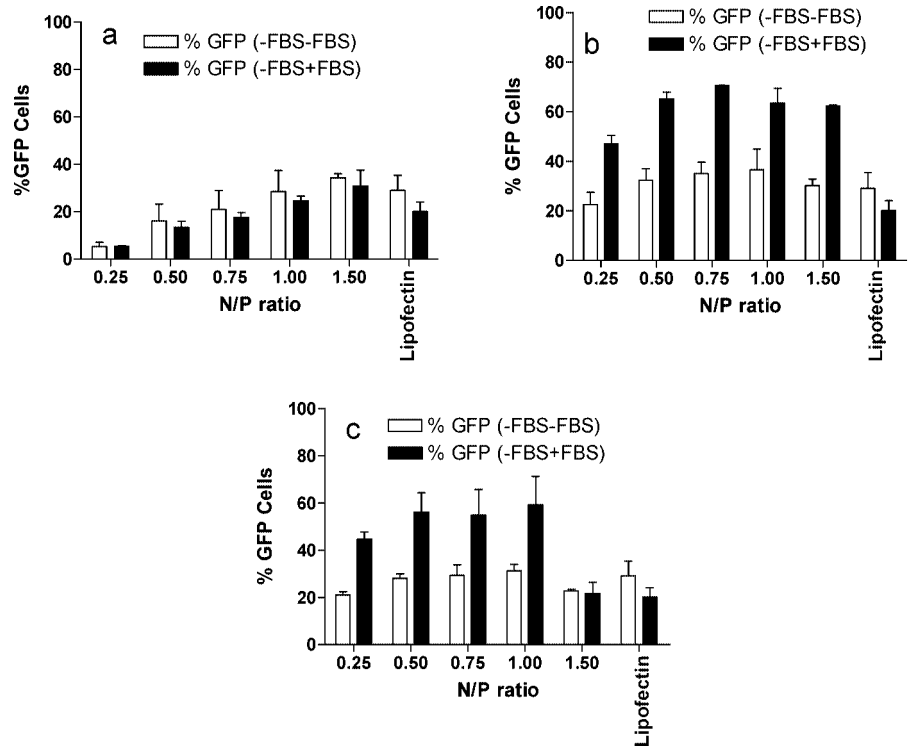

Figure 7. Transfection efficiencies of gemini lipids using optimized lipid/DOPE formulations at various N/P ratios in the absence (-FBS − FBS) and the presence (-FBS + FBS) of serum. (a) **4a**; (b) **4b**; (c) **4c**. Concentration of the DNA = 0.8 μg/well. Data expressed as number of GFP-positive cells as obtained from flow cytometry analysis.

the absence of serum, lipid **3a** and **3b** formulations showed nearly the same MFI as observed in the case of Lipofectin, whereas lipid **3c** formulation was able to deliver more than twice the DNA compared to Lipofectin in the absence of serum as observed by MFI from flow cytometric analysis. In the presence of serum, there was no change in MFI in the case of lipid **3a** formulation, whereas lipid **3b** formulation showed 2-fold enhancement in the MFI in the presence of serum. However, in case of lipid **3c** formulation, there was a decrease in MFI in the presence of serum. Overall, lipid **3b** formulation was able to transfect nearly twice the number of cells with more than two times the MFI as compared to Lipofectin, and lipid **3c** formulation was able to transfect less cells with nearly three times the MFI as compared to Lipofection in the absence of serum.

Among DOPE-containing **4a**−**4c** formulations, all were found to be as effective as Lipofectin in the absence of serum (Figure 7), whereas at least 4-fold enhancement was observed in the number of transfected cells in case of lipid **4b** formulation in the presence of serum (Figure 8). Lipid **4c** formulation showed nearly 2-fold enhancement in the number of transfected cells in the presence of serum as compared to Lipofectin. In terms of MFI, all (**4a**−**4c**) formulations were found to be as effective as Lipofectin with or without serum, except lipid **4c** formulation, which showed nearly 2-fold increase in MFI as compared to Lipofectin. Overall, lipid formulations **4b** and **4c** were highly effective in the presence of serum as compared to that without serum and Lipofectin.

Cell Viability. MTT-based cell viability assays were performed in HeLa cells at the optimized lipid/DNA charge ratios (N/P) used in the transfection experiments. Percentage cell viabilities of all the gemini lipids except lipids **1c** and **2d** were found to be more than 75% (Figure 9). Lipid **1c** and **2d** formulations showed nearly 70% cell viability.

Characterization of Lipid/DNA Complexes. *Gel Electrophoresis.* To characterize the electrostatic binding interactions between the plasmid DNA and the mixed cationic liposomes as a function of different N/P charge ratios (or lipid/DNA mole ratios), we performed conventional electrophoretic gel retardation assays using optimized cationic lipid/DOPE liposomes (Figures 10 and 11). Polymethylene spacer-based gemini lipid formulations except **1d** and **2d** were able to retard the plasmid DNA from the well at N/P ratio of 0.75, whereas **1d** and **2d** showed retardation at N/P ratio of 1.0. Among oxyethylene spacer-based gemini lipids, **4a** and **4c** were found to be most effective in DNA retardation, showing complexion at N/P ratio of 0.75, whereas in case of other lipid formulations, plasmid DNA retardation was observed at N/P ratio of 1.0. It should be noted that every gemini lipid molecule possesses two hard cationic charges, which indicates that the whole plasmid DNA gets retarded at lipid/DNA mole ratio of 0.375−0.5.

Electron Microscopy. To get further insights into the lipid−DNA complexation, we examined these complexes at the optimized lipid/DNA charge ratios by transmission electron microscopy (*11*, *35*, *39*, *63–66*). Representive electron micrographs of the lipid−DNA complexes are shown in Figures 12 and 13. Most of the lipid formulations formed spherical lipid−DNA complexes, whereas lipid **1d** lipoplexes did not possess regular shapes. Lipoplexes from lipid **4a** and **4d** showed the existence of clustering of small spheres and were found to be smaller than other lipoplexes observed.

Role of Surface Hydration. Cationic lipids interact with the plasmid DNA *via* electrostatic interactions, mainly between the headgroup region of the lipid molecules and the phosphate backbone of the DNA. Therefore, the alterations in the headgroups should influence the interactions of the liposomes with the DNA. In turn, this lipid−DNA complexation directly influences the transfection activities of the liposomes. In the case of gemini lipids, we have another parameter that influences these interactions, which is the spacer between the headgroups in each gemini lipid. As in the case of gemini lipids, this spacer is embedded between the headgroups; it influences the hydration behavior of the headgroups in gemini lipid liposomes depending on its folding at the interfaces. The hydration on the membrane

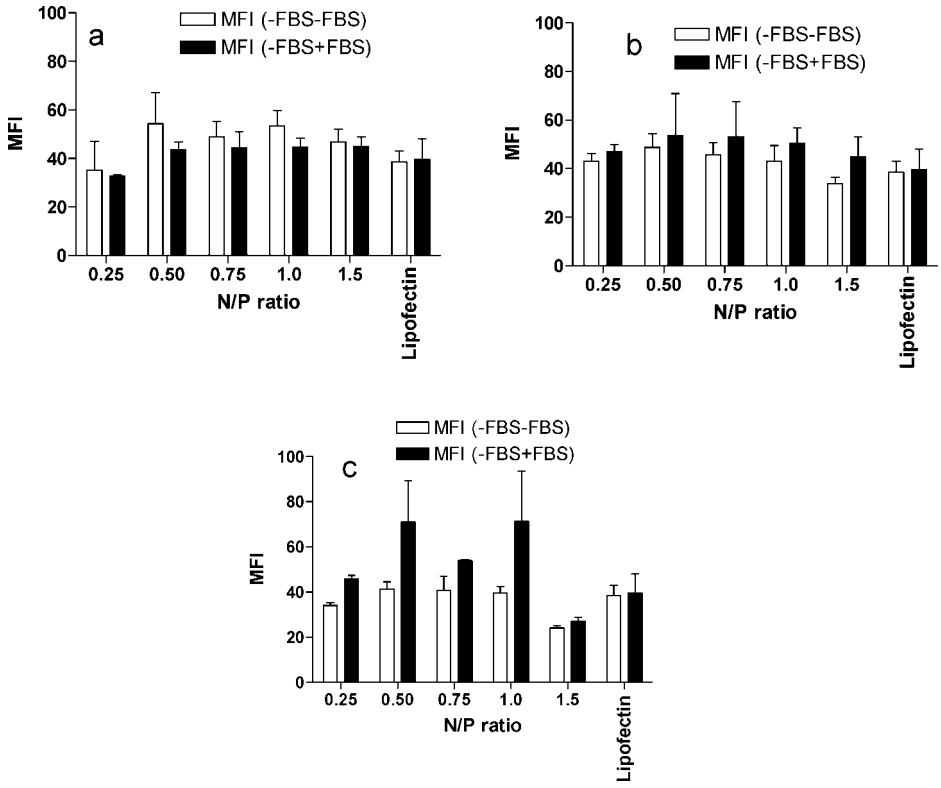

Figure 8. Transfection efficiencies of gemini lipids using optimized lipid/DOPE formulations at various N/P ratios in the absence (-FBS − FBS) and the presence (-FBS + FBS) of serum. (a) **4a**; (b) **4b**; (c) **4c**. Concentration of the DNA = 0.8 μg/well. Data expressed as MFI as obtained from flow cytometry analysis.

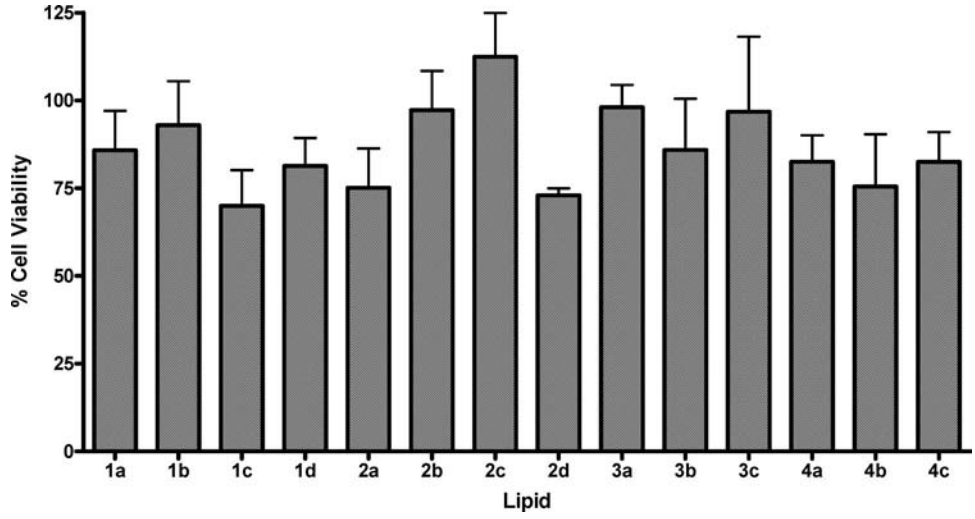

Figure 9. MTT assay-based cellular cytotoxicity of gemini lipids against HeLa cells. The percent viability values shown are averages of duplicate experiments performed on the same day.

surface will also have direct bearing on the complexation between the DNA and the liposomes. DNA has a spine of hydration, and during its complexation with lipid counterion, the "ordered" water molecules are released, giving rise to an entropic gain. When lipid membranes are highly hydrated, there is also a possibility of exchange of water molecules bound to DNA with that associated with membranes depending on the hydration requirements. The balance of these two aspects determines the efficiency of liposome−DNA complexation.

In the present investigation, as we have varied the length and the nature of the spacer from flexible hydrophobic polymethylenic to hydrophilic oxyethylene segments, we also investigated the effect of hydration environment around the liposomes on transfection activities. In case of lipid molecules **1a**−**1d**, transfection activities were found to increase with the decrease in hydration, as maximum transfection activity was found with lipid **1c** formulation having -$(CH_2)_8$- spacer, which also demonstrated the minimum hydration in this series of lipids (Figure 14). Similarly in the case of lipid molecules **2a**−**2d**, lipid **2b** afforded maximum transfection activity as compared to other lipid molecules in the series, which (except **2a**) showed high hydration as compared to **2b** liposomes. Low transfection activity of lipid **2a** formulation in spite of low hydration could be because of the high phase transition temperature of its liposomes (see below). In the case of the gemini lipids possessing an oxyethylene spacer, we found that, in general, with an increase in apparent hydration, the transfection activity increased as compared to the gemini lipids possessing a

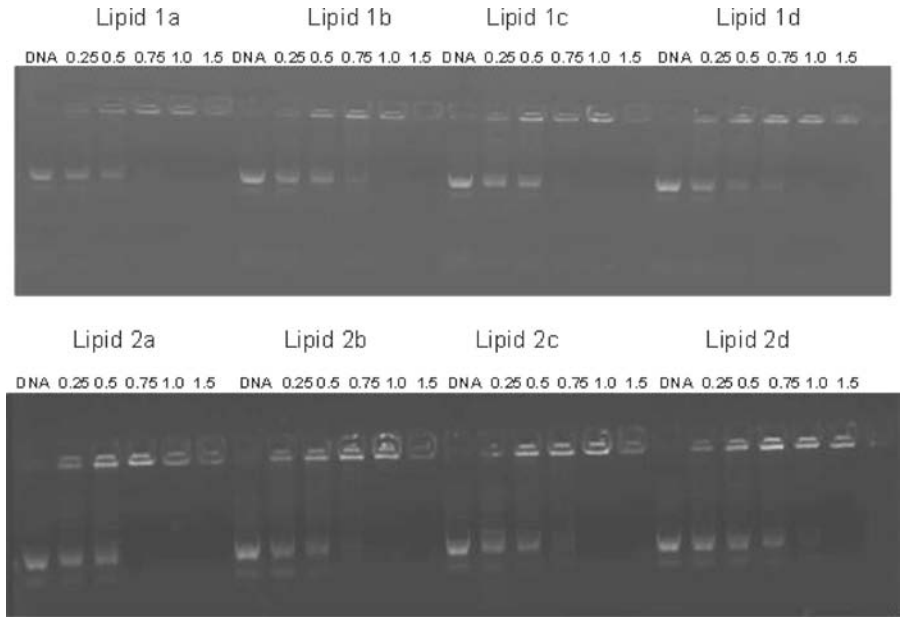

Figure 10. Electrophoretic gel patterns for lipoplex-associated DNA in gel retardation for gemini lipids possessing polymethylene spacers. The N/P ratios are indicated at the top of each lane.

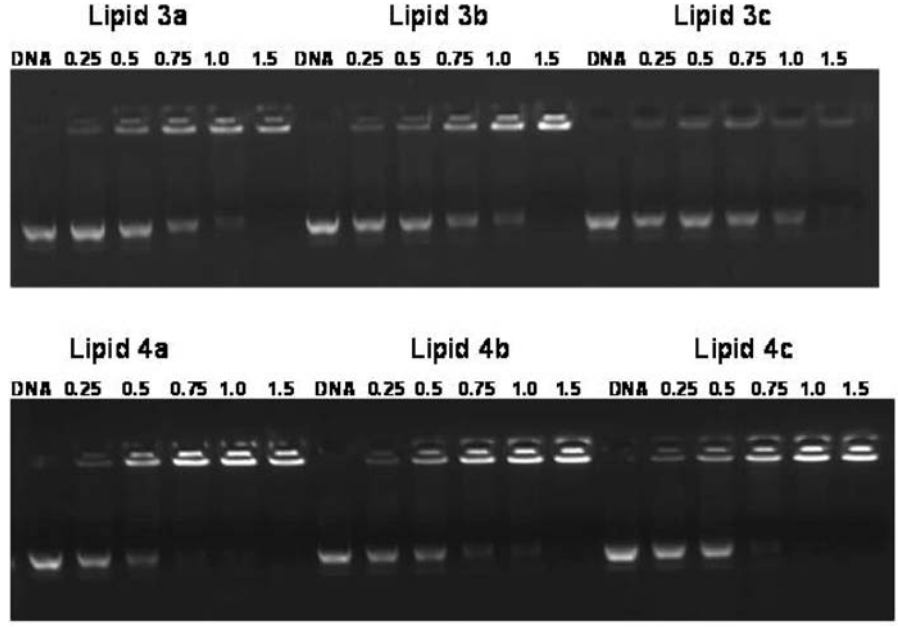

Figure 11. Electrophoretic gel patterns for lipoplex-associated DNA in gel retardation for gemini lipids possessing oxyethylene spacers. The N/P ratios are indicated at the top of each lane.

polymethylene spacer, where transfection activity increased with a decrease in the membrane hydration (Figure 14). In the case of lipid molecules **3a**−**3c**, the transfection activities increased with an increase in hydration around the liposomes. Similarly, in the case of **4a**−**4c**, the transfection activity decreased with a decrease in lipid surface hydration, except **4c** where transfection decreased despite the increase in lipid hydration. However, the lipid **4c** formulation was the one found to be the most effective recipe even in the presence of high percentages of serum. This complex behavior of this lipid formulation is immediately apparent. This opposite behavior of oxyethylene spacer-based liposomes with respect to its polymethylene counterpart indicates that the DNA complexation by gemini lipids strongly depends upon the nature of the spacer, as oxyethylene spacers might be folded in a way facilitating some different mode of interaction with DNA as compared to those with polymethylene spacers.

Lipid Melting Temperatures and Transfection Activity. Lipid phase transition temperatures (T_m) for lipid formulations are shown in Table 1. As expected, the lipids possessing *n*-$C_{16}H_{33}$ chains showed higher T_m compared to the lipids bearing *n*-$C_{14}H_{29}$ chains. Among the polymethylene spacer based gemini lipids, **1a** and **2a** bearing a -$(CH_2)_3$- spacer possessed the highest T_m among its other analogues having the same hydrocarbon chain lengths. The high T_m values of the lipid aggregates could be responsible for their low transfection activity, as at 37 °C, the corresponding membranes may be too "rigid" to effect good transfection. Similarly, among oxyethylene spacer based gemini lipids, **3a** and **4a** bearing a -CH_2−CH_2−O−CH_2−CH_2- spacer possessed the highest T_m among all the lipids in the series. It was found that lipid **3a** showed the lowest transfection activity within the series, whereas lipid **4a** showed reasonable MFI but the number of transfected cells was very low.

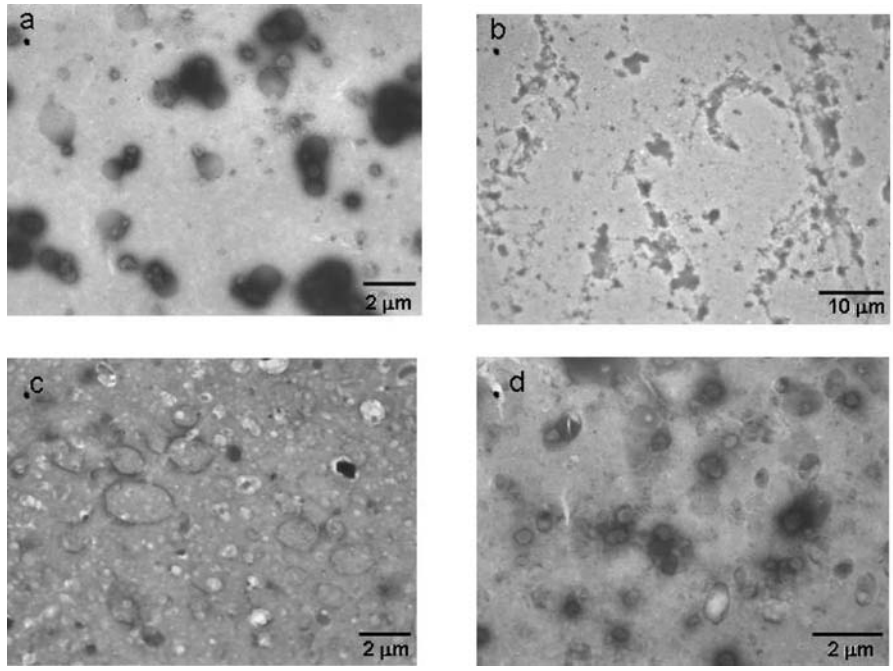

Figure 12. Representive transmission electron micrographs for the lipoplexes prepared from gemini lipid/DOPE liposome/DNA complexes at the optimized N/P ratio. (a) **1b**; (b) **1d**; (c) **2b**; (d) **2c**.

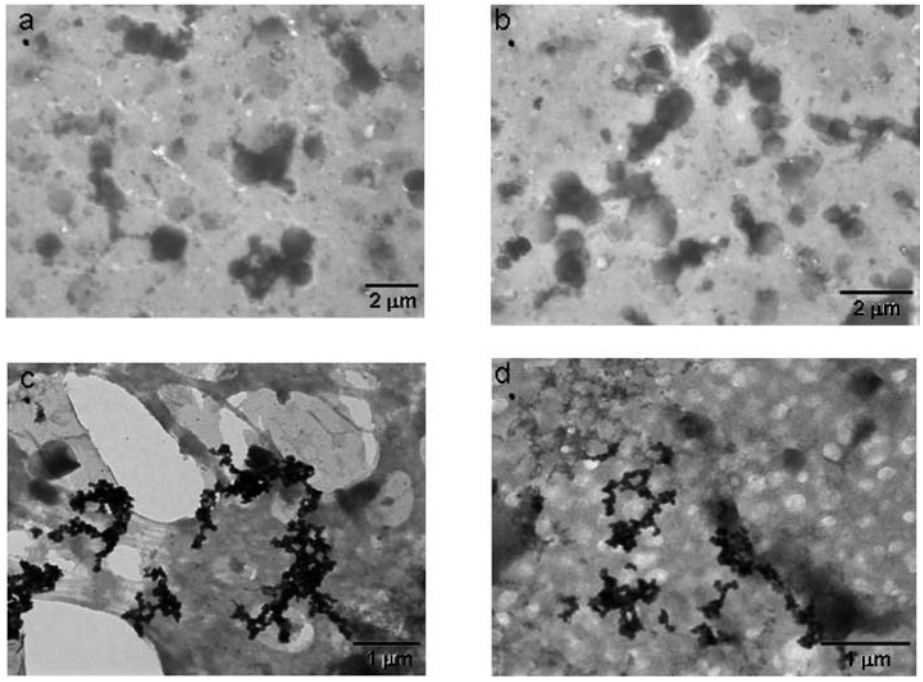

Figure 13. Representive transmission electron micrographs for the lipoplexes prepared from gemini lipid/DOPE liposome/DNA complexes at the optimized N/P ratio. (a) **3a**; (b) **3b**; (c) **4a**; (d) **4d**.

It is evident from the hydration and calorimetric studies that the transfection properties of pseudoglyceryl gemini lipid formulations are dependent upon the hydration and T_m of their liposome formulations, which are in turn controlled by hydrocarbon chain lengths and the length and nature of the spacer between the cationic ammonium headgroups. Although gene trafficking inside eukaryotic cells is a very complicated phenomenon, in order to understand variation in the transfection activity and lipid−DNA complexation of different lipids, we performed ethidium bromide exclusion assay and anionic SDS induced release of the DNA from preformed lipid−DNA complexes.

DNA Complexation by Cationic Liposomes. Various complexes of cationic liposomes with calf-thymus DNA (CT-DNA) were examined using several physical methods to gain insight into the nature of interaction among the various components. We first looked into the effect of the addition of different positively charged liposomes to CT-DNA. For this, the fluorescence experiments were performed by exposing *ds*-DNA molecules to ethidium bromide (EB) that acts as a fluorescent probe upon intercalation with DNA base pairs. Progressive addition of a given cationic liposome into the EB/CT-DNA complex led to a gradual quenching of the EB fluorescence eventually leading to saturation. Quenching of the

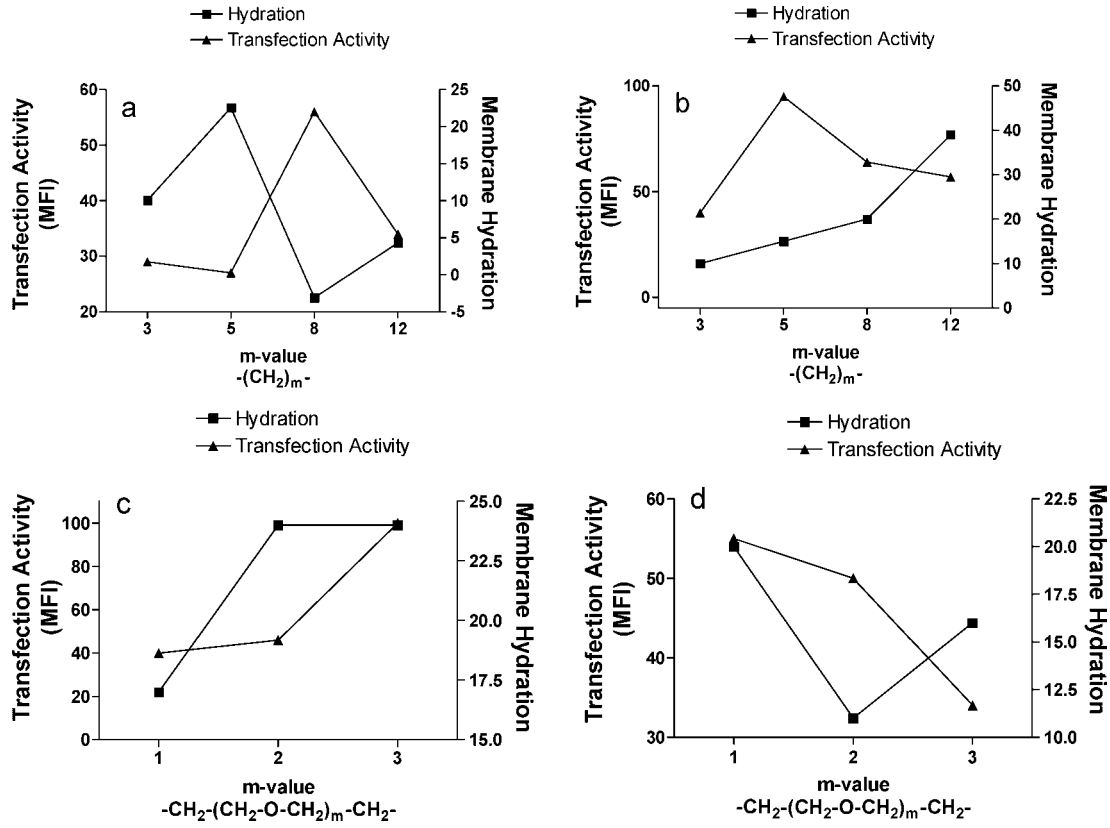

Figure 14. Effect of hydration of the gene transfection efficacies of pseudoglyceryl gemini lipids differing in the nature and length of the spacer and possessing different hydrocarbon chain lengths. (a) and (c) *n*-$C_{14}H_{29}$ hydrocarbon chain based lipids, (b) and (d) *n*-$C_{16}H_{33}$ hydrocarbon chain based lipids. Membrane hydration was calculated from the GP values using Paldan as membrane probe as discussed in the Experimental Procedures section.

Table 1. Phase Transition Temperatures of Gemini Lipid Aggregates

lipid	T_m	lipid	T_m	lipid	T_m	lipid	T_m
1a	43.2	**2a**	59.3	**3a**	38.9	**4a**	53.9
1b	28.6	**2b**	46.2	**3b**	26.6	**4b**	44.2
1c	30.6	**2c**	48.6	**3c**	27.1	**4c**	44.9
1d	29.6	**2d**	47.3				

fluorescence intensity (FI) at 590 nm upon addition of cationic liposomes is due to the gradual release of free EB out of the EB/CT-DNA complex (*67*). This could be explained on the basis of the cationic liposome induced compaction formation of DNA, which facilitates the dissociation of EB from the EB−DNA complex. Although the fluorescence quenching was seen in all the instances, there were significant differences in the minimum concentration (*c*) of the liposomes required for inducing saturation in the fluorescence quenching. The percentage decreases of FI (FI %) until saturation for given liposomes also were found to depend on the molecular structure of the cationic lipid. Figure 15 shows how various cationic lipid suspensions promote dissociation of EB from EB−DNA complexes.

Lipid **2d** induced nearly 90% dissociation of EB at N/P ratio of 1.0, whereas **2a** was able to induce ∼90% dissociation at N/P ratio of 2.0. The maximum ethidium bromide dissociation for liposomes from **2b** and **2c** were found to be at N/P ratio 1.0−2.0. For all the liposomes showing complexion with DNA, the saturation value of FI that could be attained ranged from 80% to 90% of the original value. This value is plotted as the percentage decrease in FI as shown in Figure 15. The % decrease in FI is a direct measure of the strength of the DNA−cationic liposome complex. This also reflects the ability of the given cationic liposome to complex with DNA. However, the ability of a lipid aggregate to attain saturation appeared to be related to the lipid molecular structure. The ease of the abilities of the cationic lipids possessing *n*-$C_{16}H_{33}$ chains to bring about compaction of the DNA followed the order **2d** > **2c** > **2b** > **2a**. It indicates that the binding of the liposomes depends on the spacer length between the cationic headgroups in a gemini lipid. Lipids bearing longer spacers bind at lower N/P ratios, whereas those with shorter spacers bind at higher N/P ratios. However, there was no such pronounced effect of the spacer on DNA complexation when liposomes of *n*-$C_{14}H_{29}$ chain-based lipids were used, as such lipid suspensions showed ∼90% decrease in FI at N/P ratio of 0.75. Among oxyethylene spacer-based lipids, the order was **3a** > **3b** > **3c**. Among the oxyethylene spacer-based lipids with *n*-$C_{16}H_{33}$ chains, the order was **4a** > **4c** > **4b**. This clearly indicates that, among oxyethylene spacer-based gemini lipids, lipids possessing shorter oxyethylene spacers are more efficient at DNA binding.

SDS-Induced Release of DNA from Cationic Liposome−DNA Complexes. It is generally believed that the endosomal layers of the cell, which are rich in negatively charged lipids, facilitate release of DNA from its complexes with cationic liposomes. To study this aspect in a model situation, we have used negatively charged SDS micelles to induce release of DNA from various cationic liposome−DNA complexes. An aqueous solution of EB (25 μM) gave a broad λ_{max} at 590 nm when excited at 526 nm. In the presence of CT-DNA (40 μM base molarity), the FI at 590 nm due to intercalated EB increases more than 5-fold. Addition of an aqueous solution of a given cationic liposome to the EB/DNA complex resulted in quenching of the FI as discussed previously. Progressive addition of SDS triggers the dissociation of cationic lipids from the cationic liposome/DNA complex. This in turn facilitates the reintercalation of EB into CT-DNA that gets released from the lipoplex. The increase in the fluorescence intensity reached a plateau at

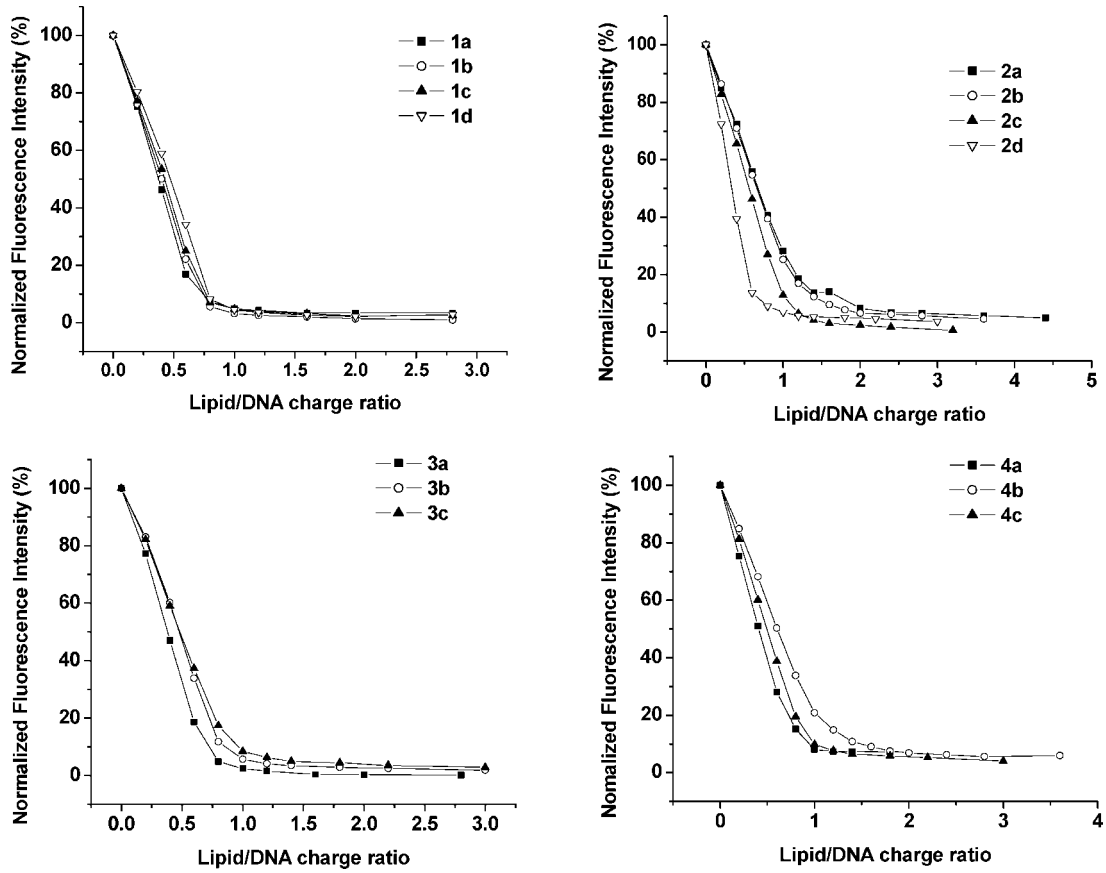

Figure 15. Release of the ethidium bromide (EB) from the DNA−EB complexes upon addition of the liposomes at different lipid/DNA charge ratios.

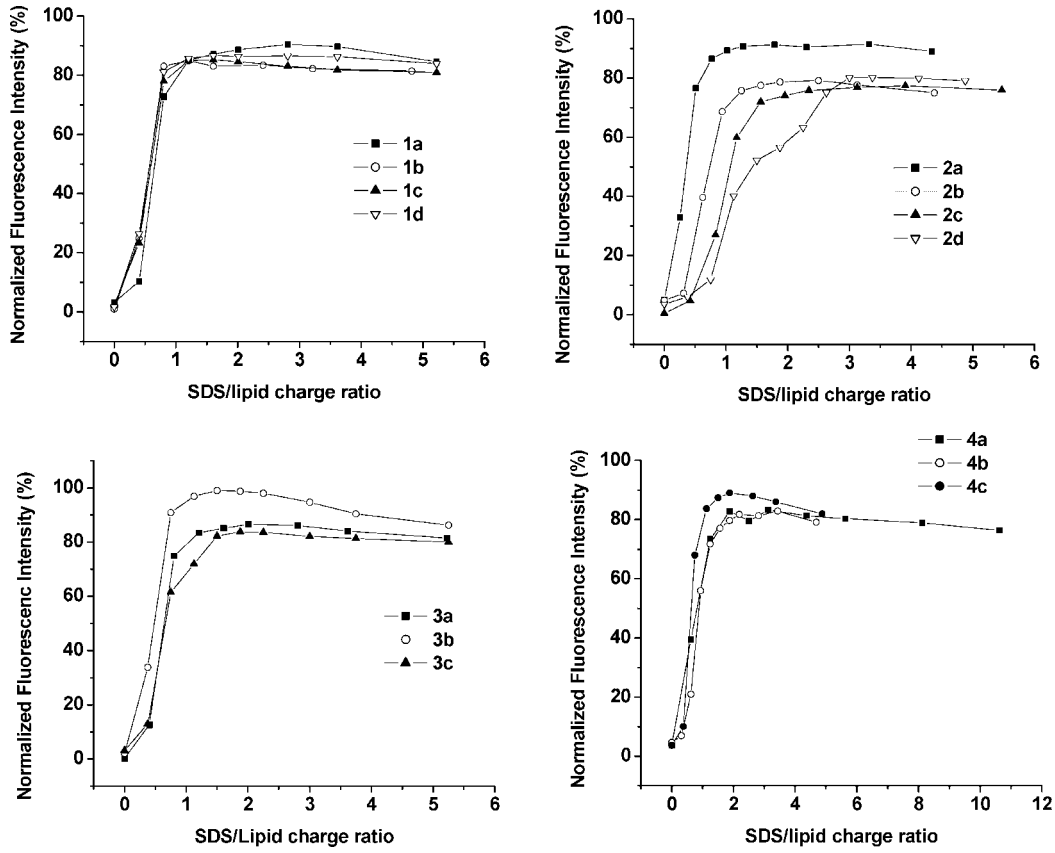

Figure 16. Reintercalation of the ethidium bromide to the DNA upon release of the DNA from lipid/DNA complexes upon addition of SDS at different SDS/lipid charge ratios.

a particular concentration of SDS for a given cationic liposome/DNA complex. Beyond this concentration, further addition of SDS did not result in any additional extent of fluorescence recovery as shown in Figure 16.

Examination of the profiles obtained by SDS promoted the DNA release from a given cationic liposome/DNA complex revealed significant differences. For instance, the amount of SDS required to reach a saturation value of FI was not the same for different cationic liposome/DNA complexes. The complexes of liposomal **2a** with DNA showed 90% recovery of FI at SDS/lipid charge ratio of 1.0, whereas **2d** liposomes needed the highest SDS concentration for DNA release from complexes. The order of ease of fluorescence recovery upon addition of SDS was **2a** > **2b** > **2c** > **2d**. At SDS/lipid charge ratio of 0.75, the order of recovery of fluorescence among n-$C_{14}H_{29}$ chain-based lipids was **1b** > **1d** > **1c** > **1a**, and among oxyethylene-based gemini lipids **3b** > **3a** > **3c**. Among oxyethylene spacer-based gemini lipids with n-$C_{16}H_{33}$ chains, addition of SDS induced release of liposomes **4c** from the DNA much more easily as compared to other lipids of the series. It should be noted that this lipid-based formulation was found to be the best transfecting agent in the presence of serum.

CONCLUSIONS

We have undertaken a chemical biological investigation on the gene delivery efficacies of pseudoglyceryl-based gemini lipid based liposomes. Fourteen gemini lipids, differing in the hydrocarbon chain lengths and the nature of spacer between the headgroups, were investigated. These lipids formed stable suspensions in water easily. These gemini lipid formulations showed a significant enhancement in the gene transfection activities as compared to that of Lipofectin, a monomeric lipid related to this series of gemini lipids investigated herein.

Serum is known to be a major impediment to the applications of cationic lipids for their use in vivo (*68*). So, there is always a challenge to design such cationic lipids, which can be useful for transfection studies in the presence of serum. The present set of gemini lipids were found to be serum compatible, and even the presence of serum caused enhancement of the gene transfection activities of the lipid **3b**, **4b**, and **4c** formulations. We have been able to reduce their cytotoxicity and enhance the transfection efficiency significantly. The simplicity of the use of pseudoglyceryl backbone and their high chemostability and long shelf-lives make these formulations particularly attractive for further applications in biological research.

Although the DNA delivery to eukaryotic cells involves several steps (*69*) and the precise mechanisms of many of these steps are not clearly understood at the molecular level at this point in time, it would be important to note that some correlation could be achieved between the molecular structures of these new gemini lipids and their membrane level properties and transfection properties. Regardless of the actual mechanism for transfection mediated by this class of gemini lipid formulations, the results obtained with these gemini lipids should be of interest to researchers working in the design of non-viral vectors.

ACKNOWLEDGMENT

This work was supported by Department of Biotechnology, Government of India, New Delhi, India. Avinash Bajaj is thankful to the CSIR for senior research fellowship. We thank Dr. Omana Joy and Ms. Padmini for their help during the work.

LITERATURE CITED

(1) Verma, I. M., and Somia, N. (1997) Gene therapy - promises, problems and prospects. *Nature 389*, 239–242.

(2) Hattori, Y., and Maitani, Y. (2005) Folate-linked nanoparticle-mediated suicide gene therapy in human prostate cancer and nasopharyngeal cancer with herpes simplex virus thymidine kinase. *Cancer Gene Ther. 12*, 796–809.

(3) Pakunlu, R. I., Wang, Y., Saad, M., Khandare, J. J., Starovoytov, V., and Minko, T. (2006) In vitro and in vivo intracellular liposomal delivery of antisense oligonucleotides and anticancer drug. *J. Controlled Release 114*, 153–162.

(4) Bhattacharya, S., and Bajaj, A. (2005) Recent advances in lipid molecular design. *Curr. Opin. Chem. Biol. 9*, 647–655.

(5) Aissaoui, A., Martin, B., Kan, E., Oudrhiri, N., Hauchecorne, M., Vigneron, J.-P., Lehn, J.-M., and Lehn, P. (2004) Novel cationic lipids incorporating an acid-sensitive acylhydrazone linker: synthesis and transfection properties. *J. Med. Chem. 47*, 5210–5223.

(6) Martin, B., Sainlos, M., Aissaoui, A., Oudrhiri, N., Hauchecorne, M., Vigneron, J. P., Lehn, J. M., and Lehn, P. (2005) The design of cationic lipids for gene delivery. *Curr. Pharm. Des. 11*, 375–394.

(7) Sainlos, M., Hauchecorne, M., Oudrhiri, N., Zertal-Zidani, S., Aissaoui, A., Vigneron, J.-P., Lehn, J. M., and Lehn, P. (2005) Kanamycin A-derived cationic lipids as vectors for gene transfection. *ChemBioChem 6*, 1023–1033.

(8) Behr, J. P., Demeneix, B., Loeffler, J. P., and Perez-Mutul, J. (1989) Efficient gene transfer into mammalian primary endocrine cells with lipopolyamine-coated DNA. *Proc. Natl. Acad. Sci. U.S.A. 86*, 6982–6986.

(9) Gao, X., and Huang, L. (1991) A novel cationic liposome reagent for efficient transfection of mammalian cells. *Biochem. Biophys. Res. Commun. 179*, 280–285.

(10) Okayama, R., Noji, M., and Nakanishi, M. (1997) Cationic cholesterol with a hydroxyethylamino head group promotes significantly liposome-mediated gene transfection. *FEBS Lett. 408*, 232–234.

(11) Smisterova, J., Wagenaar, A., Stuart, M. C. A., Polushkin, E., Brinke, G. t., Hulst, R., Engberts, J. B. F. N., and Hoekstra, D. (2001) Molecular shape of the cationic lipid controls the structure of cationic lipid/dioleylphosphatidylethanolamine-DNA complexes and the efficiency of gene delivery. *J. Biol. Chem. 276*, 47615–47622.

(12) Ewert, K., Ahmad, A., Evans, H. M., Schmidt, H. W., and Safinya, C. R. (2002) Efficient synthesis and cell-transfection properties of a new multivalent cationic lipid for nonviral gene delivery. *J. Med. Chem. 45*, 5023–5029.

(13) Heyes, J. A., Niculescu-Duvaz, D., Cooper, R. G., and Springer, C. J. (2002) Synthesis of novel cationic lipids: effect of structural modification on the efficiency of gene transfer. *J. Med. Chem. 45*, 99–114.

(14) Kumar, V. V., Pichon, C., Refregiers, M., Guerin, B., Midoux, P., and Chaudhuri, A. (2003) Single histidine residue in head-group region is sufficient to impart remarkable gene transfection properties to cationic lipids: evidence for histidine-mediated membrane fusion at acidic pH. *Gene Ther. 10*, 1206–1215.

(15) Dileep, P. V., Antony, A., and Bhattacharya, S. (2001) Incorporation of oxyethylene units between hydrocarbon chain and pseudoglyceryl backbone in cationic lipid potentiates gene transfection efficiency in the presence of serum. *FEBS Lett. 509*, 327–331.

(16) Ewert, K., Ahmad, A., Evans, H. M., and Safinya, C. R. (2005) Cationic lipid-DNA complexes for non-viral gene therapy: relating supramolecular structures to cellular pathways. *Exp. Opin. Biol. Ther. 5*, 33–53.

(17) Bhattacharya, S., and Dileep, P. V. (2004) Cationic oxyethylene lipids. Synthesis, aggregation, and transfection properties. *Bioconjugate Chem. 15*, 508–519.

(18) Narang, A. S., Thoma, L., Miller, D. D., and Mahato, R. I. (2005) Cationic lipids with increased DNA binding affinity for nonviral gene transfer in dividing and nondividing cells. *Bioconjugate Chem. 16*, 156–168.

(19) Chabaud, P., Camplo, M., Payet, D., Serin, G., Moreau, L., Barthelemy, P., and Grinstaff, M. W. (2006) Cationic nucleoside lipids for gene delivery. *Bioconjugate Chem. 17*, 466–472.

(20) Ewert, K. K., Evans, H. M., Zidovska, A., Bouxsein, N. F., Ahmad, A., and Safinya, C. R. (2006) A columnar phase of dendritic lipid-based cationic liposome-DNA complexes for gene delivery: hexagonally ordered cylindrical micelles embedded in a DNA honeycomb lattice. *J. Am. Chem. Soc. 128*, 3998–4006.

(21) Ilies, M. A., Seitz, W. A., Johnson, B. H., Ezell, E. L., Miller, A. L., Thompson, E. B., and Balaban, A. T. (2006) Lipophilic pyrylium salts in the synthesis of efficient pyridinium-based cationic lipids, gemini surfactants, and lipophilic oligomers for gene delivery. *J. Med. Chem. 49*, 3872–3887.

(22) Jewell, C. M., Hays, M. E., Kondo, Y., Abbott, N. L., and Lynn, D. M. (2006) Ferrocene-containing cationic lipids for the delivery of DNA: Oxidation state determines transfection activity. *J. Controlled Release 112*, 129–138.

(23) Gardner, R. A., Belting, M., Svensson, K., and Phanstiel, O., IV. (2007) Synthesis and transfection efficiencies of new lipophilic polyamines. *J. Med. Chem. 50*, 308–318.

(24) Koiwai, K., Tokuhisa, K., Karinaga, R., Kudo, Y., Kusuki, S., Takeda, Y., and Sakurai, K. (2005) Transition from a normal to inverted cylinder for an amidine-bearing lipid/pDNA complex and its excellent transfection. *Bioconjugate Chem. 16*, 1349–1351.

(25) Isobe, H., Nakanishi, W., Tomita, N., Jinno, S., Okayama, H., and Namamura, E. (2006) Nonviral gene delivery by tetraamino fullerene. *Mol. Pharmaceut. 3*, 124–136.

(26) Kish, P. E., Tsume, Y., Kijek, P., Lanigan, T. M., Hilfinger, J. M., and Roessler, B. J. (2007) Bile acid-oligopeptide conjugates interact with DNA and facilitate transfection. *Mol. Pharmaceut. 4*, 95–103.

(27) Antipina, M. N., Schulze, I., Dobner, B., Langer, A., and Brezesinski, G. B. (2007) Physicochemical investigation of a lipid with a new core structure for gene transfection:2-amino-3-hexadecyloxy-2-(hexadecyloxymethyl)propan-1-ol. *Langmuir 23*, 3919–3926.

(28) Seo, Y. J., Jeong, H. S., Bang, E.-K., Hwang, G. T., Jung, J. H., Jang, S. K., and Kim, B. H. (2006) Cholesterol-linked fluorescent molecular beacons with enhanced cell permeability. *Bioconjugate Chem. 17*, 1151–1155.

(29) Hardy, J. G., Kostiainen, M. A., Smith, D. K., Gabrielson, N. P., and Pack, D. W. (2006) Dendrons with spermine surface groups as potential building blocks for nonviral vectors in gene therapy. *Bioconjugate Chem. 17*, 172–178.

(30) Fayazpour, F., Lucas, B., Alvarez-Lorenzo, C., Sanders, N. N., Demeester, J., and Smedt, S. C. D. (2006) Physicochemical and transfection properties of cationic hydroxyethylcellulose/DNA nanoparticles. *Biomacromolecules 7*, 2856–2862.

(31) Ghosh, Y. K., Visweswariah, S. S., and Bhattacharya, S. (2000) Nature of linkage between the cationic headgroup and cholesteryl skelton controls gene transfection efficiency. *FEBS Lett. 473*, 341–344.

(32) Ghosh, Y. K., Visweswariah, S. S., and Bhattacharya, S. (2002) Advantage of the ether linkage between the positive charge and the cholesteryl skeleton in cholesterol-based amphiphiles as vectors for gene delivery. *Bioconjugate Chem. 13*, 378–384.

(33) Rosen, M. J., and Tracy, D. J. (1998) Gemini surfactants. *J. Surfactants Deterg. 1*, 547–554.

(34) Menger, F. M. (1999) New and unusual surfactants. Book of Abstracts, 218th ACS National Meeting, New Orleans, Aug. 22−26, COLL-003.

(35) Jennings, K. H., Marshall, I. C. B., Wilkinson, M. J., Kremer, A., Kirby, A. J., and Camilleri, P. (2002) Aggregation properties of a novel class of cationic gemini surfactants correlate with their efficiency as gene transfection agents. *Langmuir 18*, 2426–2429.

(36) Kirby, A. J., Camilleri, P., Engberts, J. B. F. N., Feiters, M. C., Nolte, R. J. M., Soderman, O., Bergsma, M., Bell, P. C., Fielden, M. L., Garcia Rodriguez, C. L., Guedat, P., Kremer, A., McGregor, C., Perrin, C., Ronsin, G., and Van Eijk, M. C. P. (2003) Gemini surfactants: new synthetic vectors for gene transfection. *Angew. Chem., Int. Ed. 42*, 1448–1457.

(37) Bell, P. C., Bergsma, M., Dolbnya, I. P., Bras, W., Stuart, M. C. A., Rowan, A. E., Feiters, M. C., and Engberts, J. B. F. N. (2003) Transfection mediated by gemini surfactants: engineered escape from the endosomal compartment. *J. Am. Chem. Soc. 125*, 1551–1558.

(38) Bombelli, C., Faggioli, F., Luciani, P., Mancini, G., and Sacco, M. G. (2005) Efficient transfection of DNA by liposomes formulated with cationic gemini amphiphiles. *J. Med. Chem. 48*, 5378–5382.

(39) Bombelli, C., Borocci, S., Diociaiuti, M., Faggioli, G., Galantini, L., Luciani, P., Mancini, G., and Sacco, M. G. (2005) Role of the spacer of cationic gemini amphiphiles in the condensation of DNA. *Langmuir 21*, 10271–10274.

(40) Bello, C., Bombelli, C., Borocci, S., di Profio, P., and Mancini, G. (2006) Role of the spacer stereochemistry on the aggregation properties of cationic gemini surfactants. *Langmuir 22*, 9333–9338.

(41) Wang, C., Wettig, S. D., Foldvari, M., and Verrallb, R. E. (2007) Synthesis, characterization, and use of asymmetric pyrenyl-gemini surfactants as emissive components in DNA-lipoplex systems. *Langmuir 23*, 8995–9001.

(42) Bhattacharya, S., De, S., and George, S. K. (1997) Synthesis and vesicle formation from novel pseudoglyceryl dimeric lipids. Evidence of formation of widely different membrane organizations with exceptional thermotropic properties. *Chem. Commun.* 2287–2288.

(43) Bhattacharya, S., and De, S. (1999) Synthesis and vesicle formation from dimeric pseudoglyceryl lipids with (CH_2)m spacers: pronounced m-value dependence of thermal properties, vesicle fusion, and cholesterol complexation. *Chem. Eur. J. 5*, 2335–2347.

(44) Bhattacharya, S., and De, S. (1999) Vesicle formation from dimeric ion-paired amphiphiles. Control over vesicular thermotropic and ion-transport properties as a function of intra-amphiphilic headgroup separation. *Langmuir 15*, 3400–3410.

(45) Ahmed, O. A. A., Pourzand, C., and Blagbrough, I. S. (2006) Varying the unsaturation in N4,N9-dioctadecanoyl spermines: nonviral lipopolyamine vectors for more efficient plasmid DNA formulation. *Pharm. Res. 23*, 31–40.

(46) Chien, P.-Y., Wang, J., Carbonaro, D., Lei, S., Miller, B., Sheikh, S., Ali, S. M., Ahmad, M. U., and Ahmad, I. (2005) Novel cationic cardiolipin analog-based liposome for efficient DNA and small interfering RNA delivery in vitro and in vivo. *Cancer Gene Ther. 12*, 321–328.

(47) Grunner, S. M., and Jain, M. K. (1985) X-ray diffraction demonstrates that phosphatidyldiacylglycerol and phosphatidylcholesterol are not lamellar above the main transition temperature. *Biochim. Biophys. Acta 818*, 352.

(48) DeRosa, M., and Gambacorta, A. (1988) The lipids of archaebacteria. *Prog. Lipid Res. 27*, 153–175.

(49) Hubner, W., Mantsch, H. H., and Kates, M. (1991) Intramolecular hydrogen bonding in cardiolipin. *Biochim. Biophys. Acta 1066*, 166–174.

(50) Bhattacharya, S., and Bajaj, A. (2007) Membrane-forming properties of pseudoglyceryl backbone based gemini lipids possessing oxyethylene spacers. *J. Phys. Chem. B 111*, 2463–2472.

(51) Bhattacharya, S., and Bajaj, A. (2007) Thermotropic and hydration studies of membranes formed from gemini pseudoglyceryl lipids possessing polymethylene spacers. *Langmuir 23*, 8988–8994.

(52) Bhattacharya, S., and Bajaj, A. (2007) Membrane-forming properties of gemini lipids possessing aromatic backbone between the hydrocarbon chains and the cationic headgroup. *J. Phys. Chem. B 111*, 13511–13519.

(53) Bajaj, A., Kondiah, P., and Bhattacharya, S. (2007) Design, synthesis and in vitro gene transfection efficacies of cholesterol based gemini lipids and their serum compatibility: a structure activity relationship. *J. Med. Chem. 50*, 2432–2442.

(54) Bajaj, A., Kondaiah, P., and Bhattacharya, S. (2007) Synthesis and gene transfer activities of novel serum compatible cholesterol based gemini lipids possessing oxy-ethylene type spacers. *Bioconjugate Chem. 18*, 1537–1546.

(55) Bajaj, A., Kondaiah, P., and Bhattacharya, S. (2007) Gene transfer efficacies of novel cationic gemini lipids possessing aromatic backbone and oxy-ethylene spacers. *Biomacromolecules 9*, 991–999.

(56) Bajaj, A., Paul, B., Indi, S. S., Kondaiah, P., and Bhattacharya, S. (2007) Effect of the hydrocarbon chain lengths and spacer lengths on gene transfection efficacies of gemini lipids based on aromatic backbone. *Bioconjugate Chem. 18*, 2144–2158.

(57) Mosmann, T. (1983) Rapid colorimetric assay for cellular growth and survival: application to proliferation and cytotoxicity assays. *J. Immunol. Methods 65*, 55–63.

(58) Hansen, M. B., Nielsen, S. E., and Berg, K. (1989) Re-examination and further development of a precise and rapid dye method for measuring cell growth/cell kill. *J. Immunol. Methods 119*, 203–210.

(59) Choi, J. S., Lee, E. J., Jang, H. S., and Park, J. S. (2001) New cationic liposomes for gene transfer into mammalian cells with high efficiency and low toxicity. *Bioconjugate Chem. 12*, 108–113.

(60) Bajaj, A., Mishra, K. S., Kondaiah, P., and Bhattacharya, S. (2008) Effect of the headgroup variation on the gene transfer properties of cholesterol based cationic lipids possessing ether linkage. *Biochim. Biophys. Acta, Biomembr. 1778*, 1222–1236.

(61) Kates, M., Chan, T. H., and Stanacev, N. Z. (1963) Aliphatic diether analogs of glyceride-derived lipids. I. Synthesis of D-dialkyl glyceryl ethers. *Biochemistry 2*, 394–397.

(62) Felgner, J. H., Kumar, R., Sridhar, C. J., Wheeler, Y. J., Tsai, R., Border, P., Ramsey, M., Martin, C. N., and Felgner, P. L. (1994) Enhanced gene delivery and mechanism studies with a novel series of cationic lipid formulations. *J. Biol. Chem. 269*, 2550–2561.

(63) Bhattacharya, S., and Mandal, S. S. (1997) Interaction of surfactants with DNA. Role of hydrophobicity and surface charge on intercalation and DNA melting. *Biochim. Biophys. Acta Biomembr. 1323*, 29–44.

(64) May, S., and Ben-Shaul, A. (1997) DNA-lipid complexes: stability of honeycomb-like and spaghetti-like structures. *Biophys. J. 73*, 2427–2440.

(65) Huebner, S., Battersby, B. J., Grimm, R., and Cevc, G. (1999) Lipid-DNA complex formation: reorganization and rupture of lipid vesicles in the presence of DNA as observed by cryoelectron microscopy. *Biophys. J. 76*, 3158–3166.

(66) Simberg, D., Danino, D., Talmon, Y., Minsky, A., Ferrari, M. E., Wheeler, C. J., and Barenholz, Y. (2001) Phase behavior, DNA ordering, and size instability of cationic lipoplexes. *J. Biol. Chem. 276*, 47453–47459.

(67) Bhattacharya, S., and Mandal, S. S. (1998) Evidence of inter-lipidic ion-pairing in anion-induced DNA release from cationic amphiphile-DNA complexes. mechanistic implications in transfection. *Biochemistry 37*, 7764–7777.

(68) Li, S., Tseng, W. C., Stolz, D. B., Wu, S. P., Watkins, S. C., and Huang, L. (1999) Dynamic changes in the characteristics of cationic lipidic vectors after exposure to mouse serum: implications for intravenous lipofection. *Gene Ther. 6*, 585–594.

(69) Xu, Y., and Szoka, F. C., Jr. (1996) Mechanism of DNA Release from cationic liposome/DNA complexes used in cell transfection. *Biochemistry 35*, 5616–23.

BC700474R

A Novel Prosthetic Group for Site-Selective Labeling of Peptides for Positron Emission Tomography

Dag Erlend Olberg,*[,†] Ole Kristian Hjelstuen,[†,‡] Magne Solbakken,[‡] Joseph Arukwe,[‡] Hege Karlsen,[‡] and Alan Cuthbertson[‡]

University of Tromsø, Institute of Pharmacy, Department of Pharmaceutics and Biopharmaceutics, N- 9037 Tromsø, Norway, and GE Healthcare, Medical Diagnostics Discovery Research, P.O. Box 4220, 0401 Oslo, Norway. Received January 7, 2008; Revised Manuscript Received April 4, 2008

Efficient methodologies for the radiolabeling of peptides with [^{18}F]fluoride are a prerequisite to enabling commercialization of peptide-containing radiotracers for positron emission tomography (PET) imaging. It was the purpose of this study to investigate a novel chemoselective ligation reaction comprising conjugation of an [^{18}F]-*N*-methylaminooxy-containing prosthetic group to a functionalized peptide. Twelve derivatives of general formula R_1-CO-NH-Lys-Gly-Phe-Gly-Lys-OH were synthesized where R_1 was selected from a short list of moieties anticipated to be reactive toward the *N*-methylaminooxy group. Conjugation reactions were initially carried out with nonradioactive precursors to assess, in a qualitative manner, their general suitability for PET chemistry with only the most promising pairings progressing to full radiochemical assessment. Best results were obtained for the ligation of *O*-[2-(2-[^{18}F]fluoroethoxy)ethyl]-*N*-methyl-*N*-hydroxylamine **18** to the maleimidopropionyl-Lys-Gly-Phe-Gly-Lys-OH precursor **10** in acetate buffer (pH 5) after 1 h at 70 °C. The non-decay-corrected isolated yield was calculated to be 8.5%. The most encouraging result was observed with the combination **18** and 4-(2-nitrovinyl)benzoyl-Lys-Gly-Phe-Gly-Lys-OH, **9**, where the conjugation reaction proceeded rapidly to completion at 30 °C after only 5 min. The corresponding non-decay-corrected radiochemical yield for the isolated ^{18}F-labeled product **27** was 12%. The preliminary results from this study demonstrate the considerable potential of this novel strategy for the radiolabeling of peptides.

INTRODUCTION

In recent years, ^{18}F-labeled peptides have gained increasing interest as an important class of radiotracer well-suited to functional imaging with PET (*1–3*). The intrinsic pharmacokinetic properties, high affinity, and versatility of solid-phase chemistry make small proteins and peptides attractive candidates for diagnostic imaging.

The short-lived positron emitter fluorine-18 is currently the radionuclide of choice from the perspective of radiotracer manufacturability and distribution. It has excellent physical characteristics including a relatively low positron energy of 635 keV and a half-life of 109.7 min. This allows for extended radiochemical synthesis times and prolonged PET imaging protocols. There are, however, still considerable challenges to finding faster, more efficient methods for radiolabeling of peptides with this radionuclide. Although direct labeling routes have been described (*4*), the most common method utilizes a two-step process whereby the fluorine-18 is first introduced into a prosthetic group followed by conjugation to the peptide. This strategy separates the harsh reaction conditions required for [^{18}F]fluoride incorporation from the mild conditions preferred for conjugation, ameliorating the risk of significant degradation of the peptide precursor. A variety of ^{18}F-labeled prosthetic groups have been developed for incorporation into peptides, exploiting many different chemical reactions. These include acylation, alkylation, oxime formation, hydrazone formation, and 1,3-dipolar cycloaddition (*4–7*). Although alkylation and Michael-type reactions are often used in conjugation chemistry, there are limited cases reported for peptide labeling with ^{18}F-containing prosthetic groups. Examples include the [^{18}F]thiol conjugation to α-haloacetylated or maleimide-modified peptides and [^{18}F]maleimide conjugation to peptides bearing a free thiol group (*7, 8*). Thiols however, have the potential to oxidize to disulfides and readily take part in exchange reactions under a variety of conditions leading to complex mixtures (*9*). 4-[^{18}F]Fluorobenzaldehyde has been demonstrated to be a useful prosthetic group in the labeling of peptides bearing an aminooxy function (*10–13*). Oxime-bond formation proceeds rapidly and in good yield but often requires heating during the conjugation step, leading in some cases to the accelerated degradation of the peptide. In addition, the high reactivity of the aminooxy group complicates the routine handling and storage of the precursors and demands high quality standards for the reagents and solvents used in the process.

In contrast to aminooxy, the *N*-methylaminooxy group is unreactive toward aldehydes and ketones but reacts with Michael acceptors and a wide range of alkyl halides (*14*). The *N*-methylaminooxy nitrogen can also be selectively reacted with active esters at slightly acidic pH in the presence of competing nucleophiles such as the thiol group of cysteine or amino group of lysine (*15*). Peptides containing *N*-methylaminooxy amino acids have been chemoselectively alkylated with allylic, benzylic, and α-haloacetyl, *N*-ethylmaleimide, and hexyl acrylate groups in mildly acidic aqueous/organic solutions (*14, 16*). It was therefore postulated that an ^{18}F-labeled *N*-methylaminooxy prosthetic group could provide a useful addition to the toolbox of PET labeling strategies. This study reports on the radiosynthesis of the novel prosthetic *O*-[2-(2-[^{18}F]fluoroethoxy)ethyl]-*N*-methyl-*N*-hydroxylamine **18** and demonstrates its suitablility for radiolabeling in a model peptide system. Conjugation proceeded rapidly to completion in acetate buffer at pH 5 with

* Dag Erlend Olberg. E-mail: dag.erlend.olberg@farmasi.uit.no. Tel. +47 23185213. Fax +47 23186014.

† University of Tromsø.

‡ GE Healthcare.

10.1021/bc800007h CCC: $40.75 © 2008 American Chemical Society
Published on Web 05/29/2008

4-(2-nitrovinyl)benzoyl-Lys-Gly-Phe-Gly-Lys-OH, **9**, at 30 °C after only 5 min. The desired conjugate **27** was isolated after purification with a non-decay-corrected radiochemical yield of 12%.

MATERIAL AND METHODS

General. 9-Fluorenylmethoxycarbonyl (Fmoc) amino acids, Fmoc-Lys(Boc)-Sasrin resin, and peptide coupling reagents were purchased from Novabiochem, Bachem, and Applied Biosystems, respectively. All other reagents and solvents were purchased from Acros, Fluka, and Sigma-Aldrich. Mass spectra were recorded on a LCQ DECA XP MAX instrument using electrospray ionization (ESI) operated in positive mode at 4.5 kV and scan rate 5500 Da/s coupled to Finnigan Surveyor PDA chromatography system. Accurate mass spectra were recorded on a QToF-micro orthogonal acceleration time-of-flight mass spectrometer (Micromass UK Ltd., Manchester, UK) coupled to an Agilent 1100 chromatography system (Agilent Technology, Stockport, UK) using Leucine Enkephalin (Sigma Aldrich, St Louis, MO, USA) as reference compound. Data acquisition and processing were performed using *Masslynx 4.0* data system.

All NMR-spectra were recorded at 25 °C in 5 mm tubes on a Varian Unity Inova 500 NMR spectrometer using a ^{1}H{broadband} indirect detection pfg probe.

Thin layer chromatography (TLC) was run on precoated plates of silica gel 60F_{254} (Merck). Analytical and preparative reversed-phase HPLC runs were performed on Finnigan, Shimadzu, and Beckman chromatography systems. Purification of nonradioactive compounds, with the exception of the peptide derivatives, was performed using standard manual flash chromatography or an automated flash chromatography instrument (Combiflash companion, Teledyne ISCO). Details on HPLC and LC-MS conditions and analytical results are deposited as Supporting Information.

Preparation of Peptide Precursors. Assembly of the resin-bound amino acid sequence Lys(Boc)-Gly-Phe-Gly-Lys(Boc)-OH was done using fully automated synthesis (ABI 433A synthesis machine) on Fmoc-Lys(Boc)-Sasrin resin (0.25 mmol) with 2-(1*H*-benzotriazole-1-yl)-1,1,3,3-tetramethylaminium hexafluorophosphate (HBTU) activation. Further derivatization of the peptide to yield compounds **1**−**12** was performed on the solid phase using a manual nitrogen bubbler apparatus (0.05−0.1 mmol peptide loading). Anhydride formation was mediated by *N*,*N*′-dicyclohexylcarbodiimide in dichloromethane. Coupling reactions were monitored by the Kaiser test (*17*). Simultaneous removal of the peptides from the resin and deprotection of side-chain protecting groups was carried out in trifluoroacetic acid containing triisopropylsilane and water (95:2.5:2.5 v/v/v). After filtration, the solution was concentrated under reduced pressure and the residue was washed with diethyl ether. Crude products were purified by reversed-phase preparative HPLC and isolated by lyophilization.

Chloroacetyl-Lys-Gly-Phe-Gly-Lys-OH (1). Freshly prepared chloroacetic anhydride (0.4 mmol) and diisopropylethylamine (DIPEA) (0.4 mmol) were added to a suspension of the resin-bound peptide (0.05 mmol) in dimethylformamide (DMF) (5 mL). The reaction was run until complete conversion was achieved (1 h). After cleavage, the crude material was purified yielding 13 mg (42%).

Bromoacetyl-Lys-Gly-Phe-Gly-Lys-OH (2). The compound was synthesized as described for the corresponding chloro compound **1** yielding 17 mg (52%) after purification.

Acryloyl-Lys-Gly-Phe-Gly-Lys-OH (3). Acrylic acid (0.25 mmol) was preactivated for 3 min using (7-azabenzotriazol-1-yloxy)tripyrrolidinophosphonium hexafluorophosphate (PyAOP) (0.25 mmol) and DIPEA (0.4 mmol) in DMF (3 mL). The mixture was added to the resin-bound peptide (0.06 mmol) and left to react until complete conversion (2 h). Yield after cleavage and purification was 18 mg (51%).

2-Fluoroacryloyl-Lys-Gly-Phe-Gly-Lys-OH (4). A solution of freshly prepared 2-fluoroacrylic anhydride (0.2 mmol) in DMF (5 mL) was added to the resin-bound peptide (0.05 mmol) and left to react for 2 h. The procedure was repeated until complete conversion was achieved. After cleavage, the crude material was purified affording 24 mg (79%).

2-(Trifluoromethyl)acryloyl-Lys-Gly-Phe-Gly-Lys-OH (5). 2-(Trifluoromethyl)acryloyl chloride was prepared from 2-(trifluoromethyl)acrylic acid following the procedure by Yamazaki et al. (*18*). Coupling of the acid chloride (0.3 mmol) to the resin-bound peptide (0.1 mmol) in dry dichloromethane containing sym-collidine (0.1 mmol) was performed as described by Volonterio et al. (*19*) at 0 °C for 1 h and was repeated until complete conversion was achieved. After cleavage, the crude product was purified affording 13 mg (23%).

4-Bromocrotonoyl-Lys-Gly-Phe-Gly-Lys-OH (6). Freshly prepared 4-bromocrotonic anhydride (0.3 mmol) was added to a suspension of the resin-bound peptide (0.1 mmol) in DMF (3 mL) and left to react until complete conversion was achieved (2 h). After cleavage, the crude material was purified affording 50 mg (70%).

4-(Bromomethyl)benzoyl-Lys-Gly-Phe-Gly-Lys-OH (7). 4-(Bromomethyl)benzoic acid (0.15 mmol) was preactivated for 3 min using a solution of PyAOP (0.15 mmol) and DIPEA (0.3 mmol) in DMF (3 mL). The mixture was added to the resin-bound peptide (0.05 mmol) and left to react until complete conversion was achieved (2 h) followed by cleavage. The product was identified but decomposed during purification.

4-(Bromoacetyl)benzoyl-Lys-Gly-Phe-Gly-Lys-OH (8). Freshly prepared 4-(bromoacetyl)benzoic acid anhydride (0.3 mmol) was added to the resin-bound peptide (0.1 mmol) and left to react until complete conversion was achieved (2 h). After cleavage, the crude product was purified affording 17 mg (22%).

4-(2-Nitrovinyl)benzoyl-Lys-Gly-Phe-Gly-Lys-OH (9). 4-[(1*E*)-2-Nitrovinyl]benzoic acid (0.3 mmol), prepared according to a method of Park and Pei (*20*), was preactivated for 3 min in a solution of PyAOP (0.3 mmol) and DIPEA (0.6 mmol) in DMF (5 mL). The mixture was added to the resin-bound peptide (0.1 mmol) and left to react until complete conversion was achieved (1 h). After cleavage, the crude material was purified affording 50 mg (70%).

3-(Maleimido)propionyl-Lys-Gly-Phe-Gly-Lys-OH (10). To a suspension of the resin-bound peptide (0.1 mmol) in DMF (3 mL) were added 3-(maleimido)propionic acid *N*-hydroxysuccinimide ester (0.3 mmol) and DIPEA (0.35 mmol). The mixture was left to react until a complete conversion was achieved (4 h). After cleavage, the crude product was purified affording 60 mg (87%).

Vinylsulfonyl-Lys-Gly-Phe-Gly-Lys-OH (11). The vinylsulfonyl derivative was prepared following a procedure by Li et al. (*21*). To a stirred suspension of the resin-bound peptide (0.05 mmol) in dichloromethane (3 mL) cooled to 0 °C were added 2-chloroethanesulfonyl chloride (0.375 mmol) and triethylamine (0.375 mmol). The mixture was stirred for 1 h at room temperature. Triethylamine (3.75 mmol) was added and the mixture was stirred for 1 h to effect elimination and formation of the vinylsulfone. The product was cleaved off the resin and purified to give 24 mg (76%).

2-Methyloxirane-2-carbonyl-Lys-Gly-Phe-Gly-Lys-OH (12). 2-Methyloxirane-2-carboxylic acid was prepared by hydrolysis of methyl 2-methyloxirane-2-carboxylate following a procedure by Roush et al. (*22*). Freshly prepared 2-methyloxirane-2-caboxylic acid anhydride (0.4 mmol) was added to the resin-bound peptide (0.1 mmol) in DMF and left to react until

a complete conversion was achieved (1 h). After cleavage, the crude product was purified affording 28 mg (45%).

Methyl[4-[[(4-methylphenyl)sulfonyl]oxy]butoxy]carbamic Acid *t*-Butyl Ester (13). *N*-Boc-*N*-methylhydroxylamine was synthesized from *N*-methylhydroxylamine after a procedure by Tamura et al. (*23*).

To a solution of 4-bromo-1-butanol (2.80 g, 18.0 mmol) and DIPEA (10 mL) in dichloromethane (10 mL) was added diphenyl-*t*-butylsilyl chloride (5.0 mL, 18 mmol) under argon atmosphere. The solution was stirred at room temperature for 2 h, concentrated *in vacuo*, and purified by flash chromatography (hexane/ethyl acetate, 10:1) to afford (4-bromobutoxy)(*t*-butyl)-diphenylsilane as a colorless oil (4.39 g, 62%). ^{1}H NMR ($CDCl_3$, 500 MHz) δ 1.05 (9H, s, (CH_3)$_3$), 1.69 (2H, m, CH_2), 1.98 (2H, m, CH_2), 3.42 (2H, t, J = 6.8 Hz, CH_2Br), 3.69 (2H, t, J = 6.1 Hz, CH_2O), 7.41 (3H, m, 3 × Ar*H*), 7.66 (2H, m, 2 × Ar*H*).

A solution of *N*-Boc-*N*-methylhydroxylamine (0.74 g, 5.0 mmol) in DMF (10 mL) was treated with sodium hydride (200 mg, 60% dispersion in mineral oil, 4.80 mmol) and stirred for 1 h under argon. To the mixture was added a solution of (4-bromobutoxy)(*t*-butyl)diphenylsilane (1.56 g, 4.00 mmol) in DMF (10 mL) at 0 °C. The reaction mixture was stirred at 0 °C for 3 h and then concentrated. The residue was taken up in ethyl acetate (150 mL) and washed with 0.1 M NaOH (5 × 50 mL), water (50 mL), 0.1 M $KHSO_4$, and brine (50 mL), and dried ($MgSO_4$). After concentration, the residue was purified by flash chromatography (hexane/ethyl acetate, 10:1) affording [4-[[(*t*-butyl)diphenylsilyl]oxy]butoxy]methylcarbamic acid *t*-butyl ester as a colorless oil (0.59 g, 24%). ^{1}H NMR ($CDCl_3$, 500 MHz) δ 1.04 (9H, s, (CH_3)$_3$), 1.48 (9H, s, (CH_3)$_3$), 1.69 (4H, m, 2 × CH_2), 3.07 (3H, s, CH_3O), 3.68 (2H, t, J = 6.2 Hz, 2 × CH_2O), 3.83 (2H, t, J = 6.2 Hz, 2 × CH_2O), 7.39 (6H, m, 6 × Ar*H*), 7.66 (4H, m, 4 × Ar*H*). ESI-MS: found m/z = 457.8 $(MH)^+$, calcd m/z = 458.3.

Tetrabutylammonium fluoride (TBAF) (1 M solution in THF, 1.6 mL, 1.6 mmol) was added to a solution of [4-[[(*t*-butyl)diphenylsilyl]oxy]butoxy]methylcarbamic acid *t*-butyl ester (0.59 g, 1.2 mmol) in dry THF (20 mL). The reaction was stirred overnight under argon. Saturated ammonium chloride solution (40 mL) was added to the mixture and THF was evaporated off. The product was extracted into dichloromethane and dried (Na_2SO_4). The organic phase was removed under reduced pressure and the residue was purified by flash chromatography (hexane/ethyl acetate 1:1) affording (4-hydroxybutoxy)methylcarbamic acid *t*-butyl ester as a colorless oil (0.17 g, 63%). ^{1}H NMR ($CDCl_3$, 500 MHz) δ 1.49 (9H, s, (CH_3)$_3$), 1.71 (4H, m, 2 × CH_2), 1.78 (1H, t, J = 5.3 Hz, O*H*), 3.10 (3H, s, CH_3O), 3.69 (2H, m, CH_2OH), 3.89 (2H, m, CH_2O). ESI-MS: found m/z = 241.9 $(M+Na)^+$, calcd m/z = 242.1.

To a stirred solution of (4-hydroxybutoxy)methylcarbamic acid *t*-butyl ester (170 mg, 0.800 mmol) and triethylamine (161 μL, 1.16 mmol) in dry dichloromethane (10 mL) was added tosyl chloride (191 mg, 1.00 mmol) in dry dichloromethane (5 mL). The reaction mixture was stirred overnight under argon. The organic phase was washed with 10% $NaHCO_3$ (3 × 10 mL) and dried ($MgSO_4$). After concentration, the residue was purified by flash chromatography (hexane/ethyl acetate 8:2) to give **13** as a colorless oil (64 mg, 22%). ^{1}H NMR ($CDCl_3$, 500 MHz) δ 1.47 (9H, s, (CH_3)$_3$), 1.64 (2H, m, CH_2), 1.79 (2H, m, CH_2), 2.45 (3H, s, ArCH_3), 3.05 (3H, s, CH_3N), 3.79 (2H, t, J = 6.1 Hz, CH_2O), 4.07 (2H, t, J = 6.3 Hz, CH_2O), 7.34 (2H, m, 2 × Ar*H*), 7.79 (2H, m, 2 × Ar*H*). ESI-MS: found m/z = 396.1 $(M+Na)^+$, calcd m/z = 396.2.

(4-Fluorobutoxy)methylcarbamic Acid *t*-Butyl Ester (14). A mixture of potassium fluoride (4.64 mg, 0.0800 mmol) and 4,7,13,16,21,24-hexaoxa-1,10-diazabicylo[8.8.8]hexacosane (Kryptofix 222) (30.1 mg, 80.0 μmol) in dry acetonitrile (0.75 mL) was stirred for 5 min. A solution of **13** (15 mg, 40 μmol) in dry acetonitrile (0.250 mL) was added and the mixture was heated at 60 °C for 1 h. After concentration, the residue was purified by flash chromatography (hexane/ethyl acetate, 1:1) affording **14** as a colorless oil (4.5 mg, 51%). ^{1}H NMR ($CDCl_3$, 500 MHz) δ 1.49 (9H, s, (CH_3)$_3$), 1.73 (2H, m, CH_2), 1.82 (2H, m, CH_2), 3.10 (3H, s, CH_3N), 3.87 (2H, t, J = 6.2 Hz, CH_2O), 4.49 (2H, d of t, J_{HF} = 47.2 Hz, J = 6.0 Hz, CH_2F). ESI-MS: found m/z = 221.7 $(M+H)^+$, calcd m/z = 222.2.

Methyl[2-[2-[[(4-methylphenyl)sulfonyl]oxy]ethoxy]ethoxy]carbamic Acid *t*-Butyl Ester (16). To a stirred solution of diethylene glycol (22.0 g, 208 mmol) and triethylamine (10.5 g, 104 mmol) in dichloromethane (100 mL) was added tosyl chloride (9.9 g, 52 mmol). The solution was stirred at room temperature for 1 h. The reaction mixture was washed with aqueous 0.1 M $KHSO_4$ and 5% $NaHCO_3$ and dried (Na_2SO_4). After concentration, the residue was purified by flash chromatography (hexane/ethyl acetate, 1:1) to give 2-(2-hydroxyethoxy)ethyl tosylate as a colorless oil (7.62 g, 56%). ^{1}H NMR ($CDCl_3$, 500 MHz) δ 1.86 (1H, s, O*H*), 2.45 (3H, s, ArCH_3), 3.54 (2H, m, CH_2O), 3.67 (2H, m, CH_2O), 3.70 (2H, m, CH_2O), 4.20 (2H, m, CH_2O), 7.35 (2H, m, 2 × Ar*H*), 7.81 (2H, m, 2 × Ar*H*). ESI-MS: found m/z = 261.3 $(M+H)^+$, calcd m/z = 261.1.

To a solution of 2-(2-hydroxyethoxy)ethyl tosylate (7.62 g, 29.3 mmol) in dichloromethane (30 mL) containing DIPEA (6.0 mL, 35 mmol) were added diphenyl-*t*-butylsilyl chloride (9.0 mL, 35 mmol) and a catalytic amount of 4-dimethylaminopyridine under argon atmosphere. The solution was stirred at room temperature for 48 h. The reaction mixture was diluted with dichloromethane (100 mL) and washed with water (2 × 100 mL) and brine (2 × 50 mL) and dried ($MgSO_4$). After concentration, the residue was purified by automated flash chromatography (RediSep 120 g column, flow 85 mL/min) using a gradient of 0−50% ethyl acetate in hexane over 30 min affording 2-[2-[[(*t*-butyl)diphenylsilyl]oxy]ethoxy]ethyl tosylate as a colorless oil (9.2 g, 63%). ^{1}H NMR ($CDCl_3$, 500 MHz) δ 1.03 (9H, s, (CH_3)$_3$), 2.41 (3H, s, ArCH_3), 3.52 (2H, m, CH_2O), 3.67 (2H, m, CH_2O), 3.73 (2H, m, CH_2O), 4.17 (2H, m, CH_2O), 7.28 (2H, m, 2 × Ar*H*), 7.37 (4H, m, 4 × Ar*H*), 7.42 (2H, m, 2 × Ar*H*), 7.66 (4H, m, 4 × Ar*H*), 7.78 (2H, m, 2 × Ar*H*). ESI-MS: found m/z = 499.2 $(M+H)^+$, calcd m/z = 499.2.

A solution of *N*-Boc-*N*-methylhydroxylamine (1.53, 1.04 mmol) in THF (5 mL) was added slowly to a stirred suspension of sodium hydride (60% in mineral oil, 0.48 g, 12 mmol) in THF (5 mL) under argon. The reaction mixture was stirred for 30 min until no more gas evolution was observed and then cooled to 0 °C. 2-[2-[[(*t*-Butyl)diphenylsilyl]oxy]ethoxy]ethyl tosylate (4.0 g, 8.0 mmol) was added and the solution was stirred at 0 °C for 30 min and then at room temperature overnight. After concentration, the residue was taken up in ethyl acetate (200 mL) and washed consecutively with 0.1 M NaOH (5 × 50 mL), water (50 mL), 0.1 M $KHSO_4$ (50 mL), and brine (50 mL); dried ($MgSO_4$), and concentrated. The product was purified by flash chromatography (RediSep 40 g column, flow 40 mL/min) using a gradient 0−20% methanol in dichloromethane over 20 min affording [2-[2-[[(*t*-butyl)diphenylsilyl]oxy]ethoxy]ethoxy]methylcarbamic acid *t*-butyl ester as a colorless oil (3 g, 78%). ^{1}H NMR ($CDCl_3$, 500 MHz) δ 1.05 (9H, s, (CH_3)$_3$), 1.48 (9H, s, (CH_3)$_3$), 3.09 (3H, s, CH_3N), 3.61 (2H, m, CH_2O), 3.68 (2H, m, CH_2O), 3.81 (2H, m, CH_2O), 3.98 (2H, m, CH_2O), 7.37 (4H, m, 4 × Ar*H*), 7.42 (2H, m, 2 × Ar*H*), 7.68 (4H, m, 4 × Ar*H*). ESI-MS: found m/z = 496.1 $(M+Na]^+$, calcd m/z = 496.3.

TBAF (1 M solution in THF, 6.8 mL, 6.8 mmol) was added to a stirred solution of [2-[2-[[(*t*-butyl)diphenylsilyl]oxy]ethoxy]ethoxy]methylcarbamic acid *t*-butyl ester (3.0 g, 6.0 mmol) in dry THF (15 mL). The reaction was stirred overnight at room

temperature. After concentration, the residue was taken up in dichloromethane and washed consecutively with saturated ammonium chloride solution (40 mL), water (2 × 50 mL), and brine (2 × 50 mL); dried ($MgSO_4$), and concentrated. The product was purified by automated flash chromatography (RediSep 40 g column, flow 30 mL/min) using gradient 0−5% methanol in dichloromethane over 20 min affording [2-(2-hydroxyethoxy)ethoxy]methylcarbamic acid *t*-butyl ester as a colorless oil (1.36 g, 91%). ^{1}H NMR (CD_2Cl_2, 500 MHz) δ 1.46 (9H, s, (CH_3)$_3$), 2.41 (1H, t, J = 6.2 Hz, O*H*), 3.08 (3H, s, CH_3N), 3.57 (2H, m, CH_2O), 3.65 (2H, m, CH_2O), 3.67 (2H, m, CH_2O), 3.97 (2H, m, CH_2O). ESI-MS: found m/z = 258.2 $(M+Na)^+$, calcd m/z = 258.1.

A solution of tosyl chloride (1.6 mg, 8.5 mmol), [2-(2-hydroxyethoxy)ethoxy]methylcarbamic acid *t*-butyl ester (1.0 g, 4.3 mmol), and triethylamine (1.25 mL, 9.00 mmol) in dry dichloromethane (30 mL) was stirred under argon overnight. Dichloromethane (50 mL) was added and the reaction mixture was washed consecutively with 5% $NaHCO_3$ (100 mL), brine (100 mL), and water (2 × 100 mL); dried ($MgSO_4$) and concentrated. The product was purified by automated flash chromatography (RediSep 40 g column, flow 40 mL/min) using gradient 10−65% ethyl acetate in hexane over 20 min to give **16** as a colorless oil (1.23 g, 74%). ^{1}H NMR ($CDCl_3$, 500 MHz) δ 1.48 (9H, s, (CH_3)$_3$), 2.45 (3H, s, ArCH_3), 3.07 (3H, s, CH_3N), 3.62 (2H, m, CH_2O), 3.70 (2H, m, CH_2O), 3.95 (2H, m, CH_2O), 4.17 (2H, m, CH_2O), 7.34 (2H, m, 2 × Ar*H*), 7.80 (2H, m, 2 × Ar*H*). ESI-MS: found m/z = 412.0 $(M+Na)^+$, calcd m/z = 412.2.

[2-(2-Fluoroethoxy)ethoxy]methylcarbamic Acid *t*-Butyl Ester (17). A mixture of potassium fluoride (58 mg, 1.0 mmol) and Kryptofix 222 (376 mg, 1.00 mmol) in dry acetonitrile (3 mL) was stirred for 5 min. A solution of **16** (230 mg, 0.600 mmol) in dry acetonitrile (2 mL) was added and the mixture was heated at 80 °C for 1 h. After concentration, the residue was purified by flash chromatography (hexane/ethyl acetate, 1:1) affording **17** as a colorless oil (83 mg, 58%). ^{1}H NMR ($CDCl_3$, 500 MHz) δ 1.49 (9H, s, (CH_3)$_3$), 3.12 (3H, s, CH_3N), 3.73 (2H, m, CH_2O), 3.76 (2H, d of m, J_{HF} = 29.5 Hz, FCH_2CH_2O), 4.03 (2H, m, CH_2O), 4.57 (2H, d of m, J_{HF} = 47.6 Hz, FCH_2CH$_2$O). ESI-MS: found m/z = 260.0 $(M+Na)^+$, calcd m/z = 260.1.

Compounds 10−31. General Conjugation Procedure. To a conical vial charged with **14** or **17** (2 mg, 8 μmol) was added 2 M HCl in diethylether (0.3 mL), and the reaction mixture was left at room temperature for 5 min removing the Boc-groups quantitatively to give **15** and **18**, respectively. The solution was concentrated to dryness under reduced pressure and a solution of peptide derivative (3 mg, 2.8−5.1 μmol) in 0.4 M sodium acetate buffer pH 5 (0.8 mL) was added. Progress of the reaction was monitored by LC-MS analysis. If formation of conjugate could not be detected after reaction at room temperature for 30 min, temperature was increased to 70 °C and aliquots were analyzed at 45, 60, 90, and 120 min reaction times. Analytical results are deposited as Supporting Information.

Radiochemistry. All anhydrous chemicals were purchased from Sigma-Aldrich (Norway). HPLC solvents were obtained from Merck KGaA (VWR). Radiochemistry and semipreparative HPLC purifications were performed using the TracerLab Fx_{FN} (GE Medical Systems) with manual interventions when required. Thin layer chromatography (TLC) was run on precoated plates of silica gel $60F_{254}$ (Merck) developed in hexane/ethyl acetate (1:1). Instant Imager (Packard BioScience) was used to measure the Radio-TLC scan. Analytical HPLC was performed on an Agilent system (1100 series) with UV detection equipped in series with a γ-detector (Bioscan flow-count). Preparative purification was run on a TracerLab HPLC system. [^{18}F]Fluoride was produced by a cyclotron (GE PETtrace 6) using ^{18}O(p,n)^{18}F nuclear reaction with a 16.5 MeV proton irradiation of an enriched [^{18}O]H_2O target.

Preparation of the K[^{18}F]F−K_{222} Complex. Aqueous [^{18}F]fluoride (1 mL, 150−250 MBq) was passed through an anion-exchange resin (Sep-Pak light Waters Accell Pluss QMA Cartridge, preconditioned with K_2CO_3). The [^{18}F]fluoride was then eluted from the resin into the TracerLab reaction vessel using a solution of Kryptofix 222 (56 mg) and K_2CO_3 (10 mg) in a mixture of water (215 μL) water and acetonitrile (785 μL). The solution was then concentrated to dryness by heating at 100 °C under reduced pressure and a flow of nitrogen for 2 min. Acetonitrile (0.8 mL) was added and evaporated off as above. This step was repeated twice.

(4-[^{18}F]Fluorobutoxy)methylcarbamic Acid *t*-Butyl Ester ([^{18}F]14). To the dried K[^{18}F] F−K_{222} complex was added a solution of **13** (3 mg, 8 μmol) in acetonitrile (1 mL). The sealed reaction vessel was heated at 70 °C for 20 min and then analyzed by TLC and HPLC. The reaction mixture was passed through an alumina column (Sep-Pak, Waters) removing free [^{18}F]F^-. Finally, the reaction vessel was rinsed with acetonitrile (1 mL) and this solution was passed through the same alumina column to isolate as much of the labeled material as possible.

[2-(2-[^{18}F]Fluoroethoxy)ethoxy]methylcarbamic Acid *t*-Butyl Ester ([^{18}F]17). To the dried K[^{18}F] F−K_{222} complex was added a solution of **16** (3.0 mg, 7.7 μmol or 5.0 mg, 12.5μmol) acetonitrile (1 mL). The sealed reaction vessel was heated to 90 °C for 10 min. and then analyzed by TLC and HPLC. The reaction mixture was diluted with water (9 mL) and loaded onto an Oasis HLB Sep-Pak column (Waters). The column was rinsed with 25% methanol in water solution (50 mL) and then dried with a flow of nitrogen. The labeled product was eluted off the column using acetonitrile (1.5 mL).

[^{18}F]23. Conjugation of Prosthetic Group [^{18}F]15 to Peptide 10. The solution of [^{18}F]**14** in acetonitrile (2 mL) from the labeling procedure was evaporated to dryness at 70 °C under vacuum. To the residue was added 2 M HCl in diethyl ether (1 mL) and the reaction mixture was stirred for 5 min. The mixture was concentrated at 65 °C under reduced pressure with a flow of nitrogen. To the residue was added a solution of peptide **10** (5.0 mg, 7.3 μmol) in 0.4 M sodium acetate buffer pH 5 (0.8 mL). The reaction mixture was heated to 70 °C and aliquots were removed after 20, 40, and 60 min reaction time. HPLC analysis showed reappearance of free [^{18}F]fluoride, unreacted [^{18}F]**15**, and the desired peptide conjugate [^{18}F]**23**.

[^{18}F]27. Conjugation of Prosthetic Group [^{18}F]18 to Peptide 9. To the solution of [^{18}F]**17** in acetonitrile (1.5 mL) from the labeling procedure was added 2 M HCl in diethyl ether (0.2 mL) and the reaction mixture was stirred for 5 min. The mixture was concentrated at 65 °C under reduced pressure with a flow of nitrogen for 3 min. Acetonitrile (0.8 mL) was added and the concentration procedure was repeated. To the residue was added a solution of peptide **9** (5 mg, 7 μmol) in 0.4 M sodium acetate buffer pH 5 (0.8 mL). The reaction mixture was heated at 30 °C for 5 min, diluted with water (3 mL), and analyzed by HPLC showing unreacted [^{18}F]**18** and desired conjugate [^{18}F]**27**. The labeled peptide was purified on a preparative HPLC and shown to coelute with reference standard **27**.

[^{18}F]28. Conjugation of Prosthetic Group [^{18}F]18 to Peptide 10. The deprotection of Boc-protected [^{18}F]**17** and removal of the organic solvents was carried out in the same manner as that described in the section above. The dry residue was reconstituted in 0.8 mL of 0.4 M sodium acetate buffer containing 5 mg (7.3 μmol) of peptide derivative **10**. The reaction mixture was left for 60 min at 70 °C. After diluting the reaction mixture with 3 mL of water, an aliquot was analyzed

Table 1. Structures of the Peptide Derivatives Studied

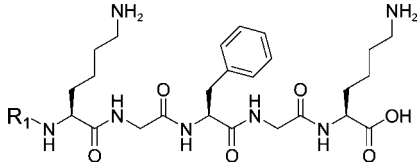

Compound	R_1	Compound	R_1
1	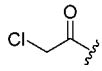	**7**[a]	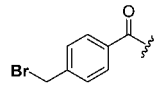
2	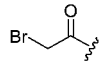	**8**	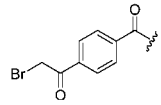
3	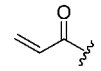	**9**	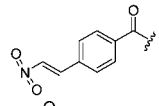
4	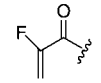	**10**	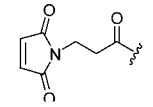
5	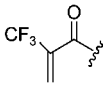	**11**	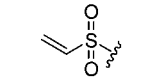
6	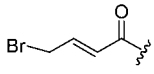	**12**	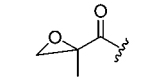

[a] indicates product degradation on purification.

by HPLC showing [18F]**18** and [18F]**28**. The reaction mixture was subjected to preparative HPLC and the isolated fraction was shown to colelute with reference standard **28**.

RESULTS AND DISCUSSION

The aim of this study was to investigate the utility of two novel 18F-containing prosthetic groups bearing the *N*-methylaminooxy functionality as a new methodology for the radiolabeling of peptides. Because of the alpha effect, *N*-methylaminooxy compounds are much more powerful nucleophiles than the ε-amino group of lysine, allowing site-specific conjugation under mildly acidic conditions (*24*). Furthermore, although structurally related, the *N*-methylaminooxy group has a quite different set of reactivities compared to aminooxy being unreactive toward aldehydes and ketones (*14*).

Carrasco et al. reported site-specific ligations of *N*-methylaminooxy groups in peptide systems to Michael-type acceptors and halides through nucleophilic substitution (*16*). One potential drawback however in applying this chemistry to the labeling of peptides for PET imaging was the relatively long reaction times reported for the conjugation step. We therefore adopted a strategy designed to rapidly screen a range of reactive groups linked to the *N*-terminal end of the model peptide KGFGK. Our approach was to assess, in a qualitative manner, the suitability and general applicability to PET chemistry. The conjugation reactions were first carried out using nonradioactive compounds with promising chemistries transferred to full radiochemical evaluation with [18F]fluoride. Table 1 shows a list of peptide derivatives synthesized for the initial conjugation studies.

The reactivity of peptide precursors **1**−**12** were then assessed using the two prosthetic groups **15** and **18** whose structures and synthetic routes are illustrated in Scheme 1 below.

Starting from 4-bromo-1-butanol, **13** was readily prepared in 4 steps by protection of the hydroxyl group as the *t*-butyl diphenyl silyl ether followed by reaction with the anion of *N*-Boc-*N*-methylhydroxylamine generated by sodium hydride, removal of the silyl ether with TBAF and reaction with tosyl chloride. The Boc-protected product **14** was obtained by direct fluorination of **13** with the KF-Kryptofix complex. Subsequent removal of the Boc-group with 2 M HCl in ether produced **15** in quantitative yield.

In a similar manner, **16** was prepared from diethylene glycol by monotosylation of the diol followed by protection as the *t*-butyl diphenyl silyl ether. Once again, reaction with the anion of *N*-Boc-*N*-methylhydroxylamine generated by sodium hydride, TBAF mediated removal of the silyl ether, and subsequent reaction with tosyl chloride gave the desired product in acceptable yield. The fluorinated compound **18** was prepared by reaction of **16** with KF-Kryptofix 222 followed by removal of the Boc-group with 2 M HCl in ether.

Nonradioactive conjugations were performed with prosthetic groups **15** and **18** and peptide derivatives **1**−**12** dissolved in 0.4 M acetate buffer at pH 5. The reactions were initially stirred for 30 min at room temperature and an aliquot analyzed by LC-MS. In cases where no detectable product had formed, the temperature of the solution was elevated to 70 °C and further aliquots removed for LC-MS analysis at 45, 60, 90, and 120 min. The reactions were performed on a milligram scale using 2 equiv of the prosthetic group and conjugation yields and product identity were confirmed by HPLC and mass spectrometry respectively.

Table 2 summarizes the test reactions carried out with peptide derivatives **1**, **3**, **5**, **6**, and **10** in combination with prosthetic group **15**.

Precursors **1** and **3** reacted sluggishly with **15**, forming only low yields of the conjugates **19** and **20** and were not selected for further evaluation. Although the 2-trifluormethyl derivative **5** gave product **21** in a 17% yield after 45 min at 70 °C, significant degradation of the starting material was observed by HPLC, complicating the analysis of the product mixture. A similar observation was made for peptide derivative **6**. Indeed, the complexity of the product mixtures led us to exclude these derivatives, and no attempt at radiochemical assessment was made. In contrast, the maleimide derivative **10** gave a 28% yield of **23** after 90 min at 70 °C, and the conjugate could be readily isolated from the starting material by HPLC.

In a similar set of experiments, the prosthetic group **18** was used to prepare conjugates with the peptide derivatives **2**, **4**, **8**, **9**, **10**, **11**, and **12**, and the yields are shown in Table 3 below.

Interestingly, the conjugation yields were in general higher using **18** compared to **15**. The maleimide derivative **10** was converted in 50% yield to product **28** with heating to 70 °C for 45 min. Most significantly, the 4-(2-nitrovinyl)benzoyl derivative **9** was converted to conjugate **27** in greater than 90% yield at 30 °C. Indeed, the reaction time could be reduced from 30 min to only 5 min with no significant impact on yield. The vinylsulfonamide **11** gave a clean reaction product, but the reaction was slower than for both maleimide and 4-(2-nitrovinyl)benzoyl-functionalized peptides. Once again, significant degradation of all other derivatives was observed, and from the initial round of screening, derivatives **9** and **10** were selected for full radiochemical assessment.

Radiochemical Assessment. Incorporation of [18F]fluoride into precursor **13** using [18F]KF-Kryptofix/ carbonate in acetonitrile at 70 °C for 20 min typically gave ~60% yield of [18F]**14** as analyzed by radio-TLC. Removal of free fluoride was performed on an alumina column (Sep-Pak, Waters) before cleavage of the Boc group with 2 N HCl in diethyl ether to quantitatively liberate [18F]**15**. The organic phase was evaporated *in vacuo* and the product reconstituted by addition of sodium acetate buffer pH 5. On subsequent reaction with the maleimide derivative **10** at 70 °C, the presence of a new

Scheme 1. Preparation of Prosthetic Groups 15 and 18 from Corresponding Tosylates 13 and 16[a]

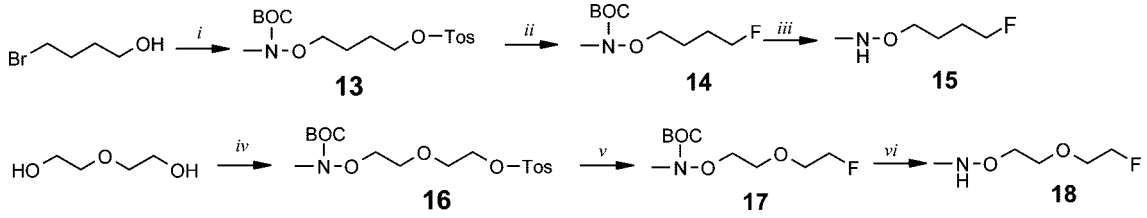

[a] Reagents and conditions: (i) 1. *t*-BDPSiCl, *i*-PrNEt, 24 h; 2. *N*-*tert*-butoxycarbonyl-*N*-methylhydroxylamine, NaH, 4 h; 3. TBAF, 24 h; 4. TosCl, *i*-PrNEt, 12 h; (ii) KF, Kryptofix, 70 °C, 60 min; (iii) 2 M HCl in diethylether, 5 min; (iv) 1. TosCl, *i*-PrNEt, 2 h; 2. *t*-BDPSiCl, *i*-PrNEt, 48 h; 3. *N*-*tert*-butoxycarbonyl-*N*-methylhydroxylamine, NaH, 12 h; 4. TBAF, 24 h; 5. TosCl, *i*-PrNEt, 24 h; (v) KF, Kryptofix, 70 °C, 60 min; (vi) 2 M HCl in diethyl ether.

Table 2. Reaction Yields of Prosthetic Group 15 with Peptide 1, 3, 5, 6, and 10

Compound	From peptide derivative	Conjugate R_2 = NH-KGFGK-OH	Time (min)	Reaction temp. (°C)	Yield[a] (%)
19	**1**	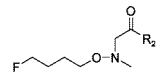	60	70	<5
20	**3**	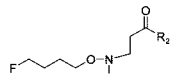	120	70	<5
21	**5**	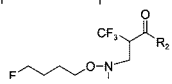	45	70	17[b]
22	**6**	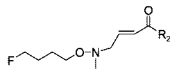	90	70	15[b]
23	**10**	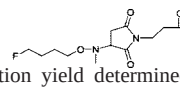	90	70	28

[a] indicates conjugation yield determined by HPLC integration (UV detection at 254 nm) of all peptide products relative to starting peptide. [b]indicates significant degradation of starting peptide.

Table 3. Reaction Yields of Prosthetic Group 18 with Peptide 2, 4, 8, 9, 10, 11, and 12

Compound	From peptide derivative	Conjugate R_3 = NH-KGFGK-OH	Time (min)	Reaction temp. (°C)	Yield[a] (%)
24	**2**	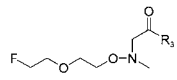	60	70	35[b]
25	**4**	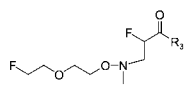	60	70	No detectable product
26	**8**	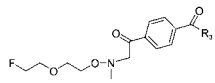	60	70	<5[b]
27	**9**	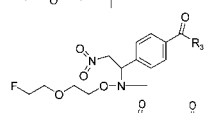	5	30	>90
28	**10**	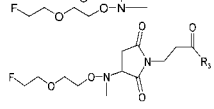	45	70	50
29	**11**	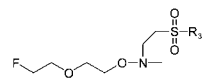	60	70	30
30	**12**	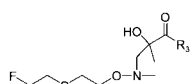	60	70	23[b]

[a] indicates conjugation yield determined by HPLC integration (UV detection at 254 nm) of all peptide products relative to starting peptide. [b] indicates significant degradation of starting peptide.

radioactive peak corresponding to the desired product **23** was observed (peak C, Figure 1). However, a second, more prominent peak was also present eluting in the void volume (peak A, Figure 1). This byproduct could be explained by

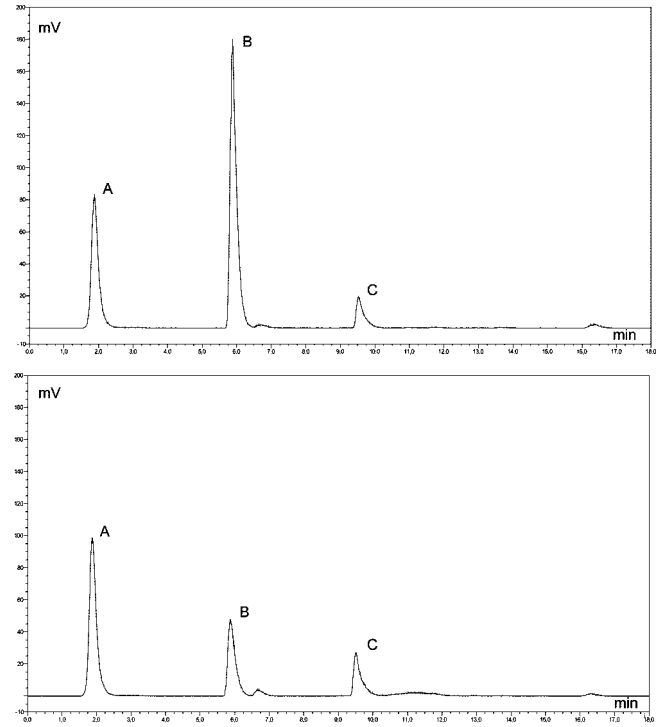

Figure 1. Radioactive HPLC analysis of [^{18}F]**15** in the presence of peptide **10** after heating to 70 °C for (top) 20 min and (bottom) 60 min in 0.4 M sodium acetate buffer at pH 5. Peak A = [^{18}F]fluoride, B = [^{18}F]**15**, and C = [^{18}F]**23**.

Scheme 2. Proposed Route of Degradation of [^{18}F]15 at 80 °C in 0.4 M Sodium Acetate Buffer at pH 5

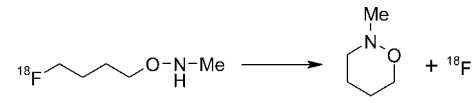

15 **31**

liberation of [^{18}F]fluoride through cyclization of the prosthetic group to give the six-membered ring **31** as shown in Scheme 2. Figure 1 shows the radiochromatograms of [^{18}F]**15** (peak B) on heating for 20 and 60 min at 70 °C in the presence of peptide derivative **10**. The presence of product **31** in the reaction mixture was confirmed by mass spectrometry. This was surprising, as direct nucleophilic substitution on alkyl fluorides is relatively uncommon; one example found in the literature relates to their reactivity with hydrazines (*25*). As a result of these findings, no further work was carried out on [^{18}F]**15**.

Radiolabeling of precursor **16** gave [^{18}F]**17** in typical radiochemical yields ranging 60−80% (n = 9) starting with 5 mg (12.9 μmol) of precursor at 90 °C for 5 min in 1 mL acetonitrile. Increasing the reaction time to either 10 or 15 min had no detectable impact on yield, as the tosylate **16** appeared to rapidly

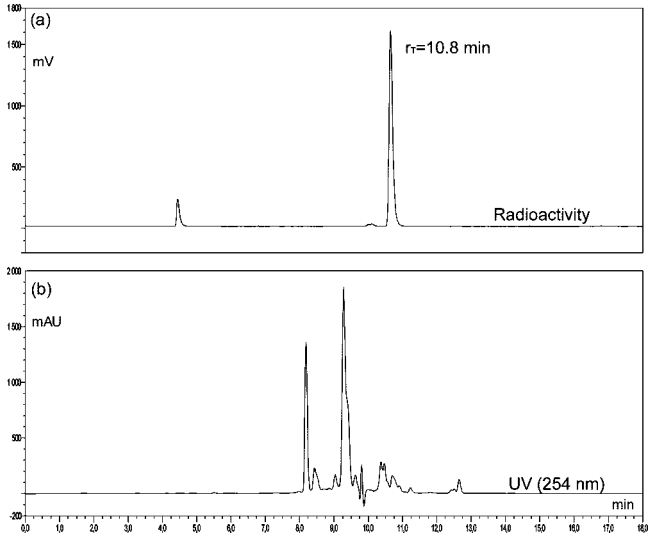

Figure 2. Analysis of an aliquot taken from the crude reaction mixture after 5 min at 30 °C. (a) Radioactivity channel, (b) UV channel at 254 nm. [18F]**27**, retention time = 10.8 min.

hydrolyze to the alcohol. This was not observed for **13** and may reflect a neighboring group effect of the ether oxygen. Purification was carried out by trapping the products of the reaction mixture on an Oasis HLB Sep-Pak cartridge, first eluting the excess alcohol with five aliquots of 10 mL 25% aqueous MeOH. Product [18F]**17** was then eluted in 1.5 mL acetonitrile with a radiochemical purity of greater than 95% and a preparation time of 35 min. This compares well with the 50% radiochemical yield and synthesis time of 30−55 min reported for [18F]FB-CHO by Phoetko et al. (*10*). The amount of alcohol carried over to the conjugation stage was found to have an impact on the final conjugation yield. Reducing the amount of precursor **16** to 3 mg (8 μmol) gave an isolated yield of [18F]**17** after Oasis Sep-Pak purification (decay-corrected) of 43 ± 4% (n = 13).

Removal of the Boc group was performed by addition of 0.2 mL 2 M HCl in diethyl ether as previously described, liberating [18F]**18**. Excess solvent was removed *in vacuo* at 65 °C under a stream of nitrogen for 3 min. To the residue was added a further 0.8 mL aliquot of acetonitrile and the drying process repeated before progressing to the next step. Conjugation was then initiated by dissolving [18F]**18** in 0.4 M acetate buffer pH 5 (0.8 mL), followed by addition of either **9** or **10**. In contrast to the [18F]**15**, [18F]**18** was found to be stable with no observable cyclization in solution following Boc deprotection. Efficient conjugation with the maleimide precursor **10** was achieved by heating for 1 h at 70 °C giving [18F]**28** in yields ranging 64−78% (n = 3) as analyzed by radio-HPLC. In contrast, peptide **9**, which in the nonradioactive experiments had proven to be the most reactive compound, demonstrated excellent reactivity at 30 °C forming [18F]**27** in yields ranging 80−89% (n = 5) after only 5 min (Figure 2a, 10.8 min). Indeed, the clean conjugation of the prosthetic group to the precursor was considered noteworthy, as closely eluting radioactive byproducts can be difficult to remove even by HPLC. These results generally compare favorably with other methodologies currently being employed in PET chemistry such as the [18F]Galacto-RGD radiosynthesis using the prosthetic group [18F]fluoropropionate, which has a reported RCY for the acylation step of ~85% (*26*). The thiol-based prosthetic groups gave comparable conjugation yields but required heating to 70−80 °C for 30 min (*7*). Likewise, for an aminooxy-modified somatostatin analogue, conjugation with [18F]FB-CHO gave a 60% RCY after 15 min at 60 °C, and for an RGD peptide, 60−80% RCY after 10−15 min at 60 °C has been reported (*10*).

Table 4. Radiochemical Yields (not corrected for decay) for [18F]27 and [18F]28

peptide conjugate	reaction temp (°C)	conjugation time (min)	% isolated yield[a]	total synthesis time[b] (min)	% RCP[c]
27	30	5	12.0 (n = 3)	80	>99
28	70	60	8.5 (n = 3)	140	>99

[a] Yields of isolated [18F]fluoropeptide, based on starting [18F]fluoride (not corrected for decay). [b] Time of synthesis measured from incoming [18F]fluoride to end of purification. [c] Radiochemical purity analyzed by radio-HPLC.

The overall efficiency of the reaction sequence was calculated from starting activity of [18F]fluoride following isolation of final product by reversed-phase chromatography. Isolated yields of 12.0% and 8.5% were achieved for [18F]**27** and [18F]**28**, respectively, as summarized in Table 4.

The major significance of these preliminary findings were the rapid kinetics demonstrated by the *N*-methylaminooxy prosthetic group [18F]**18** in combination with peptide precursor **9** at 30 °C. By avoiding high-temperature conjugation reactions, we can improve the chemical purity of the final conjugation mixture and reduce the complexity of the purification process. Peptides are known to have an inherent instability at elevated temperatures, and strategies which minimize the formation of byproduct are advantageous. We therefore anticipate that the methodology described in this study will provide a useful alternative for radiolabeling sensitive peptides for PET imaging.

CONCLUSION

18F-Containing *N*-methylaminooxy compounds are useful prosthetic groups suitable for labeling of peptides. The 4-(2-nitrovinyl)benzoyl moiety covalently linked to a model peptide was found to be highly reactive and selective toward the prosthetic group, enabling efficient labeling at 30 °C after 5 min in sodium acetate buffer at pH 5. This protocol therefore represents a novel methodology for the radiolabeling of peptides.

ACKNOWLEDGMENT

We would like to thank David Grace and Tone Hauk Fritzell (GE Healthcare) for kindly supplying the NMR spectra. We finally thank Roger Smeets and the staff at Kjeller for technical assistance.

Supporting Information Available: Additional information as described in the text. This material is available free of charge via the Internet at http://pubs.acs.org.

LITERATURE CITED

(1) Okarvi, S. M. (2004) Peptide-based radiopharmaceuticals: Future tools for diagnostic imaging of cancers and other diseases. *Med. Res. Rev. 24*, 357–397.
(2) Massoud, T. F., and Gambhir, S. S. (2003) Molecular imaging in living subjects: seeing fundamental biological processes in a new light. *Genes Dev. 17*, 545–580.
(3) Lundqvist, H., and Tolmachev, V. (2002) Targeting peptides and positron emission tomography. *Biopolymers (Peptide Science) 66*, 381–392.
(4) Okarvi, S. M. (2001) Recent progress in fluorine-18 labelled peptide radiopharmaceuticals. *Eur. J. Nucl. Med. 28*, 929–938.
(5) de Bruin, B., Kuhnast, B., Hinnen, F., Yaouancq, L., Amessou, M., Johannes, L., Samson, A., Boisgard, R., Tavitian, B., and Dollé, F. (2005) 1-[3-(2-[18F]Fluoropyridin-3-yloxy)propyl]pyrrole-2,5-dione: Design, synthesis, and radiosynthesis of a new [18F]Fluoropyridine-based maleimide reagent for the labeling of peptides and proteins. *Bioconjugate Chem. 16*, 406–420.
(6) Marik, J., and Sutcliffe, J. L. (2006) Click for PET: rapid preparation of [18F]fluoropeptides using CuI catalyzed 1,3-dipolar cycloaddition. *Tetrahedron Lett. 47*, 6681–6684.

(7) Glaser, M., Karlsen, H., Solbakken, M., Arukwe, J., Brady, F., Luthra, S. K., and Cuthbertson, A. (2004) ^{18}F-Fluorothiols: A new approach to label peptides chemoselectively as potential tracers for positron emission tomography. *Bioconjugate Chem. 15*, 1447–1453.

(8) Cai, W., Zhang, X., Wu, Y., and Chen, X. (2006) A thiol-reactive ^{18}F-labeling agent, N-[2-(4-[^{18}F)fluorobenzamido)ethyl]maleimide, and synthesis of RGD peptide-based tracer for PET imaging of $\alpha v\beta 3$ integrin expression. *J. Nucl. Med. 47*, 1172–1180.

(9) Moroder, L., Musiol, H. J., Schaschke, L., Chen, B., Hargittal, B., and Barany (2004) *Thiol group. Synthesis of peptides and peptidomimetics* (G. Goodman, M., Felix, A., Moroder, L. and Toniolo, C., Eds) pp 384−423, Chapter *2*, Houben-Weyl, New York.

(10) Poethko, T., Schottelius, M., Thumshirn, G., Hersel, U., Herz, M., Henriken, G., Kessler, H., Schwaiger, M., and Wester, H. J. (2004) Two-step methodology for high-yield routine radiohalogenation of peptides: ^{18}F-labeled RGD and octreotide analogs. *J. Nucl. Med. 45*, 892–902.

(11) Cuthbertson, A., Solbakken, M., Arukwe, J., Karlsen, H., and Glaser, M. WO Patent 2004/080492.

(12) Schottelius, M., Poethko, T., Herz, M., Reubi, J-C., Kessler, H., Schwaiger, M., and Wester, H-J. (2004) First ^{18}F-labeled tracer suitable for routine clinical imaging of SST receptor-expressing tumors using positron emission tomography. *Clin. Cancer. Res. 10*, 3593–3606.

(13) Glaser, M., Morrison, M., Solbakken, M., Arukwe, J., Karlsen, H., Wiggen, U., Champion, S., Kinberg, G. M., Cuthbertson, A. (2008) Radiosynthesis and biodistribution of cyclic RGD peptides conjugated with novel [^{18}F]fluorinated aldehyde-containing prosthetic groups *Bioconjugate Chem. 19*, 951–957.

(14) Carrasco, M. (2005) *N*-Alkylaminooxy amino acids as versatile derivatives for"post translation"modifications of synthetic peptides, In *Understanding Biology Using Peptides* (Blondelle, S. E., Ed) pp 300−302, Springer, New York.

(15) Bark, S. J., Schmid, S., and Hahn, K. M. (2000) A highly efficient method for site-specific modification of unprotected peptides after chemical synthesis. *J. Am. Chem. Soc. 122*, 3567–3573.

(16) Carrasco, M., Silva, O., Rawls, K. A., Sweeney, M. S., and Lombardo, A. A. (2006) Chemoselective alkylation of N-alkylaminooxy-containing peptides. *Org. Lett. 8*, 3529–3532.

(17) Kaiser, E., Colescott, R. L., Bossinger, C. D., and Cook, P. I. (1970) Color test for detection of free terminal amino groups in the solid-phase synthesis of peptides. *Anal. Biochem. 34*, 595–598.

(18) Yamazaki, T., Ichige, T., and Kitazume, T. (2002) Convenient preparation of 2-phenylethyl 3,3-difluoro-2-methylpropionate. *Collect. Czech. Chem. Commun. 67*, 1479–1485.

(19) Volonterio, A., Chiva, G., Fustero, S., Piera, J., Rosello, M. S., Sani, M., and Zanda, M. (2003) Stereocontrolled solid-phase synthesis of fluorinated partially-modified retropeptides via tandem aza-Michael/enolate-protonation. *Tetrahedron Lett. 44*, 7019–7022.

(20) Park, J., and Pei, D. (2004) trans-β-Nitrostyrene derivatives as slow inhibitors of protein tyrosine phosphatases. *Biochemistry 43*, 15014–15021.

(21) Li, M., Wu, R. S., Tsai, J. S. C., and Salamone, S. J. (2003) Evaluation of vinylsulfamides as sulfhydryl selective alkylation reagents in protein modification. *Bioorg. Med. Chem. Lett. 13*, 383–386.

(22) Roush, W. R., Hernandez, A. A., and Zepeda, G. (1999) A new synthesis of peptidyl epoxysuccinates for probing cysteine protease-inhibitor P3/S3 binding interactions. *Synthesis* 1500–1504.

(23) Tamura, Y., Ikeda, H., Morita, I., Tsubouchi, H., and Ikeda, M. (1982) O-Arenesulfonyl-N-alkylhydroxylamines as aminating reagents. *Chem. Pharm. Bull. 30*, 1221–1224.

(24) Langenhan, J. M., and Thorson, J. S. (2005) Recent carbohydrate-based chemoselective ligation applications. *Curr. Org. Synth. 2*, 59–81.

(25) Thomesen, B., Bols, E., and Bols, M. (1997) Synthetic studies of fluorinated analogues of 1-azafagomine: Remarkable nucleophilic substitution of fluorine by hydrazine. *Tetrahedron 53*, 9357–9364.

(26) Haubner, R., Kuhnast, B., Mang, C., Weber, W. A., Kessler, H., Wester, H., and Schwaiger, M. (2004) [^{18}F]Galacto-RDG: Synthesis, radiolabeling, metabolic stability, and radiation dose estimates. *Bioconjugate Chem. 15*, 61–69.

BC800007H

Aptamer-Targeted Gold Nanoparticles As Molecular-Specific Contrast Agents for Reflectance Imaging

David J. Javier,[†] Nitin Nitin,[†] Matthew Levy,[‡] Andrew Ellington,[‡] and Rebecca Richards-Kortum*[,†]

Department of Bioengineering, Rice University, Houston, Texas 77005, and Institute for Cellular and Molecular Biology, University of Texas at Austin, Austin, Texas 78712. Received March 25, 2008; Revised Manuscript Received April 22, 2008

Targeted metallic nanoparticles have shown potential as a platform for development of molecular-specific contrast agents. Aptamers have recently been demonstrated as ideal candidates for molecular targeting applications. In this study, we investigated the development of aptamer-based gold nanoparticles as contrast agents, using aptamers as targeting agents and gold nanoparticles as imaging agents. We devised a novel conjugation approach using an extended aptamer design where the extension is complementary to an oligonucleotide sequence attached to the surface of the gold nanoparticles. The chemical and optical properties of the aptamer−gold conjugates were characterized using size measurements and oligonucleotide quantitation assays. We demonstrate this conjugation approach to create a contrast agent designed for detection of prostate-specific membrane antigen (PSMA), obtaining reflectance images of PSMA(+) and PSMA(−) cell lines treated with the anti-PSMA aptamer−gold conjugates. This design strategy can easily be modified to incorporate multifunctional agents as part of a multimodal platform for reflectance imaging applications.

I. INTRODUCTION

Most contrast agents for molecular imaging couple a targeting molecule to a reporter moiety. For example, monoclonal antibodies are frequently used as targeting agents coupled to reporting agents. Recently, the use of aptamers for molecular targeting has been advocated due to several advantages relative to traditional antibody-based approaches (*1, 2*). Aptamers are generally smaller in size (3−5 nm) than antibodies (∼12−15 nm). The high affinity and specificity of aptamers make them ideal targeting agents. In contrast to antibodies, aptamers can be chemically synthesized in bulk amounts at a reasonable price. Another advantage of aptamers is that they can be generated using modified nucleotides, and the incorporation of these non-natural analogues can greatly increase nuclease stability. Moreover, oligonucleotide extensions can be easily incorporated in the aptamer's backbone to separate the conjugating arm from the targeting arm. This eliminates the need for direct modifications to the aptamer binding site. In the case of antibodies, the addition of reporting molecules is normally accomplished by modifying functional groups on the peptide backbone which can potentially compromise the affinity of the antibody.

The use of gold nanoparticles as reporting agents for reflectance-based molecular imaging applications has recently been reported as alternative to fluorescence-based methods (*3–5*). Gold nanoparticles have strong localized surface plasmon resonance that makes them ideal for reflectance imaging. The extinction coefficients of gold nanoparticles are higher than organic fluorophores; the scattering signal from a single nanoparticles is approximately equivalent to 10^6 fluorophores in a homogeneous environment (*6, 7*). Gold nanoparticles are good candidates for in vivo applications since their material composition is less cytotoxic compared to organic fluorescent dyes and quantum dots. Moreover, generation of reflectance imaging using gold nanoparticles also requires less complicated instrumentation compared to fluorescence methods.

In a previous study, we demonstrated the development of aptamer-based quantum dot conjugates for molecular imaging where the conjugation of the aptamers to the quantum dot is facilitated using biotin−avidin interactions (*8*). In this paper, we developed aptamer-targeted gold nanoparticles for use as contrast agents for reflectance imaging. In this approach, shown schematically in Figure 1, conjugation of the aptamers to gold nanoparticles is accomplished using an extended aptamer design where the extension is complementary to an oligonucleotide sequence attached to the surface of gold nanoparticles. This novel approach provides a simple conjugation method and offers the potential for multiplexing capabilities.

We demonstrate this conjugation approach to create a contrast agent designed for the detection of prostate-specific membrane antigen (PSMA). PSMA is a cell surface antigen commonly present in prostate cancer cells. Anti-PSMA aptamers were conjugated to 20 nm gold nanoparticles and the optical and chemical properties of the conjugates were characterized. The potential of the conjugates for molecular imaging was demonstrated by obtaining reflectance images of PSMA(+) and PSMA(−) cell lines treated with the anti-PSMA aptamer−gold conjugates.

II. MATERIALS AND METHODS

A. Synthesis of Aptamer−Gold Conjugates. The anti-PSMA aptamer used in the study is an A9 RNA aptamer. The selection and characterization of A9 RNA aptamers have been previously described in another paper (*9*). Here, we added an extension to the aptamer to serve as a hybridization site for complementary oligonucleotide-coated gold nanoparticles. The sequence of the A9 RNA aptamer showing the extended sequence (underlined) is 5′ GGG AGG ACG AUG CGG ACC GAA AAA GAC CUG ACU UCU AUA CUA AGU CUA CGU UCC CAG ACG ACU CGC CCG AGA AUU AAA UGC CCG CCA UGA CCA G. The extended A9 aptamer (100 μM concentration) was obtained from the Ellington laboratory at the University of Texas at Austin.

* E-mail: rkortum@rice.edu.
[†] Rice University.
[‡] University of Texas at Austin.

10.1021/bc8001248 CCC: $40.75 © 2008 American Chemical Society
Published on Web 05/31/2008

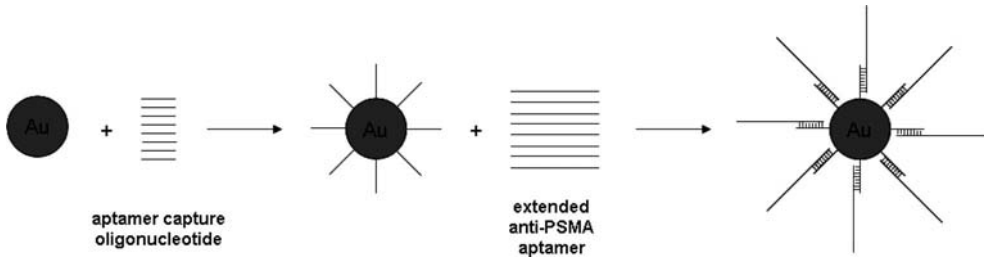

Figure 1. Schematic diagram for the conjugation of anti-PSMA aptamers to gold nanoparticles.

Gold nanoparticles (20 nm gold nanospheres, citrate-stabilized, Ted Pella, Inc.) were coated with capture oligonucleotide which was complementary to the aptamer extension sequence. The aptamer capture oligonucleotide was functionalized with thiol group (C6 S−S spacer) and hexa(ethylene glycol) (18-atom spacer) on the 5′ terminal position. The HPLC-purified aptamer capture oligonucleotide was obtained from IDT DNA Technologies with the following sequence: 5′/ThioMC6-D/Sp18/CTG GTC ATG GCG GGC ATT TAA TTC. To prepare the capture oligonucleotide-coated gold nanoparticles, 5 uM of aptamer capture oligonucleotide was reduced with TCEP (tris(2-carboxyethyl)phosphine hydrochloride, Pierce Chemical) for 30 min and added to 1.0 mL of 20 nm colloidal gold nanoparticles (7.0×10^{11} Au nanoparticles per mL). The conjugate was slowly aged with increasing concentration of PBS for 24 h until a 1× PBS concentration was reached. The unreacted capture oligonucleotide was removed from the oligonucleotide-coated gold nanoparticles by centrifugation (2×) at 12 000 *g* for 30 min. The detailed oligonucleotide coating process is described in a previous paper (*10*).

The anti-PSMA aptamer (50 μL of 100 μM stock solution or 5 nmol) was hybridized to 1.0 mL of capture oligonucleotide-coated gold nanoparticles (suspended in 1× PBS) by initially heating the solution at 70 °C for 5 min followed by incubation at room temperature for 30 min. The unreacted anti-PSMA aptamers were removed from the aptamer−gold conjugates by centrifugation (2×) at 12 000 *g* for 30 min.

B. Characterization of Aptamer−Gold Conjugates. The characterization experiments were designed to determine the size of the conjugates and the amount of aptamer-capture oligonucleotide and the extended anti-PSMA aptamers conjugated to the gold nanoparticles. We used 1.0 mL of 20 nm Au nanoparticles (7.0×10^{11} Au nanoparticles per mL) for all experiments.

The hydrodynamic size of the functionalized gold nanoparticles was measured using dynamic light scattering (Brookhaven Instruments). Triplicate runs were performed at 25 °C and 3 min analysis time to determine the average hydrodynamic diameter of the conjugates.

The amount of aptamer-capture oligonucleotide coated to gold nanoparticles was determined by fluorescence measurements using the Quant-iT OliGreen ssDNA assay kit from Invitrogen. The gold nanoparticles were first dissolved in 500 μM KCN before performing the assay. A standard curve was generated using the aptamer-capture oligonucleotide. The fluorescence intensity ($\lambda_{exc} = 480$ nm, $\lambda_{em} = 520$ nm) of the samples and standards was measured using a plate reader (SpectraMax, Molecular Devices).

The amount of extended anti-PSMA aptamer hybridized to the gold nanoparticles coated with capture oligonucleotides was estimated by using a fluorescently labeled oligonucleotide. Gold nanoparticles coated with capture oligonucleotides were hybridized with a shorter analogue of the anti-PSMA aptamer with a Cy5 modification on the 5′ terminus. The sequence of the oligonucleotide obtained from IDT DNA Technologies is 5′ Cy5\GAA TTA AAT GCC CGC CAT GAC CAG. The oligonucleotide-Cy5 was also used as a standard to generate a calibration curve. The amount of the aptamers hybridized to the gold nanoparticles was estimated by measuring the fluorescence intensity of the oligonucleotide-Cy5 upon dissolution of the gold nanoparticles with KCN and comparing the measured intensity to the standard curve. The solution was treated with KCN to dissolve the gold and release the oligonucleotides, thus preventing the plasmon resonance of gold nanoparticles from interfering with fluorescence measurements.

C. Optical Imaging of Aptamer−Gold Conjugates. LNCaP cells and PC3 prostate cancer cells were obtained from ATCC. LNCaP is used as PSMA(+) cell line, while PC3 served as PSMA(−) cell line. The cells were grown in RPMI media with 5% FBS at 37 °C until they were 80−90% confluent. The cells were trypsinized, washed, and resuspended in 1× PBS before labeling. For cell labeling, the aptamer−gold conjugates (500 μL each) were added to LNCaP and PC3 cell suspensions for 30 min at 37 °C. The cells were centrifuged twice (1 min, 800 *g*) to remove unbound aptamer−gold conjugates. Reflectance imaging of the labeled cells was performed with confocal microscopy (Zeiss LSM510) in reflectance mode (633 nm laser, 63× objective). *Image J* software was used to compare the signal intensity of the reflectance images obtained from the two cell lines.

III. RESULTS AND DISCUSSION

Figure 1 illustrates the steps involved in conjugating anti-PSMA aptamers to gold nanoparticles. Gold nanoparticles are first coated with aptamer capture oligonucleotides via the gold−sulfur interactions between the lattice structure of the gold nanoparticles and the thiol groups of the aptamer capture oligonucleotide. Due to the strong gold−sulfur binding energy (*11*), most conjugation approaches to gold nanoparticles are based on this interaction. A PEG spacer is added between the thiol and the complementary capture sequence of the oligonucleotide to improve hybridization efficiency by minimizing steric hindrance between the gold surface and the hybridization site. The use of oligonucleotide coating on gold nanoparticles has several advantages. First, the negatively charged phosphate groups present on the oligonucleotides prevent aggregation of the nanoparticles via electrostatic repulsion. This results in stable gold nanoparticles that do not aggregate even in high salt environments (i.e., physiological buffers). Second, the presence of the capture oligonucleotides on the gold nanoparticles can be used to easily conjugate other targeting moieties which incorporate a complementary sequence. In this study, an extended anti-PSMA aptamer is then hybridized to the aptamer-capture oligonucleotides on the gold nanoparticles. A major advantage of this conjugation approach is that it prevents any direct modification of the aptamer sequence involved in the binding process, since conjugation to gold nanoparticles is facilitated via the oligonucleotide extension. A longer spacer composed of PEG, polyA's, or polyT's can also be used if larger gold nanoparticles (40−100 nm diameter) are desired. Larger

Table 1. Characterization of Aptamer−Gold Conjugates

	hydrodynamic size (diameter), nm	number of oilgonucleotide per Au nanoparticle
bare Au nanoparticle	19.3 ± 0.6	N/A
Au nanoparticle + aptamer capture oilgonucleotide	25.5 ± 1.2	376 ± 25 (aptamer capture)
Au nanoparticle + aptamer capture oilgonucleotide + anti-PSMA aptamer	39.6 ± 3.8	213 ± 12 (anti-PSMA aptamer)

nanoparticles can provide higher contrast images but can present difficulties during delivery and clearance routes.

Table 1 summarizes the characteristics of the gold nanoparticle conjugates used in this study. The bare gold nanoparticles were measured to have an average hydrodynamic diameter of 19.3 nm. The addition of the aptamer-capture oligonucleotide resulted in nanoparticles with an average diameter of 25.5 nm, an increase of 6.2 nm. This is consistent with the expected size contribution of the added aptamer-capture oligonucleotide (24 nucleotides + hexa(ethylene glycol) spacer) of about ∼3 nm on each side based on the predicted hairpin structure. Upon hybridization of the anti-PSMA aptamers, the average nanoparticle size was 39.6 nm, an increase of 20.3 nm compared to the bare gold nanoparticles. Again, the expected size contribution of the added extended A9 anti-PSMA aptamer (94 nucleotides) is between 8 and 10 nm on each side based on the predicted m-fold RNA secondary structure. In summary, the measured sizes of the functionalized gold conjugates are within the expected size contribution of the added oligonucleotides. Determining the size of the gold conjugates is an important consideration in the delivery and clearance of the contrast agents for imaging applications.

We also determined the average number of oligonucleotides (both aptamer capture and anti-PSMA aptamers) present per gold nanoparticle (Table 1). Based on measurements using the oligonucleotide quantitation assay, there are approximately 376 aptamer-capture oligonucleotides per gold nanoparticle. This number represents the possible number of hybridization sites for the anti-PSMA aptamers and is consistent with literature values for oligonucleotide coating on various sizes of Au nanoparticles (*12*). Using a fluorescently labeled anti-PSMA aptamer analogue, we determined that there are approximately 213 anti-PSMA aptamer analogues per gold nanoparticle. This represents a 57% conjugation efficiency which can be attributed to the steric hindrance upon hybridization between the aptamer capture oligonucleotide and the anti-PSMA aptamer analogue. The efficiency may be further reduced when using larger oligonucleotides like the extended A9 anti-PSMA aptamer. We did not determine this efficiency directly because of difficulties in modifying the aptamer with fluorescent dyes. Direct quantitation of the aptamer conjugated to gold nanoparticles using oligonucleotide assays is difficult because of the contribution of the aptamer capture oligonucleotide. However, we validated the incorporation of the extended A9 anti-PSMA aptamers on the gold nanoparticles using reflectance imaging. Ideally, only a few copies of the aptamers per gold nanoparticles are necessary to develop a molecular-specific contrast agent for reflectance imaging.

Figure 2 shows the brightfield and reflectance confocal images of PSMA negative (PC3) and PSMA positive (LNCaP) cells labeled with anti-PSMA aptamer−gold conjugates. The reflectance images of the LNCaP positive cell lines show strong labeling with the aptamer−gold conjugates. Minimal labeling was observed for the PC3 negative cell lines. The labeling on the LNCaP positive cells occurs around the cellular membrane, consistent with the expected pattern, since the PSMA target is a membrane-bound glycoprotein. The reflectance images also

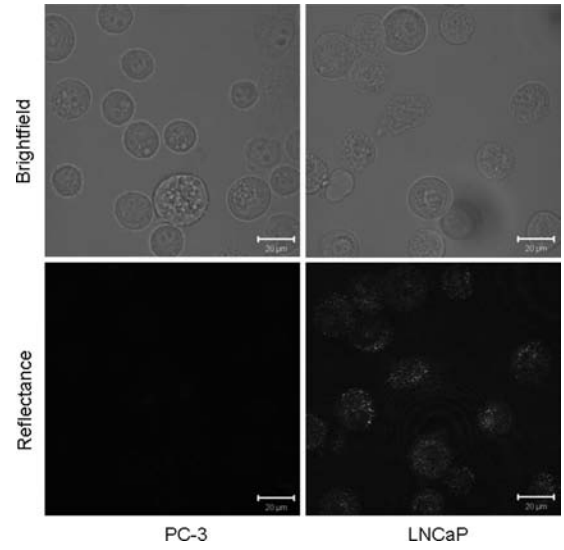

Figure 2. Reflectance imaging using aptamer−gold conjugates. Scale bar is 20 μm.

suggest possible endocytosis of the aptamer−gold conjugates during the labeling process. Analysis of signal intensity using *Image J* software shows a 3−5-fold increase in the reflectance intensity of the positive cell lines compared to intensity of the negative cell lines. For imaging applications, an increase of 1.5- to 3.0-fold in contrast intensity is considered significant (*13*).

There are other important considerations in the use of aptamer−gold conjugates as molecular-specific contrast agents for clinical imaging. For example, the cytotoxicity of the contrast agents should be carefully evaluated. In a previous paper, we evaluated the cytotoxicity of the oligonucleotide-coated gold nanoparticles using standard cell viability assays (*14*). Delivery and clearance routes of the contrast agents are also important factors. We are currently exploring these areas in order to facilitate translation of this type of contrast agents for molecular imaging applications.

IV. CONCLUSION

The study illustrates the feasibility of using aptamer−gold nanoparticles as molecular-specific contrast agents for reflectance imaging. We introduced a new method for conjugating aptamers via hybridization reactions on oligonucleotide-coated gold nanoparticles. An alternative approach for introducing aptamers to gold nanoparticles is the direct use of thiolated aptamers, which has recently been reported (*15*). However, the approach presented in this study has several advantages over the use of thiolated aptamers. First, the integrity and stability of the aptamers is easily preserved during the bioconjugation process since the aptamers are only introduced for a short period of time during the hybridization process. Second, a smaller amount of aptamers can be used for binding to gold nanoparticles, in contrast to thiolated aptamers where significant amounts of aptamers are necessary to coat and stabilize the gold nanoparticles. In our approach, the use of shorter and cheaper complementary oligonucleotides facilitates better coating and stabilization of the gold nanoparticles prior to bioconjugation of the aptamers. Last, our approach offers possible multiplexing capabilities where other types of molecules (targeting, delivery, imaging, or therapeutic) can be incorporated in the design of the contrast agents. In a previous study, we have demonstrated a multimodal reporting system (reflectance and fluorescence) using oligonucleotide−dye conjugates hybridized on complementary oligonucleotides functionalized on gold nanoparticles (*14*). Moreover, therapeutic molecules can be incorporated to

the aptamer-gold nanoparticles to develop multimodal theranostic agents. For example, protein-based therapeutic agents (*16*) can be functionalized via oligonucleotide−protein linkage to aptamer−gold conjugates with the advantage of controlling the amount of therapeutic agents per nanoparticle. The ability to incorporate multifunctional agents into a single construct can be a useful technique in developing multimodal platforms for various clinical applications.

ACKNOWLEDGMENT

We would like to acknowledge Vivian Mack for preparing the cell cultures and BRP R01CA103830 NCI and Center for Biological and Environmental Nanotechnology (CBEN) for funding. Nitin Nitin contributed equally to this manuscript.

LITERATURE CITED

(1) Bunka, D. H., and Stockley, P. G. (2006) Aptamers come of age - at last. *Nat. Rev. Microbiol. 4*, 588–96.

(2) Brody, E. N., and Gold, L. (2000) Aptamers as therapeutic and diagnostic agents. *J. Biotechnol. 74*, 5–13.

(3) Aaron, J., Nitin, N., Travis, K., Kumar, S., Collier, T., Park, S. Y., Jose-Yacaman, M., Coghlan, L., Follen, M., Richards-Kortum, R., and Sokolov, K. (2007) Plasmon resonance coupling of metal nanoparticles for molecular imaging of carcinogenesis in vivo. *J. Biomed. Opt. 12*, 034007. /1−034007/11.

(4) Nitin, N., Javier, D. J., Roblyer, D. M., and Richards-Kortum, R. (2007) Widefield and high-resolution reflectance imaging of gold and silver nanospheres. *J. Biomed. Opt. 12*, 051505. /1−051505/10.

(5) Sokolov, K., Follen, M., Aaron, J., Pavlova, I., Malpica, A., Lotan, R., and Richards-Kortum, R. (2003) Real-time vital optical imaging of precancer using anti-epidermal growth factor receptor antibodies conjugated to gold nanoparticles. *Cancer Res. 63*, 1999–2004.

(6) Aslan, K., Lakowicz, J. R., and Geddes, C. D. (2004) Nanogold-plasmon-resonance-based glucose sensing. *Anal. Biochem. 330*, 145–55.

(7) Aslan, K., Zhang, J., Lakowicz, J. R., and Geddes, C. D. (2004) Saccharide sensing using gold and silver nanoparticles−a review. *J. Fluoresc. 14*, 391–400.

(8) Chu, T. C., Shieh, F., Lavery, L. A., Levy, M., Richards-Kortum, R., Korgel, B. A., and Ellington, A. D. (2006) Labeling tumor cells with fluorescent nanocrystal-aptamer bioconjugates. *Biosens. Bioelectron. 21*, 1859–66.

(9) Lupold, S. E., Hicke, B. J., Lin, Y., and Coffey, D. S. (2002) Identification and characterization of nuclease-stabilized RNA molecules that bind human prostate cancer cells via the prostate-specific membrane antigen. *Cancer Res. 62*, 4029–33.

(10) Mirkin, C. A., Letsinger, R. L., Mucic, R. C., and Storhoff, J. J. (1996) A DNA-based method for rationally assembling nanoparticles into macroscopic materials. *Nature 382*, 607–9.

(11) Rodriguez, J. A., Dvorak, J., Jirsak, T., Liu, G., Hrbek, J., Aray, Y., and Gonzalez, C. (2003) Coverage effects and the nature of the metal-sulfur bond in S/Au(111): high-resolution photoemission and density-functional studies. *J. Am. Chem. Soc. 125*, 276–85.

(12) Hurst, S. J., Lytton-Jean, A. K., and Mirkin, C. A. (2006) Maximizing DNA loading on a range of gold nanoparticle sizes. *Anal. Chem. 78*, 8313–8.

(13) Adams, K. E., Ke, S., Kwon, S., Liang, F., Fan, Z., Lu, Y., Hirschi, K., Mawad, M. E., Barry, M. A., and Sevick-Muraca, E. (2007) Comparison of visible and near-infrared wavelength-excitable fluorescent dyes for molecular imaging of cancer. *J. Biomed. Opt. 12*, 024017. /1−024017/9.

(14) Nitin, N., Javier, D. J., and Richards-Kortum, R. (2007) Oligonucleotide-coated metallic nanoparticles as a flexible platform for molecular imaging agents. *Bioconjugate Chem. 18*, 2090–6.

(15) Medley, C. D., Smith, J. E., Tang, Z., Wu, Y., Bamrungsap, S., and Tan, W. (2008) Gold nanoparticle-based colorimetric assay for the direct detection of cancerous cells. *Anal. Chem. 80*, 1067–1072.

(16) Chu, T. C., Marks, J. W., III, Lavery, L. A., Faulkner, S., Rosenblum, M. G., Ellington, A. D., and Levy, M. (2006) Aptamer:toxin conjugates that specifically target prostate tumor cells. *Cancer Res. 66*, 5989–92.

BC8001248

TECHNICAL NOTES

Evaluation of Ketone-Oxime Method for Developing Therapeutic On-Demand Cleavable Immunoconjugates

Pappanaicken R. Kumaresan,* Juntao Luo, Aimin Song, Jan Marik, and Kit S. Lam. Received January 17, 2008; Revised Manuscript Received March 31, 2008

The use of antibody molecules in immunoassay, molecular targeting, or detection techniques encompasses a broad variety of applications affecting nearly every field of medical science. In cancer therapy, monoclonal antibodies (mAb) have been used as vehicles to deliver radionuclides, toxins, or drugs to the target cancer cells. New conjugation methods are most needed to conjugate a wide variety of targeting small molecules and peptidomimatic compounds. Here, we exploited a keto-oxime method for conjugation of protease susceptible linkers to an antibody. This modified method involves two steps: (i) introduction of methyl ketone linkers (referred to as linker moiety) to the primary amines present in the antibody and (ii) conjugation of ketone linkers to aminoxy functional group present in the conjugated moiety (referred to as functional moiety). We have optimized this conjugation method and shown that ~10 functional moieties can be conjugated to antibody. Conjugation was verified by MALDI-TOF MS and Western blot analysis. The acidic pH conditions used in this method did not change the immune reactivity of the Ab. In addition, *in vitro* protease susceptibility assay was performed to validate this method for prodrug release assay as well as to remove excess radioimmune conjugates from circulation. This orthogonal method is compatible with peptides containing a thiol, amino, or carboxyl groups in the conjugation moiety.

1. INTRODUCTION

Ketones selectively react with amino-oxy groups and form oxime bonds at slightly acidic pH. This type of chemoselective ligation is more preferable for making bioconjugates because it does not require anhydrous conditions, excessive heat, or any catalyst (*1, 2*). It is also tolerant of a wide range of functional groups that are found in proteins and oligonucleotides. This ligation has been successfully used in various applications such as making small molecule drug conjugates (*3*), peptide and oligonucleotide conjugates (*4*), protein conjugates (*5*), glycoconjugates (*2*), polymer conjugates (*6, 7*), and coating biomolecules on plannar microarray slides (*8*) and sialoglycoproteins present on cell wall (*9, 10*). Except for N-terminal labeling (*11*), this ligation method has not been used to make antibody drug conjugates especially in the area of cancer targeted therapy. Antibodies are important biomolecules developed by nature to protect hosts by eliminating disease-causing pathogens. Several conjugation methods have been developed to conjugate radionuclides, toxins, or drugs to antibody for cancer therapy (*12–17*). Here, we report conjugation of tissue plasminogen activator (t-PA) substrate rqYKYkf (*18*) to ChL6 antibody by the keto-oxime method. Chemical synthesis of methylketo linkers, aminoxy-functional peptides and optimization of conjugation method and its bioapplications are discussed.

2. MATERIALS AND METHODS

Rink amide MBHA resin (0.45 mmol/g) was purchased from Tianjin Nankai Hecheng (Tianjin, China). Levulinate *N*-succinimidyl ester was prepared using our previously published procedure (*8*). All the amino acid derivatives and HOBt (1-hydroxybenzotriazole) were purchased from CPC (San Jose, CA). DIC (diisopropylcarbodiimide) was purchased from Advanced ChemTech (Louisville, KY). DMF (*N*,*N*-dimethylformamide) was purchased from VWR (Brisbane, CA). DCM (dichloromethane), MeOH (methanol), diethyl ether, and acetonitrile were purchased from Fisher (Houston, TX). All other chemical reagents were purchased from Aldrich (Milwaukee, WI). Analytical HPLC analyses (Vydac column, 4.6 mm × 250 mm, 5 μm, 300 Å, C_{18}, 1.0 mL/min, 25 min gradient from 100% aqueous media (0.1% TFA) to 100% CH_3CN (0.1% TFA), 214, 220, 254, and 280 nm) and preparative HPLC purification (Vydac column, 20 mm × 250 mm, 5 μm, 300 Å, C_{18}, 7.0 mL/min, 45 min gradient from 100% aqueous media (0.1% TFA) to 100% CH_3CN (0.1% TFA), 254 nm) were performed on a Beckman System Gold HPLC system (Fullerton, CA). MALDI-TOF MS analysis was performed on a Bruker BIFLEX III mass spectrometer (Billerica, MA). All of the experiments are carried out at room temperature unless otherwise noted. ChL6 (Bristol-Myers Squibb Pharmaceutical Research Institute, Seattle, WA) was a chimera consisting of human IgG1-constant regions and the murine L6 mAb antigen-binding site.

2.1. Synthesis of Biotin-rqYKYkf-spacer-K(Aoa)-NH_2 Peptide. Solid-phase synthesis of biotin-rqYKYkf was carried out using Rink amide MBHA resin after the treatment of resin with 20% piperidine solution in DMF (2 mL) for 15 min to remove Fmoc protecting group. Onto the Rink resin (200 mg, 0.09 mmol) with free amino groups, Fmoc-Lys(Alloc)-OH (122.2 mg, 0.27 mmol) was coupled following the standard Fmoc chemistry using HOBt (36.5 mg, 0.27 mmol) and DIC (42.3 μL, 0.27 mmol) as coupling agents. The coupling was monitored using ninhydrin test agents until a negative result was obtained. The resin was washed with DMF, MeOH, and DCM 3 times,

* Corresponding author. Pappanaicken R. Kumaresan, 4501 X-street, UC Davis Medical Center, Sacramento, CA-95817. Ph: 916-734-0905(off). Ph: 916-734-6414(lab). Fax: 916-734-6415. E-mail: pkumaresan@ucdavis.edu.

10.1021/bc800024v CCC: $40.75 © 2008 American Chemical Society
Published on Web 05/22/2008

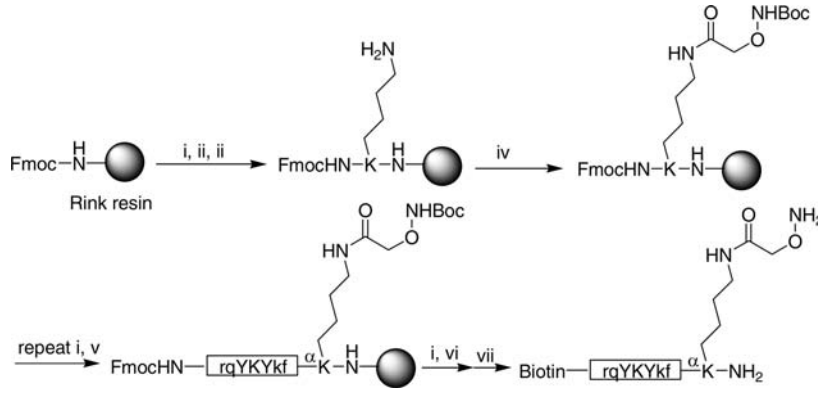

Figure 1. Schematic representation of the synthesis of aminoxy peptide. (i) 20% Piperidine in DMF; (ii) Fmoc-Lys(Alloc)-OH, DIC/HOBt; (iii) $Pd(PPh_3)_4/PhSiH_3$; (iv) Boc-Aoa-OH, DIC/HOBt; (v) Fmoc-AA_i, DIC/HOBt; (vi) Biotin, HBTU/DIEA; (vii) K Reagent (TFA/phenol/thioanisole/water/propylsilane, 82.5/7.5/5/5/2.5, v/w/v/v/v.

respectively. The resin was treated twice with $Pd(PPh_3)_4$ (26.0 mg, 0.0225 mmol) in the presence of excessive $PhSiH_3$ (266.5 μL, 2.16 mmol) in DCM under argon for 30 min to remove the alloc protecting groups on the side chain of lysine. After thoroughly washing the resin with DCM, DMF, MeOH, and DMF, Boc-Aoa-OH (51.6 mg, 0.27 mmol) was coupled onto the resin using HOBt (36.5 mg, 0.27 mmol) and DIC (42.3 μL, 0.27 mmol) as coupling agents until the ninhydrin test was negative. After deprotection of Fmoc groups by piperidine treatment, a linear hydrophilic linker was coupled to the α-amino group of the lysine as a spacer following a published procedure (*19*). The peptide was constructed on the linker using standard Fmoc chemistry using DIC/HOBt as coupling agents (*20*). After the coupling of the last amino acid, the N-terminus Fmoc protection group was removed by piperidine treatment. The resin was treated with a solution of biotin (44.0 mg, 0.18 mmol), DIEA (diisopropylethylamine, 42.3 μL, 0.36 mmol), and HBTU (*O*-(benzotriazol-1-yl)-*N*,*N*,*N*′,*N*′-tetramethyluronium hexafluorophosphate, 68.3 mg, 0.18 mmol) in DMF (2 mL) until the ninhydrin test was negative. The resin was thoroughly washed with DMF, MeOH, and DCM, and then dried *in vacuo*. To the dried resin was added 4 mL of cleavage mixture (TFA (trifluoroacetic acid)/phenol/thioanisole/water/TIS (triisopropylsilane), 82.5:7.5:5:5:2.5, v/w/v/v/v) at ice-bath temperature. The mixture was slowly warmed to room temperature and allowed to agitate for 6 h. The supernatant was then collected and the resin was washed with TFA (3 × 1 mL). The combined supernatants were concentrated to 1 mL under a stream of nitrogen. The peptide was precipitated by dilution with cold ethyl ether (10 mL), collected by centrifuge, washed with ethyl ether, and dried *in vacuo*. The crude peptide was analyzed and purified by HPLC, and characterized by MALDI-TOF MS.

2.2. Antibody Conjugation. This keto-oxime method has two steps. First, ketone linkers will be conjugated to primary amines of the antibody followed by conjugation of functional derivatives such as DOTA chelators, immunotoxin, or chemotoxin. Before conjugation, the required amounts of antibody were purified by passing through a Sephadex-G100 molecular sieving column to remove impurities and are equilibrated with 40 mM of ketone linker conjugation buffer triethanolamine (pH 7.8). The linker conjugation can be done with phosphate buffer 50 mM (pH 7.8). In order to identify optimum ketone group introduction to Ab, conjugation was done with antibody at different molar ratios (10:1, 20:1, 30:1, and 300:1) for 1 h at room temperature. After conjugation, the excess free linkers were removed by passing through the Sephadex-G100 spin columns. In the second step, aminoxy functional conjugates were conjugated to the ketone linker of Ab with different molar ratios of linker to Ab (10:1, 20:1, and 30:1) at RT for 4 h in the present of TEA (40 mM, pH 5.5). We have selected a biotin-tagged

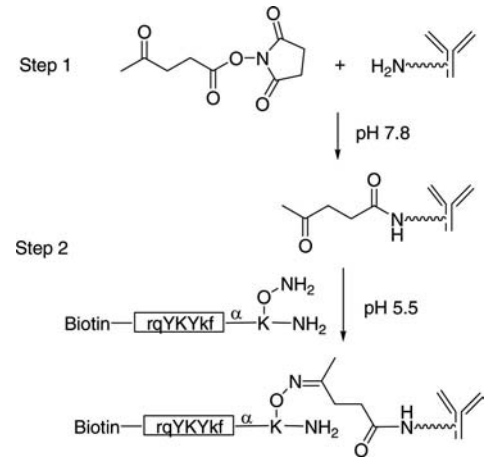

Figure 2. Schematic representation of ketone-oxime conjugation reaction.

Table 1. Optimization of Ketone Linkers Per Ab Molecule

linker moiety / Ab ratio	# linker moiety per Ab molecule	# functional moieties per Ab molecule*
5:1	none	none
10:1	none	none
30:1	5−6	1−3
300:1	~ 80	7−11

* Functional moiety conjugation was done at 30:1 ratio with antibody.

rqYKYkf peptide, which is cleavable by tissue plasminogen activator (t-PA, recombinant version of t-PA, trade name TNKase) (*18*), as a functional derivative to verify this conjugation method for antibody studies. Conjugation was confirmed by determining the mass of the antibody and peptide conjugated antibody by using MALDI-TOF mass spectrometry.

2.3. Western Blot Analysis and Protease Cleavage Studies. Breast adenocarcinoma cancer cell targeting antibody (ChL6) (*21*) and biotin-rqYKYkf-conjugated ChL6 was separated at 10% SDS-PAGE gel and transferred onto nitro cellulose membrane. The transferred membrane was blocked with 1% BSA for 3 h at RT and incubated with HRPO-conjugated avidin for 30 min. Unbound avidin was removed by washing three times with TBS containing 0.2% Tween-20 and bands were developed by ECL method (Perkin-Elmer life Sciences). Biotinylated anti-insulin antibody was used as control. For protease susceptibility studies, biotin-rqYKYkf-conjugated ChL6 was incubated with TNKase at different concentrations (0, 10, and 25 μg/mL) in TBS buffer pH 8.0 for 1 h at 37 °C. Digested

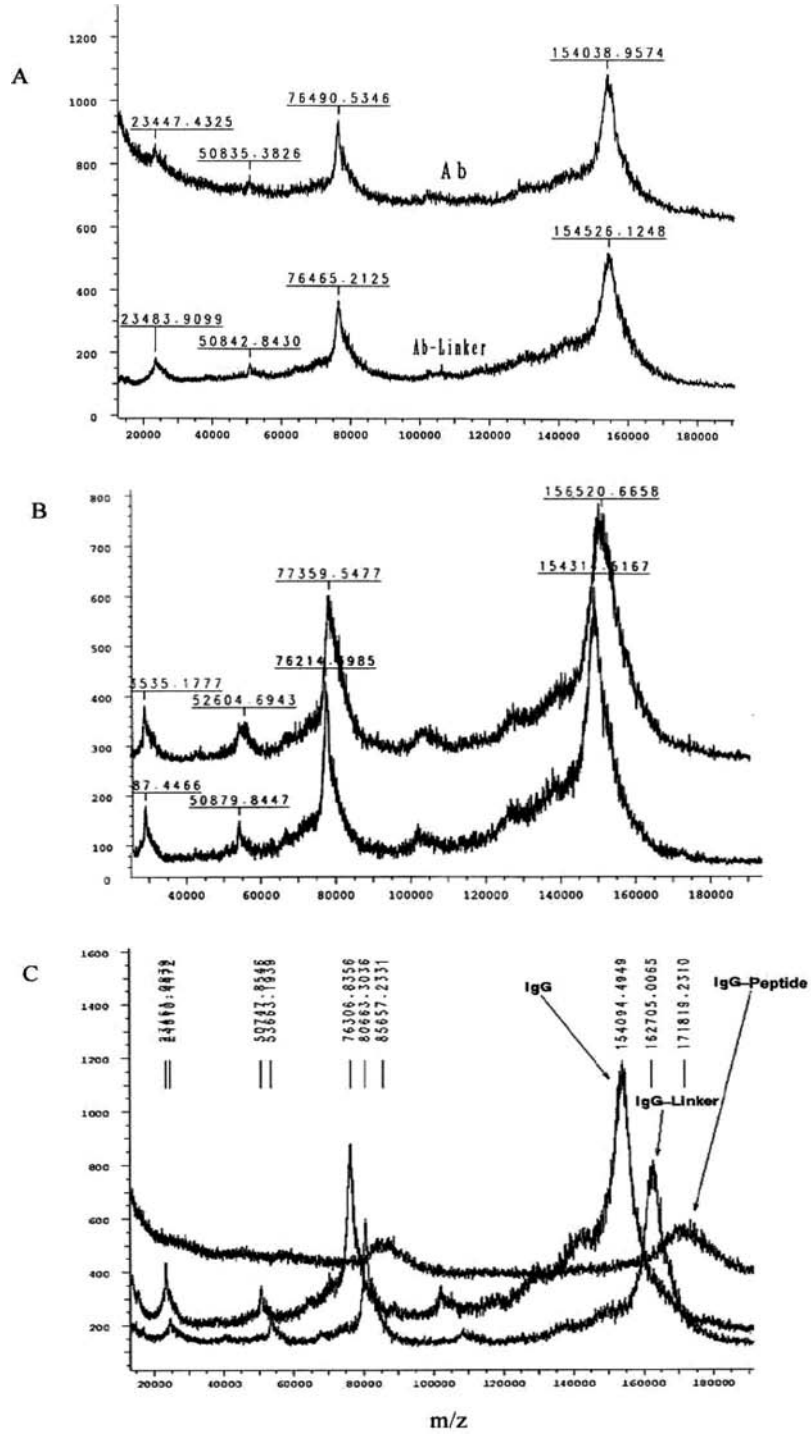

Figure 3. MALDI-MS analysis of ChL6 Ab, ChL6-linker moiety, and ChL6-functional moiety: (A) At 30:1 molar ratio of linker to Ab, ~5−6 linker moiety was conjugated to ChL6 Ab. (B) At 30:1 molar ratio, ~1−3 functional moiety (MW 1688) was conjugated to ChL6. (C) At 300:1 molar ratio, ~7−11 functional moieties were conjugated. The average incorporated values are shown. At this ratio, ChL6 with linker moiety showed a distinct peak suggesting that most of the primary amines in ChL6 are conjugated with linker moiety.

products are separated, transferred to membrane, and stained with avidin-HRPO as described above.

2.4. Immunohistochemistry. Breast adenocarcinoma cancer cells were seeded on a six-well plate one day before the experiments were performed. 1 μg of ChL6 and biotin-rqYKYkf-conjugated ChL6 were added directly into 1 mL of growth media in duplicate and kept for 1 h on ice. Unbound antibodies were removed by washing three times with PBS containing 1% BSA. FITC-conjugated streptavidin was added to each well and kept on ice for 30 min, followed by washing three times with PBS containing 1% BSA to remove the unbound streptavidin. Fluorescent staining was observed under the fluorescence microscope in green filter (U-M51004 F/R-V2; Olympus).

3. RESULTS AND DISCUSSION

3.1. Characterization of Biotin-rqYKYkf-spacer-K [Aminoxy (Aoa)]-NH_2 Peptide. The methyl ketone linker (Levulinate *N*-succinimidyl ester) was synthesized according to the reported procedure using levulinic acid and *N*-hydroxyl succinimide as starting materials and 85% yield was obtained (*8, 22*). Synthetic

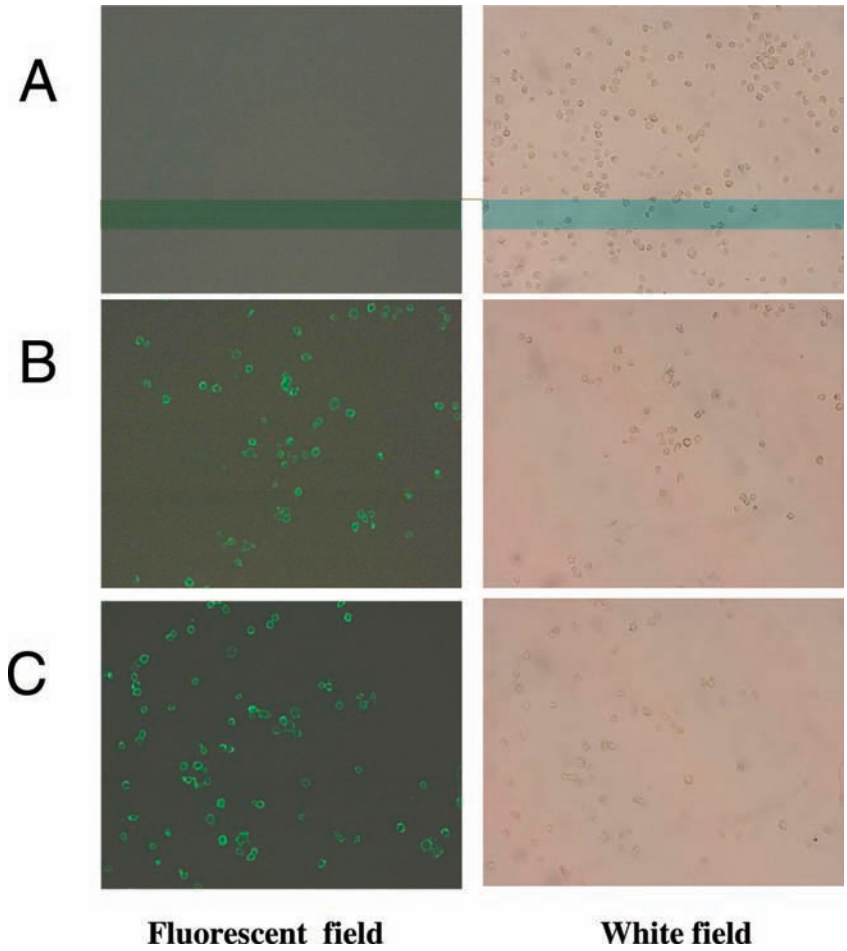

Figure 4. Immunoreactivity assay: Breast cancer cells (HBT) were incubated with ChL6 (B) and ChL6 conjugated to functional moiety (C) followed by FITC conjugated murine antihuman Ab. ChL6 conjugated with functional moiety (C) showed binding as good as native unaltered ChL6 (B). FITC conjugated murine antihuman IgG did not show any binding (A).

scheme of biotin-rqYKYkf-spacer-K(Aoa)-NH_2 peptide was shown in Figure 1. A total of 25 mg of biotin-rqYKYkf-spacer-K(Aoa)-NH_2 was obtained from 200 mg of resin (yield: 16%). The synthetic product was verified by MALDI-TOF MS $(M+H)^+$ calculated: 1688.9; found: 1688.5.

3.2. Optimization of Ketone-Oxime Conjugation. This modified ketone-oxime method has two steps. (i) introduction of the NHS-ketone linkers (referred as linker moiety) to the primary amines present in the antibody and (ii) conjugation of ketone group to aminoxy functional group present in the conjugated moiety (referred to as functional moiety). Steps involved in this conjugation are shown in Figure 2.

First, ketone linkers were introduced by reacting the NHS group with primary amines of the antibody at various molar ratio (L/Ab 5:1, 10:1, 30:1, and 300:1). MALDI-MS results revealed that antibody derivatives occurred when a 20-fold excess or more of ketone linker was used in the initial antibody modification step. No conjugation was observed when 5:1 or 10:1 molar ratio of L/Ab was used. Table 1 summarizes the level of antibody derivatives under various L/Ab ratios. At 30:1 (L/Ab) ratio, ~5−6 linker moieties were conjugated to each Ab molecule (Figure 3A). The same preparation will yield 1−3 functional conjugates (Figure 3B). At (L/Ab) ratio of 300:1, mass spectrometry analysis of ChL6 Ab showed a distinct peak (Figure 3C) suggesting that most of the primary amines present in the Ab were conjugated. When functional moiety is conjugated at 30 molar ratio to an antibody, ~3 functional moieties were generated from this preparation. Previous reports have shown that, in order to retain the biological function of antibodies, conjugation of a functional moiety should not exceed 8. Therefore, we have selected 30:1 L/Ab ratio to perform our conjugation studies.

3.3. Immunoreactivity Assay. CHL6, a chimeric antibody that targets a breast cancer antigen, was used for conjugation studies (*21*). To verify that this conjugation method does not alter antigen binding properties of CHL6 antibody, it was conjugated with biotin-tagged peptide at 30:1 L/Ab ratio, and immunoreactivity assay was performed on breast cancer cells (HBT). Figure 3 shows that both conjugated and unconjugated ChL6 antibody were binding HBT breast cancer cells with similar intensity, confirming that the conjugation method did not alter the antigen binding property of CHL6 (Figure 4).

3.4. Protease Susceptibility Assay. In clinics, antibodies have been used for targeting as well as delivering therapeutic drugs, especially prodrugs to eliminate infected and transformed cells. These nontoxic prodrugs get converted to a toxic metabolite when it is cleaved by a specific protease such as Cathepsin-B at the target site (*23*). A similar strategy has been used in radioimmunotherapy (RIT), to remove circulating radioimmunoconjugates after tumor targeting. This will boost the therapeutic potential of RIT which was greatly limited by exposure of radiation to vital organs (liver, bone marrow) during the treatment. These linkers can be cleaved either internally by proteases expressed in vital organs such as the liver (e.g., Cathepsin-D) (*24*) or externally by administering enzymes such as β-lactamase (*25*) and TNKase (*18*). We have selected TNKase as an on-demand cleavable enzyme because it is already in clinical use to dissolve fibrin clots (*26, 27*). Protease susceptibil-

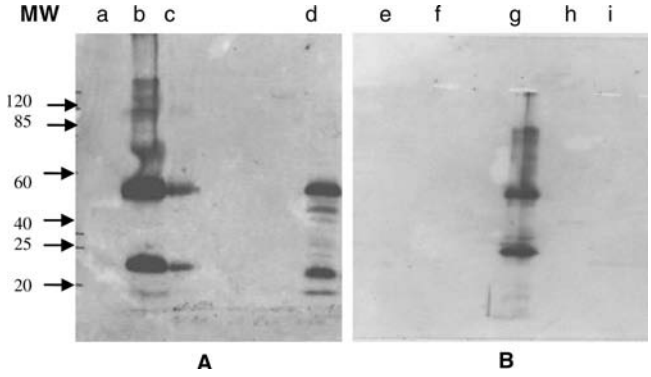

Figure 5. Western blot and protease susceptibility analysis: (A) ChL6−10μg (a), ChL6-conjugated with biotin-rqYKYkf−10μg (b), ChL6-conjugated with biotin-rqYKYkf−1μg (c), biotinylated anti-insulin Ab (d) was electrophoresed in 10% SDS-PAGE gel and developed using ECL after transferring to a nylon membrane. Positive bands appeared only on conjugated ChL6 (b,c,d) and not the native ChL6 (a). (B) To evaluate protease susceptibility of the functional moiety (t-PA substrate), conjugated ChL6 was incubated with various concentrations of TNKase, 0 μg/mL (g),10 μg/mL (h), and 25 μg/mL (i). The band has disappeared in TNKase-treated lanes (h,i) and not in untreated lanes (g). Native ChL6 and TNKase were run together as a negative control. Standard MW markers are shown on the left side of the figure.

ity was evaluated by incorporating t-PA substrate "rqYKYkf", identified by screening one-bead−one-compound combinatorial chemistry libraries in linker moiety with biotin tag (*18*). After conjugation with ChL6 at 30:1 molar ratio, 5 μg/mL samples were taken in triplicate and digested with 0, 10, and 25 μg/mL of recombinant t-PA (TNKase) for 2 h at RT. Digested samples were identified by Western blot analysis as described in the Materials and Methods section. ECL showed bands only in the conjugated ChL6 and not with ChL-6 alone or in TNKase-digested conjugated ChL6 samples, suggesting that biotin was removed by protease digestion. This confirms that this method can be used as an alternative method to conjugate therapeutic drugs, especially prodrugs (Figure 5).

CONCLUSION

Previously, we used the methods described here to print peptides and small molecules in microarrays over a planar surface (*8*). Previously, *in vivo* small molecule drug conjugate studies have demonstrated oxime bond stability at the physiological pH of body fluids (*28*, *29*). Here, we have demonstrated this method to conjugate protease (TNKase) cleavable peptides to antibodies without affecting their antigen binding properties. We also showed that conjugated substrates were susceptible to TNKase at the clinical dosage. We conclude that the ketone-oxime method can be substituted in place of other methods like maleimide (*12*) and click chemistry conjugation (*30*) for making therapeutic antibody conjugates. This method is compatible with peptides containing a thiol, amino, or carboxyl group in the conjugation moiety.

ACKNOWLEDGMENT

Author greatly appreciated Dr. Sally Denardo for providing ChL6 antibody and HBT cells and Dr. Seth Dixon for proofreading. This study was supported by funds from NIH Grant P01-CA047829-15A2 and DOD-CM064046.

LITERATURE CITED

(1) Hovinen, J. (2006) Synthesis of aminooxy-functionalized lanthanide(III) chelates for carbonyl-group conjugation. *Chem. Biodiversity 3*, 296–303.

(2) Langenhan, J. M., and Thorson, J. S. (2005) Recent carbohydrate-based chemoselective ligation applications. *Curr. Org. Synth. 2*, 59–81.

(3) Burkhart, D. J., Kalet, B. T., Coleman, M. P., Post, G. C., and Koch, T. H. (2004) Doxorubicin-formaldehyde conjugates targeting $\alpha_v\beta_3$ integrin. *Mol. Cancer Ther. 3*, 1593–604.

(4) Zatsepin, T. S., Stetsenko, D. A., Arzumanov, A. A., Romanova, E. A., Gait, M. J., and Oretskaya, T. S. (2002) Synthesis of peptide-oligonucleotide conjugates with single and multiple peptides attached to 2'-aldehydes through thiazolidine, oxime, and hydrazine linkages. *Bioconjugate Chem. 13*, 822–30.

(5) Kubler-Kielb, J., Liu, T. Y., Mocca, C., Majadly, F., Robbins, J. B., and Schneerson, R. (2006) Additional conjugation methods and immunogenicity of Bacillus anthracis poly-γ-D-glutamic acid-protein conjugates. *Infect. Immunol. 74*, 4744–9.

(6) Gaertner, H. F., and Offord, R. E. (1996) Site-specific attachment of functionalized poly(ethylene glycol) to the amino terminus of proteins. *Bioconjugate Chem. 7*, 38–44.

(7) Vilaseca, L. A., Rose, K., Werlen, R., Meunier, A., Offord, R. E., Nichols, C. L., and Scott, W. L. (1993) Protein conjugates of defined structure: synthesis and use of a new carrier molecule. *Bioconjugate Chem. 4*, 515–20.

(8) Xu, Q., Miyamoto, S., and Lam, K. S. (2004) A novel approach to chemical microarray using ketone-modified macromolecular scaffolds: application in micro cell-adhesion assay. *Mol. Diversity 8*, 301–10.

(9) Lemieux, G. A., and Bertozzi, C. R. (1998) Chemoselective ligation reactions with proteins, oligosaccharides and cells. *Trends Biotechnol. 16*, 506–513.

(10) Lemieux, G. A., Yarema, K. J., Jacobs, C. L., and Bertozzi, C. R. (1999) Exploiting differences in sialoside expression for selective targeting of MRI contrast reagents. *J. Am. Chem. Soc. 121*, 4278–4279.

(11) Scheck, R. A., and Francis, M. B. (2007) Regioselective labeling of antibodies through N-terminal transamination. *ACS Chem. Biol. 2*, 247–51.

(12) Traut, R. R., Casiano, C., and Zecherle, N. (1989) Cross-linking of protein subunits and ligands by the introduction of disulfide bonds, in *Protein Function-a Practical Approach* (Creighton, T. E., Ed.) pp 101−133, IRL Press, Oxford University, Oxford, U.K.

(13) Hermanson, T. G. (1996) Bioconjugates and applications, in *Bioconjugate chemistry* (Hermanson, T. G., Ed.), Academic Press, London.

(14) Dixon, H. B. F. (1984) N-Terminal modification of proteins-a review. *J. Protein Chem. 3*, 99–108.

(15) Gilmore, J. M., Scheck, R. A., Esser-Kahn, A. P., Joshi, N. S., and Francis, M. B. (2006) N-terminal protein modification through a biomimetic transamination reaction. *Angew. Chem., Int. Ed. 45*, 5307–5311.

(16) Wu, P., and Brand, L. (1997) N-terminal modification of proteins for fluorescence measurements. *Methods Enzymol. 278*, 321–330.

(17) Natarajan, A., Du, W. J., Xiong, C. Y., DeNardo, G. L., DeNardo, S. J., and Gervay-Hague, J. (2007) Construction of di-scFv through a trivalent alkyne-azide 1,3-dipolar cycloaddition. *Chem. Commun.* 695–697.

(18) Kumaresan, P. R., Natarajan, A., Song, A. M., Wang, X. B., Liu, R. W., DeNardo, G., DeNardo, S., and Lam, K. S. (2007) Development of tissue plasminogen activator specific "on demand cleavable" (ODC) linkers for radioimmunotherapy by screening one-bead-one-compound combinatorial peptide libraries. *Bioconjugate Chem. 18*, 175–182.

(19) Song, A. M., Wang, X. B., Zhang, J. H., Marik, J., Lebrilla, C. B., and Lam, K. S. (2004) Synthesis of hydrophilic and flexible linkers for peptide derivatization in solid phase. *Bioorg. Med. Chem. Lett. 14*, 161–165.

(20) Fields, G. B., and Noble, R. L. (1990) Solid-phase peptide-synthesis utilizing 9-fluorenylmethoxycarbonyl amino-acids. *Int. J. Pept. Protein Res. 35*, 161–214.

(21) Goodman, G. E., Hellstrom, I., Yelton, D. E., Murray, J. L., Ohara, S., Meaker, E., Zeigler, L., Palazollo, P., Nicaise, C., Usakewicz, J., and Hellstrom, K. E. (1993) Phase-I trial of chimeric (human-mouse) monoclonal-antibody L6 in patients with non-small-cell lung, colon, and breast-cancer. *Cancer Immunol. Immunother. 36*, 267–273.

(22) Lee, J. H., Baker, T. J., Mahal, L. K., Zabner, J., Bertozzi, C. R., Wiemer, D. F., and Welsh, M. J. (1999) Engineering novel cell surface receptors for virus-mediated gene transfer. *J. Biol. Chem. 274*, 21878–84.

(23) Jeffrey, S. C., Torgov, M. Y., Andreyka, J. B., Boddington, L., Cerveny, C. G., Denny, W. A., Gordon, K. A., Gustin, D., Haugen, J., Kline, T., Nguyen, M. T., and Senter, P. D. (2005) Design, synthesis, and in vitro evaluation of dipeptide-based antibody minor groove binder conjugates. *J. Med. Chem. 48*, 1344–58.

(24) DeNardo, G. L., DeNardo, S. J., Peterson, J. J., Miers, L. A., Lam, K. S., Hartmann-Siantar, C., and Lamborn, K. R. (2003) Preclinical evaluation of cathepsin-degradable peptide linkers for radioimmunoconjugates. *Clin. Cancer Res. 9*, 3865S–72S.

(25) Beeson, C., Butrynski, J. E., Hart, M. J., Nourigat, C., Matthews, D. C., Press, O. W., Senter, P. D., and Bernstein, I. D. (2003) Conditionally cleavable radioimmunoconjugates: a novel approach for the release of radioisotopes from radioimmunoconjugates. *Bioconjugate Chem. 14*, 927–33.

(26) Falk, A., and Harbour, K. (2005) Tenecteplase in the treatment of thrombosed hemodialysis grafts. *Cardiovasc. Interventional Radiol. 28*, 472–475.

(27) Guerra, D. R., Karha, J., and Gibson, C. M. (2003) Safety and efficacy of tenecteplase in acute myocardial infarction. *Expert Opin. Pharmacother. 4*, 791–798.

(28) Wilde, M. 1., Plosker, G. L., and Benfield, P. (1993) Fluvoxamine - an updated review of its pharmacology, and therapeutic use in depressive-illness. *Drugs 46*, 895–924.

(29) Pozsgay, V., Kubler-Kielb, J., Schneerson, R., and Robbins, J. B. (2007) Effect of the nonreducing end of Shigella dysenteriae type 10-specific oligosaccharides on their immunogenicity as conjugates in mice. *Proc. Natl. Acad. Sci. U.S.A. 104*, 14478–14482.

(30) Baskin, J. M., and Bertozzi, C. R. (2007) Bioorthogonal click chemistry: Covalent labeling in living systems. *QSAR Comb. Sci. 26*, 1211–1219.

BC800024V

Hyaluronic Acid−Paclitaxel Conjugate Micelles: Synthesis, Characterization, and Antitumor Activity

Hyukjin Lee, Kyuri Lee, and Tae Gwan Park*

Department of Biological Sciences, Korea Advanced Institute of Science and Technology, Daejeon 305-701, South Korea.
Received February 11, 2008; Revised Manuscript Received April 8, 2008

Chemical conjugates of paclitaxel and hyaluronic acid (HA) were synthesized by utilizing a novel HA solubilization method in a single organic phase. Hydrophilic HA was completely dissolved in anhydrous DMSO with addition of poly(ethylene glycol) (PEG) by forming nanocomplexes. Paclitaxel was then chemically conjugated to HA in the DMSO phase via an ester linkage without modifying extremely hydrophilic HA. A series of HA−paclitaxel conjugates with different conjugation percentages were synthesized and characterized. HA−paclitaxel conjugates self-assembled in aqueous solution to form nanosized micellar aggregates, as characterized by dynamic light scattering (DLS), atomic force microscopy (AFM), and transmission electron microscopy (TEM). An intact form of paclitaxel was regenerated from HA−paclitaxel conjugate micelles at acidic pH conditions. HA−paclitaxel conjugate micelles exhibited more pronounced cytotoxic effect for HA receptor overexpressing cancer cells than for HA receptor deficient cells, suggesting that they can be potentially utilized as tumor-specific nanoparticulate therapeutic agents.

INTRODUCTION

Paclitaxel is a powerful anticancer drug originally isolated from the bark of pacific yew (*Taxus brevifolia*) and is well-known for its antimitotic activity that promotes tubulin assembly into stable microtubules (*1*–*3*). Paclitaxel prevents the depolymerization of polymerized microtubules, thus inhibiting cell replication in the late G_2/M phase of the cell cycle (*4*, *5*). Although paclitaxel has shown remarkable potential as an anticancer drug, its poor solubility in water has limited widespread use in cancer therapy. Current clinical formulation such as Taxol contains a 50:50 mixture of Cremophore EL and ethanol to enhance the solubility of paclitaxel in water. However, a large number of studies have reported various side effects of Cremophore EL such as hypersensitivity, neurotoxicity, and neuropathy (*6*–*8*). Previous attempts to overcome the serious side effects include formulating paclitaxel in various carriers such as polymer conjugates, liposomes, polymeric micelles, emulsions, and nanospheres (*9*–*12*).

Among them, drug−polymer conjugates have distinctive advantages over conventional polymeric nanosized carriers by demonstrating high drug content and good solubility in water, increasing drug half-life in the body, and enhancing antitumor effects (*13*). Although various water-soluble synthetic polymers have been widely exploited for conjugation of hydrophobic drugs, naturally occurring polymers with intrinsic cell specific binding capacity have tremendous potential as a target specific drug carrier. For example, hyaluronic acid (HA), a naturally occurring polysaccharide composed of *N*-acetyl-D-glucosamine and D-glucuronic acid, has a strong affinity with cell-specific surface markers such as CD44 and RHAMM (*14*). HA plays important roles in biological functions, such as stabilizing and organizing the ECM, regulating cell adhesion and motility, and mediating cell proliferation and differentiation (*15*–*17*). HA is also closely related to angiogenesis in many types of tumors, in which HA receptors (CD44 and RHAMM) are abundantly overexpressed on the surface. Thus, malignant cells with high metastatic activities often exhibit enhanced binding and uptake of HA (*18*–*20*). More recently, HA and its derivatives have been popularly used as target-specific drug delivery vehicles for various therapeutic agents (*21*–*23*).

Chemical modification and conjugation of HA have been achieved in aqueous solution by utilizing reactive functional groups in HA such as carboxylic groups and hydroxyl groups and a reducing end (*24*–*26*). However, its extreme hydrophilicity and poor solubility in most organic solvents restrict the direct conjugation of HA with hydrophobic polymers, drugs, and lipids. To circumvent the above problems, various solubilization methods were utilized to obtain a homogeneous mixture of HA and hydrophobic reactants in a common solvent. For example, a mixture of polar organic solvent and water (i.e., DMSO/H_2O or DMF/H_2O) was used to codissolve *N*-hydroxysuccinimide-activated paclitaxel and adipic dihydrazide functionalized HA for conjugation (*27*). Polyanionic HA was physically complexed with aliphatic quaternary ammonium compounds or chemically blocked to enhance the solubility of HA in the mixed organic solvents for further modification (*28*). However, the above methods have shown some limitations such as multiple activation steps required for conjugation in mixed water/organic solvent phase and utilizing environmentally cytotoxic ammonium surfactants that are not preferred for biomedical and drug delivery applications.

Previously, we reported the solubilization of DNA in organic solvents using biocompatible poly(ethylene glycol) (PEG) by forming nanoscale complexes (*29*). More recently, other hydrophilic biomacromolecules such as proteins and carbohydrates could also be solubilized in organic solvents by using PEG as a nanocomplexing agent (*30*). Since PEG can act as both hydrogen bonding donor and acceptor, it was hypothesized that the addition of PEG in organic solvents could also facilitate the formation of HA/PEG nanocomplexes by inter- and intrahydrogen bonds (*31*). In the present study, HA was solubilized in anhydrous DMSO by complexing with dimethoxy poly(ethylene glycol) (dmPEG). It was expected that HA soluble in DMSO could be readily conjugated by various hydrophobic drugs, thus generating HA−drug bioconjugates with high yield without using any salts and blocking agents. A typical water-insoluble anticancer drug, paclitaxel, was chosen for HA−drug conjuga-

* Corresponding author. Tel: +82-42-869-2621; Fax: +82-42-869-2610; E-mail address: tgpark@kaist.ac.kr (T.G. Park).

10.1021/bc8000485 CCC: $40.75 © 2008 American Chemical Society
Published on Web 05/16/2008

Table 1. HA−Paclitaxel Conjugates Prepared by Different Conditions

sample number	HA (mg)	DCC/DMAP molar ratio to −COOH	Paclitaxel in feed (mg)	Paclitaxel amount in the conjugates (mg)	Paclitaxel conjugation yield (%)	Paclitaxel loading amount (w/w %)
1	100	0.5	10	1.18 ± 0.03	11.8	1.17
2	100	1.0	10	3.26 ± 0.05	32.6	3.16
3	100	3.0	10	5.96 ± 0.08	59.6	5.62
4	100	3.0	20	12.16 ± 0.16	60.8	10.84

tion in organic solvents. HA−paclitaxel conjugate was synthesized and their self-assembly properties in aqueous solution were characterized using dynamic light scattering (DLS), atomic force microscopy (AFM), and transmission electron microscopy (TEM). Critical aggregation concentration (CAC) was also determined by employing hydrophobic fluorescence probes. Target-specific antitumor activities were comparatively evaluated using HA-receptor positive and negative cells.

EXPERIMENTAL PROCEDURES

Materials. Hyaluronic acid (HA) sodium salt (MW: 64 kDa) was purchased from Lifecore Biomedical (Chaska, MN). Poly(ethylene glycol) dimethyl ether (dmPEG) (MW: 2000 Da), 1,3-dicyclohexylcarbodiimide (DCC), 4-dimethylaminopyridine (DMAP), propidium iodide (PI), pyrene, and anhydrous dimethyl sulfoxide (DMSO) were all obtained from Sigma-Aldrich (St. Louis, MO). Paclitaxel was purchased from TCI (Tokyo, Japan). Cell counting kit-8 (CCK-8) was obtained from Dojindo laboratories (Kumamoto, Japan). All other chemicals and reagents were of analytical grade and used as received.

Preparation of HA/dmPEG Complexes and Solubilization of HA/dmPEG in DMSO. For desalting process, 1 g of HA (64k Da) was dissolved in 100 mL of deionized water, dialyzed (MWCO: 1k Da) for 24 h, and lyophilized. A blend mixture of desalted HA and dmPEG at four different dmPEG/HA weight ratios (0.5, 1, 5, and 10) was added in 25 mL of deionized water. The solution was well-stirred and lyophilized to obtain dry HA/dmPEG complex powder. A total of 600 mg of lyophilized HA/dmPEG complexes was added in 5 mL of anhydrous DMSO under dry N_2. After the solution was vigorously stirred at 80 °C for 2 h, the transmittance value was measured at 400 nm using a spectrophotometer (UV-1601, Shimadzu, Japan) to verify the solubilization of HA/dmPEG complexes in DMSO as a function of added dmPEG amount.

Synthesis of HA−Paclitaxel Conjugate. A total of 600 mg of HA/dmPEG powder prepared at 5 weight ratios of dmPEG/HA was dissolved in 5 mL of anhydrous DMSO with addition of DCC and DMAP at different molar ratios. The solution was stirred for 1 h to activate carboxylic groups of HA. Paclitaxel with different amounts (10 and 20 mg) was dissolved in 1 mL of anhydrous DMSO and slowly added to the above solution using a syringe under dry N_2. The mixture was then stirred for 2 days at 40 °C. The resultant solution was dialyzed against DMSO for 1 day and deionized water for 3 days using a dialysis membrane (MWCO: 3500 Da) to remove unreacted paclitaxel and dmPEG. HA−paclitaxel conjugate was collected and lyophilized for 3 days and analyzed. Five different HA−paclitaxel conjugates were synthesized depending on the molar ratio of paclitaxel, DCC, and DMAP. ^{1}H NMR spectra of HA−paclitaxel conjugate was obtained by a Bruker 400 MHz NMR spectrometer (Bruker, Germany) using D_2O and DMSO-d_6. The amount of paclitaxel conjugated to HA was determined by an HPLC (1100 series, Agilent Technologies, Palo Alto, CA, USA) using a reversed-phase column (Waters Spherisorb ODS2: 4.6 mm ID × 250 mm). The mobile phase consisting of acetonitrile/water (50/50 (v/v)) was used to fully expose conjugated paclitaxel molecules in the cosolvent phase for UV detection. The solvent was delivered at a flow rate of 0.8 mL/min for the HPLC analysis and eluted peaks were monitored (λ_{max}: 227 nm, $\epsilon = 2.81 \times 10^4$ $M^{-1}cm^{-1}$). Free paclitaxel was used to generate a standard curve for the estimation of paclitaxel content in HA−paclitaxel conjugates. There was no difference in the molar extinction coefficient of paclitaxel molecule before and after the conjugation.

Characterization of Self-Assembled HA-Paclitaxel Conjugate Micelles in Aqueous Solution. The formation of HA−paclitaxel conjugate micelles in aqueous solution was characterized by measuring their hydrodynamic diameter using a dynamic light scattering instrument (Zeta-Plus, Brookhaven, NY). The size measurement was carried out ($n = 6$) at a concentration of 5.0 mg/mL of HA−paclitaxel conjugate (sample #4 in Table 1) in deionized water at 25 °C. Nanosized HA−paclitaxel micelles were also visualized by atomic force microscopy (AFM) and transmission electron microscopy (TEM). For AFM image, 100 μL of HA−paclitaxel micelle solution (5.0 mg/mL) was placed on a clean mica surface and then air-dried overnight. The image was obtained with a PSIA XE-100 AFM system (Santa Clara, CA) in a noncontact mode with a scanned area of 5 × 5 μm. For TEM image, HA−paclitaxel micelles were analyzed by Zeiss Omega 912 transmission electron microscope (TEM) (Carl Zeiss, Germany). TEM sample was prepared by depositing 20 μL of HA−paclitaxel solution (5.0 mg/mL) on a 300 mesh copper TEM grid with a carbon film and air-dried at room temperature. Critical aggregation concentration (CAC) of HA−paclitaxel conjugate was estimated by employing a hydrophobic fluorescence probe, pyrene, as described previously (*32*). A pyrene stock solution prepared in deionized water was prepared at a concentration of 6.0×10^{-7} M. Different amounts of HA−paclitaxel conjugate ranging from 0.1 μg to 1 mg/mL were dissolved in the pyrene stock solution. At an emission wavelength at 390 nm, excitation spectra of HA−paclitaxel micelle solution with pyrene were monitored by a spectrofluorometer (Shimadzu, Japan).

pH Dependent Release of Paclitaxel from HA−Paclitaxel Conjugate Micelles. HA−paclitaxel conjugate micelles were formed in deionized water at a concentration of 10 mg/mL. pH of the sample solution was adjusted from 1 to 7 using 0.1 M NaOH or HCl. After gentle mixing for 3 h at 37 °C, the solution was filtered using a 0.45 μm syringe filter. The amount of paclitaxel cleaved from the conjugate was monitored by HPLC as described above using a reverse-phase column (Waters Spherisob ODS2: 4.6 mm ID × 250 mm) with a refractive index (RI) detector (RI-71, Shodex, Japan).

***In Vitro* Antitumor Activities of HA−Paclitaxel Conjugate Micelles.** HCT-116 and MCF-7 cells were used as CD44 overexpressing cancer cell lines to verify *in vitro* cell-specific targeted delivery of HA−paclitaxel conjugate micelles (*21, 27*). NIH-3T3 cells were used as a CD44 deficient cell line. Cells were plated in a 96-well plate at a density of 1×10^4 cells per well and grown in RPMI medium supplemented with 10% (v/v) fetal bovine serum for 24 h at 37 °C. Cytotoxicity of HA−paclitaxel conjugate micelles was evaluated by treating cells with different concentrations of HA−paclitaxel conjugates for 2 days at 37 °C. For comparison, Taxol was prepared as described elsewhere and used as a positive control (*32*). Cell viability were determined by a CCK-8 cell viability assay kit (*33*).

An apoptotic event such as DNA fragmentation was observed using a confocal laser microscope (LSM 510, Carl-Zeiss Inc., USA) and a flow cytometer (FACSCalibur, USA). HCT-116 cells were

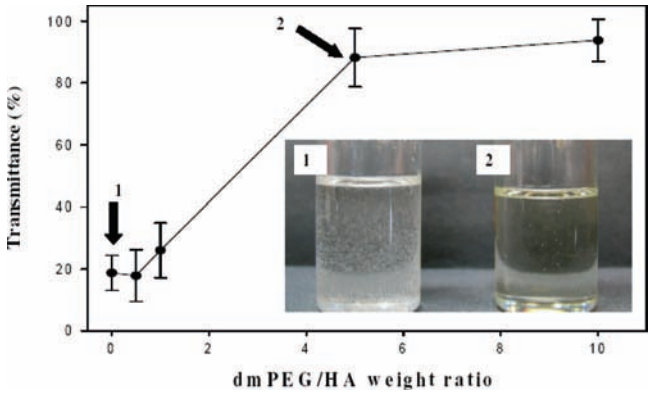

Figure 1. Transmittance of HA/dmPEG solubilized DMSO after 2 h of mixing at 80 °C as a function of dmPEG amount. Note that the inset shows the photographic image of DMSO solution at the pointed samples.

plated in a chamber slide at a density of 1.0×10^5 cells/mL and treated with Taxol formulation or HA−paclitaxel conjugate micelle formulation at an equivalent paclitaxel concentration of 1 μg/mL for 24 h at 37 °C. The cells were fixed with 1% paraformaldehyde and then incubated with a propodium iodide (PI) staining solution (0.25 mg/mL PI and 0.1 mg/mL RNase A in PBS solution) at a concentration of 1×10^6 cells/mL for 30 min at 37 °C. Stained cells were visualized at an excitation wavelength of 543 nm using a confocal microscope. For flow cytometric analysis, the stained cells were collected and resuspended in 1.5 mL PBS solution (pH 7.4). The PI fluorescence of each nucleus was analyzed using *CELLQUEST* software (PharMingen, USA).

RESULTS AND DISCUSSION

The formulation of paclitaxel with biocompatible materials has been examined in depth to increase its solubility in aqueous solution. Among the formulations using nanoscale particulates and polymer conjugates, polyglutamic acid and polypeptides were previously used to chemically conjugate paclitaxel to enhance the solubility (*34–36*). Paclitaxel-conjugated polyglutamic acid, as a prodrug, showed promising antitumor effect *in vivo* and is now in clinical trial. HA, a naturally occurring biocompatible polysaccharide, was also used for the conjugation of paclitaxel. Adipic dihydrazide functionalized HA was reacted with active ester derivatized paclitaxel in DMF/H_2O mixture for HA−paclitaxel conjugation (*27*). Although HA−paclitaxel conjugates prepared in the mixed-solvent system showed enhanced solubility of paclitaxel in aqueous medium with good cytotoxicity results, their synthetic method required multiple cumbersome steps for direct conjugation of paclitaxel on the backbone of HA. This is because HA is not soluble in most organic solvents mainly due to extremely hydrophilic nature with strong inter/intramolecular hydrogen bonding (*14,15*). To make HA soluble in polar organic solvents, HA was physically complexed with cationic salts and surfactants to shield highly anionic carboxylic acid groups and to disrupt inter/intramolecular hydrogen bonds in HA. Alternatively, functional groups in HA were partially protected by hydrophobic blocking agents and deprotected after the conjugation with hydrophobic molecules (*25, 28*).

We recently discovered a novel solubilization method of various biomacromolecules, such as plasmid DNA, proteins, and carbohydrates, in selected organic solvents by nanocomplexing with poly(ethylene glycol) (PEG) (*29, 30*). In this study, HA was solubilized using dmPEG as nanoscale complexes in anhydrous DMSO. Figure 1 shows transmittance value of the DMSO solution as a function of dmPEG/HA weight ratio. The inset displays photographs of the DMSO solution containing dmPEG/HA mixture taken at the indicated points. The dmPEG/HA/DMSO solution at a dmPEG/HA weight ratio of 5 became transparent with a transmittance value greater than 90%, while the HA/DMSO solution without adding dmPEG was turbid with a much lower transmittance value as expected. It is likely that HA and dmPEG interacted together to form HA/dmPEG nanocomplexes in DMSO phase via hydrogen bonding as reported earlier (*30*). The size of HA/dmPEG complexes was 120 ± 6.3 nm in DMSO, as determined by dynamic light scattering technique, sufficiently small to not scatter visible light, resulting in a homogeneous and clear solution. Paclitaxel was then conjugated to HA/dmPEG nanocomplexes finely dispersed in the DMSO phase.

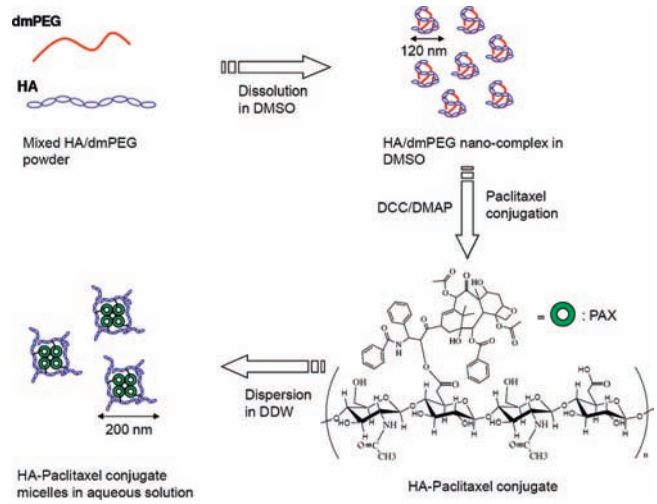

Figure 2. Synthetic scheme of HA−paclitaxel conjugation.

A synthetic scheme for the HA−paclitaxel conjugate is shown in Figure 2. Hydroxyl groups of paclitaxel were directly conjugated to carboxylic groups of HA in a single organic phase using DCC/DMAP as coupling agent (*37, 38*). The resultant HA−paclitaxel conjugate had an acid-cleavable ester linkage. In this study, dimethoxy-PEG (dmPEG) was used for solubilization of HA in DMSO instead of dihydroxyl-PEG to avoid any unfavorable conjugation of hydroxyl group terminated PEG to HA during the HA−paclitaxel conjugation. It should be noted that HA in the HA/dmPEG nanocomplexes was also partially cross-linked by the DCC/DMAP coupling process because it has both hydroxyl and carboxylic acid groups. However, it was most likely that paclitaxel was conjugated to HA mainly at the surface of compactly formed nanocomplexes, limiting self-cross-linking between dmPEG-bound HA molecules. The synthesis of HA−paclitaxel conjugate was verified by ^{1}H NMR analysis (Figure 3). Two different solvents were used to obtain characteristic proton peaks of paclitaxel and HA. In the case of D_2O, a strong acetyl (-NHCOCH_3) peak was identified at 1.86 ppm along with glucosidic H (10*H*) at 3.0−4.0 ppm and anormeric H (2*H*) at 4.30 and 4.40 ppm, while characteristic peaks of paclitaxel such as multiplets in aromatic rings (7.37−7.58 and 7.74−7.85 ppm) were minimal. When DMSO-d_6 was used as a solvent, the characteristic peaks of paclitaxel strongly appeared in the ^{1}H NMR spectra along with the disappearance of HA specific acetyl peaks at 1.86 ppm and reduced anormeric H (2*H*) peak at 4.33 ppm. However, the specific conjugation site in paclitaxel could not be identified. According to the previous reports, it appears that the 2′-hydroxyl group in paclitaxel was preferentially conjugated to HA rather than the 7′-hydroxyl group because it is less sterically hindered (*34*). From the ^{1}H NMR results, it is conceivable that HA−paclitaxel conjugate micelles were formed in aqueous solution by hydrophobic interaction between paclitaxel molecules conjugated to the HA backbone. Although the paclitaxel specific peaks were observed

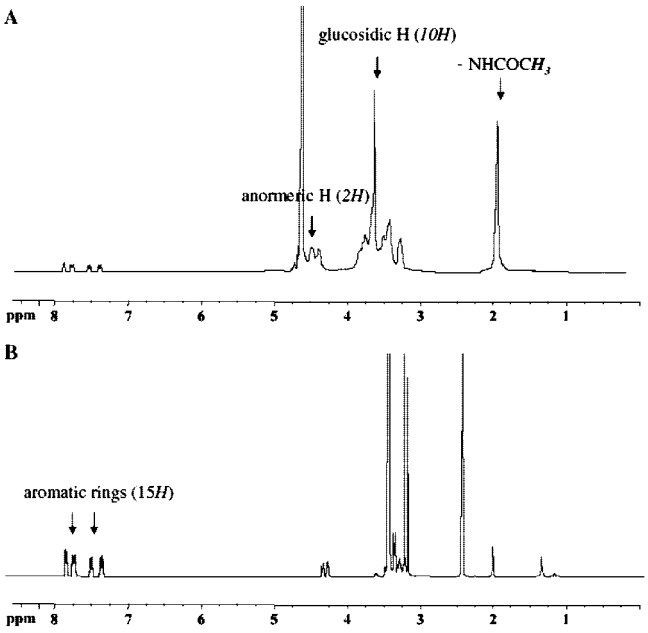

Figure 3. ^{1}H NMR spectra of HA−paclitaxel in (A) D_2O and (B) DMSO-d_6. HA and paclitaxel specific peaks are indicated with arrows.

in ^{1}H NMR in the polar organic phase, the shielding and deshielding effects of paclitaxel and HA peaks made it difficult to accurately estimate the conjugation extent of paclitaxel to HA. Therefore, the conjugation percent of paclitaxel to HA and the yield of each batch sample were determined by an HPLC using a 50:50 mixture of acetonitrile and water as a cosolvent, and the results were summarized in Table 1. As the molar excess of DCC/DMAP increased, the yield of HA−paclitaxel conjugate increased and reached about 60%. The most paclitaxel conjugated sample exhibited ca. 10.8% of paclitaxel loading content (w/w %), which means approximately nine paclitaxel molecules were bound to each HA chain. These data demonstrate that the feed ratio of DCC/DMAP was a critical factor in conjugating paclitaxel to HA.

The size of HA−paclitaxel conjugate micelles was measured by DLS (Figure 4A). The HA−paclitaxel conjugate micelles showed an average diameter of 196 ± 9.6 nm with a narrow size distribution. It is well-known that amphiphilic copolymers, such as Pluronic copolymers, poly(lactic-*co*-glycolic acid) (PLGA)-PEG block copolymers, and PLGA-poly(L-lysine) graft copolymers self-assemble to produce nanosized micelles in aqueous solution via hydrophobic interactions (*39–41*). To visualize HA−paclitaxel conjugate micelles, AFM and TEM images were obtained (Figure 4B,C). From AFM images, round-shaped HA−paclitaxel conjugate micelles were observed with an average diameter of 232.0 ± 28.2 nm (n = 30), which corresponds well to the size as measured by DLS. TEM image also provided evidence for the spherical morphology (183 ± 17.8 nm, n = 30). HA−paclitaxel conjugate micelles were likely to have a core/shell structure composed of a hydrophobic inner core containing aggregated paclitaxel molecules and a hydrophilic HA shell layer.

The self-assembly behavior of HA−paclitaxel conjugate in aqueous solution was characterized by measuring the critical aggregation concentration (CAC) of HA−paclitaxel conjugate using pyrene as a hydrophobic fluorescence probe (*32*, *42*). It is known that pyrene can partition into the hydrophobic core of polymer micelles and exhibits aggregation-induced enhanced emission (AIEE) in aqueous solution. Excitation spectra were measured and the intensity ratio of I_{339}/I_{334} of pyrene was evaluated as a function of HA−paclitaxel conjugate concentration (Figure 4D). A rapid increase of fluorescence intensity and a red shift of pyrene were observed when increasing the concentration of HA−paclitaxel conjugate. From the plot of intensity ratios (I_{339}/I_{334}), the CAC value was estimated to be 7.8 μg/mL. This value is similar to those of polymeric micelles such as poly(L-lactic acid) grafted chondroitin sulfate (5.0 μg/mL) and PLGA grafted poly(L-lysine) (1.0−9.6 μg/mL), but significantly lower than those of Pluronic copolymers (1−24

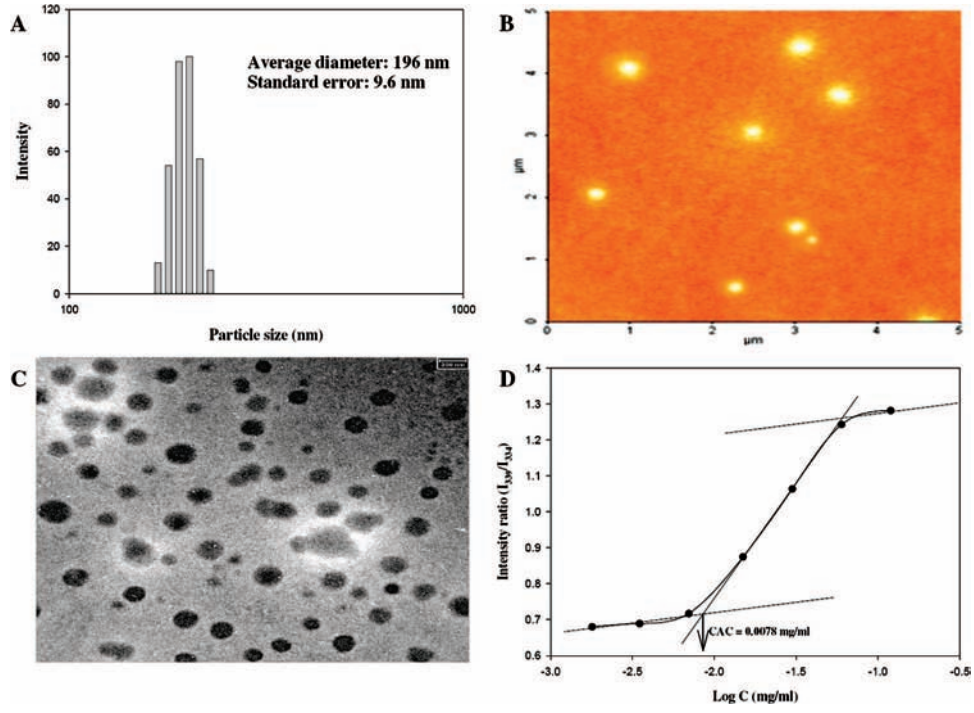

Figure 4. Measurement of HA−paclitaxel conjugate micelles by (A) DLS, and the images of HA−paclitaxel nanoparticle by (B) AFM and (C) TEM. (D) Critical aggregation concentration (CAC) measurement by pyrene: plot of intensity ratio between I_{339} and I_{334} as a function of concentration.

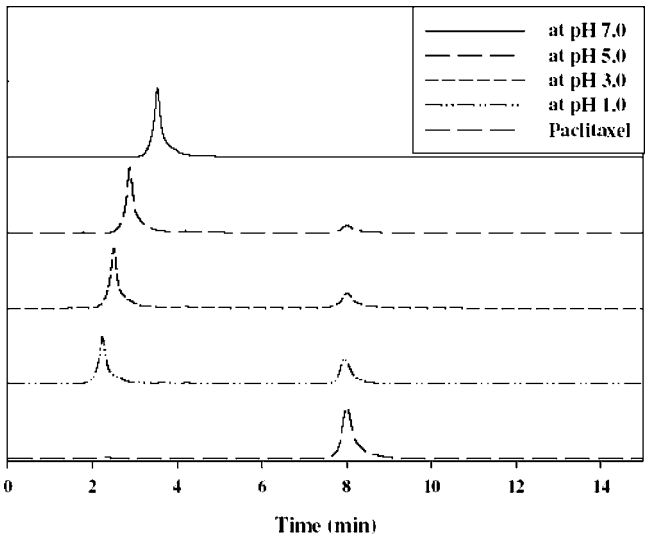

Figure 5. HPLC measurement of released paclitaxel from HA−paclitaxel conjugate micelles after 3 h incubation at different pH values. Paclitaxel is used as a positive control.

mg/mL) (*41*, *43*). Since paclitaxel was conjugated to HA via an acid-cleavable ester linkage, an intact form of paclitaxel was cleaved from the conjugate at slightly acidic environments such as extracellular solid tumor tissues and intracellular endosomal and lysosomal vesicles. After 3 h incubation of the HA−paclitaxel conjugate at four different pH conditions, the release of paclitaxel was monitored using reversed-phase HPLC. As shown in Figure 5, an intact paclitaxel peak appears to a greater extent at more acidic pH. In addition, the gradual left-shift of the HA−paclitaxel conjugate peak was also observed at acidic pH, because the hydrophobicity of the HA−paclitaxel conjugate started to decrease with the gradual cleavage of paclitaxel. It is likely that the release of free paclitaxel from the conjugate micelles was also dependent on the incubation pH. Since acidic physiological condition is in the range of pH 5.0 to 6.0, slow release of paclitaxel from HA−paclitaxel conjugates was observed. Therefore, the pH-dependent release behavior would play a favorable role in enhancing the cytotoxicity effect of free paclitaxel to acidic tumor cells.

In vitro cytotoxicity of HA−paclitaxel conjugate micelles was monitored by a cell viability assay using CCK-8 (Figure 6) (*21*, *33*). As compared to the commercially available Taxol formulation, HA−paclitaxel conjugate micelles exhibited more cytotoxicity for HCT-116 and MCF-7 cells, but reduced cytotoxicity for NIH-3T3 cells. HCT-116 and MCF-7 cells are known to overexpress HA recognizable CD44 receptors on the cell membrane, while NIH-3T3 cells do not overexpress CD44 receptors. Our data suggested that HA−paclitaxel conjugate micelles were internalized to a greater extent within HCT-116 and MCF-7 cells via HA receptor-mediated endocytosis than paclitaxel in the Taxol formulation, resulting in higher cytotoxic effect. Taxol is supposed to transport into cells by a passive diffusion mechanism, but HA−paclitaxel conjugate micelles are likely to be internalized within cells via a HA-receptor-mediated endocytosis process. The cytoxicity effect of HA−paclitaxel conjugate micelles was lower than that of the Taxol formulation for NIH-3T3 cells, probably due to their reduced extent of cellular uptake. It seems that negatively charged HA prohibits the anticancer effect of paclitaxel to HA receptor-deficient cells like NIH-3T3 by reducing nonselective uptake of HA−paclitaxel conjugate micelles.

Previously, we showed that HA nanogels physically encapsulating small interfering RNA (siRNA) could be delivered to HCT-116 cells in a HA receptor-mediated, target-specific

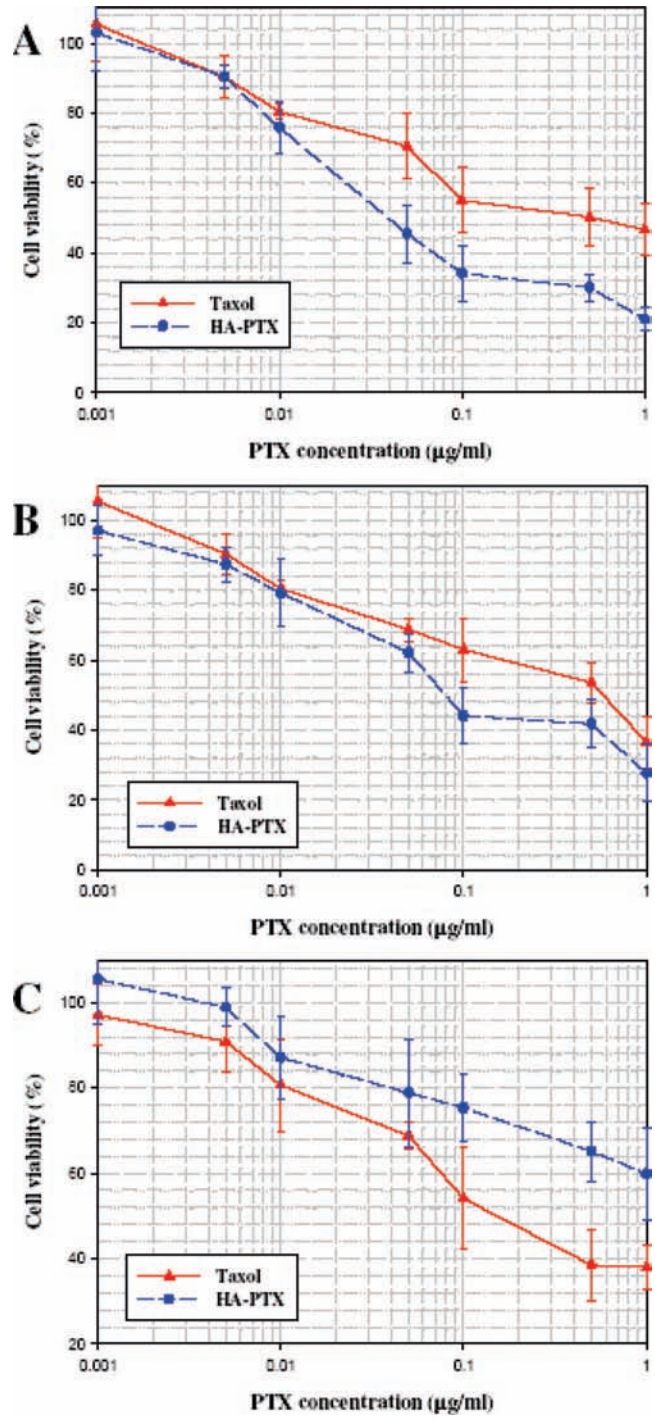

Figure 6. *In vitro* cytotoxicity of HA−paclitaxel conjugate micelles and Taxol against three different cell lines (A) HCT-116, (B) MCF-7, and (C) NIH-3T3.

manner (*21*). Similarly, it is conceivable that HA−paclitaxel conjugate micelles could be utilized for targeted delivery of paclitaxel to many tumor cells overexpressing HA receptors. To verify the apoptosis-inducing effect of HA−paclitaxel conjugate micelles, confocal microscopy and flow cytometric analyses were performed for HCT-116 cells. Figure 7 illustrates the confocal microscopic images of HCT-116 cells followed by incubation with various paclitaxel formulations at an equivalent paclitaxel concentration of 1 μg/mL. Morphological change of the cell nuclei such as DNA fragmentation was visualized by propodium iodide (PI) staining to confirm paclitaxel-induced apoptotic cell death. Since HCT-116 cells treated with the control formulation (20 μg/mL of HA) without

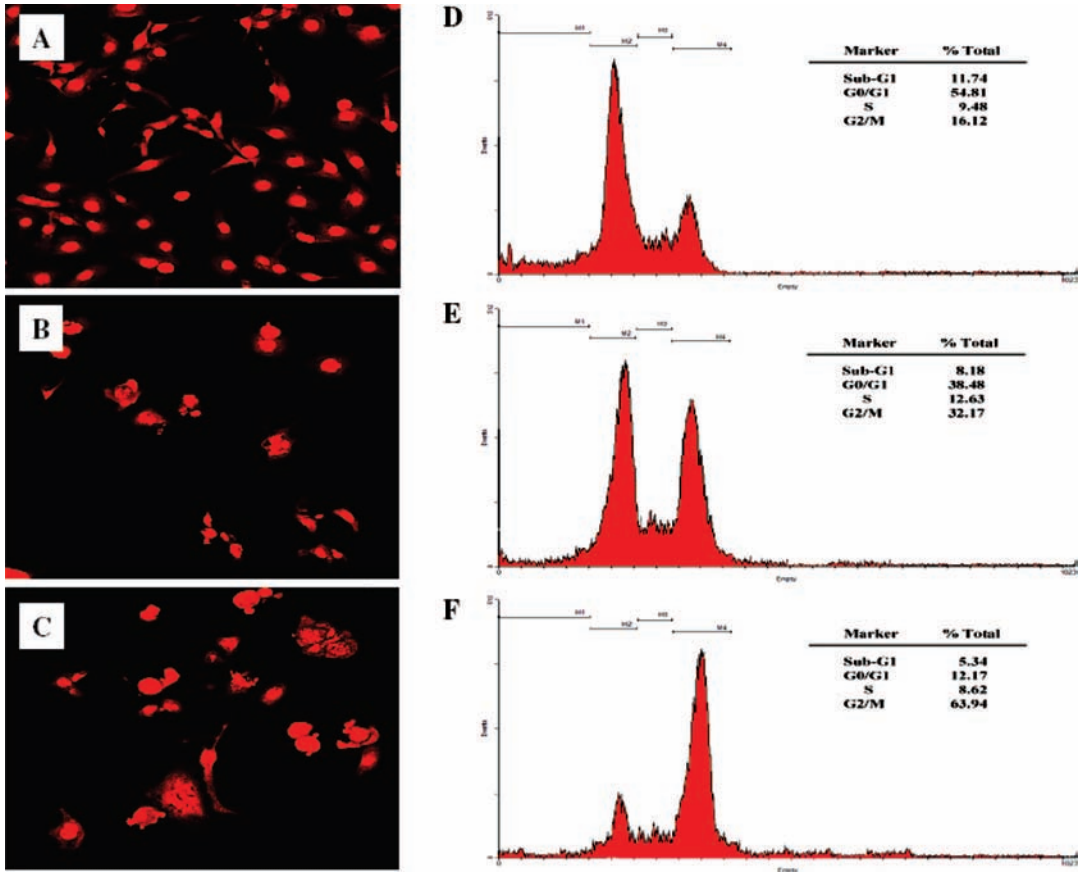

Figure 7. Confocal images of PI stained HCT-116 cells: (A) control, (B) Taxol, and (C) HA−paclitaxel. FACS analysis of apoptotic effects on HCT-116 cells: (D) control, (E) Taxol, and (F) HA_-paclitaxel conjugate micelles. All paclitaxel formulations have 1 μg/mL of equivalent paclitaxel concentration.

paclitaxel were nonapoptotic, strong red fluorescence was detected homogeneously within the nucleus (Figure 7A). In contrast, after incubation with Taxol or HA−paclitaxel conjugate micelles, HCT-116 cells displayed apparent evidence of apoptosis such as segregation and fragmentation of cell nucleus into dense and tiny granules (Figure 7 B,C). It was thought that the activation of endogenous nucleases was associated during the apoptosis which cleaved chromosomal DNA into oligonucleosomal fragments (*44*, *45*). The extent of apoptosis was quantitatively assessed by flow cytometric analysis. Since the cytotoxic activity of paclitaxel is mainly due to its stabilizing effect on polymerized microtubules necessary for spindle formation and cell division, paclitaxel has been shown to cause a cell cycle arrest in the G2/M phase and finally cell death through an apoptotic mechanism (*4*, *5*). As shown in Figure 7D−F, HA−paclitaxel conjugate micelles induced a significant increase in G2/M cell population (64.9%), compared to that of the control (16.1%) and Taxol (31.2%). Consequently, these results demonstrate that HA−paclitaxel conjugate micelles were readily taken up by CD44 overexpressing cells and significantly enhanced the extent of apoptosis-inducing cell death. Nanosized and self-assembled HA−paclitaxel conjugate micelles could be utilized as efficient all-in-one carriers not only for the solubilization of paclitaxel, but also for its passive and active targeted delivery to cancer cells.

CONCLUSIONS

In this study, paclitaxel, a very hydrophobic anticancer drug, was directly conjugated to HA in DMSO by forming HA/PEG nanocomplexes without using any ionic surfactants, salts, and blocking agents to functional groups in HA. HA−paclitaxel conjugates were self-assembled to form nanosized spherical micelles in aqueous solution. HA−paclitaxel conjugate micelles exhibited greater cytotoxicity to HA recognizable CD44 overexpressing cells than the conventional paclitaxel formulation, suggesting that they could be efficiently delivered to cancer cells that overexpress HA receptors.

ACKNOWLEDGMENT

This study was supported by the National Research Laboratory grant from the Ministry of Science and Technology, Republic of Korea.

LITERATURE CITED

(1) Spencer, C. M., and Faulds, D. (1994) Paclitaxel: a review of its pharmacodynamic and pharmacokinetic properties and therapeutic-potential in the treatment of cancer. *Drugs 48*, 794–847.
(2) Rowinsky, E. K., Onetto, N., Canetta, R. M., and Arbuck, S. G. (1992) Taxol: the first of the taxanes, an important new class of antitumor agents. *Semin. Oncol. 19*, 646–662.
(3) Thigpen, J. T., Blessing, J. A., Ball, H., Hummel, S. J., and Barrett, R. J. (1994) Phase II trial of paclitaxel in patients with progressive ovarian carcinoma after platinum-based chemotherapy. *J. Clin. Oncol. 12*, 1748–1753.
(4) Schiff, P., Fant, J., and Horwitz, S. B. (1979) Promotion of microtubule assembly in vitro by taxol. *Nature 277*, 665–667.
(5) Rowinsky, E. K., Donehower, R. C., Jones, R. J., and Tucker, R. W. (1988) Microtubule changes and cytotoxicity in leukemic cell lines treated with taxol. *Cancer Res. 48*, 4093–4100.
(6) Onetto, N., Canetta, R., Winograd, B., Catane, R., Grechko, J., Burroughs, J., and Rozencweig, M. (1993) Overview of taxol safety. *J. Natl. Cancer Inst. Monogr. 15*, 131–139.
(7) Mazzo, D., Nguyen-Huu, J. J., Pagniez, S., and Denis, P. (1997) Compatibility of docetaxel and paclitaxel in intravenous solutions

with polyvinyl chloride infusion materials. *Am. J. Health Syst. Pharm. 54*, 566–569.
(8) Gregory, R., and DeLisa, A. F. (1993) Paclitaxel: a new antineoplastic agent for refractory ovarian cancer. *Clin. Pharm. 12*, 401–415.
(9) Crosasso, P., Ceruti, M., Brusa, P., Arpicco, S., Dosio, F., and Cattel, L. (2000) Preparation, characterization and properties of sterically stabilized paclitaxel-containing liposomes. *J. Controlled Release 63*, 19–30.
(10) Bae, K. H., Lee, Y., and Park, T. G. (2007) Oil-encapsulating PEO-PPO-PEO shell crosslinked nanocapsules for target-specific delivery of paclitaxel. *Biomacromolecules 8*, 650–656.
(11) Tarr, B. D., Sambandan, T. G., and Yalkowsky, S. H. (1987) A new parenteral emulsion for the administration of taxol. *Pharm. Res. 4*, 162–165.
(12) Dordunoo, S. K., Jackson, J. K., Arsenault, L. A., Oktaba, A. M. C., Hunter, W. L., and Burt, H. M. (1995) Taxol encapsulation in poly(ϵ-caprolactone) microspheres. *Cancer Chemother. Pharmacol. 36*, 279–282.
(13) Maeda, H., Seymour, L. W., and Miyamoto, Y. (1992) Conjugates of anticancer agents and polymers: advantages of macromolecular therapeutics in vivo. *Bioconjugate Chem. 3*, 351–362.
(14) Laurent, T. C. (1987) Biochemistry of hyaluronan. *Acta Otolaryngol Suppl. 442*, 7–24.
(15) Turley E. A. (1989) *The biology of hyaluronan*, pp 121−137, CIBA Foundation, J. Wiley & Sons, Ltd., Chichester, U.K.
(16) Knudson, C. B., and Knudson, W. (1993) Hyaluronan-biding proteins in development, tissue homeostasis, and disease. *FASEB J. 7*, 1233–1241.
(17) Entwistle, J., Hall, C. L., and Turley, E. A. (1996) HA receptors: regulators of signaling to the cytoskeleton. *J. Cell. Biochem. 61*, 569–577.
(18) Herrlich, P., Sleeman, J., Wainwright, D., Konig, H., Sherman, L., and Ponta, H. (1998) How tumor cells make use of CD44. *Cell Adhes. Commun. 6*, 141–147.
(19) Hall, C. L., Yang, B., Yang, X., Zhang, S., Turley, M., Samuel, S., Lange, L. A., Wang, C., Curpen, G. D., Savani, R. C., Greenburg, A. H., and Turley, E. A. (1995) Overexpression of the hyaluronan receptor RHAMM is transforming and is also required for h-ras transformation. *Cell 82*, 19–28.
(20) Hua, Q., Knudson, C. B., and Knudson, W. J. (1993) Internalization of hyaluronan by chondrocytes occurs via receptor-mediated endocytosis. *J. Cell Sci. 106*, 365–375.
(21) Lee, H., Mok, H., Lee, S., Oh, Y. K., and Park, T. G. (2007) Target-specific intracellular delivery of siRNA using degradable hyaluronic acid nanogels. *J. Controlled Release 119*, 245–252.
(22) Kurisawa, M., Chung, J. E., Yang, Y. Y., Shu, J., and Uyama, H. (2005) Injectable biodegradable hydrogels composed of hyaluronic acid-tyramine conjugates for drug delivery and tissue engineering. *Chem. Commun. 34*, 4312–4314.
(23) Larsen, N. E., and Balazs, E. A. (1991) Drug delivery systems using hyaluronan and derivatives. *Adv. Drug Delivery Rev. 7*, 279–293.
(24) Luo, Y., and Prestwich, G. D. (2001) Hyaluronic acid-N-hydroxysuccinimide: A useful intermediate for bioconjugation. *Bioconjugate Chem. 12*, 1085–1088.
(25) Zhang, M., and James, S. P. (2005) Synthesis and properties of melt-processable hyaluronan esters. *J. Mater. Sci. 16*, 587–593.
(26) Ruhela, D., Riviere, K., and Szoka, F. C. (2006) Efficient synthesis of an aldehyde functionalized hyaluronic acid and its application in the preparation of hyaluronan-lipid conjugates. *Bioconjugate Chem. 17*, 1360–1363.
(27) Luo, Y., and Prestwich, G. D. (1999) Synthesis and selective cytotoxicity of a hyaluronic acid-antitumor bioconjugate. *Bioconjugate Chem. 10*, 755–763.
(28) Zhang, M., and James, S. P. (2005) Silylation of hyaluronan to improve hydrophobicity and reactivity for improved processing and derivatization. *Polymer 46*, 3639–3648.
(29) Mok, H., and Park, T. G. (2006) PEG-assited DNA solubilization in organic solvents for preparing cytosol specifically degradable PEG/DNA nanogels. *Bioconjugate Chem. 17*, 1369–1372.
(30) Mok, H., Kim, H. J., Park, T. G. (2008) Dissolution of biomacromolecules in organic solvents by nano-complexing with poly(ethylene glycol), *Int. J. Pharm.* doi:10.1016/j.ijpharm.2008.01.033.
(31) Sheth, S. R., and Leckband, D. (1997) Measurements of attractive forces between proteins and end-grafted poly(ethylene glycol) chains. *Proc. Natl. Acad. Sci. U.S.A. 94*, 8399–8404.
(32) Lee, C. S., and Jeong, S. Y. (2003) Polymeric micelles of poly(2-ehyl-2-oxazoline)-block-poly(ϵ-caprolactone) copolymer as a carrier for paclitaxel. *J. Controlled Release 89*, 437–446.
(33) Itano, N., Atsumi, F., Sawai, T., Yamada, Y., Miyaishi, O., Senga, T., Hamaguchi, M., and Kimata, K. (2002) Abnormal accumulation of hyaluronan matrix diminishes contact inhibition of cell growth and promotes cell migration. *Proc. Natl. Acad. Sci. U.S.A. 99*, 3609–3614.
(34) Li, C., Yu, D. F., Newman, R. A., Cabral, F., Stephens, L. C., Hunter, N., Milas, L., and Wallace, S. (1998) Complete regression of well-established tumors using a novel water-soluble poly(L-glutamic acid)-paclitaxel conjugate. *Cancer Res. 58*, 2404–2409.
(35) Auzenne, E., Donato, N. J., Li, C., Leroux, E., Price, R. E., Farquhar, D., and Klostergaard, J. (2002) Superior therapeutic profile of poly-L-glutamic acid-paclitaxel copolymer compared with Taxol in xenogeneic compartmental models of human ovarian carcinoma. *Clin. Cancer Res. 8*, 573–581.
(36) Chen, X., Plasencia, C., Hou, Y., and Neamati, N. (2005) Synthesis and biological evaluation of dimeric RGD peptide-paclitaxel conjugate as a model for integrin-targeted drug delivery. *J. Med. Chem. 48*, 1098–1106.
(37) Zhang, X., Li, Y., Chen, X., Wang, X., Xu, X., Liang, Q., Hu, J., and Jing, X. (2005) Synthesis and characterization of the paclitaxel/MPEG-PLA block copolymer conjugate. *Biomaterials 26*, 2121–2128.
(38) Jung, S. W., and Kim, S. H. (2005) Drug release from core-shell type nanoparticles of poly(DL-lactide-co-glycolide)-grafted dextran. *J. Microencapsulation 22*, 901–911.
(39) Choi, S. H., Lee, J. H., Choi, S. M., and Park, T. G. (2006) Thermally reversible Pluronic/heparin nanocapsules exhibiting 1,000-fold volume transition. *Langmuir 22*, 1758–1762.
(40) Yoo, H. S., and Park, T. G. (2001) Biodegradable polymeric micelles composed of doxorubicin conjugated PLGA-PEG block copolymer. *J. Controlled Release 70*, 63–70.
(41) Jeong, J. H., Byun, Y., and Park, T. G. (2003) Synthesis and characterization of poly(L-lysine)-g-poly(D,L-lactic-co-glycolic acid) biodegradable micelles. *J. Biomater. Sci.: Polym. Edn. 14*, 1–11.
(42) Zhao, C. L., Winnik, M. A., Riess, G., and Croucher, M. D. (1990) Fluorescence probe technique used to study micelle formation in water soluble block copolymers. *Langmuir 6*, 514–516.
(43) Lee, C. T., Huang, C. P., and Lee, Y. D. (2006) Preparation of amphiphilic poly(L-lactide)-graft-chondroitin sulfate copolymer self-aggregates and its aggregation behavior. *Biomacromolecules 7*, 1179–1186.
(44) Martin, S. J., Green, D. R., and Cotter, T. G. (1994) Dicing with death: dissecting the components of the apoptosis machinery. *Trends Biochem. Sci. 19*, 26–30.
(45) Bacso, Z., Everson, R. B., and Eliason, J. F. (2000) The DNA of annexin V-binding apoptotic cells is highly fragmented. *Cancer Res. 60*, 4623–4628.

BC8000485

Bioconjugate Chemistry

2008
Volume 19, Number 7

© Copyright 2008 by the American Chemical Society

REVIEWS

Re-Engineering Biopharmaceuticals for Delivery to Brain with Molecular Trojan Horses

William M. Pardridge*

Department of Medicine, University of California at Los Angeles, Los Angeles, California 90024. Received April 9, 2008; Revised Manuscript Received May 7, 2008

Biopharmaceuticals, including recombinant proteins, monoclonal antibody therapeutics, and antisense or RNA interference drugs, cannot be developed as drugs for the brain, because these large molecules do not cross the blood−brain barrier (BBB). Biopharmaceuticals must be re-engineered to cross the BBB, and this is possible with genetically engineered molecular Trojan horses. A molecular Trojan horse is an endogenous peptide, or peptidomimetic monoclonal antibody (mAb), which enters brain from blood via receptor-mediated transport on endogenous BBB transporters. Recombinant neurotrophins, single chain Fv antibodies, or therapeutic enzymes may be re-engineered as IgG fusion proteins. The engineering of IgG-avidin fusion proteins enables the BBB delivery of biotinylated drugs. The IgG fusion proteins are new chemical entities that are dual or triple function molecules that bind multiple receptors. The fusion proteins are able both to enter the brain, by binding an endogenous BBB receptor, and to induce the desired pharmacologic effect in brain, by binding target receptors in the brain behind the BBB. The development of molecular Trojan horses for BBB drug delivery allows the re-engineering of biopharmaceuticals that, owing to the BBB problem, could not otherwise be developed as new drugs for the human brain.

INTRODUCTION

Biopharmaceuticals include recombinant proteins, monoclonal antibodies (mAb), and antisense drugs including RNA interference (RNAi) therapeutics. However, short of a trans-cranial injection of drug into the brain, biopharmaceuticals cannot presently be developed as new drugs for human brain diseases, because these drugs do not cross the brain capillary endothelial wall, which forms the blood−brain barrier (BBB) in vivo. While it is generally assumed that small molecules cross the BBB, in fact, <2% of all small molecules cross the BBB in pharmacologically active amounts (*1*). The BBB is the most important factor limiting the development of new drugs for the brain, and particularly, large molecule biopharmaceuticals.

The BBB phenomenon is illustrated in Figure 1A, which is a whole body autoradiogram of a mouse 30 min after the intravenous injection of radiolabeled histamine, a small molecule of just 111 Da (*2*). The histamine readily crosses the porous vascular barrier in all organs of the body except for the brain and spinal cord. The capillaries in the brain lack the pores found in microvessels in peripheral tissues (*3*). The microvasculature of the brain is shown in Figure 1B, which is a vascular cast of the human brain cortex (*4*). The distance between brain capillaries is about 40 μm, which provides space for approximately 2 neurons between 2 capillaries in the brain.

* To whom correspondence should be addressed: UCLA Warren Hall 13-164 900 Veteran Ave. Los Angeles, CA 90024. Ph: (310) 825-8858. Fax: (310) 206-5163. E-mail: wpardridge@mednet.ucla.edu.

10.1021/bc800148t CCC: $40.75 © 2008 American Chemical Society
Published on Web 06/12/2008

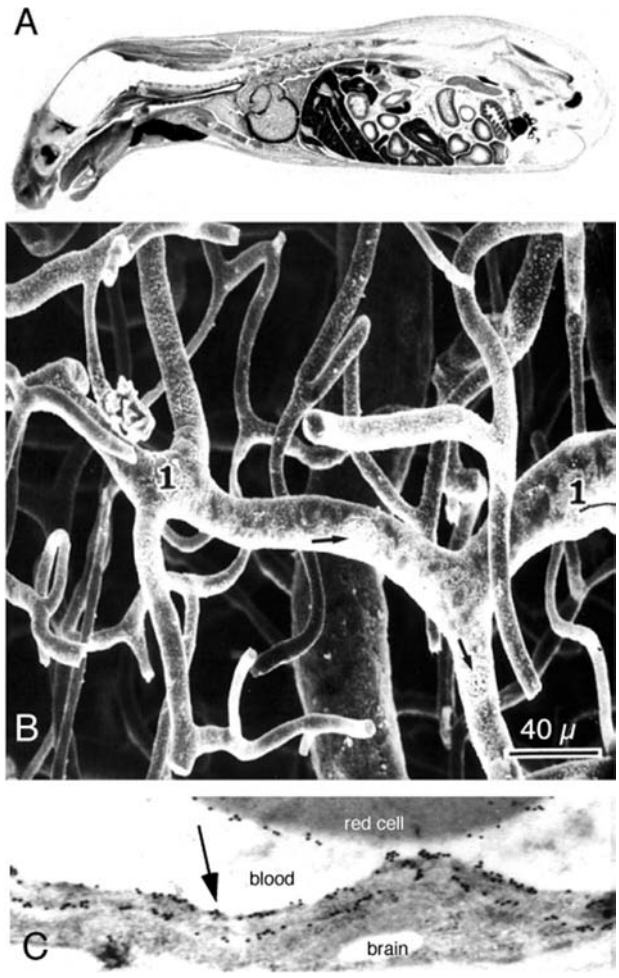

Figure 1. Location of endogenous BBB transporters. (A) Whole body autoradiogram of an adult mouse sacrificed 30 min after intravenous injection of radiolabeled histamine, a small molecule that readily traverses the capillary barrier in all organs of the body, except for the brain and spinal cord. From ref (*2*). (B) Scanning electron micrograph of the human cortex. The distance between capillaries in the human brain is approximately 40 μm. From ref (*4*). (C) Electron microscopic immunogold study of human brain with a rabbit polyclonal antibody to the human GLUT1 glucose transporter, and a secondary antibody conjugated with 10 nm gold. The localization of the gold particles (arrow) shows the expression of a model endogenous BBB transporter (the GLUT1 glucose transporter) at the luminal and abluminal membranes of the brain capillary endothelial cell. GLUT1 is also visible on the plasma membrane of an erythrocyte within the capillary lumen. From ref (*8*).

Therefore, each neuron in perfused by its own blood vessel. Once the biopharmaceutical crosses the brain microvascular barrier, the drug is delivered to the "doorstep" of every neuron in the brain. Diffusion plays a minimal role in the distribution of drugs within the brain following entry via the trans-vascular route, owing to the short intercapillary distance.

The BBB is expressed in the brain of all vertebrates, and is laid down within the first trimester of human fetal life (*5*). The anatomical basis of the BBB is the presence of epithelial-like tight junctions within the capillary endothelial cells of the brain (*3*). Unlike capillaries in peripheral tissues, which have porous endothelial barriers, the endothelial cells of brain microvessels are fused together by the high-resistance tight junctions. The electrical resistance across the brain capillary endothelial cell is as high as 8000 ohm$\cdot$cm^2 (*6*), which is as high as any cellular barrier in biology. Owing to the presence of the endothelial tight junctions at the cerebral microvasculature, circulating molecules gain access to brain interstitial fluid only via one of two transport

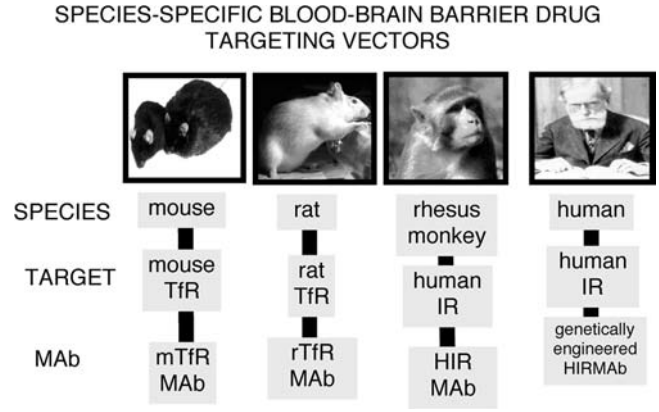

Figure 2. BBB molecular Trojan horses. Panel of species-specific monoclonal antibodies (mAb) against either the rodent transferrin receptor (TfR) or the human insulin receptor (IR). From ref (*19*).

pathways: lipid-mediated free diffusion, which is available to a restricted class of lipid-soluble small molecules; and catalyzed transport via endogenous BBB transporters.

There are two broad classes of endogenous BBB transporters that mediate the uptake of circulating molecules by brain. Carrier-mediated transporters (CMT) allow for the selective uptake of water-soluble small molecule nutrients that have an affinity for specialized CMT systems within the BBB, including the glucose transporter, the amino acid transporter, and other transporters (*7*), which are generally expressed by genes within the solute carrier (SLC) gene family (*1*). The expression of the GLUT1 glucose transporter on the luminal and abluminal membranes of the brain capillary endothelial cell is illustrated with the electron microscopic immunogold study shown in Figure 1C (*8*). The endogenous transporter is expressed on both luminal and abluminal membranes, which are separated by about 200 nm of endothelial cytoplasm. Similar to CMT systems, such as the glucose transporter, the BBB also expresses endogenous receptor-mediated transport (RMT) systems for certain endogenous large molecules in the circulation, such as the insulin receptor or the transferrin receptor (TfR) (*9*). The rapid receptor-mediated transport of insulin or transferrin across the BBB in vivo was demonstrated with thaw mount autoradiography of brain following the intracarotid arterial infusion of radiolabeled insulin or transferrin (Tf) (*10, 11*). The RMT pathway was shown to be a transcytosis process with electron microscopy of brain following the intracarotid arterial infusion of conjugates of 5 nm gold and a mAb against the TfR (*12*).

BLOOD−BRAIN BARRIER MOLECULAR TROJAN HORSES

The discovery of endogenous RMT systems within the BBB, such as the insulin receptor or the TfR, led to the development of the molecular Trojan horse hypothesis. Certain endogenous peptides, such as insulin or Tf, could be used as molecular Trojan horses to ferry drugs across the BBB following attachment of the drug to the endogenous insulin or Tf. In addition, certain peptidomimetic MAbs to the endogenous BBB RMT systems could also be used as molecular Trojan horses. A panel of species-specific molecular Trojan horses has been developed for mice, rats, Rhesus monkeys, and humans, as shown in Figure 2. A rat mAb to the mouse TfR is used as a Trojan horse for drug delivery in the mouse (*13*). This mAb is not active in rats or other species. A murine mAb to the rat TfR is used for drug delivery in rats (*14*), and this mAb is not active in mice or other species. A murine mAb to the human insulin receptor (HIR) cross reacts with the insulin receptor of Old World primates such as the Rhesus monkey (*15*). The murine HIRMAb is not

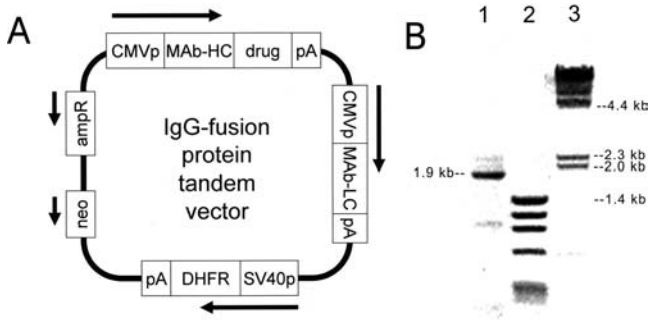

Figure 3. Tandem vector for expression of IgG fusion proteins. (A) A tandem vector contains the separate expression cassettes for the IgG heavy chain (HC) fusion gene, the IgG light chain (LC) gene, the dihydrofolate reductase (DHFR) gene, and the neomycin resistance gene (neo). The HC and LC genes are bordered by the cytomegalovirus (CMV) promoter and the bovine growth hormone (BGH) polyA (pA) transcription termination sequence. The DHFR gene is bordered by the SV40 promoter (SV40p) and the hepatitis B virus pA sequence; ampR = ampicillin resistance gene. (B) PCR amplification of the 1.9 kb cDNA encoding the human α-L-iduronidase (IDUA) (lane 1); DNA size standards are shown in lanes 2 and 3. From ref (*20*).

active in New World primates such as the squirrel monkey. The murine HIRMAb cannot be used for drug delivery in humans owing to immune reactions to a mouse protein. Therefore, both a chimeric HIRMAb and a humanized HIRMAb have been developed for drug delivery in humans (*16*). A genetically engineered TfRMAb could be used for drug delivery across the human BBB. However, the HIRMAb is 900% more active as a BBB drug delivery vector than any known mAb to the human TfR (*17*). The TfRMAb is used as a molecular Trojan horse in rodents, because there is no known mAb to the rat or mouse insulin receptor that can be used as a molecular Trojan horse for drug delivery in these species.

The availability of the genes encoding the heavy chain (HC) and the light chain (LC) of the genetically engineered HIRMAb allows for the bioengineering of IgG fusion proteins for drug delivery of recombinant proteins and MAbs across the human BBB (*16*). The recombinant protein or single chain Fv (ScFv) monoclonal antibody is fused to the heavy chain, or light chain, of the HIRMAb. If the therapeutic protein functions as a dimer, then fusion of the amino terminus of the therapeutic protein to the carboxyl terminus of the heavy chain of the HIRMAb restores the natural dimeric configuration of the therapeutic protein. Many proteins, such as neurotrophins, ScFv antibodies, or avidin, have preferred dimeric configurations. To facilitate the isolation of high expressing mammalian host cell systems, the genes encoding the heavy chain fusion gene and the light chain gene, as well as the gene encoding for a selectable marker such as dihydrofolate reductase (DHFR), are placed on a single piece of DNA called a tandem vector (Figure 3A). The HC expression cassette, the LC expression cassette, and the DHFR expression cassette, are are all contained within the tandem vector, which also encodes the neomycin resistance gene and the ampicillin resistance gene (*18*). The heavy chain expression cassette and the light chain expression cassette are both driven by tandem cytomegalovirus (CMV) promoters and both expression cassettes have separate and tandem bovine growth hormone (BGH) polyA (pA) transcription termination sequences. A unique restriction endonuclease sequence is engineered at the 3′ end of the heavy chain expression cassette. This allows for the facile insertion of a cDNA encoding the therapeutic protein into the tandem vector for expression of a new fusion protein, which is composed of the HIRMAb heavy chain fused to the nontransportable therapeutic protein. The cDNA encoding for the nontransportable therapeutic protein is generated by the polymerase chain reaction (PCR) and the PCR amplification of the cDNA encoding human α-L-iduronidase (IDUA) is shown in Figure 3B. Following the engineering of the tandem vector, the engineering of new vectors expressing new HIRMAb fusion proteins is a relatively rapid process.

Table 1. Partial Lists of Protein Drugs That Could Enter Drug Development Should the Protein be Enabled to Cross the Blood−Brain Barrier[a]

recombinant proteins
Brain derived neurotrophic factor
Fibroblast growth factor (FGF)-2
Multiple FGFs
Nerve growth factor
Neurotrophin (NT)-3
NT-4/5
Glial derived neurotrophic factor
Ciliary neurotrophic factor
Neurturin
Neuregulins
Interleukins
Transforming growth factor (TGF)-α
TGF-β
Vasoactive intestinal peptide
Epidermal growth factor (EGF)
Erythropoietin
Hepatocyte growth factor
Platelet derived growth factor
Artemin
Persephin
Netrins
Cardiotrophin-1
Stem cell factor
Midkine
Pleiotrophin
Bone morphogenic proteins
Saposins
Semaphorins
Leukemia inhibitory factor
monoclonal antibodies
Anti-Aβ for Alzheimer's disease
Anti-HER2 for breast cancer in brain
Anti-EGF receptor for primary brain cancer
Anti-nogo A for brain injury
Anti-TRAIL for HIV
Anti-α-synuclein for Parkinson's
Anti-htt for Huntington's
Anti-prion for mad cow disease
Anti-West Nile virus
lysosomal enzymes
α-L-iduronidase
iduronate-2-sulfatase
N-acetyl-galactosamine-6-sulfatase
arylsulphatase B
acid α-glucosidase
acid sphingomyelinase

[a] TRAIL: tumor necrosis factor-related apoptosis-inducing ligand; HIV: human immunodeficiency virus.

There are almost an endless number of therapeutic proteins that could be fused to the HIRMAb to create new chemical entities, which are composed of the HIRMAb fused to the therapeutic protein. A partial list of recombinant proteins that could be developed for drugs for the brain is given in Table 1, and these are broadly classified as recombinant proteins, recombinant monoclonal antibodies, or recombinant lysosomal enzymes. There are many highly neuroprotective neurotrophins which could be developed as neuropharmaceuticals for a variety of brain diseases (*21*), should these molecules be made transportable through the human BBB, and a partial list is shown in the recombinant protein section of Table 1. There are multiple therapeutic monoclonal antibodies that could be developed for brain diseases, and a partial list is shown in the monoclonal antibody section of Table 1. There are different approaches that could be used for the genetic engineering of a fusion antibody

Table 2. IgG Fusion Proteins and Therapeutic Applications for the Brain[a]

therapeutic protein	therapeutic application
BDNF	stroke, neurodegeneration
GDNF	stroke, Parkinson's disease, motor neuron disease
Aβ ScFv	Alzheimer's disease
IDUA	MPS type I
Avidin	biotinylated drugs, including siRNA

[a] BDNF = brain-derived neurotrophic factor; GDNF = glial derived neurotrophic factor; ScFv = single chain Fv antibody; IDUA = iduronidase; MPS = mucopolysaccharidosis; siRNA = short interfering RNA.

composed of the HIRMAb and a therapeutic antibody (*22*, *23*). The approach described below involves the fusion of a therapeutic ScFv to the heavy chain of the HIRMAb. In addition, many enzymes are potential therapeutic proteins for brain diseases such as lysosomal storage disorders or other conditions, and a partial list of potential enzyme therapeutics for the brain is given in the lysosomal enzyme section of Table 1. This review will discuss the recent genetic engineering and testing of HIRMAb fusion proteins which encode for neurotrophins such as brain-derived neurotrophic factor (BDNF), glial derived neurotrophic factor (GDNF), a ScFv against the Aβ amyloid peptide of Alzheimer's disease (AD), the lysosomal enzyme IDUA, and avidin (Table 2).

BLOOD−BRAIN BARRIER DELIVERY OF IgG-NEUROTROPHIN FUSION PROTEINS

Neurotrophins are potential neuroprotective agents for the brain (Table 1), including stroke. However, neurotrophins do not cross the BBB, and have not been effective in the treatment of human stroke. In experimental stroke, or other brain diseases, it is necessary to deliver the neurotrophin to brain via a transcranial injection, owing to the BBB problem. Recently, two model neurotrophins, BDNF (*18*) and GDNF (*24*), have been re-engineered for delivery across the human BBB.

Glial-Derived Neurotrophic Factor (GDNF). The cDNA encoding human prepro GDNF was produced by PCR and cDNA generated from RNA isolated from human U87 glioma cells (*24*). The cDNA encoding the mature 134 amino acid GDNF was subsequently produced by PCR from the prepro GDNF template and subcloned into the HIRMAb heavy chain expression cassette. COS cells were dual lipofected with separate expression plasmids encoding the HIRMAb light chain and the fusion gene of the HIRMAb heavy chain and the GDNF (*24*). The HIRMAb-GDNF fusion protein was purified from conditioned serum-free medium with protein A affinity chromatography. Western blot analysis with primary antibodies to either human IgG or human GDNF is shown in Figure 4. The size of the HC of the HIRMAb-GDNF fusion protein is about 15 kDa larger than the HC of the original HIRMAb using either the antihuman IgG primary antibody or the antihuman GDNF primary antibody (Figure 4). Both the HIRMAb and the HIRMAb-GDNF fusion protein have the same immunoreactive light chain in the IgG Western blot, since both proteins share the same light chain. The GDNF antibody is immunoreactive with the HIRMAb-GDNF fusion protein and with recombinant human GDNF, but not with the HIRMAb (Figure 4). Similarly, the antihuman IgG primary antibody is immunoreactive with the HIRMAb and the HIRMAb-GDNF fusion protein, but not with recombinant GDNF (Figure 4). The affinity of the HIRMAb-GDNF fusion protein for the HIR extracellular domain (ECD) was determined with a ELISA-based binding assay following the initial affinity purification of the HIR ECD from serum-free medium conditioned by Chinese hamster ovary (CHO) cells permanently transfected with the cDNA encoding

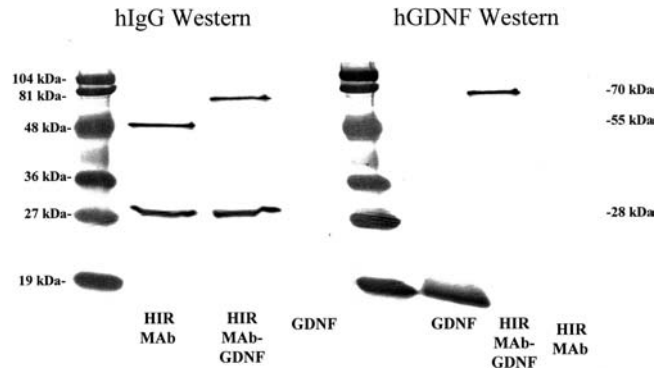

Figure 4. GDNF Western blot. Western blot with either antihuman (h) IgG primary antibody (left panel) or an antihuman GDNF primary antiserum (right panel). The immunoreactivity of the HIRMAb-GDNF fusion protein is compared to the HIRMAb and to recombinant GDNF. Both the HIRMAb-GDNF fusion protein and the HIRMAb have identical light chains on the anti-hIgG Western. The HIRMAb-GDNF fusion heavy chain reacts with both the anti-hIgG and the antihuman GDNF antibody, whereas the HIRMAb heavy chain only reacts with the anti-hIgG antibody. The size of the HIRMAb-GDNF fusion heavy chain, 70 kDa, is about 15 kDa larger than the size of the heavy chain of the HIRMAb, owing to the fusion of the 15 kDa GDNF to the 55 kDa HIRMAb heavy chain. From ref (*24*).

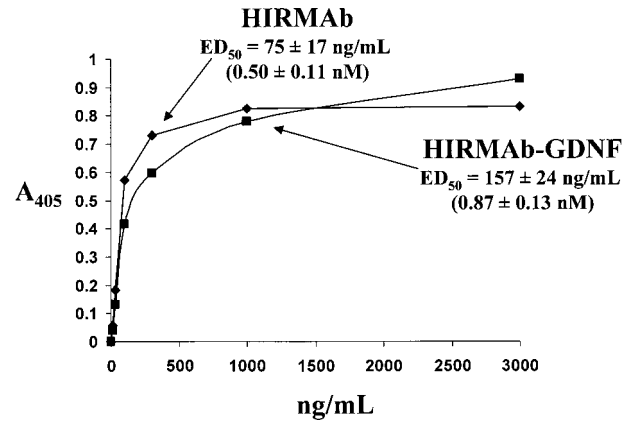

Figure 5. Fusion protein binding to the human insulin receptor. Binding of either the HIRMAb or the HIRMAb-GDNF fusion protein to the HIR extracellular domain (ECD) is saturable. The ED50 of HIRMAb-GDNF binding to the HIR ECD is comparable to the ED50 of the binding of the HIRMAb. From ref (*24*).

the HIR ECD (*25*). The HIR binding assay shows that the affinity of the HIRMAb-GDNF for the HIR is comparable to the original HIRMAb and both proteins have high affinity for the insulin receptor with an ED50 of 0.5−1.0 nM (Figure 5). The binding of the HIRMAb-GDNF fusion protein to the GDNF receptor was demonstrated with a separate binding assay, which measured the affinity of the fusion protein for the ECD of the human GDNF receptor (GFR)-α1. In a cell free binding assay, human GDNF bound to the recombinant GFR-α1 ECD with an ED50 of 1.03 ± 0.18 nM. The affinity of the HIRMAb-GDNF fusion protein for the GFR-α1 was also high with ED50 of 1.68 ± 0.17 nM (*24*). The original HIRMAb had no affinity for the GFR-α1. The activation of the GFR-α1 dependent signal transduction pathways within human neural cells by the HIRMAb-GDNF fusion protein was evaluated in a cell-based bioassay (Figure 6A). Human neural SK-N-MC cells were dual transfected with a cDNA encoding for the c-ret kinase and a luciferase reporter gene driven by the tyrosine hydroxylase (TH) promoter (*28*). Addition of GDNF to the medium of these cells activates the TH promoter via the GFR-α1/c-ret kinase system, and this leads to increased cellular luciferase expression (Figure

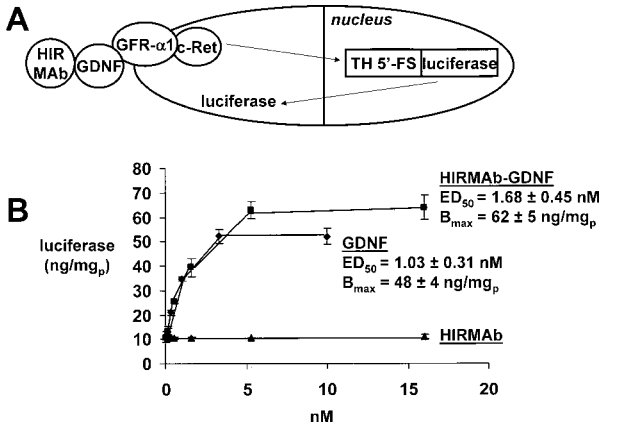

Figure 6. Cell-based bioassay of fusion protein potency. (A) Binding by either GDNF or the HIRMAb-GDNF fusion protein to the GFRα1 on the cell membrane of c-ret kinase transfected human neural SK-N-MC cells activates the tyrosine hydroxylase (TH) 5′-flanking sequence (FS), which drives luciferase gene expression. (B) Both GDNF and the HIRMAb-GDNF fusion protein activate luciferase gene expression in a saturable manner, with comparable ED50 values. There is no activation of luciferase gene expression by the HIRMAb. From ref (*24*).

6B). GDNF increased luciferase expression with an ED50 of 1.03 ± 0.31 nM, and the HIRMAb-GDNF also increased luciferase expression with an ED50 of 1.68 ± 0.45 nM (Figure 6B). The original HIRMAb was biologically inactive in this bioassay (Figure 6B). The biological activity of the HIRMAb-GDNF fusion protein was also evaluated with an in vivo bioassay using a middle cerebral artery occlusion (MCAO) stroke model in the adult rat (*24*). Since the HIRMAb portion of the HIRMAb-GDNF fusion protein does not recognize the rat insulin receptor, the HIRMAb-GDNF fusion protein could not be delivered to rat brain following intravenous administration. However, the fusion protein was delivered to ischemic rat brain following permanent occlusion of the middle cerebral artery with an intracerebral injection for the purposes of demonstrating neural cell neuroprotection in vivo. The intracerebral injection of the HIRMAb-GDNF fusion protein resulted in a 77% reduction in the hemispheric stroke volume from 331 ± 33 mm^3 to 77 ± 22 mm^3 (as shown in Figure 7A), and this reduction in stroke volume was significant at the $p < 0.001$ level. Similarly, the stroke volume in the cortex was significantly reduced 86% and the subcortical stroke volume was reduced significantly 52% by the administration of the HIRMAb-GDNF fusion protein (Figure 7A). The volume of the infarcted area in brain was measured by histochemistry using 2% 2,3,5-triphenyltetrazolium chloride (TTC). A representative TTC stain of the rat brain 24 h after occlusion of the middle cerebral artery and intracerebral injection of either saline or the HIRMAb-GDNF fusion protein is shown in Figure 7B,C, respectively (*24*). The neurologic deficit score was 3.0 ± 0.7 and 1.3 ± 0.6 in the saline treated and HIRMAb-GDNF treated rats, respectively, and this difference is statistically significant (*24*). The recent work with HIRMAb-GDNF fusion protein demonstrates that GDNF can be re-engineered to enable transport across the human BBB so that this neurotrophin can be pharmacologically active in brain following intravenous administration. GDNF could be a new pharmaceutical for the treatment of both acute and chronic brain diseases including acute stroke, Parkinson's disease, or motor neuron disease (Table 2).

Brain-Derived Neurotrophic Factor (BDNF). BDNF is a potent neuroprotective molecule when injected directly into the brain (*29, 30*). However, BDNF is not pharmacologically active in the brain following intravenous administration in the absence of BBB disruption (*31, 32*), because BDNF does not cross

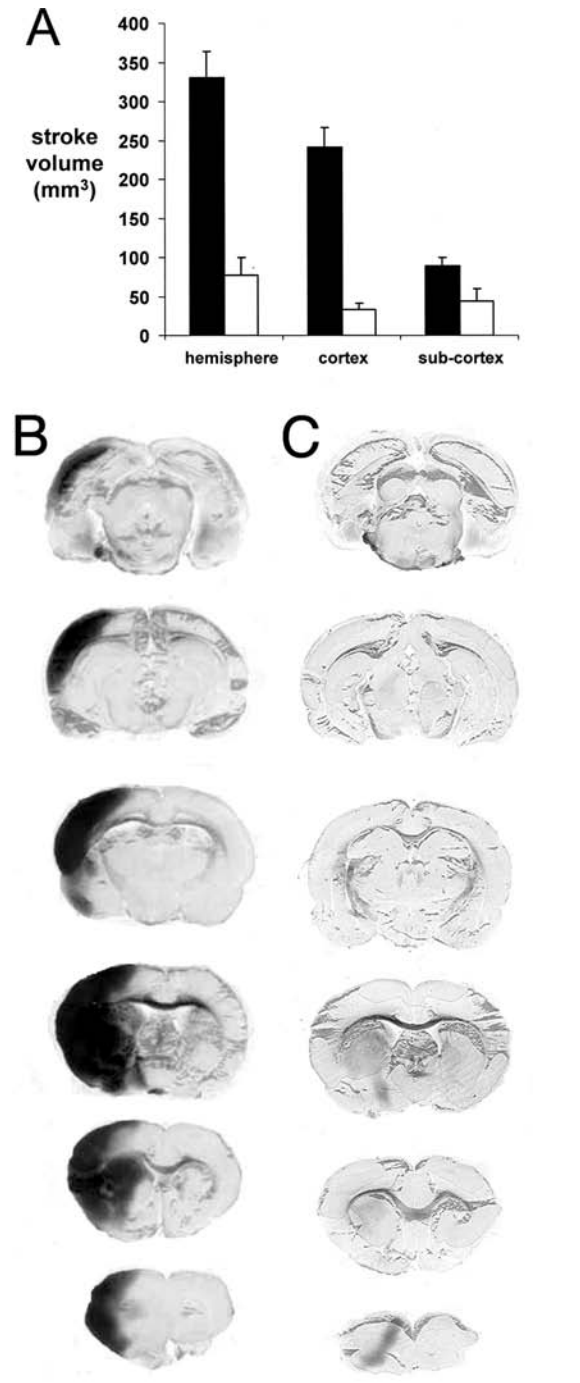

Figure 7. In vivo bioassay of fusion protein potency. (A) Stroke volumes in rats subjected to a 24 h permanent middle cerebral artery occlusion (MCAO) and treated with either intracerebral saline (closed bar) or the HIRMAb-GDNF fusion protein (open bar). Data are mean ± SE ($n = 5-6$ rats per group). (B, C) TTC stains of serial coronal sections of rat brain at 24 h after permanent MCAO and intracerebral saline (B) or HIRMAb-GDNF fusion protein (C). A representative stain is shown for 1 rat from each treatment group. In these inverted gray-scale images, the infarcted brain is black, and the healthy brain is white. The most rostral section is top and the most caudal section is bottom. From ref (*24*).

the BBB (*33*). Therefore, if BDNF is to be developed as a new pharmaceutical for the brain, the BDNF must be re-engineered to cross the human BBB. A HIRMAb-BDNF fusion protein was genetically engineered and a tandem vector encoding this fusion protein was permanently inserted into CHO cells with electroporation (*18*). Following amplification of cell lines with methotrexate (MTX) and dilutional cloning of the cell line, a

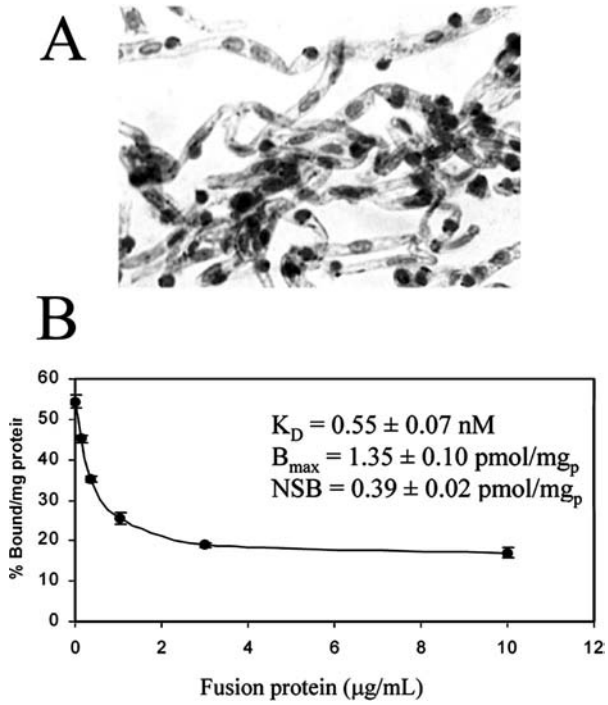

Figure 8. Fusion protein binding to the human BBB. (A) Light micrograph of capillaries isolated from human brain, used as an in vitro model system of the human BBB. (B) Radio-receptor assay of binding of [^{3}H]-HIRMAb-BDNF fusion protein to the HIR on the human BBB; the binding is self-inhibited by unlabeled fusion protein. Fitting the saturation data to a Scatchard plot with a nonlinear regression analysis yields the binding parameters: $K_D = 0.55 \pm 0.07$ nM, $B_{max} = 1.35 \pm 0.10$ pmol/mg_p, NSB $= 0.39 \pm 0.02$ pmol/mg_p, where B_{max} is the maximal saturable binding, and NSB is the nonsaturable binding. From ref (*18*).

high producing CHO line was isolated. The fusion protein was affinity purified by protein A affinity chromatography. The high-affinity binding of the HIRMAb-BDNF fusion protein to the human BBB was evaluated with a radioreceptor assay (RRA) using isolated human brain microvessels. Capillaries can be isolated from human autopsy brain free of adjoining brain tissue, as illustrated in Figure 8A. Binding of ligands to the endogenous human BBB insulin receptor can be measured with the isolated human brain capillary RRA. The fusion protein was tritiated with [^{3}H]-*N*-succinimidylpropionate. The binding of the [^{3}H]-HIRMAb-BDNF fusion protein to isolated human brain capillaries was saturable and the K_D was 0.55 ± 0.07 nM (Figure 8B). This K_D is identical to the K_D of binding of the original murine HIRMAb to the isolated human brain capillary (*15*). These observations indicate there is no change in affinity of the HIRMAb for binding to the intact HIR at the human BBB following fusion of a BDNF molecule to each of the two heavy chains of the HIRMAb. The transport of the HIRMAb-BDNF fusion protein across the BBB in the Rhesus monkey in vivo was measured following the intravenous injection of the [^{3}H]-HIRMAb-BDNF fusion protein (*18*). The fusion protein was rapidly cleared from blood at a rate comparable to the rate of clearance of the original murine HIRMAb (Figure 9A). The comparable clearance of the HIRMAb-BDNF fusion protein, and the HIRMAb, demonstrates that fusion of a highly cationic protein, such as BDNF, to the HIRMAb does not cause an acceleration of the removal of the IgG from the bloodstream. In contrast, the highly cationic BDNF is rapidly removed from blood, and is rapidly degraded following an intravenous administration (*33*). The metabolic stability of BDNF in vivo is increased following fusion of the neurotrophin to the IgG. The differential trichloroacetic acid (TCA) precipitability of the serum radioactivity of radiolabeled HIRMAb-BDNF fusion protein and native BDNF is shown in Figure 9B. The much higher TCA precipitability of the HIRMAb-BDNF fusion protein, as compared to BDNF, shows that the metabolic stability of the BDNF is increased following re-engineering of the neurotrophin as an IgG fusion protein. The concentration of the HIRMAb-BDNF fusion protein in primate brain following intravenous administration of a subtherapeutic dose of fusion protein is many-fold greater than the concentration of endogenous BDNF (Figure 9C). This demonstrates that brain BDNF can be elevated by administration of the HIRMAb-BDNF fusion protein. The increased brain uptake of the HIRMAb-BDNF is due to actual transport through the microvascular barrier, and into brain parenchyma. This was demonstrated with the capillary depletion technique (Figure 9D). The equivalence of the volume of distribution (VD) of the labeled fusion protein in the total brain homogenate versus the postvascular supernatant (Figure 9D) indicates the HIRMAb-BDNF fusion protein is not sequestered within the microvascular compartment of brain (*18*). In summary, recent work shows that BDNF can be developed as a new pharmaceutical for human brain disease, providing this neurotrophin is re-engineered to cross the human BBB. BDNF could be used for the treatment of acute stroke or head injury, or for the treatment of chronic neurodegeneration.

BLOOD−BRAIN BARRIER DELIVERY OF THERAPEUTIC MONOCLONAL ANTIBODIES

A new therapeutic for the treatment of AD is a mAb against the Aβ amyloid peptide of Alzheimer's disease. The dementia of AD correlates with the deposition of Aβ amyloid plaques in brain (*34*), which accumulate over many years prior to the development of dementia. AD transgenic mouse models have been developed which similarly demonstrate Aβ amyloid deposits in brain as well as deterioration of neuro-behavioral function which progresses in parallel with accumulation with age of Aβ amyloid plaque in brain (*35*). The intracerebral injection of a monoclonal antibody against the Aβ peptide results in rapid disaggregation of the Aβ amyloid plaque (*36, 37*). This plaque disaggregation is followed by repair of dystrophic neurites in the region previously occupied by the amyloid plaque (*36, 37*), which correlates with improvement in neuro-behavioral function. Similar results were reported with passive immune therapy in AD transgenic mice, which involves the systemic administration of large doses of an anti-Aβ mAb (*38, 39*). However, the passive immune therapy of AD does not address the question as to how the circulating anti-Aβ mAb gains access to the brain amyloid plaque, which resides behind the BBB. The pharmacologic effects of passive immune therapy in transgenic mouse models of AD may be due to inadvertent BBB disruption. A consistent finding of passive immune therapy in rodents is the development of cerebral microhemorrhage (*40, 41*). Such BBB disruption would allow the circulating anti-Aβ mAb to gain access to brain amyloid. The cause of cerebral microhemorrhage is not known. However, it is known that the plasma level of the Aβ peptide increases from very low levels to nearly 1 μM following the intravenous administration of an anti-Aβ mAb for the passive immune therapy of AD (*42*). It is also known that elevations in the plasma concentration of the Aβ peptide following the infusion of Aβ peptide into the blood of rodents also results in microhemorrhage and BBB disruption (*43*). These findings suggest that the cerebral microhemorrhage of passive immune therapy may be caused by the large increase in plasma Aβ concentration. Therefore, it is possible that passive immune therapy will lead to cerebral microhemorrhage in humans similar to that observed in rodents. What is needed is a re-engineering of the anti-Aβ mAb, such that the therapeutic mAb gains access to plaques in brain following receptor-

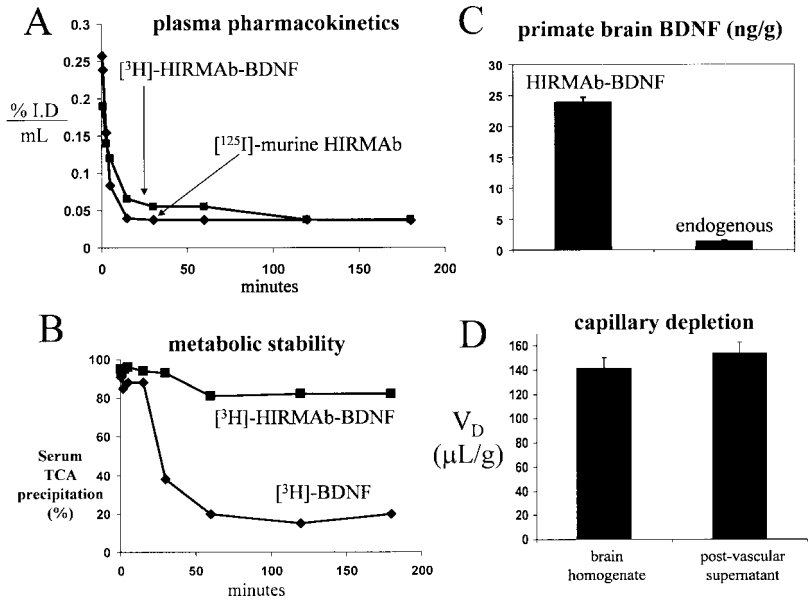

Figure 9. Fusion protein pharmacokinetics and brain uptake in the Rhesus monkey. Pharmacokinetics and brain uptake of HIRMAb-BDNF fusion protein in the adult Rhesus monkey. (A) The serum concentration of [^{3}H]-HIRMAb-BDNF, or [^{125}I]-murine HIRMAb, is plotted vs time after a single intravenous injection of either protein in anesthetized adult Rhesus monkeys. (B) The serum radioactivity that is precipitable by trichloroacetic acid (TCA) is plotted vs time after a single intravenous injection of either [^{3}H]-HIRMAb-BDNF in the anesthetized adult Rhesus monkey, or [^{3}H]-BDNF in the anesthetized adult rat. (C) Primate brain concentrations of HIRMAb-BDNF fusion protein at 180 min after an intravenous injection of 70 μg/kg fusion protein, as compared to the endogenous concentration of BDNF in the adult primate brain. (D) Capillary depletion analysis of brain volume of distribution (V_D) at 180 min after a single intravenous injection of the [^{3}H]-HIRMAb-BDNF fusion protein in the anesthetized adult Rhesus monkey. The V_D is shown for the total brain homogenate and the postvascular supernatant. From ref (*18*).

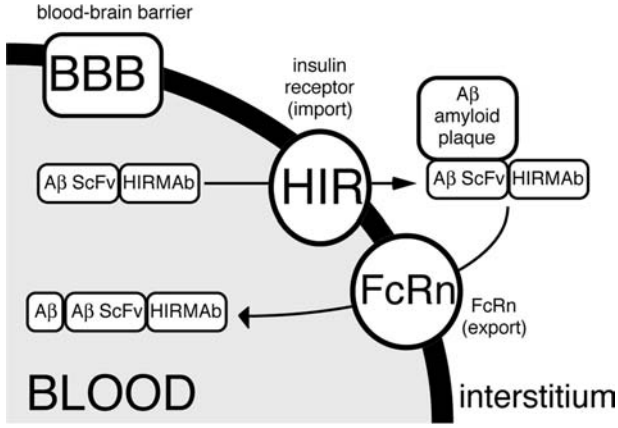

Figure 10. Import−export model of Aβ antibody therapeutics. The fusion antibody of the HIRMAb and the anti-Aβ single chain Fv antibody (ScFv) clears amyloid from brain in AD via 3 sequential steps, and each of these 3 sequential steps uses separate parts of the fusion antibody molecule. Step 1 is the influx of the fusion antibody from blood to brain across the BBB, which is mediated by binding of the fusion antibody to the BBB HIR. Step 2 is binding of the fusion antibody to the amyloid plaque in AD, which promotes disaggregation of the amyloid plaque, and this binding to the plaque is mediated by the anti-AβScFv part of the fusion antibody. Step 3 is the efflux of the fusion antibody from brain to blood across the BBB, which is mediated by binding of the fusion antibody to the BBB FcRn at the CH_2-CH_3 interface of the Fc region of the fusion antibody. From ref (*26*).

mediated transport across the BBB. Such a molecule would be rapidly cleared from the blood, as compared to a conventional anti-Aβ mAb (*26*), and this rapid clearance would minimize the accumulation of the Aβ peptide in the blood compartment.

The bidirectional BBB transport of a fusion antibody of the HIRMAb and an anti-Aβ ScFv is illustrated in Figure 10, which depicts the influx of the fusion antibody from blood into brain via transport on the endogenous HIR (*26*). Once in brain, the fusion antibody is free to bind to the Aβ amyloid plaque and promote disaggregation of the plaque. However, there must also be also a mechanism for efflux of the fusion antibody from brain to blood; otherwise, there would be no net decrease in the brain Aβ amyloid peptide burden. The fusion antibody is able to rapidly exit the brain via reverse transcytosis across the BBB, because the BBB expresses an Fc receptor (FcR), which functions as an IgG efflux system (*44*). IgG molecules injected directly into the brain are rapidly transported to blood via reverse transcytosis across the BBB, which is mediated by the brain microvascular FcR (*44*). The most widely expressed FcR on the BBB is the neonatal FcR, also called the FcRn (*45*). The BBB FcR mediates the asymmetric reverse transcytosis of IgG molecules from brain back to blood, but does not mediate the uptake or influx of IgG molecules in the blood to brain direction. The FcRn binding site on an IgG molecule is the CH_2-CH_3 interface (*46*). This region of the IgG molecule is retained following the engineering of the HIRMAb-ScFv fusion antibody, which is depicted in Figure 11. The genes encoding the variable region of heavy chain (VH) and the variable region of light chain (VL) of a murine mAb against the amino terminal portion of the Aβ peptide were spliced together with a linker peptide to form a ScFv molecule (*26*). The amino terminal portion of this anti-Aβ ScFv was fused to the carboxyl terminus of the CH_3 region of the HIRMAb to produce the fusion antibody shown in Figure 11. The fusion antibody is a trifunctional molecule that binds the HIR on the BBB to mediate influx from blood into the brain; binds to the BBB FcRn at the CH_2-CH_3 interface to mediate efflux from brain back to blood; and binds and disaggregates the Aβ amyloid plaque of AD. These three functionalities of the fusion antibody were all demonstrated in vivo in different animal models (*26*). The fusion antibody was radiolabeled with 125-iodine, and coinjected intravenously into the adult Rhesus monkey with [^{3}H]-labeled anti-Aβ mAb (*26*). The HIRMAb-ScFv fusion antibody was rapidly removed from blood, similar to the rapid removal from blood of the HIRMAb-BDNF fusion protein shown in Figure 9A. In contrast, the conventional anti-Aβ mAb had a very long blood residence time,

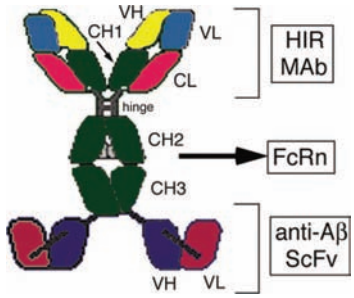

Figure 11. Antibody fusion protein with 3 functional domains. The first domain, the HIRMAb, binds the BBB HIR to trigger influx across the BBB. The second domain, the anti-AβScFv fused to the CH_3 region, binds to the Aβ amyloid peptide of AD to cause disaggregation of amyloid plaque in brain. The third domain, the CH_2-CH_3 interface of the Fc region, binds to the BBB FcRn to trigger efflux of the fusion antibody from brain back to blood, resulting in a net depletion of amyloid plaque in brain. From ref (*26*).

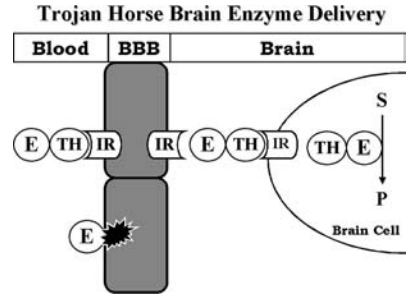

Figure 12. Antibody−lysosomal enzyme fusion protein. The fusion protein is composed of an engineered mAb to the human insulin receptor (IR), which acts as a molecular Trojan horse (TH), and IDUA, a lysosomal enzyme (E). By itself, the IDUA does not cross the blood−brain barrier (BBB). However, following fusion of the IDUA to the TH, the enzyme is able to cross the BBB, and the brain cell membrane, by trafficking on the IR, which is expressed at both membranes in the brain. Once inside brain cells, the IDUA moiety of the fusion protein degrades lysosomal storage substrate (S) into low molecular weight products (P). From ref (*20*).

and was not measureably removed from blood during the experimental time period (*26*). As expected, the anti-Aβ mAb was not taken up by brain (*26*). In contrast, high brain uptake of the fusion antibody was observed owing to transport into brain on the endogenous insulin receptor of the primate BBB (*26*). Although the rat insulin receptor does not recognize the HIRMAb, the rat FcRn does recognize human IgG (*47*). Therefore, the rapid efflux of the fusion antibody from the brain to blood compartments across the BBB could be demonstrated with the brain efflux index method following the intracerebral injection of the fusion antibody into adult rat brain (*26*). The binding of the fusion antibody to the $A\beta^{1-40}$ peptide was confirmed with an immunoradiometric assay in vitro (*26*). The binding of the fusion antibody to the Aβ amyloid plaque was demonstrated in vivo following the intracerebral injection of the fusion antibody into the brain of a double transgenic mouse model of AD (*26*). A single intracerebral injection of 20 pmol of the fusion antibody into the transgenic mouse brain resulted in a 40% reduction in amyloid plaque in both the hippocampus and the cortex within 48 h. In summary, if mAb therapeutics, such as a mAb against the Aβ amyloid of Alzheimer's disease, are to be developed as human neurotherapeutics, these therapeutic MAbs must be reengineered to cross the human BBB. The ability of the fusion antibody to traverse the BBB in both directions may be controlled by the genetic engineering. If the intent is to minimize efflux from brain, then the fusion antibody could be engineered without a constant region CH_2-CH_3 interface, so as to eliminate affinity of the fusion protein for the BBB FcR IgG efflux system. There are multiple genetic engineering approaches that can be taken to develop antibody fusion proteins that cross the BBB in either direction.

BLOOD−BRAIN BARRIER DELIVERY OF THERAPEUTIC ENZYMES

There are over 40 lysosomal storage disorders and approximately 75% of these affect the brain (*48*). The standard therapy for lysosomal storage disorders is enzyme replacement therapy (ERT) (*49*). However, recombinant enzymes do not cross the BBB and do not treat the brain in patients with lysosomal storage diseases. A common lysosomal storage disorder is mucopolysaccharidosis (MPS) type I, also called Hurler's syndrome, which is caused by the mutation of the gene encoding for the IDUA lysosomal enzyme. Recombinant human IDUA is produced in CHO cells (*50, 51*) for the ERT of Hurler's syndrome. The delivery of IDUA from blood to a neuronal lysosomal compartment requires transport of the lysosomal enzyme across two membranes in series: the BBB and the neuronal plasma membrane, as shown in Figure 12. Owing to the high expression of the insulin receptor on the neuronal plasma membrane (*52*), the HIRMAb acts as a molecular Trojan horse to ferry the lysosomal enzyme not only across the BBB, but also across the neuronal plasma membrane (Figure 12). Following the PCR amplification of a 1.9 Kb cDNA encoding for the human IDUA, minus its signal peptide (Figure 3B), the IDUA cDNA was fused to the 3′-terminus of the cDNA encoding the heavy chain of the HIRMAb (*20*). The HIRMAb-IDUA fusion protein was expressed in COS cells and purified from conditioned serum-free medium with protein A affinity chromatography. The HIRMAb-IDUA fusion protein was added to the medium of MPS type I fibroblasts and the localization of the fusion protein within these cells 24 h later was detected with confocal microscopy and primary antibodies to either human IDUA (Figure 13A) or human lysosomal associated membrane protein (LAMP)-1 (Figure 13B). As shown in the overlay study (Figure 13C), there is localization of the HIRMAb-IDUA fusion protein in the lysosomal compartment of MPS type I fibroblasts. Figure 13D is an overlap image of the negative control primary antibodies. The HIRMAb-IDUA fusion protein was radiolabeled with 125-iodine and chloramine T. The [^{125}I]-HIRMAb-IDUA fusion protein was injected intravenously into the adult Rhesus monkey. At 2 h after injection, the animal was euthanized, the brain was removed, and 20 μm frozen sections were prepared for film autoradiography. The brain autoradiography study demonstrated a robust uptake of the HIRMAb-IDUA fusion protein in all parts of the Rhesus monkey brain following intravenous administration with a higher uptake in gray matter as compared to white matter (Figure 13E). Owing to the greater microvascular density of gray matter as compared to white matter, there is a higher vascular density of insulin receptor in gray matter as compared to white matter (*15*). The primate brain uptake of the HIRMAb-IDUA fusion protein was 1.05 ± 0.05% of injected dose (ID) per 100 g brain (*20*). Since the size of the Rhesus monkey brain is approximately 100 g, the amount of injected fusion protein that distributed to primate brain was approximately 1%. A standard dose of intravenous common IDUA in the ERT of Hurler's syndrome is 0.6 mg/kg (*53*). Given this injection dose in a 50 kg patient, and given the brain uptake of the fusion protein expressed as percent of injected dose per gram, and given the IDUA enzyme-specific activity of 363 units/μg protein for the HIRMAb-IDUA fusion protein (*20*), the brain IDUA enzyme activity is predicted to be 1.1 units of IDUA enzyme activity per mg of protein following the intravenous administration of the therapeutic dose of the HIRMAb-IDUA fusion protein (*20*). This level of IDUA enzyme activity is normal for the human brain, where the IDUA

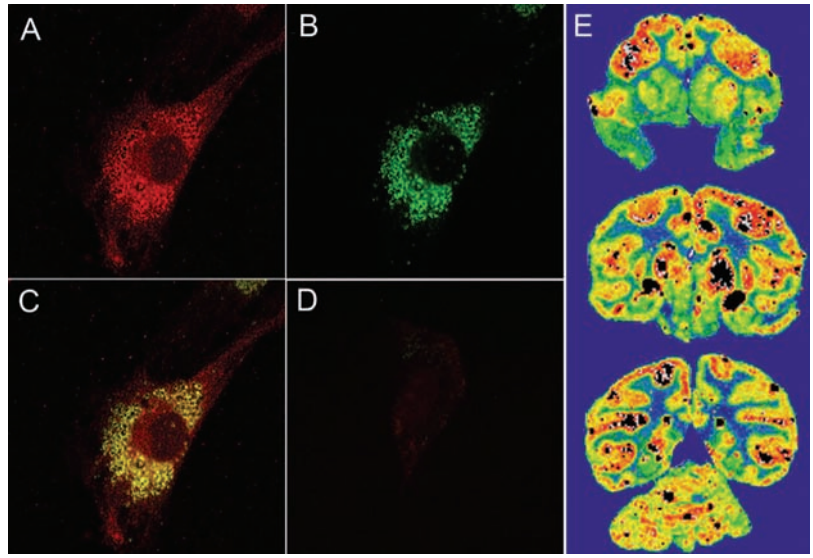

Figure 13. Delivery of IDUA by Trojan horse in cell culture and in vivo in the Rhesus monkey brain. (A, B, C, D) Hurler fibroblasts were incubated with HIRMAb-IDUA fusion protein for 24 h and then fixed and immune stained for confocal microscopy. The fixed cells were stained with an antibody to human IDUA (panel A: red channel), and a mouse monoclonal antibody to human lysosomal associated membrane protein (LAMP)-1 (panel B: green channel). The overlap image in panel C shows sequestration of the HIRMAb-IDUA fusion protein within lysosomes. Panel D is an overlap image of negative control primary antibodies. (E) Film autoradiography of Rhesus monkey brain removed 2 h after an intravenous administration of [^{125}I]-HIRMAb-IDUA fusion protein. Coronal sections through the forebrain (top panel), midbrain (middle panel), and hindbrain/cerebellum (bottom panel) are shown. Gray matter is red−yellow and white matter is blue−green. From ref (*20*).

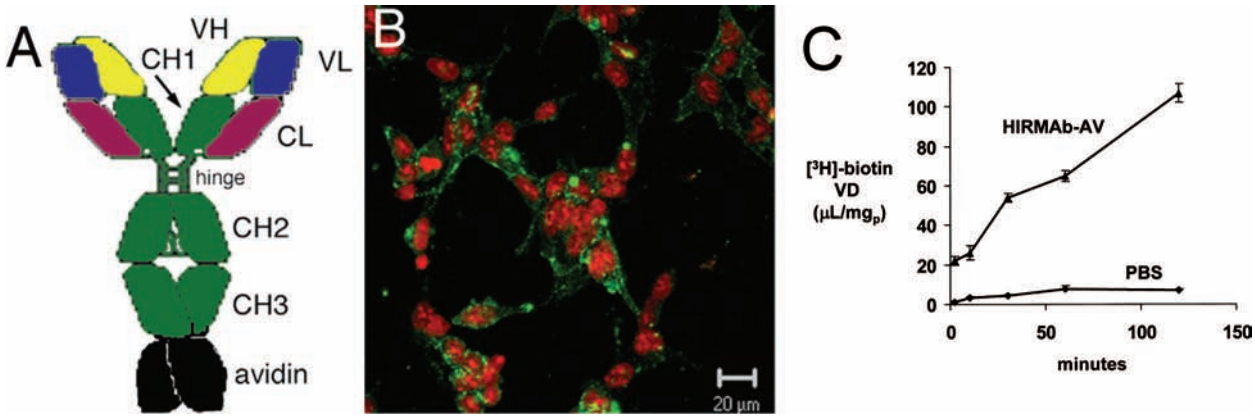

Figure 14. Antibody-avidin fusion protein. (A) Structure of the HIRMAb-avidin fusion protein showing fusion of the amino terminus of the mature avidin (AV) monomer to the carboxyl terminus of the CH_3 region of the heavy chain of the engineered HIRMAb. The fusion protein is a bifunctional molecule. The fusion protein binds the HIR at the BBB, to mediate transport into the brain, and binds biotinylated pharmaceuticals, to mediate high-affinity attachment of the pharmaceutical to the HIRMAb molecular Trojan horse. (B) Confocal microscopy of human 293 cells showing the intracellular distribution (green) of fluorescein-biotin conjugated to the HIRMAb-AV fusion protein. The nuclei are stained by propidium iodide (red). (C) Volume of distribution (VD) of [^{3}H]-biotin in human 293 cells at 2 to 120 min of incubation at 37 °C after comixture of the labeled biotin with either phosphate buffered saline (PBS) or the HIRMAb-AV fusion protein. Data points are mean ± SE (n = 4 dishes per time point). From ref (*27*).

enzyme activity ranges from 0.5 to 1.5 units/mg protein (*54*). Therefore, the IDUA enzyme activity in the brain of patients with Hurler's syndrome may be normalized following the intravenous administration of therapeutic doses of the HIRMAb-IDUA fusion protein. This is made possible following the re-engineering of IDUA to enable transport of this recombinant enzyme across the human BBB (Table 2).

ENGINEERING OF IgG-AVIDIN FUSION PROTEINS FOR DELIVERY OF BIOTINYLATED DRUGS

It is not feasible to engineer IgG fusion proteins for certain types of biotherapeutics including oligopeptides, antisense drugs, or short interfering RNA (siRNA). However, the delivery of monobiotinylated therapeutics or siRNA across the BBB is possible with the genetic engineering and expression of a HIRMAb-avidin fusion protein. Avidin has been administered to humans without immunologic reactions (*55, 56*). The binding of biotin by avidin is characterized by very high affinity, with a $K_D = 10^{-15}$ M and a dissociation $t_{1/2} = 89$ days (*57*). Therefore, the avidin−biotin system provides the high stability of the bond between the drug and the Trojan horse that is required for in vivo drug delivery. The avidin cDNA was produced by PCR and following engineering of the heavy chain-avidin fusion gene, and transfection of COS or CHO cells, the HIRMAb-avidin (AV) fusion protein was expressed and purified (*27*). The amino terminus of the avidin monomer was fused to the carboxyl terminus of the CH_3 region of the HIRMAb heavy chain, as depicted in Figure 14A. Engineering the IgG-avidin fusion protein in this manner places the avidin monomer in a dimeric configuration which replicates the natural configuration of avidin, which is a dimer of dimers (*58*). A high producing CHO line was isolated, which allowed for purification of the

HIRMAb-avidin fusion protein. Initial work showed the biotin binding site of the HIRMAb-AV fusion protein was completely saturated by the high biotin content of cell culture medium. However, the CHO line could be maintained for up to a month in biotin-free medium, and the HIRMAb-AV fusion protein produced under these conditions avidly bound biotin (*27*). The biologic activity of the HIRMAb-avidin fusion protein was demonstrated in cell culture using human 293 epithelial cells. The intracellular distribution of biotin-fluorescein in 293 cells was demonstrated with confocal microscopy following attachment of the biotin-fluorescein to the HIRMAb-AV fusion protein (Figure 14B). There is no measurable cell uptake of the biotin-fluorescein in the absence of the HIRMAb-AV fusion protein (*27*). The uptake by these cells of ^{3}H-biotin was increased many-fold following attachment of the biotin to the HIRMAb-AV fusion protein as compared to biotin alone (Figure 14C). The use of avidin−biotin technology in drug delivery has advantages over other methods for attachment of ligands to an antibody transport vector and may be particularly advantageous in the delivery of siRNA therapeutics. The BBB delivery of siRNA was validated with an intracranial brain cancer model in rats. Rat glial tumors permanently transfected with the luciferase gene were implanted in adult rat brain. A monobiotinylated siRNA against the luciferase mRNA was attached to a conjugate of streptavidin and the mAb against the rat TfR (*59*). Intravenous administration of the siRNA alone caused no knockdown in brain tumor luciferase gene expression. However, the biotinylated siRNA caused a 69−81% reduction in luciferase gene expression following intravenous administration of the siRNA conjugated to the TfRMAb molecular Trojan horse (*59*). Therefore, the availability of the HIRMAb-AV fusion protein may allow for the delivery of siRNA across the human BBB. The HIRMAb-AV fusion protein is a universal Trojan horse, and almost any monobiotinylated drug could be delivered to brain with this delivery system. The formulation of human therapeutics with the IgG-avidin fusion protein technology is facilitated by a "two-vial" approach. The HIRMAb-AV fusion protein is formulated in one vial, and the monobiotinylated therapeutic is formulated in a second vial. The two vials are mixed just prior to administration. Owing to the very high affinity of avidin binding of biotin, there is instantaneous capture of the biotinylated drug by the HIRMAb-AV fusion protein.

CONCLUSIONS

The BBB problem has been the rate-limiting step in brain drug development. Prior attempts to deliver pharmaceuticals to the brain include BBB disruption, by either osmotic (*60*) or biochemical agents (*61*), or trans-cranial approaches using intracerebroventricular (ICV) injection (*62*) or convection-enhanced diffusion (CED) (*63*). BBB disruption is associated with chronic neuropathologic changes (*64*), which may be related to the toxic effects of plasma proteins on brain cells (*65*). Administration of drug by ICV injection only distributes drug to the ependymal surface of the brain, and this approach was not successful in the delivery of GDNF for Parkinson's disease (PD) (*66*). The delivery of GDNF for PD via CED was not successful in clinical trials (*67*), and this was subsequently shown to be due to limited distribution of the neurotrophin in brain distal to the perfusion catheter (*68*). An alternative approach to either the disruption of the BBB, or the trans-cranial delivery of drug to the brain, is the targeting of drug to brain via the trans-vascular route utilizing endogenous BBB transporters. This approach requires the re-engineering of biopharmaceuticals so that these molecules can access the endogenous BBB receptor-mediated transport systems.

The re-engineering of therapeutic proteins for drug delivery across the human BBB represents a merger of biopharmaceutical drug discovery and drug delivery. The presence of the BBB, and the fact that all large molecule biopharmaceuticals do not cross this barrier, represents an insurmountable barrier for CNS drug developers. Brain drug development programs that are focused solely on CNS drug discovery, in the absence of a parallel effort in CNS drug delivery, are destined to fail, owing to the BBB problem. There are many protein drugs for the brain that have already been discovered (Table 1). However, these drugs do not cross the BBB, and cannot enter into a CNS drug development program because of the BBB problem. The availability of these drugs allows a CNS drug delivery program to short-circuit CNS drug discovery. The drugs have already been discovered; the problem is BBB drug delivery. The BBB drug delivery problem can be solved by re-engineering existing biopharmaceuticals for transport across the human BBB using genetically engineered molecular Trojan horses. Future clinical trials with fusion proteins will address immunogenicity in humans, and off-target side effects. However, human Fc:soluble extracellular domain receptor fusion proteins such as etanercept (*69*) are FDA approved biopharmeuticals, and have low immunogenicity in humans, and safety profiles consistent with minimal off-target side effects (*70*).

ACKNOWLEDGMENT

The author is indebted to colleagues Drs. Ruben Boado, Yun Zhang, and Yufeng Zhang, of ArmaGen Technologies, for many valuable discussions.

LITERATURE CITED

(1) Pardridge, W. M. (2005) The blood-brain barrier: bottleneck in brain drug development. *NeuroRx 2*, 3–14.
(2) Pardridge, W. M. (1986) Biochemistry of the human blood-brain barrier. In: Blood-brain barrier: interface between internal medicine and the brain. *Ann. Intern. Med. 105*, 82–95.
(3) Brightman, M. W. (1977) Morphology of blood-brain interfaces. *Exp. Eye Res. 25*, 1–25.
(4) Duvernoy, H., Delon, S., and Vannson, J. L. (1983) The vascularization of the human cerebellar cortex. *Brain Res. Bull. 11*, 419–480.
(5) Saunders, N. R., and Mollgard, K. (1984) Development of the blood-brain barrier. *J. Dev. Physiol. 6*, 45–57.
(6) Smith, Q. R., and Rapoport, S. I. (1986) Cerebrovascular permeability coefficients to sodium, potassium, and chloride. *J. Neurochem. 46*, 1732–1742.
(7) Oldendorf, W. H. (1971) Brain uptake of radiolabeled amino acids, amines, and hexoses after arterial injection. *Am. J. Physiol. 221*, 1629–1639.
(8) Cornford, E. M., Hyman, S., Cornford, M. E., and Caron, M. J. (1996) Glut1 glucose transporter activity in human brain injury. *J. Neurotrauma 13*, 523–536.
(9) Pardridge, W. M. (1986) Receptor-mediated peptide transport through the blood-brain barrier. *Endocr. Rev. 7*, 314–330.
(10) Duffy, K. R., and Pardridge, W. M. (1987) Blood-brain barrier transcytosis of insulin in developing rabbits. *Brain Res. 420*, 32–38.
(11) Skarlatos, S., Yoshikawa, T., and Pardridge, W. M. (1995) Transport of [125I]transferrin through the rat blood-brain barrier. *Brain Res. 683*, 164–171.
(12) Bickel, U., Kang, Y. S., Yoshikawa, T., and Pardridge, W. M. (1994) In vivo demonstration of subcellular localization of anti-transferrin receptor monoclonal antibody-colloidal gold conjugate in brain capillary endothelium. *J. Histochem. Cytochem. 42*, 1493–1497.
(13) Lee, H. J., Engelhardt, B., Lesley, J., Bickel, U., and Pardridge, W. M. (2000) Targeting rat anti-mouse transferrin receptor monoclonal antibodies through blood-brain barrier in mouse. *J. Pharmacol. Exp. Ther. 292*, 1048–1052.

(14) Pardridge, W. M., Buciak, J. L., and Friden, P. M. (1991) Selective transport of an anti-transferrin receptor antibody through the blood-brain barrier in vivo. *J. Pharmacol. Exp. Ther. 259*, 66–70.
(15) Pardridge, W. M., Kang, Y. S., Buciak, J. L., and Yang, J. (1995) Human insulin receptor monoclonal antibody undergoes high affinity binding to human brain capillaries in vitro and rapid transcytosis through the blood-brain barrier in vivo in the primate. *Pharm. Res. 12*, 807–816.
(16) Boado, R. J., Zhang, Y., and Pardridge, W. M. (2007) Humanization of anti-human insulin receptor antibody for drug targeting across the human blood-brain barrier. *Biotechnol. Bioeng. 96*, 381–391.
(17) Pardridge, W. M. (1997) Drug delivery to the brain. *J. Cereb. Blood Flow Metab. 17*, 713–731.
(18) Boado, R. J., Zhang, Y., and Pardridge, W. M. (2007) Genetic engineering, expression, and activity of a fusion protein of a human neurotrophin and a molecular Trojan horse for delivery across the human blood-brain barrier. *Biotechnol. Bioeng. 97*, 1376–1386.
(19) Pardridge, W. M. (2001) *Brain Drug Targeting; The Future of Brain Drug Development*, pp 1−370, Cambridge University Press, Cambridge, United Kingdom.
(20) Boado, R. J., Zhang, Y., Xia, C. F., Wang, Y., and Pardridge, W. M. (2008) Genetic engineering of a lysosomal enzyme fusion protein for targeted delivery across the human blood-brain barrier. *Biotechnol. Bioeng. 99*, 475–484.
(21) Hefti, F. (1997) Pharmacology of neurotrophic factors. *Annu. Rev. Pharmacol. Toxicol. 37*, 239–267.
(22) Merchant, A. M., Zhu, Z., Yuan, J. Q., Goddard, A., Adams, C. W., Presta, L. G., and Carter, P. (1998) An efficient route to human bispecific IgG. *Nat. Biotechnol. 16*, 677–681.
(23) Miller, K., Meng, G., Liu, J., Hurst, A., Hsei, V., Wong, W. L., Ekert, R., Lawrence, D., Sherwood, S., DeForge, L., Gaudreault, J., Keller, G., Sliwkowski, M., Ashkenazi, A., and Presta, L. (2003) Design, construction, and in vitro analyses of multivalent antibodies. *J. Immunol. 170*, 4854–4861.
(24) Boado, R. J., Zhang, Y., Wang, Y., and Pardridge, W. M. (2007) GDNF fusion protein for targeted-drug delivery across the human blood-brain barrier Biotechnol. Bioeng. *100*, 387–396.
(25) Coloma, M. J., Lee, H. J., Kurihara, A., Landaw, E. M., Boado, R. J., Morrison, S. L., and Pardridge, W. M. (2000) Transport across the primate blood-brain barrier of a genetically engineered chimeric monoclonal antibody to the human insulin receptor. *Pharm. Res. 17*, 266–274.
(26) Boado, R. J., Zhang, Y., Xia, C. F., and Pardridge, W. M. (2007) Fusion antibody for Alzheimer's disease with bidirectional transport across the blood-brain barrier and abeta fibril disaggregation. *Bioconjugate Chem. 18*, 447–455.
(27) Boado, R. J., Zhang, Y., Xia, C. F., Wang, Y., and Pardridge, W. M. (2008) Genetic engineering, expression, and activity of a chimeric monoclonal antibody-avidin fusion protein for receptor-mediated delivery of biotinylated drugs in humans. *Bioconjugate Chem. 19*, 731–739.
(28) Tanaka, M., Xiao, H., Hirata, Y., and Kiuchi, K. (2003) A rapid assay for glial cell line-derived neurotrophic factor and neurturin based on transfection of cells with tyrosine hydroxylase promoter-luciferase construct. *Brain Res. Brain Res. Protoc. 11*, 119–122.
(29) Schabitz, W. R., Schwab, S., Spranger, M., and Hacke, W. (1997) Intraventricular brain-derived neurotrophic factor reduces infarct size after focal cerebral ischemia in rats. *J. Cereb. Blood Flow Metab. 17*, 500–506.
(30) Yamashita, K., Wiessner, C., Lindholm, D., Thoenen, H., and Hossmann, K. A. (1997) Post-occlusion treatment with BDNF reduces infarct size in a model of permanent occlusion of the middle cerebral artery in rat. *Metab. Brain Dis. 12*, 271–280.
(31) Wu, D., and Pardridge, W. M. (1999) Neuroprotection with noninvasive neurotrophin delivery to the brain. *Proc. Natl. Acad. Sci. U.S.A. 96*, 254–259.
(32) Zhang, Y., and Pardridge, W. M. (2001) Conjugation of brain-derived neurotrophic factor to a blood-brain barrier drug targeting system enables neuroprotection in regional brain ischemia following intravenous injection of the neurotrophin. *Brain Res. 889*, 49–56.
(33) Pardridge, W. M., Wu, D., and Sakane, T. (1998) Combined use of carboxyl-directed protein pegylation and vector-mediated blood-brain barrier drug delivery system optimizes brain uptake of brain-derived neurotrophic factor following intravenous administration. *Pharm. Res. 15*, 576–582.
(34) Cummings, B. J., and Cotman, C. W. (1995) Image analysis of beta-amyloid load in Alzheimer's disease and relation to dementia severity. *Lancet 346*, 1524–1528.
(35) Savonenko, A., Xu, G. M., Melnikova, T., Morton, J. L., Gonzales, V., Wong, M. P., Price, D. L., Tang, F., Markowska, A. L., and Borchelt, D. R. (2005) Episodic-like memory deficits in the APPswe/PS1dE9 mouse model of Alzheimer's disease: Relationship to β-amyloid deposition and neurotransmitter abnormalities. *Neurobiol. Dis. 18*, 602–617.
(36) Lombardo, J. A., Stern, E. A., McLellan, M. E., Kajdasz, S. T., Hickey, G. A., Bacskai, B. J., and Hyman, B. T. (2003) Amyloid-beta antibody treatment leads to rapid normalization of plaque-induced neuritic alterations. *J. Neurosci. 23*, 10879–10883.
(37) Brendza, R. P., Bacskai, B. J., Cirrito, J. R., Simmons, K. A., Skoch, J. M., Klunk, W. E., Mathis, C. A., Bales, K. R., Paul, S. M., Hyman, B. T., and Holtzman, D. M. (2005) Anti-Abeta antibody treatment promotes the rapid recovery of amyloid-associated neuritic dystrophy in PDAPP transgenic mice. *J. Clin. Invest. 115*, 428–433.
(38) Hartman, R. E., Izumi, Y., Bales, K. R., Paul, S. M., Wozniak, D. F., and Holtzman, D. M. (2005) Treatment with an amyloid-beta antibody ameliorates plaque load, learning deficits, and hippocampal long-term potentiation in a mouse model of Alzheimer's disease. *J. Neurosci. 25*, 6213–6220.
(39) Brody, D. L., and Holtzman, D. M. (2008) Active and passive immunotherapy for neurodegenerative disorders Annu. Rev. Neurosci., in press.
(40) Wilcock, D. M., Rojiani, A., Rosenthal, A., Subbarao, S., Freeman, M. J., Gordon, M. N., and Morgan, D. (2004) Passive immunotherapy against Abeta in aged APP-transgenic mice reverses cognitive deficits and depletes parenchymal amyloid deposits in spite of increased vascular amyloid and microhemorrhage. *J. Neuroinflammation 1*, 24.
(41) Racke, M. M., Boone, L. I., Hepburn, D. L., Parsadainian, M., Bryan, M. T., Ness, D. K., Piroozi, K. S., Jordan, W. H., Brown, D. D., Hoffman, W. P., Holtzman, D. M., Bales, K. R., Gitter, B. D., May, P. C., Paul, S. M., and DeMattos, R. B. (2005) Exacerbation of cerebral amyloid angiopathy-associated microhemorrhage in amyloid precursor protein transgenic mice by immunotherapy is dependent on antibody recognition of deposited forms of amyloid beta. *J. Neurosci. 25*, 629–636.
(42) Wilcock, D. M., Alamed, J., Gottschall, P. E., Grimm, J., Rosenthal, A., Pons, J., Ronan, V., Symmonds, K., Gordon, M. N., and Morgan, D. (2006) Deglycosylated anti-amyloid-beta antibodies eliminate cognitive deficits and reduce parenchymal amyloid with minimal vascular consequences in aged amyloid precursor protein transgenic mice. *J. Neurosci. 26*, 5340–5346.
(43) Su, G. C., Arendash, G. W., Kalaria, R. N., Bjugstad, K. B., and Mullan, M. (1999) Intravascular infusions of soluble beta-amyloid compromise the blood-brain barrier, activate CNS glial cells and induce peripheral hemorrhage. *Brain Res. 818*, 105–117.
(44) Zhang, Y., and Pardridge, W. M. (2001) Mediated efflux of IgG molecules from brain to blood across the blood-brain barrier. *J. Neuroimmunol. 114*, 168–172.
(45) Schlachetzki, F., Zhu, C., and Pardridge, W. M. (2002) Expression of the neonatal Fc receptor (FcRn) at the blood-brain barrier. *J. Neurochem. 81*, 203–206.
(46) Martin, W. L., West, A. P., Jr., Gan, L., and Bjorkman, P. J. (2001) Crystal structure at 2.8 A of an FcRn/heterodimeric Fc

complex: mechanism of pH-dependent binding. *Mol. Cell 7*, 867–877.
(47) Ober, R. J., Radu, C. G., Ghetie, V., and Ward, E. S. (2001) Differences in promiscuity for antibody-FcRn interactions across species: implications for therapeutic antibodies. *Int. Immunol. 13*, 1551–1559.
(48) Cheng, S. H., and Smith, A. E. (2003) Gene therapy progress and prospects: gene therapy of lysosomal storage disorders. *Gene Ther. 10*, 1275–1281.
(49) Brady, R. O., and Schiffmann, R. (2004) Enzyme-replacement therapy for metabolic storage disorders. *Lancet Neurol. 3*, 752–756.
(50) Kakkis, E. D., Matynia, A., Jonas, A. J., and Neufeld, E. F. (1994) Overexpression of the human lysosomal enzyme alpha-L-iduronidase in Chinese hamster ovary cells. *Protein Expr. Purif. 5*, 225–232.
(51) Unger, E. G., Durrant, J., Anson, D. S., and Hopwood, J. J. (1994) Recombinant alpha-L-iduronidase: characterization of the purified enzyme and correction of mucopolysaccharidosis type I fibroblasts. *Biochem. J. 304*, 43–49.
(52) Zhao, W., Chen, H., Xu, H., Moore, E., Meiri, N., Quon, M. J., and Alkon, D. L. (1999) Brain insulin receptors and spatial memory. Correlated changes in gene expression, tyrosine phosphorylation, and signaling molecules in the hippocampus of water maze trained rats. *J. Biol. Chem. 274*, 34893–34902.
(53) Wraith, J. E., Clarke, L. A., Beck, M., Kolodny, E. H., Pastores, G. M., Muenzer, J., Rapoport, D. M., Berger, K. I., Swiedler, S. J., Kakkis, E. D., Braakman, T., Chadbourne, E., Walton-Bowen, K., and Cox, G. F. (2004) Enzyme replacement therapy for mucopolysaccharidosis I: a randomized, double-blinded, placebo-controlled, multinational study of recombinant human alpha-L-iduronidase (laronidase). *J. Pediatr. 144*, 581–588.
(54) Crow, J., Gibbs, D. A., Cozens, W., Spellacy, E., and Watts, R. W. (1983) Biochemical and histopathological studies on patients with mucopolysaccharidoses, two of whom had been treated by fibroblast transplantation. *J. Clin. Pathol. 36*, 415–430.
(55) Paganelli, G., Magnani, P., Zito, F., Lucignani, G., Sudati, F., Truci, G., Motti, E., Terreni, M., Pollo, B., Giovanelli, M., Canal, N., Scotti, G., Comi, G., Koch, P., Maecke, H. R., and Fazio, F. (1994) Pre-targeted immunodetection in glioma patients: tumour localization and single-photon emission tomography imaging of [99mTc]PnAO-biotin. *Eur. J. Nucl. Med. 21*, 314–321.
(56) Samuel, A., Paganelli, G., Chiesa, R., Sudati, F., Calvitto, M., Melissano, G., Grossi, A., and Fazio, F. (1996) Detection of prosthetic vascular graft infection using avidin/indium-111-biotin scintigraphy. *J. Nucl. Med. 37*, 55–61.
(57) Green, M. (1975) Avidin. *Adv. Protein Chem. 29*, 85–133.
(58) Hendrickson, W. A., Pahler, A., Smith, J. L., Satow, Y., Merritt, E. A., and Phizackerley, R. P. (1989) Crystal structure of core streptavidin determined from multiwavelength anomalous diffraction of synchrotron radiation. *Proc. Natl. Acad. Sci. U.S.A. 86*, 2190–2194.
(59) Xia, C. F., Zhang, Y., Boado, R. J., and Pardridge, W. M. (2007) Intravenous siRNA of brain cancer with receptor targeting and avidin-biotin technology. *Pharm. Res. 24*, 2309–2316.
(60) Neuwelt, E. A., and Rapoport, S. I. (1984) Modification of the blood-brain barrier in the chemotherapy of malignant brain tumors. *Fed. Proc. 43*, 214–219.
(61) Cloughesy, T. F., Black, K. L., Gobin, Y. P., Farahani, K., Nelson, G. P., Villablanca, P., Kabbinavar, F., Viñeula, F., and Wortel, C. H. (1999) Intra-arterial Cereport (RMP-7) and Carboplatin: a dose escalation study for recurrent malignant gliomas. *Neurosurgery 44*, 270–278.
(62) Yan, Q., Matheson, C., Sun, J., Radeke, M. J., Feinstein, S. C., and Miller, J. A. (1994) Distribution of intracerebral ventricularly administered neurotrophins in rat brain and its correlation with trk receptor expression. *Exp. Neurol. 127*, 23–36.
(63) Ai, Y., Markesbery, W., Zhang, Z., Grondin, R., Elseberry, D., Gerhardt, G. A., and Gash, D. M. (2003) Intraputamenal infusion of GDNF in aged rhesus monkeys distribution and dopaminergic effects. *J. Comp. Neurol. 461*, 250–261.
(64) Salahuddin, T. S., Johansson, B. B., Kalimo, H., and Olsson, Y. (1988) Structural changes in the rat brain after carotid infusions of hyperosmolar solutions. *Acta Neuropathol. 77*, 5–13.
(65) Nadal, A., Fuentes, E., Pastor, J., and McNaughton, P. A. (1995) Plasma albumin is a potent trigger of calcium signals and DNA synthesis in astrocytes. *Proc. Natl. Acad. Sci. U.S.A. 92*, 1426–1430.
(66) Nutt, J. G., Burchiel, K. J., Comella, C. L., Jankovic, J., Lang, A. E., Laws, E. R., Lozano, A. M., Penn, R. D., Simpson, R. K., Stacy, M., and Wooten, G. F. (2003) Randomized, double-blind trial of glial cell line-derived neurotrophic factor (GDNF) in PD. *Neurology 60*, 69–73, ICV GDNF Study Group.
(67) Lang, A. E., Gill, S., Patel, N. K., Lozano, A., Nutt, J. G., Penn, R., Brooks, D. J., Hotton, G., Moro, E., Heywood, P., Brodsky, M. A., Burchiel, K., Kelly, P., Dalvi, A., Scott, B., Stacy, M., Turner, D., Wooten, V. G., Elias, W. J., Laws, E. R., Dhawan, V., Stoessl, A. J., Matcham, J., Coffey, R. J., and Traub, M. (2006) Randomized controlled trial of intraputamenal glial cell line-derived neurotrophic factor infusion in Parkinson disease. *Ann. Neurol. 59*, 459–466.
(68) Salvatore, M. F., Ai, Y., Fischer, B., Zhang, A. M., Grondin, R. C., Zhang, Z., Gerhardt, G. A., and Gash, D. M. (2006) Point source concentration of GDNF may explain failure of phase II clinical trial. *Exp. Neurol. 202*, 497–505.
(69) Tzu, J., and Kerdel, F. (2008) From conventional to cutting edge: the new era of biologics in treatment of psoriasis. *Dermatol. Ther. 21*, 131–141.
(70) Dore, R. K., Mathews, F., Schechtman, J., Surbeck, W., Mandel, D., Patel, A., Zhou, L., and Peloso, P. (2007) The immunogenicity, safety, and efficacy of etanercept liquid administered once weekly in patients with rheumatoid arthritis. *Clin. Exp. Rheumatol. 25*, 40–46.

BC800148T

COMMUNICATIONS

Design of an Optical Switch for Studying Conformational Dynamics in Individual Molecules of GroEL

Gabriel A. Frank,[†,§] Yakov Kipnis,[§] Elena Smolensky,[§] Shirley S. Daube,[‡] Amnon Horovitz,*[,§] and Gilad Haran*[,†]

Departments of Chemical Physics, Chemical Research Support, and Structural Biology, Weizmann Institute of Science, Rehovot 76100, Israel. Received March 21, 2008; Revised Manuscript Received May 15, 2008

We describe the design of an optical switch in the chaperonin GroEL that is opened and closed by its ATP- and cochaperonin GroES-driven conformational changes. The switch, based on a fluorophore and a quencher, is engineered into the single-ring variant of the chaperone, and shows dramatic modulation of its fluorescent intensity in response to the transition of the protein between its allosteric states. It, therefore, forms a sensitive probe for the dynamics of the allosteric transitions of this machine, both in the bulk and in single molecules.

Many proteins operate as molecular machines, using chemical energy to drive them through a functional cycle that involves multiple conformational states (*1*). The *E. coli* molecular chaperone GroEL is a machine that assists protein folding by undergoing allosteric transitions between protein substrate binding (T) and release (R) states (*2*). Fluorescence spectroscopy has been used for studying the functional cycle of GroEL in both ensemble (*3, 4*) and single-molecule experiments (*5*). However, it has been difficult to devise methods that allow probing the conformational dynamics of the chaperone itself at the single-molecule level. We designed an optical switch that is opened and closed by the conformational changes of GroEL, showing a dramatic modulation of its fluorescent intensity. This optical switch was demonstrated to be a sensitive probe of ATP- and cochaperone-driven allosteric transitions, both in the bulk and in individual molecules.

GroEL is made up of two homoheptameric rings, stacked back-to-back, with a cavity at each end (*6*), in which protein folding can take place. GroEL functions in conjunction with a heptameric ring-shaped cochaperonin, GroES, that caps the cavity of the so-called *cis* ring, thereby triggering dissociation of bound protein substrates into the cavity (*7*). The allosteric transitions of GroEL are induced by ATP binding that occurs with positive cooperativity within rings and negative cooperativity between rings (*8*). The intraring positive cooperativity is an outcome of a concerted switch of its rings between the T and R conformations. The structure of the GroEL-GroES-ADP_7 complex has been determined at atomic resolution (*9*). A single-ring version of GroEL (SR1) displays similar positive cooperative behavior with respect to ATP binding (*10*) but, unlike GroEL, its complex with GroES is long-lived since the trigger for GroES dissociation is ATP binding to the opposite ring (*11*). In the rest of this Communication, we concentrate on SR1.

The switch we built into the structure of SR1 is based on the quenching of oxazine derivatives by tryptophan (Trp) (*12*). This electron transfer-based quenching reaction has been used previously to study folding dynamics in peptides and small proteins (*13, 14*). It requires the formation of a ground-state complex between an appropriate fluorophore (attached to the side chain of an amino acid residue) and the side chain of a tryptophan residue, and can thus operate only if the two are in close proximity to each other. The quenched state has low fluorescence intensity. A conformational change that increases the distance between the fluorophore and the quencher should, in principle, lead to a large increase in emission. The design of the optical switch that is described below was based on our knowledge of the structures of two conformations of GroEL (*9*).

The fluorophore we used in this work was the maleimide derivative of the oxazine dye Atto 655 (Atto-tec). The switch based on this dye requires inserting a cysteine residue (to be labeled) and a Trp residue at appropriate positions. To identify such positions, we first listed all pairs of amino acid residues (either within one subunit or in neighboring subunits) that are separated by a distance short enough to allow contact formation between the fluorophore and the Trp side chain in the T conformation, but too long for quenching to take place in the R′ (GroES-bound) conformation. All pairs in this list in which the interaction between the fluorophore and the Trp in the T conformation might be hindered by other amino acids were discarded. This analysis resulted in 51 suitable pairs that are listed in Table 1 of the Supporting Information. Pairs of mutations that were not likely, on the basis of the literature, to affect the protein's stability and activity are highlighted in Table 1. One of these pairs, on which we focused, involves residue 44 in one subunit and residue 327 in the nearest-neighbor subunit in the counterclockwise direction. The mutations F44W and K327C were each characterized before and found to have only minor effect on the protein's stability and activity (*15, 16*). In the T conformation, the distance between the C_α atoms of these residues is ∼17 Å, allowing interaction of a dye molecule with the Trp side chain. In the R′ conformation, this distance grows to ∼46 Å, thereby preventing this interaction. A molecular graphics program was used to build a subset of the fluorophore's rotamers into the two structures of GroEL with the above

* gilad.haran@weizmann.ac.il; amnon.horovitz@weizmann.ac.il.
† Department of Chemical Physics.
‡ Department of Chemical Research Support.
§ Department of Structural Biology.

10.1021/bc800118j CCC: $40.75 © 2008 American Chemical Society
Published on Web 06/24/2008

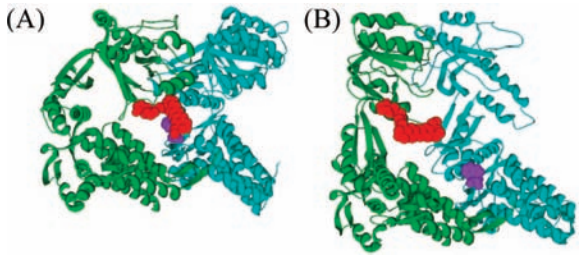

Figure 1. The optical switch in single-ring GroEL (SR1) molecules. (A) The fluorescence of the oxazine dye at position 327 (in red) is quenched by Trp44 (in violet) in the T conformation of GroEL. (B) In the R′ conformation, the quenching is removed. The structures shown in A and B are those of two adjacent subunits in the *trans* and *cis* rings, respectively, of the GroEL-GroES-ADP_7 complex (*9*).

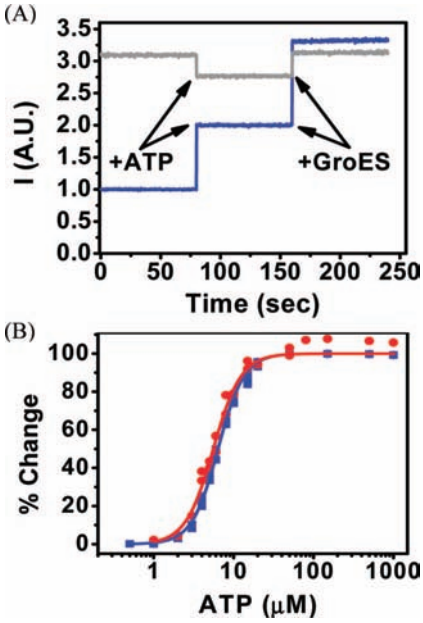

Figure 2. Response of the optical switch to conformational changes. (A) Response of SR1WC (blue) and SR1C (gray) to the addition of 1 mM ATP followed by addition of 50 nM GroES. (B) ATP titration curves of labeled SR1WC molecules obtained in the bulk (blue) and on a glass surface (red). Data were fitted to the Hill equation (lines).

mutations, and test that the fluorophore is indeed in contact with the Trp side chain in the T conformation (Figure 1).

We generated SR1 molecules with the replacements F44W and K327C (SR1WC), using standard site-directed mutagenesis techniques, and labeled Cys327 with Atto655. Under the labeling conditions we used, wild-type cysteines are essentially unreactive (*17*). Care was taken so that less than one subunit in each SR1 molecule would be labeled on average. We also purified and labeled the Trp-lacking single mutant SR1-K327C (SR1C) as a control.

The addition of 1 mM ATP to 25 nM labeled SR1WC molecules generated a strong response, doubling the fluorescence intensity (Figure 2A, blue line). Addition of 50 nM GroES shortly after the addition of ATP (Figure 2A) essentially doubled the signal again. In contrast, the baseline fluorescence of labeled SR1C molecules (without ATP and GroES) was almost as high as the maximal fluorescence of SR1WC molecules in the presence of both additives (Figure 2A, gray line). Addition of ATP and GroES to the Trp-lacking molecules barely changed their fluorescence, thereby showing that the fluorescence changes observed in SR1WC molecules are related to the removal of Trp quenching. In the absence of GroES and as ATP was consumed with time, SR1WC molecules reverted to their initial

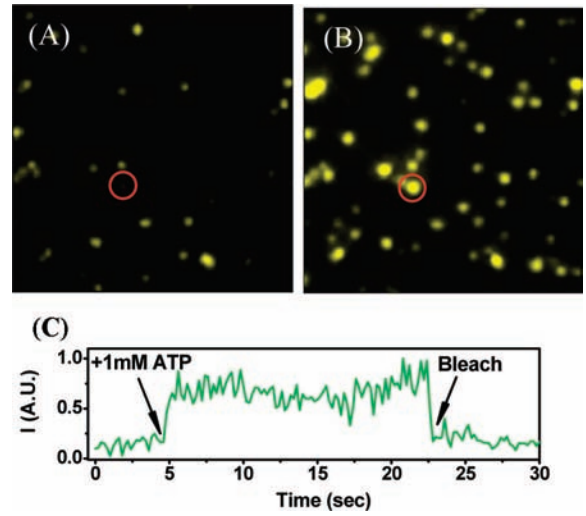

Figure 3. Activity of the optical switch in labeled SR1WC molecules deposited on a glass surface, monitored at the single molecule level. Changes in fluorescence after addition of (A) buffer only and (B) 1 mM ATP. (C) Temporal trajectory of the molecule marked with a red circle in (A) and (B).

conformation and the fluorescence returned essentially to its baseline (not shown). The optical switch, thus, operates as designed.

The observation that the fluorescence intensity of labeled SR1WC, in the presence of ATP and GroES, is similar to the baseline fluorescence of the Trp-lacking mutant suggests that the SR1-GroES complex is in a conformation in which the interaction between Trp44 and the label is not possible. On the other hand, the fluorescence intensity attained with a saturating concentration of ATP is only about half of the value when GroES is also present. This suggests that ATP-bound SR1 molecules are in dynamic equilibrium with conformations in which the quenched state can be formed. This intriguing observation awaits further study.

ATP titration experiments with the labeled double mutant revealed a gradual increase in fluorescence with a sigmoidal dependence on ATP concentration (Figure 2B, blue points), indicating a cooperative behavior. Fitting the data to the Hill equation yielded a Hill coefficient of 2.65 ± 0.05, similar to a previously published value for SR1 based on its ATPase activity (2.87 ± 0.16) (*10*), thus showing that the labeled protein is fully functional.

In order to test the applicability of the design for single-molecule experiments, we deposited labeled SR1WC molecules on a glass slide and observed them under a fluorescence microscope. First, a dense molecular layer was formed, and a titration curve was obtained by registering fluorescence changes upon gradual addition of ATP. The surface titration curve was similar to the bulk titration curve (Figure 2B, red), indicating that the deposition of the protein on the surface does not significantly change its activity. Washing the surface following ATP addition led to a return of the fluorescence intensity to baseline levels, establishing reversibility of the optical switch.

A sparse layer of protein molecules was then formed, and fluorescence changes were monitored on the single-molecule level. Figure 3 shows a typical microscope field before (A) and after (B) addition of 1 mM ATP. A strong increase in the fluorescence of many of the molecules is readily observed. The temporal trajectory of the fluorescence of one of these (circles in Figure 3A,B) is shown in Figure 3c.

We have shown here how an optical switch can be incorporated into the structure of GroEL to report on its structural changes. This switch has several advantages over other fluo-

rescence-based methods for probing conformational transitions. First, it provides a very large dynamic range, as the signal is large in one conformation and essentially null in the other. Second, labeling with only one dye is required in contrast with FRET which usually necessitates labeling with two different dyes. The optical switch built into SR1 now provides us with a convenient and powerful route for studying its dynamics on the single-molecule level, which we hope to report soon.

ACKNOWLEDGMENT

This research was made possible by the historic generosity of the Perlman Family, and financial support from the NIH (GM080515 to G.H.) and the ISF (67/05 to A.H.).

Supporting Information Available: A detailed description of materials and methods and a table of potential pairs of residues for the construction of the optical switch. This material is available free of charge via the Internet at http://pubs.acs.org.

LITERATURE CITED

(1) Chiu, W., Baker, M. L., and Almo, S. C. (2006) Structural biology of cellular machines. *Trends Cell Biol. 16*, 144–150.

(2) Horovitz, A., and Willison, K. R. (2005) Allosteric regulation of chaperonins. *Curr. Opin. Struct. Biol. 15*, 646–651.

(3) Rye, H. S. (2001) Application of fluorescence resonance energy transfer to the GroEL-GroES chaperonin reaction. *Methods 24*, 278–288.

(4) Kim, S. Y., Semyonov, A. N., Twieg, R. J., Horwich, A. L., Frydman, J., and Moerner, W. E. (2005) Probing the sequence of conformationally induced polarity changes in the molecular chaperonin GroEL with fluorescence spectroscopy. *J. Phys. Chem. B 109*, 24517–24525.

(5) Taguchi, H., Ueno, T., Tadakuma, H., Yoshida, M., and Funatsu, T. (2001) Single-molecule observation of protein-protein interactions in the chaperonin system. *Nat. Biotechnol. 19*, 861–865.

(6) Braig, K., Otwinowski, Z., Hegde, R., Boisvert, D. C., Joachimiak, A., Horwich, A. L., and Sigler, P. B. (1994) The crystal structure of the bacterial chaperonin GroEL at 2.8 Å. *Nature 371*, 578–586.

(7) Xu, Z., and Sigler, P. B. (1998) GroEL/GroES: structure and function of a two-stroke folding machine. *J. Struct. Biol. 124*, 129–141.

(8) Yifrach, O., and Horovitz, A. (1995) Nested cooperativity in the ATPase activity of the oligomeric chaperonin GroEL. *Biochemistry 34*, 5303–5308.

(9) Xu, Z., Horwich, A. L., and Sigler, P. B. (1997) The crystal structure of the asymmetric GroEL-GroES-$(ADP)_7$ chaperonin complex. *Nature 388*, 741–750.

(10) Inobe, T., Makio, T., Takasu-Ishikawa, E., Terada, T. P., and Kuwajima, K. (2001) Nucleotide binding to the chaperonin GroEL: non-cooperative binding of ATP analogs and ADP, and cooperative effect of ATP. *Biochim. Biophys. Acta 1545*, 160–173.

(11) Rye, H. S., Burston, S. G., Fenton, W. A., Beechem, J. M., Xu, Z., Sigler, P. B., and Horwich, A. L. (1997) Distinct actions of cis and trans ATP within the double ring of the chaperonin GroEL. *Nature 388*, 792–798.

(12) Marme, N., Knemeyer, J. P., Sauer, M., and Wolfrum, J. (2003) Inter- and intramolecular fluorescence quenching of organic dyes by tryptophan. *Bioconjugate Chem. 14*, 1133–1139.

(13) Neuweiler, H., Schulz, A., Bohmer, M., Enderlein, J., and Sauer, M. (2003) Measurement of submicrosecond intramolecular contact formation in peptides at the single-molecule level. *J. Am. Chem. Soc. 125*, 5324–5330.

(14) Neuweiler, H., Doose, S., and Sauer, M. (2005) A microscopic view of miniprotein folding: enhanced folding efficiency through formation of an intermediate. *Proc. Natl. Acad. Sci. U.S.A. 102*, 16650–16655.

(15) Yifrach, O., and Horovitz, A. (1998) Transient kinetic analysis of adenosine 5′-triphosphate binding-induced conformational changes in the allosteric chaperonin GroEL. *Biochemistry 37*, 7083–7088.

(16) Shiseki, K., Murai, N., Motojima, F., Hisabori, T., Yoshida, M., and Taguchi, H. (2001) Synchronized domain-opening motion of GroEL is essential for communication between the two rings. *J. Biol. Chem. 276*, 11335–11338.

(17) Yamasaki, R., Hoshino, M., Wazawa, T., Ishii, Y., Yanagida, T., Kawata, Y., Higurashi, T., Sakai, K., Nagai, J., and Goto, Y. (1999) Single molecualr observation of the interaction of GroEL with substrate proteins. *J. Mol. Biol. 292*, 965–972.

BC800118J

Charge Dependence of Ligand Release and Monolayer Stability of Gold Nanoparticles by Biogenic Thiols

Apiwat Chompoosor, Gang Han, and Vincent M. Rotello*

Department of Chemistry, University of Massachusetts, 710 North Pleasant Street, Amherst, Massachusetts 01003, Department of Chemistry, University of Massachusetts, Amherst 01003. Received February 22, 2008; Revised Manuscript Received May 19, 2008

The effect of surface charge on the stability of gold nanoparticles (AuNPs) to the biogenic thiols glutathione (GSH), dihydrolipoic acid (DHLA), and cysteine was quantified. It was observed that the rate of release of fluorescein-tagged ligand was determined by the surface charge of the AuNPs, with cationic particles much more labile than anionic analogues. This ability to tune stability is significant for the design of both delivery vehicles and intracellular probes.

The design of functional materials that are capable of controlled release of therapeutic materials is of great importance in biomedical and materials chemistry (*1, 2*). Numerous drug release strategies have been employed, including those relying on external stimuli (e.g., photochemical (*3, 4*) or ultrasound *5, 6*) or intracellular environment (e.g., enzymes (*7, 8*) or pH *9, 10*).

One of the most promising intracellular release strategies relies on glutathione (GSH) (*11, 12*). GSH is the most abundant thiol species inside the cell and plays an essential role in protecting organisms from free radical damage and oxidative stress through balancing the GSH/oxidized glutathione (GSSG) equilibrium (*13*). The concentration of GSH is significantly lower in the extracellular environment than inside the cell (10 μM in blood plasma (*14*) vs 10 mM in liver cells (*15*)). This 1000-fold difference in concentration makes GSH a promising trigger for intracellular release, a method that has been exploited through disulfide-bond based drug delivery systems (*16*). Other biogenic thiols are found in cells, including DHLA (*17*) and cysteine (*18*).

Recent interest has been focused on drug delivery using gold nanoparticles (AuNPs). The core of AuNPs are essentially inert and nontoxic, and the capability to tune the core size and surface functionalities provide convenient access to explore and optimize delivery parameters (*19, 20*). These materials also offer controlled release of payload through place-exchange of GSH with thiols on the AuNP surface, thus leading to efficient protein (*21*), DNA (*22*), and small molecular drug payload release *in vitro* and inside cells (*11*). However, it will be very desirable to develop a simple approach to modulate payload release kinetics by systemic alteration of functionalities of AuNPs (*23*).

Here, we report the use of a series of fluorophore-labeled gold nanoparticles with varied surface charges to investigate the role of particle charge on the stability of gold nanoparticles to thiols. Our hypothesis was that the systemic tuning of the surface charge on AuNP would affect the electrostatic interaction between AuNPs surface and anionic GSH molecule, thus alternating concomitant payload release. In addition, intracellular thiols DHLA and cysteine were systematically examined.

Monolayer-protected AuNPs of 2 nm diameter featuring controlled surface charge were synthesized by the Brust-Schiffrin reduction (*24*) followed by the Murray place-exchange reaction (*25*). The charges on these particles range from positive to negative (Figure 1). Briefly, the cationic AuNPs (**NP1**−**NP4**) were fabricated with different ratios of tetra(ethylene glycol) (TEG) ligands onto 1-pentanethiol AuNPs, while the anionic AuNP (**NP5**) was obtained in analogous fashion using a carboxylate-terminated tetra(ethylene glycol) (TCOOH) ligand (see Supporting Information). In placed-exchanged protocol, the fluorophore was also incorporated onto these water-soluble nanoparticles (≤1% loading as determined by NMR) with fluorescein-functionalized thiol **FITC-SH**. The obtained AuNPs were subjected to dialysis to remove excess fluorophore and displaced ligands. The ligand ratios for the cationic and neutral ligands were determined through NMR endgroup analysis; the fluorescein ligand was at concentrations too low to quantify. As expected, the zeta potential tracked qualitatively with ligand ratio for the particles (Figure 1).

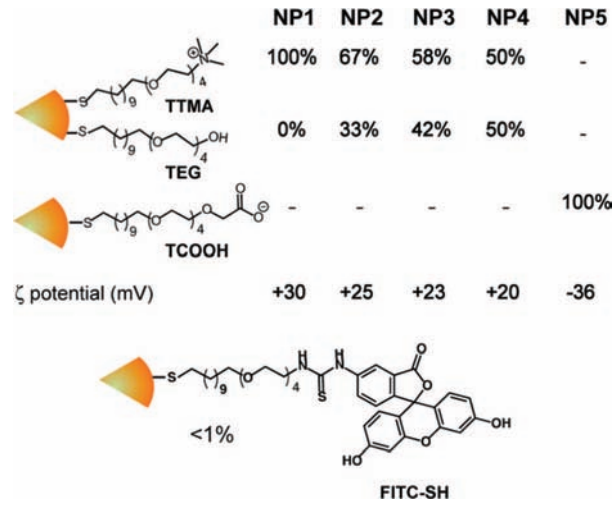

Figure 1. Ligand ratios as determined by NMR for **NP1**−**NP5**.

The rate of ligand release from the nanoparticles was determined using fluorescence spectroscopy, exploiting the efficient quenching of fluorophores by the Au core of the particles. The increase in light emission observed upon GSH-mediated displacement of the fluorophores provides a direct tool for the quantification of release *in vitro* and in the cellular environments (*11*). The fluorophore-conjugated AuNPs **NP1**−**NP5** were treated with GSH solution (Figure 2). Upon place exchange with GSH, the fluorescent ligands are released from the AuNP surface and the fluorescence recovered. The

* E-mail: rotello@chem.umass.edu.

10.1021/bc8000694 CCC: $40.75 © 2008 American Chemical Society
Published on Web 06/14/2008

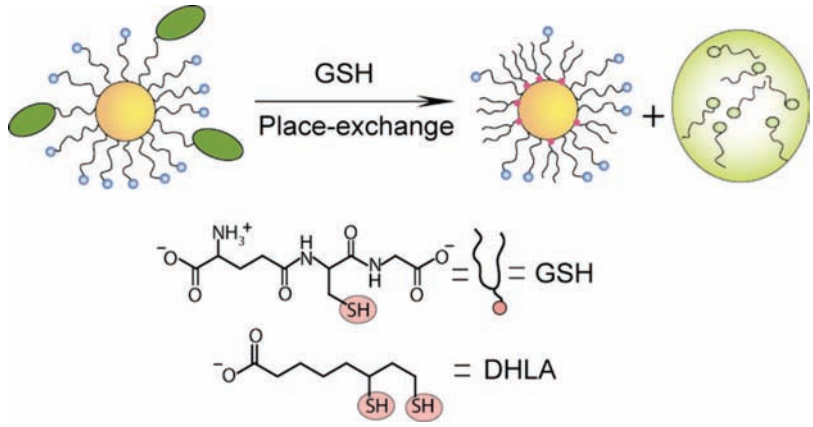

Figure 2. Schematic representation of GSH-mediated ligand release.

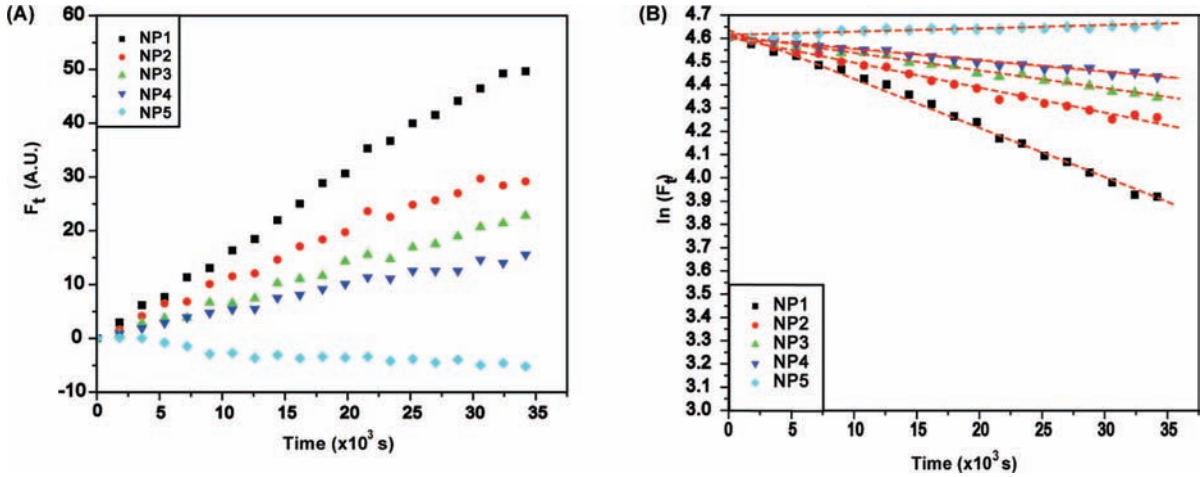

Figure 3. Percentage (A) and rate (B) for GSH-mediated release of fluorophores from different NPs. The fraction of the released **FITC-SH** ligand (F_t) at a given incubation time point (t). The concentration of AuNPs was 1.5 μM in PBS buffer (pH $\sim$ 7.4) at 37 °C.

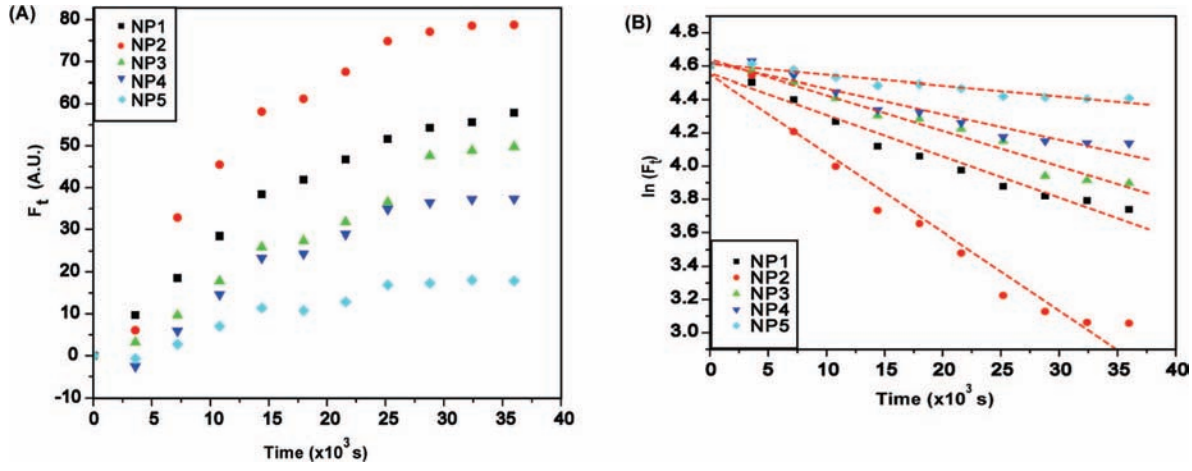

Figure 4. Percentage (A) and rate (B) for DHLA-mediated release of fluorophore. The fraction of the released **FITC-SH** ligand (F_t) at a given incubation time point (t). The concentration of AuNPs was 1.5 μM in PBS buffer (pH $\sim$ 7.4), at 37 °C.

fluorescence intensity thus corresponds to the amount of fluorophore that is released from the NP surface (Figure 3).

From Figure 3, it is evident that fluorophore release from the AuNPs surface is time- and charge-dependent. Moreover, the kinetic analysis of the parameter of ln F_t (logarithm of the normalized percentage of fluorophore release) as a function of time shows a linear dependency with respect to time, indicating pseudo first-order kinetics (see Supporting Information).

In addition to GSH, the AuNPs were investigated in the presence of other biologically relevant free thiols, i.e., DHLA and cysteine. In comparison with GSH, dihydrolipoic acid (DHLA) features two thiols and a higher degree of hydrophobicity and has been used to functionalize nanoparticles, including quantum dots. The results from DHLA-mediated release of FITC from AuNP surface are shown in Figure 4. Cysteine, a zwiterionic thiol, was likewise tested (Figure 5). In both cases, pseudo first-order kinetics were observed.

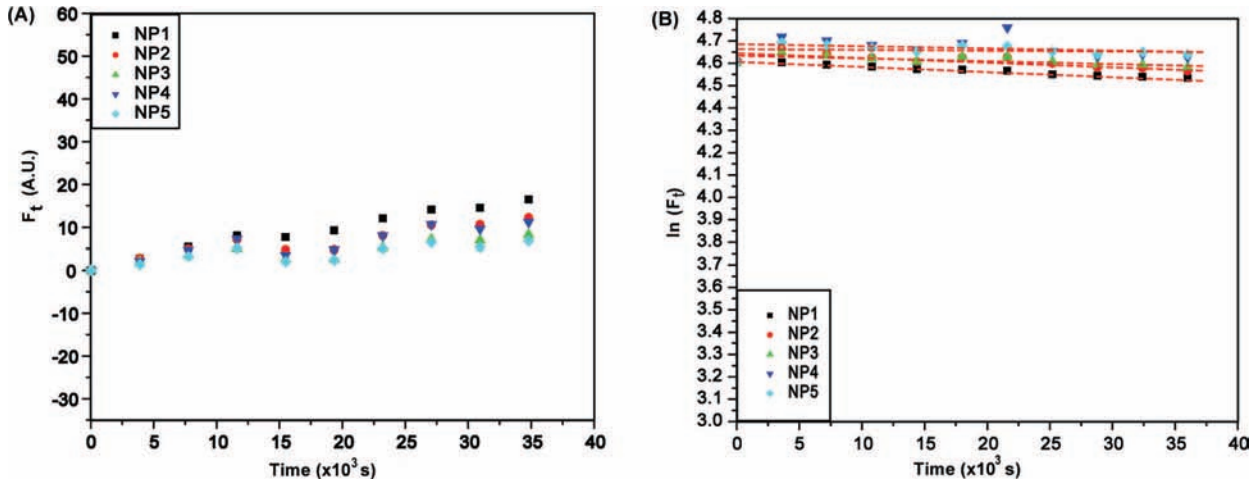

Figure 5. Percentage (A) and rate (B) for cysteine-mediated release of fluorophores from different NPs. The fraction of the released **FITC-SH** ligand (F_t) at a given incubation time point (t). The concentration of AuNPs was 1.5 μM in PBS buffer (pH $\sim$ 7.4). at 37 °C.

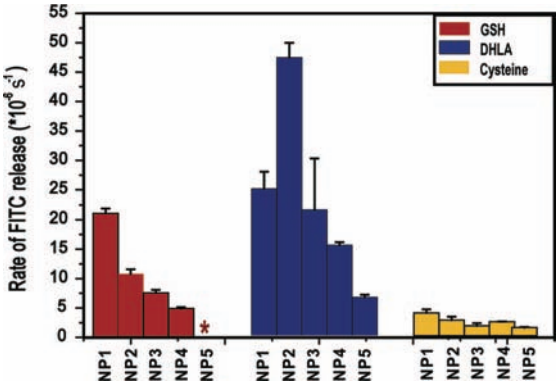

Figure 6. Summary of release rates at 20 mM thiol concentration.

The pseudo first-order rate constants of **NP1**−**NP5** with GSH, DHLA, and cysteine are shown in Table 1 and summarized in Figure 6. Of the particles, **NP1** (100% positively charged) shows the highest release rate with GSH, presumably due to the strong electrostatic interaction between the positive charge on the particle surface and the negative charge on the thiol molecule (Figure 7). The rate of release with the other positively charged NPs show that increasing positive charge results in more rapid fluorophore release. In the case of negatively charged AuNPs, no measurable change in fluorescence was observed, indicating complete nanoparticle stability. This low reactivity presumably arises due to repulsion between the negatively charged NP surface and negative charge on the GSH (Figure 7).

DHLA-mediated release was qualitatively similar to that observed with GSH. The one major difference is that **NP2** shows

Table 1. Summary Rate of FITC Release Mediated by Different Thiol Species at 20 mM Concentration

	rate of release ($\times 10^{-6}$ s^{-1})		
AuNPs	GSH	DHLA	cysteine
NP1	21.10	24.90	3.90
NP2	10.80	47.20	2.69
NP3	7.59	21.40	1.72
NP4	4.91	15.40	2.42
NP5	-	6.55	1.41

the highest release rate. This behavior suggests that the hydrophobic properties and electrostatic interaction of **NP2** interact in a cooperative fashion. As expected, release by DHLA is more rapid than with GSH, as DHLA is both more hydrophobic and contains a dithiol in the molecule facilitating interactions with the AuNP core. Cysteine, while zwitterionic, will be partially anionic (pI = 5.07) under the conditions studied. The rate of release with cysteine was very slow, with the most rapid release occurring with **NP1**, as expected based on electrostatic arguments presumably the slow rate of exchange arises from the lack of hydrophobicity of the highly charged amino acid.

In summary, we found that the stability of gold nanoparticles toward thiols is governed by the surface charge of AuNPs. The ability to control the rate of release of ligands via place exchange provides a potentially potent tool for drug delivery applications. Likewise, these studies provide a strategy for enhancing the stability of nanoparticles in cells, and important consideration for the design of imaging agents.

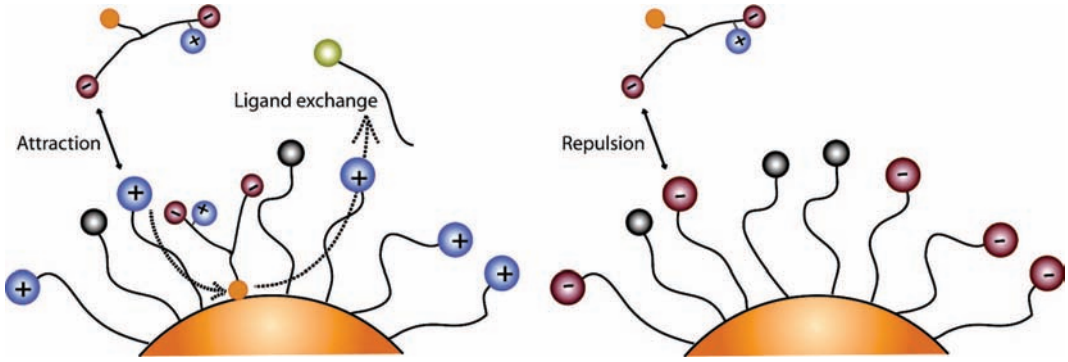

Figure 7. Proposed mechanism for GSH-mediated FITC release from cationic and anionic AuNPs surface.

ACKNOWLEDGMENT

This research is supported by the Center for Hierarchical Manufacturing (NSEC, DMI-0531171), MRSEC facilities, and National Institute of Health (NIH, GM077173).

Supporting Information Available: Synthesis of ligands and particles, data analysis. This material is available free of charge via the Internet at http://pubs.acs.org.

LITERATURE CITED

(1) Santini, J. T., Cima, M. J., and Langer, R. (1999) A controlled-release microchip. *Nature 397*, 335–338.
(2) Rosler, A., Vandermeulen, G. W. M., and Klok, H. A. (2001) Advanced drug delivery devices via self-assembly of amphiphilic block copolymers. *Adv. Drug Delivery Rev. 53*, 95–108.
(3) Chandra, B., Subramaniam, R., Mallik, S., and Srivastava, D. K. (2006) Formulation of photocleavable liposomes and the mechanism of their content release. *Org. Biomol. Chem. 4*, 1730–1740.
(4) Shum, P., Kim, J. M., and Thompson, D. H. (2001) Phototriggering of liposomal drug delivery systems. *Adv. Drug Delivery Rev. 53*, 273–284.
(5) Skirtach, A. G., De Geest, B. G., Mamedov, A., Antipov, A. A., Kotov, N. A., and Sukhorukov, G. B. (2007) Ultrasound stimulated release and catalysis using polyelectrolyte multilayer capsules. *J. Mater. Chem. 17*, 1050–1054.
(6) Kim, H. J., Matsuda, H., Zhou, H. S., and Honma, I. (2006) Ultrasound-triggered smart drug release from a poly(dimethylsiloxane)-mesoporous silica composite. *Adv. Mater. 18*, 3083–3088.
(7) Thornton, P. D., Mart, R. J., and Ulijn, R. V. (2007) Enzyme-responsive polymer hydrogel particles for controlled release. *Adv. Mater. 19*, 1252–1256.
(8) Meers, P. (2001) Enzyme-activated targeting of liposomes. *Adv. Drug Delivery Rev. 53*, 265–272.
(9) Bae, Y., Nishiyama, N., Fukushima, S., Koyama, H., Yasuhiro, M., and Kataoka, K. (2005) Preparation and biological characterization of polymeric micelle drug carriers with intracellular pH-triggered drug release property: Tumor permeability, controlled subcellular drug distribution, and enhanced in vivo antitumor efficacy. *Bioconjugate Chem. 16*, 122–130.
(10) Hiller, J., and Rubner, M. F. (2003) Reversible molecular memory and pH-switchable swelling transitions in polyelectrolyte multilayers. *Macromolecules 36*, 4078–4083.
(11) Hong, R., Han, G., Fernandez, J. M., Kim, B. J., Forbes, N. S., and Rotello, V. M. (2006) Glutathione-mediated delivery and release using monolayer protected nanoparticle carriers. *J. Am. Chem. Soc. 128*, 1078–1079.
(12) Han, G., Chari, N. S., Verma, A., Hong, R., Martin, C. T., and Rotello, V. M. (2005) Controlled recovery of the transcription of nanoparticle-bound DNA by intracellular concentrations of glutathione. *Bioconjugate Chem. 16*, 1356–1359.
(13) Sies, H. (1999) Glutathione and its role in cellular functions. *Free Radical Biol. Med. 27*, 916–921.
(14) Jones, D. P., Carlson, J. L., Mody, V. C., Cai, J. Y., Lynn, M. J., and Sternberg, P. (2000) Redox state of glutathione in human plasma. *Free Radical Biol. Med. 28*, 625–635.
(15) Anderson, M. E. (1998) Glutathione: an overview of biosynthesis and modulation. *Chem.-Biol. Interact. 112*, 1–14.
(16) Saito, G., Swanson, J. A., and Lee, K. D. (2003) Drug delivery strategy utilizing conjugation via reversible disulfide linkages: role and site of cellular reducing activities. *Adv. Drug Delivery Rev. 55*, 199–215.
(17) Lockwood, T. D. (2002) Cathepsin B responsiveness to glutathione and lipoic acid redox. *Antioxidants Redox Signaling 4*, 681–691.
(18) Griffith, O. W. (1999) Biologic and pharmacologic regulation of mammalian glutathione synthesis. *Free Radical Biol. Med. 27*, 922–935.
(19) Connor, E. E., Mwamuka, J., Gole, A., Murphy, C. J., and Wyatt, M. D. (2005) Gold nanoparticles are taken up by human cells but do not cause acute cytotoxicity. *Small 1*, 325–327.
(20) Joshi, H. M., Bhumkar, D. R., Joshi, K., Pokharkar, V., and Sastry, M. (2006) Gold nanoparticles as carriers for efficient transmucosal insulin delivery. *Langmuir 22*, 300–305.
(21) Verma, A., Simard, J. M., Worrall, J. W. E., and Rotello, V. M. (2004) Tunable reactivation of nanoparticle-inhibited beta-galactosidase by glutathione at intracellular concentrations. *J. Am. Chem. Soc. 126*, 13987–13991.
(22) Han, G., Chari, N. S., Verma, A., Hong, R., Martin, C. T., and Rotello, V. M. (2005) Controlled recovery of the transcription of nanoparticle-bound DNA by intracellular concentrations of glutathione. *Bioconjugate Chem. 16*, 1356–1359.
(23) Templeton, A. C., Hostetler, M. J., Kraft, C. T., and Murray, R. W. (1998) Reactivity of monolayer-protected gold cluster molecules: Steric effects. *J. Am. Chem. Soc. 120*, 1906–1911.
(24) Brust, M., Walker, M., Bethell, D., Schiffrin, D. J., and Whyman, R. (1994) Synthesis of Thiol-Derivatized Gold Nanoparticles in a 2-Phase Liquid-Liquid System. *J. Chem. Soc.: Chem. Commun.* 801–802.
(25) Hostetler, M. J., Wingate, J. E., Zhong, C. J., Harris, J. E., Vachet, R. W., Clark, M. R., Londono, J. D., Green, S. J., Stokes, J. J., Wignall, G. D., Glish, G. L., Porter, M. D., Evans, N. D., and Murray, R. W. (1998) Alkanethiolate gold cluster molecules with core diameters from 1.5 to 5.2 nm: Core and monolayer properties as a function of core size. *Langmuir 14*, 17–30.

BC8000694

ARTICLES

Preparation of Sodium Deoxycholate (DOC) Conjugated Heparin Derivatives for Inhibition of Angiogenesis and Cancer Cell Growth

Kwang Jae Cho,[†,‡] Hyun Tae Moon,[†,§] Go-eun Park,[‡] Ok Chul Jeon,[§] Youngro Byun,*[,∥] and Yong-kyu Lee*[,⊥]

Department of Otolaryngology, Head and Neck Surgery, The Catholic University of Korea, College of Medicine Uijeongbu, St. Mary's Hospital, Kyunggi-Do 480-717, Korea, Mediplex Corporation, Seoul 135-729, Korea, College of Pharmacy, Seoul National University, San 56-1, Sillim-dong, Gwanak-gu, Seoul 151-742, Korea, and Department of Chemical and Biological Engineering, Chungju National University, Chungbuk 380-702, Korea. Received April 28, 2008; Revised Manuscript Received May 19, 2008

We describe new DOC (sodium deoxycholate)−heparin nanoparticles for *in vivo* tumor targeting and inhibition of angiogenesis based on chemical conjugation and the enhanced permeability and retention (EPR) effect. Heparin has been used as a potent anticoagulant agent for 70 years, and has recently been found to inhibit the activity of growth factors which stimulate the smooth muscle cells around tumor. From the results, DOC and heparin were conjugated by bonding carboxyl groups of heparin with amine groups of aminated sodium deoxycholate. Larger antitumor effects of the DOC−heparin VI (8.5 mol of DOC coupled with 1.0 mol heparin) were achieved in animal studies, compared to heparin alone. We confirmed that the conjugated heparin retained its ability to inhibit binding with angiogenic factor, showing a significant decrease in endothelial tubular formation. These results provide new insights into the nontoxic anticancer drug carrier as well as the design of multifunctional bioconjugates for targeted drug delivery.

INTRODUCTION

Tumors produce a number of growth factors stimulating angiogenesis via affinity for receptors on endothelial cells. Low molecular weight heparin (LMWH) appears to have a greater inhibitory effect on angiogenesis than unfractioned heparin (*1–4*). It has been shown that LMWH, as a result of its smaller size and in contrast to unfractioned heparin, can reduce binding of growth factors to their receptors. Fragments of fewer than 18 saccharides reduce the activity of vascular endothelial growth factor (VEGF), and fragments of fewer than 10 saccharides inhibit the activity of basic fibroblast growth factor (bFGF) (*5, 6*). Small molecular heparins (smaller than 6000 Da) are more effective than unfractionated heparin (UFH) for inhibition of VEGF- and bFGF-mediated angiogenesis *in vivo* (*3, 4*).

Heparin has highly hydrophilic properties due to the negatively charged group such as sulfonyl, carboxyl, and hydroxyl within its structure (*7–9*). To treat tumor with heparin, we need new structure designs to allow the use of a reduced dose to achieve the same therapeutic response with a consequent decrease in systemic toxicity and side reactions. Recently, a heparin-based drug carrier has been developed to deliver an anticancer drug to tumor sites by the EPR effect (*10, 11*). In our previous study, a chemically modified unfractionated heparin derivative for delivery of the anticancer doxorubicin was developed and proven a safe drug carrier without the risk of inducing hemorrhage and other side effects (*11*). Other studies have developed polysaccharides such as chitosan and curdlan as anticancer drug carriers with inhibition of tumor growth (*12, 13*).

In this study, we propose a new anticancer drug conjugate system for the treatment of tumor and tumor vasculature by using DOC−heparin nanoparticles. To obtain the optimized anticancer effect of heparin, we designed DOC−heparin conjugates by modification of the C3-hydroxyl group of DOC with 4-nitrophenyl chloroformate (4-NPC) and ethylenediamine (EDA). Through the conjugation method, many DOC molecules were allowed to bind freely with one heparin structure. In addition, the conjugated heparin retained its ability to inhibit binding with angiogenic factors, which can induce proliferation of smooth muscle cells. The rationale for conjugating DOC to the polysaccharide heparin was to specifically target tumor and tumor vasculature and to circumvent adverse reactions from drug toxicity and bleeding by reducing the binding affinity with anticoagulant factors such as factor Xa.

MATERIALS AND METHODS

Materials. Fraxiparin (101 IU/mg, heparin) of average molecular weight ca. 5000 Da was purchased from GlaxoSmith-Kline (Brentford, Middlesex, UK). Sodium deoxycholate (DOC), 4-nitrophenyl chloroformate, triethylamine, dicyclohexylcarbodiimide (DCC), hydroxysuccinimide (HOSu), 4-methylmorpholine, ethylene diamine, dimethyl sulfoxide (DMSO), and ethyl acetate were purchased from Sigma Chemical Co. (St. Louis, MO). Formamide was obtained from Merck (Darmstadt, Germany). Coatest Factor Xa assay kits were from Chromogenix

* Corresponding authors. E-mail: yrbyun@snu.ac.kr and leeyk@cjnu.ac.kr. Tel.: +82-2-880-7866, Fax: +82-2-872-7864 (Y. Byun). Tel.: +82-43-841-5224, Fax: +82-43-841-5220 (Y. Lee).

† Dr. Cho and Dr. Moon are equal contributors to this article.

‡ The Catholic University of Korea.

§ Mediplex Corporation.

∥ Seoul National University.

⊥ Chungju National University.

10.1021/bc800173m CCC: $40.75 © 2008 American Chemical Society
Published on Web 06/28/2008

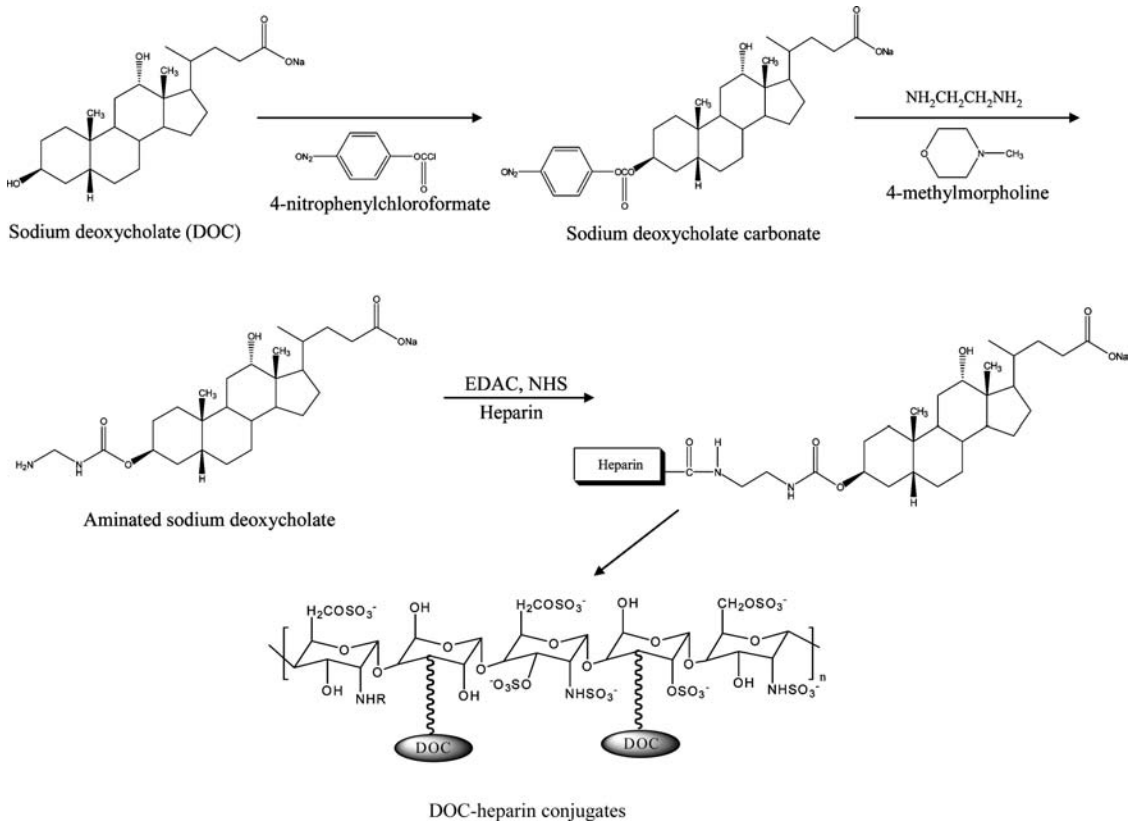

Figure 1. Synthesis and schematic structure of DOC−heparin conjugate.

(Milano, Italy). All reagents were of analytical grade and were used without further purification.

Preparation of DOC−Heparin Conjugates (Figure 1). For amination of sodium deoxycholate (DOC), DOC (0.93 mmol) in 5 mL DMSO was reacted with 4-nitrophenyl chloroformate (4-NPC, 4.65 mmol) and triethylamine (5.58 mmol) for 6 h at room temperature. After reaction, the precipitant was removed by 0.45 μm filter membrane. The filtrate was extracted with 25 mL ethyl acetate and 25 mL water. The crude product from aqueous solution was washed with ethyl acetate three times, and then DOC carbonate was obtained as a powder type after freeze-drying. To obtain aminated DOC, DOC carbonate was reacted with 4-methylmorpholine (1.42 mmol) and ethylenediamine (0.071 mmol) overnight at room temperature. The product was concentrated by rotary evaporation and then precipitated by adding acetonitrile. The precipitated product was dried under vacuum for 24 h.

For preparation of the DOC-heparin conjugate, heparin (0.01 mmol) was dissolved in water and adjusted to pH 5.0 by adding 0.1 M HCl solution. The solution was mixed with EDAC (0.04 mmol), NHS (0.04 mmol), and aminated DOC (0.044 mmol). After 30 min, the mixture was dialyzed (MWCO: 2000) against water to remove unreacted NHS, EDAC, and aminated DOC. The final product, DOC−heparin, was obtained and stored at 4 °C after freeze-drying. The dried DOC−heparin conjugate was analyzed by ^{1}H NMR and FT-IR (Bruker, Germany). Values for ^{1}H NMR of heparin (D_2O) were: δ 5.38 [H1 of glucosamine residue (A)], δ 5.04 [H1 of iduronic acid residue (I)], δ 4.84 [I-5], δ 4.36−4.23 [A-6], δ 4.12−4.40 [I-3], δ 4.08 [I-4], δ 4.02 [A-5], δ 3.78 [I-2], δ 3.71 [A-4], δ 3.65−3.69 [A-3], δ 3.24 [A-2]. Values for ^{1}H NMR of aminated DOC (D_2O) were: δ 1.2−1.9 [m, five and six rings of DOC, 1H], δ 2.1−2.3 [m, CH_3 of DOC, 1H], δ 3.15[d, 12α-OH of DOC, 2H], δ 8.0 [H of CONH]. Values of 1H-NMR of DOC−heparin conjugates (D_2O) were: δ 1.2−1.9 [m, five and six rings of DOC, 1H], δ 3.24−5.38 [A or I of heparin], δ 8.0−8.2 [H of CONH of DOC−heparin].

Ninhydrin Colorimetric Method. For the coupling ratio of DOC in the DOC−heparin conjugate, the ninhydrin colorimetric method was used as described previously (*14*). In brief, 80 μL of the ninhydrin solution was added to 300 μL aminated DOC and the test tube covered with a piece of paraffin film to avoid the loss of solvent due to evaporation. With gentle stirring, the solution was heated for 5 min at 100 °C. After cooling to room temperature in a cold water bath, the absorbance was recorded with a spectrophotometer at 570 nm in wavelength. With the standard curves of aminated DOC, the coupling ratios of DOC−heparin conjugates were determined by subtracting the OD values of remaining aminated DOC.

Anticoagulant Activity of DOC−Heparin Conjugates. DOC−heparin conjugate (100 μL) was mixed with 100 μL of antithrombin III (ATIII) solution to make DOC−heparin conjugate−ATIII complexes, where ATIII concentration was in excess of the DOC−heparin conjugate concentration. The solution was incubated at 37 °C for 3 min, and 100 μL of FXa was added to the solution. The resulting solution was then incubated for an additional 30 s. The concentration of FXa was also in excess of the DOC−heparin conjugate concentration. The substrate (200 μL, 0.8 μmol/mL) was then added and incubated at 37 °C for 3 min. The reaction was terminated by adding 300 μL of 20% acetic acid. The bioactivity and the concentration of DOC−heparin conjugate were calculated from the absorbance at 405 nm.

Endothelial Tubular Formation. Human endothelial cells were resuspended at 4×10^5 cells/mL phenol red−free RPMI containing glutamine (2 mM). Then, 100 μL growth factor-free Matrigel with or without SDF-1α (200 ng/mL) was plated into 96-well plates (Costar, Corning, NY) and incubated at 37 °C for 30 min for gelation. Thereafter, cells were seeded in gelated Matrigel in the presence of different stimuli. Plates were

Table 1. Reaction Condition and Coupled Ratio of DOC in DOC−Heparin Conjugates

	DOC−heparin I	DOC−heparin II	DOC−heparin III	DOC−heparin IV	DOC−heparin V	DOC−heparin VI
Fraxiparin (Ca^{2+},mol)	1	1	1	1	1	1
EDAC (mol)	1.2	2.4	3.6	4.8	6	12
HOSu (mol)	1.2	2.4	3.6	4.8	6	12
Aminated DOC (mol)	1.3	2.6	4	5.2	6.7	13.3
Coupling ratio	0.9	2.1	3.2	3.9	4.2	8.5

incubated for 24 h, and then tubular formation was analyzed after 6 h of incubation. For inhibition experiments, heparin or DOC−heparin conjugates were used at 10, 50, and 250 μg/mL and added together with the cells before seeding the cells on Matrigel. After 6 h of incubation, cell growth and three-dimensional organization were observed through a reverse-phase-contrast photomicroscope (Olympus 1 × 71), and the results were expressed as the mean number of junctions/5 fields at × 100 original magnification. Tubular formation and inhibition of tubular formation experiments were performed in duplicate and repeated at least 3 times.

Human Tumor Xenograft. Four- to six-week-old Athymic BALB/c-nu/nu female nude mice (14−18 g) were purchased from SLC Inc. (Japan) and maintained under specific pathogen-free conditions. All experiments were approved by the institutional guidelines of the Institutional Animal Care and Use Committee (IACUC) of the Catholic University of Korea College of medicine in accordance with the NIH Guidelines. Cultured KB cells (ATCC, Rockville, MD) were trypsinized, washed twice with serum-free EMEM medium (ATCC), and suspended at 1 × 10^7cells/mL PBS buffer. 50 μL of the suspended cells was subcutaneously injected into the back of the mice. On day 12−15 after tumor injection, the resulting tumors reached a volume of 45−55 mm^3. According to body weight and tumor size, the animals were divided into four experimental groups of five mice each: groups A, B, C, and D, respectively, received through the tail vein injections of 100 μL of saline as control (Group A, $n = 5$), heparin (10 mg/kg, Group B, $n = 5$), DOC−heparin VI (5 mg/kg, Group C, $n = 5$), and DOC−heparin VI (10 mg/kg, Group D, $n = 5$). Each drug was administered twice a week for four weeks after tumor inoculation. Data are expressed as means ± SE. One-way ANOVA was used to compare groups, where P values of <0.05 were considered significant.

RESULTS AND DISCUSSION

We synthesized DOC−heparin conjugates for cancer targeting and angiogenesis inhibition by linking the polysaccharide heparin (about 5000 Da) with sodium deoxycholate (DOC). Conjugation between the carboxyl groups of polysaccharide heparin and the amine groups of DOC was confirmed by the presence of signals at δ 8.0−8.2 ppm in the ^{1}H NMR spectrum. The selective modification of C3-OH was conducted by a suitable protected side chain of C12-OH group. It also took advantage of the known reactivity order of the two hydroxyl groups in DOC structure, C3-OH > C12-OH (*15*). We also found a sharp peak at δ 2.0 ppm, indicating the presence of a hydroxyl group at the C12-OH position. The amount of DOC conjugated to polysaccharide heparin estimated by the ninhydrin colorimetric method was maximized to 8.5 mol based on 1 mol of heparin (DOC-heparin VI) as shown in Table 1. By changing feed mole ratio of heparin, EDAC, HOSu, and aminated DOC, we controlled the coupling ratio between DOC and heparin. When dissolved in water, the DOC−heparin conjugates produced a clear solution at a concentration of 50 mg/mL. AFM and size measurement showed that the particles formed uniform spheres with a narrow size distribution as shown in Figure 2. The mean diameter of the nanoparticles (DOC-heparin IV) was 185 nm with a standard deviation of 2.8 nm, as determined by dynamic light scattering. A nanoparticle size of about 100−300 nm is considered to be suitable for passive targeted delivery utilizing the EPR effect. Several research groups using liposomes and other macromolecules have shown that particles with small size (less than 400 nm and ideally less than 200 nm) are more efficient in cell targeting than larger particles (*16*).

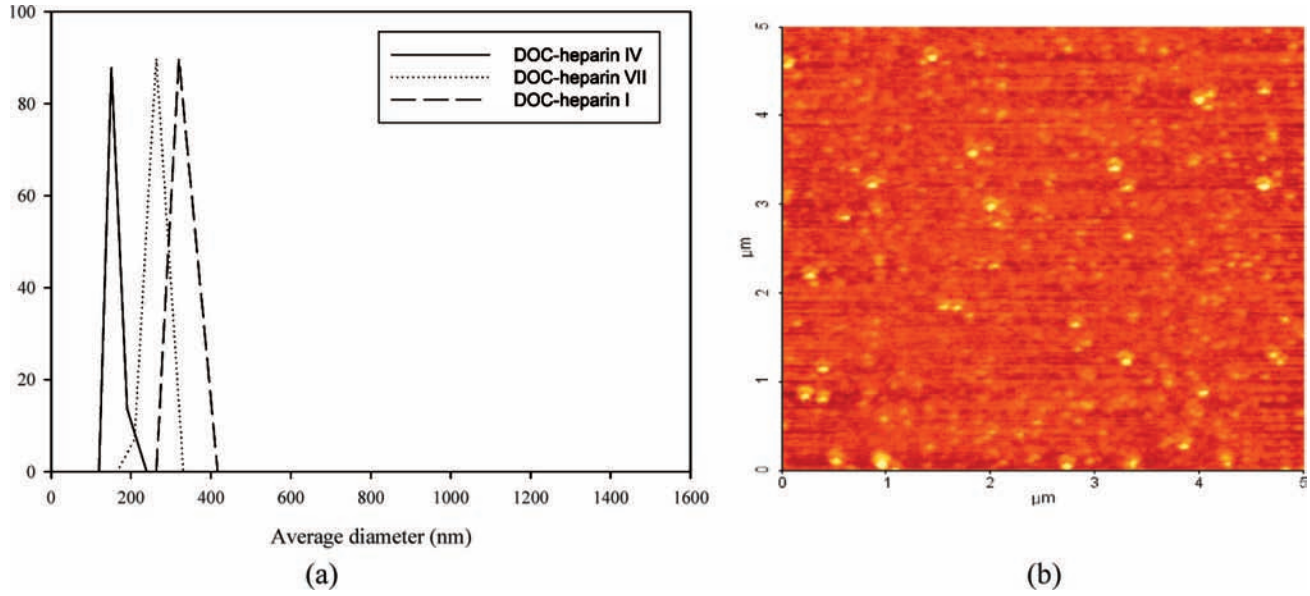

Figure 2. Size distribution and AMF image of DOC−heparin conjugate. (a) Size distribution of DOC−heparin conjugates by dynamic light scattering. (b) AFM image of DOC−heparin nanoparticles.

Table 2. Bioactivity of DOC−Heparin Conjugates

sample	absolute bioactivity (IU/mg)	SD
Fraxiparine (Ca^{2+})	101 IU/mg	-
DOC−heparin I	106.7 IU/mg	1.5
DOC−heparin II	109.8 IU/mg	2.1
DOC−heparin III	92.6 IU/mg	2.0
DOC−heparin IV	86.5 IU/mg	5.7
DOC−heparin V	86.0 IU/mg	2.7
DOC−heparin VI	75.1 IU/mg	1.0

Biological Activity. Antifactor Xa activity of DOC−heparin conjugates measured by chromogenic assay decreased with the increase of coupled DOC in DOC−heparin as shown in Table 2. When the carboxyl group of heparin is modified by conjugation, its affinity to factor Xa and/or antithrombin and thus its anticoagulant activity diminishes (*17–19*). The conjugated heparin presents several advantages as an anticancer drug carrier: (i) More DOC−heparin conjugates can access cancer cells, bypassing the coagulation cascade. (ii) Conjugation to DOC in DOC−heparin reduces the amount of negative charges of heparin, decreasing side effects such as heparin-induced thrombocytopenia (HIT) or bleeding that arise from the charge and size of heparin (*20*, *21*). (iii) Through the intact sulfate group, the conjugated heparin retains its ability to inhibit binding with angiogenic factors, which can induce proliferation of smooth muscle cells. It is widely known that a high degree of sulfation and optimum saccharide chain length are essential for recognition of angiogenic growth factors such as bFGF and VEGF (*22–27*). All of the advantages suit our purpose to develop a biocompatible novel drug carrier that acts as an efficient antitumor agent, and is free of undesired interactions with blood and vessel components.

DOC−Heparin Conjugates Inhibit Tumor Vasculature

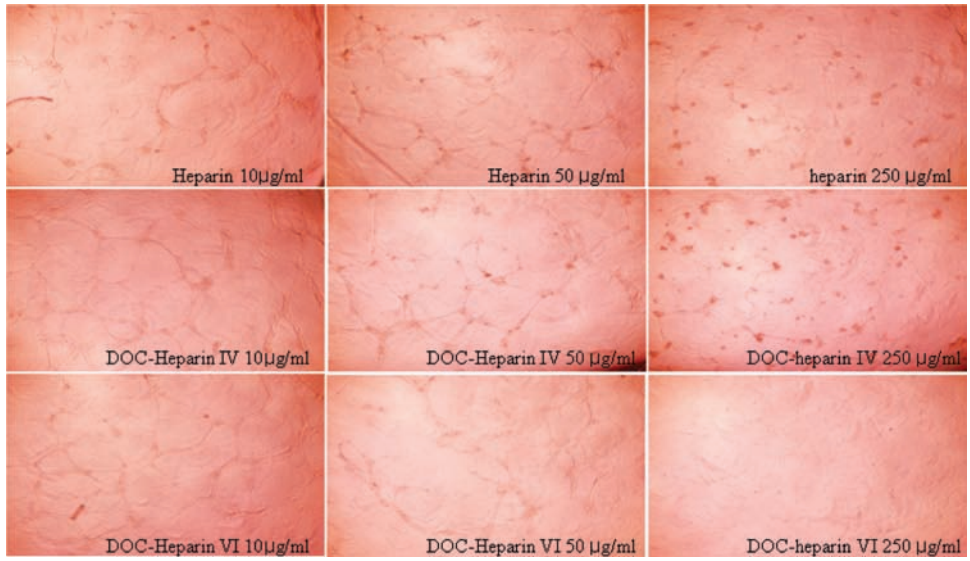

Figure 3. Inhibition of tubular formation by heparin and DOC−heparin conjugates at different concentrations.

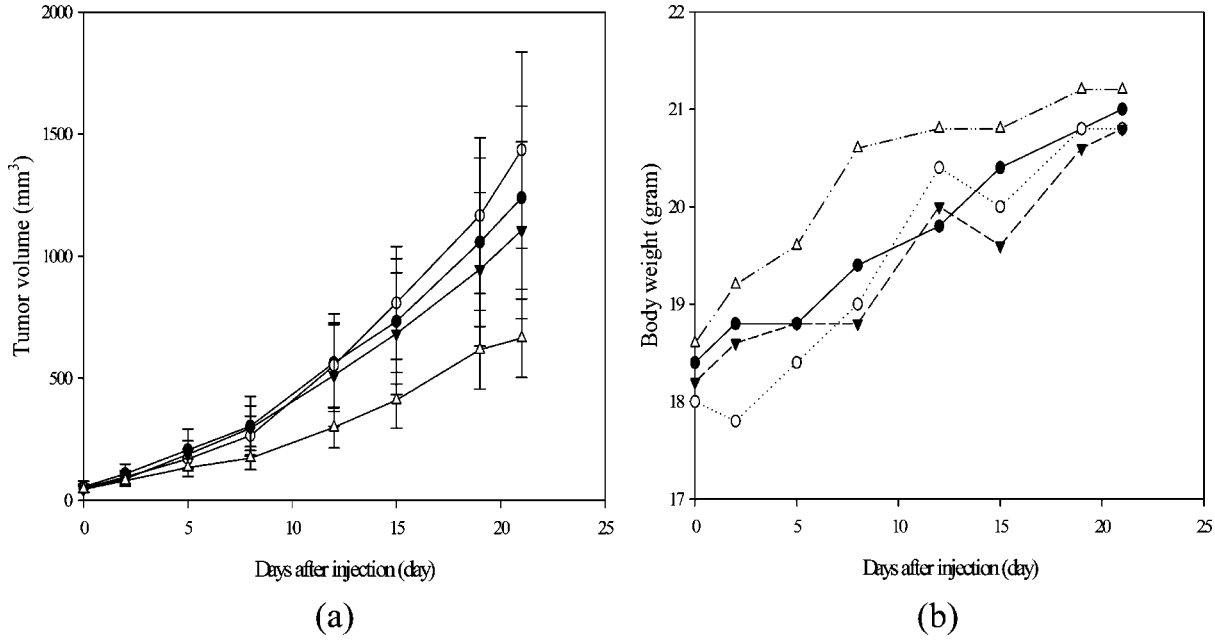

Figure 4. Antitumor effects of DOC−heparin conjugates. (a) Shrinkage in tumor volume and (b) changes in body weight after treatment with saline (□), 10 mg/kg heparin (•), 5 mg/kg of DOC−heparin VI (▼), and 10 mg/kg of DOC−heparin VI (Δ), respectively. All data represent mean ± s.e.

Growth. We sought to determine whether DOC−heparin conjugates would block angiogenesis that accompanies tumor growth. After heparin or DOC−heparin conjugates were added on Matrigel that included human endothelial cells, we observed the endothelial tubular formation and counted the number of tubes formed by a reverse-phase contrast photomicroscope as shown in Figure 3. When treated with heparin at 10, 50, and 250 μg/mL, no inhibitory effect of tubular formation was observed. On the other hand, DOC−heparin VI showed significant decrease in tubular formation at 50 μg/mL. For endothelial cells treated with 250 μg/mL of DOC−heparin VI, tubular formation was completely removed.

From the results, we believe that blood vessels surrounding the tumor treated with DOC−heparin VI have almost disappeared whereas a number of capillaries near the tumor excised from nude mice treated with saline remained intact (data not in shown). A significant decrease of angiogenesis was seen in *in vitro* treatment with DOC−heparin VI, indicating that DOC−heparin inhibits tumor vasculature growth in mice.

DOC−Heparin Conjugate Showed Remarkable Tumor Growth Inhibition. To determine whether heparin or DOC−heparin conjugates can reduce tumor growth rate, athymic BALB/c-nu/nu female nude mice bearing KB tumors (human epidermoid carcinoma cells) were used. Tumor growth and body weight were monitored after treatment. The antitumor effect of DOC−heparin conjugate against KB tumor cells was remarkably better than that of heparin. The tumor volume of mice treated with injection of DOC−heparin VI was about 550 mm^3, indicating shrinkage in initial tumor volume and inhibition of tumor growth by 37% ($p < 0.01$) compared to the control group (saline injection) as shown in Figure 4. The DOC−heparin conjugates did not induce death due to toxicity or body weight loss during treatment.

By itself, however, polysaccharide heparin is ineffective in inhibiting solid tumor growth. When intravenously injected at 10 mg/kg, most of the polysaccharide heparin will be systemically distributed into blood vessels, bind preferably with Factor Xa, and act as a highly potent anticoagulant, leaving only a few polysaccharide heparin molecules available to reach cancer cells. A high concentration of heparin or anticancer drug may circumvent this problem, but not without the accompanying side effects such as bleeding, thrombocytopenia, and general complications similar to those of chemotherapy. Therefore, the need arises for a strategy to facilitate specific interaction between polysaccharide heparin and tumor cells. The binding affinity to Factor Xa is markedly diminished when the carboxyl groups of heparin are modified to anchor DOC (Figure 1). The extent of antiangiogenesis *in vitro* would be ranked as follows: DOC−heparin VI > DOC−heparin IV > heparin > saline. The reduction of tumor vasculature when treated with the DOC−heparin VI implies that heparin, in addition to its targeted carrier role, may strongly interact with angiogenic stimulators to inhibit tumor vasculature growth. From the slowly halted tumor growth at 21 days, we concluded that it was likely that most of the residual solid tumors perished after treating with DOC−heparin VI for 21 days. The treated tumor cells had irregular structure with nuclei exposed to the outside of the cell membrane, indicating necrosis and cell malfunction.

In addition, this study introduces new prospects for the delivery of macromolecular drugs. As an antitumor agent, DOC−heparin conjugate can efficiently be delivered to solid tumors via intravenous injection. The conjugates were shown to produce certain therapeutic effects on human tumor implanted in BALB/c mice. It may become a new compound, but further studies still need to be conducted to explore *in vivo* metabolic profiles. Also, this approach can be used as a method to prove certain interaction between angiogenesis and tumor growth.

CONCLUSION

This study demonstrated that the DOC−heparin conjugate can specifically target tumor and tumor vasculature with minimized side effects. The main advantage of these novel biomolecular nanoparticles is the superior antitumor effect *in vivo*. By design, the self-assembled nanoparticles accumulate in tumors by passive targeting mechanisms. The conjugate inhibited tumor growth in mice without decrease in body weight. Our findings in animal studies suggest that the DOC−heparin VI has high antitumor activity and selective toxicity, yielding 34% tumor inhibition compared with tumor volume treated heparin. The results are consistent with tumor angiogenesis inhibition, showing a less detectable tumor vasculature after DOC−heparin VI treatment.

ACKNOWLEDGMENT

This work was supported by a grant of the Korea Health 21 R&D Project, Ministry of Health & Welfare, Republic of Korea. (A060699). This work was also in part supported by the BioImaging Research Center at GIST, and the Catholic Cancer Center, the Catholic University of Korea College of Medicine.

LITERATURE CITED

(1) Hejna, M., Raderer, M., and Zielinski, C. C. (1999) Inhibition of metastases by anticoagulants. *J. Natl. Cancer Inst. 91*, 22–26.

(2) Smorenburg, S. N., and Van Noorden, C. J. F. (2001) The complex effects on heparins on cancer progression and metastasis in experimental studies. *Pharmacol. Rev. 53*, 93–105.

(3) Norrby, K. (1993) Heparin and angiogenesis: a low-molecular-weight fraction inhibits and a high-molecular-weight fraction stimulates angiogenesis systemically. *Haemostasis 23*, 141–149.

(4) Norrby, K., and Ostergaard, P. (1996) Basic-fibroblast-growth-factor-mediated de novo angiogenesis is more effectively suppressed by low-molecular-weight than by high-molecular-weight heparin. *Int. J. Microcirc. Clin. Exp. 16*, 8–15.

(5) Jayson, G., and Gallagher, J. T. (1997) Heparin oligosaccharides: inhibitors of the biological activity of bFGF on Caco-2 ells. *Br. J. Cancer 75*, 9–16.

(6) Soker, S., Goldstaub, D., Svahn, C. M., Vlodavski, I., Levi, B. Z., and Neufeld, G. (1994) Variation in the size and sulfation of heparin modulate the effect of heparin on the binding of VEGF 165 to its receptors. *Biochem. Biophys. Res. Commun. 203*, 1339–1347.

(7) Linhardt, R. J. (2003) Heparin: structure and activity. *J. Med. Chem. 46*, 2551–2564.

(8) Ishihara, M., and Ono, K. (1998) Structure and function of heparin and heparan sulfate: heparinoid library and modification of FGF-activities. *Trends Glycosci. Glycotechnol. 10*, 223–233.

(9) Casu, B., and Lindahl, U. (2001) Structure and biological interactions of heparin and heparan sulfate. *Adv. Carbohydr. Chem. Biochem. 57*, 159–206.

(10) Yu, M. K., Lee, D. Y., Kim, Y. S., Park, K., Park, S. A., Son, D. H., Lee, G. Y., Nam, J. H., Kim, S. Y., Kim, I. S., Park, R. W., and Byun, Y. (2007) Antiangiogenic and apoptotic properties of a novel amphiphilic folate-heparin-lithocholate derivative having cellular internality for cancer therapy. *Pharm. Res. 24*, 705–714.

(11) Park, K., Lee, G. Y., Kim, Y. S., Yu, M., Park, R. W., Kim, I. S., Kim, S. Y., and Byun, Y. (2006) Heparin-deoxycholic acid chemical conjugate as an anticancer drug carrier and its antitumor activity. *J. Controlled Release 114*, 300–306.

(12) Na, K., Park, K., Kim, S. W., and Bae, Y. H. (2000) Self-assembled hydrogel nanoparticles from Curdlan derivatives: characterization, anticancer drug release and interaction with a

hepatoma cell line (HepG2). *J. Controlled Release 69*, 225–236.
(13) Kwon, S., Park, J., Chung, H. H., Kwon, I. C., and Jeong, S. Y. (2003) Physicochemical characteristics of self-assembled nanoparticles based on glyco chitosan bearing 5¥â-cholanic acid. *Langmuir 19*, 10188–10193.
(14) Hwang, M., and Ederer, G. M. (1975) Rapid hippurate hydrolysis method for presumptive identification of group B streptococci. *J. Clin. Microbiol. 1*, 114–115.
(15) von Geldern, T. W., Tu, N., Kym, P. R., Link, J. T., Jae, H. -S., Lai, C., Apelqvist, T., Rhonnstad, P., Hagberg, L., Koehler, K., Grynfarb, M., Goos-Nilsson, A., Sandberg, J., Osterlund, M., Barkhem, T., Hoglund, M., Wang, J., Fung, S., Wilcox, D., Nguyen, P., Jakob, C., Hutchins, C., Farnegardh, M., Kauppi, B., Ohman, L., and Jacobson, P. B. (2005) Liver-selective glucocorticoid antagonists: a novel treatment for type 2 diabetes. *J. Med. Chem. 48*, 2724–2724.
(16) Kong, G., Braun, R. D., and Dewhirst, M. W. (2000) Hyperthermia enables tumor-specific nanoparticle delivery: Effect of particle size. *Cancer Res. 60*, 4440–4445.
(17) Lee, Y., Nam, J. H., Shin, H. C., and Byun, Y. (2001) Conjugation of low molecular weight heparin and deoxycholic acid for development of new oral anticoagulant agent. *Circulation 104*, 3116–3120.
(18) Lee, Y., Moon, H. T., and Byun, Y. (1998) Preparation of slightly hydrophobic heparin derivatives which can be used for solvent casting in polymeric formulation. *Thromb. Res. 92*, 149–156.
(19) Lee, Y., Kim, S. K., Lee, D. Y., Lee, S., Kim, C. Y., Shin, H. C., Moon, H. T., and Byun, Y. (2006) Efficacy of orally active chemical conjugate of low molecular weight heparin and deoxycholic acid in rats, mice and monkeys. *J. Controlled Release 111*, 290–298.
(20) Petitou, M., Hérault, J. P., Bernat, A., Driguez, P. A., Duchaussoy, P., Lormeau, J. C., and Herbert, J. M. (1999) Synthesis of thrombin-inhibiting heparin mimetics without side effects. *Nature 398*, 417–422.
(21) Casu, B. (1985) Structure and biological activity of heparin. *Adv. Carbohydr. Chem. Biochem. 43*, 51–134.
(22) Parish, C. R., Freeman, C., Brown, K. J., Francis, D. J., and Cowden, W. B. (1999) Identification of sulfated oligosaccharide-based inhibitors of tumor growth and metastasis using novel in vitro assays for angiogenesis and heparanase activity. *Cancer Res. 59*, 3433–3441.
(23) Jayne, D. G., Perry, S. L., Morrison, E., Farmery, S. M., and Guillou, P. J. (2000) Activated mesothelial cells produce heparin-binding growth factors: implications for tumor metastases. *Br. J. Cancer 82*, 1233–1238.
(24) Li, H. L., Ye, K. H., Zhang, H. W., Luo, Y. R., Ren, X. D., Xiong, A. H., and Situ, R. (2001) Effect of heparin on apoptosis in human nasopharyngeal carcinoma CNE2 cells. *Cell. Res. 11*, 311–315.
(25) Meyer, T., and Hart, I. R. (1998) Mechanisms of tumour metastasis. *Eur. Cancer 34*, 214–221.
(26) Zacharski, L. R., and Ornstein, D. R. (1998) Heparin and cancer. *Thromb. Haemost. 80*, 10–23.
(27) Elias, E. G., Shukla, S. K., and Mink, I. B. (1975) Heparin and chemotherapy in the management of inoperable lung carcinoma. *Cancer 36*, 129–136.

BC800173M

PEGylation of Human Serum Albumin: Reaction of PEG-Phenyl-Isothiocyanate with Protein

Fantao Meng,[†] Belur N. Manjula,[†] Paul K. Smith,[§] and Seetharama A. Acharya*[,†,‡]

Department of Physiology and Biophysics and Department of Medicine, Albert Einstein College of Medicine, Bronx, New York 10461, and BioAffinity Systems, Rockford, Illinois 61109. Received October 18, 2007; Revised Manuscript Received May 21, 2008

Successful and cost-effective PEGylation protocols require pure functionalized PEG reagents, which can be synthesized by simple and efficient procedures, exhibit high stability against hydrolysis, and maintain a level of reactivity with protein functional groups under mild reaction conditions. PEG-phenyl-isothiocyanate (PIT-PEG) is a new functionalized PEG having these characteristics, and has been synthesized by condensation of the bifunctional reagent 4-isothiocyanato phenyl isocyanate with monomethoxy PEG (mPEG). The data of ^{1}H NMR and colormetric analysis of the new PEG reagent establish that the mPEG has been quantitatively functionalized. The $t_{1/4}$ values for the hydrolysis of PIT-PEG5K in 100 mM phosphate solution at pH 6.5 and 9.2 are about 95 and 40 h, respectively. Incubation of human serum albumin (HSA, 0.5 mM) with a 10-fold molar excess of PIT-PEG (3K or 5K) at pH 6.5 and 9.2 generated PEG-HSA conjugates with average of 3.5 and 6.0 PEG chains per HSA molecule, respectively. The circular dichroism spectra of the conjugates showed that PEGylation of HSA has little influence on the secondary structure of HSA. The hexaPEGylated HSA, $(TCP\text{-}PEG5K)_6$-HSA, exhibited very high hydrodynamic volume, and the molecular radius of HSA increased from 3.95 to 6.57 nm on hexaPEGylation. The hexaPEGylation also increased the viscosity of 4% HSA from 1.05 to 2.10 cP, and the colloid osmotic pressure from 15.2 to 48.0 mmHg. The large increase in the hydrodynamic volume and the solution properties of $(TCP\text{-}PEG5K)_6$-HSA suggest that it could be a potential candidate as a plasma volume expander. PIT-PEG is a useful addition to the spectrum of functionalized PEG reagents available for surface decoration of proteins with PEG.

INTRODUCTION

Advances in biotechnology, in particular recombinant DNA technology, have made a large number of proteins available for application as novel drugs. Most of these therapeutic proteins suffer from short circulating life due to their proteolytic degradation and/or rapid clearance. Immunogenic reaction of the therapeutic proteins is another major concern in developing protein-based drugs. This in effect decreases their therapeutic efficacy (*1*). Covalent attachment of natural or synthetic polymers to therapeutic proteins with the purpose of generation of hybrid biomacromolecules with unique and improved molecular properties has become a popular approach to overcome these limitations of therapeutic proteins (*2*). Many polymers have been studied for these applications, and the most popular one is poly(ethylene glycol) (PEG), which is nontoxic, nonimmunogenic, highly soluble in water, and FDA approved. Since the pioneering experiments on PEGylation of proteins by Abuchowski et al. (*3, 4*), the application of this strategy to improve the therapeutic efficacy of protein drugs has been very clearly demonstrated (*1, 5, 6*).

PEGylation of a protein, peptide, or nonpeptide molecule involves the covalent attachment of one or more copies of PEG chains to the desired molecule. Functionalization of the PEG chain with a choice reactive functional group is the first step in carrying out PEGylation of macromolecules. Several PEG reagents, which facilitate the formation of bioconjugates (*7–9*), have been developed over the years, and are commercially available now.

Active esters of PEG, in particular the *N*-hydroxysuccinimde (NHS) esters of PEG acids are the most commonly used PEG reagents to target PEGylation to surface amino groups of protein. The half-life of the NHS esters of PEG acids for hydrolysis is in the range from 1 min (or less) to about 45 min at pH 8.0 and 25 °C (*10, 11*). As the reactivity of PEG-NHS toward amino groups of proteins goes up, the half-life of the PEG reagent in aqueous buffer decreases. Accordingly, a large excess of PEG reagents over protein have to be used for achieving desired levels of PEGylation.[1]

In contrast to the NHS ester of PEG acid, a maleimide-activated PEG, which reacts with the thiols of cysteine residues of protein to form stable thioether linkage with the protein, exhibits a much higher stability against hydrolysis, and accordingly PEG-maleimide reagents have been one of most desired PEGylation reagents. The maleimide moiety reacts rapidly with the thiol group without hydrolysis around neutral pH. The reaction is very selective as well as nearly quantitative. Accordingly, we have developed a new strategy that takes advantage of the high selectivity and efficiency of the thiol-

* Corresponding author. Professor Seetharama A. Acharya, Professor of Medicine and of Physiology and Biophysics, Albert Einstein College of Medicine, 1300 Morris Park Avenue, Bronx, NY 10461. Phone 718-430-2133. Fax: 1-718-430-8819. E-mail: acharya@aecom.yu.edu.

[†] Department of Physiology and Biophysics, Albert Einstein College of Medicine.

[‡] Department of Medicine, Albert Einstein College of Medicine.

[§] BioAffinity Systems.

[1] Abbreviations: CD, circular dichroism; COP, colloid osmotic pressure; Hb, hemoglobin; HSA, human serum albumin; PBS, phosphate buffer saline; PEG, poly(ethylene glycol); PEG5K, PEG with Mw of 5000 dalton; mPEG, monomethoxy PEG; PEGylation, conjugation with PEG; PIT-PEG, PEG-phenyl-isothiocyanate; SEC, size exclusion chromatography; $(TCP\text{-}PEG5K)_n$-HSA, thiocarbamoyl phenyl PEG-HSA conjugate with *n* copies of PEG5K chains.

10.1021/bc7003878 CCC: $40.75 © 2008 American Chemical Society
Published on Web 06/24/2008

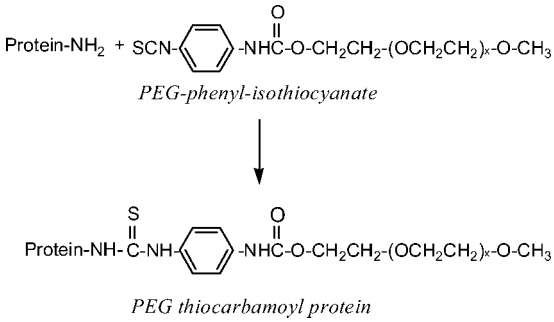

Figure 1. Schematic representation of the reaction of PEG-phenyl-isothiocyanate with protein amino groups.

maleimide reaction to develop a new PEGylation platform, referred to as the extension arm facilitated (EAF) PEGylation. This procedure targets the PEGylation reaction to the reactive surface amino groups of the proteins. Hemoglobin, albumin, and red blood cell have been surface-decorated with multiple copies of PEG chains very efficiently using this simple and cost-effective PEGylation protocol (*12–15*). In this PEGylation protocol, protein can be incubated with both the thiolating reagent (2-iminothiolane) and PEG-maleimide simultaneously. As new thiol groups are generated *in situ* as a result of reaction of iminothiolane with protein amino group, they are trapped by the PEG-maleimide. The application of this protocol for surface decoration of protein and cells is further facilitated by the development of a single-step procedure for functionalization of the mPEG as PEG-maleimide. An easy and nearly quantitative reaction of aromatic isocyanates with aliphatic hydroxyl that generates a carbamate linkage has been used to functionalize the PEG (*16, 17*). This approach of using a low molecular weight bifunctional reagent, phenyl isocynanate, carrying the desired functional group at the *p*-position is advanced as a modular approach for functionalizing PEG.

Phenyl isothiocyanate is a well-known reagent for carrying out Edman degradation (*18*) and amino acid analyses by HPLC (*19*). Some isothiocyanates were used to modify hemoglobin (Hb) in an attempt to correlate the structure with function (*20, 21*) and to introduce cross-links into Hb (*22, 23*). In all these reactions, isothiocyanates showed a high reactivity with the N-terminal valine residues of Hb. Isothiocyanate reacts with nucleophiles such as amines, sulfhydryls, and the phenolate ion of tyrosine side chains. The only stable product of these reactions, however, is with the primary amino groups (*24*). Therefore, isothiocyanate compounds are very selective reagents for modifying ϵ- and N-terminal amines in proteins. Besides, phenyl isothiocyanate is a stable reagent that can be stored at room temperature. Accordingly, it is reasonable to expect that PEG activated with a phenyl isothiocyanate group will exhibit high stability against hydrolysis and also a good level of reactivity with the α-amino groups and the low pK_a amino groups of proteins to generate thiocarbamoyl protein conjugate (Figure 1). Under the conditions where the NHS esters of PEG acids readily undergo hydrolysis, PEG-isothiocyanate could serve as an alternate reagent for PEGylation.

To functionalize PEG with isothiocyanato moiety, we have translated the one-step modular approach that we had developed earlier to functionalize PEG with a maleimide moiety, i.e., condensation of *p*-maleimide phenyl isocyanate with mPEG (*16,17*). Accordingly, for functionalizing mPEG with an isothiocyanato moiety, the synthesis of *p*-isothiocyanato phenyl isocyanate and the condensation of this reagent with mPEG have been pursued (*25*). The application of this reagent for PEGylation of protein has been investigated using human serum albumin (HSA) as a model protein.

HSA is an abundant negatively charged plasma protein, with ligand binding and transport functions, antioxidant functions, and enzymatic activities (*26, 27*). We choose HSA as a model protein for PEGylation with multiple copies of PEG chains using this new reagent, in view of our interest in the application of PEGylated albumin as a plasma volume expander to improve microcirculatory function in various clinical settings (*28, 29*).

Here, we describe the functionalization of PEG as PEG-phenyl-isothiocyanate (PIT-PEG), its stability against hydrolysis, its reactivity with HSA, and optimization of its reaction with HSA for generation of hexaPEGylated albumin. To assess the feasibility of using these new PEG-HSA conjugates as plasma volume expanders, the solution properties (including hydrodynamic molecular radius, viscosity, and colloid osmotic pressure) of the new PEG-HSA conjugates, influence of PEGylation on the secondary structure, and overall conformation of HSA have also been studied.

MATERIALS AND METHODS

Synthesis of PEG-Phenyl-Isothiocyanate. Monomethoxy PEG-phenyl-isothiocyanate, namely, PIT-PEG, was synthesized as described earlier (*25*). As shown in Figure 2A, the synthesis of PIT-PEG can be achieved in a one-step reaction, activating the mPEG with a small molecular weight bifunctional reagent, 4-isothiocyanato-phenyl isocyanate. The synthesis of the bifunctional reagent can be divided into three steps as schematically represented in Figure 2B: (i) synthesis of 4-carboxy phenyl isothiocyanate from *p*-amino benzoic acid; (ii) the conversion of 4-carboxy phenyl isothiocyanate to 4-isothiocyanato benzoyl azide; (iii) the synthesis of 4-isothiocyanato phenyl isocyanate.

(i) Synthesis of 4-Carboxy Phenyl Isothiocyanate. Para-aminobenzoic acid (0.2 mol; 26 g) was dissolved in acetone (400 mL) at room temperature. Activated carbon, (about 5 g, Darco, G60) was added and the mixture was stirred (using magnetic stir bar) for 5 to 10 min. The entire solution was filtered, yielding a much lighter colored solution of *p*-aminobenzoic acid. Sodium acetate (0.3 mol, 26 g) was dissolved in about 200 mL of deionized water, and added to the above filtrate of *p*-aminobenzoic acid, now contained in a 4 L vacuum flask. A vacuum was applied to the flask with an intermediate dry ice/acetone trap connected between the flask and the vacuum pump.

Thiophosgene (about 40 g of neat red liquid) was added to the cooled acetone stripped slurry of *p*-aminobenzoic acid, while stirring rapidly with an overhead paddle stirrer. A tan precipitate formed almost immediately upon the addition of the thiophosgene along with considerable foaming. After the foaming subsided (about 10 min), the insoluble precipitate was filtered and dried under vacuum to get a powdery material. The crude product was recrystallized from hot (80 °C) glacial acetic acid to yield yellow needles of 4-carboxy phenyl isothiocyanate (about 16 g) after drying under vacuum.

Elemental analysis of the yellow crystals yielded: Carbon (found 53.38%, theory 53.63%); hydrogen (found 2.76%, theory 2.79%); nitrogen (found 7.58%, theory 7.82%). The crystals darkened but did not melt at 220 °C.

(ii) Synthesis of 4-Isothiocyanato Benzoyl Azide. 15 g of the 4-carboxyphenyl isothiocyanate was suspended in 200 mL of dry methylene chloride in a 1 L sidearm vacuum flask, along with 16 g of pyridine (0.2 M), phenyl dichlorophosphate (0.1 M), and 6.5 g of sodium azide (0.1 M). This mixture was stirred overnight at room temperature. The stirred mixture was then washed in a separatory funnel with 200 mL of water and then with 200 mL of 0.05 M sulfuric acid. The acid-washed methylene chloride layer was dried with anhydrous magnesium sulfate. The dried methylene chloride reaction solution was evaporated under vacuum in a rotary evaporator at room temperature. The resulting light tan crystals were dissolved in

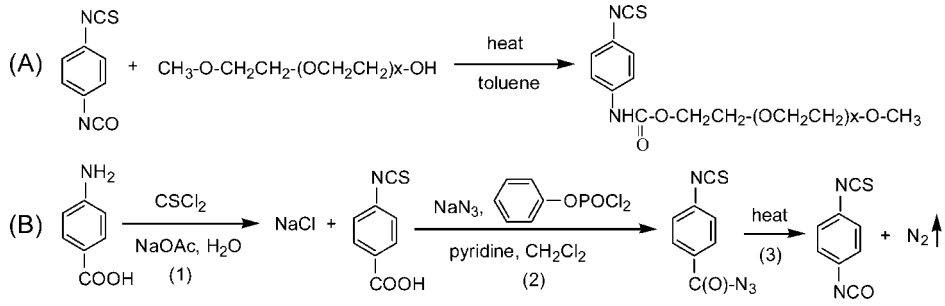

Figure 2. Schematic representation functionalization of mPEG as PEG-phenyl-isothiocyanate. (A) The one-step functionalization procedure. (B) The synthesis of 4-isothiocyanato phenyl isocyanate.

a minimal amount of ethyl ether at room temperature. The recrystallization solution was treated with activated carbon (Darco G 60) and filtered. The resulting light-colored solution was evaporated to dryness at room temperature. White crystals were obtained which melted at 68 to 72 °C with the evolution of nitrogen consistent with azide decomposition.

The elemental analysis of the 4-isothiocyano benzoyl azide crystals gave the following results: Carbon (found 46.85%, theory 47.05%); hydrogen (found 2.09%, theory 1.96%); nitrogen (found 26.87%, theory 27.45%). The infrared spectrum of the crystals (FTIR) conformed to 4-isothiocyanobenzoyl azide (e.g., strong broadband from about 2000 to about 2200 cm^{-1} is from N═C═O and N═C═S stretching modes; and a strong absorption due to azide at about 980−1000 cm^{-1}). The compound is stable at room temperature but was stored in the freezer.

(iii) Synthesis of 4-Isothiocyanato Phenyl Isocyanate. The 4-isothiocyanobenzoyl azide was thermally decomposed at about 75−104 °C (Curtius rearrangement) smoothly and quantitatively as a solution in dry refluxing of a toluene solution to 4-isothiocyanato phenyl isocyanate. The 4-isothiocyanate phenyl isocyanate was not isolated, but reacted as formed *in situ* with the hydroxyl-containing PEG according to the following description. An infrared spectrum of the composition containing 4-isothiocyanate phenyl isocyanate showed the decrease in the azide band at about 980−1000 cm^{-1} along with increased complexity of the absorbance in the N═C═O and N═C═S region of the spectrum from about 2000 to about 2300 cm^{-1}.

(iv) Functionalization of mPEG to PIT-PEG. 50 g of mPEG5K having a low diol content (NOF Corporation, Japan) was dissolved in 500 mL of toluene in a 2 L, three-necked flask equipped with a thermometer, overhead stirrer with motorized drive, and a Dean−Stark trap and condenser. The solution was stirred and heated to reflux (about 104 °C) and any water present was azeotropically removed as it accumulated in Dean−Stark trap. When no more additional water could be removed, the refluxing was discontinued and the contents were cooled under a dry nitrogen blanket to about 60 °C. To this reaction mixture, *p*-isothiocyanato benzoyl azide (0.5 g) was added and heating was resumed. Nitrogen was evolved during the initial 15 to 30 min after the heating was resumed. Heating was continued (reflux) for an additional hour. Heating was discontinued and the contents of the flask was allowed to cool to room temperature, and the reaction mixture now contained the desired product, PEG5K-phenyl-isothiocyanate. The reaction mixture was concentrated under vacuum using a rotary evaporator into viscous oil. This was treated with anhydrous ethyl ether to induce the crystallization of the activated mPEG5K. Ethyl ether also extracted the unreacted *p*-isothiocyanatophenyl isocyanate.

The crude PIT-PEG was purified with filtration in water, extraction with methylene chloride twice, then recrystallization in mixed solvent of methylene chloride/anhydrous ether twice. Finally, the purified white solid (48 g) was dried at room temperature under vacuum overnight. The purity of PIT-PEG was estimated as described below.

Estimation of Phenyl Isothiocyanato Moiety in Functionalized PEG. The concentration of phenyl isothiocyanato moiety in PIT-PEG was assayed by a colorimetric method developed by Zhang et al. (*30*). The principle of the method is that phenyl isothiocyanate reacts with 1,2-benzenedithiol to yield 1,3-benzodithiole-2-thione (λ_{max} = 365 nm and ϵ_m = 23 000 M^{-1} cm^{-1}). A final volume of 2.0 mL reaction mixture contains 900 μL of 100 mM potassium phosphate solution (pH 8.5), 900 μL of methanol, 100 μL of a solution of the isothiocyanate to be determined (0.5 mM), and 100 μL of 80 mM 1,2-benzenedithiol in methanol. The reactions were carried out in 5 mL of screwtop glass vials. The vials containing the reaction mixture were heated at 65 °C for 1 h and then cooled to room temperature. The absorbance at 365 nm was determined against a solvent blank. Each sample to be analyzed was accompanied by a paired blank containing all ingredients, except 1,2-benzedithiol. Each set of determinations also included a control vessel that contained the 1,2-benzedithiol but no isothiocyanate. A typical calibration curve for 0.1−1.0 mM phenyl isothiocyanate was generated with each testing of samples.

Hydrolysis Kinetics of Isothiocyanate of PIT-PEG5K. 25.9 mg of PIT-PEG5K dissolved into 1 mL (5 mM) of 100 mM potassium phosphate solution at different pH values, i.e., 5.5, 6.5, 7.4, and 9.2. The PIT-PEG5K solutions were incubated at room temperature. 40 μL of aliquots were pipetted out from the 5 mM of PIT-PEG5K solution at regular time intervals, and the concentrations of isothiocyanate in the incubation mixtures were estimated by colorimetric method as described above.

PEGylation of HSA with PIT-PEG. 0.5 mM HSA (Sigma, 99.9% free from acid) was incubated with a desired concentration of PIT-PEG reagent in 0.5 mL of 10 mM phosphate solution, at pH 8.5, at room temperature. The unreacted PIT-PEG was removed by centrifugal filtration using Centricon (50 KD cutoff membrane, Millipore Corp.) at 5000 rpm for 30 min four times. To study the kinetics of PEGylation (pH 9.2), 40 μL of reaction mixture was pipetted out at regular time intervals and diluted to 300 μL, and then analyzed by size exclusion chromatography (SEC) to measure the amount of unreacted PIT-PEG. For large preparation of PEGylated HSA, 1 g of HSA was incubated with 0.48 g of PIT-PEG3K or 0.78 g of PIT-PEG5K (HSA: PIT-PEG = 0.5:5 mM) in 30 mL of 10 mM phosphate solution, pH 6.5 or 9.2, at room temperature for 6 h. The unreacted PIT-PEG was removed by tangential flow ultrafiltration against phosphate buffer serum (PBS), using Minim from PALL Corporation and a 70 KD cutoff membrane. The progress of the removing of unreacted PIT-PEG from the products was monitored by the absorbance at 280 nm using a SEC.

Analytical Methods. SEC was performed on a Pharmacia FPLC system, at 25 °C using two HR10/30 Superose 12 columns connected in series with a 100 μL loop. The columns

were equilibrated and eluted with PBS, pH 7.4, at a flow rate of 0.5 mL/min. The effluent was monitored at 280 nm. SDS-PAGE analysis was carried out using a 6% Tris-glycine gel from Invitrogen Corp. as described previously (*31*).

HSA Content Assay. The concentration of HSA was determined from the absorbance at 279 nm (1 mg/mL, OD = 0.531; $\epsilon_m = 35\,300\ M^{-1}\ cm^{-1}$). The concentrations of PEG-HSA conjugates were determined by the standard procedure of Bio-Rad protein assay (*32*).

^{1}H NMR Analysis. ^{1}H NMR spectra were recorded using D_2O as the solvent and terimethylsilopropionate as the internal standard on a Bruker DRX 300 NMR spectrometer at 300 MHz. 10 mg samples (either PIT-PEG reagents or PEG-HSA conjugates) were dissolved in 0.1 mL of D_2O and their ^{1}H NMR spectra were scanned for 1.3 s. Pure sample of mPEG (10 mg) in D_2O (0.1 mL) served as standard. The integrated signal characteristic for mPEG was recorded for all samples, and by reference to the standard, the amount of functionalized group in PIT-PEG or the amount of mPEG in the conjugates was calculated (*33*).

Solution Properties of PEGylated HSA. The hydrodynamic molecular radius of the PEGylated HSA was determined at 22 °C at 1 mg/mL by dynamic light scattering measurements on a DynaPro molecular sizing instrument (Protein Solutions, Charlottesville, VA). The viscosity of the PEGylated HSA was measured with a cone and plate rheometer (Brookfield, Middleboro, MA) at 37 °C in PBS. The instrument was calibrated with water prior to measurements of the viscosity of the HSA samples. The colloid osmotic pressure (COP) of the PEGylated HSA was determined using a Wescor 4420 Colloidal Osmometer (Wescor, Logan, UT, USA) with a 30 KD Mw cutoff membrane at room temperature in PBS. The instrument was calibrated with Osmocoll reference standard prior to measurements of the samples. Each sample was measured at least twice and the average of the measurements is presented.

Spectroscopic Studies of PEGylated HSA. CD (circular dichroism) spectra for HSA and PEGylated HSA were recorded on a JASCO-720 spectropolarimeter (Tokyo, Japan) at 25 °C using a 0.2 cm light path cuvette (310 μL). All the samples (3 μM) were scanned in the range 200−250 nm in PBS, pH 7.4. The CD results were expressed in terms of mean residue ellipticity (MRE) [θ] in deg.cm^2/dmol. The fluorescence measurements of HSA and PEGylated HSA samples (3 μM) were performed using a Shimadzu RF-5301 spectrofluorimeter at room temperature. The emission spectra were recorded from 305 to 400 nm using an excitation wavelength of 295 nm. A cuvette with a 1 cm path length was used in all these stuides.

RESULTS

Isolation and characterization of PIT-PEG. PIT-PEG was isolated by recrystallization as described in Methods and Materials. The ^{1}H NMR spectrum of mPEG5K functionalized with 4-isothiocyanato phenyl isocyanate is compared with that of mPEG5K in Figure 3. The ^{1}H NMR spectrum of the functionalized PEG clearly "fingerprints" the signature of phenyl ring introduced, and the methylene groups of PEG that are connected to the phenyl ring through a carbamate linkage. The NMR data confirmed the expected molecular structure of PIT-PEG. The chemical shifts and assignments of the protons in the PEG reagent are as follows: δ 3.3 (s, 3H, mPEG, CH_3O-); δ 3.5−3.8 (s, PEG backbone, -CH_2CH_2O-); δ 4.3 (t, 2H, carbamate PEG linker, -CH_2-OC(O)-); and δ 7.2−7.5 (q, 4H, phenyl ring, -C_6H_4-).

Purity of PIT-PEG. The purities of PIT-PEGs are calculated from the estimation of isothiocyanato moiety in the functionalized PEG by colorimetric method and by ^{1}H NMR method (*34*), and presented in Table 1. The colorimetric method

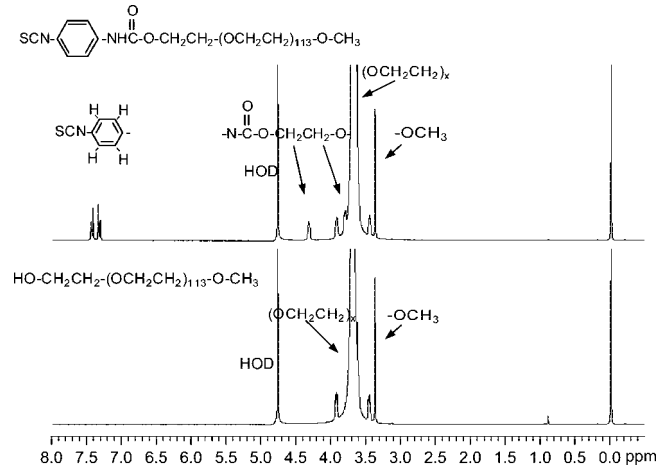

Figure 3. ^{1}H NMR spectra (D_2O, 300 MHz) of mPEG5K and PIT-PEG5K.

Table 1. Extent of Functionalization of PEG by Isothiocyanato Phenyl Isocyanate

	extent of functionalization	
	colorimetry method	^{1}H NMR method
PIT-PEG3K	109%	93%
PIT-PEG5K	112%	96%

estimates the purity higher than 100%. ^{1}H NMR spectroscopy estimates the purity of PIT-PEG3K and PIT-PEG5K as about 93% and 96%, respectively. The purity of PIT-PEG5K was obtained by quantitating the integrated areas of hydrogen of backbone PEG (113 × 4H) with that of phenyl ring (4H). The purities estimated by both methods indicate that the mPEG appears to be essentially fully functionalized.

Stability of PIT-PEG. The PEG-isothiocyanate is an electrophilic reagent, which can react with a weak nucleophile like hydroxyl ion. In neutral aqueous solution, the hydrolysis of PIT-PEG is relatively very slow, but proceeds more rapidly in aqueous alkaline solutions. The hydrolysis of PEG-isothiocyanate forms corresponding PEG-aniline, carbon dioxide, and hydrogen sulfide (*35*). The kinetics of hydrolysis of PIT-PEG5K (5 mM) in 100 mM phosphate solution as a function of pH is shown in Figure 4. The hydrolysis rate of PIT-PEG5K increases with the increase of pH. It may be noted that only a negligible amount of PIT-PEG5K hydrolyzed at all the pH within the first 12 h. The $t_{1/4}$ for the hydrolysis of PIT-PEG5K in different buffers of pH 5.5, 6.5, 7.4, and 9.2 (curve a, b, c, and d, respectively) are approximately 105, 95, 70, and 40 h, respectively.

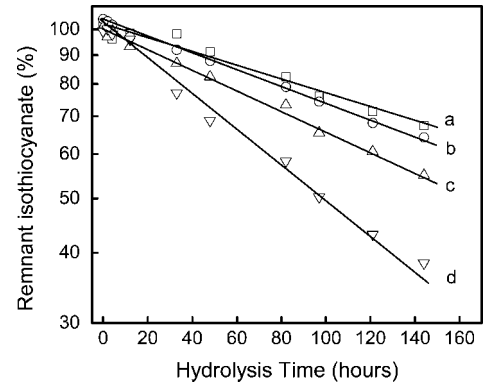

Figure 4. Hydrolysis kinetics of PIT-PEG5K (5 mM) in 100 mM of phosphate solutions at different pH (pH 5.5, 6.5, 7.4, and 9.2; curves a−d) at room temperature.

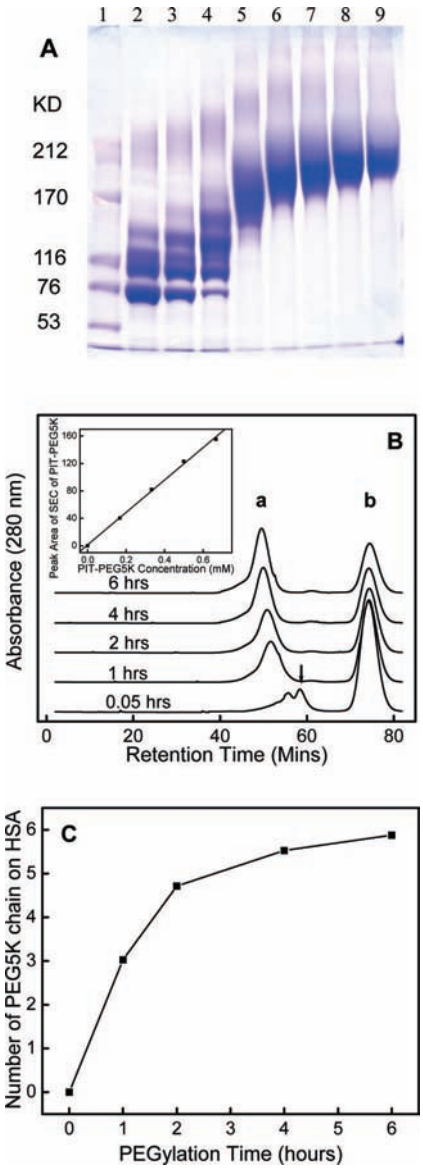

Figure 5. (A) The SDS-PAGE analysis of HSA and PEG-HSA conjugates prepared at the different ratio in 10 mM phosphate solution at pH 8.5 at room temperature for 6 h. Lane 1, marker; Lanes 2 to 9, 0.5 mM albumin reacted with 0.25, 0.5, 1.0, 4.0, 8.0, 10.0, 15.0, and 20.0 mM PIT-PEG5K, respectively. (B) SEC analysis of HSA (0.5 mM) reacted with PIT-PEG5K (5 mM) in 10 mM phosphate solution (pH 9.2) at room temperature. 20 μL of reaction mixture was diluted to 150 μL and uploaded into SEC (100 μL of loop) at 0.05, 1, 2, 4, and 6 h. The arrow points at the unmodified HSA. Inset is the standard curve of the peak area in SEC as a function of concentration of PIT-PEG5K. (C) The kinetic curve of PEGylation of HSA with PIT-PEG5K (0.5:5 mM) reacted in 10 mM phosphate solution (pH 9.2) at room temperature.

Reactivity of PIT-PEG. *(i) Modification of HSA by PIT-PEG5K as a Function of Molar Excess of the Reagent.* The reactivity of the isothiocyanato moiety of PIT-PEG with a protein amino group has been investigated using HSA as the model protein. SDS-PAGE pattern of HSA (0.5 mM) incubated with 0.5- to 40-fold molar equivalents of PIT-PEG5K (0.25 to 20 mM) in 10 mM phosphate solution, pH 8.5, at room temperature for 6 h is shown in Figure 5A. As the molar equivalents of PIT-PEG5K to HSA increase, HSA with an apparent molecular size of approximately 70 KD is converted into higher molecular weight species. Apparently, the new protein bands generated in these reactions represent PEG-HSA conjugates with number of PEG chains. When the PIT-PEG is only 0.5 equiv (0.25 mM, lane 2 in Figure 5A), most of the HSA remains unPEGylated, but three well-resolved bands are present besides the unmodified HSA. When the PIT-PEG is increased to 1 equiv (lane 3 in Figure 5A), the amount of the HSA band decreases with a concomitant increase in the other three bands and the generation of the fourth band. As the PIT-PEG5K increased further to 2 equiv (lane 4 in Figure 5A), the HSA band becomes a minor species, with generation of the new fifth band (diffused) of higher molecular size. This reflects the high reactivity of PEG-isothiocyanate with the amino groups of HSA. When the PIT-PEG is increased to 8 equiv (lane 5 in Figure 5A), PEGylated HSA moves as a diffused band in the apparent molecular weight range of 130 to 170 kD. With 16-fold molar equiv (lane 6 in Figure 5A) of PIT-PEG, almost all modified HSA appears as a diffused band in the molecular weight range 170−212 kD. Further increase in the amount of PIT-PEG does not increase the apparent molecular mass of the modified PEG significantly, but the product moves as a more compact band.

(ii) Kinetics of PEGylation of HSA by PIT-PEG. The kinetics of PEGylation of HSA with PIT-PEG5K (0.5:5 mM) in 10 mM phosphate solution (pH 9.2) at room temperature is studied by SEC and shown in Figure 5B. The decrease in the retention time and the increasing peak area of albumin as reflect by the absorbance at 280 nm (peak **a** in Figure 5B), suggest that the molecular size of albumin and its absorbance at 280 nm increase as PEG is coupled to HSA gradually with the incubation time increasing (the linkage between the PEG and HSA has a strong UV absorption due to presence of the phenyl ring and thiourea bond). Meanwhile, the amount of the PIT-PEG5K (peak **b** in Figure 5B) decreases as the reaction proceeds.

In view of the high stability of PIT-PEG (Figure 4), peak **b** represents the unreacted PIT-PEG in the reaction mixture, and it is conceivable that quantitation of this peak can be used to estimate the PEGylation of the protein. The inset curve in the Figure 5B depicts the linear correlation of that the peak area of PIT-PEG5K in SEC as a function of its concentration loaded into SEC (100 μL of loop). From the standard curve and the integrated area of unreacted PIT-PEG5K (peak **b** in Figure 5B), the amount of PIT-PEG5K coupled to albumin (the number of PEG5K chains on HSA) in each of the PEG-HSA conjugate can be calculated.

The kinetic curve of PEGylation of HSA with PIT-PEG5K is shown in Figure 5C. The PEGylation proceeds very fast in the first 2 h, and is almost complete with about 5 copies of PEG chains coupled to albumin molecule. As the reaction is going on, the rate of PEGylation slows down, and only about 1 copy of additional PEG chain is coupled on each molecule in the following 4 h. After 6 h of reaction, there are about 5.9 copies of PEG5K chains attached on HSA molecule. In view of the high stability of the reagent, and the fact that only 50% of the reagent is used by 2 h, the second phase of the kinetics of PEGylation represents an increasing resistance of PEG-HSA conjugate as the number of PEG chains on the protein molecule increases.

(iii) Influence of pH and Length of PEG Chain on the PEGylation of HSA. The influences of reaction pH and length of PEG chain on the PEGylation of HSA have been studied by incubating HSA with PIT-PEG3K and PIT-PEG5K at pH 6.5 and 9.2. Incubation of 0.5 mM HSA with 5 mM PIT-PEG3K or PIT-PEG5K in 10 mM phosphate solution, at pH 6.5 and 9.2, at room temperature for 6 h, resulted in a quantitative modification of HSA as anticipated, and a concomitant significant enhancement in apparent molecular size of HSA as shown by SEC pattern (Figure 6A). The HSA modified with PIT-PEG3K at pH 6.5 (curve 2) elutes close to the position of HSA dimer, while the PEG-HSA generated at pH 9.2 with PIT-

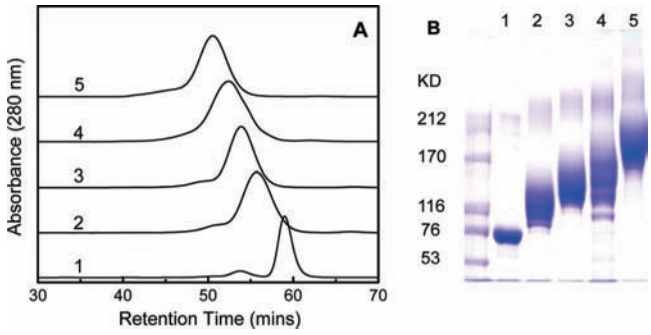

Figure 6. SEC analysis (A) and SDS-PAGE analysis (B) of native HSA (1), PEG3K-HSA generated at pH 6.5 (2), PEG3K-HSA generated at pH 9.2 (3), PEG5K-HSA generated at pH 6.5 (4), and PEG5K-HSA generated at pH 9.2 (5). The reaction condition is described in context. The unreacted PIT-PEG were removed using tangential flow ultrafiltration.

Table 2. Influence of Reaction pH and PEG Chain Length of PIT-PEG on the PEGylation of HSA

		average copies of PEG chains on HSA molecule	
pH	ITP-PEGMw	SEC method	^{1}H NMR method
6.5	PEG3K	3.3	3.6
6.5	PEG5K	3.7	3.4
9.2	PEG3K	5.5	5.9
9.2	PEG5K	6.0	6.0

PEG3K (curve 3) is slightly larger than the HSA dimer. Similarly, the hydrodynamic molecular size of PEG5K-HSA conjugate generated at pH 6.5 (curve 4) is smaller than that of PEG5K-HSA conjugate generated at pH 9.2 (curve 5). The numbers of PEG chains on the four PEGylated samples are calculated from their SEC results (data not shown) before removing unreacted PIT-PEG and presented in Table 2. In the reactions at pH 9.2, approximately 6 copies of PEG chains (either PEG3K or 5K) are conjugated to HSA, whereas in the reactions at pH 6.5, about 3.5 copies of PEG chains are linked to HSA. Therefore, it is clear that modulation of pH of the reaction mixture will be a good approach to control the extent of PEGylation, and that the PEG chain length of PIT-PEG has little influence on the PEGylation of HSA.

The SDS-PAGE analysis of the four PEG-HSA conjugates are shown in Figure 6B. From the gel, it is confirmed that the PEG-HSA conjugates generated at pH 9.2 (Lanes 3 and 5) exhibit higher level of PEGylation than the PEG-HSA conjugates generated at pH 6.5 (Lanes 2 and 4). The distribution of the PEGylated materials (based on the number of PEG chains) of Lanes 2 and 4 (conjugates generated at pH 6.5) is wider as compared to the distribution of the PEGylated material in Lanes 3 and 5 (conjugates generated at pH 9.2). Therefore, the PEG-HSA conjugates generated at pH 6.5 appear to be much more heterogeneous as compared to the products generated at pH 9.2.

The SEC and SDS-PAGE results suggest that the level of PEGylation increases with the increase of the pH of the PEGylation reaction, as more ϵ-amino groups of HSA are deprotonated at higher pH.

Solution Properties of PEG-HSA Conjugates. Four PEG-albumin conjugates were prepared in large scale (1 g HSA) and purified using tangential flow ultrafiltration. Two PEG-HSA conjugates have been generated at pH 6.5 using PIT-PEG3K and PIT-PEG5K, respectively, and the another two conjugates have been generated at pH 9.2 again using the same two PEG reagents.

(i) Molecular Mass of PEG Conjugated to Albumin. The amount of PEG conjugated to albumin in the four PEG-HSA conjugates have been calculated by the ^{1}H NMR approach (*33*) and compared with the amount calculated by spectrophotometric/SEC approach in Table 2. The PEGylation at pH 6.5 couples an average of 3.5 PEG chains on each albumin molecule. Comparatively, the PEGylation at pH 9.2 couples 6 copies of PEG chains. According to the number of PEG chains attached on HSA molecule, the PEG-HSA conjugates generated at pH 6.5 are referred to as tetraPEGylated HSA [named (TCP-PEG3K)$_4$-HSA or (TCP-PEG5K)$_4$-HSA], and those generated at pH 9.2 as hexaPEGylated HSA [named (TCP-PEG3K)$_6$-HSA or (TCP-PEG5K)$_6$-HSA].

Table 3. Comparison of Solution Properties of PEG-HSA Conjugates

sample HSA	hydrodynamic[a] radius/nm	PEG mass[b] /kD (n PEG)	viscosity[c] /cP	COP[d] /mmHg
HSA	3.95	0	1.05	15.2
(TCP-PEG3K)$_4$-HSA	4.83	10.8 (3.6)	1.12	21.3
(TCP-PEG5K)$_4$-HSA	5.79	17.0 (3.4)	1.34	33.2
(TCP-PEG3K)$_6$-HSA	5.57	17.7 (5.9)	1.46	26.9
(TCP-PEG5K)$_6$-HSA	6.57	30.0 (6.0)	2.03	46.8

[a] Measured by DynaPro, concentration = 1.0 mg/mL, 22 °C. [b] Calculated by ^{1}H NMR. [c] Albumin concentration = 4.0 g/100 mL, 37 °C. [d] Albumin concentration = 4.0 g/100 mL, 25 °C.

(ii) Solution Properties of PEGylated Albumins. Molecular Radius of the PEGylated Albumins. The molecular radius of native HSA is around 3.95 nm (Table 3). The hexaPEGylated HSA with PEG5K chains, (TCP-PEG5K)$_6$-HSA, has the largest radius of 6.57 nm. The tetraPEGylated HSA with the least amount of PEG, (TCP-PEG3K)$_4$-HSA exhibits the smallest molecular radius, i.e., 4.83 nm. (TCP-PEG3K)$_6$-HSA has a molecular radius of 5.57 nm, while (TCP-PEG5K)$_4$-HSA exhibits a radius of 5.79 nm (Table 3). It may be noted that, although (TCP-PEG3K)$_6$-HSA carries a little more amount of PEG on HSA than that on (TCP-PEG5K)$_4$-HSA (17.7 KD vs 17.0 KD, Table 3), the former conjugate exhibits a smaller radius than the latter conjugate (5.57 nm vs 5.79 nm in Table 3, and Curve 3 vs 4 in Figure 6A). This is probably because, although (TCP-PEG3K)$_6$-HSA carries more PEG chains than (TCP-PEG5K)$_4$-HSA does, the PEG shell of the former conjugate is fixed on the albumin surface through 6 anchors and the PEG shell of the latter one is fixed through fewer locating sites, 4 anchors. The PEG shell of (TCP-PEG3K)$_6$-HSA, therefore, appears more compact than that of (TCP-PEG5K)$_4$-HSA. This result is different from that reported by Fee et al. (*36*), who suggested that the hydrodynamic radii of PEGylated proteins depend on the total weight of grafted PEG but not on PEG molecular weight, or PEG-to-protein molar grafting ratio.

Colloid Osmotic Pressure of PEGylated Albumins. The COP of PEGylated albumins hs been studied as a function of protein concentration and compared with that of unmodified albumin (Figure 7A). The COP of albumin shows only a marginal increase when measured as a function of the protein concentration, and this small increase is linear over the range of the protein concentration studied. On the other hand, the COP values of PEGylated albumin samples are higher than that of native HSA and exhibit an exponential increase as a function of the protein concentration. The increased COP resulting from PEGylation as a function of PEG mass conjugated to HSA at different protein concentration is shown in the inset of Figure 7A. The increase in COP as a function of PEG mass conjugated is also exponential.

Viscosity of PEGylated Albumins. The viscosities of PEGylated albumins are compared with that of unmodified albumin as a function of the protein concentration (Figure 7B). The viscosity of HSA does not increase significantly upon increasing the protein concentration. On the other hand, the viscosities of the four PEGylated albumins exhibit an exponential increase as a function of the protein concentration. The correlation of

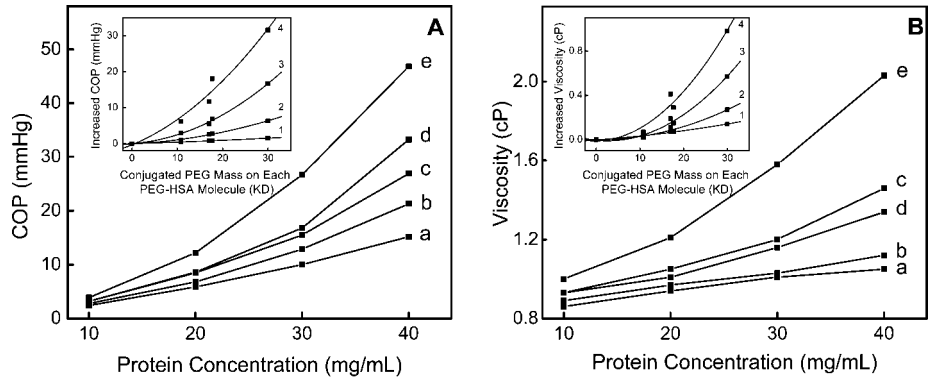

Figure 7. Colloid osmotic pressure (A) and viscosity (B) of HSA (a) and PEG-HSA conjugates, $(TCP\text{-}PEG3K)_4$-HSA (b), $(TCP\text{-}PEG5K)_4$-HSA (c), $(TCP\text{-}PEG3K)_6$-HSA (d), and $(TCP\text{-}PEG5K)_6$-HSA (e) as a function of the protein concentration. Inset A, relationships of conjugated PEG masses on PEG-HSA conjugates and the increased COP at different protein concentrations. Inset B, relationships of conjugated PEG masses on PEG-HSA conjugates and the increased viscosity at different protein concentrations. Curve 1, 1 g/dL; curve 2, 2 g/dL; curve 3, 3 g/dL; curve 4, 4 g/dL.

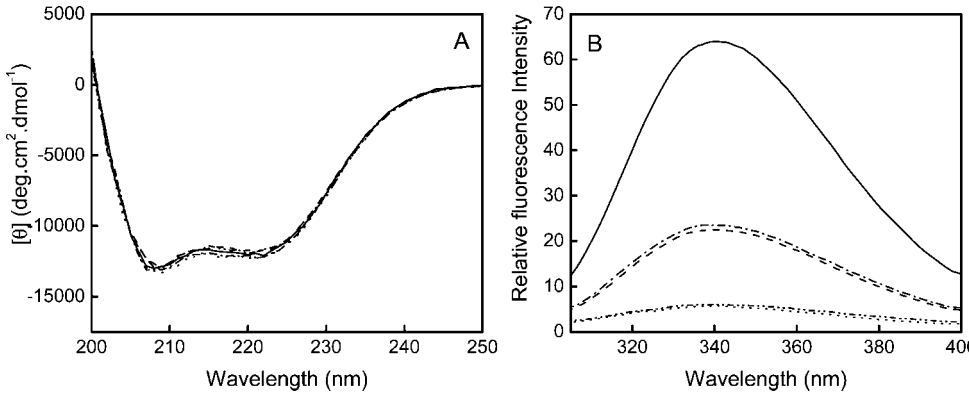

Figure 8. Circular dichroism (A) and intrinsic fluorescence emission (B) spectra of HSA (solid line) and conjugates $(TCP\text{-}PEG3K)_4$-HSA (dash), $(TCP\text{-}PEG3K)_6$-HSA (dot), $(TCP\text{-}PEG5K)_4$-HSA (dash dot), and $(TCP\text{-}PEG5K)_6$-HSA (dash dot dot).

increased viscosity as a function of PEG mass conjugated to HSA is presented in the inset of Figure 7B. Again, the viscosity as a function of the molecular mass of PEG in the conjugate increased exponentially, especially at high protein concentration.

(iii) Influence of PEGylation on the Conformation of HSA: Influence of PEGylation on the Secondary Structure of HSA. The CD spectra of PEGylated HSA in the far-UV region (200 to 250 nm) is compared with that of the unmodified HSA (Figure 8A). The CD spectra of PEG-HSA conjugates and albumin in the far ultraviolet region are essentially identical. Only very few changes are seen in the CD spectra, particularly in terms of the values of mean residue ellipticity [θ] at 208 and 222 nm, as a consequence of PEGylation. The results suggest that the α-helical conformation of HSA is not influenced by the PEGylation. Thus, the secondary structure of HSA is not adversely influenced on its PEGylation with PIT-PEG.

Intrinsic Fluorescence Measurement. The intrinsic fluorescence spectra of the PEG-HSA conjugates are analyzed to evaluate the conformational changes around the tryptophan residue (Trp 214) in HSA. When excited at 295 nm, all the PEGylated samples and HSA showed maximum emission intensity at the same wavelength (340 nm) (Figure 8B). The fluorescence intensity of PEGylated HSA, however, showed a significant decrease as compared to that of HSA, indicating that attachment of PIT-PEG on HSA quenched the intrinsic fluorescence of the Trp 214 residue of HSA. The fluorescence intensities of the two conjugates generated at pH 6.5 (using PIT-PEG3K and PIT-PEG5K) are similar; the PEG-HSA adducts generated at pH 9.2 also have a similar level of fluorescence quenching. Thus, the total amount of coupled PEG on the surface of HSA molecule does not dictate fluorescence of PEGylated HSA. The level of quenching of fluorescence is dictated by the pH of PEGylation reaction, i.e., by the extent of PEGylation. The quenching effect is apparently a consequence of the specific formation of thiocarbamoyl-phenyl linker between protein amino group and PEG chain. The hydrophobic phenyl linker section binds near the Trp 214 or its proximity and acts like some small hydrophobic molecules quenching the fluorescence of Trp 214 (*37, 38*). The quenching of the Trp 214 fluorescence clearly indicates that the conformation of the hydrophobic binding pocket in the second α-helix domain is affected.

DISCUSSION

Functionalizing PEG chains by quantitative modification of the hydroxyl group of methoxy PEG is a very crucial step in achieving a high-purity, reliable, and reproducible PEGylation reagent. If mPEG is subjected to multiple steps of organic synthetic reactions during the process of functionalization, the yield and/or purity of the final PEG reagent will decrease. A one-step functionalization process using a small molecular weight heterobifunctional reagent will minimize the exposure of mPEG to a multistep synthetic protocol. A quantitative modification of mPEG by the heterobifunctional reagent will significantly simplify the subsequent purification of the funationalized PEG. We have now developed such a one-step protocol for functionalizing the mPEG with a desired functional group. The reaction of phenyl isocyanate with hydroxyl group of mPEG is simple and quantitative and can serve as a prototype reaction for attaching a bifunctional reagent that carries the desired functional group at its distal end to the mPEG. The one-step functionalization of PEG by isothiocyanato phenyl isocy-

anate as PEG-phenyl-isothiocyanate proceeds very efficiently. The functionalization of both mPEG3K and mPEG5K are nearly quantitive as assayed by the colorimetric method and ^{1}H NMR method (Table 1).

The isolation of the small molecular bifunctional reagent, isothiocyanato phenyl isocyanate, is not required in the synthesis of PIT-PEG, because its precursor, an azide, can be quantitively converted *in situ* before its reaction with mPEG. However, in the case of synthesis of PEG-maleimides by this approach, the isolation of the small molecular weight bifunctional reagent, *p*-maleimido phenyl isocyanate, is preferred, as it gives a better preparation of PEG-maleimide (*39*).

The PIT-PEG exhibits a high stability against hydrolysis at room temperature. When PIT-PEG was dissolved in phosphate solution of different pH values (from pH 5.5 to 9.2) at room temperature, only a negligible level of hydrolysis occurred within the first 12 h. The high stability of the PIT-PEG permits the use of the high pH as well as room temperature for PEGylation, as far as the protein is stable under these conditions. The high stability of the PIT-PEG has also made it possible to develop an analytical procedure to calculate the amount of consumed PEG in reaction (i.e., conjugated to protein) using a SEC, that facilitates the easy calculation of the extent of PEGylation.

Generally, when a protein chemical modification reagent exhibits a high stability against hydrolysis, it will exhibit a low reactivity for PEGylation of protein. In spite of the high stability of the PEG-isothiocyanate against hydrolysis, it displays an acceptable level of reactivity to modify HSA at room temperature. Incubation of 0.5 mM HSA and a 10-fold molar excess of PIT-PEG at room temperature for 6 h at pH 9.2 generates hexaPEGylated HSA, i.e., 60% of PEG reagent is utilized and conjugated to HSA. The reaction of PEG-isothiocyanate with an amino group in albumin involves the nucleophilic attack of the amino group and the generation of a stable linkage, thiocarbamoyl linkage, between the PEG and the albumin. PIT-PEG reacts better at slightly alkaline pH, as more amino groups on proteins will be unprotonated. Nearly identical levels of PEGylation of HSA by PIT-PEG3K and PIT-PEG5K at both pH 6.5 and 9.2 reflect that the PEGylation reaction is correlated to the pH and the length of PEG chain of PIT-PEG has limited influence on the PEGylation reaction under the present reaction condition.

PEGylation of HSA with PIT-PEG proceeds very fast in beginning, and then slows down after 2 h reaction (Figure 5C). The PEGylation is expected to target the single α-amino group of amino-terminal Asp and the ε-amino groups of internal Lys residues. HSA has a single free SH group, which is a nucleophile. To establish whether the thiol has been conjugated with PEG, we measured the number of SH group on HSA (lyophilized powder, the thiol group was blocked to prevent dimerization) by reaction with 4-PDS (40), and it is 0.32. After hexaPEGylation, the number of SH groups on modified HSA is about 0.31. The results suggested that the PIT-PEG does not react with the thiol group on HSA. The observation that PEGylation of HSA proceeds very fast in the beginning and then slows down after 2 h reaction can be a reflection of one or both of these aspects: (i) the reaction rate slows down as the low pK_a amino groups have been modified; and (ii) PEG chains that are already conjugated to albumin molecules make it difficult to conjugate new PEG chains to the PEGylated albumin molecule. As a combination of these molecular aspects of the PEGylation of HSA with PIT-PEG, at pH 9.2 the hexaPEGylation of HSA appears to be complete under the present experimental condition. Increasing the concentration of PEG reagent from 20- to 40-fold molar excess of HSA has very little influence on the extent of PEGylation (Lanes 7 to 9, Figure 5A), which is consistent with the above conclusion. This suggests that the strong rule of steric factors is slowing down the PEGylation reaction on hexaPEGylation of proteins of molecular size of 65 KD. A similar conclusion has been made with regard to the hexaPEGylation of Hb (*41*).

The PEGylation studies of Hb exposed that the unique molecular properties could be engineered into proteins by the conjugation of PEG chains, namely, unusually enhanced hydrodynamic volume, high viscosity, and high COP (*12, 14, 15, 40–42*). These molecular properties, which are also the unique properties of plasma volume expanders that endow unique microvascular properties to the molecules, have been attributed to the nonhypertensive property of PEGylated Hb (*12*). Accordingly, we have considered the PEGylated albumin generated by extension arm facilitated protocol as plasma volume expanders; and the studies of both dodecaPEGylated and hexaPEGlated albumin with animal models have indeed established that PEGylated albumin is a new therapeutic protein with some unique potential as a plasma volume expander (*28, 29*). Therefore, we suggest that $(TCP\text{-}PEG5K)_6$-HSA is also potential therapeutic protein as a plasma volume expanders.

PEGylation of HSA has little influence on the secondary structure of HSA. On the other hand, the fluorescence of HSA (Trp 214) is influenced by PEGylation. The extent of quenching of fluorescence is dependent on the extent of PEGylation, that is, the number of copies of PEG chains conjugated, however, not on the size of PEG chain conjugated. Apparently, it is the phenyl linker that quenched the fluorescence of Trp-214 on HSA, and clearly suggests the proximity of the conjugated chains to the Trp reside.

In summary, we have designed and developed a novel PEGylation reagent, PEG-phenyl-isothiocyanate. The new PEG reagent displays a high stability against hydrolysis around neutral pH, and also displays a good level of chemical reactivity with protein amino groups.

ACKNOWLEDGMENT

We thank Dr. Parimala Nacharaju, Dr. Tao Hu, Dr. Dongxia Li, and Dr. Ananda U for critical review of this paper prior to submission. We would like to acknowledge the assistance of Dr. Sean Cahill for the help in ^{1}H NMR analysis. This work was supported by a grant-in-aid from the American Heart Association Heritage Affiliate 9951021T, the National Institutes of Health grants HL58247, HL71064, and U.S. Army grant PR023085.

LITERATURE CITED

(1) Harris, J. M., and Chess, R. B. (2003) Effect of PEGylation on pharmaceuticals. *Nat. Rev. Drug Discovery 2*, 214–221.
(2) Veronese, F. M., and Morpurgo, M. (1999) Bioconjugation in pharmaceutical chemistry. *I1 Farmaco 54*, 497–516.
(3) Abuchowski, A., Van Es, T., Palczuk, N. C., and Davis, F. F. (1977) Alteration of immunological properties of bovine serum by covalent attachment of polyethylene glycol. *J. Biol. Chem. 252*, 3578–3581.
(4) Abuchowski, A., McCoy, T. J. R., Palczuk, N. C., Van Es, T., and Davis, F. F. (1977) Effect of covalent attachment of polyethylene glycol on immunogenicity and circulating life of bovine liver catalase. *J. Biol. Chem. 252*, 3583–3586.
(5) Pasut, G., and Veronese, F. M. (2006) PEGylation of proteins as tailored chemistry for optimized bioconjugates. *Adv. Polym. Sci. 192*, 95–134.
(6) Hamidi, M., Azadi, A., and Rafiei, P. (2006) Pharmacokinetic consequences of PEGylation. *Drug Delivery 13*, 399–409.
(7) Kumar, S., Soppimath, K., and Nachaegari, S. (2006) Novel delivery technologies for protein and peptide therapeutics. *Curr. Pharm. Biotechnol. 7*, 261–276.

(8) Zalipsky, S. (1995) Chemistry of polyethylene glycol conjugates with biologically active molecules. *Adv. Drug Delivery Rev. 16*, 157–182.
(9) Roberts, M. J., Bentley, M. D., and Harris, J. M. (2002) Chemistry for peptide and protein PEGylation. *Adv. Drug Delivery Rev. 54*, 459–476.
(10) Greenwald, R. B., Pendri, A., Martinez, A., Gilbert, C., and Bradley, P. (1996) PEG thiazolidine-2-thione, a novel reagent for facile protein modification: conjugation of bovine hemoglobin. *Bioconjugate Chem. 7*, 638–641.
(11) http://www.sejinbio.co.kr/Catalogue/Nektar. Nektar Catalog 2005−2006, p 11.
(12) Acharya, S. A., Friedman, J., Manjula, B. N., Intaglietta, M., Tsai, A., Winslow, R., Malavalli, A., Vandegriff, K., and Smith, P. (2005) Enhanced molecular volume of conservatively pegylated Hb: (SP-PEG5K)6-HbA is non-hypertensive. *Artif/ Cells Blood Substit. Immobil. Biotechnol. 33*, 239–255.
(13) Nacharaju, P., Boctor, F. N., Manjula, B. N., and Acharya, S. A. (2005) Surface decoration of red blood cells with maleimidophenyl-polyethylene glycol facilitated by thiolation with iminothiolane: an approach to mask A, B, and D antigens to generate universal red blood cells. *Transfusion 45*, 374–383.
(14) Manjula, B. N., Tsai, A., Upadhya, R., Perumalsamy, K., Smith, P. k., Malavalli, A., Vandegriff, K. D., Winslow, R. M., Intaglietta, M., Prabhakaran, M., Friedman, J. M., and Acharya, A. S. (2003) Site-specific PEGylation of hemoglobin at Cys-93(β): Correlation between the colligative properties of the PEGylated protein and the length of the conjugated PEG chain. *Bioconjugate Chem. 14*, 464–472.
(15) Manjula, B. N., Tsai, A. G., Intaglietta, M., Tsai, C-H., Ho, C., Smith, P. K., Perumalsamy, K., Kanika, N. D., Friedman, J. M., and Acharya, A. S. (2005) Conjugation of multiple copies of polyethylene glycol to hemoglobin facilitated through thiolation: influence on hemoglobin structure and function. *Protein J. 24*, 133–146.
(16) Acharya, A. S., Manjula, B. N., Smith., P. Hemoglobin crosslinkers, US patent 585,484, December 17, 1996.
(17) Acharya, A. S., Manjula, B. N., Smith.,P. Hemoglobin crosslinkers, US patent 017,943, January 25, 2000.
(18) Stryer, L. (1995) Exploring proteins. In *Biochemistry*, 4th ed., Stryer, L. Ed.) pp 45−74, Chapter 3, W. H. Freeman and Company, New York.
(19) Heinrikson, R. L., and Meredith, S. C. (1984) Amino acid analysis by reverse-phase high-performance liquid chromatography: precolumn derivatization with phenylisothiocyanate. *Anal. Biochem. 136*, 65–74.
(20) Currell, D. L., Nguyen, D. M., Ng, S., and Hom, M. (1982) The effect of 4-isothiocyanatobenzoic acid on the oxygen-linked chloride binding sites in human hemoglobin: influence on the alkaline Bohr effect. *Biochem. Biophys. Res. Commun. 106*, 1325–1330.
(21) Bellelli, A., Ippoliti, R., Currell, D., Condo, S. G., Giardina, B., and Brunori, M. (1986) On the oxygen-linked anion-binding sites in human hemoglobin: functional properties of human hemoglobin reacted with 4-isothiocyanatobenzenesulphonic acid and its hybrids. *Eur. J. Biochem. 161*, 329–333.
(22) Manning, L. R., Morgan, S., Beavis, R. C., Chait, B. T., Manning, J. M., Hess, J. R., Cross, M., Currell, D. L., Marini, M. A., and Winslow, R. M. (1991) Preparation, properties, and plasma retention of human hemoglobin derivatives: comparison of uncrosslinked carboxymethylated hemoglobin with crosslinked tetrameric hemoglobin. *Proc. Natl. Acad. Sci. U.S.A. 88*, 3329–3333.
(23) Kavanaugh, M. P., Shih, D. T. B., and Jones, R. T. (1988) Affinity labeling of hemoglobin with 4,4′-diisothiocyanostilbene-2,2′-disulfonate: cocvalent cross-linking in the 2,3-disphosphoglycerate binding site. *Biochemistry 27*, 1804–1808.
(24) Hermanson, T., G. (1995) *The Chemistry of Reactive Group. Bioconjugate Techniques*, pp 138−168, Pierce Chemical Company, Rockford, IL.
(25) Smith, P. K. Activated Polyethylene Glycol Compounds, US Patent 6,737,524, May, 18, 2004.
(26) Assaly, R. A., Azizi, M., Kennedy, D. J., Amauro, C., Zaher, A., Houts, F. W., Habib, R. H., Shapiro, J. I., and Dignam, J. D. (2004) Plasma expansion by polyethylene-glycol-modified Albumin. *Clin. Sci. 107*, 263–272.
(27) Quinlan, G. J., Martin, G. S., and Evans, T. W. (2005) Albumin: biochemical properties and therapeutic potential. *Hepatology 41*, 1211–1219.
(28) Hangai-Hoger, N., Nachara, P., Manjula, B., Cabrales, P., Tsai, A., Acharya, S., and Intaglietta, M. (2006) Microvascular effects following treatment with polyethylene glycol-albumin in lipopolysaccharide-induced endotoxemia. *Crit. Care Med. 34*, 108–17.
(29) Cabrales, P., Nacharaju, P., Manjula, B. N., Tsai, A. G., Acharya, S. A., and Intalietta, M. (2005) Early difference in tissue pH and microvascular hemodynamics in hemorrhagic shock resuscitation using polyethylene glycol-albumin- and hydroxyethyl starch-based plasma expanders. *Shock 24*, 66–73.
(30) Zhang, Y., Cho, C., Posner, G. H., and Talalay, P. (1992) Spectrascopic quantitation of organic isothiocyanates by cyclocondensation with vicinal dithiols. *Anal. Biochem. 205*, 100–107.
(31) Manjula, B. N., Malavalli, A., Smith, P. K., Chan, N. L., Arnone, A., Friedman, J. M., and Acharya, A. S. (2000) Cys-93-betabeta-succinimidophenyl polyethylene glycol 2000 hemoglobin A. Intramolecular cross-bridging of hemoglobin outside the central cavity. *J. Biol. Chem. 275*, 5527–5534.
(32) Bradford, M. (1976) A rapid and sensitive method for quantitation of microgram quantities of protein utilizing the principle of protein-dye-binding. *Anal. Biochem. 72*, 248–254.
(33) Jackson, C. J., Charlton, J. L., Kuzminski, K., Lang, G. M., and Sehon, A. H. (1987) Synthesis, isolation, and characterization of conjugates of ovalbumin with monomethoxypolyethylene glycol using cyanuric chloride as the coupling agent. *Anal. Biochem. 165*, 114–127.
(34) Dust, J. M., Fang, Z., and Harris, J. M. (1990) Proton NMR characterization of poly(ethylene glycols) and derivatives. *Macromolecules 23*, 3742–3746.
(35) Satchell, D. P. N., and Satchell, R. S. (1991) The kinetics and mechanism of the hydrolysis of *p*-nitrophenyl isothiocyanate promoted by soft metal ions. *J. Chem. Soc., Perkin Trans. 2*, 303–306.
(36) Fee, C. J., and Van Alstine, J. M. (2004) Prediction of the viscosity radius and the size exclusion chromatography behavior of PEGylated proteins. *Bioconjugate Chem. 15*, 1304–1313.
(37) Trynda-Lemiesz, L. (2004) Paclitaxel-HSA interaction. Binding sites on HSA molecule. *Bioorg. Med. Chem. 12*, 3269–3275.
(38) Chadborn, N., Bryant, J., Bain, A. J., and O'Shea, P. (1999) Ligand-dependent conformational equilibra of setum albumin revealed by tryptophan fluorescence quenching. *Biophys. J. 76*, 2198–2207.
(39) Ananda, K., Nacharaju, P., Smith, P. K., Acharya, S. A., and Manjula, B. N. (2008) Analysis of functionalization of methoxy-PEG as maleimide-PEG. *Anal. Biochem. 374*, 231–242.
(40) Hu, T., Prabhakaran, M., Acharya, S. A., and Manjula, B. N. (2005) Influence of the chemistry of conjugation of poly(ethylene glycol) to Hb on the oxygen-binding and solution properties of the PEG-Hb conjugate. *Biochem. J. 392*, 555–564.
(41) Li, D., Manjula, B. N., and Acharya, A. S. (2006) Extension arm facilitated PEGylation of hemoglobin: correlation of the properties with the extent of PEGylation. *Protein J. 25*, 263–274.
(42) Hu, T., Manjula, B., Brenowitz, M., and Acharya, S. (2007) Influence of intramolecular cross-links on the molecular, structural and functional properties of PEGylated haemoglobin. *Biochem. J. 402*, 143–151.

BC7003878

Peptide−Oligonucleotide Conjugates Form Stable and Selective Complexes with Antibody and DNA

Tuula Tennilä, Maxim Antopolsky, Alex Azhayev, and Elena Azhayeva*

Department of Pharmaceutical Chemistry, University of Kuopio, FIN-70211 Kuopio, Finland. Received December 12, 2007; Revised Manuscript Received April 9, 2008

The present work demonstrates that the relatively low molecular weight synthetic peptide−oligonucleotide conjugates are capable of stable and selective three-component complex formation with complementary 72−100mer DNA oligonucleotides and a cardiac troponin I monoclonal antibody. Neither the Watson−Crick-type interaction between peptide−oligonucleotide conjugate and DNA nor the conjugate−antibody interaction dramatically hampers the other. These interactions remain selective and specific in the presence of several other conjugates not specific to cardiac troponin I monoclonal antibody as well as in the presence of control 100mer DNA oligonucleotides. The data herein demonstrate the feasibility of the synthetic peptide−oligonucleotide conjugates as convenient molecular tools, e.g., for antibody epitope mapping.

INTRODUCTION

Applications for semisynthetic nucleic acid−protein conjugates (NAPCs) (*1–4*) in array technology (*5, 6*) and nanobiotechnology (*7, 8*) have received increasing interest. Moreover, immuno-PCR (*9–11*) and even magneto-immuno-PCR (*12*) employing NAPCs are established and substantially developed.

Methods for the covalent synthesis of peptide−oligonucleotide conjugates (POCs) have drawn a considerable amount of attention during the past 20 years (*13–17*). Undoubtedly, low molecular weight POCs are easier to obtain (*13–17*) and properly characterize (*18*) by chemical methods than high molecular weight NAPCs.

Nowadays, linear POCs where the N- or C-terminus of a peptide is covalently linked to either 3′- or 5′-terminus of an oligonucleotide are available commercially on virtually any scale from Thermo Scientific (www.thermo.com/biopolymers). Moreover, the oligonucleotide moiety of these custom-synthesized oligomers may incorporate modified nucleosides as well as additional dye modification (fluorescein, Cy3, etc.). In other words, it seems fair to claim that at least small libraries of POCs are easily available for a variety of applications as molecular tools.

Limited data are currently available on the applicability of POCs as molecular tools for the life sciences. To our knowledge, the only publication closely related to the subject of this investigation was the demonstration that oligodeoxyribonucleotides, PNA−peptide conjugates (PPCs), and antibodies form stable ternary complexes that can be used for quantification of antibodies (*19*).

Recently, a high-complexity, multiplexed solution-phase assay for profiling protease activity on microarrays was reported (*20*). In this assay, the sets of peptide sequences that serve as protease substrates were conjugated to oligonucleotide sequences (from 100 to 1000 POCs in a set) complementary to the oligo tags on randomly assembled bead arrays. The assay was successfully employed for the measurement of protease activity in complex samples.

* To whom correspondence should be addressed. Department of Pharmaceutical Chemistry, University of Kuopio, Harjulantie 1A, FIN-70211 Kuopio, Finland. E-mail: Elena.Azhayeva@uku.fi. Tel: +358-17-16-3128.

POC libraries may also find use for epitope mapping, employing immuno-PCR. Obviously, it is possible to construct POC libraries where every oligonucleotide unequivocally corresponds to certain peptide. With the help of such libraries, the task of the epitope mapping can be thus translated into oligonucleotide sequence estimation provided that the antibody−POC−DNA triple complex is strong and specific enough.

The objective of this work was to demonstrate the feasibility of a predesigned complex formation, based on simultaneous antigen−antibody and Watson−Crick interactions. We investigated DNA−POC−mAb complexes involving two different DNA templates capable of binding one or four POCs. In an attempt to study possible applications of the complexes mentioned above, we constructed a very simple model system, comprising a small library of several POCs, a small library of longer DNA oligomers, and an immobilized mAb. The small POC library incorporated a single POC, bearing a peptide sequence specific to the solid phase bound mAb, while the POCs of the control library contained only nonspecific peptides. The aim of the experiment was to show that incubation of the POC library with the support-bound mAb and DNA library results in the formation of a specific triple complex with the single antibody-specific POC and the single DNA. This DNA (and the oligonucleotide part of POC accordingly) sequence was estimated after PCR amplification of the bound oligonucleotide. In the control case, no amplification of the longer DNA sequence was observed, since no POC was capable of binding the antibody. In our opinion, this simple testing revealed the ability of POCs to simultaneously display efficient and selective Watson−Crick base-pairing and efficient and selective epitope−antibody recognition. Our experiments, described below, may serve as a basis for future development of more complex essays, exploiting the three-component complex formation.

EXPERIMENTAL PROCEDURES

General Procedures. Cardiac Troponin I monoclonal antibody, clone 19C7 (**mAb1**), Sepharose-bound **mAb1**, and Sepharose-bound antibody to precursor of brain natriuretic peptide (**mAb2**) were from HyTest. γ-^{32}P ATP and γ-^{33}P ATP was from Perkin-Elmer; polynucleotide kinase and CycleReader DNA Sequencing Kit were from Fermentas. Oligonucleotides were assembled on the Biosset ASM 800 synthesizer, using

10.1021/bc700457y CCC: $40.75 © 2008 American Chemical Society
Published on Web 06/05/2008

reagents from Glen Research. Peptide−oligonucleotide conjugates were prepared and characterized as reported earlier (*14*, *15*, *18*). PAGE was run on a Hoefer SE600 unit. PCR experiments were conducted on a BioRad iCycler. Manual DNA sequencing was performed on a Pharmacia Biotech Macrophor electrophoresis unit with a thermostatic plate.

Labeling of the Oligonucleotides and POCs. Mixtures of 250 pmol of the oligonucleotide or **POC1**, 1 μM ATP, 1 mM cystamine, 5−10 units of polynucleotide kinase, 70 μCi of γ-^{32}P ATP in buffer, containing 10 mM Tris-acetate, 10 mM magnesium acetate, and 50 mM potassium acetate, were incubated at 37 °C for 30−60 min, heated 5 min at 65 °C, centrifuged, and finally kept on ice.

Template T72-POC1-mAb1 Complexes. Complex formation was performed in two steps. In the first step, 100−130 pmol of the oligonucleotide **T72** and 400−530 pmol of **POC1**, 2.5 pmol of 5′-^{32}P-**POC1**, or 5′-^{32}P- **T72** were mixed. Samples were annealed in buffer, containing 10 mM Tris, 15 mM $MgCl_2$, and 150 mM NaCl, pH 7.5, by heating to 85 °C and slowly decreasing the temperature to 25 °C. The resulting samples were stored at 4 °C. In the second step, **mAb1** was incubated with template−conjugate complexes at different **mAb1**/complex ratios. Each sample usually contained 128 pmol of **T72**, 512 pmol of **POC1**, and **mAb1** at 2:1, 1:1, 0.5:1, and 0.1:1 ratios. Samples were incubated for 30−60 min at room temperature and finally analyzed by nondenaturing 5−20% (or 3−17%) gradient PAGE. The gel was autoradiographed and subsequently stained with Coomassie Blue.

Template T75-POC3-mAb1 Complexes. Complex formation was performed essentially as described above. In the case of **POC3**, the peptide moiety was linked to the 5′-terminus of oligonucleotide; only the 5′-^{32}P-**T75** was employed in the present experiment.

Complex Formation on the Sepharose-Bound Cardiac Troponin I mAb. Sets of samples, containing 1 μM of oligonucleotide−peptide conjugates and DNA template **T100a**, as well as different control mixtures with control templates in the PCR buffer, were prepared for annealing. After heating for 3 min at 87 °C, the samples were left for 6 h in a thermoblock and then transferred to 4 °C. Several small columns were packed with 50 μL of Sepharose-bound **mAb1**, washed with 2 × 900 μL of 0.1 M glycine buffer, and then equilibrated with 3 × 900 μL of PCR buffer (10 mM Tris−HCl, 50 mM KCl, 3 mM $MgCl_2$, pH 8.3). 100 μL of annealed samples were applied and incubated with Sepharose for 2 h at room temperature (samples were shaken every 0.5 h). Control Sepharose-bound **mAb2**was treated in the same way. After incubation, the unbound template−conjugate complexes were washed off with 2 × 900 μL of the PCR buffer, then with 900 μL of PCR buffer containing 0.3 M NaCl, and finally with 4 × 900 μL of PCR buffer. 70 μL of PCR buffer was added and 30 μL Sepharose suspension containing antibody/conjugate/template complexes was transferred to Eppendorf tubes and taken for PCR. **Pr1** and **Pr2** were used for the initial amplification of the complex-bound template. The PCR was run in touchdown mode, at an initial annealing temperature of 50 °C, at 15 cycles with 1 °C decrease per cycle, T_{amp} 72 °C, and 25 additional cycles with T_{ann} 36 °C, T_{amp} 72 °C. After PCR amplification, samples were analyzed by 15% PAGE (ethidium bromide staining). The final verification of amplified product was performed by sequencing. **Pr1** or **Pr3** was labeled with γ-^{33}P ATP and polynucleotide kinase, and subsequently used in conjunction with the CycleReader DNA Sequencing Kit, where 8 μL of amplified product was used as a template in the sequencing mixture. The reaction was run as follows: 94 °C for 3 min; 35 cycles at 94 °C for 30 s, 50 °C for 30 s, and 72 °C for 1 min. Samples were applied to the sequencing gel, which was autoradiographed after electrophoresis. A similar experiment was conducted with the consequent application of conjugates and templates. Initially, 1 μM conjugates or mixtures of conjugates were applied to Sepharose-bound **mAb1** and incubated at room temperature for 1−1.5 h. After incubation, the columns were washed with 2 × 900 μL of PCR buffer, then with 900 μL of PCR buffer containing 0.3 M NaCl, and finally with 4 × 900 μL of PCR buffer. Mixtures containing 1 μM oligonucleotides **T100a**−**T100e** or their mixtures were applied, incubated for 2−3 h, and washed with 2 × 900 μL of PCR buffer, then with 900 μL of PCR buffer containing 0.3 M NaCl, and finally with 4 × 900 μL of PCR buffer. Samples were subjected to PCR as previously described herein and sequenced.

RESULTS AND DISCUSSION

Three-Component Complex formation. Ketomäki and Lönnberg (*19*) have demonstrated applicability of ternary complexes formed by oligodeoxyribonucleotides, PPCs, and mAbs for quantification of antibodies. In their study, they employed conjugates of PNAs and peptides rather than POCs and demonstrated the possibility of quantification of antibodies. Although this approach seems to be undoubtedly attractive, in some cases, PPCs may display certain disadvantage, when applied for broader use in diagnostics. Noteworthy are the higher costs associated with PNA synthesis and the potentially poor solubility of PNAs (*21*, *22*) and some PPCs in aqueous solutions (when compared to highly soluble POCs). It seems also important to consider a potential hydrophobic interaction of some PNA moieties with certain peptides or stabilization of PNA−DNA duplex formation by polycationic peptide moieties of some PPCs (*23*, *24*). Evidently, no data are available on the influence of these factors upon the selectivity and stability of ternary complexes formed by oligodeoxyribonucleotides, PPCs, and antibodies. In principle, however, these interactions may hamper selective antibody−epitope recognition.

Likewise, no knowledge is available on the selectivity and stability of three-component complexes formed by oligodeoxyribonucleotides, POCs, and antibodies. According to Harrison and Balasubramanian (*25*), the polycationic peptide moiety of POC is able to considerably stabilize duplex formation by preferable association with the single-stranded overhand of 16mer oligonucleotide. This phenomenon in principle may seriously affect the antibody−epitope interaction and, as a result, oligodeoxyribonucleotide, POC, and antibody ternary complex formation.

Our initial objective was to demonstrate the feasibility of a predesigned complex formation, based on simultaneous antigen−antibody and Watson−Crick interactions. Thus, the components of the complex included **POC1** (Figure 1), 72mer DNA oligonucleotide **T-72**, and **mAb1**. **POC1** contained peptide sequence **P1**, capable of specific and selective interaction with **mAb1** and a 14mer oligonucleotide sequence (complementary to the 72mer DNA oligonucleotide **T-72**). **T-72** contained four identical short stretches for interaction with conjugate **POC1** (Figure 2A). Complexes were preformed in two steps as discussed below.

In the first step, Watson−Crick complexes of **T72** and **POC1** were formed, with a molar ratio of **POC1** to **T72** of 4:1, in accordance with the number of complementary stretches on the 72mer. Either **POC1** or oligomer **T72** was radioactively 5′-^{32}P-labeled. In the second step, **mAb1** was incubated with the previously formed template−conjugate duplexes at antibody−Watson−Crick complex ratios of 2:1, 1:1, 0.5:1, and 0.1:1. Theoretically, in such a case, each antibody may bind up to two POCs. A maximum of four **POC1** molecules may bind to the 72-base oligonucleotide template. In other words, a variety of multicomponent complexes and even supramolecular struc-

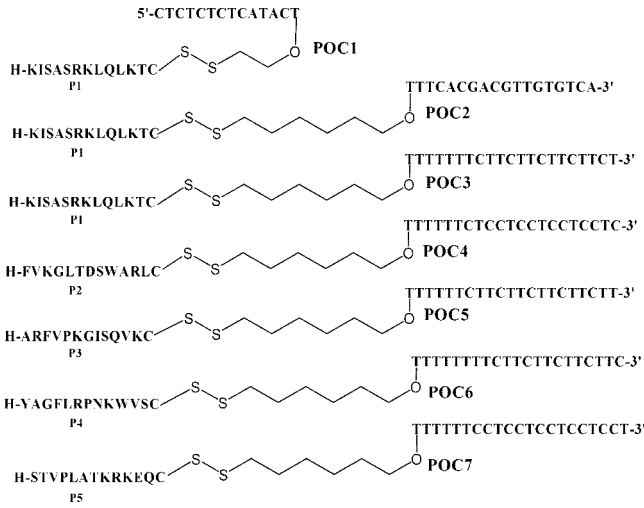

Figure 1. Structures of **POC1**−**POC7**, employed in the present study. Peptide sequences are abbreviated as **P1**, **P2**, **P3**, **P4**, and **P5**, correspondingly.

tures may exist in POC−template−antibody mixture. One of these three-component complexes, incorporating only a single template molecule, with up to four POC molecules and up to four antibodies is shown in Figure 2A.

Thus, the resulting complexes from this experiment were analyzed by a nondenaturing gradient (3−17%) PAGE. After electrophoresis, the gel was autoradiographed and subsequently stained with Coomassie Blue. Figure 3 was obtained by overlaying two images of this PAGE.

In Figure 3, it can be seen that the **POC1** demonstrates a distinct interaction with **mAb1** (Figure 3, lanes 9−11) and the resulting complex migrates some distance further on the gel, probably due to the increased total negative charge, whereas no interactions of **mAb1** and 5′-**T72** template are evident (Figure 3, lanes 12−14). Lanes 3−5 (**mAb1**-**T72**-5′-^{32}P-**POC1** mixtures) as well as lanes 6−8 (**mAb1**−5′-^{32}P-**T72**−**POC1** mixtures) characterize the mixture of two-component and three-component complexes. The presence of the radioactive bands (Figure 3, lanes 3, 4, 5 and 6, 7, 8) close to or coinciding with two-component antibody−conjugate complexes (Figure 3, lanes 9, 10, 11) in the case of mixtures containing labeled **T72** template (Figure 3, lanes 6, 7, 8) but not the labeled conjugate (Figure 3, lanes 3, 4, 5) can only be explained by the formation of the three-component complexes. The mobility rates of **mAb1**-**T72**-**POC1** complexes are influenced by both the large molecular mass of the antibody molecule (probably one in this case) and a significant combined negative charge of the 72-mer template and the 14-mer conjugate. It seems rather difficult to precisely characterize the exact molecular composition of the described three-component complexes, due to their intricate behavior under conditions of electrophoresis.

As follows from Figure 3, lane 5, some slower-moving radioactive structures were observed to migrate similarly to **mAb1** alone, or even slower (red arrow). These complexes may be attributed to some higher degree of complexity for the three-component structures. One can also notice certain associates not entering the gel, but which were stained by Coomassie Blue and incorporated the radioactive label (green arrow). At higher **mAb1** concentrations (Figure 3, lanes 3, 4 and 7, 8), the three-component structures having a low degree of complexity (blue arrow) disappear. In parallel to that, the amount of radioactive structures migrating on the gel similarly to the antibody alone (red arrow), but more slowly than **mAb1**-(5′-^{32}P-**POC1**) complex (blue arrow), distinctly increases. In addition, the amount of material both radioactive and stained by Coomassie Blue and not entering the gel (green arrow) also increases. We are tempted to speculate that the data discussed above points to the presence of multiple types of three-component structures of diverse complexity. As for the non-entering components on the gel, both radioactive and stained with Coomassie Blue, these may correspond to multicomponent supramolecular species that exist in **POC1**−**T72**-**mAb1** mixtures.

In a similar experiment, the 75mer DNA oligonucleotide **T75** incorporated only one region, complementary to the oligonucleotide moiety of **POC2** (Figure 2B). Apparently, a somewhat simpler three-component structure may be expected in the case of the **POC2**-**T75** complex interaction with **mAb1** (Figure 2B).

The resulting complexes from this experiment were analyzed by a nondenaturing gradient (3−17%) PAGE (Figure 4), as described above. Again, the presence of radioactivity at the **mAb1**-**POC2** two-component associate position (Figure 4, lanes 2, 3, 4; blue arrow) supports our interpretation of these bands as being a mixture of two- and three-component complexes. It is assumed that the component composition of complexes in these bands is characterized by the ratio 1:2:2 (**mAb1**-**POC2**-**T75**). The bands indicated by the red arrow in Figure 4 may be interpreted accordingly as the three-component complexes with the ratio composition of 1:1:1 (**mAb1**-**POC2**-**T75**).

The detailed study of the three-component complex stoichiometry was not an aim of the present work. In fact, the feasibility of a stable selective DNA−POC−antibody complex formation was the primary focus, as a basis for the further development of practical applications. Both experiments described above, however interesting, do not give any clear-cut answer to the main question of this work—i.e., are the POC−DNA −antibody complexes stable and selective enough to be employed as reliable molecular tools?

Indeed, from a thorough inspection of numerous gradient nondenaturing PAGEs, similar to those given in Figures 3 and 4, it became obvious that the presence or absence of radioactive and Coomassie Blue stained spots corresponded to various types of three-component complexes (simpler triple complexes, complexes of a higher order, and possibly even supramolecular structures) were strongly dependent on the exact conditions while conducting the electrophoresis. Therefore, it seemed apparent that certain additional experiments were absolutely imperative to understand if the stability and selectivity of POC−DNA−antibody complexes would be suitable for development of a simple model system for the immuno-PCR-based antibody epitope mapping.

Complex Formation on the Sepharose-Bound Cardiac Troponin I mAb. For the additional experiments, a 100mer template **T100a** was synthesized to incorporate three regions that were complementary to three different peptide−oligonucleotide conjugates (**POC1**−**POC3**), and bearing peptide moiety **P1** (Figure 5). The main difference among these peptides was that, whereas the **POC1** was a 3′-conjugate and incorporated a shorter disulfide linker, bridging the peptide **P1** directly with the oligonucleotide sequence complementary to template **T100a**, **POC2** and **POC3** were 5′-conjugates and incorporated a longer disulfide linker, bridging the peptide **P1** with the oligonucleotide sequence complementary to template **T100a** *via* two (**POC2**) or five (**POC3**) noncomplementary thymidine residues. By employing these three different conjugates, we hoped to understand whether the orientation of conjugation and the linker size would noticeably affect our results.

The complementary sequences were designed in the central region of the template in order to enable the sequencing of this region at the final stage of the experiment. For this purpose, **T100a** incorporated regions, complementary to initial PCR (**Pr1**, **Pr2**) and sequencing (**Pr1**, **Pr3**) primers (Figure 6A). In addition, four 100mer control templates (**T100b**−**T100e**) were synthesized. These control templates contained the same PCR

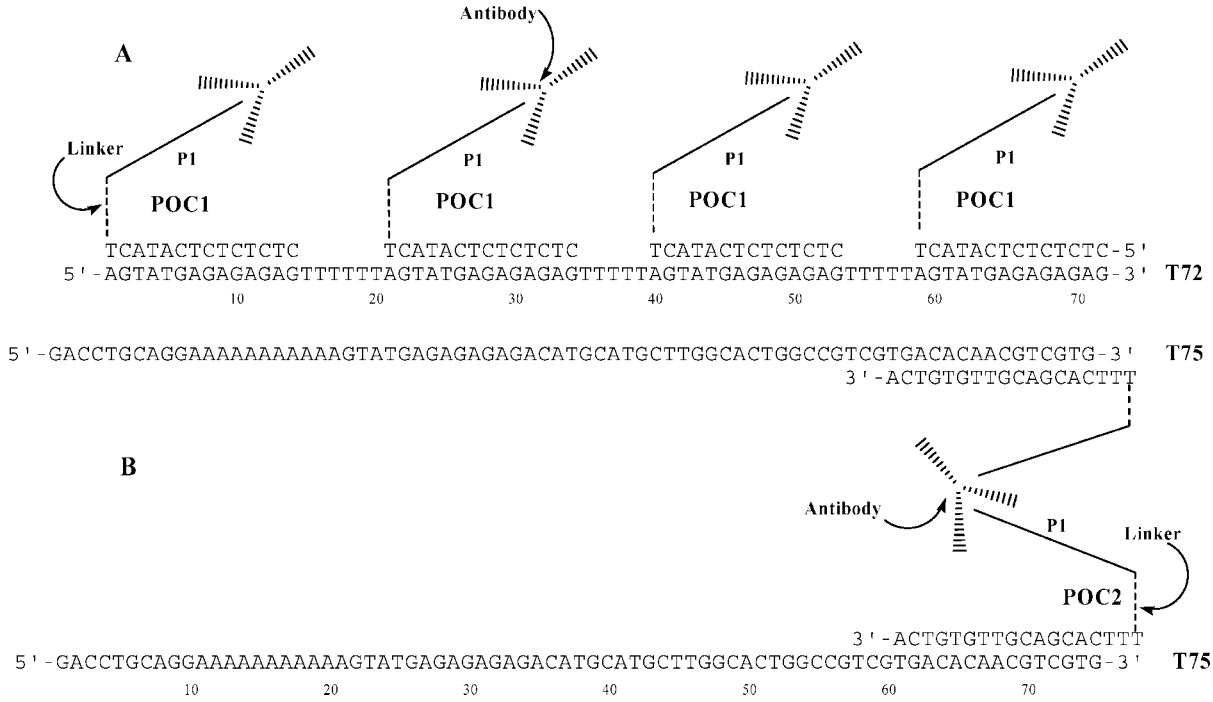

Figure 2. (A) Three-component complex, incorporating only a single template **T72** molecule, four **POC1** molecules, and four antibodies **mAb1**. (B) Three-component complex, incorporating only a single antibody **mAb1**, two template **T75** molecules, and two **POC2** molecules.

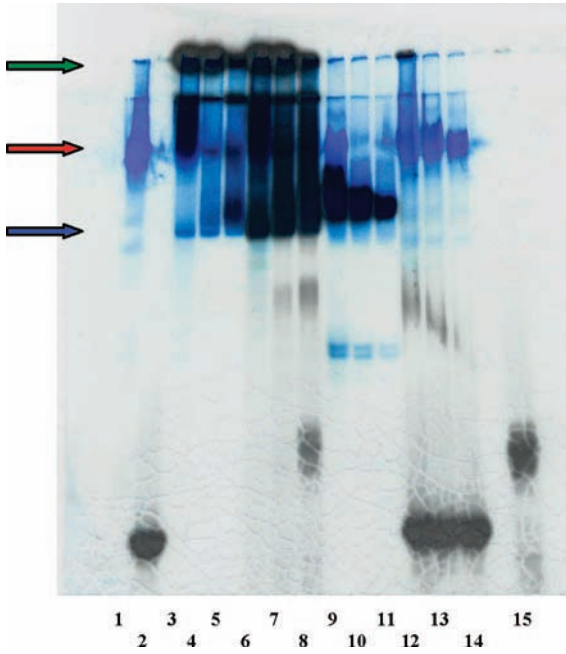

Figure 3. Overlay of two images of autoradiographed and Coomassie Blue stained 3−17% gradient nondenaturing PAGEs of the **T72-POC1-mAb1** three-component complexes. Controls: Lane 1,**mAb1**; Lane 2, 5′-^{32}P-**T72**; Lanes 12−14, **mAb1** and 5′-^{32}P-**T72** mixtures (2:1; 1:1; 0.5:1 correspondingly). Two-component complexes: Lane 15, **T72**-5′-^{32}P-**POC1** complex (1:4); Lanes 9−11, **mAb1**-5′-^{32}P-**POC1** complexes (2:1; 1:1; 0.5:1 correspondingly). Three-component complexes: Lanes 3−5, **mAb1**-(**T72**-5′-^{32}P-**POC1**) complexes (2:1; 1:1; 0.5:1 correspondingly); Lanes 6−8, **mAb1**-(5′-^{32}P-**T72**−**POC1**) complexes (2:1; 1:1; 0.5:1 correspondingly). Blue arrow: three-component low-complexity structures. Red arrow: three-component higher-complexity structures. Green arrow: multicomponent associates not entering the gel.

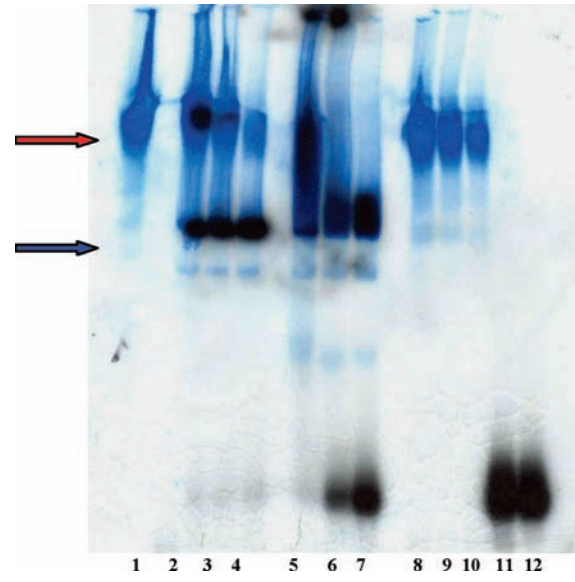

Figure 4. Overlay of two images of autoradiographed and Coomassie Blue stained 3−17% gradient nondenaturing PAGE of the **T75-POC2-mAb1** three-component complexes. Controls: Lane 1, **mAb1**; Lanes 8−10, **mAb1** and 5′-^{32}P-**T75** mixtures (2:1; 1:1; 0.5:1 correspondingly). Two-component complexes: Lanes 11, 12, 5′-^{32}P-**T75-POC2** complex (1:1 and 1:4 correspondingly). Three-component complexes: Lanes 2−4, **mAb1**-5′-^{32}P-**T75**−**POC2** complexes (2:1:1; 1:1:1; 0.5:1:1 correspondingly); Lanes 5−7, **mAb1**-5′-^{32}P-**T75**−**POC2** complexes (2:1:4; 1:1:4; 0.5:1:4 correspondingly). Blue arrow: three-component low-complexity structures. Red arrow: three-component higher-complexity structures.

and sequencing primer regions as **T100a**, but no complementary regions for the POCs (Figure 6B). Four control conjugates (**POC4**−**POC7**, Figure 1) were also prepared that incorporated 13mer peptide moieties (**P2**, **P3**, **P4**, **P5**), which displayed no affinity to **mAb1**, and the oligonucleotide sequences were noncomplementary to **T100a** (Figures 1, 5).

Sets of samples containing POCs, template **T100a**, as well as different control mixtures with control templates in PCR buffer were prepared, annealed, and applied onto the **mAb1**-Sepharose columns. The control **mAb2**-Sepharose columns were treated in the same way. After 2 h incubation at room

3′-GTTGGTATGGCTCGATGAGATATTCATTTTC**GAGAGAGAGTATGA**GTGCTGCAACACAGTTAGAAGAAGAAGAAGATGACATCTGATCGAATCCCGCAAA-5′ **T100a**
5′-**CTCTCTCTCATACT-P1**
POC1

3′-GTTGGTATGGCTCGATGAGATATTCATTTTCGAGAGAGAGTATGAGTGCTGCAACACAGTT**AGAAGAAGAAGAAGA**TGACATCTGATCGAATCCCGCAAA-5′ **T100a**
P1-TTTTT**TCTTCTTCTTCTTCT-3′**
POC3

3′-GTTGGTATGGCTCGATGAGATATTCATTTTCGAGAGAGAGTATG**AGTGCTGCAACACAGT**TAGAAGAAGAAGAAGATGACATCTGATCGAATCCCGCAAA-5′ **T100a**
P1-TT**TCACGACGTTGTGTCA-3′**
POC2

Figure 5. Template **T100a** incorporating three regions complementary to **POC1**, **POC2**, or **POC3** (**POC1**, **POC2**, and **POC3** and complementary stretches of **T100a** are in bold).

A

Pr1 3′-**TCTCATCGAGCCATACCA**-5′
5′-AAACGCCCTAAGCTAGTCTACAGTAGAAGAAGAAGAAGATTGACACAACGTCGTGAGTATGAGAGAGAGCTTTTACTTATA**GAGTAGCTCGGTATGGT**TG-3′ **T100a**
3′-**TTGCGGGATTCGATCAGA**TGTCATCTTCTTCTTCTTCTAACTGTGTTGCAGCACTCATACTCTCTCTCGAAAATGAATATCTCATCGAGCCATACCA-5′
5′-**CTAAGCTAG**-3′ **Pr2**
5′-**AACGCCCTAAGCTAGTCT**-3′ **Pr3**

B

5′-AAACGCCCTAAGCTAGTCTACAGTAGAAGAAGAAGAAGATTGACACAACGTCGTGAGTATGAGAGAGAGCTTTTACTTATAGAGTAGCTCGGTATGGTTG-3′ **T100a**

5′-AAACGCCCTAAGCTAGTCTATTCACGGGGATTGGCTCAAGAGGAGGAGGAGGAGTAAACCAATGGCTGAATCCTACTTATAGAGTAGCTCGGTATGGTTG-3′ **T100b**

5′-AAACGCCCTAAGCTAGTCTATTCAAAACCAATGGCTGAAGAAGAAGAAGAACAAACCTGGTATCCATTTATTTTACTTATAGAGTAGCTCGGTATGGTTG-3′ **T100c**

5′-AAACGCCCTAAGCTAGTCTATTCAAACCTGGTATCCATTTTAAAGAAGAAGAAGAAGGGATTGGCTCAAATCCTACTTATAGAGTAGCTCGGTATGGTTG-3′ **T100d**

5′-AAACGCCCTAAGCTAGTCTATTCACGGGGAGGAGGAGGAGGAGGGATTGGCTCAAAAACCAATGGCTGAATCCTACTTATAGAGTAGCTCGGTATGGTTG-3′ **T100e**

Figure 6. (A) Template **T100a** and complementary strand, incorporating stretches for initial amplification primers **Pr1** and **Pr2** and sequencing primers **Pr1** and **Pr3**. (B) Control 100mer templates **T100b**, **T100c**, **T100d**, **T100e**.

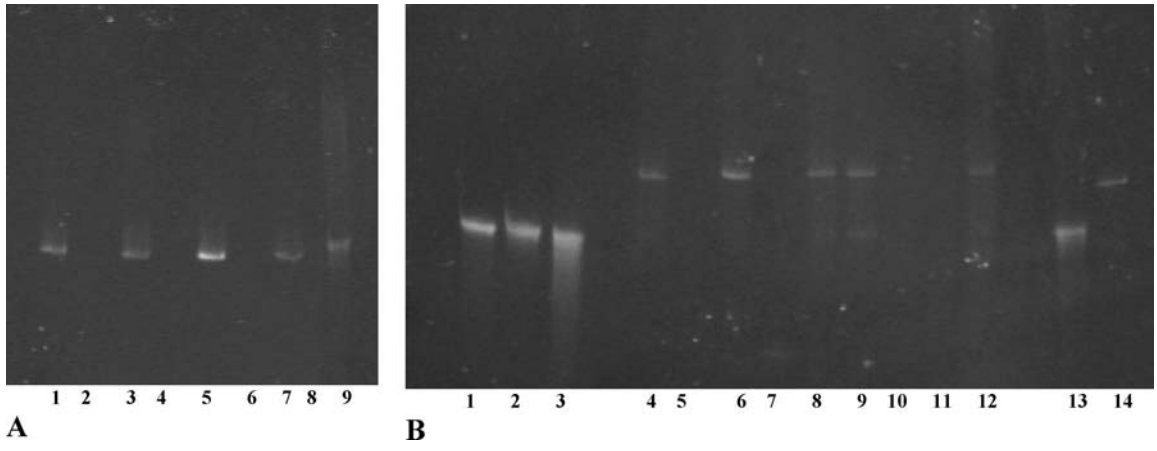

Figure 7. PCR products, obtained after selective three-component complex formation on Sepharose-bound **T100a**. PCR products, resulting from selective interaction of 100mer matrix/POC Watson−Crick complexes and Sepharose-bound **mAb1**. Watson−Crick complexes of 100mer matrixes and POCs were formed by annealing, applied to the columns, containing Sepharose-bound **mAb1**. Columns were washed, and Sepharose with bound complexes was subjected to PCR (see Experimental Procedures). (A) Standard: Lane 9, template **T100a**. PCR products resulting from annealed mixtures, containing: Lane 1, 1 μM of **POC3** and 1 μM of **T100a**; Lane 2, 1 μM of **POC3**; Lane 3, 1 μM of **POC2** and 1 μM of **T100a**; Lane 4, 1 μM **POC2**; Lane 5, 1 μM **POC1** and 1 μM of **T100a**; Lane 6, 1 μM of **POC1**; Lane 7, 1 μM of each-**POC3**, control conjugates **POC4**−**POC7** with 1 μM of **T100a**; Lane 8, 1 μM of each - **POC3**, control conjugates **POC4**−**POC7** without template. (B) Standards: Lane 1, control template **T100b**; Lane 2, control **T100c**; Lane 3, control **T100d**; Lane 13, **T100a**; Lane 14, control PCR with **T100a** as template. PCR products resulting from annealed mixtures, containing: Lane 4, 1 μM of **POC3** and 1 μM of **T100a**; Lane 5, 1 μM of **POC3**; Lane 6, 1 μM of **POC2** and 1 μM of **T100a**; Lane 7, 1 μM **POC2**; Lane 8, 1 μM of **POC3** and 1 μM of each **T100a**, **T100b**, **T100c**, **T100d**, **T100e**; Lane 9, 1 μM of each **POC1**, **POC2**, **POC3** with 1 μM of each **T100a**, **T100b**, **T100c**, **T100d**, **T100e**; Lane 10, 1 μM of each control conjugates **POC4**−**POC7** and 1 μM of **T100a**; Lane 11, 1 μM of each control conjugates **POC4**−**POC7** and 1 μM of each **T100b**, **T100c**, **T100d**, **T100e**; Lane 12, 1 μM of each **POC2**, control conjugates **POC4**−**POC7** and 1 μM of each **T100a**, **T100b**, **T100c**, **T100d**, **T100e**. All PCR mixtures contained 30 μL of Sepharose suspension, 0.1 μM primers, and 10 μM dNTPs. PCR products in part B are double-stranded, as they were not efficiently denatured during electrophoresis, which explains higher band position on the gel.

temperature, the samples of Sepharose were thoroughly washed, equilibrated with the PCR buffer, suspended in the PCR buffer, and taken for PCR, using **Pr1** and **Pr2** (Figure 6A) as initial amplification primers. Several sets of primers with different melting temperatures were previously tested in order to optimize the selectivity of PCR.

The results of the PCR experiments are shown in Figure 7A,B. Neither template (not shown) nor conjugate alone treated samples (Figure 7A, lanes 2, 4, 6; Figure 7B, lanes 5, 7), nor any samples with control **mAb2**-Sepharose (data not shown) resulted in any detectable PCR product. The mixture of control POCs (**POC4**−**POC7**) annealed with (a) control templates

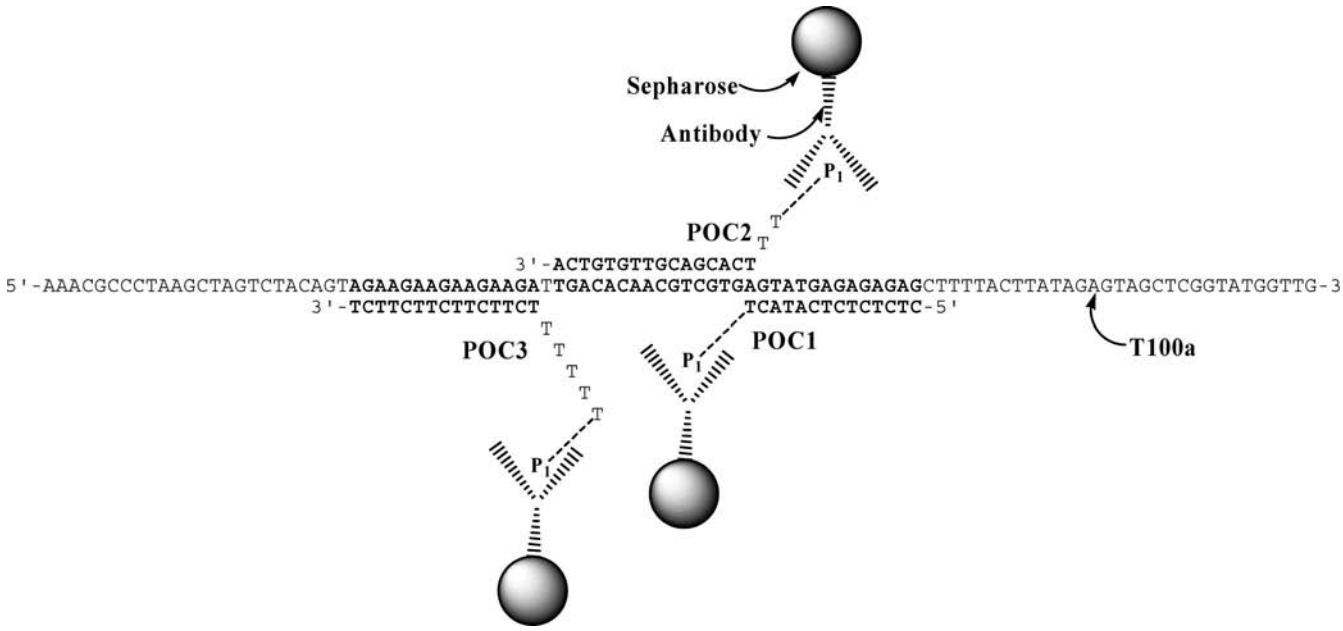

Figure 8. Three-component complex, incorporating Sepharose-bound antibody **mAb1**, template **T100a** and **POC1**, **POC2**, or **POC3**.

T100b−**T100e** (Figure 7B, lane 11) and (b) template **T100a** (Figure 7B, lane 10) also did not result in any detectable PCR product. All three conjugates were studied individually: **POC3** (Figure 7A, lane 1; Figure 7B, lane 4), **POC2** (Figure 7A, lane 3; Figure 7B, lane 6), and **POC1** (Figure 7A, lane 5), or in the mixture (Figure 7A, lane 7; Figure 7B, lanes 8, 9), and were able to form the three-component complexes with template **T100a** and Sepharose-bound **mAb1**, thus resulting in the 100-mer PCR product. From the mixture of various **POC1**−**POC7**, only those incorporating **mAb1** specific peptide **P1** were selectively binding to the complex (compared with no product in Figure 7B, lines 10, 11).

The final verification of the amplified product was performed by sequencing, using either ^{33}P-**Pr3** and **Pr1** or ^{33}P-**Pr1** and **Pr3** primers and CycleReader DNA Sequencing Kit (Fermentas). Results obtained confirmed that the product amplified from the three-component Sepharose-bound **mAb1**/**POC1**, **POC2**, or **POC3**/template DNA complex had a sequence of **T100a** (Supporting Information).

Additionally, the same experiment was conducted with the consequent application of conjugates and templates. Initially, individual conjugates **POC1**, **POC2**, or **POC3** or mixtures of POCs (**POC1**−**POC7**) were applied to the Sepharose-bound **mAb1** column. After incubation for 1−1.5 h at room temperature, the columns were washed and the oligonucleotide templates or their mixtures were applied, incubated for 2−3 h, and finally washed. Samples were subjected to PCR and sequenced as described previously herein. These results confirmed that the amplified sequences were that of **T100a** (Supporting Information). This experiment clearly demonstrates not only that preformed POC−template duplexes are capable of selectively and efficiently binding the antibody, but also that the formation of a selective POC−mAb complex does not hamper the Watson−Crick base pairing between the oligonucleotide template and complementary oligonucleotide moiety of **POC1**, **POC2**, or **POC3** (Figure 8). It is noteworthy that differences in orientation of conjugation and linker size had no effect on our result with **POC1**−**POC3**. Within our experiments, all three POCs were capable of engaging in selective three-component complex formation, leading to identical results, when used in a model system for the immuno-PCR-based antibody epitope mapping.

In the investigation of 49 POCs library (*25*), positively charged peptides incorporated in POCs along within 8mer oligonucleotide parts were causing the additional electrostatic rather than sequence-dependent interactions with overhang of complementary 16mer oligonucleotide. However, no data are available on how the DNA−POC (bearing the polycationic peptide) interaction may influence the antibody−peptide recognition, when forming ternary complexes.

In this study, the 12mer peptide portion **P1** of **POC1**−**POC3** incorporated 4 basic (two Lys and two Arg) and 8 neutral amino acid residues. These 4 basic residues according to (*25*) had to be engaged in the association of **POC1**−**POC3** and the single-stranded overhangs of oligomers **T72**, **T75**, and **T100a**. However, at least under the conditions of our experiments, this kind of interaction did not dramatically hamper the **P1**−**mAb1** recognition, and we were capable of testing the simple model system for the immuno-PCR based antibody epitope mapping. To our mind, experiments described herein may be extended to construction of considerably more complex protocols for epitope mapping that employ representative POC libraries.

CONCLUSIONS

The present work demonstrates that the relatively low molecular weight POCs that incorporate, for example, 14mer peptide and 13−15 oligonucleotide moieties are capable of a stable and selective three-component complex formation with DNA and mAb. Neither the Watson−Crick type interaction between POC and DNA nor the POC-antibody interaction dramatically hamper the other. In our experiments, the selectivity of three-component complex formation resulted in only one 100mer oligonucleotide **T100a**, associated with Sepharose-bound **mAb1** *via* **POC1**, **POC2**, or **POC3**, bearing peptide moiety **P1**. It was noteworthy that any of these POCs or their mixture brought about a similar result. Neither the control POCs nor control 100mer oligonucleotides interfered with this process, and, as a result, only a single sequence of **T100a** was clearly readable on the verification gel.

We conclude that the synthetic POCs may be successfully employed in a variety of practical applications, e.g., the immuno-PCR based antibody epitope mapping, employing representative POC libraries.

ACKNOWLEDGMENT

We are grateful to Dr. Maria Severina and Dr. Alexei Katrukha of HyTest Ltd. for providing antibodies and valuable discussions. We thank Dr. James Callaway for reading the manuscript. Financial support by the Finnish Funding Agency for Technology and Innovation (TEKES) is gratefully acknowledged.

Supporting Information Available: Sequencing of PCR products, obtained in the experiments with complexes selectively formed on Sepharose-bound **mAb1**. This material is available free of charge *via* the Internet at http://pubs.acs.org.

LITERATURE CITED

(1) Niemeyer, C. M. (2001) Semi-synthetic nucleic acid-protein conjugates: applications in life sciences and nanobiotechnology. *Rev. Mol. Biotechnol. 82*, 47–66.

(2) Lovrinovic, M., Spengler, M., Deutsch, C., and Niemeyer, C. M. (2005) Synthesis of covalent DNA-protein conjugates by expressed protein ligation. *Mol. BioSyst. 1*, 64–69.

(3) Lovrinovic, M., and Niemeyer, C. M. (2005) Rapid synthesis of DNA-cysteineconjugates for expressed protein ligation. *Biochem. Biophys. Res. Commun. 335*, 943–948.

(4) Lovrinovic, M., and Niemeyer, C. M. (2007) Microtiter plate-based screening for the optimization of DNA-protein conjugate synthesis by means of expressed protein ligation. *ChemBioChem 8*, 61–67.

(5) Wacker, R., Schröder, H., and Niemeyer, C. M. (2004) Performance of antibody microarrays fabricated by either DNA-directed immobilization, direct spotting, or streptavidin-biotin attachment: a comparative study. *Anal. Biochem. 330*, 281–287.

(6) Lovrinovic, M., and Niemeyer, C. M. (2005) DNA microarrays as decoding tools in combinatorial chemistry and chemical biology. *Angew. Chem., Int. Ed. 44*, 3179–3183.

(7) Hazarika, P., Ceyhan, B., and Niemeyer, C. M. (2004) Reversible switching of DNA-gold nanoparticle aggregation. *Angew. Chem., Int. Ed. 43*, 6469–6471.

(8) Kukolka, F., Schoeps, O., Woggon, U., and Niemeyer, C. M. (2007) DNA-directed assembly of supramolecular fluorescent protein energy transfer systems. *Bioconjugate Chem. 18*, 621–627.

(9) Niemeyer, C. M., Adler, M., Pignataro, B., Lenhert, S., Gao, S., Chi, L., Fuchs, H., and Blohm, D. (1999) Self-assembly of DNA-streptavidin nanostructures and their use as reagents in immuno-PCR. *Nucleic Acids Res. 27*, 4553–4561.

(10) Niemeyer, C. M., Wacker, R., and Adler, M. (2003) Combination of DNA-directed immobilization and immuno-PCR: very sensitive antigen detection by means of self-assembled DNA-protein conjugates. *Nucleic Acids Res. 31*, e90.

(11) Niemeyer, C. M., Adler, M., and Wacker, R. (2005) Immuno-PCR: high sensitivity detection of proteins by nucleic acid amplification. *Trends Biotechnol. 23*, 208–216.

(12) Wacker, R., Ceyhan, B., Alhorn, P., Schueler, D., Lang, C., and Niemeyer, C. M. (2007) Magneto Immuno-PCR: A novel immunoassay based on biogenic magnetosome nanoparticles. *Biochem. Biophys. Res. Commun. 357*, 391–396.

(13) Tung, C. H., and Stein, S. (2000) Preparation and applications of peptide-oligonucleotide conjugates. *Bioconjugate Chem. 11*, 605–618.

(14) Antopolsky, M., Azhayeva, E., Tengvall, U., Auriola, S., Jääskeläinen, I., Rönkkö, S., Honkakoski, P., Urtti, A., Lönnberg, H., and Azhayev, A. (1999) Peptide-oligonucleotide phosphorothioate conjugates with membrane translocation and nuclear localization properties. *Bioconjugate Chem. 10*, 598–606.

(15) Antopolsky, M., and Azhayev, A. (2001) Synthesis of peptide-oligonucleotide phosphorothioate conjugates by convergent or stepwise solid-phase strategies. *Nucleosides, Nucleotides Nucleic Acids 20*, 539–550.

(16) Zubin, E. M., Romanova, E. A., and Oretskaya, T. S. (2002) Modern methods for the synthesis of peptide-oligonucleotide conjugates. *Russ. Chem. Rev. 71*, 239–264.

(17) Pierce, T. L., White, A. R., Tregear, G. W., and Sexton, P. M. (2005) Peptide-oligonucleotide hybrids in Antisence therapy. *Mini Rev. Med. Chem. 5*, 41–55.

(18) Tengvall, U., Auriola, S., Antopolsky, M., Azhayev, A., and Beigelman, L. (2003) Characterization of antisense oligonucleotide-peptide conjugates with negative ionization electrospray mass spectrometry and liquid chromatography-mass spectrometry. *J. Pharm. Biomed. Anal. 32*, 581–590.

(19) Ketomäki, K., and Lönnberg, H. (2006) Mixed-phase immunoassay based on simultaneous binding of fluorescently tagged and PNA-conjugated peptide epitopes on antibodies: Quantification on PNA-coated microparticles. *Bioconjugate Chem. 17*, 1063–1068.

(20) Kozlov, I. A., Melnyk, P. C., Hachmann, J. P., Srinivasan, A., Shults, M., Zhao, C., Musmacker, J., Neison, N., Barker, D. L., and Lebl, M. (2008) A high-complexity, multiplexed solution-phase assay for profiling protease activity on microarrays. *Comb. Chem. High Throughput Screen. 11*, 24–35.

(21) Koppelhus, U., Awasthi, S. K., Zachar, V., Holst, H. U., Ebbesen, P., and Nielsen, P. E. (2002) Cell-dependent differential uptake of PNA, peptides, and PNA-peptide conjugates. *Antisense Nucleic Acid Drug Dev. 12*, 51–63.

(22) de Koning, M. C., van der Marel, G. A., and Overhand, M. (2003) Synthetic developments towards PNA-peptide conjugates. *Curr. Opin. Chem. Biol. 7*, 734–740.

(23) Abibi, A., Protozanova, E., Demidov, V., and Frank-Kamenetskii, M. D. (2004) Specific versus nonspecific binding of cationic PNAs to duplex DNA. *Biophys. J. 86*, 3070–3078.

(24) Gildea, B. D., Casey, S., MacNeill, J., Perry-O'Keefe, H., Sorensen, D., and Coull, J. M. (1998) PNA solubility enhancers. *Tetrahedron Lett. 39*, 7255–7258.

(25) Harrison, J. G., and Balasubramanian, S. (1998) Synthesis and hybridization analysis of small library of peptide-oligonucleotide conjugates. *Nucleic Acids Res. 26*, 3136–3145.

BC700457Y

Novel Thermoresponsive Nonviral Gene Vector: P(NIPAAm-*co*-NDAPM)-*b*-PEI with Adjustable Gene Transfection Efficiency

Han Cheng, Jing-Ling Zhu, Yun-Xia Sun, Si-Xue Cheng, Xian-Zheng Zhang,* and Ren-Xi Zhuo

Key Laboratory of Biomedical Polymers of Ministry of Education and Department of Chemistry, Wuhan University, Wuhan 430072, P. R. China. Received December 21, 2007; Revised Manuscript Received May 7, 2008

A thermoresponsive cationic copolymer, poly(*N*-isopropylacrylamide-*co*-*N*-(3-(dimethylamino)propyl)methacrylamide)-*b*-polyethyleneimine (P(NIPAAm-*co*-NDAPM)-*b*-PEI), was designed and synthesized as a potential nonviral gene vector. The lower critical solution temperature (LCST) of P(NIPAAm-*co*-NDAPM)-*b*-PEI in water measured by UV−vis spectroscopy was 38 °C. P(NIPAAm-*co*-NDAPM)-*b*-PEI as the gene vector was evaluated in terms of cytotoxicity, buffer capability determined by acid−base titration, DNA binding capability characterized by agarose gel electrophoresis and particle size analysis, and in vitro gene transfection. P(NIPAAm-*co*-NDAPM)-*b*-PEI copolymer exhibited lower cytotoxicity in comparison with 25 kDa PEI. Gel retardation assay study indicated that the copolymer was able to bind DNA completely at N/P ratios higher than 30. At 27 °C, the mean particle sizes of P(NIPAAm-*co*-NDAPM)-*b*-PEI/DNA complexes decreased from 1200 to 570 nm corresponding to the increase in N/P ratios from 10 to 60. When the temperature changed to 37 °C, the mean particle sizes of complexes decreased from 850 to 450 nm correspondingly within the same N/P ratio range due to the collapse of thermoresponsive PNIPAAm segments. It was found that the transfection efficiency of P(NIPAAm-*co*-NDAPM)-*b*-PEI/DNA complexes was higher than or comparable to that of 25 kDa PEI/DNA complexes at their optimal N/P ratios. Importantly, the transfection efficiency of P(NIPAAm-*co*-NDAPM)-*b*-PEI/DNA complexes could be adjusted by altering the transfection and cell culture temperature.

INTRODUCTION

For human gene therapy, genes are introduced to cells to be transfected and produce therapeutic proteins (*1–6*). However, due to the lack of vectors that can safely and efficiently deliver nucleic acids to the target cells, gene therapy has not fulfilled its potential. Both viral and nonviral delivery systems for delivering genes into cells have been extensively investigated. Since viral vectors are limited due to the issues of safety, immunogenicity, and mutagenesis, there is a limited amount of genomic information, although they have high efficiency (*7–10*). Nonviral vectors such as liposomes and cationic polymers have been developed to overcome these limitations (*1, 11*). Water-soluble cationic polymers such as poly(ethyleneimine)s (PEIs) and their block copolymers have been studied as nonviral vectors for effective and safe gene delivery systems (*11, 12*). Although cationic polymers can carry much larger pieces of DNA as compared with the viral vectors, they also exhibit some problems such as the aggregation of complexes at physiological conditions and possible cytotoxicity on the target cells due to the high surface charge.

The transfection efficiency and cytotoxicity of PEIs depend on the molecular weight greatly. As we know, the high molecular weight PEIs exhibit high transfection activity as well as high cytotoxicity compared with the low molecular weight PEIs. For example, the well-known commercial linear and branched 25 kDa PEIs, as an effective transfection reagent in vitro and in vivo, have high transfection efficiency but have high cytotoxicity at the same time. In order to enhance the transfection efficiency and decrease the cytotoxicity, synthetic cationic copolymers based on PEIs and stimuli-responsive polymers were investigated as nonviral gene vectors. The introduction of the stimuli-responsive polymers not only reduces the excess positive charge but also shows variable physiochemical characteristics under different cellular environments. Among various stimuli-responsive polymers, the most popular thermoresponsive polymer is poly(*N*-isopropylacrylamide) (PNIPAAm), which exhibits a phase transition at its lower critical solution temperature (LCST) around 32−33 °C. Several research groups reported temperature-sensitive vectors based on the PNIPAAm-derived polymers (*13–17*).

In this study, a novel thermoresponsive P(NIPAAm-*co*-NDAPM)-*b*-PEI copolymer as gene vector was synthesized by a coupling reaction between P(NIPAAm-*co*-NDAPM)-COOH and 800 Da PEI. The copolymer as the gene vector was evaluated based on the cytotoxicity, buffer capability determined by acid−base titration, DNA binding capability characterized by agarose gel electrophoresis and particle size analysis, and in vitro gene transfection. It was found that the copolymer exhibited different binding capabilities with DNA upon temperature changes. In addition, the temperature-dependent transfection efficiency demonstrated that P(NIPAAm-*co*-NDAPM)-*b*-PEI copolymer had great potential as a nonviral gene vector with low cytotoxicity and adjustable gene transfection efficiency.

EXPERIMENTAL PROCEDURES

Materials. *N*-Isopropylacrylamide (NIPAAm) and 3-mercaptopropionic acid (MPA) were purchased from ACROS and used as received. *N*,*N*′-Carbonyldiimidazole (CDI) and branched PEIs (25 kDa and 800 Da) were purchased from Sigma and used as received. *N*-(3-(Dimethylamino)propyl)methacrylamide (NDAPM) was purchased from Japan Mark lot. *N*,*N*′-Dimethylformamide (DMF) was obtained from Shanghai Chemical Reagent Co. and used after distillation under reduced pressure.

* Corresponding author. Tel. & Fax: 86-27-6875 4509. E-mail address: xz-zhang@whu.edu.cn (X.-Z. Zhang).

10.1021/bc700478s CCC: $40.75 © 2008 American Chemical Society
Published on Web 07/16/2008

N,*N*′-Azobisisobutyronitrile (AIBN) was purchased from Shanghai Chemical Reagent Co., China, and used after recrystallization with 95% ethanol. Plasmid pGL-3 control with SV40 promoter and enhancer sequences encoding luciferase was obtained from Promega, Madison, WI, USA. Plasmid pEGFP-C1 encoding a red-shifted variant of wild-type green fluorescent protein (GFP) was purchased from Clontech, Mountain View, CA, USA. All other chemicals were analytical grade and used as received.

Plasmid DNA Preparation and Purification. PGL-3 and EGFP-C1 plasmids were used for in vitro gene transfections. The former was transformed in *E. coli* JM109 and the latter was transformed in *E. coli* DH5α. Both plasmids were amplified in Luria−Bertani (LB) medium at 37 °C overnight at 250 rpm. Then, the plasmids were purified as described by means of EndoFree plasmid purification. The purified plasmids were diluted by TE buffer solution and stored at −20 °C. The integrity of the plasmid was confirmed by agarose gel electrophoresis. The purity and concentration of plasmids were determined by ultraviolet (UV) absorbance at 260 and 280 nm.

Synthesis of P(NIPAAm-*co*-NDAPM)-*b*-PEI. P(NIPAAm-*co*-NDAPM)-COOH was synthesized by free-radical copolymerization of NIPAAm (2.74 g) and NDAPM (150 μL) in DMF (10 mL) using AIBN (0.021 g) and MPA (0.418 g) as an initiator and a chain transfer reagent, respectively. After all the reactants were dissolved in DMF, the solution was degassed by bubbling with nitrogen for 30 min. Then the polymerization reaction was carried out at 70 °C under N_2 atmosphere for 24 h. The P(NIPAAm-*co*-NDAPM)-COOH was obtained by precipitating the reaction mixture into diethyl ether. The precipitated polymer was isolated by filtration, dried under vacuum, and then reprecipitated from diethyl ether. Subsequently, resultant P(NIPAAm-*co*-NDAPM)-COOH (0.8348 g) and CDI (28 mg) were dissolved in DMSO (10 mL) and stirred for 3 h at room temperature. The solution was added quickly to a large excess of 800 Da PEI in DMSO (5 mL) with vigorous stirring. After 24 h, the product was precipitated in diethyl ether. The precipitated polymer was isolated by filtration and dried in a vacuum. Then, the dried polymer was further purified by dialysis against distilled water (MWCO 8000−12000) to remove the unreacted 800 Da PEI and other residues.

Characterizations. Fourier transformed infrared (FTIR) spectra were recorded on a Lambda Bio40 UV−vis spectrometer (Perkin-Elmer). ^{1}H nuclear magnetic resonance (NMR) spectra were recorded on a Varian Unity 300 MHz spectrometer using $CDCl_3$ as a solvent.

LCST Measurement. Optical absorbance of P(NIPAAm-*co*-NDAPM)-COOH, P(NIPAAm-*co*-NDAPM)-*b*-PEI, and P(NIPAAm-*co*-NDAPM)-*b*-PEI/DNA complexes at various temperatures was measured at 542 nm using a Lambda Bio40 UV−vis spectrometer (Perkin-Elmer). Sample cells were thermostatted in a refrigerated circulator bath at different temperatures from 31 to 60 °C prior to measurement. The heating rate was set at 0.1 °C/min. The LCSTs of the polymers and complexes were defined as the temperature showing a 50% change in the total optical absorbance.

Cell Culture. Human embryonic kidney 293 cells (HEK293) were incubated in Dulbecco's Modified Eagle's Medium (DMEM) containing 10% fetal bovine serum (FBS) and 1% antibiotics (penicillin−streptomycin, 10000 U/mL) at 37 °C in a humidified atmosphere containing 5% CO_2.

Cell Viability Assay. For cell viability assay, the HEK293 cells (2500 cells/well) were seeded into 96-well plates. The cells were then incubated in culture medium containing polymer with a particular concentration for 48 h. After that, the medium was replaced with 200 μL of fresh medium, and 20 μL of sterile filtered MTT (3-(4,5-dimethylthiazol-2-yl)-2,5-diphenyl tetrazolium bromide) (5 mg/mL) stock solution in PBS was added to each well, reaching a final concentration of 0.45 mg/mL. After 4 h, unreacted dye was removed by aspiration. The formazan crystals were dissolved in 200 mL DMSO per well and measured spectrophotometrically in an ELISA plate reader (model 550, Bio-Rad) at a wavelength of 570 nm. The cell survival was expressed as follows.

$$\text{cell viability} = (\text{OD}_{\text{treated}}/\text{OD}_{\text{control}}) \times 100\%$$

where $\text{OD}_{\text{control}}$ was obtained in the absence of polymers and $\text{OD}_{\text{treated}}$ was obtained in the presence of polymers.

Acid−Base Titration. The buffer capability of PEIs and P(NIPAAm-*co*-NDAPM)-*b*-PEI were determined by acid−base titration assay over the pH from 10 to 2 as described by Benns et al. (*18, 19*). Briefly, 0.2 mg/mL of each sample solution was prepared in 30 mL 150 mM NaCl solution. The pH value of the sample solution was adjusted to 10 by adding 0.1 M NaOH, and then the solution was titrated by 0.1 M HCl. During titration, the pH value of the mixture was measured using a microprocessor pH meter (pH 211, Germany).

Polymer/DNA Complex Formation. P(NIPAAm-*co*-NDAPM)-*b*-PEI was dissolved in NaCl solution (150 mM, pH 7.4) to form a solution with a concentration of 1 mg/mL. A plasmid DNA stock solution (120 ng/μL) was prepared in Tris-HCl buffer solution (pH 7.4). The total volumes of polycation solution and DNA stock solution were adjusted to 50 μL with 150 mM NaCl solution, respectively, and then two solutions were mixed together to form complexes with different N/P (the primary amino groups of PEI in the P(NIPAAm-*co*-NDAPM)-*b*-PEI to phosphate groups) ratios. The formation of complexes was carried out for 30 min at 37 °C after vortexing polymer/DNA mixture for 5 s.

Agarose Gel Retardation Assay. The complexes at different N/P ratios were prepared by adding appropriate volumes of P(NIPAAm-*co*-NDAPM)-*b*-PEI (in 150 mM NaCl solution) to 96 ng of plasmid EGFP-C1 DNA (120 ng/μL in 40 mM Tris-HCl buffer solution), and the complexes were diluted by 150 mM NaCl solution to 6 μL, then the complexes were incubated at 37 °C for 30 min. After that, the complexes were loaded on the 0.7% (w/v) agarose gel containing GelRed with Tris-acetate (TAE) running buffer at 80 V for 80 min. DNA was visualized with a UV lamp using a Vilber Lourmat imaging system (France).

Particle Size Measurements. The P(NIPAAm-*co*-NDAPM)-*b*-PEI/DNA complexes at various N/P ratios were prepared by adding appropriate volumes of P(NIPAAm-*co*-NDAPM)-*b*-PEI (in 150 mM NaCl solution) to 10 μg of plasmid DNA (in 40 mM Tris-HCl buffer solution), then the complexes were diluted by 150 mM NaCl solution to 1 mL and incubated at 27 and 37 °C for 30 min, respectively. The particle size was measured by Nano-ZS ZEN3600 (MALVERN Instruments) at 27 and 37 °C, respectively.

Gene Transfection. For in vitro transfection study, the HEK293 cells were split one day prior to transfection and seeded in 24-well plates at a density of 5×10^4 cells/well. Before transfection, the cell culture medium was replaced with serum-free DMEM. The cells were transfected with P(NIPAAm-*co*-NDAPM)-*b*-PEI/DNA complexes containing 1 μg of plasmid DNA at 25 and 37 °C for 4 h, respectively. Then, the complexes were removed and incubated in fresh DMEM with 10% FBS at 37 °C for another 48 h. Altogether, for the thermo-controlled assay, the complexes were incubated following the two different temperature programs: (1) 37 °C (4 h) → 37 °C (48 h) and (2) 27 °C (4 h) → 37 °C (48 h).

Cell Tracing Assay. GelRed was used as a molecular probe to show the transport of P(NIPAAm-*co*-NDAPM)-*b*-PEI/DNA complexes into cells. Complexes were incubated with serum-free DMEM in 24-well plates following the above two tem-

Scheme 1. Schematic Illustration of the Synthesis of P(NIPAAm-*co*-NDAPM)-*b*-PEI

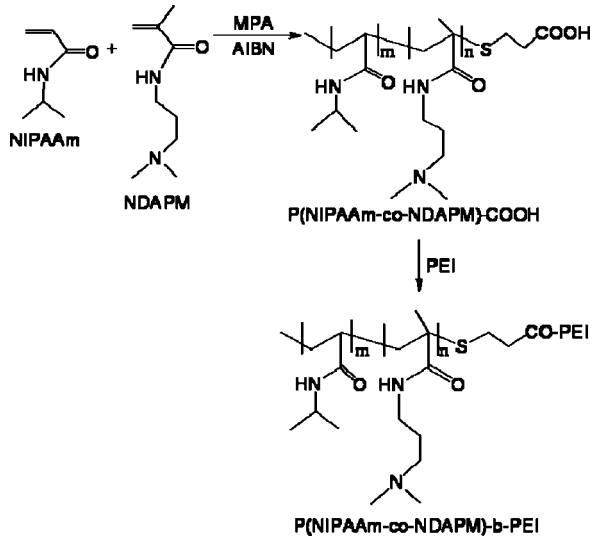

perature-controlled programs for 4 h. After that, the GelRed solution (at 1/5000 volume of the transfection medium) was added to 24-well plates and incubated 10 min before the serum-free DMEM was replaced by fresh DMEM with 10% FBS. Then, the cells were directly observed by an inverted microscope (TE-2000U, NIKON, JAPAN) after incubation for 4 and 12 h in DMEM with 10% FBS.

Luciferase Assay. The cells were washed by PBS and lysed with the reporter lysis buffer (Promega, USA). The luciferase activity in cell extracts was measured using a luciferase assay kit (Promega, USA). Each measurement was carried out for 10 s in a single-well luminometer (Berthold Lumat LB 9507, Germany). The relative light units (RLU) were normalized by the total protein concentration of the cell extracts, and the total protein was measured with a BCA protein assay kit (PERBIO, USA). Luciferase activity was expressed as RLU/mg protein.

GFP Detection. The cells which expressed green fluorescent proteins were directly observed by inverted microscope (IX 70, OLYMPUS, JAPAN).

RESULTS AND DISCUSSION

Synthesis of P(NIPAAm-*co*-NDAPM)-*b*-PEI. PNIPAAm has been frequently used as a thermoresponsive segment to form block polymers with the LCST of around 32−33 °C (*20*). In the present study, a block copolymer of P(NIPAAm-*co*-NDAPM)-*b*-PEI was prepared. The hydrophilic NDAPM units were used to adjust the LCST of P(NIPAAm-*co*-NDAPM)-*b*-PEI copolymer. The synthesis of the P(NIPAAm-*co*-NDAPM)-*b*-PEI copolymer involved two steps as illustrated in Scheme 1. P(NIPAAm-*co*-NDAPM)-COOH was synthesized by free-radical polymerization using AIBN as an initiator, and MPA as a chain transfer agent. Then, P(NIPAAm-*co*-NDAPM)-*b*-PEI was prepared by coupling reaction between P(NIPAAm-*co*-NDAPM)-COOH and PEI, using CDI as a coupling reagent. During the coupling reaction, the large excess 800 Da PEI was added to make sure that one PEI molecule would react with one P(NIPAAm-*co*-NDAPM)-COOH molecule, and the P(NIPAAm-*co*-NDAPM)-COOH would be consumed completely.

The structure of polymers was confirmed by FTIR and ^{1}H NMR spectroscopies. As shown in Figure 1, the absorbance of amide carbonyl groups in P(NIPAAm-*co*-NDAPM)-COOH occurred at 1630 cm^{-1} and the bending frequency of the amide N−H appeared at 1580 cm^{-1}. The FTIR spectrum of P(NIPAAm-*co*-NDAPM)-*b*-PEI was similar to that of P(NIPAAm-*co*-NDAPM)-COOH due to the fact that the amide N−H peak of PEI overlapped the one of PNIPAAm. However, it was found that the absorbance of amide N−H in P(NIPAAm-*co*-NDAPM)-*b*-PEI was greatly enhanced (Figure 1b) as compared with that of P(NIPAAm-*co*-NDAPM)-COOH, which indicated that the PEI was successfully grafted on P(NIPAAm-*co*-NDAPM)-COOH.

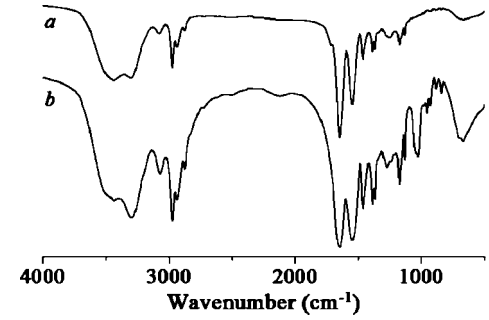

Figure 1. FTIR spectra of P(NIPAAm-*co*-NDAPM)-COOH (a) and P(NIPAAm-*co*-NDAPM)-*b*-PEI (b).

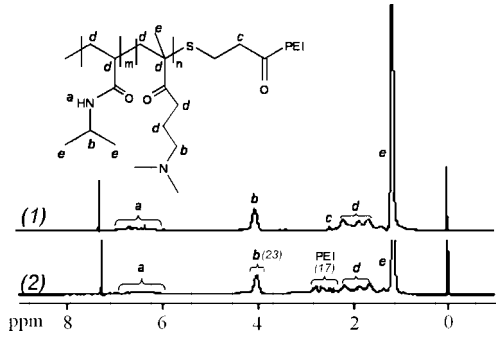

Figure 2. The ^{1}H NMR spectra of (1) P(NIPAAm-*co*-NDAPM)-COOH and (2) P(NIPAAm-*co*-NDAPM)-*b*-PEI in $CDCl_3$.

The ^{1}H NMR spectra of P(NIPAAm-*co*-NDAPM)-COOH and P(NIPAAm-*co*-NDAPM)-*b*-PEI in $CDCl_3$ are shown in Figure 2. Figure 2(1) and (2) both showed a single peak at δ 3.9−4.1 ppm, which could be attributed to the hydrogen of NC*H*$(CH_3)_2$ in the PNIPAAm segment. Besides, there existed a signal at around δ 1.0 ppm which could be assigned to the methyl in the PNIPAAm. In Figure 2(2), the broad peak δ 2.5−3.3 ppm was assigned to the methylene of branched 800 Da PEI. The integrals of signal δ 3.9−4.1 ppm and signal δ 2.5−3.3 ppm were 23 and 17, respectively. In addition, the molecular weights (M_n) of the polymers were calculated from the ratio of these two integrals. The M_n of P(NIPAAm-*co*-NDAPM)-COOH and P(NIPAAm-*co*-NDAPM)-*b*-PEI were 1.14×10^4 and 1.22×10^4, respectively.

LCST Determination. The phase transition of thermoresponsive polymers in aqueous solution is attributed to a change in the hydrophilic/hydrophobic equilibrium of the polymers with respect to their hydrogen bonding between the polymer chains and water molecules. The light transmittance of a polymer solution could be examined as a function of temperature, and the LCST of the polymer was defined as the temperature producing a half-decrease of the total decrease in light transmittance. Generally, PNIPAAm itself exhibits a temperature-induced phase transition at around 32−33 °C (*20*), and the complete transition occurs within a narrow temperature range. As shown in Figure 3, the LCST values of P(NIPAAm-*co*-NDAPM)-COOH, P(NIPAAm-*co*-NDAPM)-*b*-PEI, and P-(NIPAAm-*co*-NDAPM)-*b*-PEI/DNA complexes are around 42, 38, and 37 °C, respectively. A well-recognized mechanism for the phase transition of the PNIPAAm polymer is the result of

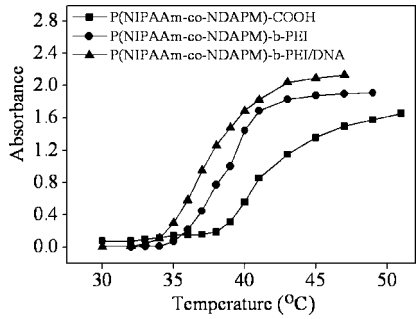

Figure 3. Thermoresponsive behavior of P(NIPAAm-*co*-NDAPM)-COOH, P(NIPAAm-*co*-NDAPM)-*b*-PEI, and P(NIPAAm-*co*-NDAPM)-*b*-PEI/DNA complexes.

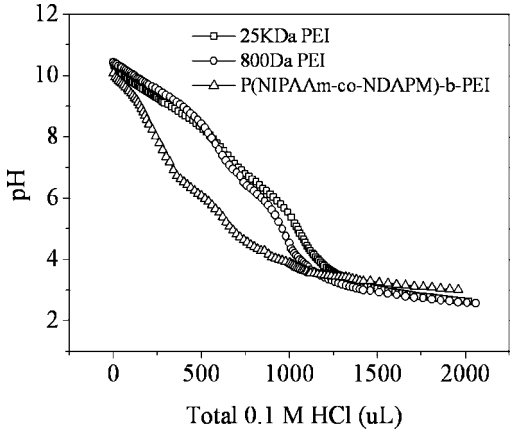

Figure 4. Acid−base titration curves of 25 kDa PEI, 800 Da PEI, and P(NIPAAm-*co*-NDAPM)-*b*-PEI in 150 mM NaCl solution.

a balance between hydrophilicity and hydrophobicity in the polymer chain. When a hydrophilic moiety is copolymerized into a PNIPAAm segment, the hydrophilic/hydrophobic balance shifts to a more hydrophilic nature, and the LCST would shift to a higher temperature accordingly (*21*, *22*).

The P(NIPAAm-*co*-NDAPM)-COOH and P(NIPAAm-*co*-NDAPM)-*b*-PEI exhibited higher LCSTs compared with pure PNIPAAm, ascribed to the incorporation of hydrophilic NDAPM units. The fact that the LCST of P(NIPAAm-*co*-NDAPM)-COOH was higher than that of P(NIPAAm-*co*-NDAPM)-*b*-PEI is due to the end group effect of terminal carboxylic acid groups (*23*, *24*).

Acid−Base Titration. The buffer capabilities of 25 kDa PEI, 800 Da PEI, and P(NIPAAm-*co*-NDAPM)-*b*-PEI are shown in Figure 4. It was found that the buffer capabilities of 25 kDa and 800 Da PEIs are similar, that is to say that the buffer capability is not directly correlated with the molecular weight. It was reported that the buffer capability depends on the primary, secondary, and ternary amines. Hence, the buffer capability of P(NIPAAm-*co*-NDAPM)-*b*-PEI, which is slightly lower than that of PEIs, could be ascribed to the reduction of positive charge density owing to the introduction of neutral PNIPAAm chains.

Characterization of Polymer/DNA Complexes. The binding capability between the polycation and DNA is a prerequisite for the gene vector. When the DNA is condensed by the polycation, the condensed form can protect the DNA against digestion by enzymes. In addition, the compact unit facilitates the escape of the complex from endosomes into the cytoplasm, and then the DNA accumulates in the nucleus of the targeted cell where the gene is expressed. In order to study the ability of the polymer to condense DNA, the agarose gel assay was conducted. As shown in Figure 5, the plasmid DNA was retarded partly at the N/P ratio of 10. With an increase in N/P ratio, the

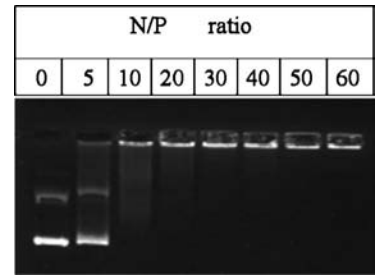

Figure 5. Agarose gel electrophoresis retardation assay of P(NIPAAm-*co*-NDAPM)-*b*-PEI/DNA complexes at different N/P ratios of 0, 5, 10, 20, 30, 40, 50, and 60.

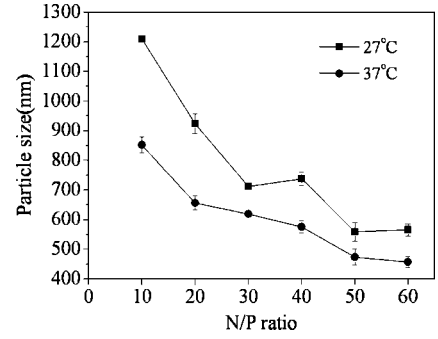

Figure 6. Particle size of P(NIPAAm-*co*-NDAPM)-*b*-PEI/DNA complexes at N/P ratios ranging from 10 to 60 at different temperatures (27 and 37 °C). Data were shown as mean ± SD ($n = 3$).

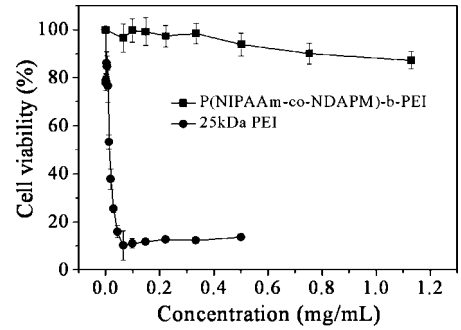

Figure 7. Cytotoxicity of P(NIPAAm-*co*-NDAPM)-*b*-PEI for HEK293 cells in comparison to 25 kDa PEI.

DNA binding capability of P(NIPAAm-*co*-NDAPM)-*b*-PEI was improved and the copolymer was able to bind DNA completely at N/P ratio higher than 30.

Particle Size Measurement. The particle sizes of the polymer/DNA complexes at different N/P ratios at 27 and 37 °C are shown in Figure 6. The effect of the N/P ratio on the complex size shows a similar trend at 27 and 37 °C. At 27 °C, with an increase in the N/P ratio from 10 to 60, the particle size decreases from 1200 to 600 nm. At 37 °C, with an increase in N/P ratio from 10 to 60, the particle size decreases from 860 to 450 nm.

It is obvious that the particle size of complexes depends on the temperature, and the particle size at 27 °C is larger than that at 37 °C at the same N/P ratio. As we know, at a higher temperature, the PNIPAAm chains collapse to form highly compact structure. At a lower temperature, the PNIPAAm chains get expanded to promote the dissociation of complexes. In the current study, at a lower N/P ratio, the complexes at both 27 and 37 °C form larger particles attributed to the weaker electrostatic interaction between P(NIPAAm-*co*-NDAPM)-*b*-PEI and DNA. With increasing N/P ratio, the electrostatic interaction becomes stronger and more compact complexes are

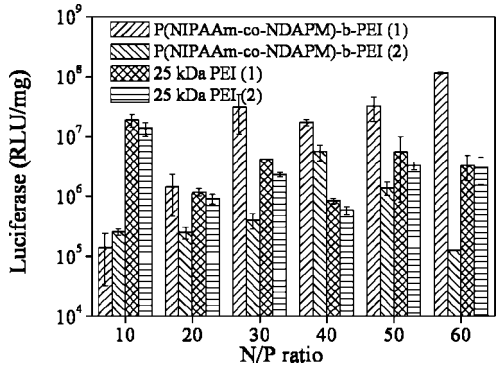

Figure 8. Transfection efficiency of P(NIPAAm-*co*-NDAPM)-*b*-PEI/DNA and 25 kDa PEI/DNA complexes evaluated at N/P ratios range from 10 to 60 at two different cultured temperature programs: (1) 37 °C (4 h) → 37 °C (48 h); (2) 27 °C (4 h) → 37 °C (48 h). Data were shown as mean ± SD ($n = 3$).

formed (*25*), and so, the particle size at 37 °C is smaller than that at 27 °C (*25*, *26*), which implies that the particle size of P(NIPAAm-*co*-NDAPM)-*b*-PEI/DNA complexes might be adjusted by changing the temperature.

Cytotoxicity of Polymers. Low cytotoxicity is a very important requirement for gene vectors. In this study, the cytotoxicity of P(NIPAAm-*co*-NDAPM)-*b*-PEI was evaluated in HEK293 cells by MTT assay using 25 kDa PEI as the control. As shown in Figure 7, the viability of HEK293 cells treated with P(NIPAAm-*co*-NDAPM)-*b*-PEI at the concentration of 1.1 mg/mL is above 80%, indicating that the cytotoxicity of P(NIPAAm-*co*-NDAPM)-*b*-PEI is lower than that of 25 kDa PEI. Moreover, the cytotoxicity of P(NIPAAm-*co*-NDAPM)-*b*-PEI increases slightly with increasing polymer concentration.

The cytotoxicity of a polymer is correlated with the molecular weight as well as the cell binding between the polymer and cellular surfaces (*27*). The lower cytotoxicity of P(NIPAAm-*co*-NDAPM)-*b*-PEI is attributed to the lower molecular weight of PEI and the shielding function of PNIPAAm chains, which can partially prevent the combination between P(NIPAAm-*co*-NDAPM)-*b*-PEI and cellular surfaces.

In Vitro Transfection. The commercially available branched 25 kDa PEI was used as the positive control due to its high transfection efficiency in vitro and in vivo. The plasmid PGL-3 was used as a reporter gene. In order to examine the influence of temperature on the transfection efficiency, the complexes were incubated following two different temperature programs: (1) 37 °C (4 h) → 37 °C (48 h) and (2) 27 °C (4 h) → 37 °C (48 h). The efficiency of P(NIPAAm-*co*-NDAPM)-*b*-PEI/DNA complexes was evaluated at N/P ratios from 10 to 60, and the efficiency of 25 kDa PEI at the optimal ratio (N/P = 10) was used as the control. As shown in Figure 8, the luciferase activities of P(NIPAAm-*co*-NDAPM)-*b*-PEI/DNA complexes at various N/P ratios are 1.38×10^5 RLU/mg, 1.44×10^6 RLU/mg, 3.11×10^7 RLU/mg, 1.72×10^7 RLU/mg, 3.21×10^7 RLU/mg, and 1.16×10^8 RLU/mg under the constant temperature program (1). However, under the condition of nonconstant temperature program (2), the luciferase activities of P(NIPAAm-*co*-NDAPM)-*b*-PEI decrease 0.5−1000-fold as compared with that of the constant temperature program (1). As also shown in Figure 8, the efficiency of P(NIPAAm-*co*-NDAPM)-*b*-PEI/DNA complexes at certain N/P ratios is higher than that of 25 kDa PEI/DNA complexes at its optimal N/P ratio under constant temperature program (1).

To further illuminate the effect of temperature on the transfection efficiency, the tracing analysis was carried out using fluorescent microscopy, showing transport of the complexes into the cells. As shown in Figure 9, the GelRed labeled P(NIPAAm-*co*-NDAPM)-*b*-PEI/DNA complexes initially dispersed on the cell surface after incubation in DMEM with 10% FBS for 4 h following two temperature programs (Figure 9a,c, arrows). After the complexes were incubated in DMEM with 10% FBS for 12 h, the labeled DNA was clearly restricted to the periphery

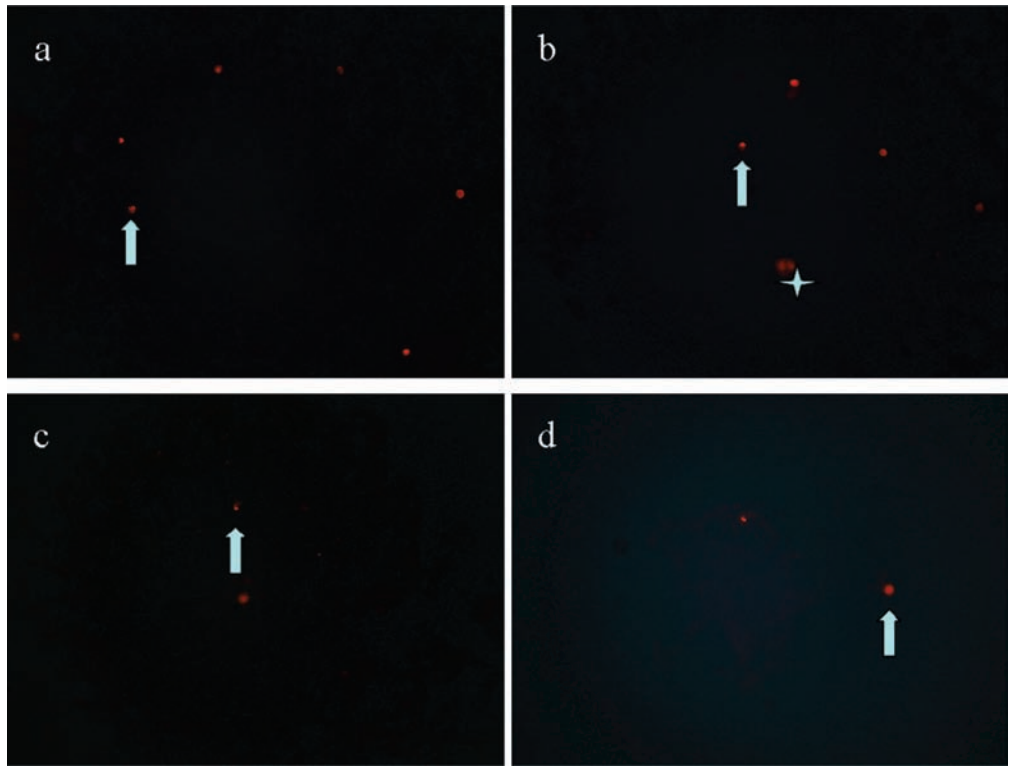

Figure 9. Cell tracing of GelRed labeled P(NIPAAm-*co*-NDAPM)-*b*-PEI/DNA complexes in HEK293 cells at two different cultured temperature programs: (1) 37 °C (4 h) → 37 °C (48 h) for 4 h (a) and 12 h (b); (2) 27 °C (4 h) → 37 °C (48 h) for 4 h (c) and 12 h (d). The images were obtained at magnification of 100×.

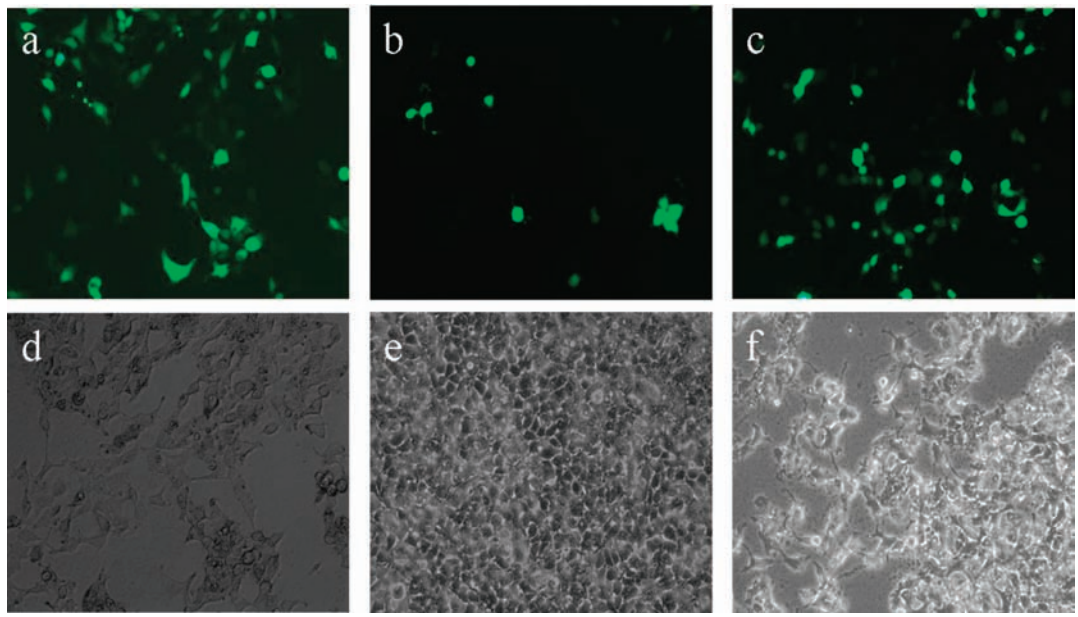

Figure 10. The transfected HEK293 cells by P(NIPAAm-*co*-NDAPM)-*b*-PEI/DNA complexes and 25 kDa PEI/DNA complexes observed by inverted microscope. The images in a, b, and c are the fluorescent images, and the images in d, e, and f are the bright-field images. The images (a, d) of P(NIPAAm-*co*-NDAPM)-*b*-PEI/DNA complexes were obtained under the temperature program (1) with N/P ratio of 60, images (b, e) of P(NIPAAm-*co*-NDAPM)-*b*-PEI/DNA complexes under the temperature program (2) with N/P ratio of 60, and images (c, f) of 25 kDa PEI/DNA complexes with N/P ratio of 10. The images were obtained at magnification of 100×.

of the nucleus following temperature program (1) (Figure 9b, asterisk). However, it was difficult to identify any labeled DNA entering the cells, and it was still dispersed on the cell surface after incubation in DMEM with 10% FBS for 12 h following temperature program (2) (Figure 9d, arrow). The results indicate that the transfection efficiency of P(NIPAAm-*co*-NDAPM)-*b*-PEI/DNA complexes is adjustable through temperature control.

However, the transfection result of P(NIPAAm-*co*-NDAPM)-*b*-PEI/DNA complexes is partially different from that of the previously studied thermoresponsive complexes at two different temperature programs (*13, 28*). The difference was attributed to the different transfection methods. In this study, when the P(NIPAAm-*co*-NDAPM)-*b*-PEI/DNA complexes were incubated in DMEM for 4 h at 37 °C, the complexes got associated compactly for cell uptake and prevention of DNA degradation; hence, the gene expression was conducted successfully. When the P(NIPAAm-*co*-NDAPM)-*b*-PEI/DNA complexes were incubated in DMEM for 4 h at 27 °C, the P(NIPAAm-*co*-NDAPM)-*b*-PEI could not condense DNA compactly, as demonstrated by the particle size analysis and tracing assay. The transgene expression was limited and thus resulted in low transfection efficiency at 27 °C. In the literature reports (*13, 28*), the thermoresponsive complexes were first incubated for a few hours at 37 °C, and the complexes got associated tightly for cell uptake. After that, the complexes were further incubated for a couple of hours at temperatures below the LCST, resulting in the dissociation of the complexes, and then the free DNA would enter the nucleus easily. As a result, the transfection efficiency of the complexes incubated for a couple of hours at temperatures below the LCST is higher than that at temperature above the LCST. In a word, the transfection efficiency of thermoresponsive polymer/DNA complexes could be adjusted by altering the cultured temperature.

In order to directly visualize the infected cells expressing GFP, EGFP-C1 encoded a red-shifted variant of wild-type GFP with optimized brighter fluorescence and higher expression in mammalian cell was used as a reporter gene. The cells expressing green fluorescence were observed by inverted microscope at the optimal N/P ratio for the polymer/DNA complexes. The transfection results are presented in Figure 10. Figure 10a,b,c represents the fluorescent images, and Figure 10d,e,f represents the bright-field images. GFP is successfully expressed in HEK293 cells, the number of green fluorescent cells increases with increasing N/P ratio, and the nonconstant temperature program results in less GFP expression compared with the constant temperature program, which is consistent with luciferase reporter system.

CONCLUSIONS

A novel thermoresponsive P(NIPAAm-*co*-NDAPM)-*b*-PEI block copolymer was prepared by the coupling reaction between P(NIPAAm-*co*-NDAPM)-COOH and 800 Da PEI. Compared with 25 kDa PEI, P(NIPAAm-*co*-NDAPM)-*b*-PEI copolymer exhibits much lower cytotoxicity. The particle size of P(NIPAAm-*co*-NDAPM)-*b*-PEI/DNA complexes could be adjusted by varying the culture temperature. In vitro gene transfection reveals that the transfection efficiency of P(NIPAAm-*co*-NDAPM)-*b*-PEI/DNA complexes is comparable to or even higher than that of 25 kDa PEI/DNA complex (N/P = 10). Importantly, the gene transfection efficiency of P(NIPAAm-*co*-NDAPM)-*b*-PEI/DNA complexes could be adjusted by altering the transfection and incubation temperature, suggesting that the P(NIPAAm-*co*-NDAPM)-*b*-PEI has great potential as an intelligent and effective nonviral gene vector.

ACKNOWLEDGMENT

This work was supported by National Key Basic Research Program of China (2005CB623903), National Natural Science Foundation of China (20504024, 50633020), and Ministry of Education of China (Cultivation Fund of Key Scientific and Technical Innovation Project 707043).

LITERATURE CITED

(1) Laporte, L. D., Rea, J. C., and Shea, L. D. (2006) Design of modular non-viral gene therapy vectors. *Biomaterials 27*, 947–954.

(2) Zhang, X. J., and Godbey, W. T. (2006) Viral vectors for gene delivery in tissue engineering. *Adv. Drug Delivery Rev. 58*, 515–534.

(3) Olefsky, J. M. (2000) DiabetesGene therapy for rats and mice. *Nature 408*, 420–421.

(4) Song, S., Goudy, K., Campbell-Thompson, M., Wasserfall, C., Scott-Jorgensen, M., Wang, J., Tang, Q., Crawford, J. M., Ellis, T. M., Atkinson, M. A., and Flotte, T. R. (2004) Recombinant adeno-associated virusmediated alpha-1 antitrypsin gene therapy prevents type I diabetes in NOD mice. *Gene Ther. 11*, 181–186.

(5) El-Aneed, A. (2004) An overview of current delivery systems in cancer gene therapy. *J. Controlled Release 94*, 1–14.

(6) Merdan, T., Kopecek, J., and Kissel, T. (2002) Prospects for cationic polymers in gene and oligonucleotide therapy against cancer. *Adv. Drug Delivery Rev. 54*, 715–758.

(7) Lehrman, S. (1999) Virus treatment questioned after gene therapy death. *Nature 401*, 517–518.

(8) Liu, Q., and Muruve, D. A. (2003) Molecular basis of the inflammatory response to adenovirus vectors. *Gene Ther. 10*, 935–940.

(9) Sun, J. Y., Anand-Jawa, V., Chatterjee, S., and Wong, K. K. (2003) Immune responses to adeno-associated virus and its recombinant vectors. *Gene Ther. 10*, 964–976.

(10) Gore, M. E. (2003) Adverse effects of gene therapy, gene therapy can cause leukaemia, no shock, mild horror but a probe. *Gene Ther. 10*, 4–4.

(11) Kunath, K., Harpe, A. V., Fischer, D., Petersen, H., Bickel, U., Voigt, K., and Kissela, T. (2003) Low-molecular-weight polyethylenimine as a non-viral vector for DNA delivery, comparison of physicochemical properties, transfection efficiency and in vivo distribution with high-molecular-weight polyethylenimine. *J. Controlled Release 89*, 113–125.

(12) Itaka, K., Yamauchi, K., Harada, A., Nakamura, K., Kawaguchi, H., and Kataoka, K. (2003) Polyion complex micelles from plasmid DNA and poly(ethyleneglycol)-poly(L-lysine) block copolymer as serum-tolerable polyplex system, physicochemical properties of micelles relevant to gene transfection efficiency. *Biomaterials 24*, 4495–4506.

(13) Kurisawa, M., Yokoyama, M., and Okano, T. (2000) Gene expression control by temperature with thermo-responsive polymeric gene carriers. *J. Controlled Release 69*, 127–137.

(14) Türk, M., Dinçer, S., Yulug̃, I. G., and Pişkin, E. (2004) In vitro transfection of HeLa cells with temperature sensitive polycationic copolymers. *J. Controlled Release 96*, 325–340.

(15) Twaites, B. R., Alarcón, C. H., Lavigne, M., Saulnier, A., Pennadam, S. S., Cunliffe, D., et al. (2005) Thermoresponsive polymers as gene delivery vectors, cell viability, DNA transport and transfection studies. *J. Controlled Release 108*, 472–483.

(16) Twaites, B. R., Heras Alarcón, C., Cunliffe, D., Lavigne, M., Pennadam, S., and Smith, J. R. (2004) Thermo and pH responsive polymers as gene delivery vectors, effect of polymer architecture on DNA complexation in vitro. *J. Controlled Release 97*, 551–566.

(17) Bisht, H. S., Manickam, D. S., You, Y. Z., and Oupicky, D. (2006) Temperature-controlled properties of DNA complexes with poly(ethylenimine)-graft-poly(N-isopropylacrylamide). *Biomacromolecules 7*, 1169–1178.

(18) Benns, J. M., Choi, J. S., Mahato, R. I., Park, J. S., and Kim, S. W. (2000) pH-Sensitive cationic polymer gene delivery vehicle N-ac-poly(L-histidine)-graft-poly(L-lysine) comb shaped polymer. *Bioconjugate Chem. 11*, 637–645.

(19) Benns, J. M., Mahato, R. I., and Kim, S. W. (2002) Optimization of factors influencing the transfection efficiency of folate-PEG-folate-graft-polyethylenimine. *J. Controlled Release 79*, 255–269.

(20) Li, Y. Y., Zhang, X. Z., Cheng, H., Zhu, J. L., Cheng, S. X., and Zhuo, R. X. (2006) Self-assembled, thermoresponsive PCL-g-P(NIPAAm-co-HEMA) micelles for drug delivery. *Macromol. Rapid Commun. 27*, 1913–1919.

(21) Vernon, B., Kim, S. W., and Ba, Y. H. (2000) Thermoreversible copolymer gels for extracellular matrix. *J. Biomed. Mater. Res. 51*, 69–79.

(22) Shibayama, M., Fujikawa, Y., and Nomura, S. (1996) Dynamic light scattering study of poly(N-isopropylacrylamide-co-acrylic acid) gels. *Macromolecules 29*, 6535–6540.

(23) Kujawa, P., Segui, F., Shaban, S., Diab, C., Okada, Y., Tanaka, F., and Winnik, F. M. (2006) Impact of end-group association and main-chain hydration on the thermosensitive properties of hydrophobically modified telechelic poly(*N*-isopropylacrylamides) in water. *Macromolecules 39*, 341–348.

(24) Xia, Y., Burke, N. A. D., and Stöver, H. D. H. (2006) End group effect on the thermal response of narrow-disperse poly(*N*-isopropylacrylamide) prepared by atom transfer radical polymerization. *Macromolecules 39*, 2275–2283.

(25) Cheng, N., Liu, W. G., Cao, Z. Q., Ji, W. H., Liang, D. C., Guo, G., and Zhang, J. Y. (2006) A study of thermoresponsive poly(N-isopropylacrylamide)/polyarginine bioconjugate non-viral transgene vector. *Biomaterials 27*, 4984–4992.

(26) Sun, S. J., Liu, W. G., Cheng, N., Zhang, B. Q., Cao, Z. Q., Yao, K. D., Liang, D. H., Zuo, A. J., Guo, G., and Zhang, J. Y. (2005) A thermoresponsive chitosan-NIPAAm/vinyl laurate copolymer vector for gene transfection. *Bioconjugate Chem. 16*, 972–980.

(27) Clements, B. A., Bai, J., Kucharski, C., Farrell, L. L., Lavasanifar, A., Ritchie, B., Ghahary, A., and Uludag, H. (2006) RGD conjugation to polyethyleneimine does not improve DNA delivery to bone marrow stromal cells. *Biomacromolecules 7*, 1481–1488.

(28) Lavigne, M. D., Pennadam, S. S., Ellis, J., Yates, L. L., Alexander, C., and Górecki, D. C. (2007) Enhanced gene expression through temperature profile-induced variations in molecular architecture of thermoresponsive polymer vectors. *J. Gene Med. 9*, 44–54.

BC700478S

Novel Cell-Penetrating Calpain Substrate

Zoltán Bánóczi,[†] Anita Alexa,[‡] Attila Farkas,[‡] Péter Friedrich,[‡] and Ferenc Hudecz*[,†,§]

Research Group of Peptide Chemistry, Eötvös L. University, Hungarian Academy of Sciences, P.O. Box 32, 1518 Budapest, 112 Hungary, Institute of Enzymology, Biological Research Center, Hungarian Academy of Science, P.O. Box 7, 1518 Budapest, Hungary, and Department of Organic Chemistry, Eötvös L. University, Pázmány P. S 1/A, H-1117 Budapest, Hungary. Received January 17, 2008; Revised Manuscript Received April 15, 2008

The calpain enzymes play important roles in numerous processes in the cell. *In vivo* analysis of calpain activity might be useful for clarification of their role in different diseases. Our early results suggested that a peptide substrate, *Dabcyl*-TPLKSPPPSPR-*EDANS*, based on the calpain cleavage sequences is suitable for developing a new cell-penetrating calpain substrate. This conjugate with the Dabcyl and EDANS fluorophores as a FRET pair is specific for calpain even in cell lysate, but unfortunately has poor cell uptake. Therefore, we have modified this sequence by C-terminal elongation with heptaarginine unit possessing cell-penetrating activity. In order to preserve the necessary distance between the two FRET partners, we inserted a Glu residue between the substrate and heptaarginine parts of the peptide. Thus, the cell-penetrating substrate *Dabcyl*-TPLKSPPPSPRE(*EDANS*)R_7 was synthesized. This peptide not only retained the substrate property, but was a better substrate of Calpain B enzyme. The cell uptake of the substrate conjugate was studied by fluorescence microscopy and flow cytometry. The results showed that the conjugate enters COS-7 cells more efficiently than the peptide substrate without heptaarginine. The uptake occurs already at low concentration and the compound is distributed homogeneously inside cells. These observations might indicate that this new cell-penetrating substrate could be useful for determining calpain activity in cell lysate or in intact cells of various origins.

INTRODUCTION

Calpains are intracellular cysteine proteases whose catalytic site is analogous to that of the papain-like protease domain (*1, 2*). The family has 14 members showing various patterns of expression. The ubiquitous forms of them are the μ- and m-calpains (calpains 1 and 2, respectively). Calpains play crucial roles in cell adhesion and motility, exocytosis, signal transduction, cell cycle progression, and regulation of gene expression (*3–7*). Calpain overactivation is associated with the pathogenesis of a wide range of disorders (*8*). For *in vitro* study of calpain activity, short peptide sequences were used with modification by a fluorophore (*9*). Since these substrates are not specific to calpain and are quite poor in kinetic terms, there have been attempts to create better substrates for specific applications. The study of a huge number of cleavage sites of calpain in different substrates resulted in an amino acid preference matrix in the P1−P7′ position (*10*). From the most preferred amino acids, a new substrate, *Dabcy*l-TPLKSPPPSPR-*EDANS*, was prepared. By this peptide substrate, it was possible to measure calpain activation in COS-7 cell lysates, and only after lipofection intracellular calpain activity in *Drosophila* S2 cells. However, this construct was not able to penetrate cells.

For *in vivo* measurement of calpain activity, Vanderklish et al. (*11*) constructed a vector encoding for an 11 amino acid long sequence of α-spectrin flanked by two fluorescent protein domains to serve as an *in vivo* FRET substrate. This construct led to identifying dendritic spines in which calpain is activated during the excitatory synaptic activity. Mittoo et al. followed a similar approach to design two FRET substrates using the same α-spectrin sequence (*12*). In the third case, protein−substrate of calpain, MAP2, labeled with DTAF to monitor calpain continuously was used (*13*).

Another strategy is the application of a small labeled dipeptide calpain substrate (Boc-LM-CMAC) for *in vivo* activity measurement. In this case, calpain activity could be determined by measuring the hydrolysis of the dipeptide substrate using fluorescence microscopy (*14*) with the excitation and emission wavelengths $\lambda = 350$ and $\lambda = 430$ nm, or by flow cytometry (*15*). After the internalization, the nonfluorescent dipeptide substrate is conjugated to an intracellular thiol group via chloromethyl group of aminocoumarin (CMAC), resulting in a membrane-impermeable form allowing substrate accumulation within the cell (*16*). The proteolytic cleavage of this peptide by calpain produces aminocoumarin derivative, which possesses blue fluorescence.

Several oligopeptides of natural and/or synthetic origin have been discovered with cell membrane penetrating capability. The first peptide sequences came from the HIV-1 Tat (*17, 18*) and the Antennapedia protein of *Drosophila* (*19*). Based on the polycationic nature of the cell-penetrating peptides, the ability to enter cells of oligomers of 3−9 Arg, Lys, Orn, or His residues were tested. It was found that hexa- and octaarginine were taken up far more effectively than other polycationic oligopeptides of equal length (*20–22*). These peptides could go through the cell membrane with different covalently attached cargos (peptides, peptide-nucleic acid, oligonucleotide) (review (*23*)).

Our aim was to synthesize a new cell-penetrating substrate of calpain, based on the *Dabcyl*-TPLKSPPPSPR-*EDANS* peptide, by conjugation with octaarginine. Considering that the sequence contains one Arg at the C-terminal, and it is not necessary to have all eight Arg residues in one block in the sequence (*24*), in our design−*Dabcyl*-TPLKSPPPSPRE-(*EDANS*)R_7−a Glu residue was inserted between the substrate and the heptaarginine parts of the target peptide−conjugate. Thus, in this construct we also preserved the necessary distance between the two FRET partners. The substrate properties of the

* Address correspondence to Ferenc Hudecz, Tel.: +36-1-2090-555/6428, Fax: +36-1-372-2620; E-mail: fhudecz@ludens.elte.hu.
[†] Research Group of Peptide Chemistry, Eötvös L. University.
[‡] Biological Research Center, Hungarian Academy of Science.
[§] Department of Organic Chemistry, Eötvös L. University.

10.1021/bc800021y CCC: $40.75 © 2008 American Chemical Society
Published on Web 06/05/2008

new construct were studied by using calpain B enzyme. We report here also that the cell-penetrating variant not only retained the substrate properties, but was even better than the free peptide substrate. In contrast to the free peptide, we found that the conjugate internalized efficiently and distributed nearly homogeneously in COS-7 cells as demonstrated by fluorescent microscopy studies. As the concentration dependence of internalization studied by flow cytometry indicates, the conjugate had already penetrated with high efficiency at low concentration. We have also demonstrated that the enzyme activity could be suitably measured in cell lysate and living cells by this new conjugate. These data suggest its potential for measurements of calpain activity *in vivo*.

EXPERIMENTAL PROCEDURES

Materials. All amino acid derivatives were purchased from Bachem (Bubendorf, Switzerland) and Reanal (Budapest, Hungary), while thioanisole, ethandithiol (EDT), *N*-diisopropylethylamine (DIEA), 1-hidroxybenztriazole (HOBt), benztriazol-1-yloxy)tris(dimethyl-amino)phosphonium-hexafluorophosphate (BOP), *N*,*N*′-diisopropylcarbodiimide (DIC), piperidine, 1,8-diazabicyclo[5.4.0]undec-7-ene (DBU), trifluoracetic acid (TFA), and 5(6)-carboxyfluorescein (cf) were Fluka (Buchs, Switzerland) products. The Rink-amide MBHA resin and *N*-{4-[4′-(dimethylamino)phenylazo]benzoyloxy}succinimide (Dabcyl-OSu) were purchased from Novabiochem (Laufelfingen, Switzerland). The 5-(2-aminoethylamino)-1-naphtalenesulfonic acid (EDANS) was purchased from Sigma-Aldrich Kft. (Budapest, Hungary). Solvents (DMF, DCM, diethyl ether, acetonitrile) for synthesis and purification were obtained from Reanal (Budapest, Hungary).

The fluorescent substrate LY-AMC (catalog no. S 1153) and all other chemicals used in biological experiments were purchased from Sigma. The buffers were prepared with ion-exchanged distilled water.

Analytical RP-HPLC. Analytical HPLC was performed on a Knauer (Herbert Knauer GmbH, Berlin, Germany) system using a Phenomenex SYNERGI MAX-RP column (250 × 4.6 mm i.d., 4 μm silica, 80 Å pore size) (Torrance, CA) as a stationary phase. Linear-gradient elution (0 min 0% B; 5 min 0% B; 50 min 90% B) was generated using 0.1% TFA in water as eluent A and 0.1% TFA in acetonitrile−water (80:20, V/V) as eluent B. A flow rate of 1 mL/min was applied at ambient temperature. Peaks were detected at $\lambda = 220$ nm. The samples were dissolved in eluent B. The crude products were purified on a semipreparative Phenomenex Jupiter C18 column (250 × 10 mm i.d., 10 μm silica, 300 Å pore size) (Torrance, CA). The flow rate was 4 mL/min. Peaks were detected at $\lambda = 220$ nm.

Mass Spectrometry. The molecular mass of the conjugates was measured by ESI-MS. Positive ion electrospray ionization mass spectrometric analysis was performed on a Bruker Daltonics Esquire 3000 plus (Germany). The samples were dissolved in acetonitrile−water (50:50, V/V), containing 0.1% acetic acid.

Synthesis of Dabcyl-TPLKSPPPSPRE(EDANS)RRRR-RRR-NH_2 Peptide. This conjugate was synthesized manually by solid-phase methodology on Rink-amide resin (0.230 g, 0.7 mmol/g) by Fmoc/^{t}Bu strategy. Fmoc protection from the N^α-amino group was removed with 2% piperidine and 2% DBU in DMF (2 + 2 + 5 + 10 min) followed by washing with DMF (8 × 0.5 min). Amino acid derivatives, DIC, and HOBt were dissolved in DMF in 3 molar excess for the resin capacity to the coupling proceeded for 60 min at RT. Then, the resin was washed (DMF (2 × 0.5 min), DCM (3 × 0.5 min)). The efficiency of the coupling was checked by ninhydrin (*25*) or isatin (*26*) tests. After the removal of the last N^α-Fmoc group, a Dabcyl group was introduced to the *N*-terminus of the peptidyl-resin by 1.5 equiv Dabcyl-OSu dissolved in DMF. The reaction was carried out overnight. Peptide was cleaved by 10 mL TFA, using 0.75 g phenol, 0.5 mL distilled ion-exchanged water, 0.5 mL thioanisole, and 0.25 ethandithiol as scavengers. Crude product was precipitated by dry diethyl ether, dissolved in 10% acetic acid, and freeze-dried. Crude *Dabcyl*-TPLKSPPPSPRERRRRRRR-NH_2 (21 mg, 8 μmol) was dissolved in 1 mL DMF, and 2 equiv Fmoc-OSu (5 mg, 16 μmol) and 1 equiv DIEA (2 μL, 8 μmol) were added to the solution. The reaction was performed for 3 h; after the mixture was purified by RP-HPLC, gradient was 0 min 20% B, 7 min 20% B, 52 min 85% B. The EDANS was coupled to the *Dabcyl*-TPLK(*Fmoc*)SPPPSPRERRRRRRR-NH_2 peptide (20 mg, 7 μmol) in 1 mL DMF. 2 equiv EDANS (4 mg, 14 μmol), BOP (6 mg, 14 μmol), HOBt (2 mg, 14 μmol), and 4 equiv DIEA (5 μL, 28 μmol) were used in the coupling reaction. After 1 day, the solution was purified by RP-HPLC, gradient was 0 min 35% B, 7 min 35% B, 52 min 80% B. The product was not pure but this fraction was used in the next step. Fmoc group was removed by 20% piperidine in DMF. After acidification, the cleavage mixture was purified by RP-HPLC; gradient was 0 min 20% B, 7 min 20% B, 52 min 85% B.

Synthesis of 5(6)-Carboxyfluorescein Labeled Peptides. The *H*-TPLKSPPPSPRE-NH_2 peptide amide was synthesized by solid-phase methodology on Rink-amide resin (50 mg, 0.72 mmol/g) using Fmoc chemistry on a Syro (Multisyntech, Written, Germany) peptide synthesizer. The Fmoc protection from the N^α-amino groups was removed with 40% piperidine in DMF (2 + 15 min) followed by washing with DMF (6 × 0.5 min). For coupling, amino acid derivatives, DIC and HOBt dissolved in DMF were used in 4 molar excess for the resin capacity. The reaction proceeded for 60 min at RT. Then, the resin was washed (DMF (4 × 0.5 min) and the coupling process was repeated. After the removal of last N^α-Fmoc group, a Dabcyl group was introduced to the *N*-terminus of the peptidyl-resin by 1.5 equiv Dabcyl-OSu dissolved in DMF. The reaction was carried out overnight. Peptide was cleaved by 10 mL TFA, using 0.75 g phenol, 0.5 mL D.I. water, 0.5 mL thioanisole, and 0.25 ethandithiol as scavengers. Crude product was precipitated by dry diethyl ether, dissolved in 10% acetic acid, and freeze-dried. The crude product was purified on FPLC System (Pharmacia, Uppsala, Sweden). 5 mg (3.2 μmol) *Dabcyl*-TPLKSPPPSPRE-NH_2 was reacted with 2.5 mg (4 μmol) pentachlorophenyl ester of 5(6)-carboxyfluorescein (cf-OPcp) in 0.5 mL DMF in the presence of 0.8 μL (4.8 μmol) DIEA overnight. The cf labeled substrate was purified by RP-HPLC. Linear gradient elution was applied: 0 min 25% B, 8 min 25% B, 53 min 75% B.

Dabcyl-TPLK(*cf*)SPPPSPRERRRRRRR-NH_2 was prepared in solution. 5 mg (2 μmol) *Dabcyl*-TPLKSPPPSPRERRRRRRR-NH_2 was reacted with 2 mg (3.2 μmol) cf-OPcp in DMF in the presence of 0.5 μL (3 μmol) DIEA overnight. The reaction mixture was purified by RP-HPLC system. Linear gradient elution was applied: 0 min 5% B, 10 min 25% B, 55 min 70% B.

Enzyme Assay. Kinetic analysis was carried out with cell-penetrating substrate using *Drosophila* Calpain B enzyme in a Jasco FP-6300 spectrofluorometer (Essex, U.K.), in a 3 × 3 mm quartz cuvette at room temperature. The excitation wavelength was $\lambda = 320$ nm, and emission was monitored at $\lambda = 480$ nm. The reactions were carried out in 50 μL calpain buffer (50 mM TRIS, 150 mM NaCl, 1 mM EDTA, pH 7.5), which contained 20 mM $CaCl_2$, 0.5 μM Calpain B, and the cell-penetrating substrate with concentration in the range 1−200 μM. The reaction was followed by continuously recording the increase of fluorescence intensity corresponding to the cleavage of the substrate. The initial rate of change of the fluorescence

intensity was determined from the progress curves, using *MicroCal Origin* software.

Analysis of Cellular Uptake by Fluorescent Microscopy. COS-7 cells were grown in Dulbecco's modified Eagle's medium (Sigma-Aldrich Kft, Budapest, Hungary) at 37 °C and 5% CO_2 content. The substrates were dissolved in 0.01 M PBS (pH = 7.4) and used at a final concentration of 330 μM. Cells were incubated for 4 h with substrates, then washed with PBS. The fluorescence of cells after fixation (3% *para*-formaldehyde for 10 min) mounted with MOWIOL 4−88 (Calbiochem, MERCK Kft., Budapest, Hungary) was analyzed by a Leica DMLS fluorescent microscope equipped with a Spot RT color digital camera (Diagnostic Instruments, Livingston, U.K.).

Analysis of Cellular Uptake by Flow Cytometry. COS-7 cells were plated into 24 well plates 24 h prior to treatment. Cells were washed twice with serum-free medium. The cells were incubated with the labeled peptides and conjugates for 3 h at 37 °C. Following the incubation, cells were trypsinized with PBS containing 5 mg/mL trypsin and 2 mg/mL EDTA. The change of cellular fluorescence was analyzed by flow cytometry on a BD LSR II cytometer. Data were analyzed with FACSDiVa and *WinMDI 2.9* software. Fluorescence mean values of untreated control were subtracted from the mean fluorescence of treated samples. Statistical analysis of data was performed using Student's *t* test at the 95% confidence level.

Measurement of Intracellular Calpain Activity. *Drosophila melanogaster* Schneider S2 cells ($1-1.5 \times 10^7$) were collected by centrifugation at 2000 rpm for 5 min and washed three times with 10 mL of 0.01 M PBS (pH 7.4). Collected cells were resuspended in 300 μL 0.05 M TRIS buffer containing 0.15 M NaCl, 10 mM EDTA, 10 mM β-mercaptoethanol, 10 mM benzamidine, and 1 mM phenylmethylsulphonyl fluoride, and then were sonicated (16 μm, MSE sonicator, West Sussex, U.K.) four times for 10 s with 1 min breaks at 0 °C. After sonication, the cell lysate was centrifuged at 100 000 × *g* for 20 min at 4 °C, and the supernatant was used for fluorometric calpain activity measurement. In the case of the induction of the exogenous calpain gene, cells were incubated with 0.7 μM $CuSO_4$ for 12−16 h before collection.

1 mM LY-AMC or 100 μM *Dabcyl*-TPLKSPPPSPRE(*EDANS*)RRRRRRR-NH_2 were used as substrate for fluorometric calpain activity measurement in 50 μL calpain buffer (50 mM TRIS, 150 mM NaCl, 1 mM EDTA, pH 7.5), which contained 25 μL S2 cell lysate, 5 mM EDTA, or 10 mM free Ca^{2+}. The final concentration of the inhibitor (Calpain Inhibitor I) was 20 μM. The excitation and emission wavelengths were $\lambda = 320$ nm and $\lambda = 480$ nm, respectively.

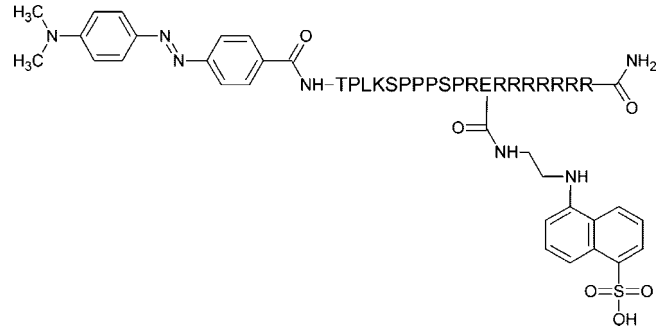

Figure 1. Structure of cell-penetrating calpain substrate.

Activity Measurement with Cells Incubated with Cell-Penetrating Substrate. Confluent S2 cells were incubated with 150 μM *Dabcyl*-TPLKSPPPSPRE(*EDANS*)RRRRRRR-NH_2 substrate in 1 mL Drosophila-SFM medium at 25−28 °C for 20 h. After incubation, cells were washed with 0.01 M PBS (pH 7.4) three times and then gently suspended in 1 mL calpain buffer (50 mM TRIS, 150 mM NaCl, 1 mM EDTA, pH 7.5) without EDTA. Cells were collected by centrifugation (2000 rpm × 5 min) and washed calpain buffer without EDTA until the supernatant became colorless. Washed cells, $1-1.2 \times 10^7$ in 300 μL calpain buffer without EDTA, were separated into two: one-half of them were used for *in vivo* activity measurement (with the cells intact) and the other half were lysed and used for fluorometric calpain activity measurement as described above.

In vivo activity measurements were carried out in a Jasco FP-6300 spectrofluorometer (Essex, U.K.), in a 3 × 3 mm quartz cuvette at room temperature using 50 μL cell suspension. Fluorescence intensity was monitored continuously from the start, and at about 1000 s after the initiation of the measurement, 20 μM ionomycin (from 1 mM stock solution) was added. After 1200 s, the fluorimeter was restarted, keeping the cuvette untouched, and an additional 500 s later, the cells were stirred up and the measurement was continued.

RESULTS

Synthesis of Cell-Penetrating Calpain Substrate. For the synthesis of new cell-penetrating calpain substrate, the peptide substrate (*10*) was elongated by a Glu and seven Arg residues at its C-terminus (Figure 1). The modified substrate sequence was prepared by solid-phase peptide synthesis using Fmoc/^{t}Bu strategy as outlined in Scheme 1. After the cleavage of the last N^{α}-Fmoc protecting group, Dabcyl fluorophore was coupled to the *N*-terminal amino group of resin-bound peptide by using

Scheme 1. Outline of the Synthesis of Cell-Penetrating Calpain Substrate

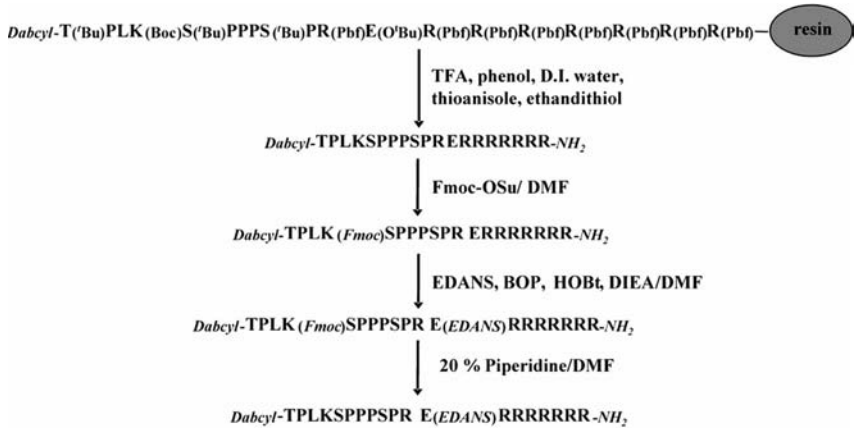

Table 1. Characteristics of Substrate Peptides

compounds	R_t[a] (min)	$[M+H]^{+b}$ $M_{cal.}$	$[M+H]^{+b}$ $M_{meas.}$
Dabcyl-TPLKSPPPSPRE (*EDANS*)RRRRRRR-NH_2	26.5	2897.0	2896.9
Dabcyl-TPLK(*cf*)SPPPSP RERRRRRR-NH_2	31.5	3007.0	3007.2
Dabcyl-TPLK(*cf*)SPPPSP RE-NH_2	33.2	1914.2	1913.6

[a] Column: Phenomenex Jupiter C18 (250 × 4.6 mm, 5 μm, 300 Å). Linear gradient elution (0 min 0% B; 5 min 0% B; 50 min 90% B) with eluent A (0.1% TFA in water) and eluent B (0.1% TFA in acetonitrile−water (80:20, V/V)) was used at a flow rate of 1 mL/min at ambient temperature. Peaks were detected at λ = 220 nm. [b] ESI-MS, masses presented as $[M+H]^+$ were calculated from multiple charged ions.

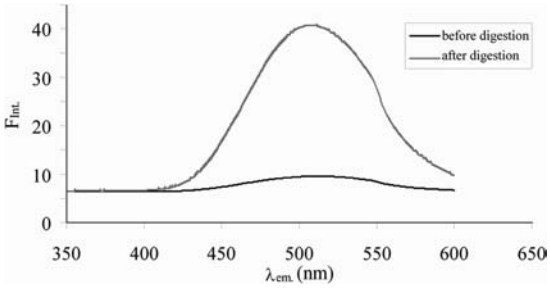

Figure 2. Fluorescence intensity before and after digestion of cell-penetrating substrate by isolated Calpain B enzyme. The substrate (200 μM) was digested by Calpain B enzyme (0.5 μM) in calpain buffer (50 mM TRIS, 150 mM NaCl, 1 mM EDTA, pH 7.5) for 40 min, and the fluorescence spectrum of the substrate was recorded before (solid line) and after (dashed line) digestion.

its active ester derivative (Dabcyl-OSu). The substrate containing Dabcyl group was cleaved from the resin by TFA cleavage mixture. The crude peptide was used in the next reactions without purification. The ϵ-amino group of Lys residue in the sequence was temporarly protected by Fmoc group, coupled in solution. Then, the EDANS fluorophore was attached to the semiprotected peptide by BOP/HOBt coupling reagent. The cell-penetrating FRET substrate was isolated by RP-HPLC purification after the cleavage of Fmoc group (Scheme 1). The compounds were characterized by analytical RP-HPLC and ESI-MS (Table 1). Their purity was higher than 95% based on analytical HPLC.

Enzyme Kinetics. The kinetic parameters of cell-penetrating FRET substrate (*Dabcyl*-TPLKSPPPSPRE(*EDANS*)RRRRRRR-NH_2) were studied by using Calpain B enzyme. Data are summarized in Figure 2. Before cleavage by calpain, the level of fluorescence is low, but calpain cleavage results in an about 4-fold increase in fluorescence intensity. The increase in the fluorescence intensity indicated that cell-penetrating substrate is cleaved by Calpain B enzyme and this level of the change is enough for the kinetic measurements.

Kinetic parameters were determined with digestion of cell-penetrating substrate using it in the 1−200 μM concentration range. The change of fluorescence intensity was recorded and parameters were calculated. Based on the kinetic parameters one could appreciate that the cell-penetrating substrate conjugate is an appropriate substrate of Calpain B enzyme (k_{cat} = 0.2 s^{-1} and k_{cat}/K_M = 5000 M^{-1} s^{-1}). In comparison to the free peptide substrate (*Dabcyl*-TPLKSPPPSPR-*EDANS*) (k_{cat} = 0.17 s^{-1} and k_{cat}/K_M = 680 M^{-1} s^{-1}) (*10*), the conjugation with heptaarginine not only preserved but increased the sensitivity of Calpain B enzyme. However, the molar change in the fluorescence intensity is dependent on the initial concentration of cell-penetrating

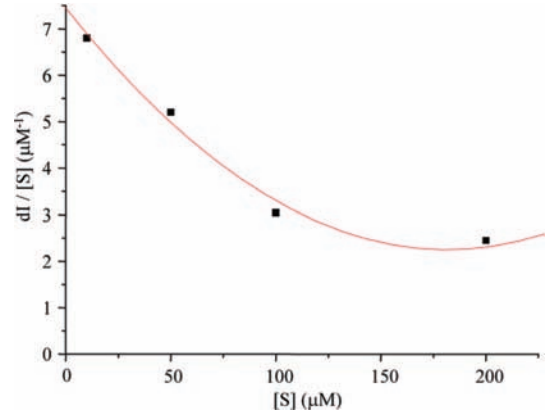

Figure 3. Molar change of fluorescence intensity as a function of the initial concentration of cell-penetrating substrate conjugate. The substrate at different concentrations was digested by Calpain B enzyme (0.5 μM) in calpain buffer (50 mM TRIS, 150 mM NaCl, 1 mM EDTA, pH 7.5) for 10 min, and the fluorescence spectrum of the substrate was recorded.

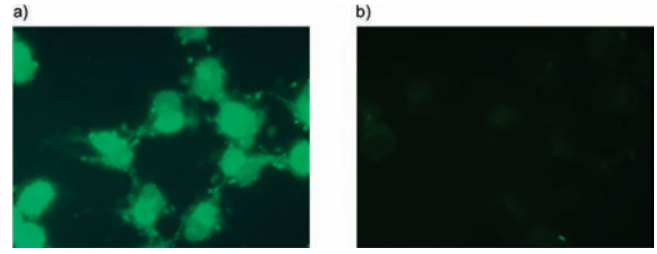

Figure 4. Internalization of substrates into COS-7 cells. The COS-7 cells were treated with 330 μM solution of (a) cell-penetrating substrate conjugate, (b) free peptide substrate for 4 h at 37 °C, and then the fixed cells were examined by fluorescence microscopy.

substrate (Figure 3). At low concentration, the degree of change was decreased steeply and at c = 100 μM reached minimum value.

Internalization of Calpain Substrates into COS-7 Cells. The internalization properties of the substrates were studied first by fluorescence microscopy. COS-7 cells were treated by the peptide substrate (*Dabcyl*-TPLKSPPPSPR-*EDANS*) and cell-penetrating substrate conjugate (*Dabcyl*-TPLKSPPPSPRE(*EDANS*)RRRRRRR-NH_2), then the fluorescence intensity of cells was recorded (Figure 4). In case of the free peptide substrate, the cells had almost no fluorescence intensity. When the cells were treated by cell-penetrating substrate conjugate, high fluorescence was detected and the fluorescence intensity was found to be homogeneous in cells.

The concentration dependence of cell uptake of cf labeled substrates was studied by flow cytometry. COS-7 cells were treated with the labeled substrates (*Dabcyl*-TPLK(*cf*)SPPPSPRE-NH_2 and *Dabcyl*-TPLK(*cf*)SPPPSPRERRRRRRR-NH_2), and then cells were trypsinised and their fluorescence intensity was measured by flow cytometry (Figure 5). Peptide substrate showed poor internalization at 10 μM concentration (F_{mean} = 334), which could be increased by elevation of the concentration (at 50 μM concentration F_{mean} = 1159.5). On the other hand, uptake of cell-penetrating substrate conjugate was significant (F_{mean} = 15 097.5) at 10 μM concentration. At higher concentration, the efficiency of penetration was at a similar level (at 50 μM, F_{mean} = 12 724.5).

Measurement of Intracellular Calpain Activity. Considering that the cell-penetrating substrate conjugate seemed to be a good substrate *in vitro* (Figure 2) and could translocate into COS-7 cells (Figures 4 and 5), we extended our studies to evaluate its applicability for measurements of intracellular

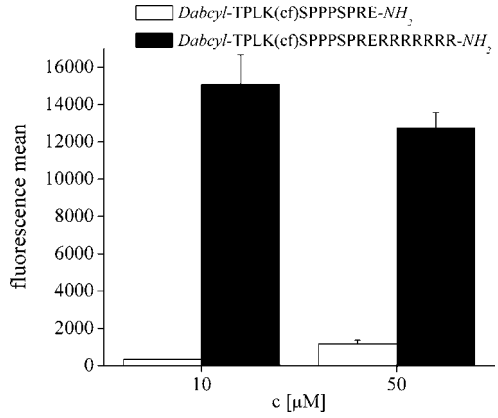

Figure 5. Concentration-dependent cell uptake of *Dabcyl*-TPLK(cf)-SPPPSPRE-NH_2 and *Dabcyl*-TPLK(cf)SPPPSPRERRRRRRR-NH_2 by COS-7 cells. COS-7 cells were incubated with the solution of substrates at $c = 10$ or 50 μM for 3 h. Then, the cells were trypsinized and fluorescence intensity was measured by flow cytometry.

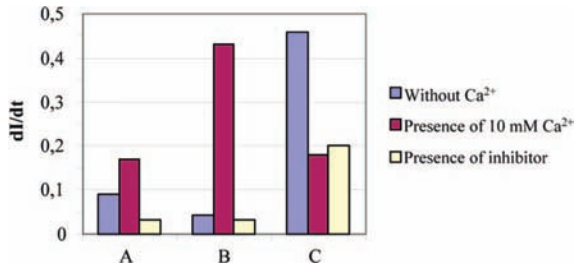

Figure 6. Change in the fluorescence intensity of *Dabcyl*-TPLKSP-PPSPRE(*EDANS*)RRRRRRR-NH_2 A. *Dabcyl*-TPLKSPPPSPRE(*EDAN-S*)RRRRRRR-NH_2 added to S2 cell lysate. B. *Dabcyl*-TPLKSP-PPSPRE(*EDANS*)RRRRRRR-NH_2 added to lysate of S2 cell overexpressing calpain. C. LY-AMC added to lysate of S2 cell overexpressing calpain.

calpain activity. Therefore, first we used cell-penetrating substrate to determine calpain activity in the lysate of *Drosophila melanogaster* S2 cells. The cell-penetrating substrate conjugate was added to the cell lysate and the change in the fluorescence intensity was measured. We found that the substrate was cleaved in the cell lysate, which could be inhibited by Calpain inhibitor I (Figure 6 column A). The increase of the fluorescence intensity was the largest in presence of Ca^{2+}. In order to prove the calpain cleavage of substrate, lysate of cells overexpressing calpain was used (Figure 6 column B). We observed the same phenomenon as in case of normal cells. It is interesting to note that the differences between the fluorescence intensity changes recorded in the absence or in the presence of Ca^{2+} were more expressed. As control, the commercially available LY-AMC substrate was also included into experiments with cell lysate of calpain-overexpressing cells (Figure 6 column C). No change in the fluorescence intensities was detected in relation to calpain activity.

What happens with the substrate in the cells is an important question. Does it remain intact or is it digested intracellular by enzyme? To address this, the S2 cells were treated with the solution of cell-penetrating substrate conjugate and were lysed. The activity of endogenous calpain in the lysate was measured after Ca^{2+} activation. Data are summarized in Figure 7. In the absence of Ca^{2+} ion, only the base fluorescence intensity was detected. This was not altered until the time point of Ca^{2+} ion addition (0−700 s). The addition of Ca^{2+} initiated the increase in the fluorescence intensity, an indication of the activation of calpain.

In the third experiment, the activity of endogenous calpain was measured in living cells. The S2 cells were treated with

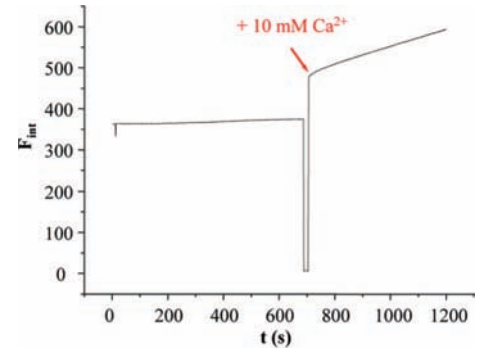

Figure 7. Change of fluorescence intensity of lysate of cells treated with cell-penetrating substrate conjugate. The change of fluorescence intensity in the presence of Ca^{2+} indicates the difference of enzyme activity in the lysate of S2 cells after treatment by cell-penetrating substrate. $\lambda_{ex.} = 320$ nm, $\lambda_{em.} = 480$ nm.

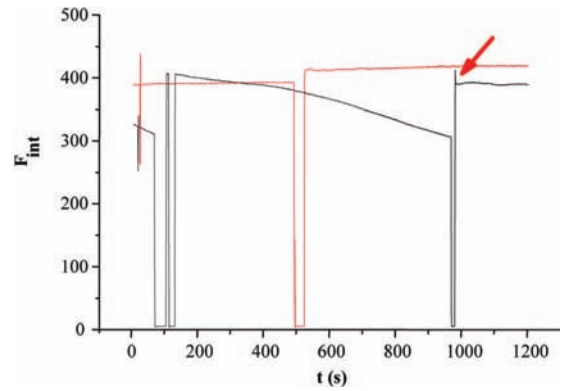

Figure 8. Change in the fluorescence intensity of the S2 cell suspension. The S2 cells were incubated with cell-penetrating substrate and the fluorescence intensity of cell suspension was detected. The black curve shows the decreasing fluorescence intensity, due to the sedimentation of cells. After addition of ionomicin (red arrow), a slight increase in the fluorescence intensity was measured (red curve).

cell-penetrating substrate; then, ionomycin was added to the cells and the fluorescence intensity was monitored. Results outlined in Figure 8 show that the fluorescence intensity is decreased (black curve) due to the sedimentation of cells. After the addition of 10 μM ionomycin (red arrow), the fluorescence intensity slightly increased, indicating calpain activation and substrate cleavage.

DISCUSSION

The calpains, Ca^{2+} dependent Cys proteases, play important roles in many different physiological and pathological processes. To study their function, dipeptide substrates are widely used. To understand better the calpain cleavage specificity, the preferred amino acids in the P_4-P_7' position of 101 calpain cleavage site was studied and a preference matrix was constructed (*10*). We found earlier that the FRET derivative of peptide (*Dabcyl*-TPLKSPPPSPR-*EDANS*) derived from the preference matrix was a better substrate than the LY-AMC dipeptide (*10*).

Our aim was to prepare a conjugate of the matrix substrate to enhance the internalization efficiency and to measure the activity of intracellular calpain by conjugation with heptaarginine. Considering the presence of an Arg residue in the substrate sequence, seven Arg residues were attached to the C-terminus of substrate. For the FRET analysis, the chromophore and the fluorophore must be within a given distance. In the free substrate peptide, the distance of the two groups was appropriate for FRET. In our cell-penetrating

substrate conjugate, incorporation of seven Arg residues between the chromophores might diminish FRET. To avoid this, a Glu residue was inserted between the substrate and the heptaarginine part. In this case, the eight Arg residues do not connect continuously. It was demonstrated before that the number of Arg residues in the sequence is important for sufficient penetration, but not their linear connection (*24*). The Dabcyl chromophore was attached at the *N*-terminus of the cell-penetrating peptide, while the EDANS fluorophore to the γ-carboxylic group of Glu residue.

Though the sequence of substrate was only slightly modified in respect to FRET pairs, first the FRET phenomenon was studied. Our result suggests that the distance between the FRET pair was not higher than their Förster radius (33 Å), and the change in fluorescence intensity was sufficient for the detection of calpain activation *in vitro*.

Next, the substrate properties of the conjugate were studied. We observed that the presence of seven Arg residues does not interfere with the substrate properties, but rather improves them. The k_{cat}/K_M of cell-penetrating substrate was higher, indicating that it is a better substrate than the free peptide. The mechanism of the effect of heptaarginine had not been studied. Considering that this part of the conjugate is outside the sequence responsible for FRET, cleavage(s) in this part of the molecule were not detected in the experiments. It is attractive to speculate that the presence of heptaarginine results in such a conformer, which could fit better into the substrate pocket, or the positively charged heptaarginine could improve the substrate binding to the enzyme. The molar fluorescence intensity change is dependent on the concentration of cell-penetrating substrate. At low concentrations, the change was higher and decreased steeply on increasing concentration.

The internalization and distribution of the conjugate in COS-7 cells were followed by fluorescent microscopy. As expected, the free peptide substrate did not exhibit internalization; the cells had no fluorescence. In contrast, if the cells were treated with cell-penetrating substrate conjugate, high fluorescence intensity was observed. The internalized cell-penetrating substrate distributed nearly homogeneously in the cytosol. Based on these results, one could conclude that the conjugation of seven Arg residues resulted in marked and detectable internalization of the peptide substrate.

For studying the effect of substrate concentration, cell uptake was also monitored by flow cytometry. It should be noted that for the sake of comparison the Glu-modified substrate, as a component of the cell-penetrating substrate conjugate, was used. The free substrate peptide showed poor internalization at 10 μM concentration. The conjugation of seven Arg residues resulted in highly efficient translocation even at this concentration. The increase of concentration (to 50 μM) could slightly improve the cell uptake of substrate peptide; however, the cell-penetrating substrate internalized almost with the same efficiency. The results suggest that the cell-penetrating substrate can efficiently penetrate into cells even at low concentration.

The substrate properties of new cell-penetrating substrate conjugate and its efficient internalization into COS-7 cells suggest that this compound could be suitable for *in vivo* measurement of calpain activity. To study the specificity of the new substrate, calpain activity was measured in S2 cell lysate in comparison with commercially available LY-AMC substrate. While the dipeptide substrate did not signal calpain activation, the conjugate was able to detect calpain activity after addition of Ca^{2+} ion. The differences between the signal with and without Ca^{2+} addition suggest that this substrate is appropriate for activity measurement in cell lysate. To prove the calpain function in the substrate cleavage, lysate of S2 cells overexpressing calpain was also examined. In this case, the fluorescence intensity change in the presence of Ca^{2+} was remarkably higher as compared to the effect observed in the absence of the ion.

In order to have some information about the fate of the conjugate after internalization, S2 cells were treated with the cell-penetrating substrate conjugate and lysed after. We found that Ca^{2+} addition resulted in increased fluorescence intensity. This might be indicative of retained substrate integrity and cleavage only after activation of calpain. The fluorescence intensity of cell-penetrating substrate conjugate treated S2 cell suspension increased significantly after addition of ionomycin. This result indicates that intracellular release of Ca^{2+} could induce activation as well and might suggest that the new cell-penetrating substrate conjugate is suitable for measurement of intracellular calpain activity.

ACKNOWLEDGMENT

This study was supported by grants: OTKA K 68285, OTKA NK-60-723, GVOP-3.2.1-2004-04-0352/3.0, GVOP-3.2.1-2004-04-0005/3.0, Medichem2, NKFP-1A005-04. A.A. acknowledges the support of a Bolyai János Scholarship.

LITERATURE CITED

(1) Sorimachi, H., Ishiura, S., and Suzuki, K. (1997) Structure and physiological function of calpains. *Biochem. J. 328*, 721–732.

(2) Sorimachi, H., and Suzuki, K. (2001) The structure of calpain. *J. Biochem. (Tokyo) 129*, 653–664.

(3) Goll, D. E., Thompson, V., Li, F. H., Wei, W., and Cong, J. (2003) The calpain system. *Physiol. Rev. 83*, 731–801.

(4) Glading, A., Lauffenburger, D. A., and Wells, A. (2002) Cutting to the chase: calpain proteases in cell motility. *Trends Cell Biol. 12*, 46–54.

(5) Sato, K., and Kawashima, S. (2001) Calpain function in the modulation of signal transduction molecules. *Biol. Chem. 382*, 743–751.

(6) Rutledge, T. W., and Whiteheart, S. W. (2002) SNAP-23 is a target for calpain cleavage in activated platelets. *J. Biol. Chem. 277*, 37009–37015.

(7) Franco, S. J., and Huttenlocher, A. (2005) Regulating cell migration: calpains make the cut. *J. Cell Sci. 118*, 3829–3838.

(8) Huang, Y., and Wang, K. K. (2001) The calpain family and human disease. *Trends Mol. Med. 7*, 355–362.

(9) Sasaki, T., Kikuchi, T., Yumoto, N., Yoshimura, N., and Murachi, T. (1984) Comparative specificity and kinetic studies on porcine Calpain I and Calpain II with naturally occurring peptides and synthetic fluorogenic substrates. *J. Biol. Chem. 259*, 12489–12494.

(10) Tompa, P., Buzder-Lantos, P., Tantos, Á., Farkas, A., Szilágyi, A., Bánóczi, Z., Hudecz, F., and Friedrich, P. (2004) On the sequential determinants of calpain cleavage. *J. Biol. Chem. 279*, 20775–20785.

(11) Vanderklish, P. W., Krushel, L. A., Holst, B. H., Gally, J. A., Crossin, K. L., and Edelman, G. M. (2000) Marking synaptic activity in dendritic spines with a calpain substrate exhibiting fluorescence resonance energy transfer. *Proc. Natl. Acad. Sci. U.S.A. 97*, 2253–2258.

(12) Mittoo, S., Sundstrom, L. E., and Bradley, M. (2003) Synthesis and evaluation of fluorescent probes for the detection of calpain activity. *Anal. Biochem. 319*, 234–238.

(13) Tompa, P., Schád, E., Baki, A., Alexa, A., Batke, J., and Friedrich, P. (1995) An ultrasensitive, continuous fluorometric assay for calpain activity. *Anal. Biochem. 228*, 287–293.

(14) Glading, A., Uberall, F,., Keyse, S. M., Lauffenburger, D. A., and Wells, A. (2001) Membrane proximal ERK signaling is required for M-calpain activation downstream of epidermal growth factor receptor signaling. *J. Biol. Chem. 276*, 23341–23348.

(15) Niapour, M., and Berger, S. (2007) Flow cytometric measurement of calpain activity in living cells. *Cytometry A 71*, 475–85.

(16) Rosser, B. G., Powers, S. P., and Gores, G. J. (1993) Calpain activity increases in hepatocytes following addition of ATP. Demonstration by a novel fluorescent approach. *J. Biol. Chem. 268*, 23593–23600.

(17) Frankel, A. D., and Pabo, C. O. (1988) Cellular uptake of the Tat protein from human immunodeficiency virus. *Cell 55*, 1189–1193.

(18) Green, M., and Loewenstein, P. M. (1988) Autonomous functional domains of chemically synthesized humanism immunodeficiency virus Tat trans-activator protein. *Cell 55*, 1179–1186.

(19) Joliot, A., Pernelle, C., Deagostini-Bazin, H., and Prochiantz, A. (1991) Antennapedia homeobox peptide regulates neural morphogenesis. *Proc. Natl. Acad. Sci. U.S.A. 88*, 1864–1868.

(20) Mitchell, D. J., Kim, D. T., Steinman, L., Fathman, C. G., and Rothbard, J. B. (2000) Polyarginine enters cells more efficiently than other polycationic homopolymers. *J. Pept. Res. 56*, 318–325.

(21) Wender, P. A., Mitchell, D. J., Pattabiraman, K., Pelkey, E. T., Steinman, L., and Rothbard, J. B. (2000) The design, synthesis, and evaluation of molecules that enable or enhance cellular uptake: Peptoid molecular transporters. *Proc. Natl. Acad. Sci. U.S.A. 97*, 13003–13008.

(22) Futaki, S., Suzuki, T., Ohashi, W., Yagami, T., Tanaka, S., Ueda, K., and Sugiura, Y. (2001) Arginine-rich peptides. An abundant source of membrane-permeable peptides having potential as carriers for intracellular protein delivery. *J. Biol. Chem. 276*, 5836–5840.

(23) Hudecz, F., Bánóczi, Z., and Csík, G. (2005) Medium-sized peptides as built in carriers for biologically active compounds. *Med. Res. Rev. 25*, 679–736.

(24) Futaki, S., Nakase, I., Suzuki, T., Youjun, Z., and Sugiura, Y. (2002) Translocation of branched-chain arginine peptides through cell membranes: Flexibility in the spatial disposition of positive charges in membrane-permeable peptides. *Biochemistry 41*, 7925–7930.

(25) Kaiser, E., Colescott, R. L., Bossinger, C. D., and Cook, P. I. (1970) Color test of detection of free amino groups in the solid phase synthesis of peptides. *Anal. Biochem. 34*, 595–598.

(26) Kaiser, E., Bossinger, C. D., Colescott, R. L., and Olsen, D. B. (1980) Color test for terminal prolyl residues in the solid phase synthesis of peptides. *Anal. Chim. Acta 118*, 149–151.

BC800021Y

Enhanced Intracellular Delivery of the Reactive Oxygen Species (ROS)-Generating Copper Chelator D-Penicillamine via a Novel Gelatin−D-Penicillamine Conjugate

Anshul Gupte,[†] Saurabh Wadhwa,[‡] and Russell J Mumper*[,‡,§]

Department of Pharmaceutical Sciences, College of Pharmacy, University of Kentucky, Lexington, Kentucky 40536-0082, Division of Molecular Pharmaceutics, Eshelman School of Pharmacy, Center for Nanotechnology in Drug Delivery, and UNC Lineberger Comprehensive Cancer Center, University of North Carolina at Chapel Hill, North Carolina 27599-7360. Received January 31, 2008; Revised Manuscript Received May 15, 2008

D-Penicillamine (D-pen) is an established copper chelator. We have recently shown that the copper-catalyzed D-pen oxidation generates concentration-dependent hydrogen peroxide (H_2O_2). Additionally, D-pen coincubated with cupric sulfate resulted in cytotoxicity in human leukemia and breast cancer cells due to the extracellular generation of reactive oxygen species (ROS). The inherent physicochemical properties of D-pen such as its short *in vivo* half-life, low partition coefficient, and rapid metal catalyzed oxidation limit its intracellular uptake and the potential utility as an anticancer agent *in vivo*. Therefore, to enhance the intracellular delivery and to protect the thiol moiety of D-pen, we designed, synthesized, and evaluated a novel gelatin-D-pen conjugate. D-pen was covalently coupled to gelatin with a biologically reversible disulfide bond with the aid of a heterobifunctional cross-linker (*N*-succinimidyl-3-(2-pyridyldithio)-propionate) (SPDP). Additionally, fluorescein-labeled gelatin-D-pen conjugate was synthesized for cell uptake studies. D-pen alone was shown not to enter leukemia cells. In contrast, the qualitative intracellular uptake of the conjugate in human leukemia cells (HL-60) was shown with confocal microscopy. The conjugate exhibited slow cell uptake (over the period of 48 to 72 h). A novel HPLC assay was developed to simultaneously quantify both D-pen and glutathione in a single run. The conjugate was shown to completely release D-pen in the presence of glutathione (1 mM) in approximately 3 h in PBS buffer, pH 7.4. The gelatin−D-pen conjugate resulted in significantly greater cytotoxicity compared to free D-pen, gelatin alone, and a physical mixture of gelatin and D-pen in human leukemia cells. Further studies are warranted to assess the potential of D-pen conjugate in the delivery of D-pen as a ROS generating anticancer agent.

INTRODUCTION

D-Penicillamine (D-pen) is a copper chelating agent that is currently approved by the FDA for the treatment of Wilson's disease and rheumatoid arthritis. In recent years, there has been immense interest in the use of copper chelators including D-pen as antiangiogenic agents (*1*, *2*). This is due to the now-established role of copper in angiogenesis. Copper is known to act as a cofactor for a variety of important endogenous pro-angiogenic compounds such as fibroblast growth factor (FGF) and vascular endothelial growth factor (VEGF) (*2*). Thus, it has been proposed that copper chelation by D-pen could lead to an antiangiogenic effect. It is also known that the interaction of D-pen with copper during chelation leads to the generation of hydrogen peroxide (H_2O_2) and other reactive oxygen species (ROS) (*1*, *3*, *4*). We have recently confirmed, both qualitatively and quantitatively, that copper-catalyzed D-pen oxidation generated concentration-dependent H_2O_2 (*5*). In addition, we have shown that D-pen coincubated with cupric sulfate resulted in concentration-dependent cytotoxicity in both human breast cancer (MCF-7, BT474) and leukemia cells (HL-60, HL-60/VCR) in culture (*6*).

As copper levels have been reported to be significantly elevated in the serum (*7*, *8*) and the tumor tissue (*9*–*11*) of cancer patients, we believe that our studies in the investigation of D-pen cytotoxicity in the presence of copper have significant potential. Therefore, we hypothesized that novel formulation strategies that could increase the intracellular delivery of D-pen would potentially lead to the use of D-pen as a dual anticancer agent via (1) cytotoxicity, through the intracellular generation of H_2O_2 and other ROS, (2) antiangiogenesis, through the well-known copper chelation process. However, the physicochemical properties of D-pen would limit the anticancer efficacy of D-pen *in vivo*. These limiting properties include (i) extreme hydrophilicity (Log $P = -0.39$) (*12*), thus limiting its intracellular uptake in cancer cells (*13*, *14*), (ii) rapid elimination from the blood exhibiting biphasic kinetics (*15*, *16*), and (iii) sensitivity to oxidation. The thiol group of D-pen is critical to both copper chelation and H_2O_2 generation; however, D-pen is prone to oxidation resulting in the formation of inactive D-pen disulfide or mixed disulfides. Therefore, the efficacy of D-pen as an anticancer agent would depend on its successful delivery to cancer cells in its reduced form or a modified form which could then be reversibly converted intracellularly to bioactive D-pen.

We have previously reported on a novel D-pen-nanoparticle formulation for metal chelation therapy (*17*). Also, Chvapil et al. recently reported on the synthesis of a hexyl-D-pen-ester that converted D-pen to a more lipophilic form (Log $P = 1.61$) (*12*, *18*). The ester prodrug strategy for D-pen delivery could potentially have problems such as (i) the lack of protection

* Corresponding author: Russell J. Mumper, Ph.D., John A. McNeill Distinguished Professor, Director, Center for Nanotechnology in Drug Delivery, Division of Molecular Pharmaceutics, Eshelman School of Pharmacy, CB # 7360 University of North Carolina at Chapel Hill, Chapel Hill, NC 27599-7360. E-mail: mumper@email.unc.edu. Phone: (919) 966-1271. Fax: (919) 966-0197.

[†] University of Kentucky.

[‡] School of Pharmacy and Center for Nanotechnology in Drug Delivery, University of North Carolina at Chapel Hill.

[§] UNC Lineberger Comprehensive Cancer Center.

10.1021/bc800042s CCC: $40.75 © 2008 American Chemical Society
Published on Web 06/21/2008

of the critical thiol group and (ii) the slow rate of D-pen release from the lipophilic ester prodrug. This could result in less than effective free D-pen concentrations *in vivo*. To overcome these potential problems, we designed a novel conjugate of D-pen wherein D-pen was linked to a macromolecular polymer via a biologically reversible disulfide bond. In recent years, the covalent conjugation of low molecular weight drugs with soluble macromolecular carriers (peptides, protein, and polymers) has been the focus of considerable research (*19, 20*).

Gelatin is a partially hydrolyzed form of collagen (*19*). Gelatin has been used in oral delivery technologies such as hard and soft capsules and is recently being examined as a carrier in novel drug delivery (*21*). Gelatin has been reported to be both biocompatible and biodegradable (*21, 22*). These and other desirable physiochemical properties of gelatin make it a suitable carrier for the delivery of genes (*23–25*), and chemotherapeutic agents formulated as conjugates (*19, 20, 26, 27*), nanoparticles (*21, 28–31*), complex coacervates (*24*), and as microspheres (*21, 25*). Both the carboxyl and the amino groups of gelatin have been modified for drug conjugation (*22, 27*).

In the present studies, we describe the synthesis of a soluble gelatin-D-pen conjugate through the modification of gelatin with the aid of a heterobifunctional cross-linker, sulfosuccinimidyl 6-(3′(2-pyridyldithio)-propionamido) hexanoate (sulfo-LC-SPDP) (water-soluble derivative of SPDP). Gelatin was coupled to D-pen using SPDP to form a potentially biologically reversible disulfide bond. The disulfide bond was an attractive strategy for D-pen delivery due to (i) enhanced protection of the thiol group of D-pen from oxidation before it reaches the site of action, (ii) its potential for intracellular reversibility (due to the presence of ∼1−11 mM of glutathione inside the cells) (*32–34*), and (iii) its reported relative stability in plasma (*35*).

The overall objectives of the present studies were to (1) synthesize and characterize a novel disulfide gelatin−D-pen conjugate; (2) evaluate the *in vitro* release of D-pen from the gelatin-D-pen conjugate as a function of glutathione concentration, time of incubation with glutathione, and pH; (3) evaluate the intracellular uptake of free D-pen and fluorescein labeled gelatin−D-pen conjugate in human leukemia cells (HL-60); and (4) investigate the *in vitro* cytotoxicity of gelatin−D-pen conjugate in HL-60 cells compared to free D-pen, gelatin alone, and the physical mixture of gelatin with D-pen.

EXPERIMENTAL PROCEDURES

Materials. Type B gelatin (75 bloom strength) with 100−115 mmol of carboxylic acid per 100 g of protein, an isoelectric point of 4.7−5.2, and an average molecular weight of 20 000−25 000 Da, D-penicillamine (D-pen), D-penicillamine disulfide, glutathione, glutathione disulfide, dithiothreitol (DTT) were purchased from Sigma-Aldrich Chemical Co. (St. Louis, MO). Sulfosuccinimidyl 6-(3′(2-pyridyldithio)-propionamido) hexanoate (Sulfo-LC-SPDP), 2,4,6-trinitrobenzene sulfonic acid (TNBS) reagent, *N*-hydroxysuccinimide-fluorescein (NHS-Fluorescein), M-PER mammalian cell extraction reagent were purchased from Pierce Biotech Inc. (Rockford, IL). Acetonitrile and *o*-phosphoric acid (85%) were purchased from Fisher Scientific (Pittsburgh, PA). Microcon (YM-10, MWCO: 10 kDa) centrifugal filter devices were purchased from Millipore (Billerica, MA). All aqueous solutions were prepared in deionized distilled water (MilliQ, Millipore Inc.).

Cell Lines and Culture Conditions. The human leukemia cell line (HL-60) was purchased from American type Cell Culture Collection (ATCC, Rockville, MD). Cells were routinely cultured in RPMI-1640 media (Invitrogen, Carlsbad, CA) supplemented with 100 U/mL penicillin, 100 μg/mL streptomycin, and 10% fetal bovine serum (FBS) (ATCC, Rockville, MD) and maintained at 37 °C in a humidified 5% CO_2 incubator. Plasmocin (5 μg/mL) (InvivoGen, San Diego, CA) was added to the cell culture media as a prophylactic measure to prevent mycoplasma contamination. Cell viability was regularly determined by Trypan blue dye (0.4% in phosphate buffered saline) (ATCC, Rockville, MD).

Synthesis and Purification of the Gelatin−D-Pen Conjugate. A heterobifunctional cross-linker (sulfo-LC-SPDP) was employed to conjugate D-pen with gelatin. Sulfo-LC-SPDP has an amine reactive *N*-hydroxysuccinimide (NHS) and a thiol-reactive 2-pyridylthio group. The conjugate synthesis was performed in two steps. Briefly, gelatin (2 mg/mL) was incubated with SPDP for 2 h at room temperature in PBS, pH 7.4. After incubation, excess SPDP was separated from gelatin with microcon centrifugation devices (MWCO: 10 kDa). As described below, the pyridine-2-thione and the TNBS assays were performed to determine the degree of SPDP modification of gelatin. The SPDP-modified gelatin was then incubated with excess D-pen. The gelatin−D-pen conjugate was separated from the unconjugated D-pen with microcon centrifugal devices. The HPLC assay as described below was performed on the filtrate and retentate to determine the amount of D-pen conjugated to gelatin.

The complete and efficient separation of gelatin from unreacted SPDP or D-pen was performed with microcon centrifugation filter devices (MWCO: 10 kDa). Briefly, 500 μL of reaction mixture was added to the microcon filter device, the mixture was centrifuged at 14 000 *g* for 30 min at room temperature. The filtrate was then collected and the retentate was washed twice with 400 μL of fresh PBS buffer. The retentate was finally collected by centrifuging at 3000 *g* for 5 min. Gelatin and D-pen concentration both in the filtrate and in the retentate were quantified as described below.

Synthesis and Purification of the Fluorescein Labeled Gelatin−D-Pen Conjugate. The fluorescent labeling of the conjugate was performed with the aid of an amine-reactive fluorescent probe, NHS-fluorescein. Briefly, NHS-fluorescein was added to gelatin in a 1:1 mol ratio and the mixture was incubated with constant shaking for 1 h at room temperature. The unreacted free fluorescein was separated from fluorescein−gelatin using the microcon centrifugal filter devices. The fluorescein−gelatin was washed three times with PBS, pH 7.4, until the free fluorescein was completely removed. The fluorescein−gelatin was then used to synthesize the conjugate as described above.

CHARACTERIZATION OF THE GELATIN−D-PEN CONJUGATE

Amino Content Determination. 2,4,6-Trinitrobenezene sulfonic acid (TNBS) is a rapid and sensitive assay reagent employed for the determination of free amino groups. Briefly, 50 μL of 0.01% (w/v) TNBS was added to 100 μL of either gelatin or SPDP-modified gelatin in PBS buffer, pH 7.4, and was incubated for 2 h at 37 °C. 25 μL of 1 N HCl was added to stop the reaction. The resulting absorbance was recorded at 335 nm with the Synergy 2 Multi-Detection Microplate Reader (Biotek, Winooski, VT). A standard curve for amino groups was generated using known concentrations of D-pen. The primary amino group was expressed as the amount of TNBS reactive amino groups in 1 g of gelatin. The % amino groups conjugated was calculated as follows: % amino groups conjugated = (amino groups of SPDP modified gelatin/amino groups in gelatin alone) × 100%.

Gelatin Determination. The gelatin concentration was analyzed using the Coomassie Plus assay. Briefly, 10 μL of standard or sample was added to 150 μL of Coomassie Plus Protein Assay Reagent (Pierce Biotech, Rockford, IL), mixed

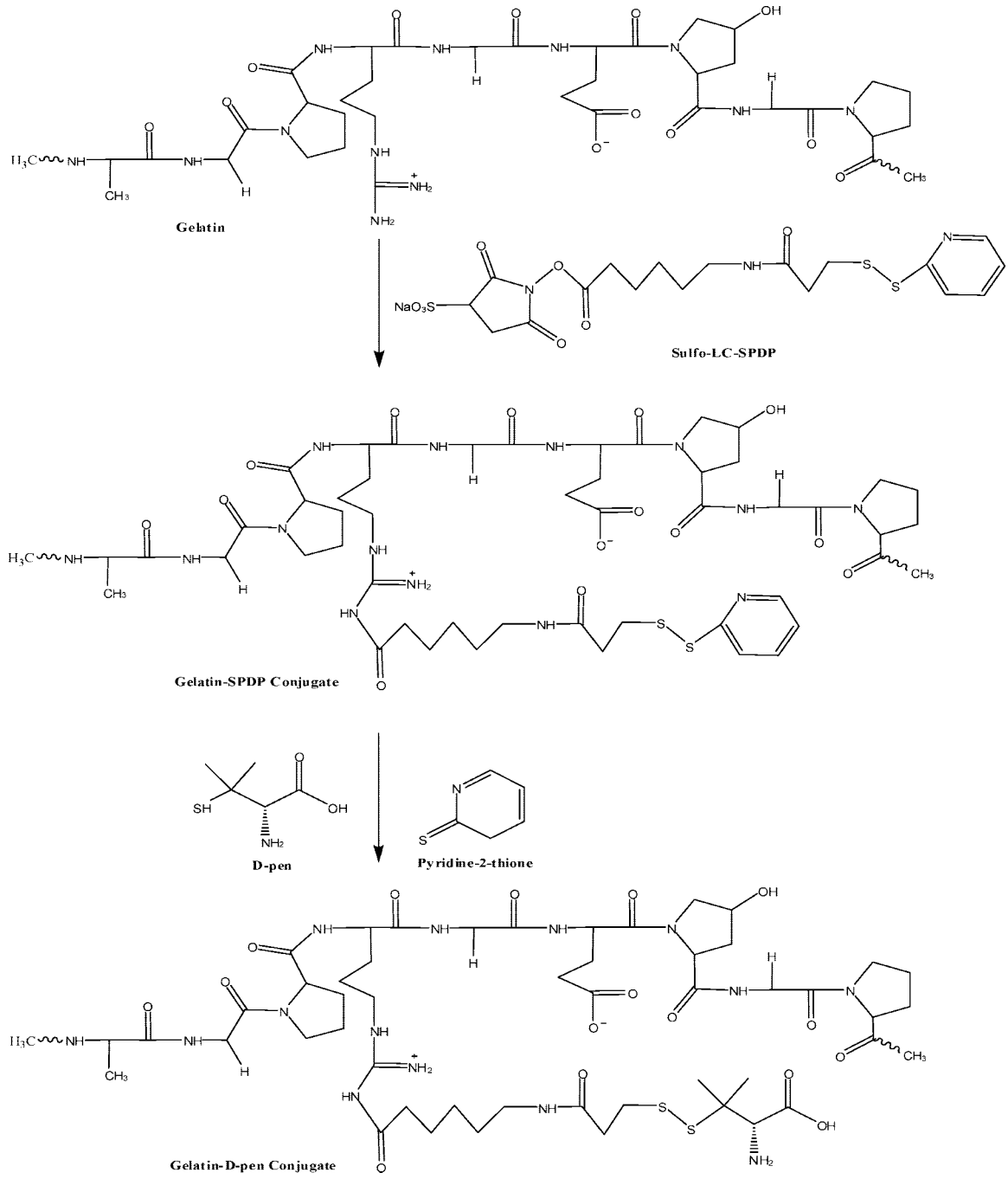

Figure 1. Schematic illustration of gelatin−D-pen conjugate synthesis. The amino group of gelatin was modified with the amine-reactive *N*-hydroxysuccinimide (NHS) portion of sulfo-SPDP and D-pen was conjugated to the SPDP modified gelatin by reacting with sulfhydryl reactive 2-pyridothione.

and incubated for 10 min at room temperature and the absorbance was read at 595 nm with the microplate reader.

Determination of the Level of SPDP Modification. The degree of SPDP modification of gelatin was determined by quantifying the release of pyridine-2-thione group after exposure of the SPDP-modified gelatin with DTT. Briefly, 100 μL purified SPDP-modified gelatin was diluted to 1 mL with PBS buffer, pH 7.4. 10 μL DTT (15 mg/mL) was added and samples were incubated for exactly 15 min, and the absorbance was recorded at 343 nm with the microplate reader. The molar ratio of SPDP to gelatin modification was calculated as follows = ($\Delta A \times 8080$) $\times$ (average MW of gelatin $\times$ mg/mL of gelatin), where the value 8080 reflects the extinction coefficient (8.08×10^3 M^{-1} cm^{-1}) for pyridine-2-thione at 343 nm.

HPLC Determination of D-Pen and Glutathione. D-pen and glutathione were simultaneously analyzed with a modification of our previously reported HPLC method (*5*). Briefly, a HPLC system (Finnigan Surveyor System (Thermo Electron Corp., San Jose, CA)) was used and the data were analyzed with *ChromQuest* software version 4.2. The mobile phase employed was a 50:50% v/v mixture of solvent A (50 mM *o*-phosphoric acid) and solvent B (50 mM *o*-phosphoric acid + 5% acetonitrile), both adjusted to pH 2.5, and pumped at a flow rate of 1 mL/min. Both D-pen and glutathione were detected by UV absorption at 214 nm with retention times of 3.1 ± 0.01 and 2.79 ± 0.01 min, respectively. Sample concentrations (μM) were obtained from the regression line of peak area versus standard sample concentration (μM). These were calculated

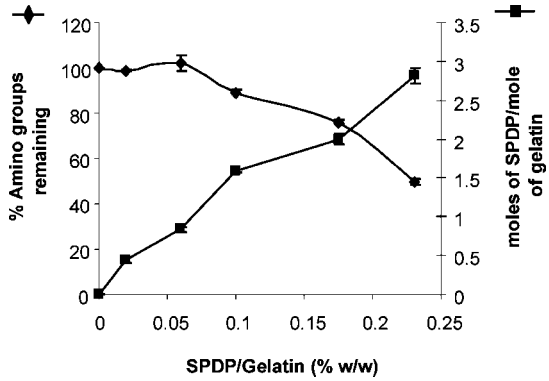

Figure 2. Effect of increasing SPDP concentration on the modification of gelatin. The amine groups and moles of SPDP conjugated to gelatin. The pyridine-2-thione assay was used to determine the SPDP modification of gelatin. The TNBS assay was used to determine the level of SPDP modification of gelatin. Each value represents mean ± SD.

Table 1. Effect of SPDP/Gelatin Concentration on the Amount of D-Pen Conjugated to Gelatin[a]

SPDP/gelatin (% w/w)	D-pen (μmol)/gelatin (g) ± SD	D-pen (mg)/gelatin (g) ± SD
0.02	20.5 ± 0.5	3.1 ± 0.07
0.06	52.8 ± 2.0	7.8 ± 0.3
0.1	58.8 ± 0.9	8.7 ± 0.14
0.18	84.3 ± 9.1	12.6 ± 1.3
0.23	102.4 ± 1.4	15.3 ± 0.2

[a] Each value represents the mean ± SD ($n = 3$).

using a ten-point calibration curve of D-pen and glutathione dissolved in PBS buffer, pH 7.4.

D-Pen Release from the Conjugate under Reducing Conditions. To evaluate the amount of D-pen released from the conjugate under reducing conditions, the gelatin−D-pen conjugate was incubated in PBS buffer, pH 6.2 and 7.4, with increasing concentrations of glutathione (0, 0.1, 1, and 10 mM) for 2 h at 37 °C. Additionally, D-pen release from the conjugate at various times was also determined in PBS at pH 6.2 and 7.4 after incubation in the presence of 1 mM of glutathione at 37 °C.

CANCER CELL UPTAKE STUDIES

Quantitative Cell Uptake of Free D-Pen. The quantitative cell uptake of free D-pen was investigated in HL-60 cells. Briefly, D-pen (100 μM) was incubated with HL-60 (1×10^6) cells in PBS, pH 7.4, at 37 °C in a 5% CO_2 incubator. Cells were incubated for 1−4 h. At a predetermined time, the cells were separated by centrifugation and the supernatant was analyzed for the remaining concentration of D-pen present as either free D-pen or D-pen disulfide using the HPLC assay previously described (5).

Intracellular Uptake of the Conjugate. The uptake of the fluorescein-gelatin-D-pen conjugate was determined qualitatively using confocal microscopy. HL-60 cells (1×10^5) were suspended in a 24 well plate in the medium alone (control) or containing either fluorescein-gelatin (fluorescein-labeled gelatin) (control) or fluorescein-gelatin-D-pen conjugate. At 4, 24, 48, and 72 h post-treatment, cells were transferred to a centrifuge tube, washed twice with PBS, and resuspended in 200 μL fresh Phenol red free media. Cells were transferred onto a slide for visualizing using Zeiss 510 Meta laser scanning confocal microscope (Carl Zeiss, Thornwood, NY). Differential interference contrast (DIC) images, fluorescence images, and the overlapped images taken from the microscope were visualized using the Zeiss AIM Viewer (Carl Zeiss, Thornwood, NY).

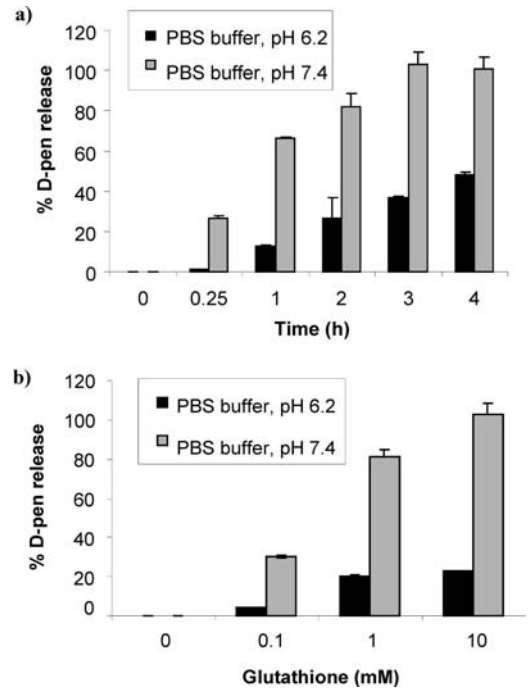

Figure 3. Release of D-pen from the gelatin−D-pen conjugate under reducing conditions. (a) The gelatin−D-pen conjugate was incubated with glutathione (1 mM) at 37 °C in phosphate buffer saline (PBS, pH 7.4 and pH 6.2) and the release of D-pen was analyzed with HPLC. Each value represents mean ± SD ($n = 3$). (b) The gelatin−D-pen conjugate was incubated with increasing concentration of glutathione (0, 0.1, 1, 10 mM) at 37 °C for 2 h. D-pen release was analyzed with HPLC. Each value represents mean ± SD ($n = 3$).

Additionally, to support the qualitative cell uptake of the conjugate, we measured the lysate fluorescence of the fluorescein-gelatin-D-pen conjugate treated HL-60 cells. Briefly, after treatment and washing with PBS as described above the HL-60 cells were lysed with M-PER mammalian cell extraction reagent. The fluorescence of the cell lysate was measured at 485 ± 20 nm (excitation) and 520 ± 25 nm (emission).

Gelatin−D-Pen Conjugate Cytotoxicity. HL-60 cells were plated in 48 well plates at 20 000 cells/well. The cells were treated with the gelatin−D-pen conjugate (1 mg/mL conjugate, corresponding to 100 μM D-pen), D-pen (100 μM), gelatin (1 mg/mL), a physical mixture of gelatin (1 mg/mL) plus D-pen (100 μM). The medium was replaced every 2 days, and no further dose of any treatment group was added. Cytotoxicity was determined on the 2nd, 4th, 6th, 8th, and 10th day using the MTT assay.

Statistical Analysis. Statistical analysis was performed with GraphPad *Prism 4* software (GraphPad software Inc., San Diego, CA). The data represented in Figure 7 were analyzed with two-way analysis of variance (ANOVA) followed by Bonferonni's post test, where significance was set at $p < 0.05$.

RESULTS AND DISCUSSION

Synthesis of Gelatin−D-Pen Conjugate. The gelatin−D-pen conjugate was prepared by a simple two-step reaction as shown in Figure 1: (i) gelatin was modified with the heterobifunctional cross-linker (sulfo-LC-SPDP); (ii) D-pen was conjugated to the modified gelatin (SPDP-gelatin) with simple thiol exchange. The choice of the amine-thiol reactive heterobifunctional cross-linker (sulfo-LC-SPDP) was based on two important properties: (i) availability of amino groups in gelatin for chemical modification, (ii) the protection of the thiol group of D-pen, through a reversible bond between polymer (gelatin) and

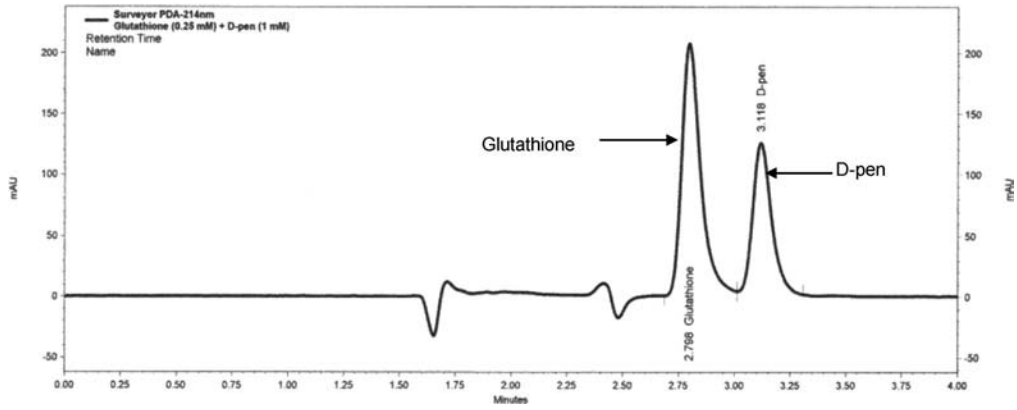

Figure 4. HPLC chromatogram showing glutathione and D-pen elution.

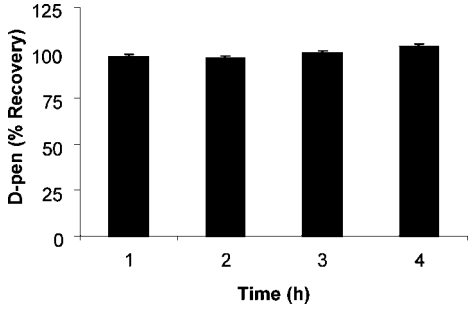

Figure 5. Cell uptake of D-pen. D-pen (100 μM) was added to HL-60 (1×10^6) cells in PBS (pH 7.4) in a 24 well plate at 37 °C in 5% CO_2 incubator. Cells were separated by centrifugation and the supernatant was analyzed by HPLC assay for D-pen concentration. Data represent mean ± SD ($n = 4$).

the drug (D-pen). A disulfide bond compared to the irreversible (maleimide) bond provides potential biological reversibility.

As shown in Figure 2, the amino group content of gelatin was reduced to approximately 50% of the original gelatin as the ratio of SPDP added to gelatin increased to 0.23% w/w. To confirm and quantify the amount of SPDP modification of gelatin in the process of loss of amino groups, the SPDP-modified gelatin was incubated with DTT to release the pyridine-2-thione group. Figure 2 shows that approximately 3 mol of SPDP was conjugated per mole of gelatin as SPDP added to gelatin increased to 0.23% w/w. This corresponded to 20.5 ± 0.5 to 102.4 ± 1.4 μmol D-pen/g gelatin or 3.1 ± 0.07 to 15.3 ± 0.2 mg D-pen/g gelatin as the ratio of SPDP to gelatin was increased from 0.02% to 0.23% w/w (shown in Table 1).

Synthesis of Fluorescein Labeled Gelatin−D-Pen Conjugate. A fluorescein-gelatin-D-pen conjugate was synthesized for cell uptake studies. The degree of labeling of fluorescein on gelatin was 0.1 mol of fluorescein per mole of gelatin. Gelatin was labeled with fluorescein through the reaction of the NHS-fluorescein with gelatin to form fluorescein-labeled gelatin. The fluorescein-gelatin was then conjugated to D-pen as described above to form the fluorescein-gelatin-D-pen conjugate. Fluorescein-gelatin alone was used as a control for cell uptake studies.

D-Pen Release in the Presence of Glutathione. The stability of the disulfide bond between D-pen and gelatin was investigated using glutathione, an endogenous reducing agent. The intracellular glutathione concentration has been reported to range from 1 to 11 mM (*33*). Therefore, *in vitro* release studies were performed in the presence of both low (1 mM) and high (10 mM) concentrations of glutathione. The selection of pHs 6.2 and 7.4 were based on the reported pH of the early endosome and cytosol, respectively. In the presence of 1 mM glutathione

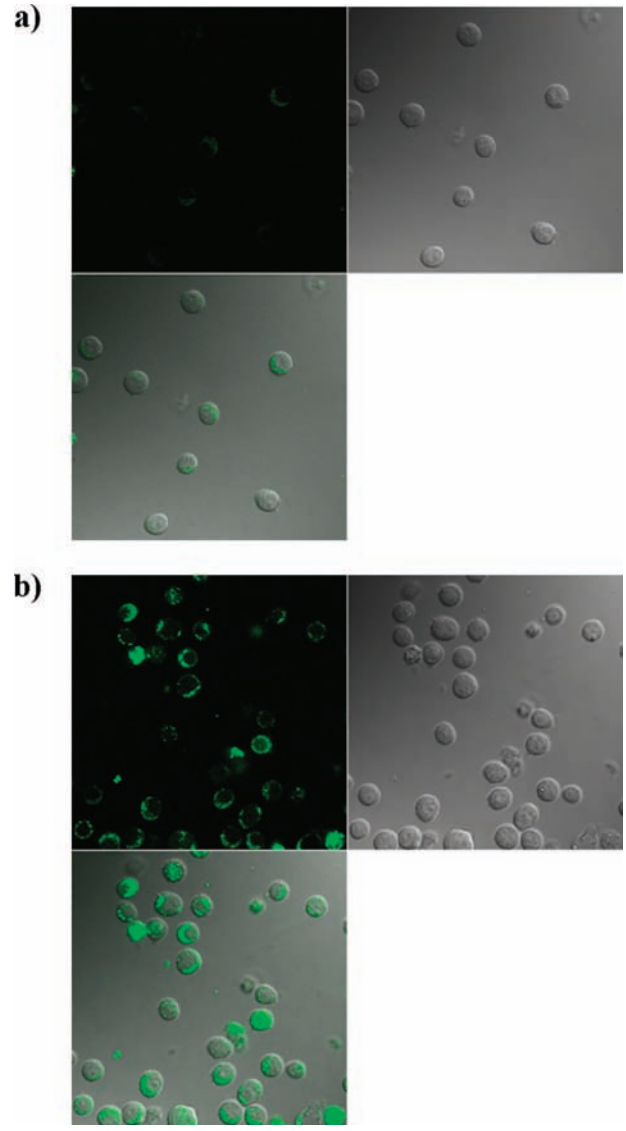

Figure 6. Intracellular uptake of gelatin−D-pen conjugate. HL-60 cells were incubated with the fluorescein-labeled gelatin−D-pen conjugate at 37 °C for (a) 4 and (b) 72 h. Cells were washed twice with PBS and cells then suspended in Phenol red free RPMI media. Cells were imaged by confocal laser scanning microscopy. Fluorescence (left), differential contrast (DIC) (right), and overlapped images (bottom).

in pH 7.4, D-pen was completely released in 4 h, while only ~50% D-pen was released at pH 6.2 (Figure 3a). As shown in Figure 3b, 2 h incubation of the conjugate with glutathione

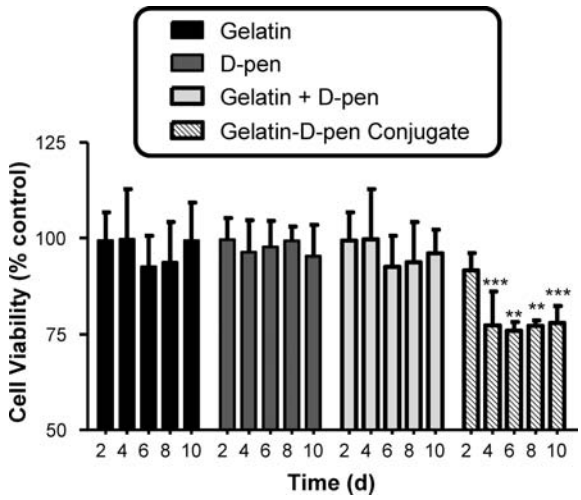

Figure 7. Cytotoxicity of the gelatin-D-pen conjugate in HL-60 cells. Cells (2×10^4) were incubated with gelatin alone (1 mg/mL), D-pen alone (100 μM), gelatin (1 mg/mL) plus D-pen (100 μM), and gelatin−D-pen conjugate (1 mg/mL) After every 2 day interval, media was replaced with fresh media. MTT assay was performed on day 2, 4, 6, 8, and 10. Data represent mean ± SD ($n = 6$). $^{**}p < 0.01$ and $^{***}p < 0.001$ compared to gelatin plus D-pen ($n = 3$).

(0.1−10 mM) at pH 7.4 resulted in the release of approximately 30%, 80%, and 100% of D-pen in the presence of 0.1, 1, and 10 mM glutathione, respectively. In contrast, the D-pen release at pH 6.2 was approximately 5%, 20% in the presence of 0.1, 1, and 10 mM glutathione, respectively. D-pen and glutathione were simultaneously quantitated as shown in Figure 4. These studies underline the significance of interaction of the conjugate at favorable pH and local concentration of glutathione for successful D-pen release and the subsequent cytotoxicity.

Intracellular Uptake of Free D-Pen. Lodemann et al. reported the inability of D-pen to cross cell membrane of mammalian cells (*36*). The inability to be transported is likely explained by the three highly ionizable functional groups of D-pen. The novel HPLC assay developed provides accurate determination of both D-pen and D-pen disulfide. As shown in Figure 5, when the supernatant was analyzed for remaining D-pen at 1, 2, 3, and 4 h postincubation, approximately 100% D-pen was recovered. These results support the previously reported studies by Lodemann et al. (*36*) and signify the need for developing a novel delivery system for D-pen to enhance intracellular delivery.

Gelatin−D-Pen Conjugate Uptake. The intracellular uptake of the gelatin−D-pen conjugate and fluorescein-labeled gelatin alone in HL-60 cells was studied using confocal laser scanning microscopy. The fluorescein-gelatin-D-pen conjugate uptake into HL-60 cells was a slow process with maximum uptake seen at the 72 h (Figure 6b) compared to 4 h (Figure 6a). Similar slow cell uptake was seen with the fluorescein-labeled gelatin (data not shown). Both the conjugate and gelatin alone were seen to accumulate in the cells in a uniform, nonpunctate manner. However, there was a trend for increased fluorescence associated with the cell membrane as compared to the cytoplasm. There were no apparent differences between the cellular uptake of gelatin and the gelatin−D-pen conjugate. Ofner et al. previously showed a similar cellular distribution and slow uptake (over 96 h) of fluorescein-labeled gelatin in HL-60 cells (*20*). We have confirmed the cell uptake of the conjugate by measuring the cell lysate fluorescence of the conjugate-treated HL-60 cells (data not shown). We are currently examining the cellular uptake profiles of other polymers such as polyglutamic acid to further improve intracellular D-pen delivery. For example, we have preliminary data that the uptake of the polyglutamic acid−D-pen conjugate is much more rapid than that of gelatin−D-pen conjugate and results in dose-dependent increase in intracellular ROS leading to cytotoxicity in HL-60 cells within 8 h. Moreover, the levels of ROS produced by gelatin−D-pen conjugate (equivalent to 500 μM D-pen dose) is comparable to that caused by 100 μM H_2O_2 (data not shown), whereas free D-pen causes no increase in intracellular ROS since it is cell-impermeable.

Conjugate Cytotoxicity in HL-60 Cells. We have reported that D-pen alone in the presence of cupric sulfate was more cytotoxic in leukemia cells compared to breast cancer cells (*6*). The data suggest that this may be due to the higher innate copper levels in the cultured leukemia cells compared to breast cancer cells (unpublished data). Therefore, the cytotoxicity of the conjugate was evaluated in human HL-60 leukemia cells. HL-60 cells were treated with gelatin and D-pen alone, a physical mixture of gelatin plus D-pen and the gelatin-D-pen conjugate. As the conjugate was shown to enter the cells, the differences in cytotoxicity of the conjugate were compared with the free gelatin and D-pen and the physical mixture of gelatin plus D-pen in the presence of innate levels of intracellular copper in HL-60 cells. During the studies, media was replaced every two days. As shown in Figure 7, the conjugate exhibited significantly increased cytotoxicity compared to all the controls ($p < 0.001$ on days 4 and 10 and $p < 0.01$ on days 6 and 8, respectively). As we have reported earlier, the mechanism of D-pen cytotoxicity is due to the generation of H_2O_2 and other ROS in the presence of copper (*5*, *6*). Thus, the intracellular efficacy of D-pen is dependent upon two important processes, namely, (i) the interaction of the conjugate with glutathione and the subsequent release of D-pen and (ii) the interaction of the released D-pen with the intracellular innate copper present in leukemia cells to produce its cytotoxic effect. We are presently investigating the intracellular D-pen release from the conjugate and the localization of intracellular copper to improve the conjugate anticancer effect. Other conjugates are being designed and synthesized that may increase the rate and extent of uptake and the subsequent D-pen release.

CONCLUSIONS

A method for the synthesis and characterization of a novel gelatin−D-pen conjugate is described. The disulfide bond between gelatin and D-pen in the conjugate provides protection of D-pen from oxidation. Additionally, the disulfide bond in the conjugate was shown to be biologically reversible through the complete release of D-pen only in the presence of biologically relevant concentration of glutathione. It was shown that free D-pen does not enter cells. The delivery of D-pen as a novel gelatin-D-pen conjugate was shown to increase the intracellular accumulation of conjugate in cancer cells over time, and this directly led to enhanced cytotoxicity in human leukemia cells. The cytotoxicity of the conjugate in leukemia cells was sustained and significant compared to the physical mixture of gelatin and D-pen, indicating the importance of the disulfide bond between gelatin and D-pen. To further improve the conjugate cytotoxicity, we are currently examining the intracellular interaction of the D-pen released from the conjugate with the cellular copper either free or bound to proteins.

ACKNOWLEDGMENT

The authors would like to thank Wendy Salmon at the Michael Hooker Microscopy Facility at the University of North Carolina at Chapel Hill for her help and guidance in the confocal microscopy studies.

LITERATURE CITED

(1) Brem, S., Grossman, S. A., Carson, K. A., New, P., Phuphanich, S., Alavi, J. B., Mikkelsen, T., and Fisher, J. D. (2005) Phase 2 trial of copper depletion and penicillamine as anti-angiogenesis therapy of glioblastoma. *Neuro-Oncol. 7*, 246–253.

(2) Brewer, G. J. (2005) Anticopper therapy against cancer and diseases of inflammation and fibrosis. *Drug Discovery Today 10*, 1103–1109.

(3) Lipsky, P. E., and Ziff, M. (1980) Inhibition of human helper T cell function in vitro by D-penicillamine and $CuSO_4$. *J. Clin. Invest. 65*, 1069–1076.

(4) Starkebaum, G., and Root, R. K. (1985) D-penicillamine: analysis of the mechanism of copper catalyzed hydrogen peroxide generation. *J. Immunol. 134*, 3371–3378.

(5) Gupte, A., and Mumper, R. J. (2007) An investigation into copper catalyzed D-penicillamine oxidation and subsequent hydrogen peroxide generation. *J. Inorg. Biochem. 101*, 594–602.

(6) Gupte, A., and Mumper, R. J. (2007) Copper chelation by D-penicillamine generates reactive oxygen species that are cytotoxic to human leukemia and breast cancer cells. *Free Radical Biol. Med. 43*, 1271–1278.

(7) Yucel, I., Arpaci, F., Ozet, A., Doner, B., Karayilanoglu, T., Sayar, A., and Berk, O. (1994) Serum copper and zinc and copper/zinc ratio in patients with breast cancer. *Biol. Trace Elem. Res. 40*, 31–38.

(8) Zuo, X. L., Chen, J. M., Zhou, X., Li, X. Z., and Mei, G. Y. (2006) Levels of selenium, zinc, copper and antioxidant enzyme activity in patients with leukemia. *Biol. Trace Elem. Res. 114*, 41–53.

(9) Geraki, K., Farquharson, M. J., and Bradley, D. A. (2002) Concentration of Fe, Cu and Zn in breast tissue: a synchrotron XRF study. *Phys. Med. Biol. 47*, 2327–2339.

(10) Kuo, H. W., Chen, S. F., Wu, C. C., Chen, D. R., and Lee, J. H. (2002) Serum and tissue trace elements in patients with breast cancer in Taiwan. *Biol. Trace Elem. Res. 89*, 1–11.

(11) Sharma, K., Mittal, D. K., Kesarwani, R. C., Kamboj, V. P., and Chowdhery. (1994) Diagnostic and prognostic significance of serum and tissue trace elements in breast malignancy. *Ind. J. Med. Sci. 48*, 227–232.

(12) Chvapil, M., Kielar, F., Liska, F., Silhankova, A., and Brendel, K. (2005) Synthesis and evaluation of long acting D-penicillamine derivatives. *Connect. Tissue Res. 46*, 242–250.

(13) Joyce, D. A. (1989) D-penicillamine pharmacokinetics and pharmacodynamics in man. *Pharmac. Ther. 42*, 405–427.

(14) Joyce, D. A. (1990) D-penicillamine. *Bailliere's Clin. Rheum. 4*, 553–574.

(15) Lu, J. X., Jr. (1992) Penicillamine: pharmacokinetics and differential effects on zinc and copper status in chicks. *J. Nutr. 122*, 355–362.

(16) Netter, P., Bannwarth, B., Pere, P., and Nicolas, A. (1987) Clinical pharmacokinetics of D-penicillamine. *Clin. Pharmacokinetics 13*, 317–333.

(17) Cui, Z., Lockman, P. R., Atwood, C. S., Hsu, C-H., Gupte, A., Allen, D. D., and Mumper, R. J. (2005) Novel D-penicillamine carrying nanoparticles for metal chelation therapy in Alzheimer's and other CNS diseases. *Eur. J. Pharm. Biopharm. 59*, 263–272.

(18) Chvapil, M., and Dorr, R. (2005) Single intratumoral injection of long acting benzyl ester of D-penicillamine inhibits the growth of melanoma tumor in mice. *Anti-cancer Drugs 16*, 757–762.

(19) Bowman, B. J., and Ofner, C. M. III. (2000) Characterization and in-vitro methotrexate release from methotrexate/gelatin conjugates of opposite bond polarity. *Pharm. Res. 17*, 1309–1315.

(20) Ofner, C. M., Pica, K., Bowman, B. J., and Chen, C. S. (2006) Growth inhibition, drug load, and degradation studies of gelatin/methotrexate conjugates. *Int. J. Pharm. 308*, 90–99.

(21) Young, S., Wong, M., Tabata, Y., and Mikos, A. G. (2005) Gelatin as a delivery vehicle for the controlled release of bioactive molecules. *J. Controlled Release 109*, 256–274.

(22) Kommareddy, S., and Amiji, M. (2005) Preparation and evaluation of thiol-modified gelatin nanoparticles for intracellular DNA delivery in response to glutathione. *Bioconjugate Chem. 16*, 1423–1432.

(23) Bhavsar, M. D., and Amiji, M. M. (2007) Gastrointestinal distribution and in vivo gene transfection studies with nanoparticles-in-microsphere oral system (NiMOS). *J. Controlled Release 119*, 339–348.

(24) Thakor, D., Spigelman, I., Tabata, Y., and Nishimura, I. (2007) Subcutaneous peripheral injection of cationized gelatin/DNA polyplexes as a platform for non-viral gene transfer to sensory neurons. *Mol. Ther. 15*, 2124–2131.

(25) Xia, Z., Abe, K., Furusu, A., Miyazaki, M., Obata, Y., Tabata, Y., Koji, T., and Kohno, S. (2008) Suppression of renal tubulointerstitial fibrosis by small interfering RNA targeting heat shock protein 47. *Am. J. Nephrol. 28*, 34–46.

(26) Chung, J. E., Kurisawa, M., Uyama, H., and Kobayashi, S. (2003) Enzymatic synthesis and antioxidant property f gelatin-catechin conjugates. *Biotechnol. Lett. 25*, 1993–1997.

(27) Pica, K., Tchao, R., and Ofner, C. M., III (2006) Gelatin-methotrexate conjugate microspheres as a potential drug delivery system. *J. Pharm. Sci. 95*, 1896–1908.

(28) Azarmi, S., Huang, Y., Chen, H., McQuarrie, S., Abrams, D., Roa, W., Finaly, W. H., Miller, G. G., and Lobenberg, R. (2006) Optimization of a two step desolvation method for preparing gelatin nanoparticles and cell uptake studies in 143B osteosarcoma cancer cells. *J. Pharm. Pharmaceut. Sci 9*, 124–132.

(29) Kaul, G., and Amiji, M. (2002) Long circulating poly (ethylene glycol)-modified gelatin nanoparticles for intracellular delivery. *Pharm. Res. 19*, 1061–1067.

(30) Kommareddy, S., and Amiji, M. (2007) Biodistribution and pharmacokinetic analysis of long circulating thiolated gelatin nanoparticles following systemic administration in breast cancer-bearing mice. *J. Pharm. Sci. 96*, 397–407.

(31) Xu, X., Capito, R. M., and Spector, M. (2008) Delivery of plasmid IGF-1 to chondrocytes via cationized gelatin nanoparticles. *J. Biomed. Mater. Res. A 84*, 73–83.

(32) Saito, G., Swanson, J. A., and Lee, K. D. (2003) Drug delivery strategy utilizing conjugation via reversible disulfide linkages: role and site of cellular reducing activities. *Adv. Drug Delivery Rev. 55*, 199–215.

(33) Schafer, F. Q., and Buettner, G. R. (2001) Redox environment of the cell as viewed through the redox state of the glutathione disulfide/glutathione couple. *Free Radical Biol. Med. 30*, 1191–1212.

(34) Cavallaro, G., Campisi, M., Licciardi, M., Orgis, M., and Giammona, G. (2006) Reversible stable thiopolyplexes for intracellular delivery of genes. *J. Controlled Release 115*, 322–334.

(35) Jones, D. P., Carlson, J. L., Mody, V. C., Cai, J., Lynn, M. J., and Sternberg, P. (2000) Redox state of glutathione in human plasma. *Free Rad. Biol. Med. 28*, 625–635.

(36) Lodemann, E. (1981) Transport of D- and L-penicillamine by mammalian cells. *Biochem. Biophys. Res. Commun. 102*, 775–783.

BC800042S

Islets Surface Modification Prevents Blood-Mediated Inflammatory Responses

Yuji Teramura and Hiroo Iwata*

Department of Nano-Medicine Merger Education Unit and Department of Polymer Chemistry, Graduate School of Engineering, Kyoto University, and Institute for Frontier Medical Sciences, Kyoto University, 53 Kawara-cho, Shogoin, Sakyo-ku, Kyoto, 606-8507, Japan. Received February 16, 2008; Revised Manuscript Received May 11, 2008

Transplantation of islets of Langerhans (islets) is a promising technique for treating insulin-dependent diabetes mellitus (type I). One unresolved issue is early graft loss due to inflammation triggered by blood coagulating on the surface of islets after transplantation into the portal vein. Here, we describe a versatile method for modifying the surface of islets with an ultrathin membrane carrying the fibrinolytic enzyme urokinase or the anticoagulant heparin. The surface of islets was modified with a poly(ethylene glycol)−phospholipid conjugate bearing a biotin group (biotin-PEG-lipids, PEG MW: 5000). Biotin-PEG-lipids were anchored to the cell membranes of islets, and the PEG-lipid layer on the islets was further covered by streptavidin and biotin−bovine serum albumin conjugate using a layer-by-layer method. The surface was further activated with oxidized dextran. Urokinase was anchored to the islets through Schiff base formation. Heparin was anchored to the islets through polyion complex formation between anionic heparin and a cationic protamine coating on the islets. No practical islet volume increase was observed after surface modification, and the modifications did not impair insulin release in response to glucose stimulation. The anchored urokinase retained high fibrinolytic activity, which could help to improve graft survival by preventing thrombosis on the islet surface.

INTRODUCTION

The success achieved with the Edmonton protocol has established clinical islet transplantation as an alternative to pancreas transplantation (*1*, *2*). Transplantation of islets of Langerhans (islets) has been proposed as a safe and effective method for treating patients with insulin-dependent diabetes mellitus (type I). However, it still remains an experimental procedure for late-stage diabetics who can no longer control diabetes with insulin injection. Some improvements in islet transplantation are needed, including increasing islet isolation efficiency, improving islet preservation, increasing the efficacy of immunosuppressive drug dosage protocols, and reducing islet loss in the early phase following transplantation. Among these, graft loss poses the most serious limitations for current islet transplantation protocols. Even though sufficient numbers of islets from multiple donors are transplanted to one patient, only 30% of patients treated become insulin-independent (*2*), suggesting that many islets are lost early after intraportal transplantation.

Innate immune reactions are involved in the destruction of islets exposed to blood in the portal vein (*3*–*6*). The blood coagulation and complement systems are activated when islets are exposed to fresh blood in the portal vein. Chemotactic factors, tissue factor, chemokines, and other inflammatory mediators are released during this early phase. These factors induce instant blood-mediated inflammatory reactions that result in graft loss (*7*). Some methods of regulating early coagulation and blood-mediated inflammatory reactions have been investigated, such as administering the thrombin inhibitor Melagatran (*8*), activated protein C (*9*), dextran sulfate (*10*), and the water-soluble domain of complement receptor I (*11*). Control of these reactions has promoted the transplantation success by reducing islet loss in animal models; however, it is difficult to apply these methods in the clinical environment because systemic administration is associated with an increased risk of bleeding. Recently, Nilsson et al. proposed an original method for preventing instant blood-mediated inflammatory reactions by coating islets with heparin to inhibit surface thrombosis formation following transplantation (*12*). Although it is a challenging method to reduce islet loss in the early phase of transplantation, it has been experimentally under examination. At this point, it is valuable to propose several alternative methods to modify islet surface.

In our previous studies (*13*, *14*), islets were enclosed in a thin synthetic polymer membrane through poly(ethylene glycol)-conjugated phospholipid (PEG−lipids) derivatives that had been anchored in the membranes of islets cells. The PEG−lipid derivatives can be immobilized on the cell surface through hydrophobic interactions between the lipid bilayer and the PEG−lipid, without any effect on cell viability or function. The polymer membrane can be covered further using the layer-by-layer method (*13*, *14*). In this report, we propose a versatile method for immobilizing enzyme and glycosaminoglycans, such as urokinase and heparin, to the surface of islets utilizing this layer-by-layer method. In addition, the results of detailed studies on the fibrinolytic properties of islet-anchored urokinase are reported.

EXPERIMENTAL PROCEDURES

Materials. α-*N*-Hydroxysuccinimidyl-*ω*-*tert*-butoxycarbonyl poly(ethylene glycol) (NHS-PEG-Boc, MW 5000) was purchased from Nektar Therapeutics (San Carlos, CA). 1,2-Dipalmitoyl-*sn*-glycerol-3-phosphatidylethanolamine (DPPE) was purchased from NOF Corporation (Tokyo, Japan). Dichloromethane, chloroform, *N*,*N*-dimethylformamide (DMF), diethyl ether, *N*,*N*′-dicyclohexylcarbodiimide (DCC), D-biotin, streptavidin from Streptomyces avidin, dextran (MW 200 000−300 000), protamine sulfate (from Salmon), and heparin sodium salt were purchased from Nacalai Tesque (Kyoto, Japan). Sodium perio-

* To whom correspondence should be addressed. E-mail: iwata@frontier.kyoto-u.ac.jp, Tel/Fax: +81-75-751-4119.

10.1021/bc800064t CCC: $40.75 © 2008 American Chemical Society
Published on Web 06/06/2008

date ($NaIO_4$) was purchased from Wako Pure Chemcal (Osaka, Japan). Fluorescein isothiocyanate (FITC) was purchased from Dojindo Laboratories (Kumamoto, Japan). Urokinase was purchased from Calbiochem Inc. (La Jolla, CA). Biotinylated bovine serum albumin (biotin-BSA, biotin/BSA = 9, by molar ratio) was purchased from Pierce Biotechnology Inc. (Rockford, IL). Fibrinogen (human) and FITC-labeled BSA (FITC-BSA) were purchased from Sigma-Aldrich Co. (St Louis, MO). Thrombin was purchased from Kayaku CO. Ltd. (Saitama, Japan). FITC-streptavidin was purchased from Zymed laboratories (South San Francisco, CA). Biotinylated poly(ethylene glycol) alkanethiol was purchased from SensoPath Technologies Inc. (Bozeman, MT). Minimum essential medium (MEM), HEPES buffer solution, and Medium 199 were purchased from Invitrogen Co. (Carlsbad, CA). Fetal bovine serum (FBS) was purchased from BioWest (Miami, FL). Phosphate-buffered saline (PBS) was purchased from Nissui Pharmaceutical Co. Ltd. (Tokyo, Japan).

Synthesis of Biotinylated PEG-Conjugated DPPE. NH_2-PEG-lipid was synthesized from DPPE and NHS-PEG-Boc, which carries an activated ester (NHS) to react with an amino group of DPPE, and a protective group (Boc) for the amino group, as reported previously (*13*). Briefly, NHS-PEG-Boc (175 mg) and DPPE (21 mg) were dissolved in 5 mL of dichloromethane solution, and stirred for 3 days at room temperature (RT). Then, a solution of TFA (2 mL) was added and stirred for 20 min at 4 °C to remove Boc groups. The crude product was purified by precipitation with diethyl ether. After extraction into chloroform and evaporation, NH_2-PEG-lipid was obtained as a white solid (115 mg, yield 66%). D-Biotin (20 mg) and DCC (21 mg) were dissolved into DMF and stirred for 3 h at RT. Then, NH_2-PEG-lipid (22 mg) was added to the solution and stirred for 7 days at RT. This solution was filtered through a glass filter and the DMF was evaporated *in vacuo*; then, chloroform was added. After precipitation with diethyl ether, biotin-PEG-lipid was obtained as a white powder (10 mg, yield 40%). Biotin-PEG-lipid: ^1H NMR ($CDCl_3$, 400 MHz, δ ppm): 0.88 (t, 6H, -CH_3), 1.25 (br, 52H, -CH_2-, DPPE), 3.18 (d, 2H, C-CH_2-S, biotin), 3.24 (q, 1H, S-CH(-C)-C, biotin), 3.64 (br, 460H, PEG). 4.52 (m, 2H, C-CH(-C)-N, biotin), 5.15 (s, 2H, C-NH-C, biotin).

Forming Biotin-BSA and Streptavidin-Based Multilayers. A multilayered protein membrane was formed with biotin-BSA and streptavidin using the layer-by-layer method. To examine the formation of the multilayered membrane, we employed an in-house-designed surface plasmon resonance (SPR) instrument (*15*). Gold-coated BK-7 glass plates were immersed in a biotin-SAM (1 mM) methanol solution for 24 h, and the biotin-SAM formed on the surface of the gold-coated glass plates. Before SPR measurements, the plates were sequentially washed thoroughly with pure water and 2-propanol. A glass plate was set in an SPR flow cell, and a solution of strepavidin (20 μg/mL in PBS) was allowed to flow onto the surface, followed by a solution of biotin-BSA (40 μg/mL in PBS). These procedures were repeated several times to form multiple layers of BSA and streptavidin by the layer-by-layer method. The reaction solutions and PBS were allowed to circulate through the flow cell at 4.0 mL/min, and all SPR measurements were performed at 30 °C.

Modifying a Single Cell Surface with Biotin-PEG-Lipid and Streptavidin Complex. CCRF-CEM cells (acute lymphoblastic leukemia T-cells) were used as model cells for the surface modification of single cells. Biotin-PEG-lipids were dispersed in MEM and added to a CCRF-CEM cell suspension (1×10^6 cells in MEM, [biotin-PEG-lipids] = 100 μM), the cell suspension was incubated for 30 min at RT. The cells were washed with MEM and centrifuged at 180 $\times$ *g* for 5 min at RT. This procedure was repeated twice. The biotin-PEG-modified cells were resuspended in 80 μL of MEM. Then, 20 μL of FITC-labeled streptavidin was added to the cell suspension (100 μg/mL) and incubated at RT for 5 min. Cell viability was assessed by the Trypan blue exclusion method. FITC-labeled streptavidin-modified cells were observed by confocal laser scanning microscopy (FLUOVIEW FV500, Olympus, Tokyo).

Islets Surface Modification. Islets were isolated from the pancreas of Syrian hamsters (7−8 weeks old, female, Japan SLC, Inc., Shizuoka, Japan) by the collagenase digestion method (*24*). The islets were maintained in culture medium (Medium 199 with 10% FBS, 8.8 mM HEPES buffer, 100 units/mL penicillin, 100 μg/mL streptomycin, and 8.8 U/mL heparin). A large amount release of insulin was observed from damaged islets during a few days culture after the islet isolation. Isolated islets were cultured for 7 days to remove damaged cells before surface modification. Effect of surface modification on islet functions could be clearly seen after this 7 days culture. A biotin-PEG-lipid solution was added to islets suspended in MEM (100 islets, [biotin-PEG-lipid] = 500 μM 100 μL of MEM), and the mixture was incubated at RT for 1.5 h. After washing three times with MEM, the biotin-PEG-lipid modified islets were mixed with a solution of streptavidin (50 μg/mL in PBS) and allowed to react for 10 min at RT. Streptavidin-modified islets were washed three times with MEM. The modified islets were then added to a solution of biotin-BSA (100 μg/mL in PBS) and left for 10 min at RT. The layer-by-layer modification with streptavidin and biotin-BSA was repeated 10 times to form 20 layers on the surface of the islets. In order to visualize the surface of islets by confocal laser scanning microscopy), FITC-labeled streptavidin (30 μg/mL in PBS) was used for the 21st layer.

Anchoring Bioactive Molecules onto the Surface-Modified Islets. The surface-modified islets were further modified with the fibrinolysis enzyme urokinase or with heparin, using dialdehyde dextran (*16*) or protamine. $NaIO_4$ (107 mg) was added to a dextran (250 mg) solution in pure water (5 mL) and the reaction mixture was stirred for 2 h at RT. Oxidation of dextran by $NaIO_4$ causes cleavage of the carbon−carbon bonds within each monosaccharide unit of the dextran chain, transforming the 1−2 hydroxyl groups into dialdehyde groups. After precipitation with acetone and dialysis against PBS, dialdehyde dextran was obtained as a white solid (220 mg). Biotin-BSA/streptavidin-modified (20 layers) islets were then activated using the dialdehyde dextran solution (5 mg/mL in PBS) for 30 min at 37 °C, and then incubated in urokinase solution (1000 IU/mL in PBS) for 60 min at 37 °C to anchor the urokinase onto the islets. Urokinase-islets were cultured in Medium 199 supplemented with FBS, heparin, and HEPES for a specified number of days at 37 °C in 5% CO_2.

Fibrinolytic activity of the anchored urokinase was determined by the fibrin plate method (*17*). Briefly, 10 mL of a fibrinogen solution (10 mg/mL in saline) (ϕ = 9.5 cm) and 60 μL of a thrombin solution (60 IU/mL) was mixed well. Plasminogen was not added to the fibrinogen solution, because plasminogen is included in fibrinogen prepared by the standard preparation (*17*). Naïve islets and urokinase-anchored islets (50 islets) collected after 0, 1, 3, and 7 days of culture were spotted onto the fibrin plate and incubated at 37 °C for 12 h. The size of the area of dissolved fibrin around the islet spot was determined as a measure of urokinase fibrinolytic activity.

For anchoring heparin, the BSA and streptavidin-modified islets (total layers, 10) were further treated with polycation, protamine (150 μg/mL in HBSS), for 5 min at RT. Most of polycations are cytotoxic toward many cell types. In this study, protamine was used as a polycation, because it is the least cytotoxic polycation as could be expected from the fact that it

Scheme 1[a]

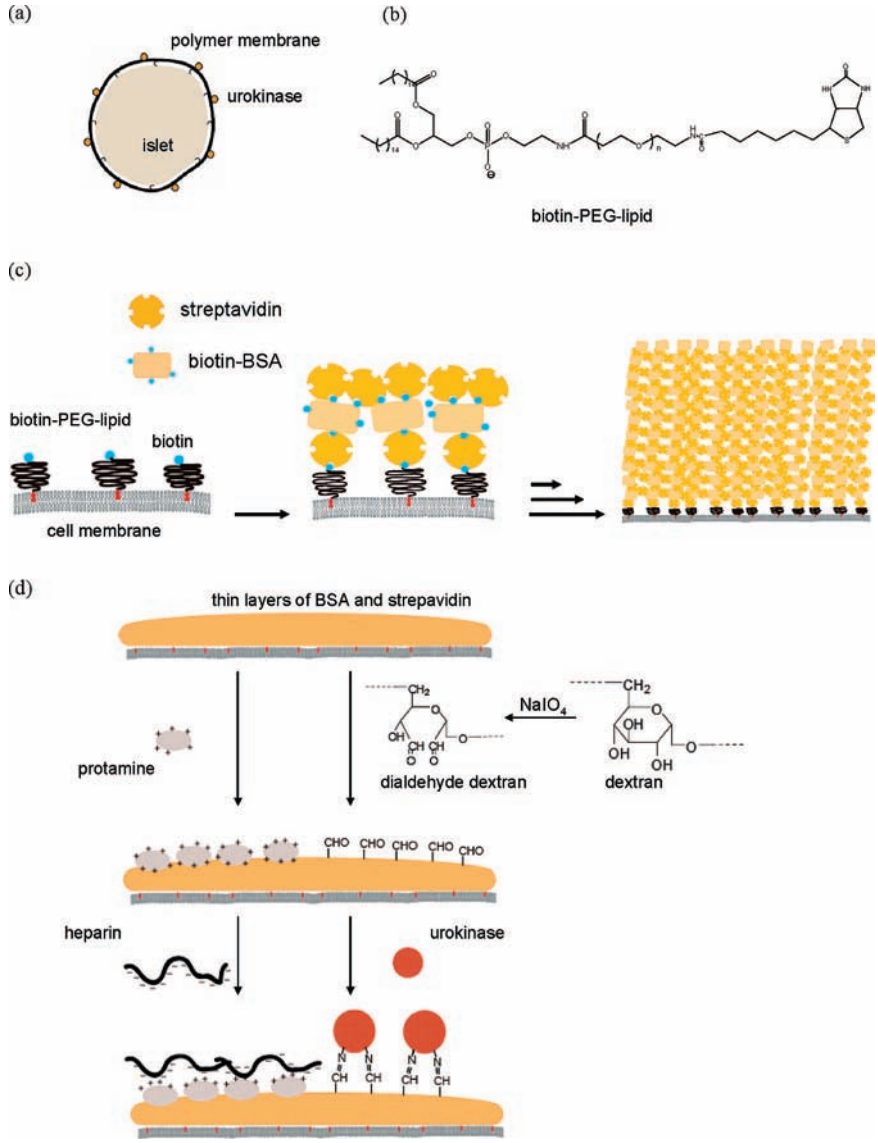

[a] (a) Scheme for anchoring urokinase on surface of islets by constructing a multilayered membrane composed of streptavidin and biotin-BSA. (b) Chemical structure of biotin-PEG-conjugated DPPE (biotin-PEG-lipid). (c) Biotin-BSA/streptavidin multilayered membrane formation. The first biotin-PEG layer was anchored to the surface through hydrophobic interactions. Then, streptavidin and biotin-BSA were chemically reacted to the surface, layer-by-layer. (d) Dextran was oxidized to produce aldehyde groups on the surface of islets, providing a means for urokinase immobilization through Schiff base formation. Heparin was anchored to the surface of islets after treatment with protamine.

is administered to reverse heparin action in the clinical setting. Then, heparin was added for 15 min at RT (5 mg/mL in HBSS). For visualization, the heparin had been labeled with FITC. Heparin (40 mg/mL in pure water) was reacted with FITC (2.6 mg in 100 μL of DMSO) for 3 h at RT, precipitated in acetone at −20 °C for 24 h, evaporated, and washed three times with acetone. Finally, the precipitate was dialyzed against PBS for 2 days (MWCO; 3500 Da) to obtain FITC-heparin (FITC/heparin = 2.5 by molar ratio).

Glucose Stimulation Test. A static glucose-responsive insulin assay (*13*) was performed on biotin-BSA/streptavidin-encapsulated islets, activated dextran modified-encapsulated islets, and urokinase-immobilized islets after 1 and 7 days in culture. After the modified islets were washed several times with Krebs-Ringer solution, they were incubated in 0.1 g/dL, 0.3 g/dL, and then 0.1 g/dL glucose in Krebs-Ringer solution for 1 h each at 37 °C. The insulin concentration in the supernatant at each step was determined by an enzyme-linked immunosorbent assay (ELISA; Shibayagi Co. Ltd., Gunma, Japan).

Statistical Analyses. Comparisons between two groups were performed by Student's *t* test. $P < 0.05$ was considered statistically significant. All statistical calculations were performed using the software *JMP v.5.1.1*.

RESULTS

Forming Multilayered Biotin-BSA and Streptavidin Membranes on Surface of Islets. A nanometer-thick membrane composed of streptavidin and biotin-BSA layers formed on cell surfaces using biotin-PEG-lipid and the layer-by-layer method, as shown in Scheme 1. Biotin and streptavidin interact to form a stable conjugate (association constant was $\sim 10^{15}$ M^{-1}) under physiological conditions, so this system can be used to form a multilayered membrane without damaging the surface of the living cell. To confirm the formation of a multilayered biotin-BSA and streptavidin membrane, the SPR method, which can detect small changes in refractive index on the surface of a gold thin film in real time, was employed. Figure 1 shows the SPR profiles of layer-by-layer reactions between streptavidin and

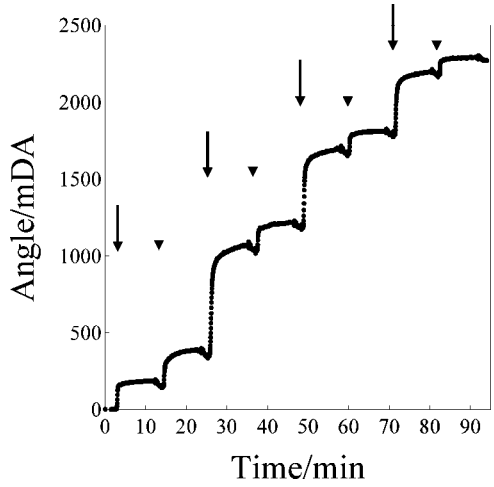

Figure 1. SPR-monitoring of multilayered streptavidin and biotin-BSA membrane formation on the biotin-SAM surface. Stepwise SPR profile indicates sequential formation of a protein multilayer. Arrows and arrowheads indicate the addition of streptavidin and biotin-BSA solutions, respectively.

biotin-BSA. A solution of streptavidin was flowed onto an SPR sensor with a self-assembled monolayer of biotinylated poly(ethylene glycol) alkanethiol (biotin-SAM) as indicated by the first arrow in Figure 1 and Supporting Information Figure S1. The streptavidin layer was formed on a biotin-SAM formed on the sensor surface. Then, biotin-BSA was flowed onto the surface (indicated by the first arrowhead), and BSA was trapped on the streptavidin layer through the biotin/streptavidin reaction. Afterward, streptavidin and biotin-BSA solutions were alternately applied to the surface. The refractive index increased in a stepwise manner indicating the formation of a multilayered membrane composed of streptavidin and biotin-BSA. After this procedure was repeated 10 times, the thickness of the multilayered membrane was about 30 nm as indicated by an SPR shift when the refractive index of the BSA and streptavidin layer was assumed to be 1.45.

Modifying the Surface of Islets with the Multilayered Membrane. In order to construct a biotin-BSA/streptavidin multilayer on the membranes of islets, a hydrophobic lipid chain conjugated hydrophilic PEG chain carrying a biotin molecule was applied to the cell suspension. When a biotin-PEG-lipid dispersion is mixed with the islets suspension, it is expected to incorporate into cell membranes spontaneously via hydrophobic interactions between the hydrophobic part of biotin-PEG-lipid and the lipid bilayer of the cell membrane. Hydrophilic PEG chains remain on the outer surface of the cell, as illustrated in Scheme 1.

First, the surface of single CCRF-CEM cells (floating cells, acute lymphoblastic leukemia T-cells) was treated with biotin-PEG-lipid to confirm the occurrence of the reaction. After incubation of the cells in biotin-PEG-lipid dispersion, FITC-labeled streptavidin was applied. Figure 2a shows the microscopic images of cells modified with FITC-labeled streptavidin/biotin-PEG-lipid. Fluorescence from FITC-streptavidin was visible at the periphery of the each cell, indicating that FITC-streptavidin had formed a complex with the biotin-PEG-lipid on the cell membrane. No fluorescence was observed for cells not treated with biotin-PEG-lipid. Thus, the hydrophobic lipid of the biotin-PEG-lipid was anchored in the lipid bilayer of the cell membrane as shown in Scheme 1. Cell viability as assessed by Trypan blue exclusion was 89% after the modification. There was no statistically significant difference in cell viability between cells modified with streptavidin/biotin-PEG-lipid conjugates and cells prior to modification. Therefore, the surface modification was not toxic to the living cells.

Islets were sequentially treated with biotin-PEG-lipid and FITC-streptavidin. Their fluorescent images taken with a confocal laser-scanning microscope are shown in Figure 2b. Clear fluorescence is seen at the periphery of each islet; no fluorescence was observed on islets treated with FITC-streptavidin when the biotin-PEG-lipid treatment was skipped. These observations indicate that biotin groups can be introduced on the surface of islets using biotin-PEG-lipid and that streptavidin can be anchored to the islet surface via biotin without damaging islet morphology. To form a multilayered membrane of streptavidin and biotin-BSA, the biotinylated islet surface was treated sequentially with streptavidin and biotin-BSA; this procedure was repeated several times. Finally, FITC-streptavidin was used for the 21st layer to allow visualization under a confocal laser-scanning microscope. Figure 2c shows fluorescent images of islets encapsulated with 21 layers of biotin-BSA and streptavidin. A strongly fluorescing layer was observed at the periphery of all islets, indicating the presence of multilayered membranes of biotin-BSA and streptavidin.

Immobilization of Bioactive Molecules to the Surface of Encapsulated Islets. Urokinase is a serine protease that activates plasminogen. Activation of plasminogen triggers a proteolysis cascade that participates in thrombolysis. Immobilizing urokinase on the surface of islets is expected to help dissolve small blood clots that may form on islets, thereby suppressing blood-mediated inflammatory reactions. Multilayered membrane-modified islets were further modified with dialdehyde dextran to introduce aldehyde groups on the surface of islets. Urokinase was immobilized on the islets surface through Schiff base formation between the aldehyde groups with primary amines of urokinase. FITC-labeled BSA was reacted with the aldehyde groups in place of urokinase, allowing direct visualization (Figure 2d). Fluorescence from FITC-BSA was observed at the periphery of all islets, indicating the presence of FITC-BSA. On the other hand, no fluorescence was observed on islets without treatment with activated dextran (Supporting Information Figure S2 (a)). Islets after treatment with biotin-BSA and streptavidin were also used to immobilize heparin at the surface. Protamine was immobilized on islets with biotin-BSA as an outermost surface and then anionic heparin was immobilized on the protamine layer through polyion complex formation. Fluorescence from FITC-heparin was observed at the periphery of all islets (Figure 2e), indicating the presence of FITC-heparin on the islets. There was no fluorescence on islets without the protamine layer (Supporting Information Figure S2 (b)). Thus, our technique enables various bioactive molecules to be immobilized on the surface of islets.

A fibrin plate-based assay was performed to assess the function of the urokinase anchored on the islets. Urokinase transforms plasminogen into active plasmin, which can dissolve fibrin. To assess the activity of the membrane-anchored urokinase, we spotted the modified islets on a fibrin gel, and measured the area of dissolved fibrin around the spotted urokinase-islets. Figure 3a shows the fibrin plate at 12 h after urokinase-islets spotting. A large transparent area was observed around the urokinase-islets, indicating urokinase activity. The transparent area was small around naïve islet spots. The small transparent area might be due to small amounts of urokinase secreted by the islet itself (*18*). Islets with anchored urokinase were cultured in Medium 199 supplemented with 10% FBS. Urokinase activity during culture was followed and is shown in Figure 3b. The fibrinolytic activity of urokinase was retained for 3 days, and then decreased to 25% after 7 days in culture. The stability of the surface modifications was also examined by observing the morphology of islets treated with a multilayered membrane (total layer number = 20). Their outermost layer was treated with FITC-streptavidin and fixed with dialdehyde dextran. Figure 4

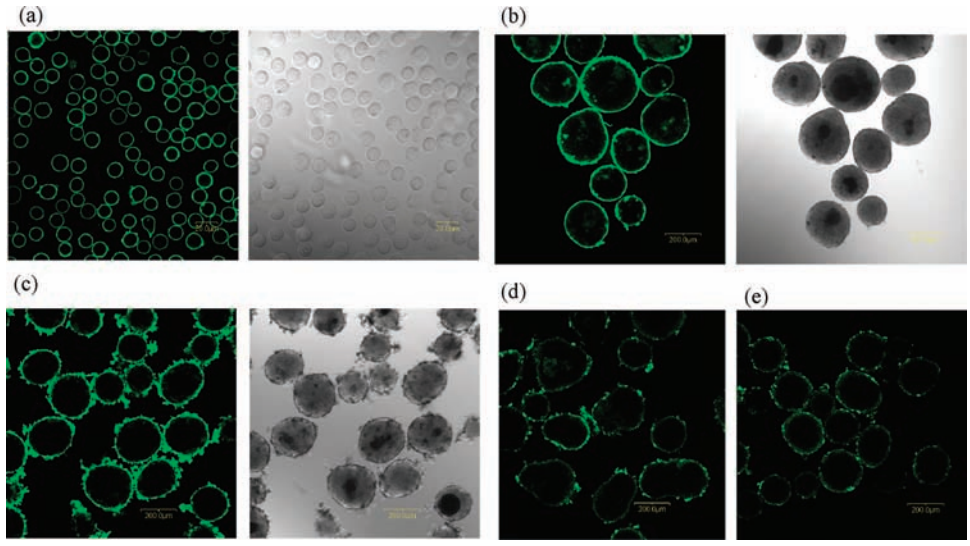

Figure 2. Images of surface-modified cells and islets observed under confocal laser and differential interference microscopy. (a) CCRF-CEM cells were sequentially modified with biotin-PEG-lipid and FITC-labeled streptavidin. (b) Hamster islets were sequentially modified with biotin-PEG-lipid and FITC-labeled streptavidin. (c) Hamster islets modified with biotin-PEG-lipid were sequentially coated with streptavidin and biotin-BSA (20 times); the 21st layer was FITC-streptavidin. (d) Islets covered with a multilayered biotin-BSA/streptavidin membrane were activated with oxidized dextran. FITC-BSA was anchored to the islets through Schiff base formation. (e) Multilayered islets were coated with cationic protamine and FITC-labeled heparin (anionic) was immobilized on the islets through polyion complex formation. Scale bars: 20 μm for (a), and 200 μm for (b), (c), (d), and (e).

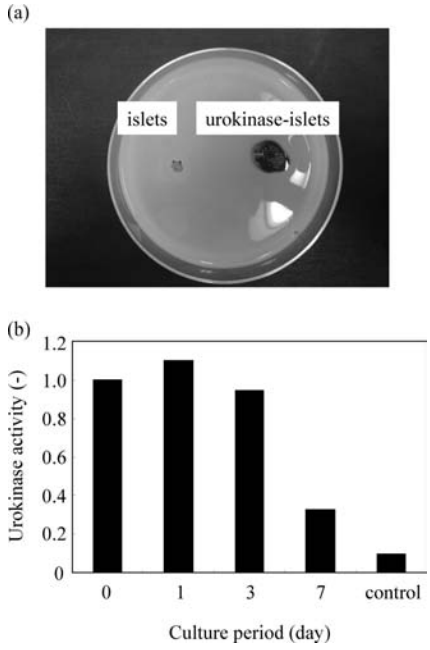

Figure 3. Fibrin plate assay for islet-anchored urokinase. (a) 100 naïve islets and 100 urokinase-modified islets were spotted on the left and right sides of a fibrin plate, respectively, and incubated at 37 °C for 12 h. (b) Bar graph illustrating the change in islet-anchored urokinase activity during culture in medium. Activity is expressed as the area of dissolved fibrin around urokinase-islet spots normalized to the area at day zero (see Experimental Section).

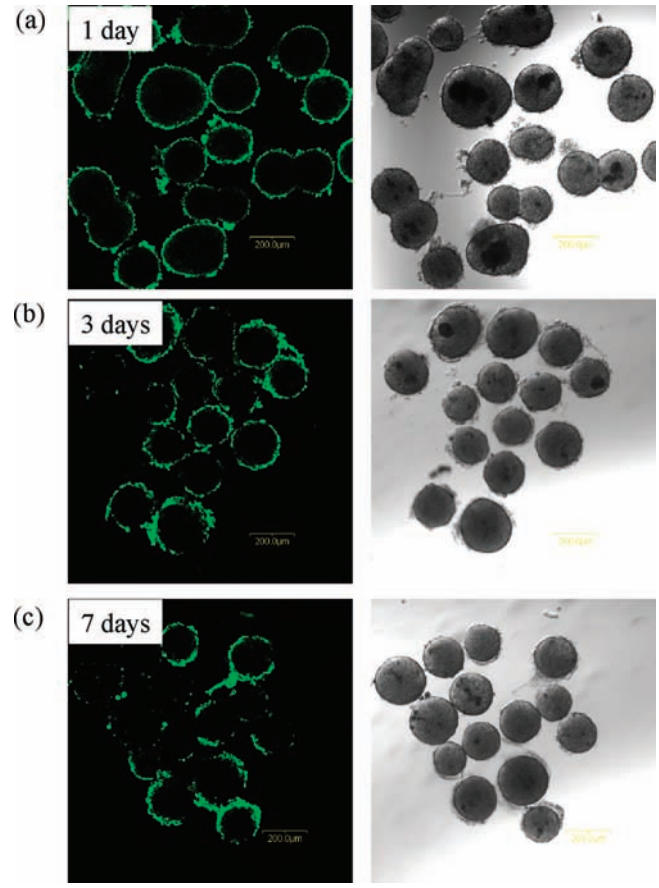

Figure 4. Changes in multilayered membranes on islets after (a) 1, (b) 3, and (c) 7 days in culture. Islets had been coated with a multilayered biotin-BSA/streptavidin membrane on biotin-PEG-lipid modified surface, followed by reaction with activated dextran and culture in Medium 199.

shows the microphotographs of islets at 1, 3, and 7 days of culture. The membrane gradually deteriorated over time, although islet morphology was well-maintained. Thus, urokinase could have detached from the islets, which could account for the decrease in urokinase activity.

Glucose-Stimulated Insulin Release by Surface-Modified Islets. A glucose stimulation test was performed in order to examine the ability of the modified islets to control insulin release in response to glucose level changes; the results are summarized in Figure 5. When the glucose concentration was increased from 0.1 g/dL to 0.3 g/dL, islets in all groups increased insulin release from basal levels. Insulin release returned to the basal level when islets were re-exposed to 0.1 g/dL, indicating

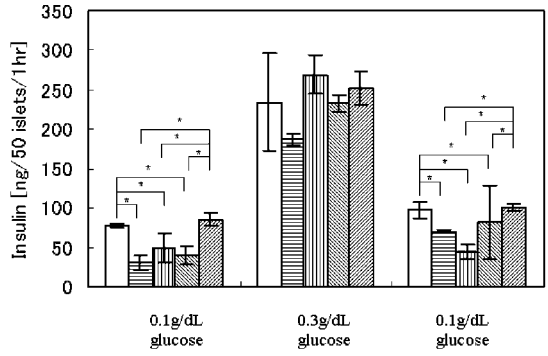

Figure 5. Glucose stimulation test. Bars from left indicate (1) islets without surface modification, (2) islets modified with a multilayered biotin-BSA/streptavidin membrane, (3) periodate-activated dextran-treated islets, (4) urokinase-anchored islets at day zero, and (5) urokinase-anchored islets after 7 days of culture in Medium 199 at 37 °C. The amounts of insulin secreted from modified islets in response to glucose concentration changes (0.1, 0.3, and 0.1 g/dL) were determined by ELISA. ($n = 3$). * indicates a statistically significance difference ($p < 0.01$).

that islets after surface modification normally response to the glucose changes. At low glucose level, the insulin secretion rates in groups of islets after surface modification are slower than that of control group, whereas it was the same level among all groups at high glucose level. However, the all insulin secretion rates were recovered to the basal level after seven days culture. These results indicate that the surface modifications and urokinase anchoring did not influence the islets' ability to regulate and release insulin.

DISCUSSION

Recently, Nilsson et al. reported that the graft survival of porcine islets could be improved by modifying the surface of islets with heparin (*12*), and Chaikof et al. reported immobilizing thrombomodulin to the surface of islets (*19*). In their approaches, biotin molecules were conjugated to amino groups of islets surface proteins in order to cover the surface with avidin for immobilizing heparin, and it is necessary to covalently conjugate phosphine molecules to surface protein amino groups to anchor thrombomodulin. Although they reported some improvements in the graft survival by their modification methods, their method is not sufficient enough to solve all of the problems related with the graft loss in the islet transplantation. It is meaningful to increase options to modify islet surface.

In this study, we develop a versatile method for anchoring bioactive substances onto the surface of islets. First, biotin-PEG-lipid was anchored to the lipid bilayer of the cell membrane through hydrophobic interactions. This modification had no influence on cell viability. The biotin molecule on the cell surface was used to add multilayered membranes of streptavidin and biotin-BSA. Then, a fibrinolytic enzyme, urokinase or anticoagulant heparin, was immobilized to the outermost surface to prevent the instant blood-mediated inflammatory reaction. Our methods can much more easily immobilize enzymes and polysaccharide on islet surfaces. The surface modifications did not influence the glucose-responsive insulin-secreting ability of islets, and anchored urokinase retained its fibrinolytic properties at least for 7 days. Therefore, thrombosis that form immediately after transplantation would be prevented from using these modified islets for transplantation. Immobilizing urokinase and heparin on the surface of islets is an attractive method because it would prevent systemic administration of anticoagulants, which is associated with an increased risk of bleeding after intraportal transplantation.

As shown Figure 2c, a strong fluorescence layer was observed at the periphery of all islets. Multilayered membranes of biotin-BSA and streptavidin seem to be formed on islets from the microphotographs and SPR monitoring shown in Supporting Information Figure S1. Although the surface of islets treated with a single layer was smooth, the surface became rough and some debris-like material was found on the surface of islets coated with the 21 layers. The internal tension in the coated membranes is expected to increase with a number of the layer-by-layer sequences. The layer formed was peeled off when the internal tension became larger than the anchoring strength of the PEG-lipid into the lipid bilayer. Bovine serum albumin is a globular protein and is expected not to form a mechanical strong film. We will examine synthetic linear polymers, such as poly(vinyl alcohol) and cellulose derivatives, which have been used to prepare tough membranes in industrial applications.

The number of amino groups in urokinase (25 lysine residues in a molecule) is less than that of BSA (59 lysine residue in a molecule) and the reaction used to immobilize proteins was Schiff base formation which is considered to be a reversible reaction. Although urokinase seems to be easily released from the islet surface, the fibrinolytic activity of urokinase immobilized on islets retained 25% of its initial activity after 7 days in culture. Activated dextran carries a number of aldehyde groups in a molecule. The interaction between the activated dextran and urokinase becomes stronger and more stable due to multibond formation between these molecules, even though each Schiff base is unstable by itself. Our technique using activated dextrane enables various bioactive proteins to be immobilized on the surface of islets.

Islets microencapsulated within an alginate-poly-(L-lysine) membrane and an agarose hydrogel membrane have been investigated for use as a bioartificial pancreas (*20–26*). Many groups have reported that a long-term normoglycemia in a diabetic small animal, such as a mouse or a rat, can be realized by transplanting microencapsulated islets into its peritoneal cavity. However, in clinical settings, about 10 mL of islet suspension should be injected through a catheter into the portal vein in liver. The diameter of microencapsulated islets was several times larger than that of islets, which could result in plugged vessels if infused into the portal vein. As shown in Figure 1 for SPR examinations, the thickness of the membrane increases stepwise using the streptavidin/biotin-BSA multilayer method. We examined the possibility of enclosing islets within a thin membrane using this layer-by-layer method. After forming 21 layers, the multilayer thickness reached tens of nanometers, as evaluated by SPR method and microscopy (Figures 1 and 2). The thickness was enough to the cover islet surface, but the islets' volume increase was small. Our method holds promise as a means to enclose islets without increasing volume. Immunoisolative efficacy of the layer-by-layer membrane is carefully being examined in islet transplantation studies; the results will be reported.

We examined membrane stability and found that the membrane gradually deteriorated over time (Figure 4). Either the mechanical strength of the streptavidin and biotin-BSA membrane is not strong enough for long-term encapsulation or enzymes secreted from the cells degraded the membranes. In addition, it would be necessary to carefully examine the effect of urokinase and heparin immobilized to the surface of islets *in vivo*. Future work will focus on maintaining the integrity of the multilayer membrane for longer periods and graft survivals will be carefully examined.

In conclusion, thin-layered membranes were formed on the surface of islets via biotin-PEG-lipids and the biotin/streptavidin system without increasing cell volume. Further, urokinase was anchored to the membrane, and its high fibrinolytic ability was maintained for seven days in culture. This novel method for

constructing a bioartificial pancreas provides a promising means for improving graft survival following intraportal transplantation.

ACKNOWLEDGMENT

This study was supported in part by R&D Projects for Economic Reinvigoration (Leading Projects) and by Grant-in-Aid for Scientific Research (A) (no. 18200034) from the Ministry of Education, Culture, Sports, Science, and Technology (MEXT) of Japan.

Supporting Information Available: Additional information as described in the text. This material is available free of charge via the Internet at http://pubs.acs.org.

LITERATURE CITED

(1) Shapiro, A. M, Lakey, J. R., Ryan, E. A., Korbutt, G. S., Toth, E, Warnock, G. L., Kneteman, N. M., and Rajotte, R. V. (2000) Islet transplantation in seven patients with type 1 diabetes mellitus using a glucocorticoid-free immunosuppressive regimen. *N. Engl. J. Med. 343*, 230–238.

(2) Ryan, E. A., Lakey, J. R., Rajotte, R. V., Korbutt, G. S., Kin, T., Imes, S., Rabinovitch, A., Elliott, J. F., Bigam, D., Kneteman, N. M., Warnock, G. L., Larsen, I., and Shapiro, A. M. (2001) Clinical outcomes and insulin secretion after islet transplantation with the Edmonton protocol. *Diabetes 50*, 710–719.

(3) Moberg, L., Johansson, H., Lukinius, A., Berne, C., Foss, A, Kallen, R., Ostraat, O., Salmela, K., Tibell, A., Tufveson, G., Elgue, G., Ekdahl, K., Korsgren, O., and Nilsson, B. (2002) Production of tissue factor by pancreatic islet cells as a trigger of detrimental thrombotic reactions in clinical islet transplantation. *Lancet 360*, 2039–2045.

(4) Piemonti, L., Leone, B. E., Nano, R., Saccani, A., Monti, P., Maffi, P., Bianchi, G., Sica, A., Peri, G., Melzi, R., Aldrighetti, L., Secchi, A., Di Carlo, V., Allavena, P., and Bertuzzi, F. (2002) Human pancreatic islets produce and secrete MCP-1/CCL2: relevance in human islet transplantation. *Diabetes 51*, 55–65.

(5) Johansson, H., Lukinius, A., Moberg, L., Lundgren, T., Berne, C., Foss, A., Felldin, M., Kallen, R., Salmela, K., Tibell, A., Tufveson, G., Ekdahl, K. N., Elgue, G., Korsgren, O., and Nilsson, B. (2005) Tissue factor produced by the endocrine cells of the islets of Langerhans is associated with a negative outcome of clinical islet transplantation. *Diabetes 54*, 1755–1762.

(6) Moberg, L. (2005) The role of the innate immunity in islet transplantation. *Ups. J. Med. Sci. 110*, 17–55.

(7) van der Windt, D. J., Bottino, R., Casu, A., Campanile, N., and Cooper, D. K. (2007) Rapid loss of intraportally transplanted islets: an overview of pathophysiology and preventive strategies. *Xenotransplantation 14*, 288–297.

(8) Ozmen, L., Ekdahl, K. N., Elgue, G., Larsson, R., Korsgren, O., and Nilsson, B. (2002) Inhibition of thrombin abrogates the instant blood-mediated inflammatory reaction triggered by isolated human islets: possible application of the thrombin inhibitor melagatran in clinical islet transplantation. *Diabetes 51*, 1779–1784.

(9) Contreras, J. L., Eckstein, C., Smyth, C. A., Bilbao, G., Vilatoba, M., Ringland, S. E., Young, C., Thompson, J. A., Fernandez, J. A., Griffin, J. H., and Eckhoff, D. E. (2004) Activated protein C preserves functional islet mass after intraportal transplantation: a novel link between endothelial cell activation, thrombosis, inflammation, and islet cell death. *Diabetes 53*, 2804–2814.

(10) Johansson, H., Goto, M., Dufrane, D., Siegbahn, A., Elgue, G., Gianello, P., Korsgren, O., and Nilsson, B. (2006) Low molecular weight dextran sulfate: a strong candidate drug to block IBMIR in clinical islet transplantation. *Am. J. Transplant. 6*, 305–312.

(11) Bennet, W., Sundberg, B., Lundgren, T., Tibell, A., Groth, C. G., Richards, A., White, D. J., Elgue, G., Larsson, R., Nilsson, B., and Korsgren, O. (2000) Damage to porcine islets of Langerhans after exposure to human blood in vitro, or after intraportal transplantation to cynomologus monkeys: protective effects of sCR1 and heparin. *Transplantation 69*, 711–719.

(12) Cabric, S., Sanchez, J., Lundgren, T., Foss, A., Felldin, M., Kallen, R., Salmela, K., Tibell, A., Tufveson, G., Larsson, R., Korsgren, O., and Nilsson, B. (2007) Islet surface heparinization prevents the instant blood-mediated inflammatory reaction in islet transplantation. *Diabetes 56*, 2008–2015.

(13) Miura, S., Teramura, Y., and Iwata, H. (2006) Encapsulation of islets with ultra-thin polyion complex membrane through poly(ethylene glycol)-phospholipids anchored to cell membrane. *Biomaterials 27*, 5828–5835.

(14) Teramura, Y., Kaneda, Y., and Iwata, H. (2007) Islet-encapsulation in ultra-thin layer-by-layer membranes of poly-(vinyl alcohol) anchored to poly(ethylene glycol)-lipids in the cell membrane. *Biomaterials 28*, 4818–4825.

(15) Hirata, I., Morimoto, Y., Murakami, Y., Iwata, H., Kitano, E., Kitamura, H., and Ikada, Y. (2000) Study of complement activation on well-defined surfaces using surface plasmon resonance. *Colloid Surf., B: Biointerfaces 18*, 285–292.

(16) Hermanson, G. T., Mallia, A. K., Smith, P. K. *Immobilized affinity ligand techniques*, Academic Press, London.

(17) Edward, N. (1972) Methods for improving the sensitivity and specificity of the fibrin plate. *J. Clin. Pathol. 25*, 335–337.

(18) Virji, M. A., and Dimasi, M. J. (1987) Selective secretion of only the urokinase plasminogen activator from rat islets of Langerhans. *Diabetes Res. 6*, 9–13.

(19) Stabler, C. L., Sun, X. L., Cui, W., Wilson, J. T., Haller, C. A, and Chaikof, E. L. (2007) Surface re-engineering of pancreatic islets with recombinant azido-thrombomodulin. *Bioconjugate Chem. 18*, 1713–1715.

(20) Lin, F., and Sun, A. M. (1980) Microencapsulated islets as bioartificial endocrine pancreas. *Science 210*, 908–910.

(21) O'Shea, G. M., Goosen, M. F. A., and Sun, A. M. (1984) Prolonged survival of transplanted islets of Langerhans encapsulated in a biocompatible membrane. *Biochim. Biophys. Acta 804*, 133–136.

(22) Fritschy, W. M., Wolters, G. H., and van Schilfgaarde, R. (1991) Effect of alginate-polylysine-alginate microencapsulation on *in vitro* insulin release from rat pancreatic islets. *Diabetes 40*, 37–43.

(23) Sakai, S., Ono, T., Ijima, H., and Kawakami, K. (2002) In vitro and in vivo evaluation of alginate/sol-gel synthesized aminopropyl-silicate/alginate membrane for bioartificial pancreas. *Biomaterials 23*, 4177–4183.

(24) Iwata, H., Takagi, T., Shimizu, H., Yamashita, K., Kobayashi, K., and Akutsu, T. (1992) Agarose for bioartificial pancreas. *J. Biomed. Mater. Res. 26*, 967–977.

(25) Iwata, H., Kobayashi, K., Takagi, T., Oka, T., Yang, H., Amemiya, H., Tsuji, T., and Ito, F. (1994) Feasibility of agarose microbeads with xenogeneic islets as a bioartificial pancreas. *J. Biomed. Mater. Res. 28*, 1003–1011.

(26) Kobayashi, T., Aomatsu, Y., and Iwata, H. (2003) Indefinite islet protection from autoimmune destruction in nonobese diabetic mice by agarose microencasulation without immunosupression. *Transplantation 75*, 619–625.

BC800064T

Surface-Modified and Internally Cationic Polyamidoamine Dendrimers for Efficient siRNA Delivery

Mahesh L. Patil,[†] Min Zhang,[†] Seema Betigeri,[†] Oleh Taratula,[‡] Huixin He,[‡] and Tamara Minko*[,†]

Department of Pharmaceutics, Rutgers, The State University of New Jersey, Piscataway, New Jersey 08854, and Department of Chemistry, Rutgers, The State University of New Jersey, Newark, New Jersey 07102. Received February 22, 2008; Revised Manuscript Received May 27, 2008

A novel internally quaternized and surface-acetylated poly(amidoamine) generation four dendrimer (QPAMAM-NHAc) was synthesized and evaluated for intracellular delivery of siRNA. The proposed dendrimer as a nanocarrier possesses the following advantages: (1) modified neutral surface of the dendrimer for low cytotoxicity and enhanced cellular internalization; (2) existence of cationic charges inside the dendrimer (not on the outer surface) resulting in highly organized compact nanoparticles, which can potentially protect nucleic acids from degradation. The properties of this dendrimer were compared with PAMAM-NH_2 dendrimer, possessing surface charges, and with an internally quaternized charged and hydroxyl-terminated QPAMAM-OH dendrimer. Atomic force microscopy studies revealed that internally charged and surface neutral dendrimers, QPAMAM-OH and QPAMAM-NHAc, formed well-condensed, spherical particles (polyplexes) with siRNA, while PAMAM-NH_2 resulted in the formation of nanofibers. The modification of surface amine groups to amide significantly reduced cytotoxicity of dendrimers with QPAMAM-NHAc dendrimer showing the lowest toxicity. Confocal microscopy demonstrated enhanced cellular uptake and homogeneous intracellular distribution of siRNA delivered by the proposed QPAMAM-NHAc nanocarrier. The results clearly demonstrated distinct advantages of developed QPAMAM-NHAc/siRNA polyplexes over the existing nucleic acid dendrimeric carriers.

INTRODUCTION

Short or small interfering RNA (siRNA) is a class of short double-stranded RNA molecules composed of 20−25 nucleic acids. siRNA is involved in the RNA interference (RNAi) pathway to inhibit gene expression of a specific gene (*1–3*). In addition, siRNA also acts in RNAi-related pathways, e.g., as an antiviral mechanism or in shaping the chromatin structure of a genome. Despite several potential therapeutic applications, the efficiency of siRNA *in vivo* is limited by its low resistance against enzymatic degradation, limited permeability across cell membrane, and substantial liver and renal clearance (*4*). Therefore, in order to exploit potential therapeutic applications of siRNA, the effective delivery of siRNA to the site of action and into targeted cells is required. While considerable efforts have recently been made to develop new siRNA carriers, the research on the delivery of siRNA is still in a preliminary stage (*5–11*).

One of the most common methods used for the delivery of charged nucleic acids involves their electrostatic interaction with cationic carriers. Several types of cationic carriers such as liposome/lipids, dendrimers, and polymeric amines have been successfully used for the delivery of plasmid DNA and oligonucleotides (*12, 13*). Even though siRNA is structurally similar to plasmid DNA with negatively charged anionic phosphodiester backbones, electrostatic interaction of siRNA largely differs from that of plasmid DNA (*14*). The molecular weight and molecular topography of siRNA and plasmid DNA play an important role in their electrostatic interaction with cationic agents. Nonviral vectors, and especially polymers, form looser complexes with siRNA than with plasmid DNA, and incomplete encapsulation of the nuclear acid leads to the exposure of siRNA to enzymatic or physical degradation prior to delivery to the targeted cells. Consequently, carriers that are successfully used for the delivery of plasmid DNA cannot be efficiently employed for the delivery of siRNA, and a different approach is required.

Polycationic dendrimers such as poly(amidoamine) (PAMAM) dendrimers have been extensively studied as efficient vehicles for the delivery of genes and therapeutic drugs (*15–17*). Dendrimers are a type of regular and highly branched, monodisperse, spherical nanomaterials with dense peripheral groups that can be functionalized with drugs, targeting moieties, and other biologically active components (*18, 19*). Biodistribution studies showed that the higher molecular mass and/or more branched dendrimers exhibited longer circulation half-lives due to slower excretion into the urine when compared with lower molecular mass carriers, less branched dendrimers, or linear polymers (*20*). Dendrimers such as poly(amidoamine) and poly(propylenimine) possess cationic primary amine groups at the surface, which participate in the DNA binding process and increase the cellular uptake of DNA by transforming the entire complex into nanoscale polyplexes (*12–15, 17*). However, these highly efficient delivery systems have been less explored for siRNA delivery. It has been shown that PAMAM dendrimers or their conjugates are more efficient in delivering antisense oligonucleotides or plasmid DNA than siRNA (*21*).

Lee et al. have demonstrated synthesis of internally quaternized PAMAM-OH dendrimers and their efficiency in the delivery of plasmid DNA (*22, 23*). Although the internally charged PAMAM dendrimers formed stable polyplexes with plasmid DNA, their transfection ability was far lower than polyplexes of the poly(ethyleneimine) or PAMAM dendrimer.

* To whom correspondence should be addressed: Professor Tamara Minko, Ph.D., Department of Pharmaceutics, Ernest Mario School of Pharmacy, Rutgers, The State University of New Jersey, 160 Frelinghuysen Road, Piscataway, NJ 08854-8020, Phone: 732-445-3831x 214, Fax: 732-445-3134, Email: minko@rci.rutgers.edu.

[†] Department of Pharmaceutics.

[‡] Department of Chemistry.

10.1021/bc8000722 CCC: $40.75 © 2008 American Chemical Society
Published on Web 06/25/2008

It is generally believed that the neutral surface of a dendrimer results in low transfection efficiency. In contrast, cationic dendrimers with positive surface charge interact with negatively charged cell membranes and permeate more easily than the neutral or anionic dendrimers. However, such a positive surface charge renders cytotoxicity to the cationic dendrimers, which limits their clinical applications. Recently, it has been shown that modification of surface amine groups of PAMAM dendrimer reduced their cytotoxicity (*22, 24*).

Herein, we describe synthesis of surface-modified and an internally quaternized PAMAM dendrimer that possesses low cytotoxicity and at the same time offers internal positive charges for electrostatic interaction with negatively charged siRNA. A novel QPAMAM-NHAc dendrimer in which surface amine groups were modified with acetyl group and internal tertiary nitrogens were quaternized was prepared and evaluated for siRNA delivery.

EXPERIMENTAL PROCEDURES

Materials. Generation four PAMAM-NH_2 (Mw ~14 214 Da, 64 amine end groups), generation four PAMAM-OH dendrimer (Mw ~14 277 Da, 64 hydroxyl end groups), acetic anhydride and methyl iodide were purchased from Sigma-Aldrich Co. (St. Louis, MO). Spectra/Pore dialysis membrane with molecular weight cutoff of 2000 Da was obtained from Spectrum Laboratories, Inc. (Rancho Dominguez, CA). Fluorescent RNA duplex−siRNA labeled with Pierce NuLight DY-547 fluorophores (si*GLO* Red Transfection Indicator, red fluorescence) was obtained from Applied Biosystems (Ambion, Inc., Foster City, CA). All other chemicals were purchased from Fisher Scientific (Fairlawn, NJ).

Cell Line. The human ovarian carcinoma A2780 cell line was obtained from Dr. T. C. Hamilton (Fox Chase Cancer Center). Cells were cultured in RPMI 1640 medium (Sigma, St. Louis, MO) supplemented with 10% fetal bovine serum (Fisher Scientific, Fairlawn, NJ). Cells were grown at 37 °C in a humidified atmosphere of 5% CO_2 (v/v) in air. All experiments were performed on cells in the exponential growth phase.

Synthesis of Internally Quaternized QPAMAM-OH Dendrimer. A slightly modified previously described procedure was used for synthesis of QPAMAM-OH dendrimer (*23*). Briefly, PAMAM-OH generation four (172 mg, 0.012 mmol) was dissolved in *N*,*N*′-dimethylformamide (DMF, 1 mL) and excess methyl iodide (MeI, 0.5 mL) was added. The reaction mixture was sealed and stirred at 50 °C for 48 h. The reaction mixture was then precipitated into diethyl ether to obtain a solid, which was dried under a vacuum and redissolved in water (1 mL). The resulting solution was dialyzed against 2 M NaCl and deionizer water successively using dialysis membrane (molecular mass cutoff 2000 Da) and then lyophilized to afford a white solid (Figure 1A).

Synthesis of Acetylated PAMAM-NHAc Dendrimer (Figure 1B). Triethylamine (0.17 mL, 1.2 mmol) was added to a stirred solution of PAMAM-NH_2 generation four (172 mg, 0.012 mmol) dissolved in anhydrous methanol (10 mL) followed by the addition of excess acetic anhydride (0.1 mL, 0.96 mmol). The resulting mixture was stirred at room temperature for 24 h. Methanol was evaporated under reduced pressure and the resulting residue was dissolved in water (2 mL). Further purification by extensive dialysis against deionizer water using dialysis membrane (molecular mass cutoff 2000 Da) and freeze-drying afforded acetylated PAMAM dendrimer.

Synthesis of Acetylated and Internally Quaternized QPAMAM-NHAc Dendrimer (Figure 1B). PAMAM-NHAc (100 mg, 0.0059 mmol) was dissolved in DMF (1 mL) and excess methyl iodide (0.5 mL) was added. The reaction mixture was sealed and stirred at 50 °C for 48 h. The reaction mixture was then precipitated into diethyl ether to obtain a solid, which was dried under a vacuum and redissolved in water (1 mL). The resulting solution was dialyzed against 2 M NaCl and deionizer water successively using dialysis membrane (molecular mass cutoff 2000 Da) and then lyophilized to afford a white solid.

Proton nuclear magnetic resonance spectroscopy (^{1}H NMR). ^{1}H NMR was performed on a Varian VNMRS 400 MHz NMR spectrometer (Varian, Inc., Palo Alto, CA). The chemical shift was expressed as parts per million (ppm) and a solvent peak was used as reference (D_2O, 4.8 ppm). The following abbreviations are used in the Results section to identify multiplicities: s, singlet; m, multiplet; br, broad.

Atomic Force Microscopy. The samples of siRNA/dendrimer condensates were imaged with a tapping mode atomic force microscope (Nanoscope III A, Veeco Digital Instruments, Chadds Ford, PA). During imaging, a 125 μm long rectangular silicon cantilever/tip assembly was used with a spring constant of 40 N/m, resonance frequency of 315−352 kHz, and tip radius of 5−10 nm. The images were generated by the change in amplitude of the free oscillation of the cantilever as it interacts with the sample. The height differences on the surface are indicated by the color code: lighter regions indicate higher heights. In order to image siRNA condensates, 5 μL of dendrimer/siRNA solutions was deposited on freshly cleaved mica. After 3−5 min of incubation, the mica surface was rinsed with 3 drops of deionized water 4 times and dried under a flow of nitrogen.

Gel Electrophoresis. The complexes of dendrimers (PAMAM-NH_2, QPAMAM-OH, and QPAMAM-NHAc) and siRNA were prepared in water at N/P (negative to positive) charge ratios ranging 0−1.5 and incubated at room temperature for 30 min. The charge ratio was calculated by relating the number of positive charges on dendrimer (primary amine groups of PAMAM-NH_2 and quaternary amine groups of QPAMAM-OH and QPAMAM-NHAc) with the number of negatively charged phosphate groups of siRNA. Dendrimer-free siRNA was used as the control. Double-stranded RNA ladder (New England Biolabs) with the smallest number of base pairs at 21 was used as a size reference. The samples were further diluted with DPBS buffer and electrophoresed with ethidium bromide in 4% agarose gel at 100 V for 50 min in Tris-Borate-EDTA buffer. siRNA bands on the gel were visualized under ultraviolet light.

Dynamic Light Scattering (DLS) Analysis. Three types of complexes with N/P charge ratios of 1, 1.5, and 3 were prepared from dendrimers (PAMAM-NH_2, QPAMAM-OH, and QPAMAM-NHAc) and siRNA in water. The resulting complexes were incubated for 30 min and the size was determined using the DynePro-MS800 dynamic light scattering/molecular sizing instrument with argon laser wavelength $\lambda = 830$ nm, a detector angle 90°, and typical sample volume of 20 μL. Each light scattering experiment consisted of 20 or more independent readings, each 10 s in duration. Data analysis was conducted using DynaPro Instrument Control Software for Molecular Research DYNAMICS (version 5.26.60). The obtained DLS data represents the average of three runs.

Cellular Internalization of siRNA and Dendrimer/siRNA Complex. To analyze cellular internalization and intracellular localization of siRNA, fluorophore-labeled siRNA (si*GLO* Red, red fluorescence) either free or complexed with dendrimer (N/P = 3) was incubated for 75 min with living A2780 human ovarian cancer cells. Fluorescence and its distribution within the cell were examined every minute using a confocal microscope. Fluorescent images were digitally scanned and fluorescence inside cells (that reflects cellular accumulation of labeled siRNA) was expressed in arbitrary units.

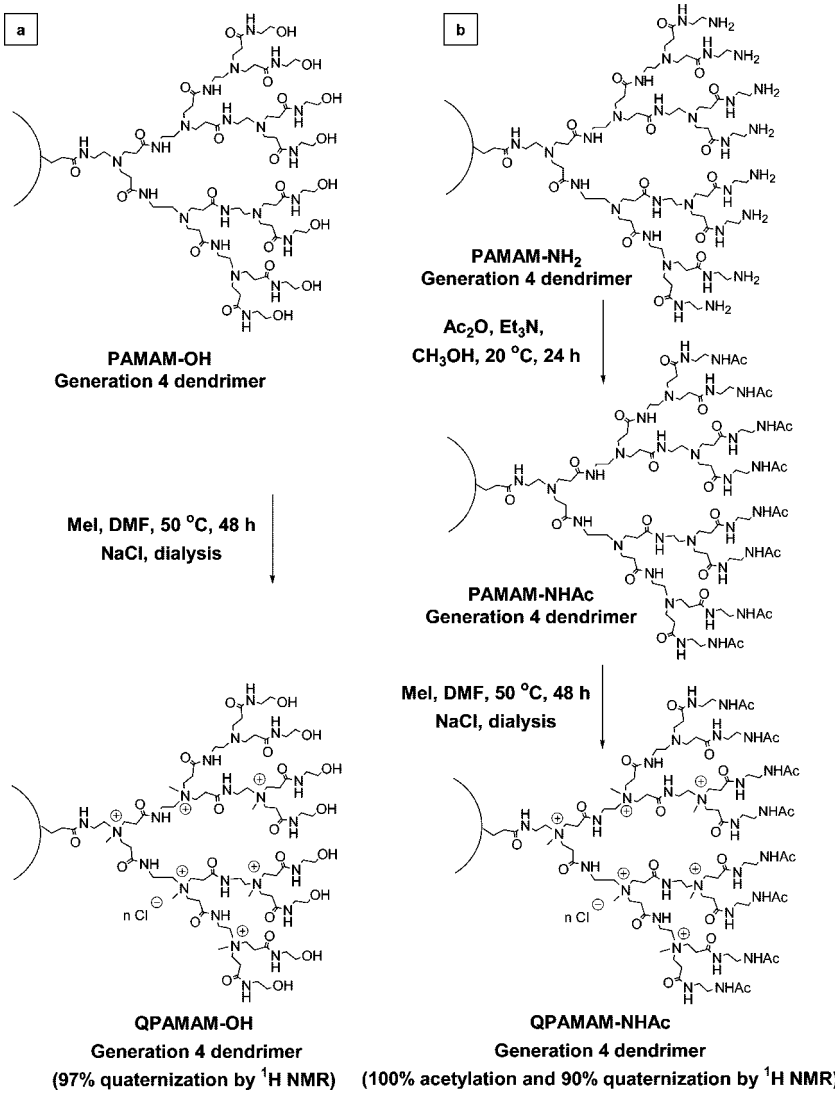

Figure 1. Synthesis of dendrimers. (a) PAMAM-OH dendrimer was internally quaternized to form QPAMAM-OH dendrimer with inner cationic charges. (b) PAMAM-NH_2 dendrimer was acetylated to form PAMAM-NHAc dendrimer. Surface acetylated PAMAM-NHAc dendrimer was internally quaternized to form QPAMAM-NHAc dendrimer possessing internal cationic charges.

***In Vitro* Cytotoxicity.** A modified MTT (3-(4,5-dimethylthiazol-2-yl)-2,5-diphenyltetrazolium bromide) assay was used to assess the cyctotoxicity of three dendrimers as previously described (*25*). To measure cytotoxicity, cells were separately incubated in a microtiter plate with different concentrations of PAMAM-NH_2, QPAMAM-OH, and QPAMAM-NHAc dendrimers. Control cells received an equivalent volume of fresh medium. The duration of incubation was 24 h. On the basis of these measurements, cellular viability was calculated for each dendrimer concentration. A decrease in the cellular viability indicated an increase in dendrimer toxicity.

RESULTS

Synthesis and Characterization of Internally Quaternized PAMAM Dendrimer (QPAMAM-OH). The internal quaternization of PAMAM-OH dendrimer was carried out according to a previously described procedure (*23*) with a slight modification (Figure 1A). Excess methyl iodide was added to ensure complete quaternization of internal tertiary amine groups. Analysis of dendrimer by ^{1}H NMR (400 MHz, D_2O) revealed the following major peaks (Figure 2): δ 2.83−2.98 (br m, $\underline{CH_2}CONH$), 3.16 (br s, $N^+\underline{CH_3}$), 3.32−3.38 (br m, $\underline{CH_2}CH_2OH$), 3.46−3.57 (br m, $CONHCH_2\underline{CH_2}N^+$), 3.62−3.78 (br m, $N^+\underline{CH_2}CH_2CONH$ and $\underline{CH_2}OH$). The degree of quaternization was confirmed by ^{1}H NMR spectroscopy. Proton peaks arising from the (-$CH_2\underline{CH_2}$N-) methylene group adjacent to

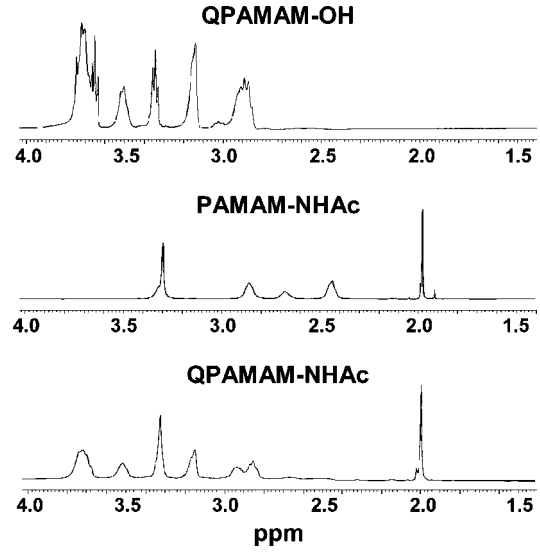

Figure 2. Typical proton nuclear magnetic resonance (^{1}H NMR) spectra of different dendrimers.

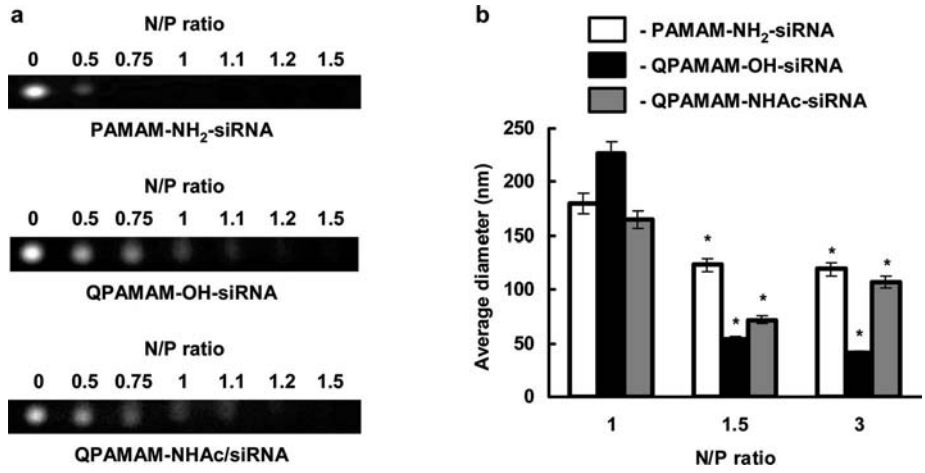

Figure 3. Influence of negative to positive charge ratios on dendrimer−siRNA complex formation and particle size. (a) Typical agarose gel electrophoresis images of the siRNA−dendrimer complexes at different N/P (negative to positive) charge ratios. The dendrimer−siRNA complex formation led to the disappearance of siRNA bands from agarose gels. (b) Average particle size of different siRNA−dendrimer complexes determined by dynamic light scattering. Means ± SD are shown. *P < 0.05 when compared with N/P ratio equal 1.

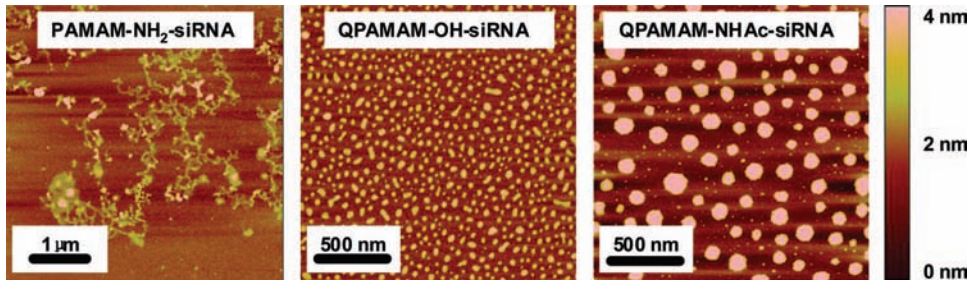

Figure 4. Typical atomic force microscope images of the condensates formed by siRNA in the presence of different dendrimers. The images were made in a tapping mode. The height differences on the surface are indicated by the color code: lighter regions indicate higher heights.

tertiary nitrogen were completely shifted, suggesting almost complete quaternization. Furthermore, the exact degree of quaternization (97%) was determined by comparing the integrated peak area of newly introduced methyl group (N^+-CH_3) at δ 3.16 to that of the unmodified methylene protons (−$\underline{CH_2}CH_2OH$) at δ 3.32−3.38.

Synthesis and Characterization of Surface-Modified and Internally Quaternized PAMAM Dendrimer (QPAMAM-NHAc). The surface-modified and internally quaternized dendrimer QPAMAM-NHAc was synthesized in two steps (Figure 1B). During the first step, the primary amine groups of PAMAM-NH_2 dendrimer were modified with acetyl group to yield fully acylated PAMAM-NHAc (*23*). ^{1}H NMR (400 MHz, D_2O) spectral data for this dendrimer are (Figure 2): δ 1.98 (s, CO$\underline{CH_3}$), 2.40−2.50 (br m, $\underline{CH_2}$CONH), 2.62−2.73 (br m, CONHCH$_2\underline{CH_2}$N), 2.82−2.92 (br m, N$\underline{CH_2}CH_2$CONH), 3.26−3.37 (m, CONH$\underline{CH_2}$ and $\underline{CH_2}$NHCOCH$_3$). The degree of acetylation was confirmed by ^{1}H NMR spectra by relating the integrated peak area of signal appeared at δ 1.98 ppm (-NHCO$\underline{CH_3}$) to that of methylene protons of PAMAM dendrimer (δ 2.40−3.37). During the second step, internal tertiary amine groups of the surface-modified PAMAM-NHAc dendrimer were quaternized by treatment with excess methyl iodide in *N*,*N*′-dimethylformamide at 50 °C. ^{1}H NMR (400 MHz, D_2O) spectral data for this dendrimer are as follows (Figure 2): δ 2.00 (s, CO$\underline{CH_3}$), 2.81−2.99 (br m, $\underline{CH_2}$CONH), 3.16 (br s, $N^+\underline{CH_3}$), 3.29−3.38 (br m, CONH$\underline{CH_2}$ and $\underline{CH_2}$NHCOCH$_3$), 3.47−3.58 (br m, CONHCH$_2\underline{CH_2}N^+$), 3.66−3.81 (br m, $N^+\underline{CH_2}$-CH_2CONH). The degree of quaternization was estimated using ^{1}H NMR spectroscopy by comparing the integrated peak area of newly introduced methyl group (N^+-CH_3) at δ 3.16 to that of the unmodified methylene protons (CONH$\underline{CH_2}$ and $\underline{CH_2}$NHCOCH$_3$) at δ 3.29−3.38.

Analysis of Dendrimer/siRNA Complex Formation by Agarose Gel Electrophoresis. Three types of dendrimers, PAMAM-NH_2, QPAMAM-OH, and QPAMAM-NHAc, were mixed with siRNA in water at various N/P charge ratios and were subjected to electrophoresis in agarose gel (Figure 3a). The complex formation was observed for all three dendrimers as evidenced by oligonucleotide bands disappearance from agarose gels. Interestingly, QPAMAM-OH and QPAMAM-NHAc dendrimers displayed a comparable ability to form complexes with siRNA, and no significant difference was observed in their band intensities.

Analysis of Particle Size of Dendrimer/siRNA complexes. The particle size of each of the dendrimer/siRNA complexes was determined by dynamic light scattering. Measured sizes of dendrimer/siRNA complexes at charge ratios ranging from 1 to 3 rel. units are shown in Figure 3b. The complexes formed using PAMAM-NH_2 and QPAMAM-OH dendrimers exhibited a decrease in particle size as the charge ratio was increased. These results are in agreement with previous studies by Lee et al. on dendrimer/pDNA polyplexes, where the particle size decreased systematically as the charge ratio was increased (*23*). The complexes formed with QPAMAM-NHAc dendrimer showed an initial decrease in average particle size from 165 to 72 nm as N/P ratio increased from 1 to 1.5 rel. units. However, the particle size did not decrease further with the increase in the N/P ratio to 3 rel. units.

Atomic Force Microscopy. The size and morphology of all three dendrimer/siRNA complexes at N/P ratio of 3 rel. units were also determined by atomic force microscopy (Figure 4).

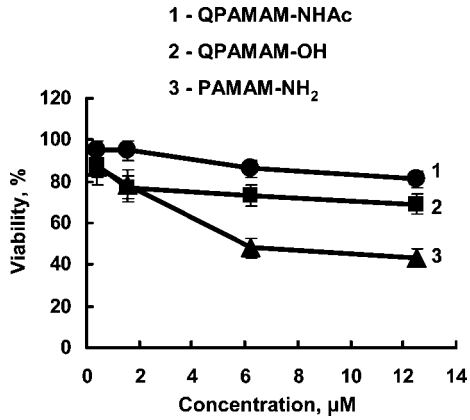

Figure 5. Cytotoxicity of dendrimers. Cellular viability was evaluated by the modified MTT (3-(4,5-dimethylthiazol-2-yl)-2,5-diphenyltetrazolium bromide) assay. Means ± SD are shown.

It was found that well-condensed spheroidal particles were formed with internally quaternized QPAMAM-OH and QPAMAM-NHAc dendrimers, while the PAMAM-NH_2 dendrimer resulted in nanofiber-shaped structures. The particle size distribution was consistent with the dynamic light scattering data.

***In Vitro* Cytotoxicity.** The cytotoxicity evaluation of each dendrimer at various concentrations revealed a relationship between dendrimer surface charge and cellular cytotoxicity (Figure 5). An increase in surface charge led to the increase in cytotoxicity of the dendrimer. The PAMAM-NH_2 dendrimer showed highest toxicity, while a significant decrease in toxicity was observed for QPAMAM-OH dendrimer. Notably, among all three dendrimers, QPAMAM-NHAc was the least toxic even at higher concentrations.

Cellular Uptake of siRNA. The cellular uptake of fluorophore-labeled siRNA (si*GLO* Red, red fluorescence) either naked or complexed with different dendrimers (N/P = 3) was analyzed using confocal fluorescent microscopy. In this series, A2780 human ovarian cancer cells were separately incubated 80 min with naked siRNA or dendrimer−siRNA complexes, and fluorescence distribution within the cell was examined every minute using a confocal microscope. The naked siRNA without any complexation with cationic dendrimers failed to internalize cells, which was evident by the absence of measurable red fluorescence in the cell cytoplasm and nuclei (Figure 6). Similarly, PAMAM-NH_2/siRNA and QPAMAM-OH/siRNA complexes did not penetrate into cellular cytoplasm within the incubation time. In contrast, the QPAMAM-NHAc-siRNA complex was internalized by the cells and distributed uniformly inside the cytoplasm and nuclei by the end of the incubation period.

DISCUSSION

Given the ability to knock down any gene of interest, siRNA has generated a considerable interest as a novel and very effective tool for basic research and applied medicine. However, poor cell penetration ability and facile enzymatic degradation of siRNA limit its effective use (*14*). The presence of a hydroxyl group at the 2′ position of the pentose ring in the RNA favors hydrolysis of the phosphodiester backbone of nucleic acid by serum nucleases (*26*). Consequently, the development of efficient delivery systems which will protect siRNA from degradation during the voyage in the bloodstream and organs and facilitate its uptake by the targeted cells is one of the major challenges in the therapeutic application of siRNA.

Similar to the delivery of plasmid DNA, electrostatic interaction of siRNA with cationic carriers is expected to enhance cellular uptake and protect it from enzymatic degradation. Cationic liposomes and dendrimers are considered two of the most promising nanocarriers for the effective delivery of plasmid DNA, antisense oligonucleotides, and siRNA. Cationic liposomes interact with siRNA leading to a relatively large size of complexes due to uncontrolled and incomplete encapsulation of nucleic acid, thereby exposing siRNA to enzymatic degradation prior to delivery to the cell (*27*). Dendrimers have been extensively studied for the efficient delivery of plasmid DNA and antisense oligonucleotides. However, they have been explored less for the delivery of siRNA. Moreover, the relatively high cytotoxicity of cationic PAMAM-NH_2 dendrimer due to nonspecific interaction of primary amine groups with the cell membrane is the main concern for their potential applications as nanocarriers.

In the present study, two different approaches have been used to reduce the cytotoxicity of PAMAM dendrimers. First, an internally quaternized PAMAM dendrimer (QPAMAM-OH) that forms less toxic complexes with negatively charged plasmid DNA (*23*) was prepared and tested as a nanocarrier to deliver siRNA. Second, the surface primary amine groups of the PAMAM-NH_2 dendrimer were modified by acetylation followed by internal quaternization resulting in novel internally quaternized QPAMAM-NHAc dendrimer. While most traditional cationic nanocarriers have an electrical charge on their surface, both of the developed dendrimers possess neutral outer surfaces with internal positive charges. Therefore, one can hypothesize that siRNA could be internalized (at least partially) inside the dendrimer. This hypothesis is based on a report by Lee et al. (*23*) that large plasmid DNA can be incorporated in the inner space of dendrimers. Since siRNA are smaller than DNA, we suggest that it can easily penetrate between dendrimer branches. It is possible that siRNA was partially accommodated inside the dendrimer branches and the remaining part of siRNA was internalized in another molecule of dendrimer. Thus, at N/P ratio 1, an interpolyelectrolyte complex would be formed which is supported by the fact that siRNA/dendrimer complex at N/P charge ratio 1 showed a larger diameter. On the other hand, at higher N/P charge ratio, several dendrimer molecules were available to accommodate siRNA in parts and thus exhibited a decrease in diameter. These results might suggest that siRNA is partially internalized in dendrimer branches and is covered by several dendrimers, thus limiting the exposure of siRNA to nucleases. Therefore, siRNA is likely to be shielded by the dendrimer surface, which in turn limited the exposure of siRNA to a hazardous environment. This could potentially improve the stability of the entire system during its journey toward the site of action. Present experimental data confirmed that acetylated quaternized dendrimers containing siRNA are taken up to a higher extent than other dendrimers or siRNA alone.

Agarose gel retardation studies clearly indicated that both synthesized QPAMAM-OH and QPAMAM-NHAc dendrimers, as well as commercially available PAMAM-NH_2 dendrimer, interacted with siRNA irrespective of internal or surface positive charges. As anticipated, surface modification of PAMAM-NH_2 dendrimers significantly reduced their cytotoxicity. It was found that the QPAMAM-NHAc dendrimer showed the least toxicity among all three tested nanocarriers. These results are consistent with previously published data (*24*) and confirm that prevention of nonspecific nanocarrier−cell interactions caused by surface amine groups decreases the cytotoxicity of the PAMAM dendrimer. Furthermore, dynamic light scattering studies revealed condensation of siRNA into particles of nanometer dimensions when complexed with the dendrimers. The particle size dramatically decreased with an increase in N/P, which is in good agreement with the assumption that the dendrimer acts as a cross-linker, and the particle size increases if the complexation is not complete. It is interesting that hydroxyl-terminated

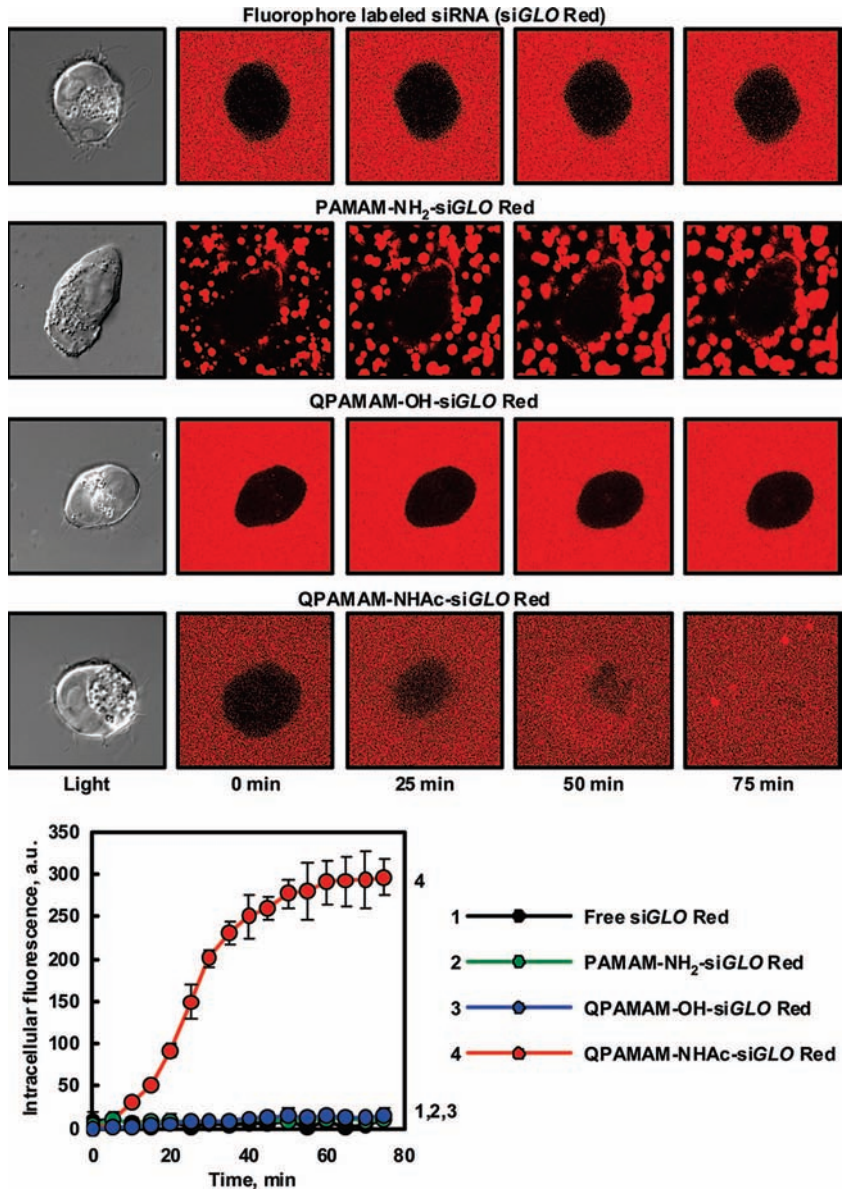

Figure 6. Cellular internalization of free siRNA and siRNA delivered by different dendrimers. Typical confocal microscopy images of living A2780 cells incubated with fluorophore-labeled siRNA (si*GLO* Red, red fluorescence) and dendrimer−siRNA complexes and time course of fluorescence intensity of si*GLO* accumulated inside cells. Means ± SD are shown.

dendrimers have lower average diameters at 1.5 and 3 N/P ratios. These results are consistent with observations made by Lee et al. (*23*). It is believed that at N/P ratio 1 the dendrimer acts as a cross-linker leading to a large-sized interpolyelectrolyte complex. Such a mechanism is supported by the fact that a siRNA/dendrimer complex at N/P charge ratio 1 showed a larger diameter. On the other hand, at higher N/P charge ratio, a higher number of dendrimers are available to form complexes with siRNA. Therefore, the net number of dendrimer/siRNA would be considerably reduced in the complex, which in turn decreased the diameter of the particles. The reason for the slight increase in particle size of the QPAMAM-NHAc/siRNA complex at charge ratio of 3 rel. units is unknown. However, all dendrimer/siRNA complexes were small enough to be internalized by cells via an adsorptive nonspecific endocytosis pathway (*28*).

The particle size distribution of synthesized nanocarriers was further supported by atomic force microscope experiments, which also revealed very interesting morphological features of the studied dendrimer/siRNA complexes at charge N/P ratio of 3.0 rel. units. The internally quaternized and surface-neutral dendrimers QPAMAM-OH and QPAMAM-NHAc formed complexes with siRNA resulting into more compact spherical nanometer particles. In contrast, the PAMAM-NH_2 dendrimer possessing cationic amino groups at the surface formed ribbon-like nanofibers, probably originating from the interpolyelectrolyte complexation with siRNA. Previous studies on understanding the condensation mechanism of DNA and dendrimers proposed a model that involves binding of one dendrimer molecule to two or more DNA chains (*29*). Apparently, such complexation leads to the formation of nanofiber-shaped structures (*30*); however, the dendrimer generation and charge ratio could also contribute to determining the morphology of the complexes. Based on these observations, we believe that internal positive charges in QPAMAM-OH or QPAMAM-NHAc dendrimer play a significant role in controlling the morphology of the complexes by shielding siRNA with the dendrimer surface. Apparently, at high N/P ratios, siRNA could be encapsulated by several QPAMAM-OH or QPAMAM-NHAc dendrimers to produce compact and spherical particles. On the other hand, surface-charged PAMAM-NH_2 probably is involved in linking two or more siRNA molecules to form higher molecular weight polymer chains.

In addition to enzymatic degradation, low cellular uptake of naked siRNA is one of the serious problems that limit their potential applications. Since siRNAs are negatively charged in the physiological range of pH, the cellular internalization of naked siRNA through a negatively charged cell membrane is considerably low. In fact, our confocal microscope studies demonstrated that naked siRNAs are not internalized by cells. Similar to plasmid DNA, complexation of siRNA with cationic agents such as polymers, liposomes, or dendrimers increases cell permeability. Alternatively, the backbone of all bases in oligonucleotides (DNA and RNA) can potentially be modified to neutralize their electric charge, enhance nuclease resistance, and increase the incorporation efficacy into liposomes or other neutral nanocarriers (*31–33*). Previously, we successfully used both approaches utilizing neutral and cationic liposomes for effective delivery of P-ethoxy antisense oligonucleotides and siRNA, respectively (*34–37*). In the present study, we exploited complexation of siRNA to the cationic outer surface or inner core of dendrimers in order to facilitate the uptake of siRNA by cells. However, our data showed that the complexation of siRNA with surface-charged PAMAM-NH_2 and internally charged QPAMAM-OH dendrimers could not improve the siRNA cell permeability. Although the exact reason for inefficiency of these types of dendrimers is unknown, we believe that size and morphology of siRNA/PAMAM-NH_2 complex and neutral surface of QPAMAM-OH dendrimers contributed to the registered low cellular uptake. In contrast, the surface-modified and internally quaternized QPAMAM-NHAc showed excellent cell permeability resulting in a substantial accumulation of siRNA in cells within 80 min. These results are in agreement with the observations made by Kolhatkar and coauthors that surface-acetylated PAMAM dendrimers showed good permeability across the cell membrane (*24*). The authors suggested a paracellular transport route for increased permeability of acetylated dendrimers due to reduced nonspecific interaction of dendrimers with cell membrane leading to an increase in concentration of dendrimers across the apical side of the membrane. It is possible that a similar mechanism was responsible for a higher uptake of acetylated dendrimers. Cellular uptake is a complex mechanism and involves several important factors that include concentration of penetrating material across the cell membrane, surface charge, and hydrogen bonding with the cell membrane. Increased permeability of surface-modified dendrimers due to reduced nonspecific interaction of dendrimers with cell membranes leading to an increase in concentration of dendrimers across the apical side of the membranes was suggested (*24*). Alternatively, amide groups on the surface of the dendrimer may also offer hydrogen bonding with cell membranes to enhance the cellular uptake of the complex. Wender et al. demonstrated the importance of hydrogen bonding in the mechanism of translocation of guanidinium-rich peptides into cells (*38*). It was found that charge is necessary, but not sufficient for cellular uptake, and hydrogen bonds with H-bond acceptor functionality on the cell surface increased uptake significantly. It is possible that these mechanisms could also be responsible at least in part for higher penetration ability of the QPAMAM-NHAc/siRNA complex. However, further studies are required to elucidate the exact mechanism for cell permeability of acetylated and internally quaternized QPAMAM-NHAc dendrimer and its complex with siRNA.

CONCLUSIONS

In summary, we have demonstrated surface-modified and internally quaternized PAMAM dendrimers as novel siRNA delivery systems. Three types of dendrimers were examined for their cytotoxicity and siRNA delivery in A2780 ovarian cancer cells. The modification of surface amine groups of PAMAM dendrimers to amide and internal quaternization proved to play a critical role for the reduced cytotoxicity and efficient cell permeability of the dendrimer−siRNA complex.

ACKNOWLEDGMENT

The research was supported in part by NIH grants CA100098 and CA111766 from the National Cancer Institute.

LITERATURE CITED

(1) Dave, R. S., and Pomerantz, R. J. (2003) RNA interference: on the road to an alternate therapeutic strategy! *Rev. Med. Virol. 13*, 373–385.

(2) Eccleston, A., and Eggleston, A. (2004) RNA interference. *Nature 431*, 337–338.

(3) Riddihough, G. (2005) In the forests of RNA dark matter. *Science 309*, 1507–1533.

(4) Paroo, Z., and Corey, D. R. (2004) Challenges for RNAi in vivo. *Trends Biotechnol. 22*, 390–394.

(5) Chu, T. C., Twu, K. Y., Ellington, A. D., and Levy, M. (2006) Aptamer mediated siRNA delivery. *Nucleic Acids Res. 34*, e73.

(6) Derfus, A. M., Chen, A. A., Min, D. H., Ruoslahti, E., and Bhatia, S. N. (2007) Targeted quantum dot conjugates for siRNA delivery. *Bioconjugate Chem. 18*, 1391–1396.

(7) Hu-Lieskovan, S., Heidel, J. D., Bartlett, D. W., Davis, M. E., and Triche, T. J. (2005) Sequence-specific knockdown of EWS-FLI1 by targeted, nonviral delivery of small interfering RNA inhibits tumor growth in a murine model of metastatic Ewing's sarcoma. *Cancer Res. 65*, 8984–8992.

(8) Itaka, K., Kanayama, N., Nishiyama, N., Jang, W. D., Yamasaki, Y., Nakamura, K., Kawaguchi, H., and Kataoka, K. (2004) Supramolecular nanocarrier of siRNA from PEG-based block catiomer carrying diamine side chain with distinctive pKa directed to enhance intracellular gene silencing. *J. Am. Chem. Soc. 126*, 13612–13613.

(9) Schiffelers, R. M., Ansari, A., Xu, J., Zhou, Q., Tang, Q., Storm, G., Molema, G., Lu, P. Y., Scaria, P. V., and Woodle, M. C. (2004) Cancer siRNA therapy by tumor selective delivery with ligand-targeted sterically stabilized nanoparticle. *Nucleic Acids Res. 32*, e149.

(10) Song, E., Zhu, P., Lee, S. K., Chowdhury, D., Kussman, S., Dykxhoorn, D. M., Feng, Y., Palliser, D., Weiner, D. B., Shankar, P., Marasco, W. A., and Lieberman, J. (2005) Antibody mediated in vivo delivery of small interfering RNAs via cell-surface receptors. *Nat. Biotechnol. 23*, 709–717.

(11) Soutschek, J., Akinc, A., Bramlage, B., Charisse, K., Constien, R., Donoghue, M., Elbashir, S., Geick, A., Hadwiger, P., Harborth, J., John, M., Kesavan, V., Lavine, G., Pandey, R. K., Racie, T., Rajeev, K. G., Rohl, I., Toudjarska, I., Wang, G., Wuschko, S., Bumcrot, D., Koteliansky, V., Limmer, S., Manoharan, M., and Vornlocher, H. P. (2004) Therapeutic silencing of an endogenous gene by systemic administration of modified siRNAs. *Nature 432*, 173–178.

(12) Kawakami, S., Higuchi, Y., and Hashida, M. Nonviral approaches for targeted delivery of plasmid DNA and oligonucleotide, *J. Pharm. Sci.* in press.

(13) Park, T. G., Jeong, J. H., and Kim, S. W. (2006) Current status of polymeric gene delivery systems. *Adv. Drug Delivery Rev. 58*, 467–486.

(14) Gary, D. J., Puri, N., and Won, Y. Y. (2007) Polymer-based siRNA delivery: perspectives on the fundamental and phenomenological distinctions from polymer-based DNA delivery. *J. Controlled Release 121*, 64–73.

(15) Haensler, J., and Szoka, F. C., Jr. (1993) Polyamidoamine cascade polymers mediate efficient transfection of cells in culture. *Bioconjugate Chem. 4*, 372–379.

(16) Khandare, J. J., Jayant, S., Singh, A., Chandna, P., Wang, Y., Vorsa, N., and Minko, T. (2006) Dendrimer versus linear conjugate: Influence of polymeric architecture on the delivery and anticancer effect of paclitaxel. *Bioconjugate Chem. 17*, 1464–1472.

(17) Kukowska-Latallo, J. F., Bielinska, A. U., Johnson, J., Spindler, R., Tomalia, D. A., and Baker, J. R., Jr. (1996) Efficient transfer of genetic material into mammalian cells using Starburst polyamidoamine dendrimers. *Proc. Natl. Acad. Sci. U.S.A. 93*, 4897–4902.

(18) Gillies, E. R., and Frechet, J. M. (2005) Dendrimers and dendritic polymers in drug delivery. *Drug Discovery Today 10*, 35–43.

(19) Grainger, D., and Okano, T. (2003) Biomedical micro- and nano-technology. *Adv. Drug Delivery Rev. 55*, 311–313.

(20) Gillies, E. R., Dy, E., Frechet, J. M., and Szoka, F. C. (2005) Biological evaluation of polyester dendrimer: poly(ethylene oxide) "bow-tie" hybrids with tunable molecular weight and architecture. *Mol. Pharm. 2*, 129–138.

(21) Kang, H., DeLong, R., Fisher, M. H., and Juliano, R. L. (2005) Tat-conjugated PAMAM dendrimers as delivery agents for antisense and siRNA oligonucleotides. *Pharm. Res. 22*, 2099–2106.

(22) Lee, J. H., Lim, Y. B., Choi, J. S., Choi, M. U., Yang, C. H., and Park, J. S. (2003) Quaternized polyamidoamine dendrimers as novel gene delivery systems: Releationship between degree of quaternization and their influences. *Bull. Korean Chem. Soc. 24*, 1637–1640.

(23) Lee, J. H., Lim, Y. B., Choi, J. S., Lee, Y., Kim, T. I., Kim, H. J., Yoon, J. K., Kim, K., and Park, J. S. (2003) Polyplexes assembled with internally quaternized PAMAM-OH dendrimer and plasmid DNA have a neutral surface and gene delivery potency. *Bioconjugate Chem. 14*, 1214–1221.

(24) Kolhatkar, R. B., Kitchens, K. M., Swaan, P. W., and Ghandehari, H. (2007) Surface acetylation of polyamidoamine (PAMAM) dendrimers decreases cytotoxicity while maintaining membrane permeability. *Bioconjugate Chem. 18*, 2054–2060.

(25) Minko, T., Kopeckova, P., and Kopecek, J. (1999) Comparison of the anticancer effect of free and HPMA copolymer-bound adriamycin in human ovarian carcinoma cells. *Pharm. Res. 16*, 986–996.

(26) Banan, M., and Puri, N. (2004) The ins and outs of RNAi in mammalian cells. *Curr. Pharm. Biotechnol. 5*, 441–450.

(27) Spagnou, S., Miller, A. D., and Keller, M. (2004) Lipidic carriers of siRNA: differences in the formulation, cellular uptake, and delivery with plasmid DNA. *Biochemistry 43*, 13348–13356.

(28) Perales, J. C., Ferkol, T., Molas, M., and Hanson, R. W. (1994) An evaluation of receptor-mediated gene transfer using synthetic DNA-ligand complexes. *Eur. J. Biochem. 226*, 255–266.

(29) Chen, W., Turro, N. J., and Tomalia, D. A. Using ethidium bromide to probe the interactions between DNA and dendrimers*Langmuir 16*, 15–19.

(30) Kabanov, V. A., Sergeyev, V. G., Pyshkina, O. A., Zinchenko, A. A., Zezin, A. B., Joosten, J. G. H., Brackman, J., and Yoshikawa, K. (2000) Interpolyelectrolyte complexes formed by DNA and astramol poly(propylene imine) dendrimers. *Macromolecules 33*, 9587–9593.

(31) Gutierrez-Puente, Y., Tari, A. M., Ford, R. J., Tamez-Guerra, R., Mercado-Hernandez, R., Santoyo-Stephano, M., and Lopez-Berestein, G. (2003) Cellular pharmacology of P-ethoxy antisense oligonucleotides targeted to Bcl-2 in a follicular lymphoma cell line. *Leuk. Lymphoma 44*, 1979–1985.

(32) Gutierrez-Puente, Y., Tari, A. M., Stephens, C., Rosenblum, M., Guerra, R. T., and Lopez-Berestein, G. (1999) Safety, pharmacokinetics, and tissue distribution of liposomal P-ethoxy antisense oligonucleotides targeted to Bcl-2. *J. Pharmacol. Exp. Ther. 291*, 865–869.

(33) Konopleva, M., Tari, A. M., Estrov, Z., Harris, D., Xie, Z., Zhao, S., Lopez-Berestein, G., and Andreeff, M. (2000) Liposomal Bcl-2 antisense oligonucleotides enhance proliferation, sensitize acute myeloid leukemia to cytosine-arabinoside, and induce apoptosis independent of other antiapoptotic proteins. *Blood 95*, 3929–3938.

(34) Betigeri, S., Pakunlu, R. I., Wang, Y., Khandare, J. J., and Minko, T. (2006) JNK1 as a molecular target to limit cellular mortality under hypoxia. *Mol. Pharm. 3*, 424–430.

(35) Pakunlu, R. I., Cook, T. J., and Minko, T. (2003) Simultaneous modulation of multidrug resistance and antiapoptotic cellular defense by MDR1 and BCL-2 targeted antisense oligonucleotides enhances the anticancer efficacy of doxorubicin. *Pharm. Res. 20*, 351–359.

(36) Pakunlu, R. I., Wang, Y., Tsao, W., Pozharov, V., Cook, T. J., and Minko, T. (2004) Enhancement of the efficacy of chemotherapy for lung cancer by simultaneous suppression of multidrug resistance and antiapoptotic cellular defense: novel multicomponent delivery system. *Cancer Res. 64*, 6214–6224.

(37) Wang, Y., and Minko, T. (2004) A novel cancer therapy: combined liposomal hypoxia inducible factor 1 alpha antisense oligonucleotides and an anticancer drug. *Biochem. Pharmacol. 68*, 2031–2042.

(38) Rothbard, J. B., Jessop, T. C., Lewis, R. S., Murray, B. A., and Wender, P. A. (2004) Role of membrane potential and hydrogen bonding in the mechanism of translocation of guanidinium-rich peptides into cells. *J. Am. Chem. Soc. 126*, 9506–9507.

BC8000722

Controlling the Reactivity of Ampiphilic Quantum Dots in Biological Assays through Hydrophobic Assembly of Custom PEG Derivatives

Michael R. Warnement, Ian D. Tomlinson, Jerry C. Chang, Michael A. Schreuder, Courtney M. Luckabaugh, and Sandra J. Rosenthal*

Department of Chemistry, Vanderbilt University, Station B, 351822, Nashville, Tennessee, 37235-1822. Received March 12, 2008; Revised Manuscript Received April 28, 2008

Modifications of the quantum dot (QD) surface are routinely performed via covalent biomolecule attachment, and poly(ethylene glycol) (PEG) derivatization has previously been shown to limit nonspecific cellular interactions of QD probes. Attempts to functionalize ampiphilic QDs (AMP-QDs) with custom PEG derivatives having a hydrophobic terminus resulted in self-assembly of these PEG ligands to the AMP-QD surface in the absence of covalent coupling reagents. We demonstrate, via electrophoretic characterization techniques, that these self-assembled PEG-QDs exhibit improved passivation in biological environments and are less susceptible to unwanted protein adsorption to the QD surface. We highlight the artifactual fluorescent response protein adsorption can cause in biological assays, and discuss considerations for improved small molecule presentation to facilitate specific QD interactions.

INTRODUCTION

Quantum dots (QDs) were first reported as improved fluorophores for biological imaging applications in 1998 (*1, 2*), and have since seen increasing incorporation into numerous biological assays ranging from multiplexed fluorescent detection (*3, 4*) to tumor targeting *in vivo* (*5, 6*). Their remarkable photostability has permitted biological processes to be observed on time scales unattainable with conventional organic fluorophores (*7*). Recently, an increasing number of reports have utilized QDs to visualize trafficking dynamics of individual proteins (*8–11*); these processes are readily observable due to the enhanced brightness of these QD probes, with attainable quantum yields approaching unity (*12*). Their inorganic composition, which gives rise to these robust, size-dependent optical properties, is not conducive, however, to direct integration into biological assays. Surface modifications are initially required to permit dispersion in aqueous environments, and further functionalization is necessary to facilitate specific biological interactions. Initial attempts at water solubilization generally involved the displacement of organic capping ligands present on the quantum dot surface (*1, 2, 13*), but these approaches generally had a deleterious effect on the QD optical properties as well as reduced colloid stability. Retention of these organic capping ligands seemingly results in improved fluorophores; as such, encapsulation in phospholipids (*14*) or ampiphilic polymers (*15, 16*) has been widely used to confer water solubility. Biological specificity can subsequently be introduced through biomolecule attachment (see (*17*) for a comprehensive review). Consequently, the surface of a biologically active QD probe is surprisingly complex, with alternating regions of hydrophobicity and hydrophilicity, the possibility of a net positive or negative surface charge depending on functionalization, as well as the presence of numerous reactive chemical functionalities. A better understanding of this potentially reactive surface is required and will ultimately result in improved surface passivation and the elimination of undesirable biological interferences.

* To whom correspondence should be addressed. E-mail: sandra.j.rosenthal@vanderbilt.edu. Phone: 615-322-2633. Fax: 615-343-1234.

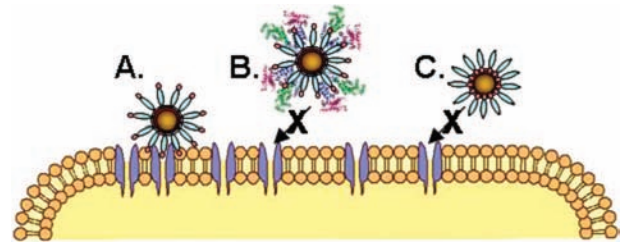

Figure 1. Cartoon schematic illustrating (a) small molecule QD targeting approach, (b) potential interferences due to protein adsorption and (c) ineffective ligand presentation as a result of ligand interaction with the QD surface.

A majority of fluorescent imaging applications involving QD probes utilize antibody conjugation to introduce biological specificity. Our own laboratory has demonstrated the utility of biologically active small molecule QD conjugates for targeting membrane-associated receptors (*13, 18*). Small molecule conjugates have the potential to provide several advantages over antibody recognition. Notably, the large size of antibodies (~150 kDa) adds significant steric bulk to an already sizable QD probe, whereas small molecule attachment provides minimal additional bulk. Despite the fact that antibodies can be designed to recognize virtually any biological target, the antibody−antigen interaction varies dramatically from antibody to antibody, and the associated cost of antibody production significantly limits their utility. Small molecules, on the other hand, can have significantly reduced costs associated with synthesis, and the strength of the ligand−receptor interaction can be optimized through iterative ligand development. Additionally, a wide variety of cellular targets are available based on drug candidates from the known pharmocopia, and these improved probes would be of immediate benefit for various drug discovery applications. Our small molecule QD targeting approach is schematically illustrated in Figure 1a. This ligand design incorporates a biologically active drug derivative (pink) on one end of a poly(ethylene glycol) (PEG) chain (blue). The PEG chain acts to reduce nonspecific interactions (*19–21*) as well as provide additional degrees of freedom for the drug derivative to interact with its cellular target. The terminus of the PEG chain is

10.1021/bc800104n CCC: $40.75 © 2008 American Chemical Society
Published on Web 06/05/2008

designed with a chemical functionality to facilitate attachment to the QD surface. Generally, a terminal amine is utilized in conjunction with standard carbodiimide coupling chemistry to covalently modify carboxylic acid derivatized AMP-QDs (ITK Qdots, Invitrogen Corp., formerly Quantum Dot Corp.). Alternately, a biotin can be introduced at this terminus to assemble ligands on commercially available streptavidin QDs, utilizing the extremely high affinity streptavidin−biotin interaction. Fluorescent imaging applications utilizing this small molecule architecture have remained elusive, however, due to technical difficulties involving ligand design and associated ligand presentation on the QD surface.

It is apparent that ligand presentation on the QD surface must be optimized to facilitate specific binding of the small molecule−QD conjugate to a cellular target. Furthermore, nonspecific protein adsorption to the QD surface, specifically adsorption of the serum protein albumin, significantly inhibits the ability of a ligand to interact with a cellular target. Albumin, a 66 kDa serum protein present in standard blocking solutions and widely used in biological protocols, has previously been shown to complex to reactive QD surfaces and facilitate QD endocytosis (*22*). This protein adsorption, or "biofouling" as it has been called, on the QD surface is less problematic in the case of the larger antibody (∼150 kDa) or streptavidin (∼50 kDa) QD conjugates, but it has a dramatic effect for the ligand−QD conjugates due to the added size and steric bulk of adsorbed protein (illustrated schematically in Figure 1b). PEG modification reportedly prevents serum protein adsorption (*23*), but in this manuscript, we demonstrate continued protein adsorption despite PEG surface modification. Additionally, we show that PEG derivatives with increasingly hydrophobic targeting functionalities have the ability to self-assemble to the surface of ampiphilic QDs in the absence of any added coupling reagents (Figure 1c). This hydrophobic ligand self-assembly results in a passivated, nontargeted QD surface better suited to prevent nonspecific protein adsorption. In this manuscript, we discuss electrophoretic characterization techniques useful for the identification of adsorbed proteins on the QD surface and demonstrate improved surface passivation resulting from the hydrophobic self-assembly of PEGylated ligands. Fluorescence microscopy further demonstrates the utility of these improved probes in reducing the QD background signal *in vitro*, and illustrates the artifact endosomal fluorescence staining which results from albumin adsorption.

EXPERIMENTAL METHODS

Reagents. Ampiphilic poly(acrylic acid) polymer-coated quantum dots, commercially available as ITK Qdots, were purchased from the Invitrogen Corporation (Carlsbad, CA). Core/shell cadmium selenide/zinc sulfide quantum dots emitting at 605 nm were utilized in this study. Quantum dot concentrations were determined by UV−vis spectroscopy using a NanoDrop ND-1000 spectrophotometer (Nanodrop Technologies, Wilmington, DE). Concentrations were calculated from absorbance readings at 350, 405, 488, and 532 nm, each with reported extinction coefficients of 4 400 000, 2 800 000, 1 100 000, and 580 000 M^{-1} cm^{-1}, respectively (*24*), and then averaged to yield a final concentration. 5-Methoxyindol, 5-cyanoindol, 4-piperidone hydrochloride monohydrate, octanoic acid, *N*-hydroxy succinimide (NHS), methoxy-PEG2000, 2-(2-bromoethyl)isoindoline-1,3-dione, 1-(3-dimethylaminopropyl)-3-ethylcarbodiimide hydrochloride (EDC), and dicyclohexylcarbodimide (DCC) were obtained from the Sigma Aldrich corporation (Milwaukee, WI). Boc-PEG3400-NHS and biotin-PEG5000-NHS were obtained from Nektar Therapeutics (Huntsville, AL). Borate buffer, supplied as a 5× concentrate, was obtained from Polysciences, Inc. (Warrington, PA). Ultrapure agarose and Tris-acetate-EDTA (TAE) buffer were purchased from Invitrogen, while all equipment and supplies required for polyacrylamide gel preparation (30% acrylamide solution, Tris-HCl buffer, ammonium persulfate (APS), *N*,*N*,*N*′,*N*′,-tetramethyl ethylenediamine (TEMED), Tris-borate-EDTA (TBE) running buffer, and Coomassie brilliant blue staining and destaining solutions) were purchased from Bio-Rad Laboratories. SephadexTM G-50 from Amersham Biosciences (Uppsala, Sweden) and 100K molecular weight centrifugal filters from Millipore (UFV5BHK00, Billerica, MA) were used for QD conjugate purification. Deuterium oxide for NMR experiments was purchased from Cambridge Isotope Laboratories (Andover, MA). Unless otherwise noted, all reagents were used as supplied without further purification.

Ligand Synthesis. The synthesis of custom PEG derivatives utilized in this study is outlined in Scheme 1. This approach initially involves the synthesis of 3-(4-piperidinyl)indole derivatives, previously shown to have a high affinity for the serotonin transporter (SERT) (*25*, *26*), and their subsequent attachment to either amine- or biotin-terminated PEG chains. The use of either 2-(2-bromoethyl)isoindoline-1,3-dione (**IIa**) or 2-(11-bromoundecyl)isoindoline-1,3-dione (**IIb**), as described by Tomlinson et al. (*25*), allows for the incorporation of a variable-length alkyl spacer between the SERT-selective 3-(4-piperidinyl)indole derivative and the PEG chain. This alkyl spacer region appears to have a significant effect on the ligand's affinity for SERT, and ongoing investigations are focused toward specifically targeting SERT utilizing QD conjugates which incorporate a long alkyl chain spacer. Additionally, alternate PEG derivatives without SERT-specificity (IDT352, IDT353, and IDT363) were synthesized in a one-step coupling to either a mono-amino-methoxy-terminated PEG2000, as previously described (*20*), or a biotin-PEG5000-NHS. These nontargeting ligands were used to determine the chemical functionality required to drive the interaction with the QD surface, and not employed for any biological labeling application. Specific synthetic details are as follows:

5-Methoxy-3-(1,2,3,6-tetrahydropyridin-4yl)-1*H*-indole (Ia). 5-Methoxyindole (5 g, 34 mmol) was dissolved in methanol (200 mL) containing potassium hydroxide (22.4 g, 0.4 mol). 4-Piperidone hydrochloride monohydrate (14 g, 91 mmol) was added to the resulting solution and the mixture was heated at reflux for 18 h, after which it was cooled to ambient temperature and added to deionized water (2000 mL). The product crystallized from solution over a 48 h period and was removed by filtration to give 2.3 g (30% yield) of 5-methoxy-3-(1,2,3,6-tetrahydropyridin-4yl)-1*H*-indole (**Ia**) as a pale brown sold. This was used without further purification.

3-(1,2,3,6-Tetrahydropyridin-4-yl)-1*H*-indole-5-carbonitrile (Ib). 5-Cyanoindole (5 g, 35 mmol) and 4-piperidone hydrochloride monohydrate (14 g, 91 mmol) were heated at reflux for 18 h in methanol (200 mL) containing potassium hydroxide (22.4 g, 0.4 mol). The solution was cooled and added to deionized water (1000 mL). The aqueous solution was extracted with methylene chloride (3 × 200 mL) and the combined organic extracts were dried over magnesium sulfate. The organic solution was filtered and evaporated to yield a brown solid which was purified by column chromatography on silica eluted with ethyl acetate to give 1.8 g of the desired product in a 22% yield.

2-(2-(4-(5-Methoxy-1*H*-indol-3-yl)-5,6-dihydropyridin-1(2*H*)-yl)ethyl)isoindoline-1,3-dione (IIIa). 5-Methoxy-3-(1,2,3,6-tetrahydropyridin-4yl)-1*H*-indole (2 g, 8.7 mmol) was dissolved in acetonitrile (100 mL). Triethylamine (2 mL) and 2-(2-bromoethyl)isoindoline-1,3-dione (2.7 g, 10 mmol) were added and the mixture was heated at reflux for 18 h, after which the solvent was evaporated under reduced pressure and the product

Scheme 1. Synthesis of Ligand-Conjugated PEG Derivatives[a]

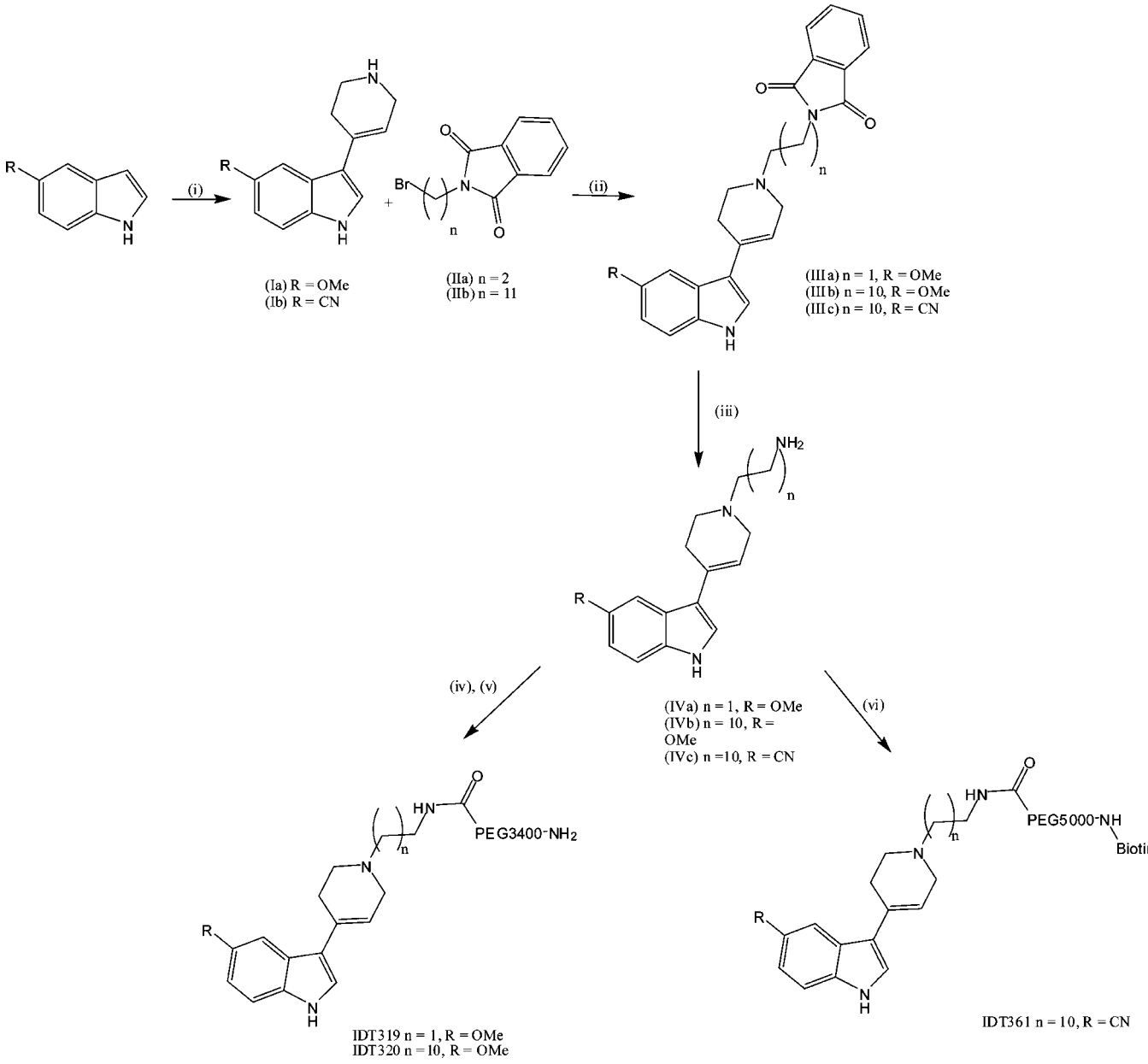

[a] (i) KOH, methanol, 4-piperidone hydrochloride monohydrate, reflux 18 h; (ii) triethylamine, acetonitrile, reflux 18 h; (iii) (a) Hydrazine monohydrate, ethanol, ambient temperature, 2 h, (b) methylene chloride, ambient temperature, 18 h; (iv) BOC-PEG3400-NHS, methylene chloride, ambient temperature, 18 h; (v) TFA; (vi) Biotin-PEG5000-NHS, (**IVc**), methylene chloride ambient temperature.

was recrystallized from methanol to give 2-(2-(4-(5-methoxy-1*H*-indol-3-yl)-5,6-dihydropyridin-1(2*H*)-yl)ethyl)isoindoline-1,3-dione (**IIIa**) in a 29% yield as a pale brown solid.

2-(2-(4-(5-Methoxy-1*H*-indol-3-yl)-5,6-dihydropyridin-1(2*H*)-yl)undecyl)isoindoline-1,3-dione (IIIb). 5-Methoxy-3-(1,2,3,6-tetrahydropyridin-4yl)-1*H*-indole (2 g, 8.7 mmol) was dissolved in acetonitrile (100 mL). Triethylamine (10 mL) and 2-(11-bromoundecyl)isoindoline-1,3-dione (3.8 g, 10 mmol) were added and the mixture was heated at reflux for 18 h. Upon cooling, the solvent was removed under reduced pressure and the product was recrystallized from acetonitrile to give 1.7 g of 2-(2-(4-(5-methoxy-1*H*-indol-3-yl)-5,6-dihydropyridin-1(2*H*)-yl)undecyl)isoindoline-1,3-dione as a pale brown solid in a 36% yield.

3-(1-(11-(1,3-Dioxoisoindolin-2-yl)undecyl)-1,2,3,6-tetrahydropyridin-4-yl)-1*H*-indole-5-carbonitrile (IIIc). 3-(1,2,3,6-Tetrahydropyridin-4-yl)-1*H*-indole-5-carbonitrile (0.9 g, 4 mmol) was added to 2-(11-bromoundecyl)isoindoline-1,3-dione (1.7 g, 4.4 mmol) in acetonitrile (100 mL) and triethylamine (5 mL). The mixture was heated at reflux for 18 h, cooled, and then evaporated to yield the crude product as a yellow solid. This was purified by column chromatography on silica gel eluted with ethyl acetate/methanol (95:5) followed by recrystallization from acetonitrile to give 1 g (50%) of the product as a pale yellow solid.

2-(4-(5-Methoxy-1*H*-indol-3-yl)-5,6-dihydropyridin-1(2*H*)-yl)ethanamine (IVa). 2-(2-(4-(5-Methoxy-1*H*-indol-3-yl)-5,6-dihydropyridin-1(2*H*)-yl)ethyl)isoindoline-1,3-dione (0.9 g, 0.2 mmol) was dissolved in absolute ethanol (50 mL) and hydrazine monohydrate (3 mL) was added. The solution was stirred at ambient temperature for 18 h, then evaporated under reduced pressure. Methylene chloride (100 mL) was added and the solution was stirred for 18 h. The resulting 2,3-dihydrophthalazine-1,4-dione was removed by filtration and the filtrate was evaporated under reduced pressure. 2-(4-(5-Methoxy-1*H*-indol-3-yl)-5,6-dihydropyridin-1(2*H*)-yl)ethanamine was recrystallized

from acetonitrile to give 0.5 g of the desired product as a pale brown solid in a 90% yield.

11-(4-(5-Methoxy-1*H*-indol-3-yl)-5,6-dihydropyridin-1(2*H*)-yl)undecan-1-amine (IVb). Using the same procedure as was used to synthesize (**IVa**), 11-(4-(5-methoxy-1*H*-indol-3-yl)-5,6-dihydropyridin-1(2*H*)-yl)undecan-1-amine was obtained in a 100% yield as a brown solid from 2-(2-(4-(5-methoxy-1*H*-indol-3-yl)-5,6-dihydropyridin-1(2*H*)-yl)undecyl)isoindoline-1,3-dione (**IIIb**).

3-(1-(11-Aminoundecyl)-1,2,3,6-tetrahydropyridin-4-yl)-1*H*-indole-5-carbonitrile (IVc). 11-(4-(5-Methoxy-1*H*-indol-3-yl)-5,6-dihydropyridin-1(2*H*)-yl)undecan-1-amine (0.8 g, 1.5 mmol) was dissolved in ethanol (50 mL) and hydrazine monohydrate (5 mL) was added. The mixture was stirred at ambient temperature for 2 h and then evaporated. Methylene chloride (100 mL) was added and the solution was stirred at ambient temperature for 18 h. The solution was filtered and evaporated, and the product was recrystallized from acteonitrile to give 0.37 g of (**IVc**) as a pale yellow solid in a 60% yield.

IDT-319. BOC-PEG3400-NHS (0.8 g) was dissolved in methylene chloride (20 mL) and 2-(4-(5-methoxy-1*H*-indol-3-yl)-5,6-dihydropyridin-1(2*H*)-yl)ethanamine (0.6 g, 0.025 mmol) was added. The solution was stirred at ambient temperature for 18 h and evaporated. The resulting t-BOC-protected intermediate was washed with diethyl ether (5 × 100 mL) and dried under reduced pressure. The intermediate was dissolved in methylene chloride (50 mL), and trifluoroacetic acid (2 mL) was added. This solution was stirred at ambient temperature for 18 h and evaporated to yield 0.076 g of IDT-319 which was used without further purification.

IDT-320. 0.086 g of IDT-320 was obtained using the same synthetic protocol employed for the synthesis of IDT-319, substituting compound (**IVb**) in place of (**IVa**), and was used without further purification.

IDT-352. Mono-amino-methoxy-terminated PEG2000 (0.5 g, 0.25 mmol) and octanoic acid (28.6 mg, 0.25 mmol) were placed in a 100 mL round-bottom flask equipped with a stir bar, and methylene chloride (50 mL) was added. *N*-Hydroxysuccinimide (0.03 g, 0.26 mmol) was added, and the solution was cooled to 0 °C. Then, a solution of dicyclohexylcarbodimide (0.054 g, 0.25 mmol) dissolved in methylene chloride (10 mL) was added dropwise, and the solution was stirred overnight. The solution was filtered to remove the resulting urea and evaporated under reduced pressure. The crude product was washed with diethyl ether (5 × 100 mL) resulting in 0.5 g of IDT-352, which was used without further purification.

IDT-353. Mono-amino-methoxy-terminated PEG2000 (0.2 g) was placed in a 100 mL round-bottom flask equipped with a magnetic stir bar. To this, methylene chloride (50 mL) and indole-3-butyric acid NHS ester (0.33 g, 1.1 mmol) was added. The solution was stirred at ambient temperature for 18 h, evaporated, and washed with diethyl ether (5 × 100 mL). This gave 0.15 g of IDT-353 as a colorless solid which was used without further purification.

IDT-363. Biotin-PEG5000-NHS (0.15 g) was dissolved in methylene chloride (50 mL) and dodecan-1-amine (1 g, 5.4 mmol) was added. The solution was stirred at ambient temperature for 18 h, evaporated, and the resulting material was washed with diethyl ether (5 × 100 mL). This gave 0.13 g of IDT-363 as a colorless solid, which was used without further purification.

IDT-361. 0.16 g of 11-(4-(5-cyano-1*H*-indol-3-yl)-5,6-dihydropyridin-1(2*H*)-yl)undecan-1-amine (**IVc**) was added to biotin-PEG5000-NHS (0.2 g) dissolved in methylene chloride (50 mL). The solution was stirred at ambient temperature for 18 h, evaporated, and washed with diethyl ether (5 × 100 mL). This gave 0.13 g of IDT-361 as a pale yellow solid, which was used without further purification.

QD Conjugate Preparation. Covalent attachment of amine-terminated ligands was performed through the use of an EDC coupling reaction. We have previously reported optimized coupling conditions which result in PEG ligand attachment while retaining optimal fluorescent QD emission (*20*). These optimized conditions were retained with a slight modification; the conjugation reaction was performed with a higher ratio of ligands in order to ensure complete QD surface coverage. Consequently, EDC couplings were performed in borate buffer by reacting 8000 mol equiv of amine-terminated ligand with 6000 mol equiv of both EDC and NHS to each molar equivalent of quantum dots. The reaction was allowed to proceed for 1 h with stirring at room temperature.

While the EDC coupling reaction is intended to result in a covalent attachment of the ligand's terminal amine to a carboxylic acid on the polymeric QD coating, we also demonstrate surface modification in the absence of added coupling reagents. For these self-assembly reactions, 8000 mol equiv of ligand for each molar equivalent of quantum dot were stirred together in borate buffer for 1 h at room temperature. Surface modifications resulting from this approach cannot be due to covalent attachment, due to a lack of added coupling reagents. Through the testing of a variety of PEG derivatives, each with differing terminal functionalities, we have demonstrated that this self-assembly results from hydrophobic interactions with the QD surface.

Gel Electrophoresis Characterization. Ligand conjugation to the QD surface was confirmed using agarose gel electrophoresis. Gels were prepared at a concentration of 1% agarose in TAE buffer, and run for 80 min at a constant 80 V in TAE running buffer. Fluorescent images of gels were acquired on an AlphaImager 2000 imaging station (Alpha Innotech Corp.). Since surface modification acts both to passivate charged residues on the QD surface and increase the overall probe size, successful ligand attachment results in an overall reduction of the observed electrophoretic mobility.

Since PEG-QD conjugates exhibit a significantly reduced electrophoretic mobility in agarose gels, subsequent protein adsorption does not result in any observable electrophoretic difference. Consequently, a nondenaturing polyacrylamide gel electrophoresis (PAGE) approach was developed to verify protein adsorption to the QD surface. PAGE provides the capability to initially separate QDs from any unadsorbed protein and subsequently stain to determine protein distribution. Native, nondenaturing polyacrylamide gels were prepared according to established protocols (*27*) utilizing a 2.5% polyacrylamide stacking gel with a 10% polyacrylamide resolving gel. QD conjugates, with and without added albumin, were run at a constant 25 mAmp for 2.5 h. A fluorescent image was then recorded using the AlphaImager 2000 imaging station to verify location of QD bands present in the gel. The gel was subsequently removed from its glass cassette and stained for protein distribution using a Coomassie Blue staining solution overnight as per manufacturer's instructions (note: fluorescent images of the gel must be acquired prior to protein staining since the Coomassie solution quenches the QD fluorescence). A bright field image following gel destaining provides a colorimetric determination of protein content throughout the gel. Protein adsorption to the QD surface is clearly resolved using this approach, as it results in protein bands which colocalize with the previously observed QD bands.

NMR Spectroscopy. ^{1}H NMR experiments were performed to provide spectroscopic proof of QD-ligand complexes. For these reactions, QD conjugation was carried out as before, with and without EDC coupling reagents, for both IDT-319 and IDT-320 ligands. Following conjugation, the reaction mixtures were run through Sephadex G-50 columns to help eliminate any

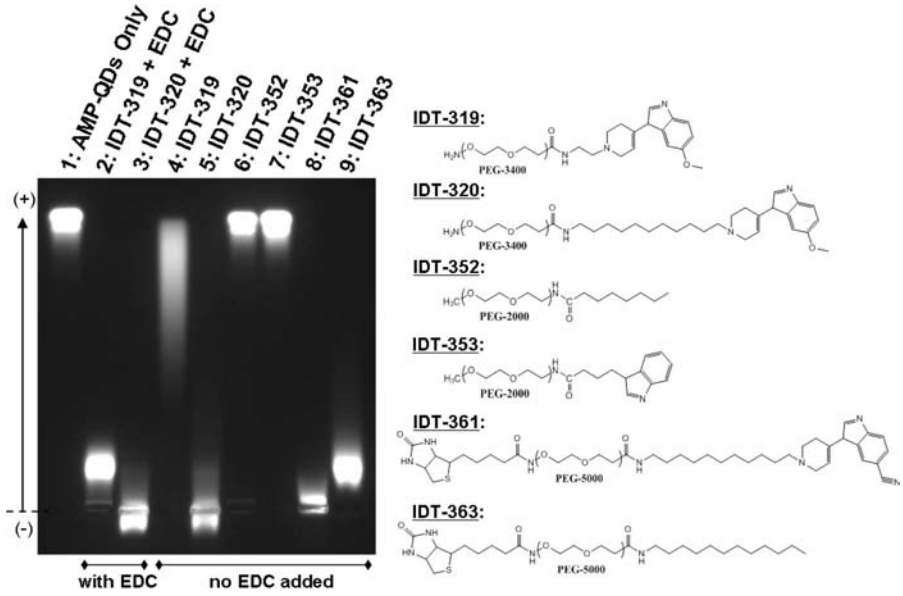

Figure 2. Agarose gel electrophoresis demonstrating assembly of PEG derivatives to QD surface. QD conjugates were run on a 1% agarose gel in TAE buffer for 80 min with a constant applied potential of 80 V. Unconjugated AMP-QDs (lane 1) have a characteristic electrophoretic mobility due to the deprotonated carboxylic acid residues on their surface. Ligand conjugation to the QD surface retards the observed electrophoretic mobility, as seen for both IDT-319 conjugates (lane 2) and IDT-320 conjugates (lane 3). A diminished electrophoretic mobility is also observed for these ligands without added EDC coupling reagent, indicative of self-assembly to the QD surface. Simply mixing IDT-319 with QDs (lane 4) results in conjugates which streak on the gel, indicating differential ligand loading; while IDT-320 completely passivates the QD surface without covalent attachment (lane 5). Other ligands were assayed in an attempt to understand the chemical functionality required to drive surface modification. PEG derivatives with either a short alkyl chain (IDT-352, lane 6) or an indole terminus (IDT-353, lane 7) both failed to drive surface modification in the absence of added coupling reagent. Self-assembly is driven by added hydrophobicity at the PEG terminus, as illustrated for both IDT-361 (lane 8) and IDT-363 (lane 9). Structures of various compounds are illustrated on the right.

unconjugated PEG ligands, and only the fluorescent QD fraction was collected. These QD solutions were then concentrated by means of 100K molecular weight centrifugal filters (Millipore), with one added rinse to ensure complete removal of any unbound ligand, to a final volume of ~20 μL. This concentrated QD solution was then diluted in deuterium oxide to a final concentration of 200 nM, and UV−vis absorption measurements were then made to ensure identical QD concentrations for each NMR sample. All ^{1}H spectra were then recorded on a Bruker 501 spectrometer at ambient temperature in D_2O. A small portion of the residual H_2O signal was suppressed. The resulting spectra were analyzed using *TopSpin 2.0* software.

Cell Culture. LLC-PK1 cell cultures were supplied as a gift from the laboratory of Dr. Randy Blakely (Vanderbilt University, Nashville, TN) and maintained according to established protocols (*28*). Briefly, cells cultured in Dulbecco's Modified Eagle's Medium (DMEM, GIBCO) supplemented with 10% fetal bovine serum, 2 mM L-glutamine, 100 units/mL penicillin, and 100 mg/mL streptomycin were maintained at 37 °C with 5% CO_2. For fluorescent microscopy experiments, cells were initially plated on coverglass bottom cell culture dishes (MatTek Corp., Ashland, MA) approximately 24−48 h prior to imaging, and allowed to reach ~80% confluency. Once cells reached the desired confluency, they were rinsed once with PBS and exposed to a 10 nM solution of QD conjugates for 30 min at room temperature. Cells were then rinsed three times with cold PBS and imaged immediately.

Fluorescence Microscopy. Fluorescent imaging was carried out using a Zeiss Axiovert 200 M inverted fluorescent microscope equipped with a Photometrics HQ2 high-resolution CCD camera, a HBO-100 mercury arc lamp for fluorescent excitation, and Metamorph image analysis software. Bright field images were acquired using differential interference contrast microscopy, while fluorescent images were obtained using a filter set designed for optimal QD detection (XF304−1, Omega Optical) All images were acquired using an oil-immersion 100× objective (Zeiss) and thresholded equivalently for clear comparison.

RESULTS AND DISCUSSION

Initial efforts were focused on the development of small molecule QD conjugates which would specifically interact with the serotonin transporter (SERT) membrane bound receptor. As such, custom ligands were synthesized to include a SERT selective terminus as well as a reactive amine terminus on either side of a PEG spacer. The amine functionality permitted covalent attachment to the carboxylic acid functionality on the surface of commercially available water-soluble ITK QDs, while the SERT selective small molecule would presumably be able to interact with its biological target. Agarose gel electrophoresis was used as verification of successful QD surface modification subsequent to covalent attachment of PEG ligands. As illustrated in Figure 2, the addition of PEG ligands acts both to decrease QD surface potential, by derivatizing negatively charged carboxylic acid residues, as well as increase the overall probe volume, cumulatively resulting in a decreased electrophoretic mobility. Consequently, unconjugated QDs (lane 1) have an increased electrophoretic mobility in a 1% agarose gel as compared to IDT-319 (lane 2) or IDT-320 (lane 3) QD-conjugates. Unexpectedly, however, there was an observable difference between the relative mobility of IDT-319 and IDT-320 QD-conjugates. The only difference between these two ligands is a nine carbon alkyl linker between the PEG and the SERT-selective terminus, a seemingly negligible difference which should not result in any sizable disparity in electrophoretic mobilities, especially given the large overall molecular weight (~3400 Da) of the PEG ligand. This electrophoretic difference could therefore be attributed to differential ligand loading at the QD surface for these two similar ligands, perhaps mediated by added hydrophobicity at the IDT-320 terminus.

To verify the possibility that a hydrophobic terminus could interact with the QD surface and cause self-assembly, the

conjugation reaction was carried out without added EDC or NHS. EDC is a reagent that enables the formation of an amide bond between the terminal amine of the PEG ligand and carboxylic acid functionalities at the QD surface. Consequently, any observed surface modification in the absence of these coupling reagents would have to result from interactions with the ligand's more hydrophobic SERT-selective region. The absence of added coupling reagents, presumably resulting in no ligand attachment, should result in products with the same electrophoretic mobility of unconjugated AMP-QDs. However, it is apparent that QD surface modifications do occur in the absence of added coupling reagents, most notably for increasingly hydrophobic PEG ligands (lanes 4−9, Figure 2). QDs mixed with IDT-319 only resulted in partial surface modification (lane 4), suggesting that ligand attachment is at least partially dependent upon amide bond formation. The streaking observed in the IDT-319 QD product in the absence of EDC and NHS is indicative of differential ligand loading at the QD surface. The IDT-320 QD product (lane 5), however, results in complete surface modification and faithfully reproduces the electrophoretic mobility observed when the conjugation was carried out in the presence of EDC and NHS (lane 3). This indicates that IDT-320 assembles independent of covalent ligand attachment and acts to passivate the reactive AMP-QD surface.

Additionally, alternate PEG ligands were synthesized to further elucidate the chemical functionality required to drive the self-assembly of PEG ligands to the AMP-QD surface in the absence of coupling reagents. PEG ligands terminated with either a seven-carbon alkyl chain (IDT-352, lane 6) or an indole ring (IDT-353, lane 7) did not result in QD surface modification. A PEG derivative with a longer twelve-carbon alkyl chain (IDT-363, lane 9), however, did result in ligand assembly to the QD surface, as illustrated by a characteristic retardation of electrophoretic mobility. Taken together, these data indicate that this self-assembly of PEG ligands to the QD surface is driven by hydrophobic/hydrophilic interactions, and not a result of a specific chemical functionality present in the SERT-selective termini. Additionally, an alternate SERT-selective cyano derivative (IDT-361, lane 8), with a chemical functionality similar to IDT-320 but synthesized via different intermediates, results in self-assembly to the QD surface; this further corroborates the importance of added hydrophobicity for driving assembly of PEG ligands to the QD surface.

While agarose gel electrophoresis characterization qualitatively indicate the self-assembly of hydrophobic PEG derivatives to the QD surface, additional spectroscopic proof of this interaction is certainly necessary for verification of any such claims. As a result, a NMR experiment was devised to provide spectroscopic characterization of these QD-ligand structures and help quantify ligand coverage to verify any conclusions drawn from electrophoretic mobility measurements. Given the large number of structurally equivalent hydrogen atoms in their long PEG chains, the ^{1}H NMR spectra of IDT-319 and IDT-320 predominately consist of a single large peak around 3.64 ppm (Supporting Information, Figure S2). The ^{1}H spectrum of unconjugated AMP-QDs (also Supporting Information Figure S2) has no such feature present at that chemical shift, indicating the utility of this spectral feature in assessing ligand conjugation to the QD surface. NMR samples were diluted into deuterium oxide following QD conjugation to either IDT-319 or IDT-320, carried out as before both with and without added EDC coupling reagents, and special care was taken to eliminate any unbound ligand following conjugation (see Experimental Methods section). The ^{1}H NMR spectra of IDT-319 and IDT-320 conjugates, presented in Figure 3, illustrate IDT-320 conjugation to the QD regardless of any coupling reagents, an indication that the observed differences in electrophoretic mobilities result directly from PEG surface modifications. A large PEG peak is apparent for both the IDT-319 and IDT-320 QD-conjugates synthesized in the presence of EDC coupling reagents (Figure 3A). While this peak remains for IDT-320 conjugates synthesized in the absence of any added coupling reagents, a demonstration that these hydrophobic PEG derivatives self-assemble to the QD surface, the IDT-319 peak is significantly diminished in the absence of EDC (Figure 3B). The presence of additional peaks from the AMP-QD, presumably due to protons present in its ampiphilic polymer coating, permit normalization of integral areas with respect to QD concentration and facilitate straightforward sample-to-sample comparisons for determination of relative ligand loading. As expected, the integral areas for these

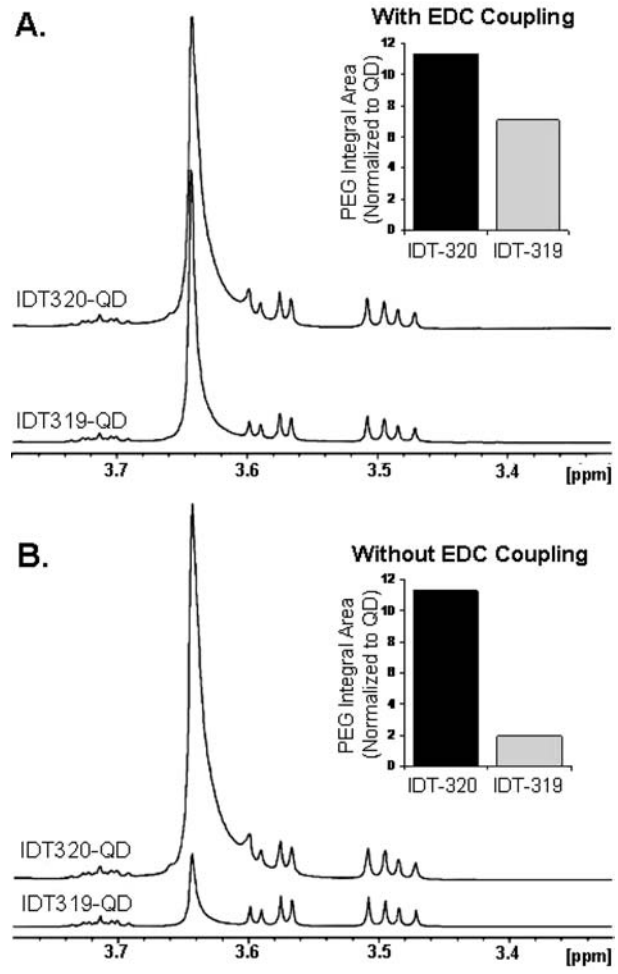

Figure 3. ^{1}H NMR characterization of QD-ligand conjugates. QD conjugation reactions to either IDT-319 or IDT-320 were carried out (A) with the addition of EDC coupling reagents or (B) in the absence of any coupling reagents; conjugates were then purified of any unbound ligand before analysis. Consequently, the presence of a peak at 3.64 ppm in the ^{1}H NMR spectra, due to the long PEG chain present in each ligand, is indicative of ligand attachment to the QD surface. (A) In the presence of EDC coupling reagents, both IDT-320 (upper spectrum) and IDT-319 (lower spectrum) present a spectral feature indicating ligand attachment. (B) Without added coupling reagents, the feature is still clearly present for the IDT-320 conjugates (upper spectrum), while this peak is greatly diminished for IDT-319 conjugates (lower spectrum). The integral area of each PEG peak, which is directly proportional to the amount of ligand present, is therefore indicative of ligand loading, but all areas must be first be normalized to a QD feature to permit any sample-to-sample comparison. (Inset) Quantification of integral areas, each normalized to the AMP-QD doublet of doublets at 3.5 ppm, clearly demonstrate equivalent ligand loading for IDT-320 conjugates regardless of added coupling reagents, while the IDT-319 conjugates demonstrate a roughly 4-fold decrease in ligand attachment in the absence of coupling reagents.

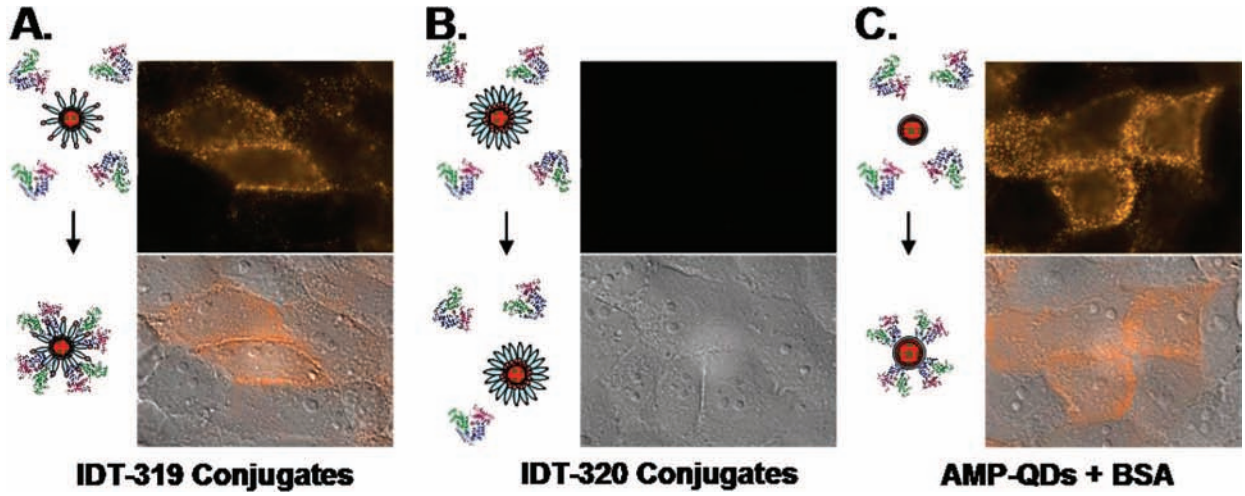

Figure 4. Cellular imaging with QD conjugates. SERT-expressing LLC-PK1 cells were incubated with various QD conjugates in the presence of BSA, a standard blocking agent. QD fluorescence micrographs (top) and corresponding bright field composite overlay images (bottom) are shown for IDT-319 QD-conjugates (A), IDT-320 QD-conjugates (B), and unconjugated AMP-QDs (C). The fluorescent staining observed for the IDT-319 conjugates is not ligand-mediated, since the same pattern is observed with unconjugated AMP-QDs; rather, this artifactual staining is apparently the result of albumin adsorption (illustrated schematically at left). No such albumin associated artifactual staining is observed for IDT-320 QD conjugates, owing to the improved passivation of the IDT-320 QD surface.

QD-conjugates, each normalized to a doublet of doublets at 3.47 ppm from the AMP-QD, clearly indicate a similar ligand loading for IDT-320 regardless of coupling reagents, while the IDT-319 conjugates have approximately a 4-fold decrease in ligand loading without covalent attachment (Figure 3, inset). These results are obviously consistent with the results of the agarose electrophoresis experiment, in which any added ligand loading results in a diminished electrophoretic mobility. Taken together, these data provide an unambiguous demonstration of the attachment of PEG derivatives to the QD surface and provide an additional means to determine and compare ligand loading.

The utility of this surface modification approach, and the improved QD surface passivation, could be of great importance to biological imaging applications. Our own efforts have been focused toward the development of small molecule conjugated QDs for biological imaging application, and these custom PEG ligands should ultimately facilitate specific QD recognition of SERT. An initial attempt to demonstrate specific targeting of SERT in a cellular assay using these custom PEG derivatives, however, produced intriguing results. For this assay, SERT-expressing LLC-PK1 cells were incubated with either IDT-319 or IDT-320 ligand-conjugated QDs in a bovine serum albumin (BSA) blocking solution for 30 min at 37 °C, rinsed three times with cold PBS, and immediately imaged with a fluorescent microscope at 100× magnification. The observed fluorescent staining pattern for IDT-319 QD conjugates (Figure 4A) was dramatically different from the negligible fluorescent staining observed for IDT-320 conjugates (Figure 4B). This staining pattern observed for the IDT-319 conjugates was not uniform across the field of view, but isolated to individual cells, an indication of specificity and apparently not the result of nonspecific QD interactions with the cellular membrane. This labeling, however, could not be blocked with the selective serotonin reuptake inhibitor paroxetine, and was apparent in parental cell lines which do not express SERT (data not shown), a clear demonstration that the custom PEG ligands were not mediating specific labeling of SERT. Additional imaging experiments indicated that the observed QD staining pattern involved active intracellular transport, demonstrated a cell cycle dependence, and could not be blocked with free ligand (Supporting Information). It became apparent that albumin was mediating this effect when AMP-QDs, without any added surface modification, recapitulated the same fluorescent staining pattern following an initial incubation in a solution containing BSA (Figure 4C). Taken together, these data indicate that BSA adsorption (illustrated schematically in Figure 4) to AMP-QDs and IDT-319 QD conjugates result in an endosomally associated fluorescent staining pattern, while improved surface passivation of IDT-320 QD conjugates prevent protein adsorption and any associated artifactual cellular labeling.

QD-BSA conjugates are reportedly photostable endosomal markers (*22*), but it was assumed that PEG surface modification would passivate the reactive QD surface and eliminate any undesirable protein associations. Our own prior investigation has highlighted the utility of PEG to significantly reduce nonspecific interactions of AMP-QDs in live cell assays (*20*), but these previous results were collected in the absence of serum protein blocking conditions and any potential protein interference was consequently not explored. It is now apparent that nontargeted PEG-QDs result in an endosomal fluorescent staining pattern for cellular assays where serum protein blocking conditions are employed (Supporting Information Figure S4). These cellular imaging results seem to indicate that BSA adsorption occurs despite PEG modification; yet, this protein adsorption to the QD surface must first be verified in order to validate these assumptions. Gel-filtration chromatography has previously been employed as an analytical tool to assess serum protein interactions with QD surfaces (*23*), and has proven useful in identifying electrostatic interactions as the most likely cause of serum protein adsorption to QD surfaces (*29*). We have focused instead on an alternate approach using polyacrylamide gel electrophoresis (PAGE) to assess protein−QD interactions, without the added expense of gel-filtration chromatography instrumentation. Previous work has identified the utility of PAGE for characterization of QDs covalently modified with BSA (*30*, *31*), but these studies focused on denaturing SDS-PAGE given the covalent nature of the QD surface modification. A nondenaturing, native gel was chosen for our assay in order to maintain the interaction which causes albumin adsorption to reactive QD surfaces. This approach initially facilitates electrophoretic separation of QDs from unconjugated protein, owing to a significant size difference; additionally, the resulting resolved gel can subsequently be stained to assess protein localization. Colocalization of a protein band, visualized via colorimetric detection, with the QD band, as determined by fluorescence, is therefore indicative of a protein−QD interaction;

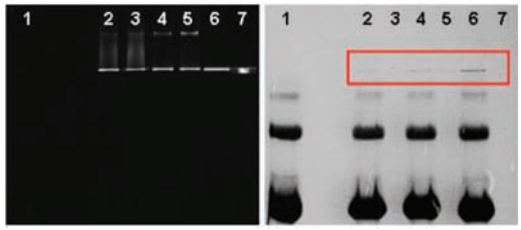

Figure 5. Polyacrylamide gel electrophoretic determination of albumin adsorption to reactive QD surfaces. A fluorescent image (left) illustrates QD accumulation at the interface between the 2.5% stacking gel and the 10% resolving gel. A bright field image following Coomassie Blue staining (right) confirms protein localization. Unassociated BSA is evident in the resolving gel as three characteristic bands. Albumin adsorbed to the QD surface, however, colocalizes with the QD fluorescent bands (highlighted with a red box). Lane 1: BSA without any QDs. Lane 2: IDT-320 QDs with BSA. Lane 3: IDT-320 QDs, no BSA. Lane 4: IDT-319 QDs with BSA. Lane 5: IDT-319 QDs, no BSA. Lane 6: AMP-QDs with BSA. Lane 7: AMP-QDs, no BSA. The passivated IDT-320 QD show minimal albumin adsorption (lane 2) compared to IDT-319 conjugates (lane 4), while AMP-QDs show the highest degree of albumin association (lane 6).

conversely, complete separation of protein from QDs occurs in the absence of any protein−QD interaction.

Protein analysis is routinely performed using PAGE and frequently incorporates both a lower percentage polyacrylamide stacking gel with a higher percentage resolving gel. The QD characterization technique developed in this study makes use of a 2.5% polyacrylamide stacking gel and a 10% resolving gel. As large particles experience a decreased electrophoretic mobility with increasing polyacrylamide concentration, the initial 2.5% gel facilitates QD migration and protein separation, while the 10% resolving gel acts a barrier to the QDs, concentrating them to an individual band (Figure 5, left). A Coomassie Blue stain after electrophoretic separation subsequently permits colorimetric determination of protein localization (Figure 5, right). Using this approach, free BSA separates into three distinct bands, characteristic of albumin monomers, dimers, and globulins (Figure 5, lane 1), but BSA adsorbed to the QD surface appear as an additional band coincidental with the QD fluorescence (highlighted with red box). Of particular notice, the dark band associated with AMP-QDs (lane 6) indicates a large degree of albumin association. Additionally, IDT-319 conjugates (lane 4) have an increased albumin adsorption as compared to their IDT-320 counterparts (lane 2), consistent with the cellular imaging observations. The covalent PEG attachment for the IDT-319 conjugates does act to reduce the amount of albumin adsorption as compared to AMP-QDs, but apparently this minimal amount of protein is still sufficient to cause the observed artifact in fluorescent imaging experiments. Control samples consisting of QD conjugates without added BSA (lanes 3, 5, and 7) provide verification that the observed staining is not due to QD interferences. While this PAGE characterization may lack the sensitivity of a comparable gel-filtration approach, it does serve as a facile tool to quickly assess potential protein interactions at the QD surface without any significant instrumentation expenditure.

CONCLUSIONS

In this report, we have demonstrated that increasingly hydrophobic ligands will self-assemble to the QD surface, presumably through an interaction with the hydrophobic organic capping ligands present on the QD surface. Our own small molecule approach to specifically target membrane-associated receptors is critically dependent upon ligand presentation at the QD surface, and it is now apparent that increasingly hydrophobic targeting molecules will be unavailable to interact with their intended targets due to this unexpected association with the QD surface. An improved architecture for optimal ligand presentation on the surface of AMP-QDs must therefore incorporate a less hydrophobic targeting compound, as is the case for our own $GABA_c$ receptor-specific muscimol−QD derivatives (*18*). In the instance that a biological target requires a hydrophobic compound for effective labeling, a two-step labeling approach can be employed, utilizing biotinylated ligands to initially facilitate a specific interaction, and subsequently be recognized by a streptavidin-conjugated QD (*32*). Alternately, effective presentation of these hydrophobic drug derivatives may ultimately be accomplished through a complete displacement of any organic capping ligands, although issues regarding diminished colloidal stability and fluorescence quenching are still of concern for these type of conjugates (*33*, *34*). In addition to these observations regarding ligand presentation, we have demonstrated the improved passivation resulting from self-assembly of PEG derivatives, which have proven to be even less reactive than covalently modified PEG-QDs. These self-assembled conjugates may ultimately provide a useful platform for biological applications owing to their ability to eliminate unwanted protein adsorption and other associated interferences.

Previous reports have focused on identifying appropriate blocking strategies and surface modifications which limit biological recognition of nanoparticles and reduce their nonspecific binding to cellular membranes. We have demonstrated the potential interference protein adsorption can cause in cellular assays which incorporate QD probes, despite efforts to limit QD reactivity through PEG surface modification, and it is apparent that the observed endosomal staining could easily be mistaken for a specific interaction. Serum protein adsorption, and in particular albumin adsorption, is likely to occur in any *in vivo* analysis and is also likely to occur in numerous *in vitro* assays, where serum blocking is widely employed to limit unwanted fluorescent background staining. While the use of serum proteins is generally accepted in biological protocols, and furthermore necessary for maintaining long-term cellular viability, their potential reactivity with QD probes is frequently neglected. At least one study has demonstrated the importance of selecting an appropriate blocking solution for effective and specific QD labeling (*35*), and our results provide further insight into the persistent nature of this problematic interference. An alternate report has highlighted a potential application utilizing protein adsorption on gold nanoparticles to facilitate intracellular delivery and mediate materials transfection (*36*), consistent with the intracellular staining observed with our own albumin-modified QDs. Consequently, protein adsorption can present either a desirable result or an unwanted interference, depending on the nature of the biological assay in question, highlighting the importance of improved approaches to control the QD surface and mediate biomolecule attachment.

ACKNOWLEDGMENT

We would like to thank Brian O. Bachman for providing access to gel imaging equipment and Frederick R. Haselton for access to a Nanodrop spectrophotometer. We would also like to thank Randy D. Blakely for helpful discussion throughout the course of this work and providing us with the LLC-PK1 cell line employed in this study. This work was supported by the National Institutes of Health under Grants EB003728 and GM72048-02. M.R.W. gratefully acknowledges a fellowship from the Vanderbilt Institute of Nanoscale Science and Engineering (VINSE) and additional funding through the Vanderbilt Institute for Integrative Biosystems Research and Education (VIIBRE).

Supporting Information Available: Additional experimental details demonstrating protein adsorption and characterization of the *in vitro* cellular response of albumin−QD conjugates. This material is available free of charge via the Internet at http://pubs.acs.org.

LITERATURE CITED

(1) Bruchez, M., Moronne, M., Gin, P., Weiss, S., and Alivisatos, A. P. (1998) Semiconductor nanocrystals as fluorescent biological labels. *Science 281*, 2013–2016.

(2) Chan, W. C. W., and Nie, S. M. (1998) Quantum dot bioconjugates for ultrasensitive nonisotopic detection. *Science 281*, 2016–2018.

(3) Chattopadhyay, P. K., Price, D. A., Harper, T. F., Betts, M. R., Yu, J., Gostick, E., Perfetto, S. P., Goepfert, P., Koup, R. A., DeRosa, S. C., Bruchez, M. P., and Roederer, M. (2006) Quantum dot semiconductor nanocrystals for immunophenotyping by polychromatic flow cytometry. *Nat. Med. 12*, 972–977.

(4) Fountaine, T. J., Wincovitch, S. M., Geho, D. H., Garfield, S. H., and Pittaluga, S. (2006) Multispectral imaging of clinically relevant cellular targets in tonsil and lymphoid tissue using semiconductor quantum dots. *Mod. Path. 19*, 1181–1191.

(5) Kim, S., Lim, Y. T., Soltesz, E. G., DeGrand, A. M., Lee, J., Nakayama, A., Parker, J. A., Mihaljevic, T., Laurence, R. G., Dor, D. M., Cohn, L. H., Bawendi, M. G., and Frangioni, J. V. (2004) Near-infrared fluorescent type II quantum dots for sentinel lymph node mapping. *Nat. Biotechnol. 22*, 93–97.

(6) Akerman, M. E., Chan, W. C. W., Laakkonen, P., Bhatia, S. N., and Ruoslahti, E. (2002) Nanocrystal targeting in vivo. *Proc. Natl. Acad. Sci. U.S.A. 99*, 12617–12621.

(7) Lidke, D. S., Nagy, P., Heintzmann, R., ArndtJovin, D. J., Post, J. N., Grecco, H. E., JaresErijman, E. A., and Jovin, T. M. (2004) Quantum dot ligands provide new insights into erbB/HER receptor-mediated signal transduction. *Nat. Biotechnol. 22*, 198–203.

(8) Dahan, M., Levi, S., Luccardini, C., Rostaing, P., Riveau, B., and Triller, A. (2003) Diffusion dynamics of glycine receptors revealed by single-quantum dot tracking. *Science 302*, 442–445.

(9) Sundara Rajan, S., and Vu, T. Q. (2006) Quantum dots monitor TrkA receptor dynamics in the interior of neural PC12 cells. *Nano Lett. 6*, 2049–2059.

(10) Bouzigues, C., Morel, M., Triller, A., and Dahan, M. (2007) Asymmetric redistribution of GABA receptors during GABA gradient sensing by nerve growth cones analyzed by single quantum dot imaging. *Proc. Natl. Acad. Sci. U.S.A. 104*, 11251–11256.

(11) Cui, B. X., Wu, C. B., Chen, L., Ramirez, A., Bearer, E. L., Li, W. P., Mobley, W. C., and Chu, S. (2007) One at a time, live tracking of NGF axonal transport using quantum dots. *Proc. Natl. Acad. Sci. U.S.A. 104*, 13666–13671.

(12) McBride, J., Treadway, J., Feldman, L. C., Pennycook, S. J., and Rosenthal, S. J. (2006) Structural basis for near unity quantum yield core/shell nanostructures. *Nano Lett. 6*, 1496–1501.

(13) Rosenthal, S. J., Tomlinson, I., Adkins, E. M., Schroeter, S., Adams, S., Swafford, L., McBride, J., Wang, Y., DeFelice, L. J., and Blakely, R. D. (2002) Targeting cell surface receptors with ligand-conjugated nanocrystals. *J. Am. Chem. Soc. 124*, 4586–4594.

(14) Dubertret, B., Skourides, P., Norris, D. J., Noireaux, V., Brivanlou, A. H., and Libchaber, A. (2002) In vivo imaging of quantum dots encapsulated in phospholipid micelles. *Science 298*, 1759–1762.

(15) Wu, X. Y., Liu, H. J., Liu, J. Q., Haley, K. N., Treadway, J. A., Larson, J. P., Ge, N. F., Peale, F., and Bruchez, M. P. (2003) Immunofluorescent labeling of cancer marker Her2 and other cellular targets with semiconductor quantum dots. *Nat. Biotechnol. 21*, 41–46.

(16) Petruska, M. A., Bartko, A. P., and Klimov, V. I. (2004) An amphiphilic approach to nanocrystal quantum dot-titania nanocomposites. *J. Am. Chem. Soc. 126*, 714–715.

(17) Warnement, M. R., Tomlinson, I. D., and Rosenthal, S. J. (2007) Fluorescent imaging applications of Quantum Dot probes. *Curr. Nanosci. 3*, 273–284.

(18) Gussin, H. A., Tomlinson, I. D., Little, D. M., Warnement, M. R., Qian, H., Rosenthal, S. J., and Pepperberg, D. R. (2006) Binding of muscimol-conjugated quantum dots to GABAc receptors. *J. Am. Chem. Soc. 128*, 15701–15713.

(19) Ballou, B., Lagerholm, B. C., Ernst, L. A., Bruchez, M. P., and Waggoner, A. S. (2004) Noninvasive imaging of quantum dots in mice. *Bioconjugate Chem. 15*, 79–86.

(20) Bentzen, E. L., Tomlinson, I. D., Mason, J., Gresch, P., Warnement, M. R., Wright, D., Sanders-Bush, E., Blakely, R., and Rosenthal, S. J. (2005) Surface modification to reduce nonspecific binding of quantum dots in live cell assays. *Bioconjugate Chem. 16*, 1488–1494.

(21) Tomlinson, I. D., Gies, A. P., Gresch, P. J., Dillard, J., Orndorff, R. L., Sanders-Bush, E., Hercules, D. M., and Rosenthal, S. J. (2006) Universal polyethylene glycol linkers for attaching receptor ligands to quantum dots. *Bioorg. Med. Chem. Lett. 16*, 6262–6266.

(22) Hanaki, K., Momo, A., Oku, T., Komoto, A., Maenosono, S., Yamaguchi, Y., and Yamamoto, K. (2003) Semiconductor quantum dot/albumin complex is a long-life and highly photostable endosome marker. *Biochem. Biophys. Res. Commun. 302*, 496–501.

(23) Zimmer, J. P., Kim, S. W., Ohnishi, S., Tanaka, E., Frangioni, J. V., and Bawendi, M. G. (2006) Size series of small indium arsenide-zinc selenide core-shell nanocrystals and their application to in vivo imaging. *J. Am. Chem. Soc. 128*, 2526–2527.

(24) Invitrogen Corporation. Qdot® streptavidin conjugates user's manual. Appendix 3: Extinction coefficients. http://probes.invitrogen.com/media/pis/mp19000.pdf (accessed May 2008).

(25) Tomlinson, I. D., Warnement, M. R., Mason, J. N., Vergne, M. J., Hercules, D. M., Blakely, R. D., and Rosenthal, S. J. (2007) Synthesis and characterization of a pegylated derivative of 3-(1,2,3,6-tetrahydro-pyridin-4yl)-1H-indole (IDT199): A high affinity SERT ligand for conjugation to quantum dots. *Bioorg. Med. Chem. Lett. 17*, 5656–5660.

(26) Gueremy, C., Audiau, F., Champseix, A., Uzan, A., Lefur, G., and Rataud, J. (1980) 3-(4-Piperidinylalkyl)indoles, selective inhibitors of neuronal 5-hydroxytryptamine uptake. *J. Med. Chem. 23*, 1306–1310.

(27) Walker, J. M. (2002) Nondenaturing polyacrylamide gel electrophoresis of proteins., in *The protein protocols handbook* (Walker, J. M., Ed.) pp 57−60, Humana Press, Totowa, NJ.

(28) Gu, H. H., Ahn, J., Caplan, M. J., Blakely, R. D., Levey, A. I., and Rudnick, G. (1996) Cell-specific sorting of biogenic amine transporters expressed in epithelial cells. *J. Biol. Chem. 271*, 18100–18106.

(29) Choi, H. S., Liu, W., Misra, P., Tanaka, E., Zimmer, J. P., Ipe, B. I., Bawendi, M. G., and Frangioni, J. V. (2007) Renal clearance of quantum dots. *Nat. Biotechnol. 25*, 1165–1170.

(30) Wang, S. P., Mamedova, N., Kotov, N. A., Chen, W., and Studer, J. (2002) Antigen/antibody immunocomplex from CdTe nanoparticle bioconjugates. *Nano Lett. 2*, 817–822.

(31) Wang, Q., Kuo, Y. C., Wang, Y. W., Shin, G., Ruengruglikit, C., and Huang, Q. R. (2006) Luminescent properties of water-soluble denatured bovine serum albumin-coated CdTe quantum dots. *J. Phys. Chem. B 110*, 16860–16866.

(32) Orndorff, R. L., Warnement, M. R., Mason, J. N., Blakely, R. D., and Rosenthal, S. J. (2008) Quantum dot ex vivo labeling of neuromuscular synapses. *Nano Lett. 8*, 780–785.

(33) Liu, W., Choi, H. S., Zimmer, J. P., Tanaka, E., Frangioni, J. V., and Bawendi, M. (2007) Compact cysteine-coated CdSe(ZnCdS) quantum dots for in vivo applications. *J. Am. Chem. Soc. 129*, 14530–14531.

(34) Liu, W., Howarth, M., Greytak, A. B., Zheng, Y., Nocera, D. G., Ting, A. Y., and Bawendi, M. G. (2008) Compact biocompatible quantum dots functionalized for cellular imaging. *J. Am. Chem. Soc. 130*, 1274–1284.

(35) Pathak, S., Cao, E., Davidson, M. C., Jin, S. H., and Silva, G. A. (2006) Quantum dot applications to neuroscience: New tools for probing neurons and glia. *J. Neurosci. 26*, 1893–1895.

(36) Giljohann, D. A., Seferos, D. S., Patel, P. C., Millstone, J. E., Rosi, N. L., and Mirkin, C. A. (2007) Oligonucleotide loading determines cellular uptake of DNA-modified gold nanoparticles. *Nano Lett. 7*, 3818–3821.

BC800104N

In Vitro and *in Vivo* Evaluation of Doxorubicin Conjugates with the Divalent Peptide E-[c(RGDfK)$_2$] that Targets Integrin $\alpha_v\beta_3$

Claudia Ryppa,[†] Hagit Mann-Steinberg,[‡] Iduna Fichtner,[§] Holger Weber,[||] Ronit Satchi-Fainaro,[‡] Martin L. Biniossek,[⊥] and Felix Kratz*,[†]

Tumor Biology Center, Breisacher Straβe 117, 79106 Freiburg, Federal Republic of Germany, Department of Physiology and Pharmacology, Sackler School of Medicine, Tel-Aviv University, Tel-Aviv 69978, Israel, Max-Delbrück Center, Robert-Rössle-Straβe 10, 13122 Berlin, ProQinase, Breisacher Straβe 117, 79106 Freiburg, and Institut für Molekulare Medizin and Zellforschung, Zentrum für Biochemie and Molekulare Zellforschung, Stefan-Meier-Straβe 17, 79104 Freiburg, Federal Republic of Germany. Received March 20, 2008; Revised Manuscript Received May 15, 2008

Integrins, especially integrin $\alpha_v\beta_3$, are attractive receptors for vascular targeting strategies. Recently, a divalent RGD peptidomimetic, E-[c(RGDfK)$_2$], has been described that demonstrates increased uptake in human ovarian carcinoma OVCAR-3 xenograft tumors. Inspired by these results, we set out to develop doxorubicin conjugates with E-[c(RGDfK)$_2$] by binding two different maleimide derivatives of doxorubicin to E-[c(RGDfK)$_2$] that was thiolated with iminothiolane. In this way, two water-soluble derivatives were obtained, E-[c(RGDfK)$_2$]-DOXO-1 and E-[c(RGDfK)$_2$]-DOXO-2. In E-[c(RGDfK)$_2$]-DOXO-1, doxorubicin was bound to the peptide through a stable amide bond, and in E-[c(RGDfK)$_2$]-DOXO-2, a MMP-2/MMP-9 cleavable octapeptide was introduced between doxorubicin and the peptide. The rationale for a MMP-2/MMP-9-cleavable linker was that MMP-2 and MMP-9 bind to integrin $\alpha_v\beta_3$ and both are overexpressed in tumor vasculature. In addition, analogous control doxorubicin-containing peptides bearing c(RADfK) that does not bind to integrin $\alpha_v\beta_3$ were synthesized, i.e., c(RADfK)-DOXO-1 and c(RADfK)-DOXO-2. Whereas E-[c(RGDfK)$_2$]-DOXO-2 was cleaved effectively by MMP-2 and in OVCAR-3 tumor homogenates releasing a doxorubicin-tetrapeptide or doxorubicin as the final cleavage product, no release of doxorubicin was observed for E-[c(RGDfK)$_2$]-DOXO-1. Proliferation of HUVEC in the presence of MMP-2-cleavable doxorubicin-containing peptides exhibited 6- to 10-fold increased inhibition compared to the amide-linked doxorubicin-containing peptides. In addition, inhibition of HUVEC sprouting during a 24 h exposure was approximately 3-fold stronger for E-[c(RGDfK)$_2$]-DOXO-2 and 20-fold stronger for the reference peptide conjugate c(RADfK)-DOXO-2 than for doxorubicin alone. *In vivo* studies in an OVCAR-3 xenograft model demonstrated no or only moderate antitumor efficacy for either E-[c(RGDfK)$_2$], E-[c(RGDfK)$_2$]-DOXO-1, E-[c(RGDfK)$_2$]-DOXO-2, or c(RADfK)-DOXO-2, even at doses of 3 × 24 mg/kg doxorubicin equivalents, compared to an improved antitumor effect for doxorubicin at 2 × 8 mg/kg.

INTRODUCTION

Vascular targeting agents interact with receptors on endothelial cells and, unlike antiangiogenic drugs that inhibit the formation of new vessels, destroy or occlude pre-existing blood vessels of solid tumors (*1*). Vascular targeting agents can act as inhibitors of endothelial growth such as combretastatins or receptor antagonists or they comprise ligand-based drugs consisting of a targeting moiety and an effector molecule. Suitable receptors on endothelial cells for ligand-directed approaches are the VEGF[1] receptors, the fibronectin ED-B domain, endoglin, NG2 proteoglycan, prostate-specific membrane antigen (PSMA), as well as cell adhesion receptors such as vascular cell adhesion molecule 1 (VCAM-1), E-selectins, and integrins (*1–4*). The latter have perhaps been the most intensely studied as endothelial targets for vascular targeting agents (*5*). Integrins are heterodimeric cell surface receptors of which several such as integrin $\alpha_v\beta_3$, $\alpha_v\beta_5$, and $\alpha_5\beta_1$ are overexpressed in the blood vessels of solid tumors and mediate adhesion between cells and the extracellular matrix, thus promoting tumor cell migration and tumor growth (*3*). A characteristic feature of integrins is their high binding affinity for arginyl-glycyl-aspartic acid (RGD) sequences exposed on endogenous or exogenous ligands. Using an *in vivo* phage display technology, Arap and co-workers discovered cyclic RGD-4C peptides that bind avidly to integrin $\alpha_v\beta_3$ and $\alpha_v\beta_5$ (*6, 7*). A number of doxorubicin conjugates have been developed with a divalent RGD-4C peptide (ACDCRGDCFCG). The first by Arap et al. who coupled the 3′-amino position of doxorubicin to one or two of the free carboxylate groups of RGD-4C by activating the latter with 1-ethyl-3-(3,3-dimethylaminopropyl)carbodiimide and *N*-hydroxysuccinimide. This conjugate showed improved activity and toxicity profile over doxorubicin in a MDA-MB-435 mammary carcinoma model

* To whom correspondence should be addressed. Dr. Felix Kratz, Tumor Biology Center, Department of Medical Oncology, Clinical Research, Breisacher Straβe 117, D-79106 Freiburg, Federal Republic of Germany. Tel.: 0049-761-2062930. Fax: 0049-761-2062905. E-mail: felix@tumorbio.uni-freiburg.de.

[†] Tumor Biology Center.

[‡] Tel-Aviv University.

[§] Max-Delbrück Center.

[||] ProQinase.

[⊥] Institut für Molekulare Medizin and Zellforschung.

[1] Abbreviations: VEGF, vascular endothelial growth factor; OVCAR, ovarian carcinoma; MMP, matrix metalloprotease; HUVEC, human umbilical vein endothelial cells; AcN, acetonitrile; TFA, trifluoroacetic acid; EX, excitation; EM, emission; TOF, time of flight; APMA, *p*-aminophenylmercuric acetate; Tris, Tris-(hydroxymethyl)-aminomethane; EBM-2, endothelial cell basal medium 2; EGM-2, endothelial growth medium 2; FBS, fetal bovine serum; EC, endothelial cells; nu/nu, Nude; i.v., intravenous; s.c., subcutaneous; i.p., intraperitoneal; ID/g, injected doses/gram; MTD, maximum tolerated dose; T/C, tumor volume test/control; BWC, body weight change.

10.1021/bc800117r CCC: $40.75 © 2008 American Chemical Society
Published on Web 06/26/2008

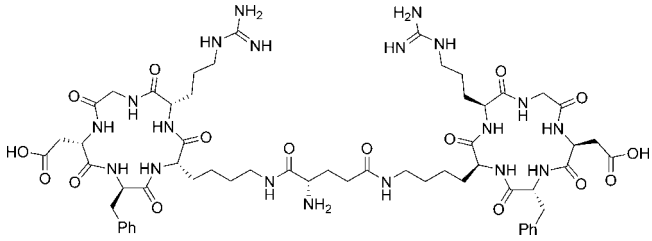

Figure 1. Structure of E-[c(RGDfK)$_2$].

in which integrin $\alpha_v\beta_3$ is expressed in the tumor vessels as well as on the tumor cell themselves (*7, 8*). Superior efficacy of the RGD-4C-doxorubicin conjugate was confirmed in another model (hepatoma) in which the tumor cells did not express integrin $\alpha_v\beta_3$ suggesting that a direct endothelial effect was responsible for tumor growth inhibition (*8*). The precise structure and mode of action of these conjugates has not been reported, but conjugation at the 3′-amino group seems likely resulting in a stable amide bond between doxorubicin and the divalent peptide which presumably cannot be readily cleaved *in vivo*. This led de Groot et al. to develop a prodrug with RGD-4C and a plasmin-cleavable substrate D-Ala-Phe-Lys that showed comparable *in vitro* cytotoxicity to doxorubicin after activation by plasmin (*9*). Unfortunately, no *in vivo* efficacy has been reported for this conjugate. Due to the presence of two disulfide bridges in the structure of RGD-4C that are prone to cleavage during synthesis or in biological media, a stable peptide derivative E-[c(RGDfK)$_2$] based on the integrin $\alpha_v\beta_3$ antagonist Cilengitide has been developed that shows specific tumor targeting properties (*10–13*). The presence of the glutamic acid residue makes it an ideal ligand for further chemical conjugation. Burkhart et al. conjugated a doxorubicin prodrug, doxsaliform, to this position and showed that the resulting conjugate bound specifically to vitronectin and that *N*-methylhydroxyl-doxorubicin is released by hydrolysis as the highly cytotoxic doxorubicin derivative, but no *in vivo* data were reported (*14*).

Further diagnostic studies by Janssen et al. demonstrated that a dimeric form of c(RGDfK) (Figure 1), i.e. E-[c(RGDfK)$_2$], has improved tumor targeting properties over the monomeric form (*12, 14*). Subsequent biodistribution studies with radiolabeled E-[c(RGDfK)$_2$] showed an uptake of up to 7.5% injected dose/g in OVCAR-3 xenograft tumors (*12*).

Inspired by these results, we set out to develop doxorubicin conjugates with E-[c(RGDfK)$_2$]. Our aim was to (a) develop a stable drug derivative as well as a prodrug with RGD peptides, (b) to establish the *in vitro* properties of these drug conjugates including analogously constructed conjugates with the nonintegrin $\alpha_v\beta_3$ binding control peptide c(RADfK), and (c) to compare the *in vivo* efficacy of the RGD doxorubicin conjugates in the human ovarian carcinoma OVCAR-3 xenograft model which was used by Janssen et al. for biodistribution studies with E-[c(RGDfK)$_2$], in the hope of answering some of the open questions regarding cleavability and *in vivo* potential that have arisen in this particular area of doxorubicin conjugates.

As starting materials for the intended doxorubicin RGD-based peptide conjugates, we used the 6-maleimidocaproyl amide derivative of doxorubicin **1** as a stable derivative and the maleimidotriethylene glycol peptide derivative **2** that contains an octapeptide that is cleaved by matrix metalloproteases 2 and 9 (MMP-2 and MMP-9) (Figure 2). A MMP-2/-9 cleavable prodrug seemed suitable for our vascular targeting strategy considering that MMP-2 and MMP-9 bind to integrin $\alpha_v\beta_3$ and both are overexpressed in tumor vasculature (*15–17*) which could ensure that sufficient amounts of these proteases are present at the molecular target after binding of the doxorubicin RGD peptides to integrin $\alpha_v\beta_3$. In addition, compound **2**, developed as an albumin binding prodrug, demonstrated superior *in vivo* efficacy compared to doxorubicin in a melanoma xenograft model (*18*).

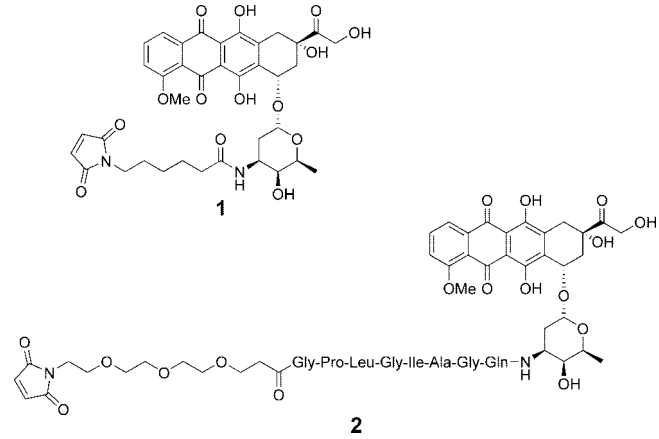

Figure 2. Stable 6-maleimidocaproyl amide derivative of doxorubicin **1** and the MMP-2 cleavable maleimidotriethylene glycol peptide derivative **2**.

EXPERIMENTAL PROCEDURES

Materials and Instrumental. Doxorubicin hydrochloride was purchased from Yick-Vic (Hong Kong, PRC); E-[c(RGDfK)$_2$] and c(RADfK) were purchased from Peptides International (Louisville, KY, USA); organic solvents: HPLC grade (Labscan Ltd., Dublin, Ireland; Roth, Karlsruhe, FRG; Merck, Darmstadt, FRG). Compound **2** was prepared as described in the literature (*18*). All other chemicals used were at least reagent grade and obtained from Sigma-Aldrich (Deisenhofen, FRG), Roth, or Merck and used without further purification; buffers were vacuum-filtered through a 0.2 μm membrane (Sartorius, Göttingen, FRG) and thoroughly degassed with nitrogen prior to use. ^{1}H, ^{13}C NMR: Bruker AM 400 (internal standard: TMS); analytical HPLC were performed with a Kontron 422 pump and a Kontron 430 detector (at 495 and 254 nm). For peak integration, *Geminyx* software (v 1.91 by Goebel Instrumentelle Analytik, FRG) was used; column: Machery-Nagel, 100 Å, Nucleosil 100−5 C18 [4 × 250 mm] with precolumn; chromatographic conditions: flow: 1.0 mL/min, mobile phase A: AcN/0.05% aq. TFA (30/70, v/v), mobile phase B: AcN/0.05% aq. TFA (70/30, v/v), gradient: 0−1.5 min 100% mobile phase A; 1.5−40 min increase to mobile phase B; 40−46.5 min decrease to initial mobile phase A; injection volume: 20 μL. Cleavage studies with MMP-2 and in OVCAR-3 tumor homogenates were performed following a modified method according to the literature (*18*) with a Kontron 422 pump and a Merck F-1050 fluorescence spectrophotometer (EX 490 nm, EM 540 nm). For peak integration, *Geminyx* software was used; column: Waters WAT106151, Symmetry 300, C18 5 μ [4.6 × 250 mm] with precolumn WAT106166; chromatographic conditions: flow: 1.0 mL/min, mobile phase A: AcN/0.05% aq. TFA (25/75, v/v), mobile phase B: AcN/0.05% aq. TFA (55/45, v/v), gradient: 0−25 min 100% mobile phase A; 25−40 min increase to mobile phase B; 40−50 min 100% mobile phase B; 50−60 min decrease to initial mobile phase A; injection volume: 20 μL. Preparative HPLC for the separation of E-[c(RGDfK)$_2$]-DOXO-1, E-[c(RGDfK)$_2$]-DOXO-2, c(RADfK)-DOXO-1, and c(RADfK)-DOXO-2 was performed with a BioLogic Duo-Flow System from Biorad (München, FRG) which was connected with a Lambda 1010 visible monitor from Bischoff (at λ = 495 nm); UV-detection at λ = 254 nm from Biorad; column: Machery-Nagel, 100 Å, Nucleosil 100−7 C18 [21 × 250 mm] with precolumn; chromatographic conditions: flow: 10 mL/min,

mobile phase A: AcN/0.05% aq. TFA (30/70, v/v), mobile phase B: AcN/0.05% aq. TFA (70/30, v/v), gradient: 0−1 min 100% mobile phase A; 1−44 min increase to mobile phase B; 41−46 min decrease to initial mobile phase A; injection volume: 2 mL. MALDI-TOF mass spectra were acquired on a Reflex III mass spectrometer (Bruker Daltonik GmbH, Bremen, FRG) in the reflector mode (positively charged ions) with external calibration. Samples were prepared with an adapted thin-layer technique (*19*). α-Cyano-4-hydroxycinnamic acid (97%, Aldrich, Taufkirchen, FRG) was used as matrix and nitrocellulose (Biorad, Trans-Blot Transfer Medium) as additive. The samples were washed with 0.1% TFA. Monoisotopic peaks were used for data analysis. ESI-TOF mass spectra were acquired on an Agilent 6210 system, consisting of an Agilent 1100 HPLC system with a diode array detector and an ESI-MSD TOF by Agilent Technologies (Böblingen, FRG).

Synthesis of 6-Maleimidocaproylamide Derivate of Doxorubicin 1. Doxorubicin hydrochloride (500 mg, 0.86 mmol, 1 equiv), 6-maleimidocaproylic acid *N*-hydroxysuccinimide ester (292 mg, 0.95 mmol, 1.1 equiv), and triethyl amine (239 μL, 1.74 mmol, 2 equiv) were dissolved in DMF (30 mL) and stirred for 2 h at room temperature. The solution was precipitated in diethyl ether (10 mL), washed with dry diethyl ether (2 × 5 mL), filtered and dried *in vacuo* to obtain red crystals in 91% yield (574 mg, 0.78 mmol); HPLC analysis: 14.4 min, 96% of peak area, 495 nm; MS (ESI-TOF) m/z = 775.21 $[M + K]^+$, 759.24 $[M + Na]^+$.

General Procedure for the Synthesis of E-[c(RGDfK)$_2$]-DOXO-1, E-[c(RGDfK)$_2$]-DOXO-2, c(RADfK)-DOXO-1, and c(RADfK)-DOXO-2. The doxorubicin derivatives **1** (20 mM solution in DMF) or **2** (1 equiv) and E-[c(RGDfK)$_2$] or c(RADfK) (1 equiv) were dissolved in 10 mM sodium phosphate buffer (8−20 mL, containing 1 mM EDTA, pH 7.5). A 72.7 mM solution of 2-iminothiolane (1 equiv) in 10 mM sodium phosphate buffer (containing 1 mM EDTA, pH 7.5) was added to the clear red solution and the mixture was kept overnight at room temperature. The solvent was removed *in vacuo*; the residue was dissolved in 2 mL AcN/0.05% aq. TFA (30/70, v/v) and purified by preparative HPLC.

E-[c(RGDfK)$_2$]-DOXO-1. Red crystals were obtained in 44% yield (42 mg, 0.017 mmol). HPLC analysis: 10.3 min, >97% of peak area, 495 nm; MS (TOF) m/z = 2177.90 $[M + Na]^+$, 2155.93 $[M + H]^+$, 1759.84 $[C_{79}H_{119}N_{22}O_{22}S]^+$.

E-[c(RGDfK)$_2$]-DOXO-2. Red crystals were obtained in 62% yield (60 mg, 0.018 mmol). HPLC analysis: 12.1 min, 95% of peak area, 495 nm; MS (TOF) m/z = 2939.35 $[M + H]^+$, 2543.27 $[C_{113}H_{176}N_{31}O_{34}S]^+$.

c(RADfK)-DOXO-1. Red crystals were obtained in 29% yield (43 mg, 0.026 mmol). HPLC analysis: 11.3 min of peak area, 95%, 495 nm; MS (TOF) m/z = 1455.61 $[M + H]^+$, 1059.55 $[C_{48}H_{75}N_{12}O_{13}S]^+$.

c(RADfK)-DOXO-2. Red crystals were obtained in 43% yield (81 mg, 0.033 mmol). HPLC analysis: 12.9 min, 91% of peak area, 495 nm; MS (TOF) m/z = 2261.04 $[M + Na]^+$, 2239.06 $[M + H]^+$, 1842.97 $[C_{82}H_{132}N_{21}O_{25}S]^+$.

Cleavage Studies of E-[c(RGDfK)$_2$]-DOXO-2 with 58.8 mU/μL Activated MMP-2. A 200 μM solution of E-[c(RGDfK)$_2$]-DOXO-2 in 50 mM Tris·HCl buffer (pH 7.5) was prepared. A 10 mM stock solution of *p*-aminophenylmercuric acetate (APMA, 3.9 mg) in 0.1 M NaOH (1 mL) was diluted with 50 mM Tris·HCl buffer (3 mL, pH 7.5) to obtain a 2.5 mM APMA solution which was adjusted to pH 7.2. MMP-2 (58.8 mU) was activated for 30 min at 37 °C with 7.5 μL of the 2.5 mM APMA solution. 100 μL of the E-[c(RGDfK)$_2$]-DOXO-2 stock solution (200 μM) were mixed with activated MMP-2 and incubated at 37 °C. Samples were collected and analyzed by HPLC over 3 h.

Cleavage Studies of E-[c(RGDfK)$_2$]-DOXO-2 with OVCAR-3 Tumor Homogenates. For preparing the tumor homogenates, tissues of OVCAR-3 xenografts were cut into small pieces, and 200 mg samples were transferred in a 2 mL Eppendorf tube to which was added 800 μL of buffer (50 mM Tris·HCl buffer, pH 7.4, containing 1 mM monothioglycerol). Homogenization was carried out with a microdissmembrator at 2000 rpm for 2 × 10 min with the aid of glass balls. Subsequently, the samples were centrifuged at 10 000 rpm for 10 min at 4 °C. The supernatant was aliquoted and kept frozen at −78 °C prior to use.

100 μL of the E-[c(RGDfK)$_2$]-DOXO-2 stock solution (200 μM) were mixed with OVCAR-3 tumor homogenate at pH 7.4 and incubated at 37 °C. Samples were collected and analyzed by HPLC over 75 min.

Endothelial Cell Proliferation Assay. HUVEC were plated onto 24-well plate (1.5×10^4 cells/well) in EBM-2 medium (Clonetics, Walkersville, MD, USA) supplemented with 5% FBS and incubated for 24 h (37 °C; 5% CO_2). On the following day, the cultured medium was removed and cells were exposed to serial dilutions of doxorubicin derivatives prepared in a fresh mixture of EBM-2 medium and EGM-2 complete medium (Clonetics) (1:1, v/v). Cell proliferation was assessed after 72 h by means of direct counting using a Z1 Coulter Particle Counter (Beckman Coulter, Luton, England). As positive control, cells were grown without treatment. Each treatment was assayed in triplicates and the experiment was repeated independently. Proliferation of endothelial cells was normalized to percent cell growth compared to the cell growth of the positive untreated control cells. Error bars represent the standard deviation of the mean.

Endothelial Cell Sprouting Assay. HUVEC were purchased from PromoCell (Heidelberg, FRG) and used at passage 3−4. The experiments were pursued in modification of the originally published protocol (*20, 21*). In brief, spheroids were prepared as described by pipetting 500 endothelial cells (EC) in a hanging drop on plastic dishes to allow overnight spheroid aggregation. 50 EC spheroids were then seeded in 0.9 mL of a collagen solution and pipetted into individual wells of a 24 well plate to allow polymerization. The test compounds were added after 30 min by pipetting 100 μL of a 10-fold concentrated working dilution on top of the polymerized gel in combination with VEGF-A (25 ng/mL, ProQinase, Freiburg, FRG). Plates were incubated at 37 °C for 24 h and fixed by adding 4% paraformaldehyde. Sprouting intensity of EC spheroids was quantitatively determined by the cumulative sprout length per spheroid using an inverted microscope and the digital imaging software *Analysis 3.2* from Soft Imaging System (Münster, FRG). The mean of the cumulative sprout length of 10 randomly selected spheroids was analyzed as an individual data point and the relative inhibition by the test compounds determined. Fitting of IC_{50} curves and calculation of IC_{50} values was performed with *GraphPad Prism 5.01*.

***In Vivo* Experiments.** For the *in vivo* testing of E-[c(RGDfK)$_2$], E-[c(RGDfK)$_2$]-DOXO-1, E-[c(RGDfK)$_2$]-DOXO-2, and c(RADfK)-DOXO-2 in comparison with doxorubicin female NMRI: nu/nu mice (M&B A/S, Ry, Denmark) were used. The mice were held in laminar flow shelves under sterile and standardized environmental conditions (25 ± 2 °C room temperature, 50 ± 10% relative humidity, 12 h light−dark rhythm). They received autoclaved food and bedding (ssniff, Soest, FRG) and acidified (pH 4.0) drinking water *ad libitum*. All animal experiments were performed under the auspices of the German Animal Protection Law. Orientating toxicity study with E-[c(RGDfK)$_2$]-DOXO-2 was carried out at doses of 8, 16, and 24 mg/kg doxorubicin equivalents. E-[c(RGDfK)$_2$]-DOXO-2 was dissolved in glucose phosphate buffer (10 mM

Scheme 1. Preparation of E⁻[c(RGDfK)$_2$]-DOXO^{-1} and E⁻[c(RGDfK)$_2$]-DOXO^{-2}

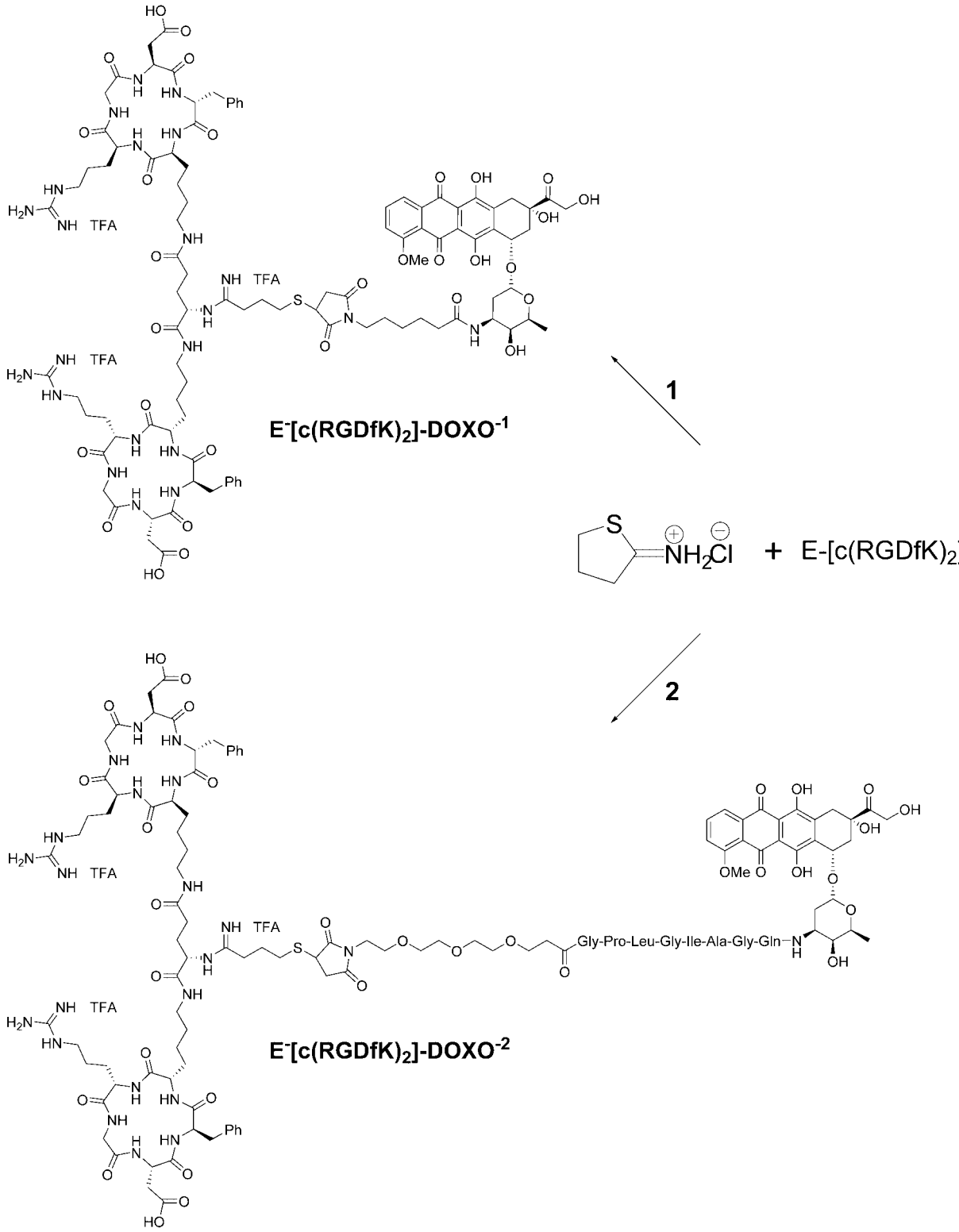

sodium phosphate, 5% D-(+)-glucose, pH 5.8) at a concentration of 3 mM and administered intravenously (i.v.) in a weekly schedule. For experiments in tumor-bearing animals, 10^7 cells of human ovarian cancer cells OVCAR-3 from *in vitro* culture were transplanted subcutaneously (s.c.) into the flank region of anaesthetized (40 mg/kg i.p. Radenarkon, Asta Medica, Frankfurt, FRG) mice on day zero. Mice were randomly distributed to the experimental groups (8 mice for control, 6 mice each for the treatment groups). When the tumors were grown to a palpable size, treatment was initiated (Figure 8). Mice were treated intravenously at day 10, 17, and 24 with glucose phosphate buffer (10 mM sodium phosphate, 5% D-(+)-glucose, pH 5.8), E-[c(RGDfK)$_2$], dissolved in glucose phosphate buffer (10 mM sodium phosphate, 5% D-(+)-glucose, pH 5.8) at a concentration of 7 mM (3 × 54.5 mg/kg), doxorubicin (2 × 8 mg/kg), E-[c(RGDfK)$_2$]-DOXO-1, dissolved in glucose phosphate buffer (10 mM sodium phosphate, 5% D-(+)-glucose, pH 5.8) at a concentration of 4 mM (3 × 24 mg/kg), E-[c(RGDfK)$_2$]-DOXO-2, dissolved in glucose phosphate buffer (10 mM sodium phosphate, 5% D-(+)-glucose, pH 5.8) at a concentration of 3

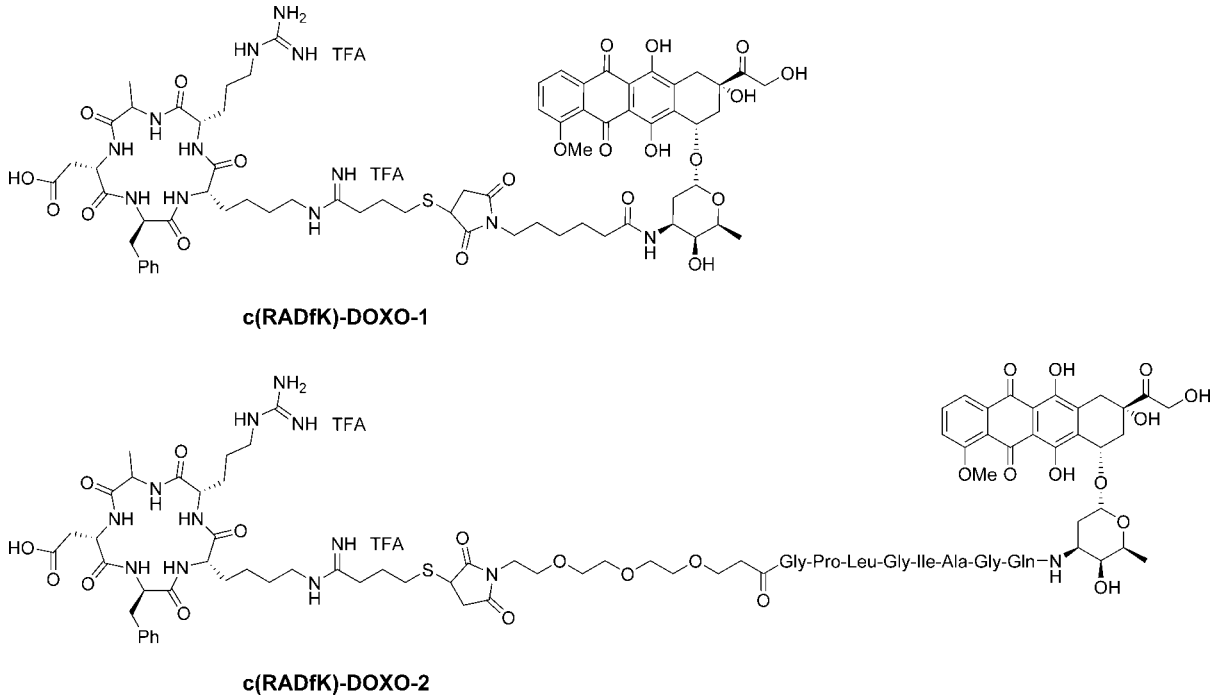

Figure 3. Structure of c(RADfK)-DOXO-1 and c(RADfK)-DOXO-2.

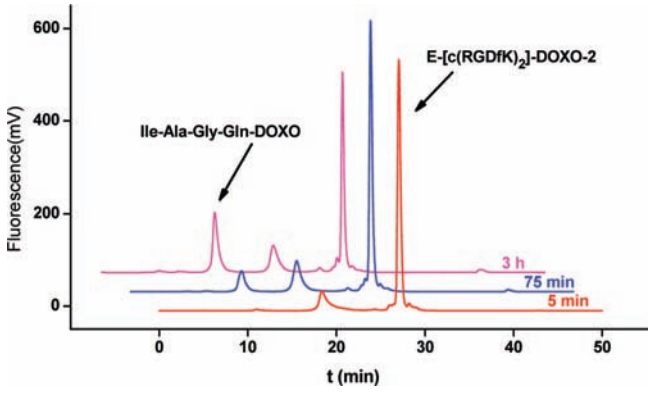

Figure 4. Chromatograms of incubation studies of a 200 μM solution of E-[c(RGDfK)$_2$]-DOXO-2 with 58.8 mU activated MMP-2 at 37 °C. Chromatographic conditions: see Experimental Procedures.

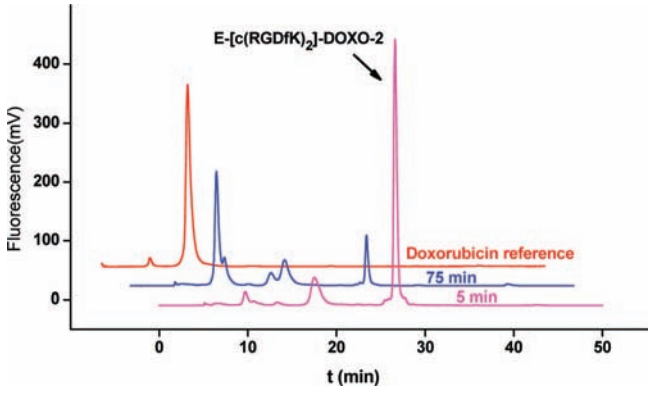

Figure 5. Chromatograms of incubation studies of a 100 μM solution of E-[c(RGDfK)$_2$]-DOXO-2 with OVCAR-3 tumor homogenates at 37 °C. Chromatographic conditions: see Experimental Procedures.

mM (2 × 8 mg/kg, 3 × 24 mg/kg), or c(RADfK)-DOXO-2, dissolved in glucose phosphate buffer (10 mM sodium phosphate, 5% D-(+)-glucose, pH 5.8) at a concentration of 6 mM (3 × 24 mg/kg) freshly dissolved in glucose phosphate buffer.

Tumor size was measured twice weekly with a caliper-like instrument in two dimensions. Individual tumor volumes (V) were calculated by the formula $V = (\text{length} + [\text{width}]^2)/2$ and related to the values on the first day of treatment (relative tumor volume, RTV). Statistical analysis was performed with the U-test (Mann and Whitney) with $p < 0.05$. The body weights of mice were determined every 3 to 4 days.

RESULTS

Chemistry. A series of acid-sensitive and enzymatically cleavable maleimide drug derivatives have been developed in our group that react specifically and selectively with thiol groups, e.g., with the cysteine-34 position of circulating albumin (*18, 22–28*). Maleimide doxorubicin derivatives were therefore an obvious choice for developing conjugates with E-[c(RGDfK)$_2$]. The precursor **1** for the stable conjugates was obtained by reaction of doxorubicin hydrochloride and 6-maleimidohexanoic acid *N*-hydroxysuccinimide ester. By introducing a thiol group with 2-iminothiolane (Traut's reagent) at the α-amino position of the glutamic acid moiety of E-[c(RGDfK)$_2$], we discovered that doxorubicin conjugates with **1** and **2** could be conveniently synthesized in a one-pot reaction of 2-iminothiolane, E-[c(RGDfK)$_2$], and the respective 6-maleimide derivate **1** or **2**. Subsequently, the resulting conjugates were isolated by preparative HPLC, thus obtaining E-[c(RGDfK)$_2$]-DOXO-1 and E-[c(RGDfK)$_2$]-DOXO-2 (Scheme 1). The analogously constructed doxorubicin conjugates with the control peptide c(RADfK), c(RADfK)-DOXO-1, and c(RADfK)-DOXO-2 were obtained in the same manner (Figure 3 and Experimental Procedures section). The conjugates showed good water solubility in glucose phosphate buffer (10 mM sodium phosphate, 5% D-(+)-glucose, pH 5.8) of ~10 mg/mL for E-[c(RGDfK)$_2$]-DOXO-1, c(RADfK)-DOXO-1, and c(RADfK)-DOXO-2 and ~20 mg/mL for E-[c(RGDfK)$_2$]-DOXO-2. The conjugates were characterized by analytical HPLC and MALDI TOF (see Experimental Procedures section).

Stability and Cleavage Properties of RGD Doxorubicin Conjugates. Stability of E-[c(RGDfK)$_2$]-DOXO-2 was studied at pH 7.0 (FPLC buffer; 150 mM NaCl, 4 mM Na_2HPO_4) at room temperature. Chromatograms were recorded over a period of 24 h showing minor decomposition of 17% (data not shown).

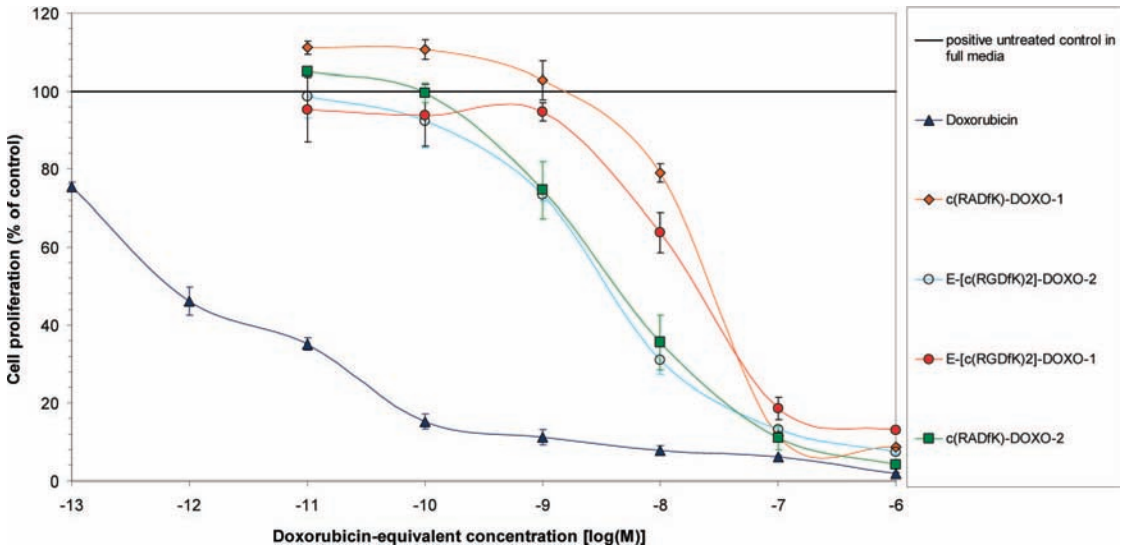

Figure 6. HUVEC proliferation assay treated with free doxorubicin (closed triangles, mean IC_{50} = 700 fM) and doxorubicin derivatives: E-[c(RGDfK)$_2$]-Doxo-1 (closed circles, mean IC_{50} = 20 nM), E-[c(RGDfK)$_2$]-Doxo-2 (open circles, mean IC_{50} = 3.5 nM), c(RADfK)-Doxo-1 (closed diamond, mean IC_{50} = 28 nM), and c(RADfK)-Doxo-2 (closed squares, mean IC_{50} = 4.2 nM). Solid line represents positive control of HUVEC proliferation in the presence of growth factors. Data represents mean ± standard deviation of the mean. HUVEC proliferation was significantly inhibited by free doxorubicin, while it was inhibited to a lesser extent by doxorubicin derivatives.

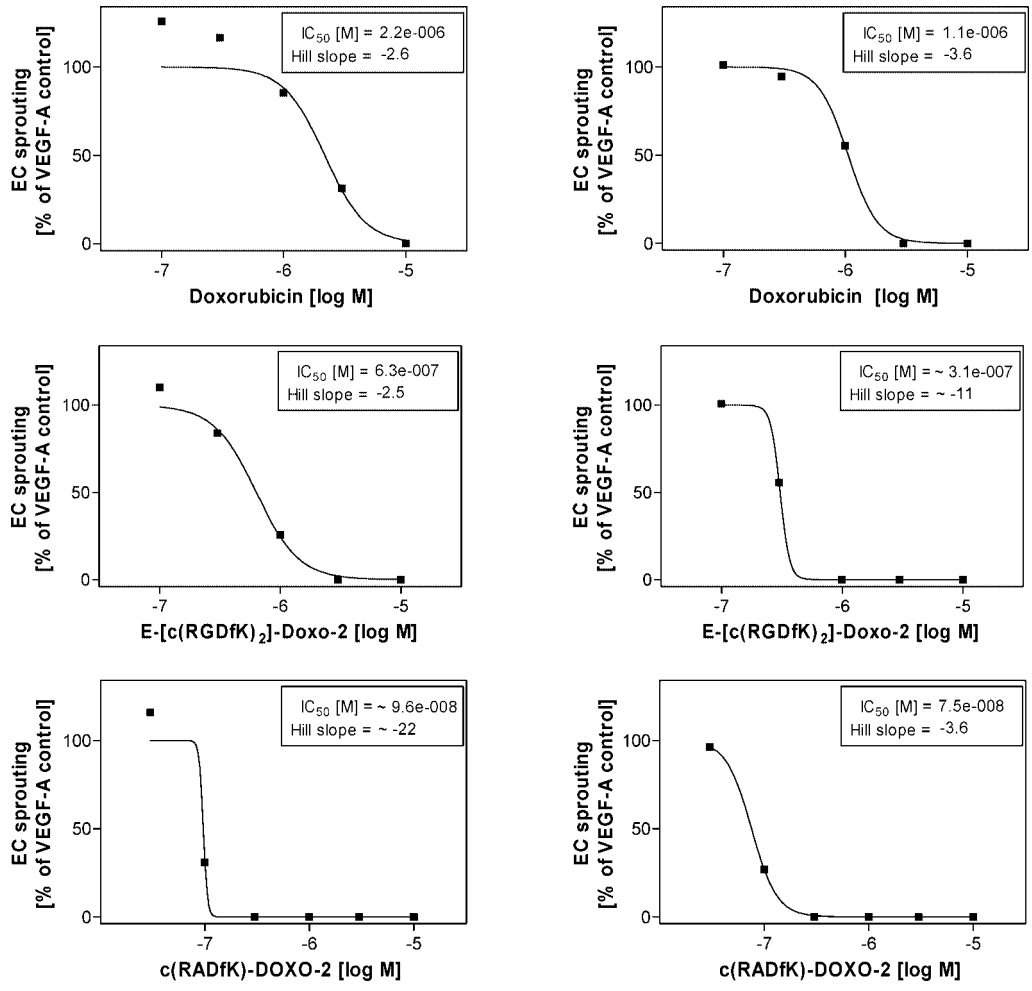

Figure 7. 3D spheroid-based angiogenesis assay. HUVEC spheroids were embedded in a 3D collagen gel, stimulated with VEGF-A [25 ng/mL], and treated for 24 h with different concentrations of doxorubicin, E-[c(RGDfK)$_2$]-DOXO-2, and c(RADfK)-DOXO-2 (in [log *M*], as indicated). The cumulative sprout length of 10 randomly selected spheroids per data point was analyzed and the relative inhibition by the test compounds determined. Two independent experiments were performed. Fitting of IC_{50} curves and calculation of IC_{50} values was performed with *GraphPad Prism 5.01*. HUVEC sprouting was inhibited approximately 3.5-fold more strongly with E-[c(RGDfK)$_2$]-DOXO-2 [mean IC_{50} = 470 nM] and approximately 20-fold stronger with c(RADfK)-DOXO-2 [mean IC_{50} = 86 nM] compared to doxorubicin [mean IC_{50} = 1700 nM].

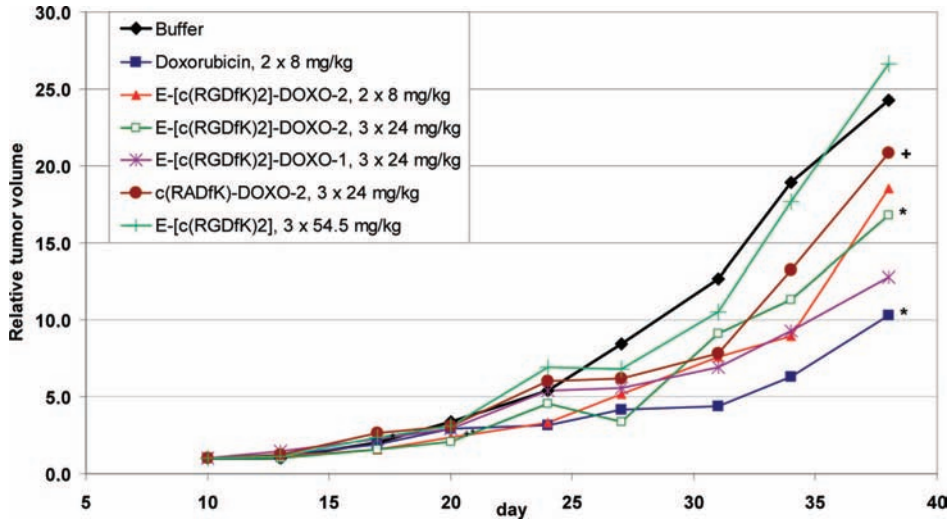

Figure 8. Curves depicting tumor growth inhibition of subcutaneously OVCAR-3 xenografts under therapy with RGD- and RAD-doxorubicin derivatives, doxorubicin, and E-[c(RGDfK)$_2$]; * significant to control; + significant to doxorubicin $p < 0.05$.

Table 1. Dose Schedule, Mortality, Body Weight Change, and Antitumor Activity of RGD- and RAD-Doxorubicin Derivatives, Doxorubicin, and E-[c(RGDfK)$_2$] against Human Ovarian Cancer Xenografts (OVCAR-3) *in Vivo*

substance	nu/nu mice	treatment (d)	dose (mg/kg/inj.)	toxic deaths (d)	BWC (%) d 10−17	optimum T/C (%) [at day]
5% Glucose-P-Buffer	8	10, 17, 24			−2	
Doxorubicin	6	10, 17	8	0	−2	33 [34][a]
E-[c(RGDfK)$_2$]-DOXO-2	6	10, 17	8	0	−3	47 [34]
E-[c(RGDfK)$_2$]-DOXO-2	6	10, 17, 24	24	1 (25)	−2	40 [27][a]
c(RADfK)-DOXO-2	6	10, 17, 24	24	3 (18, 18, 25)	−2	49 [34]
E-[c(RGDfK)$_2$]-DOXO-1	6	10, 17, 24	24	3 (18, 25, 25)	−1	70 [34][b]
E-[c(RGDfK)$_2$]	6	10, 17, 24	54, 5	0	0	80 [27]

[a] Significant to control. [b] Significant to doxorubicin $p < 0.05$.

Subsequent cleavage studies of E-[c(RGDfK)$_2$]-DOXO-2 were carried out following a modified method of Mansour et al. (*18*). The octapeptide Gly-Pro-Leu-Gly-Ile-Ala-Gly-Gln in **2** is specifically cleaved by MMP-2 and MMP-9 releasing the doxorubicin-tetrapeptide Ile-Ala-Gly-Gln-DOXO as previously shown (*18, 29*). Incubation studies of E-[c(RGDfK)$_2$]-DOXO-2 with activated MMP-2 showed a major peak at 27 min for E-[c(RGDfK)$_2$]-DOXO-2 min in the HPLC chromatogram after 5 min incubation time which decreased with time and an unidentified peak at 18 min (Figure 4). Furthermore, a peak at 13 min was observed which increased during 3 h and which we assigned as Ile-Ala-Gly-Gln-DOXO by comparison with our data from refs (*18, 29*). In OVCAR-3 tumor homogenates, the major cleavage product was doxorubicin after 75 min incubation (Figure 5). Identification of doxorubicin as the cleavage product was verified with a doxorubicin standard and spiking with doxorubicin in the cleavage experiment. In contrast, no release of doxorubicin was observed for E-[c(RGDfK)$_2$]-DOXO-1 in OVCAR-3 tumor homogenates (data not shown).

***In Vitro* Activity.** *Endothelial Cell Proliferation and Sprouting Is Inhibited by Doxorubicin-Containing RGD Peptides.* The effect of doxorubicin, and the doxorubicin derivatives E-[c(RGDfK)$_2$]-DOXO-1, E-[c(RGDfK)$_2$]-DOXO-2, c(RADfK)-DOXO-1, and c(RADfK)-DOXO-2 on endothelial cells was tested in two independent assays. First, the ability of doxorubicin derivatives to inhibit HUVEC proliferation was assessed using a standard 72 h proliferation assay. Free doxorubicin inhibited HUVEC proliferation more efficiently than the four peptide-containing doxorubicin derivatives, demonstrating an IC_{50} value of 700 fM compared to 20 nM for E-[c(RGDfK)$_2$]-DOXO-1, 3 nM for E-[c(RGDfK)$_2$]-DOXO-2, 30 nM for c(RADfK)-DOXO-1, and 5 nM for c(RADfK)-DOXO-2 (Figure 6). The E-[c(RGDfK)$_2$] peptide inhibited HUVEC proliferation by itself but only at high concentrations of 100−1000 nM. c(RADfK) peptide showed no effect even at those high concentrations (data not shown).

In a second assay, HUVEC spheroids were embedded in a 3D collagen gel, stimulated with VEGF-A, and treated for 24 h with different concentrations of doxorubicin, E-[c(RGDfK)$_2$]-DOXO-2, and c(RADfK)-DOXO-2 (in [log *M*], as indicated). As shown in Figure 7, HUVEC sprouting was inhibited ~3.5-fold stronger with E-[c(RGDfK)$_2$]-DOXO-2 [mean IC_{50} = 470 nM] and ~20-fold stronger with c(RADfK)-DOXO-2 [mean IC_{50} = 86 nM] compared to doxorubicin [mean IC_{50} = 1700 nM]. In contrast, the free peptides E-[c(RGDfK)$_2$] and c(RADfK) as well as the stable doxorubicin amide derivatives E-[c(RGDfK)$_2$]-DOXO-1 and c(RADfK)-DOXO-1 showed no activity at the highest concentration of ~10 000 nM (data not shown).

***In Vivo* Activity.** Subsequently, the *in vivo* antitumor efficacy of E-[c(RGDfK)$_2$], doxorubicin, and the doxorubicin derivatives E-[c(RGDfK)$_2$]-DOXO-1, E-[c(RGDfK)$_2$]-DOXO-2, and c(RADfK)-DOXO-2 was evaluated in xenografted nu/nu mice (human ovarian carcinoma OVCAR-3), this model being chosen because Janssen et al. showed a high uptake of radiolabeled E-[c(RGDfK)$_2$] of up to 7.5% ID/g in subcutaneously growing OVCAR-3 tumors (*11*).

Based on an orientating toxicity study with E-[c(RGDfK)$_2$]-DOXO-2 that showed a maximum tolerated dose (MTD) of 24 mg/kg doxorubicin equivalents, the following doses were chosen: doxorubicin (2 × 8 mg/kg), E-[c(RGDfK)$_2$]-DOXO-1 (3 × 24 mg/kg doxorubicin equivalents), E-[c(RGDfK)$_2$]-DOXO-2 (2 × 8 mg/kg, and 3 × 24 mg/kg doxorubicin equivalents), c(RADfK)-DOXO-2 (3 × 24 mg/kg doxorubicin equivalents), and E-[c(RGDfK)$_2$] (3 × 54.5 mg/kg, corresponding to the amount present in 3 × 24 mg/kg E-[c(RGDfK)$_2$]-DOXO-2) (Table 1). The results of the xenograft experiment are summarized in Table 1 and Figure 8. Treatment with

doxorubicin resulted in a moderate, but statistically significant, antitumor effect at its optimal dose in nu/nu mice models of 2 × 8 mg/kg (T/C max. 33%). In contrast, the free peptide E-[c(RGDfK)$_2$] and the stable amide derivative E-[c(RGDfK)$_2$]-DOXO-1 were inactive, with the latter also being toxic with a mortality of 50%. The prodrug E-[c(RGDfK)$_2$]-DOXO-2 at 2 × 8 mg/kg and 3 × 24 mg/kg showed a very moderate inhibition of tumor growth, which was statistically significant versus control only for the high-dose group. One animal died in this group. The prodrug c(RADfK)-DOXO-2 with the nonintegrin $\alpha_v\beta_3$ binding control peptide showed a high mortality at 3 × 24 m/kg and doxorubicin equivalents (50%). The remaining three animals showed a slightly better antitumor efficacy than the five animals treated with E-[c(RGDfK)$_2$]-DOXO-2, although this antitumor effect was not statistically significant compared to the control.

DISCUSSION

Integrins, especially integrin $\alpha_v\beta_3$, have served as an attractive target for designing drug delivery systems ranging from RGD-based liposomes (*30*, *31*), protein (*32*) or polymer conjugates (*33*), and nanoparticles (*34*).

A key result in this field was the discovery of the divalent RGD-4C peptide using a phage-display library (*7*). Subsequent development and evaluation of doxorubicin conjugates with RGD-4C have, however, not resulted in a clear picture of the structural requirements that a doxorubicin RGD conjugate should have for effective *in vivo* vascular targeting. In this work, we therefore developed doxorubicin conjugates with the divalent RGD peptide, E-[c(RGDfK)$_2$], which is more stable than RGD-4C and meanwhile commercially available. Synthesis of the conjugates was achieved by thiolating the free amino group of E-[c(RGDfK)$_2$] or of the control peptide c(RADfK) and reacting the stable maleimide doxorubicin derivative **1** or a MMP-2 cleavable doxorubicin derivative **2** with the introduced thiol group yielding E-[c(RGDfK)$_2$]-DOXO-1 and E-[c(RGDfK)$_2$]-DOXO-2, c(RADfK)-DOXO-1, and c(RADfK)-DOXO-2. E-[c(RGDfK)$_2$]-DOXO-2 was effectively cleaved by MMP-2 and in OVCAR-3 tumor homogenates releasing a doxorubicin-tetrapeptide or doxorubicin as the final cleavage product demonstrating a clear prodrug nature for **2**. In contrast, E-[c(RGDfK)$_2$]-DOXO-1 was stable in OVCAR-3 tumor homogenates. In a cytotoxicity assay against HUVEC, E-[c(RGDfK)$_2$]-DOXO-1 and E-[c(RGDfK)$_2$]-DOXO-2 as well as their c(RADfK) analogues showed cytotoxicity in the low nanomolar range, the cytotoxicity being more dependent on the cleavability than the nature of the RGD peptide (Figure 6). Surprisingly, in a HUVEC sprouting assay the doxorubicin prodrug with the control peptide, c(RADfK)-DOXO-2, was more active than E-[c(RGDfK)$_2$]-DOXO-2 (Figure 7), whereas E-[c(RGDfK)$_2$]-DOXO-1 and c(RADfK)-DOXO-1 were inactive, indicating that interactions with other membrane-associated targets besides integrin $\alpha_v\beta_3$ could be important.

In vivo, neither doxorubicin conjugates with E-[c(RGDfK)$_2$] nor c(RADfK) showed convincing antitumor efficacy. This result is disappointing considering that much larger doses (3 × 24 mg/kg doxorubicin equivalents) than the MTD of doxorubicin in nu/nu mice models (2 × 8 mg/kg) were administered. In contrast, the albumin-binding prodrug **2** has shown superior efficacy compared to doxorubicin in a melanoma xenograft model (*18*). There are a number of reasons that could explain the lack of efficacy of our new conjugates: (1) The targeting potential of the new conjugates is insufficient, although this explanation does not seem likely considering the convincing evidence of tumor uptake that Janssen et al. has collected with radiolabeled E-[c(RGDfK)$_2$] in the OVCAR-3 xenograft model (*12*), the same that model that we used in our studies. (2) After binding of E-[c(RGDfK)$_2$] to endothelial cells, the doxorubicin conjugates are taken up rapidly by endocytosis that would prevent the cleavage of E-[c(RGDfK)$_2$]-DOXO-2 by the extracellular proteases MMP-2 and MMP-9. There are data supporting an internalization of RGD peptides in integrin $\alpha_v\beta_3$ expressing and nonexpressing melanoma cells by an integrin-independent fluid-phase endocytosis pathway (*35*). Our own investigations do not support cleavage of the MMP-2 cleavable octapeptide when tumor homogenates at pH 5.0 are used that preserve activity of lysosomal proteases (*36*). (3) The potency of doxorubicin is not sufficient for receptor targeting of integrin $\alpha_v\beta_3$. The interaction of E-[c(RGDfK)$_2$]-DOXO-2 with integrin might be limited due to an insufficient receptor density on endothelial cells or a rapid clearance of E-[c(RGDfK)$_2$]-DOXO-2 leading to low amounts of doxorubicin reaching endothelial cells. Thus, targeting of integrin $\alpha_v\beta_3$-expressing cells could be improved by using highly potent cytotoxic drugs in line with the clear trend of using such agents for the development of drug antibody conjugates that are designed for receptor or antigen targeting (*37*, *38*).

In our current work, we are addressing the nature of the enzymatically cleavable linker as well as the drug component on RGD-based drug conjugates.

ACKNOWLEDGMENT

The support of the Deutsche Forschungsgemeinschaft (DFG) is gratefully acknowledged. This study was supported by a Postdoctoral Fellowship (HMS) from the Israel Cancer Research Fund. This research was supported by The Israel Science Foundation (grant No. 1300/06) and the Igal Alon Fellowship (RSF).

Supporting Information Available: MALDI-TOF and ESI-TOF spectra of compound **1**, E-[c(RGDfK)$_2$]-DOXO-1, E-[c(RGDfK)$_2$]-DOXO-2, c(RADfK)-DOXO-1, and c(RADfK)-DOXO-2.This material is available free of charge via the Internet at http://pubs.acs.org.

LITERATURE CITED

(1) Maier, J. A., Delia, D., Thorpe, P. E., and Gasparini, G. (1997) In vitro inhibition of endothelial cell growth by the antiangiogenic drug AGM-1470 (TNP-470) and the anti-endoglin antibody TEC-11. *Anticancer Drugs 8*, 238–244.

(2) Neri, D., and Bicknell, R. (2005) Tumour vascular targeting. *Nat. Rev. Cancer 5*, 436–446.

(3) Ruoslahti, E. (2002) Drug targeting to specific vascular sites. *Drug Discovery Today 7*, 1138–1143.

(4) Satchi-Fainaro, R. (2002) Targeting tumor vasculature: reality or a dream? *J. Drug Targeting 10*, 529–533.

(5) Temming, K., Schiffelers, R. M., Molema, G., and Kok, R. J. (2005) RGD-based strategies for selective delivery of therapeutics and imaging agents to the tumour vasculature. *Drug Resist. Update 8*, 381–402.

(6) Pasqualini, R., Koivunen, E., and Ruoslahti, E. (1997) Alpha v integrins as receptors for tumor targeting by circulating ligands. *Nat. Biotechnol. 15*, 542–546.

(7) Arap, W., Pasqualini, R., and Ruoslahti, E. (1998) Cancer treatment by targeted drug delivery to tumor vasculature in a mouse model. *Science 279*, 377–380.

(8) Kim, J. W., and Lee, H. S. (2004) Tumor targeting by doxorubicin-RGD-4C peptide conjugate in an orthotopic mouse hepatoma model. *Int. J. Mol. Med. 14*, 529–535.

(9) de Groot, F. M., Broxterman, H. J., Adams, H. P., van Vliet, A., Tesser, G. I., Elderkamp, Y. W., Schraa, A. J., Kok, R. J., Molema, G., Pinedo, H. M., and Scheeren, H. W. (2002) Design, synthesis, and biological evaluation of a dual tumor-specific motive containing integrin-targeted plasmin-cleavable doxorubicin prodrug. *Mol. Cancer Ther. 1*, 901–911.

(10) Haubner, H., Gratias, R., Diefenbach, B., Goodman, S. L., Jonczyk, A., and Kessler, H. (1996) Structural and functional aspects of RGD-containing cyclic pentapeptides as highly potent and selective integrin alpha(v)beta(3) antagonists. *J. Am. Chem. Soc. 118*, 7461–7472.

(11) Janssen, M., Oyen, W. J., Massuger, L. F., Frielink, C., Dijkgraaf, I., Edwards, D. S., Radjopadhye, M., Corstens, F. H., and Boerman, O. C. (2002) Comparison of a monomeric and dimeric radiolabeled RGD-peptide for tumor targeting. *Cancer Biother. Radiopharm. 17*, 641–646.

(12) Janssen, M. L., Oyen, W. J., Dijkgraaf, I., Massuger, L. F., Frielink, C., Edwards, D. S., Rajopadhye, M., Boonstra, H., Corstens, F. H., and Boerman, O. C. (2002) Tumor targeting with radiolabeled alpha(v)beta(3) integrin binding peptides in a nude mouse model. *Cancer Res. 62*, 6146–6151.

(13) Janssen, M., Frielink, C., Dijkgraaf, I., Oyen, W., Edwards, D. S., Liu, S., Rajopadhye, M., Massuger, L., Corstens, F., and Boerman, O. (2004) Improved tumor targeting of radiolabeled RGD peptides using rapid dose fractionation. *Cancer Biother. Radiopharm. 19*, 399–404.

(14) Burkhart, D. J., Kalet, B. T., Coleman, M. P., Post, G. C., and Koch, T. H. (2004) Doxorubicin-formaldehyde conjugates targeting alphavbeta3 integrin. *Mol. Cancer Ther. 3*, 1593–1604.

(15) Deryugina, E. I., Ratnikov, B., Monosov, E., Postnova, T. I., DiScipio, R., Smith, J. W., and Strongin, A. Y. (2001) MT1-MMP initiates activation of pro-MMP-2 and integrin alphavbeta3 promotes maturation of MMP-2 in breast carcinoma cells. *Exp. Cell Res. 263*, 209–223.

(16) Deryugina, E. I., and Quigley, J. P. (2006) Matrix metalloproteinases and tumor metastasis. *Cancer Metastasis Rev. 25*, 9–34.

(17) Rolli, M., Fransvea, E., Pilch, J., Saven, A., and Felding-Habermann, B. (2003) Activated integrin alphavbeta3 cooperates with metalloproteinase MMP-9 in regulating migration of metastatic breast cancer cells. *Proc. Natl. Acad. Sci. U.S.A. 100*, 9482–9487.

(18) Mansour, A. M., Drevs, J., Esser, N., Hamada, F. M., Badary, O. A., Unger, C., Fichtner, I., and Kratz, F. (2003) A new approach for the treatment of malignant melanoma: enhanced antitumor efficacy of an albumin-binding doxorubicin prodrug that is cleaved by matrix metalloproteinase 2. *Cancer Res. 63*, 4062–4066.

(19) Kussmann, M., Lässing, U., Stürmer, C. A., Przybylski, M., and Roepstorff, P. (1997) Matrix-assisted laser desorption/ionization mass spectrometric peptide mapping of the neural cell adhesion protein neurolin purified by sodium dodecyl sulfate polyacrylamide gel electrophoresis or acidic precipitation. *J. Mass Spectrom. 32*, 483–493.

(20) Korff, T., and Augustin, H. G. (1998) Integration of endothelial cells in multicellular spheroids prevents apoptosis and induces differentiation. *J. Cell Biol. 143*, 1341–1352.

(21) Korff, T., and Augustin, H. G. (1999) Tensional forces in fibrillar extracellular matrices control directional capillary sprouting. *J. Cell Sci. 112* (Pt 19), 3249–3258.

(22) Schmid, B., Chung, D. E., Warnecke, A., Fichtner, I., and Kratz, F. (2007) Albumin-binding prodrugs of camptothecin and doxorubicin with an Ala-Leu-Ala-Leu-linker that are cleaved by cathepsin B: synthesis and antitumor efficacy. *Bioconjugate Chem. 18*, 702–16.

(23) Schmid, B., Warnecke, A., Fichtner, I., Jung, M., and Kratz, F. (2007) Development of albumin-binding camptothecin prodrugs using a Peptide positional scanning library. *Bioconjugate Chem. 18*, 1786–99.

(24) Kratz, F., Warnecke, A., Scheuermann, K., Stockmar, C., Schwab, J., Lazar, P., Drückes, P., Esser, N., Drevs, J., Rognan, D., Bissantz, C., Hinderling, C., Folkers, G., Fichtner, I., and Unger, C. (2002) Probing the cysteine-34 position of endogenous serum albumin with thiol-binding doxorubicin derivatives: improved efficacy of an acid-sensitive doxorubicin derivative with specific albumin-binding properties compared to that of the parent compound. *J. Med. Chem. 45*, 5523–5533.

(25) Kratz, F. (2007) DOXO-EMCH (INNO-206): the first albumin-binding prodrug of doxorubicin to enter clinical trials. *Expert Opin. Invest. Drugs 16*, 855–866.

(26) Kratz, F., Mansour, A., Soltau, J., Warnecke, A., Fichtner, I., Unger, C., and Drevs, J. (2005) Development of albumin-binding doxorubicin prodrugs that are cleaved by prostate-specific antigen. *Arch. Pharm. (Weinheim) 338*, 462–472.

(27) Warnecke, A., Fichtner, I., Garmann, D., Jaehde, U., and Kratz, F. (2004) Synthesis and biological activity of water-soluble maleimide derivatives of the anticancer drug carboplatin designed as albumin-binding prodrugs. *Bioconjugate Chem. 15*, 1349–1359.

(28) Warnecke, A., and Kratz, F. (2003) Maleimide-oligo(ethylene glycol) derivatives of camptothecin as albumin-binding prodrugs: synthesis and antitumor efficacy. *Bioconjugate Chem. 14*, 377–387.

(29) Kratz, F., Drevs, J., Bing, G., Stockmar, C., Scheuermann, K., Lazar, P., and Unger, C. (2001) Development and in vitro efficacy of novel MMP2 and MMP9 specific doxorubicin albumin conjugates. *Bioorg. Med. Chem. Lett. 11*, 2001–2006.

(30) Schiffelers, R. M., Molema, G., ten Hagen, T. L., Janssen, A. P., Schraa, A. J., Kok, R. J., Koning, G. A., and Storm, G. (2002) Ligand-targeted liposomes directed against pathological vasculature. *J. Liposome Res. 12*, 129–135.

(31) Xiong, X. B., Huang, Y., Lu, W. L., Zhang, X., Zhang, H., Nagai, T., and Zhang, Q. (2005) Enhanced intracellular delivery and improved antitumor efficacy of doxorubicin by sterically stabilized liposomes modified with a synthetic RGD mimetic. *J. Controlled Release 107*, 262–275.

(32) Temming, K., Meyer, D. L., Zabinski, R., Senter, P. D., Poelstra, K., Molema, G., and Kok, R. J. (2007) Improved efficacy of alphavbeta3-targeted albumin conjugates by conjugation of a novel auristatin derivative. *Mol. Pharm. 4*, 686–694.

(33) Mitra, A., Coleman, T., Borgman, M., Nan, A., Ghandehari, H., and Line, B. R. (2006) Polymeric conjugates of mono- and bi-cyclic alphaVbeta3 binding peptides for tumor targeting. *J. Controlled Release 114*, 175–183.

(34) Xie, J., Shen, Z., Li, K. C., and Danthi, N. (2007) Tumor angiogenic endothelial cell targeting by a novel integrin-targeted nanoparticle. *J. Nanomedicine 2*, 479–485.

(35) Castel, S., Pagan, R., Mitjans, F., Piulats, J., Goodman, S., Jonczyk, A., Huber, F., Vilaró, S., and Reina, M. (2001) RGD peptides and monoclonal antibodies, antagonists of alpha(v)-integrin, enter the cells by independent endocytic pathways. *Lab. Invest. 81*, 1615–1626.

(36) Werle, B., Ebert, W., Klein, W., and Spiess, E. (1994) Cathepsin B in tumors, normal tissue and isolated cells from the human lung. *Anticancer Res. 14*, 1169–1176.

(37) Kratz, F., Müller, I. A., Ryppa, C., and Warnecke, A. (2008) Prodrug strategies in anticancer chemotherapy. *ChemMedChem 3*, 20–53.

(38) Wu, A. W., and Senter, P. D. (2005) Arming antibodies. *Nat. Biotechnol. 23*, 1137–1146.

BC800117R

Synthesis and Characterization of Star Poly(ε-caprolactone)-*b*-Poly(ethylene glycol) and Poly(L-lactide)-*b*-Poly(ethylene glycol) Copolymers: Evaluation as Drug Delivery Carriers

Fei Wang,*,† Tatiana K. Bronich,‡ Alexander V. Kabanov,‡ R. David Rauh,† and Jacques Roovers§

EIC Laboratories, Incorporated, 111 Downey Street, Norwood, Massachusetts 02062, and Department of Pharmaceutical Science, University of Nebraska Medical Center, 986025 University Medical Center, Omaha, Nebraska 68198-6025. Received November 20, 2007; Revised Manuscript Received May 22, 2008

Two types of 32 arm star polymers incorporating amphiphilic block copolymer arms have been synthesized and characterized. The first type, stPCL-PEG_{32}, is composed of a polyamidoamine (PAMAM) dendrimer as the core with radiating arms having poly(ε-caprolactone) (PCL) as an inner lipophilic block in the arm and poly(ethylene glycol) (PEG) as an outer hydrophilic block. The second type, stPLA-PEG_{32}, is similar but with poly(L-lactide) (PLA) as the inner lipophilic block. Characterization with SEC, ^{1}H NMR, FTIR, and DSC confirmed the structure of the polymers. Micelle formation by both star copolymers was studied by fluorescence spectroscopy. The stPCL-PEG_{32} polymer exhibited unimolecular micelle behavior. It was capable of solubilizing hydrophobic molecules, such as pyrene, in aqueous solution, while not displaying a critical micelle concentration. In contrast, the association behavior of stPLA-PEG_{32} in aqueous solution was characterized by an apparent critical micelle concentration of ca. 0.01 mg/mL. The hydrophobic anticancer drug etoposide can be encapsulated in the micelles formed from both polymers. Overall, the stPCL-PEG_{32} polymer exhibited a higher etoposide loading capacity (up to 7.8 w/w % versus 4.3 w/w % for stPLA-PEG_{32}) as well as facile release kinetics and is more suitable as a potential drug delivery carrier.

INTRODUCTION

Micelles formed from amphiphilic block copolymers have recently attracted significant attention in diverse fields of medicine and biology. In particular, polymeric micelles have been developed as drug and gene delivery systems (*1*–*3*) as well as carriers for various contrast agents in diagnostic imaging applications (*4*). In an aqueous environment, the hydrophobic blocks of the copolymer are expected to segregate into the core of the micelle, while the hydrophilic blocks form the corona or outer shell. Such a core−shell architecture is essential for the utility of the polymeric micelles as functional materials for pharmaceutical applications. The hydrophobic micelle core serves as a microenvironment for the incorporation of various therapeutic compounds, while the corona, the outer shell, serves as a stabilizing interface between the hydrophobic core and the external medium. As a result, polymeric micelles can be used as effective "nanocontainers" for reagents with poor solubility and/or low stability in physiological environments (*5*, *6*). Interest in polymeric micelles for drug delivery has increased rapidly since the late 1980s (*7*). Most of the work has focused on classical micelles formed by intermolecular aggregation of amphiphilic block copolymers as the drug delivery vehicle, and the advantages of using their micelle structures as drug delivery systems have been demonstrated (*8*, *9*).

The major factors that influence the performance of polymeric micelles for drug delivery are loading capacity, release kinetics, circulation time, biodistribution, size, stability, and stability on dilution (*2*). One of the approaches to improve the micelles' stability is to develop star-shaped molecules in which the lipophilic components are covalently bound together within the micelle core. Core polymerization is an effective method to prevent dissociation of the block copolymer micelle. Kataoka's group has successfully employed this idea (*10*). In their study, the micelles were prepared from an amphiphilic block copolymer in which the hydrophobic block contained a polymerizable end group. After micellation, the end groups on the hydrophobic block were polymerized to form a stable core for the star-shaped polymer structure. The resulting micelles showed fairly high stability and maintained their small size. As anticipated, the core-polymerized micelle showed excellent solubilization of rather large molecules such as taxol (*11*). Another approach was reported by Uhrich et al. (*12*) with a star-shaped polymer composed of mucic acid substituted with a fatty acid as the lipophilic inner block and PEG as the hydrophilic outer block. This new type of molecule was capable of encapsulating a hydrophobic model drug in aqueous media.

The increased interest in amphiphilic star polymers for drug delivery has been demonstrated by several more recent publications. One paper (*13*) described the synthesis of a 4 arm star block copolymer of PCL and PEG using chemistry similar to that reported in this manuscript. Another report (*14*) described the preparation of a 4 arm star PCL-b-PEG polymer using a diethyl zinc catalyst. However, the molecular weight distribution of the block copolymer was unacceptably wide. Allen et al. (*15*) described the synthesis of a 6 arm star poly(δ-valerolactone)-*b*-PEG copolymer via a cationic polymerization method using fumaric acid as a catalyst. The micelle formation and biocompatibility of the star copolymer were demonstrated.

In a previous report (*16*), we described the synthesis and characterization of a 16 arm star PCL-PEG copolymer. The star structure of the polymers was confirmed by several physicochemical methods. The micellar properties of the star amphiphilic polymer in aqueous media were characterized by

* To whom correspondence should be addressed. Phone: (781) 769-9450. Fax: (781) 551-0283. E-mail: feiwang@eiclabs.com.
† EIC Laboratories.
‡ University of Nebraska Medical Center.
§ 21 Wren Road, Ottawa, Ontario K1J 7H5, Canada.

10.1021/bc7004285 CCC: $40.75 © 2008 American Chemical Society
Published on Web 06/20/2008

fluorescence techniques and dynamic light scattering (DLS). A series of entrapment experiments showed that various drugs could be incorporated in such micelles. These results indicate that the star-PCL-PEG micelle system is a promising drug carrier for the delivery of lipophilic drugs. The aggregation from unimolecular micelles into larger associated micelles was observed by DLS and pyrene fluorescence studies. It is likely that the 16 arm star polymer forms a relatively loose outer PEG shell, which is not sufficient to hinder the intermolecular association of the inner hydrophobic PCL blocks. It is expected that more stable unimolecular micelles may be obtainable by increasing the number of block copolymer arms. It has been demonstrated that when the number of arms reaches 64, star polymers exhibit characteristics of a hard sphere, and the repulsion between the star molecules becomes much stronger (*17*).

In this paper, we describe the synthesis and characterization of two types of 32 arm star polymers composed of amphiphilic block copolymer arms. The first type, stPCL-PEG_{32}, is composed of a polyamidoamine (PAMAM) dendrimer as the core with radiating arms having poly(ε-caprolactone) (PCL) as an inner lipophilic block in the arm and poly(ethylene glycol) (PEG) as an outer hydrophilic block. The second type, stPLA-PEG_{32}, is similar but with poly(L-lactide) (PLA) as the inner lipophilic block. The micelle formation of both star copolymers was studied by fluorescence spectroscopy. The affinity of the star polymer micelles for solubilizing small hydrophobic molecules was assessed by determining the aqueous partition coefficient of the lipophilic fluorescence probe pyrene. Finally, solubilization of the anticancer drug etoposide into the 32 arm star polymer micelles was studied to evaluate the relevance of such systems for drug delivery.

EXPERIMENTAL SECTION

Materials and Methods. PEG (M_n = 5000) with methoxy and carboxymethyl terminal groups was used as received from Nektar. ε-Caprolactone from Sigma-Aldrich was dried by stirring with CaH_2 and distilled before use. L-Lactide was from Lancaster and was recrystallized twice from ethyl acetate before use. Dichloromethane was dried by stirring over and distilling from P_2O_5. All other reagents and solvents were used as received from Sigma-Aldrich.

^{1}H NMR spectra were recorded on a Hitachi R-1500 FT-NMR spectrometer at 60 MHz. Infrared spectra were recorded on a Nicolet 750 FTIR spectrometer. UV−vis spectra were recorded on a HP 8452A UV−vis diode array spectrophotometer. Size exclusion chromatography (SEC) was used to determine the molecular weights, polydispersity, and degree of branching of the synthesized polymers. SEC measurements were conducted using a Hewlett-Packard series 1050 HPLC equipped with one Polymer Laboratories PL gel 5 μ mixed-D column and a Hewlett-Packard 1047A refractive index detector as well as Viscotek T60 light scattering (LS) and viscosity detectors. Tetrahydrofuran was used as the eluting solvent at a flow rate of 1 mL/min. Data analysis was performed using Viscotek Trisec GPC software version 3.0.

The thermal transitions of the polymers were determined using a Perkin-Elmer DSC7 differential scanning calorimeter under nitrogen purge. The samples were heated and cooled at a rate of 10 °C/min.

Synthesis of the 32 Arm Star-PCL Polymer (stPCL_{32}). A 100 mL three-neck flask equipped with a condenser and argon gas inlet was charged with PAMAM-OH Dendrimer Generation 3 with 32 terminal OH groups (20 wt % solution in methanol, 5.26 g, 0.151 mmol). Methanol was then removed under vacuum. A predetermined amount of ε-caprolactone (14.42 g, 126 mmol) followed by 15 mL toluene were added into the reaction flask. The mixture was heated to reflux using a Dean−Stark trap for 30 min, and the toluene was distilled off. The heating of the reaction mixture up to 145 °C resulted in the dissolution of the dendrimer in ε-caprolactone. After cooling the reaction mixture to 130 °C, 5 mg (0.012 mmol) of tin(II) 2-ethylhexanoate ($Sn(Oct)_2$) was introduced, followed by stirring at 115−120 °C for 20 h. The reaction mixture was cooled to room temperature, dissolved in THF, and precipitated into cold methanol. After drying, 15.3 g (99% yield) of the white solid product was obtained. The polymer was further purified by fractionation. 3.6 g of polymer was dissolved in 70 mL of THF in a round-bottom flask, and methanol was added until the solution became cloudy. The solution was heated in a water bath at 60 °C and became clear. About 10 mL of methanol was added to reach a cloudy point, and the mixture was transferred into a hot separation funnel and allowed to stand at room temperature for three days. The polymer solution separated into two layers, and the top layer was removed without disturbing the lower layer. The lower layer was diluted with THF and precipitated into cold methanol. 2.76 g of polymer was obtained. ^{1}H NMR ($CDCl_3$): δ = 4.07 (t, 2H, OCH_2), 2.31 (t, 2H, $COCH_2$), 1.1−2 (m, 6H, $(CH_2)_3$). The characteristic peaks of dendrimer and polymer were overlapping, and peak integration was inconclusive.

Synthesis of the 32 Arm Star-PCL-PEG Polymer (stPCL-PEG_{32}). The $stPCL_{32}$ (1.3 g, 0.0152 mmol), PEG (2.64 g, 0.527 mmol), and 4-(dimethylamino)pyridinium 4-toluenesulfonate (DPTS) (0.155 g, 0.527 mmol) were dissolved in 80 mL of dry CH_2Cl_2 by stirring at room temperature. Then diisopropylcarbodiimide (DIPC) (0.2 g, 1.58 mmol) was added into the reaction mixture via syringe. The reaction mixture was stirred overnight at room temperature. An additional amount of DIPC (0.15 g) was added to the reaction mixture followed by stirring for a total of 7 days. The reaction was stopped, and fractionation was used to purify the Star-PCL-PEG. Briefly, 20 mL CH_2Cl_2 was added to dilute the product. Hexane was slowly added to the resulting solution at a water bath of 45 °C until the appearance of cloudiness. Then the mixture was transferred into a hot separation funnel and was allowed to stand at room temperature. The top layer was removed, and the lower layer refractionated by the same procedure. Finally, the lower layer was diluted with CH_2Cl_2 and precipitated into hexane. After drying, 3.1 g (83% yield) of white solid product was obtained. ^{1}H NMR ($CDCl_3$): δ = 4.07 (t, 2H, $COOCH_2$), 3.64 (s, 18.8H, OCH_2CH_2O), 2.31 (t, 2H, $COCH_2$), 1.1−1.9 (m, 6H, $(CH_2)_3$).

Synthesis of the 32 Arm Star-PLA polymer (stPLA_{32}). A 100 mL three-neck flask equipped with a condenser and argon gas inlet was charged with PAMAM-OH Dendrimer Generation 3 (20 wt % solution in methanol, 5.26 g, 0.151 mmol). Methanol was then removed under vacuum. A predetermined amount of L-lactide (14.71 g, 102 mmol) followed by 15 mL toluene was added into the reaction flask. The mixture was heated to reflux using a Dean−Stark trap for 30 min and toluene was distilled off. Heating of the reaction mixture up to 135 °C resulted in the dissolution of the dendrimer in L-lactide. After cooling the reaction mixture to 125 °C, 5 mg (0.012 mmol) of $Sn(Oct)_2$ was introduced, followed by stirring at 105 °C for 20 h. The reaction mixture was cooled to room temperature, dissolved in THF, and precipitated into cold methanol. After drying, 15.4 g (97% yield) of the white solid product was obtained. SEC analysis indicated that there were some low molecular weight impurities mixed with the star polymer. The polymer was further purified by fractionation using THF as the solvent and methanol as the nonsolvent. However, after repeated trials, including the use of chloroform as the solvent, the fractionation was found to be unsuccessful. Low molecular weight materials remained in the star polymer. ^{1}H NMR ($CDCl_3$): δ = 5.17 (q, 1H,

-CH(CH_3)-), 1.57 (d, 3H, CH_3). The characteristic peaks of the dendrimer were too broad and integration was inconclusive.

Synthesis of the 32 Arm Star-PLA-PEG Polymer (stPLA-PEG$_{32}$). The stPLA$_{32}$ (1.2 g, 0.0141 mmol), PEG (2.6 g, 0.52 mmol), and DPTS (0.155 g, 0.527 mmol) were dissolved in 80 mL of dry CH_2Cl_2 by stirring at room temperature. Then DIPC (0.2 g, 1.58 mmol) was added into the reaction mixture via syringe. The reaction mixture was stirred overnight at room temperature. An additional amount of DIPC (0.15 g) was added to the reaction mixture followed by stirring for total of 7 days. The product was purified by fractionation twice with CH_2Cl_2 as the solvent and hexane as the nonsolvent. After workup and drying, 2.53 g (72% yield) of white solid product was obtained. ^{1}H NMR ($CDCl_3$): $\delta = 5.18$ (q, 1H, -C**H**(CH_3)-), 3.64 (s, 12.6H, OCH_2CH_2O), 1.58 (d, 3H, -CH_3).

Synthesis of Linear-PLA (l-PLA). A linear PLA was synthesized in a similar procedure using L-lactide (5.1 g, 35.4 mmol), di(ethylene glycol) benzyl ether (0.05 g, 0.25 mmol) as an initiator, and two drops of Sn(Oct)$_2$. Isolation was conducted with the same procedure as described previously. After drying, 4.8 g (95% yield) of the white solid product was obtained.

Preparation of Polymer Micelles. Aqueous dispersions of stPCL-PEG$_{32}$ and stPLA-PEG$_{32}$ were prepared using the dialysis technique. Initially, the copolymer was dissolved in *N*,*N*-dimethylformamide (DMF) at polymer concentrations ranging from ~100−200 mg/mL. Next, distilled water was added to the mixture dropwise in a very slow fashion (25 μL of water per 2−3 min) until the desired water content was achieved (67−87.5 vol %). Finally, the water−organic mixture was dialyzed against 3 L distilled water using Membra-Cel MD-25−03.5 membrane tubing. The water was changed every hour for the first 4 h and then every 4−6 h for the next two days. The concentration of the star copolymers after dialysis was determined gravimetrically.

Micelle Characterization. Dynamic laser light scattering (DLS) measurements on polymer micelles were carried out using a "ZetaPlus" Zeta Potential Analyzer (Brookhaven Instrument Co.) equipped with the Multi Angle Option and with a 30 mW solid state laser operated at a wavelength of 635 nm. The sizing measurements were performed at 25 °C at an angle of 90°. All solutions were filtered repeatedly through Millipore membranes with pore sizes of 0.45 and 0.22 μm prior to measurements. Software provided by the manufacturer was used to calculate the effective hydrodynamic diameters of the micelles. DLS measurements were also used to monitor the aggregation stability of micelle solutions. Consequently, size measurements were carried out every 2−3 days over a one month period. Steady-state fluorescence spectra were recorded using a Shimadzu RF5000U spectrofluorophotometer with a bandwidth of 2.5 nm for both excitation and emission. For fluorescence emission spectra, λ_{ex} was 336 nm, and for excitation spectra, λ_{em} was 390 nm. Negative staining was used for the transmission electron microscopy (TEM) studies. A drop of the filtered (0.22 μm filter) sample solution was allowed to settle on a Formvar precoated copper grid for one minute. Excess solution was wicked away with filter paper, and a drop of 1% uranyl acetate solution was allowed to contact the sample for one minute. The samples were studied using a Phillips 410LS electron microscope with a digital imaging camera. The diameters of the particles were determined using 127 measurements randomly collected from TEM images using the Image Pro program (Media Sybernetics).

Drug Encapsulation and Release. The two star copolymers with different lipophilic components were evaluated to determine which structure was more suitable for the delivery of etoposide. A micelle extraction method (*2*) was used to encapsulate etoposide into the 32 arm star polymer micelles. 100 μL of etoposide stock solution (20 mg/mL) in acetonitrile was added to the empty vial, and the solvent was evaporated to dryness. Then 1 mL of micelle solution was added to the vial and agitated for 2 days. The concentration of micelle solution was varied from 2 mg/mL to 15 mg/mL. The solution was centrifuged (5 min at 10 000 × *g*) to remove any insoluble drug. It should be noted that centrifugation of the polymer micelle solutions under these conditions did not change the polymer content in the supernatant. The etoposide concentration in the supernatant was determined by HPLC using a Shimadzu LC-10AT system equipped with a reverse-phase C18 column (4.6 mm × 15 cm), mobile phase: 25% (acetonitrile/1% acetic acid)/75% (water/1% acetic acid), flow rate at 1 mL/min, $T = 32$ °C. The detection of etoposide was performed by UV absorption at 230 nm.

The release of etoposide from the polymer micelles was evaluated by the dialysis method. The polymer micelles loaded with etoposide in phosphate buffered saline (PBS, pH 7.4, 0.14 M NaCl, 1 mL) were transferred to a dialysis bag (molecular weight cutoff 3500). The dialysis bag was immediately placed in 20 mL of PBS. At regular time intervals, 1 mL of release medium was sampled and replaced with an equal volume of PBS. The release experiments were performed at room temperature. The concentration of etoposide present in the dialysate was monitored using HPLC as described above.

RESULTS AND DISCUSSION

Synthesis of Star Copolymers. The synthesis of stPCL-PEG$_{32}$ was carried out following the synthetic scheme shown in Scheme 1. The expected PEG formula weight is 5000 D and the PCL formula weight is 3000 D, corresponding to $m = 26$. PAMAM-OH Dendrimer Generation 3 was used as the initiator core. Starting from this core, the star-PCL polymer with 32 arms was synthesized by the ring-opening polymerization of ε-caprolactone with Sn(Oct)$_2$ as the catalyst. The stPCL$_{32}$ product was obtained in almost quantitative yield. After two fractionations, the pure star polymer was obtained. Next, PEG polymers were attached to the stPCL$_{32}$ polymers using a commercial product from Nektar. The structure of this product is a PEG polymer (5000 D), with one end capped by a methoxy and the other end by a carboxylic acid group. The carboxylic acid endgroup on the PEG was esterified by the terminal hydroxyl groups in the stPCL$_{32}$ polymer to produce the desired final star polymer stPCL-PEG$_{32}$. Excess PEG polymer was used, and the reaction was allowed to continue for seven days. After the reaction was complete, the product was purified twice by fractionation to remove the excess PEG and other impurities. The final stPCL-PEG$_{32}$ polymer was obtained in 83% yield.

Using a similar approach, a 32-arm stPLA-PEG$_{32}$ was synthesized as shown in Scheme 1. Here, we started with a PAMAM-OH Dendrimer Generation 3 as the initiator to polymerize *l*-lactide, using Sn(Oct)$_2$ as a catalyst. Similar to the polymerization of ε-caprolactone, the reaction was well-controlled, and the final star-PLA polymer had an arm length determined by the feed ratio of monomer/initiator. The reaction yield was 97%. SEC analysis indicated that the star-PLA polymer contained some low molecular weight side products. Purification by fractionation was attempted but unsuccessful, possibly because of interfering crystallization (see DSC study below). The impure stPLA$_{32}$ polymer was therefore used in the next step, with the expectation that the low molecular weight side product will be removed when purifying the final product. The stPLA-PEG$_{32}$ polymer was prepared by the same esterification reaction described above. The stPLA-PEG$_{32}$ polymer was purified by two fractionations, and the yield was 72%. The low molecular weight impurity was completely removed, and pure stPLA-PEG$_{32}$ product was obtained.

To verify that L-lactide polymerization under Sn(Oct)$_2$ catalysis conditions can produce PLA with a narrow molecular

Scheme 1. Synthesis of Star Polymers

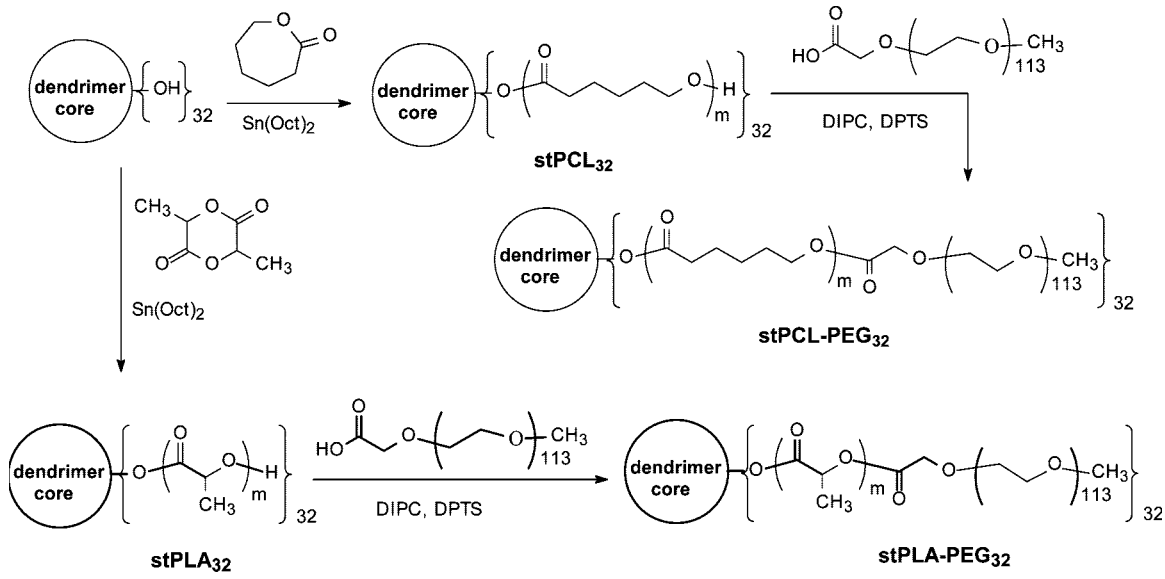

Table 1. SEC Results for the Polymers

	theoretical mol. wt	number-average mol. wt	weight-average mol. wt	polydispersity M_w/M_n
$stPCL_{32}$	102 900	89 200	92 600	1.04
$stPCL\text{-}PEG_{32}$	262 900	215 400	231 400	1.07
$stPLA_{32}$	102 900	80,500[a]	87,100[a]	1.08
$stPLA\text{-}PEG_{32}$	262 900	221 400	230 000	1.04
Linear-PLA	20 000	18 100	19 300	1.07

[a] When calculating the molecular weights, the integration was limited only to the major star polymer peak.

weight distribution, a linear PLA polymer was synthesized using di(ethylene glycol) benzyl ether as the initiator. The yield was 94%. SEC analysis confirmed that this linear-PLA polymer indeed has a very narrow molecular weight distribution (shown in Table 1).

Characterization of Star Polymers. Spectroscopic measurements confirmed the structures of the star polymer products. In the ^{1}H NMR spectrum of $stPCL_{32}$ (shown in Figure 1), four major peaks were observed: the triplet peak at 3.98 ppm is assigned as (-C***H***$_2$-O-) protons; the triplet at 2.23 ppm is assigned as (-C***H***$_2$-CO-) protons; the multiple peak at 1.57 ppm are the protons of (-O-CH_2-C***H***$_2$-CH_2-C***H***$_2$-CH_2-CO-); the multiple peak at 1.30 ppm are the protons in the middle. The peaks from the dendrimer core have a low intensity due to the low content. The small triplet peak at 3.58 ppm is assigned as the chain end terminal protons (-C***H***$_2$-OH). The integration ratio of this peak vs peaks at 3.98 ppm is used to estimate the degree of polymerization of the PCL polymer arms and was found to be about 1/26. This corresponds to a PCL block formula weight of about 3000 D. However, this estimation is based on the ratio of a very small terminal proton peak to a large polymer peak.

In the ^{1}H NMR spectrum of $stPCL\text{-}PEG_{32}$, in addition to the peaks from PCL, the single peak at 3.56 ppm is assigned as the (-O-CH_2CH_2-O-) of the PEG unit. The integration ratio between PEG and PCL reflects the component ratio in the block copolymers and is consistent with the SEC results. The ^{1}H NMR spectrum of $stPLA\text{-}PEG_{32}$ is consistent with the structure, with a quartet peak observed at 5.08 ppm due to the (-C***H***(CH_3)-) proton; a doublet at 1.49 ppm due to the (-CH(CH_3)-) protons; and single peak at 3.56 ppm due to the (-O-CH_2CH_2-O-) in the PEG unit.

The molecular weights of the synthesized polymers were determined by SEC and are summarized in Table 1. The system is equipped with refractive index, viscosity, and light scattering detectors. The combination of these three detectors can provide the absolute molecular weights of the star polymers. The polydispersity of the star polymers was narrow ($M_w/M_n < 1.08$). All the star polymer samples had relatively low intrinsic viscosities and small radii of gyration, confirming their highly branched, compact structure. As shown in Table 1, all of the polymers had lower molecular weights than the theoretical values. This may reflect some uncertainty in the SEC-LS method. There are two possible explanations for this: (1) the polymer arms are shorter than expected; (2) the number of star polymer arms is less than desired. Data from the ^{1}H NMR study indicate that the $stPCL_{32}$ product had an arm length close to the expected value of about 3K. However, as discussed before, such an estimation is not precise. Some OH-containing impurities exist in the system that initiate the polymerization of monomer, as is evident from the low molecular weight polymer impurities in the PCL and PLA stars. These low molecular weight impurities consume some of the monomers, which can result in star polymers with shorter arms than the theoretical value. The ^{1}H NMR analysis of $stPCL\text{-}PEG_{32}$ indicates that the PEG/PCL ratio is 1.81, higher than the theoretical 1.67. This excludes a deficiency in the esterification reaction. It is also possible that our batch of PAMAM-OH dendrimer had some defects, so that the number of surface -OH groups available for polymerization was less than 32. Therefore, both shorter arms and a reduced number of arms may contribute to the overall lower molecular weight of the final star polymer. The number of arms equal to 27.8 is derived from $[M_w(stPCL\text{-}PEG_{32}) - M_w(stPCL_{32})]/M_w(PEG)$. Similarly, for $stPLA\text{-}PEG_{32}$ the calculated number of arms is 28.6. Taking into account the various uncertainties, the estimated number of arms in these star polymers is in the range 26−30.

Thermal Behavior. The thermal properties of the polymers were investigated using differential scanning calorimetry (DSC) to determine the glass transition temperature (T_g) and melt temperature (T_m). For the $stPCL_{32}$ and $stPCL\text{-}PEG_{32}$ polymers, the thermal behavior was simple: $T_m = 50$ °C was observed for $stPCL_{32}$ and $T_m = 57$ °C for $stPCL\text{-}PEG_{32}$. For the PLA polymers, interesting thermal behavior was observed. The DSCs of $stPLA_{32}$ and the linear PLA are shown in Figures 2 and 3, respectively. The heating trace for $stPLA_{32}$ shows a T_g at about

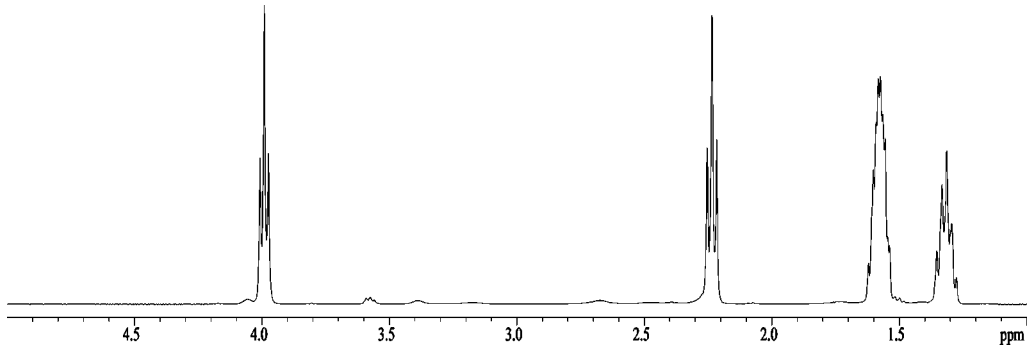

Figure 1. ^{1}H NMR spectrum of stPCL$_{32}$.

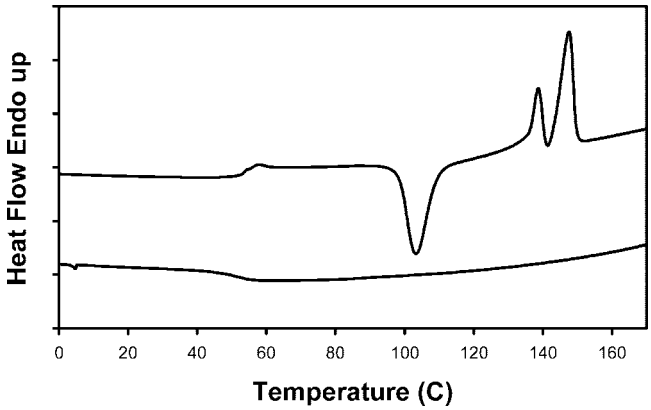

Figure 2. DSC of stPLA$_{32}$: top trace is heating and lower trace is cooling.

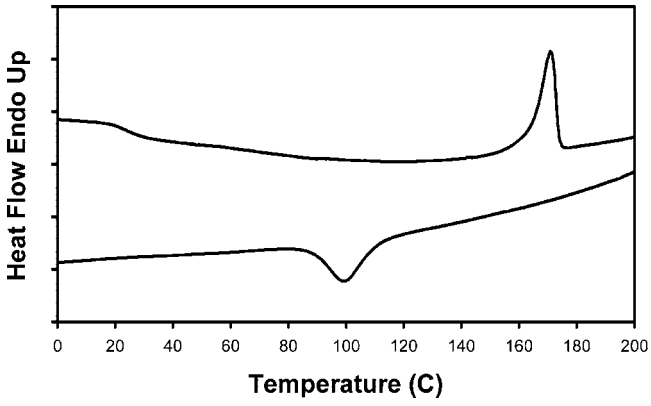

Figure 3. DSC of linear-PLA: top trace is heating and lower trace is cooling.

56 °C, a crystallization transition temperature at 103 °C, and two melting transition peaks at 139 and 148 °C. The cooling trace shows no crystallization transition, and the T_g is at about 50 °C. In contrast, the heating trace for the linear-PLA shows no T_g, and a single melting transition is observed at 171 °C. The cooling trace shows a crystallization transition at 98 °C and no T_g. The linear-PLA polymer can reorganize more freely and has a higher molecular weight of 19K. This indicates a high proportion of crystalline phase in the sample and a small amorphous phase. For the stPLA$_{32}$, the polymer chain is shorter (3K), and one end is bound to the dendrimer core. This means that it has less freedom to reorganize and therefore forms less perfect crystals and a larger amorphous fraction, leading to the observed T_g. In the cooling process, the nucleation of the crystallization (which dominates) is slow at high temperatures (above T_m), so the sample stays amorphous until it passes the T_g. In the heating process, the polymer chains become mobile

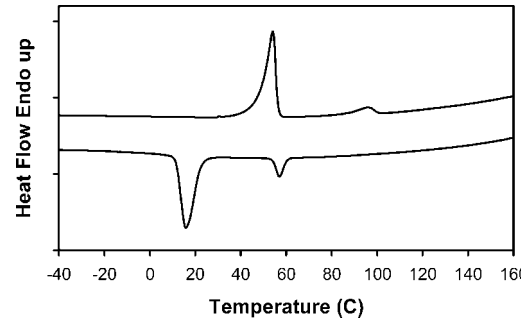

Figure 4. DSC of stPLA-PEG$_{32}$: top trace is heating and lower trace is cooling.

Table 2. Characterization of Star Polymer Micelles

	effective diameter[a], nm	polydispersity index
stPCL-PEG$_{32}$	19.0	0.19
stPLA-PEG$_{32}$	24.7	0.20

[a] Effective diameter denotes averaged value calculated from three measurements performed on each sample. The effective diameter values are within ±5 nm. Polymer concentration is 15 mg/mL.

(kinetics dominate) above the T_g. Nucleation is then very fast at low temperature (below T_m), and crystallization occurs. Since it forms less perfect crystals, the two peak melting profiles may be due to two types of crystals, or there may be a partial melting/recrystallization followed by complete melting.

The DSC of stPLA-PEG$_{32}$ in Figure 4 shows interesting behavior as well. The heating trace exhibits a large T_m at 54 °C and a small T_m at 97 °C. The cooling trace shows corresponding transitions at lower temperatures. The unusual thermal behavior of stPLA$_{32}$ was not observed here. The highly crystalline nature of the PEG plays a major role in this case. The sample may contain two types of crystals; one is the PEG crystal and the other is the less perfect PLA crystal. The majority PEG crystal melts at lower temperature and gives the large peak. The smaller amount and less perfect PLA crystals melt at a higher temperature and give a relatively small peak.

Micellar Properties of the Star Polymers. The dialysis method was employed to prepare polymeric micelles. Their effective hydrodynamic diameter was measured by DLS. The measurements performed immediately after dialysis revealed the formation of dispersions of star polymer particles with very broad distributions (polydispersity indices were more than 0.3). Removal of the large aggregates by repeated filtration (membranes with pore sizes of 0.45 and 0.22 μm) resulted in the substantial decrease of the concentration of micellar dispersions (ca. 30−50%). The effective diameters of the polymer micelles in solutions prepared by dialysis are presented in Table 2. The micelle size distribution was rather broad in all cases and varied in the range 0.13−0.21, indicating the possible existence of some aggregated species. As an example, a DLS graph of size

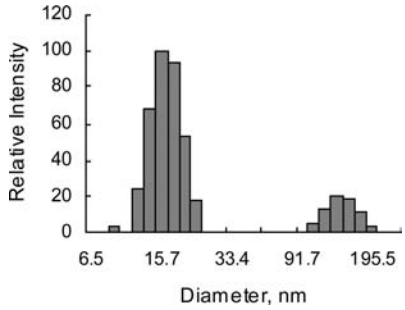

Figure 5. DLS graph of the stPCL-PEG_{32} micelle size distribution. Concentration of stPCL-PEG32 was 15 mg/mL.

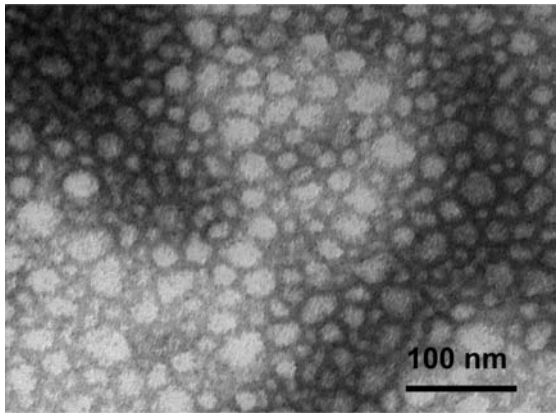

Figure 6. TEM micrograph of stPCL-PEG32 micelles obtained using uranyl acetate staining.

distribution of stPCL-PEG_{32} micelles in a polymer solution with a concentration of 15 mg/mL is shown in Figure 5. It is a bimodal distribution with a smaller size component of ~15.7 nm (85%) and a large size component of ~134 nm (15%). The size and aggregation stability of the star polymer micelles in aqueous dispersions depended on the water content in the water−organic mixture at the start of the dialysis. Specifically, micelles prepared by dialysis from the water−organic mixtures with higher water content (87.5 vol %) were characterized as having both larger particle size and polydispersity, as well as a lower degree of stability. Formation of aggregates followed by phase separation was observed in these solutions within 2−3 days. The most stable stPCL-PEG_{32} and stPLA-PEG_{32} aqueous dispersions were obtained with 67% water content in the initial dialysis mixture. Subsequent measurements of these stPCL-PEG_{32} and stPLA-PEG_{32} samples showed that the size of the particles remained practically unchanged for several weeks. Furthermore, it should be noted that the size and size distribution of the micelles formed from the same batch of polymer varied slightly due to variations in the processing parameters such as stirring conditions, rate of water addition, and so forth.

The morphology of the star polymer micelles was further examined by transmission electron microscopy (TEM) using negative staining. A representative micrograph of the stPCL-PEG_{32} micelles is presented in Figure 6. The micelles are close to spherical and have a mean number-average diameter of 11.5 ± 0.4 nm. Analysis of TEM images revealed the broad size distribution of the polymer micelles as well as the presence of large aggregates with diameters between 25 and 45 nm (frequency from 6% to 1%). The diameters of the particles determined from the TEM data were less than the effective diameter determined by DLS. This is not surprising, since the DLS determines the hydrodynamic diameter or the "equivalent sphere diameter" in solution, while TEM images were obtained in the absence of the solvent. Nevertheless, both methods exhibited the same trend in the particle sizes of the micelles.

The star polymer micelles were further characterized by fluorescence spectroscopy to determine the partition coefficient of the model hydrophobic probe pyrene between the polymer micelles and the aqueous compartment. Several aspects of the pyrene spectroscopic properties were changed as the polymer concentration increased: the total fluorescence intensity increased, and the vibrational fine structure of the emission spectra changed. This type of behavior is indicative of the partitioning of the pyrene into the more hydrophobic environment. However, the extent of these changes as a function of polymer concentration was drastically different for the polymers studied. For stPCL-PEG_{32}, the total fluorescence intensity increased steadily even in very dilute polymer solutions, and the vibrational fine structure (I_1/I_3) changed from 1.8 to 1.32. These results suggest that in dilute solutions the intact stPCL-PEG_{32} molecules formed unimolecular micelles. The calculated value for the partition coefficient (P) for pyrene between stPCL-PEG_{32} micelles and water at 22 °C was 4150, nearly double than that found for a 16 arm star-PCL-PEG polymer (P = 2410) (*16*). In contrast, the onset of the changes in the fluorescence spectra of pyrene in the stPLA-PEG_{32} aqueous dispersions was detected at a polymer concentration of ~0.01 mg/mL. The partition coefficient for pyrene in this system was found to be ~600. Furthermore, the stPLA-PEG_{32} micelle solutions were found to have an I_1/I_3 ratio of 1.6. This value is higher than the 1.32 value determined for stPCL-PEG_{32} micelles. These data suggest that the PLA cores of stPLA-PEG_{32} micelles are more polar compared to the PCL cores. As a result, the environment of the pyrene molecule in the PLA core is less hydrophobic, decreasing the solubilization capacity of stPLA-PEG_{32} micelles.

Similar studies were conducted for star polymer micelles in phosphate buffer saline (PBS). In the case of stPCL-PEG_{32}, the total fluorescence intensity steadily increased even in the very dilute polymer solutions, suggesting the presence of stPCL-PEG_{32} molecules as unimolecular micelles. The onset of the changes in the fluorescence spectra of pyrene in the stPLA-PEG_{32} aqueous dispersions was detected at a polymer concentration of ~0.067 mg/mL. The calculated values for the partition coefficient for pyrene under these conditions were 1440 for stPCL-PEG_{32} micelles and 470 for stPLA-PEG_{32} micelles.

Encapsulation and Release of Etoposide in Copolymer Micelles. Two general drug-loading methods were explored for encapsulating etoposide in stPCL-PEG_{32} micelles. In the first method (dialysis), etoposide (2 mg) was dissolved in acetonitrile and then mixed with stPCL-PEG_{32} polymer (5 mg) dissolved in DMF (1 mL). Next, distilled water was slowly added dropwise to the mixture (25 μL of water per 2−3 min) to achieve a water content of 67 vol %. Drug precipitation was not observed upon mixing water with the drug−polymer solution. The obtained water−organic solvent mixture containing etoposide and polymer was then dialyzed against water. No etoposide was detected in the final dispersions. Therefore, this technique is not applicable, possibly due to the water solubility of etoposide (ca. 0.12 mg/mL).

In the second method, micelle extraction (*2*) was used to encapsulate etoposide into the star micelles. Briefly, an aliquot of etoposide stock solution in acetonitrile was added to the empty vial, the solvent was evaporated to dryness, and 1 mL micelle solution was added to the vial and agitated for 2 days. Polymer concentrations ranging from 2 mg/mL to 15 mg/mL were used. The solution was then centrifuged to remove insoluble drug, and the etoposide concentration in the solution was determined by HPLC. The loading levels of etoposide into the copolymer micelles are presented in Table 3. The maximum etoposide loading (7.8 w/w % for stPCL-PEG_{32} and 4.3 w/w

Table 3. Etoposide Loading in stPCL-PEG$_{32}$ and stPLA-PEG$_{32}$ Polymers

polymer	polymer conc. (mg/mL)	etoposide (mg/mL)[a]	loading in polymer (w/w %)
stPCL-PEG$_{32}$	2.4	0.12	5.0
	3.0	0.23	7.8
	5.0	0.29	5.9
	8.0	0.31	3.9
	15	0.50	3.4
stPLA-PEG$_{32}$	2.4	0.05	2.2
	3.0	0.13	4.3
	5.0	0.16	3.2
	8.0	0.19	2.4
	15	0.43	2.8

[a] The etoposide concentration values are within ± 3%.

% for stPLA-PEG$_{32}$, respectively) was achieved at a polymer concentration of ca. 3 mg/mL. Further increase in the polymer concentration resulted in a decrease in the drug loading level. Such complex solubilization behavior is typical of systems where there is a strong interaction between the drug and the micelle core (*3*, *18*, *19*). In this case, the solubilization capacity might increase to a saturation level with increasing polymer concentration. As a result, the relative drug loading in the micelles will decrease. It is noteworthy that the incorporation of drug did not affect the size of the star polymer micelles. The etoposide/star polymer dispersions remained stable over several days. Furthermore, they could be stored at 4 °C for at least 24 h without precipitation of etoposide.

The drug release from the etoposide/stPCL-PEG$_{32}$ system (polymer concentration 5 mg/mL) was evaluated in phosphate buffered saline (pH 7.4, 0.14 M NaCl) by the dialysis method. About 60% of the loaded etoposide (an averaged value calculated based on three experiments) was released from the micelles during the first 24 h. Overall, these studies suggested that etoposide can be loaded and efficiently released from star polymer micelles.

Concluding Remarks. In summary, we have successfully synthesized two types of amphiphilic star-polymers with PCL and PLA as the lipophilic components. The star polymer structures were confirmed by SEC, spectroscopic, and thermal characterizations. The micelle properties of the polymers were investigated by various techniques. The formation of unimolecular micelles from the stPCL-PEG$_{32}$ has been demonstrated by pyrene fluorescence studies. The results from fluorescence, DLS, and TEM experiments have shown that unimolecular micelles and aggregated multimolecular micelles coexist in the water solution. A systematic study revealed the optimal condition for etoposide encapsulation by the polymer micelles. The stPCL-PEG$_{32}$ has a higher etoposide loading capacity than stPLA-PEG$_{32}$. This may be due to the more lipophilic properties of the PCL core. The overall etoposide loading capacity of the 32 arm star polymer is lower than the 16 arm star polymer we reported previously (*16*). One possible reason for this may be due to the higher PCL polymer density in the 32 arm star polymer micelle interior, therefore leaving less space for drug loading. The *in vivo* testing for tumor treatment by the etoposide/star polymer formulation will be report in separate paper.

ACKNOWLEDGMENT

Funding of this work by the NIH (5R44EB000551) is gratefully acknowledged. The authors thank Mr. Monsy Jacob and Mr. Sangrama K. Sahoo for help in obtaining ^{1}H NMR spectra.

LITERATURE CITED

(1) Kwon, G. S., and Kataoka, K. (1995) Block copolymer micelles as long-circulating drug vehicles. *Adv. Drug Delivery Rev. 16*, 295.

(2) Allen, C., Maysinger, D., and Eisenberg, A. (1999) Nano-engineering block copolymer aggregates for drug delivery. *Colloids Surf., B: Biointerfaces 16*, 3.

(3) Kabanov, A. V., and Alakhov, V.Yu. (2002) Pluronic block copolymers in drug delivery: From micellar microcontainers to biological response modifiers. *Crit. Rev. Ther. Drug Carrier Syst. 19*, 1.

(4) Torchilin, V. P. (1999) Polymeric micelles in diagnostic imaging. *Colloids Surf., B: Biointerfaces 16*, 305.

(5) Wilhelm, M., Zhao, C., Wang, Y., Xu, R., Winnik, M. A., Mura, J., Reiss, G., and Croucher, M. D. (1991) Poly(styrene-ethylene oxide) block copolymer micelle formation in water: a fluorescence probe study. *Macromolecules 24*, 1033.

(6) Kwon, G. S., Naito, M., Yokoyama, M., Okano, T., Sakurai, Y., and Kataoka, K. (1993) Micelles based on AB block copolymers of poly(ethylene oxide) and poly(β-benzyl L-aspartate). *Langmuir 9*, 945.

(7) Kabanov, A. V., Chekhonin, V. P., Alakhov, V. Yu., Batrakova, E. V., Lebedev, A. S., Melik-Nubarov, N. S., Arzhakov, S. A., Levashov, A. V., Morozov, G. V., Severin, E. S., and Kabanov, V. A. (1989) The neuroleptic activity of haloperidol increases after its solubilization in surfactant micelles. *FEBS Lett. 258*, 343.

(8) Hagan, S. A., Coombes, A. G. A., Garnett, M. C., Dunn, S. E., Davies, M. C., Illum, L., Davis, S. S., Harding, S. E., Purkiss, S., and Gellert, P. R. (1996) Polylactide-poly(ethylene glycol) copolymers as drug delivery system. 1. Characterization of water dispersible micelle-forming systems. *Langmuir 12*, 2153.

(9) Kataoka, K. (1993) Block copolymer micelles as vehicles for drug delivery. *J. Controlled Release 24*, 119.

(10) Iijima, M., Nagasaki, Y., Okada, T., Kato, M., and Kataoka, K. (1999) Core-polymerized reactive micelles from heterotelechelic amphiphilic block copolymers. *Macromolecules 32*, 1140.

(11) Kim, J.-H., Emoto, K., Iijima, M., Nagasaki, Y., Aoyagi, T., Okano, T., Sakurai, Y., and Kataoka, K. (1999) Core-stabilized polymeric micelle as potential drug carrier: increased solubilization of taxol. *Polym. Adv. Technol 10*, 647.

(12) Liu, H., Jiang, A., Guo, J., and Uhrich, K. E. (1999) Unimolecular micelles: synthesis and characterization of amphiphilic polymer systems. *J. Polym. Sci., Part A: Polym. Chem. 37*, 703.

(13) Kim, K. H., Cui, G. H., Lim, H. J., Huh, J., Ahn, C., and Jo, W. H. (2004) Synthesis and micellization of star-shaped poly(ethylene glycol)-block-poly(ε-caprolactone). *Macromol. Chem. Phys. 205*, 1684.

(14) Deng, M., Chen, X., Piao, L., Zhang, X., Dai, Z., and Jing, X. (2004) Synthesis of four-armed poly(ε-caprolactone)-block-poly(ethylene oxide) by diethylzinc catalyst. *J. Polym. Sci., Part A: Polym. Chem. 42*, 950.

(15) Zeng, F., Lee, H., Chidiac, M., and Allen, C. (2005) Synthesis and characterization of six-arm star poly(δ-valerolactone)-*block*-methoxy poly(ethylene glycol) copolymer. *Biomacromolecules 6*, 2140.

(16) Wang, F., Bronich, T. K., Kabanov, A. V., Rauh, R. D., and Roovers, J. (2005) Synthesis and evaluation of a star amphiphilic block copolymer from poly(-caprolactone) and poly(ethylene glycol) as a potential drug delivery carrier. *Bioconjugate Chem. 16*, 397.

(17) Roovers, J., Toporowski, P. M., and Douglas, J. (1995) Thermodynamic properties of dilute and semidilute solutions of regular star polymers. *Macromolecules 28*, 7064.

(18) Xing, L., and Mattice, W. L. (1997) Strong solubilization of small molecules by triblock-copolymer micelles in selective solvents. *Macromolecules 30*, 1711.

(19) Gadelle, F., Koros, W. J., and Schechter, R. S. (1995) Solubilization of aromatic solutes in block copolymers. *Macromolecules 28*, 4883.

BC7004285

Novel Chemically Modified Analogues of Neuropeptide Y for Tumor Targeting[§]

Denise Zwanziger,[+,†] Irfan Ullah Khan,[+,†] Ines Neundorf,[†] Stephanie Sieger,[‡] Lutz Lehmann,[‡] Matthias Friebe,[‡] Ludger Dinkelborg,[‡] and Annette G. Beck-Sickinger*[,†]

Institute of Biochemistry, Leipzig University, Brüderstr. 34, 04103 Leipzig, Germany, and Bayer Schering Pharma, Global Drug Discovery, Berlin, Germany. Received November 21, 2007; Revised Manuscript Received April 20, 2008

The successful use of peptides as potential radiopharmaceuticals essentially requires the modification of the bioactive peptide hormones to introduce chelators for radiolabeling. In this study, four Y_1/Y_2 receptor-selective NPY analogues with different receptor subtype specificities have been investigated. For *in vitro* studies, the cold metal surrogate was used. Gallium and indium complexes were introduced by using 1,4,7,10-tetraazacyclododecane-1,4,7,10-tetraacetic acid as bifunctional chelator. The peptides were synthesized by solid-phase peptide synthesis (SPPS), the chelator was coupled either at the N-terminus or at the N^{ε} side chain of Lys^4 of the resin-bound peptide, and the labeling was performed in solution after cleavage. Competitive binding assays showed high binding affinity of the receptor-selective analogues at NPY receptor expressing cells. To test internalization of the novel peptide analogues and the metabolic stability in human blood plasma, the corresponding 5(6)-carboxyfluorescein (CF) analogues were prepared and investigated. One of the most promising analogues, the Y_1-receptor selective [Lys(DOTA)^4, Phe^7, Pro^{34}]NPY was labeled with ^{111}In and injected into nude mice that bear MCF-7 breast cancer xenografts, and biodistribution studies were performed. *In vitro* and *in vivo* studies suggest that receptor-selective analogues of NPY have promising characteristics for future applications in nuclear medicine for breast tumor diagnosis and therapy.

INTRODUCTION

The use of radiolabeled receptor-mediated peptide analogues for the treatment of primary and metastatic tumors, namely, targeted radionuclide therapy, has been an important alternative to conventional therapeutic regimens. Receptor-avid peptides have been chosen as vehicles to selectively deliver cytotoxic radiation-emitting radionuclides to tumor cells, resulting in tumor cell death (*1*).

Neuropeptide Y (NPY)[1] is a 36 amino acid peptide amide of the pancreatic polypeptide family. It is expressed in the peripheral and central nervous system and is one of the most abundant neuropeptides in the brain (*2*). NPY acts peripherally as a vasoconstrictor and modulates the activity of further neurotransmitters. Several other physiological activities such as induction of food intake, inhibition of anxiety, increase in memory retention, etc., have also been attributed to NPY (*3*). Its receptors are produced in a number of neuroblastoma and cell lines derived thereof, which suggest them as optimal targets for tumor scintigraphy. So far, five receptor subtypes (Y_1, Y_2, Y_4, Y_5, y_6) have been cloned that bind NPY with nanomolar affinity (*4*). They all belong to the large family of G-protein-coupled receptors (GPCRs) with their typical seven transmembrane helix structure (*5*).

Previous studies showed that there is a molecular basis for a putative role of NPY in tumors, e.g., neuroendocrine tumors, glioblastomas, and breast cancers (*6–9*). The strong predominance of Y_1 receptors in breast carcinomas compared to Y_2 in normal breast tissue suggests that neoplastic transformation can switch the NPY receptor expression from the Y_2 to the Y_1 receptor subtype. The high incidence of Y_1 in *in situ*, invasive, and metastatic breast cancers therefore allows the possibility to target them for diagnosis and therapy with NPY Y_1 receptor-selective analogues by using an appropriate metalloradiopharmaceutical that contains, e.g., a metallic radionuclide (e.g., ^{67}Cu, ^{90}Y, ^{99m}Tc, ^{111}In, ^{177}Lu, ^{186}Re, or ^{212}Bi). Additionally, the targeting biomolecule requires a bifunctional chelator (BFC), either directly or separated by a spacer molecule to coordinate the metallic radionuclide.

[§] Dedicated to Professor Dr. Hans-Dieter Jakubke on the occasion of his 75th birthday.

* Correspondence to: Tel. +49-341-9736901; fax +49-341-9736909; Leipzig University, Brüderstr. 34, 04103 Leipzig; E-mail: beck-sickinger@uni-leipzig.de.

[+] Contributed equally.

[†] Leipzig University.

[‡] Global Drug Discovery.

[1] Abbreviations used: NPY, neuropeptide Y; Ga, gallium metal; CF, 5(6)-carboxyfluorescein; GPCRs, G-protein coupled receptors; BFC, bifunctional chelator; His, histidine; Phe, phenylalanine; Lys, lysine; Pro, proline; Asp, aspartic acid; Glu, glumatic acid; Ser, serine; Thr, threonine; Asn, asparagine; Gln, glutamine; Arg, arginine; In, indium; Y, yttrium; DOTA, 1,4,7,10-tetraazacyclododecane-1,4,7,10-tetraacetic acid; SPPS, solid phase peptide synthesis; Boc, *tert*-butyl-oxycarbonyl; Pmc, pentamethylchroman-6-sulfonyl; Dde, 4,4-dimethyl-2, 6-dioxocyclohex-1-ylidene-ethyl; DMF, *N*,*N*-dimethylformamide; DCM, dichloromethane; MeOH, methanol; Et_2O, diethyl ether; HOBt, hydroxybenzotriazole; DIC, *N*,*N*′-diisopropylcarbodiimide; DIPEA, *N*,*N*-diisopropylethylamine; ACN, acetonitrile; MEM, minimum essential medium; DMEM, Dulbecco's Modified Eagle's Medium; FCS, fetal calf serum; BSA, bovine serum albumin; EDTA, ethylenediaminetetraacetic acid; MALDI-ToF, matrix-assisted laser desorption ionization-time-of-flight; HPLC, high performance liquid chromatography; TFA, trifluoroacetic acid; NSB, nonspecific binding; $Ga(NO_3)_3$, gallium nitrate; $InCl_3$, indium chloride; $^{111}InCl_3$, ^{111}Indium chloride; PRRT, peptide receptor radiation therapy; PBS, phosphate buffered saline; Y*y* = NPY receptor subtype Y (*y* = 1, 2, or 5); PET, positron emission tomography; %ID/g, percent of injected dose per gram; HCl, hydrochloric acid; Bq, bequerel, CLSM, confocal laser scanning microscopy; BHK, baby hamster kidney.

10.1021/bc7004297 CCC: $40.75 © 2008 American Chemical Society
Published on Web 06/24/2008

We focused on the development of gallium- and indium-labeled NPY receptor-selective analogues chelated by DOTA, since this chelator is capable of forming stable complexes with various 3^+-charged radiometals, as demonstrated by the successful development of Ga-labeled somatostatin analogues (*10*). The effect on receptor binding properties was studied by labeling the DOTA-NPY analogues with nonradioactive Ga and In.

All peptides were tested for receptor binding affinity at various NPY receptor expressing cells, e.g., human neuroepithelioma (SK-N-MC), human breast adenocarcinoma (MCF-7), human neuroblastoma (SMS-KAN), and human endometrial carcinoma (HEC) cells. The SK-N-MC and MCF-7 cells selectively express NPY Y_1 receptors, while SMS-KAN cells selectively express NPY Y_2 receptors and HEC-1B$-Y_5$ cells were stable transfected with Y_5 receptors (*11*). All cell lines have frequently been used to investigate binding as well as signal transduction of NPY (*12*).

Here, we report on the influence of the linker chelator 1,4,7,10-tetraazacyclododecane-1,4,7,10-tetraacetic acid (DOTA) and conjugates of four different NPY analogues with respect to ligand binding. Interestingly, the position of the labeling of linker was of significant interest regarding the binding to the receptor. Moreover, we present the first series biodistribution data of one of the most potent Y_1 receptor selective NPY analogues [Lys(DOTA)^4, Phe^7, Pro^{34}]NPY. The peptide was successfully labeled with ^{111}In and accordingly confirms the proof of the principle. The *in vivo* characteristic of the peptide was studied in nude mice that bear MCF-7 breast cancer xenografts.

EXPERIMENTAL PROCEDURES

Materials. The N^α-Fmoc-protected amino acids were obtained from Alexis (Läufelfingen, Switzerland) and Novabiochem (Läufelfingen, Switzerland). The side chain protecting groups were *tert*-butyl for Asp, Glu, Ser, Thr, and Tyr; *tert*-butyloxycarbonyl (Boc) for Lys; trityl for Asn, Gln, and His; and 2,2,5,7,8-pentamethylchroman-6-sulfonyl (Pmc) for Arg. The 4-(2′,4′-dimethoxyphenyl-Fmoc-aminomethyl)-phenoxy (Rink Amide) resin was obtained from Novabiochem. *N*,*N*-Dimethylformamide, dichloromethane, methanol, and diethyl ether were purchased from Scharlau (La Jota, Barcelona, Spain). Physiological sodium chloride was obtained from Braun (Melsungen, Germany). 5(6)-Carboxyfluorescein (CF), 1-hydroxybenzotriazole (HOBt), thioanisole, *p*-thiocresol, piperidine, diisopropylethylamine, hydrazine monohydrate, and *tert*-butanol were purchased from Fluka (Buchs, Switzerland). *N*,*N*′-Diisopropylcarbodiimide (DIC) was purchased from Aldrich (Buchs, Switzerland). Acetonitrile (ACN) was obtained from Romil (Cambridge, England) and Merck (Darmstadt, Germany). Trifluoroacetic acid was obtained from Fluka (Buchs, Switzerland) and Merck. Ethanol (70%), water for chromatography, sodium acetate buffer, and saline solution were purchased from Merck. Dulbecco's MEM/NutMix F12 medium (50:50, v/v), Minimum Essential Medium (MEM) with Earl's salts, Dulbecco's PBS, sodium pyruvate, phosphate buffered saline (NaCl/Pi), fetal calf serum, glutamine, nonessential amino acids, and trypan blue were purchased from Gibco (Life Technologies, Basel, Switzerland). Trypsin-EDTA was obtained from Gibco (Life Technologies, Basel, Switzerland) and Biochrom (Berlin, Germany). Isofluran Curamed was purchased from Cura MED Pharma (Karlsruhe, Germany) and MatrigelTM Matrix was obtained from Becton & Dickinson (Heidelberg, Germany). Bacitracin and BSA were from Sigma (Buchs, Switzerland), while EDTA, Pefabloc SC, and all other chemicals were from Fluka. [^{3}H]propionyl-NPY and $^{111}InCl_3$ were obtained from Amersham (Buckinghamshire, United Kingdom).

Automatic Peptide Synthesis. The peptides were synthesized by fluorenylmethoxycarbonyl/*tert*-butyl (Fmoc/t-Bu) strategy with an automated multiple peptide synthesis robot system (Syro, MultiSynTech, Bochum, Germany) using Rink amide resin (30 mg, 450 μmol). Each amino acid was coupled by a double coupling procedure (two times coupling with 40 min incubation) using a 10-fold excess of N^α-Fmoc-protected amino acids and *in situ* activation with DIC and 500 μL HOBt (0.5 M in DMF) within 15 min incubation time at room temperature (*13*). The removal of the Fmoc-group was carried out with 40% piperidine in DMF (*13*). Cleavage of the peptide from the resin and of the side-chain protecting groups was accomplished in one step with 90% trifluoroacetic acid (TFA) in the presence of 10% scavengers (thioanisole/thiocresol 1:1) for 3 h. The peptides were precipitated from ice-cold diethyl ether and collected by centrifugation, resuspended in ether, and centrifuged again. This procedure was repeated four times. The identification of the products was confirmed by matrix-assisted LASER desorption ionization-time-of-flight (MALDI-ToF) mass spectrometry. The purification of the peptides was performed by a preparative RP-HPLC on a Shimadzu RP18-column (12.5 $\times$ 250 mm; 5 μm/300 Å). The pure products were characterized by analytical RP-HPLC on a Vydac RP18-column (4.6 $\times$ 250 mm; 5 μm/ 300 Å, Merck Hitachi, Darmstadt, Germany) by using a linear gradient of 0.1% TFA in water (A) and 0.08% TFA in acetonitrile (B) from 10% to 60% B in A over 30 min at a flow rate of 0.6 mL/min^{-1}. The following peptides were synthesized: NPY, [Phe^7, Pro^{34}]NPY, [Ahx$^{5-24}$]NPY, and [Ahx$^{8-20}$]NPY. The analytical data of the peptides are summarized in Table 1.

For the modification of the N^ε side chain of Lys^4, this residue was protected with 4,4-dimethyl-2,6-dioxocyclohex-1-ylideneethyl (Dde group) by using Fmoc-Lys(Dde), whereas the N-terminus was protected by the Boc-protecting group. After complete synthesis of the peptide sequence, the Dde protecting group was selectively removed from the resin by repeated washing steps with 2% hydrazine in DMF (*14*) followed by a 10 min incubation time at room temperature. The peptide remained still bound to the resin and all acid labile protecting groups remain fully protected under these conditions. After this, Lys (*4*) was labeled with the respective group (chelator or 5(6)-carboxyfluorescein), followed by the cleavage of the labeled peptide from the resin as described above.

Labeling with 5(6)-Carboxyfluorescein (CF). Prior to cleavage of the peptides, the peptides were labeled with 5(6)-carboxyfluorescein, following the procedure described by Weber et al. (*15*), in which a 10-fold excess of the CF group was used. HOBt and DIC were dissolved in DMF to give a 250 mM solution and an incubation period of 2 h was applied. Then, the resin was washed three times with 1 mL of DMF, DCM, MeOH, and Et_2O each and dried *in vacuo*. Cleavage of the peptides from the resin and identification of the CF-labeled peptides was performed as described above. The following peptides were produced: CF-NPY, [Lys(CF)^4]NPY, CF-[Phe^7, Pro^{34}]NPY, [Lys(CF)^4, Phe^7, Pro^{34}]NPY, CF-[Ahx$^{5-24}$]NPY, [Lys(CF)^4, Ahx$^{5-24}$]NPY, CF-[Ahx$^{8-20}$]NPY, and [Lys(CF)^4, Ahx$^{8-20}$]NPY.

Conjugation with DOTA. A protected DOTA analogue (DOTA-3tBu) was activated in a separate vial by 3 equiv HOBt and 3 equiv DIC in 250 μL DMF. It was transferred to the resin-bound peptide and incubated at room temperature for 2 h. The resin was washed three times with 1 mL of DMF, DCM, DMF, MeOH, and Et_2O each and dried *in vacuo*. The following peptides were synthesized: DOTA-NPY, Lys(DOTA)^4-NPY, DOTA-[Phe^7, Pro^{34}]NPY, Lys(DOTA)^4-[Phe^7, Pro^{34}]NPY, DOTA-[Ahx$^{5-24}$]NPY, Lys(DOTA)^4-[Ahx$^{5-24}$]NPY, DOTA-[Ahx$^{8-20}$]NPY, and Lys(DOTA)^4-[Ahx$^{8-20}$]NPY.

Labeling of DOTA-NPY Analogues with Ga. A mixture of 500 μg (340 μmol) of DOTA-NPY in 500 μL of 0.4 M sodium acetate buffer (pH 5) was incubated with 102 μL of a

Table 1. Analytical and Binding Data of the Modified/Labelled NPY Analogues

					pK_i			
no.	peptide	$MW_{calc.}$ [D]	$MW_{expt.}$ [D]	RT[a] [min]	SK-N-MC	MCF-7	SMS-KAN	HEC-1B-Y5
1.	NPY	4254.0	4254.8	21.8	9.5 ± 0.1	9.5 ± 0.1	8.8 ± 0.1	8.2 ± 0.1
2.	[Phe^7, Pro^{34}]NPY	4255.1	4255.4	22.1	10.3 ± 0.2	9.1 ± 0.1	7.6 ± 0.1	8.6 ± 0.5
3.	[Ahx$^{5-24}$]NPY	2220.2	2221.3	14.9	6.8 ± 0.1	n.d.[b]	9.2 ± 0.3	n.d.
4.	[Ahx$^{8-20}$]NPY	2981.0	2982.4	19.9	8.0 ± 0.1	7.7 ± 0.1	8.2 ± 0.1	6.9 ± 0.1
1a.	DOTA-NPY	4640.7	4641.5	22.3	n.d.	n.d.	n.d.	n.d.
1b.	[Lys(DOTA)^4]NPY	4640.7	4641.9	21.4	n.d.	n.d.	n.d.	n.d.
2a.	DOTA-[Phe^7, Pro^{34}]NPY	4642.0	4643.5	23.5	8.6 ± 0.2	8.9 ± 0.1	6.5 ± 0.1	7.1 ± 0.3
2b.	[Lys(DOTA)^4, Phe^7, Pro^{34}]NPY	4642.0	4643.0	22.8	9.5 ± 0.2	9.1 ± 0.1	7.2 ± 0.1	7.5 ± 0.1
3a.	DOTA-[Ahx$^{5-24}$]NPY	2607.6	2608.5	17.4	n.d.	n.d.	8.8 ± 0.1	7.0 ± 0.3
3b.	[Lys(DOTA)^4, Ahx$^{5-24}$]NPY	2607.6	2608.8	17.8	n.d.	n.d.	8.5 ± 0.1	6.8 ± 0.2
4a.	DOTA-[Ahx$^{8-20}$]NPY	3368.5	3369.6	20.5	n.d.	n.d.	n.d.	n.d.
4b.	[Lys(DOTA)^4, Ahx$^{8-20}$]NPY	3368.5	3369.3	21.1	n.d.	n.d.	n.d.	n.d.
2e.	[Lys(Ga-DOTA)^4, Phe^7, Pro^{34}]NPY	4708.6	4709.7	23.6	8.8 ± 0.1	n.d.	n.d.	n.d.
2f.	[Lys(In-DOTA)^4, Phe^7, Pro^{34}]NPY	4753.7	4754.7	21.6	8.8 ± 0.1	n.d.	n.d.	n.d.
2g.	[Lys(^{111}In-DOTA)^4, Phe^7, Pro^{34}]NPY	4753.7	n.d.	20.9	n.d.	n.d.	n.d.	n.d.
1c.	CF-NPY	4612.0	4613.1	24.8	8.2 ± 0.1	9.3 ± 0.2	n.d.	n.d.
1d.	[Lys(CF)^4]NPY	4612.0	4613.4	24.7	7.1 ± 0.1	7.2 ± 0.1	n.d.	n.d.
2c.	CF-[Phe^7, Pro^{34}]NPY	4614.1	4615.1	25.3	8.9 ± 0.2	9.5 ± 0.2	n.d.	n.d.
2d.	[Lys(CF)^4, Phe^7, Pro^{34}]NPY	4614.1	4614.5	25.1	8.1 ± 0.1	7.9 ± 0.1	n.d.	n.d.
3c.	CF-[Ahx$^{5-24}$]NPY	2578.9	2580.6	17.9	n.d.	n.d.	8.2 ± 0.1	n.d.
3d.	[Lys(CF)^4, Ahx$^{5-24}$]NPY	2578.9	2580.3	18.1	n.d.	n.d.	8.0 ± 0.1	n.d.
4c.	CF-[Ahx$^{8-20}$]NPY	3339.8	3340.8	13.3	6.8 ± 0.1	7.6 ± 0.1	8.8 ± 0.1	n.d.
4d.	[Lys(CF)^4, Ahx$^{8-20}$]NPY	3339.8	3340.8	22.8	6.8 ± 0.1	7.1 ± 0.1	7.7 ± 0.1	n.d.

[b] n.d. not determined. [a] Retention time.

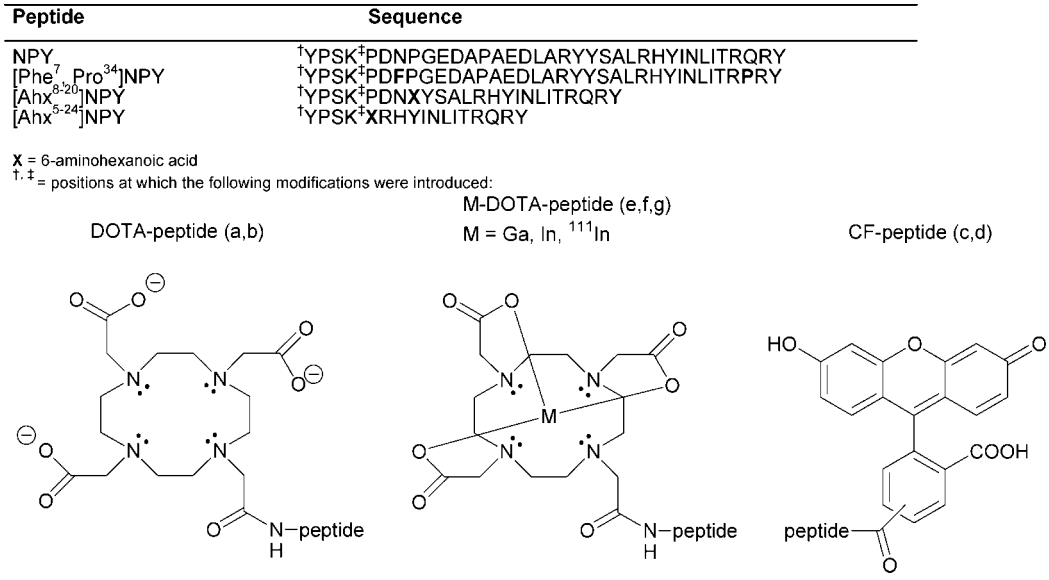

Figure 1. Sequences and modifications of the peptides used in this study: (a) modification with DOTA at the N-terminus, (b) modification with DOTA at the N^{ε} side chain of Lys^4, (e,f) modification with Ga/In, (g) modification with ^{111}In, (c) modification with CF at the N-terminus, (d) modification with CF at the N^{ε} side chain of Lys^4.

0.01 M aqueous solution of nonradioactive $Ga(NO_3)_3$ for 30 min at 37 °C and cooled to room temperature. Lys(DOTA)^4-[Phe^7, Pro^{34}]NPY was labeled with Ga to produce [Lys(Ga-DOTA)^4, Phe^7, Pro^{34}]NPY.

Labeling of DOTA-NPY Analogues with In. A mixture of 500 μg (340 μmol) of DOTA-NPY in 500 μL of 0.4 M ammonium acetate buffer (pH 5) was incubated with 100 μL of a 0.01 M aqueous solution of nonradioactive $InCl_3$ for 30 min at 37 °C and cooled to room temperature. Lys(DOTA)^4-[Phe^7, Pro^{34}]NPY was labeled with In to produce [Lys(In-DOTA)^4, Phe^7, Pro^{34}]NPY.

Labeling of DOTA-NPY Analogues with ^{111}In. A mixture of 25 μg (1 mg/0.5 mL saline solution (2.5 M)) of NPY analogue in 12.5 μL of saline solution (2.5 M) was incubated with 100 μL of $^{111}InCl_3$ (41 MBq) in 0.04 M HCl and 20 μL of a 2.5 M sodium acetate buffer (pH 5.6) for 15 min at 75 °C and cooled for 10 min (*16*). The product was analyzed by radio-HPLC. Analysis was performed on the HPLC system Agilent (Luna column 5 μm, C18, 250 × 4.6 mm), by using a linear gradient of 0.1% TFA in water (A) and 0.1% TFA in acetonitrile (ACN) (B) from 25% to 50% B in A in 30 min with a flow of 1.0 mL/min. Lys(DOTA)^4-[Phe^7, Pro^{34}]NPY was labeled with ^{111}In to produce [Lys(^{111}In-DOTA)^4, Phe^7, Pro^{34}]NPY.

Cell Culture. Cells were grown in 75 cm^2, 175 cm^2, and 225 cm^2 culture flasks at 37 °C, 5% CO_2, in a humidified atmosphere. SK-N-MC cells were cultivated in MEM with Earl's salts supplemented with 10% (v/v) heat-inactivated fetal calf serum (FCS), 4 mM L-glutamine, 0.2 mM nonessential amino acids, and 1 mM sodium pyruvate. SMS-KAN cells were grown in DMEM/nutrient mix Ham's F12 (1:1) with 15% v/v FCS, 4 mM L-glutamine, and 0.2 mM nonessential amino acids. MCF-7 cells were cultivated in DMEM/nutrient mix Ham's F12 (1:1) with 10% (v/v) FCS and 2 mM L-glutamine. All cells were grown to confluence before use.

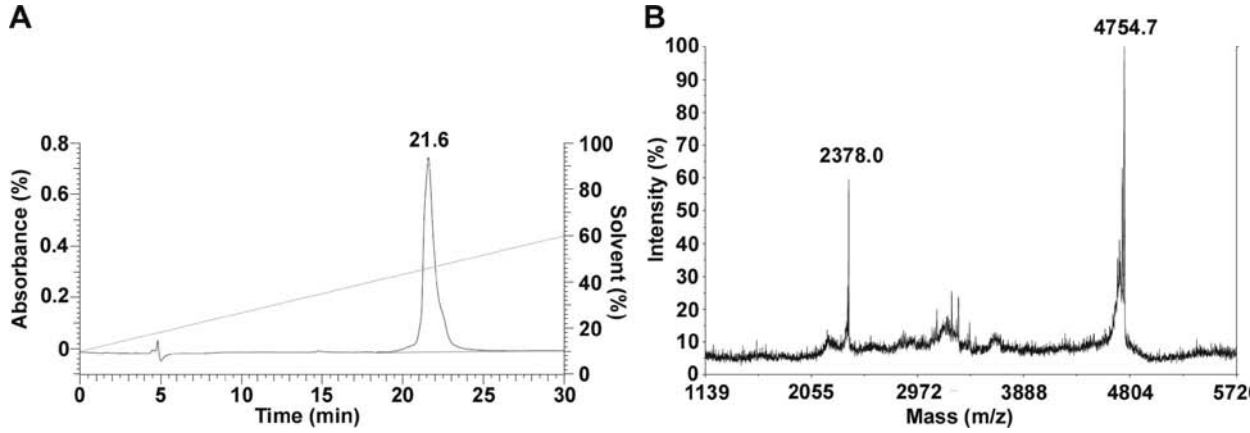

Figure 2. Typical analytical data of compound **2f** [Lys(In-DOTA)^4, Phe^7, Pro^{34}]NPY (A) HPLC chromatogram from 10% to 60% ACN in 30 min, (B) MALDI spectrum of the compound.

Receptor Binding Affinity Assays. Cells were resuspended in incubation buffer (minimal essential medium with Earl's salts containing 0.1% bacitracin, 50 mM Pefabloc SC, and 1% bovine serum albumin). A total of 200 μL of the cell suspension containing approximately 60 000 cells was incubated with 25 μL of a 10 nM solution of ^{3}H-propionyl-NPY and 25 μL of NPY or analogue in a concentration range of 10 μM to 10 pM in 1% BSA. Nonspecific binding (NSB) was defined in the presence of 1 μM unlabeled NPY. After incubating the cells for 90 min at room temperature, the incubation was terminated by centrifugation at 2000 $\times$ *g* and 4 °C for 5 min. The pellets were washed twice with 400 μL PBS (137 mM NaCl, 8 mM Na_2HPO_4/KH_2PO_4, pH 7.4), centrifuged, and resuspended in 100 μL PBS. The cell suspension was mixed with 3 mL scintillation cocktail and radioactivity was determined by using a beta-counter.

IC_{50} values of the binding curves were calculated by nonlinear regression on a sigmoidal dose−response based model by using GraphPad Software *PRISM 3.0*. Each experiment was performed 2−3 times in triplicate and $K_i \pm$ SEM values were calculated, using the Cheng-Prusoff equation (*17*). The following K_D values of the radioligand ^{3}H-NPY at the respective receptors were used: 0.18 nM at the Y_1 receptor, 0.45 nM at the Y_2 receptor, and 1.8 nM at the Y_5 receptor.

Confocal Laser Scanning Microscopy (CLSM). For confocal laser scanning microscopy, the cells were grown on Falcon Cell Culture Inserts with Cyclopore membranes or a Laboratory-Tak Chamber Slides for the observation of unfixed cells. In order to perform measurements, the Leica Confocal System TCS SP2 was used at excitation/emission wavelengths of 488/514 nm argon laser, respectively.

Metabolic Stability in Human Blood Plasma. The proteolytic degradation of the CF-labeled peptide was determined *in vitro* in human blood plasma obtained from healthy donors. 0.1 mL of plasma was incubated at 37 °C with 10 μM CF-labeled peptide for 0, 3, 6, 12, and 24 h. Then, samples were precipitated with 40 μL acetonitrile/ethanol (50:50, v/v) by incubation in ice for 30 min followed by centrifugation at 8000 rpm at 4 °C for 15 min. The supernatant was filtered through HPLC certified 220 μm filters, analyzed by HPLC on a Vydac RP18-column (4.6 $\times$ 250 mm; 5 μm/ 300 Å, Merck Hitachi, Darmstadt, Germany), and monitored by fluorescence detection. A linear gradient with 0.1% TFA in water (A) and 0.08% in acetonitrile (B) from 25% to 50% B in A over 60 min at a flow rate of 600 μL min^{-1} was used. The fluorescence labeled metabolites collected from each HPLC chromatogram were identified by MALDI-ToF as possible cleavage sites from the parent peptide.

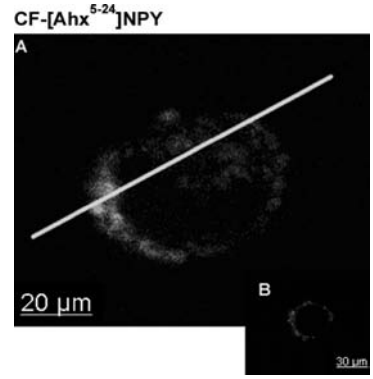

Figure 3. (A) Cellular uptake of CF-[Ahx$^{5-24}$]NPY in SMS-KAN cells. Cells were incubated with the CF-labeled peptide at a final concentration of 1 μm at 37 °C for 120 min. The CLSM view shows a slice at 3.08 μm from Z-scans (from −4.50 to 2.04 μm with an increment interval of 0.38 μm). (B) For the determination of nonspecific adsorption of the ligand, BHK cells which do not express NPY receptors were used as negative control. They were treated in parallel and observed in CLSM under the same parameters.

Inoculation of MCF-7 Tumor Cells in Immunodeficient Mice. In general, for biodistribution studies nude mice (female); app. 18 g NMRI nu/nu were used. First of all, three days before tumor cell inoculation, subcutaneous implantation of estrogen pellet in the left shoulder was affected. Mice were anesthesized with Isofluran Curamed. MCF-7 cells were resuspended in Dulbecco's PBS with Ca^{2+}/Mg^{2+} and Matrigel Matrix with growth factor. Subcutaneous injection of 100 μL of the cell suspension containing similarly 2 $\times$ 10^7 cells occurred in the right shoulder of the mice 16 days before biodistribution.

Biodistribution of Lys(^{111}In-DOTA)^4-[Phe^7, Pro^{34}]NPY in MCF-7 Tumor-Bearing Mice. The biodistribution of Lys(^{111}In-DOTA)^4-[Phe^7, Pro^{34}]NPY was studied in nude mice bearing MCF-7 tumors. Adjacent to the induction of light anesthesia with Isofluran Curamed, the animals were injected with the radiolabeled peptide via a lateral tail vein at a radioactive dose of 88 kBq ^{111}In. Following injection, animals were individually housed in metabolism cages with food and water to allow separate collection of voided urine and feces. Animals were killed after 0.5 h, 1.0 h, 2.0 h, 4.0 h, and 24 h by decapitation under anesthesia with Isofluran Curamed. Each carcass was dissected and the organs and tissues assayed for radioactivity (*18*).

RESULTS

Synthesis and Labeling of NPY Analogues. For our studies, we used the three NPY analogues [Phe^7, Pro^{34}]NPY,

[Ahx$^{5-24}$]NPY, and [Ahx$^{8-20}$]NPY as well as NPY. It has been shown that [Phe^7, Pro^{34}]NPY significantly binds to Y_1 receptors with subnanomolar affinity (*19*). For [Ahx$^{5-24}$]NPY and [Ahx$^{8-20}$]NPY, selectively binding to Y_2 receptors has been observed (*13*, *20*). The peptides were produced with either a DOTA or a CF group (Figure 1). The labels were introduced manually to the resin-bound peptides either at the N-terminus or at the selectively deprotected N$^{\varepsilon}$ side chain of Lys^4 while they were still bound to the resin. The most potent DOTA-conjugated peptide was chelated with $Ga(NO_3)_3$ and $InCl_3$. The optimum conditions at which we could obtain the Ga-DOTA-NPY analogue with a maximum yield (42%) and the In-DOTA-NPY analogue with a maximum yield (96%) included the incubation of DOTA-conjugated peptide in 0.4 M sodium acetate buffer and 0.4 M ammonium acetate buffer with 0.01 M aqueous solution of $Ga(NO_3)_3$ or $InCl_3$ for 30 min at 37 °C. All peptides were purified and analyzed by RP-HPLC and the identity was confirmed by MALDI-ToF. A typical analytical data of the compound **2f** are shown in Figure 2. In total, 23 peptides were produced and their sequences and analytical data are listed in Table 1. Numbering was performed according to the scheme described in Figure 1.

Receptor Binding Affinity. The receptor affinity was tested at cell lines that selectively express single NPY receptor subtypes by the displacement of 1 nM [^{3}H]propionyl-NPY. The experimental data showed an IC_{50} value of 2.0 ± 0.1 nM for NPY at Y_1 receptor expressing SK-N-MC cells that was transferred to a K_i value of 0.3 ± 0.02 nM, by using the Cheng-Prusoff equation (*17*). Evaluation of the binding data obtained with the modified or labeled analogues is summarized in Table 1. As shown in Table 1, the unlabeled NPY showed maximum binding at all NPY receptor expressing cells.

To test the effect of the chelator on receptor binding properties, compounds **2**−**4** were labeled with DOTA. The labeling of compound **2** as well as of NPY at the N$^{\varepsilon}$ side chain of Lys^4 with DOTA showed better binding affinities at Y_1/Y_2 receptor expressing cells compared to the labeling at the N-terminus (compound **2a** with pK_i values 8.6 ± 0.2 vs **2b** with 9.5 ± 0.2). A reversed effect was observed with compounds **3a** and **3b** at Y_2 receptors with pK_i values 8.8 ± 0.1 vs 8.5 ± 0.1, respectively.

Although some loss in affinity was found for compound **2e** (pK_i = 8.8 ± 0.1), nanomolar affinity was still found for the Ga-DOTA-labeled peptide. The same affinity could be observed for the In-DOTA-labeled peptide, compound **2f** (pK_i = 8.8 ± 0.1).

Furthermore, the DOTA conjugated compound **2a** showed constant selectivity at Y_1 receptor expressing SK-N-MC and MCF-7 cells compared to Y_2 and Y_5 receptor expressing SMS-KAN and HEC-1B−Y5 cells (compound **2a** with pK_i values of 8.6 ± 0.2 at SK-N-MC vs 6.5 ± 0.1 and 7.1 ± 0.3 at SMS-KAN and HEC-1B−Y5 cells). Same results could be observed for the compound **2b** with DOTA at N$^{\varepsilon}$ side chain of Lys^4 (compound **2b** with pK_i values of 9.5 ± 0.2 at SK-N-MC vs 7.2 ± 0.1 and 7.5 ± 0.1 at SMS-KAN and HEC-1B−Y5 cells).

To determine whether the fluorescently labeled NPY analogues had any effect on receptor affinity, CF labeled peptides were tested as well. Interestingly, the binding was found to significantly dependent on the position of the labeling, as the NPY receptor selective N-terminally labeled peptides as well as NPY were found to be mostly more biologically active at the corresponding NPY Y_1 or Y_2 receptor. The effect was pronounced at the Y_1 receptors especially in MCF-7 cells (compounds **1c** and **1d** with pK_i values of 9.3 ± 0.2 vs 7.2 ± 0.1, respectively). Similar results were also obtained with Y_2 receptor selective analogues at SMS-KAN cells (compounds **3c** and **4c** with pK_i values of 8.2 ± 0.1 and 8.8 ± 0.1 vs pK_i values of 8.0 ± 0.1 and 7.7 ± 0.1 of compounds **3d** and **4d**). All of these binding data at various receptors are summarized in Table 1. These fluorescent labeled compounds were further used in confocal microscopy for visualization of the receptor−ligand interaction in internalization assays to investigate uptake of compounds into the cells. For all analogues, receptor subtype selective uptake could be demonstrated. Figure 3 shows the cellular uptake of compound **3c** into SMS-KAN cells by using confocal laser scanning microscopy (CLSM).

Metabolic Stability in Human Blood Plasma. The metabolic stability and the main cleavage product in human blood plasma of [Lys(CF)^4, Phe^7, Pro^{34}]NPY, compound **2d**, was determined. The intact peptide found after 3 h incubation was about 95%, after 6 h as 88%, after 12 h as 74%, and after 24 h about 71%. Only one main cleavage product could be detected for the NPY analogue after 24 h, [Lys(CF)^4, Phe^7, Pro^{34}]NPY(1−35) with about 25−30%. Figure 4 shows the analytical data of metabolic degradation in human blood plasma after 24 h and the time course of degradation of [Lys(CF)^4, Phe^7, Pro^{34}]NPY.

Radiolabeling. [Phe^7,Pro^{34}]NPY has been shown to be the compound with the most significant Y_1-receptor preference with subnanomolar affinity (*19*). Accordingly, we used this NPY analogue for radiolabeling and biodistribution studies in MCF-7 tumor-bearing mice for detection of breast cancers. ^{111}In-DOTA radiolabeling of [Lys(DOTA)^4, Phe^7, Pro^{34}]NPY is also dependent on different labeling conditions, like temperature, pH, and reaction time. Optimized conditions were found for the incubation of DOTA-NPY analogue in 2.5 M saline solution and $^{111}InCl_3$ (41 MBq) in 0.04 M HCl for 15 min at 75 °C with a radiochemical yield of 80%. In contrast, a longer incubation time of 20 min and a temperature of 70 °C led to a radiochemical yield of only 6% (Figure 5A). The radiolabeled peptide was analyzed by radio-HPLC. A typical radio-HPLC chromatogram of the compound **2g** is shown in Figure 5B.

Biodistribution. The evaluation of [Lys(^{111}In-DOTA)^4, Phe^7, Pro^{34}]NPY for *in vivo* receptor targeting was performed by using biodistribution in MCF-7 tumor-bearing mice. Therefore, the nude mice were successfully inoculated with the Y_1 receptor expressing MCF-7 cell line in the right shoulder. The animals were injected with the ^{111}In-labeled peptide via a lateral tail vein (inject dose of 87.67 kBq). The radiolabeled peptide was not removed from the unlabeled peptide. Separated organs, tissues, and the blood were weighed and assayed for radioactivity using a gamma-counter for detection of ^{111}In after 0.5 h, 1.0 h, 2.0 h, 4.0 h, and 24 h respectively. Microsoft *Excel* analysis program was applied to calculate %ID/g (percent of injected dose per gram organ, tissue, or blood). The biodistribution study data of the compound **2g** demonstrated extensive accumulation in the kidney and a low tumor uptake. After intravenous injection of the ^{111}In-labeled peptide, maximum tumor uptake of 1.7%ID/g was reached after 30 min. A significant accumulation of 86.8%ID/g after 4 h was reached in the kidney. Furthermore, an increase in the uptake was found in the bone with a maximum of 1.62%ID/g after 24 h. A relatively lower concentration was detected in spleen (1.10%ID/g after 24 h). In the adrenals and blood, ^{111}In-labeled peptide concentration decreased over 24 h. The complete results of the biodistribution study are summarized in Table 2.

DISCUSSION

The prerequisite for radiolabeled receptor-binding peptides as diagnostic or therapeutic agents include therapeutic efficacy and favorable pharmacokinetics, such as rapid and high tumor uptake, extended tumor retention, high organ ratio of tumor to normal organ, and rapid whole-body clearance (*21*). In a metalloradiopharmaceutical, the targeting biomolecule is only one part of the whole molecule and the development of an efficient BFC and new

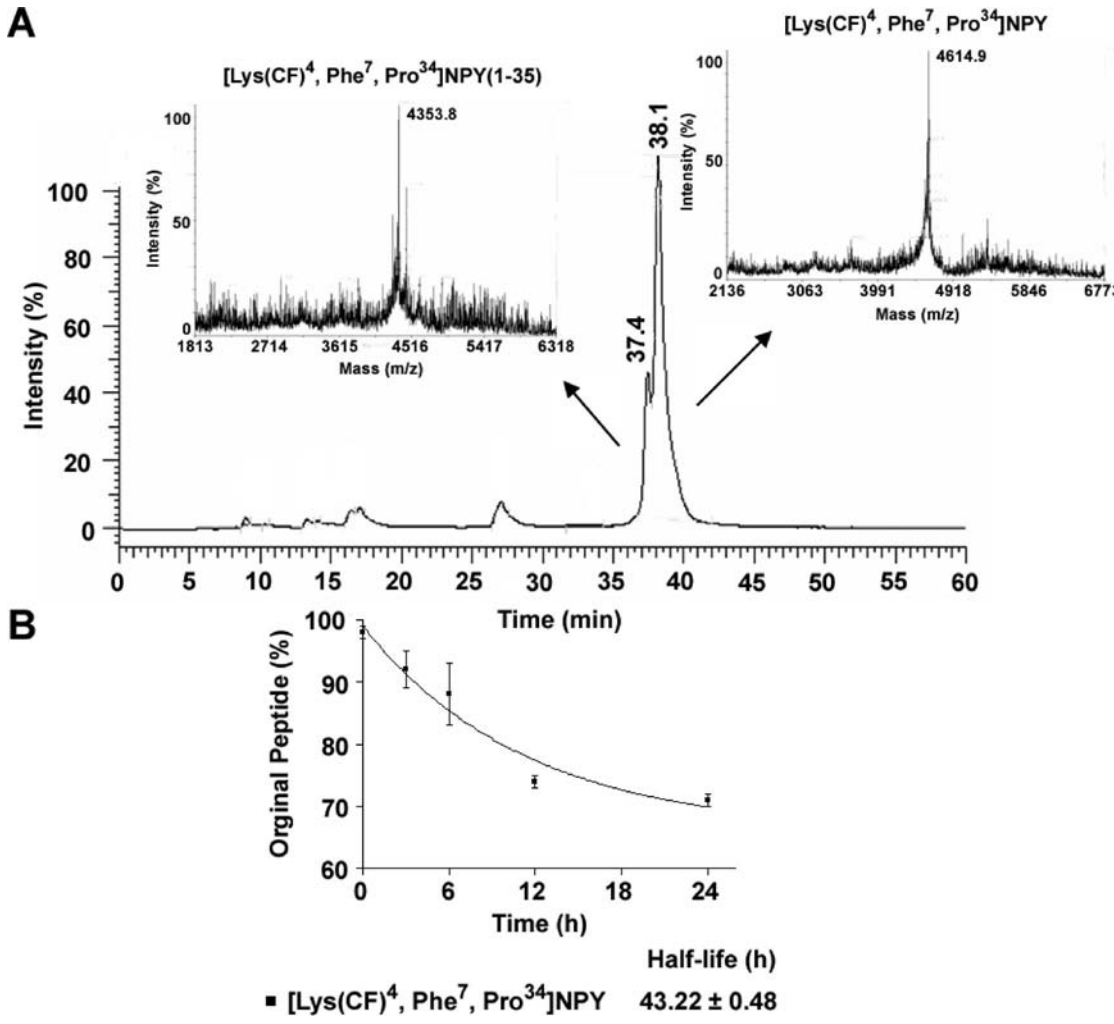

Figure 4. (A) HPLC chromatogram from 20% to 50% ACN in 60 min and MALDI spectra of fluorescence labeled metabolites of [Lys(CF)^4, Phe^7, Pro^{34}]NPY, compound **2d** after 24 h incubation at 37 °C in human blood plasma. (B) Time course of degradation after incubating compound **2d** with blood plasma at 37 °C.

radiolabeling technologies is equally important. For the receptor-based therapeutic radiopharmaceuticals, it is very important to remember that the receptor population is often limited. The use of a large amount of unlabeled bifunctional chelator−biomolecule (BFC-BM) conjugate may block the binding of the radiolabeled BFC-BM conjugate at the receptor sites. Therefore, the BFC must have very high labeling efficiency (fast and high-yield labeling) and form metal complexes with high specific activity. The choice of BFC is largely dependent upon the nature and oxidation state of the metal ion and requires a good understanding of the coordination chemistry of any given radiometal. Another point of fundamental concern in the design of radiometallated peptide constructs is to ensure the *in vivo* stability of the radiometal incorporated by the ligand framework. *In vivo* stability can be controlled by virtue of the high thermodynamic stability and the kinetic inertness of a specific metal chelation framework (*22*–*24*).

Because the DOTA macrocyclic ligand system is well-known to form kinetically inert and thermodynamically stable chelates with indium, yttrium, and lanthanides, it has received wide acceptance for *in vivo* applications with several trivalent radiometals, not only for scintigraphy but also for peptide receptor radionuclide therapy (PRRT) (*25*–*27*). Peptide ligands can be derivatized with DOTA without loss of receptor specificity and binding affinity. Recently, [DOTA^0, Tyr^3]-octreotate, labeled with the β- and γ-particle-emitting radionuclide ^{177}Lu, was reported to be very successful in terms of tumor regression and animal survival in a rat model (*28*).

Bifunctional chelating agents (BFCAs) can be incorporated into peptides by using either the prelabeling or postlabeling approach. In the postlabeling approach, a BFCA is first attached to the peptide and then the radionuclide is coupled to the free chelating group of the BFCA (*29*). This approach can be combined with the advantages of solid-phase peptide synthesis (SPPS). Applying a molar excess of BFCA, complete coupling to the resin-bound peptide can be achieved, and unreacted BFCA is easily washed away. Subsequent cleavage from the resin yields the highly pure BFCA−peptide conjugate.

Accordingly, NPY receptor-selective derivatives on Rink amide resin were synthesized, selectively deprotected N$^\varepsilon$ side chain of Lys^4 by hydrazine in DMF and coupled the BFCA either at the N$^\varepsilon$ side chain of Lys^4 or at the N-terminus, by using the postlabeling approach. Furthermore, by incorporation of Phe^7 and Pro^{34} into NPY sequence, Y_1 receptor subtype selectivity (*19*) and by replacing the sequence (5−24)NPY or (8−20)NPY with the spacer 6-aminohexanoic acid (Ahx), Y_2 receptor subtype selectivity were achieved (*30*). This can be confirmed by the binding data of compounds **2** and **3** determined with SK-N-MC and SMS-KAN cells with (pK_i values 10.3 ± 0.2 vs 7.6 ± 0.1) and (pK_i values 6.8 ± 0.1 vs 9.2 ± 0.3), respectively.

The compounds conjugated with DOTA at the N$^\varepsilon$ side chain of Lys^4 showed higher affinity compared to the N-terminally conjugated compounds with respect to native NPY and the NPY Y_1 receptor selective analogue. These effects could be due to

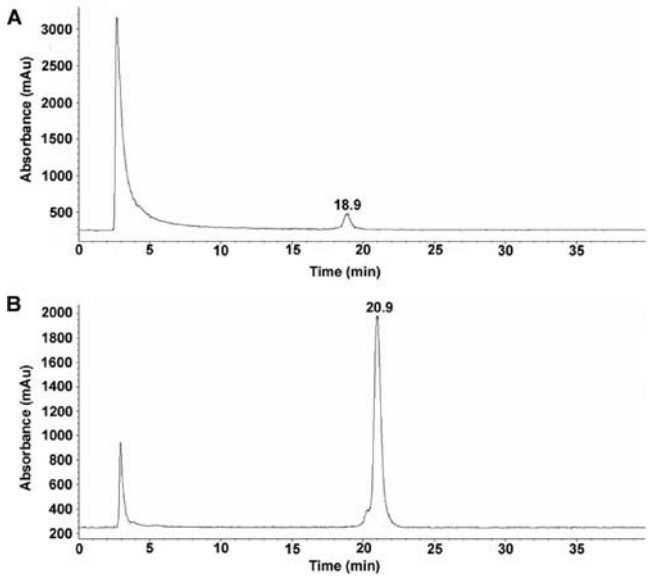

Figure 5. (A) Radio-HPLC chromatogram from 25% to 50% ACN in 30 min of [Lys(^{111}In-DOTA)^4, Phe^7, Pro^{34}]NPY, compound **2g**, after 20 min incubation at 70 °C. The radio-HPLC chromatogram shows a radiochemical yield of only 6%. (B) Radio-HPLC chromatogram from 25% to 50% ACN in 30 min of [Lys(^{111}In-DOTA)^4, Phe^7, Pro^{34}]NPY, compound **2g**, after 15 min incubation at 75 °C. The radio-HPLC chromatogram shows a radiochemical yield of 80%.

less steric hindrance encountered by more spatial availability of the N-terminus produced by labeling of the chelator at the N$^\epsilon$ side chain of Lys^4. Our results show that N-terminal flexibility is a crucial factor for the interaction of the bioconjugate with the receptor. Otherwise, the N-terminally DOTA-conjugated NPY Y_2 receptor selective analogue showed higher affinity than that conjugated at the N$^\epsilon$ side chain of Lys^4. These data can be explained by the reduced influence of the truncated N-terminus of [Ahx$^{5-24}$]NPY in receptor binding compared to NPY or [Phe^7, Pro^{34}]NPY.

Carboxyfluorescein possesses two carboxyl groups as possible reaction centers, the intrinsic carboxyl group of fluorescein in position 2 and the additional carboxyl group in position 4(5). Since the fluorescence-properties of fluorescein depend on the presence of the free carboxyl-group in position 2, this group has to remain unmodified during reaction. Our data show that the peptides labeled with CF at the N-terminus showed mostly higher affinity compared to the CF-labeling at the N$^\epsilon$ side chain of Lys^4. This also suggests that the type of modifier is involved in the Y-receptor−ligand interaction.

A metabolic stability study in human blood plasma of [Lys(CF)^4, Phe^7, Pro^{34}]NPY was performed. The peptide was found to be enzymatically more stable than native NPY (half-life of 24.66 ± 1.38 h) *in vitro* (*31*). In addition, only one main cleavage product [Lys(CF)^4, Phe^7, Pro^{34}]NPY(1−35) could be detected after 24 h incubation (*31*).

Furthermore, first results of the *in vivo* behavior of the Y_1 receptor selective neuropeptide Y (NPY) analogue [Phe^7, Pro^{34}]NPY could be obtained. Our data show that [Lys-(DOTA)^4, Phe^7, Pro^{34}]NPY was successfully labeled with ^{111}In at 75 °C for 15 min with a radiochemical yield of 80%. In contrast, by using a temperature of 70 °C and an incubation time of 20 min only a radiochemical yield of 6% could be observed. This result suggests that higher reaction temperatures could lead to more flexibility of the cage-like structure of DOTA followed by a better complexation of ^{111}In. However, higher temperatures could lead to degradation of the peptide. Different retention times in radio-HPLC (20.9 min vs 18.9 min) could be explained by distinct concentrations of the unlabeled peptide.

In the past, strong predominance of the Y_1 receptor subtype was shown in breast carcinomas (*9*). Thus, the nude mice for the biodistribution study were inoculated with the Y_1 receptor expressing MCF-7 breast cancer cell line. Our results demonstrate a high accumulation of the ^{111}In-DOTA-labeled [Phe^7, Pro^{34}]NPY in the kidney with 86.8% ID/g after 4 h. This is a common phenomenon for radiometal-chelated peptides, especially for peptides with DOTA as BFC (*32*). On the other hand, our biodistribution results show a low tumor uptake of the peptide with 1.7% ID/g after 30 min. These data indicate that the interaction between the ^{111}In-labeled peptide and the breast cancer tumor, which expresses the Y_1 receptor subtype, was disturbed by the faster accumulation in the kidney. Another reason for the low tumor uptake could be the lack of separation of the unlabeled peptide, which might have resulted in binding competition of the unlabeled and ^{111}In-labeled peptide *in vivo*. Moreover, it has been shown that the native ligand NPY exhibits rapid proteolysis in humans with a half-life of only 4 min (*33*). The differences between the metabolic stability in the body

Table 2. Biodistribution of [Lys(^{111}In-DOTA)^4, Phe^7, Pro^{34}]NPY

time	0.5 h	1.0 h	2.0 h	4.0 h	24 h
weight (g)	29.79	31.68	30.73	27.69	27.36
			%ID/g		
spleen	1.52 ± 0.27	1.36 ± 0.36	1.08 ± 0.16	1.37 ± 0.19	1.10 ± 0.24
liver	3.34 ± 0.56	3.23 ± 0.61	3.41 ± 0.23	4.20 ± 0.30	3.25 ± 0.99
kidney	60.54 ± 8.80	63.01 ± 9.40	77.11 ± 3.30	86.83 ± 11.60	67.60 ± 13.30
lung	3.04 ± 0.35	2.28 ± 0.15	1.48 ± 0.12	1.48 ± 0.13	0.48 ± 0.14
bone	1.52 ± 0.20	0.97 ± 0.10	0.86 ± 0.08	0.89 ± 0.21	1.62 ± 0.11
heart	1.62 ± 0.02	1.09 ± 0.13	0.95 ± 0.07	1.02 ± 0.21	0.36 ± 0.04
brain	0.11 ± 0.01	0.09 ± 0.04	0.07 ± 0.01	0.08 ± 0.01	0.03 ± 0.003
fat	0.50 ± 0.04	0.38 ± 0.02	0.55 ± 0.12	0.48 ± 0.14	0.68 ± 0.12
thyroid	1.70 ± 0.29	1.08 ± 0.40	0.74 ± 0.07	0.73 ± 0.11	0.52 ± 0.05
muscle	0.75 ± 0.07	0.52 ± 0.09	0.33 ± 0.09	0.42 ± 0.10	0.24 ± 0.09
tumor	1.66 ± 0.51	1.29 ± 0.33	1.13 ± 0.23	1.25 ± 0.31	1.21 ± 0.39
skin	1.93 ± 0.36	1.29 ± 0.06	0.87 ± 0.14	1.07 ± 0.09	0.99 ± 0.10
blood	3.77 ± 0.38	2.93 ± 0.36	2.41 ± 0.33	2.23 ± 0.52	0.32 ± 0.12
tail	3.74 ± 0.98	3.61 ± 2.46	5.05 ± 2.23	3.04 ± 1.36	1.15 ± 0.56
stomach	1.21 ± 0.15	0.86 ± 0.05	0.64 ± 0.06	0.64 ± 0.12	0.49 ± 0.09
ovary	1.58 ± 0.13	1.18 ± 0.21	1.38 ± 0.41	1.14 ± 0.22	0.75 ± 0.15
uterus	1.62 ± 0.28	1.51 ± 0.58	1.31 ± 0.15	1.41 ± 0.34	0.89 ± 0.16
intestine	0.89 ± 0.18	0.71 ± 0.04	0.74 ± 0.05	0.84 ± 0.13	0.65 ± 0.18
pancreas	1.13 ± 0.17	0.91 ± 0.11	0.78 ± 0.04	0.86 ± 0.13	0.63 ± 0.13
adrenals	1.69 ± 0.22	1.43 ± 0.05	1.46 ± 0.40	1.52 ± 0.24	1.03 ± 0.10

and the blood can be confirmed by our results of the fast degradation of the ^{111}In-DOTA-labeled [Phe^7, Pro^{34}]NPY in mice compared to the half-life of [Lys(CF)^4, Phe^7, Pro^{34}]NPY in human blood plasma. The development of metabolically more stable NPY analogues is a crucial step for radiopharmaceutical application.However, Y_1 receptor selective NPY analogues show good capability for future applications in tumor targeting and therapy, confirmed by some tumor uptake of [Lys(^{111}In-DOTA)^4, Phe^7, Pro^{34}]NPY.

Accordingly, we clearly could demonstrate a novel application of modified BFCA-conjugated NPY Y_1/Y_2 receptor selective analogues. Competitive binding assays showed surprisingly high affinity to the desired receptors. Based on structure−activity relationships of NPY, we found potential candidates for metal complexation. By using SPPS, stable, well-defined BFCA DOTA conjugated analogues for Ga or In and ^{111}In complexation were synthesized. These analogues are stable and selectively maintained the binding with the desired receptor. Our data show that, in spite of replacement/substitution of amino acids, introduction of spacer, and incorporation of an organometallic moiety, the binding potency of the ligand at the receptor was only slightly influenced. Moreover, the *in vivo* data show the possibility of using NPY Y_1 receptor selective analogues for future applications in tumor therapy and diagnosis, because some, although still low, tumor uptake in MCF-7 tumor-bearing mice was observed. Our *in vitro* and *in vivo* data demonstrate that modified NPY analogues are expandable candidates for further developments in the field of tumor targeting.

ACKNOWLEDGMENT

The authors thank Regina Reppich for excellent mass spectrometry and Christina Dammann for technical assistance in cell culture. This work was financially supported by DFG (FOR630, Be1264/9−1), EFRE (Grant # 3370701481201), and by Bayer Schering Pharma.

LITERATURE CITED

(1) Heppeler, A., Froidevaux, S., Eberle, A. N., and Maecke, H. R. (2000) Receptor targeting for tumor localisation and therapy with radiopeptides. *Curr. Med. Chem. 7*, 971–94.

(2) Tatemoto, K., Carlquist, M., and Mutt, V. (1982) Neuropeptide Y-a novel brain peptide with structural similarities to peptide YY and pancreatic polypeptide. *Nature 296*, 659–60.

(3) Grundemar, L. B., S.R. (1997) *Neuropeptide Y and drug developments*, p 396, Academic Press, San Diego.

(4) Michel, M. C., Beck-Sickinger, A., Cox, H., Doods, H. N., Herzog, H., Larhammar, D., Quirion, R., Schwartz, T., and Westfall, T. (1998) XVI. International Union of Pharmacology recommendations for the nomenclature of neuropeptide Y, peptide YY, and pancreatic polypeptide receptors. *Pharmacol. Rev. 50*, 143–50.

(5) Beck-Sickinger, A. (1997) The importance of various parts of the NPY molecule for receptor recognition. *Neuropept. Drug Dev.* 107–126.

(6) Korner, M., Waser, B., and Reubi, J. C. (2005) Neuropeptide Y receptors in renal cell carcinomas and nephroblastomas. *Int. J. Cancer 115*, 734–41.

(7) Korner, M., Waser, B., and Reubi, J. C. (2004) Neuropeptide Y receptor expression in human primary ovarian neoplasms. *Lab. Invest. 84*, 71–80.

(8) Reubi, J. C., Korner, M., Waser, B., Mazzucchelli, L., and Guillou, L. (2004) High expression of peptide receptors as a novel target in gastrointestinal stromal tumours. *Eur. J. Nucl. Med. Mol. Imaging 31*, 803–10.

(9) Reubi, J. C., Gugger, M., Waser, B., and Schaer, J. C. (2001) Y(1)-mediated effect of neuropeptide Y in cancer: breast carcinomas as targets. *Cancer Res. 61*, 4636–41.

(10) Breeman, W. A., Bakker, W. H., De Jong, M., Hofland, L. J., Kwekkeboom, D. J., Kooij, P. P., Visser, T. J., and Krenning, E. P. (1996) Studies on radiolabeled somatostatin analogues in rats and in patients. *Q. J. Nucl. Med. 40*, 209–20.

(11) Moser, C., Bernhardt, G., Michel, J., Schwarz, H., and Buschauer, A. (2000) Cloning and functional expression of the hNPY Y5 receptor in human endometrial cancer (HEC-1B) cells. *Can. J. Physiol. Pharmacol. 78*, 134–42.

(12) Rist, B., Ingenhoven, N., Scapozza, L., Schnorrenberg, G., Gaida, W., Wieland, H. A., and Beck-Sickinger, A. G. (1997) The bioactive conformation of neuropeptide Y analogues at the human Y2-receptor. *Eur. J. Biochem. 247*, 1019–28.

(13) Rist, B., Wieland, H. A., Willim, K. D., and Beck-Sickinger, A. G. (1995) A rational approach for the development of reduced-size analogues of neuropeptide Y with high affinity to the Y1 receptor. *J. Pept. Sci. 1*, 341–8.

(14) Bloomberg, G. B., A, D., Gargaro, A. R., and Tanner, M. J. A. (1993) Synthesis of a branched cyclic peptide using a strategy employing Fmoc chemistry and two additional orthogonal protecting groups. *Tetrahedron Lett. 34*, 4709–4712.

(15) Weber, P. J., Bader, J. E., Folkers, G., and Beck-Sickinger, A. G. (1998) A fast and inexpensive method for N-terminal fluorescein-labeling of peptides. *Bioorg. Med. Chem. Lett. 8*, 597–600.

(16) Gali, H., Sieckman, G. L., Hoffman, T. J., Owen, N. K., Chin, D. T., Forte, L. R., and Volkert, W. A. (2001) In vivo evaluation of an ^{111}In-labeled ST-peptide analog for specific-targeting of human colon cancers. *Nucl. Med. Biol. 28*, 903–9.

(17) Cheng, H. C. (2001) The power issue: determination of KB or Ki from IC50. A closer look at the Cheng-Prusoff equation, the Schild plot and related power equations. *J. Pharmacol. Toxicol. Methods 46*, 61–71.

(18) Chen, J., Giblin, M. F., Wang, N., Jurisson, S. S., and Quinn, T. P. (1999) In vivo evaluation of ^{99m}Tc/^{188}Re-labeled linear α-melanocyte stimulating hormone analogs for specific melanoma targeting. *Nucl. Med. Biol. 26*, 687–93.

(19) Soll, R. M., Dinger, M. C., Lundell, I., Larhammer, D., and Beck-Sickinger, A. G. (2001) Novel analogues of neuropeptide Y with a preference for the Y1-receptor. *Eur. J. Biochem. 268*, 2828–37.

(20) Rist, B., Zerbe, O., Ingenhoven, N., Scapozza, L., Peers, C., Vaughan, P. F., McDonald, R. L., Wieland, H. A., and Beck-Sickinger, A. G. (1996) Modified, cyclic dodecapeptide analog of neuropeptide Y is the smallest full agonist at the human Y2 receptor. *FEBS Lett. 394*, 169–73.

(21) Miao, Y., Owen, N. K., Fisher, D. R., Hoffman, T. J., and Quinn, T. P. (2005) Therapeutic efficacy of a ^{188}Re-labeled α-melanocyte-stimulating hormone peptide analog in murine and human melanoma-bearing mouse models. *J. Nucl. Med. 46*, 121–9.

(22) Otte, A., Herrmann, R., Heppeler, A., Behe, M., Jermann, E., Powell, P., Maecke, H. R., and Muller, J. (1999) Yttrium-90 DOTATOC: first clinical results. *Eur. J. Nucl. Med. 26*, 1439–47.

(23) Heppeler, A. F., S., Maecke, H. R., Jermann, E., Behe, M., Powell, P., and Hennig, M. (1999) Radiometal-labelled macrocyclic chelator-derivatised somatostatin analogue with superb tumour-targeting properties and potential for receptor-mediated internal radiotherapy. *Chem. Eur. J. 5*, 1974–1981.

(24) Behr, T. M., Jenner, N., Behe, M., Angerstein, C., Gratz, S., Raue, F., and Becker, W. (1999) Radiolabeled peptides for targeting cholecystokinin-B/gastrin receptor-expressing tumors. *J. Nucl. Med. 40*, 1029–44.

(25) Kwekkeboom, D. J., Mueller-Brand, J., Paganelli, G., Anthony, L. B., Pauwels, S., Kvols, L. K., O'Dorisio, T, M., Valkema, R., Bodei, L., Chinol, M., Maecke, H. R., and Krenning, E. P. (2005) Overview of results of peptide receptor radionuclide therapy with 3 radiolabeled somatostatin analogs. *J. Nucl. Med. 46*, 62S–6S.

(26) Ingenhoven, N., and Beck-Sickinger, A. G. (1997) Fluorescent labelled analogues of neuropeptide Y for the characterization of

cells expressing NPY receptor subtypes. *J. Recept. Signal Transduct. Res. 17*, 407–18.
(27) Gordon, E. A., Kohout, T. A., and Fishman, P. H. (1990) Characterization of functional neuropeptide Y receptors in a human neuroblastoma cell line. *J. Neurochem. 55*, 506–13.
(28) Erion, J. L. B., J. E., Schmidt, M.A., Wilhelm, R. R., and Srinivasan, A. (1999) High radiotherapeutic efficacy of [Lu-177]-DOTA-Y(3)-octreotate in a rat tumor model. *J. Nucl. Med. 40*, 223.
(29) Liu, S., and Edwards, D. S. (1999) ^{99m}Tc-labeled small peptides as diagnostic radiopharmaceuticals. *Chem. Rev. 99*, 2235–68.
(30) Cabrele, C., and Beck-Sickinger, A. G. (2000) Molecular characterization of the ligand-receptor interaction of the neuropeptide Y family. *J. Pept. Sci. 6*, 97–122.
(31) Khan, I. U., Reppich, R., and Beck-Sickinger, A. G. (2007) Identification of neuropeptide Y cleavage products in human blood to improve metabolic stability. *Biopolymers 88*, 182–9.
(32) Froidevaux, S., Calame-Christe, M., Tanner, H., and Eberle, A. N. (2005) Melanoma targeting with DOTA-α-melanocyte-stimulating hormone analogs: structural parameters affecting tumor uptake and kidney uptake. *J. Nucl. Med. 46*, 887–95.
(33) Pernow, J., Lundberg, J. M., and Kaijser, L. (1987) Vasoconstrictor effects in vivo and plasma disappearance rate of neuropeptide Y in man. *Life Sci. 40*, 47–54.

BC7004297

Novel Bimodal Bifunctional Ligands for Radioimmunotherapy and Targeted MRI

Hyun-Soon Chong,*,† Hyun A. Song,† Xiang Ma,† Diane E. Milenic,‡ Erik D. Brady,‡ Sooyoun Lim,† Haisung Lee,† Kwamena Baidoo,‡ Dengfeng Cheng,† and Martin W. Brechbiel‡

Chemistry Division, Biological, Chemical, and Physical Sciences Department, Illinois Institute of Technology, Chicago, Illinois, Radioimmune and Inorganic Chemistry Section, Radiation Oncology Branch, Center for Cancer Research, National Cancer Institute, National Institutes of Health, Bethesda, Maryland. Received February 8, 2008; Revised Manuscript Received April 22, 2008

The structurally novel bifunctional ligands *C*-NETA and *C*-NE3TA, each possessing both acyclic and macrocyclic moieties, were prepared and evaluated as potential chelates for radioimmunotherapy (RIT) and targeted magnetic resonance imaging (MRI). Heptadentate *C*-NE3TA was fortuitously discovered during the preparation of *C*-NETA. An optimized synthetic method to *C*-NETA and *C*-NE3TA including purification of the polar and tailing reaction intermediates, *tert*-butyl *C*-NETA (**2**) and *tert*-butyl *C*-NE3TA (**3**) using semiprep HPLC was developed. The new Gd(III) complexes of *C*-NETA and *C*-NE3TA were prepared as contrast enhancement agents for use in targeted MRI. The T_1 relaxivity data indicate that Gd(*C*-NETA) and Gd(*C*-NE3TA) possess higher relaxivity than Gd(*C*-DOTA), a bifunctional version of a commercially available MRI contrast agent; Gd(DOTA). *C*-NETA and *C*-NE3TA were radiolabeled with ^{177}Lu, ^{90}Y, ^{203}Pb, $^{205/6}$Bi, and ^{153}Gd; and *in vitro* stability of the radiolabeled corresponding complexes was assessed in human serum. The *in vitro* studies indicate that the evaluated radiolabeled complexes were stable in serum for 11 days with the exception being the ^{203}Pb complexes of *C*-NETA and *C*-NE3TA, which dissociated in serum. *C*-NETA and *C*-NE3TA radiolabeled ^{177}Lu, ^{90}Y, or ^{153}Gd complexes were further evaluated for *in vivo* stability in athymic mice and possess excellent or acceptable *in vivo* biodistribution profile. $^{205/6}$Bi-*C*-NE3TA exhibited extremely rapid blood clearance and low radioactivity level at the normal organs, while $^{205/6}$Bi-*C*-NETA displayed low radioactivity level in the blood and all of the organs except for the kidney where relatively high renal uptake of radioactivity is observed. *C*-NETA and *C*-NE3TA were further modified for conjugation to the monoclonal antibody Trastuzumab.

INTRODUCTION

Radioimmunotherapy (RIT) (*1*) and magnetic resonance imaging (MRI) (*2*) are promising techniques for targeted treatment or imaging of numerous cancer types. Both modalities require the use of either radioactive or nonradioactive metals, either of which can be very toxic when deposited in normal tissues *in vivo*, causing life-threatening side effects (*3*). Therefore, the success of clinical applications of both RIT and MRI depends heavily on the performance of the metal-binding ligands. RIT employs a monoclonal antibody (mAb) for selective delivery of a cytotoxic radionuclide to tumor cells while minimizing toxicity due to nonselective exposure of the radionuclide to the normal healthy cells (*4, 5*). The RIT scenario requires three components: a radionuclide, a mAb, and a bifunctional ligand (*6*). The first RIT drug, Zevalin, consists of an anti-CD20 antibody, 1B4M-DTPA (2-(4-nitrobenzyl)-6-methyl-diethylenetriaminepentaacetic acid), and ^{90}Y, and has proven to have significant potency against B-cell non-Hodgkin's lymphoma (*7, 8*). The radionuclides ^{177}Lu, ^{90}Y, ^{212}Pb, ^{212}Bi, and ^{213}Bi are all recognized as promising metallic radionuclides for effective RIT (*5, 6*). An effective bifunctional ligand conjugated to a sensitive mAb that can rapidly form a stable complex with a short-lived radionuclide must be employed to minimize toxicity due to either dissociation of metal complex or radiolytic damage resulting from extended exposure of the protein during radiolabeling (*9–11*). Although numerous RIT using the radioisotopes have been explored to treatment of various cancers, less progress has been made on development of new bifunctional ligands that might address limitations of the currently available bifunctional ligands, *C*-DOTA (2-(4-nitrobenzyl)-1,4,7,10-tetraazacyclododecane tetraacetic acid) and *C*-DTPA (2-(4-nitrobenzyl)-diethylenetriamine pentaacetic acid), that are related to slow complexation kinetics and low complex stability, respectively (*12*).

MRI is a powerful diagnostic medical tool that provides noninvasive and high-resolution imaging for a variety of applications (*2, 13*). MRI gives distribution of the MR signal intensity resulting from the longitudinal (T_1) and the transverse (T_2) magnetic relaxation times of water protons. Images with a clear contrast between tissues with different relaxation times of water protons can be obtained with MRI (*2*). The lanthanide Gd(III) is known to be an optimal paramagnetic metal for MRI due to high electronic spin (7/2) and slow electronic relaxation rate (*14*). Stable Gd(III) complexes with low toxicity and efficient excretion profiles are required for *in vivo* use since free Gd(III) is toxic causing severe side effects (*15*). A number of Gd(III) complexes such as Gd(DOTA) and Gd(DTPA) are clinically approved for use in MRI (*2*). However, most contrast agents have nonspecific extracellular distribution and the disadvantages of low relaxivity, low tissue specificity, and rapid clearance. Considerable research efforts have been directed toward developing safe Gd(III)-based MR contrast agents with high tissue specificity and sensitivity. Development of bifunctional

* To whom correspondence should be addressed. E-mail: Chong@iit.edu, Phone: 312-567-3235, Fax: 312-567-3494. Mailing address: 3101 S. Dearborn St, LS 182, Illinois Institute of Technology, Chemistry Division, Biological, Chemical, and Physical Science Department, Chicago, IL, 60616.

† Illinois Institute of Technology.

‡ National Cancer Institute.

10.1021/bc800050x CCC: $40.75 © 2008 American Chemical Society
Published on Web 06/20/2008

ligands with a functional unit for conjugation to a targeting moiety that can tightly sequester Gd(III) is required for targeted MRI with high sensitivity and specificity.

Previously, we reported NETA to be a promising chelate for RIT and MRI applications (*16*–*18*). The bimodal ligand NETA ({4-[2-(bis-carboxymethyl-amino)-ethyl]-7-carboxymethyl-[1,4,7]triazonan-1-yl}-acetic acid) possesses a parent macrocyclic ligand and a flexible acyclic multidentate pendant arm and is designed to integrate the advantages of the macrocyclic DOTA (1,4,7,10-tetraazacyclododecane-tetraacetic acid) and acyclic DTPA (diethylenetriaminepenta acetic acid) frameworks and with this hybridization to provide high thermodynamic stability and favorable formation kinetics for complexation of metal ions of interest. Indeed, nonfunctionalized NETA displayed significantly enhanced complexation kinetics with Y(III) (*16*), Lu(III) (*19*), and Bi(III) (*19*) as compared to DOTA. The NETA complexes radiolabeled with ^{90}Y (*16*), ^{177}Lu (*17*), or ^{153}Gd (*18*) exhibited excellent *in vitro* serum stability and demonstrated excellent or acceptable *in vivo* biodistribution profiles. NETA was also evaluated as the chelate of Gd(III) for MRI. NETA-Gd(III) complex displayed enhanced relaxivity comparable to that of DOTA-Gd(III) (*18*). NETA radiolabeled with ^{153}Gd was exceptionally stable in serum and mice (*18*). With the proven potential of NETA for RIT and MRI, we have moved forward with synthesis of a bifunctional version of NETA and NETA analogue possessing a linker for conjugation to a targeting moiety for RIT and for targeted MRI. In this paper, we describe the synthesis and evaluation of a bifunctional version of NETA, *C*-NETA ({4-[2-(bis-carboxymethyl-amino)-3-(4-nitro-phenyl)-propyl]-7-carboxymethyl[1,4,7]triazonan-1-yl}-acetic acid) and its heptadentate analogue *C*-NE3TA ({4-carboxymethyl-7-[2-(carboxymethyl-amino)-3-(4-nitro-phenyl)-propyl]-[1,4,7]triazo-nan-1-yl}-acetic acid) for RIT and MRI.

EXPERIMENTAL PROCEDURES

Instruments and Methods. ^{1}H and ^{13}C NMR spectra were obtained using a Bruker 300 MHz instrument and chemical shifts are reported in ppm on the δ scale relative to TMS, TSP, or solvent. Elemental microanalyses were performed by Galbraith Laboratories, Knoxville, TN. Fast atom bombardment (FAB) high-resolution mass spectra (HRMS) were obtained on JEOL double sector JMS-AX505HA mass spectrometer (University of Notre Dame, IN). Analytical HPLC was performed on Agilent 1200 instrument (Agilent, Santa Clara, CA) equipped with a diode array detector (λ = 254 and 280 nm), thermostat set at 35 °C, and a Zorbax Eclipse XDB-C18 column (4.6 × 150 mm, 80Å, Agilent, Santa Clara, CA). The mobile phase of a binary gradient (0−100% B/40 min; solvent A = 0.05 M AcOH/Et_3N, pH 6.0; solvent B = CH_3CN for method 1) or solvent A = 0.05 M AcOH/Et_3N, pH 6.0; solvent B = CH_3OH for method 2; (0−50% B/30 min solvent A = 0.05 M AcOH/Et_3N, pH 6.0; solvent *B* = CH_3OH for method 5) or a binary gradient and isocratic (0−100% B/40 min and 100% B/40−50min; solvent A = 0.05 M AcOH/Et_3N, pH 6.0; solvent B = CH_3CN for method 6) at a flow rate of 1 mL/min was used. Semiprep HPLC was performed on an Agilent 1200 equipped with a diode array detector (λ = 254 and 280 nm), thermostat set at 35 °C, and a Zorbax Eclipse XDB-C18 column (9.4 × 250 mm, 80 Å). The mobile phase of a binary gradient (0−100% B/160 min; solvent A = 0.05 M AcOH/Et_3N, pH 6.0; solvent B = CH_3CN for method 3 or 0−50% B/30 min, solvent A = H_2O; solvent B = methanol for method 4) at a flow rate of 3 mL/min was used. Size exclusion HPLC (SE-HPLC) chromatograms were obtained on a Laboratory Alliance isocratic system (model: QGrad, State College, PA) with a Waters 717plus autosampler (Milford, MA), a Gilson 112 UV detector (Middleton, WI), and an in-line IN/US γ-Ram model 2 radiodetector (Tampa, FL), fitted with a TSK G3000PW column (Tosoh Biosep, Montgomeryville, PA).

Reagents. All reagents were purchased from Sigma-Aldrich (St. Louis, MO) and used as received unless otherwise noted. Phosphate buffered saline (PBS), 1×, pH 7.4, consisted of 0.08 M Na_2HPO_4, 0.02 M KH_2PO_4, 0.01 M KCl, and 0.14 M NaCl. ^{90}Y in the chloride form was purchased from Perkin-Elmer Life Sciences (Shelton, CT). ^{177}Lu in the chloride form was obtained from NEN Perkin-Elmer. ^{86}Y,^{205,6}Bi, and ^{203}Pb were produced using a CS30 cyclotron (PET Dept, Clinical Center, NIH) and purified as described previously (*17*, *18*). *C*-DOTA was purchased from Macrocyclics (Dallas, TX). ^{153}Gd was obtained from Isotope products (Valencia, CA). ^{157}Gd and ^{115}In were obtained from Sigma-Aldrich (St. Louis, MO).

***tert*-Butyl {4-*tert*-Butoxycarbonylmethyl-7-[2-(*tert*-butoxycarbonylmethyl-amino)-3-(4-nitrophenyl)-propyl]-[1,4,7]triazonan-1-yl}-acetic Acetate (3).** To a slurry of **1** (*26*) as an acidic salt (2.27 g, 5 mmol) in DMF (50 mL) at 0 °C was added DIPEA (6.5 g, 50.25 mmol) and KI (996 mg, 6 mmol). *tert*-Butyl bromoacetate (3.22 g, 16.5 mmol) was added dropwise over 20 min. The resulting mixture was stirred for 2 h at 0 °C and for 2 h at room temperature. The reaction mixture was heated to 50 °C and stirred for 19 h after which time the reaction mixture was cooled to room temperature and then to 0 °C. 6 M HCl (3.5 mL) and heptane (30 mL) were sequentially added to the solution. The resulting solution was vigorously stirred for 5 min, and the heptane layer was separated. The aqueous layer was extracted with heptane (2 × 30 mL), and treated with 10% Na_2CO_3 (45 mL). Additional heptane (30 mL) was added into the aqueous solution, the resulting mixture was stirred for 30 min, and the heptane layer was separated. The combined heptane layers were washed with water (10 mL), dried ($MgSO_4$), filtered, and concentrated *in vacuo*. The residue was eluted on a silica gel (220−400 mesh) column with 20−30% CH_3OH/CH_2Cl_2 and 0.5 mL Et_3N in 20−30% CH_3OH/CH_2Cl_2 starting from CH_2Cl_2 to provide pure **3** (2.21 g, 68%): ^{1}H NMR ($CDCl_3$) δ 1.41 (s, 27 H), 2.30−2.52 (m, 2 H), 2.63−2.94 (m, 15 H), 3.20−3.36 (m, 6 H), 7.36 (d, J = 8.01 Hz, 2 H), 8.15 (d, J = 8.01 Hz, 2 H); ^{13}C NMR ($CDCl_3$) δ 28.98, 28.09, 39.32, 49.83, 55.84, 56.04, 56.92, 59.48, 62.62, 80.36, 80.76, 123.32, 130.11, 146.36, 147.47, 171.07, 171.40; HRMS (positive ion FAB): Calcd for $C_{33}H_{56}N_5O_8$ $[M+H]^+$ *m*/*z* 650.4129. Found: $[M+H]^+$ *m*/*z* 650.4110. Analytical HPLC (t_R = 32.6 min, method 6). Isolation of **3** from the reaction mixture was achieved using semiprep HPLC (method 3). The mixture was dissolved in 1 mL of CH_3OH, and the fractions from 79−101 min were collected, evaporated, dissolved in CH_2Cl_2, treated with H_2O, and adjusted to pH 7. The organic layer was dried, filtered, evaporated, and concentrated *in vacuo* to afford the desired **3**.

{4-Carboxymethyl-7-[2-(carboxymethyl-amino)-3-(4-nitrophenyl)-propyl]-[1,4,7]triazonan-1-yl}-acetic Acid (C-NE3TA). Compound **3** (60 mg, 0.09 mmol) was treated with 4 M HCl in 1,4-dioxane (5 mL) at 0 °C. The resulting mixture was gradually warmed to room temperature and stirred for 24 h. Diethyl ether (100 mL) was added into the reaction mixture, and the resulting mixture was placed in the freezer for 2 h. The precipitate was filtered, immediately dissolved in water (10 mL), and washed with diethyl ether (20 mL). The aqueous layer was lyophilized to provide pure *C*-NE3TA as a light brownish solid (54 mg, 95%): ^{1}H NMR (D_2O) δ 2.42−2.60 (m, 1 H), 2.80−3.39 (m, 14 H), 3.68−3.92 (m, 8 H), 7.45 (d, J = 7.9 Hz, 2 H), 8.16 (d, J = 7.9 Hz, 2 H); ^{13}C NMR (D_2O) δ 36.6, 47.5, 51.4, 52.3, 54.3, 58.6, 61.1, 126.8, 132.9, 145.7, 149.6, 171.6, 174.0. HRMS (positive ion FAB): Calcd for $C_{21}H_{32}N_5O_8$ $[M+H]^+$ *m*/*z* 482.2251. Found: $[M+H]^+$ *m*/*z* 482.2274. Analytical HPLC (t_R = 9.96 min, method 2).

***tert*-Butyl {4-[3-(4-Aminophenyl)-2-(bis-*tert*-butoxycarbonylmethylamino)-propyl]-7-*tert*-butoxycarbonylmethyl-[1,4,7]triazanonan-1-yl}-acetate (4).** To a solution of **2** (*26*) (90 mg, 0.12 mmol) in MeOH (10 mL) was added 10% Pd/C catalyst (20 mg). The resulting mixture was subjected to hydrogenolysis by agitation with excess H_2 (g) at 15 psi in a Parr hydrogenator apparatus at ambient temperature for 14 h. The reaction mixture was filtered through Celite, and the filtrate was concentrated *in vacuo* to provide pure **4** (81 mg, 92%). ^{1}H NMR ($CDCl_3$) δ 1.42 (s, 9 H), 1.44 (s, 18 H), 1.47 (s, 9 H), 2.02−2.60 (m, 5 H), 2.65−2.96 (m, 12 H), 3.30−3.80 (m, 8 H), 6.60 (d, 2 H), 6.91 (d, 2 H); ^{13}C NMR ($CDCl_3$) 28.1, 34.7, 51.6, 52.2, 53.0, 53.2, 56.8, 57.7, 60.2, 80.5, 80.7, 115.2, 128.9, 129.9, 144.3, 170.0, 170.6, 170.8. HRMS (positive ion FAB): Calcd for $C_{39}H_{67}N_5O_8$ $[M+H]^+$ *m/z* 734.5068. Found: $[M+H]^+$ *m/z* 734.5029. Analytical HPLC (t_R = 29.82 min, method 1).

***tert*-Butyl {4-[3-(4-Aminophenyl)-2-(*tert*-butoxycarbonylmethylamino)-propyl]-7-*tert*-butoxycarbonylmethyl-[1,4,7]triazonan-1-yl}-acetate (5).** To a solution of **3** (180 mg, 0.28 mmol) in MeOH (20 mL) was added 10% Pd/C catalyst (36 mg). Compound **5** (167 mg, 97%) was isolated using the same procedure described for synthesis of **4**. ^{1}H NMR ($CDCl_3$) δ 1.37−1.50 (m, 36 H), 2.24−2.49 (m, 5 H), 2.61−2.94 (m, 12 H), 3.28−3.47 (m, 8 H), 6.60 (d, 2 H), 6.92 (d, 2 H); ^{13}C NMR ($CDCl_3$) 28.05, 28.15, 38.23, 49.53, 55.09, 55.41, 56.74, 59.11, 62.23, 80.60, 80.75, 115.19, 128.38, 129.91, 144.76, 171.16, 171.41; HRMS (positive ion FAB): Calcd for $C_{33}H_{58}N_5O_6$ $[M+H]^+$ *m/z* 620.4387. Found: $[M+H]^+$ *m/z* 620.4385. Analytical HPLC (t_R = 29.82 min, method 1).

{4-[3-(4-Aminophenyl)-2-(bis-carboxymethyl-amino)-propyl]-7-carboxymethyl-[1,4,7]triazanonan-1-yl}-acetic Acid (6). Compound **4** (50 mg, 0.07 mmol) was treated with 4 M HCl in 1,4-dioxane (5 mL) at 0 °C. The resulting solution was lyophilized to provide pure **6** as a pale yellow solid (44 mg, 93%): ^{1}H NMR (D_2O) δ 2.90−3.20 (m, 6 H), 3.30−3.57 (m, 11 H), 3.72 (t, 2 H), 3.92−4.22 (m, 7 H), 4.39 (d, 1 H), 7.37 (dd, 4 H); ^{13}C NMR (D_2O) δ 33.5, 48.5, 50.2, 50.7, 51.0, 52.0, 52.7, 52.91, 53.4, 53.9, 55.9, 60.8, 123.7, 129.3, 131.0, 135.6. HRMS (positive ion FAB): Calcd for $C_{23}H_{36}N_8O_8$ $[M+H]^+$ *m/z* 510.2587. Found: $[M+H]^+$ *m/z* 510.2564. Analytical HPLC (t_R = 5.45 min, method 2; t_R = 4.74 min, method 1).

{4-[3-(4-Amino-phenyl)-2-(carboxymethylamino)-propyl]-7-carboxymethyl-[1,4,7]triazonan-1-yl}-acetic Acid (7). Compound **5** (55 mg, 0.09 mmol) was treated with 4 M HCl in 1,4-dioxane (5 mL) at 0 °C. Compound **7** (48 mg, 97%) was obtained using the same procedure described for **6**. ^{1}H NMR (D_2O) δ 2.42−2.53 (m, 2 H), 2.75−3.22 (m, 14 H), 3.51 (s, 1 H), 3.75−3.95 (m, 8 H), 7.29 (dd, 4 H); ^{13}C NMR (D_2O) δ 33.7, 44.9, 48.7, 49.5, 50.9, 51.6, 55.9, 56.3, 56.7, 58.7, 123.7, 129.1, 130.8, 136.4, 169.1, 171.1, 171.8. HRMS (positive ion FAB): Calcd for $C_{21}H_{34}N_5O_6$ $[M+H]^+$ *m/z* 452.2509. Found: $[M+H]^+$ *m/z* 452.2491. Analytical HPLC (t_R = 1.70 min, method 2).

{4-[2-(Bis-carboxymethyl-amino)-3-(4-isothiocyanatophenyl)propyl]-7-carboxymethyl-[1,4,7]triazanonan-1-yl}-acetic Acid (8). To a solution of **6** (20 mg, 0.031 mmol) in water (2 mL) was added a 1 M solution of thiophosgene in $CHCl_3$ (0.39 mL). The resulting mixture was stirred for 4 h at room temperature. The aqueous layer was decanted, and the $CHCl_3$ layer was separated and washed with water (2 × 1 mL). The combined aqueous layers were lyophilized to provide **8** as a pale yellow solid (18 mg, 85%): ^{1}H NMR (D_2O) δ 2.95−4.40 (m, 27 H), 7.18−7.42 (s, 4 H). HRMS (positive ion FAB): Calcd for $C_{24}H_{34}N_5O_8S$ $[M+H]^+$ *m/z* 552.2117. Found: $[M+H]^+$ *m/z* 552.2128. Analytical HPLC (t_R = 14.56 min, method 2).

{4-Carboxymethyl-7-[2-(carboxymethylamino)-3-(4-isothiocyanatophenyl)-propyl]-[1,4,7] triazonan-1-yl}-acetic Acid (9). To a solution of **7** (20 mg, 0.031 mmol) in water (2 mL) was added a 1 M solution of thiophosgene in $CHCl_3$ (0.39 mL). Compound **9** (19 mg, 88%) was isolated using the same procedure described for **3**. ^{1}H NMR (D_2O) δ 2.52−2.60 (m, 2 H), 2.85−3.32 (m, 15 H), 3.74−3.88 (m, 8 H), 7.21 (dd, 4 H). HRMS (positive ion FAB): Calcd for $C_{22}H_{32}N_5O_6S$ $[M+H]^+$ *m/z* 494.2073 Found: $[M+H]^+$ *m/z* 494.2081. Analytical HPLC (t_R = 16.0 min, method 1).

General Procedure for the Preparation of Gd(III) Complexes (C-DOTA, C-NETA, or C-NE3TA). The Gd^{3+} complexes were prepared by reacting the aqueous solution of the appropriate ligand (2 mM, 1 mL, *C*-NETA, *C*-NE3TA, or *C*-DOTA) and $GdCl_3$ (2 mM, 0.9 mL) at a 1:0.9 mol ratio at 90 °C overnight, and the pH of the resulting solution was adjusted to ∼7 using 1 M NaOH. No unbound Gd(III) was detected in the solution as evidenced by AAIII assay and TLC analysis. The Gd complexes were purified using semi-HPLC (method 4). Fractions centered at 20.4, 18.0, and 14.5−15.1 min were collected to provide the Gd(III) complexes of *C*-NETA, *C*-NE3TA, and *C*-DOTA, respectively. Analytical HPLC of the isolated complexes (method 5) was performed, and the data were compared to those of free ligands (Gd-*C*-NETA, t_R = 20.4 min; Gd-*C*-NE3TA, t_R = 18.0 min; Gd-*C*-DOTA, t_R = 15.4 min; *C*-NETA, t_R = 11.2 min; *C*-NE3TA, t_R = 14.2 min; *C*-DOTA, t_R = 21.6 min).

Procedure for Detection of Free Gd(III) Using AAIII Assay. AAIII assay was used for the determination of the free Gd(III) in the complex solution (*27*). A solution of AAIII (10 μM) was prepared in the acetate buffer (NH_4OAc, 0.15 M, pH 7). Droplets of AAIII (100 μL) were arranged in a 96 well plate, and a droplet of reaction mixture (5 μL) was added to AAIII solution in each well. The presence of free Gd(III) was indicated by the immediate color change from pink to green.

ICP-MS. To verify the concentration of Gd(III) in the purified complexes, ICP-MS was performed using a computer-controlled Thermo Elemental (now Thermo Fisher) PQ ExCell inductively coupled plasma mass spectrometer. Samples were prepared by nitric acid digestion (9:1 nitric acid:sample) in a 65 °C water bath. The digested samples were diluted into 15 mL conical vials with a final concentration of 3% (v/v) nitric acid. Gd(III) standards were prepared in 3% (v/v) nitric acid with values 0.1, 0.25, 0.5, 1, 5, 10, 25, and 50 ng/mL Gd(III). Indium was spiked into every sample (including standards) for a final indium concentration of 5 ng/mL. Isotopes ^{157}Gd and ^{115}In were used for determination.

Relaxivity Measurements. Relaxivity measurements were acquired by taking the slope of a plot of $1/T_1$ (s^{-1}) versus concentration (mM). The longitudinal water proton relaxation times (T_1) were determined using a Bruker mq60 NMR (Bruker Canada, Milton, ON, Canada) analyzer operating at 59.97 MHz and 37 °C. The agent was added to Millipore water and serially diluted by 0.5 to give a series of 5 concentrations (500 μL total volume) for each relaxivity trial. The T_1 relaxivity was determined using an inversion recovery pulse sequence with 10 different pulse separations per sample, 4 repetitions per echo time, phase cycling, and a recycle delay that is ≥5 times the T_1 of each given sample. All curves were fit using a monoexponential curve fitting formula.

Radiolabeling of Ligands. Each of the radionuclides (1−3 mCi in 10−20 μL of 0.1 M HCl solution) was added to 100 μL of 0.15 M NH_4OAc buffer solution (pH 4.5). 5 M NH_4OAc (pH 7.3) was added as needed to adjust pH to 4.5, and the volume of the solution was brought up to 200 μL. Separate tubes containing 7 μmol of each of the ligands were prepared, and the solids were dissolved in 200 μL of NH_4OAc (pH 4.5). The ligand solution was added to the radionuclide solution and the resulting tube was capped. The reactions were heated at 80 °C

Table 1. *In Vitro* Serum Stability of C-NETA and C-NE3TA Radiolabeled with Radioisotopes

time	C-NE3TA					C-NETA				
h	^{177}Lu	^{90}Y	$^{205/6}$Bi	^{203}Pb	^{153}Gd	^{177}Lu[a]	^{90}Y	$^{205/6}$Bi[a]	^{203}Pb	^{153}Gd
0	100	100	100	95.1	100	100	100	100	100	100
1	100	100	100	67.5	100	100	100	100	98.1	100
2	100	100	100	59.9	100	100	100	100	98.7	100
4	100	100	100	56.1	100	100	100	100	-	100
6	100	100	100	56.1	100	100	100	100	98.0	100
22	100	100	100	-	100	100	100	100	97.0	100
26	100	100	100	65.7	100	100	100	100	-	100
92	100	100	100	75.0	100	100	100	100	-	100
96	100	100	100	-	100	100	100	100	95.7	100
118	100	100	100	77.9	100	100	100	100	95.7	100
141	100	100	100	73.2	100	100	100	100	-	100
142	100	100	100	-	100	100	100	100	91.4	100
164	100	100	100	78.2	100	100	100	100	-	100
166	100	100	100	-	100	100	100	100	82.7	100
192	100	100	100	83.7	100	100	100	100	-	100
262	100	100	100	90.9	100	100	100	100	-	100

[a] The data were cited for comparison (*26*).

for 12 h, after which they were loaded onto a column of Chelex-100 resin (100−200 mesh, Na^+ form, Biorad, Richmond, CA; 1 mL volume bed, equilibrated with PBS, pH 7.4). The complexes were eluted from the resin with PBS, pH 7.4, while the resin retained the free metals.

***In Vitro* Stability of the Radiolabeled Metal Complexes.** The stability of the purified radiolabeled complexes was evaluated in human serum (Gemini Bioproducts, Woodland, CA) for up to 11 days (Table 1). The serum stability of the radiolabeled complexes was assessed by measuring the transfer of the radionuclide from each complex to serum proteins using SE-HPLC methods. Radiolabeled complexes were diluted to an appropriate volume that allowed for preparation of multiple samples containing 5−10 μCi and were filter-sterilized using a Millex-GV 0.22 μm filter. This stock solution was then mixed with 1400 μL of sterile normal human serum. Aliquots (200 μL) were drawn and separated into individual tubes for subsequent analysis using aseptic technique. The samples were incubated at 37 °C, and at designated intervals, subjected to analysis by SE-HPLC. Samples were loaded onto the HPLC and eluted with PBS, pH 7.4 isocratically at 1 mL/min. Radioactivity still associated with the chelate typically displayed a retention time of ∼8.5 min at this flow rate. Radioactivity associated with a transfer to serum proteins generally appeared at ∼6 min.

***In Vivo* Biodistribution Studies of the Radiolabeled Metal Complexes.** Female athymic mice were obtained from Charles River Laboratories (Wilmington, MA) at 4−6 weeks of age. The pH of the radiolabeled ligands was adjusted to pH ∼7.0 with 0.5 M sodium bicarbonate (pH 10.5) and diluted in phosphate-buffered saline. The radiolabeled ligands (5−10 μCi for ^{86}Y, $^{205/6}$Bi, ^{177}Lu, and ^{203}Pb) were administered to the mice in 200 μL of solution *via* tail vein injection. The mice (5 per data point) were sacrificed by exsanguination at 0.5, 1, 4, 8, and 24 h. Blood and the major organs were harvested, wet-weighed, and the radioactivity measured in a γ-scintillation counter (1480 Wizard, Perkin-Elmer). The percent injected dose per gram (% ID/g) was determined for each tissue. The values presented are the mean and standard deviation for each tissue. All animal experiments were performed in compliance with current regulations and guidelines of the U.S. Dept. of Agriculture and approved by the NCI Animal Care and Use Committee.

General Procedure for Spectroscopic Determination of Ligand to Protein Ratio. A stock solution of the Cu(II)-AAIII reagent was prepared in 0.15 M NH_4OAc, pH 7.0, by adding an aliquot of a 5.00×10^{-4} M Cu(II) atomic absorption solution (to afford a 5 μM solution of copper) to a 10 μM solution of arsenazo III. This solution was stored in the dark to avoid degradation over time. A UV/vis spectrometer was zeroed against a cuvette filled with 1.0 mL of a 0.15 M NH_4OAc solution at pH 7.0 with a window open from 250 to 700 nm. The acetate solution was removed and replaced with 1.0 mL of the Cu(II)-AAIII reagent, a spectrum was collected, and the absorbance values at 280 and 652 nm noted. 50 μL of the Cu(II)-AAIII reagent were removed and discarded. The ligand−antibody conjugate of interest was added (50 μL) and the spectrum was immediately collected. Spectra were then collected periodically until no further change was noted for the peaks at 280 and 652 nm (less than 30 min for the Cu(II)-AAIII reagent with the ligands detailed in this paper). A series of calculations detailed in the discussion allow for the determination of the concentration of ligand in the sample.

Spectroscopic Determination of Ligand to Protein Ratio. All absorbance measurements were obtained on an Agilent 8453 diode array spectrophotometer equipped with a 8-cell transport system (designed for 1 cm cells). Metal-free stock solutions of all buffers were prepared using Chelex-100 resin (100−200 mesh, Bio-Rad Laboratory, Hercules, CA). Chelex resin (5 g) was added into the buffer solution (500 mL) and the mixture was shaken for 1 h in a shaker, stored in the refrigerator overnight, and filtered through a Corning filter system (#430513, pore size 0.2 μM). Disposable PD-10 Sephadex G-25 M columns (GE Healthcare, Piscataway, NJ) were rinsed with 25 mL of the appropriate buffer prior to addition of antibody or its ligand conjugates. Centricon C-50 (50 000 MWCO) Centrifugal Filter Devices were purchased from Amicon Bioseparations (Millipore, Bedford, MA) and were rinsed several times with DI H_2O prior to use. Trastuzumab was purchased from Genentech Inc. (South San Fransico, CA). The initial concentration of Trastuzumab was determined by the Lowry method (*24*). Phosphate buffered saline (PBS) was purchased from Gibco as a 1× solution at pH 7.4 and was used as received. Ammonium acetate (0.15 M, pH 7.0, and 0.15 M, pH 4.5), bicarbonate buffer (50 mM $NaHCO_3$, 150 mM NaCl, 10 mM EDTA, pH 8.5), and conjugation buffer (50 mM HEPES, 150 mM NaCl, pH 8.6) were prepared as 10× solutions, chelexed, and then diluted to 1× solutions for use as needed with DI H_2O. Phosphate buffered saline (PBS), 1×, pH 7.4 consisted of 0.08 M Na_2HPO_4, 0.02 M KH_2PO_4, 0.01 M KCl, and 0.14 M NaCl.

Conjugation of C-NETA-NCS to Trastuzumab. Trastuzumab (9.5 mg) was added to a PD-10 column previously charged with bicarbonate buffer. Additional buffer was added in 0.5 mL portions to the PD-10 column to exchange the buffer solution of the antibody. The buffer solution collected between 3.5 and 5.0 mL was combined following confirmation of the presence of Trastuzumab via analysis of the UV/vis spectrum at 280 nm. To a sterile test tube containing the recovered Trastuzumab (5 mg) was added a 20-fold excess of *C*-NETA-NCS. The resulting solution was gently agitated overnight at room temperature. The following day, this solution was placed on a Centricon C-50 membrane and spun down to reduce volume. PBS (3 × ∼2 mL) was added to the remaining solution of the C-NETA−Trastuzumab conjugate, followed by centrifugation in order to remove unreacted ligand. The volume of purified, conjugate antibody was brought to 2.00 mL with PBS. The ligand to protein (*L*/*P*) ratio was determined by measuring the absorbance of the solution at 280 nm, which indicated that 1.45 mg (9.67×10^{-6} M, 29%) of the Trastuzumab remained after centrifugation. An aliquot of the C-NETA−Trastuzumab conjugate (50 μL) was added to the cuvette containing the Cu(II)-AAIII reagent (950 μL) and the absorbance at 652 nm was monitored over time. The reaction was complete after 20 min, and the concentration of *C*-NETA-NCS was calculated

Scheme 1. Synthesis of *C*-NE3TA

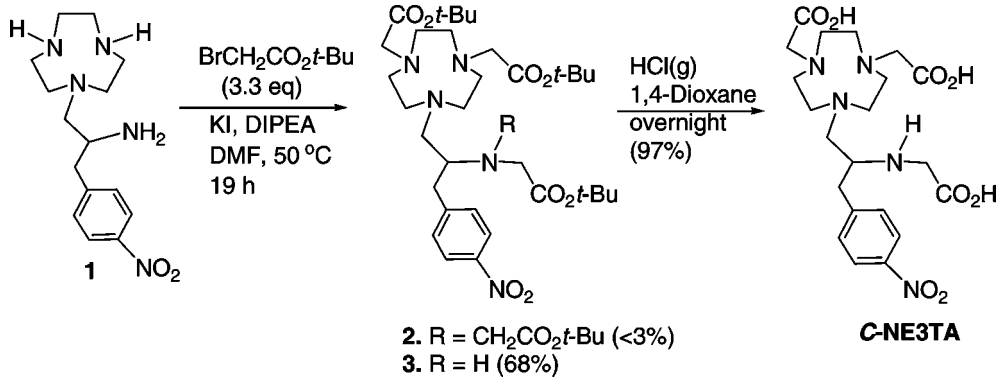

(1.48 × 10^{-5} M). The *L*/*P* for the C-NETA−Trastuzumab conjugate was found to be 1.5 to 1.

Conjugation of C-NE3TA-NCS to Trastuzumab. Trastuzumab (6.0 mg, 2.5 mL) was added to a PD-10 column previously charged with conjugation buffer. Additional conjugation buffer (3.5 mL) was added to PD-10 column to exchange the buffer solution of the antibody. The collected antibody solution (5.9 mg, 98.0%) was then added to a 10-fold excess of *C*-NE3TA-NCS. The solution was gently agitated for 24 h at room temperature. The reaction solution was then placed on a Centricon C-50 membrane and spun down to reduce volume. PBS (3 × 2 mL) was added to the remaining solution of the *C*-NE3TA−Trastuzumab conjugate, followed by centrifugation to remove unreacted ligand. The volume of purified conjugate antibody was brought to 1 mL with PBS. The analysis of the absorbance of the solution at 280 nm indicated that 5.71 mg (38.8 × 10^{-5} M, 96.8%) of the Trastuzumab remained after the processing.

A stock solution of the Cu(II)-AAIII reagent was prepared in 0.15 M NH_4OAc, pH 7.0, by adding an aliquot of a 5 μM Cu(II) atomic absorption solution to a 10 μM solution of AAIII. This solution was stored in the dark to avoid degradation over time. A UV/vis spectrometer was zeroed against a cuvette filled with 2.0 mL of a 5 μM AAIII solution at pH 4.5 with a window open from 200 to 1100 nm. The AAIII solution was removed and replaced with 2.000 mL of the Cu(II)-AAIII reagent, a spectrum was collected, and the absorbance values at 610 nm noted. Solutions of *C*-NE3TA-NO_2 were then used for generating the calibration graph. Various concentration of *C*-NE3TA-NO_2 solution (50 μL) was reacted with 1.95 mL of the Cu(II)-AAIII reagent at room temperature. Abosrbance measurements at 610 nm were taken after 5 min. An aliquot of the *C*-NE3TA−Trastuzumab conjugate (50 μL) was added to a cuvette containing the Cu(II)-AAIII reagent (1.95 mL) and the absorbance at 610 nm was monitored over time. Spectra were then collected periodically until no further change was noted for the peaks at 280 and 610 nm. The reaction was complete after 30 min, and the concentration of *C*-NE3TA was calculated (9.7 × 10^{-5} M). The *L*/*P* for the *C*-NE3TA−Trastuzumab conjugate was found to be 2.5 to 1.

RESULTS AND DISCUSSION

Synthesis of *C*-NETA and *C*-NE3TA. *C*-NE3TA was serendipitously discovered during the synthesis of *C*-NETA. *C*-NE3TA contains four amines and three carboxylates as potential donor groups. The heptadentate *C*-NE3TA forms a neutral complex with Y(III), Lu(III), Bi(III), and Gd(III) that requires no counterion and thus these formed complexes have an advantage of less protein interaction and a potentially more favorable *in vivo* tissue distribution. Synthesis of *C*-NE3TA is shown in Scheme 1. As an initial attempt to prepare *tert*-butyl *C*-NETA **2** (*26*), the free amino groups in **1** were reacted with *tert*-butyl bromoacetate in CH_3CN in the presence of diisopropylethylamine (DIPEA) as a base. However, the reaction afforded **2** in low (<35%) and nonreproducible yields. The reaction also provided a significant amount of a polyalkylated byproduct very difficult to differentiate from **2** by TLC as confirmed by NMR. To improve the synthesis of **2**, starting material **1** as a HCl salt instead of free amine was directly reacted with *tert*-butyl bromoacetate in DMF at 50 °C (Scheme 1) (*20*). Surprisingly, the reaction provided *tert*-butyl *C*-NE3TA (**3**) in 68% yield as the major product along with a small amount of **2**. This result was taken as an indication that the formation of **2** requires an elevated reaction temperature. Indeed, when starting material **1**, still as a HCl salt, was reacted with *tert*-butyl bromoacetate in DMF at 90 °C (*26*), **2** was obtained in an improved yield (54%). Although not described in detail in this paper, the preparation of **2** and **3** was not straightforward. Numerous reaction conditions varying solvents, bases, temperatures, and mole ratios of the reagents were investigated. Purification of **2** and **3** using flash silica gel (or alumina) column chromatography was found to be quite challenging due to the presence of byproduct, specifically a polyalkylated byproduct, which could not be resolved from the desired ligands by TLC. A significant amount of solvents were consumed even in small-scale column chromatographic purifications of **2** (∼100 mg) using a very gradual increase of solvent polarity. With the challenge encountered in isolation of **2** and **3** in high purity, research focused on development of a reliable and efficient purification method available for preparation of these intermediates, **2** and **3**, in high purity so that, after deprotection of the *tert*-butyl groups, the water-soluble per-acid products could be cleanly isolated. Semipreparative HPLC of the reaction mixture containing **2** and **3** eluted with a binary gradient (solvent A = 0.05 M AcOH/Et_3N, pH 6.0, and solvent B = CH_3CN) successfully separated **2** and **3** in high purity. The desired ligands, *C*-NETA (*26*) and *C*-NE3TA were then obtained by removal of the *tert*-butyl groups of **2** and **3** using HCl(g) in 1,4-dioxane. Synthesis of *C*-NE3TA-NCS and *C*-NETA-NCS having a functional linker for conjugation to an antibody is shown in Scheme 2. The nitro groups in **2** and **3** were transformed into the amino group to provide **4** and **5**, respectively. Removal of the *tert*-butyl groups in **4** and **5** followed by reaction with thiophosgene provided the desired ligands with the linker for conjugation to antibody, *C*-NETA-NCS (**8**) and *C*-NE3TA-NCS (**9**).

Relaxivities. The Gd(III) complexes of the new chelates in the nitro form were prepared and purified. The T_1 relaxivity of Gd(*C*-NETA) and Gd(*C*-NE3TA) was measured and compared to that of Gd(*C*-DOTA). Previously, we reported the Gd(III) complex of nonfunctionalized bimodal ligand NETA to be stable both in serum and *in vivo* and displayed

Scheme 2. Synthesis of *C*-NETA-NCS (8) and *C*-NE3TA-NCS (9)

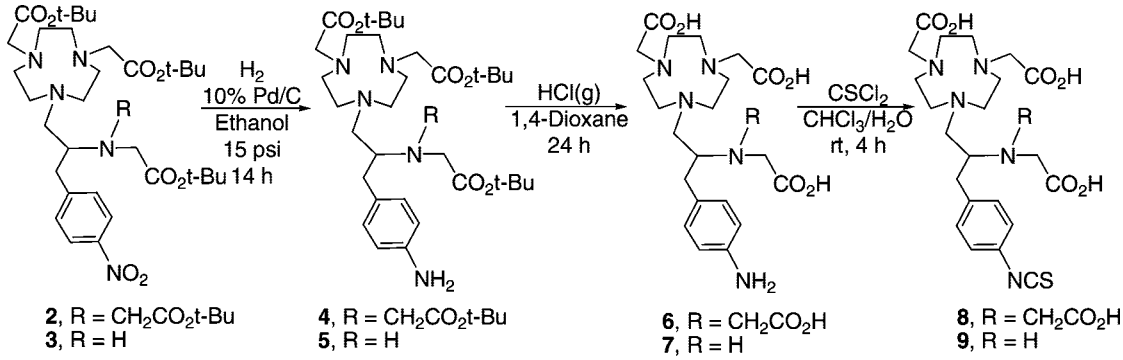

Table 2. Biodistribution of Ligands Radiolabeled with ^{177}Lu in Non-Tumor-Bearing Athymic Mice[a]

		time points (h)				
ligand	tissue	0.50	1.00	4.00	8.00	24.00
C-NE3TA	blood	0.93 ± 0.30	0.31 ± 0.04	0.12 ± 0.02	0.06 ± 0.01	0.01 ± 0.00
	liver	0.82 ± 0.27	0.69 ± 0.20	0.50 ± 0.02	0.36 ± 0.05	0.31 ± 0.04
	spleen	0.33 ± 0.08	0.28 ± 0.20	0.19 ± 0.07	0.13 ± 0.02	0.12 ± 0.05
	kidney	2.78 ± 0.99	1.57 ± 0.52	1.34 ± 0.09	1.16 ± 0.19	0.84 ± 0.08
	lung	0.87 ± 0.22	0.42 ± 0.16	0.17 ± 0.03	0.15 ± 0.03	0.07 ± 0.03
	heart	0.37 ± 0.08	0.19 ± 0.09	0.08 ± 0.02	0.10 ± 0.11	0.02 ± 0.01
	femur	1.06 ± 1.35	0.39 ± 0.13	0.36 ± 0.11	0.28 ± 0.15	0.38 ± 0.10
C-NETA[b]	blood	0.91 ± 0.41	0.34 ± 0.55	0.03 ± 0.00	0.01 ± 0.00	0.00 ± 0.00
	liver	0.56 ± 0.21	0.25 ± 0.034	0.16 ± 0.04	0.13 ± 0.03	0.08 ± 0.01
	spleen	0.54 ± 0.38	0.15 ± 0.11	0.07 ± 0.01	0.07 ± 0.03	0.05 ± 0.03
	kidney	2.98 ± 1.24	1.19 ± 0.47	1.07 ± 0.20	0.87 ± 0.24	0.59 ± 0.12
	lung	0.88 ± 0.41	0.26 ± 0.08	0.10 ± 0.06	0.04 ± 0.01	0.03 ± 0.01
	heart	0.43 ± 0.16	0.11 ± 0.04	0.04 ± 0.01	0.03 ± 0.01	0.02 ± 0.01
	femur	0.66 ± 0.13	0.53 ± 0.24	0.19 ± 0.05	0.17 ± 0.01	0.19 ± 0.08

[a] Values are the percent injected dose per gram(% ID/g) ± standard deviation;. [b] The data were cited for comparison (*26*).

considerably enhanced T_1 relaxivity compared to Gd(DOTA) where the Gd(III) is coordinated to the eight donor atoms of the ligands with one vacant coordination site available to bind a water molecule ($q = 1$) (*2*). The increase in relaxivity of Gd(NETA) as compared to Gd(DOTA) was proposed to be ascribed to a decrease in ligand denticity from eight- to seven-coordinate by one of the flexible acyclic pendant coordinating groups not being coordinated at all or from an "on"−"off" mechanism of one of the pendant coordinating groups and thus resulting in an increase in q value of the Gd(NETA) complex to an intermediate state between one coordinated water molecule ($q = 1$) and two coordinated water molecules ($q = 2$) (*18*). In the present study, the Gd(III) complexes of bifunctional ligands *C*-NETA and heptadentate *C*-NE3TA were prepared as potential MRI contrast agents. Heptadentate *C*-NE3TA was expected to provide enhanced relaxivity due to increase in hydration number (q) when compared to *C*-NETA and *C*-DOTA. The Gd(III) complexes of the bifunctional ligands were prepared and purified using semipreparative HPLC, while the presence of free Gd(III) ions was detected using an ArsenazoIII (AAIII) assay (*27*). Relaxivity of the aqueous Gd(III) complexes (∼pH 7) were measured on a Bruker MQ60 NMR analyzer, and the concentration of the Gd(III) complexes was measured by ICP-MS. The relaxivity data indicate that Gd-*C*-NETA (4.77 mM^{-1} s^{-1}) and Gd-*C*-NE3TA (5.89 mM^{-1} s^{-1}) complexes provided higher relaxivity as compared to the DOTA complex (3.96 mM^{-1} s^{-1}). Introduction of a functional nitro group into the NETA backbone did not impact the T_1 relaxivity of NETA. The difference of T_1 relaxivity (∼1 MHz) between *C*-DOTA and *C*-NETA was similar to that between DOTA and NETA. As mentioned above, the on and off binding to Gd(III) of one of the pendant coordinates would have resulted in enhanced relaxivity of Gd(*C*-NETA) as compared to Gd(*C*-DOTA). Among the evaluated Gd(III) complexes, Gd(*C*-NE3TA) gives the highest T_1 relaxivity at 60 MHz, probably due to an increase in q (*21*). The relaxation rates for the Gd(III) chelates are dominated by the inner-sphere dipolar coupling between the coordinated water molecule and the paramagnetic Gd(III). The measured relaxivities arise from the exchange between the coordinated water molecule and the surrounding water molecules in solution (*21*). An increase in the number of coordinated water molecules to the Gd(III), which could have occurred with dissociation of Gd(III) from the chelate in solution, would have resulted in a significant increase in the measured relaxivities. No indication of Gd(III) dissociation is evident from the relaxivity data, which is in agreement with the *in vitro* serum stability and *in vivo* biodistribution studies.

***In Vitro* Serum Stability.** *C*-NETA and *C*-NE3TA were radiolabeled with ^{90}Y,^{177}Lu, ^{203}Pb, $^{205/6}$Bi, or ^{153}Gd as previously described (*17, 18*). *In vitro* serum stability of the radiolabeled complexes purified via ion-exchange chromatography was performed to determine if *C*-NETA or *C*-NE3TA labeled with the radionuclides remained stable without transchelation or loss of their respective radionuclide in human serum. This was assessed by measuring the transfer of radionuclide from the complex to serum proteins over the course of 11 days. *C*-NETA and *C*-NE3TA radiolabeled with^{90}Y,^{177}Lu, $^{205/6}$Bi, and ^{153}Gd were stable in serum for up to 11 days with no measurable loss of radioactivity. However, considerable release of radioactivity into serum (∼17%) over 7 days was observed with the ^{203}Pb-labeled *C*-NETA. ^{203}Pb-*C*-NE3TA was also unstable by this assay as indicated by significant amounts of ^{203}Pb (∼40%) dissociating within 1 day.

***In Vivo* Biodistribution.** The *in vivo* stability of the radiolabeled complexes was evaluated by performing biodistribution studies in normal athymic mice. The results of the

Table 3. Biodistribution of Ligands Radiolabeled with ^{86}Y in Non-Tumor-Bearing Athymic Mice[a]

		time points (h)				
ligand	tissue	0.50	1.00	4.00	8.00	24.00
C-NE3TA	blood	1.86 ± 1.92	0.76 ± 1.09	0.05 ± 0.05	0.02 ± 0.00	0.00 ± 0.00
	liver	1.65 ± 0.59	0.88 ± 0.59	0.17 ± 0.05	0.20 ± 0.16	0.10 ± 0.03
	spleen	0.70 ± 0.15	0.47 ± 0.26	0.13 ± 0.08	0.07 ± 0.02	0.07 ± 0.02
	kidney	2.58 ± 1.04	2.00 ± 2.32	0.74 ± 0.15	0.49 ± 0.10	0.35 ± 0.05
	lung	1.64 ± 0.99	1.16 ± 0.65	0.10 ± 0.04	0.16 ± 0.22	0.23 ± 0.36
	heart	0.79 ± 0.52	0.38 ± 0.31	0.06 ± 0.02	0.05 ± 0.01	0.02 ± 0.01
	femur	1.19 ± 0.48	0.82 ± 0.26	0.30 ± 0.04	0.22 ± 0.06	0.08 ± 0.02
C-NETA	blood	0.63 ± 0.18	0.22 ± 0.04	0.05 ± 0.00	0.03 ± 0.00	0.03 ± 0.01
	liver	0.48 ± 0.08	0.32 ± 0.07	0.29 ± 0.03	0.22 ± 0.03	0.17 ± 0.02
	spleen	0.83 ± 0.50	1.02 ± 1.07	0.24 ± 0.05	0.17 ± 0.03	0.26 ± 0.03
	kidney	2.64 ± 1.18	0.79 ± 0.43	1.12 ± 0.09	0.87 ± 0.11	0.64 ± 0.08
	lung	0.73 ± 0.17	0.40 ± 0.06	0.17 ± 0.05	0.13 ± 0.01	0.16 ± 0.03
	heart	0.66 ± 0.12	0.28 ± 0.06	0.22 ± 0.05	0.15 ± 0.01	0.24 ± 0.05
	femur	1.69 ± 0.83	2.05 ± 0.20	1.79 ± 0.19	0.66 ± 0.02	0.78 ± 0.07

[a] Values are the percent injected dose per gram (% ID/g) ± standard deviation.

Table 4. Biodistribution of Ligands Radiolabeled with$^{205/6}$Bi in Non-Tumor-Bearing Athymic Mice[a]

		time points (h)				
ligand	tissue	0.50	1.00	4.00	8.00	24.00
C-NE3TA	blood	0.46 ± 0.18	0.13 ± 0.02	0.03 ± 0.00	0.02 ± 0.01	0.01 ± 0.00
	liver	1.01 ± 0.15	0.80 ± 0.16	0.52 ± 0.13	0.37 ± 0.08	0.14 ± 0.03
	spleen	0.45 ± 0.24	0.25 ± 0.02	0.18 ± 0.01	0.12 ± 0.02	0.13 ± 0.01
	kidney	5.05 ± 0.24	4.69 ± 0.55	3.42 ± 0.55	1.99 ± 0.32	0.73 ± 0.19
	lung	0.56 ± 0.13	0.25 ± 0.03	0.16 ± 0.01	0.13 ± 0.04	0.09 ± 0.01
	heart	0.36 ± 0.09	0.19 ± 0.02	0.12 ± 0.01	0.09 ± 0.01	0.08 ± 0.02
	femur	0.62 ± 0.27	0.26 ± 0.05	0.23 ± 0.06	0.14 ± 0.02	0.13 ± 0.01
C-NETA[b]	blood	0.52 ± 0.11	0.23 ± 0.07	0.09 ± 0.01	0.08 ± 0.01	0.06 ± 0.01
	liver	1.01 ± 0.05	0.92 ± 0.11	0.68 ± 0.14	0.62 ± 0.12	0.49 ± 0.04
	spleen	0.77 ± 0.18	0.60 ± 0.12	0.36 ± 0.12	0.41 ± 0.03	0.42 ± 0.02
	kidney	24.91 ± 3.48	24.63 ± 2.79	17.29 ± 3.24	10.55 ± 1.38	6.06 ± 1.34
	lung	0.85 ± 0.16	0.53 ± 0.15	0.41 ± 0.07	0.41 ± 0.06	0.33 ± 0.07
	heart	0.55 ± 0.02	0.37 ± 0.09	0.23 ± 0.04	0.29 ± 0.04	0.20 ± 0.02
	femur	1.25 ± 0.11	0.86 ± 0.11	0.66 ± 0.07	0.87 ± 0.07	0.47 ± 0.08

[a] Values are the percent injected dose per gram(% ID/g) ± standard deviation. [b] The data were cited for comparison (*26*).

Table 5. Biodistribution of Ligands Radiolabeled with ^{153}Gd in Non-Tumor-Bearing Athymic Mice[a]

		time points (h)				
ligand	tissue	0.50	1.00	4.00	8.00	24.00
C-NE3TA	blood	1.41 ± 0.57	0.20 ± 0.08	0.00 ± 0.00	0.00 ± 0.00	0.00 ± 0.00
	liver	1.74 ± 0.69	0.58 ± 0.22	0.03 ± 0.01	0.02 ± 0.00	0.02 ± 0.01
	spleen	0.50 ± 0.37	0.24 ± 0.05	0.02 ± 0.00	0.02 ± 0.00	0.01 ± 0.01
	kidney	4.28 ± 1.33	1.13 ± 0.12	0.52 ± 0.04	0.38 ± 0.06	0.16 ± 0.11
	lung	0.91 ± 0.28	0.32 ± 0.09	0.03 ± 0.00	0.02 ± 0.00	0.01 ± 0.01
	heart	0.43 ± 0.16	0.14 ± 0.06	0.01 ± 0.00	0.01 ± 0.00	0.13 ± 0.27
	femur	0.43 ± 0.14	1.30 ± 0.58	0.02 ± 0.01	0.02 ± 0.00	0.01 ± 0.00
C-NETA	blood	1.33 ± 0.32	0.39 ± 0.07	0.05 ± 0.02	0.03 ± 0.01	0.01 ± 0.01
	liver	2.79 ± 0.24	2.41 ± 0.34	3.19 ± 0.54	4.01 ± 0.53	2.98 ± 0.44
	spleen	0.63 ± 0.14	0.27 ± 0.05	0.31 ± 0.04	0.20 ± 0.02	0.24 ± 0.02
	kidney	3.37 ± 0.23	2.21 ± 0.38	2.70 ± 0.26	2.63 ± 0.43	2.18 ± 0.14
	lung	1.39 ± 0.20	0.69 ± 0.10	0.47 ± 0.09	0.40 ± 0.12	0.31 ± 0.03
	heart	0.82 ± 0.21	0.51 ± 0.18	0.31 ± 0.02	0.27 ± 0.07	0.25 ± 0.04
	femur	2.27 ± 0.23	1.79 ± 0.24	1.96 ± 0.28	2.06 ± 0.22	2.31 ± 0.40

[a] Values are the percent injected dose per gram (% ID/g) ± standard deviation.

biodistribution studies for the radiolabeled complexes are shown in Tables 2–5. Selected organs and the blood were harvested at 5 time points, 0.5, 1, 4, 8, and 24 h postinjection. *C*-NETA (*26*) and *C*-NE3TA radiolabeled with ^{177}Lu have similar biodistribution profiles, and both complexes were rapidly cleared from the blood and displayed low radioactivity levels in all organs (<0.8% ID/g at 24 h; Table 2). ^{86}Y-*C*-NETA and ^{86}Y-*C*-NE3TA resulted in rapid blood and liver clearance (Table 3). ^{86}Y-*C*-NETA displayed relatively higher uptake at the femur as compared to that of ^{86}Y-*C*-NE3TA at all time points (0.78 ± 0.07% ID/g vs 0.08 ± 0.02% ID/g at 24 h, respectively). Low radioactivity levels in other organs were observed with both complexes. *C*-NE3TA radiolabeled with $^{205/6}$Bi was rapidly cleared from the blood, lung, heart, and femur and displayed a higher radioactivity level in the kidney when compared to the other organs (Table 4). The radioactivity level of $^{205/6}$Bi-*C*-NE3TA in the kidney peaked at 5.05 ± 0.24% ID/g at 0.5 h and decreased to 0.73 ± 0.19% ID/g by 24 h. $^{205/6}$Bi-*C*-NETA exhibited extremely rapid blood clearance and low radioactivity levels at all of the organs except the kidney (<1.0% ID/g at all time points), while radioactivity in the kidney decreased rather slowly starting from 24.9 ± 3.48% ID/g to 6.06 ± 0.19% ID/g at 24 h (*26*). *C*-NE3TA radiolabeled with ^{153}Gd almost completely cleared from the blood, liver, spleen, lung, heart, and femur in less than 4 h, where the radioactivity level in the kidney was 0.16 ± 0.11% ID/g at 24 h postinjection (Table 5).

^{153}Gd-*C*-NETA also displayed extremely rapid blood clearance and low uptake at spleen, lung, and heart, while relatively increased radioactivity levels in the liver, kidney, and femur at 24 h (2.98 ± 0.44% ID/g, 2.18 ± 0.14% ID/g, 2.31 ± 0.40% ID/g, respectively) were observed with this complex (Table 5).

Conjugation of *C*-NETA-NCS and *C*-NE3TA-NCS to Trastuzumab and Determination of *L*/*P* Ratio Based on Cu(II)-AA(III) Assay. HER2 are receptors overexpressed in a variety of epithelial tumors making this an attractive target. Trastuzumab, a monoclonal antibody that selectively targets the HER2 protein and blocks its overexpression function (*22*) and has been shown to enhance a survival rate of metastatic breast cancer patients was chosen as a tumor targeting biomolecule (*23*) for the present study. *C*-NETA was conjugated with Trastuzumab by an established method (*24*). Protein concentration was quantified by the method of Lowry (*25*). The Cu(II)-AAIII based UV−vis spectrophotometric assay as described previously (*24*) was used for the determination of the number of *C*-NETA ligands linked to Trastuzumab (*L*/*P* ratio). The *L*/*P* ratios for *C*-NETA−Trastuzumab and *C*-NE3TA conjugates were found to be 1.5 and 2.5, respectively.

CONCLUSIONS

The novel bifunctional ligands, octadentate *C*-NETA and heptadentate *C*-NE3TA, were synthesized for use in RIT and MRI applications. The T_1 relaxivities of their corresponding Gd(III) complexes are reported. At clinically relevant field strength, the relaxivities of Gd(*C*-NETA) and Gd(*C*-NE3TA) are higher than that of a bifunctional version of the clinically used contrast agent, Gd(DOTA). The *in vitro* serum stability and *in vivo* biodistribution data of the ^{153}Gd-labeled complexes, Gd(*C*-NETA) and Gd(*C*-NE3TA), indicate that *C*-NETA and *C*-NE3TA bind ^{153}Gd with high complex stability. *C*-NETA and *C*-NE3TA were evaluated as chelators of ^{177}Lu, ^{90}Y, ^{212}Pb, ^{212}Bi, or ^{213}Bi for RIT applications. *C*-NETA and *C*-NE3TA radiolabeled with ^{177}Lu, ^{90}Y, and $^{205/6}$Bi were extremely stable without loss of any radioactivity from the metal complex in human serum for up to 11 days. Both ^{203}Pb-*C*-NETA and ^{203}Pb-*C*-NE3TA underwent significant dissociation of the metal from the complexes. *In vivo* biodistribution of *C*-NETA and *C*-NE3TA labeled with ^{177}Lu or ^{90}Y using athymic mice indicate that the radiolabeled complexes exhibited rapid blood clearance and relatively low radioactivity levels in the normal organs and possess a favorable biodistribution profile. $^{205/6}$Bi-*C*-NE3TA exhibited extremely rapid blood clearance and low radioactivity level in the normal organs at 24 h. $^{205/6}$Bi-*C*-NETA displayed a minimum amount of uptake of the activity in the normal organs except for the kidney. High renal uptake of the activity at all time points was observed with $^{205/6}$Bi-*C*-NETA. The bifunctional ligands, *C*-NETA and *C*-NE3TA, were successfully conjugated to trastuzumab with respective *L*/*P* product ratios of 1.5 and 2.5 as determined using a UV/vis spectrophotometric AAIII assay. The results of T_1 relaxivity, *in vitro* serum stability, and *in vivo* biodistribution studies suggest that the novel bifunctional ligands, *C*-NETA and *C*-NE3TA, are promising bifunctional ligands for disease-specific Gd(III)-based MRI and RIT of ^{177}Lu and ^{90}Y.

ACKNOWLEDGMENT

We acknowledge financial support from the National Institutes of Health (K22CA102637 and R01CA112503-01A2 to CHS). This research was supported in part by the Intramural Research Program of the NIH, National Cancer Institute, Center for Cancer Research. We thank Dr. Thomas Meade for the NMR analyzer and Mr. Keith Macrenaris for the ICP-MS data.

Supporting Information Available: Relaxivity data of Gd(*C*-NETA), Gd(*C*-NE3TA), and Gd(*C*-DOTA). This material is available free of charge via the Internet at http://pubs.acs.org/BC.

LITERATURE CITED

(1) Knox, S. J., and Meredith, R. F. (2000) Clinical radioimmunotherapy. *Semin. Radiat. Oncol. 10*, 73–93.
(2) Caravan, P., Ellison, J. J., McMurry, T. J., and Lauffer, R. B. (1999) Gadolinium(III) chelates as MRI contrast agents: structure, dynamics, and applications. *Chem. Rev. 99*, 2293–2352.
(3) Yoneda, S., Emi, N., Fujita, Y., Ohmichi, M., Hirano, S., and Suzuki, K. T. (1995) Effects of gadolinium chloride on the rat lung following intratracheal instillation. *Fundam. Appl. Toxicol. 28*, 65–70.
(4) McDevitt, M. R., Ma, D., Lai, L. T., Simon, J., Borchardt, P., Frank, R. K., Wu, K., Pellegrini, V., Curcio, M. J., Miederer, M., Bander, N. H., and Scheinberg, D. A. (2001) Tumor therapy with targeted atomic nanogenerators. *Science 294*, 1537–40.
(5) Srivastava, S., and Dadachova, E. (2001) Recent advances in radionuclide therapy. *Semin. Nucl. Med. 31*, 330–41.
(6) Milenic, D. E., Brady, E. D., and Brechbiel, M. W. (2004) Antibody-targeted radiation cancer therapy. *Nat. Rev. Drug Discovery 3*, 488–99.
(7) Borghaei, H., and Schilder, R. J. (2004) Safety and efficacy of radioimmunotherapy with yttrium 90 ibritumomab tiuxetan (Zevalin). *Semin. Nucl. Med. 34* (S1), 4–9.
(8) Jhanwar, Y. S., and Divgi, C. J. (2005) Current status of therapy of solid tumors. *Nucl. Med. 46* (S1), 141S–50S.
(9) Hassfjell, S., and Brechbiel, M. W. (2001) The development of the α-particle emitting radionuclides ^{212}Bi and ^{213}Bi, and their decay chain related radionuclides for therapeutic applications. *Chem. Rev. 101*, 2019–36.
(10) Lewis, M. R., Raubitschek, A., and Shively, J. E. (1994) A facile, water-soluble method for modification of proteins with DOTA. Use of elevated temperature and optimized pH to achieve high specific activity and high chelate stability in radiolabeled immunoconjugates. *Bioconjugate Chem. 5*, 565–76.
(11) Chakrabarti, M. C., Le, N., Paik, C. H., De Graff, W. G., and Carrasquillo, J. A. (1996) Prevention of radiolysis of monoclonal antibody during labeling. *J. Nucl. Med. 37*, 1384–8.
(12) Liu, S., and Edwards, D. S. (2001) Bifunctional chelators for therapeutic lanthanide radiopharmaceuticals. *Bioconjugate Chem. 12*, 7–34.
(13) Raymond, K. N., and Pierre, V. C. (2005) Next generation, high relaxivity gadolinum MRI agents. *Biconjugate Chem. 16*, 3–8.
(14) Banci, L., Bertini, I., and Luchinat, C. (1991) *Nuclear and Electronic Relaxation*, VCH, Weinheim.
(15) Yoneda, S., Emi, N., Fujita, Y., Ohmichi, M., Hirano, S., and Suzuki, K. T. (1995) Effects of gadolinium chloride on the rat lung following intratracheal instillation. *Fundam. Appl. Toxicol. 28*, 65–70.
(16) Chong, H. S., Garmestani, K., Milenic, D., and Brechbiel, M. W. (2002) Design, synthesis, and biological evaluation of novel macrocycles with pendant donor groups as radioimmunotherapy (RIT) agents. *J. Med. Chem. 45*, 3458–64.
(17) Chong, H. S., Milenic, D. E., Garmestani, K., Brady, E. D., Arora, H., Pfiester, C., and Brechbiel, M. W. (2006) In vitro and in vivo evaluation of novel ligands for radioimmunotherapy. *Nucl. Med. Biol. 33*, 459–67.
(18) Chong, H. S., Garmestani, K., Bryant, L. H., Jr., Milenic, D. E., Overstreet, T., Birch, N., Le, T., Brady, E. D., and Brechbiel, M. W. (2006) Synthesis and evaluation of novel macrocyclic and acyclic ligands as contrast enhancement agents for magnetic resonance imaging. *J. Med. Chem. 49*, 2055–62.
(19) Chong, H. S., Song, H. A., Birch, N., Le, T., Lim, S., and. Ma, X. (2008) Efficient synthesis and evaluation of bimodal ligand NETA. Bioorg. Med. Chem. Lett. In Press.

(20) Ameido, J. C., Jr., Bernard, P. J., and Fountain, M., Jr. (1999) A practical manufacturing synthesis of 1-(R)-hydroxymethyl-DTPA: An important intermediate in the synthesis of MRI contrast agents. *Syn. Commun. 29*, 2377–91.

(21) Kim, W. D., Kiefer, G. E., Maton, F., McMillan, K., Muller, R. N., and Sherry, A. D. (1995) Relaxometry, luminescence measurements, electrophoresis, and animal biodistribution of lanthanide(III) complexes of some polyaza macrocyclic acetates containing pyridine. *Inorg. Chem. 34*, 2233–43.

(22) Agus, D. B., Jr., Franklin, W., Garcia, M., and Ozols, R. F. (2000) HER-2/neu as a therapeutic target in non-small cell lung cancer, prostate cancer, and ovarian cancer. *Semin. Oncol. 27*, 53–63.

(23) Pietras, R. J., Pegram, M. D., Finn, R. S., Maneval, D. A., and Slamon, D. J. (1998) Remission of human breast cancer xenografts on therapy with humanized monoclonal antibody to HER-2 receptor and DNA-reactive drugs. *Oncogene 17*, 2235–49.

(24) Brady, E. D., Chong, H. S., Milenic, D. E., and Brechbiel, M. W. (2004) Development of a spectroscopy assay for bifunctional ligand-protein conjugates based on copper. *Nucl. Med. Biol. 31*, 795–802.

(25) Lowry, O. H., Rosebrough, N. J., Rarr, A. L., and Randall, A. J. (1951) Protein measurement with the folin phenol reagent. *J. Biol. Chem. 193*, 265–75.

(26) Chong, H. S., Ma, X., Le, T., Kwamena, B., Milenic, D. E., Brady, E. D., Song, H. A., and Brechbiel, M. W. (2008) Rational design and generation of a bimodal bifunctional ligand for antibody-targeted radiation cancer therapy. *J. Med. Chem. 51*, 118–25.

(27) Barge, A., Cravotto, G., Gianolio, E., and Fedeli, F. (2006) How to determine free Gd and free ligand in solution of Gd chelates. *Contrast Med. Mol. Imaging 1*, 184–8.

BC800050X

Simple Modifications of Branched PEI Lead to Highly Efficient siRNA Carriers with Low Toxicity

Arkadi Zintchenko,* Alexander Philipp, Ali Dehshahri, and Ernst Wagner

Center for Drug Research, Department of Pharmacy, Pharmaceutical Biology-Biotechnology, and Center for NanoScience (CeNS), Ludwig-Maximilians-University, Butenandstr. 5-13, D-81377 Munich, Germany. Received February 19, 2008; Revised Manuscript Received May 7, 2008

Polymer carriers like PEI which proved their efficiency in DNA delivery were found to be far less effective for the applications with siRNA. In the current study, we generated a number of nontoxic derivates of branched PEI through modification of amines by ethyl acrylate, acetylation of primary amines, or introduction of negatively charged propionic acid or succinic acid groups to the polymer structure. The resulting products showed high efficiency in siRNA-mediated knockdown of target gene. In particular, succinylation of branched PEI resulted in up to 10-fold lower polymer toxicity in comparison to unmodified PEI. Formulations of siRNA with succinylated PEI were able to induce remarkable knockdown (80% relative to untreated cells) of target luciferase gene at the lowest tested siRNA concentration of 50 nM in Neuro2ALuc cells. The polyplex stability assay revealed that the efficiency of formulations which are stable in physiological saline is independent of the affinity of siRNA to the polymer chain. The improved properties of modified PEI as siRNA carrier are largely a consequence of the lower polymer toxicity. In order to achieve significant knockdown of target gene, the PEI-based polymer has to be applied at higher concentrations, required most probably for sufficient accumulation and proton sponge effects in endosomes. Unmodified PEI is highly toxic at such polymer concentrations. In contrast, the far less toxic modified analogues can be applied in concentrations required for the knockdown of target genes without side effects.

INTRODUCTION

Since double-stranded RNA molecules were identified as the mediator of gene silencing in *C. elegans* (*1*), RNA interference (RNAi) has become a powerful strategy for intervention also in mammalian cell processes and treatment of various diseases, due to its ability to silence gene expression in a sequence-specific manner (*2–4*).

Polycations such as polyethylenimine (PEI)[1] have been introduced as nonviral gene carriers with a capability of forming stable complexes by electrostatic interactions with nucleic acids. The polyplex formation leads to improved protection of the genetic material from enzyme-mediated digestion and enhanced intracellular delivery. PEI, although it is known to be a powerful agent in plasmid-based gene delivery (*5, 6*), has been shown to be less effective in siRNA-mediated gene silencing (*7, 8*). Moreover, it is known to be toxic when applied at higher doses. The toxicity is mainly associated with a strong positive charge of this polycation, which leads to strong interaction of PEI with cell surfaces and their damage. Therefore, modifications of polymeric backbone that reduce the positive charge of PEI might be useful in order to reduce the toxicity of the polymer.

Several approaches have already been investigated in this direction. Different polymeric forms of PEI are available, the linear form (obtained via polyisoxazoline precursors) or the branched form (obtained from acid-catalyzed polymerization of aziridine), both in various degrees of polymerization that influence their biological activities (*9–12*). Backbone modification of linear PEI 22 kDa, which on its own is one of the most potent transfection agents (*6*), have reduced the high gene transfer activity (*13*). In fact, it was demonstrated that the high activity depends on complete removal of propionamide residues from the polyisoxazoline precursor polymer (*14*). Linear PEI22 on its own has limited efficiency in siRNA delivery (*7*); the activity however can be enhanced with concatemerizing "sticky" siRNA (ssiRNA) applied for polyplex formation (*15*).

Experiences with branched PEI 25 kDa gave different trends. Interestingly, partial acetylation of PEI amino groups was shown to enhance gene transfer activity (*16*). N-Acylation of PEI lowered its toxicity (*17*). Also, conjugation of acetate, butanoate, and hexanoate to branched PEI at low degree of substitution (below 25%) resulted in moderate improvement of transfection activity as demonstrated by Putnam and colleagues (*18*). The same research group compared different (linear and branched) PEIs for siRNA transfer activity; only branched PEI within a narrow window of conditions was able to mediate in vitro gene silencing in a (HR5-CL11) cell line (*8*). Reducing the surface charge of polyplexes by PEGylation of PEI positively affected the siRNA delivery capacity in the absence (*19*) or in the presence of a cell targeting molecule (*20*).

In this work, using relatively simple modification strategies, we were able to produce a number of branched PEI derivates, which were aimed at screening the positive charge of the polymer. In particular, negative charges were introduced into the polymer backbone by modification with succinic anhydride or Michael addition of ethyl acrylate followed by ester hydrolysis. Alternatively, amino groups were modified by acetylation or addition by ethyl acrylate. As was expected, all the products showed reduced toxicity in comparison to unmodified PEI. Moreover, we found that several modifications were able to greatly improve the siRNA/PEI formulation characteristics and

* Correspondence to Arkadi Zintchenko, tel +49 89 2180 77373, fax +49 89 2180 77798, e-mail arkadi.zintchenko@cup.uni-muenchen.de.

[1]Abbreviations: PEI, polyethylenimine; EA, ethyl acrylate; EtdBr, ethidium bromide; RLU, relative light units.

10.1021/bc800065f CCC: $40.75 © 2008 American Chemical Society
Published on Web 06/14/2008

silencing activities, thereby presenting easy access to promising siRNA transfection reagents.

EXPERIMENTAL SECTION

Materials. Ethyl acrylate (EA), acetic anhydride, and succinic anhydride were obtained from Sigma (Munich, Germany). The plasmid pEGFPLuc (Clontech Laboratories, Heidelberg, Germany) containing a CMV promoter-driven fusion of the genes encoding for enhanced green fluorescent protein and luciferase was used for generation of stably transfected cells. Branched PEI with an average molecular weight of 25 kDa (PEI) was obtained from Sigma-Aldrich (Munich, Germany). PEI was used as a 1−10 mg/mL stock solution neutralized with HCl. All other chemicals were purchased by Sigma-Aldrich (Munich, Germany). Cell culture media, antibiotics, and fetal calf serum (FCS) were purchased from Invitrogen (Karlsruhe, Germany). Ready to use siRNA duplexes were purchased from MWG-Biotech (Ebersberg, Germany), namely, luciferase-siRNA; GL3 luciferase duplex; 5′-CUUACGCUGAGUACUUCGAdTdT-3′; control-siRNA; nonspecific control duplex with similar GC content as antiluciferase-siRNA; 5′-AUUGUAUGCGAUCG-CAGACdTdT-3′.

Modification of PEI by Ethyl Acrylate (EA). About 1 g of PEI was dissolved in chloroform. The solution was heated to 40 °C. The desired amount of acrylate was added to the solution with stirring. The reaction proceeded for at 40 °C. After 4 h, the chloroform was removed by rotary evaporator. The waxy product was dissolved in 15 mL water and neutralized by HCl to the pH 4−5 and freeze-dried. The modification degree was analyzed by ^{1}H NMR in D_2O on a Jeol JNMR-GX400 (400 MHz) or Jeol JNMR-GX500 (500 MHz) spectrometer from the ratio between the peaks of PEI (δ 2.6−3.6 ppm) and methyl acrylate (δ = 1.3 ppm). The modification degree was expressed as a number of modifications per monomer unit of PEI × 100%. According to FTIR spectra recorded on a Jasco FT/IR-410 spectrometer (Jasco Labor- and Datentechnik GmbH, Germany), a pronounced ester peak (1730 cm^{-1}) was detected. No significant amide band (1652 cm^{-1}) was found.

Synthesis of Acetylated and Succinylated PEI. PEI (0.5 g) was dissolved in 8.5 mL of water and 1.5 mL of NaCl solution (3 M) and then adjusted to pH 5 using 1 M HCl. The desired amounts of acetic or succinic anhydride were dissolved in DMSO and added dropwise to PEI solution. The reaction was carried out at room temperature for 3 h. The crude products dialyzed (18 000 cutoff, Spectra/Por membrane) first against 0.25 M NaCl solution to remove unreacted acetate or succinate, and then twice against water at 4 °C to remove salt. After the dialysis, the aqueous solution was lyophilized. The modification degree was analyzed by ^{1}H NMR in D_2O from the ratio between the peaks of PEI (δ 2.6−3.6 ppm) and methylene of succinate (δ = 2.5 ppm) or methyl of acetate (δ = 2.1 ppm). The modification degree was expressed as a percentage of modified amines of PEI under the assumption that each amine is able to react.

Synthesis of Propionic Acid Modified PEI by Hydrolysis of EA Modified PEI. About 0.3 g of PEI-EA polymer was dissolved in 1 M HCl. The solution was incubated at 40 °C for 3 days. The final product was dialyzed against water (18 000 cutoff, Spectra/Por membrane) and freeze-dried. The extent of reaction was controlled by ^{1}H NMR in D_2O. No ethyl peak was found for all samples, indicating complete hydrolysis of the ester bond. Neither ester (1730 cm^{-1}) nor amide (1652 cm^{-1}) peak was detected by FTIR.

Polyplex Formation. In all studies, the composition of polyplexes was characterized by the w/w ratio of the polymer to nucleic acid in the mixture. The weight of unmodified PEI represents a weight of the polymer in base form. The weight of modified PEI represents the weight of lyophilized product, which was previously neutralized to pH of about 4−5 and, therefore, includes the mass of counterions (chloride). Formulations for pDNA and siRNA delivery were prepared in HBG (20 μL) as follows: First, different concentrations of the nucleic acid and PEI derivatives were diluted at various polymer/nucleic acid ratios (w/w: weight/weight) in separate tubes in HBG (HEPES-buffered glucose solution; 20 mM HEPES, 5% glucose). Then, the HBG solution of PEI was added to the HBG solution of the nucleic acid, mixed, and incubated for 30 to 40 min at room temperature to form stable polymer/nucleic acid complexes.

EtBr Exclusion Assay. The ability of the products to condense DNA or siRNA was studied using an ethidium bromide (EtBr) assay. Polymer solution was added stepwise to the solution of nucleic acid (10 μg/mL) in HBG containing EtBr (0.4 μg/mL). After each step, fluorescence intensity was monitored (λ_{ex} = 510 nm, λ_{em} = 590 nm). The fluorescence intensity of the EtBr solution in the presence of free nucleic acid corresponded to 0% condensation, whereas the fluorescence intensity without nucleic acid corresponded to 100% condensation.

Polyplex Stability Assay. Polyplexes were mixed with DNA or siRNA in HBG at a final concentration of 20 μg/mL of nucleic acid and a 1:1 w/w ratio. The particle sizes were monitored by dynamic laser light scattering using a Malvern Zetasizer 3000HS (Malvern Instruments, Worcestershire, UK). After this, 3 M NaCl solution was added stepwise to the polyplex solution. After each step, the correlation functions and scattering intensities were monitored. The dissociation of polyplexes led to the drop of scattering intensity to the level of the salt buffer and changes in correlation function (Supporting Information Figure 1). The NaCl concentration at which the dissociation of the polyplexes occurred was related to the stability of the polyplexes.

Cell Culture. For pDNA and siRNA delivery experiments, mouse melanoma cells B16F10, mouse glioblastoma cells Neuro2A, Neuro2A/EGFPLuc cells, and HUH7/EGFPLuc cells stably transfected with the EGFPLuc gene (see below) were used. B16F10 cells and Neuro2A/EGFPLuc cells were grown in Dulbecco's modified Eagle's medium (DMEM) and HUH7/EGFPLuc were grown in DMEM/Ham's F-12 medium, whereby all media were supplemented with 10% FCS, 4 mM stable glutamine, 100 U/mL penicillin, and 100 μg/mL streptomycin. All cells were seeded 24 h prior to pDNA or siRNA delivery using 5000 cells per well in 96-well plates for analysis of protein expression.

For the generation of stably transfected cells, the vector pEGFPLuc (Clontech) was linearized using the restriction enzyme Dra III, and cells were then transfected with this linearized vector using linear polyethylenimine 22 kDa (PEI 22lin; Euromedex, Souffelweyersheim, France).

Following gene transfer, Neuro2A or HUH7 cells were incubated in fresh medium for 72 h prior to selection of the stably transfected cells with 200 to 2000 μg/mL G418 (geneticine; Invitrogen, Karlsruhe, Germany). After several days, surviving cells were seeded at low density into 6-well plates in order to generate separate colonies. Single cell clones were then isolated and expanded. The generated clones were analyzed for the percentage of EGFP-positive (EGFPLuc stably transfected) cells by flow cytometry. Clones with the highest number of EGFP-positive cells were then further selectively grown up under the above-described selective conditions, and this procedure was repeated until all cells were positive for EGFP. These stably transfected cells expressing approximately 60 ng luciferase per million cells were then used for siRNA delivery experiments.

In Vitro Gene Transfer. In vitro transfection efficiency of the polymers was evaluated in B16F10 or Neuro2A cells using

pEGFPLuc (200 ng pDNA per well). In all experiments, pDNA delivery was performed in 96-well plates with 5000 cells (B16F10) or 10 000 cells (Neuro2A) per well in triplicates. Cells were seeded 24 h prior to transfection and then medium was replaced with 80 μL fresh growth medium containing 10% FCS. Transfection complexes for pDNA delivery (20 μL in HBG) at different w/w ratios were added to each well and incubated at 37 °C. After 4 h, the medium was replaced by fresh growth medium. The cells were treated with 50 μL cell lysis buffer (25 mM Tris, pH 7.8, 2 mM EDTA, 2 mM DTT, 10% glycerol, 1% Triton X-100) 24 h following pDNA transfection. Luciferase activity in cell lysate (20 μL) was measured using a luciferase assay kit (100 μL Luciferase Assay buffer, Promega, Mannheim, Germany) on a luminometer for 10 s (Lumat LB9507 instrument, Berthold, Bad Wildbad, Germany).

In Vitro Gene Silencing with siRNA. In vitro gene silencing experiments were performed in stably transfected Neuro2A/EGFPLuc and HUH7/EGFPLuc cells using LucsiRNA and MutsiRNA as a control. In all experiments, siRNA delivery was performed in 96-well plates with 5000 cells per well in triplicate. Cells were seeded 24 h prior to transfection, and then medium was replaced with 80 μL fresh growth medium containing 10% FCS. Transfection complexes for siRNA delivery (20 μL in HBG) at different w/w ratios were added to each well and incubated at 37 °C without medium change. Cells were washed with phosphate-buffered saline (PBS) and treated with 50 μL cell lysis buffer (25 mM Tris, pH 7.8, 2 mM EDTA, 2 mM DTT, 10% glycerol, 1% Triton X-100) 48 h following siRNA transfection. Luciferase activity in cell lysate (20 μL) was measured using a luciferase assay kit (100 μL luciferase assay buffer, Promega, Mannheim, Germany) on a luminometer for 10 s (Lumat LB9507 instrument, Berthold, Bad Wildbad, Germany). The relative light units (RLU) were related to untreated control cells.

Cytotoxicity Assay. Neuro2A cells were seeded into 96-well plates at a density of 1×10^4 cells/well. After 24 h, the culture medium was replaced with 100 μL/well of serial dilutions of polymer stock solutions in growth medium. Alternatively, transfection complexes for pDNA delivery (20 μL in HBG) at different C/P ratios were added. All studies were made in triplicate. After 4 h incubation, the medium was replaced by the fresh one.

After 24 h, MTT (3-(4,5-dimethylthiazol-2-yl)-2,5-diphenyltetrazolium bromide) (Sigma-Aldrich, Germany) was dissolved in phosphate buffered saline at 5 mg/mL, and 10 μL aliquots were added to each well reaching a final concentration of 0.5 mg MTT/mL. After an incubation time of 1 h, unreacted dye with medium was removed. The purple formazan product was dissolved in 100 μL/well dimethyl sulfoxide and quantified by a plate reader (Tecan, Groedig, Austria) at 590 nm with background correction at 630 nm. The relative cell viability (%) relative to control wells containing cell culture medium without polymer was calculated by [A] test/[A] control $\times$ 100.

RESULTS

Synthesis of the Polymers. The strategies for modification of branched PEI 25 kDa are presented in Figure 1. In EA and PROP series, the primary amines of PEI were transformed to the secondary amines by Michael addition. In AC and SUC series, the primary amines were acetylated to amides. Additionally, PROP and SUC series have carboxylic group in the structure.

Syntheses and characterization are described in Materials and Methods and Supporting Information. PEI was modified with ethyl acrylate via Michael addition performed at 40 °C and relatively short incubation time. Table 1 shows the degrees of modification (12−31%) depending on the ratios in the feed.

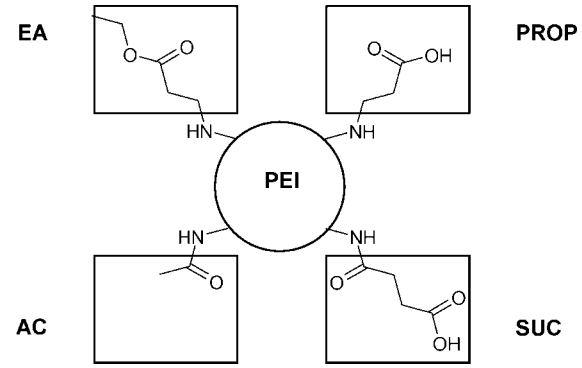

Figure 1. Strategies for modification of branched PEI.

Table 1. Composition of Modified PEIs[a]

polymer	reagent/amine*100%, feed	modification degree, %
PEI-EA 12	13%	11.5%
PEI-EA 18	26%	17.6%
PEI-EA 31	52%	31%
PEI-PROP 12	n.a.	11.5%
PEI-PROP 18	n.a.	17.6%
PEI-PROP 31	n.a.	31%
PEI-AC 12	10%	12.3%
PEI-AC 22	20%	21.8%
PEI-SUC 9	10%	8.9%
PEI-SUC 19	20%	19.4%

[a] The nomenclature of the polymers is expressed as follows: PEI-*X Y*, where *X* represents the reagent by which PEI was modified (EA, ethyl acrylate; SUC or AC, succinic or acetic anhydride, respectively) or functional group (PROP for 3-propionic acid) and *Y* represents the modification degree of the amines measured by NMR.

Longer incubation times are known to cause aminolysis of ester bond and lead to cross-linking of PEI (*21*). No amide peak was found on FTIR spectra of all polymer samples of PEI-EA series (data not shown). Therefore, no aminolysis was observed, excluding the cross-linking of PEI. No double bond peak was present in ^{1}H NMR for all samples, indicating the complete evaporation of unreacted acrylate during freeze-drying procedure and its absence in the final products.

The 3-propionic acid-modified B-PEI (PEI-PROP) was generated by acid hydrolysis of PEI-EA polymers. Complete hydrolysis was verified by disappearance of the ester protons in the NMR spectra and characteristic FTIR-band at 1730 cm^{-1}. The degrees of PEI modification with carboxylic groups were assumed to be the same as in nonhydrolyzed precursor polymers. An absence of the amide peak on FTIR spectra (1652 cm^{-1}) reveal no significant cross-linking during hydrolysis.

The modification of PEI with acetic anhydride and succinic anhydride was performed in the presence of salt in the reaction solution to avoid precipitation of the polymer. The purification of polymers via dialysis was performed against salt buffer to ensure complete exchange of acetic or succinic acid, respectively, against chloride. At low reagent/amine feed ratios (10−20%), nearly quantitative modification of PEI was achieved (Table 1).

The yields were typically 80−120%. The neutralization of the products and, consequently, the weight gain due to counterions (chloride), which was not taken into account by calculation of theoretical yields, was the reason for some of the yields being above 100%.

The pH titrations of the polymers demonstrated that the pH5 to pH7 buffer capacity did not significantly change after modification (data not shown).

Toxicity of the Polymers. The cell culture cytotoxicity profiles of modified PEIs (Figure 2) are shifted to higher polymer concentrations in comparison to PEI, demonstrating a

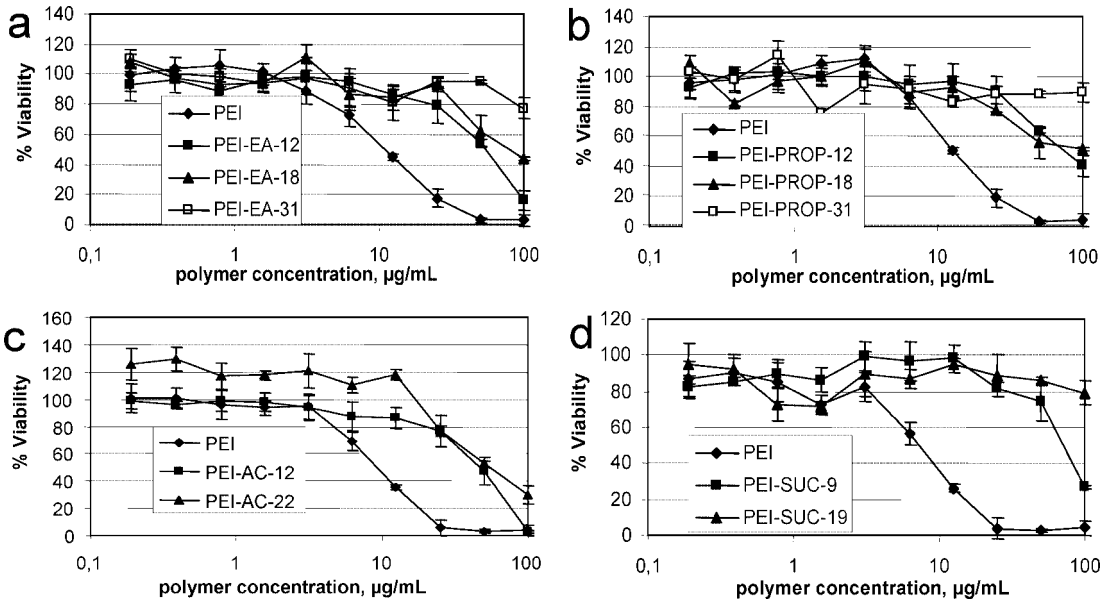

Figure 2. Cell viability of Neuro2A cells as a function of concentration of modified PEI polymers in the medium. (a) PEI-EA series, (b) PEI-PROP series, (c) PEI-AC series, (d) PEI-SUC series.

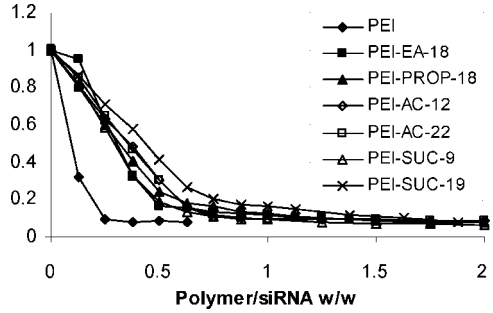

Figure 3. EtBr exclusion assay of the polymers with siRNA in HBG buffer.

decrease in toxicity. Relatively soft neutral modifications (EA and AC) have shown only moderate improvement of cell viability, whereas the incorporation of negative charges on PEI led to polymers with far less toxicity.

Chemical and Biophysical Properties of Polyplexes. In salt-free buffer, all polymers were effective in binding of siRNA (Figure 3) as well as DNA (data not shown). In comparison to PEI, the binding required higher polymer to siRNA and DNA (w/w) ratios. Such a difference is caused by the fact that for modified PEI w/w ratio was calculated from the base form. Modified PEIs were weighed in neutralized form; therefore, the counter ions (chloride) markedly contribute to mass per charge ratio. Nevertheless, at w/w ratio of 2 even the polymers with a high degree of modification show the reduction of EtBr fluorescence to less than 10%. No significant difference in binding between products of different modifications was observed in this assay. Agarose gel electrophoresis data confirmed these results (data not shown).

The analysis of the polyplex solutions mixed in HBG at w/w ratios of 2 and 4 by photon correlation spectroscopy did not show the formation of nanoparticles in the usual 30−300 nm range of standard DNA/PEI polyplexes. The scattering intensity from polyplex solution at a concentration of 5 μg/mL based on siRNA was close to that of HBG buffer, which indicates very small polyplex sizes and low aggregation number of the polymer chains. Such behavior of siRNA/PEI polyplexes has recently been shown by Meyer et al. (*22*) where particle sizes of around 25 nm were detected by fluorescent correlation spectroscopy.

The increase of the salt concentration in this solution to 150 mmol NaCl led to continuous aggregation of the initial polyplexes and formation of nanoparticles (around 500 nm after 30 min) in the case of modified PEI. Unmodified PEI without siRNA did not show any aggregation at physiological saline.

Plasmid-Based Gene Transfer. Most of the polymers were found to be effective gene transfer agents and showed transfection efficiencies comparable to branched PEI on B16F10 and Neuro2A cells (Supporting Information Figure 2). Only PEI-PROP-31 displayed relatively low efficiency. All others showed transfection efficiencies comparable to PEI. The polyplexes generated with the modified PEIs induce much less toxicity than PEI. As can be seen from Supporting Information Figure 2b,c, at w/w ratio of 4 the cell viabilities are above 80% for the modified PEI and only 20−40% for the unmodified PEI.

Gene Silencing with siRNA. Modified PEIs were found to be good DNA transfection agents. However, it is known from literature that efficient carriers of plasmid DNA are not necessarily effective for siRNA delivery (*23*). Linear polyethylenimine 22 kDa and branched polyethylenimine 25 kDa (PEI), the powerful DNA delivery agents, showed only limited efficiency in siRNA delivery (*7, 8*). Therefore, the modified PEIs were tested for their efficiency in siRNA delivery using a neuroblastoma cell line stably transfected with a luciferase marker gene. The results are presented in Figure 4. Luciferase activities were determined for cells treated either with LUC siRNA (directed against the target mRNA) or with a control siRNA (Mut siRNA), and compared with the luciferase activity of untreated control cells. Knockdown effects are real when expression decreases with Luc siRNA but not Mut siRNA. If luciferase expression decreases with both target and control siRNA, "knockdown" is mainly due to unspecific carrier toxicity. siRNA formulations with PEI were not able to facilitate knockdown of reporter gene without toxicity. High toxicity was observed for the formulations above w/w ratio of 1, indicated by decrease of luciferase level for formulations with mismatched siRNA.

Most modified PEIs (except PEI-PROP-31 and PEI-SUC-19) showed up to 80−90% of luciferase knockdown, when formulated with Luc-siRNA. The effect cannot be attributed to the toxicity of polyplexes, since the luciferase level by the formulations with mismatched siRNA was close to the control.

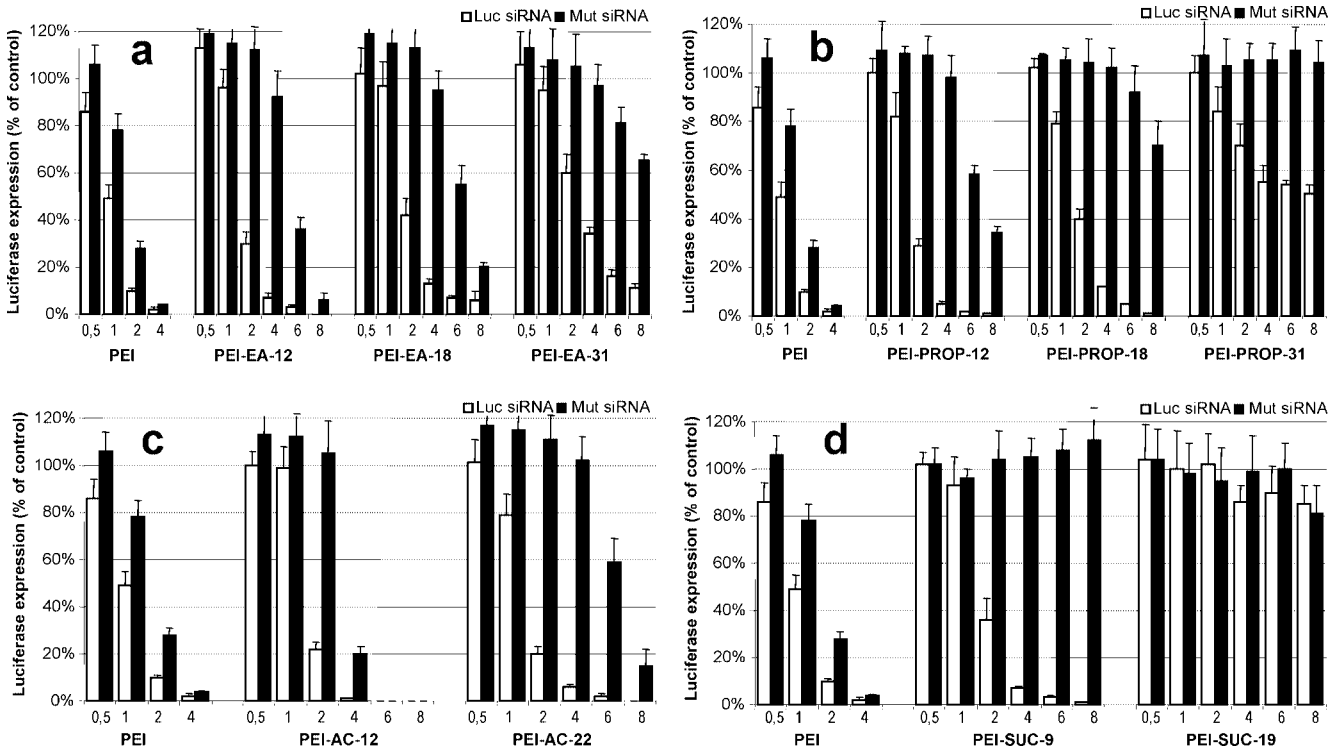

Figure 4. siRNA delivery to Neuro2A/EGFPLuc cells using modified PEI: (a) EA series, (b) PROP series, (c) AC series, (d) SUC series. The numbers on the *x*-axis represent the polymer/siRNA w/w ratios. The final siRNA concentration in culture medium was 380 nM. White bars, LucsiRNA; black bars, MutsiRNA. Luciferase expression levels are presented in % relative to untreated control cells. Luciferase expression was measured 48 h after transfection without change of the medium.

The best knockdown was achieved with PEI-SUC-9. Being nontoxic at all studied mixing ratios, it showed the gene silencing to almost less than 10% relative to the control. Further increase of the negative charge on PEI led to inactivation of this polymer; PEI-SUC-19 did not show any gene knockdown at all w/w ratios. Interestingly, PEI-EA-31 showed significant knockdown at w/w of 4 and 6, whereas the hydrolyzed analogue PEI-PROP-31 was inactive. Thus, low amounts of negatively charged groups on the polymer were able to improve the efficiency of PEI in siRNA delivery, whereas high amounts of negative charges resulted in nontoxic but also ineffective polymers.

Even with lower amounts of siRNA significant knockdown was achieved, if the polymer amount remained on the same level (Figure 5). At concentration of the polymers in transfection medium of 20 μg/mL and siRNA concentration of 50 nM, it was possible to achieve 50−80% knockdown of the luciferase gene. Decrease of siRNA concentration led to a certain increase of the toxicity of the formulations with most of the polymers, which was caused by an increasing amount of uncomplexed PEI in the transfection medium. Only PEI-SUC-9 was able to show up to 80% knockdown without any sign of toxicity at 50 nM siRNA concentration. Unmodified PEI at concentration of 2.5 μg/mL was taken as a control. As is seen, PEI was not efficient at any siRNA concentration. Higher concentrations showed unspecific knockdown due to the toxicity of the carrier.

PEI-SUC-9, as the most promising candidate, was additionally tested for siRNA delivery to another stably transfected cell line HUH7Luc (Supporting Information Figure 3). Also on this cell line, high efficiency and low toxicity of this carrier were demonstrated.

Bolcato-Bellemin et al. (*15*) postulated that the limited efficiency of PEI/siRNA formulations might be caused by low binding affinity of polycation to nucleic acid. Therefore, if the binding to PEI could be increased, the formulation with siRNA would gain efficiency. The modifications of PEI used in the

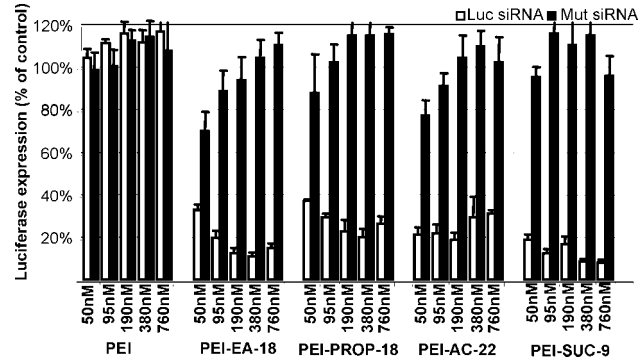

Figure 5. siRNA delivery to Neuro2A/EGFPLuc cells using modified PEI. The numbers on the *x*-axis represent the concentration of siRNA in culture medium. The concentration of PEI-EA-18, PEI-PROP-18, PEI-AC-22, and PEI-SUC-9 was kept constant at 20 μg/mL. The concentration of unmodified PEI was kept at 2.5 μg/mL. White bars, LucsiRNA; black bars, MutsiRNA. Luciferase expression levels are presented in % relative to untreated control cells. Luciferase expression was measured 48 h after transfection without change of the medium.

present paper were not expected to increase the binding with siRNA. Nevertheless, several of the modified polymers showed strongly improved siRNA activity in comparison to that of PEI. To study this discrepancy and further define the influence of PEI modification on the binding between polymer and siRNA, the stability of the polyplexes against dissociation induced by salt was studied.

Electrostatic interactions between polycations and nucleic acids are largely responsible for the stabilization of polyplexes. Contrary to long nucleotide sequences (like plasmids), for relatively short oligomers the stabilization is expected to be dependent on the number of charges per nucleic acid molecule. Low molecular salt is able to screen the electrostatic interactions and, at certain concentration, cause the dissociation of poly-

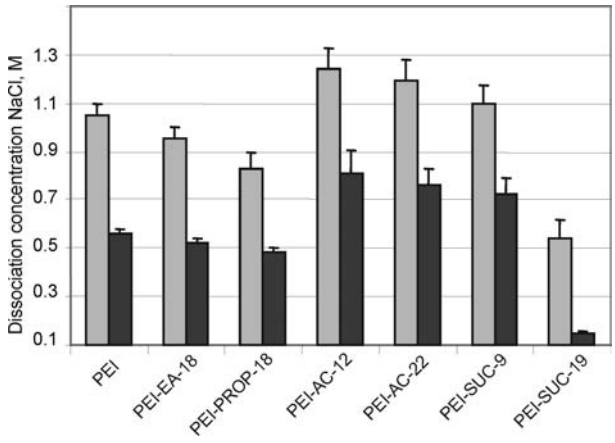

Figure 6. NaCl concentrations required for dissociation of polyplexes: gray bars, polyplexes with DNA; black bars, polyplexes with siRNA. For details, see Experimental Section and Supporting Information. Complexes were formed at concentration of 20 ug/mL nucleic acid and 1/1 w/w ratio.

plexes. The salt concentration required for the dissociation could be attributed to the stability of polyplexes. Photon correlation spectroscopy was used to detect the dissociation point. The polyplexes formed in salt-free buffer were titrated with NaCl. After each step, dynamic light scattering measurements were performed. Addition of NaCl to the polyplex solution led to aggregation of small polyplex particles, increase of scattering intensity, and shift of the correlation function to the slow-motion range (Supporting Information Figure 1). Further increase in NaCl concentration led to the dissociation point, where the scattering intensity drops to the level of NaCl buffer. The residual correlation is mainly caused by the statistically low number of foreign particles in the solution (i.e., dust) (Supporting Information Figure 1).

The NaCl concentrations required for the dissociation of the polyplexes with DNA and siRNA are presented in Figure 6. As expected, polyplexes with DNA dissociate at near two times higher salt concentration than polyplexes with siRNA. However, no correlation between the stability and knockdown efficiency within siRNA polyplexes was found, since all series of PEI modifications were found to show the efficient knockdown of the luciferase gene. According to the stability data, EA and PROP series showed lower stability than PEI, whereas in case of AC and SUC series, the stability was higher. The same dependence could be also attributed to the polyplexes with DNA. The reasons for the increased stability of the polyplexes in AC and SUC series are not clear. Additional stabilization of the polyplexes might be mediated through the hydrogen bonding between the amides in these structures and the nucleic acids (*24*).

Interestingly, the PEI-SUC-19 was able to transfect the cells, but was completely inefficient in inducing knockdown with siRNA (Figure 4d). Data from Figure 6 explain this behavior. While being relatively stable with DNA, siRNA polyplexes of this polymer are unstable at physiological salt concentration and not able to induce knockdown.

DISCUSSION

In this study, a number of PEI-based polymers were synthesized, which showed significantly lower toxicity in comparison to branched PEI. Since toxicity of PEI is mainly associated with the high positive charge of the polymer, the screening of PEI amines was performed in different ways. The Michael addition of ethyl acrylate (EA series) represents a relatively soft modification, which results in transformation of primary amines of PEI to secondary. Also, a bulky EA group is introduced to the structure, which could represent a steric barrier for interaction of PEI with negatively charged surfaces. The AC modification reduces the positive charges of PEI due to acetylation of primary amines. In the PROP series, the transformation of primary to secondary amines was combined with the introduction of negatively charged proionic acid residues. Finally, SUC series represent the strongest reduction of the positive charge of PEI by combination of acylation of primary amines and introduction of negative charges into the polymer.

As expected, the toxicity of the polymers was greatly reduced by the modifications. Even the softer PEI modifications (EA, AC) reduced the toxicity, although to a lower extent in comparison to the PROP and SUC series. These data fit very well with literature, where several modifications of branched PEI led to decreased charge and lower toxicity of the polymer (*17*, *25*). The reduction of positive charge, however, might also reduce activity of polycation in nucleic acid transfer as previously reported (*13*, *14*, *19*). Within our series of modifications, only two products with the highest degrees of modification showed inactivation: PEI-PROP-31 for both DNA and siRNA transfer, and PEI-SUC-19 for siRNA transfer. Reduced polyplex stability due to the increased density of negative charges on the cationic polymer chain is presumably responsible for this. For example, polyplexes of siRNA and PEI-SUC-19 dissociated in physiological saline. All other modified PEI products were found to show transfection efficiency with DNA comparable to that of unmodified PEI. Importantly, in contrast to unmodified PEI, they were able to induce efficient siRNA-mediated knockdown. PEI-SUC-9 was found to be the most effective delivery agent for siRNA. Low toxicity and high efficiency in knockdown, also at low concentrations of siRNA, make this PEI modification very promising for in vitro delivery of siRNA.

Possible reasons for the low efficiency of unmodified PEIs in siRNA delivery despite their high efficiency in DNA transfer might be associated with the stability of the polyplexes. Requirements for delivery of DNA and siRNA are different. DNA transfer requires nuclear uptake with subsequent unpacking and release of the plasmid. Relatively strong binding of the carrier to the pDNA might prevent the unpacking and degradation of pDNA in the cytoplasm. In case of siRNA delivery, an effective dissociation from the carrier is required within the cytoplasm. Therefore, the modifications should aim at a lower affinity of the polymer to siRNA in comparison to DNA polypexes. Another hypothesis postulates that lower affinity of siRNA to the carrier as compared to plasmid DNA may be the reason for insufficient knockdown due to polyplex instability. Therefore, in order to achieve effective knockdown formulations, the stability of the polyplexes with siRNA should be increased.

Neither of the two hypotheses seems to be true. According to the data of the present investigation, the stability of the polyplexes with siRNA is lower in comparison to the polyplexes with DNA. Although all PEI modifications in this study were expected to reduce the electrostatic affinity to nucleic acids, certain series (AC and SUC) showed even higher stability of polyplexes in comparison to unmodified PEI. Taking into account that all modification types were able to induce significant knockdown, AC and SUC series do not fit the first hypothesis as well as EA and PROP series to the second. The stability of siRNA formulations could possibly play a role during in vivo applications; however, for in vitro efficacy the extent of polyplex stability has minor importance, unless the polyplex is sufficiently stable to survive in the culture medium.

The most probable reason for the improved properties of modified PEIs in siRNA delivery in comparison to unmodified PEI is the lower toxicity of the carrier, which enables higher

amounts of PEI for transfection. This hypothesis is also supported by DNA transfection data with unmodified PEI; the increase of w/w ratio from 0.8 to 4 led to increased transfection efficiency (and toxicity). Higher amounts of PEI in the formulation and subsequently in endosomal compartments may increase escape to the cytosol due to a stronger proton sponge effect (*26, 27*). Therefore, the transfection properties of PEI can be boosted by increasing the amount of polymer.

The concentration of PEI plays a major role for efficient siRNA delivery. At small concentrations, unmodified PEI is not able to facilitate significant knockdown (Figure 5). Higher concentrations lead to high toxicity of the carrier. In the case of modified PEIs, in particular, PEI-SUC-9, higher concentrations of PEI could be applied without toxicity. At these concentrations, even small amounts of siRNA could be applied to decrease the activity of the target gene. Therefore, the reduction of the toxicity has a really decisive role for the efficiency of siRNA formulations with modified PEI.

CONCLUSIONS

The amino group modifications of branched PEI with acetamide, β-propionic acid and ethyl ester, or succinic acid as presented in this study strongly increase the efficiency in siRNA delivery. For example, PEI-SUC can mediate knockdown at siRNA concentrations as low as 50 nM. The stability of polyplexes did not correlate with the efficiency. The most probable reason for the improved characteristics is the strongly reduced cytotoxicity of the modified PEI, which allows the administration of polyplexes formulated with a larger amount of polymeric carrier.

ACKNOWLEDGMENT

This work was funded by the Excellence Cluster 'Nanosystems Initiative Munich (NIM)', SFB486 and EC project GIANT. The financial support of Ali Dehshahri by Iranian Ministry of Health and Medical Education is gratefully acknowledged.

Supporting Information Available: Additional information on dissociation of PEI polyplexes in NaCl, pDNA transfection efficiencies in B16F10 or Neuro2A cells, and siRNA delivery to HUH7/EGFPLuc cells. This material is available free of charge via the Internet at http://pubs.acs.org.

LITERATURE CITED

(1) Fire, A., Xu, S., Montgomery, M. K., Kostas, S. A., Driver, S. E., and Mello, C. C. (1998) Potent and specific genetic interference by double-stranded RNA in *Caenorhabditis elegans*. *Nature 391*, 806–811.

(2) Elbashir, S. M., Harborth, J., Lendeckel, W., Yalcin, A., Weber, K., and Tuschl, T. (2001) Duplexes of 21-nucleotide RNAs mediate RNA interference in cultured mammalian cells. *Nature 411*, 494–498.

(3) Behlke, M. A. (2006) Progress towards in vivo use of siRNAs. *Mol. Ther. 13*, 644–670.

(4) Meyer, M., and Wagner, E. (2006) Recent developments in the application of plasmid DNA-based vectors and small interfering RNA therapeutics for cancer. *Hum. Gene Ther. 17*, 1062–1076.

(5) Boussif, O., Lezoualc'h, F., Zanta, M. A., Mergny, M. D., Scherman, D., Demeneix, B., and Behr, J. P. (1995) A versatile vector for gene and oligonucleotide transfer into cells in culture and in vivo: polyethylenimine. *Proc. Natl. Acad. Sci. U.S.A. 92*, 7297–7301.

(6) Zou, S. M., Erbacher, P., Remy, J. S., and Behr, J. P. (2000) Systemic linear polyethylenimine (L-PEI)-mediated gene delivery in the mouse. *J. Gene Med. 2*, 128–134.

(7) Hassani, Z., Lemkine, G. F., Erbacher, P., Palmier, K., Alfama, G., Giovannangeli, C., Behr, J. P., and Demeneix, B. A. (2005) Lipid-mediated siRNA delivery down-regulates exogenous gene expression in the mouse brain at picomolar levels. *J. Gene Med. 7*, 198–207.

(8) Grayson, A. C., Doody, A. M., and Putnam, D. (2006) Biophysical and structural characterization of polyethylenimine-mediated siRNA delivery in vitro. *Pharm. Res. 23*, 1868–1876.

(9) Godbey, W. T., Wu, K. K., and Mikos, A. G. (1999) Size matters: molecular weight affects the efficiency of poly(ethylenimine) as a gene delivery vehicle. *J. Biomed. Mater. Res. 45*, 268–275.

(10) Wightman, L., Kircheis, R., Rossler, V., Carotta, S., Ruzicka, R., Kursa, M., and Wagner, E. (2001) Different behavior of branched and linear polyethylenimine for gene delivery in vitro and in vivo. *J. Gene Med. 3*, 362–372.

(11) Kunath, K., von Harpe, A., Fischer, D., Petersen, H., Bickel, U., Voigt, K., and Kissel, T. (2003) Low-molecular-weight polyethylenimine as a non-viral vector for DNA delivery: comparison of physicochemical properties, transfection efficiency and in vivo distribution with high-molecular-weight polyethylenimine. *J. Controlled Release 89*, 113–125.

(12) Werth, S., Urban-Klein, B., Dai, L., Hobel, S., Grzelinski, M., Bakowsky, U., Czubayko, F., and Aigner, A. (2006) A low molecular weight fraction of polyethylenimine (PEI) displays increased transfection efficiency of DNA and siRNA in fresh or lyophilized complexes. *J. Controlled Release 112*, 257–270.

(13) Brissault, B., Kichler, A., Guis, C., Leborgne, C., Danos, O., and Cheradame, H. (2003) Synthesis of linear polyethylenimine derivatives for DNA transfection. *Bioconjugate Chem. 14*, 581–587.

(14) Thomas, M., Lu, J. J., Ge, Q., Zhang, C., Chen, J., and Klibanov, A. M. (2005) Full deacylation of polyethylenimine dramatically boosts its gene delivery efficiency and specificity to mouse lung. *Proc. Natl. Acad. Sci. U.S.A. 102*, 5679–5684.

(15) Bolcato-Bellemin, A. L., Bonnet, M. E., Creusat, G., Erbacher, P., and Behr, J. P. (2007) Sticky overhangs enhance siRNA-mediated gene silencing. *Proc. Natl. Acad. Sci. U.S.A. 104*, 16050–16055.

(16) Forrest, M. L., Meister, G. E., Koerber, J. T., and Pack, D. W. (2004) Partial acetylation of polyethylenimine enhances in vitro gene delivery. *Pharm. Res. 21*, 365–371.

(17) Thomas, M., and Klibanov, A. M. (2002) Enhancing polyethylenimine's delivery of plasmid DNA into mammalian cells. *Proc. Natl. Acad. Sci. U.S.A. 99*, 14640–14645.

(18) Doody, A. M., Korley, J. N., Dang, K. P., Zawaneh, P. N., and Putnam, D. (2006) Characterizing the structure/function parameter space of hydrocarbon-conjugated branched polyethylenimine for DNA delivery in vitro. *J. Controlled Release 116*, 227–237.

(19) Mao, S., Neu, M., Germershaus, O., Merkel, O., Sitterberg, J., Bakowsky, U., and Kissel, T. (2006) Influence of polyethylene glycol chain length on the physicochemical and biological properties of poly(ethylene imine)-graft-poly(ethylene glycol) block copolymer/SiRNA polyplexes. *Bioconjugate Chem. 17*, 1209–1218.

(20) Schiffelers, R. M., Ansari, A., Xu, J., Zhou, Q., Tang, Q., Storm, G., Molema, G., Lu, P. Y., Scaria, P. V., and Woodle, M. C. (2004) Cancer siRNA therapy by tumor selective delivery with ligand-targeted sterically stabilized nanoparticle. *Nucleic Acids Res. 32*, e149.

(21) Tarcha, P. J., Pelisek, J., Merdan, T., Waters, J., Cheung, K., von Gersdorff, K., Culmsee, C., and Wagner, E. (2007) Synthesis and characterization of chemically condensed oligoethylenimine containing beta-aminopropionamide linkages for siRNA delivery. *Biomaterials 28*, 3731–3740.

(22) Meyer, M., Philipp, A., Oskuee, R., Schmidt, C., and Wagner, E. (2008) Breathing life into polycations: functionalization with pH-responsive endosomolytic peptides and polyethylene glycol enables siRNA delivery. *J. Am. Chem. Soc. 130*, 3272–3273.

(23) Leng, Q., Scaria, P., Zhu, J., Ambulos, N., Campbell, P., and Mixson, A. J. (2005) Highly branched HK peptides are effective carriers of siRNA. *J. Gene Med. 7*, 977–986.

(24) Prevette, L. E., Kodger, T. E., Reineke, T. M., and Lynch, M. L. (2007) Deciphering the role of hydrogen bonding in enhancing pDNA-polycation interactions. *Langmuir 23*, 9773–9784.

(25) Nimesh, S., Aggarwal, A., Kumar, P., Singh, Y., Gupta, K. C., and Chandra, R. (2007) Influence of acyl chain length on transfection mediated by acylated PEI nanoparticles. *Int. J. Pharm. 337*, 265–274.

(26) Sonawane, N. D., Szoka, F. C., Jr., and Verkman, A. S. (2003) Chloride accumulation and swelling in endosomes enhances DNA transfer by polyamine-DNA polyplexes. *J. Biol. Chem. 278*, 44826–44831.

(27) Boeckle, S., von Gersdorff, K., van der Piepen, S., Culmsee, C., Wagner, E., and Ogris, M. (2004) Purification of polyethylenimine polyplexes highlights the role of free polycations in gene transfer. *J. Gene Med. 6*, 1102–1111.

BC800065F

Solid-Phase Synthesis of Europium-Labeled Human INSL3 as a Novel Probe for the Study of Ligand−Receptor Interactions

Fazel Shabanpoor,[†,‡] Richard A. Hughes,[§] Ross A. D. Bathgate,[†,||] Suode Zhang,[†] Denis B. Scanlon,[⊥] Feng Lin,[†] Mohammed Akhter Hossain,[†] Frances Separovic,[‡] and John D. Wade*[,†,‡]

Howard Florey Institute, School of Chemistry, Department of Pharmacology, Department of Biochemistry and Molecular Biology, and Bio21 Institute, The University of Melbourne, Victoria 3010, Australia. Received March 27, 2008; Revised Manuscript Received May 1, 2008

An efficient solid-phase synthesis protocol has been developed which, together with regioselective sequential formation of the three disulfide bonds, enabled the preparation of specifically monolanthanide (europium)-labeled human insulin-like peptide 3 (INSL3) for the study of its interaction with its G-protein-coupled receptor, RXFP2, via time-resolved fluorometry. A commercially available chelator, diethylene triamine pentaacetic acid (DTPA), was coupled to the N-terminus of the INSL3 A-chain on the solid phase, and then a coordination complex between europium ion and DTPA was formed using $EuCl_3$ to protect the chelator from production of an unidentified adduct during subsequent combination of the A- and B-chains. The labeled peptide was purified in high yield using high-performance liquid chromatography with nearly neutral pH buffers to prevent the liberation of Eu^{3+} from the chelator. Using time-resolved fluorometry, saturation binding assays were undertaken to determine the binding affinity (pK_d) of labeled INSL3 for RXFP2 in HEK-293T cells stably expressing RXFP2. The dissociation constant of DTPA-labeled INSL3 (9.05 ± 0.03, $n = 3$) that was obtained from saturation binding experiments was comparable to that of ^{125}I-labeled INSL3 (9.59 ± 0.09, $n = 3$). The receptor binding affinity (pK_i) of human INSL3 was determined to be 9.27 ± 0.06, $n = 3$, using Eu-DTPA-INSL3 as a labeled ligand, which again is similar to that obtained when ^{125}I-INSL3 was used as labeled ligand (9.34 ± 0.02, $n = 4$). This novel lanthanide-coordinated, DTPA-labeled INSL3 has excellent sensitivity, stability, and high specific activity, properties that will be particularly beneficial in high-throughput screening of INSL3 analogues in structure−activity studies.

Insulin-like peptide 3 (INSL3), also referred to as Leydig-insulin-like (Ley-I-L) and relaxin-like factor (RLF) (*1*) is a circulating peptide hormone belonging to the relaxin-insulin superfamily of peptides. The heterodimeric peptide hormone INSL3 consists of two chains (A and B) connected via three disulfide bonds (*1–3*). INSL3 and its G-protein coupled receptor (GPCR), RXFP2 (also known as LGR8), have been shown to play important roles in the reproductive system including testicular descent during fetal development as a result of INSL3-mediated gubernacular growth (*4–6*) and meiotic progression of arrested oocytes in the female and suppression of male germ cell apoptosis (*7*). Additionally, recent studies have shown the pathological involvement of INSL3 in certain cancers, as its expression is up-regulated in human thyroid carcinoma, neoplastic Leydig cells, and mammary epithelial cells (*8*).

Recent structure−activity relationship studies have provided considerable insight into the molecular interaction of INSL3 with its receptor associated with reproductive processes. The rapidly emerging physiological and pathological importance of INSL3 has led to efforts to develop antagonists which prevent binding and signaling of INSL3. The structure-based development and discovery of such antagonists requires the design and synthesis of various analogues. In order to test these analogues for their receptor binding affinity, radioactive ^{125}I-labeled INSL3 has typically been employed. However, the use of this peptide has drawbacks including its short half-life, high cost, and the need for its preparation immediately prior to use. Additionally, there are safety concerns associated with the use of radionuclides. To overcome these problems, we undertook the development of efficient methods for the preparation of an INSL3 labeled with a lanthanide for evaluation and use in a time-resolved fluorescence receptor binding assay.

The development of such lanthanide-based assays to study ligand−receptor interactions provides an attractive alternative to the traditional radionuclide-based assays. Due to their unique fluorescent properties, chelates of specific trivalent lanthanide ions (Eu^{3+}, Tb^{3+}, and Sm^{3+}) have been coupled to molecules of biological interest and the resultant labeled molecules used as probes in various biological assays such as kinase assays (*9*), immunofluorometric detection assays (*10*), and ligand−receptor interaction assays (*11*). Normally, aqueous solutions of Eu^{3+}, Tb^{3+}, or Sm^{3+} produce such a weak fluorescence that it cannot be detected by a regular fluorometer (*12*). However, these rare earths form stable coordination complexes with appropriate signal-enhancing ligands and, following irradiation with near-ultraviolet light, the ligand is excited (*13*). Then by intersystem crossing (known as an antenna effect), energy is transferred from the signal-enhancing ligand to the central lanthanide ion, which becomes excited (*13*). When the excited lanthanide ion returns to the ground state, it emits a strong fluorescence. The signal-enhancing ligands enhance the fluorescent emission of lanthanide ions by shielding them from the quenching effects of water (*14*).

The emitted fluorescence has four attractive characteristics: (1) the emission wavelength is barely affected by the structure of the ligand. (2) It has a long fluorescence lifetime (∼ms) which

* Corresponding author. Professor John D. Wade, Howard Florey Institute, University of Melbourne, Victoria 3010, Australia. Ph: +61 3 8344 7285/Fax: +61 3 9348 1707. E-mail: john.wade@florey.edu.au.
[†] Howard Florey Institute.
[‡] School of Chemistry.
[§] Department of Pharmacology.
[||] Department of Biochemistry and Molecular Biology.
[⊥] Bio21 Institute.

10.1021/bc800127p CCC: $40.75 © 2008 American Chemical Society
Published on Web 06/05/2008

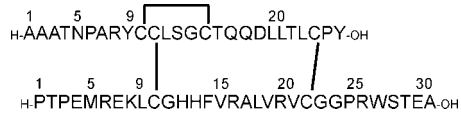

Figure 1. The primary structure of human INSL3. Of the three free amino groups, there is one each at the N-terminus of the A- and B-chains and one at the side-chain of lysine 8 on the B-chain.

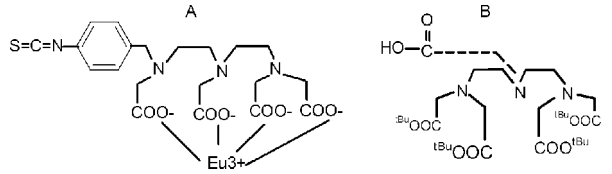

Figure 2. (A) Chemical structure of an activated Eu-DTTA chelate for postsynthesis acylation of free amino groups. (B) Chemical structure of tBu-protected DTPA for direct acylation of the N-terminal amino group in solid-phase peptide synthesis.

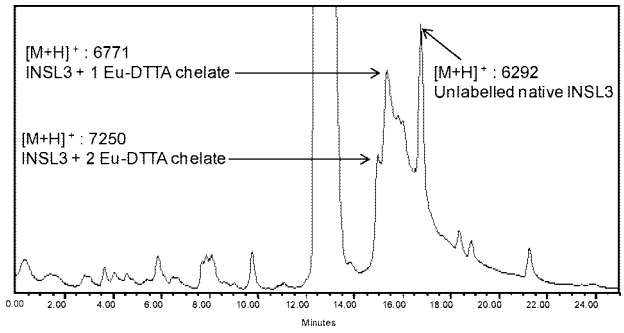

Figure 3. -HPLC chromatogram of human INSL3 following postsynthesis labeling with Eu-DTTA complex. A complex mixture of mono- and dilabeled peptides was obtained which could not be satisfactorily resolved.

allows measurement of fluorescence signal to be made after the decay of short-lived (micro- to picoseconds) background fluorescence from plates, cells, and reagents that are often a source of background in many fluorescence measurements (*10*, *15*, *16*). (3) It is characterized by a large Stokes shift (difference between the excitation maximum and emission maximum) compared to the short Stokes shift of organic fluorescent dyes in which the excitation and emission spectrum often overlap. (4) It exhibits a sharp emission peak which causes a large emission intensity that is easily detectable. These factors contribute to the low background and high sensitivity of lanthanide time-resolved fluorescence, making it comparable to that of radionuclide detection.

In this study, we have developed an efficient solid-phase synthesis technique to prepare specifically monolabeled peptide, which was subsequently shown to possess biophysical properties that render it suitable for receptor binding studies. INSL3 was labeled specifically at the *N*-terminus of the synthetic A-chain with the chelator, diethylenetriamine-*N*,*N*,*N*′′*N*′′-tetra-*tert*-butyl acetate-*N*′-acetic acid (DTPA). The labeled peptide was subsequently combined with the B-chain via regioselective disulfide bond formation. After chemical characterization of labeled INSL3, we performed saturation binding assays to determine maximum specific binding (B_{max}) and the receptor binding affinity of Eu-DTPA-labeled INSL3 (pK_d). We then performed competition binding assays to determine the binding affinity (pK_i) of the native INSL3 for RXFP2 in HEK 293 cell line using Eu-DTPA-INSL3 as labeled ligand.

EXPERIMENTAL PROCEDURES

Materials. 9-Fluorenylmethoxycarbonyl (Fmoc) protected L-α-amino acids; 1-[bis(dimethylamino)methylene]-1*H*-benzotriazolium hexafluorophosphate (HBTU), *N*,*N*-dimethylformamide (DMF), piperidine, and trifluoroacetic acid (TFA) were obtained from Auspep (West Melbourne, Australia). Fmoc-L-Tyr(tBu)-PEG-PS and Fmoc-L-Ala-PEG-PS resins with substitution of 0.20 mmol/g were purchased from Applied Biosystems (Melbourne, Australia). Methanol, diethyl ether, dichloromethane, Merck (Kilsyth, Melbourne, Australia), 3,6-dioxa-1,8-octanedithiol (DODT), triisopropylsilane (TIPS), diisopropylethylamine (DIPEA), 1,2,4,5-benzene-tetracarboxylic dianhydride (Sigma-Aldrich, Sydney, Australia), 2,2′-dipyridyl disulfide (DPDS), (Fluka-Switzerland); diethylenetriamine-*N*,*N*,*N*′′,*N*′′-tetra-*tert*-butyl acetate-*N*′-acetic acid (DTPA) (Macrocyclic, USA). N^1-(*p*-isothiocyanatobenzyl)-diethylenetriamine-*N*, N^2, *N*, N^3-tetraacetic acid (Eu-DTTA) (Perkin-Elmer, Australia). Acetonitrile and NH_4HCO_3, $(NH_4)_2CO_3$: BDH laboratory supplies, (Poole, UK) and trifluoromethanesulfonic acid (TFMSA) (MP Biomedicals, Seven Hills NSW Australia). All other reagents: Sigma Castle Hill, NSW. Dulbecco's modified Eagles' medium (DMEM), RPMI 1640 medium, 2 mM L-glutamine, fetal calf serum, and penicillin/streptomycin were all obtained from Trace Biosciences (Castle Hill, New South Wales). All other reagents were obtained from Sigma-Aldrich (New South Wales, Australia).

Peptide Synthesis. All linear precursor peptides were solid-phase synthesized (*17*) as C-terminal acids on PAC-PEG-PS resin (0.2 mmol/g loading) using Fmoc chemistry. They were assembled on a CEM Liberty microwave peptide synthesizer (Ai Scientific, Queensland, and Australia). The side chain protecting groups of trifunctional amino acids were trifluoroacetic acid labile, except for acetamidomethyl (Acm)-protected cysteines in positions A24 and B22, and *tert*-butyl (tBu)-protected cysteine in position A11. All peptides were synthesized on a 0.1 mmol scale using a 5-fold molar excess of Fmoc-protected amino acids (0.5 mmol) that were activated by using 5-fold excess of HBTU in the presence of DIEA (*18*, *19*). N^{α}-Fmoc protecting groups were removed by treating the resin-attached peptide with piperidine (20% v/v) in DMF. The coupling and deprotection were carried out at 75 °C using 25 W microwave power for 5 min and 60 W microwave power for 3 min, respectively. The chelator, DTPA-tetra(tBu ester) (3 equiv, 0.3 mmol), was coupled to the N-terminus of the solid-phase bound A-chain. The 2,4,6-trinitrobenzenesulphonic acid (TNBSA) test (*20*) was carried out to determine the success of coupling the DTPA. Each resin-bound polypeptide chain was cleaved from the solid support by treatment with a cocktail of trifluoroacetic acid (TFA)/3,6-dioxa-1,8-octanedithiol (DODT)/H_2O/triisopropylsilane (TIPS) (94%/2.5%/2.5%/1%, 20 mL) for 90 min. The cleaved peptide was precipitated in ice-cold diethyl ether and centrifuged at 3000 rpm for 3 min. The pellet was washed by resuspending it in ice-cold diethyl ether and centrifuging it again. This washing process was repeated at least three times. The stepwise synthesis of disulfide bonds was carried out by first forming the intra-A-chain disulfide bond between cysteines at positions A10 and A15. The cysteines were oxidized by first dissolving the linear A-chain in 0.1 M NH_4HCO_3 (1 mg/3 mL) to which a 1 mM solution of 2,2′-dispyridyl disulfide (DPDS) (*21*) in methanol (0.2 mL/ 1 mg peptide) was added while stirring. An aliquot of the mixture was analyzed by RP-HPLC to monitor the oxidation process. The oxidized INSL3 A-chains were analyzed and purified by preparative RP-HPLC on Waters XBridge columns (4.6 × 250 mm, C18, 5 μm) and (19 × 150 mm, C18, 5 μm), respectively, using two different buffer systems. INSL3 A-chain was purified using 0.1% trifluoroacetic acid in water (solvent A) and 0.1%

Scheme 1. Schematic Diagram of Synthesis of Eu-DTPA-INSL3 and Its Reagents and Conditions[a]

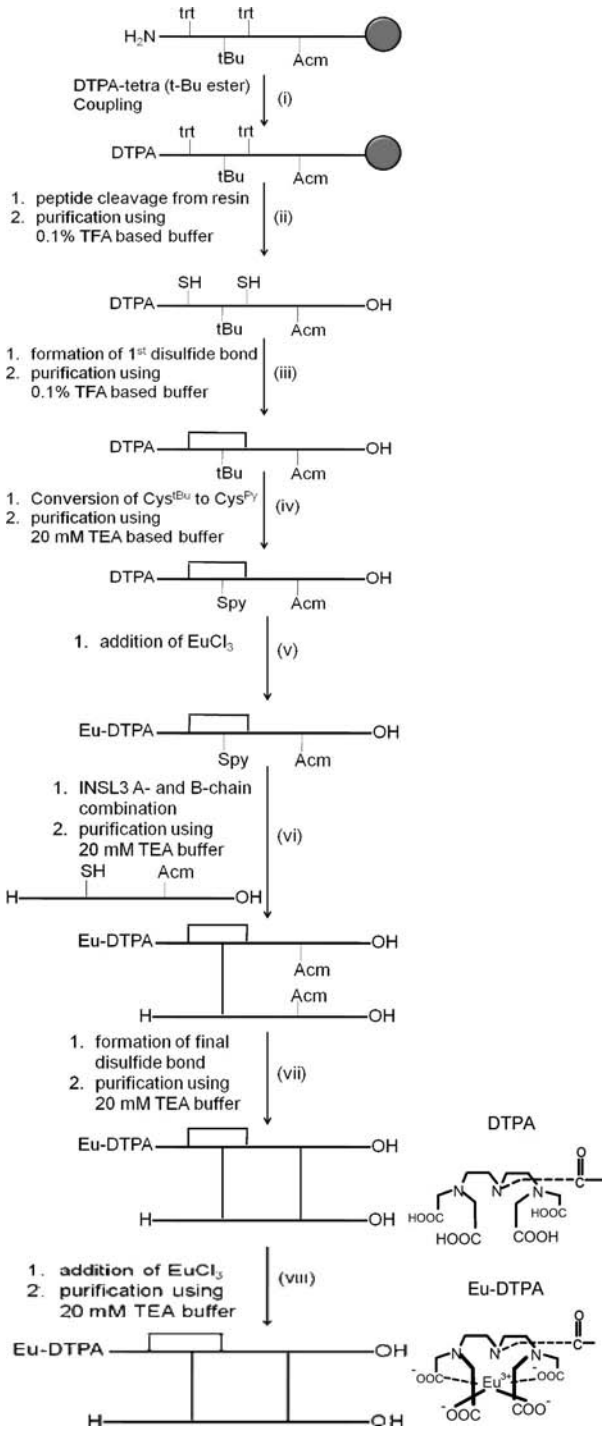

[a] (i) DTPA (3 equiv), HBTU (3 equiv), DIEA (3.5 equiv); (ii) TFA:DoDt:H_2O:TIPS (94:2.5:2.5:1); (iii) 1 mg peptide/0.2 mL of 1 mM DPDS; (iv) peptide:DPDS (1:4 μmol) dissolved in TFA: thioanisole (9:1) in 50 μg/μL, chilled on ice to 0 °C and then similar volume of TFA:TFMSA (4:1) was added; stirred for 1 hr at 0 °C and then purificaion of DTPA-INSL3 A-chain using 20 mM TEA buffer, pH 6.5, (v) DTPA-INSL3 A-chain and $EuCl_3$ (2 equiv) were dissolved in H_2O and stirred at room temperature for 30 min; (vi) Eu-DTPA-INSL3 A-chain dissolved in NH_4CO_3 mixed with INSL3 B-chain in water (1:1 mol) and stirred for 30 min; (vii) 60 mM HCl, acetic acid (2 mg/ mL), 20 mM I_2 (23 equiv/Acm), 1 h at rt, peptide was purified using 20 mM TEA based buffer, (viii) Eu-DTPA-INSL3 and $EuCl_3$ (2 equiv) were dissolved in H_2O and stirred at room temperature for 30 min and then final product was purified using 20 mM TEA based buffer to prevent the liberation of Eu^{3+} from the chelation with DTPA chelator.

trifluoroacetic acid in 100% acetonitrile (solvent B) running from 20% to 50% B at a flow rate of 10 mL/min over 30 min. In order to form the first interchain disulfide bond, the *tert*-butyl protecting group on cysteine in position A11 was converted to 2-pyridylsulfenyl derivative by dissolving the A-chain and DPDS (1:4 μmol) in TFA and thioanisole (9:1 v/v) (50 μg/ μL). The mixture was chilled on ice after which a similar volume of TFMSA in TFA (1:4 v/v) was added and the reaction continued for 45 min at 0 °C (*22*). The A-chain was precipitated with cold diethyl ether, and the pellet collected by centrifugation and washed 4 times to remove excess DPDS. The INSL3 A-chain derivative was purified using 0.1% TFA based buffers whereas the INSL3 A-chain with DTPA attached was purified using 20 mM triethylammonium acetate (TEA), pH 6.5, (solvent A) and 20 mM TEA in 90% acetonitrile (solvent B) with gradient of 20−50% B in 30 min. The first interchain disulfide bond was formed by reacting equimolar amounts of purified INSL3 B-chain with thiol-activated A-chain. The A-chain was dissolved in NH_4HCO_3, pH 8.5 and the B-chain, dissolved in water, was then added with stirring. The progress of the reaction was monitored using RP-HPLC. The reaction was complete after 30 min and the combined A- and B-chains were then purified by RP-HPLC using 0.1% TFA based buffers. In the case of INSL3 A-chain with the DTPA chelator at the N-terminus, the A-chain was first dissolved in NH_4HCO_3, pH 8.5, and then a 2-fold excess of europium chloride ($EuCl_3$) solution in water was added and the reaction was stirred for 10 min to form the complex of Eu-DTPA-A-chain before adding the equimolar amounts of INSL3 B-chain. The combined INSL3 Eu-DTPA-A-chain and B-chain was purified using 20 mM TEA based buffers. The formation of the last disulfide bond was achieved by oxidative removal of the acetamidomethyl groups in positions A24 and B22 by dissolving the peptide in 60 mM HCL (5% v/v) and acetic acid (2 mg/mL) followed by addition of 20 mM iodine (23 equiv/Acm). The reaction was stirred at room temperature for 1 h during which the progress was assessed by analytical RP-HPLC. After the completion of reaction, the mixture was poured onto chilled diethyl ether to precipitate the peptide, which was collected by centrifugation. The peptide was dissolved in water and 20 mM ascorbic acid to quench the remaining traces of iodine and then purified by preparative RP-HPLC on a Waters XBridge column (19 × 150 mm, C18, 5 μm) using 20 mM TEA-based buffers as described above. The solvent was removed by lyophilization which left a yellow oily peptide that was relyophilized in 50% acetonitrile in water to give a white powder. After purification, the labeled INSL3 containing the DTPA chelator was redissolved in H_2O and then 2 equiv of europium chloride was added and stirred for an hour. The formation of complex between europium and DTPA chelator was monitored by RP-HPLC and MALDI-TOF/TOF mass spectroscopy. The labeled INSL3 was then purified by RP-HPLC using 20 mM TEA-based buffer.

Postsynthesis Labeling of INSL3. The postsynthesis labeling of INSL3 with Eu-DTTA complex was attempted using a 10-fold excess of Eu-DTTA over peptide at three different reaction conditions: (1) 50 mM $NaHCO_3$ + 150 mM NaCl, pH 8.5 (*23*), (2) 100 mM Na_2CO_3, pH 9.2 (according to the DELFIA labeling kit form PerkinElmer), (3) 100 mM Na_2CO_3, pH 6.5. The reactions were carried out at 4 °C overnight.

Peptide Characterization. Matrix-assisted laser desorption ionization time-of-flight mass spectrometry (MALDI-TOF/TOF MS, Bruker Daltonics, Germany) was used to characterize the peptides at each intermediate step using sinapinic acid, α-cyano-4-hydroxycinnamic acid, and 2,5-dihydroxy benzoic acid (Bruker Daltonics, Germany) based on the molecular size of the peptide. The matrices were made up in 50% acetonitrile containing either 0.05% TFA or 0.05% formic acid. The peptide

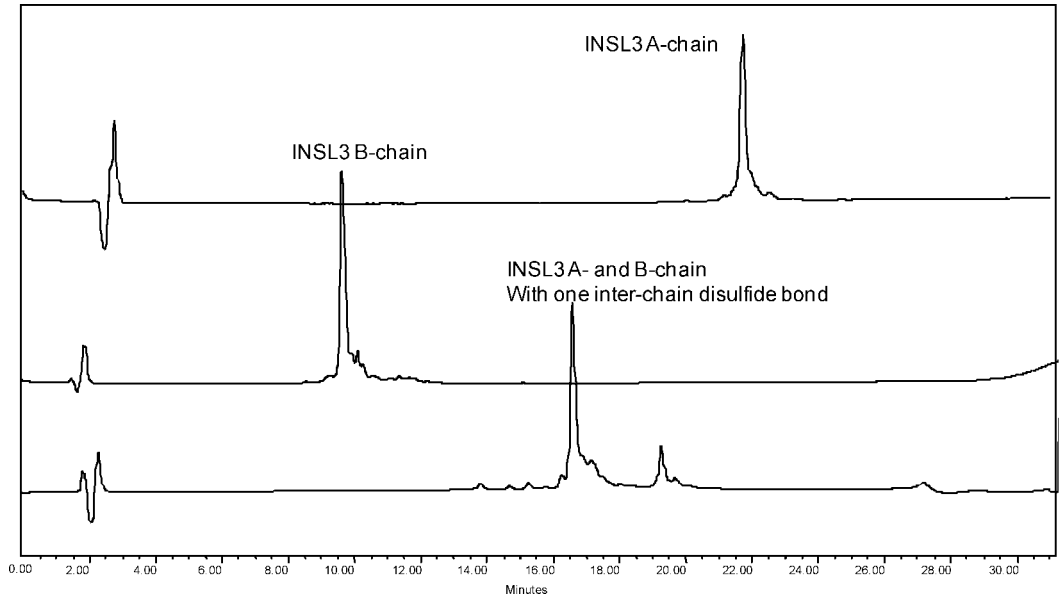

Figure 4. RP-HPLC monitoring of DTPA-INSL3 A-chain combination with INSL3 B-chain. The single-chain peptides each have a correct molecular mass as determined by MALDI-TOF/TOF. However, the combined A- and B-chain product had a *m*/*z* 55.2 higher than the expected monoisotopic mass (see Figure 5).

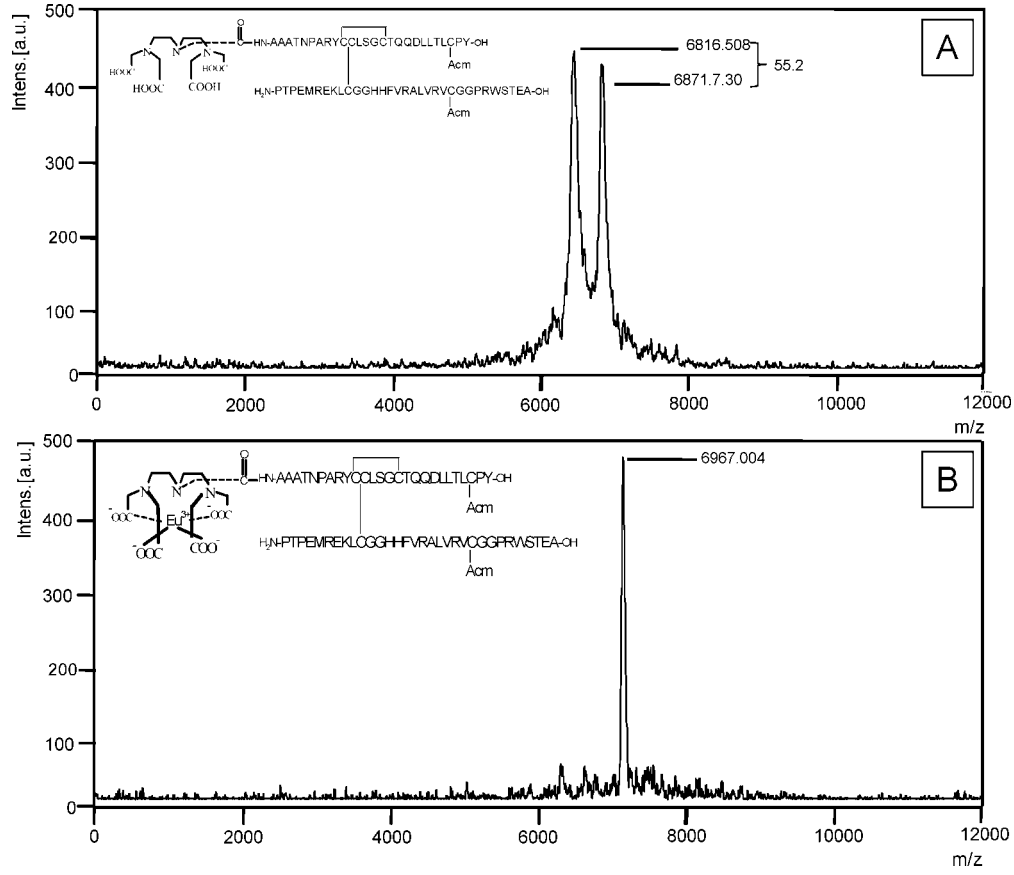

Figure 5. (A) Mass spectrum of DTPA-labeled INSL3 after the formation of first interchain disulfide bond which showed a *m*/*z* of 55.2 Da higher ($[M + H]^+ = 6724.244$) than the expected monoisotopic mass ($[M + H]^+ = 6668.989$). (B) Protection of the DTPA on the A-chain with Eu^{3+} prior to combination with B-chain gave a labeled INSL3 with the correct monoisotopic mass (expected $[M + H]^+ = 6966.85$).

content was determined using vapor-phase acid hydrolysis in 6 M HCL containing 2% phenol at 110 °C for 24 h. The individual amino acids were converted to stable, fluorescent derivatives using a Waters AccQ.Tag kit (Waters, Sydney, Australia). The derivatized amino acids were separated using a Shim-Pak XR-ODS (3 × 75 mm, 2.2 μm) column on Shimadzu RP-HPLC system (Shimadzu, Victoria, Australia).

Circular Dichroism Spectroscopy. The peptides were made up to a concentration of 0.1 μM in phosphate buffered saline (PBS: 10 mM potassium phosphate buffer containing 137 mM NaCl pH 7.4). The far UV circular dichroism (CD) spectra of peptides were acquired using a Jasco J815 spectropolarimeter between the wavelengths of 195−250 nm at room temperature with a resolution of 0.1 nm, bandwidth of 0.1 nm, and a cell of

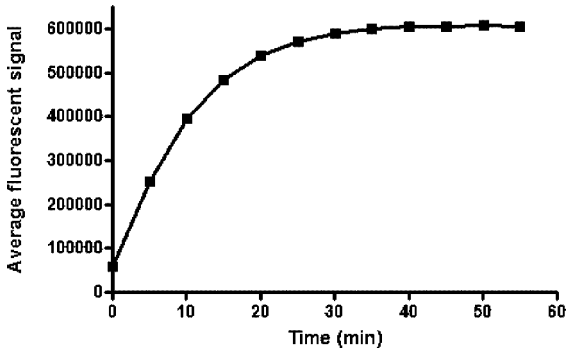

Figure 6. Measurement of Eu release from DTPA chelate. 10 μL of 10 nM Eu-DTPA-INSL3 peptide was mixed with enhancement solution in triplicate and the fluorescence was measured at 5 min interval for 60 min. The signal reached its maximum at ~600 000 average fluorescent units (AFU) at time 40 min.

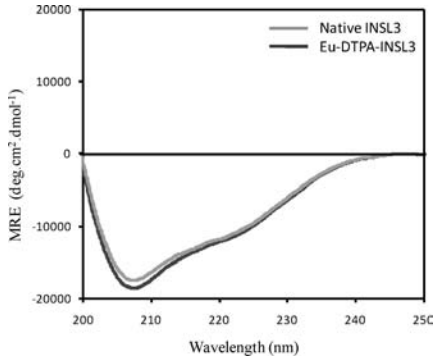

Figure 7. CD spectra of human INSL3 (solid gray line) and Eu-DTPA-INSL3 (solid black line) measured at a concentration of 0.1 μM in PBS (pH 7.4) at room temperature. The two peptides showed similar spectra and a calculated helicity of approximately 33%.

0.1 cm path length. The recorded spectra in millidegrees of ellipticity (θ) were converted to mean residue ellipticity (MRE) in deg.cm^2 dmol^{-1}.

Cell Culture and Ligand Binding Assays. Subcultures of human embryonic kidney cells (HEK 293T) stably transfected with RXFPR2 (LGR8) were plated out at a density of 80 000 cells per 200 μL per well in a 96 well Isoplate with white wall and clear bottom precoated with poly(L-lysine). The binding assay was carried out using a modification of a method previously described by us (*24*). Briefly, at the start of each experiment, cell culture medium was removed and the cells were washed with phosphate buffer saline (PBS) (250 μL per well). 1% BSA in receptor binding buffer (250 μL) was then added to each well and allowed to stand at room temperature for 1 h. The appropriate concentration of INSL3 and Eu-labeled INSL3, in 1% BSA in receptor binding buffer, was added to each well in triplicate and incubated at room temperature for 1 h. The cells were washed with PBS (250 μL) once, and then 100 μL of enhancement solution (purchased from Perkin-Elmer, composed of β-NTA, TOPO and 0.1% (w/v) Triton X-100 in 0.1 M acetic acid adjusted to pH 3.2) was added to each well, and after 45 min, the fluorescent measurement was carried out on a Victor^3 Plate Reader (Perkin-Elmer, USA) at excitation of 340 nm and emission of 614 nm with the delay time and counting time of 400 μs each.

Data Analysis. The CD spectra data were first transformed from machine unit θ to $\Delta\varepsilon$ using Graphpad *PRISM 4* (Graphpad Ins., San Diego, USA) with user-defined formula ($\varepsilon = \theta \times (0.1 \times \text{MRW})/(\text{P} \times \text{C}) \times 3298$). The converted values were then submitted to the DichroWeb server (*25–28*) for calculation of secondary structure using the CDSSTR (*29*) and K2D (*30*)

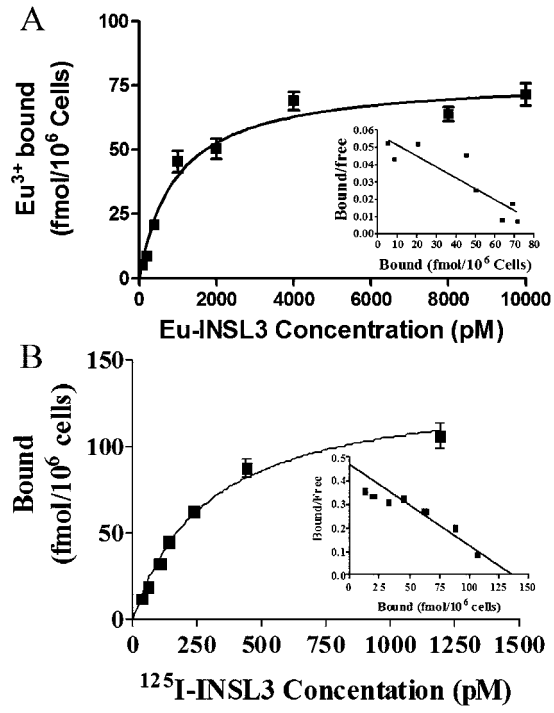

Figure 8. Saturation binding curves of Eu-DTPA-INSL3 and ^{125}I-INSL3 in HEK293T cells stably transfected to express RXFP2. Different concentrations of labeled peptides were added to cells and incubated at room temperature for 60 min. Nonspecific binding was determined in the presence of 500 nM INSL3. The pK_d and B_{max} of the labeled peptides were determined to be 9.05 $\pm$ 0.03 (n = 3); 78074 (receptors/cell) $\pm$ 15834 SEM (n = 3); and 9.59 $\pm$ 0.09; 83518 (receptors/cell) $\pm$ 13061 SEM, respectively. GraphPad *Prism* software was used to fit the data using the nonlinear regression and one site binding model.

analysis algorithms. Graphpad *PRISM 4* was used to analyze the receptor-binding assays data, which were expressed as mean $\pm$ SEM of percentage specific binding of Eu-chelate-labeled INSL3 from triplicate treatments from at least three independent experiments. The value for the dissociation constant (k_d) was determined by fitting saturation binding data to a one-site hyperbolic model. The inhibition constants were determined from IC_{50} values using the Cheng-Prusoff equation (*31*).

RESULTS AND DISCUSSION

Molecular Design and Postsynthesis Labeling. Human INSL3 has two chains (a 26 residue A-chain and a 31 residue B-chain) each containing a free terminal α-amino group. There is also an ε-amino group on the side chain of lysine B8 (Figure 1). We initially undertook postsynthesis labeling of synthetic native human INSL3 with commercially available activated Eu-DTTA chelate, N^1-(*p*-isothiocyanato benzyl)-diethylenetriamine-N,N^2,N,N^3-tetraacetic acid (Figure 2A). First, we synthesized human INSL3 by Fmoc chemistry using standard solid-phase techniques that have been optimized in our laboratory (*32*), employing regioselectively S-protecting groups for the sequential formation of each of the three disulfide bonds. The postsynthesis labeling of INSL3 was then carried out using different reaction conditions, each of which yielded a mixture of mono- and multilabeled peptides, as well as unlabeled INSL3 (Figure 3). Although it was possible to identify some of the species present in the complex mixture obtained, they were poorly resolved making their complete deconvolution and purification exceptionally difficult. As the determination of precise binding parameters requires knowledge of the true specific activity of a ligand, we thus sought an alternative approach to develop a molecularly defined Eu-labeled INSL3.

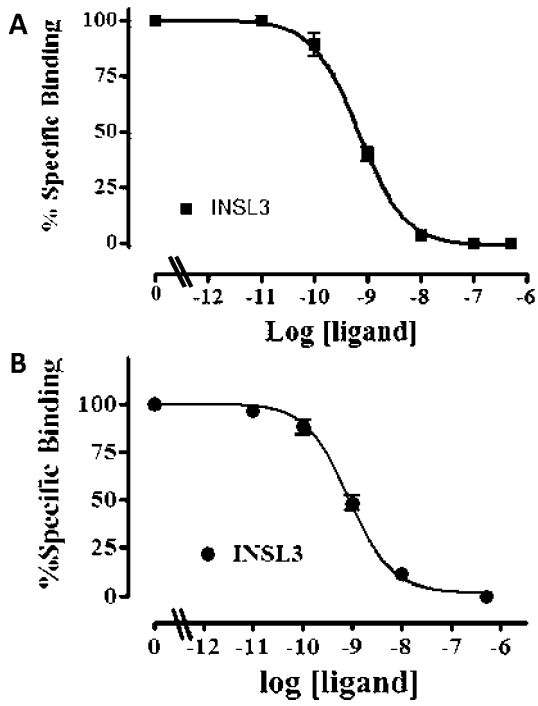

Figure 9. Competition binding curves of INSL3 using Eu-DTPA-INSL3 (A) and ^{125}I-INSL3 (B) as labeled ligand in HEK293T cells stably transfected to express RXFP2. Different concentrations of INSL3 were added to cells and incubated at room temperature for 60 min. INSL3 was competed off the receptor with 0.5 nM of Eu-DTPA-INSL3. The pK_i of INSL3 was determined to be 9.27 ± 0.06 (n = 3) using Eu-DTPA-INSL3 as labeled ligand and 9.34 ± 0.02 (n = 4) when ^{125}I-INSL3 used as labeled ligand. GraphPad *Prism* software was used to fit the data using the nonlinear regression and one site competition model.

Synthesis of INSL3 and Incorporation of DTPA Chelator on Solid Phase. Structure−activity relationship studies with INSL3, relaxin, and other members of this superfamily of peptide hormones which each have a similar core tertiary structure have shown that the N-terminus of the A-chain is tolerant to a range of chemical modifications (*33*). We thus chose to prepare a Eu-chelate labeled INSL3 in which the chelator was incorporated specifically and solely at the N-terminus of the A-chain. To do this, we first synthesized human INSL3 A-chain on the solid phase and concluded this by coupling the empty chelator DTPA (Figure 2B) (Scheme 1). Our plan was that this would allow us to use standard TFA-based HPLC buffers—these are not compatible with Eu-loaded chelates, as the chelates are unstable at low pH—rather than the less well-resolving TEA acetate buffers. Following the removal of the chelator-labeled A-chain from the solid support, the intrachain disulfide bond was formed via 2-pyridyldisulfide-mediated oxidation (*21*). The resulting modified peptide, which possessed a *tert*-butyl protecting group on the thiol of Cys 11 and a Acm group on the thiol of Cys 24, was then subjected to treatment with 2-pyridyldisulfide in TFMSA/TFA to convert the tert-butyl functionality to an S-pyridinyl group. In subsequent preliminary experiments, despite the apparent successful combination of the A- and B-chains via thiolysis of the S-pyridinyl by the free thiol of Cys 10 of the B-chain (Figure 4), MALDI-TOF MS showed the resulting product to have a molecular mass that was 55.2 higher than the expected monoisotopic mass ($[M + H]^+$= 6668.98) (Figure 5A) group. Although this modification did not hinder formation of the final disulfide bond (via iodine oxidation of the Acm groups on Cys A24 and B22), the resulting DTPA-peptide failed to form a complex with the Eu^{3+} when treated with an excess of $EuCl_3$. This suggested that the modification was of the DTPA moiety itself. In order to overcome this, we modified the protocol by loading the DTPA on the A-chain with Eu^{3+} prior to combining the two chains. This strategy effectively protected the four free carboxylic groups on the DTPA chelator during chain combination, and the resulting chain-combined peptide could thus be obtained with the correct monoisotopic mass (Figure 5B). The final stage of the synthesis (the formation of second interchain disulfide bond using iodine in acetic acid) is carried out at low pH, conditions which might be expected to lead to the loss of Eu^{3+} from the DTPA. Although MS analysis indicated that only a small proportion of Eu^{3+} was lost during the final disulfide bond formation, we nevertheless chose to reload the chelate with Eu^{3+} after this step to ensure that the final product was completely Eu-chelated. The formation of the complex between europium and DTPA-labeled INSL3 was monitored by RP-HPLC and MALDI-TOF/TOF MS. The final desired Eu-chelate labeled INSL3 was then purified by RP-HPLC buffer using TEA acetate buffer at near-neutral pH (6.5) to prevent the liberation of europium from the DTPA.

The peptide purity was shown by analytical RP-HPLC to be greater than 95%, and to have a peptide content of 64% as assessed by amino acid analysis. A monoisotopic m/z of 6821 corresponding to the singly Eu-coordinated DTPA-labeled INSL3 was obtained using MALDI-TOF MS, which contrasts to previous studies on synthetic lanthanide complexes of synthetic peptides, in which multiple isomers were obtained (*34*). The overall yield of synthesis was 7.7%, which compares favorably to that obtained for native human INSL3 (10%) obtained using a similar synthesis protocol (*35*).

In order to monitor the time that it takes for the fluorescent signal of Eu-coordinated DTPA INSL3 (as a result of the liberation of Eu^{3+} from chelation with DTPA) to reach its maximum, the release of Eu^{3+} from DTPA chelate was monitored by measuring the fluorescence of 10 μL of 10 nM Eu-DTPA-INSL3 in 100 μL of enhancement solution in triplicate at 5 min intervals for 60 min (Figure 6). The signal reached its maximum at ∼600 000 average fluorescence units (AFU) at time 40 min. This time was used in the subsequent assays as the end point for liberation of europium before measurement of fluorescent signal.

Circular Dichroism Spectroscopy. The CD spectra of synthetic native human INSL3 and DTPA-labeled INSL3 were measured in PBS (pH 7.4) (Figure 7). The two peptides showed a similar CD spectroscopic profile with calculated helicity of approximately 33%. This indicated that the coupling of DTPA to the N-terminus of the INSL3 A-chain had no apparent influence on the secondary structure of INSL3 and is therefore unlikely to have perturbed its tertiary structure.

Whole Cell Receptor Binding Assay. Eu-chelate-labeled and ^{125}I-labeled INSL3 were compared under identical saturation binding conditions using HEK293T cells stably transfected to express the INSL3 receptor RXFP2. To determine the total binding, cells were incubated with different concentrations of Eu-DTPA-INSL3 and ^{125}I-INSL3 in a 96 well plate for 60 min at room temperature to reach equilibrium. To measure the nonspecific binding, 500 nM unlabeled INSL3 was used to competitively dissociate Eu-chelate-labeled INSL3. The nonspecific binding was found to be less than 15% of total binding at any concentration of Eu-DTPA-INSL3 used. Like ^{125}I-INSL3, Eu-DTPA-INSL3 binds in a specific and saturable manner and it was best fitted to a one-site binding model (Figure 8). The calculated dissociation constant (pK_d) for Eu-DTPA-INSL3 was 9.05 ± 0.03 (n = 3) and maximal binding B_{max} was 78074 ± 15834 receptors/cell (n = 3). The pK_d and B_{max} determined for Eu-DTPA-INSL3 agreed with the pK_d (9.59 ± 0.09, n = 3) and B_{max} (83518 ± 13061 receptors/cell) values for ^{125}I-INSL3. There was a slight decrease in pK_d of Eu-DTPA-INSL3

compared to ^{125}I-INSL3 that is statistically significant ($p < 0.005$). This decline in affinity of Eu-DTPA-INSL3 for its receptor RXFP2 is possibly due to the relatively large size of the DTPA moiety compared to the smaller ^{125}I atom. This phenomenon of a slight loss in ligand−receptor affinity has also been reported in other cases where DTPA labeling of bioactive peptides has been described (*36*–*38*). Assays using the Eu-chelate-labeled INSL3 were highly reproducible, showed excellent signal-to-noise ratios, and were faster than radioisotopic-based binding assays, as the measurement can be made directly in the same plate as the assay (in the case of radionuclei-based assays, the cells need to be transferred for signal measurement).

Once the Eu-DTPA-INSL3 was characterized by saturation binding experiments, it was then used as a labeled ligand in competition binding assays (Figure 9) to determine the receptor binding affinity (pK_i) of native human INSL3 for RXFP2. INSL3 displaced Eu-DTPA-INSL3 (0.5 nM) with pK_i value of 9.27 ± 0.06 ($n = 3$), which was similar to those previously obtained using ^{125}I-INSL3 (9.34 ± 0.02, $n = 4$) (*3*).

CONCLUSION

The use of lanthanide-labeled ligands to study ligand−receptor interactions has become increasingly popular over the past decade. Such peptides have a longer shelf life compared to radiolabeled peptides, offering greater reproducibility of results, since the same stock of labeled ligand can be used over a long period of time. In this study, we have demonstrated a novel and efficient methodology for effective preparation of Eu-coordinating, DTPA-lableled INSL3 via solid-phase synthesis. The site-specific incorporation of DTPA chelator on the solid phase gives a monolabeled peptide with high yield and purity compared to the postsynthesis labeling using DTTA chelator. Eu-DTPA-labeled INSL3 showed binding properties that are comparable to that of ^{125}I-INSL3. Lanthanide detection methods are presently being applied to other members of the relaxin-insulin superfamily of peptide hormones.

ACKNOWLEDGMENT

We thank Sharon Layfield for carrying out the cell culture and Tania Ferrero for help with binding assays. This work was funded by National Health and Medical Reseach Council of Australia Project grants 350245 and 509048 to J.D.W., R.A.D.B., and R.A.H.

LITERATURE CITED

(1) Adham, I. M., Burkhardt, E., Benahmed, M., and Engel, W. (1993) Cloning of a cDNA for a novel insulin-like peptide of the testicular Leydig cells. *J. Biol. Chem. 268*, 26668–72.

(2) Hsu, S. Y. (2003) New insights into the evolution of the relaxin-LGR signaling system. *Trends Endocrinol. Metab. 14*, 303–9.

(3) Rosengren, K. J., Zhang, S., Lin, F., Daly, N. L., Scott, D. J., Hughes, R. A., Bathgate, R. A., Craik, D. J., and Wade, J. D. (2006) Solution structure and characterization of the LGR8 receptor binding surface of insulin-like peptide 3. *J. Biol. Chem. 281*, 28287–95.

(4) Nef, S., and Parada, L. F. (1999) Cryptorchidism in mice mutant for Insl3. *Nat. Genet. 22*, 295–9.

(5) Spiess, A. N., Balvers, M., Tena-Sempere, M., Huhtaniemi, I., Parry, L., and Ivell, R. (1999) Structure and expression of the rat relaxin-like factor (RLF) gene. *Mol. Reprod. Dev. 54*, 319–25.

(6) Zimmermann, S., Steding, G., Emmen, J. M., Brinkmann, A. O., Nayernia, K., Holstein, A. F., Engel, W., and Adham, I. M. (1999) Targeted disruption of the Insl3 gene causes bilateral cryptorchidism. *Mol. Endocrinol. 13*, 681–91.

(7) Kawamura, K., Kumagai, J., Sudo, S., Chun, S. Y., Pisarska, M., Morita, H., Toppari, J., Fu, P., Wade, J. D., Bathgate, R. A., and Hsueh, A. J. (2004) Paracrine regulation of mammalian oocyte maturation and male germ cell survival. *Proc. Natl. Acad. Sci. U.S.A. 101*, 7323–8.

(8) Klonisch, T., Mustafa, T., Bialek, J., Radestock, Y., Holzhausen, H. J., Dralle, H., Hoang-Vu, C., and Hombach-Klonisch, S. (2005) Human medullary thyroid carcinoma: a source and potential target for relaxin-like hormones. *Ann. N.Y. Acad. Sci. 1041*, 449–61.

(9) Braunwalder, A. F., Yarwood, D. R., Sills, M. A., and Lipson, K. E. (1996) Measurement of the protein tyrosine kinase activity of c-src using time-resolved fluorometry of europium chelates. *Anal. Biochem. 238*, 159–64.

(10) Hemmila, I., Dakubu, S., Mukkala, V. M., Siitari, H., and Lovgren, T. (1984) Europium as a label in time-resolved immunofluorometric assays. *Anal. Biochem. 137*, 335–43.

(11) Handl, H. L., Vagner, J., Yamamura, H. I., Hruby, V. J., and Gillies, R. J. (2005) Development of a lanthanide-based assay for detection of receptor-ligand interactions at the delta-opioid receptor. *Anal. Biochem. 343*, 299–307.

(12) Bunzli, J. C. (1987) Complexes with syntheic ionophores. *Handbook on the Physics and Chemistry of Rare Earth* 321.

(13) Yang, T., and Qin, W. (2007) Fluorimetric determination of traces of europium (III) using a new chelator and acetate or phosphate in dimethylsulfoxide as enhancers. *Microchim. Acta 157*, 55–61.

(14) Piszczek, G., Maliwal, B. P., Gryczynski, I., Dattelbaum, J., and Lakowicz, J. R. (2001) Multiphoton ligand-enhanced excitation of lanthanides. *J. Fluoresc. 11*, 101–107.

(15) Diamandis, E. P. (1988) Immunoassays with time-resolved fluorescence spectroscopy: principles and applications. *Clin. Biochem. 21*, 139–50.

(16) Dickson, E. F., Pollak, A., and Diamandis, E. P. (1995) Time-resolved detection of lanthanide luminescence for ultrasensitive bioanalytical assays. *J. Photochem. Photobiol., B 27*, 3–19.

(17) Merrifield, R. B. (1963) Solid phase peptide synthesis. I. The synthesis of a tetrapeptide. *J. Am. Chem. Soc. 85*, 2149–2153.

(18) Bernatowicz, M. S., Daniels, S. B., and Köster, H. (1989) A comparison of acid labile linkage agents for the synthesis of peptide C terminal amides. *Tetrahedron Lett. 30*, 4645–4648.

(19) Knorr, R., Trzeciak, A., Bannwarth, W., and Gillesen, D. (1989) New coupling reagents in peptide chemistry. *Tetrahedron Lett. 30*, 1927–1930.

(20) Hancock, W. S., and Battersby, J. E. (1976) New micro-test for detection of incomplete coupling reactions in solid-phase peptide synthesis using 2,4,6-trinitrobenzene-sulphonic acid. *Anal. Biochem. 71*, 260–264.

(21) Maruyama, K., Nagasawa, H., and Suzuki, A. (1999) 2,2′-Bispyridyl disulfide rapidly induces intramolecular disulfide bonds in peptides. *Peptides 20*, 881–4.

(22) Maruyama, K., Nagata, K., Tanaka, M., Nagasawa, H., Isogai, A., Ishizaki, H., and Suzuki, A. (1992) Synthesis of bombyxin-IV, an insulin superfamily peptide from the silkworm, *Bombyx mori*, by stepwise and selective formation of three disulfide bridges. *J. Protein Chem. 11*, 1–12.

(23) Gao, X., Hsu, C., Heinz, L. J., Morin, J., Shi, Y., Shukla, N. K., Smiley, D. L., Zhong, B., and Slieker, L. J. (2004) Europium-labeled melanin-concentrating hormone analogues: ligands for measuring binding to melanin-concentrating hormone receptors 1 and 2. *Anal. Biochem. 28*, 187–195.

(24) Muda, M., He, C., Martini, P. G., Ferraro, T., Layfield, S., Taylor, D., Chevrier, C., Schweickhardt, R., Kelton, C., Ryan, P. L., and Bathgate, R. A. (2005) Splice variants of the relaxin and INSL3 receptors reveal unanticipated molecular complexity. *Mol. Hum. Reprod. 11*, 591–600.

(25) Lees, J. G., Miles, A. J., Wien, F., and Wallace, B. A. (2006) A reference database for circular dichroism spectroscopy covering fold and secondary structure space. *Bioinformatics 22*, 1955−62.

(26) Lobley, A., and Wallace, B. A. (2001) DICHROWEB: a website for the analysis of protein secondary structure from circular dichroism spectra. *Biophys. J. 80*, 373.

(27) Lobley, A., Whitmore, L., and Wallace, B. A. (2002) DICHROWEB: an interactive website for the analysis of protein secondary structure from circular dichroism spectra. *Bioinformatics 18*, 211–2.

(28) Whitmore, L., and Wallace, B. A. (2004) DICHROWEB, an online server for protein secondary structure analyses from circular dichroism spectroscopic data. *Nucleic Acids Res. 32*, W668–73.

(29) Compton, L. A., and Johnson, W. C., Jr (1986) Analysis of protein circular dichroism spectra for secondary structure using a simple matrix multiplication. *Anal. Biochem. 155*, 155–67.

(30) Andrade, M. A., Chacon, P., Merelo, J. J., and Moran, F. (1993) Evaluation of secondary structure of proteins from UV circular dichroism spectra using an unsupervised learning neural network. *Protein Eng. 6*, 383–90.

(31) Cheng, Y.-C., and Prusoff, W. H. (1973) *Biochem. Pharmacol. 22*, 3099–3108.

(32) Rosengren, K. J., Lin, F., Bathgate, R. A., Tregear, G. W., Daly, N. L., Wade, J. D., and Craik, D. J. (2006) Solution structure and novel insights into the determinants of the receptor specificity of human relaxin-3. *J. Biol. Chem. 281*, 5845–51.

(33) Fu, P., Layfield, S., Ferraro, T., Tomiyama, H., Hutson, J., Otvos, L., Jr., Tregear, G. W., Bathgate, R. A., and Wade, J. D. (2004) Synthesis, conformation, receptor binding and biological activities of monobiotinylated human insulin-like peptide 3. *J. Pept. Res. 63*, 91–8.

(34) Gao, F., Handl, H., Vagner, J., Hruby, V., and Gillies, R. (2007) Convenient an efficient synthesis of a Lanthanide^{3+}-coordinated, Diethylene Triamine Pentaacetic Acid labeled biopolymer as an assay for the cholecystokinin B receptor. *Appl. Polym. Sci. 106*, 2683–2688.

(35) Hossain, M. A., Zhang, S., Lin, F., Ferraro, T., Bathgate, R. A. D., Tregear, G. W., and Wade, J. D. (2006) Regioselective disulfide solid phase synthesis, chemical characterization and in vitro receptor binding activity of equine relaxin. *Int. J. Pept. Res. Ther. 12*, 211–215.

(36) Bagutti, C., Stolz, B., Albert, R., Bruns, C., Pless, J., and Eberle, A. N. (1994) [^{111}In]-DTPA-Labeled analogues of a-melanocyte-stimulating horomone for melanoma targeting: Receptor binding in vitro and in vivo. *Int. J. Cancer 58*, 749–755.

(37) Mazor, O., Hillairet de Boisferon, M., Lombet, A., Gruaz-Guyon, A., Gayer, B., Skrzydelsky, D., Kohen, F., Forgez, P., Scherz, A., Rostene, W., and Salomon, Y. (2002) Europium-labeled epidermal growth factor and neurotensin: novel probes for receptor-binding studies. *Anal. Biochem. 301*, 75–81.

(38) Inglese, J., Samama, P., Patel, S., Burbaum, J., Stroke, I. L., and Appell, K. C. (1998) Chemokine receptor-ligand interactions measured using time-resolved fluorescence. *Biochem 37*, 2372–7.

BC800127P

Design and Synthesis of Dendritic Molecular Transporter that Achieves Efficient *in Vivo* Delivery of Morpholino Antisense Oligo

Yong-Fu Li* and Paul A. Morcos

Gene Tools, LLC, One Summerton Way, Philomath, Oregon 97370. Received April 4, 2008; Revised Manuscript Received May 15, 2008

Safe and efficient *in vivo* delivery of Morpholino antisense oligos was probably the last and most difficult challenge for the broad application of antisense in animal research and therapeutics. Several arginine-rich peptides effective for *in vivo* delivery of Morpholino antisense oligos require rather complex and expensive procedures for synthesis and conjugation. This work describes the design and synthesis of a dendritic transporter in a most concise manner where the selection of the core scaffold, functional group multiplication, orthogonal protecting group manipulation, solid phase conjugation, and off-resin perguanidinylation of the transporter structure are all orchestrated for efficient assembly. We utilized triazine as a core to provide a site for on-column conjugation to the Morpholino oligo and to anchor functional side arms which, after extension, multiplication, and deprotection, are subsequently converted from primary amines to the eight guanidinium headgroups that serve for transport across cell membranes. Intravenous administration of the delivery-enabled Morpholino into a splice-reporter strain of transgenic living mice results in *de novo* expression of splice-corrected green fluorescent protein in a broad range of tissues and organs in those treated mice. This rigorously demonstrates that this new dendritic transporter achieves effective delivery of a Morpholino oligo into the cytosol/nuclear compartment of cells systemically *in vivo*. The practical conjugation process may overcome any availability limitation for routine use by the scientific community, and the efficient delivery ability of this transporter may advance the application of Morpholino antisense technology in animals.

INTRODUCTION

Unlike other types of antisense oligos including siRNA, PNA, mPNA, S-DNA, and LNA, Morpholinos provide all the desired properties of stability, nuclease resistance, high efficacy, long-term activity, water solubility, low toxicity, and exquisite specificity (*1*, *2*). However, biological barriers typically limit or preclude uptake, and therefore therapeutic benefit, of large polar structures such as antisense oligos (*3*). Advanced antisense oligo types faced the lack of a safe and effective delivery component which could transport oligos into the cytosol/nuclear compartment of cells of living animals, and this constituted the last major hurdle before antisense oligos could be introduced for the treatment of a broad range of currently intractable diseases such as splice-modifying genetic defects and viral diseases. The development of novel guanidinium-rich compositions that facilitate cellular uptake of a variety of physiologically and therapeutically active biomolecules started with discovery that HIV-Tat peptide and other arginine-rich derivatives could achieve efficient intracellular delivery (*4–8*). These and other cell-permeable arginine-rich oligopeptides were capable of transporting various types of cargo, such as small polar molecules, oligonucleotides, plasmid DNA, and proteins, across the membranes of most types of animal cells (*9–15*). Structural variations on the arginine-rich peptides have shown that the length of the backbone and the spacing and composition of the side chains can be varied to adjust the uptake efficiency (*16–19*). Testing structural modifications on the arginine-rich peptides and peptoids have demonstrated that the guanidinium headgroups of the arginine residues are principally responsible for the uptake into cells, backbone chirality is not critical for cellular uptake, and about 7 to 15 guanidine headgroups are optimal for efficient uptake (*20–22*).

Arginine-rich peptides have been covalently conjugated with Morpholino antisense oligos and the conjugates were shown to enter the cytosol and nucleus of cells (*23–26*). Because of the peptidic nature, however, degradation of the peptide portion of the conjugates was found to be time- and tissue-dependent ((*27*) and references cited therein). In addition, the intensively studied cell-penetrating peptides [(R-AhxR)$_4$AhxB] showed different degrees of toxicity depending on the dose, dose frequency, and route of administration. From a practical point of view, the application of such arginine-rich peptide transporters is somewhat limited due to their high cost, scalability, and stability. Usually, these peptide transporters are prepared using a solid-phase synthesizer. Although this approach is readily automated and allows for efficient synthesis and purification of the transporter peptides, the approach suffers drawbacks including limited scalability and the need for resin attachment and cleavage and off-column attachment. Importantly, the use of peptides risks an immune response to the conjugates, which would prevent repeated administrations for diseases requiring long-term treatment.

To develop an efficient delivery composition which is cost-effective, is not immunogenic, and is stable under physiological conditions, we sought to exploit nonlinear, nonpeptidic, and non-natural architectures. Relatively few attempts have been made to use guanidine groups in branched or dendritic structures, but those attempts have produced some useful data that helped our development process. For example, polyguanidino dendrimers using triamine-based diamino acid monomeric units to form a series of octa-guanidine dendrimers show differences in uptake efficiency related to the structural flexibility of the dendritic architecture (*28*). Branched-chain arginine peptides translocate through cell membranes and bring exogenous proteins into cells; eight arginine residues was the number that exhibited the most

* Corresponding author. Telephone: 541-929-7840, ext. 1035. Fax: 541-929-7841. E-mail: yli@gene-tools.com.

10.1021/bc8001437 CCC: $40.75 © 2008 American Chemical Society
Published on Web 06/20/2008

efficient internalization (*29*). Dendritic oligoguanidines based on amino triol subunits translocate through the cell membrane (*30*). An alternative architecture based on an amino triacid scaffold demonstrated that dendritic molecular transporters can not only enable transport of bioactive cargo across the cell membrane, but can also direct the delivery into particular intracellular compartments (*31*). However, the reported syntheses of dendritic oligoguanidines are lengthy or involve expensive reagents for their assembly. We directed our efforts to developing a dendritic structure which mimics features of branched octaguanidines but provides cost-effective synthesis, convenient conjugation with bioactive molecules (Morpholino in this study), and superior performance in transporting compounds across biological barriers.

For a molecular transporter to possess the aforementioned features, we proposed that the constitution of the dendritic scaffold should allow assembly of the oligoguanidine through a variant of a segment-multiplying strategy and had to allow attachment of a bioactive substance to its orthogonal functional site. We chose triazine as a trifunctional entity on which two sites could be used for branching side arms while a Morpholino oligo could be linked to its third functional site. To construct the molecular transporter in a cost-effective manner, we used diethanolamine to displace two chlorine atoms, yielding a tetra-alcohol intermediate. After formation of a tetra-carbonate from the corresponding alcohols, a secondary amine from a triamine moiety in which the two terminal primary amines are in a protected form was contacted with the tetra-carbonate to give octa-amine, thus providing eight side chains each containing a terminal primary amino group in a protected form. To the third functional site of triazine, a reactive linking group which could conjugate with a Morpholino oligo was installed. Conjugation on synthesis resin allowed convenient removal of excess reagents, and the conjugate thus formed was cleaved from the synthesis resin by ammonia treatment. This ammonia treatment simultaneously generated an unprotected octa-amine intermediate which was subsequently converted to octa-guanidine by a single perguanidinylation step, yielding a conjugate of Morpholino with a transporter containing a triazine as the core scaffold (Scheme 1). These conjugates which are enabled for *in vivo* delivery are referred to as "Vivo-Morpholinos". We conjugated the transporter with a Morpholino oligo targeted to block a mutant RNA splicing site whose blockage leads to normal translation of an enhanced green fluorescent protein (EGFP) reporter. Using the signal from this reporter gene, relative *in vivo* delivery efficacies were determined for a variety of tissues in transgenic mice.

Scheme 1. Structure of Vivo-Morpholino (VM), a Conjugate of Transporter Composition with a Morpholino Oligo

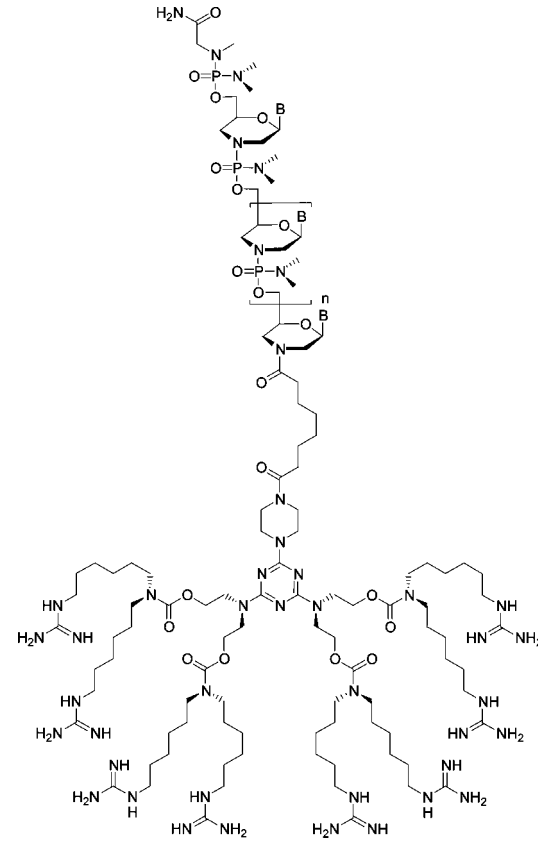

Scheme 2. Synthesis of Building Components for the Transporter Composition

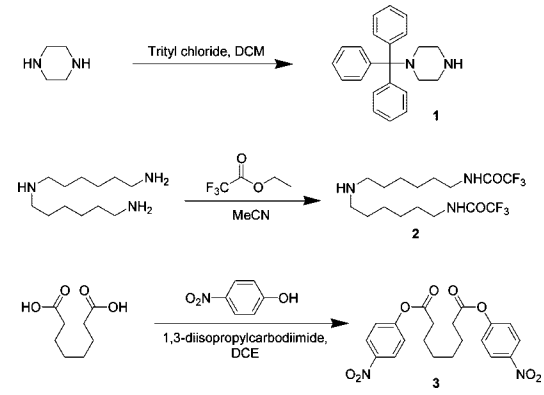

EXPERIMENTAL PROCEDURES

Materials and Methods. All reagents and solvents were purchased from commercial sources and were used as received. Components of the transporter were synthesized from readily available starting materials (Scheme 2). Analytical TLC was carried out on Baker-flex silica gel IB2-F and spots were located by UV illumination. Column chromatography was conducted through silica gel (60−200 mesh) from Fisher Scientific. All NMR spectra were measured on a 400 MHz Bruker FT-NMR spectrometer. MALDI-TOF MS were carried out on an Applied Biosystems Voyager using a matrix of 2′,4′,6′-trihydroxyacetophenone (THAP). Oasis HLB LP extraction cartridges (Waters Corporation, Milford, MA, USA) were used for purification of Vivo-Morpholino.

Synthesis of *N*-Tritylpiperazine (1). Piperazine (107.5 g, 1.25 mol) was dissolved in dichloromethane (500 mL). Trityl chloride (69.7 g, 0.25 mol) was added to the mixture cooled in an ice bath. After addition, the mixture was kept at room temperature for 30 min. The mixture was washed with water (500 mL, three times) and the organic layer was separated and dried over sodium sulfate. The solution was concentrated to ca. 100 mL and added to hexane (1 L). The solid was removed by filtration. The filtrate was evaporated to dryness to give a white solid (80 g, 97%). ^{1}H NMR (400 MHz, $CDCl_3$) $\delta = 1.31$ (br, 1H), 3.04 (br, 8H), 7.17−7.52 (m, 15H).

Synthesis of Bis(trifluoroacetamidohexyl)amine (2). To a stirred solution of bis(hexamethylene)triamine (8.62 g, 40 mmol) in acetonitrile (120 mL) cooled in an ice bath was added water (0.864 mL) and ethyl trifluoroacetate (16.7 mL, 140 mmol). After addition, the mixture was refluxed for 16 h. The solvents were removed by evaporation. The residue solidified upon storing at room temperature and was used without further purification.

Synthesis of Di(4-nitrophenyl) Suberate (3). Suberic acid (8.71 g, 50 mmol) and 4-nitrophenol (14.61 g, 105 mmol) were dissolved in dichloroethane (100 mL). 1,3-Diisopropylcarbo-

diimide (16.28 mL, 104 mmol) was added to the mixture. The mixture was kept at room temperature for 16 h. The solid was removed by filtration. The filtrate was loaded on a silica gel column (silica gel 140 g), eluting with dichloromethane. After removal of the solvent, a white solid was obtained (18.4 g, 88%). ^{1}H NMR (400 MHz, $CDCl_3$) δ = 1.54 (m, 4H), 1.84 (m, 4H), 2.66 (t, 7.44 Hz, 4H), 7.31 (d, 9.39 Hz, 4H), 8.30 (d, 9.20 Hz, 4H).

Synthesis of 2-(4-Tritylpiperazinyl)-4,6-bis(diethanolamino)triazine (4). Cyanuric chloride (922 mg, 5 mmol) was dissolved in a solution of tetrahydrofuran (10 mL) containing *N*,*N*-diisopropylethylamine (1.74 mL, 10 mmol). *N*-Tritylpiperazine (**1**) (1.642 g, 5 mmol) dissolved in tetrahydrofuran (10 mL) was added to the mixture cooled in an ice bath. The mixture was kept at 0 and 25 °C for 30 min, respectively. Diethanolamine (5 mL, 52 mmol) was added to the mixture. The mixture was heated at 70 °C for 16 h. The volatile materials were removed by evaporation. The residue was dissolved in ethyl acetate (200 mL) and washed with sodium bicarbonate (150 mL) and water (200 mL × 2) and dried over sodium sulfate. After removal of the solvent, a white solid was obtained (2.82 g, 92%). ^{1}H NMR (400 MHz, $CDCl_3$) δ = 2.36 (br, 2H), 3.70 (br, 8H), 3.71 (br, 12H), 3.83 (br, 2H), 4.01 (br, 2H), 4.39 (br, 2H), 7.17−7.50 (m, 15H).

Synthesis of 2-(4-Tritylpiperazinyl)-4,6-bis[di(4-nitrophenyloxycarbonyloxyethyl)amino]triazine (5). 2-(4-Tritylpiperazinyl)-4,6-bis(diethanolamino)triazine (**4**) (2.82 g, 4.59 mmol) was dissolved in acetone (40 mL). Triethylamine (1 mL) was added to the mixture, followed by bis(4-nitrophenyl) carbonate (8.4 g, 27.54 mmol). The mixture was kept at room temperature for 48 h. The solvent was then removed. The product was obtained by column purification to give a yellowish solid (4.8 g, 82%). ^{1}H NMR (400 MHz, DMSO-d_6) δ = 2.45 (br, 2H), 3.94 (m, 14H), 4.51 (m, 8H), 6.87 (d, 9.19 Hz, 8H), 7.17−7.49 (m, 15H), 8.07 (d, 9.19 Hz, 8H).

Synthesis of 2-(4-Tritylpiperazinyl)-4,6-bis{di[di(trifluoroacetamidohexyl)aminocarbonyloxyethyl]amino}triazine (6). 2-(4-Tritylpiperazinyl)-4,6-bis[di(4-nitrophenyloxycarbonyloxyethyl)amino]triazine (**5**) (2.03 g, 1.6 mmol) was dissolved in acetone (40 mL). *N*,*N*-Diisopropylethylamine (2.8 mL, 16 mmol) was added to the mixture, followed by bis(trifluoroacetamidohexyl)amine (**2**) (4.16 g, 8 mmol). The reaction mixture was kept at room temperature for 16 h. The volatile materials were removed by evaporation. The residue was chromatographed to give an oily foam (3.28 g, 87%). ^{1}H NMR (400 MHz, DMSO-d_6) δ = 1.21 (br, 32H), 1.42 (br, 32H), 3.07 (br, 8H), 3.15 (br, 32H), 3.72 (br, 8H), 4.08 (br, 8H), 7.19−7.45 (m, 15H), 9.35 (s, 8H). MALDI MS: calculated for $C_{102}H_{143}F_{24}N_{19}O_{16}$, 2347.3; found, 2356.9.

Synthesis of 2-[(4-Nitrophenyl)oxycarbonylhexamethylenecarbonylpiperazinyl]-4,6-bis{di[di(trifluoroacetamidohexyl)-aminocarbonyloxyethyl]amino}triazine (8). 2-(4-Tritylpiperazinyl)-4,6-bis{di[di(trifluoroacetamidohexyl)aminocarbonyloxyethyl]amino}triazine (**6**) (1.0 g, 0.43 mmol) was dissolved in methanol (3.2 mL) and the solution was mixed with 5% cyanoacetic acid in 2,2,2-trifluoroethanol (5 mL). The mixture was kept at room temperature for 10 min. The solvents were removed by evaporation. The residue was then diluted with dichloromethane (50 mL) and washed with saturated sodium bicarbonate (30 mL). The organic layer was separated and dried over sodium sulfate. After removal of the solvent, the crude product **7** was dissolved in acetone (10 mL). *N*,*N*-Diisopropylethylamine (0.4 mL, 2.3 mmol) was added to the mixture, followed by di(4-nitrophenyl) suberate (**3**) (732 mg, 1.76 mmol). The reaction mixture was kept at 50 °C for 2 h. The solvents were removed and the product was isolated from silica gel column chromatography to give an oily paste (0.95 g, 93%). ^{1}H NMR (400 MHz, DMSO-d_6) δ = 1.23 (br, 34H), 1.45 (br, 34H), 1.54 (m, 2H), 1.67 (m, 2H), 2.35 (t, 7.23 Hz, 2H), 2.64 (t, 7.43 Hz, 2H), 3.15 (m, br, 32H), 3.47 (br, 4H), 3.64 (br, 2H), 3.69 (br, 2H), 3.76 (br, 8H), 4.14 (br, 8H), 7.44 (d, 9.19 Hz, 2H), 8.31 (d, 9.19 Hz, 2H), 9.36 (s, br, 8H). MALDI MS: calculated for $C_{97}H_{144}F_{24}N_{20}O_{21}$, 2382.3; found, 2390.6.

General Procedure for Synthesis of Vivo-Morpholino 11, a Conjugate Containing the Transporter Composition and a Morpholino Antisense Oligo. The precursor transporter composition **8** (50 mg) in 1,3-dimethyl-2-imidazolidinone (0.18 mL) containing 5% of 1-hydroxybenzotriazole as catalyst and 5% of triethylamine was incubated with Morpholino (300 nmol) at 60 °C for 2 h. After removal of the solvent, concentrated ammonia (0.30 mL) was added and the mixture was incubated at 50 °C for 5 h. 18% ammonia (0.30 mL) was added to the mixture, followed by *O*-methylisourea hydrochloride (100 mg). The mixture was incubated at 65 °C for 45 min. Water was added to dilute the mixture, and the product was isolated by using Oasis HLB LP extraction cartridge to give Vivo-Morpholino.

Functional Quantitative Assessment of Delivery *in Vivo* of a Conjugate Comprising the Transporter Composition with a Morpholino. Intravenous injections of Vivo-Morpholino were carried out in Ryszard Kole's laboratory by Peter Sazani using transgenic mice that ubiquitously express a modified enhanced green fluorescent protein (EGFP) pre-mRNA containing an aberrantly spliced β-globin intron (IVS2−654) (*32*). The Vivo-Morpholino oligo called VM654−25 with the sequence 5′-TTGCTATTACCTTAACCCAGAAATT was injected i.v. into mice at 12.5 mg/kg for 4 consecutive days, sacrificed on day 5, and analyzed as described previously (*32*).

RESULTS AND DISCUSSION

We set out to design a transporter composition which could be constructed very efficiently. Therefore, many factors such as scaffold core selection, functional group multiplication, orthogonal protecting group manipulation, and methods for formation of guanidine headgroups had to be taken into consideration for overall economy of process. We chose triazine architecture since it provides three functional sites, one for installing a linking group to covalently conjugate with a Morpholino oligo and the other two for anchoring the dendritic arms. Importantly for the selection of triazine, it is unnatural and robust in the living system. This increases the likelihood of avoiding problems such as antigenicity and toxicity and improving properties such as bioavailability, stability, and safety for use *in vivo*. The synthesis uses readily available starting materials (Scheme 2). Monotritylated piperazine **1** is obtained by treating trityl chloride with an excess amount of piperazine. Reaction of bis(hexamethylene)triamine with ethyl trifluoroacetate selectively protects the two terminal primary amines and gives the intact secondary amine **2**. Homobifunctional linker **3** is obtained by formation of the nitrophenyl ester of suberic acid. The whole scheme for assembly of Vivo-Morpholino is illustrated in Scheme 3. The protected piperazine **1** reacts with cyanuric chloride to give monosubstituted dichlorotriazine. The dichloride is then treated with diethanolamine to give tetra-alcohol **4**. The hydroxyl groups are activated with bis(4-nitrophenyl) carbonate to provide tetra-carbonate **5**. The tetra-carbonate **5** is treated with a secondary amine **2** to form tetra-carbamate **6** containing octa-amine in a protected form. The secondary amine of piperazine **7** is regenerated by acidic deprotection, which reacts with the homobifunctional linker **3** to give the transporter moiety **8** with an active functional moiety at one terminus. This activated ester functional group **8** couples with a Morpholino oligo on the synthesis resin to give conjugate

Scheme 3. Synthetic Scheme for Assembly of Vivo-Morpholino

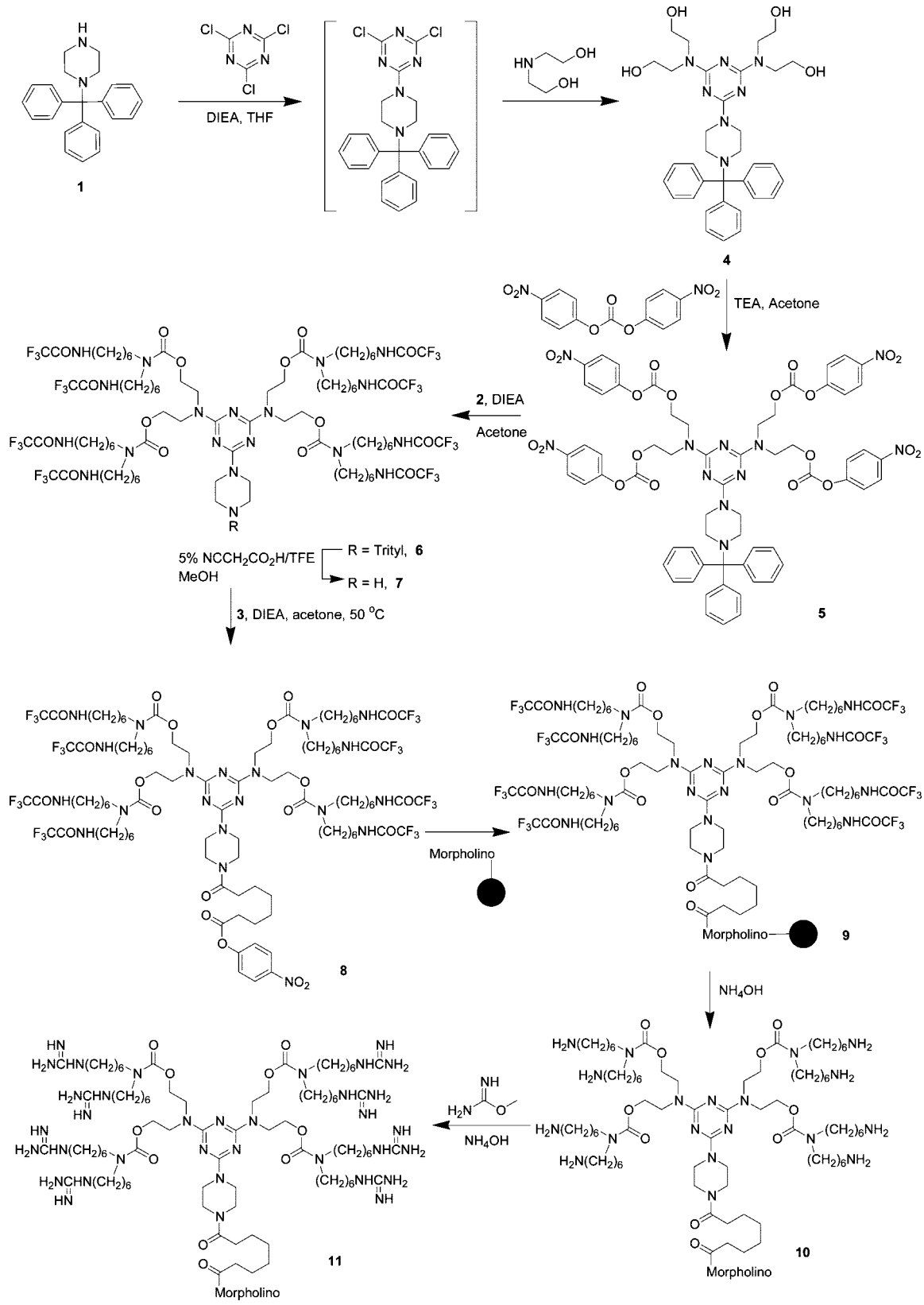

9. Exposure of **9** to concentrated ammonia cleaves the conjugate from the synthesis resin and removes all the protecting groups on the Morpholino oligo bases and the protecting groups on the octa-amines to give conjugate **10**. Perguanidinylation with *O*-methylisourea quantitatively converts all the amino groups on the dendritic scaffold to guanidine headgroups, furnishing the assembly of Vivo-Morpholino **11**.

Triazine Core and Functional Group Multiplication. Dendrimers represent an attractive transporter scaffold offering economical assembly of oligoguanidine transporters through a segment-multiplying strategy. The ease of displacement of chloride atoms in cyanuric chloride by various nucleophiles in the presence of a hydrochloride acceptor (usually tertiary amines) makes this reagent useful for preparation of mono-,

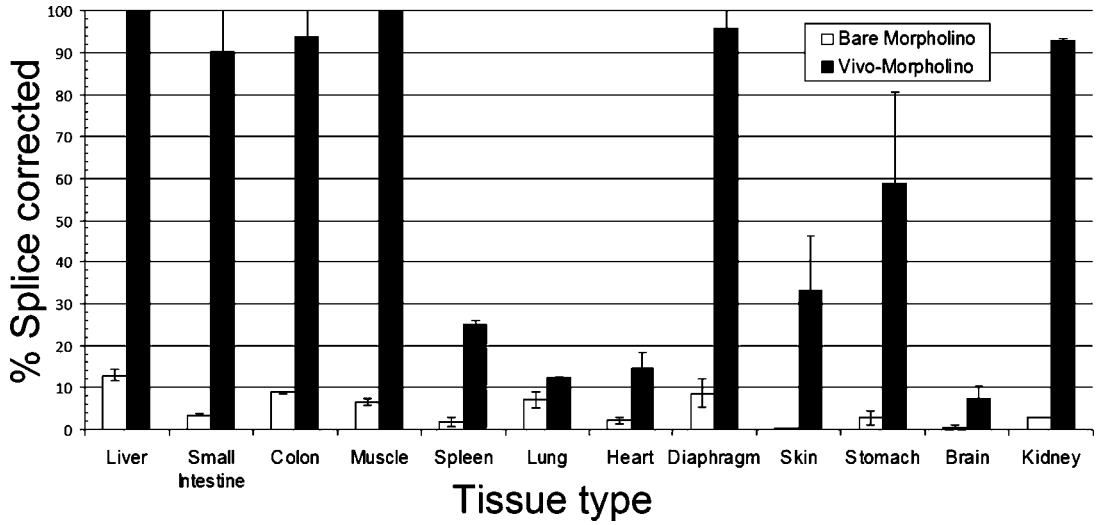

Figure 1. Densitometric analysis of RT-PCR transcripts of splice correction by Vivo-Morpholino in comparison with bare Morpholino. The data is collected from four mice, two injected with Vivo-Morpholino and two injected with bare Morpholino at 12.5 mg/kg/day i.v. for four days, followed by sacrifice and RT-PCR one day after the final injection.

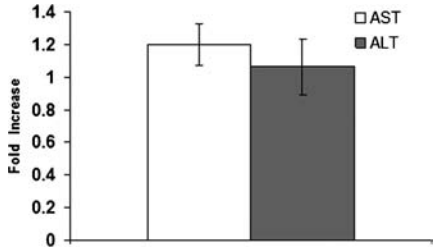

Figure 2. Assessment of liver toxicity. No significant changes in aspartate aminotransferase (AST) or alanine aminotransferase (ALT) levels in the liver were detected with Vivo-Morpholinos delivered at 12.5 mg/kg/day i.v. for four days. Data shown as fold AST or ALT over prebleed, one day after final injection.

di-, and trisubstituted 1,3,5-triazine (*33*). The substitution of chloride can be controlled by temperature to run in a stepwise manner. In this study, the first amino group from *N*-tritylpiperazine **1** was introduced to give monosubstituted triazine at 0 °C in the presence of *N*,*N*-diisopropylethylamine as base. The other two chloride atoms of the triazine were displaced at 70 °C by diethanolamine which was used in excess as base to neutralize the hydrogen chloride generated. The trityl group serves as the protecting group which, after removal at a later stage, generates an amino group for installing an active linking group to be used for conjugation with a Morpholino oligo. The formation of this intermediate provides the core scaffold on which the tetra-alcohol **4** not only extended the side-arms and doubled the number of the functional groups, but also paved the way for further multiplication of side arms. We activated the hydroxyl groups to form reactive carbonate **5**. By contacting a secondary amine of a triamine moiety in which the two terminal primary amines are in a protected form, the tetracarbonate **5** yielded an eight side chain entity **6**, each of which contains a terminal protected primary amine which forms a guanidine headgroup after deprotection and guanidinylation.

Protecting Group Manipulation. We chose bis(hexamethylene)triamine so that its secondary amine, after selective protection of two terminal primary amines, could contact reactive carbonate **5** to form carbamate **6** and double the number of side arms. The methylene units of this commercially available triamine link and spatially separate the three nitrogen atoms. After the primary amino groups are converted to guanidine headgroups, the side arms are flexibly spaced which could be beneficial for efficient contact with cell membrane surface and consequently efficient intracellular uptake. Trifluoroacetyl is selected for protecting terminal primary amines, based on the following four critical reasons: (a) Since methyl or ethyl trifluoroacetate are mild and selective reagents to protect primary amines in the presence of secondary amines (*34*), the secondary amine can remain intact while the primary amines are protected so that the secondary amine can be used to contact the carbonate **5**. (b) An orthogonal strategy has to be used since a different amino group must be selectively deprotected for ultimate conjugation with a Morpholino oligo. Acid-labile trityl group is selected for this amino group since trifluoroacetyl group is labile toward basic conditions but stable toward acidic conditions. (c) Trifluoroacetyl protecting groups on the amines can be cleaved by ammonolysis, a condition previously serving the double duty of removing protecting groups on Morpholino oligo bases and cleaving the oligo from the synthesis resin. Therefore, exposure of ammonia fits into the normal Morpholino synthesis process. This strategy proved very useful since the coupling of the transporter composition can be carried out with Morpholino antisense oligo while it is still on the synthesis resin, and subsequent ammonolytic treatment not only removes all the protecting groups on the Morpholino oligo and the oligoamine moiety, but also cleaves the Morpholino with its conjugated precursor transporter composition from the synthesis resin. The advantage of this triple duty maneuver is simple and economic production. (d) Ammonia is also a basic reagent for converting an amino group to a guanidine in the presence of a guanidinylation agent, *O*-methylisourea hydrochloride. Therefore, without any purification, the ammonia used for cleavage from resin and deprotection of protecting groups of the Morpholino oligo bases and the dendrimeric amine can be carried over for the subsequent guanidinylation. By choosing the selected protecting group (trifluoroacetyl) and the selected protecting group removal agent (ammonia), the whole process for producing a conjugate containing a Morpholino oligo and transporter composition is significantly simplified.

Perguanidinylation. In principle, guanidino groups can be installed before the whole transporter composition is conjugated with a Morpholino oligo. However, because of the nature of the guanidine moiety, it requires expensive reagents for the conversion from primary amines and for the protection of the guanidines thus formed. In this study, we adopted a postperguanidinylation performed in solution phase after deprotection and cleavage of the conjugate from the solid support with

ammonia. Without any purification, the mixture thus obtained was treated further with *O*-methylisourea hydrochloride, giving Vivo-Morpholino, the conjugate of transporter composition with a Morpholino oligo. *O*-Methylisourea hemisulfate could also be used for the conversion, but side products corresponding to the incomplete guanidinylation were observed, which was in agreement with the reported results (*35*). We did not find any side reactions toward the other amino groups present in the bases of Morpholino oligo under the guanidinylation conditions. This off-resin method to convert amino functions quantitatively into guanidines proves a concise and straightforward means to obtain the target compounds.

Systemic Delivery of Vivo-Morpholino in Transgenic Mice. Kole and co-workers have developed a strain of transgenic mice modeled after their test system used in cell culture (*36*) but replacing the luciferase component with enhanced green fluorescent protein (EGFP) (*37*). That RNA transcript, expressed in all tissues of the mice, contains a globin intron mutation that causes a splicing error which prevents expression of the EGFP. Annealing an appropriate Morpholino antisense oligo to the mutant splice site corrects the splicing error and results in the expression of EGFP. Thus, the technology of visualizing green fluorescence in a specific tissue or evaluating the corrected transcript by RT-PCR has been used to rigorously assess cytosolic delivery into cells of that tissue *in vivo*.

The ability of Vivo-Morpholinos to achieve cytosolic delivery *in vivo* was assessed by administering a Vivo-Morpholino targeting the splice mutation site. This was introduced by intravenous injection at 12.5 mg/kg for 4 consecutive days into two of the transgenic mice harboring the splice mutation, followed by sacrifice on day 5. Delivery was assessed by densitometric RT-PCR analysis of RNA transcripts isolated from various tissues (Figure 1). Nearly complete splice correction was observed in liver, small intestine, colon, skeletal muscle, diaphragm, and kidney, indicating excellent delivery with Vivo-Morpholinos. Delivery into the spleen and stomach was also high, although not sufficient for complete splice correction at the concentration tested. Modest delivery was achieved in lung, heart, skin, and brain. The AST-ALT data were also collected (Figure 2), indicating that the Vivo-Morpholinos were not toxic to the liver in mice at 12.5 mg/kg over 4 days. These striking results show that Vivo-Morpholinos are capable of achieving a quantifiable level of delivery in all tissues tested from repeated i.v. injections. This suggests that Vivo-Morpholinos are both achieving a high level of access to the cytosol of cells within tissues and able to avoid the inhibitory effects of serum and other cellular components.

CONCLUSION

In this report, we described synthesis of a novel dendritic molecular transporter and its conjugate with a Morpholino oligo and investigated intracellular uptake of the conjugate in transgenic mice by quantitative functional assessment. The transporter composition is a compact, biocompatible dendritic scaffold with guanidine headgroups spaced in a flexible framework. The assembly of the core structure exploits trifunctional triazine both for installing a linking site for ultimate conjugation with a Morpholino oligo and for anchoring the side arms which were then multiplied to extend the number of side chains. This structure was demonstrated to provide efficient delivery into cells of transgenic mice with minimal toxicity. Further investigations will involve the studies of tissue distribution, biological stability, and pharmacokinetics of delivery-enabled Morpholino oligos. Our present results show that the synthetic approach of this molecular transporter and its highly efficient delivery ability have advanced Morpholino antisense technology into a stage where cost-effective production of delivery-enhanced Morpholino oligos for studies in living animals is now practical.

ACKNOWLEDGMENT

We would like to thank Dr. James E. Summerton for his insightful discussion. Mrs. Chandell L. Terwilliger and Mrs. Jeannine M. Turner are thanked for their analytical assistance. We are grateful to Dr. Jon D. Moulton for his critical proofreading of the manuscript.

LITERATURE CITED

(1) Summerton, J. (2004) Morpholinos and PNAs compared. *Lett. Pept. Sci. 10*, 215–236.

(2) Summerton, J. E. (2007) Morpholino, siRNA, and S-DNA compared: impact of structure and mechanism of action on off-target effects and sequence specificity. *Curr. Top. Med. Chem. 7*, 651–660.

(3) Lebleu, B. (1996) Delivering information-rich drugs — Prospects and challenges. *Trends Biotechnol. 14*, 109–110.

(4) Joliot, A., and Prochiantz, A. (2004) Transduction peptides: from technology to physiology. *Nat. Cell Biol. 6*, 189–196.

(5) Fukati, S. (2006) Oligoarginine vectors for intracellular delivery: design and cellular-uptake mechanisms. *Biopolymers 84*, 241–249.

(6) Rothbard, J. B., Jessop, T. C., and Wender, P. A. (2005) Adaptive translocation: the role of hydrogen bonding and membrane potential in the uptake of guanidinium-rich transporters into cells. *Adv. Drug Delivery Rev. 57*, 495–504.

(7) Brooks, H., Lebleu, B., and Vives, E. (2005) Tat peptide-mediated cellular delivery: back to basics. *Adv. Drug Delivery Rev. 57*, 559–577.

(8) Snyder, E. L., and Dowdy, S. F. (2004) Cell penetrating peptides in drug delivery. *Pharm. Res. 21*, 389–393.

(9) Wadia, J. S., Stan, R. V., and Dowdy, S. F. (2004) Transducible TAT-HA fusogenic peptide enhances escape of TAT-fusion proteins after lipid raft macropinocytosis. *Nat. Med. 10*, 310–315.

(10) Wender, P. A., Mitchell, D. J., Pattabiraman, K., Pelkey, E. T., Steinman, L., and Rothbard, J. B. (2000) The design, synthesis, and evaluation of molecules that enable or enhance cellular uptake: peptoid molecular transporters. *Proc. Natl. Acad. Sci. U.S.A. 97*, 13003–13008.

(11) Zhao, M., and Weissleder, R. (2004) Intracellular cargo delivery using tat peptide and derivatives. *Med. Res. Rev. 24*, 1–12.

(12) Vives, E., Brodin, P., and Lebleu, B. (1997) A truncated HIV-1 Tat protein basic domain rapidly translocates through the plasma membrane and accumulates in the cell nucleus. *J. Biol. Chem. 272*, 16010–16017.

(13) Fischer, P. M., Krausz, E., and Lane, D. P. (2001) Cellular delivery of impermeable effector molecules in the form of conjugates with peptides capable of mediating membrane translocation. *Bioconjugate Chem. 12*, 825–841.

(14) de la Fuente, J. M., and Berry, C. C. (2005) Tat peptide as an efficient molecule to translocate gold nanoparticles into the cell nucleus. *Bioconjugate Chem. 16*, 1176–1180.

(15) Torchilin, V. P., Levchenko, T. S., Rammohan, R., Volodina, N., Papahadjopoulos-Sternberg, B., and D'Souza, G. G. M. (2003) Cell transfection in vitro and in vivo with nontoxic TAT peptideliposome-DNA complexes. *Proc. Natl. Acad. Sci. U.S.A. 100*, 1972–1977.

(16) Wender, P. A., Rothbard, J. B., Jessop, T. C., Kreider, E. L., and Wylie, B. L. (2002) Oligocarbamate molecular transporters: design, synthesis, and biological evaluation of a new class of transporters for drug delivery. *J. Am. Chem. Soc. 124*, 13382–13383.

(17) Rothbard, J. B., Kreider, E., VanDeusen, C. L., Wright, L., Wylie, B. L., and Wender, P. A. (2002) Arginine-rich molecular transporters for drug delivery: role of backbone spacing in cellular uptake. *J. Med. Chem. 45*, 3612–3618.

(18) Umezawa, N., Gelman, M. A., Haigis, M. C., Raines, R. T., and Gellman, S. H. (2002) Translocation of a β-peptide across cell membranes. *J. Am. Chem. Soc. 124*, 368–369.

(19) Rueping, M., Mahajan, Y., Sauer, M., and Seebach, D. (2002) Cellular uptake studies with β-peptides. *ChemBioChem 3*, 257–259.

(20) Rothbard, J. B., Jessop, T. C., Lewis, R. S., Murray, B. A., and Wender, P. A. (2004) Role of membrane potential and hydrogen bonding in the mechanism of translocation of guanidinium-rich peptides into cells. *J. Am. Chem. Soc. 126*, 9506–9507.

(21) Mitchell, D. J., Kim, D. T., Steinman, L., Fathman, C. G., and Rothbard, J. B. (2000) Polyarginine enters cells more efficiently than other polycationic homopolymers. *J. Pept. Res. 56*, 318–325.

(22) Futaki, S., Suzuki, T., Ohashi, W., Yagami, T., Tanaka, S., Ueda, K., and Sugiura, Y. (2001) Arginine-rich peptides. an abundant source of membrane-permeable peptides having potential as carriers for intracellular protein delivery. *J. Biol. Chem. 276*, 5836–5840.

(23) Moulton, H. M., Nelson, M. H., Hatlevig, S. A., Reddy, M. T., and Iversen, P. L. (2004) Cellular uptake of antisense morpholino oligomers conjugated to arginine-rich peptides. *Bioconjugate Chem. 15*, 290–299.

(24) Wu, R. P., Youngblood, D. S., Hassinger, J. N., Lovejoy, C. E., Nelson, M. H., Iversen, P. L., and Moulton, H. M. (2007) Cell-penetrating peptides as transporters for morpholino oligomers: effects of amino acid composition on intracellular delivery and cytotoxicity. *Nucleic Acids Res. 35*, 5182–5191.

(25) Youngblood, D. S., Hatlevig, S. A., Hassinger, J. N., Iversen, P. L., and Moulton, H. M. (2007) Stability of cell-penetrating peptide-morpholino oligomer conjugates in human serum and in cells. *Bioconjugate Chem. 18*, 50–60.

(26) Amantana, A., Moulton, H. M., Cate, M. L., Reddy, M. T., Whitehead, T., Hassinger, J. N., Youngblood, D. S., and Iversen, P. L. (2007) Pharmacokinetics, biodistribution, stability and toxicity of a cell-penetrating peptide-morpholino oligomer conjugate. *Bioconjugate Chem. 18*, 1325–1331.

(27) Lebleu, B., Moulton, H. M., Abes, R., Ivanova, G. D., Abes, S., Stein, D. A., Iversen, P. L., Arzumanov, A. A., and Gait, M. J. (2008) Cell penetrating peptide conjugates of steric block oligonucleotides. *Adv. Drug Delivery Rev. 60*, 517–529.

(28) Wender, P. A., Kreider, E., Pelkey, E. T., Rothbard, J., and VanDeusen, C. L. (2005) Dendrimeric molecular transporters: synthesis and evaluation of tunable polyguanidino dendrimers that facilitate cellular uptake. *Org. Lett. 7*, 4815–4818.

(29) Futaki, S., Nakase, I., Suzuki, T., Zhang, Y., and Sugiura, Y. (2002) Translocation of branched-chain arginine peptides through cell membranes: flexibility in the spatial disposition of positive charges in membrane-permeable peptides. *Biochemistry 41*, 7925–7930.

(30) Chung, H.-H., Harms, G., Seong, C. M., Choi, B. H., Min, C., Taulane, J. P., and Goodman, M. (2004) Dendritic oligoguanidines as intracellular translocators. *Biopolymers (Pept. Sci.) 76*, 83–96.

(31) Huang, K., Voss, B., Kumar, D., Hamm, H. E., and Harth, E. (2007) Dendritic molecular transporters provide control of delivery to intracellular compartments. *Bioconjugate Chem. 18*, 403–409.

(32) Roberts, J., Palma, E., Sazani, P., Ørum, H., Cho, M., and Kole, R. (2006) Efficient and persistent splice switching by systemically delivered LNA oligonucleotides in mice. *Mol. Ther. 14*, 471–475.

(33) Blotny, G. (2006) Recent applications of 2,4,6-trichloro-1,3,5-triazine and its derivatives in organic synthesis. *Tetrahedron 62*, 9507–9522.

(34) O'Sullivan, M. C., and Dalrymple, D. M. (1995) A one-step procedure for the selective trifluoroacetylation of primary amino groups of polyamines. *Tetrahedron Lett. 36*, 3451–3452.

(35) Deglane, G., Abes, S., Michel, T., Prévot, P., Vives, E., Debart, F., Barvik, I., Lebleu, B., and Vasseur, J.-J. (2006) Impact of the guanidinium group on hybridization and cellular uptake of cationic oligonucleotides. *ChemBioChem 7*, 684–692.

(36) Kang, S.-H., Cho, M.-J., and Kole, R. (1998) Up-regulation of luciferase gene expression with antisense oligonucleotides: implications and applications in functional assay development. *Biochemistry 37*, 6235–6239.

(37) Sazani, P., Gemignani, F., Kang, S.-H., Maier, M. A., Manoharan, M., Persmark, M., Bortner, D., and Kole, R. (2002) Systemically delivered antisense oligomers upregulate gene expression in mouse tissues. *Nat. Biotechnol. 20*, 1228–1233.

BC8001437

Monosaccharide-Based Water-Soluble Fluorescent Tags

Alan R. Katritzky,* Janet Cusido, and Tamari Narindoshvili

Center for Heterocyclic Compounds, Department of Chemistry, University of Florida, Gainesville, Florida 32611-7200. Received April 9, 2008; Revised Manuscript Received May 2, 2008

Monosaccharides are fluorescently labeled under microwave irradiation by *N*-(coumarin-3-carbonyl)benzotriazole **4**. 1,2:3,4-di-*O*-isopropylidene-α-D-galactopyranose **9** gives **12** (90%), 1,2:5,6-di-*O*-isopropylidene-D-glucose **10** gives **13** (89%), 2,3:5,6-di-*O*-isopropylidene-α-D-mannofuranose **11** gives **14** (65%) (all by *O*-acylation) and 2,3,4,5-tetra-*O*-pivaloyl-*β*-D-galactopyranosylamine **15** gives **16** (60%) (by *N*-acylation). Similarly, the coumarin-containing activated lysine derivatives **7** and **8** afford the L-lysine-scaffold based coumarin labeled sugars **17**, **18a**,**b**, and **19** (67−85%) which, after removal of the diisopropylidene groups, provide water-soluble fluorescent derivatives.

INTRODUCTION

Carbohydrate moieties have pivotal roles in numerous biological processes including cell−cell communication (*1–3*), cell adhesion (*4, 5*), and protein folding and are implicit in various diseases (*6*) such as chronic inflammation, microbial infections, and cancer (*7–11*).

Glycosylation is a very common post-translational modification of proteins; in eukaryotic systems, over 50% of all protein sequences are glycosylated (*12, 13*). Glycosylated lipids constitute up to 5−10% of the membrane content in animal cells, and are involved in a wide array of pathological disorders (*14*).

Sequencing and structural analysis of an oligosaccharide chain of a glycoprotein or glycolipid is more complicated than DNA or protein sequencing because glycolipid molecules are frequently branched and each linkage between sugar residues introduces a new α or *β* stereocenter. Preferred analytical approaches (*15, 16*) detect oligosaccharides either by mass spectrometry (MS) or by pulsed amperometry. Before release from glycoproteins or glycolipids by chemical or enzymatic methods, oligosaccharides are frequently labeled at the reducing end to increase detection sensitivity (*17*). The insertion of a fluorescent tag (*18*) followed by chromatography or electrophoresis is a common analytical practice.

Primary amine-containing fluorescence tags (FT) can be introduced by reductive amination at the reducing end of sugar chains (*11, 19–23*). Thus, saccharides **1** react with **2** containing, e.g., a 2-aminopyridine and sodium cyanoborohydrate (or sodium borohydride) to give a glycamine **3** (Scheme 1). Similar procedures are used to determine glycosyl transferase activities (*24*). However, these methods cleave the cyclic structure at the reducing end of the sugar chain, thus changing the properties of the sugar moieties.

Labeling amino groups of mono- and diaminosaccharides with a fluorescent tag is an alternative method of measuring glycosyltransferase activities (*25–27*). Coupling of 7-hydroxycoumarin-3-carboxylic acid to glycosylamine was carried out in DMF by HBTU/HOBT/DIEA (*25*). Amino-rich polysaccharides have also been labeled with the fluorescein derivative 5-([4,6-dichlorotriazine-2-yl] amino)-fluorescein (DTAF) (*26, 27*). However, classical labeling procedures applied to proteins, based on acylation of NH_2 groups, are not useful for many sugars because of the absence of free amino groups in many saccharide structures.

Scheme 1. Fluorescent Labeling of Saccharides by Reductive Amination

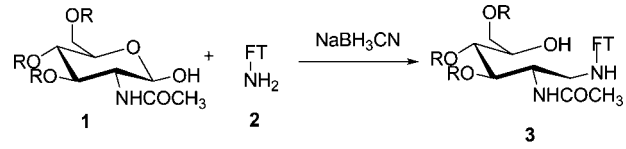

FT - Fluorescent Tag

Fluorescence detection depends on the physical characteristics of the dyes employed. Many dyes with high extinction coefficients and high quantum yields are of limited utility because of (i) poor photostability and/or (ii) poor aqueous solubility. Solubility characteristics affect the degree of self-interaction in solution of chromophores conjugated to substrates and therefore light absorption and emission properties (*28*). Bright fluorescent reagents of good aqueous solubility and affording low nonspecific staining are needed. Incorporation of sugar units confers useful water solubility to organic fluorophores without significant changes in absorption and fluorescent properties (*29, 30*).

We have disclosed *N*-(coumarin-3-carbonyl)benzotriazole **4** as a useful starting material for convenient and reliable fluorescent labeling of amino acids and dipeptides (*31*). Such coumarin-labeled lysines, including N^{ϵ}-coumarin-labeled N^{α}-protected-L-lysines **5**,**6** (*31*) are of considerable interest for the design and synthesis of fluorogenic substrates for the analysis of matrix metalloproteinases (MMP) (*32–34*). Our successful labeling of amino acids in solution phase also utilized **7** (*31*), a benzotriazole-activated **5** (Scheme 2).

We recently reported efficient *O*-acylations of diisopropylidene-protected sugars with readily available *N*-(Cbz-α-aminoacyl)benzotriazoles under microwave irradiation (*35*). We now present the convenient and efficient fluorescent labeling of disopropylidene-protected sugars **9**−**11** by *O*-acylation and of pivaloyl-protected amino sugar **15** by *N*-acylation utilizing as acylating agents (i) *N*-(coumarin-3-carbonyl)benzotriazole **4** and (ii) **7**, **8**, the benzotriazole derivatives of N^{ϵ}-coumarin-labeled N^{α}-protected-L-lysines **5**, **6**. Acylation reactions were carried out at 60 °C under microwave irradiation or at ambient temperature. Monosaccharide-containing Fmoc-lysine fluorescent building blocks could be useful as water-soluble organic fluorophores for peptide labeling at the C-terminus in inverse solid-phase peptide synthesis (SPPS) (*36*).

* katritzky@chem.ufl.edu.

10.1021/bc8001369 CCC: $40.75 © 2008 American Chemical Society
Published on Web 06/21/2008

Scheme 2

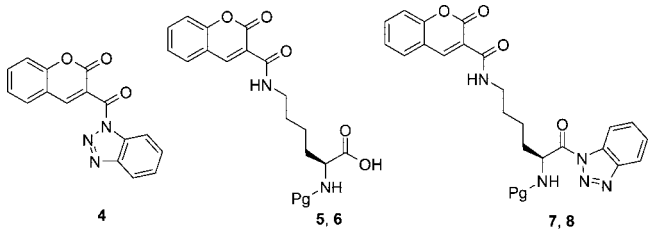

EXPERIMENTAL PROCEDURES

General Procedure for the Preparation of *O*-(Coumarin)Diacetonide Sugars 12−14 under Microwave Irradiation. A dried, heavy-walled Pyrex tube containing a small stir bar was charged with *N*-coumarinoylbenzotriazole **4** (1.0 mmol), sugar (**9**−**11**) (1 mmol), DMAP (1 mmol), and CH_2Cl_2 (1 mL). The reaction mixture was exposed to microwave irradiation (100 W) for 45 min to obtain products (**12**−**14**) at a temperature of 60 °C. After the irradiation, the reaction mixture was allowed to cool until the temperature had fallen below 30 °C (ca. 10 min). CH_2Cl_2 (20 mL) was added to the reaction mixture, and the whole washed with 4 N HCl soln (3 × 15 mL), brine (10 mL), and dried over $MgSO_4$. The solution was concentrated under reduced pressure and the crude product was crystallized from CH_2Cl_2/hexanes for elemental analysis.

*6-O-Coumarin-3-carbonyl-1,2:3,4-di-O-isopropylidene-*α*-D-galactopyranose,* ***12.*** White microcrystals (90%), mp 146.2−148.0 °C, ^{1}H NMR ($CDCl_3$): δ 1.34 (s, 3H), 1.36 (s, 3H), 1.48 (s, 3H), 1.54 (s, 3H), 4.16−4.23 (m, 1H), 4.33−4.40 (m, 2H), 4.47 (dd, J = 11.4, 7.6 Hz, 1H), 4.55 (dd, J = 11.5, 4.9 Hz, 1H), 4.66 (dd, J = 7.8, 2.3 Hz, 1H), 5.56 (d, J = 4.9 Hz, 1H), 7.30−7.38 (m, 2H), 7.58−7.70 (m, 2H), 8.53 (s, 1H). ^{13}C NMR ($CDCl_3$): δ 24.4, 24.9, 25.9, 26.0, 64.5, 65.9, 70.5, 70.6, 70.9, 96.2, 108.9, 109.6, 116.8, 117.8, 117.9, 124.8, 129.5, 134.4, 148.8, 155.1, 156.5, 162.6. Anal. Calcd for $C_{22}H_{24}O_9$: C, 61.11; H, 5.59. Found: C, 61.06; H, 5.71.

*4-O-Coumarin-3-carbonyl-1,2:5,6-di-O-isopropylidene-*α*-D-glucose,* ***13.*** White microcrystals (89%), mp 65.1−66.7 °C, ^{1}H NMR ($CDCl_3$): δ 1.32 (s, 3H), 1.33 (s, 3H), 1.43 (s, 3H), 1.56 (s, 3H), 4.07 (dd, J = 8.8, 4.7 Hz, 1H), 4.15 (dd, J = 8.7, 5.9 Hz, 1H), 4.29 (dd, J = 8.5, 3.0 Hz, 1H), 4.45−4.51 (m, 1H), 4.68 (d, J = 3.8 Hz, 1H), 5.48 (d, J = 3.0 Hz, 1H), 5.97 (d, J = 3.8 Hz, 1H), 7.32−7.40 (m, 2H), 7.60−7.72 (m, 2H), 8.53 (s, 1H). ^{13}C NMR ($CDCl_3$): δ 25.2, 26.1, 26.7, 26.9, 67.4, 72.4, 77.6, 79.9, 83.1, 105.1, 109.4, 112.3, 116.8 (2C), 117.6, 124.9, 129.6, 134.7, 149.3, 155.2, 156.2, 162.1. Anal. Calcd for $C_{22}H_{24}O_9$: C, 61.11; H, 5.59. Found: C, 60.91; H, 5.72.

General Procedure for the Preparation of L-Lysine Scaffold Based Coumarin Labeled Sugars 17, 18a,b, 19, 20 at 20 °C. To a mixture of sugar (**9**, **10**, **11**, **12**) (1.0 mmol), N^{ϵ}-coumarin-3-carbonyl-N^{α}-Cbz-L-lysine benzotriazole **7** (to obtain **18a**) or N^{ϵ}-coumarin-3-carbonyl-N^{α}-Fmoc-L-lysine benzotriazole **8** (to obtain **17**, **18b**, **19**, **20**) (1.0 mmol) and DMAP (1.0 mmol), was added dry CH_2Cl_2 (3−5 mL), and the mixture stirred at room temperature for 16−24 h. The reaction mixture was then diluted by 30 mL of CH_2Cl_2 and washed with 4 N HCl (3 × 15 mL), brine (20 mL), and dried over $MgSO_4$. The solution was concentrated under reduced pressure and crude product was crystallized from CH_2Cl_2/hexanes mixture for elemental analysis.

*6-O-(N^{α}-(9-Fluorenylmethoxycarbonyl)-N^{δ}-(coumarin-3-carbonyl)-L-lysine)-1,2:3,4-di-O-isopropylidene-*α*-D-galactopyranose,* ***17.*** White microcrystals (85%), mp 122.3−124.1 °C. $[\alpha]^{23}_D$ = −4.69 (*c* 1.60, DMF); ^{1}H NMR ($CDCl_3$): δ 1.24−1.30 (m, 2H), 1.33 (s, 6H), 1.46 (s, 3H), 1.52 (s, 3H), 1.63−2.30 (m, 4H), 3.40−3.57 (m, 2H), 4.01−4.08 (m, 1H), 4.20−4.29 (m, 2H), 4.30−4.46 (m, 6H), 4.62 (dd, J = 7.8, 2.3 Hz, 1H), 5.54 (d, J = 4.9 Hz, 1H), 5.60 (d, J = 8.0 Hz, 1H), 7.29−7.43 (m, 6H), 7.54 (d, J = 7.7 Hz, 1H), 7.60−7.67 (m, 3H), 7.72−7.78 (m, 2H), 8.82−8.88 (m, 1H), 8.90 (s, 1H). ^{13}C NMR ($CDCl_3$): δ 22.3, 24.4, 24.9, 25.9, 26.0, 29.0, 31.9, 39.2, 47.1, 53.8, 64.2, 66.0, 67.0, 70.3, 70.7, 70.9, 96.2, 108.8, 109.7, 116.5, 118.3, 118.6, 119.9, 125.2, 127.0, 127.6, 129.7, 133.9, 141.2, 143.8, 148.3, 154.3, 155.9, 161.4, 161.7, 172.3. Anal. Calcd for $C_{43}H_{46}N_2O_{12}$: C, 65.97; H, 5.92; N, 3.58. Found: C, 65.63; H, 6.04; N, 3.62.

*4-O-(N^{α}-Carbobenzyloxy-N^{δ}-coumarin-3-carbonyl)-L-lysine)-1,2:5,6-di-O-isopropylidene-*α*-D-glucose,* ***18a.*** White microcrystals (82%), mp 123.0−124.0 °C. ^{1}H NMR ($CDCl_3$): δ 1.29 (s, 3H), 1.31 (s, 3H), 1.38 (s, 3H), 1.41−1.48 (m, 2H), 1.51 (s, 3H), 1.58−1.98 (m, 4H), 3.38−3.58 (m, 2H), 3.97 (dd, J = 8.6, 4.2 Hz, 1H), 4.07 (dd, J = 8.6, 5.1 Hz, 1H), 4.14−4.25 (m, 2H), 4.29−4.40 (m, 1H), 4.48 (d, J = 3.4 Hz, 1H), 5.07 (d, J = 12.2 Hz, 1H, B part of AB system), 5.13 (d, J = 12.2 Hz, 1H, A part of AB system), 5.40−5.52 (m, 1H), 5.65 (d, J = 7.4 Hz, 1H), 5.82 (d, J = 3.4 Hz, 1H), 7.28−7.43 (m, 7H), 7.50 (d, J = 7.1 Hz, 1H), 7.62−7.72 (m, 1H), 8.82−8.96 (m, 2H). ^{13}C NMR ($CDCl_3$): δ 22.2, 25.2, 26.2, 26.7, 26.8, 29.1, 31.3, 38.7, 54.0, 66.9, 67.2, 72.4, 76.9, 79.7, 83.0, 105.0, 109.3, 112.4, 116.5, 116.5, 118.2, 118.6, 125.3, 128.0, 128.2, 128.5, 129.8, 134.1, 136.2, 148.6, 154.3, 156.0, 161.5, 161.9, 171.0. Anal. Calcd for $C_{36}H_{42}N_2O_{12}$: C, 62.24; H, 6.09; N, 4.03. Found: C, 62.34; H, 6.11; N, 4.09.

*4-O-(N^{α}-(9-Fluorenylmethoxycarbonyl)-N^{δ}-(coumarin-3-carbonyl)-L-lysine)-1,2:5,6-di-O-isopropylidene-*α*-D-glucose,* ***18b.*** White microcrystals (67%), mp 118.2−120.4. $[\alpha]^{23}_D$ = −10.4 (*c* 1.74, DMF); ^{1}H NMR ($CDCl_3$): δ 1.29 (s, 3H), 1.31 (s, 3H), 1.38 (s, 3H), 1.51 (s, 3H), 1.60−2.00 (m, 6H), 3.40−3.62 (m, 2H), 3.95−4.14 (m, 2H), 4.19−4.27 (m, 3H), 4.30−4.45 (m, 3H), 4.51 (d, J = 3.4 Hz, 1H), 5.30 (s, 1H), 5.77 (d, J = 7.6 Hz, 1H), 5.86 (d, J = 3.6 Hz, 1H), 7.25−7.46 (m, 7H), 7.60−7.67 (m, 3H), 7.72−7.79 (m, 2H), 8.84−8.96 (m, 2H). ^{13}C NMR ($CDCl_3$): δ 22.2, 25.1, 26.2, 26.7, 26.8, 29.0, 31.3, 38.7, 47.1, 53.9, 60.4, 67.0, 67.2, 72.3, 79.7, 83.1, 105.0, 109.4, 112.4, 116.5, 118.1, 118.5, 120.0, 125.1, 125.1, 125.2, 127.1, 127.7, 129.7, 134.0, 141.2, 143.6, 143.8, 148.6, 154.3, 156.0, 161.5, 162.0, 171.1. Anal. Calcd for $C_{43}H_{46}N_2O_{12}$: C, 65.97; H, 5.92; N, 3.58. Found: C, 65.63; H, 6.04; N, 3.62.

General Procedure for the Cleavage of Diisopropylidene Group Present in Coumarin Labeled Glycoconjugates 13, 17. TFA-H_2O (4−0.2 mL) mixture was added to **13**, **17** (0.100 g) at room temperature and the reaction mixture was stirred until **13**, **17** were completely consumed as monitored by TLC (5−7 min). Solvent was then removed under reduced pressure, followed by subsequent washing with acetonitrile and diethyl ether (2−3 times). The residue solid was filtered off and dried to give **21**, **22** in yields of 97−98%.

4-O-Coumarin-3-carbonyl-D-glucose, ***21.*** White microcrystals (97%), diastereomixture of α and β forms (α:β; 0.4:0.6); mp 205−207 °C. ^{1}H NMR (DMSO-d_6): δ 3.17−3.31 (m, 2H), 3.39−3.57 (m, 2H), 3.60−3.75 (m, 1H), 4.43−4.56 (m, 1H), 4.64 (t, J = 5.7 Hz, 0.6H), 4.46−5.44 (m, 1.4H), 5.18−5.30 (m, 2H), 6.60 (d, J = 4.3 Hz, 0.4 H), 6.88 (d, J = 6.5 Hz, 0.6 H), 7.39−7.48 (m, 2H), 7.72−7.81 (m, 1H), 7.93 (d, J = 7.6 Hz, 1H), 8.82 (s, 1H). ^{13}C NMR (DMSO-d_6): δ 60.7, 67.9, 70.3, 71.9, 72.7, 76.3, 77.3, 79.5, 92.2, 96.7, 116.2, 117.7, 117.8, 125.0, 130.3, 134.6, 148.7, 148.8, 154.6, 156.0, 156.0, 161.7, 161.8. Anal. Calcd for $C_{16}H_{16}O_9 \cdot H_2O$: C, 51.89; H, 4.90. Found: C, 51.51; H, 4.54.

6-O-(N^{α}-(9-Fluorenylmethoxycarbonyl)-N^{δ}-(coumarin-3-carbonyl)-L-lysine)-D-galactose, ***22.*** White microcrystals (98%), diastereomixture of α and β forms (α:β; 0.5:0.5); mp 199−201 °C. $[\alpha]^{23}_D$ = +9.42 (*c* 1.59, DMF); ^{1}H NMR (DMSO-d_6): δ

Scheme 3. Syntheses of *O*-(Coumarin-3-Carbonyl)Diisopropylidene Sugars 12, 13, 14 and *N*-(Coumarin-3-Carbonyl)Tetrapivaloyl Sugar 16

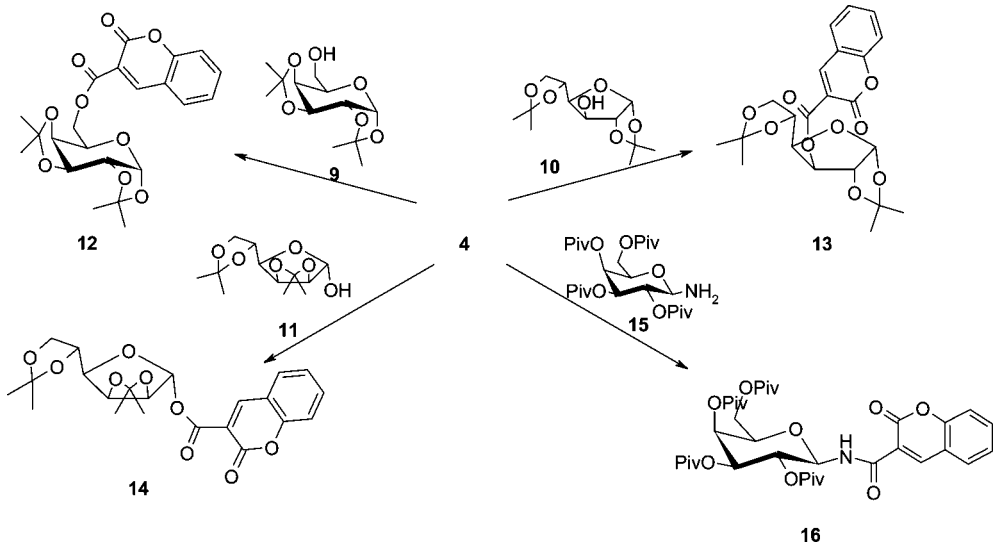

Scheme 4. Preparation of *O*- and *N*-(N^{ϵ}-coumarin-3-carbonyl)-N^{α}-(Fmoc or Cbz-L-lys)-Protected Sugars 17, 18a,b, 19, and 20

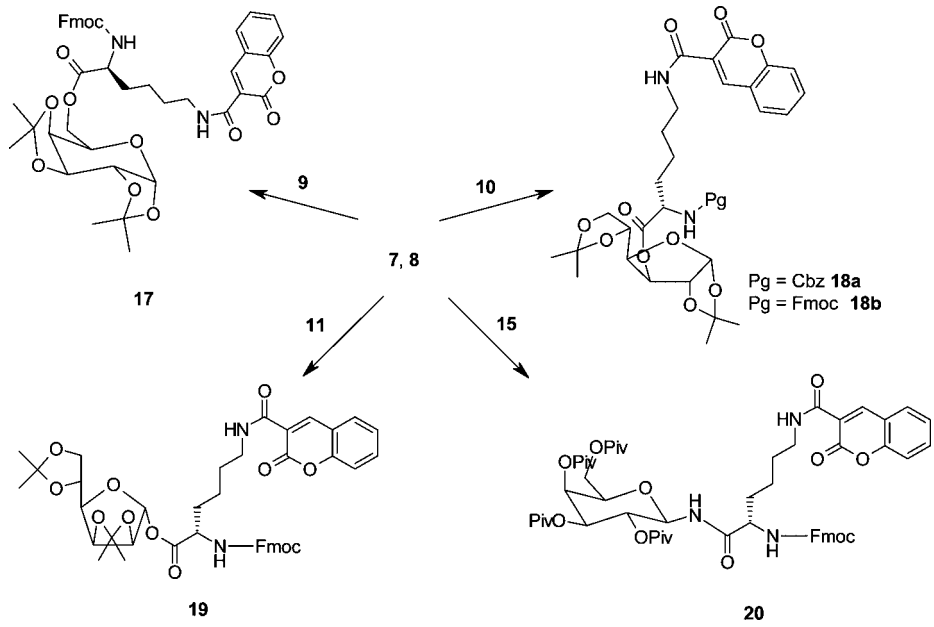

Scheme 5

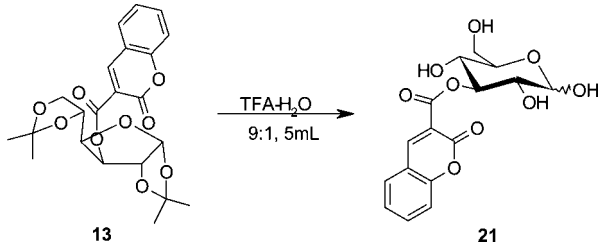

1.30−1.45 (m, 2H), 1.46−1.60 (m, 2H), 1.61−1.80 (m, 2H), 3.18−3.40 (m, 3H), 3.46−3.70 (m, 2H), 3.94−4.06 (m, 2H), 4.08−4.18 (m, 2H), 4.18−4.38 (m, 4H), 4.56 (d, J = 4.3 Hz, 1H), 4.61 (d, J = 4.2 Hz, 0.5 H), 4.70−4.80 (m, 1H), 4.90−4.97 (m, 0.5H), 6.24 (d, J = 4.7 Hz, 0.5 H), 6.59 (d, J = 6.9 Hz, 0.5H), 7.27−7.54 (m, 6H), 7.66−7.82 (m, 6H), 7.96 (d, J = 7.6 Hz, 1H), 8.66−8.77 (m, 1H), 8.84 (s, 1H). ^{13}C NMR (DMSO-d_6): δ 23.0, 28.6, 30.4, 46.6, 53.8, 64.4, 65.7, 67.5, 67.6, 68.5, 68.6, 69.0, 69.1, 71.7, 71.8, 73.0, 92.7, 97.4, 116.1, 118.5, 119.1, 120.1, 125.1, 125.3, 127.1, 127.6, 130.2, 134.0, 140.7, 143.8, 143.8, 147.3, 153.8, 156.2, 160.4, 161.1, 172.5. Anal. Calcd for $C_{37}H_{38}N_2O_{12}$0.5 H_2O: C, 62.58; H, 5.30; N, 3.89. Found: C, 62.53; H, 5.30; N, 3.71.

RESULTS AND DISCUSSION

Preparation of N^{ϵ}-Coumarin-Labeled N^{α}-Fmoc-L-Lysine Benzotriazolide 8. N^{ϵ}-Coumarin-3-carbonyl-N^{α}-Fmoc-L-lysine benzotriazole **8** (Scheme 2) was prepared (87%) from coumarin-labeled N^{α}-Fmoc-protected lysine **6** according to the benzotriazole methodology optimized in our laboratories (*37*–*43*), by reaction with 1*H*-benzotriazole and thionyl chloride in CH_2Cl_2 at 20 °C for 2 h.

Preparation of coumarin-O-tagged monosaccharides: *O*-(coumarin-3-carbonyl)diisopropylidene sugars 12, 13, 14. *O*-Coumarin-labeled diisopropylidene sugars **12**, **13**, **14** were prepared by coupling of **4** with the 6-OH of 1,2:3,4-di-*O*-isopropylidene-α-D-galactopyranose **9**, 3-OH of 1,2:5,6-di-*O*-isopropylidene-α-D-glucose **10**, and 1-OH of 2,3:5,6-di-*O*-

Scheme 6

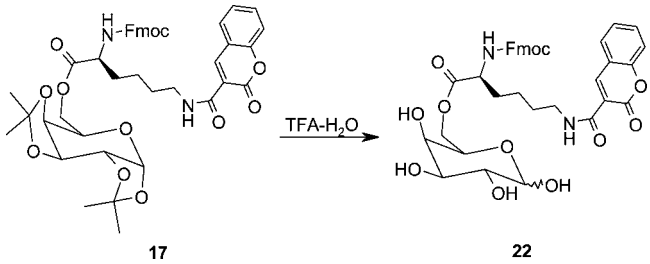

Table 1. Absorption and Fluorescence Data of Coumarin-Labeled Conjugates

entry	compound	$\lambda_{Abs.}$ [nm][a]	$\lambda_{Em.}$ [nm][a]
1	**12**	294	422
2	**13**	304	423
3	**14**	294	422
4	**16**	293	419
5	**17**	299	407
6	**18a**	296	406
7	**18b**	294	407
8	**19**	299	408
9	**20**	299	406
10	**21**	292	416
11	**22**	299	409

[a] Determined in 95% methanol.

isopropylidene-α-D-mannofuranose **11**, respectively, in CH_2Cl_2 utilizing 1 equiv of DMAP, under 100 W microwave irradiation at 60 °C for 45 min (Scheme 3). The products were isolated after simple acid workup without chromatography in 65−90% yields.

Preparation of Coumarin-N-Tagged Monosaccharide: *N*-(Coumarin-3-Carbonyl)Tetrapivaloyl Sugar 16. 2,3,4,6-Tetra-*O*-pivaloyl-*β*-D-galactopyranosylamine **15** couples with *N*-(coumarin-3-carbonyl) benzotriazole **4** in dry CH_2Cl_2 in the presence of 1 equiv of DMAP during 24 h at 20 °C (Scheme 3). After acid workup and silica-gel column chromatography using EtOAc /hexane (1:2) as eluent, product **16** was isolated in 60% yield.

Preparation of *O*- and *N*-(N^{ϵ}-Coumarin-3-Carbonyl-N^{α}(Fmoc or Cbz-L-lys)-Protected Sugars 17, 18a,b, 19, 20. L-Lysine scaffold-based coumarin-labeled sugars **17**, **18a**,**b**, **19**, and **20** were synthesized by *O*-acylation of the free OH groups of diacetonide-protected sugars **9**, **10**, and **11** and *N*-acylation of the NH_2 group of **15** by N^{ϵ}-coumarin-3-carbonyl-N^{α}-Cbz or Fmoc-L-lysine benzotriazoles **7**, **8** (Scheme 4).

Coupling reactions were carried out in dry CH_2Cl_2, in the presence of 1 equiv of DMAP, at room temperature for 16−24 h. After washing with 4 N HCl, products **17** and **18a**,**b** were obtained without chromatography in 67−85% yields. Compounds **19** and **20** were isolated using chromatography in 74% and 40% yields, respectively. Under microwave irradiation at 60 °C, the preparation of **18a** (yield 83%) took 1 h; however, for the other products **17**, **18b**, **19**, and **20** lower yields in comparison to those obtained with room-temperature conditions were obtained.

Deprotection of the Diisopropylidene Groups of O-(Coumarin-Labeled) Diisopropylidene Sugars 13 and 17. Deprotection of the diacetonide groups of **13** and **17** were achieved in aqueous TFA at 20 °C in 5−7 min. The coumarin-free sugar **21** (Scheme 5) and coumarin-L-lysine-free sugar conjugates **22** (Scheme 6) were obtained in quantitative yields and characterized by ^1H and ^{13}C NMR spectroscopy, elemental analysis, melting point, and ORP.

Absorption ($\lambda_{Abs.}$) and fluorescence ($\lambda_{Em.}$) wavelength maxima were measured for each compounds (Table 1).

In conclusion, we have demonstrated a convenient and efficient *O*-fluorescent labeling of diisopropylidene protected sugars **12**−**14** and *N*-labeling of pivaloyl protected amino sugar **15** in yields of 60−90% by *N*-(coumarin-3-carbonyl)benzotriazole **4**. Fmoc and Cbz protected L-lysine scaffold-based coumarin-labeled protected sugars **17**, **18a**,**b**, **19**, and **20** were obtained from **7** and **8**. Deprotection of diisopropylidene groups from **13** and **17** provide water-soluble conjugates **21** and **22** in quantitative yields. Sugar-Fmoc-lysine fluorescent building blocks **17** and **18b** and **19** are expected to be useful fluorescent markers for peptide labeling in SPPS; deprotection of diisopropylidene protecting groups will provide better water solubility of coumarin-labeled peptides.

Supporting Information Available: Procedures for preparation and compound characterization data for **4**−**8** and characterization data for **14**, **16**, **19** and **20**. This material is available free of charge via the Internet at http://pubs.acs.org.

LITERATURE CITED

(1) Boons, G. J. (1996) Synthetic oligosaccharides: recent advances. *Drug Discovery Today 1*, 331–342.
(2) Karlsson, K. A. (1991) Glycobiology - a growing field for drug design. *Trends Pharmacol. Sci. 12*, 265–272.
(3) Sharon, N., and Lis, H. (1993) Carbohydrates in cell recognition. *Sci. Am. 268*, 82–89.
(4) Dwek, R. A. (1996) Glycobiology: Toward understanding the function of sugars. *Chem. Rev. 96*, 683–720.
(5) Varki, A. (1993) Biological roles of oligosaccharides: All of the theories are correct. *Glycobiology 3*, 97–130.
(6) Barkley, A., and Arya, P. (2001) Combinatorial chemistry toward understanding the function(s) of carbohydrates and carbohydrate conjugates. *Chem. Eur. J. 7*, 555–563.
(7) Fukuda, M. (2002) Roles of mucin-type O-glycans in cell adhesion. *Biochim. Biophys. Acta 1573*, 394–405.
(8) Ohyama, C., Tsuboi, S., and Fukuda, M. (1999) Dual roles of sialyl Lewis X oligosaccharides in tumor metastasis and rejection by natural killer cells. *EMBO J. 18*, 1516–1525.
(9) Macmillan, D., and Daines, A. M. (2003) Recent developments in the synthesis and discovery of oligosaccharides and glycoconjugates for the treatment of disease. *Curr. Med. Chem. 10*, 2733–2773.
(10) Feizi, T., and Childs, R. A. (1985) Carbohydrate structures of glycoproteins and glycolipids as differentiation antigens, tumor-associated antigens and components of receptor systems. *Trends Biochem. Sci. 10*, 24–29.
(11) Park, J., Lee, H. Y., Cho, M-H., and Park, S. B. (2007) Development of a Cy3-labeled glucose bioprobe and its application in bioimaging and screening for anticancer agents. *Angew. Chem., Int. Ed. 46*, 2018–2022.
(12) Apweiler, R., Hermjakob, H., and Sharon, N. (1999) On the frequency of protein glycosylation, as deduced from analysis of the SWISS-PROT database. *Biochim. Biophys. Acta 1473*, 4–8.
(13) Kunz, H. (2003) Synthetic glycopeptides for the development of tumor-selective vaccines. *J. Pept. Sci. 9*, 563–573.
(14) Kolter, K., and Sandhoff, K. (1999) Spingolipids-their metabolic pathways and the pathobiochemistry of neurodegenerative diseases. *Angew.Chem., Int. Ed. 38*, 1532–1568.
(15) Dell, A., and Morris, H. R. (2001) Glycoprotein structure determination by mass spectrometry. *Science 291*, 2351–2356.
(16) Morelle, W., and Michalski, J. C. (2005) The mass spectrometric analysis of glycoproteins and their glycan structures. *Curr. Anal. Chem. 1*, 29–57.
(17) Mechref, Y., and Novotny, M. (2002) Structural investigations of glycoconjugates at high sensitivity. *Chem. Rev. 102*, 321–369.
(18) Tinnefeld, P., and Sauer, M. (2005) Branching out of single-molecule fluorescence spectroscopy: challenges for chemistry and influence of biology. *Angew. Chem., Int. Ed. 44*, 2642–2671.

(19) Malsch, R., Guerrini, M., Torri, G., Löhr, G., Casu, B., and Harenberg, J. (1994) Synthesis of a N′-alkylamine anticoagulant active low-molecular-mass heparin for radioactive and fluorescent labeling. *Anal. Biochem. 217*, 255–264.

(20) Uozumi, N., Tadashi, T., Yamamoto, T., Nishikawa, A., Gao, Y., Miyoshi, E., Gao, C., Noda, K., Ismal, K. N., Ihara, Y., Fujii, S., Shiba, T., and Taniguchi, N. (1996) A fluorescent assay method for GRD-L-Fuc:N-acetyl-β-D-glucosaminide α1−6Fucosyltransferase activity, involving high performance liquid chromatography. *J. Biochem. 120*, 385–392.

(21) Hase, S., Ibuki, T., and Ikenaka, T. (1984) Reexamination of the pyridylamination used for fluorescence labeling of olygosaccharides and its application to glycoproteins. *J. Biochem. 95*, 197–203.

(22) Tomiya, N., Kurono, M., Ishihara, H., Tejima, S., Endo, S., Arata, Y., and Takahashi, N. (1987) Structural analisis of N-linked oligosaccharides by acombination of glycopeptidase, exoglycosidases, and high-performance liquid chromatography. *Anal. Biochem. 163*, 489–499.

(23) Gross, H. J., Sticher, U., and Brossmer, R. (1990) A highly sensitive fluorometric assay for sialyltrasferase using CMP-9fluoresceinyl-NeuAc as donor. *Anal. Biochem. 186*, 127–134.

(24) Taniguchi, N., Nishikawa, A., Fujii, S., and Gu, J. (1989) Glycosyltransferase assays using pyridylaminated acceptors: N-acetylglucosamnyltransferase III, IV and V. *Methods Enzymol. 179*, 397–408.

(25) Higai, K., Masuda, D., Matsuzawa, Y., Saton, T., and Matsumoto, K. (1999) A fluorometric assay for glycosyltransferase activities using sugars aminated and tagged with 7-hydroxycoumarin-3-carboxylic acid as substrates and high performance liquid chromatography. *Biol. Pharm. Bull. 22*, 333–338.

(26) Prigel-Richard, S., Cansell, M., Vassy, J., Viron, A., Puvion, E., Jozefonvicz, J., and Letourneur, D. (1998) Fluorescent and radiolabeling of polysaccharides: binding and internalization experiments of vascular cells. *J. Biomed. Mater. Res. 40*, 275–281.

(27) Blakeslee, D., and Baines, M. G. (1976) Immunofluorescence using dichlorotriazinylaminofluorescein (DTAF) I. Preparation and fractionation of labeled IgG. *J. Immunol. Methods 13*, 305–320.

(28) Brelje, T. C., Wessendorf, M. W., and Sorenson, R. L. (1993) Multicolor laser scanning confocal imunofluorescence microscopy: practical application and limitations. *Methods Cell Biol. 38*, 97–181.

(29) Reddington, M. V. (1998) New glycoconjugated cyanine dyes as fluorescent labeling reagents. *J. Chem. Soc., Perkin Trans. 1*, 143–147.

(30) Esteves, A. P., Rodrigues, L. M., Silva, M. E., Gupta, S., Oliviera-Campos, A. M. F., Machalicky, O., and Mendonca, A. J. (2005) Synthesis and characterization of novel fluorescent N-glycoconjugates. *Tetrahedron 61*, 8625–8632.

(31) Katritzky, A. R., Narindoshvili, T., and Angrish P. (2008) Chiral coumarin-3 carbonyl-α-aminoacids: fluorescent markers for aminoacids and dipeptides, *Synthesis*. in press.

(32) Shi, Y., Xiang, R., Horvath, C., and Wilkins, J. A. (2005) Design and synthesis of a solid-phase fluorescent mass tag. *J. Sep. Sci. 28*, 1812–1817.

(33) Lauer-Fields, J. L., Kele, P., Sui, G., Nagase, H., Leblanc, R. M., and Fields, G. B. (2003) Analysis of matrix metalloproteinase triple-helical peptidase activity with substrates incorporating fluorogenic L- or D-amino acids. *Anal. Biochem. 321*, 105–115.

(34) Lauer-Fields, J. L., Broder, T., Sritharan, Th., Chung, L., Nagase, H., and Fields, G. B. (2001) Kinetic analysis of matrix mettaloprotainase activity using fluorogenic triple-helical substrates. *Biochemistry 40*, 5795–5803.

(35) Katritzky, A. R., Angrish, P., and Narindoshvili, T. (2007) Chiral O-(Z-α-aminoacyl)sugars: convenient building blocks for glycopeptides libraries. *Bioconjugate Chem. 18*, 994–998.

(36) Johansson, A., Akerblom, E., Ersmark, K., Lindeberg, G., and Hallberg, A. (2000) An improved procedure for N-and C-directed (inverse) solid-phase peptide synthesis. *J. Comb. Chem. 2*, 496–507.

(37) Katritzky, A. R., Yang, H. F., Zhang, S. M., and Wang, M. Y. (2002) An efficient conversion of carboxylic acids into Weinreb amides. *ARKIVOC (xi)* 39–44.

(38) Katritzky, A. R., Suzuki, K., and Singh, S. K. (2004) Highly diastereoselective peptide chain extensions of unprotected amino acids with N-(Z-α-aminoacyl)benzotriazoles. *Synthesis 16*, 2645–2652.

(39) Katritzky, A. R., Angrish, P., Hur, D., and Suzuki, K. (2005) N-(Cbz- and Fmoc-alpha-aminoacyl)benzotriazoles: stable derivatives enabling peptide coupling of Tyr, Trp, Cys, Met, and Gln with free amino acids in aqueous media with complete retention of chirality. *Synthesis 3*, 397–402.

(40) Katritzky, A. R., Angrish, P., and Suzuki, K. (2006) The efficient preparation of di- and tripeptides by coupling N-(Cbz- or Fmoc-alpha-aminoacyl)benzotriazoles with unprotected amino acids. *Synthesis 3*, 411–424.

(41) Katritzky, A. R., Narindoshvili, T., Dragichi, B., and Angrish, P. (2008) Regioselective syntheses of β-N-linked glycoaminoacids and glycopeptides. *J. Org. Chem. 73*, 511–516.

(42) Katritzky, A. R., Meher, G., and Angrish, P. (2006) Peptides by extension at the N- or C-terminii of lysine. *Chem. Biol. Drug Des. 68*, 326–333.

(43) Katritzky, A. R., Mohapatra, P. P., Fedoseyenko, D., Duncton, M., and Steel, P. J. (2007) 1-Benzotriazol-1-yl-3,3,3-trifluoro-2-methoxy-2-phenylpropan-1-ones: Mosher-Bt reagents. *J. Org. Chem. 71*, 4268–4271.

BC8001369

TECHNICAL NOTES

Synthesis of a Cross-Bridged Cyclam Derivative for Peptide Conjugation and ^{64}Cu Radiolabeling

C. Andrew Boswell,[⊥,†] Celeste A. S. Regino,[‡] Kwamena E. Baidoo,[†] Karen J. Wong,[‡] Ambika Bumb,[†] Heng Xu,[†] Diane E. Milenic,[†] James A. Kelley,[§] Christopher C. Lai,[§] and Martin W. Brechbiel*[,†]

Radioimmune and Inorganic Chemistry Section, Radiation Oncology Branch, and Molecular Imaging Program, Center for Cancer Research, National Cancer Institute, National Institutes of Health, 10 Center Drive, Bethesda, Maryland 20892-1088, and Laboratory of Medicinal Chemistry, Center for Cancer Research, National Cancer Institute, National Institutes of Health, 376 Boyles Street, NCI-Frederick, Frederick, Maryland 21702. Received January 30, 2008; Revised Manuscript Received May 28, 2008

The increased use of copper radioisotopes in radiopharmaceutical applications has created a need for bifunctional chelators (BFCs) that form stable radiocopper complexes and allow covalent attachment to biological molecules. Previous studies have established that 4,11-bis-(carbo-*tert*-butoxymethyl)-1,4,8,11-tetraazabicyclo[6.6.2]hexadecane (H_2CB-TE2A), a member of the ethylene "cross-bridged" cyclam (CB-cyclam) class of bicyclic tetraaza macrocycles, forms highly kinetically stable complexes with Cu(II) and is less susceptible to *in vivo* transchelation than its nonbridged analogue, 1,4,8,11-tetraazacyclotetradecane-1,4,8,11-tetraacetic acid (TETA). Herein, we report a convenient synthesis of a novel cross-bridged BFC that is structurally analogous to CB-TE2A in that it possesses two coordinating acetate arms, but in addition possesses a third orthogonally protected arm for conjugation to peptides and other targeting agents. Application of this strategy to cross-bridged chelators may also enable the development of even further improved agents for ^{64}Cu-mediated diagnostic positron emission tomography (PET) imaging as well as for targeted radiotherapeutic applications.

INTRODUCTION

The syntheses of 1,4,8,11-tetraaza-bicyclo[6.6.2]hexadecane (CB-cyclam) and related cross-bridged tetraamine ligands having non-adjacent nitrogens connected by an ethylene (CH_2CH_2) bridge (Figure 1) have been reported by Weisman and Wong (*1–3*). These ligands are remarkably efficient proton sponges and form complexes with small metal ions including Cu(II) by adopting low-energy conformations having all four nitrogen lone pairs convergent upon a three-dimensional cleft (*1*). Several related cross-bridged Cu(II) complexes have been synthesized (*2*), including those bearing pendant carboxymethyl arms that fully envelop the six-coordinate cation and neutralize its dicationic charge (*3*). Additional ethylene cross-bridged Cu(II) complexes have been explored by Busch (*4–7*), while other bridged bicyclic ligands have been reported by Springborg (*8–11*) and Micheloni (*12–16*). The coordination chemistry of bicyclic tetraaza ligands has been thoroughly reviewed by Springborg (*17*).

Copper-64 is an attractive radionuclide for use in both positron emission tomography (PET) imaging and targeted radiotherapy due to its half-life ($t_{1/2}$ = 12.7 h), its decay characteristics (β^+ (19%); β^- (39%)) and its compatibility with large-scale production at high specific activities using a biomedical cyclotron (*18*). Increased use of ^{64}Cu and other copper radioisotopes in nuclear medicine and in preclinical applications has produced a need for copper chelators with high stability against metal loss (*19–23*). Development of optimal metal chelators is a critical step in designing systems for the *in vivo* delivery of copper radioisotopes (*21, 23–25*).

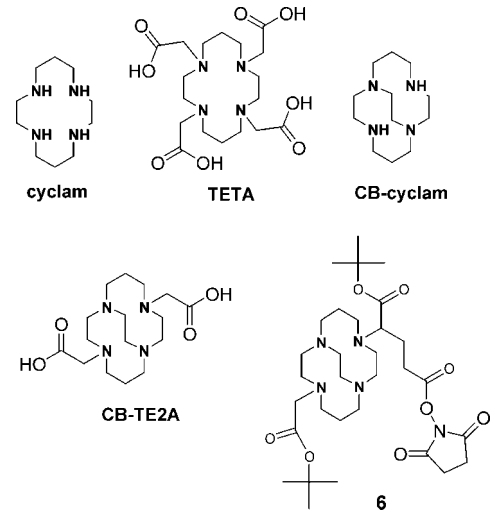

Figure 1. Structures of cyclam, TETA, CB-cyclam, CB-TE2A, and **6**.

* Correspondence to Martin W. Brechbiel, Ph.D., Radioimmune & Inorganic Chemistry Section, Radiation Oncology Branch, NCI, NIH, Building 10, Room 1B40, 10 Center Drive, Bethesda, MD 20892-1088. Fax: (301) 402-1923. E-mail: martinwb@mail.nih.gov.

† Radioimmune and Inorganic Chemistry Section, Radiation Oncology Branch.

‡ Molecular Imaging Program.

§ Laboratory of Medicinal Chemistry.

⊥ Current address: Genentech, Inc., 1 DNA Way, MS 70, South San Francisco, CA 94080.

10.1021/bc800039e CCC: $40.75 © 2008 American Chemical Society
Published on Web 07/03/2008

1,4,8,11-Tetraazacyclotetradecane-1,4,8,11-tetraacetic acid (TETA) has been extensively used as a BFC for copper radionuclides in clinical imaging and therapy studies involving both antibodies and peptides (Figure 1) (*19, 20*). Seminal work performed by Moi, Denardo, Meares, and co-workers pursued the development of TETA-based bifunctional chelators for attaching the low-energy β-emitting isotope ^{67}Cu to monoclonal antibodies for targeted radioimmunotherapy of lymphoma (*26–29*). Despite widespread use, TETA is not an optimal BFC for biomedical applications, as Anderson and co-workers have demonstrated the dissociation of ^{64}Cu from TETA-D-Phe^1-octreotide (TETA-OC) in rat liver and subsequent binding to superoxide dismutase (SOD) (*25, 30*). Copper complexes of the cross-bridged cyclam derivative CB-TE2A (Figure 1) were shown to possess superior *in vivo* stability over TETA (*25*), and a ^{64}Cu-labeled peptide conjugate of CB-TE2A demonstrated superior imaging characteristics over the corresponding TETA−peptide conjugate (*31*). However, one of the two metal coordinating carboxylic acid arms was sacrificed in order to achieve CB-TE2A peptide conjugation (*31*), leaving the Cu(II) in a less than ideal coordination geometry, as both carboxylic acid moieties would be necessary in order to fully saturate the coordination sphere of the six-coordinate cation and neutralize its +2 charge (*3*).

A recent investigation by Sprague and co-workers evaluated both the structure and the *in vivo* behavior of 4-acetamido-11-carboxymethyl-1,4,8,11-tetraazabicyclo[6.6.2]hexadecane (CB-TEAMA), a hybrid monoamide analogue of CB-TE2A, as a model for a CB-TE2A−peptide conjugate (*32*). X-ray crystallography studies have revealed a distorted octahedral coordination geometry for both Cu(II)-CB-TE2A (*3*) and Cu(II)-CB-TEAMA (*32*), with coordination from the carbonyl oxygen of the amide pendant arm in the latter case (*32*). Interpretation of the corresponding *in vivo* data for ^{64}Cu-CB-TEAMA, however, must be approached with great caution due to differences in complex lipophilicity (log *P*) as well as the potential scenario (proposed by the authors) of hepatic enzymatic hydrolysis of ^{64}Cu-CB-TEAMA to ^{64}Cu-CB-TE2A, secretion of the radiometabolite(s) into blood, and subsequent clearance via the kidneys (*32*). In any event, an orthogonal bifunctional chelator having two pendant negatively charged carboxylic acid groups and a third arm for the sole purpose of conjugation would (1) saturate the Cu(II) coordination sphere while neutralizing its dicationic charge and (2) simplify conjugation chemistry by providing a selective site for peptide conjugation. The current study addresses these issues through the synthesis and development of a novel cross-bridged bifunctional chelator *via* a monopendant-armed cross-bridged tetraamine intermediate. This approach allows greater control of conjugation chemistry and may also serve to enhance metal complex *in vivo* stability in diagnostic and therapeutic applications involving copper radionuclides.

EXPERIMENTAL SECTION

General Methods. ^{1}H NMR and ^{13}C NMR spectra were obtained using a Varian Gemini 300 MHz instrument, and the chemical shifts are reported in ppm on the δ scale relative to internal TMS or TSP. Proton chemical shifts are annotated as follows: ppm (multiplicity, integration). Resonance assignments are established with the aid of NOESY, COSY, or HETCOR. Electrospray ionization time-of-flight mass spectra were obtained on a Waters LCT Premier time-of-flight mass spectrometer using electrospray ionization (ESI/TOF/MS) operated in positive ion mode. The electrospray capillary voltage was 3 kV, and the sample cone voltage was 60 V. The desolvation temperature was 225 °C, and the desolvation nitrogen gas flow rate was 300 L/h. Accurate masses were obtained using the lock spray mode with Leu-Enkephalin as the external reference compound. Fast-atom bombardment (FAB) mass spectra were run on a VG 7070E-HF double-focusing mass spectrometer and were obtained in positive ion mode except where noted. A sample matrix of either glycerol (GLY) or 3-nitrobenzyl alcohol (NBA) was employed and ionization was effected by a beam of xenon atoms generated in a saddle-field ion gun at 8.0 ± 0.5 kV. Nominal mass MS were obtained at a resolution of 1200, while accurate mass analysis (high-resolution FAB/MS) was carried out at a resolution of approximately 5000. For the latter, a limited-range V/E scan was employed under control of a MASPEC-II data system for Windows (MasCom GmbH, Bremen, Germany). For these analyses, 1.0 μL 1.0 N KCl in 90% methanol/H_2O was added to the sample before mixing with the NBA matrix so that the matrix-derived ions, utilized as the internal mass references for accurate mass determinations, also included K^+ adducts. In these analyses, molecular identity could usually be confirmed by formation of a $[M + K]^+$ species. Both ^{1}H and ^{13}C NMR data, in conjunction with the observed isotopic distribution of $[M + H]^+$, were used to set constraints for the calculation of all possible elemental compositions within 20 ppm of the measured accurate mass. In all cases, a unique molecular formula could be determined by consideration of the molecular ion species and appropriate fragment ions. Positive ion MALDI mass spectra were obtained on a Shimadzu-Biotech Axima-CRF time-of-flight mass spectrometer using α-cyano-4-hydroxycinnamic acid as the sample matrix. Peptide standards of appropriate molecular weight to bracket the mass of the sample were used to provide internal mass reference peaks for accurate mass measurement. In all cases, the number of significant figures reported is determined by the experimental precision expressed in ppm and is related to the resolution and performance characteristics of the instrument used as well as the internal mass references employed in accurate mass measurement.

Semipreparative reversed-phase HPLC was performed using two Gilson model 303 pumps, a Gilson 803C manometric module, a Gilson 811B dynamic mixer, a Knauer ultraviolet detector, and an INUS λ-Ram radioactive detector all connected through a Gilson 506C system interface module and operated by *UniPoint* version 1.65 software. Analytical HPLC of synthetic products **4**, **5**, and **6** and all peptide conjugates was achieved with a Hamilton Prp-1 polymer reversed-phase semipreparative column (10 μm, 7.0 mm × 30.5 cm) using a flow rate of 3 mL/min; purification of all peptide conjugates was performed using identical conditions. Size-exclusion HPLC (SE-HPLC) was performed using the same system in a single pump mode using a Tosohaas G3000SW, 10 μm, 7.8 mm × 30 cm column with phosphate buffered saline solution as the eluent (0.5 mL/min).

Materials. Solvents were used as purchased. *tert*-Butyl bromoacetate, *N*-hydroxysuccinimide, *N*-ethyl-*N*′-(3-dimethylaminopropyl)carbodiimide hydrochloride (EDCI), and peptide sequence grade trifluoroacetic acid were purchased from the Aldrich Chemical Co. Sodium borohydride powder and 10% Pd/C were purchased from Lancaster Synthesis, Incorporated. CB-cyclam (*3*) and 2-bromo-pentanedioic acid 5-benzyl ester 1-*tert*-butyl ester (*33*) were prepared as reported in the literature. The integrin $\alpha_v\beta_3$-binding peptide c(RGDfK(S)) was purchased from Peptides International. All experiments with moisture- and/or air-sensitive compounds were carried out under a dry Ar atmosphere. For column chromatography, Merck 60 Silica Gel (70−230 mesh) was used. Thin-layer chromatography (TLC) was performed on silica gel 60 F-254 plates from EM Reagents. All water used was purified using a Hydro Ultrapure Water Purification system.

2-(1,4,8,11-Tetraaza-bicyclo[6.6.2]hexadec-4-yl)-pentanedioic Acid 5-Benzyl Ester 1-*tert*-Butyl Ester (3). To a solution of CB-cyclam (**1**) (1 g, 4.42 mmol) in anhydrous CH_3CN was added K_2CO_3 (0.914 g, 6.61 mmol). The solution was shielded from light, and a solution of 2.36 g (6.63 mmol) of 2-bromopentanedioic acid 5-benzyl ester 1-*tert*-butyl ester in CH_3CN was added dropwise *via* an addition funnel over 1 h with constant stirring. The resulting mixture was allowed to react for 24 h in darkness under argon with constant stirring. Excess salt was removed by filtration and solvent removed by rotary evaporation. The resulting residue was dissolved in minimal CH_2Cl_2 and subjected to flash chromatography using a slowly increasing gradient from 100% CH_2Cl_2 to 15% MeOH in CH_2Cl_2. The relevant fractions were identified by ^{1}H NMR spectroscopy, combined, and solvent removed (0.43 g of protonated (HBr) product). The resulting residue was dissolved in $CHCl_3$, chilled, and quickly extracted once with 20% NaOH (aq) at 0 °C. The organic phase was dried with Na_2SO_4 and solvent removed to yield **3** as a pale yellow oil (0.36 g, 16.2% yield). ^{1}H NMR (300 MHz, $CDCl_3$, TMS) δ 1.45 (s, 9H), 1.38−1.62 (m, 7H), 1.80−1.96 (m, 1H), 1.97−2.12 (m, 1H), 2.13−2.24 (m, 2H), 2.28−3.40 (m, 16H), 3.12−3.34 (m, 2H), 4.78−4.98 (br s, 1H), 5.12 (s, 2H), 7.33−7.37 (m, 5H); ^{13}C NMR (75 Hz, $CDCl_3$, TMS) δ 25.08, 25.91, 27.46, 28.26, 31.36, 48.63, 48.68, 48.86, 49.17, 51.74, 53.89, 54.05, 57.65, 58.88, 60.17, 61.63, 66.12, 80.79, 128.12, 128.45, 135.88, 172.22, 172.85. High resolution ESI/TOF/MS: $[M + H]^+$ for $C_{28}H_{47}N_4O_4$ 503.3597, found 503.3604.

2-(11-*tert*-Butoxycarbonylmethyl-1,4,8,11-tetraaza-bicyclo[6.6.2]hexadec-4-yl)-pentanedioic Acid 5-Benzyl Ester 1-*tert*-Butyl Ester (4). To a solution of **3** (0.180 g, 0.360 mmol) in dry CH_3CN was added K_2CO_3 (0.0494 g, 0.357 mmol) and *tert*-butyl bromoacetate (0.070 g, 0.359 mmol) in one portion. The mixture was constantly stirred in darkness for 24 h under argon. Salts were removed by filtration, and the solvent removed by rotary evaporation. The residue was placed under reduced pressure to give the HBr salt of **4** with no further purification necessary to proceed to the next step in the synthesis. For characterization, the residue was dissolved in $CHCl_3$ and quickly extracted once with 20% NaOH (aq) at 0 °C. The organic phase was dried with Na_2SO_4 and solvent removed to yield **4** as a pale yellow oil (0.21 g, 95.0% yield). ^{1}H NMR (300 MHz, $CDCl_3$, TMS) δ 1.45 (d, 18H), 1.22−1.52 (m, 7H), 1.78−1.92 (m, 1H), 1.93−2.10 (m, 1H), 2.30−3.25 (m, 22H), 5.12 (s, 2H), 7.27−7.37 (m, 5H); ^{13}C NMR (75 Hz, $CDCl_3$, TMS) δ 26.14, 27.84, 27.88, 28.32, 28.44, 31.45, 51.13, 51.38, 52.83, 53.01, 55.99, 56.39, 56.57, 57.69, 59.13, 59.18, 61.72, 66.23, 80.43, 80.73, 128.24, 128.26, 128.59, 136.08, 171.80, 172.62, 173.20. High-resolution FAB/MS: $[M + H]^+$ for $C_{34}H_{57}N_4O_6$ 617.4281, found 617.4276.

2-(11-*tert*-Butoxycarbonylmethyl-1,4,8,11-tetraaza-bicyclo[6.6.2]hexadec-4-yl)-pentanedioic Acid 1-*tert*-Butyl Ester (5). To a solution of **4** (0.350 g, 0.568 mmol)) in dry MeOH (15 mL) was added 88% HCO_2H (0.0594 g, 1.3 mmol) followed by 0.10 g of Pd/C (Degussa type E101 NE/W). The round-bottom flask with magnetic stir bar was sealed using a rubber septum. The flask was evacuated and recharged three times using a balloon filled with H_2 gas. The mixture was maintained under the balloon of H_2 for 4 h with constant stirring. The mixture was filtered through Celite 535 prewetted with MeOH, and solvent removed to yield **5** as a pale yellow solid (0.300 g, >99% yield). ^{1}H NMR (300 MHz, $CDCl_3$, TMS) δ 1.46 (d, 18H), 1.45−2.11 (m, 7H), 2.48−3.59 (m, 22H), 3.90−4.08 (br m, 1H), 4.10−4.80 (br s, 2H); ^{13}C NMR (75 Hz, $CDCl_3$, TMS) δ 22.77, 24.96, 27.81, 27.87, 31.21, 47.82, 48.25, 49.46, 50.20, 50.67, 52.89, 55.39, 55.85, 58.10, 59.24, 61.75, 81.94, 81.76, 169.98, 171.10, 174.96. High-resolution FAB/MS: $[M + H]^+$ for $C_{27}H_{51}N_4O_6$ 527.381, found 527.3794.

2-(11-*tert*-Butoxycarbonylmethyl-1,4,8,11-tetraaza-bicyclo[6.6.2]hexadec-4-yl)-pentanedioic Acid 5-*tert*-Butyl Ester 1-(2,5-dioxo-pyrrolidin-1-yl) Ester (6). To a solution of **5** (0.100 g, 0.190 mmol) in dry CH_3CN was added *N*-hydroxysuccinimide (0.026 g, 0.23 mmol) and EDCI (0.044 g, 0.23 mmol) in one portion. The resulting solution was maintained under argon for 10 h with constant stirring. Solvent was removed under reduced pressure, and the residue was dissolved in $CHCl_3$. The solution was extracted twice with brine and once with water. Solvent was removed from the organic phase by rotary evaporation to yield **6** as a pale yellow solid (0.102 g, 86.1% yield). ^{1}H NMR (300 MHz, $CDCl_3$, TMS) δ 1.41 (d, 18H), 1.50−2.15 (m, 5H), 2.40−3.65 (m, 28H), 3.65−3.80 (m, 1H), 3.80−4.00 (m, 1H); ^{13}C NMR (75 Hz, $CDCl_3$, TMS) δ 22.80, 23.23, 25.59, 25.60, 25.73, 28.13, 28.21, 28.32, 48.14, 48.38, 50.21, 50.42, 51.23, 53.55, 53.70, 55.54, 55.95, 56.43, 57.62, 59.89, 61.47, 82.15, 82.36, 168.20, 169.22, 170.40, 170.70. High-resolution FAB/MS: $[M + H]^+$ for $C_{31}H_{54}N_5O_8$ 624.3973, found 624.3941; $[MH\text{-}C_4H_3O_2N]^+$ 527.383, found 527.381; $[MH\text{-}2C_4H_8]^+$ 512.271, found 512.272.

2-(11-Carboxymethyl-1,4,8,11-tetraaza-bicyclo[6.6.2]hexadec-4-yl)-pentanedioic Acid 5-Benzyl Ester (7). Neat trifluoroacetic acid (15 mL) was added to **4** (0.100 g, 0.162 mmol) in a round-bottom flask. The mixture was stirred for 10 h under argon. Excess acid was removed by rotary evaporation. The residue was dissolved in CH_2Cl_2 (20 mL) and solvent removed by rotary evaporation; this process was repeated exhaustively to remove residual acid. The resulting yellow oil was triturated with Et_2O and by submerging the flask into an ultrasonicating bath. Upon solidification, the solid was allowed to settle, and the ethereal wash was carefully pipetted away from the product. Residual solvent was removed to give a hygroscopic pale yellow solid **7** (0.109 g, 91.6% yield including 1.5 associated TFA molecules and 1 H_2O). ^{1}H NMR (300 MHz, CD_3CN) δ 1.60−2.35 (m, 8H), 2.45−3.40 (m, 20H), 3.40−3.85 (m, 3H), 5.24 (s, 2H), 7.48−7.53 (m, 5H), 9.00−9.60 (br s, 2H); ^{13}C NMR (75 Hz, CD_3CN) δ 23.11, 24.53, 25.16, 32.33, 48.79, 49.61, 51.49, 52.75, 53.98, 56.74, 57.84, 58.22, 60.24, 65.03, 67.35, 116.13, 118.69, 120.00, 129.50, 129.92, 137.84, 161.25, 172.83, 173.96, 174.11. Elemental analysis calculated for $C_{26}H_{40}N_4O_6 \cdot (TFA)_{1.5}(H_2O)$: C, 50.20; H, 6.32; N, 8.08. Found: C, 49.95; H, 6.09; N, 7.99.

CB-TE2A Di-*tert*-butyl Ester-(propionamide linker)-c(RGDfK(S)). To c(RGDfK(S)) (0.025 g, 0.036 mmol) in DMF (250 μL) was added **6** (0.0282 g, 0.045 mmol) in one portion. The reaction mixture was stirred at 25 °C for 16 h under argon. The mixture was subjected to purification by semipreparative reversed-phase HPLC using a gradient from 100% 0.1% TFA in H_2O (pH 2.5) to 60% 0.1% TFA in CH_3CN over 30 min. Solvent was removed under reduced pressure, and the remaining aqueous solution was lyophilized to give fluffy white solid CB-TE2A di-*tert*-butyl ester-(propionamide linker)-c(RGDfK(S)) (0.017 g, 39.2% yield). ^{1}H NMR (300 MHz, D_2O, TSP) δ 0.95−1.05 (br s, 3H), 1.12−2.05 (m, 7H), 1.53 (d, 18H), 2.18−2.40 (br s, 4H), 2.40−2.65 (br s, 3H), 2.75−2.90 (m, 2H), 2.90−4.00 (m, 33H), 4.15−4.25 (m, 1H), 4.30−4.8 (m, 5H), 7.18−7.45 (m, 5H). High resolution MALDI/MS: $[M + H]^+$ for $C_{57}H_{95}N_{14}O_{14}$ 1199.72, found 1199.74.

CB-TE2A-(propionamide linker)-c(RGDfK(S)). Neat trifluoroacetic acid (15 mL) was added to CB-TE2A di-*tert*-butyl ester-(propionamide linker)-c(RGDfK(S)) (0.012 g, 0.010 mmol), and the reaction was stirred at 25 °C under for 16 h under argon. Excess acid was removed by rotary evaporation. The residue was dissolved in CH_2Cl_2 (20 mL) and solvent removed by rotary evaporation; this process was repeated exhaustively to remove

Scheme 1. Synthetic Route to the Cross-Bridged Cyclam Bifunctional Chelator

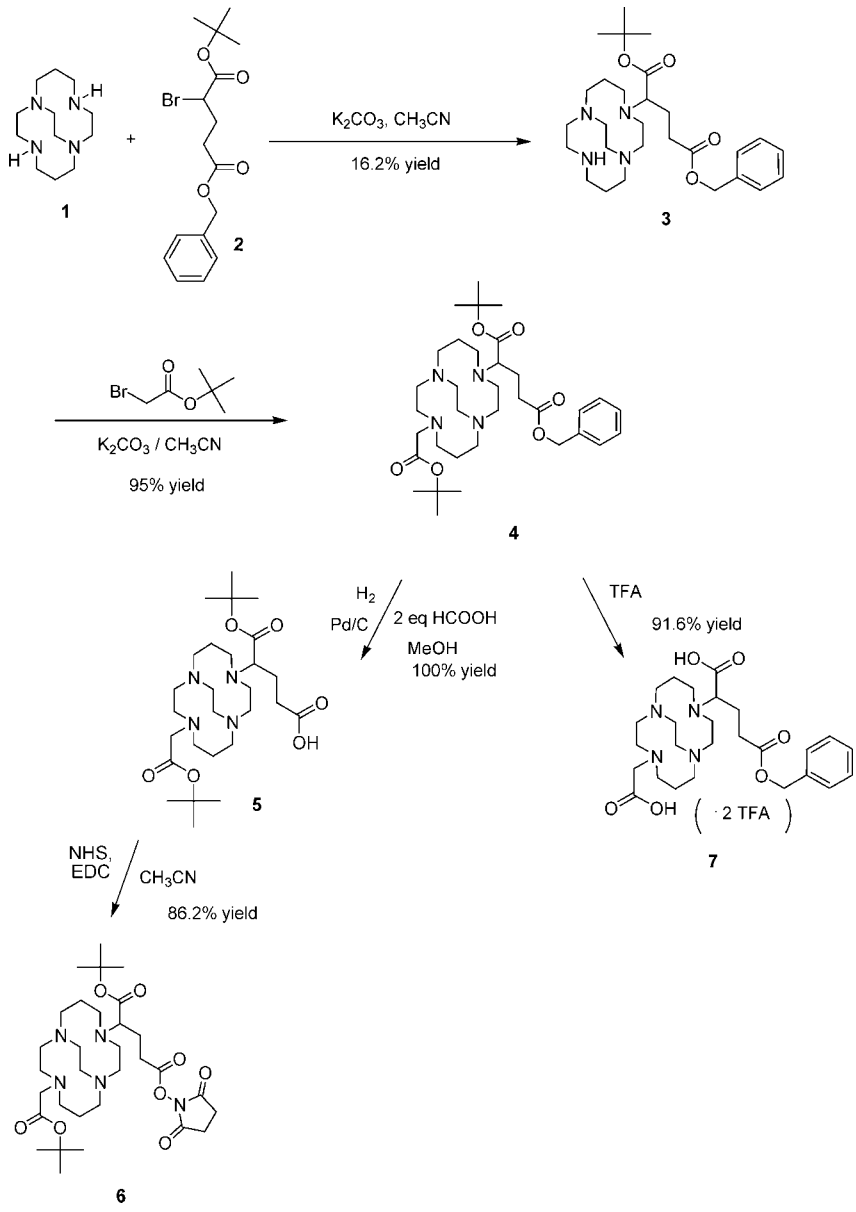

residual acid. A 20 mL aliquot of Et_2O was added to the residue to induce solidification. Solvent removal under reduced pressure gave 0.013 g (>99% assuming two associated TFA molecules) of fluffy white solid CB-TE2A-(propionamide linker)-c(RGDfK(S)). ^{1}H NMR (300 MHz, D_2O, TSP) δ 0.80−1.10 (br s, 2H), 1.30−2.00 (m, 12H), 2.22−2.45 (m, 3H), 2.45−2.60 (m, 2H), 2.65−2.85 (m, 3H), 2.90−4.00 (m, 33H), 4.00−4.30 (m, 2H), 4.35−4.45 (m, 2H), 4.65−4.75 (m, 1H), 7.20−7.45 (m, 5H). High resolution MALDI/MS: $[M + H]^+$ for $C_{49}H_{79}N_{14}O_{14}$ 1087.59, found 1087.55.

Radiochemistry—Synthesis of ^{64}Cu-CB-TE2A-(propionamide linker)-c(RGDfK(S)). *Caution: ^{64}Cu ($t_{1/2}$ = 12.7 h) is a (β^+ (19%); β^- (39%)) emitting radionuclide. Appropriate shielding and handling protocols should be in place when using this radionuclide.* $^{64}CuCl_2$ was purchased from MDS Nordion (Vancouver, BC, Canada). To CB-TE2A-(propionamide linker)-c(RGDfK(S)) (15 μg) in 0.1 M NH_4OAc (200 μL) (pH 8.0) was added $^{64}CuCl_2$ (1 mCi in 0.1 M HCl). The reaction mixture was heated for 1 h at 95 °C. Unchelated ^{64}Cu was removed from ^{64}Cu-CB-TE2A-(propionamide linker)-c(RGDfK(S) by ion exchange chromatography using Chelex-100 (100−200 mesh, Na^+ form, Bio-Rad Laboratories, Hercules, CA). The radiochemical yield was 64%. To generate analytical radio-HPLC data, a portion of the purified radiolabeled peptide was subjected to reversed-phase HPLC using a gradient from 100% 0.1% TFA in H_2O (pH 2.5) to 60% 0.1% TFA in CH_3CN over 30 min. In addition, the resulting peak fraction was collected, frozen, lyophilized, and subjected to analytical radio-HPLC using the same column and flow rate but different solvent conditions: 0.15 M NH_4OAc (pH 7.0) with 0% to 80% MeOH over 30 min (Supporting Information).

Serum Stability. An aliquot of ^{64}Cu-CB-TE2A-(propionamide linker)-c(RGDfK(S)) (3 μCi) was added to 25 μL of human serum (NHS Gemini Cat # 100−110) or to 25 μL of saline in a 100 μL microcentrifuge tube for each time point. The samples were capped and placed in a 37 °C incubator. At the appropriate time points, samples were analyzed by SE-HPLC. The % radioactivity associated with protein versus low molecular weight species was determined by integration.

RESULTS AND DISCUSSION

Ligand Synthesis and Rationale. The overall synthetic approach is presented in Scheme 1, wherein the bifunctional

Scheme 2. Conjugation of Cyclic Peptide, c(RGDfK(S)), to the Succinimidyl Ester 6 and Subsequent TFA Deprotection of the Resulting Peptide−Chelate Conjugate

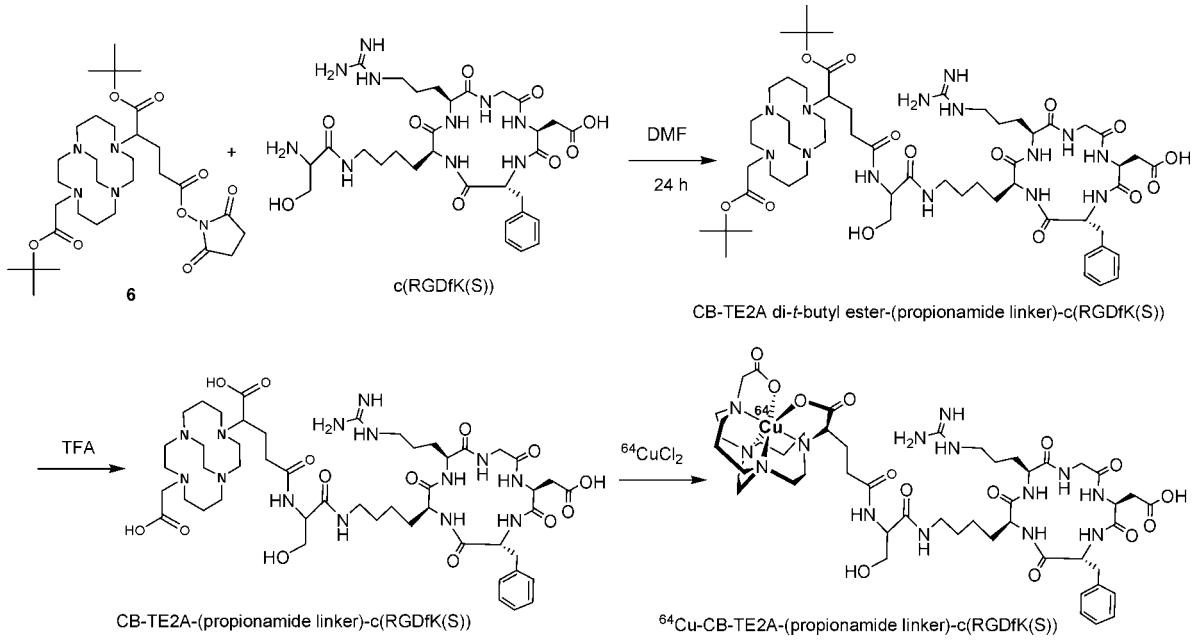

chelator derivative of CB-TE2A is synthesized for the ultimate purpose of conjugation to peptides and subsequent targeted PET imaging of tumor receptors using ^{64}Cu. It should be noted, however, that targeted radiotherapy of small to medium tumor burden may also be realized through use of the low energy β-emitting sister isotope, ^{67}Cu ($t_{1/2}$ = 61.92 h; β^- ($E_{\beta[avg]}$= 141 keV; R_{mean}= 0.24 mm)). For the synthesis of a bifunctional chelator derivative of CB-TE2A compatible with solid-phase peptide synthesis, an orthogonally protected, bromide-functionalized glutamic acid derivative (**2**) was synthesized as previously described by Mäcke and co-workers (*33*). Reaction of cross-bridged cyclam (*3*), **1**, with **2** resulted in the formation of the desired hybrid-arm construct (**3**) (Scheme 1). Our previous attempts at coupling **2** with the bisaminal resulting from condensation of cyclam with glyoxal were unsuccessful (data not shown). Reversing the sequence, alkylating **1** with **2** after reacting with *tert*-butyl bromoacetate, was found to be less desirable (data not shown). Steric effects greatly reduced the reaction yield, and the initial alkylation results in a statistical mixture of products. Unlike the more statistical product distribution achieved by alkylation with *tert*-butyl bromoacetate, alkylation of **1** using **2** tends to greatly favor the 1:1 macrocycle-arm product, even in the presence of excess alkylating agent. Interestingly, the alkylation of **3** proceeds even in $CHCl_3$ without the use of a carbonate base (data not shown); however, use of K_2CO_3 in CH_3CN reduces the reaction time from 3 days to 1 day and increases the yield of **4**.

Debenzylation of **4** was achieved by catalytic hydrogenolysis in the presence of formic acid to yield monoacid **5**. Our initial hydrogenation attempts in the absence of formic acid were completely unsuccessful, resulting in unexpected partial intramolecular transfer of the benzyl group to macrocyclic amines with concomitant formation of ethyl ester when the reaction was performed in EtOH (data not shown). This behavior was attributed to the remarkable basicity of the amines, and formic acid was chosen to acidify the reaction and to act as an additional hydrogen source for the hydrogenation. Subsequent reaction of **5** with NHS and EDCI gave the desired bifunctional chelating agent, succinimidyl ester **6**, ready for immediate conjugation to peptides. Purification of **6** was achieved by solvent extraction as described in the Experimental Methods section. The purity of this ester was acceptable by NMR and HPLC; therefore, no further purification was pursued. We observed a broad peak at ~10 ppm in the ^{1}H NMR spectrum of **6**; a similar peak was also observed for the HBr salts of **3** and **4** following column chromatography but prior to basic extraction into $CHCl_3$ (data not shown). We therefore attribute this peak to protonation of these remarkably basic amines. We are unsure of whether the proton is inside the "clamshell" cavity or not, but this is a possibility. Following the basic extraction workup of **3** and **4**, the peak at ~10 ppm was not present (Supporting Information). Unfortunately, it is impossible to use extraction to deprotonate **5** and **6** due to a polar carboxylic acid and a base-sensitive succinimidyl ester, respectively.

Compound **7** was synthesized for two reasons: (1) to further demonstrate the orthogonality of our protection scheme and (2) in hopes that crystals of Cu(II)-**7** might be obtained for structure determination. Successful deprotection of the *tert*-butyl esters using neat TFA was achieved with retention of the benzyl protection on the third pendant carboxylic acid arm. Unfortunately, all attempts at forming Cu(II)-**7** for crystallization were thwarted by partial benzyl deprotection due to the requisite complexation conditions, namely, the addition of NaOH followed by reflux in ethanol.

We have previously used a similar approach to synthesize a bifunctional chelator derivative of the acyclic ligand, CHX-A″-DTPA, that is likewise compatible with off-line tagging of peptides following Fmoc solid-phase peptide synthesis (*34*) Synthesis of a carbon backbone-functionalized isothiocyanate-bearing bifunctional chelator derivative of CB-TE2A has been reported by Archibald and co-workers (*35*, *36*). This work involved a relatively high yielding six-step synthesis of a C-functionalized nitrobenzyl bisaminal intermediate (*35*), that was further reacted to a diacid, monoisothiocyanate bifunctional chelating agent in seven additional steps (*ca.* 20% overall yield from the bisaminal) followed by conjugation to biotin (*36*). While isothiocyanate derivatives of chelators are routinely used by our laboratory and others for antibody/protein conjugation, the orthogonally protected bifunctional chelator presented here may offer advantages in peptide synthesis studies due to the clean reactions afforded by succinimidyl ester coupling chemistry. In addition, fewer synthetic steps are involved in the current approach: only four steps from **1**, which is accessible from commercially available cyclam in only four steps (*3*). The

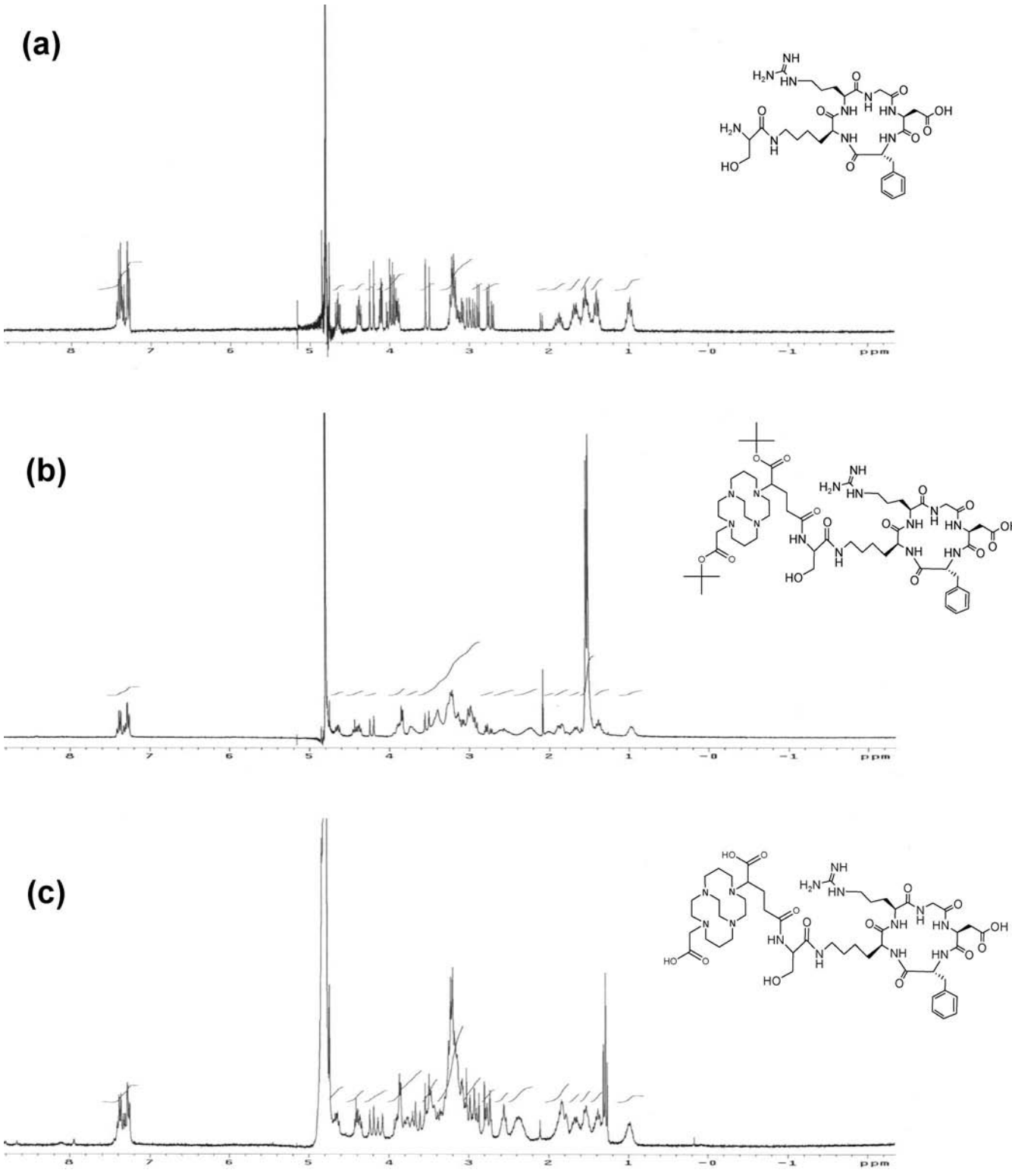

Figure 2. ^{1}H NMR spectra in D_2O of (a) c(RGDfK(S)), (b) CB-TE2A-c(RGDfK(S)) di-*tert*-butyl ester, and (c) CB-TE2A-c(RGDfK(S)) after TFA deprotection.

only major disadvantage of the current approach is the low yield obtained for the coupling reaction of CB-cyclam to the bifunctional glutamic acid-derived arm (*ca.* 16%). This low yield reflects the necessity of column chromatography to separate the desired product **3** from a structurally related analog that is also formed during the alkylation (data not shown). This side product is a quaternary ammonium compound having the same mass where alkylation on one of the bridgehead (tertiary) amines instead of on a secondary (NH) amine has occurred. Formation of significant amounts of this product is attributed to steric factors as the alkylating agent **2**, a secondary bromide, is somewhat bulky.

Peptide Conjugation, Radiolabeling with ^{64}Cu, and Serum Stability Studies. To validate the utility of our agent, we chose to conjugate our novel bifunctional cross-bridged cyclam chelator **6** to a cyclic RGD peptide, c(RGDfK(S) (Scheme 2). The peptide−chelator conjugate readily formed in DMF and, following chromatographic purification, was characterized by

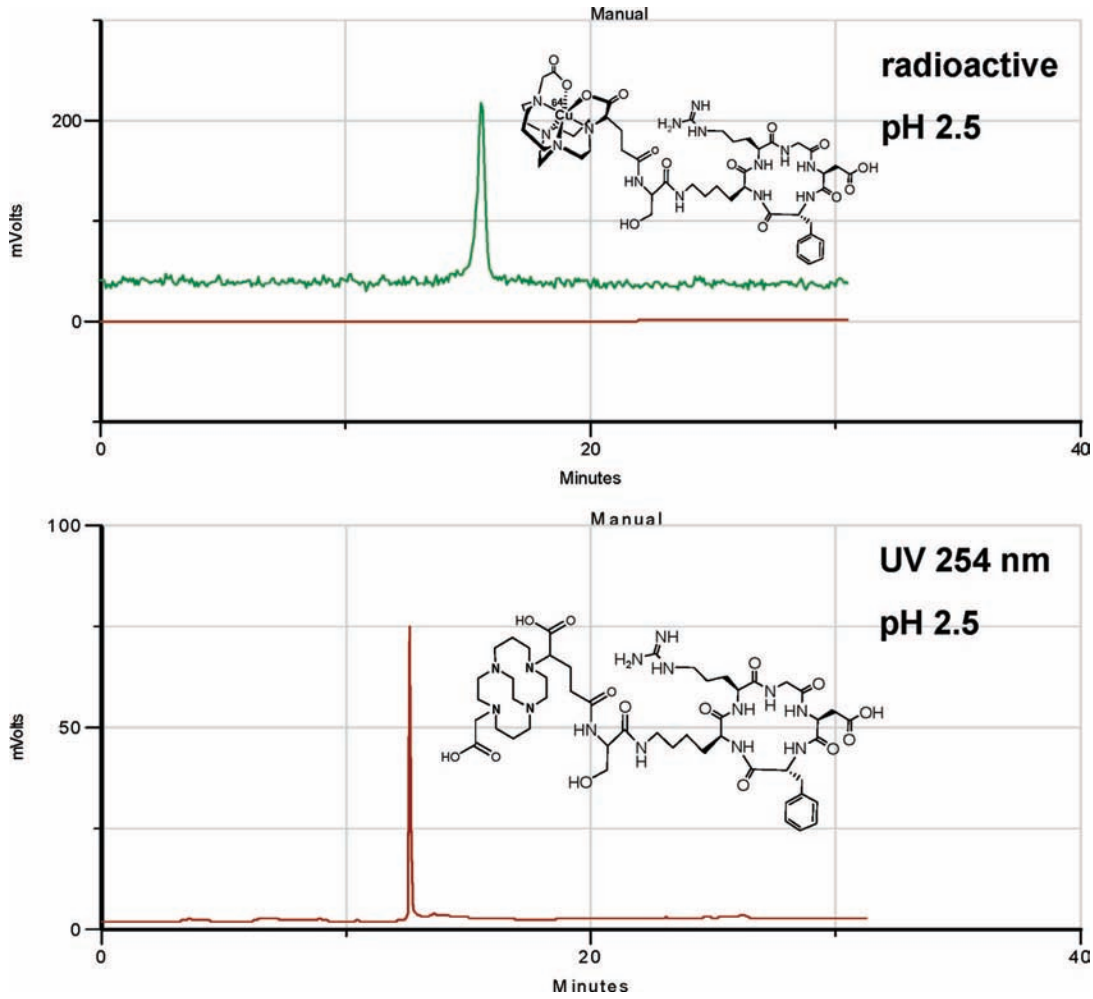

Figure 3. Radio-HPLC chromatogram of ^{64}Cu-CB-TE2A-c(RGDfK(S)) including the radioactive trace (top) and the corresponding UV trace due to CB-TE2A-c(RGDfK(S)) (bottom) on a C18 column at 3 mL/min flow rate with the following gradient: 0.1% TFA in H_2O with 0% to 60% 0.1% TFA in CH_3CN over 30 min.

NMR spectroscopy (Figure 2). This conjugate was amenable to acid deprotection of the *tert*-butyl esters and subsequent radiolabeling with ^{64}Cu (Scheme 2) as demonstrated by the ^{1}H NMR spectra (Figure 2) and HPLC data (see Figure 3 and Supporting Information), respectively. In addition, *in vitro* evaluation of the radiolabeled peptide conjugate in human serum demonstrated a stably complexed radiocopper ion with no evidence of transchelation of ^{64}Cu into serum proteins for up to 48 h (Supporting Information).

The radiochemical yield obtained was 64%. We did not attempt to optimize the radiolabeling since our overall goal in demonstrating the conceptual functionality of our bifunctional chelator was achieved. The incorporation of ^{64}Cu into our peptide conjugate was lower than previously reported for a CB-TE2A-somatostatin analogue under the same conditions (*31*). Many factors may have contributed to our lower yield, including the nature of the peptide (structure, solubility, etc.), the structural difference in our novel chelate relative to the parent CB-TE2A, and possible noncovalent intramolecular interactions between the chelate and the peptide.

Identical radiolabeling conditions (1 h, pH 8, 95 °C) were previously used to radiolabel the CB-TE2A conjugate of a somatostatin peptide analogue (*31*). Although many immunoglobulins can tolerate pH 8 and even slightly more alkaline conditions, this temperature requirement unfortunately precludes the use of cross-bridged cyclam chelators for conjugation and subsequent radiolabeling of antibodies and other heat-sensitive biological macromolecules. By using our bifunctional chelator, however, it may be possible to first form the ^{64}Cu complex using the two closest free acids and then activate the third, more distant carboxylate group unused for Cu chelation for subsequent coupling to proteins; the possibility of this approach warrants further investigation.

In vitro evaluation of the radiolabeled peptide conjugate in human serum demonstrated a stably complexed radiocopper ion with no evidence of transchelation of ^{64}Cu into serum proteins for up to 48 h (Supporting Information). This is consistent with *in vitro* stability data for the structurally related complex, ^{64}Cu-CB-TE2A, which showed no evidence of transchelation of ^{64}Cu into serum proteins for up to 24 h (*37*). A true test of *in vivo* kinetic stability, however, would require future *in vivo* metabolism studies to test for radiometal transchelation into blood and liver proteins. For example, previous studies within our laboratory have revealed that ^{64}Cu-TETA exhibits high *in vitro* serum stability (*38*): however, the situation for ^{64}Cu-TETA *in vivo* is much different in that transchelation of ^{64}Cu to superoxide dismutase and other proteins has been reported (*25, 30, 39*).

CONCLUSSIONS

A cross-bridged BFC derivative of CB-TE2A has been synthesized in four steps with reasonable (*ca.* 13 %) overall yield from CB-cyclam. The novel agent is directly structurally analogous to the parental CB-TE2A in that it possesses the identical ligand donor set arranged in the same geometry for high kinetic stability with Cu(II) radionuclides, while also

featuring a third orthogonally protected arm for conjugation to peptides and other targeting agents. This work may also enable the development of improved agents for diagnostic positron emission tomography (PET) imaging as well as for targeted radiotherapeutic applications.

ACKNOWLEDGMENT

This research was supported by the Intramural Research Program of the NIH, National Cancer Institute, Center for Cancer Research.

Supporting Information Available: ^{1}H, ^{13}C, and analytical HPLC results of relevant intermediates and compounds. This material is available free of charge via the Internet at http://pubs.acs.org.

LITERATURE CITED

(1) Weisman, G. R., Rogers, M. E., Wong, E. H., Jasinski, J. P., and Paight, E. S. (1990) Cross-bridged cyclam. Protonation and Li^{+} complexation in a diamond-lattice cleft. *J. Am. Chem. Soc. 112*, 8604–8605.

(2) Weisman, G. R., Wong, E. H., Hill, D. C., Rogers, M. E., Reed, D. P., and Calabrese, J. C. (1996) Synthesis and transition-metal complexes of new cross-bridged tetraamine ligands. *J. Chem. Soc. Chem. Commun.* 947–948.

(3) Wong, E. H., Weisman, G. R., Hill, D. C., Reed, D. P., Rogers, M. E., Condon, J. P., Fagan, M. A., Calabrese, J. C., Lam, K.-C., Guzei, I. A., and Rheingold, A. L. (2000) Synthesis and characterization of cross-bridged cyclams and pendant-armed derivatives and structural studies of their copper(II) complexes. *J. Am. Chem. Soc. 122*, 10561–10572.

(4) Hubin, T. J., Alcock, N. W., and Busch, D. H. (2000) Copper(I) and copper(II) complexes of an ethylene cross-bridged cyclam. *Acta Crystallogr., Sect. C 56*, 37–39.

(5) Hubin, T. J., Alcock, N. W., Morton, M. D., and Busch, D. H. (2003) Synthesis, structure, and stability in acid of copper(II) and zinc(II) complexes of cross-bridged tetraazamacrocycles. *Inorg. Chim. Acta 348*, 33–40.

(6) Hubin, T. J., McCormick, J. M., Alcock, N. W., Clase, H. J., and Busch, D. H. (1999) Crystallographic characterization of stepwise changes in ligand conformation as their internal topology changes and two novel cross-bridged tetraazamacrocyclic copper(II) complexes. *Inorg. Chem. 38*, 4435–4446.

(7) Hubin, T. J., McCormick, J. M., Collinson, S. R., Alcock, N. W., and Busch, D. H. (1998) Ultra rigid cross-bridged tetraazamacrocycles as ligands - the challenge and the solution. *J. Chem. Soc., Chem. Commun.* 1675–1676.

(8) Springborg, J., Glerup, J., and Sotofte, I. (1997) Synthesis and crystal structure of a compound with three [24.31]adamanzanecopper(II) species coordinated to one carbonate ion, m3-carbonatotris-{1,4,7,10-tetraazabicyclo[5.5.3]pentadecanecopper(II)} perchlorate dihydrate. *Acta Chem. Scand. 51*, 832–838.

(9) Springborg, J., Kofod, P., Olsen, C. E., and Sotofte, I. (1995) Synthesis and crystal structure of a small bicyclic tetraaza proton sponge, 1,4,7,10-tetraazabicyclo[5.5.3]pentadecane dibromide perchlorate. *Acta Chem. Scand. 49*, 547–554.

(10) Springborg, J., Pretzmann, U., Nielsen, B., Olsen, C. E., and Sotofte, I. (1998) Synthesis of [35]adamanzane, 1,5,9,13-tetraazatricyclo[7.7.3]nonadecane, by oxidative C-N cleavage of [36]adamanzane, 1,5,9,13-tetraazatricyclo[7.7.3.35,13]docosane, and crystal structure of the tetraprotonated bromide salt of [35]adamanzane. *Acta Chem. Scand. 52*, 212.

(11) Springborg, J., and Sotofte, I. (1997) Synthetic, thermodynamic and crystallographic studies of pentacoordinated copper(II) complexes with [24.31]adamanzane, 1,4,7,10-tetrazabicyclo-[5.5.3]pentadecane, and bromide, iodide, hydroxide, water, or ammonia. *Acta Chem. Scand. 51*, 357–366.

(12) Bencini, A., Bianchi, A., Bazzicalupi, C., Ciampolini, M., Dapporto, P., Fusi, V., Micheloni, M., Nardi, N., Paoli, P., and Valtancoli, B. (1993) Synthesis and characterization of and azacage behaving as a 'proton sponge'. Crystal structures of its mono- and tri-protonated species. *J. Chem. Soc., Perkin Trans. 2*, 115–120.

(13) Bencini, A., Bianchi, A., Bazzicalupi, C., Ciampolini, M., Dapporto, P., Fusi, V., Micheloni, M., Nardi, N., Paoli, P., and Valtancoli, B. (1993) Synthesis and characterization of an azacage, basicity behaviour and crystal structure of its diprotonated species. *J. Chem. Soc., Perkin Trans. 2*, 715–720.

(14) Bencini, A., Bianchi, A., Borselli, A., Ciampolini, M., Micheloni, M., Paoli, P., Valtancoli, B., Garcia-Espana, E., and Ramirez, J. A. (1990) Structural aspects of the protonation of small cages. Preparation of the new aza-cage 12,17-dimethyl-1,9,12,17-tetraazabicyclo[7.5.5]nonadecane (L). Thermodynamic studies on solution equilibria. Crystal structures of $[H_2L][CoCl_4]$ and $[H_2L1][CoCl_4]$ salts. *J. Chem. Soc., Perkin Trans. 2*, 209–214.

(15) Bencini, A., Fusi, V., Giorgi, C., Micheloni, M., Nardi, N., and Valtancoli, B. (1996) Aza-macrocycles bearing lipophilic functions. Their synthesis and selective lithium complexation. *J. Chem. Soc., Perkin Trans. 2*, 2297–2302.

(16) Bianchi, A., Micheloni, M., and Paoletti, P. (1991) Thermodynamic aspects of the polyazacycloalkane complexes with cations and anions. *Coord. Chem. Rev. 110*, 17–113.

(17) Springborg, J. (2003) Adamanzanes - bi- and tricyclic tetraamines and their coordination compounds. *Dalton Trans.* 1653–1665.

(18) McCarthy, D. W., Shefer, R. E., Klinkowstein, R. E., Bass, L. A., Margenau, W. H., Cutler, C. S., Anderson, C. J., and Welch, M. J. (1997) The efficient production of high specific activity Cu-64 using a biomedical cyclotron. *Nucl. Med. Biol. 24*, 35–43.

(19) Anderson, C. J., Dehdashti, F., Cutler, P. D., Schwarz, S. W., Laforest, R., Bass, L. A., Lewis, J. S., and McCarthy, D. W. (2001) Copper-64-TETA-octreotide as a PET imaging agent for patients with neuroendocrine tumors. *J. Nucl. Med. 42*, 213–221.

(20) Anderson, C. J., Jones, L. A., Bass, L. A., Sherman, E. L. C., McCarthy, D. W., Cutler, P. D., Lanahan, M. V., Cristel, M. E., Lewis, J. S., and Schwarz, S. W. (1998) Radiotherapy, toxicity and dosimetry of copper-64-TETA-octreotide in tumor-bearing rats. *J. Nucl. Med. 39*, 1944–1951.

(21) Anderson, C. J., and Lewis, J. S. (2000) Radiopharmaceuticals for targeted radiotherapy of cancer. *Exp. Opin. Ther. Patents 10*, 1057–1069.

(22) Anderson, C. J., Pajeau, T. S., Edwards, W. B., Sherman, E. L. C., Rogers, B. E., and Welch, M. J. (1995) In vitro and in vivo evaluation of copper-64-labeled octreotide conjugates. *J. Nucl. Med. 36*, 2315–2325.

(23) Anderson, C. J., and Welch, M. J. (1999) Radiometal-labeled agents (non-technetium) for diagnostic imaging. *Chem. Rev. 99*, 2219–2234.

(24) Boswell, C. A., McQuade, P., Weisman, G. R., Wong, E. H., and Anderson, C. J. (2005) Optimization of labeling and metabolite analysis of copper-64-labeled azamacrocyclic chelators by radio-LC-MS. *Nucl. Med. Biol. 32*, 29–38.

(25) Boswell, C. A., Sun, X., Niu, W., Weisman, G. R., Wong, E. H., Rheingold, A. L., and Anderson, C. J. (2004) Comparative in vivo stability of copper-64-labeled cross-bridged and conventional tetraazamacrocyclic complexes. *J. Med. Chem. 47*, 1465–1474.

(26) Moi, M. K., Meares, C. F., McCall, M. J., Cole, W. C., and DeNardo, S. J. (1985) Copper chelates as probes of biological systems: stable copper complexes with a macrocyclic bifunctional chelating agent. *Anal. Biochem. 148*, 249–253.

(27) Moi, M. K., DeNardo, S. J., and Meares, C. F. (1990) Stable bifunctional chelates of metals used in radiotherapy. *Cancer Res. (Suppl.) 50*, 789s–793s.

(28) DeNardo, G. L., DeNardo, S. J., Meares, C. F., Kukis, D. L., Diril, H., McCall, M. J., Adams, G. P., Mausner, L. F., Moody, D. C., and Deshpande, S. V. (1991) Pharmacokinetics of copper-67 conjugated Lym-1, a potential therapeutic radioimmunoconjugate, in mice and in patients with lymphoma. *Antibody*

Immunoconjugates Radiopharm. 4, 777–785.

(29) DeNardo, G. L., Kukis, D. L., Shen, S., DeNardo, D. A., Meares, C. F., and DeNardo, S. J. (1999) ^{67}Cu- versus ^{131}I-labeled Lym-1 antibody: comparative pharmacokinetics and dosimetry in patients with non-Hodgkin's lymphoma. *Clin. Cancer Res. 5*, 533–541.

(30) Bass, L. A., Wang, M., Welch, M. J., and Anderson, C. J. (2000) In vivo transchelation of copper-64 from TETA-octreotide to superoxide dismutase in rat liver. *Bioconjugate Chem. 11*, 527–532.

(31) Sprague, J. E., Peng, Y., Sun, X., Weisman, G. R., Wong, E. H., Achilefu, S., and Anderson, C. J. (2004) Preparation and biological evaluation of copper-64-labeled Tyr^3-octreotate using a cross-bridged macrocyclic chelator. *Clin. Cancer Res. 10*, 8674–8682.

(32) Sprague, J. E., Peng, Y., Fiamengo, A. L., Woodin, K. S., Southwick, E. A., Weisman, G. R., Wong, E. H., Golen, J. A., Rheingold, A. L., and Anderson, C. J. (2007) Synthesis, characterization and in vivo studies of Cu(II)-64-labeled cross-bridged tetraazamacrocycle-amide complexes as models of peptide conjugate imaging agents. *J. Med. Chem. 50*, 2527–2535.

(33) Eisenwiener, K. P., Powell, P., and Maecke, H. R. (2000) A convenient synthesis of novel bifunctional prochelators for coupling to bioactive peptides for radiometal labelling. *Bioorg. Med. Chem. Lett. 10*, 2133–2135.

(34) Clifford, T., Boswell, C. A., Biddlecombe, G. B., Lewis, J. S., and Brechbiel, M. W. (2006) Small animal PET/CT imaging using ^{86}Y-CHX-A"-octreotide: validation of a novel CHX-A" derivative suitable for peptide conjugation. *J. Med. Chem. 49*, 4297–4304.

(35) Lewis, E. A., Allan, C. C., Boyle, R. W., and Archibald, S. J. (2004) Efficient N- and C-functionalization of cyclam macrocycles utilizing bisaminal methodology. *Tetrahedron Lett. 45*, 3059–3062.

(36) Lewis, E. A., Boyle, R. W., and Archibald, S. J. (2004) Ultrastable complexes for in vivo use: a bifunctional chelator incorporating a cross-bridged macrocycle. *Chem. Commun.* 2212–2213.

(37) Sun, X., Wuest, M., Weisman, G. R., Wong, E. H., Reed, D. P., Boswell, C. A., Motekaitis, R., Martell, A. E., Welch, M. J., and Anderson, C. J. (2002) Radiolabeling and in vivo behavior of copper-64-labeled cross-bridged cyclam ligands. *J. Med. Chem. 45*, 469–477.

(38) Ma, D., Lu, F., Overstreet, T., Milenic, D. E., and Brechbiel, M. W. (2002) Novel chelating agents for potential clinical applications of copper. *Nucl. Med. Biol. 29*, 91–105.

(39) Jones-Wilson, T. M., Deal, K., Anderson, C. J., McCarthy, D. W., Kovacs, Z., Motekaitis, R. J., Sherry, A. D., Martell, A. E., and Welch, M. J. (1998) The in vivo behavior of copper-64-labeled azamacrocyclic complexes. *Nucl. Med. Biol. 25*, 523–530.

BC800039E

Improved Procedure for Direct Coupling of Carbohydrates to Proteins via Reductive Amination

Jeffrey C. Gildersleeve,*,† Oyindasola Oyelaran,† John T. Simpson,‡ and Benjamin Allred†

Laboratory of Medicinal Chemistry, Center for Cancer Research, National Cancer Institute, NIH, 376 Boyles Street, Building 376, Room 109, Frederick, Maryland 21702, and Protein Chemistry Laboratory, Advanced Technology Program, SAIC — Frederick, Inc., NCI — Frederick, Frederick, Maryland 21702. Received April 14, 2008; Revised Manuscript Received May 29, 2008

Carbohydrate-protein conjugates are utilized extensively in basic research and as immunogens in a variety of bacterial vaccines and cancer vaccines. As a result, there have been significant efforts to develop simple and reliable methods for the construction of these conjugates. While direct coupling via reductive amination is an appealing approach, the reaction is typically very inefficient. In this paper, we report improved reaction conditions providing an approximately 500% increase in yield. In addition to optimizing a series of standard reaction parameters, we found that addition of 500 mM sodium sulfate improves the coupling efficiency. To illustrate the utility of these conditions, a series of high mannose BSA conjugates were produced and incorporated into a carbohydrate microarray. Ligand binding to ConA could be observed and apparent affinity constants (K_ds) measured using the array were in good agreement with values reported by surface plasmon resonance. The results show that the conditions are suitable for microgram-scale reactions, are compatible with complex carbohydrates, and produce biologically active conjugates.

INTRODUCTION

Carbohydrate−protein conjugates play a key role in basic and applied research (for some recent reviews, see refs *1–5*). Several polysaccharide−protein conjugate vaccines such as Prevnar, Menactra, and HIBTiter are FDA approved and used routinely for the prevention of invasive bacterial infections. Many others are in clinical trials for the prevention of infections and for treatment of cancer (*1, 6*). In basic research, carbohydrate−BSA (bovine serum albumin) conjugates have been used for years to study molecular recognition of carbohydrates (*7, 8*). As a result, there has been significant effort to develop simple and efficient methods to covalently couple carbohydrate molecules to proteins (*7, 9*); however, existing methods are not ideal and pursuit of improved methods remains an active area of research.

Carbohydrate−protein conjugates are frequently made via multistep procedures involving modification of the carbohydrate to introduce reactive functionality (e.g., addition of a linker, oxidation of hydroxyls) followed by coupling to the protein. One of the most appealing strategies is direct coupling of oligosaccharides to proteins in a single step. Glycans containing a free reducing end can be covalently attached to protein amino groups via reductive amination (*10*). The reducing end of a sugar exists as an equilibrium mixture composed of the cyclic hemiacetal form (lactol) and the open-chain aldehyde form (see Scheme 1). Under suitable conditions, amine groups will condense with the aldehyde to form an iminium ion which can be reduced to an amine. The process results in ring opening of the reducing end monosaccharide. When coupling to proteins, this reaction is carried out in aqueous buffer.

Several factors make reductive amination of sugars to proteins challenging. First, the reducing agent must be stable in water, unreactive with aldehydes, and yet reactive with iminium ions. Sodium cyanoborohydride meets these requirements and is by far the most common reducing reagent used for reductive amination of aldehydes to proteins. Second, the equilibrium between aldehyde and lactol form of sugars highly favors the lactol; therefore, the concentration of free aldehyde is low. Third, the high concentration of water in aqueous buffer sets up an equilibrium that disfavors release of a water molecule, a process that is required to form the iminium ion. Due to the second and third features, reductive amination of carbohydrates directly to proteins is slow and inefficient. As a result, one typically uses large excesses of sugar (∼300 equiv), high concentrations (∼60 mM), and long reaction times. Therefore, direct reductive amination has been limited to sugars that are readily available in large quantities.

Our group has been using carbohydrate−protein conjugates and glycoproteins for the construction of carbohydrate microarrays (*11–14*). Carbohydrate microarrays contain diverse sets of glycans immobilized on a solid support in a spatially defined arrangement (*15–21*). Using a carbohydrate microarray, one can evaluate binding of a protein, cell, or virus to all of the carbohydrate ligands simultaneously. While reductive amination is an attractive approach for obtaining glycoconjugates, many biologically interesting carbohydrates such as N-linked sugars are very difficult to obtain. Microgram amounts of these sugars (20−200 μg) can be very expensive or require considerable time and effort to isolate and purify from natural sources; therefore, one cannot afford to use 300 equiv and waste >95% of the material in the coupling process. Moreover, the volume of buffer required to achieve high concentrations can be completely impractical when working with micrograms of material. For example, to obtain a 60 mM solution starting with 100 μg of Man9, one would require a final reaction volume of only 1 μL. Clearly, methods to improve the efficiency and facilitate coupling on a small scale were needed. Improved conditions would also be beneficial for the development and production of carbohydrate−protein conjugate vaccines.

MATERIALS AND METHODS

General. Unless indicated otherwise, all chemicals and reagents were purchased from Sigma-Aldrich (St. Louis, MI)

* To whom correspondence should be addressed. E-mail: gildersleevej@ncifcrf.gov.
† National Cancer Institute.
‡ Advanced Technology Program.

10.1021/bc800153t CCC: $40.75 © 2008 American Chemical Society
Published on Web 07/03/2008

Scheme 1. Reductive Amination of Proteins

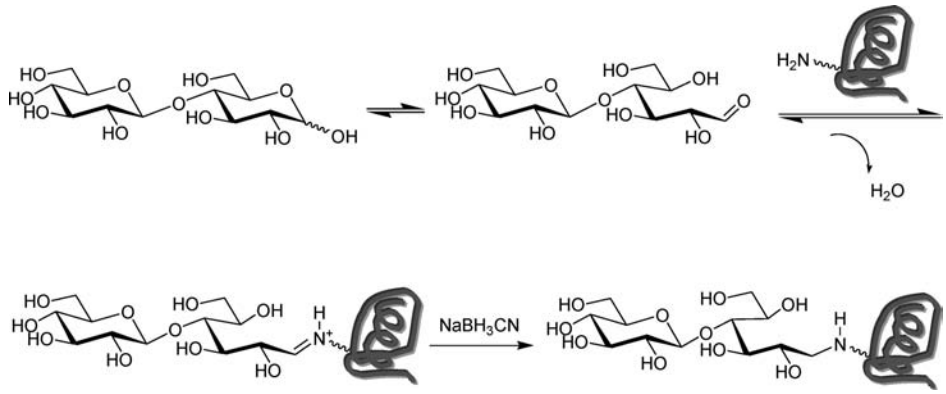

and used without further purification. LNT, LSTa, and Man8D1D3 were purchased from Glycotech (Gaithersburg, MD). Tetra-*N*-acetylchitotetraose, Man3, Man7D1, and Man7D3 were purchased from Dextra laboratories (Reading, UK). Man6 was purchased from IsoSep (Tullinge, Sweden). Man5 and Man9 were generous gifts from Dr. Lai-Xi Wang.

General Procedure for Reductive Amination. Bovine serum albumin (BSA; 2 μL of a 150 mg/mL solution; fraction V), sodium borate (5.5 μL of a 400 mM solution, pH 8.5), sodium sulfate (3.7 μL of a 3 M solution, 50 °C), oligosaccharide (3.3 μL of a 20 mM solution for 15 equiv), H_2O (5.3 μL), and sodium cyanoborohydride (2.2 μL of a 3 M solution) were combined in a 200 μL PCR tube. The tube was capped and then incubated in a PCR thermal cycler at 56 °C for 96 h with a heated lid. The reaction was diluted with H_2O (100 μL), transferred to a 500 μL dialysis tube (MWCO 10 000, Slide-A-Lyzer MINI Dialysis Unit, Pierce, Rockford, IL), and then dialyzed against H_2O (2.5 L) three times. Conjugates were diluted with H_2O to a final concentration of 1 mg/mL and then analyzed by matrix-assisted laser desorption ionization time-of-flight mass spectrometry (MALDI-TOF MS) to determine the extent of conjugation.

Mass Spectrometric Analysis of Glycoconjugates. MALDI-TOF mass spectrometric analysis of the glycoconjugates was performed on an Applied Biosystems Voyager-DE Pro time-of-flight mass spectrometer. The accelerating voltage was 25 kV, guide wire 0.15% and grid voltage 91.5%. The instrument was operated in linear mode under positive ion conditions. A nitrogen laser was used at 337 nm with 250 laser shots averaged per spectrum. Sinapinic acid (3,5-dimethoxy-4-hydroxycinnamic acid, Aldrich Chemicals, St. Louis, MO) was used as the matrix for all experiments. Matrix was prepared as a saturated solution in 50% acetonitrile/0.1% trifluoroacetic acid (v/v). Sample preparation was a modified "dried droplet" procedure (*22*), whereby 0.3 μL of sample was spotted onto the MALDI target followed by 0.3 μL of matrix. The mixture was then allowed to air-dry prior to analysis. External calibration was performed using bovine serum albumin as a standard. Data analysis was carried out using *Data Explorer* software resident on the Voyager mass spectrometer. Representative spectra can be found in the Supporting Information.

Evaluation of Neoglycoconjugate Activity by Enzyme-Linked Lectin Assay (ELLA). BSA conjugates (50 μL of a 10 μg/mL solution in PBS) were added to wells of a 96 well plate (white Maxisorp, Nunc, Rochester, NY) and incubated for 2 h at room temperature. Liquid was removed and the wells were blocked with BSA (200 μL/well of a 3% solution in PBS). After removal of the liquid, the wells were incubated with various concentrations of biotinylated wheat germ agglutinin (WGA; Vector laboratories, Burlingame, CA) diluted in 3% BSA/PBS solution. After 2 h, wells were emptied and washed 3 times with PBS. Next, wells were incubated with streptavidin−alkaline phosphatase (2 μg/mL in 3% BSA/PBS) for 1 h and then washed 7 times with PBS. Wells were then incubated with methyl umbelliferryl phosphate (50 μL of a 100 μM solution in Tris buffer at pH 9.0). After 15 min of incubation, the fluorescence intensities for each well were measured using an FL_X800 plate reader.

Carbohydrate Microarray Fabrication. Carbohydrate arrays were printed with Stealth Micro Spotting Pins (SMP3; TeleChem, Sunnyvale, CA) using a robotic array spotter (Genomic Solutions, BioRobotics MicroGrid II 600/610). Conjugates and glycoproteins were distributed into 384-well plates at 4 wells per sample and 20 μL per well. Each component was prepared at 125 μg/mL in print buffer (1× PBS: 140 mM NaCl, 3 mM KCl, 10 mM Na_2HPO_4, 2 mM KH_2PO_4, pH 7.4), 2.5% glycerol, 0.006% Triton-X 100) onto ArrayIt SuperEpoxy 2 Protein glass slides. The pins were dipped into the sample wells and blotted 10 times before printing. The humidity level in the arraying chamber was maintained at about 65% during printing. Each of the components was printed in duplicate in a grid of 110 μm diameter spots with 220 μm pitch. Sixteen complete arrays were printed on each slide. Printed slides were allowed to dry, protected from light, for about 14 h at room temperature, and then stored at −20 °C until use.

Carbohydrate Microarray Binding Assay. The binding experiment was carried out in triplicate. Slides were assembled on 16-well slide holders (ProPlate, Grace Bio-Laboratories) and blocked with 3% BSA/PBS overnight at 4 °C, then washed 6 × 200 μL PBST0.05 (PBS with 0.05% Tween 20). A dilution series of biotinylated Concanavalin A (ConA) was prepared in 25 mM Tris, 124 mM NaCl, pH 7.6, at concentrations ranging from 0.03 nM to 48 μM. Lectin solutions were added to arrays, covered tightly with a seal strip, and allowed to incubate for 1 h at room temperature. After washing unbound lectin with 3 × 200 μL PBST0.05, detection of bound lectin was carried out by incubating with Cy3-streptavidin in 3% BSA/PBS (5 μg/mL) for 30 min at room temperature. Slides were then washed 7 × 200 μL PBST0.05, removed from holders, immersed in wash buffer for 5 min, and then centrifuged at 453*g* for 5 min.

Image Processing and Calculation of Apparent Dissociation Constant. Slides were scanned with a Genepix 4000B microarray scanner (Molecular Devices Corporation, Union City, CA) at PMT voltage settings where no saturated pixels were obtained. Image analysis was carried out with *Genepix Pro 6.0* analysis software (Molecular Devices Corporation, Union City, CA). Spots were defined as circular features with maximum diameter of 100 μm. Local background subtraction was performed and features were allowed to be resized to 70 μm as needed. The background-corrected median feature intensity, *F532median-B532*, was used for initial data processing, which was performed with Microsoft *Excel*. The means for replicate

spots for each array component was calculated, and then the mean and standard deviations for the 3 replicate experiments were obtained and used for subsequent K_d determination.

Apparent dissociation constants were determined using the scientific graphing and analysis software *Origin* (OriginLab). For each glycoconjugate, the mean intensity of 3 replicate experiments was plotted as a function of ConA concentration on a logarithmic scale. Nonlinear line-fitting to the equation

$$F_{obs} = \frac{F_{max}}{\frac{K_D}{[L]} + 1} \quad (1)$$

was performed, where F_{obs} is the mean intensity of the replicate spots for ConA binding at a particular concentration, F_{max} is the maximum fluorescence intensity, K_d is the apparent dissociation constant for interaction between lectin and immobilized glycoconjugate, and [L] is the concentration of ConA. For each glycoconjugate, the reported values are the apparent K_d of the mean ± the standard deviation of 3 replicate experiments.

RESULTS AND DISCUSSION

The protocol most frequently used for direct reductive amination of carbohydrates was developed by Roy et al. (*23*). Typical reaction conditions involve coupling protein (200 μM) with sugar (60 mM) in the presence of $NaBH_3CN$ (300 mM) and aqueous sodium borate buffer (200 mM, pH 9.0) for 10−24 h at 37−50 °C. Borate buffer appears to significantly enhance the yield of coupling when compared to other buffers, although the exact role of borate is not well understood.

We began by evaluating reactions of several sugars with bovine serum albumin (BSA) under the Roy conditions but with only 15−30 equiv of sugar (3−6 mM). In addition, the reaction volume was limited to 20−50 μL to assess couplings on the small scale. The extent of conjugation was evaluated by MALDI-TOF MS. Initially, reactions were carried out in Eppendorf tubes heated either in a water bath or on a heat block. Due to the small volumes, evaporation with condensation on the lid became a serious problem resulting in highly variable results. To avoid this problem, all subsequent reactions were carried out in PCR tubes and heated in a PCR thermal cycler with a heated lid. Under these conditions, results were much more reproducible and evaporation was not observed.

After surveying a variety of oligosaccharides, the yield was found to be highly dependent on the identity of the reducing end sugar. Cummings group has also observed substrate-dependent coupling efficiency (*24*). Saccharides with a reducing end glucose residue such as maltose, LNT, and LSTa (see Figure 1) coupled efficiently. For example, reactions utilizing 30 equiv of sugar produced conjugates with an average of 10 oligosaccharide chains per molecule of BSA (after 24 h at 50 °C). In contrast, sugars with mannose (Man), *N*-acetylglucosamine (GlcNAc), or galactose (Gal) at the reducing end coupled much less efficiently yielding conjugates with an average of 0−1 oligosaccharide chain per molecule of BSA. These results were disheartening since many interesting N-linked oligosaccharides have a GlcNAc at the reducing end (see Man3−9, Figure 1); therefore, efforts to improve efficiency were investigated.

To increase the yield, a number of reaction parameters such as the temperature, time, and pH were systematically varied. While conceptually straightforward, it was not known if changes such as higher temperatures and longer reaction times would compromise the biological activity of the resulting conjugates. Tetra-*N*-acetylchitotetraose, a sugar containing GlcNAc at the reducing end (see Figure 1), was used as a model oligosaccharide in couplings to BSA. Differences in pH ranging from 8.5 to 10.0 had no effect on the ratio (data not shown), but changes to the time and temperature led to improvements. Increasing the reaction time from 24 to 96 h improved the ratio about 2-fold (see Table 1). Raising the temperature from 50 to 56 °C led to a 1.5-fold increase. Further increases in temperature resulted in precipitate formation, presumably due to denaturation of the protein. Changes to the concentration of $NaBH_3CN$ from 50−500 mM had no effect.

Formation of the key imine intermediate requires expulsion of a molecule of water. In an aqueous solution, this equilibrium is highly disfavored. It was anticipated that high salt concentrations might make the expulsion of water somewhat less

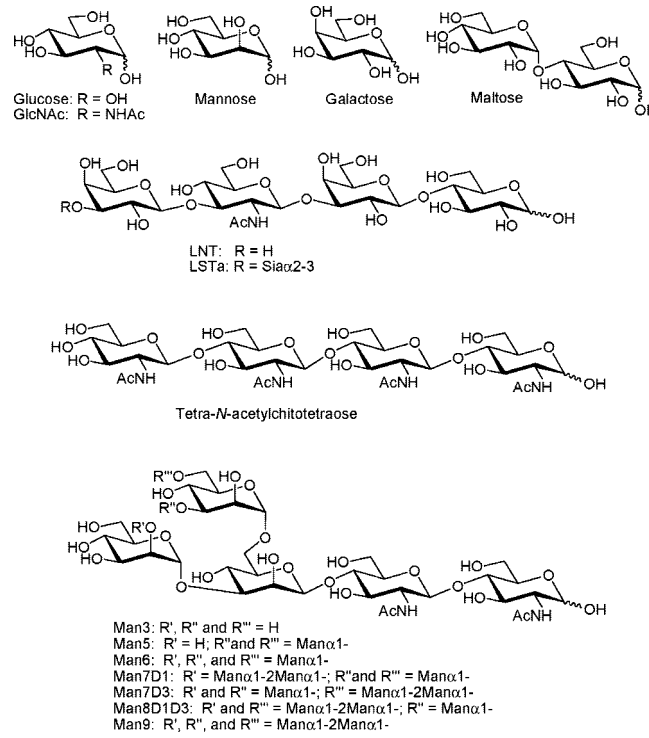

Figure 1. Representative oligosaccharide structures.

Table 1. Efficiency of Reductive Amination Using Various Reaction Conditions[a]

#	equiv	temp (°C)	salt	time (h)	ratio[b]
1	15	50	none	24	1.0
2	15	50	none	96	2.2
3	15	56	none	96	3.0
4	15	56	0.5 M NaCl	96	3.3
5	15	56	1 M NaCl	96	4.1
6	15	56	2 M NaCl	96	3.8
7	15	56	1 M KCl	96	3.3
8	15	56	1 M NaBr	96	2.6
9	15	56	1 M $MgCl_2$	96	ppt
10	15	56	1 M LiCl	96	ppt
11	15	56	1 M NaOAc	96	3.8
12	15	56	0.5 M Na_3Citrate	96	3.8
13	15	56	0.5 M $MgSO_4$	96	4.5
14	15	56	1 M $MgSO_4$	96	4.5
15	15	56	0.5 M Na_2SO_4	96	5.1
16	15	56	1 M Na_2SO_4	96	ppt
17	15	60	0.5 M Na_2SO_4	96	ppt
18	30	56	0.5 M Na_2SO_4	96	8.2
19	30	37	No salt	96	1.0
20	30	37	0.5 M Na_2SO_4	96	2.7
21	300	50	No salt; Roy conditions [c]	24	9.2

[a] Tetra-*N*-acetylchitotetraose (3−6 mM) was coupled with BSA (200 μM) in 100 mM sodium borate buffer (pH 8.5). [b] The number of sugars attached to BSA after reductive amination as determined by MALDI-MS. ppt = protein precipitated and the ratio could not be determined. [c] See ref (*23*).

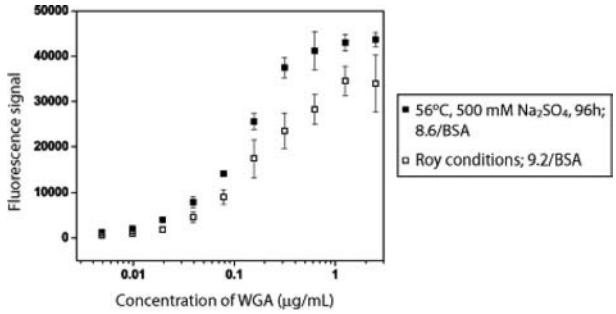

Figure 2. Comparison of wheat germ agglutinin binding to N-acetylchitotriose-BSA prepared using the Roy conditions (open squares) vs 56 °C for 96 h with 500 mM Na_2SO_4 (closed squares).

unfavorable, facilitating formation of the imine. In addition, high salt concentrations can have a substantial effect on protein structure and solubility. For example, high salt concentrations are reported to reduce the rate of aggregation of BSA (*25*); therefore, a series of salt additives was examined next.

As a first test case, NaCl was added at concentrations of 0.5 M, 1.0 M, and 2.0 M. A measurable increase in conjugation ratio was observed, with 1.0 M giving the best result. A number of other salt additives were investigated (see Table 1) and many improved the yield of the reaction. Overall, addition of 0.5 M Na_2SO_4 produced the best results. A 1.0 M Na_2SO_4 solution occasionally produced even higher ratios but frequently resulted in precipitate formation and unrecoverable protein. The added salt also improved the conjugation efficiency at lower temperatures; at 37 °C, added salt produced a nearly 3-fold increase in conjugation efficiency relative to the absence of salt (compare entries 19 and 20, Table 1). This result indicates that addition of salt may be especially useful when coupling sugars to proteins that are sensitive to high temperatures.

Overall, the combination of higher temperatures, longer reaction times, and added salt produced about a 5-fold increase in the amount of sugar conjugated to BSA and an overall yield of about 33% with 15 equiv of sugar. Higher ratios could be obtained with 30 equiv of sugar, albeit with slightly lower yield (based on sugar). This level of incorporation and efficiency was judged to be suitable for making a variety of BSA conjugates for the array.

To determine whether the altered reaction conditions affect the biological activity or binding capacity of the final conjugate, binding of biotinylated wheat germ agglutinin (WGA) was measured over a range of concentrations using an ELLA assay. Binding could be detected down to concentrations of 10 ng/mL (277 pM). For comparison, a conjugate with a similar ratio of tetra-*N*-acetylchitotetraoses to BSA (9.2/BSA) was prepared using the Roy conditions (entry 21, Table 1). Both conjugates displayed similar binding by ELLA (see Figure 2) indicating that the modified reaction conditions do not reduce the biological activity of the conjugate.

Next, the modified reaction conditions were applied to a series of biologically interesting high-mannose oligosaccharides. 30 equiv (200−300 μg, 100−200 nmol) of Man3, Man5, Man6, Man7D1, Man7D3, Man8D1D3, and Man9 were coupled to BSA (250−400 μg, 3.5−6 nmol) in 20−25 μL reactions containing 100 mM sodium borate at pH 8.5, 300 mM sodium cyanoborohydride, and 500 mM sodium sulfate. Reactions were incubated in the PCR thermal cycler at 56 °C for 96 h and then dialyzed extensively with water. MALDI-TOF MS analysis (see Supporting Information) showed that the resulting glycoconju-

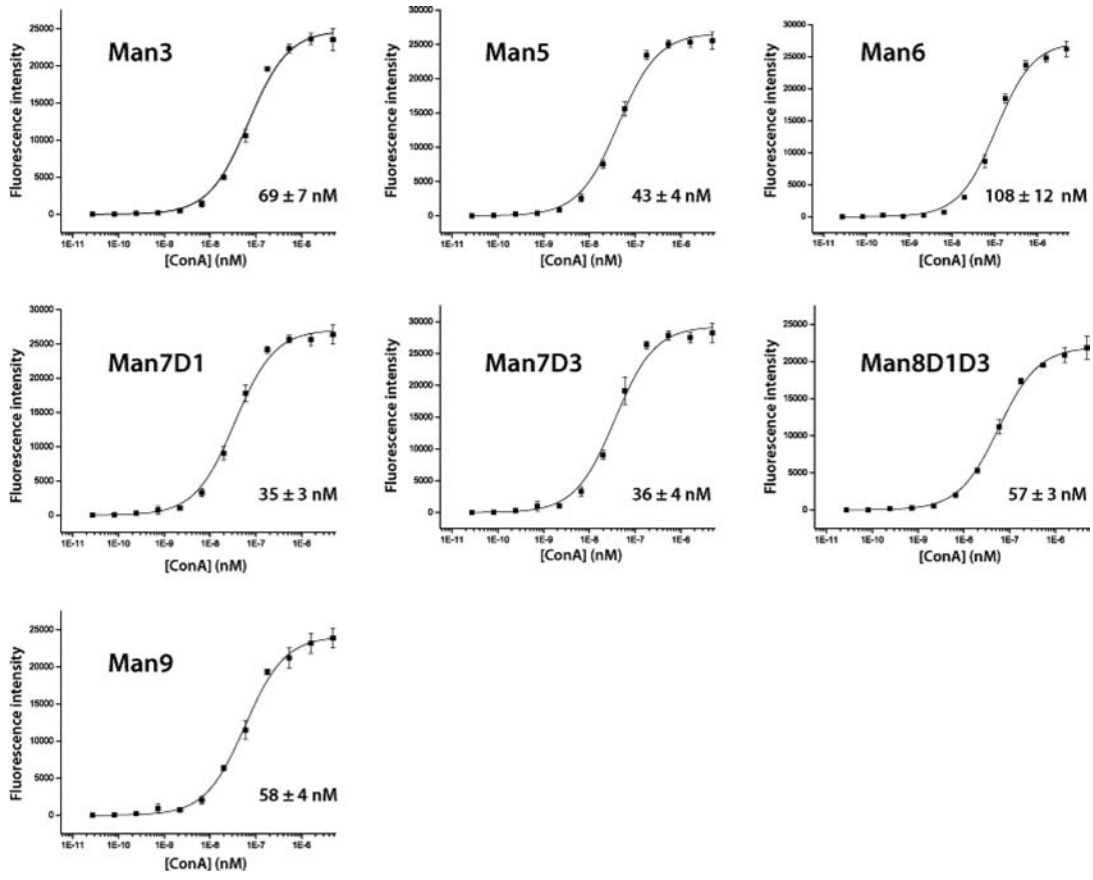

Figure 3. Binding of ConA to high mannose oligosaccharides on the carbohydrate microarray. Biotinylated ConA was incubated on the carbohydrate microarray at various concentrations. After washing, the array was incubated with Cy3-labeled streptavidin and fluorescence intensities were measured using a Genepix microarray scanner. The apparent K_ds for each high-mannose sugar are listed in the bottom right corner of each panel.

gates contained an average of 7 oligosaccharide chains per molecule of BSA. The results verify that the improved conditions for reductive amination can be successfully applied to a variety of expensive, complex oligosaccharides on a microgram scale. Using our current printing conditions for the carbohydrate microarrays, 250 μg of BSA conjugate is sufficient for over 100 000 array experiments.

To verify that the high-mannose sugars were structurally intact and suitable for use in a carbohydrate microarray, binding to concanavalin A was examined. Con A is a mannose binding lectin that has been used extensively as a research tool for detection of mannose containing glycans. It has been studied at length and is frequently used as a test lectin to validate assays. Mannose conjugates were printed on epoxide-coated glass microscope slides as reported previously (*11–13*). Binding was assessed by incubating the array with a range of concentrations of biotinylated ConA, washing away excess lectin, and incubating the array with Cy3-labeled streptavidin. After washing, fluorescent spots were detected and intensities quantitated using a DNA microarray scanner with GenePix software. Apparent K_ds were determined on the array using the method of MacBeath (*26*). K_d values are shown in Figure 3 and are in good agreement with values previously obtained for ConA with related sugars measured by surface plasmon resonance (*27*), frontal affinity chromatography (*28*), and carbohydrate microarray (*29*). Thus, the neoglycoconjugates appear to retain appropriate bioactivity.

CONCLUSSIONS

In summary, improved conditions for the direct conjugation of oligosaccharides to proteins using reductive amination are described. The conditions are compatible with microgram quantities of sugar and provide biologically active conjugates suitable for use in ELISA/ELLA assays and incorporation into microarrays. The conditions were successfully applied to a series of mannose containing oligosaccharides and these neoglycoconjugates were shown to bind to ConA. Improved conditions for reductive amination should prove useful for the preparation of glycoconjugates for both basic and applied research.

ACKNOWLEDGMENT

We thank Lai-Xi Wang for the generous gift of high mannose sugars. This research was supported by the Intramural Research Program of the NIH, NCI. This project has been funded in whole or in part with federal funds from the National Cancer Institute, National Institutes of Health, under contract N01-CO-12400. The content of this publication does not necessarily reflect the views or policies of the Department of Health and Human Services, nor does mention of trade names, commercial products, or organizations imply endorsement by the U.S. Government.

Supporting Information Available: MALDI-TOF MS data for coupling of tetra-*N*-acetylchitotetraose to BSA under various conditions and the coupling of Man3, Man5, Man6, Man7D1, Man7D3, Man8D1D1, and Man9 to BSA. This material is available free of charge via the Internet at http://pubs.acs.org.

LITERATURE CITED

(1) Vliegenthart, J. F. G. (2006) Carbohydrate based vaccines. *FEBS Lett. 580*, 2945.
(2) Seeberger, P. H., and Werz, D. B. (2007) Synthesis and medical applications of oligosaccharides. *Nature 446*, 1046.
(3) Oppenheimer, S. B., Alvarez, M., and Nnoli, J. (2008) Carbohydrate-based experimental therapeutics for cancer, HIV/AIDS and other diseases. *Acta Histochem. 110*, 6.
(4) Cipolla, L., Peri, F., and Airoldi, C. (2008) Glycoconjugates in cancer therapy. *Anti-cancer agents in medicinal chemistry 8*, 92.
(5) Pozsgay, V., Coxon, B., Glaudemans, C. P. J., Schneerson, R., and Robbins, J. B. (2003) Towards an oligosaccharide-based glycoconjugate vaccine against Shigella dysenteriae type 1. *Synlett* 743.
(6) Freire, T., Bay, S., Vichier-Guerre, S., Lo-Man, R., and Leclerc, C. (2006) Carbohydrate antigens: Synthesis aspects and immunological applications in cancer. *Mini Rev. Med. Chem. 6*, 1357.
(7) Bovin, N. V. (2002) Neoglycoconjugates: Trade and art. *Biochem. Soc. Symp. 69*, 143.
(8) Wong, S. Y. C. (1995) Neoglycoconjugates and their applications in glycobiology. *Curr. Opin. Struct. Biol. 5*, 599.
(9) Brinkley, M. (1992) A brief survey of methods for preparing protein conjugates with dyes, haptens, and cross-linking reagents. *Bioconjugate Chem. 3*, 2.
(10) Gray, G. R. (1974) The direct coupling of oligosaccharides to proteins and derivatized gels. *Arch. Biochem. Biophys. 163*, 426.
(11) Manimala, J., Li, Z., Jain, A., VedBrat, S., and Gildersleeve, J. C. (2005) Carbohydrate array analysis of anti-Tn antibodies and lectins reveals unexpected specificities: implications for diagnostic and vaccine development. *ChemBioChem 6*, 2229–2241.
(12) Manimala, J. C., Roach, T. A., Li, Z., and Gildersleeve, J. C. (2006) High-throughput carbohydrate microarray analysis of 24 lectins. *Angew. Chem., Int. Ed. Engl. 45*, 3607–3610.
(13) Manimala, J. C., Roach, T. A., Li, Z., and Gildersleeve, J. C. (2007) High-throughput carbohydrate microarray profiling of 27 antibodies demonstrates widespread specificity problems. *Glycobiology 17*, 17C–23C.
(14) Hsu, K.-L., Gildersleeve, J. C., and L.K., M. (2008) A simple strategy for the creation of a recombinant lectin microarray. *Mol. BioSyst.* 654–662.
(15) de Paz, J. L., and Seeberger, P. H. (2006) Recent advances in carbohydrate microarrays. *QSAR Comb. Sci. 25*, 1027–1032.
(16) Dyukova, V. I., Shilova, N. V., Galanina, O. E., Rubina, A. Y., and Bovin, N. (2006) Design of carbohydrate multiarrays. *Biochem. Biophys. Acta 1760*, 603–609.
(17) Feizi, T., Fazio, F., Chai, W., and Wong, C.-H. (2003) Carbohydrate microarrays- a new set of technologies at the frontiers of glycomics. *Curr. Opin. Struct. Biol. 13*, 637–45.
(18) Oyelaran, O., and Gildersleeve, J. C. (2007) Application of carbohydrate array technology to antigen discovery and vaccine development. *Exp. Rev. Vaccines 6*, 957.
(19) Paulson, J. C., Blixt, O., and Collins, B. E. (2006) Sweet spots in functional glycomics. *Nat. Chem. Biol. 2*, 238–248.
(20) Shin, I., Park, S., and Lee, M. R. (2005) Carbohydrate microarrays: An advanced technology for functional studies of glycans. *Chem. Eur. J. 11*, 2894–2901.
(21) Liang, P.-H., Wu, C.-Y., Greenberg, W. A., and Wong, C.-H. (2008) Glycan arrays: biological and medical applications. *Curr. Opin. Chem. Biol. 12*, 86.
(22) Karas, M., and Hillenkamp, F. (1988) Laser desorption ionization of proteins with molecular masses exceeding 10,000 daltons. *Anal. Chem. 60*, 2299–2301.
(23) Roy, R., Katzenellenbogen, E., and Jennings, H. J. (1984) Improved procedures for the conjugation of oligosaccharides to protein by reductive amination. *Can. J. Chem. 62*, 270–275.
(24) Stowell, S. R., Dias-Baruffi, M., Penttila, L., Renkonen, O., Nyame, A. K., and Cummings, R. D. (2004) Human galectin-1 recognition of poly-N-acetyllactosamine and chimeric polysaccharides. *Glycobiology 14*, 157.
(25) Bagger, H. L., Ogendal, L. H., and Westh, P. (2007) Solute effects on the irreversible aggregation of serum albumin. *Biophys. Chem. 130*, 17.

(26) Jones, R. B., Gordus, A., Krall, J. A., and MacBeath, G. (2006) A quantitative protein interaction network for the ErbB receptors using protein microarrays. *Nature 439*, 168.
(27) Smith, E. A., Thomas, W. D., Kiessling, L. L., and Corn, R. M. (2003) Surface plasmon resonance imaging studies of protein-carbohydrate interactions. *J. Am. Chem. Soc. 125*, 6140–6148.
(28) Ohyama, Y., Kasai, K., Nomoto, H., and Inoue, Y. (1985) Frontal affinity chromatography of ovalbumin glycoasparagines on a concanavalin A-sepharose column. A quantitative study of the binding specificity of the lectin. *J. Biol. Chem. 260*, 6882–6887.
(29) Liang, P. H., Wang, S. K., and Wong, C. H. (2007) Quantitative analysis of carbohydrate-protein interactions using glycan microarrays: determination of surface and solution dissociation constants. *J. Am. Chem. Soc. 129*, 11177–11184.

BC800153T

Minimal Chemical Modification of Reductive End of Dextran to Produce an Amphiphilic Polysaccharide Able to Incorporate onto Lipid Nanocapsules

Antoine Richard,[†] Alexandre Barras,[†] Amena Ben Younes,[‡] Nicole Monfilliette-Dupont,*[,†] and Patricia Melnyk[†]

Laboratoire de Chimie et MicroNanotechnologie à Visée Thérapeutique, UMR 8161 CNRS-Université de Lille 2-Université de Lille 1-Institut Pasteur de Lille, and INSERM IFR 142 Institut Pasteur de Lille-Institut de Biologie de Lille, Institut de Biologie de Lille, 1 Rue du Pr. Calmette, 59021 Lille cedex, France. Received December 4, 2007; Revised Manuscript Received May 19, 2008

In order to graft an amphiphilic polysaccharide to lipid nanocapsules, we present here a new method of dextran lipidation. The lipidation strategy is based on the formation of an oxime linkage between the amphiphilic hydroxylamine $\mathbf{C_{16}E_{20}ONH_2}$ and the reductive end of a 40 kDa dextran. This chemoselective reaction allows us to control the lipidation site and the number of lipid introduced on the dextran molecule. This new amphiphilic dextran was used to coat the surface of lipid nanocapsules. The coating efficiency was followed by dynamic light scattering and the presence of the polysaccharide was confirmed by ^{1}H NMR and observed by electronic microscopy.

INTRODUCITON

Since the development of liposomes, many other drug carriers in the nanometer range have been in development: polymer particles, solid lipid nanoparticles, lipid nanocapsules, and dendrimers (*1*). In order to extend the release of a drug and/or to address nanoparticles to the target cells or organ to treat, much attention has been devoted to increasing the blood half-time of these nanocarriers. Indeed, due to their interaction with the reticulo-endothelial system, their blood half-life is very low (*2, 3*). Toward this aim, nanoparticles were usually covered by a hydrophilic polymer, often a poly(ethylene glycol) (PEG). The longer the PEG, the more the blood half-time increases. Usually, medium molecular weight PEGs (2000−5000 Da) were used (*2, 3*).

Instead of PEG, biopolymers like polysaccharides can be used. Some authors reported the coating of liposome with dextran or chitosan (*4–9*). In order to anchor the polymer onto the liposome surface, a chemical modification of the polysaccharide with a hydrophobic function is necessary. These hydrophobic moieties, such as cholesteryl derivatives, were generally grafted in a statistically random manner on hydroxyl or amine functional groups present on the carbohydrate (*4, 5, 10*). By modulating the polysaccharide/lipophilic molecule ratio, it is possible to control the number of lipid moieties attached to the polysaccharide. Nevertheless, the reaction could occur anywhere on the reactive functions of the polymer.

We propose here a lipidation method of a dextran to attach a single lipid molecule at the polysaccharide reductive end. This coupling was achieved by forming an oxime bond as described by Dumy et al. (*11–13*) The oxime formation was achieved by reaction of a hydroxylamine with native dextran in aqueous medium. This chemoselective method can be used while maintaining biological properties (aqueous solubility, molecular recognition, etc.) and chemical functions which can be present on the polysaccharide chain. Moreover, by anchoring the sugar by one of its ends on the particle, we take advantage of its full length, which is impossible with statistical "lipidation" on the polymer.

As a proof of concept, the amphiphilic derivative **3** of dextran T40 (40 kDa) was synthesized and was anchored onto lipid nanocapsules. These nanocapsules consist of an oily liquid triglyceride core surrounded by a tensioactive cohesive interface. This tensioactive cohesive interface was mainly constituted of solutol HS15 which exposes a medium PEG chain containing an average of 15 ethylene glycol units (*14, 15*). To minimize the nanocapsule disturbance by the carbohydrate moiety, a PEG chain of an average of 20 ethylene glycol units was introduced between the polysaccharide and a C16 alkyl chain.

EXPERIMENTAL SECTION

Chemicals and Materials. Mass spectra were recorded on a Perspective Biosystems Voyager-DE STR, Biospectrometry Workstation MALDI-TOF spectrometer, and measurements were acquired after deposition on a dihydroxybenzoic acid (DHB) matrix. NMR spectra were recorded on a 300 MHz Bruker spectrometer. Chemicals reagents were purchased from Sigma-Aldrich. Lipid nanocapsules were made of labrafac lipophile WL 1349, soy lecithin Phospholipon 90G, and Solutol HS 15 were generously provided by Gattefossé SA, Phospholipid, and BASF, respectively.

Anchor Synthesis. Compound **1**: Under nitrogen atmosphere, 1 g (0.89 mmol, 1 equiv) of Brij-58P, 0.698 g (2.66 mmol, 3 equiv) of PPh_3, and 0.349 g (2.14 mmol, 2.4 equiv) of *N*-hydroxyphthalimide were dissolved in 20 mL of THF freshly distilled over sodium in the presence of benzophenone. 560 μL (2.66 mmol, 3 equiv) of DIAD were then added dropwise. The reaction medium was stirred for 3 h under nitrogen atmosphere and was concentrated under vacuum. The residue was precipitated in 50 mL of dry diethyl ether at 4 °C and then centrifuged. The resulting solid was collected and triturated twice with diethyl ether. The white solid obtained was dried under vacuum in the presence of P_2O_5 overnight. 952 mg of the phthalimide derivative was collected. Yield: 84%. ^{1}H NMR, $CDCl_3$, ppm: 7.83 (m, 2H); 7.76 (m, 2H); 4.38 (t, 4.5 Hz, 2H); 3.88 (t, 5 Hz, 2H); 3.65 (s, 42H); 3.44 (t, 6.8 Hz, 2H); 1.57 (m, 2H); 1.25 (s, 28H); 0.88 (t, 6.7 Hz, 3H).

Compound **2**: 952 mg (0.75 mmol, 1 equiv) of compound **1** was dissolved in 20 mL of absolute ethanol and 1 mL (20 mmol, 27 equiv) of hydrazine hydrate was added. After 4 h, the reaction medium was filtered and the solvent was evaporated under reduced pressure. The crude product was dissolved in diethyl

* To whom correspondence should be addressed. Phone: +33 3 20 87 12 20. Fax +33 3 20 87 12 33. E-mail: Nicole.dupont@ibl.fr.
[†] UMR 8161 CNRS.
[‡] INSERM IFR 142.

10.1021/bc700444t CCC: $40.75 © 2008 American Chemical Society
Published on Web 06/21/2008

ether, precipitated at 4 °C, and centrifuged. The solid was collected, dissolved in CH_2Cl_2, and precipitated twice with diethyl ether. The white solid obtained was then dried overnight under vacuum in the presence of P_2O_5. 789 mg of the hydroxylamine derivative **2** was collected. Yield: 92%. MALDI-TOF MS: Two Gaussian distributions of peaks separated by $m/z = 44$ corresponding to ethylene glycol monomer. The first Gaussian corresponds to the $[M + H^+]$ centered on $m/z = 1138.9$ and the second one corresponds to the $[M + Na^+]$ centered on $m/z = 1160.9$. ^{1}H NMR, $CDCl_3$, ppm: 3.84 (t, 4.6 Hz, 2H); 3.65 (s, 88H); 3.57, (m, 2H); 3.44 (t, 6.8 Hz, 2H); 1.54 (m, 2H); 1.25 (s, 28H); 0.88 (t, 6.7 Hz, 3H). ^{13}C NMR, $CDCl_3$, ppm: 74.9; 71.7; 70.7; 70.2; 69.7; 32.1; 29.8; 29.6. 29.5; 26.2; 22.8; 14.3.

Dextran Coupling. Compound **3**: 1.6 g (40 μmol, 1 equiv) of dextran T40 and 174 mg (140 μmol, 3.5 equiv) of **2** were dissolved in 3 mL of a 100 mM acetate buffer pH 5.5. After 72 h, the reaction medium was poured onto 50 mL of methanol and centrifuged. The solid was dissolved twice in water, precipitated again in methanol, and centrifuged. Finally, the amphiphilic dextran was dissolved in water and lyophilized. 1.531 g of a white powder was collected. Yield: 93%. ^{1}H NMR: 7.47 (d, 6.2 Hz, 0.8H); 6.83 (d, 6.6 Hz, 0.2H); 4.85 (d, 3.3 Hz, 247H); 3.8 (m, 443H); 3.6 (m, 564H); 3.4 (m, 400H); 1.45 (s, 2H); 1.18 (s, 30H); 0.79 (t, 6.1 Hz, 3H).

Nanocapsules. The preparation of lipid nanocapsules was based on a phase inversion method that allows the preparation of very small nanocapsules by thermal manipulation of an oil/water system as described by Heurtault et al. (*14*). Briefly, 420 mg of labrafac, 37.5 mg of phospholipon P90, 240 mg of solutol, 22 mg of NaCl, and 540 μL of distilled water were mixed at 80 °C. The mixture was subjected to 3 temperature cycles from 70 to 90 °C under magnetic stirring; then, it was cooled to 78 °C, 3.3 mL of 0 °C water were added, and the suspension was stirred at room temperature.

Lipodextran Insertions into Preformed Nanocapsules. Lipodextran nanocapsules were obtained by two postinsertion methods. First method: plain nanocapsules (15 mg LN/mL) were incubated for 24 h with lipodextran (10 mg/mL of LN) under magnetic stirring at room temperature. Second method: plain nanocapsules (15 mg LN/mL) were incubated for 120 min with 100 μL/mL of LN of an aqueous micellar solution of lipodextran (100 mg/mL) under magnetic stirring at 60 °C. The suspension was then dialyzed (pore size: 300 000 Da) against distilled water overnight to remove any uninserted lipodextran from the external volume of nanoparticles.

Lipid Nanoparticle Characterization. The average diameter and polydispersity of the particle were determined by photon correlation spectroscopy at 25 °C using a DynaProMS800. Nanoparticle suspensions were diluted at 1/2000 (v/v) in distilled water and filtered over 0.22 μm. Mean results were given for 100 acquisitions, and measurements were performed in triplicate. The zeta potential was determined with a Malvern Zetasizer Nano ZS (Malvern Instruments S.A., Worcestershire, UK).

Electron Microscopy. Samples were studied using a slightly modified version of the negative staining method as previously described by Op De Beeck et al. (*16*); 20 μL droplets of free and covered nanocapsule preparations were adsorbed for 1 min onto Formvar carbon-coated nickel grids (400 mesh, Electron Microscopy Science, Washington, PA). The grids were dried by absorption with a filter paper, stained for 1 min on a drop of 2% uranyl acetate stain, air-dried for less than 2 min, and immediately examined under a transmission electron microscope (TEM, Hitachi 7500, Japan) at 80 kV and HR conditions. Because of their rapid degradation, every sample is processed for electron microscopy and immediately examined under TEM.

Scheme 1. Synthesis of the Amphiphilic Hydroxylamine $C_{16}E_{20}ONH_2$

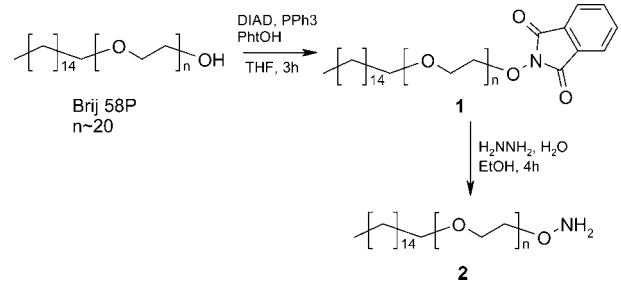

Scheme 2. Coupling of Dextran to Amphiphilic Hydroxylamine 2

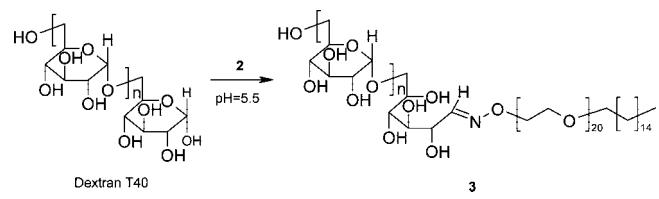

RESULTS AND DISCUSSION

Synthesis. The amphiphilic hydroxylamine moiety **2** was synthesized in two steps. First, the hydroxylamine function was introduced by coupling the *N*-hydroxyphthalimide by means of a Mitsunobu reaction. Second, the phthalimide group was

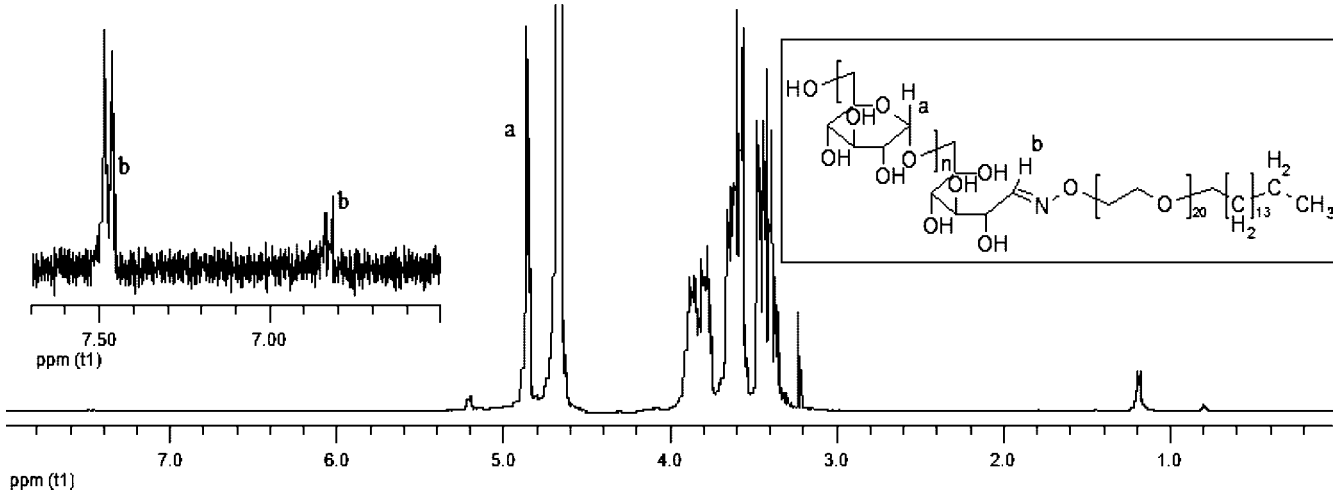

Figure 1. Analysis of oxime ^{1}H of amphiphilic dextran **3** by NMR spectroscopy.

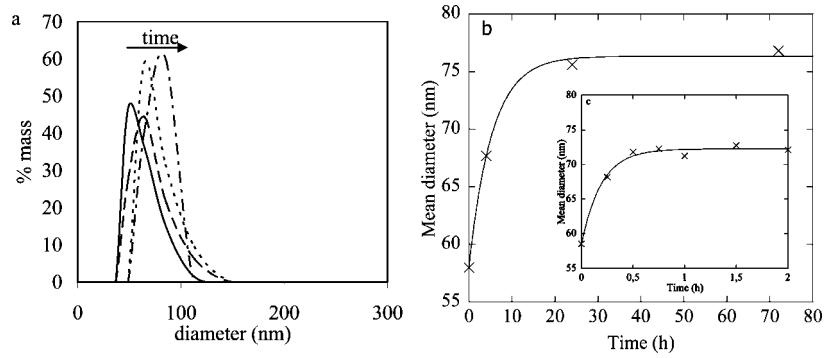

Figure 2. (a) Size distribution evolution of lipid nanocapsules in presence of amphiphilic dextran **3**. −− $t = 0$ h, — $t = 4$ h, •••• $t = 24$ h, — • — • $t = 72$ h. (b) Evolution of the mean diameter of lipid nanocapsules with time at room temperature. (c) Evolution of the mean diameter of lipid nanocapsules with time at 60 °C.

Table 1. Fitting Results of the Evolution of Nanocapsule Mean Diameter with Eq 1 in the Presence of Amphiphilic Dextran 3

postinsertion	room temperature		60 °C	
parameter	value	error	value	error
A	58.03 nm	0.7 nm	58.53 nm	0.6 nm
B	18.3 nm	0.9 nm	13.7 nm	0.7 nm
τ	5.4 h	0.7 h	0.2 h	0.03 h
R^2	0.9978	-	0.9945	-

removed by hydrazinolysis (Scheme 1). The starting product was the commercial nonionic detergent Brij 58P which consists of a C16 alkyl chain bearing a PEG chain of an average of 20 ethylene glycol units with a free hydroxyl group at the chain end.

The coupling of hydroxylamine **2** with dextran T40 occurs in an aqueous solvent at high concentration (at less than 10 mM) with an excess of compound **2** (Scheme 2). The hydroxylamine reacts with the reductive end of dextran in 72 h at room temperature to form the corresponding oxime compound. Taking advantage of dextran insolubility in methanol, buffer salt and excess reagent can be removed by precipitation in methanol to give the amphiphilic dextran **3** in an overall yield of 72% for the three steps.

^{1}H NMR of compound **3** shows the presence of a doublet at 7.47 ppm and another one at 6.83 ppm, which confirms the presence of the oxime link between the dextran and the hydroxylamine **2** (Figure 1). Moreover, taking the acetal proton (4.85 ppm) of the glucose unit of dextran (247 H for Dextran T40) as integration reference, the doublet at 7.47 ppm integrates for roughly 0.8 H and the one at 6.83 ppm for roughly 0.2 H. It is thus concluded that the oxime link is in E configuration at 80% and in Z at 20%.

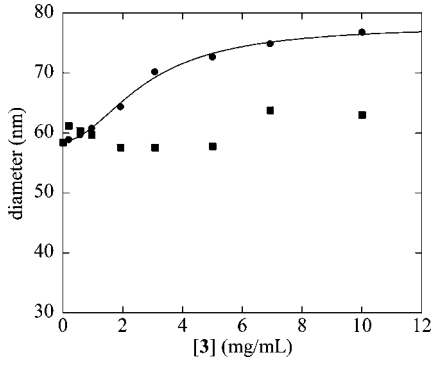

Figure 3. Evolution of nanocapsules mean diameter as a function of dextran concentration: •, amphiphilic dextran; ■, commercial dextran of 40 kDa.

Table 2. Lipid Nanoparticles Characterization (NP, lipid nanoparticles without amphiphilic dextran; and Dextran NP, lipid nanoparticles with amphiphilic dextran).

			zeta potential	
	mean particle size (nm)	polydispersity (nm)	peak (mV)	width (mV)
NP	59.2 ± 2.9	6.8 ± 1.6	−4.08	10.4
Dextran NP (RT)	71.9 ± 1.5	6.2 ± 1.4	−2.86	6.0
Dextran NP (60 °C)	73.8 ± 2.1	9.4 ± 1.4	−1.67	3.5

After three consecutive dialyses (1:1000 in water), NMR spectra do not change (data not shown), which allows us to conclude that the oxime link is stable.

Dextran Incorporation onto Nanocapsules. The dextran T40 average diameter was measured by dynamic light scattering at 9 nm. So, if we anchor this polysaccharide uniformly on the nanocapsules surface, their mean diameter should grow by approximately 20 nm. The size of our nanocapsules, initially close to 58 nm, which were suspended in an amphiphilic dextran solution at 10 mg/mL in water, was in accordance with this hypothesis (Figure 2).

The increase of particle mean diameter with time could be well fitted by a monoexponential curve as defined in eq 1

$$\bar{d} = A + B \cdot \left[1 - \exp\left(-\frac{t}{\tau}\right)\right] \quad (1)$$

in which d is the mean diameter, A the starting diameter of nanoparticles (without dextran), B the mean diameter raise, and τ the characteristic time of dextran insertion.

The fitting results of this equation are given in Table 1.

We found an increase in diameter of 18.3 ± 0.9 nm. This is in accordance with a full coverage of nanocapsules by a 40 kDa dextran. The anchorage of amphiphilic dextran was complete in 24 h when postinsertion was realized at room temperature with a characteristic time of 5 h 20 min ± 42 min and was complete in 45 min when postinsertion was realized at 60 °C with characteristic time of 12 min ± 1.8 min.

For a second time, taking advantage of the hydroxylamine reactivity in aqueous medium, we tried to form the oxime **3** directly on to the nanoparticles. This strategy was already employed to link peptides to lipid vesicles by an oxime bond (*17*). To this end, compound **2** was first incorporated during the formulation of nanocapsules. These nanocapsules were suspended in dextran solution, but the dextran concentration required (around 10 mM) for the reaction to occur with the hydroxylamine carried by particles was incompatible with nanocapsule stability. Furthermore, the coformulation of the amphiphilic dextran **3** with other components does not yield the expected particles. Thus, the postinsertion method seems to be the most efficient to coat these lipid nanocapsules with our dextran.

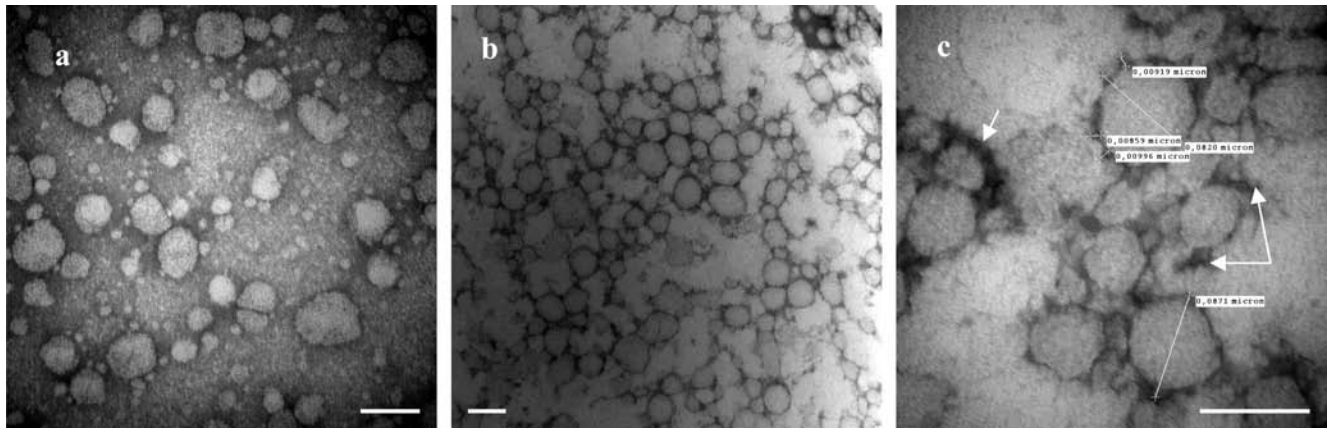

Figure 4. TEM visualization of lipid nanocapsules. Bar scale represents 100 nm. (a) Lipid nanocapsules without dextran. (b) Lipid nanocapsules in the presence of 5 mg/mL of amphiphilic dextran **3**. (c) Enlargement of (b); white arrows show a deposit attributed to dextran.

The presence of the C16 alkyl chain is a necessary condition to achieve the nanoparticles coverage: only polysaccharide **3** brings about a significant increase of nanocapsules diameter. But, as can be seen in Figure 3, a sufficient polysaccharide concentration was needed to obtain a size increase of 18 nm, corresponding to an entire coverage of particles by dextran. In our case, the concentration should be greater than 5 mg/mL to complete the postinsertion.

As shown in Table 2, the zeta potential of the nanoparticles measured was slightly influenced by the presence of dextran on the surface. Zeta potential of almost neutral value (−2.86 and −1.67 mV for postinsertion at room temperature and 60 °C, respectively) was measured for the nanoparticles prepared by postinsertion with amphiphilic dextran, which is a neutral polysaccharide.

To confirm this result, the nanocapsules were observed by transmission electron microscopy using the negative staining method (Figure 4). A dark deposit dense to electrons was observed on the nanocapsules surface only if the nanocapsules were incubated with amphiphilic dextran. The same experiment was carried out with the nanocapsules in the presence of lipodextran without incubation or free dextran T40 and no dark deposit dense to electrons was observed. This observation suggests that the amphiphilic dextran coats the surface of lipid nanocapsules. In addition, the size of this deposit, as determined from the TEM micrograph, corresponds to the size of 40 kDa dextran.

To corroborate our direct observation by electron microscopy, we wanted to have a spectrometric signature of the dextran presence on the nanocapsules surface. Thus after gel filtration through a sephacryl 500HR column, a ^{1}H NMR spectrum of the nanocapsule fraction in H_2O/D_2O 95/5 solvent was acquired. As the NMR spectra show (Figure 5), specific signals of dextran were detected (in the region between 3.8 and 4.0 ppm) with amphiphilic dextran. In the control experiment with commercial dextran T40, no dextran peak was found on nanoparticles NMR spectrum. Thus, the lipid tail link to dextran allows the polysaccharide fixation onto the surface of nanocapsules. The quantification of lipodextran has been investigated by the ^{1}H NMR method (see Supporting Information for quantitative analysis of lipodextran incorporation onto nanocapsules by ^{1}H NMR). Integration of the signals indicates the quantity of lipodextran on the surface of nanocapsules (5.1% mass incorporation of nanocapsules at RT and 10.1% mass incorporation of nanocapsules at 60 °C). The results indicate that the postinsertion method at 60 °C allows us to introduce approximately twice as much lipodextran on the surface of nanocapsules as at RT.

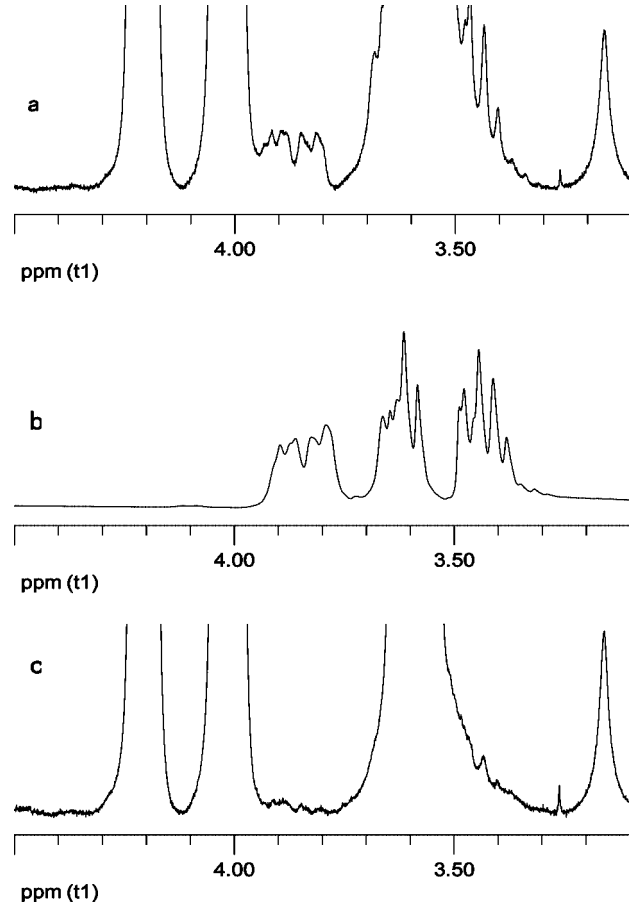

Figure 5. NMR spectra in H_2O/D_2O 95/5 of (a) nanocapsules in the presence of amphiphilic dextran **3** after gel filtration, (b) commercial dextran T40, and (c) nanocapsules in the presence of commercial dextran T40 after gel filtration.

Full Conclusion. We have developed here an efficient and convenient method to anchor a polysaccharide onto the surface of lipid nanocapsules. The formation of amphiphilic dextran as well as the formulation of nanocapsules were performed under aqueous conditions without organic solvent. This is an important parameter when biological or pharmaceutical applications are engaged. We have shown that only one alkyl C16 chain is sufficient to anchor a 40 kDa dextran. Moreover, the postinsertion of this carbohydrate can be achieved under mild conditions: at room temperature in less than one day. This method could constitute an attractive alternative to the use of

PEG and could be useful for decorating lipid particles with functionalized polysaccharide with the aim of active cell targeting.

ACKNOWLEDGMENT

This work was financially supported by "La ligue contre le cancer" and "La Cancéropôle Nord-Ouest". We gratefully acknowledge CNRS, Université de Lille 2, Université de Lille 1, Institut Pasteur de Lille for logistical support, Hervé Drobecq for MALDI-TOF acquisitions, Gérard Montagne for NMR acquisitions, Ludivine Houelrenault for TEM micrographs, and Clement Roux for proof reading.

Supporting Information Available: Details of the quantification of lipodextran by ^{1}H NMR method. This material is available free of charge via the Internet at http://pubs.acs.org.

LITERATURE CITED

(1) Couvreur, P., and Vauthier, C. (2006) Nanotechnology: intelligent design to treat complex disease. *Pharm. Res. 23*, 1417–50.

(2) Drummond, D. C., Meyer, O., Hong, K., Kirpotin, D. B., and Papahadjopoulos, D. (1999) Optimizing liposomes for delivery of chemotherapeutic agents to solid tumors. *Pharmacol Rev 51*, 691–743.

(3) Lasic, D. D., and Needham, D. (1995) The "stealth" liposome: a prototypical biomaterial. *Chem. Rev. 95*, 2601–2828.

(4) Mumper, R. J., and Hoffman, A. S. (2000) The stabilization and release of hirudin from liposomes or lipid-assemblies coated with hydrophobically modified dextran. *AAPS PharmSciTech 1*, E3.

(5) Sihorkar, V., and Vyas, S. P. (2001) Potential of polysaccharide anchored liposomes in drug delivery, targeting and immunization. *J. Pharm. Pharm. Sci. 4*, 138–58.

(6) Pain, D., Das, P. K., Ghosh, P., and Bachhawat, B. K. (1984) Increased circulatory half-life of liposomes after conjunction with dextran. *J. Biosci. 6*, 811–816.

(7) De Campos, A. M., Sanchez, A., Gref, R., Calvo, P., and Alonso, M. J. (2003) The effect of a PEG versus a chitosan coating on the interaction of drug colloidal carriers with the ocular mucosa. *Eur. J. Pharm. Sci. 20*, 73–81.

(8) Bertholon, I., Hommel, H., Labarre, D., and Vauthier, C. (2006) Properties of polysaccharides grafted on nanoparticles investigated by EPR. *Langmuir 22*, 5485–90.

(9) Letourneur, D., Parisel, C., Prigent-Richard, S., and Cansell, M. (2000) Interactions of functionalized dextran-coated liposomes with vascular smooth muscle cells. *J. Controlled Release 65*, 83–91.

(10) Cansell, M., Parisel, C., Jozefonvicz, J., and Letourneur, D. (1999) Liposomes coated with chemically modified dextran interact with human endothelial cells. *J. Biomed. Mater. Res. 44*, 140–8.

(11) Forget, D., Boturyn, D., Defrancq, E., Lhomme, J., and Dumy, P. (2001) Highly efficient synthesis of peptide-oligonucleotide conjugates: chemoselective oxime and thiazolidine formation. *Chemistry 7*, 3976–84.

(12) Edupuganti, O. P., Singh, Y., Defrancq, E., and Dumy, P. (2004) New strategy for the synthesis of 3′,5′-bifunctionalized oligonucleotide conjugates through sequential formation of chemoselective oxime bonds. *Chemistry 10*, 5988–95.

(13) Edupuganti, O. P., Renaudet, O., Defrancq, E., and Dumy, P. (2004) The oxime bond formation as an efficient chemical tool for the preparation of 3′,5′-bifunctionalised oligodeoxyribonucleotides. *Bioorg. Med. Chem. Lett. 14*, 2839–42.

(14) Heurtault, B., Saulnier, P., Pech, B., Proust, J. E., and Benoit, J. P. (2002) A novel phase inversion-based process for the preparation of lipid nanocarriers. *Pharm. Res. 19*, 875–80.

(15) Heurtault, B., Saulnier, P., Pech, B., Venier-Julienne, M. C., Proust, J. E., Phan-Tan-Luu, R., and Benoit, J. P. (2003) The influence of lipid nanocapsule composition on their size distribution. *Eur. J. Pharm. Sci. 18*, 55–61.

(16) Op De Beeck, A., Molenkamp, R., Caron, M., Ben Younes, A., Bredenbeek, P., and Dubuisson, J. (2003) Role of the transmembrane domains of prM and E proteins in the formation of yellow fever virus envelope. *J. Virol. 77*, 813–20.

(17) Richard, A., and Bourel-Bonnet, L. (2005) Internalization of a peptide into multilamellar vesicles assisted by the formation of an alpha-oxo oxime bond. *Chemistry 11*, 7315–21.

BC700444T

Synthesis of ^{64}Cu-Labeled Magnetic Nanoparticles for Multimodal Imaging

Benjamin R. Jarrett, Björn Gustafsson, David L. Kukis, and Angelique Y. Louie*

Department of Biomedical Engineering, University of California-Davis, Davis, California 95616. Received March 13, 2008; Revised Manuscript Received May 21, 2008

Complementary imaging modalities provide more information than either method alone can yield and we have developed a dual-mode imaging probe for combined magnetic resonance (MR) and positron emission tomography (PET) imaging. We have developed dual-mode PET/MRI active probes targeted to vascular inflammation and present synthesis of (1) an aliphatic amine polystyrene bead and (2) a novel superparamagnetic iron oxide nanoparticle targeted to macrophages that were both coupled to positron-emitting copper-64 isotopes. The amine groups of the polystyrene beads were directly conjugated with an amine-reactive form (isothiocyanate) of aza-macrocycle 1,4,7,10-tetraazacyclo-dodecane-1,4,7,10-tetraacetic acid (DOTA). Iron oxide nanoparticles are dextran sulfate coated, and the surface was modified to contain aldehyde groups to conjugate to an amine-activated DOTA. Incorporation of chelated Cu-64 to nanoparticles under these conditions, which is routinely used to couple DOTA to macromolecules, was unexpectedly difficult and illustrates that traditional conjugation methods do not always work in a nanoparticle environment. Therefore, we developed new methods to couple Cu-64 to nanoparticles and demonstrate successful labeling to a range of nanoparticle types. We obtained labeling yields of 24% for the amine polystyrene beads and 21% radiolabeling yield for the anionic dextran sulfate iron oxide nanoparticles. The new coupling chemistry can be generalized for attaching chelated metals to other nanoparticle platforms.

1. INTRODUCTION

Challenges in diagnostic imaging have led to an explosion of interest in combining modalities to more accurately interpret disease and abnormalities in vivo. Combinations of imaging modalities are being investigated for a synergistic effect, and the combination of positron emission tomography/magnetic resonance imaging (PET/MRI) has raised expectations for highly sensitive and high-resolution imaging (*1*, *2*). PET and MRI are complementary to each other given the high anatomical spatial resolution of MRI and the unparalleled sensitivity and functional imaging of PET (*3*). Noninvasive monitoring of physiological abnormalities in vivo promises to greatly enhance our knowledge and treatment of diseases.

Concomitant with the development of dual-mode imaging systems has been an increase in interest for dual-mode molecular imaging probes that are targeted for very specific clinical applications, e.g., imaging of tumors and atherosclerotic plaques (*4*–*7*). Most of the reported dual-mode agents have been combinations of either PET or MRI agents with optical agents (*6*, *8*–*12*). Reports of SPIOs with dual-modality properties are increasing in the literature, with the focus primarily on probes with magnetic and optical properties suitable for imaging (*13*–*18*). Very recently, a trimodal PET/CT/optical agent based on iron oxide nanoparticles was developed (*19*). In this work, we describe development of a combined MRI/PET agent composed of iron oxide nanoparticles coupled to chelated positron emitting ions.

A commonly used method to radiolabel macromolecular targeting agents for imaging with any PET active metal is to chelate the metal to a bifunctional polyazacarboxylate- (*20*) or a tetraaza-macrocycle (*21*). The isotope ^{64}Cu, with a half-life of 12.7 h, has expanded in use as a positron emitter (*22*) for PET and metabolic radiotherapy (*23*, *24*) due to the additional high-energy β^- particle and Auger electron emissions of this nucleus. The ligand−cage pairs of polyazacarboxylate- or tetraaza-macrocycle form thermodynamically stable complexes with Cu^{2+} ($\log K = 20-28$) (*25*, *26*). The copper chelate could then be conjugated to the superparamagnetic iron oxide nanoparticle to develop a dual-modality probe for MRI and PET imaging. We found that the development of an iron oxide conjugated to a copper chelate was synthetically difficult using traditional bioconjugation methods.

Herein, we report ^{64}Cu radiolabeling of dextran sulfate coated superparamagnetic iron oxide nanoparticles; these are targeted toward inflammatory events, such as atherosclerotic plaques. The labeling was done by coordination of the ^{64}Cu to the chelating bifunctional ligand *S*-2-(4-isothiocyanatobenzyl)-1,4,7,10-tetraazacyclododecane-1,4,7,10-tetraacetic acid (*p*-SCN-Bz-DOTA) and then conjugation to the nanoparticle. We also describe a synthetic route for a ^{64}Cu-radiolabeled model imaging probe utilizing an aliphatic amine polystyrene microsphere as another example for radiolabeling of nanoparticles.

2. EXPERIMENTAL PROCEDURES

2.1. General. Ferric chloride hexahydrate (99%, Acros Organics, (Geel, Belgium)), ferrous chloride tetrahydrate (>99%, Fluka (Buchs, Switzerland)), dextran sulfate, sodium salt (Fluka (Buchs, Switzerland)), ammonium hydroxide solution (~30%, EM Science (Lawrence, KS)), ethylenediamine (>99.8%, Fluka (Buchs, Switzerland)), sodium cyanoborohydride (≥95%, Fluka (Buchs, Switzerland)), periodic acid (reagent grade, Fisher Scientific (Waltham, MA)), surfactant-free aliphatic amine polystyrene beads (1 μm, 2.0% w/w, Molecular Probes, Invitrogen (Carlsbad, CA)), *S*-2-(4-isothiocyanatobenzyl)-1,4,7,10-tetraazacyclododecane-1,4,7,10-tetraacetic acid (*p*-SCN-Bz-DOTA, Macrocyclics (Dallas, TX)), *S*-2-(4-aminobenzyl)-1,4,7,10-tetraazacyclododecane tetraacetic acid (*p*-NH_2-Bz-DOTA, Macrocyclics (Dallas, TX), cupric chloride (97%, Aldrich (St. Louis, MO)), and cupric-64 chloride solution (MDS Nordion (Ottawa, Canada)) were used as purchased. Nanopure

* Corresponding author.

10.1021/bc800108v CCC: $40.75 © 2008 American Chemical Society
Published on Web 06/26/2008

Scheme 1. Amination of ADIO Nanoparticles[a]

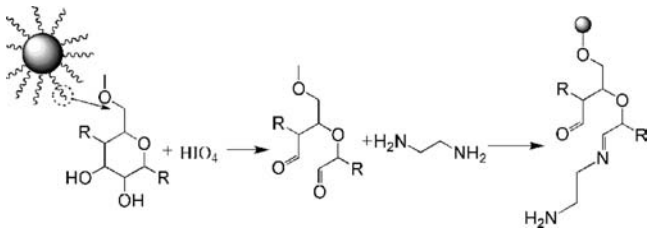

[a] The dextran coating was opened with periodic acid and the aldehyde group conjugated to ethylenediamine to generate amine functionalized nanoparticles. The bifunctionality of the ethylenediamine lead to cross-linking of the nanoparticles. R = OSO_3^- or OH.

water (18.0 MΩ·cm) was from a Barnstead nanopure filtration unit. Dextran (10 095 MW, Sigma (St. Louis, MO)) was reduced and purified according to Paul et al. (*27*).

2.2. Preparation of Polystyrene Beads and Dextran Sulfate Coated Iron Oxide Nanoparticles Labeled with "Cold" Copper. *2.2.1. Prechelation of "Cold" Copper into p-SCN-Bz-DOTA Followed by Conjugation to Polystyrene Beads.* $CuCl_2$ (1.29 mg; 9.57 μmol in 20 μL nanopure H_2O) was added to p-SCN-Bz-DOTA (5.26 mg; 7.656 μmol in 1.0 mL nanopure H_2O) and stirred for 2 h. The reaction solution was then purified by size exclusion chromatography (SEC) on a Sephadex G-25 column. UV−vis spectra of the purified product were used to determine the fraction corresponding to the *p*-SCN-Bz-DOTA(Cu^{2+}) complex based on the absorption of the benzyl group and copper ion. UV−vis was not used to assess the purity of the product. The *p*-SCN-Bz-DOTA-Cu solution was then added to tetramethylammonium phosphate solutions (pH 8) of both 78 nm and 1 μm sized polystyrene beads in molar ratios of approximately 5000:1 and 218 000:1, respectively. The reactions were stirred at room temperature overnight and purified by dialysis against 4 L nanopure water for ~2 days with 6 changes of water. Inductively coupled mass spectrometry (ICP-MS) was used to determine amounts of conjugated copper.

2.2.2. Labeling of ADIO Nanoparticles with "Cold" Copper to Determine Affect of Labeling on Particle Size. Dextran sulfate coated iron oxide nanoparticles (anionic dextran sulfate iron oxide, ADIO) were synthesized as described previously (*28*). It was found that amination of the ADIO nanoparticles leads to cross-linking as the ethylenediamine is bifunctional (Scheme 1); therefore, we sought to avoid particle cross-linking by attaching the ethylenediamine to the *p*-SCN-Bz-DOTA instead. In this way, any dimer formation of *p*-SCN-Bz-DOTA-amine complexes would be unreactive and not contribute to particle aggregation. Synthesis of copper-labeled dextran sulfate nanoparticles was achieved by conjugation of an amine reactive *p*-SCN-Bz-DOTA with the dextran sulfate coating.

The *p*-SCN-Bz-DOTA (9.82 mg; 16.70 μmol in 14.28 mL DMSO), was mixed in a 1:1 molar ratio with a solution of $CuCl_2$ (1.92 mg of $CuCl_2$ in 0.465 mL nanopure water) and incubated at room temperature for 15 min. Next, the *p*-SCN-Bz-DOTA-Cu was amine-activated by coupling ethylenediamine to the *p*-SCN-Bz-DOTA to form a urea bond (Scheme 2). A 0.1 M triethanolamine acetate (TEAA) (pH 8) buffer was added to the *p*-SCN-Bz-DOTA-Cu solution (7 mL added, 0.032 M TEAA final) and ethylenediamine (1 μL) was mixed in a 1:1 molar ratio with the *p*-SCN-Bz-DOTA and incubated at room temperature for 15 min. To couple the amine group to the particle surface (Scheme 3a), the dextran sulfate particles were prepared by the ring-opening reaction with periodic acid (*29*). Depending on the amount of labeling desired, 1% periodic acid was mixed with a 1.41 mM Fe solution (2 mL particles) of dextran sulfate particles in an Fe/HIO_4 molar ratio of 15.2:1, 5:1, or 2.5:1 (4.25, 12.75, 25.5 μL HIO_4, respectively). Then, 0.404 mL, 1.212 mL, or 2.424 mL of the amine-activated *p*-SCN-Bz-DOTA-Cu (Fe/*p*-SCN-Bz-DOTA molar ratio of 11.4:1, 3.8:1, 1.9:1) was added to the particles and stirred at room temperature for 2 h. Next, 0.6 mL ethylene glycol was added to quench the reaction, followed by 15 min of stirring. This was followed by the addition of ~5 to 15 mg solid sodium cyanoborohydride to reduce the imine bond (Schiff base) and stirred for an additional 20 min. The product was purified by gel chromatography on a Sephadex G-25 (fine bead size, Sigma (St. Louis, MO)) column equilibrated with 1× phosphate buffered saline (PBS). Fractions corresponding to the particles were collected and pooled together.

2.3. Preparation of Copper-64 Labeled Polystyrene Beads and Dextran Sulfate Coated Iron Oxide Nanopart icles (ADIO-(DOTA-Cu)). *2.3.1. Labeling of Polystyrene Beads with Copper-64.* $^{64}CuCl_2$ (2.35 mCi, approximately 0.6 nmol, in 50 μL of 10 mM HCl) was buffered with 1 M TEAA buffer, pH 8 (5 μL), then added to *p*-SCN-Bz-DOTA (0.120 μmol in 6 μL of 0.1 M TEAA buffer, pH 8). Pure triethanolamine (1 μL) was added to adjust the final pH to 8. This reaction mixture was then incubated for 20 min at 40 °C and added to a solution of polystyrene beads (1 μm; 5.2 mg in 440 μL of 0.1 M TEAA buffer, pH 8), and incubated for 2 h at 40 °C. After incubation, 10 mM EDTA (100 μL) was added to scavenge any free metal ions. To purify, the beads were centrifuged at 7500 rpm for 5 min, the supernatant was drawn off, and the beads were resuspended in water (300 μL). The purification procedure was performed three times.

2.3.2. Labeling of ADIO Nanoparticles with Copper-64 for Multimodal Imaging. The protocol described for the "cold" copper in section 2.3.1 was used with the following modifications. Ethylenediamine (at least 1 μL was used) was mixed in a 1:1, 2:1, or 30:1 molar ratio with the *p*-SCN-Bz-DOTA and incubated at room temperature for 4 h to generate amine-Bz-DOTA (2-*p*-(3-aminopropylthioureido)benzyl-1,4,7,10-tetraazacyclododecane-tetraacetic acid). If a 2:1 or 30:1 molar ratio was used, the product was purified by size exclusion gel chromatography (SEC) on a Sephadex G-25 column equilibrated with 50 mM ammonium bicarbonate. To couple the amine group to the particle surface (Scheme 3b), the dextran sulfate particles were prepared by the ring-opening reaction with periodic acid (*29*).

Briefly, amine-Bz-DOTA was synthesized by combining a buffered solution of *p*-SCN-Bz-DOTA (2.8 mg; 4.07 μmol dissolved in 408 μL 0.1 M carbonate buffer (pH 9.2)) with ethylenediamine. Within 1 min of preparation of the aqueous *p*-SCN-Bz-DOTA, ethylenediamine (8.2 μL; 122.4 μmol, 30 equiv) was added and stirred at room temperature for 4 h. The product was then purified by SEC on a Sephadex G-25 column equilibrated with 50 mM ammonium bicarbonate. Fractions corresponding to amine-Bz-DOTA were pooled (confirmed spectrophotometrically by a broad absorbance at 260−280 nm). Second, the ADIO polysaccharide surface was modified with aldehyde groups by mixing 0.5 mL ADIO (5.64 mM Fe) with 0.25 mL 1% HIO_4 (3.9 equiv) at room temperature for 4 h. The modified particles were then purified by SEC on a Sephadex G-25 column equilibrated with nanopure water. The purified amine-Bz-DOTA was then mixed with 930 μCi (~0.2 nmol) $^{64}CuCl_2$ at room temperature for 20 min. The amine-Bz-DOTA(^{64}Cu) was then added to the aldehyde-ADIO particles and stirred at room temperature for 1.5 h. The reaction was completed by the addition of ~3 mg solid sodium cyanoborohydride to reduce the imine bond formed. The labeled nanoparticles were then purified by SEC on a Sephadex G-25 column equilibrated with 1× PBS.

2.3.3. Comparison of p-NH_2-Bz-DOTA with the Synthesized Amine-Bz-DOTA for Labeling of ADIO Nanoparticles with Copper-64. *S*-2-(4-Aminobenzyl)-1,4,7,10-tetraazacyclododecane tetraacetic acid (*p*-NH_2-Bz-DOTA) was used in parallel

Scheme 2. Amine "Activation" of the *p*-SCN-Bz-DOTA for Coupling to the Dextran Sulfate Coated Nanoparticles

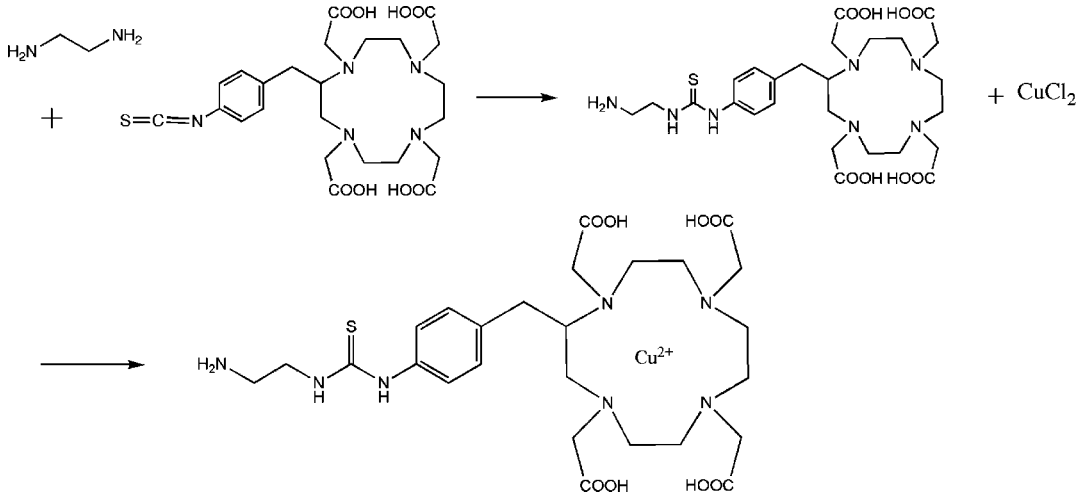

with amine-Bz-DOTA for comparison of labeling efficiency. Amine-Bz-DOTA was synthesized by reacting *p*-SCN-Bz-DOTA (1.09 μmol, 10 mM) with 30 mol equiv of ethylenediamine in 0.1 M sodium bicarbonate buffer (pH 9.0) for 3 h at room temperature (RT). The amine-Bz-DOTA product was then purified by SEC on a Sephadex G-25 column equilibrated with 50 mM ammonium bicarbonate using the Panofsky method (centrifuge at 2000 rpm for 2 min). This was repeated 2 times to yield amine-Bz-DOTA.

Next, aldehyde-terminated ADIO nanoparticles were generated by incubating 1 mol equiv (Fe/HIO_4) of 1% HIO_4 with ADIO nanoparticles at RT for 3 h (6.36 μmol Fe, 85 μL of a 74.8 mM Fe solution in 0.9% NaCl). The product was purified by SEC on a Sephadex G25 column equilibrated with nanopure water using centrifugation (2000 rpm, 2 min). This was repeated 2 times to yield the aldehyde-modified ADIO nanoparticles.

Then, copper-64 was chelated by *p*-NH_2-Bz-DOTA or amine-Bz-DOTA by first mixing $^{64}CuCl_2$ in 10 mM HCl (30 μL) with 1 M triethanolamine acetate (pH 8, 7 μL) to form a ^{64}Cu-actetate complex in a solution with a pH of 8.0. Then, the *p*-NH_2-Bz-DOTA (1.07 μmol) in 50 mM ammonium bicarbonate or amine-Bz-DOTA ($\sim$1.09 μmol) in 50 mM ammonium bicarbonate was mixed with 37 μL of the copper acetate solution at RT for 30 min.

The aldehyde-ADIO nanoparticles (110 μL) were then reacted with either *p*-NH_2-Bz-DOTA(^{64}Cu) (263 μCi) or amine-Bz-DOTA(^{64}Cu) (246 μCi) at RT for 2 h. Then, 0.5 mg solid $NaCNBH_3$ was added and allowed to incubate with the nanoparticles for an additional 20 min at RT to reduce the imine bond formed between the chelator and the nanoparticle to form a stable product. The nanoparticles were then purified by SEC on a Sephadex G25 column equilibrated with 0.9% NaCl using centrifugation (2000 rpm, 2 min). This was repeated 3 times to yield ADIO-DOTA(^{64}Cu) using either *p*-NH_2-Bz-DOTA or amine-Bz-DOTA. The activity was then measured and the radiolabeling yield determined.

2.4. Characterization. *2.4.1. Iron and Copper Quantification.* The iron and copper content of the labeled ADIOs was determined by atomic absorbance spectroscopy (AAS) using a Varian SpectrAA 220FS (Varian (Palo Alto, CA)) to verify iron concentration and the number of "cold" copper coordinated *p*-SCN-Bz-DOTA ligands were conjugated to each ADIO particle. The AAS samples were prepared in 3% HCl and five standard solutions with known iron and copper concentrations were used to generate standard curves.

Copper content of the polystyrene bead comparable experiments with "cold" copper were analyzed by inductively coupled plasma mass spectrometry (ICP-MS) on an Agilent 7500a (Agilent Technologies (Santa Clara, CA)) quadrupole ICP-MS. The ICP-MS samples were prepared as 10 mL triplicates in 3% HNO_3. In order to correct for instrumental drift during analysis, germanium solution was mixed with all sample and standard solutions as an internal standard.

2.4.2. Characterization of Amine-Bz-DOTA (2-p-(3-aminopropylthioureido)Benzyl-1,4,7,10-Tetraazacyclododecane-Tetraacetic Acid). Amine-Bz-DOTA was generated by reacting 8.26 mg *p*-SCN-Bz-DOTA with 30 mol equiv of ethylenediamine in 0.1 M sodium carbonate buffer (pH 9.0, 10 mM DOTA solution). After purification by SEC on a Sephadex G-25 column equilibrated with 50 mM ammonium bicarbonate, the amine-Bz-DOTA product was then dialyzed (MWCO = 100) against 4 L of nanopure water for 18 h with 2 water changes to remove salts. The product ($\sim$3.3 mg, 40% yield) was then lyophilized ($-$48 °C, 0.002 mTorr, 3 days) and analyzed by ^{1}H NMR and mass spectrometry. A small portion was dissolved in nanopure water for ESI^+ MS. The instrument was a Thermo LCQ ion trap (San Jose, CA) operated with an electrospray source in positive ion mode under standard conditions. The remaining sample (3.3 mg) was resuspended in D_2O (750 μL) for ^{1}H NMR (500 MHz, 300 K, Bruker, Billerica, MA). The *p*-SCN-Bz-DOTA was also dissolved in nanopure water for ESI^+ MS and DMSO-d_6 for ^{1}H NMR.

The ^{1}H NMR spectra for the final product, amine-Bz-DOTA (2-*p*-(3-aminopropylthioureido)benzyl-1,4,7,10-tetraazacyclododecane-tetraacetic acid), is presented in Supporting Information Figure S1. Amine-Bz-DOTA, ^{1}H NMR (D_2O): δ 1.9$-$2.4 (4H, m, CH_2), δ 2.4$-$2.7 (4H, m, CH_2), δ 2.745 (1H, s, CS-NH-Ar), δ 2.78$-$2.9 (4H, m, N-CH_2 and Ar-CH_2), δ 2.9$-$3.9 (21H, m, CH_2), δ 7.128 (2H, s, ArH), δ 7.225 (2H, s, ArH). ESI^+ MS (100% H_2O): *m/z* found 612.5 (100%, calc. M + H = 612.67), 634.5 (12%, M + Na^+, calc. 635.66), 306.8 (22%, [M + H]$^{2+}$, calc. 306.34), 552.5 (5%, *p*-SCN-Bz-DOTA calc. 552.4), 1223.8 (6%, dimmer + NaCl, calc. 1221.77). The ^{1}H NMR of *p*-SCN-Bz-DOTA is presented in Supporting Information Figure S2. *p*-Bz-DOTA, ^{1}H NMR (DMSO-d_6): δ 2.6$-$4.2 (43H, m, CH_2), δ 7.424 (4H, s, ArH), δ 12.5$-$14 (3H, m, COOH). ESI^+ MS (100% H_2O): *m/z* found 552.4 (100%, calc. M + H = 552.4).

2.4.3. Size Measurements. Dynamic light scattering (DLS) was used to determine the overall particle size in solution (expressed as the volume weighted diameter) with a Nanotrac 150 particle size analyzer (Microtrac, Inc. (Montgomeryville, PA)). A geometric eight-root regression, with no residuals, was used to fit the data. The Nanotrac 150 has a built-in thermometer

Scheme 3. Conjugation of *p*-SCN-Bz-DOTA-Copper to the Dextran Sulfate Coated Nanoparticles[a]

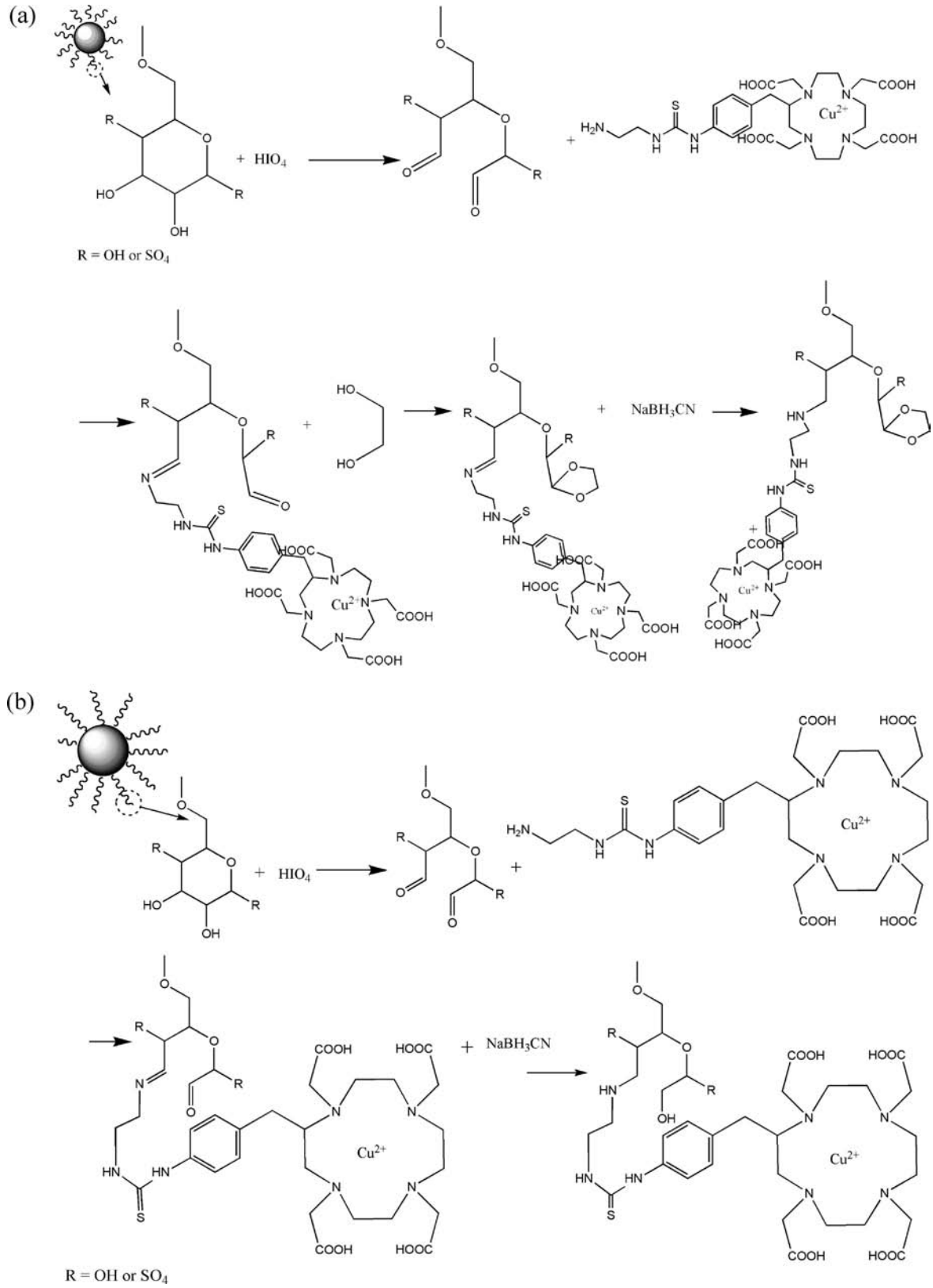

[a] (a) Initial synthesis where ethylene glycol was used to quench the HIO_4. (b) No ethylene glycol is used and SEC is used to purify the aldehyde modified nanoparticles and the final product after reduction of the imine bond between the amine-Bz-DOTA(^{64}Cu) and the nanoparticles.

to measure the cell temperature, from which the viscosity is calculated; the nanorange option was enabled and a scan time of 30 s was used. Particle size is expressed as the mean volume diameter ± one standard deviation.

3. RESULTS AND DISCUSSION

In previous work, the synthetic strategy for conjugating fluorescent dyes to nanoparticles has been to form an amide

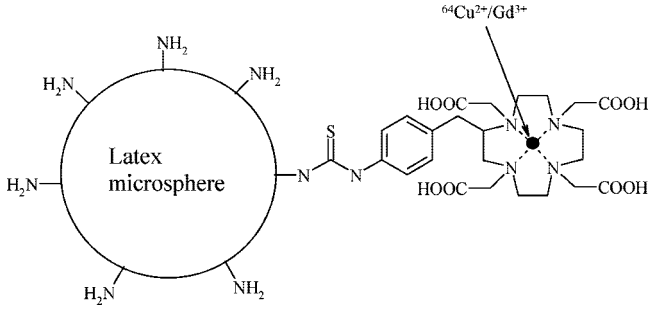

Figure 1. A schematic illustration of the conjugation of the metal chelating ligand to the surface of a polystyrene bead.

bond between the dye and the amine sites on the coating of the SPIO, or a linker connecting to the SPIO through a disulfide or a thioether linkage (*9, 13*). Our initial labeling approach was based on a similar theory. For the dextran sulfate coated nanoparticles, the particle surface is modified to contain aldehyde groups, which can be conjugated to the amine-reactive *p*-SCN-Bz-DOTA chelator. For the polystyrene beads, the chelating ligand is directly conjugated to the aliphatic amine groups on their surfaces.

3.1. Nanoparticles are Not Labeled if DOTA is Conjugated to the Particle before Chelation of Copper. *3.1.1. Polystyrene Beads As a Model Compound: Conjugation of DOTA to the Particle Surface.* To conveniently explore and develop the chemistry of the labeling of surface-modified nanoparticles, we utilized a system consisting of aliphatic amine polystyrene beads. The polystyrene beads are inexpensive, commercially available, and mimic the surface environment of amine-functionalized ADIO nanoparticles, or alternatively, different functionality if the ADIO particles are aldehyde-terminated. Because the polystyrene beads are fundamentally different from the aldehyde-modified ADIO nanoparticles (size, surface charge, and functional groups), labeling of these particles presents an opportunity to create a labeling method that can be applied to a broad range of nanoparticle systems.

The amine-reactive, metal chelating ligand (*p*-SCN-Bz-DOTA) was attached by direct linkage to the amine groups of the bead by the formation of a thiourea bond (Figure 1) described earlier by Mirazdeh et al. (*30*). We found for the aliphatic amine polystyrene bead system that labeling is not achieved if the chelator is conjugated to the nanoparticles before the copper is introduced. This has previously been observed for the 1,4,8,11-tetraazacyclotetradecane-*N*,*N*′,*N*″,*N*‴-tetraacetic acid (TETA) chelator by other researchers (*31*). In the study, by Moi et al. labeling antibodies with copper-64 TETA, it was found that labeling was only achievable if the copper was preinserted into the TETA before conjugation to the antibody (*31*).

In our polystyrene system, for example, if 0.5 mL of the 1 μm PS beads were first coupled to *p*-SCN-Bz-DOTA ($\sim$20 400 DOTA molecules per bead), purified and then mixed with a Cu^{2+} chloride solution (molar ratio of Cu^{2+}/*p*-SCN-Bz-DOTA = 2.1:1), no copper was detected in the product after purification. We believe that that lack of coupling is due to competition for binding of copper by the numerous free amines available at the surface. Each nonconjugated 1 μm sized bead had an average of 157 000 amines on the surface. Even with a 100% conjugation of the *p*-SCN-Bz-DOTA (in this case 20 400 per bead), the free surface amine groups remaining on each bead could bind up to approximately 130 000 copper(II) ions and might thereby compete with, and prevent, chelation by the DOTA groups. Therefore, prechelation of the copper ion must first be performed in a separate step.

3.1.2. Conjugation of DOTA to the ADIO Particles before Chelation of Copper Did Not Result in Labeling. The ADIOs were previously shown to have small size and good magnetic properties to work as a MR imaging contrast enhancing agent. The relaxivities were determined to $r_1 = 14.46\ mM^{-1}\ s^{-1}$ and $r_2 = 72.55\ mM^{-1}\ s^{-1}$ at 60 MHz, 37 °C, and the overall particle diameter was measured as 32.3 $\pm$ 11.8 nm (*28*).

A literature procedure for coupling fluorescein isothiocyanate was modified to couple *p*-SCN-Bz-DOTA to the nanoparticles after amination of the dextran (sulfate) coating (Scheme 1) (*29*). After amination of the ADIO particles, *p*-SCN-Bz-DOTA was conjugated to the nanoparticles through the amine groups.

We found that, for both nanoparticle systems, aliphatic amine polystyrene beads and dextran sulfate coated iron oxides, labeling with copper was not possible if the metal chelator was conjugated to the nanoparticle surface before chelation; only after preinsertion of the metal into the chelator before conjugation to the nanoparticle surface was labeling achievable. As observed for the polystyrene bead system, if the *p*-SCN-Bz-DOTA was first conjugated to the particle surface before the chelation of copper, there was inhibition of the labeling (Table 1). In agreement with the previous study by Moi et al., for our nanoparticle systems, we found that prechelation of copper-64 was necessary for both polystyrene beads and dextran sulfate coated iron oxide nanoparticles (*31*).

Table 1. Radiolabeling of ADIO Nanoparticles[a]

particle[b]	E.D.:*p*-SCN-Bz-DOTA	% yield (^{64}Cu)
ADIO	1:1	0[c]
ADIO	1:1	1
ADIO	2:1	5.2
ADIO	30:1	21.5

[a] The yield was determined by measuring the activity level before conjugation and then after purification of the final product. Size was determined by DLS. [b] Particle size of the ADIO before labeling was 32 $\pm$ 11.8 nm as determined by DLS and was 26.6 $\pm$ 7.3 nm after labeling with copper-64 (for the product that had a yield of 21.5%. [c] Copper-64 was not prechelated into the *p*-SCN-Bz-DOTA and no labeling was achieved.

Table 2. Conjugation of *p*-SCN-Bz-DOTA-Cu to the Polystyrene Bead Surface[a]

size of PS-bead	*p*-SCN-Bz-DOTA:bead	number DOTA-Cu/bead	% yield (Cu)
78 nm	4 968: 1	150	3
1000 nm	218 000:1	40 000	18

[a] The amount of Cu was determined by ICP-MS after particle purification. Particle size was given by the manufacturer and confirmed by DLS.

3.2. Chelation of the Copper by the DOTA before Conjugation to the Nanoparticles Results in Some Labeling at Low Yield. *3.2.1. Preinsertion of Copper into the p-SCN-Bz-DOTA Resulted in Labeling of Polystyrene Beads.* By first chelating the copper ion in the DOTA complex, and then conjugating the *p*-SCN-Bz-DOTA(Cu) to the PS, bead labeling was achieved (Table 2). The higher degree of labeling for the 1 μm PS beads (18%) compared to the 78 nm beads (3%) could have been due to several factors. First, the amount of *p*-SCN-Bz-DOTA was 43 times greater for the 1 μm beads, and this may have resulted in the higher labeling efficiency. Another possible explanation for the higher labeling efficiency of the larger beads could have been due to the surface density of the amine groups. For a 1 μm particle (surface area of 3 141 593 Å^2), the surface density for 157 000 amines would be approximately 1 amine group every 20 Å^2. For the 78 nm beads (1 911 345 Å^2), the surface density of 54 000 amines would be 1 amine every 36 Å^2. The surface charge of the larger particles has a greater charge density and therefore may result in a more efficient attraction and subsequent coupling between the chelator and the bead.

Table 3. Conjugation of *p*-SCN-Bz-DOTA-Cu to ADIO Surface[a]

molar ratio Fe/*p*-SCN-Bz-DOTA	particle size	number *p*-SCN-Bz-DOTA-Cu/ADIO	% yield (Cu)
11.4: 1	31.6 ± 9.1	7.0	0.8
3.8: 1	33.1 ± 8.4	16.1	0.6
1.9: 1	36.5 ± 10.4	328.8	6.0

[a] The amount of Fe and Cu were determined by AAS after particle purification. The amount of iron per core was calculated based on an average particle size of 7.9 nm and one core per ADIO particle was assumed. Particle size in solution was determined by DLS.

3.2.2. Preinsertion of Copper into the p-SCN-Bz-DOTA Resulted in Labeling of ADIO Nanoparticles, But Cross-Linking Lead to Aggregation. A literature procedure for coupling fluorescein isothiocyanate was modified to couple *p*-SCN-Bz-DOTA to the nanoparticles after amination of the dextran (sulfate) coating (Scheme 1) (*29*). After amination of the ADIO particles, *p*-SCN-Bz-DOTA was conjugated to the nanoparticles through the amine groups. We found that amination of the ADIO particles led to irreversible cross-linking and flocculation. The cross-linking is most likely due to the ethylenediamine being equally reactive at both ends. The ADIO nanoparticles were 32 nm before surface modification and 133 nm after amination.

Particle size plays an integral role in clearance from the body, and iron oxide particles larger than 50 nm have been shown to be rapidly cleared by the liver (*32–34*). To target specific sites of interest, particle size is to be kept small, smaller than ~30 nm, to increase circulation time to allow the particles to reach targets of interest (*32, 35, 36*). To avoid the irreversible cross-linking of the ADIO nanoparticles, we opted to modify the synthesis by introducing amine groups to the *p*-SCN-Bz-DOTA rather than the ADIO nanoparticles (Scheme 2). In this revised chemistry, we attach the ethylenediamine to the *p*-SCN-Bz-DOTA rather than the ADIO surface. If dimers of the DOTA form, they cannot react with the nanoparticles, and can be removed by purification, and thus the aggregation seen with functionalizing the ADIO nanoparticles was avoided.

3.2.3. Cross-Linking of ADIO Nanoparticles Avoided by Amination of the p-SCN-Bz-DOTA but Cu Labeling Yield Remains Low. After preinsertion of the copper into the *p*-SCN-Bz-DOTA (Scheme 2), the chelator was conjugated to the nanoparticle surface (Scheme 3a). The *p*-SCN-Bz-DOTA was modified to have an amine group and this could then react with the aldehyde group on the ADIO surface (Scheme 3a). By coupling the ethylenediamine to the *p*-SCN-Bz-DOTA instead of the ADIO nanoparticles, we were able to avoid the cross-linking of the particles. Results for the degree of "cold" copper labeling of the ADIO nanoparticles are shown in Table 3. As expected, the degree of labeling increased with additional HIO_4 (more binding sites) and the addition of extra *p*-SCN-Bz-DOTA(Cu^{2+}). Approximately 7 *p*-SCN-Bz-DOTA(Cu^{2+}) molecules were conjugated to the particle surface with a Fe/*p*-SCN-Bz-DOTA molar ratio 11.4:1 and the number of conjugated *p*-SCN-Bz-DOTA(Cu^{2+}) molecules increased to 328 with a Fe/*p*-SCN-Bz-DOTA molar ratio of 1.9:1 (Table 3). Interestingly, a 3-fold increase in the *p*-SCN-Bz-DOTA, from 11.4:1 to 3.8:1, did not result in an increased labeling yield (Table 3); only when a 6-fold increase in *p*-SCN-Bz-DOTA (1.9:1) was used did the labeling yield increase from 0.8% to 6%. The DOTA/HIO_4 was kept constant in all three instances, approximately 1:1; therefore, the increase in labeling yield (6%) for the highest concentration of HIO_4 (25.5 μL HIO_4, Fe/*p*-SCN-Bz-DOTA = 1.9:1) must have been more efficient compared to lower concentrations of HIO_4 for creating more reaction sites in the dextran coating on the nanoparticles. The higher acid concentration (25.5 μL HIO_4) may have been necessary to decrease the pH significantly to drive the ring opening reaction (on the polysaccharide nanoparticle coating) (Scheme 3a).

Table 4. Radiolabeling of Polystyrene Beads[a]

size of PS bead	*p*-SCN-Bz-DOTA:bead	activity used (mCi ^{64}Cu)	labeled activity (mCi ^{64}Cu)	% yield (^{64}Cu)
78	1.13×10^6: 1	2.35	0.571	24
78	1.31×10^6: 1	2.9	0.639	22
1000	1.54×10^8: 1	4.02	0.272	6.8

[a] The yield was determined by measuring the activity level before conjugation and then after purification of the final product.

The particle size increased slightly as the amount of *p*-SCN-Bz-DOTA added increased (Table 3). The size of the particles with 7 DOTA(Cu^{2+}) moieties attached was 31.6 nm and was 36.5 nm for particles with 329 DOTA(Cu^{2+}) attached. This was most likely the result of an added hydration layer due to the nitro and carboxyl groups added by the additional DOTA moieties. Dynamic light scattering measures the hydrodynamic radius, the particle size plus surface-bound water, and therefore as the number of DOTA moieties increased the hydration layer also increased, resulting in a larger particle diameter (Table 3).

3.3. Modification of the Chemistry Resulted in Greater Labeling Yields for Both Nanoparticle Systems. Initially, by attempting conjugation of *p*-SCN-Bz-DOTA chelator to an amine-coated nanoparticle, polystyrene beads or dextran sulfate coated nanoparticles, before insertion of the metal (Cu^{2+}) no labeling was achievable. By preinserting the copper into the DOTA chelator before conjugation to the nanoparticle surface, labeling was accomplished. However, for each system, there were limitations in labeling efficiency that warranted improved chemistry. In the polystyrene bead system, labeling with copper took several days, which is not desirable for a radionuclide with a limited lifetime. Therefore, we sought to obtain similar labeling yields (at least 18%) of the polystyrene beads with more rapid chemistry and purification. For the ADIO nanoparticle system, labeling was achievable and particle cross-linking avoidable by generating a amine-Bz-DOTA(Cu) complex to conjugate to the ADIO surface; however, the yields were very low, <1% for ^{64}Cu, and therefore we sought to improve the chemistry to obtain higher labeling yields.

3.3.1. Radiolabeling of Polystyrene Beads with Improved Chemistry. The radiolabeling for the polystyrene beads with copper-64 was modified from the "cold" copper labeling to minimize the reaction time to avoid unnecessary decay of the radionuclide. For the "cold" copper labeling, the copper was incubated with the DOTA at a 1.25:1 molar ratio for 2 h in diH_2O at room temperature and then purified by SEC. As for the copper-64, it was supplied in a 10 mM HCl solution, and we therefore adjusted the pH to 8 with TEAA and incubated at 40 °C for 20 min (compared to 2 h). The solution was buffered, as it is known that the stability of the copper-DOTA complex decreases as the pH decreases (*37, 38*). Furthermore, no SEC was used for purification after chelation of the copper-64 by DOTA as the *p*-SCN-Bz-DOTA was in excess. The use of an acetate buffer, TEAA, in this work is similar to the work by Sun et al. in which copper-64 was chelated by 1,4,8,11-tetraazacyclododecane-1,4,8,11-tetraacetic acid (TETA) in ammonium acetate (pH 7) at 43 °C for 2 h (*39*).

The conjugation of the *p*-SCN-Bz-DOTA(^{64}Cu) to the polystyrene beads was done at 40 °C and the incubation was 2 h compared to overnight for labeling the PS beads with the "cold" copper. Finally, similar to the work by Sun et al. (*39*), we used centrifugation to purify the radiolabeled beads in favor of dialysis.

These time reduction steps, utilizing an elevated temperature, resulted in a radiolabeling yield for the [(*p*-SCN-Bz-DOTA)-^{64}Cu] on the polystyrene beads of 7% to 24% (Table 4). The radiolabeling for the 78 nm particles increased to 22−24% (Table 4), compared to the 3% labeling with the "cold" copper (Table 2). This increase

in labeling yield was most likely due to the increased *p*-SCN-Bz-DOTA/bead ratio for the radiolabeling. However, the radiolabeling of the 1 μm PS beads was only ~7% compared to 18% for the "cold" copper (Tables 1 and 3). This may have been due to a large change in pH during the addition of the buffer with a large amount of the copper-64, 4.02 mCi, compared to the smaller amount used for the 78 nm PS beads.

3.3.2. Labeling of ADIO with Modification of the Chemistry Resulted in Greater Labeling Yields. As was the case with the "cold" copper labeling of ADIO particles and PS beads, if the copper-64 was not chelated by the *p*-SCN-Bz-DOTA before conjugation to the nanoparticle there was no labeling achieved (Table 1). Following the preinsertion scheme and molar ratios of starting materials developed during the cold copper experiments (ratio of ethylenediamine/*p*-SCN-Bz-DOTA = 1:1) (Schemes 2 and 3a), labeling the ADIO nanoparticles with copper-64 had a yield of 1% (Table 1). This was most likely due to the dimerization of *p*-SCN-Bz-DOTA and was alleviated by increasing the amount of ethylenediamine.

The amine-Bz-DOTA was purified by SEC (Schemes 2 and 3b) and excess ethylenediamine removed before addition to the aldehyde-modified nanoparticles or the excess ethylenediamine would react with adjacent nanoparticles and cause flocculation. A molar ratio of the ethlyenediamine/*p*-SCN-Bz-DOTA of 2:1 and purification with SEC increased the labeling yield from 1% to ~5% (Table 1). By further increasing the ratio to 30:1, the labeling yield increased to ~20% (Table 1). After the radioactivity had decayed, the particles that had the ~20% yield were sized by DLS and found to be 26.6 ± 7.3 nm in diameter, which is of similar size to the starting ADIO material (32 ± 11.8 nm). This demonstrates that the radiolabeling did not affect the overall particle size. Due to the low yields, the other labeled particles were not sized by DLS.

The increase in yields using SEC to purify the aldehyde-modified ADIO nanoparticles and amine-Bz-DOTA (Scheme 3b) had a strong affect on radiolabeling. The amine-Bz-DOTA was purified by SEC purification not only to remove excess ethylenediamine, but also for the removal of sodium to avoid competition between the copper-64 and sodium by the DOTA macrocycle. Additionally, by using SEC to purify the aldehyde-modified ADIO nanoparticles, the HIO_4 could be removed without the use of ethylene glycol, which could have had two effects on the outcome of the labeling.

Chromatography ensured the removal of all HIO_4 so that the solution was not acidic during the conjugation of the *p*-SCN-Bz-DOTA complex to the nanoparticle. It is known that if the pH drops below about 4 the DOTA can no longer conjugate the copper as the amines in the ring become protonated. Second, by avoiding ethylene glycol any dioxane formation at the aldehyde groups on the nanoparticle surface was avoided, which would block reaction sites for the amine-Bz-DOTA(^{64}Cu).

Low labeling yields, around 1−5%, were observed for both the cold-copper and copper-64 labeling in TEAA buffer and a 1:1 ethylenediamine/*p*-SCN-Bz-DOTA molar ratio (Tables 2 and 4). The reaction between the aldehyde group on the nanoparticle and the amine of the amine-Bz-DOTA is more efficient at a higher pH, around 9, compared to neutral or slightly basic (conditions seen with the TEAA, pH 8). We therefore used a more basic buffer, sodium carbonate buffer, pH 9.2 (versus pH 8 for the TEAA), for ethylenediamine/*p*-SCN-Bz-DOTA molar ratios of 2:1 and 30:1 (Scheme 3b). By increasing the ratio of ethylenediamine to *p*-SCN-Bz-DOTA and increasing the pH of the reaction during the copper-64 labeling, the highest labeling yield, ~20%, was achieved without an increase in particle size.

Table 5. Radiolabeling Yield for ADIO-DOTA(^{64}Cu)[a].

chelator	labeling yield (%)
p-NH_2-Bz-DOTA	6.2
amine-Bz-DOTA	9.1

[a] Running the labeling procedure in parallel using the same batch of ^{64}CuCl, the radiolabeling was more efficient (32%) using the synthesized amine-Bz-DOTA.

3.4. Labeling of ADIO with the Synthesized Amine-Bz-DOTA Resulted in a Greater Labeling Yield Compared to the Commercially Available *p*-NH_2-Bz-DOTA. The two chelators, amine-Bz-DOTA and the commercially available *p*-NH_2-Bz-DOTA, were incubated with ^{64}Cu and then conjugated to the ADIO nanoparticles in parallel (Scheme 3b). The radiolabeling using each of the DOTA derivatives is shown in Table 5, and the labeling efficiency for the amine-Bz-DOTA was ~32% greater than that of the *p*-NH_2-Bz-DOTA. This could have been due to the ethylenediamine linker, which may decrease the steric hindrance between the DOTA and the nanoparticle.

4. CONCLUDING REMARKS

From iron oxides for magnetic resonance imaging (MRI) to quantum dots for optical imaging, nanotechnology has come to play an important role in many imaging applications. The highly complementary nature of MRI and PET has resulted in great interest in combined MR/PET imaging (*2, 40*); however, there are very few reports of multimodal PET/MRI contrast agents (*5, 19*). Our recent successes in synthesizing dextran sulfate coated iron oxide nanoparticles (ADIO) (*28*) and acquiring simultaneous PET and MR images (*1*), as well as the scarcity of suitable imaging probes for PET/MR imaging made it desirable to synthesize nanoparticles labeled with ^{64}Cu. Labeling was recalcitrant to traditional coupling methods and new syntheses had to be developed to achieve labeling of nanoparticles with ^{64}Cu.

In summary, radiolabeling was not achievable for either nanoparticle system if the metal (Cu^{2+}) was not first chelated in the DOTA before conjugation. Radiolabeling yields for the polystyrene beads was 24% and was achieved by conjugating the *p*-SCN-Bz-DOTA(Cu^{2+}) to the amines on the polystyrene surface. For the ADIO nanoparticles, however, amine groups had to be introduced onto the *p*-SCN-Bz-DOTA to avoid the cross-linking that occurred when the bifunctional ethylenediamine was used functionalize the ADIO surface. Radiolabeling of the aldehyde-functionalized ADIO nanoparticles with amine-Bz-DOTA(Cu^{2+}) was improved from 1% to 5% by using SEC instead of ethylene glycol to remove the HIO_4 during purification of the aldehyde-functionalized ADIO nanoparticles. Further improvement of radiolabeling of the ADIO nanoparticles was achieved by increasing the molar ratio of ethylenediamine to *p*-SCN-Bz-DOTA to 30:1 from 1:1. Furthermore, the synthesized amine-Bz-DOTA [2-*p*-(3-aminopropylthioureido)benzyl-1,4,7,10-tetraazacyclododecane-tetraacetic acid] had a radiolabeling yield that was 32% more efficient compared to the commercially available *p*-NH_2-Bz-DOTA. This increase in labeling of the amine-Bz-DOTA was most likely due to the extended linker that the ethylenediamine provided, compared to the NH_2 group directly off of the benzyl group of the commercial compound, and thus resulted in less steric hindrance. The radiolabeling yield for the *p*-SCN-Bz-DOTA on the ADIO was ~21%, which is ample for our imaging applications; due to the extreme sensitivity of PET, even modest levels of labeling are sufficient for detection of the compound.

It is important to note that the presence of amines on a surface does not guarantee that traditional amine-coupling methods will work, as we found with the nanoparticles of two different types. The nanoparticle environment posed an unexpected challenge

for conjugation. For example, compared to the dextran-coated particles described by Nahrendorf et al., where the authors first chelate the DTPA to the nanoparticle surface and then purify the nanoparticle-DTPA(^{64}Cu) by centrifugation (*19*), we found that, if the DOTA was chelated to the nanoparticle (e.g., polystyrene) and then incubated with ^{64}Cu, centrifugation alone did not remove surface-bound (not chelated) ^{64}Cu. In our polystyrene system, this surface-bound ^{64}Cu was easily removed by chromatography. The stability constants for DTPA or DOTA complexes with copper are similar, 21.5 and 22.25, respectively (*25, 41*), but slightly higher for DOTA. It is possible for the polystyrene bead system that the large number of amine groups at the particle surface presented a competition binding site for the Cu^{2+}; if the metal was not preinserted into the chelator before conjugation to the nanoparticle surface, then the Cu^{2+} bound to the surface of the nanoparticle rather than the DOTA and could be removed by chromatography. Similarly, the Cu^{2+} could have interacted with high negative charge on the surface of dextran sulfate coated particles (ADIO) rather than the DOTA, which could explain why in our ADIO system we had to preinsert the Cu^{2+} into the DOTA before conjugation compared the method used by Nahrendorf et al. with the more neutral charge of the dextran-coated particles.

Additionally, for the polysaccharide-coated (dextran sulfate) iron oxide nanoparticles there were several parameters that had to be considered, including the affect of surface modification on particle aggregation (e.g., functionalizing ADIO surface with ethylenediamine) and preinsertion of the metal into the chelator before conjugation to the nanoparticle surface. The ethylenediamine used here to introduce amine groups most likely resulted in cross-linking between nanoparticles as a result of the bifunctionality of the ethylenediamine and numerous aldehyde groups present on the nanoparticle surface.

The methods developed here can be applied to other nanoparticle systems with amine-functionalized surfaces, or it can be used with other functional groups such as *N*-hydroxysuccinimide esters, thiol, or carboxyl functional groups. One can envision the use of the multimodal contrast agent developed here for whole body screening using PET to identify potential lesions, then applying MRI to obtain detailed information on plaque structure and composition. We are currently applying these probes for multimodal imaging in an animal modal of atherosclerosis.

ACKNOWLEDGMENT

B.R.J. was supported by the National Institutes of Health Training Grant (T32-EB003827). This work was supported by the American Heart Association (0365016Y) and the National Institutes of Health (EB000993-01A1). We thank Jacob Vogan for assistance with syntheses and Elizabeth Osborne and Dr. Chuqiao Tu for assistance with NMR and MS. We thank the laboratory of Dr. Claude Meares for providing the *S*-2-(4-aminobenzyl)-1,4,7,10-tetraazacyclododecane tetraacetic acid (*p*-NH_2-Bz-DOTA).

Supporting Information Available: ^{1}H NMR spectra of the amine-Bz-DOTA and p-SCN-Bz-DOTA. This material is available free of charge via the Internet at http://pubs.acs.org/BC.

LITERATURE CITED

(1) Catana, C., Wu, Y. B., Judenhofer, M. S., Qi, J. Y., Pichler, B. J., and Cherry, S. R. (2006) Simultaneous acquisition of multislice PET and MR images: Initial results with a MR-compatible PET scanner. *J. Nucl. Med. 47*, 1968–1976.

(2) Cherry, S. R. (2006) The 2006 Henry N.Wagner lecture: Of mice and men (and positrons) - Advances in PET imaging technology. *J. Nucl. Med. 47*, 1735–1745.

(3) Cherry, S. R. (2001) Fundamentals of positron emission tomography and applications in preclinical drug development. *J. Clin. Pharmacol. 41*, 482–491.

(4) Mulder, W. J. M., Koole, R., Brandwijk, R. J., Storm, G., Chin, P. T. K., Strijkers, G. J., Donega, C. D., Nicolay, K., and Griffioen, A. W. (2006) Quantum dots with a paramagnetic coating as a bimodal molecular imaging probe. *Nano Lett. 6*, 1–6.

(5) Gustafsson, B., Youens, S., and Louie, A. Y. (2006) Development of contrast agents targeted to macrophage scavenger receptors for MRI of vascular inflammation. *Bioconjugate Chem. 17*, 538–547.

(6) Houston, J. P., Ke, S., Wang, W., Li, C., and Sevick-Muraca, E. M. (2005) Quality analysis of in vivo near-infrared fluorescence and conventional gamma images acquired using a dual-labeled tumor-targeting probe. *J. Biomed. Opt. 10*.

(7) Kelly, K. A., Allport, J. R., Tsourkas, A., Shinde-Patil, V. R., Josephson, L., and Weissleder, R. (2005) Detection of vascular adhesion molecule-1 expression using a novel multimodal nanoparticle. *Circ. Res. 96*, 327–336.

(8) Huber, M. M., Staubli, A. B., Kustedjo, K., Gray, M. H. B., Shih, J., Fraser, S. E., Jacobs, R. E., and Meade, T. J. (1998) Fluorescently detectable magnetic resonance imaging agents. *Bioconjugate Chem. 9*, 242–249.

(9) Josephson, L., Tung, C. H., Moore, A., and Weissleder, R. (1999) High-efficiency intracellular magnetic labeling with novel superparamagnetic-tat peptide conjugates. *Bioconjugate Chem. 10*, 186–191.

(10) Schellenberger, E. A., Sosnovik, D., Weissleder, R., and Josephson, L. (2004) Magneto/optical annexin V, a multimodal protein. *Bioconjugate Chem. 15*, 1062–1067.

(11) Tsourkas, A., Shinde-Patil, V. R., Kelly, K. A., Patel, P., Wolley, A., Allport, J. R., and Weissleder, R. (2005) In vivo imaging of activated endothelium using an anti-VCAM-1 magnetooptical probe. *Bioconjugate Chem. 16*, 576–581.

(12) Wang, W., Ke, S., Kwon, S., Yallampalli, S., Cameron, A. G., Adams, K. E., Mawad, M. E., and Sevick-Muraca, E. M. (2007) A new optical and nuclear dual-labeled imaging agent targeting interleukin 11 receptor alpha-chain. *Bioconjugate Chem. 18*, 397–402.

(13) Josephson, L., Kircher, M. F., Mahmood, U., Tang, Y., and Weissleder, R. (2002) Near-infrared fluorescent nanoparticles as combined MR/optical imaging probes. *Bioconjugate Chem. 13*, 554–560.

(14) Medarova, Z., Pham, W., Kim, Y., Dai, G. P., and Moore, A. (2006) In vivo imaging of tumor response to therapy using a dual-modality imaging strategy. *Int. J. Cancer 118*, 2796–2802.

(15) Schellenberger, E. A., Reynolds, F., Weissleder, R., and Josephson, L. (2004) Surface-functionalized nanoparticle library yields probes for apoptotic cells. *ChemBioChem 5*, 275–279.

(16) Sosnovik, D. E., Schellenberger, E. A., Nahrendorf, M., Novikov, M. S., Matsui, T., Dai, G., Reynolds, F., Grazette, L., Rosenzweig, A., Weissleder, R., and Josephson, L. (2005) Magnetic resonance imaging of cardiomyocyte apoptosis with a novel magneto-optical nanoparticle. *Magn. Reson. Med. 54*, 718–724.

(17) Veiseh, O., Sun, C., Gunn, J., Kohler, N., Gabikian, P., Lee, D., Bhattarai, N., Ellenbogen, R., Sze, R., Hallahan, A., Olson, J., and Zhang, M. Q. (2005) Optical and MRI multifunctional nanoprobe for targeting gliomas. *Nano Lett. 5*, 1003–1008.

(18) Zhao, M., Josephson, L., Tang, Y., and Weissleder, R. (2003) Magnetic sensors for protease assays. *Angew. Chem., Int. Ed. 42*, 1375–1378.

(19) Nahrendorf, M., Zhang, H. W., Hembrador, S., Panizzi, P., Sosnovik, D. E., Aikawa, E., Libby, P., Swirski, F. K., and Weissleder, R. (2008) Nanoparticle PET-CT imaging of macrophages in inflammatory atherosclerosis. *Circulation 117*, 379–387.

(20) Kukis, D. L., Diril, H., Greiner, D. P., DeNardo, S. J., DeNardo, G. L., Salako, Q. A., and Meares, C. F. (1994) A comparative study of copper-67 radiolabeling and kinetic stabili-

ties of antibody-macrocycle chelate conjugates. *Cancer 73*, 779–786.
(21) Boswell, C. A., Sun, X. K., Niu, W. J., Weisman, G. R., Wong, E. H., Rheingold, A. L., and Anderson, C. J. (2004) Comparative in vivo stability of copper-64-labeled cross-bridged and conventional tetraazamacrocyclic complexes. *J. Med. Chem. 47*, 1465–1474.
(22) Smith, S. V.(. (2004) Molecular imaging with copper-64. *J. Inorg. Biochem. 98*, 1874–1901.
(23) Anderson, C. J., Connett, J. M., Schwarz, S. W., Rocque, P. A., Guo, L. W., Philpott, G. W., Zinn, K. R., Meares, C. F., and Welch, M. J. (1992) Copper-64-labeled antibodies for pet imaging. *J. Nucl. Med. 33*, 1685–1691.
(24) Barbaro, P., Bianchini, C., Capannesi, G., Di Luca, L., Laschi, F., Petroni, D., Salvadori, P. A., Vacca, A., and Vizza, F. (2000) Synthesis and characterization of the tetraazamacrocycle 4,10-dimethyl-1,4,7,10-tetraazacyclododecane-1,7-diacetic acid (H(2)Me(2)DO2A) and of its neutral copper(II) complex [Cu(Me(2)DO2A)]. A new Cu-64-labeled macrocyclic complex for positron emission tomography imaging. *J. Chem. Soc., Dalton Trans.* 2393–2401.
(25) Chaves, S., Delgado, R., and Dasilva, J. (1992) The stability of the metal-complexes of cyclic tetra-aza tetraacetic acids. *Talanta 39*, 249–254.
(26) Di Bartolo, N., Sargeson, A. M., and Smith, S. V. (2006) New Cu-64 PET imaging agents for personalised medicine and drug development using the hexa-aza cage, SarAr. *Org. Biomol. Chem. 4*, 3350–3357.
(27) Paul, K. G., Frigo, T. B., Groman, J. Y., and Groman, E. V. (2004) Synthesis of ultrasmall superparamagnetic iron oxides using reduced polysaccharides. *Bioconjugate Chem. 15*, 394–401.
(28) Jarrett, B. R., Frendo, M., Vogan, J., and Louie, A. Y. (2007) Size-controlled synthesis of dextran sulfate coated iron oxide nanoparticles for magnetic resonance imaging. *Nanotechnology 18*, 035603.
(29) Liberda, J., Ticha, M., and Jonakova, V. (1997) Preparation of fluorescein-labelled and biotinylated derivatives of polysaccharides for lectin-saccharide binding studies. *Biotechnol. Techniques 11*, 265–267.
(30) Mirzadeh, S., Brechbiel, M. W., Atcher, R. W., and Gansow, O. A. (1990) Radiometal labeling of immunoproteins: covalent linkage of 2-(4-isothiocyanatobenzyl)diethylenetriaminepentaacetic acid ligands to immunoglobulin. *Bioconjugate Chem. 1*, 59–65.
(31) Moi, M. K., Meares, C. F., McCall, M. J., Cole, W. C., and Denardo, S. J. (1985) Copper-chelates as probes of biological-systems - stable copper-complexes with a macrocyclic bifunctional chelating agent. *Anal. Biochem. 148*, 249–253.
(32) Briley-Saebo, K. C., Johansson, L. O., Hustvedt, S. O., Haldorsen, A. G., Bjornerud, A., Fayad, Z. A., and Ahlstrom, H. K. (2006) Clearance of iron oxide particles in rat liver - Effect of hydrated particle size and coating material on liver metabolism. *Invest. Radiol. 41*, 560–571.
(33) Majumdar, S., Zoghbi, S. S., and Gore, J. C. (1990) Pharmacokinetics of superparamagnetic iron-oxide mr contrast agents in the rat. *Invest. Radiol. 25*, 771–777.
(34) Yancy, A. D., Olzinski, A. R., Hu, T. C. C., Lenhard, S. C., Aravindhan, K., Gruver, S. M., Jacobs, P. M., Willette, R. N., and Jucker, B. M. (2005) Differential uptake of ferumoxtran-10 and ferumoxytol, ultrasmall superparamagnetic iron oxide contrast agents in rabbit: Critical determinants of atherosclerotic plaque labeling. *J. Magn. Reson. Imaging 21*, 432–442.
(35) Thorek, D. L. J., Chen, A., Czupryna, J., and Tsourkas, A. (2006) Superparamagnetic iron oxide nanoparticle probes for molecular imaging. *Ann. Biomed. Eng. 34*, 23–38.
(36) Weissleder, R., Elizondo, G., Wittenberg, J., Rabito, C. A., Bengele, H. H., and Josephson, L. (1990) Ultrasmall superparamagnetic iron-oxide - characterization of a new class of contrast agents for mr imaging. *Radiology 175*, 489–493.
(37) Kotek, J., Kalman, F. K., Hermann, P., Brucher, E., Binnemans, K., and Lukes, I. (2006) Study of thermodynamic and kinetic stability of transition metal and lanthanide complexes of DTPA analogues with a phosphorus acid pendant arm. *Eur. J. Inorg. Chem.* 1976–1986.
(38) Anderegg, G., Arnaud-Neu, F., Delgado, R., Felcman, J., and Popov, K. (2005) Critical evaluation of stability constants of metal complexes of compexones for biomedical and environmental applications. *Pure Appl. Chem. 77*, 1445–1495.
(39) Sun, X. K., Rossin, R., Turner, J. L., Becker, M. L., Joralemon, M. J., Welch, M. J., and Wooley, K. L. (2005) An assessment of the effects of shell cross-linked nanoparticle size, core composition, and surface PEGylation on in vivo biodistribution. *Biomacromolecules 6*, 2541–2554.
(40) Jacobs, R. E., and Cherry, S. R. (2001) Complementary emerging techniques: high-resolution PET and MRI. *Curr. Opin. Neurobiol. 11*, 621–629.
(41) Jaszberenyi, Z., Banyai, I., Brucher, E., Kiraly, R., Hideg, K., and Kalai, T. (2006) Equilibrium and NMR studies on Gd-III, Y-III, Cu-II and Zn-II complexes of various DTPA-N,N″-bis(amide) ligands. Kinetic stabilities of the gadolinium(III) complexes. *Dalton Trans.* 1082–1091.

BC800108V

AUGUST 2008
Volume 19, Number 8

© *Copyright 2008 by the American Chemical Society*

Bioconjugate Chemistry

COMMUNICATIONS

A β-Cyclodextrin "Click Cluster" Decorated with Seven Paramagnetic Chelates Containing Two Water Exchange Sites

Joshua M. Bryson,[†] Wen-Jang Chu,[§] Jing-Huei Lee,[‡,§] and Theresa M. Reineke*[,†]

The Department of Chemistry at Virginia Tech, Blacksburg, Virginia 24061, and the Departments of Psychiatry, and Biomedical Engineering, at the University of Cincinnati, Cincinnati, Ohio 45221. Received May 18, 2008; Revised Manuscript Received June 19, 2008

The development of novel macromolecular contrast agents that offer enhanced relaxivity profiles at high magnetic fields have the potential to greatly improve the diagnosis, understanding, and treatment of disease. To this end, we have designed a monodiperse paramagnetic β-cyclodextrin click cluster decorated with seven paramagnetic arms. A novel alkyne-functionalized diethylenetriaminetetraacetic acid (DTTA) chelate (**6**) has been created and coupled to a per-azido-β-cyclodextrin core (**7**) to yield the precursor macromolecule (**8**). After removal of the protecting groups and titrating with Gd^{3+}, the final paramagnetic click cluster, **Gd10**, was obtained. Luminescence measurements were carried out in H_2O and D_2O on an analogous structure, **Eu10**, and indicated that at each lanthanide has an average of 1.8 water exchange sites, which is important for enhancing relaxivity and MRI resolution. This discrete paramagnetic click cluster yields a high relaxivity profile (43.4 mM^{-1} s^{-1} per molecule and 6.2 mM^{-1} s^{-1} per Gd^{3+} at 9.4 T) and enhanced contrast on a human MRI scanner as compared to a commercial agent, Magnevist (3.2 mM^{-1} s^{-1} at 9.4 T). Moreover, the useful inclusion properties exhibited by β-cyclodextrin also make this an excellent host scaffold to functionalize via noncovalent assembly with receptor specific targeting moieties for biomolecular imaging.

Advancements in the design of novel imaging agents have the potential to transform biomedical research. Indeed, the ability to diagnose a disease at the earliest stage of onset and to understand the pathophysiological and treatment mechanisms of disease *in vivo* could revolutionize medicine. With such potential, magnetic resonance imaging (MRI) is a safe yet powerful diagnostic technique for visualizing soft tissue often with the aid of paramagnetic contrast agents (*1–3*). Chelate structures that contain Gd^{3+} improve imaging contrast by increasing the longitudinal relaxation time (T_1) of proximal water protons, which appear brighter in the T_1-weighted image (*4*). To further increase resolution, MRI scanners are rapidly being developed with higher magnetic field strengths (*5*, *6*). Considerable efforts to create innovative agents that exhibit high relaxivities ($\mathbf{r}_1$) and tissue contrast at higher magnetic fields must follow suit (*1–6*).

Although current FDA-approved small molecule Gd^{3+}-chelates provide some contrast enhancement, they do not have optimal relaxivity profiles at high magnetic fields (*5*, *6*). Likewise, small agents do not provide contrast at very low concentrations, which is essential for biomolecular and targeted imaging (*1–6*). Conversely, macromolecular contrast agents show great promise for enhancing contrast, sensitivity, and diagnostic imaging time, as they reveal slow vascular diffusion

* Corresponding author.
[†] Department of Chemistry, Virginia Tech.
[‡] Department of Biomedical Engineering, University of Cincinnati.
[§] Department of Psychiatry, University of Cincinnati.

10.1021/bc800200q CCC: $40.75 © 2008 American Chemical Society
Published on Web 07/12/2008

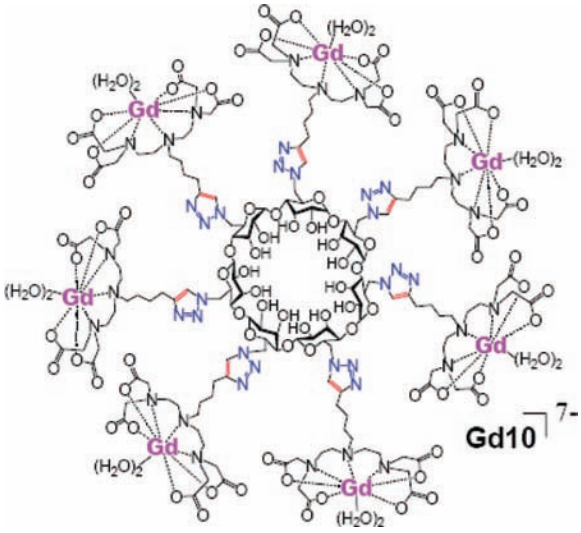

Figure 1. The target structure **Gd10**.

and clearance rates, and they can house multiple lanthanide chelates (*7–12*). However, a major drawback of existing paramagnetic macromolecules is that they suffer from polydispersity and difficulties in characterization, which could drastically affect clinical approval for diagnostic use (*9–13*).

To this end, we present our efforts toward designing a novel macromolecular MRI contrast agent that is completely monodisperse, has a multivalent loading of Gd^{3+} chelates that house two water exchange sites (Figure 1), and reveals a high relaxivity profile at high magnetic fields. This architecture has been inspired by the biocompatibility of our polycationic β-cyclodextrin "click clusters", which are highly efficient nucleic acid delivery vehicles previously created by our laboratory (*13*). The structure has also been motivated by the interesting inclusion properties of the β-cyclodextrin scaffold. The hydrophobic cup can act as a host, endowing this macromolecule with a versatile modification method via noncovalent inclusion of hydrophobic guests that are linked to receptor-specific biomolecules (*14, 15*). This potentially allows a multitude of targeted imaging applications for visualizing specific cell and tissue types, biomarkers, or receptors, and enhancing diagnosis and treatment monitoring. Indeed, it is no surprise that others have realized the potential of the cyclodextrin scaffold with related designs (*16*), particularly in a recently published paper developed in parallel to our work (*17*).

A convergent synthetic approach was designed to yield our target structure. The synthesis of the novel dendrons, the alkyne functionalized Gd^{3+} chelates, was inspired by the works of Merbach et al. (*18*). Their studies have shown that DTTA-type ligands have high lanthanide binding stability, fast water exchange, and multiple water coordination sites, which yield excellent relaxivity profiles (*18, 19*). In addition to the multivalent architecture, the key feature of our structure is the design of the arms, which consist of a chelate structure that has two open water exchange sites on the lanthanide for enhancing relaxivity. Scheme 1 was initialized with an amino bis-ethylphthalimide (**1**), which was prepared as previously reported (*20*). Next, the secondary amine was protected with a benzyl carbomate (Cbz) group (**2**) and the primary amines were liberated via hydrazine hydrate in acetronitrile, affording the diamine, **3**. This structure was then reacted with *t*-butyl bromoacetate, creating the functionalized tertiary amine (**4**), and the CBz removed via hydrogenation yielding the chelate precursor (**5**). It is worth mentioning that *t*-butyl bromoacetate was utilized in this synthetic route as the related *n*-methyl bromoacetate analogue (potentially milder basic deprotection) allowed an intramolecular cyclization to occur with the free secondary amine upon CBz removal, which could not be carried forth in the reaction scheme. A simple nucleophilic addition of **5** to 6-bromohexyne resulted in the desired protected DTTA-hexyne dendron (**6**). A crucial step in the formation of these *monodisperse* click clusters is the synthesis of the acetylated per-azido-β-cyclodextrin core (**7**) moiety. It is important to note here that the commercially available per-halogenated β-cyclodextrin analogues have an unacceptable percentage of lesser substituted impurities (up to 10%, as noted by the manufacturer), which ultimately lead to contamination of the final structure with lesser-substituted products. Because of the negative implication of a polydisperse final product, it was important to synthesize the pure acetylated per-azido-β-cyclodextrin core (**7**) according to previous reports, which produces a monodisperse final product (*vide infra*) (*13, 21, 22*).

The key step in the assembly of the target click cluster was carried out via the click reaction, which promotes regiospecific coupling in high yield even in sterically hindered environments (*23, 24*). As shown in Scheme 2, the protected DTTA-hexyne dendron (**6**) was coupled to the acetylated per-azido-β-cyclodextrin (**7**). The clean formation of the fully substituted 1,4-regioisomer (**8**) was evidenced by mass spectra (Figure 2) and NMR (see Supporting Information). Because both the DTTA carboxylates and the β-cyclodextrin hydroxyls are protected, chelation of copper from the catalyst and retention of this metal in the final product was not found. Next, the acetyl and *t*-butyl groups on the click cluster were deprotected via conventional methods creating **9**, which was then titrated with $GdCl_3$, yielding the target paramagnetic macromolecule, **Gd10**. This β-cyclodextrin click cluster was purified via exhaustive dialysis in ultra pure water. Quantification of Gd^{3+} loading and full chelation was revealed via mass spec and ICP-MS analysis, which showed the presence of seven loaded chelates without lower chelation products or excess Gd^{3+}.

Contrast agent efficacy is influenced by the chelation environment and water coordination number (q). To gain insight into the average q value, **9** was chelated with Eu^{3+}, creating **Eu10**, a luminescent analogue of **Gd10**. As Eu^{3+} and Gd^{3+} have identical coordination chemistry (*25*), q can be determined with **Eu10** from the proportionality between the luminescence decay in H_2O and D_2O via the Horrocks equation [$q = 1.11\ (kH_2O - kD_2O - 0.31)$] (*26*). Typically, Gd^{3+} and Eu^{3+} prefer nonadentate coordination and the DTTA-like chelate usually forms a heptadentate complex; therefore, a q value of 2 is predicted. From this experiment, a q value of 1.8 was calculated, which is within reasonable error of the predicted value. It has been shown that hydroxyls on adjacent groups can block water coordinate sites within related lanthanide chelates (*27*). However, this study of the analogous **Eu10** structure suggests that the two open coordination sites on the lanthanide chelates are available for water exchange, which is essential for maximal relaxivity enhancement, particularly at higher fields.

The relaxivity for **Gd10** was determined at a high magnetic field (9.4 T, 400 MHz, 37 °C) by measuring the T_1 values of several aqueous solutions and plotting $1/T_1$ versus concentration. As a control, the results were compared to Magnevist ($Gd\text{-}DTPA^{2-}$), a common clinically approved contrast agent. As shown in Figure 3a, at this high magnetic field, Magnevist has a relaxivity value of 3.2 $mM^{-1}\ s^{-1}$. However, the molecular relaxivity calculated for the entire **Gd10** cluster was found to be 43.4 $mM^{-1}\ s^{-1}$, which is an exceptionally high value. When we calculated the relaxivity value on a per Gd^{3+} basis for **Gd10**, it was found to be 6.2 $mM^{-1}\ s^{-1}$. This value represents a 94% increase in the relaxation efficiency over Magnevist at 9.4 T and is likely related to the higher q value and larger molecular size that can increase the rotational correlation time (*10–13*). It

Scheme 1. Synthetic Protocol for Alkyne-DTTA Arm Synthesis[a]

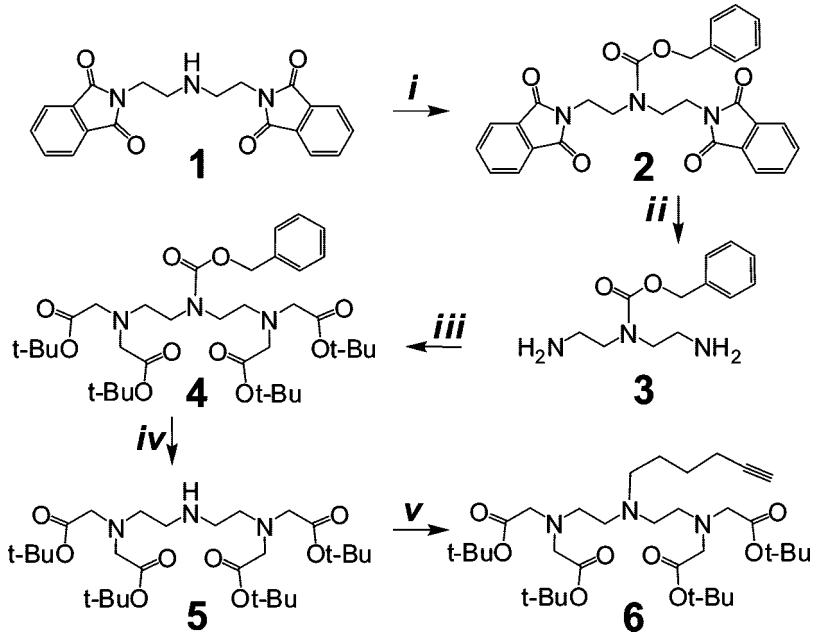

[a] (*i*) Benzylchloroformate, DIPEA, DMAP, CH_2Cl_2; (*ii*) hydrazine monohydrate, MeCN; (*iii*) *t*-butyl bromoacetate, DMF, $KHCO_3$; (*iv*) H_2, Pd/C 10%, MeOH; (*v*) 6-bromo-1-hexyne, $KHCO_3$, DMF.

Scheme 2. Synthesis of the Paramagnetic Click Cluster, Gd10[a]

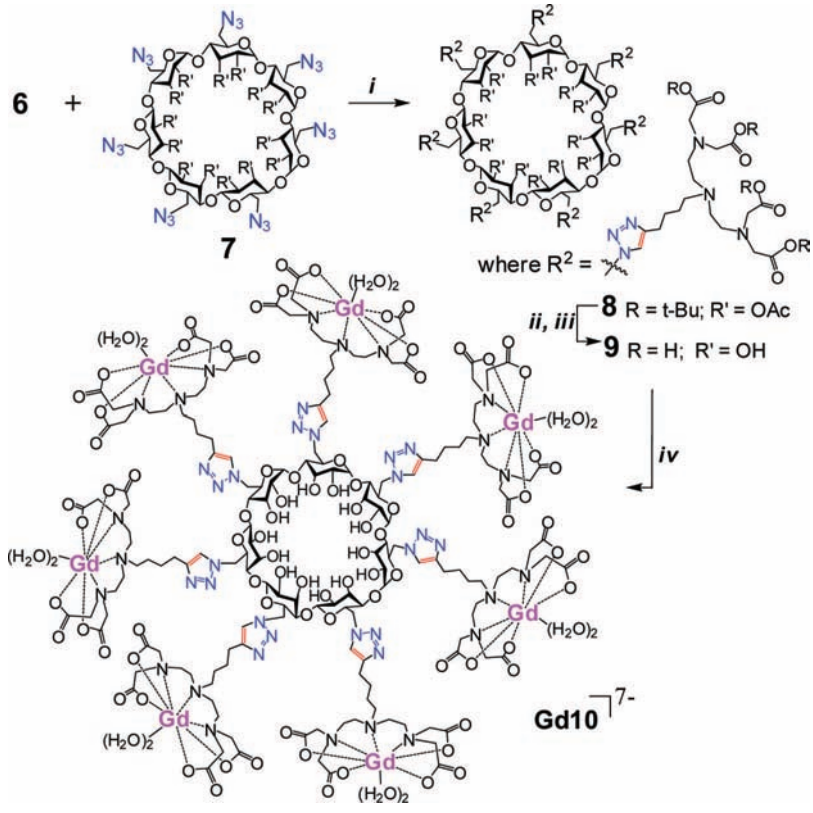

[a] (*i*) $CuSO_4 \cdot 5H_2O$, Sodium Ascorbate, THF:H_2O (1:1), 60°C; (*ii*) NaOMe, MeOH, 24 h; (*iii*) TFA, 3 h; (*iv*) $GdCl_3$, $NaHCO_3$, pH = 6−8.

should be noted that these values are predicted to be much higher at lower magnetic fields by the Solomon-Bloembergen-Morgan (SBM) equations (*1–4, 21*). To directly visualize the enhanced relaxivity for **Gd10** and potential for increasing resolution, we imaged 25 mL vials filled with Magnevist, **Gd10,** and water together on a Varian 4T human MRI scanner, keeping the gadolinium concentration constant, $[Gd^{3+}] = 1.11$ mM (Figure 3b). With respect to water, Magnevist reveals a higher contrast; however, **Gd10** clearly reveals the brightest signal and highest contrast even at a low macromolecule concentration.

In summary, the development of novel macromolecular contrast agents that offer enhanced relaxivity profiles at high magnetic fields have the potential to greatly improve the diagnosis, understanding, and treatment of disease. For this purpose, a novel β-cyclodextrin click cluster has been creatively endowed with seven paramagnetic arms that each contain two

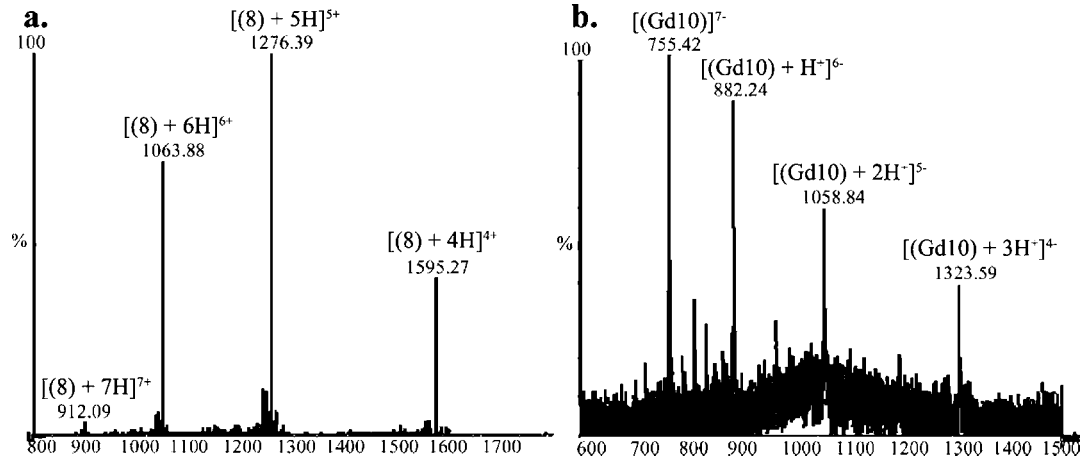

Figure 2. (a) ES-MS (positive ion mode) of **8** showing the observed monoisotopic ions. The M_{obs} {[**8** + H^+] calculated *m*/*z*: 6377.70, found *m*/*z*: 6377.38} is a deconvoluted mass of the compound from the multiply charged ions, and (b) ES-MS (negative ion mode) of **Gd10** showing the ionic distribution of 7-, 6-, 5-, and 4- species.

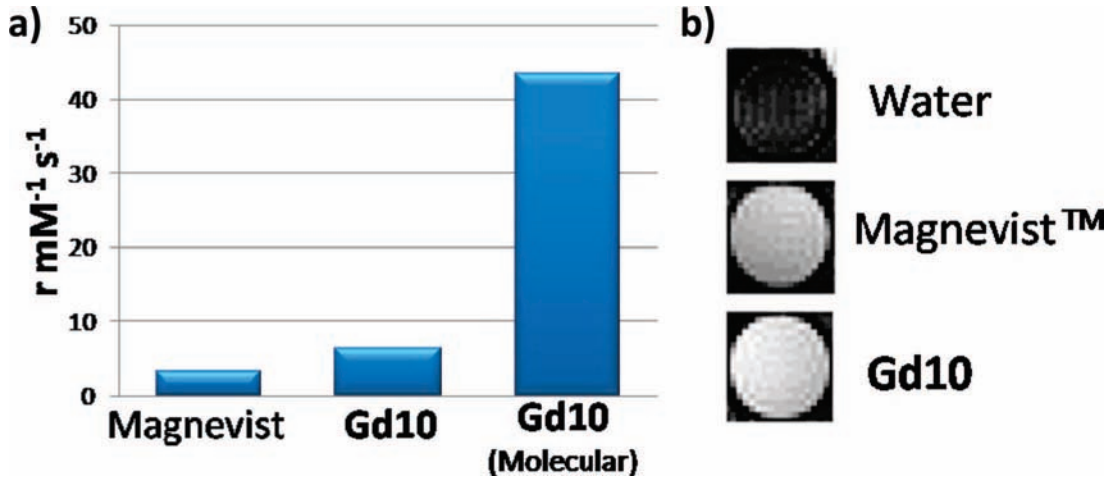

Figure 3. Relaxivity of Magnevist and **Gd10**. (a) The bars reveal the relaxivities at 9.4 T. (b) The inset images show the T_1-weighted MR images of water, Magnevist, and **Gd10** solutions acquired on a 4 T MRI scanner.

water exchange sites. This discrete paramagnetic agent yields an exceptionally high relaxivity profile (43.4 mM^{-1} s^{-1} at 9.4 T) and enhanced contrast on a human MRI scanner. Moreover, the useful inclusion properties exhibited by β-cyclodextrin also make this an excellent host scaffold to functionalize via noncovalent assembly with biological receptor-specific targeting moieties. Investigations are underway to study the limitless potential of this contrast agent for targeted MRI applications.

ACKNOWLEDGMENT

We thank Kirk Lokits for ICP-MS, Andrew Wolf for some synthetic studies, and Dr. Stephan Macha for ESI-MS acquisitions. This work was supported by the National Institutes of Health (1-R21-EB007244-01), the University of Cincinnati, and the Alfred P. Sloan Foundation.

Supporting Information Available: Experimental details of the synthesis and characterization of compounds **3**−**10** and **8**−**10** and of the water coordination, inversion recovery, and T_1-weighted images. This material is available free of charge via the Internet at http://pubs.acs.org.

LITERATURE CITED

(1) Lauffer, R. B. (1987) Paramagnetic metal complexes as water proton relaxation agents for NMR imaging: theory and design. *Chem. Rev. 87*, 901–927.

(2) Tóth, É., Merbach, A. E., Helm, L. (2001) *Relaxivity of Gd(III) complexes: Theory and mechanism*, Wiley, Chichester.

(3) Caravan, P., McMurry, T. J., and Lauffer, R. B. (1999) Gadolinium(III) chelates as MRI contrast agents: Structure, dynamics, and applications. *Chem. Rev. 99*, 2293–2352.

(4) Caravan, P. (2006) Strategies for increasing the sensitivity of gadolinium based MRI contrast agents. *Chem. Soc. Rev. 35*, 512–523.

(5) Livramento, J. B., Helm, L., Sour, A., O'Neil, C., Merbach, A. E., and Tóth, É. (2008) A benzene-core trinuclear Gd^{III} complex: towards the optimization of relaxivity for MRI contrast agent applications at high magnetic field. *Dalton Trans. 9*, 1195–1202.

(6) Pierre, V. C., Botta, M., Aime, S., and Raymond, K. N. (2006) Fe(III)-templated Gd(III) self-assemblies-A new route toward macromolecular MRI contrast agents. *J. Am. Chem. Soc. 128*, 9272–9273.

(7) Tóth, É., Helm, L., and Merbach, A. E. (2004) Metal complexes as MRI contrast enhancement agents. *Comprehensive Coordinate Chemistry II 9*, 841–881.

(8) Mohs, A. M., and Lu, Z. -R. (2007) Gadolinium(III)-based blood-pool contrast agents for magnetic resonance imaging: status and clinical potential. *Expert Opin. Drug Delivery 4*, 149–164.

(9) Torchilin, V., Babich, J., and Weissig, V. (2000) Liposomes and micelles to target the blood pool for imaging purposes. *J. Liposome Res. 10*, 483–499.

(10) Mohs, A. M., Wang, X., Goodrich, K. C., Zong, Y., Parker, D. L., and Lu, Z. -R. (2004) PEG-*g*-poly(GdDTPA-*co*-L-cystine): A biodegradable macromolecular blood pool contrast agent for MR imaging. *Bioconjugate Chem. 15*, 1424–1430.

(11) Langereis, S., Dirksen, A., Hackeng, T. M., Van Genderen, M. H. P., and Meijer, E. W. (2007) Dendrimers and magnetic resonance imaging. *New J. Chem. 31*, 1152–1160.

(12) Ranganathan, R. S., Fernandez, M. E., Kang, S. I., Nunn, A. D., Ratsep, P. C., Pillai, K. M. R., Zhang, X., and Tweedle, M. F. (1998) New multimeric magnetic resonance imaging agents. *Invest. Radiol. 33*, 779–797.

(13) Srinivasachari, S., Fichter, K. M., and Reineke, T. M. (2008) Polycationic β-cyclodextrin "click clusters": Monodisperse and versatile scaffolds for nucleic acid delivery. *J. Am. Chem. Soc. 130*, 4618–4627.

(14) Bartlett, D. W., and Davis, M. E. (2008) Impact of tumor-specific targeting and dosing schedule on tumor growth inhibition after intravenous administration of siRNA-containing nanoparticles. *Biotechnol. Bioeng. 99*, 975–985.

(15) Bellocq, N. C., Pun, S. H., Jensen, G. S., and Davis, M. E. (2003) Transferrin-containing, cyclodextrin polymer-based particles for tumor-targeted gene delivery. *Bioconjugate Chem. 14*, 1122–1132.

(16) Aime, S., Botta, M., Fedeli, F., Gianolio, E., Terreno, E., and Anelli, P. (2001) High-relaxivity contrast agents for magnetic resonance imaging based on multisite interactions between a β-cyclodextrin oligomer and suitably functionalized Gd(III) chelates. *Chem.-Eur. J. 7*, 5261–5269.

(17) Song, Y., Kohlmeir, E. K., Meade, T. J. (2008) Synthesis of multimeric MR contrast agents for cellular imaging. *J. Am. Chem. Soc.* ASAP DOI:10.1021/ja0777990.

(18) Ruloff, R., van Koten, G., and Merbach, A. E. (2004) Novel heteroditopic chelate for self-assembled gadolinium(III) complex with high relaxivity. *Chem. Commun. 7*, 842–843.

(19) Ruloff, R., Muller, R. N., Pubanz, D., and Merbach, A. E. (1998) A tripod gadolinium (III) poly(amino carboxylate) relevant to magnetic resonance imaging: structural and dynamical ^{17}O NMR and ^{1}H NMRD studies. *Inorg. Chim. Acta 275*, 15–23.

(20) Davies, J. S., and Al-Jamri, L. (2002) Synthesis of *N*-Boc-N^{ϵ}-tetrabenzyl-DTPA-L-lysine and N^{ϵ}-Fmoc-N^{ϵ}-tetra-t-butyl-DTPA-L-lysine, building blocks for solid phase synthesis of DTPA-containing peptides. *J. Pept. Sci. 8*, 663–670.

(21) Boger, J., Corcoran, R. J., and Lehn, J. -M. (1978) Cyclodextrin chemistry. Selective modification of all primary hydroxyl groups of α- and β-cyclodextrins. *Helv. Chim. Acta 61*, 2190–2218.

(22) Ashton, P. R., Koniger, R., Stoddart, J. F., Alker, D., and Harding, V. D. (1996) Amino acid derivitives of beta-cyclodextrin. *J. Org. Chem. 61*, 903–908.

(23) Rostovtsev, V. V., Green, L. G., Fokin, V. V., and Sharpless, K. B. (2002) A stepwise Huisgen cycloaddition process: Copper(I)-catalyzed regioselective "ligation" of azides and terminal alkynes. *Angew. Chem., Int. Ed. 41*, 2596–2599.

(24) Mynar, J. L., Choi, T. -L., Yoshida, M., Kim, V., Hawker, C. J., and Fréchet, J. M. J. (2005) Doubly-dendronized linear polymers. *Chem. Commun.* 5169–5171.

(25) Johnson, D. A. (1980) Principles of lanthanide chemistry. *J. Chem. Educ. 57*, 475–476.

(26) Supkowski, R. M., and Horrocks, W. D., Jr. (2002) On the determination of the number of water molecules, q, coordinated to europium(III) ions in solution from luminescence decay lifetimes. *Inorg. Chim. Acta 340* 44–48.

(27) Urbanczyk-Pearson, L. M., Fermia, F. J., Smith, J., Parigi, G., Duimstra, J. A., Eckermann, A. L., Luchinat, C., and Meade, T. J. (2008) Mechanistic investigation of β-galactosidase-activated MR contrast agents. *Inorg. Chem. 47*, 56–68.

BC800200Q

A β-Cyclodextrin "Click Cluster" Decorated with Seven Paramagnetic Chelates Containing Two Water Exchange Sites

Joshua M. Bryson,[†‡] Wen-Jang Chu,[§] Jing-Huei Lee,[€] and Theresa M. Reineke[†‡]*

[†]*The Department of Chemistry at Virginia Tech, Blacksburg, VA 24061*
The Departments of Chemistry,[‡] Psychiatry,[§] and Biomedical Engineering[€] at the University of Cincinnati, Cincinnati, OH 45221

General. β-cyclodextrin was purchased from Wacker Chemie AG (Munich, Germany) and 6-bromohexyne was acquired from ChemSampCo (Philadelphia, PA). All other chemicals unless specified otherwise were purchased from Alfa Aeser Chemical Co. (Boston, MA) and were used without further purification. Acetylated per-azido-β-cyclodextrin, **7**, was synthesized according to a published procedures (*1*). The mass spectra were obtained on an IonSpec HiResESI mass spectrometer. NMR spectra were collected on a Bruker AV-400MHz spectrometer and relaxivity measurements were carried out on a Bruker AMX-400MHz spectrometer. Determination of the percentage of gadolinium content was determined with a Perkins-Elmer ELAN 6000 Inductively-Coupled Plasma Mass Spectrometer. Luminescence studies were performed using a Varian Cary Eclipse Fluorescence Spectrophotometer. Thin-layer chromatography (TLC) was performed using TLC plastic sheets (silica gel 60 F_{254}) from Merck (Darmstadt, Germany). Dialysis membranes [1000 molecular weight cutoff (MWCO)] were manufactured by Spectrum Laboratories, Inc. (Rancho Dominguez, CA). Magnetic resonance images were acquired with a Varian 4 Tesla MRI/MRS human scanner (170.35MHz).

Synthesis.

N^1,N^3-Bis(phthalimido)-N^2-benzoxycarbonyl-diethylenetriamine (2). 1,7-Bis(phthalimido)-1,4,7-triazaheptane, **1** (9.21g, 25.2 mmol), prepared by a previously published procedure (*2*), was slurried in 80ml of dichloromethane at 0°C under brisk stirring. 4-Dimethylaminopyridine (1.25g, 10.2 mmol) and diisopropylethylamine (4.85g, 37.5 mmol) were then added to the slurry. Benzylchloroformate (5.12g, 30.0 mmol) was separately dissolved in 30ml of dichloromethane and added dropwise to the slurry over a period of 10 min, after which the reaction mixture became clear. The solution was then allowed to stir an additional 18h, after which the mixture was washed several times with 3 x 75ml acidic water (pH adjusted to 4 with 1M HCl), with saturated bicarbonate (1 x 75ml), and finally with ultrapure water (1 x 75ml). The washed organic fraction was dried over sodium sulfate and evaporated to give the crude product as an off-white solid. The crude solid was slurried in anhydrous diethylether, filtered, and washed again with ether (200mL) to remove the benzylchloroformate starting material. The final product was recovered and dried *in vacuo* yielding **2** a white solid (7.22g, 57.5%). ^{1}H-NMR ($CDCl_3$, 400MHz): δ = 3.62 (t, 4H), 3.91 (dt, 4H), 4.84 (s, 2H), 7.19 (d, 2H), 7.30 (m, 3H), 7.64 - 7.83 (m, 8H). ^{13}C-NMR ($CDCl_3$, 100MHz): δ = 35.7, 45.8, 67.3, 123.3, 127.6, 127.7, 128.3, 131.8, 134.0, 136.2, 156.1, 168.2. ES-MS positive ion mode: calculated *m/z* 520.148, [**2** + H^+]. Found *m/z*: 520.127.

N^2-Benzoxycarbonyl-diethylenetriamine (3). Compound **2** (7.22g, 14.5 mmol), was slurried in 25ml of acetonitrile. Hydrazine hydrate (5.80g, 116 mmol) was added to the mixture and after 10min of stirring, the solution became clear. After stirring the solution for approximately 4h, a precipitate formed, and after 24h, the reaction was complete (as determined via TLC). The white precipitate was filtered from the solution and washed thoroughly with acetonitrile. The initial solution was combined with the washings and dried *in vacuo* yielding the final product, **3**, as a viscous orange oil. (3.20g, 95.1%). ^{1}H-NMR ($CDCl_3$, 400MHz): δ = 1.93 (bs, 4H), 2.91 (s, 4H), 3.38 (s, 4h), 5.13 (s, 2H), 7.37 (m,

5H). ^{13}C-NMR ($CDCl_3$, 100MHz): δ = 38.4, 53.1, 67.3, 127.1, 127.6, 130.0, 136.1, 152.1. ES-MS positive ion mode: calculated *m/z* 238.156, [**3** + H^+]. Found *m/z*: 238.120.

N^2-Benzoxycarbonyl-diethylenetriamine-tetra-*t*-butylacetate (4). Compound **3** (3.20g, 13.5mmol) was dissolved in 22ml of DMF containing $KHCO_3$ (7.02g, 70.1 mmol) under stirring at room temperature. *Tert*-butyl-bromoacetate (13.7g, 70.1 mmol) was added directly to the stirred solution, which caused mild heat evolution. The reaction was allowed to stir for 48h at room temperature and then for an additional 2h at 60°C. The solution was then partitioned between diethyl ether and saturated sodium bicarbonate (50ml of each). After stirring for 5 min, the ether layer was retained and washed with ultrapure water (2 x 50ml), dried over anhydrous sodium sulfate, and evaporated to yield the crude product as a light yellow oil. The crude product was loaded onto a silica column and eluted using a solvent gradient (CH_2Cl_2 to 10% EtOAc : 90% CH_2Cl_2). The fractions containing the final product (second elution band) were combined and dried in vacuo yielding **4** (5.48g, 58.5%). ^{1}H-NMR ($CDCl_3$, 400MHz): δ = 1.46 (s, 36H), 2.88 (m, 4H), 3.40 (s, 8H), 3.47 (m, 4H), 5.12 (s, 2H), 7.36 (m, 5H). ^{13}C-NMR ($CDCl_3$, 100MHz): δ = 28.2, 46.5, 52.7, 56.1, 67.0, 80.9, 127.8, 127.9, 128.5, 137.1, 156.0, 170.6. ES-MS positive ion mode: calculated *m/z* 694.428, [**4** + H^+]. Found *m/z*: 694.448.

Diethylenetriamine-tetra-*t*-butylacetate (5). A 50ml round bottom flask containing a solution of **4** (3.34g, 4.8 mmol) dissolved in 25ml of MeOH, was purged with $Ar_{(g)}$ to remove dissolved $O_{2\ (g)}$. To remove the Cbz groups, catalyst (334 mg of Pd/C) was added to the flask which was again purged with $Ar_{(g)}$. Next, a balloon containing $H_{2\ (g)}$, fitted with a syringe, was used to bubble several liters of $H_{2\ (g)}$ through the solution at room temperature, and the solution was then allowed to stir overnight. The solution was then filtered through celite to remove the catalyst and dried *in vacuo,* yielding compound **5** (2.43g, 90%) as a yellow oil. ^{1}H-NMR ($CDCl_3$, 400MHz): δ = 1.47 (s, 36H), 2.68 (t, 4H), 2.87 (t, 4H),

3.45 (s, 8H). ^{13}C-NMR ($CDCl_3$, 100MHz): δ = 28.0, 47.9, 54.3, 56.3, 80.8, 170.8. ES-MS positive ion mode: calculated *m/z* 560.390, [**5** + H^+]. Found *m/z*: 560.394.

N^2-(Hex-5-yne)-diethylenetriamine-tetra-*t*-butylacetate (6). Compound **5** (629mg, 1.12 mmol), 6-bromohexyne (322mg, 1.69 mmol), and $KHCO_3$ (113mg, 1.12mmol) were dissolved in 2 ml of DMF. The solution was allowed to stir for 48h at room temperature and then for 2h at 60°C. This solution was then added to a partition of diethyl ether and saturated sodium bicarbonate solution and stirred for 5 min. The ether layer was recovered and washed with ultrapure water (2 x 50ml), dried over anhydrous sodium sulfate, and evaporated *in vacuo* affording the crude product as a light yellow oil. The crude product was purified via silica gel flash chromatography using a solvent gradient (CH_2Cl_2 → 20% EtOAc: 80% CH_2Cl_2 →45% EtOAc: 45% CH_2Cl_2: 10% MeOH). The final compound was eluted out with the final gradient system, and the corresponding fractions were combined and dried *in vacuo* yielding **6** (324mg, 45.2%) as a yellow oil. ^{1}H-NMR ($CDCl_3$, 400MHz): δ = 1.47 (s, 36H), 1.54 (m, 4H), 1.95 (s, 1H), 2.20 (m, 2H), 2.48 (t, 2H), 2.61 (t, 4H), 2.80 (t, 4H), 3.46 (s, 8H) ^{13}C-NMR ($CDCl_3$, 100MHz): δ = 14.1, 18.2, 21.0, 26.2, 28.1, 52.9, 56.2, 60.3, 68.4, 80.8, 170.6. ES-MS positive ion mode: calculated *m/z* 640.454, [**7** + H^+]. Found *m/z*: 640.456.

Heptakis{2,3-di-*O*-acetyl-6-*N*-[(diethylenetriamine-tetra-*t*-butylacetate)butyl]-6-(1,2,3-triazole)} cyclomaltoheptaose (8). Compounds **6** (69.5mg, 1.09 x 10^{-4} mol) and **7** (29.4mg, 1.55 x 10^{-5} mol) were dissolved in 2.6 ml of a 1:1 THF:water solution. Fresh solutions of 1M $CuSO_4 \cdot 5H_2O$ and 1M sodium ascorbate were prepared and used to introduce the catalyst 5% $CuSO_4$ and 10% sodium ascorbate (as molar percent of **6**) to the reaction mixture to promote the click coupling reaction using similar conditions developed by Hawker, Frechét and coworkers (*3*). This mixture was stirred briefly at 60°C to promote dispersion and was then stirred at room temperature until the solution became turquoise-blue (after about 8h), which signified reaction completion. The reaction mixture was then

partitioned between water and dichloromethane (10ml of each) and stirred for 2 min. The dichloromethane layer was retained and washed with a 0.1M Na^+ EDTA solution (2 x 10ml) and ultrapure water (2 x 10mL). The organic layer was dried over sodium sulfate and evaporated *in vacuo* yielding **8** (95mg, 96%) as a viscous yellow oil. ^{1}H-NMR ($CDCl_3$, 400MHz): δ = 1.23 (m, 14H), 1.42 (s, 252H), 1.53 (m, 14H), 1.61 (m, 14H), 1.98 (s, 21H), 2.03 (s, 21H), 2.48 (d, 14H), 2.59 (bs, 28H), 2.77 (bs, 28H), 2.95 (m, 14H), 3.41 (s, 56H), 4.44 (m, 7H), 4.70 (d, 7H), 4.91 (m, 7H), 5.31 (m, 7H), 5.59 (s, 7H), 7.53 (s, 7H). ^{13}C-NMR ($CDCl_3$, 100MHz): δ = 20.8, 25.6, 25.7, 27.4, 27.9, 28.2, 29.7, 50.9, 52.2, 53.1, 54.8, 67.9, 70.9, 80.7, 96.2, 100.0, 123.5, 148.3, 168.2, 170.6. ES-MS positive ion mode M_{obs}: Calculated *m/z* 1595.43, [**8** + $4H^+$]. Found *m/z*: 1595.27. Calculated *m/z*: 1276.54, [**(8)** + $5H^+$]. Found *m/z*: 1276.40. Calculated *m/z* 1063.95, [**(8)** + $6H^+$]. Found *m/z*: 1063.88. Calculated *m/z* 912.107, [**(8)** +$7H^+$]. Found *m/z*: 912.028. Deconvolution of spectrum: Found *m/z*: 6377.38. Calculated *m/z* 6377.70, [**8** + H^+].

Heptakis{6-*N*-[(diethylenetriamine-tetraaceticacid)butyl]-6-(1,2,3-triazole)} cyclomaltoheptaose (9). Compound **8** (85mg, 1.33 x 10^{-5} mol) was dissolved in 2ml of MeOH, the solution was adjusted to a pH = 8 with NaOMe, and the mixture was allowed to stir overnight. The pH was brought back to neutral using Amberlyst® strong cation exchange resin, the resin was filtered from the mixture, and the solvent was removed to yield the deacetylated product. This product was then redissolved in 2ml of dichloromethane and cooled to 0°C. Triethyl silane (TES) was added (100µl), followed by 1ml of trifluoroacetic acid (TFA). The solution was warmed to room temperature and stirred for 3h, after which the TFA/TES mixture was removed *in vacuo* leaving a viscous oil. Anhydrous ether was added to the oil and allowed to sonicate for 5 min, yielding a fine white precipitate. The white powder was recovered and dissolved in 2ml of water, brought to pH = 7 with $NaHCO_3$ and dialyzed extensively

against ultrapure water in a 1000 MWCO membrane. The purified solution was lyophilized to dryness yielding **9** (41mg, 73%) as a fluffy white solid. It should be noted that this product (**9**) is very hygroscopic and rapidly uptakes water from the air if not stored in a dessicator. ^{1}H-NMR (D_2O, 400MHz): δ = 1.80 (bs, 14H), 1.86 (bs, 14H), 1.92 (bs, 14H), 2.07 (bs, 14H), 2.39 (s, 14H), 2.30 (bs, 28H), 3.32 (bs, 28H), 3.44 (m, 7H), 3.58 (m, 7H), 3.84 (m, 7H), 3.93 (m, 7H), 3.99 (m, 7H), 4.16 (s, 56H), 7.87 (s, 7H). ^{13}C-NMR (D_2O, 100MHz): δ = 20.5, 24.8, 27.4, 48.1, 52.1, 52.8, 57.3, 58.0, 70.1, 70.6, 71.4, 76.8, 95.5, 125.1, 135.4, 170.8, 172.8. ES-MS positive ion mode deconvoluted mass [9 + H^+]$^{1+}$: Calculated *m/z* 4216.79, Found *m/z*: 4217.97. FT-IR: (KBr pellets, cm^{-1}) 3430.7, 2910.2, 1681.75, 1600.2, 1404.6, 1204.6, 1136.8, 1049.0.

Heptakis{6-*N*-[(Gd(III)-diethylenetriamine-tetraaceticacid)butyl]-6-(1,2,3-triazole)} cyclomaltoheptaose (Gd10). Compound **9** (25.2mg, 5.98 x 10^{-6}mol) was dissolved in 5ml of ultrapure water and the solution was adjusted to pH=7 with sodium bicarbonate. Gadolinium chloride hexahydrate (15.6mg, 4.18 x 10^{-5}mol) was dissolved in 1ml of ultrapure water and added to the solution of **9** in 3 separate aliquots. After the addition of each aliquot, the pH was adjusted back to a pH between 8-9 using a 0.1M potassium carbonate solution. The solution was allowed to stir for 30min to allow for Gd chelation to occur, dialyzed against ultrapure water for 18h, and lyophilized to yield **Gd10** as a fluffy white solid (27.3mg, 78%). ICP-MS: %Gd(III): theoretical for {$C_{168}H_{238}Gd_7K_7N_{42}O_{84}$ + $(H_2O)_{14}$} = 18.9%; Found 18.8%. The ES-MS for **Gd10** is displayed below in Figure S2. ES-MS negative ion mode: calculated *m/z* 755.863 [**(Gd10)**]$^{7-}$. Found *m/z*: 755.421. Calculated *m/z:* 882.070 [**(Gd10)** + H^+] $^{6-}$. Found *m/z*: 882.239. Calculated *m/z:* 1058.61 [**(Gd10)** + $2H^+$]$^{5-}$. Found *m/z*: 1058. 84. Calculated *m/z:* 1323.51 [**(Gd10)** + $3H^+$] $^{4-}$. Found *m/z*: 1323.59. FT-IR: (KBr pellets, cm^{-1}) 3422.5, 2935.9, 1750.0, 1609.9, 1402.7, 1248.9, 1048.0.

Heptakis{6-*N*-[(Eu(III)-diethylenetriamine-tetraaceticacid)butyl]-6-(1,2,3-triazole)} cyclomaltoheptaose (Eu10). Compound **9** (2.10mg, 4.98 x 10^{-7} mol) was dissolved in 0.5ml of ultrapure water and the solution was adjusted to pH=7 with sodium bicarbonate. A freshly prepared 1mM solution $EuCl_3 \cdot 6H_2O$ (498µl, 4.98 x 10^{-7} mol) was added to the solution of compound **9** in a similar manner to **Gd10**. The pH was then adjusted back to 7 - 8 using a 0.1M potassium carbonate solution. The solution was dialyzed against water and lyophilized to give **Eu10** (1.7mg, 65%) as a fluffy white solid. ICP-MS: %Eu(III): Theoretical for $\{C_{168}H_{238}Eu_7K_7N_{42}O_{84} + (H_2O)_{14}\}$ = 18.4%; Found = 22.0%. ES-MS negative ion mode: calculated *m/z* 750.717 [**(Eu10)**]$^{7-}$. Found *m/z*: 750.352. Calculated *m/z:* 875.838 [**(Eu10)** + H^+] $^{6-}$. Found *m/z*: 875.732. Calculated *m/z:* 1051.21 [**(Eu10)** + $2H^+$]$^{5-}$. Found *m/z*: 1051.42. Calculated *m/z:* 1314.26 [**(Eu10)** + $3H^+$] $^{4-}$. Found *m/z*: 1314.33. FT-IR: (KBr pellets, cm^{-1}) 3421.1, 2936.1, 1750.0, 1610.1, 1401.8, 1248.8, 1047.9.

ICP-MS for Lanthanide Quantification

$GdCl_3$ and $EuCl_3$ 1,000ppm lanthanide standard solutions in 1% HNO_3 (Aldrich, St. Lois, MO) were used to prepare a stock solution containing 1.00 ppm of both Eu^{3+} and Gd^{3+}, which was used to prepare 500, 250, 100, 50, 10, and 5 ppb solutions. These solutions were analyzed for four Gd^{3+} isotopes (156, 157, 158, 160), and 2 Eu^{3+} isotopes (151, 153). This data was used to generate a calibration curves for both Gd(III) and Eu(III). Solutions of **Gd10** and **Eu10** (100 ppb) were prepared, analyzed, and the lanthanide content was determined for each sample according to the calibration curve. The Gd^{3+} content in **Gd10** was found to be 18.8 ppb and the Eu^{3+} content for **Eu10** was found to be 22.0 ppb.

Determination of the water coordination number (*q*) (*4*)

Determination of the luminescence lifetime (τ) of **Eu10** was performed in both H_2O and D_2O (5.0×10^{-5} M) with a delay time of 0.05 ms, a gate time of 0.2 ms, λ_{ex} = 395, and λ_{em} = 614 nm. Excitation and emission slits were set to 10 nm. Calculations of *q*, were carried out in Graphpad prism v10.0 using the equation of $q = 1.11 [k_{H2O} - k_{D2O} - 0.31]$, where k is the rate of luminescence decay.

Relaxivity Measurements

Stock solutions of Magnevist™ and **Gd10** (2.95mM = $[Gd^{3+}]$) were prepared in H_2O and diluted to make 1.48 mM and 0.738 mM solutions. The longitudinal relaxation time (T_1) for the six solutions and water were measured using an inversion recovery pulse sequence (180° – d_t – 90° – acquire) carried out on a Bruker AMX-400 MHz spectrometer at 310K. Arrayed data ($n(d_t) = 14$) was processed using NUTS software and fit to a three-parameter model. Relaxivity was acquired from a linear least squares fit of the slope of the line obtained from plotting $1/T_1$ vs. [Gd].

T_1 weighted Images

Solutions of Magnevist™ and **Gd10**, were prepare so $[Gd^{3+}]$ = 1.11mM, and put in 25mL vials to be imaged. The images were acquired with gradient echo pulse sequence using a TEM (transverse electromagnetic) volume coil. Acquisition parameters are as follows: TR (repetition time) = 50 msec, TE (echo time) = 5 msec, FOV (field of view) = 200x200 mm and matrix size = 128x128. Contrast was adjusted relative to the controls.

References:

(1) Ashton, P. R., Koniger, R., Stoddart, J. F., Alker, D., and Harding, V. D. (1996) Amino Acid Derivitives of beta-Cyclodextrin. *J. Org. Chem. 61*, 903-908.

(2) Schneider, P. W., Collman, J. P. (1968) Complexes of cobalt(III) with the two isomeric diethylenetriamineacetic acids. *Inorg. Chem. 7*, 2010-2015.

(3) Mynar, J. L., Choi, T.-L., Yoshida, M., Kim, V., Hawker, C. J., Fréchet, J.M. J. (2005) Doubly-Dendronized linear polymers. *Chem. Commun.* 5169-5171.

(4) Supkowski, R. M., Horrocks, J., W. D. (2002) On the determination of the number of water molecules, *q*, coordinated to europium(III) ions in solution from luminescence decay lifetimes. *Inorg. Chim. Acta*. *340*, 44-48.

Cellular Entry and Nuclear Targeting By a Highly Anionic Molecular Umbrella

Mohamed Mehiri,[†] Bingwen Jing,[†] Danielle Ringhoff,[†] Vaclav Janout,[†] Lynne Cassimeris,[‡] and Steven L. Regen*[,†]

Departments of Chemistry and Biological Sciences, Lehigh University, Bethlehem, Pennsylvania 18015. Received May 6, 2008; Revised Manuscript Received July 14, 2008

A fluorescently labeled, persulfated molecular umbrella (**1**) has been synthesized from cholic acid, lysine, spermine, and Coumarin 343 and found capable of entering live HeLa cells. The distributions of **1** throughout the cytoplasm and the nucleus were diffuse and punctate, respectively. This finding, together with its ability to cross liposomal membranes by passive diffusion, suggests that passive diffusion plays a significant role in the ability of **1** to enter cells. The fact that **1** is concentrated at the nucleus raises the possibility that molecular umbrellas of this type could be used for the nuclear targeting of drugs.

Molecular umbrellas are a unique class of conjugates that are composed of two or more facial amphiphiles that are covalently bound to a central scaffold. Such molecules have been found to possess the ability of crossing liposomal membranes by passive diffusion (*1*−*4*). Our working hypothesis has been that the amphiphilic "wings" of a molecular umbrella first bind to the surface of the liposomal membrane, that translocation proceeds through a shielded conformation in which the hydrophilic faces of the molecule point toward one another as it passes through the hydrocarbon interior, and that the umbrella is then released from the adjacent monolayer into the adjoining aqueous phase. In Scheme 1, we illustrate our current model for umbrella transport of a hydrophilic agent across a lipid bilayer. Here, the shaded and unshaded rectangles represent hydrophobic and hydrophilic faces of the facially amphiphilic units, respectively, and the lightly shaded oval represents a covalently attached, hydrophilic agent. Thus, the umbrella first approaches the membrane in a fully exposed conformation (structure **A**). Hydrophobic interactions with the membrane interior then lead to an adsorbed state in which the hydrophilic faces are in contact with the polar headgroup region and the hydrophobic faces are in intimate contact with the hydrocarbon region of the lipid bilayer (structure **B**). Subsquent absorption into the interior of the membrane, being driven by hydrophobic forces, then affords structure **C**. Translocation to the adjoining leaflet, 180° rotation, and reversal of steps **B** and **A** (not shown) then releases the conjugate from the other side of the membrane. In essence, we have postulated that the molecular umbrella masks its own hydrophilicity as well as that of an attached polar agent as it crosses the hydrocarbon interior of the bilayer.

In the work that is reported herein, we sought to answer a long-standing question that bears directly on the potential of molecular umbrellas as drug carriers. Specifically, can a molecular umbrella that is capable of crossing liposomal membranes also cross cellular membranes? To address this question, we designed a fluorescently labeled molecular umbrella (**1**) and investigated its interaction with live HeLa cells (Chart 1). We also compared the transport properties of **1** with a non-umbrella analogue that is similar in size and charge, but devoid of facial amphiphilicity (i.e., **2**). Previously, we showed that a nonfluorescently labeled form of **1** escapes the aqueous interior of liposomes, leaving behind a much smaller, hydrophilic peptide (i.e., glutathione) (*4*). This selective release established that the much larger molecular umbrella crosses lipid bilayers without damaging them.

In Scheme 2, we outline the method that was used to prepare **1**. Thus, activation of the carboxyl group of Coumarin 343, followed by condensation with α-*t*-BOC-lysine afforded **3**. Subsequent formation of the corresponding *N*-hydroxylsuccinate ester and acylation of one of the terminal amino groups of spermine produced **4**. Finally, deprotection to give **5**, total acylation with lysine dicholamide [activated with 3-hydroxy-1,2,3-benzotriazin-4(3H)-one] to give **6**, and persulfation with pyridine sulfur trioxide afforded **1** (6683 Da). Scheme 3 shows the approach that was used to prepare **2** (5 ± 1 kDa). Thus, activation of PRO 2000 (a gift from Indevus Pharmaceuticals, Lexington, MA) with sulfonyl chloride, followed by condensation with less than 1 mol % of a monoconjugate made from Courmarin 343 and putrescine (i.e., **7**) and subsequent hydrolysis afforded **2**.

Before examining the ability of **1** and **2** to enter HeLa cells, we first compared their ability to cross liposomal membranes by passive diffusion. Using experimental methods similar to those previously described, liposomes (200 nm, extrusion) were prepared from 40 mg of a mixture of 1-palmitoyl-2-oleyol-*sn*-glycero-3-phosphocholine (POPC) and 1-palmitoyl-2-oleoyl-*sn*-glycero-3-phosphatidylglycerol (POPG) [POPC/POPG, 95/5, mol/mol] and 2 mL of phosphate buffered saline [10 mM phosphate, 150 mM NaCl, pH 7.4, PBS] that was 0.5 mM in **1** or **2** (*4*). After dialysis for 52 h at 23 °C, the percentage of liposome-entrapped **1** or **2** was monitored as a function of time (Figure 1). In contrast to **1**, which exhibited a first-order release, liposome-entrapped **2** showed no detectable release.

To determine whether **1** can enter live HeLa cells, confocal microscopy was used to section optically through the cellular volume to ascertain whether the fluorescent label was dispersed within the cell and not bound to its outer surface. Cells were also labeled with Syto-59 to mark their nucleus and their cytoplasm. After a 90-min incubation period with 4 μM of **1**, the molecular umbrella was detected inside the cells (Figure 2). Similar micrographs were observed after 10 min. That **1** had been internalized within the cells was confirmed from profile views that were obtained by computer-based rotation of the image stacks (Figure 2, bottom). Here, the red fluorescence of Syto-59 marks each cell, the fluorescence of Coumarin 343 is

* slr0@lehigh.edu.
[†] Department of Chemistry.
[‡] Department of Biological Sciences.

10.1021/bc8001826 CCC: $40.75 © 2008 American Chemical Society
Published on Web 08/06/2008

Scheme 1

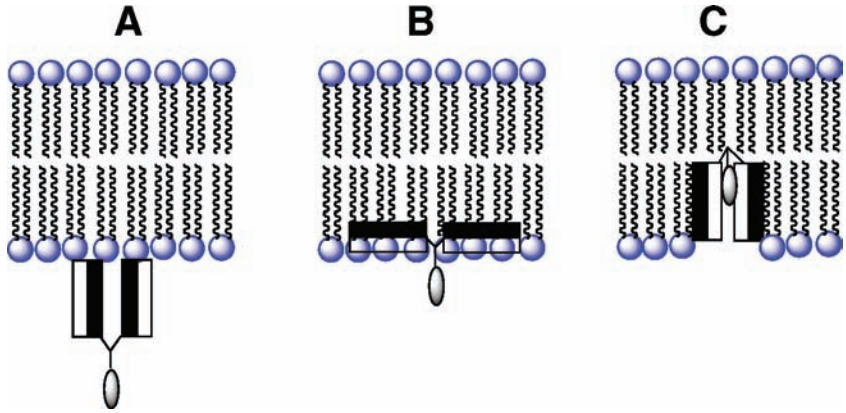

Chart 1

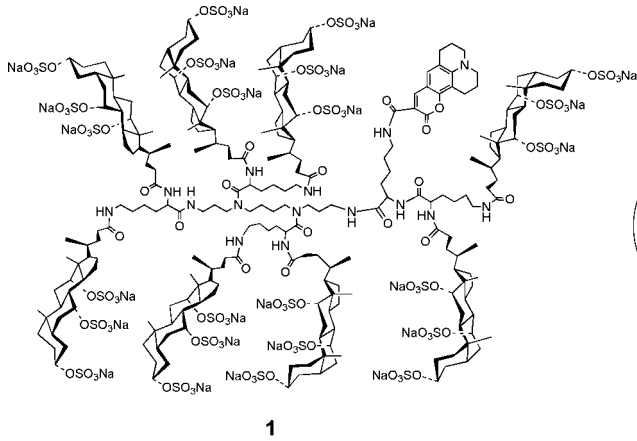

1

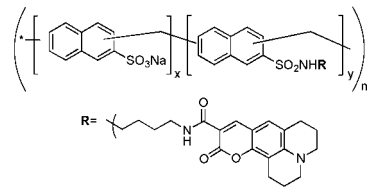

2, n_{av} = 20; y<1 mol%

Scheme 2

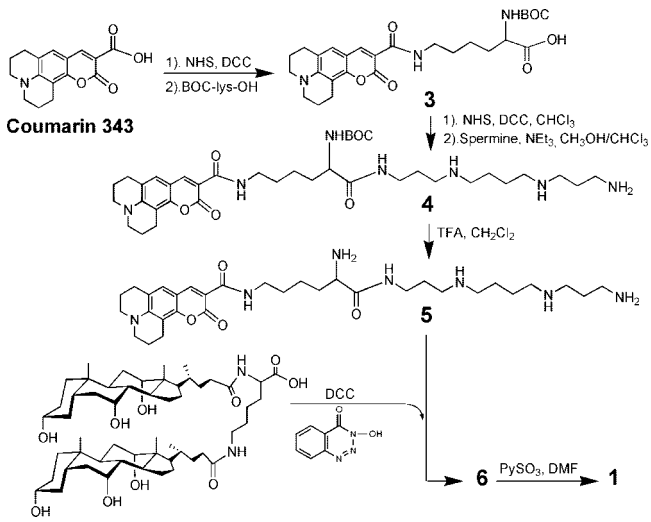

Scheme 3

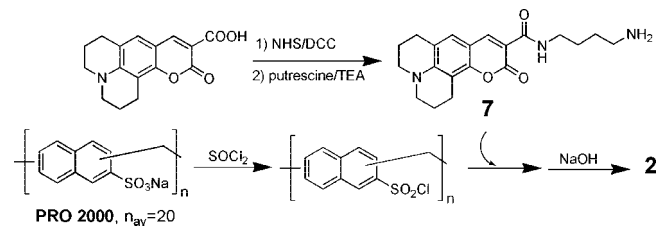

PRO 2000, n_{av}=20

shown in green, and the overall cell is revealed by the differential interference contrast (DIC) micrographs. Both the Coumarin 343 and merged micrographs in Figure 2 show a distribution of **1** that is diffuse in the cytoplasm and punctate in the nucleus. The former is generally considered to be an indication of cellular entry via passive diffusion (*5*, *6*). In addition, the molecular umbrella that was found in the nucleus was bound in spots that colocalize with nucleoli within the nucleus. At present, the nature of this binding is unclear, although we believe that the high density of the sulfate groups within each facial amhiphile is likely to play a key role. It should be noted that no cellular damage of any sort was ever observed in any of these experiments. Specifically, the cells appeared healthy throughout these experiments, as indicated by the fact that they did not retract and that they maintained attachments to the substrate. It is also noteworthy that incubation with **1** for 30 min showed negligible toxicity (<5% cell death) as judged by propidium iodide exclusion measurements. Related studies that have been carried out with CaSki cells, which were fixed with 4% paraformaldehyde, have also shown nuclear localization after 15 min of incubation with **1** (*7*).

In sharp contrast to **1**, which was consistently taken up by the HeLa cells in more than 20 independent experiments, the internalization of **2** was variable. *In most cases no cellular uptake was observed!* When cellular uptake was found, **2** entered all of the cells; that is, its uptake was either all or none. Another peculiar feature of **2** was that it induced a redistribution of Syto-59 within the HeLa cells. Examples of cellular uptake of **2**, in those few cases where internalization was observed, are shown in Figure 2. In contrast to **1**, the distribution of **2** within the cytoplasm and the nucleus was punctate and diffuse, respectively. The former implies that **2** enters HeLa cells by a fundamentally different pathway,

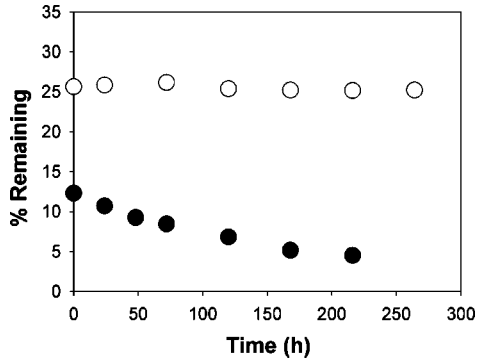

Figure 1. Plot of percentage of liposome-entrapped **1** (●) and **2** (○) remaining as a function of dialysis time at 23 °C, after an initial dialysis of 52 h. Experimental methods used were similar to those previously described (*4*). Here, release of **1** was monitored by removing aliquots of the liposomal dispersion during dialysis, destroying the liposomes with an ethanolic solution of sodium dodecyl sulfate, and analyzing for residual Cascade Blue (460 nm). The half-lives for **1** and **2** diffusing across the dialysis membrane were 3.5 and 7 h, respectively.

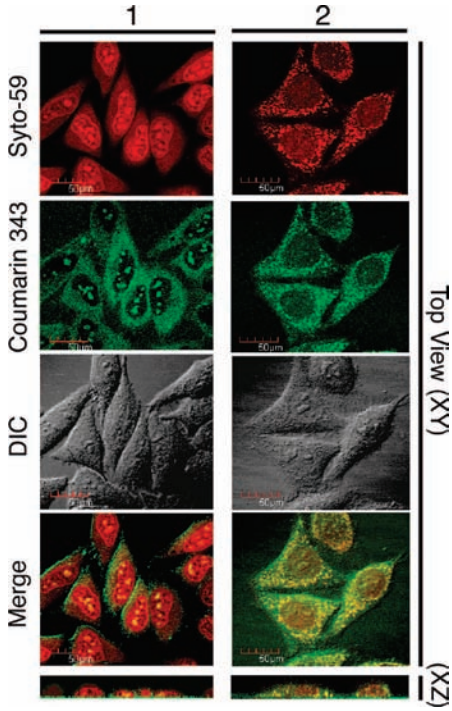

Figure 2. Confocal micrographs of HeLa cells incubated with 4 μM of **1** or **2** for 90 min. Living cells were treated with Syto-59 (red in the merged image to mark the nuclei and cytoplasm) and Coumarin 343-labeled **1** or **2** (green in merged images). Single image planes from the centers of the cells are shown. Syto-59 (red), Coumarin 343 (green), and DIC are shown in the $X-Y$ dimension (top view) and in the $X-Z$ dimension (profile, bottom). NOTE: The addition of **2** (but not **1**) to HeLa cells led to a redistribution of Syto-59.

most probably via endocytosis. Because of the poor reproducibility of cellular internalization by **2**, and because it led to a peculiar redistribution of Syto-59, this *non-umbrella* analogue was not investigated further.

The fact that **1** is capable of crossing liposomal membranes, together with its diffuse distribution within the cytoplasm, suggests that passive diffusion plays an important role in its cellular entry. The reason for the slow rate at which **1** is released from liposomes relative to the rapid internalization by cells is not presently clear. Since cell membranes are rich in proteins, one explanation for this difference would be that lipid/protein interfaces provide a pathway for the molecular umbrellas to "slip across" the membrane, possibly via some type of protein-induced "flip-flop" mechanism. Alternatively, rapid cellular entry of **1** could be related to a higher intrinsic affinity of **1** to cellular membranes. In addition, we cannot rule out the possibility that other mechanisms may be contributing to the cellular entry of **1**. In preliminary studies, treatment of HeLa cells with NaN_3 and 2-deoxyglucose (to deplete ATP production) only modestly inhibited the cellular uptake of **1** (see Supporting Information). Control experiments that were carried out under similar conditions with fluorescently labeled transferrin, however, showed a very substantial inhibition of endocytotic uptake. This finding is fully consistent with passive diffusion of **1** across lipid bilayers. Although no cellular uptake of **1** was found at 4 °C, which is consistent with an endocytotic pathway for cellular entry, we believe that the ATP-depletion experiment is a more reliable indicator of probable mechanism of cellular entry. Specifically, we believe that the lowering of the temperature to 4 °C is a more severe perturbation of cellular conditions than ATP-depletion, since it is likely to result in a major reorganization of the two-dimensional structure of the plasma membrane.

The ability of this highly *anionic* molecular umbrella (**1**) to enter live cells is in sharp contrast to many cationic cellular delivery systems that have been reported in the literature; e.g., arginine-rich, cell-penetrating peptides (*8*). This anionic character may well be responsible for the ability of **1** to concentrate at the nucleus of cells. Efforts currently in progress are aimed at defining the relationships that exist between the structure and composition of molecular umbrellas and their ability to diffuse across hydrophobic barriers, enter cells, and concentrate at the nucleus of cells. The results of these studies will be reported in due course.

ACKNOWLEDGMENT

We are grateful to the National Institutes of Health (PHS Grants GM51814 to SLR and GM58025 to LC) for support of this research and to Prof. Susan Fueshko Perry (Lehigh) for valuable discussions.

Supporting Information Available: Experimental procedures. This material is available free of charge via the Internet at http://pubs.acs.org.

LITERATURE CITED

(1) (a) Janout, V., Lanier, M., and Regen, S. L. (1996) Molecular umbrellas. *J. Am. Chem. Soc. 118*, 1573–1574. (b) Janout, V., Lanier, M., and Regen, S. L. (1997) Design and synthesis of molecular umbrellas. *J. Am. Chem. Soc. 119*, 640–647.

(2) Janout, V., DiGiorgio, C., and Regen, S. L. (2000) Molecular umbrella-assisted transport of a hydrophilic peptide across a phospholipid membrane. *J. Am. Chem. Soc. 122*, 2671–2672. (b) Janout, V., Jing, B., and Regen, S. L. (2005) Molecular umbrella-assisted transport of an oligonucleotide across cholesterol-rich phospholipid bilayers. *J. Am. Chem. Soc. 127*, 15862–15870.

(3) Janout, V., Staina, I. V., Bandyopadhyay, P., and Regen, S. L. (2001) Evidence for an umbrella mechanism of bilayer transport. *J. Am. Chem. Soc. 123*, 9926–9927.

(4) Jing, B., Janout, V., Herold, B. C., Klotman, M. E., Heald, T., and Regen, S. L. (2004) Persulfated molecular umbrellas as anti-HIV and anti-HSV agents. *J. Am. Chem. Soc. 126*, 15930–15931.

(5) Farrera-Sinfreu, J., Giralt, E., Castel, S., Albericio, F., and Royo, M. (2005) Cell-penetrating cis-gamma-amino-L-proline-derived peptides. *J. Am. Chem. Soc. 127*, 9459–9468.

(6) Fillon, A., Anderson, J. P., and Chmielewski, J. (2005) Cell-

penetrating agents based on a polyproline helix scaffold. *J. Am. Chem. Soc. 127*, 11798–11803.

(7) Madan, R. P., Mesquita, P. M. M., Cheshenko, N., Jing, B., Shende, V., Guzman, E., Heald, T., Keller, M. J., Regen, S. L., Shattock, R. J., and Herold, B. C. (2007) Molecular umbrellas: a novel class of candidate topical microbicides to prevent human immunodeficiency virus and herpes simplex virus infections. *J. Virol. 81*, 7636–7646.

(8) Yandek, L. E., Pokorny, A., Floren, A., Knoelke, K., Langel, U., and Almeida, P. F. (2007) Mechanism of the cell-penetrating peptide transportan10 permeation of lipid bilayers. *Biophys. J. 92*, 2434–2444.

BC8001826

Cellular Entry and Nuclear Targeting By a Highly Anionic Molecular Umbrella

Mohamed Mehiri, Bingwen Jing,† Danielle Ringhoff, Vaclav Janout, Lynne Cassimeris, and

Steven L. Regen

Departments of Chemistry and Biological Sciences, Lehigh University, Bethlehem, Pennsylvania 18015

Supporting Information

Materials. Coumarin 343 (Sigma-Aldrich) and PRO 2000 (Indevus Pharmaceuticals, Lexington, MA) were used as obtained. BOC-lys-OH was obtained from Fluka.

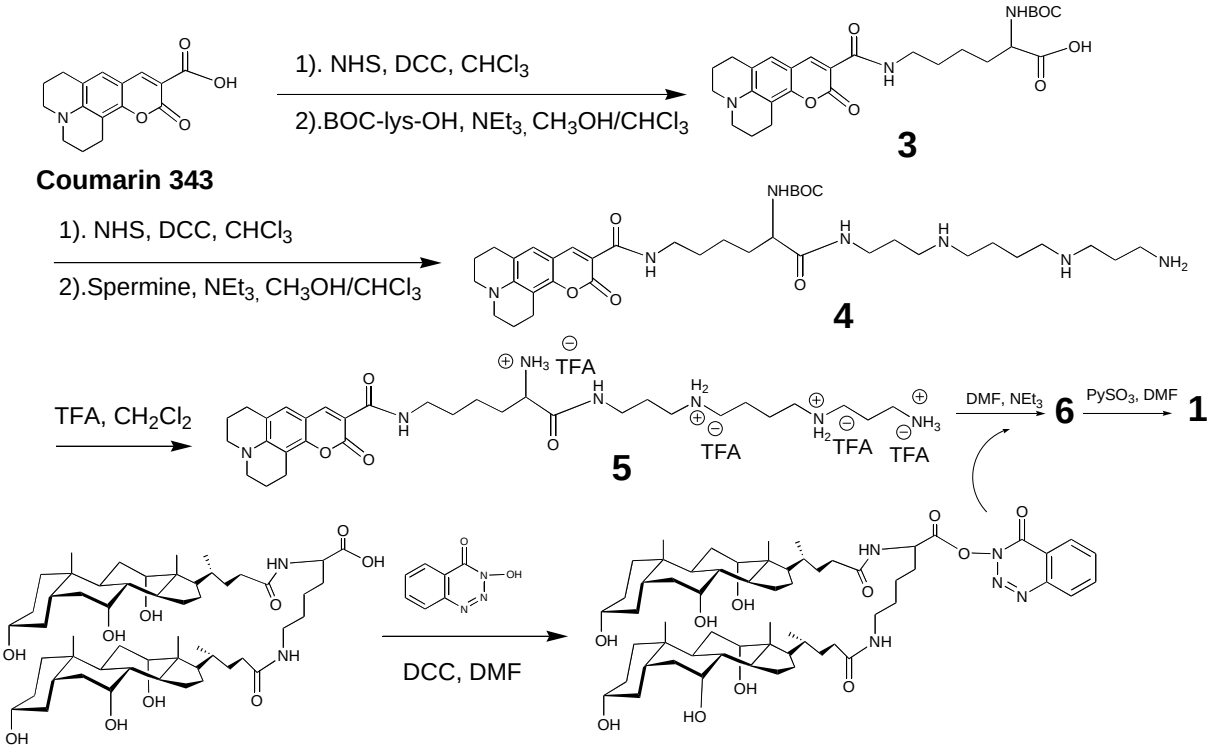

Coumarin 343-BOC–lysine (3). To a solution that was made from 300 mg (1.05 mmol) of Coumarin 343, 145 mg (1.26 mmol) of N-hydroxyl succinimide and 20 mL of chloroform was added 260 mg (1.26 mmol) of DCC. After stirring for 3 h at room temperature, the insoluble urea was removed by filtration, and the filtrate was concentrated to ca. 10 mL. The resulting chloroform solution, which contained the NHS-ester of Coumarin, was then added to a solution that was made from 271 mg (1.1mmol) of BOC-lys-OH and 460 µL (3.3 mmol) of triethylamine in 4 mL of methanol. The reaction mixture was stirred at room temperature overnight. Removal of solvent under reduced pressure and purification of the crude product by silica gel column chromatography using chloroform/methanol (10:1, v/v, R_f=0.24) as the eluant afforded 274 mg (51%) of **5** as a yellow solid and ^{1}HNMR ($CDCl_3$): 1.40-2.0(m, 19H), 2.73(t, 2H), 2.83(t, 2H), 3.30-3.50(m, 6H), 4.29(br, 1H), 5.34(s, 1H, -OCON**H**-), 6.99(s, 1H), 8.66(s, 1H). MALDI-TOF MS: *m/z* **514** ($[M+H]^+$).

Coumarin 343-BOC-lysine-spermine (4). An activated form of **3** was prepared by dissolving 205 mg (0.4 mmol) of the conjugate in 20 mL of chloroform along with 51 mg (0.44 mmol) of N-hydroxysuccinimide and 91 mg (0.44 mmol) of DCC. After stirring at room temperature for 3 h, the insoluble urea was removed by filtration and the filtrate then added, dropwise, to a stirred solution that was made from 405 mg (2 mmol) of spermine, 167 µL (1.2 mmol) of triethylamine and 50 mL of methanol. The mixture was then stirred for 1 h at room temperature, and the solvent removed under reduced pressure. The resulting residue was purified by silica gel column chromatography using chloroform/methanol/ammonium hydroxide (30%) (60/40/10, v/v/v) as the eluant, affording 187 mg (67%) of **4** having a R_f of 0.28 and ^{1}HNMR (CD_3OD): 1.40-1.80(m, 23H), 1.96(m, 4H), 2.55-2.86(m, 14H), 3.18-3.29(m, 2H), 3.33-3.45(m, 6H), 3.95(s, 1H), 7.06(s, 1H), 8.45(s, 1H). MALDI-TOF MS: *m/z* **698** ($[M+H]^+$).

Coumarin 343-lysine-spermine-TFA salt (5). A solution was prepared by dissolving 151 mg (0.216 mmol) of **4** in 2 mL of a 1/1 mixture of trifluoroacetic acid/chloroform (v/v) at 0°C, and the mixture then stirred at room temperature for 5 h. Removal of solvent under reduced pressure and subsequent

freeze drying overnight afforded 230 mg (91%) of **5** having ^{1}HNMR (CD_3OD): 1.35-2.10(m, 18H), 2.72-2.78(m, 4H), 3.00-3.15(m, 10H), 3.30-3.50(m, 8H), 3.84(t, 1H), 7.03(s, 1H), 8.41(s, 1H). MALDI-TOF MS: *m/z* **598** ($[M+H]^+$).

Conjugate 6. A solution was prepared by dissolving 300 mg (0.323 mmol) of lysine dicholamide, 56 mg (0.344 mmol) of 3-hydroxy-1,2,3-benzotriazin-4(3H)-one, and 72 mg (0.349 mmol) of DCC in 1.5 mL of DMF.[1] The mixture was stirred at room temperature for 3 h, followed by the addition of 71 mg (0.0608 mmol) of **5** and 94 μL (0.674 mmol) of triethylamine. The resulting solution was stirred at room temperature overnight and then poured into 10 mL of an aqueous saturated sodium bicarbonate solution. The precipitate was collected by filtration and purified by silica gel column using chloroform/methanol/ammonium hydroxide (30%) (40/10/1, v/v/v) as the eluant to give 134 mg (52%) of **6**, which was further purified by preparative TLC (silica gel), using the same eluant as that which was used in the column chromatography. Conjugate **6** had an R_f=0.31 and ^{1}HNMR (CD_3OD): 0.69(s, 24H), 0.90-2.40(m, 282H), 2.79(t, 2H), 2.84(t, 2H), 3.16(m, 12H), 3.32-3.50(m, 22H), 3.8(s, 8H), 3.93(s, 8H), 4.16-4.40(br, 3H), 4.76(br, 2H), 7.13(s, 1H), 8.51(s, 1H). MALDI-TOF MS: *m/z* **4258** ($[M+Na]^+$).

Conjugate 1. To 1 mL of DMF was added 67 mg (0.018 mmol) of **6** and 182 mg (1.143 mmol) of pyridine sulfur trioxide at 0 ^{0}C. The reaction mixture was stirred at room temperature overnight and neutralized by addition of cold saturated sodium bicarbonate having a pH of ca. 10. After removal of solvent under reduced pressure, the residue was purified by silica gel column using chloroform/methanol/water (50/50/10, v/v/v) as the eluant to give 90 mg (85%) of **1** having R_f=0.42 ($CHCl_3/CH_3OH/H_2O$, 4/4/1, v/v/v) and ^{1}HNMR (CD_3OD): 0.75-2.40(m, 306H), 2.80(t, 2H), 2.86(t, 2H), 3.14(m, 12H), 3.33-3.50(m, 14H), 4.13(s, 8H), 4.26(br, 3H), 4.44(s, 8H), 4.65(s, 8H), 4.76(br, 2H), 7.15(s, 1H), 8.55(s, 1H).

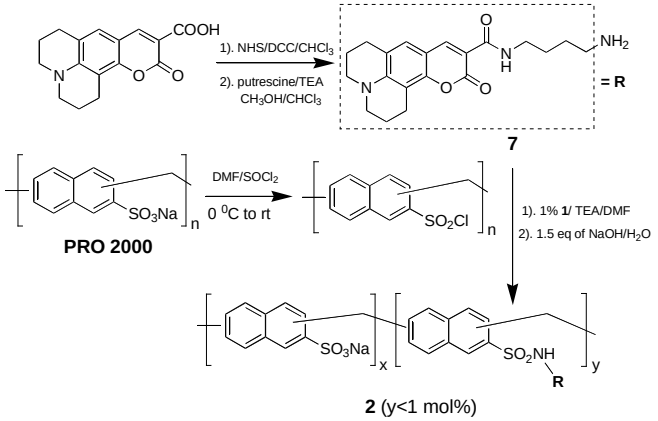

1, 4'-Aminobutylcoumarin 343 amide (7). To a solution that was prepared by dissolving 200 mg (0.7 mmol) of Coumarin 343 in 10 mL of chloroform was added 100 mg (0.87 mmol) of N-hydroxylsuccinimide and 180 mg (0.87 mmol) of DCC. After stirring for 5 h at room temperature, the insoluble urea was removed by filtration. The filtrate was then diluted with 50 mL of chloroform and the resulting solution added in a dropwise manner (within 1 h) to a stirred solution made from 176 mg (1.4 mmol) of putrescine and 293 µL (2.1 mmol) of triethylamine in 100 mL of methanol. After stirring for 3 h at room temperature, the solvent was removed under reduced pressure and the residue purified by silica gel column chromatography using chloroform/methanol/ammonium hydroxide (30%) (50/10/1, v/v/v, R_f=0.7) affording 133 mg 53% of **7** having ^{1}HNMR (500 MHz, CD_3OD, rt): 1.78(m, 4H), 2.05(m, 4H), 2.81(t, 2H), 2.88(t, 2H), 3.03(t, 2H), 3.42(m, 4H), 3.50(m, 2H), 7.17(s, 1H), 8.57(s, 1H). MALDI-TOF MS: *m/z* **356** ($[M+H]^+$).

Fluorescent Labeling of PRO 2000 (2). The procedure that was used for activating PRO 2000 was similar to that used for forming chlorosulfonate derivatives of aromatic compounds.[2,3] Thus, a suspension that was prepared from 200 mg of PRO 2000 in 1 mL of DMF was cooled to 0°C, followed by addition of 200 µL (2.75 mmol) of thionyl chloride. After stirring for 10 min, the mixture was allowed to reach room temperature and stirred for an additional 5 h. The product mixture was poured into 25 mL of ice water, vortex mixed for 5 min, and centrifuged. The aqueous solution was then removed and an additional 25 mL of ice water added to the precipitate. Further centrifugation and

removal of the aqueous phase, followed by freeze drying overnight to give 180 mg of a chlorosulfonated form of the polymer as a pale powder.

To a solution that was prepared by dissolving 80 mg of this activated form of PRO 2000 in 1 mL of DMF was added 0.5 mL of a DMF solution containing 1.2 mg (0.00337 mmol) of **7**, (corresponding to less than 1% mol of the pendant sulfonate groups present in solution) plus 100 µL (0.717 mmol) of triethylamine. This solution was stirred at room temperature for 4 h, followed by addition of an alkaline solution that was prepared by dissolving 25 mg (0.628 mmol) of NaOH in 1 mL of water. After stirring the solution for an additional 2 h, the solvent was removed under reduced pressure. The residue was dissolved in 1 mL of water and passed through a C-18 reverse-phase column using pure water as eluant. The first fraction (yellow) that was eluted from the column was concentrated under reduced pressure. Additional purification of this residue was carried out by preparative thin layer chromatography (silica gel, two chromatographs) using chloroform/methanol/water (40/40/10, v/v/v) as the eluant. The polymer was then dialyzed against pure water for 24 h, using dialysis tubing having a 500 MW cutoff. Concentration of the dialyzed product under reduced pressure afforded 53 mg of **2** as a yellow powder.

Binding to Liposomal Membranes. Binding of **1** to liposomal membranes was measured via an equilibrium dialysis cell having 2.0 mL compartments (Fisher Scientific, Bel-Art Scienceware), using a Nuclepore membrane (100 nm diameter pores) to separate the two compartments. To the "source" side was added 0.5 mL of a 500 µM solution of **1** in PBS plus 0.5 mL of a liposomal dispersion made from 10 mg of POPC/POPG (95/5, mol/mol, 200 nm diameter, extrusion) in PBS. To the "receiving side" was added 1.0 mL of PBS. The UV absorption (460 nm) in the "receiving" side of the cell was then monitored as a function of time at room temperature with gentle rocking of the cell until equilibrium was reached (24 h). Under these conditions, the amount of the molecular umbrella that was bound to the liposomes corresponded to 0.002 mole of **1** per mole of phospholipid.

Cell Entry Experiments. HeLa (human epithelial cervical carcinoma) cells were cultivated in Minimum Essential Medium (MEM, Invitrogen) supplemented with 10% fetal bovine serum (FBS) at

37°C in a humidified atmosphere containing 5% CO_2. For all experiments, exponentially growing cells were detached from the culture flasks using a trypsin-0.125% EDTA solution, counted using a hemocytometer and the trypan blue dye. The cell suspension was seeded at a concentration of 20×10^4 cells/cm^2 onto a 42 mm glass round coverslip (Hemogenix). Experiments were carried out 24 h later, at a confluence level of approximately 60%-70%. To ensure consistency in uptake, cells were passaged biweekly and discarded after 20 passages.

Compound **1** or **2** was dissolved in PBS Ca^{2+} and Mg^{2+} free (Invitrogen) at a concentration of 150 µM. Before all experiments, compound **1** or **2** stock solutions were diluted to a concentration of 4 µM in 2 mL of DMEM (Invitrogen) lacking both phenol red and fetal bovine serum.

In a typical experiment, the coverslip with the monolayer of HeLa cells was mounted in a POC chamber (PeCon GmbH, Erbach, Germany) and washed three times with 2 mL PBS of Ca^{2+} and Mg^{2+} free to remove nonadherent cells. The attached cells were then labeled with 1 µM Styo-59 (Molecular Probes) in 2 mL of DMEM at 37 °C in CO_2 atmosphere for 20 min. Cells were imaged to measure their autofluorescence prior a cellular entry experiment. The medium was then discarded and the cells were incubated with 2 mL of 4 µM of compound **1** or **2** in DMEM at 37 °C for the indicated time prior image acquisition.

Confocal laser scanning microscopy was performed with an Olympus Fluoview 1000 confocal microscope (Olympus FV 1000, Tokyo, Japan) using a 60X/1.4 NA plan-apochromatic objective. Coumarin 343 was excited by both the 458 nm and 488 nm lines from an argon ion laser. Syto-59 was excited using a 543 nm HeNe laser. The microscope settings were maintained identical for both compounds. Images, usually 1024 x 1024 or 512 x 512 pixels, were acquired using 2-line mean averaging. Optical sections have a depth of 0.75 µm. The background from a region lacking cells was subtracted from each image. The fluorescence intensity (measured using Image J software) within each cell was measured from single optical sections located at the center of the cell (Z dimension). The autofluorescence of the cells was subtracted from each measurement. For presentation, image stacks

were converted to maximum intensity projections using the Olympus Fluoview ver.1.6 viewer software. The Fluoview software was also used to rotate 3-D projections to visualize the X – Z dimension. Images were exported as TIFF files and printed using Photoshop 7.0 (Adobe).

Similar procedures were used for experiments in which cells were depleted of ATP.[4-6] In this case, the cells were incubated in saline containing 5 mM NaN_3 and 1 mM 2-deoxyglucose for 4-5 minutes.[6] The efficiency of inhibition of energy-dependent endocytosis was determined by incubation in saline containing 10 mM Alexa Fluor 488-labeled transferrin (5 mM stock solution in 1x PBS; Molecular Probes) for 3 min, fixation in 2% *p*-formaldehyde, and microscopic examination of either ATP-depleted or untreated cells.

(1) Chen, W. H.; Shao, X.B.; Regen, S. L. *J. Am. Chem. Soc*., **2005**, *127*, 12717-12735.

(2) Bosshard, H. H.; Mory, R.; Schmid, M.; Zollinger, Hch. *Helv. Chim. Acta*, **1959**, *42*, 1653-1658.

(3) Loewenthal, H. J. E.; Gottlieb, L. *J. Org. Chem.*, **1992**, *57*, 2631-2641.

(4) Cassimeris, L.; Morabito, J. *Mol. Biol. Cell*., **2004**, *15*, 1580-1590.

(5) Piehl, M.; Cassimeris, L. *Mol. Biol. Cell*., **2003**, *14*, 916-925.

(6) Howell, B.; Hoffman, D. B.; Fang, G.; Murray, A. W.; Salmon, E.D. *J. Cell Biol*.,

Effectiveness of ATP depletion on cellular uptake of AlexaFluor 488-Transferrin:

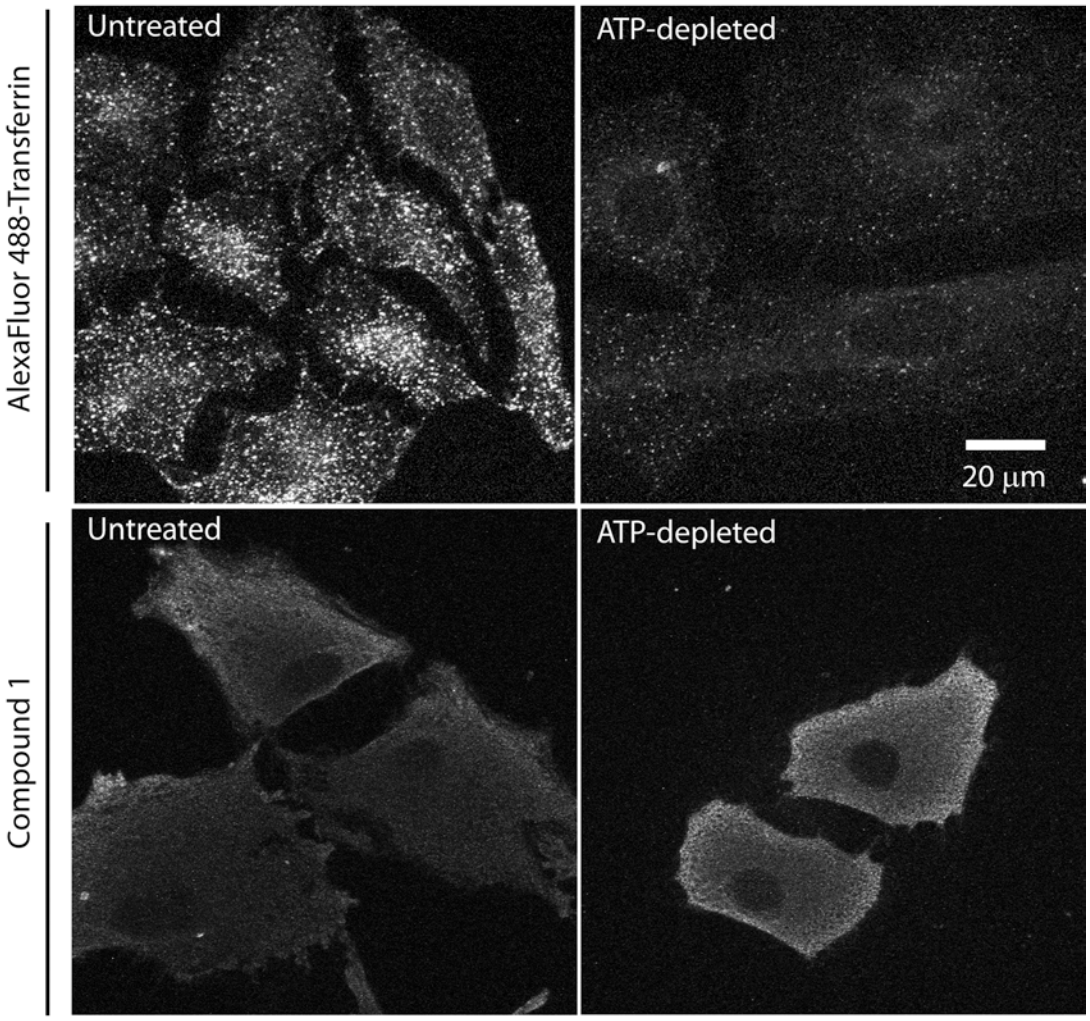

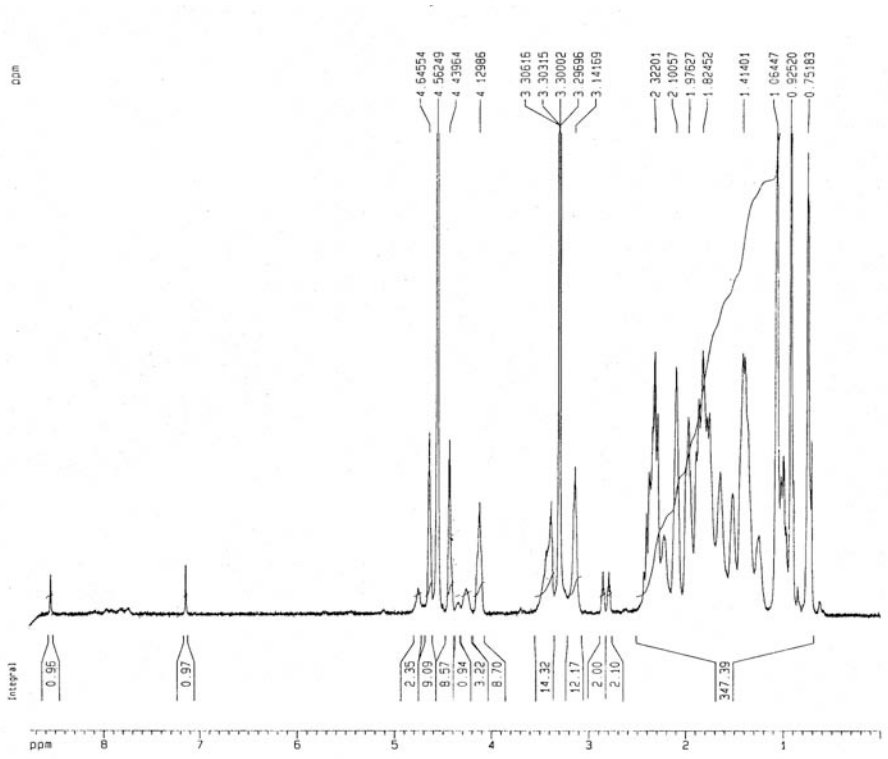

Current Data Parameters
NAME pBchas2gw
EXPNO 1
PROCNO 1

F2 - Acquisition Parameter
Date_ 20060501
Time 10.08
INSTRUM spect
PROBHD 5 mm PHBBO BB-
PULPROG zg
TD 32768
SOLVENT MeOD
NS 32
DS 0
SWH 5000.000 Hz
FIDRES 0.152588 Hz
AQ 3.2769499 se
RG 128
DW 100.000 us
DE 7.00 us
TE 323.2 K
D1 1.00000000 se

======== CHANNEL f1 ======
NUC1 1H
P1 5.00 us
PL1 -4.00 dB
SFO1 500.1319002 MH

F2 - Processing parameters
SI 16384
SF 500.1300157 MH
WDW no
SSB 0
LB 0.00 Hz
GB 0
PC 4.00

1D NMR plot parameters
CX 20.00 cm
CY 100.00 cm
F1P 9.000 pp
F1 4501.17 Hz
F2P 0.000 pp
F2 0.00 Hz
PPMCM 0.45000 pp
HZCM 225.05850 Hz

1

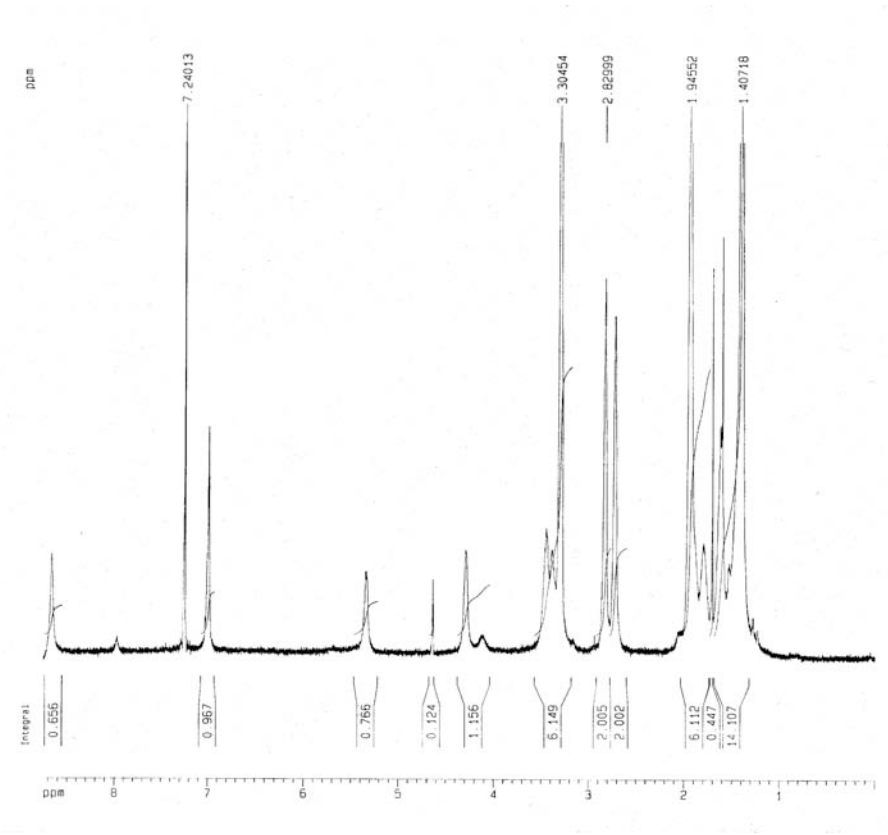

Current Data Parameters
NAME 1yBOC-coumarin343
EXPNO 1
PROCNO 1

F2 - Acquisition Parameters
Date_ 20060412
Time 16.29
INSTRUM spect
PROBHD 5 mm PHBBO BB-
PULPROG zg
TD 32768
SOLVENT CDCl3
NS 4
DS 0
SWH 5000.000 Hz
FIDRES 0.152588 Hz
AQ 3.2769499 sec
RG 161.3
DW 100.000 use
DE 7.00 use
TE 300.1 K
D1 1.00000000 sec

======== CHANNEL f1 =======
NUC1 1H
P1 5.00 use
PL1 -4.00 dB
SFO1 500.1319002 MHz

F2 - Processing parameters
SI 16384
SF 500.1300224 MHz
WDW no
SSB 0
LB 0.00 Hz
GB 0
PC 4.00

1D NMR plot parameters
CX 20.00 cm
CY 100.00 cm
F1P 9.000 ppm
F1 4501.17 Hz
F2P 0.000 ppm
F2 0.00 Hz
PPMCM 0.45000 ppm
HZCM 225.05852 Hz/

3

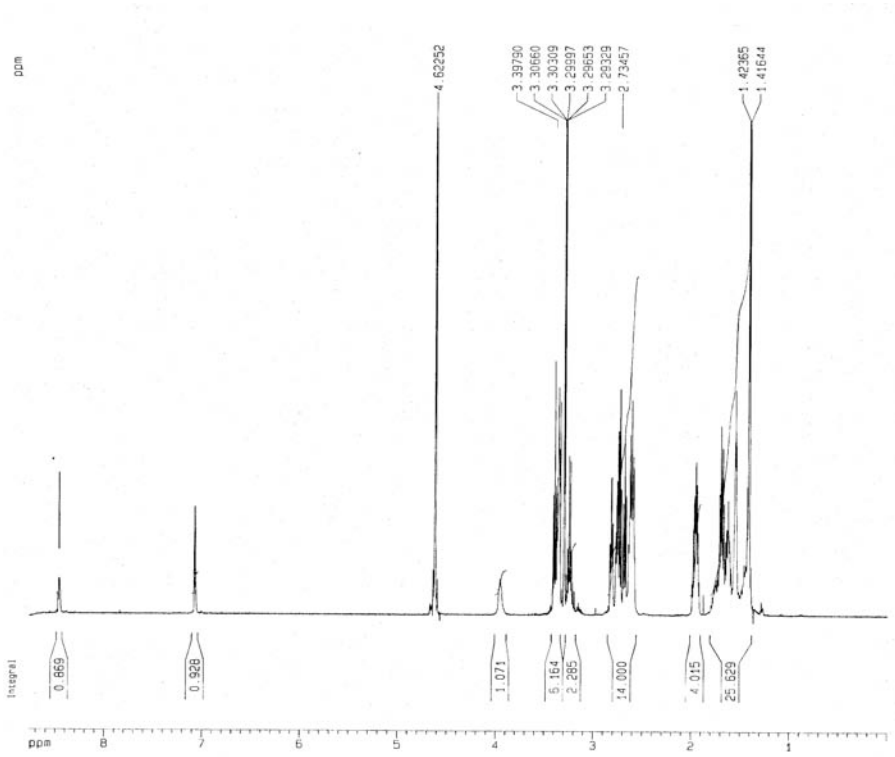


```
Current Data Parameters
NAME        1yBOC-coum-spmgw
EXPNO                      1
PROCNO                     1

F2 - Acquisition Parameter
Date_               20060414
Time                    9.51
INSTRUM                spect
PROBHD   5 mm PHBBO BB-
PULPROG                  zg
TD                    32768
SOLVENT                MeOD
NS                        8
DS                        0
SWH              5000.000 Hz
FIDRES           0.152588 Hz
AQ               3.2769499 se
RG                      114
DW               100.000 us
DE                 7.00 us
TE                318.2 K
D1            1.00000000 se

======== CHANNEL f1 ======
NUC1                      1H
P1                  5.00 us
PL1                -4.00 dB
SFO1          500.1319002 MH

F2 - Processing parameters
SI                    16384
SF           500.1300157 MH
WDW                      no
SSB                       0
LB                 0.00 Hz
GB                        0
PC                     4.00

1D NMR plot parameters
CX                 20.00 cm
CY                100.00 cm
F1P                9.000 pp
F1              4501.17 Hz
F2P                0.000 pp
F2                 0.00 Hz
PPMCM          0.45000 pp
HZCM          225.05850 Hz
```

4

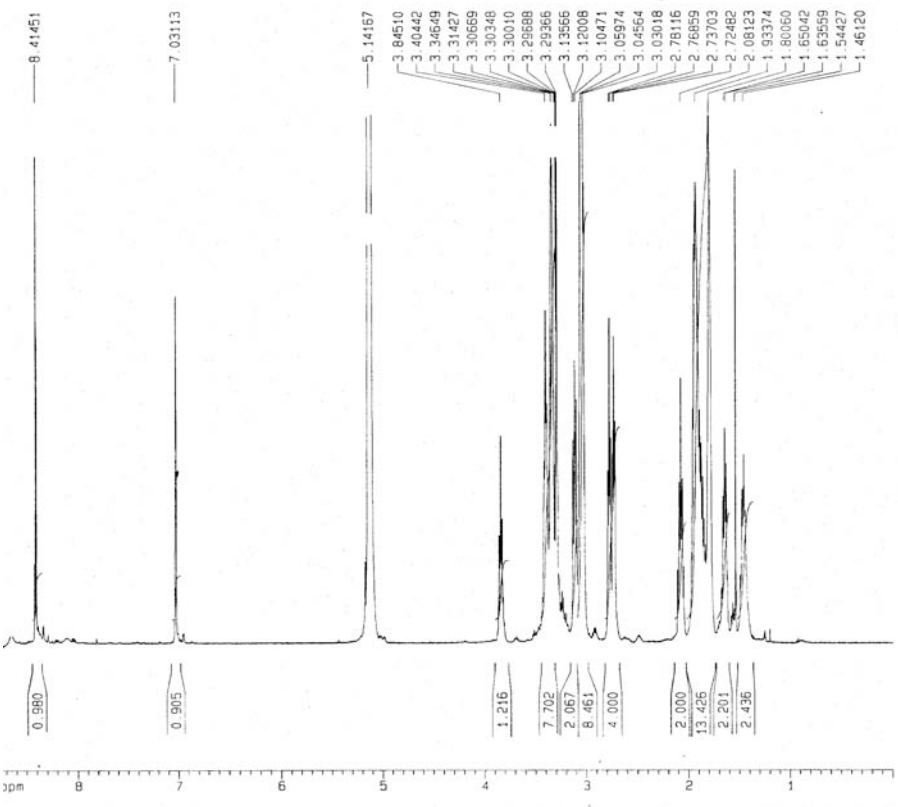


```
Current Data Parameters
NAME          1y-coum-spm
EXPNO                    1
PROCNO                   1

F2 - Acquisition Parameter
Date_             20060417
Time                 13.56
INSTRUM             spect
PROBHD   5 mm PHBBO BB-
PULPROG                zg
TD                  32768
SOLVENT              MeOD
NS                      8
DS                      0
SWH            5000.000 Hz
FIDRES         0.152588 Hz
AQ             3.2769499 se
RG                     57
DW             100.000 us
DE               7.00 us
TE              300.2 K
D1          1.00000000 se

======== CHANNEL f1 ======
NUC1                    1H
P1                5.00 us
PL1              -4.00 dB
SFO1        500.1319002 MH

F2 - Processing parameters
SI                  16384
SF         500.1300160 MH
WDW                    no
SSB                     0
LB               0.00 Hz
GB                      0
PC                   4.00

1D NMR plot parameters
CX               20.00 cm
CY               50.00 cm
F1P              9.000 pp
F1            4501.17 Hz
F2P              0.000 pp
F2               0.00 Hz
PPMCM        0.45000 pp
HZCM        225.05850 Hz
```

5

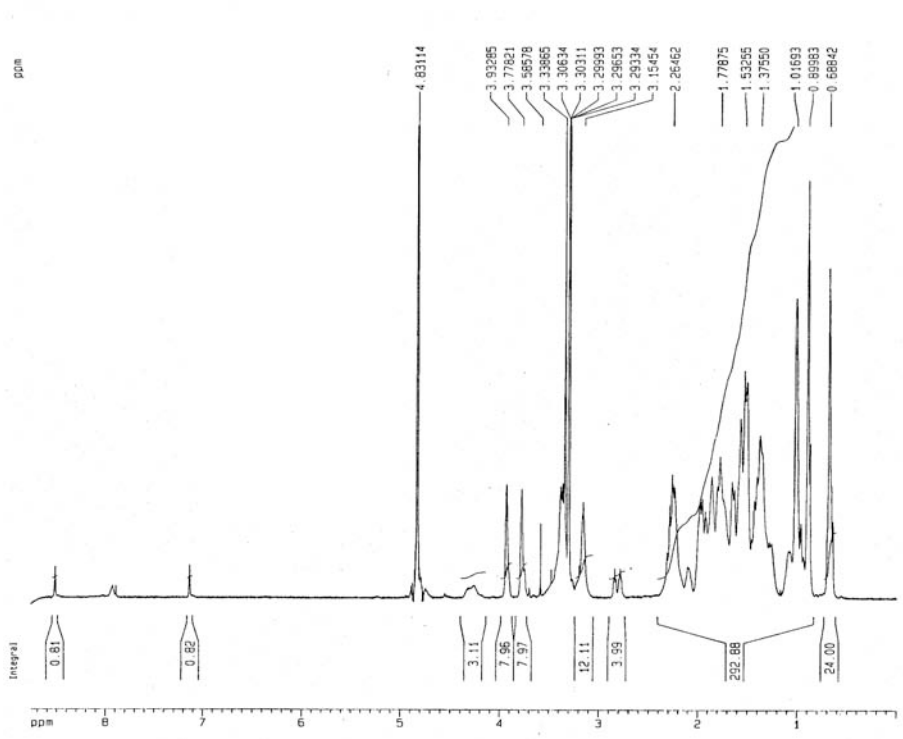


```
Current Data Parameters
NAME                  probe8CHA
EXPNO                         1
PROCNO                        1

F2 - Acquisition Parameter
Date_                  20060421
Time                      14.16
INSTRUM                   spect
PROBHD    5 mm PHBBO BB-
PULPROG                     zg
TD                       32768
SOLVENT                   MeOD
NS                           8
DS                           0
SWH                5000.000 Hz
FIDRES             0.152588 Hz
AQ                 3.2769499 se
RG                        90.5
DW                  100.000 us
DE                    7.00 us
TE                    300.0 K
D1                1.00000000 se

======== CHANNEL f1 ======
NUC1                        1H
P1                        5.00 us
PL1                      -4.00 dB
SFO1              500.1319002 MH

F2 - Processing parameters
SI                       16384
SF                500.1300160 MH
WDW                         no
SSB                          0
LB                    0.00 Hz
GB                           0
PC                        4.00

1D NMR plot parameters
CX                       20.00 cm
CY                      150.00 cm
F1P                      9.000 pp
F1                    4501.17 Hz
F2P                      0.000 pp
F2                       0.00 Hz
PPMCM                 0.45000 pp
HZCM                225.05850 Hz
```

6

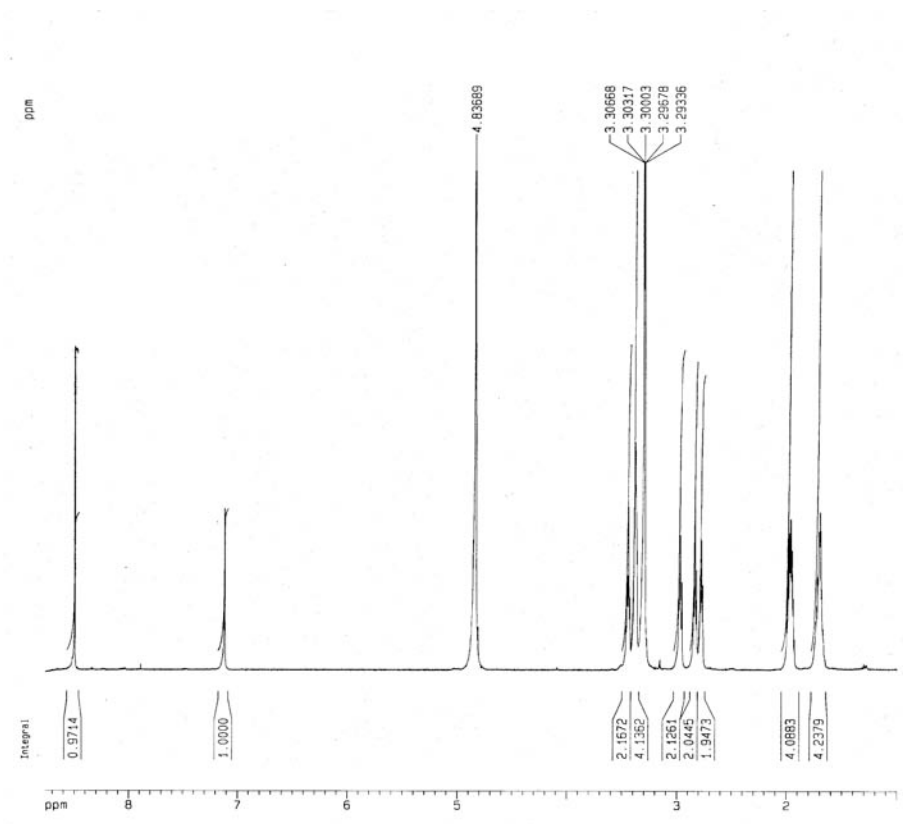


```
Current Data Parameters
NAME          Coumarin-pu
EXPNO                    1
PROCNO                   1

F2 - Acquisition Parameter
Date_             20060816
Time                 11.15
INSTRUM              spect
PROBHD    5 mm PHBBO BB-
PULPROG                zg
TD                  32768
SOLVENT              MeOD
NS                     32
DS                      0
SWH           5000.000 Hz
FIDRES        0.152588 Hz
AQ            3.2769499 se
RG                   161.3
DW             100.000 us
DE               7.00 us
TE               299.6 K
D1           1.00000000 se

======== CHANNEL f1 ======
NUC1                   1H
P1                   5.00 us
PL1                 -4.00 dB
SFO1         500.1319002 MH

F2 - Processing parameters
SI                  16384
SF           500.1300160 MH
WDW                    no
SSB                     0
LB               0.00 Hz
GB                      0
PC                   4.00

1D NMR plot parameters
CX                  20.00 cm
CY                  80.00 cm
F1P                 9.000 pp
F1               4501.17 Hz
F2P                 1.000 pp
F2                500.13 Hz
PPMCM            0.40000 pp
HZCM           200.05200 Hz
```

7

Low Res. Mass Spectrum for Compound 1

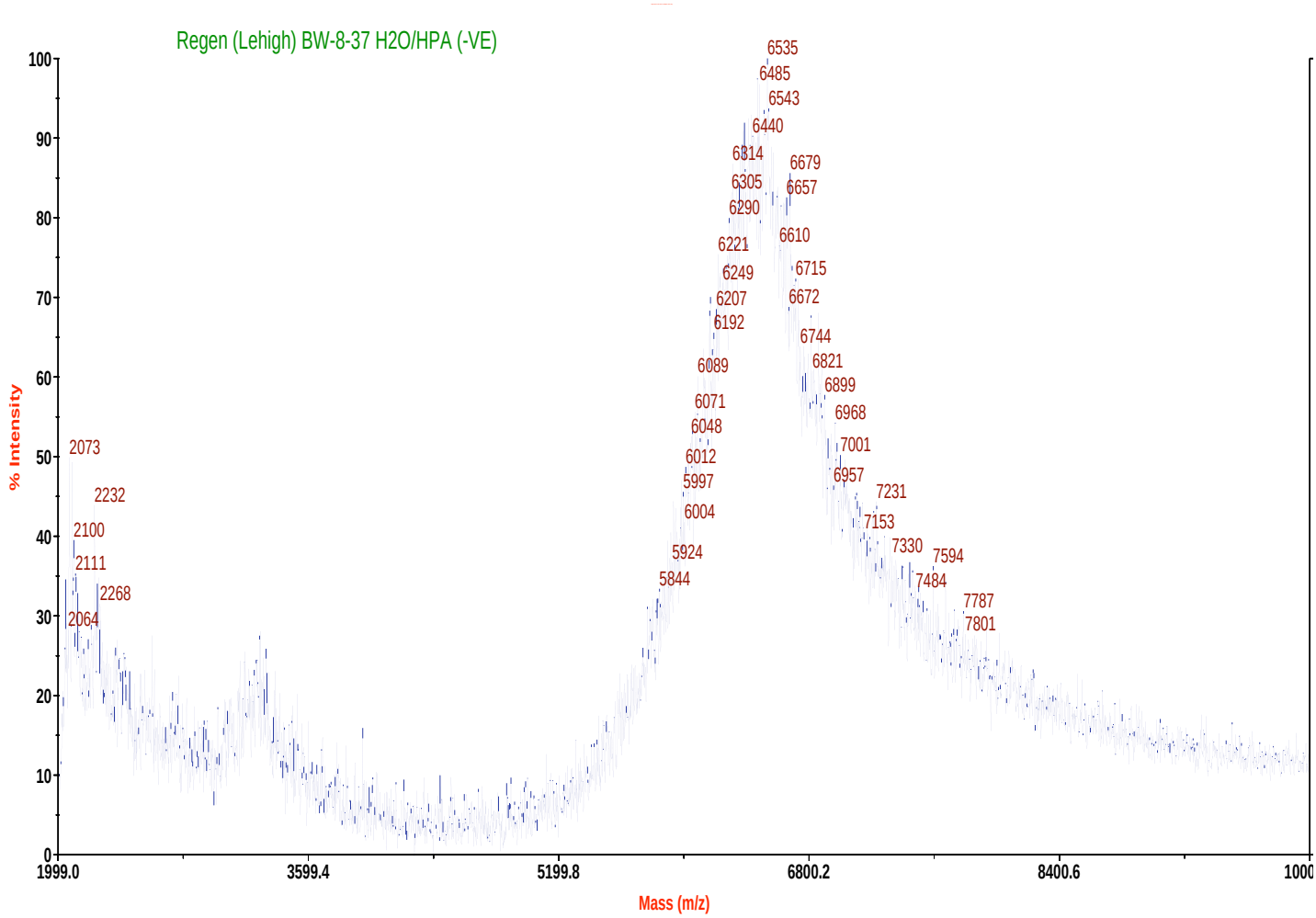

Moving Known Libraries to an Addressable Array: A Site-Selective Hetero-Michael Reaction

Melissae Stuart,[†] Karl Maurer,[‡] and Kevin D. Moeller*[,†]

Department of Chemistry, Campus Box 1134, Washington University, St. Louis, Missouri 63130, and CombiMatrix Corporation, 6500 Harbor Heights Parkway, Suite 301, Mukilteo, Washington 98275. Received January 21, 2008; Revised Manuscript Received June 6, 2008

A two-step, Michael reaction-based strategy for site-selectively placing molecules by unique electrodes in an addressable microelectrode array has been developed. The strategy is compatible with the use of polypeptide nucleophiles and works with microelectrode arrays having either 1024 electrodes/cm^2 or 12 544 electrodes/cm^2. The chemistry should allow for the transfer of existing molecular libraries to microelectrode array devices for analysis.

INTRODUCTION

Microarray technology allows for the placement of a molecular library in a small area and simultaneous screening of the library members for binding to a receptor (*1–4*). Our group is interested in using addressable microelectrode arrays as a platform for these efforts (*5, 6*). The goal is to build molecular libraries so that each unique member of the library is located next to unique, individually addressable microelectrodes in the array. The electrodes can then be used to monitor the binding of molecules in the library with biological receptors as the events happen (in "real time") (*7*).

With this in mind, we have been developing synthetic methodology for site-selectively building molecules on microelectrode arrays (*8–12*). In these efforts, the array is first coated with a porous polymer. The microelectrodes in the array are then used to covalently attach substrates to the polymer proximal to every electrode. The substrates are then site-selectively manipulated by using the microelectrodes to generate reagents that effect chemical reactions involving the polymer-bound substrates. The site-selectivity is achieved by covering the entire array with a solution containing a second substrate that destroys the reagent generated at the microelectrodes. The result is a competition between generation of a reagent at the microelectrodes and destruction of the reagent in solution. Reactions involving the polymer-bound substrate near a microelectrode occur when generation of the reagent at the electrode overwhelms the solution phase reaction. In this way, the location of reactions on the array is controlled by the selection of electrodes used.

In addition to building molecules on the microelectrode arrays, we would like to have the capability to move existing small, targeted molecular libraries to the arrays so that their binding to biological receptors can also be monitored in "real time". Accomplishing this goal requires transferring the library to the microelectrode array in a manner that places each individual member of the library proximal to a single microelectrode. For this purpose, we selected the known coupling between a thiol and either a maleimide or acrylate Michael acceptor. This reaction is often used to attach peptides, sugars, or DNA to a functionalized surface because it occurs quickly with simple incubation at neutral pH in aqueous buffer (*13–15*).

However, how can this coupling reaction be performed site-selectively on a microelectrode array having either 1024 electrodes/cm^2 (1K-chip) or 12 544 electrodes/cm^2 (12K-chip)? The more dense 12K-chips are required for analytical screening (*7*). In this case, the overall strategy involves a two-step sequence (attachment of the Michael acceptor to the polymer and then thiol addition (Scheme 1)) and hence two possible steps for effecting site-selectivity. Since the Michael reaction will occur without a catalyst (*16, 17*), it appeared that the best step for controlling the site-selectivity of the process was the step placing the Michael acceptor onto the polymer. We report here that this step can be controlled with an extremely high degree of site-selectivity.

We began our investigation with two different Michael acceptors, *N*-acryloxysuccinimide **1** and *N*-succinimidyl-3-maleimidopropionate **2** (Figure 1). In the first experiment, *N*-acryloxysuccimide **1** was placed on the surface of an agarose coated 1K-chip using the electrochemically generated base conditions employed previously for placing substrates by all of the microelectrodes in the array. However, in this case, a checkerboard pattern of electrodes was selected for the reaction. The base was generated by using the microelectrodes as cathodes to reduce vitamin B_{12}, catalyzing a transesterification between the activated ester substrate and the hydroxyls on the surface of the agarose coating the chip (Scheme 1).

The site-selectivity of the process was controlled by using a high concentration (20 mM) of activated ester in the experiment. Deprotonation of an alcohol by the radical anion of vitamin B_{12} can be expected to occur quickly. Hence, any migration of base away from the region surrounding a selected electrode would involve the formation of methoxide, either by direct deprotonation of the methanol solvent by the vitamin B_{12} radical anion or as a result of equilibration between the alkoxides generated on the surface of the agarose by the radical anion and methanol. In either case, the excess activated ester in solution would be expected to react with the methoxide to generate a methyl ester and prevent migration of the base to remote locations on the array.

The success of the reaction was determined by conducting a subsequent Michael reaction using the same electrogenerated base conditions and the same checkerboard pattern of selected electrodes. Pyrene-thiol **3** was used as the nucleophile for this test because of its fluorescence properties. Along these lines,

* Corresponding author. E-mail: moeller@wustl.edu. Phone: 314-935-4270. Fax: 314-935-4481.
[†] Washington University, St. Louis.
[‡] CombiMatrix Corporation.

10.1021/bc800025z CCC: $40.75 © 2008 American Chemical Society
Published on Web 07/25/2008

Scheme 1. Site-Selective Michael Reaction

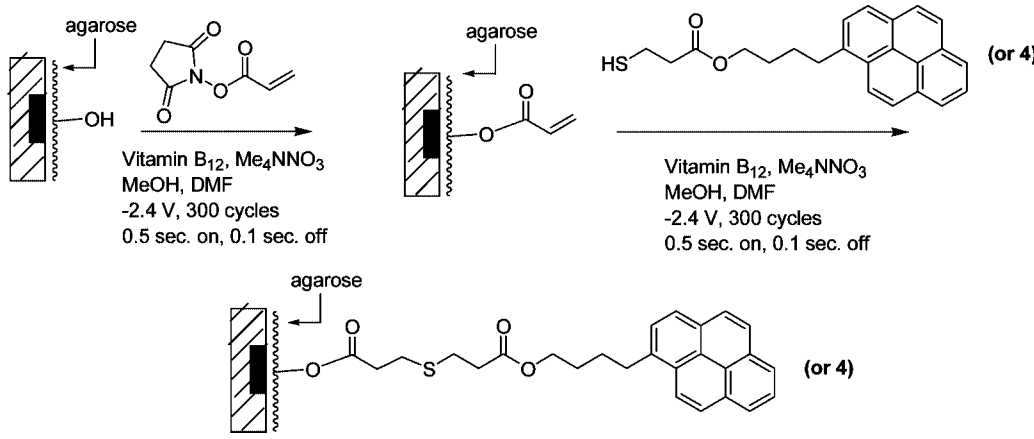

imaging the microelectrode array with a fluorescence microscope showed a bright checkerboard pattern (Figure 2A). Clearly, the two-step procedure led to the desired site-selectivity.

A control experiment confirmed that placing the Michael acceptor on the agarose was indeed necessary for attachment of the thiol to the agarose polymer. When an agarose coated chip without the Michael acceptor was treated with the pyrene-thiol **3** and electrochemically generated base, there was no reaction between the thiolate generated and the agarose polymer; no fluorescent spots were observed.

The argument that the site-selectivity of the two-step process originated with placement of the Michael acceptor and not the Michael reaction itself was supported with a second control experiment. In this study, the Michael acceptor was placed by every microelectrode in an array and then the thiolate nucleophile for the Michael reaction was generated in a checkerboard pattern. The result was the generation of Michael product and the appearance of bright fluorescent spots by every electrode in the array.

Since the site-selectivity of the process does not depend on the Michael reaction, the thiolate addition does not need to be electrochemically catalyzed. For example, an acrylic acid-patterned chip can be incubated in a solution containing the pyrene-thiol **3** to add the pyrene to the surface of the microelectrode array. Although these conditions do work, most organic solvents damage or dissolve the agarose polymer used to fix the substrates to the surface of the array during the time frame needed for the coupling reaction. Hence, for libraries that are soluble in organic solvents it is still best to use the electrochemical conditions to accelerate the coupling step and minimize damage to the agarose polymer.

To screen libraries for binding to a receptor using a microelectrode array, the libraries need to be placed on a 12K-array (*7*). While moving to a microelectrode array with a larger density of electrodes can present a problem for the site-selectivity of a reaction, in the current case the optimal conditions with the acrylate linker that gave confinement on a 1K-chip (95 μm electrode diameter) also gave confinement to a single electrode on a 12K-array (45 μm electrode diameter) (Figure 2B). When the maleimide linker **2** was used, the reaction was not confined to a single electrode. Instead, the fluorescent spot observed was roughly the same size as an electrode on a 1K-array. Since the use of the acrylate linker led to cleaner reactions, it was selected for use in subsequent studies.

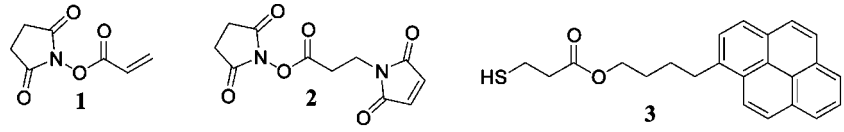

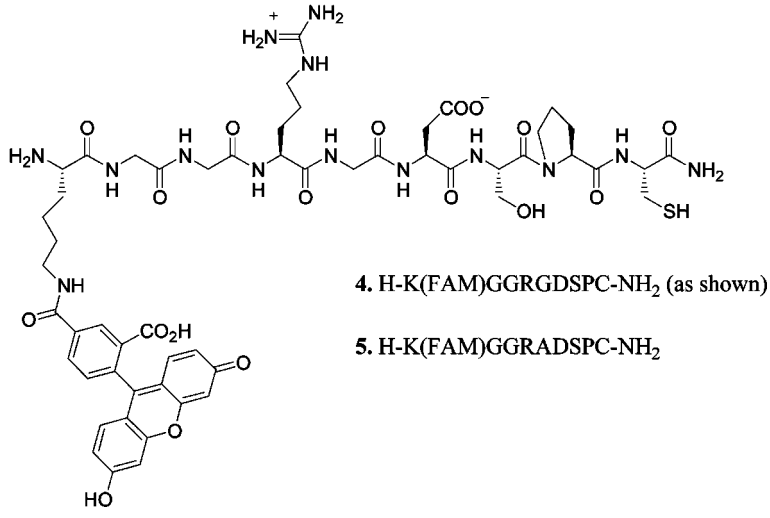

4. H-K(FAM)GGRGDSPC-NH_2 (as shown)

5. H-K(FAM)GGRADSPC-NH_2

Figure 1. Molecules used in this study.

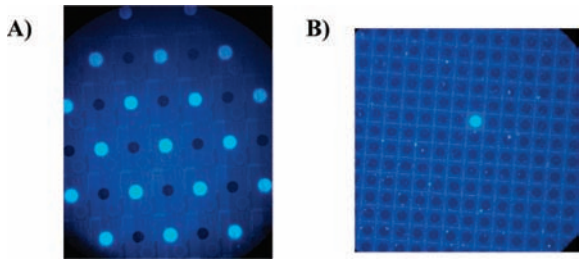

Figure 2. (A) Scheme 1, on a 1K-chip. (B) Scheme 1, on a 12K-chip.

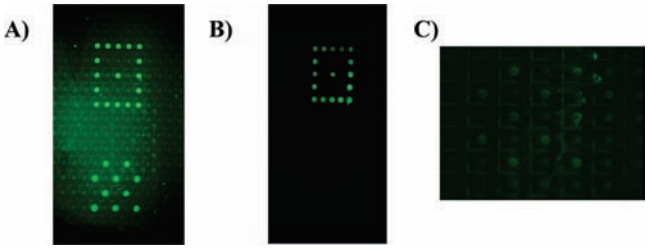

Figure 3. (A) Two patterns with acrylate linker **2** and peptide **4** as the thiol source. (B) Control experiment using 10 mM 2-hydroxyethane thiol as the initial nucleophile for the checkerboard pattern. (C) Blow-up of the checkerboard region of the array in B at longer exposure time.

Having established that the hetero-Michael reaction can be used to put a small organic molecule onto the surface of a microelectrode array, we turned our attention to the placement of water soluble biomolecules such as peptides, proteins, or DNA onto the microelectrode arrays. In these cases, it is best to site-selectively functionalize the polymer coating the array with the Michael acceptor and then incubate the functionalized array with an aqueous solution having a pH consistent with a thiol being more nucleophilic than alcohols or amines (*17*), a scenario that favors the cysteine moiety serving as the nucleophile for the hetero-Michael reaction. For example, consider the placement of a short RGD-based peptide onto a microelectrode array. Peptides containing a RGD sequence are known to bind to integrins, cell-surface receptors that mediate cell attachment (*18–20*). The peptide H-K(FAM)GGRGDSPC-NH_2, with 5(6)-carboxyfluorescein attached to the amine of the lysine side chain (**4**), was synthesized using Fmoc solid phase peptide synthesis. The acrylate acceptor **1** was placed on the surface of a microelectrode array in a checkerboard pattern using 10 electrodes of a 1K-microelectrode array. The chip was then incubated in a 7.6 mM solution of the peptide in 5 × PBS, pH 6.0. Following this step, the acrylate placement was repeated this time to give a box and dot pattern. The peptide was then placed onto the newly selected microelectrodes by incubating the array in a 7.6 mM solution of peptide in 10 × PBS, pH 4.0, while using the selected electrodes as cathodes (*21*). The change in pH for the second step was made in order to maximize the stability of the peptide already placed onto the array. The use of the selected microelectrodes as cathodes effectively raises the pH of the solution proximal to the electrodes thereby assisting the addition step in those regions. Following the second addition, the microelectrode array was imaged using a fluorescence microscope (Figure 3A). Clearly, multiple reactions can be performed with this coupling strategy, allowing attachment of different thiol-containing library members to the polymer above selected electrodes in the array.

One control experiment is very important for supporting this conclusion. In this experiment, the sequence of events used to generate the image in Figure 3A was repeated. However, in this case the initial peptide substrate used to make the checkerboard pattern was replaced with 10 mM 2-hydroxyethane thiol. The second step to make the box and dot pattern was repeated just like before using peptide **4**. The microelectrode array was then imaged using a fluorescence microscope as before (Figure 3B). A faint checkerboard pattern could be observed, although it is not observable unless the initial region of the chip is exposed for longer time periods (Figure 3C). Quantitative analysis of the spots revealed that the "bleed-over" of the peptide to the original set of electrodes was minimal.

The small amount of "bleed-over" observed could be explained by either the presence of unreacted Michael acceptor after placement of the 2-hydroxyethane thiol on the microelectrode array, or an equilibration of the product on the array following the second step. In order to address this issue, a second control study was performed. In this experiment labeled peptide was placed on the array using either the maleimide- or acrylate-based hetero-Michael reaction. A second step was then used to place a Michael acceptor at remote sites on the array. The resulting chip was incubated for 45 min in the buffer solution used for the Michael reaction, and then the array imaged to see if the peptide migrated from its original location to the remote sites. In this experiment, use of the maleimide acceptor did lead to a small amount of peptide migration. However, no such migration was detected when the acrylate acceptor was employed. Hence, the "bleed-over" observed during the previous

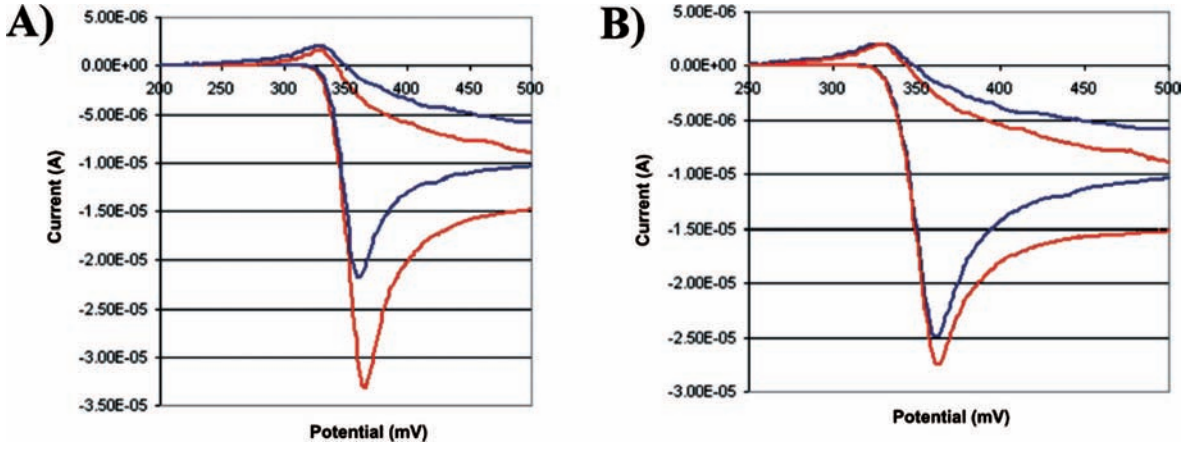

Figure 4. Red line, no receptor; blue line, with receptor. (A) CV data for the best binding peptide H-K(FAM)GGRGDSPC-NH_2 (**4**). (B) CV data for the weaker binding peptide H-K(FAM)GGRADSPC-NH_2 (**5**). In each case, 10 microelectrodes on a 12K-microelectrode array were used for the experiment. The experiments used 8 mM $K_3Fe(CN)_6$ in 30% glycerol, 100 mM NaCl, 20 mM Tris-HCl, 1 mM $CaCl_2$, and a scan rate of 10 mV/s.

study was due to a small amount of unreacted Michael acceptor in the first step, a situation that can most likely be avoided by optimizing the percent conversion of the first Michael reaction.

Peptides placed on the surface of the array using the chemistry described are available for binding ligands in solution. This was demonstrated with the electrochemical impedance experiment illustrated in Figure 4. In this experiment, a 12K-microelectrode array was functionalized with two peptides each being placed next to 10 microelectrodes. The first, peptide **4**, is known to bind the integrin receptor well (*22*). The second, peptide H-K(FAM)GGRADSPC-NH_2 (**5**), is known to bind weakly to the integrin receptor. After placing the peptides onto the array, the array was inserted into an electrolysis solution containing potassium ferricyanide along with a Pt wire auxiliary electrode. Current was then passed through the solution using the microelectrode array as the anode and the Pt wire as the cathode. The current associated with the oxidation of ferrous ion in solution (made at the cathode) was measured and the red line in both Figure 4A and Figure 4B recorded.

To the solution was then added an integrin receptor (Integrin $\alpha_{IIb}\beta_{III}$ (GPIIb/IIIa)). In an impedance experiment, the binding of a receptor to molecules on the surface of the microelectrode array blocks the ferrous ion from the neighboring microelectrode causing a dropoff in the current measured. The binding between the solution phase integrin receptor and the microelectrode array bound **4** can be seen in Figure 4A by observing the dropoff in current associated with the blue line (measured for the oxidation of ferrous ion after addition of the integrin receptor) relative to the initial red line. The significantly smaller dropoff observed in Figure 4B indicates the weaker binding event occurring next to the electrodes associated with the second peptide.

In conclusion, we have found that the base catalyzed placement of Michael acceptors on a microelectrode array can be accomplished in a highly site-selective fashion. The placement of peptides onto the array can then be accomplished in a selective fashion with a minimal amount of crossover (5%) between sites on the array. The resulting array can be used to monitor binding events between the peptides placed on the array and a receptor in solution. Work to optimize the selectivity of the placement reactions and establish the utility of the microelectrode arrays for monitoring the binding behavior of molecules in a library with a biological receptor is underway.

ACKNOWLEDGMENT

We thank Dr. Joshua Maurer for his help with the solid phase peptide synthesis and fluorescent imaging. This work is generously supported by the National Science Foundation (CHE-9023698). We also gratefully acknowledge the Washington University High Resolution NMR facility, partially supported by NIH grants RR02004, RR05018, and RR07155, and the Washington University Mass Spectrometry Resource Center, partially supported by NIHRR00954, for their assistance.

Supporting Information Available: Sample procedures, images from experiments with different linkers, and images for control experiments conducted. This material is available free of charge via the Internet at http://pubs.acs.org.

LITERATURE CITED

(1) Lipshutz, R. J., Fodor, S. P. A., Gingeras, T. R., and Lockhart, D. J. (1999) High density synthetic oligonucletide arrays. *Nat. Genet. 21*, 20–24.

(2) Pirrung, M. (1997) Spatially addressable combinatorial libraries. *Chem. Rev. 97*, 473–488.

(3) Webb, S. M., Miller, A. L., Johnson, B. H., Fofanov, Y., Li, T., Wood, T. G., and Thompson, E. B. (2003) Gene networks in glucocorticoid-evoked apoptosis of leukemic cells. *J. Steroid Biochem. Mol. Biol. 85*, 183–193.

(4) Shih, S.-R., Wang, Y.-W., Chen, G.-W., Chang, L.-Y., Lin, T.-Y., Tseng, M.-C., Chiang, C., Tsao, K.-C., Huang, C. G., Shio, M.-R., Tai, T.-H., Wang, S.-H., Kuo, T.-L., and Liu, W.-T. (2003) Serotype-specific detection of enterovirus 71 in clinical specimens by DNA microchip array. *J. Virol. Methods 111*, 55–60.

(5) Dill, K., Montgomery, D. D., Wang, W., and Tsai, J. C. (2001) Antigen detection using microelectrode array microchips. *Anal. Chim. Acta 444*, 69–78.

(6) Roth, K. M., Peyvan, K., Schwarzkopf, D. R., and Ghindilis, A. (2006) Electrochemical detection of short DNA oligomer hybridization using the CombiMatrix ElectraSense microarray reader. *Electroanalysis 18*, 1982–1988.

(7) Tesfu, E., Roth, K., Maurer, K., and Moeller, K. D. (2006) Building addressable libraries: Site selective coumarin synthesis and the "real-time" signaling of antibody-coumarin binding. *Org. Lett. 8*, 709–712.

(8) Tian, J., Maurer, K., Tesfu, E., and Moeller, K. D. (2005) Building addressable libraries: The use of electrochemistry for spatially isolating a Heck reaction on a chip. *J. Am. Chem. Soc. 127*, 1392–1393.

(9) Tesfu, E., Maurer, K., Ragsdale, S. R., and Moeller, K. D. (2004) Building addressable libraries: The use of electrochemistry for generating reactive Pd(II) reagents at preselected sites on a chip. *J. Am. Chem. Soc. 126*, 6212–6213.

(10) Chen, C., Nagy, G., Walker, A. V., Maurer, K., McShea, A., and Moeller, K. D. (2006) Building addressable libraries: The use of a mass spectrometry cleavable linker for monitoring reactions on a microelectrode array. *J. Am. Chem. Soc. 128*, 16020–16021.

(11) Tesfu, E., Maurer, K., and Moeller, K. D. (2006) Building addressable libraries: Spatially isolated, chip-based reductive amination reactions. *J. Am. Chem. Soc. 128*, 70–71.

(12) Maurer, K., McShea, A., Strathmann, M., and Dill, K. (2005) The removal of the t-BOC group by electrochemically generated acid and use of an addressable electrode array for peptide synthesis. *J. Comb. Chem. 7*, 637–640.

(13) Xiao, S.-J., Textor, M., Spencer, N. D., and Sigrist, H. (1998) Covalent attachment of cell-adhesive, (Arg-Gly-Asp)-containing peptides to titanium surfaces. *Langmuir 14*, 5507–5516.

(14) Houseman, B. T., Gawalt, E. S., and Mrksich, M. (2003) Maleimide-functionalized self-assembled monolayers for the preparation of peptide and carbohydrate biochips. *Langmuir 19*, 1522–1531.

(15) Schlapak, R., Pammer, P., Armitage, D., Zhu, R., Hinterdorfer, P., Vaupel, M., Frühwirth, T., and Howorka, S. (2006) Glass surfaces grafted with high-density poly(ethylene glycol) as substrates for DNA oligonucleotide microarrays. *Langmuir 22*, 277–285.

(16) Brinkley, M. (1992) A brief survey of methods for preparing protein conjugates with dyes, haptens and crosslinking reagents. *Bioconjugate Chem. 3*, 2–13.

(17) Gregory, J. D. (1955) The stability of N-ethylmaleimide and its reaction with sulfhydryl groups. *J. Am. Chem. Soc. 77*, 3922–3923.

(18) Pierschbacher, M. D., and Ruoslahti, E. (1984) Cell attachment activity of fibronectin can be duplicated by small synthetic fragments of the molecule. *Nature 309*, 30–33.

(19) Pierschbacher, M. D., and Ruoslahti, E. (1984) Variants of the cell recognition site of fibronectin that retain attachment-promoting activity. *Proc. Natl. Acad. Sci. U.S.A. 81*, 5985–5988.

(20) Ruoslahti, E. (1996) RGD and other recognition sequences for integrins. *Annu. Rev. Cell. Dev. Biol. 12*, 697–715.

(21) Shi, B., and Greaney, M. F. (2005) Reversible Michael addition of thiols as a new tool for dynamic combinatorial chemistry. *Chem. Commun.* 886–888.

(22) Pierschbacher, M. D., and Ruoslahti, E. (1984) Variants of the cell recognition site of fibronectin that retain attachment-promoting activity. *Proc. Natl. Acad. Sci. U.S.A. 81*, 5985–5988.

BC800025Z

Moving Known Libraries to an Addressable Array: Site-Selective Michael Reaction

Melissae Stuart,[a] Karl Maurer,[b] and Kevin D. Moeller[a]

[a]*Department of Chemistry, Washington University, St. Louis, Missouri 63130, and* [b]*CombiMatrix Corporation, 6500 Harbor Heights Parkway, Suite 301, Mukilteo, Washington 98275*

E-mail: moeller@wuchem.wustl.edu

Supporting Information

Synthetic Procedures

General:

3-Mercaptopropionic acid, 1-pyrenebutanol, *p*-toluenesulfonic acid, benzene, *N*-acryloxysuccinimide, vitamin B_{12} (cyanocobalamin), tetramethylammonium nitrate, diisopropylethylamine, piperidine, DMF, MeOH, CH_2Cl_2, HPLC-grade H_2O and MeCN were purchased from Aldrich and used as received. *N*-Succinimidyl 3-maleimidopropionate was purchased from VWR. Boc-Lys(Fmoc)-OH, Fmoc-Gly-OH, Fmoc-Arg(Pbf)-OH, Fmoc-Asp(OBut)-OH, Fmoc-Ser(But)-OH, Fmoc-Pro-OH, Fmoc-Cys(Trt)-OH, Fmoc-Ala-OH, HBTU, and Rink resin SS (200-400 mesh) were purchased from Advanced ChemTech. HOAT was purchased from AKScientific (Mountain View, CA) and PyAOP was purchased from Oakwood Products, Inc. (West Columbia, SC). 5(6)-Carboxyfluorescein was purchased from Acros. Integrin $\alpha_{IIb}\beta_{III}$(GPIIbIIIa) was purchased from Calbiochem. The peptides were synthesized on a CS Bio Company solid phase peptide synthesizer (model CS136XT). ^{1}H and ^{13}C NMR were obtained on a Varian Mercury (300 MHz). Analytical HPLC was performed on a HP1100 instrument with a UV detector. Fluorescence images in Figure 2 and 3 (A and B) were taken with an Olympus IX70 epifluorescence microscope (pyrene filter excitation wavelengths 320-400 nm, emission 420-540 nm; fluorescein filter excitation wavelengths 475-525 nm, emission 530 nm). The fluorescence image in Figure 3C was taken with a Nikon TE-2000E epifluorescence microscope. Cyclic voltammetry was performed using the ElectraSense Reader (Combimatrix, Mukilteo, WA, http://www.combimatrix.com/products_electrasense.htm) connected to a Bioanalytical System 100B/W potentiostat (Bloomington, IN) running proprietary software.

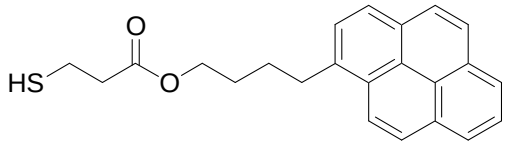

4-(pyren-2-yl)butyl 3-mercaptopropionate (3):

3-mercaptopropionic acid (261 µL, 3 mmol), 1-pyrenebutanol (0.822 g, 3 mmol), *p*-toluenesulfonic acid (0.050 g, 0.3 mmol) were added to a flame-dried three-neck flask fitted with a Dean-Stark trap under argon. The reaction mixture was dissolved in 6 mL benzene and heated to reflux. When the starting materials were consumed as indicated by thin-layer chromatography, the reaction was cooled to room temperature. The benzene was removed *in vacuo* and the residue was dissolved in 10 mL CH_2Cl_2. The organic layer was washed twice with 10 mL 5% aqueous $NaHCO_3$, twice with 10 mL H_2O, dried over Na_2SO_4, and concentrated. The crude residue was purified by silica gel chromatography (6:1 hexane: EtOAc) to provide the desired compound (0.850 g, 75% yield). IR (thin film, KBr plate): 3041, 2935, 2892, 2567, 1725, 841, 763, 710 cm^{-1}; ^1H NMR (300 MHz, $CDCl_3$): δ = 8.27 (d, J = 9.3 Hz, 1H), 8.19-8.12 (m, 4H), 8.04 (AB, J =9.0 Hz, 2H), 8.00 (t, J = 7.8 Hz, 1H), 7.87 (d, J = 7.8 Hz, 1H), 4.20 (t, J = 6.3 Hz, 2H), 3.40 (t, J = 7.5 Hz, 2H), 2.75 (dt, J = 9.6, 5.1 Hz, 2H), 2.64 (t, J = 6.6 Hz ,2H), 1.96-1.91 (m, 2H), 1.88-1.78 (m, 2H), 1.6 (t, J = 8.4 Hz,1H) ppm; ^{13}C NMR (75 MHz, $CDCl_3$): δ = 171.9, 136.5, 131.7, 131.1, 130.1, 128.8, 127.7, 127.5, 127.4, 126.9, 126.1, 125.4, 125.1, 125.03, 124.96, 123.5, 64.8, 38.7, 33.2, 28.8, 28.3, 20.0 ppm.
HR MS (FAB) *m/z* calculated for $C_{23}H_{22}O_2S$: 369.1495, measured: 369.1488.

Fmoc solid phase synthesis of *KGGRGDSPC (4) and *KGGRADSPC (5):

Rink amide resin SS, 200-400 mesh, (0.2148g, 0.1074 mmol) was swelled in 5.0 mL DMF three times. After washing with 2 x 5.0 mL DMF, the resin was treated with 4.0 mL 20% piperidine in DMF and mixed for 5 min. The resin was then treated with another 4.0 mL 20% piperidine in DMF, mixed by inversion for 20 min, and washed with 2 x 4.0 mL DMF, 2 x 5.0 mL CH_2Cl_2, and 2 x 5.0 mL DMF. Then a solution of 0.4 mmol (4 eq.) protected amino acid and 0.4 mmol HBTU in 5.0 mL DMF was mixed with 3.0 mL 0.16M DIPEA (8 eq.) in DMF. This solution was added to the resin and mixed by inversion for 45 min. The resin was then washed with 2 x 5.0 mL DMF, 5.0 mL CH_2Cl_2, and 5.0 mL DMF. The cycle began again with the Fmoc deprotection step followed by amino acid coupling. The last step, coupling the 5(6)-carboxyfluorescein, used the more reactive coupling agents HOAt and PyAOP (0.4 mmol, 4 eq. of each) instead of HBTU. Following the synthesis, the resin was collected and dried by vacuum filtration. The resin was added to a cleavage cocktail containing 9.5 mL TFA, 0.5 mL triisopropylsilane, 0.3 mL H_2O in a 15 mL conical tube. The mixture was shaken in the dark for 2 hours. After that time, the mixture was vacuum filtered and the filtrate was collected in a 50 mL conical tube. To the tube was added 40 mL ice cold Et_2O was added, yielding a yellow precipitate. The mixture was centrifuged at 10,000 rpm for 5 min and the liquid was decanted. The yellow pellet was washed twice with 30 mL cold Et_2O, centrifuging each time as before. After the final centrifugation, the yellow pellet was dissolved in 5 mL diH_2O, transferred to a tared 100 mL round bottom flask, and rolled in a dry ice/acetone bath for 10 minutes to shell freeze the liquid. The flask was connected to a vacuum line overnight, yielding 90 mg lyophilized peptide.

ESI-MS *m/z* calculated for $C_{54}H_{68}N_{14}O_{18}S$ **(4)**: 1232.45, measured: 1233.5
ESI-MS *m/z* calculated for $C_{55}H_{70}N_{14}O_{18}S$ **(5)**: 1246.47, measured: 1247.4

RP-HPLC of peptides:

Column: Supelco Discovery HS C18 column, 5 µm, 4.6 × 250 mm. MeCN and H_2O, each with 0.1% TFA added, were used as eluents. 20 µL of peptide in H_20 was injected and a linear gradient was run from 10-40% MeCN over 20 minutes, flow rate 1.0 mL/min. UV detection was at 214 nm.

t_R = 5.22 (unlabeled), 11.04, 11.21 (labeled, 2 isomers of FAM) min for **4**
t_R = 5.81 (unlabeled), 14.98, 15.30 (labeled, 2 isomers of FAM) min for **5**

General procedure for conducting Michael additions on a 1K chip:

1. A chip containing 1000 electrodes/cm^2 was spin coated (3000 rpm, 60s) with freshly prepared 3% agarose in water and let to dry for 1 hour. For the electrolysis, 6.0 mg *N*-acryloxysuccinimide (30 µmol) was dissolved in 100 µL DMF in a 1.7 mL Eppendorf tube. To this solution was added 1.5 mL MeOH containing 2.77 mg Vitamin B_{12} and 13.6 mg tetramethylammonium nitrate. The chip was immediately exposed to this solution and selected electrodes were pulsed at -2.4V for 0.5 sec and 0V for 0.1 sec for 300 cycles. The chip was then washed with an excess of EtOH, H_2O, and EtOH and let to dry. For the other Michael acceptors, 9.6 mg N-succinimidyl 6-maleimidocaproate (30 µmol) or 8.1 mg N-succinimidyl 3-maleimidopropionate (30 µmol) were used.

2. For the Michael addition, the procedure was followed as above except 5.0 mg **3** was dissolved in 100 µL DMF instead of *N*-acryloxysuccinimide. Following this reaction, the counter electrode was polished with alumina to remove tarnish. The chip was visualized with a fluorescence microscope and a pyrene filter.

3. For the Michael addition with the peptide, N-acryloxysuccinimide (9.1 mg) was placed on the chip in a small checkerboard pattern as above. Following the electrolysis, the chip was washed with EtOH, H_2O, and 5xPBS. The chip was incubated in a 7.6 mM solution of the peptide (or 10 mM β-mercaptoethanol) in 1.7 mL 10xPBS, pH 7, for 45 minutes. Following the incubation, the chip was washed with 5xPBS and visualized using a fluorescence microscope. Then, the same Michael acceptor (10.2 mg) was attached to the array in box and dot pattern following the same procedure as above. The chip was washed with H_2O and 5xPBS. The chip was then placed in a 7.6 mM solution of the peptide in 10xPBS, pH 4 and the same electrodes (box and dot pattern) were activated as cathodes. The chip was washed with H_2O and visualized as above.

General procedure for conducting Michael additions on a 12K chip:

A plasma-cleaned chip containing 12,000 electrodes/cm^2 was spin coated (1500 rpm, 30s) with freshly prepared 3% agarose in 9:1 DMF:H_2O and let to dry for 1 hour. The electrolysis solution for the coupling of the Michael acceptor, either *N*-acryloxysuccinimide or N-succinimidyl 3-maleimidopropionate, was prepared as above. The slide was exposed to 100 µL of the reaction solution and selected electrodes were grounded, while a potential of +1.5 V was applied to the auxiliary electrode (making the microelectrode array negative) for 60 s. The washing procedure

was the same as above. The electrolysis solution for the addition of **3** was prepared as above. The slide was exposed to this solution and selected electrodes were grounded, while a potential of +1.5 V was applied to the auxiliary electrode for 60 s. The chip was washed as above and visualized with a fluorescence microscope.

Cyclic voltammetry:

1. A 12K chip, cleaned with 9:1 3% H_2O_2: conc. H_2SO_4 for 30 min at 65°C, was coated as above. The chip was treated with 100 µL of the base electrolysis solution containing 8.0 mg N-acryloxysuccinimide using the electrolysis conditions as above for the 12K chip, selecting only 10 electrodes. Following reaction, the chip was washed with EtOH and H_2O. The chip was then incubated in 100 µL of 7.6 mM solution of peptide **4** in 5xPBS (pH 7) for 45 minutes. After this time, the chip was washed with H_2O and let to dry. The Michael acceptor placement was repeated as above using a neighboring 10-electrode block, the chip was washed as before, and put to soak in 100 µL of 7.6 mM solution of peptide **5** in 5xPBS (pH 7) for 45 minutes. The chip was then washed and visualized using a fluorescence microscope to confirm placement of each peptide.

2. The chip was covered with 200 µL of a solution containing 8 mM $K_3Fe(CN)_6$, 30% glycerol, 100mM NaCl, 20 mM Tris-HCl, 1 mM $CaCl_2$, pH 7.2 and was placed in the ElectraSense reader. One 10-electrode block was activated and cyclic voltammetry was performed, scanning from 700-0 mV to generate some Fe(II), then cycling from 0-750 mV with a scan rate of 10 mV/s. The counter electrode was a platinum plate of area of 0.75 cm^2 and held 650-800 µm away from the chip by an O-ring. The background scan was repeated with the other 10-electrode block. Next, the chip was covered with 200 µL of the same solution above, also containing 30 µg integrin $\alpha_{IIb}\beta_{III}$ and cyclic voltammetry was repeated as above for each block. The same protein solution was used while each block was scanned.

Images used for fluorescence quantification:

Images were taken with an EXFO X-CITE lamp at 12% power and a FITC filter with excitation wavelengths of 465-495 nm and emission at 515-555 nm. The images are 12-bit with no binning and exposure time of 700 ms.

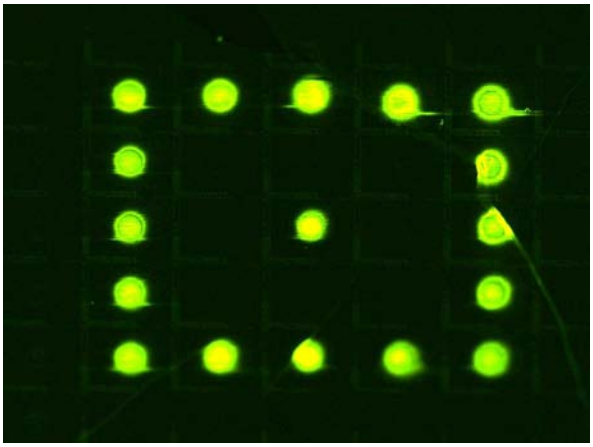

Figure S1: Box and dot pattern of chip prepared as in Figure 3B. Mean intensity of whole pattern corrected for background 700 ± 100.

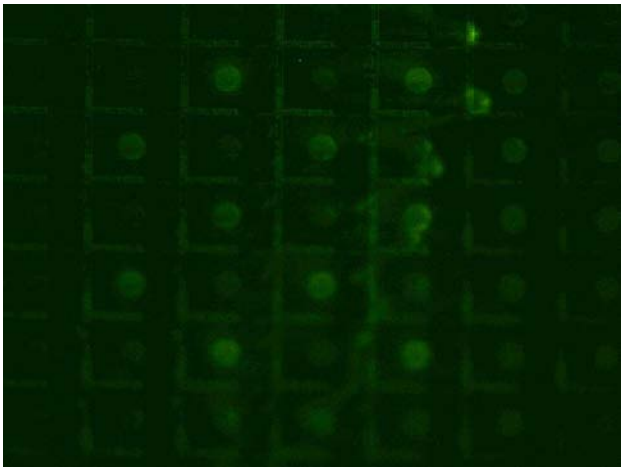

Figure S2: Checkerboard pattern on chip prepared as in Figure 3B. Mean intensity of whole pattern corrected for background 20 ± 10.

Control Experiments:

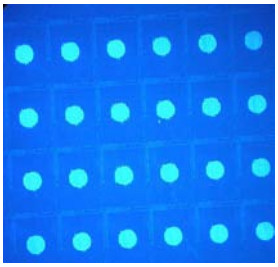

Figure S3: *Selectivity of Michael addition*
Following the above procedure for electrochemical deposition of the Michael acceptor on a 1K chip, 8.0 mg N-succinimidyl 3-maleimidopropionate was placed over every electrode. After washing as above, 5.5 mg **4** was reacted as above in a checkerboard pattern. Fluorescence was observed over every electrode, where the maleimide linker was placed. Similar results were obtained when N-acryloxysuccinimide was used as the linker.

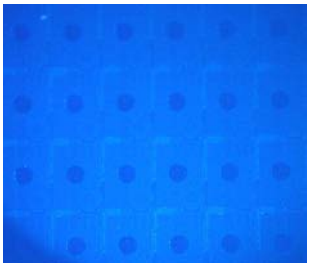

Figure S4: *Reaction of thiolate with agarose (No Michael acceptor):*
A 1K chip, coated as above, was reacted with 5.3 mg **3** under the same electrochemical conditions as above. No fluorescence was observed on any electrodes.

Other linker:

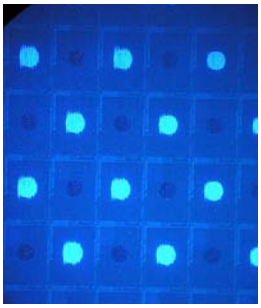

Figure S5: *Linker 2, N-succinimidyl 3-maleimidopropioate*
Following procedure for reaction on a 1K chip, using 8.1 mg N-succinimidyl 3-maleimidopropioate and 5.4 mg **3**

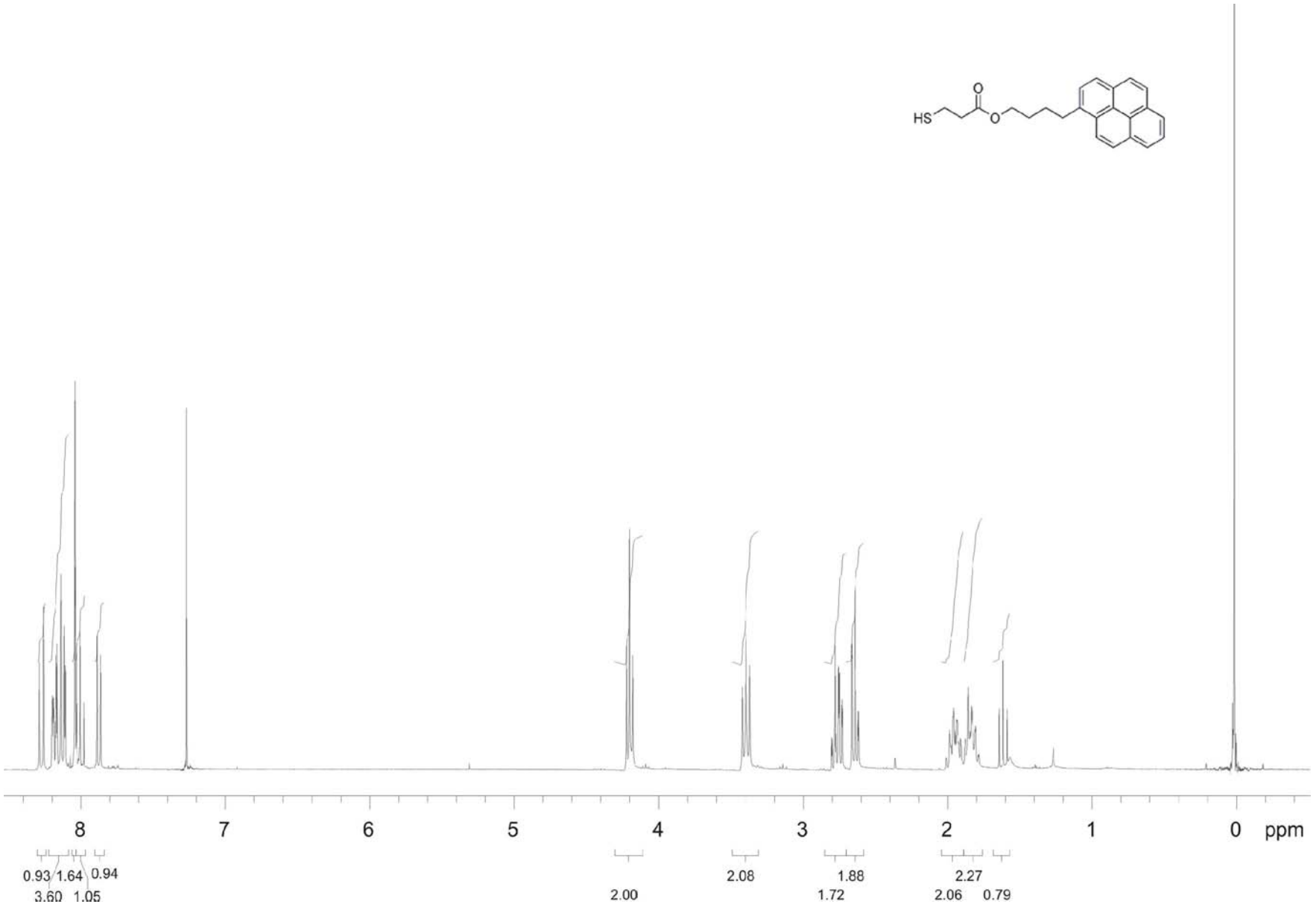
HS
O
O
8
7
6
5
4
3
2
1
0
ppm
0.93
1.64
0.94
3.60
1.05
2.00
2.08
1.88
1.72
2.27
2.06
0.79

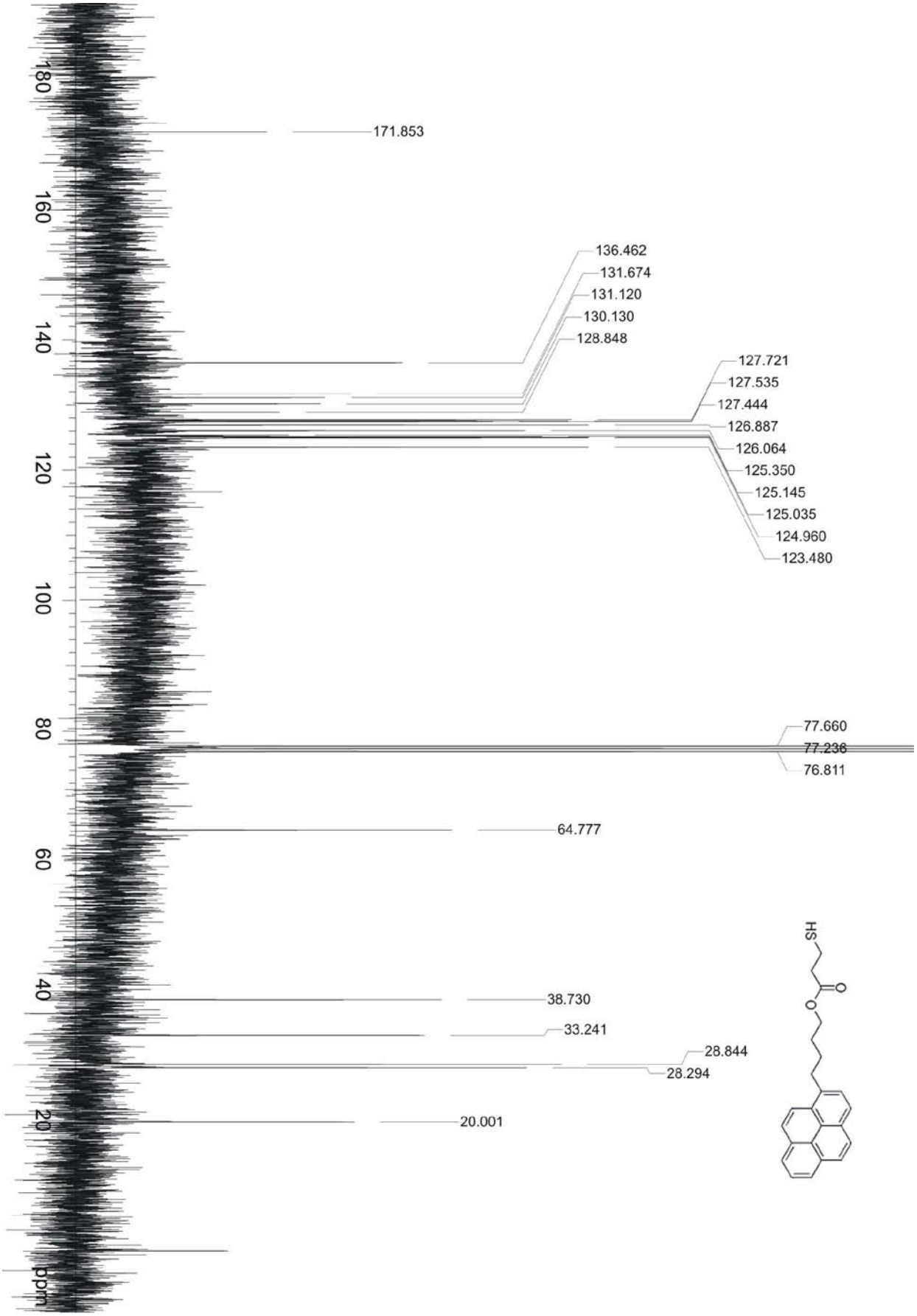
171.853
136.462
131.674
131.120
130.130
128.848
127.721
127.535
127.444
126.887
126.064
125.350
125.145
125.035
124.960
123.480
77.660
77.236
76.811
64.777
38.730
33.241
28.844
28.294
20.001
HS
O
O
180
160
140
120
100
80
60
40
20
ppm

RP-HPLC of H-K(FAM)GGRGDSPC-NH_2 (4):

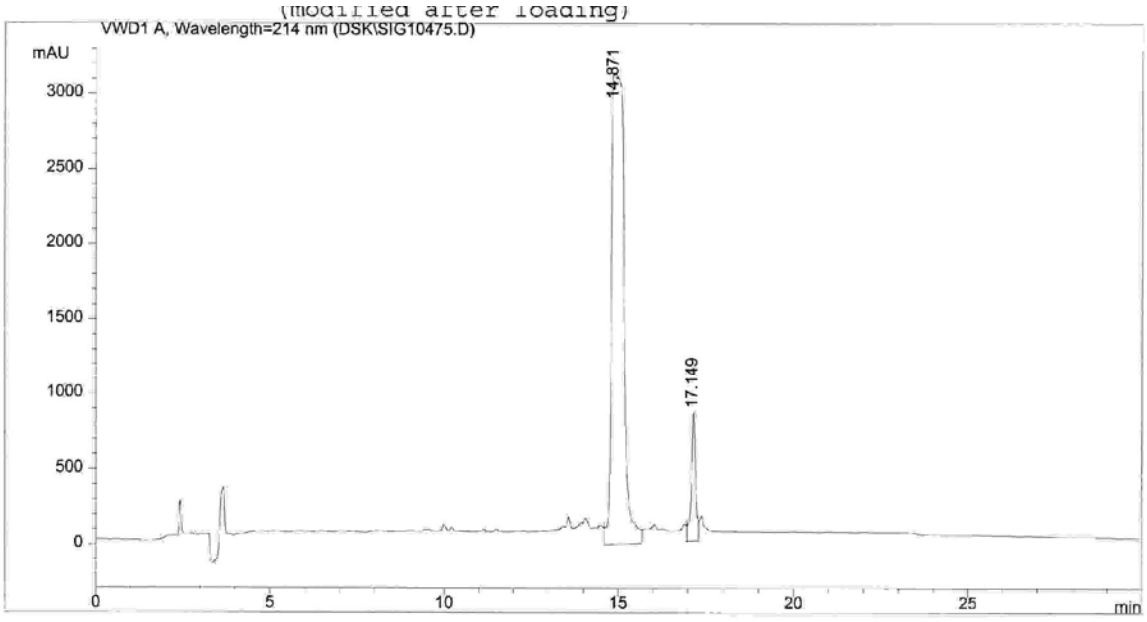

Area Percent Report

Sorted By : Signal
Multiplier : 1.0000
Dilution : 1.0000

Signal 1: VWD1 A, Wavelength=214 nm
Results obtained with standard integrator!

Peak #	RetTime [min]	Type	Width [min]	Area mAU *s	Height [mAU]	Area %
1	14.871	VV	0.3956	7.73478e4	3143.16284	91.3859
2	17.149	VV	0.1282	7290.87891	849.44257	8.6141
Totals :				8.46387e4	3992.60541	

ESI-MS of H-K(FAM)GGRGDSPC-NH_2 (4):

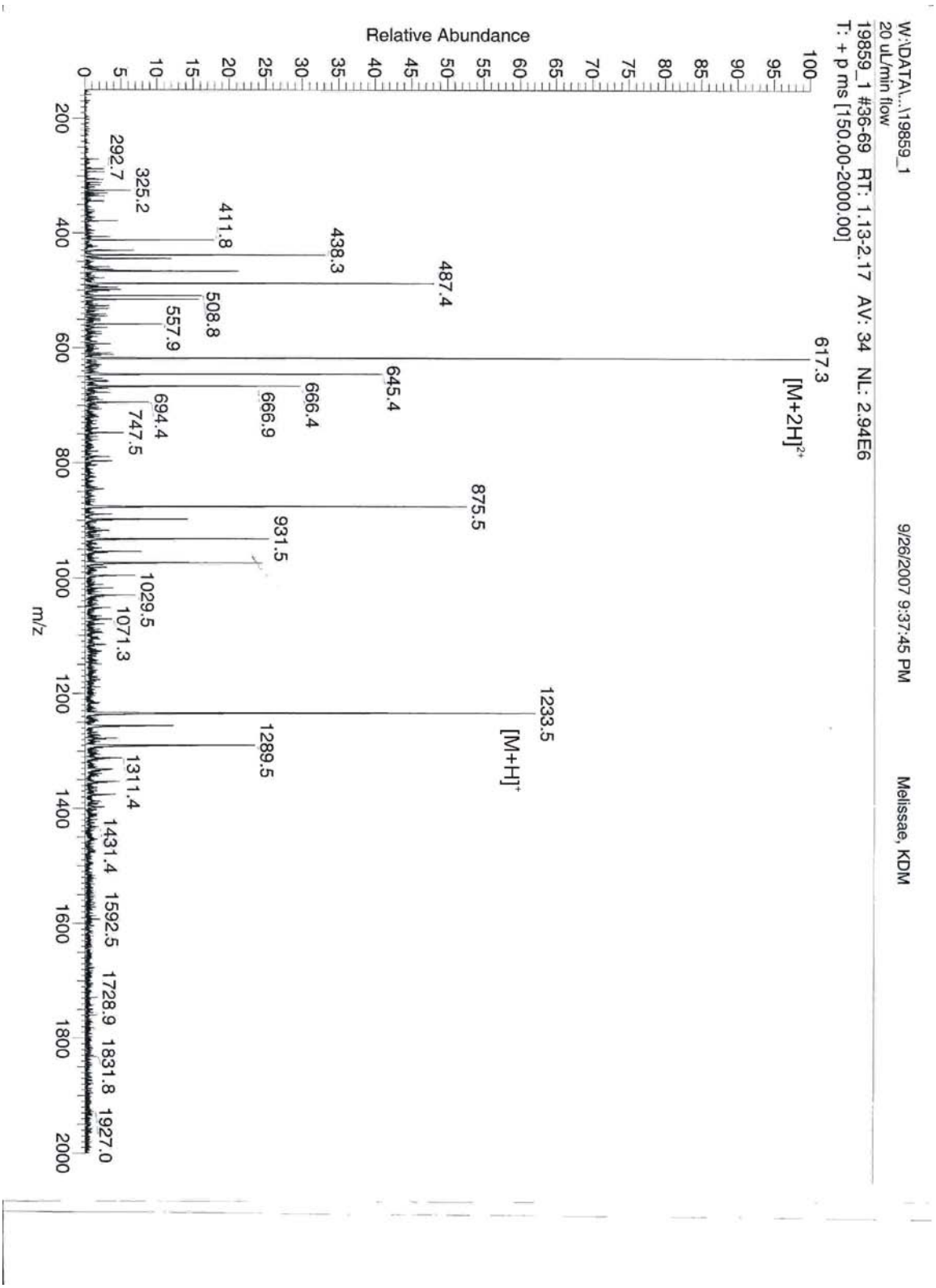

RP-HPLC of H-K(FAM)GGRADSPC-NH_2 (5):

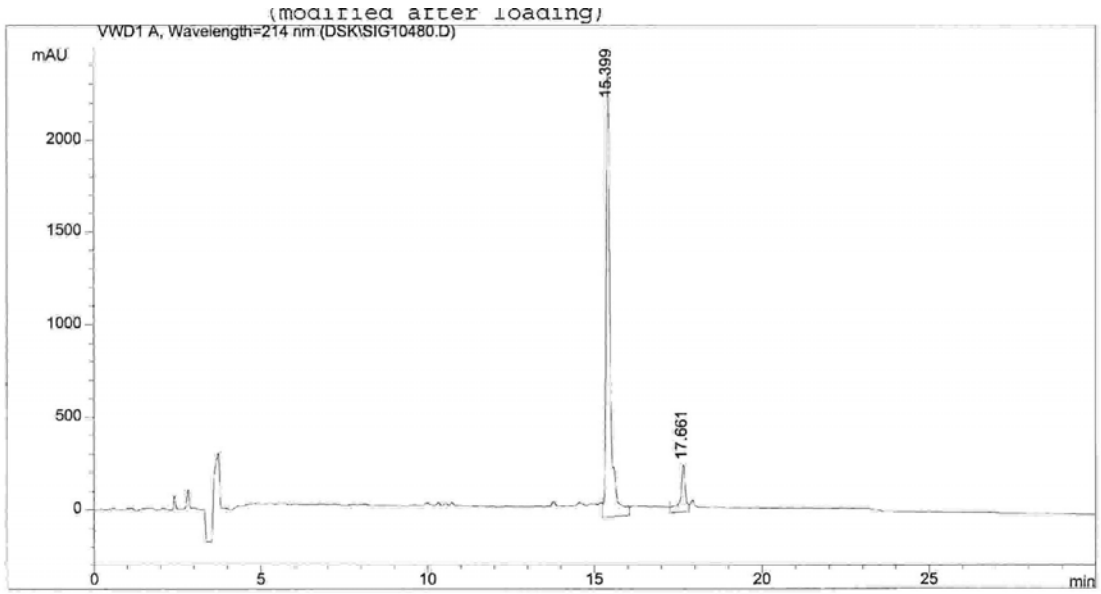


```
================================================================================
                            Area Percent Report
================================================================================

Sorted By             :      Signal
Multiplier            :      1.0000
Dilution              :      1.0000

Signal 1: VWD1 A, Wavelength=214 nm
 Results obtained with standard integrator!

Peak RetTime Type  Width     Area      Height     Area
  #   [min]       [min]  mAU   *s   [mAU   ]      %
----|-------|----|-------|----------|----------|--------|
   1  15.399 VV    0.1319 2.09069e4  2394.61401  88.4209
   2  17.661 VV    0.1495 2737.85889  259.89993  11.5791

Totals :                  2.36448e4  2654.51395
```

ESI-MS of H-K(FAM)GGRADSPC-NH_2 (5):

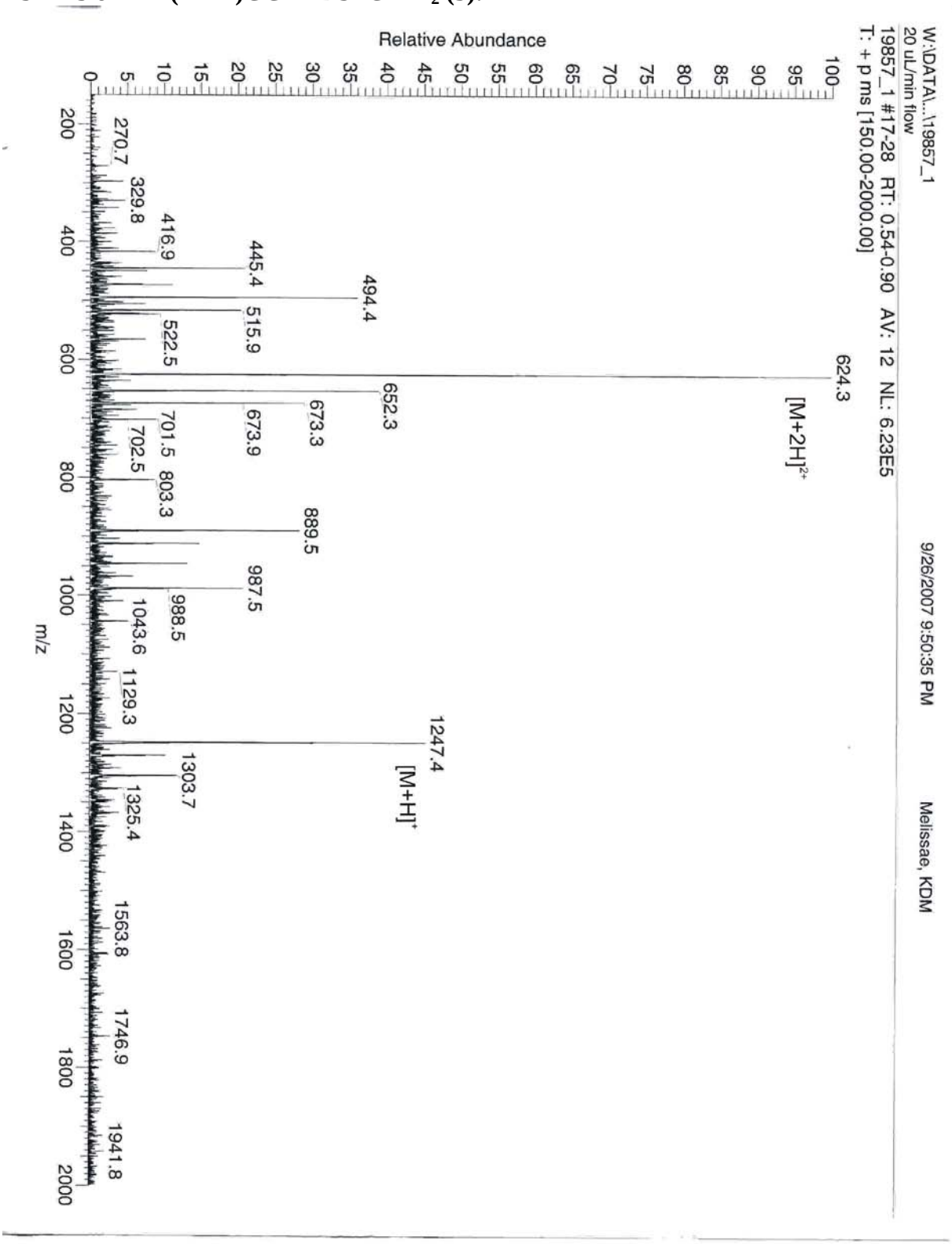

ARTICLES

Synthesis and in Vitro Characterization of a Dendrimer−MORF Conjugate for Amplification Pretargeting

Xiangji Chen, Shuping Dou, Guozheng Liu, Xinrong Liu, Yi Wang, Ling Chen, Mary Rusckowski, and Donald J. Hnatowich*

Division of Nuclear Medicine, Department of Radiology, University of Massachusetts Medical School, 55 Lake Avenue North, Worcester, Massachusetts 01655. Received March 11, 2008; Revised Manuscript Received June 12, 2008

Amplification pretargeting can play an important role in molecular imaging by significantly increasing the accumulation of signal in target tissues. Multiple-step amplification pretargeting offers the potential to greatly improve target localization of effector molecules through the intermediate use of polymers conjugated with multiple copies of complementary oligomers. In this study, PAMAM dendrimer generation 3 (G3) was conjugated with multiple copies of a phosphorodiamidate morpholino (MORF) oligomer. Characterization of the conjugate by native-PAGE and SE-HPLC demonstrated that the conjugation was successful. The average numbers of MORF groups in the G3-MORF conjugate, both attached and accessible to the ^{99m}Tc labeled complementary MORF (cMORF), were determined. The antitumor antibody CC49 was conjugated with both MORF and cMORF (collectively (c)MORF) at an average of about one group per molecule. Nine of the 32 carboxyl groups of the dendrimer were modified with MORF, of which 90% were accessible in solution to ^{99m}Tc-cMORF. After purification, the G3-MORF was radiolabeled with tracer ^{99m}Tc-labeled cMORF (i.e., G3-MORF/^{99m}Tc-cMORF) and added to the antibody CC49 previously conjugated with cMORF (i.e., CC49-cMORF/G3-MORF/^{99m}Tc-cMORF), the complex demonstrated a single peak on SE-HPLC as evidence of complete hybridization between G3-MORF/^{99m}Tc-cMORF and CC49-cMORF. The CC49-(c)MORF were bound to both Protein G and Protein L coated plates, and G3-MORF was added to hybridize with CC49-cMORF before the ^{99m}Tc-cMORF was added to test amplification pretargeting. In comparison to conventional pretargeting without the G3-MORF, the signal was amplified about 6 and 14 times, respectively, showing that the G3-MORF participated in amplifying the signal. Further amplification studies using the CC49-(c)MORF for LS174T tumor cells in tissue culture also demonstrated clear evidence of signal amplification.

INTRODUCTION

Conventional nuclear medicine imaging with radiolabeled tumor specific agents such as antitumor antibodies can provide high tumor/nontumor ratios but usually with slow signal localization and clearance. Pretargeting is one approach that provides useful tumor/nontumor radioactivity ratios more rapidly by placing the effector carrying the radioactivity or other label on a small molecule designed to clear from the circulation and whole body rapidly (*1*). Pretargeting requires at least two steps in which the targeting macromolecule, usually an antibody, is administered first followed by the radioactive effector. The pretargeting approaches that have been reported thus far use (strep)avidin, bispecific antibodies, or oligonucleotides (*2*–*5*). One advantage of (strept)avidin for pretargeting is the 4-fold valency of this protein for biotin, providing the potential of modest signal amplification (*2*). However, a polymer conjugate with multiple copies of oligomers such as peptide nucleic acids (PNAs) or phosphorodiamidate morpholinos (MORFs), administered intermediately between the antitumor antibody and the small effector, provides a potential for amplification far in excess of four (*6*–*8*). In comparison to conventional pretargeting, the three-step amplification pretargeting approach is obviously more complex, but with the potential to greatly increase the localization of radioactivity in the target. Multivalent bispecific antibody and enzyme catalytic systems have also been considered for signal amplification (*9*, *10*).

The choice of polymer is critical for successful amplification pretargeting. It should be large enough to carry sufficient numbers of oligomers; after conjugation it should be water soluble and stable in vivo; it should have favorable pharmacokinetics; and the oligomers must be arranged on the polymer in such a way that they can be easily accessed by their effector. In our previous amplification pretargeting studies, polylysine (PL) and poly(methyl vinyl ether-*alt*-maleic acid) (PA) and other linear polymers provided lower amplification factors than expected. However, the concept has now been shown to be feasible (*6*–*8*), although further studies for optimization are required.

Recently, there has been interest in exploring dendrimers as potential drug delivery vehicles (*11*–*19*). Dendrimers are branched polymers with highly reactive pendant functional groups (Figure 1) that can be used for covalent conjugation of drugs, ligands, and antibodies for targeted delivery (*20*–*34*).

* Corresponding author: Donald. J. Hnatowich, Ph.D., Professor of Radiology, Division of Nuclear Medicine, Department of Radiology, University of Massachusetts Medical School, Worcester, MA 01655, USA. Tel: (508) 856-4256. Fax: (508) 856-6363. E-mail: donald.hnatowich@umassmed.edu.

10.1021/bc8001024 CCC: $40.75 © 2008 American Chemical Society
Published on Web 07/23/2008

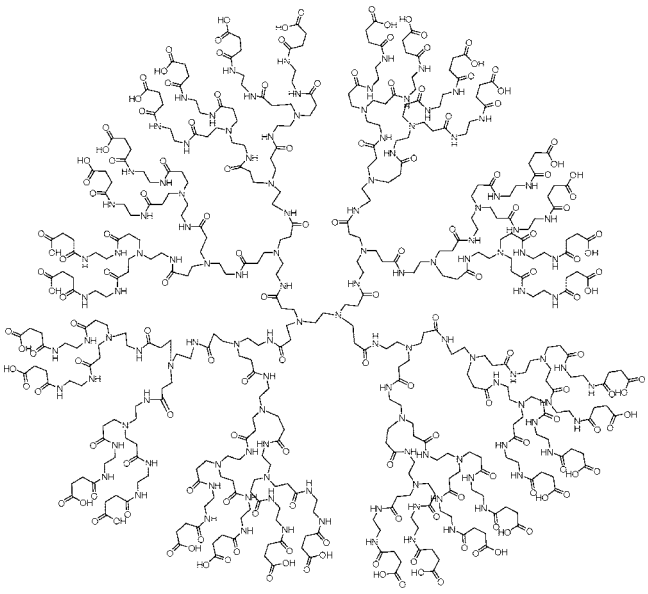

Figure 1. Two-dimentional representation of a PAMAM-succinamic acid dendrimer generation 3 with 32 carboxyl groups on its surface.

Unlike the linear PA and PL polymers, steric hindrances diminishing the accessibility of the conjugated oligomers to their complements should be minimal in the case of dendrimers because of their spherical geometry. The goal of this investigation was to use a dendrimer to achieve a higher degree of amplification pretargeting. As the first step toward this goal, a small dendrimer, generation 3 (G3) with 32 carboxyl groups on its surface, was conjugated with MORF and the in vitro properties of the conjugated polymer evaluated for amplification pretargeting.

EXPERIMENTAL PROCEDURES

Materials and Instruments. The 18-mer MORF and its complement, cMORF (collectively (c)MORF), were purchased from Gene-Tools (Philomath, OR) with 3′-amine modification and with the same base sequences used in this laboratory in connection with conventional pretargeting (*35, 36*). The base sequences and molecular weights were: MORF, 5′-TCTTC-TACTTCACAACTA-3-C-linker-amine, 6059 Da; cMORF, 5′-TAGTTGTGAAGTAGAAGA-3-C-linker-amine, 6317 Da. The cDNA phosphorothioate oligomer was purchased from IDT (Coralville, IA). PAMAM-succinamic acid dendrimer generation 3 (10111 Da), 1-[3-(dimethylamino)propyl]-3-ethylcarbodiimide methiodide (EDC-methiodide) and antimouse $F(ab')_2$ fragment-R-phycoerythrin antibody were purchased from Sigma-Aldrich (St. Louis, MO). *N*-hydroxysuccinimidyl S-acetylmercaptoacetyl-triglycine (NHS-MAG_3) was synthesized in house (*37*) and its structure was confirmed by elemental analysis, proton magnetic resonance, and mass spectrometry. The human colon cancer cell line (LS174T) was obtained from the American Type Culture Collection (Manassas, VA). Microcon YM-30 centrifugal filter devices were purchased from Millipore Corporation (Bedford, MA). Tris-glycine gradient precast polyacrylamide gels (4−20%) were purchased from Bio-Rad Laboratories (Hercules, CA). The antiTAG-72 IgG antibody CC49 was prepared by Strategic Biosolutions (Newark, DE) from the CC49 murine hybridoma cell line, a gift from Jeffery Schlom Ph.D. (Laboratory of Tumor Immunology and Biology, Center for Cancer Research, NCI, NIH, Bethesda, MD). The Hydralink kit was purchased from Solulink (San Diego, CA). The P-4 resin (Bio-Gel P-4, medium) was purchased from Bio-Rad and the Sephadex G-100 resin from Pharmacia Biotech (Piscataway, NJ). Protein G and Protein L coated plates were obtained from Pierce (Rockford, IL). All other chemicals were reagent grade and were used without purification. The ^{99m}Tc-pertechnetate was eluted from a ^{99}Mo-^{99m}Tc generator (Bristol-Myers Squibb Medical Imaging, N. Billerica, MA). The SE-HPLC system is consisted of one Waters 515 pump, one 2487 dual λ absorbance detector and one radioactivity detector. The Superose 12/30 HR column was purchased from GE Healthcare (Piscataway, NJ) and the mobile phase was 0.2 M phosphate buffer (pH 7.0).

Preparation of ^{99m}Tc-Labeled cMORF. The conjugation of cMORF with MAG_3 and subsequent labeling were as previously described (*38*). Briefly, the cMORF was first conjugated with S-acetyl NHS-MAG_3 via the 3′-derivatized amine in pH 8.0 HEPES buffer. After purification on a P-4 column with NH_4OAc buffer, the peak fractions were pooled and underwent a preliminary purification procedure consisting of the labeling procedure described below but without radioactivity followed by another P-4 column purification. For radiolabeling, 10 μL of ^{99m}Tc-pertechnetate generator eluate was introduced into a solution consisting of 3 μL (0.88 μg) of MAG_3-cMORF in pH 5.2 NH_4OAc buffer, 4 μL of 50 μg/μL sodium tartrate in a pH 9.2 buffer, and 1.5 μL of 4 μg/μL $SnCl_2 \cdot 2H_2O$ in ascorbate−HCl solution (1 μg/μL sodium·ascorbate in 10 mM HCl). The solution was heated to 100 °C for 20 min. The labeling efficiency was routinely greater than 95% as determined by SE-HPLC.

G3-MORF Conjugation. To 2.4 mg of EDC-methiodide (8.1 μmol) was added 10 μL of 1% PAMAM-succinamic acid dendrimer G3 (10 nmol). The mixture was gently vortexed at ambient temperature for 2 min and a 1 nmol/μL solution of MORF in distilled water was added at five different MORF/dendrimer molar ratios. Each conjugation mixture was incubated at ambient temperature overnight.

Native polyacrylamide gel electrophoresis (PAGE) conditions similar to those described elsewhere for analysis of dendrimers were used for the analysis of G3-MORF polymers (*31, 39, 40*). The free MORF, free dendrimer, and one of the G3-MORF conjugation mixtures (prepared at a 16:1, MORF/dendrimer molar ratio) before purification were analyzed using a 4−20% Tris-glycine gradient gel under native conditions. The running buffer was 2.5 mM Tris and 19.2 mM glycine at pH 8.2. Since MORF is uncharged, negatively charged cDNA (cDNA) was added to form a charged duplex that would migrate in the gel and also can be stained with ethidium bromide. Ten microliters of each of the three samples were mixed with 10 μL PBS containing equal molar cDNA at room temperature for 20 min. To each mixture, 10 μL of 50% sucrose and 1% bromophenol blue was added. The gel was run at low voltage (80 V) on a vertical gel electrophoresis system and then stained with ethidium bromide solution (0.5 μg/mL) at ambient temperature in the dark. After staining, the gel was first imaged with UV light on a Kodak Imaging Station 440CF (Eastman Kodak Co., New Haven, CT). The gel was then stained with 2.5% Coomassie Blue-R250 solution in 10% acetic acid and 50% methanol at room temperature for 2 h and destained in 10% acetic acid with 50% methanol for 4 h at room temperature and then in water overnight.

The absorbance at 265 nm of an aliquot of the conjugation mixture before purification was used to determine the average number of MORFs bonded to each dendrimer (i.e., groups of MORF per conjugate molecule (GPM)) by SE-HPLC analysis. Since the dendrimer does not appreciably absorb in the UV at 265 nm, unlike MORF, the UV peak areas of free MORF and the MORF coupled dendrimer were used to calculate the attached GPM. Since GPM accessible to radiolabled cMORF is a more important parameter than the attached GPM, the average number of MORFs accessible in solution was determined by a SE-HPLC shift assay in which ^{99m}Tc-cMORF at

Table 1. Experimental Procedures for Amplification Pretargeting and Conventional Pretargeting on Protein G and Protein L Coated Plates

	amplification pretargeting	nonspecific amplification	conventional pretargeting	nonspecific pretargeting
1st incubation	CC49-cMORF	PBS	CC49-MORF	PBS
2nd incubation	G3-MORF	G3-MORF	PBS	PBS
3rd incubation	^{99m}Tc-cMORF	^{99m}Tc-cMORF	^{99m}Tc-cMORF	^{99m}Tc-cMORF

trace concentration was added to the conjugation mixture before purification. The hybridization was carried out for 20 min at room temperature followed by SE-HPLC analysis to measure the radioactivity bound to free MORF and that bound to the G3-MORF. The areas of G3-MORF/^{99m}Tc-cMORF and MORF/^{99m}Tc-cMORF peaks on the radioactivity trace were compared with the corresponding peaks on the UV trace. Since accessibility of the ^{99m}Tc-cMORF to free MORF is assumed to be 100%, the identical ratio of G3-MORF to free MORF by radioactivity and UV detection would imply that the accessibility of the ^{99m}Tc-cMORF to G3-MORF was also 100%.

Since the free MORF (MW 6 KDa) and the coupling reagent EDC-methiodide (MW < 400 Da) are of low molecular weight, they could be removed from the high molecular weight product by filtration. The reaction mixture was repeatedly centrifuged using the Microcon YM-30 (MWCO 30 KDa) centrifugal filter devices to near dryness with water added between centrifugations until there was no evidence of free MORF or coupling agents by SE-HPLC. Stability of the conjugation mixture at room temperature in water was measured by monitoring the UV signal on SE-HPLC for more than one week.

Preparation of CC49-(c)MORF. The CC49 antibody was conjugated with either MORF or cMORF using a commercial Hydralink linker following the instruction of the manufacturer and experiences in this laboratory (*41*). Briefly, the antibody was first modified with succinimidyl 4-hydrazinonicotinate acetone hydrazone, while the (c)MORF was modified with succinimidyl 4-formylbenzoate. After purification, combining the hydrazine-modified antibody and the benzaldehyde-modified (c)MORF resulted in hydrazone formation. Purification of the antibody-(c)MORF from the free (c)MORF was achieved on Sephadex G-100 1 × 30 cm Econo-column using 100 mM PBS (pH 7.2) as eluent. The GPM was determined by SE-HPLC using the UV signal at both 265 and 280 nm. Under the assumption that the absorption coefficients of CC49 (280 nm) and (c)MORF (265 nm) do not change after conjugation, the concentration of CC49 and the (c)MORF GPM was calculated as described previously (*41, 42*).

Preserved immunoreactivities of CC49-(c)MORF were confirmed by flow cytometry with native CC49 as the positive control and the incubation medium as the negative control. Briefly, 2×10^5 LS174T cells in 100 μL of PBS were incubated with each antibody (3 μg) at room temperature for 30 min in the dark. The cells were washed three times using PBS, then gently resuspended in ice cold PBS, and phycoerythrin labeled secondary antibody, sheep antimouse F(ab′)$_2$, in 100 μL of 3% BSA/PBS was added. After 30 min incubation at room temperature in the dark, the cells were washed with PBS three times and resuspended in ice cold 3% BSA/PBS for analysis of immunoreactive fraction on a Becton-Dickinson FACSCalibur system (San Jose, CA). Background fluorescence was measured on a set of cells treated with secondary antibody alone. The immunoreactive fraction was well known to be the percentage of antibody preserving the immunoreactivity after conjugation compared with unmodified antibody. The percentage of fluorescence shift in the FACS study was used to calculate the immunoreactive fraction.

Hybridization in Solution. To confirm that the G3-MORF can link the CC49-cMORF and ^{99m}Tc-cMORF together in solution, the G3-MORF (4.75 μg, 2.5 μL) was mixed with 5 μL of ^{99m}Tc-cMORF (0.13 μg, 82.5 μCi) at room temperature and, after 30 min, 2 μL of the mixture was added to 40 uL of CC49-cMORF (4.3 μg). After a further 30 min, the mixture was analyzed by SE-HPLC by monitoring both radioactivity and UV signals.

Signal Amplification on Plates. The experimental procedure is outlined in Table 1. Both the CC49-(c)MORF antibodies were first immobilized on both the Protein G and Protein L coated 96-well flat-bottomed plates, via their Fc and VLκ regions, respectively, according to the manufacturer's instructions and the plates were rinsed three times using 200 μL of washing buffer (0.1 M PBS, pH 7.2, with 0.05% Tween-20). To two sets of wells was added 100 μL of each CC49-(c)MORF solution (about 3.3 μg/mL) containing the same amount of (c)MORF (2 pmol). As controls, to an equal number of wells only PBS was added in place of the antibodies. The plates were incubated for 60 min at room temperature and then rinsed with 3 × 200 μL of washing buffer. To the wells containing CC49-cMORF and one set of PBS control wells, 100 μL of G3-MORF (2.4 μg/mL in PBS, pH 7.2, containing 1% BSA) was added. The plates were incubated for 30 min at room temperature and then rinsed with 3 × 200 μL of washing buffer. To each well, 50 μL of ^{99m}Tc-cMORF (2 μCi in PBS, pH 7.2, containing 1% BSA) was added. The plates were incubated for another 30 min at room temperature and the free ^{99m}Tc-cMORF was removed with 3 × 200 μL of washing buffer. The radioactivity bound to the plates was removed with 2 × 200 μL of 1% sodium dodecyl sulfate (SDS) in 0.2 N NaOH and 200 μL of 2 M hydrochloride for counting in a NaI(Tl) well counter. To the wells containing CC49-MORF rather than CC49-cMORF and one set of PBS control wells was added 100 μL of PBS (pH 7.2, containing 1% BSA). The plates were incubated for 30 min at room temperature before the wells were rinsed with 3 × 200 μL of washing buffer. To each well 50 μL of ^{99m}Tc-cMORF was added and the studies performed as described above. The amplification factor (AF) was calculated from the percentage of bound radioactivity removed from the wells of all four studies. AF = (Amplification pretargeting − Nonspecific amplification)/(Conventional pretargeting − Nonspecific pretargeting). An identical study was performed on the Protein L coated plate.

Signal Amplification on Cells. The cell amplification pretargeting was performed similarly to that described in Table 1. Cells were suspended in Minimum Essential Medium (MEM) with 10% FBS and were seeded in 12-well flat-bottomed plates at 1 mL/well. The cells were used when 80% confluence was reached and the medium was changed to MEM with 1% FBS. First, 100 μL of CC49-(c)MORF solution (about 3.3 μg/mL) containing the same amount of (c)MORF (2 pmol) was added to each well in the two groups followed by incubation at 4 or 37 °C for 1 h (the 4 °C incubations were included to evaluate the influence of internalization). Thereafter, 100 μL of G3-MORF (2.4 μg/mL in PBS, pH 7.2, containing 1% BSA) was added to the CC49-cMORF wells and to one set of PBS control wells; 100 uL of PBS without G3-MORF was added to the CC49-MORF wells and one set of PBS control wells. After incubation for 30 min, the cells were rinsed with 2 × 0.5 mL of MEM with 1% FBS and 2 μCi of ^{99m}Tc-cMORF in 50 μL of PBS (containing 1% BSA) was added to each well followed by 30 min incubation. The cell medium was then carefully removed, and the cells were rinsed with 2 × 0.5 mL of cold PBS. The cells were then lysed with 1% SDS in 0.2 N NaOH,

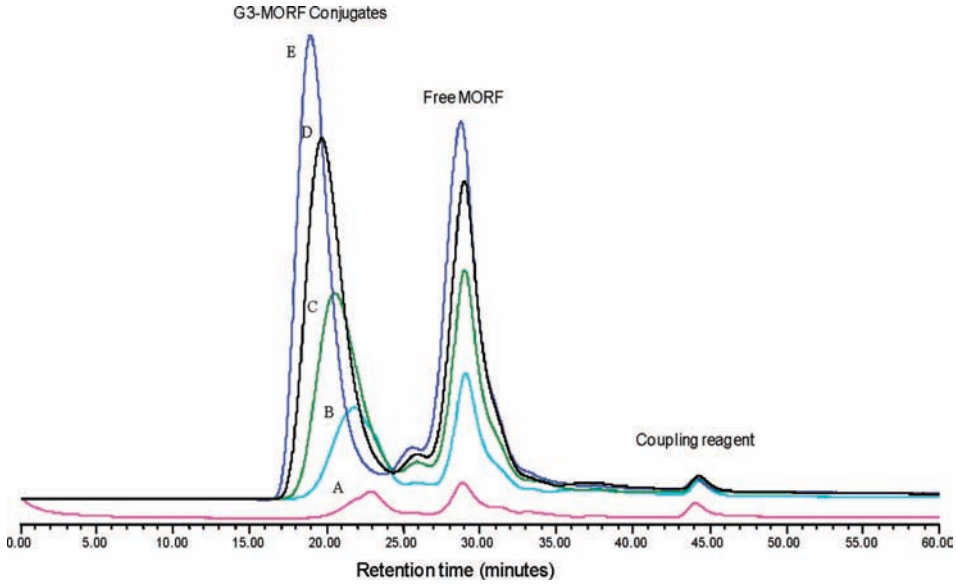

Figure 2. SE-HPLC UV chromatograms at 265 nm of G3-MORF prepared at different molar ratios of MORF to dendrimer: 1:1 (trace A), 2:1 (trace B), 4:1 (trace C), 8:1 (trace D), and 16:1 (trace E). Flow rate was 0.6 mL/min.

and the radioactivity in the medium and cells was measured in the well gamma counter.

RESULTS

G3-MORF Conjugation. In the SE-HPLC UV traces of G3-MORF before purification (Figure 2), the peak at early retention time (18.9−22.9 min) is due to the conjugated G3-MORF while the peak appearing later is due to free MORF. The conjugate prepared at higher molar ratio demonstrated shorter retention time on the SE-HPLC indicating higher molecular weight. Since these traces were obtained before purification, the ratio of peak areas is a measure of the conjugation efficiency (i.e., GPM). As shown, the average GPM increased with increasing molar ratio of MORF to dendrimer as expected. However, molar ratios higher than 16:1 did not further increase the average GPM (data not shown). The possibility that the MORF was bound to the dendrimer noncovalently even in part was excluded by the results of an identical study without coupling agent under the same conditions that demonstrated only individual peaks corresponding to unconjugated dendrimer and free MORF. The conjugate was stable at room temperature for at least one week as monitored by SE-HPLC.

As shown in Figure 3, one conjugation mixture (prepared at a 16:1 MORF/dendrimer molar ratio) was also analyzed by native PAGE following the addition of cDNA and staining with Coomassie Blue (panel A) or ethidium bromide (panel B). The migration of the conjugated dendrimer (lanes 2) was distinctly slowed compared to that of the free dendrimer (lanes 1) indicating a higher molecular weight after conjugation with MORF. The somewhat broad band for the G3-MORF indicates that the conjugate consisted of several G3-MORFs with different GPMs. Both results also demonstrate that there was no unreacted dendrimer left after conjugation. The multiple bands for the free MORF (lane 3) may indicate impurities in the commercial product.

Analysis of the conjugation mixture prepared at the 16:1 molar ratio on SE-HPLC is shown in Figure 4. UV chromatogram (top trace) indicates that this G3-MORF contained an average of 9 GPM. Since there are 32 carboxyl groups on the surface of the G3 dendrimer, the average conjugation efficiency was 28%. After adding a trace level of ^{99m}Tc-cMORF to the conjugation mixture, the ratio of radioactivity peak intensity of G3-MORF/^{99m}Tc-cMORF to MORF/^{99m}Tc-cMORF was compared with that of the UV trace. Since the accessibility of the ^{99m}Tc-cMORF tracer to free MORF may be assumed to be 100%, the comparison shows that about 90% of the MORF groups on the dendrimer formed a duplex with ^{99m}Tc-cMORF. Thus about 8 of the 9 MORF groups in the polymer were accessible to ^{99m}Tc-cMORF in solution.

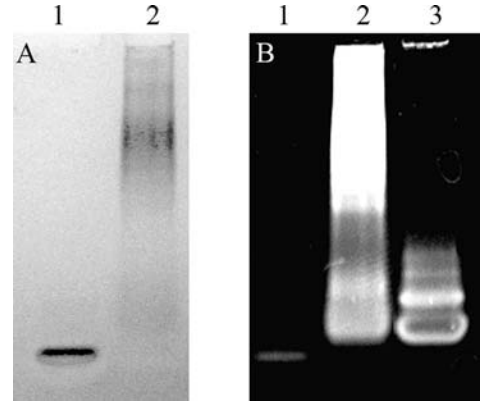

Figure 3. Native PAGE of G3-MORF analyzed before purification and after mixing with cDNA and staining with Coomassie Blue (panel A) or ethidium bromide (panel B). Lane 1 contains free dendrimer, lane 2 contains MORF conjugated dendrimer, and lane 3 (panel B only) contains free MORF.

Preparation of CC49-(c)MORF. The CC49-(c)MORF was successfully synthesized with an average GPM in the range of 1.0−1.3 by the method described previously (*41*). The flow cytometry results of Figure 5 show that both the CC49-MORF and CC49-cMORF retained more than 90% of the immunoreactive fraction of the native CC49.

Hybridization in Solution. The SE-HPLC trace for the CC49-cMORF/G3-MORF/^{99m}Tc-cMORF complex prepared by mixing the ^{99m}Tc-cMORF tracer with the G3-MORF followed by hybridization to the CC49-cMORF is shown in Figure 6. The radioactivity profile shows only a single peak with a high molecular weight retention time of 16.8 min and no evidence of free G3-MORF/^{99m}Tc-cMORF signifying complete hybridization of the G3-MORF/^{99m}Tc-cMORF to the CC49-cMORF antibody. The UV profile also shows only a single peak with the identical 16.8 min retention time (data not presented) and therefore provides further evidence of complete hybridization.

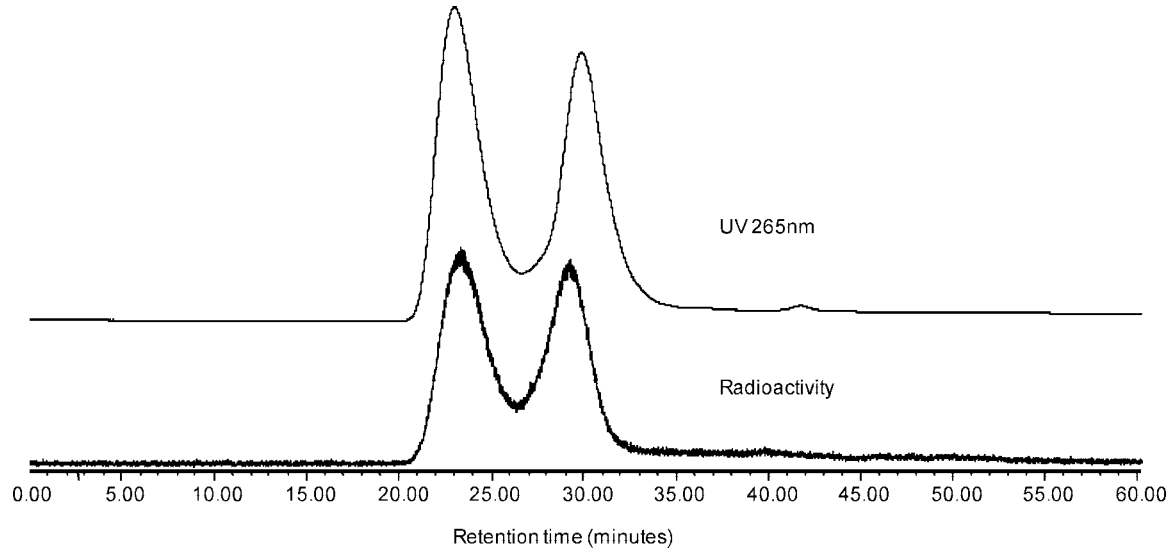

Figure 4. SE-HPLC chromatograms with UV 265 nm detection (top trace) and radioactivity detection (bottom trace) of one G3-MORF (prepared at a 16:1 MORF/dendrimer molar ratio) following addition of trace ^{99m}Tc-cMORF. Flow rate was 0.5 mL/min.

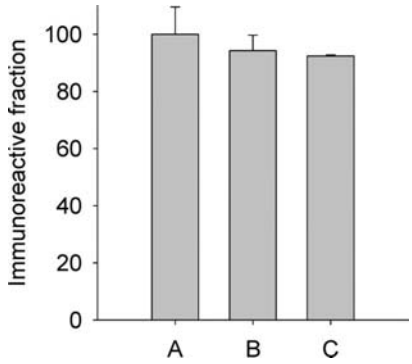

Figure 5. Histograms representing the immunoreactive fractions of native and modified CC49 detected using flow cytometry analysis. A: native CC49. B: CC49-MORF. C: CC49-cMORF. Results are averages, error bars represent 1 s.d ($N = 3$).

Signal Amplification on Plates. Figure 7 presents histograms showing the percentage of radioactivity bound to wells used for amplification pretargeting and conventional pretargeting on Protein G (panel A) and Protein L (panel B) coated plates as described above.

As shown in Figure 7, on Protein G, the amplification factor was about 6 while on Protein L this factor was about 14. The differences between amplification and controls in both cases are significant (Student's *t*-Test, $P < 0.05$). In both cases the G3-MORF therefore played an important role in the accumulation of radioactivity.

Signal Amplification on Cells. The results of the cell signal amplification studies are shown in Figure 8 for incubations at both 4 and 37 °C. Cell accumulations of ^{99m}Tc-cMORF by amplification pretargeting were significantly higher (Student's *t*-Test, $P < 0.05$) at both temperatures by up to 2.5 times that of conventional pretargeting without the G3-MORF. The percentage of radioactivity increased in all study groups except for amplification pretargeting when incubation temperature was increased to 37 °C.

DISCUSSION

In this investigation, a generation 3 PAMAM dendrimer was conjugated with multiple copies of MORF and used in combination with the CC49 antibody conjugated with cMORF and with the cMORF labeled with ^{99m}Tc for in vitro amplification pretargeting. For this investigation, the PAMAM dendrimer, anionic at neutral pH, was selected because anionic dendrimers have shown lower toxicity and a longer clearance time from circulation than cationic dendrimers (*43–46*) and because the carboxyl groups may be readily modified with amine-modified MORF using carbodiimides. Furthermore, PAMAM dendrimers are commercially available in a variety of generations. In addition, the spherical geometry of dendrimers may decrease steric hindrance compared to linear polymers. In this investigation, we determined that increasing the conjugation molar ratio of MORF to dendrimer beyond 16:1 did not increase the number of attached GPM, possibly due to steric hindrance. The maximum average number of MORF that was attached (i.e., GPM) was 9 under the conditions of this investigation. Higher generation dendrimers may therefore be required if higher GPM values are needed. Adding *N*-hydroxysulfosuccinimide (Sulfo-NHS) to improve the degree of conjugation was unsuccessful.

The conjugation was confirmed by native PAGE analysis. As expected, the broad band on native PAGE in Figure 3 indicates that the G3-MORF used in this investigation consisted of conjugates with a range of GPM with an average of 9. Analysis of the dendrimer after conjugation but before purification, when stained with ethidium bromide, provided a G3-MORF band that is much brighter than that of the unconjugated MORF which suggests a high degree of conjugation. The average molecular weight of G3-MORF was about 64 KDa or about 7.2 KDa per MORF, and therefore lower than that of the PA (9.1 KDa/MORF) and PL (10.7 KDa/MORF) polymers studied previously. Although the experimental protocols were very different, the fact that the spherical dendrimer demonstrated higher conjugation efficiency (28%) than the linear PA (19%) or PL (11%) polymers supports a suggestion that the spherical geometry of the dendrimer may be helpful in reducing steric hindrances. Possibly for the same reason, accessibility of the MORF in the G3-MORF conjugate was higher at 90% compared to 50−60% for PL-MORF and PA-MORF conjugate (*7*). As shown in Figure 4, when added at a 1:1 molar ratio, the ^{99m}Tc-cMORF completely hybridized to the G3-MORF and MORF mixture and the G3-MORF completely hybridized to the CC49-cMORF as shown in Figure 6 demonstrating uninhibited accessibility in solution in both cases.

The results presented in Figure 7 clearly demonstrate that the G3-MORF participated in signal amplification on both Protein G and Protein L coated plates in that significantly more

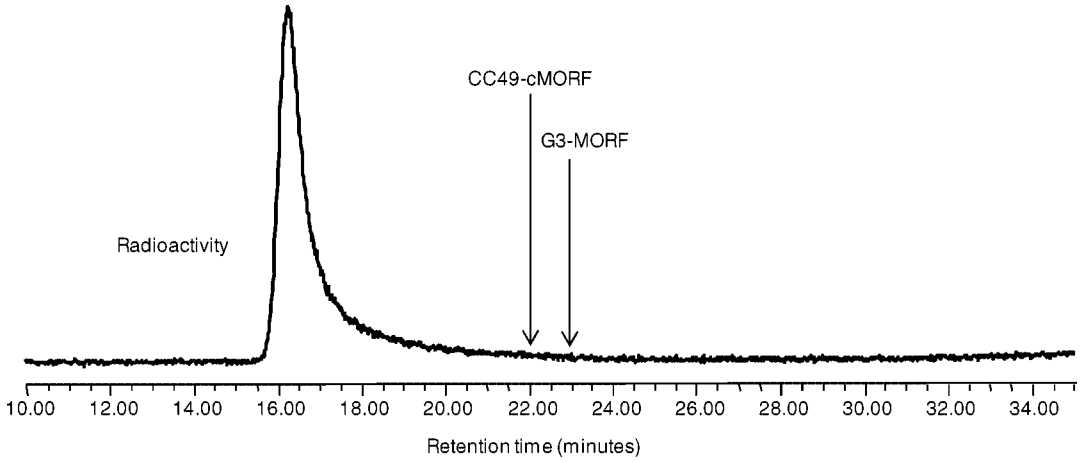

Figure 6. SE-HPLC radioactivity chromatographic profile for the CC49-cMORF/G3-MORF/^{99m}Tc-cMORF complex. The retention times for CC49-cMORF and G3-MORF are indicated by arrows. Flow rate was 0.5 mL/min.

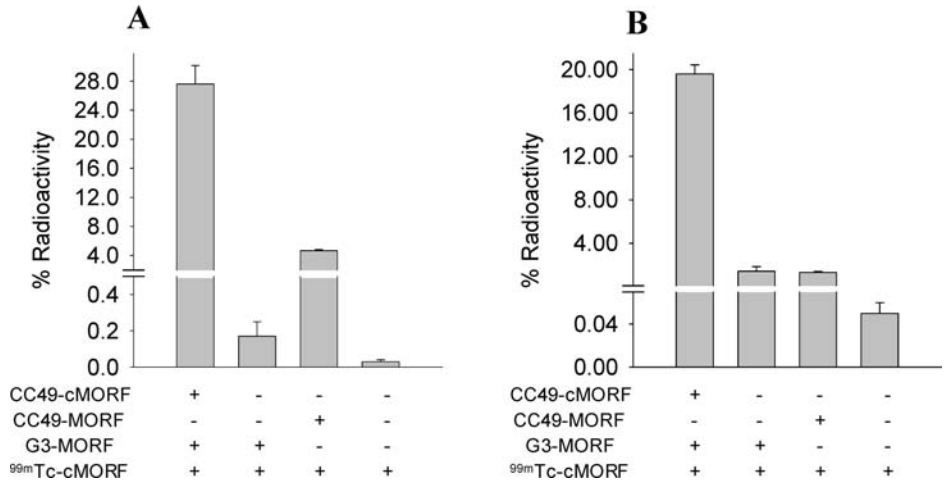

Figure 7. Histograms presenting the percentage on radioactivity obtained in Protein G (panel A) and Protein L (panel B) coated plates by amplification pretargeting and conventional pretargeting and two control studies in which the antibody or both the antibody and the polymer were eliminated. Results are averages; error bars represent 1 s.d ($N = 5$).

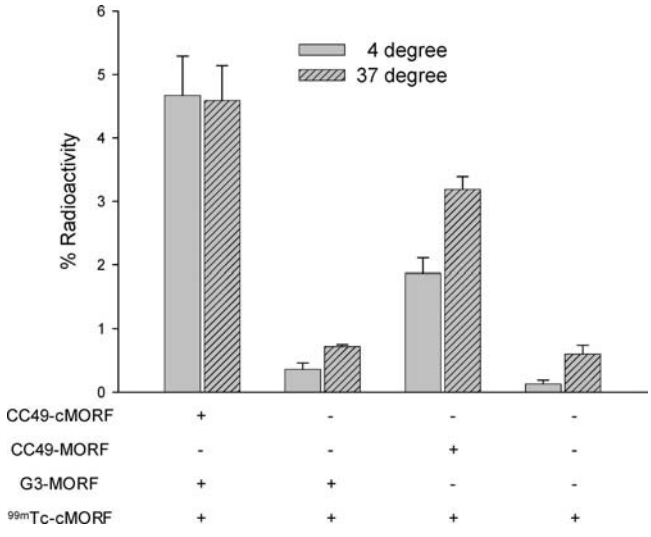

Figure 8. Histograms presenting the percentage of radioactivity accumulated in cells by amplification pretargeting, conventional pretargeting, and their control studies without antibodies, performed at 4 °C (solid bars) and 37 °C (hatched bars). Results are averages; error bars represent 1 s.d ($N = 3$).

^{99m}Tc-cMORF effector accumulated in the amplification studies compared with the conventional pretargeting studies and provided an amplification factor of about 14 in the case of the Protein L coated plate. Because the molecular volume of G3-MORF is fairly large, steric hindrance may restrict its hybridization to CC49-cMORF. The fact that the CC49 antibody was immobilized on Protein G and Protein L coated plates via Fc and VLκ regions, respectively, should result in different orientations of the bound antibodies, which in turn could expose different aspects of the antibody-bound cMORF for G3-MORF binding and may explain the differences in amplification between the two plates.

While the results of studies in cell culture showed that signal was also amplified, the amplification factor was not as high as that on the plates. Studies subsequent to those reported herein suggest that accessibility of the cMORF on antibody to G3-MORF after binding to the antigen may be restricted on the cell membrane compared to the accessibility on either Protein G or Protein L on the plate, although further studies will be required to establish the reason for this observation. As shown in Figure 8, performing the amplification pretargeting at 4 °C to eliminate any influence of internalization made no significant difference to suggest that internalization was not a significant factor in this study.

Measurements of specific binding on plates or cells in wells are usually complicated by the unavoidable contribution of nonspecific binding. It was for this reason that multiple controls were necessary in this investigation. Thus in the plate study,

the nonspecific amplification binding of the ^{99m}Tc-cMORF effector to the intermediate G3-MORF was evaluated by leaving out the CC49-cMORF and the nonspecific conventional pretargeting binding of the ^{99m}Tc-cMORF to the well surface was evaluated by leaving out the G3-MORF and the antibody, as described in Table 1. Fortunately as shown in Figure 7, the nonspecific binding of the G3-MORF in the amplification pretargeting to both Protein G and Protein L coated plates was much lower than the amplification binding. As shown in Figure 8, the identical controls were used in the cell study and again the G3-MORF did not increase the nonspecific binding on cells.

To exclude the possibility that the differences in amplification factors between the plate and cell studies may be due to the different media used, an amplification pretargeting was performed on Protein L coated plate as before but using the cell culture medium as in the cell study. In one additional control group, the protein L coated plates were first incubated with the CC49-MORF instead of CC49-cMORF, followed by the G3-MORF and finally the ^{99m}Tc-cMORF exactly as before, except now in culture media. The results (not presented) showed that the amplification factor was still about 14 as in the former study indicating that the cell culture medium cannot explain the lower amplification factors in the cell study and that the nonspecific binding of G3-MORF to the antibody was very low.

CONCLUSIONS

A G3 dendrimer-MORF conjugate was synthesized with 9 of the 32 surface groups modified with MORF, of which 90% were accessible in solution to ^{99m}Tc-cMORF. The conjugated dendrimer showed unhindered hybridization to ^{99m}Tc-cMORF and CC49-cMORF. On Protein G and Protein L coated plates, the signal was amplified by up to 14-fold that of conventional pretargeting, showing that the dendrimer−MORF conjugate participated in amplifying the signal. Although not as positive, similar studies in the LS174T tumor cells in culture also demonstrated evidence of signal amplification.

ACKNOWLEDGMENT

The authors are grateful to Dr. Schlom (Laboratory of Tumor Immunology and Biology, Center for Cancer Research, NCI, NIH, Bethesda, MD) for providing the CC49 hybridoma. Financial support from NIH (CA 94994 and CA107360) is gratefully acknowledged.

LITERATURE CITED

(1) Goodwin, D. A., Meares, C. F., McCall, M. J., McTigue, M., and Chaovapong, W. (1988) Pre-targeted immunoscintigraphy of murine tumors with indium-111-labeled bifunctional baptens. *J. Nucl. Med. 29*, 226–234.

(2) Hnatowich, D. J., Virzi, F., and Rusckowski, M. (1987) Investigations of avidin and biotin for imaging applications. *J. Nucl. Med. 28*, 1294–1302.

(3) Bos, E. S., Kuijpers, W. H. A., Meesterswinters, M., Pham, D. T., Dehaan, A. S., Vandoornmalen, A. M., Kaspersen, F. M., Vanboeckel, C. A. A., and Gougeonbertrand, F. (1994) In-vitro evaluation of DNA-DNA hybridization as a 2-step approach in radioimmunotherapy of cancer. *Cancer Res. 54*, 3479–3486.

(4) Chang, C. H., Sharkey, R. M., Rossi, E. A., Karacay, H., McBride, W., Hansen, H. J., Chatal, J. F., Barbet, J., and Goldenberg, D. M. (2002) Molecular advances in pretargeting radioimunotherapy with bispecific antibodies. *Mol. Cancer Ther. 1*, 553–563.

(5) Rusckowski, M., Qu, T., Chang, F., and Hnatowich, D. J. (1997) Pretargeting using peptide nucleic acid. *Cancer 80*, 2699–2705.

(6) Wang, Y., Chang, F., Zhang, Y., Liu, N., Liu, G., Gupta, S., Rusckowski, M., and Hnatowich, D. J. (2001) Pretargeting with amplification using polymeric peptide nucleic acid. *Bioconjugate Chem. 12*, 807–816.

(7) He, J., Liu, G., Zhang, S., Rusckowski, M., and Hnatowich, D. J. (2003) Pharmacokinetics in mice of four oligomer-conjugated polymers for amplification targeting. *Cancer Biother. Radiopharm. 18*, 941–947.

(8) He, J., Liu, G., Gupta, S., Zhang, Y., Rusckowski, M., and Hnatowich, D. J. (2004) Amplification targeting: A modified pretargeting approach with potential for signal amplification - Proof of a concept. *J. Nucl. Med. 45*, 1087–1095.

(9) Sharkey, R. M., Cardillo, T. M., Rossi, E. A., Chang, C. H., Karacay, H., McBride, W. J., Hansen, H. J., Horak, I. D., and Goldenberg, D. M. (2005) Signal amplification in molecular imaging by pretargeting a multivalent, bispecific antibody. *Nat. Med. 11*, 1250–1255.

(10) Bogdanov, A., Kang, H. W., Querol, M., Pretorius, P. H., and Yudina, A. (2007) Synthesis and testing of a binary catalytic system for imaging of signal amplification in vivo. *Bioconjugate Chem. 18*, 1123–1130.

(11) Malik, N., and Duncan, R. (2002) Dendritic-platinate drug delivery system, U. S. Patent 6,585,956.

(12) Kolhe, P., Misra, E., Kannan, R. M., Kannan, S., and Lieh-Lai, M. (2003) Drug complexation, in vitro release and cellular entry of dendrimers and hyperbranched polymers. *Int. J. Pharm. 259*, 143–160.

(13) Kannan, S., Kolhe, P., Raykova, V., Glibatec, M., Kannan, R. M., Lieh-Lai, M., and Bassett, D. (2004) Dynamics of cellular entry and drug delivery by dendritic polymers into human lung epithelial carcinoma cells. *J. Biomater. Sci.-Polym. Ed. 15*, 311–330.

(14) Patri, A. K., Kukowska-Latallo, J. F., and Baker, J. R. (2005) Targeted drug delivery with dendrimers: Comparison of the release kinetics of covalently conjugated drug and non-covalent drug inclusion complex. *Adv. Drug Delivery Rev. 57*, 2203–2214.

(15) Kukowska-Latallo, J. F., Candido, K. A., Cao, Z., Nigavekar, S. S., Majoros, I. J., Thomas, T. P., Balogh, L. P., Khan, M. K., and Baker, J. R. (2005) Nanoparticle targeting of anticancer drug improves therapeutic response in animal model of human epithelial cancer. *Cancer Res. 65*, 5317–5324.

(16) Bai, S., Thomas, C., Rawat, A., and Ahsan, F. (2006) Recent progress in dendrimer-based nanocarriers. *Crit. Rev. Ther. Drug Carrier Syst. 23*, 437–495.

(17) Kolhe, P., Khandare, J., Pillai, O., Kannan, S., Lieh-Lal, M., and Kannan, R. M. (2006) Preparation, cellular transport, and activity of polyamidoamine-based dendritic nanodevices with a high drug payload. *Biomaterials 27*, 660–669.

(18) Chandrasekar, D., Sistla, R., Ahmad, F. J., Khar, R. K., and Diwan, P. V. (2007) The development of folate-PAMAM dendrimer conjugates for targeted delivery of anti-arthritic drugs and their pharmacokinetics and biodistribution in arthritic rats. *Biomaterials 28*, 504–512.

(19) Chandrasekar, D., Sistla, R., Ahmad, F. J., Khar, R. K., and Diwan, P. V. (2007) Folate coupled poly(ethyleneglycol) conjugates of anionic poly(amidoamine) dendrimer for inflammatory tissue specific drug delivery. *J. Biomed. Mater. Res.: Part A 82A*, 92–103.

(20) Quintana, A., Raczka, E., Piehler, L., Lee, I., Myc, A., Majoros, I., Patri, A. K., Thomas, T., Mule, J., and Baker, J. R. (2002) Design and function of a dendrimer-based therapeutic nanodevice targeted to tumor cells through the folate receptor. *Pharm. Res. 19*, 1310–1316.

(21) Nakanishi, H., Mazda, O., Satoh, E., Asada, H., Morioka, H., Kishida, T., Nakao, M., Mizutani, Y., Kawauchi, A., Kita, M., Imanishi, J., and Miki, T. (2003) Nonviral genetic transfer of Fas ligand induced significant growth suppression and apoptotic tumor cell death in prostate cancer in vivo. *Gene Ther. 10*, 434–442.

(22) Thomas, T. P., Patri, A. K., Myc, A., Myaing, M. T., Ye, J. Y., Norris, T. B., and Baker, J. R. (2004) In vitro targeting of synthesized anti body-conjugated dendrimer nanoparticles. *Biomacromolecules 5*, 2269–2274.

(23) Khandare, J., Kolhe, P., Pillai, O., Kannan, S., Lieh-Lai, M., and Kannan, R. M. (2005) Synthesis, cellular transport, and activity of polyamidoamine dendrimer-methylprednisolone conjugates. *Bioconjugate Chem. 16*, 330–337.

(24) Thomas, T. P., Majoros, I. J., Kotlyar, A., Kukowska-Latallo, J. F., Bielinska, A., Myc, A., and Baker, J. R. (2005) Targeting and inhibition of cell growth by an engineered dendritic nanodevice. *J. Med. Chem. 48*, 3729–3735.

(25) Arima, H., Chihara, Y., Arizono, M., Yamashita, S., Wada, K., Hirayama, F., and Uekama, K. (2006) Enhancement of gene transfer activity mediated by mannosylated dendrimer/alpha-cyclodextrin conjugate (generation 3, G3). *J. Controlled Release 116*, 64–74.

(26) Khandare, J. J., Jayant, S., Singh, A., Chandna, P., Wang, Y., Vorsa, N., and Minko, T. (2006) Dendrimer versus linear conjugate: Influence of polymeric architecture on the delivery and anticancer effect of paclitaxel. *Bioconjugate Chem. 17*, 1464–1472.

(27) Ke, T., Feng, Y., Guo, J., Parker, D. L., and Lu, Z. R. (2006) Biodegradable cystamine spacer facilitates the clearance of Gd(III) chelates in poly(glutamic acid) Gd-DO3A conjugates for contrast-enhanced MR imaging. *Magn. Reson. Imaging 24*, 931–940.

(28) Shukla, R., Thomas, T. P., Peters, J. L., Desai, A. M., Kukowska-Latallo, J., Patri, A. K., Kotlyar, A., and Baker, J. R. (2006) HER2 specific tumor targeting with dendrimer conjugated anti-HER2 mAb. *Bioconjugate Chem. 17*, 1109–1115.

(29) Rudovsky, J., Botta, M., Hermann, P., Hardcastle, K. I., Lukes, I., and Aime, S. (2006) PAMAM dendrimeric conjugates with a Gd-DOTA phosphinate derivative and their adducts with polyaminoacids: The interplay of global motion, internal rotation, and fast water exchange. *Bioconjugate Chem. 17*, 975–987.

(30) Fu, Y., Nitecki, D. E., Maltby, D., Simon, G. H., Berejnoi, K., Raatschen, H. J., Yeh, B. M., Shames, D. M., and Brasch, R. C. (2006) Dendritic iodinated contrast agents with PEG-cores for CT imaging: Synthesis and preliminary characterization. *Bioconjugate Chem. 17*, 1043–1056.

(31) Wang, X., Inapagolla, R., Kannan, S., Lieh-Lai, M., and Kannan, R. M. (2007) Synthesis, characterization, and in vitro activity of dendrimer-streptokinase conjugates. *Bioconjugate Chem. 18*, 791–799.

(32) Tsutsumi, T., Hirayama, F., Uekama, K., and Arima, H. (2007) Evaluation of polyamidoamine dendrimer/alpha-cyclodextrin conjugate (generation 3, G3) as a novel carrier for small interfering RNA (siRNA). *J. Controlled Release 119*, 349–359.

(33) Battah, S., Balaratnam, S., Casas, A., O'Neill, S., Edwards, C., Batlle, A., Dobbin, P., and MacRobert, A. J. (2007) Macromolecular delivery of 5-aminolaevulinic acid for photodynamic therapy using dendrimer conjugates. *Mol. Cancer Ther. 6*, 876–885.

(34) Myc, A., Majoros, I. J., Thomas, T. P., and Baker, J. R. (2007) Dendrimer-based targeted delivery of an apoptotic sensor in cancer cells. *Biomacromolecules 8*, 13–18.

(35) Liu, G., He, J., Dou, S., Gupta, S., Vanderheyden, J., Rusckowski, M., and Hnatowich, D. J. (2004) Pretargeting in tumored mice with radiolabeled morpholino oligomer showing low kidney uptake. *Eur. J. Nucl. Med. Mol. Imaging 31*, 417–424.

(36) Liu, G., He, J., Dou, S., Gupta, S., Rusckowski, M., and Hnatowich, D. J. (2005) Further investigations of morpholino pretargeting in mice-establishing quantitative relations in tumor. *Eur. J. Nucl. Med. Mol. Imaging 32*, 1115–1123.

(37) Winnard, P., Chang, F., Rusckowski, M., Mardirossian, G., and Hnatowich, D. J. (1997) Preparation and use of NHS-MAG_3 for technetium-99m labeling of DNA. *Nucl. Med. Biol. 24*, 425–432.

(38) Liu, G., Dou, S., He, J., Yin, D., Gupta, S., Zhang, S., Wang, Y., Rusckowski, M., and Hnatowich, D. J. (2006) Radiolabeling of MAG_3-morpholino oligomers with ^{188}Re at high labeling efficiency and specific radioactivity for tumor pretargeting. *Appl. Radiat. Isot. 64*, 971–978.

(39) Sharma, A., Desai, A., Ali, R., and Tomalia, D. (2005) Polyacrylamide gel electrophoresis separation and detection of polyamidoamine dendrimers possessing various cores and terminal groups. *J. Chromatogr., A 1081*, 238–244.

(40) Shi, X., Patri, A. K., Lesniak, W., Islam, M. T., Zhang, C., Baker, J. R., and Balogh, L. P. (2005) Analysis of poly(amidoamine)-succinamic acid dendrimers by slab-gel electrophoresis and capillary zone electrophoresis. *Electrophoresis 26*, 2960–2967.

(41) He, J., Liu, G., Dou, S., Gupta, S., Rusckowski, M., and Hnatowich, D. J. (2007) An improved method for covalently conjugating morpholino oligomers to antitumor antibodies. *Bioconjugate Chem. 18*, 983–988.

(42) Liu, G., Zhang, S., He, J., Liu, N., Gupta, S., Rusckowski, M., and Hnatowich, D. J. (2002) The influence of chain length and base sequence on the pharmacokinetic behavior of Tc-99m-morpholinos in mice. *Q. J. Nucl. Med. 46*, 233–243.

(43) Malik, N., Wiwattanapatapee, R., Klopsch, R., Lorenz, K., Frey, H., Weener, J. W., Meijer, E. W., Paulus, W., and Duncan, R. (2000) Dendrimers: Relationship between structure and biocompatibility in vitro, and preliminary studies on the biodistribution of I-125-labelled polyamidoamine dendrimers in vivo. *J. Controlled Release 65*, 133–148.

(44) Jevprasesphant, R., Penny, J., Jalal, R., Attwood, D., McKeown, N. B., and D'Emanuele, A. (2003) The influence of surface modification on the cytotoxicity of PAMAM dendrimers. *Int. J. Pharm. 252*, 263–266.

(45) Duncan, R., and Izzo, L. (2005) Dendrimer biocompatibility and toxicity. *Adv. Drug Delivery Rev. 57*, 2215–2237.

(46) Svenson, S., and Tomalia, D. A. (2005) Commentary - Dendrimers in biomedical applications - reflections on the field. *Adv. Drug Delivery Rev. 57*, 2106–2129.

BC8001024

Improved Cellular Activity of Antisense Peptide Nucleic Acids by Conjugation to a Cationic Peptide-Lipid (CatLip) Domain

Uffe Koppelhus,[#,§] Takehiko Shiraishi,[§] Vladimir Zachar,[#] Stanislava Pankratova, and Peter E. Nielsen*

Department of Cellular and Molecular Medicine, The Panum Institute, Faculty of Health Sciences, University of Copenhagen, Blegdamsvej 3c, DK-2200 Copenhagen N, Denmark. Received February 22, 2008; Revised Manuscript Received June 20, 2008

Conjugation to cationic cell penetrating peptides (such as Tat, Penetratin, or oligo arginines) efficiently improves the cellular uptake of large hydrophilic molecules such as oligonucleotides and peptide nucleic acids, but the cellular uptake is predominantly via an unproductive endosomal pathway and therefore mechanisms that promote endosomal escape (or avoid the endosomal route) are required for improving bioavailability. A variety of auxiliary agents (chloroquine, calcium ions, or lipophilic photosensitizers) has this effect, but improved, unaided delivery would be highly advantageous in particular for future *in vivo* applications. We find that simply conjugating a lipid domain (fatty acid) to the cationic peptide (a CatLip conjugate) increases the biological effect of the corresponding PNA (CatLip) conjugates in a luciferase cellular antisense assay up to 2 orders of magnitude. The effect increases with increasing length of the fatty acid (C_8-C_{16}) but in parallel also results in increased cellular toxicity, with decanoic acid being optimal. Furthermore, the relative enhancement is significantly higher for Tat peptide compared to oligoarginine. Confocal microscopy and chloroquine enhancement indicates that the lipophilic domain increases the endosomal uptake as well as promoting significantly endosomal escape. These results provide a novel route for improving the (cellular) bioavailability of larger hydrophilic molecules.

INTRODUCTION

Bioavailability in general and effective cellular delivery in particular are major challenges for nucleic acid derived gene targeting agents and thus for drug discovery and development of such agents. Delivery of large DNA vectors for cellular transfection and gene therapy and of smaller oligonucleotides for antisense and RNA interference approaches is effectively accomplished by lipofection using a variety of cationic lipids (*1–4*). Unfortunately, this method is not without complications for *in vivo* use mainly due to toxicity. Neutral (or positively charged) antisense agents such as peptide nucleic acids (PNAs) (*5*) or morpholino oligomers (*6*) cannot effectively be delivered via lipofection, but codelivery with a partially cDNA oligonucleotide is possible (*7–9*) as is delivery of PNA oligomers conjugated to a variety of lipophilic ligands such a fatty acids (*10*) or polyaromates (*11*).

Several years ago it was discovered that a group of cationic peptides of biological origin as exemplified by the HIV derived Tat-peptide (*12, 13*) and the Antennapedia peptide, penetratin (*14*) (which is contained in a transcription factor form *Drosophila*), are taken up by eukaryotic cells and are able to deliver a conjugated molecular cargo to such cells. These so-called cell penetrating peptides (CPP) (*15*) typically contain multiple arginines, and indeed simple oligoarginines exhibit good cellular delivery activity (*16–18*). Although the first reports claimed that the cellular uptake of CCPs was exclusively a physical phenomenon involving binding to negatively charged sites on the membrane followed by internalization by transient membrane destabilization or by pore formation by the peptides, a range of recent studies have reached the consensus that the major cellular port of entrance for the cationic CPPs is via endocytosis (*19–22*), maybe predominantly macropinocytosis (*23–25*). Consequently, delivery is to endosomes (which eventually turn into lysosomes), and therefore the biological effect is very limited, as the compounds are trapped in these compartments and cannot reach their biological target in the cytoplasm or in the nucleus. Thus one of the major challenges for exploiting CPPs for drug delivery is the discovery of methods or mechanisms that allow efficient endosomal escape of the drugs. This may be accomplished by using auxiliary agents such as chloroquine (*26, 27*), calcium ions (*26*), or lipophilic photosensitizers (*28, 29*), but delivery may also be improved by chemical modification of the peptide. Most obviously, addition of a (viral) endosome disruption domain to the peptide should increase efficiency as already demonstrated (*25*), and more complex "chimeric" peptides such as arginine modified penetratin (*30*) and especially transportan also appear more effective (at least in a PNA context) than simple cationic peptides (*17*), although the mechanism(s) of uptake is still very poorly understood.

The galanin domain of transportan is rather hydrophobic while the mastoparan domain contains the only cationic moieties of this peptide. It would therefore appear that the cellular uptake of transportan could rely more on hydrophobic interactions with the membrane than on electrostatic interactions. It is of course reasonable that both membrane binding as well as membrane penetration should be facilitated by lipophilic ligands. On the other hand a cationic domain would contribute both electrostatic cellular adhesion as well as increased aqueous solubility of the ligand. The efficiency of cationic lipids for cellular delivery of (anionic) oligonucleotides and DNA is well established (*31*), and recently it was shown that fatty acid conjugates of oligoarginines may also be successfully exploited as delivery vehicles for DNA and RNA (*32*). In this case, however, the main function of the cationic peptide most likely is condensation of the anionic nucleic acids. We set out to study the cellular delivery properties of cationic peptides containing a simple lipophilic domain, in the form of a fatty acid. We have

* Corresponding author. Telephone: 0045 3532 7762. Fax: 0045 35396042. E-mail: pen@imbg.ku.dk.

[#] Laboratory for Stem Cell Research, Institute for Health Technologies, Aalborg University, Fredrik Bajers Vej 3B, DK-9220 Aalborg Ø, Denmark.

[§] These authors contributed equally.

10.1021/bc800068h CCC: $40.75 © 2008 American Chemical Society
Published on Web 07/23/2008

Table 1. List of PNAs

no.	name	sequence[a]
2395	Tat-PNA	H-GRKKRRQRRRPPQ-eg1-CCT CTT ACC TCA GTT ACA-NH_2
2456	Deca-PNA	Deca-eg1-CCT CTT ACC TCA GTT ACA-NH_2
2534	Tat-Deca-PNA	H-GRKKRRQRRRPPQ-Lys(Deca)-Gly-CCT CTT ACC TCA GTT ACA -NH_2
2821	Deca-Tat-Deca-PNA	H-Lys(Deca)-GRKKRRQRRRPPQ-Lys(Deca)-Gly-CCT CTT ACC TCA GTT ACA-NH_2
2785	(D-Arg)$_7$-PNA	H-(D-Arg)$_7$-Gly-CCT CTT ACC TCA GTT ACA-NH_2
2801	(D-Arg)$_7$-Deca-PNA	H-(D-Arg)$_7$-Lys(Deca)-Gly-CCT CTT ACC TCA GTT ACA-NH_2
2786	Deca-(D-Arg)$_7$-PNA	Deca-(D-Arg)$_7$-Gly-CCT CTT ACC TCA GTT ACA-NH_2
2787	(D-Arg)$_8$-PNA	H-(D-Arg)$_8$-Gly-CCT CTT ACC TCA GTT ACA-NH_2
2802	(D-Arg)$_8$-Deca-PNA	H-(D-Arg)$_8$-Lys(Deca)-Gly-CCT CTT ACC TCA GTT ACA-NH_2
2788	Deca-(D-Arg)$_8$-PNA	Deca-(D-Arg)$_8$-Gly-CCT CTT ACC TCA GTT ACA-NH_2
2752	mismatch[b]	H-GRKKRRQRRRPPQ-Lys(Deca)-Gly-CCT CT**G** ACC TCA **T**TT ACA-NH_2
2591	(Arg)$_6$-Deca-PNA	H-(Arg)$_6$-Lys(Deca)-Gly-CCT CTT ACC TCA GTT ACA -NH_2
3100	(Arg)$_7$-Deca-PNA	H-(Arg)$_7$-Lys(Deca)-Gly-CCT CTT ACC TCA GTT ACA -NH_2
3101	(Arg)$_8$-Deca-PNA	H-(Arg)$_8$-Lys(Deca)-Gly-CCT CTT ACC TCA GTT ACA -NH_2
2592	(Arg)$_9$-Deca-PNA	H-(Arg)$_9$-Lys(Deca)-Gly-CCT CTT CTT ACC TCA GTT ACA -NH_2
2739	(D-Arg)$_6$-Deca-PNA	H-(D-Arg)$_6$-Lys(Deca)-Gly-CCT CTT ACC TCA GTT ACA-NH_2
2740	(D-Arg)$_9$-Deca-PNA	H-(D-Arg)$_9$-Lys(Deca)-Gly-CCT CTT ACC TCA GTT ACA-NH_2
2646	(Arg)$_6$-Octa-PNA	H-(Arg)$_6$-Lys(Octa)-CCT CTT ACC TCA GTT ACA-NH_2
2647	(Arg)$_6$-Dodeca-PNA	H-(Arg)$_6$-Lys(Dodeca)-CCT CTT ACC TCA GTT ACA-NH_2
2648	(Arg)$_6$-Hexadeca-PNA	H-(Arg)$_6$-Lys(Hexadeca)-CCT CTT ACC TCA GTT ACA-NH_2
2822	(RK)$_3$-PNA	H-(D-Arg D-Lys)$_3$-Gly-CCT CTT ACC TCA GTT ACA-NH_2
2823	Deca-(RK)$_3$-PNA	H-Lys(Deca)-(D-Arg D-Lys)$_3$-Gly-CCT CTT ACC TCA GTT ACA-NH_2
2824	(RK)$_4$-PNA	H-(D-Arg D-Lys)$_4$-Gly-CCT CTT ACC TCA GTT ACA-NH_2
2825	Deca-(RK)$_4$-PNA	H-Lys(Deca)-(D-Arg D-Lys)$_4$-Gly-CCT CTT ACC TCA GTT ACA-NH_2
2826	(RRA)$_3$-PNA	H-(D-Arg D-Arg Ala)$_3$-Gly-CCT CTT ACC TCA GTT ACA-NH_2
2827	Deca-(RRA)$_3$-PNA	H-Lys(Deca) (D-Arg D-Arg Ala)$_3$ Gly-CCT CTT ACC TCA GTT ACA-NH_2
2828	(RRA)$_4$-PNA	H-(D-Arg D-Arg Ala)$_4$-Gly-CCT CTT ACC TCA GTT ACA-NH_2
2829	Deca-(RRA)$_4$-PNA	H-Lys(Deca) (D-Arg D-Arg Ala)$_4$-Gly-CCT CTT ACC TCA GTT ACA-NH_2
2830	R_4K_4−PNA	H-(D-Arg)$_4$(D-Lys)$_4$-Gly-CCT CTT ACC TCA GTT ACA-NH_2
2831	Deca-R_4K_4−PNA	H-Lys(Deca) (D-Arg)$_4$(D-Lys)$_4$-Gly-CCT CTT ACC TCA GTT ACA-NH_2
2832	$K_2R_4K_2$−PNA	H-(D-Lys)$_2$(D-Arg)$_4$(D-Lys)$_2$-Gly-CCT CTT ACC TCA GTT ACA-NH_2
2833	Deca-$K_2R_4K_2$−PNA	H-Lys(Deca) (D-Lys)$_2$(D-Arg)$_4$(D-Lys)$_2$-Gly-CCT CTT ACC TCA GTT ACA-NH_2
2738	(D-Arg)$_9$-PNA	H-(D-Arg)$_9$-Gly-CCT CTT ACC TCA GTT ACA-NH_2
3016	Chol-(Arg)$_7$-PNA	Cholesteryl hemisuccinate-(Arg)$_7$-eg1-CCT CTT ACC TCA GTT ACA-NH_2
3266	Fl-(Arg)$_8$-PNA	H-Flk-(D-Arg)$_8$-AAT CTC ACC TGA TAG T-NH_2
3265	Fl-(Arg)$_8$-Deca-PNA	H-Deca-Flk-(D-Arg)$_8$-AAT CTC ACC TGA TAG T-NH_2

[a] The sequences of the PNAs are written from N-terminal to C-terminal end. Cell penetrating peptides, decanoic acid (Deca) or Lys(Deca) moietiy was covalently linked to PNA at the N-terminal through an ethyleneglycol linker (eg1: 8-amino-3,6-dioxaoctanoic acid) or glycine (Gly) via continuous synthesis. [b] Mismatch PNA for the Tat-Deca-PNA (PNA2534) whereas two mismatches are indicated in bold. Flk, fluorescein (Fl) attached to the ε-amino group of a lysine residue (Lohse, J., Nielsen, P. E., Harrit, N., Dahl, O. (1997) *Bioconjugate Chem. 8*, 503−509).

characterized such two-domain "CatLip" peptides in a PNA antisense context (Table 1) using the quantitative and very sensitive and accurate mRNA splicing correction luciferase pLuc HeLa cell system (*33*, *34*), and we find that adding a fatty acid moiety increases the biological activity of Tat and oligoarginine CPP-PNA conjugates by up to 2 orders of magnitude.

EXPERIMENTAL PROCEDURES

PNA Synthesis. The sequences of the PNAs used are listed in Table 1. PNA synthesis was carried out by the standard Boc strategy as reported previously (*35*). Peptides were linked to the PNA at the N-terminal through an ethylene glycol linker (eg1: 8-amino-3,6-dioxaoctanoic acid) or glycine via continuous solid phase synthesis. The fatty acid was conjugated to the ε-amino group of a lysine moiety during synthesis using orthogonal Fmoc protection. The PNA conjugates were purified by HPLC and characterized by MALDI-TOF mass spectrometry (see Supporting Information). The PNAs were lyophilized and stored at 4 °C until use.

Cell Culture. HeLa pLuc705 cells were purchased from Gene Tools (USA). Cells were grown in RPMI1640 medium (Sigma) supplemented with 10% fetal bovine serum (FBS, Sigma), 1% glutamax (Gibco), 100 U/mL penicillin (Gibco), and 100 μg/mL streptomycin (Gibco) at 37 °C in humidified air with 5% CO_2. For studies of HeLa pLuc705 cells in 96 well plate format, cells were trypsinized and seeded (1.2×10^4 cells/well) 16 h before treatment. For studies in 24-well plate, 7.2×10^4 cells/well were used.

PNA Treatment. The cells, replated in 96 well (Nunc) or 24 well plates (Nunc) 16−24 h earlier, were treated with 100 μL/well (for 96 well plate) or 0.3 mL/well (for 24 well plate) of OPTI-MEM (Gibco) containing the PNA at the desired concentration for 4 h. After PNA treatment, cells were supplemented with the 100 μL/well (for 96 well plate) or 0.3 mL/well (for 24 well plate) of RPMI1640 medium (containing 20% FBS and 1% Glutamax), incubated further for 24 h, and subjected to the desired analysis unless otherwise stated. For the endosome disruption treatments, cells were treated as reported previously (*36*). Briefly, for photochemical internalization (PCI) treatment, cells were plated the day before PNA treatment with the antibiotics free growth medium containing 5 μg/mL aluminum phthalocyanine ($AlPcS_{2a}$, Frontier Scientific, Logan, USA). After the 4 h PNA treatment, the medium was replaced with fresh growth medium (RPMI1640 containing 10%

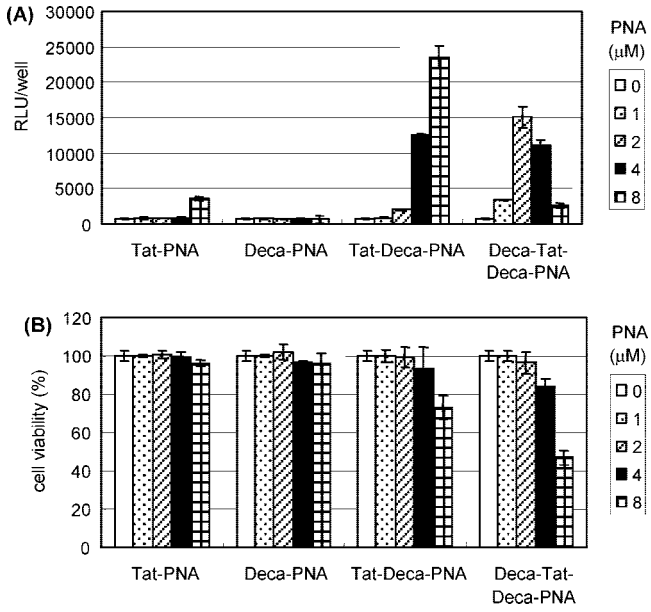

Figure 1. Relative cellular luciferase antisense activity and cellular toxicity in HeLa pLuc705 cells of PNAs conjugated to Tat-peptide and/or decanoic acid (attached to the ε-amino group of a lysine). Cells plated in the 96 well plates were treated with PNAs (Tat-PNA, Deca-PNA, Tat-Deca-PNA, and Deca-Tat-Deca-PNA) for 4 h in OPTI-MEM medium at the designated concentrations (0−8 μM) and incubated further for 24 h after addition of serum-containing growth medium (without removing the PNA solution). The cell samples were then subjected to luciferase analysis and cellular viability test. All tests were performed in triplicate and the results are given as the average values ± standard deviations (SD). (A) Luciferase activities were analyzed by Blight-Gro reagent (Promega) and given as relative light units (RLU/well). (B) Cellular viabilities were analyzed by MTS assay (Promega) and obtained values were normalized to the average value of non-PNA-treated sample.

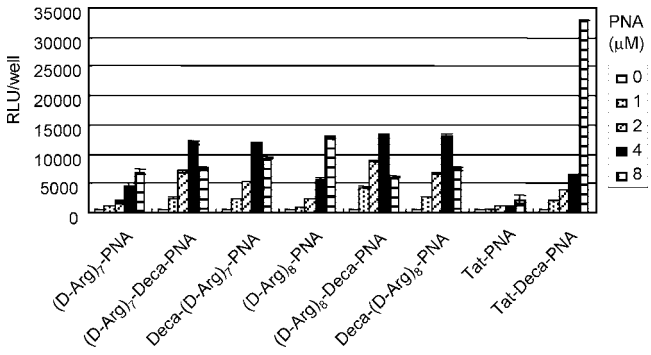

Figure 2. Relative cellular luciferase antisense activity in HeLa pLuc705 cells of PNAs conjugated to a cell penetrating peptide ((D-Arg)$_7$-, (D-Arg)$_8$-, or Tat-) and/or a decanoic acid (attached to the ε-amino group of a lysine). Cells plated in 96 well plate were treated with PNAs (0−8 μM) for 4 h in OPTI-MEM medium and incubated further for 24 h after addition of serum-containing growth medium without removing the transfection solution. Then the cell samples were subjected to luciferase analysis. Luciferase activities were analyzed by Blight-Gro reagent (Promega) and given as relative light units (RLU/well). All tests were performed in triplicate and the results are given as the average values ± standard deviations (SD).

FBS and 1% glutamax) and incubated for 4 h before irradiation with a fluorescence light tube (Alcadia, FO18) at 7.77 μW/cm^2 at 660 nm (15 nm bandwidth). Following irradiation, cells were incubated for additional 24 h before subjected to further analysis. For the chloroquine (CQ) treatment and Ca^{2+} treatment, cells were treated with PNA in OPTIMEM containing 120 μM CQ or 6 mM $CaCl_2$, respectively.

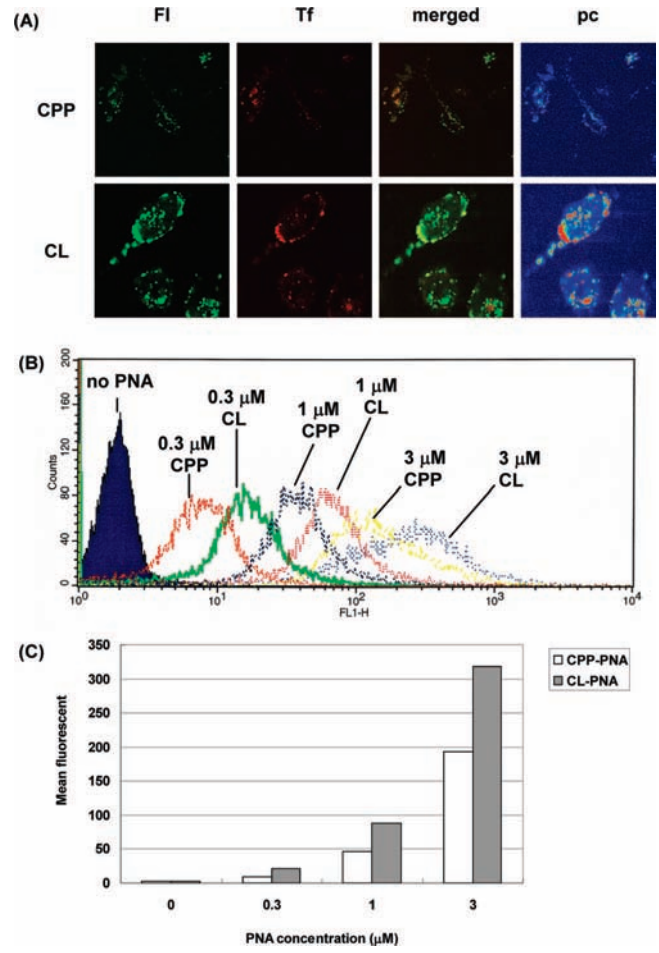

Figure 3. (A) Confocal fluoresence microscopy analysis of the cellular uptake of PNAs in HeLa pLuc705 cells. The fluorescein (Fl)-labeled PNAs (Fl-(Arg)$_8$-PNA (PNA3266) and Fl-(Arg)$_8$-Deca-PNA (PNA3265) were used. The cells were treated with 0.5 μM of PNA together with 20 μg/mL of tranferrin (Tf) for 24 h and analyzed by confocal fluoresence microscopy. Merged images (merged) and pseudocolor (ps) images were created by using the *Lasersharp 2000* software package (BioRad). (B) Flow cytometric analysis of HeLa pLuc705 cells treated with PNAs (Fl-(Arg)$_8$-PNA (CPP) or Fl-(Arg)$_8$-Deca-PNA (CL)) at three different concentrations (0.3, 1, and 3 μM) for 24 h and collected by pipetting using 1% BSA solution (in PBS) for the flow cytometric analysis. Cells (10 000 events for each sample) were analyzed using BD FACSCalibur cytometer and the data were analyzed by the *CellQuest* software. The histogram data of the cells treated with the PNAs at three different concentrations were superimposed. (C) Histogram representation of mean fluorescence of the cells.

Luciferase Assay. At 24 h after the PNA treatment, the cells were subjected to luciferase activity analysis by using the Bright-Glo Luciferase assay system (Promega) or the Luciferase Assay System (Promega) for the cells in 96 well plates or the cells in 24 well plates, respectively. Measurements were performed according to the manufacturer's instructions. Luminescence readings obtained with the Bright-Glo-Luciferase assay system were background-subtracted and are presented as relative light units (RLU/well). For the luciferase assay with the Luciferase Assay System, the cells were lysed with 0.1 mL/well of Passive Lysis Buffer (Promega) and used for both luciferase analysis and RNA extraction as mentioned below. Luminescence readings obtained with the Luciferase Assay System were background-subtracted and normalized by protein concentrations and were presented as RLU/μg protein. Protein concentrations were determined by the BCA protein assay (Pierce) according to the manufacturer's instruction.

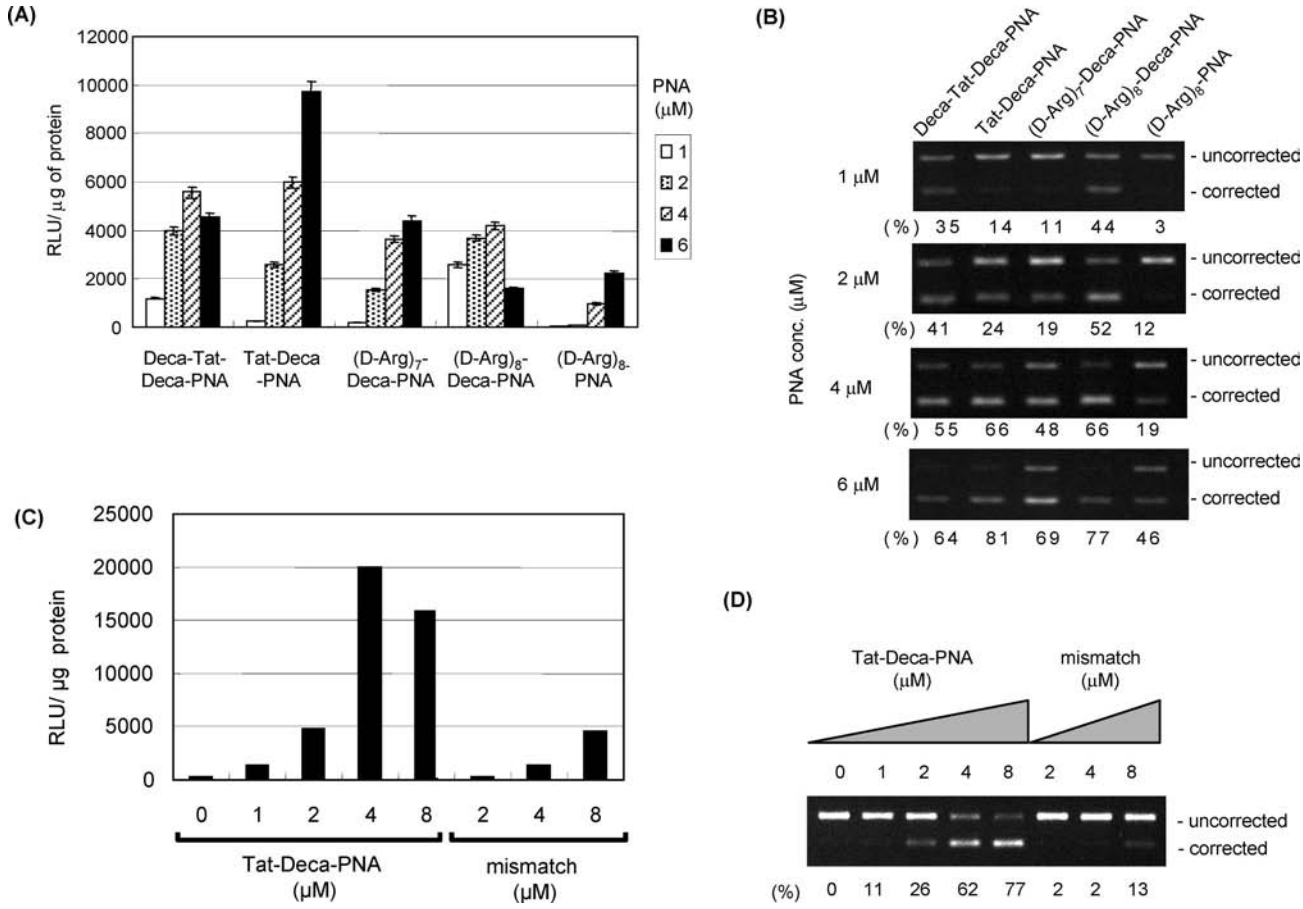

Figure 4. Relative cellular luciferase antisense activity in HeLa pLuc705 cells of PNAs conjugated to a cell penetrating peptide ((D-Arg)$_7$-, (D-Arg)$_8$-, or Tat-) and/or a decanoic acid (attached to the ε-amino group of a lysine). The cells were treated as described in Figure 1. Then cells were subjected to the further analysis. (A and B) PNAs (Deca-Tat-Deca-PNA (PNA2821), Tat-Deca-PNA (PNA2534), (D-Arg)$_7$-Deca-PNA (PNA2801), (D-Arg)$_8$-Deca-PNA (PNA2802), and (D-Arg)$_8$-PNA (PNA2787)) were used at the indicated concentrations (0−6 μM). (A) Luciferase activity was measured by Luciferase assay system (Promega), normalized to protein concentration and given as RLU/ μg of protein. (A) RT-PCR analysis of the splicing correction of pre-mRNAs by PNAs. Total RNA was extracted from the cells after the PNA treatment and subjected to RT-PCR analysis. Uncorrected indicates the 268 bp fragment without mis-splicing correction, and corrected indicates the 142 bp correctly spliced fragment. Numbers under each lane indicate the amount of the corrected form relative to the sum of corrected form and uncorrected form. (C and D) Comparison of Tat-Deca-PNA (PNA2534) with its mismatch PNA (mismatch, PNA2752). PNAs were used at the indicated concentrations (0−8 μM). Analysis was performed as described in (A and B). (C) Luciferase activity was measured and normalized to protein concentration. (D) RT-PCR analysis of mis-splicing correction by PNAs.

Cytotoxicity Test. Cells in 96 well plates were subjected to the MTS assay for cell viability test by using the CellTiter 96 Aqueous Non-Radioactive Cell Proliferation Assay (Promega) according to the manufacturer's instructions. The absorbance is presented as relative cellular viability (absorbance from non-PNA treated cells was set as 100%).

RT-PCR. Total RNA was extracted from the cellular lysate (see the luciferase assay section) by using RNeasy Mini kit (Qiagen) and subjected to RT-PCR analysis. A total of 3 ng RNA was used for each RT-PCR reaction (20 μL). RT-PCR was performed by using OneStep RT-PCR kit (Qiagen) following the manufacture's instructions. Primers for the RT-PCR were as follows: forward primer, 5′-TTGATATGTGGATTTC-GAGTCGTC-3′; reverse primer, 5′-TGTCAATCAGAGT-GCTTTTGG-CG-3′. The RT-PCR program was as follows: [(55 °C, 35 min) × 1 cycle, (95 °C, 15 min) × 1 cycle, (94 °C, 0.5 min; 55 °C, 0.5 min; 72 °C, 0.5 min) × 29 cycles]. RT-PCR products were analyzed on 2% agarose gel with 1× TBE buffer and visualized by ethidium bromide staining. Gel images were captured by ImageMaster (Pharmacia Biotech) and analyzed by UN-SCAN-IT software (Silk Scientific corporation).

Confocal Microscopy. Exponentially growing HeLa pLuc705 cells were plated in 8 well Laboratory-Tek Chambered Coverglass (Nunc) at a cell density of 5×10^4 cells/well the day before transfection. Following 16−24 h incubation, the cells were treated with PNA by incubation in OPTI-MEM medium (0.25 mL/well) containing the fluorescein-labeled PNA at the desired concentration and 20 μg/mL Alexa Fluor 633-conjugated human transferrin (80 kDa, Molecular Probes) for 4 h. Then the cells were incubated further for 20 h after supplement of RPMI 1640 growth medium containing 20% FBS (0.25 mL/well). Subsequently, the cells were washed with Hank's solution and subjected to microscopy analysis in this solution using a MultiProbe 2001 laser scanning confocal system equipped with an argon laser and a red laser diode (excitation wavelength 488 and 638 nm, Radiance2000, BioRad) connected to a Nicon eclipse TE200 microscope (oil immersion 60× 1.4 NA objective, Nikon, Tokyo, Japan). The *Lasersharp 2000* software package (BioRad) was used for image acquisition and processing.

Flow Cytometry. Exponentially growing HeLa pLuc705 cells were plated in 24 well plates at 1.0×10^5 cells/well the day before PNA treatment. After 16−24 h incubation, the cells were treated with fluorescein-labeled PNA as described above. After 24 h, the cells were washed twice with phosphate buffered saline (PBS) containing 1% BSA and collected by pipetting from the BSA/PBS solution. Then the cells were filtered with the cell strainer (70 μM, BD falcon) and subjected to flow cytometric analysis (10 000 events for each samples) using a BD FACS-

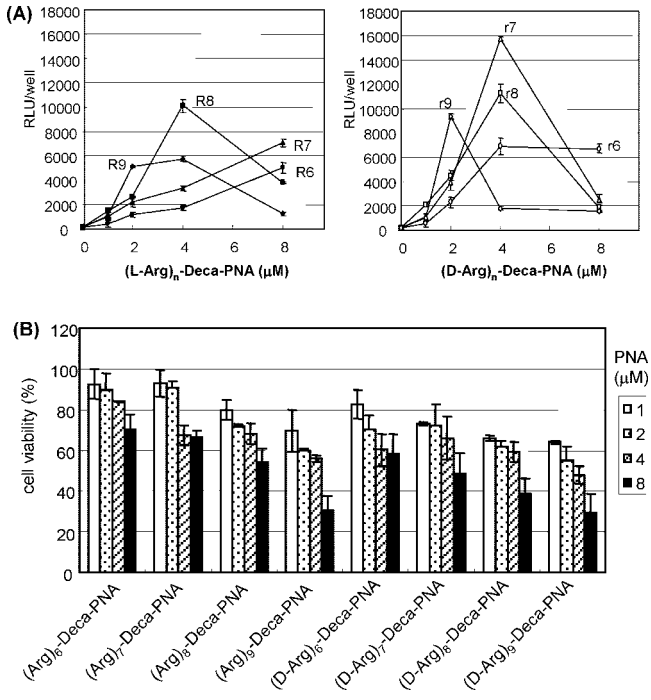

Figure 5. Relative cellular luciferase antisense activity in HeLa pLuc705 cells of PNAs conjugated to decanoic acid and different L-arginine or oligo D-arginine peptides: PNAs 2591 (R6, $(Arg)_6$-Deca-PNA), 3100 (R7, $(Arg)_7$-Deca-PNA); 3101(R8, $(Arg)_8$-Deca-PNA); 2592 (R9, $(Arg)_9$-Deca-PNA); 2739 (r6, $(D\text{-}Arg)_6$-Deca-PNA); 2801 (r7, $(D\text{-}Arg)_7$-Deca-PNA); 2802 (r8, $(D\text{-}Arg)_8$-Deca-PNA), and 2740 (r9, $(D\text{-}Arg)_9$-Deca-PNA) were used. Experimental details as in Figure 1. All tests were performed in triplicate and the results are given as the average values ± standard deviations (SD). (A) Luciferase activities were analyzed by Blight-Gro reagent (Promega) and given as relative light units (RLU/well). (B) Cellular viability was analyzed by the MTS-assay (Promega) and the data were normalized to the average value of non-PNA-treated sample.

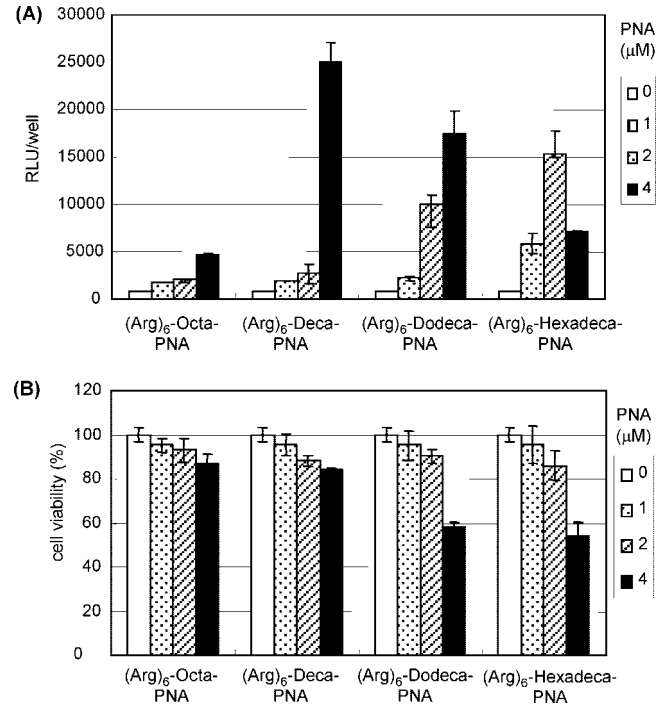

Figure 6. Relative cellular luciferase antisense activity and cellular toxicity in HeLa pLuc705 cells of hexaarginine-PNAs conjugated to different fatty acids (octanoic acid, decanoic acid, dodecanoic acid, or hexadecanoic acid) for the cellular uptake and the cellular toxicity in the HeLa pLuc705 ells. Experimental details as in Figure 1 using PNAs 2646 ($(Arg)_6$-Octa-PNA), 2591 ($(Arg)_6$-Deca-PNA), 2647 ($(Arg)_6$-Dodeca-PNA), and 2648 ($(Arg)_6$-Hexadeca-PNA). All tests were performed in triplicate and the results are given as the average values ± standard deviations (SD). (A) Luciferase activity was analyzed by Blight-Gro reagent (Promega) and is presented as relative light units (RLU/well). (B) Cellular viability was analyzed by MTS assay (Promega) and the data normalized to the average value of non-PNA-treated sample.

Calibur cytometer, and the mean fluorescence signal was calculated by *CellQuest* software.

RESULTS

The Tat peptide belongs to the group of cell penetrating peptides that was originally introduced for cellular delivery (*13*) and for which it has subsequently been shown that, although cellular uptake is quite efficient, this is almost exclusively via an endosomal pathway (*19*, *21*). Thus antisense PNA−Tat conjugates show only very limited activity in cell culture (*17*). However, the activity is dramatically enhanced by endosome disruption agents such as chloroquine (*26*) or lipophilic photosensitizers (*29*), as well as by calcium ions (*26*). Therefore we chose to prepare antisense PNA-Tat-fatty acid conjugates targeted to the aberrant splice site in the engineered luciferase gene in pLucHeLa 705 cells. This antisense assay yields a positive readout (luciferase activation) that is readily quantified with high sensitivity (*33*, *34*), and therefore allows reliable and quantitative comparison of different delivery methods (for antisense agents) (*9*, *11*).

The results presented in Figure 1 clearly demonstrate that while the PNA−Tat conjugate shows only very weak antisense activity in this assay, the analogous conjugate containing a decanoic acid attached to the ε-amino group of a lysine (Tat-Deca-PNA) is dramatically more active. Thus, at 2, 4, and 8 μM, the PNA−Tat conjugate induced luciferase activities of 80, 165, and 2832 RLU; while the corresponding values for the Tat-Deca-PNA were 1275, 11 696, and 22 747, respectively. The activity is further enhanced by having two decanoic acids in the conjugate (Deca-Tat-Deca-PNA) resulting in a luciferase activity of 14 310 at 2 μM—more than 150 times higher than that found for the pure Tat−PNA conjugate at this concentration. However, increased cellular toxicity is observed for the Tat−fatty acid conjugates and this is especially pronounced for the difatty acid compound. Thus, at higher concentrations (4 and 8 μM) the luciferase activation by this conjugate is markedly reduced, due to cellular toxicity. The control fatty acid−PNA conjugate (Deca-PNA) showed no activity.

In order to address whether conjugation of a lipophilic moiety (a fatty acid) to a cationic cell penetrating peptide domain could be a general principle to obtain increased cellular bioavailability we made a series of PNA conjugates based on oligo-arginines. The results presented in Figure 2 show that although hepta- and octa-arginine PNA conjugates as reported previously (*17*) show significantly higher antisense activity than the PNA−Tat conjugate, the activity is further enhanced several fold by fatty acid conjugation, and this enhancement is more pronounced at lower concentrations (1 and 2 μM), but is not seen at 8 μM due to increased toxicity of the fatty acid conjugates (Figures 2 and 5A,B). We also note that although the Tat-Deca-PNA conjugate is slightly less active than the Arg-Deca-PNA conjugates at lower concentrations, it exhibits the highest activity at 8 μM because of lower toxicity. The results also show that the position of the fatty acid relative to the peptide (amino terminal (e.g., Deca-$(D\text{-}Arg)_7$-PNA) or C-terminal between the peptide and the PNA (e.g., $(D\text{-}Arg)_7$-Deca-PNA) does not seem of major importance for activity.

In order to trace the intracellular path of the CatLip PNA a series of experiments were performed using fluorescein labeled

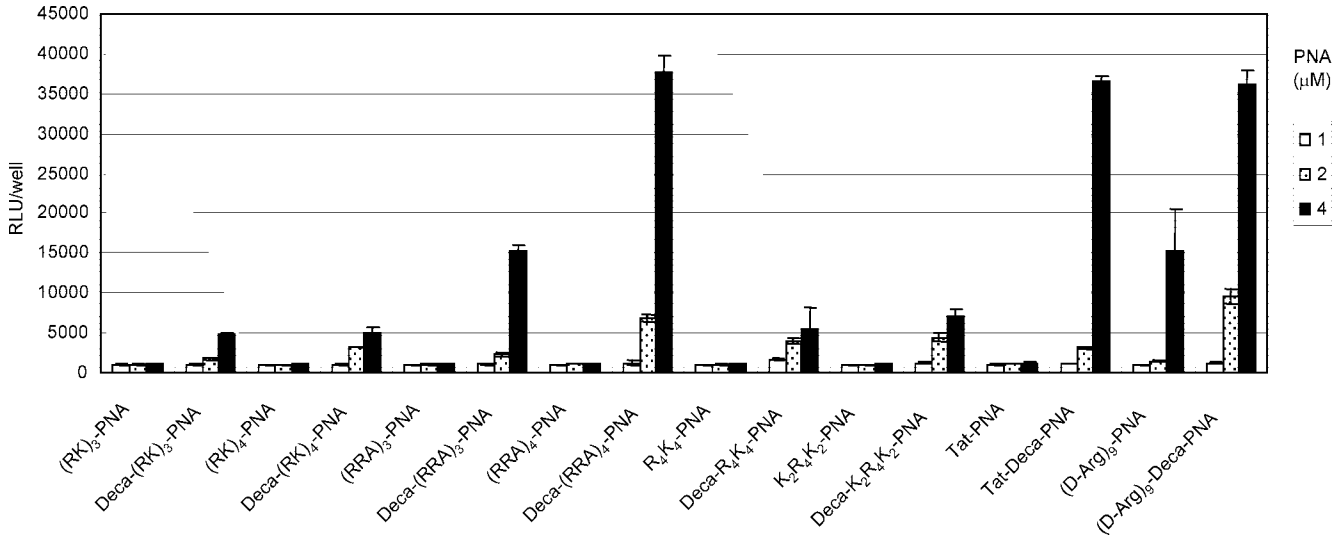

Figure 7. Relative cellular luciferase antisense activity in HeLa pLuc705 cells of PNAs conjugated to a cell penetrating peptide (CPP) or conjugated to both CPP and a decanoic acid. Experimental details as in Figure 1 using PNAs $(RK)_3$-PNA, Deca-$(RK)_3$-PNA, $(RK)_4$-PNA, Deca-$(RK)_4$-PNA, $(RRA)_3$-PNA, Deca-$(RRA)_3$-PNA, $(RRA)_4$-PNA, Deca$(RRA)_4$-PNA, R_4K_4−PNA, Deca-R_4K_4−PNA, $K_2R_4K_2$−PNA, Deca-$K_2R_4K_2$−PNA, Tat-PNA, Tat-Deca-PNA, $(D\text{-Arg})_9$-PNA, $(D\text{-Arg})_9$-Deca-PNA). Luciferase activity was analyzed by Blight-Gro reagent (Promega) and are presented as relative light units (RLU/well). All tests were performed in triplicate and the results are given as the average values ± standard deviations (SD).

octa-arginine PNA conjugates in combination with FACS and fluorescence microscopy analyses. These experiments first of all demonstrate that the lipophilic domain significantly increases the cellular attachment and possibly the uptake of, in this case, the PNA as indicated from the increased intracellular fluorescence observed by confocal fluorescence microscopy (Figure 3A), and quantitatively confirmed by FACS analysis (Figure 3B,C). However, it is quite clear from the fluorescence micrographs that the major part of the fluorescence still appears associated with endosomes, although some increase in diffuse cytoplasmatic and nuclear fluorescence may be present. Therefore, these results would indicate that the enhancing effect of the lipophilic domain on the nuclear antisense activity has contributions from both an increase in cellular (endosomal) uptake as well as a more favorable intracellular distribution with (slightly) reduced endosomal confinement, although even for these improved conjugates, most of the uptake is still within endosomal entrapment (*vide infra*).

The luciferase activity reading is a secondary effect from the molecular event of splicing redirection by the PNA, and we therefore found it important to verify the antisense effect directly at the mRNA level. The results show a very good correlation between the luciferase activity (Figure 4A) and the relative amount of correctly spliced luciferase mRNA (Figure 4B) at PNA concentrations up to 4 μM. However, at 6 μM where toxicity becomes a limiting factor and where the luciferase readings are reduced for two of the conjugates (Deca-Tat-Deca-PNA and $(D\text{-Arg})_8$-Deca-PNA), the RNA data shows increased relative correction activity also for these two PNAs, indicating an expected dose response on splice correction in spite of a decreased amount of total mRNA due to general toxicity.

The RNA data also confirm the strong enhancement exerted by the lipid moiety. Thus at 1 μM a relatively efficient peptide such as $(D\text{-Arg})_8$ only promotes 3% splicing correction when conjugated to the PNA, while $(D\text{-Arg})_8$-Deca-PNA under similar conditions promotes 44% splicing correction, corresponding to more than 10-fold enhancement. At higher concentrations the relative enhancement decreases gradually to less than 2-fold at 6 μM (Figure 4B). The CatLip conjugates are amphiphiles and thus most probably shall form micelles at a well defined cmc (critical micelle concentration). If micelle formation was instrumental for delivery efficiency, a clear concentration threshold (cooperative) effect would be expected. However, the data (e.g., Figure 5) do not specifically support such an effect, although some experiments may hint at nonlinearity of the dose dependence (e.g., Figures 1and 4). Thus more elaborate dose response studies are warranted to specifically address the issue of possible micelle formation by the conjugates and the eventual importance of such putative micelles on cellular uptake and also on toxicity. In this context it is also worth noting that toxicity of the conjugates does appear to be correlated to disruption of the cell membrane integrity as assayed using propidium iodide staining (Supporting Information) (which very much parallel the MTS toxicity assay), thereby indicating a direct physical membrane disturbance by the amphiphilic CatLip conjugates.

As a control for the sequence specificity of the antisense effect we synthesized a double base pair mismatch derivative of identical base composition (two base interchange) of the Tat-Deca-PNA and tested this. As expected, this PNA exhibited dramatically reduced activity both in terms of luciferase activity as well as in terms of mRNA correction activity (Figure 4C,D).

A comparison between D-Arg and L-Arg conjugates (Figure 5A) shows slightly higher activity of the non-natural D-form, clearly arguing against the involvement of specific receptor interactions of the peptide. These data also stress the very fine balance between uptake and toxicity. At 2 μM the activity increases with increasing number of arginines, but as the concentration increases, this order changes as the conjugates of the longer oligo-arginines are relatively more toxic than those of the shorter ones. Finally, the D-Arg conjugates show higher antisense activity but in parallel are also more toxic to the cells (Figure 5B).

This delicate activity/toxicity balance is further illustrated when analyzing the effect of the length of the fatty acid. For this experiment we chose the less active and less toxic hexa-arginine conjugate (Figure 6). Clearly, at lower PNA concentrations (up to 2 μM) the conjugates with longer fatty acid tails are the more active, but as the dodeca- and hexadeca- conjugates are clearly more toxic than the deca- conjugate, the latter shows the highest activity at 4 μM. Thus increased fatty acid length, and thus lipophilicity, produces more potent antisense agents but also compounds of higher cellular toxicity, and decanoic acid appears as a good compromise. A small series of arginine-rich peptides were tested for enhancement by fatty acid acylation

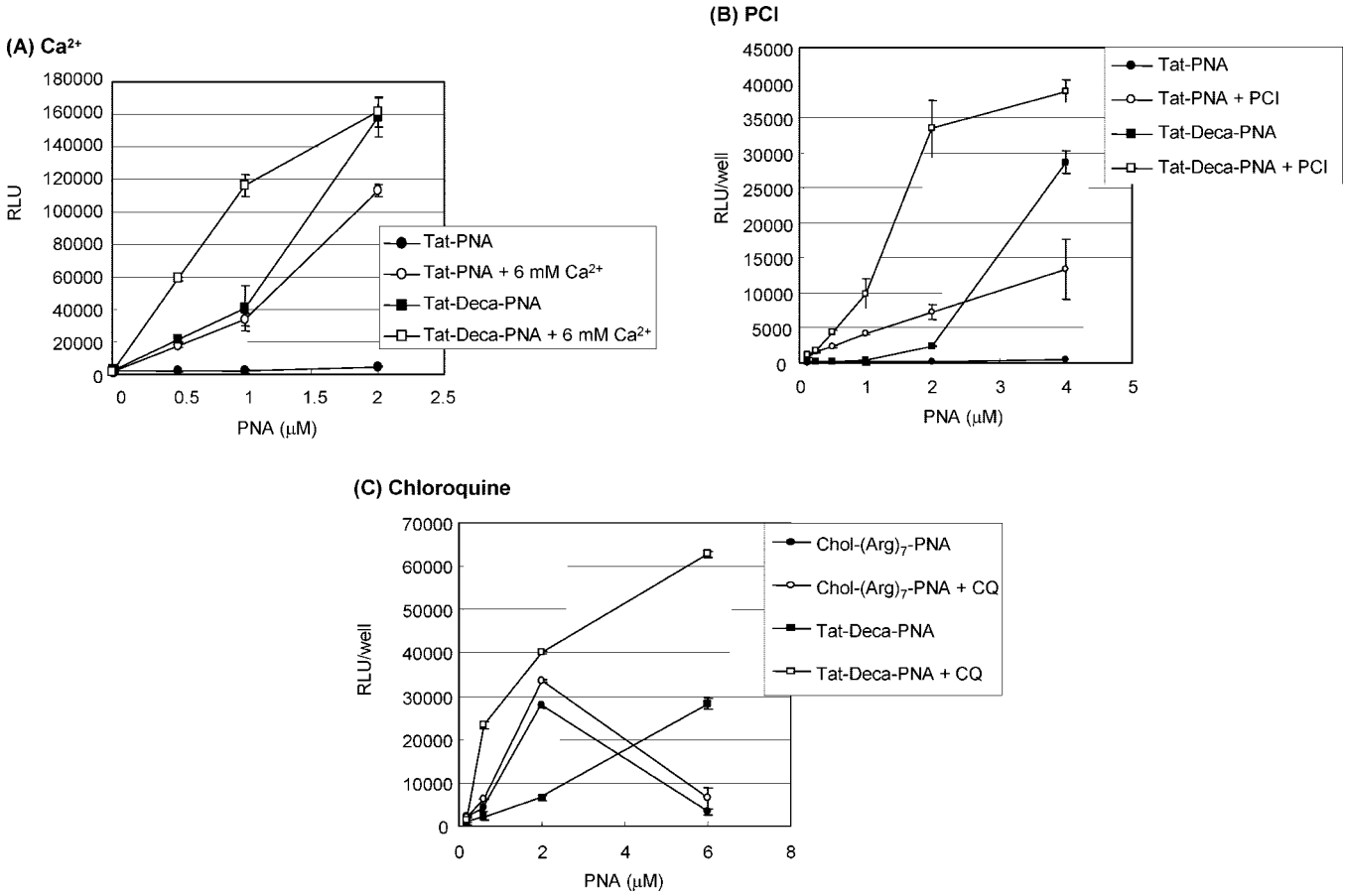

Figure 8. Effects of the endosome disruption agents on the cellular luciferase antisense activity in HeLa pLuc705 cells of PNA conjugates. HeLa pLuc705 cells (plated in the 96 well plate) were treated with the PNA in combination with one of the endosome disruption treatments (chloroquine (CQ), photochemical treatment (PCI) or Ca^{2+} treatment) and subjected to luciferase analysis. Luciferase activity was analyzed by Blight-Gro reagent (Promega) and are presented as relative light units (RLU/well). All tests were performed in triplicate and the results are given as the average values ± standard deviations (SD). (A) Cells were treated with the PNA (Tat-PNA, Tat-Deca-PNA) in combination with the Ca^{2+} treatment. For the Ca^{2+} treatment, cells were incubated with the PNA for 4 h in OPTI-MEM medium containing 6 mM Ca^{2+} and incubated further for 24 h after addition of the serum-containing growth medium without removing the OPTI-MEM medium. (B) Cells were treated with the PNA (2395, Tat-PNA; 2534, Tat-Deca-PNA) in combination with PCI treatment. For the administration of the photosensitizer, cells were incubated with 5 μg/mL $AlPcS_{2a}$ in the growth medium for 16−24 h before being subjected to the PNA treatment. Cells were then treated with the PNA for 4 h in OPTI-MEM medium and incubated further for 4 h after the replacement of the PNA solution with fresh serum-containing growth medium. Then cells were subjected to 10 min red light irradiation and incubated further for 24 h before being subjected to the luciferase analysis.

as illustrated by the data presented in Figure 7. It is clear that for all conjugates the acylated form exhibits superior activity relative the nonacylated form, but it is also noteworthy that the relative enhancement differs significantly for the various peptides as already demonstrated by the difference between the Tat and oligo-arginine conjugates. In particular, the very dramatic enhancement (up to 2 orders of magnitude) of the $(Arg\text{-}Arg\text{-}Ala)_4$ conjugate upon fatty acid conjugation is interesting in terms of the molecular mechanism(s) of the cellular uptake as this conjugate resembles the behavior of the Tat peptide more than that of the oligo-arginines. These data indicate a clear possibility for optimizing the peptide-fatty acid (CatLip) moiety in terms of delivery/toxicity ratio.

We have previously found that the antisense activity of CPP−PNA conjugates is significantly augmented in the presence of submillimolar concentrations of chloroquine or millimolar concentrations of calcium ions (*26*) or by photochemical internalization (PCI) using photosensitizers (*29*), agents that all promote endosome disruption. In order to address whether these agents could also enhance the effect of the fatty acid conjugates, we studied the effect of chloroquine, Ca^{2+}, and PCI treatment on the antisense activity of the Tat-Deca-PNA conjugate. In all cases a significant enhancement was observed especially at lower concentrations (Figure 8). However, the relative enhancement is much more pronounced for the Tat-PNA (10−25-fold) than for the Tat-Deca-PNA (1−15-fold) (Figure 8A), possibly indicating that the fatty acid moiety is facilitating endosomal escape or is supporting a nonendosomal pathway for uptake. Interestingly, we note that a CatLip construct based on a cholesterol ester (PNA 3016) which exhibits considerably higher antisense activity than the Tat−decanoic acid conjugate (PNA 2534) (but also higher cellular toxicity) is not enhanced by chloroquine (Figure 8C). Further studies are needed to determine whether this very interesting behavior is due to a nonendosomal route of entry or to efficient endosomal escape by this type of CatLip conjugates.

CONCLUSIONS

The present results clearly demonstrate that the nuclear antisense activity of PNA oligomers can be dramatically enhanced by conjugation to a CatLip domain consisting of a cationic peptide and a fatty acid, and that this enhancement (dependent on the specific peptide) is up to 2 orders of magnitude higher than that obtained by using the peptide alone. The antisense effect of the CatLip PNAs is further enhanced by endosome disruptive agents but the enhancing effect is significantly less than that seen for the corresponding PNA−peptide conjugates, thereby giving a clear indication that part, but not all, of the effect of the lipophilic domain is due to facilitation of endosomal escape. Obviously the lipophilic

domain supports the interaction of the PNA conjugates with the cellular (and endosomal) membranes and most likely contributes to membrane destabilization (as also indicated by the increased cellular toxicity of these conjugates), which could also facilitate nonendosomal, direct passage through the membrane. Increased cellular association was indeed observed through FACS and fluorescence microscopy analyses. These experiments also illustrate that even for the most effective CatLip conjugates a major part of the antisense agent was still trapped in endosomes and increased activity could be obtained using endosome releasing agents such as chloroquine. The cholesteryl conjugate (which also exhibit high toxicity) could be an example of a conjugate for which the endosomal route is not the more significant one. Clearly, the present results open the door to a new family of drug delivery conjugates, and further studies will reveal the interplay between different (peptidic as well as nonpeptidic) cationic domains and lipophilic domains in terms of cellular delivery potency, mechanism(s) of cellular entry and toxicity in various cell types. Furthermore, the behavior of such conjugates for increasing the *in vivo* bioavailability of potential drugs could be very interesting. Finally, there is little doubt that the delivery properties of CatLip domains may be optimized far beyond the limited examples studied so far.

ACKNOWLEDGMENT

This work was supported by the Lundbeck Foundation, The Danish Cancer Foundation and the European Commission (6th FP EMIL and SNIPER contracts LSHC-CT-2004−503569 & LSHB-CT-2004−005204). The authors would like to acknowledge Dr. Anders E. Pedersen for help with flow cytometry, Dr. Darya Kiryushko for help with confocal laser microscopy, and Ms. Jolanta Ludvigsen and MSc. Nadia Bendifallah for synthesizing the PNA conjugates.

Supporting Information Available: Additional information as described in the text. This material is available free of charge via the Internet at http://pubs.acs.org.

Note Added after ASAP Publication: This paper was modified on August 6, 2008, to include the following additional information. The authors note that a paper reporting analogous delivery strategy has been published. See: Hu, J., and Corey, D. R. (2007) Inhibiting Gene Expression with Peptide Nucleic Acid (PNA)-Peptide Conjugates That Target Chromosomal DNA. *Biochemistry 46*, 7581−7589.

LITERATURE CITED

(1) Dass, C. R. (2004) Lipoplex-mediated delivery of nucleic acids: factors affecting in vivo transfection. *J. Mol. Med. 82*, 579–91.
(2) Kumar, V. V., Singh, R. S., and Chaudhuri, A. (2003) Cationic transfection lipids in gene therapy: successes, set-backs, challenges and promises. *Curr. Med. Chem. 10*, 1297–306.
(3) Liu, D., Ren, T., and Gao, X. (2003) Cationic transfection lipids. *Curr. Med. Chem. 10*, 1307–15.
(4) Nicolazzi, C., Garinot, M., Mignet, N., Scherman, D., and Bessodes, M. (2003) Cationic lipids for transfection. *Curr. Med. Chem. 10*, 1263–77.
(5) Nielsen, P. E., Egholm, M., Berg, R. H., and Buchardt, O. (1991) Sequence-selective recognition of DNA by strand displacement with a thymine-substituted polyamide. *Science 254*, 1497–500.
(6) Summerton, J., and Weller, D. (1997) Morpholino antisense oligomers: design, preparation, and properties. *Antisense Nucleic Acid Drug Dev. 7*, 187–95.
(7) Hamilton, S. E., Simmons, C. G., Kathiriya, I. S., and Corey, D. R. (1999) Cellular delivery of peptide nucleic acids and inhibition of human telomerase. *Chem. Biol. 6*, 343–51.
(8) Morcos, P. A. (2001) Achieving efficient delivery of morpholino oligos in cultured cells. *Genesis 30*, 94–102.
(9) Rasmussen, F. W., Bendifallah, N., Zachar, V., Shiraishi, T., Fink, T., Ebbesen, P., Nielsen, P. E., and Koppelhus, U. (2006) Evaluation of transfection protocols for unmodified and modified peptide nucleic acid (PNA) oligomers. *Oligonucleotides 16*, 43–57.
(10) Bendifallah, N., Kristensen, E., Dahl, O., Koppelhus, U., and Nielsen, P. E. (2003) Synthesis and properties of ester-linked peptide nucleic acid prodrug conjugates. *Bioconjugate Chem. 14*, 588–92.
(11) Shiraishi, T., Bendifallah, N., and Nielsen, P. E. (2006) Cellular delivery of polyheteroaromate-peptide nucleic acid conjugates mediated by cationic lipids. *Bioconjugate Chem. 17*, 189–94.
(12) Silhol, M., Tyagi, M., Giacca, M., Lebleu, B., and Vives, E. (2002) Different mechanisms for cellular internalization of the HIV-1 Tat-derived cell penetrating peptide and recombinant proteins fused to Tat. *Eur. J. Biochem. 269*, 494–501.
(13) Vives, E., Brodin, P., and Lebleu, B. (1997) A truncated HIV-1 Tat protein basic domain rapidly translocates through the plasma membrane and accumulates in the cell nucleus. *J. Biol. Chem. 272*, 16010–7.
(14) Derossi, D., Joliot, A. H., Chassaing, G., and Prochiantz, A. (1994) The third helix of the Antennapedia homeodomain translocates through biological membranes. *J. Biol. Chem. 269*, 10444–50.
(15) Mae, M., and Langel, U. (2006) Cell-penetrating peptides as vectors for peptide, protein and oligonucleotide delivery. *Curr. Opin. Pharmacol. 6*, 509–14.
(16) Moulton, H. M., Nelson, M. H., Hatlevig, S. A., Reddy, M. T., and Iversen, P. L. (2004) Cellular uptake of antisense morpholino oligomers conjugated to arginine-rich peptides. *Bioconjugate Chem. 15*, 290–9.
(17) Bendifallah, N., Rasmussen, F. W., Zachar, V., Ebbesen, P., Nielsen, P. E., and Koppelhus, U. (2006) Evaluation of cell-penetrating peptides (CPPs) as vehicles for intracellular delivery of antisense peptide nucleic acid (PNA). *Bioconjugate Chem. 17*, 750–8.
(18) Wender, P. A., Mitchell, D. J., Pattabiraman, K., Pelkey, E. T., Steinman, L., and Rothbard, J. B. (2000) The design, synthesis, and evaluation of molecules that enable or enhance cellular uptake: peptoid molecular transporters. *Proc. Natl. Acad. Sci. U.S.A. 97*, 13003–8.
(19) Koppelhus, U., Awasthi, S. K., Zachar, V., Holst, H. U., Ebbesen, P., and Nielsen, P. E. (2002) Cell-dependent differential cellular uptake of PNA, peptides, and PNA-peptide conjugates. *Antisense Nucleic Acid Drug Dev. 12*, 51–63.
(20) Drin, G., Cottin, S., Blanc, E., Rees, A. R., and Temsamani, J. (2003) Studies on the internalization mechanism of cationic cell-penetrating peptides. *J. Biol. Chem. 278*, 31192–201.
(21) Richard, J. P., Melikov, K., Vives, E., Ramos, C., Verbeure, B., Gait, M. J., Chernomordik, L. V., and Lebleu, B. (2003) Cell-penetrating peptides. A reevaluation of the mechanism of cellular uptake. *J. Biol. Chem. 278*, 585–90.
(22) Fotin-Mleczek, M., Fischer, R., and Brock, R. (2005) Endocytosis and cationic cell-penetrating peptides-a merger of concepts and methods. *Curr. Pharm. Des. 11*, 3613–28.
(23) Nakase, I., Niwa, M., Takeuchi, T., Sonomura, K., Kawabata, N., Koike, Y., Takehashi, M., Tanaka, S., Ueda, K., Simpson, J. C., Jones, A. T., Sugiura, Y., and Futaki, S. (2004) Cellular uptake of arginine-rich peptides: roles for macropinocytosis and Actin rearrangement. *Mol. Ther. 10*, 1011–22.
(24) El-Andaloussi, S., Johansson, H. J., Lundberg, P., and Langel, U. (2006) Induction of splice correction by cell-penetrating peptide nucleic acids. *J Gene Med*.
(25) Wadia, J. S., Stan, R. V., and Dowdy, S. F. (2004) Transducible TAT-HA fusogenic peptide enhances escape of TAT-fusion proteins after lipid raft macropinocytosis. *Nat. Med. 10*, 310–5.

(26) Shiraishi, T., Pankratova, S., and Nielsen, P. E. (2005) Calcium ions effectively enhance the effect of antisense peptide nucleic acids conjugated to cationic tat and oligoarginine peptides. *Chem. Biol. 12*, 923–9.

(27) Turner, J. J., Ivanova, G. D., Verbeure, B., Williams, D., Arzumanov, A. A., Abes, S., Lebleu, B., and Gait, M. J. (2005) Cell-penetrating peptide conjugates of peptide nucleic acids (PNA) as inhibitors of HIV-1 Tat-dependent trans-activation in cells. *Nucleic Acids Res. 33*, 6837–49.

(28) Boe, S., Longva, A. S., and Hovig, E. (2007) Photochemically induced gene silencing using small interfering RNA molecules in combination with lipid carriers. *Oligonucleotides 17*, 166–73.

(29) Shiraishi, T., and Nielsen, P. E. (2006) Photochemically enhanced cellular delivery of cell penetrating peptide-PNA conjugates. *FEBS Lett. 580*, 1451–6.

(30) Abes, S., Turner, J. J., Ivanova, G. D., Owen, D., Williams, D., Arzumanov, A., Clair, P., Gait, M. J., and Lebleu, B. (2007) Efficient splicing correction by PNA conjugation to an R6-Penetratin delivery peptide. *Nucleic Acids Res. 35*, 4495–502.

(31) Azzam, T., and Domb, A. J. (2004) Current developments in gene transfection agents. *Curr. Drug Delivery 1*, 165–93.

(32) Futaki, S., Ohashi, W., Suzuki, T., Niwa, M., Tanaka, S., Ueda, K., Harashima, H., and Sugiura, Y. (2001) Stearylated arginine-rich peptides: a new class of transfection systems. *Bioconjugate Chem. 12*, 1005–11.

(33) Kang, S. H., Cho, M. J., and Kole, R. (1998) Up-regulation of luciferase gene expression with antisense oligonucleotides: implications and applications in functional assay development. *Biochemistry 37*, 6235–9.

(34) Kang, S. H., Zirbes, E. L., and Kole, R. (1999) Delivery of antisense oligonucleotides and plasmid DNA with various carrier agents. *Antisense Nucleic Acid Drug Dev. 9*, 497–505.

(35) Christensen, L., Fitzpatrick, R., Gildea, B., Petersen, K. H., Hansen, H. F., Koch, T., Egholm, M., Buchardt, O., Nielsen, P. E., Coull, J., and Berg, R. H. (1995) Solid-phase synthesis of peptide nucleic acids. *J. Pept. Sci. 1*, 175–83.

(36) Shiraishi, T., and Nielsen, P. E. (2006) Enhanced delivery of cell-penetrating peptide-peptide nucleic acid conjugates by endosomal disruption. *Nat. Protocols 1*, 633–36.

BC800068H

Supporting Information

PNA cellular uptake studies with propidium iodide (PI) counter staining. For uptake analysis, exponentially growing HeLa pLuc705 cells were plated in 4-well chamber slides (Nunc) the day before treatment. The cells were treated with the fluorescein-labeled PNA (Fl-CPP-PNA(3266), Fl-CL-PNA(3265)) by incubating with the PNAs (0.6, 2 and 6 μM) in OPTI-MEM medium (serum free) for 4 h and further 20 h after adding the equal volume of growth medium (including 20% FBS) without removing the PNA solutions. After 24 h the cells were counter stained with 1 μg/ml PI for 10 min at 37 ^{o}C before subjected to microscopy. Living cells (without fixation) were visualized using a fluorescence microscope (DIALUX 22EB, LEITZ WETZLAR (Germany)) at 500x magnification with appropriate filter blocks (I2/3 and N2 respectively for PI and FITC).

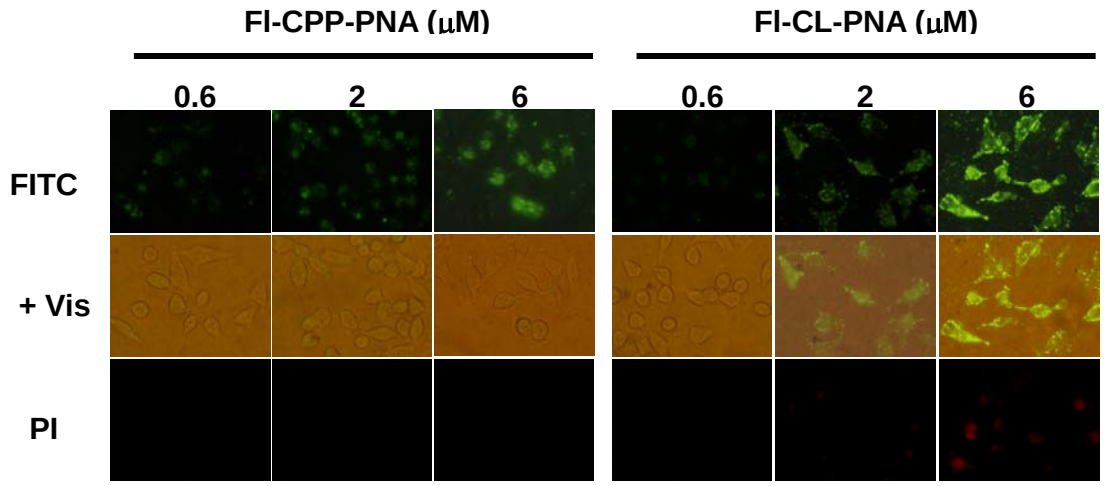

PNA CatLip Conjugates. Sequences, names and HPLC & MALDI-TOF mass spectrometry characterization

PNA no.	Name	Sequence[a]	Mass: found(calcd)	Purity (%)[b]
2395	Tat-PNA	H-GRKKRRQRRRPPQ-eg1-CCTCTTACCTCAGTTACA-NH_2	6611 (6612)	95
2456	Deca-PNA	Deca-eg1-CCTCTTACCTCAGTTACA-NH_2	5064 (5065)	98
2534	Tat-Deca-PNA	H-GRKKRRQRRRPPQ-Lys(Deca)-Gly-CCTCTTACCTCAGTTACA-NH_2	6808 (6808)	98
2821	Deca-Tat-Deca-PNA	H-Lys(Deca)GR KKR RQR RRP PQ-Lys(Deca)-Gly-CCTCTTACCTCAGTTACA-NH_2	7086 (7088)	90
2785	(D-Arg)7-PNA	H-$(D\text{-}Arg)_7$-Gly-CCTCTTACCTCAGTTACA-NH_2	5913 (5916)	90
2801	(D-Arg)7-Deca-PNA	H-$(D\text{-}Arg)_7$-Lys(Deca)-Gly-CCTCTTACCTCAGTTACA-NH_2	6194 (6198)	98
2786	Deca-(D-Arg)7-PNA	Deca-$(D\text{-}Arg)_7$-Gly-CCTCTTACCTCAGTTACA-NH_2	6075 (6070)	90
2787	(D-Arg)8-PNA	H-$(D\text{-}Arg)_8$-Gly-CCTCTTACCTCAGTTACA-NH_2	6068 (6072)	90
2802	(D-Arg)8-Deca-PNA	H-$(D\text{-}Arg)_8$-Lys(Deca)-Gly-CCTCTTACCTCAGTTACA-NH_2	6357 (6354)	95
2788	Deca-(D-Arg)8-PNA	Deca-$(D\text{-}Arg)_8$-Gly-CCTCTTACCTCAGTTACA-NH_2	6226 (6226)	90
2752	Mismatch 2534	H-GRKKRRQRRRPPQ-Lys(Deca)-Gly-CCTCT**G**ACCTCA**T**TTACA-NH_2	6808 (6808)	98
2591	(Arg)6-Deca-PNA	H-$(Arg)_6$-Lys(Deca)-Gly-CCTCTTACCTCAGTTACA-NH_2	6043 (6042)	90
3100	(Arg)7-Deca-PNA	H-$(L\text{-}Arg)_7$-Lys(Deca)-Gly-CCTCTTACCTCAGTTACA-NH_2	6202 (6199)	95
3101	(Arg)8-Deca-PNA	H-$(L\text{-}Arg)_8$-Lys(Deca)-Gly-CCTCTTACCTCAGTTACA-NH_2	6358 (6355)	95
2592	(Arg)9-Deca-PNA	H-$(Arg)_9$-Lys(Deca)-Gly-CCTCTTACCTCAGTTACA-NH_2	6508 (6510)	95
2739	(D-Arg)6-Deca-PNA	H-$(D\text{-}Arg)_6$-Lys(Deca)-Gly-CCTCTTACCTCAGTTACA-NH_2	6055 (6042)	95
2740	(D-Arg)9-Deca-PNA	H-$(D\text{-}Arg)_9$-Lys(Deca)-Gly-CCTCTTACCTCAGTTACA-NH_2	6502 (6511)	98
2646	(Arg)6-Octa-PNA	H-$(Arg)_6$-Lys(Octa)-CCTCTTACCTCAGTTACA-NH_2	5960 (5958)	#
2647	(Arg)6-Dodeca-PNA	H-$(Arg)_6$-Lys(Dodeca)-CCTCTTACCTCAGTTACA-NH_2	6017 (6014)	90
2648	(Arg)6-Hexadeca-PNA	H-$(Arg)_6$-Lys(Hexadeca)-CCTCTTACCTCAGTTACA-NH_2	6077 (6070)	95
2822	(RK)3-PNA	H-$(D\text{-}Arg\text{-}D\text{-}Lys)_3$-Gly-CCTCTTACCTCAGTTACA-$NH_2$	5675 (5676)	90

2823	Deca-(RK)3-PNA	H-Lys(Deca)-(D-Arg-D-Lys)$_3$-Gly-CCTCTTACCTCAGTTACA-NH_2	5957 (5958)	75
2824	(RK)4-PNA	H-(D-Arg D-Lys)$_4$-Gly-CCTCTTACCTCAGTTACA-NH_2	5959 (5960)	90
2825	Deca-(RK)4-PNA	H-Lys(Deca)-(D-Arg D-Lys)$_4$-Gly-CCTCTTACCTCAGTTACA-NH_2	6242 (6243)	75
2826	(RRK)3-PNA	H-(D-Arg D-Arg-Ala)$_3$-Gly-CCTCTTACCTCAGTTACA-NH_2	5971 (5973)	90
2827	Deca-(RRK)3-PNA	H-Lys(Deca)-(D-Arg-D-Arg Ala)$_3$-Gly-CCTCTTACCTCAGTTACA-NH_2	6253 (6255)	75
2828	(RRK)4-PNA	H-(D-Arg D-Arg Ala)$_4$-Gly-CCTCTTACCTCAGTTACA-NH_2	6349 (6352)	90
2829	Deca-(RRK)4-PNA	H-Lys(Deca)-(D-Arg-D-Arg Ala)$_4$-Gly-CCTCTTACCTCAGTTACA-NH_2	6637 (6639)	75
2830	R4K4-PNA	H-(D-Arg)4(D-Lys)4-Gly-CCTCTTACCTCAGTTACA-NH_2	5960 (5960)	75
2831	Deca-R4K4-PNA	H-Lys(Deca)-(D-Arg)4(D-Lys)$_4$-Gly-CCTCTTACCTCAGTTACA-NH_2	6242 (6243)	75
2832	K2R4K2-PNA	H-(D-Lys)$_2$(D-Arg)$_4$(D-Lys)$_2$-Gly-CCTCTTACCTCAGTTACA-NH_2	5962 (5960)	75
2833	Deca-K2R4K2-PNA	H-Lys(Deca)-(D-Lys)$_2$(D-Arg)4(D-Lys)$_2$-CCTCTTACCTCAGTTACA-NH_2	6242 (6243)	90
2738	(D-Arg)9-PNA	H-(D-Arg)$_9$-Gly-CCTCTTACCTCAGTTACA-NH_2	6235 (6228)	90
3016	Chol-(Arg)7-PNA	Cholesteryl hemisuccinate-(Arg)$_7$-eg1-CCTCTTACCTCAGTTACA-NH_2	6474 (6472)	98
3266	Fl-(Arg)8-PNA	H-Flk-(D-Arg)$_8$-AATCTCACCTGATAG T-NH_2[c]	6100 (6107)	98
3265	Fl-(Arg)8-Deca-PNA	Deca-Flk-(D-Arg)$_8$-AATCTCACCTGATAGT-NH_2	6255 (6261)	98

[a)]The sequences of cell-penetrating peptides are written using the standard one-letter amino acid symbols. The sequences of PNA conjugates are written from N-terminal-end to C-terminal –end. eg1 (8-amino-3,6-dioxaoctanoic acid) is an ethylene glycol linker. [b)]98 corresponds to single peak; 95 corresponds to single peak with slight foot; 90 corresponds to single peak with slight foot and/or shoulder peak; 75 corresponds to single peak with significant foot and/or shoulder/satellite peaks; # the HPLC analysis showed a close, sharp double peak, whereas the MALDI analysis showed only one signal of the expected mass. [c)] Flk is a monomer with fluorescein (Fl) attached to the ε-amino group of a lysine residue (Lohse J, Nielsen PE, Harrit N, Dahl O *Bioconjugate Chemistry* 1997, 8: 503-509.).

Octa-Substituted Anionic Porphyrins: Topoisomerase I Inhibition and Tumor Cell Apoptosis Induction

Baoping Zhai,[†,‡] Li Shuai,[†,‡] Li Yang,[‡] Xiaocheng Weng,[‡] Lin Wu,[‡] Shaoru Wang,[‡] Tian Tian,[‡] Xiaojun Wu,[‡] Xiang Zhou,*[,‡,§] and Congyi Zheng[§]

College of Chemistry and Molecular Sciences, State Key Laboratory of Virology, and School of Life Science, Wuhan University, Hubei, Wuhan 430072, PR China. Received December 17, 2007; Revised Manuscript Received March 30, 2008

β-Octabromo-*meso*-tetra(4-carboxyl)phenyl porphyrin **6** and β-octaphenyl-*meso*-tetra(4-carboxyl)phenyl porphyrin **8** were synthesized and fully characterized by ^{1}H NMR, UV, and HRMS. Their cytotoxicities to tumor cells were tested using MTT assays. One kind of tumor cell apoptosis induced by these anionic porphyrins under irradiation was examined by flow cytometric analysis. The inhibition of Topo I (Topoisomerase I) indicates that Topo I preferentially binds to the synthesized compounds, thus blocking the interaction between Topo I and DNA. The results implied that compounds **4**, **6**, and **8** are potential inhibitors to Topo I, which might be one of the important factors inducing apoptosis of tumor cells.

INTRODUCTION

Porphyrins have found wide application in catalysis, materials, and medicine (*1–6*) because of their physical, chemical, and biological properties. When porphyrin molecules are modified by the use of peripheral substitutents, they could show very interesting functions due to the change in electronic and steric properties (*7–9*). Therefore, the substitution at β-positions is of extraordinary importance. It has been found that substitutents at the β-positions of porphyrins exert much larger steric and electronic effects on the porphyrin ring than substiutents at the *meso*-aryl positions. What's more, β-substitutents can induce the porphyrin ring into a nonplanar conformation, which might mimic control of the the biological properties in tetrapyrrole systems like the photosynthetic centers, vitamin B12 and P-450 (*10–12*).

Since Fiel and collaborators studied the interaction between porphyrins and nucleic acid (*13*), a variety of porphyrins have been synthesized and their abilities to bind to DNA have been confirmed (*14–16*). Several kinds of porphyrins have been found to induce cell apoptosis (*17*). Nevertheless, so far most reported works concerning either the interaction between porphyrins and DNA or the induction of tumor cell apoptosis are chiefly concentrated on cation porphyrins such as TMPyP (tetra-(4-*N*-methylpyridium)porphyrin). In fact, as is proven in previous work, negatively charged porphyrins are more membrane permeable than cation porphyrins, which makes the porphyrin molecules biologically more active (*18*). Recently, Vicente and co-workers (*19*) have reported the cellular uptake and animal toxicity of a anionic porphyrin, tetra(carboranylphenyl)-tetrabenzoporphyrin. Their results suggest that anionic porphyrins might have more favorable abilities to interact with tumor cells. In this paper, we have designed and synthesized a series of anionic porphyrins with β-octabromo or β-octaphenyl substitution; meanwhile, carboxyl groups are introduced onto the *meso*-aryl positions. Some initial studies on the inducement of tumor cell apoptosis by the synthesized compounds have also been carried out. The results reveal that the inhibition of topoisomerase I activity by the synthesized compounds might be one of the key points to tumor cell apoptosis, which is in accord with the reported fact that DNA topoisomerases are responsible for cell death via the apoptosis pathway (*20, 21*).

EXPERIMENTAL PROCEDURES

Synthesis of Test Compounds. Desired compounds were synthesized according to the procedures shown in Scheme 1. Compound **5** was synthesized with reference to Day's report (*8*). The synthesis of β-octasubstituted-*meso*-tetra-(4-carboxyl)phenyl porphyrin **6** and **8** was involved in Suzuki coupling chemistry starting from β-octabromoporphyrin. Porphyrins **3** (*22*) and **4** (*23*) were obtained from mixing methyl 4-formylbenzoate **1** or 4-carboxybenzaldehyde **2** and pyrrole in refluxing propionic acid with yields of 22.4% and 10.5%, respectively. β-Octabromo-substituted porphyrin **5** was prepared from porphyrin **3**. Porphyrins **6** and **8** were traced by HPLC (Supporting Information, Figure S1).

Synthesis of β-octabromo-*meso*-tetrakis (4-carboxyphenyl)porphyrin methyl ester (**5**). Porphyrin **3** (400 mg, 0.47 mmol) was dissolved in 150 mL of chloroform followed by the addition of $Cu(OAc)_2 \cdot H_2O$ (760 mg, 3.81 mmol, 8 equiv). The reaction mixture was stirred at reflux for 30 min. After complete conversion to copper porphyrin as detected by TLC, 4 mL liquid Br_2 was added to the reaction mixture directly. The solution was continually stirred for about 1 day at room temperature. Aqueous solution of sodium thiosulfate was added to quench the reaction. After removal of the excessive bromine, the reaction mixture was washed by H_2O several times, and then 30 mL of perchloric acid was added to the solution. The reaction mixture was stirred for about 12 h for demetallization. The organic layer was separated and washed with aqueous and a solution of sodium bicarbonate and water, and dried over anhydrous Na_2SO_4. The organic mixture was rotary-evaporated to give a solid. The crude product was purified by column chromatography on silica gel using chloroform/ethyl acetate 60:1 as eluent to give porphyrin **5** (478 mg, 68.4% yield). ^{1}H NMR

* Corresponding author. Prof. Xiang Zhou, Tel: (086) 027-61056559. Fax: (086) 027-87663380. E-mail: xzhou@whu.edu.cn.

† Both authors contributed equally to this work.

‡ College of Chemistry and Molecular Sciences, State Key Laboratory of Virology.

§ State Key Laboratory, School of Life Science.

[1]Abbreviations: Topo I, Topoisomerase I; TMPyP, tetra-(4-*N*-methylpyridium) porphyrin; CPT, camptothecin; CT DNA, calf thymus DNA.

10.1021/bc7004686 CCC: $40.75 © 2008 American Chemical Society
Published on Web 07/30/2008

Scheme 1[a]

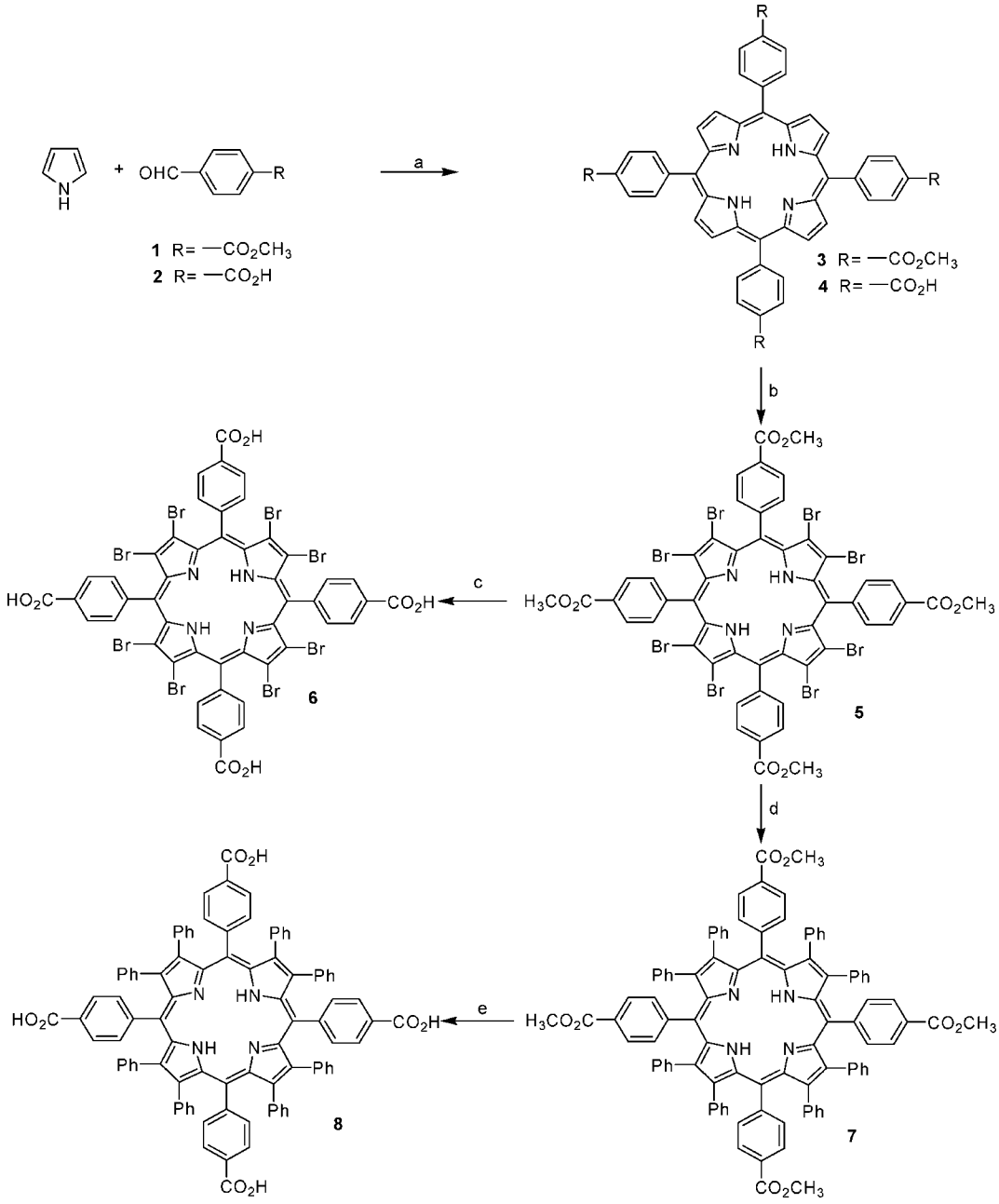

[a] (a) Propionic acid, reflux, **3** 22.4%, **4** 10.5%; (b) (1) $Cu(OAc)_2$, $CHCl_3$, reflux, 0.5 h; (2) Br_2, $CHCl_3$, rt, 1 day; (3) $HClO_4$, $CHCl_3$, rt, 12 h, 68.4%; (c) THF, 2 N KOH 3 day, 86.7%; (d) $PhB(OH)_2$, K_2CO_3, $Pd(Ph_3P)_4$, toluene/DMF(v/v 9:1), 95−105 °C, 7 days, **7** 52.9%; (e) THF, 2 N KOH 3 day, 92.1%.

($CDCl_3$, 300 MHz): δ (ppm), 8.47−8.44 (d, J = 7.8 Hz, 8 H), 8.32−8.30 (d, J = 8.1 Hz, 8 H), 4.10 (s, 12 H). UV−vis ($CHCl_3$): λ_{max} (nm, log ϵ) = 370 (4.40), 472 (5.26), 625 (4.10). MALDI-TOF HRMS for $C_{52}H_{30}Br_8N_4O_8$ [M^+ + H] calcd 1478.5527, found 1478.5382.

Synthesis of β-octaphenyl-*meso*-tetrakis(4-carboxyphenyl)porphyrin methyl ester (**7**). A 100 mL Teflon-stoppered flask was charged with porphyrin **5** (400 mg 0.27 mmol), $PhB(OH)_2$ (656 mg, 5.4 mmol, 20 equiv), $(Ph_3P)_4Pd$ (96 mg, 0.08 mmol, 0.3 equiv), anhydrous K_2CO_3 (1500 mg, 10.8 mmol, 40 equiv), DMF (6 mL), and toluene (54 mL). The brown suspension was degassed by the freeze−pump−thaw method (three cycles), and then was heated at 90−100 °C under N_2 for 7 days. The reaction mixture was worked up by extracting with 50 mL $CHCl_3$ and washed with water and brine. The organic layer was dried over anhydrous Na_2SO_4 and rotary-evaporated to dryness. The crude product was purified by column chromatography on silica gel using chloroform/ethyl acetate 20:1 as eluent to give porphyrin **7** (208 mg, 52.9% yield). ^{1}H NMR ($CDCl_3$, 300 MHz): δ (ppm), 7.63−7.60 (d, J = 7.2 Hz, 8 H), 7.40−7.37 (d, J = 9.1 Hz, 8 H), 6.69−6.67 (m, 40 H), 3.99 (s, 12 H). UV−vis ($CHCl_3$): λ_{max} (nm, log ϵ) = 467 (5.19), 562 (4.03), 611 (3.96). ESI HRMS for $C_{100}H_{70}N_4O_8$ [M^+ + H] calcd 1455.5266, found 1455.5310.

Synthesis of β-octabromo-*meso*-tetrakis(4-carboxyphenyl)porphyrin (**6**). Porphyrin **5** (30 mg, 0.02 mmol) was dissolved in 5 mL of THF and 3 mL of a 2 M aqueous solution of potassium hydroxide was added. The solution was stirred in a sealed flask at room temperature, for 3 days. The aqueous phase was collected and the pH lowered, using a 1 M solution of hydrochloric acid, until precipitation of the porphyrin. The precipitate was washed with water and dried under vacuum to

Table 1. Inhibitory Percentage of Porphyrins 6, 8, and 4 to Tumor Cell Line 7901 (%)

Concentration of compounds (μM)		0.01	0.1	0.5	1	5	10	15	20	25	30	50	100
6	irradiation	23.59	18.50	21.09	18.54	23.47	52.13		71.17		96.46	99.33	99.63
	dark	−10.67	−4.70	1.17	−3.4	−6.2	4.9		31.41		60.38	97.54	94.13
8	irradiation	−2.94	−0.07	−3.04	−5.08	−3.74	5.22	33.79	52.00	66.80	88.50	96.63	97.79
	dark	−0.41	2.42	−0.64	1.12	5.73	12.08	32.64	44.45	58.05	69.84	95.44	95.65
4	irradiation	19.40	19.65	16.23	28.87	69.91	95.39		99.72		98.96	99.76	100.5
	dark	2.09	3.26	−0.16	7.95	10.66	22.26		59.11		89.96	99.35	99.84

The various concentration porphyrins were added, and the cells were irradiated for 30 min by a 50 W high-pressure mercury lamp at a distance of 13 cm after incubation for 4 h.Then, the cells were treated for 72 h and incubated with 5 mg·mL^{-1} MTT for 4 h. The amount of MTT formazan produced was determined by measuring absorbance at 570 nm (*24*). All data are represented as the mean values obtained from eight separate cultures, RSD < 0.05.

give porphyrin **6** (25 mg, 86.7% yield). ^{1}H NMR ([d^6]-DMSO, 300 MHz): δ (ppm), 8.49−8.40 (m, 8 H), 8.37−8.30 (m, 8 H). UV−vis (DMSO): λ_{max} (nm, log ϵ): 489.0 (5.15), 672 (4.28). MALDI-TOF HRMS for $C_{48}H_{22}Br_8N_4O_8$ [M+] calcd 1422.4911, found 1422.4856.

Synthesis of β-octaphenyl-*meso*-tetrakis (4-carboxyphenyl)porphyrin (**8**). Porphyrin **7** (36 mg, 0.025 mmol) was dissolved in 5 mL of THF and 3 mL of a 2 M aqueous solution of potassium hydroxide was added. The solution was stirred in a sealed flask at room temperature, for 3 days. The aqueous phase was collected and the pH lowered, using a 1 M solution of hydrochloric acid, until precipitation of the porphyrin. The precipitate was washed with water and dried under vacuum to give porphyrin **8** (32 mg, 92.1% yield). ^{1}H NMR ([d^6]-DMSO, 300 MHz): δ (ppm), 8.36 (s, 4 H), 7.41−7.38 (d, J = 9.0 Hz, 8 H), 7.22−7.19 (d, J = 9.0 Hz, 8 H), 6.70 (s, 40 H). UV−vis (DMSO): λ_{max} (nm, log ϵ): 450 (5.25), 555 (4.21), 594 (3.98). ESI HRMS for $C_{96}H_{62}N_4O_8$ [M^+] calcd 1397.4484, found 1397.4437.

Cell Incubation and Cell Survival Assay (*24*). The SGC7901 cells were obtained from China Center for type Culture Collection (CCTCC) and grown in MEM supplemented with 10% FBS (fetal bovine serum), incubated at 37 °C in a 5% CO_2, 95% air atmosphere, and were subcultured every two to three days as necessary. The cells (about 3×10^3) were added to a 96-well plate and incubated for 24 h at 37 °C in a 5% CO_2 incubator. Then, the as-synthesized porphyrins at various concentrations were added. After incubation for 4 h at 37 °C in a 5% CO_2 incubator, the cells were irradiated for 30 min by a 50 W high-pressure mercury lamp at a distance of 13 cm. Then, the cells were allowed to incubate for another 72 h. MTT formazan (10 μL, 5 mg/mL) was added to each well and incubated for another 4 h. The cells were centrifuged at 2000 rpm for 10 min, and then the medium was removed. With addition of 100 μL of DMSO to each well, the values of OD were detected at 570 nm. The cytotoxicity data were presented as IC_{50} values.

Flow Cytometric Determination of Apoptosis (*17*). The cells were cultured as above. 5×10^4 cells of each well were seeded in a 24-well plate. After 24 h, various concentrations of porphyrins were added and trireplicated. Then, the plate was irradiated for 30 min by a 50 W high-pressure mercury lamp. After 72 h, the cells of each well were harvested by using typsin. After centrifugation and being washed two times with PBS, these cells were fixed in an ice-cold 70% ethanol solution at −20 °C overnight. The 100 μL of suspended single cell solution in PBS were obtained by further centrifugation and washing. Sample wells prepared for the flow cytometry analysis were treated with RNase (1 mg/mL) for 30 min at 37 °C. The mixture was suspended in 1 mL of PBS solution containing propidium iodide PI (100 μg/mL). Then, the cells were incubated for 1 h at room temperature in the dark and analyzed on a flow cytometer (Beckmen Coulter Eltra flow cytometer). The linear DNA content data were analyzed by MultiCycle DNA Content and Cell Analysis software for cell cycle analysis. Cell apoptosis was measured as a sub-G0-G1 hypodiploid peak and indicated with the fluorescence intensity of FITC.

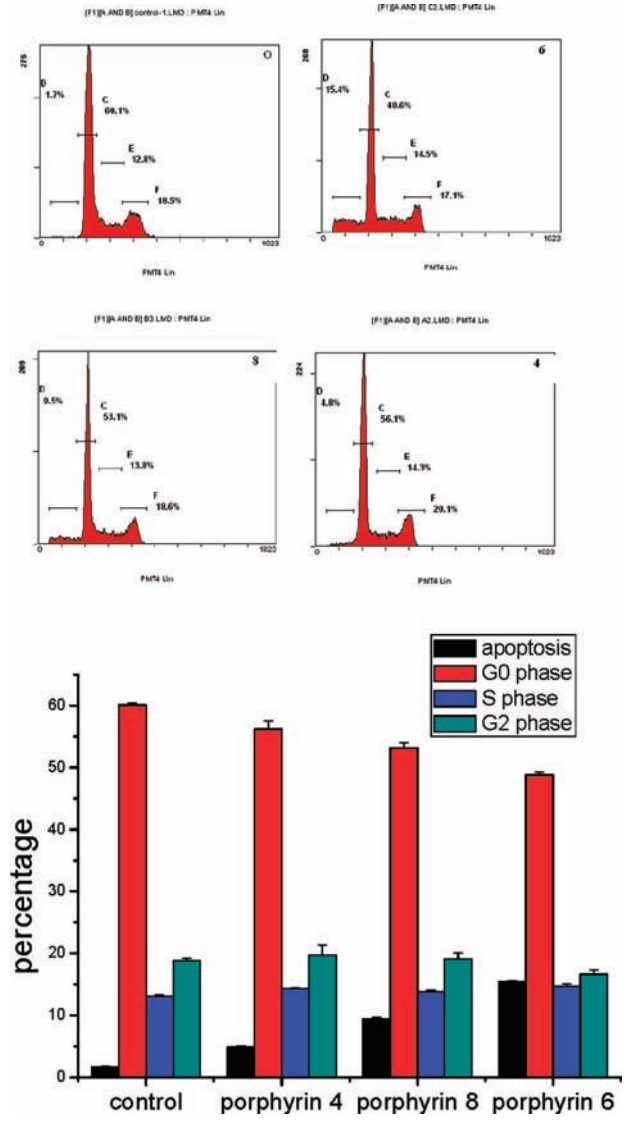

Figure 1. The histogram drug-induced cell cycle arrest and apoptosis of porphyrin (10 μM) in 7901 cells as measured by flow cytometric analysis. The *x*-axis is the DNA content and the *y*-axis is the number of cells with that fluorescence intensity. **6**, **8**, and **4** represent cells that were treated with 10 μM porphyrins **6**, **8**, and **4**, respectively, for 72 h (O is control) and irradiated by light for 30 min, respectively. The rate of apoptosis: 15.4 ± 0.15%, 9.5 ± 0.25%, and 4.8 ± 0.21%, respectively.

Assessment of Intracellular Caspase-3 Activity (*25*). The CaspGLOW Fluorescein Active Caspase-3 Staining Kit was used to monitor the intracellular caspase-3 activities according to the manufacturer's recommendations (Biovision, USA). The assay utilizes the caspase-3 inhibitor DEVD-FMK conjugated

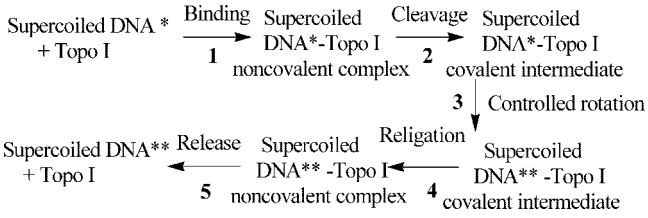

Figure 2. Mechanism of human topoisomerase I. * means the τ of this supercoiled DNA is n. ** means the τ of this supercoiled DNA is $n - 1$.

to FITC (FITC-DEVD-FMK) as the fluorescent in situ marker. FITC-DEVD-FMK is cell-permeable, nontoxic, and irreversibly binds to activated caspase-3 in apoptotic cells. The FITC label allows for direction of activated caspases in apoptotic cells by flow cytometry. The cells were cultured as above. 2×10^5 cells of each well were seeded in a 6-well plate. After 24 h, various concentrations of porphyrins were added and trireplicated. The cells were irradiated for 30 min by a 50 W high-pressure mercury lamp at a distance of 13 cm after incubation for 4 h at 37 °C in a 5% CO_2 incubator. The cells of each well were harvested by using typsin at given time intervals. Aliquots (300 μL) of each treatment were added into microtubes. With the addition of 1 μL of FITC-DEVD-FMK, the tubes were incubated for 0.5 h at 37 °C in an incubator with 5% CO_2. Cells were centrifuged at 3000 rpm for 5 min and supernatant was removed. The cells were then resuspended in 0.5 mL of wash buffer, and centrifuged again. For flow cytometric analysis, cells were resuspended in 500 μL of wash buffer. Samples were put on ice and analyzed by flow cytometry (Beckman-Coulter, Eltra flow cytometer) using the FL-1 channel.

Measurement of Relaxation Activity Topo I (*26*). Functional activity of Topo I[1] was assayed by relaxation of supercoiled plasmid DNA. Briefly, relaxation of 50 ng of supercoiled DNA pBR322 (0.1 U of Topo I) was performed in 10 μL of Topo I relaxation buffer (20 mM Tris pH 7.5, 0.1 mM Na_2EDTA, 10 mM $MgCl_2$, 50 mg/mL acetylated-BSA, 100 mM KCl) at 37 °C for 30 min in the presence or absence of the porphyrins dissolved in DMSO solution. Control groups were either DNA alone or DNA treated with Topo I only. Incubation at 37 °C for time course was terminated by addition of 0.5% (w/v) SDS and proteinase K. The mixtures were run in a 0.8% agarose gel. Gels were stained with ethidium bromide (EB) and visualized by UV and photographed using Vilber Lourmat video system.

Measurement of Topo I Mediated DNA Cleavage (*27*). With addition of excessive enzymes (i.e., 0.3 U of Topo I), topoisomerase I reactions were performed in topoisomerase I relaxation buffer at 37 °C for 30 min. Reactions were terminated with 0.5% (w/v) SDS. After digestion with proteinase K, open circular and linear DNA were separated from intact supercoiled and relaxed forms by agarose gel electrophoresis in the presence of 0.5 mg/mL of EB under the same conditions as for the relaxation assay. CPT was used as the reference drug.

Analysis of Binding with Topo I and pBR 322 (*28*). The supercoiled DNA pBR322 (50 ng) or the Topo I enzyme (0.2 U) was preincubated at 4 °C for 15 min in Topo I relaxation buffer with the indicated concentrations of compound **6**. Then, Topo I (0.2 U) or supercoiled DNA pBR322 (50 ng) was added and incubated with compound **6** for 30 min at 37 °C and analyzed on 0.8% agarose gels at 4.5 V/cm. The control shows the electrophoretic mobility of pBR 322 DNA alone.

Analysis of Topoisomerase−DNA Binding by Electrophoretic Mobility Shift Assay (EMSA) (*28*). During analysis of Topo I/DNA binding by EMSA, supercoiled DNA pBR322 was incubated with 0.3 U of topoisomerase I for 1 min at 37

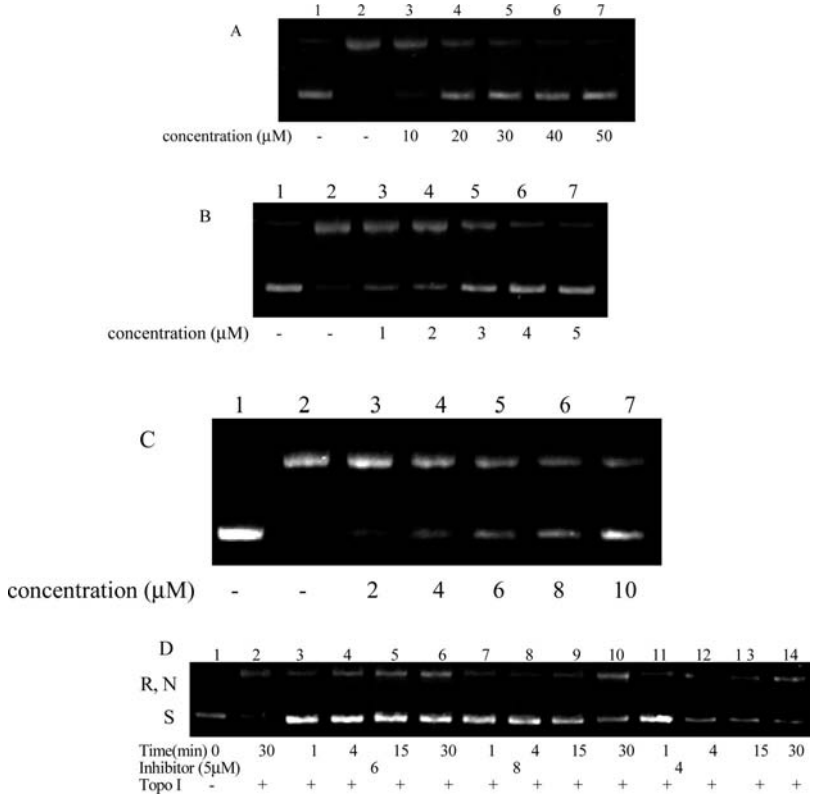

Figure 3. (A) The gradient agarose gel assays of compound **4**. (B) The gradient agarose gel assays of compound **6**. (C) The gradient agarose gel assays of compound **8**. (D) Activity inhibition of Topoisomerase I. Agarose gel electrophores from 1 to 30 min. Relaxed DNA (R) and nicked DNA (N) slowly migrate in the gel for a cell free DNA relaxation assay of a pBR322 DNA treated with Topo I inhibitors as compared to supercoiled DNA (S).

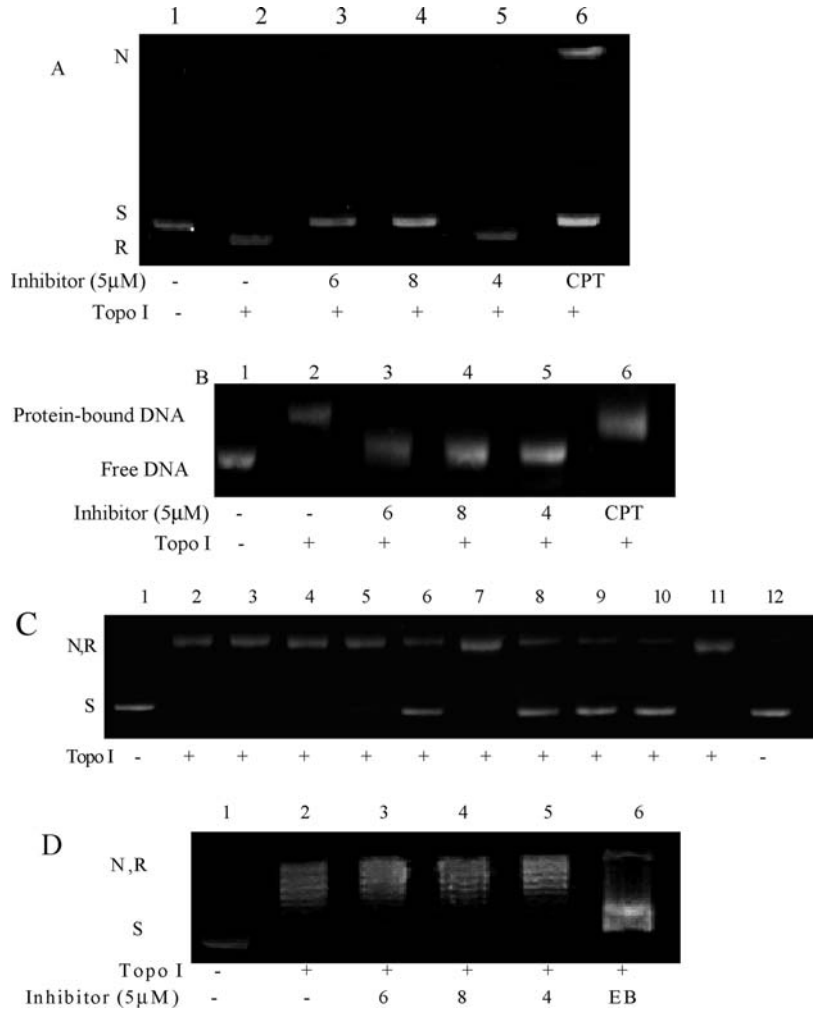

Figure 4. Mechanism of Topo I inhibition. (A) Representative image of agarose gel electrophoresis of the cleavage assay. pBR322 DNA (50 ng) was incubated in the presence of Topo I (0.1 U) and with or without Topo I inhibitors. Only CPT induced the formation of a slowly migrating complex formed by enzyme, drug, and DNA; whereas drug **6**, **8**, and **4** were unable to interfere. (B) Prevent binding of Topo I to substrate DNA. EMSAs of Topo I incubated with appropriate DNA are shown. Samples contained pBR322 DNA (50 ng), each inhibitor, and excess of topoisomerase I (0.3 U) to allow the strongest possible DNA shift. (C) Inhibition of Topo I catalyzed pBR 322 DNA relaxation by compound **6**. Relaxation of 50 ng of pBR 322 DNA by 0.2 units of human topoisomerase I was incubated with compound **6** for 30 min at 37 °C and analyzed on 0.8% agarose gels. The DNA−substrate (lanes 1 to 6) or the enzyme (lanes 7 to 12) were preincubated at 4 °C for 15 min with the indicated concentrations of compound **6**. (D) interaction of drug **6**, **8**, and **4** with DNA was measured in an unwinding assay. All experiments were repeated three times with similar results.

°C. SDS denaturation and proteinase K digestion were omitted. Samples were immediately loaded onto the 0.8% agarose gel with 0.5 mg/mL of ethidium bromide in TBE buffer and separated by electrophoresis for 6 h.

Measurement of DNA Intercalation (*29, 30*). DNA intercalation was measured with the unwinding assay. Supercoiled pBR322 DNA was relaxed with 0.3 U of Topo I at 37 °C for 10 min in Topo I relaxation buffer. To confirm full relaxation of DNA, the sample was terminated with SDS after 10 min. Porphyrins were added and the mixture was allowed to incubate for another 30 min. A parallel experiment ensured that Topo I retained its activity in the presence of the compounds used. The reaction was terminated by addition of 0.5% (w/v) SDS and followed by digestion with proteinase K as described above. Excess porphyrins were removed by extraction with chloroform/isoamyl alcohol (24:1). Reaction samples were loaded onto the 0.8% agarose gel. At this moment, EB was used as the reference.

CT DNA topoisomerase I (Topo I) (20 U/μL) and supercoiled pBR322 plasmid DNA were purchased from Toyobo (Osaka, Japan). Camptothecin (CPT) was purchased from Acros. Human gastric carcinoma cell line SGC7901 was obtained from China Center for Type Culture Collection (CCTCC).

RESULTS

Cell Survival Assay. For initial investigation, we chose tumor cell line 7901 as the target to study the anticancer abilities of the synthesized porphyrins. The effect of the compounds on proliferation of cancer cell lines was determined using the standard MTT assay under irradiation (*24*). All the stock solutions were dissolved in DMSO and diluted with water, and the final DMSO concentration is less than 0.1%. Results from MTT assay are shown in Table 1.

Cell Cycle and Apoptosis analysis. In further research, we investigated the effects of anionic porphyrins on the growth of tumor cells through cell cycle and apoptosis analysis. Normally, there is a cell cycle in the proliferation of cells. If the cell cycle was perturbed and was not successfully repaired by itself, the cell will go to death (necrosis or apoptosis). Apoptosis is a physiological "cell suicide" program, and is the normal pathway for clearance of defective or aged cells in the body (*31, 32*). It is also the key pathway in animal development (*33*). The

apoptosis analysis was conducted by flow cytometry assay staining with propidium iodide (Figure 1).

Assessment of Intracellular Caspase-3 Activity. Caspase-3 is a member of the cysteine aspartic-acid-specific protease family. As the enzyme takes part in the execution phase of programmed cell death, it plays a key role in early phases of apoptosis in mammalian cells (*34*). Therefore, the activity of the enzyme is an important biochemical indicator of the apoptosis procedure. We studied the enzymatic activity of caspase-3 in cells incubated with the synthesized compounds using the CaspGLOW Fluorescein Active Caspase-3 Staining Kit.

Inhibition of Topoisomerase I Activity. The mechanism of human Topo I (topoisomerase I) has been well-established, as is shown in Figure 2 (*35*). CPT (camptothecin) binds to the supercoiled DNA*−Topo I covalent intermediate after cleavage and inhibits subsequent religation. It means that CPT can inhibit step 4 in the procedure. Our results indicate that porphyrins **4**, **6**, and **8** could bind to free Topo I and subsequently inhibit the binding of the free enzyme to the DNA cleavage site, and thus prevent all following steps of the catalytic cycle. Such a hypothesis is supported by CT DNA (calf thymus DNA) Topo I activity in a cell-free system was evaluated with relaxation assay. We tested whether these compounds could inhibit Topo I relaxation activity of a supercoiled DNA pBR322. The experimental data are shown in Figure 3. Figure 3A,B,C are gradient agarose gel assays which show the inhibition of these compounds. The IC_{50} value for the inhibition of the catalytic activity of Topo I by **6**, **8**, and **4** were 2.34 μM, 3.40 μM, and 11.75 μM, respectively.

Mechanism of Interaction between Topo I and Porphyrins. It is known that Topo I is a single-stranded endonuclease and ligase. CPT, which is used as our control, is known to inhibit ligase without affecting the cleavage step (*36*, *37*). Therefore, CPT shows a slowly migrating complex, which is named a cleavable complex, formed with the enzyme and drug and DNA, As we have found that **4**, **6**, and **8** could inhibit Topo I activity, we try to understand their working sites of compounds **4**, **6**, and **8** either as pure catalytic inhibitors or as topoisomerase poisons, stabilizing the cleavable complex (*27*). Figure 4A shows that CPT could stabilize the Topo I cleavable complex, resulting in the generation of open-circle plasmid DNA (*28*). In contrast, open-circle DNA was not observed with **4**, **6**, or **8**.

These findings encouraged us to consider that **4**, **6**, and **8** might exert their effect on Topo I before DNA cleavage (*29*). To verify such a hypothesis, we performed the EMSA (electrophoretic mobility shift assay) experiments between supercoiled pBR322 DNA and Topo I and investigated the impact of these compounds on Topo I. We used CPT as a control, which inhibits the ligase activity without interfering with the binding of the enzyme to DNA. Figure 4B demonstrates that **4**, **6**, and **8** inhibit the formation of these enzyme−DNA complexes. In contrast, DNA binding of Topo I is not affected by CPT (Figure 4B, lane 6). These observations are inconsistent with the mechanism of CPT, and thus we suggested that drugs could interfere in the binding of Topo I to DNA (*30*).

DISCUSSION

As expected, data in Table 1 show good abilities of porphyrins **6**, **8**, and **4** to inhibit the growth of the 7901 cell line at low concentrations. Under light irradiation, the IC_{50} values of **6**, **8**, and **4** are 13.6 ± 1.5, 18.7 ± 0.7, and 3.7 ± 0.4 μM, respectively; while the values in the absence of light irradiation are 24.6 ± 1.6, 21.6 ± 0.9, and 17.5 ± 1.1 μM. These data indicate that light irradiation has not resulted in significant changes in the IC_{50} values; i.e., the inhibitory efficiency of **4** and **6** with irradiation are 5 times and 2 times higher than in the dark. For compound **6** at a concentration of 10 μM, as seen in Table 1, the proliferation of cells is inhibited to 52% in the light, whereas the inhibitory percentage is only 4.9% in the dark, which shows good photoactivity of this compound. To further elucidate the mechanism of the cytotoxicity of these compounds, their abilities to induce apoptosis are investigated.

Table 2. Caspase-3 Activity Induced by Compound 6[a]

samples	control 1	control 2	22 h	44 h	96 h
10 μM	0%	2.2%	9.5%	13.6%	25.8%
20 μM	0%	2.2%	14.8%	27.2%	34.6%

[a] Percentages refer to the ratio of caspase-3-activated cells. Control 1: cells without any compounds or Z-VAD-FMK. Control 2: cells with Z-VAD-FMK but without compounds.

The apoptosis analysis indicated that compound **6** can significantly induce apoptosis of 7901 cells at a 10 μM concentration, while under the same conditions, compounds **8** and **4** have much slighter effects as compared to **6**. From the analysis of the cell cycle, we found that all three compounds can disturb the cell cycle of the 7901 cell line, which is shown with the decreased G0−G1 phase and increased S phase. Obviously, compound **6** has the most significant effect on cell cycle compared to the other two compounds. The G0−G1 phase percentage of **6** decreases from 60.1 ± 0.35% to 48.6 ± 0.40%. The apoptosis of tumor cells 7901 resulting from porphyrins causes the decrease of cells in the G0 phase. This is because the activation of endonucleases following the apoptosis of cells plays a direct and important role in DNA fragmentation, which results in the decrease of cells in the G0 phase (*38*). The outstanding inhibiting ability of compound **6** might be attributed to the electron-deficient property of the molecule resulting from the strong electron-withdrawing effect of the eight bromine atoms at β-positions.

The preliminary results of intracellular caspase-3 activity have shown that cells incubated with **6** exhibits significant caspase-3 activity as compared to the negative control (Table 2). Data in Table 2 also show that the caspase-3 activity increases with prolonged the incubation time. After incubating for 96 h, the percentages of apoptosis cells are 25.8% and 34.6%, respectively, with 10 μM and 20 μM of **6**. Another clear trend is that, at the same incubation time, the higher concentration of the compound leads to higher caspase-3 activity. We also examined **8** and **4** with the same method. However, no caspase-3 activity was detected in the cells incubated with these two compounds. Thus, it is concluded that the cell death induced by **6** is via an apoptosis pathway.

Mechanism of interaction between Topo I and porphyrins has been studied and experimental data shown in Figure 4A,B give a clear indication that the inhibition of the catalytic activity of Topo I by **4**, **6**, and **8** is due to the inhibition of the DNA binding of the enzyme. The effect of **4**, **6**, and **8** could be achieved by intercalation of these compounds into partially relaxed plasmid DNA or by a direct interaction of the drugs with the enzyme itself. To distinguish between these possibilities and further elucidate the mechanism of topoisomerase inhibition, we carried out further experiments with the results shown in Figure 4C,D (*25*, *30*, *31*). Upon preincubation of **6** with enzyme, effective inhibition of topoisomerase I-catalyzed pBR 322 DNA relaxation could be obviously observed at 1 μM concentration, whereas in the case when the porphyrin was preincubated with pBR322, 3 μM **6** was needed to observe the DNA relaxation. Results in Figure 4C further indicate that the enzyme preferentially combines with the drug molecule; hence, the interaction of enzyme with DNA is blocked and the enzymatic activity is weakened. The inhibitory effect of **4**, **6**, and **8** on Topo I-mediated DNA relaxation can be enhanced by preincubation with the enzyme before addition of the DNA plasmid. On the

other hand, we employed a DNA unwinding assay to assess any possible impact of **4**, **6**, and **8** on the superhelical state of closed circular DNA. This assay is based on the ability of intercalating compounds to unwind the DNA duplex and thereby change the DNA twist. These drug-induced changes in DNA twist also induce structural tension in the DNA backbone, and this tension can be relieved by topoisomerases (*35*). On removal of both topoisomerase and intercalating agent, the unwinding effect of the intercalating compound is no longer present and the DNA returns to a supercoiled state. Figure 4D shows that **4**, **6**, and **8** were unable to modulate DNA unwinding, whereas EB, used as a positive control, did it. These findings therefore indicate that the mechanism through which **4**, **6**, and **8** inhibit topoisomerases was independent of DNA intercalation. Taken together, these data suggest that **4**, **6**, and **8** bind directly to Topo I. For porphyrin **6**, it has a potent ability to inhibit Topo I comparing with porphyrins **4** and **8**.

In all, we have synthesized two β-substituted anionic porphyrinsm, and their bioactivities were evaluated. Through MTT and flow cytometric analysis, their abilities to induce cell apoptosis and kill tumor cells were investigated. The β-octabromo porphyrin **6** was preliminarily proven to potentially be a strong anticancer agent. Meanwhile, we found that compound **6** has a stronger ability to inhibit Topo I, and it might be one of the factors that induce tumor cell apoptosis. Further research concerning the mechanism of inducing apoptosis as well as factors affecting the induction are currently in process.

ACKNOWLEDGMENT

Author thanks financial support by the National Science of Foundation of China (No. 20272046, 20425206, 20621502), the Cultivation Fund of the Key Scientific and Technical Innovation Project, the Ministry of Education of China (No. 706040), Open funds supported by The State Key Laboratory of Natural and Biomimetic Drugs of China, State Key Laboratory of Applied Organic Chemistry of China.

Supporting Information Available: HPLC as described in the text. This material is available free of charge via the Internet at http://pubs.acs.org.

LITERATURE CITED

(1) Bonnett, R., and Martinez, G. (2001) Photobleaching of sensitisers used in photodynamic therapy. *Tetrahedron 57*, 9513–9547.

(2) Detty, M. R., Gibson, S. L., and Wagner, S. J. (2004) Current clinical and preclinical photosensitizers for use in photodynamic therapy. *J. Med.Chem. 47*, 3897–3915.

(3) Dozzo, P., Koo, M-S., Berger, S., Forter, T. M., and Kahl, S. B. (2005) Synthesis, characterization, and plasma lipoprotein association of a nucleus-targeted boronated porphyrin. *J. Med. Chem. 48*, 357–359.

(4) Nishiyama, N., Stapert, H. R., and and Zhang, G. D. (2003) Light-harvesting ionic dendrimer porphyrins as new photosensitizers for photodynamic therapy. *Bioconjugate Chem. 14*, 58–66.

(5) Lottner, C., Bart, K.-C., Bernhardt, G., and Brunner, H. (2002) Hematoporphyrin-derived soluble porphyrin-platinum conjugates with combined cytotoxic and phototoxic antitumor activity. *J. Med. Chem. 45*, 2064–2078.

(6) Ochsenbein, P., Ayougou, K., Mandon, D., Fischer, J., Weiss, R., Austin, R. N., Jayaraj, K., Gold, A., Terner, J., and Fajer, J. (1994) Conformational effects on the redox potentials of tetraarylporphyrins halogenated at the β-pyrrole positions. *Angew. Chem., Int. Ed. Engl. 33*, 348–350.

(7) Nurco, D. J., Medforth, C. J., Forsyth, T. P., Olmstead, M. M., and Smith, K. M. (1996) Conformational flexibility in dodecasubstituted porphyrins. *J. Am. Chem. Soc. 118*, 10918–10919.

(8) Kachadourian, R., Flaherty, M. M., Crumbliss, A. L., Patel, M., and Day, B. J. (2003) Synthesis and in vitro antioxidant properties of manganese (III) β-octabromo-meso-tetrakis(4-carboxyphenyl)porphyrin. *J. Inorg. Biochem 95*, 240–248.

(9) Bhyrappa, P., and Krishnan, V. (1991) Octabromotetraphenylporphyrin and its metal derivatives: Electronic structure and electrochemical properties. *Inorg. Chem. 30*, 239–245.

(10) Gust, D., Moore, T. A., and Moore, A. L. (2001) Mimicking photosynthetic solar energy transduction. *Acc. Chem. Res. 34*, 40–48.

(11) Palacio, M., Loire, V., Mansuy-Mouries, G., LeBarch-Ozette, K., Leduc, P., Barkigia, K. M., Fajer, J., Battioni, P., and Mansuy, D. (2000) A new general method for selectiveβ-polynitration of porphyrins; preparation and redox properties of Zn-porphyrins bearing one through to eight β-nitro substituents and X-ray structure of the first Znβ-pernitro porphyrin. *J. Chem. Soc.: Chem. Commun. 19*, 1907–1908.

(12) Grinstaff, M. W., Hill, M. G., Labinger, J. A., and Gray, H. B. (1994) Mechanism of catalytic oxygenation of alkanes by halogenated iron porphyrins. *Science 264*, 1311–1313.

(13) Fiel, R. J., Howard, J. C., Mark, E. H., and Datta-Gupta, N. (1979) Interaction of DNA with a porphyrin ligand: evidence for intercalation. *Nucleic Acids Res. 6*, 3093–3118.

(14) Pasternack, R. F., Brigandi, R. A., Abrams, M. J., Williams, A. P., and Gibbs, E. J. (1990) Interactions of porphyrins and metalloporphyrins with single-stranded poly(dA). *Inorg. Chem. 29*, 4483–4486.

(15) Gibbs, E. J., Maurer, M. C., Zhang, J. H., Reiff, W. M., Hill, D. T, Maliska-Blaskiewicz, M., McKinnie, R. E., Liu, H. Q., and Pasternack, R. F. (1988) Interactions of porphyrins with purified DNA and more highly organized structures. *J. Inorg. Biochem. 32*, 39–65.

(16) Sari, M. A., Battioni, J. P., Dupre, D., and Pecq, J. B. (1990) Interaction of cationic porphyrins with DNA: importance of the number and position of the charges and minimum structural requirements for intercalation. *Biochemistry 29*, 4205–4215.

(17) He, H. P., Zhou, Y., Liang, F., Li, D. Q., Wu, J. J., Yang, L., Zhou, X., Zhang, X. L., and Cao, X. P. (2006) Combination of porphyrins and DNA-alkylation agents: Synthesis and tumor cell apoptosis induction. *Bioorg. Med. Chem. 14*, 1068–1077.

(18) Krishnamurthy, P. C., Du, G., Fukvda, Y., Sun, D., Sampath, J., Mercer, K. E., Wang, J., Sosa-Pineda, B., Murti, K. G., and Schuetz, J. D. (2006) Identification of a mammalian mitochondrial porphyrin transporter. *Nature 443*, 586–589.

(19) Gottumukkala, V., Ongayi, O., Baker, D. G., Lomax, L. G., and Vicente, M. G. H. (2006) Synthesis, cellular uptake and animal toxicity of a tetra(carboranylphenyl)-tetrabenzoporphyrin. *Bioorg. Med. Chem. 14*, 1871–1879.

(20) Lansiaux, A., Laine, W., Baldeyrou, B., Mahieu, C., Wattez, N., Vezin, H., Martinez, F. J., Pineyro, A., and Bailly, C. (2001) DNA topoisomerase II inhibition by peroxisomicine A1 and its radical metabolite induces apoptotic cell death of HL-60 and HL-60/MX2 human leukemia cells. *Chem. Res. Toxicol. 14*, 16–24.

(21) Froelich-Ammon, S. J., and Osheroff, N. (1995) Topoisomerase poisons: harnessing the dark side of enzyme mechanism. *J. Biol. Chem. 271*, 21429–21432.

(22) Naomi, A., Sayo, U., Tomoya, K., Hiroaki, A., and Tadashi, M. (2007) Synthesis of biladienone and bilatrienone by coupled oxidation of tetraarylporphyrins. *J. Org. Chem. 72*, 5320–5326.

(23) Bradshaw, J. E. K., Gillogly, A., Wilson, L. J., Kumar, K., Wan, X. M., Tweedle, M. F., Hernandez, and BryantG. R. G. (1998) New non-ionic water-soluble porphyrins: evaluation of manganese (III) polyhydroxylamide porphyrins as MRI contrast agents. *Inorg. Chim. Acta 275−276*, 106–116.

(24) Alley, M. C., Scudiero, D. A., Monks, A., Hyrsey, M. L., Czerwinski, M. J., Fine, D. L., Abbott, B. J., Mayo, J. G.,

Shoemaker, R. H., and Boyd, M. R. (1988) Feasibility of drug screening with panels of human tumor cell lines using a microculture tetrazolium assay. *Cancer Res. 48*, 589–601.

(25) Yu, D. Y., Matsuya, Y., Zhao, Q. L., Ahmed, K., Wei, Z. L., Nemoto, H., and T., Kondo. (2007) Enhancement of hyperthermia-induced apoptosis by a new synthesized class of furan-fused tetracyclic compounds. *Apoptosis 12*, 1523–1532.

(26) Raspaglio, G., Ferlini, C., Mozzetti, S., Prislei, S., Gallo, D., Das, N., and Scambia, G. (2005) Thiocolchicine dimers: a novel class of topoisomerase-I inhibitors. *Biochem. Pharmacol. 69*, 113–121.

(27) Y, Pommier. (2006) Topoisomerase I inhibitors: camptothecins and beyond. *Nat. Rev. Cancer 6*, 789–802.

(28) Hsiang, Y. H., Hertzberg, R., Hecht, S., and Liu, L. F. (1985) Camptothecin induces protein-linked DNA breaks via mammalian DNA topoisomerase I. *J. Biol. Chem. 260*, 14873–14878.

(29) Habermeyer, M., Fritz, J., Barthelmes, H. U., Christensen, M. O., Larsen, M. K., Boege, F., and Marko, D. (2005) Camptothecin induces protein-linked DNA breaks via mammalian DNA topoisomerase I. *Chem. Res. Toxicol. 18*, 1395–1404.

(30) Boege, F., Straub, T., Kehr, A., Boesenberg, C., Christiansen, K., Andersen, A., Jakob, F., and Kohrle, J. (1996) Selected novel flavones inhibit the DNA binding or the DNA religation step of eukaryotic topoisomerase I. *J. Biol. Chem. 271*, 2262–2270.

(31) Alam, J. J. (2003) Apoptosis: target for novel drugs. *Trends Biotechnol. 21*, 479–483.

(32) Wylli, A. H. (1980) Glucocorticoid-induced thymocyte apoptosis is associated with endogenous endonuclease activation. *Nature 284*, 555–556.

(33) Huang, Z. (2002) The chemical biology of apoptosis: Exploring protein-protein interactions and the life and death of cells with small molecules. *Chem. Biol. 9*, 1059–1072.

(34) Datta, R., Kojima, H., Yoshida, K., and Kufe, D. (1997) Caspase-3-mediated cleavage of protein kinase C θ in induction of apoptosis. *J. Biol. Chem. 272*, 20317–20320.

(35) Stewart, L., Redinbo, M. R., Qiu, X. Y., Hol, W. G. J., and Champoux, J. J. (1998) A model for the mechanism of human topoisomerase I. *Science 279*, 1534–1541.

(36) Syrovets, T., Buchele, B., Gedig, E., Slupsky, J. R., and Simmet, T. (2000) Acetyl-boswellic acids are novel catalytic inhibitors of human topoisomerases I and II alpha. *Mol. Pharm. 58*, 71–81.

(37) Raspaglio, G., Ferlini, C., Mozzetti, S., Prislei, S., Gallo, D., Das, N., and Scambia, G. (2005) Thiocolchicine dimers: a novel class of topoisomerase-I inhibitors. *Biochem. Pharmacol. 69*, 113–121.

(38) Moosavi, M. S., Yazdanparast, R., and Lotfi, A. (2006) GTP induces S-phase cell-cycle arrest and inhibits DNA synthesis in K562 cells but not in normal human peripheral lymphocytes. *J. Biochem. Mol. Biol. 39*, 492–501.

BC7004686

Supprting Information

Octa-substituted Anionic Porphyrins: Topoisomerase I Inhibition and Tumor Cell Apoptosis Induction

Baoping Zhai[‡,§] *, Li Shuai*[‡,§]*, Li Yang*[‡]*, Xiaocheng Weng*[‡]*, Lin Wu*[‡]*, Shaoru Wang*[‡]*, Tian Tian*[‡]*, Xiaojun Wu*[‡] *Xiang Zhou*[‡,*]*, Congyi Zheng*[‖]

[‡]College of Chemistry and Molecular Sciences, Wuhan University, Hubei, Wuhan 430072, PR China

‖ School of Life Science, Wuhan University, Hubei, Wuhan 430072, PR China

HPLC trace of porphyrins **6** and **8:**

SHIMADZU LC-10AT*VP*

Reversed-phase HPLC analysis: The samples were analyzed on a AT.ChromC18 column (4.6×250mm).

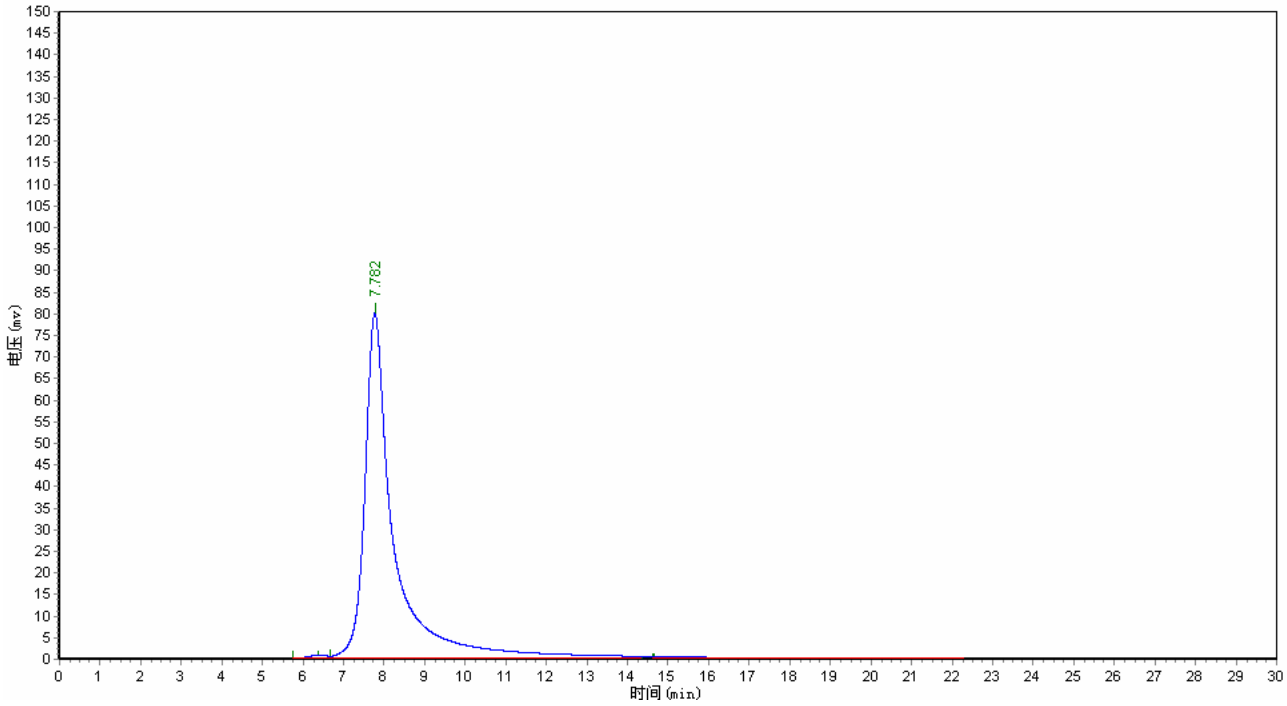

Porphyrin **6**. Detection at 489 nm, CH_3OH : 2% HOAc aqueous solution 85 : 15, 1 mL/min, retention time is 7.782min.

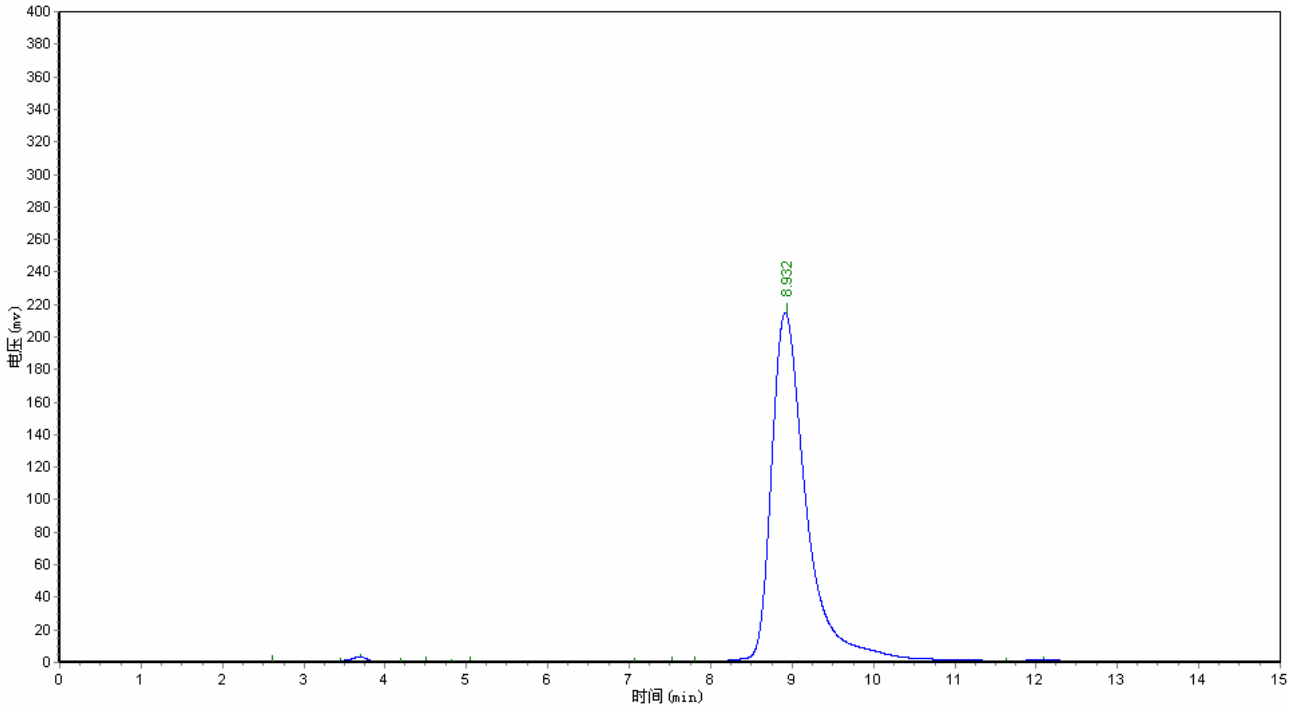

Porphyrin **8**: Detection at 449 nm, CH_3OH: 2% HOAc aqueous solution 95 : 5, 1 mL/min, retention time is 8.932 min.

Covalent Modifications of Antitetanus $F(ab')_2$ Fragments with Natural and Synthetic Polyamines and Their Effects on the Antibody Endocytosis in Cultured HL60 Cells

Françoise Hervé,*,† Nicolae Ghinea,‡ Philippe D'Athis,§ Pierre-Alain Carrupt,|| and Jean-Michel Scherrmann⊥

CNRS, UPR2228, Université Paris Descartes, UFR Biomédicale, 45 rue des Saints-Pères, F-75270 Paris Cedex 06, France, INSERM, U841-EQ07, Université Paris 12, Faculté de Médecine, 8 rue du Général Sarrail, F-94010 Créteil Cedex, France, Service de Biostatistique et Informatique Médicale, Centre Hospitalier Universitaire de Dijon, F-21034 Dijon Cedex, France, Unité de Pharmacochimie, Section des Sciences Pharmaceutiques, Université de Genève, Université de Lausanne, Quai Ernest-Ansermet 30, CH-1211, Genève 4, Switzerland, and INSERM, U705, CNRS, UMR7157, Université Paris Diderot, Université Paris Descartes, Hôpital Fernand Widal, 200 rue du Faubourg Saint-Denis, F-75475 Paris Cedex 10, France. Received February 3, 2008; Revised Manuscript Received May 26, 2008

For antibody therapeutics to succeed when intracellular target molecules are involved, a strategy must be applied to increase the delivery of antibodies into cells to reach their targets. Antibody cationization by chemical conjugation of a polyamine could be one such strategy. Both natural polyamines with increasing net charge valencies (putrescine, PUT; spermidine, SPD; and spermine, SPM) and a synthetic polyamine (hexamethylenediamine, HMD) can be used to cationize antibodies, but no comparison of the respective effects of these polyamines on intracellular delivery of antibodies has been performed yet. This study describes the covalent modification of antitetanus $F(ab')_2$ with these four polyamines using different reaction conditions, and compares the effects of these modifications on antibody interaction with cultured HL60 cells. The cationized antibodies retained ≥80% of the binding activity of the unmodified $F(ab')_2$ with regard to tetanus toxin, as measured by an antigen-binding capture enzyme immunoassay. This same method was used to quantify the amount of cell-associated $F(ab')_2$ following incubation with HL60 cells. Cationization was shown to enhance cell interaction of the $F(ab')_2$: the higher the number of coupled polyamine molecules, the greater the amount of antibody associated with the cells. Moreover, coupling the $F(ab')_2$ to the SPD and SPM polyamines had greater effect on cell interaction than coupling the $F(ab')_2$ to the PUT and HMD diamines. Internalization of the cationized antibodies by the HL60 cells was demonstrated by confocal microscopy. This technique also showed that SPD and SPM were more effective than PUT and HMD in terms of intracellular delivery of the $F(ab')_2$. It follows from all these results that electrostatic interaction involving charge density plays a predominant role in the endocytic transport mechanism of the $F(ab')_2$ modified with these polyamines. However, coupling the $F(ab')_2$ to SPM and SPD yielded the same maximum effects in terms of cell interaction, although coupling SPM was expected to increase the antibody net charge valency more than coupling SPD. This finding suggests that the effective global charge for the cell interaction and uptake of polyamine-modified antibodies does not simply correspond to the addition of the ionizable amine functions on the coupled polyamines, and that other factors may come into play.

INTRODUCTION

The potential of antibodies as diagnostic and therapeutic agents is limited, especially when intracellular target molecules are involved, because antibodies are poorly internalized by cells. Indeed, these hydrophilic molecules cannot cross the lipid matrix of the cell plasma membrane efficiently, and so cannot gain access to the cell interior or the different cellular compartments to reach the target molecules.

The high adsorptive property of cationic proteins to anionic sites present on all cell surfaces has provided the basis for the development of cationization strategies for delivering proteins into cells (*1*, *2*). Proteins can be cationized through the chemical conversion of their surface carboxylic acid groups into basic moieties by covalent coupling of polyamines. Not only can the positively charged proteins thus formed bind to the various negatively charged plasma membrane components surrounding the cells, but the bound proteins are also internalized into cells in a receptor- and transporter-independent manner, by adsorptive-mediated endocytosis (AME[1]) (*3*).

The ability of cationized antibodies or fragments to undergo enhanced cellular uptake (*3*–*6*) and exert intracellular activity (*7*, *8*) has been demonstrated in different in vitro cell models.

* Corresponding author. Dr. Françoise Hervé, CNRS UPR2228, Université Paris Descartes, UFR Biomédicale, 45 rue des Saints-Pères, F-75270 Paris Cedex 06, France. Phone: 33 (1) 42 86 20 51. Fax: 33 (1) 42 60 55 37. Email: francoise.herve@univ-paris5.fr.

† CNRS, UPR2228.

‡ INSERM, U841-EQ07.

§ Centre Hospitalier Universitaire de Dijon.

|| Université de Genève, Université de Lausanne.

⊥ INSERM, U705, CNRS, UMR7157.

[1]Abbreviations: AME, adsorptive-mediated endocytosis; BSA, bovine serum albumin; C.V., coefficient of variation; EDC, 1-ethyl-3-(3-dimethylaminopropyl) carbodiimide; ELISA, enzyme-linked immunosorbent assay; HBSS, Hanks' balanced saline solution; HBSS/BSA, HBSS containing 0.2% BSA; Hepes, *N*-2-hydroxyethylpiperazine-*N*′-2-ethanesulfonic acid; HMD, hexamethylediamine; IEF, isolectric focusing; IgG, immunoglobulin G; Mes, 2-(*N*-morpholino)ethanesulfonic acid; MWCO, molecular weight cutoff; PBS, phosphate-buffered saline; pI, isolectric point; PUT, putrescine; RPMI 1640, Roswell Park Memorial Institute 1640 medium; S.D., standard deviation; SDS, sodium dodecyl sulfate; SDS-PAGE, sodium dodecyl sulfate polyacrylamide gel electrophoresis; SPD, spermidine; SPM, spermine.

10.1021/bc800045x CCC: $40.75 © 2008 American Chemical Society
Published on Web 07/17/2008

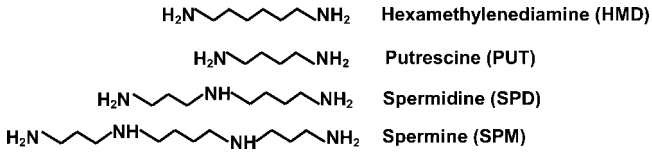

Figure 1. Structures of the synthetic diamine, hexamethylenediamine (HMD), and of the natural polyamines, putrescine (PUT), spermidine (SPD), and spermine (SPM). Due to coupling, each polyamine is found with one less primary amino group, i.e., one less positive charge, at neutral pH.

Moreover, it has also been shown that cationized antibodies can be transported across complex physiological barriers, such as the blood-brain barrier (*1*), indicating that cationization is a strategy able to increase both target cell endocytosis and *trans*-endothelial migration of antibodies.

Antibody cationization has most generally been accomplished by coupling antibodies to the synthetic diamine molecule known as hexamethylenediamine (HMD) (Figure 1). In addition, a different type of protein cationization involving the covalent attachment of putrescine (PUT), spermidine (SPD), and spermine (SPM), a series of endogenously occurring polyamines with increasing net charge valencies (Figure 1), has also been described (*9*). The covalent modification of a variety of proteins with PUT, SPD, and/or SPM has been shown to facilitate the delivery of these proteins into the brain in vivo. More specifically, a remarkable increase in brain transfer was observed for PUT-modified immunoglobulin G (IgG) relative to the native protein (*9*). However, no comparison of the respective effects of PUT, SPD, and SPM on the cellular internalization of antibodies in vitro or their brain transfer in vivo has been performed yet. The same holds true for HMD in that it has yet to be shown whether synthetic polyamines are more, less, or equally effective as natural polyamines. Therefore, we chose to perform a study which included all of the aforementioned polyamines for antibody cationization in order to investigate these questions and to select the most effective polyamine in terms of intracellular delivery.

Using polyclonal antitetanus $F(ab')_2$ fragments as an antibody model, the present study describes their covalent modification with HMD, PUT, SPD, and SPM and the effects of these modifications on antibody cell interaction and internalization in an in vitro model with HL60 cells. Optimization of the conditions of modification yielded two sets of $F(ab')_2$ with increasing net charge valencies: one set with an increasing number of coupled polyamine molecules, and the other with increasing charge densities associated with the polyamines after antibody modification. We then measured the antigen-binding activity of the modified $F(ab')_2$ samples, and quantitatively analyzed their interaction with the HL60 cells by an ELISA method which has been especially developed for these measurements (*10*). Finally, the distribution of these antibodies at the cellular level was visualized by confocal microscopy.

EXPERIMENTAL PROCEDURES

Materials. The antitetanus toxoid horse polyclonal $F(ab')_2$ fragments (batch no U-5000-2) and the tetanus anatoxin were gifts from Aventis-Pasteur (Marcy l'Etoile, France). The HL60 (Human Caucasian promyelocytic leukemia) cell line was obtained from the European Collection of Animal Cell Cultures (Salisbury, Wiltshire, UK). Putrescine • 2HCl, spermidine • 3HCl, spermine • 4HCl, hexamethylenediamine, and 1-ethyl-3-(3-dimethylaminopropyl)carbodiimide (EDC) were from Fluka (Saint-Quentin Fallavier, France). [2,3-^{3}H-(*N*)]putrescine (1243.2 GBq/mmol; 185 MBq/mL) and [terminal methylenes-^{3}H-(*N*)]spermidine (919.5 GBq/mmol; 185 MBq/mL) were obtained from PerkinElmer Life Sciences (Boston, MA), and [1,4-^{14}C]spermine (4.07 GBq/mmol; 1.85 MBq/mL) from GE Healthcare (Orsay, France). Alkaline phosphatase-labeled streptavidin, *p*-nitrophenyl phosphate, protamine base, and 2-(*N*-morpholino)ethanesulfonic acid (Mes) were purchased from Sigma-Aldrich (Saint-Quentin Fallavier, France). Rabbit biotin conjugated affinity purified antihorse IgG ($F(ab')_2$ specific) was from Rockland (Gilbertsville, PA). The following chemicals were obtained from Invitrogen (Cergy Pontoise, France): streptavidin conjugated to Alexa Fluor 488, toto-3 iodide, Roswell Park Memorial Institute 1640 medium (RPMI 1640), Hepes buffer solution 1 M, Hanks' balanced saline solution (HBSS), and 7.5% (w/v) bovine serum albumin (BSA) solution. All other chemicals were of the purest grade available and purchased from VWR (Fontenay-sous-Bois, France) unless otherwise noted. Milli-Q Plus purified water (Millipore, Bedford, MA) was used throughout.

Preparation of Polyamine-Modified Antitetanus $F(ab')_2$. The method used for antibody modification was similar to that described previously (*10*). The polyamines, HMD, PUT, SPD, and SPM, respectively, were covalently attached to carboxylic acid groups of the $F(ab')_2$ using EDC. A sample of the native $F(ab')_2$ diluted in 0.1 M Mes buffer with a pH of 4.5, 5.5, or 6.5 was added to the desired polyamine in water while stirring. This was followed by the addition of water-soluble EDC, and the modification reaction was allowed to proceed for 4 h at 4 °C in the dark. The concentrations of tested polyamine, EDC, and antibody in the EDC(+) mixture (50 mL) were 50 mM, 0.96 mg/mL, and 0.5 mg/mL, respectively. The reaction was quenched with the addition of an equal volume of 0.1 M sodium acetate buffer, pH 5.0. To remove the excess of polyamine and EDC, the product was first filtered on Omega-50 membrane filter with a MWCO of 50 000 (Pall/Gelman Sciences, Ann Arbor, MI), and then on Bio-Gel 10DG column (Bio-Rad, Marnes-la-Coquette, France), and finally dialyzed against water with multiple changes for 60 h at 4 °C using Spectra/Por CE membrane with a MWCO of 25 000 (VWR). Concurrently, $F(ab')_2$ samples were treated under the same conditions as those described above, except that water was used in place of EDC. These EDC(−) $F(ab')_2$ samples were used as controls throughout this study. The cationized and the control antibody preparations were analyzed for protein content using the Bio-Rad DC Protein Assay kit with bovine IgG as a standard (Bio-Rad). The antibody solutions were then individually aliquoted and stored at −20 °C for subsequent use. These aliquots were stable over a one-year storage period at this temperature.

Estimation of the Polyamine Substitution Ratio of the $F(ab')_2$. The polyamine, PUT, SPD, or SPM, was added to two samples of the $F(ab')_2$ in 0.1 M Mes buffer with the desired pH, ranging from 4.5 to 6.5, and the samples spiked with known amounts of [^{3}H]PUT, [^{3}H]SPD, or [^{14}C]SPM. Then, EDC was added to one $F(ab')_2$ sample (EDC(+)) and water to the other (EDC(−)). The concentrations of polyamine and $F(ab')_2$ in the EDC(+) and EDC(−) samples (each 5 mL), and the concentration of EDC in the EDC(+) sample were the same as those used above. The concentration of radioactive polyamine in each sample was 2 μM for [^{3}H]PUT and for [^{3}H]SPD and 10 μM for [^{14}C]SPM. After incubation followed by the addition of 0.1 M sodium acetate buffer, pH 5.0 (5 mL), the EDC(+) and EDC(−) $F(ab')_2$ samples were individually filtered and dialyzed as described. Dialysis was stopped when no radioactivity was detected in the EDC(−) sample (generally after 48−60 h dialysis), indicating that all free polyamine had been removed from both samples. Radioactivity counting was performed using liquid β-scintillation spectrometry (Tri-Carb 1900-TR model, Packard Instruments, Les Ulis, France). The dialyzed EDC(+) $F(ab')_2$ sample was analyzed for radioactivity and protein

content to determine its polyamine substitution ratio (i.e., the number of coupled polyamine molecules per antibody molecule).

Characterization of the Polyamine-Modified $F(ab')_2$ by Electrophoresis. The control $F(ab')_2$ and the polyamine-modified $F(ab')_2$ samples were analyzed by sodium dodecyl sulfate-polyacrylamide gel electrophoresis (SDS-PAGE), using gels with an acrylamide monomer concentration of either 12% or 8% T and 2.67% C, and a Tris-glycine buffer system (*11*). Protein samples were solubilized in SDS under reducing conditions with 2-mercaptoethanol, and under nonreducing conditions. This step was followed by electrophoresis and staining with Coomassie Blue R-250. Gels were run at constant voltage with the Mini-Gel apparatus (Bio-Rad), according to the manufacturer's instructions. Protein standards used were the Precision Plus protein standards from Bio-Rad or the high molecular weight calibration kit from GE Healthcare. Isoelectric focusing (IEF) was performed as described previously (*10*), using ampholine polyacrylamide gel plates of 1mm thickness, with acrylamide monomer concentration of 5% T and 3% C and 2.2% carrier ampholytes pH 3.5−9.5 (GE Healthcare). IEF standards from GE Healthcare were used containing 11 proteins with isoelectric points in the range of 3.5−9.3. The proteins were visualized with Coomassie Blue R-250.

Determination of the Antigen-Binding Activity of the Antitetanus $F(ab')_2$. An antigen-binding capture enzyme-linked immunosorbent assay (ELISA) for the antitetanus $F(ab')_2$ (*10*) was performed on preparations of control and polyamine-modified antitetanus $F(ab')_2$ to determine their binding activity. The protocol followed was the same as that reported in ref (*10*). Briefly, the method used tetanus anatoxin coated on microtiter plates as capture antigen (0.5 μg/well) to bind the $F(ab')_2$, with the amount of antibody binding being quantified using, first, a rabbit biotinylated antihorse $F(ab')_2$ (60 ng/well), and then a streptavidin-alkaline phosphatase conjugate (0.15 μg/well). Substrate for making the color reaction was *p*-nitrophenyl phosphate (100 μg/well). A solution of HBSS supplemented with 0.2% (w/v) BSA (HBSS/BSA) was used as assay diluent for the $F(ab')_2$ samples. Each dilution of samples (over the concentration range 2.5−25 ng/mL for both the control and polyamine-modified $F(ab')_2$) was assayed in duplicate. Blanks (HBSS/BSA) were included in each assay. The color was developed for 60 min in the dark at room temperature and the enzyme reaction stopped with 1 M NaOH (100 μL/well). Plates were read on a Bio-Tek ELX 800 microplate reader (Winooski, VT) at a wavelength of 405 nm.

Linear regression curves were determined by plotting the concentrations of the control or polyamine-modified $F(ab')_2$ versus the absorbance according to the following equation:

$$y = a \times x + b \tag{1}$$

where y is the absorbance at 405 nm, x the antibody concentration in ng/mL, and a and b are the slope and intercept of the curve, respectively.

HL60 Cell Assays and Measurement of Cell-Associated $F(ab')_2$. HL60 cells were grown in suspension cultures as reported (*6*), using a RPMI 1640 medium with 10% fetal calf serum, and maintained in a logarithmic growth phase at a maximum density of $\sim 1.5 \times 10^6$ cells/mL by subculturing every 3 days. For the assays with the polyamine-modified and control $F(ab')_2$, the HL60 cells were harvested from cultures by centrifugation at 200 × *g* (5 min, room temperature), washed three times with RPMI 1640 containing 10 mM Hepes buffer (pH 7.0) and 0.2% (w/v) BSA, and suspended to a density of $\sim 2 \times 10^6$ cells/mL. The cell suspension was divided between two sample sets of polypropylene centrifuge tubes (1 mL/tube): one set was incubated at 4 °C and the other at 37 °C. To each tube was then added 1 mL of dilutions of either the polyamine-modified or the control $F(ab')_2$ prepared in RPMI 1640/10 mM Hepes/0.2% (w/v) BSA. Dilutions of each antibody were made up to give $F(ab')_2$ concentrations of 5, 12.5, 25, or 50 μg/mL. Each antibody level was tested in duplicate. The tubes were then incubated for 120 min at 4 or 37 °C. Kinetic experiments using SPD-$F(ab')_2$ showed that cellular antibody concentrations reached steady state at 120 min of incubation at 37 °C. The kinetic results were similar to those obtained with PUT-$F(ab')_2$ in a previous study (*10*). After incubation, the cells were immediately centrifuged at 200 × *g* (5 min, 4 °C) and washed three times with ice-cold HBSS to remove the unbound antibody. Cells were then suspended in 1 mL of ice-cold HBSS and finally lysed on ice by ultrasound sonication for 10 s. Blank cell lysates from HL60 cells incubated without antibodies were prepared as stated above. Each cell lysate was then separated into two parts, the first part for the cellular protein assay and the second for the measurement of cell-associated $F(ab')_2$. The term cell-associated $F(ab')_2$ includes the surface-bound antibody plus the internalized antibody, if any. Protein determination was performed in duplicate as described above, using BSA (Bio-Rad) as a standard. The concentrations of the antitetanus $F(ab')_2$ in total cell lysates were determined by ELISA. Prior to this, the total lysates were supplemented with BSA (0.2%, final w/v), and dilutions ranging from 1/2 to 1/50 were then prepared in HBSS also containing 0.2% BSA. The dilutions were assayed by ELISA concurrently with dilutions of a $F(ab')_2$ standard, i.e., the same $F(ab')_2$ as that used for the assays with the HL60 cells. Standards were prepared in HBSS/BSA over the concentration range 2.5−25 ng/mL for both the control and the polyamine-modified $F(ab')_2$. Blanks (HBSS/BSA) were included in each assay. The plates were then processed as described above. A linear regression curve was calculated for the standard and used to compute antibody levels in cell lysates. The amount of cell-associated $F(ab')_2$ was normalized to milligrams of cell proteins.

Inhibition Assays. HL60 cells ($\sim 2 \times 10^6$ cells in RPMI 1640/10 mM Hepes/0.2% (w/v) BSA) were incubated for 120 min at 37 °C with 50 μg/mL of control or SPD-modified $F(ab')_2$ and different concentrations of inhibitor, SPD, or protamine base. SPD was used in the concentration range 1.25−1250 μg/mL, and protamine in the range 0.205−1025 μg/mL. After incubation, the cells were centrifuged and washed with ice-cold HBSS to remove the excess unbound antibody and inhibitor. The cells in each tube were then suspended in 1 mL HBSS and lysed using ultrasound sonication. Each cell lysate was analyzed for protein content and its antitetanus $F(ab')_2$ level as already described. The amount of cell-associated $F(ab')_2$ was normalized to milligrams of cell proteins.

The relationship between the amount of cell-associated $F(ab')_2$ (C) and the concentration of inhibitor (I_t) was modeled with the following equation

$$C/C_{max} = IC_{50}/(IC_{50} + I_t) \tag{2}$$

where C_{max} is the maximum amount of cell-associated antibody measured in the absence of inhibitor, and IC_{50} is the theoretical concentration of inhibitor producing a 50% decrease in C_{max}. IC_{50} was estimated with its standard deviation by nonlinear regression analysis using Micro-Pharm software (*12*).

Confocal Laser Microscopy. The polyamine-modified and control $F(ab')_2$ (each used at a concentration of 50 μg/mL) were incubated with HL60 cells at either 4 or 37 °C, as described above. Following incubation, the cells were centrifuged and washed with ice-cold HBSS to remove the unbound antibody. The cells ($\sim 2 \times 10^6$ cells/tube) were then fixed with 1 mL of 4% (w/v) paraformaldehyde in 10 mM phosphate buffer/138 mM NaCl/2.7 mM KCl, pH 7.4, (PBS) for 60 min. All subsequent steps were performed at room temperature, and PBS was used as washing buffer between each step. After washing,

the cells were suspended in 0.4 mL PBS and then immobilized on the glass surface of Lab-Tek II chambers (Nunc, Roskilde, Denmark) previously coated with 0.1% (w/v) poly(L-lysine) (Sigma-Aldrich) in water. The immobilized cells were permeabilized with 0.2% (v/v) Triton X-100 in PBS for 10 min, and the free aldehyde groups then blocked with 0.8% (w/v) glycine in PBS for 30 min. Thereafter, the cells were successively incubated with 2% (v/v) rabbit serum (Sigma-Aldrich) in PBS for 30 min, rabbit biotinylated antihorse $F(ab')_2$ (8 μg/mL in PBS containing 2% (v/v) rabbit serum) for 60 min in the dark, and finally with a streptavidin-Alexa Fluor 488 conjugate (2 μg/mL in PBS containing 1% (w/v) BSA) for 30 min in the dark. The biotinylated secondary antibody was the same antibody as that used in ELISA. For specific nuclear labeling, the cells were incubated with toto-3 (1 μg/mL in PBS) for 10 min in the dark. The internalization of antibodies was examined using a confocal microscope (Zeiss LSM 510) and a 63/1.4× oil immersion objective. Confocal optical sections were obtained through the nuclear plane of the cells. As controls, we used HL60 cells which were incubated without antitetanus $F(ab')_2$ at either 4 or 37 °C. These cells were then treated in exactly the same way as those incubated with antibodies.

Statistical Analysis. Data analyzed with the Triomphe software (*13*) are presented as mean ± standard deviation (S.D.). Coefficient of variation (C.V. = S.D./mean) was used to evaluate variation between measures. To study the variation in antigen binding activity between the different $F(ab')_2$ preparations, we used a two-way analysis of variance (*14*) to compare mean values of antibody binding, and an analysis of covariance (*15*) to compare the slopes of the titration curves of the $F(ab')_2$. The analysis of variance studied the effects of the reaction pH on the $F(ab')_2$ cell interaction, as well as the effects of cationization at the different pH values, for each temperature and each antibody. It also studied the variation in amount of cell-associated antibody between the different $F(ab')_2$, and between temperatures for each antibody. Statistical significance was set at the $p < 0.05$ level.

RESULTS

Polyamine Modification of the Antitetanus $F(ab')_2$. The antitetanus $F(ab')_2$ was covalently modified with PUT, SPD, SPM, or HMD, by activating carboxylic acid groups to the reactive ester with water-soluble carbodiimide (EDC), and then by reacting with each polyamine as the nucleophilic reagent (*16*). A large excess of the polyamines was used in the reaction to ensure that only one primary amine group of the molecules would couple with one carboxylic acid group on the antibody, and thus avoid intermolecular cross-linking and the formation of $F(ab')_2$ polymers (*2*). Following the reaction, the excess of polyamine was removed from the polyamine-$F(ab')_2$ conjugates using a three-step purification procedure.

The conditions for the carbodiimide-mediated amidation of the $F(ab')_2$ carboxylic acid groups were optimized as follows. Because the initial phase of the reaction depends on the ionization of carboxylic acid, preliminary experiments using PUT and [^{3}H]PUT were conducted to adjust the ionization of the $F(ab')_2$ carboxylic acid groups with pH. As illustrated in Figure 2, reactions at different pH values decreasing from 7.0 to 4.5 demonstrated increasing degrees of modification of the $F(ab')_2$ which reached a maximum value of ~3 molecules of PUT coupled per antibody molecule at pH 4.5. Decreasing the pH to values below 4.5 did not further increase the amount of coupling and led to the risk of antibody denaturation. Another variable that can influence the extent of cationization of a protein is the molar excess of polyamine relative to the carboxyl groups (*17*). Therefore, experiments were conducted where the $F(ab')_2$ was modified with PUT and [^{3}H]PUT at pH 4.5, using different molar ratios of polyamine over antibody. The amount of coupling was shown to increase almost linearly from 0.02 to 3.2 molecules of PUT per $F(ab')_2$ molecule when the molar ratio of polyamine over antibody increased from 100 to 10 000. The use of PUT/$F(ab')_2$ ratios higher than 10 000 resulted in a contamination of the antibody conjugate by free polyamine which could not be removed by two successive filtrations on Omega-50 membrane filter and Bio-Gel 10DG column, followed by dialysis, even when dialysis was continued for more than 7 days.

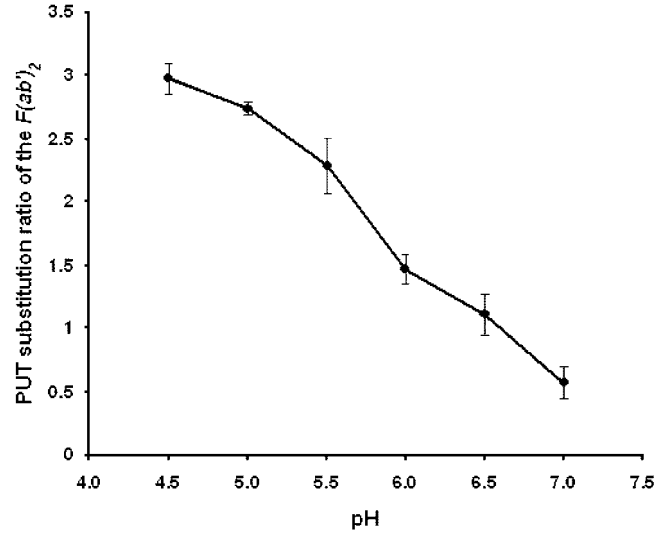

Figure 2. The effect of pH on the EDC-mediated polyamine modification of the antitetanus $F(ab')_2$. The average number of PUT molecules coupled per $F(ab')_2$ molecule (●) estimated at each pH value is shown along with its S.D., and is the result of five independent experiments.

Table 1. Polyamine Substitution Ratio of the Antitetanus $F(ab')_2$[a]

polyamine	pH of the reaction	cationized antibody	substitution ratio
PUT	6.5	PUT-$F(ab')_2$	1.11 ± 0.16
PUT	5.5	PUT-$F(ab')_2$	2.29 ± 0.22
PUT	4.5	PUT-$F(ab')_2$	2.98 ± 0.12
SPD	4.5	SPD-$F(ab')_2$	2.68 ± 0.11
SPM	4.5	SPM-$F(ab')_2$	2.89 ± 0.19
HMD	4.5	HMD-$F(ab')_2$	*nd*[b]

[a] The results are presented according to the polyamine and pH used in the modification reaction. The substitution ratio of the $F(ab')_2$ corresponds to the number of polyamine molecules coupled per antibody molecule. Mean values are shown in all cases along with their S.D., and are the results of five independent experiments. [b] *nd*, not determined.

On the basis of these results, the antitetanus $F(ab')_2$ was modified with PUT at pH 6.5, 5.5, and 4.5. Table 1 shows that these modifications resulted in substitution ratios of roughly 1, 2, and 3 coupled PUT molecules per antibody molecule, yielding a set of antibodies with increasing positive charge valencies due to the number of coupled polyamine molecules. Using the same maximized reaction conditions as for PUT, the $F(ab')_2$ was modified with either HMD, SPD, or SPM, resulting in a second set of antibodies with different charge valencies due to the different number of corresponding protonated amino groups left after coupling (Figure 1). The substitution ratios determined for the $F(ab')_2$ modified with SPD and SPM at pH 4.5 and using a molar polyamine/antibody ratio of 10 000 were both close to 3 (Table 1). The coupling was reproducible in all cases (C.V. <15%). As no radioisotope for HMD is commercially available, it was assumed that similar results of coupling obtained for PUT, SPD, and SPM at pH 4.5 could also be obtained for HMD coupled to the $F(ab')_2$ (i.e., 3 coupled HMD molecules per antibody molecule).

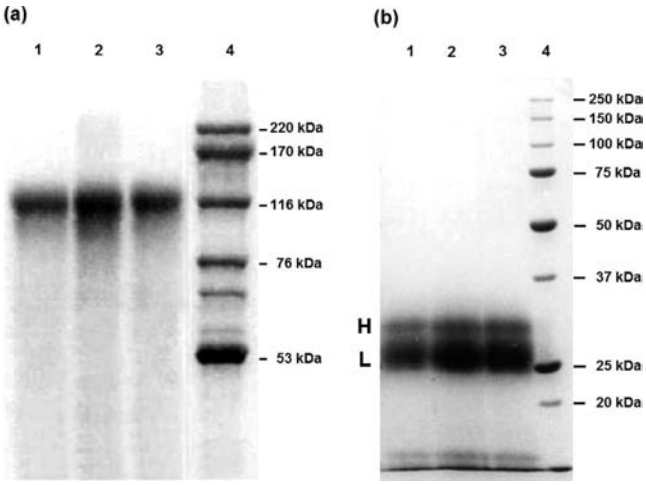

Figure 3. Analysis of polyamine-modified antitetanus $F(ab')_2$ by SDS-PAGE. (a) Coomassie Blue stain of nonreducing SDS-PAGE of PUT-$F(ab')_2$ after modification at pH 4.5 (lane 1), the corresponding control $F(ab')_2$ (lane 2), and the native $F(ab')_2$ (lane 3). (b) Coomassie Blue stain of reducing SDS-PAGE of PUT-$F(ab')_2$ modified at pH 4.5 (lane 1), the corresponding control $F(ab')_2$ (lane 2), and the native $F(ab')_2$ (lane 3). The migration of the heavy chain fragments (H) and light chains (L) of the $F(ab')_2$ is shown on the left-hand border. Five micrograms of each $F(ab')_2$ was applied to the gel, along with molecular weight standards (lanes 4 in (a) and (b)). The molecular weights of the standards are shown on the right-hand border. Reducing and nonreducing SDS-PAGE analysis of all the other polyamine-modified $F(ab')_2$ and the corresponding control $F(ab')_2$ yielded similar results, respectively, to those shown for the PUT-$F(ab')_2$ and its control.

For both the cationized and control $F(ab')_2$, the amount of antibody recovered after the reaction followed by purification represented ≥75% of the amount of $F(ab')_2$ in the starting material. The loss observed for both the cationized and control antibodies was tolerable and likely due to the nonspecific adsorption of these antibodies to the ultrafiltration or dialysis membranes, or the gel particles (or to all three), which were used in the three-step purification procedure.

SDS-PAGE and IEF Analysis of the Polyamine-Modified Antitetanus $F(ab')_2$. When SDS-PAGE was performed under nonreducing conditions, both the control and cationized $F(ab')_2$ migrated with one single protein band at a molecular weight of ~110 kDa, which was identical to that exhibited by native antitetanus $F(ab')_2$ (Figure 3a). This result indicates that polyamine modification of the $F(ab')_2$ and the conditions used therein did not result in any intermolecular cross-linking of the antibody, nor in its degradation. In addition, the results of SDS-PAGE under reducing conditions demonstrated two protein bands at molecular weights of ~30 and ~25 kDa for both the control and modified forms of the $F(ab')_2$, which corresponded to the monomeric heavy chain fragments and to the light chains of the native $F(ab')_2$ (Figure 3b).

As determined by IEF, the isoelectric point (pI) of the native antitetanus $F(ab')_2$ varied over a wide pI range 5.2−8.4, with a predominant distribution in the high pI range (Figure 4). The control $F(ab')_2$ samples also had multiple species whose pIs and distribution were similar to those of the native antibody, indicating that the conditions used in the reaction caused minimal changes in the antibody pI forms. Very different IEF results were obtained with the cationized $F(ab')_2$. Modification with PUT at pH 6.5, 5.5, and 4.5 resulted in a graded shift to increasing pIs that was in the order of pH 6.5 < 5.5 < 4.5 (Figure 4a). Concurrently, the proportions of residual unmodified isoforms gradually decreased. These results were consistent with the increasing amounts of coupling determined at these three pH values (Table 1). The IEF profiles of the $F(ab')_2$ modified with HMD, SPD, and SPM at pH 4.5 (Figure 4b) were similar to that of the PUT-$F(ab')_2$ modified at the same pH value. All these antibodies showed two major isoforms: one had an average pI of ~8.8 and the other a pI ≥ 9.3. They also contained some minor isoforms in the pI range ~7.4−8.6.

Antigen-Binding Activity of the Polyamine-Modified Antitetanus $F(ab')_2$. The effects of HMD, PUT, SPD, and SPM modifications on the biological activity of the $F(ab')_2$ were evaluated by assaying dilutions of decreasing concentrations of the polyamine-modified and control antibodies by a specific ELISA method (*10*). Because this assay was also intended to be used for the quantitative analysis of the $F(ab')_2$ in HL60 cell lysates, a HBSS solution with 0.2% BSA (HBSS/BSA) was used as assay diluent. Representative examples of the titration curves obtained for the polyamine-modified and control $F(ab')_2$ are presented in Figure 5. Linear dose-response curves were obtained for all the antibodies when titration was performed over the concentration range 2.5−25 ng/mL. Linearity was determined by checking five titration curves over five days for each antibody (duplicate measurements per level on each day). For all the antibodies assayed, the coefficients of correlation of the titration curves were ≥0.9951. The slope of each titration curve reflects the antigen binding activity of the antibody. As illustrated in Figure 5, low background levels (≤0.107 absorbance units) were measured in both the assays using the polyamine-modified $F(ab')_2$ and the control $F(ab')_2$, indicating that the ELISA was not affected by nonspecific adsorption of these antibodies to the coated plates (*10*). The precision for concentrations at 5, 7.5, 10, 12.5, 15, 17.5, and 20 ng/mL on these curves was always C.V. ≤15%, and the accuracy within the interval of ±15% of the nominal values. The precision for both the lower and upper concentrations on the curves (2.5 and 25 ng/mL, respectively) was C.V. ≤20%, and the accuracy within ± 20% of the nominal values. These results satisfactorily met current acceptance criteria for validation of standard curves (*18*), so these curves were used to determine the concentrations of polyamine-modified and control $F(ab')_2$ in cell lysate samples.

As shown by the slopes of the titration curves for the PUT-$F(ab')_2$ (Figure 5), the antigen binding activity of the antibody decreases with the pH of the modification reaction: the decrease did not exceed 3% of the control when modification was performed at pH 6.5, and reached values up to ~20% by reducing the pH to 4.5 ($p < 0.01$ in all cases). Modification of the $F(ab')_2$ with SPD, SPM, and HMD at pH 4.5, respectively, also resulted in a decrease of roughly 20% in antigen binding activity, as compared with the corresponding control antibodies ($p < 0.001$ in all cases) (not illustrated). Furthermore, the similar results obtained with the $F(ab')_2$ modified with PUT, SPD, SPM, and HMD at pH 4.5 ($p = 0.305$) indicated that the type of coupled polyamine did not influence the antigen-binding activity of the $F(ab')_2$. Only small and nonsignificant differences were observed among the activities of the control antibodies ($p > 0.500$). Moreover, these activities were very similar to that determined for the native antitetanus $F(ab')_2$ in a previous study (*10*), also using HBSS/BSA as assay diluent.

Quantification of Antitetanus $F(ab')_2$ in HL60 Cell Lysates by ELISA. The quantitative analysis of cationized and control $F(ab')_2$ which were associated to the HL60 cells following incubation at 4 and 37 °C, respectively, was performed with an ELISA method (*10*) using total cell lysates. Thus, all cell-associated $F(ab')_2$, including surface-bound and internalized antibodies, were measured. Because this method is an antigen-binding capture ELISA, the antibodies measured are necessarily active antibodies. The results for the PUT-$F(ab')_2$ and the corresponding control $F(ab')_2$ are presented in Figure 6, and those for the HMD-, SPM-, and SPD-$F(ab')_2$ and their respective controls in Figure 7.

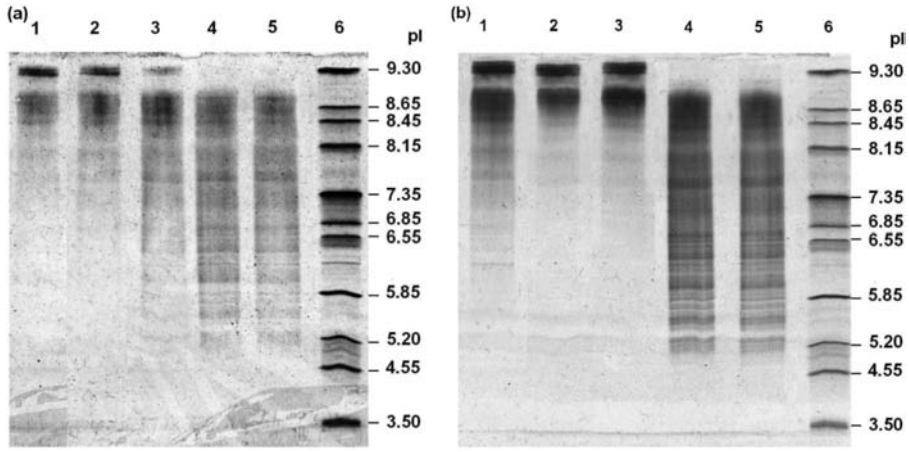

Figure 4. Analysis of polyamine-modified antitetanus $F(ab')_2$ by IEF. (a) Coomassie Blue stain of polyacrylamide gel IEF of PUT-$F(ab')_2$ modified at pH 4.5 (lane 1) along with the corresponding control $F(ab')_2$ (lane 4), and PUT-$F(ab')_2$ modified at pH 5.5 (lane 2) and pH 6.5 (lane 3), and the native $F(ab')_2$ (lane 5). (b) Coomassie Blue stain of polyacrylamide gel IEF of HMD-$F(ab')_2$ (lane 1), SPD-$F(ab')_2$ (lane 2), SPM-$F(ab')_2$ (lane 3) along with the corresponding control $F(ab')_2$ (lane 4), and the native $F(ab')_2$ (lane 5). Twenty micrograms of each $F(ab')_2$ were applied to the gel in (a), and 25 μg in (b), along with pI standards (lanes 6 in (a) and (b)). The pIs of the standards are shown on the right-hand border.

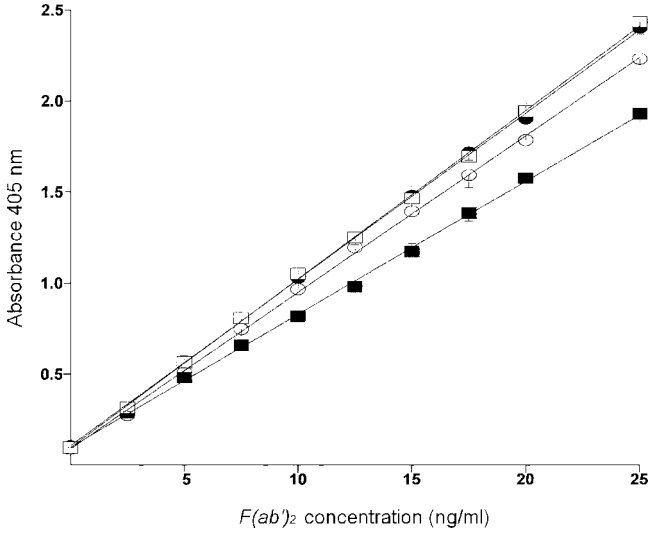

Figure 5. Titration curves measured by ELISA for the PUT-$F(ab')_2$ modified at pH 6.5 (●), pH 5.5 (○), and pH 4.5 (■), along with the control $F(ab')_2$ (□) corresponding to the latter. All antibodies were assayed at concentrations of 2.5, 5, 7.5, 10, 12.5, 15, 17.5, 20, and 25 ng/mL (duplicate measurements per level). Each titration curve was determined from the data of five different ELISA experiments. The experimental points correspond to mean values which are shown along with their S.D.. The solid lines are computer-estimated values. The equations of the titration curves for the PUT-$F(ab')_2$ modified at pH 6.5 and 5.5 are $y = -0.0913x + 0.107$ and $y = -0.0860x + 0.090$, respectively. The coefficients of correlation (r) of these curves were 0.9985 and 0.9976. The equations of the curves for the PUT-$F(ab')_2$ modified at pH 4.5 and the corresponding control are $y = -0.0729x + 0.099$ ($r = 0.9977$) and $y = -0.0925x + 0.097$ ($r = 0.9988$). x is the concentration of the $F(ab')_2$ in ng/mL, and y is the absorbance. The titration results for the SPD-, SPM-, and HMD-$F(ab')_2$ modified at pH 4.5 were not significantly different from those obtained with the PUT-$F(ab')_2$ modified at pH 4.5. No significant differences were found between the various control samples.

The amounts of cell-associated $F(ab')_2$ were greater at 37 than at 4 °C for the cationized and the control antibodies ($p < 0.001$). The amounts also increased as the initial antibody concentration was increased in the incubation medium ($p < 0.001$), the effect of concentration being greater at 37 °C than at 4 °C ($p < 0.001$ for the temperature-concentration interaction). No $F(ab')_2$ was measured in the blank cell samples (no antibody present).

Effect of the Degree of Antibody Modification on Cell Interaction. As shown in Figure 6, the amounts of PUT-$F(ab')_2$ associated with the cells increased as the number of coupled PUT molecules increased. The amounts measured at 4 or 37 °C for the $F(ab')_2$ coupled with three PUT molecules (the antibody modified at pH 4.5) were approximately 1.5 times higher, on average, than that measured for the $F(ab')_2$ coupled with two PUT molecules (the antibody modified at pH 5.5) and 2 times higher than that coupled with one PUT molecule (the antibody modified at pH 6.5). All the differences observed were significant ($p < 0.05$). The cell-associated amounts of all the PUT-$F(ab')_2$ were significantly higher than those of the corresponding control $F(ab')_2$ at each temperature and antibody level tested ($p < 0.05$). When the pH of the modification reaction decreased from 6.5 to 4.5, the variation between the cationized and control antibodies was accentuated. Small, albeit statistically significant, differences in cell-associated amounts were observed between the various control $F(ab')_2$ at both 4 and 37 °C ($p < 0.05$ for each temperature). These differences increased as the pH decreased. This suggests that the accessibility and/or relative distribution of amino acid side-chain groups on the antibody surface may be slightly changed by the pH of the reaction, thus mildly affecting the interaction of the control antibodies with the cells. Nonetheless, this was seen to have minimal effect on the IEF profiles of the control $F(ab')_2$ and none on their antigen-binding activities relative to the native antibody.

Effect of the Charge Valency of $F(ab')_2$ Coupled Polyamine. The amounts of cell-associated antibody measured for the $F(ab')_2$ modified with HMD, SPD, and SPM at pH 4.5 are shown in Figure 7. These antibodies had substitution ratios of approximately 3 coupled polyamine molecules per antibody molecule, which were similar to that of the PUT-$F(ab')_2$ modified at pH 4.5 (Table 1). Since 1 protonated amino group is left on a HMD or PUT molecule after coupling, and 2 and 3 of these groups are left on SPD and SPM molecules, respectively (Figure 1), the expected number of positive charges associated with these polyamines after coupling should increase in the order of HMD or PUT < SPD < SPM, with a corresponding increase in the antibody net charge valency of +3, +6, and +9, respectively. At all antibody concentrations tested, both at 4 and at 37 °C, the amounts of cell-associated HMD-$F(ab')_2$ (Figure 7) were similar to those measured for the PUT-$F(ab')_2$ modified at pH 4.5 (C.V. <18%) (Figure 6). These amounts were ~2.5 times lower, on average, than those measured for the $F(ab')_2$ modified with SPD or SPM at each temperature (p

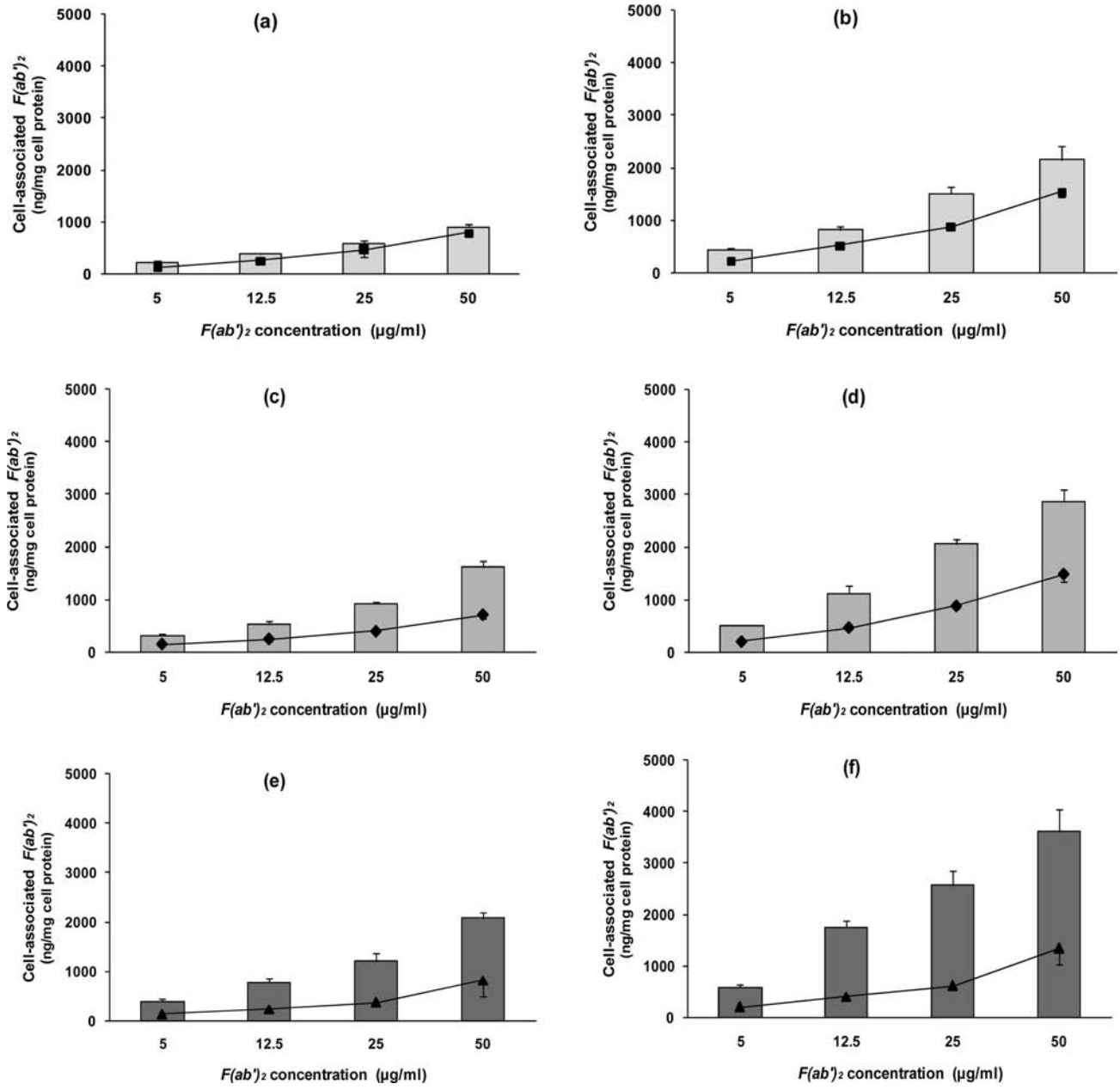

Figure 6. Cell-associated PUT-$F(ab')_2$ and control-$F(ab')_2$ measured by ELISA following incubation with HL60 cells at 4 and 37 °C. Cells were incubated for 120 min with different concentrations (5, 12.5, 25, or 50 μg/mL) of the PUT-$F(ab')_2$ modified at pH 6.5 (a and b), pH 5.5 (c and d), and pH 4.5 (e and f), at either 4 °C (a, c, and e) or 37 °C (b, d, and f). The figures also show the amounts of cell-associated antibody measured for the corresponding control $F(ab')_2$ (■, ◆, and ▲, respectively) after incubation with HL60 cells at these two temperatures. The results for the cationized $F(ab')_2$ are presented in bar graphs where the different shades of gray indicate different antibodies. The corresponding control $F(ab')_2$ are superimposed (-■-,-◆-, or -▲-). Mean values for the cationized $F(ab')_2$, as well as for the control $F(ab')_2$, are shown along with their S.D. These values are the results of three to seven independent experiments (each antibody level tested in duplicate in each experiment).

< 0.05 in each case) (Figure 7). However, the SPD-$F(ab')_2$ and SPM-$F(ab')_2$ showed similar cell-associated amounts at either 4 or 37 °C (C.V. <7%), indicating that an increase in the $F(ab')_2$ charge valency from +6 to +9 after coupling of SPD and SPM does not further increase the interaction of the antibody with the HL60 cells. In comparison, the cell-associated amounts of all three control antibodies for the HMD-, SPD-, and SPM-$F(ab')_2$ were significantly lower ($p < 0.05$ at each temperature and antibody concentration). Indeed, the amounts for the control antibodies corresponding to the SPD- and SPM-$F(ab')_2$ were up to 8 times lower, on average, when compared to the cationized antibodies. Only small differences were observed among all three control antibodies at either 4 or 37 °C (C.V. <13%). The cell viability checks performed throughout these experiments by Trypan blue exclusion indicated that none of the antibodies used at the present doses exerted cellular toxicity (cell viability ≥90% in all cases).

Inhibition of the Interaction of the Polyamine-Modified $F(ab')_2$ with HL60 Cells. Figure 8 illustrates the inhibition of the cell interaction of SPD-$F(ab')_2$ and that of the corresponding control $F(ab')_2$ by addition of (free) SPD and protamine. Higher concentrations of (free) SPD (Figure 8a) were needed to decrease the amounts of cell-associated SPD-$F(ab')_2$ relative to protamine (Figure 8b): the IC_{50} values calculated for these inhibitors were 568 ± 17 and 348 ± 10 μg/mL, respectively. Much lower inhibitory potencies were found for SPD and protamine when they were used to inhibit the cell interaction of the control $F(ab')_2$, with IC_{50} values of 1807 ± 61 and 988 ± 44 μg/mL. Moreover, the amounts of cell-associated antibody were reduced by only 50% for the control $F(ab')_2$ versus 75%

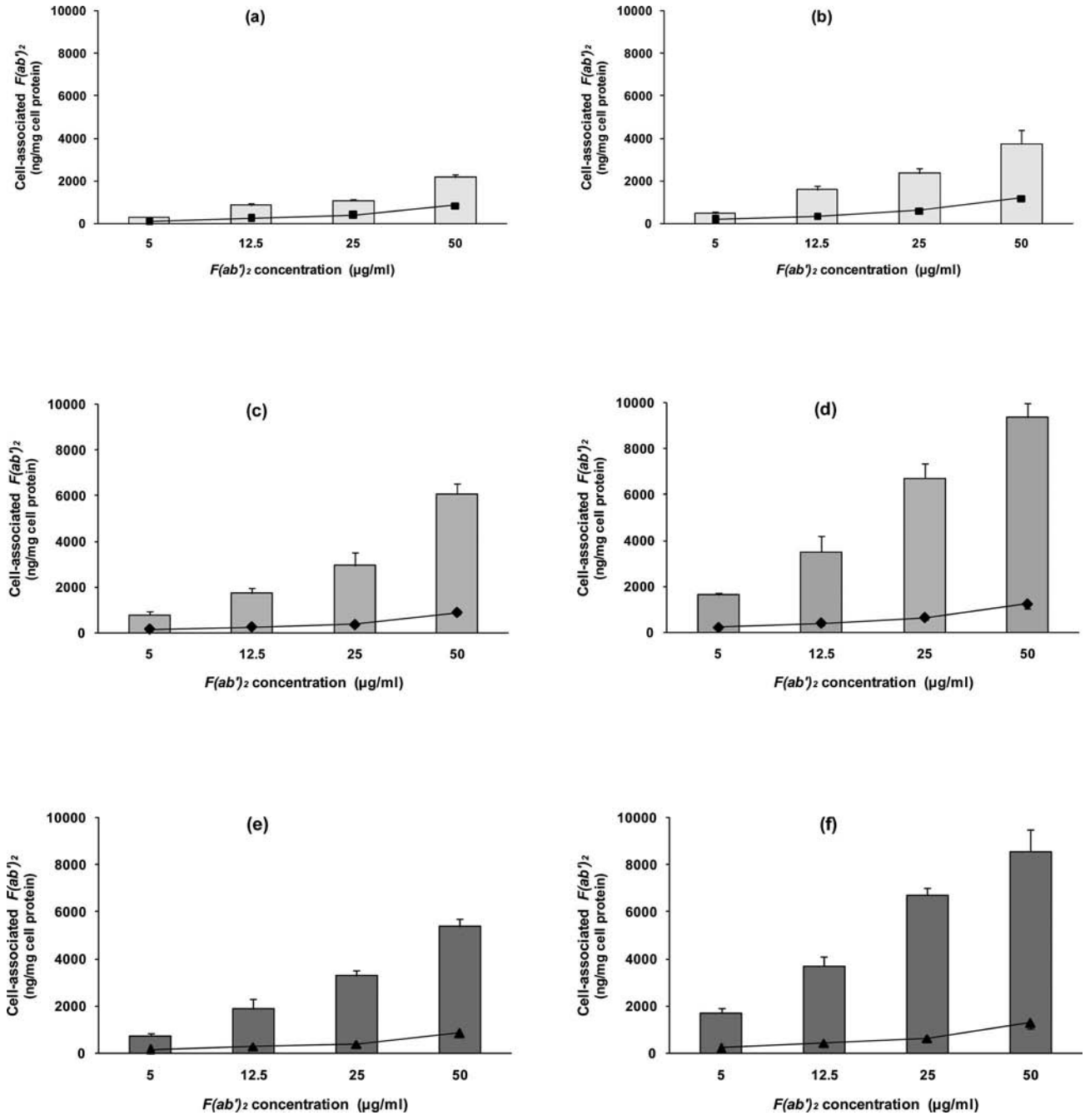

Figure 7. Cell-associated HMD-, SPD-, and SPM-$F(ab')_2$ and corresponding control-$F(ab')_2$ measured by ELISA following incubation with HL60 cells at 4 and 37 °C. Cells were incubated for 120 min with different concentrations (5, 12.5, 25, or 50 μg/mL) of the HMD-$F(ab')_2$ (a and b), SPD-$F(ab')_2$ (c and d), and SPM-$F(ab')_2$ (e and f), at either 4 °C (a, c, and e) or 37 °C (b, d, and f). The pH used in the modification reaction of the $F(ab')_2$ with HMD, SPD, or SPM was 4.5. The figures also show the amounts of cell-associated antibody measured for the corresponding control $F(ab')_2$ (■, ◆, ▲, respectively) after incubation with HL60 cells at these two temperatures. The results for the cationized $F(ab')_2$ are presented in bar graphs where the different shades of gray indicate different antibodies. The corresponding control $F(ab')_2$ are superimposed (-■-,-◆-, or -▲-). Mean values for the cationized $F(ab')_2$, as well as for the control $F(ab')_2$, are shown along with their S.D. These values are the results of three to seven independent experiments (each antibody level tested in duplicate in each experiment). Note that the scale on the *y*-axis is two times greater than that in Figure 6.

or more for the polyamine-modified antibody, at the highest inhibitor concentrations used.

Confocal Microscopic Studies. Two different antibody detection procedures were tested in preliminary experiments: a one-step procedure using a secondary antihorse $F(ab')_2$ conjugated to Texas red, and a two-step procedure that used first a secondary biotinylated antihorse $F(ab')_2$ and then a streptavidin-Alexa Fluor 488 conjugate. The two-step detection procedure gave better results than the other in terms of sensitivity, probably because of the signal amplification effect brought about through the biotin-streptavidin system. This procedure also had the advantage of using the same secondary antibody as in the ELISA assays. Figure 9 shows representative confocal microscopy images of HL60 cells incubated with either polyamine-modified or control $F(ab')_2$, using the biotin-streptavidin system for detection.

Wide-field images at low magnification (×10) of all the HL60 cells incubated with the various cationized $F(ab')_2$ at 37 °C gave comparable results in that all incubated cells showed the presence of associated antibodies which included both surface-

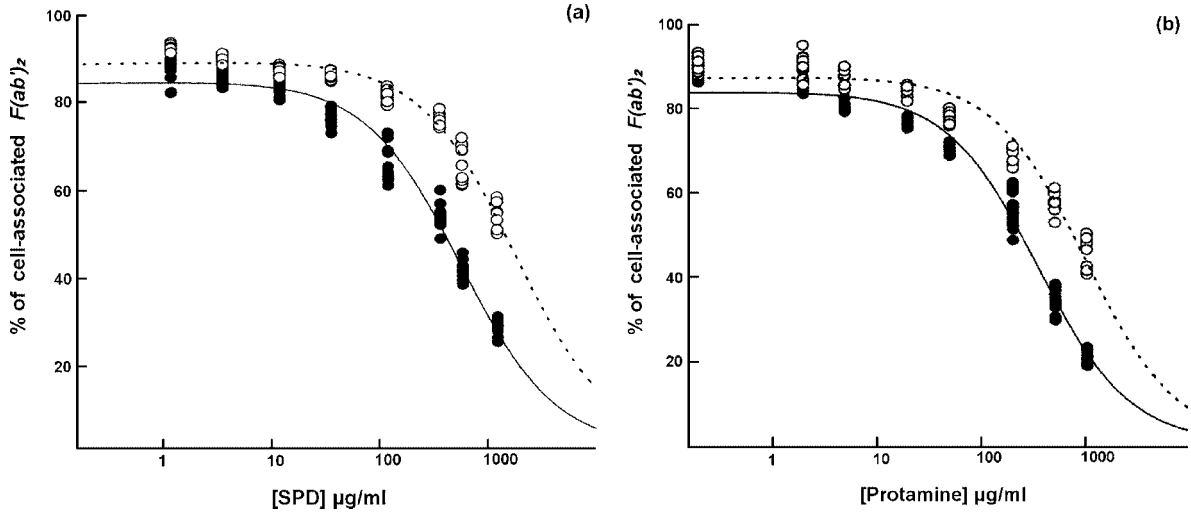

Figure 8. Inhibition of the interaction of SPD-$F(ab')_2$ (●; solid line) and corresponding control $F(ab')_2$ (○; dotted line) with HL60 cells by addition of free SPD (a) and protamine (b). Each antibody used at a concentration of 50 μg/mL was incubated with the cells in the presence of increasing concentrations of (free) SPD or protamine for 120 min at 37 °C. The inhibitor concentrations were 1.25, 3.75, 12.5, 37.5, 125, 375, 600, and 1250 μg/mL for SPD, and 0.205, 2.05, 5.125, 20.5, 51.25, 205, 512.5, and 1025 μg/mL for protamine. The percentage shown of cell-associated $F(ab')_2$ is the ratio of the cell-associated amount in the presence of inhibitor to the cell-associated amount in the absence of inhibitor. All the values shown are mean values from five independent experiments for the SPD-$F(ab')_2$ and four experiments for the control $F(ab')_2$ (each inhibitor concentration tested in duplicate in each experiment). The solid or dotted lines are computer-estimated values. The IC_{50} values of the inhibitors calculated from the inhibition data are given in the text along with their S.D.

bound and internalized $F(ab')_2$. However, a more detailed examination of the fluorescence pattern at ×40 or ×63 magnification, in combination with Nomarski images of the cells, showed specific differences between the cells incubated with the PUT- and HMD-$F(ab')_2$ conjugates and those incubated with the SPD- and SPM-$F(ab')_2$ conjugates. An intense punctured fluorescence was observed in the cytoplasm of the cells incubated with the various conjugates (Figures 9b and d), indicating that all of these conjugates were actually internalized at 37 °C. However, the fluorescence in cells incubated with the SPD-$F(ab')_2$ (Figure 9d) or the SPM-$F(ab')_2$ (not illustrated) was greater than the fluorescence in cells incubated with the PUT-$F(ab')_2$ (Figure 9b) or the HMD-$F(ab')_2$ (not illustrated). The different fluorescent intensities observed suggested that the HL60 cells internalized more of the antibodies cationized with SPD or SPM. This observation was consistent with the greater amounts of cell-associated antibody measured for the SPD- and the SPM-$F(ab')_2$ by ELISA relative to the PUT- and HMD-$F(ab')_2$ (Figures 6 and 7). For all internalized polyamine-$F(ab')_2$, fluorescence was localized in vesicular-like structures which may correspond to endosomes and/or lysosomes. In contrast to the results at 37 °C, fluorescence was associated only with the plasma membrane of the cells incubated with the cationized $F(ab')_2$ at 4 °C (Figure 9a,c). On the other hand, in HL60 cells incubated with the control $F(ab')_2$ at either 4 °C (Figure 9e) or 37 °C (Figure 9f), the fluorescence was very weak, and no fluorescence was detected in the cytoplasm, demonstrating that the $F(ab')_2$ did not undergo significant endocytosis when it was not cationized. No fluorescence was detected in the blank HL60 cells incubated without antitetanus $F(ab')_2$ but with all other reagents.

Estimation of Internalized Amounts of the Cationized $F(ab')_2$. Considering the ELISA results in light of those obtained by microscopy, we concluded that the cationized $F(ab')_2$ which were associated with the cells at 4 °C corresponded to surface-bound antibodies only (endocytosis is blocked at 4 °C (*19*)), while those at 37 °C corresponded to internalized antibodies as well as surface-bound antibodies. The cell-associated amounts of control $F(ab')_2$ at 4 °C was ascribed to nonspecific binding, and the amounts at 37 °C ascribed to nonspecific binding and perhaps nonspecific endocytosis (the contribution due to non-specific endocytosis must be small, since no control $F(ab')_2$ was detected inside the cells (Figure 9f)).

Using the ELISA measurements (Figures 6 and 7), we estimated the cell-internalized amounts of HMD-, SPD-, and SPM-$F(ab')_2$ as well as those for PUT-$F(ab')_2$ cationized at pH 4.5, all having the same maximum coupling. We did not include the PUT-$F(ab')_2$ modified at pH 5.5 and 6.5 because the interaction of these antibodies with the HL60 cells was less successful. For these calculations, the amounts of cell-associated control $F(ab')_2$ at 37 and 4 °C were subtracted from the amounts of cell-associated cationized $F(ab')_2$ at 37 and 4 °C, respectively, to eliminate any possible contribution due to nonspecific binding and/or nonspecific endocytosis. The amount of internalized cationized $F(ab')_2$ was then calculated as the difference between the cell-associated amounts at 37 °C and those at 4 °C. This calculation assumes that the amounts of cationized $F(ab')_2$ bound to the HL60 cell surface via electrostatic interaction were similar at both 4 and 37 °C, which seems reasonable because, as far as electrostatic interaction is concerned, the binding of cationic substances to anionic surfaces slightly increases when the temperature decreases if the process is enthalpy-driven (*20–22*). Therefore, this assumption could only lead to an underestimation of the amount of internalized antibody.

The results corresponding to these calculations are presented in Figure 10. The endocytosis of the cationized $F(ab')_2$ was concentration-dependent, but the relationship between the amount of antibody taken up by the cells and the corresponding concentration of cationized $F(ab')_2$ was not linear: the amount of internalized $F(ab')_2$ increased for concentrations ranging from 5 to 25 μg/mL, but reached a plateau for concentrations greater than 25 μg/mL. This could reflect a saturation in the internalization process of these antibodies by HL60 cells. The maximum amounts of SPD- and SPM-$F(ab')_2$ internalized by the cells were similar and amounted to ~3000 ng/mg cell protein. These values were approximately three times higher than those calculated for the PUT-$F(ab')_2$ as well as for the HMD-$F(ab')_2$. These results indicate that coupling the antitetanus $F(ab')_2$ to SPD and SPM in order to deliver this antibody into HL60 cells is more efficient

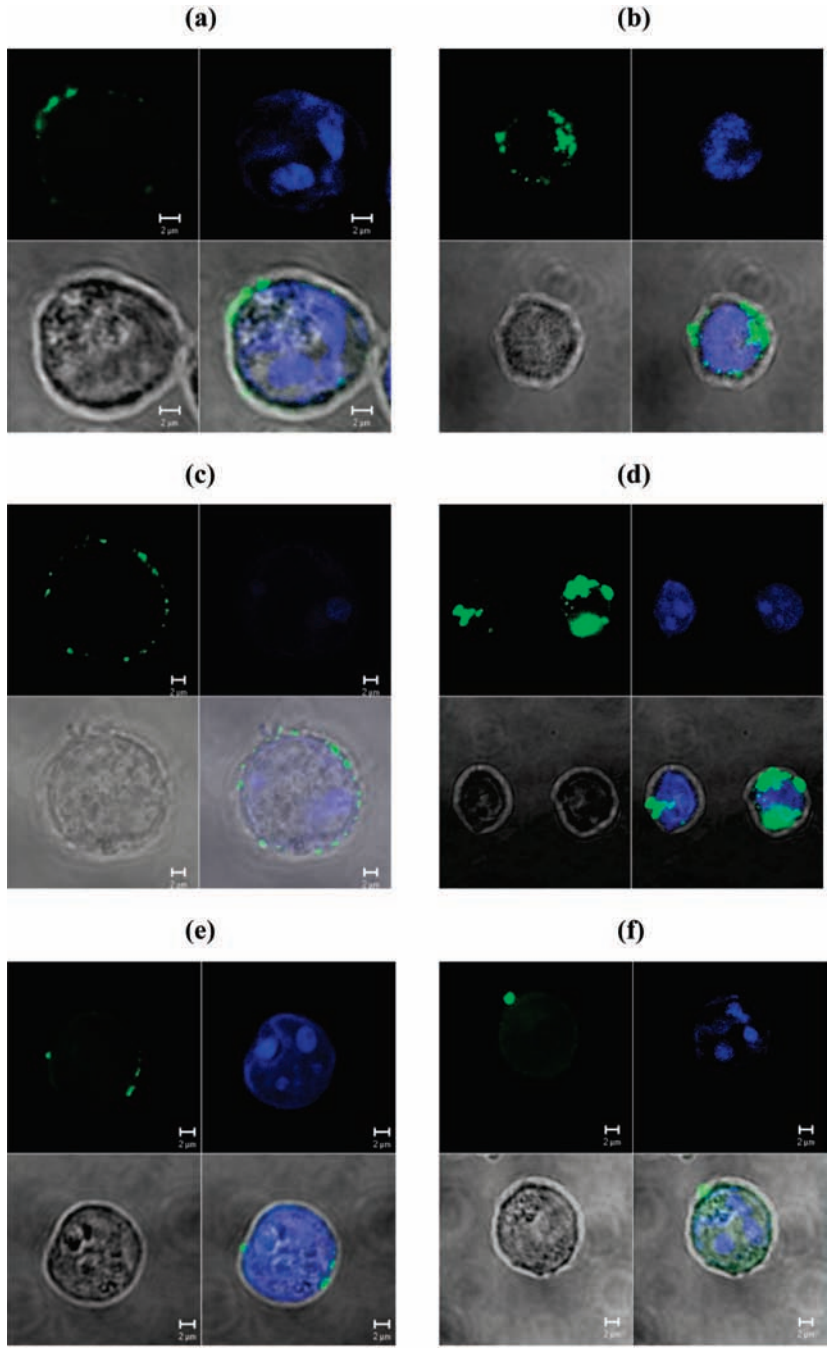

Figure 9. Internalization of cationized antitetanus $F(ab')_2$ fragments by HL60 cells, and effect of modification with different polyamines. Cells were incubated for 120 min with PUT-$F(ab')_2$ (a and b), SPD-$F(ab')_2$ (c and d), and control unmodified $F(ab')_2$ (e and f), at either 4 °C (a, c, and e) or 37 °C (b, d, and f). Bound and internalized $F(ab')_2$ fragments (green) were detected by immunofluorescence confocal microscopy using a biotinylated antihorse $F(ab')_2$ antibody/streptavidin−Alexa 488 conjugate system. Nuclear labeling (blue) was performed using toto-3. Nomarski images were used to visualize the cells. Scale bar = 2 μm.

than coupling to PUT and HMD, probably owing to the larger number of positive charges left after coupling on SPD and SPM.

DISCUSSION

As was stipulated in the introduction, our aim was to compare both the natural PUT, SPD, and SPM polyamines and the synthetic HMD polyamine after antibody cationization in order to, at the outcome, select the most effective polyamine in terms of antibody intracellular delivery. To this end, we used a systematic approach that encompassed (i) the cationization of polyclonal antitetanus $F(ab')_2$ with these polyamines, (ii) the degree of modification of the $F(ab')_2$ conjugates, (iii) their biological activity, and (iv) their interaction with HL60 cells. For these last two points, we used an ELISA method especially developed both to measure antibody binding activity after cationization and to quantify cell-associated antibodies after interaction with HL60 cells (*10*). Our choice of HL60 cells as a model is justified in that these cells have already shown their viability in other cellular internalization studies, one using antitetanus $F(ab')_2$ cationized with PUT (*10*), and another concerning IgG and its *Fab* fragments cationized with HMD (*6*).

By coupling HMD, PUT, SPD, or SPM to surface carboxyl groups of the $F(ab')_2$, we showed that the degree of modification of the antibody could be controlled by varying the pH of the reaction or the molar excess of polyamine relative to the

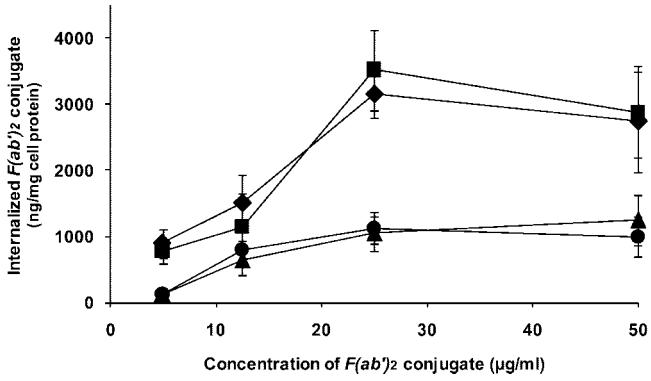

Figure 10. Internalization of cationized $F(ab')_2$ in HL60 cells estimated from ELISA-based measurements: effect of antibody cationization at pH 4.5 with various polyamines. The amounts of internalized PUT-$F(ab')_2$ modified at pH 4.5 (●) and HMD- (▲), SPD- (■), and SPM-$F(ab')_2$ (◆) were calculated from the data shown in Figures 6 and 7. The values of internalized antibody amounts are mean values, and are shown along with their standard deviation. Details of the calculations are described in the text.

antibody carboxyl groups, yielding a coupling of one, two, or three polyamine molecules per $F(ab')_2$ molecule. This study has taken protein cationization one step further compared to other studies where the different stages of cationization were evaluated only by the increase in the protein pI (*6, 17, 23–25*). In our study, we developed a procedure that quantitatively determines the degree of polyamine coupling of the antitetanus $F(ab')_2$. A definite cationization of the $F(ab')_2$ was achieved by high excess of polyamine, thus reducing the risk of cross-linking between $F(ab')_2$ molecules. Dialysis used alone was not found to be a sufficient method in eliminating the excess polyamine from the $F(ab')_2$ following cationization, as seen in other studies (*17*). Therefore, we were very careful in purifying the cationized $F(ab')_2$. Purification was obtained by a three-step procedure: ultrafiltration, gel filtration, and dialysis of the reaction products. The maximum coupling of three polyamine molecules per antitetanus $F(ab')_2$ molecule was relatively low. This result may not be surprising since, in its native form, this polyclonal antibody is characterized by a large content of high pI forms, indicating a low abundance of accessible carboxyl groups. The shift to high pIs observed after polyamine modification confirmed that the $F(ab')_2$ was readily cationized. In addition, this shift was more pronounced in the acidic $F(ab')_2$ species than in the other ones, and also when the antibody was modified at pH 4.5 rather than at higher pH levels.

The antigen-binding activity of cationized antibodies is critical to their use as potential drugs. Because cationization may compromise the antibody activity, we came up with an antigen-binding capture ELISA (*10*) which would quantify the biological activity of the cationized $F(ab')_2$, as well as the HL60 cellular interaction and the active amounts of cell-associated antibodies. There was a gradual decrease in the activity of the $F(ab')_2$ when cationized at decreasing pH values. The highest decrease observed was comparable to that reported for other cationized polyclonal antibodies (*26*) and stayed within tolerable limits. It was also consistent with the absence of structural changes in the antibody that would have altered mobility on SDS-PAGE. Accordingly, there was no need to perform cationization with antibody site protection.

To sum up, the HL60 cellular interaction of the cationized and control $F(ab')_2$ was quantified by ELISA, and the localization of these antibodies at the cellular level was visualized by confocal microscopy. The ELISA-based measurements showed that cationization of the $F(ab')_2$ significantly enhanced the interaction of the antibody with the cells, compared to control $F(ab')_2$. They also highlighted an increasing cell interaction of the polyamine-modified $F(ab')_2$ when the degree of polyamine coupling increased. Moreover and for similar degrees of coupling, the $F(ab')_2$ modified with the polyamines SPD and SPM (+6 and +9 positive charges, respectively, expected after modification) exhibited higher interactions with the HL60 cells than the antibodies modified with the diamines PUT and HMD (+3 positive charges expected for each). The HL60 cellular interaction was seen to depend on both temperature and antibody concentration. Furthermore, the confocal microscopy studies demonstrated clear internalization of the cationized $F(ab')_2$ by the HL60 cells at 37 °C, but not at 4 °C. In addition, the relationship between the estimated amount of internalized antibody and the tested dose of cationized $F(ab')_2$ indicated that the cell uptake of these antibodies reached a plateau. These results were consistent with those of previous studies which also showed that the internalization of HMD-cationized IgG and *Fab* fragments by HL60 cells (*6*), and the cell uptake of other HMD-modified antibodies using other cell models (*3, 5, 27*) was inhibited at low temperatures, and could become saturated. In contrast, and in spite of the preponderance of alkaline isoforms, the control antitetanus $F(ab')_2$, like the native $F(ab')_2$ (*10*), bound only in small amounts to the surface of the cells and did not undergo detectable endocytosis, showing that a basic pI in this context is not sufficient to cause significant antibody internalization, as observed in other studies (*4, 5*).

Taken together, these results suggest that the mechanism involved in cellular internalization of the polyamine-modified $F(ab')_2$ is an adsorptive-mediated endocytosis (AME). Indeed, AME is a temperature- and concentration-dependent transport process (*1, 28*) which depends predominantly on charge-charge interaction between the transported molecule and the cell surface (*3*). It typically becomes saturated and/or inhibited at higher doses than receptor-mediated endocytosis (*1*). These features are consistent with the particularly high concentrations of SPD and protamine needed to inhibit the HL60 cellular interaction of SPD-$F(ab')_2$. Moreover, the greater IC_{50} value determined for SPD in relation to protamine showed that protamine was a more potent inhibitor of the SPD-$F(ab')_2$ interaction with the HL60 cells than SPD, probably owing to its larger number of positive charges. Nonetheless, if the cationized $F(ab')_2$ enter the HL60 cells by virtue of charge interaction, our results raise the question as to why no further increase in cell uptake was observed when the number of ionizable amine groups left on the polyamine after protein coupling increased from +6 (for the SPD-$F(ab')_2$) to +9 (for the SPM-$F(ab')_2$), coupling to these two polyamines having the same maximum effect.

As has been established (*29, 30*), the protonation schema of (free) SPD and SPM showed normal first and second protonation reactions of their amine functions, while for the third protonation (and also the fourth for SPM) the basicity of the amine functions decreased. These variations of the macro-ionization constants are consistent with the difficulty of adding another positive charge on a molecule that is already positively charged, owing to repulsive interactions between electric charges of the same sign accumulating in a confined space (*29*). According to the pK_a values reported for SPD (10.8, 9.58, and 7.82) and for SPM (10.7, 9.7, 8.31, and 7.18), an SPD molecule will carry 2.8 positive charges at neutral pH, and an SPM molecule only 3.3 charges, although these values can change when electrolytes are present in the medium (*29, 30*). After protein coupling, the SPD molecule is expected to carry 2 positive charges, and an SPM molecule a maximum of 2.8 charges since the third protonation of coupled SPM remains difficult for electrostatic reasons. Moreover, the proximity of the third ionizable amine function of SPM to the site of coupling can decrease its accessibility to the solvent and affect its protonation, possible interaction of this function with vicinal charged amino acid side

chain groups on the protein surface notwithstanding. Owing to this, the global charge of SPM after protein coupling may only be due to the protonation of its two most external amine functions. In this case, the effective global charge brought about by coupling of SPM to $F(ab')_2$ would be similar to that of SPD; the respective effects thereof on antibody cell interaction and uptake would also be similar.

Due to the abundance of polyanions that surround cells, cationization of proteins is a reasonable method to endow them with the ability to penetrate cells via AME. In this study, we explored the idea of cationization via the carbodiimide-mediated amidation of the $F(ab')_2$. Nevertheless, other successful cationization methods have also been described, involving the chemical conjugation of proteins to polycationic polymers or to arginine/lysine-rich peptides (*2*). Another strategy for improving the cell entry of proteins is the covalent attachment of these molecules to cell-penetrating peptides (CPPs) (*31*). These peptides are heterogeneous in size and sequence, but they have an obvious common feature in their cationic nature. The uptake mechanisms of CPPs still remain ambiguous in that different CPPs can utilize diverse uptake mechanisms, depending on their cargo and biophysical properties. However, several studies have highlighted the crucial role of CPPs' basic residues in the translocating ability of these peptides (*31*). Various CPPs, including the Tat-derived peptides (*31*) and Syn-B peptides (*32*), have been associated with AME. There is experimental evidence that heparan sulfate proteoglycans (HSPG) (*33*), as well as other negatively charged cell surface components (*31*), are involved in the cell uptake of these peptides, thus reinforcing the possibility of an adsorptive endocytic process for some CPPs.

In conclusion, this is the first study, to our knowledge, which uses both synthetic and natural polyamines for antibody cationization and compares the effects of these modifications on antibody cell interaction and uptake. Modification of the antitetanus $F(ab')_2$ with the synthetic diamine HMD was as effective as with the natural diamine PUT, in terms of intracellular delivery. In comparison, modification with SPD or SPM gave better results, indicating that the increase in cell uptake observed after polyamine modification was, to a certain degree, dependent on the charge density associated with the coupled polyamine. The similar results for SPD- and SPM-$F(ab')_2$ suggest that the effective global charge for the cell uptake of polyamine-modified antibody may not simply correspond to the addition of the ionizable amine functions in the polyamine, but may also be related to differences in protonation between these functions, and to the reduced accessibility of the most internal amine function of SPM when it is coupled to $F(ab')_2$. In view of this, both the intrinsic properties of polyamines and the effect of protein coupling on the accessibility/protonation of their amine functions should be taken into account when planning to use these molecules as vectors to improve the intracellular delivery of proteins. Finally, a good example of a potential use for cationized antibodies would be a treatment for tetanus. This severe disease, caused by a bacterial toxin targeting the central nervous system (*34*), is currently treated with antitoxin antibodies. But while these antibodies can neutralize the toxin in the blood, they are ineffective when the toxin enters the nerve cells (*35*). It has been shown that cationization has the potential to facilitate transcytosis of antitetanus $F(ab')_2$ across an in vitro blood-brain barrier model (*36*). The present study showed robust internalization of this antibody following cationization with SPD and SPM, with retention of antigen binding activity after uptake. The cationized $F(ab')_2$ were localized in vesicle-like structures which may correspond either to endosomes or to lysosomes. The exact fate of cationized $F(ab')_2$ after internalization is unknown, but some of these proteins may be released by vesicular disruption and may gain access to the cytoplasm where they can bind and neutralize the toxin. Although these studies are encouraging, there is much to be learned before any cationization-mediated strategy can be developed to deliver antitetanus antibodies across the blood−brain barrier and into nerve cells, and also before the potential of cationized antitetanus antibodies as therapeutic substances for the treatment of tetanus can be pharmacologically exploited.

ACKNOWLEDGMENT

We would like to thank Dr. Charles Lutsch and the Aventis-Pasteur Company (Marcy l'Etoile, France) for providing us with the antitetanus $F(ab')_2$ fragments and tetanus anatoxin. This work was supported by a grant from INSERM.

LITERATURE CITED

(1) Bickel, U., Yoshikawa, T., and Pardridge, W. M. (2001) Delivery of peptides and proteins through the blood-brain barrier. *Adv. Drug Delivery Rev. 46*, 247–279.

(2) Futami, J., Kitazoe, M., Murata, H., and Yamada, H. (2007) Exploiting protein cationization techniques in future drug development. *Expert Opin. Drug Discovery 2*, 261–269.

(3) Kumagai, A. K., Eisenberg, J. B., and Pardridge, W. M. (1987) Absorptive-mediated endocytosis of cationized albumin and a beta-endorphin-cationized albumin chimeric peptide by isolated brain capillaries. Model system of blood-brain barrier transport. *J. Biol. Chem. 262*, 15214–15219.

(4) Pardridge, W. M., Kang, Y-S., Yang, J., and Buciak, J. L. (1995) Enhanced cellular uptake and in vivo distribution of a monoclonal antibody following cationization. *J. Pharm. Sci. 84*, 943–948.

(5) Pardridge, W. M., Buciak, J., Yang, J., and Wu, D. (1998) Enhanced endocytosis in cultured human breast carcinoma cells and *in vivo* distribution in rats of a humanized monoclonal antibody after cationization of the protein. *J. Pharmacol. Exp. Ther. 286*, 548–554.

(6) Hong, G., Chappey, O., Niel, E., and Scherrmann, J. M. (2000) Enhanced cellular uptake and transport of polyclonal immunoglobulin G and Fab after their cationization. *J. Drug Target. 8*, 67–77.

(7) Pardridge, W. M., Bickel, U., Buciak, J., Yang, J., and Diagne, A. (1994) Enhanced endocytosis and anti-HIV-1 activity of anti-rev antibodies after cationization. *J. Infect. Dis. 169*, 55–61.

(8) Pardridge, W. M., Kang, Y-S., Diagne, A., and Zack, J. A. (1996) Cationized hyperimmune immunoglobulins: pharmacokinetics, toxicity evaluation and treatment of human immunodeficiency virus-infected human-peripheral blood lymphocytes-severe combined immune deficiency mice. *J Pharmacol. Exp. Ther. 276*, 246–252.

(9) Poduslo, J. F., and Curran, G. L. (1996) Polyamine modification increases the permeability of proteins at the blood-nerve and blood-brain barriers. *J. Neurochem. 66*, 1599–1609.

(10) Welfringer, F., d'Athis, P., Scherrmann, J. M., and Hervé, F. (2005) Development and validation of an antigen-binding capture ELISA for native and putrescine-modified anti-tetanus F(ab′)2 fragments for the assessment of the cellular uptake and plasma kinetics of the antibodies. *J. Immunol. Methods 307*, 82–95.

(11) Laemmli, U. K. (1970) Cleavage of structural proteins during the assembly of the head of bacteriophage T4. *Nature 227*, 680–685.

(12) Urien, S. (1995) MicroPharm-K, a microcomputer interactive program for the analysis and simulation of pharmacokinetic processes. *Pharmacol. Res. 12*, 1225–1230.

(13) Gex-Fabry, M., and Balant, L. P. (1994) Pharmacokinetics of drugs. Considerations on data analysis using computer methods and currently available software for personal computers. *Handbook of Experimental Pharmacology* (Balant, L. P., and Welling, P. G., Eds) Vol *110*, pp 507−527, Springer Verlag, New York.

(14) Snedecor, G. W., and Cochran, W. G. (1957) Two-way classifications. *Statistical Methods*, 6th ed., pp 299−338, Chapter 11, The Iowa State University Press, Ames, IO.

(15) Snedecor, G. W., and Cochran, W. G. (1957) Analysis of covariance. *Statistical Methods*. 6th ed., pp 419−436, Chapter 14, The Iowa State University Press, Ames, IO.

(16) Hoare, D. G., and Koshland, D. E. (1967) A method for the quantitative modification and estimation of carboxylic acid groups in proteins. *J. Biol. Chem. 242*, 2447–2453.

(17) Bickel, U. (1995) Antibody delivery through the blood-brain barrier. *Adv. Drug Delivery Rev. 15*, 53–72.

(18) Shah, V. P., Midha, K. K., Findlay, J. W., Hill, H. M., Hulse, J. D., McGilveray, I. J., McKay, G., Miller, K. J., Patnaik, R. N., Powell, M. L., Tonelli, A., Viswanathan, C. T., and Yacobi, A. (2000) Bioanalytical method validation−a revisit with a decade of progress. *Pharm. Res. 17*, 1551–1557.

(19) Brickman, M. J., Cook, J. M., and Balber, A. E. (1995) Low temperature reversibly inhibits transport from tubular endosome to a perinuclear, acidic compartment in African trypanosomes. *J. Cell Sci. 108*, 3611–3621.

(20) Blouin, C., Guillemette, J. G., and Wallace, C. J. (2002) Probing electrostatic interactions in cytochrome c using site-directed chemical modification. *Biochem. Cell Biol. 80*, 197–203.

(21) Brandenburg, K., David, A., Howe, J., Koch, M. H., Andrä, J., and Garidel, P. (2005) Temperature dependence of the binding of endotoxins to the polycationic peptides polymyxin B and its nonapeptide. *Biophys. J. 88*, 1845–1858.

(22) Zhang, X., and Bruice, T. C. (2006) Temperature dependence of the structure of the substrate and active site of the Thermus thermophilus chorismate mutase E x·S complex. *Biochemistry 45*, 8562–8567.

(23) Poduslo, J. F., and Curran, G. L. (1996) Increased permeability of superoxide dismutase at the blood-nerve and blood-brain barriers with retained enzymatic activity after covalent modification with the naturally occurring polyamine, putrescine. *J. Neurochem. 67*, 734–741.

(24) Wengenack, T. M., Curran, G. L., Olson, E. E., and Poduslo, J. F. (1997) Putrescine-modified catalase with preserved enzymatic activity exhibits increased permeability at the blood nerve and blood-brain barriers. *Brain Res. 767*, 128–135.

(25) Poduslo, J. F., Curran, G. L., and Gill, J. S. (1998) Putrescine-modified nerve growth factor: bioactivity, plasma pharmacokinetics, blood-brain/nerve barrier permeability, and nervous system biodistribution. *J. Neurochem. 71*, 1651–1660.

(26) Gauthier, V. J., Mannik, M., and Striker, G. E. (1982) Effect of cationized antibodies in preformed immune complexes on deposition and persistence in renal glomeruli. *J. Exp. Med. 156*, 766–777.

(27) Triguero, D., Buciak, J. B., Yang, J., and Pardridge, W. M. (1989) Blood-brain barrier transport of cationized immunoglobulin G: enhanced delivery compared to native protein. *Proc. Natl. Acad. Sci. U.S.A. 86*, 4761–4765.

(28) Audus, K. L., Chikhale, P. J., Miller, D. W., Thompson, S. E., and Borchardt, R. T. (1992) Brain uptakes of drugs: the influence of chemical and biological factors. *Adv. Drug Res. 23*, 1–64.

(29) De Robertis, A., Foti, C., Giuffre, O., and Sammartano, S. (2001) Dependence on ionic strength of polyamine protonation in NaCl aqueous solution. *J. Chem. Eng. Data 46*, 1425–1435.

(30) De Stefano, C., Giuffre, O., and Sammartano, S. (2005) Protonation constants of ethylenediamine, diethylenetriamine, and spermine in NaCl(aq), $(CH_3)_4NCl$(aq), and $(C_2H_5)_4NI$(aq) at different ionic strengths and $t = 25°C$. *J. Chem. Eng. Data 50*, 1917–1923.

(31) Tréhin, R., and Merkle, H. P. (2004) Chances and pitfalls of cell penetrating peptides for cellular drug delivery. *Eur. J. Pharm. Biopharm. 58*, 209–223.

(32) Drin, G., Cottin, S., Blanc, E., Rees, A. R., and Temsamani, J. (2003) Studies on the internalization mechanism of cationic cell-penetrating peptides. *J. Biol. Chem. 278*, 31192–31201.

(33) Belting, M. (2003) Heparan sulfate proteoglycan as a plasma membrane carrier. *Trends Biochem. Sci. 28*, 145–151.

(34) Grumelli, C., Verderio, C., Pozzi, D., Rossetto, O., Montecucco, C., and Matteoli, M. (2005) Internalization and mechanism of action of clostridial toxins in neurons. *Neurotoxicology 26*, 761–767.

(35) Scherrmann, J. M. (1994) Antibody treatment of toxin poisoning: recent advances. *J Toxicol. Clin. Toxicol. 32*, 363–375.

(36) Girod, J., Fenart, L., Regina, A., Dehouck, M. P., Hong, G., Scherrmann, J. M., Cecchelli, R., and Roux, F. (1999) Transport of cationized antitetanus Fab'_2 fragments across an *in vitro* blood-brain barrier model: involvement of the transcytosis pathway. *J. Neurochem. 73*, 2002–2008.

BC800045X

Structure, Photophysical Property, and Cytotoxicity of Human Serum Albumin Complexed with Tris(dicarboxymethylene)[60]fullerene

Xue Qu,[†] Teruyuki Komatsu,*[,†,‡] Takaaki Sato,[†] Otto Glatter,[§] Hirohisa Horinouchi,[||] Koichi Kobayashi,[||] and Eishun Tsuchida*[,†]

Research Institute for Science and Engineering, Waseda University, 3-4-1 Okubo, Shinjuku-ku, Tokyo 169-8555, Japan, PRESTO, Japan Science and Technology Agency (JST), Institute of Chemistry, University of Graz, Heinrichstrasse 28, A-8010 Graz, Austria, and Department of Thoracic Surgery, School of Medicine, Keio University, 35 Shinanomachi, Shinjuku-ku, Tokyo 160-8582. Received February 6, 2008; Revised Manuscript Received June 18, 2008

We present structure, photoexcited triplet-state property, and singlet oxygen ($^1O_2$) generation capability of human serum albumin complexed with a tris(dicarboxymethylene)[60]fullerene C_3-isomer (HSA−CF). Small angle X-ray scattering measurements showed that a globular size-dimension and surface charge distribution of HSA were unaltered by monomolecular complexation of CF into the hydrophobic cavity. Laser flash photolysis to the HSA−CF solution yielded a photoexcited triplet state of the CF chromophore (^{3}CF*) with lifetime of 46 μs. In the presence of O_2, energy transfer occurred from HSA−^{3}CF* to O_2 to generate $^1O_2$; the quenching rate constant [$k_q(O_2)$] was determined to be 2.2×10^8 M^{-1} s^{-1}. The HSA−CF showed strong photoresistence relative to HSA complexed with a protoporphyrin IX. The quantum yield of $^1O_2$ production for this artificial protein was compared to those of other photosensitizing agent. The HSA−CF did not show a dark cytotoxicity, but induced cell death efficiently under visible light irradiation.

INTRODUCTION

Photodynamic therapy (PDT) is a nonsurgical cancer treatment that combines a photosensitizing medication with exposure to visible light (*1, 2*). Highly cytotoxic singlet oxygen ($^1O_2$) formed by energy transfer from photoexcited sensitizer to molecular O_2 has been implicated as an intermediary species leading to cell death in tumors. To accelerate this $^1O_2$ generation, a range of organic dyes, especially porphyrin compounds, have been synthesized as photosensitizers (*3*). The most widely used reagent in clinical PDT is Photofrin, which is a heterogeneous mixture of hematoporphyrin oligomers (*1, 2, 4*). Several porphyrin or chlorin derivatives are also being tested as second generation (*1, 2, 5, 6*). Another well-known agent approved by the FDA is Levulan; 5-aminolevulinic acid (ALA) (*7–9*). ALA-induced photosensitization is unique approach that utilizes the heme biosynthetic pathway to produce endogenous protoporphyrin IX (PP). When ALA enters cancer cells, it triggers the synthesis of PP, which acts as an active sensitizer. Wavelengths typically used in PDT are between 600 and 800 nm, because light below 600 nm is absorbed by tissues and hemoglobin (Hb). Photofirin is normally excited by a red light (630 nm) using an Excimer dye-laser (*1, 2*). The ALA-PDT also uses the 630 nm laser, while the irradiation using a metal halide lamp or xenon arc lamp is still popular, because this is reasonable in comparison to the expensive laser pulse system and suitable for irradiation of the wide area of the diseased part (*9*). In fact, the light source approved in the U.S. for ALA-PDT was halogen lamp (λ_{exc} = 410 nm). Buckminster[60]fullerene (C_{60}) produces $^1O_2$ by energy transfer with extremely high quantum yield (Φ_Δ: 0.96, λ_{exc} = 532 nm) (*10, 11*) and generally shows strong photoresistance compared to the porphyrins. Consequently, various water-soluble fullerenes and fullerene−polymer hybrids have been prepared as a new class of photosensitizer for $^1O_2$ production (*11–16*). However, we would like to emphasize herein that most exogenous compounds administered into our bloodstream are immediately captured by human serum albumin (HSA, Mw: 66.5 kDa), which is the major protein component in our blood plasma (*17, 18*). To evaluate the biological performance of the fullerene, we must investigate the structure and function of the HSA−fullerene complex. Despite that necessity, photochemistry of the HSA−fullerene complex has never been studied to date. In this paper, we report for the first time the structure and photoexcited triplet-state properties of HSA complexed with a tris(dicarboxymethylene)[60]fullerene C_3-isomer (HSA−CF) and highlight its photoinduced energy transfer to O_2 to produce $^1O_2$. Furthermore, cytotoxicity of HSA−CF in vitro has also been evaluated. It is known that CF acts as a neuroprotective agent (*19*) and binds to HSA (*20*), but its photophysical behavior and cytotoxicity under visible light irradiation have not been elucidated.

EXPERIMENTAL PROCEDURES

Materials and Apparatus. All reagents were purchased from commercial sources as special grades and used without further purification. Recombinant HSA expressed in *Pichia pastoris* was purchased from Sigma-Aldrich Corp. Tris(dicarboxymethylene)-[60]fullerene C_3-isomer (CF) was purchased from Axxora LLC and 2-[4-(2-hydroxyethoxy)phenyl]-1,3-dioxolo-4*a*,5*a*-[60]fullerene (HF) was purchased from FLOX Corp. Protoporphyrin IX (PP), protoporphyrin IX dimethyl ester (PPDME), and [60]fullerene (C_{60}) were purchased from Sigma-Aldrich Corp. The water was deionized using a Millipore Elix and Simpli Laboratory-UV. The UV−vis absorption spectra for the potassium phosphate buffered (PB) solution (pH 7.0, 50 mM) of the HSA−fullerene complex (normally 20 μM) were recorded using an Agilent 8453 UV−visible spectrophotometer with an Agilent

* Corresponding author. (E.T.) Tel: +81-3-5286-3120, Fax: +81-3-3205-4740, E-mail: eishun@waseda.jp. (T.K.) E-mail: teruyuki@waseda.jp.
[†] Waseda University.
[‡] PRESTO, JST.
[§] University of Graz.
[||] Keio University.

10.1021/bc800207j CCC: $40.75 © 2008 American Chemical Society
Published on Web 07/22/2008

89090A temperature control unit. The CD spectra for the PB solution of the HSA−fullerene complex were measured using a JASCO J-820 circular dichrometer. The concentration of the HSA sample was 2 μM and a quartz cuvette with a 2.0 mm thickness was used for measurements in the range 195−250 nm. Mass spectroscopic analyses were performed using a JEOL JMS-T100CS ESI-TOF mass spectrometer.

Preparations of HSA−Fullerene Complexes. Typically, 3.92 mL of a PB solution (pH 7.0, 50 mM) of HSA (0.25 mM) was mixed with 1.0 mL of 0.98 mM CF in PB (CF/HSA molar ratio of 1:1) and incubated for 12 h with rotation in the dark at room temperature. The complex was then diluted with 50 mM PB solution and concentrated to the initial volume using a Vivaspin 20 centrifuge filter (5 kDa MW cutoff) at 4000 × *g* using a Beckman Coulter Allegra X-15R centrifuge. In the case of HSA−HF, 4.29 mL of PB solution (pH 7.0, 50 mM) of HSA (42 μM) was mixed with 0.67 mL of 0.267 mM HF in DMSO (HF/HSA molar ratio of 1:1) and incubated for 12 h with rotation in the dark at room temperature ([DMSO] = 13.5 vol %). The complex was then diluted using 50 mM PB solution and concentrated to the initial volume using a Vivaspin 20 centrifuge filter at 4000 × *g*. These dilution/concentration cycles were repeated to reduce the DMSO concentration to <0.1 vol %. The obtained protein solution was loaded on a Superdex 75 g gel-permeation column by elution of 50 mM PB using an ÄKTA Prime Plus FPLC system; only one band was observed during the chromatography. The PB solutions (pH 7.0, 50 mM) of HSA−CF and HSA−HF ([HSA]: 20 μM) in a 10-mm-path length optical quartz cuvette sealed with a rubber septum was degassed and purged using N_2 prior to use. The HSA complexed with PP (HSA−PP) was also prepared by the same procedure as HSA−HF.

HPLC. HPLC measurement of the HSA−fullerene complex was carried out using an HPLC system consisted of a Shimadzu LC-8A pump and a Shimadzu SPD-10A UV detector. A Shodex Protein KW-803 column was used with PB (pH 7.0, 10 mM) as the mobile phase at 22 °C (1.0 mL min^{-1}).

Isoelectric Focusing (IEF). The IEF was performed using an Amersham Biosciences Electrophoresis Power Supply EPS 301 with an Invitrogen Novex pH 3−7 IEG Gel. The protein marker used was a GE Healthcare IEF calibration kit Low Range *p*I (pH 2.5−6.5). The voltage was gradually raised to 300 V for 4 h. The gels were stained by a Daiichi Pure Chemicals PAGE Blue 83 and distained by washing with aqueous ethanol/acetic acid and 10% acetic acid.

Small-Angle X-ray Scattering (SAXS). SAXS experiments were carried out using an Anton Paar SAXSess camera in the *q*-range 0.10−9.0 nm^{-1}. Deionization of the protein sample was performed by dilution/concentration cycles with pure water using Vivaspin 20 centrifuge filter (5 kDa MW cutoff) at 4000 × *g*, giving an aqueous solution of the HSA−CF complex. Washing with phosphate buffered saline (PBS) solution (pH 7.4, 150 mM) gave the PBS solution of the protein. The scattered intensity $I(q)$ was generally given as $I(q) = nP(q)S(q)$ for globular particle system, where n is the particle number density, $P(q)$ is the form factor, and $S(q)$ is static structure factor. The measured intensities were normalized to give the uniform primary intensity at $q = 0$ and converted into absolute scale using water as a secondary standard. A model-independent collimation-correction procedure was made via an indirect Fourier transformation (IFT) technique. The pair-distance distribution functions $p(r)$ of HSA and HSA−CF in solution, which are given as inverse Fourier transformations of the form factor $P(q)$ into real space, were obtained using IFT technique for a highly diluted sample ($S(q) \sim 1$) and its generalized version (GIFT) for $c > 1$ g dL^{-1}. The GIFT technique enables splitting of $I(q)$ into $P(q)$ and $S(q)$, letting $P(q)$ and the resulting $p(r)$ virtually model free, where we assumed a screened Coulomb (Yukawa) potential and Rogers-Young (RY) closure relation. We made a complementary analysis to deduce the experimental structure factor, $S(q)^{exp}$, by dividing the normalized intensity $I(q)/c$ by the experimental form factor $P(q)^{exp}$ determined at very low concentration, which confirms the validity of the GIFT results.

Laser Flash Photolysis. The transient absorption spectra and triplet lifetime measurements were carried out using a Unisoku TSP-1000WK time-resolved spectrophotometer with a Spectron Laser Systems SL803G-10 Q-switched Nd:YAG laser, which generated a second-harmonic (532 nm) pulse of 6 ns duration (10 Hz) (*21*). The samples (20 μM) of the PB solutions (50 mM, pH. 7.0) of HSA−CF, HSA−HF, HSA−PP, THF solution of PPDME, and toluene solution of C_{60} were held in a quartz cuvette (optical path length; 10 mm); experiments were carried out at 22 °C. The gas mixture with the desired partial pressure of O_2/N_2 prepared by a KOFLOC Gasbrender GB-2C was flowed into the sample cuvette for 20 min for equilibration.

Near-Infrared Photo-Counting Measurement. The emission spectrum of $^1O_2$ ($^1\Delta_g \rightarrow {}^3\Sigma_g^-$) was measured using a Hamamatsu Photonics C8282W Near-Infrared Photo-Counting System equipped with a Hamamatsu Photonics R5509 photomultiplier and a Q-switched Nd:YAG laser, which generated a second-harmonic (532 nm) pulse (20 Hz, 60 μJ/pulse at the sample position). The gate time width was 2−100 μs. The samples (40 μM) were held in a quartz cuvette (optical path length 10 mm). The experiments were carried out in air at 22 °C. Quantum yield of $^1O_2$ (Φ_Δ) production by HSA−CF was determined using rose bengal as the standard compound.

In Vitro Cytotoxicity Evaluation. The LY80 tumor cell, a variant of the Yoshida sarcoma, was kindly gifted from Dr. Katsuyoshi Hori, Tohoku University. The cells were grown at 37 °C in DMEM supplemented with 10% fetal bovine serum (FBS) and penicillin (100 IU/cm^3) in 95% air−5% CO_2 humidified incubator. The cell solution (2.5×10^5 cells/mL, 0.16 mL) was mixed with PBS (0.04 mL) or PBS solution of HSA−CF (100 μM, 0.04 mL) in a Corning Costar 3596 cell culture plate (96 well) and incubated in the dark. Then the plate was irradiated by visible light using a 500 W halogen lamp in conjunction with a HOYA HA30 heart absorption filter (330−700 nm). The power at the cell level was monitored using a Gentec Power Meter and adjusted to 20 mW cm^{-2}. The temperature was kept at 36 ± 1 °C during the irradiation. As a negative control, we examined another PBS group in the same culture plate without light irradiation. After 2 h, the cell numbers were counted using microscopy under tripan blue staining.

RESULTS AND DISCUSSION

Structure of HSA−Fullerene Complexes. The HSA−fullerene complexes were prepared essentially as described previously for HSA−hemin complexes (*21*). A phosphate buffered (PB) solution (pH 7.0, 50 mM) of HSA was mixed with PB solution of CF (CF/HSA molar ratio of 1:1) and incubated for 12 h. The complex was then concentrated to the initial volume using a centrifuge filter (Figure 1 inset photograph). The filtrate was colorless during the centrifugation. The gel permeation chromatogram (Superdex 75 g) of the orange-colored protein exhibited only a single elution peak. These results indicate that CF is efficiently incorporated into HSA. For comparison, hydrophobic fullerene, 2-[4-(2-hydroxyethoxy)-phenyl]-1,3-dioxolo-4a,5a-[60]fullerene (HF), was also complexed with HSA to give HSA−HF. The obtained HSA−fullerene solutions can be concentrated up to 3.75 mM (25 g dL^{-1}); they were stable for a year without precipitation.

The UV−vis absorption spectroscopic features of the HSA−CF solution are the sum of those from the individual HSA and CF (Figure 1), which indicates that CF is monomolecularly

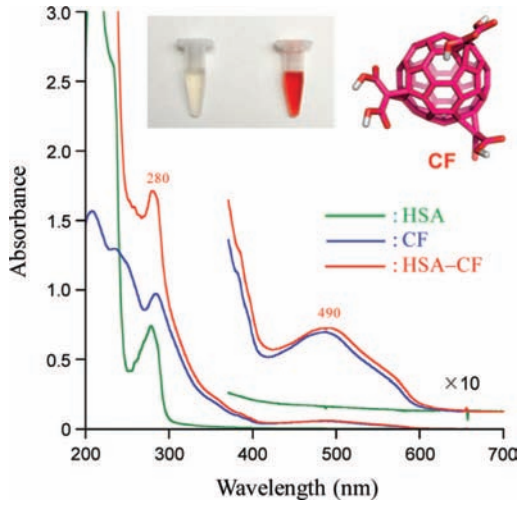

Figure 1. UV−vis absorption spectrum of HSA−CF complex, CF and HSA (20 μM) in PB solution (pH 7.0, 50 mM) at 22 °C. Inset photographs are 5 g dL^{-1} HSA (left) and HSA−CF (right) solutions.

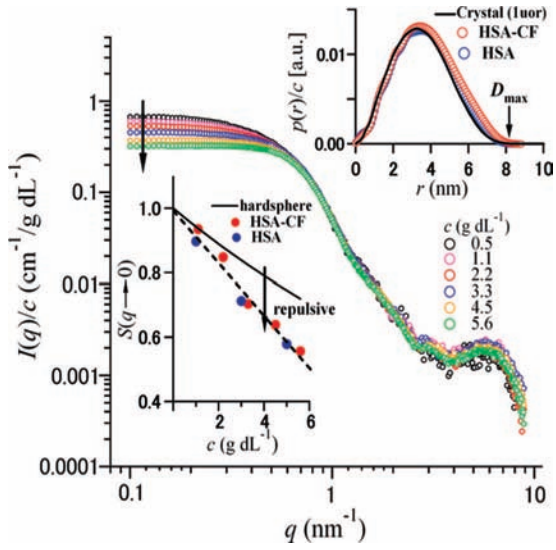

Figure 2. Normalized SAXS intensities [$I(q)/c$] of HSA−CF complex in 150 mM PBS solutions (c = 0.5−5.6 g dL^{-1}). The upper and lower insets show pair-distance distribution functions [$p(r)$] and extrapolated structure factors [$S(q\to 0)$] of HSA−CF and HSA, respectively.

incorporated into HSA and no specific interaction between the two molecules at the ground state. In contrast, the absorption spectrum of the brown-colored HSA−HF solution did not coincide with the superposition of the HSA and HF spectra (Figure S1). The increased absorbance at 380−550 nm suggests the formation of HF clusters in the protein (*11, 16*).

The HSA−CF complex was sufficiently stable to apply the HPLC measurement. In the elution profile, a single peak appeared at a retention time of 7.64 min, which was slightly earlier than that of HSA itself (7.75 min) (Figure S2). The ratio of the peak intensity monitored at 280 nm (based on HSA) and at 490 nm (based on CF) (I_{280}/I_{490} = 30) was exactly the same as the absorbance ratio at 280 and 490 nm in the UV−vis absorption spectrum (A_{280}/A_{490}) of HSA−CF, which implies that all CF molecules were eluted within the HSA fraction.

The ESI-TOF mass spectroscopy of HSA−CF showed a distinct ion peak at 67 587 Da, which corresponds to the mass of the equivalent complex of HSA−CF. On the other hand, two separated peaks were observed in the HSA−HF spectrum at 66 585 (free HSA) and 68 296 Da, that reveals 1:2 stoichiometry for HSA/HF and the formation of HF clusters in the protein. The CD spectral patterns and intensities of HSA−CF and HSA−HF were identical to those of HSA (Figure S3). We inferred that fullerene binding did not change the highly ordered structure of the host HSA.

The incorporation of negatively charged CF having hexacarboxyl groups might influence the surface charge distribution of albumin. However, isoelectric focusing of HSA−CF indicated the same isoelectric point (*p*I) with HSA. This contrasts sharply to the fact that fatty acid binding induced the reduction of the *p*I value because of partial neutralization of the molecular charge (*22*). We then used small-angle X-ray scattering (SAXS) to evaluate the globular particle structure and protein−protein interactions of HSA−CF (Figure 2) (*23*). The pair-distance distribution functions [$p(r)$] of HSA−CF and HSA were almost identical to the curve calculated from crystallographic data of HSA (1uor) (Figure 2 upper inset). It demonstrates that the maximum diameter (D_{max}: *ca.* 8 nm) and three-dimensional particle shape of HSA were unaltered by complexation of CF. The normalized SAXS intensities [$I(q)/c$] of HSA−CF at the low q range [$I(q\to 0)/c$] monotonously decreases with increasing protein concentration. In the PBS solution, the long-range electrostatic repulsion between HSA−CFs is efficiently screened, so that the suppressed forward intensity could be mainly due to excluded volume effect. However, the extrapolated structure factors [$S(q\to 0)$] of HSA−CF and HSA, which reflect the net repulsive forces between the protein molecules, were systematically lower than that predicted for hardsphere with an identical volume fraction (Figure 2 lower inset). The negative deviations are attributed to the electrostatic repulsion between the proteins. It is remarkable that the plots of $S(q\to 0)$ for HSA−CF and HSA perfectly lie on the same line, suggesting that HSA preserves its surface net charges upon the CF binding. On the basis of these results, we conclude that (i) CF is accommodated into the deep hydrophobic cavity of HSA with internal charge neutralization, and (ii) it does not induce marked changes in the globular particle size and surface charge distribution of HSA.

Photoexcited Triplet State of HSA−CF Complex and $^1O_2$ Formation. Photoexcitation of the fullerenes generates the singlet state, which undergoes intersystem crossing to the triplet state in high yield (*10, 11*). Laser flash photolysis (SHG of Nd:YAG, 532 nm, 6 ns) of the HSA−CF solution under an N_2 atmosphere gave a triplet−triplet (T-T) absorption spectrum of the ^{3}CF* chromophore (λ_{max} = 740 nm) (Figure 3) (*11, 13, 24*). The time course of the absorbance decay was composed of a single exponential kinetics with a lifetime (τ_T) of 46 μs (Figure 3 inset). The peaks of maximum absorption and τ_T value resembled those of the aqueous CF solution (τ_T: 43 μs). These observations again support that CF is held monomolecularly within the HSA interior.

Although HF in DMSO exhibited clear triplet absorption (τ_T: 31 μs), HSA−HF showed no signals in this wavelength range (Figure S4). The extremely short triplet lifetime of HSA−HF is probably attributed to T-T annihilation of the HF aggregates in the protein (*11*). If this is the case, the lifetime should become longer when the laser pulse energy is decreased. However, the decay was too fast to analyze precisely even under the weak laser flash photolysis.

In the presence of O_2, the triplet lifetime of HSA−CF significantly decreased. Energy transfer occurred from HSA−^{3}CF* to the O_2 molecule to generate active $^1O_2$. The Stern-Volmer plot clearly depicts a linear correlation for O_2 concentrations of 0−1.0 mM, giving the Stern-Volmer constant (K_{SV}) and quenching rate constant [$k_q(O_2)$] (Figure 4) [Note: $\tau_T^0/\tau_T = K_{SV}[O_2]$ (τ_T^0 and τ_T represent triplet lifetimes in the absence and presence of O_2)].The $k_q(O_2)$ of HSA−CF was 2.2 $\times$ 10^8 M^{-1} s^{-1}, which is one-seventh that of the monomeric

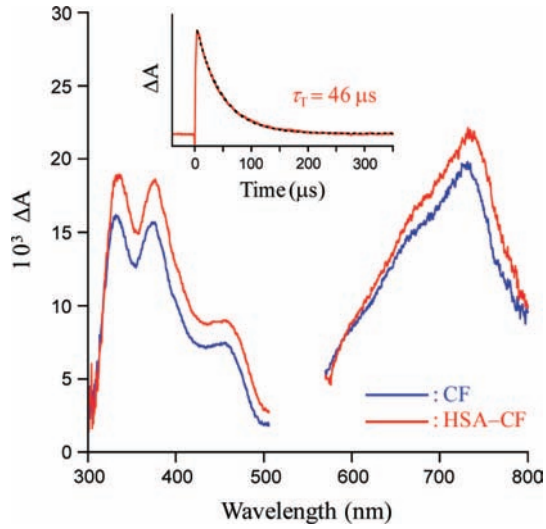

Figure 3. Triplet−triplet absorption spectra of HSA−CF complex and CF in PB solution (pH 7.0, 50 mM) under N_2 atmosphere at 22 °C; Ex. at 532 nm. The inset shows absorption decay of HSA−^{3}CF* complex at 734 nm, which was fitted by single exponential relaxation curve (black dotted line).

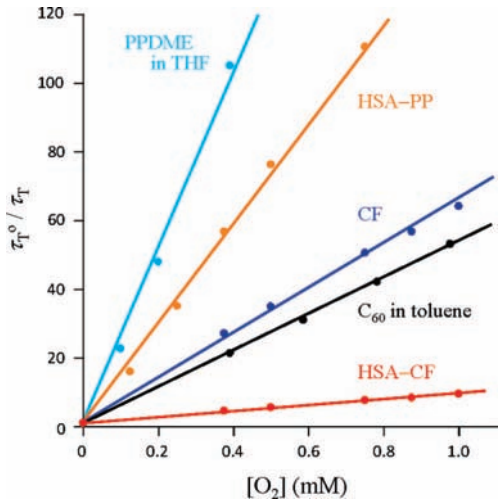

Figure 4. Stern-Volmer plots of triplet state quenching of HSA−CF complex and other compounds by O_2 at 22 °C. The HSA−CF, HSA−PP, and CF were in PB solution (pH 7.0, 50 mM).

Table 1. Quenching Rate Constants of the Photoinduced Excited Triplet States of HSA−CF Complex and Other Compounds by O_2 at 22 °C

compound	solvent	$k_q(O_2)$ (M^{-1} s^{-1})
HSA−CF	PB (pH 7.0, 50 mM)	2.2×10^8
CF	PB (pH 7.0, 50 mM)	1.6×10^9
HSA−PP	PB (pH 7.0, 50 mM)	1.3×10^8
PPDME	THF	1.6×10^9
C_{60}	toluene	1.6×10^9
		1.9×10^{9a}

[a] ref 10.

CF solution (1.6×10^9 M^{-1} s^{-1}) (Table 1). The HSA−PP complex in PB also showed smaller $k_q(O_2)$ (1.3×10^8 M^{-1} s^{-1}) compared to that of the protoporphyrin IX dimethylester (PPDME) in THF (*25*). The slow $k_q(O_2)$ values of the protein systems suggest that the quenching reaction is almost diffusion controlled. The intensity of the visible band of HSA−CF (λ_{max} = 490 nm) did not changed after 10^3 laser flash photolysis (λ_{ex} = 532 nm, 0.5 W) in air, indicating no photodegradation of the CF chromophore. In contrast, the Soret band of HSA−PP was

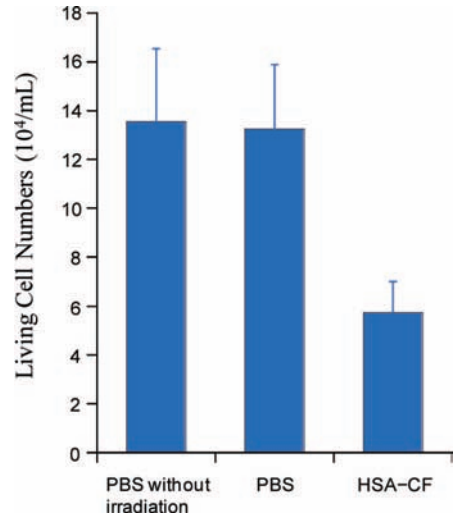

Figure 5. Living cell numbers of LY80 with HSA−CF and PBS after visible light irradiation (20 mW cm^{-2}, 2 h, 36 ± 1 °C). Each value represents the mean ± SD (n = 4).

≈6% photobleached after the identical flash irradiations. It can be concluded that the light resistance of CF is significantly higher than that of PP, which is an active photosensitizer in ALA-PDT.

We observed the near-infrared luminescence of the produced $^1O_2$ (λ_{max} 1270 nm) and evaluated the quantum yield of $^1O_2$ production (Φ_Δ) for HSA−CF from the value of emission intensity at 1270 nm (I) using rose bengal as a standard (*26*). The Φ_Δ value of HSA−CF (0.46) was in the same range as those of monomeric CF (0.48), methylene blue (0.52), PPDME in benzene (0.59) (*26*), and substituted fullerenes in organic solvent (*27, 28*), but somewhat lower than those of rose bengal (0.75), hematoporphyrin in methanol (0.74) (*29*), and C_{60} (0.96) in benzene (*10*). It is known that the substitution of the pristine C_{60} causes a perturbation of the electronic structure of the fullerene core, and thereby results in a decrease in the quantum yield for the $^1O_2$ formation (*27, 28*).

Cytotoxicity of HSA−CF Complex. Finally, we measured the cytotoxicity and photodynamic activity of the HSA−CF complex to the LY80 tumor cells in vitro. The cell cultures were first incubated for 24 h in the dark with HSA−CF (20 μM) at 37 °C under 5% CO_2. The cell numbers after the incubation were identical to that of control group with the PBS solution, indicating that the HSA−CF complex does not have dark cytotoxicity. The cell culture plates were then exposed to visible light of 350−600 nm (20 mW cm^{-2}) for 2 h at 36 ± 1 °C. Some of the cells mixed with HSA−CF showed abnormal shape after the light irradiation, whereas the PBS group did not show any morphological changes of the cells. The living cell numbers of the PBS groups with and without light irradiation were almost the same (Figure 5), which means that the light exposure did not affect the LY80 tumor cells in this experimental condition. On the other hand, the living cell numbers of the HSA−CF group were markedly lower than that of the PBS group; 57% cell death occurred by visible light irradiation. This result clearly implies that the HSA−CF complex acts as a photosensitizer for PDT.

CONCLUSIONS

The HSA−CF complex having identical molecular shape and surface charge distribution with HSA is easily excited by visible light and shows a high charge transfer rate constant for molecular O_2. The efficiency of the $^1O_2$ production of this artificial protein is in the same range as well-known dye

sensitizers, such as methylene blue and PPDME. In general, water-soluble drugs administrated into our bloodstream are quickly eliminated from the body. On the contrary, the HSA hybrid can remain in the circulatory system and/or tissues with a long persistence; therefore, the $^1O_2$ generation by albumin-based photosensitizer might be of clinical importance for photodynamic cancer therapy. The HSA−CF complex does not show dark cytotoxicity, but engenders cell death efficiently under visible light irradiation. Recombinant HSA is currently manufactured on an industrial scale using yeast species *Pichia pastoris* (*30*), which allows the use of the HSA−fullerene complex in practical applications.

ACKNOWLEDGMENT

This work was supported by PRESTO, JST, and Grant-in-Aid for Scientific Research from JSPS (No. 20350058), and Health Science Research Grants from MHLW, Japan. The authors acknowledge Dr. Akifumi Kamiya (Hamamatsu Photonics KK) for near-infrared photocounting measurements. X.Q. thanks a JSPS Postdoctoral Fellowship for Foreign Researchers.

Supporting Information Available: Figures S1−S4. This material is available free of charge via the Internet at http://pubs.acs.org.

LITERATURE CITED

(1) Dougherty, T. J., Gomer, C. J., Henderson, B. W., Jori, G., Kessel, D., Korbelik, M., Moan, J., and Peng, Q. (1998) Photodynamic therapy. *J. Natl. Cancer Inst. 90*, 889–905.

(2) Sharman, W. M., Allen, C. M., and Lier, J. E. (1999) Photodynamic therapeutics: basic principles and clinical applications. *Drug Discovery Today 4*, 507–517.

(3) Sternberg, E. D., Dolphin, D., and Bruckner, C. (1998) Porphyrin-based photosensitizers for use in photodynamic therapy. *Tetrahedron 54*, 4151–4202.

(4) Dougherty, T. J. (1987) Studies on the structure of porphyrins contained in Photofrin-II. *Photochem. Photobiol. 46*, 569–573.

(5) Aveline, B., Hasen, T., and Redmond, R. W. (1994) Photophysical and photosensitizing properties of benzoporphyrin derivative monoacid ring A (BPD-MA). *Photochem. Photobiol. 59*, 328–335.

(6) Kato, H., Furukawa, K., Sato, M., Okunaka, T., Kusunoki, Y., Kawahara, M., Fukuoka, M., Miyazawa, T., Yana, T., Matsui, K., Shiraishi, T., and Horinouchi, H. (2003) Phase II clinical study of photodynamic therapy using mono-L-aspartyl chlorine e6 and diode laser for early superficial squamous cell carcinoma of the lung. *Lung Cancer 42*, 103–111.

(7) Kennedy, J. C., Pottier, R. H., and Pross, D. C. (1990) Photodynamic therapy with endogeneous protoporphyrin IX: basic principles and present clinical experience. *J. Photochem. Photobiol. B 6*, 143–148.

(8) Lopez, R. F. V., Lange, N., Guy, R., and Bentley, M. V. L. B. (2004) Photodynamic therapy of skin cancer: controlled drug delivery of 5-ALA and its esters. *Drug Delivery Rev. 56*, 77–94.

(9) Peng, Q., Warloe, T., Berg, K., Moan, J., Kongshaug, M., Giercksky, K. E., and Nesland, J. M. (1997) 5-Aminolevulic acid-based photodynamic therapy -clinical research and future challenges. *Cancer 79*, 2282–2308.

(10) Arbogast, J. W., Darmanyan, A. P., Foote, C. S., Rubin, Y., Diederich, F. N., Alvarez, M. M., Anz, S. J., and Whetten, R. L. (1991) Photophysical properties of C_{60}. *J. Phys. Chem. 95*, 11–12.

(11) Guldi, D. M., and Prato, M. (2000) Excited-state properties of C_{60} fullerene derivatives. *Acc. Chem. Res. 33*, 695–703.

(12) Nakamura, E., and Isobe, H. (2003) Functionalized fullerene in water. The first 10 years of their chemistry, biology, and nanooscience. *Acc. Chem. Res. 36*, 807–815.

(13) Andersson, T., Nilsson, K., Sundahl, M., Westman, G., and Wennerström, O. (1992) C_{60} embedded in γ-cyclodextrin: a water-soluble fullerene. *Chem. Commun.* 604–606.

(14) Yoshida, Z., Takekuma, H., Takekuma, S., and Matsubara, Y. (1994) Molecular recognition of C_{60} with γ-cyclodextrin. *Angew. Chem., Int. Ed. 33*, 1597–1599.

(15) Islam, S. D.-M., Fjitsuka, M., Ito, O., Ikeda, A., Hatano, T., and Shinkai, S. (2000) Photoexcited state properties of C_{60} encapsulated in a water-soluble calixarene. *Chem. Lett.* 78–79.

(16) Buvári-Barcza, A., Rohonczy, J., Rozlosnik, N., Gilányi, T., Szabo, B., Lovas, G., Braun, T., Samu, J., and Barcza, L. J. (2001) Aqueous solubilization of [60]fullerene via inclusion complex formation and the hydration of C_{60}. *J. Chem. Soc., Perkin Trans. 2*, 191–196.

(17) Kragh-Hansen, U. (1981) Molecular aspects of ligand binding to serum albumin. *Pharmacol. Rev. 33*, 17–53.

(18) Peters, T. (1996) *All about albumin: biochemistry, genetics and medical applications*, Academic Press Inc., San Diego.

(19) Dugan, L. L., Turetsky, D. M., Du, C., Lobner, D., Wheeler, M., Almli, C. R., Shen, C. K.-F., Luh, T.-Y., Choi, D. W., and Lin, T.-S. (1997) Carboxyfullerenes as neuroprotective agents. *Proc. Natl. Acad. Sci. U.S.A. 94*, 9434–9439.

(20) Benyamini, H., Shulman-Peleg, A., Wolfson, H. J., Belgorodsky, B., Fadeev, L., and Gozin, M. (2006) Formation and characterization of stable human serum albumin-tris-malonic acid [C_{60}]fullerene complex. *Bioconjugate Chem. 17*, 378–386.

(21) (a) Komatsu, T., Ohmichi, N., Nakagawa, A., Zunszain, P. A., Curry, S., and Tsuchida, E. (2005) O_2 and CO binding properties of artificial hemoproteins formed by complexing iron protoporphyrin IX with human serum albumin. *J. Am. Chem. Soc. 127*, 15933–15942. (b) Komatsu, T., Wang, R.-M., Zunszain, P. A., Curry, S., and Tsuchida, E. (2006) Photosensitized reduction of water to hydrogen using human serum albumin complexed with zinc-protoporphyrin IX. *J. Am. Chem. Soc. 128*, 16297–16301. (c) Komatsu, T., Matsukawa, Y., and Tsuchida, E. (2002) Effect of heme structure on O_2-binding properties of human serum albumin-heme hybrids: intramolecular histidine coordination provides a stable O_2-adduct complex. *Bioconjugate Chem. 13*, 397–402.

(22) Evenson, M. A., and Deutsch, H. F. (1978) Influence of fatty acids on the isoelectric point properties of human serum albumin. *Clin. Chim. Acta 89*, 341–354.

(23) Fritz, G., Bergmann, A., and Glatter, O. (2000) Evaluation of small-angle scattering data of charged particles using the generalized indirect Fourier transformation technique. *J. Chem. Phys. 113*, 9733–9740.

(24) Anderson, J. L., An, Y.-Z., Rubin, Y., and Foote, C. S. (1994) Photophysical characterization and singlet oxygen yield of a dihydrofullerene. *J. Am. Chem. Soc. 116*, 9763–9764.

(25) Kubát, P., Zelinger, Z., and Jirsa, M. (1997) The effect of the irradiation wavelength on the processes sensitized by protoporphyrin IX dimethyl ester. *Radiat. Res. 148*, 382–385.

(26) Wilkinson, F., Helman, W. P., and Rossa, A. B. (1993) Quantum yields for the photosensitized formation of the lowest electronically excited singlet-state of molecular-oxygen in solution. *J. Phys. Chem. Ref. Data 22*, 113–262.

(27) Hamano, T., Okuda, K., Mashino, T., Hirobe, M., Arakane, K., Ryu, A., Mashiko, S., and Nagano, T. (1997) Singlet oxygen production from fullerene derivatives: effect of sequential functionalization of the fullerene core. *Chem. Commun.* 21–22.

(28) Prat, F., Stackow, R., Bernstein, R., Qian, W., Rubin, Y., and Foote, C. S. (1999) Triplet-state properties and singlet oxygen generation in a homologous series of functionalized fullerene derivatives. *J. Phys. Chem. A 103*, 7230–7235.

(29) Tanielian, C., Wolff, C., and Esch, M. (1996) Singlet oxygen production in water: aggregation and charge-transfer effects. *J. Phys. Chem. 100*, 6555–6560.

(30) Kobayashi, K. (2006) Summary of recombinant human serum albumin development. *Biologicals 34*, 55–59.

BC800207J

=Supporting Information=

Structure, Photophysical Property, and Cytotoxcity of Human Serum Albumin Complexed with Tris(dicarboxylmethylene)[60]fullerene

Xue Qu,[†] Teruyuki Komatsu,*[,†,‡] Takaaki Sato,[†] Otto Glatter,[¶] Hirohisa Horinouchi,[§] Koichi Kobayashi,[§] Eishun Tsuchida*[,†]

[†]*Research Institute for Science and Engineering, Waseda University, 3-4-1 Okubo, Shinjuku-ku, Tokyo 169-8555, Japan,* [‡]*PRESTO, Japan Science and Technology Agency (JST),* [¶]*Institute of Chemistry, University of Gratz, Heinrichstrasse 28, A-8010 Graz, Austria,* [§]*Department of Thoracic Surgery, School of Medicine, Keio University, 35 Shinanomachi, Shinjuku-ku, Tokyo*

E-mail: teruyuki@waseda.jp (T.K.), eishun@waseda.jp (E.T.)

Human Serum Albumin Complexed with Fullerene

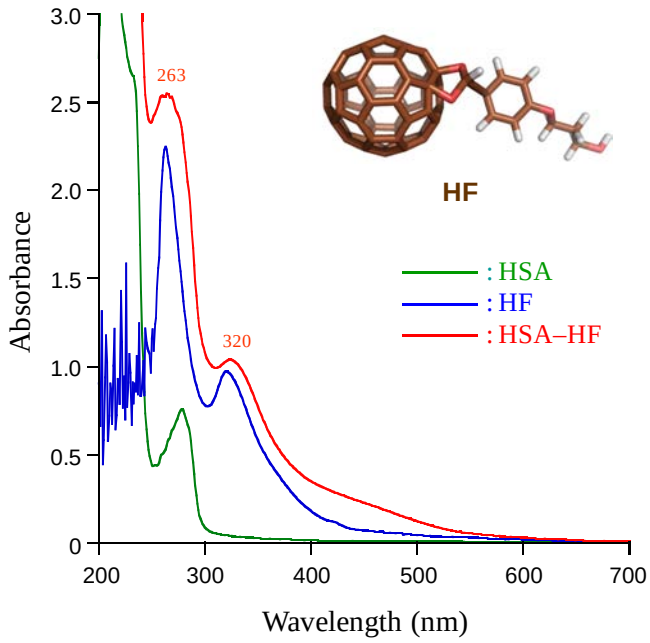

Figure S1. UV-vis absorption spectra of HSA–HF complex and HSA (20 μM) in PB solution (pH 7.0, 50 mM) and HF (20 μM) in DMSO solution at 22°C.

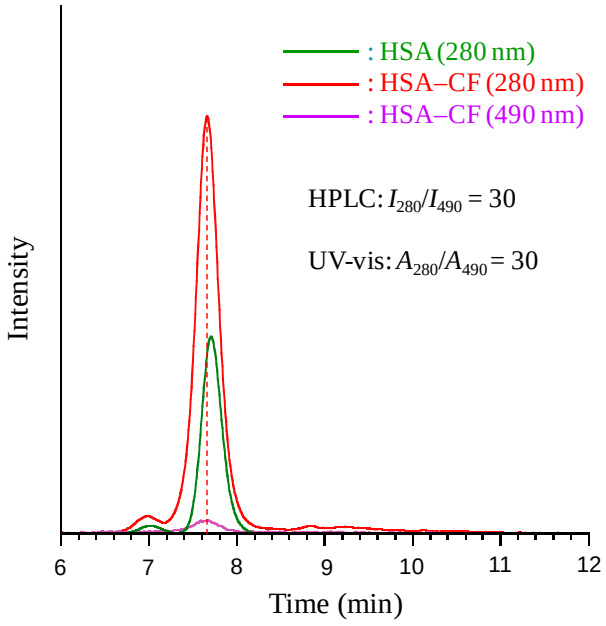

Figure S2. HPLC elution profiles of HSA–CF complex and HSA (detected at 280 nm and 490 nm).

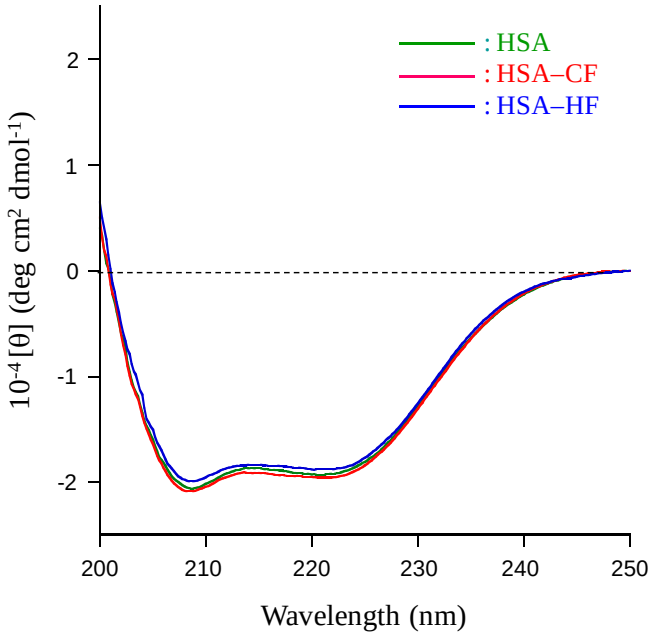

Figure S3. CD spectra of HSA–fullerene complexes in PB solution (pH 7.0, 50 mM) at 22°C.

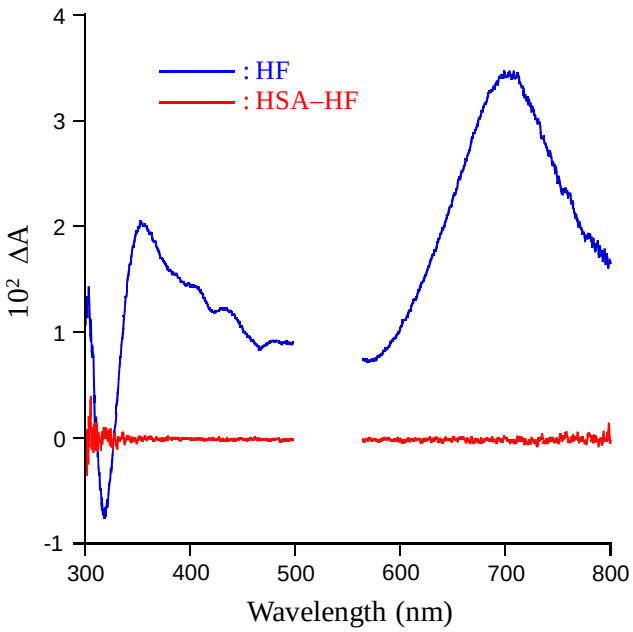

Figure S4. Triplet-triplet absorption spectra of HSA–HF complex in PB solution (pH 7.0, 50 mM) and HF in DMSO solution under N_2 atmosphere at 22°C; Ex. at 532 nm.

Antibody Targeting of Camptothecin-Loaded PLGA Nanoparticles to Tumor Cells

Paul A. McCarron,[†] Waleed M. Marouf,[‡] Derek J. Quinn,[†] Francois Fay,[†] Roberta E. Burden,[†] Shane A. Olwill,[§] and Christopher J. Scott*,[†]

School of Pharmacy, Queen's University Belfast, Medical Biology Centre, 97 Lisburn Road, Belfast BT9 7BL, U.K., Hikma Pharmaceuticals (Jordan), P.O. Box 182400, Amman 11118, Jordan, and Fusion Antibodies Ltd., Springbank Industrial Estate, Pembroke Loop Road, Belfast, BT17 0QL, U.K. Received February 12, 2008; Revised Manuscript Received May 26, 2008

Antibody targeting of drug substances can improve the efficacy of the active molecule, improving distribution and concentration of the drug at the site of injury/disease. Encapsulation of drug substances into polymeric nanoparticles can also improve the therapeutic effects of such compounds by protecting the molecule until its action is required. In this current study, we have brought together these two rationales to develop a novel immuno-nanoparticle with improved therapeutic effect against colorectal tumor cells. This nanoparticle comprised a layer of peripheral antibodies (Ab) directed toward the Fas receptor (CD95/Apo-1) covalently attached to poly(lactide-*co*-glycolide) nanoparticles (NP) loaded with camptothecin. Variations in surface carboxyl density permitted up to 48.5 μg coupled Ab per mg of NP and analysis of nanoparticulate cores showed efficient camptothecin loading. Fluorescence visualization studies confirmed internalization of nanoconstructs into endocytic compartments of HCT116 cells, an effect not evident in NP without superficial Ab. Cytotoxicity studies were then carried out against HCT116 cells. After 72 h, camptothecin solution resulted in an IC_{50} of 21.8 ng mL^{-1}. Ab-directed delivery of NP-encapsulated camptothecin was shown to be considerably more effective with an IC_{50} of 0.37 ng mL^{-1}. Calculation of synergistic ratios for these nanoconstructs demonstrated synergy of pharmacological relevance. Indeed, the results in this paper suggest that the attachment of anti-Fas antibodies to camptothecin-loaded nanoparticles may result in a therapeutic strategy that could have potential in the treatment of tumors expressing death receptors.

INTRODUCTION

Targeting of tumor-associated antigens using specific antibodies forms the basis of a drug delivery strategy to circumvent difficulties and side effects associated with nonspecific drug dosing. In the design of any immuno-nanoparticulate system, the choice of peripheral antibody, its conjugation chemistry, and therapeutic payload will depend on the intended target cell and associated cell-surface biomarker. One such cell-surface target, amenable to binding by antibodies, is the Fas (CD95/Apo-1) receptor. Fas is a 45 KDa type 1 membrane protein and a member of the tumor necrosis factor (TNF) super family. It is found on the plasma membrane of a variety of cancer cell lines (*1*) and has been identified as a target for antibodies that induce apoptosis in various human cell lines (*2, 3*). Fas is present on the cell surface as a homotrimer (*4*). Upon Fas ligand (FasL) or agonist antibody binding, activation of the Fas receptor trimer results in recruitment of the death inducing signaling complex (DISC) to its intracellular domain leading to activation of pro-caspase 8 (*5, 6*). Pro-caspase 8 is autocatalytically activated (*6*), and in turn cleaves and activates several downstream substrates including the effector caspases 3 and 7, cumulating in a proteolytic cascade that leads to the death of the cell (*7*).

The cell surface expression of Fas has been shown to be modulated by treatment of cells with drugs such as the quinoline-based plant alkaloids found in the wood, bark, and fruit of the Asian tree *Camptotheca acuminate*. The most utilized of these is camptothecin (CPT) which selectively inhibits mammalian topoisomerase I, a DNA replication enzyme overexpressed in a wide range of tumors, including advanced human colon, ovarian, and esophageal carcinomas (*8*). CPT exhibits antitumorigenic effects by trapping topoisomerase-I with DNA in topoisomerase I-cleavage complexes (*9*). This inhibition results in the stalling of DNA replication, subsequent S-phase arrest, and initiation of apoptotic cell death in tumor cells (*10*). Previously, it has been observed that agonistic Fas antibodies potentiated the cytotoxicity caused by CPT treatment (*11*). Specifically, results demonstrated that sublethal concentrations of CPT up-regulated Fas and other pro-apoptotic proteins, such as Fas ligand, Bax, and p21. Similarly, Xia and co-workers demonstrated that CPT significantly increased the glioblastoma cell death response to Fas receptor activation using agonist antibodies (*12*). Furthermore, a study using CPT-11 (irinotecan), a water-soluble, semisynthetic prodrug of CPT, found up-regulation of cell-surface Fas expression in colorectal cancer cells, independent of *p53* status. Interestingly, by combination treatments with CPT-11 and agonistic Fas antibody, it was shown that this surface up-regulation could be exploited to produce synergistic tumor cell cytotoxicity (*13*).

Despite the demonstration that CPT has efficacious activity toward tumor cells, drawbacks remain with its clinical application. CPT is particularly active when in its lactone form, but is easily converted at physiological conditions to a less active carboxylate form, which gives rise to increased side effects (*14–16*). Moreover, human serum albumin binds to the carboxylate form preferentially, driving the equilibrium in favor of carboxylate formation in the systemic circulation (*17, 18*).

* Corresponding author. Dr. Christopher J. Scott, School of Pharmacy, Queen's University Belfast, Medical Biology Centre, 97 Lisburn Road, Belfast BT9 7BL, U.K. Tel: +44 (0) 28 90 972 350, Fax:+44 (0) 28 90 247 794, E-mail: c.scott@qub.ac.uk.

[†] Queen's University Belfast.

[‡] Hikma Pharmaceuticals (Jordan).

[§] Fusion Antibodies Ltd.

10.1021/bc800057g CCC: $40.75 © 2008 American Chemical Society
Published on Web 07/16/2008

Additionally, CPT is poorly water-soluble (*19*), and formulations frequently require addition of cosolvents, such as poly(ethylene glycol) (PEG) 400, prior to administration (*20*). It is believed that these drawbacks contribute to the considerable variability in patient response after oral or intravenous administration, observed for the entire CPT drug class (*21*). Furthermore, as an S phase-specific drug, CPT requires prolonged exposure to the tumor to ensure efficacy (*11, 22, 23*). *In vivo* studies examining the pharmacokinetic profile of CPT have shown that large doses administered over extended intervals are poorly effective when compared to continual low doses or frequently fractioned dosing (*24*). Consequently, irinotecan (CPT-11) was developed in an effort to circumvent these problems. Although intentionally more water-soluble than CPT, it exhibits much lower antitumor activity, with an IC_{50} of 1200 μM compared to CPT with an IC_{50} of 23 μM in L1210 murine leukemia cells. Furthermore, CPT-11 has a lower activity on topoisomerase-I inhibition, with an $IC_{50} > 100$ μM, compared to an IC_{50} of 0.6−1.4 μM for CPT (*25*).

Although clinically effective, the reduced potency of CPT-11 means that the ability to use CPT still remains an attractive goal for cancer therapy. As an alternative to cosolvent approaches, the *in vitro* antitumor activity of CPT has been enhanced by loading into colloidal drug delivery systems, such as mixed micellar systems (PEG)-phosphatidylethanolamine conjugate with D-α-tocopheryl poly(ethylene glycol) 1000 succinate (*26*) and sterically stabilized phospholipid micelles (*23*). Similarly, the improved efficacy of CPT-loaded methoxy-poly(ethylene glycol)-poly(DL-lactic acid) nanoparticles (NP) lead to a combination of longer plasma retention times with more efficient tumor localization (*27*).

In this present study, the application of antibody-targeted nanoparticle conjugates containing CPT has been investigated. It was hypothesized that a nanoparticulate system containing CPT and bearing antibodies toward Fas would be simultaneously beneficial. The study aimed to investigate if the combination of Fas targeting and intracellular CPT delivery would improve the efficacy of the drug over solution-based delivery. The results show that entrapment of CPT within the NP improves their efficacy toward tumor cells which is further improved by direct targeting and triggering of receptor-mediated endocytosis via antibody directed interaction with Fas receptor to deliver CPT intracellularly to its site of action.

EXPERIMENTAL PROCEDURES

Materials. (*S*)-(+)-CPT was purchased from Sigma-Aldrich, Germany. PLGA (Resomer RG 502 H) with an acid value of 9 mg KOH per g PLGA, molecular weight 12 kDa and inherent viscosity of 0.22 dL g^{-1} at 0.1% (w/v) in chloroform at 25 °C, was a generous gift from Mr. Markus Weingärtner, Boehringer Ingelheim, Germany. PLGA (Resomer RG 505 S) with an acid value of <1 mg KOH per g PLGA, molecular weight 80 kDa and inherent viscosity of 0.7 dL g^{-1} at 0.1% (w/v) in chloroform at 25 °C, was purchased from Boehringer Ingelheim, Germany. A water-soluble carbodiimide, *N*-ethyl-*N*(3-dimethylaminopropyl) carbodiimide hydrochloride (EDC), was obtained from Fluka, Slovakia. *N*-Hydroxysuccinimide (NHS) and poly(vinyl alcohol) (PVA), 87−89% hydrolyzed with molecular weight 13−23 kDa, were obtained from Aldrich, Germany. Magnesium chloride hexahydrate ($MgCl_2 \cdot 6H_2O$), 2-morpholinoethanesulfonic acid monohydrate (MES), polyoxyethylenesorbitan monooleate (Tween 80), and 3-(4,5-dimethyl-2-thiazolyl)-2,5-diphenyl-2*H*-tetrazolium bromide (MTT reagent) were obtained from Sigma, Germany. Anti-Fas human mAb and IgG Isotype mAb were supplied by Fusion Antibodies Ltd., Northern Ireland. The microBCA kit was purchased from Pierce, USA. Acridine Orange dye was obtained from Sigma, USA. Acetone (Fisher Scientific, UK) was used as a water-miscible solvent during NP preparation, while dichloromethane (DCM) (Riedel-de Haën, Germany) was used as a water-immiscible solvent. Dimethyl sulfoxide (DMSO) and acetonitrile were from (BDH, UK). Phenol Red-free medium (RPMI 1640 with L-glutamine) and McCoy's 5A medium with L-glutamine were obtained from Invitrogen USA. A human colorectal cancer cell line (HCT116) was obtained from the American Tissue Culture Collection. All chemicals were used without further purification.

Preparation of CPT-Loaded and AO-Loaded PLGA NP. CPT-loaded NP were prepared by dissolving CPT (0.2 mg) in 200 μL DCM and 100 μL DMSO to give the 100:1 PLGA/CPT weight ratio nanoparticulate formulation. DMSO was introduced as a cosolvent to ensure complete CPT dissolution in the organic phase. NP with the 10:1 weight ratio were prepared by addition of 2.0 mg CPT to the DCM/DMSO phase. The CPT solution was added to a 500.0 μL organic solution of acetone containing 20 mg PLGA. The ratio of total water-miscible organic solvents (acetone/DMSO) to DCM was maintained at 3:1 v/v. The organic phase (ice-cold) was injected under moderate stirring into 3.0 mL of ice-cold pH 5.0 MES buffer (25 mM) solution containing 2.5% (w/v) PVA and 45% (w/v) $MgCl_2 \cdot 6H_2O$. Both phases were then sonicated in an ice bath for three minutes, at 50−55 W in pulse mode. An additional 5.0 mL of pH 5.0 MES buffer (25 mM) solution containing 2.5% (w/v) PVA was added under moderate stirring to initiate acetone-DMSO diffusion. Samples were kept stirring overnight to allow organic solvent evaporation.

NP were prepared using RG 502 H alone (NP-100), which gave a maximum carboxylic acid density on the peripheral surface. Also, a 20% w/w blend of RG 502 H with 80% w/w RG 505 S (NP-20), which gave a lower peripheral carboxylic acid density, was prepared. Blank NP were prepared as described above, but without CPT. Acridine Orange (AO)-loaded NP without CPT incorporation were prepared using the procedure described above, with AO replacing CPT in the organic phase.

NP Purification. NP were filtered through a No. 1 sintered glass filter, centrifuged at 50 000 × *g* for 1 h at 10 °C, then washed using suspension-spin cycles with pH 5.0 MES buffer. NP loaded with AO were washed repeatedly, until a clear supernatant was evident, to eliminate any loosely adsorbent materials, be it CPT or free dye. Nanoparticulate pellets were resuspended to give 1.0 mg NP mL^{-1} in pH 5.0 MES buffer prior to further use.

CPT Entrapment Efficiency. The purified nanoparticulate pellet was dissolved in DMSO and acetonitrile (ACN) added to bring the volume ratio to 1:1 (DMSO/ACN). Samples were diluted further using this 1:1 volume ratio solvent (DMSO/ACN) and measured using UV−vis spectrophotometry at 365 nm. Results were compared to a standard calibration curve of CPT solution in DMSO/ACN at a 1:1 volume ratio. Entrapment efficiency was calculated using eq 1.

$$\text{Entrapment efficiency (\%)} = \frac{\text{Mass of drug determined (mg)}}{\text{Mass of drug added (mg)}} \times 100 \quad (1)$$

***In Vitro* Evaluation of CPT Release from PLGA NP.** Release profiles of CPT from nanoparticulate suspensions (100:1 weight ratio loading) were determined using a dialysis-based procedure. CPT-loaded NP were dispersed in a release medium (phosphate buffered saline (PBS), pH 7.4 containing 2% (w/v) Tween 80) (*28*) with the amount of available CPT for release and the volume of release medium adjusted so as to maintain optimal sink conditions. A mass of NP, equivalent to 300 μg CPT, was dispersed in 12 mL of a pH 7.4 PBS solution containing 2% (w/v) Tween 80. This was injected into a Slide-A-Lyzer dialysis cassette with a 10K molecular weight cutoff

(Pierce, USA) and immersed in 138 mL of a pH 7.4 PBS solution containing 2% (w/v) Tween 80 under conditions of continuous stirring. Samples (5.0 mL) of receiver phase were withdrawn at selected time points and replaced with equivalent volumes of fresh medium. CPT concentration in the receiver medium was measured using spectrofluorometry (emission at 435 nm and excitation at 374 nm) and compared with a calibration curve for standard CPT solutions prepared under similar conditions.

The diffusion of CPT from a standard solution across the dialysis membrane served as a control, representing a situation where formulation-based sustained effects were not exerted. In this study, 300 μg CPT was dissolved in 12 mL of a pH 7.4 PBS containing 2% (w/v) Tween 80 and introduced into the dialysis cassette. Sample were withdrawn and analyzed as described above.

Particle Size and Zeta Potential Measurements. Nanoparticulate size and zeta potential were measured using photon correlation spectroscopy (ZetaSizer 3000 HS, Malvern instruments, UK). Measurements were carried out using monochromatic coherent He−Ne laser light of fixed wavelength (633 nm) at 90° and at room temperature (25 °C), with each sizing determination done in triplicate and an average particle size expressed as the mean diameter (Z_{ave}).

NP Activation with NHS and Carbodiimide. Purified NP (100:1 weight ratio loading) were used as the core platform for antibody conjugation and subsequent *in vitro* evaluations. They were suspended in 20 mL pH 5.0 MES buffer and activated using NHS-carbodiimide chemistry, as described previously (*29*). Briefly, activation was achieved by adding 200 μL of 0.1 M EDC and 200.0 μL of 0.7 M NHS, both dissolved in pH 5.0 MES, to the nanoparticulate suspension, which was kept at room temperature for 1 h under conditions of moderate stirring. Samples were centrifuged at 50 000 × *g* for 1 h at 10 °C, and the NP collected, washed three times in pH 7.4 PBS using suspension-spin cycles to eliminate unused adsorbent reagents, and finally resuspended at 1 mg mL^{-1} in PBS.

Peripheral Anti-Fas mAb and IgG Isotype mAb Conjugation. Anti-Fas human mAb (100 μL of 1.0 mg mL^{-1} solution) or IgG isotype mAb, which was used as a control for anti-Fas mAb (100 μL of 1.0 mg mL^{-1} solution), were added to a 1 mL suspension of 1 mg mL^{-1} activated NP in 1.5 mL Eppendorf tubes. Samples were vortexed and incubated at 4 °C overnight, centrifuged at 22 000 × *g* (Sigma 3−18 K Centrifuge) for one hour at 10 °C and washed twice with PBS using suspension-spin cycles to remove excess unconjugated antibody. Antibody conjugation was quantified spectrophotometrically at 562 nm (Tecan Spectra III, Austria) using a microBCA kit (Pierce, USA) as per the manufacturer instructions.

Fluorescence Microscopy Imaging. HCT116 cells were cultured in Phenol Red free medium (RPMI 1640) containing L-glutamine, sodium pyruvate (5 mM), and 10% v/v fetal calf serum. Cells were grown to a confluency of 70% before seeding in six-well plates at 1.0 × 10^5 cells per well. This was followed by 90 min of incubation at 37 °C and 5% CO_2 with 100.0 μL dispersion of 1.0 mg mL^{-1} AO-loaded NP-100 conjugated to anti-Fas human mAb suspended in PBS. All NP preparations were diluted 10-fold, where 10.0 μL of 1.0 mg mL^{-1} of NP suspension was made up to 100.0 μL using PBS. Naked AO-loaded NP-100 were used as corresponding controls. Cells were washed three times with ice-cold PBS before observation using fluorescence microscopy (Nikon Eclipse TE 300, Japan). The *X*/*Y Y*/*Z* section analysis was performed using confocal scanning laser microscopy (Leica Confocal TCS Sp2, Germany). Excitation was done using laser illumination at 450 nm for green fluorescence and 540 nm for red fluorescence.

Table 1. Glossary and Summary of Different NP Preparations Prepared for Cell-Based Assays

abbreviation	loading[a]	antibody conjugated
20% RG 502 H (w/w) - Low Carboxylic Acid Density on NP Surface		
NP-20	none	none
NP-20-CPT	CPT	none
NP-20-CPT-CtrlAb	CPT	IgG Isotype control antibody
NP-20-Fas	none	Anti-Fas mAb
NP-20-CPT-Fas	CPT	Anti-Fas mAb
100% RG 502 H (w/w) - High Carboxylic Acid Density on NP Surface		
NP-100	none	none
NP-100-CPT	CPT	none
NP-100-CPT-CtrlAb	CPT	IgG Isotype control antibody
NP-100-Fas	none	Anti-Fas mAb
NP-100-CPT-Fas	CPT	Anti-Fas mAb

[a] CPT = camptothecin.

***In Vitro* Antitumor Activity of CPT-Loaded NP.** HCT116 cells were plated in 96-well microplates at 5.0 × 10^3 cells per well in 190.0 μL of complete medium and allowed to adhere under incubation at 37 °C and 5% CO_2. Twenty-four hours later, 10.0 μL of medium containing different CPT solutions or nanoparticulate suspensions were added to wells and incubated for 24, 48, and 72 h. Preparations were made for anti-Fas human mAb, either as solutions or conjugated to the surface of NP, which were themselves either blank or CPT-loaded (Table 1). IgG1 isotype control mAb were presented to cells after being conjugated to the surface of CPT-loaded NP to act as a control for corresponding anti-Fas conjugated NP. CPT was presented either as a solution in 10.0% (v/v) DMSO or loaded in NP, either naked or conjugated to antibody (Table 1). Wells containing control cells for all preparations were treated with 10 μL of medium, except for CPT solution preparations, where 10 μL medium containing 10% (v/v) DMSO was used resulting in a final concentration of 0.5% (v/v) DMSO in the medium. At this concentration the DMSO had no measurable effect on cell viability.

Percentage cell survival after each time point was determined by the MTT colorimetric assay. The medium was replaced by 200 μL of MTT solution prepared in media to give a final concentration of 0.5 mg mL^{-1}. This was incubated for 2 h at 37 °C and 5% CO_2 to allow for the formation of purple water-insoluble formazan. MTT solution was replaced with 100 μL DMSO and incubated at 37 °C and 5% CO_2 for 2 h to dissolve formazan. Optical density was measured at 570 nm using a microwell plate reading spectrophotometer (Tecan Spectra III, Austria) and compared to control cells. Cell survival was then expressed as a percentage of the control cells, which were taken to represent the 100% cell survival for each respective time point.

***In Vitro* Caspase 8 Activation.** Cultured HCT116 cells were seeded in flat-bottomed, 6-well plates (250 000 cells/well) and allowed to adhere overnight. Cells were treated with a solution of blank NP coated with anti-Fas mAb or isotype IgG mAb (0.18 mg PLGA per well, corresponding to 0.1 μg of conjugated mAb per 1000 cells) for 48 h. Cells were harvested and centrifuged at 2000 × *g* for 10 min at 4 °C and the pellet resuspended in 10 μL of PBS and stored at −80 °C until required.

Whole cell lysates (25 μL) were electrophoresced on 10% Tris-SDS-PAGE gels (Bio-Rad Laboratories, Hercules, CA) and electroblotted onto a polyvinylidene difluoride (PVDF) membrane (Bio-Rad Laboratories) using standard techniques. The PVDF membrane was blocked with 3% (w/v) bovine serum albumin in PBS prior to detection with anticaspase-8 (1:700) (Alexia Corporations, San Diego, CA) and a HRP-conjugated goat antimouse secondary antibody (1:3000, BioRad, Hercules,

Table 2. Particle Size, Zeta Potential, CPT Entrapment Efficiency, and Antibody Conjugation of NP Prepared from Different PLGA Blends

NP formulation	PLGA/CPT ratio w/w	particle size (nm) [a]	entrapment efficiency[b]	anti-Fas conjugation (μg mg^{-1})[c]
100% RG 502 H				
	Blank	116.5 ± 1.6	N/A	48.3 ± 1.9
	100:1	127.2 ± 1.5	100% ± 1.7	47.6 ± 0.8
	10:1	170.8 ± 2.5	100% ± 2.1	48.5 ± 1.1
20% RG 502 H				
	Blank	123.1 ± 0.8	N/A	12.4 ± 3.4
	100:1	139.3 ± 2.4	100.0% ± 1.2%	11.9 ± 2.2
	10:1	187.1 ± 1.1	100.0% ± 0.8%	12.1 ± 1.7

[a] Mean of three determinations ± standard deviation. [b] Efficiency expressed as a percentage mean of three determinations ± standard deviation of CPT weight recovered in NP compared to theoretical loaded weight and referring to purified samples. [c] Antibody conjugation is expressed as average of three determinations in μg antibody per mg NP ± standard deviation N/A: Not applicable.

CA, USA) followed by visualization using Supersignal West Femto Chemiluminescent Substrate (Pierce, Rockford, IL).

Data Analysis. Statistical analyses were performed using analysis of variance (one-way and two-way ANOVA), with either followed by Bonferoni's test to compare all pairs of preparations (Graph-Pad Prism, San Diego, CA, USA). Rejection of the null hypothesis was considered when the P value is <0.05. IC_{50} values, defined as the concentration of a preparation which will result in a 50% cell survival, were used to compare potency of different preparations. The IC_{50} value for a preparation was obtained by plotting log(concentration) against percentage cell survival and then applying a nonlinear sigmoidal dose response curve fitting function (Graph-Pad Prism, San Diego, CA, USA).

The nature of the interaction obtained by conjugating anti-Fas human mAb to CPT-loaded NP was determined by calculating the synergistic ratio (SR) (*30*), as shown in eq 2

$$\mathrm{SR} = \frac{S_{\mathrm{exp}}}{S_{\mathrm{obs}}} \quad (2)$$

where the expected HCT116 cell survival (S_{exp}) was defined as the product of the HCT116 cell survival observed for CPT-loaded NP alone and the HCT116 cell survival observed for anti-Fas mAb conjugated to the surface of blank NP alone.

$$S_{\mathrm{exp}} = (\text{Survival CPT-loaded NP}) \times (\text{Survival anti-Fas mAb conjugated to blank NP}) \quad (3)$$

The actual HCT116 cell survival observed for anti-Fas mAb conjugated to the surface of CPT-loaded NP was defined as S_{obs}. Synergy was defined as an SR greater than unity (SR > 1.0). SR values of 1.0 or less indicated the absence of synergy. A synergistic interaction may be of pharmacological interest when SR values are around 2.0 (*31*).

RESULTS

The evaluation of CPT entrapped in PLGA NP and anti-Fas conjugated PLGA NP was undertaken, using different blends of PLGA polymer. Changes in particle size, zeta potential, CPT entrapment efficiency, and antibody conjugation of NP prepared from different PLGA blends were analyzed (Table 2). Modulation of non-end-capped density by way of variation of PLGA composition had a significant effect ($P < 0.05$) on the NP size and amount of antibody conjugation, but did not affect CPT entrapment efficiency. NP-100, prepared using 100% (w/w) RG 502 H, were significantly smaller when compared to NP-20, prepared using 20% RG 502 H ($P < 0.05$). Entrapment efficiencies for both the 100:1 and 10:1 CPT loadings where

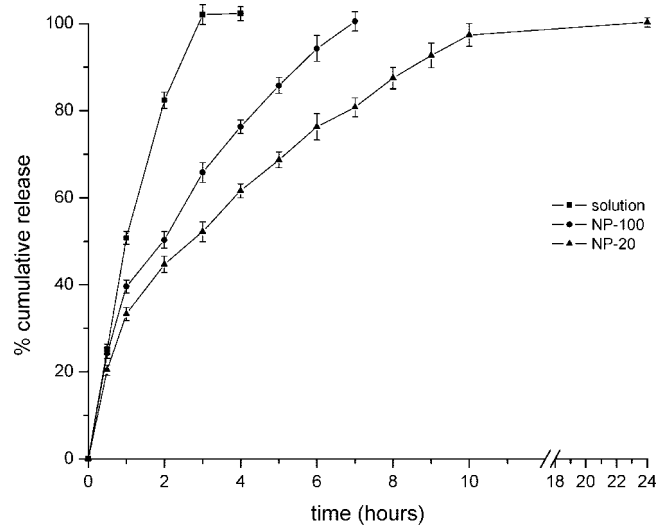

Figure 1. The effect of PLGA composition on *in vitro* release of CPT from the 100:1 weight ratio loading, showing cumulative release from NP formulations, NP-100 (▲), NP-20 (•), and from CPT solution (□), which was used as a control for equilibrium across the dialysis membrane. (Results are mean ± SD, $n = 3$).

shown to be almost complete, with PLGA composition not affecting this parameter. As expected, antibody conjugation was more effective when the 100% (w/w) RG 502 H composition was used as this formulation exposes more peripheral carboxyl coupling functionality in comparison to the to the 20% RG 502 H variant. This was demonstrated by conjugation levels in NP prepared using 100% RG 502 H polymer, which resulted in 48.3 μg coupled antibody per mg of NP, in comparison to NP prepared with only 20% RG 502 H, giving instead only 12.4 μg antibody per mg NP (Table 2). These results show clearly that the amount of anti-Fas mAb that could be conjugated to the NP using a two-step carbodiimide activation was dependent on the ratio of non-end-capped to endcapped PLGA types. In addition, it was observed that anti-Fas conjugation was not affected by CPT loading with no significant differences observed between conjugation to blank NP or those loaded with CPT.

CPT release profiles from the 100:1 weight ratio NP formulations, evaluated by a dialysis procedure, enabled determination of free CPT concentration without the need for prolonged centrifugation. Care was taken to ensure sink conditions and that the maximum concentration possible of CPT remained below 10% of the solubility of CPT in the release medium, previously reported as 79 μg mL^{-1} (*28*). Calibration procedures showed a linear correlation between fluorescent emission intensity and CPT concentration in the range of 20 ng mL^{-1} to 80 ng mL^{-1} ($r^2 = 0.992$). The effect of both PLGA compositions on *in vitro* cumulative release profiles from NP prepared using either 100% RG 502 H or 20% RG 502 H is shown in Figure 1. In both formulations, a rapid initial release of CPT was observed. However, beyond 60 min distinct differences in drug release were observed with 34% CPT release observed for 20% RG 502 H NP compared with 39% in 100% RG 502 H NP. By 3 h, the observed release was 50% for the 20% RG 502 H NP, compared to 65% from 100% RG 502 H NP. Both types of PLGA NP had achieved almost 100% release by 10 h. Although not instantaneous, the equilibrium of the CPT control solution across the dialysis membrane was more rapid, reaching an approximate value of 82% (w/v) CPT diffused into the receiver phase after 2 h.

The application of mAb-NP formulations were then examined in cell-based assays using the HCT116 colorectal carcinoma cells, previously shown to express Fas (*33*). To permit the visualization of the mAb-NP conjugates in association with cells,

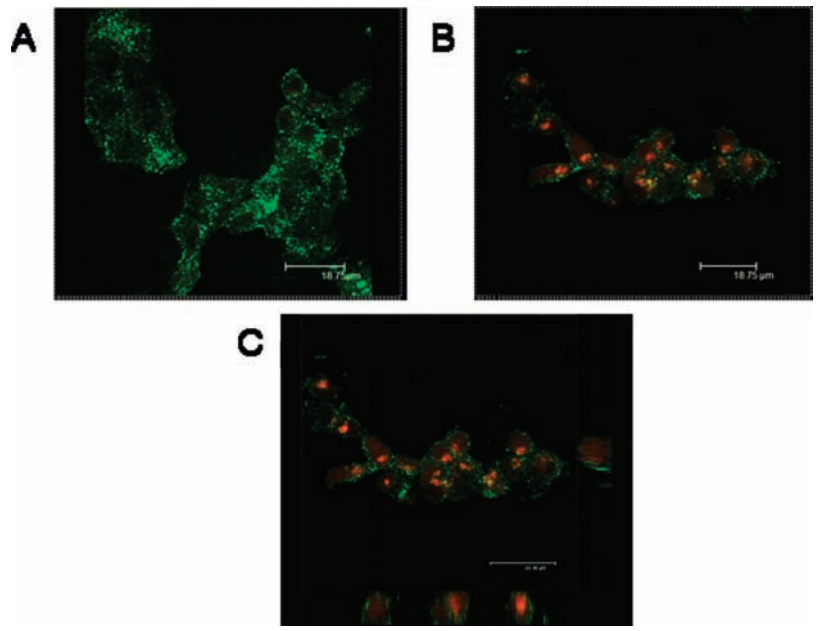

Figure 2. Fluorescence microscopy images for HCT116 cells incubated with (A) a 100 μL suspension of naked AO-loaded NP-100 in PBS, (B) a 100 μL suspension of AO-loaded NP-100 with 4.67 μg of conjugated anti-Fas mAb, and (C) *X*/*Y Y*/*Z* confocal section analysis of HCT116 cells incubated with a 100 μL PBS dispersion of AO-loaded NP-100 with anti-Fas mAb conjugated peripherally. Cells were exposed to NP dispersions over a 90-min incubation period at 37 °C and 5% CO_2. Cells were washed three times with ice-cold PBS before observation using confocal laser scanning microscopy with excitation at 450 nm for green fluorescence and 540 nm for red fluorescence.

NP were prepared containing acridine orange (AO), as employed previously to visualize uptake of the conjugates into cells using fluorescence microscopy (*33*). Furthermore, results have determined that the release of AO from the PLGA NP *in vitro* amounts to approximately 10% of the total encapsulated AO over 4 h (data not shown), barely detectable at concentrations and length of study (90 min) employed in these cellular studies presented here. Therefore, the intense fluorescence arising from endosomal space is almost exclusively AO still entrapped within PLGA cores. AO fluoresces in a pH-dependent manner, with a green emission spectra at neutral or basic pH, shifting to red/orange fluorescence in acidic conditions (*34*, *35*). Substantial differences in subcellular fluorescence was observed in HCT116 cells, dependent on the nature of the conjugate applied, with the presence of red fluorescent foci in cells treated with mAb-NP, which was not observed in the presence of unconjugated NP (Figure 2a,b). This finding is consistent with internalization of the antibody-conjugated particles localizing in acidic vesicles, suggesting that binding of anti-Fas conjugated NP to the surface of HCT116 cells leads to internalization into endocytic acidic compartments. Further analysis of this internal fluorescence was undertaken using an *X*/*Y Y*/*Z* confocal section analysis confirming the intracellular localization of the AO-loaded NP (Figure 2c). Conversely, in the control nonconjugated particles, only green fluorescence is visualized suggesting that these NP, at the concentrations and mild washing conditions employed here, have adhered or internalized into the cells in a nonspecific nonreceptor mediated manner. Crucially, however, and in line with our previous findings (*33*), is the difference in fluorescence observed with the two formulations indicating the receptor specific nature of the internalization with antibody-conjugated NP.

Next, the ability of the nanoparticle formulations were analyzed in their ability to attenuate the proliferation of tumor cells. HCT116 cells were exposed to CPT as a solution in 10% (v/v) DMSO (CPT solution) or CPT-loaded NP prepared with 100% (NP-100-CPT) or 20% (NP-20-CPT) RG 502H. NP were either naked or conjugated with anti-Fas monoclonal antibody (NP-100-CPT-Fas or NP-20-CPT-Fas), or conjugated with isotype IgG control antibody (NP-100-CPT-ContAb or NP-20-CPT-ContAb). As a further control, Anti-Fas mAb alone was presented to cells either in solution (Fas solution) or conjugated to non-drug-loaded NP (NP-100-Fas or NP-20-Fas). The viability of cell populations were then assessed at 24 h, 48 h, and 72 h time points. After 24 h, no significant variances in cell viability were measured with the formulations (Table 3), but by 48 h the dose-dependent cytotoxic effect of the CPT solution was evident cumulating in approximately 25% HCT116 survival at 100 ng mL^{-1} with an IC_{50} of 21.8 ng mL^{-1} after 72 h (Figure 3 and Table 3). The incorporation of CPT into the NP resulted in significant improvements in potency of both PLGA formulations examined (*P* value <0.01). However, the full extent of the cytotoxic potency of CPT-loaded NP was found to be dependent on the PLGA blend used to prepare the NP and concentration of available CPT. After 72 h of incubation, the

Table 3. IC_{50} Values Calculated after Nonlinear Dose-Response Curve Fitting of the HCT116 Cell Survival Results

NP formulation	time from treatment	IC_{50} (ng mL^{-1})
CPT solution	24 h	<450
	48 h	231.2 (±10.2)
	72 h	21.8 (±1.4)
NP-20 CPT	24 h	<450
	48 h	48.9 (±9.9)
	72 h	7.8 (±0.9)
NP-20 CPT and control antibody	24 h	<450
	48 h	75.9 (±9.8)
	72 h	14.1 (±0.9)
NP-20 CPT Fas antibody	24 h	<450
	48 h	31.6 (±6.8)
	72 h	5.6 (±0.5)
NP-100 CPT	24 h	<450
	48 h	47.9 (±6.1)
	72 h	15.8 (±1.2)
NP-100 CPT and control antibody	24 h	<450
	48 h	28.8 (±9.5)
	72 h	6.8 (±0.7)
NP-100 CPT and Fas antibody	24 h	398 (±46)
	48 h	25.1 (±3.4)
	72 h	0.37 (±0.1)

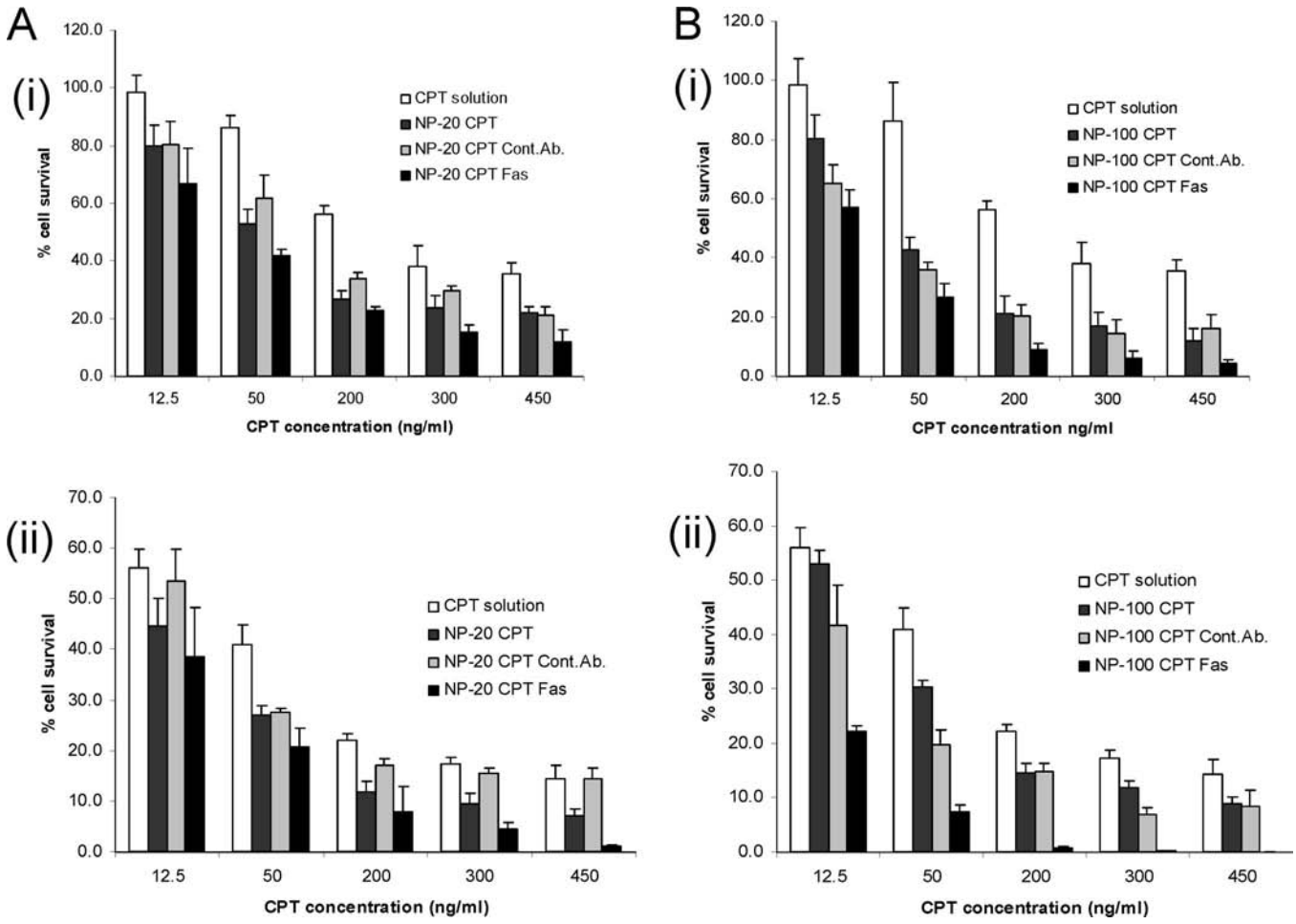

Figure 3. Percentage HCT116 cell survival (MTT assay) after treatment with different formulations of CPT and/or anti-Fas mAb. (A) Graphs show the determined survival for NP-20 prepared using 20% RG 502 H at 48 (panel i) and 72 h (panel ii). (B) Graphs show the determined survival for NP-100 prepared using 100% RG 502 H at 48 (panel i) and 72 h (panel ii). (Results are mean ± SD, $n = 5$).

NP-20-CPT formulation was found to be significantly more potent than NP-100-CPT ($P < 0.05$), as demonstrated by the calculated NP-20-CPT IC_{50} of 7.8 ng mL^{-1} in comparison to 15.8 ng mL^{-1} for NP-100-CPT (Figure 3A panel (ii); Figure 3B panel (ii), and Table 3).

The attachment of antibodies to the surface of the CPT-loaded particles resulted in further improvements in cytotoxic effects over both CPT solution and CPT containing NP. This was particularly evident at the 72 h time point, with cytotoxicity at 200 ng mL^{-1} reaching almost 100% (IC_{50} of 0.37 ng mL^{-1}) using NP-100-CPT-Fas (Figure 4A). Use of the NP-20-CPT-Fas formulation resulted in similar cytotoxicity trends, but with a less potent IC_{50} of 5.6 ng mL^{-1} (Table 3).

The possible cytotoxic effects mediated by the antibodies themselves on the surface of the NP conjugates were also examined using blank NP-mAb conjugates comprising cores made using both polymer ratios (NP-20-Fas and NP-100-Fas). Results demonstrated that the conjugated antibodies on their own had a minimal effect. Over 24 and 48 h of incubation, there was no effect on cell viability (data not shown). At the 72 h time point, a small divergent effect is seen at higher antibody concentrations in both NP polymer formulations, with up to 20% cell death (Figure 4A). Due to the high density of the IgG antibody on the surface of the NP, it was hypothesized that this antibody could be promoting the cross-linking of the Fas receptor and activation of the extrinsic apoptotic pathway through activation of caspase 8. To examine this, anti-Fas NP and anti-isotype control NP conjugates were incubated for 48 h in the presence of HCT116 and whole cell lysates were analyzed by Western blot for activation of caspase 8 (Figure 4B). It was found that caspase 8 cleavage was evident in these cells treated with the Fas-conjugated NP, indicative of its activation.

Analysis of the cytotoxicity results, by calculation of a synergistic ratio (SR), showed that the combined effects of CPT and anti-Fas antibodies were indeed synergistic, as shown by SR results in excess of unity (Figure 5). Pharmacologically relevant SR (values above 2, indicated by dashed line, Figure 5), showed that, after 72 h exposure with both formulations of NP, synergy could be seen with higher concentrations of CPT in the NP-20 formulations, but in the NP-100 formulations, which present higher concentrations of anti-Fas antibody (Table 2), the pharmacologically relevant synergy was observed at all concentrations used, demonstrating the effectiveness of this combination of antibody and chemotherapy in NP formulations.

DISCUSSION

Although numerous targeting methodologies have been proposed and reviewed at length, such as those based on immunoliposomes (*36*) and polymeric constructs (*37*), the evaluation of novel nanoparticulate systems remains an area of active investigation (*38*). In this present study we have investigated the application of the chemotherapeutic agent CPT in targeted immunoconjugates. CPT and derivatives are therapeutic chemotherapeutics with potent antitumor activity that has been shown previously to up-regulate the expression of the death receptor Fas on the surface of tumor cells (*11–13*); exploitable by the application of agonist anti-Fas antibodies to trigger

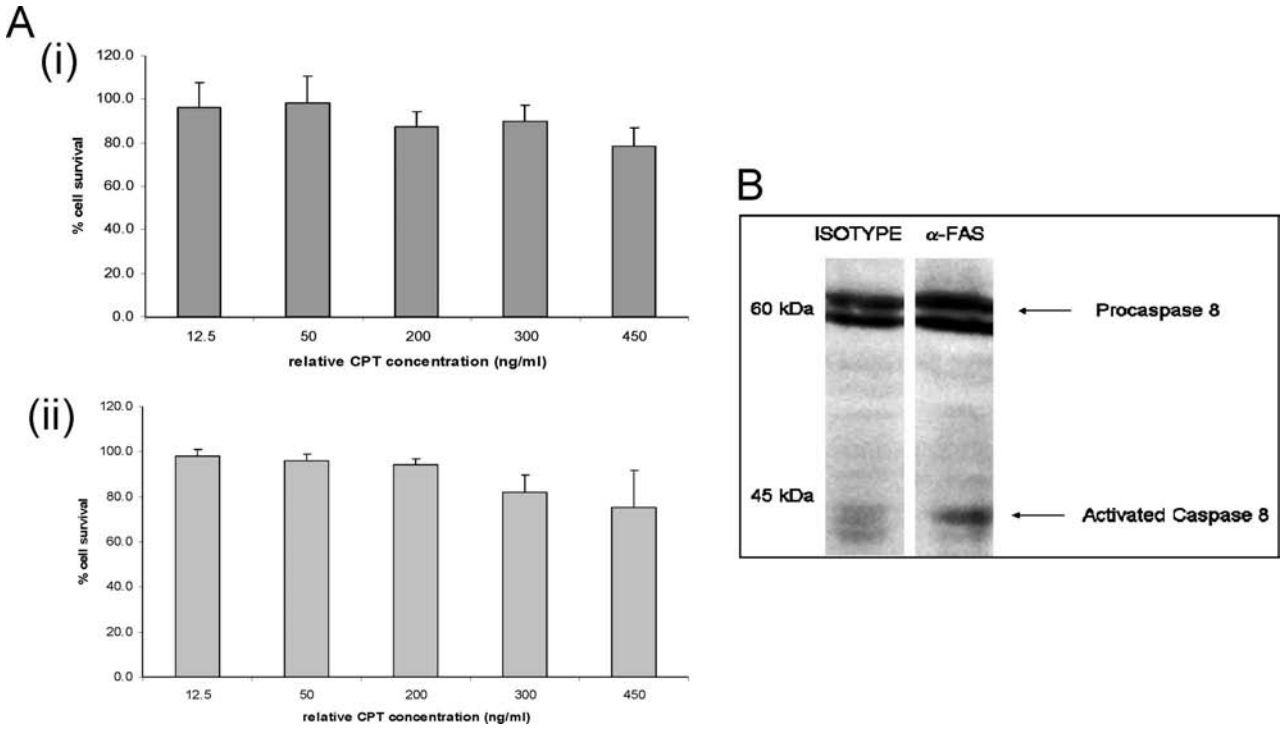

Figure 4. (A) Cell survival in the presence of "empty" NP-20 coated with anti-Fas antibody at 72 h (panel i) or NP-100 (panel ii). The *X* axis represents the relative CPT concentration that would be present if the NP were loaded with CPT as in Figure 3. (Results are mean ± SD, $n = 5$). (B) Caspase 8 activation following exposure of blank NP coated with anti-Fas antibody, demonstrating activation of Fas receptor and initiation of extrinsic apoptotic pathway.

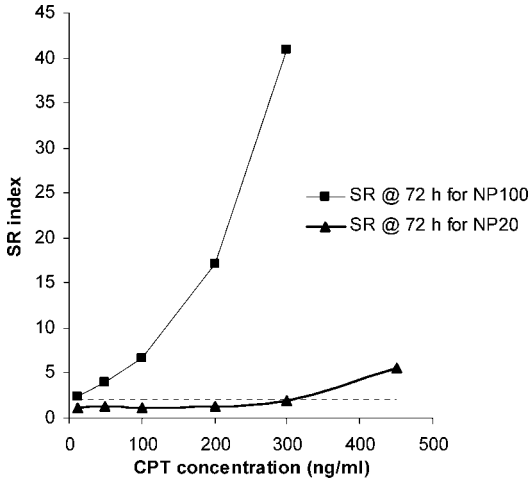

Figure 5. Synergistic ratio (SR) values after 72 h of exposure. SR values were calculated based on HCT116 cell survival obtained in Figure 3 for NP-100 CPT Fas in comparison with NP-100 loaded with CPT and "empty" NP-100 Fas (□) and NP-100 CPT Fas in comparison with NP-100 loaded with CPT and "empty" NP-100 Fas (▲). Pharmacological relevance (SR ≥ 2) is represented as the dashed line.

extrinsic apoptotic cell pathways to improve cytotoxicity over treatment with CPT alone. Therefore, the application of these two therapeutic approaches was pursued in the form of a immunoconjugate consisting of a nanoparticle, loaded with CPT and coated in anti-Fas antibodies.

The initial focus of this work was to incorporate CPT into PLGA NP. A novel aspect to this work was the simultaneous use of two PLGA polymers, one with a low molecular weight and high acid value (RG 502 H) and the other with a higher molecular weight variant with low acid value (RG 505 S). This enables the manufacture of NP with different matrix properties, but more importantly, with different densities of superficial carboxyl functionality. Conjugation of anti-Fas human monoclonal antibodies to PLGA NP using a water-soluble carbodiimde/NHS procedure was found to be dependent on carboxylic acid density on the NP surface (Table 2). NP made with 100% RG 502 H (low molecular weight) permitted increased antibody conjugation than NP made from the 20/80 blend (NP-20), which possessed less peripheral -COOH. This relationship between carboxylic acid density on the NP surface and amount of conjugated antibody indicated that chemical linkage is dominant over nonspecific physical adsorption.

The entrapment efficiency of CPT into NP manufactured from both PLGA blends, and at the two loading ratios tested, was essentially 100% within the concentration ranges analyzed here and did not depend on the PLGA compositions used. Further investigations revealed that the nature of the initial organic solution of CPT affected incorporation, with DMSO a requisite solvent during this process. In the absence of DMSO, entrapment efficiency fell to approximately 60% (data not shown). Previously, it has been shown that CPT exists in a crystalline form at 10% w/w of CPT loaded in PLGA microspheres and is molecularly dispersed at 1.2% w/w of CPT loaded in PLGA microspheres (*19*). The formation of a crystalline state of CPT in the initial organic solution could explain the observations see in Table 2, where larger NP were obtained as the drug loading was increased from 100:1 to 10:1. The subsequent release of entrapped CPT, loaded at 100:1 weight ratio was shown to be dependent on the PLGA composition (Figure 1). Similar release profiles generated using the 10:1 loading (not shown) were generally more prolonged and were not ideally suited to the time frame used during the *in vitro* cellular exposures. For this reason, the 100:1 PLGA:CPT weight ratio was the preferred loading. In all NP preparations tested, 100% RG 502 H (NP-100) showed a faster release when compared to 20% RG 502 H, as its low molecular weight and high acid value results in faster hydration when compared to the high molecular weight, low acid value RG 505 S, which forms the majority (80% w/w) of NP prepared using 20% RG 502 H (NP-20).

Importantly, though, once entrapped within a PLGA-based NP, the CPT is exposed to an acidic microclimate, which has been shown to stabilize the active lactone structure of this compound (*39*). The approach taken in this work, whereby CPT is loaded into PLGA NP, is expected to maintain CPT in its active lactone form for sustained periods of time and also to protect it from blood and human serum albumin, which readily hydrolyze CPT into its carboxylate form with a hydrolysis half-life of 54 min (*40*). The carboxylate form also has a high binding affinity to human serum albumin (*41*) enhancing its formation and resulting in reduced activity (*15*) and increased side effects (*14*). Particulate delivery of CPT was reported to enhance *in vitro* antitumor effects, such as seen with PLGA microspheres (*42*). Thus, stabilizing the lactone form and sustaining its release may explain the higher potency observed for NP-100-CPT (IC_{50} of 47.9 and 15.8 ng mL^{-1} after 48 and 72 h exposure, respectively) and NP-20-CPT (IC_{50} of 48.9 and 7.8 ng mL^{-1}, respectively) compared to CPT solution (IC_{50} of 231.2 ng mL^{-1} and 21.8 ng mL^{-1}, respectively). The ability of NP-20-CPT to show longer sustained release may also explain its higher potency when compared to NP-100-CPT. Similar improvements have previously been observed with poly(ϵ-caprolactone) microspheres (*28*), poly(ethylene glycol)-CPT conjugates (*43*), water-soluble poly(L-glutamic acid)-Gly-CPT conjugates (*44*), and long-circulating polymeric micelles (*20*).

Internalization of antibody-conjugated NP was examined by fluorescent microscopy, which indicated the selective localization of NP unto the surface of the HCT116 cells using an anti-Fas monoclonal antibody. Furthermore, the NP localization within acidified lysosomes, as shown in Figure 2, was in accordance with the findings of Algeciras-Scimnich et al. (*45*),who reported internalization of activated Fas through an endosomal pathway. Interestingly, localization of CPT NP in lysosomes may improve the stability of CPT as the acidic pH in this compartment will help maintain the lactone form of the drug.

Although this work has shown that NP can sustain CPT release and induce NP uptake through targeting of the Fas receptor, it is possible that the targeting of the Fas receptor with a CPT-loaded delivery system has added advantages. It was hypothesized that the display of anti-Fas antibody on the surface of the NP may enhance Fas-mediated caspase 8 activation. The detection of caspase 8 cleavage in the presence of "empty" particles displaying anti-Fas antibodies suggest that the NP conjugates promote their cytotoxic effects via activation of both the intrinsic and extrinsic apoptotic pathways with CPT initiating DNA damage and the antibody initiating caspase 8 activation.

Previously, studies using HCT116 cells demonstrated that the application of the cross-linking IgM anti-Fas antibody CH11 could be used in combination with CPT-11 to produce a synergistic cytotoxic effect (*13*). In agreement with these previous studies, it was shown in this current work that a combination of a CPT-loaded PLGA NP and a peripheral coating of anti-Fas mAb resulted in significant synergetic cytotoxicity. NP-20-CPT-Fas showed less significant potency and a lower SR values when compared to NP 100, as shown in Figure 5. This may be due to lower amounts of anti-Fas human monoclonal antibody conjugated to the NP surface. This lower density of antibody presentation on the NP may result in lower Fas activation, but this observation and the full intent of exstrinic apoptosis induction through Fas will require further investigation.

In conclusion, this work has demonstrated the application of CPT using PLGA NP coated with an antibody targeting Fas. This drug delivery system directs and selectively targets cells expressing Fas receptor and through receptor-mediated internalization results in the uptake of the drug-loaded NP. Furthermore, as well as mediating its cytotoxic effect through DNA damage induced by CPT, these particles may result in the activation of Fas receptor and initiation of the extrinsic apoptotic pathway. Furthermore, as it is known that CPT up-regulates Fas cell surface expression, this antibody drug conjugate further potentiates cytotoxicity through two independent mechanisms resulting in synergy that could be pharmaceutically useful. This study paves the way for examination of other drug and receptor relationships were combinations of antibody and drug payload could produce conjugates with improved targeting and efficacy for treatment of cancer and other conditions.

LITERATURE CITED

(1) Leithäuser, F., Dhein, J., Mechtersheimer, G., Koretz, K., Brüderlein, S., Henne, C., Schmidt, A., Debatin, K. M., Krammer, P. H., and Möller, P. (1993) Constitutive and induced expression of APO-1 a new member of the nerve growth factor/tumor necrosis factor receptor superfamily, in normal and neoplastic cells. *Lab Invest. 69*, 415–29.

(2) Trauth, B. C., Klas, C., Peters, A. M., Matzku, S., Möller, P., Falk, W., Debatin, K. M., and Krammer, P. H. (1989) Monoclonal antibody-mediated tumor regression by induction of apoptosis. *Science 245*, 301–5.

(3) Suda, T., and Nagata, S. (1994) Purification and characterization of the Fas-ligand that induces apoptosis. *J. Exp. Med. 179*, 873–9.

(4) Papoff, G., Hausler, P., Eramo, A., Pagano, M. G., Di Leve, G., Signore, A., and Ruberti, G. (1999) Identification and characterization of a ligand-independent oligomerization domain in the extracellular region of the CD95 death receptor. *J. Biol. Chem. 274*, 38241–38250.

(5) Ashkenazi, A., and Dixit, V. M. (1998) Death receptors: signaling and modulation. *Science 281*, 1305–1308.

(6) Medema, J. P., Scaffidi, C., Kischkel, F. C., Shevchenko, A., Mann, M., Krammer, P. H., and Peter, M. E. (1997) FLICE is activated by association with the CD95 death-inducing signaling complex (DISC). *EMBO J. 16*, 2794–2804.

(7) Muzio, M., Salvesen, G. S., and Dixit, V. M. (1997) FLICE induced apoptosis in a cell-free system. Cleavage of caspase zymogens. *J. Biol. Chem. 272*, 2952–2956.

(8) Giovanella, B. C., Stehlin, J. S., Wall, M. E., Wani, M. C., Nicholas, A. W., Liu, L. F., Silber, R., and Potmesil, M. (1989) DNA topoisomerase I-targeted chemotherapy of human colon cancer in xenografts. *Science 246*, 1046–1048.

(9) Pommier, Y., Pourquier, P., Fan, Y., and Strumberg, D. (1998) Mechanism of action of eukaryotic DNA topoisomerase I and drugs targeted to the enzyme. *Biochim. Biophys. Acta 1400*, 83–105.

(10) Goldwasser, F., Shimizu, T., Jackman, J., Hoki, Y., O'Connor, P. M., Kohn, K. W., and Pommier, Y. (1996) Correlations between S and G2 arrest and the cytotoxicity of camptothecin in human colon carcinoma cells. *Cancer Res. 56*, 4430–4437.

(11) Shao, R. G., Cao, C. X., Nieves-Neira, W., Dimanche-Boitrel, M. T., Solary, E., and Pommier, Y. (2001) Activation of the Fas pathway independently of Fas ligand during apoptosis induced by camptothecin in p53 mutant human colon carcinoma cells. *Oncogene 20*, 1852–1859.

(12) Xia, S., Rosen, E. M., and Laterra, J. (2005) Sensitization of glioma cells to Fas-dependent apoptosis by chemotherapy-induced oxidative stress. *Cancer Res. 65*, 5248–5255.

(13) McDermott, U., Longley, D. B., Galligan, L., Allen, W., Wilson, T., and Johnston, P. G. (2005) Effect of p53 status and STAT1 on chemotherapy-induced, Fas-mediated apoptosis in colorectal cancer. *Cancer Res. 65*, 8951–8960.

(14) Hertzberg, R. P., Caranfa, M. J., Holden, K. G., Jakas, D. R., Gallagher, G., Mattern, M. R., Mong, S. M., Bartus, J. O., Johnson, R. K., and Kingsbury, W. D. (1989) Modification of the hydroxy lactone ring of camptothecin: inhibition of mammalian topoisomerase I and biological activity. *J. Med. Chem. 32*, 715–720.

(15) Fassberg, J., and Stella, V. J. (1992) A kinetic and mechanistic study of the hydrolysis of camptothecin and some analogues. *J. Pharm. Sci. 81*, 676–684.
(16) Potmesil, M. (1994) Camptothecins: from bench research to hospital wards. *Cancer Res. 54*, 1431–1439.
(17) Burke, T. G., and Mi, Z. (1994) The structural basis of camptothecin interactions with human serum albumin: impact on drug stability. *J. Med. Chem. 37*, 40–46.
(18) Burke, T. G., Munshi, C. B., Mi, Z., and Jiang, Y. (1995) The important role of albumin in determining the relative human blood stabilities of the camptothecin anticancer drugs. *J. Pharm. Sci. 84*, 518–519.
(19) Ertl, B., Platzer, P., Wirth, M., and Gabor, F. (1999) Poly(D,L-lactic-co-glycolic acid) microspheres for sustained delivery and stabilization of camptothecin. *J. Controlled Release 61*, 305–317.
(20) Kawano, K., Watanabe, M., Yamamoto, T., Yokoyama, M., Opanasopit, P., Okano, T., and Maitani, Y. (2006) Enhanced antitumor effect of camptothecin loaded in long-circulating polymeric micelles. *J. Controlled Release 112*, 329–332.
(21) Gupta, E., Vyas, V., Ahmed, F., Sinko, P. J., Cook, T., and Rubin, E. (2000) Pharmacokinetics of orally administered camptothecins. *Ann. N.Y. Acad. Sci. 922*, 195–204.
(22) Garcia-Carbonero, R., and Supko, J. G. (2002) Current perspectives on the clinical experience, pharmacology, and continued development of the camptothecins. *Clin. Can. Res. 8*, 641–661.
(23) Koo, O. M., Rubinstein, I., and Onyuksel, H. (2005) Camptothecin in sterically stabilized phospholipid micelles: a novel nanomedicine. *Nanomedicine 1*, 77–84.
(24) O'Leary, J., and Muggia, F. M. (1998) Camptothecins: A review of their development and schedules of administration. *Eur. J. Cancer 34*, 1500–1508.
(25) Srivastava, V., Negi, A. S., Kumar, J. K., Gupta, M. M., and Khanuja, S. P. (2005) Plant-based anticancer molecules: a chemical and biological profile of some important leads. *Bioorg. Med. Chem. 13*, 5892–5908.
(26) Mu, L., Elbayoumi, T. A., and Torchilin, V. P. (2005) Mixed micelles made of poly(ethylene glycol)-phosphatidylethanolamine conjugate and d-alpha-tocopheryl polyethylene glycol 1000 succinate as pharmaceutical nanocarriers for camptothecin. *Int. J. Pharm. 306*, 142–149.
(27) Miura, H., Onishi, H., Sasatsu, M., and Machida, Y. (2004) Antitumor characteristics of methoxypolyethylene glycol-poly(DL-lactic acid) nanoparticles containing camptothecin. *J. Controlled Release 97*, 101–113.
(28) Dora, C. L., Alvarez-Silva, M., Trentin, A. G., de Faria, T. J., Fernandes, D., da Costa, R., Stimamiglio, M., and Lemos-Senna, E. (2001) Evaluation of antimetastatic activity and systemic toxicity of camptothecin-loaded microspheres in mice injected with B16-F10 melanom A cells. *J. Pharm. Pharm. Sci. 9*, 22–31.
(29) Mo, Y., and Lim, L. Y. (2005) Preparation and in vitro anticancer activity of wheat germ agglutinin (WGA)-conjugated PLGA nanoparticles loaded with paclitaxel and isopropyl myristate. *J. Controlled Release 107*, 30–42.
(30) Kern, D. H., Morgan, C. R., and Hildebrand-Zanki, S. U. (1988) In vitro pharmacodynamics of 1 beta-D-arabinofuranosylcytosine: synergy of antitumor activity with cis-diamminedichloroplatinum(II). *Cancer Res. 48*, 117–121.
(31) Romanelli, S., Perego, P., Pratesi, G., Carenini, N., Tortoreto, M., and F.Zunino, F. (1998) In vitro and in vivo interaction between cisplatin and topotecan in ovarian carcinoma systems. *Cancer Chemother. Pharmacol. 41*, 385–390.
(32) Garnett, C. T., Palena, C., Chakraborty, M., Tsang, K. Y., Schlom, J., and Hodge, J. W. (2004) Sublethal irradiation of human tumor cells modulates phenotype resulting in enhanced killing by cytotoxic T lymphocytes. *Cancer Res. 64*, 7985–7994.
(33) Scott, C. J., Marouf, W. M., Quinn, D. J., Buick, R. J., Orr, S. J., Donnelly, R. F., and McCarron, P. A. (2008) Immunocolloidal targeting of the endocytotic siglec-7 receptor using peripheral attachment of siglec-7 antibodies to poly(lactide-co-glycolide) nanoparticles. *Pharm. Res. 25*, 135–46.
(34) Lake, J. R., Van Dyke, R. W., and Scharschmidt, B. F. (1987) Acidic vesicles in cultured rat hepatocytes. Identification and characterization of their relationship to lysosomes and other storage vesicles. *Gastroenterology 92*, 1251–1261.
(35) Butor, C., Griffiths, G., Aronson Jr, N. N., and Varki, A. (1995) Co-localization of hydrolytic enzymes with widely disparate pH optima: implications for the regulation of lysosomal pH. *J. Cell Sci. 108*, 2213–2219.
(36) Mastrobattista, E., Koning, G. A., and Storm, G. (1999) (1999)Immunoliposomes for the targeted delivery of antitumor drugs. *Adv. Drug Delivery Rev. 40*, 103–127.
(37) Minko, T., and Khandare, J. (2006) Polymer-drug conjugates: Progress in polymeric prodrugs. *Prog. Polym. Sci. 31*, 359–397.
(38) Brannon-Peppas, L., and Blanchette, J. O. (2004) Nanoparticle and targeted systems for cancer therapy. *Adv. Drug Delivery Rev. 56*, 1649–1659.
(39) Shenderova, A., Burke, T. G., and Schwendeman, S. P. (1999) The acidic microclimate in poly (lactide-co-glycolide) microspheres stabilizes camptothecins. *Pharm. Res. 16*, 241–248.
(40) Opanasopit, P., Yokoyama, M., Watanabe, M., Kawano, K., Maitani, Y., and T.Okano, T. (2005) Influence of serum and albumins from different species on stability of camptothecin-loaded micelles. *J. Controlled Release 104*, 313–321.
(41) Scott, D. O., Bindra, D. S., and Stella, V. J. (1993) Plasma pharmacokinetics of lactone and carboxylate forms of 20 (S)-camptothecin in anesthetized rats. *Pharm. Res. 10*, 1451–1457.
(42) Tong, W., Wang, L., and D'Souza, M. J. (2003) Evaluation of PLGA microspheres as delivery system for antitumor agent-camptothecin. *Drug Dev. Ind. Pharm. 29*, 745–756.
(43) Yu, D., Peng, P., Dharap, S. S., Wang, Y., Mehlig, M., Chandna, P., Zhao, H., Filpula, D., Yang, K., Borowski, V., Borchard, G., Zhang, Z., and Minko, T. (2005) Antitumor activity of poly(ethylene glycol)-camptothecin conjugate: the inhibition of tumor growth in vivo. *J. Controlled Release 110*, 90–102.
(44) Singer, J. W., Bhatt, R., Tulinsky, J., Buhler, K. R., Heasley, E., Klein, P., and P., and de Vries, P. (2005) Water-soluble poly-(L-glutamic acid)-Gly-camptothecin conjugates enhance camptothecin stability and efficacy in vivo. *J. Controlled Release 74*, 243–247.
(45) Algeciras-Schimnich, A., Shen, L., Barnhart, B. C., Murmann, A. E., Burkhardt, J. K., and Peter, M. E. (2002) Molecular ordering of the initial signaling events of CD95. *Mol. Cell. Biol. 22*, 207–220.

BC800057G

In Vivo Tumor Cell Targeting with "Click" Nanoparticles

Geoffrey von Maltzahn,[†,‡] Yin Ren,[†,‡] Ji-Ho Park,[||] Dal-Hee Min,[‡] Venkata Ramana Kotamraju,[§] Jayanthi Jayakumar,[‡] Valentina Fogal,[§] Michael J. Sailor,[||] Erkki Ruoslahti,[§] and Sangeeta N. Bhatia*[,‡,⊥]

Harvard-MIT Division of Health Sciences and Technology, Cambridge, Massachusetts, Cancer Research Center, Burnham Institute for Medical Research, La Jolla, California, Vascular Mapping Center, Burnham Institute for Medical Research at University of California Santa Barbara, Santa Barbara, California, Materials Science and Engineering Program, Department of Chemistry and Biochemistry, University of California, San Diego, La Jolla, California 92093, and Electrical Engineering and Computer Science, MIT/Brigham & Women's Hospital, Boston, Massachusetts. Received March 3, 2008; Revised Manuscript Received May 7, 2008

The *in vivo* fate of nanomaterials strongly determines their biomedical efficacy. Accordingly, much effort has been invested into the development of library screening methods to select targeting ligands for a diversity of sites *in vivo*. Still, broad application of chemical and biological screens to the *in vivo* targeting of nanomaterials requires ligand attachment chemistries that are generalizable, efficient, covalent, orthogonal to diverse biochemical libraries, applicable under aqueous conditions, and stable in *in vivo* environments. To date, the copper(I)-catalyzed Huisgen 1,3-dipolar cycloaddition or "click" reaction has shown considerable promise as a method for developing targeted nanomaterials *in vitro*. Here, we investigate the utility of "click" chemistry for the *in vivo* targeting of inorganic nanoparticles to tumors. We find that "click" chemistry allows cyclic LyP-1 targeting peptides to be specifically linked to azido-nanoparticles and to direct their binding to p32-expressing tumor cells *in vitro*. Moreover, "click" nanoparticles are able to stably circulate for hours *in vivo* following intravenous administration (>5 h circulation time), extravasate into tumors, and penetrate the tumor interstitium to specifically bind p32-expressing cells in tumors. In the future, *in vivo* use of "click" nanomaterials should expedite the progression from ligand discovery to *in vivo* evaluation and diversify approaches toward multifunctional nanoparticle development.

INTRODUCTION

The ability to target nanomaterials to precise biological locations would have wide-ranging impact in biology and medicine. In living systems, highly controlled transportation networks continually shuttle payloads to and from specific molecular addresses. The efficiency of these systems provides strong motivation for the advancement of targeted nanoparticle technologies, particularly for the diagnosis and treatment of human diseases. Toward this goal, high throughput strategies for ligand discovery have generated a multitude of chemical and biological motifs with the potential to direct nanomaterials to specific biomolecular targets. However, translation of these ligands toward *in vivo* nanoparticle targeting has been limited by the number of nanoparticle attachment methods that are efficient, generalizable, aqueous compatible, chemically orthogonal to broad ranges of functional groups, and suitable for *in vivo* applications.

Previous work has demonstrated that *in vivo* bacteriophage display may be used to select for peptide sequences that mimic the ability of endogenous shuttles to target vascular and parenchymal tissue addresses (*1*–*5*). Already, linear peptide candidates of phage screens, as well as small molecule targeting candidates, have been translated toward nanomaterial targeting (*6*–*9*), primarily via use of exogenous or nonessential thiols, carboxylic acids, or amines. Still, some of the most powerful targeting motifs developed to date are those that contain essential thiol, amine, and carboxyl groups, thereby prohibiting their specific attachment via traditional methods. In particular, conformationally constrained, disulfide-cyclized targeting peptides are desirable for their enhanced affinity to biological receptors (*10*, *11*), and resistance to proteolytic degradation *in vivo* relative to their linear counterparts (*12*, *13*). However, specific intramolecular cyclization makes it difficult to add exogenous cysteine residues, while essential amines and carboxyl groups prohibit selective conjugation via exogenous lysine, aspartic acid, or glutamic acid residues. Additionally, noncovalent methods of ligand attachment relying on hydrophobic or electrostatic effects, although widely used *in vitro* (*14*–*16*), are unlikely to remain stable in blood or to resist rapid clearance *in vivo*. Recently, copper(I)-catalyzed "click" chemistry has emerged as an extraordinarily selective chemistry and an attractive solution in applications where commonly used thiol-reactive (maleimide, 2-pyridyldithio, iodoacetyl) or amine-reactive (NHS, epoxy, aldehyde, EDC) chemistries are not suitable (*17*). *In vitro* "click" chemistry has been utilized to generate functionalized polymers, (*18*–*20*), surfaces (*21*–*23*), and nanoparticles (*24*–*32*), and meets the previously mentioned criteria for broad utility in nanoparticle functionalization (chemical orthogonality, aqueous efficiency, applicability for diverse substrates). However, the use of "click" nanoparticles for *in vivo* applications has not been investigated. Particularly, as opposed to small molecule reagents with circulation times on the order of minutes (*8*), ligand attachments on long circulating nanomaterials must remain stable against *in vivo* degradation for hours while nanoparticles circulate systemically and identify molecular targets.

* Correspondence should be addressed to Sangeeta N. Bhatia, MD, PhD; Director, Laboratory for Multiscale Regenerative Technologies; Massachusetts Institute of Technology; E19-502D Cambridge, MA 02139. Phone: 617-324-0221. E-mail: sbhatia@mit.edu.

[†] These authors contributed equally.

[‡] Harvard-MIT Division of Health Sciences and Technology.

[§] Cancer Research Center, Burnham Institute for Medical Research, and Vascular Mapping Center, Burnham Institute for Medical Research at University of California Santa Barbara.

[||] University of California, San Diego.

[⊥] MIT/Brigham & Women's Hospital.

10.1021/bc800077y CCC: $40.75 © 2008 American Chemical Society
Published on Web 07/09/2008

Scheme 1. Design of a "Click" Nanoparticle That Targets Tumor Cells *in Vitro* and *in Vivo*[a]

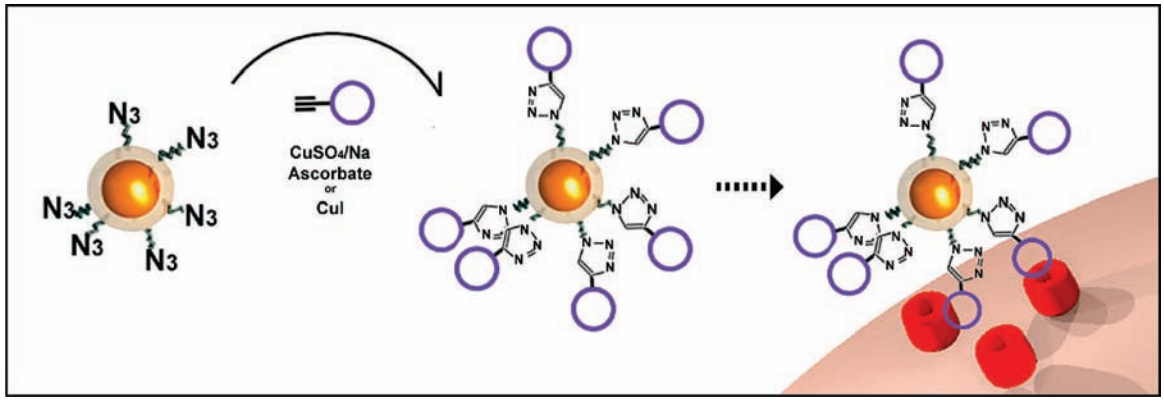

[a] Cross-linked, fluorescent, superparamagnetic iron oxide nanoparticles are modified to display azido-PEG groups. Conjugation of cyclic targeting peptides (purple circles) bearing pendant alkynes to azido-PEG nanoparticles via the copper(I)-catalyzed Huisgen 1,3-dipolar cycloaddition ("click" reaction) allows specific targeting of the nanoparticles to cells expressing the receptor (red).

Here, we find that alkyne-azide "click" chemistry provides a facile, single-step method for specifically linking the cyclic tumor-targeting peptide LyP-1 (CGNKRTRGC (*1*, *33*);), which contains essential thiol and amine groups, to polymer-coated magnetofluorescent nanoparticles. LyP-1 binds to p32, a mitochondrial proteins that is both overexpressed and aberrantly localized at the cell surface of tumor cells, macrophages and lymphatic endothelial cells in certain experimental tumors and in human cancers (*34*, *35*). We find that "click" LyP-1 nanoparticles are able stably traverse the systemic circulation, extravasate into tumors, and penetrate the tumor interstitium to specifically bind to receptors on p32-expressing cells in the tumors. Together, these results provide strong motivation for future use of "click" functionalization as a strategy for developing nanoparticles for *in vivo* biomedical applications (Scheme 1).

EXPERIMENTAL SECTION

Unless otherwise stated all reagents were purchased from Sigma-Aldrich and all reactions were performed at room temperature.

Iron Oxide Nanoparticle Synthesis. Cross-linked, aminated, fluorescent, superparamagnetic iron oxide nanoparticles were synthesized according to the published protocol (*36*, *37*). Briefly, dextran-coated iron oxide nanoparticles were synthesized, purified, and subsequently cross-linked using epichlorohydrin. After exhaustive dialysis, particles were aminated by adding 1:10 v/v ammonium hydroxide (30%) and incubated on a shaker overnight. Aminated nanoparticles were subsequently purified from excess ammonia using a Sephadex G-50 column and concentrated using a high-gradient magnetic-field filtration column (Miltenyi Biotec). The near-infrared-fluorochrome VivoTag 680 was added to remotely detect particle accumulation *in vitro* and *in vivo* by reacting in 0.1 M HEPES buffer with 0.15 M NaCl at pH 7.2. DMSO-solubilized fluorochromes were added into particle solutions at 4 °C under mixing and allowed to warm to room temperature to react for 2 h. The yield was approximately 10 fluorochromes per nanoparticle for all experiments.

Succinimidyl 4-Azidobutyrate Synthesis (Scheme 2A). *Ethyl 4-azidobutyrate (***1***).* To a solution of ethyl 4-bromobutyrate (5.85 g, 30 mmol) in dimethyl sulfoxide (DMSO, 20 mL), sodium azide (2.925 g, 45 mmol) was added with stirring. The reaction mixture was stirred for 22 h at 55 °C, and cooled to room temperature. Water was added to the reaction mixture and extracted with ethyl ether (3 × 30 mL). The combined organic layer was washed with water and brine, and reduced in vacuo to afford 3.80 g of the azido compound **1**.

*4-Azidobutyric acid (***2***).* Ethyl 4-azidobutyrate **1** (3.14 g, 20 mmol) was dissolved in aqueous sodium hydroxide solution (1 N, 24 mL) with a minimum amount of methanol to make the solution homogeneous. The reaction mixture was stirred for 3 h at room temperature. After removal of methanol *in vacuo*, the aqueous solution was acidified to pH 0 with HCl and extracted with ethyl ether (3 × 50 mL). The ether layer was then dried over sodium sulfate and filtered. Removal of solvent gave the acid **2** (2.25 g).

*Succinimidyl 4-Azidobutyrate (***3***).* To a solution of *N*-hydroxyl succinimide (1.65 g, 14.3 mmol) in methylene chloride (100 mL) was added acid **2** (1.68 g, 13 mmol) followed by 1-ethyl-3-[3-dimethylaminopropyl]carbodiimide hydrochloride (EDAC, 2.74 g, 14.3 mmol). After stirring for 4 h at room temperature, the reaction mixture was washed with water and brine, dried over sodium sulfate, and filtered. Solvent was removed under reduced pressure to yield 1.15 g of the succinimidyl 4-azidobutyrate **3**.

Peptide Synthesis. Peptides were synthesized in the MIT Biopolymers Laboratory and their composition was confirmed via HPLC and mass spectrometry. The LyP-1 and LyP-1CTL peptides were synthesized with either heptynoic acid or propargylglycine at the N-terminus for conjugation. Each peptide is also labeled with a TAMRA fluorophore (Anaspec) via a lysine residue separated by an aminohexanoic acid (Ahx) spacer. (final sequence for LyP-1: Heptynoic acid or propargylglycine-K(Tamra)[Ahx]-CGNKRTRGC; for LyP-1CTL: Heptynoic acid or propargylglycine-K(Tamra)[Ahx]-CRVRTRSGC). Peptides were cyclized by bubbling air into 10 μM aqueous peptide solutions overnight. Finally, peptide solutions were lyophilized for subsequent use.

"Click" Attachment of Peptides to Nanoparticles. Succinimidyl 4-azidobutyrate was linked to 5 kDa thiol-PEG-amine polymers in 0.1 M HEPES 0.15 M NaCl pH 7.2 for 1 h at a 2:1 molar ratio between linker and polymer. Simultaneously, amino-modified, fluorochrome-labeled nanoparticles were activated with *N*-[γ-maleimidobutyryloxy] succinimide ester (GMBS) (dissolved in DMSO) cross-linker under similar conditions at a 200:1 molar ratio between cross-linker and nanoparticles. To remove excess GMBS, nanoparticle samples were filtered on a G50 column into 50 mM Na phosphate buffer at pH 7.2 supplemented with 10 mM EDTA. Purified nanoparticles were then combined with the polymer reaction mixture and allowed to react at room temperature overnight. Azido-PEG-nanoparticles were then purified from excess polymer and succinimidyl 4-azidobutyrate on a size exclusion column (ACA-44 media: Pall) into 0.1 M HEPES pH 7.2 buffer. Finally, the

Scheme 2. Synthesis of LyP-1-Coated Nanoparticles Using "Click" Chemistry[a]

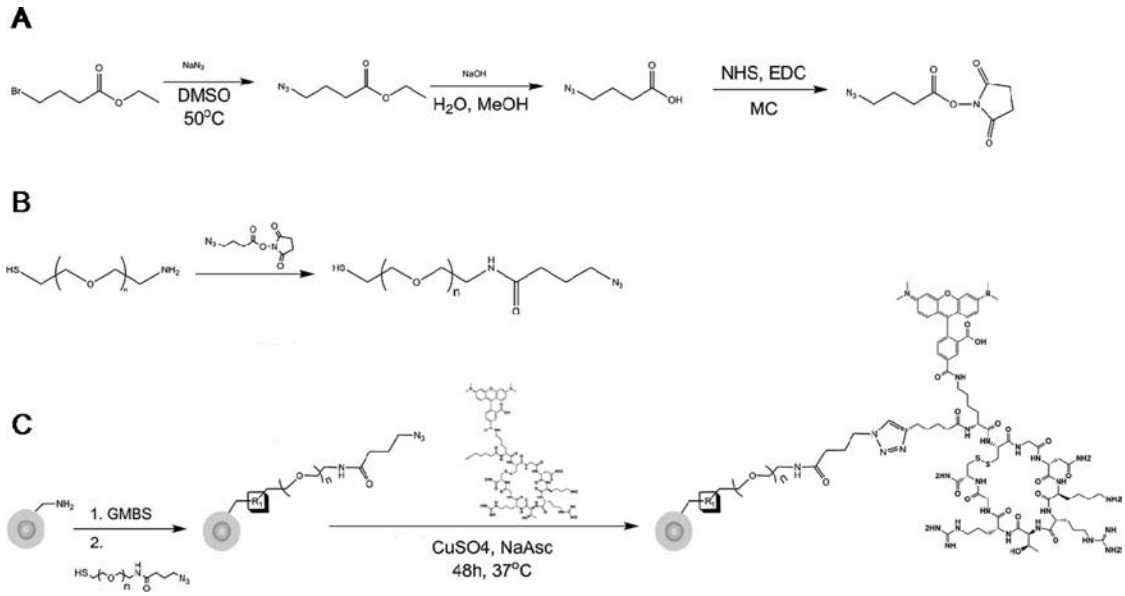

[a] (A) Synthesis of succinimidyl 4-azidobutyrate. (B) Synthesis of azide-PEG-thiol by linking succinimidyl 4-azidobutyrate to a 5 kDa thiol-PEG-amine. (C) Aminated, cross-linked, fluorochrome-labeled superparamagnetic iron-oxide nanoparticles are activated with GMBS, filtered, and then reacted with the thiol-PEG-azide from (B) to yield azido-PEG bearing nanoparticles. After purification, the particle solutions were reacted with alkyne-bearing LyP-1 peptides with $CuSO_4$/Na Ascorbate as catalysts to yield LyP-1-coated nanoparticles for *in vitro* and *in vivo* use.

azide-PEG-bearing particles were concentrated using Amicon Ultra-4 (Millipore) filters and stored at 4 °C.

To optimize catalyst concentrations for the "click" reaction by HPLC, a 10-fold excess of azido-PEG-NH_2 or *O*-(2-aminoethyl)-*O′*-(2-azidoethyl)pentaethylene glycol (Polypure) was added to a 100 μM peptide solution. $CuSO_4$ and Na ascorbate were dissolved in H_2O and added to the reaction mixture to final concentrations of 1 mM/5 mM and 10 mM/50 mM $CuSO_4$/Na Ascorbate. This mixture was shaken at 37 °C for various times (1 day to 3 days), after which it was characterized via HPLC.

Alkyne-bearing peptides (70:1 peptide/nanoparticle molar ratio), $CuSO_4$ (1 mM), and sodium ascorbate (5 mM) in H_2O were added to a solution of particles and the mixture was shaken at 37 °C for 48 h. Following the reaction, nanoparticles were purified from copper catalyst and excess peptides by filtration in ACA-44 size exclusion media into 0.1 M HEPES 0.15 M NaCl pH 7.2 buffer.

Cell Culture. Cell uptake experiments were performed using a human MDA-MB-435 cancer cell line. Grow media was minimum essential medium eagle (Invitrogen) with fetal bovine serum (10%; Invitrogen). Cells were passaged into 96-well plates and used at 60−80% confluency.

For peptide uptake experiments (Figure 1), LyP-1 or LyP-1CTL peptides were added to cell monolayers in serum-containing media at a final concentration of 10 μM. After 45 min of incubation at 37 °C, cells were washed with media, PBS, treated with trypsin (0.25%) and EDTA, and resuspended in 1% BSA (in PBS) for flow cytometry (BD LSRII). Fluorescence data on 10 000 cells was collected for each sample.

For nanoparticle uptake experiments (Figure 2), particles bearing an LyP-1, LyP-1CTL, or terminal azides were added to the cells in serum media at a final concentration of 100 nM. After 2 h of incubation, cells were trypsinized and assayed for particle fluorescence by flow cytometry. For peptide inhibition experiments, free LyP-1 peptides (10 μM to 100 μM) were first incubated with the cells for 1 h. The cells were then washed with media and 100 nM of LyP-1-coated nanoparticles were added to the cell culture. For imaging, cells were washed with PBS and observed using a 20× objective. Images were captured with a CCD camera mounted on a Nikon TE200 inverted epifluorescence microscope.

In Vivo Studies of Nanoparticle Targeting. Nude athymic mice were inoculated subcutaneously with human cancer cells (MDA-MB-435). After tumors had reached ~0.5 cm^3 in size, LyP-1- and azide-bearing nanoparticles were injected intravenously in the tail vein (1 mgFe/kg). Twenty-four hours after the injection, tumor tissues were excised, snap−frozen, and cut into 15 μm histological sections. Rat antimouse CD-31 (1:50, BD Pharmingen) and polyclonal anti-p32 antibody (1:200 (*34*)) were used for immunohistochemical staining of frozen tissue sections. The corresponding secondary antibodies were added and incubated for 1 h at room temperature: Alexa Fluor 594 goat antirat IgG (1:500, Invitrogen) for CD-31 and Alexa Fluor 594 goat antirabbit IgG (1:500, Invitrogen) for p32 antibody. The slides were washed three times with PBS and mounted in Vectashield Mounting Medium with DAPI (Vector Laboratories). The stained tumor sections were observed with a fluorescence microscope (Nikon, Tokyo, Japan). Histological quantitation of nanoparticles localization was done using *ImageJ* software. Stacks of CD31-stained sections and nanoparticle fluorescence images were utilized for intra- and extravascular particle distribution quantitation. Regions with CD31-staining were selected to denote intravascular accumulation of nanoparticles and surrounding areas were classified as extravascular. The net nanoparticle fluorescence signal above background was quantified for each of these regions to determine the approximate percent of nanoparticle fluorescence localized to the vasculature vs the extravascular space. Three sections from each set of mice were randomly chose for analysis.

RESULTS AND DISCUSSION

In order for "click" chemistry to be applied to the development of peptide-targeted nanomaterials, peptides must be able to harbor pendant alkyne or azide moieties without abating peptide activity. To investigate the efficacy of targeting peptides harboring pendant alkyne moieties, LyP-1 peptide (CGNKRTRGC) and untargeted cyclic control peptide, LyP-1CTL (CRVRTRSGC) in which the essential NKRTR motif is replaced with

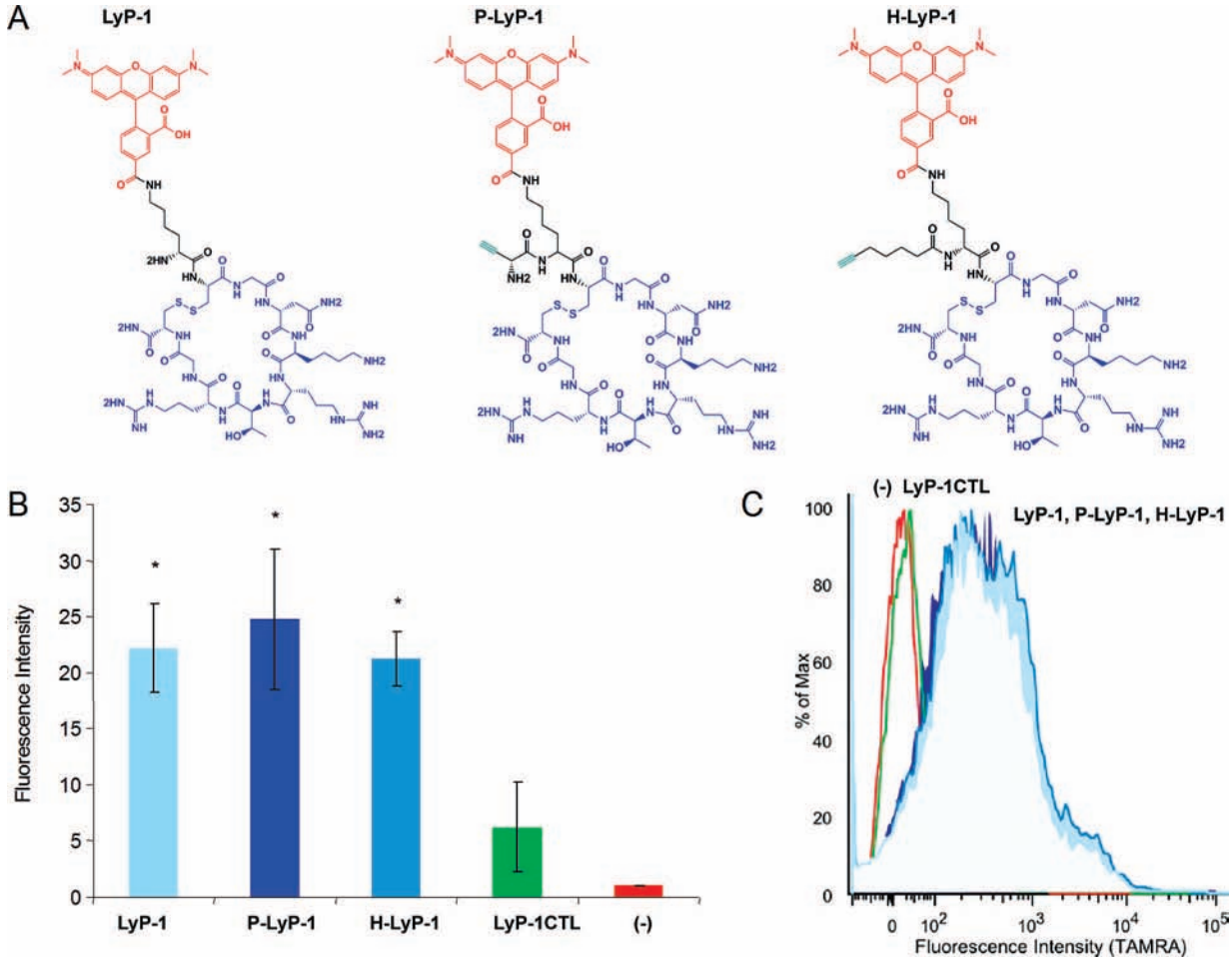

Figure 1. Native and alkyne-bearing LyP-1 peptides target p32-expressing MDA-MB-435 cells *in vitro*. (A) Structures of LyP-1, propargylglycine-LyP-1, and heptynoic acid-LyP-1, all labeled with a TAMRA fluorophore (red). The cyclic nonapeptide is in blue. The pendant alkyne moieties were conjugated to the N-terminus of the peptide during standard FMOC peptide synthesis. (B) Flow cytometry shows that peptides bearing different alkyne groups target MDA-MB-435 cancer cells similarly, while a scrambled control (LyP-1CTL) do not target (P = propargylglycine, H = 6-heptynoic acid, $*p < 0.01$, unpaired Student's *t*-test). **(**C) Flow cytometry histogram shows LyP-1, P-LyP-1, and H-LyP-1 peptides (in different shades of blue) target MDA-MB-435 cells *in vitro*, while LyP-1CTL peptide (green) did not show targeting relative to peptide-free control cells (red).

RVRTR to maintain net charge but abate p32 targeting (*33*), were synthesized to incorporate either of two alkyne moieties (the unnatural amino acid propargylglycine or 6-heptynoic acid) and a 5,6-carboxytetramethylrhodamine fluorophore (TAMRA) (Figure 1A; spectra: Supporting Information Figure 1). Because the alkyne moieties provide molecularly small chemical handles that may be incorporated in FMOC synthesis to either the N- or C-terminal of essential peptide sequences, we hypothesized their presence could be tailored to allow chemical attachment to azido-nanomaterials without interfering with LyP-1 peptide activity. In previous investigations, we found that N-terminal addition of visible and near-infrared fluorophores do not disrupt peptide binding to its receptors (*1, 33*). Accordingly, we reasoned alkyne moieties located near the N-terminus would be well-tolerated by the peptide (Figure 1A). To verify the specificity and efficacy of alkyne-LyP-1 targeting, 10 μM of LyP-1, bearing propargyl glycine, heptynoic, or no alkyne group were incubated for 45 min on monolayers of MDA-MB-435 human tumor cells, which have been shown to bind and internalize LyP-1 and express p32 at the cell surface (*33, 34*), LyP-1CTL peptides were included as a control sequence to verify targeted enhancement of uptake over nonspecific cyclic peptide structures. Cellular uptake of LyP-1 peptide was quantified via flow cytometry (Figure 1B) and plotted as the populational fluorescent intensity, relative to cells incubated with vehicle alone. *In vitro* targeting of LyP-1 peptides bearing either propargylglycine or 6-heptyoic acid was similar to that of native LyP-1 and control peptides (Figure 1C), indicating that alkyne modifications N-terminal to targeting sequences were innocuously chaperoned by peptides and did not affect cell binding.

We next probed the effect of three variables on "click" reaction conditions between our peptides and an azido-PEG-amine (catalyst, catalyst concentration, and reaction time). Azido-PEG-amine was chosen to emulate the azido-PEG surface of the nanoparticles to be used subsequently and to provide a model reaction amenable to HPLC quantitation of product formation. Copper(I) catalyst was added either directly as an iodinated salt (Cu(I)I), or indirectly as soluble copper sulfate ($Cu(II)SO_4$) and reduced by sodium ascorbate *in situ*. The degree of product formation was measured via HPLC with mass spectrometric verification of product identity. The addition of the azido-PEO-amine rendered peptides more hydrophilic and decreased retention times compared to unconjugated peptides. As shown in Supporting Information Table S1, product formation proceeded more completely in the tested reaction conditions for the heptynoic acid-LyP-1, likely due to reduced steric hindrance provided by the extended hydrocarbon chain. Optimal reaction conditions were found to be either 1 mM $CuSO_4$/5 mM Na ascorbate or 1 mM −100 mM CuI for 72 h. Notably, the reaction yields with 10 mM $CuSO_4$ levels were dramatically

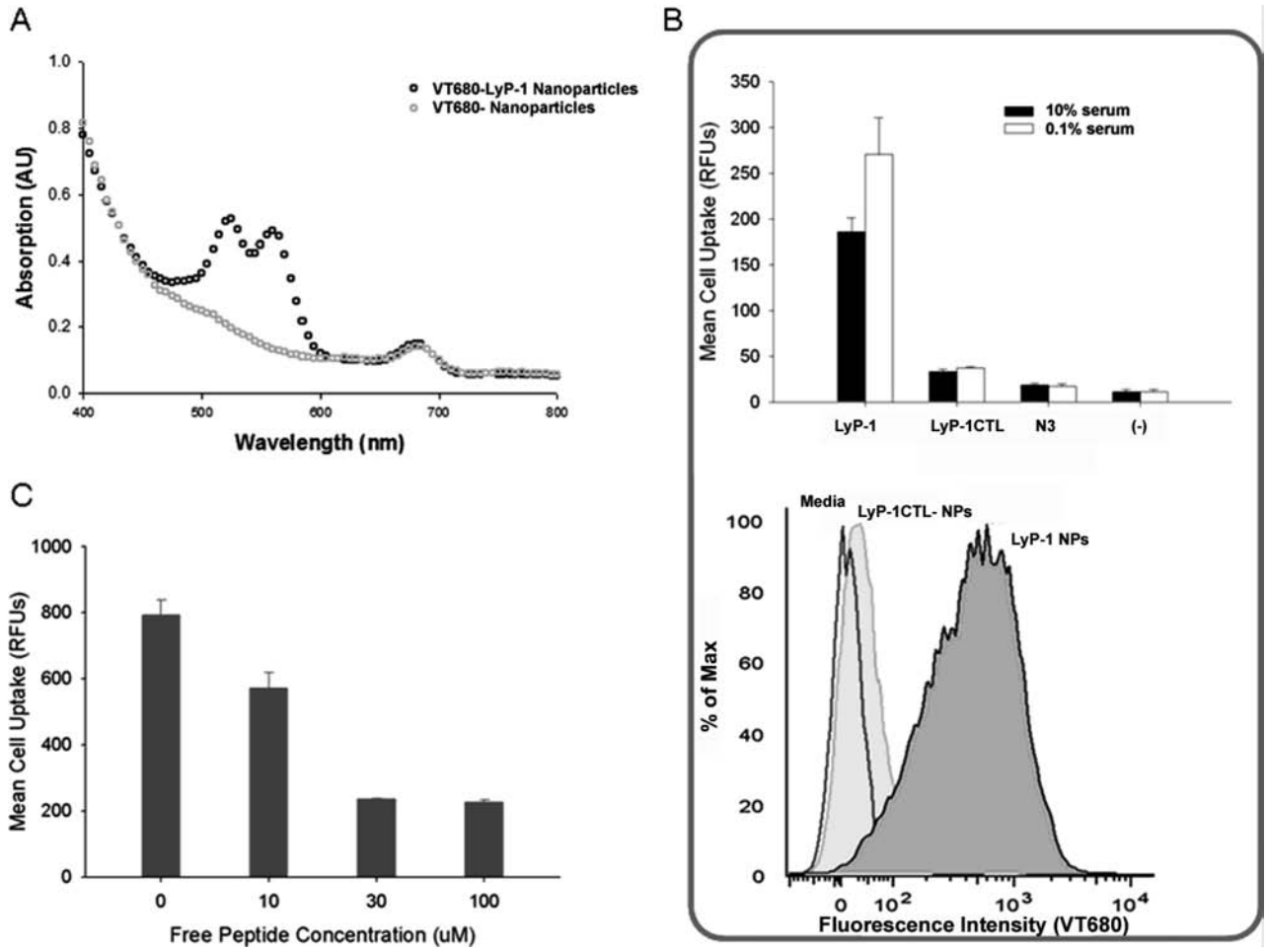

Figure 2. LyP-1-conjugated nanoparticles target p32-expressing MDA-MB-435 cells *in vitro*, while nanoparticles conjugated to control cyclic peptides (LyP-1CTL) do not target. (A) The amount of peptide bound per particle was quantified spectrophotometrically by measuring the absorbance of the TAMRA dyes added following the click reaction. With the addition of catalyst $CuSO_4$/Na ascorbate (dark circles), the TAMRA absorbance at 555 nm was quantified to equal approximately 30 peptides per particle, whereas no TAMRA signal was observed without catalyst (light circles). (B) LyP-1-nanoparticles or control LyP-1CTL-nanoparticles (both at ~30 peptides per particle), or parent azido-bearing particles (N3), were added to MDA-435-MB cancer cells in normal 10% serum (black bars) and 0.1% serum-starved (light bars) conditions. Flow cytometry histogram shows marked increase in uptake of LyP-1-nanoparticles (black contour) vs LyP-1CTL-nanoparticles (light gray contour) and particle-free control cells (dark gray contour). Each error bar represents 6 parallel experiments. (C) Addition of free LyP-1 peptides at concentrations from 10 to 100 uM inhibited cellular uptake of LyP-1-coated nanoparticles, suggesting that the LyP-1 peptide and LyP-1-labeled particles target the same receptor.

lower than 1 mM, likely due to global precipitation of reduced Cu(I) in solution. Nevertheless, we found 1 mM $CuSO_4$ reactions to yield more reliable conjugations than 1 to100 mM CuI reactions, possibly because the insolubility of CuI in aqueous solutions produced variations in the amount of available catalyst delivered to the reactions. Therefore, the optimal conditions for subsequent nanoparticle modification were determined to be 1 mM $CuSO_4$ and 5 mM Na ascorbate. Under these conditions, we did not observe any reduction of peptide disulfide bonds due to copper catalyst or Na ascorbate reduction as determined by MALDI mass spectrometry and HPLC analysis (data not shown).

Having verified that alkyne-bearing LyP-1 peptides could effectively target p32-expressing MDA-MB-435 cancer cells and become linked to azido-bearing PEG polymers, we next developed a protocol for linking these peptides onto azido-PEG bearing, near-infrared fluorochrome-labeled (VivoTag 680) iron oxide nanoparticles. Dextran-caged iron oxide nanoparticles were used as the parent formulation to provide a highly stable, relatively noncytotoxic, and *in vivo*-tested nanoparticle scaffold. Briefly, a heterobifunctional linker bearing an azide on one end an N-hydroxysuccinimide leaving group on the other was synthesized and attached to an amine-PEG-thiol polymer (MW 5000 Da) via its terminal amine (Scheme 2A,B). Azido-PEG-thiol polymers were subsequently linked to surface of cross-linked, aminated, and fluorochrome-labeled dextran-coated iron oxide nanoparticles via the linker *N*-[γ-maleimidobutyryloxy] succinimide ester (GMBS) (Scheme 2C). Long PEG polymers were utilized to carry pendant azide groups in order to enhance particle circulation time *in vivo* and to provide a generalizable nanoparticle surface, whereby optimized "click" attachment conditions might be applicable to other PEG-coated organic and inorganic nanomaterials in the future. Azido-PEG particles were purified from excess polymer and linked to alkyne-bearing peptides in 1 mM $CuSO_4$, 5 mM Na ascorbate. Finally, the conjugated nanoparticles were purified and sterile filtered for *in vitro* and *in vivo* applications.

Peptide valency on nanoparticles was assessed spectrophotometrically by quantifying the number of TAMRA dyes added onto nanoparticles following "click" reaction (Figure 2A). In the presence of catalyst, approximately 30 peptides were added per nanoparticle for both LyP-1 and LyP-1CTL peptides, whereas no addition was observed in the absence of catalyst (Figure 2A). LyP-1 nanoparticles, LyP-1CTL nanoparticles, or azide nanoparticles were incubated over MDA-MB-435 tumor cells for 2 h and nanoparticle accumulation was quantified using flow cytometry (Figure 2B). LyP-1-nanoparticles showed significant tumor cell accumula-

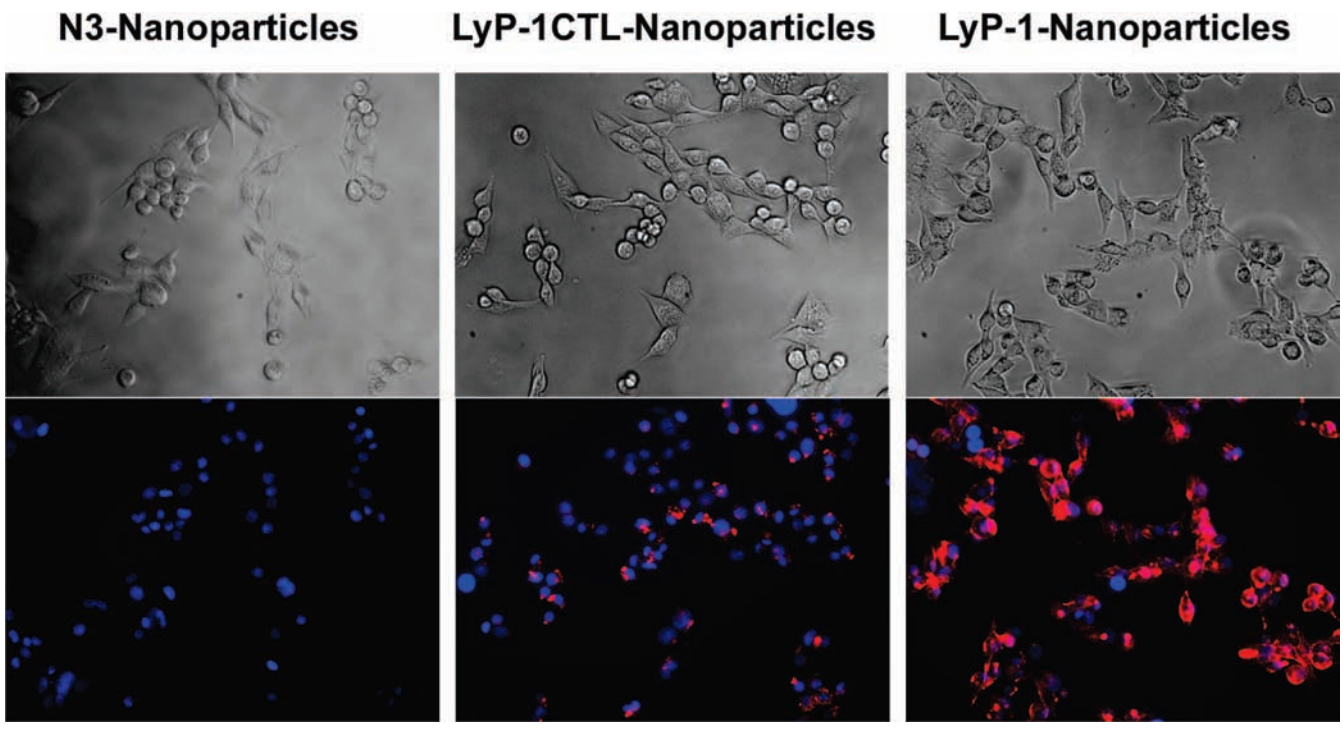

Figure 3. LyP-1-nanoparticles target MDA-MB-435 cancer cells (right). Fluorescence imaging of cells incubated with LyP-1-nanoparticles showed increased near-infrared fluorescence (red). Uptake of azido-bearing or scrambled control peptide (LyP-1CTL)-bearing nanoparticles are not visible or show minor background (left and middle).

tion, while LyP-1CTL-nanoparticles or azide-nanoparticles displayed minimal cell uptake (Figure 2B). The effect of serum on nanoparticle uptake was also studied, as low serum levels enhance the stress-induced expression of the p32 receptor (*33*). The slight increase in LyP-1-nanoparticle targeting in lower serum levels provided further validation of receptor-specific targeting, as decreased serum protein concentrations lowers the likelihood of nonspecific serum protein mediated uptake. To further confirm the uptake specificity of LyP-1-nanoparticles, free LyP-1 peptide was added to cells along with LyP-1-particles (Figure 2C). Dose-dependent inhibition of uptake was observed with LyP-1 peptide concentrations from 10 to 100 μM, suggesting the free LyP-1 and LyP-1-labeled particles share common cellular receptors. We attribute the large excess of free peptide required for inhibition compared to the concentration of nanoparticles used (100 nM) to the presence of multiple copies of the LyP-1 peptide on each nanoparticle, thus improving nanoparticle avidity to receptors through polyvalent binding (*38*). In order to visualize LyP-1 peptide-mediated cell uptake, nanoparticles bearing pendant LyP-1 peptides, control LyP-1CTL peptides, or azides were incubated over MDA-MB-435 cells for 30 min, washed, incubated with a nuclear stain, and imaged via epifluorescence microscopy (Figure 3). LyP-1-nanoparticles were seen associated with cells, while markedly less binding of azide-bearing or control peptide-bearing nanoparticles was not observed. If the same staining procedure was instead performed at 24 h post-incubation, LyP-1-nanoparticles were seen in punctate locations consistent with sequestration in endosome-like compartments (Supporting Information Figure 2). To assess the cytotoxicity of "click" nanoparticles, NH_2-PEG-, azido-PEG-, and peptide-conjugated nanoparticles were incubated for 24 h above HeLa cell cultures (Supporting Information Figure 3). In all three formulations, the TC50 is >7 mM Fe, or over 16 times higher than maximal blood concentrations during *in vivo* experiments performed here and 32 times higher than concentrations used *in vitro* here.

Having found that "click" attachment of homing peptides could mediate the targeting nanoparticles *in vitro*, we evaluated the ability of "click" chemistry to direct nanoparticle targeting to specific tumor cells *in vivo*. Again, near-infrared fluorochrome-labeled (VivoTag 680) nanoparticles were "clicked" to LyP-1 peptides, resulting on average of ~30 LyP-1 peptides per particle, while the parent azido-PEG nanoparticles were used as a negative control. Each population of nanoparticles was injected intravenously into mice bearing human MDA-MB-435 cancer xenografts. Nanoparticles were allowed to circulate and distribute in mice for 24 h, after which the mice were sacrificed and organs collected for immunohistochemical or whole organ fluorescence analysis. Vascular staining with anti-CD31 antibodies showed that azide nanoparticles in tumors remained localized within the immediate periphery of blood vessels (Figure 4B). This perivascular distribution of untargeted nanomaterials is in agreement with previous histological and intravital observations of passive liposomal accumulation in tumors (*39, 40*). By contrast, LyP-1 "click" nanoparticles appeared to have extravasated from the tumor vasculature, penetrated into the interstitial space of the tumor, and bound to p32-expressing cells (Figure 4B,C). As a result, the fraction of LyP-1 nanoparticles that get sequestered beyond the perivascular space was significantly higher than that of azido nanoparticles (Figure 4D) ($P < 0.005$). This pattern was observed in all injected mice and is characteristic of LyP-1 peptide and phage homing observed previously (*1*). Interestingly, previous LyP-1 bacteriophage experiments showed that the LyP-1-expressing phage concentrate in nonvascularized sites of tumors within minutes after injection while insertless phage do not reach these regions (*1*). Thus, there may be unique transportation pathways within tumors that are exploited by this ligand after extravasation that are not available to untargeted materials. In the future, the localization of LyP-1 nanoparticles in avascular tumor regions may be of use for directing therapeutics into hypoxic regions of tumors, where most nanoparticle therapies do not reach. Whole organ assessment

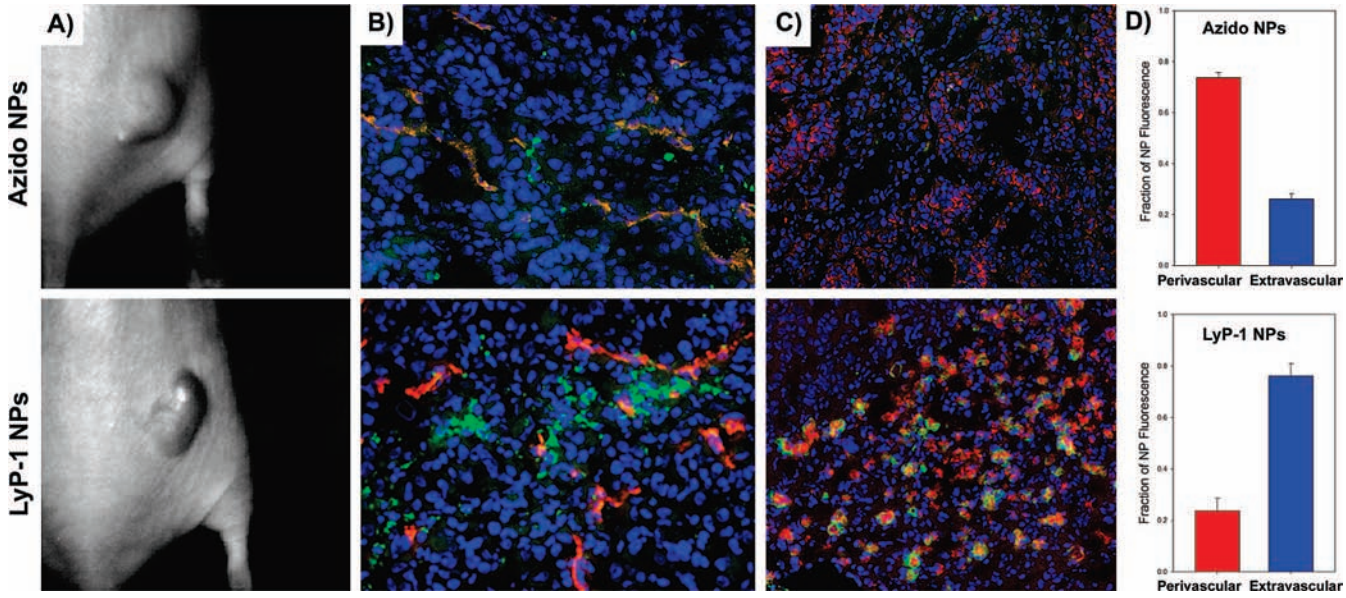

Figure 4. "Click" LyP-1-nanoparticle targeting to tumor cells *in vivo*. Nanoparticles bearing only azide groups (top) or labeled with LyP-1 peptides (bottom) that are matched in circulation time were injected intravenously via the tail vein into mice bearing human MDA-MB-435 cancer xenografts. Histological sections were obtained 24 h postinjection. (A) Light reflectance images of mice bearing the tumor xenografts. (B) Fluorescent LyP-1-nanoparticles (VT680 fluorescence pseudocolored as green) did not colocalize with CD31, a blood vessel marker (red), while untargeted azide-PEG nanoparticles remained localized to the blood vessels or their immediate periphery. (C) LyP-1-nanoparticles (green) accumulated in regions of high p32 expression (red), whereas untargeted, azido-bearing nanoparticles did not accumulate in these areas. (D) Histological quantitation using CD31 stain to assess nanoparticle localization to immediate periphery of blood vessels. The fraction of LyP-1 nanoparticles outside of the perivascular space of CD31-stained blood vessels is significantly higher than azido-nanoparticles ($P < 0.005$) as assessed from three randomly chosen views in each set of mice ($n = 3$). Together, LyP-1-coated nanoparticles penetrate into the tumor interstitium to target p32-expressing cells.

of near-infrared tumor fluorescence demonstrated that, despite the distinct microscopic behavior of LyP-1 nanoparticles, the macroscopic tumor accumulation of LyP-1 nanoparticles and PEG-azide nanoparticles was similar (Supporting Information Figure 4), indicating that the targeted accumulation of LyP-1-nanoparticles was on par with passive delivery, whereby long-circulating materials accumulate in tumors via their hyperporous vasculature over time (*41*, *42*). These results are in accordance with data showing that the development of targeted nanoparticle formulations that amplify the macroscopic accumulation in tumors requires systematic *in vivo* optimization of multiple material parameters, including target avidity, circulation time, and particle size (*43*, *44*). Experiments of this kind are ongoing in order to probe the power of the LyP-1 targeting ligand for amplifying the accumulation and efficacy of nanoparticle-based imaging and therapeutic agents.

CONCLUSION

In this work, we have demonstrated that "click" chemistry may be used to develop nanoparticles that seek out specific cells *in vivo* based on their surface expression of protein markers. Ultimately, these findings suggest that "click" chemistry meets the criteria of being applicable under aqueous conditions, efficient, orthogonal to thiol- and amine-containing targeting motifs, and stable in the complex *in vivo* environments of the blood and tumor milieu. In the future, this work may empower the development of "click" nanomaterials that seek out specific tumor cell types, including tumor stem cells and angiogenic endothelial cells, or amplify the macroscopic accumulation of imaging agents or therapeutics in tumors. Further, the modularity of this "click" attachment strategy should allow it to be adapted to a diversity of *in vivo* nanoparticle platforms and both biological and synthetic ligands, potentially empowering novel on-nanoparticle screen approaches to targeted nanomaterial development.

ACKNOWLEDGMENT

The authors acknowledge financial support from NIH (BRP: 1R01CA124427-01), NIH/NCI (U54 CA119349-01, U54 CA119335), Packard Fellowship (1999-1453A), Whitaker Foundation Graduate Fellowship (G. v. M.), NSF Graduate Fellowship (G. v. M.), and Medical Scientist Training Program (Y.R.). The authors declare no competing financial interests.

Supporting Information Available: Studies on the optimization of the "click" reaction by HPLC, LyP-1 peptide spectra, localization of LyP-1 nanoparticles in endosomal-like compartments, nanoparticle cytotoxicity, and LyP-1 and azido nanoparticle tumor accumulation. This material is available free of charge via the Internet at http://pubs.acs.org.

LITERATURE CITED

(1) Laakkonen, P., Porkka, K., Hoffman, J. A., and Ruoslahti, E. (2002) A tumor-homing peptide with a targeting specificity related to lymphatic vessels. *Nat. Med. 8*, 751–5.
(2) Lee, S. M., Lee, E. J., Hong, H. Y., Kwon, M. K., Kwon, T. H., Choi, J. Y., Park, R. W., Kwon, T. G., Yoo, E. S., Yoon, G. S., Kim, I. S., Ruoslahti, E., and Lee, B. H. (2007) Targeting bladder tumor cells in vivo and in the urine with a peptide identified by phage display. *Mol. Cancer Res. 5*, 11–9.
(3) Rajotte, D., and Ruoslahti, E. (1999) Membrane dipeptidase is the receptor for a lung-targeting peptide identified by in vivo phage display. *J. Biol. Chem. 274*, 11593–8.
(4) Porkka, K., Laakkonen, P., Hoffman, J. A., Bernasconi, M., and Ruoslahti, E. (2002) A fragment of the HMGN2 protein homes to the nuclei of tumor cells and tumor endothelial cells in vivo. *Proc. Natl. Acad. Sci. U.S.A. 99*, 7444–9.
(5) Ruoslahti, E. (2004) Vascular zip codes in angiogenesis and metastasis. *Biochem. Soc. Trans. 32*, 397–402.
(6) Simberg, D., Duza, T., Park, J. H., Essler, M., Pilch, J., Zhang, L., Derfus, A. M., Yang, M., Hoffman, R. M., Bhatia, S., Sailor, M. J., and Ruoslahti, E. (2007) Biomimetic amplification of

nanoparticle homing to tumors. *Proc. Natl. Acad. Sci. U.S.A. 104*, 932–6.

(7) Reddy, G. R., Bhojani, M. S., McConville, P., Moody, J., Moffat, B. A., Hall, D. E., Kim, G., Koo, Y. E., Woolliscroft, M. J., Sugai, J. V., Johnson, T. D., Philbert, M. A., Kopelman, R., Rehemtulla, A., and Ross, B. D. (2006) Vascular targeted nanoparticles for imaging and treatment of brain tumors. *Clin. Cancer Res. 12*, 6677–86.

(8) Zhang, C., Jugold, M., Woenne, E. C., Lammers, T., Morgenstern, B., Mueller, M. M., Zentgraf, H., Bock, M., Eisenhut, M., Semmler, W., and Kiessling, F. (2007) Specific targeting of tumor angiogenesis by RGD-conjugated ultrasmall superparamagnetic iron oxide particles using a clinical 1.5-T magnetic resonance scanner. *Cancer Res. 67*, 1555–62.

(9) Weissleder, R., Kelly, K., Sun, E. Y., Shtatland, T., and Josephson, L. (2005) Cell-specific targeting of nanoparticles by multivalent attachment of small molecules. *Nat. Biotechnol. 23*, 1418–23.

(10) Giordano, R. J., Anobom, C. D., Cardo-Vila, M., Kalil, J., Valente, A. P., Pasqualini, R., Almeida, F. C., and Arap, W. (2005) Structural basis for the interaction of a vascular endothelial growth factor mimic peptide motif and its corresponding receptors. *Chem. Biol. 12*, 1075–83.

(11) Colombo, G., Curnis, F., DeMori, G. M., Gasparri, A., Longoni, C., Sacchi, A., Longhi, R., and Corti, A. (2002) Structure-activity relationships of linear and cyclic peptides containing the NGR tumor-homing motif. *J. Biol. Chem. 277*, 47891–7.

(12) Rozek, A., Powers, J. P., Friedrich, C. L., and Hancock, R. E. (2003) Structure-based design of an indolicidin peptide analogue with increased protease stability. *Biochemistry 42*, 14130–8.

(13) Ruoslahti, E., and Pierschbacher, M. D. (1987) New perspectives in cell adhesion: RGD and integrins. *Science 238*, 491–7.

(14) Green, J. J., Chiu, E., Leshchiner, E. S., Shi, J., Langer, R., and Anderson, D. G. (2007) Electrostatic ligand coatings of nanoparticles enable ligand-specific gene delivery to human primary cells. *Nano Lett. 7*, 874–9.

(15) Sokolov, K., Follen, M., Aaron, J., Pavlova, I., Malpica, A., Lotan, R., and Richards-Kortum, R. (2003) Real-time vital optical imaging of precancer using anti-epidermal growth factor receptor antibodies conjugated to gold nanoparticles. *Cancer Res. 63*, 1999–2004.

(16) Huang, X., El Sayed, I. H., Qian, W., and El Sayed, M. A. (2006) Cancer cell imaging and photothermal therapy in the near-infrared region by using gold nanorods. *J. Am. Chem. Soc. 128*, 2115–20.

(17) Kolb, H. C., Finn, M. G., and Sharpless, K. B. (2001) Click Chemistry: Diverse Chemical Function from a Few Good Reactions. *Angew. Chem., Int. Ed. 40*, 2004–2021.

(18) Lee, J. W., Kim, J. H., Kim, H. J., Han, S. C., Kim, J. H., Shin, W. S., and Jin, S. H. (2007) Synthesis of symmetrical and unsymmetrical PAMAM dendrimers by fusion between azide- and alkyne-functionalized PAMAM dendrons. *Bioconjugate Chem. 18*, 579–84.

(19) Wu, P., Malkoch, M., Hunt, J. N., Vestberg, R., Kaltgrad, E., Finn, M. G., Fokin, V. V., Sharpless, K. B., and Hawker, C. J. (2005) Multivalent, bifunctional dendrimers prepared by click chemistry. *Chem. Commun. (Cambridge)* 5775–7.

(20) Shi, Q., Chen, X., Lu, T., and Jing, X. (2008) The immobilization of proteins on biodegradable polymer fibers via click chemistry. *Biomaterials 29*, 1118–26.

(21) Rozkiewicz, D. I., Gierlich, J., Burley, G. A., Gutsmiedl, K., Carell, T., Ravoo, B. J., and Reinhoudt, D. N. (2007) Transfer printing of DNA by "click" chemistry. *ChemBioChem 8*, 1997–2002.

(22) Ciampi, S., Bocking, T., Kilian, K. A., James, M., Harper, J. B., and Gooding, J. J. (2007) Functionalization of acetylene-terminated monolayers on Si(100) surfaces: a click chemistry approach. *Langmuir 23*, 9320–9.

(23) Such, G. K., Tjipto, E., Postma, A., Johnston, A. P., and Caruso, F. (2007) Ultrathin, responsive polymer click capsules. *Nano Lett 7*, 1706–10.

(24) Li, H., Cheng, F., Duft, A. M., and Adronov, A. (2005) Functionalization of single-walled carbon nanotubes with well-defined polystyrene by "click" coupling. *J. Am. Chem. Soc. 127*, 14518–24.

(25) Cavalli, S., Tipton, A. R., Overhand, M., and Kros, A. (2006) The chemical modification of liposome surfaces via a copper-mediated [3 + 2] azide-alkyne cycloaddition monitored by a colorimetric assay. *Chem. Commun. (Cambridge)* 3193–5.

(26) Fischler, M., Sologubenko, A., Mayer, J., Clever, G., Burley, G., Gierlich, J., Carell, T., and Simon, U. (2008) Chain-like assembly of gold nanoparticles on artificial DNA templates via 'click chemistry'. *Chem. Commun. (Cambridge)* 169–71.

(27) Opsteen, J. A., Brinkhuis, R. P., Teeuwen, R. L., Lowik, D. W., and van Hest, J. C. (2007) "Clickable" polymersomes. *Chem. Commun. (Cambridge)* 3136–8.

(28) Antoni, P., Nystrom, D., Hawker, C. J., Hult, A., and Malkoch, M. (2007) A chemoselective approach for the accelerated synthesis of well-defined dendritic architectures. *Chem. Commun. (Cambridge)* 2249–51.

(29) Zeng, Q., Li, T., Cash, B., Li, S., Xie, F., and Wang, Q. (2007) Chemoselective derivatization of a bionanoparticle by click reaction and ATRP reaction. *Chem. Commun. (Cambridge)* 1453–5.

(30) Brennan, J. L., Hatzakis, N. S., Tshikhudo, T. R., Dirvianskyte, N., Razumas, V., Patkar, S., Vind, J., Svendsen, A., Nolte, R. J., Rowan, A. E., and Brust, M. (2006) Bionanoconjugation via click chemistry: The creation of functional hybrids of lipases and gold nanoparticles. *Bioconjugate Chem. 17*, 1373–5.

(31) Sun, E. Y., Josephson, L., and Weissleder, R. (2006) "Clickable" nanoparticles for targeted imaging. *Mol. Imaging 5*, 122–8.

(32) Said Hassane, F., Frisch, B., and Schuber, F. (2006) Targeted liposomes: convenient coupling of ligands to preformed vesicles using "click" chemistry. *Bioconjugate Chem. 17*, 849–54.

(33) Laakkonen, P., Akerman, M. E., Biliran, H., Yang, M., Ferrer, F., Karpanen, T., Hoffman, R. M., and Ruoslahti, E. (2004) Antitumor activity of a homing peptide that targets tumor lymphatics and tumor cells. *Proc. Natl. Acad. Sci. U.S.A. 101*, 9381–6.

(34) Fogal, V., Zhang, L., and Ruoslahti, E. Mitochondrial/cell surface protein p32/gC1qR as a molecular target in tumor cells and tumor stroma. *Cancer Res.* (Submitted).

(35) Rubinstein, D. B., Stortchevoi, A., Boosalis, M., Ashfaq, R., Ghebrehiwet, B., Peerschke, E. I., Calvo, F., and Guillaume, T. (2004) Receptor for the globular heads of C1q (gC1q-R, p33, hyaluronan-binding protein) is preferentially expressed by adenocarcinoma cells. *Int. J. Cancer 110*, 741–50.

(36) Shen, T., Weissleder, R., Papisov, M., Bogdanov, A., Jr., and Brady, T. J. (1993) Monocrystalline iron oxide nanocompounds (MION): physicochemical properties. *Magn. Reson. Med. 29*, 599–604.

(37) Josephson, L., Tung, C. H., Moore, A., and Weissleder, R. (1999) High-efficiency intracellular magnetic labeling with novel superparamagnetic-Tat peptide conjugates. *Bioconjugate Chem. 10*, 186–91.

(38) Montet, X., Funovics, M., Montet-Abou, K., Weissleder, R., and Josephson, L. (2006) Multivalent effects of RGD peptides obtained by nanoparticle display. *J. Med. Chem. 49*, 6087–93.

(39) Unezaki, S., Maruyama, K., Hosoda, J., Nagae, I., Koyanagi, Y., Nakata, M., Ishida, O., Iwatsuru, M., and Tsuchiya, S. (1996) Direct measurement of the extravasation of polyethyleneglycol-coated liposomes into solid tumor tissue by in vivo fluorescence microscopy. *Int. J. Pharm. 144*, 11–17.

(40) Son, D. H., Park, S. A., Lee, S. W., Cho, Y. W., Roh, J. L., and Kim, S. Y. (2006) In vivo tumor targeting and radionuclide imaging with self-assembled nanoparticles: Mechanisms, key factors, and their implications. *EJC Suppl. 4*, 47–47.

(41) Moghimi, S. M., and Szebeni, J. (2003) Stealth liposomes and long circulating nanoparticles: critical issues in pharmacokinetics,

opsonization and protein-binding properties. *Prog. Lipid Res. 42*, 463–78.

(42) Moghimi, S. M., Hunter, A. C., and Murray, J. C. (2001) Long-circulating and target-specific nanoparticles: theory to practice. *Pharmacol. Rev. 53*, 283–318.

(43) Bartlett, D. W., Su, H., Hildebrandt, I. J., Weber, W. A., and Davis, M. E. (2007) Impact of tumor-specific targeting on the biodistribution and efficacy of siRNA nanoparticles measured by multimodality in vivo imaging. *Proc. Natl. Acad. Sci. U.S.A. 104*, 15549–54.

(44) Gu, F., Zhang, L., Teply, B. A., Mann, N., Wang, A., Radovic-Moreno, A. F., Langer, R., and Farokhzad, O. C. (2008) Precise engineering of targeted nanoparticles by using self-assembled biointegrated block copolymers. *Proc. Natl. Acad. Sci. U.S.A. 105*, 2586–2591.

BC800077Y

	Degree of Functionalization	
Catalyst [mM], Time	Propargylglycine-Lyp1	Heptynoic Acid-Lyp1
CuSO4 [1mM], 24 h	44%	48%
CuSO4 [1mM], 72 h	80%	82%
CuSO4 [10mM], 24h	0%	0.5%
CuSO4 [10mM], 72h	0%	13%
CuI [1mM], 24 h	70%	70%
CuI [1mM], 72 h	76%	95%
CuI [10mM], 24 h	68%	76%
CuI [10mM], 72 h	77%	100%
CuI [100mM], 24 h	75%	83%
CuI [100mM], 72 h	79%	89%
No Catalyst, 72h	0%	0%

Table S1. Optimization of the "click" reaction. The rate of product conversion in the "click" reaction is measured as a function of product formation in HPLC. The reaction is performed in various catalysts (CuSO4 or CuI) and concentrations, in 24h or 72h reactions, using LyP-1 peptides bearing either propargylglycine or 6-heptynoic-acid.

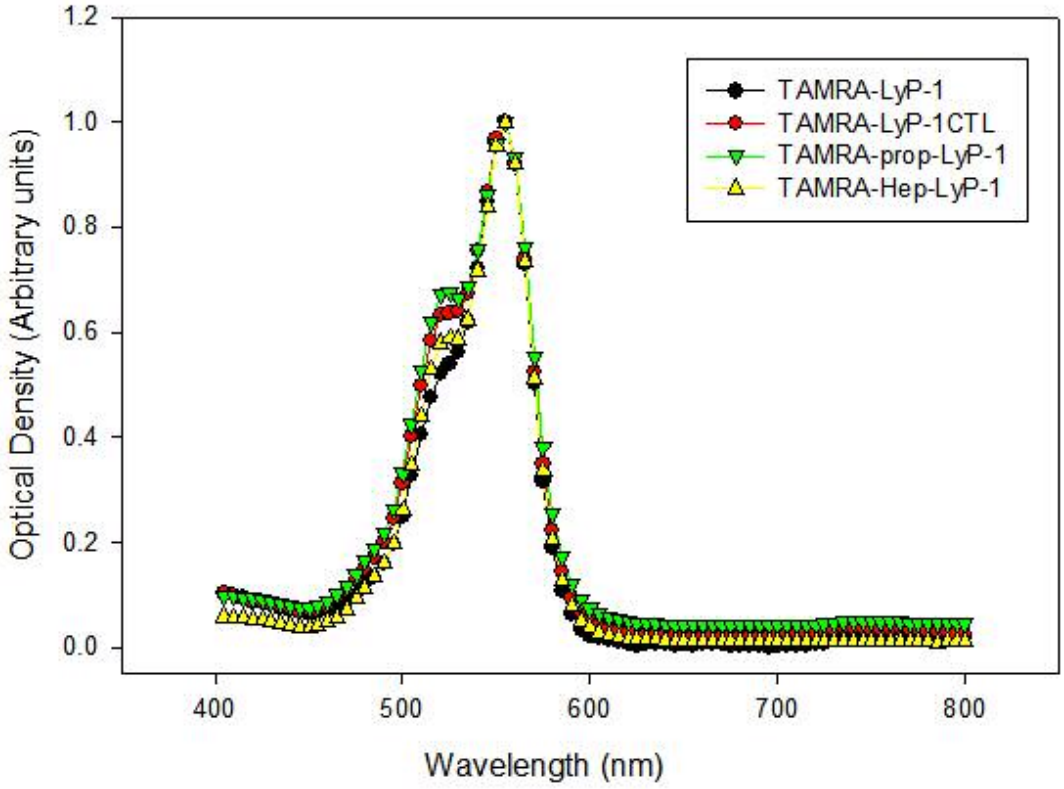

Supplementary Figure 1. *Fluorophore-labeled LyP-1 Peptide Spectra.* UV-Vis spectra for LyP-1 and LyP-1CTL peptides synthesized with varying pendant alkyne groups (prop= propargylglycine; Hep=heptynoic acid)

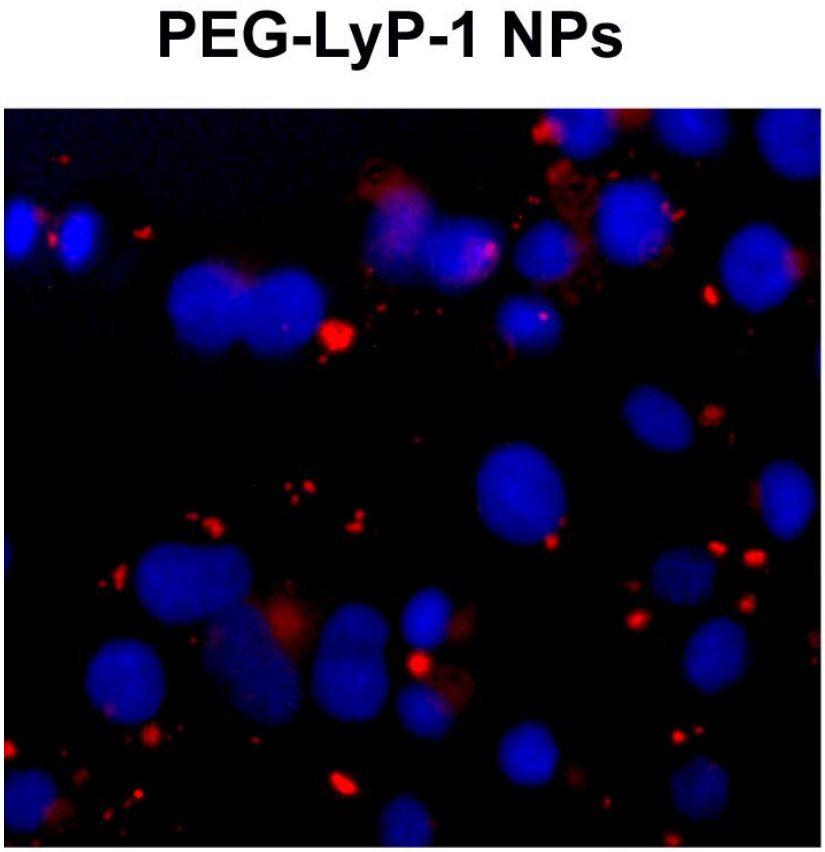

Supplementary Figure 2. LyP-1-nanoparticles target MDA-MB-435 cancer cells and become localized in endosome-like compartments over 24hrs in vitro. Cells were incubated with LyP-1-nanoparticles for 30min, washed, and incubated for 24hrs before nuclear staining and imaging. PEG-LyP-1 nanoparticles no longer show diffuse membranous staining, but have become localized into punctuate compartments, implying endosomal sequestration away from cell surface.

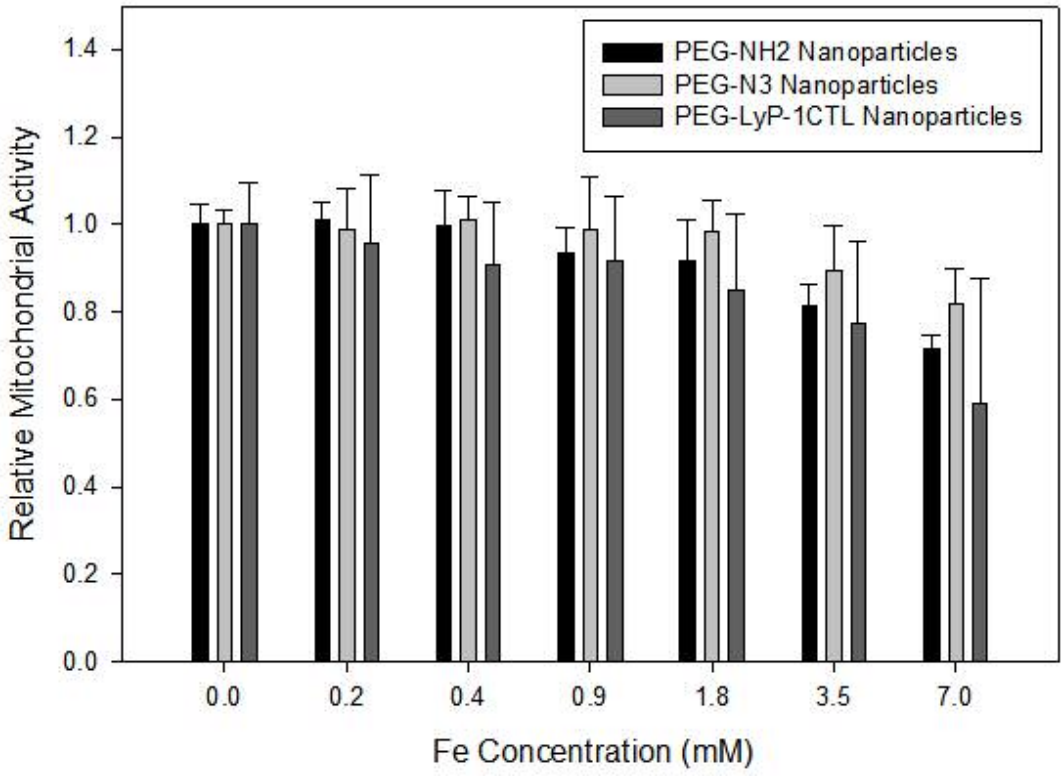

Supplementary Figure 3. *Probing "Click" Nanoparticle Cytotoxicity to Human Cell Cultures.* Human HeLa cervical cancer cells were incubated with parent NH2-PEG-NPs, PEG-N3-NPs, or PEG-LyP-1CTL-NPs at varying concentrations for 24 hrs, rinsed, and incubated with media containing thiazolyl blue tetrazolium bromide (MTT reagent) at 0.5mg/ml. After 3hr, blue precipitates begin to form within cells as a result of mitochondrial activity. Quantitaion of cellular viability via absorbance of DMSO:isopropanol-solubilized MTT reagent showed that all three NP peparations have TC_{50} values of greater than 7mM, which is over 35-times that used in vitro here (100nM NPs used in cell culture and FACS expts = 0.2mM Fe) and greater than sixteen times the maximum blood concentrations during *in vivo* experiments (200nM NP concentration in blood immediately after injection = 0.4mM Fe).

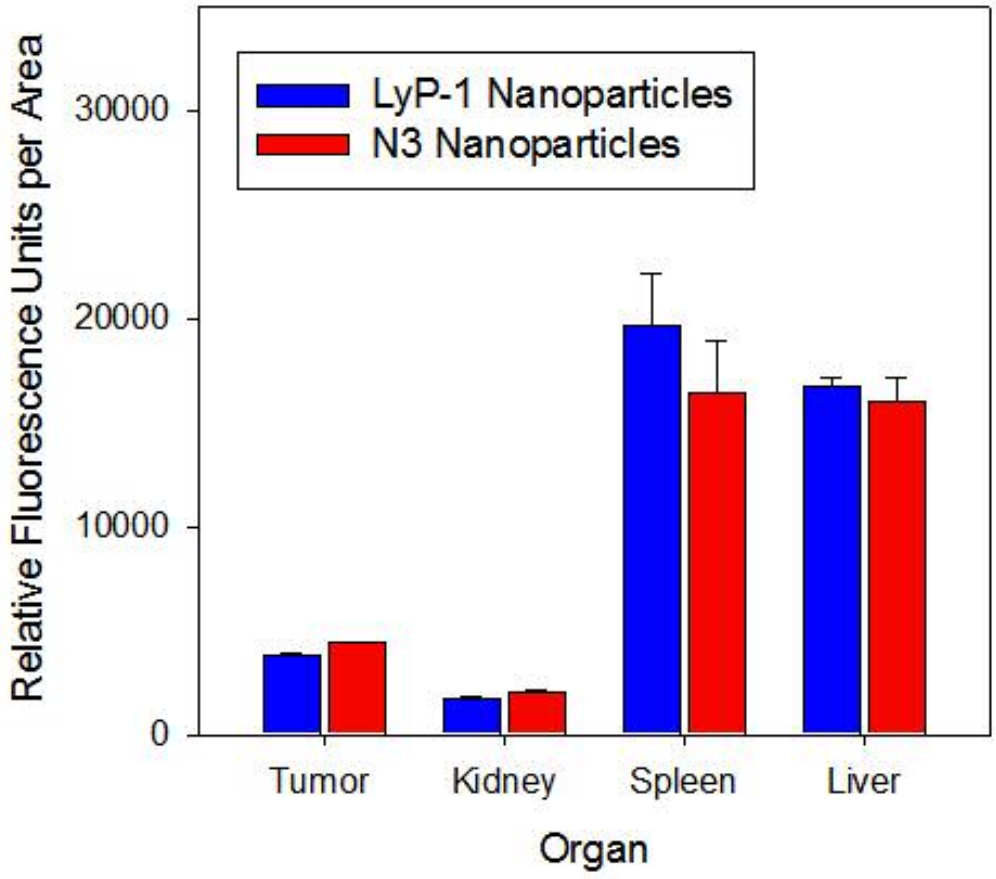

Supplementary Figure 4. *Near-Infrared Fluorescence Analysis of LyP-1- and Azido-Nanoparticle Tumor Accumulation.* Near-infrared fluorochrome-labeled nanoparticles bearing terminal azide groups (red) or LyP-1 peptides (blue) were injected intravenously via the tail vein into mice bearing human MDA-MB-435 cancer xenografts (4 mice). After particles had cleared the systemic circulation (24hrs), mice were sacrificed and tumor, liver, spleen, and kidneys were fluorescently imaged for nanoparticle accumulation (LI-COR Odyssey). As expected for nanoparticles above the renal filtration limit, clearance was predominately via reticuloendothelial system uptake (liver and

spleen). Nanoparticle accumulation in tumors was slightly decreased for peptide-modified nanoparticles, likely due to a decrease in the particle circulation time following cationic peptide attachment and concomitant decrease in the passive targeting.

Evaluation of a Maleimido Derivative of CHX-A″ DTPA for Site-Specific Labeling of Affibody Molecules

Vladimir Tolmachev,[†,‡,§] Heng Xu,[||] Helena Wållberg,[‡] Sara Ahlgren,[§] Magnus Hjertman,[‡] Anna Sjöberg,[‡] Mattias Sandström,[⊥] Lars Abrahmsén,[‡] Martin W. Brechbiel,[||] and Anna Orlova*[,†,‡]

Division of Biomedical Radiation Sciences, Rudbeck Laboratory, Uppsala University, Uppsala, Sweden, Affibody AB, Bromma, Sweden, Division of Nuclear Medicine, Department of Medical Sciences, Uppsala University, Uppsala, Sweden, Radiation Oncology Branch, National Cancer Institute, National Institutes of Health, 10 Center Drive, Bethesda, Maryland 20892-1088, USA, and Hospital Physics, Department of Oncology, Uppsala University Hospital, Uppsala, Sweden. Received March 16, 2008; Revised Manuscript Received May 25, 2008

Affibody molecules are a new class of small targeting proteins based on a common three-helix bundle structure. Affibody molecules binding a desired target may be selected using phage-display technology. An Affibody molecule $Z_{HER2:342}$ binding with subnanomolar affinity to the tumor antigen HER2 has recently been developed for radionuclide imaging *in vivo*. Introduction of a single cysteine into the cysteine-free Affibody scaffold provides a unique thiol group for site-specific labeling of recombinant Affibody molecules. The recently developed maleimido-CHX-A″ DTPA was site-specifically conjugated at the C-terminal cysteine of $Z_{HER2:2395}$-C, a variant of $Z_{HER2:342}$, providing a homogeneous conjugate with a dissociation constant of 56 pM. The yield of labeling with ^{111}In was >99% after 10 min at room temperature. *In vitro* cell tests demonstrated specific binding of ^{111}In-CHX-A″ DTPA-Z_{2395}-C to HER2-expressing cell-line SKOV-3 and good cellular retention of radioactivity. In normal mice, the conjugate demonstrated rapid clearance from all nonspecific organs except kidney. In mice bearing SKOV-3 xenografts, the tumor uptake of ^{111}In-CHX-A″ DTPA-Z_{2395}-C was 17.3 ± 4.8% IA/g and the tumor-to-blood ratio 86 ± 46 (4 h postinjection). HER2-expressing xenografts were clearly visualized 1 h postinjection. In conclusion, coupling of maleimido-CHX-A″ DTPA to cysteine-containing Affibody molecules provides a well-defined uniform conjugate, which can be rapidly labeled at room temperature and provides high-contrast imaging of molecular targets *in vivo*.

INTRODUCTION

Progress in molecular tumor biology is a foundation for increasing specificity of cancer therapy by targeting of molecular structures, which are uniquely expressed or overexpressed on the surface of cancer cells. Since such overexpression occurs only in a fraction of tumors, specific therapy has to be personalized, i.e., patients should be carefully stratified to optimize targeted therapy while avoiding over- or undertreatment. The use of radionuclide molecular imaging can be an important tool for detection of expression of a particular molecular target in the primary tumor and metastases of a patient. Successful molecular imaging depends on the availability of imaging agents that are capable of providing a specific and high contrast imaging of cancer-associated targets *in vivo*.

Three years ago, a preclinical evaluation of a new class of targeting proteins, Affibody molecules, was initiated (*1–3*). Affibody molecules are three helix bundle proteins, derived from staphylococcal protein A. Phage display enables selection of Affibody molecules with a low picomolar affinity (*4*). A small size, about 7 kDa, enables rapid tumor localization of Affibody molecules and their fast clearance from nonspecific compartments. For example, the $Z_{HER2:342}$ Affibody molecule, which binds HER2[1] antigen with an affinity of 22 pM (*4*), demonstrated clear visualization of murine xenografts at 1 h postinjection (pi) (*5*). Recently, Affibody molecules were developed against another tumor-associated target, EGFR (*6–8*).

Successful molecular imaging depends both on a targeting protein providing specific accumulation of radionuclide in the tumor and on a label, i.e., a combination of a particular radionuclide and a linker that provides a stable attachment to the targeting protein. The use of different labeling methods influences not only the stability of the attachment of the radionuclide to the targeting proteins, but also the charge and the lipophilicity of the conjugate, which may influence uptake in healthy tissues and the excretion route. Alternative labeling of Affibody molecules has previously been demonstrated to result in different biodistribution of the radioactivity (*9–16*). Different macrocyclic and acyclic chelators have been evaluated for labeling of Affibody molecules with the radionuclide ^{111}In ($T_{1/2}$ = 2.8 days). Initial evaluation was done using isothiocyanate derivatives of DTPA (*17*), DOTA (*15*), and CHX-A″ DTPA (*18*). Though all these conjugates demonstrated good targeting properties, isothiocyanate-mediated coupling to amino

* Address for correspondence: Anna Orlova, Biomedical Radiation Sciences, Rudbeck Laboratory, Uppsala University, S-751 81 Uppsala, Sweden. Phone: +46 18 471 3829; Fax: + 46 18 471 3432; E-mail anna.orlova@bms.uu.se.

† Rudbeck Laboratory, Uppsala University.

‡ Affibody AB.

§ Department of Medical Sciences, Uppsala University.

|| National Cancer Institute, National Institutes of Health.

⊥ Uppsala University Hospital.

[1] Abbreviations: HER2, human epidermal growth factor receptor type 2, known also as neu, c-ErbB2, p185; EGFR, human epidermal growth factor receptor type 1; DTPA, diethyleneaminepentaacetic acid; DOTA, l,4,7,10-tetraazacyclododecane tetraacetic acid; CHX-A″ DTPA, *N*-[(*R*)-2-Amino-3-(*p*-aminophenyl)propyl]-*trans*-(*S,S*)-cyclohexane-1,2-diamine-*N,N,N′,N″,N″*-pentaacetic acid; Maleimido CHX-A″ DTPA, [[2-(Bis-carboxymethyl-amino)-cyclohexyl]-(2-bis-carboxymethyl-amino)-3-{4-[7-(2,5-dioxo-2,5-dihydro-pyrrol-1-ul)-heptanoylamino]-phenyl}-propyl)-amino]-acetic acid.

10.1021/bc800110y CCC: $40.75 © 2008 American Chemical Society
Published on Web 07/12/2008

groups is not site-specific, and the labeled product presented as a distribution of conjugates with chelators at different positions and therefore potentially with different targeting properties. The use of peptide synthesis enabled production of a homogeneous conjugate of the anti-HER2 Affibody molecule $Z_{HER2:342}$ with DOTA attached site-specifically to the *N*-terminal amine (*5*). After labeling with ^{111}In, this conjugate demonstrated excellent targeting of HER2-expressing xenografts in mice (*5*). However, a site-specific method for labeling of Affibody molecules made by recombinant production would be attractive.

One approach to site-specific labeling of recombinant Affibody molecules is based on the fact that the protein lacks cysteines. Therefore, introduction of a single cysteine into the Affibody molecule provides a unique thiol group, which can be used for site-specific labeling. Previously, this approach has been used for labeling of Affibody molecules with radiohalogens for *in vivo* imaging (*9*), and Oregon Green and horseradish peroxidase (HRP) for *in vitro* detection of HER2 (*19*). Recently, we reported the use of this approach for labeling of the anti-HER2 Affibody molecule $Z_{HER2:2395}$-Cys (a variant of anti-HER2 Affibody molecule $Z_{HER2:342}$, which contains a cysteine at C terminus) with ^{111}In using a maleimido-derivative of DOTA (*20*). The resulting conjugate, ^{111}In-DOTA-$Z_{HER2:2395}$-C, demonstrated a tumor-to-blood ratio similar to the ratio observed with the synthetic ^{111}In-DOTA-$Z_{HER2:342}$ conjugate in a murine xenograft model (*5*).

The semirigid acyclic chelator CHX-A″ DTPA, which forms stable complexes with a number of radiometals of interest for radionuclide imaging, might be an alternative to DOTA for labeling of Affibody molecules. Amino-reactive derivatives of CHX-A″ DTPA demonstrated suitability for labeling of proteins and peptides with ^{111}In (*21*, *22*). Of particular importance, the isothiocyanate derivative of CHX-A″ DTPA provided the best tumor-to-blood ratio among all non-site-specifically ^{111}In-labeled Affibody conjugates (*18*). A thiol-reactive derivative of CHX-A″ DTPA, maleimido CHX-A″ DTPA, has recently been reported (*23*) and is now evaluated here for the site-specific conjugation and radiolabeling of Affibody molecules.

The goals of the study were (a) to prepare a maleimido CHX-A″ DTPA conjugate of anti-HER2 Affibody molecule $Z_{HER2:2395}$-Cys; (b) to evaluate targeting properties of the Affibody molecule $Z_{HER2:2395}$ site-specifically labeled with ^{111}In using maleimido CHX-A″ DTPA (^{111}In-CHX-A″ DTPA-Z_{2395}-C); and (c) to compare this product with $Z_{HER2:2395}$ site-specifically labeled with DOTA (^{111}In-DOTA-Z_{2395}-C) and with $Z_{HER2:342}$ nonspecifically labeled using the isothiocyanate derivative of CHX-A″ DTPA (^{111}In-CHX-A″ DTPA-Z_{342}). The chelators used in this study are presented in Figure 1.

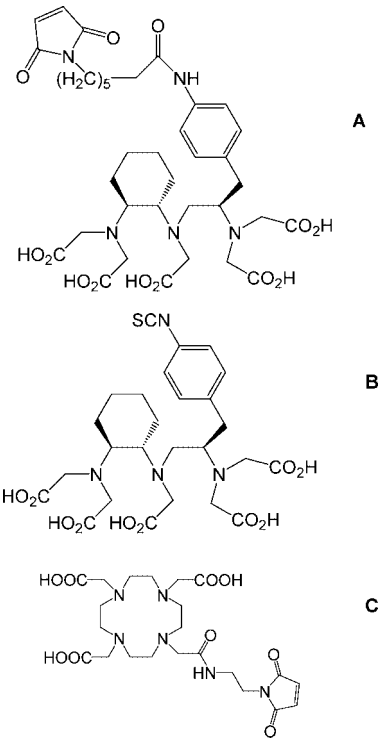

Figure 1. Structures of maleimido-CHX-A″ DTPA (A), CHX-A″ DTPA (B), and maleimido-monoamine-DOTA (C).

MATERIALS AND METHODS

Material. A cysteine-containing variant of $Z_{HER2:342}$, $Z_{HER2:2395}$-C, and its derivatives DOTA-Z_{2395}-C and ^{111}In-DOTA-Z_{2395}-C were produced according to ref (*20*). MMA-DOTA and isothiocyanante-CHX-A″ DTPA were purchased from Macrocyclics (Dallas, TX, USA). The maleimido CHX-A″ DTPA was prepared as previously reported (*23*). A ^{111}In-CHX-A″ DTPA-Z_{342} was produced and labeled according to ref (*18*). Purity and identity of all macromolecules and their conjugates was confirmed using high performance liquid chromatography with on line mass spectrometric detection, as described in the Instrumentation subsection. All purified proteins demonstrated a single peak with a mass, coinciding with the theoretically calculated with an accuracy of ± 1.5 Da, which is within the accuracy of the instrument. Buffers, such as 0.1 M phosphate buffered saline (PBS), pH 7.5, and 0.2 M ammonium acetate, pH 5.5, were prepared using common methods from chemicals supplied by Merck (Darmstadt, Germany). High-quality Milli-Q water (resistance higher than 18 MΩ cm) was used for preparing solutions. Buffers, which were used for conjugation and labeling, were purified from metal contamination using Chelex 100 resin (Bio-Rad Laboratories, Richmond, CA, USA). NAP-5 size exclusion columns were from Amersham Biosciences, Uppsala, Sweden. [^{111}In]indium chloride was purchased from Tyco. Silica gel impregnated glass fiber sheets for instant thin layer chromatography (ITLC SG) were from Gelman Sciences Inc. For cell studies, the HER2-expressing ovarian carcinoma cell line SKOV-3 (ATCC, purchased via LGC Promochem, Borås, Sweden), displaying approximately 1.2×10^6 HER2 receptors per cell (*24*) was used. The cell line was cultured in McCoy's medium (Flow Irvine, UK). The medium was supplemented with 10% fetal calf serum (Sigma, USA), 2 mM L-glutamine, and PEST (penicillin 100 IU/mL and 100 μg/mL streptomycin), all from Biokrom Kg, Germany. Ketalar [ketamine] (50 mg/mL, Pfizer, NY, USA), Rompun [xylazin] (20 mg/mL, Bayer, Leverkusen, Germany), and Heparin (5000 IE/mL, Leo Pharma, Copenhagen, Denmark) were obtained commercially. Data on cellular uptake and biodistribution were analyzed by unpaired, two-tailed *t*-test using GraphPad *Prism* (version 4.00 for Windows GraphPad Software, San Diego, CA, USA) in order to determine any significant differences ($P < 0.05$).

Instrumentation. The radioactivity was measured using an automated gamma counter with 3 in NaI(Tl) detector (1480 WIZARD, Wallac Oy, Turku, Finland). ^{111}In was measured with the use of both photopeaks and summation peak (energy setting from 140 to 507 keV). SDS-PAGE analysis was performed using NuPAGE 4−12% Bis-Tris Gel (Invitrogen) in MES buffer (200 V constant). Distribution of radioactivity along the ITLC strips and SDS-PAGE gels was measured on a Cyclone Storage Phosphor System (further referred to as PhosphorImager) and analyzed using the OptiQuant image analysis software. Cells were counted using electronic cell counter (Beckman Coulter). Affibody samples were analyzed by high performance liquid chromatography with on line mass spectrometric detection (Agilent 1100 HPLC/MSD). The mass spectrometer consisted of a single quadropole mass analyzer with an electrospray

ionization (ESI) interface used in positive ion mode. The software used for analysis and evaluation was Chemstation Rev. B.02.01. (Agilent Technologies). For HPLC-MS analysis, 10 μL sample (1:1 dilution with solution A: 0.1% TFA in Milli-Q water) was loaded onto a Zorbax 300SB-C8 (2.1 × 150 mm, 3.5 μm) RPC-column equilibrated with solution A with 10% solution B (0.1% TFA in acetonitrile) at a flow rate of 0.5 mL/min. After 2 min, the proteins were eluted using a linear gradient, 10−70% solution B in 15 min. For purification, a semipreparative column Zorbax 300SB-C8, 9.4 × 250 mm, 5 μm) was used. The flow rate was 5 mL/min and fractions were collected according to the peak detection settings specified in the chromatographic method.

Preparation and Characterization of ^{111}In-CHX-A″ DTPA-Z_{2395}-C. Conjugation of maleimido CHX-A″ DTPA to $Z_{HER2:2395}$ was performed with calculated chelator to protein ratios of 1:1, 2:1, and 3:1. To reduce any spontaneously forming disulfide bonds, 0.5 mL of $Z_{HER2:2395}$ (stock solution, 3.91 mg/mL) was incubated for 2 h in 30 mM DTT at 37 °C. After incubation, the reduced $Z_{HER2:2395}$ was purified using NAP-5 column pre-equilibrated and eluted with degassed 0.02 M ascorbic acid. Three aliquots of eluant (concentration 2 mg/mL), 200 μL each, were used for coupling. Aliquots were mixed with a precalculated amount of 1 M NH_4OAc, pH 5.5, (degassed by sonication) and with freshly prepared solution of maleimido CHX-A″ DTPA (1 mg/mL in degassed Milli-Q water). The vial was filled with argon gas, and the mixture was incubated at 37 °C for 18 h (overnight). After the end of incubation, the reaction mixture was analyzed using HPLC-MS, as described in the Instrumentation section. Purification of conjugates was performed using semipreparative HPLC, and buffer was changed to 0.2 M NH_4OAc, pH 5.5, using NAP-5 column. Exact concentration of protein was determined by amino acid analysis (Aminosyraanalyscentralen, Uppsala, Sweden). Affinity of conjugate to HER2 was measured using a Biacore 2000 instrument (Biacore, Uppsala, Sweden) according to the method described earlier (*5*).

For a labeling, 180 μL of conjugate solution (containing 20 μg of conjugate in 0.2 M NH_4OAc, pH 5.5) was mixed with 25 μL of ^{111}In in 0.05 M HCl (18 MBq). The mixture was incubated at room temperature. At 10, 20, and 30 min after the start of incubation, a small (0.8 μL) aliquot was taken from the reaction mixture and analyzed using ITLC SG eluted with 0.2 M citric acid. To confirm stable chelation, an aliquot of solution was incubated in 500-fold molar excess of EDTA for 4 h, and then analyzed using ITLC. This stability test was repeated twice.

Binding and Processing of ^{111}In-CHX-A″ DTPA-Z_{2395}-C by HER2-Expressing SKOV-3 Cell Line *in Vitro*. To evaluate cellular processing of ^{111}In-CHX-A″ DTPA-Z_{2395}-C, the labeled conjugate was added in 1 mL complete medium to a series of Petri dishes containing 250 000 cells at an equimolar ratio of Affibody molecules to HER2 receptors. Dishes were incubated for 1 h at 4 °C, and the incubation medium was removed. Cells were washed 3 times with ice-cold serum-free medium and, after addition of 1 mL complete medium, cell dishes were incubated further at 37 °C. At designed times of incubation (0, 0.5, 1, 1.5, 2, 3, 4, 8, and 24 h), one set of 3 dishes was analyzed for cell-associated radioactivity. Medium was collected, and the cells were washed 3 times with ice-cold serum-free medium and treated with 0.5 mL 4 M urea solution in 0.2 M glycine buffer, pH 2.0, with 0.15 M NaCl for 5 min at 4 °C (according to method described in ref (*25*)). Solution was collected and cells were additionally rinsed with 0.5 mL of the same buffer. The radioactivity, which was removed by acid wash, was considered as the membrane bound fraction. After addition of 0.5 mL 1 M NaOH solution, the cells were incubated for 1 h at 37 °C and the solution was collected. Cell dishes were subsequently rinsed with 0.5 mL of alkaline solution. Pooled alkaline fractions represented internalized conjugate. The radioactivity content of the samples was measured using the automated gamma counter.

To confirm that binding of conjugate was receptor-specific, a 100-fold excess of nonlabeled Affibody molecules was added 5 min before the labeled ones to 3 culture dishes and cell-bound radioactivity was measured after treatment with trypsin-EDTA solution (0.25% trypsin, 0.02% EDTA in buffer, Biochrom AG, Berlin, Germany).

To assess the fraction of the conjugate that dissociated intact from the cells, the media was collected after 1, 4, 8, and 24 h of incubation at 37 °C and analyzed using disposable NAP-5 size-exclusion columns (cutoff size 5 kDa) pre-equilibrated with 2.5% bovine serum albumin solution in PBS. Separation on high and low molecular weight fractions was done according to the manufacturer's descriptions. Radioactivity in a high molecular weight fraction was considered intact dissociated conjugate.

Animal Studies. The animal experiments were planned and performed in accordance with the national regulation on laboratory animals' protection. The animal study plans have been approved by the local Ethics Committee for Animal Research in Uppsala. Biodistribution studies in non-tumor-bearing mice were performed in female immunocompetent Naval Medical Research Institute (NMRI) mice. In all experiments on tumor-bearing mice, female outbreed BALB/c nu/nu mice were used. The mice were kept using standard diet, bedding, and environment with free access to food and water. All mice were acclimatized for one week at the Rudbeck Laboratory animal facility before any experimental procedures. Xenografts of HER2-expressing SKOV-3 ovarian carcinoma cell line, 10^7 SKOV-3 cells per animal, were subcutaneously implanted in right hind leg.

In each biodistribution experiment, mice were randomized into groups of four. Animals were injected intravenously (tail vein) with 1 μg conjugate (50 kBq) in 100 μL PBS. At the predetermined time point, a mixture of Ketalar-Rompun (20 μL of solution per gram body weight; Ketalar, 10 mg/mL; Rompun, 1 mg/mL) was intraperitonealy injected and the mice were euthanized by a heart puncture using a 1 mL syringe, prewashed with diluted heparin (5000 IE/mL). Blood as well as lung, liver, spleen, kidneys, tumor (from xenografted mice), samples of muscle and bone, gastrointestinal tract (with its content), and remaining carcass were collected in preweighed plastic vials. Organs and tissue samples were weighed and measured for radioactivity using an automatic gamma counter. The tissue uptake values were calculated as percent injected activity per gram tissue (% IA/g), except for the gastrointestinal tract and the carcass, which were calculated as % IA per whole sample. The radioactivity in the gastrointestinal tract with its content was used as a measure of hepatobiliary excretion.

Biodistributions of the three differentially labeled constructs (two site-specifically labeled at C-terminal, ^{111}In-CHX-A″ DTPA-Z_{2395}-C and ^{111}In-DOTA-Z_{2395}-C, and one labeled using amino-directed chemistry, ^{111}In-CHX-A″ DTPA-Z_{342}) were determined in NMRI mice at 4 and 24 h pi.

Tumor targeting and biodistribution of ^{111}In-CHX-A″ DTPA-Z_{2395}-C at 1, 4, and 24 h pi. were studied in immunodeficient mice bearing SKOV-3 xenografts. To confirm that xenograft accumulation of ^{111}In-CHX-A″ DTPA-Z_{2395}-C was HER2-specific, receptors in one additional group of mice were presaturated by subcutaneous injection of 520 μg of unlabeled $Z_{HER2:342}$ 45 min prior to injection of radiolabeled Affibody molecule. Mice in this group were sacrificed 4 h after injection. For comparison, biodistributions of ^{111}In-DOTA-Z_{2395}-C and ^{111}In-CHX-A″ DTPA-Z_{342} were studied in the same batch of SKOV-3-grafted mice, 4 h pi.

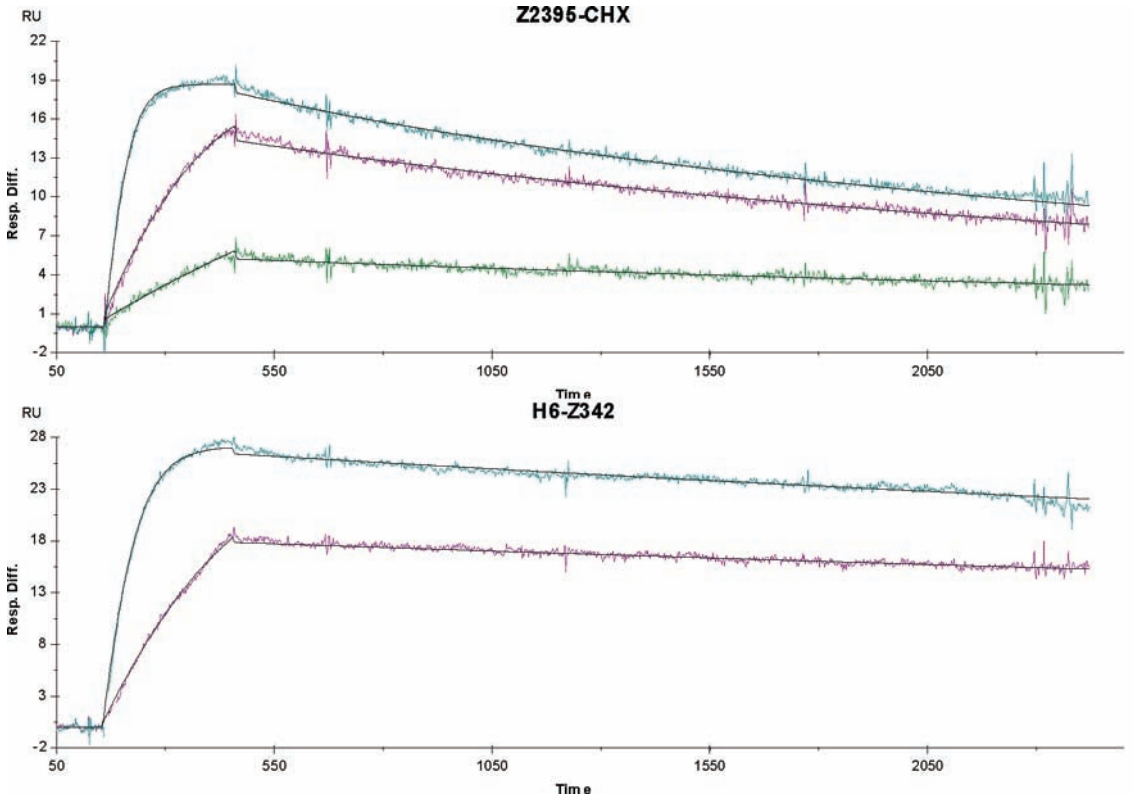

Figure 2. Biosensor binding study using surface plasmon resonance. Sensorgrams obtained after injection of the CHX-A″ DTPA-Z_{2395}-C conjugate (upper panel) and parental His_6-$Z_{HER2:342}$ (lower panel) over a sensor chip flow-cell surface containing amine-coupled HER2-Fc fusion protein. CHX-A″ DTPA-Z_{2395}-C was injected at concentrations of 5 nM, 1.2 nM, and 0.31 nM. His_6-$Z_{HER2:342}$ was injected at concentrations of 6 nM and 1.5 nM. Experimental curves were fitted to a 1:1 (Langmuir) binding model with correction for mass transfer effects.

For gamma camera imaging, four SKOV-3 xenograft bearing mice were injected with 2.7 MBq ^{111}In-CHX-A″ DTPA-Z_{2395}-C (amount of protein 3 μg). 1 and 4 h postinjection, two animals were sacrificed by overdosing Ketalar/Rompun followed by cervical dislocation. After euthanasia, the urine bladders were excised and cadavers were stored on ice until imaging. Imaging was performed at the department of Nuclear Medicine at Uppsala University Hospital using a Millennium GE gamma camera equipped with a medium energy general purpose (MEGP) collimator. Static images (10 min), obtained with a zoom factor of 2, were digitally stored in a 256 × 256 matrix. The evaluation of the images was performed using a Hermes system (Hermes Medical Solutions, Stockholm). In each animal, a region of interest (ROI) was drawn around the tumor. The same region was copied to a contralateral thigh. Tumor-to-contralateral thigh ratios were calculated based on total counts in the ROIs.

RESULTS

Preparation and Characterization of ^{111}In-CHX-A″ DTPA-Z_{2395}-C. HPLC-MS analysis demonstrated that 83% of the $Z_{HER2:2395}$ Affibody molecules were conjugated with chelator, when coupling of maleimido-CHX-A″ DTPA was performed using equimolar amount of chelator and protein. When maleimido-CHX-A″ DTPA was used in a 2- or 3-fold molar excess, no unconjugated Affibody molecules were detected after incubation during 18 h at 37 °C, demonstrating that a uniform 1:1 product was produced. Semi-preparative HPLC using Zorbax 300SB-C8 column provided complete separation from nonconjugated chelator.

Measurement of the binding kinetics of CHX-A″ DTPA-Z_{2395}-C to extracellular domain of HER2 (Figure 2) suggested that the association rate (k_a) was $7.4 \pm 0.5 \times 10^6$ M^{-1} s^{-1} (an average of two measurements ± maximum error of measurement), and dissociation rate $4.1 \pm 0.2 \times 10^{-4}$ s^{-1}, resulting in an equilibrium dissociation constant of 56 ± 6.5 pM. Affinity measurement of His_6-$Z_{HER2:342}$ gave a value of 29 pM, which is in a good agreement with previously published data (22 pM (*4*)). Apparently, coupling of maleimido-CHX-A″ DTPA had no major negative effect on the affinity of the conjugate toward HER2.

Labeling performed at specific radioactivity of 0.9 MBq/μg (6.3 GBq/μmol) provided nearly quantitative yield (99.7 ± 0.3%) after 10 min. Extension of the labeling time to 30 min did not increase the labeling yield. Incubation with 500-fold molar excess of EDTA for 4 h did not decrease conjugate-associated radioactivity, indicating that the labeling was fully mediated by CHX-A″ DTPA, not by any weak chelating pocket that might be formed by amino acid residues.

Binding and Processing of ^{111}In-CHX-A″ DTPA-Z_{2395}-C by HER2-Expressing SKOV-3 Cell Line *in Vitro*. Binding of ^{111}In-CHX-A″ DTPA-Z_{2395}-C to HER2-expressing SKOV-3 cells was specific, since presaturation of receptors with a 100-fold excess of nonlabeled Affibody molecules prevented binding nearly completely, from 35 ± 0.5% to 0.06 ± 0.01% of added radioactivity ($p < 0.0001$).

The results of cellular processing experiments indicated that retention of the conjugate was good; 81 ± 0.5% of radioactivity was still associated with cells 24 h after change of the media (Figure 3, left panel). Interestingly, internalization was rather slow as only 16.6 ± 1.4% of the radioactivity initially associated with cells was internalized at 24 h. Excretion of degraded conjugate was also slow and at early time points the majority of noncell-bound radioactivity was presented by intact conjugates that dissociated from cells. This observation is in agreement with known good intracellular retention of radiometal

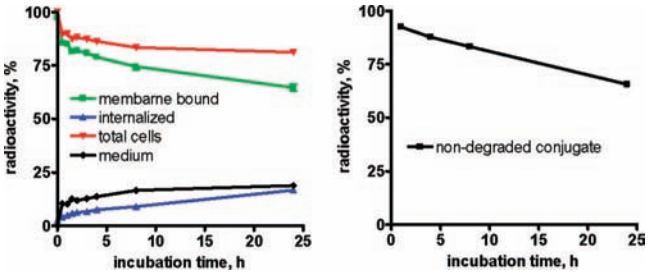

Figure 3. Left panel: cellular retention and internalization of ^{111}In-CHX-A″ DTPA-Z_{2395}-C by HER2-expressing SKOV-3 ovarian carcinoma cell line after inrerrupted incubation. Right panel: percentage of nondegraded conjugate in cell culture media (high-molecular-weight fraction in size-exclusion chromatography using NAP-5 columns) as a function of time after interrupted incubation and media change. Data presented as an average from three cell culture dishes ± SD. Error bars may be not seen since they are smaller than point symbols.

labels (*26*). Excreted radiocatabolites could be detected in the media 24 h after change, but amounted to only 6.5% of the initial radioactivity. Thus, the favorable cellular retention was mainly due to strong binding (very slow off-rate) to cell membrane target.

Animal Studies. To evaluate influence of maleimido-CHX-A″ DTPA conjugation on the biodistribution of the HER2-binding Affibody molecule, the biodistribution of ^{111}In-CHX-A″ DTPA-Z_{2395}-C was compared with that of ^{111}In-DOTA-Z_{2395}-C (site-specifically labeled at the C-terminal using DOTA) and with that of ^{111}In-CHX-A″ DTPA-Z_{342} (labeled via CHX-A″ DTPA coupled using isothiocyanate) in NMRI mice, at 4 and 24 h pi. The results of the biodistribution experiments are presented in Table 1. All conjugates demonstrated rapid clearance from blood and the majority of normal organs and tissues. The renal excretion was dominating, which resulted in a low radioactivity accumulation in the gastrointestinal tract, but high uptake in kidneys. There were, however, some differences. Though radioactivity accumulation in bone was low, the use of DOTA provided lower bone uptake than CHX-A″ DTPA. At the same time, bloodborne radioactivity was higher at both time points for ^{111}In-DOTA-Z_{2395}-C than for both CHX-A″ DTPA-containing conjugates. Hepatic accumulation of the radioactivity was also higher for ^{111}In-DOTA-Z_{2395}-C at 24 h pi. Interestingly, the overall clearance of ^{111}In-CHX-A″ DTPA-Z_{342} from blood and tissues was more rapid than clearance of both site-specifically labeled conjugates.

Targeting of HER2 *in vivo* using ^{111}In-CHX-A″ DTPA-Z_{2395}-C was evaluated in BALB/C nu/nu mice bearing SKOV-3 xenografts (Figure 4 and Tables 2 and 3). The average tumor size was 0.57 ± 0.39 g at the time for the experiment. In agreement with biodistribution data for NMRI mice, ^{111}In-CHX-A″ DTPA-Z_{2395}-C cleared rapidly from normal tissue and blood, with a rather high degree of renal reabsorption. Tumor targeting was also rapid, and already at 1 h pi, the tumor uptake was higher than uptake in any other organ or tissue, except kidney. At 4 h pi, the tumor uptake had not changed significantly in comparison with that at 1 h pi, but tumor-to-organ ratios increased significantly for blood, lung, muscle, and bone due to clearance from normal tissues. Only tumor-to-lung and tumor-to-muscle increased by 24 h pi in comparison with the 4 h pi time point. In order to verify the specificity of ^{111}In-CHX-A″ DTPA-Z_{2395}-C accumulation in HER2-expressing xenografts, its biodistribution (4 h pi) was studied after saturating the binding epitope of HER2 by preinjection of 520-fold molar excess of nonlabeled $Z_{HER2:342}$.The tumor uptake was reduced from 17.3 ± 4.8% to 1.7 ± 0.2% IA/g ($p < 0.001$), demonstrating specific HER2-binding of ^{111}In-CHX-A″ DTPA-Z_{2395}-C in the xenografts.

The targeting properties were assessed at 4 h pi to compare ^{111}In-CHX-A″ DTPA-Z_{2395}-C with the two most favorable HER2-targeting Affibody conjugates, ^{111}In-DOTA-Z_{2395}-C (site-specifically labeled at C-terminal using DOTA (*20*)) and ^{111}In-CHX-A″ DTPA-Z_{342} (labeled via CHX-A″ DTPA coupled using isothiocyanate (*18*)). The results of this comparison are presented in Tables 2 and 3.

Images acquired after the i.v. injection of the ^{111}In-CHX-A″ DTPA-Z_{2395}-C into mice bearing SKOV-3 xenografts confirmed the capacity of this conjugate to visualize HER2-expression (Figure 5). In agreement with the biodistribution data, tumors were clearly visualized already at 1 h pi (tumor-to-contralateral thigh ratio 20 ± 6). By 4 h pi, the contrast of imaging increased due to decrease of the background radioactivity (tumor-to-contralateral thigh ratio 37 ± 8). Due to the renal excretion, high radioactivity was accumulated also in kidneys.

DISCUSSION

Personalizing cancer treatment requires methods for detection of a variety of tumor-specific cell-surface antigens for patient stratification. The Affibody technology of small robust high-affinity binders may be a convenient platform for development of molecular imaging agents to be used for noninvasive assessment of responsiveness to patient-specific therapy (*1–3*). The rapid tumor localization of Affibody-based targeting conjugates and their rapid clearance from blood and healthy tissues (except kidneys) result in high-contrast *in vivo* imaging of tumor biomarkers shortly after injection. However, careful studies on structure−property relationships are required for design of optimal Affibody-based conjugates. Selection of suitable chelators for labeling with radiometals is one important direction for such studies. Thiol-directed chemistry is of particular interest, since it can provide exquisite site-specific coupling of chelators to both chemically and recombinantly produced Affibody molecules having a unique cystein, thereby increasing the flexibility of manufacturing.

HER2 is a transmembrane tyrosine kinase receptor, which is overexpressed in a fraction of breast, ovary and urinary bladder carcinomas (*27–29*). Blocking of HER2 signaling in breast carcinomas using the monoclonal antibody trastuzumab (Herceptin) results in increase of survival and is approved for clinical use both in Europe and North America for patients with HER2-overexpressing tumors. Besides, targeted therapy of HER2-expressing tumors using radionuclides (*30–33*) and drugs (*34*) is under development. Both the American Association of Clinical Oncology (*35*) and the European Group on Tumour Markers (*36*) recommend detecting HER2 expression in each new breast tumor or recurrence in order to select patients who would benefit from trastuzumab therapy. Presently, the assessment of HER2 expression is done based on histopathological examination. Unfortunately, the results of such tests may be affected by sampling errors, discordance in HER2 expression in primary tumors and metastasis, and experience of a laboratory performing analysis (*37*). In contrast, molecular imaging would allow an assessment of the global HER2 expression. An example of clinical utility of radionuclide imaging of HER2 expression in breast cancer patients has been presented by Behr and co-workers (*38*). It was shown that the use of ^{111}In-DTPA-trastuzumab identify not only of patients responding to trastuzumab treatment (alone or in combination with chemotherapy) but also patients who may suffer from cardiac toxicity associated with such treatment.

The choice of the chelator moiety contributes to the overall charge and lipophilicity of the conjugate, and could in addition have an effect on the conformation of the tracer. The present study focused on the effects of different labeling methods on $Z_{HER2:2395}$-C, a cysteine-containing derivative of anti-HER2

Table 1. Biodistribution of Different anti-HER2 Affibody Conjugates after iv Injection in NMRI Mice

	uptake, % IA/g[a]					
	4 h pi			24 h pi		
	^{111}In-CHX-A″ DTPA-Z_{2395}-C	^{111}In-DOTA-Z_{2395}-C	^{111}In-CHX-A″ DTPA-Z_{342}	^{111}In-CHX-A″ DTPA-Z_{2395}-C	^{111}In-DOTA-Z_{2395}-C	^{111}In-CHX-A″ DTPA-Z_{342}
blood	$0.069 \pm 0.003^{c,d}$	0.18 ± 0.07	0.04 ± 0.01^{c}	$0.023 \pm 0.003^{c,d}$	0.05 ± 0.01	0.011 ± 0.002^{c}
lung	0.34 ± 0.04	0.27 ± 0.04	0.24 ± 0.06	0.158 ± 0.009^{d}	0.14 ± 0.03	0.107 ± 0.008
liver	1.1 ± 0.1^{d}	1.01 ± 0.05	0.32 ± 0.07^{c}	$0.65 \pm 0.05^{c,d}$	0.85 ± 0.01	0.17 ± 0.03^{c}
spleen	0.30 ± 0.04	0.32 ± 0.03	0.2 ± 0.1	0.21 ± 0.02^{d}	0.23 ± 0.02	0.13 ± 0.02^{c}
kidney	234 ± 20^{c}	183 ± 12	217 ± 21	135 ± 9^{d}	126 ± 12	109 ± 8
muscle	0.08 ± 0.01^{c}	0.055 ± 0.006	0.06 ± 0.04	0.05 ± 0.01^{d}	0.035 ± 0.003	0.029 ± 0.009
bone	0.38 ± 0.08^{c}	0.15 ± 0.03	0.4 ± 0.3	0.245 ± 0.03^{d}	0.099 ± 0.008	0.17 ± 0.05^{c}
GI tract[b]	2.0 ± 0.4	2.3 ± 0.7	1.9 ± 0.6	0.87 ± 0.02	0.8 ± 0.2	0.6 ± 0.2
carcass[b]	3.8 ± 0.4	3.4 ± 0.6	2.6 ± 1.0	2.3 ± 0.4^{d}	1.9 ± 0.2	1.2 ± 0.1^{c}

[a] Data presented as average ± SD ($n = 4$) of percent of injected activity per gram (% IA/g). [b] For intestine (together with content) and carcass, data presented as percent of injected activity per whole sample (% IA). [c] Significant difference ($p < 0.05$) with ^{111}In-DOTA-Z_{2395}-C at the same time point. [d] Significant difference ($p < 0.05$) with ^{111}In-CHX-A″ DTPA-Z_{342} at the same time point.

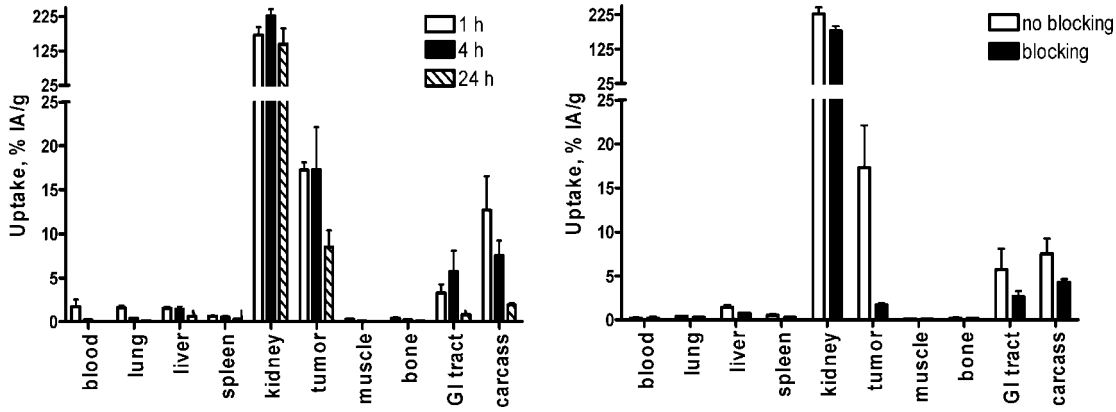

Figure 4. Targeting of HER2-expressing xenografts *in vivo*. Left panel: Biodistribution of ^{111}In-CHX-A″ DTPA-Z_{2395}-C 1, 4, and 24 h pi. Right panel: Specificity of ^{111}In-CHX-A″ DTPA-Z_{2395}-C tumor uptake in SKOV-3 xenografts, 4 h pi. In order to saturate HER2 receptors in tumors, one group of animals was preinjected with 520 μg nonlabeled $Z_{HER2:342}$ 45 min before injection of radiolabeled conjugate (designated as blocking). All animals were injected with 1 μg of labeled Affibody molecules. Data are expressed as % IA/g (percent of injected radioactivity per gram tissue) and presented as an average from four animals ± SD. Data for the gastrointestinal tract (with its content) and for carcass are presented as % IA per whole sample.

Table 2. Biodistribution of ^{111}In-CHX-A″ DTPA-Z_{2395}-C, ^{111}In-DOTA-Z_{2395}-C, and ^{111}In-CHX-A″ DTPA-Z_{342} Affibody Conjugates 4 h after iv Injection in BALB/C nu/nu Mice Bearing SKOV-3 Xenografts

	uptake, % IA/g[a]		
	^{111}In-CHX-A″ DTPA-Z_{2395}-C	^{111}In-DOTA-Z_{2395}-C	^{111}In-CHX-A″ DTPA-Z_{342}
blood	0.22 ± 0.05^{d}	0.25 ± 0.09	0.04 ± 0.01^{c}
lung	$0.42 \pm 0.03^{c,d}$	0.31 ± 0.06	0.15 ± 0.05^{c}
liver	1.4 ± 0.3^{d}	1.6 ± 0.6	0.63 ± 0.08^{c}
spleen	0.5 ± 0.1^{d}	0.5 ± 0.2	0.16 ± 0.02^{c}
kidney	$227 \pm 18^{c,d}$	169 ± 36	184 ± 17
tumor	17 ± 5^{d}	8 ± 2	8 ± 2
muscle	$0.12 \pm 0.03^{c,d}$	0.07 ± 0.02	0.03 ± 0.01^{c}
bone	0.21 ± 0.05^{d}	0.2 ± 0.2	0.09 ± 0.03
GI tract[b]	6 ± 2^{c}	0.9 ± 0.2	4.6 ± 0.3^{c}
carcass[b]	$8 \pm 2^{c,d}$	2.9 ± 0.3	1.9 ± 0.4^{c}

[a] Data presented as average ± SD ($n = 4$) of percent of injected activity per gram (% IA/g). [b] For intestine (together with content) and carcass, data presented as percent of injected activity per whole sample (% IA). [c] Significant difference ($p < 0.05$) with ^{111}In-DOTA-Z_{2395}-C at the same time point. [d] Significant difference ($p < 0.05$) with ^{111}In-CHX-A″ DTPA-Z_{342} at the same time point.

Affibody molecule $Z_{HER2:342}$ (*4*). Previous data have shown that coupling with the chelator DOTA followed by labeling with ^{111}In result in a favorable molecular imaging agent, ^{111}In-DOTA-Z_{2395}-C (*20*), superior to ^{111}In-Bz-DOTA- Z_{342}, bearing Bz-DOTA randomly coupled to amino groups (*15*). In contrast to DOTA, CHX-A″ DTPA is a semirigid chelator that provides stable labeling at ambient temperature with a range of medically useful radionuclides (*18*, *21*, *39*, *40*). A maleimido derivative of the CHX-A″ DTPA was developed for use in site-directed maleimide−thiol Michael addition conjugation chemistry (*23*). Site-specific coupling of the maleimido-CHX-A″ DTPA to $Z_{HER2:2395}$-C had no major effect on affinity, suggesting that no major structural changes resulted from the conjugation. The cellular processing was essentially unchanged in comparison with ^{111}In-DOTA-Z_{2395}-C (*20*). Although ^{111}In-CHX-A″ DTPA-Z_{2395}-C demonstrated strong membrane binding, internalization was as slow as for ^{111}In-DOTA-Z_{2395}-C (Figure 3). In normal mice, ^{111}In-CHX-A″ DTPA-Z_{2395}-C as well as ^{111}In-DOTA-Z_{2395}-C and ^{111}In-CHX-A″ DTPA-Z_{342} were rapidly cleared from the blood and the majority of tissues, accompanied by a high degree of renal reabsorption of radioactivity. Interestingly, the ^{111}In-CHX-A″ DTPA-Z_{342} conjugate (with the chelators conjugated via a thiourea bond) cleared more rapidly than the site-specifically labeled conjugates. The same was observed in

Table 3. Tumor-to-Organ Ratios in BALB/C nu/nu Mice Bearing SKOV-3 Xenografts[a]

	^{111}In-CHX-A″ DTPA-Z_{2395}-C			^{111}In-DOTA-Z_{2395}-C	^{111}In-CHX-A″ DTPA-Z_{342}
	1 h	4 h	24 h	4 h	4 h
blood	12 ± 5^{b}	86 ± 46	157 ± 49	36 ± 10	$195 \pm 13^{e,f}$
lung	11 ± 2^{b}	42 ± 14^{c}	67 ± 9	27 ± 8	61 ± 16^{f}
liver	11.5 ± 0.7	12 ± 3	14 ± 3	6 ± 2^{d}	13 ± 3^{f}
spleen	28 ± 4	35 ± 9	32 ± 7	18 ± 4^{d}	$53 \pm 10^{e,f}$
kidney	0.10 ± 0.01	0.08 ± 0.02	0.06 ± 0.01	0.05 ± 0.01	0.05 ± 0.01^{e}
muscle	61 ± 13^{b}	157 ± 64^{c}	246 ± 29	125 ± 26	$325 \pm 89^{e,f}$
bone	42 ± 8^{b}	83 ± 9	109 ± 35	53 ± 25	103 ± 23^{f}

[a] Data are presented as an average for four animals ± SD. [b] Significant difference ($p < 0.05$) between tumor-to-organ ratios at 1 and 4 h pi. for ^{111}In-CHX-A″ DTPA-Z_{2395}-C. [c] Significant difference ($p < 0.05$) between tumor-to-organ ratios at 4 and 24 h pi. for ^{111}In-CHX-A″ DTPA-Z_{2395}-C. [d] Significant difference ($p < 0.05$) between tumor-to-organ ratios 4 h pi. for ^{111}In-CHX-A″ DTPA-Z_{2395}-C and ^{111}In-DOTA-Z_{2395}-C. [e] Significant difference ($p < 0.05$) between tumor-to-organ ratios 4 h pi. for ^{111}In-CHX-A″ DTPA-Z_{2395}-C and ^{111}In-CHX-A″ DTPA-Z_{342}. [f] Significant difference ($p < 0.05$) between tumor-to-organ ratios 4 h pi. for ^{111}In-DOTA-Z_{2395}-C and ^{111}In-CHX-A″ DTPA-Z_{342}.

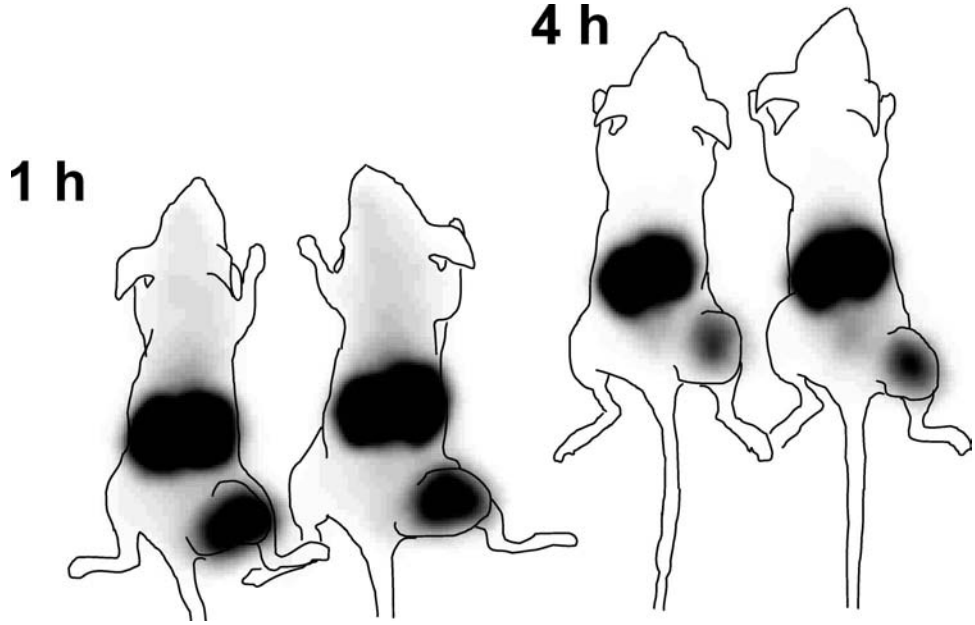

Figure 5. Anterior gamma-camera images of nude mice bearing HER2-expressing SKOV-3 xenografts 1 h (left) and 4 h (right) after injection of ^{111}In-CHX-A″ DTPA-Z_{2395}-C. Contours derived from a digital photographs were superimposed over gamma-camera images to facilitate interpretation. Besides tumors (right hind legs), only kidneys are visualized.

tumor-bearing mice. In our previous study (*20*), an ^{111}In-Bz-DTPA-Z_{342} conjugate with an acyclic chelator randomly amine-coupled demonstrated a more rapid clearance than ^{111}In-DOTA-Z_{2395}-C having DOTA site-specifically coupled. One might hypothesize that a decrease in positive charge resulting from reaction of the isothiocyanate with ϵ-amines of the lysine residues or the N-terminus amine facilitates clearance. In tumor-bearing mice, ^{111}In-CHX-A″ DTPA-Z_{2395}-C displays rapid tumor localization, enabling high tumor-to-organ ratios as early as 1 h pi (Table 3). These results were confirmed by γ-camera imaging (Figure 5). By 4 h pi, the contrast had improved further. Also, the tumor-to-lung and tumor-to-bone ratios were sufficient for imaging at 4 h pi, although these ratios were significantly increased by 24 h. At 4 h pi, the tumor-to-blood ratio of ^{111}In-CHX-A″ DTPA-Z_{2395}-C (86:1) greatly exceeded reported values of any non-Affibody-based HER2-targeting agent, including the ^{111}In-DOTA(GSG)-KCCYSL peptide (tumor-to-blood ratio of 3:1 (*41*)) or ^{111}In-CHX-A″ DTPA-C6.5K-A diabody (tumor-to-blood ratio of 1.34:1 (*21*)).

The high kidney uptake of ^{111}In-CHX-A″ DTPA-Z_{2395}-C might be of some concern, although the radiation dose is most likely not a radiation safety issue. The present data are insufficient for a detailed dosimetry evaluation, but a dose estimate has been performed for another Affibody molecule, ^{111}In-DOTA-$Z_{HER2:342}$, which displayed somewhat higher uptake in kidneys (*5*). Dosimetry modeling suggested that the renal dose from ^{111}In-DOTA-$Z_{HER2:342}$ would be 1.8 mSv/MBq, or 200 mSv if 111 MBq is given to the patient. This is comparable to the 124 mSv/185 MBq for ^{111}In-ProstaScint (data from package insert). It should be noted that renal doses as high as 45 Gy (after more than 90 GBq injected radioactivity) did not cause negative effects on the kidneys in clinical trials using ^{111}In-octreotide for therapy (*42, 43*). The high renal uptake might complicate imaging of metastases close to kidney; however, contemporary reconstruction algorithms may minimize this problem. Handling of renal uptake of radiometal-labeled Affibody molecules is discussed in more detail in a recent publication (*20*).

The chelator CHX-A″ DTPA may be used for labeling with different nuclides. As illustrated here, SPECT studies with ^{111}In are possible. PET imaging is possible after labeling with ^{86}Y, granted that the half-life of only 14.7 h is compatible with the half-life of the tracer (*44*). The half-life of this nuclide would facilitate distribution of radiolabeled conjugates from a central cyclotron-equipped dispensary to satellite PET centers. The use of PET might improve of sensitivity of imaging, including the possibility of visualizing smaller metastases or tumors in the vicinity of kidneys or urinary bladder. The chelator may also be used with a number of therapeutic radionuclides, including ^{90}Y (*21, 22, 45*), ^{114m}In (*18*), ^{177}Lu (*28, 32*), and the α-emitting nuclides ^{212}Bi and ^{213}Bi (*39, 46, 47*). High renal uptake would, most likely, prevent systemic therapy using radiolabeled CHX-

A″ DTPA-Z_{2395}-C. However, locoregional therapy of bladder carcinoma or brain metastases of breast cancer (using short-lived α-emitters) deserves further investigations. The maleimido-CHX-A″ DTPA is of course not limited to the labeling of Affibody molecules, but may be used with any targeting protein containing an unpaired cysteine residue, including Fab′ fragments of monoclonal antibodies and scFv with an engineered cysteine. The final choice of tracer to carry the nuclide will depend on several factors. Besides pharmacokinetics and biodistribution discussed in the present report, multiple administrations may require a low immunogenic response to the tracer. Preliminary data suggest that the Affibody molecules display a low immunogenic potential, possibly due to rapid clearance from the body (*48*).

CONCLUSION

The use of maleimido-CHX-A″ DTPA enables facile and stable site-specific labeling of Affibody molecules with ^{111}In under mild conditions. The conjugate demonstrated preserved binding to HER2-expressing cells and good cellular retention of the radioactivity. In BALB/c nu/nu mice bearing HER2-expressing xenografts, the tumors were clearly visualized 1 and 4 h pi. This suggests that the Affibody molecule-maleimido-CHX-A″ DTPA conjugates possess a high potential for *in vivo* imaging of tumor-associated targets and, possibly, for radionuclide therapy. Apparently, the maleimido-CHX-A″ DTPA can be a suitable chelator for site-specific labeling of other targeting proteins, including Fab′-fragments.

ACKNOWLEDGMENT

This research was supported in part by the Intramural Research Program of the NIH, National Cancer Institute, Center for Cancer Research and by grant from Swedish Cancer Society (Cancerfonden).

LITERATURE CITED

(1) Tolmachev, V., Orlova, A., Nilsson, F. Y., Feldwisch, J., Wennborg, A., and Abrahmsén, L. (2007) Affibody molecules: potential for *in vivo* imaging of molecular targets for cancer therapy. *Expert Opin. Biol. Ther. 7*, 555–568.

(2) Nilsson, F. Y., and Tolmachev, V. (2007) Affibody molecules: new protein domains for molecular imaging and targeted tumor therapy. *Curr. Opin. Drug Discovery Dev. 10*, 167–175.

(3) Orlova, A., Feldwisch, J., Abrahmsén, L., and Tolmachev, V. (2007) Update: affibody molecules for molecular imaging and therapy for cancer. *Cancer Biother. Radiopharm. 22*, 573–584.

(4) Orlova, A., Magnusson, M., Eriksson, T. L., Nilsson, M., Larsson, B., Höidén-Guthenberg, I., Widström, C., Carlsson, J., Tolmachev, V., Ståhl, S., and Nilsson, F. Y. (2006) Tumor imaging using a picomolar affinity HER2 binding affibody molecule. *Cancer Res. 66*, 4339–4348.

(5) Orlova, A., Tolmachev, V., Pehrson, R., Lindborg, M., Tran, T., Sandström, M., Nilsson, F. Y., Wennborg, A., Abrahmsén, L., and Feldwisch, J. (2007) Synthetic affibody molecules: a novel class of affinity ligands for molecular imaging of HER2-expressing malignant tumors. *Cancer Res. 67*, 2178–2186.

(6) Friedman, M., Nordberg, E., Höidén-Guthenberg, I., Brismar, H., Adams, G. P., Nilsson, F. Y., Carlsson, J., and Ståhl, S. (2007) Phage display selection of Affibody molecules with specific binding to the extracellular domain of the epidermal growth factor receptor. *Protein Eng. Des. Sel. 20*, 189–199.

(7) Nordberg, E., Friedman, M., Göstring, L., Adams, G. P., Brismar, H., Nilsson, F. Y., Ståhl, S., Glimelius, B., and Carlsson, J. (2007) Cellular studies of binding, internalization and retention of a radiolabeled EGFR-binding affibody molecule. *Nucl. Med. Biol. 34*, 609–618.

(8) Friedman, M., Orlova, A. , Johansson, E., Eriksson, T., Höidén-Guthenberg, I., Tolmachev, V., Nilsson, F. Y., and Ståhl S. (2008) Directed evolution to low nanomolar affinity of an epidermal growth factor receptor 1-binding Affibody molecule. *J. Mol. Biol. 376*, 1388–1402.

(9) Mume, E., Orlova, A., Larsson, B., Nilsson, A. S., Nilsson, F. Y., Sjöberg, S., and Tolmachev, V. (2005) Evaluation of ((4-hydroxyphenyl)ethyl)maleimide for site-specific radiobromination of anti-HER2 affibody. *Bioconjugate Chem. 16*, 1547–1555.

(10) Orlova, A., Nilsson, F. Y., Wikman, M., Widström, C., Ståhl, S., Carlsson, J., and Tolmachev, V. (2006) Comparative *in vivo* evaluation of technetium and iodine labels on an anti-HER2 affibody for single-photon imaging of HER2 expression in tumors. *J. Nucl. Med. 47*, 512–519.

(11) Engfeldt, T., Orlova, A., Tran, T., Bruskin, A., Widström, C., Karlström, A. E., and Tolmachev, V. (2007) Imaging of HER2-expressing tumours using a synthetic Affibody molecule containing the ^{99m}Tc-chelating mercaptoacetyl-glycyl-glycyl-glycyl (MAG3) sequence. *Eur. J. Nucl. Med. Mol. Imaging 34*, 722–733.

(12) Tran, T., Orlova, A., Sivaev, I., Sandström, M., and Tolmachev, V. (2007) Comparison of benzoate- and dodecaborate-based linkers for attachment of radioiodine to HER2-targeting Affibody ligand. *Int. J. Mol. Med. 19*, 485–493.

(13) Tran, T., Engfeldt, T., Orlova, A., Widström, C., Bruskin, A., Tolmachev, V., and Karlström, A. E. (2007) *In vivo* evaluation of cysteine-based chelators for attachment of 99mTc to tumor-targeting Affibody molecules. *Bioconjugate Chem. 18*, 549–558.

(14) Engfeldt, T., Tran, T., Orlova, A., Widström, C., Feldwisch, J., Abrahmsen, L., Wennborg, A., Karlström, A. E., and Tolmachev, V. (2007) ^{99m}Tc-chelator engineering to improve tumour targeting properties of a HER2-specific Affibody molecule. *Eur. J. Nucl. Med. Mol. Imaging 34*, 1843–1853.

(15) Orlova, A., Tran, T., Widström, C., Engfeldt, T., Eriksson Karlström, A., and Tolmachev, V. (2007) Pre-clinical evaluation of [^{111}In]-benzyl-DOTA-$Z_{HER2:342}$, a potential agent for imaging of HER2 expression in malignant tumors. *Int. J. Mol. Med. 20*, 397–404.

(16) Tran, T., Engfeldt, T., Orlova, A., Sandström, M., Feldwisch, J., Abrahmsén, L., Wennborg, A., Tolmachev, V., and Karlström, A. E. (2007) sup > 99mTc-maEEE-$Z_{HER2:342}$, an Affibody molecule-based tracer for the detection of HER2 expression in malignant tumors. *Bioconjugate Chem. 18*, 1956–1964.

(17) Tolmachev, V., Nilsson, F. Y., Widström, C., Andersson, K., Rosik, D., Gedda, L., Wennborg, A., and Orlova, A. (2006) ^{111}In-benzyl-DTPA-ZHER2:342, an affibody-based conjugate for in vivo imaging of HER2 expression in malignant tumors. *J. Nucl. Med. 47*, 846–853.

(18) Orlova, A., Rosik, D., Sandström, M., Lundqvist, H., Einarsson, L., and Tolmachev, V. (2007) Evaluation of [$^{111/114m}$In]CHX-A″-DTPA-ZHER2:342, an Affibody ligand coniugate for targeting of HER2-expressing malignant tumors. *Q. J. Nucl. Med. Mol. Imaging 51*, 314–323.

(19) Lundberg, E., Höidén-Guthenberg, I., Larsson, B., Uhlén, M., and Gräslund, T. (2007) Site-specifically conjugated anti-HER2 Affibody molecules as one-step reagents for target expression analyses on cells and xenograft samples. *J Immunol. Methods. 319*, 53–63.

(20) Ahlgren, S., Orlova, A., Rosik, D., Sandström, M., Sjöberg, A., Baastrup, B., Widmark, O., Fant, G., Feldwisch, J., and Tolmachev, V. (2008) Evaluation of maleimide derivative of DOTA for site-specific labeling of recombinant Affibody molecules. *Bioconjugate Chem. 19*, 235–243.

(21) Adams, G. P., Shaller, C. C., Dadachova, E., Simmons, H. H., Horak, E. M., Tesfaye, A., Klein-Szanto, A. J., Marks, J. D., Brechbiel, M. W., and Weiner, L. M. (2004) A single treatment of yttrium-90-labeled CHX-A"-C6.5 diabody inhibits the growth of established human tumor xenografts in immunodeficient mice. *Cancer Res. 64*, 6200–6206.

(22) Parry, R., Schneider, D., Hudson, D., Parkes, D., Xuan, J. A., Newton, A., Toy, P., Lin, R., Harkins, R., Alicke, B., Biroc, S.,

Kretschmer, P. J., Halks-Miller, M., Klocker, H., Zhu, Y., Larsen, B., Cobb, R. R., Bringmann, P., Roth, G., Lewis, J. S., Dinter, H., and Parry, G. (2005) Identification of a novel prostate tumor target, mindin/RG-1, for antibody-based radiotherapy of prostate cancer. *Cancer Res. 65*, 8397–8405.

(23) Xu, H., Baidoo, K. E., Wong, K. J., and Brechbiel, M. W. (2008) A novel bifunctional maleimido CHX-A″ chelator for conjugation to thiol-containing biomolecules. *Bioorg. Med. Chem. Lett. 18*, 2679–83.

(24) Persson, M., Tolmachev, V., Andersson, K., Gedda, L., Sandstrom, M., and Carlsson, J. (2005) [^{177}Lu]pertuzumab: experimental studies on targeting of HER-2 positive tumour cells. *Eur. J. Nucl. Med. Mol. Imaging 32*, 1457–1462.

(25) Wållberg, H., Orlova, A. (2008) Slow internalization of anti-HER2 synthetic Affibody monomer ^{111}In-DOTA-$Z_{HER2:342-pep2}$: implications for development of labeled tracers, *Cancer Biother. Radiopharm.*, in press.

(26) Shih, L. B., Thorpe, S. R., Griffiths, G.L., Diril, H., Ong, G. L., Hansen, H. J., Goldenberg, D. M., and Mattes, M. J. 1994) The processing and fate of antibodies and their radiolabels bound to the surface of tumor cells in vitro: a comparison of nine radiolabels. *J. Nucl. Med. 35*, 899–908.

(27) Aunoble, B., Sanches, R., Didier, E., and Bignon, Y. J. (2000) Major oncogenes and tumor suppressor genes involved in epithelial ovarian cancer (review). *Int. J. Oncol. 16*, 567–576.

(28) Carlsson, J., Nordgren, H., Sjostrom, J., et al. (2004) HER2 expression in breast cancer primary tumours and corresponding metastases. Original data and literature review. *Br. J. Cancer 90*, 2344.

(29) Gardmark, T., Wester, K., de la Torre, M., Carlsson, J., and Malmstrom, P. U. (2005) Analysis of HER2 expression in primary urinary bladder carcinoma and corresponding metastases. *BJU Int. 95*, 982–986.

(30) Brechbiel, M. W., and Waldmann, T. A. (2000) Anti-HER2 radioimmunotherapy. *Breast Dis. 11*, 125–132.

(31) Milenic, D. E., Garmestani, K., Brady, E. D., Albert, P. S., Ma, D., Abdulla, A., and Brechbiel, M. W. (2004) Targeting of HER2 antigen for the treatment of disseminated peritoneal disease. *Clin. Cancer Res. 10*, 7834–7841.

(32) Tolmachev, V., Orlova, A., Pehrson, R., Galli, J., Baastrup, B., Andersson, K., Sandström, M., Rosik, D., Carlsson, J., Lundqvist, H., Wennborg, A., and Nilsson, F. Y. (2007) Radionuclide therapy of HER2-positive microxenografts using a ^{177}Lu-labeled HER2-specific Affibody molecule. *Cancer Res. 67*, 2773–2782.

(33) Milenic, D. E., Garmestani, K., Brady, E. D., Albert, P. S., Ma, D., Abdulla, A., and Brechbiel, M. W. (2005) Alpha-particle radioimmunotherapy of disseminated peritoneal disease using a ^{212}Pu-labeled radioimmunoconjugate targeting HER2. *Cancer Biother. Radiopharm. 20*, 557–568.

(34) Mandler, R., Wu, C., Sausville, E. A., Roettinger, A. J., Newman, D. J., Ho, D. K., King, C. R., Yang, D., Lippman, M. E., Landolfi, N. F., Dadachova, E., Brechbiel, M. W., and Waldmann, T. A. (2000) Immunoconjugates of geldanamycin and anti-HER2 monoclonal antibodies: antiproliferative activity on human breast carcinoma cell lines. *J. Natl. Cancer. Inst. 92*, 1573–1581.

(35) Bast, R. C. Jr., Ravdin, P., Hayes, D. F., Bates, S., Fritsche, H.Jr., Jessup, J. M., Kemeny, N., Locker, G. Y., Mennel, R. G., and Somerfield, M. R. (2001) American society of clinical oncology tumor markers expert panel 2000 update of recommendations for the use of tumor markers in breast and colorectal cancer: clinical practice guidelines of the american society of clinical oncology. *J.Clin. Oncol 19*, 1865–1878.

(36) Molina, R., Barak, V., van Dalen, A., Duffy, M. J., Einarsson, R., and Gion, M. (2005) Tumor markers in breast cancer-European group on tumor markers recommendations. *Tumour Biol. 26*, 281–293.

(37) Perez, E. A., Suman, V. J., Davidson, N. E., Martino, S., Kaufman, P. A., Lingle, W. L., Flynn, P. J., Ingle, J. N., Visscher, D., and Jenkins, R. B. (2006) HER2 testing by local, central, and reference laboratories in specimens from the North Central Cancer Treatment Group N9831 intergroup adjuvant trial. *J. Clin. Oncol. 24*, 3032–3038.

(38) Behr, T. M., Behe, M., and Wormann, B. (2001) Trastuzumab and breast cancer. *N. Engl. J. Med. 345*, 995–996.

(39) Nikula, T. K., McDevitt, M. R., Finn, R. D., Wu, C., Kozak, R. W., Garmestani, K., Brechbiel, M. W., Curcio, M. J., Pippin, C. G., Tiffany-Jones, L., Geerlings, M. W. Sr., Apostolidis, C., Molinet, R., Geerlings, M. W. Jr., Gansow, O. A., and Scheinberg, D. A. (1999) Alpha-emitting bismuth cyclohexylbenzyl DTPA constructs of recombinant humanized anti-CD33 antibodies: pharmacokinetics, bioactivity, toxicity and chemistry. *J. Nucl. Med. 40*, 166–176.

(40) Milenic, D. E., Garmestani, K., Chappell, L. L., Dadachova, E., Yordanov, A., Ma, D., Schlom, J., and Brechbiel, M. W. (2002) *In vivo* comparison of macrocyclic and acyclic ligands for radiolabeling of monoclonal antibodies with ^{177}Lu for radioimmunotherapeutic applications. *Nucl. Med. Biol. 29*, 431–442.

(41) Kumar, S. R., Quinn, T. P., and Deutscher, S. L. (2007) Evaluation of an ^{111}In-radiolabeled peptide as a targeting and imaging agent for ErbB-2 receptor - expressing breast carcinomas. *Clin. Cancer Res. 13*, 6070–6079.

(42) Valkema, R., De Jong, M., Bakker, W. H., Breeman, W. A., Kooij, P. P., Lugtenburg, P. J., De Jong, F. H., Christiansen, A., Kam, B. L., De Herder, W. W., Stridsberg, M., Lindemans, J., Ensing, G., and Krenning, E. P. (2002) Phase I study of peptide receptor radionuclide therapy with [In-DTPA]octreotide: the Rotterdam experience. *Semin. Nucl. Med. 32*, 110–122.

(43) Kwekkeboom, D. J., Mueller-Brand, J., Paganelli, G., Anthony, L. B., Pauwels, S., Kvols, L. K., O'dorisio, T. M., Valkema, R., Bodei, L., Chinol, M., Maecke, H. R., and Krenning, E. P. (2005) Overview of results of peptide receptor radionuclide therapy with 3 radiolabeled somatostatin analogs. *J. Nucl. Med. 46* (Suppl 1), 62S–66S.

(44) Clifford, T., Boswell, C. A., Biddlecombe, G. B., Lewis, J. S., and Brechbiel, M. W. (2006) Validation of a novel CHX-A″ derivative suitable for peptide conjugation: small animal PET/CT imaging using yttrium-86-CHX-A″-octreotide. *J. Med. Chem. 49*, 4297–4304.

(45) Lee, F. T., Mountain, A. J., Kelly, M. P., Hall, C., Rigopoulos, A., Johns, T. G., Smyth, F. E., Brechbiel, M. W., Nice, E. C., Burgess, A. W., and Scott, A. M. (2005) Enhanced efficacy of radioimmunotherapy with ^{90}Y-CHX-A″-DTPA-hu3S193 by inhibition of epidermal growth factor receptor (EGFR) signaling with EGFR tyrosine kinase inhibitor AG1478. *Clin. Cancer Res. 11*, 7080s–7086s.

(46) McDevitt, M. R., Barendswaard, E., Ma, D., Lai, L., Curcio, M. J., Sgouros, G., Ballangrud, A. M., Yang, W. H., Finn, R. D., Pellegrini, V., Jr., Lee, M., Brechbiel, M. W., Bander, N. H., Cordon-Cardo, C., and Scheinberg, D. A. (2000) An alpha-particle emitting antibody ([^{213}Bi]J591) for radioimmunotherapy of prostate cancer. *Cancer Res. 60*, 6095–6100.

(47) Kelly, M. P., Lee, F. T., Tahtis, K., Smyth, F. E., Brechbiel, M. W., and Scott, A. M. (2007) Radioimmunotherapy with alpha-particle emitting ^{213}Bi-C-functionalized trans-cyclohexyl-diethylenetriaminepentaacetic acid-humanized 3S193 is enhanced by combination with paclitaxel chemotherapy. *Clin. Cancer Res. 13*, 5604s–5612s.

(48) Feldwisch, J., Unpublished results.

BC800110Y

Effect of Transferrin As a Ligand of pH-Sensitive Fusogenic Liposome−Lipoplex Hybrid Complexes

Naoki Sakaguchi,[†] Chie Kojima,[†] Atsushi Harada,[†] Kazunori Koiwai,[‡] Nobuhiko Emi,[§] and Kenji Kono*[,†]

Department of Applied Chemistry, Graduate School of Engineering, Osaka Prefecture University, 1-1 Gakuen-cho, Nakaku, Sakai, Osaka 599-8531, Research and Develop Center, Terumo Corporation, 1500 Inokuchi, Nakai-machi, Ashigarakamigun, Kanagawa 259-0151, and Department of Hematology, Fujita Health University School of Medicine, 1-98 Dengakugakubo, Kutsukake, Toyoake, Aichi 470-1192, Japan. Received March 27, 2008; Revised Manuscript Received May 22, 2008

We previously developed potent nonviral vectors based on complexation of lipoplexes and pH-sensitive fusogenic liposomes, which achieve efficient transfection through membrane fusion with intracellular acidic compartments such as endosomes. Because transferrin receptor is known to be overexpressed in cancer cells, in this study, we investigated the effect of transferrin as a ligand for transfection of various cancer-derived cell lines mediated by the liposome−lipoplex hybrid complexes. Results showed that these hybrid complexes with transferrin exhibited higher transfection efficiency toward these cells than complexes without transferrin, but the extent of the transferrin-induced enhancement was dependent on the cell line. Conjugation of transferrin increased their transfection activity for HeLa and KB cells, although it only slightly enhanced transfection for HT1080, HepG2, and K562. Transferrin receptors in HT1080, HepG2, and K562 cells were internalized slowly, whereas those in HeLa and KB cells were internalized quickly and actively. These results indicate that transfection mediated by the ligand-attached hybrid complex does not correlate with the amount of transferrin receptor in the cell surface but correlate with the activity of internalization of transferrin receptor into the cells.

INTRODUCTION

For the establishment of gene therapy, safe and efficient vectors must be developed to deliver DNA into cells to express proteins (*1*–*5*). Although vectors are classified roughly as viral and nonviral vectors, nonviral vectors are attractive because of their low immunogenicity and lack of pathogenicity (*6*, *7*).

To date, several cellular processes have been shown to affect transfection efficiency mediated by nonviral vectors: cellular binding and internalization, transfer from endosome to cytosol, and entry into the nucleus (*8*–*12*). Inefficient internalization and degradation in lysosomes are important problems that must be solved during development of potent nonviral vectors. Modification with appropriate ligands and incorporation of endosomelytic molecules to vectors might overcome these hindrances (*8*, *13*–*19*).

We previously synthesized a pH-sensitive fusogenic polymer, succinylated poly(glycidol) (SucPG), and used it for preparation of pH-sensitive fusogenic liposomes that generate fusion ability under weakly acidic conditions (Figure 1) (*20*, *21*). Because SucPG-modified liposomes are negatively charged, they form a complex with positively charged vector systems, such as lipoplexes, through electrostatic interaction, and impart fusion ability to them (*22*).

Complexation with SucPG-modified liposomes shields positive charges of lipoplexes, reducing their affinity to cell membranes. However, once appropriate ligands are attached to the liposomes, their complexes might exhibit efficient transfection through specific ligand−receptor interaction and fusion with intracellular acidic compartments, such as endosome (*22*, *23*).

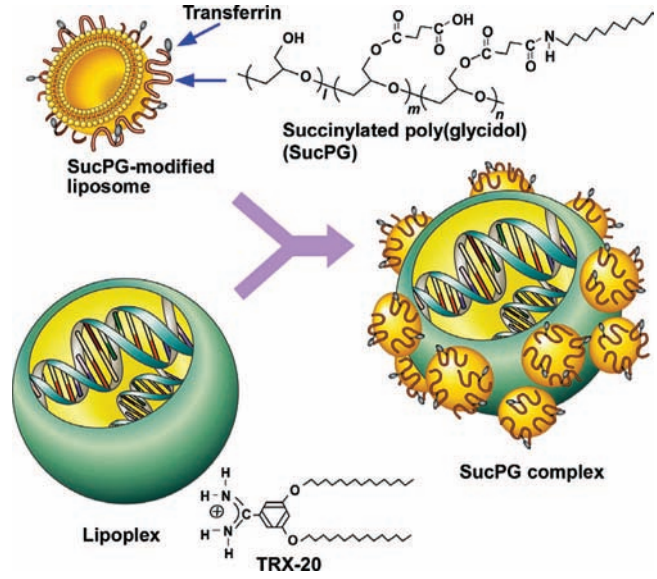

Figure 1. Preparation of SucPG complex.

Transferrin is a glycoprotein transporting iron into cells. Its receptors are expressed on the cell surface and are constitutively taken up through clathrin-dependent endocytosis (*24*, *25*). After internalization, transferrin and its receptors are recycled to the cellular surface via the recycling pathway (*26*, *27*). Therefore, transferrin is considered an appropriate ligand, which provides nonviral vectors with properties of target-specific binding and efficient internalization (*28*).

Complexation of lipoplexes with SucPG-modified liposomes bearing transferrin generates hybrid complexes, which transfect HeLa cells efficiently, as we showed recently (Figure 1) (*22*, *23*).

* Corresponding author. Kenji Kono, Department of Applied Chemistry, Graduate School of Engineering, Osaka Prefecture University, 1-1 Gakuen-cho, Nakaku, Sakai, Osaka 599-8531, Japan. Tel: + 81-722-54-9330; Fax: +81-722-54-9330; E-mail kono@chem.osakafu-u.ac.jp.

[†] Osaka Prefecture University.

[‡] Terumo Corporation.

[§] Fujita Health University School of Medicine.

10.1021/bc800126s CCC: $40.75 © 2008 American Chemical Society
Published on Web 07/16/2008

Considering that many types of cancer cells are known to overexpress transferrin receptors, the transferrin-conjugated hybrid complexes are expected to achieve efficient transfection toward these cancer cells. For the present study, we applied the transferrin-conjugated hybrid complexes, which are termed SucPG complexes, to various types of human cancer-derived cells. We then investigated the relation between their transferrin receptor expression and transfection efficiency. Results showed that attachment of transferrin enhanced the transfection activity of the hybrid complexes, but the extent of the transferrin-induced enhancement was dependent on the cell line. Correlation between the transferrin-induced enhancement of the hybrid complex-mediated transfection and the cellular internalization efficiency of transferrin receptors is described.

EXPERIMENTAL PROCEDURES

Materials. Dioleoylphosphatidyleyhanolamine (DOPE) and egg yolk phosphatidylcholine (EYPC) were kindly donated by NOF Co. (Tokyo, Japan). 3,5-Dipentadecyloxybenzamidine hydrochloride (TRX-20) was kindly donated by Terumo Co. (Kanagawa Japan). Dilauroylphosphatidylcholine (DLPC) was obtained from Wako Pure Chemical Industries (Osaka, Japan). Dulbecco's modified Eagle's medium (DMEM) was from Nissui Pharmaceutical (Tokyo, Japan). Lipofectamine 2000 and SuperFect were purchased from Invitrogen (Carlsbad, CA) and Qiagen (Hilden, Germany), respectively. 1-Ethyl-3-(3-dimethylaminopropyl) carbodiimide (EDC) was obtained from Dojin Laboratories (Kumamoto, Japan). Bovine serum albumin (BSA) was purchased from Sigma (St. Louis, MO). *N*-(7-Nitrobenz-2-oxa-1,3-diazol-4-yl)-1,2-dihexadecanoyl-*sn*-glycero-3-phosphoethanolamine (NBD-PE) was purchased from Molecular Probes Inc., (Eugene, OR). FITC-labeled anti-transferrin receptor was obtained from Dainippon Pharmaceutical Co. (Osaka, Japan). Succinylated poly(glycidol) having *n*-decyl groups (Figure 1) was prepared using poly(glycidol) with the number average molecular weight of 16 400 according to the method previously reported (*20*). Mole percents of glycidol, succinylated glycidol, and *n*-decylamine-attached residues in the SucPG were determined by ^{1}H NMR to be 5, 85, and 10, respectively.

Preparation of Lipoplex and SucPG Complex. Lipoplexes were prepared as reported previously (*29*). To a dry thin membrane of a mixture of TRX-20, DLPC, DOPE (0.26 μmol, 0.26 μmol, 0.52 μmol), 5% glucose solution (2 mL) was added and sonicated for 2 min using a bath-type sonicator to afford a cationic liposome suspension. Plasmid DNA (1.0 μg), p10 (*22*, *23*), which contains a firefly luciferase coding sequence derived from pGL3-basic (Promega) between Raus sarcoma virus LTR and polyadenylation signal, or pEGFP-C1 (Clontech), in 5% glucose solution (25 μL) was added a given volume of the liposome suspension (37.5 μL), and they were incubated for 10 min on ice to afford a lipoplex. SucPG-modified liposomes were prepared by suspending a mixture of SucPG (3 mg) and EYPC (7 mg) in 5% glucose solution (2 mL) using a bath-type sonicator and subsequent extrusion through a polycarbonate membrane with a pore size of 50 nm. To the liposome suspension was added EDC (0.7 mg) at pH 6.0 and stirred for 2 h at 4 °C. Then, transferrin (3 mg) and 0.5 M ferric citrate (5 μL) were added to the liposome suspension, and the suspension was kept at 4 °C overnight. After the liposome suspension was adjusted to pH 7.4, the transferrin-conjugated SucPG-modified liposome was purified using a Sepharose 4B column at 4 °C with 5% glucose. A suspension of SucPG-modified liposome with or without ligand (0−50 μL) was added to the lipoplex suspension and incubated for 10 min in an ice bath.

Cell Culture. HeLa (human cervical cancer cell line), HepG2 (human hepatoma line), KB (human epidermoid adenocarcinoma line), and HT1080 (human fibrosarcoma line) cells were grown in DMEM supplemented with 10% FBS (MP Biomedical, Inc.) and antibiotics at 37 °C. K562 (human leukemia line) cells were grown in RPMI 1640 supplemented with 10% FBS (MP Biomedical, Inc.) and antibiotics at 37 °C.

Transfection. For luciferase assay, transfection to HeLa cells was done according to our previous report (*29*). HeLa cells were seeded in 24 well culture plates at 5.0×10^4 cells per well the day before transfection. The cells were washed with PBS containing 0.36 mM $CaCl_2$ and 0.42 mM $MgCl_2$ [PBS (+)] and then covered with DMEM supplemented with 10% FCS (0.9 mL). The vector solution (62.5−122.5 μL) containing plasmid DNA (1.0 μg) was added and incubated at 37 °C for 4 h. Then, the cells were rinsed with PBS (+), covered with DMEM supplement with 10% FCS, and incubated at 37 °C for 40 h. The cells were washed and lysed by adding 50 μL of Luc-PGC-50 detergent (Toyo Ink, Tokyo, Japan). A 20 μL aliquot from each dish was used for one luciferase assay according to a protocol of a kit (Toyo Ink, Tokyo, Japan) and a Lumat LB9507 luminometer (Berthold, Bad Wildbad, Germany). The protein content of the lysate was measured by Coomassie Protein Assay Reagent (Pierce, IL, USA) using bovine serum albumin as the standard. For GFP expression, the various kinds of cells were seeded in 0.5 mL of DMEM supplemented with 10% FCS in 12-well culture plates at 1.0×10^5 cells per well and allowed to grow for 24 h. The cells were washed with PBS (+) and covered with DMEM supplemented with 10% FCS (1.96 mL). SucPG complexes (36.3 μL) or the lipoplex (31.3 μL) containing pEGFP-C1 (0.5 μg) were added gently to the cells and incubated at 37 °C for 4 h. After that, the cells were washed with PBS three times, followed by the incubation in culture medium at 37 °C for 24 h. Then, GFP-transfected cells were evaluated using flow cytometry (*29*). Superfect (QIAGEN) and Lipofetamine 2000 (Invitrogen) were also used according to the manufacturer's instructions.

Cellular Uptake of SucPG Complex and Inhibition by Free Transferrin. HT1080, HepG2, K562, KB, and HeLa cells (1.0×10^5 cells) cultured for one day in a 12-well plate were washed with PBS (+) and then incubated in the culture medium (1.96 mL). The fluorescence-labeled SucPG complex was prepared by using a lipoplex in which DOPE was substituted by NBD-PE (2 mol %). SucPG complexes (36.3 μL) or the lipoplexes (31.3 μL) containing plasmid DNA (0.5 μg) were added gently to the cells and incubated for 4 h at 37 or 4 °C. In the case of the experiments at 4 °C, cells were preincubated at 4 °C for 2 h. The cells were washed with PBS (+), and detached using trypsin. Then, cellular fluorescence was evaluated by flow cytometry (EPICS XL, Beckman Coulter, Inc.). For inhibition assay, cells were preincubated at varying concentrations of free transferrin for one hour before the incubation with the NBD-PE labeled complexes.

Evaluation of Intracellular Uptake of Transferrin Receptor. HT1080, HepG2, K562, KB, and HeLa cells (1.0×10^5 cells) cultured for one day in a 12-well plate were washed with PBS (+) and then covered with the DMEM supplemented with 10% FCS and 1% BSA (440 μL). FITC-labeled anti-transferrin receptor (60 μL), which was dissolved in the DMEM supplemented with 10% FCS and 1% BSA was added gently to the cells to a final antibody concentration of 6 μg/mL and incubated for 3 h at 37 or 4 °C. In the case of the experiments at 4 °C, cells were preincubated at 4 °C for 2 h. Cells were washed with PBS (+), and harvested using 2 mol % EDTA containing PBS. Fluorescence intensity of cells was evaluated by flow cytometry (EPICS XL, Beckman Coulter, Inc.). Microscopic analysis of

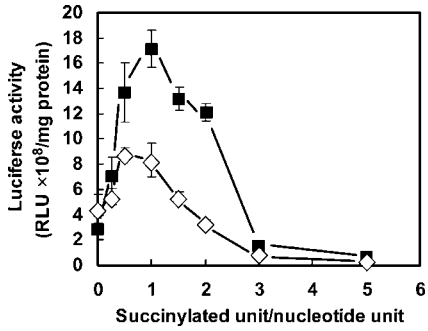

Figure 2. Expression of luciferase in HeLa cells treated with transferrin-conjugated (closed squares) and plain (open diamonds) SucPG complexes with varying compositions. The composition of SucPG complexes was expressed as the ratio of succinylated units of SucPG-modfied liposomes to DNA nucleotide units. The TRX-20 lipoplex with the (±) charge ratio of 1.5 was used for the preparation of SucPG complexes.

these cells was performed using a fluorescence microscopy (BX51WI, Olympus).

RESULTS AND DISCUSSION

Transfection Activity of SucPG Complexes. We have developed hybrid complexes of transferrin-conjugated SucPG-modified liposomes and lipoplexes, designated as SucPG complexes (*22*). Although SucPG complexes have been prepared in PBS, we found recently that SucPG complexes prepared in an aqueous glucose solution generate SucPG complexes with much smaller diameters and much higher transfection activity toward HeLa cells than do complexes prepared in PBS (*29*). Because HeLa cells express transferrin receptors on their cell membrane, specific interaction between transferrin and its receptor might contribute to their high transfection activity. Therefore, we first examined how this specific interaction influences the transfection efficiency.

First, we examined transfection of HeLa cells using the transferrin-conjugated and plain SucPG complexes prepared by complexation of the lipoplex with varying amounts of SucPG-modified liposomes with or without transferrin (Figure 2). Their compositions were expressed as the ratio of succinylated units of SucPG-modified liposomes to nucleotide units of plasmid DNA included in the lipoplex. Transfection activity of the plain SucPG complexes increased with the increasing succinylated unit/nucleotide unit ratio by 0.5. This result suggests that complexation of the SucPG liposomes with the lipoplex indeed enhanced the transfection activity of the lipoplex, probably because their complexation might result in the complex with higher fusion ability under the weakly acidic condition of endosomes (*22*). However, a further increase in the succinylated unit/nucleotide unit ratio decreased the transfection activity. The complex with the succinylated unit/nucleotide unit of 0.5 corresponds to a charge-neutral complex. Therefore, complexes with reduced transfection activity are expected to be negatively charged (*22*). It is likely that the negatively charged surface of the complexes strongly suppressed their association with the cellular surfaces and subsequent internalization into the cells.

The composition dependence of transfection activity for transferrin-conjugated complexes is also shown in Figure 2. Their transfection activity increased concomitantly with the increase in the succinylated unit/nucleotide unit ratio and reached the highest value at the succinylated unit/nucleotide unit ratio of 1, where the activity was twice as high as that without transferrin, as reported previously (*29*). The ligand-conjugated SucPG complexes retained high activity at the succinylated unit/nucleotide unit ratio by 2, where the transferrin-conjugated complex exhibited about four-times-higher efficiency than the plain complex of the same composition. These results indicate that transferrin plays an important role in the enhanced transfection efficiency.

The effect of transferrin conjugation on the transfection activity of the SucPG complex was examined further using EGFP gene. HeLa cells were treated with SucPG complexes with succinylated unit/nucleotide unit ratio of 1, which achieved the highest activity, and expression of EGFP was observed using a fluorescence microscope (Figure 3A,B). More intensive fluorescence was observed for cells treated with the transferrin-conjugated complex than for cells treated with the complex without the ligand. The EGFP expression of HeLa cells treated with the SucPG complexes were also evaluated using flow cytometry (Figure 3C). Although the untreated cells showed very weak fluorescence intensity of less than 10^0, the SucPG complex-treated cells displayed much stronger fluorescence with intensity of around 10^1-10^2. In addition, cells treated with the transferrin-conjugated complex exhibited stronger fluorescence and a higher fraction of EGFP-expressing cells than cells treated with the plain SucPG complex (see also Figure 9). These results demonstrate that the conjugation of transferrin induced both transfection efficiency and elevation of transfection activity induced by the transferrin conjugation.

Cellular Uptake of the SucPG Complex Bearing Transferrin. We next investigated cellular association of these complexes to elucidate the effect of transferrin on transfection. The HeLa cells were treated with the transferrin-conjugated or plain SucPG complexes of varying compositions labeled with fluorescent lipid NBD-PE at 37 °C (*29, 30*). Irrespective of the presence of transferrin, the cellular association of these complexes decreased concomitantly with increasing amounts of SucPG-modified liposomes in the complexes (Figure 4A). Probably, the negatively charged SucPG-modified liposomes shield positive charges of the lipoplex moiety of the complex. We showed in an earlier study that the SucPG complexes at the succinylated unit/nucleotide unit of more than 1 have a negatively charged surface (*29*). However, when SucPG complexes with the same composition were compared, markedly higher amounts of cellular association were observed for transferrin-conjugated complexes, especially those with the succinylated unit/nucleotide unit ratio of 1−1.5, which achieved efficient transfection of HeLa cells (Figure 2).

We also examined internalization of SucPG complexes into the cell by comparing the cellular association of the fluorescent lipid-labeled SucPG complexes at 4 °C, at which cellular endocytosis was blocked, with that at 37 °C (*31, 32*). We used SucPG complexes with the succinylated unit/nucleotide unit ratio of 1, which achieved the highest transfection activity (Figure 2). Figure 4A portrays the mean fluorescence intensity of the cells treated with the SucPG complexes or the parent lipoplex as evaluated using flow cytometry. The cellular fluorescent intensity decreased in the order of lipoplex > transferrin-conjugated SucPG complex > plain SucPG complex at 4 °C, which indicates that positively charged lipoplexes had higher affinity to the cell than SucPG complexes with transferrin.

Intracellular uptake of the complexes was estimated from the difference in fluorescence intensities of the treated cells between 4 and 37 °C (Figure 4B). Calculations show that the amounts of internalization of lipoplex and the transferrin-conjugated SucPG complex were 1.3 and 2.0 times higher, respectively, than that of the plain SucPG complex. In addition, differences in the amounts of the associated complexes between 4 and 37 °C suggest that only 39% of the bound lipoplex particles were internalized into the cell during the cellular treatment, although the amount of internalized transferrin-conjugated SucPG complex particles was 1.6 times that of the SucPG complex bound to the cell surface. This observation indicates that transferrin

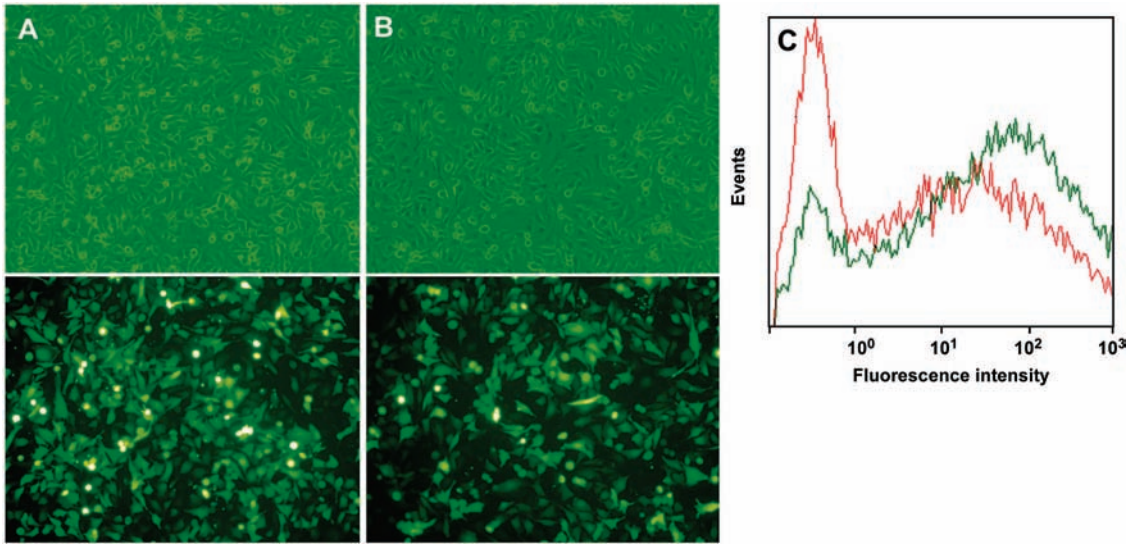

Figure 3. Expression of EGFP in HeLa cells treated with SucPG complexes. Phase contrast and fluorescence micrographs of HeLa cells treated with transferrin-conjugated (A) and plain (B) SucPG complexes. (C) Expression of EGFP in HeLa cells treated with transferrin-conjugated (green line) and plain (red line) SucPG complexes detected using flow cytometry. SucPG complexes with the succinylated unit/nucleotide unit ratio of 1 were used.

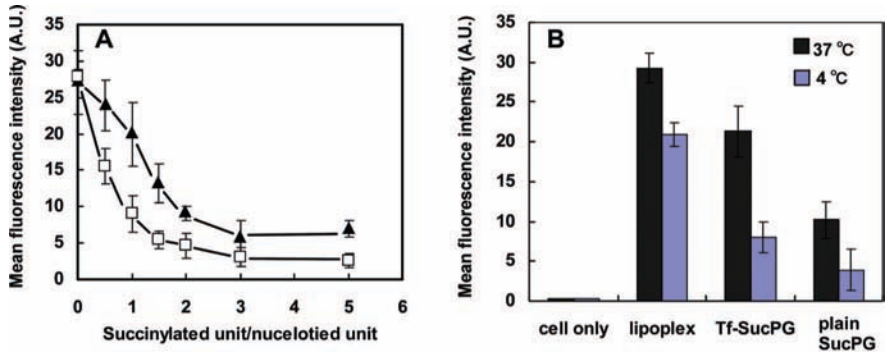

Figure 4. (A) Association of SucPG complexes with HeLa cells. Mean fluorescence intensities of cells treated with fluorescence lipid-labeled transferrin-conjugated (closed triangles) and plain (open squares) SucPG complexes with varying compositions at 37 °C. (B) Mean fluorescence intensities of cells treated with fluorescence lipid-labeled transferrin-conjugated and plain SucPG complexes and the parent lipoplex at 37 °C (black bars) and 4 °C (purple bars). Mean fluorescence intensities of cells without the treatment were also given. SucPG complexes with the succinylated unit/nucleotide unit ratio of 1 was used.

conjugated to SucPG complex enhanced not only its binding to the cell surface but also its internalization into the cell. It is likely that the specific interaction between transferrin and its receptor contributed to these enhancements.

We further examined inhibitory effects of free transferrin on their interaction to confirm the specificity of the interaction between the transferrin-conjugated SucPG complex and HeLa cell. The HeLa cells were treated with the fluorescent lipid-labeled SucPG complex bearing transferrin at varying concentrations of free transferrin. Fluorescence intensities of the treated cells were estimated using flow cytometry (Figure 5A). Apparently, fluorescence intensity of the cells decreased with increasing free transferrin concentration and reached a constant level of fluorescence intensity at free transferrin concentrations greater than 8.8 μM.

The cellular treatment with the fluorescent lipid-labeled SucPG complex without the ligand was also performed at varying concentrations of free transferrin. As presented in Figure 5B, the treated cells displayed almost identical levels of fluorescence intensity, irrespective of free transferrin concentration, indicating that free transferrin does not influence cellular association of the SucPG complex without transferrin. In addition, fluorescence intensities of both the cells treated with transferrin-conjugated SucPG complex at free transferrin concentration greater than 8.8 μM and the cells treated with the plain SucPG complex exhibited similar levels of fluorescence, suggesting that the cellular association of the transferrin-conjugated SucPG complex through the specific interaction with transferrin receptor was blocked by free transferrin under these conditions. These results demonstrate that enhancement of cellular association and uptake was induced by the specific interaction of transferrin conjugated to the SucPG complex with its receptor on the cellular surface and by subsequent internalization through the receptor-mediated endocytosis.

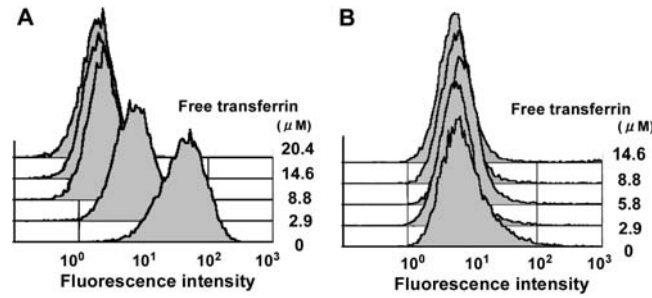

Figure 5. Cellular association of transferrin-conjugated SucPG complex (A) and plain SucPG complex (B) at varying concentrations of free transferrin.

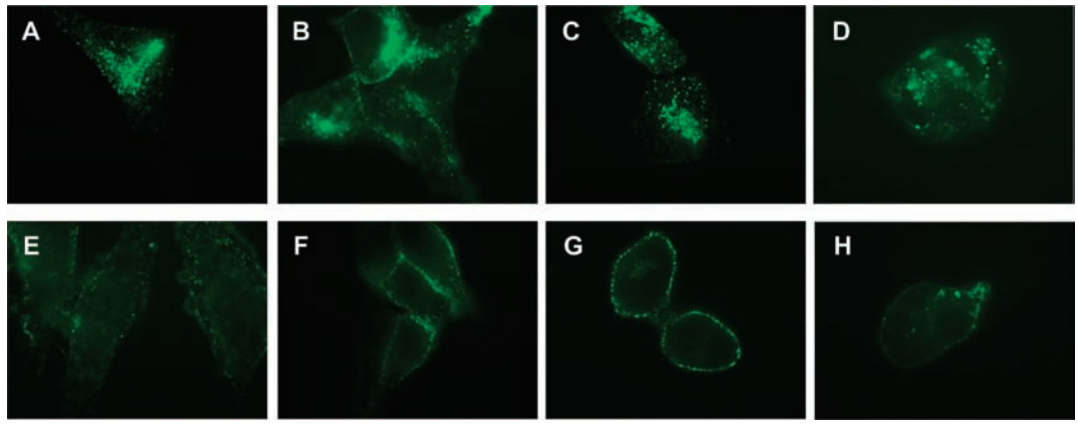

Figure 6. Localization of transferrin receptors in various cells. Fluorescence micrographs of HeLa cells (A,E), KB cells (B,F), HT1080 cells (C,G), and HepG2 cells (D,H) incubated with FITC-labeled anti-transferrin receptor at 37 °C (A−D) and 4 °C (E−H).

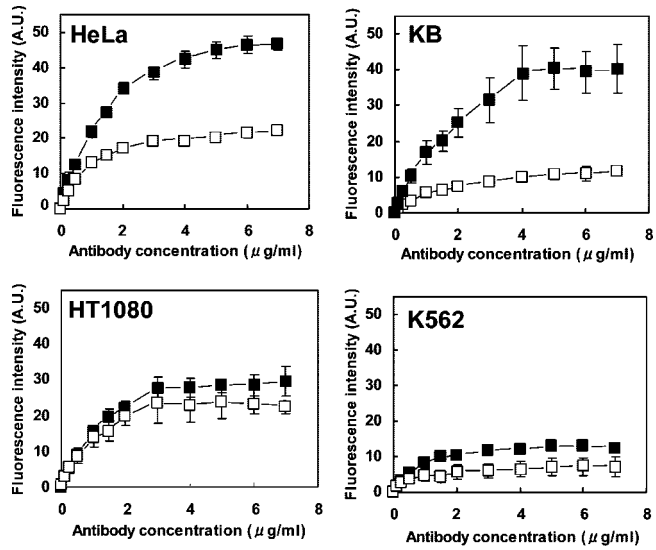

Figure 7. Association of anti-transferrin receptor with various cells. Mean fluorescence intensities of HeLa, KB, HT1080, and K562 cells treated with FITC-labeled anti-transferrin receptor at 4 °C (open symbols) and 37 °C (closed symbols) as a function of antibody concentration. Fluorescence intensity was evaluated using flow cytometry.

Expression of Transferrin Receptors. Because transferrin receptors are known to be overexpressed and actively internalized through clathrin-mediated endocytosis in various types of cancer cells, transferrin has been considered to be a suitable ligand for improving the transfection activity of nonviral vectors toward these cells (*28*). Therefore, we next examined expression and internalization of transferrin receptors in various types of cancer-derived cell lines using FITC-labeled anti-transferrin receptor.

With FITC-labeled anti-transferrin receptor at 37 or 4 °C for 3 h, we incubated five kinds of cancer-derived cells: HeLa, KB, HT1080, and HepG2. Figure 6 depicts fluorescence micrographs of these cells after incubation. Irrespective of the cell lines, at 4 °C, weak fluorescence was observed mainly in the cell periphery; at 37 °C, intensive fluorescence was visible as bright dots inside cells. This observation suggests that transferrin receptor−antibody complexes were localized on the cell surface at 4 °C, and vesicular compartments at 37 °C, which is consistent with the difference in activity of cellular endocytosis between 4 and 37 °C.

We analyzed fluorescence intensities of cells treated with FITC-labeled antibody using flow cytometry. When the FITC-labeled antibody was incubated with cells, we observed that cellular fluorescence intensity increased with time and reached a constant value after 2 h incubation (data not shown). We examined binding of the anti-transferrin receptor to various types of cancer-derived cell lines, HeLa, KB, K562, and HT1080 cells, which were incubated in the presence of various concentrations of the FITC-labeled antibody for 3 h at 37 or 4 °C (Figure 7). The same experiment was also performed for HepG2 cells (data not shown). For all of these cells, cellular fluorescence intensity increased concomitantly with increased labeled antibody concentration and then reached a constant value at labeled antibody concentrations greater than 3−6 μg/mL, which suggests that transferrin receptors on the cell membrane might be fully associated with the labeled antibody at concentrations greater than these.

Mean fluorescence intensities of the cells incubated with the FITC-antibody (6 μg/mL) at 37 and 4 °C are portrayed in Figure 8A. As described above, cellular endocytosis is active at 37 °C but is inactive at 4 °C. Therefore, fluorescence intensities of the cells with treatment at 4 °C might reflect the number of cellular transferrin receptors on the cell surface. It is apparent that expression of transferrin receptors depends on the cell line: expression of transferrin receptors is of a low level for K562 and HepG2 cells, whereas HT1080 and HeLa cells exhibited three-times-higher expression of transferrin receptors than did K562 cells.

Considering that transferrin-conjugated gene vectors, such as SucPG complexes, might deliver a gene into the cell after

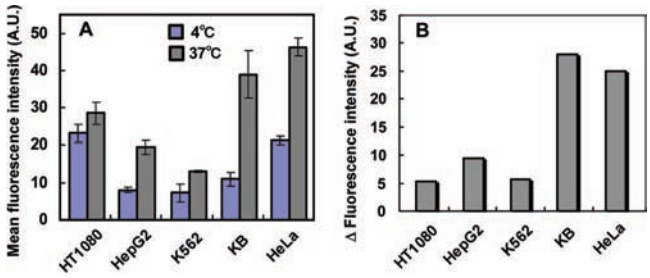

Figure 8. Association of anti-transferrin receptor with various cells. (A) Mean fluorescence intensities of HeLa, KB, HT1080, HepG2, and K562 cells treated with FITC-labeled anti-transferrin receptor at 4 or 37 °C at 6 μg antibody/mL. (B) Difference in cellular fluorescence intensities between 37 and 4 °C. Mean fluorescence intensity was evaluated using flow cytometry.

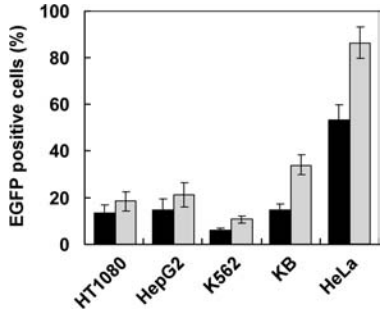

Figure 9. Transfection efficiency of HT1080, HepG2, K562, KB, and HeLa cells treated with transferrin-conjugated (gray bars) and plain (black bars) SucPG complex as evaluated using flow cytometry.

internalization through transferrin receptor-mediated endocytosis, it is likely that cellular activity for internalization of transferrin receptors influences the transfection efficiency of the cells mediated by transferrin-conjugated gene vectors. Therefore, we estimated differences in cellular fluorescence intensities between 4 and 37 °C, which were inferred to reflect the amounts of the receptor−antibody complexes internalized into the cells, at the antibody concentration of 6 μg/mL.

As presented in Figure 8B, KB and HeLa cells exhibited substantial internalization, suggesting high activity for transferrin receptor-mediated endocytosis in these cells. In contrast, much less internalization was observed for HT1080, HepG2, and K562 cells, which is indicative of low activity of the receptor-mediated endocytosis in these three cells. Interestingly, HT1080 cells showed the lowest activity of internalization among these cell species, although their transferrin receptor expression was the highest among them, suggesting that internalization through transferrin receptor-mediated endocytosis might not be induced in HT1080 cells. On the contrary, although KB cells exhibited a low level of transferrin receptors, a very high level of internalization through transferrin receptor-mediated endocytosis might be induced. This fact suggests that the extent of the receptor expression on the cell surface does not always correlate with the activity of the receptor-mediated endocytosis.

Effect of Transferrin on Transfection of Various Cancer-Derived Cells. Results of this study show that cellular expression of transferrin receptors and activity of their internalization varies depending on the cell lines. Indeed, such differences in expression and activity of transferrin receptors might affect their transfection efficiency mediated by the transferrin-conjugated SucPG complex. Therefore, we examined transfection of these cancer-derived cells using transferrin-conjugated SucPG complex and compared those results to those obtained with the plain SucPG complex. Six kinds of cancer-derived cells—HT1080, HepG2, K562, KB, and HeLa—were treated with the SucPG

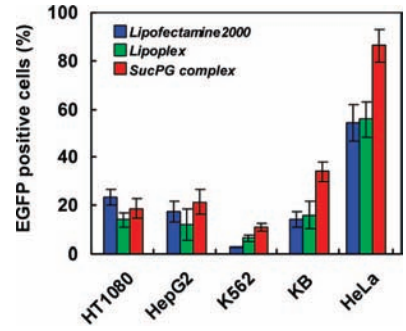

Figure 10. Transfection efficiency of HT1080, HepG2, K562, KB, and HeLa cells treated with transferrin-conjugated SucPG complex, TRX-20 lipoplex, and Lipofectamine 2000 complex as evaluated using flow cytometry.

complexes containing the EGFP gene. Then, EGFP-expressing cells were detected using flow cytometry (see Figure 3).

As presented in Figure 9, a significant difference in transfection efficiency was observed between the transferrin-conjugated complex and the plain complex for HeLa and KB cells, which respectively exhibited differences of 22% and 34% between the transferrin-conjugated and plain complexes. In contrast, HT1080, HepG2, and K562 showed only limited increases in transfection efficiency of ca. 5−6.3% by transferrin conjugation. In connection with the result of Figure 8B, apparently cells that exhibited active internalization of transferrin receptor achieved considerable enhancement of the transfection efficiency. In contrast, the cells with low transferrin receptor-mediated endocytosis displayed only limited enhancement of transfection efficiency.

Transferrin receptor is considered to pass sequentially through early endosomes and perinuclear recycling endosomes before returning to the cell membrane (*27, 33*). Early endosomes are known to be of two distinct populations: a dynamic population, which is highly mobile on microtubules and which matures quickly toward late endosomes; and a static population, which matures much more slowly (*34*). As presented in Figure 8B, in HT1080, HepG2, and K562 cells, internalization of transferrin receptor was low, implying that a large fraction of transferrin receptor was trapped in early endosome of a static nature. Therefore, after receptor-mediated endocytosis, the transferrin-conjugated SucPG complex might be mainly trapped in early endosome of a static nature, which is slowly acidified and hence slowly activates the fusion ability of the SucPG complex.

In contrast, KB and HeLa cells actively internalized transferrin receptor. Consequently, a large fraction of the transferrin receptor might be included in an early endosome of dynamic nature. Therefore, in these cells, the transferrin-conjugated SucPG complex might be trapped in an early endosome of dynamic character, which quickly matures and quickly activates the fusion ability of the SucPG complex. Cellular activity of transferrin receptor-mediated endocytosis is likely to influence the effectiveness of transferrin conjugation on transfection activity of SucPG complex for individual cell lines.

Finally, we compared the transferrin-conjugated SucPG complex with a widely used transfection reagent, Lipofectamine 2000 (*35–37*), which forms a positively charged complex with plasmid DNA. The parent TRX-20 lipoplex was also used as a control. Both the Lipofectamine 2000-plasmid DNA complex and the TRX-20 lipoplex interact with negatively charged cell membranes via nonspecific interaction through electrostatic force. As presented in Figure 10, these positively charged complexes and the transferrin-conjugated SucPG complex exhibited similar transfection efficiency toward HT1080 and HepG2 cells, both of which showed low activity of the transferrin receptor-mediated endocytosis. However, the trans-

ferrin-conjugated SucPG complex achieved much higher transfection efficiency toward KB and HeLa cells, which exhibited higher activity of the transferrin receptor-mediated endocytosis than the positively charged complexes. The transferrin-conjugated SucPG complex showed higher activity than the lipofectamine complex toward K562, whose activity of transferrin receptor-mediated endocytosis was not high. Because K562 cells are nonadhesive cells, the SucPG complex with small size might associate more efficiently with cells suspended in the medium than lipofectamine, which generally form a large aggregate with plasmid DNA. Therefore, the efficacy of the transferrin-conjugated SucPG complex on transfection of cells is related closely with the cellular activity of transferrin-mediated endocytosis.

In conclusion, results of this study show that the effects of conjugation of transferrin to the SucPG complexes on their transfection activity highly depend on cell species. This conjugation improved the transfection efficiency toward cells, which actively internalize transferrin receptor into the cells. However, the transferrin conjugation was not effective for cells with low activity of transferrin receptor-mediated endocytosis. The transferrin-conjugated SucPG complexes achieve significantly higher transfection toward several cancer-derived cells, such as KB and HeLa cells, than a widely used transfection reagent. Therefore, transfection mediated by the ligand-attached hybrid complex does not correlate with the amount of transferrin receptor in the cell surface but correlates with the activity of internalization of transferrin receptor into the cells. Toward further improvement of their transfection activity, selection of the ligand might be important to facilitate cellular internalization and acid-triggered activation of SucPG complexes. The proper ligand might differ depending on the individual cell species, because cellular functions, which affect internalization and intracellular processes of the ligand−receptor complex, might differ among individual cell species. Therefore, conjugation of appropriate ligands to SucPG complexes is expected to generate highly potent nonviral vectors, which achieve transfection of target cells through the ligand−receptor interaction, efficient internalization, and the acid-triggered activation of their fusion ability.

ACKNOWLEDGMENT

This work was supported in part by a Grant-in-aid for Scientific Research from the Ministry of Education, Science, Sports, and Culture in Japan. We thank Ms. Noriko Tano for preparation of figures.

LITERATURE CITED

(1) Ledley, F. D. (1995) Nonviral gene therapy: the promise of genes as pharmaceutical products. Hum. *Gene Ther. 6*, 1129–1144.

(2) Niidome, T., and Huang, L. (2002) Gene therapy progress and prospects: Nonviral vectors. *Gene Ther. 9*, 1647–1652.

(3) Martin, B., Sainlos, M., Aissaoui, A., Oudrhiri, N., Hauchecorne, M., Vigneron, J. -P., Lehn, J. -M., and Lehn, P. (2005) The design of cationic lipids for gene delivery. *Curr. Pharm. Des. 11*, 375–394.

(4) Harrop, R., John, J., and Carroll, M. W. (2006) Recombinant viral vectors: Cancer vaccines. *Adv. Drug Delivery Rev. 58*, 931–947.

(5) Bloquel, C., Bourges, J. L., Touchard, E., Berdugo, M., BenEzra, D., and Behar-Cohen, F. (2006) Non-viral ocular gene therapy: Potential ocular therapeutic avenues. *Adv. Drug Delivery Rev. 58*, 1224–1242.

(6) Edelstein, M. L., Abedi, M. R., and Wixon, J. (2007) Gene therapy clinical trials worldwide to 2007 - an update. *J. Gene Med. 9*, 833–842.

(7) Evans, C. H., Gouze, E., Gouze, J. N., Robbins, P. D., and Ghivizzani, S. C. (2006) Gene therapeutic approaches - transfer in vivo. *Adv. Drug Delivery Rev. 58*, 243–258.

(8) Schätzlein, A. G. (2003) Targeting of synthetic gene delivery systems. *J. Biomed. Biotechnol. 2*, 149–158.

(9) Branski, L. K., Pereira, C. T., Herndon, D. N., and Jeschke, M. G. (2007) Gene therapy in wound healing: present status and future directions. *Gene Ther. 14*, 1–10.

(10) Meyer, M., and Wagner, E. (2006) Recent developments in the application of plasmid DNA-based vectors and small interfering RNA therapeutics for cancer. *Hum. Gene Ther. 17*, 1062–1076.

(11) Pollard, H., Remy, J. -S., Loussouarn, G., Demolombe, S., Behr, J. -P., and Escande, D. (1998) Polyethylenimine but not cationic lipids promotes transgene delivery to the nucleus in mammalian cells. *J. Biol. Chem. 273*, 7507–7511.

(12) Brunner, S., Sauer, T., Carotta, S., Cotten, M., Saltik, M., and Wagner, E. (2000) Cell cycle dependence of gene transfer by lipoplex, polyplex and recombinant adenovirus. *Gene Ther. 7*, 401–407.

(13) Lu, Y., and Low, P. S. (2002) Folate-mediated delivery of macromolecular anticancer therapeutic agents. *Adv. Drug Delivery Rev. 54*, 675–693.

(14) Kichler, A., Mechtler, K., Behr, J. -P., and Wagner, E. (1997) Influence of membrane-active peptides on lipospermine/DNA complex mediated gene transfer. *Bioconjugate Chem. 8*, 213–221.

(15) Liu, D., and Huang, L. (1990) pH-sensitive, plasma-stable liposomes with relatively prolonged residence in circulation. *Biochim. Biophys. Acta 1022*, 348–354.

(16) Li, W., Nicol, F., and Szoka, F. C. (2004) GALA: a designed synthetic pH-responsive amphipathic peptide with applications in drug and gene delivery. *Adv. Drug Delivery Rev. 56*, 967–985.

(17) Ogris, M., Carlisle, R. C., Bettinger, T., and Seymour, L. W. (2001) Melittin enables efficient vesicular escape and enhanced nuclear access of nonviral gene delivery vectors. *J. Biol. Chem. 276*, 47550–47555.

(18) Seki, K., and Tirrell, D. A. (1984) pH-dependent complexation of poly(acrylic acid) derivatives with phospholipid vesicle membrane. *Macromolecules 17*, 1692–1698.

(19) Fujiwara, M., Grubbs, R. H., and Baldeschwieler, J. D. (1997) Characterization of pH-dependent poly(acrylic acid) complexation with phospholipid vesicles. *J. Colloid Interface Sci. 185*, 210–216.

(20) Kono, K., Zenitani, K., and Takagishi, T. (1994) Novel pH-sensitive liposomes: liposomes bearing a poly(ethylene glycol) derivative with carboxyl groups. *Biochim. Biophys. Acta 1193*, 1–9.

(21) Kono, K., Igawa, T., and Takagishi, T. (1997) Cytoplasmic delivery of calcein mediated by liposomes modified with a pH-sensitive poly(ethylene glycol) derivative. *Biochim. Biophys. Acta 1325*, 143–154.

(22) Kono, K., Torikoshi, Y., Mitsutomi, M., Itoh, T., Emi, N., Yanagie, H., and Takagishi, T. (2001) Novel gene delivery systems: complexes of fusogenic polymer-modified liposomes and lipoplexes. *Gene Ther. 8*, 5–12.

(23) Sakaguchi, N., Kojima, C., Harada, A., Koiwai, K., Shimizu, K., Emi, N., and Kono, K. (2006) Enhancement of transfection activity of lipoplexes by complexation with transferrin-bearing fusogenic polymer-modified liposomes. *Int. J. Pharm. 325*, 186–90.

(24) Aisen, P. (1980) Iron transport and strage proteins. *Annu. Rev. Biochem. 49*, 357–393.

(25) Wagner, E., Curiel, D., and Cotton, M. (1994) Delivery of drugs, proteins and genes into cells using transferrin as a ligand for receptor-mediated endocytosis. *Adv. Drug Delivery Rev. 14*, 113–135.

(26) Gruenberg, J., and Maxfield, F. R. (1995) Membrane transport in the endocytic pathway. *Curr. Opin. Cell Biol. 7*, 552–563.

(27) Sheff, D. R., Daro, E. A., Hull, M., and Mellman, I. (1999) The receptor recycling pathway contains two distinct populations of early endosomes with different sorting functions. *J. Cell Biol. 145*, 123–139.

(28) Singh, M. (1999) Transferrin as a targeting ligand for liposomes and anticancer drugs. *Curr. Pharm. Des. 5*, 443–451.

(29) Sakaguchi, N., Kojima, C., Harada, A., Koiwai, K., Shimizu, K., Emi, N., and Kono, K. (2008) Generation of highly potent nonviral gene vectors by complexation of lipoplexes and transferrin-bearing fusogenic polymer-modified liposomes in aqueous glucose solution. *Biomaterials 29*, 1262–1272.

(30) Kessner, S., Krause, A., Rothe, U., and Bendas, G. (2001) Investigation of the cellular uptake of E-Selectin-targeted immunoliposomes by activated human endothelial cells. *Biochim. Biophys. Acta 1514*, 177–190.

(31) Kheirolomoom, A., and Ferrara, K. W. (2007) Cholesterol transport from liposomal delivery vehicles. *Biomaterials 28*, 4311–4320.

(32) Muro, S., Cui, X., Gajewski, C., Murciano, J. -C., Muzykantov, V. R., and Koval, M. (2003) Slow intracellular trafficking of catalase nanoparticles targeted to ICAM-1 protects endothelial cells from oxidative stress. *Am. J. Physiol. Cell Physiol. 285*, 1339–1347.

(33) Sheff, D., Pelletier, L., O'Connell, C. B., Warren, G., and Mellman, I. (2002) Transferrin receptor recycling in the absence of perinuclear recycling endosomes. *J. Cell Biol. 156*, 797–804.

(34) Lakadamyali, M., Rust, M. J., and Zhuang, X. (2006) Ligands for clathrin-mediated endocytosis are differentially sorted into distinct populations of early endosomes. *Cell 124*, 997–1009.

(35) Dalby, B., Cates, S., Harris, A., Ohki, E. C., Tilkins, M. L., Price, P. J., and Ciccarone, V. C. (2004) Advanced transfection with Lipofectamine 2000 reagent: primary neurons, siRNA, and high-throughput applications. *Methods 33*, 95–103.

(36) Corsi, K., Chellat, F., Yahia, L'H., and Fernandes, J. C. (2003) Mesenchymal stem cells, MG63 and HEK293 transfection using chitosan-DNA nanoparticles. *Biomaterials 24*, 1255–1264.

(37) Son, K. K., Patel, D. H., Tkach, D., and Park, A. (2000) Cationic liposome and plasmid DNA complexes formed in serum-free medium under optimum transfection condition are negatively charged. *Biochim. Biophys. Acta 1466*, 11–15.

BC800126S

Detailed Analysis Concerning the Biodistribution and Metabolism of Human Calcitonin-Derived Cell-Penetrating Peptides

I. Neundorf,*,† R. Rennert,† J. Franke,† I. Közle,‡ and R. Bergmann‡

Faculty of Life Science, Pharmacy and Psychology, Institute of Biochemistry, Brüderstr 34, D-04103 Leipzig, Germany, and Research Center Dresden-Rossendorf, Institute of Radiopharmacy, Bautzner Landstrasse 128, D-01328 Dresden, Germany.
Received April 10, 2008; Revised Manuscript Received June 17, 2008

The interest in using small peptides for therapeutic and diagnostic *in vivo* applications is based on several advantageous features such as good penetration into tissues and rapid clearance from the body. Because of their size, they can easily be synthesized chemically. The recently discovered cell-penetrating peptides (CPP) and among them CPP derived from the native peptide hormone human calcitonin (hCT) could meet these requirements. Therefore, they are nowadays widely used as delivery vectors for a variety of bioactive molecules. However, the knowledge about the distribution and metabolism of CPP *in vivo* is very limited. Hence, evaluation of the pharmacological features of any promising peptide is a crucial challenge in its development process. Herein, we studied the *in vivo* radiopharmacology of ^{68}Ga radiolabeled DOTA-modified, hCT-derived CPP in rats using small animal PET. Furthermore, the arterial blood at different time points and urine were analyzed for radiometabolites. It was shown that D-amino acid modifications of the sequence hCT(9−32) resulted in an increased *in vivo* stability and lower retention in the kidney cortex of this peptide.

INTRODUCTION

During the past decade, the interest in using cell-penetrating peptides (CPP) as vectors for drug delivery has dramatically increased (*1*, *2*). By using CPP, it is possible to introduce membrane-impermeable substances into mammalian cells. There is a growing demand for such delivery strategies since many pharmacologically interesting molecules provide on the one hand promising therapeutic properties *in vitro* but are on the other hand often poorly bioavailable *in vivo*. Because of their physicochemical properties, the transport of such substances into cells and to their biological target is often restricted. That is the reason why during the last few years delivery systems using CPP as drug carriers have been under intense investigation. Meanwhile, a number of different cargos have been transported successfully into various cells, e.g., peptide nucleic acids (PNA) (*3*), proteins (*4*), oligonucleotides (*5*), or nanoparticles (*6*).

Cell-penetrating properties have been described also for the peptide hormone human calcitonin (hCT). Human calcitonin consists of 32 amino acids and is C-terminally amidated and secreted in the thyroid gland. Because of a high permeability through the nasal epithelium, it is applied as an intranasal therapeutic in the treatment of several bone diseases (*7*). Recently, the truncated sequence hCT(9−32) was shown to translocate through cell membranes, although its N-terminal part (residues 1−8) responsible for receptor activation was lacking (*8*). By using hCT(9−32), it was possible to efficiently shuttle different cargos such as the antiproliferative drug daunorubicin, fluorophores, or even large molecules such as the enhanced green fluorescent protein (eGFP) into cells (*9*–*11*).

The interest in using cell-penetrating peptides for therapeutic *in vivo* applications is based on some advantageous features: these small peptides penetrate more readily into tissues, are distributed more uniformly, and disappear more rapidly from the body than larger molecules such as antibodies. However, major drawbacks in using such peptides as *in vivo* therapeutics are their low resistance against proteolytic enzymes and their rapid clearance by the kidneys.

The enzymatic degradation can effectively be inhibited by molecular modifications such as the introduction of D-amino acids or amino-alcohols and the insertion of unnatural amino acids or side chains (*12*). Recently, we modified the N-terminally truncated hCT fragment hCT(9−32) by the introduction of either D-phenylalanine or *N*-methylphenylalanine at positions 12 and 16, which were previously shown to be the initial cleavage sites for an enzymatic digestion *in vitro* (*13*). We could demonstrate that the half-lives of these modified peptides were increased *in vitro* in human blood plasma as well as in the cell culture supernatant (*14*).

Although several examples for successful drug delivery *in vivo* exist (*15*–*18*), so far a careful analysis of the *in vivo* behavior of these hCT-derived peptides as well as for most of the CPP described in the literature is missing. Moreover, in most studies the therapeutic potential of CPP is evaluated by using tissue culture models. However, the evaluation of pharmacological features is a crucial challenge not only in drug discovery but also in the drug development process. Therefore, by detailed studies, it should be possible to design molecules possessing on the one hand the desired biological activity and on the other hand the required pharmacological potency and metabolic stability. Furthermore, the results of such studies could help to decide whether or not a further development of a compound makes sense.

An elegant possibility to investigate the three-dimensional distribution of radiolabeled compounds *in vivo* is the positron emission tomography (PET). PET provides noninvasive and nondestructive quantitative measurements of the time course of biomolecules within living subjects (*19*). The prerequisite for PET studies is the labeling of the compound of interest with a positron-emitting radionuclide, e.g., ^{68}Ga. This isotope has

* Corresponding author. Dr. Ines Neundorf, Faculty of Life Sciences, Pharmacy and Psychology, Institute of Biochemistry, Brüderstr 34, D-04103 Leipzig, Germany. Phone: +49 (0) 341 97 36 832. Fax: +49 (0) 341 97 36 909. E-mail: neundorf@uni-leipzig.de.
† Institute of Biochemistry.
‡ Institute of Radiopharmacy.

10.1021/bc800149f CCC: $40.75 © 2008 American Chemical Society
Published on Web 07/24/2008

the advantage of an appropriate half-life of 68 min and can be easily obtained from a $^{68}Ge/^{68}Ga$ radionuclide generator (*20*). For the binding of such trivalent metal cations to peptides, DOTA (1,4,7,10-tetraazacyclotetradecane-*N*,*N*′,*N*″,*N*‴ tetraacetic acid) has proven to be a very suitable chelator (*21, 22*).

The aim of the present work was to evaluate the *in vivo* biodistribution and the metabolic stability of hCT(9−32) and a D-phenylalanine-modified analogue, [$f^{12,16}$]-hCT(9−32). For this purpose, both peptides were equipped with the chelator DOTA and subsequently labeled with the radioisotope ^{68}Ga. By analyzing blood and urine fractions, it was shown that the amino acid modifications indeed improve the *in vivo* stability of the hCT(9−32) analogue.

MATERIALS AND METHODS

Materials. For peptide synthesis, Nα-Fmoc-protected amino acids, 1-hydroxybenzotriazole (HOBt) and 4-(2′,4′-dimethoxyphenyl-Fmoc-aminomethyl)-phenoxy (Rink amide) resin were purchased from NovaBiochem (Läufelfingen, Switzerland). The side chain protecting groups for the amino acids were *tert*-butyl (*t*Bu) for Tyr and Thr; *tert*-butyloxy (*t*BuO) for Asp; trityl (Trt) for Asn, Gln, and His; and either *tert*-butyloxycarbonyl (Boc) or 1-(4,4-dimethyl-2,6-dioxocyclohex-1-ylidene)ethyl (Dde) for Lys according to the synthesis strategy. *N*,*N*′-diisopropylcarbodiimide (DIC) was obtained from Sigma-Aldrich (Taufkirchen, Germany). Trifluoroacetic acid (TFA), *N*,*N*-diisopropylethylamine (DIEA), thioanisole, *p*-thiocresole, hydrazine hydrate solution, and piperidine were purchased from Fluka (Taufkirchen, Germany). Acetonitrile (ACN for HPLC) was obtained from Merck (Darmstadt, Germany). Diethyl ether, dichloromethane and *N*,*N*-dimethylformamide (DMF, peptide synthesis grade) were obtained from Biosolve (Valkenswaard, Netherlands). DOTA (1,4,7,10-tetraazacyclotetradecane-*N*,*N*′,*N*″,*N*‴ tetraacetic acid) was purchased as *t*-Bu-ester from Macrocyclics (Dallas, USA).

Peptide Synthesis. Peptides were synthesized according to the Fmoc-strategy by using an automated multiple solid-phase peptide synthesizer (Syro, MultiSynTech, Bochum, Germany) on Rink amide resin (30 mg, resin loading 0.5 mmol g^{-1}). The following peptides were synthesized as C-terminal amides: hCT(9−32), LGTYTQDFNKFHTFPQTAIGVGAP; [$f^{12,16}$]-hCT(9−32), LGTfTQDfNKFHTFPQTAIGVGAP; and random (rd)-hCT(9−32), FLTAGQNTIQTPVKTGGHFPFADY.

To equip the peptides N-terminally with the chelator DOTA, the preswollen resin was incubated with 3 equiv of DOTA-tris (*t*-Bu-ester), 3 equiv of HOBt, and 3 equiv of DIC for 3 h at room temperature.

Finally, the peptides were cleaved from the resin by using a mixture of TFA/thioanisole/thiocresole (90:5:5, v/v/v) within 3 h at room temperature, simultaneously removing all acid-labile protecting groups. Subsequently, the peptides were precipitated from ice cold diethyl ether, collected by centrifugation, washed four times, and lyophilized from water/*tert*-butyl alcohol (3:1, v/v).

Purification of the peptides was achieved by preparative RP-HPLC on a RP C-18 column (Vydac, 250 × 25 mm, 10 μm) with a gradient of 20−60% B in A (A = 0.1% TFA in water; B = 0.08% TFA in acetonitrile) over 50 min and a flow of 10 mL min^{-1}.

The peptides were analyzed by MALDI-TOF mass spectrometry (Voyager RP, Perseptive Biosystems) and by analytical RP-HPLC on a Vydac RP18-column (4.6 × 250 mm; 5 μm, 300 Å) using a linear gradient of 10−60% B in A over 30 min and a flow rate of 0.6 mL min^{-1}. The experimentally detected masses were in full agreement with calculated masses, and the purity of all peptides was >95% according to analytical RP-HPLC.

Radiolabeling. Two hundred microliters of $^{68}Ga^{3+}$-eluate was added to 60 μL of DOTA-modified peptide (1 mM in 40% propylenglycol). The pH was adjusted to 3.7 − 4.1 by the addition of 0.5 M ammonium acetate. The solution was stirred at 90 °C for 10 min. Then, 10 μL (10 mM) of EDTA was added, the solution was incubated for 10 min at 40 °C, and the success of the ^{68}Ga complexation was controlled by radio-thin layer chromatography (radio-TLC) and radio-HPLC. Analysis by radio-TLC was carried out on Merck-RP-18 sheets using either a 10% aqueous ammonium acetate solution (v/v) or a 4:6 mixture (v/v) of ACN (0.05% TFA) and H_2O (0.05% TFA) as mobile phases. One micorliter of the sample was run on the sheet, subsequently the sheet was dried, and the activity spot was detected by using a Fujifilm Imaging Plate and a Bas Reader 2000 (Fuji, Raytest). The reaction mixture was applied to size exclusion chromatography (HiTrap 5 mL column, elution with isotonic sodium chloride containing 1% propylenglycol), and the radioactive peptide fraction was used in the experiments.

The HPLC system consisted of a Beckman System Gold 125 solvent module equipped with a UV detector (Hewlett-Packard Series 1100) and an external radiochemical detector (RFT 20 046). Analysis was performed on a Zorbax C18 column with a gradient of 10−90% B (ACN with 0.05% TFA) in A (H_2O with 0.05% TFA) over 13 min and a flow of 2 mL min^{-1}.

Animals, Feeding, Husbandry, and Biodistribution Studies in Rats. The animal research committee of the Regierungspräsidium Dresden approved the animal facilities and the experiments according to institutional guidelines and the German animal welfare regulations. The experimental procedure used conforms to the *European Convention for the Protection of Vertebrate Animals used for Experimental and other Scientific Purposes (ETS No. 123)*, to the *Deutsches Tierschutzgesetz*, and to the *Guide for the Care and Use of Laboratory Animals* published by the US National Institutes of Health (DHEW Publication No. (NIH) 82−23, Revised 1996, Office of Science and Health Reports, DRR/NIH, Bethesda, MD 20205).

Wistar rats (Wistar Unilever, HsdCpb:Wu, Harlan Winkelmann GmbH, Borchen, Germany) were housed under standard conditions with free access to standard food and tap water. Animals were between 7 and 9 weeks of age. The rats were housed in an Animal Biosafety Level 1 (ABSL-1) acclimatized facility with a temperature of 23 ± 2 °C and humidity of 55 ± 5%. Animals were under a 12 h light cycle in temperature (27 ± 1 °C)-controlled airflow cabinets. The animals had free access to standard pellet feed and water. Four animals (body weight 191 ± 9 g) for each time point were intravenously injected into a tail vein with approximately 55 μCi (2 MBq) ^{68}Ga-DOTA-hCT(9−32), ^{68}Ga-DOTA-[$f^{12,16}$]-hCT(9−32), or ^{68}Ga-DOTA-rd-hCT(9−32) in 0.5 mL of electrolyte solution E-153 (Serumwerk Bernburg, Germany) supplemented with 0.1% (w/v) human serum albumin (Serumwerk Bernburg, Germany). Animals were euthanized at 5 and 60 min post injection. Blood and the major organs were collected, wet-weighed, and counted in a Wallac WIZARD Automatic Gamma Counter (PerkinElmer, Germany). The radioactivity of the tissue samples was decay-corrected and calibrated by comparing the counts in tissue with the counts in aliquots of the injected tracer that had been measured in the gamma counter at the same time. The activity in the selected tissues and organs was expressed as percent-injected dose per organ (% ID) or as standardized uptake value (SUV) according to the following equation:

$$SUV = \frac{tissue_tracer_concentration}{injected_dose} \times body_weight = \frac{(Bq/g)}{Bq} \times g = \frac{\%ID/g}{100\%} \times g$$

The values are quoted as the means ± standard deviation (mean ± SD) for each group of four animals.

PET Imaging. General anesthesia of rats was induced with inhalation of desflurane 9% (v/v) (Suprane, Baxter, Germany) in 40% oxygen/air (gas flow 1 L/min), and was maintained with desflurane 6% (v/v). For arterial blood sampling, a 3.5 Fr umbilical vessel catheter prefilled with heparinized saline was inserted into the right carotid artery, and 200 μL blood samples were taken at 1.5, 3, 5, 10, 20, 30, and 60 min after tracer application. The volume was substituted by E-153. In the PET experiments, 0.5 mCi (18 MBq) of ^{68}Ga-DOTA-hCT(9−32), ^{68}Ga-DOTA-[f^{12,16}]-hCT(9−32), or ^{68}Ga-DOTA-rd-hCT(9−32) in 0.5 mL was administered intravenously over 1 min into a tail vein. PET imaging in rat was performed over 60 min with a microPET P4 scanner (Siemens CTI Molecular Imaging Inc., Knoxville). Data acquisition was performed in 3D list mode. A transmission scan was carried out prior to the injection of the radiolabeled peptides using a ^{57}Co point source. Emission data were collected continuously for 60 min after injection of the ^{68}Ga-labeled peptides. The list mode data were sorted into sinograms using a framing scheme of 15 × 10 s, 5 × 30 s, 5 × 60 s, 4 × 300 s, and 4 × 600 s frames. The data were attenuation corrected, and frames were reconstructed by Ordered Subset Expectation Maximization applied to 3D sinograms (OSEM3D) with 14 subsets, 6 OSEM3D iterations, 2 maximum a posteriori (MAP) iterations, and 0.05 β-value for smoothing. The pixel size was 0.3 by 0.3 by 1.21 mm in a matrix of 256 × 256 × 63, and the resolution in the center of field of view was 1.85 mm. No correction for recovery and partial volume effects was applied. The image files were processed using the *ROVER* software (ABX GmbH, Radeberg, Germany). Summed frames from 30 to 90 s post injection (p.i.) and 30 to 90 min p.i. were used to define the regions of interest (ROI). The data were normalized to the injected radioactivity by using standards from the injection solution measured in a γ-well counter (Isomed 2000, Dresden, Germany) cross-calibrated to the PET scanner and expressed in %ID or SUV.

Statistical Analysis. The data are expressed as the means ± SD. One-way analysis of variance (ANOVA) was used for statistical evaluation. Means were compared using Student's *t*-test. A P value of <0.05 was considered significant and indicated by an asterisk symbol (*), hash mark (#), or paragraph (§) symbol dependent on the compared data sets.

Metabolite Analysis. The 0.5 mCi (18 MBq) of ^{68}Ga-DOTA-hCT(9−32), ^{68}Ga-DOTA-[f^{12,16}]-hCT(9−32) or ^{68}Ga-DOTA-rd-hCT(9−32) in 0.5 mL were injected intravenously, and seven arterial blood samples were drawn at 90, 180, 300, 600, 1200, 1800, and 3600 s after application. Aliquots (50 μL) of arterial blood samples were taken for the total blood activity measurement. The blood plasma was separated by centrifugation (11,000g × 3 min) from the blood cells. Plasma proteins were precipitated by mixing of 1 volume plasma with 2 volumes acetonitrile followed by freezing in liquid nitrogen. After thawing, the samples were centrifuged (11,000g × 3 min), the clear supernatant was used for radio-HPLC analysis, and aliquots were measured for ^{68}Ga-activity determination. The hematocrit was determined from the blood sample 1 (90 s p.i.) with the classical capillary centrifugation method. The hematocrit was calculated as the mean of four determinations.

The chromatographic system of Agilent 1100 LC series, Agilent Technologies, Germany consisted of an autosampler with a 0.9 mL sample loop, a quaternary pump with degasser, thermostat column compartment, VWD detector and a radio-chromatography detector RAMONA (raytest Isotopenmessgeräte GmbH, Germany). The samples were analyzed using a ZORBAX III 300SB-C-18 250 × 9, 4 mm, 5 μm column with a binary gradient (eluent A, water with 0.05% TFA; eluent B, acetonitrile with 0.04% TFA; 20 min from 5 to 70% B, 1 min to 90% B, 9 min at 90% B). The flow was constant at 3 mL/min, the UV-signals were measured at 210 and 254 nm, and the radioactivity was registered with a time constant of 1 s. The data were expressed as the metabolite fraction in the rat plasma. These data were used to calculate the amount of original compounds in the arterial blood.

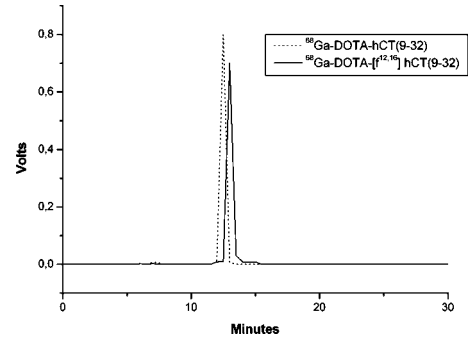

Figure 1. Radio-HPLC elution profiles of ^{68}Ga-DOTA-[f^{12,16}]-hCT(9−32) and ^{68}Ga-DOTA-hCT(9−32).

MALDI-TOF Analysis of the Metabolites. The RP-HPLC system (Agilent series), applied for metabolite analysis, was equipped with an UV detector and an external radiochemical detector (RFT 20 046). HPLC was performed by using a Zorbax C18 column with a gradient of 10−90% B (ACN with 0.05% TFA) in A (H_2O with 0.05% TFA). The plasma and urine samples were detected by their radioactive signals. Peaks appearing in the urine samples were collected, and after activity was decayed, they were examined by MALDI-TOF mass spectrometry on a Voyager-DE RP workstation (Perseptive Biosystems).

RESULTS

Peptide Synthesis and Radiolabeling. The hCT-derived peptides hCT(9−32), [f^{12,16}]-hCT(9−32) as well as a random sequence were prepared with high yields by automated solid-phase peptide synthesis according to standard Fmoc/*t*Bu-methodology. The Rink amide resin was used to obtain C-terminal peptide amides. After completion of the solid-phase synthesis, the bifunctional chelator DOTA was manually introduced at the N-terminus of the peptides by activating the *tert*-butyl ester of DOTA with HOBt/DIC. After deprotection and cleavage from the resin with trifluoroacetic acid, the labeled peptides were purified by preparative RP-HPLC. The purity (>95%) and identity was controlled by RP-HPLC and MALDI-TOF mass spectrometry, respectively.

Subsequently, the DOTA-labeled peptides were complexed with ^{68}Ga in 0.5 ammonium acetate (containing approximately 230 MBq), at pH 3.5−4.2 for 10 min at 90 °C. The reaction mixtures were analyzed by radio-TLC and radio-HPLC (see Figure 1 for ^{68}Ga-DOTA-hCT(9−32) and ^{68}Ga-DOTA-[f^{12,16}]-hCT(9−32)). The radiochemical yield of 32% ± 5 (decay-corrected) was obtained with a radiochemical purity of >90% for all preparations according to the radio-HPLC measurements.

Biodistribution. ^{68}Ga-DOTA-hCT(9−32), ^{68}Ga-DOTA-[f^{12,16}]-hCT(9−32), and the ^{68}Ga-labeled random peptide were injected intravenously into a tail vein in male Wistar rats. After 5 and 60 min postinjection, the rats were euthanized, and the radioactivity of the blood and the tissue samples were determined. The results of the biodistribution studies are summarized in Figure 2 (see Supporting Information for detailed data Tables 1−4).

The activity in the selected tissues and organs was expressed as percent-injected dose (%ID) (see Figure 2A) or as standardized uptake value (SUV) (see Figure 2B). It can be seen that the peptides left the blood stream immediately after injection and that the general retention in the body was low. However,

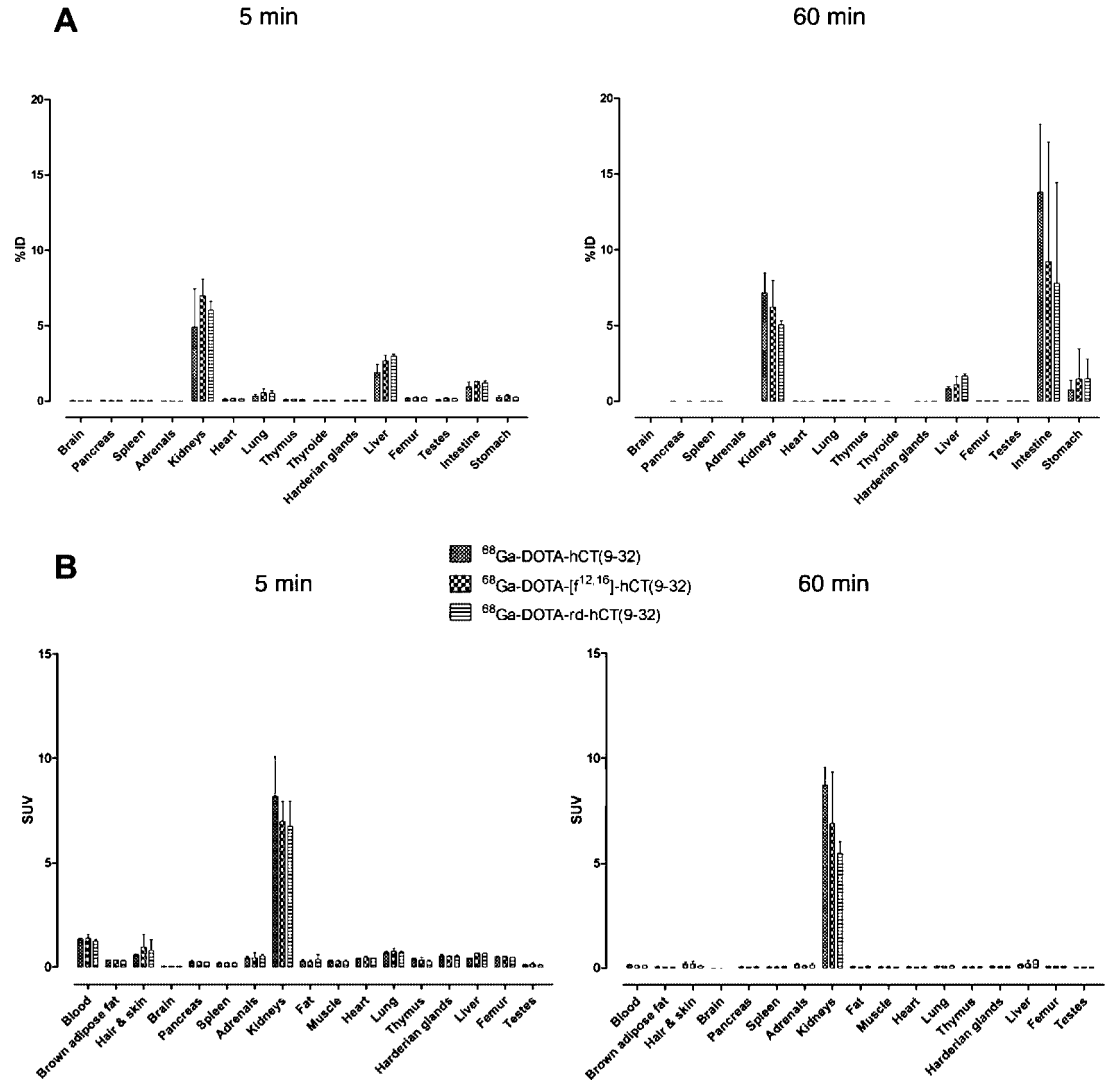

Figure 2. Biodistribution of ^{68}Ga-DOTA-hCT(9−32), ^{68}Ga-DOTA-[f^{12,16}]-hCT(9−32), ^{68}Ga-DOTA-rd-hCT(9−32) in male Wistar rats 5 and 60 min after single intravenous application represented as %ID ± SD (A) and as SUV ± SD (B) (4 animals per time point).

they were rapidly taken up by kidneys and liver and substantially excreted into the intestine. High activity was observed after 5 min in the kidneys (4.90 ± 2.55%ID per gram tissue for ^{68}Ga-DOTA-hCT(9−32), 6.99 ± 1.09%ID g^{-1} for ^{68}Ga-DOTA-[f^{12,16}]-hCT(9−32) and 6.03 ± 0.60%ID g^{-1} for ^{68}Ga-DOTA-rd-hCT(9−32)). Interestingly, ^{68}Ga-DOTA-[f^{12,16}]-hCT(9−32) had a lower retention in the kidney cortex, and the activity of the parent ^{68}Ga-DOTA-hCT(9−32) peptide increased here after 60 min i. v. injection to 7.17 ± 1.30%ID g^{-1}. Some amount of the peptides was metabolized by the hepatobiliary tract too, as was indicated by the detected activities in the liver (1.91 ± 0.52%ID g^{-1} for ^{68}Ga-DOTA-hCT(9−32), 2.67 ± 0.39%ID g^{-1} for ^{68}Ga-DOTA-[f^{12,16}]-hCT(9−32), and 2.98 ± 0.14%ID g^{-1} for ^{68}Ga-DOTA-rd-hCT(9−32)).

No relevant accumulation in other tissues was observed. Furthermore, as detected by the low activities in the brain none of the tested peptides was able to cross the blood-brain barrier.

PET Imaging Studies. Dynamic PET studies were carried out to validate the data from the biodistribution experiments and to study the kinetics of the radiolabeled hCT-derived peptides. Therefore, whole body PET scans were carried out over 60 min postinjection of ^{68}Ga-DOTA-hCT(9−32), ^{68}Ga-DOTA-[f^{12,16}]-hCT(9−32), and ^{68}Ga-DOTA-rd-hCT(9−32). A fast clearance out of the body was observed (see Supporting Information, Figure 1 for PET maximum intensity projections of ^{68}Ga-DOTA-[f^{12,16}]-hCT(9−32) distribution at different time points). Figure 3A and B show coronal PET images of the three peptides distribution in male Wistar rats 45 min after single intravenous application. High activity accumulations were observed in the kidneys.

Furthermore, the *in vivo* kinetic of the labeled peptides was analyzed within regions-of-interest (ROI). Figure 3C displays time−activity curves of ^{68}Ga-DOTA-hCT(9−32), ^{68}Ga-DOTA-[f^{12,16}]-hCT(9−32), and ^{68}Ga-DOTA-rd-hCT(9−32) in the kidneys of male Wistar rats after single intravenous application in SUV as calculated from kidney ROI. These data were in agreement with the corresponding results obtained from biodistribution experiments and show again the activity retention in the kidneys. The increasing activity in the kidneys of ^{68}Ga-DOTA-[f^{12,16}]-hCT(9−32) in the second half of the measurement was a result of low urine flow in this rat and not a sign of changed metabolism.

Additionally, we determined metabolite corrected blood time−activity curves of the three radiolabeled injected peptides. The data were calculated from heart ROI and the metabolite fraction in the blood at seven different time points after tracer application (see Figure 4). We could estimate that the blood clearance of the original peptides reached terminal half-lives of ^{68}Ga-DOTA-hCT(9−32) 15.9 min, ^{68}Ga-DOTA-[f^{12,16}]-hCT(9−32) 20.9 min, and ^{68}Ga-DOTA-rd-hCT(9−32) 15.8 min.

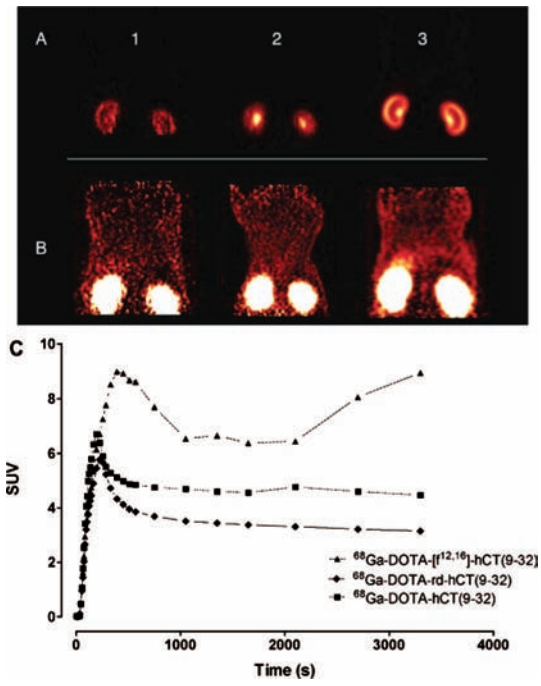

Figure 3. (A and B) Coronal PET images of ^{68}Ga-DOTA-hCT(9−32) (1), ^{68}Ga-DOTA-[f^{12,16}]-hCT(9−32) (2), and ^{68}Ga-DOTA-rd-hCT(9−32) (3) distribution in male Wistar rats 45 min after single intravenous application. The color scales of the upper images (A) are normalized to the maximum, and the color scales of the lower images (B) are expanded to show the background activity distribution. (C) Time−activity curves of ^{68}Ga-DOTA-hCT(9−32) (■), ^{68}Ga-DOTA-[f^{12,16}]-hCT(9−32) (▲), and ^{68}Ga-DOTA-rd-hCT(9−32) (♦) in the kidneys of male Wistar rats after single intravenous application in SUV. The data were calculated from kidney ROI.

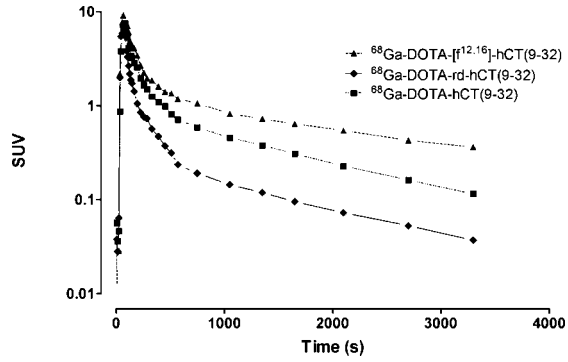

Figure 4. Metabolite corrected blood time−activity curves of ^{68}Ga-DOTA-hCT(9−32) (■), ^{68}Ga-DOTA-[f^{12,16}]-hCT(9−32) (▲), and ^{68}Ga-DOTA-rd-hCT(9−32) (♦) in male Wistar rats after single intravenous application in SUV. The data were calculated from heart ROI and metabolite fraction in the blood at 1, 3, 5, 10, 20, 30, and 60 min after tracer application.

Metabolite Analysis in Blood Samples. Metabolic stability of the parent radiometal-labeled peptides was determined in arterial blood samples at seven different time points (1.5, 3, 5, 10, 20, 30, and 60 min postinjection). Analysis by radio-HPLC showed different cleavage patterns for the distinct peptides (see Supporting Information, Figure 2). Unfortunately, the concentrations of the collected peaks from the radio-HPLC were too low for further mass spectrometric analysis of the evolved metabolites. However, the random peptide was cleaved very rapidly in a set of metabolites. After 30 min postinjection, the HPLC-chromatograph revealed seven different peaks, whereas one could be attributed to the original compound ^{68}Ga-DOTA-rd-hCT(9−32). In contrast to this, the cleavage patterns of the two peptides ^{68}Ga-DOTA-hCT(9−32) and ^{68}Ga-DOTA-[f^{12,16}]-hCT(9−32) displayed fewer radio-metabolites. After 30 min postinjection, three major peaks arose (in which one could be related to the parent compound) but to different extents, indicating the higher metabolic stability of the D-Phe-modified hCT peptide.

Analysis of the Metabolites in the Urine. We also analyzed the urine for metabolite content by using radio-HPLC. The metabolite patterns found in the urine samples of rats injected with ^{68}Ga-DOTA-hCT(9−32) allowed a differentiation of eight peaks with retention times from 5.5 min−11.2 min (data not shown), whereas no unaffected peptide could be found (12.8 min, see Figure 1). The main peak was detected at 7.0 min. Unfortunately, the fractionated peptide concentrations were too low for mass spectrometric metabolite analysis.

In contrast, the radio-HPLC of urine samples derived from rats injected with ^{68}Ga-DOTA-[f^{12,16}]-hCT(9−32) showed only three peaks, eluting from 12.0 to 13.1 min. These peaks were collected and analyzed by MALDI-TOF mass spectrometry. As presented in Figure 5, three major metabolites were identified: ^{68}Ga-DOTA-[f^{12,16}]-hCT(9−17), ^{68}Ga-DOTA-[f^{12,16}]-hCT(9−18), and ^{68}Ga-DOTA-[f^{12,16}]-hCT(9−19) (see also Table 1).

DISCUSSION

During the past decade, the successful application of a number of peptides in *in vitro* studies has raised the hope of their therapeutic and diagnostic application *in vivo*. Indeed, the demand on such small peptides as therapeutic or diagnostic agents is increasing, for instance as delivery vectors for membrane-impermeable drugs (*1*) or as radiopharmaceuticals in nuclear medicine (*23*). However, even if a peptide is well characterized *in vitro*, the prediction of its *in vivo* behavior is difficult because of the countless factors that may influence the route of the peptide inside the body, its structural integrity, or its clearance. Therefore, it is likely that a careful investigation of the pharmacological features of a promising peptide is one major prerequisite for its possible future application *in vivo*. Concerning the family of cell-penetrating peptides, until now only few studies exist that investigated these features (*2, 24, 32*). Thus, the true potential of CPP *in vivo* remains to be elucidated.

One of the major problems in the application of peptides is often their short biological half-life due to proteolytic cleavage. Also for the parent hormone human calcitonin, poor absorption and rapid proteolytic degradation are described. Therefore, the oral route is limited by extensive proteolytic degradation in the GI lumen and low intrinsic intestinal membrane permeability (*25*). However, it was shown that enzymatic degradation can be inhibited by modifications of the peptide sequence, e.g., by replacement of L-amino acids by D-amino acids (*26*) or the insertion of unnatural amino acids or side chains (*12*). Accordingly, we modified recently the cell-penetrating peptide hCT(9−32) by the introduction of D-phenylalanine at amino acid positions 12 and 16. *In vitro* stability tests in heparinised human blood plasma revealed a significantly increased metabolic stability of the resulting novel peptide [f^{12,16}]-hCT(9−32) (*14*). But although the *in vivo* stability of peptides in blood might be well modeled by *in vitro* stability tests in heparinised plasma (*27, 28*), this approach neglects for instance the renal and hepatic clearance that will occur *in vivo*. Therefore, the aim of this work was a systematic examination of the *in vivo* stability and biodistribution of the hCT-derived cell-penetrating peptides hCT(9−32) and [f^{12,16}]-hCT(9−32). To exclude any artifacts, we also investigated the tissue distribution of a radiolabeled random hCT(9−32) sequence.

Therefore, the two peptides as well as the random sequence were N-terminally labeled with DOTA and subsequently complexed with ^{68}Ga. We recently showed for the peptides DOTA-

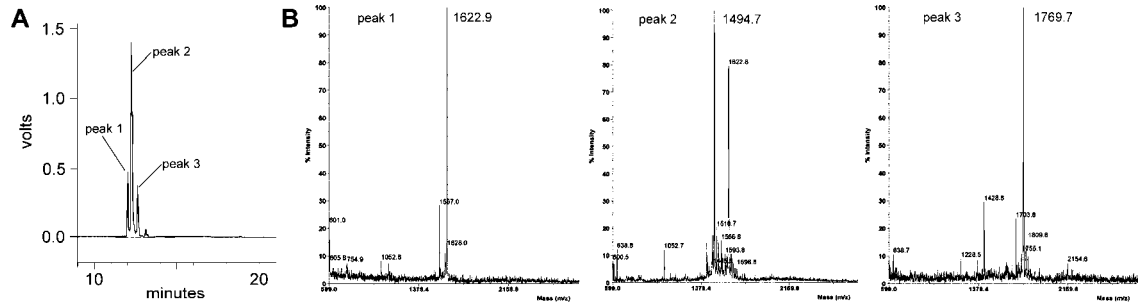

Figure 5. (A) Radio-HPLC of urine samples derived from rats injected with ^{68}Ga-DOTA-[f^{12,16}]-hCT(9−32). (B) MALDI-TOF analysis of the collected peaks.

Table 1. Peptide Sequences as Well as Calculated and Experimentally Determined Molecular Weights of the Cleavage Products of ^{68}Ga-DOTA-[f^{12,16}]-hCT(9-32) Found in Urine Samples by MALDI-TOF Analysis

peak	name	sequence	$MW_{exp.}$	$MW_{calc.}$
1	Ga-DOTA-[f^{12,16}]-hCT(9−18)	Ga-DOTA-LGTfTQDfNK	1622.8	1621.9
2	Ga-DOTA-[f^{12,16}]-hCT(9−17)	Ga-DOTA-LGTfTQDfN	1494.7	1493.8
3	Ga-DOTA-[f^{12,16}]-hCT(9−19)	Ga-DOTA-LGTfTQDfNKF	1769.7	1769.0

hCT(9−32) and DOTA-[f^{12,16}]-hCT(9−32) complexed with cold gallium that they are still internalized in HEK 293 and HeLa cells, respectively (*29*). Hence, we conclude that the labeling did not influence the cell-penetrating properties of the two peptides when applied in *ex vivo* studies.

The radiolabeled peptides were then injected in male Wistar rats, and their tissue distribution was determined. A relatively high kidney uptake is typical for all radioconjugates, which are small enough to pass through glomerular membranes and hydrophilic enough to undergo renal clearance (*30*). This was the case for ^{68}Ga-DOTA-hCT(9−32) and for the modified analogue ^{68}Ga-DOTA-[f^{12,16}]-hCT(9−32). Also, the random sequence was excreted mostly by the renal pathway. All peptides were metabolized to some extent by the hepatobiliary tract too and showed some excretion into the intestine. It was important for us to demonstrate that our CPP are not nonselectively accumulated in a specific tissue. Accumulation in the reticuloendothelial system is often observed for large or aggregated structures and can cause side effects in future *in vivo* applications (*31*). Recently, studies with a fusion protein of TAT and β-galactosidase showed distribution to all tissues in mice, including the brain (*2, 24*). In our experiments, no delivery over the blood−brain barrier was observed. Another preliminary study concerning the *in vivo* behavior of the sweet arrow peptide demonstrated uptake in blood cells (*32*). Whether our peptides have been indeed taken up in blood cells or in liver or kidney cells has not been elucidated yet. From *in vitro* studies with HT-29 colon carcinoma cells, we know that hCT(9−32) can transfer the ^{68}Ga-DOTA label effectively into the cell interior (data not shown). However, the transfer of bioactive cargos *in vivo* will be the focus of future studies.

All the results observed in the biodistribution studies could be confirmed by using small animal PET imaging. Strong ^{68}Ga activities in the kidneys and the bladder were detected that indicate renal peptide elimination. The corresponding kinetic supports this picture and demonstrates a very rapid peptide clearance from the blood and the kidneys. Furthermore, with the calculated time−activity curves in blood we could demonstrate the higher stability of the ^{68}Ga-DOTA-[f^{12,16}]-hCT(9−32) peptide. The estimated terminal half-life of 20.9 min was clearly higher than that of ^{68}Ga-DOTA-hCT(9−32) (15.9 min).

To analyze the metabolic stability of the peptides, radio-HPLC was used to identify the labeled compounds in blood as well as in urine samples. Because of the low peptide content, the blood samples could not be further characterized by MALDI-TOF mass spectrometry. But this is not surprising since a very rapid peptide clearance from the blood was observed. Nevertheless, from the radio-HPLC chromatographs it was concluded that the random peptide was relatively fast degraded in blood in a lot of metabolites. In contrast to this, the original CPP ^{68}Ga-DOTA-[f^{12,16}]-hCT(9−32) and ^{68}Ga-DOTA-hCT(9−32) were metabolically more stable, whereas the D-Phe modified hCT-analogue had the highest stability. These results confirm well our recently performed *in vitro* studies (*14*).

More results about the cleavage pattern were obtained from urine fractions that were collected 60 min postinjection. By using radio-HPLC, in the case of ^{68}Ga-DOTA-hCT(9−32) eight radiolabeled peaks were detected with retention times between 5.5−11.2 min. Since the retention time of 12.8 min of the unaffected peptide was lacking, this result indicates the complete proteolytic degradation of ^{68}Ga-DOTA-hCT(9−32). The obviously low metabolic stability of this peptide is in good agreement with previous *in vitro* studies (*13, 14*). Unfortunately, it was not possible to identify any cleavage products of ^{68}Ga-DOTA-hCT(9−32) by using MALDI-TOF mass spectrometry. Therefore, an enzymatic cleavage at the former *in vitro* identified labile positions 12 and 16 can neither be proven nor excluded.

However, in the case of the D-amino acid-modified ^{68}Ga-DOTA-[f^{12,16}]-hCT(9−32), radio-HPLC revealed three ^{68}Ga-labeled compounds in urine. The smallest peak (retention time 13.0 min) might be the uncleaved parent compound, but because of its low peptide content, this could not be confirmed by MALDI-TOF mass spectrometry. Nevertheless, HPLC analysis indicated that the parent compound was proteolytically degraded resulting in at least three ^{68}Ga-labeled metabolites. By analyzing these metabolites with MALDI-TOF mass spectrometry, three cleavage products were identified: ^{68}Ga-DOTA-[f^{12,16}]-hCT(9−17), ^{68}Ga-DOTA-[f^{12,16}]-hCT(9−18), and ^{68}Ga-DOTA-[f^{12,16}]-hCT(9−19). As the major cleavage product, ^{68}Ga-DOTA-[f^{12,16}]-hCT(9−17) was found. Interestingly, the same metabolite was recently detected by our group in preliminary *in vitro* studies (*14*). However, the *in vivo* identified cleavage sites after Lys^{18} and Phe^{19} were not observed in the *in vitro* study. Probably ^{68}Ga-DOTA-[f^{12,16}]-hCT(9−32) is proteolytically cleaved *in vivo* between Asn^{17}-Lys^{18} by an endopeptidase resulting in the fragment ^{68}Ga-DOTA-[f^{12,16}]-hCT(9−17). In addition, two cleavage sites in the C-terminal part of the peptide (Gln^{24}-Thr^{25} and Ala^{26}-Ile^{27}) that were found *in vitro* were not detected in the present *in vivo* study. But more interestingly, no further N-terminal cleavage site was observed, probably indicating the increased stability of the modified hCT(9−32) analogue, which would be in good agreement with our *in vitro*

data. It is obvious that a peptide modification with D-amino acids can provide protection against metabolic degradation not only *in vitro* but also *in vivo*.

CONCLUSIONS

The results of the presented *in vivo* examination show that ^{68}Ga-DOTA-hCT(9−32) and ^{68}Ga-DOTA-[f^{12,16}]-hCT(9−32) do not accumulate in a specific tissue. As other investigated radiolabeled peptides, they were relatively rapidly excreted out of the body mostly by the renal system. The blood clearance and the elimination of the ^{68}Ga-DOTA-peptides were relatively high and may be decreased by further structural changes. This will be investigated in more detail in future studies. In addition, we could prove the increased metabolic stability of the modified peptide [f^{12,16}]-hCT(9−32) peptide. Furthermore, the results of this *in vivo* degradation study supported very well the results we gained in previous *in vitro* experiments. All in all, these studies demonstrate that it is very important to define the pharmacokinetic characteristics of an assumed biologically active compound. The future application of CPP *in vivo* will hardly depend on such pharmacological issues.

ACKNOWLEDGMENT

We gratefully thank R. Herrlich for performing the biodistribution studies, A. Suhr for performing the analysis of the metabolites, and R. Reppich-Sacher for the MALDI-TOF measurements. I.N. thanks Professor Dr. A. G. Beck-Sickinger for generous access to all facilities of the institute.

Supporting Information Available: Supplementary tables and figures including biodistribution data, representative PET images, and radio-HPLC elution profiles. This material is available free of charge via the Internet at http://pubs.acs.org.

LITERATURE CITED

(1) Mae, M., and Langel, U. (2006) Cell-penetrating peptides as vectors for peptide, protein and oligonucleotide delivery. *Curr. Opin. Pharmacol. 6*, 509–514.

(2) Schwarze, S. R., and Dowdy, S. F. (2000) In vivo protein transduction: intracellular delivery of biologically active proteins, compounds and DNA. *Trends Pharmacol. Sci. 21*, 45–48.

(3) Turner, J. J., Ivanova, G. D., Verbeure, B., Williams, D., Arzumanov, A. A., Abes, S., Lebleu, B., and Gait, M. J. (2005) Cell-penetrating peptide conjugates of peptide nucleic acids (PNA) as inhibitors of HIV-1 Tat-dependent trans-activation in cells. *Nucleic Acids Res. 33*, 6837–6849.

(4) Gros, E., Deshayes, S., Morris, M. C., Aldrian-Herrada, G., Depollier, J., Heitz, F., and Divita, G. (2006) A non-covalent peptide-based strategy for protein and peptide nucleic acid transduction. *Biochim. Biophys. Acta 1758*, 384–393.

(5) Turner, J. J., Arzumanov, A. A., and Gait, M. J. (2005) Synthesis, cellular uptake and HIV-1 Tat-dependent trans-activation inhibition activity of oligonucleotide analogues disulphide-conjugated to cell-penetrating peptides. *Nucleic Acids Res. 33*, 27–42.

(6) Lewin, M., Carlesso, N., Tung, C. H., Tang, X. W., Cory, D., Scadden, D. T., and Weissleder, R. (2000) Tat peptide-derivatized magnetic nanoparticles allow in vivo tracking and recovery of progenitor cells. *Nat. Biotechnol. 18*, 410–414.

(7) Sexton, P. M., Findlay, D. M., and Martin, T. J. (1999) Calcitonin. *Curr. Med. Chem. 6*, 1067–1093.

(8) Rennert, R., Neundorf, I., and Beck-Sickinger, A. G. (2008) Calcitonin-derived carrier peptides: Mechanism and application. *Adv. Drug. Delivery Rev. 60*, 485–498.

(9) Machova, Z., Muhle, C., Krauss, U., Trehin, R., Koch, A., Merkle, H. P., and Beck-Sickinger, A. G. (2002) Cellular internalization of enhanced green fluorescent protein ligated to a human calcitonin-based carrier peptide. *ChemBioChem 3*, 672–677.

(10) Krauss, U., Muller, M., Stahl, M., and Beck-Sickinger, A. G. (2004) In vitro gene delivery by a novel human calcitonin (hCT)-derived carrier peptide. *Bioorg. Med. Chem. Lett. 14*, 51–54.

(11) Krauss, U., Kratz, F., and Beck-Sickinger, A. G. (2003) Novel daunorubicin-carrier peptide conjugates derived from human calcitonin segments. *J. Mol. Recognit. 16*, 280–287.

(12) Powell, M. F., Grey, H., Gaeta, F., Sette, A., and Colon, S. (1992) Peptide stability in drug development: a comparison of peptide reactivity in different biological media. *J. Pharm. Sci. 81*, 731–735.

(13) Trehin, R., Nielsen, H. M., Jahnke, H. G., Krauss, U., Beck-Sickinger, A. G., and Merkle, H. P. (2004) Metabolic cleavage of cell-penetrating peptides in contact with epithelial models: human calcitonin (hCT)-derived peptides, Tat(47−57) and penetratin(43−58). *Biochem. J. 382*, 945–956.

(14) Rennert, R., Wespe, C., Beck-Sickinger, A. G., and Neundorf, I. (2006) Developing novel hCT derived cell-penetrating peptides with improved metabolic stability. *Biochim. Biophys. Acta 1758*, 347–354.

(15) Schwarze, S. R., Ho, A., Vocero-Akbani, A., and Dowdy, S. F. (1999) In vivo protein transduction: delivery of a biologically active protein into the mouse. *Science 285*, 1569–1572.

(16) Zielinski, J., Kilk, K., Peritz, T., Kannanayakal, T., Miyashiro, K. Y., Eiriksdottir, E., Jochems, J., Langel, U., and Eberwine, J. (2006) In vivo identification of ribonucleoprotein-RNA interactions. *Proc. Natl. Acad. Sci. U.S.A. 103*, 1557–1562.

(17) Senatus, P. B., Li, Y., Mandigo, C., Nichols, G., Moise, G., Mao, Y., Brown, M. D., Anderson, R. C., Parsa, A. T., Brandt-Rauf, P. W., Bruce, J. N., and Fine, R. L. (2006) Restoration of p53 function for selective Fas-mediated apoptosis in human and rat glioma cells in vitro and in vivo by a p53 COOH-terminal peptide. *Mol. Cancer Ther. 5*, 20–28.

(18) Jiang, T., Olson, E. S., Nguyen, Q. T., Roy, M., Jennings, P. A., and Tsien, R. Y. (2004) Tumor imaging by means of proteolytic activation of cell-penetrating peptides. *Proc. Natl. Acad. Sci. U.S.A. 101*, 17867–17872.

(19) Tai, Y. C., Chatziioannou, A. F., Yang, Y., Silverman, R. W., Meadors, K., Siegel, S., Newport, D. F., Stickel, J. R., and Cherry, S. R. (2003) MicroPET II: design, development and initial performance of an improved microPET scanner for small-animal imaging. *Phys. Med. Biol. 48*, 1519–1537.

(20) Schuhmacher, J., Zhang, H., Doll, J., Macke, H. R., Matys, R., Hauser, H., Henze, M., Haberkorn, U., and Eisenhut, M. (2005) GRP receptor-targeted PET of a rat pancreas carcinoma xenograft in nude mice with a 68Ga-labeled bombesin(6−14) analog. *J. Nucl. Med. 46*, 691–699.

(21) De Leon-Rodriguez, L. M., Kovacs, Z., Dieckmann, G. R., and Sherry, A. D. (2004) Solid-phase synthesis of DOTA-peptides. *Chemistry 10*, 1149–1155.

(22) Meyer, G. J., Macke, H., Schuhmacher, J., Knapp, W. H., and Hofmann, M. (2004) 68Ga-labeled DOTA-derivatised peptide ligands. *Eur. J. Nucl. Med. Mol. Imaging 31*, 1097–1104.

(23) Blok, D., Feitsma, R. I., Vermeij, P., and Pauwels, E. J. (1999) Peptide radiopharmaceuticals in nuclear medicine. *Eur. J. Nucl. Med. 26*, 1511–1519.

(24) Cai, S. R., Xu, G., Becker-Hapak, M., Ma, M., Dowdy, S. F., and McLeod, H. L. (2006) The kinetics and tissue distribution of protein transduction in mice. *Eur. J. Pharm. Sci. 27*, 311–319.

(25) Lee, Y. H., and Sinko, P. J. (2000) Oral delivery of salmon calcitonin. *Adv. Drug Del. Rev. 42*, 225–231.

(26) Elmquist, A., and Langel, U. (2003) In vitro uptake and stability study of pVEC and its all-D analog. *Biol. Chem. 384*, 387–393.

(27) Powell, M. F., Stewart, T., Otvos, L., Jr., Urge, L., Gaeta, F. C., Sette, A., Arrhenius, T., Thomson, D., Soda, K., and Colon,

S. M. (1993) Peptide stability in drug development. II. Effect of single amino acid substitution and glycosylation on peptide reactivity in human serum. *Pharm. Res. 10*, 1268–1273.

(28) Velikyan, I., Sundberg, A. L., Lindhe, O., Hoglund, A. U., Eriksson, O., Werner, E., Carlsson, J., Bergstrom, M., Langstrom, B., and Tolmachev, V. (2005) Preparation and evaluation of (68)Ga-DOTA-hEGF for visualization of EGFR expression in malignant tumors. *J. Nucl. Med. 46*, 1881–1888.

(29) Franke, J., Rennert, R., Beck-Sickinger, A. G., and Neundorf, I. (2007) In *Proceedings of the 5th Fall Conference on Metallobiolomics*, pp 153−158, Herbert Utz Verlag, München.

(30) Behr, T. M., Goldenberg, D. M., and Becker, W. (1998) Reducing the renal uptake of radiolabeled antibody fragments and peptides for diagnosis and therapy: present status, future prospects and limitations. *Eur. J. Nucl. Med. 25*, 201–212.

(31) Akermann, M. E., Chan, W. C., Laakkonen, P., Bhatia, S. N., and Ruoslahti, E. (2002) Nanocrystal targeting in vivo. *Proc. Natl. Acad. Sci. U.S.A. 99*, 12617–12621.

(32) Pujals, S., Sabido, E., Tarrago, T., and Giralt, E. (2007) All-D proline rich cell-penetrating peptides: a preliminary in vivo internalization study. *Biochem. Soc. Trans. 35*, 794–796.

BC800149F

Detailed Analysis Concerning Biodistribution and Metabolism of hCT-Derived Cell-Penetrating Peptides

I. Neundorf, R. Rennert, J. Franke, I. Közle, R. Bergmann

Supporting Information

List of Contents

Tables 1-4 Biodistribution data

Figure 1 PET maximum intensity projections of ^{68}Ga-DOTA-[f^{12,16}]-hCT(9-32)

Figure 2 Radio-HPLC elution profiles of radio-peptides

Table 1. Biodistribution of ^{68}Ga-DOTA-hCT(9-32), ^{68}Ga-DOTA-[f^{12,16}]-hCT(9-32), ^{68}Ga-DOTA-rd-hCT(9-32) in male Wistar rats 5 min after single intravenous application represented as %ID±SD (4 animals per time point).

%ID 5 min p.i.	**^{68}Ga-DOTA-hCT(9-32)**			**^{68}Ga-DOTA-[f^{12,16}]-hCT(9-32)**			**^{68}Ga-DOTA-rd-hCT(9-32)**			
Brain	0.033	±	0.016	0.031	±	0.003	0.036	±	0.009	#§
Pancreas	0.036	±	0.020	0.035	±	0.012	0.048	±	0.003	#§
Spleen	0.036	±	0.013	0.046	±	0.003	0.044	±	0.004	#§
Adrenals	0.010	±	0.002	0.012	±	0.002	0.011	±	0.002	#§
Kidneys	4.90	±	2.55	6.99	±	1.09	6.03	±	0.60	#§
Heart	0.121	±	0.043	0.162	±	0.018	0.155	±	0.014	#§
Lung	0.332	±	0.130	0.559	±	0.260	0.520	±	0.163	#§
Thymus	0.096	±	0.038	0.136	±	0.002	0.097	±	0.029	#§
Thyroide	0.041	±	0.024	0.058	±	0.025	0.057	±	0.013	#§
Harderian glands	0.051	±	0.023	0.068	±	0.006	0.068	±	0.009	#§
Liver	1.91	±	0.52	2.67	±	0.39	2.98	±	0.14	*#§
Femur	0.181	±	0.079	0.239	±	0.053	0.245	±	0.024	#§
Testes	0.097	±	0.044	0.186	±	0.063	0.164	±	0.047	#§
Intestine	0.939	±	0.342	1.29	±	0.03	1.20	±	0.15	#§
Stomach	0.245	±	0.145	0.360	±	0.078	0.265	±	0.028	#§
Carcass	74.8	±	14.7	65.3	±	10.0	61.1	±	9.4	#§
Urine	14.9	±	10.7	19.9	±	9.7	25.3	±	10.1	#§

* P<0.05 comparison of ^{68}Ga-DOTA-hCT(9-32) and ^{68}Ga-DOTA-[f^{12,16}]-hCT(9-32); # P<0.05 comparison of ^{68}Ga-DOTA-hCT(9-32) and ^{68}Ga-DOTA-rd-hCT(9-32); § P<0.05 comparison of ^{68}Ga-DOTA-[f^{12,16}]-hCT(9-32) ^{68}Ga-DOTA-rd-hCT(9-32).

Table 2. Biodistribution of ^{68}Ga-DOTA-hCT(9-32), ^{68}Ga-DOTA-[f^{12,16}]-hCT(9-32), ^{68}Ga-DOTA-rd-hCT(9-32) in male Wistar rats 60 min after single intravenous application represented as %ID±SD (4 animals per time point).

%ID 60 min p.i.	**^{68}Ga-DOTA-hCT(9-32)**			**^{68}Ga-DOTA-[f^{12,16}]-hCT(9-32)**			**^{68}Ga-DOTA-rd-hCT(9-32)**			
Brain	0.006	±	0.001	0.005	±	0.001	0.004	±	0.00	*#§
Pancreas	0.009	±	0.002	0.006	±	0.002	0.009	±	0.00	#§
Spleen	0.014	±	0.002	0.013	±	0.000	0.015	±	0.00	#§
Adrenals	0.004	±	0.002	0.003	±	0.000	0.004	±	0.00	#§
Kidneys	7.17	±	1.30	6.22	±	1.76	5.06	±	0.27	#§
Heart	0.017	±	0.006	0.013	±	0.000	0.016	±	0.00	#§
Lung	0.067	±	0.007	0.054	±	0.004	0.066	±	0.02	#§
Thymus	0.018	±	0.006	0.016	±	0.002	0.017	±	0.00	#§
Thyroide	0.009	±	0.001	0.006	±	0.002	0.006	±	0.00	*#§
Harderian glands	0.011	±	0.003	0.008	±	0.001	0.010	±	0.00	#§
Liver	0.842	±	0.135	1.102	±	0.554	1.674	±	0.15	*#§
Femur	0.040	±	0.007	0.032	±	0.002	0.036	±	0.01	#§
Testes	0.038	±	0.005	0.034	±	0.000	0.039	±	0.01	#§
Intestine	13.8	±	4.5	9.21	±	7.89	7.80	±	6.64	#§
Stomach	0.746	±	0.642	1.48	±	1.99	1.51	±	1.30	#§
Carcass	27.0	±	1.17	20.1	±	11.2	14.0	±	3.3	*#§
Urine	50.0	±	6.6	61.5	±	18.4	69.6	±	8.3	*#§

* P<0.05 comparison between ^{68}Ga-DOTA-hCT(9-32) and ^{68}Ga-DOTA-[f^{12,16}]-hCT(9-32); # P<0.05 comparison between ^{68}Ga-DOTA-hCT(9-32) and ^{68}Ga-DOTA-rd-hCT(9-32); § P<0.05 comparison between ^{68}Ga-DOTA-[f^{12,16}]-hCT(9-32) and ^{68}Ga-DOTA-rd-hCT(9-32).

Table 3. Biodistribution of ^{68}Ga-DOTA-hCT(9-32), ^{68}Ga-DOTA-[f^{12,16}]-hCT(9-32), ^{68}Ga-DOTA-rd-hCT(9-32) in male Wistar rats 5 min after single intravenous application represented as SUV±SD (4 animals per time point).

SUV 5 min p.i.	**^{68}Ga-DOTA-hCT(9-32)**			**^{68}Ga-DOTA-[f^{12,16}]-hCT(9-32)**			**^{68}Ga-DOTA-rd-hCT(9-32)**			
Blood	1.371	±	0.012	1.399	±	0.178	1.262	±	0.083	#§
Brown adipose fat	0.336	±	0.025	0.326	±	0.024	0.300	±	0.055	#§
Hair & skin	0.578	±	0.044	0.974	±	0.603	0.814	±	0.511	#§
Brain	0.049	±	0.020	0.043	±	0.010	0.041	±	0.011	#§
Pancreas	0.256	±	0.040	0.256	±	0.014	0.236	±	0.026	#§
Spleen	0.200	±	0.023	0.201	±	0.004	0.191	±	0.023	#§
Adrenals	0.439	±	0.060	0.446	±	0.247	0.546	±	0.079	#§
Kidneys	8.17	±	1.91	6.99	±	0.95	6.75	±	1.18	#§
Fat	0.290	±	0.082	0.262	±	0.066	0.374	±	0.217	#§
Muscle	0.296	±	0.029	0.291	±	0.005	0.268	±	0.039	#§
Heart	0.408	±	0.029	0.467	±	0.031	0.428	±	0.027	#§
Lung	0.688	±	0.088	0.764	±	0.156	0.693	±	0.079	#§
Thymus	0.395	±	0.012	0.333	±	0.147	0.273	±	0.056	#§
Harderian glands	0.538	±	0.052	0.521	±	0.033	0.498	±	0.070	#§
Liver	0.418	±	0.001	0.669	±	0.014	0.653	±	0.010	*#§
Femur	0.476	±	0.060	0.488	±	0.023	0.459	±	0.012	#§
Testes	0.108	±	0.008	0.140	±	0.061	0.103	±	0.010	#§

* P<0.05 comparison between ^{68}Ga-DOTA-hCT(9-32) and ^{68}Ga-DOTA-[f^{12,16}]-hCT(9-32); # P<0.05 comparison between ^{68}Ga-DOTA-hCT(9-32) and ^{68}Ga-DOTA-rd-hCT(9-32); § P<0.05 comparison between ^{68}Ga-DOTA-[f^{12,16}]-hCT(9-32) and ^{68}Ga-DOTA-rd-hCT(9-32).

Table 4. Biodistribution of ^{68}Ga-DOTA-hCT(9-32), ^{68}Ga-DOTA-[f^{12,16}]-hCT(9-32), ^{68}Ga-DOTA-rd-hCT(9-32) in male Wistar rats 60 min after single intravenous application represented as SUV±SD (4 animals per time point).

SUV 60 min p.i.	**^{68}Ga-DOTA-hCT(9-32)**	**^{68}Ga-DOTA-[f^{12,16}]-hCT(9-32)**	**^{68}Ga-DOTA-rd-hCT(9-32)**	
Blood	0.137 ± 0.025	0.109 ± 0.013	0.114 ± 0.029	#§
Brown adipose fat	0.047 ± 0.009	0.033 ± 0.008	0.036 ± 0.009	#§
Hair & skin	0.186 ± 0.080	0.184 ± 0.144	0.097 ± 0.017	#§
Brain	0.008 ± 0.001	0.006 ± 0.002	0.005 ± 0.001	#§
Pancreas	0.053 ± 0.008	0.038 ± 0.007	0.046 ± 0.013	#§
Spleen	0.052 ± 0.006	0.046 ± 0.009	0.055 ± 0.013	#§
Adrenals	0.160 ± 0.060	0.105 ± 0.024	0.132 ± 0.091	#§
Kidneys	8.70 ± 0.87	6.89 ± 2.45	5.46 ± 0.57	#§
Fat	0.054 ± 0.019	0.035 ± 0.004	0.061 ± 0.050	#§
Muscle	0.047 ± 0.012	0.036 ± 0.022	0.031 ± 0.013	#§
Heart	0.050 ± 0.012	0.036 ± 0.002	0.044 ± 0.014	#§
Lung	0.105 ± 0.010	0.087 ± 0.011	0.101 ± 0.026	#§
Thymus	0.052 ± 0.014	0.050 ± 0.005	0.053 ± 0.013	#§
Harderian glands	0.086 ± 0.025	0.057 ± 0.004	0.071 ± 0.014	#§
Liver	0.155 ± 0.034	0.214 ± 0.130	0.362 ± 0.040	*#§
Femur	0.081 ± 0.008	0.067 ± 0.006	0.069 ± 0.013	#§
Testes	0.032 ± 0.002	0.028 ± 0.002	0.032 ± 0.006	#§

* P<0.05 comparison between ^{68}Ga-DOTA-hCT(9-32) and ^{68}Ga-DOTA-[f^{12,16}]-hCT(9-32); # P<0.05 comparison between ^{68}Ga-DOTA-hCT(9-32) and ^{68}Ga-DOTA-rd-hCT(9-32); § P<0.05 comparison between ^{68}Ga-DOTA-[f^{12,16}]-hCT(9-32) and ^{68}Ga-DOTA-rd-hCT(9-32).

Figure 1

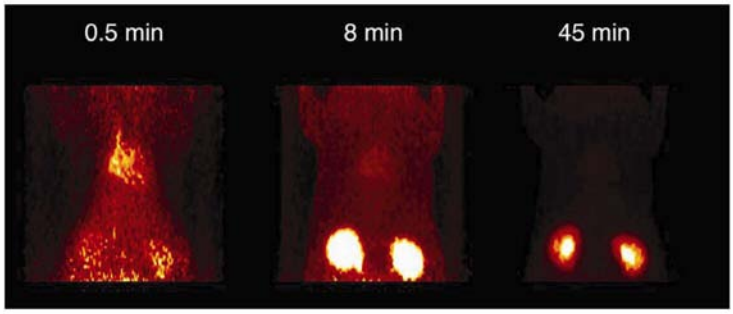

Figure 1. PET maximum intensity projections in coronal planes of ^{68}Ga-DOTA-[f^{12,16}]-hCT(9-32) distribution in a male Wistar rat 0.5, 8, and 45 min after single intravenous application.

Figure 2

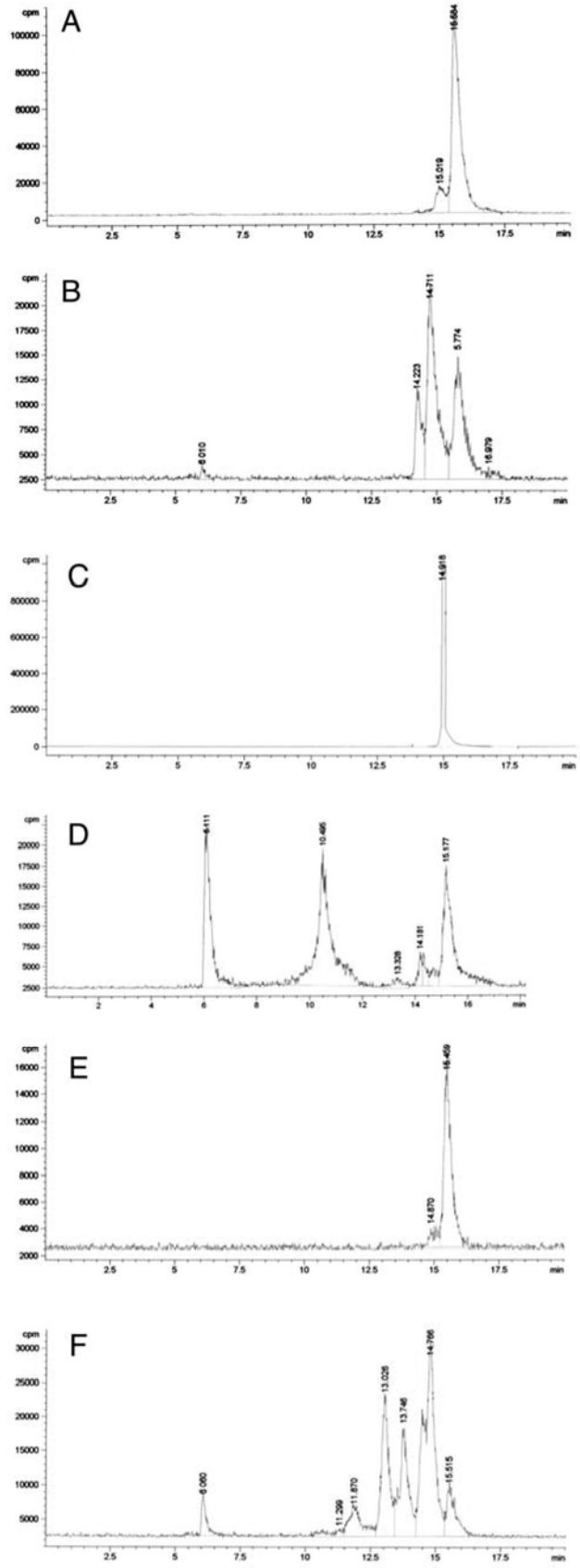

Figure 2. Radio-HPLC elution profiles of radio-peptides at 1.5 min and 30 min after single intravenous application in arterial rat blood, ^{68}Ga-DOTA-[f^{12,16}]-hCT(9-32) (A 1.5 min, B 30 min), ^{68}Ga-DOTA-hCT(9-32) (C 1.5 min, D 30 min), ^{68}Ga-DOTA-rd-hCT(9-32) (E 1.5 min, F 30 min).

Biophysical and Biochemical Approach to Locating an Inhibitor Binding Site on Cholesteryl Ester Transfer Protein

David Cunningham, Wen Lin, Lise R. Hoth, Dennis E. Danley, Roger B. Ruggeri, Kieran F. Geoghegan, Boris A. Chrunyk, and James G. Boyd*

Pfizer Global Research and Development, Groton, Connecticut 06340. Received April 22, 2008; Revised Manuscript Received June 20, 2008

Cholesteryl ester transfer protein (CETP) transfers neutral lipids between different types of plasma lipoprotein. Inhibitors of CETP elevate the fraction of plasma cholesterol associated with high-density lipoproteins and are being developed as new agents for the prevention and treatment of cardiovascular disease. The molecular basis of their function is not yet fully understood. To aid in the study of inhibitor interactions with CETP, a torcetrapib-related compound was coupled to different biotin-terminated spacer groups, and the binding of CETP to the streptavidin-bound conjugates was monitored on agarose beads and in a surface plasmon resonance biosensor. CETP binding was poor with a 2.0 nm spacer arm, but efficient with polyethyleneglycol spacers of 3.5 or 4.6 nm. The conjugate based on a 4.6 nm spacer was used for further biosensor experiments. Soluble inhibitor blocked the binding of CETP to the immobilized drug, as did preincubation with a disulfide-containing covalent inhibitor. To provide a first estimate of the binding site for torcetrapib-like inhibitors, CETP was modified with a disulfide-containing agent that modifies Cys-13 of CETP. Mass spectrometry of the modified protein indicated that a single half-molecule of the disulfide was covalently bound to CETP, and peptide mapping after digestion with pepsin confirmed previous reports based on mutagenesis that Cys-13 was the site of modification. Modified CETP was unable to bind to the biosensor-mounted torcetrapib analog, indicating that the binding site on CETP for torcetrapib is in the lipid-binding pocket near the N-terminus of the protein. The crystal structure of CETP shows that the sulfhydryl group of Cys-13 resides at the bottom of this pocket.

INTRODUCTION

Cardiovascular disease is the major cause of premature death in Western societies (*1*). Decades of epidemiological analysis has led to the recognition of multiple distinct risk factors for this syndrome, among which unhealthful elevation of the level of low-density lipoprotein (LDL) cholesterol is the best-known example. This can be treated successfully with statins, which block cholesterol production in the liver, but it still represents only about 30% of the total risk for acquiring the disease. There remains an urgent need for therapies that reduce other elements of the risk burden.

One example is suboptimal levels of high-density lipoprotein (HDL) cholesterol. HDL collect cholesterol from the vascular periphery, and return it (as cholesteryl esters) to the liver for excretion. Despite some advances, there are not yet any approved drugs that elevate the level of HDL cholesterol successfully enough (and in a manner sufficiently free of undesirable side effects) to make major inroads against atherosclerotic disease. Currently, however, there are intensive efforts to evaluate inhibitors of cholesteryl ester transfer protein (CETP) for this purpose.

CETP is a circulating hydrophobic glycoprotein with a polypeptide molecular mass of 53 kDa and three or four N-linked glycans. It transfers neutral lipids between lipoproteins of different classes (other functions await recognition), and reductions in this activity by drug action or genetic change lead to an elevation of HDL cholesterol. When a CETP inhibitor (torcetrapib) was coadministered with atorvastatin, quite dramatic changes in the plasma lipid profile were obtained of a kind corresponding to a highly desirable shift in the levels of both biomarkers (*2*). Torcetrapib, unfortunately, was recently withdrawn from development because of surprising adverse events (*3*), but it continues to be medically and scientifically important to elucidate the function of CETP at a molecular level and the manner in which its inhibitors bind to it and block its function.

Kinetic analysis of CETP function indicated that it is a shuttle protein (*4*), optionally binding to lipoproteins of different classes, extracting a small number of molecules of their predominant neutral lipids in exchange for lipids previously bound, and presumably existing as a soluble protein when not bound to a lipoprotein. A recent report of its crystal structure suggested how these functions might occur, showing that neutral lipids are carried in a 6 nm tunnel formed inside the protein's elongated body, while each orifice of the tunnel is plugged with an amphiphilic phospholipid (*5*). Keen interest now centers on how CETP inhibitors bind to the protein and affect its function as a lipid shuttle.

Several important clues are already available. Torcetrapib has been shown to increase the relative affinity of CETP for HDL by a factor of 5 (*6*). As a shuttle carrier must have finely balanced relative affinities for the different states that it populates, this effect is clearly sufficient to disable lipid transfer by CETP. It is also known that torcetrapib binds to CETP with 1:1 stoichiometry (*6*), but the binding pocket that it occupies on CETP has not been determined.

CETP possesses two large binding pockets for neutral lipids which form a continuous interior cavity within the protein (*5*), but are demarcated from each other by a constriction in the cavity that has been termed the neck. To date, there have been no direct reports of the structures of CETP-inhibitor complexes, but there has been biochemical and mutagenesis-based evidence that two distinct disulfide containing inhibitors each modify Cys-

* Corresponding author. Tel: 860-441-1580. Fax: 860-441-3858. E-mail: james_g_boyd@pfizer.com.

10.1021/bc800165n CCC: $40.75 © 2008 American Chemical Society
Published on Web 07/23/2008

13 in the N-terminal region of CETP (*7*, *8*). Another report suggested that a mercurial cholesterol analog inhibits by modifying Cys-333 in the C-terminal lipid binding region (*9*). In the present study, a close analog of torcetrapib was adapted for use in a biosensor instrument by coupling it to biotin-terminated spacers of different lengths, and the resulting conjugates were characterized for their ability to bind CETP. The ability to measure the binding of CETP to an immobilized inhibitor provided a basis for experiments probing the ability of different inhibitors to compete with one another for binding sites, and has led to the discovery that torcetrapib apparently occupies the same pocket as one of the covalent inhibitors for which the site of action was previously implied by mutagenesis and was directly determined in the present study.

EXPERIMENTAL SECTION

CETP Mutant 444. A mutant form of CETP (C1A, C131A, N88D, N240D, N341D) was prepared as described (*5*). The expressed protein, designated CETP 444, was composed of the 493-residue polypeptide given in Genbank accession M30185 with the five mutations as listed. Amino-acid numbering (including the mutations) refers to mature CETP lacking the 17-residue signal sequence, i.e., the eighteenth residue of the gene product is designated Cys-1. The mutant showed activity equal to that of recombinant wild-type CETP in cholesteryl ester transfer assays. For mass spectrometry of the intact protein, it was deglycosylated using peptide N-glycosidase F.

Reagents and Conditions. Guanidine hydrochloride (Sigma Ultra) and iodoacetamide were purchased from Sigma (St Louis, MO). Hydrochloric acid and Tris base were from J. T. Baker (Phillipsburg NJ). DTT was from BioVectra (PEI, Canada). TFA was from Applied Biosystems (Foster City, CA). All other solvents were from J. T. Baker or Applied Biosystems were used as purchased. Phosgene (2.0 M in toluene) was purchased from Fluka (St. Louis, MO), and 6-amino-1-hexanol and *tert*-butyl dicarbonate were from Aldrich. *N*-Fmoc-8-Amino-3,6-dioxaoctanoic acid was from Chem-Impex (Wood Dale, IL). 1-Amino-11-azido-3,6,9-trioxoundecane was from Toronto Research Chemicals (North York, Ontario, Canada). NHS-LC-Biotin and TFP-PEO-Biotin were purchased from Pierce (Rockford, IL). Boc-6-Amino-1-hexanol was prepared from commercially available *tert*-butyl dicarbonate and amino alcohol as described (*10*).

NMR was performed on a 400 MHz field strength spectrometer from Varian Inc. (Palo Alto, CA) in CD_3OD or $CDCl_3$. Chemical shifts are reported in parts-per-million (ppm). Residual solvent was used as reference (CD_3OD = 3.32 ppm, $CDCl_3$ = 7.27 ppm). Preparative HPLC was performed using a BISCHOFF (Atlanta, GA) C_{18} column (50 × 20 mm, part # B025 0F185PS050), eluting with a linear slope gradient of water/acetonitrile/TFA (95:5:0.1 to 20:80:0.1) over 10 min, then isocratic 80% acetonitrile for 5 min, and flow rate of 10 mL/min). Analytical samples for liquid chromatography electrospray mass spectrometry (LC ESMS) were dissolved in methanol. 5−10 μL each of these were injected onto a Phenomenex 4.6 × 50 mm C_{18} Jupiter column and eluted using a linear gradient from 0.1% TFA, 5% acetonitrile in water to 100% acetonitrile over 10 min with a flow rate of 1 mL/min. Mass detection was performed using a Micromass LCT spectrometer employing external calibration with sodium iodide/cesium iodide clusters to determine experimental masses. Observed peaks were evaluated by summing those scans at one-half peak height. Compound purity was assessed by C_{18} reversed phase HPLC (RP HPLC) methods using diode array UV detection. Biotinyl compounds were >89% pure when measured at 214 nm and >99% pure when measured at 250 nm.

Preparation of Affinity Columns. A stock solution of biotinyl ligand was prepared by dissolving compound **8**, **9**, or **13** (0.5 μmol) in 2.5 mL ethanol and diluting with 7.5 mL phosphate buffered saline (pH 7.0). An aliquot of the stock solution (5 μL) was diluted with 95 μL methanol and set aside as an HPLC standard. A 1 mL HiTrap Streptavidin HP column (GE Healthcare, catalog # 17−5112−01) was pre-equilibrated with 10 mL of 20% ethanol in pH 7.0 phosphate buffer. The 10 mL of ligand stock solution was passed over the column using a syringe at a flow rate of about 1 mL/min and the flow-through fraction collected. The column was washed with 10 mL of 20% ethanol in phosphate buffer and the eluant collected. The stock solution, flow-through, and wash fractions were assayed by RP HPLC. No ligand was detected in the eluants indicating complete loading on the column.

(±) Benzyl [(2*R*,4*S*)-2-ethyl-6-(trifluoromethyl)-1,2,3,4-tetrahydroquinolin-4-yl]carbamate (1). 4-Trifluoromethylaniline (1.2 g, 7.4 mmol) and propionaldehyde (0.5 g, 8.6 mmol) were combined in dichloromethane (30 mL) and treated with anhydrous sodium sulfate (2.5 g). After stirring 1 h at room temperature, the reaction mixture was filtered and to the resulting solution was added *N*-vinyl-*O*-benzylcarbamate (1 equivalent) and a drop of borontrifluoride etherate. After stirring for 90 min at room temperature the reaction mixture was concentrated onto silica gel employing a rotary evaporator and purified by silica gel chromatography eluting with 5−10% ethyl acetate in hexanes to afford 1.0 g of the racemic product (47%). ^{1}H NMR ($CDCl_3$): δ 7.32 − 7.41 (m, 5H), 7.22 (dd, 1H, *J* = 8.3, 2.1 Hz), 6.46 (d, 1H, *J* = 8.51 Hz), 5.18 (s, 2 H), 5.03 (td, 1H, *J* = 10.5, 5.5 Hz), 4.87 (d, 1H, *J* = 9.6 Hz), 4.06 (bs, 1H), 3.35 − 3.45 (m, 1H), 2.32 (ddd, 1H, *J* = 12.3, 5.5, 2.6 Hz), 1.54 (d, 1H, *J* = 6.4 Hz), 1.51 − 1.58 (m, 1 H), 1.45 (td, 1H, *J* = 11.6 Hz), 0.98 (t, 3H, *J* = 7.5 Hz).

Benzyl [(2*R*,4*S*)-2-ethyl-1-(trifluoroacetyl)-6-(trifluoromethyl)-1,2,3,4-tetrahydroquinolin-4-yl]carbamate (2). Compound **1** (1.0 g, 2.6 mmol) and triethylamine (1 mL, 7.2 mmol) were dissolved in 30 mL of dichloromethane and cooled in an ice/water bath as trifluoroacetic anhydride (0.5 mL, 3.5 mmol) was added. After 4 h, the reaction mixture was combined with an aqueous 1 N HCl solution, and the organic phase washed with a saturated aqueous $NaHCO_3$ solution, dried over $MgSO_4$, filtered and concentrated under reduced pressure to afford the racemic product (85%). The enantiomers were separated by regular phase HPLC using a Chiralcel OD column eluting with 20% isopropanol in heptane. The later eluting peak contains the desired THQ enantiomer with the (2*R*, 4*S*) stereochemistry. ^{1}H NMR ($CDCl_3$): δ 7.60 (s, 1 H), 7.57 (d, 1 H, *J* = 7.5 Hz), 7.39 (m, 6 H), 5.19 (s, 2 H), 4.97 (d, 1 H, *J* = 9.1 Hz), 4.79 (bs, 1 H), 4.66 (bs, 1 H), 2.69 (m, 1 H), 1.48 (m, 1 H), 1.37 (m, 2 H), 0.97 (t, 3 H, *J* = 7.5 Hz).

(2*R*,4*S*)-2-Ethyl-1-(trifluoroacetyl)-6-(trifluoromethyl)-1,2,3,4-tetrahydroquinolin-4-amine (3). Compound **2** (1.0 g, 2.1 mmol) was dissolved in 30 mL each of absolute ethanol and cyclohexene. The resulting solution was treated with 10% Pd on carbon (200 mg, 50% by weight with water) and heated at reflux. After 1 h, the reaction mixture was filtered through a pad of Celite and concentrated under reduced pressure to afford the title compound. ^{1}H NMR ($CDCl_3$): δ 7.82 (s, 1H), 7.58 (ddd, 1H *J* = 8.3, 1.4, 0.7 Hz), 7.33 (bs, 1H), 4.71 (bs, 1H), 3.83 (dd, 1H, *J* = 11.4, 5.2 Hz), 2.64 (ddd, 1H, *J* = 12.5, 8.8, 5.3 Hz), 1.42 − 1.51 (m, 1H), 1.29 − 1.41 (m, 1H), 1.18 (bs, 1H), 0.88 (t, 3H, *J* = 7.5 Hz).

***N*-[3,5-Bis(trifluoromethyl)benzyl]-*N*-[(2*R*,4*S*)-2-ethyl-1-(trifluoroacetyl)-6-(trifluoromethyl)-1,2,3,4-tetrahydroquinolin-4-yl]acetamide (4).** Compound **3** (0.5 g, 1.5 mmol) and 3,5-(bis)trifluoromethylbenzaldehyde (0.36 g, 1.5 mmol) were combined in 40 mL of 1,2-dichloroethane at room temperature. After 1 h, sodium triacetoxyborohydride (0.21 g, 7.5 mmol) was added and the mixture stirred for 18 h. An aqueous 2 N

KOH solution was added to the reaction mixture, the organic phase was separated, dried over $MgSO_4$, filtered and concentrated under reduced pressure to afford 0.65 g crude amine. The amine was dissolved in 1.0 mL pyridine and 20 mL dichloromethane, and the resulting mixture cooled with an ice/water bath. Acetyl chloride (0.5 mL, 7.0 mmol) was added slowly by syringe and the reaction stirred at room temperature for 4 h. Aqueous 1 N HCl solution was added to the reaction mixture, the organic layer was separated, washed once with an aqueous saturated sodium bicarbonate solution, dried over magnesium sulfate, filtered and concentrated under reduced pressure. The resulting material was purified by chromatography on silica eluting with 20% ethyl acetate in hexanes to afford the title compound (44%). ^{1}H NMR ($CDCl_3$): [~2:1 mixture of rotamers] δ 7.74 − 7.88 (m, 1H), 7.67 (s, 1H), 7.65 − 7.73 (m, 1H), 7.48 (bs, 1H), 7.27 (s, 1H), 5.59 (d, 1H, J = 16 Hz), 4.84 (dd, 1H, J = 11.9, 4.7 Hz), 4.55 − 4.71 (m, 1H), 3.96 (d, 1H, J = 16.2 Hz), 2.35 (bs, H), 2.26 (bs, 1H), 2.24 (s, 2H), 2.08 (s, 1H), 1.43 − 1.61 (m, 1H), 1.27 − 1.43 (m, 2H), 0.78 (t, 3H, J = 7.4 Hz).

***N*-[3,5-Bis(trifluoromethyl)benzyl]-*N*-[(2*R*,4*S*)-2-ethyl-6-(trifluoromethyl)-1,2,3,4-tetrahydroquinolin-4-yl]acetamide (5).** Compound **4** (400 mg, 0.66 mmol) was dissolved in 10 mL THF, combined with 5 mL of an aqueous 2 N LiOH solution, and stirred at room temperature for 4 h. The reaction mixture was concentrated under reduced pressure, the residue diluted with water and $MgSO_4$, filtered, and concentrated under reduced pressure to afford the title compound. ^{1}H NMR ($CDCl_3$): [~2:1 mixture of rotamers] δ 7.54 − 7.83 (m, 3H), 7.21 − 7.27 (m, 1H), 6.92 − 7.01 (m, 1H), 6.49 − 6.57 (m, 1H), 5.26 (dd, 1H, J = 11.8, 5.6 Hz), 4.59 − 4.89 (m, 1H), 3.99 − 4.14 (m, 1H), 3.99 − 4.29 (m, 1H), 3.40 (bs, 1H), 2.38 (s, 2H), 2.14 (s, 1H), 1.94 − 2.09 (m, 1H), 1.37 − 1.66 (m, 3H), 0.93 (t, 2H, J = 7.4 Hz), 0.89 (t, 1H, J = 7.7 Hz).

(6-[(*tert*-Butoxycarbonyl)amino]hexyl) (2*R*,4*S*)-4-{acetyl[3,5-bis(trifluoromethyl)benzyl]amino}-2-ethyl-6-(trifluoromethyl)-3,4-dihydroquinoline-1(2H)-carboxylate (6a). To a solution of 300 mg compound **5** in 5 mL toluene was added 3 mL of 20% phosgene (6 mmol) in toluene. The reaction was refluxed for 6 h, cooled to room temperature, and the excess phosgene was driven into a trap by a stream of nitrogen. The residual solvent was evaporated on rotovap followed by high vacuum, leaving the carbamoyl chloride as a waxy solid. LCMS showed it to be a mixture of 95% carbamoyl chloride and 5% **5,** which is stable at room temperature for at least 30 days (ESMS: calculated m/z for $[M+H]^+$ = 575.11, found = 575.22). To 50 mg carbamoyl chloride (0.087 mmol) was added 1.0 mL toluene, 95 mg Boc-6-amino-1-hexanol (0.44 mmol) and 0.1 mL DIEA. The reaction was refluxed for 24 h, cooled, evaporated, dissolved in 0.5 mL methanol and directly purified by preparative HPLC as described in Reagents and Conditions. Collected fractions were analyzed by analytical LCMS and those judged as having adequate purity were pooled and lyophilized. The purity of the product was 90% as determined by HPLC at 215 nm. Yield = 15 mg (23%). ^{1}HNMR (CD_3OD): δ 7.92 (s, 2H), 7.84 (s, 1H), 7.6 (dd, 2H), 7.06 (s, 1H), 5.3 (d, 1H, J = 16 Hz), 5.14 (dd, 1H), 4.35 (m, 1H), 4.29 (d, 1H, J = 16 Hz), 4.16 (t, 2H), 2.99 (t, 2H), 2.28 (m, 1H), 2.26 (s, 3H), 1.67 (m, 4H), 1.5−1.3 (m, 8H), 1.40 (s, 9H), 0.72 (t, 3H). ESMS: calculated m/z for $[M+H]^+$ = 756.30, found = 756.51.

6-Aminohexyl (2*R*,4*S*)-4-{acetyl[3,5-bis(trifluoromethyl)benzyl]amino}-2-ethyl-6-(trifluoromethyl)-3,4-dihydroquinoline-1(2*H*)-carboxylate (6b), TFA Salt. Boc protected urethane **6a** (15 mg) was treated with 0.5 mL TFA for 10 min at room temperature. The TFA was evaporated under a stream of nitrogen, then at high vacuum. The purity of the amine TFA salt was 90% as determined by HPLC at 214 nm. Yield = 15 mg (100%). ESMS: calculated m/z for $[M+H]^+$ = 656.25, found = 656.38. HRMS: calculated m/z for $[M+H]^+$ = 656.2529, found = 656.2526.

(6-({[2-(2-Aminoethoxy)ethoxy]acetyl}amino)hexyl) (2*R*,4*S*)-4-{acetyl[3,5-bis(trifluoromethyl)benzyl]amino}-2-ethyl-6-(trifluoromethyl)-3,4-dihydroquinoline-1(2*H*)-carboxylate (7), TFA Salt. To a solution of 7.0 mg (18 μmol) Fmoc-8-amino-3,6-dioxaoctanoic acid in 36 μL of a 0.5 M DMF solution of HOBT/HBTU (18 μmol) was added 10 μL (60 μmol) DIEA. After 2 min, 6.0 mg (9.1 μmol) of TFA salt **6b** was added and the solution allowed to react for 1 h. The reaction solution was diluted with 10 mL ethyl ether, and washed with 0.1 M HCl, 0.1 M $NaHCO_3$, saturated NaCl, and dried over $MgSO_4$. The ether was filtered and concentrated to an oily solid. The solid was treated with 0.1 mL 30% piperidine/DMF for 20 min, then 30 μL acetic acid was added to quench the reaction. The solution was fractionated by direct injection onto a C_{18} preparative HPLC column as for **5**, and appropriate fractions were pooled and lyophilized. Yield = 2.0 mg (28%). ESMS: calculated m/z for $[M+H]^+$ = 801.33, found = 801.36.

(6-{[6-({5-[(3a*S*,4*S*,6a*R*)-2-Oxohexahydro-1*H*-thieno[3,4-*d*]imidazol-4-yl]pentanoyl}amino)hexanoyl]amino}hexyl)(2*R*,4*S*)-4-{acetyl[3,5-bis(trifluoromethyl)benzyl]amino}-2-ethyl-6-(trifluoromethyl)-3,4-dihydroquinoline-1(2*H*)-carboxylate (8). To a solution of 5.0 mg (7.6 μmol) TFA salt **6b** in 50 μL DMF was added 10 mg (22 μmol) NHS-LC-Biotin and 5 μL DIEA. After 1 h, the product was purified by direct injection onto a C_{18} preparative HPLC column as for **5**. Appropriate fractions were pooled and lyophilized. HPLC purity at 214 nm = 94%, at 250 nm >99%. Yield = 6.2 mg (65%). ESMS: calculated m/z for $[M+H]^+$ = 995.41, found = 995.61. HRMS: calculated m/z for $[M+H]^+$ = 995.4145, found = 995.4142.

(8,11,27-Trioxo-31-[(3a*S*,4*S*,6a*R*)-2-oxohexahydro-1*H*-thieno[3,4-*d*]imidazol-4-yl]-16,19,22-trioxa-7,12,26-triazahentriacont-1-yl) (2*R*,4*S*)-4-{acetyl[3,5-bis(trifluoromethyl)benzyl]amino}-2-ethyl-6-(trifluoromethyl)-3,4-dihydroquinoline-1(2*H*)-carboxylate (9). To a solution of 4.0 mg (6.1 μmol) TFA salt **6b** in 50 μL DMF was added 16 mg (23 μmol) TFP-PEO-Biotin (Pierce, catalog # 21336) and 5 μL DIEA. After 1 h, the product was purified by direct injection onto a C_{18} preparative HPLC column as for **5**. Appropriate fractions were pooled and lyophilized. HPLC purity at 214 nm = 89%, at 250 nm >99%. Yield = 4.0 mg (55%). ESMS: calculated m/z for $[M+H]^+$ = 1184.51, found = 1184.75. HRMS: calculated m/z for $[M+2H]^{+2}$ = 592.7609, found = 592.7632.

(8,17,20,36-Tetraoxo-40-[(3a*S*,4*S*,6a*R*)-2-oxohexahydro-1*H*-thieno[3,4-*d*]imidazol-4-yl]-10,13,25,28,31-pentaoxa-7,16,21,35-tetraazatetracont-1-yl) (2*R*,4*S*)-4-{acetyl[3,5-bis(trifluoromethyl)benzyl]amino}-2-ethyl-6-(trifluoromethyl)-3,4-dihydroquinoline-1(2*H*)-carboxylate (10). TFP-PEO-Biotin was allowed to react with 2.0 mg (2.2 μmol) of TFA salt **7** as described for the synthesis of **9**. HPLC purity at 214 nm = 94%, at 250 nm >99%. Yield = 1.5 mg (51%). ESMS: calculated m/z for $[M+H]^+$ = 1329.73, found = 1329.59. HRMS: calculated m/z for $[M+2H]^{+2}$ = 665.2979, found = 665.3000.

Methyl [(2*S*,4*R*)-1-(13-azido-5,8,11-trioxa-2-azatridecan-1-oyl)-2-ethyl-6-(trifluoromethyl)-1,2,3,4-tetrahydroquinolin-4-yl]carbamate (12). In a 1.5 mL Eppendorf tube 150 mg (0.50 mmol) of methyl [(2*S*,4*R*)-2-ethyl-6-(trifluoromethyl)-1,2,3,4-tetrahydroquinolin-4-yl]carbamate (**11**) (*11*) was dissolved in 0.10 mL THF. *p*-Nitrochloroformate (200 mg, 2.0 equiv) was added and the resulting solution was shaken at 40 °C for 16 h. The THF was evaporated and residue was dissolved in 1.5 mL methanol, 0.35 mL DIEA. 400 mg (4.0 equiv) 1-amino-11-azido-3,6,9-trioxoundecane was added and the resulting solution was shaken at 70 °C for 48 h. The product was purified by

direct injection onto preparative HPLC as for compound **5** except a shallower solvent gradient to 50% acetonitrile was employed. Yield = 99 mg (36%). ESMS: calculated *m*/*z* for $[M+H]^+$ = 547.25, found = 547.24.

Methyl [(2*S*,4*R*)-1-{15,22-dioxo-26-[(3a*S*,4*S*,6a*R*)-2-oxohexahydro-1H-thieno[3,4-d]imidazol-4-yl]-5,8,11-trioxa-2,14,21-triazahexacosan-1-oyl}-2-ethyl-6-(trifluoromethyl)-1,2,3,4-tetrahydroquinolin-4-yl]carbamate (13). 4.2 mg (7.7 μmol) of compound **12** was dissolved in 2 mL THF. Three mg Pd/C was added and the mixture shaken under 50 psi H_2 for 5 h. The reaction was filtered through a plug of celite and evaporated. LCMS showed >99% conversion of the azide to the amine (ESMS: calculated *m*/*z* for $[M+H]^+$ = 521.26, found = 521.22). The amine was dissolved in 100 μL DMF and 10 μL DIEA. NHS-LC-Biotin (14 mg, 4.0 equiv) was added and the solution shaken for 1 h at room temperature The product was purified by direct injection onto preparative HPLC as for compound **5**. HPLC purity at 214 nm = 95%, at 250 nm >99%. ESMS: calculated *m*/*z* for $[M+H]^+$ = 860.42, found = 860.57. HRMS: calculated *m*/*z* for $[M+H]^+$ = 860.4198, found = 860.4196.

Covalent Modification of CETP. CETP (18 μM) was incubated with **14** (50 μM) in 20 mM Tris, 150 mM NaCl, pH 7.5 for 36 h at room temperature, after which it was dialyzed exhaustively against the same buffer at 4 °C.

Biosensor Analyses. SPR measurements were performed using a Biacore 3000 system (GE Healthcare, Piscataway, NJ). In typical experiments, biotinylated drug analogs were immobilized onto standard Biacore streptavidin-coated biosensor chips. CETP binding was measured at 25 °C in 20 mM Tris pH 7.4, 150 mM NaCl, 0.005% Tween 20, 1% DMSO using a flow rate of 100 μL/min. The underivatized streptavidin surface was used as a reference. Surfaces were regenerated between injections by two sequential three-second pulses of 0.1% SDS. Data were processed using Scrubber 2 software (BioLogic Software) to y-zero, x-align and double reference against buffer injections and a streptavidin surface lacking any immobilized ligand. Kinetic analyses were conducted using BIAeval software (GE Healthcare, Piscataway, NJ.).

Acetone Precipitation of CETP. HCl (0.005 mL, 0.5 M) was added to 0.042 mL of CETP (2.4 mg/mL) to give a final HCl concentration of 0.05 M. 0.150 mL of cold acetone was added and the sample was allowed to stand at −20 °C for 2 h, after which the sample was centrifuged for 10 min at 14,000 rpm in a microfuge. The supernatant was discarded and the pellet was dried in a centrifugal concentrator to remove residual acetone.

Peptic Digestion/Reduction. The acetone precipitate (~0.1 mg CETP) was dissolved in 0.1 mL of 0.05 M HCl, 8 M guanidine hydrochloride, and incubated at 50 °C for 15 min. The sample was diluted to 3 M guanidine hydrochloride, 0.001 mL of pepsin at 2 mg/mL was added, and the sample was digested for 19 h at 23 °C. The samples was then divided into two portions: (i) Nonreduced, non-neutralized sample: 0.002 mL water was added to 0.010 mL of the pepsin digest. (ii) Reduced sample: 0.001 mL 1 M Tris base and 0.001 mL 1 M DTT was added to 0.01 mL of the pepsin digest.

Reversed-Phase Liquid Chromatography−Mass Spectrometry. Peptide mapping by reversed-phase HPLC-MS was conducted by capillary HPLC using a Vydac type 218MS5.510 column (0.5 × 100 mm) running at 0.005 mL/min on an Agilent 1100 chromatograph based on a Model G1376A capillary pump and interfaced with a Thermo Finnigan LCQ ion-trap mass spectrometer. The HPLC solvents were: A, 0.02% TFA; B, 0.02% TFA in acetonitrile. From initial conditions of 1.6% B (0−2 min), the gradient consisted of steps from 1.6−35% B (2−100 min), and 35−80% B (100−110 min). The standard Finnigan electrospray interface was modified by replacing the sample needle with a coated fused silica tip (TaperTip; part number TT150−50−50-CE-5, New Objective Inc., Woburn, Massachusetts). The LCQ was controlled by Xcalibur 1.2 software (Thermo Finnigan) and set to perform data-dependent MS/MS analysis ("triple play") as described. Peptides were identified by searching the Swiss-Prot sequence database using Sequest as implemented under license by Thermo Finnigan (Sequest Browser), or the Mascot search engine (Matrix Sciences) (*12*).

Size-Exclusion Chromatography−Mass Spectrometry. SEC-MS was conducted with a Phenomenex Bio-SEC-S3000 column (300 × 4.6 mm) run at 0.2 mL/min on an Agilent 1100 chromatograph based on a Model G1312A binary pump and interfaced with a Micromass LCT electrospray/time-of-flight mass spectrometer. The HPLC solvent was 0.045% TFA in 40% acetonitrile. The LCT was controlled by MassLynx 4.0 software (Waters).

RESULTS

Affinity Ligand Synthesis. Compound **4**, a close-in analog of torcetrapib (Scheme 1), was selected as the starting structure for elaboration to potential affinity ligands. Internal (unpublished) torcetrapib SAR had shown that the methoxycarbonyl at the tetrahydroquinoline (THQ) 4-amino position could be replaced with acetyl without loss of affinity for CETP. More importantly for the present investigations, replacement of the ethyl chain of the THQ 1 position carbamate with longer alkyl chains only slightly reduced CETP binding. Hence, we investigated the value of placing different biotin-terminated spacer arms in this substituent. Condensation of 4-trifluoromethylaniline with propionaldehyde followed by addition to *N*-vinyl-*O*-benzylcarbamate provided a direct route to racemic cis-4-aminocarbobenzyloxy (Cbz) protected THQ **1**. Trifluoroacetylation of the THQ 1-amine affords an intermediate that can be readily separated into its constitutive enantiomers by chiral HPLC methods. Thus **2** was obtained, which following hydrogenation provides the suitably protected primary amine **3**. Reductive coupling of **3** with 3,5-bis-trifluoromethylbenzaldehyde followed by acetylation of the alkylated 4-amino group led to intermediate **4**. Removal of the trifluoroacetyl group with lithium hydroxide delivered key THQ **5**. Reaction of **5** with phosgene in toluene followed by evaporation of the solvent provided a carbamoyl chloride crude product in about 95% purity. We found that the THQ carbamoyl chloride reacted readily with amines, but the product ureas had significantly reduced affinity for CETP. Synthesis of high affinity urethane compounds was significantly more difficult, but reaction with excess *N*-Boc protected 6-aminohexanol in refluxing toluene did provide compound **6a** in modest yield. Finally, removal of the Boc group of compound **6a** with TFA afforded amine salt **6b**.

Putative CETP affinity ligands were prepared as shown in Scheme 2. TFA salt **6b** was coupled directly with a long chain *N*-hydroxysuccinimidyl ester of biotin (NHS-LC-Biotin) to produce compound **8**, which was purified by reverse phase HPLC. Similarly, **6b** was coupled to Fmoc-8-amino-3,6-dioxaoctanoic acid with HBTU activation, and the resulting intermediate was deblocked with piperidine/DMF and purified by preparative HPLC to provide amine salt **7**. Amines **6b** and **7** were allowed to react with the tetrafluorophenyl (TFP) ester of a PEG-biotin reagent (TFP-PEO-Biotin) to prepare compounds **9** and **10**, respectively. Control urea compound **13** was prepared from chiral THQ **11** (*11*), which features the opposite THQ stereochemistry of torcetrapib (Scheme 3). Activation of the THQ nitrogen of **11** with *p*-nitrophenylchloroformate followed by reaction with a commercially available heterobifunctional linker provided urea azide **12**, a compound that lacks

Scheme 1[a]

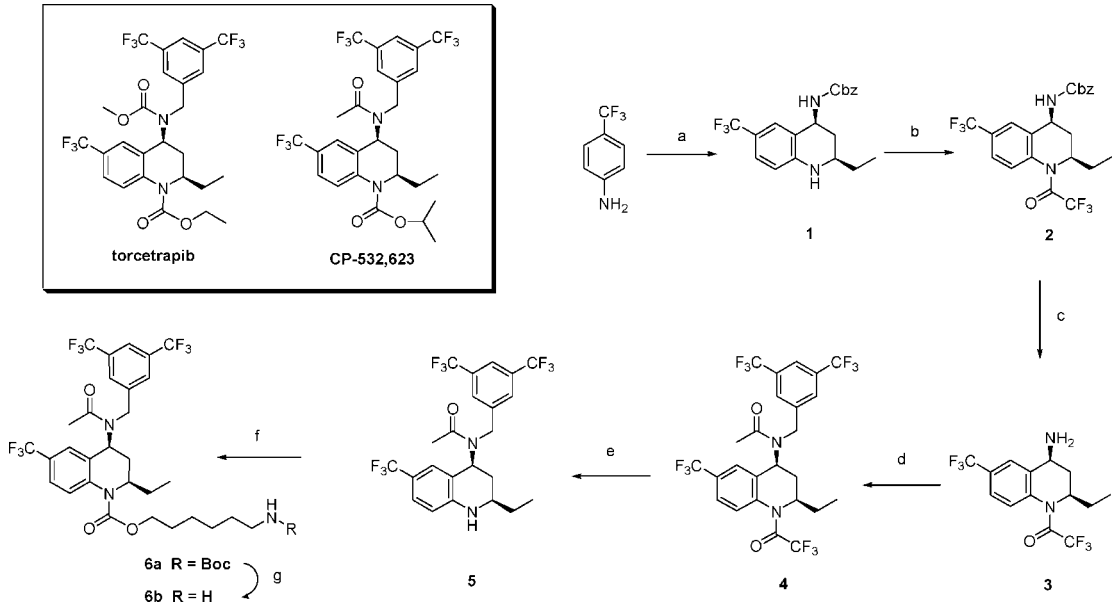

[a] Reagents and conditions: (a) (i) propionaldehyde (1.2 equiv), anhyd. Na_2SO_4, DCM, room temp, 1 h, (ii) *N*-vinyl-*O*-benzylcarbamate (1 equiv), cat. BF_3 Et_2O, room temp, 1.5 h, 47%; (b) (i) TFAA (1.3 equiv), DCM, 0−5 °C, 4 h, 85%, (ii) chiral column resolution; (c) wet 10% Pd/C, cyclohexane/EtOH, reflux, 1 h; (d) (i) 3,5-(bis)trifluoromethylbenzaldehyde (1.0 equiv), $NaBH(AcO)_3$, DCE, room temp, 18 h, (ii) AcCl (5.0 equiv), pyridine/DCM, 0 °C then room temp, 4 h, 44%; (e) LiOH, THF/water, room temp, 4 h; (f) (i) $COCl_2$ (10 equiv), toluene, reflux, 6 h, (ii) Boc-6-amino-1-hexanol (5 equiv), toluene, DIEA, reflux 24 h, 23%; (g) neat TFA, 5 min, 100%.

Scheme 2[a]

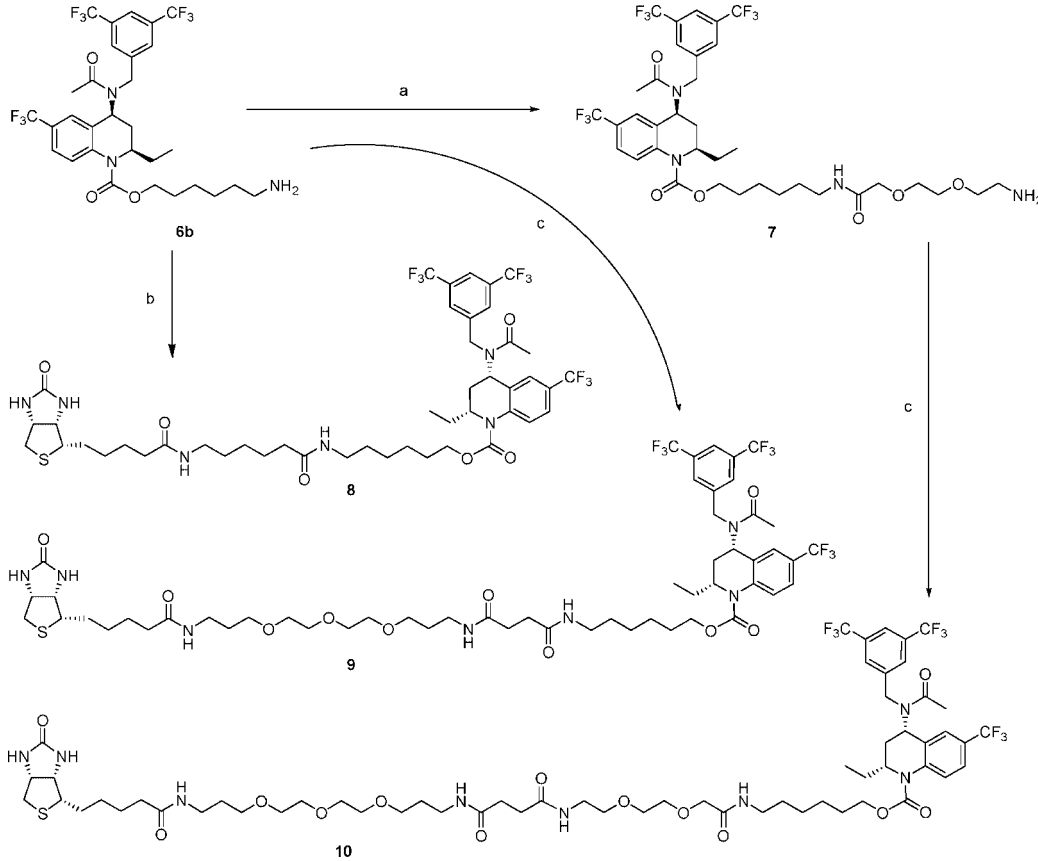

[a] Reagents and conditions: (a) (i) Fmoc-8-amino-3,6-dioxaoctanoic acid, HBTU (2 equiv.), DIEA, DMF, room temp, 1 h, (ii) piperidine (20 equiv), 28%; (b) NHS-LC-Biotin (3 equiv), DIEA, DMF, room temp, 1 h, 65%; (c) TFP-PEO-Biotin (3.8 equiv.), DIEA, DMF, room temp, 1 h, 51−55%.

detectable CETP affinity for CETP. Catalytic hydrogenation of the azide to primary amine followed by acylation with NHS-LC-Biotin provided the desired negative control compound **13**.

CETP Inhibition and Affinity Column. Compounds **6a**, **8**, **9**, and **10**, were tested for their ability to inhibit the CETP-mediated transfer of ^{3}H-labeled cholesteryl oleate from HDL

Scheme 3[a]

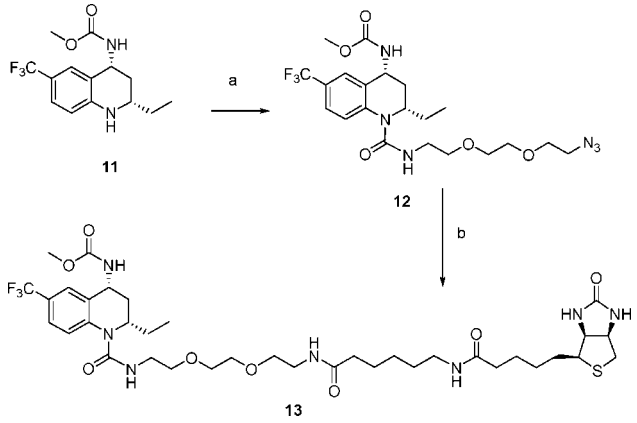

[a] Reagents and conditions: (a) (i) *p*-nitrophenyl chloroformate (2.0 equiv), THF, 40 °C, 15 h, (ii) 1-amino-11-azido-3,6,9-trioxoundacane (4.0 equiv), MeOH, DIEA, 70 °C, 48 h, 36%; (b) (i) H_2, cat. Pd/C, THF, room temp, 5 h, (ii) NHS-LC-biotin (3.5 equiv), DMF, DIEA, room temp, 1 h.

Table 1. Effects of Immobilization and Spacer Arm Length on CETP Binding

compound	phase	IC50[b] (μM)	% CETP bound[c]	capacity (μg/mL)	spacer length[e] atoms[d]	spacer length[e] nm
6a	solution	1.5	NA[a]	NA	NA	NA
8	agarose	2.3	20	75	16	2.1
9	agarose	2.6	>98	1100	28	3.5
10	solution	0.72	NA	NA	37	4.6
12	solution	>300	NA	NA	NA	NA
13	agarose	ND	19	70	21	2.5
none	agarose	NA	<3	<10	NA	NA

[a] NA = not applicable; ND = not determined. [b] Average of two determinations. [c] Reported as the percent missing from the flow-through fraction and washings as measured by SDS−PAGE, and absorbance at 280 nm following a 0.375 mg load. Additional 0.375 mg aliquots of CETP were used to determine column capacity. [d] Number of atoms between the THQ 1 position and the carboxyl group of the biotin affinity handle. [e] Estimated for fully extended conformation using average bond length = 1.48 Å and the formula (average bond length)(cos 35)(# atoms + 1).

to LDL or VLDL in 90% human plasma (*13*). All three compounds showed similar affinities for CETP, with IC_{50} values in the low micromolar range (Table 1). By comparison, the reported IC_{50} value for torcetrapib is 47 nM (*6*), indicating that the aminohexanol-derived spacers caused a 30- to 50-fold loss in binding affinity. Control compound **12,** which had the opposite stereochemistry of torcetrapib and lacked the 3,5-(bis)trifluoromethylbenzyl group, did not inhibit CETP.

Biotinyl compounds **8**, **9**, and **13** were evaluated as potential ligands for immobilization of CETP. A 0.5 mg sample of each compound was allowed to bind to 1 mL of Streptavidin Sepharose, a maximum loading density of 0.5 mg/mL agarose (~0.5 mM). Solutions of purified CETP were passed over the columns as well as over a column of Streptavidin Sepharose containing no biotinyl ligand, and the flow-through fractions were assayed for protein using SDS-PAGE and absorbance at 280 nm. When 0.37 mg of CETP was passed over Streptavidin Sepharose lacking affinity ligand, >97% of the protein was recovered from the flow-through and wash fractions, indicating no detectable binding to the matrix (Table 1). When 0.37 mg of CETP was passed over the column prepared with ligand **8**, 0.30 mg (81%) was recovered in the flow-through. Additional aliquots of protein were passed over the column of immobilized **8**, but no additional CETP bound, indicating that its total capacity for CETP was 0.07 mg/mL. This result was essentially identical to that seen with a column made from biotinylated

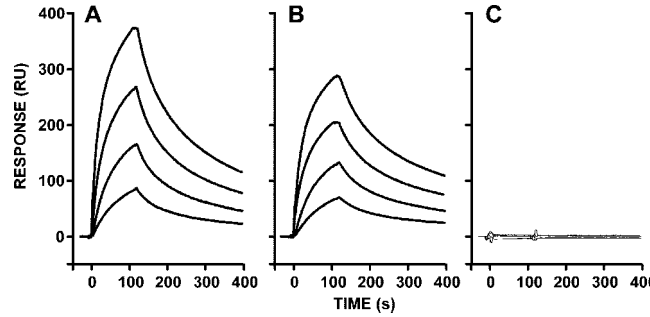

Figure 1. The effect of spacer arm length on the binding of CETP to immobilized inhibitor. Wild-type CETP at 1.7, 0.56, 0.18, and 0.06 μM was injected over (A) compound **10** (spacer 4.6 nm); (B) compound **9** (spacer 3.5 nm), and (C) compound **8** (spacer 2.9 nm). Each compound was immobilized to give a surface density of ~150 RU on the streptavidin biosensor surfaces.

control compound **13**, and suggests that CETP binding to columns of immobilized **8** and **13** was compound-dependent but nonspecific, and likely due to hydrophobic interaction with the THQ rather than to specific binding of the immobilized torcetrapib analog. In contrast, when CETP was passed over columns of immobilized **9**, essentially all of the protein bound to the column and none was detected in the flow-through fraction. By passing additional aliquots of protein over a column of **9** until overloading occurred, the CETP capacity was determined to be about 1.1 mg/mL. When dissolved in plasma, ligands **8** and **9** had similar potencies in the CE transfer assay, but **8** did not specifically bind CETP when immobilized. This strongly suggested that there was a dependence on linker length, and that the 16-atom spacer of **8** was too short for the THQ group to access the torcetrapib binding pocket when the biotin residue was bound to streptavidin.

Biosensor Analysis. Initial SPR experiments evaluated the effect of spacer length on CETP binding. When CETP was injected over biotinyl compounds **8**, **9**, and **10** immobilized on a streptavidin-coated biosensor, binding results were similar to those seen when the compounds were immobilized on Streptavidin Sepharose. No specific CETP binding was observed with **8** (Figure 1), confirming that its 16-atom spacer is too short to allow the THQ group to reach the torcetrapib binding pocket. While both **9** and **10** bound CETP (Figure 1), compound **10** had approximately 25% greater binding capacity than **9**, suggesting that the 37-atom spacer of **10** allowed greater access to the torcetrapib site than did the 28-atom spacer of **9**. All subsequent SPR experiments used immobilized **10**. A kinetic analysis of CETP binding at concentrations ranging from 2.8 μM to 0.1 μM indicated that binding was somewhat complex. However, a reasonable global fit could be made using the 1:1 Langmuir model that indicated a K_D of approximately 0.3 μM with an on-constant of 22 000 ± 200 $M^{-1}s^{-1}$ and an off-constant of 0.0064 ± 0.0001 s^{-1} (data not shown). This value correlated well with the IC_{50} of 0.7 μM obtained for **10** in the transfer assay (Table 1). Though IC_{50} is dependent on the conditions of the assay, which are different from those used in the SPR assay, a value consistent in magnitude to the calculated K_D suggests that the assay is relevant to specific binding of the compound and target. For a competitive inhibitor K_D relates to IC_{50} by the equation $K_D = IC_{50}/(1+[S]/K_m)$. When CETP was preincubated with an equimolar concentration of either torcetrapib (not shown) or its close analog CP-532,623 (*14*), binding to **10** was substantially inhibited (Figure 2), providing good evidence that immobilized **10** binds specifically to CETP in the same pocket as torcetrapib.

The test of ability to bind to immobilized **10** could then be used to survey inhibitors for evidence of binding in the

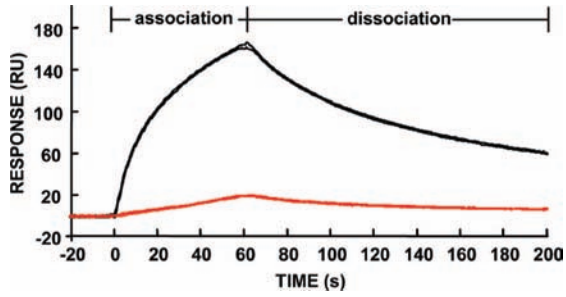

Figure 2. Preincubation with inhibitor prevents CETP binding to immobilized torcetrapib analog. Mutant CETP 444 at 1 μM was preincubated 30 min with (red) or without (black) torcetrapib analog CP-532,623 (1 μM) and injected in duplicate over immobilized 10.

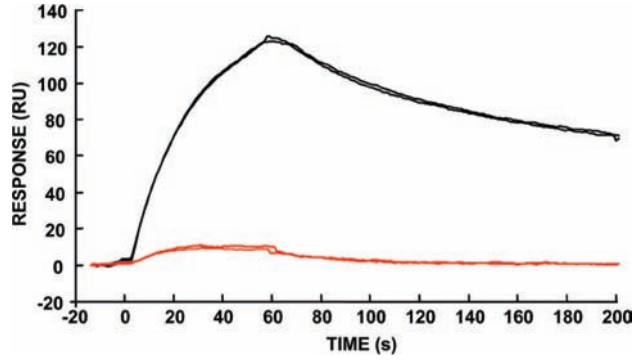

Figure 3. Modification with **14** prevents CETP binding to immobilized torcetrapib analog. Mutant CETP 444 modified with compound **14** (red) or unmodified control (black) each at 1 μM was injected in duplicate over immobilized compound **10**.

Scheme 4

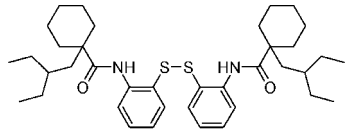

14

torcetrapib pocket. When the reportedly covalent disulfide inhibitor **14** (compound 4 of reference (*7*)) was preincubated with CETP, it blocked binding of CETP to immobilized **10** (Figure 3) and lowered its cholesteryl ester transfer activity by >90% (data not shown). The action of this compound was investigated in more detail to enhance its value as an indicator of the binding site of torcetrapib.

Stoichiometry of Modification. Site-directed mutagenesis implicated Cys-13 as the reaction site on CETP for **14** (*7*) (see Scheme 4 for structure), but could not exclude the possibility of additional modifications at other cysteine residues. To check the stoichiometry of modification, modified CETP 444 was subjected to electrospray/time-of-flight mass spectrometry using size-exclusion chromatography in 40% acetonitrile as the desalting method (Figure 4). To obtain interpretable spectra, it was necessary to remove the lone glycan on Asn-296 of CETP 444 using peptide N-glycosidase F. For unmodified CETP 444, the mass of 53 052 Da (Figure 4A) agreed acceptably well with the theoretical value of 53 046 Da, which assumes a disulfide bond between Cys-143 and Cys-184 and conversion of Asn-296 to Asp-296 during deglycosylation. The minor peak came from protein lacking residues 1−3, as verified by Edman sequencing (mass obsd. 52 765 Da; mass theor. 52 760 Da)

Peaks in the mass spectrum of CETP 444 treated with **14** gained 326 Da (major) and 321 Da (minor), respectively,

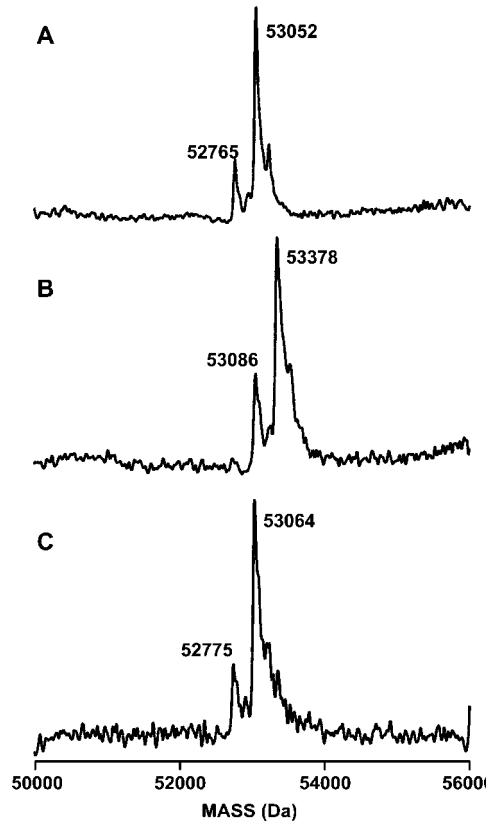

Figure 4. Mass spectrometry of CETP 444 (A) before and (B) after modification with **14** and (C) after treatment of the modified protein with dithiothreitol. The theoretical mass for deglycosylated unmodified CETP 444 (major peak) was 53046 Da, and for the same protein lacking amino acids 1−3, it was 52760 Da. The theoretical mass increase resulting from the formation of a mixed disulfide with a half-molecule of **14** was 317 Da.

consistent in this method with addition of a single half-molecule of **14** as a mixed disulfide with a protein thiol (theoretical increase 317 Da) (Figure 4B). Treatment with dithiothreitol reversed the modification, supporting the interpretation (Figure 4C).

Site of Modification by 14. The site at which **14** modified CETP 444 was determined by peptide mapping, using pepsin as the agent of digestion. Pepsin was chosen not only for its broad specificity and preference for hydrophobic sites, but also because digesting CETP at pH 2 lowered the risk of disulfide interchange reactions. In the map of the modified protein (Figure 5), new peaks in the 100−108 min range (see asterisks in Figure 5B) were attributed on the bases of novelty, mass and MS/MS-derived sequencing (not shown) to fragments containing Cys-13 disulfide-linked to the half-molecule of **14**. The peaks at 100, 104 and 108 min were attributed to fragments 1−20, 4−20 and 11−20 of CETP 444, respectively, each modified by the addition of 317.5 Da at Cys-13. Also detected, but in much lower abundance, were the modified peptides 1−21, 4−21 and 11−21. No other cysteine was modified. Peptides from unmodified CETP 444 containing Cys-13 as a free thiol were absent from the digest of the modified form (not shown). Treating the digest of the modified protein with dithiothreitol abolished the modification, confirming that it was based on a disulfide (Figure 5C).

DISCUSSION

SPR-based biosensors detect changes in refractive index that occur when molecules in solution bind to their immobilized partners in the molecular layer adjacent to the biosensor surface

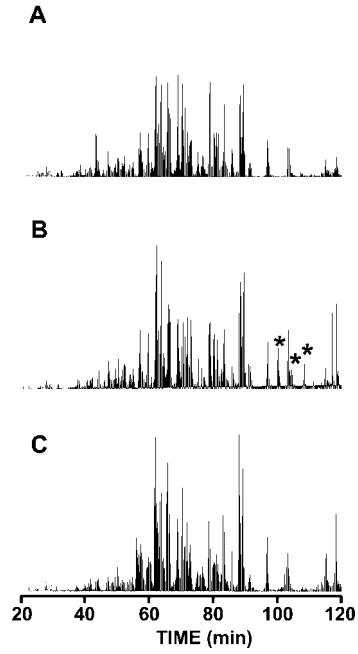

Figure 5. Base peak chromatograms from LC-MS peptide mapping analysis of (A) CETP 444; (B) CETP 444 after modification with **14**; and (C) after treatment of the modified CETP with dithiothreitol. Asterisks in panel B mark the three major peaks attributed to peptides containing the mixed disulfide bond between Cys-13 of CETP and one-half-molecule of **14**. From left to right, the three marked peaks were attributed to peptides 1−20, 4−20, and 11−20 of CETP 444 (see Table 2 for data related to the identifications).

(*15*). Early SPR technology was limited to detecting the capture of macromolecules, but refinements now make it possible to detect directly the binding of small molecules to immobilized proteins in many systems. Largely because of the availability of this technology, kinetic analyses of interactions between candidate drugs and their targets are an increasingly important aspect of drug discovery (*16*). Biosensors can now provide these analyses for a wide variety of targets beyond the classical cases of slow-binding enzyme inhibitors (*17*) and membrane-bound receptors. However, in some cases development of a method for direct biosensor kinetics is hindered by difficulties in obtaining stable and active immobilized protein or by problems associated with compound aggregation or compound binding to fluidics and reference surfaces. CETP and its inhibitors presented all of these of difficulties. (D. Cunningham, unpublished).

When direct kinetic biosensor methods are not possible, indirect inhibitor affinity data can sometimes be obtained from solution affinity experiments in which protein and ligand are mixed at various ligand concentrations and the mixtures are allowed to come to equilibrium. When the mixtures are injected over an immobilized ligand, the initial rate of protein binding to the immobilized ligand is proportional to the free (unliganded) protein concentration. For optimum results, the free protein must bind the immobilized compound to give a sufficiently robust signal when present in concentrations at or below the K_d for the competing inhibitor.

While immobilized small molecule approaches can circumvent the problems listed above, their use in SPR techniques has been limited due to the need to synthesize tagged ligands that retain useful receptor affinity when bound to SPR chips (for examples see *18–25*). In general, ligand development is an empirical process but it is aided greatly by the availability of direct structural information or compound series SAR. In the present examples we drew upon in-house (unpublished) SAR in the torcetrapib series which suggested that CETP could accommodate long linear spacer groups at the torcetrapib THQ 1 position. Thus compound **6a** was synthesized and found to exhibit an IC_{50} of 1.5 μM in a cholesteryl ester transfer assay (Table 1). The measured IC_{50} for torcetrapib in this assay is near 50 nM (*13*) indicating that **6a** suffers a 30-fold reduction in binding affinity for CETP, perhaps due to some unfavorable interactions with the protein. Nonetheless, low micromolar affinity was judged sufficient for further ligand development.

Hydrophilic spacers of different lengths were placed between biotin and the drug-like component to generate affinity ligands **8**, **9**, and **10**. In solution these ligands showed similar affinities for CETP as measured by the transfer assay but the length of the spacer arm proved to be critical for efficient CETP binding when immobilized. When the conjugates were bound to streptavidin, either on agarose matrices or biosensor surfaces, it was found that a 2.1 nm (extended length) polyethyleneglycol-based spacer was not long enough to reach the torcetrapib pocket in CETP (Figure 1). While both the 3.5 nm spacer of compound **9** and the 4.6 nm spacer of compound **10** were sufficient to allow binding to a biosensor surface, the 4.6 nm linker apparently allowed better access and provided the greatest CETP binding capacity. Preincubation of CETP with free torcetrapib analog prevented binding to immobilized **10** on a biosensor surface (Figure 2), suggesting that binding was specific and based on occupancy of the site that accommodates torcetrapib. Although the binding of CETP to the immobilized compound appeared to be complex (data not shown), a reasonable fit could be obtained using a simple 1:1 binding analysis. CETP bound to immobilized **10** with an affinity that was very similar to its affinity for **10** in solution (K_d = 0.3 μM, as compared to a transfer assay IC_{50} of 0.7 μM). This binding proved to be more than adequate for use in an affinity resin, where high immobilization densities and relatively low flow rates contribute to extensive rebinding, However, when **10** was immobilized in a biosensor for the solution affinity measurements for which it was designed, the signal was not robust at the low CETP concentrations required. This may have been in part due to variable losses of the hydrophobic CETP to instrument fluidics when injected at low concentrations.

The linker lengths reported in Table 1 are for fully extended *anti* conformations of all sp^3 hybridized linker atoms, but it is *gauche* conformations that predominate for polymers of ethylene

Table 2. Peptides Detected with the +317.2 Da Modification at Cys-13 by Peptic Peptide Mapping of CETP 444 Modified with a Half-Molecule of Disulfide 14.

fragment	sequence[a]	mass theor. (Da)[b]	mass obsd. (Da)	ions detected/theoretical[c]
1−21	ASKGTSHEAGIVC*RITKPALL	2468.4	2468.4	15/40
1−20	ASKGTSHEAGIVC*RITKPAL	2355.3	2355.5	12/36
4−21	GTSHEAGIVC*RITKPALL	2182.2	2182.0	2/30
4−20	GTSHEAGIVC*RITKPAL	2069.1	2069.1	8/28
11−21	IVC*RITKPALL	1542.9	1543.0	4/18
11−20	IVC*RITKPAL	1429.9	1430.0	10/16

[a] Asterisk indicates that the modification was at Cys-13. [b] Masses are monoisotopic. [c] Singly charged b- and y-type sequence ions in MS/MS of the peptide.

oxide (*26*). Dynamics simulation experiments performed on PEG-based linkers have shown that extended linker lengths are often overestimated and that the effective linker length of PEG linkers is probably 60−80% of that calculated here (*27*). Even taking this adjustment into account, the magnitude of the linker length dependence observed for compounds **8**, **9**, and **10** is still striking. One can rationalize this result by referring to the recently published crystal structure of CETP (*5*). The structure reveals a 6.0 nm long tunnel which traverses the length of the protein and binds two molecules of cholesteryl ester and two molecules of phospholipid. The tunnel can be accessed by either of two openings which allow entry and egress of lipid cargo molecules. The linker length data reported here support a model where torcetrapib affinity analogs enter through an opening and bind deep in the tunnel. When immobilized on an avidin support, the linker of **8** is not long enough to allow the tethered drug to reach the torcetrapib binding site (Figure 1 and Table 1). The lower CETP binding capacity observed for compound **9** relative to **10** may indicate that 3.5 nm linker length of **9** is near the minimum needed to access the torcetrapib binding site.

Despite this, the tethered torcetrapib analog proved quite valuable in another SPR application for surveying inhibitors of various chemotypes for evidence of binding either in the torcetrapib pocket or in distinct pockets (D. Cunningham, unpublished work). These experiments revealed that **14** blocks wild-type CETP binding to immobilized **10.** As **14** was thought to be a covalent inhibitor (*7*), it then became a convenient tool for the focus of the present study to locate primary sequence in proximity to the torcetrapib binding site. While a previous report provided indirect evidence for the involvement of Cys-13 in disulfide formation with a thioester closely related to **14**, the results presented demonstrated that **14** inactivates CETP by reacting with Cys-13. Mass spectrometry of the intact modified molecule demonstrated that **14** modified the simplified mutant CETP 444 with one-half-molecule of disulfide only, and peptide mapping after digestion with pepsin confirmed that the modified residue was Cys-13. Mutant CETP 444 so modified was inhibited for binding to immobilized torcetrapib analog, suggesting that torcetrapib also binds in the vicinity of Cys-13. The crystal structure of CETP (*5*) shows that indeed Cys-13 resides in the bottom of the N-terminal pocket that forms one end of the lipid-binding tunnel. This study shows that immobilized inhibitors can be useful probes in SPR even when the immobilized inhibitor has a relatively weak affinity for the target protein.

ACKNOWLEDGMENT

We are grateful to George Perkins for expert HRMS analyses.

LITERATURE CITED

(1) De Backer, G., Ambrosioni, E., Borch-Johnsen, K., Brotons, C., Cifkova, R., Dallongeville, J., Ebrahim, S., Faergeman, O., Graham, I., Mancia, G., Manger Cats, V., Orth-Gomer, K., Perk, J., Pyorala, K. L, Rodicio, J., Sans, S., Sansoy, V., Sechtem, U., Silber, S., Thomsen, T., and Wood, D. (2004) European guidelines on cardiovascular disease prevention in clinical practice. *Atherosclerosis 173*, 379–389.

(2) Brousseau, M. E., Schaefer, E. J., Wolfe, M. L., Bloedon, L. T., Digenio, A. G., Clark, R. W., Mancuso, J. P., and Rader, D. J. (2004) Effects of an inhibitor of cholesteryl ester transfer protein on HDL cholesterol. *N. Engl. J. Med. 350*, 1505–1515.

(3) Tall, A. R., Yvan-Charvet, L., and Wang, N. (2007) The failure of torcetrapib: Was it the molecule or the mechanism? *Arterioscler., Thromb., Vasc. Biol. 27*, 257–260.

(4) Connolly, D. T., McIntyre, J., Heuvelman, D., Remsen, E. E., McKinnie, R. E., Vu, L., Melton, M., Monsell, R., Krul, E. S., and Glenn, K. (1996) Physical and kinetic characterization of recombinant human cholesteryl ester transfer protein. *Biochem. J. 320*, 39–47.

(5) Qiu, X., Mistry, A., Ammirati, M. J., Chrunyk, B. A., Clark, R. W., Cong, Y., Culp, J. S., Danley, D. E., Freeman, T. B., Geoghegan, K. F., Griffor, M. C., Hawrylik, S. J., Hayward, C. M., Hensley, P., Hoth, L. R., Karam, G. A., Lira, M. E., Lloyd, D. B., McGrath, K. M., Stutzman-Engwall, K. J., Subashi, A. K., Subashi, T. A., Thompson, J. F., Wang, I.-K., Zhao, H., and Seddon, A. P. (2007) Crystal structure of cholesteryl ester transfer protein reveals a long tunnel and four bound lipid molecules. *Nat. Struct. Mol. Biol. 14*, 106–113.

(6) Clark, R. W., Ruggeri, R. B., Cunningham, D., and Bamberger, M. J. (2006) Description of the torcetrapib series of cholesteryl ester transfer protein inhibitors, including mechanism of action. *J. Lipid Res. 47*, 537–552.

(7) Okamoto, H., Yonemori, F., Wakitani, K., Minowa, T., Maeda, K., and Shinkai, H. (2000) A cholesteryl ester transfer protein inhibitor attenuates atherosclerosis in rabbits. *Nature 406*, 203–207.

(8) Hope, H. R., Heuvelman, D., Duffin, K., Smith, C., Zablocki, J., Schilling, R., Hegde, S., Lee, L., Witherbee, B., Baganoff, M., Bruce, C., Tall, A. R., Krul, E., Glenn, K., and Connolly, D. T. (2000) Inhibition of cholesteryl ester transfer protein by substituted dithiobisnicotinic acid dimethyl ester: Involvement of a critical cysteine. *J. Lipid Res. 41*, 1604–1614.

(9) Epps, D. E., and Vosters, A. F. (2002) The essential role of a free sulfhydryl group in blocking the cholesteryl site of cholesteryl ester transfer protein (CETP). *Chem. Phys. Lipids 114*, 113–122.

(10) Mattingly, P. G. (1990) Mono-protected diamines. Nα-tert-Butoxycarbonyl α,ω-alkanediamine hydrochlorides from amino alcohols. *Synthesis* 366–368.

(11) Damon, D. B., Dugger, R. W., Hubbs, S. E., Scott, J. M., and Scott, R. W. (2006) Asymmetric synthesis of the cholesteryl ester transfer protein inhibitor torcetrapib. *Org. Process Res. Dev. 10*, 472–480.

(12) Perkins, D. N., Pappin, D. J. C., Creasy, D. M., and Cottrell, J. S. (1999) Probability-based protein identification by searching sequence databases using mass spectrometry data. *Electrophoresis 20*, 3551–3567.

(13) Clark, R. W., Sutfin, T. A., Ruggeri, R. B., Willauer, A. T., Sugarman, E. D., Magnus-Aryitey, G., Cosgrove, P. G., Sand, T. M., Wester, R. T., Williams, J. A., Perlman, M. E., and Bamberger, M. J. (2004) Raising high-density lipoprotein in humans through inhibition of cholesteryl ester transfer protein: An initial multidose study of torcetrapib. *Arterioscler., Thromb., Vasc. Biol. 24*, 490–497.

(14) Kelley, R. M., McCarthy, K. E., Miller, S. A., Nesler, M. J., Schildknegt, K., Wager, C. B., and Zandi, K. S. (2004) The Synthesis of Isotopically Labeled CETP Inhibitors. *Synthesis and Applications of Isotopically Labelled Compounds*, Proceedings of the 8th International Symposium, Boston, MA, June 15, 2003, pp11−14. .

(15) Rich, R. L., and Myszka, D. G. (2007) Higher-throughput, label-free, real-time molecular interaction analysis. *Anal. Biochem. 361*, 1–6.

(16) Huber, W., and Mueller, F. (2006) Biomolecular interaction analysis in drug discovery using surface plasmon resonance technology. *Curr. Pharm. Des. 12*, 3999–4021.

(17) Morrison, J. F., and Walsh, C. T. (1988) The behavior and significance of slow-binding enzyme inhibitors. *Adv. Enzymol. Relat. Areas Mol. Biol. 61*, 201–301.

(18) Cannon, M. J., Myszka, D. G., Bagnato, J. D., Alpers, D. H., West, F. G., and Grissom, C. B. (2002) Equilibrium and kinetic analyses of the interactions between vitamin B12 binding proteins and cobalamins by surface plasmon resonance. *Anal. Biochem. 305*, 1–9.

(19) Gobi, K. V., and Miura, N. (2004) Highly sensitive and interference-free simultaneous detection of two polycyclic aromatic hydrocarbons at parts-per-trillion levels using a surface

plasmon resonance immunosensor. *Sens. Actuators, B 103*, 265–271.

(20) Jenssen, K., Sewald, K., and Sewald, N. (2004) Synthesis of marimastat and a marimastat conjugate for affinity chromatography and surface plasmon resonance studies. *Bioconjugate Chem. 15*, 594–600.

(21) Kaiser, T., Gudat, P., Stock, W., Pappert, G., Grol, M., Neumeier, D., and Luppa, P. B. (2000) Biotinylated steroid derivatives as ligands for biospecific interaction analysis with monoclonal antibodies using immunosensor devices. *Anal. Biochem. 282*, 173–185.

(22) Kanoh, N., Kyo, M., Inamori, K., Ando, A., Asami, A., Nakao, A., and Osada, H. (2006) SPR imaging of photo-cross-linked small-molecule arrays on gold. *Anal. Chem. 78*, 2226–2230.

(23) Miyashita, M., Shimada, T., Miyagawa, H., and Akamatsu, M. (2005) Surface plasmon resonance-based immunoassay for 17β-estradiol and its application to the measurement of estrogen receptor-binding activity. *Anal. Bioanal. Chem. 381*, 667–673.

(24) Schlecht, U., Nomura, Y., Bachmann, T., and Karube, I. (2002) Reversible surface thiol immobilization of carboxyl group containing haptens to a BIAcore biosensor chip enabling repeated usage of a single sensor surface. *Bioconjugate Chem. 13*, 188–193.

(25) Svedhem, S., Enander, K., Karlsson, M., Sjoebom, H., Liedberg, B., Loefas, S., Martensson, L.-G., Sjoestrand, S. E., Svensson, S., Carlsson, U., and Lundstroem, I. (2001) Subtle differences in dissociation rates of interactions between destabilized human carbonic anhydrase ii mutants and immobilized benzenesulfonamide inhibitors probed by a surface plasmon resonance biosensor. *Anal. Biochem. 296*, 188–196.

(26) Begum, R., Masatoki, S., and Matsuura, H. (1996) Conformational behavior of short poly(oxyethylene) compounds in formamide: a Raman spectroscopic study. *J. Mol. Struct. 384*, 115–120.

(27) Green, N. S., Reisler, E., and Houk, K. N. (2001) Quantitative evaluation of the lengths of homobifunctional protein cross-linking reagents used as molecular rulers. *Protein Sci. 10*, 1293–1304.

BC800165N

Chemically Reactive Derivatives of Gramicidin A for Developing Ion Channel-Based Nanoprobes

Steven Blake, Ricardo Capone, Michael Mayer,* and Jerry Yang*

Department of Chemistry and Biochemistry, University of California, San Diego, 9500 Gilman Drive, MC 0358, La Jolla, California 92093-0358, and Department of Biomedical Engineering and Department of Chemical Engineering, University of Michigan, 1101 Beal Avenue, Ann Arbor, Michigan 48109. Received May 5, 2008

Ion channel-forming peptides and proteins offer tremendous opportunities for fundamental and applied studies of function on individual molecules. An ongoing challenge in ion channel research is the lack of simple and accessible synthetic methods to engineer pores with tailored chemical and physical properties. This paper describes a practical synthetic route to rapidly generate C-terminally modified derivatives of gramicidin A (gA), an ion channel-forming peptide, through the use of two chemically reactive gA-based building blocks. These amine- and azide-containing building blocks can react readily with typical substrates for amidation and 1,3-dipolar cycloaddition ("click") reactions to present molecules with desired structure and functionality near the opening of a gA pore. These derivatives of gA are stable under typical aqueous conditions for ion channel recordings and retain characteristic single ion channel conductance properties in planar lipid bilayers. Additionally, the synthetic methods described here afford useful quantities of these gA derivatives in good purity and yield with minimal purification. We demonstrate that derivatives of gA can be used for studying, *in situ*, a change in conductance through a channel upon performing a "click" reaction on an azide moiety attached to the gA pore. We also demonstrate that these gA-based building blocks can be used to construct sensors for the recognition of specific protein−ligand binding interactions in solution. This widely accessible, enabling synthetic methodology represents a powerful new tool to study relationships between chemical structure and function on the single molecule level.

INTRODUCTION

Semisynthetic ion channels derived from natural peptides and proteins have gained increasing interest in recent years as functional nanotransducers that can amplify a signal through the transport of ions across a lipid bilayer membrane (*1–23*). Ion channels can conduct more than 10^3 ions per millisecond from a single channel opening event (*24*), making it possible to detect the ion conducting functional properties of individual supramolecular structures. This high gain amplification makes ion channels promising for fundamental studies of structure−function relationships on the single molecule level (*2–4, 25–35*) and for sensing applications (*9, 19, 36–42*). Among the most significant challenges for the development of ion channel-based probes is the lack of widely accessible, reliable, and cost-effective methods to modify these pores chemically with tailored functional groups (*43*). Here, we present a method to formally convert the C-terminal alcohol on gramicidin A (gA, **1**, a natural ion channel forming peptide) to a reactive amine or azide functionality in order to make gA readily accessible for facile and selective synthesis of ion channel-based molecular probes. We demonstrate that these two gA-based building blocks, which we call gramicidamine (**2**) and gramicidazide (**3**), are readily amenable to conventional synthetic derivatization to produce robust and active ion channels carrying tailored chemical functionality. Starting from these two building blocks, we introduce four additional, novel derivatives of gA and characterize them electrophysiologically on a single channel level. Additionally, we illustrate the usefulness of these reactive gA building blocks for development of ion channels that can be used for monitoring a "click" reaction, *in situ*, or for detecting a specific protein−ligand interaction in solution.

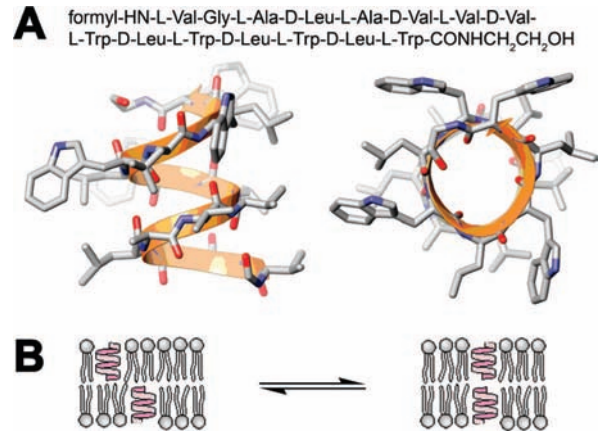

Figure 1. Cartoon showing the amino acid sequence and structure of a monomer of gramicidin A (gA) (adapted from the crystal structure of gA, 1GRM) and the reversible dimeric assembly of a gA pore in a lipid bilayer. (A) Sequence and helical structure (side view on the left and top view on the right) of gA. (B) Pore formation of gA: the reversible dimerization of two gA molecules at their N-termini via hydrogen-bonding produces an open pore that spans the lipid bilayer and conducts monovalent cations. This ion flux results in distinct and measurable conductance levels that are characteristic for certain derivatives of gA (*2, 4, 26, 43, 100, 101*).

Gramicidin A is a natural 15-amino-acid peptide (isolated from *Bacillus brevis*) that self-incorporates into lipid bilayers and facilitates a transmembrane flux of monovalent cations upon reversible head-to-head dimerization within a membrane (Figure 1). At least eight reasons make this peptide attractive as a practical molecular platform for the development of ion channel-based nanoprobes: (1) its ion conducting properties can measur-

* Author email address: jerryyang@ucsd.edu or mimayer@umich.edu. Jerry Yang: Tel 858-534-6006; Fax 858-534-4554. Michael Mayer: Tel 734-763-4609; Fax 734-647-4834.

10.1021/bc800180z CCC: $40.75 © 2008 American Chemical Society
Published on Web 07/17/2008

ably amplify a signal by monitoring a flux of ions through a single pore; (2) its current levels are distinct and quantized, which facilitate the measurement of changes in conductance on a single pore level; (3) its C-terminus is conducive to derivatization without compromising function (*2, 3, 9–12, 44–48*); (4) its availability in gram quantities from commercial sources makes it possible to generate tailored derivatives on practical scales; (5) its self-incorporation into lipid bilayers makes its use straightforward as opposed to most ion channel proteins that require incorporation into bilayers through proteoliposome fusion (*49–52*); (6) its electrophysiological characteristics are well explored, which makes it an excellent model for fundamental biophysical studies of pores in membranes; (7) its size is nanoscale, which is conducive to miniaturized device designs and may enable parallel assays developed in a high density format; and (8) its activity is localized in a membrane, a property useful for applications where control of location is important.

Figure 1A shows the sequence and helical structure of gA. Gramicidin A reversibly dimerizes in a bilayer (Figure 1B), forming an N-terminus to N-terminus dimeric structure held together by a network of hydrogen bonds (*53–55*). The C-termini in these dimeric structures are exposed to the aqueous solutions on either side of a bilayer, and C-terminal modifications affect (but do not destroy) the conductance properties of the peptide (*3, 9, 10, 12, 17*).

To date, two major synthetic approaches to install modifications at the C-terminus of gA have been employed: solid phase peptide synthesis or direct functionalization of the C-terminal alcohol of native gA. Although solid phase peptide synthesis can afford small quantities of tailored gA derivatives (*12, 27, 56–60*), esterification or carbamoylation of the C-terminal alcohol of native gA has been the dominant reported synthetic approach for constructing gA-derivatives (*3, 9–11, 25, 44, 46*). This choice of synthetic approach is presumably due to simplicity, available equipment and facilities, and cost. The poor chemical reactivity of the C-terminal alcohol on native gA, however, restricts the use of native gA for construction of gA derivatives carrying tailored functionality (*60*).

In order to develop an improved method to generate C-terminally modified derivatives of gA, we developed a practical procedure to convert large quantities of native, commercial gA to gA-based building blocks carrying reactive C-terminal functional groups. We developed a protocol to generate these gA-based building blocks with the following five goals in mind: (1) the synthetic steps must afford desired products in good purity and yield, (2) the protocol must be amenable to conversion of commercial gA on a scale of at least 100 mg, (3) the protocol must not require any HPLC purification steps (to make these gA-based building blocks readily accessible to non-synthetic laboratories), (4) the new chemical functionality introduced on the C-terminus of gA must be readily amenable to selective and chemically stable conjugation, and (5) the new chemical functionality on the C-terminus must be as close to the opening of the pore as possible (a characteristic that is, for instance, important for charge-based sensing applications *9, 10*).

Within these design constraints, we describe here a practical synthetic procedure for preparing gramicidamine **2** and gramicidazide **3**. We used these building blocks to synthesize four novel derivatives of gA and characterized them functionally by single channel recordings. We confirmed that **2** and **3** are more reactive than native gA toward desired chemical derivatization. We also demonstrated the expected increased stability under conventional ion channel recording conditions of the amide and triazole groups generated from derivatization of **2** and **3** compared to previously reported ester linkages on gA (*9–11, 25*).

To highlight the engineered, selective reactivity of the azide group in **3**, we used single channel recordings to monitor, *in situ*, a "click" reaction between **3** and propargyl sulfonate under typical conditions for 1,3-dipolar cycloaddition reactions (*61*). In addition, we demonstrated an example of a biochemically relevant sensing application of a molecule derived from **3** that reports the interaction between a sulfonamide moiety and carbonic anhydrase. Finally, we confirmed specificity of this protein−ligand interaction by competitive displacement of a gA derivative carrying a sulfonamide (**11**) with 4-carboxybenzene sulfonamide.

EXPERIMENTAL PROCEDURES

Materials. We purchased all reagents and chemicals from Sigma-Aldrich unless otherwise stated. Gramicidin A (gA) was purchased as gramicidin D from Sigma Aldrich and purified by silica chromatography using a literature procedure (*62*) (to afford a final purity of 97% of gA). Carbonic anhydrase II (CA, bovine, EC 4.2.1.1) was from Sigma-Aldrich, Inc. We purchased 1,2-diphytanoyl-*sn*-glycero-3-phosphocholine (DiPhyPC) lipids from Avanti Polar Lipids, Inc. All analyses by HPLC were performed on an Agilent Zorbax C-18 column (4.6 μm × 25 cm) using a gradient of 60% to 100% MeOH in H_2O over 52 min (flow rate = 1 mL min^{-1}.

Synthesis of 2-Aminoethyl Gramicidate (4). Gramicidin A (142 mg, 75 μmol) was added to 10 mL of acetonitrile (ACN). Phosphorus oxychloride (287 μL, 3 mmol) was added dropwise to the solution of gA and the reaction was stirred at 23 °C for 4 h. The reaction mixture was concentrated to dryness and 10 mL of a 4:1 mixture of ACN/H_2O was added. The mixture was stirred for 20 min, concentrated to dryness, and dissolved in 5 mL of a 2:1 mixture of dichloromethane (DCM)/methanol (MeOH). This mixture was added dropwise to a stirred beaker containing 200 mL of H_2O. The resulting precipitate was collected by filtration. The crude yield was 96% by weight. The retention time by HPLC was 34.7 min. ESI-MS (*m*/*z*) calculated for $C_{99}H_{140}N_{20}O_{17}$ (M^+), 1882.07; found $(M-H)^-$, 1880.85.

Synthesis of *N*-Formyl-2-aminoethyl Gramicidate. Anhydrous formic acid (0.55 mL, 14.4 mmol) was combined with acetic anhydride (1.36 mL, 14.4 mmol) and heated to 65 °C for 30 min. After cooling the formic acid/acetic anhydride solution to 23 °C, the mixture was added to 2-aminoethyl gramicidate **4** (139 mg, 72 μmol) that was dissolved in 20 mL of dry tetrahydrofuran (THF). The reaction was stirred for 3.5 h followed by concentration to dryness. We dissolved the crude product in a minimal volume of a 2:1 mixture of DCM/MeOH at 23 °C (until the solution was clear) and added this solution dropwise to a stirred beaker containing 200 mL of H_2O. The resulting precipitate was collected by filtration and taken to the next step without further purification. Note: When performing these reactions on smaller scales (<100 mg of peptides), it is possible to isolate the product by silica chromatography using DCM/MeOH (9:1) as the eluent to afford *N*-formyl-2-aminoethyl gramicidate as a white powder in 72% isolated yield. ESI-MS (*m*/*z*) calculated for $C_{100}H_{140}N_{20}O_{18}$ (M^+), 1910.07; found $(M+Na)^+$, 1932.97.

Synthesis of Desethanolamine gA (5). The crude product of *N*-formyl-2-aminoethyl gramicidate (150 mg, 78 μmol) was dissolved in 25 mL of THF. In a separate flask, $LiOH \cdot H_2O$ (327 mg, 7.8 mmol) was dissolved in 25 mL of H_2O. The two mixtures were combined and stirred at 23 °C for 3 h, followed by slow addition of 1 M HCl until the solution had a pH of 2. The reaction mixture was concentrated *in vacuo* to dryness and redissolved in 15 mL of 2:1 DCM/MeOH. The mixture was added dropwise to 150 mL of H_2O while stirring. The resulting precipitate was collected by filtration and purified by silica chromatography. The eluent initially consisted of a mixture of $CHCl_3$/MeOH/H_2O:acetic acid (750:75:10:2.5) to elute the less-polar impurities. After confirming by thin layer chromatography

(TLC) that the impurities had eluted, the eluent was changed to $CHCl_3$/MeOH/H_2O/acetic acid (200:30:4:1). The fractions containing desethanolamine gA **5** were concentrated *in vacuo*, and the resulting gel was redissolved in 15 mL of 2:1 DCM/MeOH. The mixture was added dropwise to 150 mL of H_2O while stirring. The resulting precipitate was collected by filtration to yield 93 mg of **5** (65% yield over two steps from **4**). ESI-MS (*m*/*z*) calculated for $C_{97}H_{135}N_{19}O_{17}$ $(M)^+$, 1839.03; found $(M+Na)^+$, 1861.94. The retention time by HPLC was 40.7 min.

Synthesis of Gramicidamine (2). Desethanolamine gA **5** (25 mg, 13.6 μmol) and triethylamine (7.6 μL, 54.4 μmol) were added to 1 mL of anhydrous THF and the resulting mixture was stirred and cooled to 0 °C. After adding ethyl chloroformate (5.20 μL, 54.4 μmol) to the cooled mixture, the reaction was stirred for 3.5 h at 0 °C. Mono-*tert*-butyloxycarbonyl (BOC) ethylenediamine (8.6 μL, 54.4 μmol, purchased from Alfa Aesar) was dissolved in 0.2 mL of THF and cooled to 0 °C. This solution was added to the mixture containing desethanolamine gA **5** and the resulting solution was stirred for an additional 30 min at 0 °C, followed by stirring at 23 °C for 8 h. After concentrating to dryness, the BOC-protected gramicidamine was purified using preparative silica chromatography (using a 9:1 mixture of DCM/MeOH as eluent). ESI-MS (*m*/*z*) calculated for $C_{104}H_{149}N_{21}O_{18}$ (M^+), 1981.14; found $(M-H)^-$, 1979.66. A mixture containing 1 mL of DCM, 1 mL of trifluroacetic acid (TFA), 0.1 mL of dimethylsulfide, and 0.05 mL of ethanedithiol was prepared and cooled to 0 °C. BOC-protected gramicidamine (22.4 mg, 11.3 μmol) was dissolved in the cooled mixture. The reaction was allowed to warm up to 23 °C and stirred for 3 h. The reaction mixture was concentrated *in vacuo* to dryness and purified by silica chromatography. The eluent initially consisted of a mixture of DCM/MeOH (9:1) to elute the less-polar impurities. After confirming by thin layer chromatography (TLC) that the impurities had eluted, the eluent was changed to DCM/MeOH (9:2). HR-MS (*m*/*z*) calculated for $C_{99}H_{141}N_{21}O_{16}$ $(M+H)^+$, 1881.0937; found $(M+H)^+$, 1881.0943. The retention time by HPLC was 40.5 min. The overall yield was 74% (19 mg) from desethanolamine gA **5**.

Synthesis of 7. Gramicidamine **2** (1.2 mg, 0.64 μmol), (N-BOC-protected) glycine *N*-hydroxysuccinimidyl ester (0.52 mg, 2 μmol), and diisopropylethylamine (DIEA, 0.32 μL, 2 μmol) were dissolved in 0.4 mL of THF. The reaction was stirred for 14 h at 23 °C. The product was purified by HPLC. The isolated yield of **7** was 76%. The retention time by HPLC was 43.3 min. HR-MS (*m*/*z*) calculated for $C_{106}H_{152}N_{22}O_{19}$ $(M+H)^+$, 2038.1676; found $(M+H)^+$, 2038.1661.

Synthesis of 9. Gramicidamine **2** (1.2 mg, 0.64 μmol), 4-carboxybezenesulfonamide *N*-hydroxysuccinimidyl ester (0.57 mg, 2 μmol), and DIEA (0.32 μL, 2 μmol) were dissolved in 0.4 mL of THF. The reaction was stirred for 14 h at 23 °C. The product was purified by HPLC. The isolated yield of **9** was 41%. The retention time by HPLC was 37.6 min. HR-MS (*m*/*z*) calculated for $C_{106}H_{146}N_{22}O_{19}S$ $(M+H)^+$, 2064.0928; found $(M+H)^+$, 2064.1015.

Synthesis of Sodium Propargyl Sulfonate (*63*). Propargyl bromide (1 mL, 9 mmol), purchased from Acros Organics as a solution containing 80 wt % in toluene, and sodium sulfite (1.43 g, 11.35 mmol) were dissolved in 3.5 mL of H_2O and 3.5 mL of MeOH. The mixture was stirred for 7 h at 65 °C. MeOH (60 mL) was added and the resulting precipitate was filtered and removed. The filtrate was diluted in acetone and the resulting precipitate was collected as white crystals (1.3 g, 81% yield). ESI-MS (*m*/*z*) calculated for $C_3H_3O_3S$ $(M)^+$, 118.98; found $(M)^+$, 119.04. ^{1}H NMR (D_2O, 400 MHz): δ 3.849 (d, 2H, 1.4 Hz), 2.714 (t, 1H, 1.4 Hz).

Synthesis of 2-Azidoethylammonium Chloride (*64*). Sodium azide (236 mg, 3.6 mmol) and 2-bromoethylammonium bromide (200 mg, 0.98 mmol) were dissolved in 1 mL of H_2O. The reaction was refluxed at 95 °C for 1 h. After cooling the solution to 23 °C, 1 M NaOH was added to the solution until the pH was 12. The resulting 2-azidoethylammonium chloride was then co-distilled with H_2O, acidified to pH 4 with 1 M HCl, and lyophilized to provide 76 mg of product as a white powder (65% yield). ESI-MS (*m*/*z*) calculated for $C_2H_6N_4$ $(M)^+$, 86.06; found $(M+H)^+$, 86.99. ^{1}H NMR (D_2O, 400 MHz): δ 3.414 (t, 2H, 5.6 Hz), 3.301 (t, 2H, 5.6 Hz).

Synthesis of Gramicidazide (3). Desethanolamine gA **5** (20 mg, 10.8 μmol) and DIEA (7.6 μL, 43.4 μmol) were added to 2 mL of anhydrous THF and the resulting mixture was stirred and cooled to 0 °C. After adding ethyl chloroformate (4.6 μL, 43.4 μmol) to the cooled mixture, the reaction was stirred for 3.5 h at 0 °C. Separately, 2-azidoethylammonium chloride (5.3 mg, 43.4 μmol) was dissolved in 0.2 mL of 1 M NaOH and cooled to 0 °C. This solution was added to the mixture containing desethanolamine gA and the resulting solution was stirred for an additional 30 min at 0 °C and then at 23 °C for 8 h. After concentrating to dryness, the product was purified using preparative silica chromatography (using a mixture of 9:1 DCM/MeOH as eluent) to give 14.2 mg of **3** (69% yield). HR-MS (*m*/*z*) calculated for $C_{99}H_{139}N_{23}O_{16}$ $(M+H)^+$, 1907.0842; found $(M+H)^+$, 1907.0782. The retention time by HPLC was 42.4 min.

Synthesis of 10. Gramicidazide **3** (10 mg, 5.2 μmol) and sodium propargyl sulfonate (1.2 mg, 8.6 μmol) were dissolved in 2 mL of *tert*-butanol (t-BuOH). Sodium ascorbate (8.2 mg, 41.4 μmol) was dissolved in 0.5 mL of H_2O, and $CuSO_4 \cdot 5H_2O$ (2.6 mg, 10.4 μmol) was dissolved separately in 0.5 mL of H_2O. The solution of sodium ascorbate was added to the solution of gramicidazide **3**, followed by addition of the solution of $CuSO_4 \cdot 5H_2O$. The reaction was stirred at 23 °C for 14 h. The solution was then concentrated *in vacuo* and purified by HPLC to give 32% yield of **10**. The retention time by HPLC was 36.1 min. HR-MS (*m*/*z*) calculated for $C_{102}H_{143}N_{23}O_{19}S$ $(M-H)^-$, 2025.0578; found $(M-H)^-$, 2025.0512.

Synthesis of *N*-Propargyl-4-sulfamoylbenzamide (*65*). Propargyl amine (34 μL, 0.497 mmol) and 4-carboxybenzenesulfonamide (100 mg, 0.497 mmol) were dissolved in 2 mL of dry dimethylformamide. *N*-Hydroxybenzotriazole (44.7 mg, 0.33 mmol), *O*-(benzotriazol-1-yl)-*N*,*N*,*N*′,*N*′-tetramethyluronium hexafluorophosphate (188 mg, 0.497 mmol) and DIEA (79.4 μL, 0.497 mmol) were added in this order to the stirred solution. After 4 h, the solution was evaporated to dryness and 30 mL of ethylacetate was added. The solution was washed twice with 30 mL of H_2O and with 30 mL of brine, dried over Na_2SO_4, filtered, and concentrated to dryness. The compound was purified by column chromatography using a 1:4 mixture of DCM/ethyl acetate as eluent, affording 52 mg (44% yield) as a white solid. ^{1}H NMR (DMSO-d_6, 400 MHz): δ 9.148 (t, 1H, 5.6 Hz), 8.003 (d, 2H, 8.4 Hz), 7.902 (d, 2H, 8.4 Hz), 7.506 (s, 2H), 4.075 (m, 2H), 3.172 (t, 1H, 2.4 Hz).

Synthesis of 11. Gramicidazide **3** (1.5 mg, 0.79 μmol) and *N*-propargyl-4-sulfamoylbenzamide (0.30 mg, 1.26 μmol) was dissolved in 0.2 mL of *t*-BuOH. To the solution of **3**, a solution of sodium ascorbate (1.1 mg, 5.5 μmol) dissolved in 0.05 mL of H_2O was added, followed by addition of a solution of $CuSO_4 \cdot 5H_2O$ (700 μg, 2.8 μmol) dissolved in 0.05 mL of H_2O. The reaction was stirred for 3 days. The solution was then concentrated *in vacuo* and purified by HPLC to give an 88% yield of **11**. HR-MS (*m*/*z*) calculated for $C_{109}H_{149}N_{25}O_{19}S$ $(M+H)^+$, 2145.1254; found $(M+H)^+$, 2145.1216. The retention time by HPLC was 37.6 min.

Formation of Planar Lipid Bilayers. We formed most planar lipid bilayers by the "folding technique" (*10*). Briefly, we used a Teflon film (Eastern Scientific Inc., pore diameter

0.1−0.2 mm) that we pretreated on both sides of the pore with 2 μL of 5% (v/v) hexadecane in pentane. This film was mounted using vacuum grease (Dow Corning, high vacuum grease) to a custom-made Teflon chamber separating two buffer compartments each with a volume capacity of 4 mL (*66*). After addition of 1 mL of electrolyte (20 mM KCl buffered with 0.2 mM HEPES pH 7.4 or 140 mM KCl buffered with 10 mM phosphate pH 8.0) to each compartment, we spread lipids at the air−water interface of the electrolyte solution in both compartments (specifically, we added 5 μL from a 25 mg mL^{-1} solution of 1,2-diphytanoyl-*sn*-glycero-3-phosphatidylcholine, DiPhyPC, in pentane). Three additional milliliters of the same electrolyte solution were added to each compartment to raise the liquid level above the aperture in the Teflon film. We formed the bilayers on the pore of the Teflon film by aspirating the electrolyte solution into a 3 mL syringe, followed by dispensing the electrolyte solution back into each compartment. This cycle of raising and lowering the liquid levels was repeated until we obtained a bilayer that had a minimum capacitance of 70 pF and that was stable (i.e., no significant current fluctuations above the baseline noise level) at 100 mV of applied potential for at least 2 min.

Ion Channel Measurements. We performed single channel recordings in "voltage clamp mode" using Ag/AgCl pellet electrodes (Warner Instruments) in each compartment of the bilayer setup. Data acquisition and storage was carried out using custom software in combination with an EPC-7 patch clamp amplifier from Heka (set at a gain of 10 mV pA^{-1} and a filter cutoff frequency of 3 kHz). The data acquisition board for the amplifier was set to a sampling frequency of 15 kHz. All current traces shown in the figures were further filtered using a digital Gaussian low-pass filter with a cutoff frequency of 4 Hz.

We performed the analysis of the single channel current traces by computing histograms of the currents from the original current versus time traces with *ClampFit 9.2* software from Axon Instruments. From these histograms, we extracted the main current values by fitting a Gaussian function to the peaks in the histograms. All gramicidin molecules showed a predominant conductance and occasionally subconductance states (i.e., single channel currents that were smaller than the main current values). Single channel conductances reported in this paper always refer to the main conductance state (i.e., to the dominant peaks in the current histograms). All conductance values were obtained from the slopes of current versus voltage ($I-V$) curves taken at −75, −50, +50, and +75 mV.

Monitoring a 1,3-Dipolar Cycloaddition ("Click") Reaction *in Situ* Using Single Ion Channel Recordings. We added 3 μL (from a 100 ng mL^{-1} solution in ethanol) of **3** (to afford a final concentration of 40 pM of **3**) to each compartment of a bilayer setup containing as electrolyte 20 mM KCl and 0.2 mM HEPES buffer. Solutions of sodium ascorbate and sodium propargyl sulfonate were added to both compartments to bring the final concentration of each molecule to 2 mM. We added a solution of $CuSO_4 \cdot 5H_2O$ to each compartment to a final concentration of 0.5 mM. The final pH of this solution was 6.9. In order to facilitate the analysis of single ion channel traces, we kept the concentration of **3** low (40 pM) during the reaction to minimize the possibility for multichannel events (i.e., opening of two or more channels simultaneously). This strategy made it possible to observe measured currents that would frequently return to baseline (i.e., current steps separated by no observed channel events). Consequently, we observed a small number of events over time, and thus analyzed the data over a window of time rather than at specific time points. Events were recorded over time windows of 4−15, 90−104, and 150−165 min throughout the course of the reaction. The percent composition of **3** and **10** in the reaction mixture in each time window were estimated by manually counting the number of observed single ion channel events corresponding to the conductance of **3** or **10.** For the 4−15 min time window, we measured 26 total channel events. For the 90−105 and 150−165 min time windows, we recorded 15 total channel events. Since the number of total channel events from each time window was limited to 15−26 events, the reported percent of conversion of starting material to product are estimated values. The capacitance of the folded membranes throughout the course of these studies ranged 70−88 pF. The conductivities of the buffer before and after the reaction were 323 and 336 mS cm^{-1}, respectively.

Detection of Protein−Ligand Binding Interactions Using Ion Channel Measurements. We added 1 μL (from a 100 ng mL^{-1} solution in ethanol) of **11** (to afford a final concentration of 12 pM of **11**) to each compartment of a bilayer setup containing as electrolyte 140 mM KCl and 10 mM phosphate buffer (pH 8.0). The conductance was recorded at 100 mV. Upon addition of bovine carbonic anhydrase II (CA, EC 4.2.1.1) to the trans compartment to bring the final concentration of CA to 50 μM, the membrane broke and was refolded. We recorded the conductance through the refolded membrane for 40 min to ensure that the observed reduction of ion channel activity was due to the interaction of CA with **11**. We then added 4-carboxybenzenesulfonamide (to give a final concentration of 1.5 mM of inhibitor) to the trans compartment of the bilayer setup, and again observed that the membrane broke during this addition. After refolding the membrane, we rapidly observed (within 20 s of reestablishing a planar lipid bilayer) the reemergence of significant ion channel activity. The capacitance of all folded membranes throughout the course of these studies ranged from 84−88 pF.

RESULTS AND DISCUSSION

Synthesis of Chemically Reactive Derivatives Gramicidamine 2 and Gramicidazide 3 from Native gA. In order to develop a general route to prepare functional molecular probes based on gA, we synthesized two derivatives of gA carrying chemically reactive groups on the C-terminus of the peptide. We envisioned that these reactive gA derivatives could be used as common building blocks for the synthesis of ion channels with tailored chemical functionality. One of these gA-based building blocks carried a reactive, primary amine functionality. Amines can be conjugated to readily synthesized or commercially available substrates that bear an activated ester group to form stable amide linkages (*67*). The other gA-based building block carried a C-terminal azide functionality on gA. Azides can be used as a reactive chemical group for conjugation to biomolecules due to the well-known reactivity of azides with terminal alkynes under mild conditions to furnish cycloaddition products in good yield (*61*).

To formally convert the C-terminal alcohol of native gA to an amine or azide functionality, we began with a strategy that removed the entire C-terminal ethanolamine residue of gA to afford desethanolamine gA (**5**, Scheme 1). To this end, we reacted native gA with excess $POCl_3$ to convert the C-terminal ethanolamine to a putative oxazoline intermediate, followed by treatment with H_2O in acetonitrile to afford the amino ester **4** (Scheme 1). To hydrolyze the ester in **4**, we reacted the primary amine in **4** with a formyl group (to prevent it from converting rapidly back to gA under alkaline conditions), and hydrolyzed the ester group of this *N*-formyl derivative of **4** with LiOH to give desethanolamine gA (**5**).[1] Finally, we reacted **5** with

[1]We improved on a previously reported procedure for the synthesis of **5** to afford this molecule in greater purity and with fewer purification steps compared to the original method (*J. Am. Chem. Soc.* **2007**, *129*, 9737−9745).

Scheme 1. Synthesis of Gramicidamine (2) and Gramicidazide (3)[a]

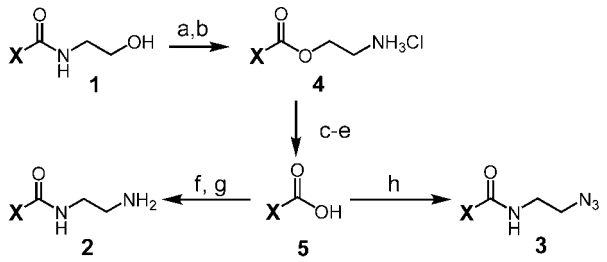

[a] (a) $POCl_3$, acetonitrile (ACN); (b) H_2O, ACN (96% yield, 2 steps); (c) acetic anhydride, formic acid, tertrahydrofuran (THF) (72% yield); (d) LiOH, H_2O, THF; (e) HCl, H_2O (65% yield, 2 steps); (f) $ClCO_2CH_2CH_3$ ($ClCO_2Et$), $N(CH_2CH_3)_3$ (NEt_3), dichloromethane (DCM) followed by *N-tert*-butyloxycarbonyl-ethylenediamine (N-BOC-ethylenediamine); (g) trifluoroacetic acid (TFA), ethanedithiol (EDT), dimethyl sulfide (Me_2S), DCM (74% yield, 2 steps); (h) $ClCO_2Et$, NEt_3, THF followed by 2-azidoethylammonium chloride, H_2O, NaOH (69% yield). All yields correspond to isolated yields.

N-BOC-ethylenediamine (followed by acidic deprotection of the BOC group) to afford the desired gramicidamine **2** or with azidoethylammonium chloride to afford the desired gramicidazide **3**.

Although the overall yields of 48% for **2** and 45% for **3** from native gA are relatively modest, we were able to convert 150 mg of native gA to 38 mg of **2** and 28 mg of **3** in two days without the need for HPLC purification (the ability to work with gA derivatives at scales above 20 mg significantly facilitates the purification of intermediates and final products by precipitation and flash column chromatography, and therefore circumvents the need for HPLC purification). Furthermore, the purities of **2** (85%) and **3** (95%) obtained from these comparably (*9, 10*) large-scale preparations were sufficient to explore the synthetic utility of these gA-based building blocks for development of four additional, novel ion channel-based probes.

Chemical Reactivity of Gramicidamine 2 and Gramicidazide 3. In order to examine whether gramicidamine **2** and gramacidazide **3** can be readily derivatized using conventional chemical methods, we tested their chemical reactivity using a set of molecules that represent typical substrates for conjugation to amine or azide groups. For gramicidamine **2**, we examined the reactivity of the amine functionality with molecules containing activated ester groups. Scheme 2 shows that **2** reacts in good yield with the *N*-hydroxysuccinimidyl (NHS) ester of *N-tert*-butyloxycarbonyl-protected (BOC-protected) glycine and with the NHS ester of 4-sulfonamidobenzoate in the presence of diisopropylethylamine (as a base catalyst). We demonstrated in several organic solvents that these common amidation conditions afforded the expected products in good yield (here, demonstrated in the case of the NHS ester of BOC-protected glycine) (Table 1), suggesting that issues of substrate solubility, which are often problematic (*68*), should not limit the ability to synthesize desired gA derivatives. For comparison, we demonstrated that native gA had little to no reactivity with the NHS ester of BOC-protected glycine in the presence of a base catalyst in a variety of organic solvents (Table 1).

Although in a few examples we and others have succeeded in esterifying the C-terminal alcohol of native gA (*9–11, 25*), these ester derivatives of gA can have limited stability under typical aqueous conditions for ion channel measurements

Scheme 2. Synthesis of gA Derivatives from gA-Based Building Blocks 2 and 3 and the Structures of Two Ester Derivatives of gA (6 and 12) Derived from Native gA[a]

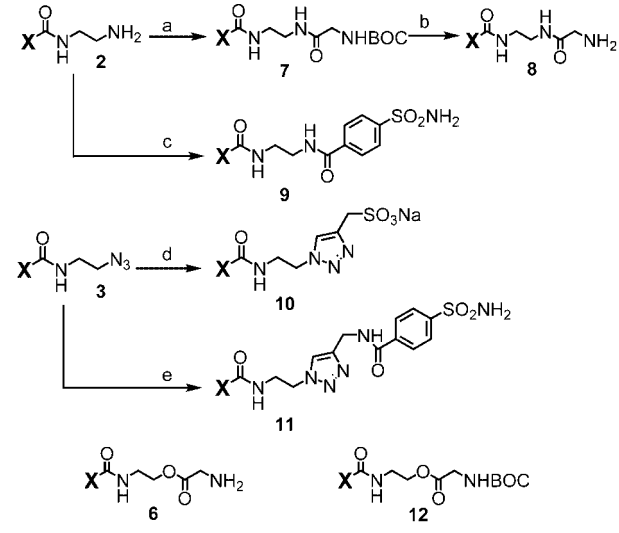

[a] (a) NHS ester of BOC-protected glycine, diisopropylethylamine (DIEA), THF; (b) TFA, Me_2S, EDT, DCM (62% yield over 2 steps); (c) NHS ester of 4-sulfonamidobenzoate, DIEA, THF (41% yield); (d) *N*-propargyl-4-sulfonamidobenzamide, $CuSO_4 \cdot 5H_2O$, sodium ascorbate, H_2O, *tert*-butanol (t-BuOH) (88% yield); (e) propargyl sulfonate, $CuSO_4 \cdot 5H_2O$, sodium ascorbate, H_2O, t-BuOH (32%).

(especially over a wide range of pH). To confirm the limited stability of ester derivatives of gA, we synthesized gramicidyl glycine (*9*) (**6**, Scheme 2) and tested its stability in acidic (pH 3.5) and in basic solutions (pH 10.4). In acidic solutions, we did not observe hydrolysis of the ester moiety of **6** after 24 h at 23 °C. We did, however, observe the expected complete hydrolysis of the ester of **6** after 3 h at 23 °C in the basic solution (as determined by HPLC analysis). For comparison, **8**, which was prepared using the method presented here and hence contained an amide linkage between the gramicidamine and a glycine group (Scheme 2) as opposed to the ester in **6**, was stable toward hydrolysis under acidic (pH 3.4) and basic (pH 10.4) conditions over a period of 24 h at 23 °C. These results highlight two important advantages of molecules derived from **2**: first, the synthetic route to molecules derived from **2** is simplified and proceeds in reasonable yield compared to molecules derived from native gA (*44*), and second, the stability of molecules derived from **2** in aqueous solutions extends the range of applications of ion channel-based probes compared to ion channels generated through direct esterification of native gA.

In addition to synthesizing gramicidamine (**2**) for direct comparison of reactivity and stability with gA, we synthesized gramicidazide (**3**) containing an azide group that is expected to have orthogonal reactivity to the C-terminal alcohol in native gA or the C-terminal amine in gramicidamine (**2**). Since organic azides undergo 1,3-dipolar cycloaddition reactions with terminal alkynes under mild conditions in water (*61*), we tested the reactivity of gramicidazide (**3**) with propargyl sulfonate and *N*-propargyl-4-sulfamoylbenzamide as representatives of typical, terminal alkyne substrates (Scheme 2). As expected, reaction of **3** with these two alkyne susbtrates in the presence of Cu^I as metal catalyst afforded triazole cycloaddition products **10** and **11** in modest to good yield (Table 1). These yields are in agreement with similar "click" reactions under comparable experimental conditions (*61*). We confirmed, as expected, that the triazole linkage in **10** resulting from conjugation of the

Table 1. Summary of Reactions of Native gA (1), Gramicidamine (2), And Gramicidazide (3) with Molecules That Represent Typical Substrates for Conjugation to Amines and Azides

compound[a]	substrate[b,c]	solvent	product	% yield[e]
2	BOC-Gly-NHS	DCM	**7**	67
2	BOC-Gly-NHS	MeCN	**7**	67
2	BOC-Gly-NHS	DMF	**7**	67
2	BOC-Gly-NHS	MeOH	**7**	65
2	BOC-Gly-NHS	THF	**7**	64
1	BOC-Gly-NHS	DCM	**12**	0
1	BOC-Gly-NHS	MeCN	**12**	0
1	BOC-Gly-NHS	DMF	**12**	0
1	BOC-Gly-NHS	MeOH	**12**	0
1	BOC-Gly-NHS	THF	**12**	0
2	NHS 4-sulfonamido-benzoate	THF	**9**	73
3	propargyl sulfonate	H_2O + *t*-BuOH[d]	**10**	32
3	*N*-propargyl-4-sulfamoyl-benzamide	H_2O + *t*-BuOH[d]	**11**	88

[a] The concentration of **1** and **2** was 1.6 mM in all cases. The concentration of **3** was 1.7 mM when reacted with sodium propargyl sulfonate and 2.6 mM when reacted with *N*-propargyl-4-sulfamoylbenzamide. [b] All reactions with **1** and **2** contained 1.5 equiv of diisopropylethylamine (DIEA) and 2 equiv of the NHS ester. The reaction between **3** and sodium propargyl sulfonate contained 8 equiv of sodium ascorbate, 3 equiv of $CuSO_4 \cdot 5H_2O$, and 1.6 equiv of sodium propargyl sulfonate. The reaction between **3** and *N*-propargyl-4-sulfamoylbenzamide contained 7 equiv of sodium ascorbate, 3.5 equiv of $CuSO_4 \cdot 5H_2O$, and 1.6 equiv of *N*-propargyl-4-sulfamoylbenzamide. [c] NHS = *N*-hydroxysuccinimidyl. [d] The solvent was a 2:1 mixture of t-BuOH:H_2O. [e] Yields were determined by HPLC.

terminal alkyne to gramicidazide is stable to acidic (pH 3.4) and basic (pH 10.4) solutions over a period of 24 h at 23 °C.

In order to demonstrate that molecules derived from **2** and **3** retained their activity as functional ion channels, we measured the single channel conductance of **2**, **3**, **7**, and **9**−**11** in planar lipid bilayers. Figure 2 shows representative single channel traces of current versus time of these gA derivatives under an applied potential of 100 mV. These current recordings illustrate that **2** and **3**, as well as derivatives generated from **2** and **3**, all retained well-defined ion channel activity.

Monitoring a "Click" Reaction *in Situ* Using Single Ion Channel Recordings. We recently reported that chemical analytes that react with (and change the charge of) functional groups attached to the opening of a gA pore can be detected using single ion channel recordings (*9, 10*). Here, we use conductance measurements to highlight the reactivity of the azide group of **3** toward reaction with terminal alkynes in the presence of a Cu^I catalyst and to demonstrate the capability to follow the course of this chemical reaction on individual pores. We used single ion channel conductance measurements to monitor, *in situ*, the conversion of the azide group in **3** to a negatively charged triazole cycloaddition product **10** (Figure 3). Since we (*10*) and others (*25, 56*) have previously shown that derivatives of gA carrying a negative charge near the opening of the pore have increased conductance compared to uncharged derivatives of gA (under conditions of low ionic strength in the recording electrolyte (*10*)), we expected the product of cycloaddition **10** to have a larger conductance than **3**. Measurement of the conductance of pure samples of **10** and **3** confirmed this prediction, indicating a single channel conductance (γ) of 4.3 ± 0.1 pS for **10** and 3.3 ± 0.1 pS for **3** under the recording conditions used to monitor the cycloaddition reaction shown in Figure 3. By making the simplifying assumption that **3** and **10** distribute equally between the bilayer and the aqueous media, we can use the difference in conductance between **3** and **10** to estimate the relative conversion of starting material **3** to product **10** throughout the course of the reaction (Figure 3).[2]

We added **3** to a final concentration of 40 pM to both 4 mL chambers of a stirred lipid bilayer setup comprised of zwitterionic 1,2-diphytanoyl-*sn*-glycero-3-phosphatidylcholine (DiPhyPC) lipids that separated two compartments containing 20 mM KCl, 0.2 mM HEPES buffer, 2 mM sodium ascorbate (as a reducing agent for Cu^{II}), and 2 mM propargyl sulfonate. The final pH of this solution was 6.9. We added $CuSO_4$ (to give a final concentration of Cu^{II} of 0.5 mM) to both chambers of the bilayer setup and recorded the single ion channel activity over time. Although we added the substrate and catalyst to both chambers of the bilayer setup, we previously showed that only changes in the chemical properties of molecules attached near the *entrance* of the pore (and not the *exit* of the pore) affect the conductance through gA-based ion channels (*3, 10*). Since we monitored this cycloaddition reaction at a constant applied potential of +75 mV, these experiments only revealed the chemical reactions on **3** occurring on the positively polarized side of the membrane (which represents the *entrance* of the pore). The table in Figure 3 summarizes the results from ion channel conductance measurements throughout the course of this reaction. When we analyzed the conductance values from ion channel events in a time window from the fourth to 15th minute after the start of the reaction, we observed that approximately 20% of the ion channel events corresponded to an ion channel with conductance value significantly higher than **3**, which we attribute to the presence of product **10.** Measurement of ion channel events over a window of time between 90−104 min of incubation revealed that the reaction between **3** and propargyl sulfonate had proceeded to give approximately 60% product. Analysis of the channel events from the reaction mixture between 150−165 min showed the same ratio of product **10** to starting material **3** as observed in the time window 90−104 min, suggesting the reaction was complete after ∼90 min. Although these reaction conditions were not optimized for this 1,3-dipolar cycloaddition reaction (*69, 70*), these results illustrate the utility of tailored gA derivatives for monitoring the progress of synthetic reactions using single ion channel conductance measurements.

Design and Synthesis of an Ion Channel-Based Sensor for Detection of Protein−**Ligand Interactions.** In order to illustrate the synthetic utility of gA-based building blocks **2** and **3** for construction of ion channel-based sensors, we carried out a proof-of-principle study for the detection of a protein−ligand interaction using ion channel recordings. In Scheme 2, we show that molecules **2** and **3** can be used to synthesize gA derivatives **9** and **11**, which both carry benzenesulfonamide moieties. Benzenesulfonamides are well-known ligands for carbonic anhydrase II (CA, EC 4.2.1.1), a Zn^{2+}-containing protein (*71–78*).

[2]This assumption is very rough since we would expect the negatively charged product **10** to partition significantly less in the membrane due its increased solubility in water compared to the neutrally "charged" starting material **3**. The yields shown in Figure 3B are, therefore, likely to be an underestimate due to the likely difference in partitioning between **3** and **10** in the membrane.

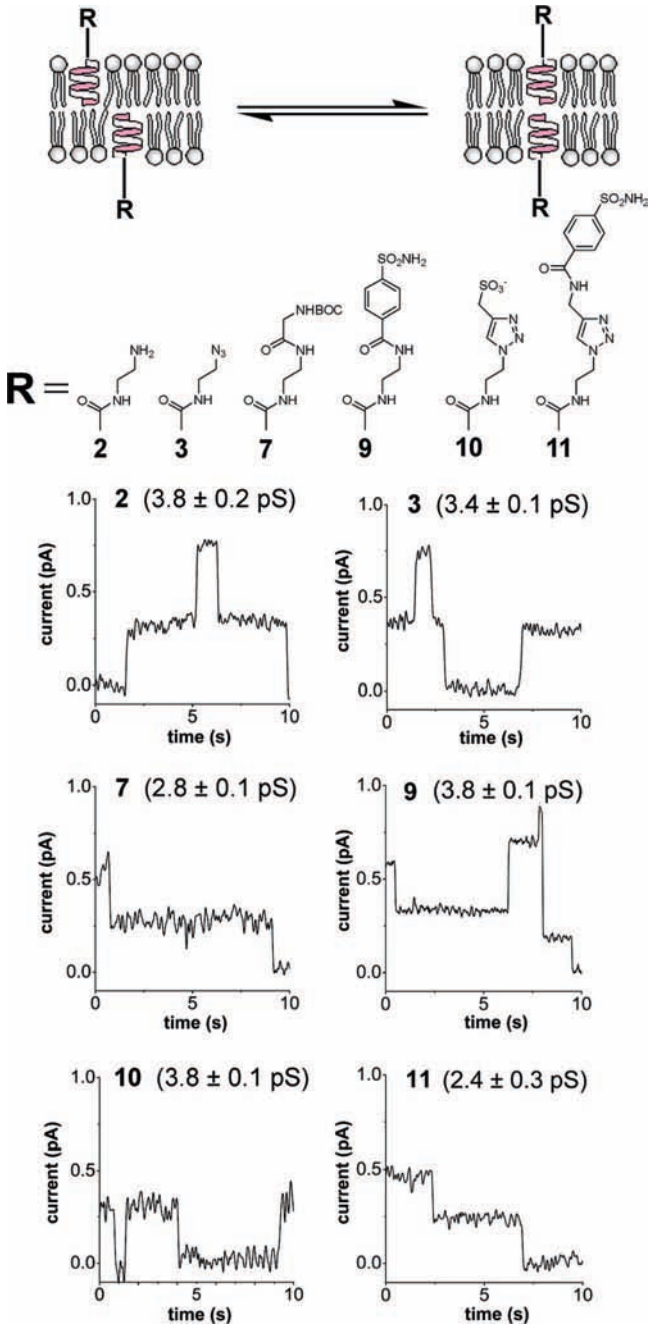

Figure 2. Cartoon illustrating the reversible dimerization of six different derivatives of gA (**2**, **3**, **7**, **9**−**11**) and original single channel traces of current versus time of all six derivatives. The applied potential was 100 mV and the electrolyte solution contained 20 mM KCl and 0.2 mM HEPES (pH 7.4) in all experiments. The conductance values (listed on top of every current trace) were determined from the slopes of current versus voltage (*I*−*V*) curves. The traces shown here were selected for clarity. Complete analysis of traces over long periods of time showed occasional subconductance states (shown here, for example, in the case of **9**). Conductance values are mean values determined from linear best fits of the *I*−*V* curves of the main conductance states in the linear range from −75 mV to +75 mV. All current traces were filtered with an analogue filter with a cutoff frequency of 3 kHz followed by filtering with a digital Gaussian filter with a cutoff frequency of 4 Hz.

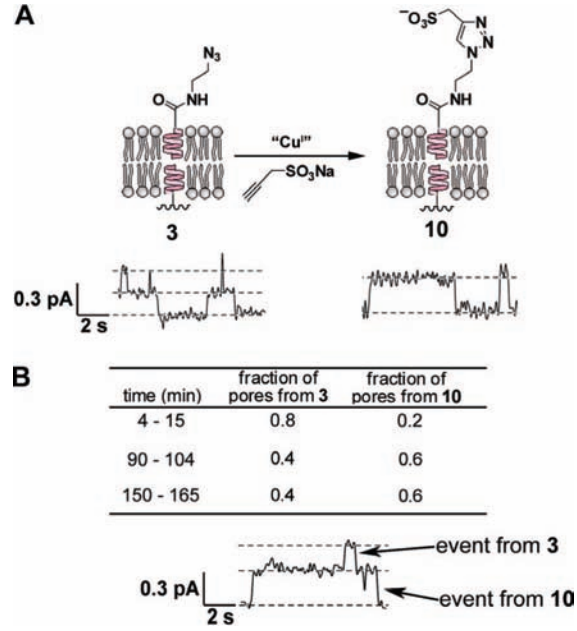

Figure 3. Conversion of gramicidazide **3** to a negatively charged triazole sulfonate **10**. (A) Cartoon of ion channels comprised of **3** and **10** in a membrane and their corresponding single ion channel conductance traces. As expected, the single channel conductance of **10** (4.3 ± 0.1 pS) was larger than the single channel conductance of **3** (3.3 ± 0.1 pS) when measured in low ionic strength recording media. (B) The table indicates the fraction of observed ion channel events that corresponded to the starting material (gramicidazide **3**) and the product of the reaction (triazole sulfonate **10**) over time windows 4−15, 90−104, and 150−165 min throughout the course of the reaction. The current versus time trace in B shows a time window during the course of the reaction where an ion channel event from **3** occured at the same time as an ion channel event from **10**. All current versus time traces were generated at an applied voltage of +75 mV in recording media containing 20 mM KCl, 0.2 mM HEPES (pH 7.4), 2 mM sodium ascorbate, 2 mM propargyl sulfonate, and 0.5 mM $CuSO_4$. The pH of the solution was 6.9. The initial concentration of **3** was 40 pM. Note: the single channel conductances of **3** and **10** are different from conductances reported in Figure 2 due to the differences in the recording buffer.

We, therefore, examined whether a derivative of gA carrying a benzenesulfonamide group could be used to detect the presence of CA in solution. In previous work, Cornell (*11*), Antonenko (*48*, *79*), and Futaki (*12*) showed the use of biotinylated derivatives of gA to detect streptavidin or an anti-biotin antibody. Here, we demonstrate that gramicidazide **3** makes it possible to expand the scope of biological interactions that can be explored using ion channel measurements by focusing on a protein−ligand interaction with a binding constant that is typically found in biology ($K_d = 10^{-6}$−10^{-9} M) such as the association of CA with a benzenesulfonamide ligand (*80*).

Figure 4A shows the conductance of multiple, simultaneous openings of pores of **11** (at a concentration of 12 pM) in a bilayer made from DiPhyPC lipids. Upon addition of CA to one side of the bilayer to give a final concentration of CA of 50 μM, we observed nearly complete suppression of ion channel activity (Figure 4B). Since the K_d for binding of benzenesulfonamides to CA can range from 10^{-6} to 10^{-9} M (*80*), it is reasonable to expect that a significant fraction of **11** would be associated with CA at these concentrations of protein and gA derivative. Two potential mechanisms can explain the decrease in observed channel activity upon binding of CA to **11** (*43*): (1) CA may have associated with **11** and caused the CA-bound **11** to partition less in the membrane compared to **11** alone (i.e., binding of CA may have extracted **11** from the bilayer), or (2) CA may have associated with membrane-bound **11** and sterically blocked ions from entering or exiting the channel (Figure 4B). Both mechanisms would result in the observed strong reduction in channel activity and they may act in parallel.

To test whether the observed strong reduction in ion channel activity shown in Figure 4B was indeed due to a specific and reversible protein−ligand binding event, we added an excess of a competitive inhibitor, 4-carboxybenzenesulfonamide, to the

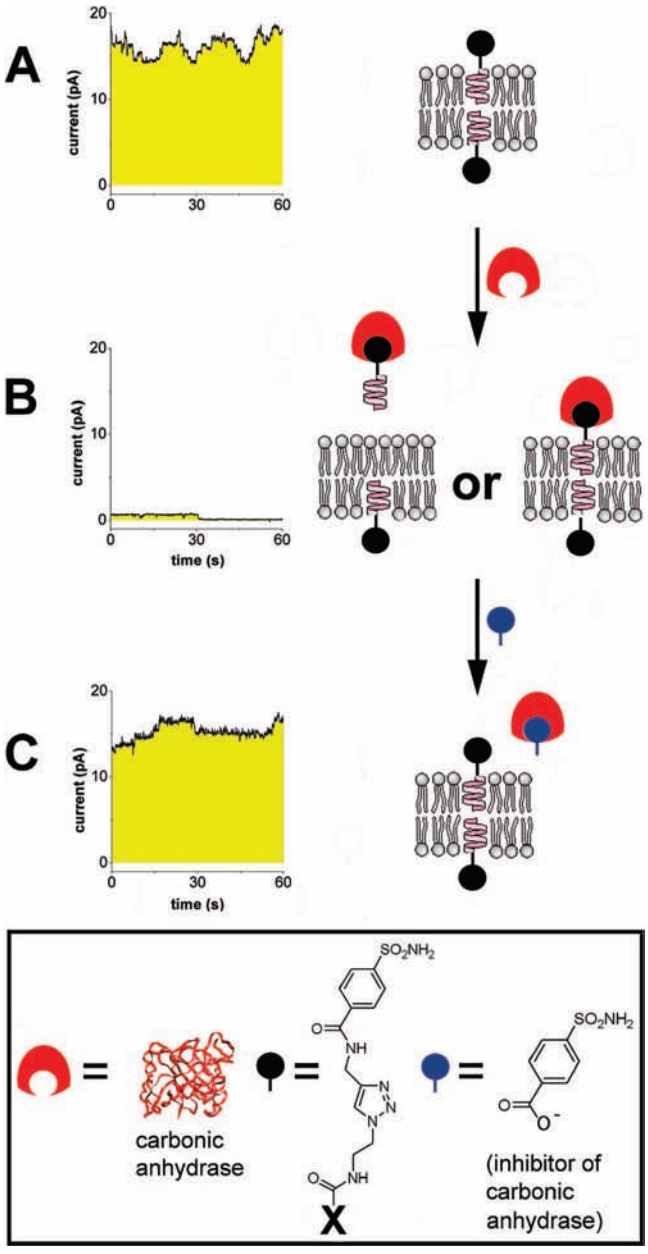

Figure 4. Detection of carbonic anhydrase (CA) with gA derivative **11**. (A) Cartoon of two molecules of **11** that dimerize to form an open pore across a membrane. The accompanying current versus time trace shows the conductance of multiple, simultaneous opening events in the membrane. (B) Binding of gA-sulfonamide **11** by CA almost completely abolished the observed transmembrane ion flux through **11**. This dramatic reduction in observed conductance could be caused either by extraction of the gA derivative from the bilayer upon binding to CA or by steric blockage of the pores by CA. (C) Addition of a competitive inhibitor of CA (4-carboxybenzenesulfonamide) restored ion channel activity and hence demonstrated specificity of binding of **11** to CA. The recording electrolyte contained 140 mM KCl and 10 mM phosphate buffer (pH 8.0). The current traces were recorded at 100 mV. **X** = HCO-Val-Gly-Ala-Leu-Ala-Val-Val-Trp-Leu-Trp-Leu-Trp-Leu-Trp-.

aqueous solution to displace **11** from CA. Upon addition of the competitive inhibitor, we observed a rapid restoration (within 20 s) of ion channel activity (Figure 4C), confirming the specificity of the interaction between CA and **11**. These results illustrate the utility of gA-based building blocks **2** and **3** for constructing specific and sensitive nanoprobes for fundamental studies of protein−ligand interactions in membranes as well as for sensing applications.

In conclusion, this paper demonstrates a practical method to synthesize chemically reactive gA-based building blocks from commercially available native gA. These amine- and azide-containing building blocks can be used to rapidly generate stable, C-terminally modified derivatives of gA that retain single channel conductance properties, and can, therefore, serve as an enabling tool for basic and applied studies on ion channels. For instance, these gA-based building blocks make it possible to tune the chemical and physical properties at the opening of the pore, which is useful for basic biophysical studies of ion channels on the single molecule level (*1*, *25*, *31*, *81*–*86*). These synthetic methods also make it possible to rapidly gain access to derivatives of gA for sensing applications, where changes in the ion flux through gA derivatives in response to a specific external stimulus can be detected using ion channel conductance measurements (*9*, *11*, *12*, *44*, *60*, *87*, *88*). Recent advances in bilayer recording technology and microfabrication (*66*, *89*–*98*) address many of the non-synthetic challenges that have also previously limited studies on ion channels such as limited mechanical stability of membranes (*6*, *19*, *66*, *89*, *99*) and poor signal-to-noise ratios for conductance measurements (*66*). A convenient and general synthetic procedure to rapidly produce gA derivatives that display specific chemical functionality, along with the availability of improved and increasingly automated commercial planar lipid bilayer setups, could make such fundamental and applied studies on ion channels accessible to a broad scientific community.

ACKNOWLEDGMENT

This work was supported by the UCSD Academic Senate, a Hellman Faculty Fellowship for J.Y., the UCSD Center for AIDS Research (NIAID 5 P30 AI36214), a National Science Foundation CAREER Award (M.M., grant No. 449088), research grant from IMRA America and AISIN USA, and seed funds from the College of Engineering, University of Michigan.

LITERATURE CITED

(1) Antonenko, Y. N., Borisenko, V., Melik-Nubarov, N. S., Kotova, E. A., and Woolley, G. A. (2002) Polyanions decelerate the kinetics of positively charged gramicidin channels as shown by sensitized photoinactivation. *Biophys. J. 82*, 1308–1318.

(2) Apell, H. J., Bamberg, E., and Alpes, H. (1979) Dicarboxylic-acid analogs of Gramicidin-A - dimerization kinetics and single channel properties. *J. Membr. Biol. 50*, 271–285.

(3) Apell, H. J., Bamberg, E., Alpes, H., and Lauger, P. (1977) Formation of ion channels by a negatively charged analog of Gramicidin-A. *J. Membr. Biol. 31*, 171–188.

(4) Apell, H. J., Bamberg, E., and Lauger, P. (1979) Effects of surface-charge on the conductance of the gramicidin channel. *Biochim. Biophys. Acta 552*, 369–378.

(5) Bayley, H. (2007) Understanding and manipulating channels and pores. *Mol. BioSyst. 3*, 645–647.

(6) Bayley, H., and Cremer, P. S. (2001) Stochastic sensors inspired by biology. *Nature 413*, 226–230.

(7) Bayley, H., and Jayasinghe, L. (2004) Functional engineered channels and pores. *Mol. Membr. Biol. 21*, 209–220.

(8) Bayley, H., Jayasinghe, L., and Wallace, M. (2005) Prepore for a breakthrough. *Nat. Struct. Biol. 12*, 385–386.

(9) Blake, S., Mayer, T., Mayer, M., and Yang, J. (2006) Monitoring chemical reactions by using ion-channel-forming peptides. *ChemBioChem 7*, 433–435.

(10) Capone, R., Blake, S., Rincon Restrepo, M., Yang, J., and Mayer, M. (2007) Designing nanosensors based on charged derivatives of Gramicidin A. *J. Am. Chem. Soc. 129*, 9737–9745.

(11) Cornell, B. A., Braach-Maksvytis, V. L. B., King, L. G., Osman, P. D. J., Raguse, B., Wieczorek, L., and Pace, R. J. (1997) A biosensor that uses ion-channel switches. *Nature 387*, 580–583.

(12) Futaki, S., Zhang, Y. J., Kiwada, T., Nakase, I., Yagami, T., Oiki, S., and Sugiura, Y. (2004) Gramicidin-based channel

systems for the detection of protein-ligand interactions. *Bioorg. Med. Chem. 12*, 1343–1350.
(13) Matile, S., Sakai, N., Mareda, J., Kumaki, J., and Yashima, E. (2006) Minireview - Sensing, threading, orienting, and cutting polymers with rigid-rod pores. *J. Recept. Signal Transduct. Res. 26*, 461–472.
(14) Ashkenasy, N., Sanchez-Quesada, J., Bayley, H., and Ghadiri, M. R. (2005) Recognizing a single base in an individual DNA strand: A step toward DNA sequencing in nanopores. *Angew. Chem., Int. Ed. 44*, 1401–1404.
(15) Banghart, M. R., Volgraf, M., and Trauner, D. (2006) Engineering light-gated ion channels. *Biochemistry 45*, 15129–15141.
(16) Gokel, G. W., Schlesinger, P. H., Djedovic, N. K., Ferdani, R., Harder, E. C., Hu, J. X., Leevy, W. M., Pajewska, J., Pajewski, R., and Weber, M. E. (2004) Functional, synthetic organic chemical models of cellular ion channels. *Bioorg. Med. Chem. 12*, 1291–1304.
(17) Hirano, A., Wakabayashi, M., Matsuno, Y., and Sugawara, M. (2003) A single-channel sensor based on gramicidin controlled by molecular recognition at bilayer lipid membranes containing receptor. *Biosens. Bioelectron. 18*, 973–983.
(18) Schoen, P., Degefa, T. H., Asaftei, S., Meyer, W., and Walder, L. (2005) Charge propagation in ion channel sensors based on protein-modified electrodes and redox marker ions. *J. Am. Chem. Soc. 127*, 11486–11496.
(19) Terrettaz, S., Mayer, M., and Vogel, H. (2003) Highly electrically insulating tethered lipid bilayers for probing the function of ion channel proteins. *Langmuir 19*, 5567–5569.
(20) Borisenko, V., Burns, D. C., Zhang, Z. H., and Woolley, G. A. (2000) Optical switching of ion-dipole interactions in a gramicidin channel analogue. *J. Am. Chem. Soc. 122*, 6364–6370.
(21) Banghart, M., Borges, K., Isacoff, E., Trauner, D., and Kramer, R. H. (2004) Light-activated ion channels for remote control of neuronal firing. *Nat. Neurosci. 7*, 1381–1386.
(22) Chambers, J. J., Banghart, M. R., Trauner, D., and Kramer, R. H. (2006) Light-induced depolarization of neurons using a modified Shaker K(+) channel and a molecular photoswitch. *J. Neurophysiol. 96*, 2792–2796.
(23) Trauner, D. (2003) Potassium channels: symmetric, selective, and sensitive. *Angew. Chem., Int. Ed. 42*, 5671–5675.
(24) Aidley, D. J., Stanfield, P. R. (1996) *Ion Channels: Molecules in Action*, Cambridge University Press, Cambridge.
(25) Bamberg, E., Alpes, H., Apell, H. J., Bradley, R., Harter, B., Quelle, M. J., and Urry, D. W. (1979) Formation of ionic channels in black lipid-membranes by succinic derivatives of Gramicidin-A. *J. Membr. Biol. 50*, 257–270.
(26) Bamberg, E., Apell, H. J., Alpes, H., Gross, E., Morell, J. L., Harbaugh, J. F., Janko, K., and Lauger, P. (1978) Ion channels formed by chemical analogs of Gramicidin-A. *Fed. Proc. 37*, 2633–2638.
(27) Bamberg, E., and Lauger, P. (1973) Channel formation kinetics of Gramicidin-A in lipid bilayer membranes. *J. Membr. Biol. 11*, 177–194.
(28) Bamberg, E., and Lauger, P. (1974) Temperature-dependent properties of Gramicidin-A channels. *Biochim. Biophys. Acta 367*, 127–133.
(29) Bamberg, E., and Lauger, P. (1977) Blocking of gramicidin channel by divalent-cations. *J. Membr. Biol. 35*, 351–375.
(30) Bamberg, E., Noda, K., Gross, E., and Lauger, P. (1976) Single-channel parameters of Gramicidin-A, Gramicidin-B and Gramicidin-C. *Biochim. Biophys. Acta 419*, 223–228.
(31) Rostovtseva, T. K., Aguilella, V. M., Vodyanoy, I., Bezrukov, S. M., and Parsegian, V. A. (1998) Membrane surface-charge titration probed by gramicidin A channel conductance. *Biophys. J. 75*, 1783–1792.
(32) Rostovtseva, T. K., Petrache, H. I., Kazemi, N., Hassanzadeh, E., and Bezrukov, S. M. (2008) Interfacial polar interactions affect gramicidin channel kinetics. *Biophys. J. 94*, L23–L25.
(33) Bamberg, E., and Benz, R. (1976) Voltage-induced thickness changes of lipid bilayer membranes and the effect of an electric field on gramicidin A channel formation. *Biochim. Biophys. Acta 426*, 570–580.
(34) Wu, M., Maier, E., Benz, R., and Hancock, R. E. (1999) Mechanism of interaction of different classes of cationic antimicrobial peptides with planar bilayers and with the cytoplasmic membrane of *Escherichia coli*. *Biochemistry 38*, 7235–7242.
(35) Boheim, G., Hanke, W., and Eibl, H. (1980) Lipid phase transition in planar bilayer membrane and its effect on carrier- and pore-mediated ion transport. *Proc. Natl. Acad. Sci. U.S.A. 77*, 3403–3407.
(36) Das, G., Talukdar, P., and Matile, S. (2002) Fluorometric detection of enzyme activity with synthetic supramolecular pores. *Science 298*, 1600–1602.
(37) Litvinchuk, S., Sorde, N., and Matile, S. (2005) Sugar sensing with synthetic multifunctional pores. *J. Am. Chem. Soc. 127*, 9316–9317.
(38) Sakai, N., Mareda, J., and Matile, S. (2007) Ion channels and pores, made from scratch. *Mol. BioSyst. 3*, 658–666.
(39) Gorteau, V., Bollot, G., Mareda, J., Pasini, D., Tran, D. H., Lazar, A. N., Coleman, A. W., Sakai, N., and Matile, S. (2005) Synthetic multifunctional pores that open and close in response to chemical stimulation. *Bioorg. Med. Chem. 13*, 5171–5180.
(40) Talukdar, P., Bollot, G., Mareda, J., Sakai, N., and Matile, S. (2005) Ligand-gated synthetic ion channels. *Chem.-Eur. J. 11*, 6525–6532.
(41) Talukdar, P., Bollot, G., Mareda, J., Sakai, N., and Matile, S. (2005) Synthetic ion channels with rigid-rod π-stack architecture that open in response to charge-transfer complex formation. *J. Am. Chem. Soc. 127*, 6528–6529.
(42) Sakai, N., Ni, C., Bezrukov, S. M., and Matile, S. (1998) Voltage-dependent ion channel formation by rigid rod-shaped polyols in planar lipid bilayers. *Bioorg. Med. Chem. Lett. 8*, 2743–2746.
(43) Mayer, M., Semetey, V., Gitlin, I., Yang, J., and Whitesides, G. M. (2008) Using ion channel-forming peptides to quantify protein-ligand interactions. *J. Am. Chem. Soc. 130*, 1453–1465.
(44) Bali, D., King, L., and Kim, S. (2003) Syntheses of new gramicidin A derivatives. *Aust. J. Chem. 56*, 293–300.
(45) Jin, X. Z., Durrant, J. D., Duffin, R., and Busath, D. D. (2004) The impact of the negative charge on cation permeation in the taurine(16)-gramicidin A channel. *Biophys. J. 86*, 206A–206A.
(46) Borisenko, V., Zhang, Z. H., and Woolley, G. A. (2002) Gramicidin derivatives as membrane-based pH sensors. *Biochim. Biophys. Acta 1558*, 26–33.
(47) Kovalchuk, S. I., Kotova, E. A., Stoilova, T. B., Sychev, S. V., Egorova, N. S., Surovoy, A. Y., Antonenko, Y. N., and Ivanov, V. T. (2007) Positively charged gramicidin A based peptides form two types of membrane channels. *Biopolymers 88*, 624–624.
(48) Antonenko, Y. N., Rokitskaya, T. I., Kotova, E. A., Reznik, G. O., Sano, T., and Cantor, C. R. (2004) Effect of streptavidins with varying biotin binding affinities on the properties of biotinylated gramicidin channels. *Biochemistry 43*, 4575–4582.
(49) Diociaiuti, M., Molinari, A., Ruspantini, I., Gaudiano, M. C., Ippoliti, R., Lendaro, E., Bordi, F., Chistolini, P., and Arancia, G. (2002) P-glycoprotein inserted in planar lipid bilayers formed by liposomes opened on amorphous carbon and Langmuir-Blodgett monolayer. *Biochim. Biophys. Acta 1559*, 21–31.
(50) Miller, C. (1986) *Ion Channel Reconstitution*, Plenum Press, New York.
(51) Ohlsson, P. A., Tjarnhage, T., Herbai, E., Lofas, S., and Puu, G. (1995) Liposome and proteoliposome fusion onto solid substrates, studies using atomic-force microscopy, quartz-crystal microbalance and surface-plasmon resonance - biological-activities of incorporated components. *Bioelectrochem. Bioenerg. 38*, 137–148.
(52) Pizzolato, F., Morelis, R. M., and Coulet, P. R. (2000) Enzymatic nanolayers from proteolipidic Langmuir-Blodgett films for biosensors. *Quim. Anal. 19*, 32–37.

(53) Gennis, R. B. (1989) *Biomembranes: Molecular Structure and Function*, Springer-Verlag, New York.
(54) Hladky, S. B., and Haydon, D. A. (1970) Discreteness of conductance change in bimolecular lipid membranes in presence of certain antibiotics. *Nature 225*, 451.
(55) Stankovic, C. J., Heinemann, S. H., Delfino, J. M., Sigworth, F. J., and Schreiber, S. L. (1989) Transmembrane channels based on tartaric acid Gramicidin-A hybrids. *Science 244*, 813–817.
(56) Roeske, R. W., Hrinyopavlina, T. P., Pottorf, R. S., Bridal, T., Jin, X. Z., and Busath, D. (1989) Synthesis and channel properties of [tau-16]Gramicidin-A. *Biochim. Biophys. Acta 982*, 223–227.
(57) Fields, C. G., Fields, G. B., Noble, R. L., and Cross, T. A. (1989) Solid phase peptide synthesis of 15N-gramicidins A, B, and C and high performance liquid chromatographic purification. *Int. J. Pept. Protein Res. 33*, 298–303.
(58) Fields, G. B., Fields, C. G., Petefish, J., Van Wart, H. E., and Cross, T. A. (1988) Solid-phase peptide synthesis and solid-state NMR spectroscopy of [Ala3−15N][Val1]gramicidin A. *Proc. Natl. Acad. Sci. U.S.A. 85*, 1384–1388.
(59) Rizzolo, F., Sabatino, G., Chelli, M., Rovero, P., and Papini, A. M. (2007) Optimized solid-phase synthesis of difficult peptide sequences: Case study of gramicidin A. *Biopolymers 88*, 620–620.
(60) Suarez, E., De, E., Molle, G., Lazaro, R., and Viallefont, P. (1998) Synthesis and characterization of a new biotinylated gramicidin. *J. Pept. Sci. 4*, 371–377.
(61) Kolb, H. C., Finn, M. G., and Sharpless, K. B. (2001) Click chemistry: Diverse chemical function from a few good reactions. *Angew. Chem., Int. Ed. 40*, 2004–2021.
(62) Stankovic, C. J., Delfino, J. M., and Schreiber, S. L. (1990) Purification of Gramicidin-A. *Anal. Biochem. 184*, 100–103.
(63) Ryu, E. H., and Zhao, Y. (2005) Efficient synthesis of water-soluble calixarenes using click chemistry. *Org. Lett. 7*, 1035–1037.
(64) Forster, M. O., and Newman, S. H. (1911) The triazo-group. Part XVII. Nitrosoazides of pinene and terpineol. *J. Chem. Soc. 99*, 244–250.
(65) Wilkinson, B. L., Bornaghi, L. F., Houston, T. A., Innocenti, A., Supuran, C. T., and Poulsen, S. A. (2006) A novel class of carbonic anhydrase inhibitors: glycoconjugate benzene sulfonamides prepared by "click"-tailing. *J. Med. Chem. 49*, 6539–6548.
(66) Mayer, M., Kriebel, J. K., Tosteson, M. T., and Whitesides, G. M. (2003) Microfabricated Teflon membranes for low-noise recordings of ion channels in planar lipid bilayers. *Biophys. J. 85*, 2684–2695.
(67) Nefkens, G. H., and Tesser, G. I. (1961) A novel activated ester in peptide synthesis. *J. Am. Chem. Soc. 83*, 1263–1263.
(68) Gee, K. R., Archer, E. A., and Kang, H. C. (1999) 4-Sulfotetrafluorophenyl (STP) esters: New water-soluble amine-reactive reagents for labeling biomolecules. *Tetrahedron Lett. 40*, 1471–1474.
(69) Rostovtsev, V. V., Green, L. G., Fokin, V. V., and Sharpless, K. B. (2002) A stepwise Huisgen cycloaddition process: Copper(I)-catalyzed regioselective "ligation" of azides and terminal alkynes. *Angew. Chem., Int. Ed. 41*, 2596–2599.
(70) Wu, P., Hilgraf, R., and Fokin, V. V. (2006) Osmium-catalyzed olefin dihydroxylation and aminohydroxylation in the second catalytic cycle. *Adv. Synth. Catal. 348*, 1079–1085.
(71) Culf, A. S., Gerig, J. T., and Williams, P. G. (1997) Tritium NMR studies of the human carbonic anhydrase I-benzenesulfonamide complex. *J. Biomol. NMR 10*, 293–299.
(72) Mahmood Ul, H., Chohan, Z. H., Scozzafava, A., and Supuran, C. T. (2004) Carbonic anhydrase inhibitors: Schiff's bases of aromatic and heterocyclic sulfonamides and their metal complexes. *J. Enzyme. Inhib. Med. Chem. 19*, 263–267.
(73) Menziani, M. C., Debenedetti, P. G., Gago, F., and Richards, W. G. (1989) The binding of benzenesulfonamides to carbonic-anhydrase enzyme - a molecular mechanics study and quantitative structure activity relationships. *J. Med. Chem. 32*, 951–956.
(74) Merz, K. M., Murcko, M. A., and Kollman, P. A. (1991) Inhibition of carbonic-anhydrase. *J. Am. Chem. Soc. 113*, 4484–4490.
(75) Saczewski, F., Innocenti, A., Brzozowski, Z., Slawinski, J., Pomarnacka, E., Kornicka, A., Scozzafava, A., and Supuran, C. T. (2006) Carbonic anhydrase inhibitors. Selective inhibition of human tumor-associated isozymes IX and XII and cytosolic isozymes I and II with some substituted-2-mercapto-benzenesulfonamides. *J. Enzyme. Inhib. Med. Chem. 21*, 563–568.
(76) Santos, M. A., Marques, S., Vullo, D., Innocenti, A., Scozzafava, A., and Supuran, C. T. (2007) Carbonic anhydrase inhibitors: Inhibition of cytosolic/tumor-associated isoforms I, II, and IX with iminodiacetic carboxylates/hydroxamates also incorporating benzenesulfonamide moieties. *Bioorg. Med. Chem. Lett. 17*, 1538–1543.
(77) Supuran, C. T., and Scozzafava, A. (2000) Carbonic anhydrase inhibitors: Aromatic sulfonamides and disulfonamides act as efficient tumor growth inhibitors - Part 95. *J. Enzyme. Inhib. 15*, 597–610.
(78) Gitlin, I., Mayer, M., and Whitesides, G. M. (2003) Significance of charge regulation in the analysis of protein charge ladders. *J. Phys. Chem. B 107*, 1466–1472.
(79) Rokitskaya, T. I., Kotova, E. A., and Antonenko, Y. N. (2003) Tandem gramicidin channels cross-linked by streptavidin. *J. Gen. Physiol. 121*, 463–476.
(80) Lahiri, J., Isaacs, L., Grzybowski, B., Carbeck, J. D., and Whitesides, G. M. (1999) Biospecific binding of carbonic anhydrase to mixed SAMs presenting benzenesulfonamide ligands: A model system for studying lateral steric effects. *Langmuir 15*, 7186–7198.
(81) Bastug, T., Gray-Weale, A., Patra, S. M., and Kuyucak, S. (2006) Role of protein flexibility in ion permeation: A case study in gramicidin A. *Biophys. J. 90*, 2285–2296.
(82) Biswas, S. C., Rananavare, S. B., and Hall, S. B. (2005) Effects of gramicidin-A on the adsorption of phospholipids to the air-water interface. *Biochim. Biophys. Acta 1717*, 41–49.
(83) Broniatowski, M., Obidowicz, K., Vila Romeu, N., Broniatowska, E., and Dynarowicz-Latka, P. (2007) Mixed Langmuir monolayers of gramicidin A and fluorinated alcohols. *J. Colloid Interface Sci. 313*, 600–607.
(84) Durrant, J. D., Caywood, D., and Busath, D. D. (2006) Tryptophan contributions to the empirical free-energy profile in gramicidin A/M heterodimer channels. *Biophys. J. 91*, 3230–3241.
(85) Portella, G., Pohl, P., and de Groot, B. L. (2007) Invariance of single-file water mobility in gramicidin-like peptidic pores as function of pore length. *Biophys. J. 92*, 3930–3937.
(86) Wang, Z., and Fried, J. R. (2007) A hierarchical approach for predicting the transport properties of the gramicidin A channel. *Soft Matter 3*, 1041–1052.
(87) Woolley, G. A., Zunic, V., Karanicolas, J., Jaikaran, A. S. I., and Starostin, A. V. (1997) Voltage-dependent behavior of a "ball-and-chain" gramicidin channel. *Biophys. J. 73*, 2465–2475.
(88) Anastasiadis, A., Morton, C. J., Talbo, G. H., Koeppe, R. E., and Separovic, F. (2006) Effect of linker length on avidin binding to biotinylated gramicidin A. *Int. J. Pept. Res. Therap. 12*, 243–252.
(89) Schmidt, C., Mayer, M., and Vogel, H. (2000) A chip-based biosensor for the functional analysis of single ion channels. *Angew. Chem., Int. Ed. 39*, 3137–3140.
(90) Uram, J. D., Ke, K., Hunt, A. J., and Mayer, M. (2006) Label-free affinity assays by rapid detection of immune complexes in submicrometer pores. *Angew. Chem., Int. Ed. 45*, 2281–2285.
(91) An, R., Uram, J. D., Yusko, E. C., Ke, K., Mayer, M., and Hunt, A. J. (2008) Ultrafast laser fabrication of submicrometer pores in borosilicate glass. *Opt. Lett. 33*, 1153–1155.
(92) Fertig, N., Meyer, C., Blick, R. H., Trautmann, C., and Behrends, J. C. (2001) Microstructured glass chip for ion-channel electrophysiology. *Phys. Rev. E: Stat. Nonlin. Soft Matter Phys. 64*, 040901.

(93) Borisenko, V., Lougheed, T., Hesse, J., Fureder-Kitzmuller, E., Fertig, N., Behrends, J. C., Woolley, G. A., and Schutz, G. J. (2003) Simultaneous optical and electrical recording of single gramicidin channels. *Biophys. J. 84*, 612–622.

(94) Jeon, T. J., Malmstadt, N., and Schmidt, J. J. (2006) Hydrogel-encapsulated lipid membranes. *J. Am. Chem. Soc. 128*, 42–43.

(95) Malmstadt, N., Jeon, L. J., and Schmidt, J. J. (2008) Long-lived planar lipid bilayer membranes anchored to an in situ polymerized hydrogel. *Adv. Mater. 20*, 84+.

(96) Malmstadt, N., Nash, M. A., Purnell, R. F., and Schmidt, J. J. (2006) Automated formation of lipid-bilayer membranes in a microfluidic device. *Nano Lett. 6*, 1961–1965.

(97) Shim, J. W., and Gu, L. Q. (2007) Stochastic sensing on a modular chip containing a single-ion channel. *Anal. Chem. 79*, 2207–2213.

(98) White, R. J., Ervin, E. N., Yang, T., Chen, X., Daniel, S., Cremer, P. S., and White, H. S. (2007) Single ion-channel recordings using glass nanopore membranes. *J. Am. Chem. Soc. 129*, 11766–11775.

(99) Peterman, M. C., Ziebarth, J. M., Braha, O., Bayley, H., Fishman, H. A., and Bloom, D. M. (2002) Ion channels and lipid bilayer membranes under high potentials using microfabricated apertures. *Biomed. Microdevices 4*, 231–236.

(100) Gross, E., Morell, J. L., Bamberg, E., and Lauger, P. (1977) The synthesis and ion transport properties of gramicidin analogs. *Fed. Proc. 36*, 864.

(101) Janko, K., Bamberg, R. R., E., Apell, H.-J., Alpes, H., Lauger P. (1983) *Peptides: Structure and Function*, Pierce Chemical Company, Rockford.

BC800180Z

Acetal Linked Oligoethylenimines for Use As pH-Sensitive Gene Carriers

Veronika Knorr,[†,‡] Verena Russ,[†,‡] Lars Allmendinger,[§] Manfred Ogris,[†,‡] and Ernst Wagner*[,†,‡]

Pharmaceutical Biology - Biotechnology and Pharmaceutical Chemistry, Department of Pharmacy Ludwig-Maximilians-Universität München, Butenandtstr. 5-13, D-81377 Munich, Germany. Received May 7, 2008; Revised Manuscript Received June 7, 2008

Two types of acid-degradable nonviral gene carriers, OEI-MK and OEI-BAA, were synthesized by polymerizing oligoethylenimine of 800 Da (OEI800) with the pH-sensitive acetone ketal cross-linker 2,2-bis(*N*-maleimidoethyloxy) propane (MK) or the 4-methoxybenzaldehyde bisacrylate acetal cross-linker 1,1-bis-(2-acryloyloxy ethoxy)-[4-methoxy-phenyl]methane) (BAA). Corresponding acid-insensitive counterparts (OEI-BM and LT-OEI-HD) were synthesized as well, representing control polymers. Kinetics of hydrolysis were measured and confirmed the pH-dependent degradation profile of the acetal functions, with short half-lives of 3 min at pH 5.0, and 5 h (OEI-MK) or 3.5 h (OEI-BAA) at physiological pH 7.4 and 37 °C. DNA polyplexes of a luciferase expression plasmid were tested for gene transfer efficiency and biocompatibility in two cell lines (B16F10 and Neuro2A). Polyplexes with acid-labile polymers showed an improved toxicity profile compared to those made with acid-stable polymer analogues. At low cation/plasmid (c/p) w/w ratios the transfection efficiency of pH-sensitive polymers was slightly reduced, but it became similar or superior to the efficiency of acid-stable polymers at higher c/p ratios. An improved *in vivo* biocompatibility of the acid-degradable polymers over the stable control polymers was confirmed by liver histology after systemic administration of polymers in Balb/c mice.

INTRODUCTION

The design of vectors that mediate gene transfer efficiently but do not cause appreciable toxic side-effects is still a major challenge in the field of nonviral gene delivery. High transfection efficiency is almost always associated with high vector toxicity. For example, polyethylenimines (PEI) of molecular weight around 22−25 kDa mediate gene transfer very effectively (*1*, *2*) but cause considerable toxic effects (*3*, *4*) and are not degradable into small excretable degradation products. In contrast, shorter polyethylenimines such as 800 Da OEI possess just negligible toxicity, but exhibit only very poor gene transfer capacity. Therefore, one approach toward safer vectors designs biodegradable polycations of adequate sizes, which allow gene transfer as effective as their stable PEI counterparts, but with time or upon a specific stimulus, decompose into nontoxic degradation products. Researchers have inserted diverse degradable functions into their polymers, including disulfide bonds (*5–9*), ester bonds (*6*, *10–12*), imines (*13*), or phosphoesters (*14*, *15*).[1]

In the current work, we focused on developing gene carriers containing acid cleavable acetal functions. Acetal groups have already been introduced into polymers (*16*, *17*) to allow triggered degradation at a slightly acidic pH such as the endosomal pH. Thus, drug carriers can be produced that are sufficient stable at physiological pH of 7.4 to mediate efficient drug delivery to the target cell. Upon endocytosis, degradation of the acid-sensitive polymeric carriers in the maturing and acidifying endosome should result in small decomposition products with enhanced biocompatibility. In this article we present the synthesis and characterization of two acetal linked polymer types: OEI-MK is generated from 800 Da oligoethylenimine (OEI) and 2,2-bis(*N*-maleimidoethyloxy) propane (MK) as pH-sensitive ketal linker (*18*), and OEI-BAA is synthesized from OEI and the 1,1-bis (2-acryloyloxy ethoxy)-[4-methoxy-phenyl]methane) (BAA) linker (*19*). To investigate a possible advantage of the pH sensitivity, the pH-labile polymers were compared with homologous acid-insensitive polymers OEI-BM and LT-OEI-HD, with the acid-sensitive functions being replaced by a stable ether or a hydrocarbon moiety, respectively.

EXPERIMENTAL SECTION

Chemicals and Reagents. Dimethylsulfoxide purissimum (DMSO) and dichloromethane purissimum (DCM) were obtained from Fluka (Fluka Chemie GmbH, Deisenhofen, Germany). Acetone and *n*-heptane were distilled prior to use. Oligoethylenimine with an average molecular mass of 800 Da (OEI800), branched PEIs with average molecular weights of 2, 10, 25, and 50 kDa (PEI2K, PEI10K, PEI25K, PEI50K), 1,6-hexanediol diacrylate (HD), *p*-methoxybenzaldehyde, 2-hydroxyethyl acrylate, *p*-toluene sulfonic acid, and triethylamine (TEA) were purchased from Sigma-Aldrich (Munich, Germany). 1,8-Bis-maleimidodiethyleneglycol (BM) was purchased from

* To whom correspondence should be addressed. Phone: ++49-89-2180-77841. Fax: + +49-89-2180-77798. E-mail: ernst.wagner@cup.uni-muenchen.de.

† Pharmaceutical Biology - Biotechnology.

§ Pharmaceutical Chemistry, Department of Pharmacy, Center for Drug Research.

‡ Center for NanoScience.

[1] Abbreviations: OEI800, oligoethylenimine with an average molecular weight of 800 Da; PEI22K, linear polyethylenimine with an average molecular weight of 22 kDa; PEI2K, PEI10K, PEI25K, PEI50K, branched polyethylenimines with an average molecular weight of 2 kDa, 10 kDa, 25 kDa or 50 kDa; MK, 2,2-bis(*N*-maleimidoethyloxy) propane; BM, 1,8-bis-maleimidodiethyleneglycol; BAA, 1,1-bis-(2-acryloyloxy ethoxy)-[4-methoxy-phenyl]methane); HD, 1,6-hexanediol diacrylate; EtBr, ethidium bromide; pDNA, plasmid DNA; RLU, relative light units; FCS, fetal calf serum; Hepes, *N*-2-hydroxyethylpiperazine-*N*′-2-ethane sulfonic acid; HBG, Hepes buffered glucose (5% (w/v) glucose, 20 mM Hepes, pH 7.4); HBS, Hepes buffered salt (5% glucose (w/v), 150 mM NaCl, 20 mM Hepes, pH 7.4); s.d., standard deviation; pDNA, plasmid DNA; c/p ratio, cation/plasmid weight/weight ratio; m.w., molecular weight; M_w, molecular weight by weight; M_n, molecular weight by number; M_p, molecular weight at peak maximum; d*n*/d*c*, differential index of refraction.

10.1021/bc8001858 CCC: $40.75 © 2008 American Chemical Society
Published on Web 07/16/2008

Pierce Biotechnology, Inc., Rockford, USA. 2,2-Bis(*N*-maleimidoethyloxy) propane (MK) can be synthesized as described (*18*) and was purchased from Organix Inc., Woburn, Massachusetts, USA. 1,1-Bis-(2-acryloyloxy ethoxy)-[4-methoxyphenyl]methane) (BAA) was synthesized as described (*19*). The resulting crude product was purified by flash column chromatography on silica gel equilibrated with the eluent (*n*-heptane/acetone 8.2/1.8 + 1% TEA) and BAA was obtained as a colorless oil with 100% purity as confirmed by ^{1}H NMR. Linear PEI of 22 kDa (PEI22K) was synthesized by acid-catalyzed deprotection of poly(2-ethyl-2-oxazoline) (50 kDa, Aldrich) in analogous form as described in ref (*20*). Superdex 75 preparative grade and Superdex 200 preparative grade were obtained from GE Healthcare Europe GmbH (Freiburg, Germany). Cell culture media, antibiotics, and fetal calf serum (FCS) were purchased from Life Technologies (Karlsruhe, Germany). Plasmid pCMVLuc (*Photinus pyralis* luciferase under control of the CMV enhancer/promoter) described in ref (*21*) was purified with the EndoFree Plasmid Kit from Qiagen (Hilden, Germany). Dialysis was performed with Spectra/Por membranes (molecular mass cutoff 3.5 kDa; Spectrum Laboratories Inc., Rancho Dominguez, CA, USA) at 4 °C. Water was used as purified, deionized water. Silica gel column chromatography was performed on silica gel 60 Å (35−70 μm) from Acros (Acros Organics, Geel, Belgium). Infrared spectra were recorded on a Jasco FT/IR-410 spectrometer (Jasco Labor und Datentechnik GmbH, Germany). ^{1}H NMR spectra were recorded on a Jeol JNMR-GX400 (400 MHz) or a Jeol JNMR-GX500 (500 MHz) spectrometer. Chemical shifts are reported in ppm; data are reported as s = singlet, d = doublet, t = triplet, m = multiplet; br = broad.

Synthesis of pH-Stable Polymer OEI-BM. BM (15.4 mg; 50 mg/mL in anhydrous DMSO) was added dropwise and under vortexing to OEI800 (40 mg; 400 mg/mL in anhydrous DMSO) and reacted for 22 h at 22 °C under constant shaking. Prior to purification, the reaction mixture was diluted 1:4 with 1 M Hepes buffer pH 7.5 containing 4 M sodium chloride. Dialysis was carried out at 4 °C in 20 mM Hepes buffer pH 7.5 containing 0.25 M sodium chloride using a Spectra/Por membrane (molecular mass cutoff 3.5 kDa). After 4 h, the buffer was exchanged against water; water was then replaced twice by fresh water. After a total dialysis duration of 26 h, the purified product was lyophilized (yield 48%) and stored at −80 °C in dry form. According to NMR analysis, the molar ratio of BM to OEI800 in the product was 1.3/1.

^{1}H NMR (500 MHz, D_2O): δ = 3.77 (t, 4H, NCH_2CH_2O), 3.69 (s, 4H, OCH_2CH_2O linker ethylene), 3.64 (t, 2H, COCHCH_2 of linker succinimide), 3.59−2.35 (br m; 72H NCH_2 of OEI ethylenes; 4H NCH_2CH_2O of linker ethylenes and 4H COCH_2CH of linker succinimide).

Synthesis of Acid-Degradable Polymer OEI-MK. MK (16.1 mg; 50 mg/mL in anhydrous DMSO) was added dropwise under vortexing to OEI800 (40 mg; 400 mg/mL in anhydrous DMSO) and the mixture was reacted for 22 h at 22 °C while shaking constantly. Purification and lyophilization were performed as indicated above for OEI-BM (yield 40%). The dry polymer was stored at −80 °C. According to NMR analysis the molar ratio of MK-linker versus acetone ketal versus OEI800 in the product was 1.03/0.93/1.

^{1}H NMR (400 MHz, D_2O): δ = 3.75 (t, 4H, OCH_2), 3.72−2.30 (br m; 72H NCH_2 of OEI ethylenes; 10H NCH_2 of linker ethylene and COCHCH_2 of linker succinimide), 1.45−1.25 (m, 6H, CH_3 linker of acetone ketal).

Synthesis of Acid-Degradable Polymers OEI-BAA. BAA (14 mg at 50 mg/mL in anhydrous DMSO for the synthesis of OEI-BAA-1 polymers, 28 mg at 50 mg/mL for the synthesis of OEI-BAA-2, or 17.5 mg at 500 mg/mL for the synthesis of BAA-1.25) was added dropwise under vortexing to OEI800 (32 mg; 400 mg/mL in anhydrous DMSO) and reacted for 3 days (OEI-BAA-1−3d, OEI-BAA-2−3d), 1.5 days (OEI-BAA-1−1.5d) or 45 min (OEI-BAA-1−45m, OEI-BAA-1.25−45m) at 22 °C with constant shaking. Purification and lyophilization were performed as indicated above for OEI-BM, with the difference that total dialysis duration at 4 °C was only 15 h to prevent degradation. The yields were 40%, 56%, and 70% in the cases of OEI-BAA-1−3d, −1.5d, and 1−45m, respectively; 50% yield in the case of OEI-BAA-2−3d; and 58% in the case of OEI-BAA-1.25−45m. Polymers were stored at −80 °C. According to NMR analysis the molar BAA/OEI800 ratios and the content of intact diester in the products were 0.3/1 and 26% for (OEI-BAA-1−3d), and 0.7/1 and 26% for OEI-BAA-2−3d. Reduction of reaction time (to 1.5 days or 45 min) increased intact BAA incorporation, providing a 0.4/1 BAA/OEI ratio with a 40% diester content for OEI-BAA-1/1−1.5d, a 0.44/1 ratio with 75% diester for OEI-BAA-1−45m, and a 0.56/1 ratio with 60% diester for OEI-BAA-1.25−45m.

^{1}H NMR (400 MHz, D_2O): δ = 7.50−7.37 (m, 2H, CHCHCOCH$_3$ of aromatic ring), 7.08−6.96 (m, 2H, CHCOCH$_3$ of aromatic ring), 5.68−5.53 (m; 1H, acetal H), 4.35−4.28 (m, COOCH_2; 2H, monoester* or 4H, diester), 4.00−2.30 (br m; 72H, NCH_2 of OEI ethylenes; 3H, OCH_3; 4H, OCH_2CH$_2$OCO; 2H, OCH$_2$CH_2OH*; 8H, OOCCH_2CH_2 and NOCCH_2CH_2*). (*Due to partial ester aminolysis, resulting in corresponding alcohol and the carboxamide).

Analysis of the Kinetics of Aminolysis by ^{1}H NMR. Synthesis of OEI-BAA-1 was performed analogously as indicated above in DMSO-d_6. The reaction mixture was analyzed by ^{1}H NMR at different time points between 0.5 h and 24 d. The degree of aminolysis was calculated by analyzing the signal of the acetal proton at 5.5 ppm, which is shifted toward the higher field when aminolysis occurs.

Synthesis of LT-OEI-HD Polymer. Synthesis of LT-OEI-HD was performed following the protocol of Kloeckner et al. (*22*). HD-linker and OEI800 were employed in the synthesis at a molar ratio of 1.2/1 (HD/OEI800) in anhydrous DMSO at 22 °C. After purification by dialysis at 4 °C using a 3.5 kDa molecular mass cutoff membrane and freeze-drying, LT-OEI-HD was obtained in 65% yield. As determined by ^{1}H NMR, the HD to OEI ratio was 1.25/1, with 77% of esters remaining intact.

Structural Analysis by FT-IR. Infrared spectra of the polymers were recorded from potassium bromide (KBr) pellets on a Jasco FT/IR-410 spectrometer.

Size Exclusion Chromatography (SEC) of Polymers. Gel filtration was performed using HR 10/30 columns containing Superdex 75 or a Superdex 200 material (GE Healthcare Bio-Sciences AB, SE-75184 Uppsala), with an HPLC 600 controller equipped with a photodiode array detector 996 from Waters (Waters GmbH Eschborn, Germany). Prior to use, column material was preconditioned with PEI25K and then washed with running buffer. A 20 mM Hepes buffer pH 7.4 with 0.25 M NaCl was chosen as running buffer. Chromatography was performed at a flow rate of 1 mL/min and sample detection was carried out at λ = 225 nm. Calibration with standard polymers of known molecular weights and of comparable chemical structure, OEI800, PEI2K, PEI10K, PEI25K, and PEI50K was performed. The term "size exclusion chromatography (SEC)" is used in the following text to describe gel filtration analysis performed on Superdex material using the described neutral buffer and equipment.

Determination of Polymer Molecular Weights by Gel Permeation Chromatography (GPC). Analysis of acid stable polymers (OEI-BM and LT-OEI-HD) was performed using an Agilent 1200 series HPLC system (Agilent Technologies, Waldbronn, Germany) equipped with a MALLS and a refractive

index detector, a NOVEMA 10-μm precolumn and a NOVEMA 300 analytical column (10 μm, 8 $\times$ 300 mm) (PSS, Mainz, Germany). The mobile phase was maintained in formic acid and sodium chloride (0.1% (v/v) HCOOH, 0.1 M NaCl, pH 2.8) at a flow rate of 1 mL/min. Samples were dissolved in the mobile phase at a concentration of 6 mg/mL; 10 μL of methanol were added to 1 mL of sample as internal standard. Results were evaluated using PSS WinGPC Unity software. Molecular weights were measured relative to Pullulan molecular weight standards that were used for preparing a standard calibration curve. This was necessary, as the d*n*/d*c* was not available for the analyzed polymers. The term "gel permeation chromatography (GPC)" is used in the following text to describe gel filtration analysis performed on NOVEMA 300 material using the described acidic buffer and GPC equipment.

Hydrolysis Assay. Aliquots of OEI-MK or OEI-BM were dissolved either in 1 mL 20 mM Hepes buffer pH 7.4 containing 0.25 M NaCl or in 1 mL 0.2 M sodium acetate buffer pH 5.0 containing 0.25 M NaCl. After incubation at 37 °C for different time periods, samples were applied to a gel filtration column (Superdex 75) either directly (pH 7.4 samples) or after neutralization with sodium hydroxide to stop hydrolysis (pH 5.0 samples). SEC was performed as indicated above. For calculation of the degradation rates, the monitored curves were segmented into three fractions: fraction I containing the polymer portion of the highest m.w., fraction II consisting of midsized m.w., and fraction III including the degradation end-products (OEI800 monomers). These fractions were integrated, and as a function of time the decrease of the AUC of fraction I and the increase of the AUC of fraction III, respectively, were set into relation. Out of this, the half-life was determined. For OEI-BAA polymers, kinetics of acetal hydrolysis was measured by monitoring the UV absorption of the emerging hydrolysis product (*p*-methoxybenzaldehyde) at 300 nm. Therefore, the polymer was diluted with 0.2 M sodium acetate buffer pH 5.0, or 0.2 M Hepes buffer pH 7.4. Samples were incubated at 37 °C and absorption was determined on a GENESYS 10 series spectrometer (Thermo Electron Corporation, Pittsford, NY) at different time points. Hydrolysis of LT-OEI-HD was monitored by ^{1}H NMR analysis, as the polymer lacks appropriate UV absorbing functions. The polymer was incubated in D_2O at pH 7.4 and 37 °C. After different periods of time (up to 14 days), NMR spectra were recorded and the decrease of the ester signal was analyzed.

Ethidium Bromide (EtBr) Exclusion Assay. Aliquots of the respective polymer were added sequentially to a DNA solution (20 μg/mL) in HBG (Hepes buffered glucose; 20 mM Hepes pH 7.4 plus 5% w/v glucose) containing 400 ng/mL EtBr, and the decrease of fluorescence was measured in a Varian Cary Eclipse fluorescence spectrometer (Varian, Mulgrave, Australia). EtBr/DNA fluorescence (λ_{ex} 510 nm and λ_{em} 590 nm) was set to 100% prior to addition of polycation.

Formation of Polyplexes. Plasmid DNA (pDNA) was mixed with the polycation at indicated cation/pDNA (c/p) ratios (w/w). PEI22K was applied at $c/p = 0.78$ which presents N/P = 6. Polycation/DNA polyplexes were prepared as described in ref (*23*) at final DNA concentrations of 100 μg/mL for biophysical analysis on the Zetasizer (see below) and 20 μg/mL for transfection experiments. Briefly, indicated amounts of pDNA and polycation were each diluted in HBG or HBS pH 7.4 and mixed rapidly by pipetting. Polyplexes were incubated at room temperature for 20 min prior to use.

Particle Size and Zeta Potential Analysis. Particle size and surface charge of polycation/DNA complexes were measured by laser-light scattering using a Malvern Zetasizer Nano ZS (Malvern Instruments, Worcestershire, UK). For measurements, the complexes (preparation in HBG pH 7.4) were diluted with the indicated buffer (HBG or HBS pH 7.4) to a final DNA concentration of 10 μg/mL (total volume 1 mL).

Cell Culture. B16F10 murine melanoma cells (kindly provided by I. J. Fidler, Texas Medical Center, Houston, TX) and murine neuroblastoma Neuro2A cells (ATCC CCI-131) were cultured in DMEM (1 g of glucose/L) supplemented with 10% FCS (v/v) and 1% penicillin/streptomycin (v/v). The cells were grown at 37 °C in 5% CO_2 humidified atmosphere.

Luciferase Reporter Gene Expression and Metabolic Activity of Transfected Cells. *In vitro* transfection experiments were performed on either B16F10 or Neuro2A cells. Two parallel transfection series were carried out in separate 96-well plates (TPP), one for the determination of reporter gene expression and one for the determination of metabolic activity. 24 h prior to transfection cells were seeded with a density of 5×10^3 (B16F10) or 1×10^5 cells (Neuro2A) in 200 μL of culture medium (DMEM supplemented with 1 g of glucose/L, 10% FCS (v/v) and 1% penicillin/streptomycin) per well. Immediately before transfection, medium was removed and 100 μL of a dilution of transfection complexes (200 ng pDNA/well) in culture medium were added to the cells. After 4 h of incubation at 37 °C complex containing medium was replaced by 100 μL of fresh medium. Transfection efficiency was evaluated 24 h after treatment by measuring luciferase reporter gene expression from cell lysates using a luminometer (Lumat LB 9507; Berthold Technologies, Bad Wildbad, Germany) as described previously (*24*). Values are given as relative light units (RLU) and represent the luciferase activity per 10^4 cells. Two ng of recombinant luciferase (Promega, Mannheim, Germany) corresponds to 10^7 light units.

Relative metabolic activity of cells was determined 24 h after transfection by the methylthiazoletetrazolium (MTT)/thiazolyl blue assay as described in ref (*25*). Optical absorbance was measured at 590 nm (reference wavelength 630 nm) using a micro plate reader (Spectrafluor Plus, Tecan Austria GmbH, Grödig, Austria). Metabolic activity was expressed relative to the metabolic activity of untreated control cells, defined as 100%.

***In Vivo* Biocompatibility Study.** Animal experiments were performed according to National Regulations and were approved by the Local Animal Experiments Ethical Committee. Female Balb/c mice were purchased from Janvier (Le Genest St Isle, France). Animals were housed in individually vented cages; food and water were provided *ad libitum*. For toxicity studies, polymers were dissolved in HBG and injected into the tail vain of the 8-week-old mice. The polymers were applied at amounts of 100 or 50 μg/20 g mouse, in an injection volume of 250 μL. At 48 h after polymer treatment, mice were killed and perfusion-fixed with formalin solution (4% paraformaldehyde in phosphate-buffered saline). Main organs were taken and embedded in paraffin. Sections of 5 μm thickness were cut and stained with hematoxylin-eosin for histological investigations. Microscopic pictures were taken with a Framos Infinity 2−3C, CCD-camera on an Axiovert 200 inverted microscope (Carl Zeiss) using a $\times$40 LC Achroplan objective.

Statistical Analysis. Results are presented as mean $\pm$ sd. Data were evaluated by variance analysis (ANOVA) using the Duncan test. *p*-values smaller than 0.05 were considered to be significant; * $p < 0.05$, ** $p < 0.01$, *** $p < 0.001$.

RESULTS

Polymer Syntheses and Structural Analysis. OEI800-based polymers were generated by Michael addition of OEI800 amines with four different bifunctional linkers (Figure 1). Maleimido-functionalized linkers, (a) the pH-labile ketal MK or (b) the nonhydrolyzable diether BM linker, were mixed with OEI800 at equimolar ratio and reacted for 22 h at 22 °C in anhydrous

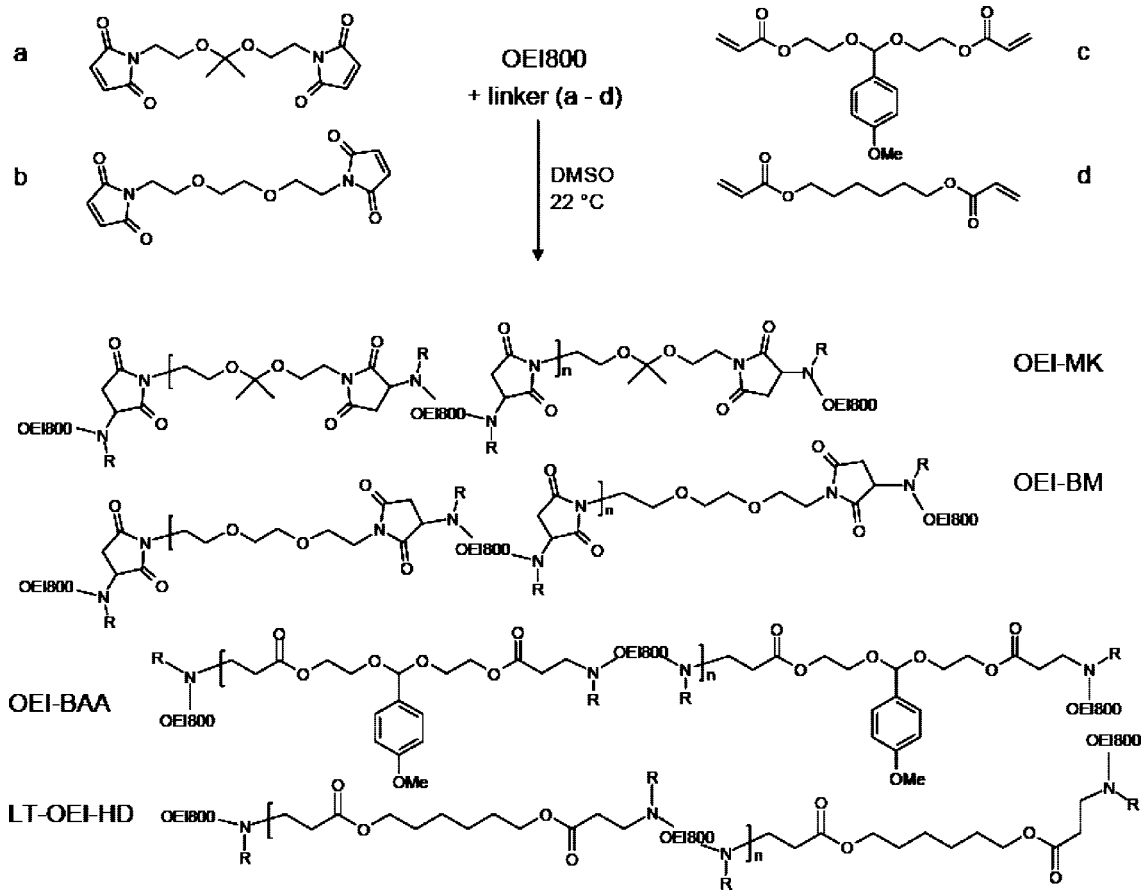

Figure 1. Syntheses of the oligoethylenimine based polymers: acid-degradable acetal-linked OEI-MK, OEI-BAA, and control polymers OEI-BM and LT-OEI-HD. (a) acid-labile MK-linker; (b) acid-stable BM-linker; (c) acid-labile BAA-linker; (d) acid-insensitive HD-linker.

Table 1. Chemical and Structural Data of OEI800 Based Conjugates[a]

			Feed Product Intact Linker [%]		
Polymer	Yield [%]	Mp [kDa]		Linker/OEI	[molar ratio]
OEI-MK	40	8−10	1	1.03	93
OEI-BM	48	8−10; 40	1	1.3	100
OEI-BAA-1−3d	40	2−3	1	0.3	26
OEI-BAA-1−1.5d	56	2−3	1	0.4	40
OEI-BAA-1−45m	70	2−3	1	0.44	75
OEI-BAA-1.25−45m	58	2−3	1.25	0.56	60
OEI-BAA-2−3d	50	4; 8−10	2	0.7	26
LT-OEI-HD	65	8−10	1.2	1.25	77

[a] Yields are given as weight to product/weight to educts [w/w] percent. Molecular weights were determined by SEC using a Superdex 75 and 200 columns.

DMSO. Purification of the products from solvent and unreacted starting material was achieved by dialysis at 4 °C using a 3.5 kDa molecular mass cutoff membrane and freeze-drying. Polymers OEI-BM and OEI-MK were then analyzed by ^{1}H NMR to investigate their linker to OEI ratio and confirm the preservation of the labile acetal functions during synthesis and purification (Table 1). For OEI-BM a linker to OEI ratio of 1.3/1 was found. For OEI-MK the linker to ketal to OEI ratio was 1.03/0.93/1, indicating a <10% hydrolysis of ketal groups in the product after workup.

To generate OEI polymers, which may degrade via acetal and ester bond cleavage, the methoxybenzaldehyde acetal diacrylate ester BAA (c) was applied, whereas 1,6-hexanediol diacrylate HD (d) was applied to synthesize the acetal-free control polymer LT-OEI-HD. LT-OEI-HD had a HD to OEI ratio of 1.25/1, with 77% of esters remaining intact. In our previous work (*22*) we found that the low temperature (LT, i.e., 22 °C, 4 days) is critical to avoid aminolysis of the ester bonds by OEI amines. For this reason also OEI-BAA synthesis was performed at 22 °C with BAA/OEI molar input ratios of 1, 1.25, and 2. Nevertheless, NMR analysis of products resulting from 3 day reactions (OEI-BAA-1−3d, OEI-BAA-2−3d) demonstrated significant aminolysis (Figure 2), resulting in polymers that contain acetal, ester, and amide bonds (see Table 1). The kinetics of the amide formation was monitored by ^{1}H NMR during a synthesis of OEI-BAA-1 performed in DMSO-d_6. By analyzing the signal of the acetal protons (5.6−5.5 ppm) the ratios of diester/monoester/diol were determined (Figure 2). Based on this analysis, and the finding that the Michael addition between BAA linker and OEI800 was largely completed within 45 min at room temperature, additional OEI-BAA polymers were synthesized by reducing the reaction time to 1.5 days and also as short as 45 min. For the OEI-BAA polymers this reduced reaction time increased the content of intact diester in the linker molecules (from 26%) to up to 75%. Infrared analysis of OEI-BAA-1−45min, OEI-BAA-1−1.5d, and OEI-BAA-2−3d confirmed the presence of amides in the polymers as well as their increase with the elongation of reaction time.

Molecular weight distribution of polymers is shown in Table 1 as analyzed by SEC. For detailed information on molecular weight determined by GPC (using a Novema 300 column) and SEC (using Superdex 75 and Superdex 200 columns) see Supporting Information (Figure S1 and Table S1). In short, GPC analysis of the pH-stable polymers OEI-BM and LT-OEI-HD displayed molecular weight distributions of $M_n = 8.5$ kDa, $M_w = 36$ kDa and $M_n = 4.9$ kDa, $M_w = 21$ kDa, respectively. These data correlated well with SEC analysis displaying peak molecular weights M_p of 8−10 kDa. Based on this good correlation

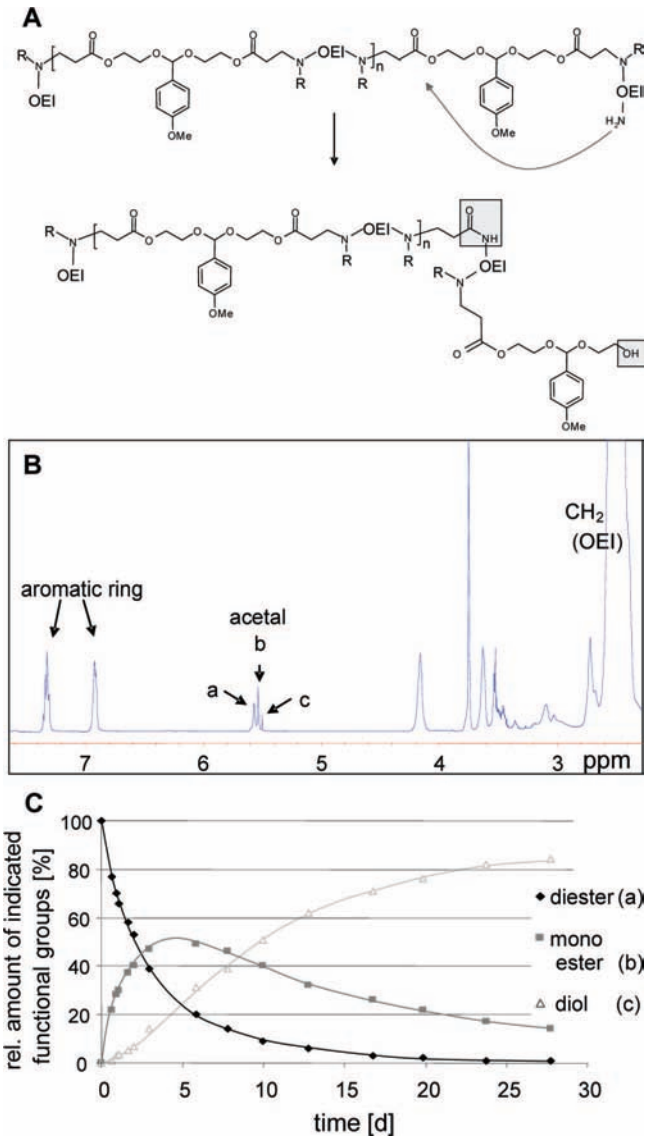

Figure 2. Structural analysis of OEI-BAA-1−3d during polymer synthesis. (A) Scheme of aminolysis reaction. (B) ^{1}H NMR spectra were recorded at different time points (shown here: reaction time 48 h) during the reaction at 22 °C in DMSO-d_6 and the degree of aminolysis was calculated on the basis of the acetal signal (5.6−5.5 ppm). This signal shows three different chemical shifts; for the intact diester at 5.57 ppm (a), for the monoester (aminolysis on one side of the linker) at 5.54 ppm (b), for the diol (aminolysis on both linker sides) at 5.50 ppm (c). (C) Diagram of the ^{1}H NMR based kinetics of BAA aminolysis over 24 days.

and the fact that the established GPC required the use of a pH 2.8 mobile phase, molecular weight distribution of the pH-labile polymers was analyzed by SEC only. Polymer OEI-MK displayed a M_p of 8−10 kDa, OEI-BAA-2−3d a main M_p of 4 kDa with a minor M_p of 8−10 kDa, and the other OEI-BAA polymers a smaller M_p range of 2−3 kDa.

Degradation Study of OEI-MK and OEI-BAA Polymers. To evaluate the pH dependency of the hydrolysis of OEI-MK and OEI-BAA polymers, degradation kinetics was measured at 37 °C and physiological pH 7.4 as well as at pH 5.0 (Figure 3). The half-life of OEI-MK was determined by detection of polymer fragments by SEC using Superdex 75 (Figure 3A). At pH 5.0, polymer hydrolysis was almost complete (98%) after 15 min, whereas at pH 7.4, the half-life was about 5 h at 37 °C. In contrast, control polymer OEI-BM was stable even after 20 h of incubation at both pH conditions and 37 °C (data not shown). Degradation of the acetal function in OEI-BAA

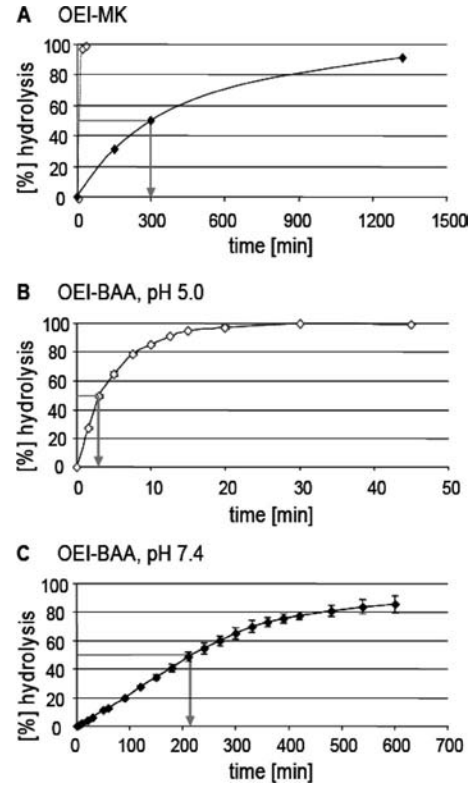

Figure 3. Kinetics of hydrolysis of acid labile polymers at 37 °C. Grey arrows mark the half-lifes of the polymers. (A) Degradation of OEI-MK at pH 5.0 (open diamonds) and at pH 7.4 (closed diamonds), values calculated from Superdex 75 SEC data (AUC at different time points after incubation). (B) Hydrolysis of OEI-BAA polymers at 37 °C, pH 5.0 and (C) at pH 7.4. UV absorbance (λ 300 nm) of the arising hydrolysis product was measured at indicated time points. Each point represents the mean ± sd of three independent experiments.

polymers was analyzed by measuring the increase of UV-absorbance of the released aromatic benzaldehyde. At pH 5.0 (Figure 3B), hydrolysis proceeded with a half-life of about 3 min and was complete in less than 30 min, while at pH 7.4, the half-life was about 3.5 h (Figure 3 C). The slower hydrolysis of the ester bonds is not detectable in this assay. It was analyzed by ^{1}H NMR using the ester bond containing control polymer LT-OEI-HD. The half-life was found to be 2 days at pH 7.4, 37 °C. At pH 5, ester-based polymers would hydrolyze significantly more slowly (*22*).

The presence of amide linkages in OEI-BAA polymers influences the size of fragments obtained by acid-catalyzed hydrolysis (see Supporting Information, Figure S2). OEI-BAA-1−45m, the polymer with the highest diester acetal linker content, degraded completely into fragments of the size of OEI800 monomers and dimers. OEI-BAA-2−3d (the polymer with the highest nonhydrolyzable amide content) hydrolyzed to monomers, dimers (M_p around 2 kDa) and considerable amounts of oligomers. Nevertheless, very profound degradation took place for all polymers, eliminating any high molecular weight fraction.

DNA Binding Assay. All polymers were analyzed for their DNA binding affinity by EtBr exclusion assay in HBG (Figure 4). The OEI-BM and -MK polymers bound to DNA more strongly than native OEI800. This was also the case for LT-OEI-HD at higher *c*/*p* ratios, while at low *c*/*p* ratios EtBr exclusion was weaker. OEI-BAA polymers showed slightly reduced binding capacity compared to OEI800.

Particle Size and Zeta Potential. Polyplexes with pDNA were formed at different *c*/*p* ratios in HBG buffer and were analyzed for their size and surface charge. Polymers formed

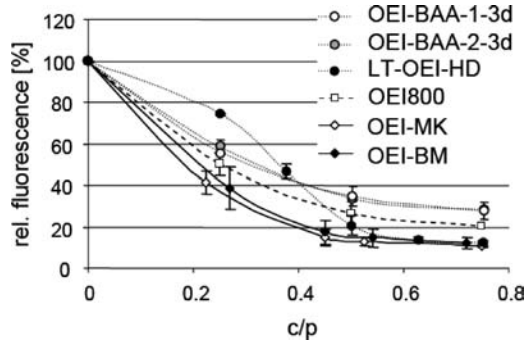

Figure 4. DNA binding affinity of polymers determined by ethidium bromide exclusion assay in HBG pH 7.4. OEI800, open squares; OEI-MK, open diamonds; OEI-BM, solid diamonds; OEI-BAA-1−3d, open circles; OEI-BAA-2−3d, gray diamonds; LT-OEI-HD, solid circles. Each point represents the mean ± sd of three independent experiments.

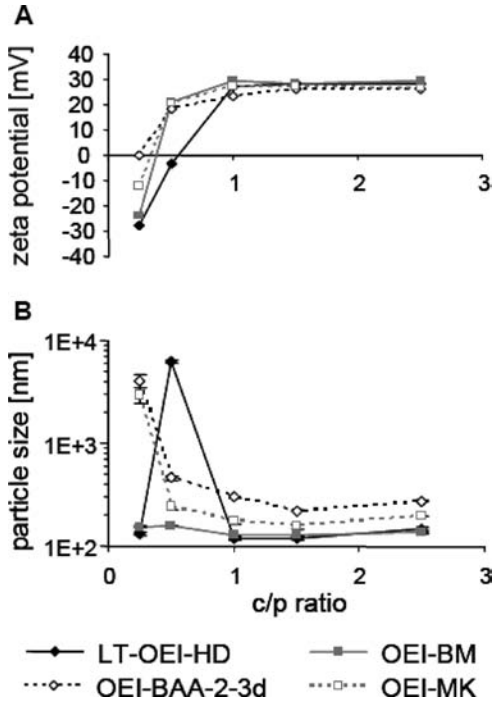

Figure 5. Surface charges (A) and sizes (B) of DNA polyplexes with OEI-MK, OEI-BM, OEI-BAA-2−3d, and LT-OEI-HD at different *c*/*p* ratios (in HBG, pH 7.4). Experiments were performed in triplicate.

polyplexes of small size (OEI-BM, OEI-MK: 130−200 nm; LT-OEI-HD, OEI-BAA: 150−300 nm) and positive surface charge (23−30 mV) at *c*/*p* ratios of 1 and higher (Figure 5), with the exception for OEI-BAA-1−3d where polyplexes aggregated with time. For lower *c*/*p* ratios of 0.5 or 0.25, surface charges of polyplexes became lower or even negative and all polymers particles tended to aggregate. Additionally, the influence of ionic strength on particle stability was investigated (data not shown). Upon the addition of salt (HBS), aggregation of particles occurred in the case of polymers with weaker DNA binding ability, i.e., OEI-BAA polymers (all *c*/*p* ratios tested) and LT-OEI-HD (for *c*/*p* ratios of 1 or less).

Luciferase Reporter Gene Expression and Metabolic Activity of Transfected Cells. In order to investigate the influence of polymer degradability on transfection efficiency and cytotoxicity, B16F10 (Figure 6) and Neuro2A cells (Figure 7) were transfected with pCMVLuc reporter gene polyplexes with the acid-labile polycations or their acid-insensitive counterparts at different *c*/*p* ratios prepared in HBG. PEI22K previously established as the gold standard was used for comparison at its optimal *c*/*p* ratio (*c*/*p* 0.78, corresponding to N/P 6) (*12*). Linear PEI22K was selected as transfection control (instead of the structurally more related branched PEI25K) because of its higher transfection activity over PEI25K in the investigated cell lines (*12*).

For B16F10 cells, the maximum transfection efficiency of both degradable OEI-MK and its stable analogue OEI-BM reached values of about 1 log unit below PEI22K (Figure 6A). For maximum efficiency, higher *c*/*p* ratios (≥5) of OEI-MK were required than for OEI-BM (optimal transfection at a *c*/*p* ratio of 2.5). For OEI-BM, further increase in *c*/*p* resulted in a reduction of transfection efficiency. This can be explained by significant cytotoxicity (Figure 6B) caused by OEI-BM at *c*/*p* ≥5. In contrast, no cytotoxicity was observed for pH-labile OEI-MK up to *c*/*p* 7.5. Consequently, at high *c*/*p* ratios the acid-labile polymer OEI-MK became superior. The starting material OEI800 shows no cytotoxicity but also no transfection efficiency, independent from the *c*/*p* ratio. PEI22K shows only moderate cytotoxicity at optimal *c*/*p* ratio of 0.78, but strong toxicity at higher *c*/*p* ratios, with relative metabolic viability of less than 50% for *c*/*p* 2 (*12*).

The OEI-BAA polymers and its acetal-free ester analogue LT-OEI-HD (Figure 6C,D) were also evaluated on B16F10 cells. Here, OEI-BAA-1−3d was the most promising polymer, with an optimal transfection efficiency at *c*/*p* of 7.5 significantly exceeding even PEI22K (Figure 6C). The acetal-free control polymer LT-OEI-HD could not reach the transfection levels of OEI-BAA-1−3d and OEI-BAA-2−3d. Although the ester-based degradable polymer LT-OEI-HD is far less cytotoxic than PEI22K, it showed some toxicity at c/*p* ≥ 5. The acetal- and ester-containing OEI-BAA counterparts showed the best biocompatibility (Figure 6D).

OEI-BAA polymers that differ in their diester acetal-linker content (i.e., low amide content) were compared in their transfection efficiency and cytotoxity profiles (Supporting Information Figure S3). A fine balance between maximum gene transfer activity and maximum biocompatibility was observed. In short, OEI-BAA-2−3d, the polymer with a considerable amide content, displayed the highest transfection activity and reduced metabolic activity of transfected cells at *c*/*p* of ≥10. The polymers with the highest diester acetal content and lower molecular weight displayed the best biocompatibility even at *c*/*p* of 20, but were least effective in gene transfer. Polymer OEI-BAA-1−1.5 was less effective as OEI-BAA-2−3d at low *c*/*p* ratios, but became almost equal at *c*/*p* 20, while remaining completely nontoxic. Therefore, within the OEI-BAA series the polymers containing acetal diesters and significant amide linkages provided the best activity and biocompatibility profile.

Transfections were also carried out with Neuro2A cells as a second cell line. In this cell line, transfection efficiencies of all polyplexes (including also the standard PEI22K) prepared in HBG buffer were low (Figure 7A, solid bars). In contrast, transfection efficiency was improved for several polymers if formulations were generated in salt-containing HBS buffer (Figure 7A, striped bars). All OEI-BAA polymers (including also those not shown in Figure 7) and PEI22K responded to this procedure with strongly (approximately 100-fold) elevated transfection levels. Cytotoxicity (Figure 7B) was not influenced remarkably by the presence of salt, except for PEI22K where metabolic activity of treated cells decreased by 20%. Interestingly, HBS had only little influence on the transfection efficiency of LT-OEI-HD and no influence on the more stable OEI-MK and OEI-BM polyplexes (data not shown).

***In Vivo* Biocompatibility Studies.** As the acid-degradable polymers showed promising results concerning biocompatibility *in vitro*, we also examined their *in vivo* toxicity. Different

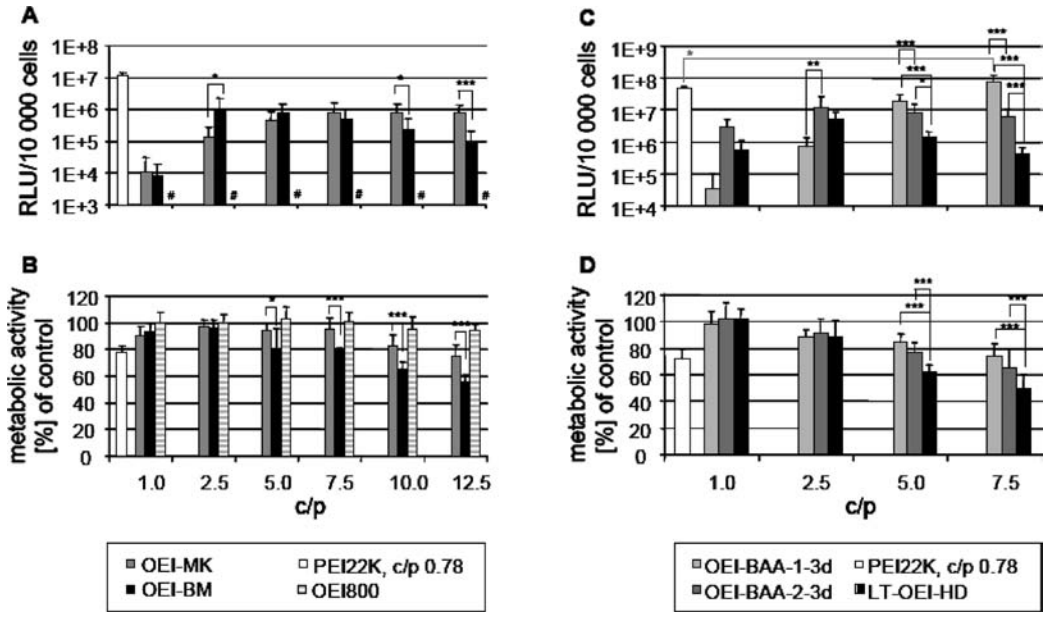

Figure 6. Transfection efficiency (luciferase assay, A,C) and metabolic activity (MTT assay, B,D) in B16F10 cells. Cells were treated with polyplexes of OEI-MK and OEI-BM in comparison to OEI800 and PEI22K (A,B), or with OEI-BAA and LT-OEI-HD (C,D). #, OEI800 <1000 RLU for all *c*/*p* ratios.

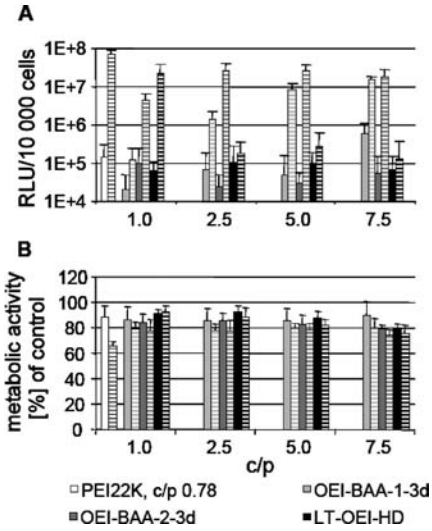

Figure 7. Transfection of Neuro2A cells. Influence of ionic strength (solid bars, HBG; striped bars, HBS) on transfection efficiency (luciferase assay, A) and cytotoxicity (MTT-assay, B). Sequence of polymer formulations (from left to right): PEI22K, *c*/*p* 0.78; OEI-BAA-1−3d; OEI-BAA2−3d; LT-OEI-HD.

amounts of selected plain polymers (OEI-BAA-2−3d, OEI-MK, or stable controls OEI-BM, LT-OEI-HD, PEI25K) were administered to 8-week-old female Balb/c mice via tail vain injection. As control polymer, branched PEI25K was chosen, because it is structurally more related to the branched OEI800 based polymers than the linear PEI22K. After PEI25K treatment, all three animals died when treated with 50 μg/20 g body weight. The dosage had to be reduced to 25 μg PEI25K/20 g mouse. Even then hepatocytes lost their normal shape indicating necrotic changes (Figure 8). Acetal comprising polymers were well-tolerated by mice at amounts of 50 μg/20 g mouse, and no changes in liver tissue were detectable (Figure 8, upper two pictures on the left). Doubling the polymer amount to 100 μg/20 g mouse was still well-tolerated for OEI-BAA-2−3d and no pathological alterations in the analyzed liver tissue were found; for OEI-MK this was also the case for two out of three mice, while one of the mice showed the first slight signs of developing a fatty liver at the 100 μg dose. In contrast, stable OEI-BM and LT-OEI-HD polymers had already caused fatty livers at 50 μg/20 g mouse (Figure 8, upper two pictures on the right), and the 100 μg dosage was lethal in the case of OEI-BM.

DISCUSSION

The aim of this study was to design degradable polycations as nucleic acid carriers, which are composed of small oligocation units linked via acid-sensitive acetal linkages. While maintaining their high molecular weight in the extracellular space, providing efficient protection and tight packaging of the nucleic acid and mediating its uptake into the cell, these polymeric carriers should degrade intracellularly into small, biocompatible decomposition products. Different approaches (i.e., vectors decomposing with different velocities upon different stimuli) have already been investigated, but currently the required optimal specific timing (minutes, hours, or days) and location (*26, 27*) of such a degradation (vesicles, cytoplasm, nucleus) remain to be determined. For example, vector decomposition that depends on endosomal milieu has to proceed fast enough to ensure that polymer degradation occurs before endosomal release into the pH-neutral cytoplasm. This might occur on a quite short time scale (minutes to less than an hour), because an efficient endosomal release of polyplexes must take place before the endosome matures into an endolysosome destroying the delivered nucleic acid. Too rapid degradation of the polymeric carrier which protects the nucleic acid would also be counterproductive. In essence, concerted polymer degradation and endosomal release is hypothesized to be preferred for pH-sensitive carriers. However, it is difficult to make specific statements on optimal location and timing, as the demands depend on the particular objective and target (nuclear DNA delivery/cytoplasmic RNA delivery) and also on the cell type. It also remains to be determined which molecular triggers for degradation, cleavage upon endosomal acidification (*16, 17, 28–31*), reductive cleavage of disulfide bonds (*27, 32*), hydrolysis of ester bonds (*6, 10, 11, 33*), alone or in combination, are most suitable for polyplex delivery.

In the current work we focused on the acidification of endosomal compartments as a specific trigger for polymer degradation. For this purpose two different acetal-based linkers were chosen for cross-linking OEI800 units into larger acid-

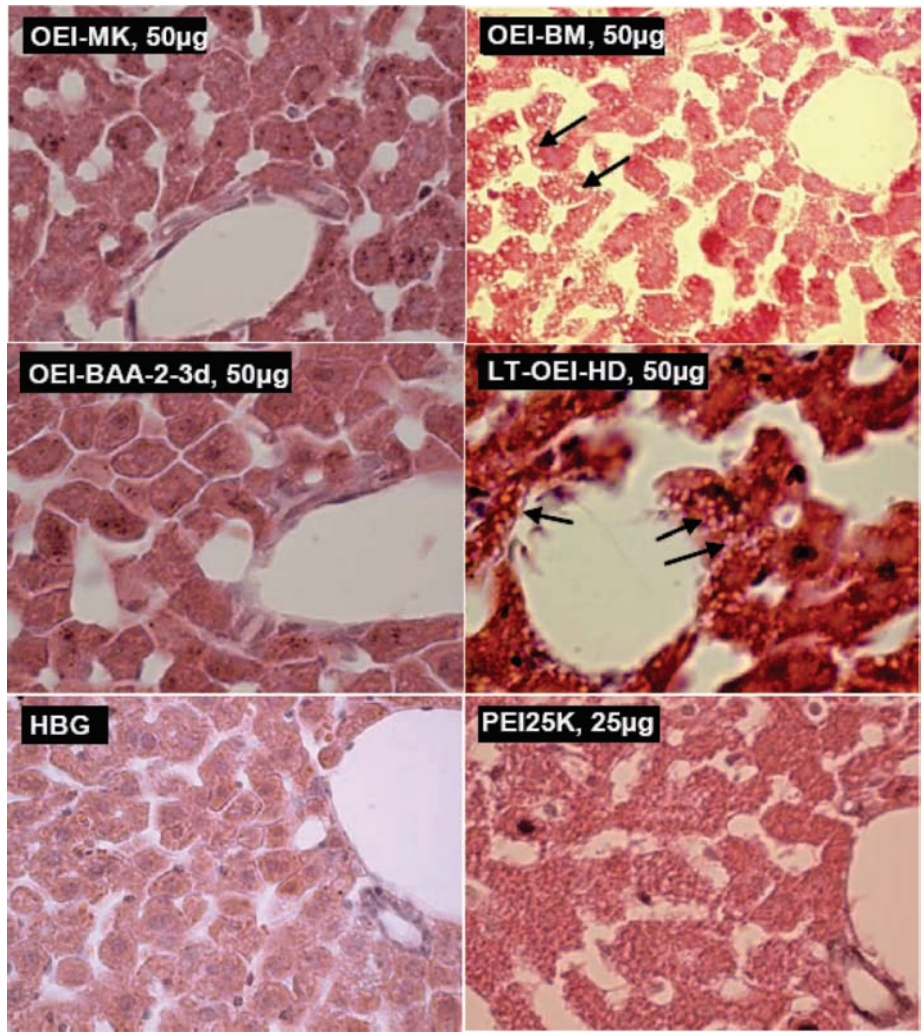

Figure 8. *In vivo* study on toxicity of the free polymers in Balb/c mice. Histological examination on liver tissue (hematoxylin and eosin staining) 48 h after i.v. administration of indicated amounts of free polymer per 20 g mouse. Application of 50 μg of acid-labile polymers OEI-MK and OEI-BAA-2 induced no histopathological changes in the liver compared to HBG-treated control animals. In contrast, the same dosage of OEI-BM and LT-OEI-HD polymers resulted in the development of fatty livers (black arrows indicate lipid droplets in hepatocytes after OEI-BM and LT-OEI-HD treatment). Mice treated with 25 μg of PEI25K even showed necrotic changes in liver tissue, which can be seen by the impaired morphology of hepatocytes in the lower right picture.

hydrolyzable polymers OEI-MK and OEI-BAA. The acetone ketal-containing linker MK (*18*) was previously introduced as reversible protein cross-linking agent, and the *p*-methoxybenzaldehyde acetal diacrylate ester BAA (*19*) previously applied in acid-cleavable polymer particles. In the case of BAA, the obtained OEI-BAA polymers contain both the acid-labile acetal groups and hydrolyzable ester groups. If polyplexes were not degraded completely until they are released from the endosome, the remaining polymer can be hydrolyzed in the cytosol at neutral pH.

The acetal containing polymers OEI-MK and OEI-BAA degrade in a pH-dependent manner, with very fast degradation kinetics (approximately 3 min half-life at 37 °C) in the acidic environment of pH 5 and much slower degradation (3.5 to 5 h half-life) at physiological pH 7.4. In contrast, the control polymers OEI-BM (as control for OEI-MK) and LT-OEI-HD (control for OEI-BAA) degraded under the same acidic conditions either very slowly (LT-OEI-HD) or not detectable at all (OEI-BM).

With regard to their application as gene vectors, DNA binding and compacting capacity of the polymers was determined by ethidium bromide (EtBr) exclusion assay and polyplex particle size and zeta potential analysis. At *c*/*p* ratios >1, stable, positively charged particles (i.e., sizes of 100−300 nm, positive zeta potential of 23−30 mV)) were obtained in salt-free buffer. The EtBr exclusion assay correlated well with the size measurements: for polymers that showed weaker DNA-binding affinity (e.g., OEI-BAA polymers) in the EtBr assay, slightly larger particles were detected by size measurements than for those made from polymers with high DNA-binding ability (e.g., OEI-MK). The firmer the DNA was condensed by the polycation, the smaller the polyplex was in size. Sizes of polyplexes from polymers with strong DNA binding (OEI-MK, OEI-BM) were not influenced by the addition of salt, while those prepared from weakly DNA-binding polymers (OEI-BAA polymers, at low *c*/*p* also LT-OEI-HD) started to grow in size and aggregated, as is also known for standard PEIs (*34*, *35*). Overall, the polyplexes showed biophysical characteristics in the range of PEI22K particles and thus should be suitable for use as gene vectors.

Polyplex transfection efficiency and toxicity were tested using B16F10 and Neuro2A cells. Concerning the biocompatibility of the formulations, the acid-degradable polymers showed a clear advantage over acid-stable analogues: the acetal containing polymers (OEI-MK and OEI-BAA) were significantly less toxic than their stable controls. This effect became more apparent with increasing *c*/*p* ratios. Regarding gene transfer efficiency, we found that polymerization of the very poorly transfecting

OEI800 to larger polycations boosts transfection efficiency levels dramatically, both for acid-stable linkages (OEI-BM, LT-OEI-HD) as well as for the acid-degradable (OEI-MK, OEI-BAA) ones. Due to better biocompatibility, for acid-labile polymers the *c*/*p* ratios leading to maximum transfection efficiency were slightly higher than those for the stable counterparts.

The OEI-BAA polymer series, containing both the acid-labile methoxybenzaldehyde acetal and hydrolyzable β-aminopropionic ester bonds, displayed the most encouraging potential as transfection agent. For example, polymer OEI-BAA-2−3d mediated gene transfer more effectively than the control ester polymer LT-OEI-HD (with similar molecular weight) at all *c*/*p* ratios tested. The smaller polymer OEI-BAA-1−3d which showed lower transfection efficiency at low *c*/*p*, exceeded OEI-BAA-2−3d with increasing *c*/*p* ratio and also the gold standard linear PEI22K. It is worth noting that the stability of the OEI-BAA polymer can be modulated by incorporation of additional amide linkages by an aminolysis process as described in the chemistry section of the paper.

In Neuro2A cells, a generally low transfection efficiency of medium-sized polyplexes (formed in HBG) is observed, presumably resulting from a generally insufficient polyplex cellular uptake. This can be overcome by salt-induced aggregated polyplexes of PEI22K and OEI-BAA polymers. Once more, the BAA polymers provided highest gene expression levels, at lowest cytotoxicity.

In vivo toxicity studies with the free polymers confirmed the encouraging biocompatibility of the acetal containing polymers. Dosages (100 μg/20 g mouse) which are lethal in case of OEI-BM, PEI25K, or PEI22K polymer and cause damage in liver tissue in the case of LT-OEI-HD, were well-tolerated in the case of OEI-MK and OEI-BAA-2−3d polymers. This emphasizes the advantage of acid degradable polymers over the controls *in vivo* also and makes them interesting candidates for use as more biocompatible gene transfer agents.

Taken together, these data clearly show an advantage of degradable acetal-linked polymers compared to acid-stable ones. The chosen acetal linkages exhibit favorable kinetics of hydrolysis: the synthesized polymers provide adequate stability for DNA polyplex formation resulting in efficient gene transfer, but also sensitivity toward a slight decrease in pH in endosomes, which causes polymer degradation and thus improved biocompatibility. The presented work did not address significant additional bottlenecks beyond biodegradability. Endosomal release is still a major limit even for PEI-type polymers despite their proton sponge activity (*36*), but might be overcome by incorporation of endosomally active components (*37, 38*). Inadvertent particle aggregation may be prevented by pH-responsive PEGylation (*31, 37, 39*). Insufficient endocytosis of polyplexes might be overcome by the integration of suitable ligands to boost specific polyplex uptake into the target cells. Such strategies remain to be investigated in the context of the polymeric carriers presented in this paper, to yield polyplexes with suitable characteristics for *in vivo* gene transfer.

ACKNOWLEDGMENT

We thank Olga Brück for skillful assistance in preparing the manuscript and Wolfgang Rödl for help with the GPC analysis. This work was supported by the DFG SFB 486, SPP1230, excellence cluster Nanosystems Initiative Munich (NIM), and by the European Community project 'GIANT'.

Supporting Information Available: Additional data on polymer characterization by SEC and GPC; degradation study of different OEI-BAA polymers; transfection efficiency of different OEI-BAA polymers and metabolic activity of transfected cells. This material is available free of charge via the Internet at http://pubs.acs.org.

LITERATURE CITED

(1) Boussif, O., Lezoualc'h, F., Zanta, M. A., Mergny, M. D., Scherman, D., Demeneix, B., and Behr, J. P. (1995) A versatile vector for gene and oligonucleotide transfer into cells in culture and in vivo: polyethylenimine. *Proc. Natl. Acad. Sci. U.S.A. 92*, 7297–7301.

(2) Zou, S. M., Erbacher, P., Remy, J. S., and Behr, J. P. (2000) Systemic linear polyethylenimine (L-PEI)-mediated gene delivery in the mouse. *J. Gene Med. 2*, 128–134.

(3) Moghimi, S. M., Symonds, P., Murray, J. C., Hunter, A. C., Debska, G., and Szewczyk, A. (2005) A two-stage poly(ethylenimine)-mediated cytotoxicity: implications for gene transfer/therapy. *Mol. Ther. 11*, 990–995.

(4) Chollet, P., Favrot, M. C., Hurbin, A., and Coll, J. L. (2002) Side-effects of a systemic injection of linear polyethylenimine-DNA complexes. *J. Gene Med. 4*, 84–91.

(5) Gosselin, M. A., Guo, W., and Lee, R. J. (2001) Efficient gene transfer using reversibly cross-linked low molecular weight polyethylenimine. *Bioconjugate Chem. 12*, 989–994.

(6) Kloeckner, J., Wagner, E., and Ogris, M. (2006) Degradable gene carriers based on oligomerized polyamines. *Eur. J. Pharm. Sci. 29*, 414–425.

(7) Read, M. L., Singh, S., Ahmed, Z., Stevenson, M., Briggs, S. S., Oupicky, D., Barrett, L. B., Spice, R., Kendall, M., Berry, M., Preece, J. A., Logan, A., and Seymour, L. W. (2005) A versatile reducible polycation-based system for efficient delivery of a broad range of nucleic acids. *Nucleic Acids Res. 33*, e86.

(8) Lee, Y., Mo, H., Koo, H., Park, J. Y., Cho, M. Y., Jin, G. W., and Park, J. S. (2007) Visualization of the degradation of a disulfide polymer, linear poly(ethylenimine sulfide), for gene delivery. *Bioconjugate Chem. 18*, 13–18.

(9) Christensen, L. V., Chang, C. W., Kim, W. J., Kim, S. W., Zhong, Z., Lin, C., Engbersen, J. F., and Feijen, J. (2006) Reducible poly(amido ethylenimine)s designed for triggered intracellular gene delivery. *Bioconjugate Chem. 17*, 1233–1240.

(10) Thomas, M., Ge, Q., Lu, J. J., Chen, J., and Klibanov, A. M. (2005) Cross-linked small polyethylenimines: while still nontoxic, deliver DNA efficiently to mammalian cells in vitro and in vivo. *Pharm. Res. 22*, 373–380.

(11) Forrest, M. L., Koerber, J. T., and Pack, D. W. (2003) A degradable polyethylenimine derivative with low toxicity for highly efficient gene delivery. *Bioconjugate Chem. 14*, 934–940.

(12) Russ, V., Elfberg, H., Thoma, C., Kloeckner, J., Ogris, M., and Wagner, E. (2008) Novel degradable oligoethylenimine acrylate ester-based pseudodendrimers for in vitro and in vivo gene transfer. *Gene Ther. 15*, 18–29.

(13) Kim, Y. H., Park, J. H., Lee, M., Kim, Y. H., Park, T. G., and Kim, S. W. (2005) Polyethylenimine with acid-labile linkages as a biodegradable gene carrier. *J. Controlled Release 103*, 209–219.

(14) Wang, J., Mao, H. Q., and Leong, K. W. (2001) A novel biodegradable gene carrier based on polyphosphoester. *J. Am. Chem. Soc. 123*, 9480–9481.

(15) Zhao, Z., Wang, J., Mao, H. Q., and Leong, K. W. (2003) Polyphosphoesters in drug and gene delivery. *Adv. Drug Delivery Rev. 55*, 483–499.

(16) Murthy, N., Thng, Y. X., Schuck, S., Xu, M. C., and Frechet, J. M. (2002) A novel strategy for encapsulation and release of proteins: hydrogels and microgels with acid-labile acetal cross-linkers. *J. Am. Chem. Soc. 124*, 12398–12399.

(17) Paramonov, S. E., Bachelder, E. M., Beaudette, T. T., Standley, S. M., Lee, C. C., Dashe, J., and Frechet, J. M. (2008) Fully Acid-degradable biocompatible polyacetal microparticles for drug delivery. *Bioconjugate Chem. 19*, 911–919.

(18) Srinivasachar, K., and Neville, D. M., Jr. (1989) New protein cross-linking reagents that are cleaved by mild acid. *Biochemistry 28*, 2501–2509.

(19) Chan, Y., Bulmus, V., Zareie, M. H., Byrne, F. L., Barner, L., and Kavallaris, M. (2006) Acid-cleavable polymeric core-shell particles for delivery of hydrophobic drugs. *J. Controlled Release 115*, 197–207.

(20) Brissault, B., Kichler, A., Guis, C., Leborgne, C., Danos, O., and Cheradame, H. (2003) Synthesis of linear polyethylenimine derivatives for DNA transfection. *Bioconjugate Chem. 14*, 581–587.

(21) Plank, C., Zatloukal, K., Cotten, M., Mechtler, K., and Wagner, E. (1992) Gene transfer into hepatocytes using asialoglycoprotein receptor mediated endocytosis of DNA complexed with an artificial tetra-antennary galactose ligand. *Bioconjugate Chem. 3*, 533–539.

(22) Kloeckner, J., Bruzzano, S., Ogris, M., and Wagner, E. (2006) Gene carriers based on hexanediol diacrylate linked oligoethylenimine: effect of chemical structure of polymer on biological properties. *Bioconjugate Chem. 17*, 1339–1345.

(23) Kircheis, R., Kichler, A., Wallner, G., Kursa, M., Ogris, M., Felzmann, T., Buchberger, M., and Wagner, E. (1997) Coupling of cell-binding ligands to polyethylenimine for targeted gene delivery. *Gene Ther. 4*, 409–418.

(24) Boeckle, S., von Gersdorff, K., van der Piepen, S., Culmsee, C., Wagner, E., and Ogris, M. (2004) Purification of polyethylenimine polyplexes highlights the role of free polycations in gene transfer. *J. Gene Med. 6*, 1102–1111.

(25) de Wolf, H. K., Luten, J., Snel, C. J., Oussoren, C., Hennink, W. E., and Storm, G. (2005)In vivo tumor transfection mediated by polyplexes based on biodegradable poly(DMAEA)-phosphazene. *J. Controlled Release*.

(26) Kulkarni, R. P., Mishra, S., Fraser, S. E., and Davis, M. E. (2005) Single cell kinetics of intracellular, nonviral, nucleic acid delivery vehicle acidification and trafficking. *Bioconjugate Chem. 16*, 986–994.

(27) Guo, X., and Szoka, F. C., Jr. (2003) Chemical approaches to triggerable lipid vesicles for drug and gene delivery. *Acc. Chem. Res. 36*, 335–341.

(28) Heller, J., Barr, J., Ng, S. Y., Abdellauoi, K. S., and Gurny, R. (2002) Poly(ortho esters): synthesis, characterization, properties and uses. *Adv. Drug Delivery Rev. 54*, 1015–1039.

(29) Murthy, N., Campbell, J., Fausto, N., Hoffman, A. S., and Stayton, P. S. (2003) Bioinspired pH-responsive polymers for the intracellular delivery of biomolecular drugs. *Bioconjugate Chem. 14*, 412–419.

(30) Li, W., Huang, Z., MacKay, J. A., Grube, S., and Szoka, F. C., Jr. (2005) Low-pH-sensitive poly(ethylene glycol) (PEG)-stabilized plasmid nanolipoparticles: effects of PEG chain length, lipid composition and assembly conditions on gene delivery. *J. Gene Med. 7*, 67–79.

(31) Knorr, V., Allmendinger, L., Walker, G. F., Paintner, F. F., and Wagner, E. (2007) An acetal-based PEGylation reagent for pH-sensitive shielding of DNA polyplexes. *Bioconjugate Chem. 18*, 1218–1225.

(32) Saito, G., Swanson, J. A., and Lee, K. D. (2003) Drug delivery strategy utilizing conjugation via reversible disulfide linkages: role and site of cellular reducing activities. *Adv. Drug Delivery Rev. 55*, 199–215.

(33) Lim, Y. B., Kim, S. M., Suh, H., and Park, J. S. (2002) Biodegradable, endosome disruptive, and cationic network-type polymer as a highly efficient and nontoxic gene delivery carrier. *Bioconjugate Chem. 13*, 952–957.

(34) Ogris, M., Steinlein, P., Kursa, M., Mechtler, K., Kircheis, R., and Wagner, E. (1998) The size of DNA/transferrin-PEI complexes is an important factor for gene expression in cultured cells. *Gene Ther. 5*, 1425–1433.

(35) Wightman, L., Kircheis, R., Rossler, V., Carotta, S., Ruzicka, R., Kursa, M., and Wagner, E. (2001) Different behavior of branched and linear polyethylenimine for gene delivery in vitro and in vivo. *J Gene Med. 3*, 362–372.

(36) Sonawane, N. D., Szoka, F. C., Jr., and Verkman, A. S. (2003) Chloride accumulation and swelling in endosomes enhances DNA transfer by polyamine−DNA polyplexes. *J. Biol. Chem. 278*, 44826–44831.

(37) Rozema, D. B., Lewis, D. L., Wakefield, D. H., Wong, S. C., Klein, J. J., Roesch, P. L., Bertin, S. L., Reppen, T. W., Chu, Q., Blokhin, A. V., Hagstrom, J. E., and Wolff, J. A. (2007) Dynamic PolyConjugates for targeted in vivo delivery of siRNA to hepatocytes. *Proc. Natl. Acad. Sci. U.S.A. 104*, 12982–12987.

(38) Meyer, M., Philipp, A., Oskuee, R., Schmidt, C., and Wagner, E. (2008) Breathing life into polycations: functionalization with pH-responsive endosomolytic peptides and polyethylene glycol enables siRNA delivery. *J. Am. Chem. Soc. 130*, 3272–3273.

(39) Walker, G. F., Fella, C., Pelisek, J., Fahrmeir, J., Boeckle, S., Ogris, M., and Wagner, E. (2005) Toward synthetic viruses: endosomal pH-triggered deshielding of targeted polyplexes greatly enhances gene transfer in vitro and in vivo. *Mol. Ther. 11*, 418–425.

BC8001858

SUPPORTING INFORMATION

Acetal linked oligoethylenimines for use as pH-sensitive gene carriers.

Veronika Knorr,[†‡] *Verena Russ,*[†‡] *Lars Allmendinger,*[§]*, Manfred Ogris,*[†‡] *Ernst Wagner*[†‡]

[†] Pharmaceutical Biology – Biotechnology, and [§] Pharmaceutical Chemistry, Department of Pharmacy, Center for Drug Research, and [‡] Center for NanoScience (CeNS), Ludwig-Maximilians-Universität Munich, Butenandtstr. 5-13, D-81377 Munich, Germany

1. Determination of Polymer Molecular Weight by GPC and SEC.

Gel Permeation Chromatography (GPC). Analysis of acid-stable polymers (OEI-BM and LT-OEI-HD) was performed using an Agilent 1200 series HPLC system (Agilent Technologies, Waldbronn, Germany) equipped with a MALLS and a refractive index detector, a NOVEMA 10-µm precolumn and a NOVEMA 300 analytical column (10 µm, 8 x 300 mm) (PSS, Mainz, Germany). The mobile phase was maintained in formic acid and sodium chloride (0.1% (v/v) HCOOH, 0.1 M NaCl, pH 2.8) at a flow rate of 1 mL/min. Samples were dissolved in the mobile phase at a concentration of 6 mg/mL; 10 µl of methanol were added to 1 mL of sample as internal standard. Results were evaluated using PSS WinGPC Unity software. Molecular weights were measured relative to Pullulan molecular weight standards that were used for preparing a standard calibration curve.

Size Exclusion Chromatography (SEC). Gel filtration was performed using HR 10/30 columns containing Superdex 75 or a Superdex 200 material (GE Healthcare Bio-Sciences AB, Uppsala, Sweden), with an HPLC 600 controller equipped with a photodiode array detector 996 from Waters (Waters GmbH Eschborn, Germany). Prior to use, column material was preconditioned with PEI25K and then washed with running buffer. A 20 mM Hepes buffer pH 7.4 with 0.25 M NaCl was chosen as running buffer. Chromatography was performed at a flow rate of 1 mL/min and sample detection was carried out at $\lambda = 225$. Calibration with standard polymers of known molecular weights and of comparable chemical structure, OEI800, PEI2K, PEI10K, PEI25K and PEI50K, was performed.

Figure S1. (A) GPC elution profiles of acid-stable OEI-BM and LT-OEI-HD on a Novema 300 column. (B-D) SEC elution profiles: OEI-MK, OEI-BM on Superdex 75 (B) and Superdex 200 (C) and OEI-BAA, LT-OEI-HD on Superdex 75 (D) column material. The scale below the diagram shows the elution times of standard PEIs of indicated molecular weight, the shaded boxes mark peaks that are induced by salt and do not refer to the samples.

Figure S1

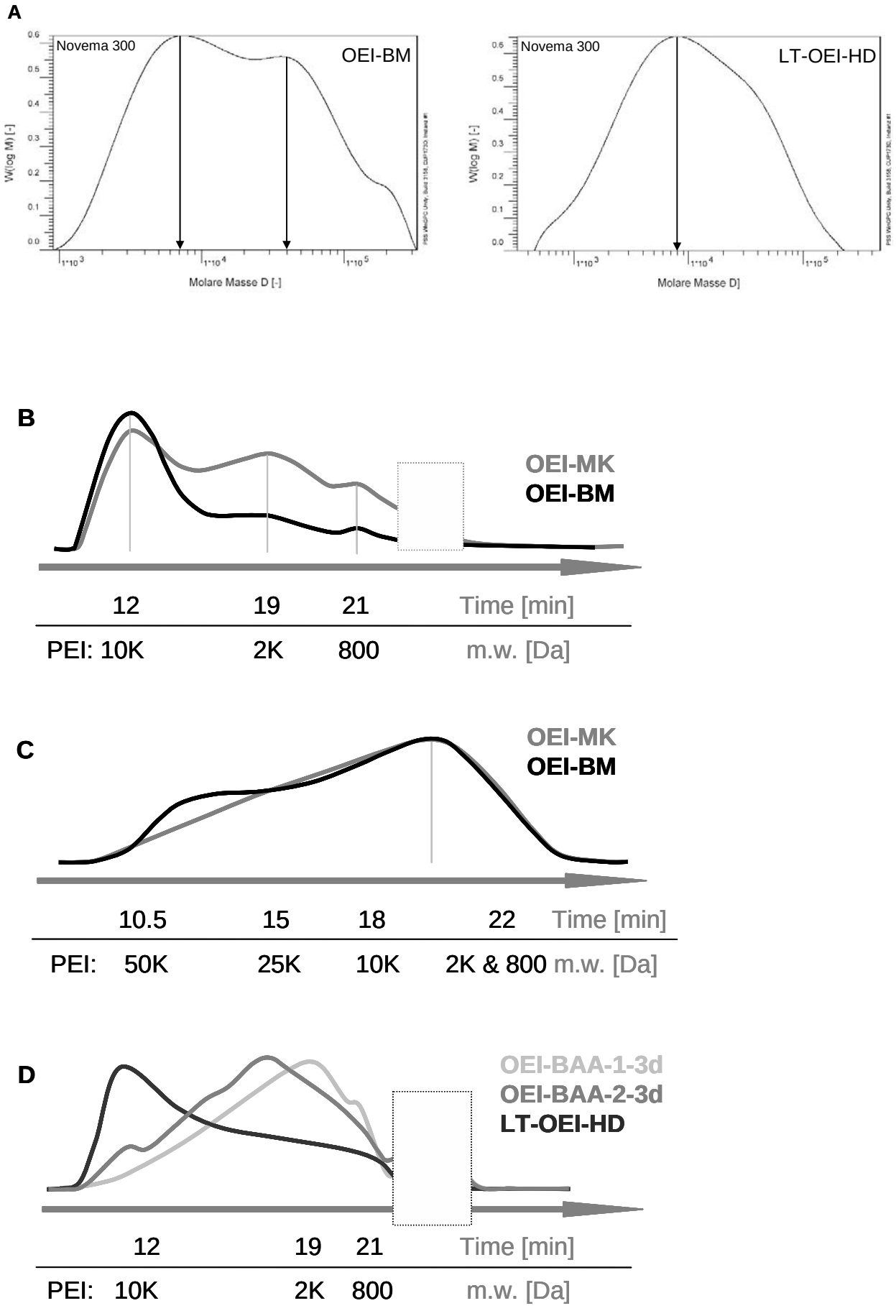
A
Novema 300
OEI-BM
W(log M) [-]
Molare Masse D [-]
Novema 300
LT-OEI-HD
W(log M) [-]
Molare Masse D]
B
OEI-MK
OEI-BM
12
19
21
Time [min]
PEI: 10K
2K
800
m.w. [Da]
C
OEI-MK
OEI-BM
10.5
15
18
22
Time [min]
PEI:
50K
25K
10K
2K & 800
m.w. [Da]
D
OEI-BAA-1-3d
OEI-BAA-2-3d
LT-OEI-HD
12
19
21
Time [min]
PEI:
10K
2K
800
m.w. [Da]

Table S1. Summary of polymer size characterization by GPC and SEC.

Polymer	**SEC**			**GPC**				
	Mp	m.w. range	Vp	Mp	Vp	Mn	Mw	PDI
OEI-BM	8-10 kDa, 40 kDa	1 kDa - >50 kDa	12 mL (Sup. 200), 20 mL (Sup. 200)	7 kDa 40 kDa	10.3 mL	8.5 kDa	36 kDa	4.2
OEI-MK	8-10 kDa	1 kDa - 50 kDa	20 mL (Sup. 200)					
LT-OEI-HD	8-10 kDa	1 kDa - 50 kDa	20 mL (Sup. 200)	8 kDa	10.1 mL	4.9 kDa	21 kDa	4.3
OEI-BAA-2-3d	4 kDa, 8-10 kDa	1 kDa - 10 kDa	20 mL (Sup. 200); 12, 14, 17mL (Sup. 75);					
OEI-BAA-1-3d	2-3 kDa	1 kDa - 10 kDa	18.5 mL (Sup. 75)					
OEI-BAA-1-1.5d	2-3 kDa	1 kDa - 10 kDa	18.5 mL (Sup. 75)					
OEI-BAA-1-45m	2-3 kDa	1 kDa - 8 kDa	18.5 mL (Sup. 75)					
OEI-BAA-1.25-45m	2-3 kDa	1 kDa - 9 kDa	18.5 mL (Sup. 75)					

2. Degradation Study for Different OEI-BAA Polymers.

Aminolysis in the OEI-BAA polymer synthesis generates amide linkages which do not degrade as fast as the acetal linkages. Therefore, dependent on their different acetal diester and amide contents, acid catalyzed hydrolysis of OEI-BAA polymers results in end-products of different sizes. To investigate this in more detail, polymers were diluted in 20 mM Hepes and adjusted at pH 1 by the addition of HCl. Samples were incubated at 37 °C for 1 h, and neutralized with NaOH. The degradation products were analyzed by SEC using a Superdex 75 column with 20 mM Hepes pH 7.4, 0.25 M NaCl as running buffer (**Figure S2**). OEI-BAA-1-45m, the polymer with the highest diester acetal linker content, degraded completely into fragments of the size of OEI800 monomers and dimers. OEI-BAA-1-1.5d (with a slightly lower acetal diester content) showed a degradation product profile shifted towards the dimers and minor amounts of oligomers. OEI-BAA-2-3d (the polymer with the highest non-hydrolyzable amide content) hydrolyzed to monomers, dimers and considerable amounts of oligomers. Despite the amide content very profound hydrolysis of the polymer took place, eliminating the high m.w. fraction of the polymer (compare Figure S1D).

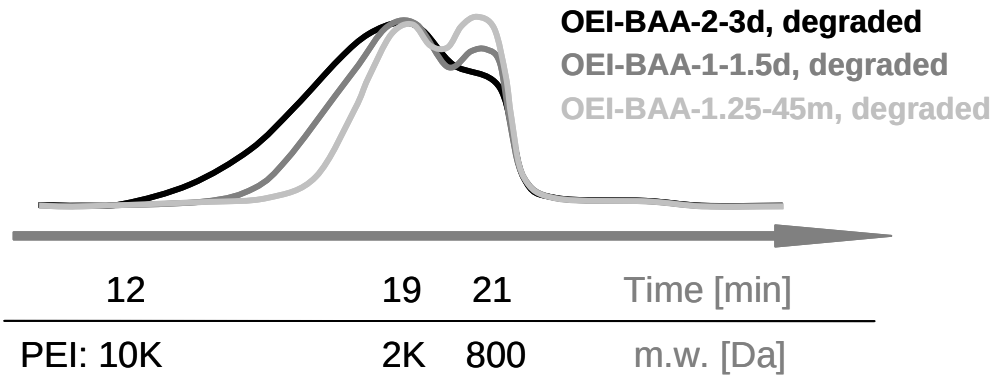

Figure S2. SEC elution profiles (Superdex 75) of degraded OEI-BAA polymers after acid treatment.

3. Comparison of Different OEI-BAA Polymers for Transfection Efficiency and Metabolic Activity of Transfected Cells.

OEI-BAA polymers that differ in their diester- and acetal-linker content were compared in their transfection efficiency (**Figure S3A**) and cytotoxity (**Figure S3B**) profiles. OEI-BAA-2-3d, OEI-BAA-1-1.5d, OEI-BAA-1-45m and OEI-BAA-1.25-45m were evaluated which form polyplexes of comparable size and surface charge. High c/p ratios (up to 20) were also tested in this experiment, to make any significant toxicity visible. A clear relationship between the content of acid degradable diester acetal linker in the polymer and its biocompatibility (i.e. low cytotoxicity) was observed. OEI-BAA-2-3d, the polymer with the lowest diester content among the tested OEI-BAAs, reduced metabolic activity of transfected cells at c/p of ≥10. Nevertheless, biocompatibility was far better than for PEI22K or the acetal-free ester analog LT-OEI-HD (see also Figure 6) and optimum transfection activity was observed at the much lower c/p 2.5. Polymers with higher acetal content (OEI-BAA-1-1.5d, OEI-BAA-1-45m, OEI-BAA-1.25-45m) displayed no detectable cytotoxicity even at the highest c/p ratio tested. These polymers however showed also the lowest transfection levels. OEI-BAA-1-1.5 was inferior to OEI-BAA-2-3d at low c/p ratios but became almost equal at higher concentrations, while still being completely non-toxic.

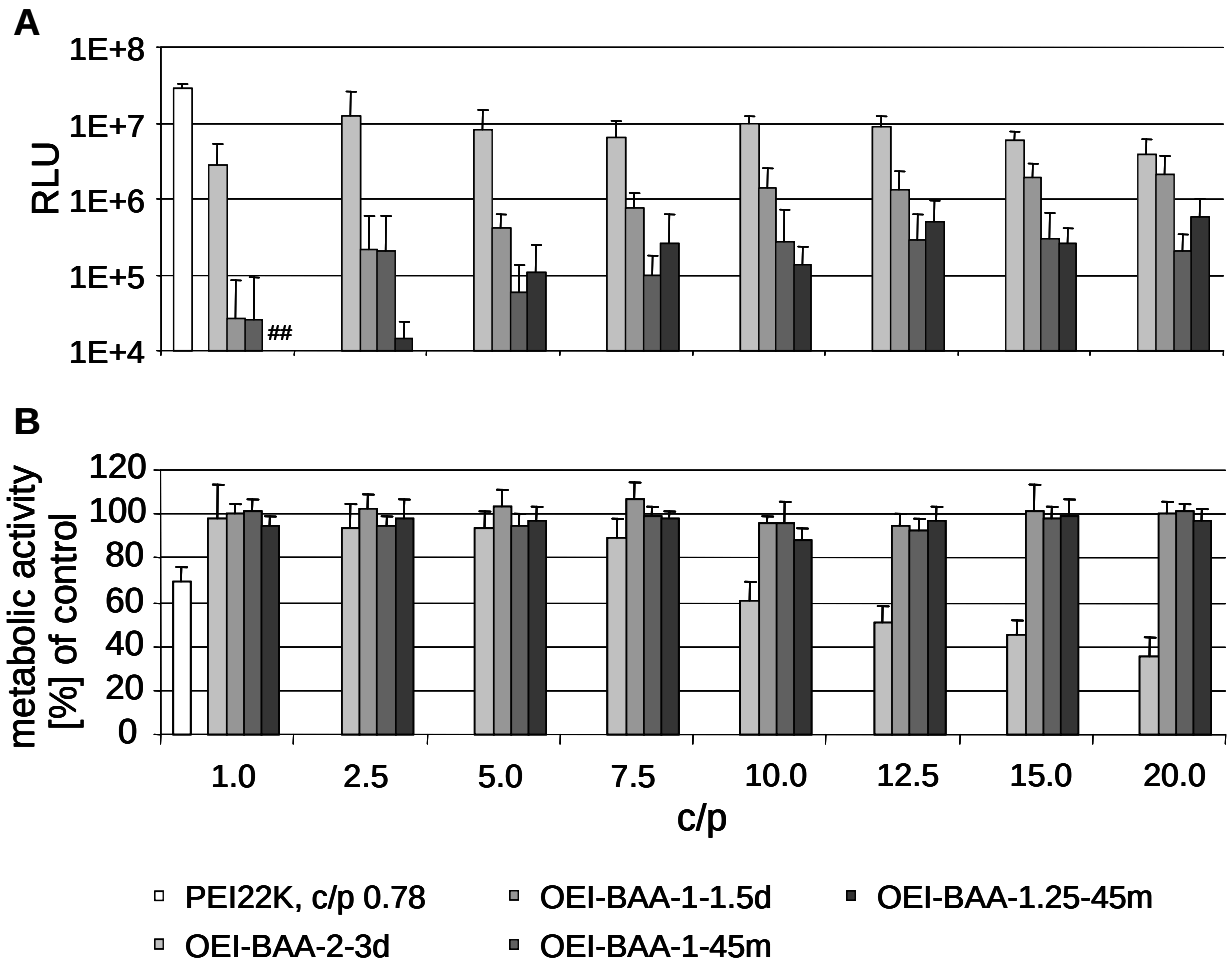

Figure S3. Influence of acetal linker content in the OEI-BAA polymers on transfection efficiency (E) and toxicity (F). ## 4540 RLU ± 920.

Near Infrared Fluorescence-Based Bacteriophage Particles for Ratiometric pH Imaging

Scott A. Hilderbrand,*[,†] Kimberly A. Kelly,[†] Mark Niedre,[†] and Ralph Weissleder[†,‡]

Center for Molecular Imaging Research and Center for Systems Biology, Massachusetts General Hospital/Harvard Medical School. Received May 9, 2008; Revised Manuscript Received June 11, 2008

Fluorogenic imaging agents emitting in the near-infrared are becoming important research tools for disease investigation *in vivo*. Often pathophysiological states such as cancer and cystic fibrosis are associated with disruptions in acid/base homeostasis. The development of optical sensors for pH imaging would facilitate the investigation of these diseased conditions. In this report, the design and synthesis of a ratiometric near-infrared emitting probe for pH quantification is detailed. The pH-responsive probe is prepared by covalent attachment of pH-sensitive and pH-insensitive fluorophores to a bacteriophage particle scaffold. The pH-responsive cyanine dye, HCyC-646, used to construct the probe, has a fluorogenic pK_a of 6.2, which is optimized for visualization of acidic pH often associated with tumor hypoxia and other diseased states. Incorporation of pH-insensitive reference dyes enables the ratiometric determination of pH independent of the probe concentration. With the pH-responsive construct, measurement of intracellular pH and accurate determination of pH through optically diffuse biological tissue is demonstrated.

INTRODUCTION

The *in vivo* investigation of biological processes at a molecular level has received considerable attention for its potential application in early diagnosis and treatment of disease. Although the disruption of acid/base homeostasis is associated with a variety of diseases such as cancer, cystic fibrosis, and immune dysfunction (*1–4*), our understanding of the direct and indirect effects of these environments is limited. Due to their sensitivity and noninvasive nature, fluorescence-based imaging methodologies are well suited for investigation of pH in biological systems.

In order to obtain useful *in vivo* pH data, methods need to be employed in which the pH response of the probe is determined in a ratiometric fashion, allowing for measurement of local pH in a probe concentration independent manner. Even though small molecule (*5–10*) and nanoparticle (*11–15*) based systems have been employed for ratiometric pH determination in solution and *in vitro*, none are suitable for *in vivo* imaging applications. These probes typically use fluorescein (*6, 8–10, 13–15*) or other pH-sensitive lumophores (*5, 7, 11, 12*) with emission in the visible region. For efficient *in vivo* optical imaging, fluorophores that emit in the NIR are necessary due to the increased optical transparency and minimal tissue autofluorescence in this regime (*16*). There are currently few reports of NIR pH-responsive fluorophores in the literature (*17–21*). These dyes have suboptimal optical and solubility properties for imaging pH *in vivo*. Often the diseased states result in pH changes that are only slightly lower than that of physiological pH. For example, typical extracellular pH values reported for tumors are between 6.3 and 7.0 (*3*). Current NIR probes are not ideal for biological imaging because they are either irreversible (*21*) or have fluorogenic pK_a values that are too high (*17, 20*) or too low (*18*) for effective imaging. Recently, we reported a new strategy for tuning the pK_a of pH-responsive cyanine dyes to address these issues (*22*).

Probes based on a nanoscaffold possess several advantages over small molecule pH sensors. Particle based approaches can easily incorporate a pH-insensitive reporter dye allowing for the determination of H^+ concentration independent of the probe concentration. In addition, multiple copies of the reference and pH-responsive dyes can be appended to a single particle, effectively increasing the brightness of the individual probe nanoparticle. Our research group has reported the development of targeted M13 bacteriophage particles functionalized with several hundred copies of NIR fluorophores for *in vitro* and *in vivo* receptor targeted imaging applications (*23, 24*). The M13 bacteriophage is a flexible heterofunctional nanoplatform (*25*) with a well investigated *in vivo* biodistribution profile (*26*). Individual bacteriophage particles are approximately 880 × 6.6 nm in size and contain 2700 copies of the p8 coat protein with their amino termini exposed to the solvent. These amine groups are available for bioconjugation (*23, 27*). The preparation of nanoscale pH-sensitive imaging agents based on these bacteriophage imaging platforms using optimized pH-responsive and pH-insensitive NIR fluorophores for potential *in vivo* imaging is detailed in this report.

EXPERIMENTAL PROCEDURES

General Considerations. All chemicals were purchased from Sigma-Aldrich (Milwaukee, WI), TCI America (Portland, OR) or Acros Organics USA (Morris Plains, NJ) and were used as received. The starting indoles, 2,3,3-trimethylindolenine-5-sulfonic acid and 1-(ε-carboxypentyl)-2,3,3-trimethylindolenium-5-sulfonate, were prepared according to published procedures (*28*). The succinimidyl esters of Cy 7 and Cy 5 were purchased from GE Lifesciences (Piscataway, NJ). All solvents, including anhydrous DMF, were purchased from Sigma-Aldrich. High performance liquid chromatography (HPLC) was performed on a Hitachi D-7000 instrument equipped with a L-7455 diode array detector. Nuclear magnetic resonance (NMR) spectra were acquired on a Bruker DPX-400 spectrometer at ambient temperature and referenced to tetramethylsilane (TMS) as an

* Corresponding author. Scott A. Hilderbrand, 149 13th St., Room 5406, Charlestown, MA 02129 USA. Phone: (617) 726-5788. Fax: (617) 726-5708. Email: Scott_Hilderbrand@hms.harvard.edu.

† Center for Molecular Imaging Research.

‡ Center for Systems Biology.

10.1021/bc800188p CCC: $40.75 © 2008 American Chemical Society
Published on Web 07/31/2008

internal standard. Absorption spectra were collected on a Varian Cary 50-Bio UV/visible spectrophotometer (Palo Alto, CA). The extinction coefficient measurements for dye **2** were determined in 50 mM glycine buffer, pH 3.0, and were performed in triplicate using reverse phase C-18 and cation exchange chromatography purified dye. For determination of the extinction coefficient, of protonated **2**, fresh stock solutions of the dye were prepared for each trial by dissolution of 2−3 mg portions of the dyes, weighed on a Mettler AT201 analytical balance with an error of ±0.01 mg, in 50 mM glycine buffer, pH 3.0, using a 10 mL volumetric flask. The extinction coefficient of the deprotonated form of **2** was determined in an analogous manner using aqueous NaOH, pH 10.0. Standard deviations for the extinction coefficient measurements were 5% or less. Fluorescence data were collected on a Horiba Jobin Yvon Fluorolog-3 spectrofluorometer (Edison, NJ) and were corrected for the detector sensitivity. Quantum yield measurements of the protonated form of **2** in 50 mM glycine, pH 3.0, were performed in triplicate following published procedures (*29*) and were collected using dilute samples (absorbance ≤0.10 OD) with Cy 5 ($\Phi = 0.27$) (*28*) in phosphate buffered saline as a standard. All samples for quantum yield determinations were excited at 610 nm. High-resolution electrospray ionization (ESI) mass spectra were collected on a Bruker Daltonics APEXII 3 T Fourier transform mass spectrometer in the Department of Chemistry Instrumentation Facility (DCIF) at the Massachusetts Institute of Technology. Low-resolution ESI mass spectra were obtained using a Waters/Micromass ZQ 4000 mass spectrometer.

Fluorescence microscopy was performed on Zeiss Axiovert 100 TV microscope with a 40X objective using filter sets from Omega Optical. The NIR reference dye, Cy 7 was imaged using a 740 ± 12.5 nm band-pass filter for excitation and a 780 nm long-pass filter for emission. The pH-sensitive dye was imaged using a 610 ± 10 nm band-pass filter for excitation and a 670 ± 20 nm band-pass filter for emission.

Fluorescence reflectance imaging (FRI) data were acquired on a Maestro imaging system from CRi (Woburn, MA). The pH-responsive HCyC-646 (**2**), was imaged using a 590 to 645 nm band-pass excitation filter and the LCD emission filter tuned to 670 nm. The pH-insensitive reference, Cy 7, was imaged using a 690 to 750 nm band-pass excitation filter and the LCD emission filter tuned to 775 nm. All Cy 7 images were exposed for 97 ms and all images using dye **2** were exposed for 68 ms.

HCyC-646 Methyl Ester, 1. To a solution of 1-(ε-carboxypentyl)-2,3,3-trimethylindoleninium-5-sulfonate (884 mg, 2.5 mmol) was added chloromalonaldehyde (266 mg, 2.5 mmol) in 15 mL of MeOH. This solution was sealed in a thick-walled glass pressure reactor and heated at 70 °C for 30 min giving a yellow-green solution. After cooling, 2,3,3-trimethylindolenine-5-sulfonic acid (598 mg, 2.5 mmol) was added, the pressure reactor was resealed, and the solution was heated at 70 °C for an additional 5 h giving a dark blue solution. After cooling to room temperature, the solvent was removed by rotary evaporation. The crude blue solid was subjected to reverse-phase C-18 column chromatography (Isolute 70 g RPC18 cartridge) eluting with increasing concentrations of CH_3CN (0, 5, and 10%) in H_2O to afford **1** (163 mg, 9.6%). HPLC analysis of the final product indicates >97% purity with dye **2** being the major contaminant. ^{1}H NMR (400 MHz, DMSO-d_6): δ 13.1 (broad s, 1H), 8.39 (d, 1H, $J = 13.8$ Hz), 8.27 (broad d, 1H, $J = 12.8$ Hz), 7.85−7.84 (two overlapping singlets, 2H), 7.67−7.63 (two overlapping doublets, 2H), 7.40 (d, 1H, $J = 8.3$ Hz), 7.23 (d, 1H, $J = 8.1$ Hz), 6.37 (broad d, 1H, $J = 13.8$ Hz), 4.13 (t, 2H, $J = 6.4$ Hz), 3.55 (s, 3H), 2.30, (t, 2H, $J = 7.3$ Hz), 1.76−1.33 (m, 18H). MS-ESI $[M+H]^+$: calcd for $C_{32}H_{38}ClN_2O_8S_2^+$ 677.2, found 677.2.

HCyC-646, 2. Intermediate **1** (102 mg, 0.15 mmol) was added to 5 mL of 1 M NaOH and heated at 80 °C for 1.5 h. After cooling, the solution was acidified by addition of 10% aqueous HCl and the solvent was removed by rotary evaporation. The blue solid was purified by reverse-phase C-18 column chromatography (Isolute 70 g RPC18 cartridge) eluting with increasing concentrations of CH_3CN (0%, 10%, and 15%) in H_2O. Following solvent removal, the product was subjected to cation exchange chromatography (Dowex 50WX8 hydrogen form resin) to give pure **2** (88 mg, 88%). ^{1}H NMR (400 MHz, DMSO-d_6): δ 13.1 (broad s, 1H), 8.39 (d, 1H, $J = 13.8$ Hz), 8.28 (d, 1H, $J = 12.7$ Hz), 7.85 (two overlapping singlets, 2H), 7.67−7.63 (two overlapping doublets, 2H), 7.40 (d, 1H, $J = 8.3$ Hz), 7.23 (d, 1H, $J = 8.1$ Hz), 6.37 (broad d, 1H, $J = 13.4$ Hz), 6.24 (d, 1H, $J = 13.4$ Hz), 4.14 (t, 2H, $J = 5.9$ Hz), 2.20 (t, 2H, 7.2 Hz), 1.76−1.37 (m, 18H). HRMS-ESI $[M+H]^+$: calcd for $C_{31}H_{36}ClN_2O_8S_2^+$ 663.1596, found 663.1613.

HCyC-646 Su, 3. To a solution of **2** (19.9 mg, 0.03 mmol) in 1 mL of anhydrous DMF was added 11.5 mg (0.045 mmol) of *N*,*N*′-disuccinimidyl carbonate (DSC) and triethylamine (31 μL, 0.225 mmol). After stirring for 4 h, the product was precipitated by addition of *tert*-butyl methyl ether to give a blue solid. This material was further purified by preparative reverse phase HPLC chromatography using a gradient of 100% H_2O with 0.1% TFA to 60% CH_3CN in H_2O with 0.1% TFA to yield **3** (18.9 mg, 83%) as a blue solid. HPLC analysis of the product indicates the presence of approximately 5% dye **2** as an impurity. ^{1}H NMR (400 MHz, DMSO-d_6): δ 13.1 (broad s, 1H), 8.38 (d, 1H, $J = 13.8$ Hz), 8.27 (broad d, 1H, $J = 13.5$ Hz), 7.85−7.84 (two overlapping singlets, 2H), 7.65−7.63 (two overlapping doublets, 2H), 7.39 (d, 1H, $J = 8.3$ Hz), 7.22 (d, 1H, $J = 8.1$ Hz), 6.37 (broad d, 1H, $J = 13.7$ Hz), 6.23 (d, 1H, $J = 13.4$ Hz), 4.14 (broad t, 2H), 2.80 (s, 4H), 2.69 (t, 2H, $J = 7.2$ Hz), 1.77−1.37 (m, 18H). HRMS-ESI $[M-H]^-$: calcd for $C_{35}H_{37}ClN_3O_{10}S_2^-$ 758.1614, found 758.1592.

Bacteriophage Preparation and Labeling. Wild type M13 bacteriophage were amplified by infection in *Escherichia coli* and their titer was determined according to published procedures (*30*). Following titer determination, the bacteriophage were labeled simultaneously with the succinimidyl esters of Cy 7 and HCyC-647 using a modified literature procedure (*31*). Briefly, Cy 7 succinimidyl ester (40 μL of a 5 μg/μL stock solution in anhydrous DMSO) and HCyC-646 (20 μL of a 5 μg/μL stock solution in anhydrous DMSO) were added to 1×10^{13} plaque forming units (pfu) of wild type M13 bacteriophage in 2 mL of 100 μM bicarbonate buffer, pH 8.3. The resulting solution was allowed to incubate for 1 h at room temperature in the dark. Following incubation, the labeled bacteriophage was precipitated by addition of 350 μL of a PEG 8000/2.5 M NaCl solution (40% w/v PEG 8000) and allowed to stand on ice for 30 min. The bacteriophage was then pelleted by centrifugation at 10 000 *g* for 15 min. After removal of the supernatant, the pellet was resuspended in 833 μL of DPBS buffer. This suspension was then subjected to two additional rounds of the PEG precipitation using 166 μL of the PEG 8000/2.5 M NaCl solution. The final labeled bacteriophage was resuspended in 1000 μL of DPBS. The concentration of the labeled bacteriophage (in pfu) was determined by comparing the absorbance values of 10-fold dilutions of the initial unlabeled bacteriophage (5×10^9 pfu/μL) to the labeled bacteriophage at 280 nm. The degree of labeling for both dyes was determined from a 10-fold dilution of the stock labeled bacteriophage in 100 μM PBS, pH 8.0, using the extinction coefficients of Cy 7 ($\varepsilon = 200\,000$ M^{-1} cm^{-1} at 750 nm) (*28*) and deprotonated HCyC-646 ($\varepsilon = 50\,000$ M^{-1} cm^{-1} at 506 nm). Typical dye labeling using this procedure gives 400−500 copies of each dye per bacteriophage particle.

Scheme 1. Synthesis of the pH-Responsive Cyanine Derivative

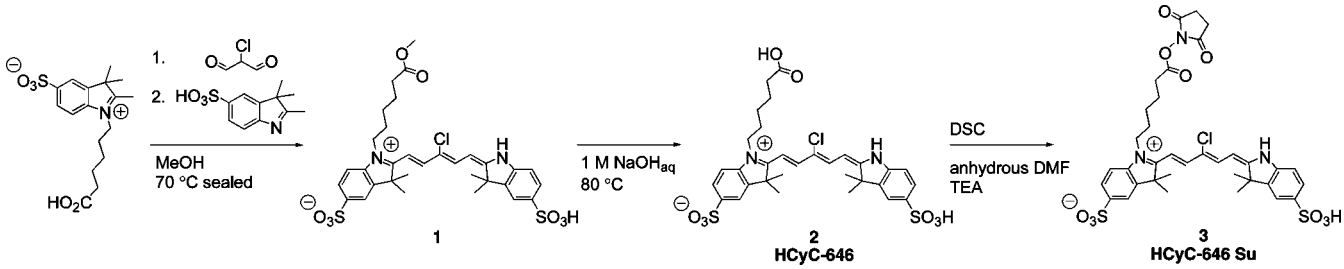

Sensor Calibration. The pH-dependent response of the sensor was determined based on the ratio of the fluorescence emission bands of the Cy 7 and HCyC-646 fluorophores on the bacteriophage particles in a series of 50 mM phosphate/citric acid buffer solutions from pH 4.9 to 9.3. For the *in vitro* calibrations, Cy 7 was excited at 715 nm and the fluorescence emission was integrated from 730 to 825 nm, whereas HCyC-646 was excited at 610 nm and the fluorescence emission was integrated from 630 to 725 nm.

For the cell imaging experiments, *in situ* standard curves were generated on the same day that the imaging was performed using a procedure modified from the literature (*5*). The ionophore nigericin was used for intracellular pH equilibration of all samples (*5*). Briefly, RAW cells on 24 well plates were first incubated at 37 °C with the pH-responsive bacteriophage (at a final concentration of 1 μM Cy 7 on the bacteriophage) in DPBS, pH 7.4 for 1 h. Following removal of the pH-sensitive bacteriophage-containing buffer, the cells were washed 2 × 100 μL with the appropriate pH nigericin solutions. Nigericin solutions were prepared by adding 100 μL of a 10× nigericin stock solution (100 μg/mL nigericin, 1.3 M KCl, and 10 mM $MgCl_2$ in distilled water) to 900 μL of 50 mM phosphate/citric acid solutions with pH values between 5.0 and 7.5 in increments of 0.5 pH units. The cells were then incubated in the different pH nigericin solutions at 37 °C for 30 min to equilibrate the intracellular pH with the buffer pH and were then imaged by fluorescence microscopy. Images of at least three cells were used to acquire the fluorescence ratio between Cy 7 and HCyC-646 at each pH value for generation of the standard curve.

In the mouse imaging experiments, standard curves were generated by acquiring fluorescence images of the Cy 7 and HCyC-646 signals from 50 μL volume phantom tubes containing the pH-responsive bacteriophage. For all phantoms, the bacteriophage was adjusted to a Cy 7 concentration of 1 μM. The bacteriophage probe was suspended in a series of 50 mM phosphate/citric acid buffer solutions with pH values between 5.0 and 7.0 in increments of 0.5 pH units. The phantoms were inserted subcutaneously into a mouse, which had been previously sacrificed, prior to imaging in order to correct for differences in light attenuation through tissue between the Cy 7 and HCyC-646 imaging channels. The fluorescence signals from the individual imaging channels were further corrected for background fluorescence by subtracting the average fluorescence intensity from a region of interest (ROI) adjacent to the bacteriophage-probe phantoms from the average signal intensity of ROIs covering the entire phantom. As with the *in vitro* and intracellular-based standard curves, the Cy 7/HCyC-646 ratios were used to generate a standard curve used for subsequent imaging experiments.

RESULTS AND DISCUSSION

The water-soluble pH sensitive dye, HCyC-646 used in this report was prepared by the condensation of 1-(ε-carboxypentyl)-2,3,3-trimethylindoleninium-5-sulfonate and 2,3,3-trimethylindolenine-5-sulfonic acid with chloromalonaldehyde and then converted to its activated succinimidyl ester for bioconjugation (Scheme 1). In acidic environments, HCyC-646, exists primarily in its protonated emissive form with absorption at 646 nm and fluorescence emission at 670 nm (Scheme 2, and Figure S1 Supporting Information). The protonated dye has an extinction coefficient of 200 000 M^{-1} cm^{-1} at 646 nm and a quantum yield of 8% in aqueous media. At neutral or basic pH, however, deprotonation of the indole nitrogen is accompanied by a large hypsochromic shift in the absorption maximum to 506 nm and loss of NIR fluorescence emission. With a pK_a of 6.2, HCyC-646 is ideally suited for potential imaging of biologically relevant acidic environments such as those found in tumors (*3*) and other disease states (*32, 33*). In addition, the long wavelength absorption and emission of HCyC-646 lie within the optimal window for *in vivo* imaging between approximately 650 and 900 nm (*16*).

Scheme 2. pH-Dependent Equilibrium of HCyC-646

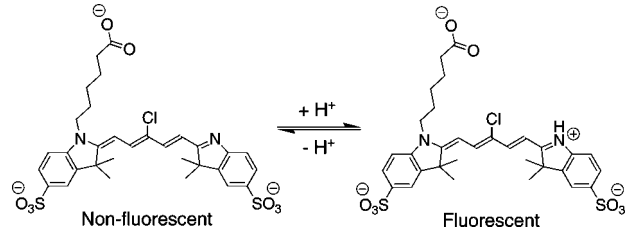

To prepare the ratiometric bacteriophage probe, the succinimidyl esters of the pH-sensitive dye and an additional pH-insensitive reference dye, Cy 7, were conjugated to the surface of the bacteriophage particles. In a typical labeling procedure approximately 400−500 copies of each dye could be attached to the surface of the bacteriophage particles. Once labeled, the bacteriophage respond to pH in a ratiometric manner with the HCyC-646 emission signal varying with pH and the Cy 7 signal remaining stable from pH 5 to 9 (Scheme 3 and Figure 1). This pH range matches well with the expected pH values in biological systems.

The labeled bacteriophage can be used for intracellular pH imaging. Incubation of the pH-responsive probe with RAW cells for one hour results in internalization of the phage particles into acidic intracellular vesicles. Cells were imaged with filter sets optimized for HCyC-646 and Cy 7. To obtain pH map data, the ratios of the Cy 7 and HCyC-646 signals were taken and then correlated to an *in situ* standard curve. Using this approach, it is possible to visualize intracellular pH (Figure 2). The cellular pH readings were found to lie between 6.5 and approximately 5.0. These values agree well with reported pH ranges for acidic intracellular vesicles such as endosomes, phagosomes, and lysosomes (*34*). These data are also in good agreement with intracellular pH readings from a recently published fluorescein-based ratiometric pH probe (*13*). In addition to the ability of the pH-responsive bacteriophage to image intracellular pH, the probe can be used to image through optically diffuse biological tissue.

Scheme 3. Fluorophore Labeled Bacteriophage Particles

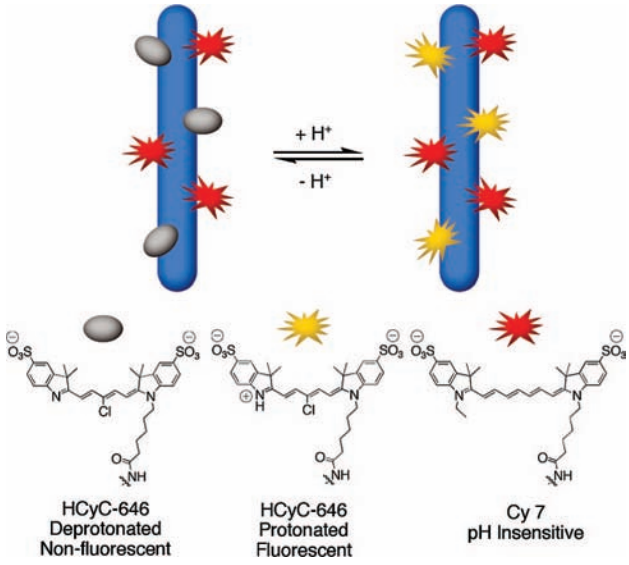

To demonstrate the ability of the phage particles for imaging through tissue, pH adjusted phantoms containing a 50 μL solution of the probe adjusted to a concentration of 1 μM with respect to Cy 7 were inserted subcutaneously into mice and visualized by fluorescence reflectance imaging (Figure 3). As with the cell imaging experiments, the fluorescence signals were ratioed and mapped to a standard curve to generate the pH maps.

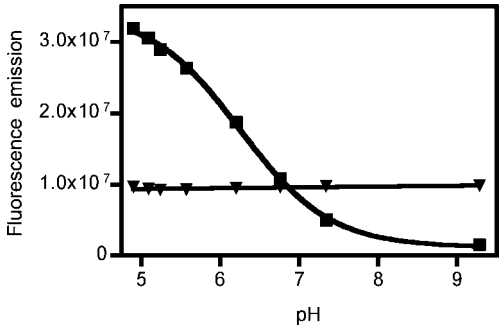

Figure 1. Fluorescence response of the labeled bacteriophage in a series of different pH 50 mM phosphate/citric acid buffers. The emission from the conjugagted HCyC-646 (squares) varies with pH, whereas the Cy 7 signal (triangles) is pH-insensitive. Excitation for HCyC-646 was at 610 nm and the emission signal was integrated from 630 to 725 nm. Excitation for Cy 7 was at 715 nm and the emission signal was integrated from 730 to 825 nm. The probe was adjusted to a concentration of 1 μM with respect to Cy 7.

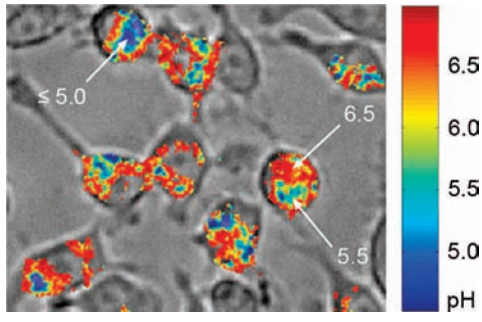

Figure 2. Intracellular ratiometric pH imaging in RAW cells with the pH-responsive bacteriophage particles. Prior to imaging, the cells were incubated with the ratiometric imaging probe in PBS, pH 7.4 adjusted to a final probe concentration of 1 μM with respect to Cy 7. The fluorescence images from the HCyC-646 and Cy 7 were ratioed and correlated to the standard curve to generate the pH map.

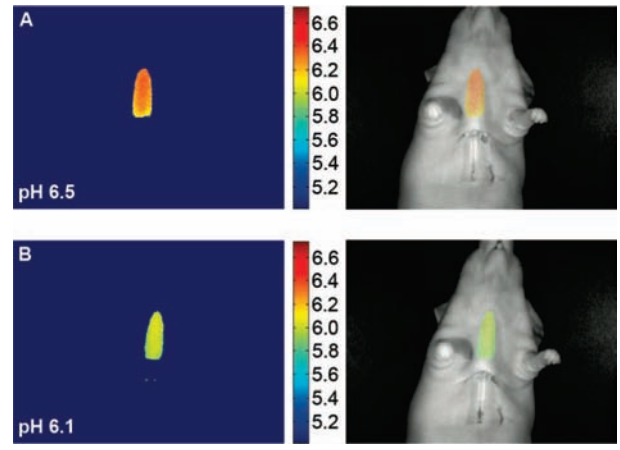

Figure 3. Fluorescence ratio pH maps through optically diffuse tissue of 50 μL phantoms containing the pH-responsive probe adjusted to a concentration of 1 μM with respect to Cy 7 in 50 μM phosphate/citric acid buffers. The left and right panels show the recconstructed pH ratio maps from the phantoms and the pH maps overlaid on the bright field images, respectively. The ratiometrically determined pH values of 6.5 (A) and 6.1 (B) match well with the corresponding pH electrode measurements of 6.60 and 6.16.

There is excellent correlation between the ratiometrically based pH readings and the electrode measured pH values of the phantoms. For example, the ratiometrically measured pH of the phantom in Figure 3a of 6.5 compares well with the actual pH of 6.60. In Figure 3b, a ratiometrically measured pH of 6.1 matches well with the actual pH of 6.16. The ability to clearly visualize different pH values in this range should prove invaluable for *in vivo* imaging of pathophysiological processes associated with acidic pH. One current limitation of this system arises from differences in the tissue penetrating ability of light at the emission wavelengths of the two fluorophores (Table S1, Supporting Information). The shorter wavelength fluorescence emission at ~670 nm from HCyC-646 shows stronger tissue absorbance than the ~775 nm emission from Cy 7. To correct for the light penetrating abilities at the different imaging wavelengths, fluorescence data for the standard curve were obtained under identical conditions to those in which the unknown pH phantoms were imaged.

In summary, we report the development of a new nanoscaffold for fluorescence-based pH imaging, both intracellular and through optically diffuse biological tissue. The pH-sensitive cyanine dye, HCyC-646, used in this report has a pK_a of 6.2, which is optimized for visualization of pH in a biologically relevant range. Through coupling of several hundred copies pH sensitive HCyC-646 and Cy 7, a pH-insensitive dye, to the surface of bacteriophage particles, a bright pH-responsive ratiometric imaging platform was obtained. With this platform, it is possible to make intracellular pH measurements as well as determine pH through optically diffuse tissue. Current research is focused on development of new nanoparticle scaffolds, for preparation of additional ratiometric pH-sensitive systems. We are also exploring strategies in which correcting for differences in light penetration through diffuse biological tissue at the different imaging wavelengths would not be necessary. One potential approach is through the use of fluorescence lifetime-based measurements using pH-sensitive and -insensitive dyes, which have identical absorption and emission wavelengths, but different fluorescence lifetimes. Once these hurdles are overcome, *in vivo* fluorescence-based imaging of pH in disease will be feasible. Such systems could prove invaluable for identification and diagnosis of tumors and other diseased states.

ACKNOWLEDGMENT

This research was funded in part by NIH grants CA119349, CA92782, and HL080731 (to R.W.).

Supporting Information Available: Spectroscopic characterization of pH-responsive dye, **2**, and signal attenuation of the fluorophores through tissue. This material is available free of charge via the Internet at http://pubs.acs.org.

LITERATURE CITED

(1) Kellum, J. A., Song, M., and Li, J. (2004) Extracellular acidosis and the immune response: clinical and physiologic implications. *Crit. Care 8*, 331–336.

(2) Coakley, R. D., Grubb, B. R., Paradiso, A. M., Gatzy, J. T., Johnson, L. G., Kreda, S. M., O'Neal, W. K., and Boucher, R. C. (2003) Abnormal surface liquid pH regulation by cultured cystic fibrosis bronchial epithelium. *Proc. Natl. Acad. Sci. U.S.A. 100*, 16083–16088.

(3) Gillies, R. J., Raghunand, N., Garcia-Martin, M. L., and Gatenby, R. A. (2004) pH Imaging. *IEEE Eng. Med. Biol. Mag. 23*, 57–64.

(4) Gillies, R. J., Schornack, P. A., Secomb, T. W., and Raghunand, N. (1999) Causes and effects of heterogenous perfusion in tumors. *Neoplasia 1*, 197–207.

(5) Overly, C. C., Lee, K.-D., Berthiaume, E., and Hollenbeck, P. J. (1995) Quantitative measurment of intraorganelle pH in the endosomal-lysosomal pathway in neurons by using ratiometric imaging with pyranine. *Proc. Natl. Acad. Sci. U.S.A. 92*, 3156–3160.

(6) Martin, G. R., and Jain, R. K. (1993) Fluorescence ratio imaging measurment of pH gradients: calibration and application in normal and tumor tissues. *Microvasc. Res. 46*, 216–230.

(7) Bassnett, S., Reinisch, L., and Beebe, D. C. (1990) Intracellular pH measurment using single excitation-dual emission fluorescence ratios. *Am. J. Physiol.-Cell Physiol. 258*, C171−C178.

(8) Murphy, R. F., Powers, S., and Cantor, C. R. (1984) Endosome pH measured in single cells by dual fluorescence flow cytometry: rapid acidification of insulin to pH 6. *J. Cell Biol. 98*, 1757–1762.

(9) Heiple, J. M., and Taylor, D. L. (1980) Intracellular pH in single motile cells. *J. Cell Biol. 86*, 885–890.

(10) Thomas, J. A., Buchsbaum, R. N., Zimniak, A., and Racker, E. (1979) Intracellular pH measurments in Ehrlich ascites tumor cells utilizing spectroscopic probes generated in situ. *Biochemistry 18*, 2210–2218.

(11) Tomasulo, M., Yildiz, I., and Raymo, F. M. (2006) pH-sensitive quantum dots. *J. Phys. Chem. B 110*, 3853–3855.

(12) Kim, S., Pudavar, H. E., and Prasad, P. N. (2006) Dye-concentrated organically modified silical nanoparticles as a ratiometric fluorescent pH probe by one- and two-photon excitation. *Chem. Commun.* 2071–2073.

(13) Burns, A., Sengupta, P., Zedayko, T., Baird, B., and Weisner, U. (2006) Core/shell fluorescent silica nanoparticles for chemical sensing: towards single-particle laboratories. *Small 2*, 723–726.

(14) McNamara, K. P., Nguyen, T., Dumitrascu, G., Ji, J., Rosenzweig, N., and Rosenzweig, Z. (2001) Synthesis, characterization, and application of fluroescence sensing lipobeads for intracellular pH measurements. *Anal. Chem. 73*, 3240–3246.

(15) Ji, J., Rosenzweig, N., Griffin, C., and Rosenzweig, Z. (2000) Synthesis and application of submicrometer fluorescence sensing particles for lysosomal pH measurments in murine macrophages. *Anal. Chem. 72*, 3497–3503.

(16) Weissleder, R., and Ntziachristos, V. (2003) Shedding light onto live molecular targets. *Nat. Med. 9*, 123–8.

(17) Zhang, Z., and Achilefu, S. (2005) Design, synthesis and evaluation of near-infrared fluorescent pH indicators in a physiologically relevant range. *Chem. Commun.* 5887–5889.

(18) Strekowski, L., Mason, J. C., Lee, H., Say, M., and Patonay, G. (2004) Water-soluble pH sensitive 2,6-bis(substituted ethylidene)-cyclohexanone/hydroxy cyanine dyes that absorb in the visible/near-infrared regions. *J. Heterocyclic Chem. 41*, 227–232.

(19) Cooper, M. E., Gregory, S., Adie, E., and Kalinka, S. (2002) pH-sensitive cyanine dyes for biological applications. *J. Fluoresc. 12*, 425–429.

(20) Snee, P. T., Somers, R. C., Nair, G., Zimmer, J. P., Bawendi, M. G., and Nocera, D. G. (2006) A ratiometric CdSe/Zns nanocrystal pH sensor. *J. Am. Chem. Soc. 128*, 13320–21.

(21) Almutairi, A., Guillaudeu, S. J., Berezin, M. Y., Achilefu, S., and Fréchet, J. M. J. (2008) Biodegradable pH-sensing dendritic nanoprobes for near-infrared fluorescence lifetime and intensity imaging. *J. Am. Chem. Soc. 130*, 444–445.

(22) Hilderbrand, S. A., and Weissleder, R. (2007) Optimized pH-responsive cyanine fluorochromes for detection of acidic environments. *Chem. Commun.* 2747–9.

(23) Hilderbrand, S. A., Kelly, K. A., Weissleder, R., and Tung, C.-H. (2005) Monofunctional near-infrared fluorochromes for imaging applications. *Bioconjugate Chem. 16*, 1275–81.

(24) Kelly, K. A., Waterman, P., and Weissleder, R. (2006) In vivo imaging of moleculary targeted phage. *Neoplasia 8*, 1011–8.

(25) Khalil, A. S., Ferrer, J. M., Brau, R. R., Kottmann, S. T., Noren, C. J., Lang, M. J., and Belcher, A. M. (2007) Single M13 bacteriophage tethering and stretching. *Proc. Natl. Acad. Sci. U.S.A. 104*, 4892–7.

(26) Zou, J., Dickerson, M. T., Owen, N. K., Landon, L. A., and Deutscher, S. L. (2004) Biodistribution of filamentous phage peptide libraries in mice. *Mol. Biol. Reports 31*, 121–129.

(27) Newton, J. R., Miao, Y., Deutscher, S. L., and Quinn, T. P. (2007) Melanoma imaging with pretargeted bivalent bacteriophage. *J. Nucl. Med. 48*, 429–36.

(28) Mujumdar, R. B., Ernst, L. A., Mujumdar, S. R., Lewis, C. J., and Waggoner, A. S. (1993) Cyanine dye labeling reagents: sulfoindocyanine succinimidyl esters. *Bioconjugate Chem. 4*, 105–11.

(29) Demas, J. N., and Crosby, G. A. (1971) The measurment of photoluminescence quantum yields. A review. *J. Phys. Chem. 75*, 991–1024.

(30) Kelly, K. A., Allport, J. R., Tsourkas, A., Shinde-Patil, V. R., Josephson, L., and Weissleder, R. (2005) Detection of vascular adhesion molecule-1 expression using a novel multimodal nanoparticle. *Circ. Res. 96*, 327–326.

(31) Jaye, D. L., Geigerman, C. M., Fuller, R. E., Akyildiz, A., and Parkos, C. A. (2004) Direct fluorochrome labeling of phage display library clones for studying binding specificities: applications in flow cytometry and fluorescence microscopy. *J. Immunol. Methods 295*, 119–127.

(32) Ricciardolo, F. L. M., Gaston, B., and Hunt, J. (2004) Acid stress in the pathology of asthma. *J. Allergy Clin. Immunol. 113*, 610–19.

(33) Song, Y., Salinas, D., Nielson, D. W., and Verkman, A. S. (2006) Hyperacidity of secreted fluid from submucosal glands in early cystic fibrosis. *Am. J. Physiol.-Cell Physiol. 290*, 741–749.

(34) Vieira, O. V., Bothelo, R. J., and Grinstein, S. (2002) Phagosome maturation: aging gracefully. *Biochem. J. 366*, 689–704.

BC800188P

Supporting Information For:

Near Infrared Fluorescnce-Based Bacteriophage Particles for Ratiometric pH Imaging

Scott A. Hilderbrand,[†*] Kimberly A. Kelly,[†] Mark Niedre,[†] and Ralph Weissleder[†§]

[*] Corresponding Author:
Scott A. Hilderbrand
149 13th St.
Room 5406
Charlestown, MA 02129 USA

Phone: (617) 726-5788
Fax: (617) 726-5708
Email: Scott_Hilderbrand@hms.harvard.edu

[†] Center for Molecular Imaging Research, Massachusetts General Hospital / Harvard Medical School
[§] Center for Systems Biology, Massachusetts General Hospital / Harvard Medical School

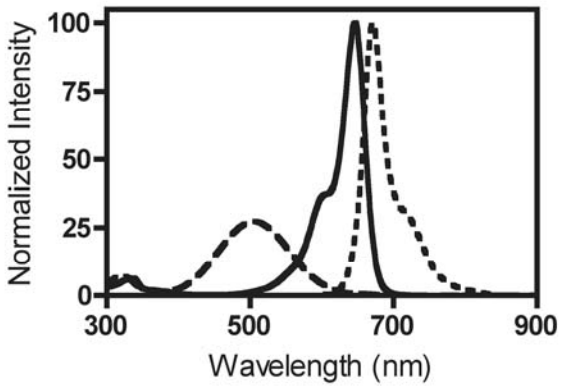

Figure S1. Normalized absorption and fluorescence emission data for 1 µM HCyC-646 in aqueous media. The absorbance trace of the deprotonated dye in pH 10.0 aqueous NaOH solution (dashed line) and the absorbance of the protonated dye in 50 mM glycine buffer, pH 3.0 (solid line) are shown. The fluorescence emission (dotted line) was obtained by excitation of the protonated dye at 610 nm in 50 mM glycine buffer, pH 3.0.

Table S1. Raw fluorescence emission signals from the Cy 7 and HCyC-646 dye labeled bacteriophage alone or through tissue (subcutaneous) collected on the Maestro imaging system showing differences in the attenuation of the two signals through tissue. For the Cy 7 data, the LCD emission filter of the imaging system was set to 775 nm, whereas for the HCy-646 data, the emission filter was set to 670 nm. The same phantom solution, 1 µM probe with respect to Cy 7 at pH 5.12, was used for the data with and without the optically diffuse tissue.

	Cy 7	HCyC-646
Phantom	3292.6	3283.3
Phantom + Tissue	2597.5	1508.2
% Attenuation	21%	54%

Synthesis and Gene Transfection Efficacies of PEI−Cholesterol-Based Lipopolymers

Avinash Bajaj,[†] Paturu Kondaiah,[‡] and Santanu Bhattacharya*[,†,§]

Department of Organic Chemistry, and Department of Molecular Reproduction, Development, and Genetics, Indian Institute of Science, Bangalore 560 012, India, and Chemical Biology Unit of JNCASR, Bangalore 560 064, India. Received October 14, 2007; Revised Manuscript Received March 18, 2008

Nine lipopolymers based on low molecular weight polyethyleneimines (PEI) and cholesterol via an ether linkage between the polymer amine and the cholesterol backbone have been synthesized. Different percentage of cholesterol moieties have been grafted on three types of PEI of molecular weights 800, 1200, and 2000. These lipopolymers were studied for gene transfection activities in HeLa cells. All the lipopolymers were first optimized for enhanced transfection efficacies as coliposomes with DOPE. All lipopolymers are better transfecting agents and highly serum compatible than commercially available PEI-25KDa. Transfection efficacies and serum compatibility of lipopolymers were found to be dependent upon the MW of PEI used for lipopolymer synthesis and percentage of cholesterol grafting on lipopolymers. Cell viability assay showed that PEI-25KDa is highly toxic as compared to all the lipopolymers. Lipopolyplexes were characterized by transmission electron microscopy, which showed the presence of spherical aggregates.

INTRODUCTION

Gene Therapy (*1*), which involves the transfer of a desired gene to a target cell, is a new hope for various disorders like cystic fibrosis (*2, 3*), diabetes, cancer (*4, 5*), AIDS (*6*), and so forth (*7*−*9*). The first major challenge of the use of gene therapy for curing disorders is to deliver the desired gene efficiently with the least toxicity and low immunogenicity. A second major challenge is to transfer such genes to the specific cells (*10*−*13*). Viruses are very potent carriers for delivery of the gene, but due to toxicity, strong immunogenicity, and its limitation to carry less DNA, various researchers are trying to develop different kinds of nonviral vectors for efficient gene delivery (*14*−*17*).

Among nonviral vectors, cationic lipids (*18, 19*), polymers (*20*), and lipopolymers (*21*) are a major focus for researchers to develop new vectors for efficient gene delivery. Various kinds of cationic lipids have been developed and investigated for their gene transfection activity (*22*−*25*). Over the past few years, we have been investigating the aggregation, transfection, and mechanistic studies of various lipid-based formulations (*26*−*32*). Among polymers, polyethylenimine (PEI[1]) (*33*), polylysine, polyornithine (*34, 35*), and so forth have been examined for gene delivery (*36*). Behr and co-workers demonstrated for the first time the transfection efficacy of PEI (*33*). PEI is also one of the main focus systems for gene delivery in many research groups because of its early endosomal release of DNA, which prevents the DNA from degradation in late endosomes (*37*). This is because of the different pK_a values of the primary, secondary, and tertiary amines in it, which give the PEI a good buffer capacity that does not allow it to lower the pH of early endosomes, which is suitable for various enzymes to act (*37*).

PEIs of different molecular weights ranging 0.6−800 kDa have been examined in gene transfection studies (*37*). PEIs of higher molecular weights (70−800 kDa) were found to be better transfecting agents for *in vitro* studies, whereas low MW PEIs have been known to show better gene delivery activity with intravenous administration. Cytotoxicities of PEI increase with increase in molecular weight. However, low MW PEIs are found to be less cytotoxic, although they are not effective as gene delivery agents. To further improve their transfection potential, PEI had been derivatized with various ligands including sugars (*10*), amino acids (*36*), poly(ethylene glycol) (*37*), long hydrocarbon chains (*38*), and even cholesterol (*39*). Hydrophobic anchors are essential for gene delivery vehicles because of increased cellular uptake and enhanced DNA stability against the bloodstream (*37*). Klibanov et al. had shown the effect of various chemical modifications of nitrogen atoms on the efficiency of PEIs as synthetic vectors for the delivery of plasmid DNA (*38*).

One of the major problems associated with the nonviral vectors for clinical application is their inefficiency in serum conditions (*40*−*43*). It has already been mentioned that a hydrophobic part is essential to enhance the stability of the lipoplex in the bloodstream and gene transfer, as the cellular uptake would be increased by favorable hydrophobic groups of gene carrier and cell membrane. Various kinds of long-chain alkyl and cholesteryl groups have been attached to PEI to enhance the efficiency of gene transfer. Modification of PEI of M_w 1800 with cholesterol at the primary amine has been shown to dramatically increase the transfection efficacy of PEI (*44*). Modification of secondary amines in PEI with cholesterol moieties was also shown to furnish better transfection activities (*45*). Kim and co-workers have shown the DNA delivery abilities of modified linear PEI (MW 25 kDa) with cholesterol (*46*). Park et al. studied the transfection properties of cholesterol and myristate-conjugated PEI (*39*). Recently, dexamethasone-conjugated low molecular weight PEI was reported for gene transfection efficacies as well (*47*).

We have previously reported the aggregation and transfection properties of different types of cationic lipids (*48*−*52*). We also

* Corresponding author. E-mail: sb@orgchem.iisc.ernet.in. Phone: (91)-80-2293-2664. Fax: (91)-80-2360-0529.

[†] Department of Organic Chemistry, Indian Institute of Science.

[‡] Development, and Genetics, Indian Institute of Science.

[§] Chemical Biology Unit of JNCASR.

[1]Abbreviations: PEI, polyethylenimine; DOPE, 1,2-dioleoyl-L-α-glycero-3-phosphatidylethanolamine; FACS, fluorescence-activated cell sorting.

10.1021/bc700381v CCC: $40.75 © 2008 American Chemical Society
Published on Web 07/11/2008

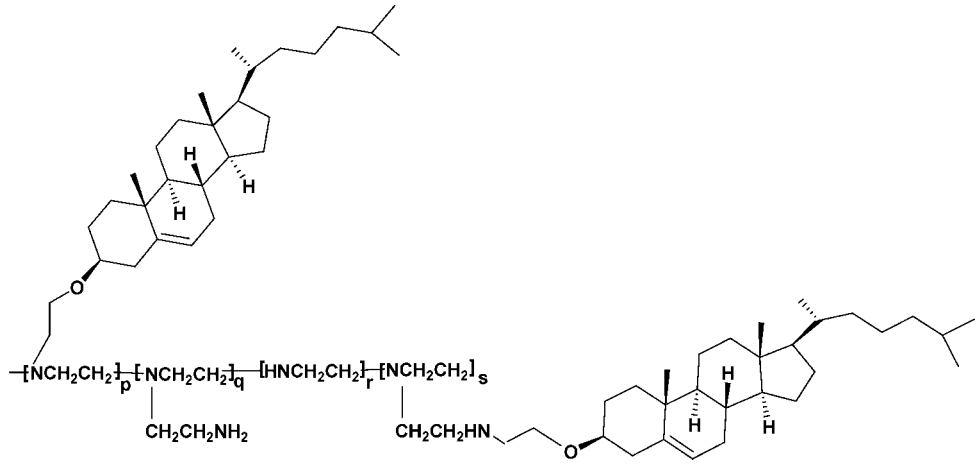

Figure 1. General structure of the PEI−cholesterol-based lipopolymers used for the study.

probed the interaction of cholesterol in membranes with cationic and phospholipids (*53, 54*). Cholesterol accordingly was used in the design of various cationic lipids and lipopolymers due to its natural occurrence, which make the vectors biocompatible. It has already been reported from this laboratory that the nature of the linkage between the hydrophobic cholesterol backbone and the headgroup plays an important role in regulating the transfection activities of cationic lipids (*55*−*59*). Thus, the cholesterol lipids possessing ether-based linkages between the cationic headgroup and steroid skeleton significantly enhanced transfection activities as compared to its ester- or urethane-based counterparts. Recently, we also showed the serum-compatible gene transfection activities of cholesterol-based gemini lipids differing in the length and nature of the spacer between the headgroups (*42, 43*).

Although few PEI−cholesterol conjugates have been reported (*39, 45, 46*), the PEI−lipid conjugates based on ether-linked cholesterol units have never been described and examined for transfection activity. Accordingly, we have synthesized nine lipopolymers with variable extent of cholesterol units to three different low molecular weight PEIs (M_w = 800 (**P8**), M_n = 1200 (**P12**), and M_w = 2000 (**P20**)) via ether-based links. We also characterized such cholesterol−PEI-based lipopolymers (Figure 1) and finally investigated their transfection efficiencies.

EXPERIMENTAL PROCEDURES

Materials and Methods. All reagents, solvents, and chemicals used in this study were of the highest purity available. The solvents were dried prior to use. Column chromatography was performed using 60−120 mesh silica gel. NMR spectra were recorded using Jeol JNM λ−300 (300 MHz for ^{1}H) spectrometer. The chemical shifts (δ) are reported in ppm downfield from the internal standard: TMS, for ^{1}H NMR. Mass spectra were recorded on a MicroMass ESI-TOF spectrometer or ESI-MS (HP1100LC-MSD). Infrared (IR) spectra were recorded on a Jasco FT-IR 410 spectrometer using KBr pellets or neat.

Synthesis (Scheme 1). *Cholest-5-en-3β-tosylate (2).* To an ice-cooled solution of cholesterol (**1**) (5.0 g, 0.013 mmol) in dry pyridine (5 mL) and dry chloroform (5 mL), *p*-tosyl chloride (3.7 g, 0.02 mmol) was added. A catalytic amount of DMAP was also added. The reaction mixture was then allowed to stir at 0 °C for 6 h, chloroform (35 mL) was added, and the resulting reaction mixture was washed with 1 N HCl (2 × 50 mL), water (50 mL), and brine (50 mL); the organic layer was separated and dried over anhydrous Na_2SO_4. Chloroform from this solution was evaporated to leave a residue. From the residue, cholest-5-en-3β-tosylate (**2**) was recrystallized using chloroform and methanol. Yield: White solid, 6.49 g., 0.012 mmol, 92.8%. m.p: 133 °C. lit m.p: 132−133 °C (*55*). IR (neat) (cm^{-1}): 2949, 2867, 1598, 1495, 1467, 1366, 1188, and 1174. ^{1}H NMR ($CDCl_3$, 300 MHz): δ 0.65 (s, 3H), 0.84−2.29 (m, 41H), 2.44 (s, 3H), 4.32 (m, 1H), 5.30 (d, 1H, J = 4.5 Hz), 7.31−7.34 (d, 2H, J = 8.1 Hz), 7.78 −7.81 (d, 2H, J = 8.1 Hz).

Scheme 1[a]

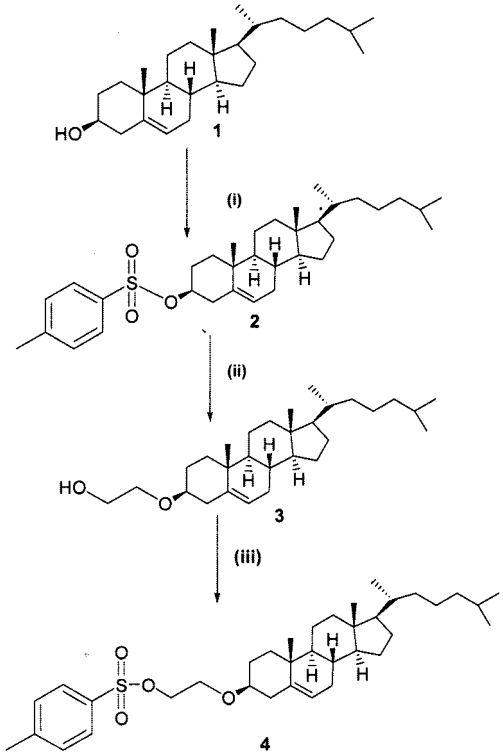

[a] Reaction conditions: (i) *p*-TsCl/Py/$CHCl_3$, 0 °C, 6 h; (ii) ethylene glycol, 1,4-dioxane, 4 h, reflux; (iii) *p*-TsCl/Py/$CHCl_3$, 0 °C, 6 h.

Cholest-5-en-3β-oxyethane (3). Chlolest-5-en-3β-tosylate (**2**) (3.5 g, 6.5 mmol) was taken in anhydrous dioxane. To this, dry ethylene glycol (10 g, 0.16 mol) was added and the mixture was refluxed under nitrogen for 4 h. The solution was cooled and solvent was removed under vacuum. A white residue was obtained which was dissolved in chloroform (50 mL) and washed with water. The organic layer was separated; washed with $NaHCO_3$ (50 mL), water (50 mL), and brine (50 mL); and dried over anhydrous Na_2SO_4. Finally, from this solvent was removed *in vacuo*, and the product cholest-5-en-3β-oxyethane (**3**) was purified by column chromatography over silica gel using a mixture of hexane and ethyl acetate. Yield: white solid, 2.3 g,

Scheme 2

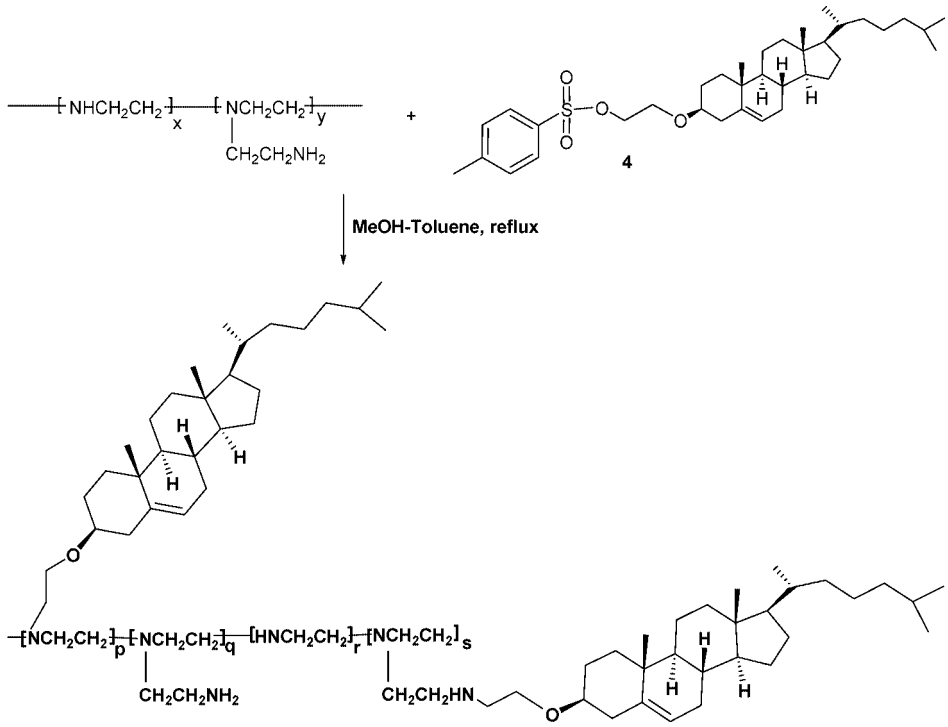

Table 1. Lipopolymers Synthesized and Percentage of Cholesterol Grafting on Lipopolymers and the Optimized Lipopolymer/DOPE Ratios

lipopolymer	PEI−MW	ΔA_{pei}	ΔA_c	% cholesterol grafting	optimized lipopolymer. DOPE
P8C1	800	5.82	3	104.7[a]	1:1
P8C2	800	8.99	3	57.22	4:1
P8C3	800	15.71	3	29.18	2:1
P12C1	1200	7.72	3	88.10	1:1
P12C2	1200	8.04	3	66.32	2:1
P12C3	1200	15.18	3	30.34	1:4
P20C1	2000	5.25	3	123[a]	1:1
P20C2	2000	8.09	3	65.68	1:0
P20C3	2000	17.17	3	26.36	1:0

[a] More then 100% cholesterol grafting indicates that the primary amines in PEI get alkylated with two cholesteryl moieties.

5.3 mmol, 85%. m.p: 99−100 °C. lit mp: 97−98 °C (*60*). IR (neat) (cm^{-1}): 3438, 2936, 2868, 1466, and 1376. ^1H NMR ($CDCl_3$, 300 MHz): δ 0.67 (s, 3H), 0.85−2.35 (m, 41H), 3.20 (m, 1H), 3.57−3.60 (t, 2H), 3.72 (t, 2H), 5.34 (d, 1H). ESI-MS: 453 ($M + Na^+$).

Cholest-5-en-3β-oxyethane tosylate (4). To an ice-cooled solution of cholest-5-en-3β-oxyethan-2-ol (**3**) (2.2 g, 5.1 mmol) in dry pyridine (5 mL) and dry chloroform (5 mL), *p*-tosyl chloride (1.5 g, 7.86 mmol) was added. The reaction mixture was allowed to stir at 0 °C for 6 h, chloroform (40 mL) was added, and then the reaction mixture was washed with 1 N HCl (2 × 50 mL), water (50 mL), and brine (50 mL). Finally, the organic layer was separated and dried over anhydrous Na_2SO_4. Solvent was removed using a rotary evaporator, and the product cholest-5-en-3β-oxyethane tosylate (**4**) was purified by column chromatography over silica gel using a mixture of hexane and ethyl acetate. Yield: 2.68 g, 7.04 mmol, 90.0%. IR (neat) (cm^{-1}): 2935, 2886, 1598, 1465, 1360, 1189, and 1177. ^1H NMR ($CDCl_3$, 300 MHz): δ 0.67 (s, 3H), 0.85−2.25 (m, 41H), 2.44 (s, 3H), 3.06−3.13 (m, 1H), 3.63−3.66 (t, 2H), 4.13−4.16 (t, 2H), 5.31 (d, 1H), 7.32−7.35 (d, 2H), 7.79−7.82 (d, 2H). ESI-MS: 607 ($M + Na^+$).

Lipopolymer Synthesis (Scheme 2). Cholest-5-en-3β-oxyethane-tosylate (**4**) (170 mg, 0.29 mmol) was taken in 3 mL of dry toluene. Desired amounts of PEI solutions (2−8 equiv) from the stock solution of PEI in dry MeOH were added to reaction mixture. The reaction mixture was refluxed, the reaction was monitored by TLC, and reflux was continued until the disappearance of cholest-5-en-3β-oxyethane-tosylate (**4**). The reaction mixture was evaporated, and 30 mL of chloroform was added to the crude mixture. The chloroform layer was washed with 5 mL of 1 N NaOH, water (5 mL), and brine solution (5 mL). The organic layer was passed through dry K_2CO_3 and evaporated to get lipopolymer. All the lipopolymers were characterized by ^1H NMR.

Transmission Electron Microscopy. Freshly prepared aqueous suspensions of lipopolymer−DNA complexes were examined under transmission electron microscopy with negative staining using 1% uranyl acetate. A 10 μL sample of the suspension was loaded onto Formvar-coated 400 mesh copper grids and allowed to remain for 1 min. Excess fluid was wicked off the grids by touching their edges to filter paper, and 10 μL of 1% uranyl acetate was applied on the same grid after which the excess stain was similarly wicked off. The grid was air-dried for 30 min, and the specimens were observed under TEM (JEOL 200-CX) operating at an acceleration voltage of 120 keV. Micrographs were recorded at a magnification of 5000−20 000×.

Plasmid DNA. pEGFP-c3 (Clontech, USA), which encodes for an enhanced green fluorescence protein (GFP) under a CMV promoter, was amplified in *Escherichia coli* (DH5α) and purified using Qiagen Midi Prep Plasmid Purification protocol (Qiagen, Germany). Purity of the plasmid was checked by electrophoresis on 1.0% agarose gel. Concentration of the DNA was estimated spectroscopically by measuring the absorption at 260 nm and confirmed by gel electrophoresis. The plasmid preparations showing a value of $OD_{260}/OD_{280} > 1.8$ were used.

Cell Culture. Cells (HeLa) were cultured in Dulbecco's Modified Eagle's Medium (DMEM; Sigma) supplemented with 10% fetal bovine serum (FBS) in T25 culture flasks (Nunc, Denmark) and were incubated at 37 °C in a humidified atmosphere containing 5% CO_2. Cells were regularly passaged

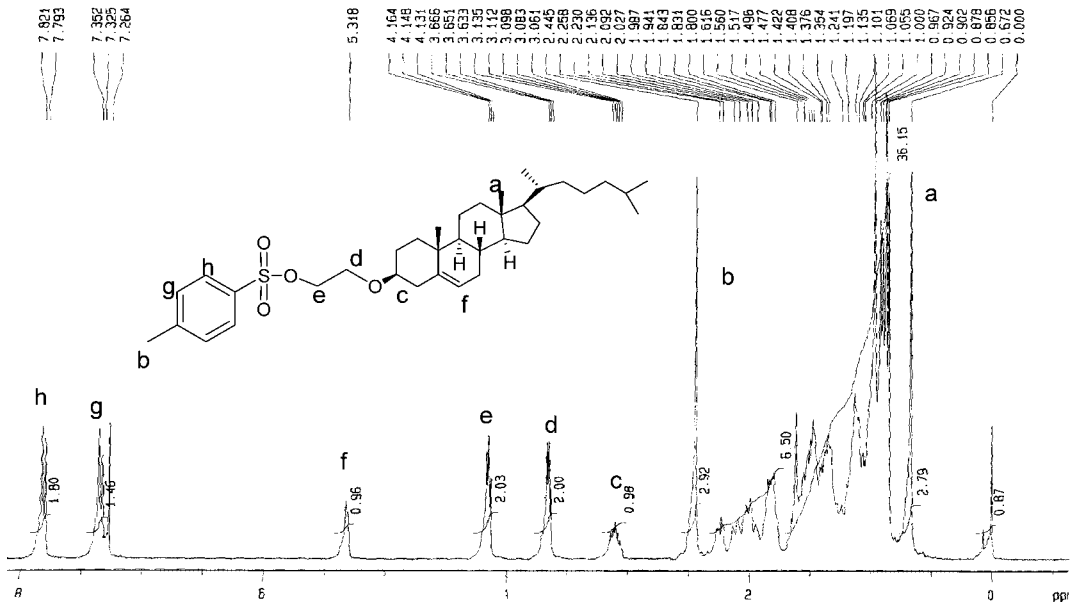

Figure 2. Representive ^{1}H NMR (300 MHz) of cholest-3β-oxyethan-tosylate.

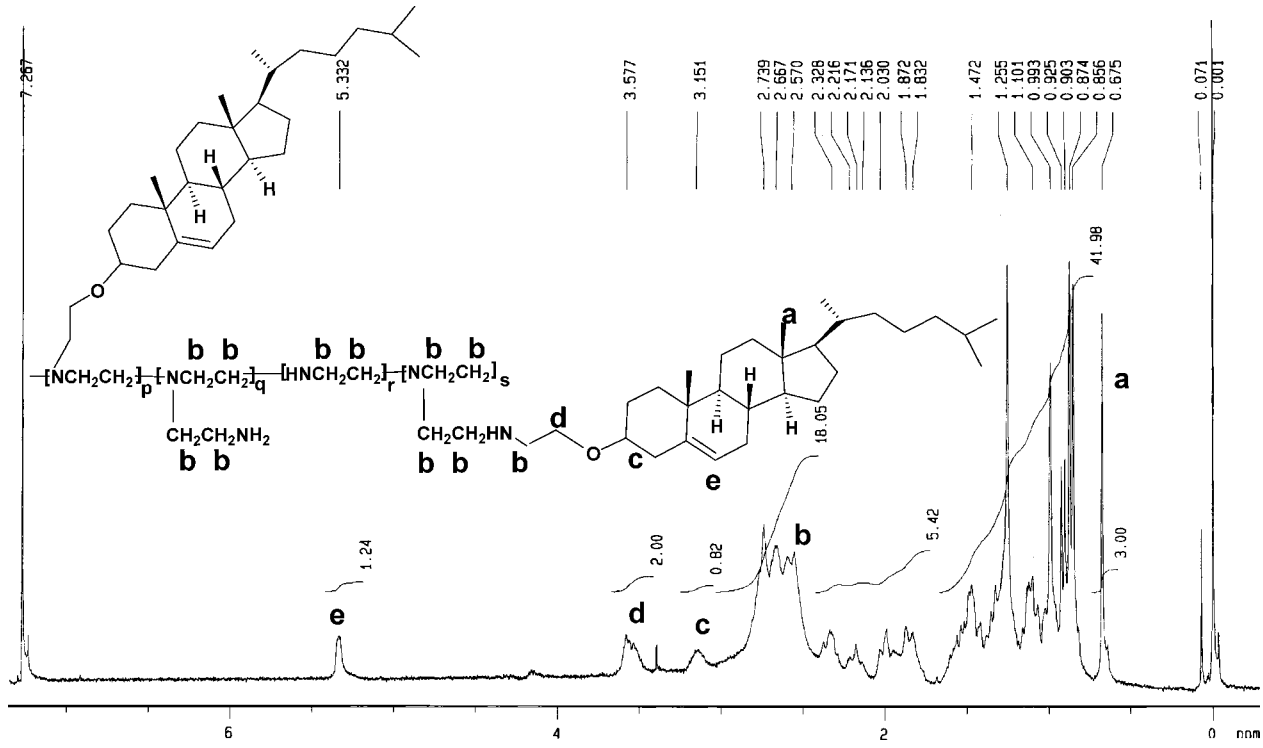

Figure 3. Representive ^{1}H NMR (300 MHz) of one lipopolymer molecule.

by trypsinization with 0.1% trypsin (EDTA 0.02%, dextrose 0.05%, and trypsin 0.1%) in PBS (pH 7.2).

Cytotoxicity. Toxicity of each lipopolymer formulation toward HeLa cells was determined using 3-(4,5-dimethylthiazole-2-yl)-2,5-diphenyltetrazolium bromide reduction assay following literature procedures (*61, 62*).

Cytotoxicity of the lipopolymer formulations optimal for transfection experiments was determined under conditions exactly the same as transfection conditions. Nearly 12 000 cells/well were plated in 96 well plates. After 24 h, optimized lipopolymer/DOPE formulations were complexed with 0.2 μg of the DNA at various N/P ratios for 30 min. DNA−lipopolymer complexes were added to the cells in the absence of serum. After 6 h of incubation, lipoplexes were removed and 200 μL of media with 10% FBS was added. After 42 h, 20 μL of MTT solution was added and the cells were incubated further for 6 h. Blue formazan crystals were seen when checked under microscope. Media was removed and 200 μL of DMSO was added per well. The absorbance was measured using a microtiter plate reader. The % viability was then calculated as [{A_{590}(treated cells) − background]/[A_{590}(untreated cells) − background}] × 100.

Transfection Procedure. All transfection experiments were carried out in HeLa Cells in antibiotic-free media unless specified otherwise. In a typical experiment, 24 well plates were seeded with 45 000 cells/well in antibiotic-free media 24 h before transfection such that they were at least ~70% confluent at the time of transfection. For transfection, lipopolymer

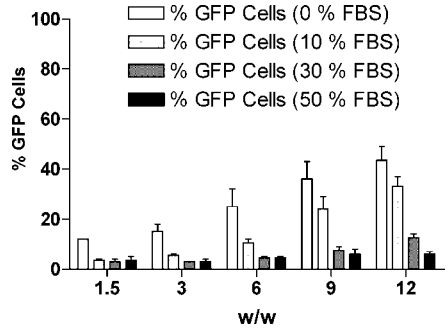

Figure 4. Transfection efficiency of PEI-25KDa at different polymer/DNA weight ratios (w/w) using EGFP-c3 plasmid in the presence of different percentages of serum.

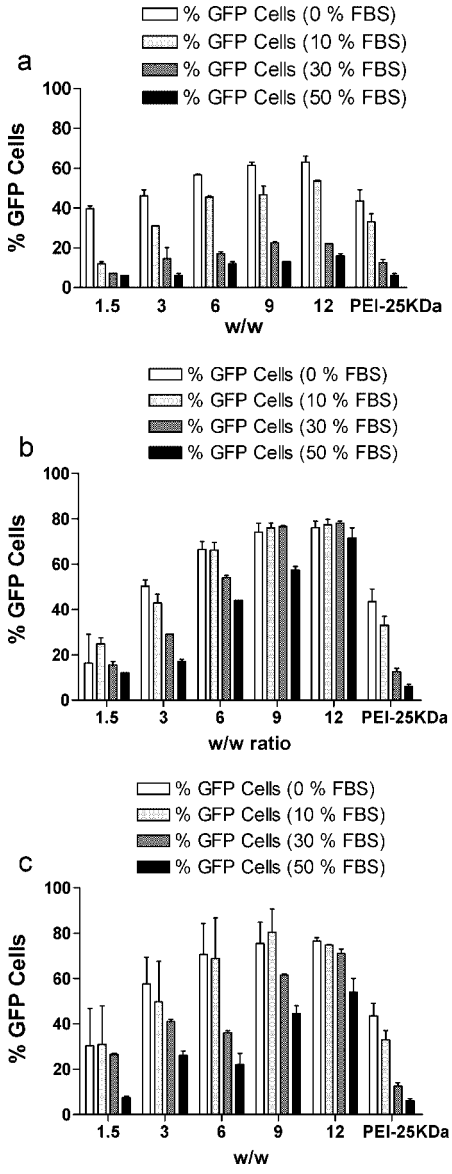

Figure 5. Transfection efficiencies of lipopolymers at different lipopolymer/DNA weight ratios (w/w) using EGFP-c3 plasmid in the presence of different percentages of serum using optimized lipopolymer/DOPE ratio: (a) **P8C1**; (b) **P8C2**; (c) **P8C3**.

formulation and DNA were serially diluted separately in DMEM containing no serum to have the required working stocks. DNA was used at a concentration of 0.8 μg/well unless specified otherwise. The lipopolymer and DNA were complexed in a volume of 200 μL by incubating the desired amount of lipopolymer formulation and DNA together at room temperature for about 30 min. The lipopolymer concentrations were varied so as to obtain the required lipopolymer/DNA (w/w) charge ratios. After 30 min of complexation, 200 μL of media was added to the complexes. Old medium was removed from the wells, cells were washed with DMEM, and lipopolymer−DNA complexes in 200 μL media were added to the cells. The plates were then incubated for 6 h at 37 °C in a humidified atmosphere containing 5% CO_2. At the end of incubation period, medium was removed, and cells were washed with DMEM, and then 500 μL of DMEM containing 10% FBS was added per well. Plates were further incubated for a period of 42 h before checking for the reporter gene expression. GFP expression was examined by fluorescence microscopy and was quantified by flow cytometry analysis. All the experiments were done in duplicate, and results presented are the average of at least two such independent experiments done on two different days.

For transfections in the presence of serum, lipopolymer and DNA were separately diluted in serum-free media as already mentioned, and the complexation was done in serum-free media (200 μL) for 30 min. The complex was then diluted to 400 μL with DMEM containing 20% FBS so as to achieve a final serum concentration of 10%. The cells were then incubated with this complex for 6 h. At the end of the incubation period, medium was removed and cells were washed with DMEM, and 500 μL of DMEM containing 10% FBS was added per well. For transfections at 30% and 50% of serum concentrations, complexes were diluted with DMEM containing 60% FBS or with neat FBS, respectively.

Flow Cytometry. The reporter gene expression was examined by fluorescence microscopy at regular intervals and was quantified 48 h post-transfection by flow cytometry. The percentages of transfected cells were obtained by determining the statistics of cells fluorescing above the control level where nontransfected cells were used as the control. Approximately 10 000 cells were analyzed to generate the statistical data, which have been presented as the average of at least two independent measurements. For the flow cytometry analysis, ~48 h post-transfection, old medium was removed from the wells; cells were washed with PBS and trypsinized by adding 100 μL of 0.1% trypsin. To each well, 200 μL of PBS containing 20% FBS was added. Duplicate cultures were pooled and analyzed by flow cytometry immediately using Becton and Dickinson flow cytometer equipped with a fixed laser source at 488 nm.

FACS Analysis. FACS data were analyzed by public domain *WinMDI* software to eliminate data from cell debris (particles smaller than cells), dead cells, and clumps of two or more cells. Subcellular debris and clumps can be distinguished from single cells by size (estimated by the intensity of low angle forward scatter). Dead cells have lower forward-scatter and higher side-scatter than living cells. The FACS scans were configured to display the fluorescence signals only from those particles with a specified set of scatter properties, namely, living single cells. This is called a scatter-gated fluorescence analysis. Therefore, the data from dead cells had been eliminated by gating out brightly fluorescent cells. We have presented the representative FACS scans (as well as scatter plots) for the transfection experiments using lipopolymers and the respective FACS scans (as well as scatter plots) of the untransfected cells in the Supporting Information. We have set up the baseline in FACS scans, so that we observed only 1−3% transfection in the untreated cells as shown by the FACS scans presented in the Supporting Information. Baseline setup for the representative FACS scans has been shown in the Supporting Information.

RESULTS

Synthesis and Characterization. Nine PEI−cholesterol-based lipopolymers were synthesized using different molecular

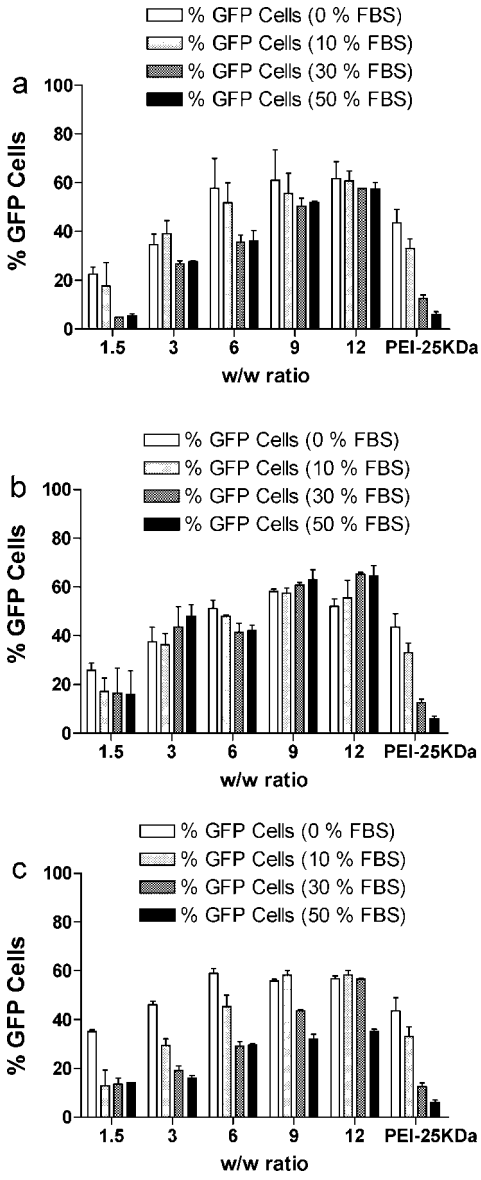

Figure 6. Transfection efficiencies of lipopolymers at different lipopolymer/DNA weight ratios (w/w) using EGFP-c3 plasmid in the presence of different percentages of serum using optimized lipopolymer/DOPE ratio: (a) **P12C1**; (b) **P12C2**; (c) **P12C3**.

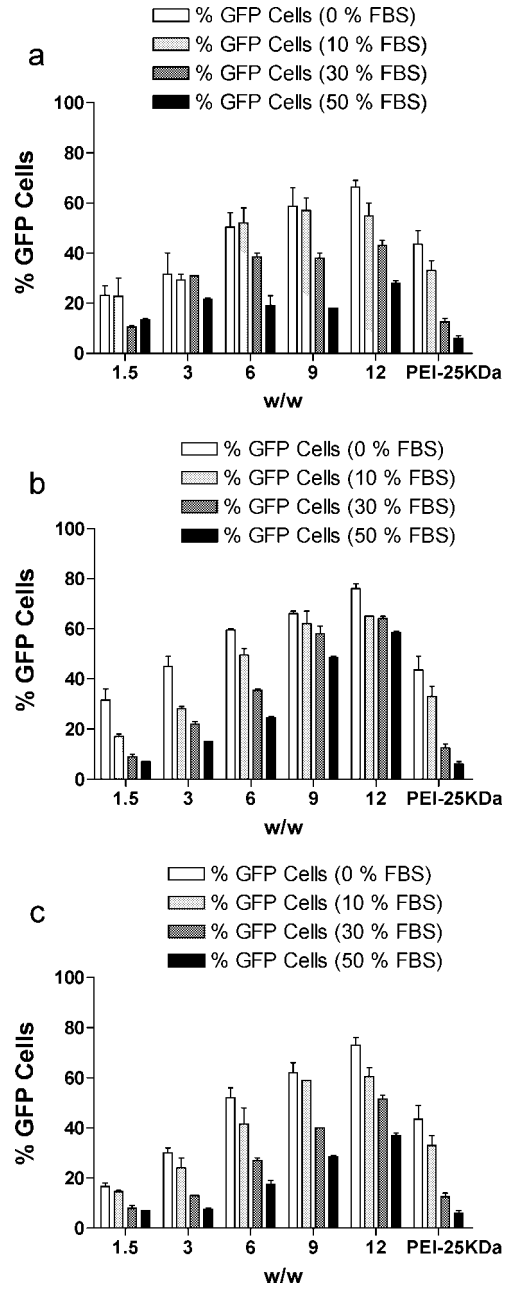

Figure 7. Transfection efficiencies of lipopolymers at different lipopolymer/DNA weight ratios (w/w) using EGFP-c3 plasmid in the presence of different percentages of serum using optimized lipopolymer/DOPE ratio: (a) **P20C1**; (b) **P20C2**; (c) **P20C3**.

weight polyethylenimines as starting materials (Figure 1, Table 1). Different percentages of cholesteryl units were incorporated covalently on PEI by its reaction with cholest-5-en-3β-oxyethane tosylate (**4**). First, cholesterol (**1**) was tosylated using *p*-toluenesulfonyl chloride in pyridine−chloroform (v/v: 1/1) with a catalytic amount of DMAP for 6 h at 0 °C in 92% yield. Cholesterol tosylate (**2**) was then subjected to a reaction with ethylene glycol in dioxane under reflux for 4 h to afford cholest-5-en-3β-oxyethan-2-ol (**3**) in 85% yield. Compound **3** was then tosylated with *p*-toluenesulfonyl chloride in pyridine−chloroform (v/v: 1/1) for 6 h at 0 °C to get **4** in 90% yield. Reaction of the tosylate (**4**) with PEI of different molecular weights in different mole ratios resulted in the formation of PEI−cholesterol-based lipopolymers. All the lipopolymers were characterized by ^{1}H NMR studies (*47*).

Characterization of Lipopolymers. Figure 2 displays the ^{1}H NMR of cholest-3β-oxyethan-tosylate (**4**). The ^{1}H peak at δ of 0.67 is due to the angular methyl group directly linked to cyclohexane and cyclopentane rings of the cholesterol backbone (signal a designated by proton a). The chemical shifts at δ 3.64 and δ 4.14 were attributed to protons d and e, respectively. The ^{1}H peaks of δ 3.09 and δ 5.3 were associated with the $-CH-$O$-$ (proton c, signal c) and $-CH=$C$-$ (proton f, signal f) protons of cholesterol, respectively. Singlets at δ 2.3 (proton b, signal b) and δ 7.3, 7.8 (protons g and h, signal g and h) were due to methyl and aromatic protons of the tosylate group. The ratio of the peak areas was determined to be 3:3:1:2:2:1:2:2 for signals/protons a:b:c:d:e:f:g:h, confirming the successful synthesis of cholest-3β-oxyethan-tosylate (**4**).

The successful synthesis of lipopolymers was evidenced by ^{1}H NMR spectra as shown in Figure 3. The ^{1}H NMR of lipopolymers illustrates peaks at δ 0.67, 3.14, and 5.3 because of the presence of protons a, c, and e due to the cholesterol moiety. Various peaks at 0.7−1.2 were also attributed to the presence of cholesterol units with polymer. The peak at 5.38 arose from the proton of =CH− in the cholesterol units (signal e). The peak at δ 0.7 was from the methyl group directly linked to the cyclic hydrocarbon (signal a). The broad peak in the

region δ 2.0−2.5 was because of the protons of the PEI backbone (signal b, protons b), which also includes the protons of $-CH_2-$ from the $-CH_2-CH_2-O-$ group of the cholesterol unit attached to the PEI backbone by alkylation. Disappearance of the peaks at δ 2.3 and δ 7−8 in ^{1}H NMR of lipopolymers (Figure 3) (signals b, g, and h observed in the case of the ^{1}H NMR spectra of cholest-3β-oxyethan-tosylate (Figure 2)) confirms the substitution of the tosylate group by the amine of PEI. The information provided by the ^{1}H NMR spectrum of lipopolymers proved that the cholesteryl group was successfully grafted onto the PEI main chain.

Degree of Cholesterol Grafting in PEI. The grafting degree was obtained from the ^{1}H NMR spectra. The degree of cholesterol grafting has been defined as the relationship of the number of amines alkylated by the cholesterol moiety to the total number of amines on the PEI chain. The signal at 0.67 is due to the protons attached to the $-CH_3$ group directly linked to the hexane and pentane cycles of the cholesterol backbone (signal a, proton a). The broad peak in the region δ 2.0−2.5 is attributed to $-CH_2-$ of the PEI backbone as well as the protons of $-CH_2-$ from the $-CH_2-CH_2-O-$ group attached to the cholesterol backbone, which are now attached to PEI backbone by alkylation. The ratio of the protons due to $-CH_3$ at δ 0.67 and $-CH_2$ from the $-CH_2-CH_2-O-$ group attached to the cholesterol backbone, which are now attached to the PEI backbone by alkylation is 3:2, or 1.5:1. Therefore, the area of the curve in the region δ 2.0−2.5 (ΔA_{pei}) also includes the area (ΔA_c/1.5) which is due to $-CH_2$ from the $-CH_2-CH_2-O-$ group attached to the cholesterol backbone, which are now attached to the PEI backbone by alkylation. Therefore, the actual area of the PEI backbone would be ($\Delta A_{pei} - \Delta A_c$/1.5). The percentage of grafting may be estimated as follows:

$$R_g = \frac{\Delta A_c \times N_{pei}}{\left(\Delta A_{pei} - \frac{\Delta A_c}{1.5}\right) \times N_c}$$

where ΔA_c is the area of the selected peak from the cholesterol backbone, ($\Delta A_{pei} - \Delta A_c$/1.5) is the area of the selected peak of the PEI backbone, N_c is the number of hydrogen atoms from the selected region of cholesterol backbone, and N_{pei} is the number of hydrogen atoms from the selected region of the PEI backbone. Only suitable protons from the pendant chain and the main chain of the polymers were selected in the calculation. The proton signal selected should not overlap with the signals from other protons. On the basis of the peak area of the signals a and b, R_g for lipopolymers was estimated as given in Table 1.

Transfection Efficacy. *Optimization of the Lipopolymer/DOPE Ratio.* Incorporation of the helper lipid, DOPE, is known to enhance the transfection efficiencies of many of cationic lipid-based formulations (*63*). Therefore, we first decided to investigate the optimized lipopolymer/DOPE mole ratios for our newly synthesized lipopolymers. These data were obtained from flow cytometric analysis (*64*). In order to determine the most effective formulations, transfections were performed with identical amounts of the DNA and lipopolymer upon variation of mole ratios of lipopolymers in DOPE. Optimized lipopolymer/DOPE mole ratios were found to depend upon the percentage of cholesterol grafting and the molecular weight of PEI. The optimized lipopolymer/DOPE ratios for all lipopolymers are given in Table 1. Lipopolymers (**P8C1**, **P12C1**, **P20C1**) with highest cholesterol drafting showed optimized transfection at lipopolymer/DOPE ratio of 1:1. In contrast, lipopolymers **P20C2** and **P20C3** showed maximum transfection activities in the absence of DOPE. In further studies, we used these optimized lipopolymer/DOPE formulations. All the optimized lipopolymer formulations were examined for transfection studies using EGFP-c3 plasmid in HeLa cells at different DNA/lipoolymer weight ratios. The transfection experiments were performed in the absence and in the presence of serum. To get further insight, we investigated the transfection activities at higher serum concentrations as well. The transfection experiments have also been performed with the unmodified polymers. We have not observed any transfection activity with these polymers. It is also well-known in the literature that low molecular weight PEI does not show transfection. Kim et al. (*45*) reported only <1% transfection efficiency of PEI of molecular weight 1800, and transfection efficiencies increases with increase in molecular weight. PEI-25KDa was found to be the best commercially available PEI polymer, and we have compared the transfection efficacies of lipopolymers with PEI-25KDa.

Optimization of Lipopolymer/DNA Ratio. After optimization of lipopolymer/DOPE mole ratio for each lipopolymer, all the lipopolymers were tested by taking an identical amount of DNA (0.8 μg) and varying the amount of lipopolymer using the respective optimized lipopolymer/DOPE ratio. We have also examined the transfection efficacies of commercially available PEI 25KDa. It showed nearly 40% GFP positive cells by FACS analysis, and even in the presence of 10% serum, nearly 30% transfection efficacy was observed (Figure 4). At higher serum concentrations of 30% and 50%, transfection activity decreases drastically. Only ∼5% transfection activity was observed in the presence of 50% serum.

Formulation from the **P8C1** lipopolymer was able to transfect nearly 60% of the cells in the absence of serum and in the presence of 10% serum; there was little decrease in the transfection activity to 50% (Figure 5). At high serum concentrations of 30% and 50%, nearly 10−20% GFP-positive cells were found by FACS analysis. Formulations based on lipopolymers **P8C2** and **P8C3** showed nearly 70% transfection activity. In the case of **P8C3** formulation, there was a decrease in the activity at higher serum concentrations, whereas in case of **P8C2** formulation, there was some decrease in the activity in the presence of 50% serum concentrations. Nearly 60% GFP-positive cells were observed at a w/w ratio of 12 at 50% serum concentrations in the case of lipopolymer **P8C2**, whereas in case of lipopolymer **P8C3**, nearly 50% transfected cells were observed.

In the case of formulations **P12C1** and **P12C2**, there was no decrease in the transfection activities at high serum concentrations (Figure 6). Nearly 50−60% transfection activities were observed in the cases of both formulations at all serum concentrations. In the case of **P12C3** formulation, transfection efficacy decreases at high serum conditions. Nearly 20−30% transfection activity was observed at 50% serum conditions, whereas 50−60% cells had been found to be positive by FACS analysis in the absence of serum.

There was a gradual decrease in the transfection efficacy with increase in the serum concentrations in the case of **P20C1** and **P20C3** formulations, where in the case of formulation **P20C2**, there was little decrease in the transfection activity at 50% serum conditions (Figure 7). Only 20−30% transfection efficiency was observed at 50% serum conditions for formulations **P20C1** and **P20C3**, whereas **P20C2** showed ∼60% efficacy at 50% serum conditions.

Figure 8 shows the comparative gene transfection efficacies of lipopolymers and PEI-25KDa in the presence of various percentages of serum, which clearly shows that all lipopolymers are better transfecting agents and highly serum compatible than PEI-25KDa. Transfection efficacy and serum compatibility are dependent upon the MW of PEI used for lipopolymer synthesis and % of cholesterol grafting on lipopolymers

Cytotoxicity. Percentage cell viabilities of PEI-25KDa and lipopolymers at different concentrations are shown in Figure 9.

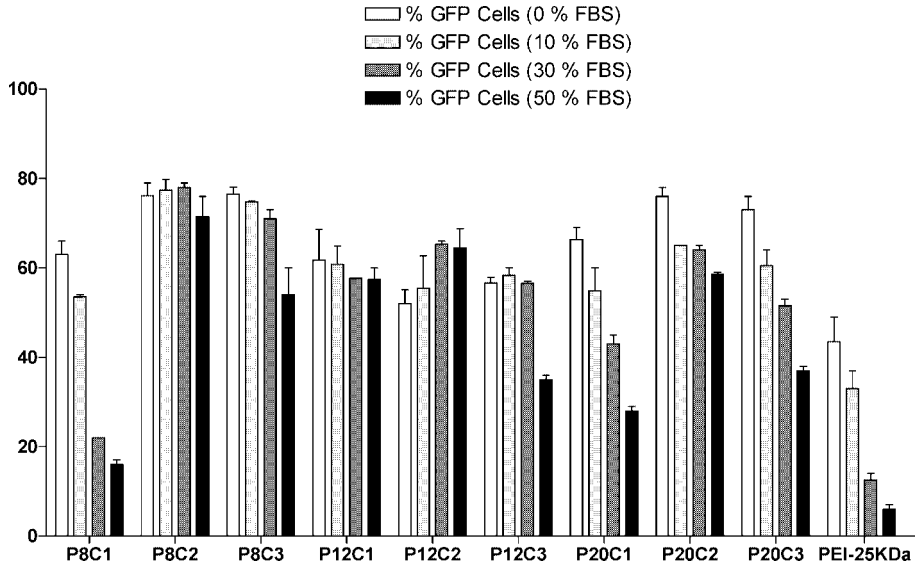

Figure 8. Comparative gene transfection efficacies of lipopolymers and PEI-25KDa in the presence of various percentages of serum using EGFP-c3 plasmid DNA at w/w ratio of 12 using optimized lipopolymer/DOPE ratio.

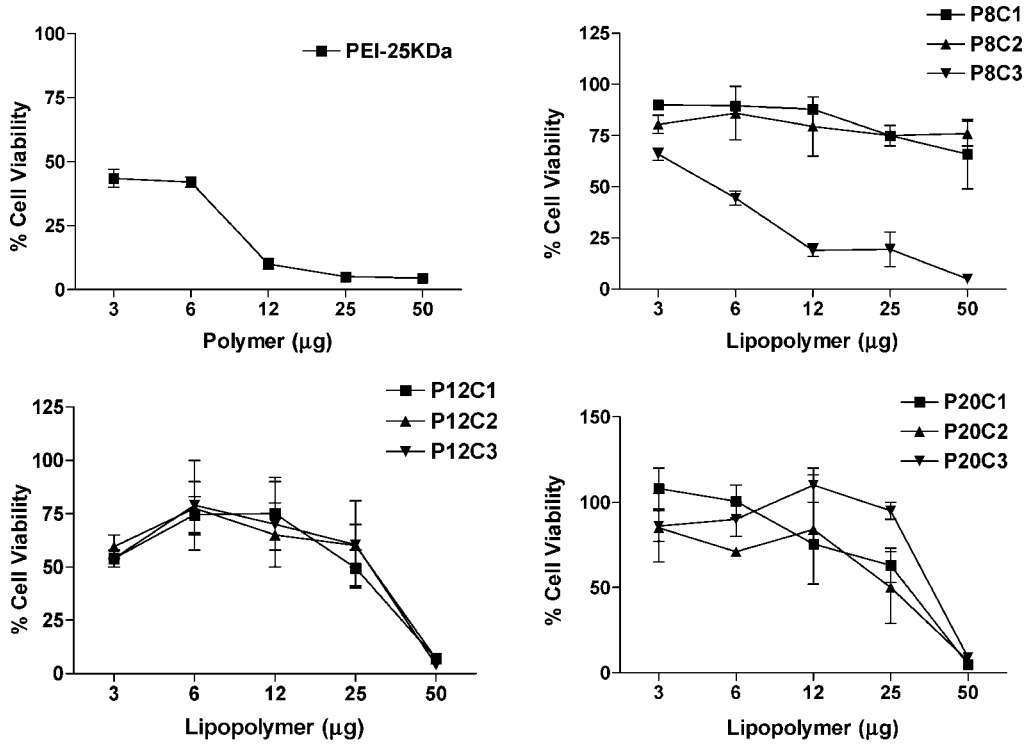

Figure 9. Percentage cell viabilities of PEI-25KDa and lipopolymers in HeLa cells at different concentrations of lipopolymers.

PEI-25KDa was found to be highly toxic as compared to all the lipopolymers. There was nearly complete cell death at 12 μg of the PEI-25KDa. In the case of lipopolymers **P8C1**, **P8C2**, and **P8C3**, % viability increases with increase in cholesterol grafting, and **P8C3** shows complete cell death at 50 μg concentration, whereas 75% cell viability was observed in the case of **P8C1** and **P8C2**. Other lipopolymers showed no cell viability at 50 μg concentration. Therefore, cell viability assays of lipopolymer formulations clearly showed that all lipopolymer formulations are much less toxic as compared to commercially available PEI-25KDa. After studying the cytotoxicity of lipopolymer formulations, we studied the cell viabilities of lipopolyplexes (lipopolymer/DNA complexes) using optimized lipopolymer/DOPE formulations at different w/w ratios at which transfection experiments were performed. Cell viabilities of lipopolyplexes at different w/w ratios are shown in Figure 10. This clearly showed that all lipopolyplexes possessed more than 80% cell viability, whereas formulations **P20C1** and **P20C2** were found to be toxic at lipopolymer/DNA weight ratio of 12, where 50% cell viability was observed.

Characterization of Lipopolyplexes. To get further insight into the lipopolymer−DNA complexes, we performed transmission electron microscopy of the lipopolymer−DNA complexes using the optimized lipopolymer/DOPE formulations. Representive electron micrographs of lipopolymer−DNA complexes have been shown in Figure 11. Most of the lipopolymer formulations formed spherical lipopolymer−DNA complexes. Lipopolymer **P8C3** formulation forms polyplexes of uniform size, whereas other lipopolymer−DNA complexes (of lipopolymers **P20C1** and **P20C2**) were found to be irregular in shape. **P8C2**

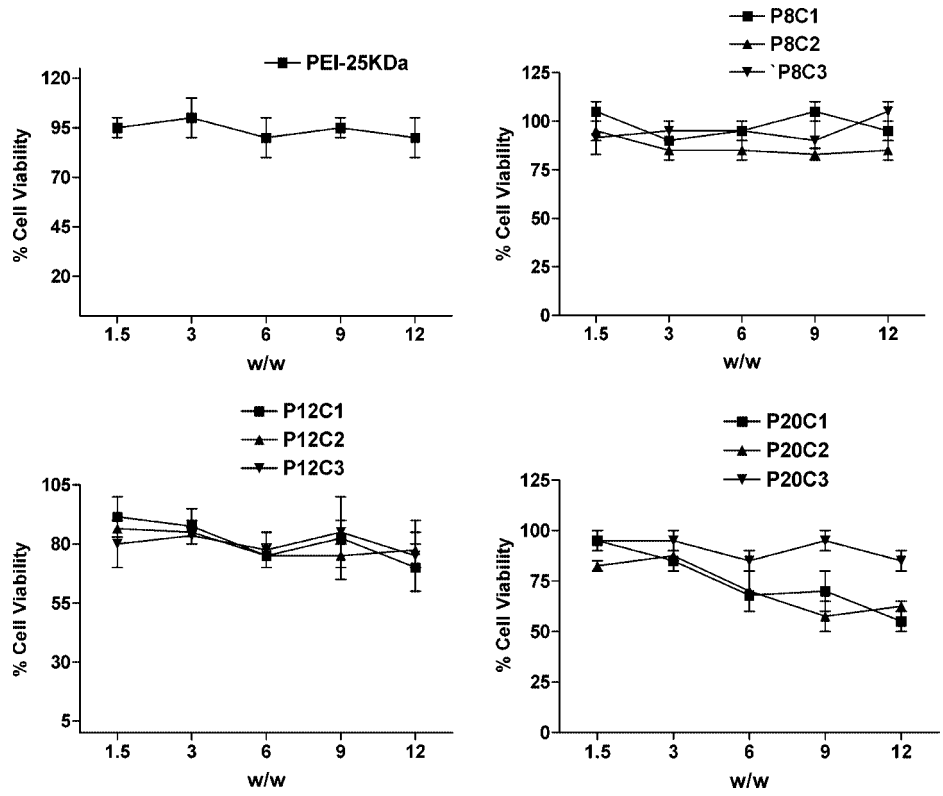

Figure 10. Percentage cell viabilities of lipopolyplexes using PEI-25KDa and lipopolymers at different lipopolymer/DNA weight ratios (w/w) using EGFP-c3 plasmid DNA in HeLa cells at different weight ratios of lipopolymers and DNA.

lipopolymer-based polyplexes showed small spherical loose aggregates. Large spherical aggregates were formed from polyplexes of lipopolymers **P8C1** and **P20C1**.

DISCUSSION

PEIs of different molecular weights have been studied for their gene delivery efficacies since the discovery of its gene transfection potential by Behr and co-workers (*33*). Various structure−activity investigations have been reported with the modification of different types of PEI to enhance the transfection activity and to reduce the toxicity. In this report, we present the effect of cholesterol modification on three different low molecular weight PEIs on cytotoxicity and gene transfection properties, as low molecular weight has been known to show low transfection activity and low cytotoxicity. We synthesized nine PEI−cholesterol-based lipopolymers by alkylation of PEI with cholest-5-en-3β-oxyethane tosylate using three PEIs of different molecular weights. Ether functionality has been incorporated between the amine backbone and cholesterol moiety, as prior studies indicated advantages from transfection with such linkages. Different amounts of cholesterol have been grafted on the PEI backbone. The transfection properties of all the lipopolymers and PEI-25KDa have been studied in HeLa cells. One of the major drawbacks of nonviral vectors for their *in vivo* use is in the inhibition of the transfection in the presence of serum (*65, 66*). Maintenance of the transfection efficiency in the absence of serum even for *in vitro* experiments is also cumbersome often due to the toxic nature of the synthetic formulations. Therefore, we have also studied the effect of the different concentrations of serum on the transfection activities of the lipopolymer formulations and compared that with commercially available PEI-25KDa. PEI-25KDa showed nearly 40% transfection efficacy, but as expected with the increase in serum concentration, the transfection efficacy decreased drastically. This is expected as the highly positively charged PEI interacts with negatively charged serum proteins, thereby triggering dissociation of the PEI−DNA complex resulting in the reduction in transfection activity. Cholesterol-based lipopolymers showed enhanced gene transfection activity as compared to PEI-25KDa. In most of the lipopolymers, gene transfection efficacies decreased expectedly with increase in the serum concentrations in the case of **P8C2**, **P12C1**, and **P12C2** lipopolymer formulations. There is no effect of the high percentages of serum on transfection activities of **P8C2** and **P12C1** lipopolymer formulations, whereas in the case of the **P12C2** lipopolymer formulation, serum was found to enhance the transfection activity. Among all the formulations, **P8C2** showed highest transfection activity. The greater serum compatibility of these lipopolymers might be caused by the cholesterol grafting, as the presence of cholesterol moieties might prevent the serum proteins to dissociate from the lipopolymer−DNA complexes. It is well-known in literature that, with increase in the molecular weight of the PEI, transfection efficiency as well as cytotoxicity increases. The unmodified low molecular weight PEIs of molecular weights 800, 1200, and 2000 do not show any transfection activity, which is consistent with the reports by Kim et al., where <1% transfection activity was reported with PEI of molecular weight 1800 (*45*). The commercially available PEI-25KDa which is known to show high transfection activity was found to be highly toxic as well. The cytotoxicity studies have shown that the presently developed lipopolymers are much less toxic as compared to the commercially available PEI-25KDa. All the lipopolymer−DNA complexes also showed low levels of cell toxicity except **P20C1** and **P20C2**, which may be because of the high molecular weight of the PEI used for these lipopolymers. Although the DNA delivery to eukaryotic cells involves several steps and the mechanism of many of these steps is not very clear at the molecular level (*31, 32, 67*−*69*), it would be important to note the high transfection properties,

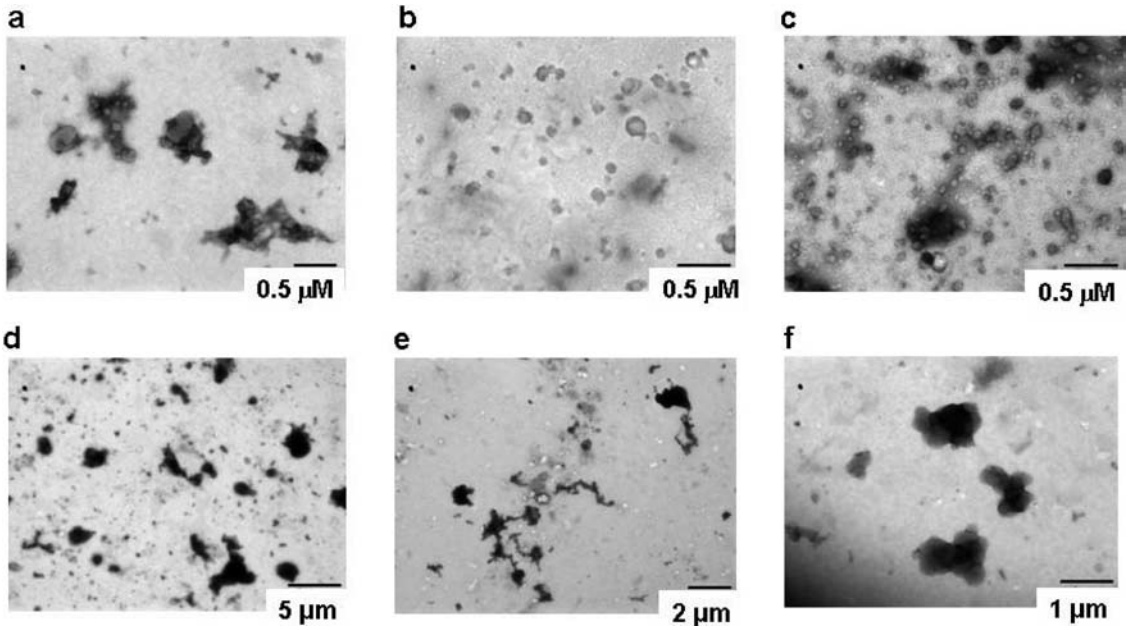

Figure 11. Representative transmission electron micrographs of the lipopolyplexes prepared from optimized lipopolymer/DOPE liposome/DNA complexes at the optimized w/w ratio of 12.0: (a) **P8C1**; (b) **P8C2**; (c) **P8C3**; (d) **P12C1**; (e) **P12C2**; (f) **P20C1**.

low cytotoxicities, and high serum compatibilities of these lipopolymer formulations.

CONCLUSIONS

PEI has been of interest to many scientists for its use in gene delivery applications. PEI can be easily derivatized with different ligands to enhance the biocompatibility and efficacies of the PEI derivatives. Toward this end, we synthesized nine PEI−cholesterol-based conjugates based on ether linkage between the polymer amine backbone and the cholesterol unit. Three low molecular weight PEIs were used for the synthesis of lipopolymers. Cholesterol tethering to PEI render them suitable for partitioning into phospholipid membranes (*70*). The transfection studies in HeLa cells showed high potency and low cytotoxicity of these lipopolymers as compared to the commercially available PEI. Commercially available PEI of molecular weight 25 kDa was found to be very toxic and less effective as compared to lipopolymers. The transfection efficacy of PEI-25 kDa decreased in the presence of high percentage of serum, whereas PEI−cholesterol-based lipopolymers were found to be effective even in the presence of high percentages of serum. The transfection efficacies and cytotoxicities of the lipopolymers were found to depend upon the percentage of cholesterol grafting and the molecular weight of PEI used for the synthesis of lipopolymers. Optimized lipopolymer−DOPE formulations were found to show higher cell viability as compared to PEI-25 kDa. All lipopolymer−DNA complexes except **P20C1** and **P20C2** formulation based lipopolyplexes showed more than 80% cell viability. Most of the lipopolymer formulations formed spherical lipopolymer-DNA complexes. The transfection activities reported in the present study manifest one of the highest efficiency among nonviral delivery reagents known. The retention of high transfection efficiency even in the presence of serum should be of interest to the researchers working in this area.

ACKNOWLEDGMENT

This work was supported by Department of Biotechnology, Government of India, New Delhi, India and by a project from FMC, India. Avinash Bajaj thanks CSIR for a senior research fellowship. We thank Dr. Omana Joy and Mr. Mani Vamsi for their help during the work.

Supporting Information Available: Scattered plots and FACS plots. This material is available free of charge via the Internet at http://pubs.acs.org.

LITERATURE CITED

(1) Verma, I. M., and Somia, N. (1997) Gene therapy - promises, problems and prospects. *Nature 389*, 2–42.
(2) Alton, E. W. F. W., and Geddes, D. M. (1995) Gene therapy for cystic fibrosis: a clinical perspective. *Gene Ther. 2*, 88–95.
(3) Griesenbach, U., Ferrari, S., Geddes, D. M., and Alton, E. W. F. W. (2002) Gene therapy progress and prospects: cystic fibrosis. *Gene Ther. 9*, 1344–1350.
(4) Anwer, K., Meaney, C., Kao, G., Hussain, N., Shelvin, R., Earls, R. M., Leonard, P., Quezada, A., Rolland, A. P., and Sullivan, S. M. (2000) Cationic lipid-based delivery system for systemic cancer gene therapy. *Cancer Gene Ther. 7*, 1156–1164.
(5) Hattori, Y., and Maitani, Y. (2005) Folate-linked nanoparticle-mediated suicide gene therapy in human prostate cancer and nasopharyngeal cancer with herpes simplex virus thymidine kinase. *Cancer Gene Ther. 12*, 796–809.
(6) Curiel, T. J., Piche, A., Kasono, K., and Curiel, D. T. (1997) Gene therapy strategies for AIDS-related malignancies. *Gene Ther. 4*, 1284–1288.
(7) Anderson, W. F. (1998) Human gene therapy. *Nature 392*, 25–30.
(8) Friedmann, T. (1996) Human gene therapy - an immature genie, but certainly out of the bottle. *Nat. Med. 2* (144), 1–47.
(9) Miller, A. D. (1992) Human gene therapy comes of age. *Nature 357*, 45–5460.
(10) Diebold, S. S., Kursa, M., Wagner, E., Cotten, M., and Zenke, M. (1999) Mannose polyethylenimine conjugates for targeted DNA delivery into dendritic cells. *Proc. Natl. Acad. Sci. U.S.A. 274*, 19087–19094.
(11) Frisch, B., Carriere, M., Largeau, C., Mathey, F., Masson, C., Schuber, F., Scherman, D., and Escriou, V. (2004) A new triantennary galactose-targeted PEGylated gene carrier, characterization of its complex with DNA, and transfection of hepatoma cells. *Bioconjugate Chem. 15*, 754–764.

(12) Hofland, H. E. J., Masson, C., Iginla, S., Osetinsky, I., Reddy, J. A., Leamon, C. P., Scherman, D., Bessodes, M., and Wils, P. (2002) Folate-targeted gene transfer in vivo. *Mol. Ther. 5*, 739–744.

(13) Jenkins, R. G., Herrick, S. E., Meng, Q. H., Kinnon, C., Laurent, G. J., McAnulty, R. J., and Hart, S. L. (2000) An integrin-targeted non-viral vector for pulmonary gene therapy. *Gene Ther. 7*, 393–400.

(14) Yang, Y., Nunes, F. A., Berencsi, K., Furth, E. E., Gonczol, E., and Wilson, J. M. (1994) Cellular immunity to viral antigens limits E1-deleted adenoviruses for gene therapy. *Proc. Natl. Acad. Sci. U.S.A. 91*, 4407–11.

(15) Yang, Y., Nunes, F. A., Berencsi, K., Goenczoel, E., Engelhardt, J. F., and Wilson, J. M. (1994) Inactivation of E2a in recombinant adenoviruses improves the prospect for gene therapy in cystic fibrosis. *Nat. Genet. 7*, 362–9.

(16) Knowles, M. R., Hohneker, K. W., Zhou, Z., Olsen, J. C., Noah, T. L., Hu, P. C., Leigh, M. W., Engelhardt, J. F., Edwards, L. J., and Jones, K. R. (1995) A controlled study of adenoviral-vector-mediated gene transfer in the nasal epithelium of patients with cystic fibrosis. *New Engl. J. Med. 333*, 823–31.

(17) Crystal, R. G., McElvaney, N. G., Rosenfeld, M. A., Chu, C.-S., Mastrangeli, A., Hay, J. G., Brody, S. L., Jaffe, H. A., Eissa, N. T., and Danel, C. (1994) Administration of an adenovirus containing the human CFTR cDNA to the respiratory tract of individuals with cystic fibrosis. *Nat. Genet. 8*, 42–51.

(18) Liu, D., Ren, T., and Gao, X. (2003) Cationic transfection lipids. *Curr. Med. Chem. 10*, 1307–1315.

(19) Bhattacharya, S., and Bajaj, A. (2005) Recent advances in lipid molecular design. *Curr. Opin. Chem. Biol. 9*, 647–655.

(20) Pack, D. W., Putnam, D., and Langer, R. (2000) Design of imidazole-containing endosomolytic biopolymers for gene delivery. *Biotechnol. Bioeng. 67*, 217–223.

(21) Mahato, R. I., Lee, M., Maheswari, A., and Kim, S. W. (2001) Intratumoral delivery of p2CMVmIL-12 using water-soluble lipopolymers. *Mol. Ther. 4*, 130–138.

(22) Ilies, M. A., Seitz, W. A., Ghiviriga, I., Johnson, B. H., Miller, A., Thompson, E. B., and Balaban, A. T. (2004) Pyridinium cationic lipids in gene delivery: a structure-activity correlation study. *J. Med. Chem. 47*, 3744–3754.

(23) Nakanishi, M. (2003) New strategy in gene transfection by cationic transfection lipids with a cationic cholesterol. *Curr. Med. Chem. 10*, 1289–1296.

(24) Niculescu-Duvaz, D., Heyes, J., and Springer, C. J. (2003) Structure-activity relationship in cationic lipid mediated gene transfection. *Curr. Med. Chem. 10*, 1233–1261.

(25) Kirby, A. J., Camilleri, P., Engberts, J. B. F. N., Feiters, M. C., Nolte, R. J. M., Soderman, O., Bergsma, M., Bell, P. C., Fielden, M. L., Garcia Rodriguez, C. L., Guedat, P., Kremer, A., McGregor, C., Perrin, C., Ronsin, G., and van Eijk, M. C. P. (2003) Gemini surfactants: New synthetic vectors for gene transfection. *Angew. Chem., Int. Ed. 42*, 1448–1457.

(26) Bhattacharya, S., and Bajaj, A. (2007) Membrane forming properties of pseudoglyceryl backbone based gemini lipids possessing oxyethylene spacers. *J. Phys. Chem. B 111*, 2463–2472.

(27) Bhattacharya, S., and Bajaj, A. (2007) Thermotropic and hydration studies of membranes formed from gemini pseudoglyceryl lipids possessing polymethylene spacers. *Langmuir 23*, 8988–8994.

(28) Bhattacharya, S., and De, S. (1999) Synthesis and vesicle formation from dimeric pseudoglyceryl lipids with $(CH_2)_m$ spacers: pronounced m-value dependence of thermal properties, vesicle fusion, and cholesterol complexation. *Chem.—Eur. J. 5*, 2335–2347.

(29) Bhattacharya, S., and Dileep, P. V. (2003) Membrane-forming properties of cationic lipids bearing oxyethylene-based linkages. *J. Phys. Chem. B 107*, 3719–3725.

(30) Bhattacharya, S., and Dileep, P. V. (2004) Cationic oxyethylene lipids. synthesis, aggregation, and transfection properties. *Bioconjugate Chem. 15*, 508–519.

(31) Bhattacharya, S., and Mandal, S. S. (1997) Interaction of surfactants with DNA. Role of hydrophobicity and surface charge on intercalation and DNA melting. *Biochim. Biophys. Acta 1323*, 29–44.

(32) Bhattacharya, S., and Mandal, S. S. (1998) Evidence of interlipidic ion-pairing in anion-induced DNA release from cationic amphiphile-DNA complexes. mechanistic implications in transfection. *Biochemistry 37*, 7764–7777.

(33) Boussif, O., Lezoualc'h, F., Zanta, M. A., Mergny, M. D., Scherman, D., Demeneix, B., and Behr, J.-P. (1995) A versatile vector for gene and oligonucleotide transfer into cells in culture and in vivo: polyethylenimine. *Proc. Natl. Acad. Sci. U.S.A. 92*, 7297–301.

(34) Abbai, M., Uludag, H., Incani, V., Olson, C., Lin, X., Acuan, B., Rutkowski, D., Ghahary, A., and Weinfeld, M. (2007) Palmitic acid-modified poly-L-lysine for non-viral delivery of plasmid DNA to skin fibroblasts. *Biomacromolecules 8*, 1059–1063.

(35) Wagneer, E., Ogris, M., and Zauner, W. (1999) Polylysine-based transfection systems utilizing receptor mediated delivery. *Adv. Drug Delivery Rev. 30*, 97–113.

(36) Wang, Y., Wang, L.-S., Goh, S.-H., and Yang, Y.-Y. (2007) Synthesis and characterization of cationic micelles self-assembled from a biodegradable copolymer for gene delivery. *Biomacromolecules 8*, 1028–1037.

(37) Kichler, A. (2004) Gene transfer with modified polyethylenimines. *J. Gene Med. 6*, S3–S10.

(38) Thomas, M., and Klibanov, A. M. (2002) Enhancing polyethylenimine's delivery of plasmid DNA into mammalian cells. *Proc. Natl. Acad. Sci. U.S.A. 99*, 14640–14645.

(39) Kim, S., Choi, J. S., Jang, H. S., Suh, H., and Park, J. (2001) Hydrophobic modification of polyethyeneimine for gene transfectants. *Bull. Chem. Soc. Jpn. 22*, 1069–1075.

(40) Bajaj, A., Kondaiah, P., and Bhattacharya, S. (2008) Effect of the nature of the spacer on gene transfer efficacies of novel thiocholesterol derived gemini lipids in different cell lines: A structure-activity investigation. *J. Med. Chem. 51*, 2533–2540.

(41) Dileep, P. V., Antony, A., and Bhattacharya, S. (2001) Incorporation of oxyethylene units between hydrocarbon chain and pseudoglyceryl backbone in cationic lipid potentiates gene transfection efficiency in the presence of serum. *FEBS Lett. 509*, 327–331.

(42) Bajaj, A., Kondaiah, P., and Bhattacharya, S. (2007) Design, synthesis and in vitro gene transfection efficacies of cholesterol based gemini lipids and their serum compatibility: a structure activity relationship. *J. Med. Chem. 50*, 2432–2442.

(43) Bajaj, A., Kondaiah, P., and Bhattacharya, S. (2007) Synthesis and gene transfection properties of novel serum compatible cholesterol based gemini lipids possessing oxyethylene spacers. *Bioconjugate Chem. 18*, 1537–1546.

(44) Han, S.-o., Mahato, R. I., and Kim, S. W. (2001) Water-soluble lipopolymer for gene delivery. *Bioconjugate Chem. 12*, 337–345.

(45) Wang, D.-a., Narang, A. S., Kotb, M., Gaber, O. A., Miller, D. D., Kim, S. W., and Mahato, R. I. (2002) Novel branched poly(ethylenimine)-cholesterol water-soluble lipopolymers for gene delivery. *Biomacromolecules 3*, 1197–1207.

(46) Furgeson, D. Y., Chan, W. S., Yockman, J. W., and Kim, S. W. (2003) Modified linear polyethylenimine-cholesterol conjugates for DNA complexation. *Bioconjugate Chem. 14*, 840–847.

(47) Bae, Y. M., Choi, H., Lee, S., Kang, S. H., Kim, Y. T., Nam, K., and Park, J. S. (2007) Dexamethasone-conjugated low molecular weight polyethylenimine as a nucleus-targeting lipopolymer gene carrier. *Bioconjugate Chem. 18* 2029–2036.

(48) Bhattacharya, S., De, S., and George, S. K. (1997) Synthesis and vesicle formation from novel pseudoglyceryl dimeric lipids. Evidence of formation of widely different membrane organizations with exceptional thermotropic properties. *Chem. Commun.* 2287–2288.

(49) Bhattacharya, S., Subramanian, M., and Hiremath, U. S. (1995) Surfactant lipids containing aromatic units produce vesicular membranes with high thermal stability. *Chem. Phys. Lipids 78*, 177–188.

(50) Bhattacharya, S., and Haldar, S. (1995) Synthesis, thermotropic behavior, and permeability properties of vesicular membranes composed of cationic mixed-chain surfactants. *Langmuir 11*, 4748–4757.

(51) Bajaj, A., Paul, B., Indi, S. S., Kondaiah, P., and Bhattacharya, S. (2007) Effect of the hydrocarbon chain lengths and spacer lengths on gene transfection efficacies of gemini lipids based on aromatic backbone. *Bioconjugate Chem. 18*, 2144–2158.

(52) Bhattacharya, S., and Bajaj, A. (2007) Membrane forming properties of gemini lipids possessing aromatic backbone between the hydrocarbon chains and the cationic headgroup. *J. Phys. Chem. B 111*, 13511–13519.

(53) Bhattacharya, S., and Haldar, S. (1996) The effects of cholesterol inclusion on the vesicular membranes of cationic lipids. *Biochim. Biophys. Acta Biomem. 1283*, 21–30.

(54) Bhattacharya, S., and Haldar, S. (2000) Interactions between cholesterol and lipids in bilayer membranes. Role of lipid headgroup and hydrocarbon chain-backbone linkage. *Biochim. Biophys. Acta Biomem. 1467*, 39–53.

(55) Bhattacharya, S., and Krishnan-Ghosh, Y. (2001) Vesicle formation from oligo(oxyethylene)-bearing cholesteryl amphiphiles: site-selective effects of oxyethylene units on the membrane order and thickness. *Langmuir 17*, 2067–2075.

(56) Ghosh, Y. K., Indi, S. S., and Bhattacharya, S. (2001) Thermal lipid order-disorder transitions in mixtures of cationic cholesteryl lipid analogues and dipalmitoyl phosphatidylcholine membranes. *J. Phys. Chem. B 105*, 10257–10265.

(57) Ghosh, Y. K., Visweswariah, S. S., and Bhattacharya, S. (2000) Nature of linkage between the cationic headgroup and cholesteryl skeleton controls gene transfection efficiency. *FEBS Lett. 473*, 341–344.

(58) Ghosh, Y. K., Visweswariah, S. S., and Bhattacharya, S. (2002) Advantage of the ether linkage between the positive charge and the cholesteryl skeleton in cholesterol-based amphiphiles as vectors for gene delivery. *Bioconjugate Chem. 13*, 378–384.

(59) Bajaj, A., Mishra, S. K., Kondaiah, P., and Bhattacharya, S. (2008) Effect of the headgroup variation on the gene transfer properties of cholesterol based cationic lipids possessing ether linkage. *Biochim. Biophys. Acta Biomem. 1778*, 1222–1236.

(60) Davis, S. C., and Szoka, F. C. J. (1998) Cholesterol phosphate derivatives: synthesis and incorporation into a phosphatase and calcium-sensitive triggered release liposome. *Bioconjugate Chem. 9*, 783–792.

(61) Hansen, M. B., Nielsen, S. E., and Berg, K. (1989) Re-examination and further development of a precise and rapid dye method for measuring cell growth/cell kill. *J. Immunol. Methods 119*, 203–210.

(62) Mosmann, T. (1983) Rapid colorimetric assay for cellular growth and survival: application to proliferation and cytotoxicity assays. *J. Immunol. Methods 65*, 55–63.

(63) Felgner, J. H., Kumar, R., Sridhar, C. J., Wheeler, Y. J., Tsai, R., Border, P., Ramsey, M., Martin, C. N., and Felgner, P. L. (1994) Enhanced gene delivery and mechanism studies with a novel series of cationic lipid formulations. *J. Biol. Chem. 269*, 2550–2561.

(64) Chabaud, P., Camplo, M., Payet, D., Serin, G., Molreau, L., Barthelemy, P., and Grinstaff, M. W. (2006) Cationic nucleoside lipids for gene delivery. *Bioconjugate Chem. 17*, 466–472.

(65) Matsui, K., Sando, S., Sera, T., Aoyama, Y., Sasaki, Y., Komatsu, T., Terashima, T., and Kikuchi, J.-I. (2006) Cerasome as an infusible, cell-friendly, and serum-compatible transfection agent in a viral size. *J. Am. Chem. Soc. 128*, 3114–3115.

(66) Zhang, C., Tang, N., Liu, X., Liang, W., Xu, W., and Torchilin, V. P. (2006) siRNA-containing liposomes modified with polyarginine effectively silence the targeted gene. *J. Controlled Release 112*, 229–239.

(67) Ewert, K., Ahmad, A., Evans, H. M., and Safinya, C. R. (2005) Cationic lipid-DNA complexes for non-viral gene therapy: relating supramolecular structures to cellular pathways. *Exp. Opin. Biol. Ther. 5*, 33–53.

(68) Xu, Y., and Szoka, F. C., Jr. (1996) Mechanism of DNA release from cationic liposome/DNA complexes used in cell transfection. *Biochemistry 35*, 5616–23.

(69) Zabner, J., Fasbender, A. J., Moninger, T., Poellinger, K. A., and Welsh, M. J. (1995) Cellular and molecular barriers to gene transfer by a cationic lipid. *J. Biol. Chem. 270*, 18997–9007.

(70) Bhattacharya, S., and Bajaj, A. (2008) Fluorescence and thermotropic studies of PEI-cholesterol based PEI-chol lipopolymers with dipalmitoyl phosphatidylcholine membranes *Biochim. Biophys. Acta Biomem.*, in press.

BC700381V

Supporting Information

Synthesis and Gene Transfection Efficacies of PEI-Cholesterol based Lipopolymers

Avinash Bajaj,[a] Paturu Kondaiah[b] and Santanu Bhattacharya[a,c,*]

[a]Department of Organic Chemistry, Indian Institute of Science, Bangalore 560 012, India.

[b]Department of Molecular Reproduction, Development and Genetics, Indian Institute of Science, Bangalore 560 012, India.

[c]Chemical Biology Unit of JNCASR, Bangalore 560 064, India.

Running Title: PEI-cholesterol lipopolymers

Keywords: Lipopolymers, PEI, Cholesterol, Gene transfection, Serum.

*Corresponding author. Email: sb@orgchem.iisc.ernet.in,

Phone: (91)-80-2293-2664.

Fax: (91)-80-2360-0529.

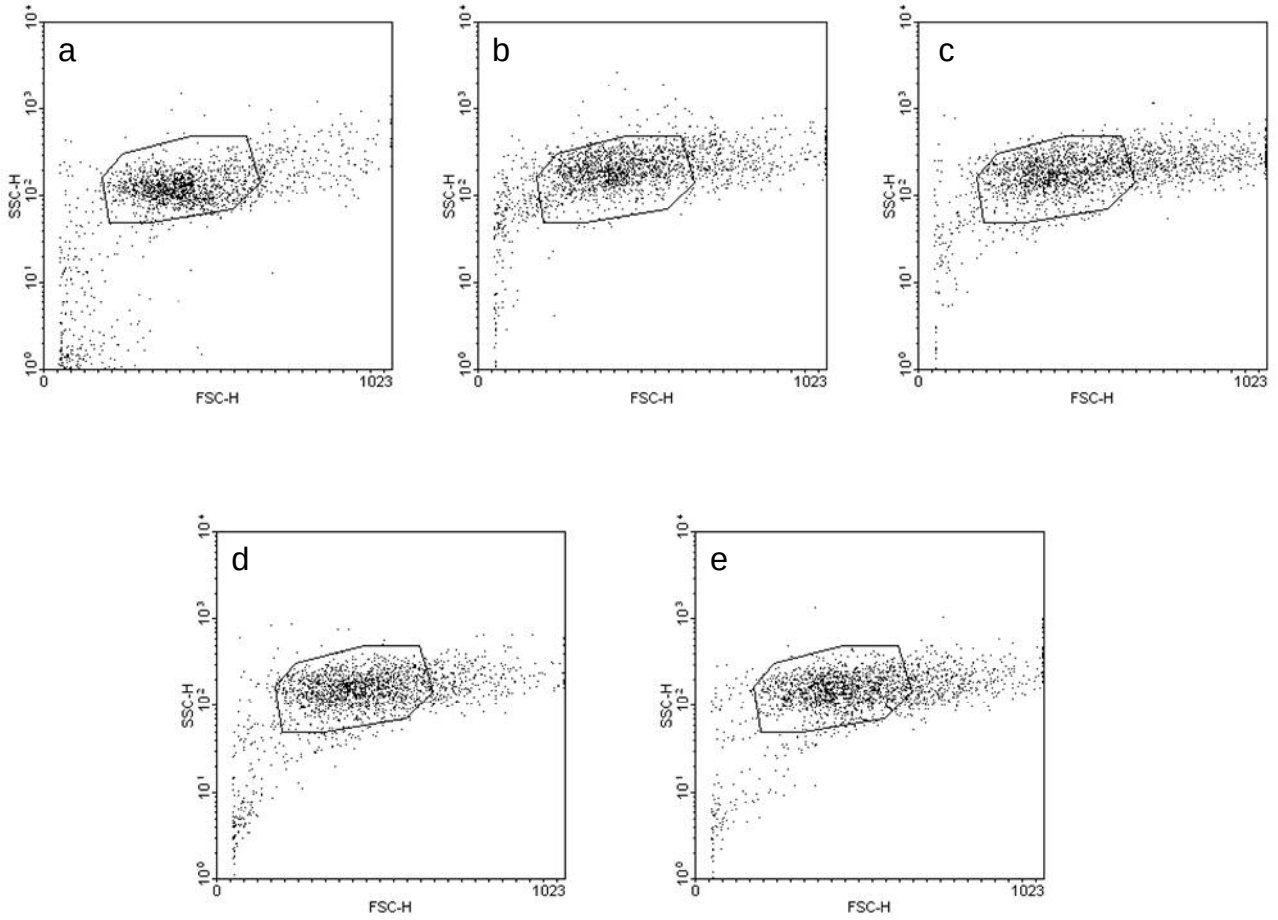

Figure S-1: Scattered plots of transfection experiments using optimized lipopolymer **P8C1**:DOPE formulations at w/w ratio of 12.0 using EGFP-c3 DNA in the presence of different percentages of serum (a) Untreated cells; (b) 0% serum; (c) 10% serum; (d) 30% serum; (e) 50% serum.

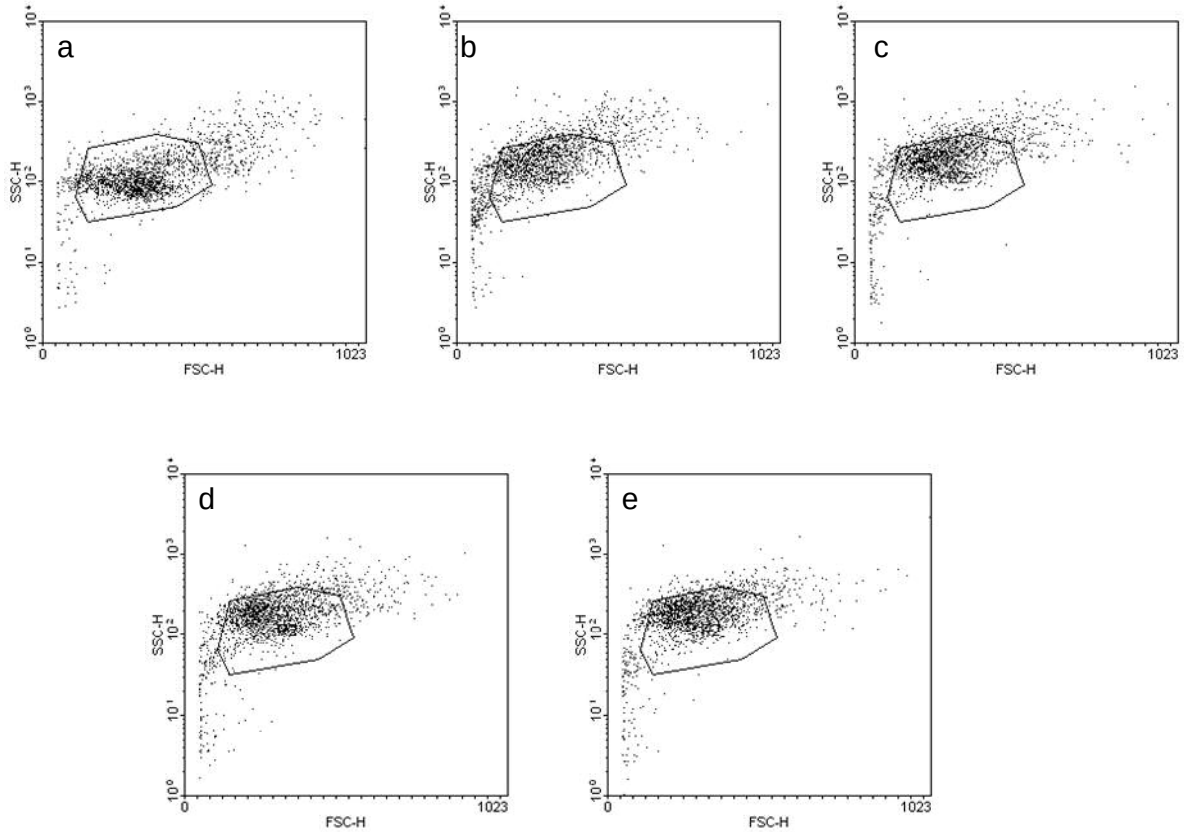

Figure S-2: Scattered plots of transfection experiments using optimized lipopolymer **P8C2**:DOPE formulations at w/w ratio of 12.0 using EGFP-c3 DNA in the presence of different percentages of serum (a) Untreated cells; (b) 0% serum; (c) 10% serum; (d) 30% serum; (e) 50% serum.

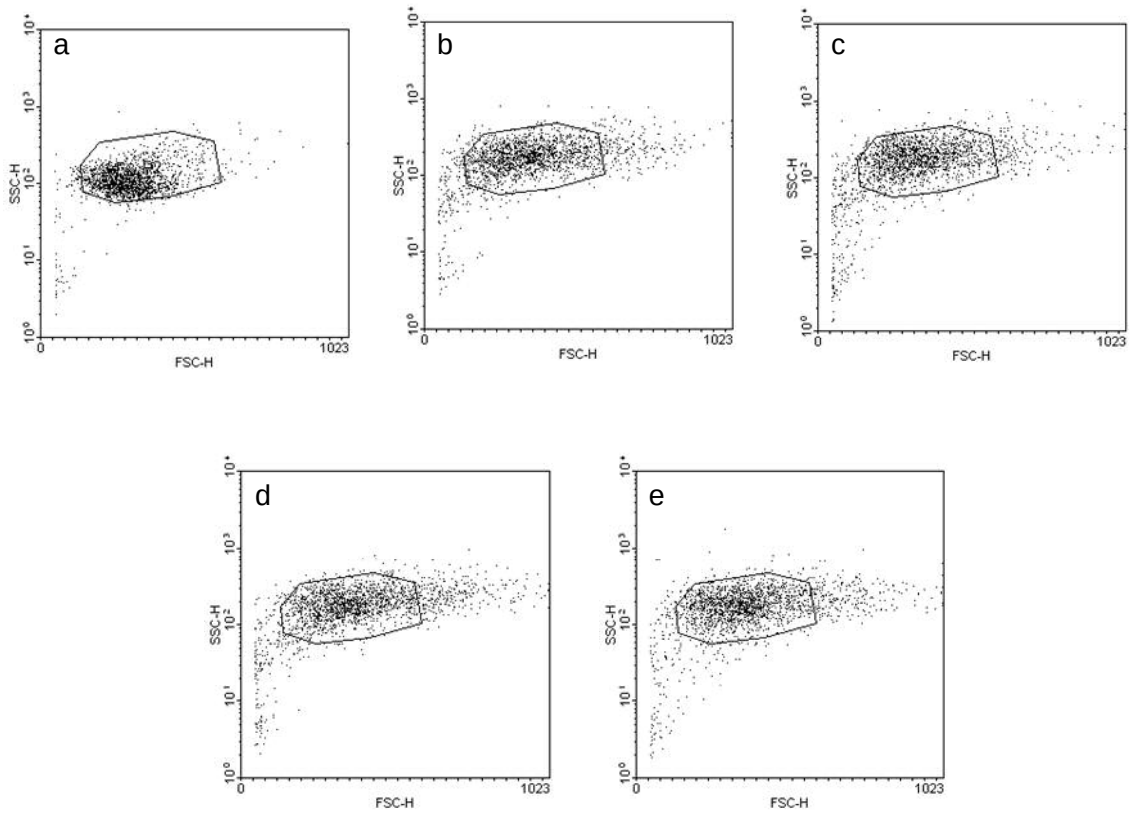

Figure S-3: Scattered plots of transfection experiments using optimized lipopolymer **P8C3**:DOPE formulations at w/w ratio of 12.0 using EGFP-c3 DNA in the presence of different percentages of serum (a) Untreated cells; (b) 0% serum; (c) 10% serum; (d) 30% serum; (e) 50% serum.

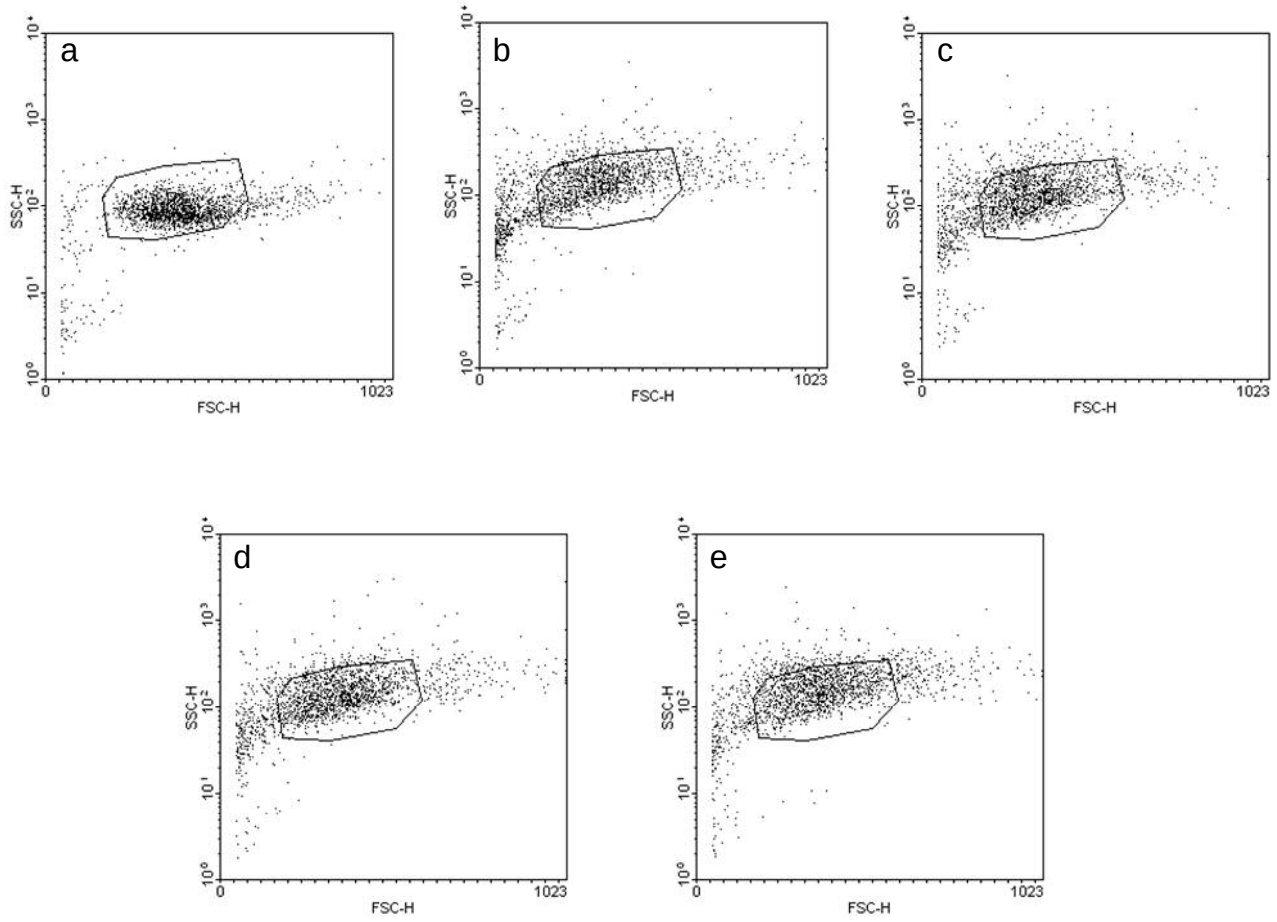

Figure S-4: Scattered plots of transfection experiments using optimized lipopolymer **P12C1**:DOPE formulations at w/w ratio of 12.0 using EGFP-c3 DNA in the presence of different percentages of serum (a) Untreated cells; (b) 0% serum; (c) 10% serum; (d) 30% serum; (e) 50% serum.

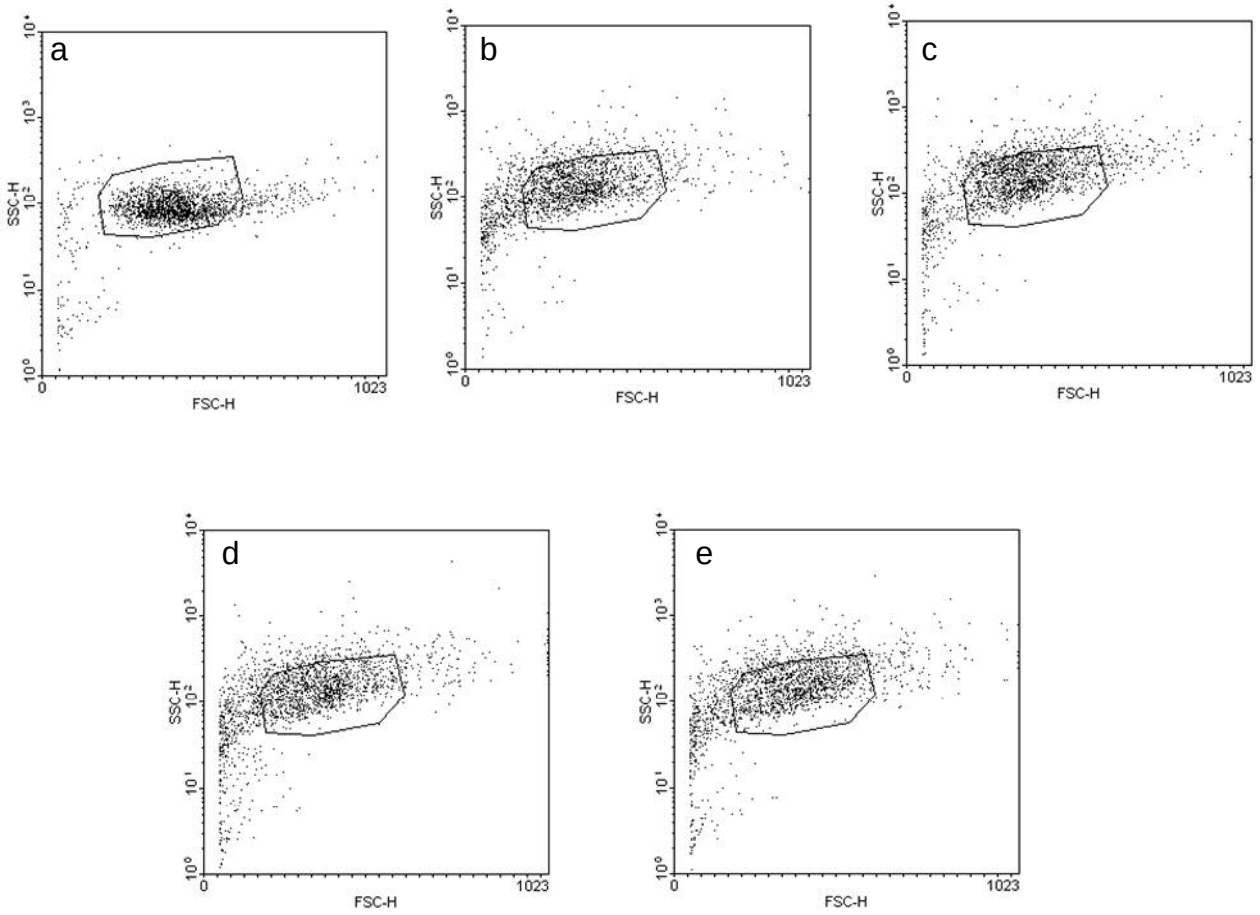

Figure S-5: Scattered plots of transfection experiments using optimized lipopolymer **P12C2**:DOPE formulations at w/w ratio of 12.0 using EGFP-c3 DNA in the presence of different percentages of serum (a) Untreated cells; (b) 0% serum; (c) 10% serum; (d) 30% serum; (e) 50% serum.

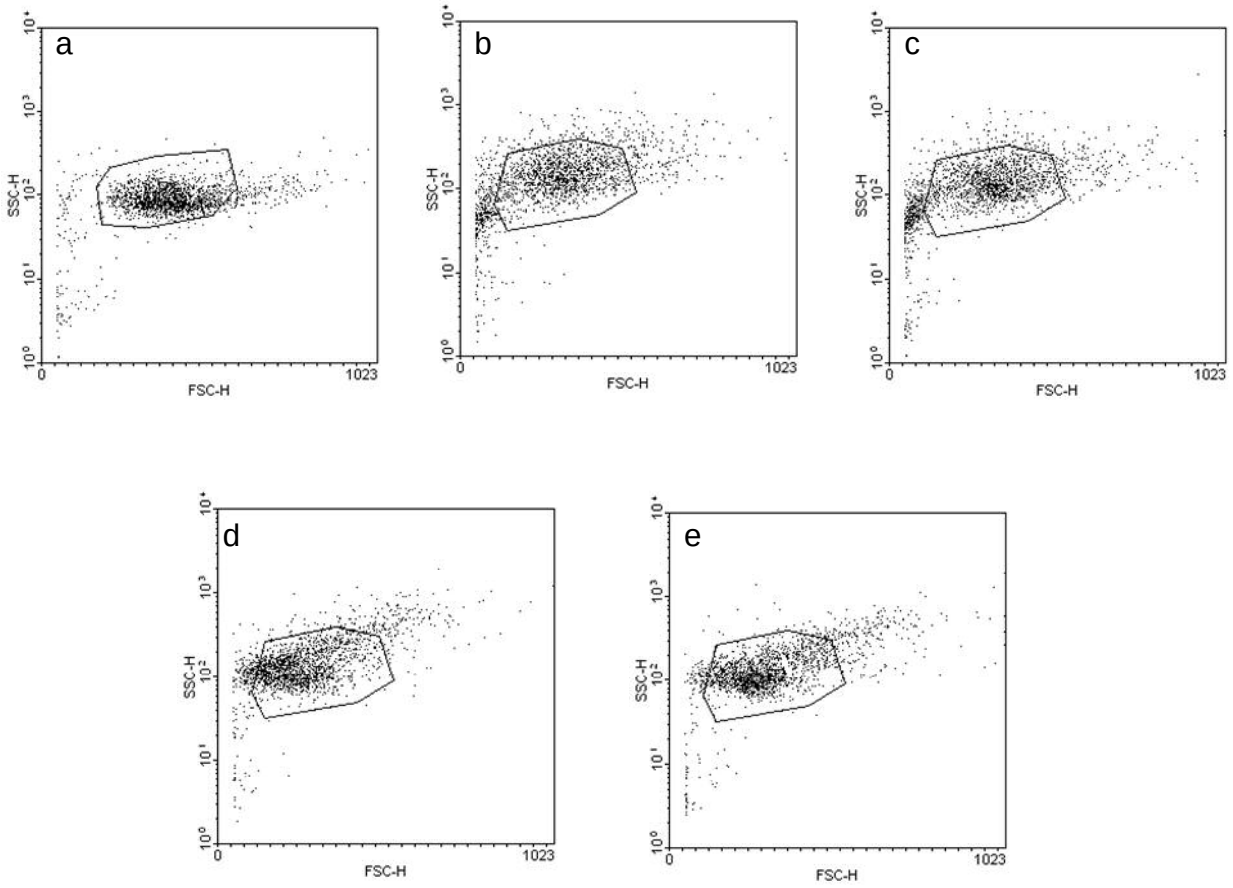

Figure S-6: Scattered plots of transfection experiments using optimized lipopolymer **P12C3**:DOPE formulations at w/w ratio of 12.0 using EGFP-c3 DNA in the presence of different percentages of serum (a) Untreated cells; (b) 0% serum; (c) 10% serum; (d) 30% serum; (e) 50% serum.

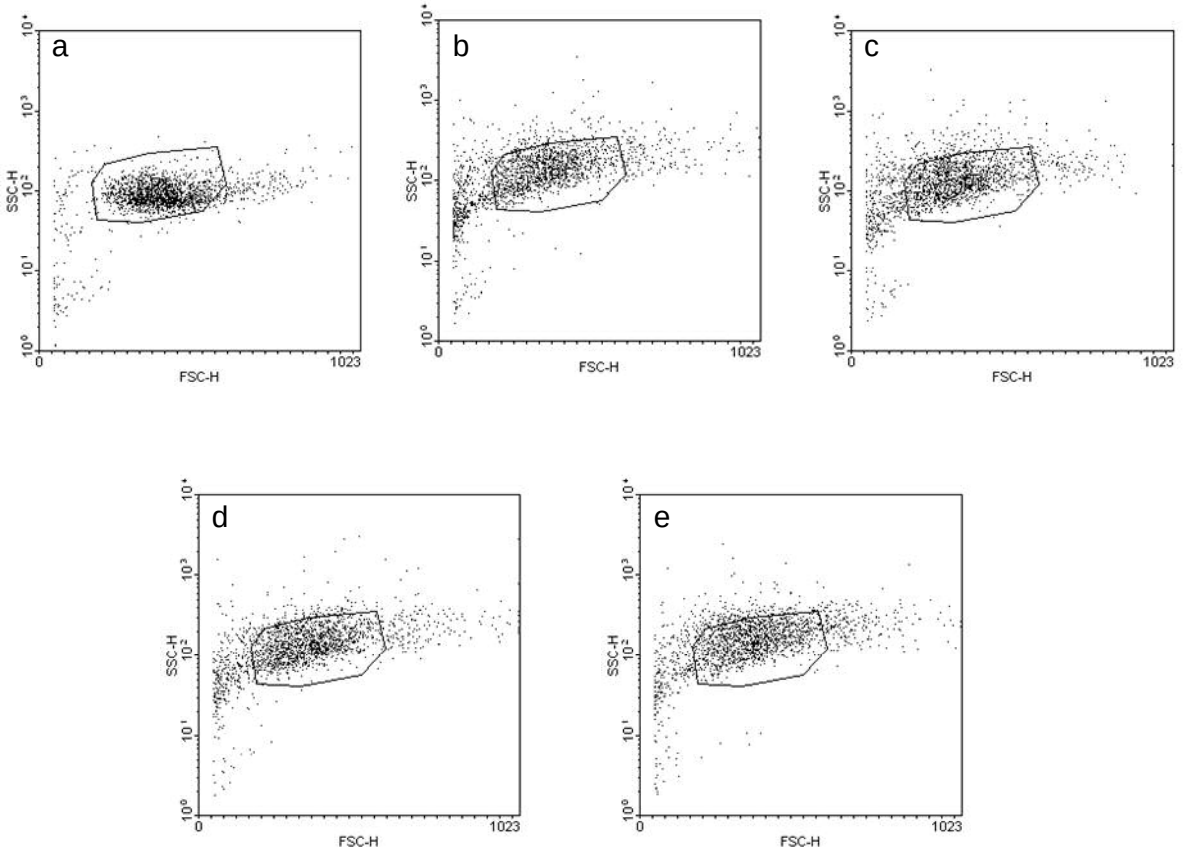

Figure S-7: Scattered plots of transfection experiments using optimized lipopolymer **P20C1**:DOPE formulations at w/w ratio of 12.0 using EGFP-c3 DNA in the presence of different percentages of serum (a) Untreated cells; (b) 0% serum; (c) 10% serum; (d) 30% serum; (e) 50% serum.

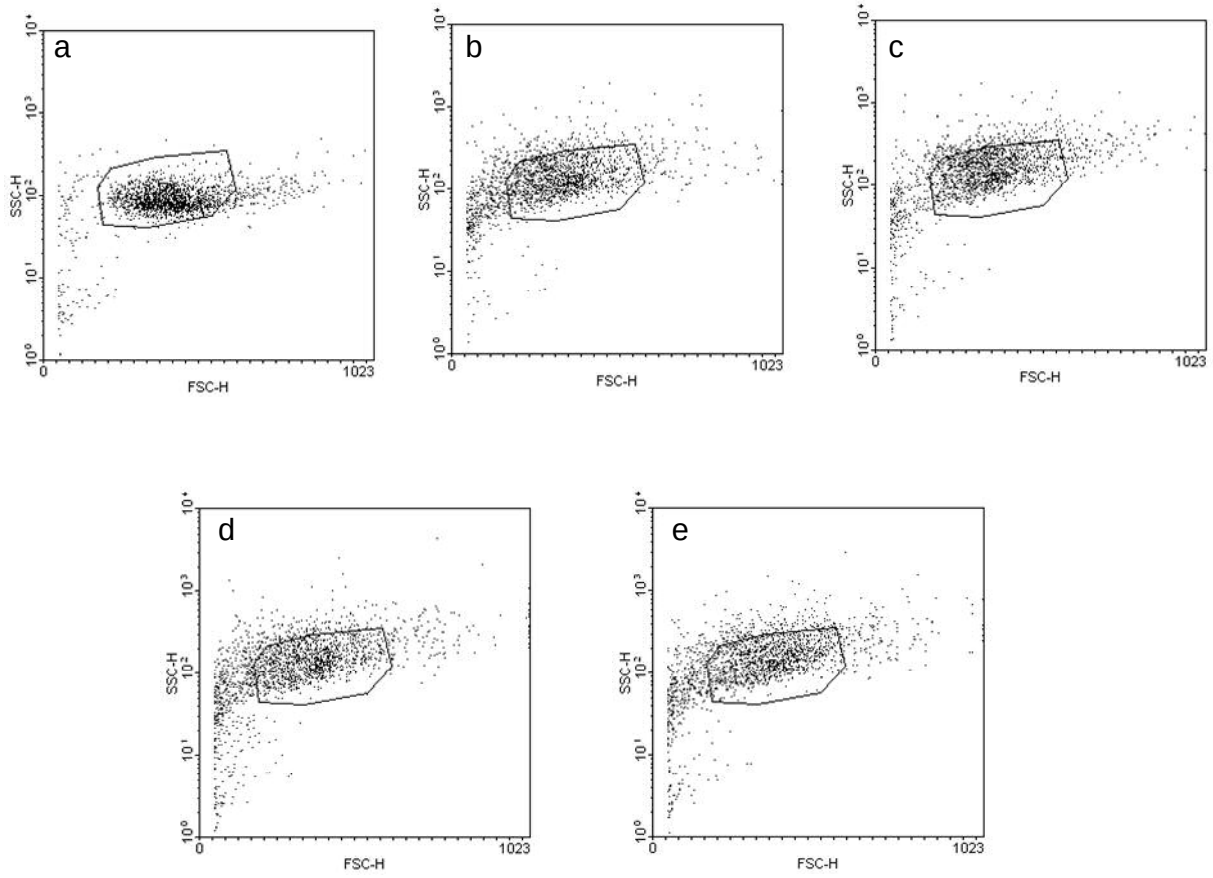

Figure S-8: Scattered plots of transfection experiments using optimized lipopolymer **P20C2**:DOPE formulations at w/w ratio of 12.0 using EGFP-c3 DNA in the presence of different percentages of serum (a) Untreated cells; (b) 0% serum; (c) 10% serum; (d) 30% serum; (e) 50% serum.

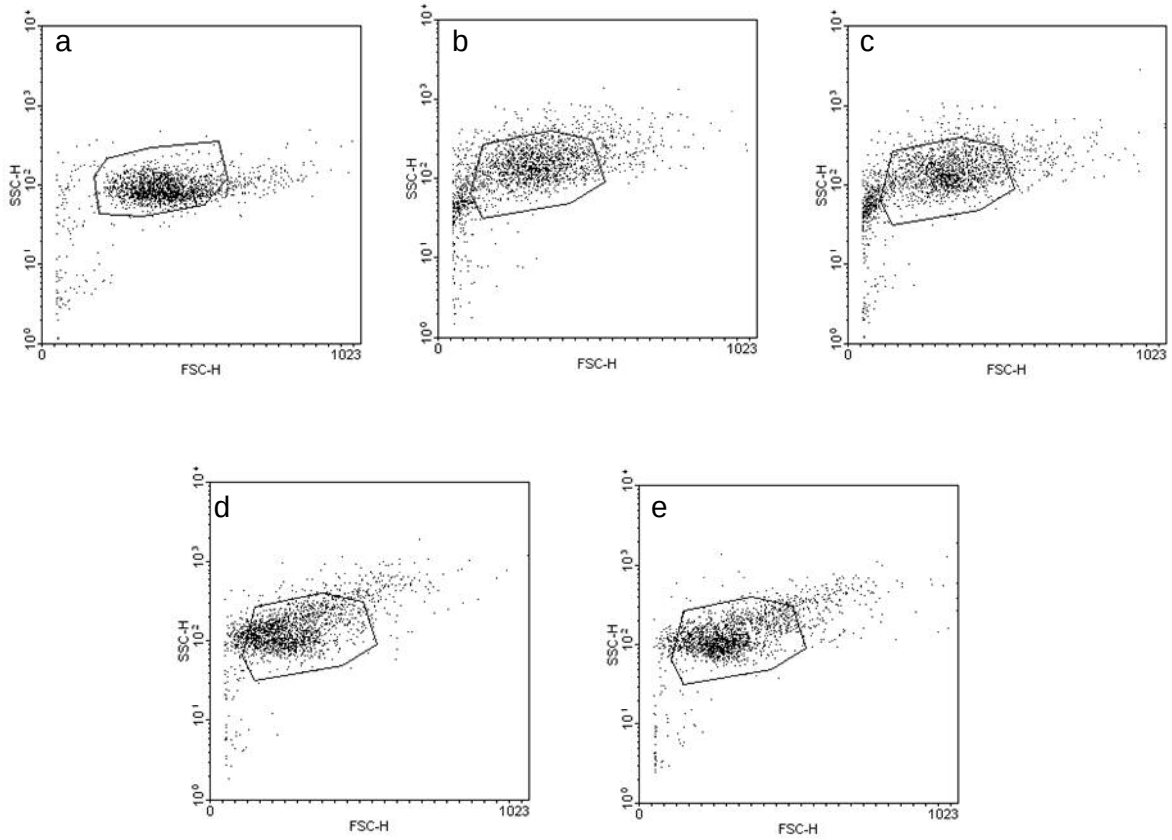

Figure S-9: Scattered plots of transfection experiments using optimized lipopolymer **P20C3**:DOPE formulations at w/w ratio of 12.0 using EGFP-c3 DNA in the presence of different percentages of serum (a) Untreated cells; (b) 0% serum; (c) 10% serum; (d) 30% serum; (e) 50% serum.

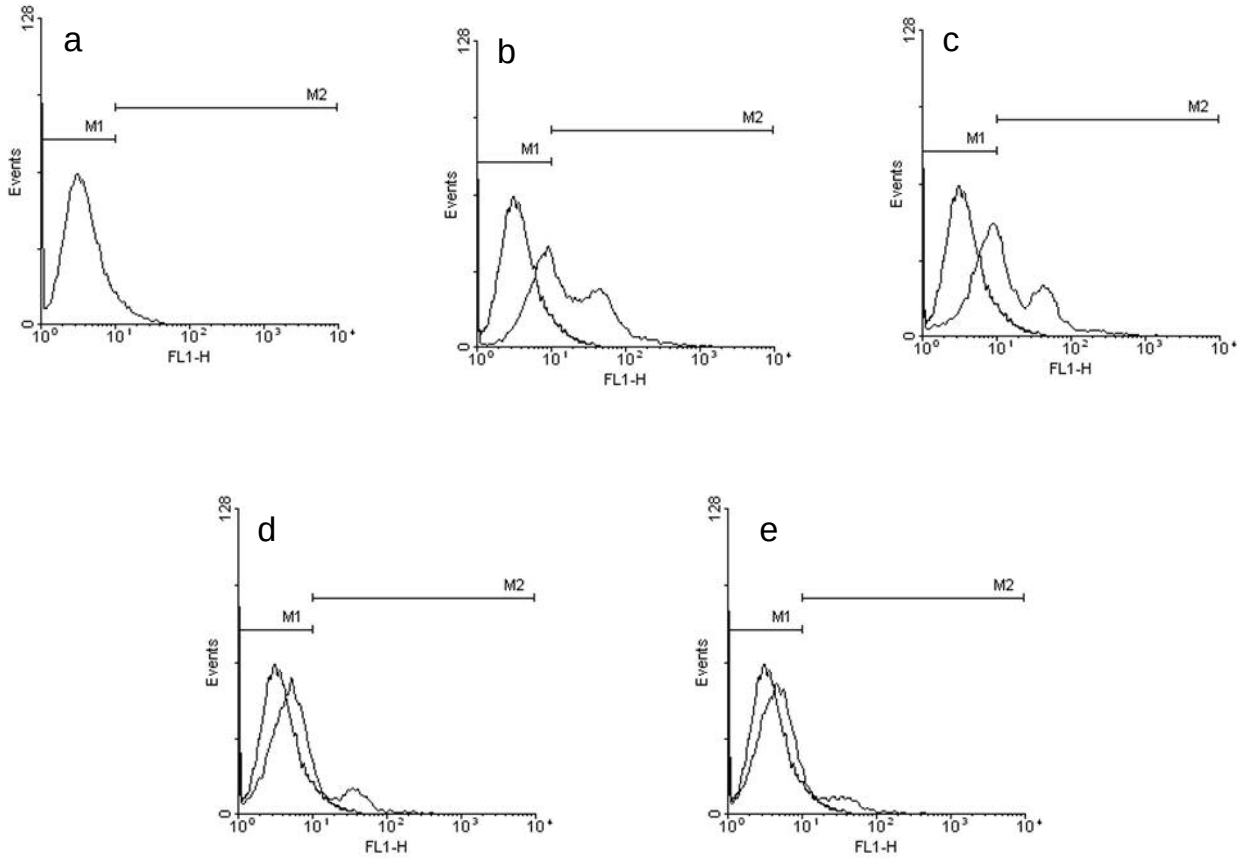

Figure S-10: FACS plots of untreated cells (a) and treated cells (b-e, overlaying with untreated facs plot) of transfection experiments using optimized lipopolymer **P8C1**:DOPE formulations at w/w ratio of 12.0 using EGFP-c3 DNA in the presence of different percentages of serum (a) Untreated cells; (b) 0% serum; (c) 10% serum; (d) 30% serum; (e) 50% serum.

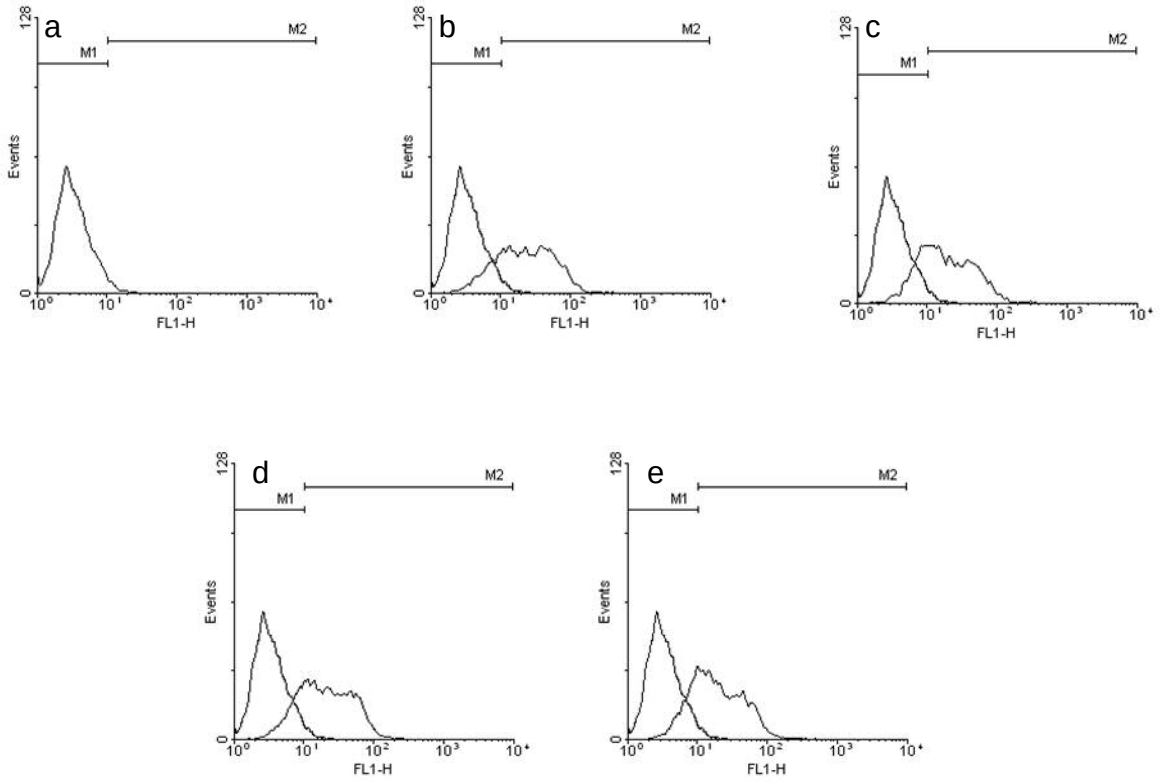

Figure S-11: FACS plots of untreated cells (a) and treated cells (b-e, overlaying with untreated facs plot) of transfection experiments using optimized lipopolymer **P8C2**:DOPE formulations at w/w ratio of 12.0 using EGFP-c3 DNA in the presence of different percentages of serum (a) Untreated cells; (b) 0% serum; (c) 10% serum; (d) 30% serum; (e) 50% serum.

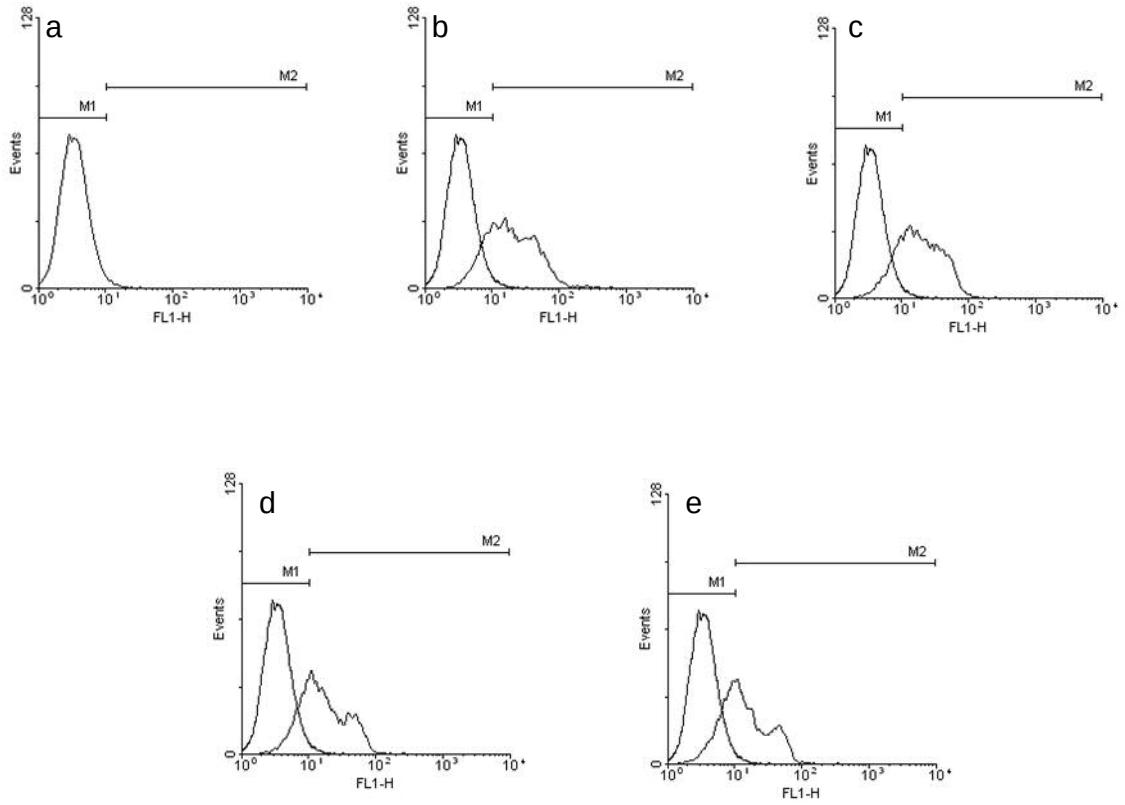

Figure S-12: FACS plots of untreated cells (a) and treated cells (b-e, overlaying with untreated facs plot) of transfection experiments using optimized lipopolymer **P8C3**:DOPE formulations at w/w ratio of 12.0 using EGFP-c3 DNA in the presence of different percentages of serum (a) Untreated cells; (b) 0% serum; (c) 10% serum; (d) 30% serum; (e) 50% serum.

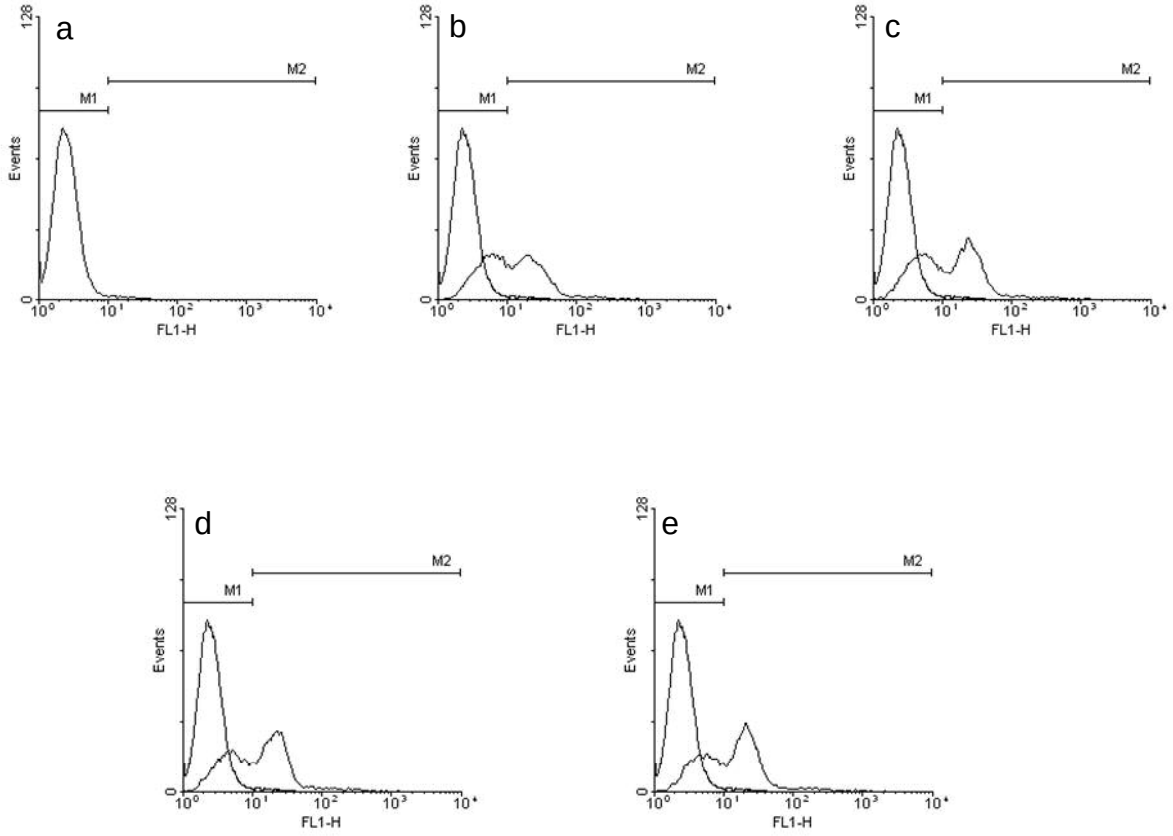

Figure S-13: FACS plots of untreated cells (a) and treated cells (b-e, overlaying with untreated facs plot) of transfection experiments using optimized lipopolymer **P12C1**:DOPE formulations at w/w ratio of 12.0 using EGFP-c3 DNA in the presence of different percentages of serum (a) Untreated cells; (b) 0% serum; (c) 10% serum; (d) 30% serum; (e) 50% serum.

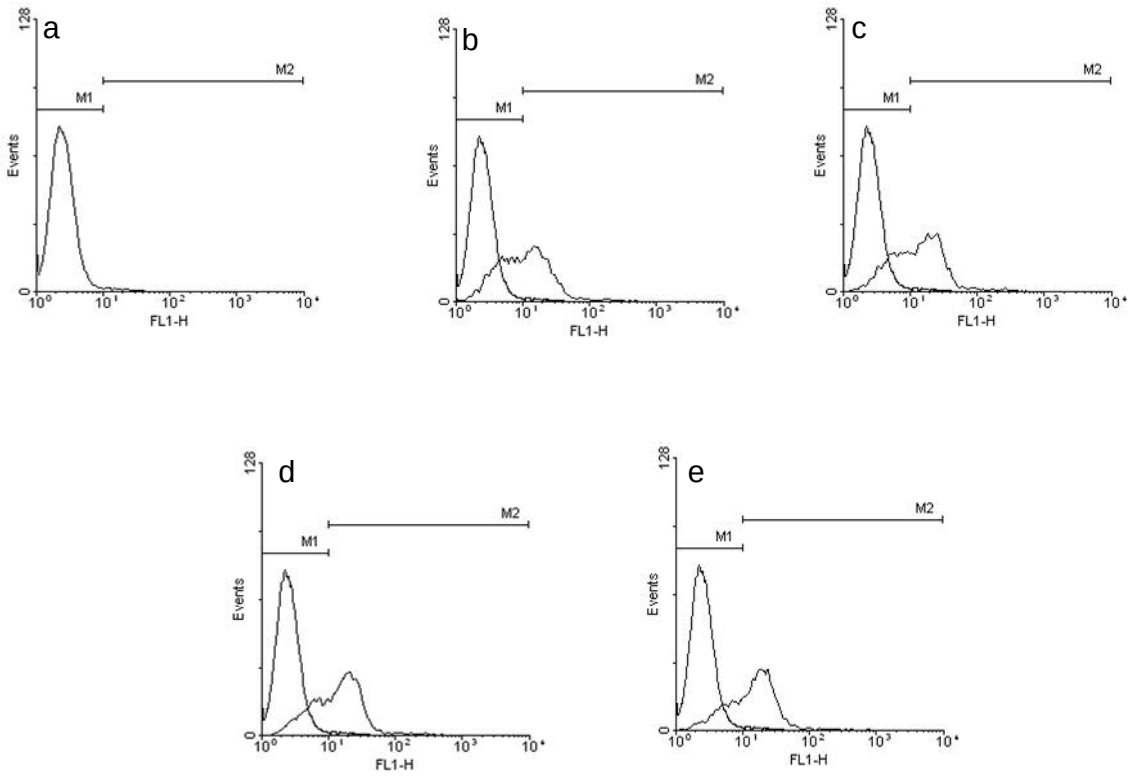

Figure S-14: FACS plots of untreated cells (a) and treated cells (b-e, overlaying with untreated facs plot) of transfection experiments using optimized lipopolymer **P12C2**:DOPE formulations at w/w ratio of 12.0 using EGFP-c3 DNA in the presence of different percentages of serum (a) Untreated cells; (b) 0% serum; (c) 10% serum; (d) 30% serum; (e) 50% serum.

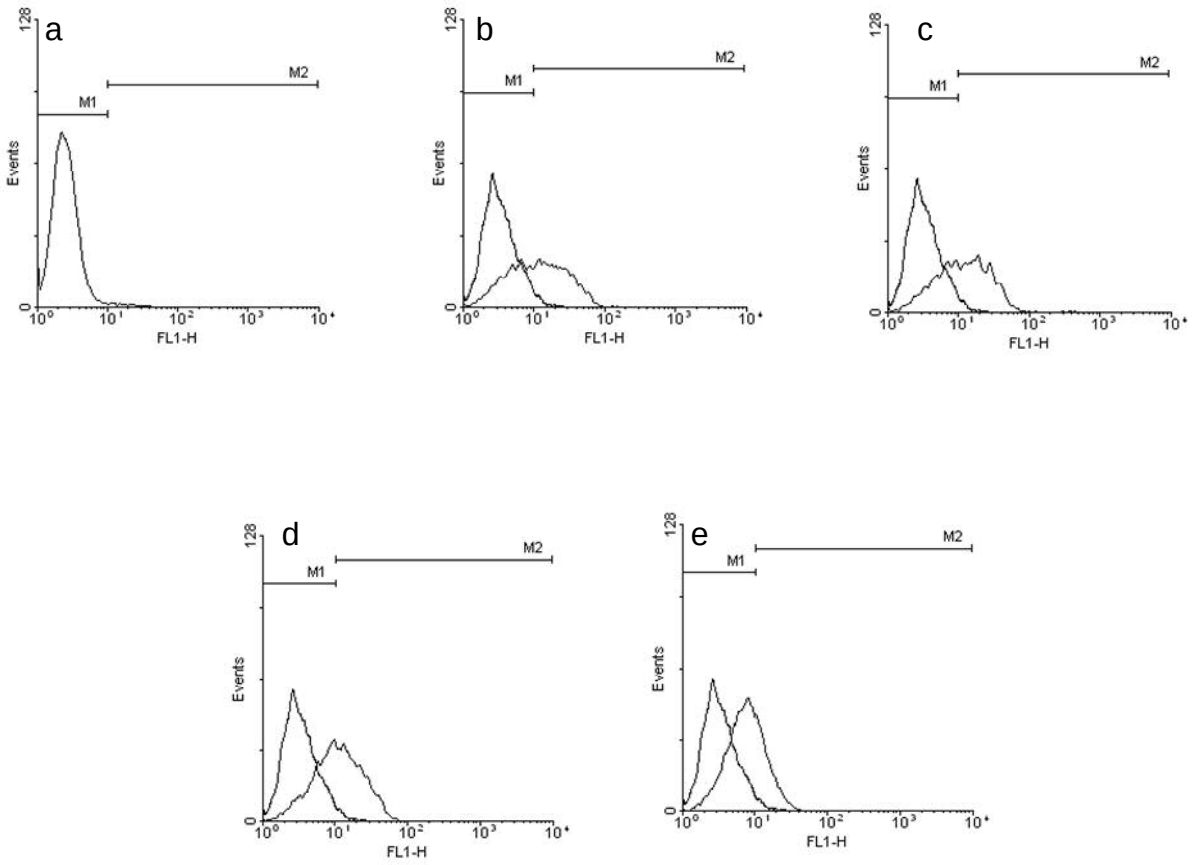

Figure S-15: FACS plots of untreated cells (a) and treated cells (b-e, overlaying with untreated facs plot) of transfection experiments using optimized lipopolymer **P12C3**:DOPE formulations at w/w ratio of 12.0 using EGFP-c3 DNA in the presence of different percentages of serum (a) Untreated cells; (b) 0% serum; (c) 10% serum; (d) 30% serum; (e) 50% serum.

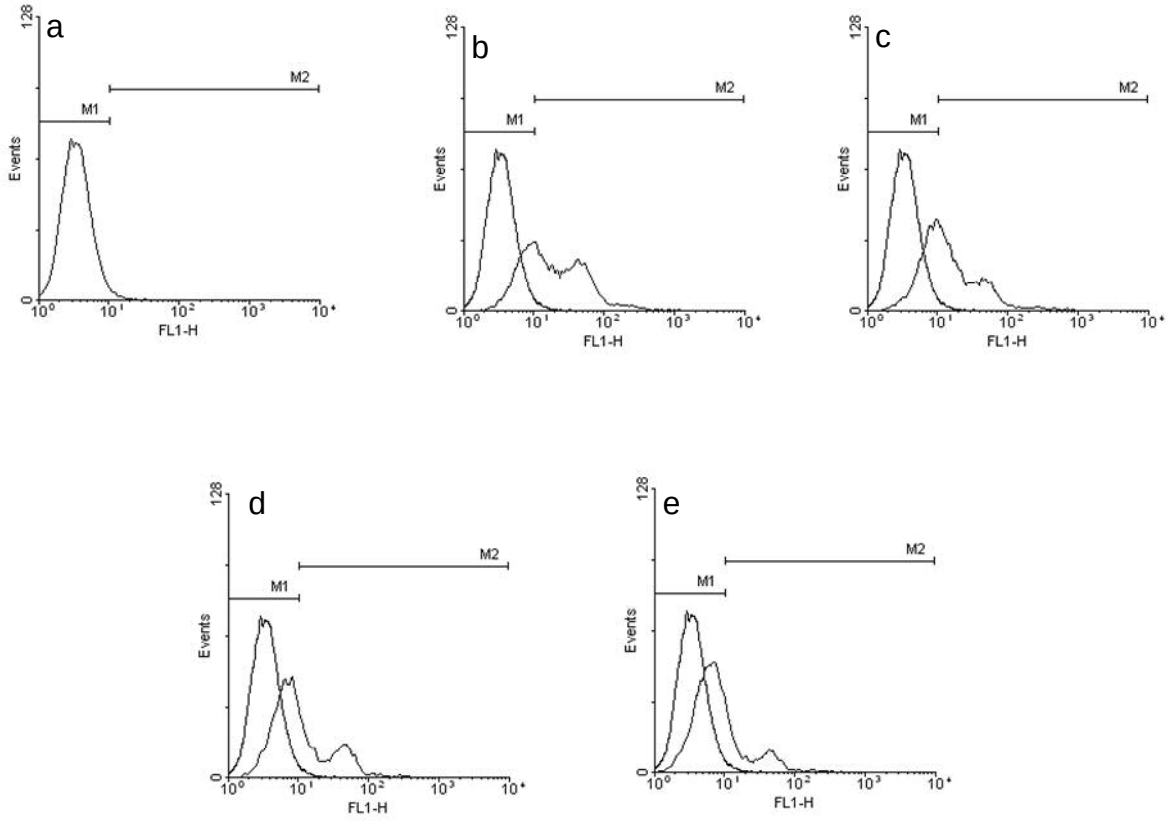

Figure S-16: FACS plots of untreated cells (a) and treated cells (b-e, overlaying with untreated facs plot) of transfection experiments using optimized lipopolymer **P20C1**:DOPE formulations at w/w ratio of 12.0 using EGFP-c3 DNA in the presence of different percentages of serum (a) Untreated cells; (b) 0% serum; (c) 10% serum; (d) 30% serum; (e) 50% serum.

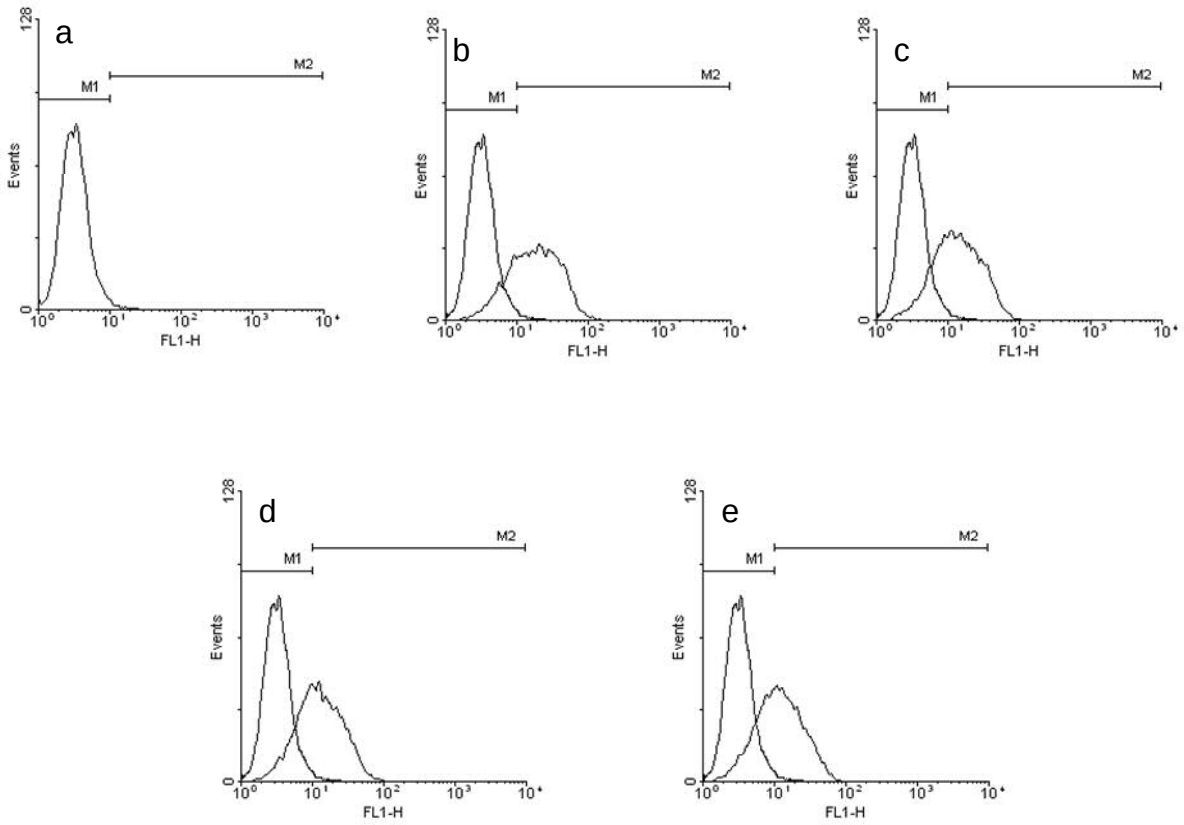

Figure S-17: FACS plots of untreated cells (a) and treated cells (b-e, overlaying with untreated facs plot) of transfection experiments using optimized lipopolymer **P20C2**:DOPE formulations at w/w ratio of 12.0 using EGFP-c3 DNA in the presence of different percentages of serum (a) Untreated cells; (b) 0% serum; (c) 10% serum; (d) 30% serum; (e) 50% serum.

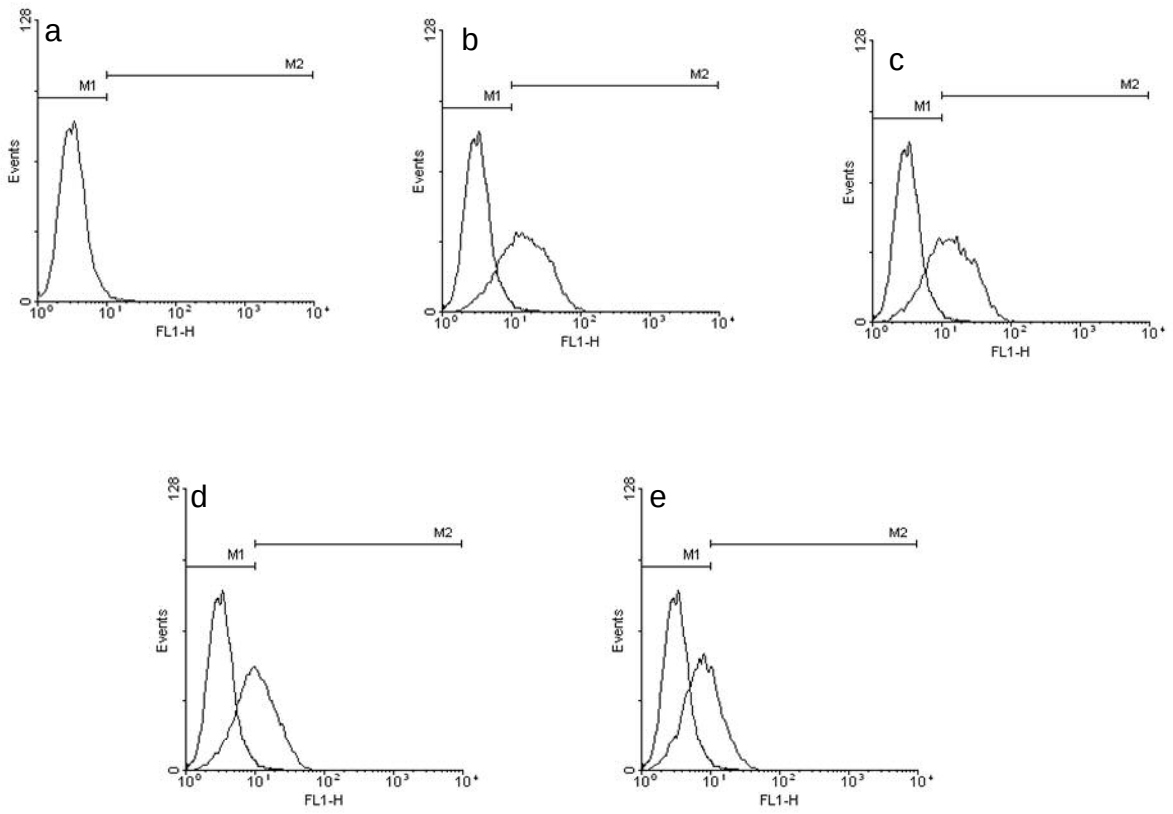

Figure S-18: FACS plots of untreated cells (a) and treated cells (b-e, overlaying with untreated facs plot) of transfection experiments using optimized lipopolymer **P20C3**:DOPE formulations at w/w ratio of 12.0 using EGFP-c3 DNA in the presence of different percentages of serum (a) Untreated cells; (b) 0% serum; (c) 10% serum; (d) 30% serum; (e) 50% serum.

Effect of Conjugation with Polypeptide Carrier on the Enzymatic Degradation of Herpes Simplex Virus Glycoprotein D Derived Epitope Peptide

Regina Tugyi,[†] Gábor Mezõ,[‡] Schlosser Gitta,[‡,⊥] Erzsébet Fellinger,[§] David Andreu,[||] and Ferenc Hudecz*[,‡,⊥]

Chemical Research Center, Institute of Biomolecular Chemistry, Hungarian Academy of Sciences, Budapest, Hungary, Research Group of Peptide Chemistry, Hungarian Academy of Sciences, Eötvös L. University, Budapest 112, P.O. Box 32, H-1518, Hungary, Department of General Zoology and Department of Organic Chemistry, Eötvös L. University, Budapest, Hungary, and Department of Experimental and Health Sciences, Universitat Pompeu Fabra, Barcelona, Spain. Received December 17, 2007; Revised Manuscript Received May 25, 2008

Two conjugates with epitope peptide ^{278}LLEDPVGTVA^{287} derived from glycoprotein D (gD-1) of Herpes simplex virus (HSV) were synthesized for analysis of the effect of conjugation on protection against enzymatic degradation. In this design, the turn-forming epitope core ^{281}DPVG^{284} was positioned in the central part of the peptide and elongated by three amino acids from the native sequence at both termini. Conjugation was achieved by the introduction of amide bond or thioether linkage between the C-terminal of the HSV peptide and the side chain of four lysine residues of the oligotuftsin derivative used as carrier molecule. We compared the proteolytic stability of the conjugates in diluted human sera as well as in rat liver lysosomal preparation. The data obtained in lysosomal preparation at two pH values (pH 3.5 and 5.0) show that the type of covalent bond between the carrier and the epitope peptide had no significant effect, as compared to the stability of the free, unconjugated peptide. Based on the identification of degradation fragments by mass spectrometry we found marked differences in the lengths and amounts of oligopeptides obtained. In contrast, in 10% and 50% human serum the conjugation provided full protection against enzymatic hydrolysis over 96 h, while the free peptide was decomposed quickly.

INTRODUCTION

One of the major limitations in the use of peptides as effective subunit vaccines is their instability in biological matrices, which is mainly due to the rapid degradation by proteases. To protect biologically active peptides from enzymatic decomposition there are various possible approaches, e.g., alteration of the peptide bond (*1*), cyclization (*2*), conjugation to carrier molecules (*3*), and incorporation of nonproteinogenic amino acids such as β-Ala (*4*) or D-amino acids (*5–7*). Conjugation could have several favorable effects on peptides: it can enhance the solubility, improve cellular uptake (*8*), provide prolonged blood circulation, alter biodistribution, and also in some cases it can diminish toxicity. Different strategies can be utilized for conjugation: the biologically active compound can be attached directly to the carrier molecule, or it is possible to use a spacer structure in between. This method is applied when the cargo has to be released on the effect of pH (for example by using a spacer sensitive to pH (*9*)) or enzymatic cleavage (e.g., by using a spacer sensitive to enzymes) and the biologically active compound can exercise its effect in the targeted compartment. When conjugated directly to a carrier molecule, different bonds could be considered: for example, amide bond formation between the amino group of the N-terminus of the cargo peptide and a side-chain carboxyl group (Glu/Asp) of the partner molecule, or between the carboxyl group of the C-terminus of the peptide and a side-chain amino group (Lys) of the carrier. A thioether link could be formed between the SH- side chain of the N- or C-terminal cystein residue of the cargo peptide and the chloroacetylated amino group of a side-chain of the carrier molecule (*10*); a disulfide bridge could be established between Cys residues present in both parties (*11*).

Literature studies mainly report on the drug release from conjugates on enzymatic effect; the enzymatic degradation of conjugates is not discussed as we know. Searle et al. studied the release of ellipticine derivative (6-(3-aminopropyl)-ellipticine) conjugated to *N*-(2-hydroxyprolyl)methacrylamide copolymer through GFLG and GG linker peptides in tritosomes (rat liver lysosomal enzymes) (*12*). Subr et al. used rat liver lysosomal preparation and cathepsin B to study the effect of Gly-Gly, Gly-Leu-Gly, and Gly-DL-Phe-Leu-Gly spacers on the release of methotrexate conjugated to hexamethylenediamine (*13*). Release of daunorubicin conjugated to succinylated serum albumin via one to four amino acids (L, AL, LAL, or ALAL) was studied in lysosomal preparation and in 95% calf serum (*14*).

Herpes simplex virus (HSV), with two closely related serotypes, HSV-1 and HSV-2, is one of the most common infectious agents in humans. Glycoprotein D (gD) of HSV type 1 or 2 is a major envelope protein, and appears to be the major target for the immune response. It has been shown that peptides from the N-terminal region of HSV-1 gD (gD-1) can induce both B and T cell responses (*14*), and the resulting antibodies are proven able to neutralize HSV-1 *in vitro* (*15–18*). Another epitope of gD-1 has been identified by monoclonal antibodies and located in the 268−287 region (*19, 20*). It was shown that the minimal epitope of this region in the HSV gD-1 was the

* Corresponding author. Professor Ferenc Hudecz, Research Group of Peptide Chemistry, Hungarian Academy of Sciences, Eötvös L. University, Budapest 112, P.O. Box 32, H-1518 Hungary. Phone: 00-36-1-209-0555/6428, E-mail: fhudecz@elte.hu.

[†] Institute of Biomolecular Chemistry, Hungarian Academy of Sciences.

[‡] Research Group of Peptide Chemistry, Hungarian Academy of Sciences.

[§] Department of General Zoology, Eötvös L. University.

[||] Department of Organic Chemistry, Eötvös L. University.

[⊥] Universitat Pompeu Fabra.

10.1021/bc700469r CCC: $40.75 © 2008 American Chemical Society
Published on Web 07/24/2008

Scheme 1. Outline of the Synthesis of Amide Bond Containing Conjugate of LLEDPVGTVA of gD-1 of HSV

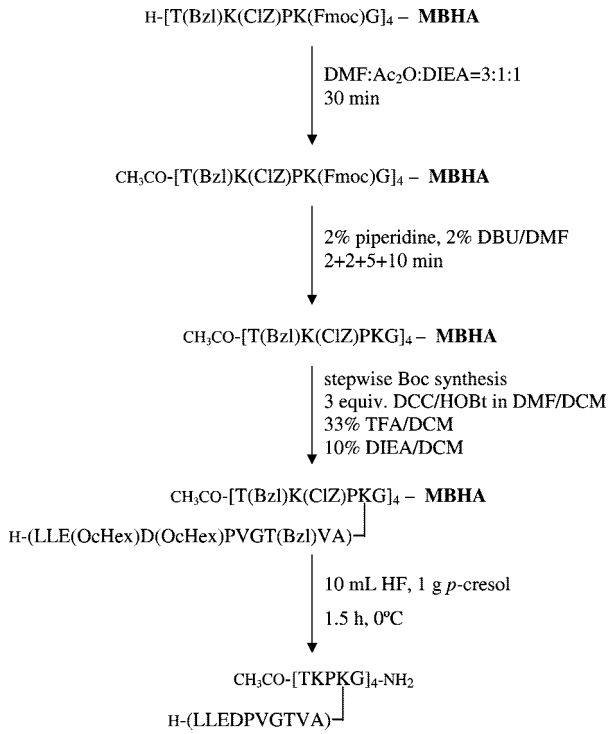

^{281}DPVG^{284} sequence (*21*) representing a turn structure that is important in the immunological recognition, as has been proven in the case of another sequence of the same protein (*22*).

The aim of this study was the analysis of the effect of conjugation on the enzymatic degradation of carrier attached epitope peptide. Therefore, conjugates containing oligotuftsin derivative as carrier and epitope peptide 278−287 with ^{281}DPVG^{284} in the central position were synthesized with amide bond or thioether link. Amide bond formation was achieved between the carboxyl group of the C-terminus of the oligopeptide and the ε-amino group of the side chain of the lysine residues in the carrier molecule (Scheme 1). For introduction of the thioether linkage, first we have elongated the peptide epitope by a C-terminally added cysteine residue. The carrier part of the conjugate was chloroacetylated and used for coupling (Scheme 2). Here we report on our findings on the enzymatic stability of the conjugated epitope peptide in complex biological fluids. The enzymatic hydrolysis of the constructs was investigated in diluted human sera (10% and 50%) and also in rat liver lysosomal preparation at two pH values (pH 3.5 and pH 5). Our data indicate that conjugates show high resistance against proteolytic degradation in diluted human sera but these compounds are degraded in lysosomal preparation.

EXPERIMENTAL PROCEDURES

Materials. Amino acid derivatives were purchased from NovaBiochem (Läufelfingen, Switzerland) and Reanal (Budapest, Hungary). 4-Methyl-benzhydrylamine (MBHA) resin was from NovaBiochem. All chemicals for coupling and cleavage (hydrogen fluoride (HF), thioanisole, *m*-cresol, *p*-cresol, *p*-thiocresol, *N,N′*-dicyclohexylcarbodiimide (DCC), 1,8-diazabicyclo[5.4.0]undec-7-ene (DBU), 1-hydroxybenzotriazole (HOBt), trifluoracetic acid (TFA), *N*-ethyldiisopropylamine (DIEA)) were obtained from Fluka (Buchs, Switzerland). All solvents for the synthesis and purification as well as $Na_2HPO_4 \cdot 2H_2O$, KH_2PO_4, Na-acetate$\cdot 3H_2O$, and acetic acid were from Reanal.

Scheme 2. Outline of the Synthesis of Thioether Bond Containing Conjugate of LLEDPVGTVA of gD-1 of HSV

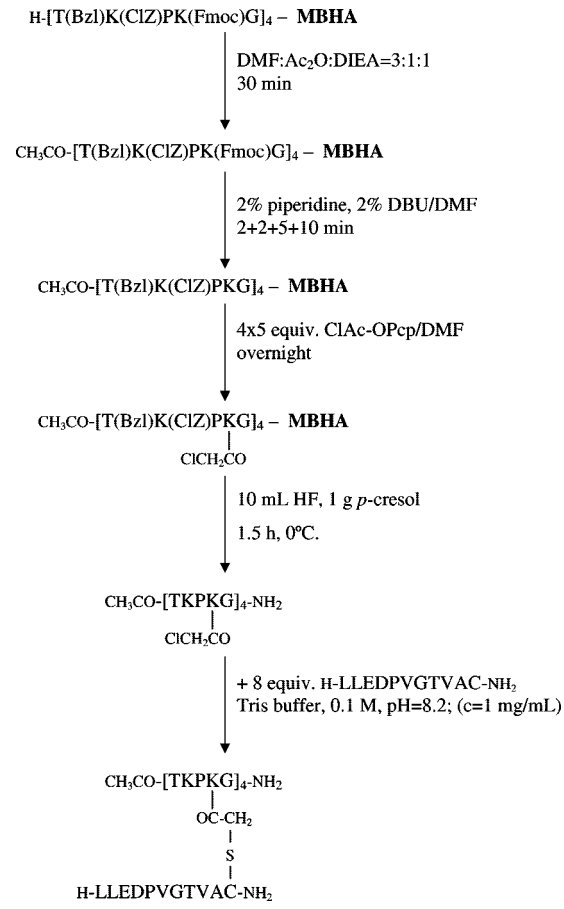

Synthesis of Conjugate with Amide Bond. Amide bond containing conjugate was prepared by solid phase methodology using 0.5 g 4-methyl-benzhydrylamine resin (1.04 mmol/g). The following side-chain protected amino acid derivatives were used: Boc-Thr(Bzl)-OH, Boc-Asp(OcHex)-OH, Boc-Glu(OcHex)-OH, Boc-Lys(Fmoc)-OH, and Boc-Lys(ClZ)-OH. Coupling was carried out by using DCC/HOBt *in situ* active ester method in 4:1 (v/v) DCM/DMF mixture. 3 equiv of amino acid derivatives and coupling reagents were used. N^{α}-Boc group was removed with 33% TFA in DCM. For neutralization 10% DIEA in DCM was applied. The success of the coupling was monitored by ninhydrine reaction (*23*) or isatine assay (*24*). The following protocol was applied: DCM washing (3 × 0.5 min); deprotection with 33% TFA/DCM (2 × 20 min); DCM washing (5 × 0.5 min); neutralization with 10% DIEA/DCM (4 × 0.5 min); DCM washing (4 × 0.5 min); coupling (60 min); DMF washing (2 × 0.5 min); DCM washing (2 × 0.5 min); ninhydrine or isatine reaction. After removal of the N^{α}-Boc group, the side-chain protected tetratuftsin derivative ([T(Bzl)K(ClZ)PK(Fmoc)G]$_4$) was acetylated at the N-terminus using a mixture of acetic anhydride and DIEA in DMF 1:1:3 (v/v/v) for 30 min. Then the Fmoc groups were removed with 2% piperidine, 2% DBU in DMF four times for 2 + 2 + 5 + 10 min. The sequence of LLEDPVGTVA decapeptide was built up stepwise on the ε-amino group of the Lys residues using suitable protected amino acids by Boc strategy. The conjugate was cleaved from the resin by the aid of anhydrous HF-*p*-cresol (10 mL/1 g) at 0 °C for 1.5 h, precipitated with dry diethyl ether, filtered, and washed several times with diethyl ether. The conjugate was dissolved in 10% acetic acid and freeze-dried.

Synthesis of Conjugate with Thioether Bond. The oligotuftsin derivative as well as peptide H-LLEDPVGTVAC-NH_2

was prepared by solid phase methodology using Boc strategy on 0.5 g 4-methyl-benzhydrylamine resin (1.04 mmol/g). The following side-chain protected amino acid derivatives were used: Boc-Cys(Mbzl)-OH, Boc-Thr(Bzl)-OH, Boc-Asp(OcHex)-OH, Boc-Glu(OcHex)-OH, Boc-Lys(Fmoc)-OH, Boc-Lys(ClZ)-OH. Synthesis was performed as described above. After the removal of the Fmoc group from the ε-amino group of the Lys residues tetratuftsin derivative was chloroacetylated at the side chain of the Lys residues. The chloroacetyl group was introduced by using chloroacetic acid pentachlorophenyl ester in 4 × 5 equiv excess (5 equiv per lysine residue) in DMF overnight at room temperature (*9*). The chloroacetylated peptide was cleaved from the resin by the aid of anhydrous HF in the presence of *m*-cresol-*p*-thiocresol (10 mL/0.5 mL/0.5 g) at 0 °C for 1.5 h (*25*).

RP-HPLC-purified chloroacetylated tuftsin oligopeptide derivative was dissolved in Tris buffer (0.1 M, pH = 8.2) at c = 1 mg/mL. Peptide H-LLEDPVGTVAC-NH_2 was added to this solution in 8 equiv excess little by little. Reaction was followed by RP-HPLC (Supelcosil C_{18} 5 μm; 4.6 mm × 250 mm column) using gradient elution. After sample application an isocratic elution with 20% eluent B was applied for 2 min, then a linear gradient from 20% to 45% eluent B was generated over 25 min at room temperature with a flow rate of 1 mL/min (eluent A, 0.1% TFA in water; eluent B, 0.1% TFA in acetonitrile−water (80:20, v/v %)). UV detection was performed at λ = 214 nm. Reaction was considered complete when no change in the position and intensity of peaks on the chromatogram was observed.

Purification by RP-HPLC. The crude products (peptides and conjugates) were purified by RP-HPLC on a Phenomenex Jupiter C_{18} column (10 μm; 300 Å, 10 mm × 250 mm), using gradient elution, where eluent A was 0.1% TFA in water, while eluent B was 0.1% TFA in acetonitrile−water (80:20, v/v %). After sample application an isocratic elution with 15% eluent B was applied for 2 min, then a linear gradient from 15% to 40% eluent B was generated over 25 min at room temperature with a flow rate of 4 mL/min. UV detection was performed at λ = 214 nm.

RP-HPLC Analysis. The homogeneity of peptides and conjugates was analyzed by RP-HPLC on a Symmetry C_{18} 3.5 μm, 4.6 mm × 150 mm column (for peptides) or on a Supelcosil C_{18} 5 μm, 4.6 mm × 250 mm column (for conjugates). After sample application an isocratic elution with 20% eluent B was applied for 2 min, then a linear gradient from 20% to 45% eluent B was generated over 25 min at room temperature with a flow rate of 1 mL/min: eluent A, 0.1% TFA in water; eluent B, 0.1% TFA in acetonitrile−water (80:20, v/v%). UV detection was performed at λ = 214 nm.

Amino Acid Analysis. The amino acid composition of compounds was determined by amino acid analysis using a Beckman model 6300 analyzer (Fullerton, CA). Prior to analysis, samples were hydrolyzed in 6 M HCl in sealed and evacuated tubes at 110 °C for 24 h.

Mass Spectrometry. Mass spectrometric experiments were performed on a Bruker Daltonics Esquire 3000plus (Germany) ion trap mass spectrometer, equipped with electrospray ionization source. Spectra were aquired in positive ionization mode, in the 50−2000 *m/z* region. Samples were dissolved in acetonitrile/water = 1:1 (v/v) mixture, containing 0.1% acetic acid. Samples were introduced into the mass spectrometer using a syringe pump, at a flow rate of 10 μL/min.

Enzymatic Digestion. *Lysosome Preparation.* For a detailed description of the lysosome preparation see Tugyi et al. (*7*). Briefly, rat livers were homogenized in 0.3 M sucrose, diluted with 0.3 M sucrose, and centrifuged. The supernatant was centrifuged again, and rehomogenized in sucrose containing 1 mM $CaCl_2$. After incubation at 37 °C for 5 min, 50% Percoll solution was added and homogenate was centrifuged again. The lysosomal fraction was obtained as a hard brown pellet. The enzymatic activity of the preparation was determined according to Dingle (*26*).

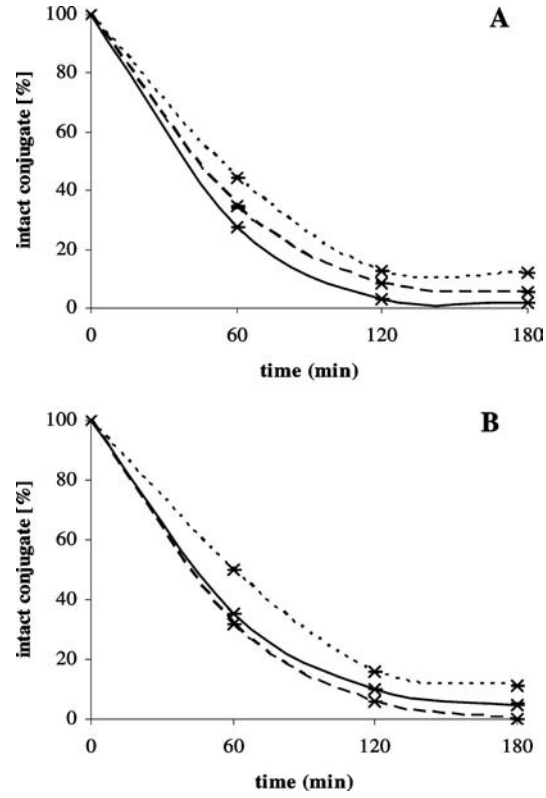

Figure 1. Degradation profile of the free peptide (H-LLEDPVGTVA-NH_2) (−x−), and its conjugates with amide (− −x− −) or thioether bond (---x---) in lysosomal preparation at pH = 3.5 (A) and at pH = 5.0 (B).

Digestion of Peptides and Conjugates in Lysosome Homogenates. Control peptide was dissolved at c = 2.5 mg/mL in 0.1 M acetate buffer, pH = 3.5 or pH = 5.0, while conjugate concentration was c = 3.76 mg/mL and c = 3.82 mg/mL for thioether and for amide conjugate, respectively. Afterward, the lysosome fraction was added ($c_{lysosomal}$ = 22 μL/mL), and peptide or conjugate samples were incubated at room temperature for 180 min. Aliquots of 100 μL were taken at 30 s and 60, 120, and 180 min. The enzymatic reaction was stopped by the addition of 5 v/v% perchloric acid. Samples were centrifuged at 4600 rpm for 5 min at 4 °C and the concentration of the intact peptide in the supernatant was determined by RP-HPLC (Supelcosil C_{18} 5 μm; 4.6 mm × 250 mm column), using calibration curves. For RP-HPLC analysis eluent A (0.1% TFA in water) and eluent B (0.1% TFA in acetonitrile−water (80:20, v/v)) were applied. A gradient 20−45% eluent B in 25 min was generated. Each sample was injected twice, and each digestion experiment was performed twice. Standard deviation of the twice-injected samples was negligible, while standard deviation for the independent studies was calculated and provided in Figure 1 and Table 2.

Digestion of Peptides and Conjugates in Human Serum. Human serum was obtained from National Institute of Haematology and Immunology (Budapest, Hungary). Control peptide was dissolved in 0.1 M phosphate buffer (pH = 7.2) containing 0%, 10%, or 50% human serum, at c = 2.5 mg/mL, while conjugate concentration was c = 3.76 mg/mL for compound with thioether linkage, and 3.82 mg/mL for the construct with amide bond. Conjugates were incubated at 37 °C up to 96 h. Samples (100 μL for 0% and 10% human sera and 140 μL for 50% human sera) were taken after 0, 24, 48, 72, and 96 h. All

Table 1. Characteristics of Conjugates and Peptide LLEDPVGTVA

	amino acid composition found (calculated)										R_t(min)[b]	[M+H]$^{+}$[c]	
peptide/conjugate	cmc[a]	Asp	Thr	Glu	Pro	Gly	Ala	Val	Leu	Lys		measured	calculated
H-LLEDPVGTVA-NH_2	-	0.9(1)	0.9(1)	1.1(1)	1.0(1)	1.2(1)	1.0(1)	1.8(2)	2.2(2)	-	16.5(*1*)	1013.2	1013.2
[TKPK(LLEDPVGTVA)G]$_4$	-	3.6(4)	7.6(8)	4.4(4)	8.0(8)	7.6(8)	4.0(4)	8.0(8)	7.6(8)	8.4(8)	24.9[2]	6084.4	6084.2
[TKPK(LLEDPVGTVAC)G]$_4$	2.8(4)	3.2(4)	3.6(4)	4.0(4)	7.6(8)	8.0(8)	4.0(4)	8.8(8)	8.4(8)	8.0(8)	24.7[2]	6724.4	6725.3

[a] cmc: measured as *S*-carboxymethyl cysteine. [b] HPLC retention time, gradient 0−2 min 15% eluent B, 2−22 min 40% eluent B (1), 0−2 min 20% eluent B, 2−27 min 45% eluent B (2), where eluent A is 0.1% TFA/water, eluent B is 0.1% TFA/acetonitrile−water 80:20 (v/v). See further details in Experimental Procedures. [c] ESI-MS measurements.

Table 2. Effect of Conjugation on the Stability of Epitope Peptide LLEDPVGTVA in Lysosomal Preparation at pH = 3.5 and pH = 5.0

	intact compound [%][a] after digestion with lysosomal preparation							
	pH = 3.5				pH = 5.0			
peptide/conjugate	0.5 min	60 min	120 min	180 min	0.5 min	60 min	120 min	180 min
H-LLEDPVGTVA-NH_2	100	28 ± 4	3 ± 4	2 ± 2	100	35 ± 2	10 ± 6	5 ± 3
[TKPK(LLEDPVGTVA)G]$_4$	100	44 ± 0,5	13 ± 0	12 ± 1	100	50 ± 0,5	16 ± 2	11 ± 3
[TKPK(LLEDPVGTVAC)G]$_4$	100	34 ± 5	9 ± 2	5 ± 1	100	31 ± 1	6 ± 0	0 ± 0

[a] Compound [%] = c_{intact}/c_{total}. The concentration of intact compound was calculated from the AUC (area under the curve) of the corresponding peak obtained after HPLC analysis as described in Experimental Procedures.

digestion experiments were performed under sterile conditions. Further treatment of the samples was identical to that described for the lysosomal digestion above.

Isolation and Identification of Degradation Fragments. Samples of the digests were analyzed by RP-HPLC using analytical column (Supelcosil C_{18} 5 μm; 4.6 mm × 250 mm column). For the RP-HPLC analysis eluent A (0.1% TFA in water) and eluent B (0.1% TFA in acetonitrile−water (80:20, v/v)) were applied. A gradient 20−45% eluent B in 25 min was generated. Fragments were collected in Eppendorf tubes and freeze-dried. Molecular mass of the fragments was detemined by mass spectrometry (see above).

RESULTS AND DISCUSSION

In order to study the effect of covalent coupling of epitope peptide on the enzymatic degradation, conjugates with an oligopeptide derived from the glycoprotein D of Herpes simplex virus were prepared. As carrier a tetratuftsin derivative composed of four tuftsin-like units, TKPKG, was used. Human tuftsin is a tetrapeptide (TKPR) present in the Fc receptor of the IgG molecule (*27*). TKPK is the canine tuftsin sequence (*28*) and the presence of the second Lys offers a new possibility to conjugate even two different entities. Both human and canine tuftsins exhibit immunostimulatory effect (*29*).

In conjugates prepared for the present study amide or thioether linkage was established between the carrier and the cargo epitope. In both cases oligopeptide ^{278}LLEDPVGTVA^{287} was attached to the tetratuftsin derivative through the C-terminal amino acid residue (Scheme 1). When a thioether bond was formed peptide 278−287 was elongated with a Cys at the C-terminal and its SH group was utilized in the conjugation (Scheme 2). The stability of conjugates with thioether link or amide bond was studied in two complex biological matrices possessing enzymatic activity. For the investigation of stability in serum we used two concentrations of the human serum (10% and 50%) under aseptic conditions. The conjugates and the free epitope peptide 278−287 were also incubated with lysosomal preparation at two different pH values (pH = 3.5 and 5.0). In experiments performed we determined the amount of intact compound. Based on the comparative analysis of these data we have documented the capability of conjugates to resist against enzymatic degradation.

Synthesis of Conjugates. The ^{278}LLEDPVGTVA^{287} region of HSV gD-1 contains the ^{281}DPVG^{284} epitope core (*21*) adopting turn structure under appropriate conditions (*30*). For our studies we have elongated the tetramer core by three amino acids from the native sequence at both termini. The amide bond containing conjugate was prepared on MBHA resin by tandem solid phase peptide synthesis. After the cleavage of all four Fmoc protecting groups from Lys residues in the carrier molecule Ac-[T(Bzl)K(ClZ)PKG]$_4$-R, the synthesis was continued using the liberated ε-amino groups of the semiprotected carrier. Thus, four copies of the decapeptide ^{278}LLEDPVGTVA^{287} were assembled as branches using the Boc strategy (Scheme 1).

For the preparation of conjugate with thioether bond, first the epitope peptide with C-terminal Cys (LLEDPVGTVAC) and the semiprotected tetratuftsin derivative carrier Ac-[T(Bzl)K(ClZ)PKG]$_4$-R was synthesized also by solid phase synthesis on MBHA resin. In this case the free side chain of four Lys residues of the carrier molecule was chloroacetylated using chloroacetic acid pentachlorophenyl ester (*11*). Finally, the chloroacetylated carrier Ac-[T(Bzl)K(ClZ)PK(ClCH$_2$CO)G]$_4$-NH_2 as well as the Cys-containing peptide, H-LLEDPVGTVAC-NH_2, were cleaved from the resin by HF. After RP-HPLC purification the oligopeptide was conjugated with the purified carrier molecule under slightly alkaline condition (0.1 M Tris buffer, pH = 8.2). Tetratuftsin derivative was dissolved at c = 1 mg/mL, then peptide H-LLEDPVGTVAC-NH_2 was added in 8 equiv excess in small portions to avoid the risk of dimerization (Scheme 2). The conjugation reaction was followed by RP-HPLC analysis. Conjugates and the free peptide used for the enzymatic studies were characterized by amino acid composition, by relative molar mass determined by ESI-MS, and by RP-HPLC retention time values (Table 1).

Enzymatic Stability of Conjugates. For *in vitro* enzymatic stability studies of peptides authors have utilized in the literature mainly isolated enzymes like carboxypeptidase A, aminopeptidase M, proteinase A, carboxypeptidase Y (*31*), α-chymotrypsin, or carboxypeptidase Y (*32*), or complex biological fluids, like human serum and urine (*33*), human plasma (*34*), or rat liver lysosomes (*35*). It is interesting to note that only a limited number of studies on peptide conjugates has been reported so far and only the liberation of the free drug has been investigated.

We have studied the enzymatic stability of two conjugates with different linkages as well as the corresponding oligopeptide, H-LLEDPVGTVA-NH_2, as control, in diluted human sera and in rat liver lysosomal preparation. We have isolated and identified the degradation products and propose a hypothesis on the involvement of potential enzymes. The data are summarized in Tables 2 and 3. The degradation profiles of all three compounds in lysosomal preparation at pH 3.5 and pH 5.0 (Figure 1A,B) are also shown.

Table 3. Effect of Conjugation on the Stability of Epitope Peptide LLEDPVGTVA in Diluted Human Serum

	intact compound [%][a] after digestion with human serum									
	10%					50%				
peptide/conjugate	0 h	24 h	48 h	72 h	96 h	0 h	24 h	48 h	72 h	96 h
H-LLEDPVGTVA-NH2	100	0	-	-	-	100	0	-	-	-
$[TKPK(LLEDPVGTVA)G]_4$	100	100	100	100	100	100	100	100	100	100
$[TKPK(LLEDPVGTVAC)G]_4$	100	100	100	100	100	100	100	100	100	100

[a] Compound [%] = c_{intact}/c_{total}. The concentration of intact compound was calculated from the AUC (area under the curve) of the corresponding peak obtained after HPLC analysis as described in Experimental Procedures.

First we have analyzed the stability of the two conjugates and compared with that of the free linear peptide, H-LLEDPVGTVA-NH_2 in rat lysosomal preparation, containing various proteolytic enzymes. Considering the lack of consensus in the literature about the pH within the lysosome we have selected two pH values (pH 3.5 and pH 5.0) to perform the assay. Harada et al. reported on a value of pH 4 (*36*); Bach et al. observed that the pH in lysosomes varies between 4.3 and 4.5 (*37*). Other groups found a different level of acidity between pH 4.5 and pH 5.0 (pH 4.5 (*38*, *39*), 4.67 (*40*), 4.75 (*41*), 5.0 (*42*)). It is also known that the optimal pH for the main lysosomal enzyme, Cathepsin D, is pH 3.5 (*43*).

Data obtained are summarized in Table 2 and Figure 1. We observed that both conjugates degraded in lysosomal preparation with a fairly similar degradation profile, in a nearly identical way to that the free peptide. However, it is interesting to note that the rate of the enzymatic hydrolysis was slightly dependent on the type of linkage present in conjugates: 88% and 89% of the amide bond containing conjugate degraded at pH = 3.5 and 5.0, respectively, while 95% and 100% of the thioether containing conjugate disappeared at pH = 3.5 and 5.0, respectively.

In the next series of experiments we have studied the enzymatic degradation of the compounds in 10% and in 50% human sera. Data, summarized in Table 3, showed no degradation when peptide was conjugated to oligotuftsin derivative as carrier under the conditions applied. However, the control linear peptide degraded along the amide bonds in 24 h even in 10% human serum.

Identification of Fragments in Lysosomal Preparation. In order to gain insight into the degradation process, fragments present in the reaction mixture were identified by mass spectrometry. We found that the fragmentation of the two conjugates differ from each other and also from that of the free peptide.

The main fragment of peptide H-LLEDPVGTVA-NH_2 is H-DPVGTVA-NH_2, but we have also detected the presence of smaller fragments like H-LLE-OH, H-DPVG-OH, and H-EDPVG-OH. The change of the pH from 3.5 to 5.0 has no significant effect on the number and composition of fragments formed.

Similarly, the pH has essentially no effect on the fragmentation profile of the amide bond containing conjugate. The quantity, number, and composition of the fragments are almost identical at the pH values used. The predominant fragment appearing at the highest quantity is a truncated conjugate missing one N-terminal LLE tripeptide unit (M: 5729.8) (Figure 2A). In marked quantity we found conjugates without (a) two LLE trimer (M: 5374.4), (b) one LLE and one LLEDPVG units (M: 5006.0), or (c) three LLE tripeptides (M: 5018.7). Accordingly we have isolated the tripeptide H-LLE-OH (M: 373.9) from the digests (Figure 2A).

In the case of the thioether conjugate the degradation was faster and the number of fragments formed was higher. In addition we observed pH-dependent fragmentation. The degradation rates of the different fragments were also pH-dependent. At pH = 3.5 the quantity of most of the fragments present after

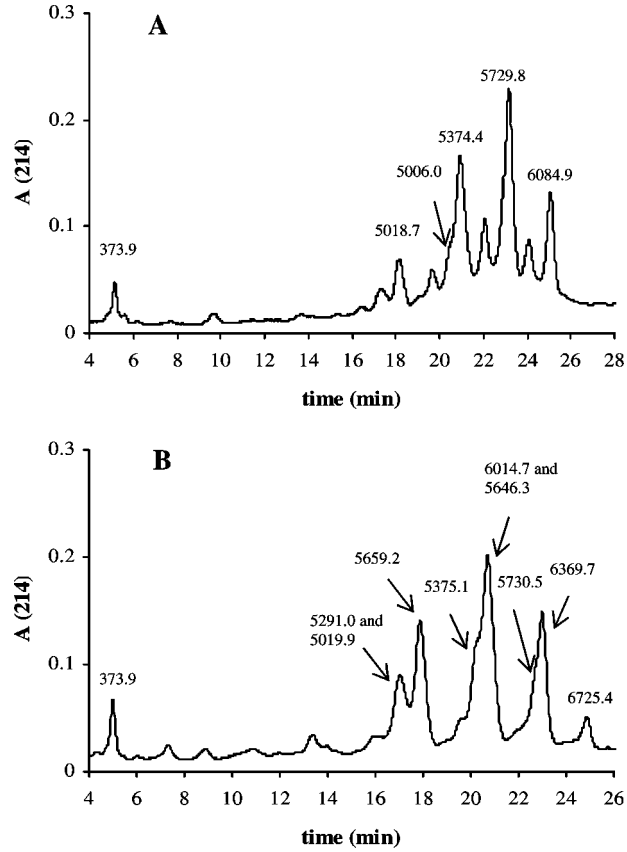

Figure 2. RP-HPLC chromatogram of digest obtained after treatment with lysosomal preparation of conjugate with amide bond at pH = 5.0 after 120 min (A); and conjugate with thioether linkage at pH = 3.5 after 120 min (B). Molecular masses of fragments identified are shown on the peaks.

60 min was increased after 120 and 180 min (Figure 3A). In contrast at pH = 5.0 the amount of the majority of the fragments present at 60 min was decreased until the end of the period studied (Figure 3B). However, the predominant fragments were found to be identical at both pH values. These are the following (see also Figure 3B): conjugate missing one, two, or three LLE tripeptides (M: 6369.7, 6014.7, and 5659.2, respectively) or one LLE tripeptide plus one LLEDPVG unit (M: 5646.3) or two LLE plus one LLEDPVG unit (M: 5019.9). The H-LLE-OH tripeptide (M: 373.9) is detectable at both pH as well as in the case of the amide bond containing conjugate. At pH = 5.0 fragments missing a full LLEDPVGTVA sequence (one LLEDPVGTVA, M: 5730.5; one LLEDPVGTVA and one LLE, M: 5375.1; one LLEDPVGTVA and two LLE, M: 5019.9) were also detectable in minor quantity. Interestingly at this pH the fragment H-LLEDPVGTVA-OH was also detectable (data not shown). The cleavage of the bond between the E and D amino acids observed in all three cases (the two conjugates and free peptide) is probably due to the presence of tripeptidyl peptidase

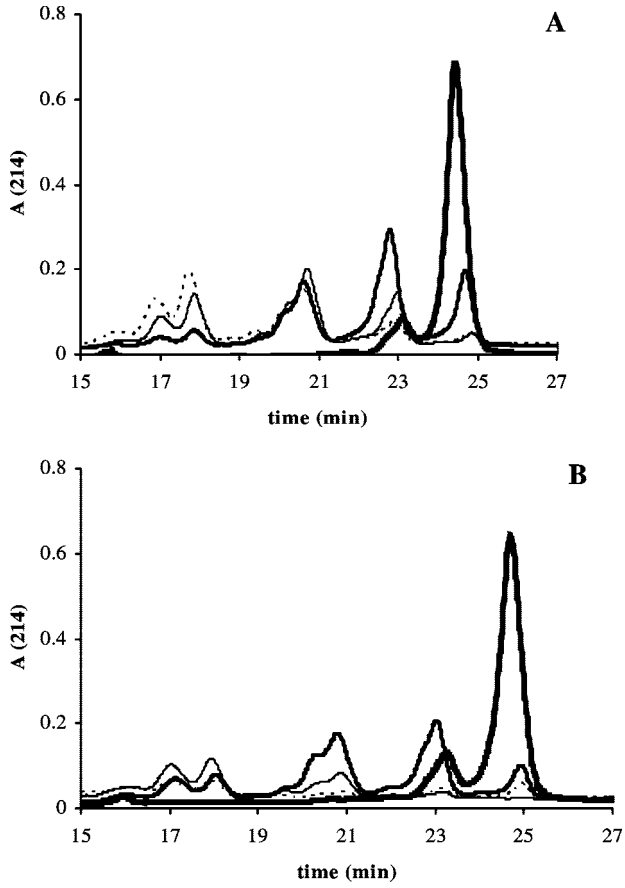

Figure 3. RP-HPLC chromatogram of digest obtained after treatment with lysosomal preparation of amide bond containing conjugate (A) and thioether linkage containing conjugate (B) after 0 (thick line), 60 (-), 120 (-), and 180 min (---).

I (*44*). The split of GT as well as AC bonds could be due presumably to the enzyme Cathepsin D (*45*).

CONCLUSION

In this study we reported on the synthesis and on proteolysis of two ^{278}LLEDPVGTVA^{287} conjugates with amide or thioether bond. We compared the stability of these conjugates in diluted human sera and in rat lysosomal preparation. The data obtained in human sera show that conjugation enhanced the stability of the epitope peptide as compared to its free form. It should be noted that the type of linkage between the peptide and the carrier part of the conjugate essentially did not influence the degradation pattern. These results also show that in diluted human sera the conjugation of an oligopeptide could provide full protection against enzymatic hydrolysis. Comparing the degradation of the two conjugates in lysosomal preparation, we found only modest differences. In the case of the conjugate with an amide bond the rate of the degradation was somewhat lower and the number of fragments were also limited as compared to the conjugate with a thioether bond. The fragment without an LLEDPVGTVA sequence appears only in the digest of the thioether conjugate. This difference could be explained by the fact that for the formation of this fragment in the case of the amide conjugate, the cleavage of the amide bond between the α-carboxyl group of Ala residue of the epitope and the ε-amino group of the Lys of the carrier molecule would be required. This cleavage probably is prevented by the fact that this is an isopeptide bond and perhaps also by steric restriction, while in the thioether conjugate the amide bond between the Ala and the Cys residue is a peptide bond and it could be more accessible because the Cys residue enhances the distance between the carrier and the peptide side chain. It is interesting to note that there is no detectable fragment from the carrier backbone of the conjugate. This observation could be explained by the conformation of the tetratuftsin derivative used as carrier (*46*), but it is more likely that the attachment of four copies of the epitope peptide to the side chains of the carrier limits the accessibility of backbone amid bonds for proteolytic enzymes.

Taken together, our results indicate that conjugation of the epitope peptide studied fully protected its degradation in diluted human sera as compared to the free linear epitope peptide, which decomposed quickly. This observation might be useful for the design of artificial immunogens. We have also demonstrated that the fragments derived from the thioether conjugate can possess the full-size epitope peptide in contrast to the amide conjugate from which only one fragment with the epitope core (DPVG) was produced. It is attractive to speculate that complete epitope peptide released from the thioether conjugate in the lysosome might be available for MHC for antigen presentation. Considering this finding, one can propose to design an amide conjugate in which a spacer unit could provide an appropriate distance between the epitope peptide and the carrier. Thus endopeptidases could have access to amide bonds and release the "full" epitope sequence.

ACKNOWLEDGMENT

These studies were supported by grants from COST Chemistry Action "Peptide based synthetic antigens against infectious diseases" (D13/0007/00), from the Hungarian-Spanish Intergovernmental Program (E-4/2003), from the Hungarian Research Fund (T-049814, K68285) and from the Ministry of Education (Medichem 2, 1/A/005/2004 NKFP). G. Schlosser acknowledges financial support by the Magyary Zoltán Higher Educational Public Fundation (Hungary).

LITERATURE CITED

(1) Meyer, J. P., Gillespie, T. J., Hom, S., Hruby, V. J., and Davis, T. P. (1995) In vitro stability of some reduced peptide bond pseudopeptide analogues of dynorphin A. *Peptides 16*, 1215–1219.

(2) Mezö, G., Hudecz, F. (2005) Synthesis of linear, branched, and cyclic peptide chimera. *Methods in Molecular Biology. Volume 298* (Howl, J., Ed), pp 63−75, Humana Press, Totowa, New Jersey.

(3) Hudecz, F. (2001) Manipulation of epitope function by modification of peptide structure: a minireview. *Biologicals 29*, 197–207.

(4) Steer, D., Lew, R., Perlmutter, P., Smith, A. I., and Aguilar, M. I. (2002) Inhibitors of metalloendopeptidase EC 3.4.24.15 and EC 3.4.24.16 stabilized against proteolysis by the incorporation of beta-amino acids. *Biochemistry 41*, 10819–26.

(5) Briand, J. P., Benkirane, N., Guichard, G., Newman, J. F., Van Regenmortel, M. H., Brown, F., and Muller, S. (1997) A retro-inverso peptide corresponding to the GH loop of foot-and-mouth disease virus elicits high levels of long-lasting protective neutralizing antibodies. *Proc. Natl. Acad. Sci. U.S.A. 94*, 12545–50.

(6) Hamamoto, K., Kida, Y., Zhang, Y., Shimizu, T., and Kuwano, K. (2002) Antimicrobial activity and stability to proteolysis of small linear cationic peptides with D-amino acid substitutions. *Microbiol. Immunol. 46*, 741–9.

(7) Tugyi, R., Uray, K., Ivan, D., Fellinger, E., Perkins, A., and Hudecz, F. (2005) Partial D-amino acid substitution: Improved enzymatic stability and preserved Ab recognition of a MUC2 epitope peptide. *Proc. Natl. Acad. Sci. U.S.A. 102*, 413–418.

(8) Hudecz, F., Bánóczi, Z., and Csík, G. (2005) Medium-sized peptides as built in carriers for biologically active compounds. *Med. Res. Rev. 25*, 679–736.

(9) Chytil, P., Etrych, T., Koňák, Č., Šírová, M., Mrkvan, T., Bouček, J., Řihová, B., and Ulbrich, K. (2008) New HPMA copolymer-based drug carriers with covalently bound hydrophobic substituents for solid tumour targeting. *J. Controlled Release 127*, 121–130.

(10) Mezö, G., de Oliveira, E., Krikorian, D., Feijlbrief, M., Jakab, A., Tsikaris, V., Sakarellos, C., Welling-Wester, S., Andreu, D., and Hudecz, F. (2003) Synthesis and comparison of antibody recognition of conjugates containing herpes simplex virus type 1 glycoprotein D epitope VII. *Bioconjugate Chem. 14*, 1260–1269.

(11) Mezö, G., Mihala, N., Andreu, D., and Hudecz, F. (2000) Conjugation of epitope peptides with SH group to branched chain polymeric polypeptides via Cys(Npys). *Bioconjugate Chem. 11*, 484–491.

(12) Searle, F., Gac-Breton, S., Keane, R., Dimitrijevic, S., Brocchini, S., Sausville, E. A., and Duncan, R. (2001) *N*-(2-Hydroxypropyl)methacrylamide copolymer-6-(3-Aminopropyl)-ellipticine conjugates. Synthesis, in vitro, and preliminary in vivo evaluation. *Bioconjugate Chem. 12*, 711–718.

(13) Subr, V., Strohalm, J., Hirano, T., and Ulbrich, K. (1997) Poly[*N*-(2-hydroxypropyl)methacrylamide] conjugates of methotrexate. Synthesis and in vitro drug release. *J. Controlled Release 49*, 123–132.

(14) Trouet, A., Masquelier, M., Baurain, R., and Deprez-De Campeneere, D. (1982) A covalent linkage between daunorubicin and proteins that is stable in serum and reversible by lysosomal hydrolases, as required for a lysosomotropic drug-carrier conjugate: *In vitro* and *in vivo* studies. *Proc. Natl. Acad. Sci. U.S.A. 79*, 626–629.

(15) Dietzschold, B., Eisenberg, R. J., Ponce de Leon, M., Golub, E., Hudecz, F., Varrichio, A., and Cohen, G. H. (1984) Fine structure analysis of type-specific and type-common antigenic sites of herpes simplex virus glycoprotein D. *J. Virol. 52*, 431–435.

(16) Eisenberg, R. J., Cerini, C. P., Heilman, C. J., Joseph, A. D., Dietzschold, B., Golub, E., Long, D., Ponce de Leon, M., and Cohen, G. H. (1985) Synthetic glycoprotein D-related peptides protect mice against herpes simplex virus challenge. *J. Virol. 53*, 634–644.

(17) Geerligs, H. J., Feijlbrief, M., Bos, C. A., Drijfhout, J. W., Welling, G. W., and Welling-Wester, S. (1990) Reactivity of human sera with overlapping synthetic peptides of herpes simplex virus type 1 glycoprotein D. *Arch. Virol. 114*, 251–258.

(18) Daurhof, R. A., Drijfhout, J. W., Scheffer, A. J., Wilterdrink, J. B., Welling, G. W., and Welling-Wester, S. (1993) T cell responses to synthetic peptides of herpes simplex virus type 1 glycoprotein D in naturally infected individuals. *Arch. Virol. 130*, 187–193.

(19) Hudecz, F., Hilbert, A., Mezö, G., Mucsi, I., Kajtár, J., Bösze, S., Kurucz, I., and Rajnavolgyi, É. (1993) Epitope mapping of the 273−284 region of HSV glycoprotein D by synthetic branched polypeptide carrier conjugates. *Pept. Res. 6*, 263–271.

(20) Isola, V. J., Eisenberg, R. J., Siebert, G. R., Heilman, C. J., Wilcox, W. C., and Cohen, G. H. (1989) Fine mapping of antigenic site II of herpes simplex virus glycoprotein D. *J. Virol. 63*, 2325–2334.

(21) Mezö, G., Dalmadi, B., Mucsi, I., Bö1sze, Sz., Rajnavölgyi, É., and Hudecz, F. (2002) Peptide based vaccine design: synthesis and immunological characterization of branched polypeptide conjugates comprising the 276−284 immunodominant epitope of HSV-1 Glycoprotein D. *J. Pept. Sci. 8*, 107–117.

(22) Krikorian, D., Stavrakoudis, A., Biris, N., Sakarellos, C., Andreu, D., de Oliveira, E., Mezö, G., Majer, Zs., Hudecz, F., Welling-Wester, S., Cung, M. T., and Tsikaris, V. (2006) Influence of sequential oligopeptide carriers on the bioactive structure of conjugated epitopes: Comparative study of the conformation of a Herpes simplex virus glycoprotein gD-1 epitope in the free and conjugated form, and protein "built-in" crystal structure. *Biopolymers 84*, 383–399.

(23) Kaiser, E., Colescott, R. L., Bossinger, C. D., and Cook, P. I. (1970) Color test for detection of free terminal amino groups in the solid-phase synthesis of peptides. *Anal. Biochem. 4*, 595–598.

(24) Kaiser, E., Bossinger, C. D., Colescott, R. L., and Olser, D. B. (1980) Color test for terminal prolyl residues in the solid-phase synthesis of peptides. *Anal. Biochem. 118*, 149–151.

(25) Ivanov, B. B., and Robey, A. F. (1996) Effective use of free thiols as scavengers for HF cocktails to deprotect bromo- and chloroacetyl synthetic peptides. *Pept. Res. 9*, 305–307.

(26) Dingle, J. T., Ed. *Lysosomes. A Laboratory Handbook*, (1972) pp 1−135, North-Holland, Amsterdam.

(27) Tzehoval, E., Segal, S., Stabinsky, Y., Fridkin, M., Spirer, Z., and Feldman, M. (1978) Tuftsin (an Ig-associated tetrapeptide) triggers immunogenic function of mactophages - implications for activation of programmed cells. *Proc. Natl. Acad. Sci. U.S.A. 75*, 3400–3404.

(28) Najjar, V., A. (1983) Tuftsin, a natural activator of phagocyte cells - an overview. *Ann. N.Y. Acad. Sci. 419*, 1–11.

(29) Fridkin, M., and Gottlieb, P. (1981) Tuftsin, Thr-Lys-Pro-Arg - anatomy of an immunologically active peptide. *Mol. Cell. Biochem. 41*, 73–97.

(30) Mezö, G., Majer, Zs., Vass, E., Jiminez, M. A., Andreu, D., and Hudecz, F. (2003) Conformational study of linear and cyclic peptides corresponding to the 276−284 epitope region of HSV gD-1. *Biophys. Chem. 103*, 51–65.

(31) Péter, A., Tóth, G., Tömböly, Cs., Laus, G., and Tourwe, D. (1999) Liquid chromatographic study of the enzymatic degradation of endomorphins, with identification by electrospray ionization mass spectrometry. *J. Chromatogr. A 846*, 39–48.

(32) Cardillo, G., Gentilucci, L., Qasem, A. R., Sgarzi, F., and Spampinato, S. (2002) Endomorphin-1 analogues containing beta-proline are mu-opioid receptor agonists and display enhanced enzymatic hydrolysis resistance. *J. Med. Chem. 45*, 2571–2578.

(33) Georgia, K. A., Samanidou, V. F., and Papadoyannis, I. N. (2001) Use of novel solid-phase extraction sorbent materials for high-performance liquid chromatography quantitation of caffeine metabolism products methylxanthines and methyluric acids in samples of biological origin. *J. Chromatogr. B 759*, 209–218.

(34) Terenius, L., Sandin, J., and Sakurada, T. (2000) Nociceptin/orphanin FQ metabolism and bioactive metabolites. *Peptides 21*, 919–922.

(35) Trouet, A., Masquelier, M., Baurain, R., and Deprez-De Campeneere, D. (1982) A covalent linkage between daunorubicin and proteins that is stable in serum and reversible by lysosomal hydrolases, as required for a lysosomotropic drug-carrier conjugate: in vitro and in vivo studies. *Proc. Natl. Acad. Sci. U.S.A. 79*, 626–629.

(36) Harada, M., Sakakibara, H., Yano, T., Suzuki, T., and Okuno, S. (2000) Determinants for the drug release from T-0128, camptothecin analogue-carboxymethyl dextran conjugate. *J. Controlled Release 69*, 399–412.

(37) Bach, G., Chen, C. S., and Pagano, R. E. (1999) Elevated lysosomal pH in Mucolipidosis type IV cells. *Clin. Chim. Acta 280*, 173–179.

(38) Yu, Z., Persson, H. L., Eaton, J. W., and Brunk, U. T. (2003) Intralysosomal iron: a major determinant of oxidant-induced cell death. *Free Radic. Biol. Med. 34*, 1243–1252.

(39) Zatta, P., Taylor, A., Zambenedetti, P., Milacic, R., and dell'Antone, P. (2000) Aluminum inhibits the lysosomal proton pump from rat liver. *Life Sci. 66*, 2261–2266.

(40) Myers, B. M., Tietz, P. S., Tarara, J. E., and LaRusso, N. F. (1995) Dynamic measurements of the acute and chronic effects

of lysosomotropic agents on hepatocyte lysosomal pH using flow cytometry. *Hepatology 22*, 1519–1526.

(41) Pshezhetsky, A. V., and Potier, M. (1993) Stoichiometry of the human lysosomal carboxypeptidase-beta-galactosidase complex. *Biochem. Biophys. Res. Commun. 195*, 354–362.

(42) King, H. D., Staab, A. J., Pham-Kaplita, K., Yurgaitis, D., Firestone, R. A., Lasch, S. J., and Trail, P. A. (2003) BR96 conjugates of highly potent anthracyclines. *Bioorg. Med. Chem. Lett. 13*, 2119–2122.

(43) Hurley, M. J., Larsen, L. B., Kelly, A. L., and McSweeney, P. L. H. (2000) Thermal inactivation kinetics of bovine cathepsin D. *Int. Dairy J. 10*, 673–681.

(44) Vines, D., and Warburton, M. J. (1998) Purification and characterisation of a tripeptidyl aminopeptidase I from rat spleen. *Biochim. Biophys. Acta 1384*, 233–242.

(45) Hughes, M. C., Healy, A., McSweeney, P. L. H., and O'Neill, E. E. (2000) Proteolytic specificity of cathepsin D on bovine F-Actin. *Meat Sci. 56*, 165–172.

(46) Mezö1, G., Kalászi, A., Reményi, J., Majer, Zs., Hilbert, Á., Láng, O., Köhidai, L., Barna, K., Gaál, D., and Hudecz, F. (2004) Synthesis, conformation, and immunoreactivity of new carrier molecules based on repeated tuftsin-like sequence. *Biopolymers 73*, 645–656.

BC700469R

Systematic Investigation of Polyamidoamine Dendrimers Surface-Modified with Poly(ethylene glycol) for Drug Delivery Applications: Synthesis, Characterization, and Evaluation of Cytotoxicity

Yoonkyung Kim,*,† Athena M. Klutz, and Kenneth A. Jacobson*

Molecular Recognition Section, Laboratory of Bioorganic Chemistry, National Institute of Diabetes and Digestive and Kidney Diseases, National Institutes of Health, Bethesda, Maryland 20892. Received January 2, 2008; Revised Manuscript Received May 21, 2008

Surface modification of amine-terminated polyamidoamine (PAMAM) dendrimers by poly(ethylene glycol) (PEG) groups generally enhances water-solubility and biocompatibility for drug delivery applications. In order to provide guidelines for designing appropriate dendritic scaffolds, a series of G3 PAMAM-PEG dendrimer conjugates was synthesized by varying the number of PEG attachments and chain length (shorter PEG_{550} and PEG_{750} and longer PEG_{2000}). Each conjugate was purified by size exclusion chromatography (SEC) and the molecular weight (MW) was determined by ^1H NMR integration and matrix-assisted laser desorption ionization time-of-flight mass spectrometry (MALDI-TOF MS). NOESY experiments performed in D_2O on selected structures suggested no penetration of PEG chains to the central PAMAM domain, regardless of chain length and degree of substitution. CHO cell cultures exposed to PAMAM-PEG derivatives (≤ 1 μM) showed a relatively high cell viability. Generally, increasing the degree of PEG substitution reduced cytotoxicity. Moreover, compared to G3 PAMAM dendrimers that were *N*-acetylated to varying degrees, a lower degree of surface substitution with PEG was needed for a similar cell viability. Interestingly, when longer PEG_{2000} was fully incorporated on the surface, cell viability was reduced at higher concentrations (32 μM), suggesting increased toxicity potentially by forming intermolecular aggregates. A similar observation was made for anionic carboxylate G5.5 PAMAM dendrimer at the same dendrimer concentration. Our findings suggest that a lower degree of peripheral substitution with shorter PEG chains may suffice for these PAMAM-PEG conjugates to serve as efficient universal scaffolds for drug delivery, particularly valuable in relation to targeting or other ligand−receptor interactions.

INTRODUCTION

Synthetic macromolecules are often employed as drug carriers to improve overall pharmacokinetic properties of monomeric drugs and to enhance their therapeutic effects (*1, 2*). For instance, one of the most successful tumor targeting approaches greatly benefits from therapeutics with macromolecules by implementing their ability to readily extravasate from the leaky tumor blood vessels and accumulate in the tumor interstitium through the enhanced permeability and retention (EPR) effect (*3*). As originally proposed by Ringsdorf and others, synthetic macromolecular carriers facilitate the incorporation of various functional units such as solubility enhancers, targeting units, and visualizing groups, in addition to the particular drug moieties of interest (*4*). Unfortunately, these carriers may suffer from an elevated toxicity and immunogenicity (i.e., low biocompatibility). Accordingly, additional modification of the structure might be necessary for a synthetic macromolecular drug delivery system to minimize undesirable properties for practical applications.

The dendrimer, one of the latest additions to the polymer family, has a globular shape and a relatively predictable size as represented by the hydrodynamic volume in a given solvent (*5–8*). Indeed, the virtue of using these (nearly) monodisperse dendrimers as drug carriers over the conventional polymeric agents relies heavily on their robust shape and controllable size and physical properties—to result in consistent biological effects—that can be attained by routine organic synthesis (*9–18*). Characteristics of dendritic structures, including toxicity, interactions with foreign objects (e.g., cells, opsonins), routes for cellular uptake, and intracellular fate will most likely be governed by the imparted surface groups (*19–21*). In contrast, such properties of conventional polymeric carriers may vary depending on their preferred folding pattern in a particular environment. Thus, a judicious choice of surface groups is crucial to optimize the pharmacological effects of a dendrimer-based drug delivery system.

Linear poly(ethylene glycol) (PEG) dissolves in water and most organic solvents and manifests crystalline properties in the solid state. Its strong but neutral hydrophilic nature without any significant toxic effect has found many applications in drug delivery as a structural modifier (*22–25*). In general, attachment of PEG (i.e., PEGylation) improves water solubility, reduces toxicity, decreases enzymatic degradation, and increases the in vivo half-lives of small-molecule drugs. A possible reduction in drug potency due to the sterics imparted by a long flexible PEG chain can be compensated by a reduced renal elimination rate.

Numerous reports described examples of attaching PEG to dendrimers through different types of *bond* formations to create hybrids of various *geometries*, among which the application for drug delivery has been most prevalent (*26*): (i) by forming either covalent (*27–33*) or electrostatic bonds (*34*) between a dendrimer and PEG groups; (ii) by attaching either linear PEG derivatives to the dendrimer periphery (i.e., unimolecular micelle) (*29, 32, 35*) or mono/multifunctional PEG derivatives to one or more core units of dendrons to form linear/branched-dendritic block

* To whom correspondence should be addressed. Y.K.: E-mail: kim_yoonkyung@yahoo.com, Phone: +82-2-958-5929, Fax: +82-2-958-5909. K.A.J.: E-mail: kajacobs@helix.nih.gov, Phone: +1-301-496-9024, Fax: +1-301-480-8422.

† Current address: Biomedical Research Center, Korea Institute of Science and Technology, 39-1 Hawolgok-dong, Seongbuk-gu, Seoul, 136-791, Korea.

10.1021/bc700483s This article not subject to U.S. Copyright. Published 2008 by the American Chemical Society
Published on Web 07/09/2008

copolymers (*27, 31, 33, 36–43*). Physical properties of these PEG-dendrimer conjugates were often dependent on the weight contribution of each block and the solvent used, occasionally exhibiting semicrystalline morphologies by phase-segregation (*37, 40, 42, 43*). Some examples involving self-assembly of amphiphilic PEG-dendritic block copolymers allowed the controlled release of electrostatically bound (*27, 44*) and/or hydrophobically encapsulated (*32, 45–47*) therapeutic agents. Intriguingly, a fully surface-PEGylated ($M_n = 2000$) dendrimer with a basic interior efficiently retained and slowly released hydrophobic anticancer drugs with acidic functionalities, in aqueous medium of a low ionic strength (*32*). Alternatively, when ligands are covalently attached (i.e., activation without chemical cleavage) to the termini of a dendrimer, the neighboring surficial PEG chains may impose a substantial steric barrier to impede the direct accessibility of ligands to their receptors. Therefore, strategies to covalently connect ligands to these dendrimer conjugates involved presenting them at the surface through peripheral PEG groups as long spacers (*28, 48, 49*) or degradable linkages (*50–53*). However, it is noteworthy that hydrophobic molecules were not well-encapsulated into a dendrimer when most of the periphery was derivatized by shorter PEG chains ($M_n = 550/750$), suggesting a relatively loose cavity (i.e., a low steric barrier) (*32, 54*).

Despite their known structural defects (*55*), poly(amidoamine) (PAMAM) dendrimers have been widely used for biomedical applications due to their commercial availability and relatively biocompatible nature (*56*). Each layer (i.e., generation) of PAMAM dendrimer is formed by a two-step procedure of double Michael addition with methyl acrylate followed by the chain extension with ethylenediamine, to present amide and tertiary amine functionalities in the interior. Of many PAMAM variations, the popularity of the amine-terminated PAMAM dendrimer, especially for oligonucleotide delivery (*27,30,33,57–62*), may arise from its unique cationic properties—a pH-dependent two-stage swelling behavior in aqueous solutions (*62, 63*). Under physiological conditions, the peripheral amino groups of PAMAM dendrimers are predominantly charged—the pK_a values of the terminal primary amine and the internal tertiary amine are 6.9 and 3.9, respectively. This is advantageous to form a charge complex with anionic drugs to allow entry into the cell mainly by endocytosis and their release under lysosomal pH conditions (*20, 21*). Unfortunately, these polycationic PAMAM dendrimers are toxic (*19, 29, 64–66*), and various strategies have been applied to conceal the terminal amino groups. Partial acetylation of the PAMAM surface, where a fraction of the toxic amino groups was left uncovered to achieve desired properties, affected water solubility and reduced the hydrodynamic volume (*67–69*). Partial conversion into lauroyl end groups increased membrane permeability and reduced cytotoxicity (*29,65*). However, this modification may increase hydrophobicity and promote aggregation in water through the attached aliphatic chains. Other examples, such as modifying into small alkyl alcohol groups, reduced the cytotoxicity and maintained water solubility (*70, 71*). Overall, PAMAM surface modification by relatively small functional groups required complex tuning of the stoichiometry for each appended functional moiety to achieve both the desired physicochemical and pharmacological properties. With the recent success of gene delivery across the blood–brain barrier (*72*), a PAMAM scaffold with peripheral PEG modifications may still be among the safest and most versatile dendritic drug carriers. Here, the synthesis, characterization, and evaluation of cytotoxicity of a series of third-generation (G3) PAMAM-PEG conjugates are explored in the context of drug delivery applications. PEG groups were attached to the surfaces of amine-terminated PAMAM dendrimers by varying their size (i.e., $M_n = 550$, 750, and 2000) and number of attachments. Each PAMAM-PEG conjugate was characterized by NMR and mass spectrometry. The cytotoxicity of each PAMAM-PEG dendrimer was evaluated in Chinese hamster ovary (CHO) cell cultures, which was compared with the cytotoxicity of acetylated G3 PAMAM structures and the commercial anionic PAMAM dendrimers of different generations.

Table 1. Structural Analysis of Acetylated PAMAM G3 Dendrimers by ^{1}H NMR and MALDI MS

	NMR		MALDI					
			DHB matrix			THAP matrix		
cmpd	no. of acetamide	MW[a]	M_n[b]	M_w[c]	PDI[d]	M_n[b]	M_w[c]	PDI[d]
1	0	6909	5772	5909	1.02	5956	6085	1.02
2	14	7497	7161	7313	1.02	6950	7125	1.03
3	20	7750	7219	7390	1.02	7036	7225	1.03
4	32	8254	7056	7256	1.03	7116	7351	1.03

[a] PAMAM dendrimer **1** used for calculation here was assumed to have 32 peripheral amino groups and no structural defects. [b] Number-average molar mass. [c] Weight-average molar mass. [d] Polydispersity index.

EXPERIMENTAL PROCEDURES

Materials and Methods. Glassware was oven-dried and cooled in a desiccator before use. All reactions were carried out under a dry nitrogen atmosphere. Solvents were purchased as anhydrous grade and used without further purification. Suppliers of the commercial compounds are listed as follows: amine-terminated G3 PAMAM dendrimer and carboxylate-terminated PAMAM dendrimers of G2.5, G3.5, and G5.5, all with the ethylenediamine as an initiator core (*8*), poly(ethylene glycol) methyl ether (M_n = 550, 750, and 2000), acetic anhydride (Ac_2O), 4-nitrophenyl chloroformate, triethylamine, *N*,*N*-diisopropylethylamine (DIEA), dimethyl sulfoxide (DMSO), methanol (MeOH), and chloroform ($CHCl_3$) were purchased from Aldrich; *N*,*N*-dimethylformamide (DMF) and tetrahydrofuran (THF) were purchased from Acros; DMSO-d_6, chloroform-*d* ($CDCl_3$), and D_2O were purchased from Cambridge Isotope Laboratories.

Preparative SEC was performed on Bio-Beads S-X1 beads (BIO-RAD, MW operating range 600−14 000 Da), 200−400 mesh, with DMF (Aldrich 99.8%, anhydrous) as an eluent at ambient pressure.

NMR spectra were recorded on either a Varian Inova 300 or a Bruker DRX-600 spectrometer at 25.0 °C under an optimized parameter setting for each sample, unless otherwise mentioned. ^{1}H NMR chemical shifts were measured relative to the residual solvent peak at 2.50 ppm in DMSO-d_6, at 7.26 ppm in $CDCl_3$, and at 4.80 ppm in D_2O. ^{13}C NMR chemical shifts were measured relative to the residual solvent peak at 39.51 ppm in DMSO-d_6 and at 77.23 ppm in $CDCl_3$. Complete NMR peak assignments were made possible with 2D COSY and NOESY experiments. For dendrimer conjugates, integrals were reported only for the peaks clearly resolved (i.e., with a relatively good baseline-separation) in the ^{1}H NMR spectra. Detailed methods for NMR analysis including peak labeling and assignments, integration, determination of the stoichiometry, and estimation of average MWs for dendrimer conjugates are described in the Supporting Information.

The electrospray ionization (ESI) MS experiments were performed on a Waters LCT Premier mass spectrometer at the Mass Spectrometry Facility, NIDDK, NIH. MALDI-TOF MS experiments were performed on an Applied Biosystems Voyager-DE STR spectrometer at the Mass Spectrometry Laboratory, University of Illinois. 2,5-Dihydroxybenzoic acid (DHB) or 2,4,6-trihydroxyacetophene (THAP) was used as the matrix for the MALDI samples. Average MWs determined by MALDI are listed in Tables 1 and 2.

Table 2. Structural Analysis of PAMAM-PEG Conjugates by ^{1}H NMR and MALDI MS

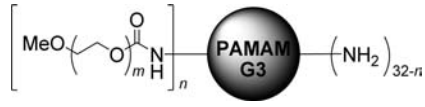

		NMR[b]			MALDI					
					DHB matrix			THAP matrix		
cmpd	M_n of **5**[a]	*m*	*n*	MW[c]	M_n[d]	M_w[e]	PDI[f]	M_n[d]	M_w[e]	PDI[f]
8	550	13	4	9432	6896[g]	7433[g]	1.08[g]	7835[g]	8091[g]	1.03[g]
9	550	12	7	11016	9035[g]	9536[g]	1.06[g]	10385[g]	10857[g]	1.05[g]
10	550	12	14	15122	13330	14009	1.05	12335	12823	1.04
11	550	12	32	25682	22039	22973	1.04	21441	22348	1.04
12	750	16	9	13775	11432	12098	1.06	9879[g]	10709[g]	1.08[g]
13	750	16	32	31321	24780	25588	1.03	25743	26202	1.02
14	2000	44	4	14894	10514[g]	12329[g]	1.17[g]	10947[g]	12533[g]	1.14[g]
15	2000	45	8	23232	19266	20019	1.04	18479[g]	19069[g]	1.03[g]
16	2000	45	17	41596	35167	36284	1.03	33054	34486	1.04
17	2000	44	32	70792	58947	60400	1.02	57626	60062	1.04

[a] M_n of PEG monomethylether **5** originally used to prepare the corresponding carbonate precursor **7**. M_n values were taken from the Aldrich bottle. [b] Based on ^{1}H NMR integration determined in DMSO-d_6. [c] PAMAM dendrimer **1** used for calculation here was assumed to have 32 peripheral amino groups and no structural defects. [d] Number-average molar mass. [e] Weight-average molar mass. [f] Polydispersity index. [g] Mass range selected for the average MW calculations contained (a part of) the peak region corresponding to the half-size of each desired compound.

General Procedure for Acetylation of PAMAM G3 Dendrimer. To a 2.68 mM DMSO solution of PAMAM G3 **1** was added slowly the corresponding amount of Ac_2O in DMSO (10%, v/v) with stirring. Reaction was stirred continuously for >24 h. Ca. 50 μL of each reaction mixture was taken, dried *in vacuo* for >2 h, and dissolved in 650−700 μL of DMSO-d_6 to determine the degree of acetylation by ^{1}H NMR. Later, it was found that the stoichiometric control of the acetylation reaction was better achieved if methanol was removed from commercial PAMAM dendrimer **1** *in vacuo*, then the dried sample was dissolved in DMSO-d_6 (ca. 1 mM), and the corresponding amount of Ac_2O (ca. 1 M in DMSO-d_6) was slowly added to the dendrimer solution. The reaction was stirred for 20−24 h, and the NMR spectrum was readily obtained by diluting an aliquot of the reaction mixture with DMSO-d_6.

Acetylated PAMAM Dendrimers 2 and 3. G3 PAMAM dendrimer **1** (2.68 mM, 5.40 mL, 14.5 μmol) was treated with Ac_2O (10% (v/v); 220 μL, ca. 233 μmol for **2**; 330 μL, ca. 349 μmol for **3**) in DMSO (total volume: 6.00 mL) and stirred for 40 h to yield a colorless glassy solid. ^{1}H NMR (600 MHz, DMSO-d_6) **2**: δ 8.15−7.81 (m, 73.18H, NH_{G0}, NH_{G1}, NH_{G2}, NH_{G3}, and NH_{Ac}), 3.09−3.07 (m, 179.31H, H_d, H_f, H_{fAc}, and H_{gAc}), 2.64−2.60 (m, 153.29H, H_b and H_g), 2.42 (m, 62.74H, H_e and H_a), 2.19−2.18 (m, 120.00H, H_c), 1.88 (s, 24.69H, CH_3CO^-), 1.79 (s, 40.60H, H_h); **3**: δ 8.14−7.81 (m, 75.79H, NH_{G0}, NH_{G1}, NH_{G2}, NH_{G3}, and NH_{Ac}), 3.09−3.07 (m, 187.24H, H_d, H_f, H_{fAc}, and H_{gAc}), 2.65−2.61 (m, 138.75H, H_b and H_g), 2.42 (m, 62.77H, H_e and H_a), 2.19−2.18 (m, 120.00H, H_c), 1.89 (s, 30.78H, CH_3CO^-), 1.79 (s, 59.22H, H_h).

Acetylated PAMAM Dendrimer 4. G3 PAMAM dendrimer **1** dried *in vacuo* (20.7 mg, 3.00 μmol) was dissolved in 1.50 mL of DMSO-d_6 and treated with Ac_2O (13.7 μL, 145 μmol). The reaction was stirred for 24 h and the ^{1}H NMR of the crude mixture was taken. Additionally, a portion of reaction mixture was purified by SEC (H 39 cm × O.D. 3.0 cm) in DMF to give **4** as a colorless glassy solid, and its ^{1}H NMR was acquired. ^{1}H NMR (600 MHz, DMSO-d_6) δ 7.94 (s, NH_{G3}), 7.88 (s, 35.05H, NH_{Ac}), 7.80 (br s, 26.41H, NH_{G0}, NH_{G1}, and NH_{G2}), 3.09−3.07 (m, 189.64H, H_d, H_{fAc}, and H_{gAc}), 2.65 (m, 116.29H, H_b), 2.42 (m, 59.60H, H_e and H_a), 2.18 (m, 120.00H, H_c), 1.79 (s, 96.34H, H_h).

General Procedure for Synthesis of PEG carbonate 7. PEG carbonate **7** was prepared following the modified procedure of Kojima et al. (*32*). To a mixture of poly(ethylene glycol) monomethyl ether **5** and 4-nitrophenylchloroformate (2 equiv) in THF was added triethylamine or DIEA (2 equiv). The reaction was stirred at room temperature for >5 d. Solvent was removed under reduced pressure, and the crude mixture was loaded on a SEC column for purification. The SEC column fractions were collected in small portions, and those verified to contain only the desired compound by ^{1}H NMR were combined. Purification by SEC was repeated, if necessary.

PEG Carbonate 7a. The reaction of poly(ethylene glycol) monomethyl ether **5a** (M_n = 550, 0.500 mL, 0.990 mmol), 4-nitrophenylchloroformate (398 mg, 1.92 mmol), and triethylamine (0.280 mL, 2.01 mmol) in THF (28 mL) gave the activated PEG carbonate **7a** as a sticky yellowish solid. ^{1}H NMR (300 MHz, $CDCl_3$) δ 8.26 (d, 2H, J = 9.5 Hz, H-3 of *p*-nitrophenol), 7.38 (d, 2H, J = 9.1 Hz, H-2 of *p*-nitrophenol), 4.42 (m, 2H, OCH_2CH_2OCO), 3.79 (m, 2H, OCH_2CH_2OCO), 3.72−3.52 (m, 55H, satellites J = 70.1 Hz, OCH_2CH_2O and OCH_2CH_2O), 3.36 (s, 3H, CH_3O); ^{13}C NMR (75 MHz, $CDCl_3$) δ 155.7, 152.6, 145.5, 125.5, 122.0, 72.1, 70.9, 70.7, 68.8, 68.5, 59.2; HRMS (ESI) Calcd for $C_{32}H_{59}N_2O_{17}$ (m = 12, M + NH_4^+): 743.3814, Found: 743.3785.

PEG Carbonate 7b. The reaction of poly(ethylene glycol) monomethyl ether **5b** (M_n = 750, 793 mg, 1.06 mmol), 4-nitrophenylchloroformate (438 mg, 2.11 mmol), and DIEA (0.370 mL, 2.12 mmol) in THF (40 mL) gave the activated PEG carbonate **7b** as a sticky yellowish solid. *The desired compound was contaminated with an inert PEG derivative, which was removed in the next step. The contaminant is suspected to be a methyl carbonate derivative of **7b** which has formed by the methanol (ca. 1 mL) added at the end of the reaction to quench the activity of excess 4-nitrophenylchloroformate. Methanol was not added for the other two reactions to make **7a** and **7c**. ^{1}H NMR (300 MHz, $CDCl_3$) δ 8.27 (d, 2H, J = 9.2 Hz, H-3 of *p*-nitrophenol), 7.38 (d, 2H, J = 9.4 Hz, H-2 of *p*-nitrophenol), 4.43 (m, 2H, OCH_2CH_2OCO), 3.80 (m, 2H, OCH_2CH_2OCO), 3.72−3.53 (m, *126H, satellites J = 70.8 Hz, OCH_2CH_2O and OCH_2CH_2O), 3.37 (s, 3H, CH_3O); ^{13}C NMR (75 MHz, $CDCl_3$) δ 125.5, 122.0, 72.1, 70.9, 70.8, 68.8, 68.5, 61.9, 59.2; HRMS (ESI) Calcd for $C_{40}H_{75}N_2O_{21}$ (m = 16, M + NH_4^+): 919.4862, Found: 919.4877.

PEG Carbonate 7c. The reaction of poly(ethylene glycol) monomethyl ether **5c** (M_n = 2000, 2.00 g, 1.00 mmol), 4-nitrophenylchloroformate (404 mg, 1.95 mmol), and triethylamine (0.280 mL, 2.01 mmol) in THF (100 mL) gave the activated PEG carbonate **7c** as a pale yellow solid. ^{1}H NMR (600 MHz, $CDCl_3$) δ 8.27 (d, 2H, J = 9.0 Hz, H-3 of

p-nitrophenol), 7.38 (d, 2H, $J = 9.2$ Hz, H-2 of *p*-nitrophenol), 4.43 (m, 2H, OCH_2CH_2OCO), 3.80 (m, 2H, OCH_2CH_2OCO), 3.69−3.53 (m, 186H, satellites $J = 70.4$ Hz, OCH_2CH_2O and OCH_2CH_2O), 3.37 (s, 3H, CH_3O); ^{13}C NMR (75 MHz, $CDCl_3$) δ 125.5, 122.0, 72.1, 70.8, 68.8, 68.5, 60.1; HRMS (ESI) Calcd for $C_{98}H_{187}N_2O_{50}Na$ ($m = 45$, $M + Na^+$): 2201.2019, Found: 2201.1978.

General Procedure for Synthesis of PAMAM-PEG Conjugates. The commercial G3 PAMAM dendrimer **1** (30−90 μL) was dried *in vacuo* to remove methanol and was weighed (50 μL gave ca. 9 mg, Aldrich). The dried dendrimer **1** was dissolved in DMSO and the corresponding amount of the activated PEG carbonate **7** was added slowly either as a solution (for PEG_{550} and PEG_{750}) in DMSO or as a solid (for PEG_{2000}). The final concentration of the dendrimer solution was ca. 1.3−1.5 mM and the reaction was stirred at room temperature for ≥4 d. The crude mixture was loaded directly on a SEC column and the fractions containing the desired product were identified by ^1H NMR. The first and last SEC fractions confirmed to contain minor amounts of the desired dendrimer by NMR were eliminated deliberately to reduce the polydispersity of the PAMAM-PEG dendrimer conjugates. In general, the yield of the each reaction calculated on the basis of the NMR-determined MW (Table 2) was nearly quantitative.

PAMAM-PEG_{550} Dendrimer Conjugate 8. To a stirred solution of G3 PAMAM dendrimer **1** (16.62 mg, 2.41 μmol) in DMSO (1.33 mL) was added PEG carbonate **7a** (6.88 mg, 9.62 μmol) in DMSO (275 μL). The mixture was continued to stir for 4 d and the crude mixture was loaded on a SEC column (H 38 cm × O.D. 4.5 cm) to isolate the desired dendrimer conjugate **8** (17.8 mg). ^1H NMR (600 MHz, DMSO-d_6) δ 8.16−7.83 (m, 57.62H, NH_{G0}, NH_{G1}, NH_{G2}, and NH_{G3}), 7.24 (br s, 3.77H, NH_{PEG} of major isomer), 6.83 (br s, 0.23H, NH_{PEG} of minor isomer), 4.03 (t, 8.47H, $J = 4.5$ Hz, H_h), 3.62−3.39 (m, 203.76H, satellites $J = 70.6$ Hz, H_i, H_j, and H_k), 3.24 (s, H_l), 3.09−3.05 (m, H_d, H_f, H_{fPEG}, and H_{gPEG}), 2.65, 2.57 (m, 157.75H, H_b and H_g), 2.43 (m, 58.97H, H_e and H_a), 2.19 (m, 120.00H, H_c).

PAMAM-PEG_{550} Dendrimer Conjugate 9. To a stirred solution of G3 PAMAM dendrimer **1** (15.7 mg, 2.27 μmol) in DMSO (1.08 mL), was added PEG carbonate **7a** (13.0 mg, 18.2 μmol) in DMSO (520 μL). The mixture was continued to stir for 4 d and the crude mixture was loaded on a SEC column (H 43 cm × O.D. 4.5 cm) to isolate the desired dendrimer conjugate **9** (21.2 mg). ^1H NMR (600 MHz, DMSO-d_6) δ 8.06−7.84 (m, 56.29H, NH_{G0}, NH_{G1}, NH_{G2}, and NH_{G3}), 7.24 (br s, 6.88H, NH_{PEG} of major isomer), 6.83 (br s, 0.54H, NH_{PEG} of minor isomer), 4.03 (t, 13.87H, $J = 4.7$ Hz, H_h), 3.62−3.38 (m, 338.47H, satellites $J = 70.9$ Hz, H_i, H_j, and H_k), 3.24 (s, 25.79H, H_l), 3.08−3.04 (m, 144.64H, H_d, H_f, H_{fPEG}, and H_{gPEG}), 2.64, 2.56 (m, 149.14H, H_b and H_g), 2.42 (m, 59.52H, H_e and H_a), 2.19 (m, 120.00H, H_c).

PAMAM-PEG_{550} Dendrimer Conjugate 10. To a stirred solution of G3 PAMAM dendrimer **1** (9.88 mg, 1.43 μmol) in DMSO (950 μL) was added PEG carbonate **7a** (16.5 mg, 23.1 μmol) in DMSO (150 μL). The mixture was continued to stir for 13 d and the crude mixture was loaded on a SEC column (H 38 cm × O.D. 3 cm) to isolate the desired dendrimer conjugate **10** (18.6 mg). ^1H NMR (600 MHz, DMSO-d_6) δ 7.97−7.86 (m, 60.53H, NH_{G0}, NH_{G1}, NH_{G2}, and NH_{G3}), 7.27 (br s, 13.07H, NH_{PEG} of major isomer), 6.85 (br s, 1.26H, NH_{PEG} of minor isomer), 4.03 (t, 27.31H, $J = 4.1$ Hz, H_h), 3.62−3.38 (m, 649.88H, satellites $J = 70.7$ Hz, H_i, H_j, and H_k), 3.23 (s, 42.76H, H_l), 3.08−3.01 (m, 158.09H, H_d, H_f, H_{fPEG}, and H_{gPEG}), 2.64, 2.54 (m, 144.01H, H_b and H_g), 2.42 (m, 57.85H, H_e and H_a), 2.19 (m, 120.00H, H_c); ^1H NMR (600 MHz, D_2O) δ 4.20, 4.16 (m, 28.00H, H_h, two isomers), 3.77−3.53 (m, 691.77H, H_i, H_j, and H_k), 3.34 (s, 46.20H, H_l), 3.25−3.20 (m, 153.89H, H_d, H_f, H_{fPEG}, and H_{gPEG}), 2.78 (m, 145.01H, H_b and H_g), 2.58 (m, 60.70H, H_e and H_a), 2.40−2.37 (m, 120.00H, H_c).

PAMAM-PEG_{550} Dendrimer Conjugate 11. To a stirred solution of G3 PAMAM dendrimer **1** (5.62 mg, 0.813 μmol) in DMSO (210 μL), was added PEG carbonate **7a** (37.4 mg, 52.3 μmol) in DMSO (340 μL). The mixture was continued to stir for 23 d and the crude mixture was loaded on a SEC column (H 38 cm × O.D. 3 cm) to isolate the desired dendrimer conjugate **11** (14.7 mg). ^1H NMR (600 MHz, DMSO-d_6) δ 7.94 (s, 33.53H, NH_{G3}), 7.79 (br s, 28.10H, NH_{G0}, NH_{G1}, and NH_{G2}), 7.23 (s, 30.00H, NH_{PEG} of major isomer), 6.80 (br s, 2.60H, NH_{PEG} of minor isomer), 4.03 (t, 63.13H, $J = 4.1$ Hz, H_h), 3.61−3.38 (m, 1540.42H, satellites $J = 69.0$ Hz, H_i, H_j, and H_k), 3.23 (s, 99.29H, H_l), 3.08−3.00 (m, 231.53H, H_d, H_{fPEG}, and H_{gPEG}), 2.64 (m, 121.74H, H_b), 2.41 (m, 58.91H, H_e and H_a), 2.17 (m, 120.00H, H_c).

PAMAM-PEG_{750} Dendrimer Conjugate 12. To a stirred solution of G3 PAMAM dendrimer **1** (11.3 mg, 1.64 μmol) in DMSO (960 μL) was added PEG carbonate **7b** (24.2 mg, 26.4 μmol) in DMSO (140 μL). The mixture was continued to stir for 23 d and the crude mixture was loaded on a SEC column (H 43 cm × O.D. 4.5 cm) to isolate the desired dendrimer conjugate **12** (18.3 mg). ^1H NMR (600 MHz, DMSO-d_6) δ 8.08−7.86 (m, 59.30H, NH_{G0}, NH_{G1}, NH_{G2}, and NH_{G3}), 7.26 (br s, 8.56H, NH_{PEG} of major isomer), 6.85 (br s, 0.51H, NH_{PEG} of minor isomer), 4.03 (t, 17.80H, $J = 4.1$ Hz, H_h), 3.62−3.38 (m, 551.24H, satellites $J = 71.1$ Hz, H_i, H_j, and H_k), 3.23 (s, 29.99H, H_l), 3.08−3.00 (m, 157.03H, H_d, H_f, H_{fPEG}, and H_{gPEG}), 2.64, 2.54 (m, 142.08H, H_b and H_g), 2.42 (m, 59.26H, H_e and H_a), 2.19 (m, 120.00H, H_c).

PAMAM-PEG_{750} Dendrimer Conjugate 13. To a stirred solution of G3 PAMAM dendrimer **1** (5.63 mg, 0.815 μmol) in DMSO (270 μL) was added PEG carbonate **7b** (48.3 mg, 52.8 μmol) in DMSO (280 μL). The mixture was continued to stir for 13 d and the crude mixture was loaded on a SEC column (H 38 cm × O.D. 4.5 cm) to isolate the desired dendrimer conjugate **13** (16.8 mg). ^1H NMR (600 MHz, DMSO-d_6) δ 7.94 (s, 34.61H, NH_{G3}), 7.79 (br s, 28.15H, NH_{G0}, NH_{G1}, and NH_{G2}), 7.23 (s, 29.94H, NH_{PEG} of major isomer), 6.81 (br s, 2.56H, NH_{PEG} of minor isomer), 4.03 (t, 63.72H, $J = 4.2$ Hz, H_h), 3.62−3.38 (m, 1949.61H, satellites $J = 70.4$ Hz, H_i, H_j, and H_k), 3.23 (s, 96.44H, H_l), 3.08−3.00 (m, 207.73H, H_d, H_{fPEG}, and H_{gPEG}), 2.64 (m, 121.55H, H_b), 2.41 (m, 59.85H, H_e and H_a), 2.17 (m, 120.00H, H_c).

PAMAM-PEG_{2000} Dendrimer Conjugate 14. A mixture of G3 PAMAM dendrimer **1** (17.0 mg, 2.45 μmol) and PEG carbonate **7c** (21.2 mg, 9.79 μmol) in DMSO (1.6 mL) was continued to stir for 5 d. The crude mixture was loaded on a SEC column (H 38 cm × O.D. 4.5 cm) to isolate the desired dendrimer conjugate **14** (35.0 mg). ^1H NMR (600 MHz, DMSO-d_6) δ 8.04−7.84 (m, 54.97H, NH_{G0}, NH_{G1}, NH_{G2}, and NH_{G3}), 7.24 (br s, 3.68H, NH_{PEG} of major isomer), 6.83 (br s, 0.19H, NH_{PEG} of minor isomer), 4.03 (t, 8.45H, $J = 4.6$ Hz, H_h), 3.62−3.39 (m, 712.46H, satellites $J = 70.8$ Hz, H_i, H_j, and H_k), 3.24 (s, H_l), 3.09−3.01 (m, 136.94H, H_d, H_f, H_{fPEG}, and H_{gPEG}), 2.64, 2.55 (m, 155.18H, H_b and H_g), 2.42 (m, 57.90H, H_e and H_a), 2.19 (m, 120.00H, H_c); ^1H NMR (600 MHz, D_2O) δ 4.20, 4.16 (m, 8.87H, H_h, two isomers), 3.78−3.54 (m, 773.85H, H_i, H_j, and H_k), 3.34 (s, 16.59H, H_l), 3.27−3.20 (m, 132.80H, H_d, H_f, H_{fPEG}, and H_{gPEG}), 2.78−2.72 (m, 158.64H, H_b and H_g), 2.58 (m, 61.43H, H_e and H_a), 2.40−2.38 (m, 120.00H, H_c).

PAMAM-PEG_{2000} Dendrimer Conjugate 15. A mixture of G3 PAMAM dendrimer **1** (15.6 mg, 2.25 μmol) and PEG carbonate **7c** (38.9 mg, 18.0 μmol) in DMSO (1.6 mL) was continued to stir for 5 d. The crude mixture was loaded on a SEC column (H 43 cm × O.D. 4.5 cm) to isolate the desired

dendrimer conjugate **15** (50.1 mg). ^{1}H NMR (600 MHz, DMSO-d_6) δ 8.02−7.83 (m, 59.93H, NH_{G0}, NH_{G1}, NH_{G2}, and NH_{G3}), 7.23 (br s, 7.63H, NH_{PEG} of major isomer), 6.82 (br s, 0.66H, NH_{PEG} of minor isomer), 4.03 (t, 15.03H, J = 4.3 Hz, H_h), 3.62−3.39 (m, 1406.73H, satellites J = 70.7 Hz, H_i, H_j, and H_k), 3.24 (s, 30.32H, H_l), 3.09−3.00 (m, 149.47H, H_d, H_f, H_{fPEG}, and H_{gPEG}), 2.64, 2.55 (m, 158.48H, H_b and H_g), 2.42 (m, 58.93H, H_e and H_a), 2.19 (m, 120.00H, H_c).

PAMAM-PEG$_{2000}$ Dendrimer Conjugate 16. A mixture of G3 PAMAM dendrimer **1** (11.2 mg, 1.62 μmol) and PEG carbonate **7c** (56.2 mg, 26.0 μmol) in DMSO (1.1 mL) was continued to stir for 25 d. The crude mixture was loaded on a SEC column (H 43 cm × O.D. 4.5 cm) to isolate the desired dendrimer conjugate **16** (53.1 mg). ^{1}H NMR (600 MHz, DMSO-d_6) δ 7.98−7.83 (m, 66.70H, NH_{G0}, NH_{G1}, NH_{G2}, and NH_{G3}), 7.25 (br s, 15.80H, NH_{PEG} of major isomer), 6.83 (br s, 1.23H, NH_{PEG} of minor isomer), 4.03 (br s, 32.67H, H_h), 3.62−3.38 (m, 3002.14H, satellites J = 70.7 Hz, H_i, H_j, and H_k), 3.23 (s, 59.22H, H_l), 3.09−3.00 (m, 166.13H, H_d, H_f, H_{fPEG}, and H_{gPEG}), 2.64, 2.55 (m, 134.95H, H_b and H_g), 2.41 (m, 58.40H, H_e and H_a), 2.18 (m, 120.00H, H_c).

PAMAM-PEG$_{2000}$ Dendrimer Conjugate 17. A mixture of G3 PAMAM dendrimer **1** (5.64 mg, 0.816 μmol) and PEG carbonate **7c** (113 mg, 52.2 μmol) in DMSO (550 μL) was continued to stir for 13 d. The crude mixture was loaded on a SEC column (H 43 cm × O.D. 4.5 cm) to isolate the desired dendrimer conjugate **17** (12.5 mg). ^{1}H NMR (600 MHz, DMSO-d_6) δ 7.93 (s, 35.70H, NH_{G3}), 7.79 (br s, 28.60H, NH_{G0}, NH_{G1}, and NH_{G2}), 7.22 (s, 29.53H, NH_{PEG} of major isomer), 6.80 (br s, 2.88H, NH_{PEG} of minor isomer), 4.03 (br s, 64.23H, H_h), 3.62−3.38 (m, 5633.29H, satellites J = 70.8 Hz, H_i, H_j, and H_k), 3.23 (s, 100.03H, H_l), 3.07−3.00 (m, 289.19H, H_d, H_{fPEG}, and H_{gPEG}), 2.63 (m, 121.87H, H_b), 2.41 (m, 58.47H, H_e and H_a), 2.17 (m, 120.00H, H_c).

Cytotoxicity Assays. Typically, a stock solution of dendrimer derivative was prepared by dissolving 0.5 μmol of a vacuum-dried solid sample in 50 μL of DMSO (10 mM solution). Dendrimers **2** and **3** used for cytotoxicity studies were not purified by SEC, in order not to disrupt the average MWs. Thus, samples **2** and **3** contained some acetic acid, and were used as reaction mixtures after drying *in vacuo* extensively. All other synthesized PAMAM-PEG dendrimer conjugates were purified by SEC. To ensure the dissolution, each 50 μL dendrimer sample in DMSO was heated at 80 °C for 30 min and then allowed to cool to room temperature. A partial gelation appeared with dendrimer conjugate **8** (see Results and Discussion section), and thus the actual concentration of assay samples of **8** may be lower. 5 mL of DMEM/F12 media (Mediatech Inc.) containing 10% fetal bovine serum and antibiotics was added to this 50 μL solution to make 1% (v/v) DMSO as a total content, which was then heated at 37 °C for another 30 min to ensure homogeneity. Any further dilutions used the media supplemented with 1% (v/v) DMSO, which was shown in control experiments not to affect the cell growth.

Serial dilutions were carried out to prepare samples of the following concentrations: 0.32, 1.0, 3.2, 10, and 32 μM for dendrimers **1**−**4** and **8**−**17**; 1.0, 3.2, 10, and 32 μM for dendrimers **18**, **19**, and **20**. 1.6 mL of each dilution was added to a six-well plate, and 30 000 cells were seeded per well. A well containing the 1.6 mL of media with 1% (v/v) DMSO was prepared simultaneously as a control along with each dendrimer series, which was seeded with the same number of cells. Two plates for each dendrimer compound were prepared so that one plate could be used for cell counting and the other plate could be used for hematoxylin staining. The cells grew for a period of 5 d, when the control well was 90% confluent. Subsequently, the media was aspirated and 1 mL of phosphate buffer saline (PBS) was added to each well and then removed. To count the cells, the cells were detached with 0.2 mL of trypsin and diluted with 2 mL of media (without the DMSO). The cell density in each well was measured using a hemocytometer to determine the effect of the added dendrimer derivative on cell survival, as an indication of cytotoxicity. Each well was homogenized and three counts were made to determine the accuracy. Thus, the percent cell survival is determined by normalizing each cell count against the value obtained from the corresponding control and is reported as mean ± standard error. For the hematoxylin staining, cells were fixed with methanol for 10 min. After PBS wash (×3) for 5 min each, the cells were stained with 4 g/L hematoxylin (containing 35.2 g/L aluminum sulfate and 0.4 g/L sodium iodate) for 10 min. The cells were washed (×3) with PBS for 5 min, allowed to air-dry, and then treated with glycerol. The image was visualized using a Zeiss bright-field microscope (*73*).

RESULTS AND DISCUSSION

Acetylation of PAMAM Dendrimers. We began our studies by preparing acetylated G3 PAMAM dendrimers. Partial acetylation of PAMAM dendrimers has been commonly applied as a way to enhance water solubility and reduce cytotoxicity of amine-terminated PAMAM dendrimers for drug delivery applications. Recent studies suggested that the partial acetylation altered the surface properties of the PAMAM dendrimer and led to a more compact structure, allowing it to better expose the attached ligands—and thus improved targeting—by suppressing the potential of backfolding (*67*, *69*). In general, commercial PAMAM dendrimers are somewhat heterogeneous, displaying a distribution of structures (i.e., defects), mainly caused by incomplete coupling and purification in each step of the divergent layer growth. Accordingly, we performed simple acetylation reactions to understand the stoichiometry involving heterogeneity and to establish the characterization method based on the ^{1}H NMR integration (Table 1). Furthermore, these partially acetylated PAMAM dendrimers may serve as controls to compare with the PEGylated PAMAM dendrimers of similar degrees of substitutions for their cytotoxic effects.

Dendrimer conjugates were synthesized from G3 PAMAM dendrimer **1** (Figure 1) with ethylenediamine as an initiator core ((*8*), Scheme 1). Initially, a stock solution of PAMAM dendrimer **1** in DMSO was prepared. In order to accurately determine the concentration of the stock solution, six individual batches containing the same volume of PAMAM stock solution, treated with different amounts of acetic anhydride in DMSO, were subjected to analysis of ^{1}H NMR integrals. Here, addition of organic base was not necessary for the acetylation reaction in DMSO, possibly due to the self-neutralizing effect of PAMAM dendrimers, which can form an ionic complex with acetic acid, the byproduct, at either the remaining peripheral amine (pK_a 6.9) or the tertiary amine (pK_a 3.9) in the interior (*62*). Next, the PAMAM dendrimer in DMSO was treated with ca. 16, 24, or 48 equiv of acetic anhydride. Typically, when the peripheral amino groups of PAMAM dendrimers were acetylated by acetic anhydride, a singlet corresponding to the methyl of acetamide appeared at 1.79 ppm ("h", Figure S1, Supporting Information) in DMSO-d_6, and a methyl peak from acetate anion was found at ca. 1.90 ppm which disappeared upon purification. When the integrals were normalized against the methylene peak of PAMAM at 2.18 ppm ("c", 120H), the internal standard of PAMAM for ^{1}H NMR integration, these dendrimers were found to contain 14, 20, and 32 acetamide groups on average, respectively (**2**, **3**, and **4**; Table 1). In fact, prior attempts to exhaustively acetylate the peripheral amino groups of PAMAM G3 dendrimers indicated that the number of terminal amino groups was close to the theoretical value of

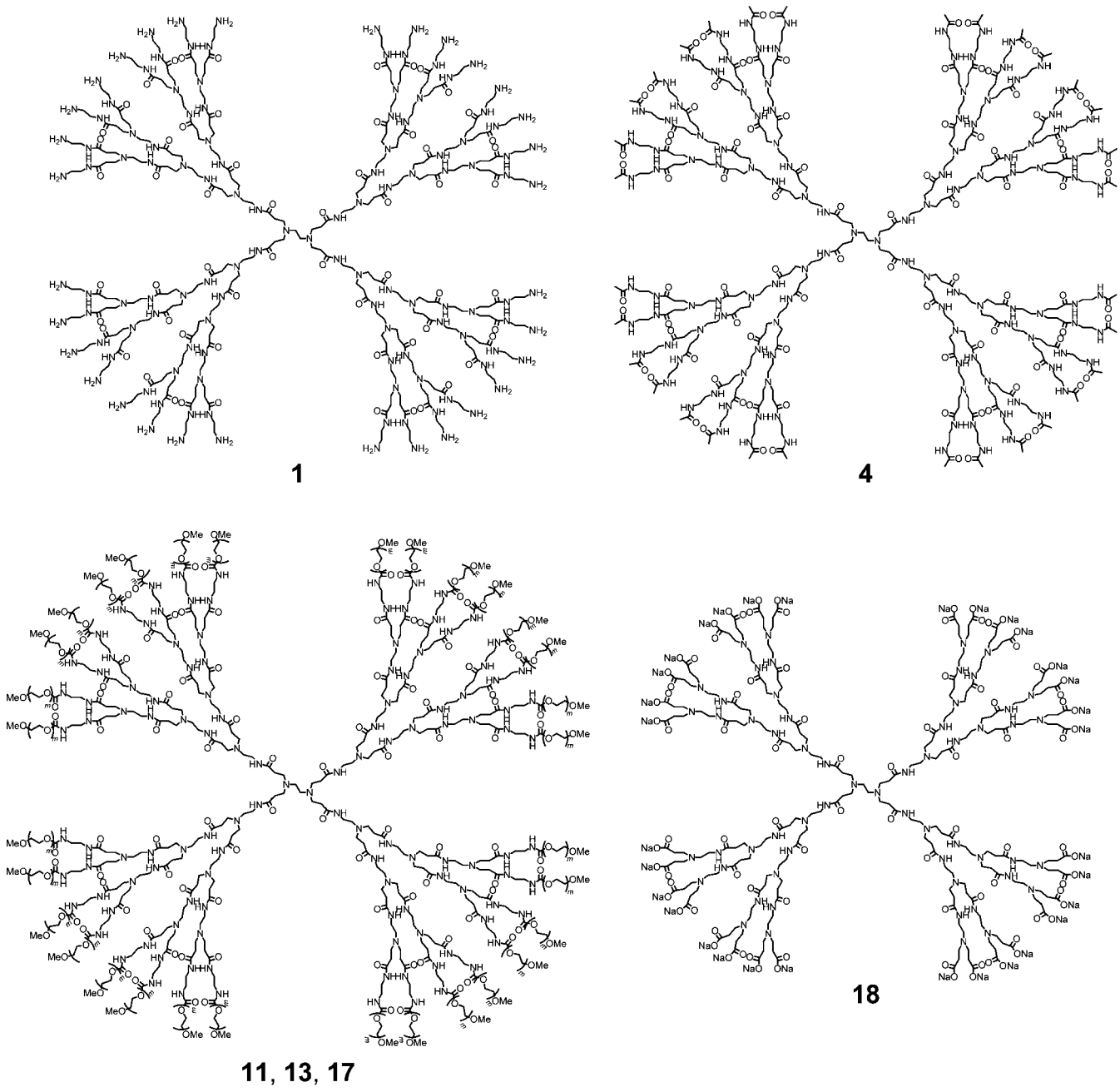

Figure 1. Structures of PAMAM dendrimer derivatives with homogeneous end groups: a commercial G3 PAMAM (**1**), acetylated G3 PAMAM (**4**), PEGylated G3 PAMAM (**11** from PEG_{550}, **13** from PEG_{750}, and **17** from PEG_{2000}), and a commercial G2.5 PAMAM with carboxylate terminal groups (**18**).

Scheme 1

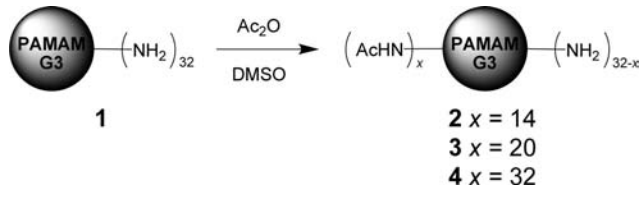

32 by this normalization method based on the internal standard "c" after purification by SEC. Thus, 32 peripheral groups were assumed for PAMAM G3 dendrimers for the remainder of our structural analysis based on the ^{1}H NMR integration. Interestingly, when a portion of either of the partially acetylated PAMAM dendrimer reaction mixtures, **2** or **3**, was passed through a SEC column in DMF, the average number of acetamide groups shifted toward higher values by ^{1}H NMR integration, whereas the value for the fully acetylated PAMAM **4** remained the same. This may have resulted from the poorer solubility of PAMAM dendrimers with a lower degree of acetylation in DMF, reducing the relative recovery after SEC compared to the recovery of dendrimers bearing more acetamide groups in the same batch.

Various matrices and conditions were attempted to obtain the mass spectra of the acetylated PAMAM dendrimers by MALDI (see Supporting Information). As reported previously, MALDI spectra obtained with either DHB or THAP as a matrix generally gave the best results for our analysis (*74*). A relatively broad major peak was observed for each acetylated dendrimer, **2**, **3**, or **4**, spanning up to the mass range corresponding to the fully acetylated PAMAM. In either matrix, the overall pattern of the peak distribution was more or less the same between these three acetylated dendrimers. A secondary broad peak region corre-

Scheme 2

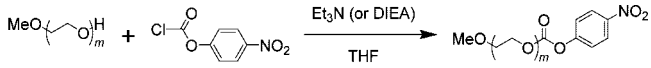

5a M_n = 550 **6** **7a**
5b M_n = 750 **7b**
5c M_n = 2000 **7c**

sponding to the half-size of the desired MW was detected in the MALDI spectra of acetylated dendrimers, **2**, **3**, and **4**, as well as for the commercial PAMAM **1**. This half-size peak may have originated from the fragmentation near the tertiary amine of the core (*75*) and/or may indeed represent G2 PAMAM derivatives which were formed by the reagents carried over to the next step without removal in the commercial PAMAM synthesis. The average MWs of **2**, **3**, and **4** determined by MALDI in either matrix were lower than those determined by ^{1}H NMR (Table 1). Unlike the analysis based on ^{1}H NMR, average MWs estimated by MALDI slightly varied depending on the specific conditions applied (e.g., sample preparation, scanned mass range, laser intensity, etc.) or by the chemical nature of samples affecting fragmentation pattern and the tendency to form matrix/salt adducts. Overall, the MALDI-estimated average MWs increased (except for **4** with DHB matrix) in both matrices as the degree of acetylation increased from **1** to **4**.

Synthesis, Purification, and Characterization of PAMAM-PEG Conjugates. In order to systematically study the influence of PEG, relative to its size and abundance on reducing the cytotoxic effect of PAMAM dendrimers, conjugates were prepared starting from three different lengths of monomethyl PEG ether **5** (i.e., M_n 550, 750, and 2000; Scheme 2) by varying the degree of PEGylation. Preparation of the activated PEG carbonate **7** followed the modified procedure of Kojima et al. (*32*). As reported previously, contamination of the commercial monomethyl PEG ether by its diol derivative produced a mixture of mono- and diactivated PEG carbonates (*23, 76*). Diactivated PEG carbonate analogue of **7** (structure not shown) may result in unwanted intra- and intermolecular cross-links, and thus a tedious and cumbersome purification was necessary to remove these species by SEC in DMF. SEC fractions verified to contain only the desired PEG derivative **7** by ^{1}H NMR were combined and were used for the next step. The average MW of each PEG derivative **7** was determined on the basis of analysis of ^{1}H NMR and MS (Table 2). Here, each purification carried out by SEC slightly shifted the distribution of PEG derivative **7** to affect the average MW. Strangely, even after repeated purification, analysis of **7b** (from PEG_{750}) by ^{1}H NMR integration indicated the number of repeat units to be approximately twice the anticipated value. Despite the suggested contamination, the mass spectrum of **7b** displayed the desired peak distribution as a major entity, and thus **7b** was used for next step (Figure S7, Supporting Information). Unlike **7a** or **7c**, conjugation of **7b** to PAMAM indeed created some discrepancies in stoichiometry (*vide infra*); however, the contaminant was successfully removed by SEC at this later step without causing any further contamination.

Next, G3 PAMAM dendrimer **1** was treated with different amounts of PEG carbonate **7** (Scheme 3). Stoichiometry of the conjugation was generally well-managed when methanol was removed *in vacuo* from the commercial PAMAM G3 dendrimer **1**, and then the corresponding amount of the activated PEG **7** was added relative to the mass of dry PAMAM **1**. Preparation of ten different PAMAM-PEG derivatives was planned by adding: 4, 8, 16, and 64 equiv of **7a** (from PEG_{550}); 16 and 65 equiv of **7b** (from PEG_{750}); 4, 8, 16, and 64 equiv of **7c** (from PEG_{2000}). Reaction was generally performed in the concentration range 1.3−1.5 mM per dendrimer, and upon addition of **7**, the colorless reaction mixture instantly turned an intense yellow color, indicating the appearance of *p*-nitrophenolate species. After stirring for ≥4 d, the reaction mixture was loaded on a SEC column with DMF as an eluent, and the desired fractions were combined after careful analyses of ^{1}H NMR spectra. Here, the first and last SEC fractions confirmed to contain minor amounts of the desired dendrimer by NMR were eliminated deliberately. This was intended to reduce the polydispersity and thus to achieve more reliable biological effects by restricting the range of structural dissimilarity in the distribution, which is a limitation of the partial derivatization method commonly applied in PAMAM dendrimer chemistry.

The stoichiometry of PAMAM-PEG conjugates was established by ^{1}H NMR integration in DMSO-d_6 (Table 2, Figures 2 and 3). Detailed methods used for the analysis of NMR data are described in the Supporting Information. In summary, PAMAM dendrimer conjugates were characterized to contain the following: 4 (**8**), 7 (**9**), 14 (**10**), and 32 (**11**) of PEG_{550} chains; 9 (**12**), and 32 (**13**) of PEG_{750} chains; 4 (**14**), 8 (**15**), 17 (**16**), and 32 (**17**) of PEG_{2000} chains. Except for the PEG_{750} derivative **12,** which was prepared from a contaminated PEG derivative **7b** (*vide supra*), stoichiometric control of the conjugation reaction was elaborately executed as planned. In addition, the NMR-based MW estimation of PAMAM-PEG derivatives in DMSO-d_6 is summarized in Table 2. Alternatively, selected structures **10** and **14** were characterized similarly by ^{1}H NMR in D_2O, to give nearly identical results (Figure S4, Supporting Information).

Overall, these PAMAM-PEG conjugates were hygroscopic and exhibited relatively good water solubility except for dendrimer **8**, which was substituted with four short chains of PEG_{550}. Surprisingly, a severe irreversible gelation occurred for a portion of compound **8**, hampering any further usage of the batch. Gelation phenomena from amine-terminated PAMAM dendrimers were noticed previously, especially with lower substitution, and neither sonication nor the treatment with various organic solvents, water, acid/base, or heat restored them to the solution state (*77*).

Next, to help predict the solution conformation of PAMAM-PEG conjugates under physiological conditions, NOESY experiments were carried out in D_2O (Figures S5 and S6, Supporting Information). Dendrimer **10** with multiple numbers of short PEG chains ($14PEG_{550}$) and dendrimer **14** substituted with fewer long PEG chains ($4PEG_{2000}$) were chosen to explore the influence of PEG chain length and population on the overall geometry in solution. No NOE cross-peaks were observed from either structure between peaks from PAMAM and PEG regions in D_2O. This strongly suggests that, in water, the terminal hydrophilic PEG groups are entirely segregated from the central PAMAM domain (i.e., no backfolding) regardless of PEG chain length studied here. Thus, the geometry of PAMAM-PEG conjugates in aqueous media may closely resemble that of the phase-separated micelle. Indeed, the concept of a dendritic/hyperbranched "unimolecular micelle" with hydrophilic end groups was introduced earlier mainly for the entrapment of small hydrophobic molecules (*35, 54, 78–82*).

MALDI mass spectra of PAMAM-PEG conjugates were obtained using 2,5-dihydroxybenzoic acid (DHB) and 2,4,6-trihydroxyacetophene (THAP) as matrices (Figure 4, Supporting Information). Generally, the desired peaks were better resolved when the MALDI scan range was narrowed. Average MWs were calculated from the mass range encompassing the desired major peak. Again, the peaks corresponding to the half-size of the desired MW were detected in all cases. In certain cases, parts of these half-size peaks were included in the mass range for MW calculation to further underestimate the MW of the

Scheme 3

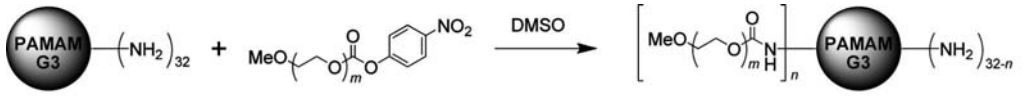

1 **7**

8 $m = 13$, $n = 4$ **13** $m = 16$, $n = 32$
9 $m = 12$, $n = 7$ **14** $m = 44$, $n = 4$
10 $m = 12$, $n = 14$ **15** $m = 45$, $n = 8$
11 $m = 12$, $n = 32$ **16** $m = 45$, $n = 17$
12 $m = 16$, $n = 9$ **17** $m = 44$, $n = 32$

desired, especially when the expected (i.e., NMR-determined) MWs of conjugates were relatively low(<25000 Da). Overall, when the half-size peak was not included, MALDI underestimated the MW of PAMAM-PEG conjugates by 7−18% compared to the MW determined by NMR. Again, broadening of peaks may have originated from random fragmentation under applied MALDI conditions (e.g., between the carbon−nitrogen bond at the interior tertiary amine), structural defects from the commercial starting material, or formation of matrix/salt adducts (*74*). Interestingly, MALDI of conjugates derivatized with fewer PEG_{2000} chains, **14** and **15**, displayed individual broad peaks separated by ca. 2000 Da, corresponding to PAMAM dendrimers with increasing numbers of PEG substitutions. MALDI-estimated average MWs of the PAMAM-PEG dendrimer conjugates in each matrix are listed in Table 2.

***In Vitro* Cytotoxicity of PAMAM Dendrimer Derivatives.** Evaluation of the cytotoxicity of PAMAM dendrimer derivatives with various surface modifications has been reported. A relevant study compared the cytotoxicity and hemolytic potential of the melamine-based dendrimers each bearing cationic (amine, guanidine), anionic (carboxylate, sulfonate, phosphonate), or neutral (PEG) hydrophilic surface group (*83*). Unfortunately, only limited systematic studies were performed to date along these lines that may provide guidelines to estimate the proper degree of peripheral substitutions needed when a particular functional group is used. Here, we examined the cytotoxic effects of dendrimer derivatives with several commonly used end groups in PAMAM-based drug delivery-acetamide, carboxylate, and PEG. Our systematic approach included varying the degree of terminal substitution for each functionality (acetamide, PEG), the size of PEG chains (PEG_{550}, PEG_{750}, and PEG_{2000}), and the generation of dendrimer (carboxylate). We investigated near the micromolar concentration range where somewhat marked differences in cytotoxicity between studied dendrimers were elicited. CHO cells were chosen as our target which were often used in our laboratory for studies on G protein-coupled receptors ((*74*) and references therein).

First, the cytotoxicity of PAMAM dendrimers with acetylated peripheries was examined (Figure 5A). Dendrimer **2** carried 14 acetamide groups (ca. 44% substitution) as analyzed by ^{1}H NMR integration method, dendrimer **3** had 20 acetamide groups (ca. 63% substitution), and dendrimer **4** was fully acetylated (100% substitution) leaving no free primary amino groups at the periphery. As expected, dendrimers with a higher degree of acetylation showed less toxicity. For instance, fully acetylated

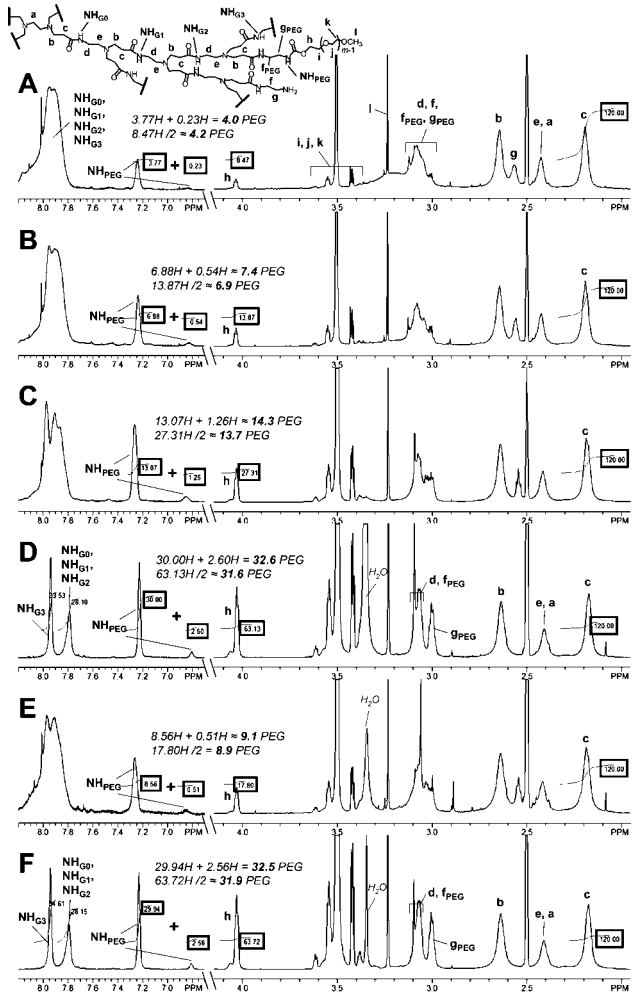

Figure 2. ^{1}H NMR spectra of PAMAM-PEG dendrimer conjugates (A) **8**, (B) **9**, (C) **10**, (D) **11**, (E) **12**, and (F) **13** in DMSO-d_6.

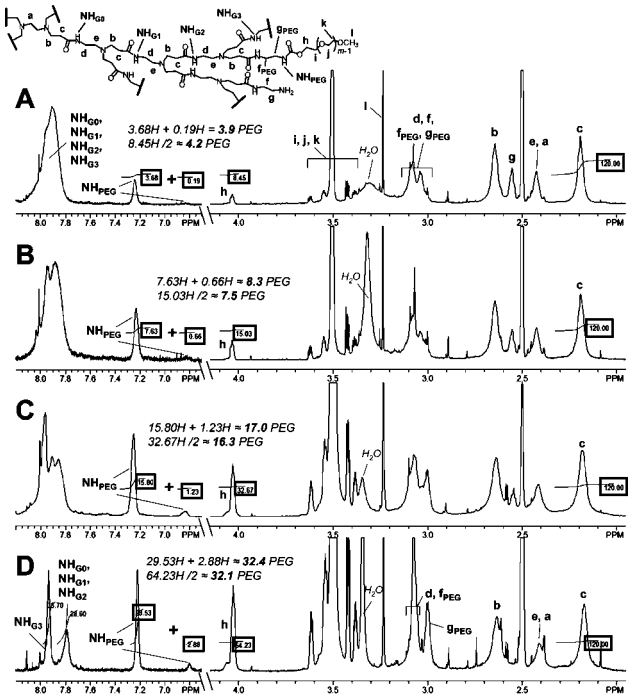

Figure 3. ^{1}H NMR spectra of PAMAM-PEG dendrimer conjugates (A) **14**, (B) **15**, (C) **16**, and (D) **17** in DMSO-d_6.

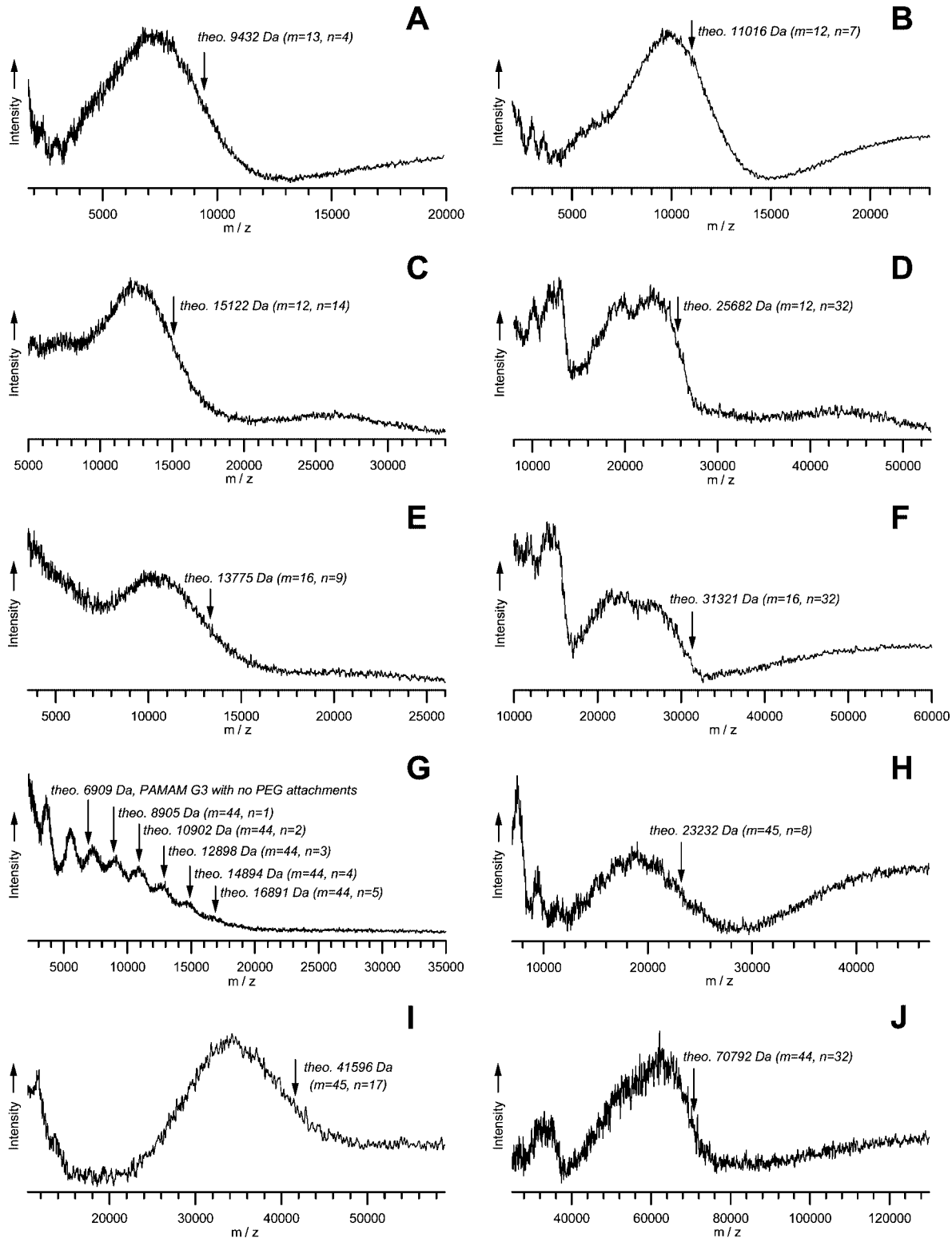

Figure 4. MALDI-TOF MS spectra of PAMAM-PEG dendrimer conjugates using DHB as a matrix: (A) **8**; (B) **9**; (C) **10**; (D) **11**; (E) **12**; (F) **13**; (G) **14**; (H) **15**; (I) **16**; (J) **17**.

dendrimer **4** exhibited ca. 75% cell survival at 32 μM (the highest concentration tested), whereas the unsubstituted PAMAM **1** and a nearly half-acetylated dendrimer **2** showed only ca. 5% cell survival. All dendrimer derivatives including the commercial PAMAM **1** exhibited >70% cell survival at $\leq$1 μM under the applied assay conditions. Recently, a similar systematic study was reported on acetylated G2 and G4 PAMAM dendrimers, which manifested concentration-dependent cytotoxic effects in Caco-2 cell cultures (*84*).

Next, our synthesized PAMAM-PEG dendrimer conjugates **8**−**17** were subjected to cytotoxicity evaluation under the same conditions in CHO cell cultures (Figure 5B,C). Generally, the cytotoxic effects of PAMAM-PEG conjugates decreased with increasing numbers of peripheral substitutions with respect to the same PEG chain length (i.e., PEG_{550}, PEG_{750}, or PEG_{2000}). Almost no cytotoxic effects were observed up to 1 μM concentration with dendrimers having a lower degree of PEG-substitution (22−28%), **9**, **12**, and **15**, which all exhibited similar

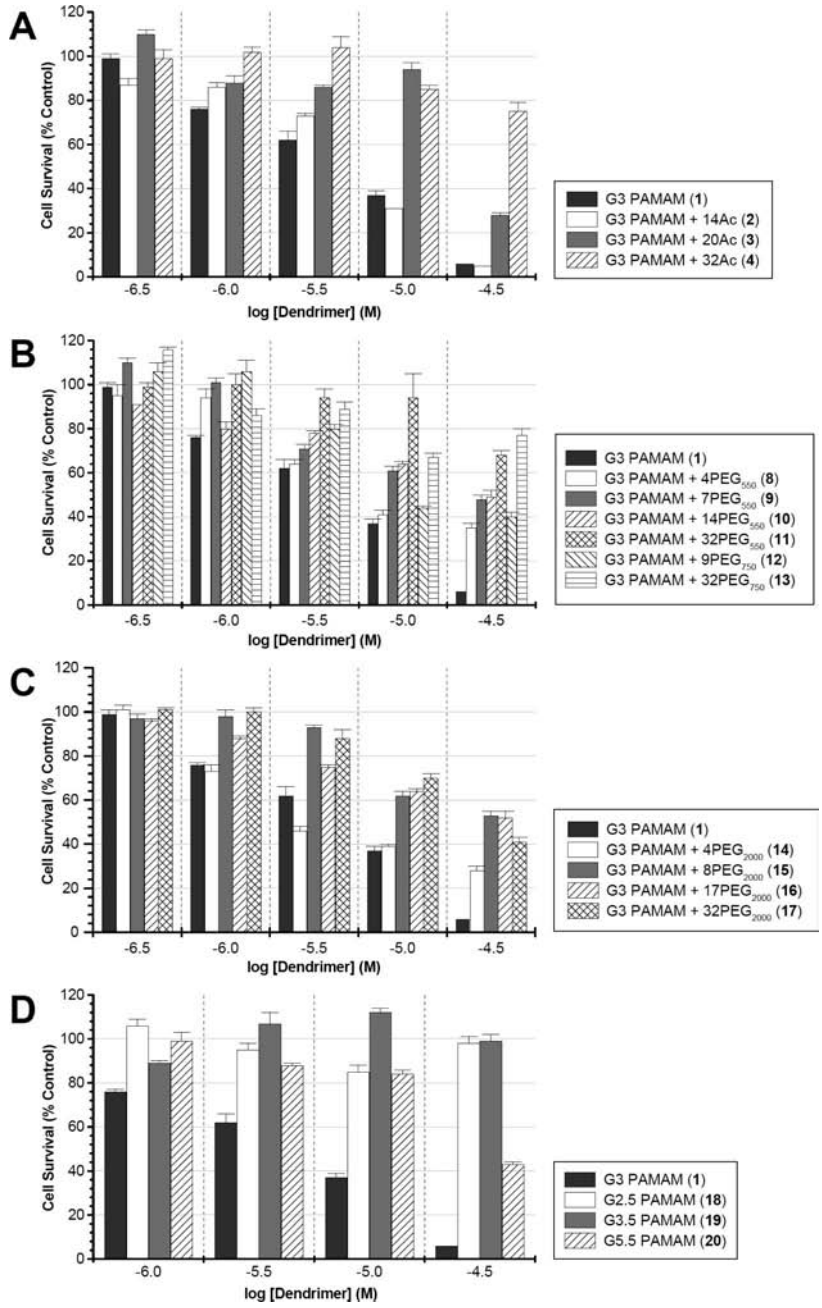

Figure 5. Cytotoxicity of dendrimers in CHO cell cultures: (A) acetylated G3 PAMAM dendrimers, G3 PAMAM dendrimers derivatized with (B) shorter PEG chains (PEG_{550}/PEG_{750}) or (C) a longer PEG chain (PEG_{2000}), and (D) anionic carboxylate PAMAM dendrimers (G2.5, G3.5, and G5.5). Each dendrimer sample was prepared using DMEM/F12 media (Mediatech, Inc.) containing 10% fetal bovine serum and antibiotics with 1% (v/v) DMSO. 30 000 cells were seeded per six-well plate containing dendrimer media, and the cells were counted after a 5 d incubation. Cell survival is reported by normalizing the cell counts to the value obtained from a control well with 1% (v/v) DMSO, which did not contain the dendrimer. Cell survival is reported as mean ± standard error.

cytotoxic values at higher concentrations within the permitted error range. Despite the limited experimental trials, when the cytotoxicity was compared between fully substituted PAMAM-PEG dendrimers, **11**, **13**, and **17** (Figure 1), interestingly, only **17** with the longest PEG groups showed a sudden drop in cell survival rate at the highest concentration of 32 μM. This dendrimer **17** was more toxic at 32 μM than the less substituted analogues, **15** and **16**, of the same chain length (PEG_{2000}). A previous report proposed the possibility of the intermolecular agglomeration and interpenetration for fully substituted PAMAM conjugates with longer PEG chains (PEG_{5000}) at higher concentrations, deterring efficient encapsulation (i.e., solubilization) of small hydrophobic molecules (*54*). Similarly, this potential agglomeration of dendrimer **17** may negatively affect cell viability at higher concentrations.

The cytotoxicity of PAMAM-PEG conjugates were then compared with that of acetylated dendrimers. At the highest concentration studied (32 μM), partially PEGylated dendrimers (**8**−**10**, **12**, and **14**−**16**) with 13−53% peripheral substitution were generally less toxic (28−53% cell survival) regardless of their chain length, compared to the partially acetylated dendrimers **2** and **3** (44−63% peripheral substitution, 5−28% cell survival). More specifically, the cytotoxicity profile of nearly half-substituted PAMAM-PEG derivatives, **10** and **16**, was more or less the same over the entire concentration range studied, suggesting negligible effects of chain length (PEG_{550} vs

PEG_{2000}). However, when these two medium-range PEG substitutions were compared to acetylated PAMAM **2** with 14 acetyl groups, cytotoxicity was significantly lower at ≥ 10 μM (49−64% cell survival for **10** and **16**; 5−31% cell survival for **2**). On the other hand, except for the dendrimer **17** with longer PEG chains, cell survival rates of fully substituted and relatively nontoxic dendrimers **4** (acetamide), **11** (PEG_{550}), and **13** (PEG_{750}) were similar. Taken together, PAMAM dendrimer with a lower degree (ca. 25% or less) of short PEG substitutions may substantially reduce the cytotoxicity of amine-terminated PAMAM dendrimers at a micromolar concentration range with good water solubility. In contrast, the smaller acetamide groups may require a higher degree of surface masking to achieve similar cell viability, limiting the number of available peripheral amino groups for further attachments of other functional moieties for drug delivery applications (e.g., drugs, targeting units, markers, etc.). Furthermore, water solubility of the final dendrimer with a partially acetylated surface may be governed more by the physical properties of these other appended moieties compared to the PEGylated surface, requiring additional fine-tuning of the stoichiometry.

Carboxylate-terminated anionic PAMAM dendrimers possess excellent water solubility. However, these derivatives have been used less frequently for drug delivery compared to the amine-terminated PAMAM dendrimers. In the same manner, we evaluated the cytotoxicity of commercial G2.5 (**18**, Figure 1), G3.5 (**19**), and G5.5 (**20**) PAMAM dendrimers with the ethylenediamine as an initiator core, which contain 32, 64, and 256 carboxylate end groups, respectively, in theory (Figure 5D). Essentially, no cytotoxic effect was observed from lower generation dendrimers, **18** and **19**, at all concentrations studied. Interestingly, for G5.5 PAMAM **20**, a sudden increase in cytotoxicity was observed at the highest concentrations (32 μM). Similar to the result obtained for dendrimer **17**, this relatively large dendrimer **20** with multiple hydrophilic end groups may aggregate intermolecularly (or alone) to display an increased level of cellular toxicity at elevated concentrations. Thus, for carboxylate PAMAM series, usage of G5.5 or higher generations may be limited to lower concentrations (≤ 10 μM) for drug delivery applications.

CONCLUSION

Attachment of PEG chains to macromolecular therapeutics generally alters the surface properties, leading to excellent water solubility and biocompatibility. PAMAM dendrimers are frequently used for dendrimer-based drug delivery applications due to their known relative biocompatibility and commercial availability. PEGylation has been applied to PAMAM dendrimers as a way to reduce toxicity of their amine termini and to offer a sufficient steric barrier for the efficient encapsulation of a drug or gene. Despite its advantageous effects, overcrowding the surface of these carriers by longer PEG chains may cause intermolecular aggregation, increase cytotoxicity, and prohibit intracellular drug release by deterring the uptake process (*9*). An estimation of minimally required PEG substitution is crucial when other functional moieties are appended on the PAMAM surface, especially when targeting or other ligand−receptor interaction is involved. Accordingly, to provide guidelines in designing PAMAM-based drug delivery agents, a series of PAMAM-PEG conjugates were prepared varying the degree of substitution and PEG chain length. Each dendrimer was purified by SEC and characterized by NMR and MALDI. A careful analysis of ^{1}H NMR integrals allowed the complete characterization of PAMAM-PEG conjugates for MW determination. NOESY experiments in D_2O confirmed the absence of back-folding of the peripheral PEG regardless of its size and population on the PAMAM surface, suggesting a micellar geometry.

The cytotoxicity of PAMAM-PEG derivatives was evaluated in CHO cell cultures. In comparison to the acetylated G3 PAMAM dendrimers, a lower degree of surface substitution was needed when PEG was present in order to achieve similar cell viability. Our systematic investigation indicated that a relatively low degree of surface modification (ca. 25% or less) by shorter PEG chains (PEG_{550}/PEG_{750}) may significantly reduce the cytotoxicity of amine-terminated PAMAM dendrimers while maintaining good water solubility.

In summary, PAMAM-PEG dendrimer conjugates may serve as universal scaffolds to build efficient and more versatile drug carriers. Current findings led us to further explore the influence of PEG chain length and number of attachments on eliciting potential pharmacological effects of ligands attached to the dendrimer surface involving receptor interactions, which will be reported in a separate manuscript.

ACKNOWLEDGMENT

This research was supported in part by the Intramural Research Program of the NIH, NIDDK. We thank Dr. Haijun Yao at the Mass Spectrometry Laboratory of the University of Illinois, for numerous attempts to obtain MALDI spectra of our PAMAM dendrimer derivatives. We are grateful to Rick Dreyfuss at ORS, NIH, who helped us to obtain the images for the cytotoxicity results. Y.K. thanks the Can-Fite Biopharma for financial support.

Supporting Information Available: ^{1}H NMR and MALDI-MS spectra, a complete list of cytotoxicity values, and selected images of cell cultures containing dendrimers used for cytotoxicity experiments. This material is available free of charge via the Internet at http://pubs.acs.org/BC.

LITERATURE CITED

(1) Haag, R., and Kratz, F. (2006) Polymer therapeutics: concepts and applications. *Angew. Chem., Int. Ed. 45*, 1198–1215.
(2) Duncan, R. (2003) The dawning era of polymer therapeutics. *Nat. Rev. Drug Discovery 2*, 347–360.
(3) Iyer, A. K., Khaled, G., Fang, J., and Maeda, H. (2006) Exploiting the enhanced permeability and retention effect for tumor targeting. *Drug Discovery Today 11*, 812–818.
(4) Ringsdorf, H. (1975) Structure and properties of pharmacologically active polymers. *J. Polym. Sci., Polym. Symp. 51*, 135–153.
(5) Tomalia, D. A. (2005) Birth of a new macromolecular architecture: dendrimers as quantized building blocks for nanoscale synthetic polymer chemistry. *Prog. Polym. Sci. 30*, 294–324.
(6) Grayson, S. M., and Fréchet, J. M. J. (2001) Convergent dendrons and dendrimers: from synthesis to applications. *Chem. Rev. 101*, 3819–3867.
(7) Zeng, F., and Zimmerman, S. C. (1997) Dendrimers in supramolecular chemistry: from molecular recognition to self-assembly. *Chem. Rev. 97*, 1681–l712.
(8) Tomalia, D. A., Naylor, A. M., and Goddard, W. A. (1990) Starburst dendrimers: molecular-level control of size, shape, surface chemistry, topology, and flexibility from atoms to macroscopic matter. *Angew. Chem., Int. Ed. Engl. 29*, 138–175.
(9) Tomalia, D. A., Reyna, L. A., and Svenson, S. (2007) Dendrimers as multi-purpose nanodevices for oncology drug delivery and diagnostic imaging. *Biochem. Soc. Trans. 35*, 61–67.
(10) Boas, U., Christensen, J. B., and Heegaard, P. M. H. (2006) *Dendrimers in medicine and biotechnology*, The Royal Society of Chemistry, Cambridge.
(11) Lee, C. C., MacKay, J. A., Fréchet, J. M. J., and Szoka, F. C. (2005) Designing dendrimers for biological applications. *Nat. Biotechnol. 23*, 1517–1526.

(12) Svenson, S., and Tomalia, D. A. (2005) Dendrimers in biomedical applications—reflections on the field. *Adv. Drug Delivery Rev. 57*, 2106–2129.
(13) Gillies, E. R., and Fréchet, J. M. J. (2005) Dendrimers and dendritic polymers in drug delivery. *Drug Discovery Today 10*, 35–43.
(14) D'Emanuele, A., and Attwood, D. (2005) Dendrimer-drug interactions. *Adv. Drug Delivery Rev. 57*, 2147–2162.
(15) Shabat, D., Amir, R. J., Gopin, A., Pessah, N., and Shamis, M. (2004) Chemical adaptor systems. *Chem. Eur. J. 10*, 2626–2634.
(16) Boas, U., and Heegaard, P. M. H. (2004) Dendrimers in drug research. *Chem. Soc. Rev. 33*, 43–63.
(17) Stiriba, S.-E., Frey, H., and Haag, R. (2002) Dendritic polymers in biomedical applications: from potential to clinical use in diagnostics and therapy. *Angew. Chem., Int. Ed. 41*, 1329–1334.
(18) Patri, A. K., Majoros, I. J., and Baker, J. R., Jr (2002) Dendritic polymer macromolecular carriers for drug delivery. *Curr. Opin. Chem. Biol. 6*, 466–471.
(19) Duncan, R., and Izzo, L. (2005) Dendrimer biocompatibility and toxicity. *Adv. Drug Delivery Rev. 57*, 2215–2237.
(20) Khalil, I. A., Kogure, K., Akita, H., and Harashima, H. (2006) Uptake pathways and subsequent intracellular trafficking in nonviral gene delivery. *Pharmacol. Rev. 58*, 32–35.
(21) Conner, S. D., and Schmid, S. L. (2003) Regulated portals of entry into the cell. *Nature 422*, 37–44.
(22) Van Vlerken, L. E., Vyas, T. K., and Amiji, M. M. (2007) Poly(ethylene glycol)-modified nanocarriers for tumor-targeted and intracellular delivery. *Pharm. Res. 24*, 1405–1414.
(23) Harris, J. M., and Chess, R. B. (2003) Effect of PEGylation on pharmaceuticals. *Nat. Rev. Drug Discovery 2*, 214–221.
(24) Greenwald, R. B., Conover, C. D., and Choe, Y. H. (2000) Poly(ethylene glycol) conjugated drugs and prodrugs: a comprehensive review. *Crit. Rev. Ther. Drug Carrier Syst. 17*, 101–161.
(25) Zalipsky, S. (1995) Chemistry of polyethylene glycol conjugates with biologically active molecules. *Adv. Drug Delivery Rev. 16*, 157–182.
(26) Gajbhiye, V., Kumar, P. V., Tekade, R. K., and Jain, N. K. (2007) Pharmaceutical and biomedical potential of PEGylated dendrimers. *Curr. Pharm. Des. 13*, 415–429.
(27) Wood, K. C., Little, S. R., Langer, R., and Hammond, P. T. (2005) A family of hierarchically self-assembling linear-dendritic hybrid polymers for highly efficient targeted gene delivery. *Angew. Chem., Int. Ed. 44*, 6704–6708.
(28) Yang, H., and Lopina, S. T. (2003) Penicillin V-conjugated PEG-PAMAM star polymers. *J. Biomater. Sci. Polymer Ed. 14*, 1043–1056.
(29) Jevprasesphant, R., Penny, J., Jalal, R., Attwood, D., McKeown, N. B., and D'Emanuele, A. (2003) The influence of surface modification on the cytotoxicity of PAMAM dendrimers. *Int. J. Pharm. 252*, 263–266.
(30) Luo, D., Haverstick, K., Belcheva, N., Han, E., and Saltzman, W. M. (2002) Poly(ethylene glycol)-conjugated PAMAM dendrimer for biocompatible, high-efficiency DNA delivery. *Macromolecules 35*, 3456–3462.
(31) Carnahan, M. A., Middleton, C., Kim, J., Kim, T., and Grinstaff, M. W. (2002) Hybrid dendritic-linear polyester-ethers for in situ photopolymerization. *J. Am. Chem. Soc. 124*, 5291–5293.
(32) Kojima, C., Kono, K., Maruyama, K., and Takagishi, T. (2000) Synthesis of polyamidoamine dendrimers having poly(ethylene glycol) grafts and their ability to encapsulate anticancer drugs. *Bioconjugate Chem. 11*, 910–917.
(33) Choi, J. S., Joo, D. K., Kim, C. H., Kim, K., and Park, J. S. (2000) Synthesis of a barbell-like triblock copolymer, poly(L-lysine) dendrimer-*block*-poly(ethylene glycol)-block-poly(L-lysine) dendrimer, and its self-assembly with plasmid DNA. *J. Am. Chem. Soc. 122*, 474–480.
(34) Chun, D., Wudl, F., and Nelson, A. (2007) Supramolecular assembly driven by complementary molecular recognition. *Macromolecules 40*, 1782–1785.
(35) Liu, M., Kono, K., and Fréchet, J. M. J. (2000) Water-soluble dendritic unimolecular micelles: Their potential as drug delivery agents. *J. Controlled Release 65*, 121–131.
(36) Gillies, E. R., Dy, E., Fréchet, J. M. J., and Szoka, F. C. (2005) Biological evaluation of polyester dendrimer: Poly(ethylene oxide) "bow-tie" hybrids with tunable molecular weight and architecture. *Mol. Pharm. 2*, 129–138.
(37) Johnson, M. A., Iyer, J., and Hammond, P. T. (2004) Microphase segregation of PEO-PAMAM linear-dendritic diblock copolymers. *Macromolecules 37*, 2490–2501.
(38) Gillies, E. R., and Fréchet, J. M. J. (2002) Designing macromolecules for therapeutic applications: Polyester dendrimer—poly(ethylene oxide) "bow-tie" hybrids with tunable molecular weight and architecture. *J. Am. Chem. Soc. 124*, 14137–14146.
(39) Yu, D., Vladimirov, N., and Fréchet, J. M. J. (1999) MALDI-TOF in the characterizations of dendritic-linear block copolymers and stars. *Macromolecules 32*, 5186–5192.
(40) Kim, Y., Zeng, F., and Zimmerman, S. C. (1999) Peptide dendrimers from natural amino acids. *Chem. Eur. J. 5*, 2133–2138.
(41) Gitsov, I., and Fréchet, J. M. J. (1996) Stimuli-responsive hybrid macromolecules: Novel amphiphilic star copolymers with dendritic groups at the periphery. *J. Am. Chem. Soc. 118*, 3785–3786.
(42) Chapman, T. M., Hillyer, G. L., Mahan, E. J., and Shaffer, K. A. (1994) Hydraamphiphiles: Novel linear dendritic block copolymer surfactants. *J. Am. Chem. Soc. 116*, 11195–11196.
(43) Gitsov, I., and Fréchet, J. M. J. (1993) Solution and solid-state properties of hybrid linear-dendritic block copolymers. *Macromolecules 26*, 6536–6546.
(44) Takahashi, T., Hirose, J., Kojima, C., Harada, A., and Kono, K. (2007) Synthesis of poly(amidoamine) dendron-bearing lipids with poly(ethylene glycol) grafts and their use for stabilization of nonviral gene vectors. *Bioconjugate Chem. 18*, 1163–1169.
(45) Kojima, C., Toi, Y., Harada, A., and Kono, K. (2007) Preparation of poly(ethylene glycol)-attached dendrimers encapsulating photosensitizers for application to photodynamic therapy. *Bioconjugate Chem. 18*, 663–670.
(46) Gillies, E. R., and Fréchet, J. M. J. (2005) pH-Responsive copolymer assemblies for controlled release of doxorubicin. *Bioconjugate Chem. 16*, 361–368.
(47) Gillies, E. R., Jonsson, T. B., and Fréchet, J. M. J. (2004) Stimuli-responsive supramolecular assemblies of linear-dendritic copolymers. *J. Am. Chem. Soc. 126*, 11936–11943.
(48) Chandrasekar, D., Sistla, R., Ahmad, F. J., Khar, R. K., and Diwan, P. V. (2007) Folate coupled poly(ethyleneglycol) conjugates of anionic poly(amidoamine) dendrimer for inflammatory tissue specific drug delivery. *J. Biomed. Mater. Res. 82A*, 92–103.
(49) Shukla, S., Wu, G., Chatterjee, M., Yang, W., Sekido, M., Diop, L. A., Müller, R., Sudimack, J. J., Lee, R. J., Barth, R. F., and Tjarks, W. (2003) Synthesis and biological evaluation of folate receptor-targeted boronated PAMAM dendrimers as potential agents for neutron capture therapy. *Bioconjugate Chem. 14*, 158–167.
(50) Kono, K., Kojima, C., Hayashi, N., Nishisaka, E., Kiura, K., Watarai, S., and Harada, A. (2008) Preparation and cytotoxic activity of poly(ethylene glycol)-modified poly(amidoamine) dendrimers bearing adriamycin. *Biomaterials 29*, 1664–1675.
(51) Guillaudeu, S. J., Fox, M. E., Haidar, Y. M., Dy, E. E., Szoka, F. C., and Fréchet, J. M. J. (2008) PEGylated dendrimers with core functionality for biological applications. *Bioconjugate Chem. 193*, 461–469.
(52) Yang, H., and Lopina, S. T. (2007) Stealth dendrimers for antiarrhythmic quinidine delivery. *J. Mater. Sci. Mater. Med. 18*, 2061–2065.

(53) De Jesús, O. L., Ihre, H. R., Gagne, L., Fréchet, J. M. J., and Szoka, F. C., Jr (2002) Polyester dendritic systems for drug delivery applications: In vitro and in vivo evaluation. *Bioconjugate Chem. 13*, 453–461.

(54) Yang, H., Morris, J. J., and Lopina, S. T. (2004) Polyethylene glycol-polyamidoamine dendritic micelle as solubility enhancer and the effect of the length of polyethylene glycol arms on the solubility of pyrene in water. *J. Colloid Interface Sci. 273*, 148–154.

(55) Shi, X., Majoros, I. J., Patri, A. K., Bi, X., Islam, M. T., Desai, A., Ganser, T. R., and Baker, J. R., Jr. (2006) Molecular heterogeneity analysis of poly(amidoamine) dendrimer-based mono- and multifunctional nanodevices by capillary electrophoresis. *Analyst 131*, 374–381.

(56) Esfand, R., and Tomalia, D. A. (2001) Poly(amidoamine) (PAMAM) dendrimers: from biomimicry to drug delivery and biomedical applications. *Drug Discovery Today 6*, 427–436.

(57) Zhou, J., Wu, J., Hafdi, N., Behr, J.-P., Erbacher, P., and Peng, L. (2006) PAMAM dendrimers for efficient siRNA delivery and potent gene silencing. *Chem. Commun.* 2362–2364.

(58) Kang, H., DeLong, R., Fisher, M. H., and Juliano, R. L. (2005) Tat-conjugated PAMAM dendrimers as delivery agents for antisense and siRNA oligonucleotides. *Pharm. Res. 22*, 2099–2106.

(59) Krämer, M., Stumbé, J.-F., Grimm, G., Kaufmann, B., Krüger, U., Weber, M., and Haag, R. (2004) Dendritic polyamines: Simple access to new materials with defined treelike structures for application in nonviral gene delivery. *ChemBioChem 5*, 1081–1087.

(60) Lee, J. H., Lim, Y.-B., Choi, J. S., Lee, Y., Kim, T.-I., Kim, H. J., Yoon, J. K., Kim, K., and Park, J.-S. (2003) Polyplexes assembled with internally quaternized PAMAM-OH dendrimer and plasmid DNA have a neutral surface and gene delivery potency. *Bioconjugate Chem. 14*, 1214–1221.

(61) Tang, M. X., Redemann, C. T., and Szoka, F. C., Jr. (1996) *In vitro* gene delivery by degraded polyamidoamine dendrimers. *Bioconjugate Chem. 7*, 703–714.

(62) Haensler, J., and Szoka, F. C., Jr. (1993) Polyamidoamine cascade polymers mediate efficient transfection of cells in culture. *Bioconjugate Chem. 4*, 372–379.

(63) Lee, I., Athey, B. D., Wetzel, A. W., Meixner, W., and Baker, J. R., Jr. (2002) Structural molecular dynamics studies on polyamidoamine dendrimers for a therapeutic application: effects of pH and generation. *Macromolecules 35*, 4510–4520.

(64) Fischer, D., Li, Y., Ahlemeyer, B., Krieglstein, J., and Kissel, T. (2003) In vitro cytotoxicity testing of polycations: influence of polymer structure on cell viability and hemolysis. *Biomaterials 24*, 1121–1131.

(65) Jevprasesphant, R., Penny, J., Attwood, D., McKeown, N. B., and D'Emanuele, A. (2003) Engineering of dendrimer surfaces to enhance transepithelial transport and reduce cytotoxicity. *Pharm. Res. 20*, 1543–1550.

(66) Malik, N., Wiwattanapatapee, R., Klopsch, R., Lorenz, K., Frey, H., Weener, J. W., Meijer, E. W., Paulus, W., and Duncan, R. (2000) Dendrimers: relationship between structure and biocompatibility in vitro, and preliminary studies on the biodistribution of ^{125}I-labelled polyamidoamine dendrimers in vivo. *J. Controlled Release 65*, 133–148.

(67) Lee, H., Baker, J. R., Jr., and Larson, R. G. (2006) Molecular dynamics studies of the size, shape, and internal structure of 0% and 90% acetylated fifth-generation polyamidoamine dendrimers in water and methanol. *J. Phys. Chem. B 110*, 4014–4019.

(68) Majoros, I. J., Keszler, B., Woehler, S., Bull, T., and Baker, J. R., Jr. (2003) Acetylation of poly(amidoamine) dendrimers. *Macromolecules 36*, 5526–5529.

(69) Quintana, A., Raczka, E., Piehler, L., Lee, I., Myc, A., Majoros, I., Patri, A. K., Thomas, T., Mulé, J., and Baker, J. R., Jr. (2002) Design and function of a dendrimer-based therapeutic nanodevice targeted to tumor cells through the folate receptor. *Pharm. Res. 19*, 1310–1316.

(70) Majoros, I. J., Thomas, T. P., Mehta, C. B., and Baker, J. R., Jr. (2005) Poly(amidoamine) dendrimer-based multifunctional engineered nanodevice for cancer therapy. *J. Med. Chem. 48*, 5892–5899.

(71) Thomas, T. P., Majoros, I. J., Kotlyar, A., Kukowska-Latallo, J. F., Bielinska, A., Myc, A., and Baker, J. R., Jr. (2005) Targeting and inhibition of cell growth by an engineered dendritic nanodevice. *J. Med. Chem. 48*, 3729–3735.

(72) Huang, R.-Q., Qu, Y.-H., Ke, W.-L., Zhu, J.-H., Pei, Y.-Y., and Jiang, C. (2007) Efficient gene delivery targeted to the brain using a transferring-conjugated polyethyleneglycol-modified polyamidoamie dendrimer. *FASEB J. 21*, 1117–1125.

(73) Mamedova, L. K., Gao, Z. G., and Jacobson, K. A. (2006) Regulation of death and survival in astrocytes by ADP activating $P2Y_1$ and $P2Y_{12}$ receptors. *Biochem. Pharmacol. 72*, 1031–1041.

(74) Kim, Y., Hechler, B., Klutz, A. M., Gachet, C., and Jacobson, K. A. (2008) Toward multivalent signaling across G protein-coupled receptors from poly(amidoamine) dendrimers. *Bioconjugate Chem. 19*, 406–411.

(75) Peterson, J., Allikmaa, V., Subbi, J., Pehk, T., and Lopp, M. (2003) Structural deviations in poly(amidoamine) dendrimers: a MALDI-TOF MS analysis. *Eur. Polym. J. 39*, 33–42.

(76) Dust, J. M., Fang, Z.-H., and Harris, J. M. (1990) Proton NMR characterization of poly(ethylene glycols) and derivatives. *Macromolecules 23*, 3742–3746.

(77) Kim, Y. Unpublished results: A rapid gelation of PAMAM dendrimer derivatives was observed from those with a lower degree of peripheral substitutions when the sample was dried *in vacuo* extensively, and then was treated with a polar aprotic solvent such as DMSO or DMF for dissolution.

(78) Morgan, M. T., Carnahan, M. A., Immoos, C. E., Ribeiro, A. A., Finkelstein, S., Lee, S. J., and Grinstaff, M. W. (2003) Dendritic molecular capsules for hydrophobic compounds. *J. Am. Chem. Soc. 125*, 15485–15489.

(79) Pistolis, G., and Malliaris, A. (2002) Study of poly(propylene imine) dendrimers in water, by exciplex formation. *Langmuir 18*, 246–151.

(80) Newkome, G. R., Moorefield, C. N., Keith, J. M., Baker, G. R., and Escamilla, G. H. (1994) Chemistry within a unimolecular micelle precursor: Boron superclusters by site- and depth-specific transformations of dendrimers. *Angew. Chem., Int. Ed. Engl. 33*, 666–668.

(81) Hawker, C. J., Wooley, K. L., and Fréchet, J. M. J. (1993) Unimolecular micelle and globular amphiphiles: Dendritic macromolecules as novel recyclable solubilization agents. *J. Chem. Soc., Perkin Trans. 1*, 1287–1297.

(82) Kim, Y. H., and Webster, O. W. (1990) Water-soluble hyperbranched polyphenylene: "A unimolecular micelle"? *J. Am. Chem. Soc. 112*, 4592–4593.

(83) Chen, H.-T., Neerman, M. F., Parrish, A. R., and Simanek, E. E. (2004) Cytotoxicity, hemolysis, and acute in vivo toxicity of dendrimers based on melamine, candidate vehicles for drug delivery. *J. Am. Chem. Soc. 126*, 10044–10048.

(84) Kolhatkar, R. B., Kitchens, K. M., Swaan, P. W., and Ghandehari, H. (2007) Surface acetylation of polyamidoamine (PAMAM) dendrimers decreases cytotoxicity while maintaining membrane permeability. *Bioconjugate Chem. 18*, 2054–2060.

BC700483S

Supporting Information for *Bioconjugate Chemistry*

Systematic Investigation of Polyamidoamine Dendrimers Surface-Modified with Poly(ethylene glycol) for Drug Delivery Applications: Synthesis, Characterization, and Evaluation of Cytotoxicity

Yoonkyung Kim,* Athena M. Klutz, Kenneth A. Jacobson*

Molecular Recognition Section, Laboratory of Bioorganic Chemistry, National Institute of Diabetes & Digestive & Kidney Diseases, National Institutes of Health, Bethesda, Maryland 20892

Table of Contents

NMR ANALYSIS OF PAMAM DENDRIMER CONJUGATES		pp. 2–3
Figure S1	^{1}H NMR spectra of acetylated PAMAM dendrimers **2**–**4**.	p. 4
Figures S2–S4	^{1}H NMR spectra of PAMAM-PEG dendrimers **8**–**17**.	pp. 5–9
Figures S5–S6	COSY and NOESY spectra of PAMAM-PEG dendrimers **10** and **14** in D_2O.	pp. 8–9
Figure S7	ESI MS of PEG derivative **7**.	p. 10
Figure S8	MALDI MS of G3 PAMAM dendrimer **1**.	p. 11
Figures S9–S11	MALDI MS of acetylated PAMAM dendrimers **2**–**4**.	pp. 12–14
Figures S12–S21	MALDI MS of PAMAM-PEG dendrimers **8**–**17**.	pp. 15–24
Figure S22	MALDI MS of commercial PAMAM G2.5, G3.5, and G5.5.	p. 25
Table S1	Cytotoxicity of PAMAM dendrimer derivatives.	p. 26
Figure S23	Cytotoxicity micrographs of PAMAM G3, G2.5, and G3.5.	p. 27

NMR ANALYSIS OF PAMAM DENDRIMER CONJUGATES

General Methods. Since each PAMAM dendrimer conjugate was not unimolecular,[1] characterization by NMR represented the average value from its polymeric distribution. The integration value of each peak was reported in two decimal places as determined by the ^{1}H NMR analysis. For G3 PAMAM dendrimer-based conjugates, a methylene peak at 2.18 ppm ("c", see Figure S2) was used as an internal standard (set at 120 H) for the integration, assuming 32 peripheral groups without any defects in the structure. Assignments of peaks were based on the labeling method shown in Figure S1 for the acetylated PAMAM dendrimers and Figure S2 for the PEGylated PAMAM dendrimers.

Determination of Stoichiometry. The stoichiometry of PAMAM-PEG conjugates was established by ^{1}H NMR integration in DMSO-d_6 (Table 2, Figures S2 and S3). A distinct methylene peak from PEG next to the carbamate bond appeared at 4.03 ppm ("h"). Similar to the integration method applied for the acetylated G3 PAMAM dendrimers, the number of PEG attachments (*n*) was determined by the integrals of peak "h" relative to the PAMAM internal standard "c" at 2.18 ppm (120 H). A methyl peak from the PEG terminus at 3.23 ppm, often used to determine the number of PEG attachments (*n*) elsewhere, was not clearly resolved in DMSO-d_6 due to the adjacent broad peaks. Alternatively, the number of PEG chains (*n*) was estimated by summing the integrals of carbamate NH peaks ("NH_{PEG}") from two conformational isomers (i.e., conformers) found at ca. 7.24 ppm (major) and ca. 6.82 ppm (minor, 5-9%), which closely matched with the values determined through the methylene peak at 4.03 ppm ("h"). In fact, the peak integrated as "h" at 4.03 ppm included a small shoulder peak (minor conformer); however, quantification of its integral was difficult due to the significant overlap with the major peak. Characterization of the *E*- and *Z*-isomers from the carbamate linkages (e.g., *tert*-butoxycarbonyl (Boc)-protected amino acids) by ^{1}H NMR and IR spectroscopic methods was described previously,[2] and the composition of isomers generally varied depending on the temperature, solvent, concentration, and adjacent substituent groups. Consequently, by taking the average of integration values determined through two different methods described here, PAMAM dendrimer conjugates were characterized to contain: 4 (**8**), 7 (**9**), 14 (**10**), and 32 (**11**) of PEG_{550}

chains; 9 (**12**), and 32 (**13**) of PEG_{750} chains; 4 (**14**), 8 (**15**), 17 (**16**), and 32 (**17**) of PEG_{2000} chains.

Estimation of Average MWs. Each purification by SEC slightly shifted the distribution of these polymeric mixtures, affecting not only the number of PEG attachments (*n*), but also the average PEG chain length (i.e., number of repeat units, *m*). In an attempt to estimate the MW of PAMAM-PEG conjugates by NMR, the total number of repeat units (*mn*) was determined by integrating the entire PEG methylene peaks (Figures S2 and S3). The major peak of PEG appeared at 3.50 ppm, and its satellite peaks were observed at 3.62 ppm and 3.38 ppm, symmetrical to each other. Unfortunately, integration of the satellite peak at 3.38 ppm was often encumbered by the presence of a nearby water peak. Thus, the same integration value as for the other at 3.62 ppm was assumed. After combining the integrals of all PEG methylene peaks including "h", the total number of repeat units (*mn*) was estimated by dividing this integral by four (number of protons from a single repeat unit). Furthermore, the number of repeat units per PEG chain (*m*) was determined by dividing the total number of repeat units (*mn*) by the number of PEG attachments (*n*) for each conjugate. Similarly, selected structures **10** and **14** were characterized in D_2O by ^1H NMR, to give nearly identical results (Figure S4). The NMR-based MW estimation of PAMAM-PEG derivatives in DMSO-d_6 is summarized in Table 2.

REFERENCES

(1) Shi, X., Majoros, I. J., Patri, A. K., Bi, X., Islam, M. T., Desai, A., Ganser, T. R., and Baker, J. R., Jr. (2006) Molecular heterogeneity analysis of poly(amidoamine) dendrimer-based mono- and multifunctional nanodevices by capillary electrophoresis. *Analyst 131*, 374−381.

(2) Branik, M., and Kessler, H. (1975) Zur konformation geschützter aminosäuren, III. NMR- und IR-untersuchungen von Boc-ω-aminosäuren. *Chem. Ber. 108*, 2176−2188.

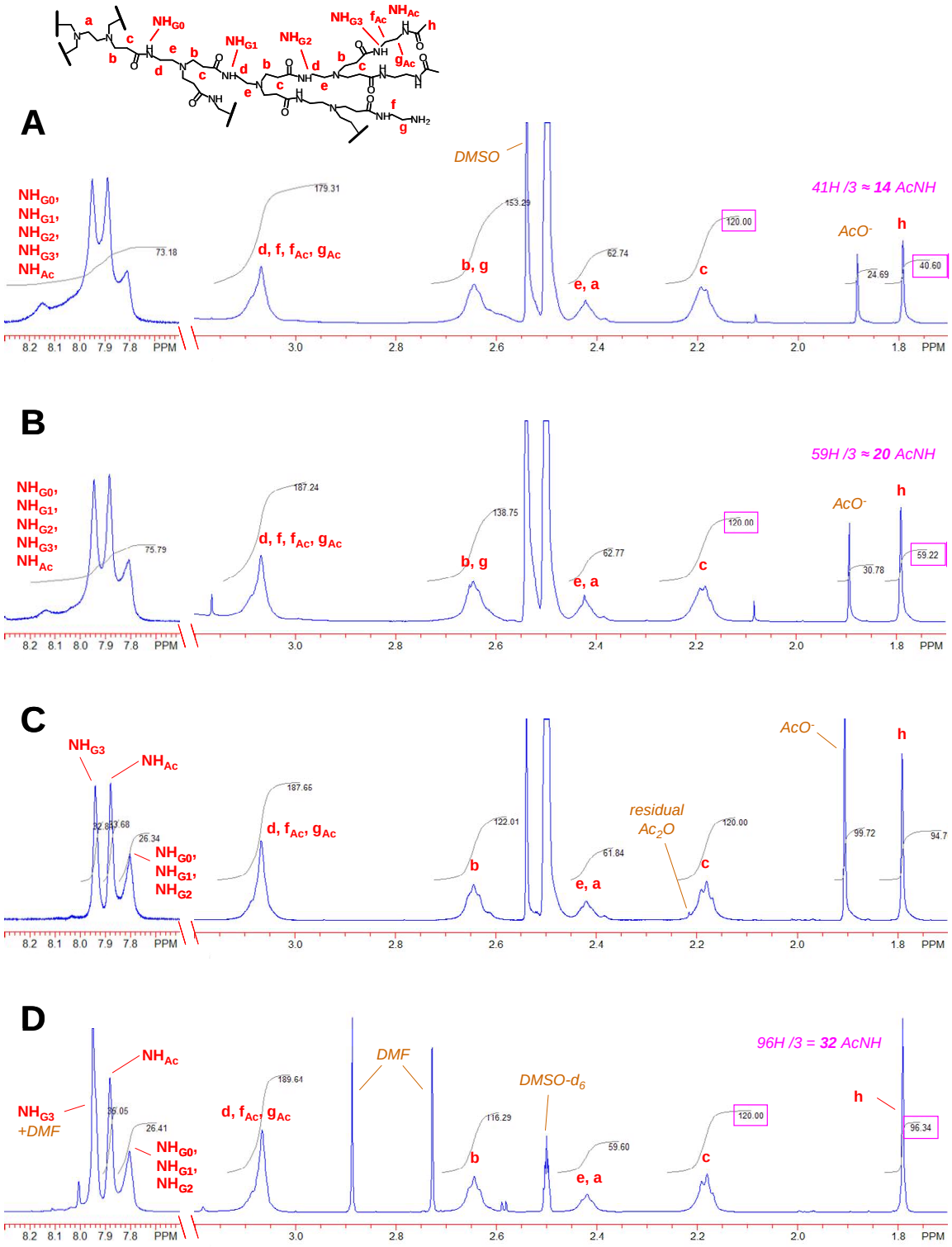

Figure S1. ^{1}H NMR spectra in DMSO-d_6 of acetylated PAMAM dendrimers (A) **2**, (B) **3**, and (C) **4** as crude reaction mixtures, and (D) **4** after purification by SEC with DMF as an eluent.

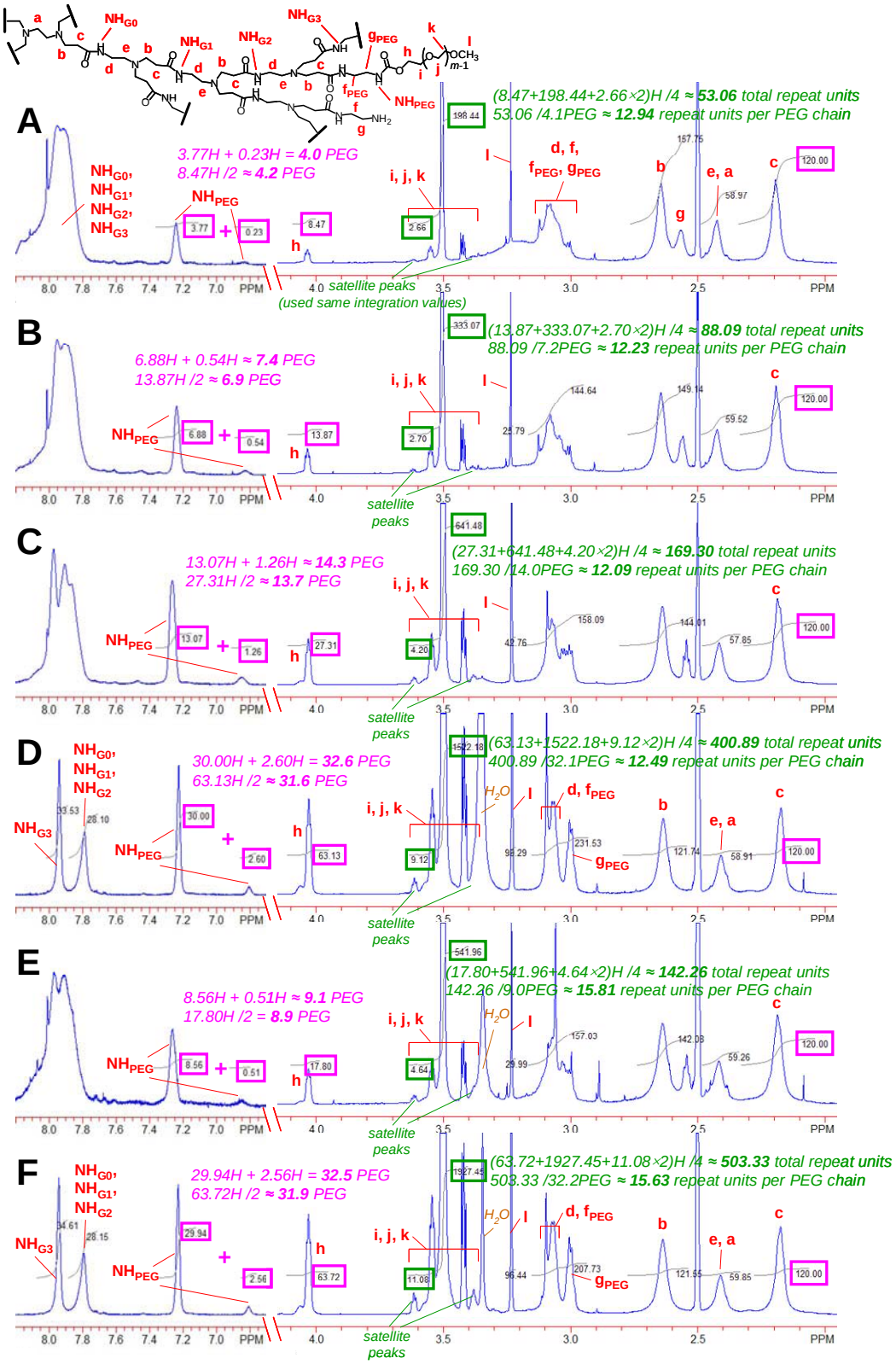

Figure S2. ^{1}H NMR spectra of PAMAM-PEG dendrimer conjugates (A) **8**, (B) **9**, (C) **10**, (D) **11**, (E) **12**, and (F) **13** in DMSO-d_6.

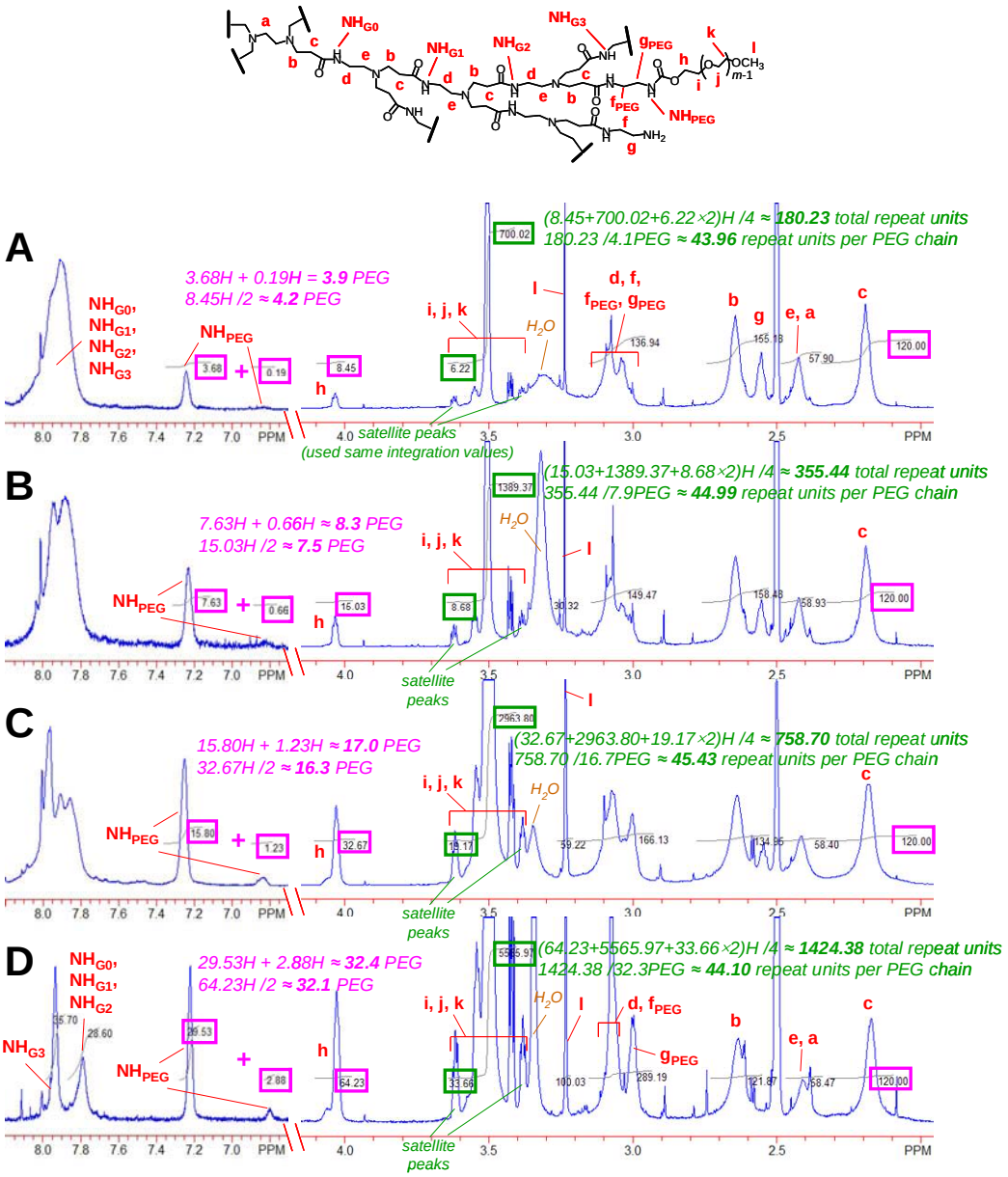

Figure S3. ^{1}H NMR spectra of PAMAM-PEG dendrimer conjugates (A) **14**, (B) **15**, (C) **16**, and (D) **17** in DMSO-d_6.

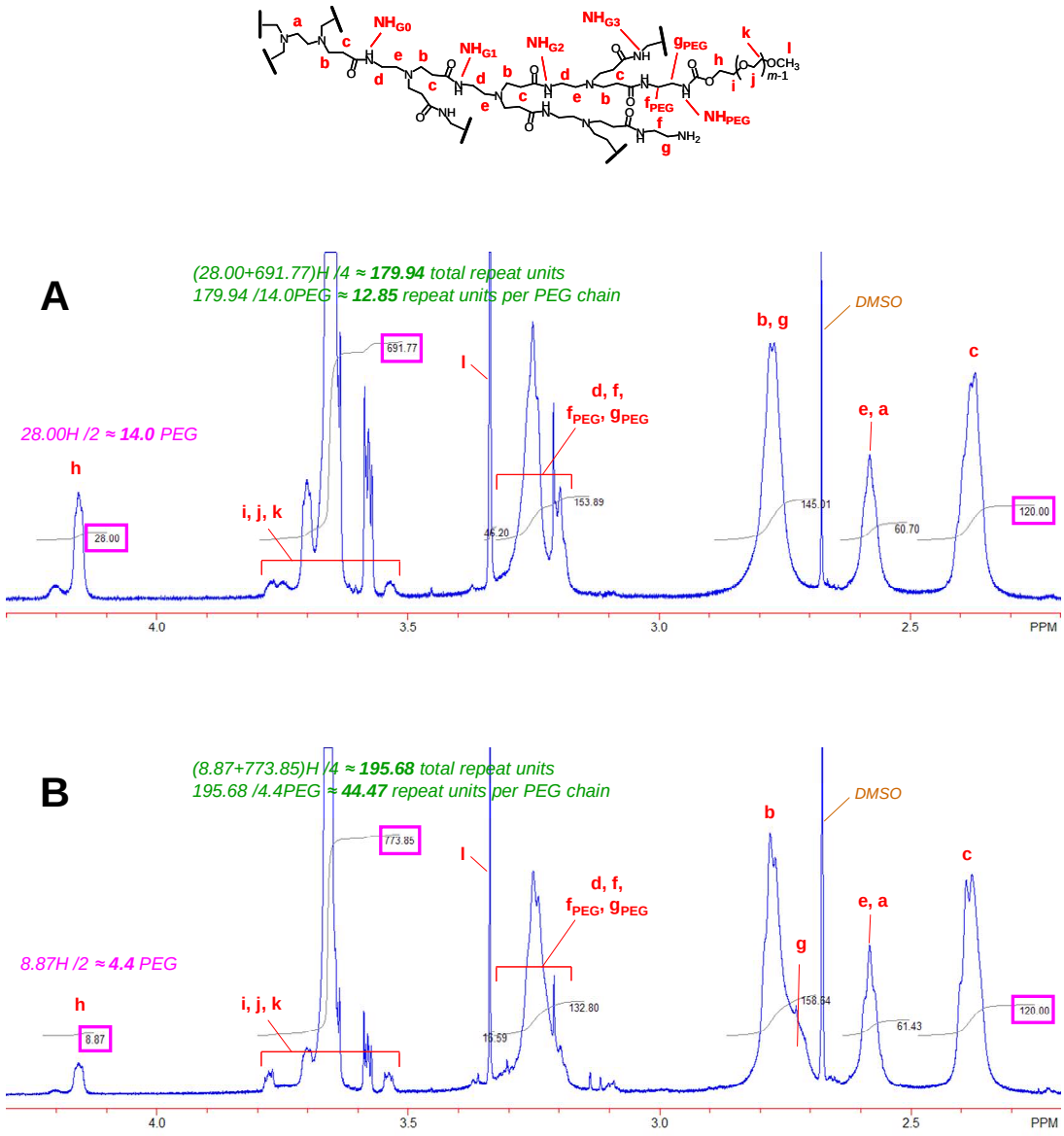

Figure S4. ^{1}H NMR spectra of PAMAM-PEG dendrimer conjugates (A) **10** and (B) **14** in D_2O.

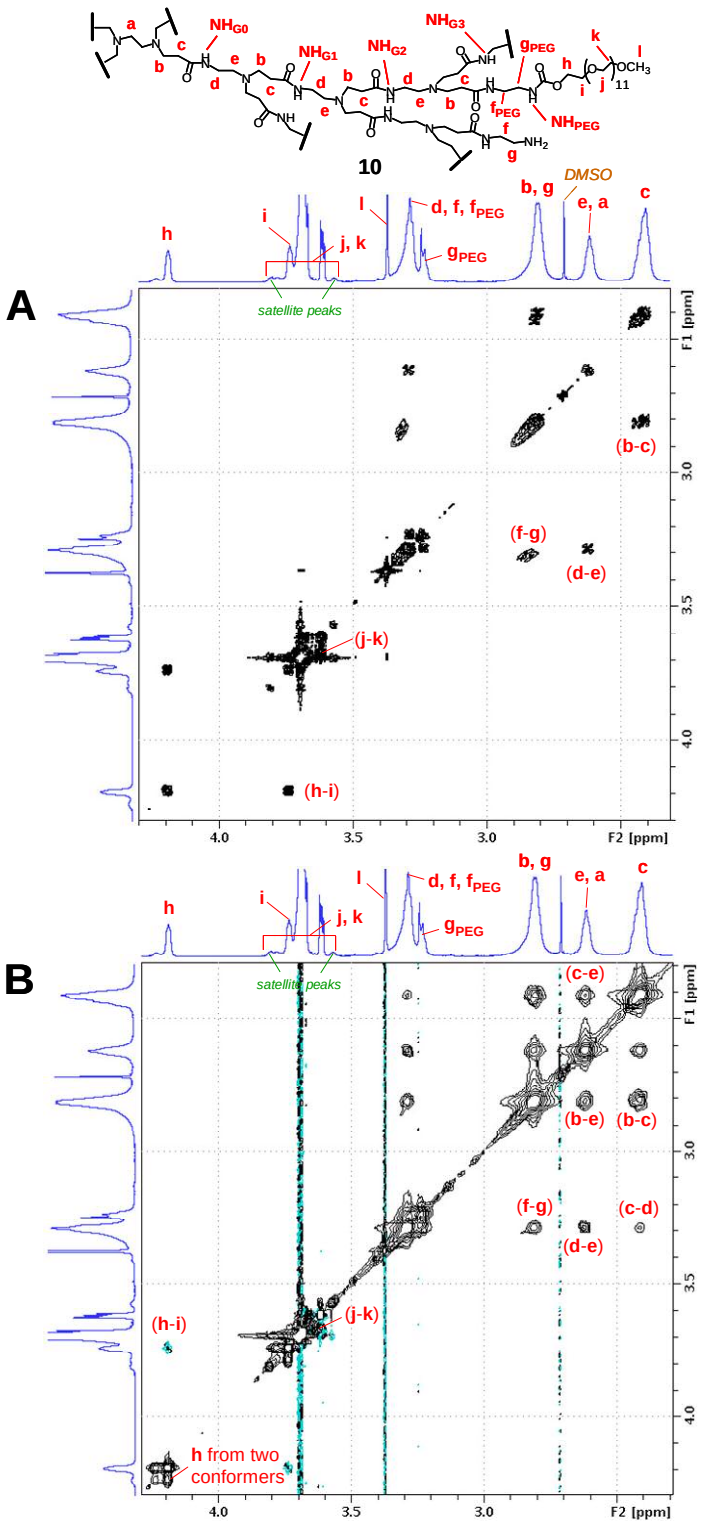

Figure S5. (A) COSY and (B) NOESY spectra of PAMAM-PEG dendrimer conjugate **10** in D_2O.

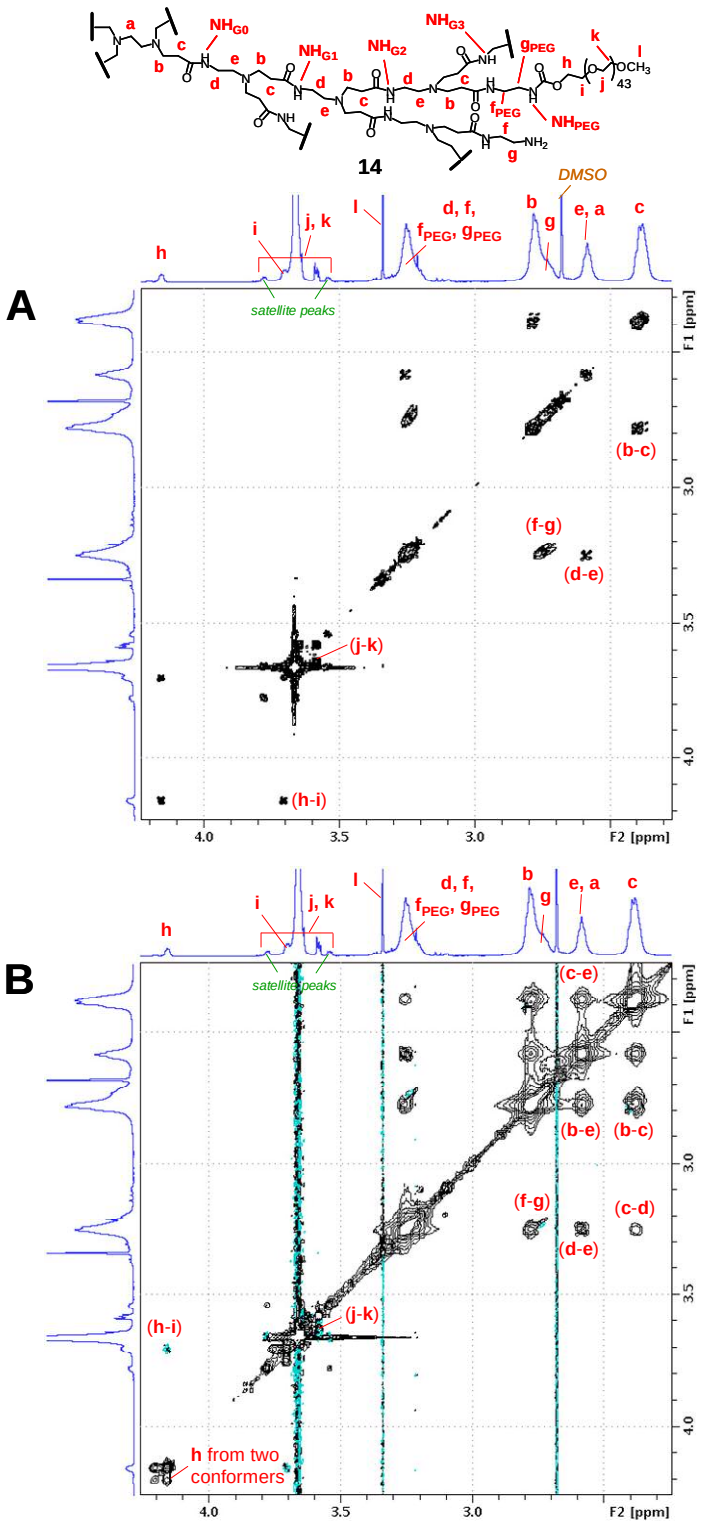

Figure S6. (A) COSY and (B) NOESY spectra of PAMAM-PEG dendrimer conjugate **14** in D_2O.

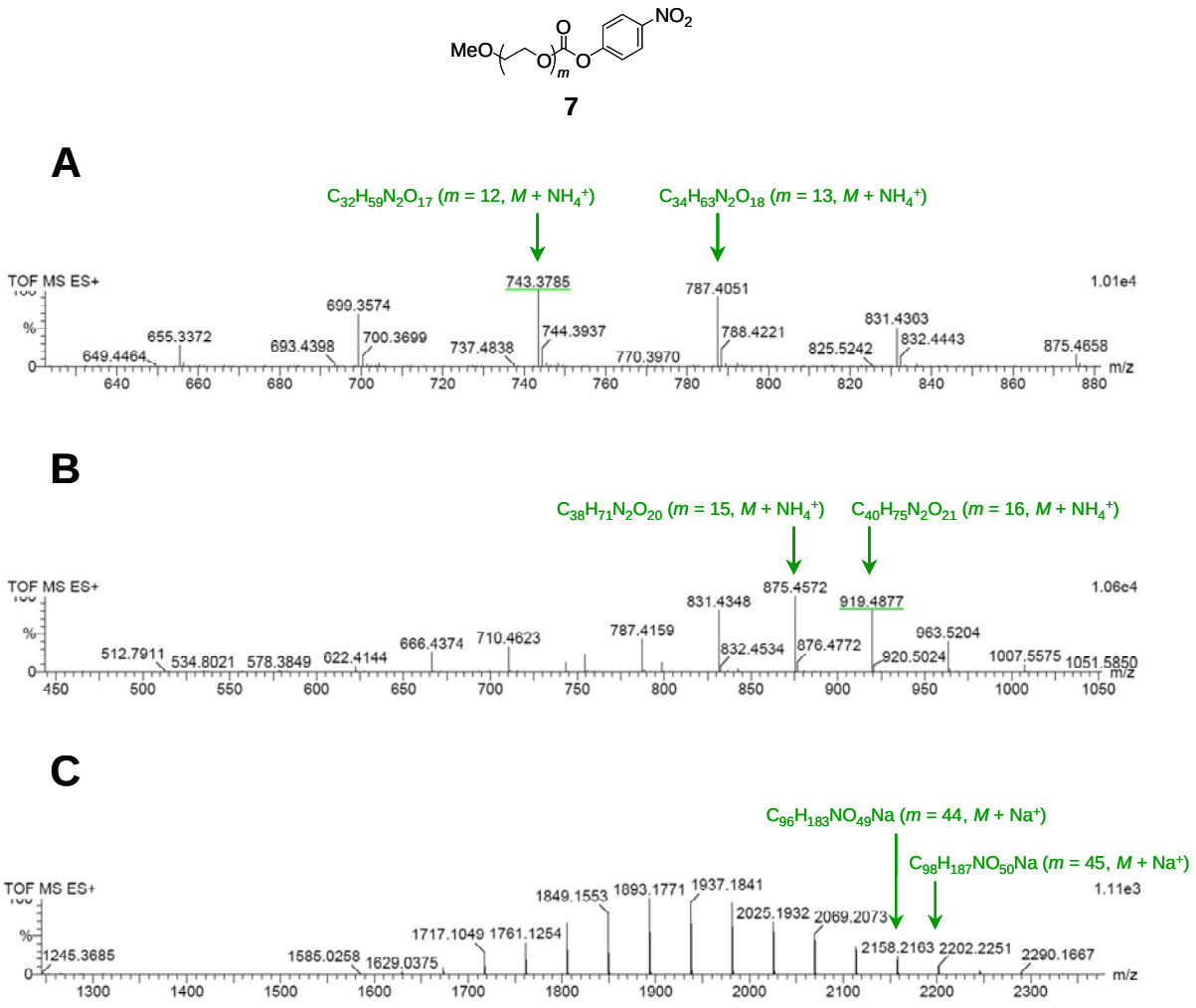

Figure S7. ESI MS of PEG derivatives (A) **7a**, (B) **7b**, and (B) **7c**. Major peaks for each spectrum are separated by c.a. 44 Da, which corresponds to the mass of a PEG repeat unit (C_2H_4O).

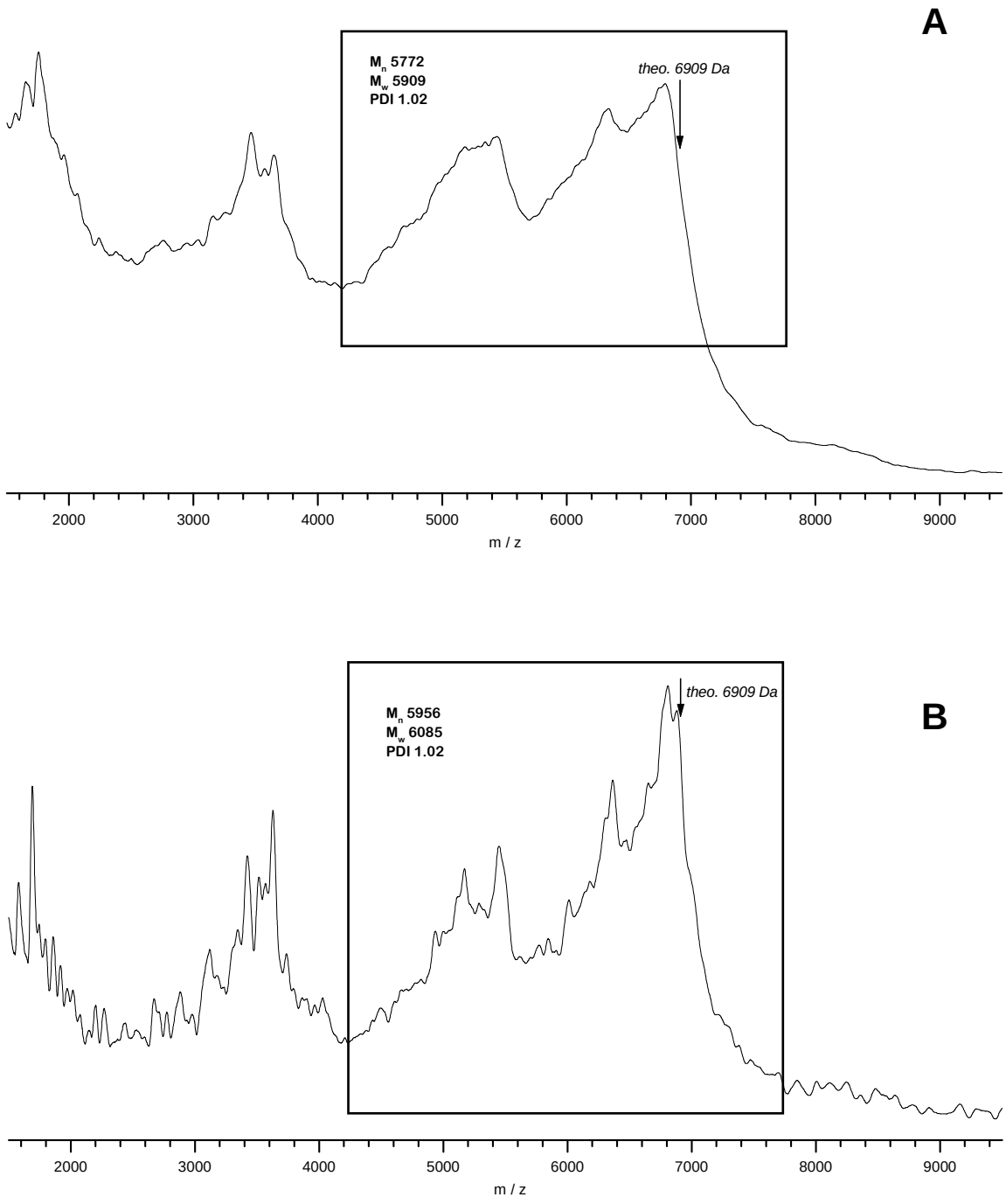

Figure S8. MALDI MS of commercial G3 PAMAM dendrimer **1**: (A) DHB as a matrix; (B) THAP as a matrix. Boxed are the regions selected for the average molecular weight calculations.

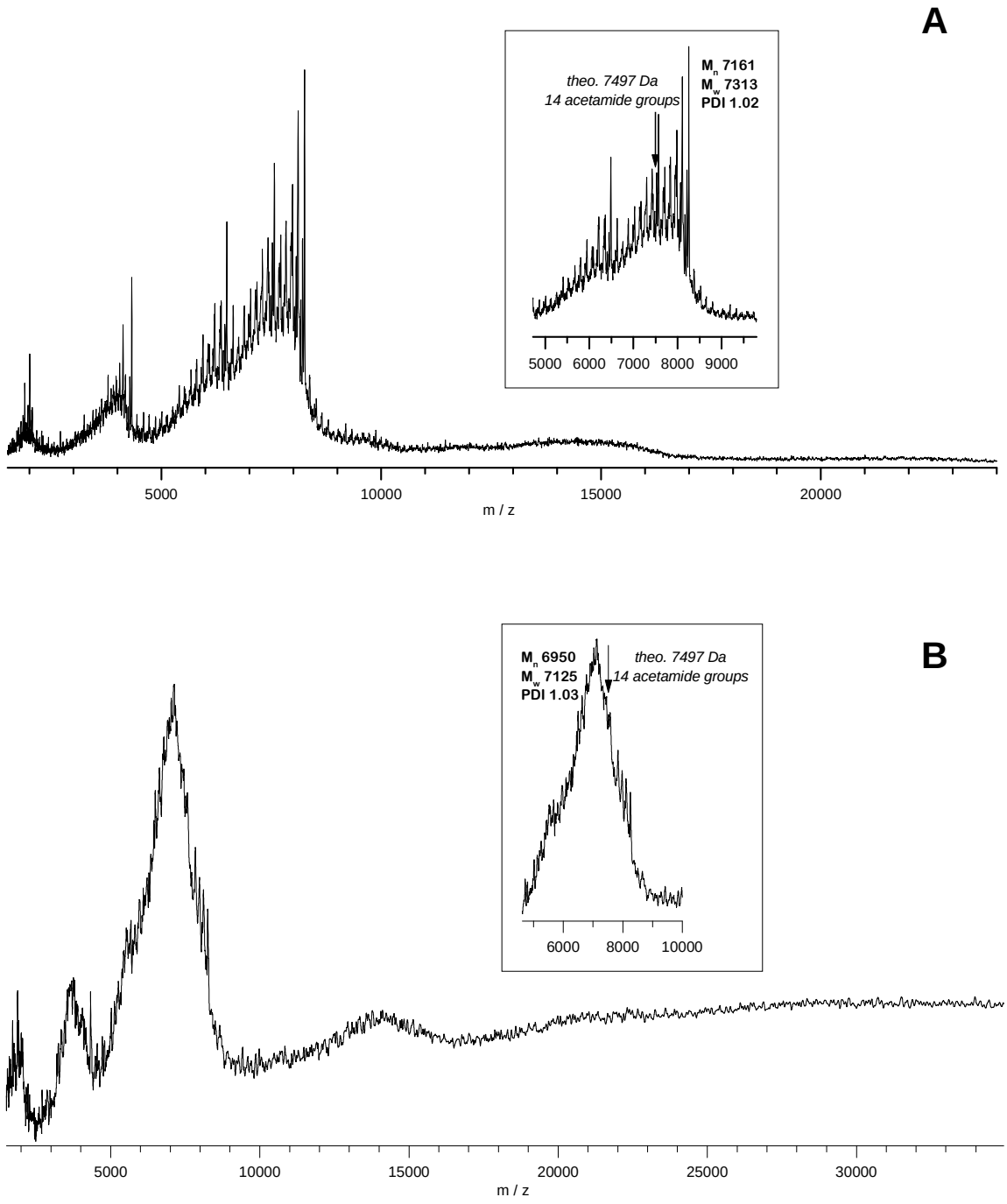

Figure S9. MALDI MS of partially acetylated PAMAM G3 dendrimer **2**: (A) DHB as a matrix; (B) THAP as a matrix. Insets are the regions taken for the average molecular weight calculations.

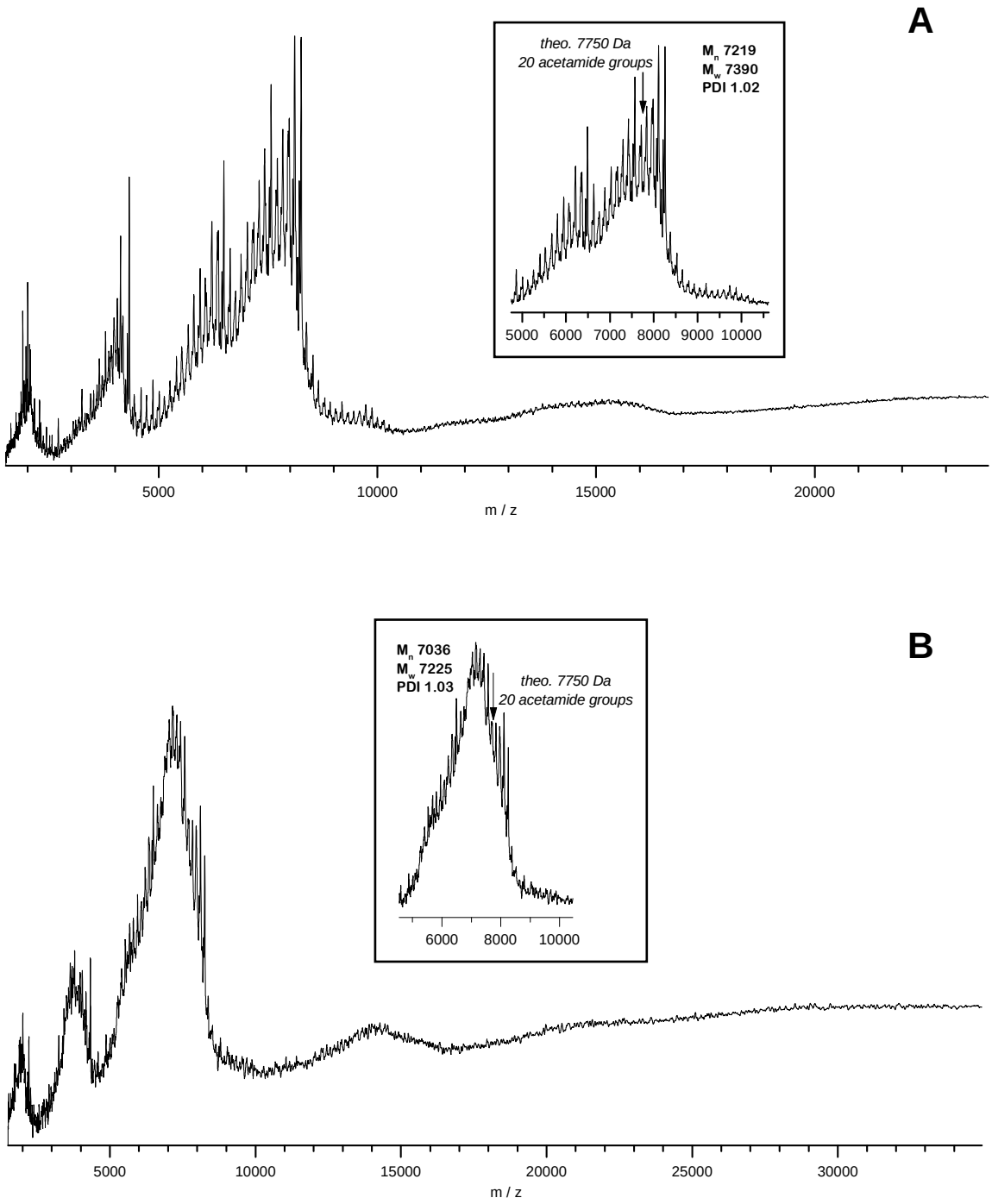

Figure S10. MALDI MS of partially acetylated PAMAM G3 dendrimer **3**: (A) DHB as a matrix; (B) THAP as a matrix. Insets are the regions taken for the average molecular weight calculations.

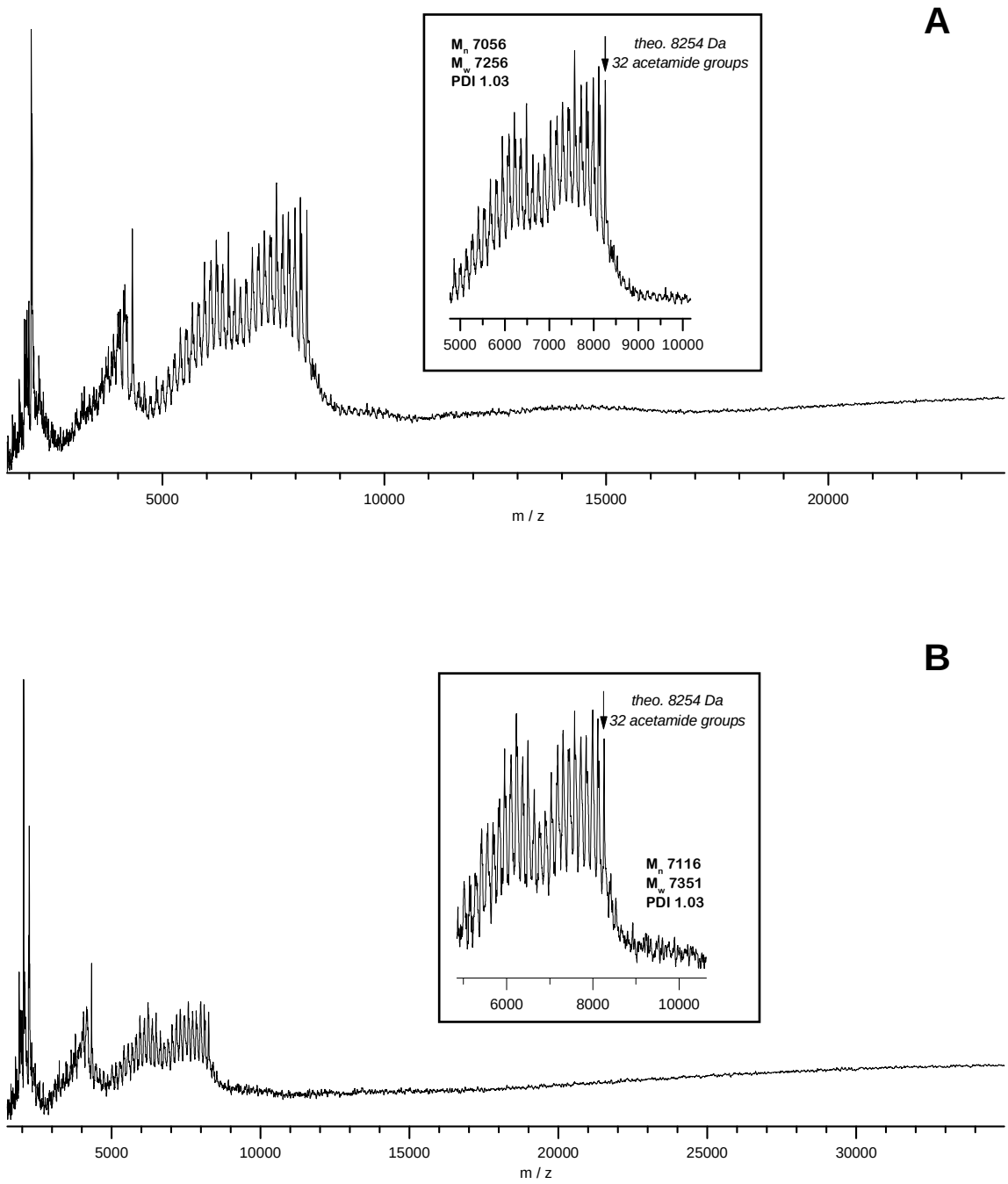

Figure S11. MALDI MS of fully acetylated PAMAM G3 dendrimer **4**: (A) DHB as a matrix; (B) THAP as a matrix. Insets are the regions taken for the average molecular weight calculations.

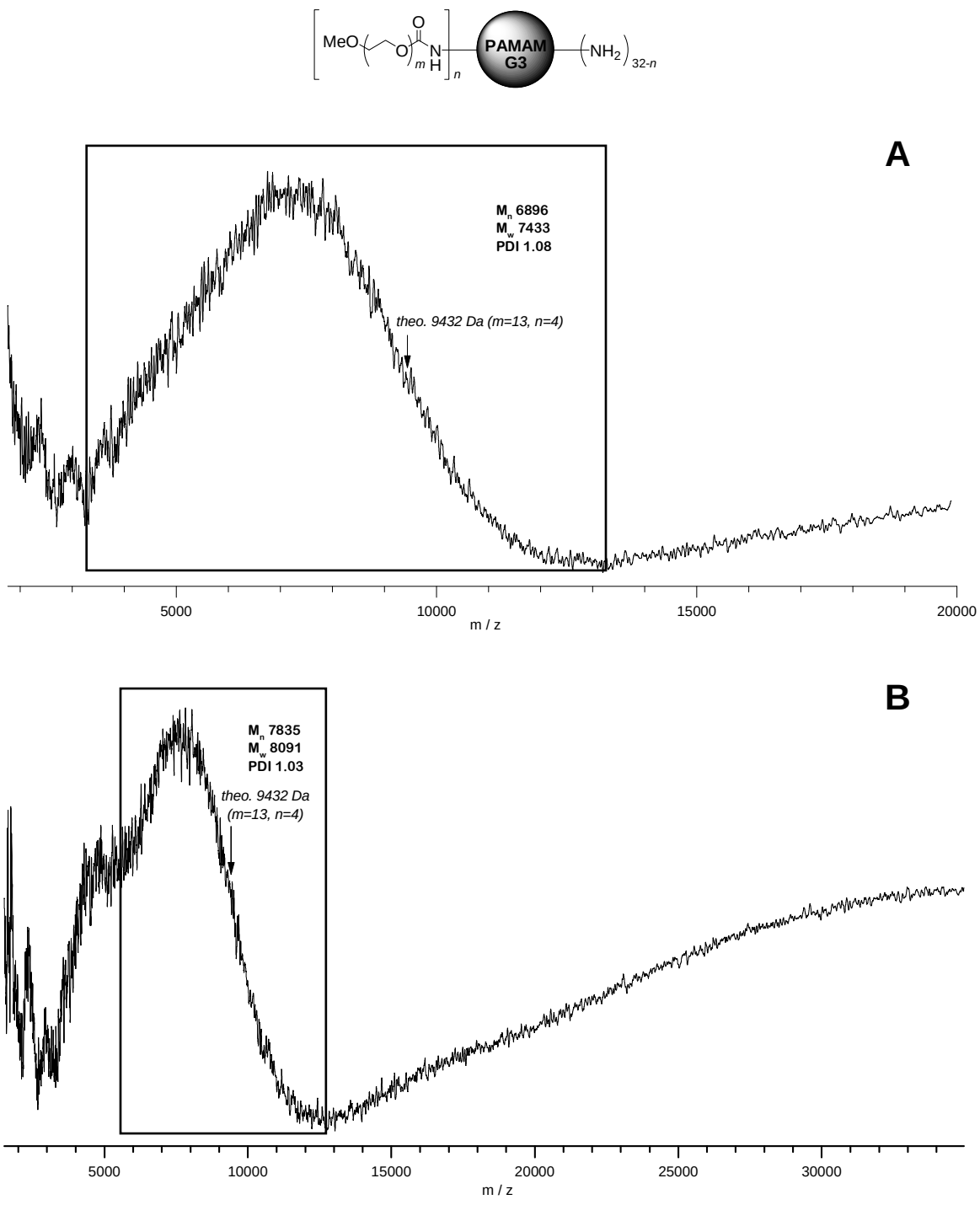

Figure S12. MALDI MS of PAMAM-PEG dendrimer conjugate **8**: (A) DHB as a matrix; (B) THAP as a matrix. Boxed are the regions selected for the average molecular weight calculations, which (partially) contained the peak region corresponding to the half-size of the desired.

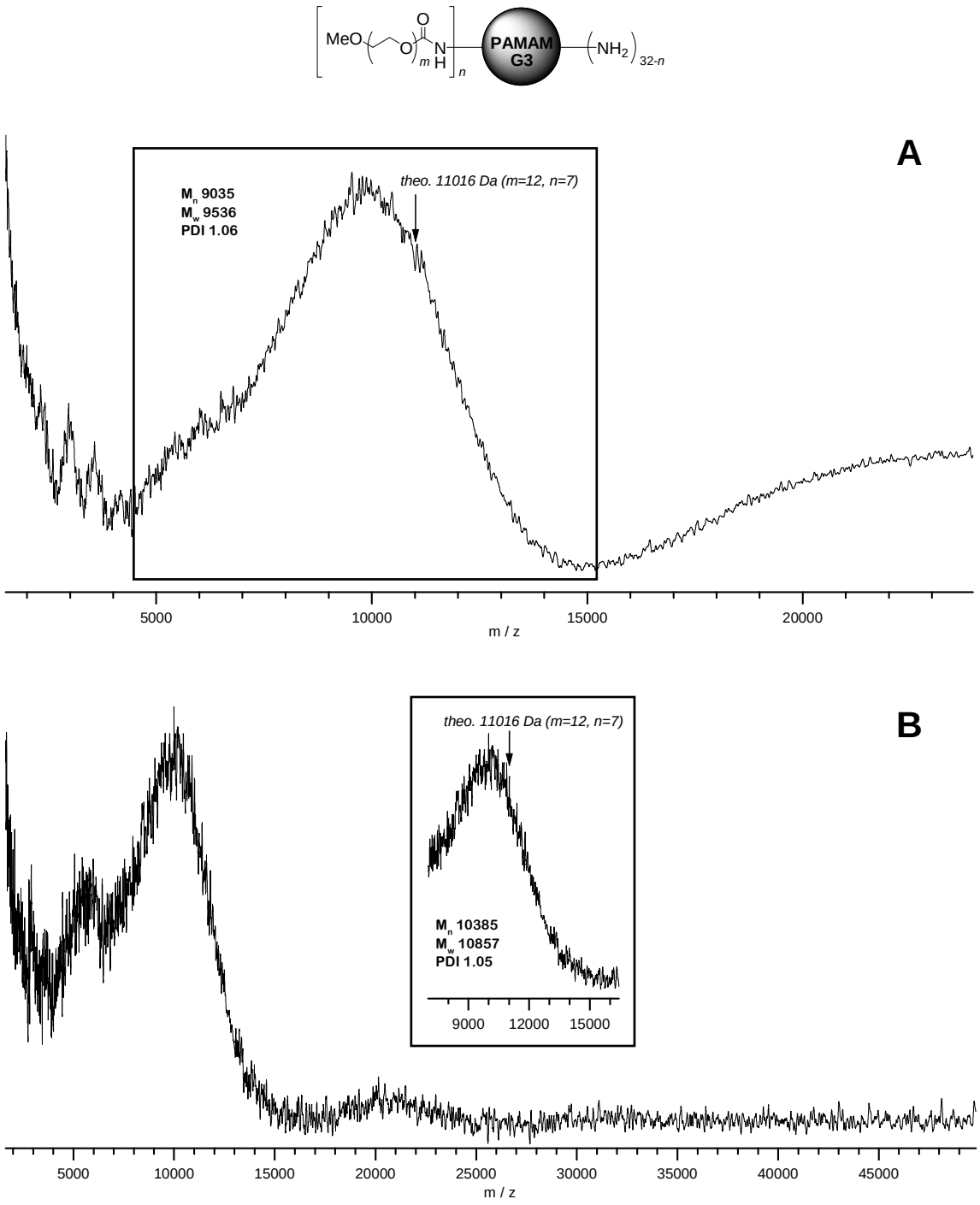

Figure S13. MALDI MS of PAMAM-PEG dendrimer conjugate **9**: (A) DHB as a matrix; (B) THAP as a matrix. Boxed are the regions taken for the average molecular weight calculations, which (partially) contained the peak region corresponding to the half-size of the desired.

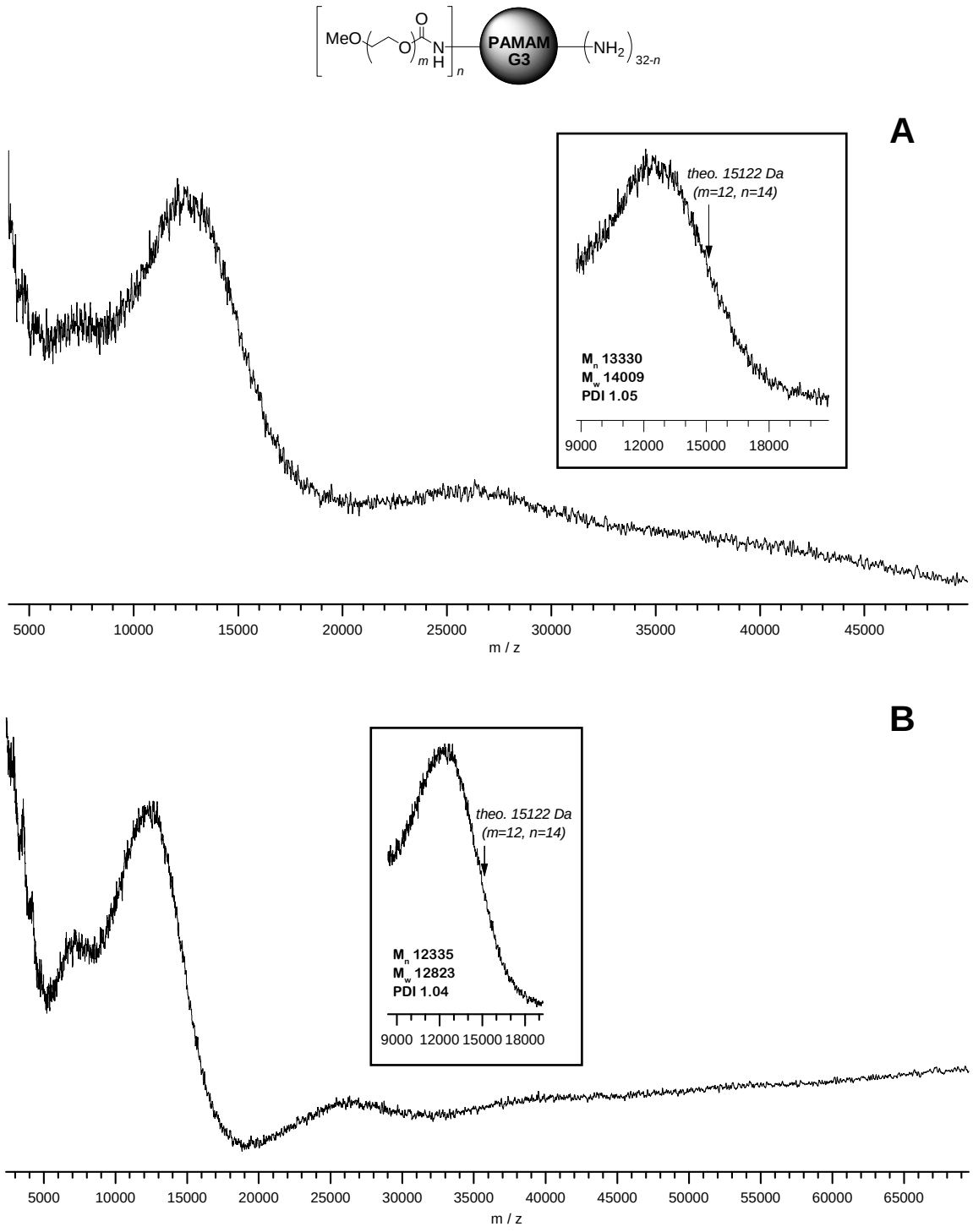

Figure S14. MALDI MS of PAMAM-PEG dendrimer conjugate **10**: (A) DHB as a matrix; (B) THAP as a matrix. Insets are the regions taken for the average molecular weight calculations.

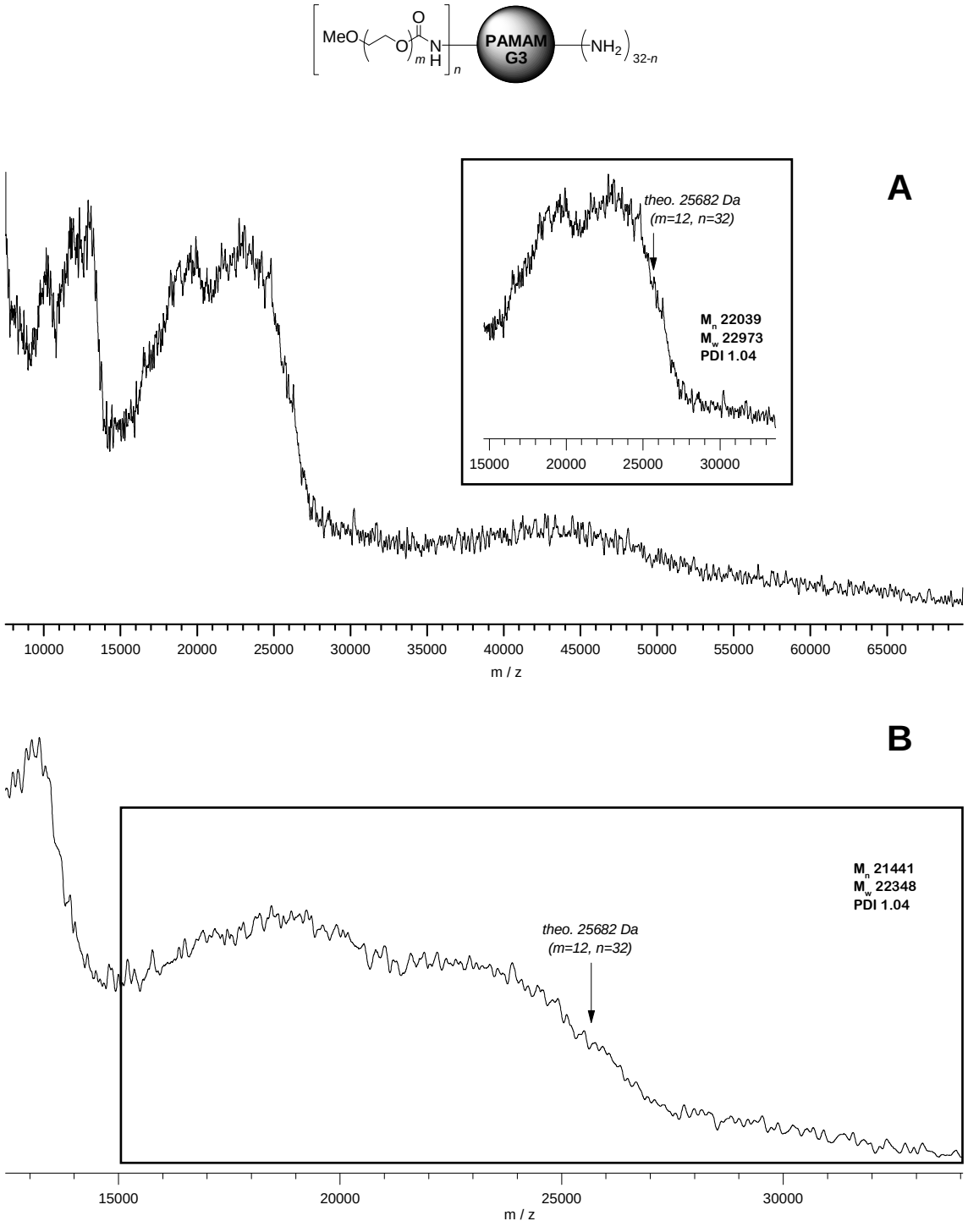

Figure S15. MALDI MS of PAMAM-PEG dendrimer conjugate **11**: (A) DHB as a matrix; (B) THAP as a matrix. Boxed are the regions taken for the average molecular weight calculations.

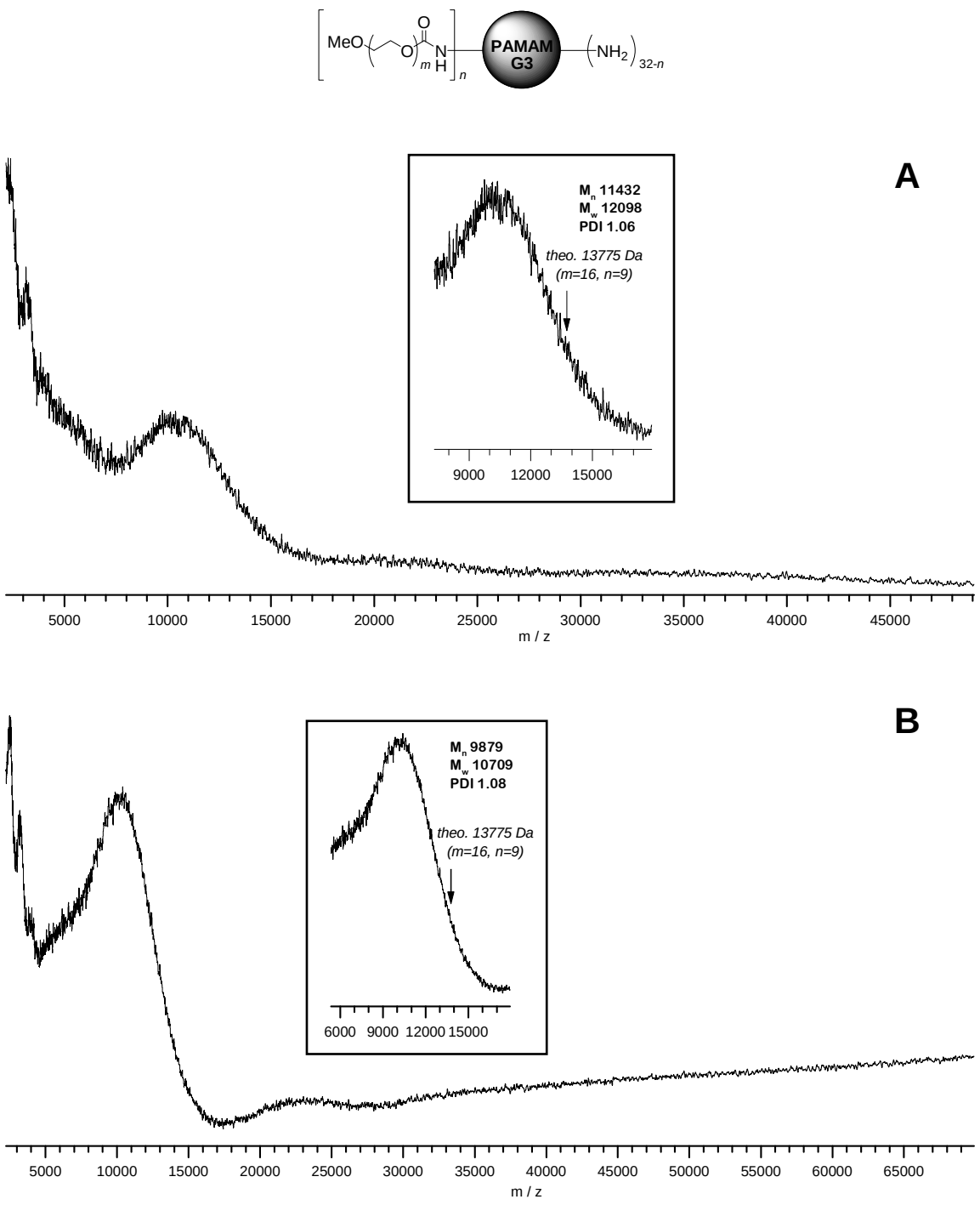

Figure S16. MALDI MS of PAMAM-PEG dendrimer conjugate **12**: (A) DHB as a matrix; (B) THAP as a matrix. Insets are the regions taken for the average molecular weight calculations: for B, the peak region corresponding to the half-size of the desired was partially included for calculations.

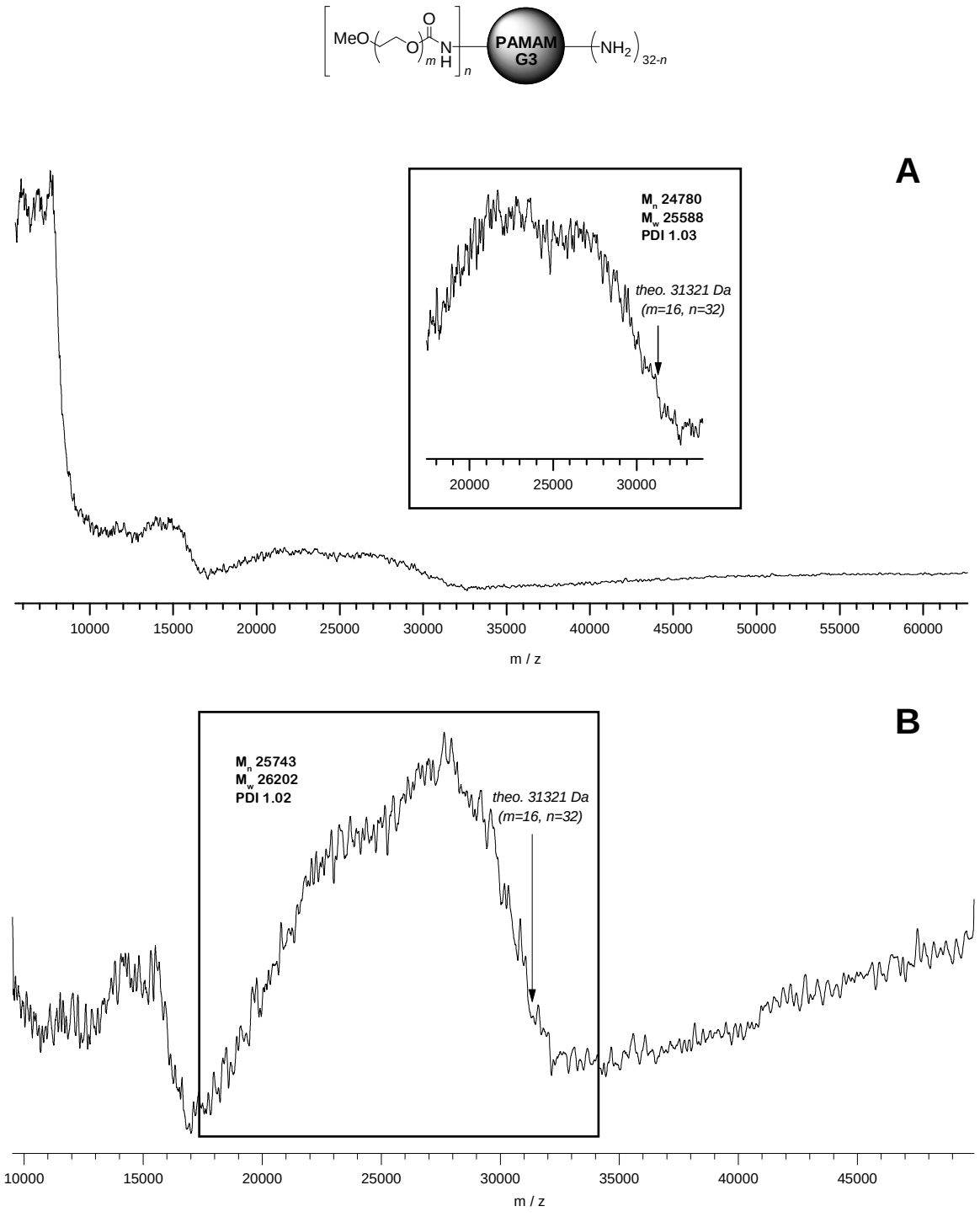

Figure S17. MALDI MS of PAMAM-PEG dendrimer conjugate **13**: (A) DHB as a matrix; (B) THAP as a matrix. Boxed are the regions taken for the average molecular weight calculations.

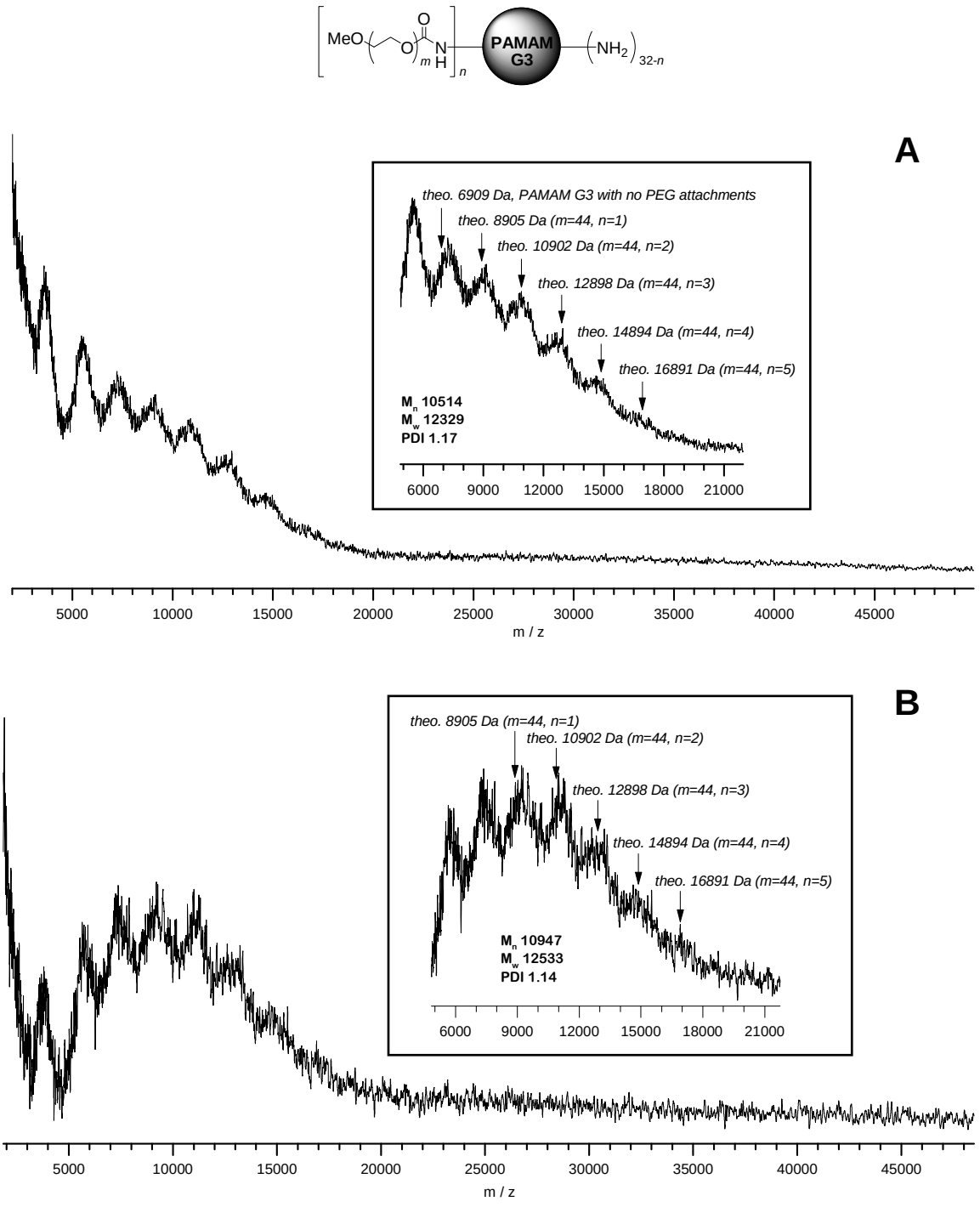

Figure S18. MALDI MS of PAMAM-PEG dendrimer conjugate **14**: (A) DHB as a matrix; (B) THAP as a matrix. Insets are the regions taken for the average molecular weight calculations, which (partially) contained the peak region corresponding to the half-size of the desired.

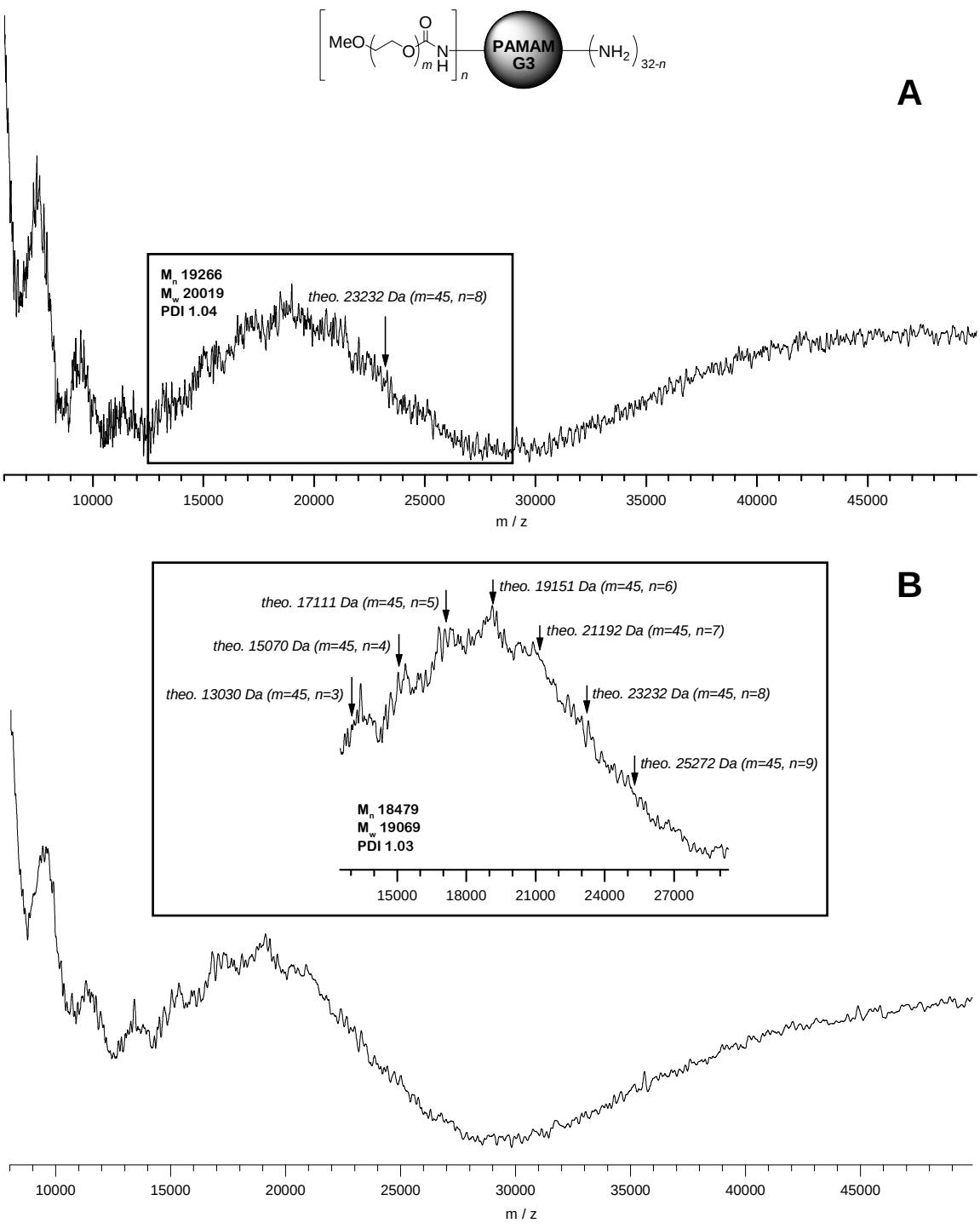

Figure S19. MALDI MS of PAMAM-PEG dendrimer conjugate **15**: (A) DHB as a matrix; (B) THAP as a matrix. Boxed are the regions taken for the average molecular weight calculations: for B, the peak region corresponding to the half-size of the desired was partially included for calculations.

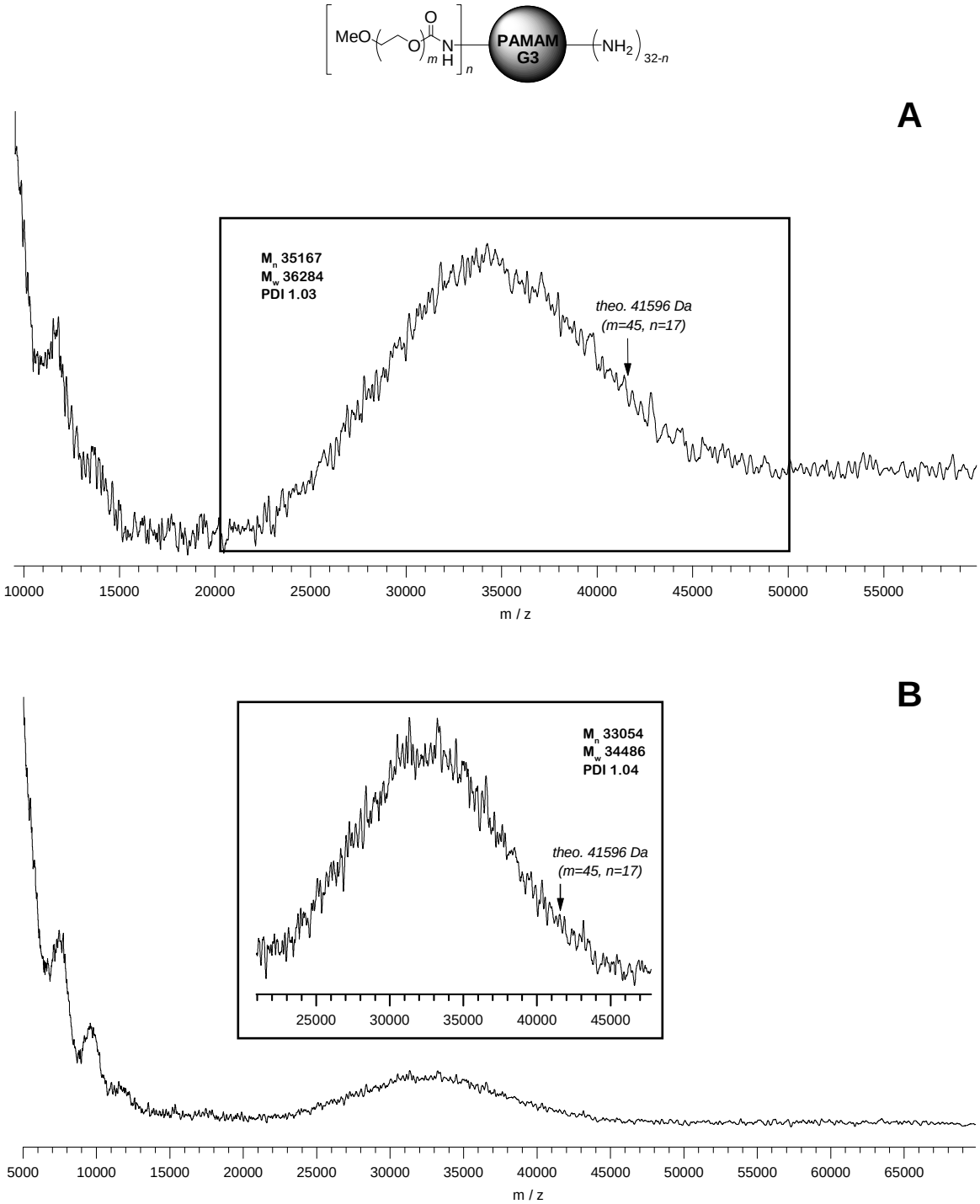

Figure S20. MALDI MS of PAMAM-PEG dendrimer conjugate **16**: (A) DHB as a matrix; (B) THAP as a matrix. Boxed are the regions taken for the average molecular weight calculations.

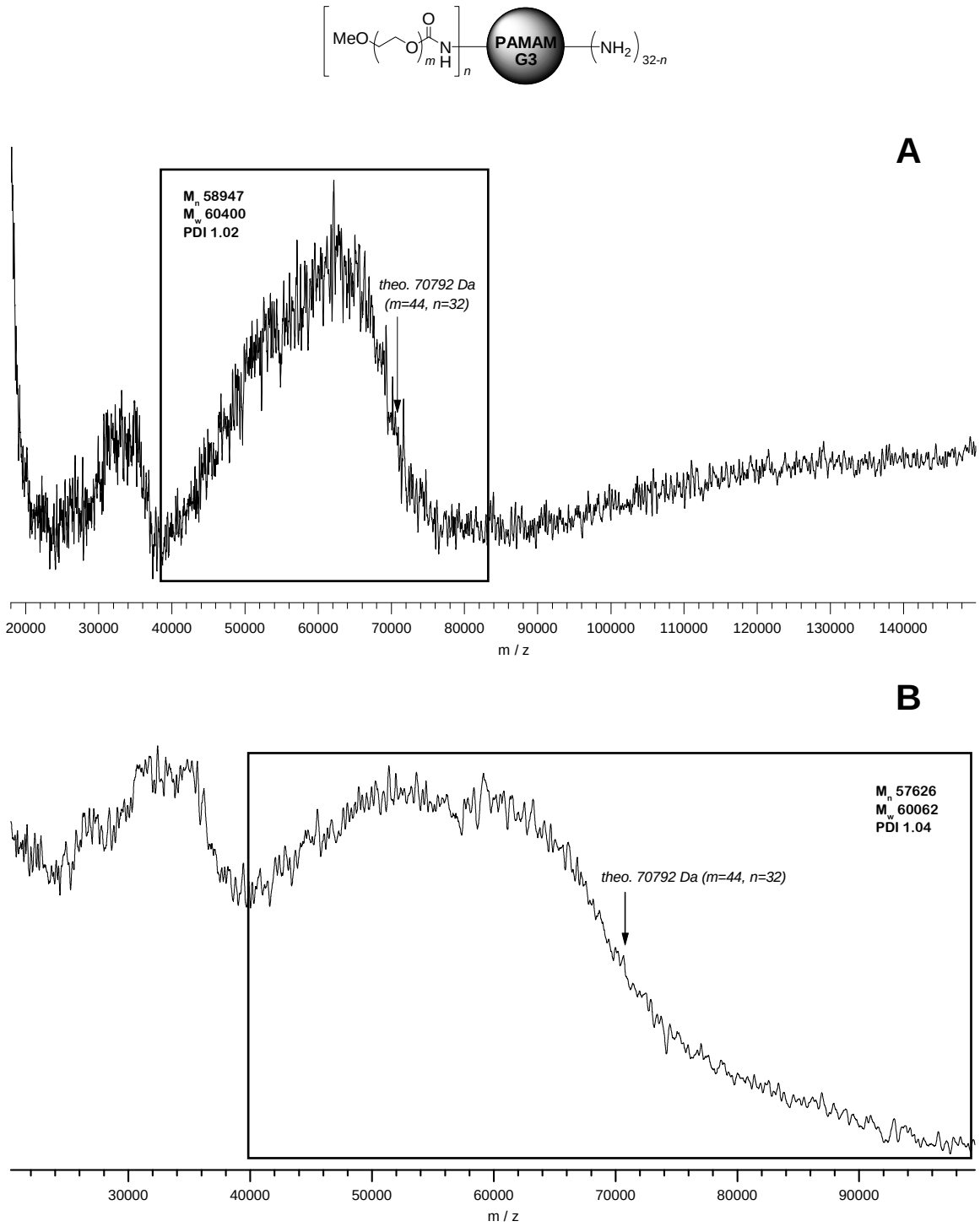

Figure S21. MALDI MS of PAMAM-PEG dendrimer conjugate **17**: (A) DHB as a matrix; (B) THAP as a matrix. Boxed are the regions taken for the average molecular weight calculations.

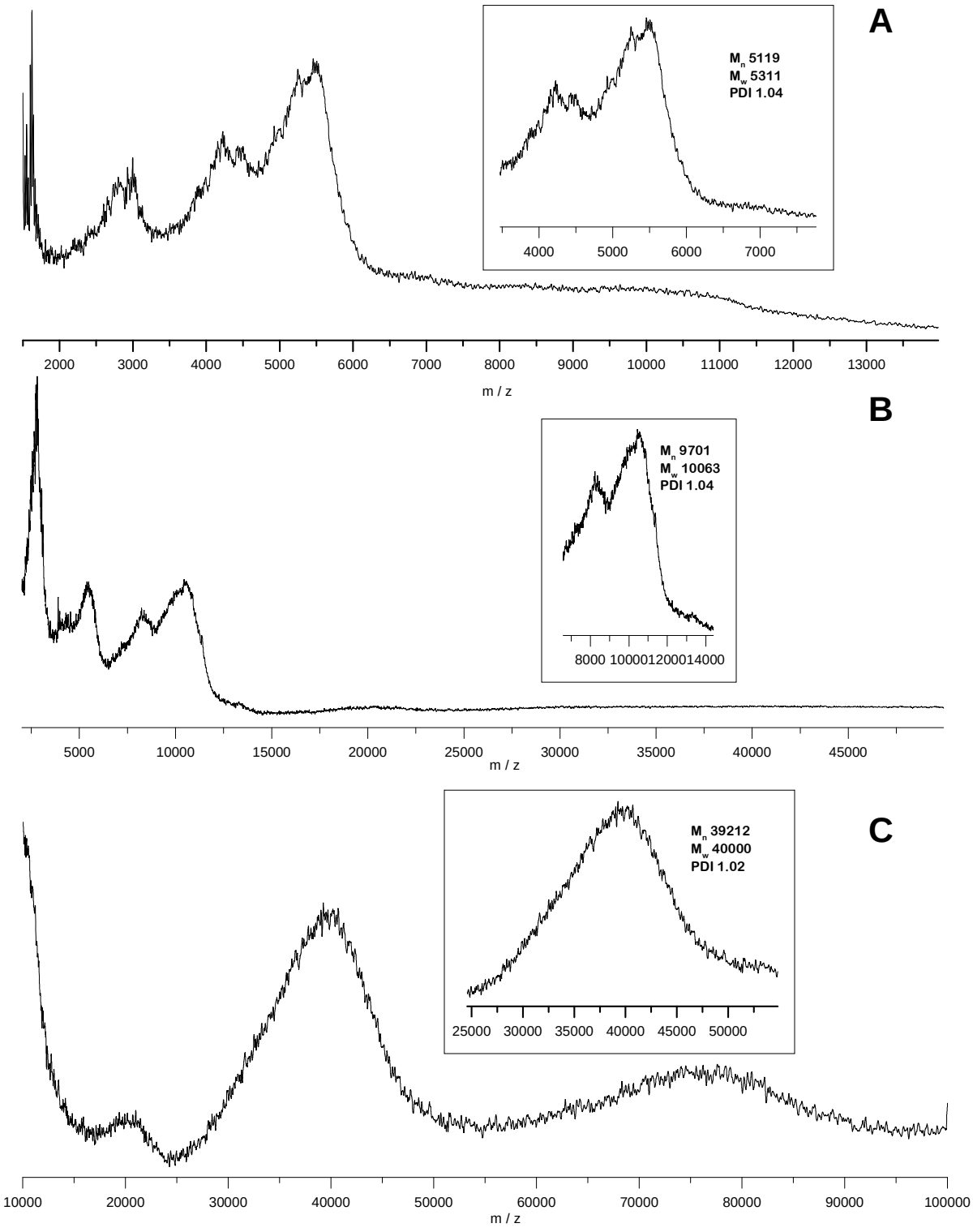

Figure S22. MALDI MS of commercial carboxylate-terminated PAMAM dendrimers each with DHB as a matrix: (A) PAMAM G2.5; (B) PAMAM G3.5; (C) PAMAM G5.5. Insets are the regions taken for the average molecular weight calculations.

Table S1. Cytotoxicity of PAMAM dendrimer derivatives.

cmpd	peripheral groups	no. of peripheral groups	degree of substitution	cell survival (% control)[d]				
				$10^{-6.5}$ M (= 0.32 μM)	$10^{-6.0}$ M (= 1.0 μM)	$10^{-5.5}$ M (= 3.2 μM)	$10^{-5.0}$ M (= 10 μM)	$10^{-4.5}$ M (= 32 μM)
1	—	—	0%	99 ± 2	76 ± 1	62 ± 4	37 ± 2	6 ± 0
2	acetamide	14	44%	87 ± 3	86 ± 2	73 ± 1	31 ± 0	5 ± 0
3	acetamide	20	63%	110 ± 2	88 ± 3	86 ± 1	94 ± 3	28 ± 1
4	acetamide	32	100%	99 ± 4	102 ± 2	104 ± 5	85 ± 2	75 ± 4
8[a]	PEG_{550}	4	13%	95 ± 5	94 ± 4	64 ± 2	41 ± 2	35 ± 2
9	PEG_{550}	7	22%	110 ± 2	101 ± 2	71 ± 2	61 ± 2	48 ± 2
10	PEG_{550}	14	44%	91 ± 0	80 ± 3	78 ± 1	64 ± 1	49 ± 3
11	PEG_{550}	32	100%	99 ± 2	100 ± 5	94 ± 4	94 ± 11	68 ± 2
12	PEG_{750}	9	28%	106 ± 4	106 ± 5	80 ± 2	44 ± 1	40 ± 2
13	PEG_{750}	32	100%	116 ± 1	86 ± 3	89 ± 3	67 ± 2	77 ± 3
14	PEG_{2000}	4	13%	101 ± 2	73 ± 3	46 ± 2	39 ± 1	28 ± 2
15	PEG_{2000}	8	25%	97 ± 2	98 ± 3	93 ± 1	62 ± 2	53 ± 2
16	PEG_{2000}	17	53%	96 ± 1	88 ± 1	75 ± 1	64 ± 1	52 ± 3
17	PEG_{2000}	32	100%	101 ± 1	100 ± 2	88 ± 4	70 ± 2	41 ± 2
18	carboxylate	32[b]	100%[c]	—	106 ± 3	95 ± 3	85 ± 3	98 ± 3
19	carboxylate	64[b]	100%[c]	—	89 ± 1	107 ± 5	112 ± 2	99 ± 4
20	carboxylate	256[b]	100%[c]	—	99 ± 4	88 ± 1	84 ± 2	43 ± 1

[a] The actual concentration of **8** used for cytotoxicity studies may not be accurate due to the lower water-solubility and partial gelation. [b] Assumed to contain theoretical numbers of peripheral groups and no structural defects. [c] Exactly, carboxylate-terminated PAMAM dendrimers were not made by the peripheral substitution, but by stopping the two-step iterative PAMAM dendrimer layer-growth after the first step. [d] Percent cell survival is reported by normalizing each cell count against the value obtained from the corresponding control without the dendrimer, and reported as mean ± standard error (see Experimental Procedures for details).

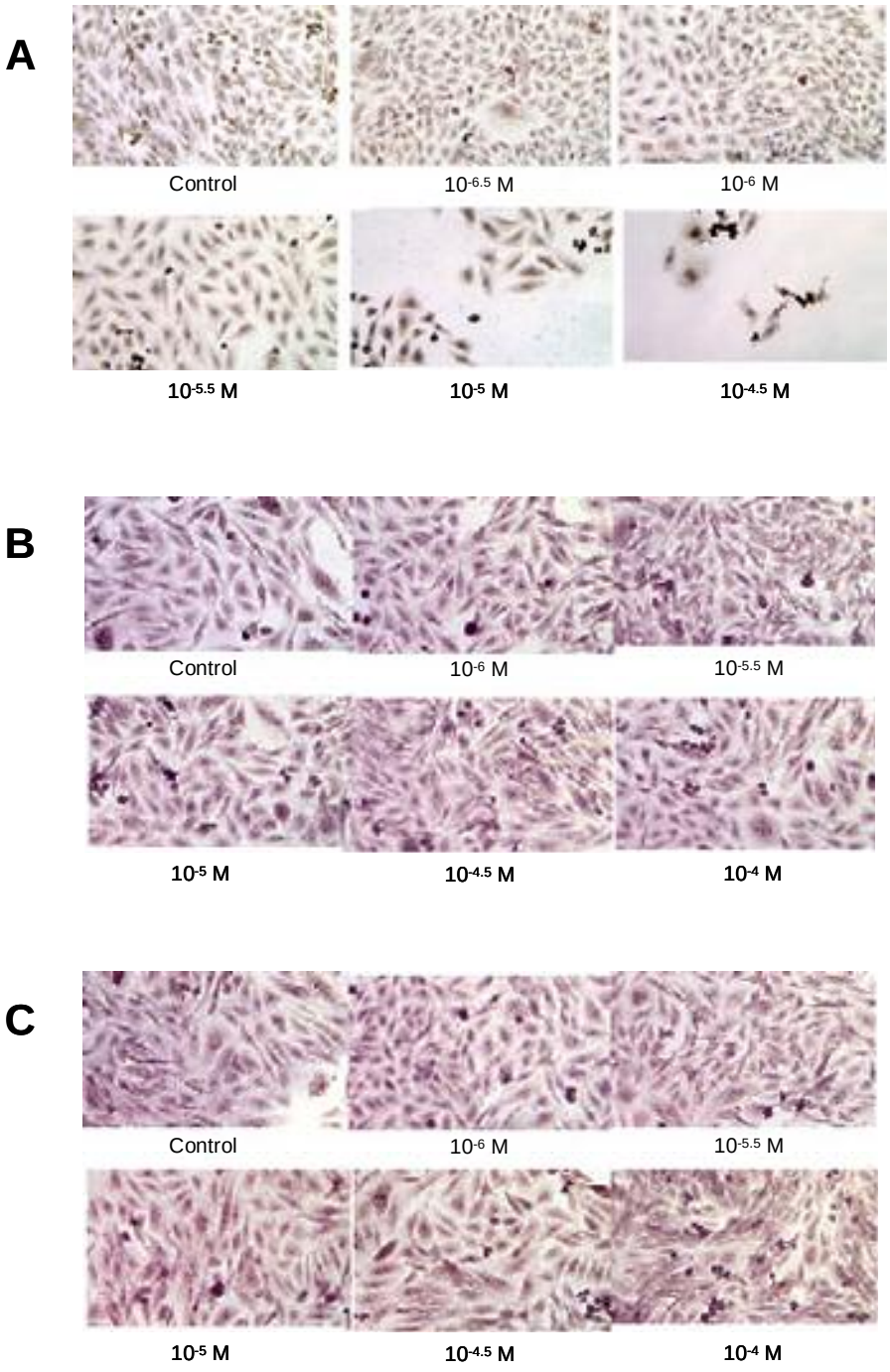

Figure S23. Cytotoxicity micrographs of (A) PAMAM G3 (**1**), (B) PAMAM G2.5 (**18**), and (C) PAMAM G3.5 (**19**) on CHO cells. Concentration of the corresponding dendrimer for control was 0 M.

Anti-CD22-MCC-DM1 and MC-MMAF Conjugates: Impact of Assay Format on Pharmacokinetic Parameters Determination

Jean-Philippe Stephan,*[,†] Pamela Chan,[†] Chien Lee,[‡] Christopher Nelson,[§] James Michael Elliott,[§] Charity Bechtel,[‡] Helga Raab,[§] David Xie,[||] Jon Akutagawa,[†] Jakub Baudys,[⊥] Ola Saad,[⊥] Saileta Prabhu,[||] Wai Lee T. Wong,[†] Richard Vandlen,[§] Fred Jacobson,[‡] and Allen Ebens[#]

Departments of Assay and Automation Technology, Protein Analytical Chemistry, Protein Chemistry, Early Development Pharmacokinetic and Pharmacodynamic Sciences, BioAnalytical Research and Development, and Translational Oncology, Genentech, Inc., 1 DNA Way, South San Francisco, California 94080. Received February 13, 2008; Revised Manuscript Received May 20, 2008

CD22 represents a promising target for antibody−drug conjugate therapy in the context of B cell malignancies since it rapidly internalizes, importing specifically bound antibodies with it. To determine the pharmacokinetic parameters of anti-CD22-MCC-DM1 and MC-MMAF conjugates, various approaches to quantifying total and conjugated antibody were investigated. Although the total antibody assay formats gave similar results for both conjugates, the mouse pharmacokinetic profile for the anti-CD22-MCC-DM1 and MC-MMAF appeared significantly different depending on the conjugated antibody assay format. Since these differences significantly impacted the PK parameters determination, we investigated the effect of the drug/antibody ratio on the total and conjugated antibody quantification using multiple assay formats. Our investigations revealed the limitations of some assay formats to quantify anti-CD22-MCC-DM1 and MC-MMAF with different drug load and in the context of a heterogeneous ADC population highlight the need to carefully plan the assay strategy for the total and conjugated antibody quantification in order to accurately determine the ADC PK parameters.

INTRODUCTION

Antibody−drug conjugate (ADC)[1] therapy, also known as antibody-targeted chemotherapy, is a therapeutic strategy designed to specifically or preferentially deliver a cytotoxic agent to tumor cells through conjugation to a monoclonal antibody that binds to a tumor-associated antigen (*1–3*). Each component of an ADC is important to achieve efficacy with minimal toxicity. First, the antibody should recognize a specific cell surface tumor antigen with no or minimal expression in vital tissue, and should preferentially trigger the internalization of its antigen. Second, the chemical linker between the antibody and the drug must be highly stable in the circulation (*4*), yet exhibit efficient release of the active drug either within the tumor cell or in its vicinity in order to mediate targeted antitumor activity. Multiple types of linker have been developed over the years, from the acid-labile hydrazones and reducible disulfides (*5–8*) to the valine-citrulline dipeptide linkers cleaved by cathepsin (*8, 9*) and the noncleavable more stable linker like the thioether (*10*) and maleimidocaproyl (*9*) linkers designed for maximum serum stability. Finally, the drug itself should be highly potent and remain active after conjugation and release from the ADC. Although the development of an efficacious ADC is in part based on rational design, it is key to keep in mind that each ADC will behave differently in terms of efficacy, toxicity, and pharmacokinetics depending on the tumor cell target. Therefore, multiple combinations of antibodies, linkers, and drugs should be investigated in order to develop the best therapeutic ADC candidate. Reliable determination of the pharmacokinetic profiles of these combinations is, therefore, a critical aspect of ADC characterization.

CD22 is a 140 kDa cell surface glycoprotein of the Siglec (sialic acid-binding immunoglobulin (Ig)-like lectins) family (*11, 12*). CD22 is expressed on the surface of B lymphocytes only during mature stages of differentiation and on their malignant counterparts, but not on other non-B lineage cells or on hematopoietic stem cells (*13–16*). Rapidly internalized, CD22 represents an attractive target for antibody−drug conjugate therapy to treat B-cell malignancies and has been investigated as such in several studies (*17–19*). We targeted CD22 using an anti-CD22 monoclonal antibody conjugated to the antitubulin agents maytansinoid (DM1) (*20, 21*) or monomethyl auristatin F (MMAF) (*9*). Both DM1 and MMAF were conjugated to the antibody through relatively stable linkers. DM1 was conjugated to the lysine residues of the antibody through a thioether linker, succinimidyl-4-(*N*-maleimidomethyl)cyclohexane-1-carboxylate (MCC) (*10*) (anti-CD22-MCC-DM1), while MMAF was coupled via a maleimidocaproyl group to the interchain cysteines (*9*) (anti-CD22-MC-MMAF). To evaluate the stability of these anti-CD22 ADCs *in vivo*, we developed two types of ELISA-based strategies allowing us to measure either the total antibody (conjugated or not) or the drug-conjugated antibody exclusively.

To measure the total anti-CD22 antibody defined as the ADC with a drug/antibody ratio higher or equal to 0, recombinant CD22 extracellular domain (ECD) was used to capture, while a goat anti-human IgG Fc horseradish peroxidase conjugated antibody (GxhFc-HRP) was used for detection. This specific total antibody assay format, which will be referred to as CD22/GxhFc-HRP, was initially compared with a generic human Fc

* Corresponding author. Jean-Philippe Stephan, Genentech, Inc., MS#98, 1 DNA Way, South San Francisco, CA94080; E-mail: stephanj@gene.com.

[†] Assay and Automation Technology.

[‡] Protein Analytical Chemistry.

[§] Protein Chemistry.

[||] Early Development Pharmacokinetic and Pharmacodynamic Sciences.

[⊥] BioAnalytical Research and Development.

[#] Translational Oncology.

[1]Abbreviations: ADC, antibody-drug conjugate; mAb, monoclonal antibody; PAb, polyclonal antibody; ECD, extra-cellular domain; DAR, drug antibody ratio; HIC, hydrophobic interaction chromatography.

10.1021/bc800059t CCC: $40.75 © 2008 American Chemical Society
Published on Web 07/19/2008

Table 1. Schematic Representation and Prevalence of the Different Subpopulations as Percentage of the Total Anti-CD22-MCC-DM1 (A and B, respectively) and Anti-CD22-MC-MMAF (C and D, respectively) ADCs[a]

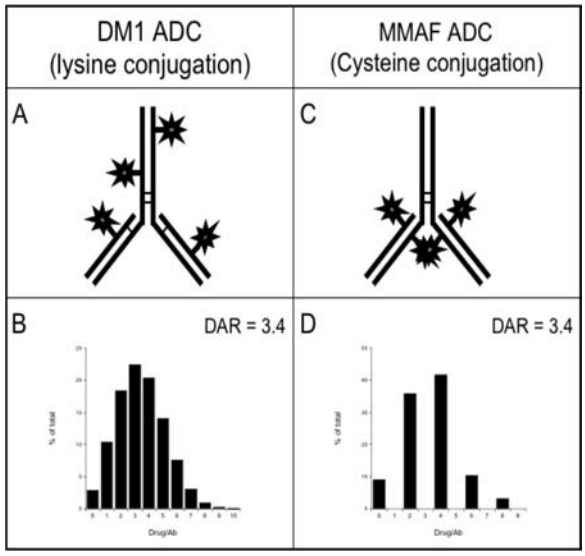

[a] A: many lysines as possible conjugation sites. C: 8 cysteines as possible conjugation sites.

IgG assay format. To measure the drug-conjugated anti-CD22 antibody defined as the ADC with a drug/antibody ratio greater than or equal to 1, recombinant CD22 ECD was used to capture, while an anti-DM1 or anti-MMAF biotinylated antibody followed by streptavidin HRP was used for detection (formats that will be referred to as CD22/xDM1-Biotin and CD22/xMMAF-Biotin assays, respectively). This assay was compared with an anti-DM1 or anti-MMAF antibody coat using biotinylated CD22-ECD combined with streptavidin-HRP to detect (later referred as xDM1/CD22-Biotin and xMMAF/CD22-Biotin assays, respectively). Noticeably, these assays generated significantly different PK profiles in a way that affected the calculation of several critical PK parameters, especially for the conjugated antibody. One critical characteristic of the conventional ADC to consider in our interpretation of the different PK assay results is the fact that maytansine and monomethyl auristatin ADC chemistry results in both positional and stoichiometric heterogeneity. Therefore, we generated anti-CD22-MCC-DM1 enriched mixtures as well as purified anti-CD22-MC-MMAF fractions with various drug loads to investigate the impact of the drug/antibody ratio on the quantification of the anti-CD22 ADCs using different total and conjugated antibody assay formats. Our investigations allowed us to define the advantages and disadvantages of each assay format depending on the anti-CD22 ADC and to highlight the limitations of some assays in their current format to solely and accurately determined the ADC concentration.

EXPERIMENTAL PROCEDURES

Preparation of Anti-CD22-ADCs. Anti-CD22 antibody (10F4v3; huIgG1) (Genentech, Inc. South San Francisco, CA, USA) was generated (*22–25*) and conjugated with SMCC-DM1 (*26*) or MC-MMAF (*9*) as previously described. The average drug to antibody ratio for both ADCs was 3.4 (Table 1).

Preparation of Anti-CD22-MCC-DM1 Enriched Mixtures. Succinimidyl-4-(*N*-maleimidomethyl)cyclohexane-1-carboxylate (SMCC)-*N*(2′)-deacetyl-*N*(2′)-(3-mercapto-1-oxopropyl)-maytansine (DM1) conjugation of anti-CD22 (10F4v3) was performed as described previously (*26*). Although SMCC-DM1 was used for the anti-CD22 antibody conjugation, the ADC is referred to here as anti-CD22-MCC-DM1 to more accurately reflect the chemical structure. The DM1 conjugation reaction was performed using various DM1/Ab ratios in order to generate anti-CD22-MCC-DM1 enriched mixtures with average DARs equal to 0, 1, 4.2, and 8.5 DM1 per Ab. The different preparations were diafiltered with PBS (20×) before characterization as described elsewhere (*26*). The 1 and 4.2 DM1/Ab enriched mixtures were analyzed by mass spectrometry. Mixing the 1 and 4.2 drug/Ab anti-CD22-MCC-DM1 enriched preparations at 2:1 and 1:2 ratios generated the 2.1 and 3.1 drug/Ab enriched mixtures, respectively. Mixing equal amounts of the 4.2 and 8.5 drug/Ab anti-CD22-MCC-DM1 enriched preparations generated the 6.3 drug/Ab enriched mixture.

Isolation of Specific DAR Species from the anti-CD22-MC-MMAF ADC. The separation of the different anti-CD22-MC-MMAF DAR species was performed with a Phenyl-5PW hydrophobic interaction chromatography column (PIN 07573, 7.5 × 75 mm, 10 μm (Tosoh Biosciences Inc., South San Francisco, CA, USA) on an Agilent 1100 HPLC system equipped with a fraction collector (Agilent Technologies Inc., Santa Clara, CA, USA). A linear gradient from 75% of mobile phase A (25% mobile phase B) to 100% mobile phase B over 16 min was used. Mobile phase A was composed of 25 mM sodium phosphate and 1.5 M ammonium sulfate at pH = 6.95. Mobile phase B contained 75% 25 mM sodium phosphate at pH = 6.95 and 25% isopropyl alcohol. The flow rate was 1 mL/min and the column was maintained at 25 °C. The anti-CD22-MC-MMAF sample loading was 1 mg for the preparative scale and 50 μg for the analytical scale. A control DAR = 0 sample was prepared by injecting 150 μg of the unconjugated anti-CD22 antibody and collecting the peak. This amount was approximately the same as that corresponding to the DAR = 0 peak (15% of the total peak area) in a 1 mg injection of the ADC. The peaks of interest (DAR = 0, 2, 4a, 4b, and 6) were collected and reinjected on the analytical column for confirmation of their purity and identity. The anti-CD22-MC-MMAF ADC, the HIC-fractionated peaks and the unconjugated anti-CD22 antibody were reduced at 2 mg/mL with 100 mM DTT in 100 mM Tris-HCl, pH 8.0, for 15 to 30 min at 37 °C. The reduced samples were analyzed on a polymeric reverse phase column (PIN 1912−1502, PLRPS 1000 Å, 50 × 2.1 mm, 5 μm (Varian Inc., Palo Alto, CA, USA)). The sample loading was 2 μg/injection. The separation was achieved at 78 °C using a linear gradient from 25% B to 50% B in 25 min at a flow rate of 0.25 mL/min. Mobile phase A was 0.05% trifluoroacetic acid in water and mobile phase B was 0.04% trifluoroacetic acid in acetonitrile. The fractionated peaks were buffer-exchanged into 10 mM sodium succinate, 10% trehalose, 0.1% PS20 at pH = 5.0 with NAP 5 Columns (GE Healthcare Life Sciences, Piscataway, NJ, USA) following collection.

Sample Generation for Pharmacokinetic Studies. Plasma pharmacokinetic study was conducted at Genentech, Inc., in compliance with National Institutes of Health guidelines for the care and use of laboratory animals and approved by the Institutional Animal Care and Use Committee (IACUC). The study was conducted in non-tumor-bearing CB-17 SCID mice. Mice were randomized into 5 groups of 20 animals such that the mean body weight was not statistically different. Animals were fasted overnight before dosing with anti-CD22 naked antibody at 5 mg/kg, anti-CD22-MCC-DM1 (DAR = 3.4)(Table 1A,B) or anti-CD22-MC-MMAF (DAR = 3.4)(Table 1C,D) at 0.5 and 5 mg/kg as a single intravenous dose. After dosing, mice (4 mice per time point, 3 time points per mouse) were anesthetized by isoflurane inhalation, and blood (200 μL) was collected, by puncture of the retro-orbital plexus at 5 min, 1 and 6 h, and 1, 2, 3, 4, 8, 10, 14, 21, 28, 35, and 44 days after injection. Blood was transferred to lithium heparin tubes and

Table 2. Different Total and Conjugated Antibody Assay Formats[a]

ELISA-based assay		Detection reagent				
		CD22-ECD-Biotin	GxhFc-HRP	GxhF(ab′)$_2$-HRP	Anti-DM1-Biotin	Anti-MMAF-Biotin
Coat reagent	CD22-ECD		Total Ab Assay (A1)	Total Ab Assay (A2)	DM1-conjugated Ab assay (C1)	MMAF-conjugated Ab assay (C2)
	RxhFc		Total Ab Assay (B1)	Total Ab assay (B2)		
	Anti-DM1	DM1-conjugated Ab assay (D1)	DM1-conjugated Ab assay (E1)	DM1-conjugated Ab assay (E2)		
	Anti-MMAF	MMAF-conjugated Ab assay (D2)	MMAF-conjugated Ab assay (E3)	MMAF-conjugated Ab assay (E4)		

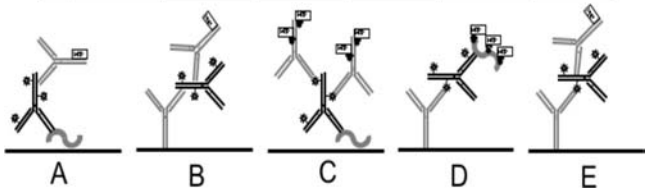

[a] For the total antibody assays various materials were used as coat reagents: CD22-ECD (Schematic A) or RxhFc (Schematic B) with GxhFc-HRP (A1, B1) or GxhF(ab′)$_2$-HRP (A2, B2) as detection reagents, respectively. For the conjugated antibody assay various materials were used as coat reagent: CD22-ECD (Schematic C) with anti-DM1-Biotin (C1) or anti-MMAF-Biotin (C2) as detection reagents; anti-DM1 (D1, E1, E2) with CD22-ECD-Biotin (Schematic D), GxhFc-HRP (schematic E) or GxhF(ab′)$_2$-HRP as detection reagents, respectively; anti-MMAF (D2, E3, E4) with CD22-ECD-Biotin (Schematic D), GxhFc-HRP (Schematic E) or GxhF(ab′)$_2$-HRP as detection reagents, respectively.

immediately placed on ice until centrifugation for collection of the plasma samples.

Total Antibody Pharmacokinetic ELISA-Based Assays. Microtiter plates (96 wells) (Nunc, Rochester, NY, USA) were coated with human CD22 (beta) extracellular domain HIS-tagged (Genentech, Inc.) at 1 μg/mL in coat buffer (0.05 M carbonate/bicarbonate buffer pH 9.6) for the CD22 coat/AffiniPure F(ab′)$_2$ fragment goat anti-human IgG, Fcγ fragment specific HRP conjugated detection (CD22/GxhFc-HRP, format A1, Table 2) and CD22 coat/AffiniPure F(ab′)$_2$ fragment goat anti-human IgG, F(ab′)$_2$ fragment specific HRP conjugated detection (CD22/GxhF(ab′)$_2$-HRP, format A2, Table 2) total assay formats. Microtiter plates (96 wells) were coated with the AffiniPure F(ab′)$_2$ fragment rabbit anti-human IgG, Fcγ fragment specific (RxhFc)(Jackson ImmunoResearch Laboratory, West Grove, PA, US) at 1 μg/mL in coat buffer for the AffiniPure F(ab′)$_2$ fragment rabbit anti-human IgG, Fcγ fragment specific coat/AffiniPure F(ab′)$_2$ fragment goat anti-human IgG, Fcγ fragment specific HRP conjugated detection (RxhFc/GxhFc-HRP, format B1, Table 2) and for the AffiniPure F(ab′)$_2$ fragment rabbit anti-human IgG, Fcγ fragment specific coat/AffiniPure F(ab′)$_2$ fragment goat anti-human IgG, F(ab′)$_2$ fragment specific HRP conjugated detection (RxhFc/GxhF(ab′)$_2$-HRP, format B2, Table 2) total assay formats. After an overnight incubation at 4 °C, assay plates were washed and treated with block buffer (PBS/0.05% Tween 20/0.05% Proclin 300 pH 7.4) for 1 to 2 h before 2 h incubation with anti-CD22-MCC-DM1 or anti-CD22-MC-MMAF standards and samples diluted in sample diluent (PBS/0.5% BSA/10 ppm Proclin/0.05% Tween 20/0.2%BGG/0.25% CHAPS/5 mM EDTA/0.35 M NaCl, pH7.4). Assay plates were first washed 6 times with wash buffer (PBS/0.05% Tween 20) and then incubated for 1 h with the AffiniPure F(ab′)$_2$ fragment goat anti-human IgG, Fcγ fragment specific HRP conjugated (GxhFc-HRP) (Jackson ImmunoResearch Laboratory) diluted to 20 ng/mL (for CD22/ GxhFc-HRP and RxhFc/ GxhFc-HRP) or the AffiniPure F(ab′)$_2$ fragment goat anti-human IgG, F(ab′)$_2$ fragment specific HRP conjugated (GxhF(ab′)$_2$-HRP)(Jackson ImmunoResearch Laboratory) diluted to 80 ng/mL (for CD22/ GxhF(ab′)$_2$-HRP and RxhFc/ GxhF(ab′)2-HRP) in assay buffer (PBS/0.5% BSA/10 ppm Proclin/0.05% Tween 20, pH7.4). After washing (6 times), detection step was done using tetramethylbenzidine (TMB) substrate (Moss, Passadena, MD, USA). Absorbance was measured at 450 nm against a reference wavelength of 620 nm.

DM1-Conjugated Antibody Pharmacokinetic ELISA-Based Assays. Microtiter plates (96 well) (Nunc) were coated either with 1 μg/mL of human CD22 (beta) extra-cellular domain HIS-tagged (Genentech, Inc.) in coat buffer for CD22 coat/biotinylated anti-DM1 antibody detection (CD22/xDM1-Biotin, format C1, Table 2) assay format or anti-DM1 antibody in coat buffer (ImmunoGen, Inc., Cambridge, MA) for anti-DM1 antibody coat/biotinylated CD22 detection (xDM1/CD22-Biotin, format D1, Table 2), anti-DM1 antibody coat/AffiniPure F(ab′)$_2$ fragment goat anti-human IgG, Fcγ fragment specific HRP conjugated detection (xDM1/GxhFc-HRP, format E1, Table 2), and anti-DM1 antibody coat/AffiniPure F(ab′)$_2$ fragment goat anti-human IgG, F(ab′)$_2$ fragment specific HRP conjugated detection (xDM1/GxhF(ab′)$_2$-HRP, format E2, Table 2) assay formats. After an overnight incubation at 4 °C, assay plates were washed and treated with block buffer for 1 to 2 h before 2 h incubation with anti-CD22-MCC-DM1 standards and samples diluted in sample diluent. Assay plates were washed 6 times with wash buffer and incubated for 1 h with either biotinylated anti-DM1 antibody at 13 ng/mL followed by streptavidin-HRP (GE Healthcare Life Sciences) (for CD22 /xDM1-Biotin assay format), human CD22 (beta) extracellular domain HIS-tagged biotinylated followed by streptavidin-HRP (for xDM1/CD22-Biotin), GxhFc-HRP diluted to 20 ng/mL (for xDM1/GxhFc-HRP) or GxhF(ab′)$_2$-HRP diluted to 40 ng/mL (for xDM1/ GxhF(ab′)$_2$-HRP) in assay buffer. After washing (6 times), detection step was carried out using TMB substrate (Moss). Absorbance was measured at 450 nm against a reference wavelength of 620 nm.

MMAF-Conjugated Antibody Pharmacokinetic ELISA-Based Assays. Microtiter plates (96 well) (Nunc) were coated with 1 μg/mL of human CD22 (beta) extracellular domain HIS-tagged (Genentech) in coat buffer for CD22 coat/biotinylated anti-MMAF antibody clone 3.247 detection (Seattle Genetics, Bothell, WA, USA) (CD22 /xMMAF-Biotin, format C2, Table 2) assay format. Microtiter plates (96 well) (Nunc) were coated with 1 μg/mL of anti-MMAF antibody clone 3.247 in coat buffer for anti-MMAF antibody coat/biotinylated CD22 detection (xMMAF/CD22-Biotin, format D2, Table 2), anti-MMAF antibody coat/AffiniPure F(ab′)$_2$ fragment goat anti-human IgG, Fcγ fragment specific HRP conjugated detection (xMMAF/GxhFc-HRP, format E3, Table 2), and anti-MMAF antibody coat/AffiniPure F(ab′)$_2$ fragment goat anti-human IgG, F(ab′)$_2$ fragment specific HRP conjugated detection (xMMAF/GxhF(ab′)$_2$-HRP, format E4, Table 2) assay formats. After an overnight incubation at 4 °C, assay plates were washed and treated with block buffer for 1 to 2 h before 2 h incubation with anti-CD22-MC-MMAF standards and samples diluted in sample diluent. Assay plates were first washed 6 times with wash buffer and then incubated for 1 h with either biotinylated anti-MMAF antibody clone 3.247 at 2.4 ng/mL followed by streptavidin-HRP (GE Healthcare Life Sciences) (for CD22/ xMMAF-Biotin assay format), human CD22 (beta) extracellular domain HIS-tagged biotinylated followed by incubation with streptavidin-HRP (for xMMAF/CD22-Biotin), GxhFc-HRP diluted to 20 ng/mL (for xMMAF/GxhFc-HRP) or GxhF(ab′)$_2$-HRP diluted to 40 ng/mL (for xMMAF/GxhF(ab′)$_2$-HRP) in

A

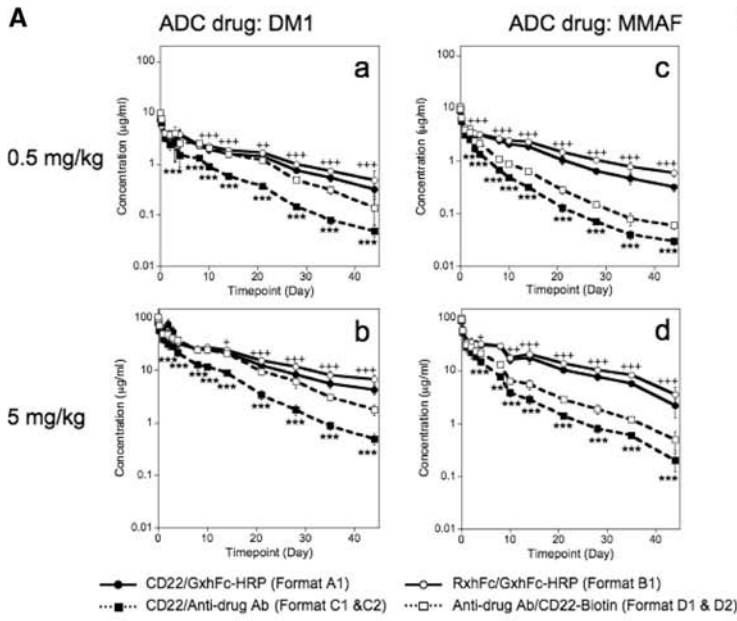

B

Total Ab assay					
		CD22/GxhuFc-HRP		*RxhuFc/GxhuFc-HRP*	
Calculated PK parameters	Dose (mg/kg)	Anti-CD22-MCC-DM1	Anti-CD22-MC-MMAF	Anti-CD22-MCC-DM1	Anti-CD22-MC-MMAF
CL (mL/kg/day)	*0.5*	7.5	7.5	6.2	5.6
	5	5.9	7.4	5.3	6.1
$t_{1/2}$ (days)	*0.5*	11	11	14	15
	5	9.1	12	14	15
V_1 (mL/kg)	*0.5*	50	50	56	46
	5	44	50	47	51
AUC (day×μg/mL)	*0.5*	67	67	81	89
	5	850	680	950	820

Conjugated Ab assay					
		CD22/Anti-drug Ab		*Anti-drug Ab/CD22-Biotin*	
Calculated PK parameters	Dose (mg/kg)	Anti-CD22-MCC-DM1	Anti-CD22-MC-MMAF	Anti-CD22-MCC-DM1	Anti-CD22-MC-MMAF
CL (mL/kg/day)	*0.5*	17	23	8.3	15
	5	14	23	7.2	16
$t_{1/2}$ (days)	*0.5*	6.6	4.8	9.3	5.9
	5	6.2	5	8.8	6.2
V_1 (mL/kg)	*0.5*	60	49	49	48
	5	55	52	47	48
AUC (day×μg/mL)	*0.5*	30	22	61	33
	5	370	210	700	310

Figure 1. (A) Mouse plasma pharmacokinetic analysis. Mice were injected with a single IV dose of anti-CD22-MCC-DM1 (a, b) or anti-CD22-MC-MMAF (c, d) at 0.5 (a, c) and 5 mg/kg (b, d) and plasma samples collected over time up to 44 days. Sample analysis was conducted using two different total assay formats: CD22/GxhFc-HRP (format A1, Table 1) (—●—) or RxhFc/GxhFc-HRP (format B1, Table 1) (—○—), and two different conjugated antibody assay formats: CD22/anti-drug-Biotin (format C1 & C2, Table 1) (--■--) or anti-drug/CD22-Biotin (format D1 & D2, Table 1) (——). For each time point the average concentrations in ng/mL ± STDEV for 4 animals is shown. Total antibody concentrations measured using CD22/GxhFc-HRP format (A1, Table 1) were compared to concentrations measured using RxhFc/GxhFc-HRP format (B1, Table 1). +, $P < 0.05$; ++, $P < 0.01$; +++, $P < 0.001$. Conjugated antibody concentrations measured using CD22/anti-drug-Biotin format (C1 & C2, Table 1) were compared to concentrations measured using anti-drug/CD22-Biotin format (D1 & D2, Table 1). *, $P < 0.05$; **, $P < 0.01$; ***, $P < 0.001$. (B) Mouse pharmacokinetic parameters. Based on the total and conjugated antibody concentrations measured using two different total assay formats (CD22/GxhFc-HRP and RxhFc/GxhFc-HRP) and two different conjugated antibody assay formats (CD22/anti-drug-Biotin and anti-drug/CD22-Biotin), pharmacokinetic parameters were calculated for anti-CD22-MCC-DM1 and anti-CD22-MC-MMAF (*CL*, $t_{1/2}$,V_1, and AUC).

assay buffer. After washing (6 times), detection step was done using TMB substrate (Moss). Absorbance was measured at 450 nm against a reference wavelength of 620 nm.

Pharmacokinetic Analysis. The mean total and conjugated 10F4v3-MCC-DM1 and 10F4v3-MC-MMAF time−concentration data were analyzed using a two-compartmental analysis (Model 200, WinNonlin-Pro, Version 5.0.1; Pharsight Corporation; Mountain View, CA) to obtain the clearance (*CL*), elimination half-life ($t_{1/2}$), volume of distribution (V_1), and drug exposure (AUC).

Statistical Analysis. Assessments of the difference between the total antibody concentrations determined using the CD22/GxhFc-HRP and RxhFc/GxhFc-HRP assay formats, and the difference between the conjugated antibody concentrations determined using the CD22/anti-drug-Biotin and anti-drug/CD22-Biotin assay formats were conducted by applying mixed-effect regression analysis of the log-ratios of the measurements from the two assay formats over the time points. Significance was defined as $P < 0.05$.

RESULTS

Mouse Plasma Pharmacokinetic Analysis Using Various Total and Conjugated Antibody Assay Formats. SCID mice received a single intravenous dose of anti-CD22-MCC-DM1 (DAR = 3.4) (Table 1A,B) or anti-CD22-MC-MMAF (DAR = 3.4) (Table 1C,D) at 0.5 (Figure 1A, panels a and c, respectively) or 5 mg/kg (Figure 1A, panels b and d, respectively). Blood was collected and plasma samples prepared at different times after injection up to 44 days. Samples were subsequently analyzed using two types of ELISA-based assays to either measure the total anti-CD22 antibody (with or without drug) or the drug-conjugated anti-CD22 antibody (defined as the ADC). Initially, two assay formats were investigated as potential total antibody assays (Figure 1A, solid lines). These assays either used CD22-ECD (Format A1, Table 2) or RxhFc to capture (Format B1, Table 2). Both of these total assays used a GxhFc-HRP for detection (see Experimental Procedures section). For both anti-CD22-MCC-DM1 and anti-CD22-MC-MMAF the two total assay formats gave similar pharmacokinetic profiles (Figure 1A). Although the total antibody concentrations measured by the RxhFc/GxhFc-HRP assay (Format B1, Table 2) were consistently slightly higher and significantly different for later time points than those measured by the CD22/GxhFc-HRP assay (Format A1, Table 2), the pharmacokinetic parameters calculated from the different total antibody profiles including clearance (*CL*), elimination half-life ($t_{1/2}$), volume of distribution (V_1), and drug exposure (AUC) were fairly equivalent (Figure 1B). As an example, for anti-CD22-MCC-DM1 the total antibody clearance was 7.5 and 5.9 mL/day/kg at 0.5 and 5 mg/kg, respectively, when assayed with CD22/GxhFc-HRP and 6.2 and 5.3 mL/day/kg at 0.5 and 5 mg/kg, respectively, when assayed with RxhFc/GxhFc-HRP (Figure 1B). Similarly, for anti-CD22-MC-MMAF the total antibody clearance was 7.5 and 7.4 mL/day/kg at 0.5 and 5 mg/kg, respectively, when assayed with CD22/GxhFc-HRP and 5.6 and 6.1 mL/day/kg at 0.5 and 5 mg/kg, respectively, when assayed with RxhFc/GxhFc-HRP (Figure 1B).

Two conjugated antibody assay formats were also implemented (Figure 1A, dotted lines) coating CD22-ECD and detecting through the biotinylated anti-drug antibody (Format C1 and C2, Table 2) or conversely coating the anti-drug antibody and detecting with biotinylated CD22-ECD (Format D1 and D2, Table 2). For both drug types (DM1 or MMAF), the ADC concentrations measured by the CD22/anti-drug-Biotin (Format

C1 and C2, Table 2) were significantly lower than those measured by the anti-drug/CD22-Biotin assays (Format D1 and D2, Table 2) (Figure 1A).

For anti-CD22-MCC-DM1, the conjugated antibody concentrations measured by the two assay formats were significantly different as early as 24 and 48 h at 0.5 and 5 mg/kg, respectively (Figure 1A, panel a and b, respectively). Anti-CD22-MCC-DM1 at 0.5 mg/kg quantified at 3.24 ± 0.46 and 4.06 ± 0.27 μg/mL (mixed-effect regression analysis $P < 0.001$) with CD22/anti-drug-Biotin and anti-drug/CD22-Biotin assay formats, respectively, after 24 h. Anti-CD22-MCC-DM1 at 5 mg/kg quantified at 32.3 ± 7.2 and 49.4 ± 10.8 μg/mL (mixed-effect regression analysis $P < 0.001$) with CD22/anti-drug-Biotin and anti-drug/CD22-Biotin assay formats, respectively, after 48 h. For later time points, the difference between the concentrations measured using the two assays increased. For example, anti-CD22-MCC-DM1 at 0.5 mg/kg quantified at 0.08 ± 0.01 and 0.31 ± 0.05 μg/mL (mixed-effect regression analysis $P < 0.001$) with CD22/anti-drug-Biotin and anti-drug/CD22-Biotin assay formats, respectively, after 35 days. Anti-CD22-MCC-DM1 at 5 mg/kg quantified at 0.9 ± 0.15 and 3.1 ± 0.47 μg/mL (mixed-effect regression analysis $P < 0.001$) with CD22/anti-drug-Biotin and anti-drug/CD22-Biotin assay formats, respectively, after 35 days. These significant differences between the anti-CD22-MCC-DM1 concentrations measured with the two conjugated assay formats resulted in marked difference in calculated PK parameters, especially for the clearance (*CL*) and the drug exposure (AUC) (Figure 1B). The calculated clearance for anti-CD22-MCC-DM1 was 17 and 14 mL/day/kg at 0.5 and 5 mg/kg, respectively, when assayed with CD22/anti-drug-Biotin and 8.3 and 7.2 mL/day/kg at 0.5 and 5 mg/kg, respectively, when assayed with anti-drug/CD22-Biotin. The drug exposure for anti-CD22-MCC-DM1 was 30 and 370 dayxμg/mL at 0.5 and 5 mg/kg, respectively, when assayed with CD22/anti-drug-Biotin and 61 and 700 day/μg/mL at 0.5 and 5 mg/kg, respectively, when assayed with anti-drug/CD22-Biotin.

For anti-CD22-MC-MMAF, the conjugated antibody concentrations measured by the two assay formats were significantly different as early as day 2 and 4 at 0.5 and 5 mg/kg, respectively (Figure 1A, panel c and d, respectively). Anti-CD22-MC-MMAF at 0.5 mg/kg quantified at 2.6 ± 0.15 and 3.5 ± 0.22 μg/mL (mixed-effect regression analysis $P < 0.001$) with CD22/anti-drug-Biotin and anti-drug/CD22-Biotin assay formats, respectively, after 2 days. Anti-CD22-MC-MMAF at 5 mg/kg quantified at 15.2 ± 2.13 and 21.7 ± 3.0 μg/mL (mixed-effect regression analysis $P < 0.001$) with CD22/anti-drug-Biotin and anti-drug/CD22-Biotin assay formats, respectively, after 4 days. For later time points, the difference between the concentrations measured using the two assays increased. For example, anti-CD22-MC-MMAF at 0.5 mg/kg quantified at 0.04 ± 0.007 and 0.08 ± 0.02 μg/mL (mixed-effect regression analysis $P < 0.001$) with CD22/anti-drug-Biotin and anti-drug/CD22-Biotin assay formats, respectively, after 35 days. Anti-CD22-MC-MMAF at 5 mg/kg quantified at 0.6 ± 0.04 and 1.2 ± 0.06 μg/mL (mixed-effect regression analysis $P < 0.001$) with CD22/anti-drug-Biotin and anti-drug/CD22-Biotin assay formats, respectively, after 35 days. These significant differences between the anti-CD22-MC-MMAF concentrations measured with the two conjugated assay formats resulted in marked difference in calculated PK parameters, especially for the clearance (*CL*) and the drug exposure (AUC) (Figure 1B). The calculated clearance was 23 mL/day/kg at 0.5 and 5 mg/kg, when assayed with CD22/anti-drug-Biotin and 15 and 16 mL/day/kg at 0.5 and 5 mg/kg, respectively, when assayed with anti-drug/CD22-Biotin. The drug exposure for anti-CD22-MC-MMAF was 22 and 210 day/μg/mL at 0.5 and 5 mg/kg, respectively, when assayed with CD22/anti-drug-Biotin and 33 and 310 day/μg/mL at 0.5 and 5 mg/kg, respectively, when assayed with anti-drug/CD22-Biotin.

From these initial investigations, we concluded that ELISA-based strategies that use different capture or detection modalities especially for the conjugated antibody assay could yield different pharmacokinetic profiles for the anti-CD22-MCC-DM1 or anti-CD22-MC-MMAF ADCs and therefore impact the calculation of critical PK parameters such as clearance and drug exposure.

Impact of the Total Antibody Assay Format on Anti-CD22-MCC-DM1 Enriched Mixtures Measurement. The differences observed between the mouse plasma pharmacokinetic profiles generated using different total and conjugated antibody assays combined with the fact that conventional ADCs are heterogeneous by nature (Table 1) prompted us to further investigate the impact of the assay format on the detection of anti-CD22-MCC-DM1 enriched mixtures with different DARs. Four total antibody assay formats using either CD22-ECD or RxhFc as coat reagents and GxhFc- or GxhF(ab′)$_2$-HRP conjugates as detection reagents were implemented (Table 2). Four conjugated antibody assay formats were also implemented for each ADC type using either CD22-ECD or anti-drug antibody as coat reagent and biotinylated anti-drug antibody, biotinylated CD22-ECD, GxhFc-HRP, or GxhF(ab′)$_2$-HRP conjugates as detection reagents (Table 2).

Enriched mixtures of anti-CD22-MCC-DM1 with average DAR equal to 0, 1, 3.1, 4.2, 6.5, and 8.5 were generated as described in the Experimental Procedures section and analyzed in four different total antibody assays. The heterogeneity of the anti-CD22-MCC-DM1 enriched mixtures at 1 and 4.2 DM1/Ab were analyzed by mass spectrometry (Figure 2A, panel a and b, respectively). For the 1 DM1/Ab enriched mixture, the range of conjugation was from 0 to 4 drugs/Ab, with the 0 and 4 DAR representing 45% and 0.32% of the entire preparation, respectively (Figure 2A, panel a). For the 4.2 DM1/Ab enriched mixture, the range of conjugation was from 0 to 9 drugs/Ab, with the 0 and 9 DAR representing 2.8% and 0.18% of the entire preparation, respectively (Figure 2A, panel b). Interestingly, similar results were observed with the CD22/GxhFc-HRP (Format A1, Table 2) (Figure 2A, panel c), CD22/GxhF(ab′)$_2$-HRP (Format A2, Table 2) (Figure 2A, panel d), and RxhFc/GxhF(ab′)$_2$-HRP (Format B2, Table 2) (Figure 2A, panel f) assay formats. With these three assay formats, increase in DM1/Ab ratio resulted in a decrease in assay signal (Figure 2A, panel c, d, and f). In addition, the biggest separation in terms of signal for the different preparations was observed with the CD22/GxhF(ab′)$_2$-HRP assay (Format A2, Table 2) (Figure 2A, panel d) with the lowest signal at 39.8% of the 0 DAR maximum absorbance, while the lowest signal was at 56.4% and 67.6% for the CD22/GxhFc-HRP (Format A1, Table 2) (Figure 2A, panel c) and RxhFc/ GxhF(ab′)$_2$-HRP (Format B2, Table 2) (Figure 2A, panel f) assays, respectively. By contrast, the assay format B1 (RxhFc/GxhFc-HRP) (Table 2) was less sensitive to drug load than the other three formats (Figure 2A, panel e). The maximum signal was observed with the anti-CD22-MCC-DM1 enriched mixture with a DM1/Ab ratio of 0 (no drug), while the lowest signal was observed with the mixture at 8.5 DM1/Ab (highest drug load). In the RxhFc/GxhFc-HRP assay (Format B1, Table 2) (Figure 2A, panel e), the different mixtures produced similar results with an average signal equal to 93.4% ± 5.5% of the 0 DAR maximum absorbance.

In conclusion, increasing DM1 load onto the anti-CD22 antibody negatively impacted the CD22/GxhFc-HRP, CD22/GxhF(ab′)$_2$-HRP, and RxhFc/ GxhF(ab′)$_2$-HRP total antibody assay formats but not the RxhFc/GxhFc-HRP assay. This result suggests that increasing stoichiometry of DM1 conjugation

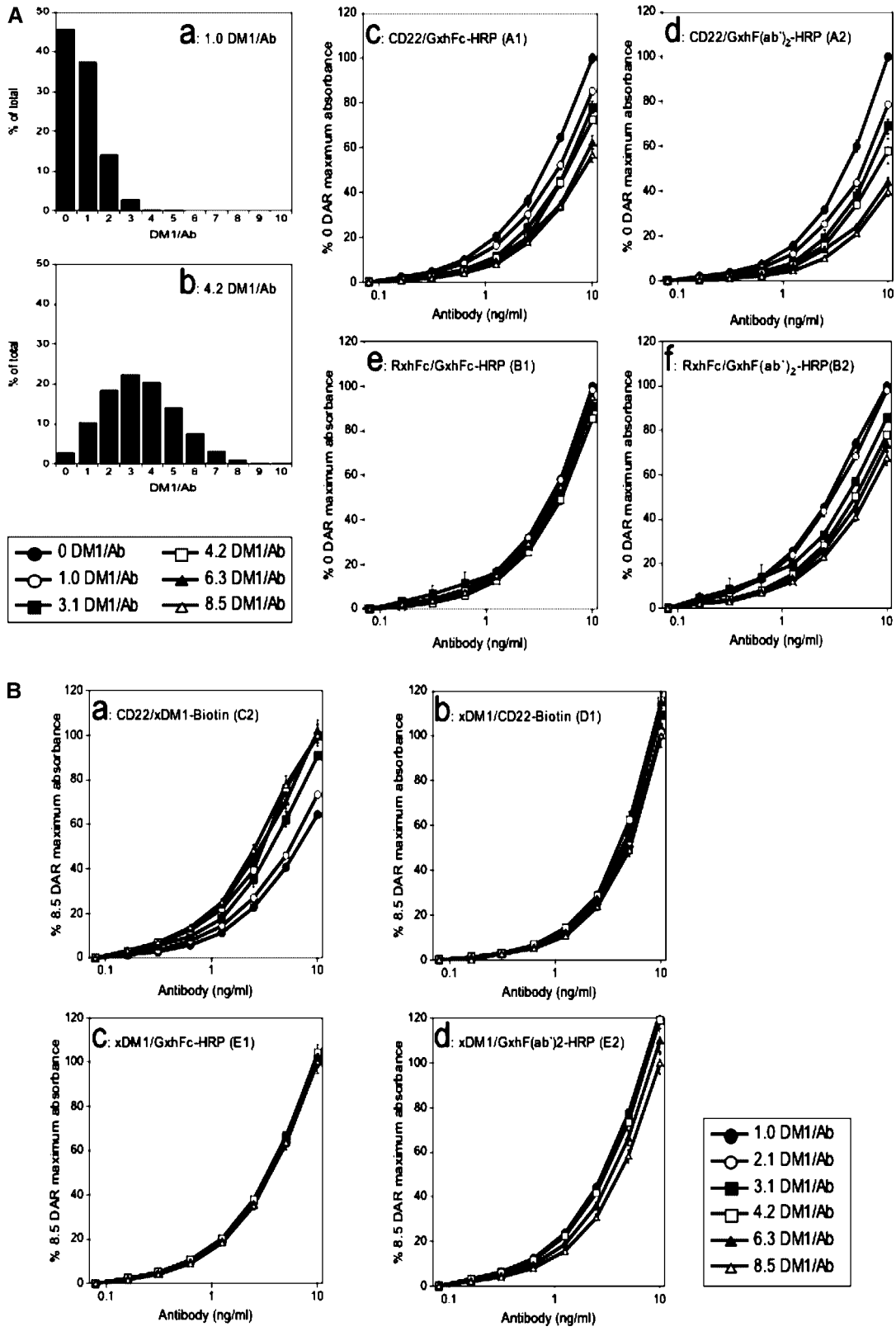

Figure 2. (A) Performances of anti-CD22-MCC-DM1 enriched mixtures in different total antibody assay formats. The heterogeneity of the anti-CD22-MCC-DM1 enriched mixtures at 1 (a) and 4.2 (b) DM1/Ab were analyzed by mass spectrometry. Anti-CD22-MCC-DM1 enriched mixtures with an average drug load of 0 (●), 1.0 (○), 3.1 (■), 4.2 (□), 6.3 (▲), and 8.5 (Δ) DM1 per antibody were assayed using various total antibody assay formats: CD22/GxhFc-HRP (c), CD22/GxhF(ab′)$_2$-HRP (d), RxhFc/GxhFc-HRP (e), RxhFc/ GxhF(ab′)$_2$-HRP (f). For the different anti-CD22-MCC-DM1 mixtures assayed from 0.16 to 10 ng/mL (1/2 serial dilution) plus blank, assay results were expressed as percentage of the maximum absorbance of 0 DM1/Ab fraction. (B) Performances of anti-CD22-MCC-DM1 enriched mixtures in different conjugated antibody assay formats. Anti-CD22-MCC-DM1 enriched mixtures with an average drug load of 1.0 (●), 2.1 (○), 3.1 (■), 4.2 (□), 6.3 (▲), and 8.5 (Δ) DM1 per antibody were assayed using various total antibody assay formats: CD22/xDM1-Biotin (a), xDM1/CD22-Biotin (b), xDM1/GxhFc-HRP (c), xDM1/ GxhF(ab′)$_2$-HRP (d). For the different anti-CD22-MCC-DM1 mixtures assayed from 0.16 to 10 ng/mL (1/2 serial dilution) plus blank, assay results were expressed as percentage of the maximum absorbance of 8.5 DM1/Ab fraction.

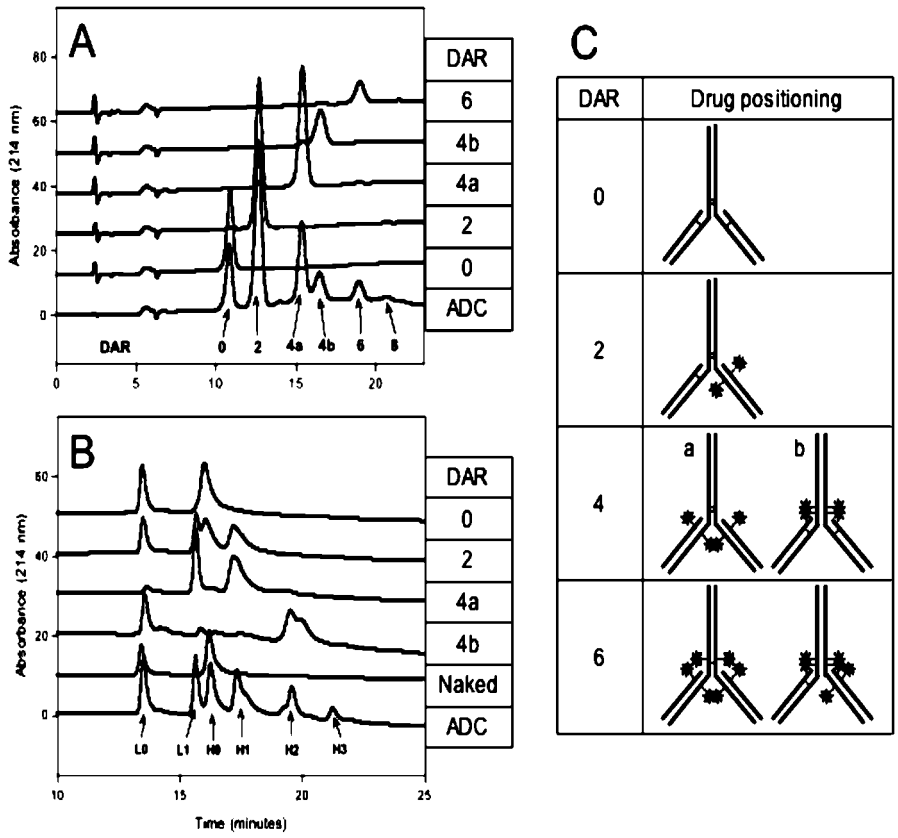

Figure 3. (A) HIC chromatograms of the anti-CD22-MC-MMAF ADC and the individual fractionated peaks at 0, 2, 4a (earlier retention time), 4b (later retention time), and 6 MMAF/Antibody. (B) RP-HPLC elution profiles of HIC purified fractions. The bottom chromatogram is the profile of the DTT reduced anti-CD22-MC-MMAF ADC. The labels L0, L1, H0, H1, H2, and H3 for the ADC profile are the free light chain, light chain with 0 drug-linker, light chain with one drug-linker, free heavy chain, heavy chain with one, two and three drug-linkers, respectively. (C) Schematic of the MMAF conjugation in different anti-CD22-MC-MMAF DAR species.

reduced binding of the anti-CD22-MCC-DM1 to CD22-ECD coat as well as binding of the GxhF(ab′)$_2$-HRP to the captured ADC.

Impact of the Conjugated Antibody Assay Format on Anti-CD22-MCC-DM1 Enriched Mixtures Measurement. The same set of anti-CD22-MCC-DM1 enriched mixtures with different DARs was analyzed using four different conjugated antibody assay formats: CD22/xDM1-Biotin (Format C1, Table 2) (Figure 2B, panel a), xDM1/CD22-Biotin (Format D1, Table 2) (Figure 2B, panel b), xDM1/GxhFc-HRP (Format E1, Table 2) (Figure 2B, panel c), and xDM1/ GxhF(ab′)$_2$-HRP (Format E2, Table 2) (Figure 2B, panel d). Regardless of the conjugated antibody assay format, no signal was observed with the 0 DM1/Ab fraction that went through the conjugation process but was not drug-modified (data not shown). In the CD22/xDM1-Biotin assay (Figure 2B, panel a), the signal increased when the ADC drug load increased. Reduction of the drug load from 3.1 to 2.1 and 1 DM1/Ab resulted in a decrease in absorbance with top signal at 10 ng/mL of ADC equal to 90.7%, 73.4%, and 64.4% of the 8.5 DAR maximum absorbance, respectively (Figure 2B, panel a). In this assay, the 8.5, 6.3, and 4.2 DM1/Ab preparations behaved similarly with an average signal equal to 100.5% ± 1.2% of the 8.5 DAR maximum absorbance. Results were markedly different when the anti-DM1 antibody was used as the coating reagent. All the differently loaded preparations behaved essentially the same in the xDM1/CD22-Biotin assay (Figure 2B, panel b) as well as in the xDM1/GxhFc-HRP assay (Figure 2B, panel c). Interestingly, some separation was observed between mixtures when GxhF(ab′)$_2$-HRP was used instead of GxhFc-HRP to detect the anti-DM1 captured ADC (Format E2, Table 2) (Figure 2B, panel d). Specifically, the two highly loaded anti-CD22-MCC-DM1 mixtures (8.5 and 6.3 DAR) generated the lowest OD signal while all the less loaded preparations (1, 2.1, 3.1, and 4.2 DM1/Ab) generated an average signal at 10 ng/mL equal to 120.3% ± 1.2% of the 8.5 DAR maximum absorbance, suggesting the GxhF(ab′)$_2$-HRP binding could be impaired by high drug load.

As expected, the signal in the CD22/xDM1-Biotin assay increased with the anti-CD22-MCC-DM1 drug load. Other assay formats were not affected by the ADC drug load except the xDM1/ GxhF(ab′)$_2$-HRP. In this assay, binding of the GxhF(ab′)$_2$-HRP appeared to be negatively impacted when the average drug load was higher or equal to 4.2 DM1/Ab.

Isolation and Characterization of Individual DAR Species from the anti-CD22-MC-MMAF ADC. Similar differences in mouse plasma pharmacokinetic profiles were observed for anti-CD22-MC-MMAF depending on the different total and conjugated antibody assays implemented (Figure 1). Since MMAF ADC is heterogeneous by nature (Table 1C,D), we investigated the impact of the assay format on the detection of ADC fractions with specific DARs purified from the anti-CD22-MC-MMAF (DAR = 3.4) use in the mouse PK study. We isolated different DAR species from the anti-CD22-MC-MMAF ADC by hydrophobic interaction chromatography. As shown in Figure 3A, anti-CD22-MC-MMAF used for this study contained 9.1%, 35.6%, 27.9%, 13.6%, and 10.4% of DAR species with 0, 2, 4a, 4b, and 6 MMAF/Ab, respectively. The individual fractions were then reduced with DTT and analyzed by reverse phase chromatography (Figure 3B) and their identities were confirmed by LC-MS (data not shown). The shoulder, which is seen at the trailing edge of the heavy chain with one drug-linker (referred to as H1, Figure 3B), and the leading as well as trailing edge of the heavy chain with two drug-linkers (referred to as H2, Figure 3B) are likely due to incomplete

reduction. The second profile from the bottom is the unconjugated anti-CD22 antibody (naked) and shows the retention times associated with reduced light and heavy chains without drug (L0 and H0). The top chromatogram (0 DAR) is identical to that of the naked anti-CD22 antibody (see above) run under the same conditions, demonstrating that there is no linker or drug attached to this fraction. The DAR 2 peak showed equal amounts of light chain and light chain with one drug-linker, as well as equal quantities of heavy chain and heavy chain with one drug-linker. Therefore, the 2 DAR species is composed of antibody with one of the two heavy chain−light chain disulfide bonds modified with drug-linker (Figure 3C) while the other disulfides are intact. Peak 4a (earlier retention time than 4b) (third profile from top, Figure 3B) showed predominantly light chain with one drug-linker and heavy chain with one drug-linker. This implies that peak 4a corresponds to an ADC in which both disulfide bonds between heavy and light chains are labeled, while the two disulfide bonds between the heavy chains at the hinge region remain intact (Figure 3C). The HIC profile of the fractionated peak 4a shows a slight contamination with the 2 DAR species (Figure 3A) that leads to the presence of the small peaks of L0 and H0. The reverse phase chromatography profile of peak 4b (later retention time than 4a) shows primarily unmodified light chain and heavy chain with two drug-linkers, with a few very minor peaks (due to some contamination of the peak with the 4a species as seen in Figure 3A). This implies that 4b corresponds to a form where both of the hinge disulfide bonds between the heavy chains are labeled, while the two disulfide bonds between heavy and light chain are unmodified (Figure 3C). Finally, characterization of the 6 drugs/Ab peak could not be conclusively performed by this technique, as the recoveries of this minor form were very low. For this fraction, assuming that only interchain disulfide bonds are involved, we hypothesize that one disulfide bond between the two heavy chains at the hinge region and both disulfide bonds between heavy and light chain or both disulfide bonds between the two heavy chains at the hinge region and one disulfide bond between heavy and light chain could be conjugated to MMAF (Figure 3C).

Impact of the Total Antibody Assay Format on Detection of Anti-CD22-MC-MMAF Fractions with Different DARs. The above purified fractions of anti-CD22-MC-MMAF ADC with drug loads of 0, 2, 4a, 4b, and 6 MMAF/Ab were assayed along with the naked anti-CD22 antibody in four different total antibody assay formats: CD22/GxhFc-HRP (Format A1, Table 2) (Figure 4A, panel a), CD22/GxhF(ab′)$_2$-HRP (Format A2, Table 2) (Figure 4A, panel b), RxhFc/GxhFc-HRP (Figure B1, Table 2) (Figure 4A, panel c), and RxhFc/GxhF(ab′)$_2$-HRP (Format B2, Table 2) (Figure 4A, panel d). In all assay formats and in the range of concentrations tested (0.16 to 10 ng/mL), these fractions generated comparable absorbance signals compared to the unmodified anti-CD22 antibody regardless of their DAR. The average signal at 10 ng/mL was 88.7% ± 6.7%, 96.3% ± 10.6%, 101.6% ± 5.3%, and 98.8% ± 5.6% of the naked antibody maximum absorbance in CD22/GxhFc-HRP (Figure 4A, panel a), CD22/ GxhF(ab′)$_2$-HRP (Figure 4A, panel b), RxhFc/GxhFc-HRP (Figure 4A, panel c), and RxhFc/ GxhF(ab′)$_2$-HRP (Figure 4A, panel d) assays, respectively.

In conclusion, increasing stoichiometry of MMAF conjugation to the anti-CD22-MC-MMAF ADC did not have any effect on the different total antibody assay tested.

Impact of the Conjugated Antibody Assay Format on Detection of anti-CD22-MC-MMAF Fractions with Different DARs. The same anti-CD22-MC-MMAF ADC purified fractions were assayed in four different conjugated antibody assay formats: CD22/xMMAF-Biotin (Format C2, Table 2) (Figure 4B, panel a), xMMAF/CD22-Biotin (Format D2, Table 2) (Figure 4B, panel b), xMMAF/GxhFc-HRP (Format E3, Table 2) (Figure 4B, panel c), and xMMAF/ GxhF(ab′)$_2$-HRP (Format E4, Table 2) (Figure 4B, panel d). As expected, regardless of the conjugated antibody assay format, no signal was observed with the 0 MMAF/Ab fraction that went through the conjugation process but was not drug-modified. In the CD22/xMMAF-Biotin assay, the signal increased when the ADC drug load increased (Figure 4B, panel a). The maximum signal was observed with the 6 MMAF/Ab fraction while signals equal to 65.3%, 57.9%, and 12% of the 6 DAR maximum absorbance was observed with the 4a, 4b, and 2 MMAF/Ab fractions, respectively. Surprisingly, in the xMMAF/CD22-Biotin assay similar signals were observed with fractions with drug loads equal to 6, 4a, and 4b MMAF/Ab with an average of 107% ± 8.5% of the 6 DAR maximum absorbance, while signal for the fraction at 2 DAR was markedly lower at 29.2% of the 6 DAR maximum absorbance (Figure 4B, panel b). In the xMMAF/GxhFc-HRP assay, a clear separation of the different fractions was observed with a signal at 77.4%, 60.3%, and 17.5% of the 6 DAR maximum absorbance with the 4b, 4a, and 2 MMAF/Ab purified fractions, respectively (Figure 4B, panel c). In the xMMAF/GxhF(ab′)$_2$-HRP assay, a separation of the different purified fractions was also observed (Figure 4B, panel d). Interestingly, the highest signal was observed with the 6 and 4b MMAF/Ab fractions while the signal for the 4a fraction was 62% lower than the one observed for the 6 MMAF/Ab fraction at 10 ng/mL. Finally, in this assay the 2 MMAF/Ab fraction also generated the lowest signal compared to the other fractions with higher DARs (Figure 4B, panel d).

To conclude, the signal generated in the CD22/xMMAF-Biotin assay was positively correlated to the anti-CD22-MC-MMAF drug load. Surprisingly, the xMMAF/GxhFc-HRP and xMMAF/GxhF(ab′)$_2$-HRP assays did not detect the ADC with 4 MMAF/Ab as efficiently as the 6 MMAF/Ab. None of the conjugated antibody assays tested efficiently detected the ADC with 2 MMAF/Ab.

DISCUSSION

As promising therapeutic candidates, the reliable determination of the pharmacokinetic profile of anti-CD22-MCC-DM1 and anti-CD22-MC-MMAF ADCs is a critical aspect of their preclinical evaluation and selection. In this study we investigated the impact of the assay format on PK parameters determination.

In mouse plasma, the two total antibody assay formats gave similar results although the CD22/GxhFc-HRP assay format measured consistently less ADCs than the RxhFc/GxhFc-HRP format. In contrast, very significant differences were observed when two conjugated antibody assay formats relying on either CD22-ECD or anti-drug antibody capture were used to quantify the ADCs. For both conjugates the CD22-ECD coat format resulted in a lower quantification of the conjugated antibody compared to the one achieved in the anti-drug antibody coat format. This difference prompted us to further investigate the impact of the assay format on ADCs quantification.

Using enriched mixtures of anti-CD22-MCC-DM1 with various DARs we demonstrated that increasing DM1 loads resulted in lower quantification of the antibody in total antibody assay formats relying on CD22-Biotin or GxhF(ab′)$_2$-HRP detection while the RxhFc/GxhFc-HRP assay was not affected. Because none of the total antibody assay formats involve the anti-DM1 antibody, this result came out as unexpected and strongly suggests that DM1 conjugation to the anti-CD22 antibody could interfere with the antigen binding ability of the antibody. This effect was observed for enriched mixtures with an average drug load as low as 1 DM1/Ab; however, considering the heterogeneity of this fraction we conclude that a conjugation ratio between 1 and 4 DM1/Ab would be sufficient to negatively

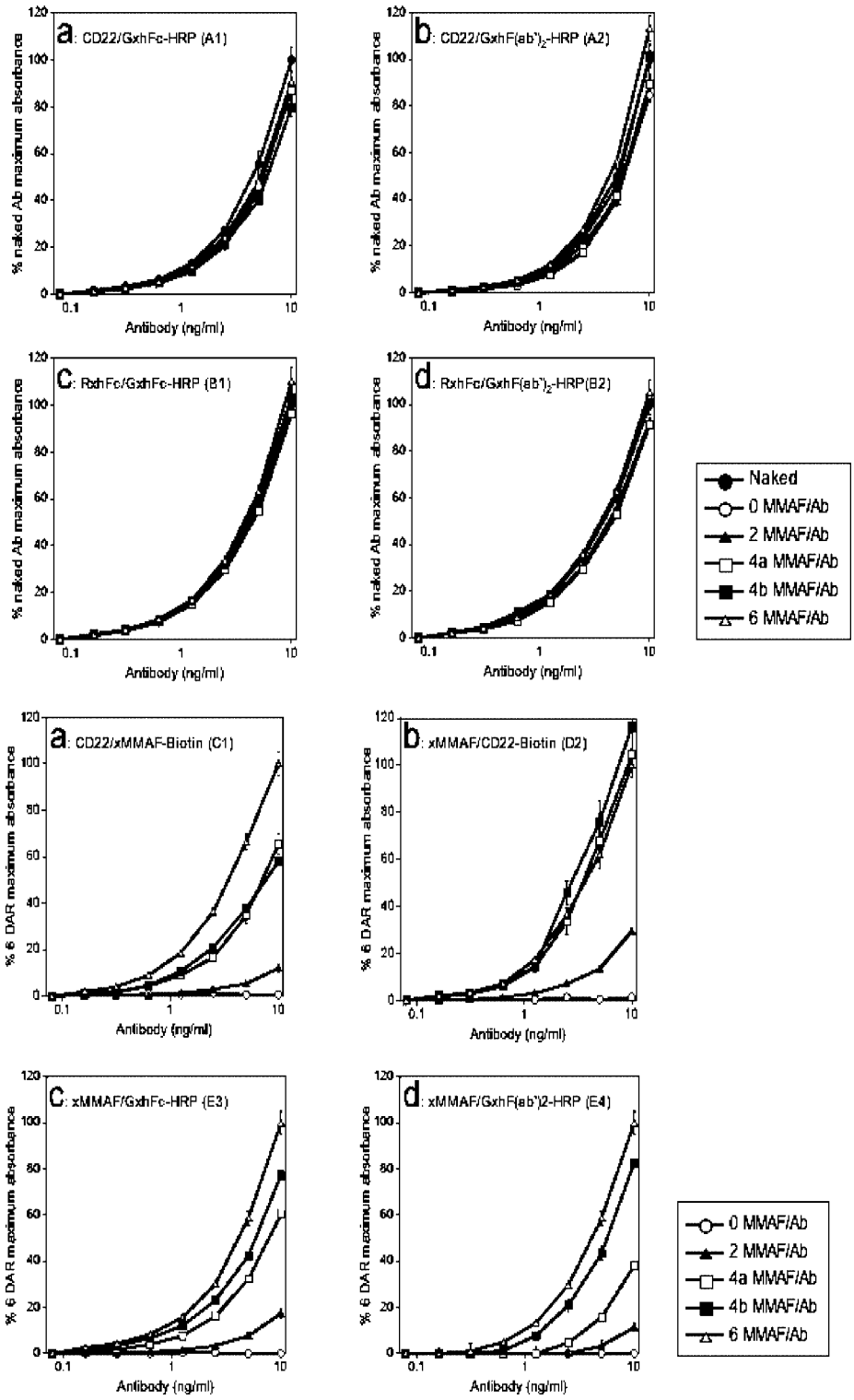

Figure 4. (A) Performances of anti-CD22-MC-MMAF HIC purified fractions in different total antibody assay formats. Unmodified anti-CD22 (●) and anti-CD22-MC-MMAF fractions with a drug load of 0 (○), 2 (▲), 4a (□), 4b (■), and 6 (Δ) MMAF per antibody were assayed using various total antibody assay formats: CD22/GxhFc-HRP (a), CD22/GxhF(ab′)$_2$-HRP (b), RxhFc/GxhFc-HRP (c), RxhFc/GxhF(ab′)$_2$-HRP (d). For the different anti-CD22-MC-MMAF fractions assayed from 0.16 to 10 ng/mL (1/2 serial dilution) plus blank, assay results were expressed as percentage of the maximum absorbance of naked antibody. (B) Performances of anti-CD22-MC-MMAF enriched fractions in different conjugated antibody assay formats. Anti-CD22-MC-MMAF fractions with a drug load of 0 (○), 2 (▲), 4a (□), 4b (■), and 6 (Δ) MMAF per antibody were assayed using various total antibody assay formats: CD22/xMMAF-Biotin (a), xMMAF/CD22-Biotin (b), xMMAF/GxhFc-HRP (c), xMMAF/GxhF(ab′)$_2$-HRP (d). For the different anti-CD22-MC-MMAF fractions assayed from 0.16 to 10 ng/mL (1/2 serial dilution) plus blank, assay results were expressed as percentage of the maximum absorbance of 6 MMAF/Ab fraction.

impact the binding of the antibody onto immobilized CD22. Based on this data, any accelerated clearance of the high DAR anti-CD22-MCC-DM1 fractions or progressive DM1 loss from these fractions would result in the CD22/GxhFc-HRP assay quantifying more than the RxhFc/GxhFc-HRP assay when using the 3.4 DAR anti-CD22-MCC-DM1 standard curve. Interestingly, this scenario does not correlate with the mouse PK data where the CD22/GxhFc-HRP assay measured consistently

slightly less total ADC than the RxhFc/GxhFc-HRP format, especially at later time points. Therefore, we hypothesized that changes in the high DAR anti-CD22-MCC-DM1 fractions would have a minor effect on the overall PK profile since these fractions represent a small percentage of the total ADC. However, changes that would result in a decrease of the anti-CD22 mAb carrying less than 3.4 DM1/Ab could affect the PK profile with the CD22/GxhFc-HRP assay quantifying less total ADC than the RxhFc/GxhFc-HRP assay when the 3.4 DAR anti-CD22-MCC-DM1 standard is use as observed in the mouse PK study.

In these conditions, our data raise the question about the best total assay format to implement to accurately evaluate the PK profile of the anti-CD22-MCC-DM1 conjugate. Although an assay format relying on antigen binding is preferred, it appeared that in this case, considering the heterogeneous nature of the anti-CD22-MCC-DM1 ADC, this type of assay could potentially introduce a bias in the total antibody quantification. Based on our data, the RxhFc/GxhFc-HRP assay format appears the most accurate in evaluating anti-CD22-MCC-DM1 pharmacokinetic profile in rodents. This total assay format was also chosen in the context of other DM1 ADCs such as Cantuzumab Mertansine (huC242-DM1), a conjugate that recognizes the tumor-selective carbohydrate epitope CanAg present on the membrane-associated mucin MUC1 (*5*). For monkey and human pharmacokinetic studies, background could interfere with the RxhFc/GxhFc-HRP assay, and therefore, the CD22/GxhFc-HRP assay format would be the best to implement although it could potentially underestimate the total circulating anti-CD22-MCC-DM1 especially at later time points.

For the conjugated antibody assays, the CD22/xDM1-Biotin assay was the only format where the signal was dependent on the drug load. This result was expected since detection of the immobilized anti-CD22-MCC-DM1 is achieved through the anti-DM1 antibody and therefore the assay signal was anticipated to be positively correlated to drug load. The other assay formats relying on the immobilized anti-DM1 antibody, assay signal was not expected to be dependent on the drug load since 1 DM1/Ab was supposed to be sufficient to optimally capture the ADC. However, in the xDM1/ GxhF(ab′)$_2$-HRP assay the signal slightly dropped for the highest DARs. This result suggests that high DM1 load could result in some modification of the anti-CD22-MCC-DM1 FAb region that impairs the GxhF(ab′)$_2$-HRP binding to the ADC captured onto the assay plate and could correlate with the total assay results suggesting that DM1 conjugation negatively impacts the binding of the antibody to the immobilized CD22. CD22/xDM1-Biotin assay would have the advantage of being able to monitor the relative circulating conjugated DM1. However, it could potentially introduce a bias in the conjugated antibody quantification, since the heterogeneous nature of the conjugate might change *in vivo* compared to the standard material. The observation that the profile generated from the xDM1/CD22-Biotin assay format separates from the total antibody profiles after 20 days indeed suggests that DM1 could be lost from the ADC, thus increasing over time the ADC fraction with 0 drug per antibody. Therefore, the xDM1/CD22-Biotin assay appears to be the format of choice to accurately quantify the anti-CD22-MCC-DM1 conjugate in circulation. A similar conjugate assay format with anti-DM1 antibody coat was also implemented by Xie et al. (*5*) to measure Cantuzumab Mertansine (huC242-DM1) in mouse plasma. In conclusion, the RxhFc/GxhFc-HRP and the xDM1/CD22-Biotin appeared to be the best assay formats to quantify the total and conjugated antibody in plasma, respectively, and interestingly these two assay formats provided similar pharmacokinetic profiles in mouse up to 20 days postinjection, suggesting that the anti-CD22-MCC-DM1 ADC defined as the antibody carrying at least one DM1 drug is relatively stable in mouse circulation at the doses studied.

Fractions of anti-CD22-MC-MMAF with 0, 2, 4, and 6 MMAF/Ab were purified using hydrophobic interaction chromatography and subsequently characterized by reverse phase chromatography. These fractions were used to investigate the impact of the MMAF load and position on the ADC quantification. Interestingly, the MMAF load on the anti-CD22 antibody did not have any major impact on the antibody quantification in any of the total antibody assay formats tested, most likely because the drug is coupled via interchain cysteines and so by definition is not near the antigen binding site. Therefore, the CD22/GxhFc-HRP assay format would be the preferred total antibody assay format to evaluate anti-CD22-MC-MMAF pharmacokinetic profiles in human, monkey, and rodent serum or plasma. This assay format relying on a specific antibody capture and an HRP-labeled anti-human IgG Ab detection was also implemented for other auristatin antibody-drug conjugates such as cAC10-Val-Cit-MMAE, an anti-CD30 MMAE conjugate, for which an anti-idiotype cAC10 monoclonal antibody was used to specifically capture the total ADC (*27*).

As expected with the conjugated antibody assay CD22/xMMAF-Biotin, the signal was positively correlated to the MMAF load. Surprisingly, similar results were observed with all other conjugated assay formats relying on immobilized anti-MMAF antibody, with a dramatic decrease in signal for the anti-CD22-MC-MMAF fraction with a DAR of 2. In addition, the position of the drug on the anti-CD22-MC-MMAF ADC affected the performance of the xMMAF/GxhF(ab′)$_2$-HRP assay suggesting that the binding of the GxhF(ab′)$_2$ antibody is clearly affected by the presence of the MMAF in the Fab region (fraction 4a), but less in the hinge region (fraction 4b). This suggests some perturbation of the antibody structure that affect more the GxhF(ab′)-HRP binding than the GxhFc-HRP binding. Our data also suggest that the anti-MMAF antibody used in our assay strongly relies on an avidity effect to capture the anti-CD22-MC-MMAF ADC. In this context, the difference between the mouse pharmacokinetic profiles generated with CD22/xMMAF-Biotin and xMMAF/CD22-Biotin assay formats was most probably due to different abilities to detect the 4 and in lesser extent the 2 MMAF/Ab fractions. Regardless of the ADC clearance mechanism, the different conjugated antibody assays described here will underestimate any increase in the proportion of circulating anti-CD22-MC-MMAF with 2 drug/Ab potentially compromising the accurate determination of the ADC PK profile and the subsequent calculation of critical PK parameters. Considering our results, either CD22/xMMAF-Biotin and xMMAF/CD22-Biotin assays could be implemented, but considering the limitations mentioned above, neither of these two assay formats will be entirely satisfying without the implementation of a conjugated MMAF assay in order to precisely determine the amount of drug associated with the circulating anti-CD22-MC-MMAF. Others implemented this strategy such as Sanderson et al. (*4*) who used a conjugated antibody assay relying on the anti-auristatin antibody to detect cAC10-Val-Cit-MMAE. Similar to our results with the CD22/anti-drug assay format, a significant reduction in assay signal was observed for the 2 DAR cAC10-Val-Cit-MMAE ADC compared to the 4 DAR, although these two fractions quantified similarly in their total assay. Interestingly, this group also determined the amount of conjugated MMAE associated with cAC10-Val-Cit-MMAE ADC using a free MMAE competition ELISA after treatment of the samples with cathepsin B (*4*).

The work presented here suggests that different total and conjugate assay formats could provide significantly different ADC PK profiles and subsequently results in the calculation of different PK parameters. Using anti-CD22-MCC-DM1 enriched

mixtures and anti-CD22-MC-MMAF purified fractions, our investigations allowed us to better understand the impact of the assay formats on the determination of the ADC PK profile and to highlight the advantages and disadvantages of various total and conjugate assay formats. The understanding of the behavior of these various assays with regard to the ADC drug load will be critical to interpret future studies geared toward the understanding of anti-CD22-MCC-DM1 and anti-CD22-MC-MMAF ADCs clearance mechanism.

ACKNOWLEDGMENT

We thank Ruth Moser and Dr. Damon Meyer (Seattle Genetics, Inc., Bothell, WA, USA) for providing us with the anti-CD22-MC-MMAF; Xingye C. Lei for her statistical analysis of the PK data; and Dr. Laura DeForge, Dr. Suzie Scales, and Dr. Lino Gonzalez for their useful comments on the manuscript.

LITERATURE CITED

(1) Garnett, M. C. (2001) Targeted drug conjugates: principles and progress. *Adv. Drug Delivery Rev. 53*, 171–216.

(2) Lambert, J. M. (2005) Drug-conjugated monoclonal antibodies for the treatment of cancer. *Curr. Opin. Pharmacol. 5*, 543–549.

(3) Polakis, P. (2005) Arming antibodies for cancer therapy. *Curr. Opin. Pharmacol. 5*, 382–387.

(4) Sanderson, R. J., Hering, M., James, S. F., Sun, M. M. C., Doronina, S. O., Siadak, A. W., Senter, P. D., and Wahl, A. F. (2005) *In vivo* drug-linker stability of an anti-CD30 dipeptide-linker auristatin immunoconjugate. *Clin. Cancer Res. 11*, 843–852.

(5) Xie, H., Audette, C., Hoffee, M., Lambert, J. M., and Blatter, W. A. (2004) Pharmacokinetics and biodistribution of the antitumor immunoconjugate, cantuzumab mertansine (huC242-DM1), and it two components in mice. *J. Pharmacol. Exp. Ther. 308*, 1073–1082.

(6) Kovtun, Y. V., Audette, C. A., Ye, Y., Xie, H., Ruberti, M. F., Phinney, S. J., Leece, B. A., Chittenden, T., Blatter, W. A., and Goldmacher, V. S. (2006) Antibody-drug conjugates designed to eradicate tumor with homogeneous and heterogeneous expression of the target antigen. *Cancer Res. 66*, 3214–3221.

(7) Hamann, P. R., Hinman, L. M., Hollander, I., Beyer, C. F., Lindh, D., Holcomb, R., Hellet, W., Tsou, H. R., Upeslacis, J., Shochat, D., Mountain, A., Flowers, D. A., and Bernstein, I. (2002) Gemtuzumab ozogamicin, a potent and selective anti-CD33 antibody-clicheamicin conjugate for treatment of acute myeloid leukemia. *Bioconjugate Chem. 13*, 47–58.

(8) Doronina, S. O., Toki, B. E., Torgov, M. Y., Mendelsohn, B. A., Cerveny, C. G., Chace, D. F., DeBlanc, R. L., Gearing, R. P., Bovee, T. D., Siegall, C. B., Francisco, J. A., Wahl, A. F., Meyer, D. L., and Senter, P. D. (2003) Development of potent monoclonal antibody auristatin conjugates for cancer therapy. *Nat. Biotechnol. 21*, 778–784.

(9) Doronina, S. O., Mendelsohn, B. A., Bovee, T. D., Cerveny, C. G., Alley, S. C., Meyer, D. L., Oflazoglu, E., Toki, B. E., Sanderson, R. J., Zabinski, R. F., Wahl, A. F., and Senter, P. D. (2006) Enhanced activity of monomethylauristatin F through monoclonal antibody delivery: effects of linker technology on efficacy and toxicity. *Bioconjugate Chem. 17*, 114–124.

(10) Erickson, H. K., Park, P. U., Widdison, W. C., Kovtun, Y. V., Garrett, L. M., Hoffman, K., Lutz, R. J., Goldmacher, V. S., and Blättler, W. A. (2006) Antibody-maytansinoid conjugates are activated in targeted cancer cells by lysosomal degradation and linker-dependent intracellular processing. *Cancer Res. 66*, 4426–4433.

(11) Nitschke, L., Floyd, H., and Croker, P. R. (2001) New functions for the sialic acid-binding adhesion molecule CD22, a member of the growing family of Siglecs. *Scand. J. Immunol. 53*, 227–234.

(12) Crocker, P. R., and Varki, A. (2001) Siglecs in the immune system. *Immunology 103*, 137–145.

(13) Crocker, P. R., and Varki, A. (2001) Siglecs, sialic acids and innate immunity. *Trends Immunol. 22*, 337–342.

(14) Hursey, M., Newton, D. L., Hansen, H. J., Ruby, D., Goldenberg, D. M., and Rybak, S. M. (2002) Specifically targeting the CD22 receptor of human B-cell lymphomas with RNA damaging agents: a new generation of therapeutics. *Leuk. Lymphoma 43*, 953–959.

(15) Moyron-Quiroz, J. E., Partida-Sanchez, S., Donis-Hernandez, R., Sandoval-Montes, C., and Santos-Argumedo, L. (2002) Expression and function of CD22, a B-cell restricted molecule. *Scand. J. Immunol. 55*, 343–351.

(16) Tedder, T. F., Tuscano, J., Sato, S., and Kehrl, J. H. (1997) CD22, a B lymphocyte-specific adhesion molecule that regulates antigen receptor signaling. *Annu. Rev. Immunol. 15*, 481–504.

(17) Kreitman, R. J. (2001) Toxin-labeled monoclonal antibodies. *Curr. Pharm. Biotechnol. 2*, 313–325.

(18) Pastan, I., and Kreitman, R. J. (2002) Immunotoxins in cancer therapy. *Curr. Opin. Invest. Drugs 3*, 1089–1091.

(19) Kreitman, R. J. (2003) Recombinant toxins for the treatment of cancer. *Curr. Opin. Mol. Ther. 5*, 44–51.

(20) Chari, R. V. J., Martell, B. A., Gross, J. L., Cook, S. B., Shah, S. A., Blättler, W. A., McKenzie, S. J., and Goldmacher, V. S. (1992) Immunoconjugates containing novel maytansinoids: Promising anticancer drugs. *Cancer Res. 52*, 127–131.

(21) Liu, C., and Chari, R. V. J. (1997) The development of antibody delivery systems to target cancer with highly potent maytansinoids. *Expert Opin. Invest. Drugs 6*, 169–172.

(22) McDonagh, C. F., Turcott, E., Westerndorf, L., Webster, J. B., Alley, S. C., Kim, K., Andreyka, J., Stone, I., Hamblett, K. J., Francsco, J. A., and Carter, P. (2006) Engineered antibody-drug conjugates with defined sites and stoichiometries of drug attachment. *Protein Eng. Des. Selection 19*, 299–307.

(23) Foote, J., and Winter, G. (1992) Antibody framework residues affecting the conformation of the hypervariable loops. *J. Mol. Biol. 224*, 487–499.

(24) Hongo, J. A., Mora-Worms, M., Lucas, C., and Fendly, B. M. (1995) Development and characterization of murine monoclonal antibodies to the latency-associated peptide of transforming growth factor beta 1. *Hybridoma 14*, 253–260.

(25) Riechmann, L., Clark, M., Waldmann, H., and Winter, G. (1988) Reshaping human antibodies for therapy. *Nature 332*, 323–327.

(26) Polson, A. G., Yu, S. F., Elkins, K., Zheng, B., Clark, S., Ingle, G. S., Slaga, D. S., Giere, L., Du, C., Tan, C., Hongo, J. A., Gogineni, A., Cole, M. J., Vandlen, R., Stephan, J. P., Young, J., Chang, W., Scales, S. J., Ross, S., Eaton, D., and Ebens, A. (2007) Antibody-drug conjugates targeted to CD79 for the treatment of non-Hodgkin's lymphoma. *Blood 110*, 616–623.

(27) Hambblett, K. J., Senter, P. D., Chace, D., F., Sun, M. M. C., Lenox, J., Cerveny, C. G., Kissler, K. M., Bernhardt, S. X., Kopcha, A. K., Zabinski, R. F., Meyer, D. L., and Francisco, J. A. (2004) Effect of drug loading on the antitumor activity of a monoclonal antibody drug conjugate. *Clin. Cancer Res. 10*, 7063–7070.

BC800059T

Site-Specific Labeling of Annexin V with F-18 for Apoptosis Imaging

Xuehe Li,[†,‡] Jeanne M. Link,*[,‡] Svetlana Stekhova,[†,‡] Kevin J. Yagle,[‡] Christina Smith,[§] Kenneth A. Krohn,[‡] and Jonathan F. Tait[§]

Department of Radiology and Department of Laboratory Medicine, University of Washington Medical Center, Seattle, Washington 98195. Received April 22, 2008; Revised Manuscript Received June 5, 2008

Annexin V is useful in detecting apoptotic cells by binding to phosphatidylserine (PS) that is exposed on the outer surface of the cell membrane during apoptosis. In this study, we examined the labeling of annexin V-128, a mutated form of annexin V that has a single cysteine residue at the NH_2 terminus, with the thiol-selective reagent ^{18}F-labeling agent N-[4-[(4-[^{18}F]fluorobenzylidene)aminooxy]butyl]maleimide ([^{18}F]FBABM). We also examined the cell binding affinity of the ^{18}F-labeled annexin V-128 ([^{18}F]FAN-128). [^{18}F]FBABM was synthesized in two-step, one-pot method modified from literature procedure. (Toyokuni et al., *Bioconjugate Chem*. **2003**, *14*, 1253−1259). The average yield of [^{18}F]FBABM was 23 ± 4% (n = 4, decay-corrected) and the specific activity was ~6000 Ci/mmol. The total synthesis time was ~92 min. The critical improvement of this study was identifying and then developing a purification method to remove an impurity *N*-[4-[(4-dimethylaminobenzylidene)aminooxy]butyl]maleimide **4**, whose presence dramatically decreased the yield of protein labeling. Conjugation of [^{18}F]FBABM with the thiol-containing annexin V-128 gave [^{18}F]FAN-128 in 37 ± 9% yield (n = 4, decay corrected). Erythrocyte binding assay of [^{18}F]FAN-128 showed that this modification of annexin V-128 did not compromise its membrane binding affinity. Thus, an *in vivo* investigation of [^{18}F]FAN-128 as an apoptosis imaging agent is warranted.

INTRODUCTION

Apoptosis, or programmed cell death, is an essential component for embryogenesis and homeostasis. Dysregulation of apoptosis is associated with many diseases such as cancer, autoimmunity, and neurodegenerative disorders (*1*). Many anticancer therapies exert their therapeutic effects by inducing apoptosis in tumor cells. A suitable *in vivo* marker for noninvasive imaging of apoptosis would be useful for both clinical care and drug development.

One of the early characteristics of apoptosis is the externalization of phosphatidylserine (PS) molecules on cell membranes, which promotes recognition and phagocytic removal (*2, 3*). In culture, once apoptosis is triggered, the PS externalization begins to occur within one hour (*2*). Annexin V, a 36 kDa endogenous cytoplasmic protein, binds with high affinity (K_d ~10 nM) to membrane-bound PS in a Ca^{2+}-dependent manner (*4*). Annexin V staining has been a standard practice for the assessment of apoptosis *in vitro* for the past decade. More recently, radiolabeled annexin V has been actively investigated to image cell death (*5–8*). ^{99m}Tc-labeled annexin V showed promising results in early clinical SPECT studies (*9–11*), but its low sensitivity has limited its broader application. To take advantage of the higher resolution and more accurate quantification of PET, labeling annexin V with short half-life positron-emitters such as ^{18}F is of particular interest.

We (*12*) and others (*13, 14*) have reported the labeling of wild-type annexin V with *N*-succinimidyl-4-^{18}F-fluorobenzoate ([^{18}F]SFB). We have also demonstrated that the ^{18}F-labeled annexin V ([^{18}F]fluoroannexin or [^{18}F]FAN) showed increased uptake in rat liver proportional to apoptosis after apoptosis was chemically induced (*15*). The rapid blood clearance and urinary excretion of [^{18}F]FAN suggest its potential as a PET imaging agent. This radiotracer, however, has its own disadvantages. The predominant renal clearance increases the radiation burden to the kidneys and bladder, and a patient would have to be catheterized if the diagnostic area of interest were in the abdomen (*15*). Moreover, this labeling method for annexin V is nonspecific, as the reaction is between the prosthetic group ([^{18}F]SFB) and any available NH_2 groups in this protein. There are at least 23 potential sites for this reaction to occur in each annexin V molecule, some near the active binding site of the protein. A recent report confirms that amine-directed chemical modification of annexin V reduces its membrane-binding activity even at low stoichiometries (*16*). Multiple substitutions of annexin V with [^{18}F]SFB could mean disproportional signaling by low-affinity molecules in PET imaging. Therefore, a site-specific method to label annexin V with only one substitution per molecule should have an advantage over the [^{18}F]SFB-modified version.

An alternative strategy to label proteins involves targeting the free thiol groups that are present only in cysteine residues. Thiol reactive agents such as N-substituted maleimides and iodoacetamide can be used to modify proteins at cysteines at specific sites (*17–20*). Annexin V-128 is a mutated form of annexin V containing only one cysteine. The initiator Met at position one is deleted and a six amino acid extension containing one cysteine is added at the N-terminus. The N-terminus does not play a role in the binding activity of annexin V and so this modification does not change the binding affinity of annexin V-128 for PS. Site-specific labeled (with ^{99m}Tc) annexin V-128 derivatives showed twice as much *in vivo* apoptosis-specific uptake in rat liver models as did amine-derivatized forms of annexin V (*16*). A previous approach to label thiol-containing molecules with *N*-[4-[(4-[^{18}F]fluorobenzylidene)aminooxy]butyl]maleimide ([^{18}F]FBABM) used a two-step/two-pot synthesis that was labor intensive and gave low yield with larger biomolecules such as 5′-S-ODN (*21*). In this paper, we report an improved synthesis and efficient purification of [^{18}F]FBABM,

* Corresponding author. Jeanne M. Link. Email: jeanne@u.washington.edu. Ph: 206-598-6256. Fax: 206-598-4192.
† Equal contribution authors.
‡ Department of Radiology.
§ Department of Laboratory Medicine.

10.1021/bc800164d CCC: $40.75 © 2008 American Chemical Society
Published on Web 07/16/2008

and the production of [^{18}F]annexin V-128 ([^{18}F]FAN-128) with this thiol-reactive reagent. The PS binding affinity of [^{18}F]FAN-128 and its potential as a PET imaging agent for cell death are also discussed.

MATERIALS AND METHODS

General. All reagents and solvents were purchased from Aldrich Chemical Co. (Milwaukee, WI) as reagent grade and were used without purification unless otherwise noted. The labeling precursor, 4-trimethylammoniumbenzaldehyde triflate **1**, was prepared as described by Haka et al. (*24*) and stored in a sealed vial over desiccant in the refrigerator. The coupling precursor, *N*-[4-(aminooxy)butyl]maleimide **3**, as a HCl salt was synthesized according to Toyokuni et al. (*21*) with modifications and stored over desiccant in the refrigerator. Enriched (97%) [^{18}O]water was obtained from Medical Isotopes, Inc. (Pelham, NH). Chromafix 30-PS-HCO_3 ^{18}F separation cartridges were obtained from GE Medical Systems and C-18 SepPak (light) cartridges were obtained from Waters Corp. (Milford, MA). The first part of the radiosynthesis (the production of the radioprecursor [^{18}F]FBABM) was performed using a GE Tracerlab FX_{FN} automatic synthesis module. The second part of the radiosynthesis (the radio-labeling of annexin V-128) was done manually outside the GE box. ^{1}H NMR data were obtained with a Varian 300 MHz NMR instrument. Quality control of the purified radioactive product was performed on a Waters 2690 HPLC module coupled with an in-line Micromass ZMD mass spectrometer.

Preparation of Annexin V-128. Annexin V-128 (~2 mg/mL in 20 mM HEPES sodium, 100 mM NaCl, pH 7.4) was prepared and purified as described (*26*). The protein was reduced with 1 mM dithiothreitol (DTT) for 15 min at 37 °C and then applied to a Sephadex G-25 column equilibrated with deoxygenated buffer (20 mM HEPES-sodium, 100 mM NaCl, pH 7.4) to remove the reductant. Protein concentration was measured by absorbance at 280 nm and the reduced protein was used for labeling within 6 h.

Synthesis of *N*-[4-[(4-Dimethylaminobenzylidene)aminooxy]butyl]maleimide 4. A solution of 4-dimethylaminobenzaldehyde (17 mg, 0.1 mmol) and **3**·HCl (20 mg, 0.09 mmol) in anhydrous DMF (1 mL) was stirred at r.t. for 16 h. The reaction mixture was then poured into water and extracted with diethyl ether. After drying over anhydrous Na_2SO_4, the ether solution was decanted, concentrated under reduced pressure, and then loaded onto a silica TLC plate (Alltech Silica Gel 60 F_{254} 5 × 20 cm). The TLC plate was developed with 40% diethyl ether in hexanes (v:v) and the product (R_f ~ 0.34) was washed off with ether as a yellowish solid (14 mg, 0.05 mmol, 50%). mp 51 °C. ^{1}H NMR ($CDCl_3$, 300 MHz) δ 1.65−1.75 (m, 4H), 2.99 (s, 6H), 3.57 (t, J = 6.0 Hz, 2H), 4.12 (t, J = 6.0 Hz, 2H), 6.66 (d, J = 9.0 Hz, 2H), 6.67 (s, 2H), 7.43 (d, J = 9.0 Hz), 7.97 (s, 1H). MS (ESI+): 316 $[M+H]^+$ HRMS (ESI+): $[M+Na]^+$ Calc. 338.1475; Found: 338.1481.

Synthesis of FBABM. A solution of 4-fluorobenzaldehyde (31 μL, 0.29 mmol) and **3**•HCl (41 mg, 0.18 mmol) in DMF (2 mL) was stirred at r.t. for 30 min. The reaction mixture was then poured into water and extracted with diethyl ether. After drying over anhydrous Na_2SO_4, the ether solution was decanted and concentrated under reduced pressure, and then loaded onto a silica flash chromatography column and eluted with 40% diethyl ether in hexanes (v:v) to give FBABM (50 mg, 0.17 mmol, 91%) as a white solid. mp 81 °C.(Lit. (*21*) 79−81 °C) ^{1}H NMR (CD_3OD, 300 MHz) δ 1.55−1.70 (m, 4H), 3.49 (t, J = 6.0 Hz, 2H), 4.09 (t, J = 6.0 Hz, 2H), 6.74 (s, 2H), 7.07 (dd, J = 9.0 Hz, 9.0 Hz, 2H), 7.57 (dd, J = 9.0 Hz, 6.0 Hz, 2H), 8.03 (s, 1H). MS (ESI+): 291 $[M+H]^+$.

Radiosynthesis of [^{18}F]FBABM. Cyclotron-produced [^{18}F]fluoride in $H_2{}^{18}O$ was forced through a Chromafix ^{18}F separation cartridge with helium pressure using a GE Tracerlab FX_{FN} automated synthesis unit. The concentrated $^{18}F^-$ on the cartridge was then eluted with 1.4 mg K_2CO_3 in 0.5 mL 1:1 (v:v) acetonitrile/water solution into the reaction vessel of the FX_{FN} box. A solution of 7.5 mg Kryptofix[2,2,2] in 2 mL anhydrous acetonitrile was then added to the same reaction vessel and the whole mixture was azeotropically evaporated to dryness under heat and reduced pressure. A solution of 4−5 mg 4-trimethylammoniumbenzaldehyde triflate **1** in 1 mL anhydrous acetonitrile was then pushed into the reactor, pressurized (~200 mbar), and heated at 100 °C. After 15 min, the reaction vessel was cooled to r.t. before 8−9 mg **3** in 1.5 mL methanol was added. After stirring at r.t. for 15 min, the mixture was slowly evaporated to <0.5 mL with heat (50 °C) under vacuum. After cooling to r.t., 1.5 mL of 45% ethanol in water (v:v) was added to the reaction vessel and the whole mixture was transferred to the HPLC loop. Semipreparative HPLC was performed with a C18 column (Phenomenex Prodigy ODS(3), 5 μm, 250 × 10 mm) eluted with 45% ethanol/water (v:v) at 3 mL/min and 50 °C. The chemically and radiochemically (>99%) pure fraction containing [^{18}F]FBABM was collected (~12 mL; t_R ~ 38−40 min). The chemical and radiochemical purity was assessed with a C18 analytical HPLC column (Phenomenex Inertisil ODS-3, 100 × 2.1 mm, 5 μm, eluted with 55% methanol/water (v:v) at 0.3 mL/min flow rate and 40 °C with in-line mass detection.

Labeling of Annexin V-128 with [^{18}F]FBABM. Purified [^{18}F]FBABM from the previous step (~12 mL) was diluted with water (~50 mL) and passed through a Waters C18 SepPak that had been preconditioned with 5 mL ethanol and 5 mL water. The SepPak was washed with additional 10 mL water and the excess water was expelled with a push of air. 2 mL of ether was then pushed through the SepPak to elute the product into a clean 5 mL glass test tube. The ether phase of the biphase mixture was drawn out and transferred into a clean 5 mL BD Vacutainer test tube. The ether was then removed by evaporation under a gentle flow of argon at 50 °C. After cooling to r.t., approximately 0.7 mg freshly prepared annexin V-128 in 0.5 mL buffer (20 mM HEPES, 100 mM NaCl, pH 7.4) was carefully added to the residual film and incubated for 15 min with periodic gentle agitation. Labeled [^{18}F]fluoroannexin V-128 ([^{18}F]FAN-128) was isolated by a semipreparative size-exclusion column (BioSep SEC-S 2000, 300 × 7.8 mm) eluted at 1 mL/min with 10 mM phosphate/150 mM NaCl (pH = 7). [^{18}F]FAN-128 was the first radioactive peak eluted from the column with a retention time of ~7−9 min.

Cell-Binding Assay of [^{18}F]FAN-128. The membrane binding affinity of [^{18}F]FAN-128 was determined following the procedure described by Tait et al. (*22, 16*) Briefly, mixtures of red blood cells (RBCs) with exposed PS on the outer surface of the cell membrane (Coulter "4C Plus" Cell Control, Fullerton, CA), [^{18}F]FAN-128 (diluted to a final concentration of 1 nM) in buffer (100 mM NaCl, 50 mM Hepes-Na, pH 7.4, 0.02% NaN_3, 1 mg/ml BSA) and $CaCl_2$ at precise concentrations (between 0 and 3 mM) were prepared. The mixtures were incubated for 10 min. at r.t. After centrifugation, the supernatant was discarded. Then the RBCs with bound [^{18}F]FAN-128 were washed with the same buffer containing $CaCl_2$ at the same concentrations and recentrifuged and the supernatant was discarded. Membrane-bound [^{18}F]FAN-128 was then released with assay buffer containing 5 mM EDTA and counted in the gamma counter.

RESULT AND DISCUSSION

Chemistry. Our synthesis of [^{18}F]FBABM builds on the approach reported by Toyokuni et al. (*21*) (Scheme 1). Briefly, triflate **1** was heated with dried [^{18}F]KF in anhydrous acetonitrile in the presence of Kryptofix[2,2,2] to generate [^{18}F]FBA **2**,

Scheme 1. Synthesis of [^{18}F]FBABM

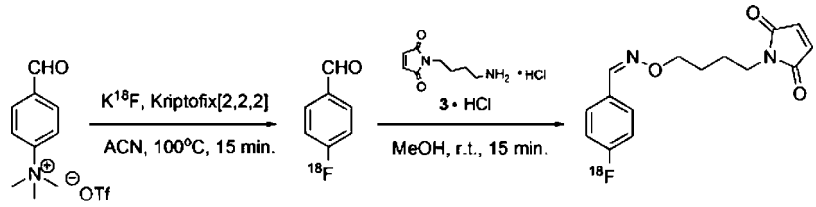

1 **2** **[^{18}F]FBABM**

Table 1. Yield of FBA (2) under Different Reaction Conditions[a]

solvent	amt. of precursor **1** (mg)	temperature (°C)	yield (%)[c]
DMSO	8	100	90
THF	4	80[b]	0
CH_3CN	2	100[b]	10
CH_3CN	3	100[b]	20
CH_3CN	4	100[b]	75
CH_3CN	8	100[b]	90

[a] All reactions were carried out by heating the precursor in 1 mL solvent for 15 min in a closed reaction vessel in a GE Tracerlab FX_{FN} automated synthesis module. [b] Heated under helium pressure (200 mbar). [c] Determined from radio-HPLC chromatograms of the crude product. Data represent an average of 3 runs.

followed by the addition of maleimide **3** in methanol and purification by HPLC. Their two-step/two-pot synthesis of [^{18}F]FBABM was used to label the thiol-containing tripeptide glutathione (GSH) and a 5′-thiol-functionalized oligodeoxynucleotide (5′-S-ODN). This synthesis started with the generation of **2** followed by a C18 SepPak purification. After coupling to the heterobifunctional linker *N*-[4-(aminoxy)butyl]maleimide **3** using the oxime O-ether formation reaction and HPLC purification, [^{18}F]FBABM was formulated in acetonitrile and successfully labeled GSH or 5′-S-ODN. This method, however, has disadvantages for routine protein labeling. First, the synthesis of [^{18}F]FBABM was labor-intensive, with a two-pot setup and a C18 SepPak purification step in between. Second, although the labeling of GSH gave good yield (70% decay corrected), the yield in labeling larger biomolecules such as 5′-S-ODN (5% decay corrected) was low. The concentrations of the GSH or the 5′-S-ODN in these reactions were 6 mM and 0.1 mM, respectively. The radiochemical yield of radiolabeled peptides/proteins or other biomolecules via prosthetic groups typically decreases as the concentration of the biomolecule decreases. For an even larger molecule such as annexin V-128, which is usually obtained in ~30 μM concentration, the radiochemical yield might be even lower than 5%. Indeed, our initial attempts to label annexin V-128 with [^{18}F]FBABM synthesized by closely following the literature procedure (*12*) gave no yield. In addition to the slow rate of reaction associated with dilute conditions, the presence of nonradioactive maleimide-containing impurities, which would compete with [^{18}F]FBABM for the available thiol groups, could be an important factor that results in the dramatic decrease in yield. In the Toyokuni report, there was little information on the chemical purity of the [^{18}F]FBABM produced. We focused our investigation on simplification of the radiosynthesis and purification of the [^{18}F]FBABM.

We found that the C18 SepPak purification was not required for [^{18}F]FBABM synthesis; the two-step reactions proceed smoothly in one pot. Starting with ~850 mCi [^{18}F]fluoride, 110 ± 14 mCi (n = 4) of purified [^{18}F]FBABM was obtained in ~92 min (23 ± 4% decay corrected radiochemical yield) with >99% radiochemical purity and a specific activity of ~6000 Ci/mmol. This yield is comparable to that from the two-pot procedure (*21*), but with a process that can be automated. Although theoretically, [^{18}F]FBABM could be formed as both *E*- and *Z*-isomers, we observed only one isomer (tentatively assigned to possess the *E*-configuration) (*21*) under our reaction condition. This was confirmed by coeluting with the cold standard of FBABM, whose NMR spectrum revealed only one isomer, on HPLC. During the preparation of this manuscript, Berndt et al. reported a one-pot method to prepare a similar thiol-reactive labeling agent *N*-[6-(4-[^{18}F]fluorobenzylidene)-aminooxyhexyl]maleimide ([^{18}F]FBAM) with similar yield to ours (*23*). Their method, however, includes an extra prepurification step using solid-phase extraction on LiChrolut RP18 cartridge before semipreparative HPLC purification.

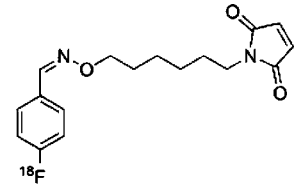

[^{18}F]FBAM

The synthesis of [^{18}F]FBA **2** from the triflate precursor **1** was traditionally carried out by heating the dried [^{18}F]KF/Kryptofix[2,2,2] in a high-boiling polar aprotic solvent such as DMSO (*24, 25*). We chose the lower boiling acetonitrile because it could be easily removed by evaporation. Compared with DMSO, the use of acetonitrile did not compromise the yield of [^{18}F]FBA (Table 1). Similar yields were obtained while the same amounts of precursors were used. A smaller amount of precursors resulted in decreased yields of **2**. Using 4 mg triflate precursor struck a balance between reasonably high yield and acceptably lower quantity of material introduced into the system. Compared to the Toyokuni report (*21*), the yield of the coupling reaction dropped from ~70% to ~40% (calculated from the yield of the first step and the overall yield), but the advantage of easier production of this radiotracer outweighed this reduction of yield. It is important to note that, because FBA is a volatile compound at elevated temperature, it is crucial to cool the reaction mixture to r.t. before opening the reaction vessel to add the coupling precursor.

The critical factor for optimal protein labeling with [^{18}F]FBABM is the chemical purity of the product. We suspected that a maleimide side product was present that would compete with [^{18}F]FBABM for reaction with thiol groups. HPLC-MS was used to identify this major contaminant as *N*-[4-[(4-dimethylaminobenzylidene)aminooxy]butyl]maleimide (**4**) (estimated >100 μg from a typical run described above) derived from the 4-dimethylaminobenzaldehyde formed inevitably during the initial nucleophilic fluorination step (Scheme 2). In a typical run, about 300 μg 4-dimethylaminobenzaldehyde was detected after this first step. The identity and quantity was determined by HPLC-MS analysis, in comparison to an authentic sample. Our initial attempt to label annexin V-128 with [^{18}F]FBABM containing **4** gave no yield, presumably due to a competition for the single thiol group by the vast molar excess of the alternative maleimide contaminant **4**. In a typical labeling reaction, the molar ratio of FBABM to annexin V-128 (generally 0.6 mg was used)

Scheme 2. Formation of 4

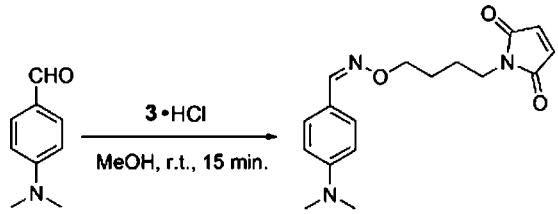

4

was approximately 1:1, whereas that of **4** was greater than 20:1. Attempts to remove the undesired 4-dimethylaminobenzaldehyde after the first step with a C18 SepPak were unsuccessful. The removal of **4** from the final product [^{18}F]FBABM proved to be challenging. The calculated log *P* values for FBABM and **4** are 1.91 and 1.85, respectively (Molinspiration program: http://www.molinspiration.com/cgi-bin/properties). The two compounds coeluted using the HPLC method from the literature (*21*). We developed a useful separation by using Phenomenex Prodigy ODS(3) 5 μm 250 × 10 mm column. At 50 °C and 45% ethanol/water as the eluent at 3 mL/min, **4** was completely removed from [^{18}F]FBABM (impurity t_R(**4**) ∼ 26−28 min, t_R(FBABM) ∼ 34−38 min). A typical semipreparative HPLC chromatogram is shown in Figure 1. No detectable amount of **4** was present in the purified [^{18}F]FBABM product. We realize that, in this isocratic HPLC method, although a complete separation of impurity **4** was achieved, the long retention time of the [^{18}F]FBABM is disadvantageous for routine production. We are currently investigating alternative purification method with gradient HPLC.

Annexin V-128 (*26*) contains one cysteine in its N-terminus. The single naturally occurring cysteine residue in its interior domain has been mutated to a serine in order to eliminate the possibility of modification by thiol-reactive prosthetic conjugating agents. Annexin V-128 is freshly reduced immediately prior to each labeling study with DTT to ensure that the free thiol is fully accessible. The protein is purified of excess DTT by eluting through a Sephadex column.

The purified [^{18}F]FBABM was concentrated onto a C18 SepPak, washed off with diethyl ether, and taken to dryness. After evaporation, the [^{18}F]FBABM was incubated with annexin V-128 in HEPES buffer (pH = 7.4, 0.5 mL). It is noted that the number of liquid transfers and the contact surface area with the reaction vessel should be minimized to reduce unnecessary loss of annexin V-128 due to surface adsorption of the protein. Even using a careful transfer technique, approximately 1/3 of the total radioactivity is typically lost in transfers for injection onto the size-exclusion column (SEC). After HPLC purification, radiochemically pure

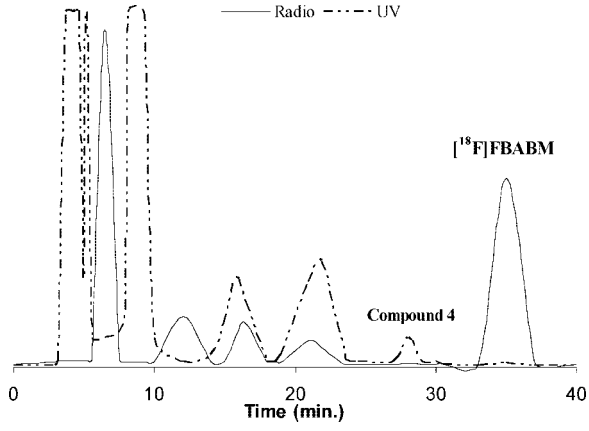

Figure 1. A typical semipreparative HPLC chromatogram for [^{18}F]FBABM purification. (Phenomenex Prodigy ODS-3, 250 × 10 mm, 5 μm, eluted with 45% ethanol/water v:v at 3 mL/min and 50 °C).

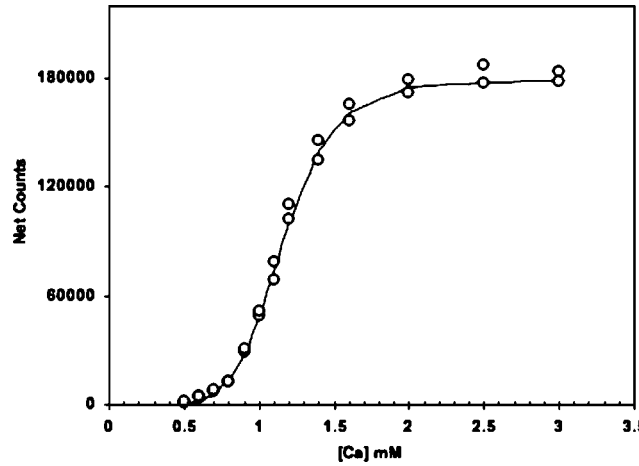

Figure 2. Typical binding curve of [^{18}F]FAN-128 to PS-enriched membranes. Typical binding curve of [^{18}F]FAN-128 as a factor of calcium concentration. [^{18}F]FAN-128 is held constant well below its K_d (at 1 nM), while calcium is titrated between 0 and 3 mM (maximal binding is observed at 2−2.5 mM Ca^{2+}). The membrane-bound radioactivity is plotted versus the concentration of Ca^{2+} present. p*K* value is calculated from slope (N) and midpoint of titration curve (EC_{50}) (*16*). Two measurements are done for each data point.

(>98%) [^{18}F]FAN-128 was obtained with 37 ± 9% yield (n = 4, decay-corrected) from [^{18}F]FBABM. The total recovery of radioactivity from the SEC was >90% with the radioactive peak at 7−9 min being [^{18}F]FAN-128. The unreacted [^{18}F]FBABM was retained for >1 h on the SEC column.

As a negative control, we repeated the reaction under the same condition using wild-type annexin V instead of mutated annexin V-128. Wild-type annexin V has one internal cysteine but it does not have a free thiol group on its N-terminus. In this reaction, the yield of ^{18}F-labeled protein was negligible (<0.2%). This result shows that, under our reaction conditions, [^{18}F]FBABM does not react with other nucleophiles such as the free NH_2 groups in annexin V, and the single cysteine residue that is present in the interior domain of wild-type annexin V is not readily accessible for maleimide binding. Therefore, we are able to conclude that the [^{18}F]FBABM labeling of annexin V-128 is site-specific. The mutation of Cys-316 to Ser in annexin V-128 may not be necessary for future annexin V based tracer design.

[^{18}F]FAN-128 PS Binding Assay. The *in vitro* membrane-binding affinity of [^{18}F]FAN-128 was determined by erythrocyte binding using the method reported by Tait et al. (*16*) The commercially available RBCs had exposed PS on their outer surfaces of the cell membranes because of the preservatives used (*27*). Annexin binding to PS is calcium dependent. By titrating calcium instead of protein, this method allows an accurate measurement of annexin binding at <1% occupancy, a value similar to that for *in vivo* imaging where the membrane is far from saturated with protein. A typical binding curve for [^{18}F]FAN-128 is presented in Figure 2. The binding affinity was measured by determining EC_{50} and slope from this experimental titration curve (*22*). The negative log of the binding constant, p*K*, is equal to $-(n \log_{10}EC_{50} + \log_{10}[\text{membrane}])$, where n is the number of Ca^{2+} ions interacting with each annexin V molecule, the EC_{50} is the molarity of Ca^{2+} at which cell binding is half of the maximal value, and [membrane] is the concentration of annexin V-binding sites in the assay (*16*). Seven batches of [^{18}F]FAN-128 gave an average p*K* of 28.5 ± 1.8, an EC_{50} of approximately 1 mM, and a slope (Hill coefficient) between 7 and 8. This compares favorably with reported values for wild-type annexin V of a p*K* around 30, EC_{50} close to 1, and a slope of 8 (*26*, *16*). These data indicate that the *in vitro* binding activity

of this site-specific, monosubstituted protein was not significantly different from that of the wild-type and an *in vivo* investigation of [^{18}F]FAN-128 as an apoptosis imaging agent is warranted.

CONCLUSION

We have developed an improved, one-pot synthesis of the thiol-reactive labeling reagent [^{18}F]FBABM. It gives satisfactory radiochemical yield and can be automated for routine production. The critical improvement was identifying and then developing a purification method to remove the impurity *N*-[4-[(4-dimethylaminobenzylidene)aminooxy]butyl]maleimide (**4**). The presence of this impurity in [^{18}F]FBABM was dramatically decreasing the yield of labeled protein by competing for the available thiol groups. To our knowledge, this is the first time that this important issue has been addressed. We have also achieved an efficient synthesis of ^{18}F-labeled annexin V-128 ([^{18}F]FAN-128), a 36 kDa protein containing a single thiol group, with the [^{18}F]FBABM radioprecursor. This maleimide modification of annexin V-128 does not compromise its membrane binding affinity.

ACKNOWLEDGMENT

Financial support was provided by NIH CA042045 for this study. We thank Robert Murano and Steve Shoner for radionuclide production.

LITERATURE CITED

(1) Johnstone, R. W., Ruefli, A. A., and Lowe, S. W. (2002) Apoptosis: a link between cancer genetics and chemotherapy. *Cell 108*, 153–164.

(2) Fadok, V. A., Voelker, D. R., Campbell, P. A., Cohen, J. J., Bratton, D. L., and Henson, P. M. (1992) Exposure of phosphatidylserine on the surface of apoptotic lymphocytes triggers specific recognition and removal by macrophages. *J. Immunol. 146* (7), 2207–2216.

(3) Martin, S. J., Reutelingsperger, C. P. M., McGahon, A. J., Rader, J. A., Van Schie, R. C. A. A., LaFace, D. M., and Grenn, D. R. (1995) Early redistribution of plasma membrane phosphatidylserine is a general feature of apoptosis regardless of the initiating stimulus: Inhibition by overexpression of Bcl-2 and Abl. *J. Exp. Med. 182*, 1545–1556.

(4) Thiagarajan, P., and Tait, J. F. (1990) Binding of annexin V/placental anticoagulant protein I to platelets. Evidence for phosphatidylserine exposure in the procoagulant response of activated platelets. *J. Biol. Chem. 265*, 17420–17423.

(5) Lahorte, C. M. M., Vanderheyden, J.-L., Steinmetz, N., Van de Wiele, C., Dierckx, R. A., and Sledgers, G. (2004) Apoptois-detecting radioligands: current state of the art and future perspectives. *Eur. J. Nucl. Med. Mol. Imaging 31*, 887–919.

(6) Blankenberg, F. G., Tait, J. F., and Strauss, H. W. (2000) Apoptotic cell death: its implications for imaging in the next millennium. *Eur. J. Nucl. Med. 27*, 359–367.

(7) Blankenberg, F. G., Mari, C., and Strauss, H. W. (2003) Imaging cell death in vivo. *Q. J. Nucl. Med. 47*, 337–48.

(8) Brauer, M. (2003) In vivo monitoring of apoptosis. *Prog. Neuro Psychopharm. Biol. Psychiatry 27*, 323–331.

(9) Belhocine, T., Steinmetz, N., Hustinx, R., Bartsch, P., Jerusalem, G., Seidel, L., Rogo, P., and Green, A. (2002) Increased uptake of the apoptosis-imaging agent ^{99m}Tc recombinant human annexin V in human tumors after one course of chemotherapy as a predictor of tumor response and patient prognosis. *Clin. Cancer Res. 8*, 2766–2774.

(10) Haas, R. L. M., De Jong, D., Olmos, R. A. V., Hoefnagel, C. A., van Heuvel, I. D., Zerp, S. F., Bartelink, H., and Verheij, M. (2004) In vivo imaging of radiation-induced apoptosis in follicular lymphoma patients. *Intl. J. Rad. Oncol. Biol. Phus. 59*, 782–787.

(11) Kartachova, M., Haas, R. L. M., Olmos, R. A. V., Hoebers, F. J. P., Zandwijk, N., and Verheij, M. (2004) In vivo imaging of apoptosis by ^{99m}Tc-Annexin V scintigraphy: visual analysis in relation to treatment response. *Radiother. Oncol. 72*, 333–339.

(12) Grierson, J. R., Yagle, K. J., Eary, J. F., Tait, J. F., Gibson, D. F., Lewellen, B., Link, J. M., and Krohn, K. A. (2004) Production of [F-18]fluoroannexin for imaging apoptosis with PET. *Bioconjugate Chem. 15*, 373–379.

(13) Toretsky, J., Levenson, A., Weinberg, I. N., Tait, J. F., Uren, A., and Mease, R. C. (2004) Preparation of F-18 labeled annexin V: a potential PET radiopharmaceutical for imaging cell death. *Nucl. Med. Biol. 31*, 747–752.

(14) Murakami, Y., Takamatsu, H., Taki, J., Tatsumi, M., Noda, A., Ichise, R., Tait, J. F., and Nishimura, S. (2004) ^{18}F-labelled annexin V: a PET tracer for apoptosis imaging. *Eur. J. Nucl. Med. Mol. Imaging 31*, 469–474.

(15) Yagle, K. J., Eary, J. F., Tait, J. F., Grierson, J. R., Link, J. M., Lewellen, B., Gibson, D. F., and Krohn, K. A. (2005) Evaluation of ^{18}F-annexin V as a PET imaging agent in an animal model of apoptosis. *J. Nucl. Med. 46*, 658–666.

(16) Tait, J. F., Smith, C., Levashova, Z., Patel, B., Blankenberg, F. G., and Vanderheyden, J.-L. (2006) Improved detection of cell death in vivo with annexin V radiolabeled by site-specific methods. *J. Nucl. Med. 47*, 1546–1553.

(17) Brinkley, M. (1992) A brief survey of methods for preparing protein conjugates with dyes, haptens, and cross-linking reagent. *Bioconjugate Chem. 3*, 2–13.

(18) Wilbur, D. S. (1992) Radiohalogenation of proteins: an overview of radionuclides, labeling methods, and reagents for conjugate labeling. *Bioconjugate Chem. 3*, 433–470.

(19) Shiue, C. Y., Wolf, A. P., and Hainfeld, J. F. (1998) Synthesis of ^{18}F-labeled N-(*p*-[^{18}F]fluorophenyl)maleimide and its derivatives for labeling monoclonal antibody with ^{18}F. *J. Labelled Compd. Radiopharm. 26*, 287–289.

(20) Bruin, B., Kuhnast, B., Hinnen, F., Yaouancq, L., Amessou, M., Johannes, L., Samson, A., Boisgard, R., Tavitian, B., and Dolle, F. (2005) 1-[3-(2-[^{18}F]Fluoropyridin-3-yloxy)propyl]pyrrole-2,5-dione: design, synthesis, and radiosynthesis of a new [^{18}F]fluoropyridine-based maleimide reagent for the labeling of peptides and proteins. *Bioconjugate Chem. 16*, 406–420.

(21) Toyokuni, T., Walsh, J. C., Domingues, A., Phelps, M. E., Barrio, J. R., Gambhir, S. S., and Satyamurthy, N. (2003) Synthesis of a new heterobifunctional linker, N-[4-(aminooxy-)butyl]maleimide, for facile access to a thio-reactive ^{18}F-labeling agent. *Bioconjugate Chem. 14*, 1253–1259.

(22) Tait, J. F., Gibson, D. F., and Smith, C. (2004) Measurement of the affinity and cooperativity of annexin V-membrane binding under conditions of low membrane occupancy. *Anal. Biochem. 329*, 112–119.

(23) Berndt, M., Pietzch, J., and Wuest, F. (2007) Labeling of low-density lipoproteins using the ^{18}F-labeled thiol-reactive reagent N-[6-(4-[^{18}F]fluorobenzylidene)aminooxyhexyl]maleimide. *Nucl. Med. Biol. 34*, 5–15.

(24) Haka, M. S., Kilbourn, M. R., Watkins, G. L., and Toorongian, S. A. (1989) Arylmethylammonium trifluoromethanesulfonates as precursors to aryl [^{18}F]fluorides: improved synthesis of [^{18}F]GBR-13119. *J. Labelled Compd. Radiopharm. 27*, 823–833.

(25) Wilson, A. A., Dannals, R. F., Ravert, H. T., and Wagner, H. N. (1990) Reductive amination of [^{18}F]fuorobenzaldehydes: radiosyntheses of 2-[^{18}F]- and 4-[^{18}F]-fluorodexetimides. *J. Labeled Compd. Radiopharm. 28*, 1189–1199.

(26) Jin, M., Smith, C., Hsieh, H.-Y., Gibson, D. F., and Tait, J. F. (2004) Essential role of B-helix calcium binding sites in annexin V-memberane binding. *J. Biol. Chem. 279*, 40351–40357.

(27) Tait, J. F., and Gibson, D. (1994) Measurement of membrane phospholipid asymmetry in normal and sickle-cell erythrocytes by means of annexin V binding. *J. Lab. Clin. Med 123* (5), 741–748.

BC800164D

"Click-to-Chelate": In Vitro and In Vivo Comparison of a $^{99m}Tc(CO)_3$-Labeled N(τ)-Histidine Folate Derivative with Its Isostructural, Clicked 1,2,3-Triazole Analogue

Thomas L. Mindt,[†] Cristina Müller,[‡] Marleen Melis,[§] Marion de Jong,[§] and Roger Schibli*[,†]

Department of Chemistry and Applied Biosciences, ETH Zurich, 8093 Zurich, Switzerland, Center for Radiopharmaceutical Science, ETH-PSI-USZ, Paul Scherrer Institute, 5232 Villigen-PSI, Switzerland, and Department of Nuclear Medicine, Erasmus Medical Center, 3015 CE Rotterdam, The Netherlands. Received May 7, 2008; Revised Manuscript Received June 26, 2008

A side-by-side comparison of the synthesis, radiolabeling, and in vitro and in vivo characterization of two new and isostructural ^{99m}Tc-tricarbonyl folic acid radiotracers comprising either a N(τ)-functionalized histidine (His) chelator or a 1,4-bifunctionalized 1,2,3-triazole His analogue is described. The 1,2,3-triazole-containing folic acid derivative was synthesized in approximately 80% yield by a short reaction sequence including application of click chemistry (the Cu(I)-catalyzed cycloaddition of azides and terminal alkynes). The synthesis of the ligand system and the functionalization of the folic acid derivative were accomplished simultaneously, which prompted us to call this approach "click-to-chelate". In comparison, the reported regioselective synthesis of the N(τ)-His compound provided the final product in only very low yields (<1%). While the efficiency of the syntheses differs considerably, the two isostructural folate derivatives exhibit virtually identical properties with respect to Tc-99m radiolabeling and in vitro and in vivo characteristics as shown by experiments performed with FR-positive KB cells and xenografted mice bearing folate receptor overexpressing tumors. We have demonstrated herein for the first time that a ligand system known to be an excellent chelator for the stable complexation of the organometallic core $[M(CO)_3]^+$ (M = Tc-99m, Re) can be replaced by an isostructural 1,2,3-triazole analogue without influencing the characteristics of the radiometal conjugate. The "click-to-chelate" strategy provides a highly efficient and convenient entry to metal conjugates suitable for diagnostic and potentially therapeutic applications. The described procedures should be readily applicable to any azide-functionalized (bio)molecule and, thus, are likely to represent the method of choice for the future development of radiopharmaceuticals radiolabeled with the organometallic precursors $[M(CO)_3(H_2O)_3]^+$ (M = ^{99m}Tc, ^{188}Re).

INTRODUCTION

A prerequisite for the use of metal probes for application in targeted imaging (using positron emission or single photon emission tomography, magnetic resonance, and fluorescence) (*1–3*) and therapy (with particle emitting radiometals) is their stable attachment to a (bio)molecule via an efficient ligand system. This can be achieved by using bifunctional chelating agents (BFCA), which comprise a ligand system for the stable chelation of the (radio)metal and a second functionality for attachment of the metal chelate to the targeting molecule. However, the preparation of BFCAs generally entails multistep syntheses and their incorporation into (bio)molecules often lacks efficiency and is further complicated by cross-reactivity with other functional groups present. Thus, novel and efficient strategies for the synthesis of metal chelating systems and their incorporation into molecules of biological interest are needed.

The organometallic precursor $[^{99m}Tc(CO)_3(H_2O)_3]^+$ (*4*) has been extensively evaluated for the radiolabeling of (bio)molecules (*5–7*). A variety of tridentate ligand systems have been reported for complexation of the Tc-99m tricarbonyl core (*6*) including examples of bifunctional chelators derived from natural amino acids or synthetic analogues (*8–10*). For example, histidine (His) derived ligand systems have been shown to be extraordinarily good chelators for the efficient and stable coordination of "$M(CO)_3$" (M = Tc-99m, Re) (*11, 12*). Unfortunately, the synthesis of BFCAs based on N(τ)-functionalized His is not straightforward. Direct alkylation of the imidazole moiety of His derivatives generally yields mixtures of N(τ)-alkylated His along with the analogous, undesired N(π)-alkylated product (Figure 1, path A) (*13*). The formation of isomers makes tedious separations necessary even if one alkylation product is formed preferentially. An elegant strategy has been reported for the regioselective preparation of N(τ)-His derivatives via alkylation of a cyclic N(π)-urea intermediate and subsequent alcohol-mediated ring opening of the resulting quaternary amine (path B) (*12, 14, 15*). However, the efficiency of the alkylation step and the ring opening reaction depends on the nature of the reagents employed, and yields of isolated N(τ)-functionalized His can vary.

We have recently reported that the imidazole heterocycle of N(τ)-functionalized histidines can be replaced with a 1,4-disubstituted 1,2,3-triazole without altering the excellent chelating properties of the ligand system with regard to complexation of "$M(CO)_3$" (M = Tc-99m, Re) (*16*). Ligand design based on a 1,2,3-triazole scaffold takes advantage of the selectivity and efficiency of the Cu(I)-catalyzed [3 + 2] cycloaddition of terminal alkynes and azides, a transformation which has been termed a "click reaction" (*17–19*). For instance, click reaction of an azide with commercial L-propargyl glycine (**1**) (*20*) quantitatively yields optically pure triazoles which are isostructural to N(τ)-functionalized histidines (Figure 1, path C). The click product derived from propargyl glycine proved to be an excellent tripodal ligand system for "$M(CO)_3$" forming stable

* Roger Schibli, Center for Radiopharmaceutical Science, ETH-PSI-USZ. Telephone: +41-56-310-2837. Fax: +41-56-310-2849. E-mail address: roger.schibli@pharma.ethz.ch.

[†] ETH Zurich.

[‡] Paul Scherrer Institute.

[§] Erasmus Medical Center.

10.1021/bc800183r CCC: $40.75 © 2008 American Chemical Society
Published on Web 07/23/2008

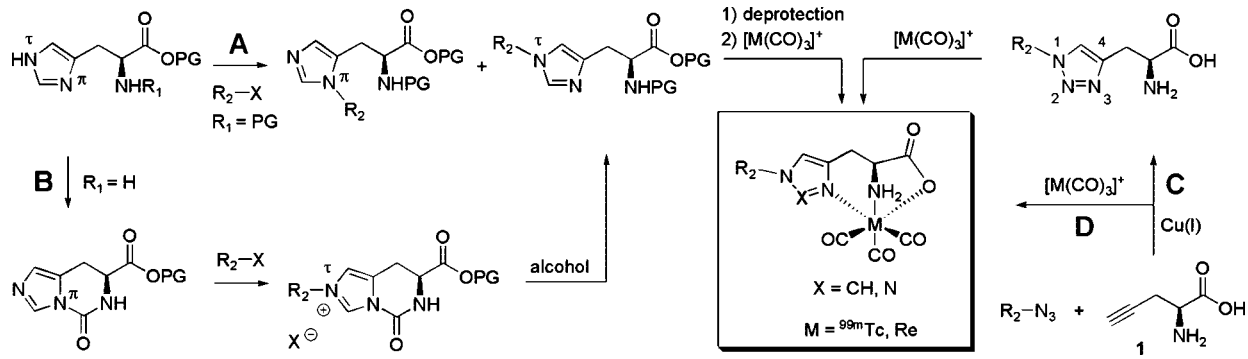

Figure 1. Synthetic strategies for the preparation of N(τ)-functionalized histidines (paths A,B), clicked 1,2,3-triazole analogues (paths C,D) and their use as BFCAs for the stable complexation of "$M(CO)_3$" (M = Tc-99m, Re). PG = protective groups; X = leaving group (e.g., halogens); R2 = organic residue or a biomolecule.

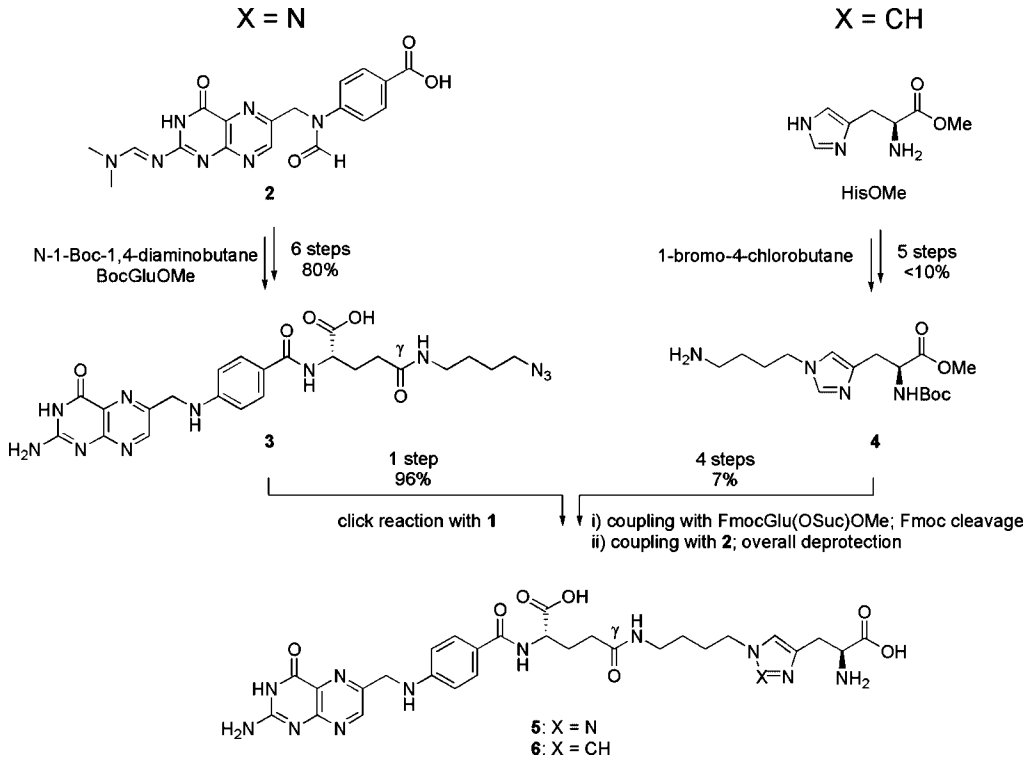

Figure 2. Comparison of the syntheses of two isostructural folic acid derivatives equipped with a 1,2,3-triazole containing chelator obtained by click chemistry (X = N) and a N(τ)-His ligand system (X = CH).

complexes by preferential coordination of the metal via nitrogen N(3) (rather than N(1) or N(2)) of the heterocycle (*16*). It is noteworthy that the synthesis of the chelating system and its attachment to a (bio)molecule is achieved simultaneously in a single step, a feature which has prompted us to call this new strategy "click-to-chelate".

In the meantime, we have reported a number of examples of the "click-to-chelate" approach for applications in radiopharmacy (*16, 21, 22*). However, a direct comparison of an N(τ)-His (radio)chelate with its 1,2,3-triazole analogue that demonstrates the chemical equivalence of the two isostructural ligand systems is still missing. We now wish to report the synthesis, Tc-99m labeling, and in vitro and in vivo characteristics of a folic acid Tc-99m radiotracer comprising a His-mimicking 1,2,3-triazole ligand system, and a side-by-side comparison with a folate conjugate equipped with a N(τ)-His chelate, the synthesis and in vivo evaluation of which has recently been described (see Figure 2) (*23, 24*).

EXPERIMENTAL PROCEDURES

Syntheses. *General Methods.* Melting points were taken on a Büchi-535 apparatus and are uncorrected. Infrared spectra were recorded on a Jasco FT/IR-6200 ATR-IR. Nuclear magnetic resonance spectra were recorded with a Bruker 400 or 500 MHz spectrometer with the corresponding solvent signals as an internal standard. Chemical shifts are reported in parts per million (ppm) relative to tetramethylsilane (0.00 ppm). Values of the coupling constant, *J*, are given in hertz (Hz); the following abbreviations are used in the experimental section for the description of ^{1}H-NMR spectra: singlet (s), doublet (d), triplet (t), quartet (q), multiplet (m), doublet of doublets (dd), and bs (broad singlet). The chemical shifts of complex multiplets are given as the range of their occurrence. For signal assignment, H/D exchange and 2D-NMR experiments (COSY, HSQC, HMBC) were performed for all new compounds. Low resolution mass spectra (LR-MS) were recorded with a Micromass Quattro micro API LC-ESI and high resolution mass spectra (HR-MS) with a Bruker FTMS 4.7 T BioAPEXII (ESI).

All water sensitive reactions were performed under argon in flame-dried glassware. Reactions were monitored by thin layer chromatography (TLC, performed on EM Science 0.25 mm thick, precoated silica gel 60 F-254 glass supported plates) or HPLC. HPLC was performed on a Merck-Hitachi L-7000 system equipped with an L-7400 tunable absorption detector and a Berthold LB 506 radiometric detector. The following systems were used for analytical HPLC: HPLC System 1: XBridge column (C18, 5 μm, 4.6 × 150 mm, Waters); 0.1% aq. TFA (solvent A), acetonitrile (solvent B); 0−1 min, 95% A; 1−15 min, 95→5% A; 15−20 min, 5% A; 20→22 min, 5→95% A; 22→25 min, 95% A; flow rate: 1 mL/min. HPLC System 2: Identical to system 1 but because of the solubility of deprotected folic acid derivatives, 10 mM NH_4HCO_3 was used instead of 0.1% aq. TFA. HPLC system 3: Tc-99m complexes were analyzed and compared with Re-analogues using a Nucleosil 5 C18 column (5 μm, 4.6 × 250 mm, Macherey-Nagel) with the following solvent system: Aqueous 0.05 M triethylammonium phosphate buffer, pH 2.25 (solvent A), methanol (solvent B), the HPLC system started with 95% A, with a linear gradient to 20% A and 80% B over 15 min, followed by 5 min of 100% A, with a flow rate of 1 mL/min. Semi preparative HPLC was performed with an XBridge column (C18, 5 μm, 10 × 150 mm, Waters) using the solvent system as indicated in the description of the individual experiments; flow rate of 3 mL/min.

[Na][$^{99m}TcO_4$] was eluted from a $^{99}Mo/^{99m}Tc$-generator (Mallinckrodt-Tyco, Petten, The Netherlands) with a 0.9% saline solution. Protected pteroic acid **2** was provided by Merck Eprova AG, Switzerland. All other commercially available reagents and solvents were purchased from Sigma-Aldrich and used as supplied unless stated otherwise. For a detailed description of the synthesis of compound **3**, see the Supporting Information.

Compound **5.** Azido folate **3** (36 mg, 0.05 mmol) was suspended in $^tBuOH/H_2O$ (1:1, 3 mL); and L-propargyl glycine (**1**, 6 mg, 0.053 mmol), $Cu(OAc)_2$ (2 mg, 20 mol %), and sodium ascorbate (4 mg, 40 mol %) were added. The mixture was stirred at 80 °C for 20 min after which HPLC (HPLC system 3) indicated completed conversion of substrate **3** and formation of a single product. The brown suspension was dissolved by addition of 2−3 drops of NaOH (1 M) and cleared by filtration through Celite. The product was precipitated by adjusting the pH of the solution to pH 2−3 with aq. HCl (1 M). The resulting suspension was centrifuged (10 min at 3500 rpm), the supernatant was decanted, and the solid was dried under reduced pressure to give the pentahydrochloride salt of triazolyl folate **5** as a orange powder (40 mg, 96%; purity according to HPLC >95%): mp >250 °C (decomposition); elemental analysis (calculated % values for $C_{28}H_{34}N_{12}O_7(HCl)_5$ in parenthesis), C 40.20 (40.37), H 5.12 (4.72), N 20.63 (20.18), O (13.45); chloride content determined by titration, 20.32 (calc. 21.28). For spectroscopic analysis, a sample of the crude product (10 mg) was purified by semipreparative HPLC (isocratic CH_3CN (10%), 0.1% aq. TFA (90%)). Lyophilization provided the tris-TFA salt, monohydrate of product **5** as a yellow powder (5 mg; purity according to HPLC >98%): IR (neat) ν 3253, 3085, 2936, 2787, 1683, 1631, 1604, 1507, 1302, 1227, 1180, 1125, 834 cm^{-1}; ^1H NMR (DMSO-d_6, using a water-signal suppressing program) δ 8.68 (bs, 1H), 8.27 (bs, 2H, exchange with D_2O), 8.20 (d, 1H, exchanges with D_2O, J = 6.8 Hz), 7.92 (s, 1H), 7.85 (t, 1H, exchanges with D_2O, J = 5.7 Hz), 7.65 (d, 2H, J = 8.1 Hz), 7.5−7.0 (multiple bs, 2H, exchange with D_2O), 6.64 (d, 2H, J = 8.1 Hz), 4.50 (s, 2H), 4.35−4.20 (m, 5H, one proton exchanges with D_2O), 3.23−3.13 (m, 2H), 3.09−2.94 (m, 2H), 2.50 (bs, 2H, exchange with D_2O), 2.18 (t, 2H, J = 8.2 Hz), 2.10−1.98 (m, 1H), 1.93−84 (m, 1H), 1.80−1.72 (m, 2H), 1.45−1.27 (m, 2H) ppm; ^{13}C NMR (DMSO-d_6) δ 173.8, 171.5, 170.1, 166.3, 160.4, 158.5, 153.5, 150.7, 149.6, 148.3, 140.4, 129.0, 127.9, 123.6, 121.4, 111.2, 52.1, 51.8, 49.0, 45.8, 37.7, 32.0, 27.2, 26.6, 26.1, 26.0 ppm; HR-MS $[M+H]^+$ = 651.2738 (calc. for $C_{28}H_{35}N_{12}O_7$ 651.2752); elemental analysis (calculated % values for $C_{28}H_{34}N_{12}O_7(TFA)_3(H_2O)$ in parenthesis), C 40.30 (40.40), H 4.20 (3.98), N 16.86 (16.63), O (22.16); fluoride content determined by titration, 15.95 (calc. 16.63).

*Compound [$^{99m}Tc(CO)_3$(**5**)]*. The precursor $[^{99m}Tc(H_2O)_3(CO)_3]^+$ was prepared according to the literature (*25*). In brief, $[^{99m}TcO_4]^-$ in 0.9% NaCl from a $^{99}Mo/^{99m}Tc$ generator was added to the IsoLink kit (Mallinckrodt-Tyco, Petten, The Netherlands) via the septum. The reaction mixture was heated for 20 min at 100 °C. The solution was cooled on ice and neutralized (pH 7.2) with 1 M phosphate buffer pH = 7.4 and 1 M HCl (1:1 mixture).

Synthesis 1: 50 μL of a stock solution of folic acid conjugate **5** (pentahydrochloride salt; 10^{-3} M in phosphate buffered saline (PBS), pH 7.4) was added to a solution of $[^{99m}Tc(CO)_3(OH_2)_3]^+$ (100 μL; ∼1 GBq/mL). PBS (pH 7.4) was added to adjust the final concentration of the ligand (10^{-4}−10^{-9} M) and the reaction mixture was heated for 30 min at 100 °C. Radiolabeling yields were determined by HPLC (γ-detection). Radiolabeling of the isostructural compound **6** was performed using the same procedure.

Synthesis 2 (one-pot, two-step procedure): Aqueous solutions azido folate **3** (100 μL, 10^{-3} M), copper (II) acetate (40 μL, 10^{-2} M), sodium ascorbate (80 μL, 10^{-2} M), and L-propargyl glycine (**1**, 150 μL, 10^{-3} M) were combined and heated at 100 °C for 30 min. After cooling to rt, $[^{99m}Tc(OH_2)_3(CO)_3]^+$ (100 μL in PBS pH 7.4; ∼1 GBq/mL) was added and the mixture was incubated at 100 °C for 30 min after which HPLC (γ-detection) indicated clean formation of product $[^{99m}Tc(CO)_3$(**5**)] (>90% purity according to HPLC).

*Compound [Re(CO)$_3$(**5**)]*. Folic acid derivative **5** (pentahydrochloride salt, 12.5 mg, 0.015 mmol) and $[Re(Br)_3(CO)_3][Et_4N]_2$ (11.5 mg, 0.015 mmol) were dissolved in water (2 mL). The pH of the solution was adjusted from pH 3 to pH 8 by addition of dilute aq. NaOH. After stirring at 50 °C for 1 h, HPLC indicated complete conversion of substrate **5** and formation of a single product. The reaction mixture was cleared by filtration through Celite and the product was precipitated at pH 2−3 by addition of dilute aq. HCl. The resulting suspension was centrifuged (10 min at 3500 rpm), the supernatant decanted, and the crude product was purified by semipreparative HPLC (isocratic CH_3CN (15%), 10 mM NH_4HCO_3 (85%)). Lyophilization provided the ammonium salt of [Re(CO)$_3$(**5**)] as a yellow solid (9.5 mg, 70%; purity according to HPLC >98%): mp >250 °C (decomposition); IR (neat) ν 3253, 3095, 2932, 2014, 1873, 1631, 1602, 1507, 1022, 821 cm^{-1}; ^1H NMR (DMSO-d_6) δ 10.55 (bs, 1H; exchanges with D_2O), 8.64 (s, 1H), 8.26 (s, 1H), 7.97 (t, 1H, J = 5.4 Hz; exchanges with D_2O), 7.80 (bs, 1H; exchanges with D_2O), 7.58 (d, 2H, J = 9.0 Hz), 7.24 (bs, 2H; exchange with D_2O), 6.91 (t, 1H, J = 5.9 Hz; exchanges with D_2O), 6.65 (d, 2H, J = 9.0 Hz), 5.95−5.91 (m, 1H, exchanges with D_2O after 5 days), 5.29 (d, 1H, J = 11.5 Hz; exchanges with D_2O after 5 days), 4.50−4.45 (m, 2H, becomes singlet (4.48 ppm) after D_2O exchange), 4.40 (t, 2H, J = 7.2 Hz), 4.12−4.03 (m, 1H; becomes triplet (4.09 ppm, J = 5.1 Hz) after D_2O exchange), 3.88−3.80 (m, 1H; becomes triplet (3.85 ppm, J = 3.9 Hz) after D_2O exchange), 3.18 (d, 2H, J = 5.0 Hz), 3.08−3.00 (m, 2H), 2.19−2.08 (m, 2H), 2.07−1.93 (m, 1H), 1.90−1.74 (m, 3H), 1.42−1.33 (m, 2H) ppm; ^{13}C NMR (DMSO-d_6) δ 199.0, 198.0, 197.3, 180.8, 174.7, 172.4, 166.2, 161.8, 156.8, 154.7, 151.1, 149.0, 148.8, 142.8, 129.1, 128.4, 126.0, 122.2, 111.7, 51.1, 51.0, 50.9, 46.4, 38.1, 32.6, 27.4, 26.5, 26.4 ppm (one CH_2 is not observed presumably due to overlapping signals); HR-MS: $[M+H]^+$ = 921.2077

(calc. for $C_{31}H_{34}N_{12}O_{10}Re$: 921.2078); elemental analysis (calculated % values for $C_{31}H_{36}N_{13}O_{10}Re$ in parenthesis) C 39.43 (39.74), H 4.02 (3.87), N 18.96 (19.23).

Determination of log *P*. The log *P* values of the Tc-99m folate tracers [$^{99m}Tc(CO)_3$(**5**)] and [$^{99m}Tc(CO)_3$(**6**)] were determined by a published procedure (*26*). In brief, samples of the HPLC-purified radiotracers (250 kBq) were mixed with equal amounts (1.5 mL) of PBS (pH 7.4) and octanol and the resulting biphasic system was mixed vigorously for 1 min. The two phases were separated by centrifugation and 0.5 mL aliquots were taken from each layer and counted for radioactivity in a γ-counter. The partition coefficient is expressed as the ratio of radioactivity (cpm) in the octanol phase to the one in the PBS phase and represents the mean (± standard deviation) of eight measurements for both compounds.

In Vitro Cell Uptake of ^{99m}Tc-Labeled Complexes. KB cells (human nasopharyngeal carcinoma cell line) were purchased from ATCC (CCL-17; American type Culture Collection, Manassas, USA). The cells were cultured as monolayers at 37 °C in a humidified atmosphere containing 5% CO_2. Importantly, the cells were cultured in FFRPMI cell culture medium (modified RPMI medium, without folic acid, vitamin B_{12}, and phenol red; Cell Culture Technologies GmbH, Gravesano/Lugano, Switzerland). FFRPMI medium was supplemented with 10% heat-inactivated fetal calf serum (FCS, as the only source of folate), L-glutamine, and antibiotics (penicillin/streptomycin/fungizone).

Eighteen hours prior to the experiment, the cells were seeded in 12-well plates (7.5×10^5 cells/well) to form confluent monolayers overnight. The experiments were performed in triplicate. Cell binding experiments of the radiofolates [$^{99m}Tc(CO)_3$(**5**)] and [$^{99m}Tc(CO)_3$(**6**)] were performed according to the following procedure: Cell monolayers were rinsed twice with PBS (pH 7.4). Pure FFRPMI medium (without FCS/L-glutamine/antibiotics, 975 μL) was added into each well. Blocking studies were performed with FFRPMI medium (475 mL) and a folic acid solution (200 μM, 500 μL). The well plates were preincubated at 37 °C for 40 min. A solution of the corresponding radiotracer (25 μL, 1.5 MBq/mL) was added, and the well plates were incubated for 1 h at 37 °C. Then, after removal of the radiotracer, the monolayers were washed two times with PBS (pH 7.4): radioactivity counted in these samples could be ascribed to the sum of FR-bound radiotracer on the cell surface and the internalized fraction. Other triplicate cell samples washed two times with stripping buffer (an aqueous solution of 0.1 M acetic acid and 0.15 M NaCl, pH 3) after the PBS wash in order to release radiotracers from FRs on the cell surface enabled determination of radioactivity of the internalized fraction only (*27*, *28*). The monolayers were lysed in 1 N NaOH (1 mL), transferred into 4 mL tubes, and homogenized by vortex. The radioactivity of each sample was measured in a γ-counter. The concentration of proteins was determined (using a commercially available kit of BioRad, Veenendaal, The Netherlands) for each sample in order to normalize measured radioactivity of the samples with respect to the averaged sample protein content. The raw data were converted from counts per minute (cpm) into percentage of total radioactivity added.

Biodistribution in Tumor Bearing Mice. All animal experiments were approved by the governing Animal Welfare Committee and conducted in accordance with the regulations of the Erasmus Medical Center, Rotterdam, The Netherlands. 8−10-week-old male, athymic nude mice (NMRI nu/nu) were purchased from Charles River Laboratories (Maastricht, The Netherlands). The animals were acclimatized and fed with a folate-deficient rodent diet starting 5 days prior to the tumor cell inoculation (*29*). The mice were inoculated subcutaneously with KB tumor cells (suspension of 5×10^6 cells in 100 μL PBS) on each shoulder. Radiofolate biodistribution studies were carried out in triplicate 14 days after tumor cell inoculation when the tumors reached a size of 0.5−1.5 cm^3. For biodistribution studies, mice were injected into a lateral tail vein with 1.5 MBq of HPLC-purified [$^{99m}Tc(CO)_3$(**5**)] and [$^{99m}Tc(CO)_3$(**6**)] respectively, in 100 μL PBS. The animals were sacrificed at 1, 4, or 24 h postinjection (p.i.) of the radiofolate. Blocking experiments were performed 4 h p.i. with mice (co)injected with excess folic acid (100 μg) shortly before injection of the radiotracer. Selected tissues and organs were removed, weighed, and counted for radioactivity in a γ-counter (Wizard, 1480, Perkin-Elmer). The results were expressed as percentage of the injected dose per gram of weight tissue [% ID/g], using reference counts from a definite sample of the original injectate counted at the same time.

RESULTS AND DISCUSSION

Folic acid is an essential dietary vitamin required by eukaryotic cells for the biosynthesis of nucleotide bases. As a consequence, acquirement of the vitamin is essential for cell survival and proliferation. A number of cancer cell lines exhibit high levels of the cell surface folate receptor (FR) while its expression is highly restricted in most normal tissues. In the past, folic acid conjugates have been successfully used to deliver specifically a variety of diagnostic and therapeutic agents to FR-positive tumors (*30*, *31*). For example, we and others have reported the attachment of radiometal chelates to folic acid for diagnostic and therapeutic applications (*32*–*38*). Although preclinical data are promising, the sometimes lengthy and inefficient syntheses of folic acid/radio metal conjugates may impede future development for radiopharmaceutical applications.

For the synthesis of compound **5**, we employed a fragment coupling strategy including as a key step the condensation of a protected pteroic acid derivative with an appropriate glutamic acid counterpart. The latter fragment was modified regioselectively at the γ-position with an azide functionality, hence providing a handle for the subsequent incorporation of a triazole-containing ligand system by click chemistry.

The synthesis of the folic acid derivative **5** is summarized in Figure 2. The required azido precursor **3** was synthesized in 6 steps and 80% yield from derivatives of glutamic acid and 1,4-diaminobutane and protected pteroic acid **2** (see Supporting Information for details). The Cu(I)-catalyzed functionalization of intermediate **3** was performed with unprotected L-propargyl glycine (**1**) (*20*) using reaction conditions similar to those initially reported by the Sharpless group (*17*). Thus, an aqueous solution of the click substrates alkyne **1** and azide **3** in the presence of catalytic amounts of in situ generated Cu(I) was heated to 80 °C for 20 min, after which HPLC indicated complete conversion of the substrates and formation of a single product. Alternatively, product **5** can be obtained at rt after stirring of the reaction mixture overnight. Conveniently, the HCl salt of triazole **5** could be isolated from the aqueous reaction mixture in pure form and in high yield by precipitation at decreased pH. Thus, precursor **5** for metal labeling was prepared in 7 steps and an overall yield of approximately 80%. In comparison, the regioselective synthesis of isostructural folate derivative **6** equipped with the N(τ)-functionalized His chelating system **4** (prepared via synthetic path B; see Figure 1) required 9 steps and provided the final product with an overall yield of <1% (Figure 1B) (*23*). Clearly, application of click chemistry led to a significant improvement of the synthetic efficiency of the preparation of functionalized folic acid derivatives.

Nonradioactive labeling of folic acid conjugate **5** was performed with the precursor $[Re(CO)_3(Br)_3][Et_4N]_2$ (*39*) using previously described procedures (Scheme 1) (*16*, *32*). Rhenium complex [$Re(CO)_3$(**5**)] was obtained as a single product and

Scheme 1. Synthesis of Folic Acid Metal Conjugates[a]

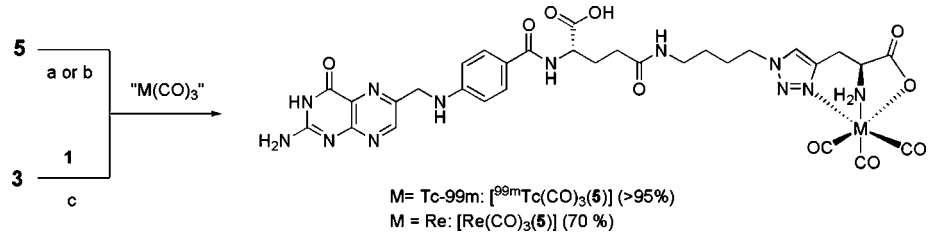

[a] (a) For $[^{99m}Tc(CO)_3(\mathbf{5})]$:$[^{99m}Tc(CO)_3(H_2O)_3]^+$, 0.15 M PBS, pH 7.4, 100 °C, 30 min; (b) For $[Re(CO)_3(\mathbf{5})]$:$[Re(Br)_3(CO)_3][Et_4N]_2$, H_2O, pH 8, 50 °C, 1 h; (c) **1**, 10 mol % $Cu(OAc)_2$/sodium ascorbate (1:2), H_2O, 30 min 100 °C, then $[^{99m}Tc(CO)_3(H_2O)_3]^+$, 30 min, 100 °C.

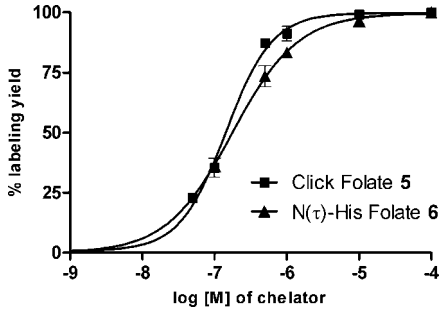

Figure 3. $^{99m}Tc(CO)_3$ labeling efficiency of the clicked 1,2,3-triazole chelator **5** and the corresponding isostructural N(τ)-His ligand system **6**, respectively, at varying concentrations (number of experiments $n = 3$).

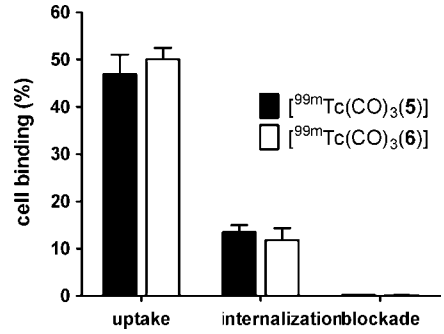

Figure 4. Uptake and internalization of complexes $[^{99m}Tc(CO)_3(\mathbf{5})]$ and $[^{99m}Tc(CO)_3(\mathbf{6})]$ using FR-positive KB cancer cells. Almost complete blockage (<1% of total added radioactivity) was found after addition of excess folic acid.

fully characterized by spectroscopic methods (NMR, MS, IR) and elemental analysis. In agreement with reported complexes of "$Re(CO)_3$" and 1,2,3-triazole-containing ligand systems (*16, 21*), NMR analysis of compound $[Re(CO)_3(\mathbf{5})]$ supports a $\kappa N(3),\kappa O,\kappa N(\alpha)$ coordination.

Derivative **5** (and **6**) could also be readily radiolabeled with $[^{99m}Tc(CO)_3(H_2O)_3]^+$ at 100 °C. Identity of $[^{99m}Tc(CO)_3(\mathbf{5})]$ was confirmed by comparison of the HPLC γ-trace with the UV-trace of $[Re(CO)_3(\mathbf{5})]$ (see Supporting Information). The labeling efficiency of folate **5** with a 1,2,3-triazole-containing chelating system was assessed and compared with the isostructural folic acid derivative **6**. Varying the concentration of the ligands gave rise to step-sigmoid curves which allowed a comparison of the labeling capacities of the two chelators (Figure 3). With both compounds, 50% labeling yield of $^{99m}Tc(CO)_3$ was achieved at ligand concentrations of $\sim 10^{-7}$ M. This demonstrates again that the N(τ)-functionalized His chelator and the 1,4-disubstituted 1,2,3-triazole analogue are equally potent ligand systems with respect to complexation of $[^{99m}Tc(CO)_3(H_2O)_3]^+$ (*16, 21*). Importantly, folic acid SPECT tracer $[^{99m}Tc(CO)_3(\mathbf{5})]$ could also be obtained directly from azide **3** by a one-pot, two-step protocol without isolation and purification of the intermediate **5**, therefore simplifying further the synthetic procedure (Figure 1, path D) (*16*). Thus, heating of an aqueous solution of azide **3** and L-propargyl glycine (**1**) in the presence of Cu(I) catalyst for 30 min followed by addition of $[^{99m}Tc(CO)_3(H_2O)_3]^+$ and heating for 30 min provided the final compound $[^{99m}Tc(CO)_3(\mathbf{5})]$ in pure form and identical in all respects to the product obtained from isolated and purified precursor **5**.

Because the lipophilicity of a radiotracer could affect the fate of the compounds after systemic administration, the log *P* values of both radiofolates $[^{99m}Tc(CO)_3(\mathbf{5})]$ and $[^{99m}Tc(CO)_3(\mathbf{6})]$ were determined. The Tc-99m complex of **5** revealed a log *P* value of -3.41 ± 0.06, whereas that of **6** was found to be -3.47 ± 0.05 (both measured at pH = 7.4). Thus, the Tc-99m complexes of compounds **5** and **6** exhibit virtually identical hydrophilic characters.

In Vitro and In Vivo Assessment. We have recently reported the assessment of a $^{99m}Tc(CO)_3$-labeled bombesin derivative which was functionalized via click chemistry (*16*). The in vitro and in vivo results were largely comparable to that of a bombesin analogue equipped with a N^{α}-AcHis chelating system. While the amino acid sequence of both peptides was identical, they differed with respect to the spacer entity (βAla vs βAla-βAla) and the site of functionalization of the chelating system (N^{α}-amino group of His vs N(1) of the 1,2,3-triazole heterocycle). In addition, the bombesin derivatives were tested in vivo at a single time point only, which did not allow a comparison of their pharmacokinetic profiles. With the isostructural folic acid derivatives $[^{99m}Tc(CO)_3(\mathbf{5})]$ and $[^{99m}Tc(CO)_3(\mathbf{6})]$ available, a more thorough and accurate evaluation and comparison in vitro and in vivo became possible.

$[^{99m}Tc(CO)_3(\mathbf{5})]$ and $[^{99m}Tc(CO)_3(\mathbf{6})]$ were assessed in vitro using FR-positive KB tumor cells (Figure 4). For both Tc-99m complexes, a cell uptake of approximately 50% of total added radioactivity was observed of which roughly one-third was found internalized. Blocking experiments with excess folic acid resulted in a decrease of cell-associated radioactivity to less than 1%, proving FR-specific uptake.

In order to assess and compare the in vivo behavior of $[^{99m}Tc(CO)_3(\mathbf{5})]$ and $[^{99m}Tc(CO)_3(\mathbf{6})]$, time-dependent biodistribution studies were performed with nude mice bearing KB tumor xenografts (Figure 5; see Supporting Information for details). On average, the two radiofolate tracers revealed a very similar biodistribution pattern. Both complexes showed a fast clearance from the blood and retention in nontargeted (FR-negative) organs and tissues was generally below 1% ID/g (4 h p.i.). Despite their almost identical lipophilicity, complex $[^{99m}Tc(CO)_3(\mathbf{6})]$ accumulated in the liver at early time points to a greater extent than $[^{99m}Tc(CO)_3(\mathbf{5})]$ (9.73 ± 1.32% ID/g vs 2.95 ± 1.02% ID/g, respectively; 1 h p.i.). However, radioactivity was completely cleared from the liver in both cases after 24 h (<1% ID/g). Tumor uptake of $[^{99m}Tc(CO)_3(\mathbf{5})]$ and $[^{99m}Tc(CO)_3(\mathbf{6})]$ 1 h after intravenous injection was 3.94 ± 0.71% ID/g and 2.63 ± 0.43% ID/g and peaked at 4 h p.i. with 4.84 ± 0.10% ID/g and 4.29 ± 0.67% ID/g, respectively. After 24 h p.i., tumor-associated radioactivity was still 3.51 ± 0.37%

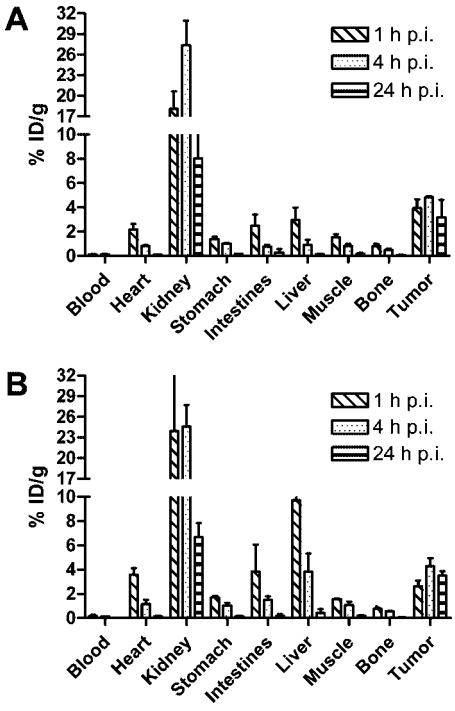

Figure 5. Time-dependent biodistribution data in selected organs and tissues at 1, 4, and 24 h p.i. of complex [^{99m}Tc(CO)$_3$(**5**)] (A) and [^{99m}Tc(CO)$_3$(**6**)] (B), respectively. Specific accumulation of the radiofolate is observed only in FR-positive tumors and kidneys. Data for compound [^{99m}Tc(CO)$_3$(**6**)] are taken from ref (*24*).

ID/g in the case of the N(τ)-His compound and 3.18 ± 1.45% ID/g for the click-derivative ($p > 0.5$). Besides in the tumor xenografts, substantial amounts of radioactivity were found in the FR-positive renal tissue. In both cases, a maximal fraction of the radiotracers was observed in the kidney at 4 h p.i. (24.56 ± 3.17% ID/g for [^{99m}Tc(CO)$_3$(**6**)] and 27.33 ± 3.61% ID/g for [^{99m}Tc(CO)$_3$(**5**)]). High renal retention of radiofolate is a known phenomenon due to substantial expression of the folate receptor at the luminal site of the proximal tubule (*40*). Biodistribution experiments performed after coinjection of excess folic acid (100 μg/mouse) confirmed specific, FR-mediated uptake of both radiofolates in the tumors and kidneys. Almost complete attenuation (<1% ID/g) of the uptake of the radiotracers was observed under these conditions (see Supporting Information).

CONCLUSIONS

A side-by-side comparison of the synthesis and in vitro and in vivo characteristics of two isostructural, organometallic ^{99m}Tc-folate radiotracers provide the final piece of evidence that (i) the "click-to-chelate" strategy improves considerably the efficiency of the preparation of Tc/Re(CO)$_3$-bioconjugates, the synthesis of which can be challenging by alternative approaches; (ii) the efficient N(τ)-derivatized histidine ligand system well suited for radiolabeling with [M(CO)$_3$(H$_2$O)$_3$]$^+$ (M = ^{99m}Tc, ^{188}Re) can be substituted by an isostructural 1,4-bifuctionalized 1,2,3-triazole-containing analogue without influencing the characteristics of the conjugate with respect to radiolabeling efficiency, in vitro uptake and internalization in a FR-overexpressing tumor cell line, and in vivo tumor-targeting capacity and pharmacokinetics.

The herein described procedures are efficient, easy to conduct, and should be readily applicable to any other type of (bio)molecule into which an azide functionality can be incorporated. It is likely that the attractive features of the "click-to-chelate" approach will make this strategy the method of choice for future development of targeted radiopharmaceuticals radiolabeled with the organometallic precursors [^{99m}Tc(CO)$_3$(H$_2$O)$_3$]$^+$ and [^{188}Re(CO)$_3$(H$_2$O)$_3$]$^+$.

ACKNOWLEDGMENT

We thank Merck Eprova AG, Switzerland for providing protected pteroic acid **2** and a sample of N(τ)-histidine folate **6**, Satish Boedhoe (Erasmus MC) for technical assistance, and Dr. Bernhard Pfeiffer and Dr. Aileen Höhne (ETH Zurich) for NMR spectroscopic measurements.

Supporting Information Available: Detailed description of the synthesis of azido folate **3**, ^{1}H and ^{13}C NMR spectra of all new compounds, HPLC chromatograms of Tc-99m and Re complexes, and complete biodistribution data of complex [^{99m}Tc(CO)$_3$(**5**)] and [^{99m}Tc(CO)$_3$(**6**)] at 1 h, 4 h, and 24 h p.i. This material is available free of charge via the Internet at http://pubs.acs.org.

LITERATURE CITED

(1) Mazzi, U., and Riondato, M. (2006) Radiometal labelled complexes for diagnostic imaging and radiotherapy. *Recent Development in Bioinorganic Chemistry: Metal Complexes of Bioactive Molecules* (Saviano, M., Ed.) pp 1−33, Transworld Research Network, Trivandrum, India.

(2) Toth, E., Helm, L., and Merbach, A. E. (2004) Metal complexes as MRI contrast enhancement agents, In *Comprehensive Coordination Chemistry II* (McCleverty, Jon A., and Meyer,Thomas J., Eds.) pp 841−881, Vol. 9, Elsevier, Oxford, UK.

(3) Buenzli, J.-C. G., and Piguet, C. (2005) Taking advantage of luminescent lanthanide ions. *Chem. Soc. Rev. 34*, 1048–1077.

(4) Alberto, R., Schibli, R., Egli, A., Schubiger, A. P., Abram, U., and Kaden, T. A. (1998) A novel organometallic aqua complex of technetium for the labeling of biomolecules: synthesis of [^{99m}Tc(OH$_2$)$_3$(CO)$_3$]$^+$ from [^{99m}TcO$_4$]$^-$ in aqueous solution and its reaction with a bifunctional ligand. *J. Am. Chem. Soc. 120*, 7987–7988.

(5) Schibli, R., and Schubiger, P. A. (2002) Current use and future potential of organometallic radiopharmaceuticals. *Eur. J. Nucl. Med. Mol. Imaging 29*, 1529–1542.

(6) Alberto, R. (2005) New organometallic technetium complexes for radiopharmaceutical imaging. *Top. Curr. Chem. 252*, 1–44.

(7) Waibel, R., Treichler, H., Schaefer, N. G., van Staveren, D. R., Mundwiler, S., Kunze, S., Kueenzi, M., Alberto, R., Nueesch, J., Knuth, A., Moch, H., Schibli, R., and Schubiger, P. A. (2008) New derivatives of vitamin B12 show preferential targeting of tumors. *Cancer Res. 68*, 2904–2911.

(8) Stephenson, K. A., Zubieta, J., Banerjee, S. R., Levadala, M. K., Taggart, L., Ryan, L., McFarlane, N., Boreham, D. R., Maresca, K. P., Babich, J. W., and Valliant, J. F. (2004) A new strategy, for the preparation of peptide-targeted radiopharmaceuticals based on ion of peptide-targeted an Fmoc-lysine-derived single amino acid chelate (SAAC). Automated solid-phase synthesis, NMR characterization, and in vitro screening of fMLF(SAAC)G and fMLF[(SAAC-Re(CO)$_3$)$^+$] G. *Bioconjugate Chem. 15*, 128–136.

(9) Banerjee, S. R., Maresca, K. P., Francesconi, L., Valliant, J., Babich, J. W., and Zubieta, J. (2005) New directions in the coordination chemistry of ^{99m}Tc: a reflection on technetium core structures and a strategy for new chelate design. *Nucl. Med. Biol. 32*, 1–20.

(10) van Staveren, D. R., Benny, P. D., Waibel, R., Kurz, P., Pak, J.-K., and Alberto, R. (2005) S-functionalized cysteine: Powerful ligands for the labelling of bioactive molecules with triaquatricarbonyltechnetium-99m(1+) ([^{99m}Tc(OH$_2$)$_3$(CO)$_3$]$^+$). *Helv. Chim. Acta 88*, 447–460.

(11) van Staveren, D. R., Waibel, R., Mundwiler, S., Schubiger, P. A., and Alberto, R. (2004) Conjugates of vitamin B12 with Nε-functionalized histidine for labeling with [^{99m}Tc(OH$_2$)$_3$(CO)$_3$]$^+$:

synthesis and biodistribution studies in tumor bearing mice. *J. Organomet. Chem. 689*, 4803–4810.
(12) Pak, J. K., Benny, P., Spingler, B., Ortner, K., and Alberto, R. (2003) Nϵ functionalization of metal and organic protected L-histidine for a highly efficient, direct labeling of biomolecules with $[^{99m}Tc(OH_2)_3(CO)_3]^+$. *Chem.-Eur. J. 9*, 2053–2061.
(13) Jones, J. H., Rathbone, D. L., and Wyatt, P. B. (1987) The regiospecific alkylation of histidine side chains. *Synthesis* 1110–1113.
(14) van Staveren, D. R., Mundwiler, S., Hoffmanns, U., Pak, J. K., Spingler, B., Metzler-Nolte, N., and Alberto, R. (2004) Conjugation of a novel histidine derivative to biomolecules and labelling with $[^{99m}Tc(OH_2)_3(CO)_3]^+$. *Org. Biomol. Chem. 2*, 2593–2603.
(15) Jain, R., and Cohen, L. A. (1996) Regiospecific alkylation of histidine and histamine at N-1 (τ). *Tetrahedron 52*, 5363–5370.
(16) Mindt, T. L., Struthers, H., Brans, L., Anguelov, T., Schweinsberg, C., Maes, V., Tourwe, D., and Schibli, R. (2006) "Click to chelate": synthesis and installation of metal chelates into biomolecules in a single step. *J. Am. Chem. Soc. 128*, 15096–15097.
(17) Rostovtsev, V. V., Green, L. G., Fokin, V. V., and Sharpless, K. B. (2002) A stepwise Huisgen cycloaddition process: copper(I)-catalyzed regioselective "ligation" of azides and terminal alkynes. *Angew. Chem., Int. Ed. 41*, 2596–2599.
(18) Tornoe, C. W., Christensen, C., and Meldal, M. (2002) Peptidotriazoles on solid phase: [1,2,3]-triazoles by regiospecific copper(i)-catalyzed 1,3-dipolar cycloadditions of terminal alkynes to azides. *J. Org. Chem. 67*, 3057–3064.
(19) Moses, J. E., and Moorhouse, A. D. (2007) The growing applications of click chemistry. *Chem. Soc. Rev. 36*, 1249–1262.
(20) Mindt, T. L., and Schibli, R. (2007) Cu(I)-catalyzed intramolecular cyclization of alkynoic acids in aqueous media: a "click side reaction. *J. Org. Chem. 72*, 10247–10250.
(21) Struthers, H., Spingler, B., Mindt, T. L., and Schibli, R. (2008) "Click-to-chelate: Design and incorporation of triazole containing metal chelating systems into biomolecules of diagnostic and therapeutic interest *Chem.-Eur. J., 14*, 6173–6183.
(22) Mindt, T. L., Ross, T., and Schibli, R. (2007) Efficient strategy for the parallel development of multi modality imaging probes using click chemistry. *J. Labelled Compd. Radiopharm. 50*, S34.
(23) Sparr, C., Michel, U., Marti, R. E., Müller, C., Schibli, R., Moser, R., and Groehn, V. (2008) Synthesis of a novel (107)-folic acid-Nτ-histidine-conjugate suitable for labelling with ^{99m}Tc and ^{188}Re *Synthesis*, accepted.
(24) Müller, C., Forrer, F., Schibli, R., Krenning, E. P., and de Jong, M. (2008) SPECT imaging studies of folate receptor-positive malignant and normal tissues in mice using a novel 99m Tc-Radiofolate. *J. Nucl. Med. 49*, 310–317.
(25) Alberto, R., Ortner, K., Wheatley, N., Schibli, R., and Schubiger, A. P. (2001) Synthesis and properties of boranocarbonate: a convenient in situ co source for the aqueous preparation of $[^{99m}Tc(OH_2)_3(CO)_3]^+$. *J. Am. Chem. Soc. 123*, 3135–3136.
(26) Rennen, H. J. J. M., van Eerd, J. E., Oyen, W. J. G., Corstens, F. H. M., Edwards, D. S., and Boerman, O. C. (2002) Effects of coligand variation on the in vivo characteristics of Tc-99m-labeled interleukin-8 in detection of infection. *Bioconjugate Chem. 13*, 370–377.
(27) Dixon, K. H., Mulligan, T., Chung, K. N., Elwood, P. C., and Cowan, K. H. (1992) Effects of folate receptor expression following stable transfection into wild type and methotrexate transport-deficient ZR-75−1 human breast cancer cells. *J. Biol. Chem. 267*, 24140–24147.
(28) Ladino, C. A., Chari, R. V., Bourret, L. A., Kedersha, N. L., and Goldmacher, V. S. (1997) Folate-maytansinoids: target-selective drugs of low molecular weight. *Int. J. Cancer 73*, 859–864.
(29) Mathias, C. J., Wang, S., Lee, R. J., Waters, D. J., Low, P. S., and Green, M. A. (1996) Tumor-selective radiopharmaceutical targeting via receptor-mediated endocytosis of gallium-67-deferoxamine-folate. *J. Nucl. Med. 37*, 1003–1008.
(30) Hilgenbrink, A. R., and Low, P. S. (2005) Folate receptor-mediated drug targeting: From therapeutics to diagnostics. *J. Pharm. Sci. 94*, 2135–2146.
(31) Low, P. S., Henne, W. A., and Doorneweerd, D. D. (2008) Discovery and development of folic-acid-based receptor targeting for imaging and therapy of cancer and inflammatory diseases. *Acc. Chem. Res. 41*, 120–129.
(32) Mueller, C., Schubiger, P. A., and Schibli, R. (2006) Synthesis and in vitro/in vivo evaluation of novel $^{99m}Tc(CO)_3$-folates. *Bioconjugate Chem. 17*, 797–806.
(33) Wang, S., Lee, R. J., Mathias, C. J., Green, M. A., and Low, P. S. (1996) Synthesis, purification, and tumor cell uptake of ^{67}Ga-deferoxamine-folate, a potential radiopharmaceutical for tumor imaging. *Bioconjugate Chem. 7*, 56–62.
(34) Wang, S., Luo, J., Lantrip, D. A., Waters, D. J., Mathias, C. J., Green, M. A., Fuchs, P. L., and Low, P. S. (1997) Design and synthesis of [^{111}In]DTPA-folate for use as a tumor-targeted radiopharmaceutical. *Bioconjugate Chem. 8*, 673–679.
(35) Ilgan, S., Yang, D. J., Higuchi, T., Zareneyrizi, F., Bayhan, H., Yu, D., Kim, E. E., and Podoloff, D. A. (1998) 99m Tc-ethylenedicysteine-folate: A new tumor imaging agent. Synthesis, labeling and evaluation in animals. *Cancer Biother. Radiopharm. 13*, 427–435.
(36) Guo, W., Hinkle, G. H., and Lee, R. J. (1999) ^{99m}Tc-HYNIC-folate: a novel receptor-based targeted radiopharmaceutical for tumor imaging. *J. Nucl. Med. 40*, 1563–1569.
(37) Mueller, C., Schubiger, P. A., and Schibli, R. (2007) Isostructural folate conjugates radiolabeled with the matched pair ^{99m}Tc/^{188}Re: A potential strategy for diagnosis and therapy of folate receptor-positive tumors. *Nucl. Med. Biol. 34*, 595–601.
(38) Leamon, C. P., Parker, M. A., Vlahov, I. R., Xu, L.-C., Reddy, J. A., Vetzel, M., and Douglas, N. (2002) Synthesis and biological evaluation of EC20: a new folate-derived, ^{99m}Tc-based radiopharmaceutical. *Bioconjugate Chem. 13*, 1200–1210.
(39) Alberto, R., Egli, A., Abram, U., Hegetschweiler, K., Gramlich, V., and Schubiger, P. A. (1994) Synthesis and reactivity of $[NEt_4]_2[ReBr_3(CO)_3]$. Formation and structural characterization of the clusters $[NEt_4][Re_3(\mu_3\text{-}OH)(\mu\text{-}OH)_3(CO)_9]$ and $[NEt_4][Re_2(\mu\text{-}OH)_3(CO)_6]$ by alkaline treatment. *J. Chem. Soc., Dalton Trans.: Inorg. Chem.* 2815–20.
(40) Birn, H., Spiegelstein, O., Christensen, E. I., and Finnell, R. H. (2005) Renal tubular reabsorption of folate mediated by folate binding protein 1. *J. Am. Soc. Nephrol. 16*, 608–615.

BC800183R

Supporting Information Available

Functionalization of Long Chain Alkylamine Controlled-Pore Glass for Thermolytic Release of DNA Oligonucleotides and Their Conjugates

Andrzej Grajkowski,[‡] *Jacek Cieślak,*[‡] *Jon S. Kauffman,*[§] *Robert Duff,*[§] *Scott Norris,*[#]

Darón I. Freedberg,[#] *and Serge L. Beaucage**[‡]

[‡]Division of Therapeutic Proteins, Center for Drug Evaluation and Research, and [#]Division of Bacterial, Parasitic & Allergenic Products, Center for Biologics Evaluation and Research, Food and Drug Administration, 8800 Rockville Pike, Bethesda, Maryland 20892, and [§]Lancaster Laboratories, 2425 New Holland Pike, Lancaster, PA 17605

Table of Contents

Materials and Methods……..S03
700 MHz ^{1}H NMR spectrum of 5'-*O*-(4,4'-dimethoxytrityl)-
3'-*O*-bis(*N*,*N*-diisopropylamino)phosphinyl-2'-deoxythymidine in C_6D_6……... S05
175 MHz ^{13}C NMR spectrum of 5'-*O*-(4,4'-dimethoxytrityl)-
3'-*O*-bis(*N*,*N*-diisopropylamino)phosphinyl-2'-deoxythymidine in C_6D_6……... S05
300 MHz ^{1}H-^{1}H TOCSYspectrum of 5'-*O*-(4,4'-dimethoxytrityl)-
3'-*O*-bis(*N*,*N*-diisopropylamino)phosphinyl-2'-deoxythymidine in C_6D_6……... S06
700 MHz ^{1}H-13C HSQC spectrum of 5'-*O*-(4,4'-dimethoxytrityl)-
3'-*O*-bis(*N*,*N*-diisopropylamino)phosphinyl-2'-deoxythymidine in C_6D_6……... S06
121 MHz ^{31}P NMR spectrum of 5'-*O*-(4,4'-dimethoxytrityl)-
3'-*O*-bis(*N*,*N*-diisopropylamino)phosphinyl-2'-deoxythymidine in C_6D_6……... S07
700 MHz ^{1}H NMR spectrum of N^4-benzoyl-5'-*O*-(4,4'-dimethoxytrityl)-
3'-*O*-bis(*N*,*N*-diisopropylamino)phosphinyl-2'-deoxycytidine in C_6D_6…….....S07
175 MHz ^{13}C NMR spectrum of N^4-benzoyl-5'-*O*-(4,4'-dimethoxytrityl)-
3'-*O*-bis(*N*,*N*-diisopropylamino)phosphinyl-2'-deoxycytidine in C_6D_6…….....S08
300 MHz ^{1}H-^{1}H TOCSYspectrum of N^4-benzoyl-5'-*O*-(4,4'-dimethoxytrityl)-
3'-*O*-bis(*N*,*N*-diisopropylamino)phosphinyl-2'-deoxycytidine in C_6D_6…….....S08
700 MHz ^{1}H-13C HSQC spectrum of N^4-benzoyl-5'-*O*-(4,4'-dimethoxytrityl)-
3'-*O*-bis(*N*,*N*-diisopropylamino)phosphinyl-2'-deoxycytidine in C_6D_6…….....S09
121 MHz ^{31}P NMR spectrum of N^4-benzoyl-5'-*O*-(4,4'-dimethoxytrityl)-
3'-*O*-bis(*N*,*N*-diisopropylamino)phosphinyl-2'-deoxycytidine in C_6D_6…….....S09

700 MHz ^{1}H NMR spectrum of N^6-benzoyl-5'-*O*-(4,4'-dimethoxytrityl)-
3'-*O*-bis(*N*,*N*-diisopropylamino)phosphinyl-2'-deoxyadenosine in C_6D_6……....S10
175 MHz ^{13}C NMR spectrum of N^6-benzoyl-5'-*O*-(4,4'-dimethoxytrityl)-
3'-*O*-bis(*N*,*N*-diisopropylamino)phosphinyl-2'-deoxyadenosine in C_6D_6……....S10
300 MHz ^{1}H-^{1}H TOCSYspectrum of N^6-benzoyl-5'-*O*-(4,4'-dimethoxytrityl)-
3'-*O*-bis(*N*,*N*-diisopropylamino)phosphinyl-2'-deoxyadenosine in C_6D_6……....S11
700 MHz ^{1}H-13C HSQC spectrum of N^6-benzoyl-5'-*O*-(4,4'-dimethoxytrityl)-
3'-*O*-bis(*N*,*N*-diisopropylamino)phosphinyl-2'-deoxyadenosine in C_6D_6……....S11
121 MHz ^{31}P NMR spectrum of N^6-benzoyl-5'-*O*-(4,4'-dimethoxytrityl)-
3'-*O*-bis(*N*,*N*-diisopropylamino)phosphinyl-2'-deoxyadenosine in C_6D_6……....S12
700 MHz ^{1}H NMR spectrum of N^2-isobutyryl-5'-*O*-(4,4'-dimethoxytrityl)-
3'-*O*-bis(*N*,*N*-diisopropylamino)phosphinyl-2'-deoxyguanosine in C_6D_6…….... S12
175 MHz ^{13}C NMR spectrum of N^2-isobutyryl-5'-*O*-(4,4'-dimethoxytrityl)-
3'-*O*-bis(*N*,*N*-diisopropylamino)phosphinyl-2'-deoxyguanosine in C_6D_6……... S13
300 MHz ^{1}H-^{1}H TOCSYspectrum of N^2-isobutyryl-5'-*O*-(4,4'-dimethoxytrityl)-
3'-*O*-bis(*N*,*N*-diisopropylamino)phosphinyl-2'-deoxyguanosine in C_6D_6……... S13
700 MHz ^{1}H-13C HSQC spectrum of N^2-isobutyryl-5'-*O*-(4,4'-dimethoxytrityl)-
3'-*O*-bis(*N*,*N*-diisopropylamino)phosphinyl-2'-deoxyguanosine in C_6D_6……... S14
121 MHz ^{31}P NMR spectrum of N^2-isobutyryl-5'-*O*-(4,4'-dimethoxytrityl)-
3'-*O*-bis(*N*,*N*-diisopropylamino)phosphinyl-2'-deoxyguanosine in C_6D_6……... S14
APESI-TOF MS spectrum of 5'-*O*-(4,4'-dimethoxytrityl)-
3'-*O*-bis(*N*,*N*-diisopropylamino)phosphinyl-2'-deoxythymidine.……S15
APESI-TOF MS spectrum of N^4-benzoyl-5'-*O*-(4,4'-dimethoxytrityl)-
3'-*O*-bis(*N*,*N*-diisopropylamino)phosphinyl-2'-deoxycytidine.……...S15
APESI-TOF MS spectrum of N^6-benzoyl-5'-*O*-(4,4'-dimethoxytrityl)-
3'-*O*-bis(*N*,*N*-diisopropylamino)phosphinyl-2'-deoxyadenosine.……S16
APESI-TOF MS spectrum of N^2-isobutyryl-5'-*O*-(4,4'-dimethoxytrityl)-
3'-*O*-bis(*N*,*N*-diisopropylamino)phosphinyl-2'-deoxyguanosine.……S16
RP-HPLC chromatograms of dinucleoside phosphate diesters that were
thermolytically released from the CPG support **7**.....S17
RP-HPLC Chromatograms of Dinucleoside Phosphorothioates that were
Thermolytically Released from the CPG support **7**……...S18
Enlarged Figure 1.……S20
Enlarged Figure 2.……S21
CHART 1. RP-HPLC analysis of unpurified 5'-d(CGACTGTGAATCGATGCCAT)
after treatment with SVP and bacterial alkaline phosphatase..……S22
CHART 2. RP-HPLC chromatograms of thymidine 3'-*O*-(1-pyrenebutyl) phosphate
that was thermolytically released from the CPG support **12**…… S23
CHART 3. RP-HPLC analysis of unpurified 3'-pyrenylated DNA oligonucleotide **14**..……S24
CHART 4. RP-HPLC analysis of the conversion of the (3',5')-heteroconjugated
DNA oligonucleotide **18** to the circular DNA oligonucleotide **19**
under "click chemistry" conditions.……..S25

Materials and Methods. Common chemicals and solvents in addition to bromoacetic acid 3*H*-1,2-benzodithiol-3-one 1,1-dioxide, Et_3N, *i*-Pr_2NEt, tripropargyl amine, benzyl azide, sodium azide, 2,6-lutidine, *O*-(2-cyanoethyl)-*O*-[3-(4,4'-dimethoxytrityl)oxy-1-propyl]-*N*,*N*-diisopropylphosphoramidite, 2-cyanoethyl-*N*,*N*-diisopropylchlorophosphoramidite, *O*-(2-cyanoethyl)-*O*-(5-hexyn-1-yl)-*N*,*N*-diisopropylphosphoramidite, bis(*N*,*N*-diisopropylamino)chlorophosphine, *O*-(2-cyanoethyl)-*O*-[6-(4-methoxytrityl)amino-1-hexyl]-*N*,*N*-diisopropylphosphoramidite, 500Å Long Chain Alkylamine Controlled-Pore Glass (CPG), tetrakis(acetonitrile)copper(I) hexafluorophosphate, copper(II) sulfate pentahydrate, sodium ascorbate, 2',4',6'-trihydroxyacetophenone monohydrate, 3-hydroxypicolinic acid, ammonium citrate tribasic, 1-methylimidazole, hydrazine hydrate, argon gas cylinder, and lecture bottles of NH_3 and CH_3NH_2 gases were all purchased from commercial sources and used without further purification. Azido acetic acid was prepared from the reaction of bromoacetic acid and sodium azide as described by Dyke, J. M. et al. (*J. Am. Chem. Soc.* **1997**, *119*, 6883-6887). Anhydrous solvents (MeCN, CH_2Cl_2, C_6H_6, pyridine, THF) and deuterated solvents (C_6D_6,) were obtained from reputable sources and used as received.

Reagents for oligonucleotide synthesis including the 5'-Deblocking solution (3% TCA in CH_2Cl_2), the Activator solution (0.25 M 5-ethylthio-1*H*-tetrazole or 0.4 M 1*H*-tetrazole in MeCN), Cap A solution (Ac_2O/pyridine/THF), Cap B solution (10% 1-methylimidazole in THF), and the Oxidizing solution (0.02 M iodine in THF/pyridine/water) were purchased from commercial sources and used as received. Succinyl long chain alkylamine controlled-pore glass functionalized with 5'-*O*-(4,4'-dimethoxytrityl)-2'-deoxythymidine as the leader nucleoside was also obtained from commercial sources and used as is. 2 M Triethylammonium acetate buffer was purchased from Applied Biosystem and diluted to 0.1 M with HPLC grade water prior to use. Snake venom phosphodiesterase (*Crotallus adamanteus*) and bacterial alkaline phosphatase were commercially available and used without further purification.

Preparative chromatographic purifications were performed on glass columns (2.5, 5.0 or 6.5 cm I.D.) packed with silica gel 60 (230-400 mesh), whereas analytical thin-layer chromatography (TLC) analyses were conducted on 2.5 cm × 7.5 cm glass plates coated with a 0.25 mm thick layer of silica gel 60 F_{254}.

RP-HPLC analyses were performed using a 5 μm Supelcosil LC-18S column (25 cm × 4.6 mm) according to the following conditions: starting from 0.1 M triethylammonium acetate pH 7.0, a linear gradient of 1% MeCN/min is pumped at a flow rate of 1 mL/min for 40 min or as indicated. Peak heights are normalized to the highest peak, which is set to 1 arbitrary unit.

All NMR experiments were performed using spectrometers at fields of 300.13 and 700.13 MHz for ^1H, 75.47 and 176.06 MHz for ^{13}C, and 121.5 MHz for ^{31}P. One-dimensional; ^1H, ^{31}P, $^1H/^{31}P$ decoupled ^{13}C, ^1H decoupled ^{13}C, and two-dimensional ^1H-^{13}C correlation (HSQC) data were acquired using a 5 mm QXI (quadruple resonance; ^1H, ^{15}N, ^{13}C, ^{31}P inverse) probe with actively shielded XYZ gradients

on the spectrometer operating at 700 MHz. ^{1}H-^{1}H total correlation (TOCSY) experiments were performed using the spectrometer operating at 300 MHz that is equipped with a TXI (triple resonance; ^{1}H, ^{15}N, ^{13}C inverse) probe with actively shielded XYZ gradients. Samples were maintained at a temperature of 298 °K. All spectra were recorded in C_6D_6 and chemical shifts δ were reported in parts per million (ppm) relative to appropriate internal references.

Accurate mass determination of each deoxyribonucleoside phosphorodiamidite **4** was performed using atmospheric pressure electrospray ionization (APESI) in the positive mode (ES^+). Samples dissolved in MeCN (~60 μg/mL) were infused directly at 2.5 mL/h into a stream of MeCN that flowed at 0.5 mL/min to obtain adequate signal intensity. A calibrant containing known ion of 922 m/z was nebulized into the chamber simultaneously with each sample. Software calibration was performed prior to the analysis to re-align the 922.0098 calibrant mass to the theoretical value. The TOF mass spectrometer was set to accurately measure masses over the range 100 to 1500 m/z. Accurate mass measurements for each sample are reported as the average of five injections.

MALDI-TOF mass spectrometric analyses were performed operating in delayed extraction reflector mode, using 3-hydroxypicolinic acid [50 mg/mL in MeCN/H_2O (1:1 v/v)] or 2',4',6'-trihydroxyacetophenone monohydrate [10 mg/mL in MeCN/H_2O (1:1 v/v)] as a matrix and ammonium citrate (50 mg/mL in H_2O) as a cation exchanger.

700 MHz ^{1}H NMR spectrum of 5'-*O*-(4,4'-dimethoxytrityl)-3'-*O*-bis(*N*,*N*-diisopropylamino)phosphinyl-2'-deoxythymidine in C_6D_6

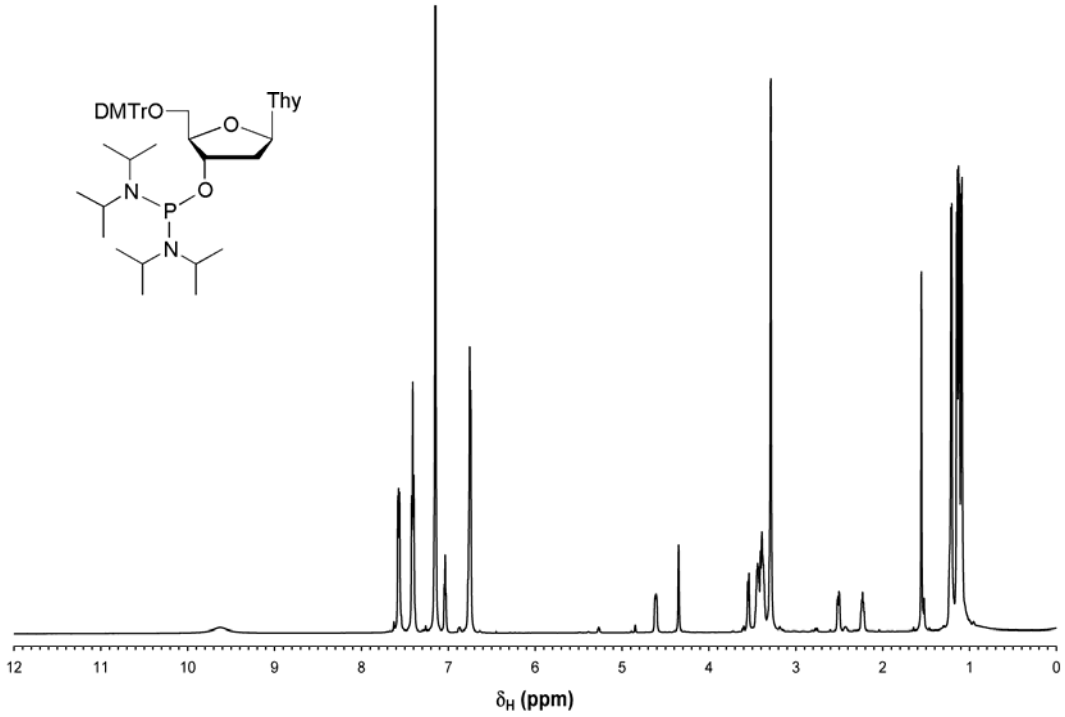

175 MHz ^{13}C NMR spectrum of 5'-*O*-(4,4'-dimethoxytrityl)-3'-*O*-bis(*N*,*N*-diisopropylamino)phosphinyl-2'-deoxythymidine in C_6D_6

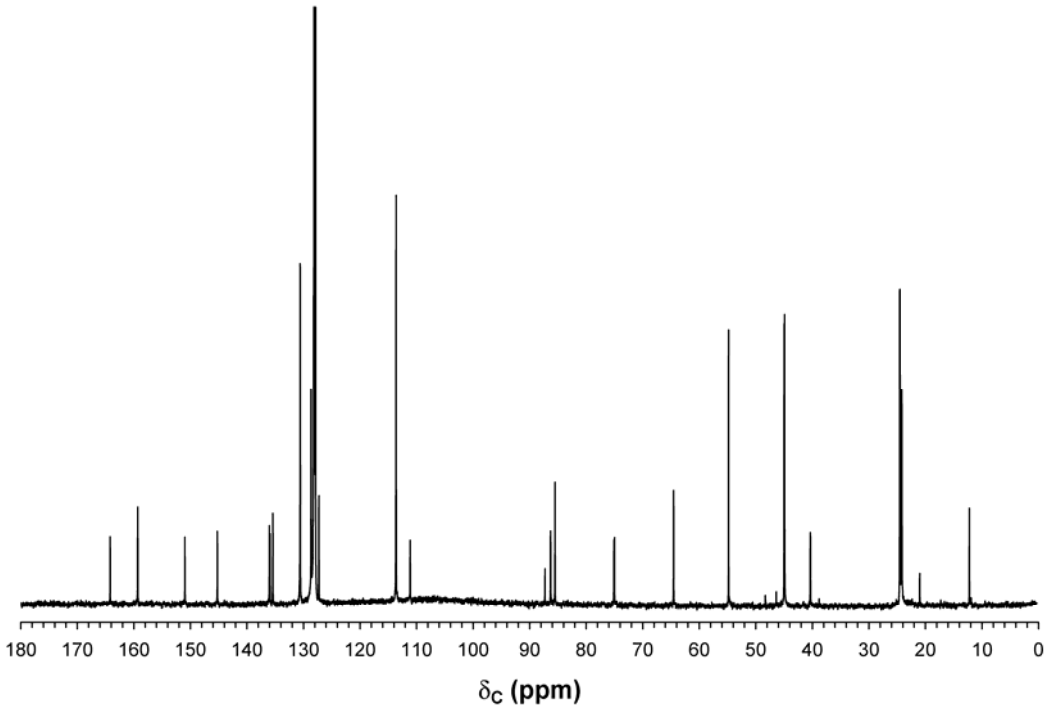

300 MHz ^{1}H-^{1}H TOCSY spectrum of 5'-*O*-(4,4'-dimethoxytrityl)-3'-*O*-bis(*N*,*N*-diisopropylamino)phosphinyl-2'-deoxythymidine in C_6D_6

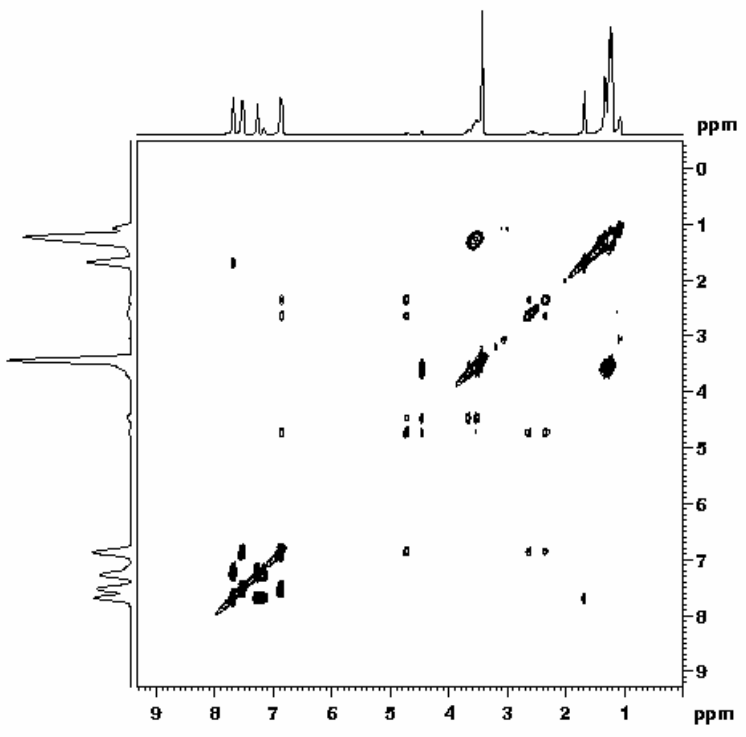

700 MHz ^{1}H-^{13}C HSQC spectrum of 5'-*O*-(4,4'-dimethoxytrityl)-3'-*O*-bis(*N*,*N*-diisopropylamino)phosphinyl-2'-deoxythymidine in C_6D_6

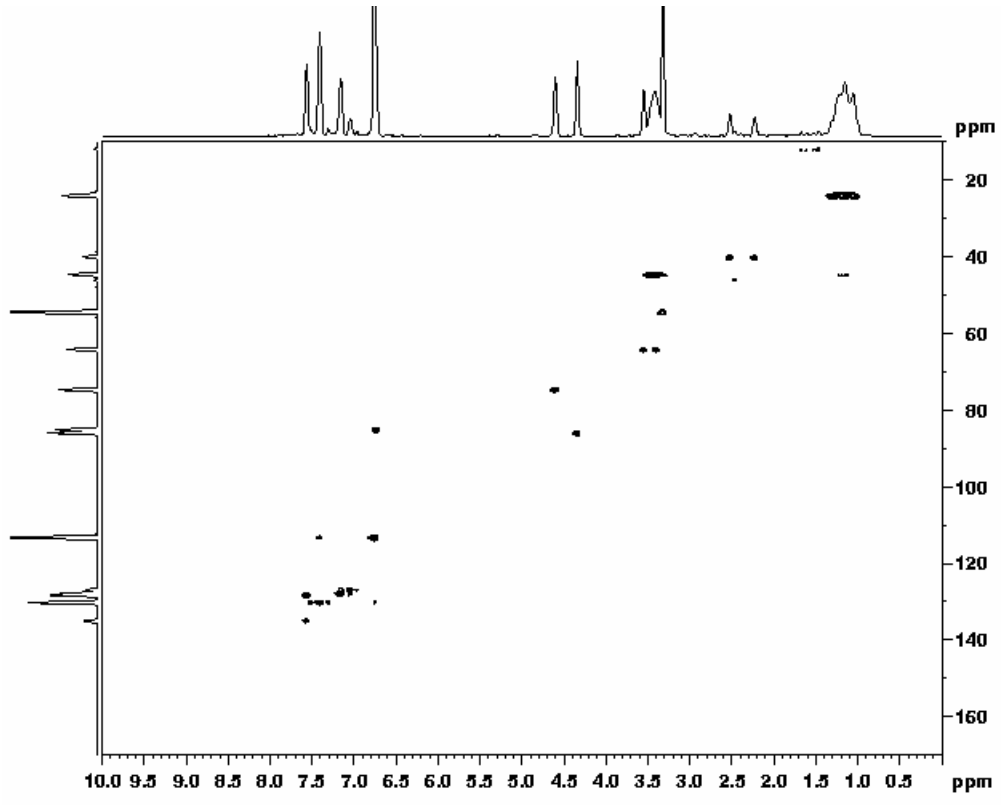

121 MHz ^{31}P NMR spectrum of 5'-*O*-(4,4'-dimethoxytrityl)-3'-*O*-bis(*N*,*N*-diisopropylamino)phosphinyl-2'-deoxythymidine in C_6D_6

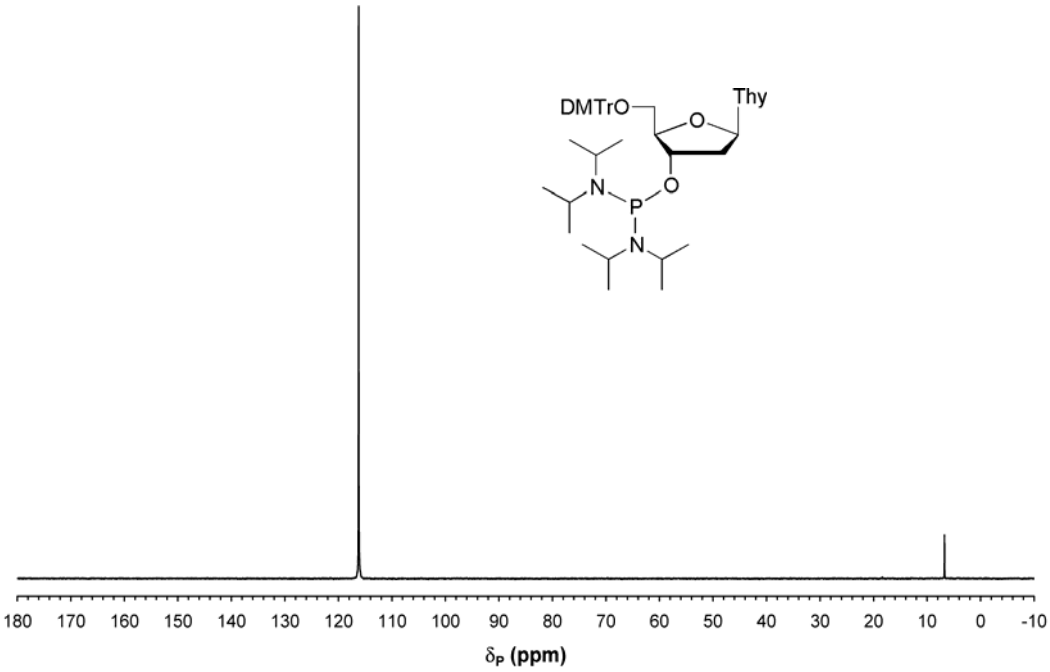

700 MHz ^{1}H NMR spectrum of N^4-benzoyl-5'-*O*-(4,4'-dimethoxytrityl)-3'-*O*-bis(*N*,*N*-diisopropylamino)phosphinyl-2'-deoxycytidine in C_6D_6

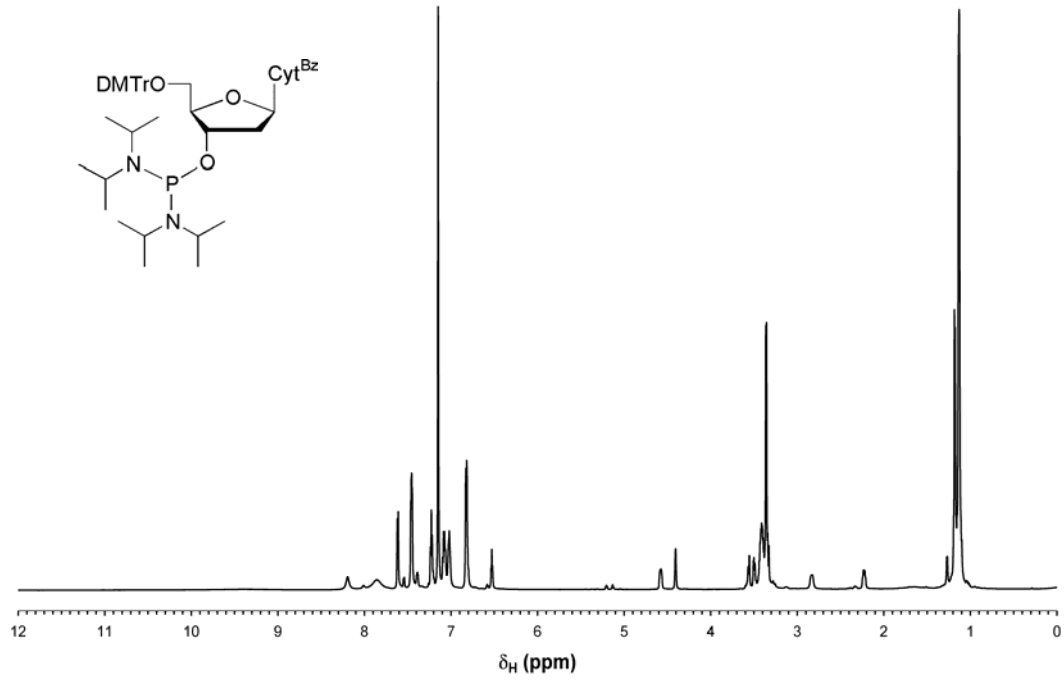

175 MHz ^{13}C NMR spectrum of N^4-benzoyl-5'-*O*-(4,4'-dimethoxytrityl)-3'-*O*-bis(*N*,*N*-diisopropylamino)phosphinyl-2'-deoxycytidine in C_6D_6

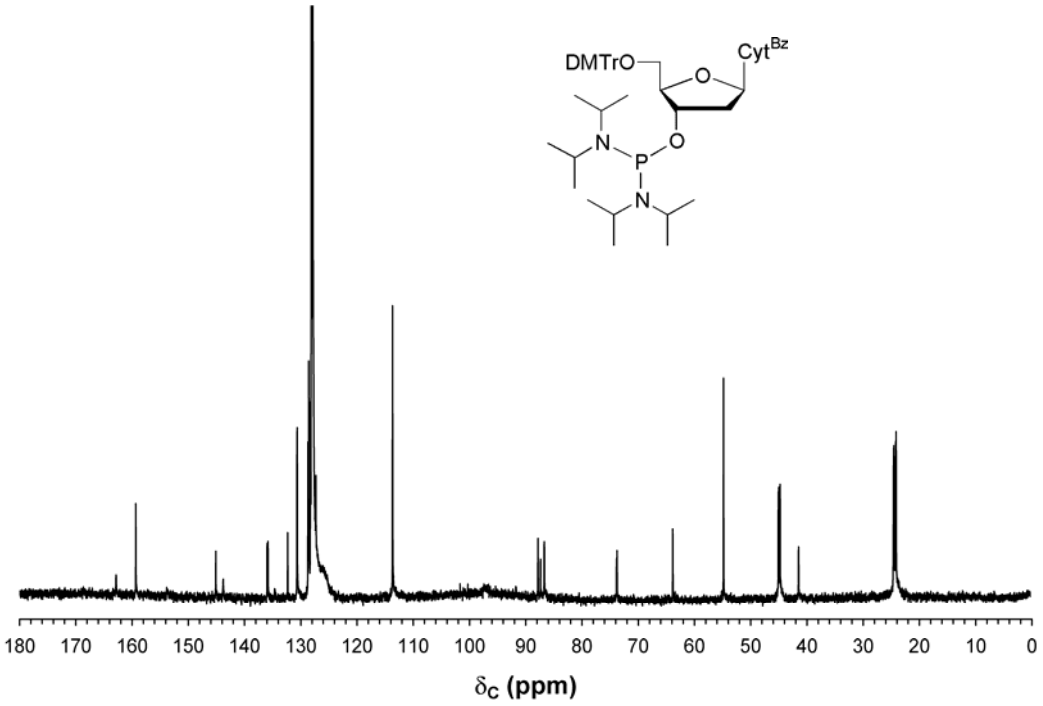

300 MHz ^{1}H-^{1}H TOCSY spectrum of N^4-benzoyl-5'-*O*-(4,4'-dimethoxytrityl)-3'-*O*-bis(*N*,*N*-diisopropylamino)phosphinyl-2'-deoxycytidine in C_6D_6

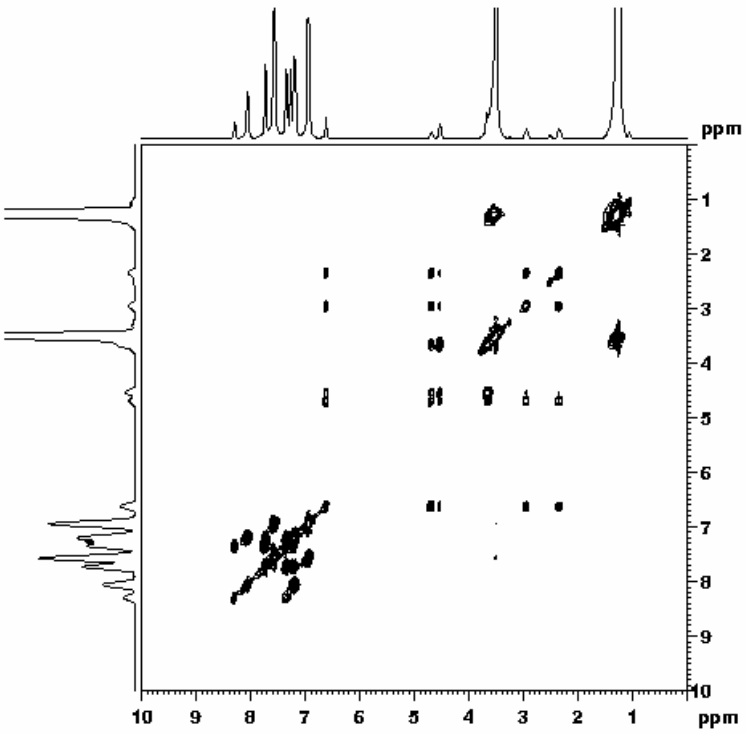

700 MHz ^{1}H-^{13}C HSQC spectrum of N^4-benzoyl-5'-*O*-(4,4'-dimethoxytrityl)-3'-*O*-bis(*N*,*N*-diisopropylamino)phosphinyl-2'-deoxycytidine in C_6D_6

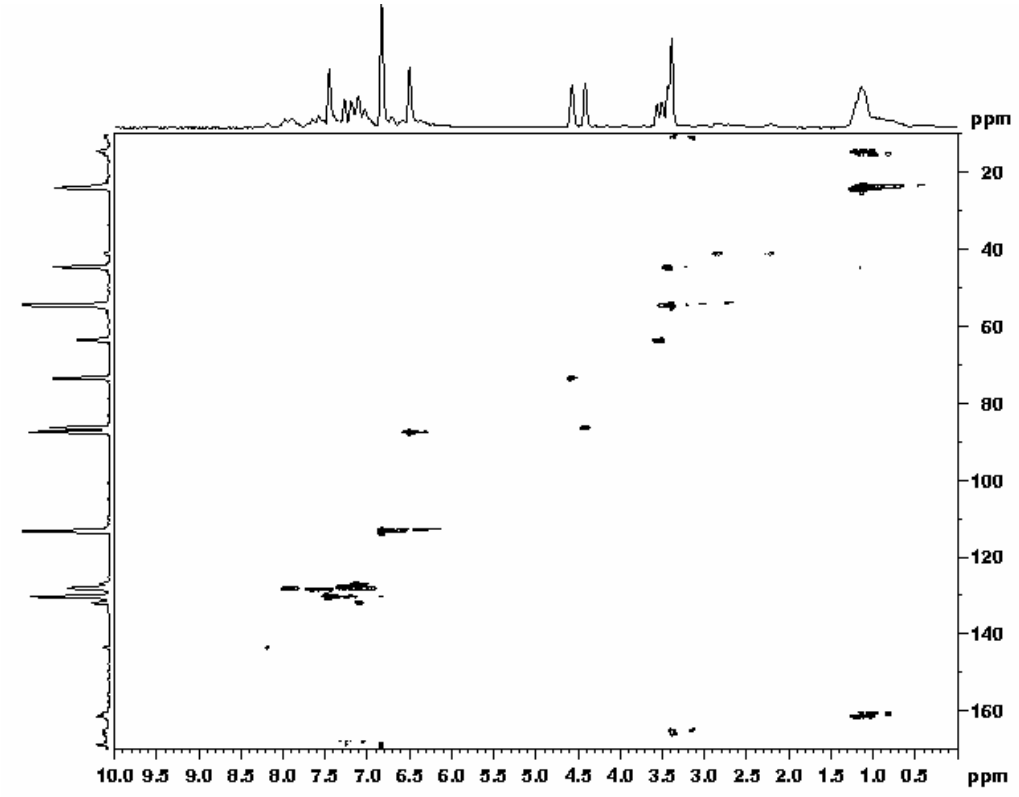

121 MHz ^{31}P NMR spectrum of N^4-benzoyl-5'-*O*-(4,4'-dimethoxytrityl)-3'-*O*-bis(*N*,*N*-diisopropylamino)phosphinyl-2'-deoxycytidine in C_6D_6

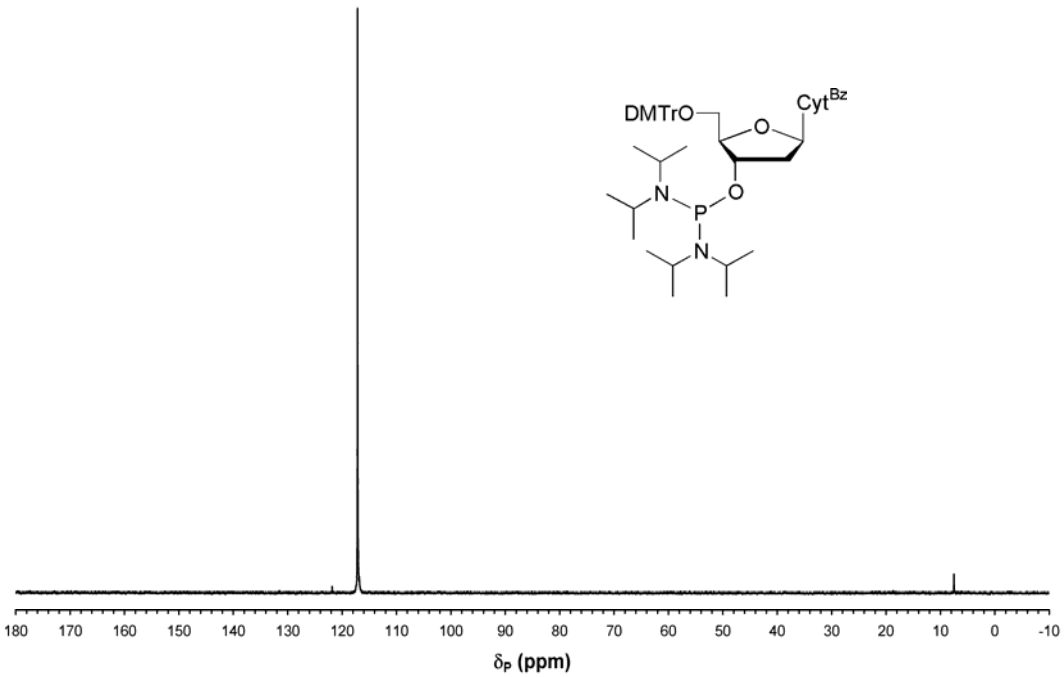

700 MHz ^{1}H NMR spectrum of N^6-benzoyl-5'-*O*-(4,4'-dimethoxytrityl)-3'-*O*-bis(*N*,*N*-diisopropylamino)phosphinyl-2'-deoxyadenosine in C_6D_6

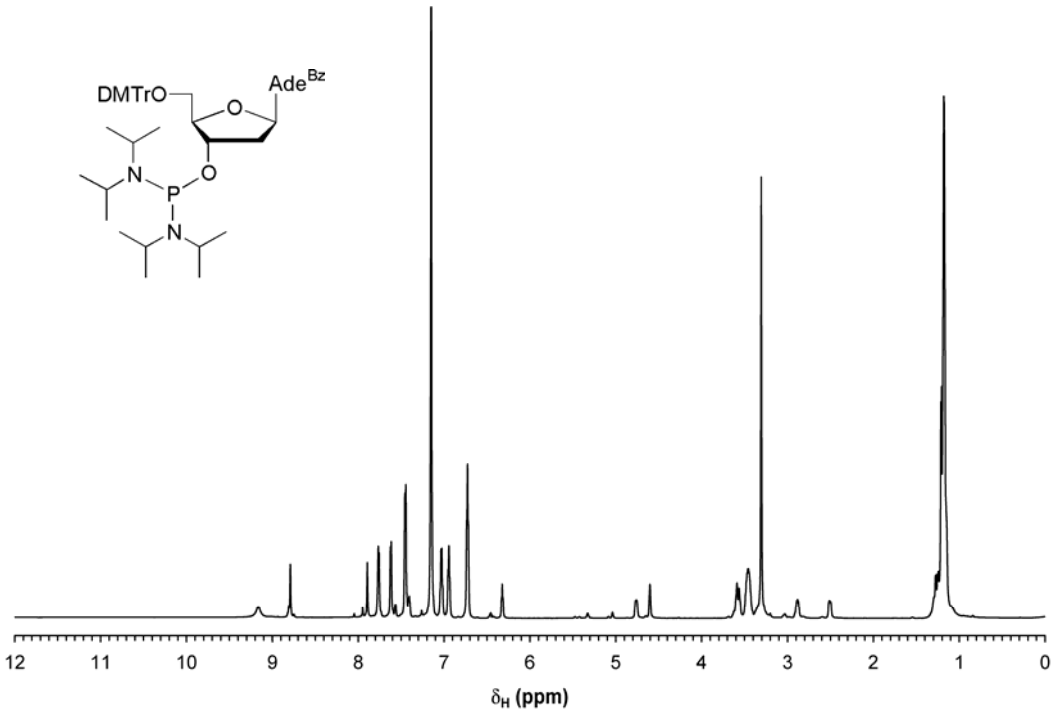

175 MHz ^{13}C NMR spectrum of N^6-benzoyl-5'-*O*-(4,4'-dimethoxytrityl)-3'-*O*-bis(*N*,*N*-diisopropylamino)phosphinyl-2'-deoxyadenosine in C_6D_6

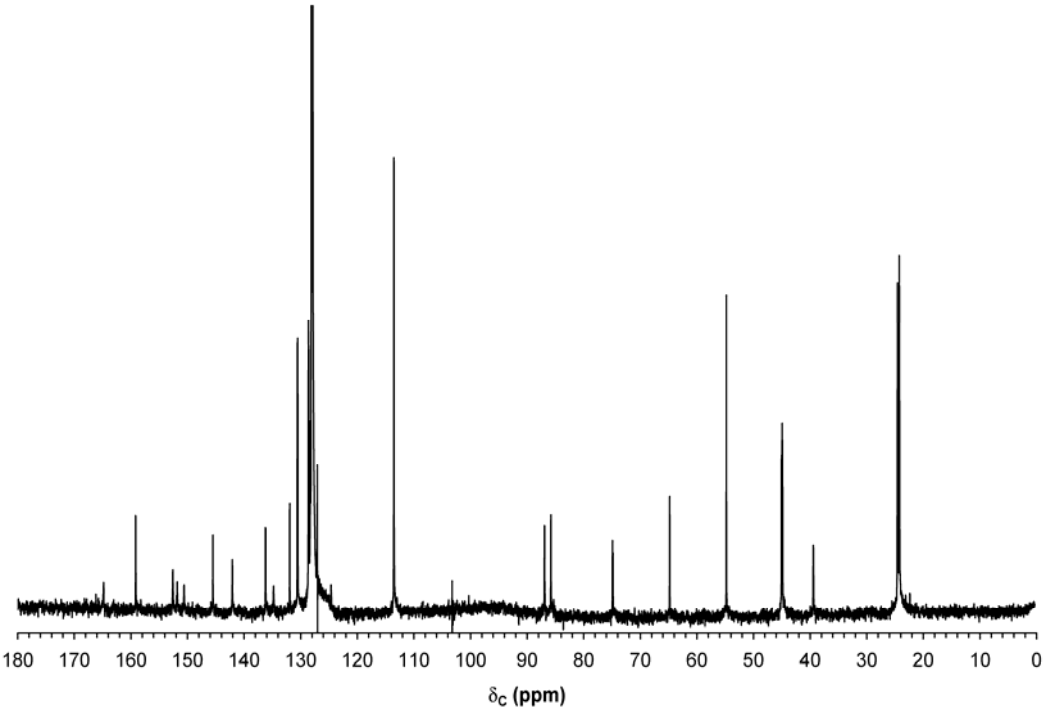

300 MHz ^{1}H-^{1}H TOCSY spectrum of N^{6}-benzoyl-5'-*O*-(4,4'-dimethoxytrityl)-3'-*O*-bis(*N*,*N*-diisopropylamino)phosphinyl-2'-deoxyadenosine in C_6D_6

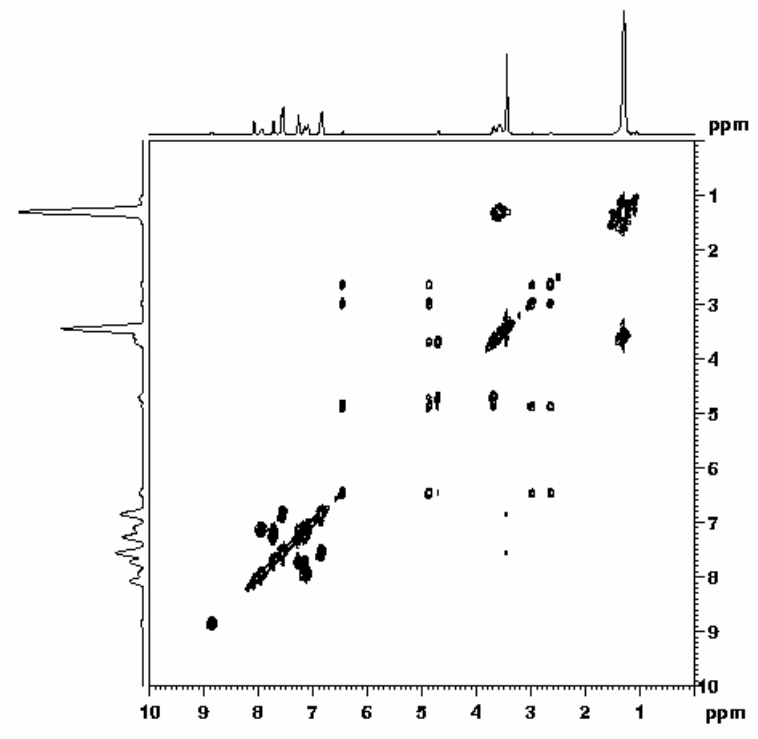

700 MHz ^{1}H-^{13}C HSQC spectrum of N^{6}-benzoyl-5'-*O*-(4,4'-dimethoxytrityl)-3'-*O*-bis(*N*,*N*-diisopropylamino)phosphinyl-2'-deoxyadenosine in C_6D_6

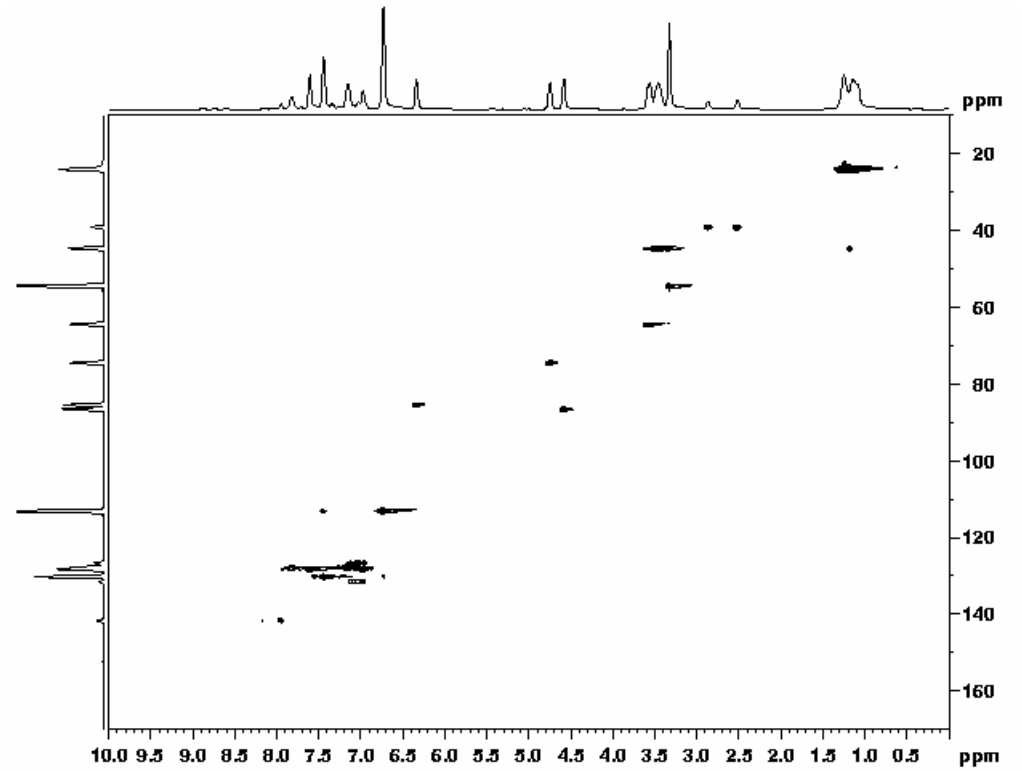

121 MHz ^{31}P NMR spectrum of N^6-benzoyl-5'-*O*-(4,4'-dimethoxytrityl)-3'-*O*-bis(*N*,*N*-diisopropylamino)phosphinyl-2'-deoxyadenosine in C_6D_6

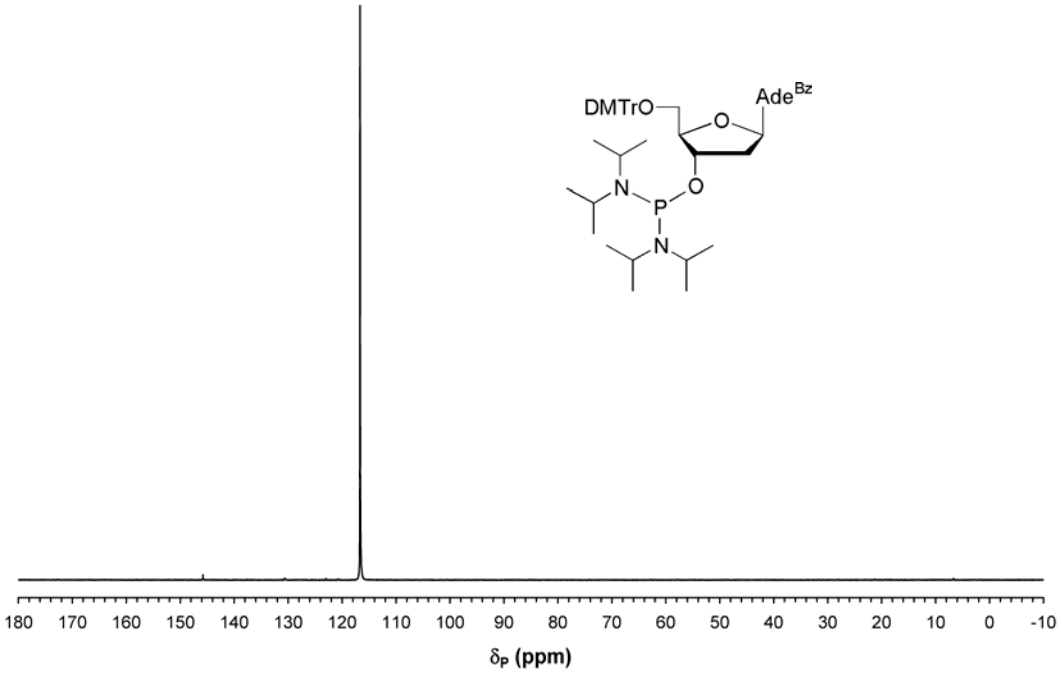

700 MHz ^{1}H NMR spectrum of N^2-isobutyryl-5'-*O*-(4,4'-dimethoxytrityl)-3'-*O*-bis(*N*,*N*-diisopropylamino)phosphinyl-2'-deoxyguanosine in C_6D_6

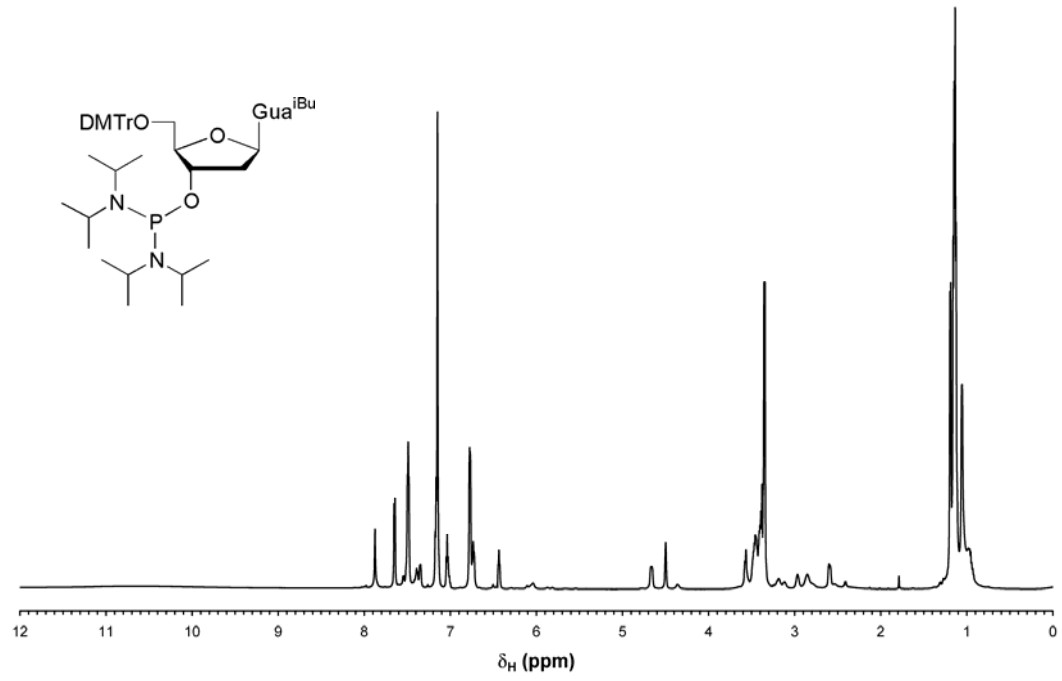

175 MHz ^{13}C NMR spectrum of N^2-isobutyryl-5'-*O*-(4,4'-dimethoxytrityl)-3'-*O*-bis(*N*,*N*-diisopropylamino)phosphinyl-2'-deoxyguanosine in C_6D_6

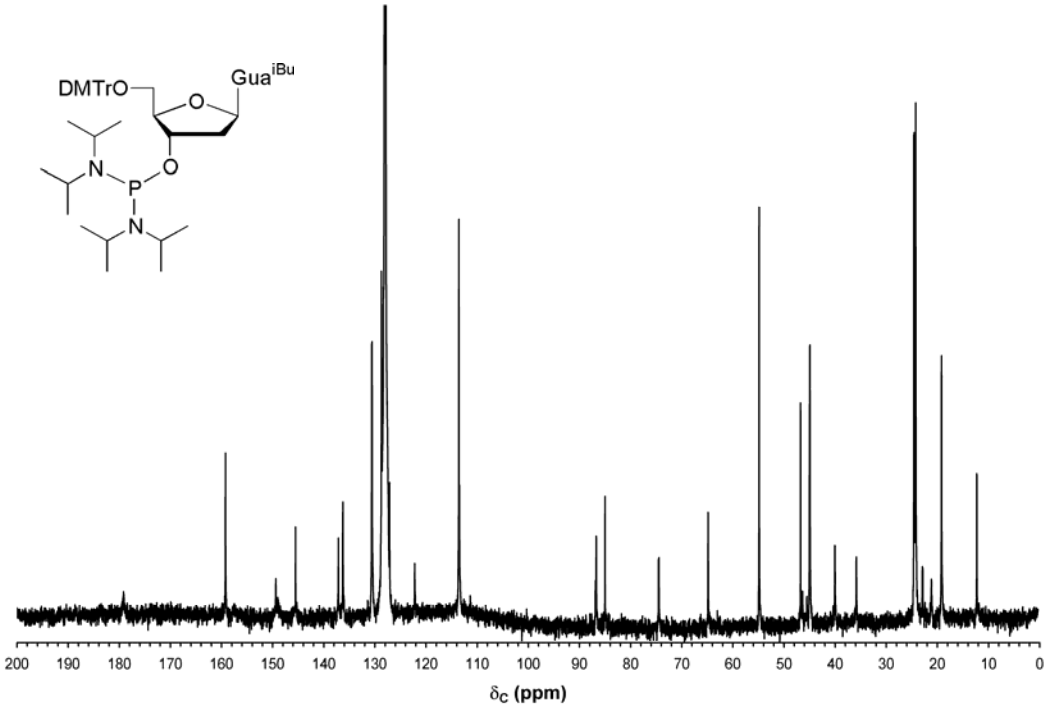

700 MHz ^{1}H-^{1}H TOCSY spectrum of N^2-isobutyryl-5'-*O*-(4,4'-dimethoxytrityl)-3'-*O*-bis(*N*,*N*-diisopropylamino)phosphinyl-2'-deoxyguanosine in C_6D_6

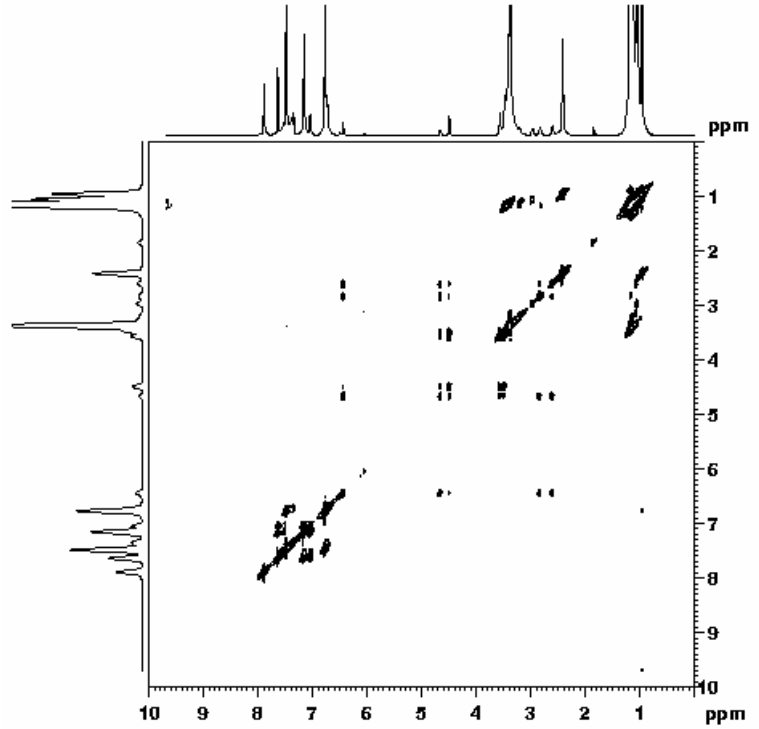

700 MHz ^{1}H-^{13}C HSQC spectrum of *N*^{2}-isobutyryl-5'-*O*-(4,4'-dimethoxytrityl)-3'-*O*-bis(*N*,*N*-diisopropylamino)phosphinyl-2'-deoxyguanosine in C_6D_6

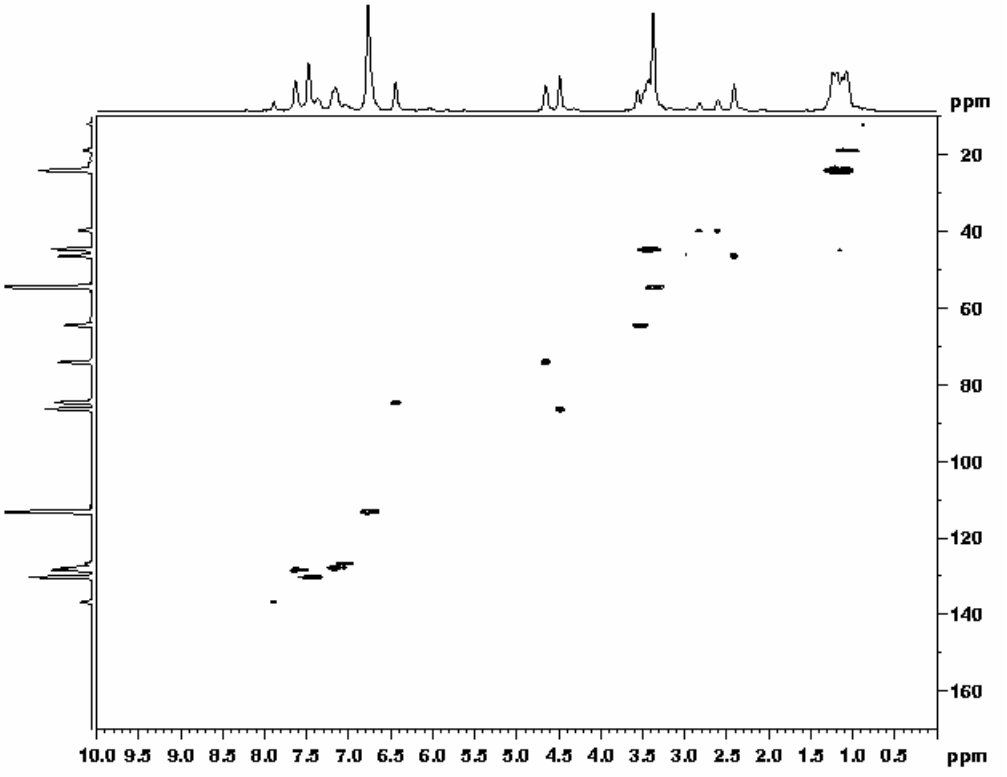

121 MHz ^{31}P NMR spectrum of *N*^{2}-isobutyryl-5'-*O*-(4,4'-dimethoxytrityl)-3'-*O*-bis(*N*,*N*-diisopropylamino)phosphinyl-2'-deoxyguanosine in C_6D_6

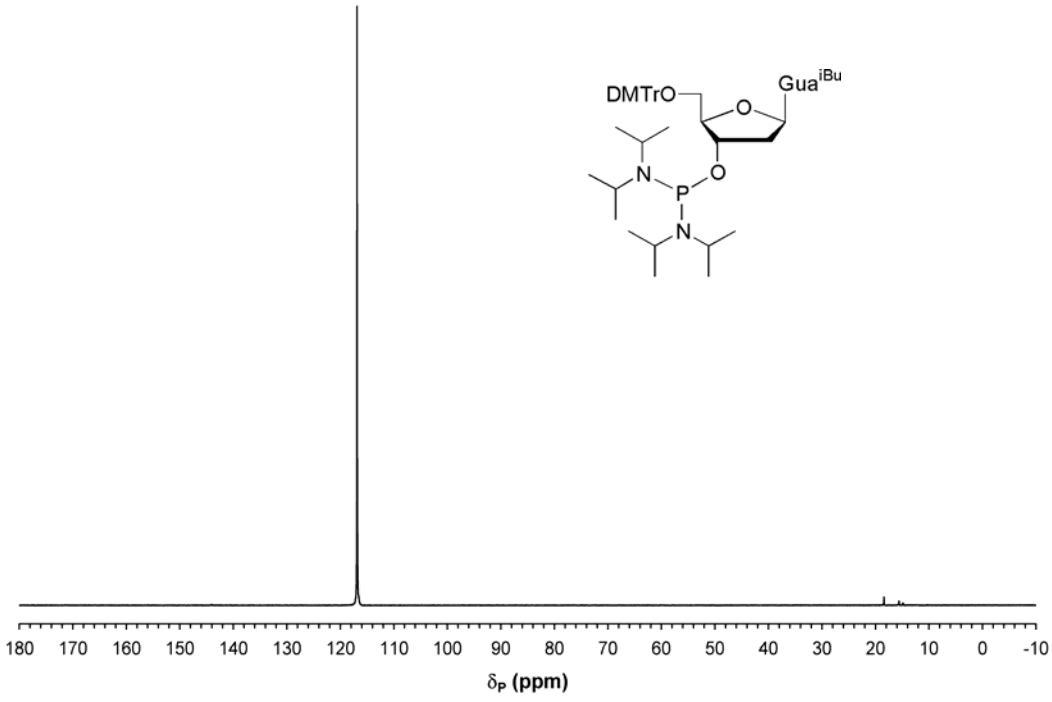

APESI-TOF MS spectrum of 5'-*O*-(4,4'-dimethoxytrityl)-3'-*O*-bis(*N*,*N*-diisopropylamino)phosphinyl-2'-deoxythymidine

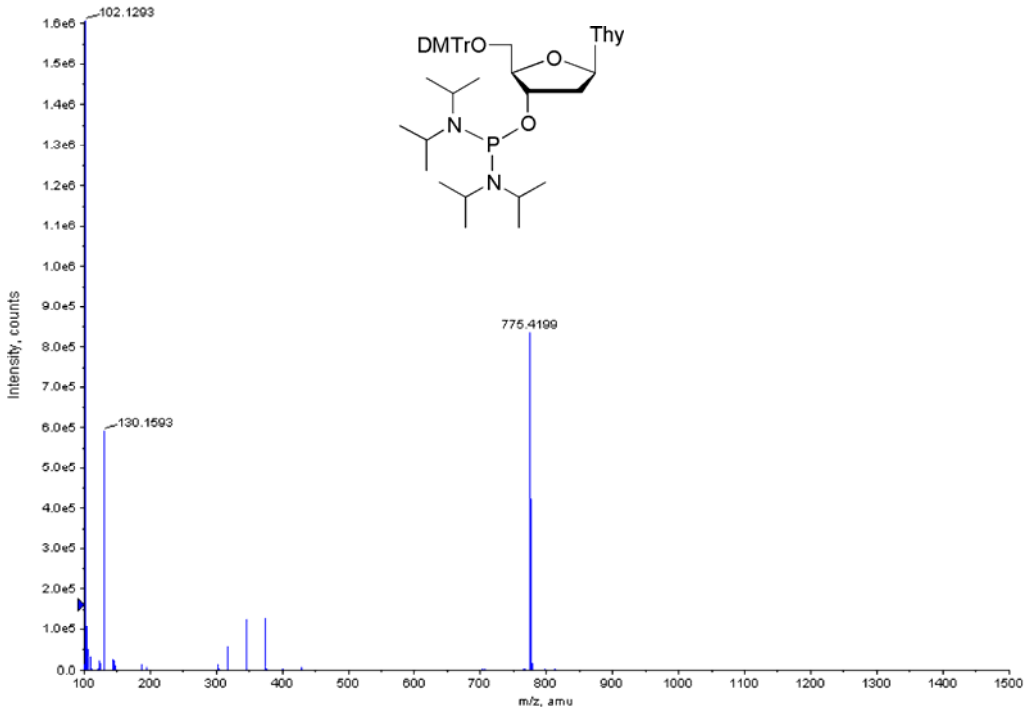

APESI-TOF MS spectrum of N^4-benzoyl-5'-*O*-(4,4'-dimethoxytrityl)-3'-*O*-bis(*N*,*N*-diisopropylamino)phosphinyl-2'-deoxycytidine

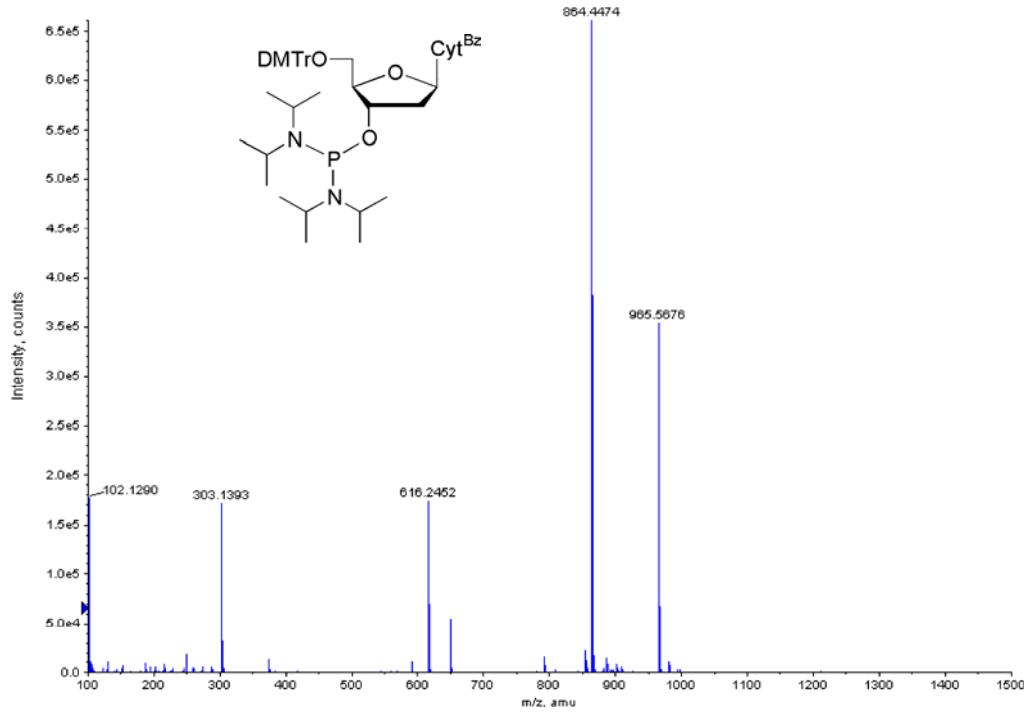

APESI-TOF MS spectrum of N^6-benzoyl-5'-*O*-(4,4'-dimethoxytrityl)- 3'-*O*-bis(*N*,*N*-diisopropylamino)phosphinyl-2'-deoxyadenosine

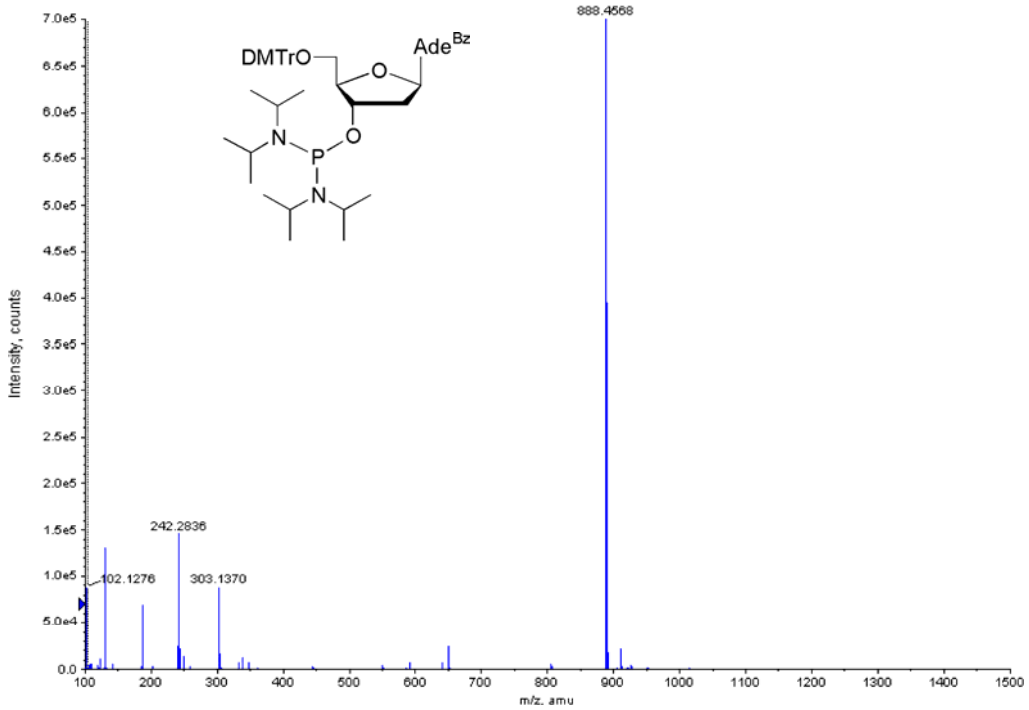

APESI-TOF MS spectrum of N^2-isobutyryl-5'-*O*-(4,4'-dimethoxytrityl)-3'-*O*-bis(*N*,*N*-diisopropylamino)phosphinyl-2'-deoxyguanosine

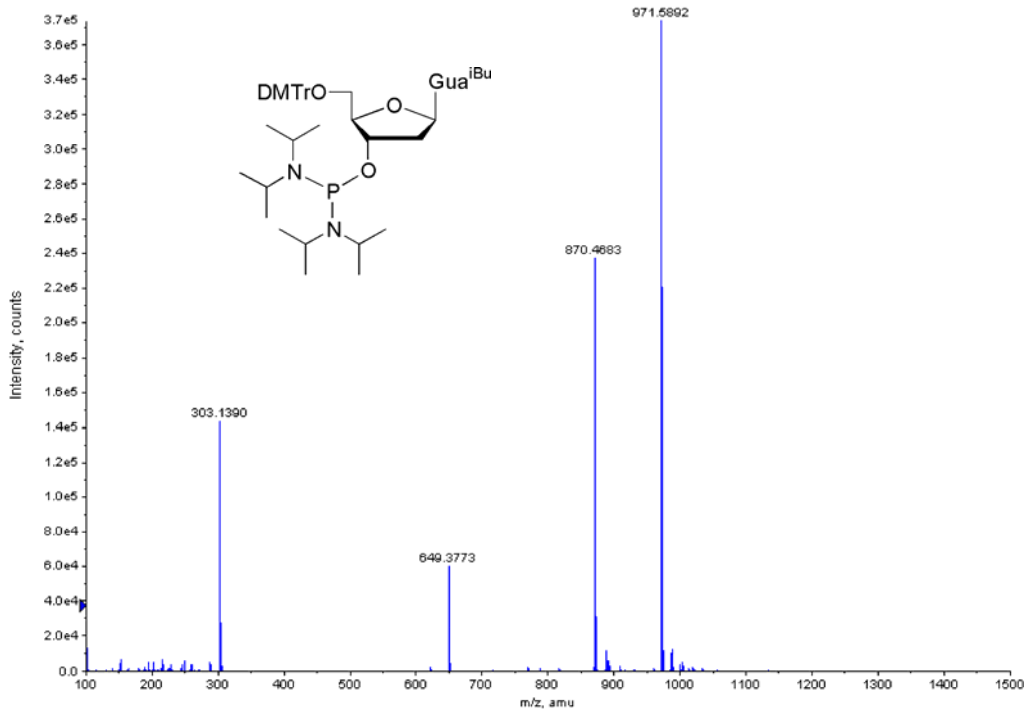

RP-HPLC chromatograms of dinucleoside phosphate diesters that were thermolytically released from the CPG support 7

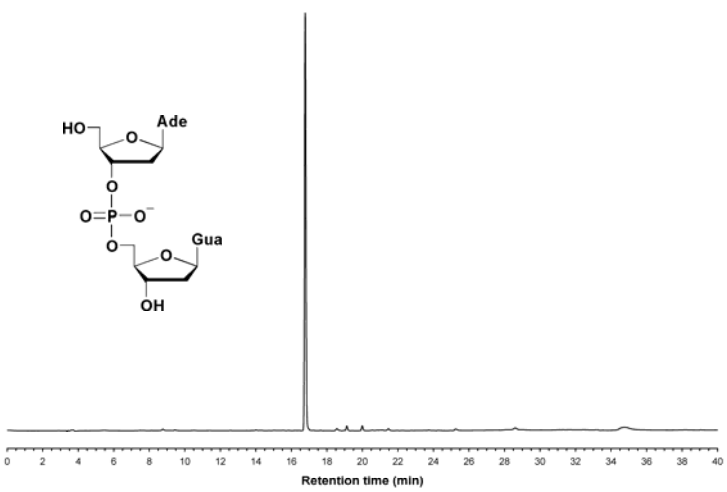

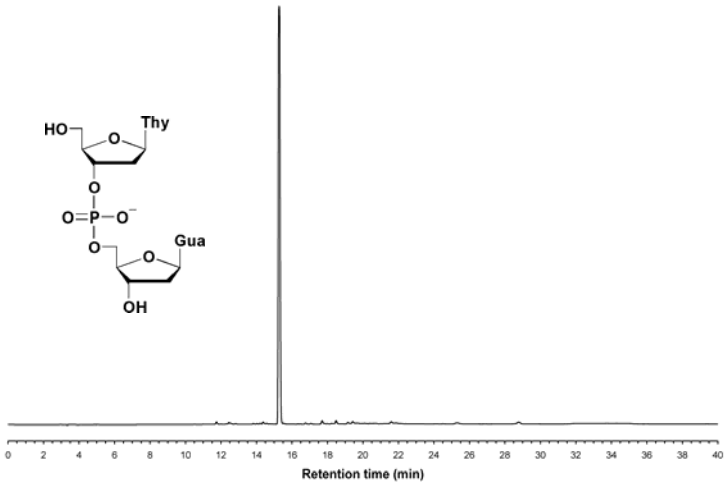

RP-HPLC chromatograms of dinucleoside phosphorothioates that were thermolytically released from the CPG support 7.

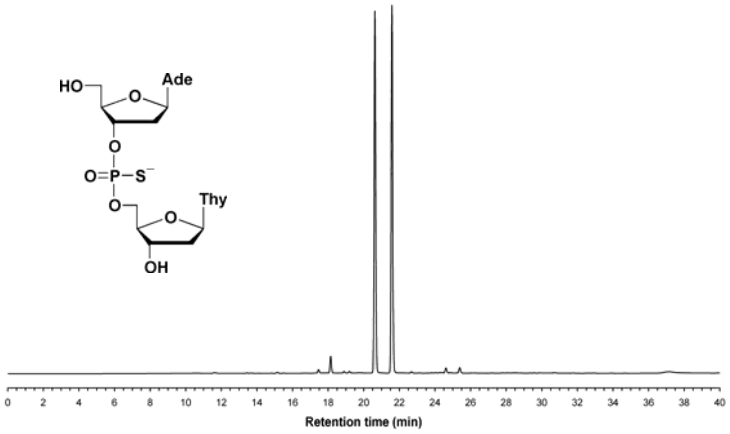

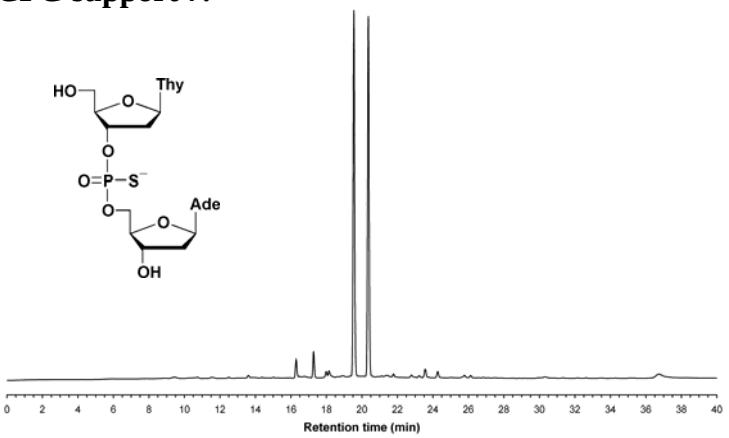

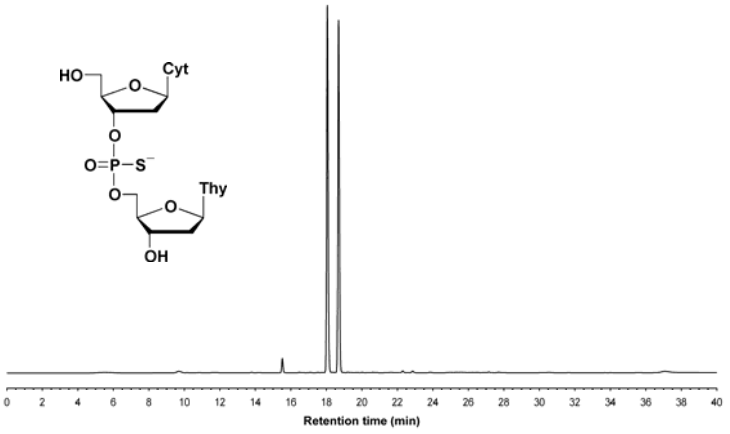

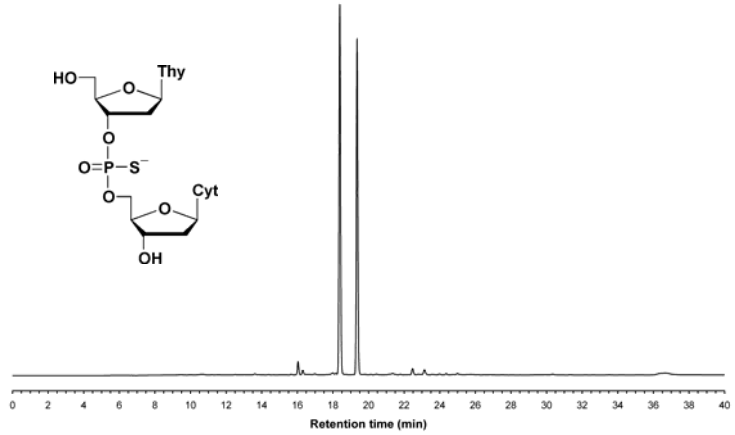

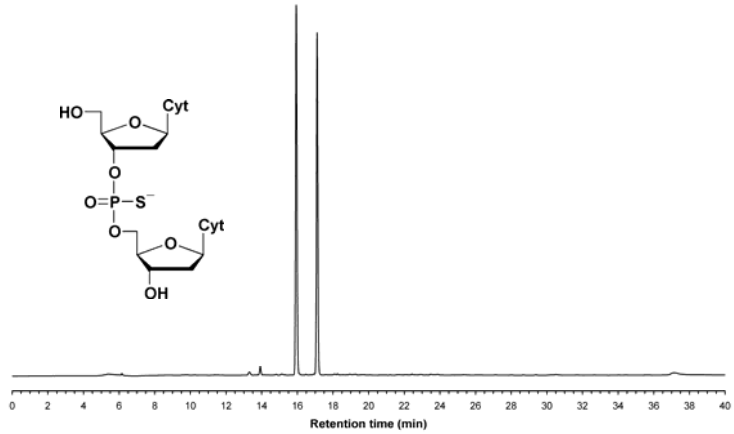

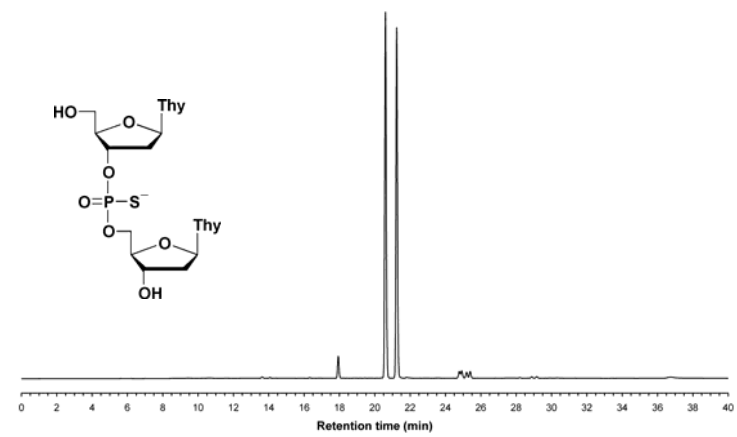

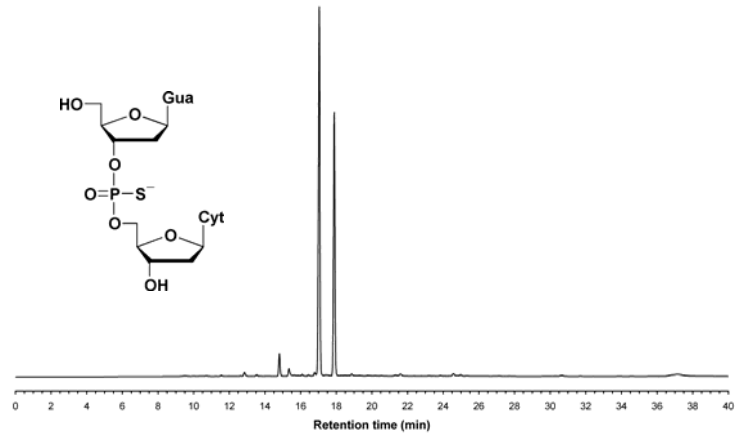

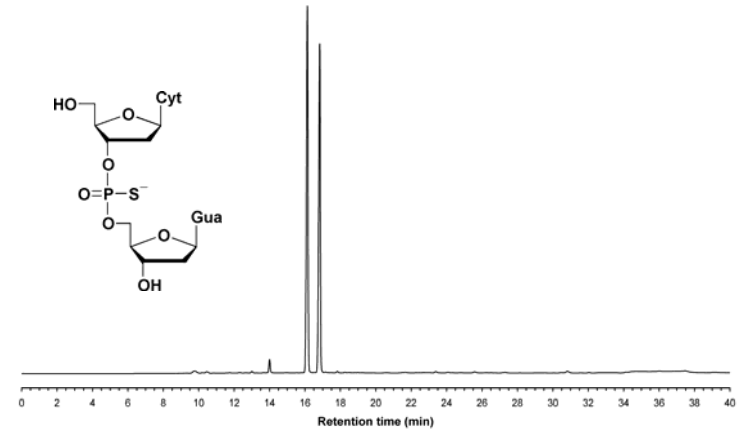

RP-HPLC chromatograms of dinucleoside phosphorothioates that were thermolytically released from the CPG support 7.

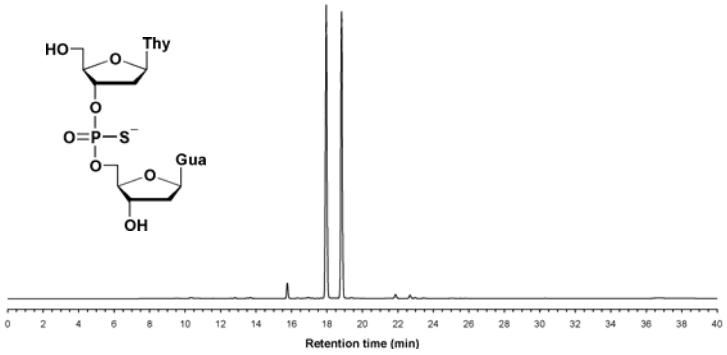

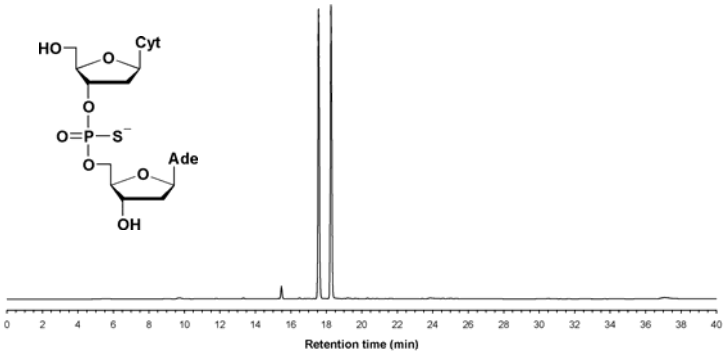

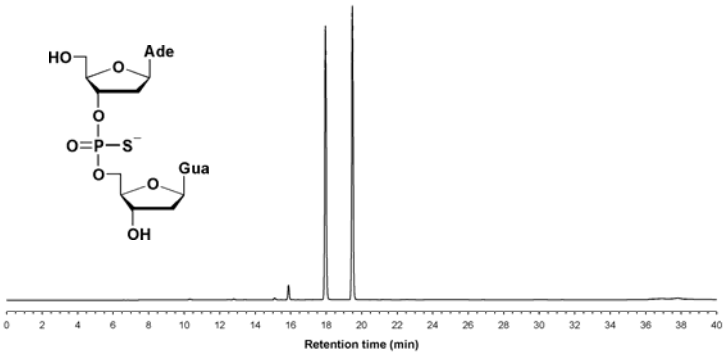

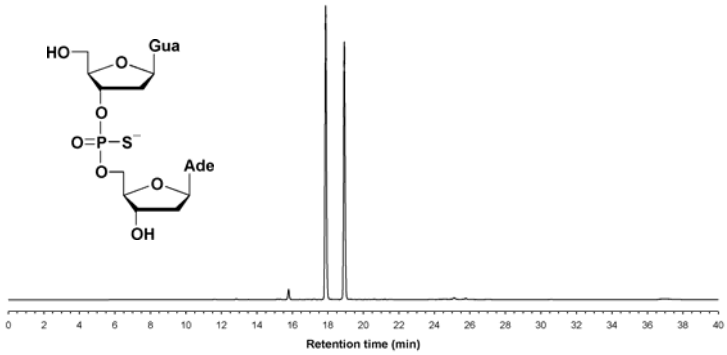

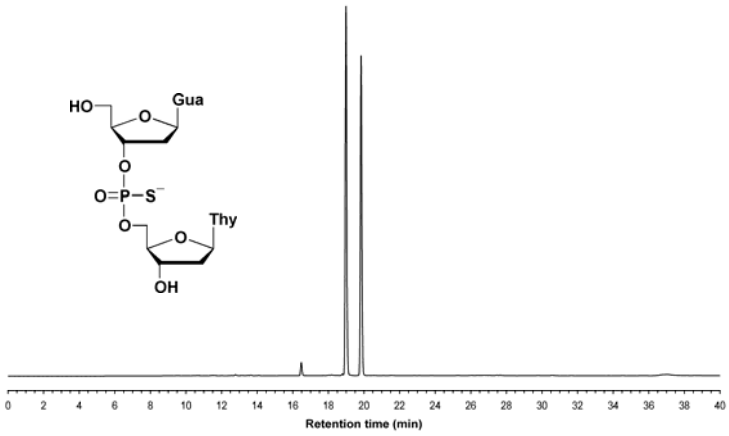

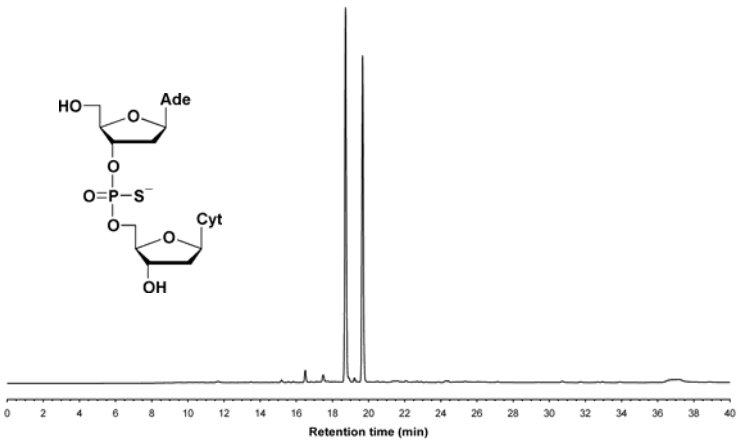

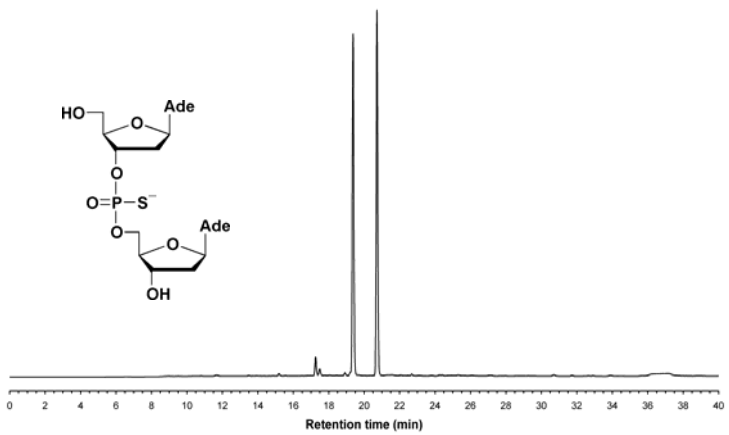

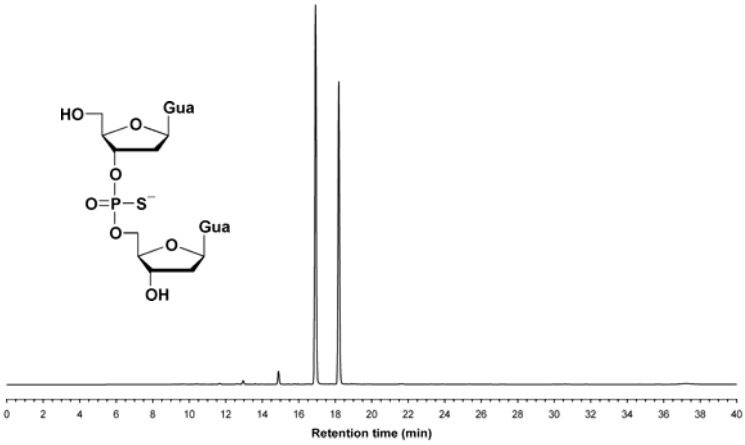

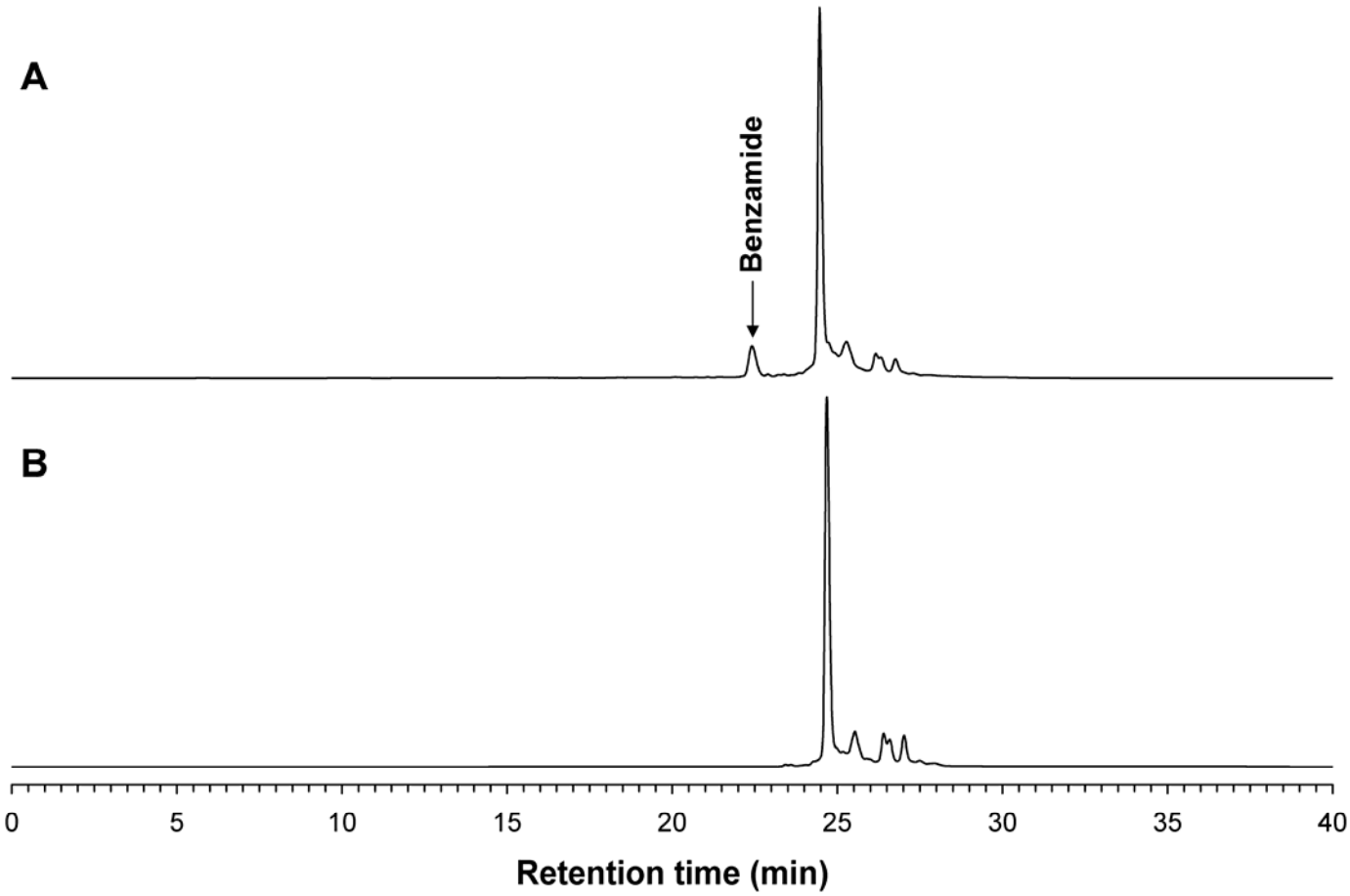

Enlarged Figure 1. RP-HPLC analysis of unpurified 5'-d(CGACTGTGAATCGATGCCAT). **A:** Chromatogram of the native 20-mer that was synthesized employing commercial CPG under standard conditions. Nucleobase and phosphate deprotection, and release of the oligomer from the support were effected by treatment with pressurized NH_3 gas (~10 bar) over a period of 16 h at 25 ºC, as described in the Experimental section. **B:** Chromatogram of the 20-mer that was synthesized using the CPG support **7** under standard conditions. After nucleobase and phosphate deprotection under the conditions described in **A**, the deprotection side products were washed away from the CPG support **8** with MeCN:H_2O (1:1 v/v). The 20-mer was thermolytically cleaved from **8** upon heating at 90 ºC in 1× PBS (pH 7.2) for 2 h. RP-HPLC analyses were performed using a 5 μm Supelcosil LC-18S column (25 cm × 4.6 mm) according to the following conditions: starting from 0.1 M triethylammonium acetate pH 7.0, a linear gradient of 0.7% MeCN/min was pumped at a flow rate of 1 mL/min for 30 min and was followed by a linear gradient of 4% MeCN for 5 min, which was held isocratically for 5 min. Peak heights are all normalized to the highest peak, which is set to 1 arbitrary unit.

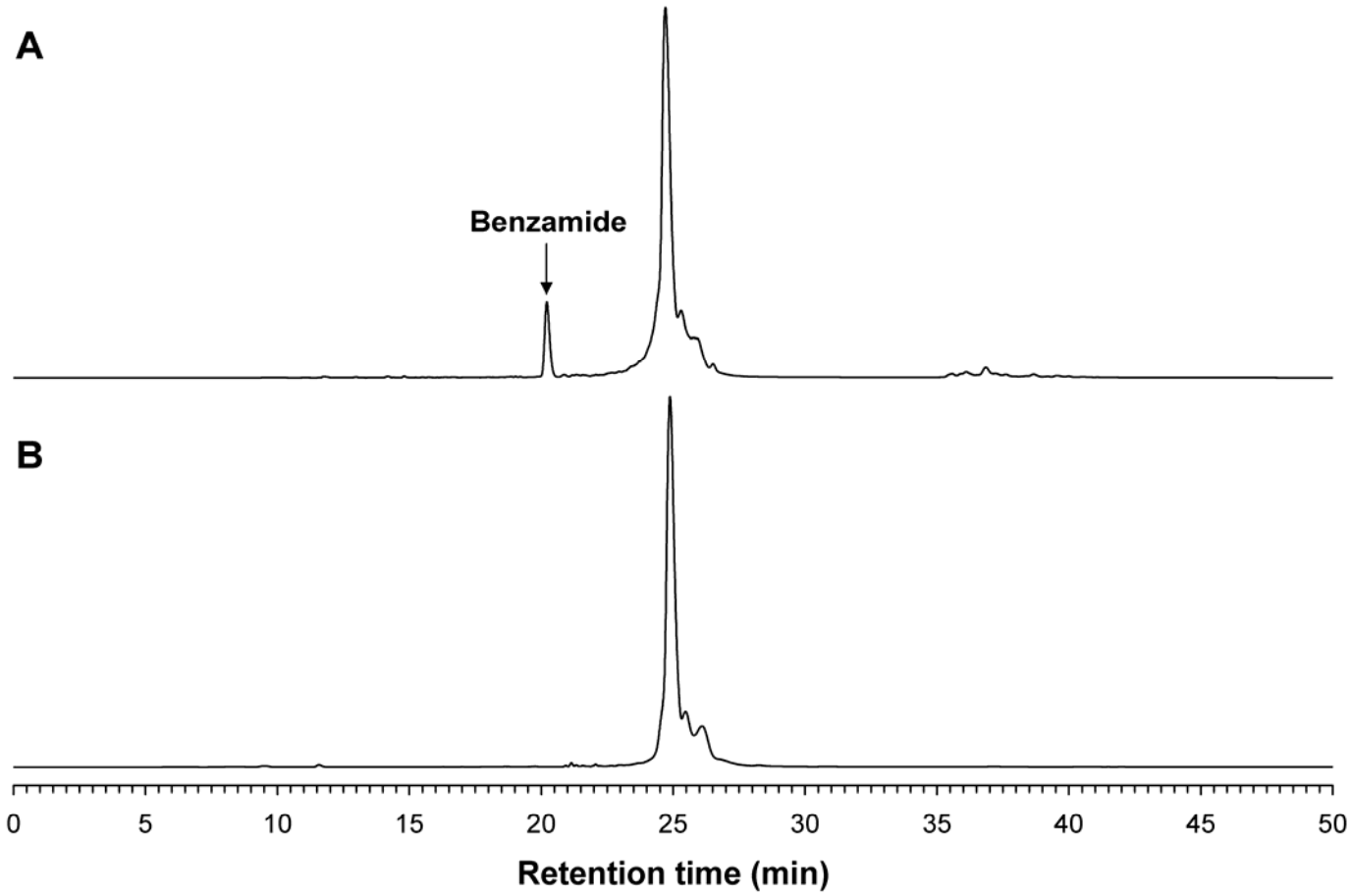

Enlarged Figure 2. RP-HPLC analysis of unpurified 5'-d($C_{PS}G_{PS}A_{PS}C_{PS}T_{PS}G_{PS}T_{PS}G_{PS}A_{PS}A_{PS}T_{PS}C_{PS}$ $G_{PS}A_{PS}T_{PS}G_{PS}C_{PS}C_{PS}A_{PS}T$). **A:** Chromatogram of the fully phosphorothioated 20-mer that was synthesized employing commercial CPG under standard conditions. Nucleobase and thiophosphate deprotection was effected by treatment with pressurized NH_3 gas (~10 bar) over a period of 16 h at 25 ºC, as described in the Experimental section. **B:** Chromatogram of the 20-mer that was synthesized using the CPG support **7** under standard conditions. After nucleobase and thiophosphate deprotection under the conditions described in **A**, the deprotection side products were washed away from the CPG support **8** with MeCN:H_2O (1:1 v/v). The 20-mer was thermolytically cleaved from the support **8** upon heating at 90 ºC in 1× PBS (pH 7.2) for 2 h. RP-HPLC analyses were performed using a 5 µm Supelcosil LC-18S column (25 cm × 4.6 mm) according to the following conditions: starting from 0.1 M triethylammonium acetate pH 7.0, a linear gradient of 1% MeCN/min was pumped at a flow rate of 1 mL/min for 40 min. Peak heights are all normalized to the highest peak, which is set to 1 arbitrary unit.

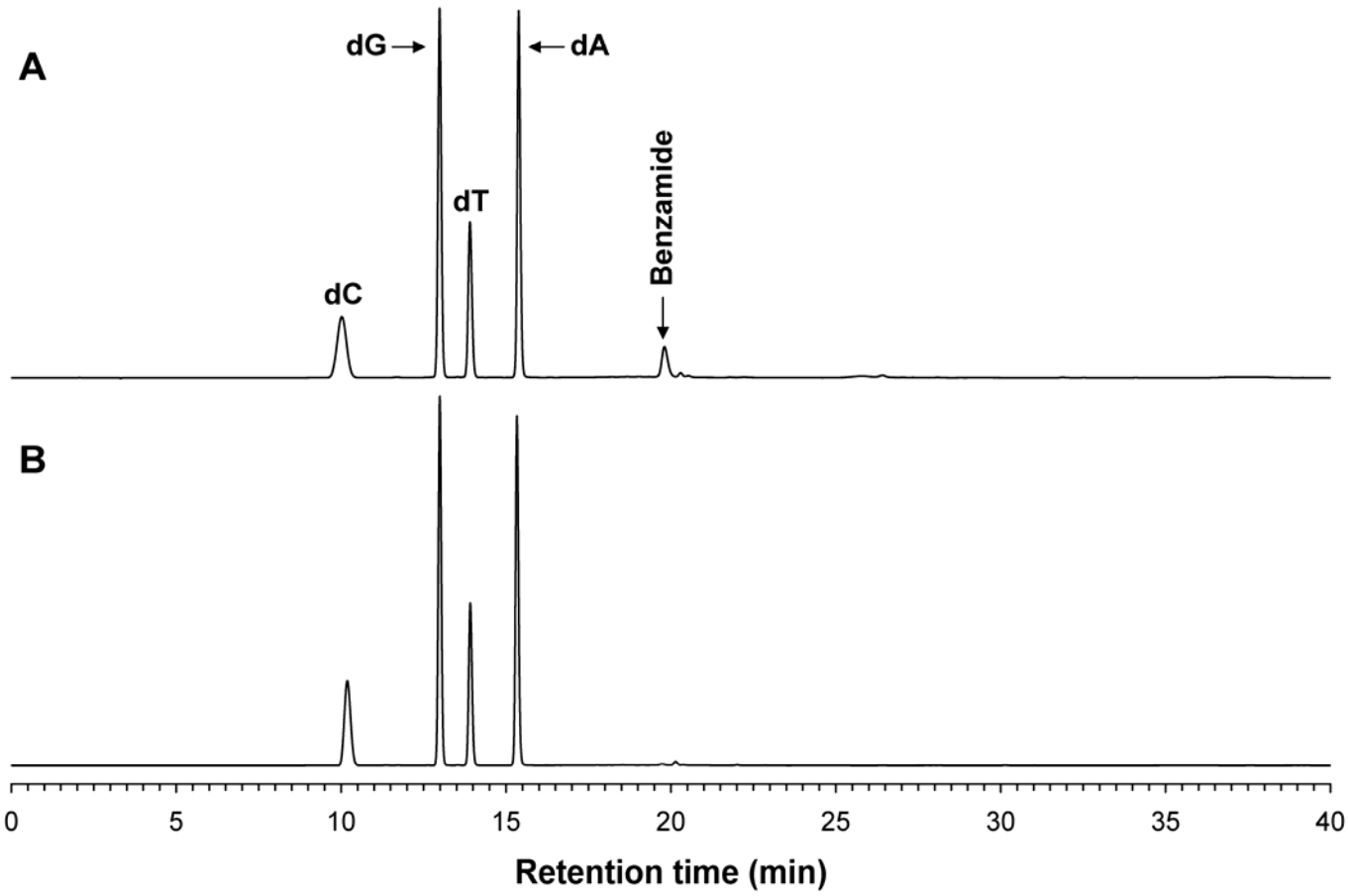

CHART 1. RP-HPLC analysis of unpurified 5'-d(CGACTGTGAATCGATGCCAT) after treatment with snake venom phosphodiesterase and bacterial alkaline phosphatase. **A:** Chromatogram of the enzymatic digest of the 20-mer described in Figure 1A. **B:** Chromatogram of the enzymatic digest of the 20-mer described in Figure 1B. Chromatographic conditions are identical to those described in the legend of Enlarged Figure 2. **dC**, 2'-deoxycytidine; **dG**, 2'deoxyguanosine; **dT**, 2'deoxythymidine; **dA**, 2'-deoxyadenosine.

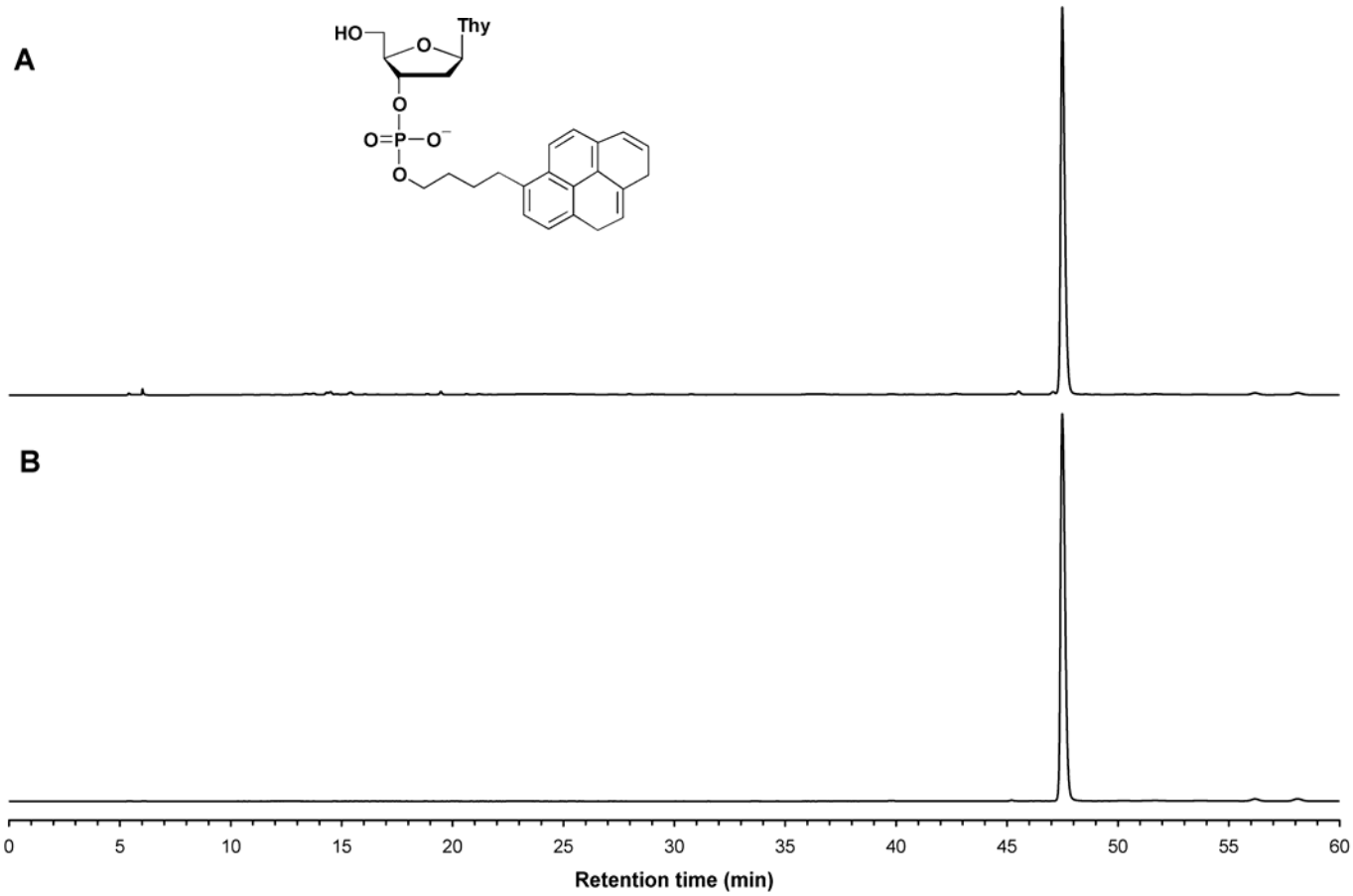

CHART 2. RP-HPLC chromatograms of unpurified thymidine 3'-*O*-(1-pyrenebutyl) phosphate that was thermolytically released from the CPG support **12**. **A:** Chromatogram of thymidine 3'-*O*-(1-pyrenebutyl) phosphate recorded at 260 nm. **B:** Chromatogram of thymidine 3'-*O*-(1-pyrenebutyl) phosphate recorded at 340 nm. RP-HPLC analyses were performed under conditions identical to those described in the legend of Enlarged Figure 2.

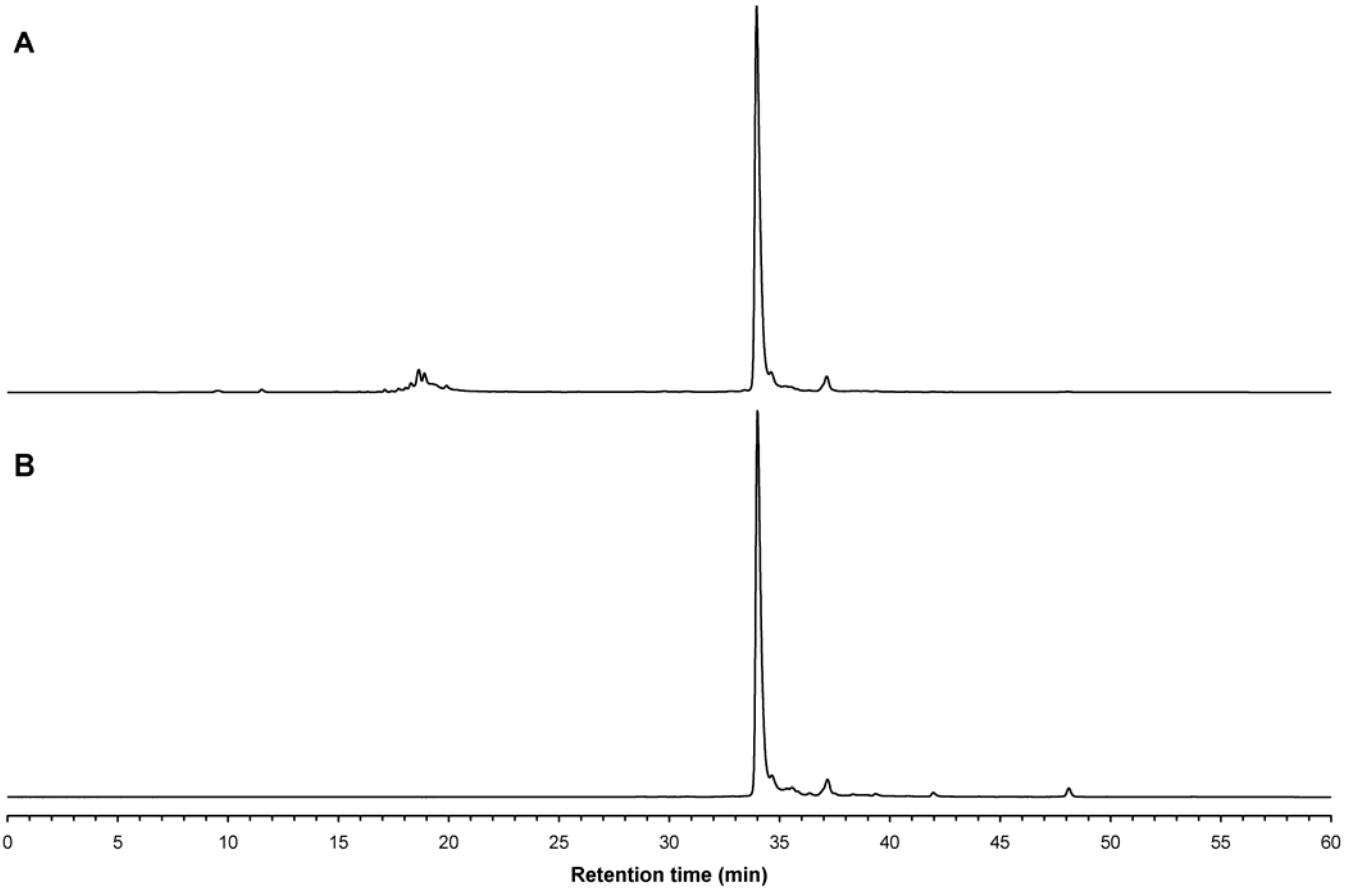

CHART 3. RP-HPLC analysis of unpurified 3'-pyrenylated DNA oligonucleotide **14**. **A:** Chromatogram of **14** recorded at 260 nm. **B:** Chromatogram of **14** recorded at 340 nm. RP-HPLC analyses were performed under conditions identical to those described in the legend of Enlarged Figure 2.

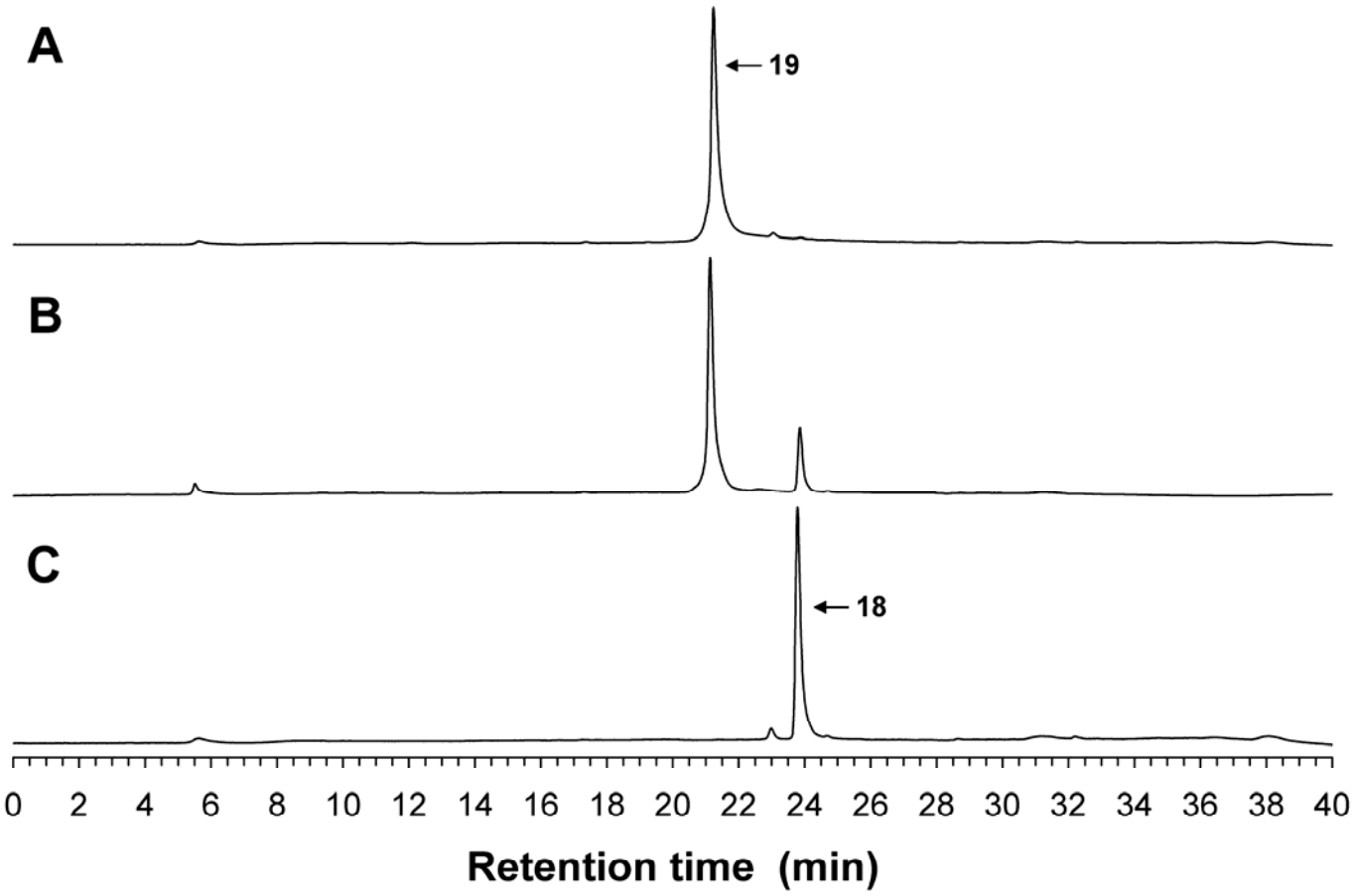

CHART 4. RP-HPLC analysis of the conversion of the (5',3')-heteroconjugated DNA oligonucleotide **18** to the circular DNA oligonucleotide **19** under "click chemistry" conditions. **A:** RP-HPLC-purified circular DNA oligonucleotide **19** (MALDI-TOF MS: calcd for $C_{209}H_{249}N_{79}O_{125}P_{21}$ $(M–H)^-$ 6517, found 6521). **B:** Chromatogram of a co-mixture of RP-HPLC-purified **19** and **18** (4:1). **C:** RP-HPLC-purified (5',3')-heteroconjugated DNA oligonucleotide **18** (MALDI-TOF MS: calcd for $C_{209}H_{249}N_{79}O_{125}P_{21}$ $(M–H)^-$ 6517, found 6522). RP-HPLC analyses were performed under conditions identical to those described in the legend of Enlarged Figure 2.

Thermolytic Release of Covalently Linked DNA Oligonucleotides and Their Conjugates from Controlled-Pore Glass at Near Neutral pH†

Andrzej Grajkowski,‡ Jacek Cieślak,‡ Jon S. Kauffman,§ Robert J. Duff,§ Scott Norris,# Darón I. Freedberg,# and Serge L. Beaucage*,‡

Division of Therapeutic Proteins, Center for Drug Evaluation and Research, and Division of Bacterial, Parasitic and Allergenic Products, Center for Biologics Evaluation and Research, Food and Drug Administration, 8800 Rockville Pike, Bethesda, Maryland 20892, and Lancaster Laboratories, 2425 New Holland Pike, Lancaster, Pennsylvania 17605. Received May 12, 2008; Revised Manuscript Received June 5, 2008

The functionalization of long chain alkylamine controlled-pore glass (CPG) with a 3-hydroxypropyl-(2-cyanoethyl)thiophosphoryl linker and its conversion to the support **7** has led to the synthesis of DNA oligonucleotides and their 3′- or (3′,5′)-conjugates. Indeed, CPG support **7** has been successfully employed in the synthesis of both native and fully phosphorothioated DNA 20-mers. Unlike conventional succinylated CPG supports, this distinctively functionalized support allows oligonucleotide deprotection and removal of the deprotection side products to proceed without releasing the oligonucleotide into the aqueous milieu. When freed from deprotection side products, the DNA oligonucleotide is thermolytically released from the support within 2 h under nearly neutral conditions (pH 7.2, 90 °C). The quality of these oligonucleotides is comparable to that of identical oligonucleotides synthesized from succinylated CPG supports in terms of shorter than full length oligonucleotide contaminants and overall yields. The versatility of the thermolytic CPG support **7** is further demonstrated by the synthesis of a DNA oligonucleotide (20-mer) and its conjugation with an azido and alkynyl groups at both 5′-and 3′-termini, respectively. The functionality of the (3′,5′)-heteroconjugated oligonucleotide **18** is verified by its circularization to the DNA oligonucleotide **19** under "click" chemistry conditions.

INTRODUCTION

Solid supports have revolutionized the synthesis of natural products such as peptides (*1, 2*), oligonucleotides (*3–6*), and carbohydrates (*7, 8*), and that of organic compounds through the development of combinatorial chemistries (*9*). The functionality of solid-supported syntheses is however critically dependent on the design and implementation of linkers for the covalent attachment of organic building blocks to solid supports (*10*). When employed in the solid-phase synthesis of oligonucleotides and their analogues or conjugates, the solid support must be functionalized efficiently with a linker designed to allow synthesis to proceed while maintaining the availability of both 5′- and 3′-terminal hydroxyls for subsequent conjugation with various functional groups. The junction linker-to-oligonucleotide and linker-to-support should ideally be stable to the reagents and conditions used during oligonucleotide synthesis and conjugation in addition to those employed for oligonucleotide deprotection. Such an attribute would facilitate the removal of side products resulting from the cleavage of nucleobase and phosphate/thiophosphate protecting groups, including those generated from terminal 5′-/3′-hydroxyl and/or functional group deprotection, by simply washing the solid support. Release of the oligonucleotide, its conjugate or analogue, from the solid support would be effected under mild and neutral thermolytic conditions, free from side products. To the best of our knowledge, the thermolytic release of oligonucleotides with free 5′- and 3′-hydroxyls from solid supports under nearly neutral conditions has not, as yet, been described in the literature. Given that modified oligonucleotides and their conjugates are valuable tools for mechanistic investigations and for therapeutic or diagnostic applications (*11–13*), we have instigated the use of versatile supports designed to enable the preparation of oligonucleotides, conjugated or not with functional groups at either the 3′-terminus or both 3′- and 5′-termini. Specifically, nucleoside or dinucleotide precursors are covalently linked to long chain alkylamine controlled-pore glass (CPG) through either a 3′- or an internucleotidic phosphotriester function. After synthesis and deprotection, release of the oligonucleotides from the support is triggered by a thermolytic intramolecular cyclodeesterification reaction (*14*) in an aqueous buffer at pH 7.2. Details regarding the functionalization of CPG and the thermolytic release of dinucleotide models are outlined in Schemes 1 and 2, respectively. The solid-phase synthesis and thermolytic release of native and modified DNA oligonucleotides in addition to oligonucleotides conjugated with functional groups at the 3′-terminus or at both 3′-and 5′-termini are also described in this report.

EXPERIMENTAL PROCEDURES

Preparation of Functionalized CPG Support 3. CPG (500 Å, 500 mg) was suspended in Et_3N/MeCN (1:1 v/v, 2 mL) in a 4 mL glass vial and was manually agitated over a period of 2 min. The suspension was vacuum-filtered using a glass sintered funnel of coarse porosity. The CPG support was washed with MeCN (10 mL) and then dried under vacuum (3 min). The support was transferred to an 8 mL glass vial, which was stoppered with a rubber septum. The vial and its contents were flushed with a flow of dry argon prior to sequentially adding, by syringe, a solution of *O*-(2-cyanoethyl)-*O*-[3-(4,4′-dimethoxytrityl)oxy-1-propyl]-*N*,*N*-diisopropylphosphoramidite (**1**, 250

* To whom correspondence should be addressed. Tel: (301)-827-5162. Fax: (301)-480-3256. Serge.Beaucage@fda.hhs.gov.

† This paper is dedicated to Professor Wojciech T. Markiewicz on the occasion of his 60th birthday.

‡ Center for Drug Evaluation and Research.

§ Lancaster Laboratories.

Center for Biologics Evaluation and Research.

10.1021/bc800189e CCC: $40.75 © 2008 American Chemical Society
Published on Web 07/23/2008

Scheme 1. Preparation of CPG Support 3 and Its Conversion to Support 7[a]

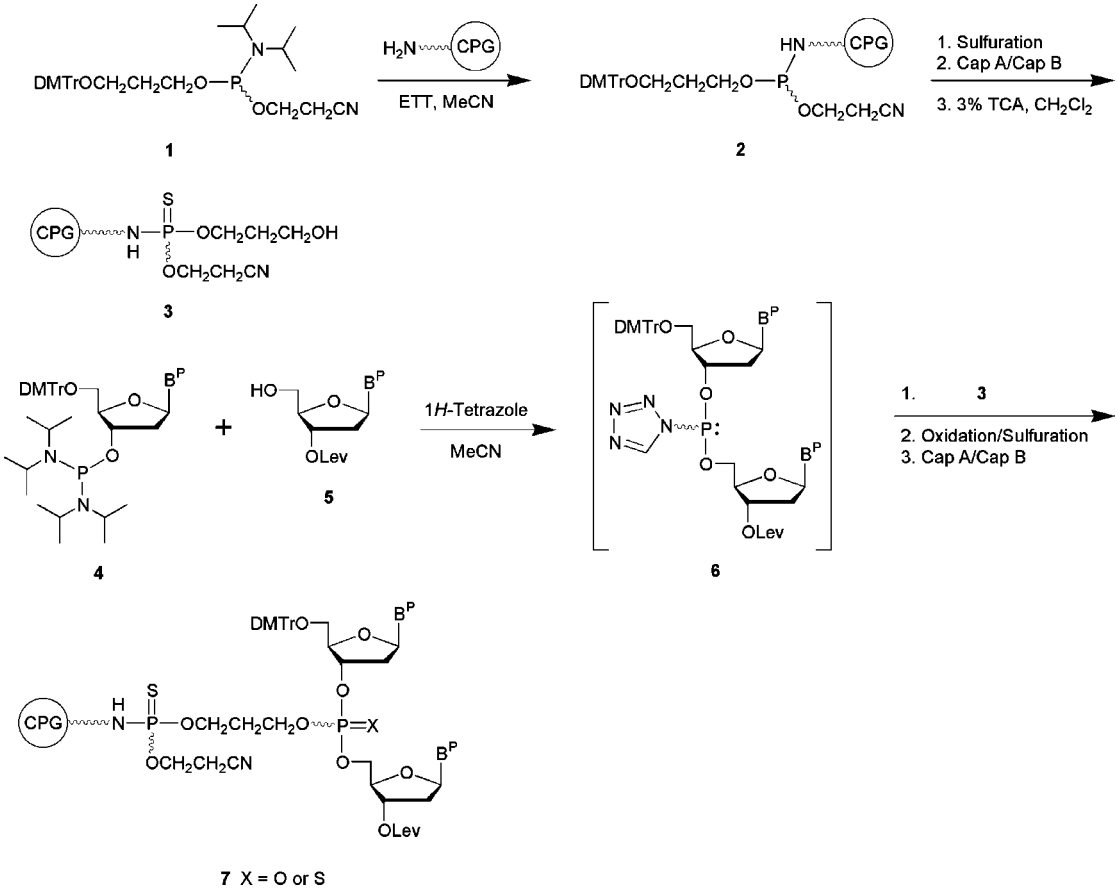

[a] Keys: DMTr, 4,4′-dimethoxytrityl; CPG, 500 Å long chain alkylamine controlled-pore glass; ETT, 5-ethylthio-1*H*-tetrazole; Cap A, acetic anhydride/pyridine/THF; Cap B, 10% 1-methylimidazole in THF; TCA, trichloroacetic acid; B^P, Thy (thymin-1-yl), Cyt^{Bz} (N^4-benzoylcytosin-1-yl), Ade^{Bz} (N^6-benzoyladenin-9-yl), or Gua^{iBu} (N^2-isobutyrylguanin-9-yl); Lev, levulinyl.

Scheme 2. Thermolytic Release of Dinucleoside Phosphate/Thiophosphate Diesters from CPG Support 8[a]

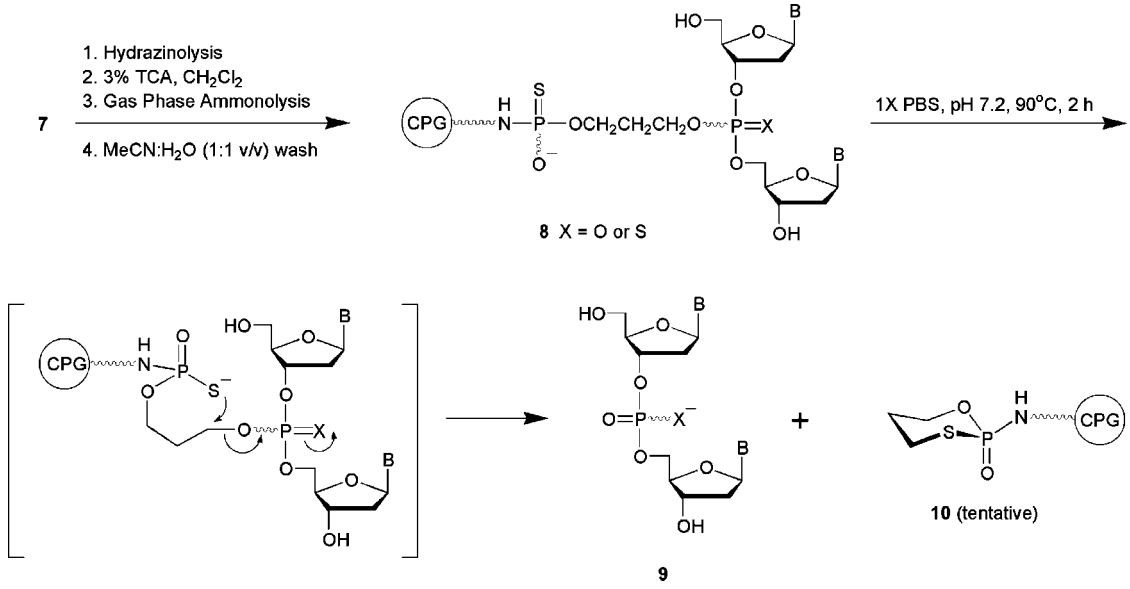

[a] Keys: B, thymin-1-yl, cytosin-1-yl, adenin-9-yl or guanin-9-yl; PBS, phosphate buffered saline.

mg, 0.43 mmol) in dry MeCN (1.2 mL) and 0.25 M 5-ethylthio-1*H*-tetrazole in dry MeCN (3.2 mL, 0.80 mmol). The suspension was agitated, manually, for 15 min under a positive pressure of argon and filtered under vacuum using a glass sintered funnel of medium porosity. The CPG support **2** was washed with MeCN (10 mL) and exposed, while in the funnel, to 0.1 M 3*H*-1,2-benzodithiol-3-one 1,1-dioxide (5 mL) for 15 min. Excess sulfuration reagent was removed from the support by vacuum filtration. The functionalized CPG support was washed with MeCN (10 mL) and was then suspended in a solution of Cap A (THF/pyridine/Ac_2O, 2.5 mL) and Cap B (1-methylimidazole/THF, 2.5 mL) for a period of 10 min. Excess capping

reagents was removed by filtration; the support was washed with MeCN (10 mL) and dried under vacuum. Dedimethoxytritylation of the support by treatment with 3% TCA (trichloroacetic acid) in CH_2Cl_2 (3 mL, 3 min) afforded the functionalized CPG support **3**. Spectrophotometric determination of the 4,4′-dimethoxytrityl cation at 498 nm revealed a hydroxyl concentration of 69 μmol/g of **3**.

General Procedure for the Preparation of Deoxyribonucleoside Phosphorodiamidites (4) (*15*). A 5′-*O*-(4,4′-dimethoxytrityl)-2′-deoxyribonucleoside (T, C^{Bz}, A^{Bz}, or G^{iBu}, 2.0 mmol) was dried by coevaporation with anhydrous pyridine (3 × 10 mL) under reduced pressure and was finally dissolved in a solution of anhydrous CH_2Cl_2 (15 mL) and *i*-Pr_2NEt (3.48 mL, 20.0 mmol). To the stirred solution was added bis((*N*,*N*-diisopropylamino)chlorophosphine (587 mg, 2.20 mmol). Progress of the reaction was monitored by TLC, which showed complete phosphinylation within 2 h at ∼25 °C. The reaction was quenched upon addition of water (15 mL); the mixture was vigorously stirred for ∼5 min prior to being transferred to a separatory funnel. The organic layer was collected and rotoevaporated to an oil under reduced pressure. The material was dissolved in a minimal amount (∼4 mL) of benzene/Et_3N (9:1, v/v) and loaded onto the top of a column packed with silica gel (∼30 g) pre-equilibrated in benzene/Et_3N (9:1, v/v). Elution of the reaction product was achieved using benzene/Et_3N (9:1, v/v) as the eluent. Fractions containing the product were identified by TLC and were pooled together. The solvent was removed by rotoevaporation under reduced pressure to afford the phosphoramidite **4** as a white foam. The material was dissolved in dry benzene (10 mL) and the resulting solution was frozen in a dry ice−acetone bath. The frozen solution was then lyophilized under high vacuum for ∼16 h to give triethylamine-free **4** as a white powder in yields of 85−95%.

5′-*O*-(4,4′-Dimethoxytrityl)-3′-*O*-bis(*N*,*N*-diisopropylamino)phosphinyl-2′-deoxythymidine. ^{1}H NMR (700 MHz, C_6D_6): δ 7.58 (q, 1H, ^4J = 1.4 Hz, H-6), 7.57 (dd, 2H, J = 8.3, 1.4 Hz, DMTr), 7.41 (d, 2H, J = 9.1 Hz, DMTr), 7.39 (d, 2H, J = 9.1 Hz, DMTr), 7.15 (m, 2H, DMTr), 7.04 (tt, 1H, J = 7.5, 1.1 Hz, DMTr), 6.76 (m, 1H, H-1′), 6.74 (d, 2H, J = 9.1 Hz, DMTr), 6.73 (d, 2H, J = 9.1 Hz, DMTr), 4.61 (m, 1H, H-3′), 4.35 (m, 1H, H-4′), 3.55 (dd, 1H, J = 10.2, 2.8 Hz, H-5′/H-5″), 3.46−3.41 (m, 2H, NC**H**$(CH_3)_2$), 3.40 (dd, 1H, J = 10.2, 3.0 Hz, H-5′/H-5″), 3.40−3.35 (m, 2H, NC**H**$(CH_3)_2$), 3.29 (s, 3H, OC**H**$_3$), 3.28 (s, 3H, OC**H**$_3$), 2.51 (m, 1H, H-2′/H-2″), 2.23 (ddd, 1H, J = 13.3, 8.8, 5.8 Hz, H-2′/H-2″), 1.56 (d, 3H, ^4J = 1.4 Hz, 5-CH_3), 1.21 (d, 6H, J = 6.6 Hz, NCH(C**H**$_3)_2$), 1.14 (d, 6H, J = 6.6 Hz, NCH(C**H**$_3)_2$), 1.12 (d, 6H, J = 6.6 Hz, NCH(C**H**$_3)_2$), 1.09 (d, 6H, J = 6.6 Hz, NCH(C**H**$_3)_2$). ^{13}C NMR (175 MHz, C_6D_6): δ 164.2 (C-4), 159.32 (DMTr), 159.31 (DMTr), 151.0 (C-2), 145.2 (DMTr), 136.0 (DMTr), 135.9 (DMTr), 135.4 (C-6), 130.60 (DMTr), 130.58 (DMTr), 128.7 (DMTr), 128.2 (DMTr), 127.3 (DMTr), 113.64 (DMTr), 113.63 (DMTr), 111.1 (C-5), 87.3 (DMTr), 86.3 (d, J_{PC} = 5.4 Hz, C-4′), 85.5 (C-1′), 75.1 (d, $^2J_{CP}$ = 19.3 Hz, C-3′), 64.5 (C-5′), 54.8 (OCH_3), 45.0 (d, $^2J_{CP}$ = 12.9 Hz, N**C**H$(CH_3)_2$), 40.4 (d, J_{CP} = 5.4 Hz, C-2′), 24.5 (d, J_{CP} = 8.6 Hz, NCH(**C**H$_3)_2$), 24.3 (d, J_{CP} = 6.4 Hz, NCH(**C**H$_3)_2$), 24.2 (d, J_{CP} = 6.4 Hz, NCH(**C**H$_3)_2$), 12.2 (5-CH_3). ^{31}P NMR (121 MHz, C_6D_6): δ 116.2. +APESI-TOF MS: calcd for $C_{43}H_{59}N_4O_7P$ $(M+H)^+$ 775.4200, found 775.4195.

***N*^{4}-Benzoyl-5′-*O*-(4,4′-dimethoxytrityl)-3′-*O*-bis(*N*,*N*-diisopropylamino)phosphinyl-2′-deoxycytidine.** ^{1}H NMR (700 MHz, C_6D_6): δ 8.18 (bs, 1H, H-6), 7.92 (m, 2H, Bz), 7.62 (dd, 2H, J = 8.6, 1.4 Hz, DMTr), 7.46 (d, 2H, J = 8.9 Hz, DMTr), 7.45 (d, 2H, J = 8.9 Hz, DMTr), 7.24 (d, 1H J = 7.5 Hz, Ar/H-5), 7.22 (d, 1H J = 7.5 Hz, Ar/H-5), 7.10 (m, 2H, Ar), 7.02 (m, 2H, Ar), 6.83 (d, 2H, J = 9.1 Hz, DMTr), 6.82 (d, 2H, J = 9.1 Hz, DMTr), 6.51 (t, 1H, J = 6.2 Hz, H-1′), 4.58 (ddd, 1H, J = 6.4, 5.8, 3.3 Hz, H-3′), 4.41 (m, 1H, H-4′), 3.56 (dd, 1H, J = 10.5, 3.3 Hz, H-5′/H-5″), 3.50 (dd, 1H, J = 10.5, 4.1 Hz, H-5′/H-5″), 3.47−3.40 (m, 4H, NC**H**$(CH_3)_2$), 3.39 (s, 3H, OC**H**$_3$), 3.38 (s, 3H, OC**H**$_3$), 2.84 (m, 1H, H-2′/H-2″), 2.23 (ddd, 1H, J = 13.6, 6.4, 6.1 Hz, H-2′/H-2″), 1.18 (d, 6H, J = 6.7 Hz, NCH(C**H**$_3)_2$), 1.15 (d, 6H, J = 6.7 Hz, NCH(C**H**$_3)_2$), 1.14 (d, 6H, J = 6.7 Hz, NCH(C**H**$_3)_2$), 1.12 (d, 6H, J = 6.7 Hz, NCH(C**H**$_3)_2$). ^{13}C NMR (175 MHz, C_6D_6): δ 162.8 (C-4), 159.4 (DMTr), 145.1 (C-2), 143.8 (C-6), 136.0 (Ar), 135.84 (Ar), 135.83 (Ar), 134.6 (Ar), 132.3 (Ar), 130.7 (DMTr), 130.6 (DMTr), 128.7 (DMTr), 128.6 (DMTr), 128.26 (Ar), 128.25 (Ar), 127.34 (Ar), 127.32 (Ar), 113.69 (DMTr), 113.68 (DMTr), 101.7 (C-5), 87.8 (DMTr), 87.4 (C-1′), 86.7 (d, J_{CP} = 4.3 Hz, C-4′), 73.8 (d, $^2J_{CP}$ = 18.3 Hz, C-3′), 63.9 (C-5′), 54.9 (OCH_3), 45.1 (d, $^2J_{CP}$ = 12.6 Hz, N**C**H$(CH_3)_2$), 44.8 (d, $^2J_{CP}$ = 12.4 Hz, N**C**H$(CH_3)_2$), 41.5 (C-2′), 24.6 (d, J_{CP} = 8.6 Hz, NCH(**C**H$_3)_2$), 24.5 (d, J_{CP} = 8.6 Hz, NCH(**C**H$_3)_2$), 24.3 (d, J_{CP} = 6.4 Hz, NCH(**C**H$_3)_2$) 24.2 (d, J_{CP} = 6.4 Hz, NCH(**C**H$_3)_2$). ^{31}P NMR (121 MHz, C_6D_6): δ 117.1. +APESI-TOF MS: calcd for $C_{49}H_{62}N_5O_7P$ $(M+H)^+$ 864.4465, found 864.4477.

***N*^{6}-Benzoyl-5′-*O*-(4,4′-dimethoxytrityl)-3′-*O*-bis(*N*,*N*-diisopropylamino)phosphinyl-2′-deoxyadenosine.** ^{1}H NMR (700 MHz, C_6D_6): δ 8.74 (bs, 1H, H-2), 7.95 (s, 1H, H-8), 7.82 (m, 2H, Bz), 7.61 (dd, 2H, J = 8.5, 1.3 Hz, DMTr), 7.44 (d, 2H, J = 9.0 Hz, DMTr), 7.43 (d, 2H, J = 9.0 Hz, DMTr), 7.15 (m, 2H, Ar), 7.06−6.96 (m, 4H, Ar), 6.73 (d, 2H, J = 9.0 Hz, DMTr), 6.72 (d, 2H, J = 9.0 Hz, DMTr), 6.34 (t, 1H, J = 6.4 Hz, H-1′), 4.75 (ddd, 1H, J = 8.7, 5.9, 3.1 Hz, H-3′), 4.59 (m, 1H, H-4′), 3.59 (dd, 1H, J = 10.2, 4.1 Hz, H-5′/H-5″), 3.55 (dd, 1H, J = 10.2, 5.1 Hz, H-5′/H-5″), 3.51−3.42 (m, 4H, NC**H**$(CH_3)_2$), 3.33 (s, 3H, OC**H**$_3$), 3.32 (s, 3H, OC**H**$_3$), 2.87 (m, 1H, H-2′/H-2″), 2.56 (ddd, 1H, J = 13.6, 6.4, 3.1 Hz, H-2′/H-2″), 1.21 (d, 6H, J = 6.7 Hz, NCH(C**H**$_3)_2$), 1.18 (d, 6H, J = 6.7 Hz, NCH(C**H**$_3)_2$), 1.17 (d, 6H, J = 6.7 Hz, NCH(C**H**$_3)_2$), 1.16 (d, 6H, J = 6.7 Hz, NCH(C**H**$_3)_2$). ^{13}C NMR (175 MHz, C_6D_6): δ 166.2 (C═O), 159.18 (DMTr), 159.16 (DMTr,) 152.6 (C-2/C-6), 151.9 (C-6/C-2), 145.5 (C-4), 142.1 (C-8), 136.24 (DMTr), 136.21 (DMTr), 132.0 (Ar), 130.6 (DMTr), 130.5 (DMTr), 128.7(DMTr) 128.6 (DMTr), 128.3 (Ar), 128.1 (Ar), 127.1 (C-5), 113.5 (DMTr), 87.0 (DMTr), 86.9 (d, J_{CP} = 5.4 Hz, C-4′), 85.8 (C-1′), 74.9 (d, $^2J_{CP}$ = 18.3 Hz, C-3′), 64.8 (C-5′), 54.8 (OCH_3), 45.0 (d, $^2J_{CP}$ = 12.9 Hz, N**C**H$(CH_3)_2$), 44.9 (d, $^2J_{CP}$ = 12.9 Hz, N**C**H$(CH_3)_2$), 39.4 (C-2′), 24.6 (d, J_{CP} = 8.6 Hz, NCH(**C**H$_3)_2$), 24.5 (d, J_{CP} = 8.6 Hz, NCH(**C**H$_3)_2$), 24.3 (d, J_{CP} = 6.4 Hz, NCH(**C**H$_3)_2$), 24.2 (d, J_{CP} = 6.4 Hz, NCH(**C**H$_3)_2$). ^{31}P NMR (121 MHz, C_6D_6): δ 116.7. +APESI-TOF MS: calcd for $C_{50}H_{62}N_7O_6P$ $(M+H)^+$ 888.4577, found 888.4574.

***N*^{2}-Isobutyryl-5′-*O*-(4,4′-dimethoxytrityl)-3′-*O*-bis(*N*,*N*-diisopropylamino)phosphinyl-2′-deoxyguanosine.** ^{1}H NMR (700 MHz, C_6D_6): δ 7.89 (s, 1H, H-8), 7.63 (dd, 2H, J = 8.6, 1.3 Hz, DMTr), 7.48 (d, 2H, J = 9.0 Hz, DMTr), 7.47 (d, 2H, J = 9.0 Hz, DMTr), 7.16 (m, 2H, DMTr), 7.04 (tt, 1H, J = 7.4, 1.3 Hz, DMTr), 6.77 (d, 2H, J = 9.0 Hz, DMTr), 6.76 (d, 2H, J = 9.0 Hz, DMTr), 6.45 (dd, 1H, J = 6.1, 5.9 Hz, H-1′), 4.66 (m, 1H, H-3′), 4.48 (m, 1H, H-4′), 3.56 (dd, 1H, J = 10.2, 3.3 Hz, H-5′/H-5″), 3.49−3.40 (m, 6H, H-5′/H-5″, COC**H**$(CH_3)_2$, NC**H**$(CH_3)_2$), 3.38 (s, 3H, OC**H**$_3$), 3.37 (s, 3H, OC**H**$_3$), 2.83 (m, 1H, H-2′/H-2″), 2.62 (ddd, 1H, J = 13.6, 5.9, 2.8 Hz, H-2′/H-2″), 1.19 (d, 6H, J = 6.7 Hz, NCH(C**H**$_3)_2$), 1.15 (d, 6H, J = 6.7 Hz, NCH(C**H**$_3)_2$), 1.14 (d, 6H, J = 6.7 Hz, NCH(C**H**$_3)_2$), 1.13 (d, 6H, J = 6.7 Hz, NCH(C**H**$_3)_2$), 1.06 (d, 3H, J = 6.7 Hz, COCH(C**H**$_3)_2$), 1.05 (d, 3H, J = 6.7 Hz, COCH(C**H**$_3)_2$). ^{13}C NMR (175 MHz, C_6D_6): δ 159.24 (DMTr), 159.23 (DMTr), 159.1 (C-6), 149.4 (C-2), 145.5 (C-4), 137.2 (C-8), 136.3 (DMTr), 136.2 (DMTr), 130.7(DMTr), 130.6 (DMTr), 128.7

(DMTr), 128.3 (DMTr), 127.1 (DMTr), 122.3 (DMTr), 113.60 (DMTr), 113.58 (DMTr), 113.5 (C-5), 86.9 (DMTr), 86.7 (d, J_{CP} = 4.3 Hz, C-4′), 85.0 (C-1′), 74.5 (d, $^2J_{CP}$ = 17.2 Hz, C-3′), 64.8 (C-5′), 54.9 (OCH_3), 45.0 (d, $^2J_{PC}$ = 12.9 Hz, N**C**H$(CH_3)_2$), 44.9 (d, $^2J_{CP}$ = 12.9 Hz, N**C**H$(CH_3)_2$), 40.0 (d, J_{CP} = 4.3 Hz, C-2′), 35.9 (CO**C**H$(CH_3)_2$), 24.6 (d, J_{CP} = 8.6 Hz, NCH(**C**$H_3)_2$), 24.3 (d, J_{CP} = 6.4 Hz, NCH(**C**$H_3)_2$), 24.2 (d, J_{CP} = 6.4 Hz, NCH(**C**$H_3)_2$), 19.19 (COCH(**C**$H_3)_2$), 19.16 (COCH(**C**$H_3)_2$). ^{31}P NMR (121 MHz, C_6D_6): δ 116.9. +APESI-TOF MS: calcd for $C_{47}H_{64}N_7O_7P$ $(M+H)^+$ 870.4683, found 870.4687.

General Procedure for Preparation of Dinucleoside Phosphorotetrazolide Intermediates (6) in Situ and for Their Covalent Attachment to CPG Support 3. Phosphorodiamidite **4** (B^P = Thy, Cyt^{Bz}, Ade^{Bz}, or Gua^{iBu}, 50 μmol), 3′-*O*-levulinyl-2′-deoxyribonucleoside **5** (B^P = Thy, Cyt^{Bz}, Ade^{Bz}, or Gua^{iBu}, 50 μmol), and sublimed 1*H*-tetrazole (11 mg, 150 μmol) were placed in a flame-dried 4 mL glass vial, which was stoppered with a rubber septum and purged with a flow of dry Argon. Anhydrous MeCN (300 μL) was syringed into the vial through the rubber septum. The coupling reaction was allowed to proceed over a period of 10 min at ~25 °C to generate the putative dinucleoside phosphorotetrazolide intermediate **6** (*16*). The reaction mixture was withdrawn from the vial and through a synthesis column filled with CPG support **3** (14.5 mg, 1 μmol) using a luer-tipped syringe connected to one end of the synthesis column and a 16-G hypodermic needle connected to the other end of the synthesis column. The coupling reaction was performed for a period of 10 min. Excess reagent was expelled from the column, which was washed with a solution of 20% 1-methylimidazole in H_2O/MeCN (1:1 v/v) for 2 min. An oxidation reaction was carried out using either 0.05 M 3*H*-1,2-benzodithiol-3-one 1,1-dioxide in MeCN or 0.02 M I_2 in THF/pyridine/H_2O for 2 min. Unreacted hydroxyl groups of support **3** were acylated when exposed to Cap A and Cap B solutions (1 mL each) for 2 min. Excess capping reagents was removed from CPG support **7** by washing with MeCN (10 mL). Spectrophotometric determination (498 nm) of the 4,4′-dimethoxytrityl cation released from **7** under acidic conditions revealed a dinucleoside phosphate triester concentration of 40 μmol/g of support.

General Procedure for the Automated Solid-Phase Synthesis of DNA Oligonucleotides Using CPG Support 7. Solid-phase synthesis of native and phosphorothioated DNA oligonucleotides was performed on a 0.2 μmol scale using a DNA/RNA synthesizer and 2-cyanoethyl deoxyribonucleoside phosphoramidites as 0.1 M solutions in dry MeCN. The reagents and conditions employed for solid-phase synthesis were those recommended by the instrument's manufacturer. However, the preparation of fully thioated oligodeoxyribonucleotides required replacement of the iodine oxidation step in the synthesis cycle with a sulfuration step employing a 0.05 M solution of 3*H*-1,2-benzodithiol-3-one 1,1-dioxide in MeCN, as recommended in the literature (*17, 18*). The capping step was performed before the oxidation step when synthesizing native DNA oligonucleotides and after the sulfuration step when synthesizing phosphorothioated DNA oligonucleotides.

General Procedure for Deprotection, Thermolytic Release, and RP-HPLC Analysis of DNA Oligonucleotides Synthesized from CPG Support 7. 5′-*O*-Dedimethoxytritylated DNA oligonucleotides that were synthesized using CPG support **7** on a 0.2 to 1 μmol scale were subjected to pressurized ammonia gas (~10 bar) for 16 h at 25 °C (*19*) to remove the nucleobase, phosphate/thiophosphate, and 3′-*O*-levulinyl protecting groups. The solid support was washed with 50% aqueous MeCN (1 mL) to eliminate the deprotection side product and was air-dried. The CPG support was transferred to a 4 mL

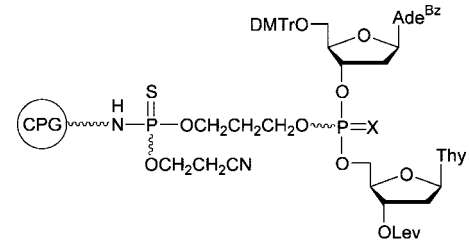

7 X = O or S

screw-capped glass vial to which was added 1 × PBS (pH 7.2, 0.5 mL); the suspension was heated for 2 h at 90 ± 2 °C. The purity of each unpurified native or phosphorothioated DNA oligonucleotide released in the aqueous buffer was assessed by RP-HPLC and compared with that of identical oligonucleotides prepared from unmodified CPG supports (data shown in Figures 1 and 2). Typically, an aliquot (20 μL) of the PBS solution of each native DNA oligonucleotide was analyzed using a 5 μm Supelcosil LC-18S column (25 cm × 4.6 mm) according to the following conditions: starting from 0.1 M triethylammonium acetate pH 7.0, a linear gradient of 0.7% MeCN/min was pumped at a flow rate of 1 mL/min for 30 min and was followed by a linear gradient of 4% MeCN/min for 5 min, which was held isocratically for 5 min.

An aliquot (60 μL) of the PBS solution of each unpurified phosphorothioated DNA oligonucleotide was analyzed under conditions similar to those used for the native DNA oligonucleotide with the following modification: starting from 0.1 M triethylammonium acetate pH 7.0, a linear gradient of 1% MeCN/min was pumped at a flow rate of 1 mL/min for 40 min. Peak heights were all normalized to the highest peak, which was set to 1 arbitrary unit.

5′-d(CGACTGTGAATCGATGCCAT) [MALDI-TOF MS]: Calcd for $C_{195}H_{227}N_{75}O_{118}P_{19}$ $(M-H)^-$ 6097, found 6102.

5′-d($C_{PS}G_{PS}A_{PS}C_{PS}T_{PS}G_{PS}T_{PS}G_{PS}A_{PS}A_{PS}T_{PS}C_{PS}G_{PS}A_{PS}T_{PS}G_{PS}C_{PS}C_{PS}A_{PS}T$) [MALDI-TOF MS]: Calcd for $C_{195}H_{227}N_{75}O_{99}P_{19}S_{19}$ $(M-H)^-$ 6402, found 6406.

Polyacrylamide Gel Electrophoresis Analysis of DNA Oligonucleotides Synthesized from CPG Support 7. To each unpurified native or phosphorothioated DNA oligonucleotide (0.25 OD_{260}) in a 1.5 mL microfuge tube was added 10 μL of Loading Buffer (10 × Tris Borate EDTA, pH 8.3, in formamide (1:4 v/v) containing 2 mg/mL bromophenol blue). The dark blue solution was vortexed vigorously and centrifuged at 16 000*g* for 5 s. Each DNA solution was syringed into a 2 cm wide well of a 20% polyacrylamide−7 M urea gel (20 cm × 40 cm × 0.75 mm). Electrophoresis was performed at 350 V, using 1 × Tris Borate EDTA (pH 8.3) as the electrolyte, until the bromphenol blue dye traveled 75% of the gel's length. The gel was immersed in a staining solution (250 mL) composed of formamide/isopropyl alcohol/ddH_2O (1:5:20 v/v/v) to which was added a solution (10 mL) of Stains-all (1 mg/mL) in formamide. The gel was stained for ~4 h in the dark. The staining solution was discarded and the gel was rinsed three times with 250 mL distilled water. The gel was exposed to natural light until the purple background disappeared. The native DNA oligonucleotides were visualized as sharp blue bands, whereas fully phosphorothioated DNA oligonucleotides appeared as dark purple bands. Photographs of the gels are shown in Figure 3.

Hydrolysis of Native DNA Oligonucleotides Catalyzed by Snake Venom Phosphodiesterase and Bacterial Alkaline Phosphatase. To 1.0 OD_{260} of lyophilized oligonucleotide was added 1 M Tris·HCl (pH 9.0, 6 μL), 1 M $MgCl_2$ (8 μL), ddH_2O to a total volume of 89 μL, snake venom phosphodiesterase (*Crotallus adamanteus*, 5 μL, 2 U/mL), and bacterial alkaline

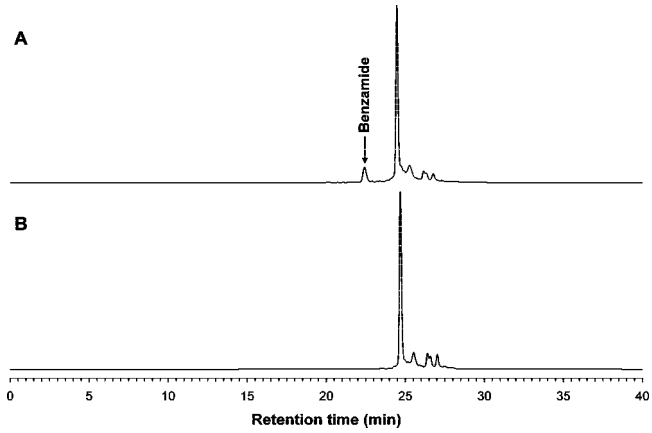

Figure 1. RP-HPLC analysis of unpurified 5′-d(CGACTGTGAATC-GATGCCAT). (A) Chromatogram of the native 20-mer that was synthesized employing unmodified CPG under standard conditions. Nucleobase and phosphate deprotection, and release of the oligomer from the support were effected by treatment with pressurized NH_3 gas (~10 bar) for 16 h at 25 °C, as described in the Experimental Procedures section. (B) Chromatogram of the 20-mer that was synthesized using CPG support **7** under standard conditions. After nucleobase and phosphate deprotection under the conditions described in (A), the deprotection side products were washed away from the modified CPG support with MeCN:H_2O (1:1 v/v). The 20-mer was thermolytically cleaved from the support upon heating at 90 °C in 1 × PBS (pH 7.2) for 2 h. Chromatographic conditions are described in the Experimental Procedures section.

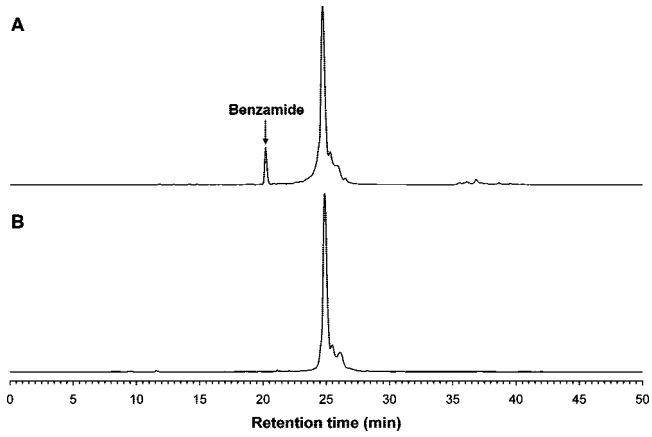

Figure 2. RP-HPLC analysis of unpurified 5′-d($C_{PS}G_{PS}A_{PS}C_{PS}T_{PS}G_{PS}$-$T_{PS}G_{PS}A_{PS}A_{PS}T_{PS}C_{PS}G_{PS}A_{PS}T_{PS}G_{PS}C_{PS}C_{PS}A_{PS}T$). (A) Chromatogram of the fully phosphorothioated 20-mer that was synthesized employing unmodified CPG under standard conditions. Nucleobase and thiophosphate deprotection was effected by treatment with pressurized NH_3 gas (~10 bar) over a period of 16 h at 25 °C, as described in the Experimental Procedures section. (B) Chromatogram of the 20-mer that was synthesized using CPG support **7** under standard conditions. After nucleobase and thiophosphate deprotection under the conditions described in (A), the deprotection side products were washed away from the modified CPG support with MeCN:H_2O (1:1 v/v). The 20-mer was thermolytically cleaved from the support upon heating at 90 °C in 1 × PBS (pH 7.2) for 2 h. Chromatographic conditions are described in the Experimental Procedures section.

phosphatase (6 μL, 0.7 U). The digestion reaction was heated for 16 h in a water bath kept at 37 °C. The digest was finally heated at 100 °C for 1 min to denature the enzymes and was centrifuged at 16 000*g* for 2 min prior to immediate analysis by RP-HPLC. The analysis was performed using a 5 μm Supelcosil LC-18S column (25 cm × 4.6 mm) according to the following conditions: starting from 0.1 M triethylammonium acetate pH 7.0, a linear gradient of 1% MeCN/min is pumped

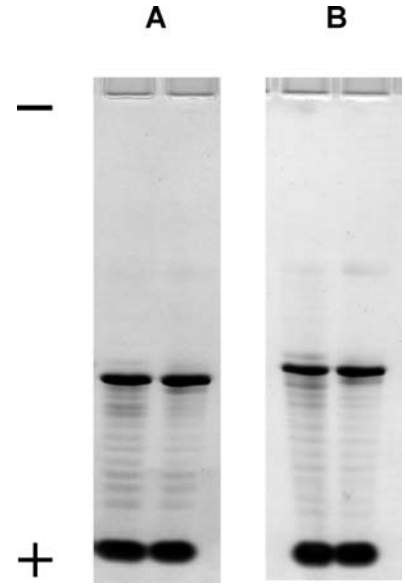

Figure 3. Polyacrylamide gel electrophoresis analysis of unpurified 5′-d(CGACTGTGAATCGATGCCAT) and 5′-d($C_{PS}G_{PS}A_{PS}C_{PS}T_{PS}G_{PS}T_{PS}$-$G_{PS}A_{PS}A_{PS}T_{PS}C_{PS}G_{PS}A_{PS}T_{PS}G_{PS}C_{PS}C_{PS}A_{PS}T$) under denaturing conditions. (A) Left lane; electrophoretic profile of the 20-mer that was synthesized employing unmodified CPG and deprotected under standard conditions, as described in the legend of Figure 1. Right lane: electrophoretic profile of the 20-mer that was synthesized using the CPG support **7** under standard conditions and deprotected as described in the legend of Figure 1. (B) Left lane: electrophoretic profile of the fully phosphorothioated 20-mer that was synthesized employing unmodified CPG and deprotected under standard conditions, as described in the legend of Figure 2. Right lane: electrophoretic profile of the fully phosphorothioated 20-mer that was synthesized using the CPG support **7** under standard conditions and deprotected as recommended in the legend of Figure 2. Electrophoretic conditions are described in the Experimental Procedures section.

at a flow rate of 1 mL/min for 40 min. Peak heights were normalized to the highest peak, which was set to 1 arbitrary unit.

Preparation of CPG-Linked Nucleotide 12. Phosphorodiamidite **4** (B^P = T, 39 mg, 50 μmol), 1-pyrenebutanol (14 mg, 50 μmol), and sublimed 1*H*-tetrazole (11 mg, 150 μmol) were placed in a flame-dried 4-mL glass vial, which was stoppered with a rubber septum and purged with a flow of dry argon. Anhydrous MeCN (300 μL) was syringed into the vial through the rubber septum. The coupling reaction was allowed to proceed for 10 min at ~25 °C to generate the deoxyribonucleoside phosphorotetrazolide intermediate **11** (Scheme 3.) The condensation of **11** with the CPG support **3** (29 mg, 2 μmol) and all subsequent processing steps were performed under conditions identical to those described above for the attachment of dinucleoside phosphorotetrazolide intermediates **6** to CPG support **3**. A fraction of CPG support **12** (2.6 mg, 0.1 μmol) was 5′-dedimethoxytritylated by treatment with 3% TCA in CH_2Cl_2 (3 mL, 3 min), washed with MeCN (10 mL), and suspended in 1 × PBS (pH 7.2, 0.5 mL). The suspension was heated for 2 h at 90 ± 2 °C. The RP-HPLC profile of thymidine 3′-*O*-(1-pyrenylbutyl)phosphate is presented in the Supporting Information.

Preparation of CPG-Linked Oligonucleotide 13. 5′-Dedimethoxytritylation of the support-linked deoxyribonucleoside phosphate triester **12** (26 mg, 1 μmol) was effected by slowly pushing 3% TCA in CH_2Cl_2 (3 mL) through the synthesis column over a period of 3 min. Automated solid-phase oligonucleotide synthesis leading to the CPG-linked oligonucleotide **13** (Scheme 3) was carried out according to the general procedure described above when employing CPG support **7**.

Scheme 3. Preparation of CPG Support 13 for the Solid-Phase Synthesis of DNA Oligonucleotide 3′-Conjugates[a]

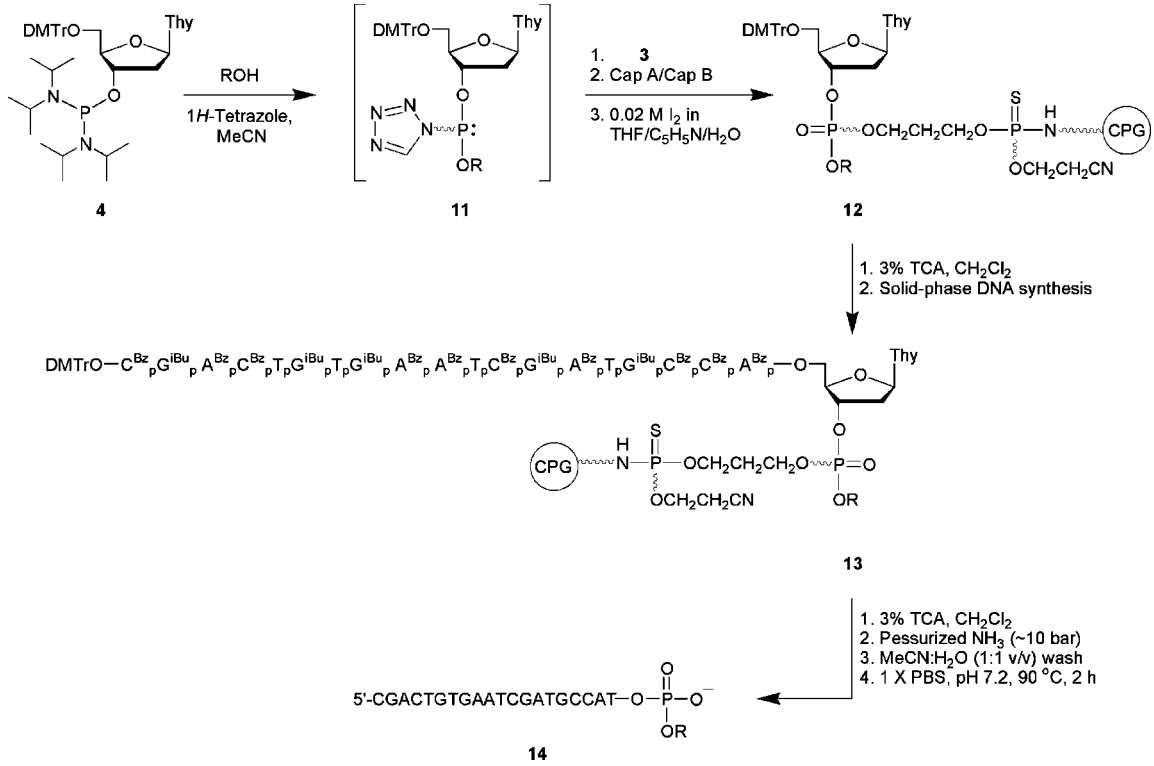

[a] Keys: R, 1-pyrenebutyl; p, 2-cyanoethyl phosphoryl.

Oligonucleotide deprotection and thermolytic release from the CPG support were performed following the general procedure described above for DNA oligonucleotides synthesized from CPG support **7**. The purity of the 3′-pyrenylated DNA oligonucleotide conjugate **14** was greater than 90%, as determined by RP-HPLC (data shown in the Supporting Information). The identity of unpurified and desalted **14** was confirmed by MALDI-TOF MS: Calcd for $C_{215}H_{243}N_{75}O_{121}P_{20}$ $(M-H)^-$ 6432, found 6437.

Preparation of CPG-Linked Dinucleotide 15. A solution of 0.5 M hydrazine hydrate in pyridine/acetic acid (3:2 v/v, 2 mL) was pushed through a synthesis column, packed with the support-linked dinucleoside phosphate triester **7** (0.2 μmol), for a period of 30 min to completely remove the 3′-*O*-levulinyl group. Dry MeCN (20 mL) was flushed through the support by syringe to carefully eliminate residual hydrazinolysis reagents and side-product. A premixed solution of 0.1 M *O*-(2-cyanoethyl)-*O*-(5-hexyn-1-yl)-*N*,*N*-diisopropylphosphoramidite (10 μmol) and 0.45 M 1*H*-tetrazole (67 μmol) in dry MeCN was syringed into the synthesis column. The suspension was manually agitated for 3 min. Excess reagents were discarded with MeCN (10 mL) and a premixed solution of Cap A and Cap B reagents (1 mL each) were syringed through the synthesis column. After a total exposure time of 1 min, the capping reagents were replaced with a solution of 0.02 M iodine in THF/pyridine/H_2O (1 mL). An oxidation time of 1 min was sufficient to complete the preparation of the CPG-linked dinucleotide **15** (Scheme 4).

Preparation of CPG-Linked DNA Oligonucleotide 16. 5′-Dedimethoxtritylation of the CPG-linked dinucleotide **15** was carried out by treatment with 3% TCA in CH_2Cl_2 (3 mL) for 3 min. A 4 mL glass vial containing 0.1 M *O*-(2-cyanoethyl)-*O*-[6-(4-methoxytrityl)amino-1-hexyl]-*N*,*N*-diisopropylphosphoramidite in dry MeCN was connected to the synthesizer at position #5 and was incorporated as such into the DNA synthesis program. The automated solid-phase oligonucleotide synthesis was achieved according to the general procedure delineated above when using CPG support **7**.

Preparation of CPG-Linked DNA Oligonucleotide 17. Removal of the terminal 4-methoxytrityl group from **16** was achieved by passing 3% TCA in CH_2Cl_2 (10 mL) through the synthesis column for a period of 10 min. Excess acid was eliminated from the column with an acetonitrile wash (20 mL) followed by a brief (30 s) Et_3N-MeCN (1:1 v/v) wash (3 mL). The resulting free terminal amino group was acylated with a solution (0.5 mL) of azidoacetic anhydride/pyridine/THF (1:1:8 v/v/v) and Cap B (0.5 mL) to produce the CPG-linked DNA oligonucleotide **17** (Scheme 4). Azidoacetic anhydride was prepared in situ from azidoacetic acid (202 mg, 2.00 mmol) and *N*,*N*′-dicyclohexylcarbodiimide (217 mg, 1.05 mmol) in dry THF (3 mL) under conditions similar to those reported for the preparation of levulinic anhydride (*20*). Oligonucleotide deprotection and thermolytic release from the CPG support were performed following the general procedure described above for DNA oligonucleotides synthesized from the CPG support **7**. The (3′,5′)-heteroconjugated DNA oligonucleotide **18** was RP-HPLC purified using the chromatographic conditions outlined above for the analysis of phosphorothioated DNA oligonucleotides; the RP-HPLC profile of **18** is shown in the Supporting Information. Identity of the desalted oligonucleotide **18** was corroborated by MALDI-TOF MS: Calcd for $C_{209}H_{249}N_{79}O_{125}P_{21}$ $(M-H)^-$ 6517, found 6522.

Conversion of Oligonucleotide 18 to Circular DNA Oligonucleotide 19. The circularization of the DNA oligonucleotide **18** was performed essentially as reported by Kumar et al. (*21*). To a solution of *tris*(benzyltriazolylmethyl)amine (1.4 μmol), sodium ascorbate (2.0 μmol), and $CuSO_4 \cdot 5H_2O$ (0.2 μmol) in 0.2 M NaCl (2.4 mL) was added **18** (5 nmol) in 0.2 M NaCl (100 μL). The reaction mixture was left standing at 25 °C for 2 h and was desalted through

Scheme 4. Preparation of CPG Support 15 for the Solid-Phase Synthesis of DNA Oligonucleotide Functionalized at Both 5′- and 3′-Termini[a]

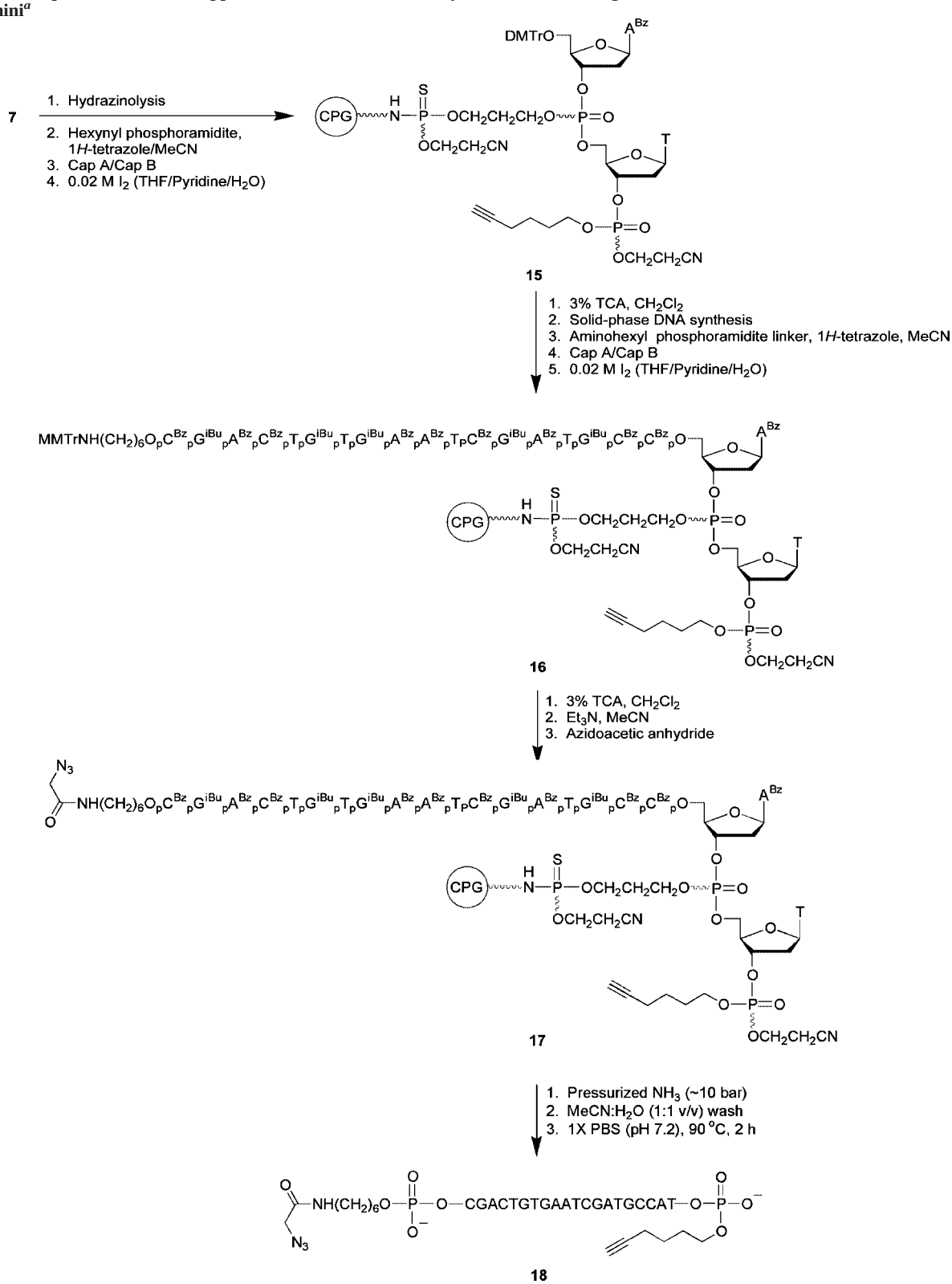

[a] Keys: MMTr, 4-methoxytrityl.

a PD-10 (Sephadex G-25M) column. The crude circular DNA oligonucleotide **19** was RP-HPLC purified under chromatographic conditions similar to those employed for the analysis of phosphorothioated DNA oligonucleotides. The RP-HPLC profile of the purified circular DNA oligonucleotide **19** is shown in the Supporting Information. The RP-HPLC retention time of **19** (t_R = 21.2 min) is shorter than that of **18** (t_R = 23.8 min) but, as expected, the molecular weight of **19**

(MALDI-TOF MS: Calcd for $C_{209}H_{249}N_{79}O_{125}P_{21}$ $(M-H)^-$ 6517, found 6521) is identical to that of **18**.

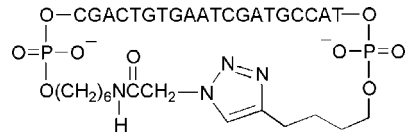

19

RESULTS AND DISCUSSION

Functionalization of CPG through 3-Hydroxypropyl Thiophosphoramidation. The amino groups of long chain alkylamine controlled-pore glass (CPG) were first activated by treatment with a solution of Et_3N in MeCN prior to reaction with a 36 mM solution of *O*-(2-cyanoethyl)-*O*-[3-(4,4′-dimethoxytrityl)oxy-1-propyl]-*N*,*N*-diisopropylphosphoramidite (**1**) and 0.25 M 5-ethylthio-1*H*-tetrazole in dry MeCN. The functionalized support **2** (Scheme 1) was washed with MeCN to remove excess reagents and was immersed into a 0.1 M solution of 1,2-benzodithiol-3-one 1,1-dioxide to oxidize the phosphoramidite entity to a thiophosphoramidate function. The unreacted amino groups of CPG were deactivated upon *N*-acetylation with an equal volume of each of the Cap A (THF/pyridine/Ac_2O) and Cap B (1-methylimidazole/THF) solutions. Subsequent dedimethoxytritylation of the support **2** under acidic conditions revealed an essentially quantitative functionalization of CPG based on an hydroxyl concentration of 69 μmol/g of **3**, which was determined by the standard trityl assay.

Attachment of Leader Dinucleoside Phosphate/Thiophosphate to CPG Support 3. The conversion of CPG support **3** to CPG support **7** began with the preparation of the deoxyribonucleoside phosphorodiamidites **4** (Scheme 1), which was reported in the literature more than 20 years ago (*15*). Typically, a 5′-*O*-(4,4′-dimethoxytrityl)-2′-deoxribonucleoside (B^P = Thy, Cyt^{Bz}, Ade^{Bz}, or Gua^{iBu}) was condensed with bis(*N*,*N*-diisopropylamino)chlorophosphine and *N*,*N*-diisopropylethylamine in anhydrous CH_2Cl_2. Complete phosphinylation was accomplished within 2 h, whereupon the crude reaction product was subjected to aqueous extractive workup and subsequent purification by chromatography on silica gel. It was necessary to equilibrate silica gel in benzene/Et_3N (9:1 v/v) to neutralize its inherent acidity and prevent acid-mediated decomposition of the reaction product. The phororodiamidites **4** were isolated as white foams, which were freed from residual moisture and Et_3N by lyophilization from dry benzene. However, depending on the variable amounts of residual moisture and Et_3N contaminating the purified phosphorodiamidites **4**, it is often preferable to precipitate **4** in cold (−78 °C) hexanes followed by lyophilization of the white precipitates from dry benzene to ensure complete removal of these contaminants. Triethylamine-free **4** were obtained as white powders, the yields of which were in the range 85−95%. The phosphorodiamidites **4** were characterized extensively using one-dimensional ^1H, ^1H decoupled ^{13}C, ^1H and ^{31}P decoupled ^{13}C, and ^{31}P NMR techniques, which were complemented with two-dimensional $^1H-^1H$ total correlation (TOCSY) and $^1H-^{13}C$ correlation (HSQC) data, and accurate mass determination by atmospheric pressure electrospray ionization time-of-flight mass spectrometry (APESI-TOF MS). The selection of an appropriate solvent for NMR characterization of the diamidites **4** is critical; the stability of **4** in a nonpolar solvent, such as benzene, is considerably higher than that observed in the relatively polar DMSO. Thus, NMR analysis of the deoxyribonucleoside phosphorodiamidites **4** was carried out in deuterated benzene (C_6D_6). All characterization data are presented in the Experimental Procedures and Supporting Information sections of this report. When pure, each deoxyribonucleoside phororodiamidite **4** is stable for months at −20 °C.

When phosphorodiamidite **4** (B^P = Thy, Cyt^{Bz}, Ade^{Bz}, or Gua^{iBu}), 3′-*O*-levulinyl-2′-deoxyribonucleoside **5** (B^P = Thy, Cyt^{Bz}, Ade^{Bz}, or Gua^{iBu}), and sublimed 1*H*-tetrazole were mixed together in a respective molar ratio of (1:1:3) in anhydrous MeCN, the putative dinucleoside phosphorotetrazolide **6** (Scheme 1) was generated within 10 min. Without isolation, **6** was mixed with support **3** and was allowed to react for 10 min at ∼25 °C. The support was washed with 20% 1-methylimidazole in H_2O/MeCN (1:1 v/v) to cleave any nucleobase adducts that might have been formed during the coupling reaction. Exposure of the support to an oxidant, namely, 0.05 M 3*H*-1,2-benzodithiol-3-one 1,1-dioxide in MeCN or 0.02 M I_2 in THF/pyridine/H_2O gave CPG support **7** (Scheme 1). The unreacted hydroxyl groups of CPG support **3** were deactivated when reacted with equal volumes of Cap A and Cap B solutions. Under these conditions, the concentration of a dinucleoside phosphate/thiophosphate on CPG support **7** averaged 40 μmol/g of support, as determined by the standard trityl assay, and is comparable to the concentration of deoxyribonucleosides linked to unmodified CPG supports.

Deprotection and release of the dinucleoside phosphate/thiophosphate triester covalently attached to CPG support **7** was initiated to evaluate the purity of each of the sixteen combinatorial dinucleoside phosphorothioate diesters and that of two exemplary dinucleoside phosphate diesters (data shown in the Supporting Information). The deprotection steps included: (i) acid-mediated cleavage of the 5′-*O*-DMTr group and (ii) exposure to pressurized ammonia gas to deprotect the nucleobase, 3′-hydroxyl, and eliminate the 2-cyanoethyl group from the phosphorothioamidate linker. The deprotection side products were conveniently eliminated from the support by washing **8** (Scheme 2) with MeCN/H_2O (1:1 v/v). The support-bound dinucleoside phosphate/thiophosphate triester **8** also served as a model for assessing the thermolytic cleavage of oligonucleotides from the CPG support. The support **8** was suspended in 1 × phosphate buffered saline (PBS, pH 7.2) and the resulting suspension was heated in a closed vial at 90 °C for 2 h. This process induced a thermolytic intramolecular cyclodeesterification reaction (*14*, *22*–*28*) resulting in the release of the dinucleoside phosphate/thiophosphate diester **9** in the aqueous buffer, whereas the putative cyclodeesterification side product remained covalently linked to CPG support **10** (Scheme 2).

Reversed-phase high performance liquid chromatography (RP-HPLC) analysis of dinucleoside phosphate/thiophosphate diesters **9** revealed clean reaction products (data shown in the Supporting Information). The purity of the dinucleoside phosphorothioate and dinucleoside phosphate diesters exceeded 95% and 98%, respectively. These encouraging results prompted the solid-phase synthesis of the native DNA oligonucleotide 5′-d(CGACTGTGAATCGATGCCAT) and that of its fully phosphorothioated analogue 5′-d($C_{PS}G_{PS}A_{PS}C_{PS}T_{PS}G_{PS}T_{PS}G_{PS}A_{PS}A_{PS}T_{PS}C_{PS}G_{PS}A_{PS}T_{PS}G_{PS}C_{PS}C_{PS}A_{PS}T$) employing the thermolytic support **7**.

Solid-Phase Oligonucleotide Synthesis on CPG Support 7 and Thermolytic Release of DNA Oligonucleotides from the Modified CPG Support. Solid-phase synthesis of DNA oligonucleotides employing the thermolytic CPG support **7** and the conventional CPG support was carried out under standard conditions (see Experimental Procedures section). Oligonucleotides sharing identical DNA sequences were prepared to demonstrate comparability of the oligonucleotides produced from the two supports in terms of identity, purity, and overall yields. The DNA oligonucleotides synthesized through CPG support **7** and the unmodified CPG support were deprotected on exposure to pressurized ammonia gas at 25 °C (*19*). After

washing away the deprotection side products from the modified support, DNA oligonucleotides were thermolytically released from the support under the conditions outlined in Scheme 2. RP-HPLC analysis of the unpurified oligonucleotides released from the modified support confirmed the absence of deprotection side products (Figures 1B and 2B) when compared to oligonucleotides prepared from the unmodified CPG support showing contamination with benzamide, one of the deprotection side products (Figures 1A and 2A). The RP-HPLC retention times of either the two native oligonucleoside phosphate diesters or the two oligonucleoside phosphorothioate diesters were identical within experimental variability (Figures 1 and 2). The polyacrylamide gel electrophoresis (PAGE) profiles of the two 20-mers produced from the use of support **7** are comparable to those produced when employing the unmodified CPG support on the basis of the amounts of less than full-length oligonucleotides contaminating the DNA oligonucleotide products (Figure 3). Each unpurified oligonucleotide was also characterized by MALDI-TOF mass spectrometry; mass determination results were consistent with the DNA sequence of each oligonucleotide (see Experimental Procedures section).

The unpurified native oligonucleoside phosphate diesters synthesized from either support **7** or the unmodified CPG support were further characterized by treatment with snake venom phosphodiesterase and bacterial alkaline phosphatase. RP-HPLC analysis of the digests revealed the expected deoxyribonucleosides without detectable nucleobase modification. These results collectively demonstrate that the idendity, purity, and overall yield of DNA oligonucleotides synthesized through the thermolytic CPG support **7** are comparable to those of identical oligonucleotides prepared from an unmodified CPG support.

Solid-Phase Synthesis and Thermolytic Release of DNA Oligonucleotides Functionalized with Functional Groups at the 3′-Terminus or at Both 5′- And 3′-Termini. The functionalization of the 3′-terminus or both 5′- and 3′-termini of DNA oligonucleotides with various functional groups is useful in the preparation of bioconjugates or in applications where both termini are required to achieve a specific function. The functionalization of a DNA oligonucleotide (20-mer) synthesized through the use of CPG support **7** was attempted after hydrazinolysis of the 3′-terminal levulinyl group. Phosphinylation of the free 3′-hydroxyl group with a commercial fluorescein-labeled phosphoramidite was unsuccessful presumably due to intermolecular crowding near the surface of the support that is commensurate with the chain length of neighboring oligonucleotides. A convenient method for the functionalization of oligonucleotides at the 3′-terminus consisted of generating a deoxyribonucleoside phosphorotetrazolide functionalized with a ligand, in situ, and covalently attaching the modified phosphorotetrazolide to CPG support **3** (Scheme 3). The ligand must however be compatible with the conditions used during oligonucleotide synthesis, oligonucleotide deprotection, and thermolytic release of the oligonucleotide from the support. Typically, condensation of the deoxyribonucleoside phosphorodiamidite **4** (B^P = Thy) with and equimolar amount of 1-pyrenebutanol and 3 molar equiv of sublimed 1*H*-tetrazole in anhydrous MeCN resulted in the formation of the pyrenylated deoxyribonucleoside phosphorotetrazolide **11** (Scheme 3) within 10 min. The hydroxylated support **3** was mixed with **11** and was allowed to react for 10 min at ~25 °C. The functionalized CPG support **12** was obtained after treatment with 20% 1-methylimidazole in H_2O/MeCN (1:1 v/v) to cleave any nucleobase adducts that might have been formed during the coupling reaction, and after oxidation effected by 0.02 M I_2 in THF/pyridine/H_2O. The unreacted CPG support **3** was suspended in Cap A/Cap B (1:1 v/v) solutions to acetylate any free hydroxyls. 5′-Dedimethoxytritylation of **12** under acidic conditions and spectrophotometric determination of the 4,4′-dimethoxytrityl cation at 498 nm indicated that the concentration of the pyrenylated deoxyribonucleoside phosphate, covalently attached to the CPG support, was 38 μmol/g of **12**. A small fraction of the CPG support **12** was heated in 1 × PBS (pH 7.2) at 90 °C for 2 h to release thymidine 3′-*O*-(1-pyrenebutyl) phosphate, the identity and purity of which was demonstrated by RP-HPLC analysis at 260 and 340 nm (data shown in the Supporting Information). The characteristic UV absorptivity of 1-pyrenebutanol at 340 nm and the absence of absorptivity at 260 nm allows for the unambiguous identification of pyrenylated nucleic acid conjugates.

Solid-phase oligonucleotide synthesis employing the CPG support **12** was carried out on a 0.2 μmol scale using commercial deoxyribonucleoside 3′-phosphoramidites under standard conditions. After the final 5′-*O*-dedimethoxytritylation, oligonucleotide deprotection was initiated by exposing the solid support to pressurized ammonia gas to cleave the nucleobase and the 2-cyanoethyl phosphate protecting groups. Removal of the deprotection side products was effected by washing the CPG support with MeCN/H_2O (1:1 v/v). The support-linked oligonucleotide was heated in 1 × PBS (pH 7.2) at 90 °C for 2 h to release the DNA oligonucleotide conjugate **14**, the identity of which was confirmed by MALDI-TOF mass spectrometry. RP-HPLC profiles of **14** at 260 nm and at 340 nm confirmed the presence of the pyrenyl group in the conjugate and captured the purity of the pyrenylated DNA oligonucleotide, which was 78% based on total peak area at 260 nm (data shown in the Supporting Information).

The versatility of this approach to the preparation of DNA oligonucleotide 3′-conjugates enables one to employ a large variety of commercial hydroxylated ligands or functional groups in the synthesis of these biomolecules, thereby avoiding the restrictions created by the use of commercial supports functionalized with a limited number of ligands or functional groups.

Solid-Phase Synthesis and Thermolytic Release of DNA Oligonucleotides Conjugated with Functional Groups at the 3′-Terminus or at Both 5′- And 3′-Termini. CPG support **7** can also be employed in the solid-phase synthesis of DNA oligonucleotides conjugated with functional groups at both 5′- and 3′-termini (Scheme 4). Hydrazinolysis of **7** followed by condensation of the free 3′-hydroxyl group with *O*-(2-cyanoethyl)-*O*-(5-hexyn-1-yl)-*N*,*N*-diisopropylphosphoramidite and 1*H*-tetrazole in MeCN produced the corresponding 3′-phosphite. Unreacted 3′-hydroxyls were acylated when treated with the Cap A/Cap B solutions and oxidation of the 3′-phosphite to the desired CPG-support **15** was effected by a solution of 0.02 M I_2 in THF/pyridine/water. 5′-Dedimethoxytritylation of **15** was performed under acidic conditions and the solid-phase synthesis of an oligonucleotide sharing a DNA sequence identical to that of conjugate **13** was initiated. Phosphitylation of the terminal 5′-hydroxyl with *O*-(2-cyanoethyl)-*O*-[6-(4-methoxytrityl)amino-1-hexyl]-*N*,*N*-diisopropylphosphoramidite in the presence of 1*H*-tetrazole gave the solid support-bound oligonucleotide **16** after standard capping and oxidation steps. Removal of the 5′-monomethoxytrityl group under acidic conditions followed by acylation of the aminoalkylated oligonucleotide by treatment with azidoacetic anhydride, generated in situ from azidoacetic acid and *N*,*N*′-dicyclohexylcarbodiimide in THF, afforded the CPG-linked oligonucleotide **17** carrying azido and alkynyl groups at the 5′- and 3′-terminus, respectively. Oligonucleotide deprotection was carried out by exposing the solid support to pressurized ammonia gas to remove the nucleobase and phosphate protecting groups, which were discarded by washing the solid support with MeCN/H_2O (1:1 v/v). The deprotected, support-linked oligonucleotide was heated in 1 × PBS at 90

°C for 2 h to release the DNA oligonucleotide **18**. The identity of RP-HPLC-purified **18** was unequivocally confirmed by MALDI-TOF mass spectrometry and the functional characterization of **18** was demonstrated by its circularization through the copper-catalyzed azide-alkyne cycloaddition reaction (*29, 30*). The circularization of **18** was carried out at a concentration of 2 μM in the presence of the Cu(I) catalyst, which was prepared in situ from Cu(II) sulfate pentahydrate, sodium ascorbate, and *tris*(benzyltriazolylmethyl)amine (*30*) in 0.2 M NaCl (*21*). The formation of the cyclic DNA oligonucleotide **19** was assessed by RP-HPLC and MALDI-TOF mass spectrometry (data shown in the Supporting Information).

In summary, the functionalization of long chain alkylamine CPG with an hydroxyalkylated thiophosphoramidate linker produced the CPG support **3**. This support allowed the covalent attachment of combinatorial dinucleoside phosphate/thiophosphate that were generated in situ from activated deoxyribonucleoside phosphorodiamidites (**4**) and 3′-*O*-levulinated deoxyribonucleosides (**5**) to produce the functionalized CPG support **7**, which in turn enabled the solid-phase synthesis of native or modified DNA oligonucleotides. These oligonucleotides can be freed from nucleobase, hydroxyl, and phosphate/thiophosphate protecting groups while being still attached to the support. The very unique feature of CPG support **7** is that fully deprotected DNA oligonucleotides can be released from the support according to a heat-driven cyclodeesterification pathway under nearly neutral conditions. In addition to the orthogonality of oligonucleotide release conditions relative to those employed in conventional solid-phase oligonucleotide synthesis, the versatility of CPG support **7** has been demonstrated in the preparation and full deprotection of a DNA oligonucleotide conjugated with two different functional groups at the 5′- and 3′-termini while still being covalently bound to the support. This approach to the preparation of DNA oligonucleotide conjugates allows the selection of a wide variety of ligands or functional groups in the synthesis of these biomolecules assuming stability of the ligands or functional groups to the conditions employed during synthesis, deprotection, and thermolytic release of the DNA conjugates. The application of the CPG support **3** to the solid-phase synthesis of oligoribonucleotides and their analogues in the context of RNA interference studies is currently being evaluated in our laboratory.

Supporting Information Available: Materials and methods; ^{1}H, ^{13}C, and ^{31}P NMR spectra of deoxyribonucleoside phosphorodiamidites **4**; ^{1}H−^{1}H TOCSY spectra and ^{1}H−^{13}C HSQC spectra of phosphorodiamidites **4**; high resolution mass spectra of phosphorodiamidites **4**; RP-HPLC chromatograms of dinucleoside phosphate diesters and dinucleoside phosphorothioate diesters that were thermolytically released from the CPG support **7**; enlarged Figures 1 and 2; RP-HPLC chromatogram of 5′-d(CGACTGTGAATCGATGCCAT) after treatment with snake venom phosphodiesterase and bacterial alkaline phosphatase; RP-HPLC chromatograms of unpurified thymidine 3′-*O*-(1-pyrenebutyl) phosphate that was thermolytically released from the CPG support **12**; RP-HPLC chromatograms of unpurified 3′-pyrenylated DNA oligonucleotide **14**; RP-HPLC chromatograms of the (3′,5′)-heteroconjugated DNA oligonucleotide **18** and of the circular DNA oligonucleotide **19**. This material is available free of charge via the Internet at http://pubs.acs.org.

LITERATURE CITED

(1) Merrifield, R. B. (1963) Solid phase peptide synthesis. I. The synthesis of a tetrapeptide. *J. Am. Chem. Soc. 85*, 2149–2154.
(2) Merrifield, R. B. (1965) Automated synthesis of peptides. *Science 150*, 178–185.
(3) Letsinger, R. L., and Mahadevan, V. (1965) Oligonucleotide synthesis on a polymer support. *J. Am. Chem. Soc. 87*, 3526–3527.
(4) Letsinger, R. L., and Mahadevan, V. (1966) Stepwise synthesis of oligodeoxyribonucleotides on an insoluble polymer support. *J. Am. Chem. Soc. 88*, 5319–5324.
(5) Beaucage, S. L., and Iyer, R. P. (1992) Advances in the synthesis of oligonucleotides by the phosphoramidite approach. *Tetrahedron 48*, 2223–2311.
(6) Pon, R. T. (2000) Solid-phase supports for oligonucleotide synthesis. *Current Protocols in Nucleic Acid Chemistry*, (Beaucage, S. L., Bergstrom, D. E., Herdewijn, P., and Matsuda, A., Eds.) pp 3.1.1−3.1.28, Vol. 1, John Wiley & Sons, New York.
(7) Seeberger, P. H., and Haase, W.-C. (2000) Solid-phase oligosaccharide synthesis and combinatorial carbohydrate libraries. *Chem. Rev. 100*, 4349–4393.
(8) Seeberger, P. H., and Werz, D. B. (2005) Automated synthesis of oligosaccharides as a basis for drug discovery. *Nat. Rev. Drug Discovery 4*, 751–763.
(9) Hermkens, P. H. H., Ottenheijm, H. C. J., and Rees, D. (1996) Solid-phase organic reactions: A review of the recent literature. *Tetrahedron 52*, 4527–4554.
(10) James, I. W. (1999) Linkers for solid phase organic synthesis. *Tetrahedron 55*, 4855–4946.
(11) Virta, P., Katajisto, J., Niittymäki, T., and Lönnberg, H. (2003) Solid-supported synthesis of oligomeric bioconjugates. *Tetrahedron 59*, 5137–5174.
(12) Beaucage, S. L. (1999) Attachment of reporter and conjugate groups to DNA. *Comprehensive Natural Products Chemistry*, (Barton, D., Nakanishi, K., Meth-Cohn, O., and Kool, E. T., Eds.) pp 153−249, Vol. 7, Elsevier, Oxford.
(13) Synthesis of modified oligonucleotides and conjugates. (2000) *Current Protocols in Nucleic Acid Chemistry* (Beaucage, S. L., Bergstrom, D. E., Herdewijn, P., and Matsuda, A., Eds.) Chapter 4, Vol. *2*, John Wiley & Sons, New York.
(14) Grajkowski, A., Ausín, C., Kauffman, J. S., Snyder, J., Hess, S., Lloyd, J. R., and Beaucage, S. L. (2007) Solid-phase synthesis of thermolytic DNA oligonucleotides functionalized with a single 4-hydroxy-1-butyl or 4-phosphato-/thiophosphato-1-butyl thiophosphate protecting group. *J. Org. Chem. 72*, 805–815.
(15) Marugg, J. E., Burik, A., Tromp, M., van der Mare1, G. A., and van Boom, J. H. (1986) A new and versatile approach to the preparation of valuable deoxynucleoside 3′-phosphite intermediates. *Tetrahedron Lett. 27*, 2271–2274.
(16) Berner, S., Mühlegger, K., and Seliger, H. (1989) Studies on the role of tetrazole in the activation of phosphoramidites. *Nucleic Acids Res. 17*, 853–864.
(17) Iyer, R. P., Phillips, L. R., Egan, W., Regan, J. B., and Beaucage, S. L. (1990) The automated synthesis of sulfur-containing oligodeoxyribonucleotides using 3*H*-1,2-benzodithiol-3-one 1,1-dioxide as a sulfur-transfer reagent. *J. Org. Chem. 55*, 4693–4699.
(18) Regan, J. B., Phillips, L. R., and Beaucage, S. L. (1992) Large-scale preparation of the sulfur-transfer reagent 3*H*-1,2-benzodithiol-3-one 1,1-dioxide. *Org. Prep. Proc. Int. 24*, 488–492.
(19) Boal, J. H., Wilk, A., Harindranath, N., Max, E. E., Kempe, T., and Beaucage, S. L. (1996) Cleavage of oligodeoxyribonucleotides from controlled-pore glass supports and their rapid deprotection by gaseous amines. *Nucleic Acids Res. 24*, 3115–3117.
(20) Hassner, A., Strand, G., Rubinstein, M., and Patchornik, A. (1975) Levulinic esters. Alcohol protecting group applicable to some nucleosides. *J. Am. Chem. Soc. 97*, 1614–1615.
(21) Kumar, R., El-Sagheer, A., Tumpane, J., Lincoln, P., Wilhelmsson, L. M., and Brown, T. (2007) Template-directed oligonucleotide strand ligation, covalent intramolecular DNA circularization and catenation using click chemistry. *J. Am. Chem. Soc. 129*, 6859–6864.
(22) Wilk, A., Grajkowski, A., Phillips, L. R., and Beaucage, S. L. (2000) Deoxyribonucleoside cyclic *N*-acylphosphoramidites as a new class of monomers for the stereocontrolled synthesis of

oligothymidylyl- and oligocytidylyl-phosphorothioates. *J. Am. Chem. Soc. 122*, 2149–2156.

(23) Grajkowski, A., Wilk, A., Chmielewski, M. K., Phillips, L. R., and Beaucage, S. L. (2001) The 2-(*N*-formyl-*N*-methyl)aminoethyl group as a potential phosphate/thiophosphate protecting group in solid-phase oligodeoxyribonucleotide synthesis. *Org. Lett. 3*, 1287–1290.

(24) Wilk, A., Chmielewski, M. K., Grajkowski, A., Phillips, L. R., and Beaucage, S. L. (2001) The 4-oxopentyl group, as a labile phosphate/thiophosphate protecting group for synthetic oligodeoxyribonucleotides. *Tetrahedron Lett. 42*, 5635–5639.

(25) Wilk, A., Chmielewski, M. K., Grajkowski, A., Phillips, L. R., and Beaucage, S. L. (2002) The 3-[(*N*-*tert*-butyl)carboxamido]-1-propyl group as an attractive phosphate/thiophosphate protecting group for solid-phase oligodeoxyribonucleotide synthesis. *J. Org. Chem. 67*, 6430–6438.

(26) Chmielewski, M. K., Marchán, V., Cieślak, J., Grajkowski, A., Livengood, V., Münch, U., Wilk, A., and Beaucage, S. L. (2003) Thermolytic carbonates for potential 5′-hydroxyl protection of deoxyribonucleosides. *J. Org. Chem. 68*, 10003–10012.

(27) Cieślak, J., and Beaucage, S. L. (2003) Thermolytic properties of 3-(2-pyridyl)-1-propyl and 2-[*N*-methyl-*N*-(2-pyridyl)]aminoethyl phosphate/thiophosphate protecting groups in solid-phase synthesis of oligodeoxyribonucleotides. *J. Org. Chem. 68*, 10123–10129.

(28) Cieślak, J., Grajkowski, A., Livengood, V., and Beaucage, S. L. (2004) The thermolytic 4-methylthio-1-butyl group for phosphate/thiophosphate protection in solid-phase synthesis of DNA oligonucleotides. *J. Org. Chem. 69*, 2509–2515.

(29) Rostovtsev, V. V., Green, L. G., Fokin, V. V., and Sharpless, K. B. (2002) A stepwise Huisgen cycloaddition process: Copper(I)-catalyzed regioselective "ligation" of azides and terminal alkynes. *Angew. Chem., Int. Ed. 41*, 2596–2599.

(30) Chan, T. R., Hilgraf, R., Sharpless, K. B., and Fokin, V. V. (2004) Polytriazoles as copper(I) stabilizing ligands in catalysis. *Org. Lett. 6*, 2853–2855.

BC800189E

Supporting Information Available

Functionalization of Long Chain Alkylamine Controlled-Pore Glass for Thermolytic Release of DNA Oligonucleotides and Their Conjugates

Andrzej Grajkowski,[‡] *Jacek Cieślak,*[‡] *Jon S. Kauffman,*[§] *Robert Duff,*[§] *Scott Norris,*[#]

Darón I. Freedberg,[#] *and Serge L. Beaucage**[‡]

[‡]Division of Therapeutic Proteins, Center for Drug Evaluation and Research, and [#]Division of Bacterial, Parasitic & Allergenic Products, Center for Biologics Evaluation and Research, Food and Drug Administration, 8800 Rockville Pike, Bethesda, Maryland 20892, and [§]Lancaster Laboratories, 2425 New Holland Pike, Lancaster, PA 17605

Table of Contents

Materials and Methods……..S03
700 MHz ^{1}H NMR spectrum of 5'-*O*-(4,4'-dimethoxytrityl)-
3'-*O*-bis(*N*,*N*-diisopropylamino)phosphinyl-2'-deoxythymidine in C_6D_6……... S05
175 MHz ^{13}C NMR spectrum of 5'-*O*-(4,4'-dimethoxytrityl)-
3'-*O*-bis(*N*,*N*-diisopropylamino)phosphinyl-2'-deoxythymidine in C_6D_6……... S05
300 MHz ^{1}H-^{1}H TOCSYspectrum of 5'-*O*-(4,4'-dimethoxytrityl)-
3'-*O*-bis(*N*,*N*-diisopropylamino)phosphinyl-2'-deoxythymidine in C_6D_6……... S06
700 MHz ^{1}H-13C HSQC spectrum of 5'-*O*-(4,4'-dimethoxytrityl)-
3'-*O*-bis(*N*,*N*-diisopropylamino)phosphinyl-2'-deoxythymidine in C_6D_6……... S06
121 MHz ^{31}P NMR spectrum of 5'-*O*-(4,4'-dimethoxytrityl)-
3'-*O*-bis(*N*,*N*-diisopropylamino)phosphinyl-2'-deoxythymidine in C_6D_6……... S07
700 MHz ^{1}H NMR spectrum of N^4-benzoyl-5'-*O*-(4,4'-dimethoxytrityl)-
3'-*O*-bis(*N*,*N*-diisopropylamino)phosphinyl-2'-deoxycytidine in C_6D_6…….....S07
175 MHz ^{13}C NMR spectrum of N^4-benzoyl-5'-*O*-(4,4'-dimethoxytrityl)-
3'-*O*-bis(*N*,*N*-diisopropylamino)phosphinyl-2'-deoxycytidine in C_6D_6…….....S08
300 MHz ^{1}H-^{1}H TOCSYspectrum of N^4-benzoyl-5'-*O*-(4,4'-dimethoxytrityl)-
3'-*O*-bis(*N*,*N*-diisopropylamino)phosphinyl-2'-deoxycytidine in C_6D_6…….....S08
700 MHz ^{1}H-13C HSQC spectrum of N^4-benzoyl-5'-*O*-(4,4'-dimethoxytrityl)-
3'-*O*-bis(*N*,*N*-diisopropylamino)phosphinyl-2'-deoxycytidine in C_6D_6…….....S09
121 MHz ^{31}P NMR spectrum of N^4-benzoyl-5'-*O*-(4,4'-dimethoxytrityl)-
3'-*O*-bis(*N*,*N*-diisopropylamino)phosphinyl-2'-deoxycytidine in C_6D_6…….....S09

700 MHz ^{1}H NMR spectrum of N^6-benzoyl-5'-*O*-(4,4'-dimethoxytrityl)-
3'-*O*-bis(*N*,*N*-diisopropylamino)phosphinyl-2'-deoxyadenosine in C_6D_6……....S10
175 MHz ^{13}C NMR spectrum of N^6-benzoyl-5'-*O*-(4,4'-dimethoxytrityl)-
3'-*O*-bis(*N*,*N*-diisopropylamino)phosphinyl-2'-deoxyadenosine in C_6D_6……....S10
300 MHz ^{1}H-^{1}H TOCSYspectrum of N^6-benzoyl-5'-*O*-(4,4'-dimethoxytrityl)-
3'-*O*-bis(*N*,*N*-diisopropylamino)phosphinyl-2'-deoxyadenosine in C_6D_6……....S11
700 MHz ^{1}H-13C HSQC spectrum of N^6-benzoyl-5'-*O*-(4,4'-dimethoxytrityl)-
3'-*O*-bis(*N*,*N*-diisopropylamino)phosphinyl-2'-deoxyadenosine in C_6D_6……....S11
121 MHz ^{31}P NMR spectrum of N^6-benzoyl-5'-*O*-(4,4'-dimethoxytrityl)-
3'-*O*-bis(*N*,*N*-diisopropylamino)phosphinyl-2'-deoxyadenosine in C_6D_6……....S12
700 MHz ^{1}H NMR spectrum of N^2-isobutyryl-5'-*O*-(4,4'-dimethoxytrityl)-
3'-*O*-bis(*N*,*N*-diisopropylamino)phosphinyl-2'-deoxyguanosine in C_6D_6…….... S12
175 MHz ^{13}C NMR spectrum of N^2-isobutyryl-5'-*O*-(4,4'-dimethoxytrityl)-
3'-*O*-bis(*N*,*N*-diisopropylamino)phosphinyl-2'-deoxyguanosine in C_6D_6……... S13
300 MHz ^{1}H-^{1}H TOCSYspectrum of N^2-isobutyryl-5'-*O*-(4,4'-dimethoxytrityl)-
3'-*O*-bis(*N*,*N*-diisopropylamino)phosphinyl-2'-deoxyguanosine in C_6D_6……... S13
700 MHz ^{1}H-13C HSQC spectrum of N^2-isobutyryl-5'-*O*-(4,4'-dimethoxytrityl)-
3'-*O*-bis(*N*,*N*-diisopropylamino)phosphinyl-2'-deoxyguanosine in C_6D_6……... S14
121 MHz ^{31}P NMR spectrum of N^2-isobutyryl-5'-*O*-(4,4'-dimethoxytrityl)-
3'-*O*-bis(*N*,*N*-diisopropylamino)phosphinyl-2'-deoxyguanosine in C_6D_6……... S14
APESI-TOF MS spectrum of 5'-*O*-(4,4'-dimethoxytrityl)-
3'-*O*-bis(*N*,*N*-diisopropylamino)phosphinyl-2'-deoxythymidine.……S15
APESI-TOF MS spectrum of N^4-benzoyl-5'-*O*-(4,4'-dimethoxytrityl)-
3'-*O*-bis(*N*,*N*-diisopropylamino)phosphinyl-2'-deoxycytidine.……...S15
APESI-TOF MS spectrum of N^6-benzoyl-5'-*O*-(4,4'-dimethoxytrityl)-
3'-*O*-bis(*N*,*N*-diisopropylamino)phosphinyl-2'-deoxyadenosine.……S16
APESI-TOF MS spectrum of N^2-isobutyryl-5'-*O*-(4,4'-dimethoxytrityl)-
3'-*O*-bis(*N*,*N*-diisopropylamino)phosphinyl-2'-deoxyguanosine.……S16
RP-HPLC chromatograms of dinucleoside phosphate diesters that were
thermolytically released from the CPG support **7**.....S17
RP-HPLC Chromatograms of Dinucleoside Phosphorothioates that were
Thermolytically Released from the CPG support **7**……...S18
Enlarged Figure 1.……S20
Enlarged Figure 2.……S21
CHART 1. RP-HPLC analysis of unpurified 5'-d(CGACTGTGAATCGATGCCAT)
after treatment with SVP and bacterial alkaline phosphatase..……S22
CHART 2. RP-HPLC chromatograms of thymidine 3'-*O*-(1-pyrenebutyl) phosphate
that was thermolytically released from the CPG support **12**…… S23
CHART 3. RP-HPLC analysis of unpurified 3'-pyrenylated DNA oligonucleotide **14**..……S24
CHART 4. RP-HPLC analysis of the conversion of the (3',5')-heteroconjugated
DNA oligonucleotide **18** to the circular DNA oligonucleotide **19**
under "click chemistry" conditions.……..S25

Materials and Methods. Common chemicals and solvents in addition to bromoacetic acid 3*H*-1,2-benzodithiol-3-one 1,1-dioxide, Et_3N, *i*-Pr_2NEt, tripropargyl amine, benzyl azide, sodium azide, 2,6-lutidine, *O*-(2-cyanoethyl)-*O*-[3-(4,4'-dimethoxytrityl)oxy-1-propyl]-*N*,*N*-diisopropylphosphoramidite, 2-cyanoethyl-*N*,*N*-diisopropylchlorophosphoramidite, *O*-(2-cyanoethyl)-*O*-(5-hexyn-1-yl)-*N*,*N*-diisopropylphosphoramidite, bis(*N*,*N*-diisopropylamino)chlorophosphine, *O*-(2-cyanoethyl)-*O*-[6-(4-methoxytrityl)amino-1-hexyl]-*N*,*N*-diisopropylphosphoramidite, 500Å Long Chain Alkylamine Controlled-Pore Glass (CPG), tetrakis(acetonitrile)copper(I) hexafluorophosphate, copper(II) sulfate pentahydrate, sodium ascorbate, 2',4',6'-trihydroxyacetophenone monohydrate, 3-hydroxypicolinic acid, ammonium citrate tribasic, 1-methylimidazole, hydrazine hydrate, argon gas cylinder, and lecture bottles of NH_3 and CH_3NH_2 gases were all purchased from commercial sources and used without further purification. Azido acetic acid was prepared from the reaction of bromoacetic acid and sodium azide as described by Dyke, J. M. et al. (*J. Am. Chem. Soc.* **1997**, *119*, 6883-6887). Anhydrous solvents (MeCN, CH_2Cl_2, C_6H_6, pyridine, THF) and deuterated solvents (C_6D_6,) were obtained from reputable sources and used as received.

Reagents for oligonucleotide synthesis including the 5'-Deblocking solution (3% TCA in CH_2Cl_2), the Activator solution (0.25 M 5-ethylthio-1*H*-tetrazole or 0.4 M 1*H*-tetrazole in MeCN), Cap A solution (Ac_2O/pyridine/THF), Cap B solution (10% 1-methylimidazole in THF), and the Oxidizing solution (0.02 M iodine in THF/pyridine/water) were purchased from commercial sources and used as received. Succinyl long chain alkylamine controlled-pore glass functionalized with 5'-*O*-(4,4'-dimethoxytrityl)-2'-deoxythymidine as the leader nucleoside was also obtained from commercial sources and used as is. 2 M Triethylammonium acetate buffer was purchased from Applied Biosystem and diluted to 0.1 M with HPLC grade water prior to use. Snake venom phosphodiesterase (*Crotallus adamanteus*) and bacterial alkaline phosphatase were commercially available and used without further purification.

Preparative chromatographic purifications were performed on glass columns (2.5, 5.0 or 6.5 cm I.D.) packed with silica gel 60 (230-400 mesh), whereas analytical thin-layer chromatography (TLC) analyses were conducted on 2.5 cm × 7.5 cm glass plates coated with a 0.25 mm thick layer of silica gel 60 F_{254}.

RP-HPLC analyses were performed using a 5 μm Supelcosil LC-18S column (25 cm × 4.6 mm) according to the following conditions: starting from 0.1 M triethylammonium acetate pH 7.0, a linear gradient of 1% MeCN/min is pumped at a flow rate of 1 mL/min for 40 min or as indicated. Peak heights are normalized to the highest peak, which is set to 1 arbitrary unit.

All NMR experiments were performed using spectrometers at fields of 300.13 and 700.13 MHz for ^1H, 75.47 and 176.06 MHz for ^{13}C, and 121.5 MHz for ^{31}P. One-dimensional; ^1H, ^{31}P, $^1H/^{31}P$ decoupled ^{13}C, ^1H decoupled ^{13}C, and two-dimensional ^1H-^{13}C correlation (HSQC) data were acquired using a 5 mm QXI (quadruple resonance; ^1H, ^{15}N, ^{13}C, ^{31}P inverse) probe with actively shielded XYZ gradients

on the spectrometer operating at 700 MHz. ^{1}H-^{1}H total correlation (TOCSY) experiments were performed using the spectrometer operating at 300 MHz that is equipped with a TXI (triple resonance; ^{1}H, ^{15}N, ^{13}C inverse) probe with actively shielded XYZ gradients. Samples were maintained at a temperature of 298 °K. All spectra were recorded in C_6D_6 and chemical shifts δ were reported in parts per million (ppm) relative to appropriate internal references.

Accurate mass determination of each deoxyribonucleoside phosphorodiamidite **4** was performed using atmospheric pressure electrospray ionization (APESI) in the positive mode (ES^+). Samples dissolved in MeCN (~60 μg/mL) were infused directly at 2.5 mL/h into a stream of MeCN that flowed at 0.5 mL/min to obtain adequate signal intensity. A calibrant containing known ion of 922 m/z was nebulized into the chamber simultaneously with each sample. Software calibration was performed prior to the analysis to re-align the 922.0098 calibrant mass to the theoretical value. The TOF mass spectrometer was set to accurately measure masses over the range 100 to 1500 m/z. Accurate mass measurements for each sample are reported as the average of five injections.

MALDI-TOF mass spectrometric analyses were performed operating in delayed extraction reflector mode, using 3-hydroxypicolinic acid [50 mg/mL in MeCN/H_2O (1:1 v/v)] or 2',4',6'-trihydroxyacetophenone monohydrate [10 mg/mL in MeCN/H_2O (1:1 v/v)] as a matrix and ammonium citrate (50 mg/mL in H_2O) as a cation exchanger.

700 MHz ^{1}H NMR spectrum of 5'-*O*-(4,4'-dimethoxytrityl)-3'-*O*-bis(*N*,*N*-diisopropylamino)phosphinyl-2'-deoxythymidine in C_6D_6

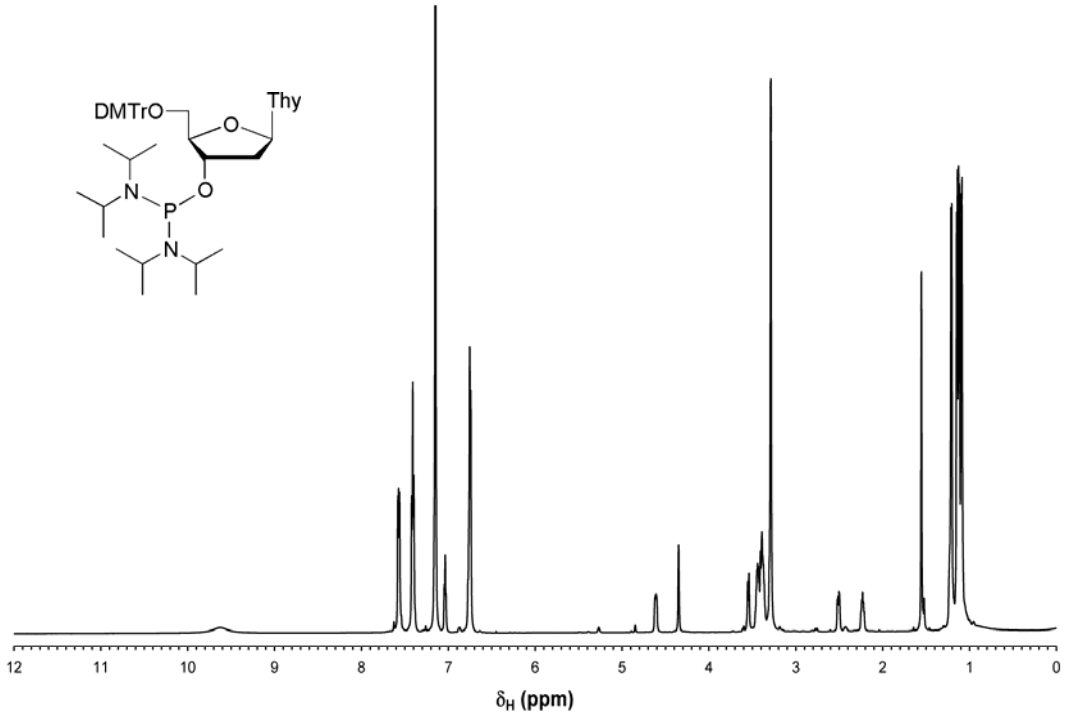

175 MHz ^{13}C NMR spectrum of 5'-*O*-(4,4'-dimethoxytrityl)-3'-*O*-bis(*N*,*N*-diisopropylamino)phosphinyl-2'-deoxythymidine in C_6D_6

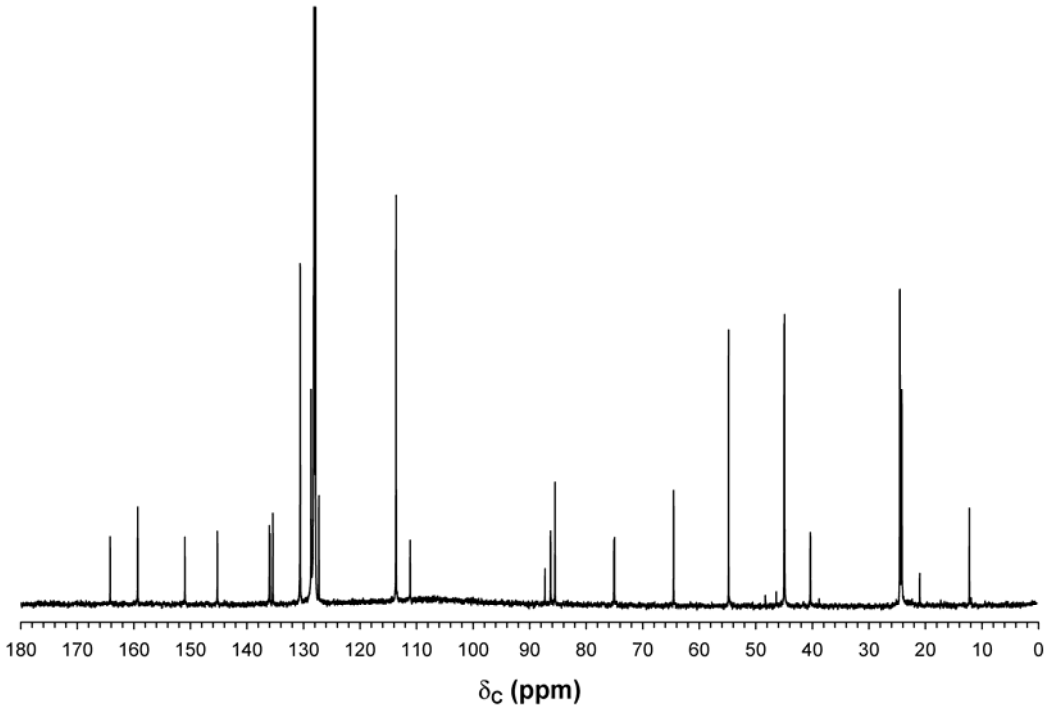

300 MHz ^{1}H-^{1}H TOCSY spectrum of 5'-*O*-(4,4'-dimethoxytrityl)-3'-*O*-bis(*N*,*N*-diisopropylamino)phosphinyl-2'-deoxythymidine in C_6D_6

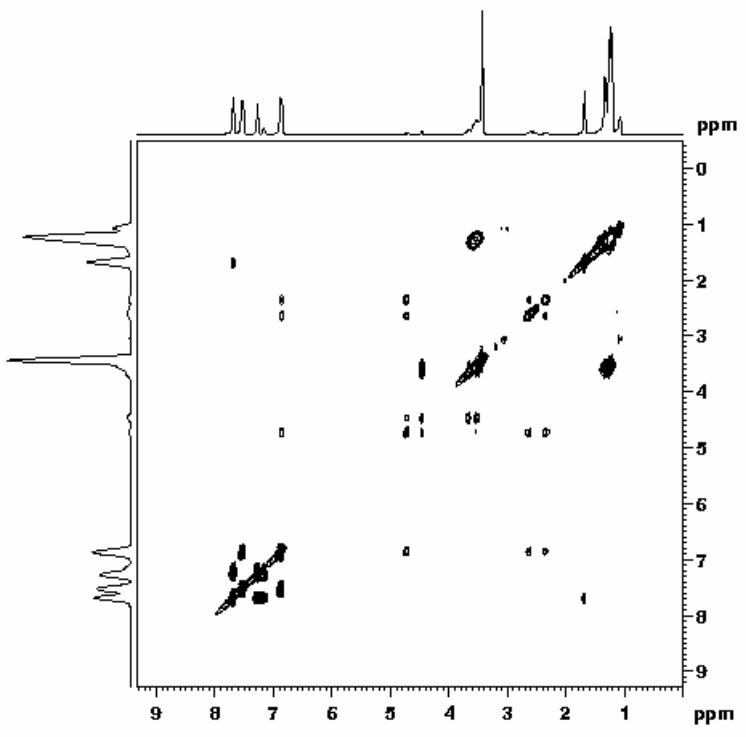

700 MHz ^{1}H-^{13}C HSQC spectrum of 5'-*O*-(4,4'-dimethoxytrityl)-3'-*O*-bis(*N*,*N*-diisopropylamino)phosphinyl-2'-deoxythymidine in C_6D_6

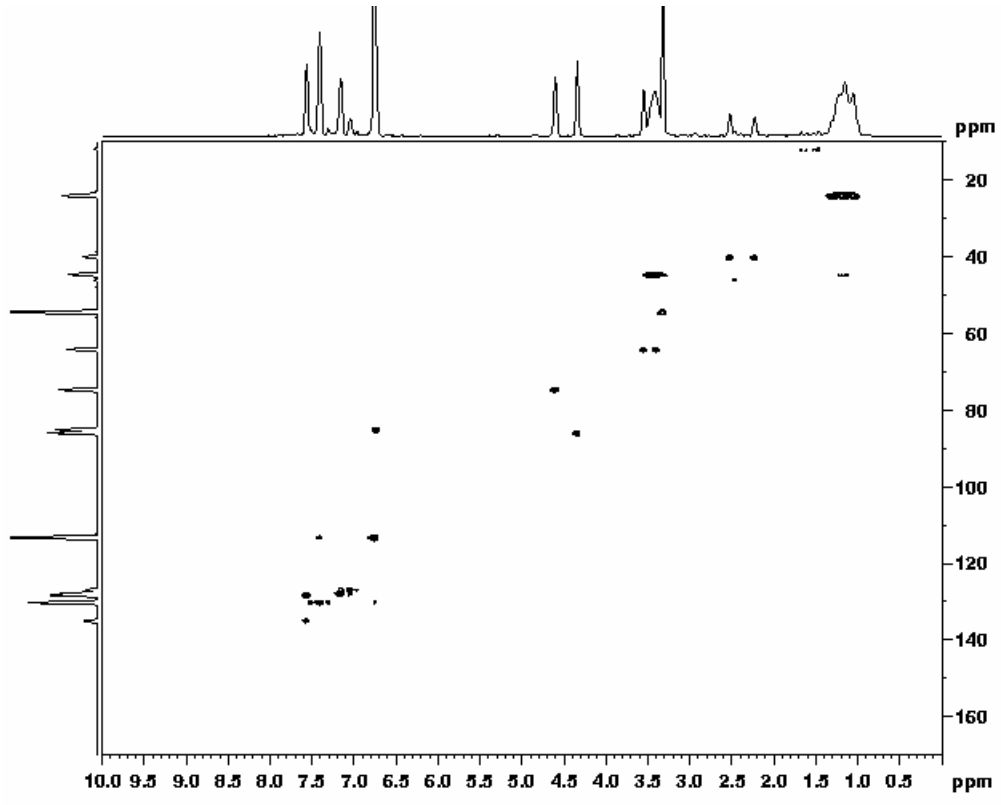

121 MHz ^{31}P NMR spectrum of 5'-*O*-(4,4'-dimethoxytrityl)-3'-*O*-bis(*N*,*N*-diisopropylamino)phosphinyl-2'-deoxythymidine in C_6D_6

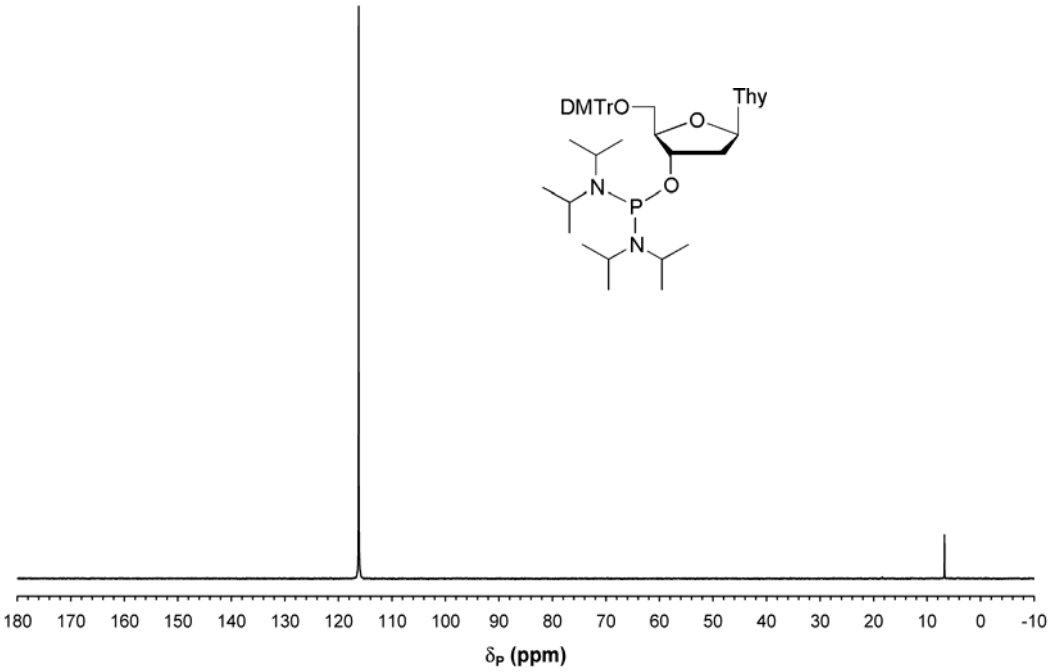

700 MHz ^{1}H NMR spectrum of N^4-benzoyl-5'-*O*-(4,4'-dimethoxytrityl)-3'-*O*-bis(*N*,*N*-diisopropylamino)phosphinyl-2'-deoxycytidine in C_6D_6

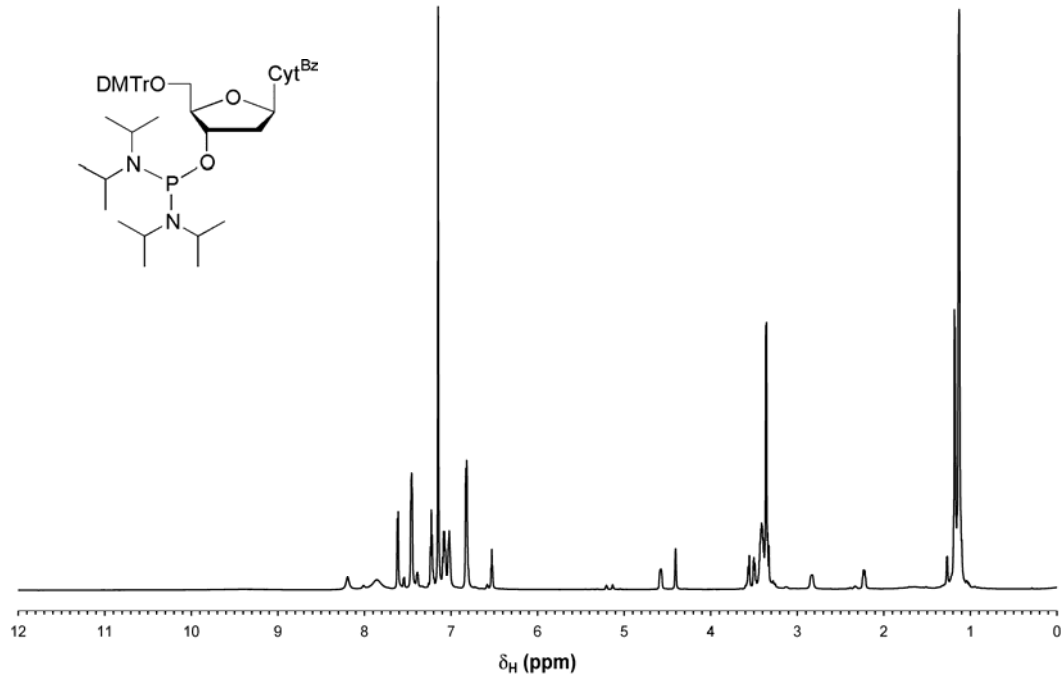

175 MHz ^{13}C NMR spectrum of N^4-benzoyl-5'-*O*-(4,4'-dimethoxytrityl)-3'-*O*-bis(*N*,*N*-diisopropylamino)phosphinyl-2'-deoxycytidine in C_6D_6

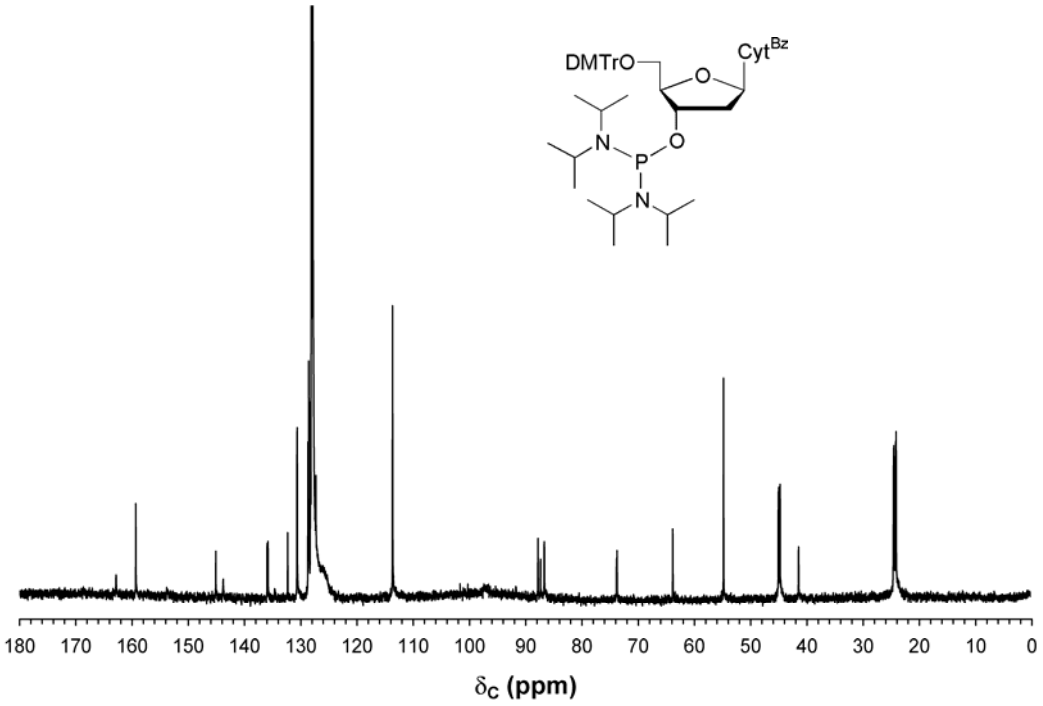

300 MHz ^{1}H-^{1}H TOCSY spectrum of N^4-benzoyl-5'-*O*-(4,4'-dimethoxytrityl)-3'-*O*-bis(*N*,*N*-diisopropylamino)phosphinyl-2'-deoxycytidine in C_6D_6

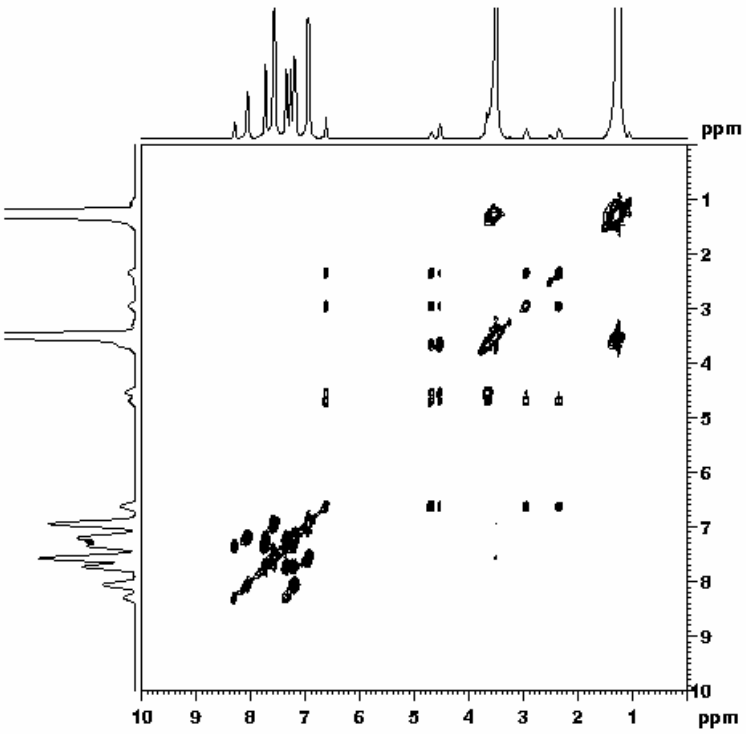

700 MHz ^{1}H-^{13}C HSQC spectrum of N^4-benzoyl-5'-*O*-(4,4'-dimethoxytrityl)-3'-*O*-bis(*N*,*N*-diisopropylamino)phosphinyl-2'-deoxycytidine in C_6D_6

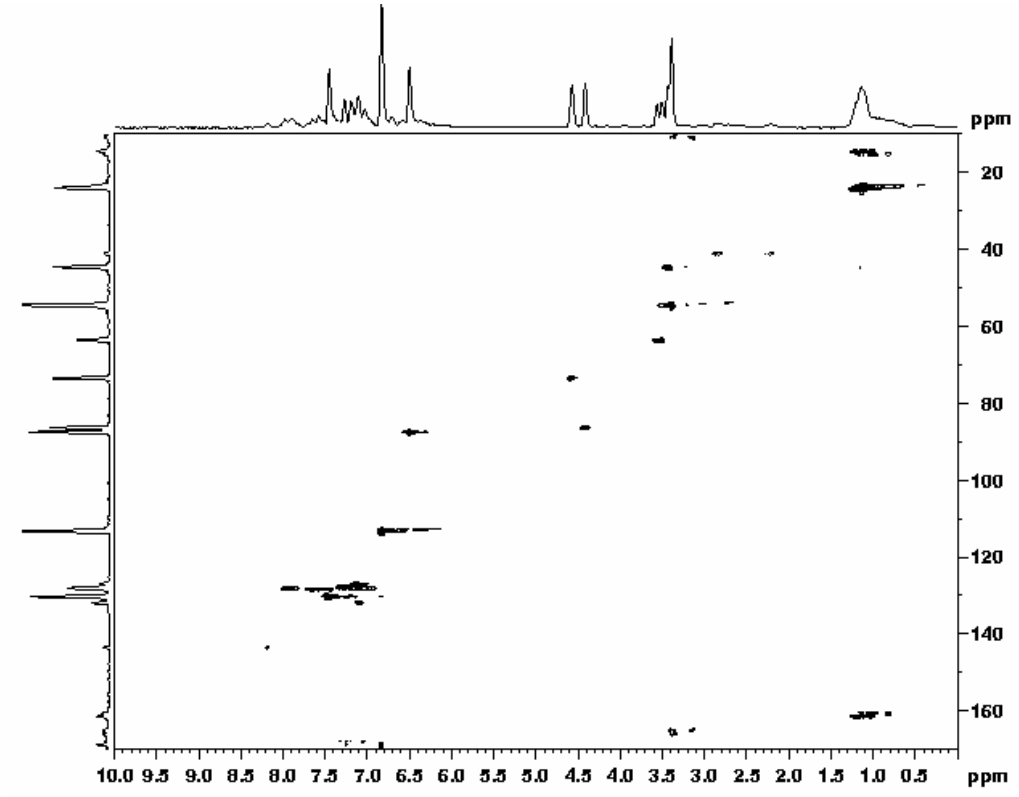

121 MHz ^{31}P NMR spectrum of N^4-benzoyl-5'-*O*-(4,4'-dimethoxytrityl)-3'-*O*-bis(*N*,*N*-diisopropylamino)phosphinyl-2'-deoxycytidine in C_6D_6

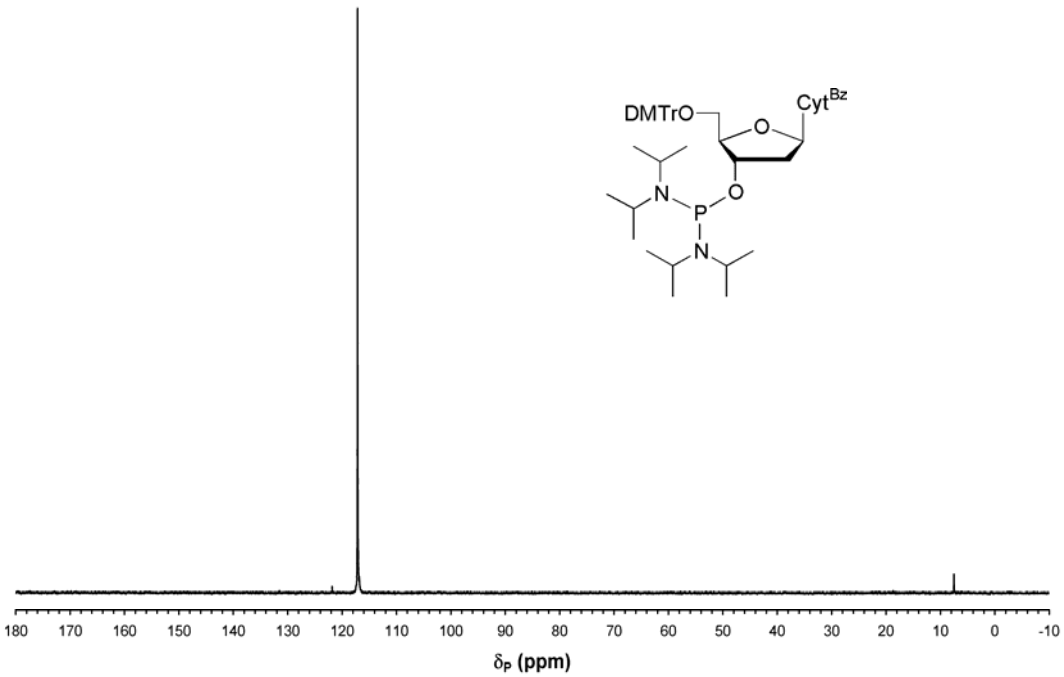

700 MHz ^{1}H NMR spectrum of N^6-benzoyl-5'-*O*-(4,4'-dimethoxytrityl)-3'-*O*-bis(*N*,*N*-diisopropylamino)phosphinyl-2'-deoxyadenosine in C_6D_6

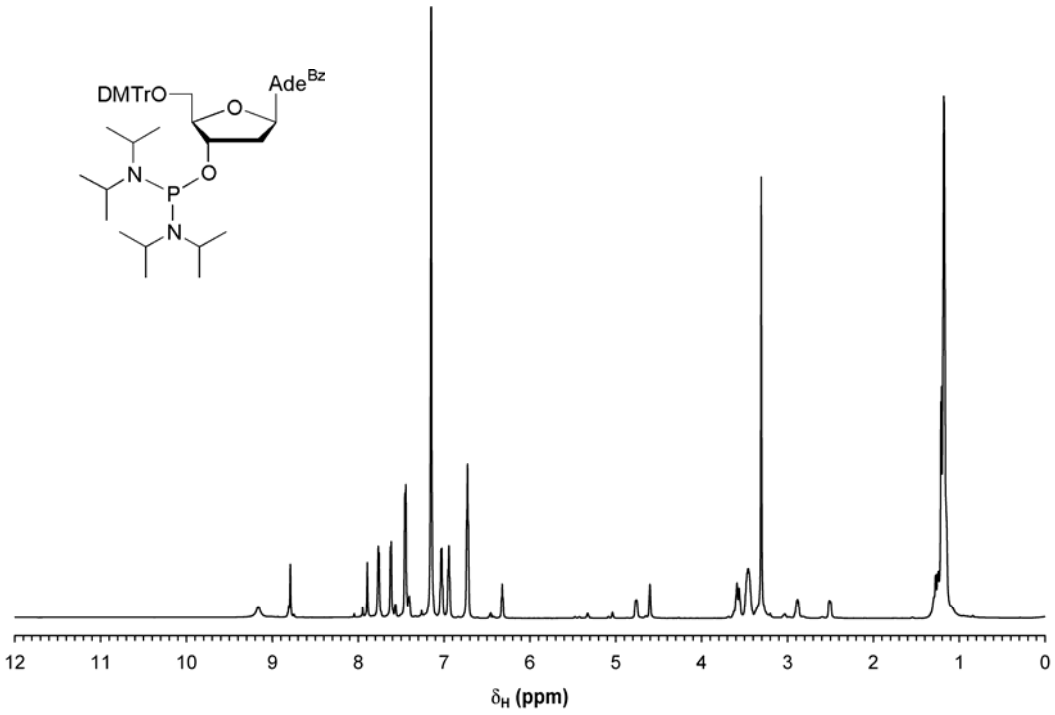

175 MHz ^{13}C NMR spectrum of N^6-benzoyl-5'-*O*-(4,4'-dimethoxytrityl)-3'-*O*-bis(*N*,*N*-diisopropylamino)phosphinyl-2'-deoxyadenosine in C_6D_6

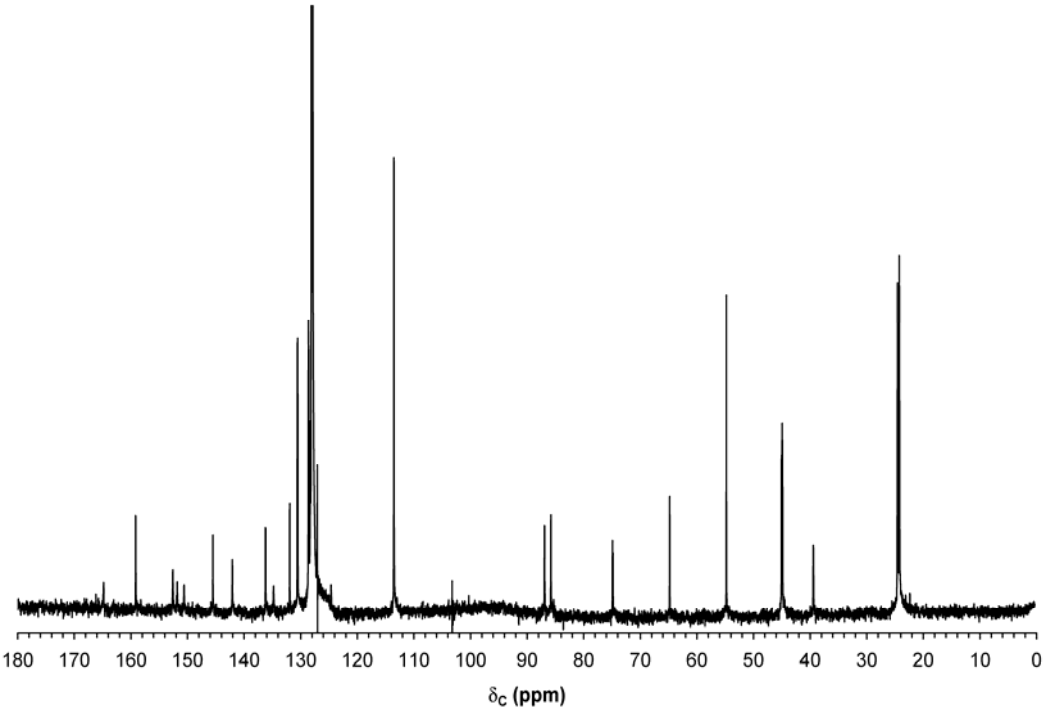

300 MHz ^{1}H-^{1}H TOCSY spectrum of N^{6}-benzoyl-5'-*O*-(4,4'-dimethoxytrityl)-3'-*O*-bis(*N*,*N*-diisopropylamino)phosphinyl-2'-deoxyadenosine in C_6D_6

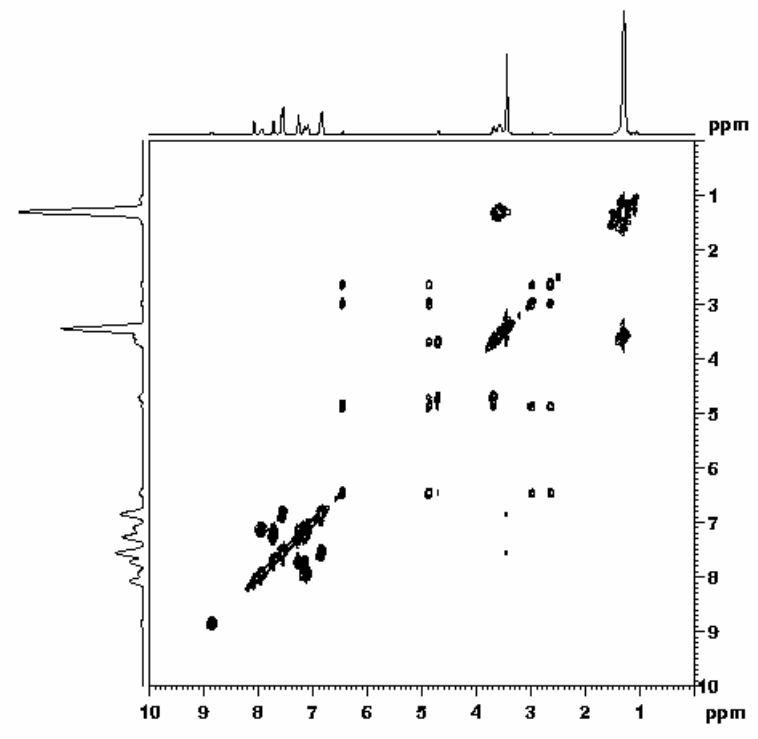

700 MHz ^{1}H-^{13}C HSQC spectrum of N^{6}-benzoyl-5'-*O*-(4,4'-dimethoxytrityl)-3'-*O*-bis(*N*,*N*-diisopropylamino)phosphinyl-2'-deoxyadenosine in C_6D_6

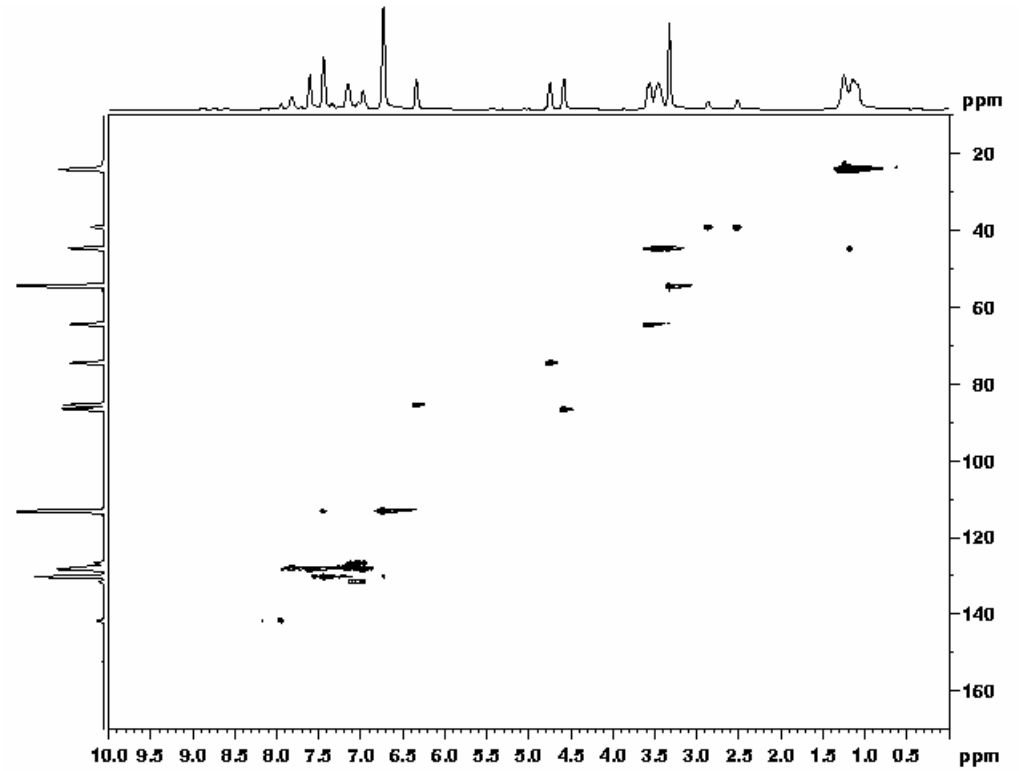

121 MHz ^{31}P NMR spectrum of N^6-benzoyl-5'-*O*-(4,4'-dimethoxytrityl)-3'-*O*-bis(*N*,*N*-diisopropylamino)phosphinyl-2'-deoxyadenosine in C_6D_6

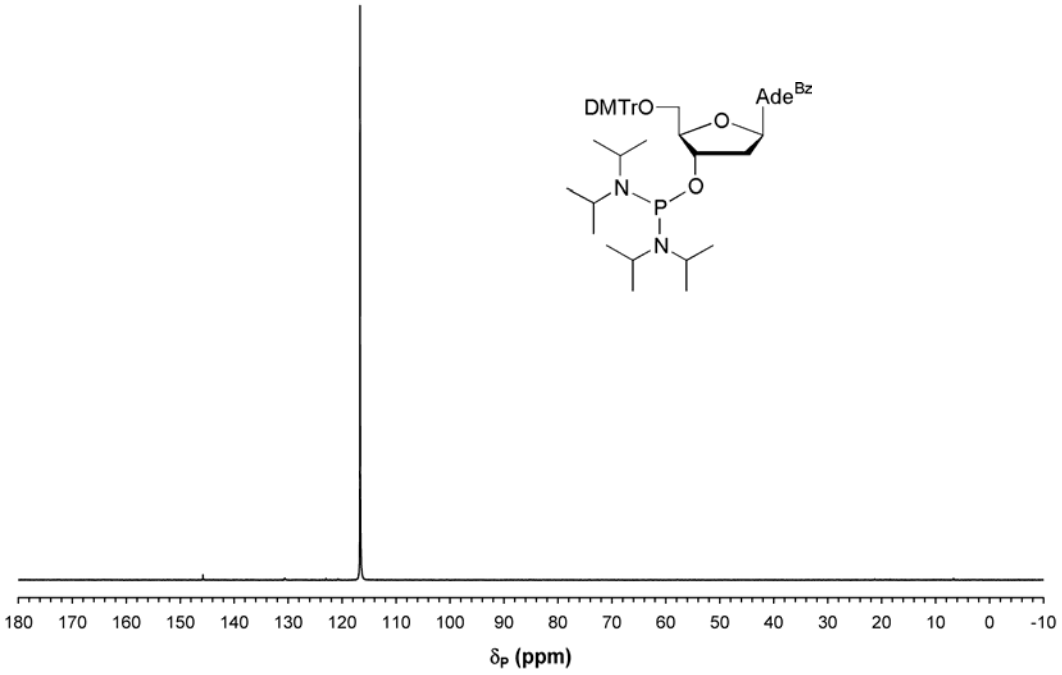

700 MHz ^{1}H NMR spectrum of N^2-isobutyryl-5'-*O*-(4,4'-dimethoxytrityl)-3'-*O*-bis(*N*,*N*-diisopropylamino)phosphinyl-2'-deoxyguanosine in C_6D_6

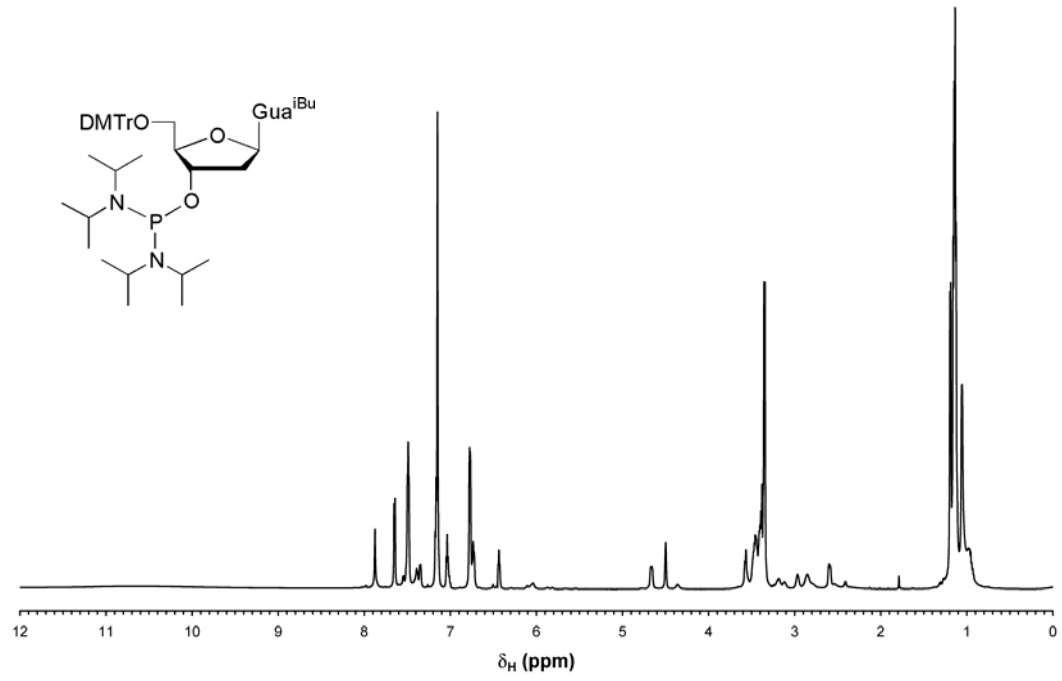

175 MHz ^{13}C NMR spectrum of N^2-isobutyryl-5'-*O*-(4,4'-dimethoxytrityl)-3'-*O*-bis(*N*,*N*-diisopropylamino)phosphinyl-2'-deoxyguanosine in C_6D_6

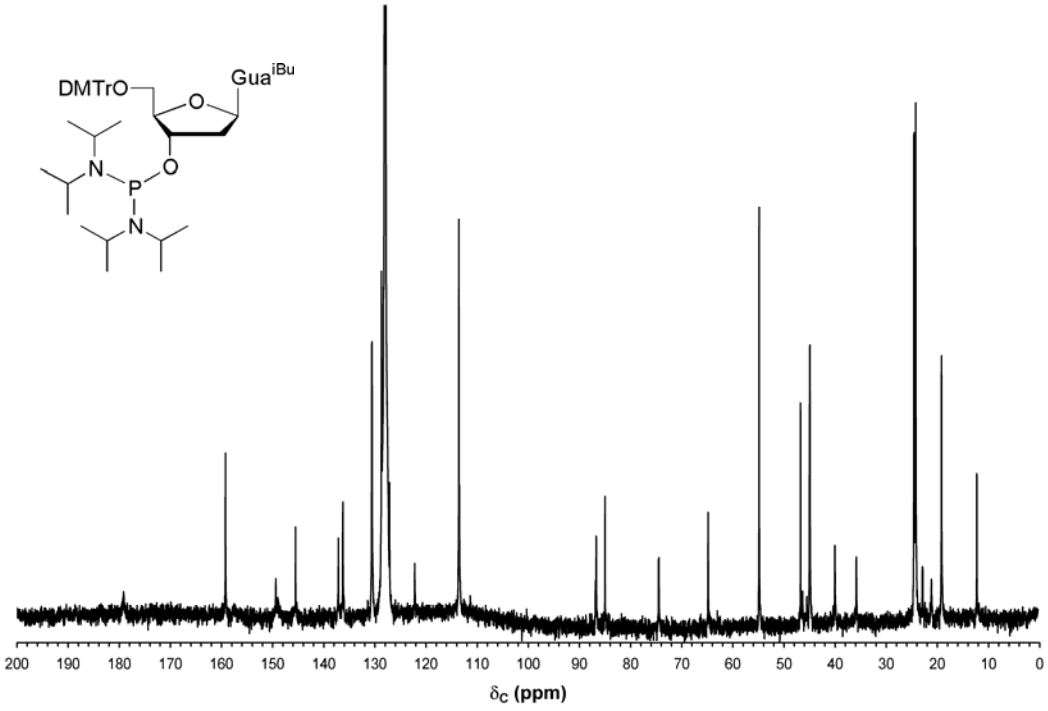

700 MHz ^{1}H-^{1}H TOCSY spectrum of N^2-isobutyryl-5'-*O*-(4,4'-dimethoxytrityl)-3'-*O*-bis(*N*,*N*-diisopropylamino)phosphinyl-2'-deoxyguanosine in C_6D_6

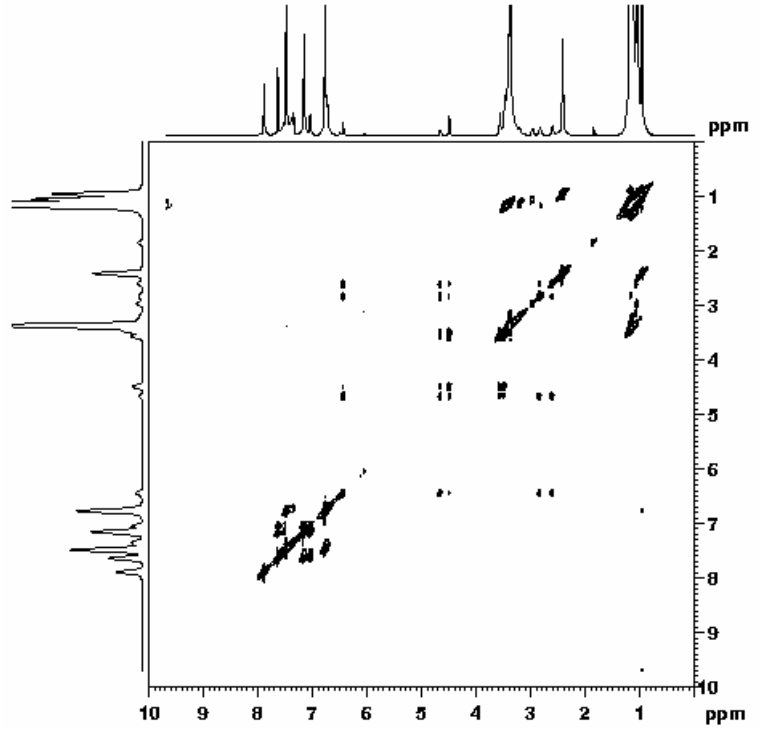

700 MHz ^{1}H-^{13}C HSQC spectrum of *N*^{2}-isobutyryl-5'-*O*-(4,4'-dimethoxytrityl)-3'-*O*-bis(*N*,*N*-diisopropylamino)phosphinyl-2'-deoxyguanosine in C_6D_6

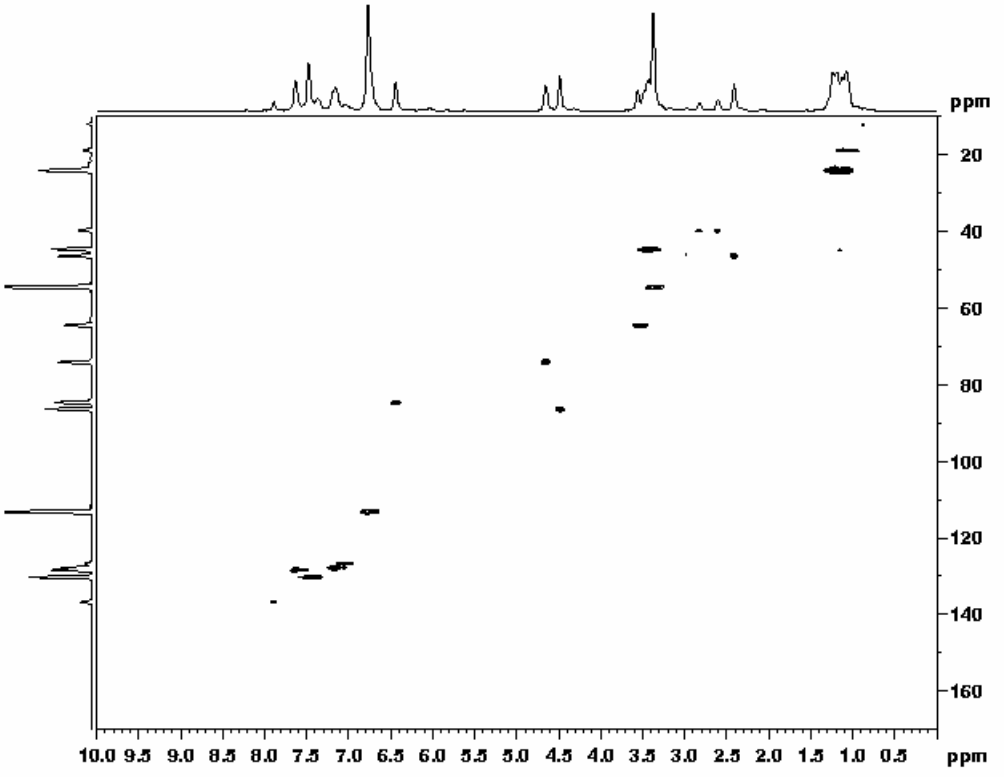

121 MHz ^{31}P NMR spectrum of *N*^{2}-isobutyryl-5'-*O*-(4,4'-dimethoxytrityl)-3'-*O*-bis(*N*,*N*-diisopropylamino)phosphinyl-2'-deoxyguanosine in C_6D_6

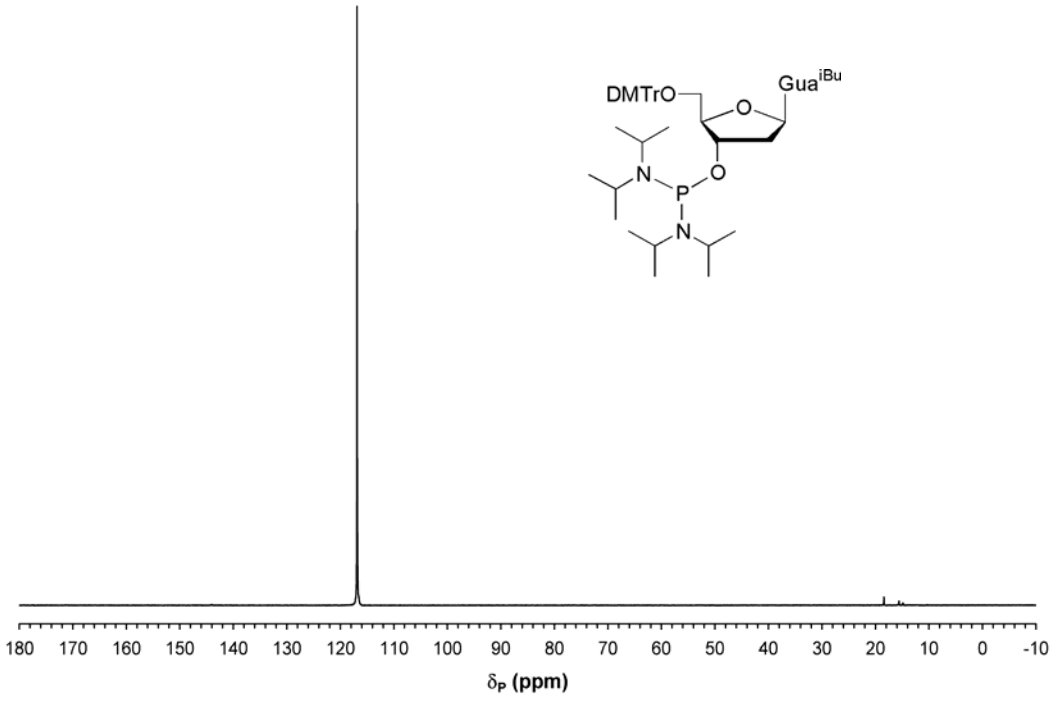

APESI-TOF MS spectrum of 5'-*O*-(4,4'-dimethoxytrityl)-3'-*O*-bis(*N*,*N*-diisopropylamino)phosphinyl-2'-deoxythymidine

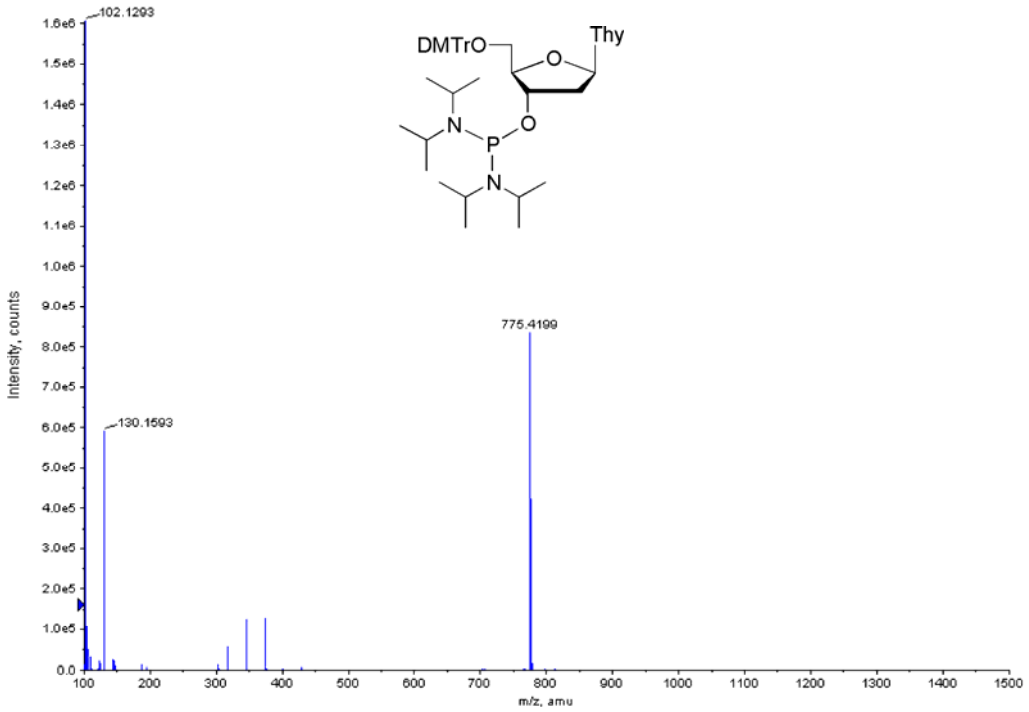

APESI-TOF MS spectrum of N^4-benzoyl-5'-*O*-(4,4'-dimethoxytrityl)-3'-*O*-bis(*N*,*N*-diisopropylamino)phosphinyl-2'-deoxycytidine

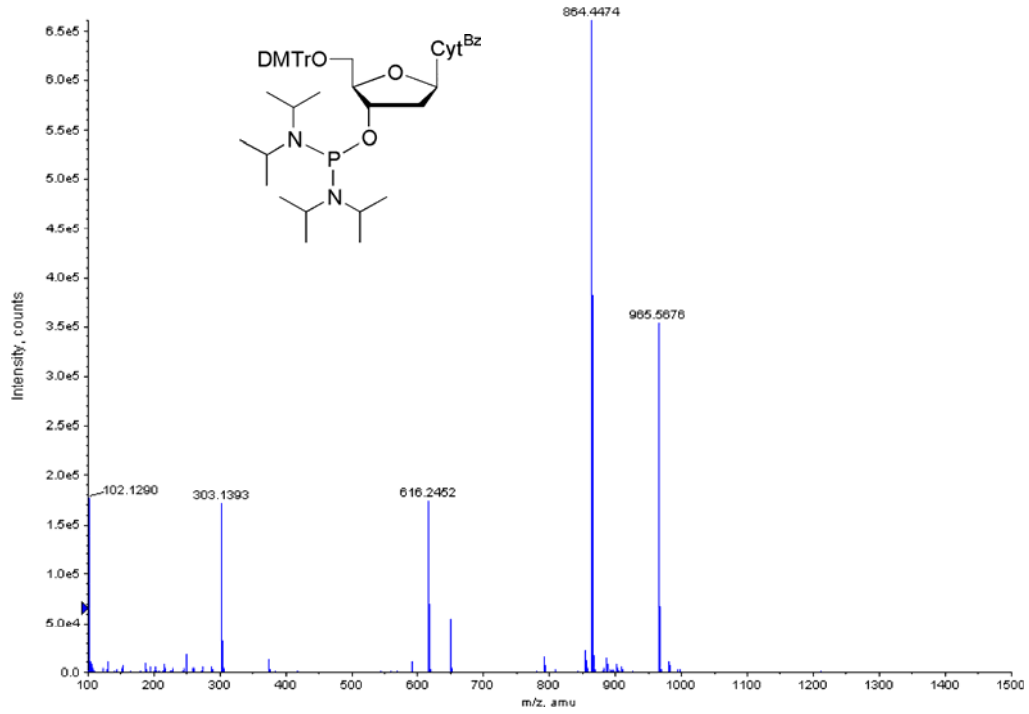

APESI-TOF MS spectrum of N^6-benzoyl-5'-*O*-(4,4'-dimethoxytrityl)- 3'-*O*-bis(*N*,*N*-diisopropylamino)phosphinyl-2'-deoxyadenosine

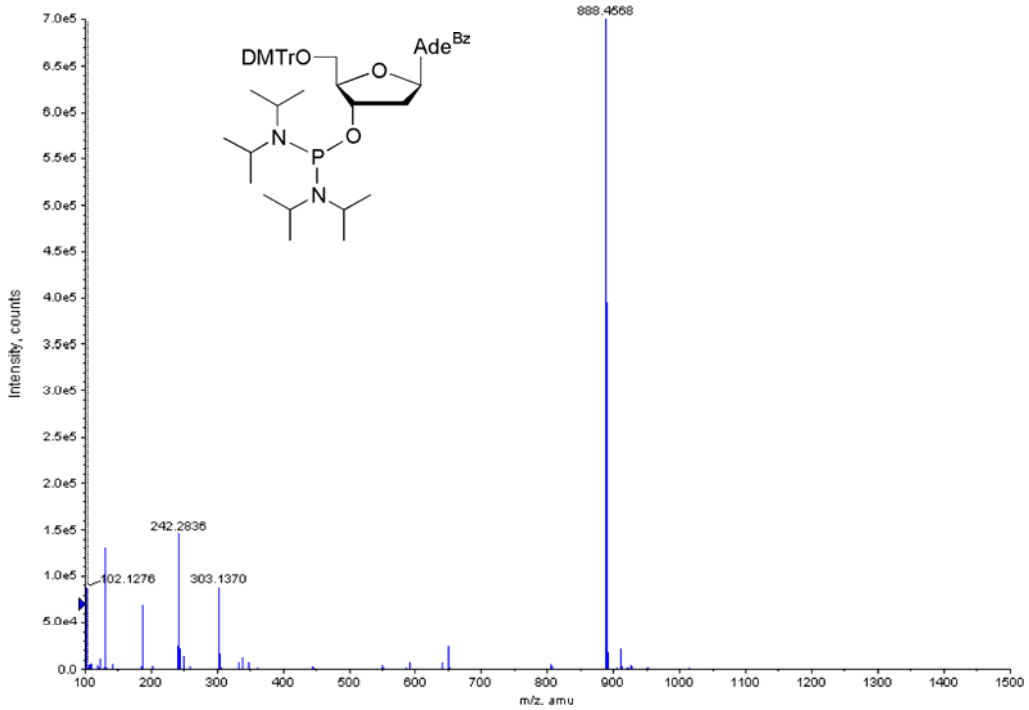

APESI-TOF MS spectrum of N^2-isobutyryl-5'-*O*-(4,4'-dimethoxytrityl)-3'-*O*-bis(*N*,*N*-diisopropylamino)phosphinyl-2'-deoxyguanosine

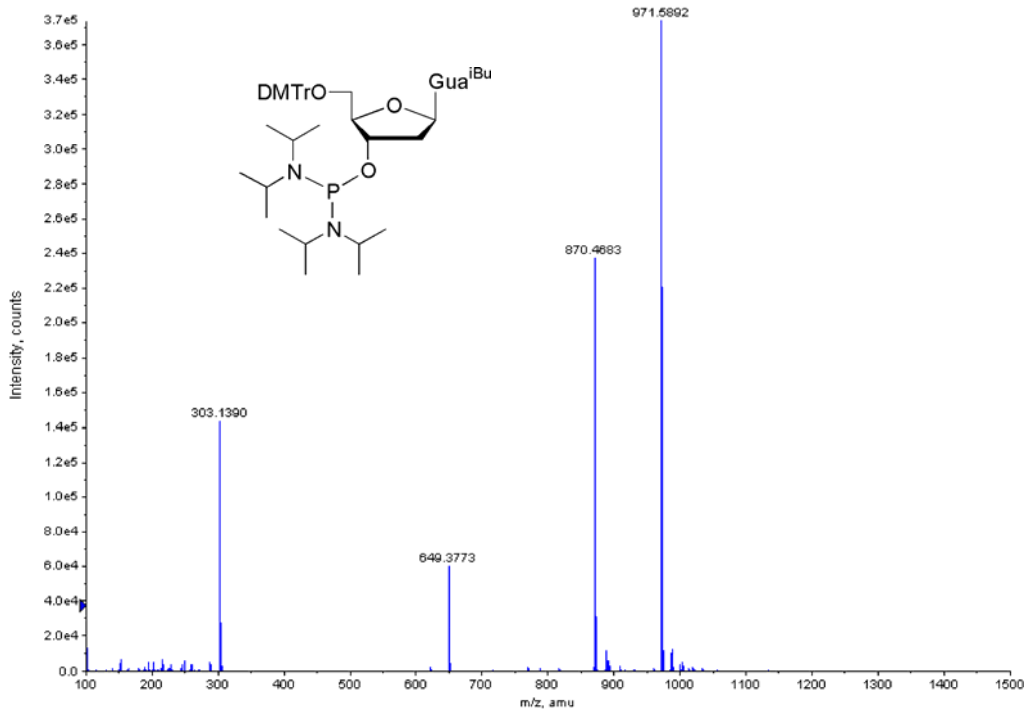

RP-HPLC chromatograms of dinucleoside phosphate diesters that were thermolytically released from the CPG support 7

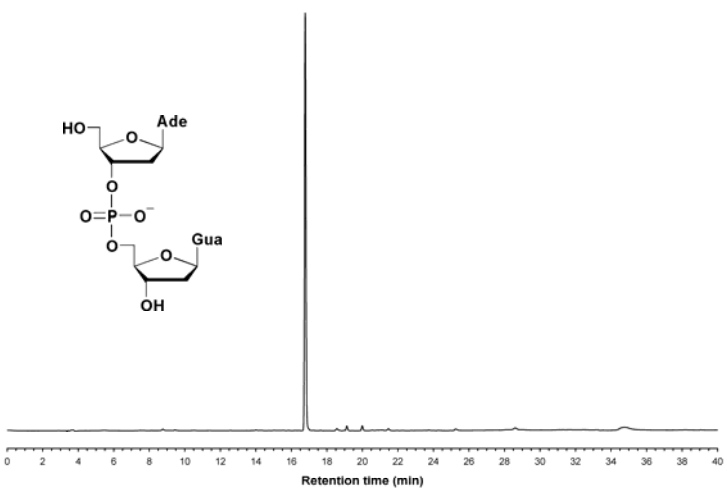

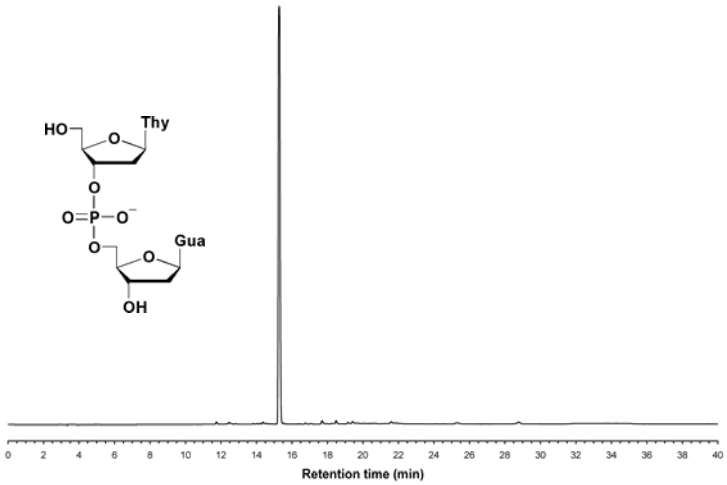

RP-HPLC chromatograms of dinucleoside phosphorothioates that were thermolytically released from the CPG support 7.

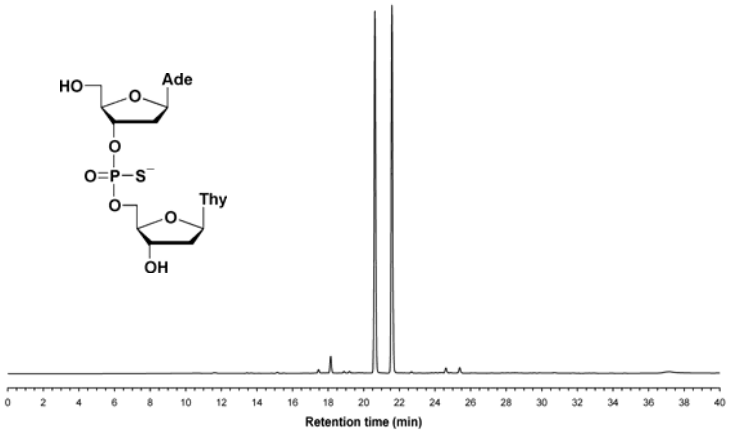

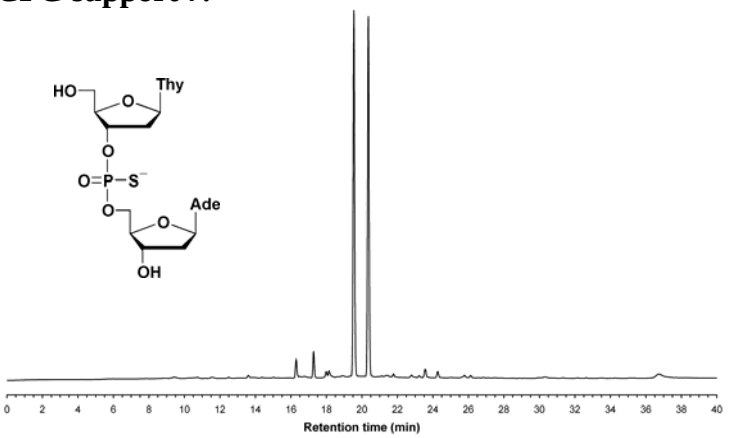

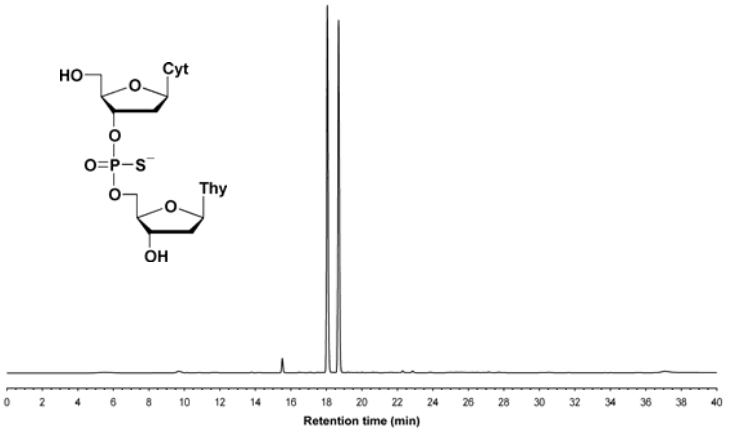

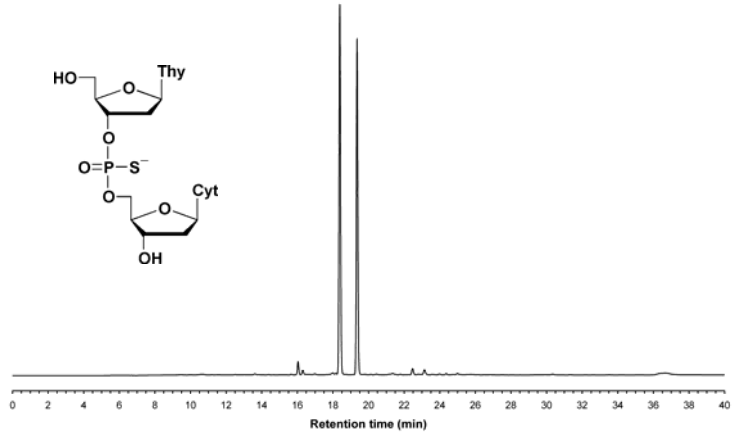

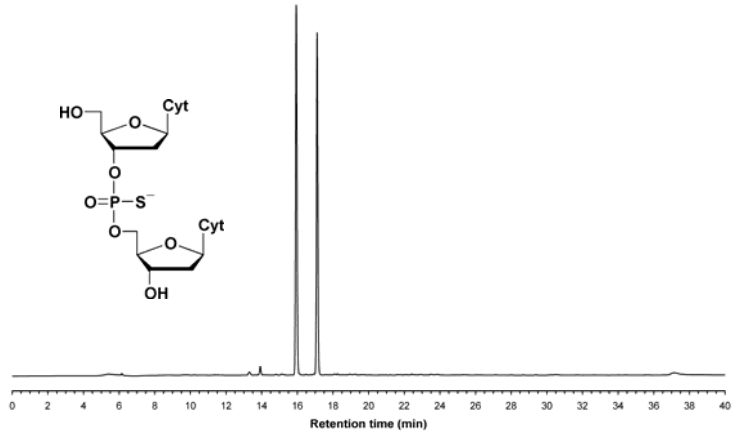

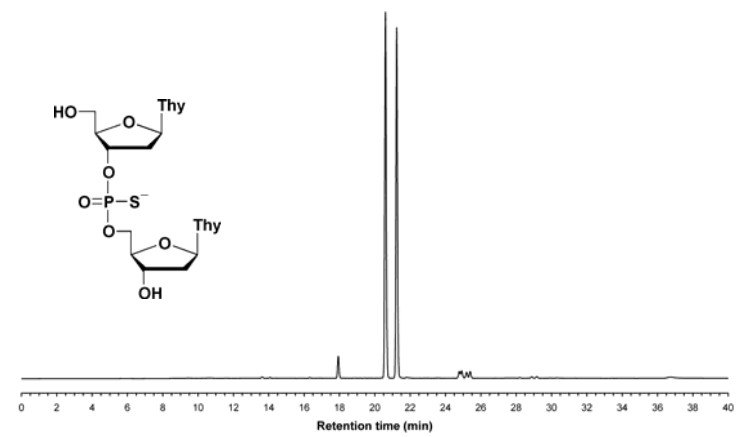

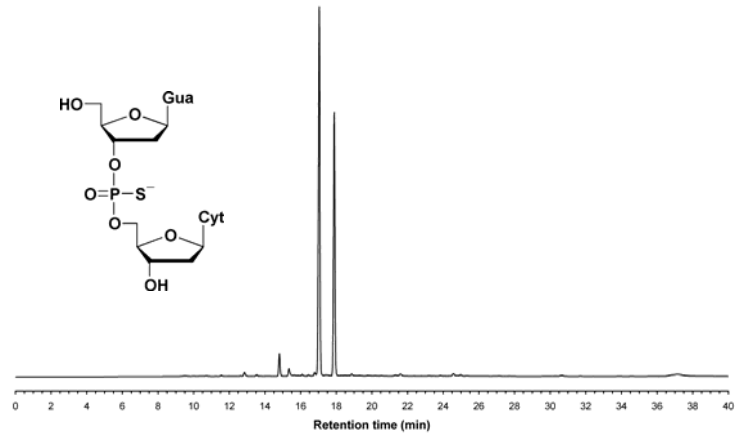

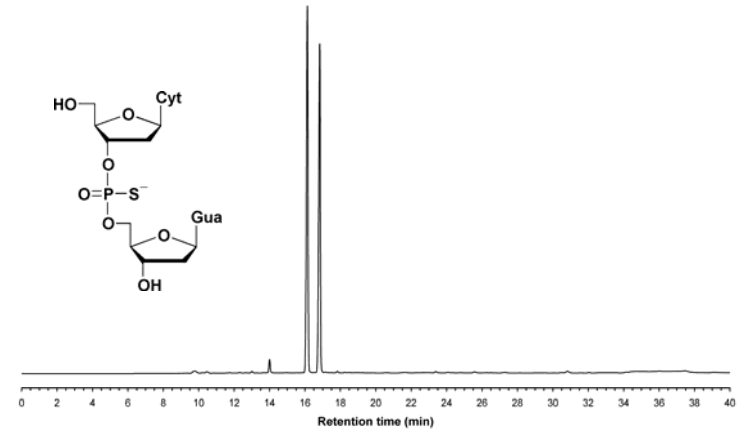

RP-HPLC chromatograms of dinucleoside phosphorothioates that were thermolytically released from the CPG support 7.

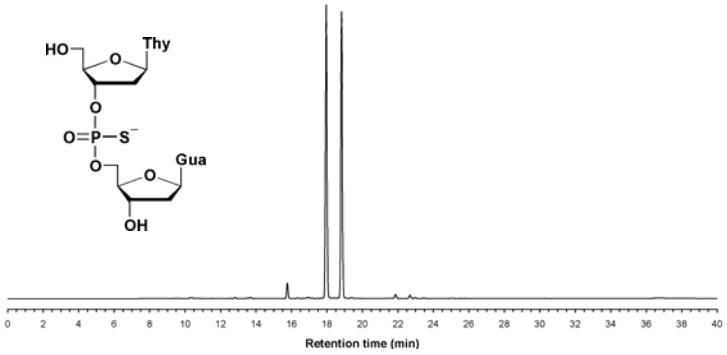

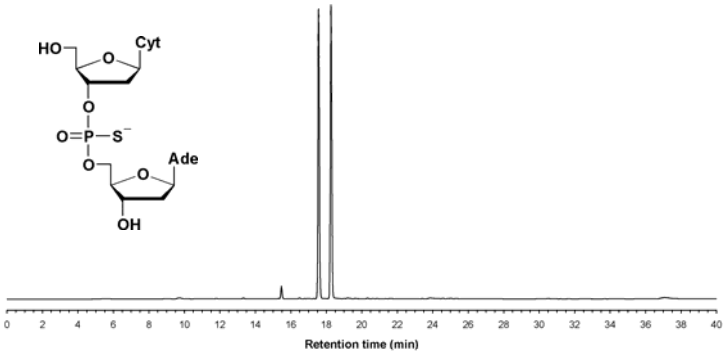

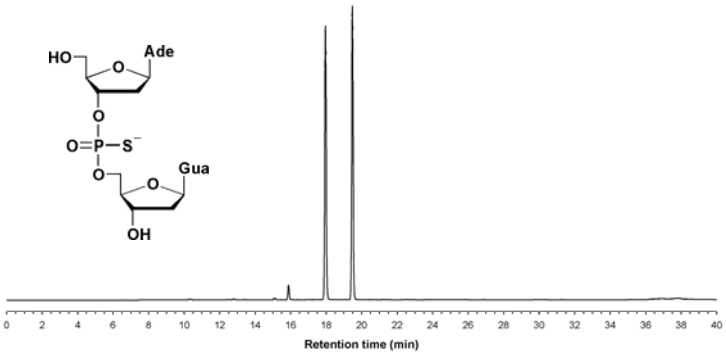

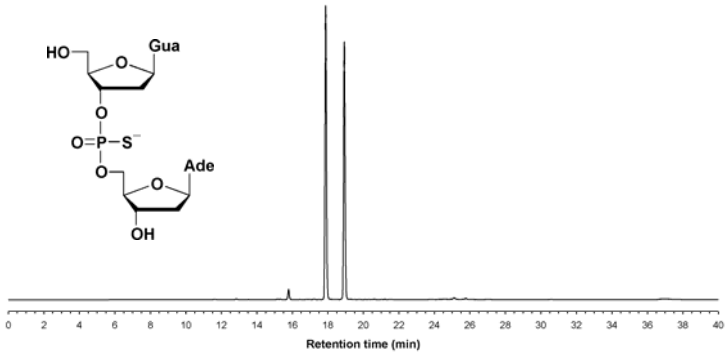

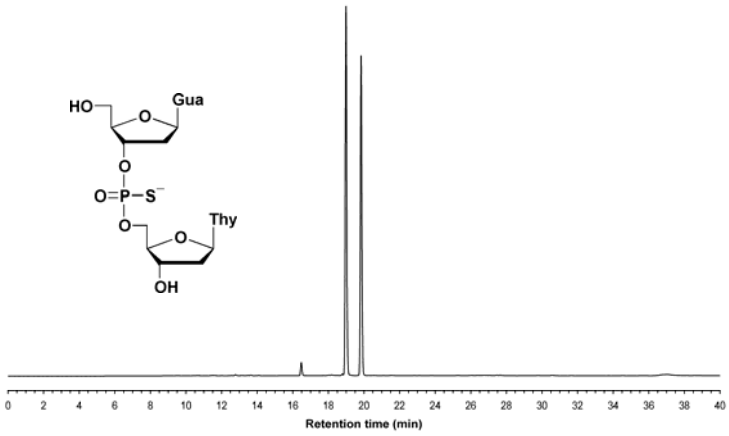

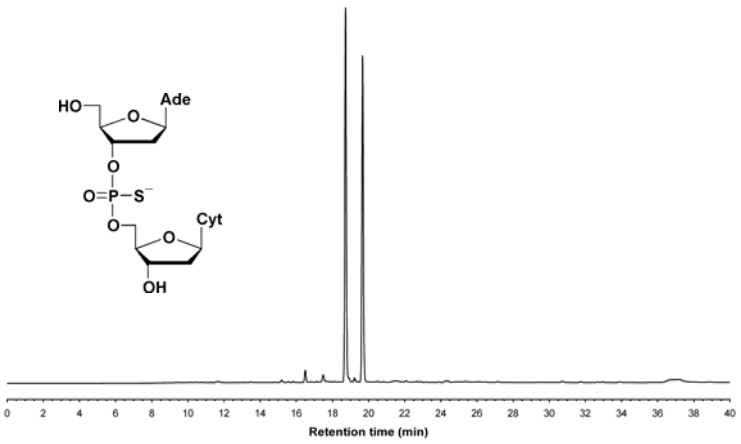

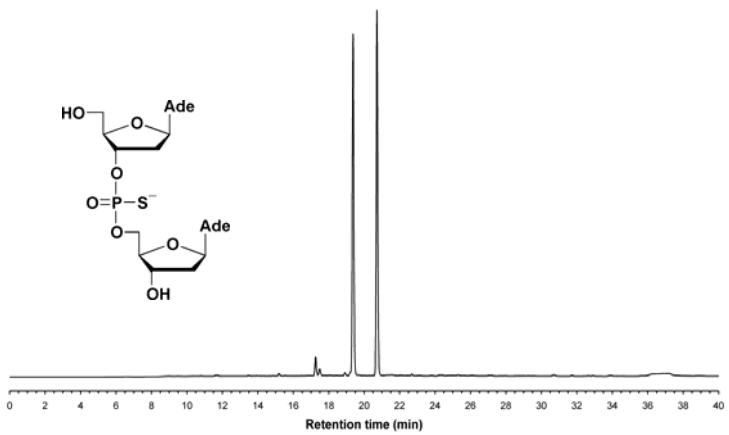

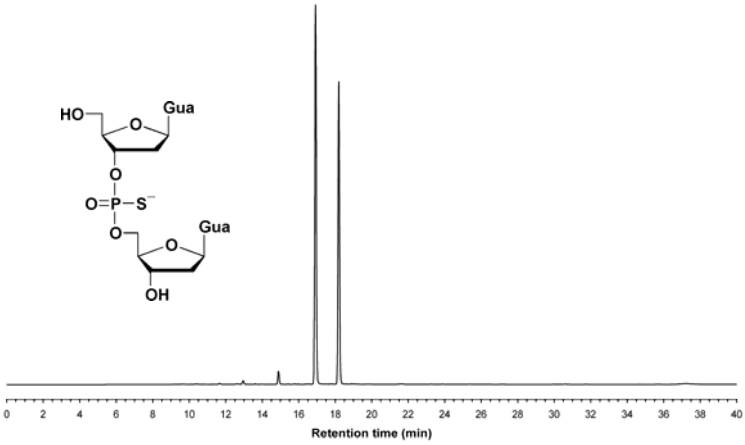

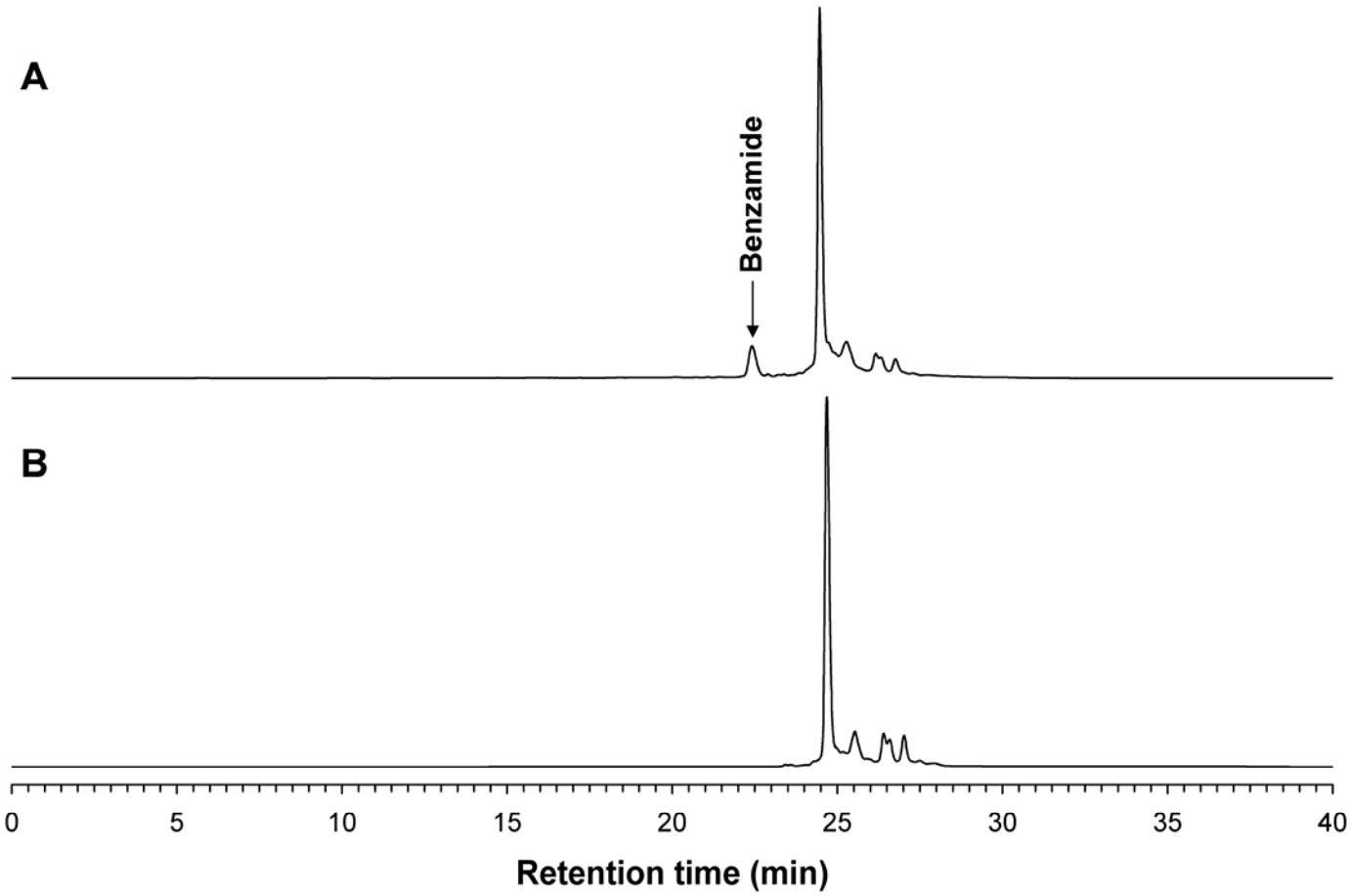

Enlarged Figure 1. RP-HPLC analysis of unpurified 5'-d(CGACTGTGAATCGATGCCAT). **A:** Chromatogram of the native 20-mer that was synthesized employing commercial CPG under standard conditions. Nucleobase and phosphate deprotection, and release of the oligomer from the support were effected by treatment with pressurized NH_3 gas (~10 bar) over a period of 16 h at 25 ºC, as described in the Experimental section. **B:** Chromatogram of the 20-mer that was synthesized using the CPG support **7** under standard conditions. After nucleobase and phosphate deprotection under the conditions described in **A**, the deprotection side products were washed away from the CPG support **8** with MeCN:H_2O (1:1 v/v). The 20-mer was thermolytically cleaved from **8** upon heating at 90 ºC in 1× PBS (pH 7.2) for 2 h. RP-HPLC analyses were performed using a 5 μm Supelcosil LC-18S column (25 cm × 4.6 mm) according to the following conditions: starting from 0.1 M triethylammonium acetate pH 7.0, a linear gradient of 0.7% MeCN/min was pumped at a flow rate of 1 mL/min for 30 min and was followed by a linear gradient of 4% MeCN for 5 min, which was held isocratically for 5 min. Peak heights are all normalized to the highest peak, which is set to 1 arbitrary unit.

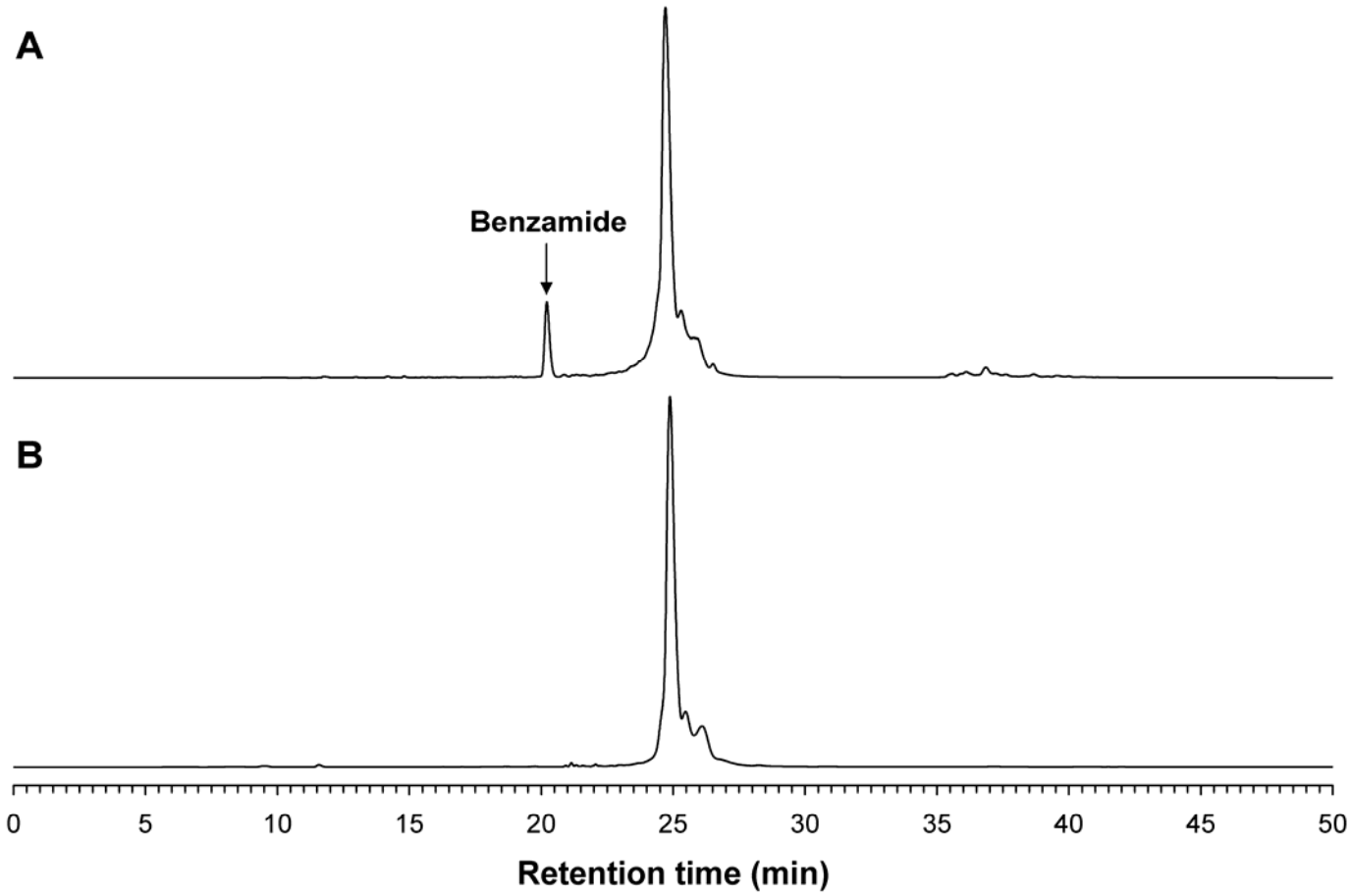

Enlarged Figure 2. RP-HPLC analysis of unpurified 5'-d($C_{PS}G_{PS}A_{PS}C_{PS}T_{PS}G_{PS}T_{PS}G_{PS}A_{PS}A_{PS}T_{PS}C_{PS}$ $G_{PS}A_{PS}T_{PS}G_{PS}C_{PS}C_{PS}A_{PS}T$). **A:** Chromatogram of the fully phosphorothioated 20-mer that was synthesized employing commercial CPG under standard conditions. Nucleobase and thiophosphate deprotection was effected by treatment with pressurized NH_3 gas (~10 bar) over a period of 16 h at 25 ºC, as described in the Experimental section. **B:** Chromatogram of the 20-mer that was synthesized using the CPG support **7** under standard conditions. After nucleobase and thiophosphate deprotection under the conditions described in **A**, the deprotection side products were washed away from the CPG support **8** with MeCN:H_2O (1:1 v/v). The 20-mer was thermolytically cleaved from the support **8** upon heating at 90 ºC in 1× PBS (pH 7.2) for 2 h. RP-HPLC analyses were performed using a 5 µm Supelcosil LC-18S column (25 cm × 4.6 mm) according to the following conditions: starting from 0.1 M triethylammonium acetate pH 7.0, a linear gradient of 1% MeCN/min was pumped at a flow rate of 1 mL/min for 40 min. Peak heights are all normalized to the highest peak, which is set to 1 arbitrary unit.

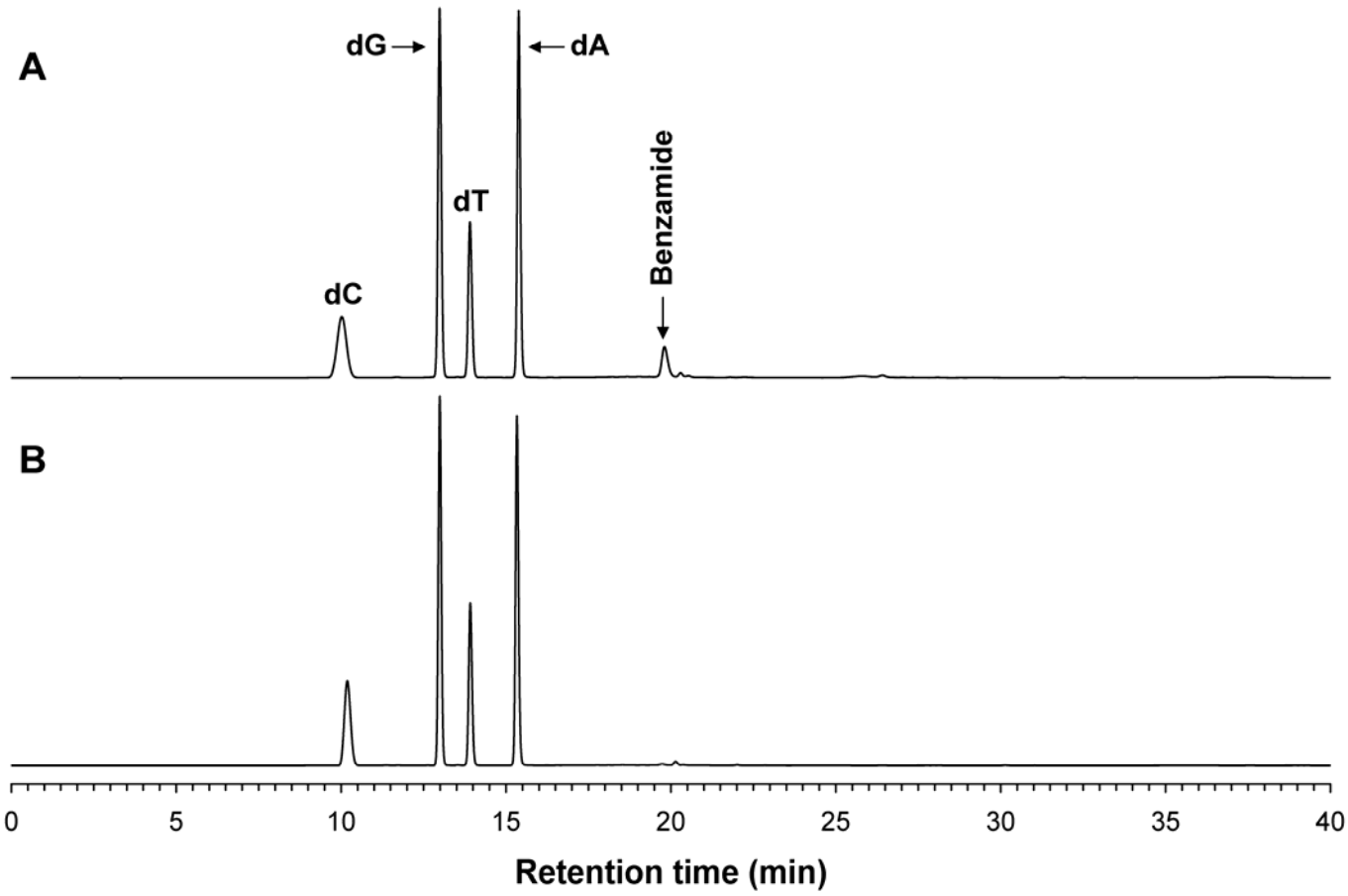

CHART 1. RP-HPLC analysis of unpurified 5'-d(CGACTGTGAATCGATGCCAT) after treatment with snake venom phosphodiesterase and bacterial alkaline phosphatase. **A:** Chromatogram of the enzymatic digest of the 20-mer described in Figure 1A. **B:** Chromatogram of the enzymatic digest of the 20-mer described in Figure 1B. Chromatographic conditions are identical to those described in the legend of Enlarged Figure 2. **dC**, 2'-deoxycytidine; **dG**, 2'deoxyguanosine; **dT**, 2'deoxythymidine; **dA**, 2'-deoxyadenosine.

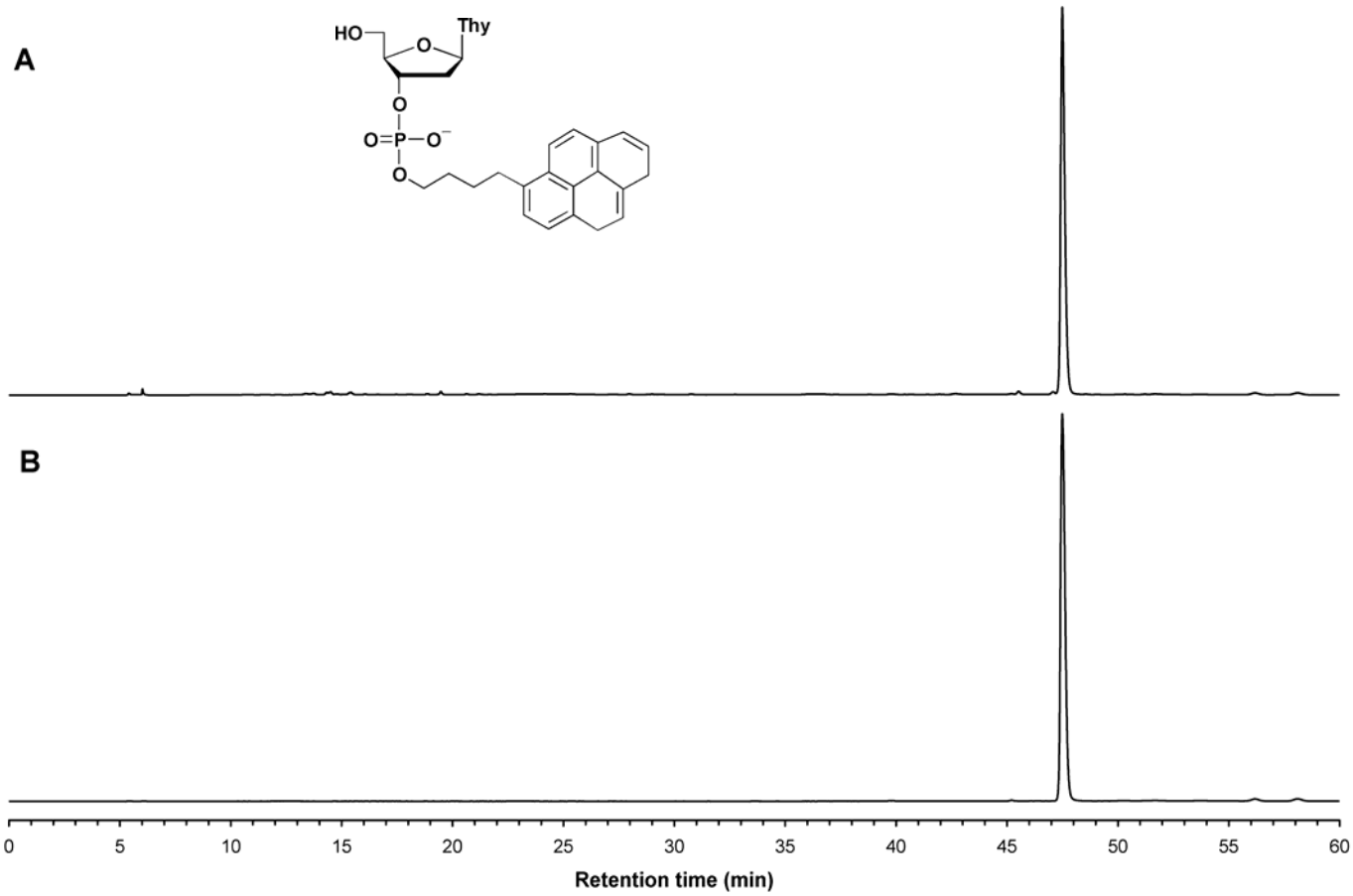

CHART 2. RP-HPLC chromatograms of unpurified thymidine 3'-*O*-(1-pyrenebutyl) phosphate that was thermolytically released from the CPG support **12**. **A:** Chromatogram of thymidine 3'-*O*-(1-pyrenebutyl) phosphate recorded at 260 nm. **B:** Chromatogram of thymidine 3'-*O*-(1-pyrenebutyl) phosphate recorded at 340 nm. RP-HPLC analyses were performed under conditions identical to those described in the legend of Enlarged Figure 2.

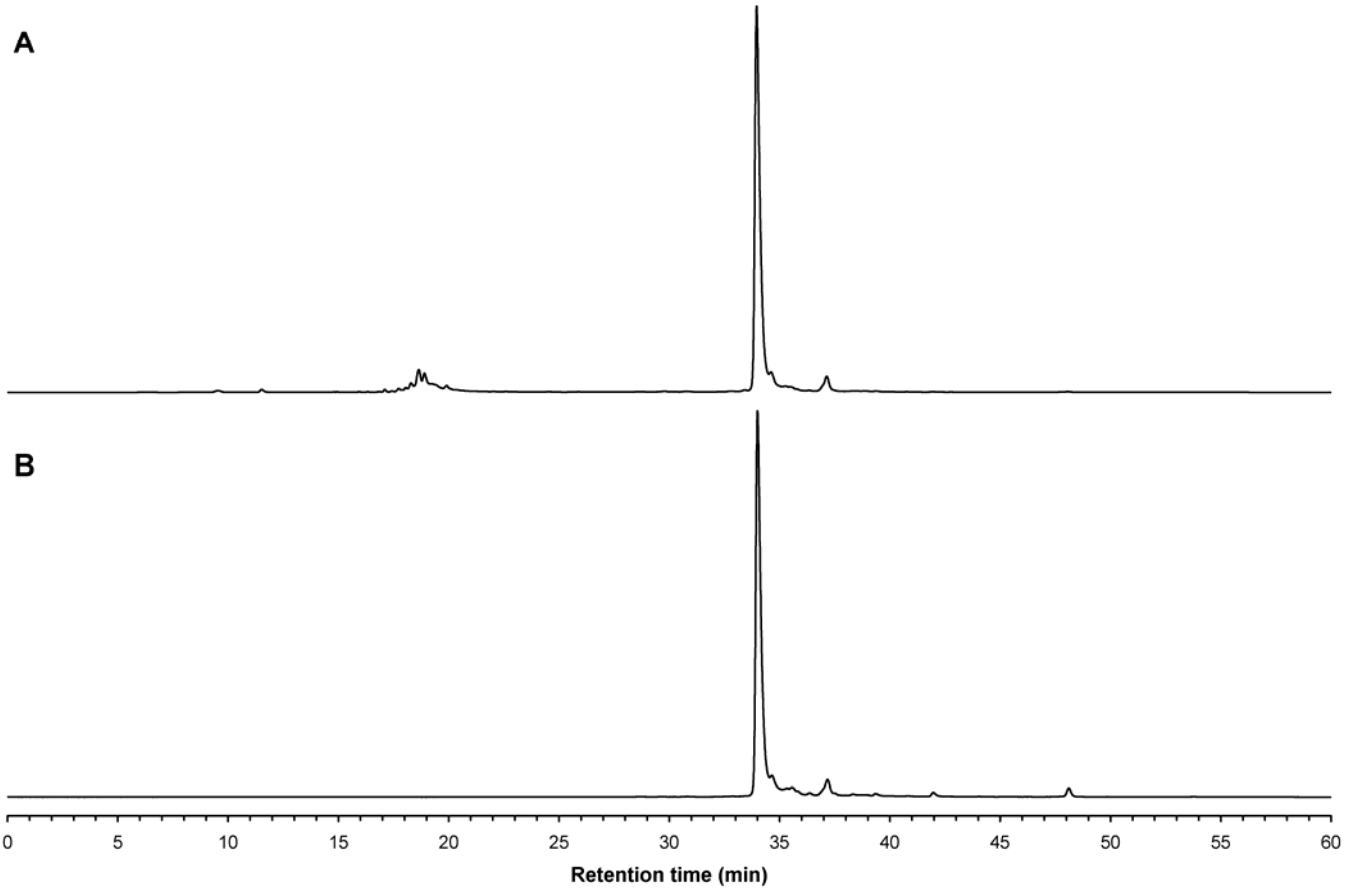

CHART 3. RP-HPLC analysis of unpurified 3'-pyrenylated DNA oligonucleotide **14**. **A:** Chromatogram of **14** recorded at 260 nm. **B:** Chromatogram of **14** recorded at 340 nm. RP-HPLC analyses were performed under conditions identical to those described in the legend of Enlarged Figure 2.

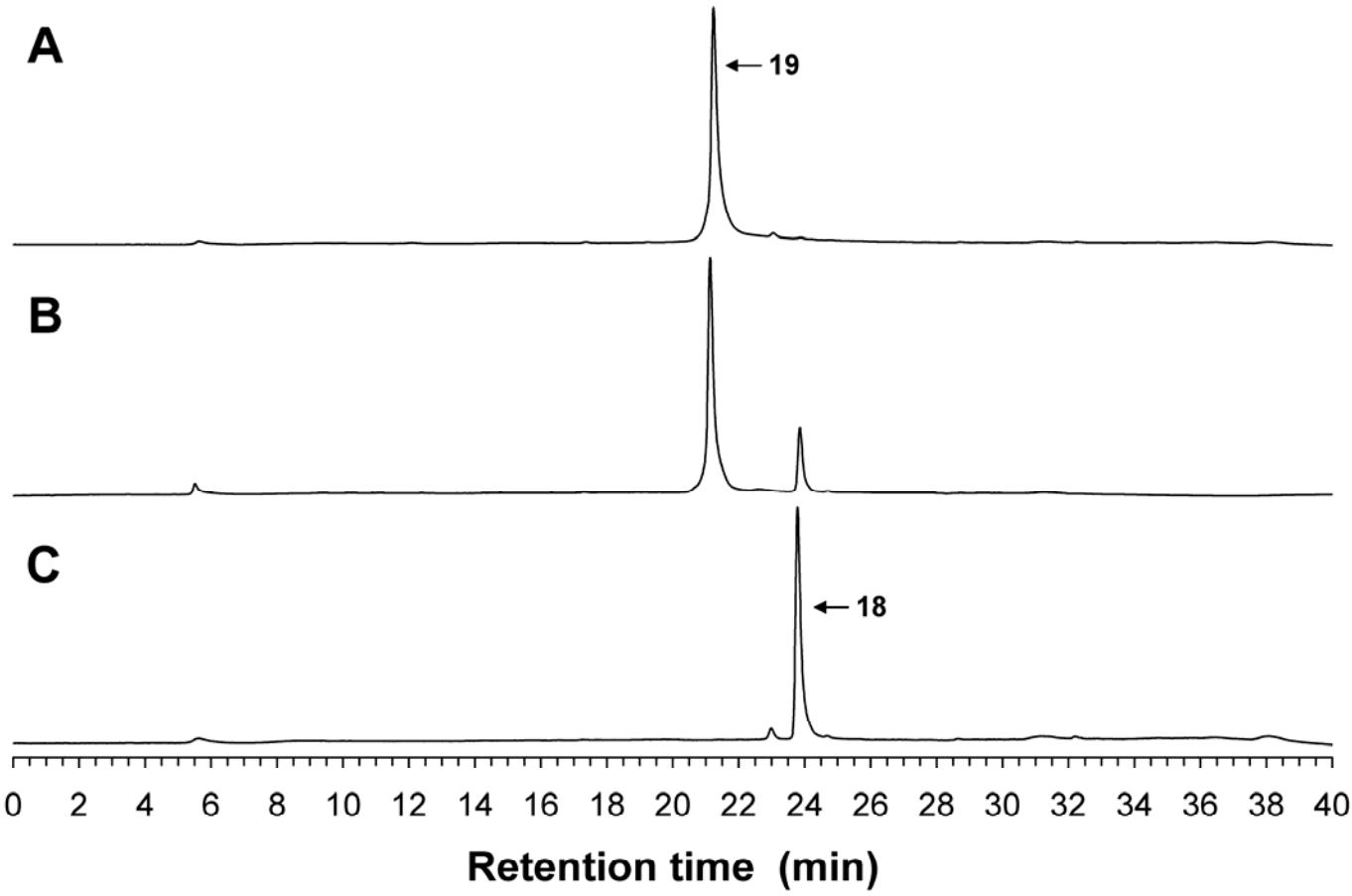

CHART 4. RP-HPLC analysis of the conversion of the (5',3')-heteroconjugated DNA oligonucleotide **18** to the circular DNA oligonucleotide **19** under "click chemistry" conditions. **A:** RP-HPLC-purified circular DNA oligonucleotide **19** (MALDI-TOF MS: calcd for $C_{209}H_{249}N_{79}O_{125}P_{21}$ $(M–H)^-$ 6517, found 6521). **B:** Chromatogram of a co-mixture of RP-HPLC-purified **19** and **18** (4:1). **C:** RP-HPLC-purified (5',3')-heteroconjugated DNA oligonucleotide **18** (MALDI-TOF MS: calcd for $C_{209}H_{249}N_{79}O_{125}P_{21}$ $(M–H)^-$ 6517, found 6522). RP-HPLC analyses were performed under conditions identical to those described in the legend of Enlarged Figure 2.

Latent Fluorophores Based on a Self-Immolative Linker Strategy and Suitable for Protease Sensing†

Jean-Alexandre Richard,[‡,§] Yves Meyer,[‡,§] Valérie Jolivel,[§,⊥,#,¶] Marc Massonneau,[§] Raphaël Dumeunier,[§] David Vaudry,[⊥,#,¶] Hubert Vaudry,[⊥,#,¶] Pierre-Yves Renard,*[,‡,¶,#,▽] and Anthony Romieu*[,‡,¶,#]

Equipe de Chimie Bio-Organique, Université de Rouen, Place Emile Blondel, 76821 Mont-Saint-Aignan, France, UMR CNRS 6014, COBRA, IRCOF, rue Lucien Tesnière, 76130 Mont-Saint-Aignan, France, QUIDD, Technopôle du Madrillet, 50, rue Ettore Bugatti, 76800 Saint-Etienne du Rouvray, France, Laboratoire de Neuroendocrinologie Cellulaire et Moléculaire, INSERM U413, Université de Rouen, 76821 Mont-Saint-Aignan, France, and Plate-forme Régionale de Recherche en Imagerie Cellulaire de Haute-Normandie, IFRMP23, Université de Rouen, 76821 Mont-Saint-Aignan, France. Received May 17, 2008; Revised Manuscript Received June 24, 2008

The self-immolative spacer *para*-aminobenzyl alcohol (PABA) was used as a key component in the design of new protease-sensitive fluorogenic probes whose parent phenol-based fluorophore is released through an enzyme-initiated domino reaction. First, the conjugation of the phenylacetyl moiety to 7-hydroxycoumarin (umbelliferone) and 7-hydroxy-9*H*-(9,9-dimethylacridin-2-one) (DAO) by means of the heterobifunctional PABA linker has led to pro-fluorophores **6a** and **6d** whose enzyme activation by penicillin amidase was demonstrated. The second part of this study was devoted to the extension of this latent fluorophore strategy to the caspase-3 protease, a key mediator of apoptosis in mammalian cells. Fluorogenic caspase-3 substrates **11** and **13** derived from umbelliferone and DAO, respectively, were prepared. It was demonstrated that pro-fluorophore **11** is a sensitive fluorimetric reagent for the detection of this cysteine protease. Furthermore, *in vitro* assays with fluorogenic probe **13** showed a deleterious effect of biological thiols on fluorescence of the released acridinone fluorophore DAO that, to our knowledge, had not been reported until now.

INTRODUCTION

Latent fluorophores (or pro-fluorophores) are molecules in which a physical property of the fluorophore is altered upon interaction with an analyte (enzyme, metal cation, reactive oxygen species, and so forth), resulting in a change in the fluorescence spectrum and/or an increase in the fluorescence quantum yield at a particular wavelength, and/or a change in some other fluorescent properties of the molecule (*1*). Most of these fluorogenic probes unmask their intense fluorescence only by a user-designated chemical reaction and so they display a unique selectivity and limited interferences associated with the probe's concentration, excitation intensity, and emission sensitivity (*2, 3*). Thus, they are widely used in many fields because of their powerful ability to improve analytical sensitivity and also because they offer greater temporal and spatial sampling capability. For example, latent fluorophores are valuable tools for modern biochemical and biological research especially for the enzyme-linked immunosorbent assay (ELISA), high-throughput screening of enzyme inhibitors, detection of DNA and RNA, and evaluation of cell viability (*4*). Furthermore, emerging and more challenging biomedical applications such as *in vivo* fluorescence imaging also require the use of such smart fluorogenic probes (*5*). Thus, numerous pro-fluorophores suitable for the vizualization of biologically relevant molecules (H_2O_2 (*6*), $O_2^{-\bullet}$ (*7–9*), $ONOO^-$ (*10*), NO (*6, 11*), cysteine/homocysteine (*12, 13*), glutathione *14–17*), and enzyme activities (esterases *1–3, 18*), caspase-3 (*19, 20*), dipeptidyl peptidase IV substrate (DPP-IV) (*21, 22*), β-galactosidase (*23, 24*), β-lactamases (*25*), phosphatases (*1*) in various *in vitro* and *in cellulo* models, have been developed. However, few of them fulfill all the requirements for *in vivo* use (i.e., far-red or near-IR excitation and emission maxima (*26*), water solubility, serum stability, cell-membrane permeability, and so forth). Inspired by prodrug design (*27–29*), Jones et al. have proposed an attractive approach to develop efficient imaging probes which relies on the conjugation of the recognition unit (responsible for the selective reaction with the target analyte) to a masked aniline-based fluorophore *via* a "self-immolative" spacer (*30*). This latter reactive linker enables the unmasking of the pro-fluorophores through a multistep cascade reaction triggered by the analyte of interest and leading to the release of the free fluorescent molecule. As the target analyte is often a hydrolytic enzyme, the presence of a spacer between the recognition unit and the bulky fluorophore is beneficial to prevent steric hindrance around the cleavage site in order to generate better enzyme substrates. Furthermore, a heterobifunctional spacer permits the conjugation of fluorescent cores that do not necessarily contain the reactive group involved in the enzyme-cleavable bond of the target pro-fluorophore and so widens the scope of fluorescent labels that can be used to prepare the fluorogenic probes (e.g., the use of phenol, thiophenol, or aniline-based fluorophores to prepare protease-sensitive fluorogenic probes). Moreover, phenol-, thiophenol-, and even aniline-based fluorescent species often are good leaving groups: direct ester, thioester, or amide linkage of the fluorescent species at the enzyme-cleavable bond thus frequently gives rise to a

* pierre-yves.renard@univ-rouen.fr or anthony.romieu@univ-rouen.fr. Phone: +33-2-35-52-24-14(or 24-15). Fax: +33-2-35-52-29-59.

† Such fluorogenic probes were covered by a patent entitled "New pro-fluorescent compounds". Renard, P.-Y., Romieu, A., Richard J.-A., and Massonneau, M. Fr. Demande (2008), FR 2910897 A1 20080704.

‡ COBRA-CNRS UMR 6014.

§ QUIDD.

⊥ INSERM U413.

IFRMP23.

¶ Université de Rouen.

▽ Institut Universitaire de France.

10.1021/bc8001997 CCC: $40.75 © 2008 American Chemical Society
Published on Web 07/22/2008

fragile bioprobe (*2, 3*), that often turns out to be sensitive to pH changes, and displays a noticeable nonspecific cleavage, often detrimental when highly sensitive phenomena are targeted. Because of the use of an intermediate self-immolative linker, the chemical functionality leading to the fluorophore release can be tuned in order to reduce drastically the background noise. Such latent fluorophore strategy was recently employed by some academic groups to prepare fluorogenic substrates of several hydrolytic enzymes (i.e., esterases (*31–33*) and β-galactosidase (*34*)) which could potentially be used for *in vivo* imaging. Surprisingly, few published works are devoted to the extension of this strategy to the design and synthesis of protease profluorescent substrates (for recent examples, see the molecular probes with UV−visible and fluorescence outputs for penicillin amidase activity, recently reported by Danieli et al. (*35*), Sicart et al. (*36*), and by us (*37*) and our akin strategy aimed at chemiluminescent probes for protease activity (*38*)). Given their critical role in numerous diseases, the evaluation of specific protease activities *in vivo* is of a great importance especially for diagnostic and therapeutic purposes. In that context, we describe here the synthesis, photophysical characterization, and preliminary biochemical studies of a new generation of fluorogenic probes resulting from the covalent association between a peptide sequence and a phenol-based fluorophore through the self-immolative spacer *para*-aminobenzyl alcohol (PABA). Latent fluorophores from two dyes (blue for **6a** and far-red for **6d**) were suitable for detecting the protease penicillin amidase (also known as penicillin G acylase, PGA) whereas fluorimetric reagents **11** and **13** were initially designed for imaging caspase-3 protease *in cellulo* and *in vivo*, respectively.

EXPERIMENTAL PROCEDURES

Chemicals and Reagents. Column chromatography purifications were performed on silica gel (40−63 μm) from SdS. TLC analyses were carried out on Merck DC Kieselgel 60 F-254 aluminum sheets. Compounds were visualized by one or both of the following methods: (1) spray with a 0.2% (w/v) ninhydrin solution in absolute ethanol, (2) spray with a 3.5% (w/v) phosphomolybdic acid solution in absolute ethanol. Acetonitrile was freshly distilled over CaH_2 under an argon atmosphere prior to use. Dichloromethane was dried by distillation over P_2O_5. Anhydrous NMP (H_2O < 100 ppm) was purchased from Fluka and stored over 4 Å molecular sieves. Pyridine was distilled over KOH and stored over BaO. DIEA and triethylamine (TEA) were distilled from CaH_2 and stored over BaO. 7-Hydroxycoumarin **5a** was purchased from Fluka. (Far)-red emitting phenol-based fluorophores 2-hydroxy Nile Red **5b**, DDAO **5c**, and DAO **5d** were synthesized according to previously reported procedures (*39–41*). The fully protected tetrapeptide Ac-Asp(OTMSE)-Glu(OTMSE)-Val-Asp(OTMSE)-OH and its PABA carboxamide derivative **8** were synthesized by using a multistep synthetic procedure recently reported by us (*38*). Recombinant human caspase-3 enzyme (5.52 U/mg) was purchased from Sigma. Penicillin amidase from *E. coli* and immobilized on Eupergit C (∼100 U/g) was purchased from Fluka. HPLC-gradient grade acetone and CH_3CN were obtained from Acros and Panreac, respectively. Buffers (caspase-3 and phosphate buffers) and aq. mobile phases for HPLC were prepared using deionized water purified with a Milli-Q system (purified to 18.2 MΩ.cm).

Instruments. ^1H and ^{13}C NMR spectra were recorded on a Bruker DPX 300 spectrometer (Bruker, Wissembourg, France). Chemical shifts are expressed in parts per million (ppm) from $CDCl_3$ ($\delta_H = 7.26$, $\delta_C = 77.36$), DMSO-d_6 ($\delta_H = 2.54$, $\delta_C = 40.45$), acetone-d_6 ($\delta_H = 2.09$, $\delta_C = 30.60$, and 205.87), or CD_3OD ($\delta_H = 3.34$, $\delta_C = 49.86$) (*42*). *J* values are expressed in Hz. Infrared (IR) spectra were recorded as thin-film on sodium chloride plates or KBr pellets using a Perkin-Elmer FT-IR Paragon 500 spectrometer. UV−visible spectra were obtained on a Varian Cary 50 scan spectrophotometer. Kinetic parameters were determined using a Molecular Devices fluorometric imaging plate reader FlexStation. Black clear-bottom 96-multiwell plates were purchased from Costar. Fluorescence spectroscopic studies were performed with a Varian Cary Eclipse spectrophotometer. Analytical HPLC was performed on a Thermo Electron Surveyor instrument equipped with a PDA detector. Semipreparative HPLC was performed on a Finnigan SpectraSYSTEM liquid chromatography system equipped with UV−visible 2000 detector. Mass spectra were obtained with a Finnigan LCQ Advantage MAX (ion trap) apparatus equipped with an electrospray source. LC-MS analyses were performed on a Thermo's Surveyor Plus HPLC system coupled with the Finnigan LCQ Advantage MAX (ionization mode, ESI±; capillary temperature, 270 °C; capillary voltage, ±10 V; tube lens offset, 0/−50 V).

HPLC Separations. Several chromatographic systems were used for the analytical experiments, the purification steps and the LC-MS analyses. Each one of these systems was optimized (except System G) in order to improve separation conditions.

System A: RP-HPLC (Thermo Hypersil GOLD C_{18} column, 5 μm, 4.6 × 150 mm) with CH_3CN and 0.1% aq. trifluoroacetic acid (aq. TFA, 0.1%, v/v, pH 2.0) as eluents [100% aq. TFA (5 min), then linear gradient from 0% to 100% (50 min) of CH_3CN] at a flow rate of 1.0 mL/min. Dual UV detection was achieved at 210 and 254 nm.

System B: System A with the following gradient [80% aq. TFA (5 min), then linear gradient from 20% to 100% (40 min) of CH_3CN].

System C1: RP-HPLC (Thermo Hypersil GOLD C_{18} column, 5 μm, 10 × 250 mm) with CH_3CN and 0.1% aq. trifluoroacetic acid (aq. TFA, 0.1%, v/v, pH 2.0) as eluents [80% aq. TFA (5 min), then linear gradient from 20% to 100% (50 min) of CH_3CN] at a flow rate of 5.0 mL/min. Dual UV detection was achieved at 254 and 320 nm.

System C2: System C1 with a Varian Kromasil C_{18} column (10 μm, 21.2 × 250 mm) running at a flow rate of 20.0 mL/min.

System D1: System C1 with visible detection at 450 nm.

System D2: System C2 with visible detection at 450 nm.

System E: RP-HPLC (Thermo Hypersil GOLD C_{18} column, 5 μm, 10 × 250 mm) with CH_3CN and aq. TFA 0.1% as eluents [100% aq. TFA (5 min), then linear gradient from 0% to 5% (10 min), 5% to 10% (10 min), and 10% to 100% (50 min) of CH_3CN] at a flow rate of 3.0 mL/min. Dual UV detection was achieved at 254 and 320 nm.

System F: System E with visible detection at 450 nm.

System G: RP-HPLC (Thermo Hypersil GOLD C_{18}, 5 μm, 2.1 × 150 mm) with CH_3CN and formic acid 0.1% (FA 0.1%) as eluents [90% FA (2 min), then linear gradient from 10 to 50% (13 min) and 50 to 90% (27 min) of CH_3CN] at a flow rate of 0.25 mL/min. UV detection was achieved at 260 nm. ESI-MS detection was achieved in both the positive and negative modes (mass range 75−750 a.m.u., centroid mode).

***N*-(4-(Hydroxymethyl)phenyl)-2-phenylacetamide (3).** *para*-Aminobenzyl alcohol **2** (322 mg, 2.61 mmol) was dissolved in a mixture of dry CH_2Cl_2/DMF (8:1, v/v, 9 mL) and the resulting solution was cooled to 0 °C. Dry pyridine (430 μL, 5.4 mmol) and phenylacetyl chloride **1** (340 μL, 2.57 mmol) were sequentially added and the reaction mixture was stirred at room temperature overnight. Thereafter, the mixture was concentrated under reduced pressure, then CH_2Cl_2 (50 mL) was added and the organic layer was washed with aq. citric acid (10%, w/v, 30 mL) and deionized water (30 mL). The aqueous layer was extracted twice with CH_2Cl_2 (30 mL); the combined organic

layers were dried over Na_2SO_4, filtered, and evaporated to dryness. The resulting residue was purified by chromatography on a silica gel column with a mixture of CH_2Cl_2/AcOEt (7:3, v/v) as the mobile phase, affording phenylacetamide **3** as a white solid (481 mg, 78%). R_f 0.5 (CH_2Cl_2/AcOEt, 7:3, v/v). IR (KBr) 3304, 3202, 3131, 1660, 1606, 1534, 1518, 1411, 1335, 1260, 1141, 1051 cm^{-1}. ^1H NMR (300 MHz, CD_3OD): δ 3.69 (s, 2H, ArCH_2), 4.57 (s, 2H, CH_2OH), 7.30−7.37 (m, 7H, 2 ArH_{PABA} + 5 ArH), 7.56 (d, J = 8.0 Hz, 2H, 2 ArH_{PABA}). ^{13}C NMR (75.4 MHz, CD_3OD): δ 44.7, 64.8, 121.2, 127.9, 128.6, 129.6, 130.1, 136.8, 138.6, 139.0, 172.3. MS (ESI, positive mode): m/z 242.27 $[M + H]^+$, calcd for $C_{15}H_{16}NO_2$ 242.12.

General Procedure for the Synthesis of the PGA Fluorogenic Probes. *(a) Preparation of the Mesylate Ester of* **4.** Alcohol **3** (443 mg, 1.84 mmol) was dissolved in dry acetone (23 mL) and the resulting solution was cooled to 0 °C. Triethylamine (770 μL, 5.5 mmol) and mesyl chloride (425 μL, 5.5 mmol) were sequentially added and the reaction mixture was stirred at room temperature overnight. Thereafter, CH_2Cl_2 (20 mL) was added and the solution was poured into cold 2 N aq HCl. The aqueous layer was extracted with CH_2Cl_2 (30 mL), and the combined organic layers were washed with deionized water (30 mL), dried over Na_2SO_4, filtered, and concentrated under reduced pressure, yielding mesylate ester **4** as a white solid. The crude product was quite unstable and was used without purification in the next step. ^1H NMR (300 MHz, $CDCl_3$): δ 3.62 (s, 3H, CH_3), 3.69 (s, 2H, ArCH_2), 4.49 (s, 2H, CH_2OH), 7.22−7.40 (m, 9H, ArH). ^{13}C NMR (75.4 MHz, $CDCl_3$): δ 44.7, 46.2, 52.8, 120.5, 127.8, 129.4, 129.6, 129.7, 133.8, 134.6, 138.0.

(b) Coupling Reaction of **4** *with the Fluorescent Label.* The phenol-based fluorophore was dissolved in dry CH_2Cl_2 (for 7-hydroxycoumarin **5a**, 0.1 M final concentration) or in dry DMF (for 2-hydroxy Nile Red **5b**, DDAO **5c** and DAO **5d**, 0.1 M final concentration). Anhydrous K_2CO_3 (2 equiv) was added and the reaction mixture was stirred at room temperature for 15 min. Then, compound **4** (1 equiv) was added and the reaction mixture was stirred at room temperature overnight. The reaction was checked for completion by RP-HPLC (system B), and evaporated under reduced pressure. CH_2Cl_2 (10 mL) was added and the organic layer was washed with deionized water, dried over Na_2SO_4, filtered, and evaporated to dryness. The crude product was purified by RP-HPLC (system C1 for **6a**, system D1 for **6b**, **6c**, and **6d**) to give after lyophilization the corresponding PGA probe in a pure form.

PGA Fluorogenic Probe (6a). White amorphous powder, overall yield 28%. R_f 0.5 (CH_2Cl_2/AcOEt, 1:1, v/v). ^1H NMR (300 MHz, $CDCl_3$): δ 3.66 (s, 2H, ArCH_2), 4.96 (s, 2H, CH_2OH), 6.15 (d, J = 9.0 Hz, 1H, ArH_{Coum}), 6.74−6.81 (m, 2H, ArH_{Coum}), 7.15−7.31 (m, 8H, ArH + ArH_{PABA} + ArH_{Coum}), 7.39 (d, J = 8.0 Hz, 2H, ArH_{PABA}), 7.54 (d, J = 9.0 Hz, 1H, ArH_{Coum}). ^{13}C NMR (75.4 MHz, $CDCl_3$): δ 45.1, 70.4, 102.2, 113.5, 113.6, 120.3, 128.0, 128.7, 129.1, 129.6, 129.8, 132.0, 134.7, 138.1, 143.8, 156.0, 161.6, 162.1, 169.6. MS (ESI, positive mode): m/z 386.33 $[M + H]^+$, calcd for $C_{24}H_{20}NO_4$ 386.14. HPLC (system B): t_R = 29.4 min (purity >95%). UV (CH_3CN, 25 °C): λ_{max} = 275 nm (63 000 M^{-1} cm^{-1}).

PGA Fluorogenic Probe (6b). Red amorphous powder, overall yield 5%. ^1H NMR (300 MHz, DMSO-d_6): δ 1.20 (t, 6H, J = 7.0 Hz, 2 CH_3), 3.55 (q, 4H, J = 7.0 Hz, 2 CH_2CH$_3$), 5.29 (s, 2H, ArCH_2CO), 6.25 (s, 1H, ArH), 6.72 (s, 1H, ArH), 6.84−6.90 (m, 1H, ArH), 7.20−7.42 (m, 6H, ArH), 7.50 (d, 2H, J = 9.0 Hz, ArH), 7.62−7.80 (m, 3H, ArH), 8.05−8.12 (m, 2H, ArH). MS (ESI, positive mode): m/z 558.27 $[M + H]^+$, calcd for $C_{35}H_{32}N_3O_4$ 558.24. HPLC (system B): t_R = 31.7 min (purity 90%). UV−vis (PB/acetone, 8:2, v/v, 25 °C): λ_{max} = 543 nm.

PGA Fluorogenic Probe (6c). Orange amorphous powder, overall yield 7%. R_f 0.5 (CH_2Cl_2/AcOEt, 3:2, v/v). ^1H NMR (300 MHz, $CDCl_3$): δ 1.78 (s, 3H, CH_3), 1.85 (s, 3H, CH_3), 3.77 (s, 2H, ArCH_2), 5.04 (s, 2H, CH_2OH), 6.66−6.69 (m, 1H, ArH_{DDAO}), 7.13 (s, 1H, ArH_{DDAO}), 7.30−7.51 (m, 10H, 5ArH + 4ArH_{PABA} + ArH_{DDAO}), 7.63 (s, 1H, ArH_{DDAO}), 7.75 (s, 1H, NH). ^{13}C NMR (75.4 MHz, $CDCl_3$): δ 29.1, 38.4, 45.2, 75.0, 114.1, 114.3, 120.0, 120.3, 128.1, 128.8, 128.9, 129.1, 129.6(6), 129.7, 129.9, 130.6, 132.5, 132.9, 133.7, 134.6, 138.3, 139.8, 140.4, 141.0, 141.3, 148.7, 153.0, 153.5, 169.5, 187.7. MS (ESI, positive mode): m/z 553.33 $[M + Na]^+$, calcd for $C_{30}H_{24}Cl_2NaN_2O_3$ 553.11. HPLC (system B): t_R = 36.8 min (purity 94%). UV−vis (PB/acetone, 8:2, v/v, 25 °C): λ_{max} = 424 nm (15 000 M^{-1} cm^{-1}).

PGA Fluorogenic Probe (6d). Orange amorphous powder, overall yield 14%. ^1H NMR (300 MHz, acetone-d_6): δ 1.57 (s, 6H, 2CH_3), 3.70 (s, 2H, ArCH_2), 5.20 (s, 2H, CH_2OH), 6.55 (dd, J = 2.0 and 10.0 Hz, 1H, ArH_{DAO}), 6.68 (d, J = 2.0 Hz, 1H, ArH_{DAO}), 7.07 (dd, J = 3.0 and 9.0 Hz, 1H, ArH_{DAO}), 7.22−7.48 (m, 9H, 5ArH + 2ArH_{PABA} + 2ArH_{DAO}), 7.60 (d, J = 9.0 Hz, 1H, ArH_{DAO}), 7.71 (d, J = 8.0 Hz, 2H, 2ArH_{PABA}). ^{13}C NMR (75.4 MHz, acetone-d_6): δ 32.2, 37.7, 44.3, 70.3, 113.4, 114.4, 119.6, 127.1, 127.6, 128.8, 129.1, 129.7, 131.3, 132.1, 134.0, 136.4, 137.2, 139.9, 140.2, 142.0, 148.1, 150.8, 161.7, 169.4, 186.8. MS (ESI, positive mode): m/z 463.13 $[M + H]^+$, calcd for $C_{30}H_{27}N_2O_3$ 463.20. HPLC (system B): t_R = 31.6 min (purity 95%). UV−vis (PB/acetone, 8:2, v/v, 25 °C): λ_{max} = 458 nm (17 000 M^{-1} cm^{-1}).

Fully Protected Caspase-3 Latent Blue Fluorophore (10). PABA carboxamide derivative **8** (152 mg, 0.16 mmol) was dissolved in dry acetone (2 mL) and the resulting solution was cooled to 0 °C. Then, triethylamine (67 μL, 0.48 mmol) and mesyl chloride (37 μL, 0.48 mmol) were sequentially added and the resulting reaction mixture was stirred at room temperature overnight. Thereafter, the reaction was quenched by dilution with CH_2Cl_2 (5 mL) and pourring in cold 2 N aq HCl. The aqueous layer was extracted with CH_2Cl_2 (2 × 10 mL). The combined organic layers were washed with deionized water (10 mL), dried over Na_2SO_4, filtered, and evaporated to dryness, affording the mesylate ester **9** as a yellow solid. This crude product was used without purification in the next step. 7-Hydroxycoumarin **5a** (29 mg, 0.18 mmol, 1.1 equiv based on the former step) was dissolved in dry CH_2Cl_2 (2 mL). Anhydrous K_2CO_3 (44 mg, 0.32 mmol, 2 equiv) was added and the mixture was stirred for 20 min, allowing the solution to become yellow-colored. Then, the crude mesylate ester in solution in dry CH_2Cl_2 (2 mL) was added and the reaction mixture was stirred at room temperature overnight. The reaction was checked for completion by RP-HPLC (system B). Thereafter, CH_2Cl_2 (10 mL) was added and the resulting solution was washed with deionized water (10 mL). The organic layer was dried over Na_2SO_4, filtered, and evaporated to dryness. The crude product was purified by RP-HPLC (system C2), to give after lyophilization the corresponding fully protected caspase-3 pro-fluorophore **10** as a white amorphous powder (32 mg, 25%). ^1H NMR (300 MHz, $CDCl_3$): δ 0.02 (s, 9H, Si(CH_3)$_3$), 0.03 (s, 9H, Si(CH_3)$_3$), 0.05 (s, 9H, Si(CH_3)$_3$), 0.96−1.02 (m, 12H, 3CH_2Si + 2CH_{3Val}), 2.07 (s, 3H, CH_3), 2.10−2.20 (m, 2H, CH_{2Glu}), 2.32−2.39 (m, 1H, CHCH$_3$), 2.51−2.62 (m, 2H, CH_2CO$_{Glu}$), 2.85−3.12 (m, 4H, 2CH_{2Asp}), 4.02−4.28 (m, 8H, C*H_{Val} + C*H_{Glu} + 3OCH_2), 4.67−4.73 (m, 1H, C*H_{Asp}), 4.95−5.12 (m, 3H, ArCH_2O + C*H_{Asp}), 6.24 (d, J = 9.0 Hz, 1H, ArH_{Coum}), 6.84−6.92 (m, 2H, 2ArH_{Coum}), 7.09 (d, J = 7.0 Hz, 1H, NH_{Asp}), 7.20 (d, J = 7.0 Hz, 1H, NH_{Val}), 7.34−7.37 (m, 3H, 2ArH_{PABA} + ArH_{Coum}), 7.58−7.64 (m, 2H, ArH_{Coum} + NH_{Asp}), 7.78 (d, J = 8.0 Hz, 2H, ArH_{PABA}), 8.47 (d, J = 3.0 Hz, 1H, NH_{Glu}), 8.67 (s, 1H, NH_{PABA}). ^{13}C NMR (75.4 MHz, $CDCl_3$): δ −1.2 (9C), 17.6

(3C), 18.1, 19.6, 23.3, 25.3, 29.3, 31.6, 36.0, 36.8, 50.3, 51.1, 56.9, 60.7, 63.6, 64.3, 64.4, 70.6, 102.3, 113.0, 113.5, 113.6, 120.6 (2C), 128.6 (2C), 129.0, 131.5, 138.7, 143.8, 156.1, 161.6, 162.2, 169.0, 171.3, 171.4, 171.9, 172.5, 172.8, 172.9, 176.0. MS (ESI, positive mode): *m/z* 1068.40 $[M + H]^+$, calcd for $C_{51}H_{78}N_5O_{14}Si_3$ 1068.49. HPLC (system A): $t_R = 42.0$ min (purity >98%).

Caspase-3 Latent Blue Fluorophore (11). Fully protected pro-fluorophore **10** (12 mg, 11.2 μmol) was dissolved in dry NMP and anhydrous CsF salt (31 mg, 210 μmol) was added. The resulting reaction mixture was stirred at room temperature. Further amounts of CsF (80 equiv and 100 equiv) were added after 16 and 30 h. The reaction was checked for completion by RP-HPLC (system A). Fully protected peptide starting material was completely consumed after 40 h. Finally, the reaction mixture was quenched by dilution with 0.1% aq TFA (3 mL) and purified by RP-HPLC (system E). The product-containing fractions were lyophilized to give the caspase-3 pro-fluorophore **11** as a pale yellow amorphous powder (8.0 mg, quantitative yield). IR (KBr) 3278, 2971, 2883, 1742, 1686, 1664, 1618, 1542, 1490, 1384, 1197, 1140 cm^{-1}. ^1H NMR (300 MHz, DMSO-d_6): δ 0.84−0.89 (m, 6H, 2CH_{3Val}), 1.70−2.10 (m, 6H, CHCH$_3$ + CH_{2Glu} + CH_3), 2.25−2.31 (m, 2H, CH_2CO$_{Glu}$), 2.52−2.80 (m, 4H, 2CH_{2Asp}), 4.15−4.21 (m, 1H, C*H_{Val}), 4.35−4.41 (m, 1H, C*H_{Glu}), 4.50−4.54 (m, 1H, C*H_{Asp}), 4.67−4.73 (m, 1H, C*H_{Asp}), 5.18 (s, 2H, ArOCH_2), 6.33 (d, $J = 9.4$ Hz, 1H, ArH_{Coum}), 7.03 (d, $J = 8.7$ Hz, 1H, ArH_{Coum}), 7.11 (s, 1H, ArH_{Coum}), 7.44 (d, $J = 8.6$ Hz, 2H, 2ArH_{PABA}), 7.66 (m, 3H, ArH_{Coum} + 2ArH_{PABA}) 7.85 (d, $J = 7.5$ Hz, 1H, NH_{Val}), 8.01−8.15 (m, 3H, ArH_{Coum} + NH_{Glu} + NH_{Asp}), 8.42 (d, $J = 6.8$ Hz, 1H, NH_{Asp}), 10.00 (s, 1H, COOH), 12.2−12.5 (m_{Broad}, 2H, 2COOH). MS (ESI, positive mode): *m/z* 768.20 $[M + H]^+$, calcd for $C_{36}H_{42}N_5O_{14}$ 768.27. HPLC (system A): $t_R = 23.6$ min (purity 95%). UV (caspase-3 buffer, 37 °C): λ_{max} = 250 and 320 nm (17 000 M^{-1} cm^{-1}).

Fully Protected Caspase-3 Latent Far-Red Fluorophore (12). 7-Hydroxy-9*H*-(9,9-dimethylacridin-2-one) (DAO) **5d** (10 mg, 42 μmol) was dissolved in dry DMF (800 μL). Anhydrous K_2CO_3 (12 mg, 84 μmol) was added and the resulting reaction mixture was stirred at room temperature for 20 min, allowing the solution to become blue-colored. Then, mesylate ester **9** (35 mg, 35 μmol) was added and the labeling reaction mixture was stirred at room temperature overnight. The reaction was checked for completion by RP-HPLC (system B). Thereafter, CH_2Cl_2 (15 mL) was added and the organic layer was washed with deionized water (7 mL), dried over Na_2SO_4, filtered, and evaporated to dryness. The crude product was purified by RP-HPLC (system D2), to give after lyophilization the corresponding fully protected caspase-3 pro-fluorophore **12** as an orange amorphous powder (4 mg, 13%). ^1H NMR (300 MHz, $CDCl_3$): δ 0.02 (s, 9H, Si(CH_3)$_3$), 0.03 (s, 9H, Si(CH_3)$_3$), 0.05 (s, 9H, Si(CH_3)$_3$), 0.78−1.02 (m, 12H, 3CH_2Si + 2CH_{3Val}), 1.19 (s, 3H, CH_{3DAO}), 1.25 (s, 3H, CH_{3DAO}), 1.95−2.20 (m, 5H, CH_{2Glu} + CH_3), 2.25−2.39 (m, 1H, CHCH$_3$), 2.45−2.62 (m, 2H, CH_2CO$_{Glu}$), 2.80−3.12 (m, 4H, 2CH_{2Asp}), 3.95−4.22 (m, 8H, C*H_{Val} + C*H_{Glu} + 3OCH_2), 4.65−4.72 (m, 1H, C*H_{Asp}), 4.95−5.09 (m, 3H, ArCH_2O + C*H_{Asp}), 6.58−6.66 (m, 3H, 3ArH_{DAO}), 6.93−6.97 (m, 1H, ArH_{DAO}), 7.08−7.12 (m, 2H, NH_{Val} + NH_{Asp}), 7.35−7.41 (m, 3H, ArH_{DAO} + 2ArH_{PABA}), 7.58−7.63 (m, 2H, NH_{Asp} + ArH_{DAO}), 7.77−7.80 (d, 2H, J = 8.7 Hz, 2ArH_{PABA}), 8.47 (d, $J = 4.2$ Hz, 1H, NH_{Glu}), 8.67 (s, 1H, NH_{PABA}). MS (ESI, positive mode): *m/z* 1145.33 $[M + H]^+$, calcd for $C_{57}H_{85}N_6O_{13}Si_3$ 1145.55. HPLC (system A): $t_R = 39.5$ min (purity 90%).

Caspase-3 Latent Far-Red Fluorophore (13). Fully protected peptide **12** (3.0 mg, 2.6 μmol) was dissolved in dry NMP. A large excess of anhydrous CsF salt (79.0 mg, 520 μmol) was added and the deprotection reaction mixture was stirred at room temperature for 48 h. The reaction was checked for completion by RP-HPLC (system A). Finally, the reaction mixture was quenched by dilution with 0.1% aq TFA (3 mL) and purified by RP-HPLC (system F). The product-containing fractions were lyophilized to give the caspase-3 pro-fluorophore **13** as an orange amorphous powder. This fluorogenic caspase-3 substrate was water-solubilized through its conversion into the tris-NH_4^+ salt by brief treatment with 5 μL of 3% aq NH_4OH followed by lyophilization. Quantification was achieved in caspase-3 buffer at $\lambda_{max} = 457$ nm by using the ε value 6500 M^{-1} cm^{-1} (yield after RP-HPLC purification: 82%). MS (ESI, negative mode): *m*/z 843.33 $[M - H]^-$, calcd for $C_{42}H_{47}N_6O_{13}$ 843.32. HPLC (system A): $t_R = 25.8$ min (purity 91%). UV−vis (caspase-3 buffer, 37 °C): λ_{max} = 247 and 457 nm (6500 M^{-1} cm^{-1}).

General Procedure for the *in Vitro* Cleavage PGA Fluorogenic Probes by Immobilized Penicillin Amidase. *(a) Fluorescence Assay.* A solution of PGA fluorogenic probe (final concentration: 2.6 μM for **6a** and 2.2 μM for **6d**) was prepared with a mixture of phosphate buffer (PB, 50 mM, pH 7.4) and acetone (PB/acetone, 8:2, v/v). 1.25 mL of this solution was transferred into a semimicro quartz fluorescence cell (Hellma, 104F-QS, 10 × 4 mm, 1400 μL) and immobilized penicillin amidase (6.4 U, 64 mg) was added. The resulting mixture was incubated at 37 °C. Fluorescence emission of the enzymatically released phenol-based fluorophore (i.e., 7-hydroxycoumarin **5a** at $\lambda = 460$ nm or DAO **5d** at $\lambda = 651$ nm) was monitored over time with measurements every 6 s, after excitation at $\lambda = 360$ nm (for **5a**) or 638 nm (for **5d**). The same conditions were applied to the control sample without adding the enzyme and no significant fluorescence signal was detected.

(b) Characterization of Cleavage by RP-HPLC. PGA fluorogenic probe was dissolved (final concentration: 1.65 mM for **6a** and 1.2 mM for **6d**) in a mixture of phosphate buffer and acetone (PB/acetone 8:2, v/v, 2 mL). For the fluorogenic probe **6d**, 2,6-di-*O*-methyl-β-cyclodextrin (46 mg, 35 μmol) was added to improve the solubility in the aq buffer. Immobilized penicillin amidase (16.7 U, 167 mg for **6a** or 15.0 U, 150 mg for **6d**) was added and the resulting suspension was stirred at 37 °C for 24 h. Periodically, 100 μL of the crude enzymatic mixture were sampled (the biocatalyst was filtered off), dissolved with 300 μL of triethylammonium acetate buffer (TEAA, 100 mM, pH 7.0), and analyzed by RP-HPLC (system A, injection volume: 10 μL). Quantification of **5a**/**6a** (or **5d**/**6d**) was achieved by measurement of the corresponding peak areas at $t_R = 15.6$ and 29.3 min (or $t_R = 21.2$ and 31.5 min).

Optical Properties of DAO 5d. The absorption spectrum of DAO was recorded (220−900 nm) in PBS (0.1 M phosphate, 0.15 M NaCl, pH 7.4) (a 4.2 mM stock solution was prepared in DMSO and diluted with PBS to reach a final concentration of 14.0 μM) at 25 °C. Emission spectrum was recorded under the same conditions after excitation at 610 nm (excitation and emission slit = 5 nm). Relative quantum yield was measured in PBS at 25 °C by a relative method using sulfocyanine dye Cy 5.0 ($\Phi_F = 0.20$ in PBS (*43*)). The following equation was used to determine the relative fluorescence quantum yield:

$$\Phi_F(\text{DAO}) = (A_{Cy5.0}/A_{DAO})(F_{DAO}/F_{Cy5.0})(n_{DAO}/n_{Cy5.0})^2\Phi F_{(Cy\ 5.0)} \quad (1)$$

where A is the absorbance (in the range 0.01−0.1 A.U.), F is the area under the emission curve (620−850 nm after excitation at 610 nm), and n is the refractive index of the solvent (at 25 °C) used in measurements ($n = 1.337$ for PBS). The slopes were determined to be: 9.65×10^4 and 2.43×10^5 ($R^2 = 0.99$) for DAO and Cy 5.0, respectively.

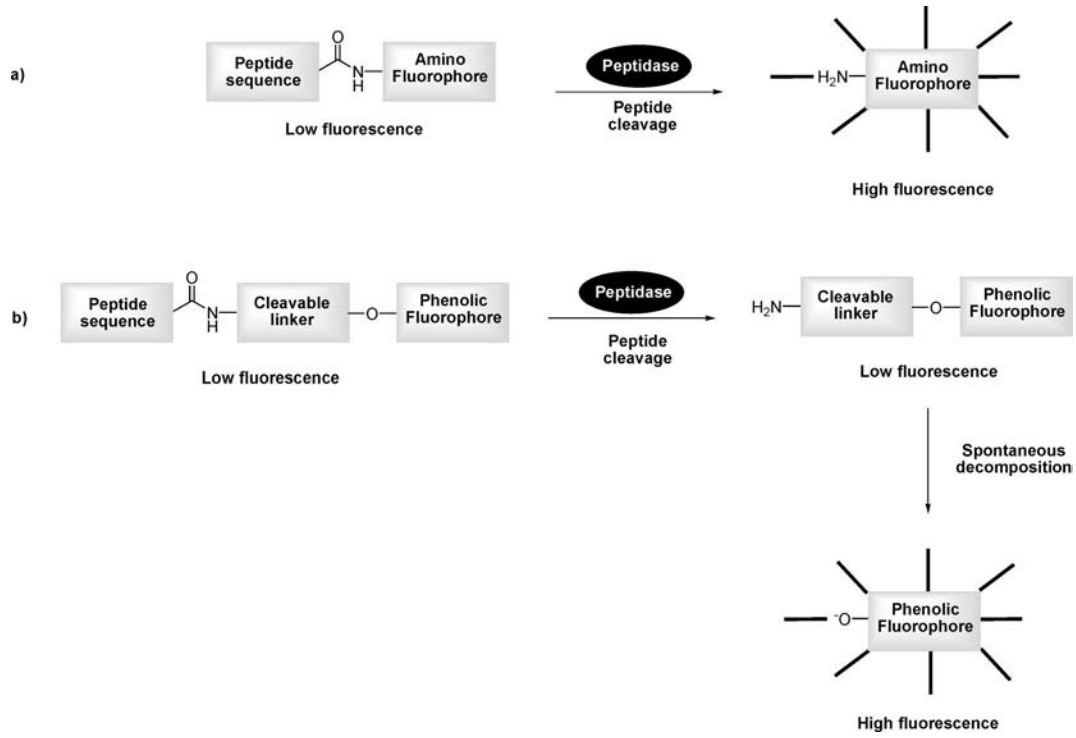

Figure 1. General mechanisms of the activation of pro-fluorophores by proteolytic enzymes. (a) Release of aniline-based fluorophores. (b) Release of phenol-based fluorophores through a self-immolative strategy.

General Procedure for the *in Vitro* Cleavage of Latent Blue and Far-Red Fluorophores 11 and 13 by Recombinant Human Caspase-3. *(a) Fluorescence Assay.* A solution of latent fluorophore (final concentration: 3.0 μM for **11** and 23.0 μM for **13**) was prepared with the following caspase-3 buffer: 100 mM NaCl, 40 mM HEPES, 10 mM DTT, 1 mM EDTA, 10% (w/v) sucrose, and 0.1% (w/v) CHAPS, pH 7.4. 50 μL of this solution were transferred into an ultramicro fluorescence cell (Hellma, 105.51-QS, 3 $\times$ 3 mm, 45 μL), human recombinant caspase-3 (1 μL, 1.6 $\times$ 10^{-3} U for **11** and 2 μL, 3.2 $\times$ 10^{-3} U for **13**) was added and the resulting mixture was incubated at 37 °C. Fluorescence emission of the enzymatically released phenol-based fluorophore (i.e., 7-hydroxycoumarin **5a** at λ = 460 nm or DAO **5d** at λ = 651 nm) was monitored over time with measurements every 5 s, after excitation at λ = 360 nm (for **5a**) or 638 nm (for **5d**). The same conditions were applied to the control sample solution without adding enzyme. No significant fluorescence signal was detected.

(b) Determination of the Kinetic Parameters for the Caspase-3 Hydrolysis of **11.** Latent blue fluorophore **11** was diluted in caspase-3 buffer at the following concentrations 100 μM, 50 μM, 25 μM, 12.5 μM, 6.25 μM, and 3.125 μM and put into a black clear-bottom 96-multiwell plate. Then, 1.0 pmol of recombinant human caspase-3 preheated during 15 min at 37 °C was added (final concentration: 20 nM). The reaction was monitored with FlexStation for 2 h with measurements every 30 s (Ex. λ = 370 nm, Em. λ = 460 nm, 37 °C, cutoff filter λ = 455 nm). A calibration curve using umbelliferone **5a** was used to convert relative fluorescence units in mole of transformed product. Initial velocity V_0 was measured for each substrate concentration, and K_M, V_{max}, k_{cat}, and k_{cat}/K_M values were determined with the double-inverse Lineweaver−Burk relationship. The determination of the kinetic parameters was performed in triplicate; the kinetic constants presented are an average of the values found.

RESULTS AND DISCUSSION

Choice of the Self-Immolative Linker. During the past decade, numerous self-immolative linker strategies have been developed for the design of efficient prodrugs of various pharmaceuticals (*29*) and functionalized solid supports suitable for the synthesis of organic compound libraries through combinatorial or parallel methods (*44–47*). As suggested in some recent publications (*30, 34*), the use of a self-cleavable linker as a spacer unit between the peptidyl substrate and a fluorescent label is potentially beneficial to improve both enzymatic reactivity and spectral properties (especially in the far-red to NIR region) and to reduce the background noise associated with nonspecific hydrolysis of the resulting pro-fluorophore compared to "standard" two-component fluorogenic protease substrates. Indeed, the self-decomposition of the linker through a protease-initiated domino reaction allows the release of a wide range of fluorophores bearing an aniline, a phenol, or a thiophenol moiety (*48*). Therefore, structures more sophisticated than basic carboxamide derivatives of fluorescent amines (i.e., 7-amino-4-methylcoumarin (AMC), rhodamine 110, or cresyl violet) can be envisaged to get protease-activated optical probes with excellent analytical properties (Figure 1). In this context, we first explored the use of the enzyme-labile safety catch linker recently reported by Grether and Waldmann, which allows the release of alcohols or amines through an original enzyme-initiated lactam-cyclization (*49, 50*). A latent blue fluorophore of penicillin amidase derived from this traceless linker was prepared in six steps from homovanilinic acid: however, *in vitro* cleavage experiments (fluorescence and HPLC assays) with PGA have clearly shown the moderate stability of its ester linkage under simulated physiological conditions due to the good leaving-group character of the 7-hydroxycoumarin fluorophore employed. Consequently, we decided to graft the phenol-based fluorophore through a less reactive ether bond by using the commercially available *para*-aminobenzyl alcohol (PABA) as the self-immolative spacer (Figure 2) (*51*). PABA is one of the most popular self-immolative linker applicable in prodrug design (*52*) and its utility in the field of spectroscopic bioprobes was recently demonstrated by Jones et al. through the design of an image contrast agent employing AMC as fluorophore and

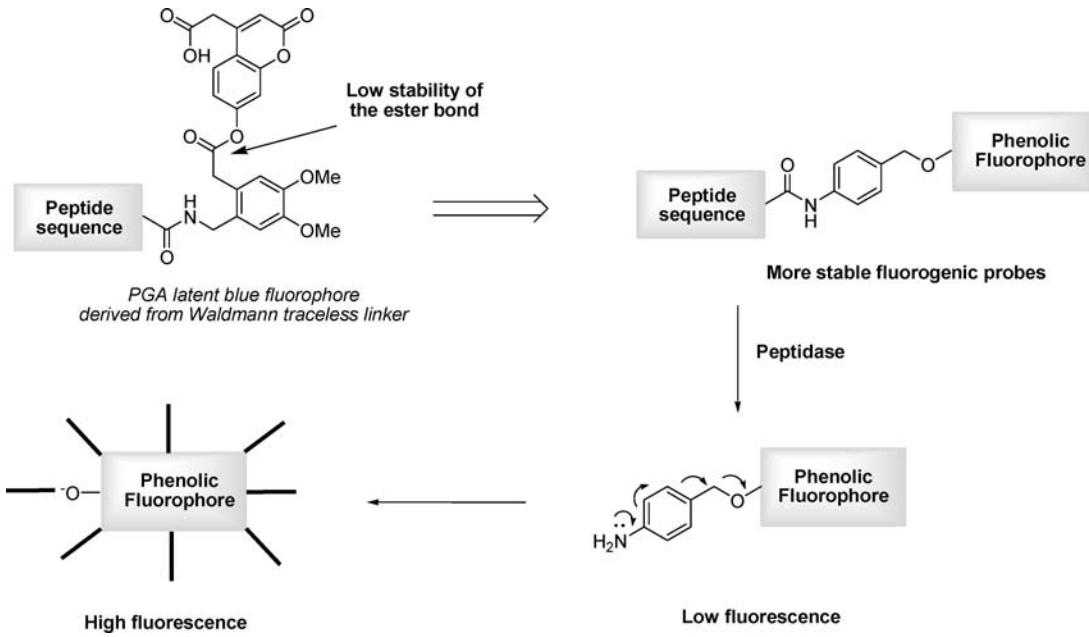

Figure 2. General structure of the first generation peptidase-sensitive pro-fluorophores based on the Waldmann enzyme-labile safety catch linker. General structure of the second generation peptidase-sensitive pro-fluorophores and principle of their activation through the self-immolation of PABA linker.

selective activation by the serine protease prostate specific antigen (PSA) (*30*).

Penicillin Amidase-Sensitive Pro-Fluorescent Probes. To validate our self-immolative approach in the context of protease-sensitive pro-fluorescent probes, we first carried out assays with penicillin amidase (PGA), a commercially available and widely used biocatalyst in the enzymatic synthesis of β-lactam antibiotics, since it allows the deprotection of phenacetyl protected amines (*53*). As this enzyme is inexpensive and readily available under an immobilized form which tolerates the use of an organic cosolvent such as acetone or methanol, it is widely employed as a suitable reagent or catalyst in organic synthesis especially for the selective deprotection of amino groups within complex molecular architectures (dendrimers (*54–56*), peptides (*57*), and so forth), both in solution or on solid phase. Interestingly, the current method for *in vitro* detection of PGA activity relies on the use of phenylacetamide derivatives of fluorescent amines (e.g., AMC) as fluorogenic substrates (*58*). Thus, we synthesized a novel class of PGA-sensitive pro-fluorescent probes in order to check if the PABA moiety inserted between the fluorophore and the protease-reactive group of our latent fluorophores was suitable to fulfill all requirements for biomolecular imaging applications: (1) changes of the fluorescence properties (especially significant increase in emission intensity) upon reaction with enzyme, (2) chemical stability under physiological conditions, and (3) efficiency of the enzyme-initiated fluorophore releasing process. Theoretically, our latent fluorophore strategy is applicable to all labeling dyes having a phenol moiety whose acylation (or alkylation) significantly affects their fluorescence properties. However, as *in cellulo* and *in vivo* applications require the use of fluorescent compounds exhibiting a significant emission in the range 450−750 nm (650−750 nm for *in vivo*) our choice was guided toward four well-known fluorescent phenols, namely, 7-hydroxycoumarin (umbelliferone) **5a**, 2-hydroxy Nile Red **5b**, 7-hydroxy-9*H*-(1,3-dichloro-9,9-dimethylacridin-2-one) (DDAO) **5c**, and 7-hydroxy-9*H*-(9,9-dimethylacridin-2-one (DAO) **5d**. The corresponding PGA-sensitive pro-fluorescent probes were prepared as shown in Scheme 1. condensation of the fluorescent phenol with the phenylacetamide derivative of PABA **3** was achieved by a nucleophilic substitution of the mesylate derivative **4**. Purification of all pro-fluorophores was performed by semipreparative RP-HPLC using 0.1% aqueous trifluoroacetic acid (TFA, pH 2.0) and acetonitrile as eluents (overall yields for two steps 10−28%). The modest isolated yields are explained by the competitive degradation of **4** under basic reaction conditions and the significant loss of fluorogenic substrate during the subsequent chromatographic purification. All spectroscopic data, especially NMR and mass spectrometry, were in agreement with the structures assigned.

The spectral properties of the four novel PGA-sensitive pro-fluorophores were evaluated, compared with those of the corresponding parent phenol-based fluorophore, and collected in Table 1 (for their emission spectra compared with those of free fluorophores, see Supporting Information). The pro-fluorescent probes **6a**, **6c**, and **6d** displayed the expected hypsochromic shift of excitation and emission spectra relative to the free fluorophores and exhibited no significant fluorescence at the maximum emission wavelength of the corresponding parent phenol dye (460 nm for **5a**, 651 nm for **5c** and **5d**). Indeed, the chemical modification of the hydroxyl group (i.e., modification of the phenol either to an ether or an ester) of a fluorescent phenol is known to effectively quench its fluorescence (*59*) and this property has already been used to design efficient fluorogenic probes for detection of β-galactosidase, β-lactamases, and phosphatases (*1*). However, we observed that this particular trend for phenol-based fluorophores was not followed by the benzophenoxazine derivative **6b**, because in our measurements, its fluorescence intensity showed only a 2-fold decrease compared to the parent 2-hydroxy Nile Red and the expected blue-shift of its maximum emission wavelength was not observed. This result is consistent with an earlier report from Briggs et al. showing that the esterification of the hydroxyl group of Nile Red derivatives does not significantly affect their optical properties and prevents the use of such phenol-based fluorophores in the context of fluorogenic probes based on the pro-fluorescence concept (*41*). Furthermore, during the course of our spectroscopic studies, we observed an anomalous behavior of the pro-fluorophore **6c** whose fluorescence significantly increases during incubation with a 8:2 mixture of phosphate buffer (PB, pH 7.4) and acetone. This nonenzymatic fluorescence unveiling of probe **6c** was attributed to the release of the DDAO dye through the hydrolytic cleavage of its ether

Scheme 1. Synthesis of PGA-Sensitive Pro-Fluorescent Probes

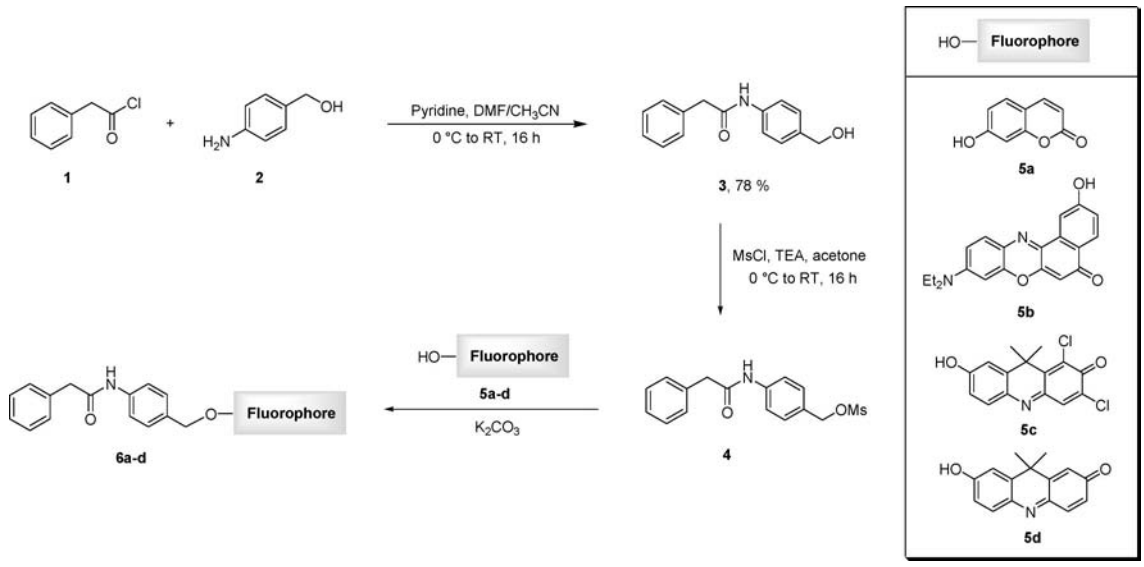

Table 1. Fluorescence Excitation and Emission Wavelengths of PGA-Sensitive Pro-Fluorophores and the Free Phenol Dyes Released by the Enzyme-Initiated Domino Reaction

	PGA pro-fluorophore[a]			free fluorophore[a]	
compound	excitation (nm)	emission (nm)	fluorescence intensity[b]	excitation (nm)	emission (nm)
6a	275	nonfl	nonfl	360	460
6b	530	652	2-fold reduction	582	655
6c	-[c]	-[c]	-[c]	636	651
6d	458	599	8.5-fold reduction	638[d]	651[d]

[a] All spectral properties were determined in a 8:2 (v/v) mixture of phosphate buffer (PB, 50 mM, pH 7.4) and acetone at 25 °C. [b] Calculated by the fluorescence intensity ratio between pro-fluorophore and free fluorophore at the same concentration. [c] Compound **6c** was found to be unstable in the mixture PB/acetone. [d] The fluorescence quantum yield of free DAO **5d** is 0.079 (determined in PBS at 25 °C by using sulfocyanine dye Cy 5.0 (Φ_F = 0.20 in PBS at 25 °C (*43*) as a standard) and the molar exctinction coefficient at λ_{max} = 633 nm is 24 450 M^{-1} cm^{-1}.

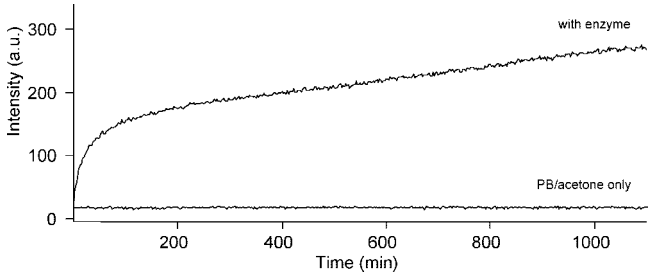

Figure 3. Fluorescence emission time course of pro-fluorescent probe **6d** (concentration 2.2 μM) with immobilized penicillin amidase (6.4 U, incubation time 24 h at 37 °C) in a 8:2 (v/v) mixture of phosphate buffer (50 mM, pH 7.4) and acetone at 651 nm (Ex. λ = 638 nm).

bond in neutral physiological conditions. Due to the presence of two chlorine atoms within its acridin-2-one core, DDAO is too good as a leaving group to be a valuable candidate for the latent fluorophore strategy. Surprisingly, the low chemical stability of fluorogenic substrates using DDAO as a pro-fluorescent label in aqueous solution has never been observed and reported in the literature, whereas some DDAO esters and ether derivatives of biomolecules (i.e., β-D-galactopyranose, nucleotide polyphosphates) have been developed and successfully used to monitor enzyme activities *in vivo* or as reagents for various homogeneous nucleic acid assays (*23, 60*).

Finally, only the two completely quenched and stable pro-fluorophores **6a** and **6d** were tested against immobilized PGA. As an illustrative example, the time-course for the amidase catalyzed hydrolysis of **6d** is shown in Figure 3 (see Supporting Information for results obtained with **6a**). After adding immobilized PGA to the substrate solution, a strong fluorescence signal generated at 651 nm indicated the catalytic cleavage of the carboxamide bond and the release of the free DAO dye. Furthermore, no nonspecific cleavage of the probe was detected in a control reaction where **6d** was incubated only with the mixture PB/acetone (8:2, v/v). Overall, these results confirm that the latent red fluorophore **6d** is a substrate for penicillin amidase. In addition to these spectral measurements, RP-HPLC analyses of the enzymatic hydrolysis mixture of **6d** were performed to prove the identity of the released fluorescent phenol (i.e., DAO, t_R = 15.6 min) and the efficacy of this release process (see Supporting Information). Thus, we validated that the connection of a protease-sensitive substrate to a phenol-base fluorophore through a self-immolative PABA linker is an efficient way to obtain activatable pro-fluorescent probes exhibiting both chemical stability and enzymatic reactivity. We then extended the scope of this approach to the detection of a more challenging protease belonging to the caspase family (i.e., caspase-3) in an attempt to perform *in cellulo* and *in vivo* imaging of apoptosis.

Synthesis of Caspase-3 Sensitive Pro-Fluorescent Probes. Caspases are Cysteine-ASpartic-acid-ProteASES that play a critical role as mediators for apoptotic cell death (*61*). Caspase-3 has been specifically identified as being a key mediator of apoptosis in mammalian cells (*62*): activation of caspase-3 indicates that the apoptotic pathway has progressed to an irreversible stage. As apoptosis disorders are involved in many diseases or malfunctionings such as ischemia, neurodegenerative diseases, or cancers, this protease is an attractive target for diagnostic and therapeutic applications through its detection in biological media using smart optical bioprobes. The main strategy for both *in vitro* and *in cellulo* sensing of caspase-3 relies on the use of fluorescent probes. Numerous

Scheme 2. Synthesis of Caspase-3 Latent Blue Fluorophore 11

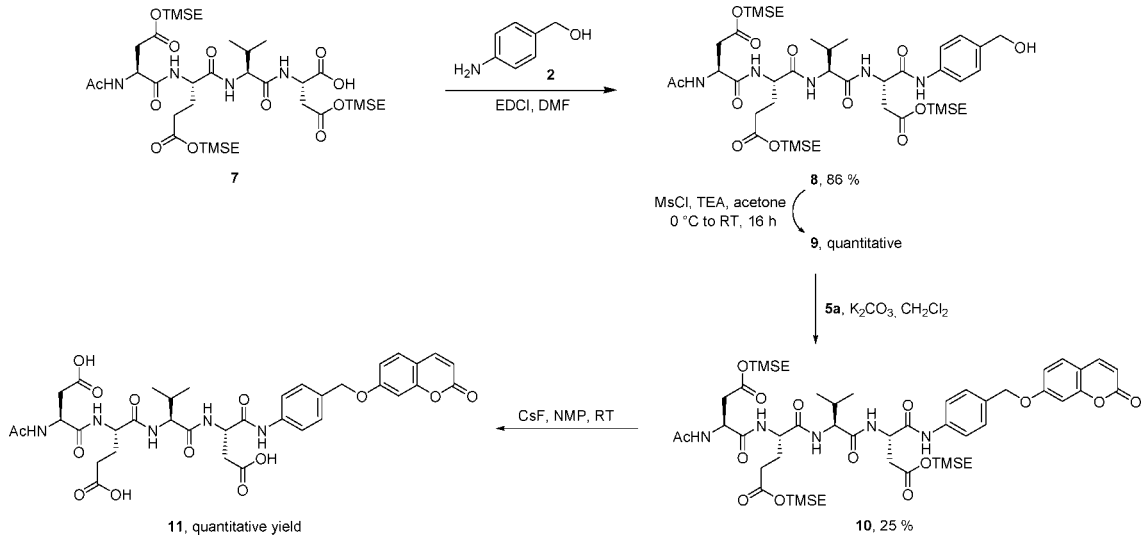

latent blue or green fluorophores (i.e., peptide conjugated to 7-aminocoumarin or rhodamine fluorescent tags) (*19, 20*) and fluorogenic probes based on the fluorescence resonance energy transfer (FRET) mechanism (*63–69*) have been developed, and some of them are routinely used as caspase-3 substrates for enzyme and cell-based fluorescent assays. All these probes are based on the fact that upon binding with caspase-3, protease-mediated cleavage of their peptide substrate occurs after the aspartic acid residue at the C-terminal side. The preferred sequence for caspase-3 cleavage is Asp-Glu-Val-Asp. To our knowledge, only one caspase-3 latent red fluorophore derived from the oxazine dye cresyl violet and marketed under the Magic Red name by ICN Biomedicals and Immunochemistry Technologies has been reported in the literature (*70*). Despite the spectral properties of cresyl violet dye in the far-red region, which enable good tissue penetration and low background noise in biological samples, the poor solubility of this fluorogenic probe in aqueous-based media and its poor kinetics due to the bulky fluorescent moiety prevents its efficient use for *in vivo* real-time imaging of caspase-3 activity. In this context, we wished to develop a novel class of water-soluble and far-red-emitting caspase-3-sensitive pro-fluorescent probes based on the validated "PABA" strategy (*vide supra*). As a first step of this challenging project, we have considered the synthesis of original caspase-3 latent fluorophores from two well-known dyes (umbelliferone **5a** and DAO **5d**), both linked by a PABA moiety to the caspase-3 tetrapeptidyl substrate (Scheme 2). First, the fully protected Ac-Asp(OTMSE)-Glu(OTMSE)-Val-Asp(OTMSE)-OH tetrapeptide **7** was synthesized on the gram scale by solution-phase peptide synthesis according to a multistep procedure developed by us (*38*). The carboxylic acid functionalities of the side chains were protected as 2-trimethylsilylethyl esters (TMSE esters) (*71, 72*). This protecting group is stable to the solution-phase peptide synthesis conditions and can be removed by treatment with various fluoride ion sources under mild conditions fully compatible with the stability of the ether bond linking the fluorescent phenol to the PABA moiety. Thereafter, the PABA linker **2** was introduced at the C-terminal side of **7** and the corresponding benzylic alcohol **8** was obtained in good yield. The introduction of the phenol-based fluorophore was achieved through nucleophilic substitution and required the activation of alcohol **8**. Mitsunobu reaction, bromination with PPh_3/CBr_4, or esterification with tosyl chloride were explored but failed to yield the target phenol-reactive derivative. Finally, we found that the only way to readily activate the alcohol was its conversion into mesylate ester **9**. We suspected that steric hindrance around the benzylic hydroxyl group probably induced by the tetrapeptide folding prevented the introduction of leaving groups bigger than mesylate. The resulting activated derivative was reacted with 7-hydroxycoumarin **5a** under mild basic conditions to give after purification by semipreparative RP-HPLC the fully protected pro-fluorescent probe **10** in 25% yield. Finally, the selective removal of the TMSE side chains protecting groups within the tetrapeptide scaffold was undertaken with different fluoride ion sources. No reaction was observed when an acidic fluoride ion source such as triethylamine-trishydrofluoride (TEA.3HF) was used. Mild basic fluoride ions provided by the tetrabutylammonium fluoride salt (TBAF or silica gel supported TBAF) allowed the complete deprotection of the TMSE esters, but isolation of the caspase-3-sensitive pro-fluorescent probe **11** in a pure form was not possible. Indeed, despite several semipreparative RP-HPLC purification runs (with aq TFA, 0.1% or deionized water as aq mobile phase), pro-fluorophore **11** was always found to be contaminated with significant amounts of tetrabutylammonium salts. This problem was circumvented by the use of tetramethylammonium fluoride (TMAF) or CsF which afforded the caspase-3 latent blue fluorophore **11** in a pure form with a quantitative yield.

To access longer wavelengths, we have applied the same synthetic strategy to the far-red dye DAO **5d** (Scheme 3). Sequential nucleophilic substitution, CsF-mediated deprotection, and final RP-HPLC purification afforded the caspase-3 latent far-red fluorophore **13** in a moderate 10% overall yield. The lower yield obtained for **11** was explained by the lower nucleophilic character of DAO compared to umbelliferone which directly affects the efficacy of the substitution step. To get a water-soluble fluorogenic caspase-3 substrate, **13** was converted into the corresponding tris-NH_4^+ salt by a brief treatment with 3% aq NH_4OH followed by lyophilization.

The structures of latent blue and far-red fluorophores **11** and **13** were confirmed by detailed analytical measurements, including ESI mass spectrometry and ^1H NMR analyses (see Figure 4 and Supporting Information).

Fluorescence Properties and Enzymatic Reactivity. Photophysical properties of fluorogenic probe **11** were evaluated in caspase-3 buffer (for the composition of this buffer, see Experimental Procedures section). This pro-fluorophore displayed the expected hypsochromic (~60 nm) and hypochromic shifts (10-fold diminution of fluorescence intensity) of emission spectrum relative to free umbelliferone (see Table 2 and Supporting Information). As this background fluorescence level

Scheme 3. Synthesis of Caspase-3 Latent Far-Red Fluorophore 13

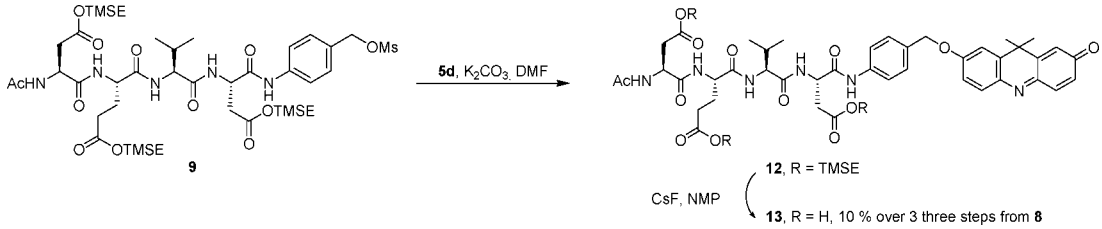

was not affected by a prolonged incubation of **11** with caspase-3 buffer, the 7-O-substituted derivative of umbelliferone proved to be fully stable in the aq solution. Concerning the reactivity of **11** as a substrate for caspase-3, *in vitro* fluorescence assay was performed with the corresponding recombinant human protease. The increase of fluorescence upon enzyme-induced hydrolytic cleavage of **11** was indicative of single hit kinetics (see Supporting Information). Kinetic constants were calculated to be $k_{cat} = 5.6\ s^{-1}$, $K_m = 65.7\ \mu M$, and $k_{cat}/K_m = 84\,852\ M^{-1}\ s^{-1}$ (Figure 5). Comparison with the apparent kinetic constants from commercially available Ac-Asp-Glu-Val-Asp-AMC fluorogenic substrate ($k_{cat} = 0.75\ s^{-1}$, $K_m = 9.0\ \mu M$, and $k_{cat}/K_m =$ 83 300 $M^{-1}\ s^{-1}$ (*73*)) shows no significant increase in the k_{cat}/K_m value, but a 7.5-fold improvement of the catalytic constant. Thus, the use of PABA linker not only maintained but even improved the recognition of the probe by the targeted enzyme. One can suspect that the beneficial effect of moving away the bulky fluorophore from peptidic substrate should be even more obvious with proteases exhibiting a lower degree of substrate tolerance. Besides this, further experiments aimed at demonstrating the utility of the pro-fluorescent reagent **11** for the measurement of apoptosis in whole cell assays are currently in progress and will be reported elsewhere.

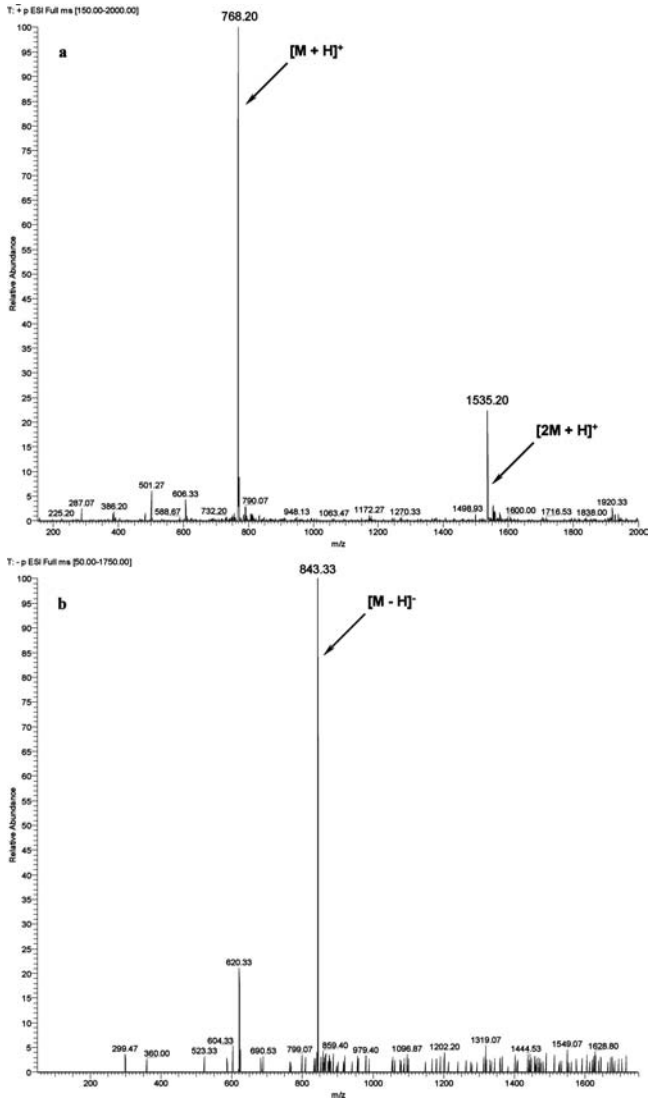

Figure 4. ESI mass spectra of caspase-3 latent fluorophores. (a) positive mode for compound **11** $[M + H]^+$: *m*/*z* calcd mass 768.27, found 768.20. (b) negative mode for compound **13** $[M - H]^-$: *m*/*z* calcd mass 843.32, found 843.33.

Table 2. Fluorescence Excitation and Emission Wavelengths of Caspase-3-Sensitive Pro-Fluorophores and the Free Phenol Dyes Released by the Enzyme-Initiated Domino Reaction

	caspase-3 pro-fluorophore[a]			free fluorophore[a]	
compound	excitation (nm)	emission (nm)	fluorescence intensity[b]	excitation (nm)	emission (nm)
11	320	397	10-fold reduction	360	460
13	460	606	12-fold reduction	638	651

[a] Spectral properties of **5a**/**11** were determined in caspase-3 buffer at 37 °C. Deionized water was used for compounds **5d**/**13** to avoid fluorescence quenching of DAO derivatives by DTT. [b] Calculated by the fluorescence intensity ratio between pro-fluorophore and free fluorophore at the same concentration.

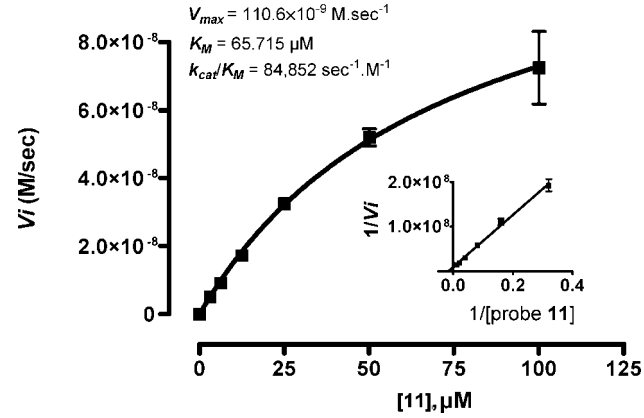

Figure 5. Michaelis−Menten plot for the hydrolysis of pro-fluorophore **11** (100 $\mu M \rightarrow 3.12\ \mu M$) by caspase-3.

The latent far-red flurophore **13** was subjected to the same fluorescence measurements. As expected, alkylation of the 7-OH group of DAO caused a blue-shift of excitation and emission peaks of this acridin-2-one dye (Ex./Em. $\lambda = 460/606$ nm compared to 638/651 nm for DAO). However, contrary to the latent blue fluorophore **11**, the *in vitro* proteolytic cleavage experiment with caspase-3 gave unexpected results. Indeed, dissolution of the pro-fluorophore **13** in caspase-3 buffer resulted in a 12-fold quenching of its residual fluorescence emission at $\lambda = 606$ nm and, after the addition of protease, the red fluorescence of the released DAO dye did appear, but only after a delay correlated with both probe and buffer amounts (around 100 min in the representative experiment displayed in Figure 6). We suspected that one chemical component of the caspase-3

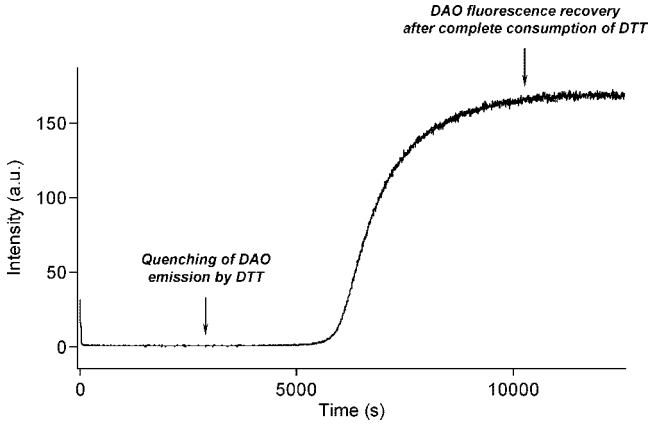

Figure 6. Fluorescence emission time course of pro-fluorescent probe **13** (concentration 23.0 μM) with recombinant human caspase-3 (3.2 10^{-3} U, form: buffered aq glycerol solution containing 100 mM NaCl, 50 mM HEPES pH 7.4, 10 mM DTT, 1 mM EDTA, 10% (w/v) glycerol, and 0.1% (w/v) CHAPS) in deionized water (37 °C) at 651 nm (Ex. λ = 638 nm). (note: The expected level of fluorescence intensity for the released DAO was not reached because of irreversible quenching of some fluorophore molecules through their reaction with DTT.)

buffer should be responsible of this temporary fluorescence extinction. Further experiments have enabled the identification of the dithiol reducing agent DTT as the sole molecule reactive toward DAO dye. LC-MS analyses of the reaction mixture of free DAO **5d** with DTT were performed to check the formation of the nonfluorescent compound and to identify its structure (see Supporting Information). By analogy with the mechanism proposed by Kitson to explain the reaction between some 7-O-substituted derivatives of resorufin and β-mercaptoethanol (*74*), we proposed a pathway compatible with both the observed on/off fluorescence switch of **5d** mediated by the dithiol-reducing agent and the mass value determined for the reaction product (Figure 7): nucleophilic addition of a thiol group of DTT to the α,β-unsaturated imine moiety followed by tautomerization to give the aromatic ring of a phenol as an intermediate nonfluorescent product; this in turn is followed by an oxidation step to reform the acridinone moiety. Thereafter, the same two-step reaction sequence (i.e., nucleophilic addition and tautomerization) occurs with the remaining free thiol group to give the nonfluorescent product **14**. This clock reaction takes place until the complete consumption of reduced DTT which is progressively oxidized either by the atmospheric oxygen dissolved in buffer or through the reverse elimination reaction giving back the fluorescent DAO dye. This unexpected competing reaction does not represent an insuperable defect for *in vitro* applications of pro-fluorescent reagent **11**. However, its evaluation as a reporter molecule for *in cellulo* and *in vivo* imaging of caspase-3 activity cannot be considered due to high levels of thiols (e.g., glutathione) in living organisms.

CONCLUSION

We have demonstrated how common phenol-based fluorophores can be converted to sophisticated molecular tools suitable for protease sensing. The use of a self-cleavable PABA linker provided pro-fluorophores with high chemical stability while maintaining enzymatic reactivity. Furthermore, the modularity of two components of our latent fluorophores (i.e., the dye and the enzyme-reactive group) was demonstrated through the preparation of blue- and far-red-emitting fluorogenic substrates of two different proteolytic enzymes: PGA and caspase-3 protease. Particularly, the implementation of this latent fluorophore strategy to *in vitro* imaging has led us to a ca. 10-fold increase of the enzyme velocity toward the fluorogenic pseudosubstrate **11** as compared to the commercially available pro-fluorophore Ac-Asp-Glu-Val-Asp-AMC. For *in vivo* imaging of protease activities, the self-immolative linker strategy has led us to explore the preparation of the original caspase-3-sensitive far-red-emitting fluorogenic probe **13** by using DAO as a fluorescent phenol. Unfortunately, our preliminary biochemical studies have allowed us to exhibit a yet unprecedented observation: the fluorescence of the enzymatically released acridinone dye is efficiently quenched in the presence of thiols, probably through a nucleophilic addition of these reducing agents to its quinonimine ring. To our knowledge, all known far-red-emitting phenol-based fluorophores (i.e., acridinone and oxazinone derivatives) contain this latter thiol-reactive moiety. Thus, the present study clearly showed the urgent need to design new red-emitting inert phenol-based fluorophores in order to expand the scope of promising latent fluorophore strategies to the visualization of various biologically relevant molecules and activities inside living cells. With this goal in mind, new conjugation-extended 7-hydroxycoumarin NIR dyes are currently under investigation in our laboratory and their use as fluorogenic labels for biomolecular imaging will be reported in due course.

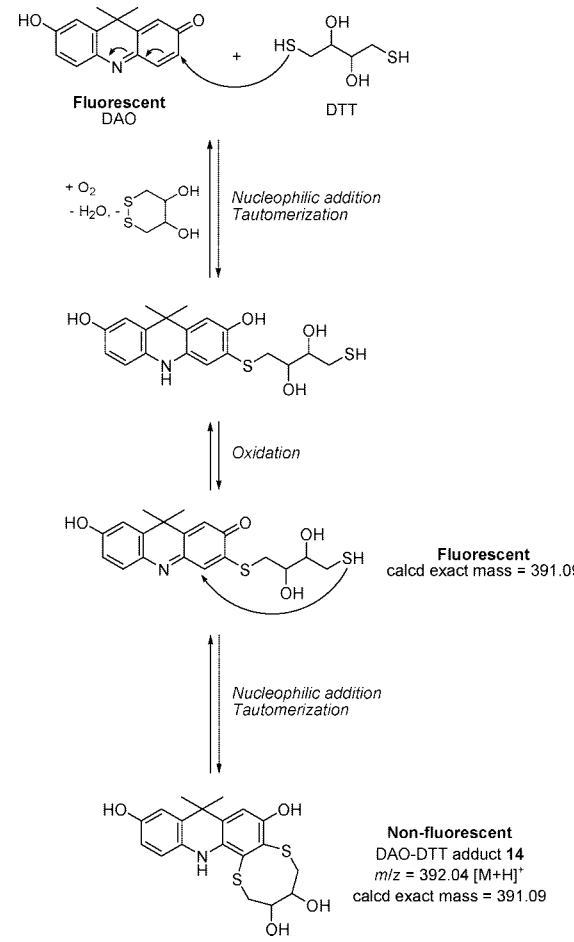

Figure 7. Proposed mechanism to explain the observed on/off fluorescence switch of the DAO dye during the caspase-3 assay with latent far-red fluorophore **13**. (note: As suggested by Kitson et al. (*74*) only the DAO derivatives bearing the quinonimine ring were considered as colored and fluorescent species.)

ACKNOWLEDGMENT

This work was supported by La Région Haute-Normandie, QUIDD and Institut Universitaire de France (IUF). We thank Elisabeth Roger (INSA de Rouen) for IR measurements and

Dr. Christophe Portal (QUIDD) for careful reading and English corrections of the manuscript.

Supporting Information Available: Characterization data for compounds **6a**, **6d**, **10**−**12**. Fluorescence and HPLC PGA assays of fluorogenic probes **6a** and **6d**. Caspase-3 assay of latent blue fluorophore **11**. LC-MS analyses of the reaction between DAO **5d** and DTT. This material is available free of charge via the Internet at http://pubs.acs.org.

LITERATURE CITED

(1) Chen, X., Sun, M., and Ma, H. (2006) Progress in spectroscopic probes with cleavable active bonds. *Curr. Org. Chem. 10*, 477–489.

(2) Goddard, J.-P., and Reymond, J.-L. (2004) Enzyme assays for high-throughput screening. *Curr. Opin. Biotechnol. 15*, 314–322.

(3) Goddard, J. P., and Reymond, J. L. (2004) Recent advances in enzyme assays. *Trends Biotechnol. 22*, 363–370.

(4) Haugland, R. P., Spence, M. T. Z., Johnson, I. D., and Basey, A. (2005) *The Handbook: A Guide to Fluorescent Probes and Labeling Technologies*, 10th ed., Molecular Probes, Eugene, OR.

(5) Johnsson, N., and Johnsson, K. (2007) Chemical tools for biomolecular imaging. *ACS Chem. Biol. 2*, 31–38.

(6) Miller, E. W., and Chang, C. J. (2007) Fluorescent probes for nitric oxide and hydrogen peroxide in cell signaling. *Curr. Opin. Chem. Biol. 11*, 620–625.

(7) Maeda, H., Yamamoto, K., Nomura, Y., Kohno, I., Hafsi, L., Ueda, N., Yoshida, S., Fukuda, M., Fukuyasu, Y., Yamauchi, Y., and Itoh, N. (2005) A design of fluorescent probes for superoxide based on a nonredox mechanism. *J. Am. Chem. Soc. 127*, 68–69.

(8) Maeda, H., Yamamoto, K., Kohno, I., Hafsi, L., Itoh, N., Nakagawa, S., Kanagawa, N., Suzuki, K., and Uno, T. (2007) Design of a practical fluorescent probe for superoxide based on protection-deprotection chemistry of fluoresceins with benzenesulfonyl protecting groups. *Chem. Eur. J. 13*, 1946–1954.

(9) Xu, K., Liu, X., and Tang, B. (2007) A phosphinate-based red fluorescent probe for imaging the superoxide radical anion generated by RAW264.7 macrophages. *ChemBioChem 8*, 453–458.

(10) Yang, D., Wang, H.-L., Sun, Z.-N., Chung, N.-W., and Shen, J.-G. (2006) A highly selective fluorescent probe for the detection and imaging of peroxynitrite in living cells. *J. Am. Chem. Soc. 128*, 6004–6005.

(11) Lim, M. H., and Lippard, S. J. (2007) Metal-based turn-on fluorescent probes for sensing nitric oxide. *Acc. Chem. Res. 40*, 41–51.

(12) Zhang, M., Yu, M., Li, F., Zhu, M., Li, M., Gao, Y., Li, L., Liu, Z., Zhang, J., Zhang, D., Yi, T., and Huang, C. (2007) A highly selective fluorescence turn-on sensor for cysteine/homocysteine and its application in bioimaging. *J. Am. Chem. Soc. 129*, 10322–10323.

(13) Bouffard, J., Kim, Y., Swager, T. M., Weissleder, R., and Hilderbrand, S. A. (2008) A Highly selective fluorescent probe for thiol bioimaging. *Org. Lett. 10*, 37–40.

(14) Ahn, Y.-H., Lee, J.-S., and Chang, Y.-T. (2007) Combinatorial rosamine library and application to in vivo glutathione probe. *J. Am. Chem. Soc. 129*, 4510–4511.

(15) Matsumoto, T., Urano, Y., Shoda, T., Kojima, H., and Nagano, T. (2007) A thiol-reactive fluorescence probe based on donor-excited photoinduced electron transfer: key role of ortho substitution. *Org. Lett. 9*, 3375–3377.

(16) Tang, B., Xing, Y., Li, P., Zhang, N., Yu, F., and Yang, G. (2007) A rhodamine-based fluorescent probe containing a Se-N bond for detecting thiols and its application in living cells. *J. Am. Chem. Soc. 129*, 11666–11667.

(17) Pires, M. M., and Chmielewski, J. (2008) Fluorescence imaging of cellular glutathione using a latent rhodamine. *Org. Lett. 10*, 837–840.

(18) Kim, Y., Choi, Y., Weissleder, R., and Tung, C.-H. (2007) Membrane permeable esterase-activated fluorescent imaging probe. *Bioorg. Med. Chem. Lett. 17*, 5054–5057.

(19) Gurtu, V., Kain, S. R., and Zhang, G. (1997) Fluorometric and colorimetric detection of caspase activity associated with apoptosis. *Anal. Biochem. 251*, 98–102.

(20) Wang, Z.-Q., Liao, J., and Diwu, Z. (2005) N-DEVD-N'-morpholinecarbonyl-rhodamine 110: novel caspase-3 fluorogenic substrates for cell-based apoptosis assay. *Bioorg. Med. Chem. Lett. 15*, 2335–2338 and references cited therein.

(21) Ho, N.-H., Weissleder, R., and Tung, C.-H. (2006) Development of a dual fluorogenic and chromogenic dipeptidyl peptidase IV substrate. *Bioorg. Med. Chem. Lett. 16*, 2599–2602.

(22) Lai, K. S., Ho, N.-H., Cheng, J. D., and Tung, C.-H. (2007) Selective fluorescence probes for dipeptidyl peptidase activity-fibroblast activation protein and dipeptidyl peptidase IV. *Bioconjugate Chem. 18*, 1246–1250.

(23) Tung, C.-H., Zeng, Q., Shah, K., Kim, D.-E., Schellingerhout, D., and Weissleder, R. (2004) In vivo imaging of β-galactosidase activity using far red fluorescent switch. *Cancer Res. 64*, 1579–1583.

(24) Urano, Y. (2008) Sensitive and selective tumor imaging with novel and highly activatable fluorescence probes. *Anal. Sci. 24*, 51–53.

(25) Gao, W., Xing, B., Tsien, R. Y., and Rao, J. (2003) Novel fluorogenic substrates for imaging β-lactamase gene expression. *J. Am. Chem. Soc. 125*, 11146–11147.

(26) Weissleder, R., and Ntziachristos, V. (2003) Shedding light onto live molecular targets. *Nat. Med. 9*, 123–128.

(27) Papot, S., Tranoy, I., Tillequin, F., Florent, J. C., and Gesson, J. P. (2002) Design of selectively activated anticancer prodrugs: elimination and cyclization strategies. *Curr. Med. Chem. 2*, 155–185.

(28) Gomes, P., Vale, N., and Moreira, R. (2007) Cyclization-activated prodrugs. *Molecules 12*, 2484–2506.

(29) Kratz, F., Muller, I. A., Ryppa, C., and Warnecke, A. (2008) Prodrug strategies in anticancer chemotherapy. *ChemMedChem 3*, 20–53.

(30) Jones, G. B., Crasto, C. F., Mathews, J. E., Xie, L., Mitchell, M. O., El-Shafey, A., D'Amico, A. V., and Bubley, G. J. (2006) An image contrast agent selectively activated by prostate specific antigen. *Bioorg. Med. Chem. 14*, 418–425.

(31) Chandran, S. S., Dickson, K. A., and Raines, R. T. (2005) Latent fluorophore based on the trimethyl lock. *J. Am. Chem. Soc. 127*, 1652–1653.

(32) Lavis, L. D., Chao, T.-Y., and Raines, R. T. (2006) Latent blue and red fluorophores based on the trimethyl lock. *ChemBioChem 7*, 1151–1154.

(33) Lavis, L. D., Chao, T.-Y., and Raines, R. T. (2006) Fluorogenic label for biomolecular imaging. *ACS Chem. Biol. 1*, 252–260.

(34) Ho, N.-H., Weissleder, R., and Tung, C.-H. (2007) A self-immolative reporter for β-galactosidase sensing. *ChemBioChem 8*, 560–566.

(35) Danieli, E., and Shabat, D. (2007) Molecular probe for enzymatic activity with dual output. *Bioorg. Med. Chem. 15*, 7318–7324.

(36) Sicart, R., Collin, M.-P., and Reymond, J.-L. (2007) Fluorogenic substartes for lipases, esterases, and acylases using a TIM-mechanism for signal release. *Biotechnol. J. 2*, 221–231.

(37) Meyer, Y., Richard, J.-A., Massonneau, M., Renard, P.-Y., and Romieu, A. (2008) Development of a new nonpeptidic self-immolative spacer. Application to the design of protease sensing fluorogenic probes. *Org. Lett. 10*, 1517–1520.

(38) Richard, J. A., Jean, L., Romieu, A., Massonneau, M., Noack-Fraissignes, P., and Renard, P. Y. (2007) Chemiluminescent probe for the in vitro detection of protease activity. *Org. Lett. 9*, 4853–4855.

(39) Bruce, J. M., and Knowles, P. (1966) Light-induced and related reactions of quinones Part III. Light-induced reactions

of some monosubstituted 1,4-benzoquinones. *J. Chem. Soc., C* , 1627–1634.
(40) Corey, P. F., Trimmer, R. W., and Biddlecom, W. G. (1991) A new chromogenic β-galactosidase substrate: 7-β-D-galactopyranosyloxy-9,9-dimethyl-9H-acridin-2-one. *Angew. Chem., Int. Ed. 103*, 1646–1648.
(41) Briggs, M. S. J., Bruce, I., Miller, J. N., Moody, C. J., Simmonds, A. C., and Swann, E. (1997) Synthesis of functionalized fluorescent dyes and their coupling to amines and amino acids. *J. Chem. Soc., Perkin Trans. 1*, 1051–1058.
(42) Gottlieb, H. E., Kotlyar, V., and Nudelman, A. (1997) NMR chemical shifts of common laboratory solvents as trace impurities. *J. Org. Chem. 62*, 7512–7515.
(43) Mujumdar, R. B., Ernst, L. A., Mujumdar, S. R., Lewis, C. J., and Waggoner, A. S. (1993) Cyanine dye labeling reagents: Sulfoindocyanine succinimidyl esters. *Bioconjugate Chem. 4*, 105–111.
(44) Bräse, S., and Dahmen, S. (2000) Traceless linkers - Only disappearing links in solid-phase organic synthesis. *Chem. Eur. J. 6*, 1899–1905.
(45) Comely, A. C., and Gibson, S. E. (2001) Tracelessness unmasked: A general linker nomenclature. *Angew. Chem., Int. Ed. 40*, 1012–1032.
(46) Wills, A. J., and Balasubramanian, S. (2003) Recent developments in linker design and application. *Curr. Opin. Chem. Biol. 7*, 346–352.
(47) Gil, C., and Bräse, S. (2004) Traceless and multifunctional linkers for the generation of small molecules on solid supports. *Curr. Opin. Chem. Biol. 8*, 230–237.
(48) Mayer, S. F., Kroutil, W., and Kurt, F. (2001) Enzyme-initiated domino (cascade) reactions. *Chem. Soc. Rev. 30*, 332–339.
(49) Grether, U., and Waldmann, H. (2000) An enzyme-labile safety catch linker for combinatorial synthesis on a soluble polymeric support. *Angew. Chem., Int. Ed. 39*, 1629–1632.
(50) Grether, U., and Waldmann, H. (2001) An enzyme-labile safety catch linker for synthesis on a soluble polymeric support. *Chem. Eur. J. 7*, 959–971.
(51) Renard, P.-Y., Romieu, A., Richard, J.-A., and Massonneau, M. New pro-fluorescent compounds Fr. Demande (2008), FR 2910897 A1 20080704.
(52) Carl, P. L., Chakravarty, P. K., and Katzenellenbogen, J. A. (1981) A novel connector linkage applicable in prodrug design. *J. Med. Chem. 24*, 479–480.
(53) Ninkovic, M., Riester, D., Wirsching, F., Dietrich, R., and Schwienhorst, A. (2001) Fluorogenic assay for penicillin G acylase activity. *Anal. Biochem. 292*, 228–233.
(54) Gopin, A., Ebner, S., Attali, B., and Shabat, D. (2006) Enzymatic activation of second-generation dendritic prodrugs: conjugation of self-immolative dendrimers with poly(ethylene glycol) via click chemistry. *Bioconjugate Chem. 17*, 1432–1440.
(55) Adler-Abramovich, L., Perry, R., Sagi, A., Gazit, E., and Shabat, D. (2007) Controlled assembly of peptide nanotubes triggered by enzymatic activation of self-immolative dendrimers. *ChemBioChem 8*, 859–862.
(56) Sagi, A., Segal, E., Satchi-Fainaro, R., and Shabat, D. (2007) Remarkable drug-release enhancement with an elimination-based AB_3 self-immolative dendritic amplifier. *Bioorg. Med. Chem. 15*, 3720–3727.
(57) Kadereit, D., and Waldmann, H. (2001) Enzymatic protecting group techniques. *Chem. Rev. 101*, 3367–3396.
(58) Scheper, T., Weiss, M., and Schuegerl, K. (1986) Two new fluorogenic substrates for the detection of penicillin-G-acylase activity. *Anal. Chim. Acta 182*, 203–206.
(59) Setsukinai, K.-I., Urano, Y., Kikuchi, K., Higuchi, T., and Nagano, T. (2000) Fluorescence switching by O-dearylation of 7-aryloxycoumarins. Development of novel fluorescence probes to detect reactive oxygen species with high selectivity. *J. Chem. Soc., Perkin Trans. 2*, 2453–2457.
(60) Sood, A., Kumar, S., Nampalli, S., Nelson, J. R., Macklin, J., and Fuller, C. W. (2005) Terminal phosphate-labeled nucleotides with improved substrate properties for homogeneous nucleic acid assays. *J. Am. Chem. Soc. 127*, 2394–2395.
(61) Denault, J.-B., and Salvesen, G. S. (2002) Caspases: Keys in the ignition of cell death. *Chem. Rev. 102*, 4489–4499.
(62) Kothakota, S., Azuma, T., Reinhard, C., Klippel, A., Tang, J., Chu, K., McGarry, T. J., Kirschner, M. W., Koths, K., Kwiatkowski, D. J., and Williams, L. T. (1997) Caspase-3-generated fragment of gelsolin: effector of morphological change in apoptosis. *Science 278*, 294–298.
(63) Mizukami, S., Kikuchi, K., Higuchi, T., Urano, Y., Mashima, T., Tsuruo, T., and Nagano, T. (1999) Imaging of caspase-3 activation in HeLa cells stimulated with etoposide using a novel fluorescent probe. *FEBS Lett. 453*, 356–360.
(64) Komoriya, A., Packard, B. Z., Brown, M. J., Wu, M.-L., and Henkart, P. A. (2000) Assessment of caspase activities in intact apoptotic thymocytes using cell-permeable fluorogenic caspase substrates. *J. Exp. Med. 191*, 1819–1828.
(65) Pham, W., Weissleder, R., and Tung, C.-H. (2002) An azulene dimer as a near-infrared quencher. *Angew. Chem., Int. Ed. 41*, 3659–3662.
(66) Bullok, K., and Piwnica-Worms, D. (2005) Synthesis and characterization of a small, membrane-permeant, caspase-activatable far-red fluorescent peptide for imaging apoptosis. *J. Med. Chem. 48*, 5404–5407.
(67) Poupart, S., Boudou, C., Peixoto, P., Massonneau, M., Renard, P.-Y., and Romieu, A. (2006) Aminopropargyl derivative of terpyridine-bis(methyl-enamine) tetraacetic acid chelate of europium (Eu (TMT)-AP3): a new reagent for fluorescent labelling of proteins and peptides. *Org. Biomol. Chem. 4*, 4165–4177.
(68) Bullok, K. E., Maxwell, D., Kesarwala, A. H., Gammon, S., Prior, J. L., Snow, M., Stanley, S., and Piwnica-Worms, D. (2007) Biochemical and in vivo characterization of a small, membrane-permeant, caspase-activatable far-red fluorescent peptide for imaging apoptosis. *Biochemistry 46*, 4055–4065.
(69) Bouteiller, C., Clavé, G., Bernardin, A., Chipon, B., Massonneau, M., Renard, P.-Y., and Romieu, A. (2007) Novel water-soluble near-infrared cyanine dyes: synthesis, spectral properties, and use in the preparation of internally quenched fluorescent probes. *Bioconjugate Chem. 18*, 1303–1317.
(70) Lee, B. W., Johnson, G. L., Hed, S. A., Darzynkiewicz, Z., Talhouk, J. W., and Mehrotra, S. (2003) DEVDase detection in intact apoptotic cells using the cell permeant fluorogenic substrate, (z-DEVD)2-cresyl violet. *BioTechniques 35*, 1080–1085.
(71) Gerlach, H. (1977) 2-(Trimethylsilyl)ethyl esters as a carboxyl protecting group; application in the synthesis of (-)-(S)-curvularin. *Helv. Chim. Acta 60*, 3039–3044.
(72) Sieber, P. (1977) The 2-trimethylsilylethyl residue, a selectively cleavable carboxyl protecting group. *Helv. Chim. Acta 60*, 2711–2716.
(73) Moretti, A., Weig, H.-J., Ott, T., Seyfarth, M., Holthoff, H.-P., Grewe, D., Gillitzer, A., Bott-Flugel, L., Schomig, A., Ungerer, M., and Laugwitz, K.-L. (2002) Essential myosin light chain as a target for caspase-3 in failing myocardium. *Proc. Nat. Acad. Sci. U.S.A. 99*, 11860–11865.
(74) Kitson, T. M. (1998) The oxidative addition reaction between compounds of resorufin (7-hydroxy-3H-phenoxazin-3-one) and 2-mercaptoethanol. *Bioorg. Chem. 26*, 63–73.

BC8001997

Supporting Information

Latent Fluorophores Based on a Self-Immolative Linker Strategy and Suitable for Protease Sensing

Jean-Alexandre Richard,[†,‡] Yves Meyer,[†,‡] Valérie Jolivel,[‡,§,#,¶] Marc Massonneau,[‡] Raphaël Dumeunier,[‡] David Vaudry,[§,#,¶] Hubert Vaudry,[§,#,¶] Pierre-Yves Renard,[*,†,¶, #,µ] and Anthony Romieu[*,†,¶,#]

Equipe de Chimie Bio-Organique, Université de Rouen, Place Emile Blondel, 76821 Mont-Saint-Aignan, France, UMR CNRS 6014, COBRA, IRCOF, rue Lucien Tesnière, 76130 Mont-Saint-Aignan, France, QUIDD, Technopôle du Madrillet, 50, rue Ettore Bugatti, 76800 Saint-Etienne du Rouvray, France, Laboratoire de Neuroendocrinologie Cellulaire et Moléculaire, INSERM U413, Université de Rouen, 76821 Mont-Saint-Aignan, France, and Plate-forme Régionale de Recherche en Imagerie Cellulaire de Haute-Normandie, IFRMP23, Université de Rouen, 76821 Mont-Saint-Aignan, France

Table of Contents

Fluorescence emission spectra of 5a and 6a (Ex. λ = 350 nm) in PB/acetone (8:2, v/v) at 25 °C (concentration 2.6 μM). S3
Fluorescence emission spectra of 5d (Ex. λ = 638 nm) and 6d (Ex. λ = 458 nm) in PB/acetone (8:2, v/v) at 25 °C (concentration 2.2 μM)..... S3
Fluorescence emission spectra of 5a (Ex. λ = 350 nm) and 11 (Ex. λ = 320 nm) in caspase-3 buffer at 37 °C (concentration 3.0 μM)..... S4
Cleavage of latent blue fluorophore 6a by immobilized PGA (2.6 μM, 37 °C) in PB/acetone (8:2, v/v). Fluorescence emission time course (Ex. λ = 360 nm) at 460 nm. S5
Cleavage of latent blue fluorophore 11 by caspase-3 (3 μM, 37 °C) in caspase-3 buffer. Fluorescence emission time course (Ex. λ = 360 nm) at 460 nm. S5
^{1}H NMR spectrum of 6a recorded in $CDCl_3$. S6
^{13}C NMR spectrum of 6a recorded in $CDCl_3$. S6
^{1}H NMR spectrum of 6d recorded in acetone-d_6..... S7
^{13}C NMR spectrum of 6d recorded in acetone-d_6. ..... S7
^{1}H NMR spectrum of 10 recorded in $CDCl_3$. S8
^{13}C NMR spectrum of 10 recorded in $CDCl_3$..... S8
^{1}H NMR spectrum of 11 recorded in DMSO-d_6. ..... S9
ESI-MS spectrum of compound 6a recorded in the positive mode..... S9
ESI-MS spectrum of compound 6b recorded in the positive mode. S10
ESI-MS spectrum of compound 6c recorded in the positive mode..... S11
ESI-MS spectrum of compound 6d recorded in the positive mode. S11
ESI-MS spectrum of compound 10 recorded in the positive mode. S12
ESI-MS spectrum of compound 12 recorded in the positive mode. S12
RP-HPLC elution profiles (system A) of the crude enzymatic reaction mixture (PGA pro-fluorophore 6a + 16.7 U of PGA in PB/acetone (8:2, v/v) 37 °C) after 0 min (a), 5 h (b) and 24 h (c). S13

RP-HPLC elution profiles (system A) of the crude enzymatic reaction mixture (PGA profluorophore 6d + 15.0 U of PGA in PB/acetone (8:2, v/v) 37 °C) after 0 min (a), 72 h (b) and 7 days (c). S14
LC-MS analysis of reaction products between DAO 5d and DTT. S15
(A) RP-HPLC elution profile (system G)[a] of DAO after incubation with 100 eq of DTT (30 min) in PBS at room temperature. S15
(B) ESI-MS spectra recorded for the peak at t_R = 17.45 min both in the positive (B1) and negative (B2) modes S16
LC-MS analysis of DAO 5d. S17
(A) RP-HPLC elution profile (system G)[a] of DAO after incubation (30 min) in PBS at room temperature. S17
(B) ESI-MS spectra recorded for the peak at t_R = 17.52 min both in the positive (B1) and negative (B2) modes S18

Fluorescence emission spectra of 5a and 6a (Ex. λ = 350 nm) in PB/acetone (8:2, v/v) at 25 °C (concentration 2.6 μM).

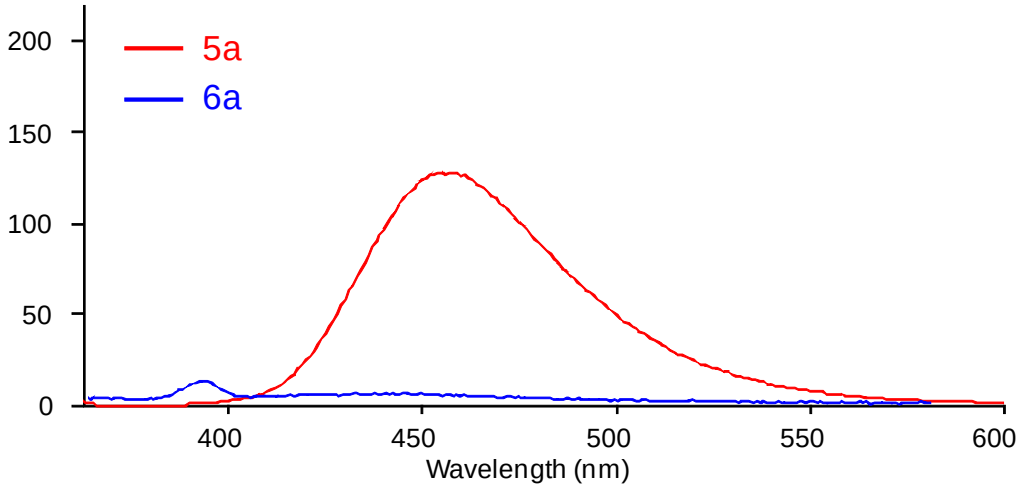

Fluorescence emission spectra of 5d (Ex. λ = 638 nm) and 6d (Ex. λ = 458 nm) in PB/acetone (8:2, v/v) at 25 °C (concentration 2.2 μM).

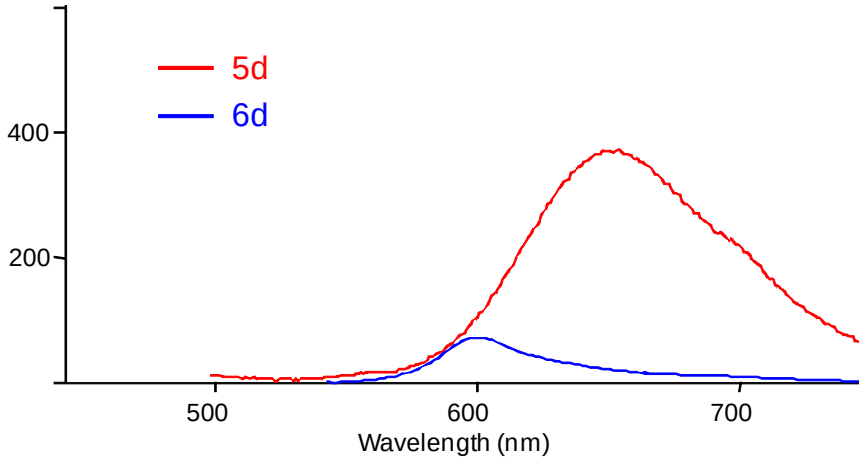

Fluorescence emission spectra of 5a (Ex. λ = 350 nm) and 11 (Ex. λ = 320 nm) in caspase-3 buffer at 37 °C (concentration 3.0 μM).

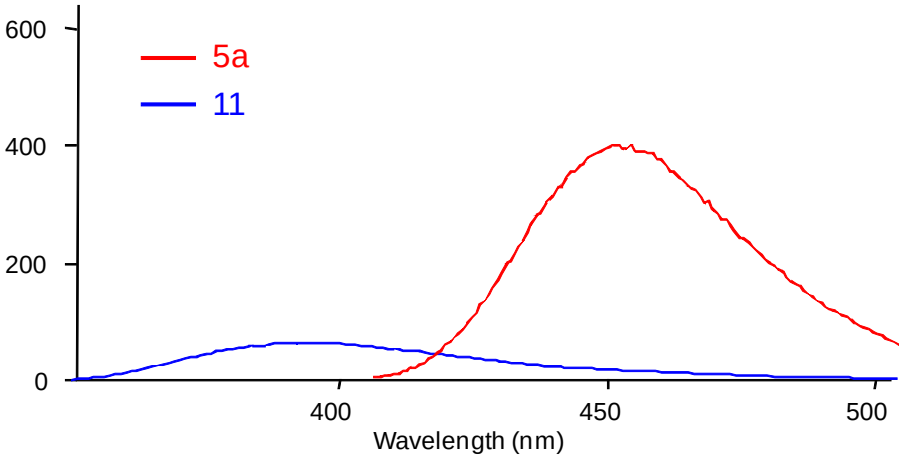

Cleavage of latent blue fluorophore 6a by immobilized PGA (2.6 μM, 37 °C) in PB/acetone (8:2, v/v). Fluorescence emission time course (Ex. λ = 360 nm) at 460 nm.

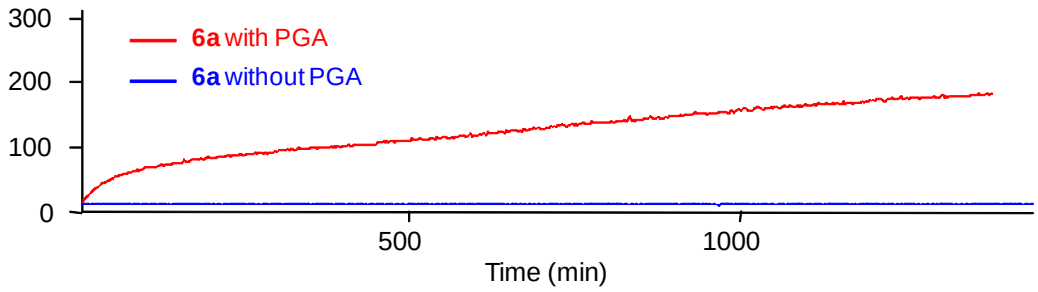

Cleavage of latent blue fluorophore 11 by caspase-3 (3 μM, 37 °C) in caspase-3 buffer. Fluorescence emission time course (Ex. λ = 360 nm) at 460 nm.

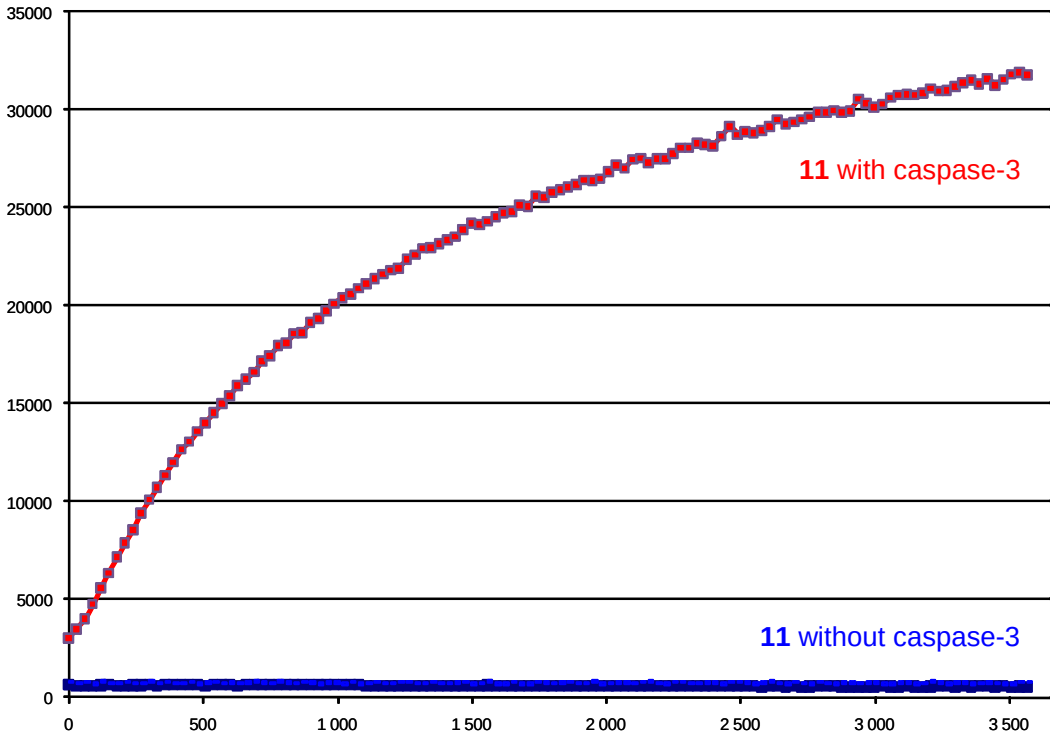

^{1}H NMR spectrum of 6a recorded in $CDCl_3$.

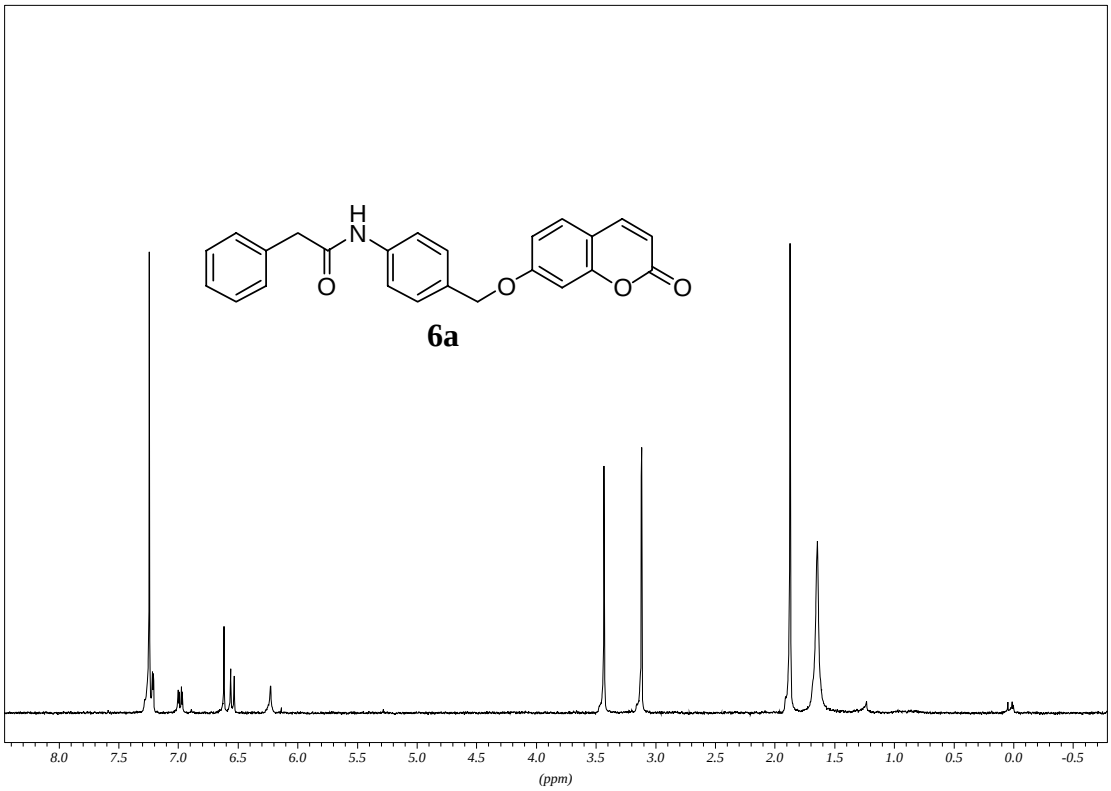

^{13}C NMR spectrum of 6a recorded in $CDCl_3$.

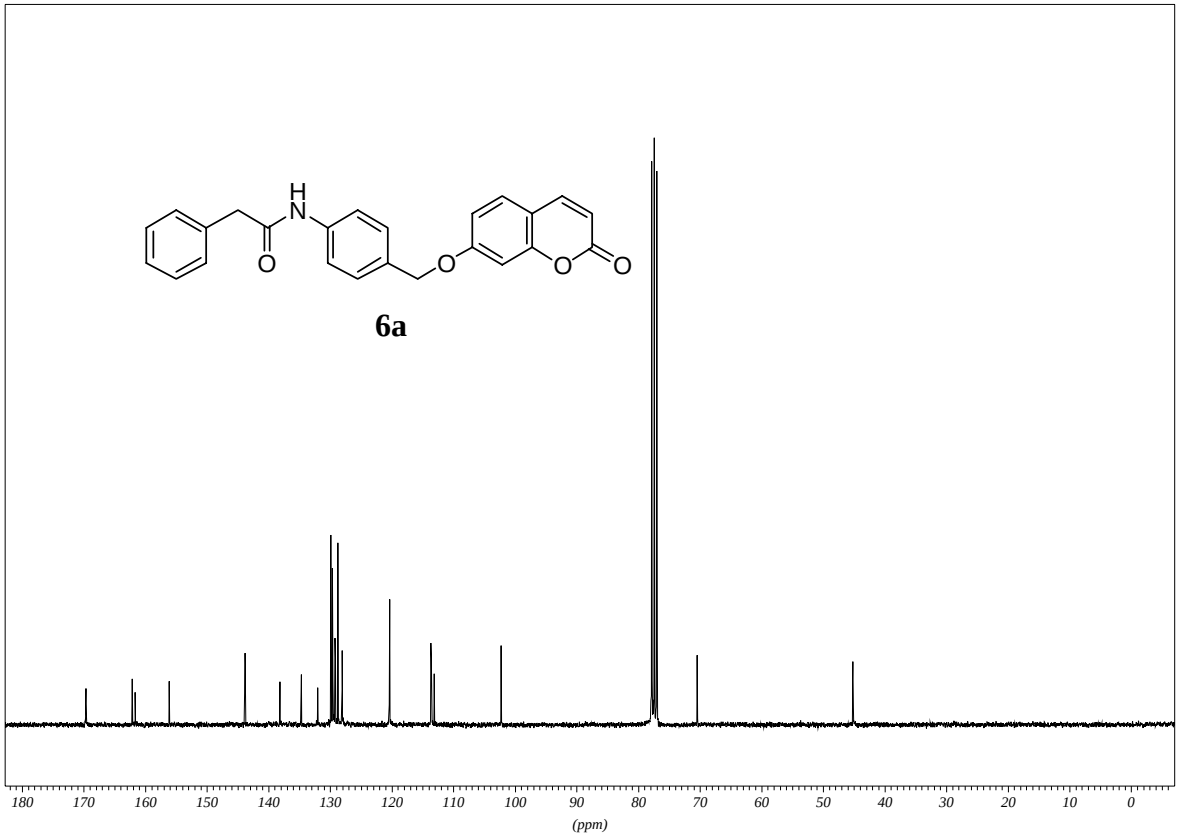

^{1}H NMR spectrum of 6d recorded in acetone-d_6.

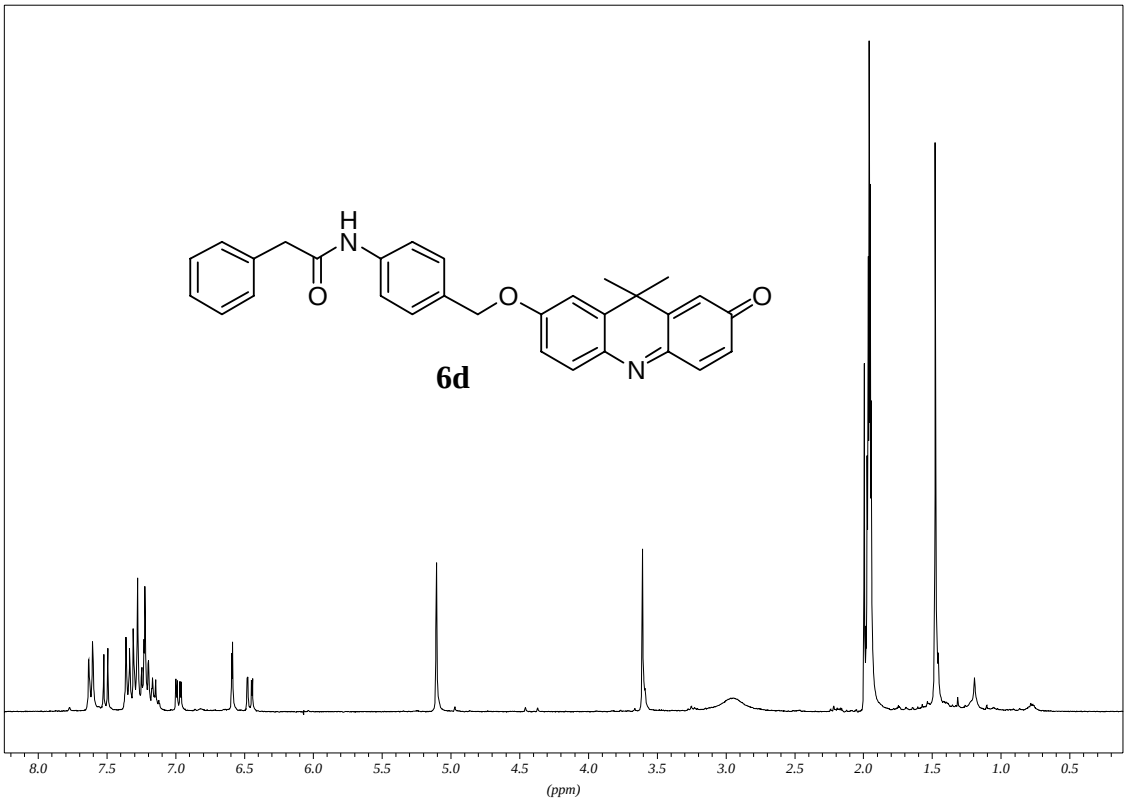

^{13}C NMR spectrum of 6d recorded in acetone-d_6.

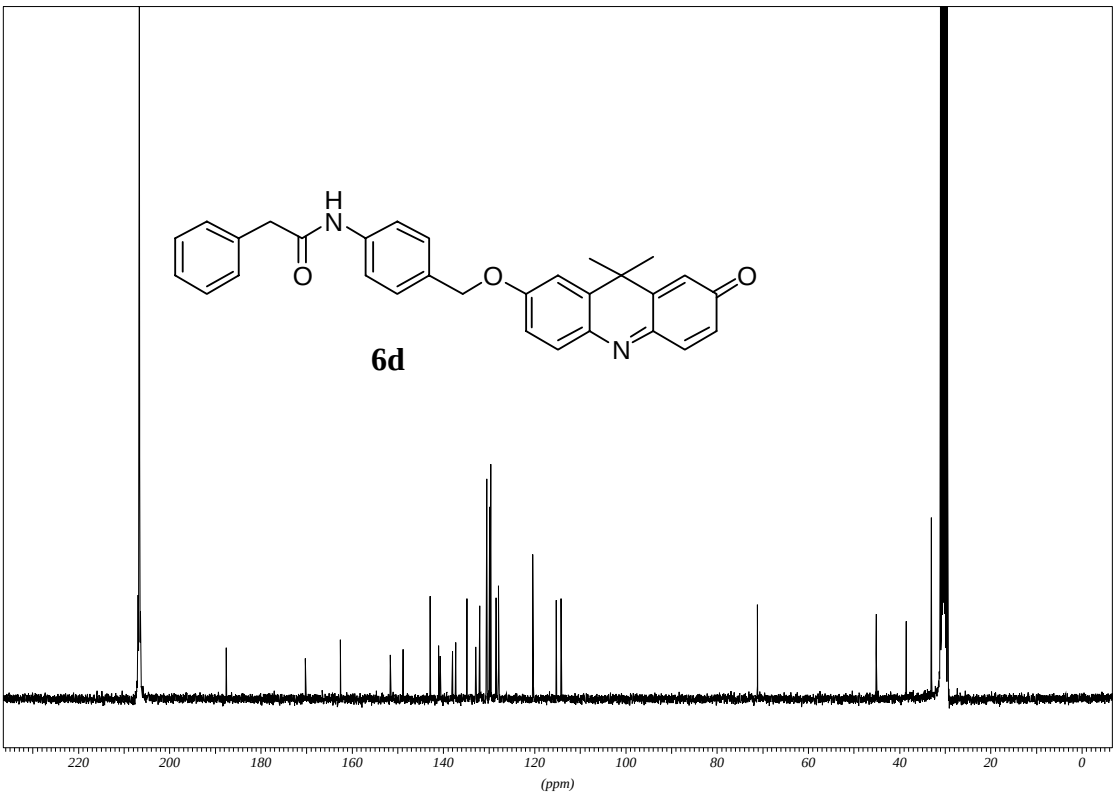

^{1}H NMR spectrum of 10 recorded in $CDCl_3$.

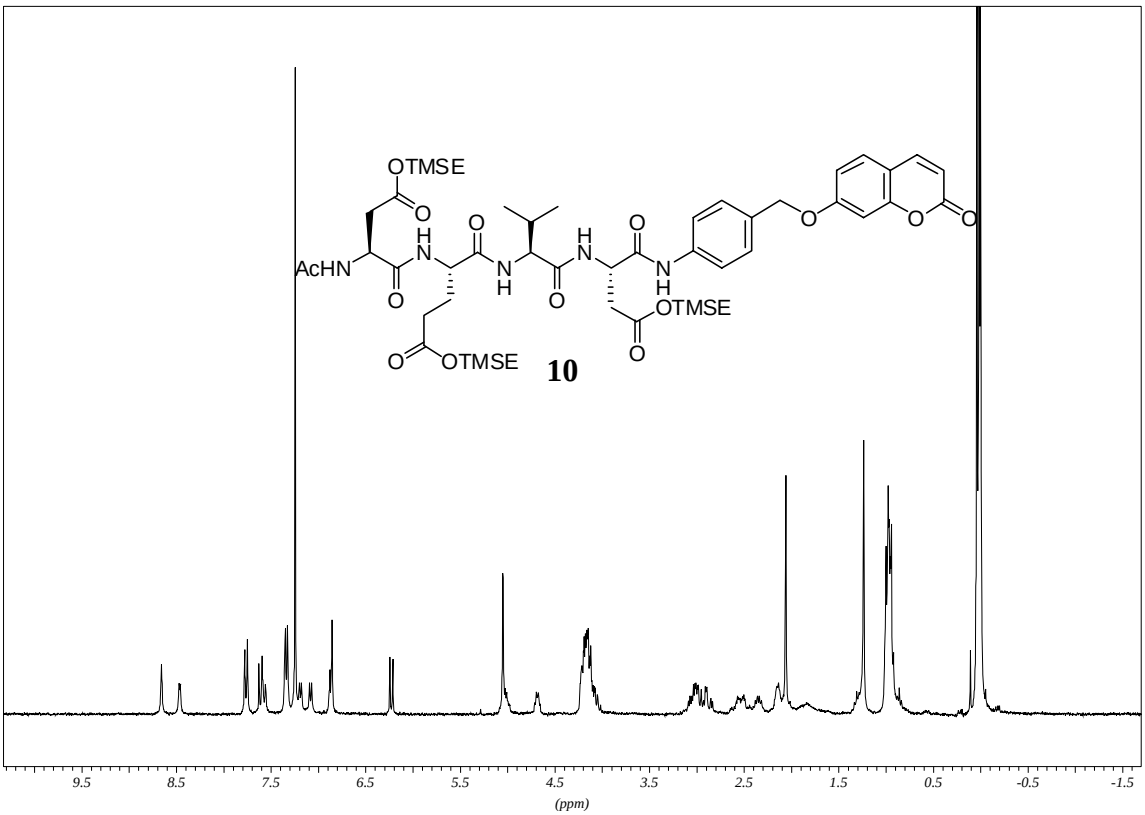

^{13}C NMR spectrum of 10 recorded in $CDCl_3$.

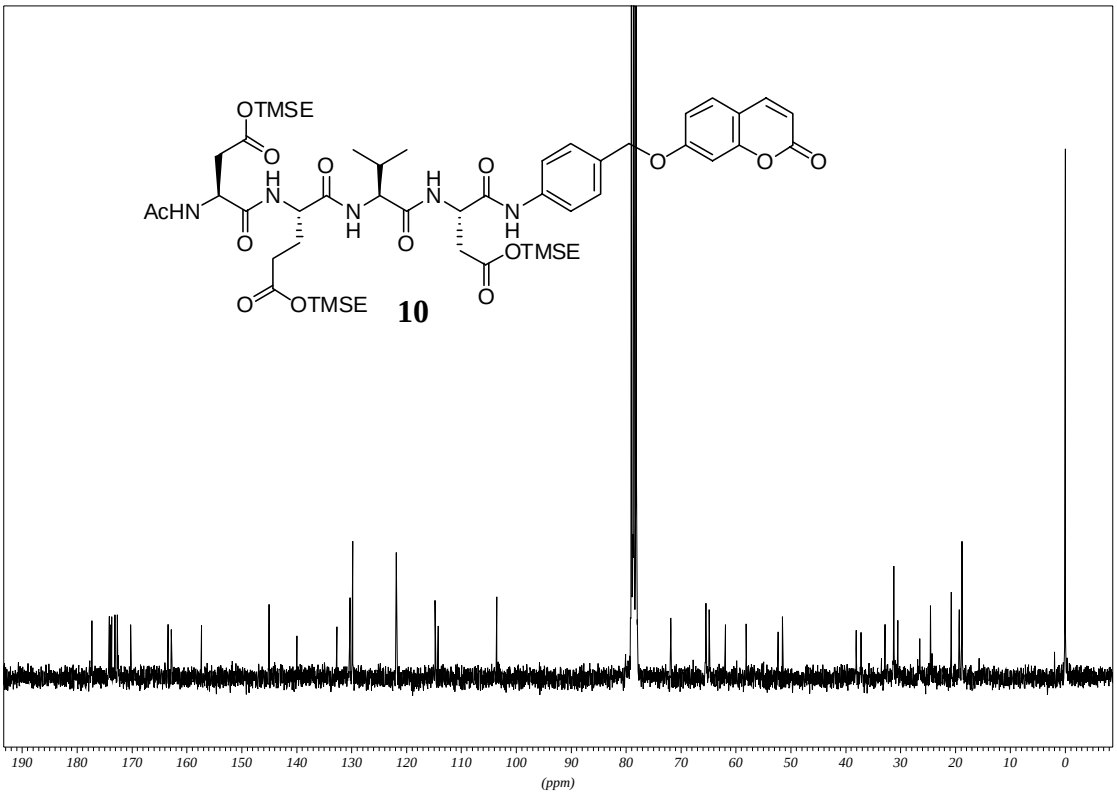

^{1}H NMR spectrum of 11 recorded in DMSO-d_6.

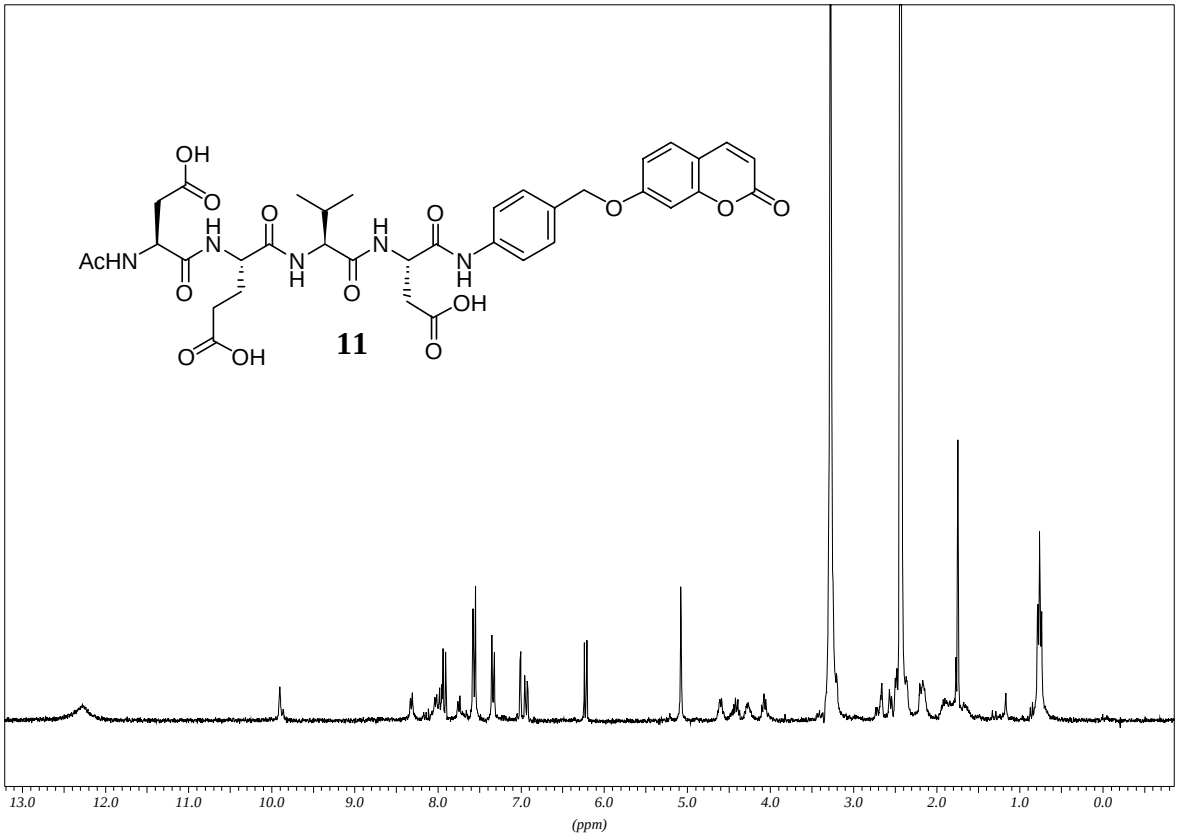

ESI-MS spectrum of compound 6a recorded in the positive mode.

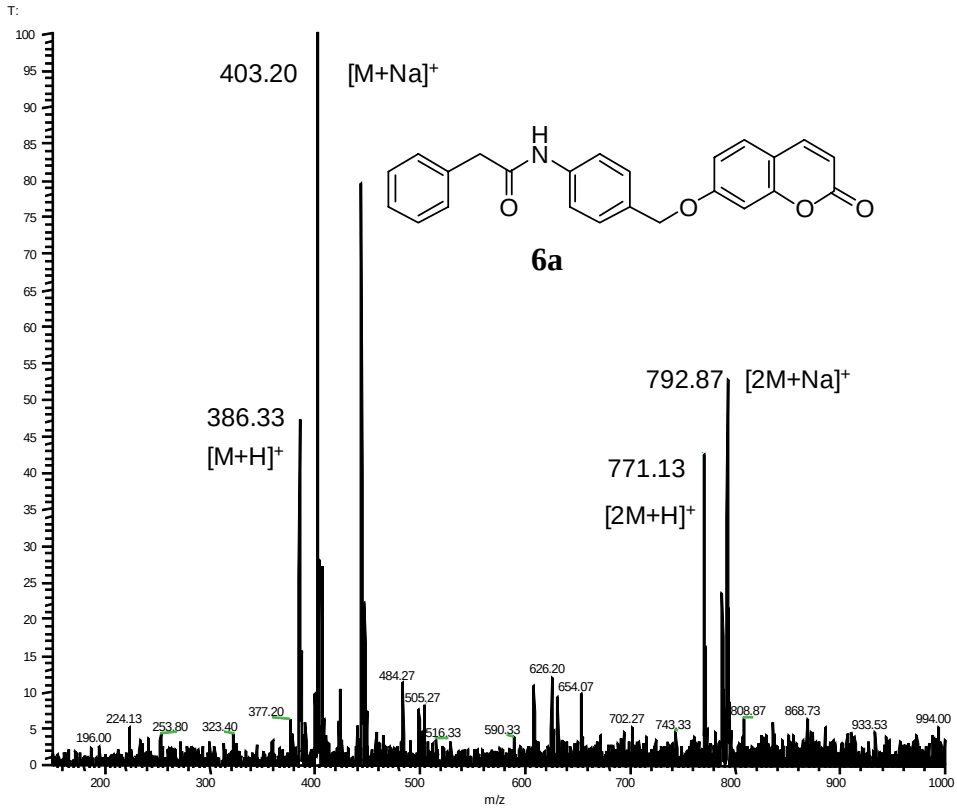

ESI-MS spectrum of compound 6b recorded in the positive mode.

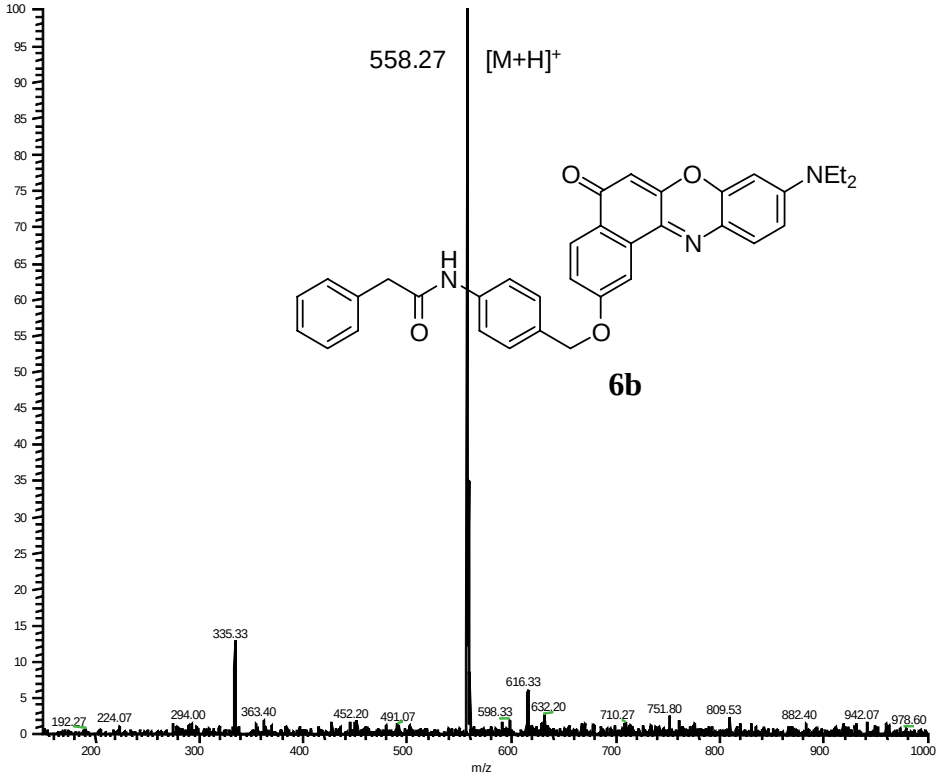

ESI-MS spectrum of compound 6c recorded in the positive mode.

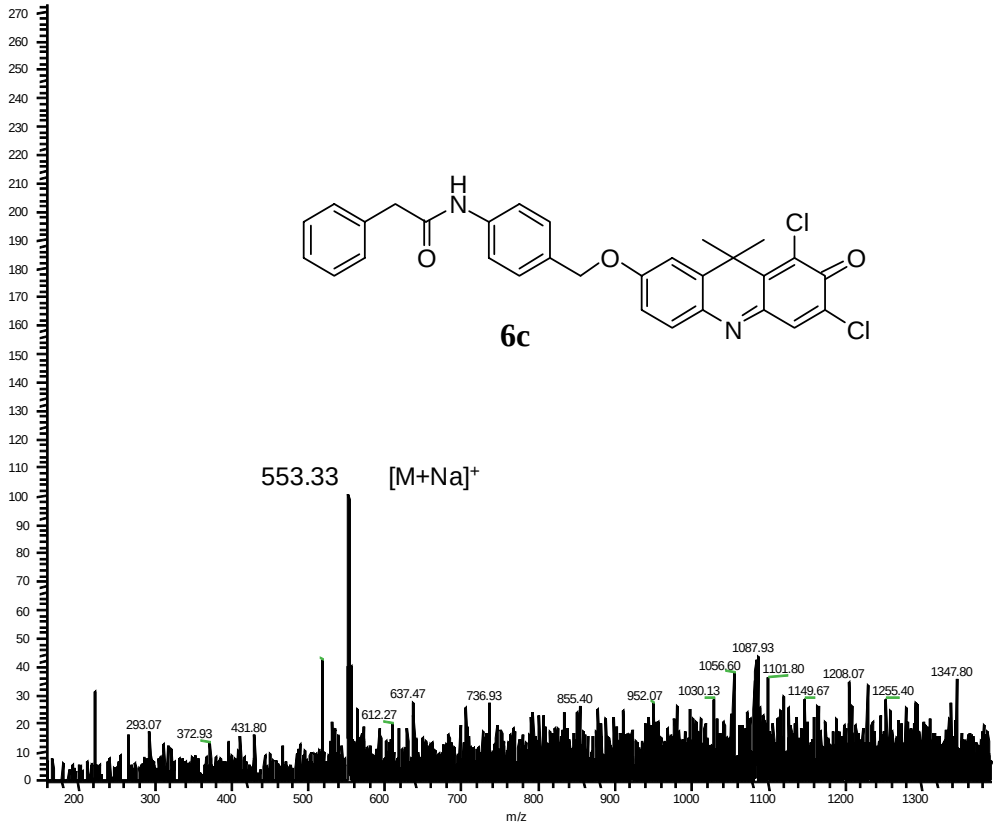

ESI-MS spectrum of compound 6d recorded in the positive mode.

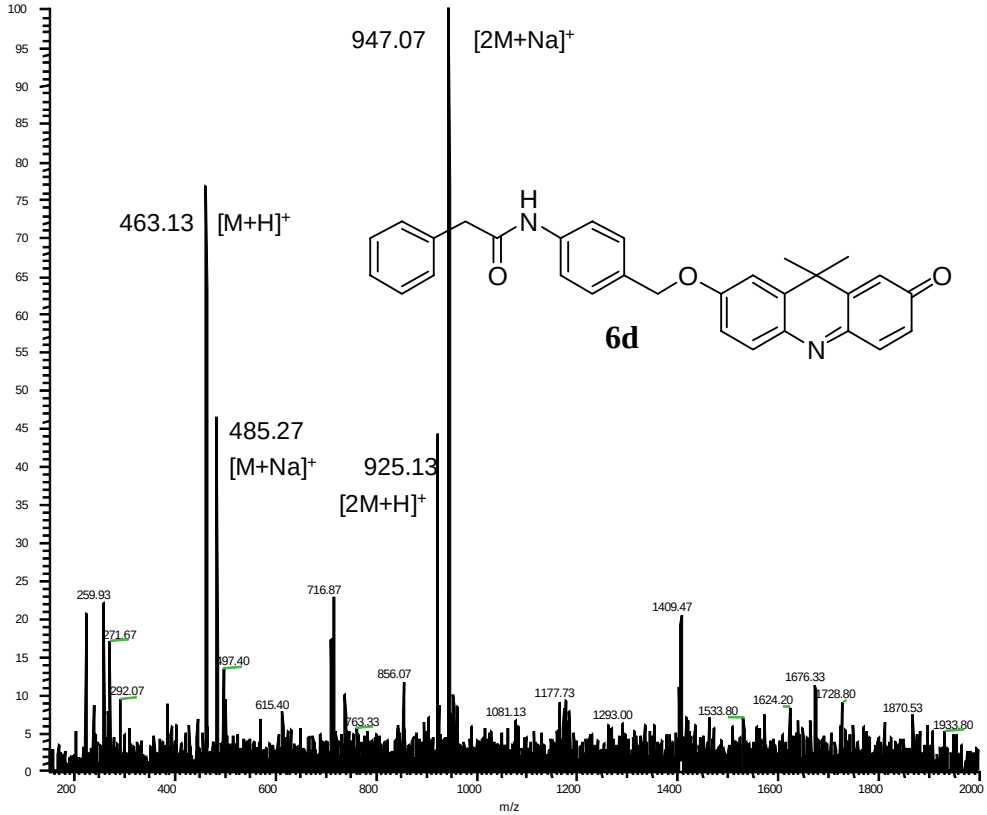

ESI-MS spectrum of compound 10 recorded in the positive mode.

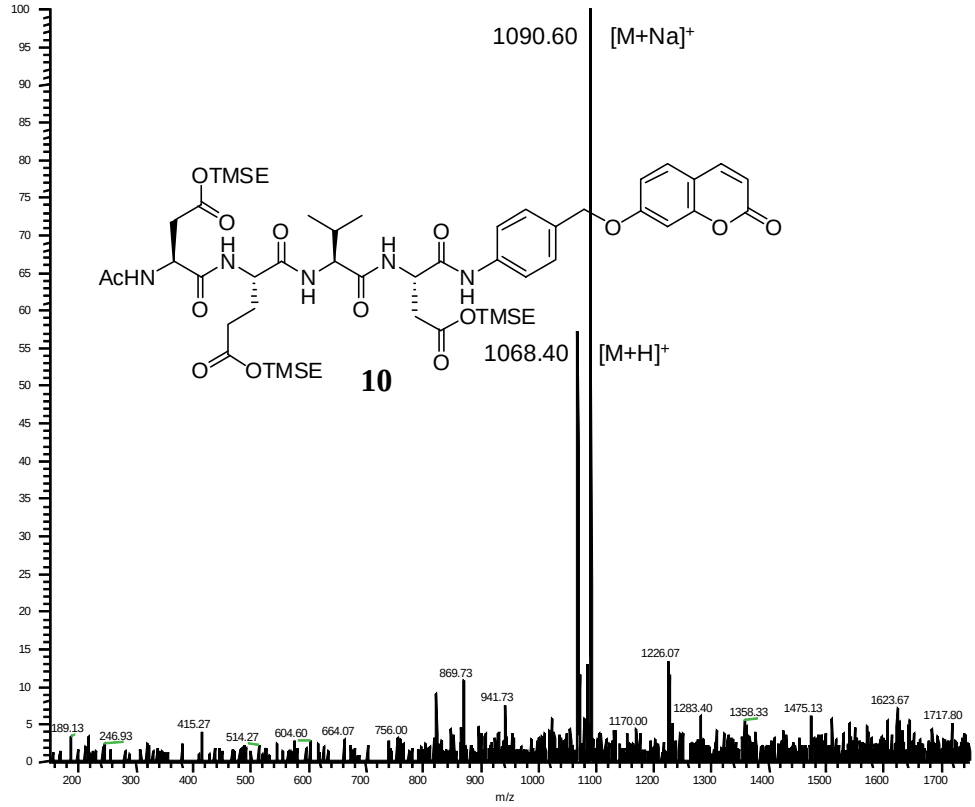

ESI-MS spectrum of compound 12 recorded in the positive mode.

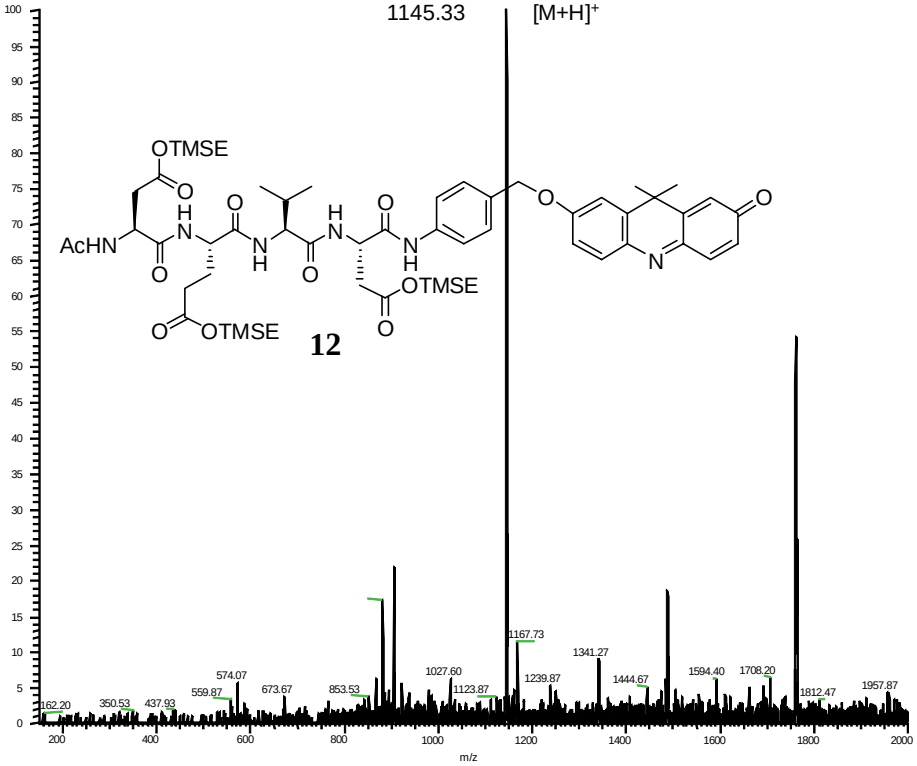

RP-HPLC elution profiles (system A) of the crude enzymatic reaction mixture (PGA pro-fluorophore 6a + 16.7 U of PGA in PB/acetone (8:2, v/v) 37 °C) after 0 min (a), 5 h (b) and 24 h (c).

a)

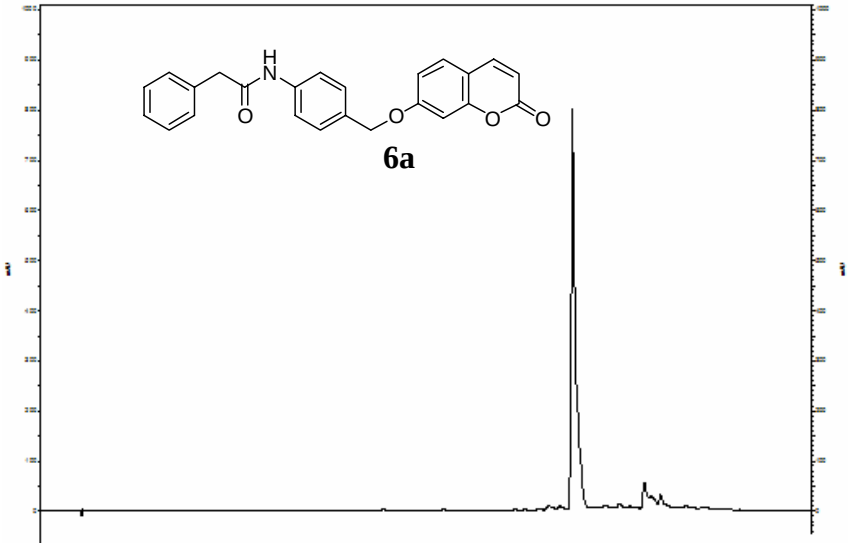

b)

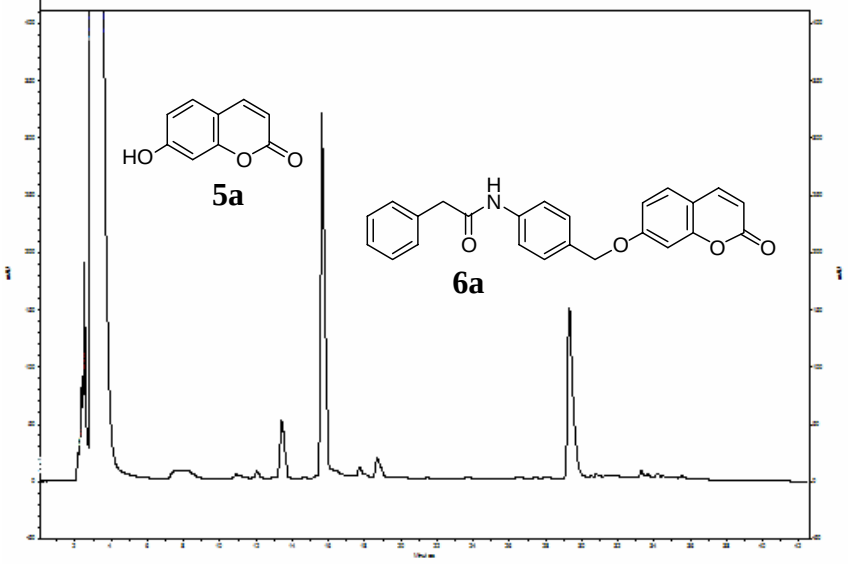

c)

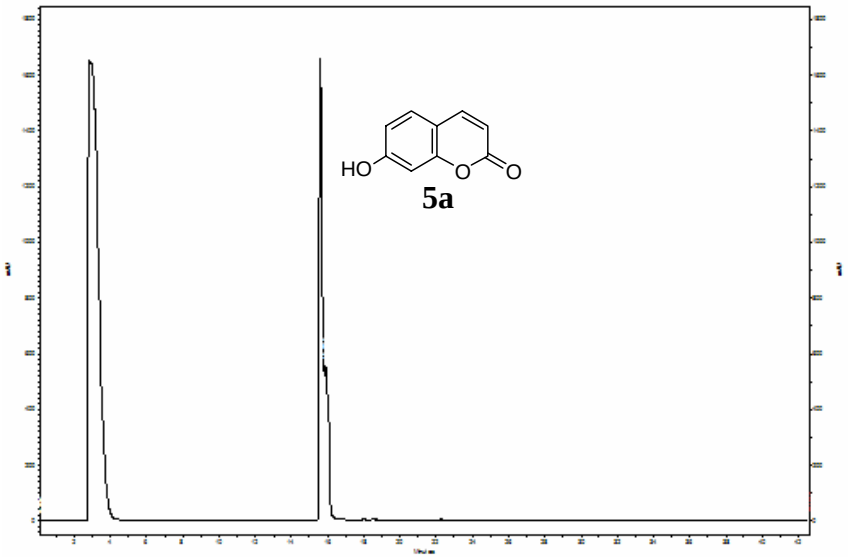

RP-HPLC elution profiles (system A) of the crude enzymatic reaction mixture (PGA pro-fluorophore 6d + 15.0 U of PGA in PB/acetone (8:2, v/v) 37 °C) after 0 min (a), 72 h (b) and 7 days (c).

a)

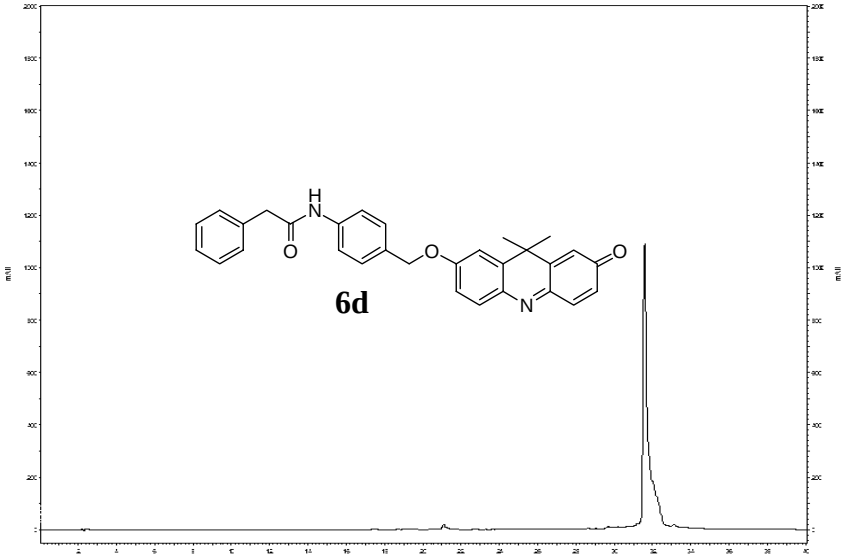

b)

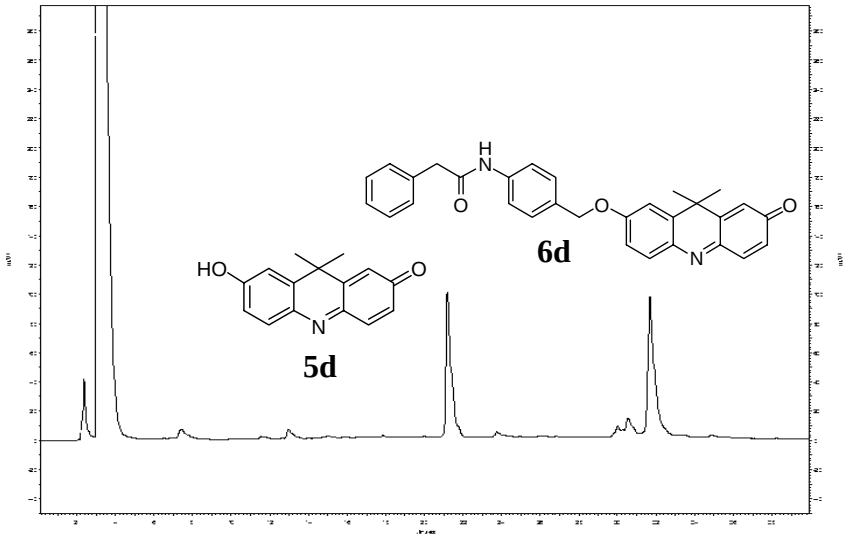

c)

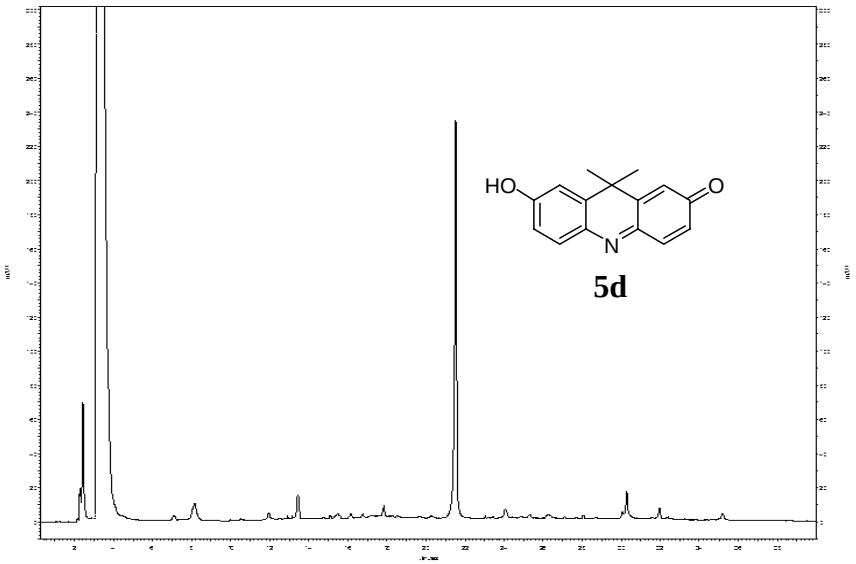

LC-MS analysis of reaction products between DAO 5d and DTT.
(A) RP-HPLC elution profile (system G)[a] of DAO after incubation with 100 eq of DTT (30 min) in PBS at room temperature.

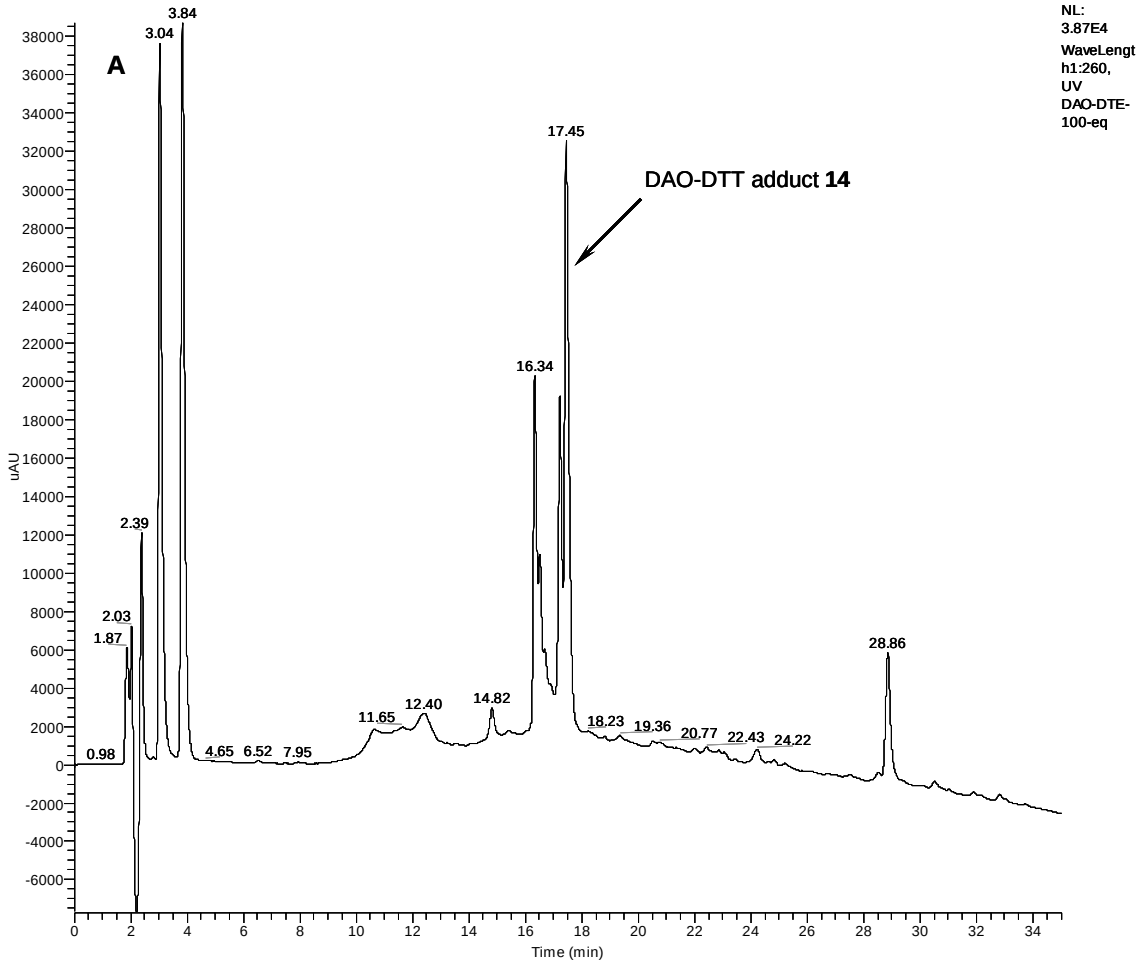

[a]Under our chromatographic conditions, DAO and compound **14** were not separated completely but easily differentiated by ESI-MS. No significant molecular ions were detected for the other peaks displayed on the chromatogram (DTT derivatives ?).

(B) ESI-MS spectra recorded for the peak at t_R = 17.45 min both in the positive (B1) and negative (B2) modes

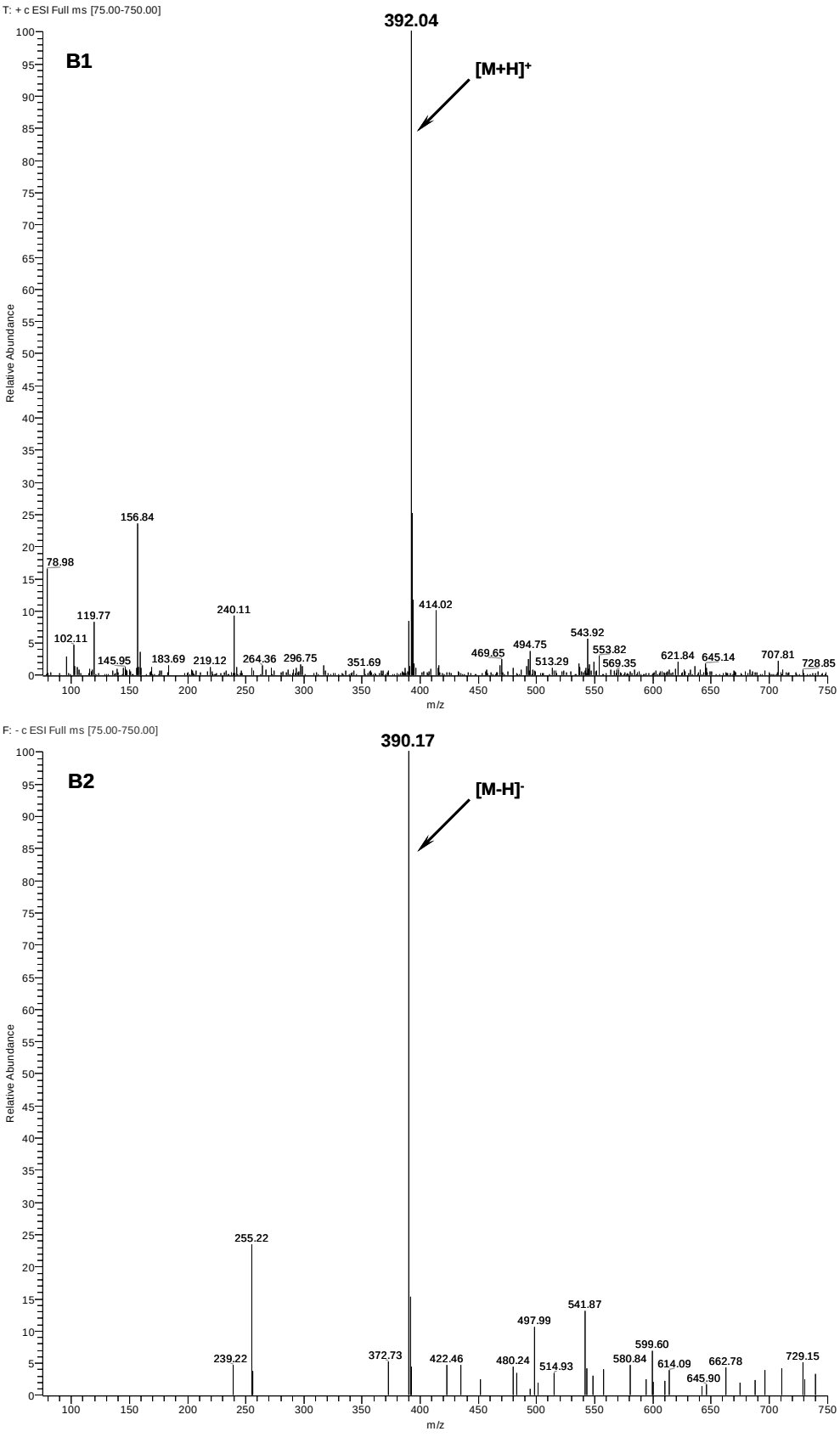

LC-MS analysis of DAO 5d.

(A) RP-HPLC elution profile (system G)[a] of DAO after incubation (30 min) in PBS at room temperature.

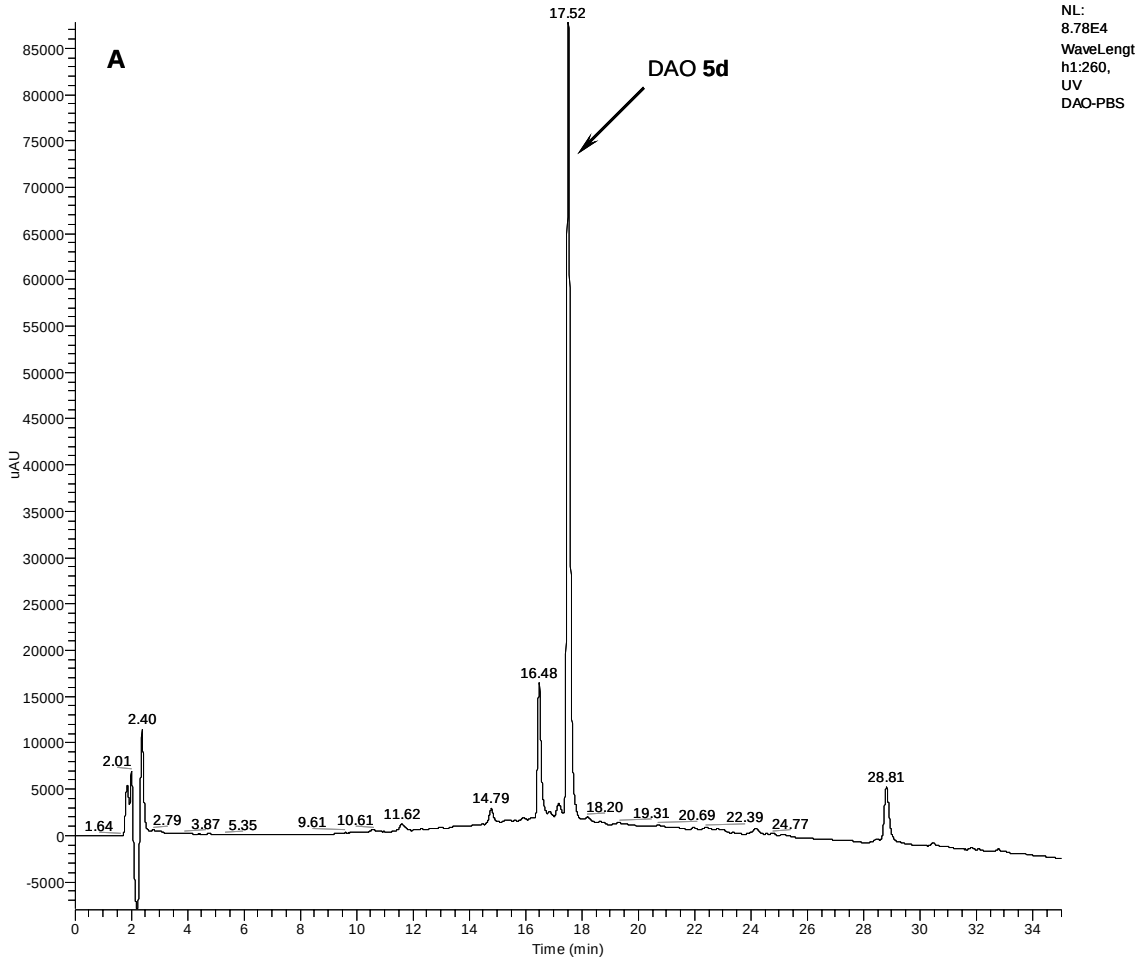

[a]Under our chromatographic conditions, DAO and compound **14** were not separated completely but easily differentiated by ESI-MS.

(B) ESI-MS spectra recorded for the peak at t_R = 17.52 min both in the positive (B1) and negative (B2) modes

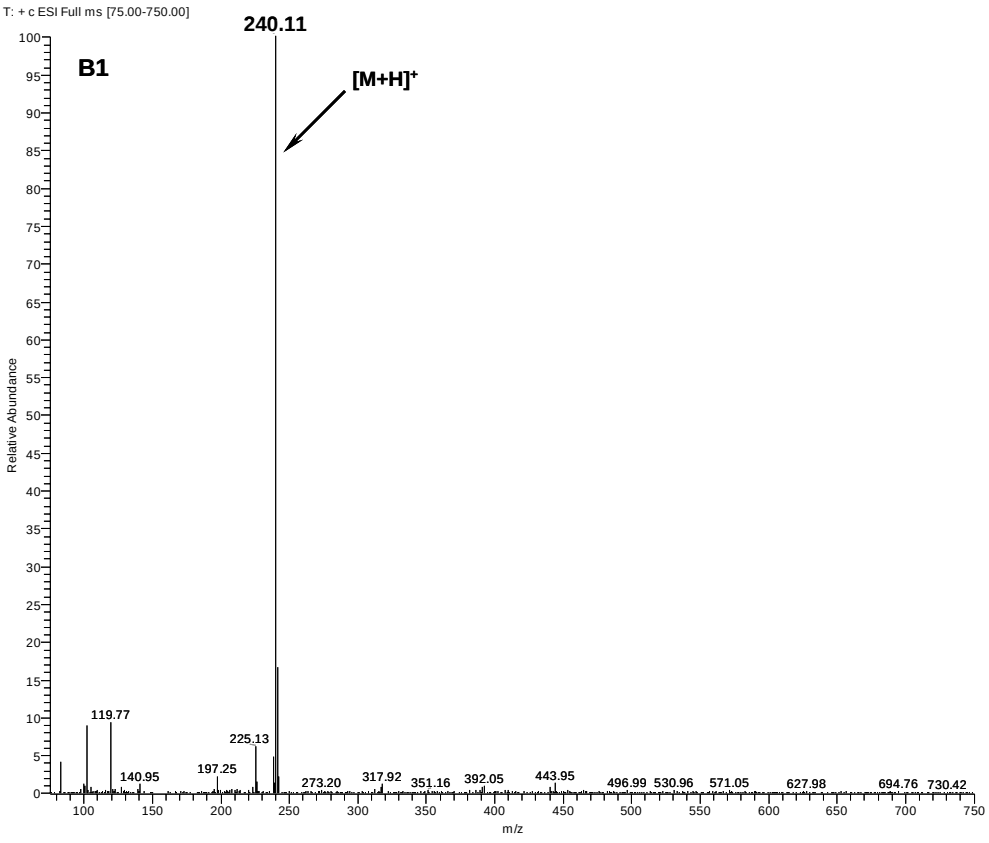

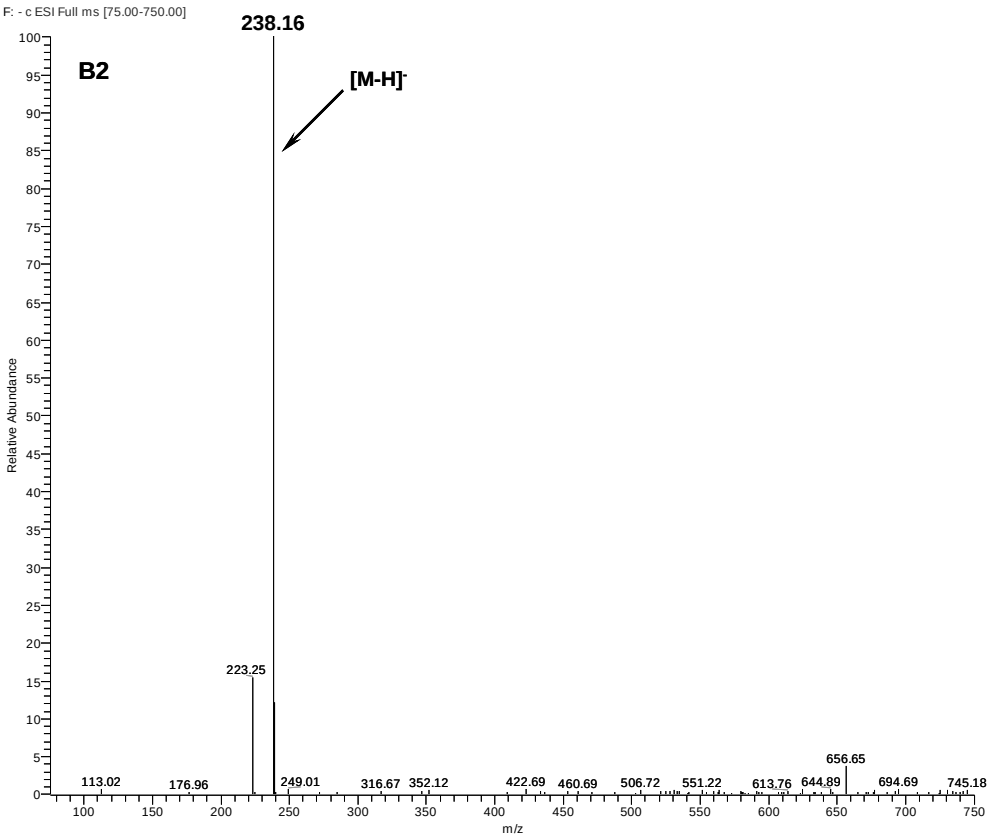

Sequence Dependence of Fluorescence Emission and Quenching of Doubly Thiazole Orange Labeled DNA: Effective Design of a Hybridization-Sensitive Probe

Shuji Ikeda,[†] Takeshi Kubota,[†] Katsuhito Kino,[‡] and Akimitsu Okamoto*[,†]

Advanced Science Institute, RIKEN (The Institute of Physical and Chemical Research), Wako, Saitama 351-0198, Japan, and Kagawa School of Pharmaceutical Sciences, Tokushima Bunri University, Shido, Kagawa 769-2193, Japan. Received May 19, 2008; Revised Manuscript Received June 26, 2008

We have designed a doubly thiazole orange labeled nucleoside showing high fluorescence intensity for a hybrid with the target DNA and effective quenching for a single-stranded state. Knowing how much the fluorescence emission and quenching of this probe depend on the probe sequence and why there is such a sequence dependence is important for effective probe design, we synthesized more than 30 probe sequences and measured their fluorescence intensities. When the probe hybridized with the target DNA strands, there was strong emission, whereas the emission intensity was much weaker before hybridization; however, self-dimerization of probes suppressed fluorescence quenching. In particular, the G/C base pairs neighboring the labeled nucleotide in a self-dimeric structure resulted in a low quenching ability for the probe before hybridization. On the other hand, mismatched base pair formation around the labeled site decreased the fluorescence intensity because the neighboring sequence is the binding site of the tethered thiazole orange dyes. The hybridization enhanced the fluorescence of the probe even when the labeled nucleotide was located at the end of the probe strand; however, the partial lack of duplex structure resulted in a decrease in the fluorescence intensity of the hybrid.

INTRODUCTION

Many fluorescent nucleic acid probes have been developed for observation of the functions of target nucleic acids (*1*−*3*). In particular, a great deal of effort has been invested in the rational design of hybridization-specific DNA detection probes to effectively detect the target DNA using on−off switching of fluorescence depending on hybridization (*4*−*10*). In designing these probes, sensitivity of the dye to the environment, higher-ordered DNA structure caused by the sequence, and quenching by electron transfer from/to nucleobases have a strong influence on fluorescence intensity and sensitivity, and they often impair our predictions.

We have designed a doubly fluorescence labeled nucleoside to achieve high fluorescence intensity for a hybrid with the target DNA and effective quenching for the single-stranded state of the probe (*11*). Two thiazole orange dyes have been linked covalently to a single nucleotide in a DNA probe (Figure 1). An excitonic interaction was produced by the formation of an H-aggregate between dyes, and as a result, emission from the probe before hybridization was suppressed. Dissociation of aggregates by hybridization with the complementary strand resulted in disruption of the excitonic interaction and strong emission from the hybrid. This clear change in fluorescence intensity depending on hybridization is useful for visible gene analysis. However, even this newly designed fluorescent probe exhibited a sequence-dependent change in the ratio of the fluorescence intensities for double- and single-stranded states, for example, $I_{ds}/I_{ss} = 14$ for 5′-d(CGCAAT**X**TAACGC)-3′ (**X**, doubly thiazole orange-labeled nucleoside) and 4.5 for 5′-d(TGAAGGGCTT**X**TGAACTCTG)-3′. To understand how much the fluorescence emission and quenching of these probes depend on the probe sequence and why such a sequence dependence of fluorescence quenching occurs is important. This knowledge facilitates prior estimation of the fluorescence properties of probes and helps in the design of highly hybridization sensitive probes.

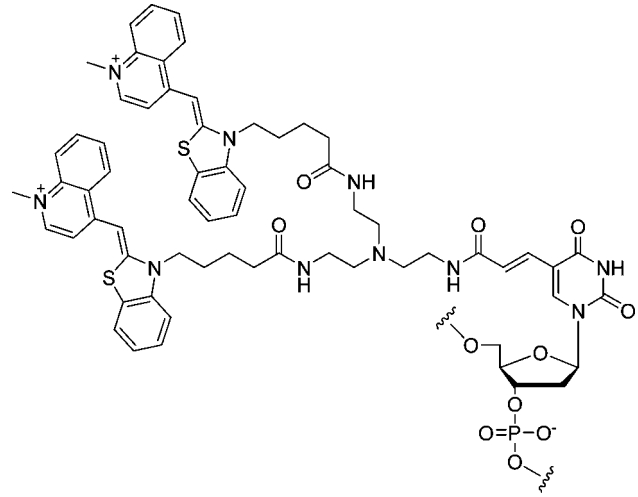

Figure 1. Newly designed nucleotide **X** controlled by excitonic interaction between thiazole orange dyes for an effective hybridization probe.

We herein report the effect of probe sequence on fluorescence emission and quenching. We synthesized a variety of probe sequences including mismatched hybrids and end-labeled probes, and measured their fluorescence intensities. The possibility of self-dimerization and location of the labeling site and mismatched base pair contributing to the fluorescence intensity of the hybrid and quenching efficiency for the single-stranded state

* To whom correspondence may be addressed. Phone: (+81) 48-467-9238. Fax: (+81) 48-467-9205. E-mail: aki-okamoto@riken.jp.
[†] RIKEN.
[‡] Tokushima Bunri University.

10.1021/bc800201m CCC: $40.75 © 2008 American Chemical Society
Published on Web 07/31/2008

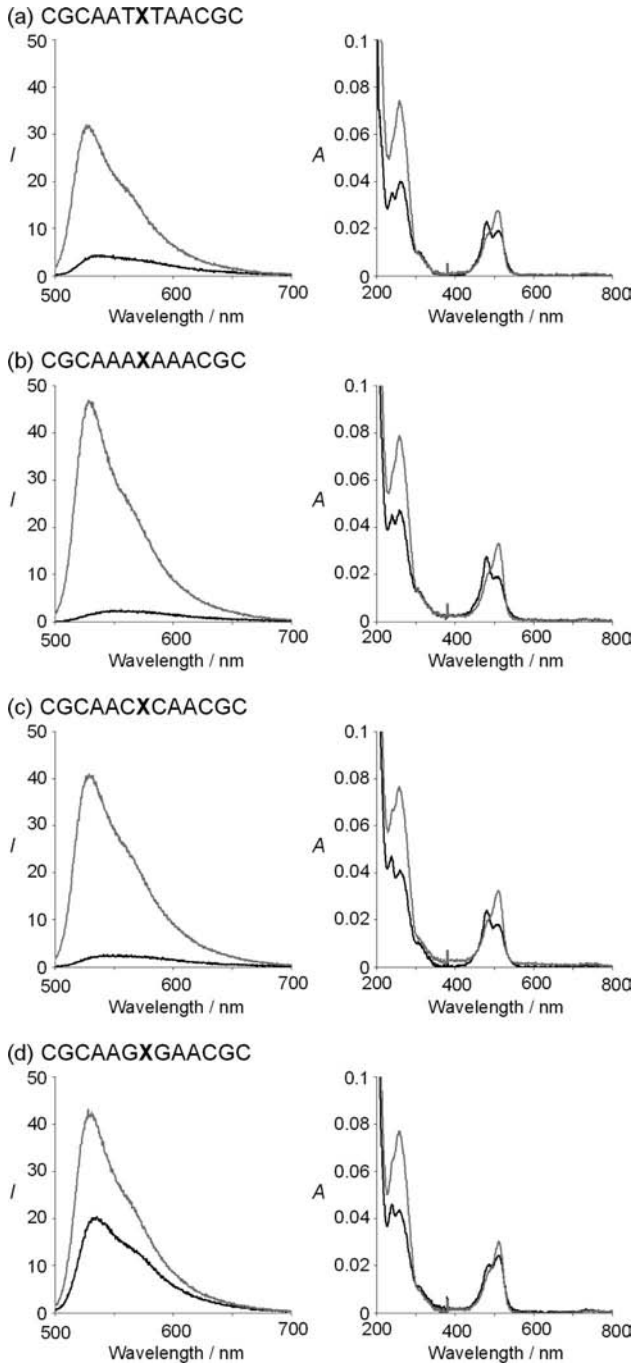

Figure 2. Emission and absorption spectra of CGCAA*N***X***N*AACGC. Emission spectra are shown in the left panels and absorption spectra are shown in the right panels. Spectra were measured in 50 mM sodium phosphate buffer (pH = 7.0) containing 100 mM sodium chloride at 25 °C. Black, spectra before hybridization; gray, spectra after hybridization with the corresponding cDNA. Emission spectra were recorded with excitation at 488 nm.

was investigated. These photophysical data can be used in practical probe design.

EXPERIMENTAL PROCEDURES

Probe Synthesis. DNA oligomers were synthesized by a conventional phosphoramidite method using an Applied Biosystems 392 DNA/RNA synthesizer. Commercially available phosphoramidites were used for dA, dG, dC, and dT. The diamino-modified nucleoside phosphoramidite, which was modified with thiazole orange dyes, was synthesized according to our previous report (*11*). The synthesized DNA oligomer was cleaved from the support with 28% aqueous ammonia and deprotected at 55 °C for 4 h and then at 25 °C for 16 h. After removal of ammonia from the solution under reduced pressure, the DNA was purified by reversed-phase HPLC on a 5-ODS-H column (10 mm × 150 mm, elution with a solvent mixture of 0.1 M triethylamine acetate (TEAA), pH 7.0, linear gradient over 30 min from 5% to 30% acetonitrile at a flow rate of 3.0 mL/min). For determination of the concentration of each DNA, the purified DNA was fully digested with calf intestine alkaline phosphatase (50 U/mL), snake venom phosphodiesterase (0.15 U/mL), and P1 nuclease (50 U/mL) at 25 °C for 16 h. Digested solutions were analyzed by HPLC on a CHEMCOBOND 5-ODS-H column (4.6 mm × 150 mm), elution with a solvent mixture of 0.1 M TEAA, pH 7.0, and flow rate of 1.0 mL/min. The concentration was determined by comparing peak areas with a standard solution containing dA, dC, dG, and dT at concentrations of 0.1 mM.

A solution of the succinimidyl ester of thiazole orange pentanoic acid (*11*) (50 equiv to an active amino group of DNA) in DMF was added to a solution of deprotected DNA in 100 mM sodium carbonate buffer (pH = 9.0), and incubated at 25 °C for 16 h. The reaction mixture was diluted with ethanol. After centrifuging at 4 °C for 20 min, the supernatant was removed. The residue was dissolved with a small amount of water and then the solution was passed through a 0.45 μm filter. The product was purified by reversed-phase HPLC on a 5-ODS-H column (10 mm × 150 mm, elution with a solvent mixture of 0.1 M TEAA, pH 7.0, linear gradient over 30 min from 5% to 30% acetonitrile at a flow rate of 3.0 mL/min). The concentration of the fluorescent DNA was determined by the same method as described in the DNA synthesis. The fluorescent DNA was identified by MALDI-TOF mass spectrometry: CGCAAT**X**TAACGC, calcd for $C_{180}H_{217}N_{56}O_{78}P_{12}S_2$ ($[M - H]^+$) 4848.8, found 4851.4; CGCAAA**X**AAACGC, calcd for $C_{180}H_{215}N_{62}O_{74}P_{12}S_2$ ($[M - H]^+$) 4866.8, found 4866.6; CGCAAC**X**CAACGC, calcd for $C_{178}H_{215}N_{58}O_{76}P_{12}S_2$ ($[M - H]^+$) 4818.8, found 4819.1; CGCAAG**X**GAACGC, calcd for $C_{180}H_{215}N_{62}O_{76}P_{12}S_2$ ($[M - H]^+$) 4898.8, found 4897.8; GCCAAG**X**GAACCG, calcd for $C_{180}H_{215}N_{62}O_{76}P_{12}S_2$ ($[M - H]^+$) 4898.8, found 4898.5; AAAAAA**X**AAAAAA, calcd for $C_{184}H_{215}N_{70}O_{68}P_{12}S_2$ ($[M - H]^+$) 4930.9, found 4930.3; CCCCCC**X**CCCCCC, calcd for $C_{172}H_{215}N_{46}O_{80}P_{12}S_2$ ($[M - H]^+$) 4642.6, found 4643.1; TTTTTA**X**ATTTTT, calcd for $C_{184}H_{225}N_{40}O_{88}P_{12}S_2$ ($[M - H]^+$) 4840.8, found 4841.0; TTTTTC**X**CTTTTT, calcd for $C_{182}H_{225}N_{36}O_{90}P_{12}S_2$ ($[M - H]^+$) 4792.7, found 4793.5; TTTTTG**X**GTTTTT, calcd for $C_{184}H_{225}N_{40}O_{90}P_{12}S_2$ ($[M - H]^+$) 4872.8, found 4872.0; TTTTGT**X**TGTTTT, calcd for $C_{184}H_{225}N_{40}O_{90}P_{12}S_2$ ($[M - H]^+$) 4872.8, found 4872.1; TTTGTT**X**TTGTTT, calcd for $C_{184}H_{225}N_{40}O_{90}P_{12}S_2$ ($[M - H]^+$) 4872.8, found 4873.0; TTGTTT**X**TTTGTT, calcd for $C_{184}H_{225}N_{40}O_{90}P_{12}S_2$ ($[M - H]^+$) 4872.8, found 4871.8; GTCCTC**X**TCGGCA, calcd for $C_{179}H_{218}N_{51}O_{82}P_{12}S_2$ ($[M - H]^+$) 4831.8, found 4832.2; TTTTAG**X**GTTGCG, calcd for $C_{183}H_{221}N_{50}O_{85}P_{12}S_2$ ($[M - H]^+$) 4916.8, found 4916.0; AGAAGA**X**GGTGGC, calcd for $C_{183}H_{216}N_{65}O_{77}P_{12}S_2$ ($[M - H]^+$) 4993.9, found 4994.9; TACCAG**X**CACCAT, calcd for $C_{179}H_{217}N_{54}O_{78}P_{12}S_2$ ($[M - H]^+$) 4808.8, found 4807.4; TATGCG**X**GATTTT, calcd for $C_{183}H_{221}N_{50}O_{84}P_{12}S_2$ ($[M - H]^+$) 4900.8, found 4900.6; CACCAG**X**CACTAC, calcd for $C_{178}H_{216}N_{55}O_{77}P_{12}S_2$ ($[M - H]^+$) 4793.8, found 4792.1; CACCAG**X**CACTGC, calcd for $C_{178}H_{216}N_{55}O_{78}P_{12}S_2$ ($[M - H]^+$) 4809.8, found 4809.1; CCGCTTAA**X**ACTGA, calcd for $C_{190}H_{230}N_{58}O_{85}P_{13}S_2$ ($[M - H]^+$) 5153.0, found 5153.4; AGATCC**X**GACAGA, calcd for $C_{181}H_{216}N_{61}O_{76}P_{12}S_2$ ($[M - H]^+$) 4897.8, found 4897.2; ACCTGCAC**X**ATAAGCAC, calcd for $C_{218}H_{265}N_{72}O_{100}P_{16}S_2$ ($[M - H]^+$) 6053.6, found 6053.1; ACAGTTCT**X**CAACTGGC,

Table 1. Photophysical Properties of Doubly Thiazole Orange Labeled DNA, CGCAA*N*X*N*AACGC [a]

sequences (5′ → 3′)	λ_{max}/nm (ε)	λ_{em}/nm[b]	Φ_f[c]	Φ_{ds}/Φ_{ss}[d]
CGCAATXTAACGC	479 (78000) 510 (52000)	538	0.059	-
CGCAATXTAACGC/GCGTTAAATTGCG	509 (89000)	528	0.272	4.6
CGCAAAXAAACGC	480 (69000) 508 (47000)	540	0.026	-
CGCAAAXAAACGC/GCGTTTATTTGCG	510 (83000)	529	0.307	12
CGCAACXCAACGC	480 (61000) 509 (45000)	538	0.034	-
CGCAACXCAACGC/GCGTTGAGTTGCG	510 (82000)	529	0.318	9.3
CGCAAGXGAACGC	486 (51000) 510 (61000)	534	0.189	-
CGCAAGXGAACGC/GCGTTCACTTGCG	511 (75000)	529	0.362	1.9

[a] 0.4 μM DNA, 50 mM sodium phosphate buffer (pH = 7.0), 100 mM sodium chloride. [b] Excited at 488 nm. [c] Excited at λ_{max} (longer wavelength when there are two λ_{max}). [d] The ratio of the quantum yields of duplex and single-stranded states.

calcd for $C_{219}H_{267}N_{68}O_{104}P_{16}S_2$ ([M − H]$^+$) 6075.6, found 6076.2; ACAAACCA**X**TATGTGCT, calcd for $C_{220}H_{267}N_{70}O_{102}P_{16}S_2$ ([M − H]$^+$) 6083.6, found 6083.5; CAAGTGCC**X**TCACTGCA, calcd for $C_{218}H_{266}N_{69}O_{103}P_{16}S_2$ ([M − H]$^+$) 6060.6, found 6061.1; CGCCAATA**X**TTACGTGC, calcd for $C_{219}H_{267}N_{68}O_{104}P_{16}S_2$ ([M − H]$^+$) 6075.6, found 6075.6; TGCAAACA**X**CCGACTGA, calcd for $C_{219}H_{265}N_{74}O_{100}P_{16}S_2$ ([M − H]$^+$) 6093.6, found 6092.4; **X**TAACGCCAAGTG, calcd for $C_{181}H_{217}N_{58}O_{78}P_{12}S_2$ ([M − H]$^+$) 4888.8, found 4888.0; **X**AAACGCCAAGTG, calcd for $C_{181}H_{216}N_{61}O_{76}P_{12}S_2$ ([M − H]$^+$) 4897.8, found 4897.5; **X**CAACGCCAAGTG, calcd for $C_{180}H_{216}N_{59}O_{77}P_{12}S_2$ ([M − H]$^+$) 4873.8, found 4872.5; **X**GAACGCCAAGTG, calcd for $C_{181}H_{216}N_{61}O_{77}P_{12}S_2$ ([M − H]$^+$) 4913.8, found 4913.0; ATTGATCATTGGTCT**X**CGCC, calcd for $C_{249}H_{306}N_{74}O_{126}P_{19}S_2$ ([M − H]$^+$) 7004.2, found 7003.5; ATTGA**X**CATTGGTCTTCGCC, calcd for $C_{249}H_{306}N_{74}O_{126}P_{19}S_2$ ([M − H]$^+$) 7004.2, found 7004.1; TTGGTCT**X**CGCCTTTCGAAG, calcd for $C_{249}H_{306}N_{74}O_{127}P_{19}S_2$ ([M − H]$^+$) 7020.1, found 7019.7.

Absorption and Fluorescence Measurements. Absorption and fluorescence spectra of the probes (0.4 μM single-stranded or duplex concentration) were measured in 50 mM sodium phosphate buffer (pH = 7.0) containing 100 mM sodium chloride using a cell with a 1 cm path length. The excitation and emission bandwidths were 1.5 nm. The fluorescence quantum yield (Φ) was determined using 9,10-diphenylanthracene as a reference, with a known Φ = 0.95 in ethanol. The quantum yield was calculated using the following equation:

$$\Phi_{(S)}/\Phi_{(R)} = [A_{(S)}/A_{(R)}] \times (\mathrm{Abs})_{(R)}/(\mathrm{Abs})_{(S)}] \times [n_{(S)}{}^2/n_{(R)}{}^2] \quad (1)$$

Here, $\Phi_{(S)}$ and $\Phi_{(R)}$ are the fluorescence quantum yields of the sample and the reference, respectively. The terms $A_{(S)}$ and $A_{(R)}$ are the areas under the fluorescence spectra of the sample and the reference, respectively, $(\mathrm{Abs})_{(S)}$ and $(\mathrm{Abs})_{(R)}$ are the optical densities of the sample and the reference solution at the wavelength of excitation, respectively, and $n_{(S)}$ and $n_{(R)}$ are the values of the refractive index for the solvents used for the sample ($n_{(S)}$ = 1.333) and the reference ($n_{(R)}$ = 1.383), respectively.

RESULTS AND DISCUSSION

Effect of Neighboring Bases. The influence of bases adjacent to the fluorescence-labeled base has often been discussed as the reason for the sequence dependence of fluorescence intensity. We initially investigated the effect of neighboring bases on the fluorescence intensity using a DNA probe 5′-d(CGCAA*N***X**-*N*AACGC)-3′ (*N* = T, A, C, or G) (Figure 2 and Table 1). When *N* was thymine, the emission spectra were observed at 538 nm as a single, broad band. Hybridization with the complementary strand enhanced the emission intensity, which is clearly distinguishable from the single-stranded state (Φ_{ds}/Φ_{ss} = 4.6). In addition, when *N* was adenine or cytosine, the probe hybridized with the target DNA strands showed strong emission, whereas the emission intensity before hybridization was much weaker. The quenching abilities were slightly higher for the single-stranded state than when *N* was thymine (Φ_{ds}/Φ_{ss} = 12 for A, 9.3 for C). On the other hand, when *N* was guanine, the probe showed a small change in emission intensity before and after hybridization (Φ_{ds}/Φ_{ss} = 1.9). The nonemissive character observed in the single-stranded state is accepted as a general feature of H-aggregates of the dyes (*12*−*14*). The excited state of the dye aggregate splits into two energy levels according to exciton coupling theory (*15*). The transition to the upper excitonic state, which is allowed for the H-aggregates, rapidly deactivates to the lower excitonic state, which is a nonemissive state. Two absorption bands were observed at 400−550 nm for all the probes. An absorption band at shorter wavelength (ca. 480 nm) appeared more strongly when the probes were in a single-stranded state, whereas an absorption band of longer wavelength (ca. 510 nm) became predominant when probes were hybridized with the complementary strands. The shift of the absorption band to 480 nm indicates aggregation of thiazole orange dyes for the single-stranded state of the probe. The ratio of absorbances at 480 and 510 nm (A_{480}/A_{510}) was 1.21, 1.48, 1.34, and 0.83 for *N* = T, A, C, and G, respectively, an order that showed good agreement with the order of Φ_{ds}/Φ_{ss}, suggesting that the aggregation of dyes affects fluorescence quenching for the single-stranded state.

The effect of the neighboring base on fluorescence quenching was also confirmed in the fluorescence measurement of another sequence, 5′-d(TTTTT*N***X***N*TTTTT)-3′ (Figure 3 and Table 2). In contrast to the low quenching ability of 5′-d(CGCAA*N***X**-*N*AACGC)-3′ for a single-stranded state when the *N* base was guanine, 5′-d(TTTTTG**X**GTTTTT)-3′ showed more effective quenching (Φ_{ds}/Φ_{ss} = 25), and aggregation of the dyes was also promoted (A_{480}/A_{510} = 1.54). The fluorescence quenching of probes for the single-stranded state was very effective, although a slight fluorescence emission was observed when *N* was adenine. Therefore, the low quenching ability of 5′-d(CGCAAG**X**GAACGC)-3′ could not be directly attributable to the guanine bases neighboring **X**.

Self-Dimerization. As another working hypothesis for the low quenching efficiency of 5′-d(CGCAAG**X**GAACGC)-3′ observed before hybridization with the target DNA, we next considered the possibility of "self-dimerization" of probes. The probe emits fluorescence when the duplex is formed. Formation of full or partial self-dimerization of the probe may maintain the fluorescence intensity. When the self-dimerized structure of 5′-d(CGCAA*N***X***N*AACGC)-3′ is assumed as the number of possible Watson−Crick base pairs around **X** becomes a maximum, the structures can be drawn as in Figure 4. When *N* is adenine or cytosine, which exhibited a larger Φ_{ds}/Φ_{ss}, two

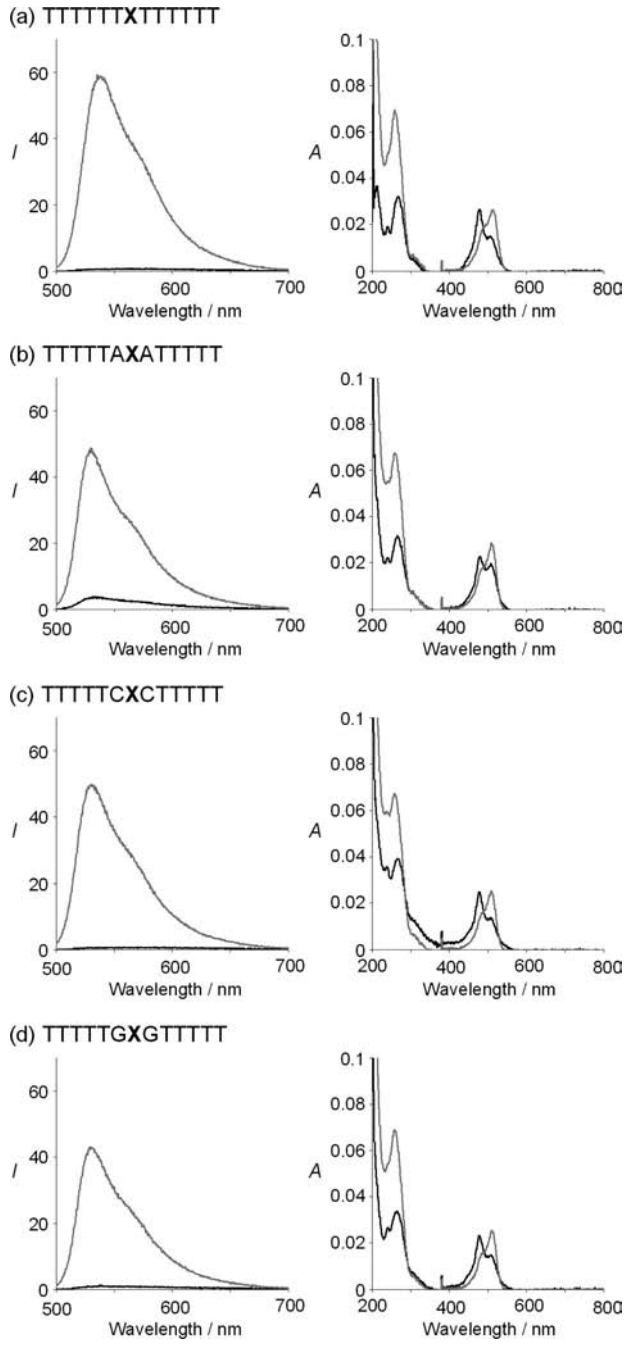

Figure 3. Emission and absorption spectra of TTTTT*N*X*N*TTTTT. Emission spectra are shown in the left panels and absorption spectra are shown in the right panels. Spectra were measured in 50 mM sodium phosphate buffer (pH = 7.0) containing 100 mM sodium chloride at 25 °C. Black, spectra before hybridization; gray, spectra after hybridization with the corresponding cDNA. Emission spectra were recorded with excitation at 488 nm.

base pairs can be formed within two bases from **X**. When *N* is thymine, four base pairs can be drawn. When *N* is guanine, which showed a lower quenching ability, the probe can also form four base pairs. The probe with N = guanine has tight G/C base pairs on both sides of **X**, and it seems to form a more stable self-dimer than when *N* is thymine. The sequence 5′-d(TTTTTA**X**ATTTTT)-3′ can also form a self-dimer with four base pairs; thus, the slight emission observed before hybridization with the target DNA may also be explained by self-dimerization.

We prepared 30 different sequences with **X**, and measured their Φ_{ds}/Φ_{ss}. We also calculated the number of possible Watson−Crick base pairs formed within two bases from **X** (N_{bp}). These data are summarized in Figure 5, which shows the relationship between Φ_{ds}/Φ_{ss} and N_{bp}. Smaller N_{bp} produced larger Φ_{ds}/Φ_{ss}, i.e., a higher efficiency of fluorescence quenching was observed. In addition, the probes with a purine-rich sequence (sequences #8 and #13) and with a sequence that can form G/C base pairs at both sides of **X** in the formation of a self-dimer (sequences #23 and #29) exhibited low Φ_{ds}/Φ_{ss} values. The "self-dimer" formed by the probe must be thermodynamically unstable because it contains many mismatched base pairs. However, this plausible self-dimeric structure may inhibit fluorescence quenching because the formation of "primer dimer" in PCR assays is known to significantly decrease amplification efficiency. The probe #29 (5′-d(AGATCC**X**GACAGA)-3′) showed a gradual sigmoid curve in the "melting temperature" measurement without the complementary strand (λ = 260 nm, T_m = 50 °C), suggesting that the self-dimeric structure exists under the condition of fluorescence measurement. When an ordered duplex structure can be maintained around **X** of the self-dimer by Watson−Crick base pairs, the neighboring base pairs would work as the binding sites of dyes.

Mismatched Base Pairs. We next examined how much mismatched base pairs affected fluorescence emission. In this experiment, we used the hybrids with the cDNA containing one or two mismatched base pairs at and around **X**. When the base opposite **X** in 5′-d(CGCAAT**X**TAACGC)-3′ was changed to a mismatched base (i.e., 5′-d(GCGTTA*N*ATTGCG)-3′ (N = C, G, or T) as the strand to be hybridized), the quantum yields of mismatched hybrids decreased to 60−85% of that of the full-matched hybrid (Table 3). On the other hand, when both or either of the base pairs neighboring **X** of 5′-d(CGCAAT**X**-TAACGC)-3′ were mismatched (i.e., 5′-d(GCGTT*NAN*′TTGCG)-3′ as the strand to be hybridized), the unique fluorescence behavior was observed. The ratio of quantum yields of T/C mismatched hybrids to the fully matched hybrid ($\Phi_{mismatch}/\Phi_{match}$) was smaller than those observed for the mismatched base pairs at **X**. The mismatched base pair formation around **X** contributes more to the decrease in fluorescence intensity rather than the mismatched base pair at **X** because the sequence neighboring **X** works as the binding site of dyes of **X**. The CD spectra of a matched duplex 5′-d(CGCAAT**X**TAACGC)-3′/5′-d(GCGTTAAATTGCG)-3′ showed a broad negative signal and a sharp positive signal at 450−550 nm, suggesting that the dyes of **X** bind to the sequence neighboring **X** through intercalation and/or binding to the major groove (*11*). The mismatched base pair formation would lower the binding affinity of dyes to DNA and induce dissociation of dyes from the DNA structure and the formation of a nonemissive bichromophoric aggregate. The decrease in fluorescence emission by mismatched base pair formation around **X** paradoxically supports the assumption that the formation of matched base pairs around **X** in the self-dimeric mode results in low fluorescence quenching. The hybrid with the strand of $N = N'$ = T also showed a lower $\Phi_{mismatch}/\Phi_{match}$ value (0.45). On the other hand, a high $\Phi_{mismatch}/\Phi_{match}$ value was observed for the hybrid with the strand of $N = N'$ = G (0.88). This is probably because T/G wobble mismatched base pairs are relatively stable and can maintain the duplex structure (*16*−*18*); thus, they do not prevent the dyes of **X** from binding to DNA.

Label on Strand End. Hybridization with the target enhanced the fluorescence intensity even when **X** was put on the end of the probe strand. We prepared the probe 5′-d(**X**TAACGC-CAAGTG)-3′ and hybridized it with 5′-d(CACTTGGCGT-TA*N*ATTGCGGTTCAC)-3′. The fluorescence intensity was enhanced by hybridization (N = A) (Table 4). However, the fluorescence quantum yield of the hybrid was lower than that of the hybrid 5′-d(CGCAAT**X**TAACGC)-3′/5′-d(GCGTTAAAT-

Table 2. Photophysical Properties of Doubly Thiazole Orange Labeled DNA, TTTTT*NXN*TTTTT[a]

sequences (5′ → 3′)	λ_{max}/nm (ε)	λ_{em}/nm[b]	Φ_f[c]	Φ_{ds}/Φ_{ss}[d]
TTTTTT**X**TTTTTT	478 (67000)	n.d.	0.010	-
	507 (38000)			
TTTTTT**X**TTTTTT/AAAAAAAAAAAAA	513 (66000)	538	0.469	47
TTTTTA**X**ATTTTT	479 (57000)	534	0.033	-
	508 (49000)			
TTTTTA**X**ATTTTT/AAAAATATAAAAA	509 (72000)	530	0.299	9.1
TTTTTC**X**CTTTTT	477 (62000)	540	0.010	-
	507 (35000)			
TTTTTC**X**CTTTTT/AAAAAGAGAAAAA	509 (63000)	530	0.390	39
TTTTTG**X**GTTTTT	477 (58000)	539	0.014	-
	508 (37000)			
TTTTTG**X**GTTTTT/AAAAACACAAAAA	510 (63000)	530	0.356	25

[a] 0.4 μM DNA, 50 mM sodium phosphate buffer (pH = 7.0), 100 mM sodium chloride. [b] Excited at 488 nm. [c] Excited at λ_{max} (longer wavelength when there are two λ_{max}). [d] The ratio of the quantum yields of duplex and single-stranded states.

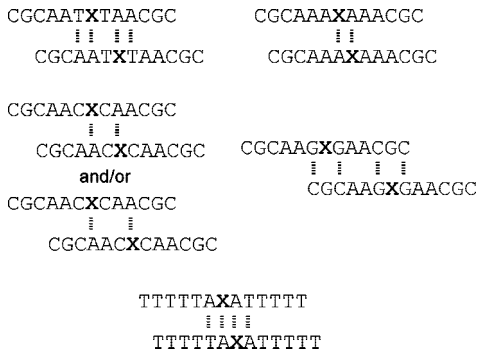

Figure 4. Plausible motifs for probe self-dimers. Watson−Crick base pairs formed within two bases from **X** are drawn by hashed lines. **X** bases can form Watson−Crick base pairs with adenine bases.

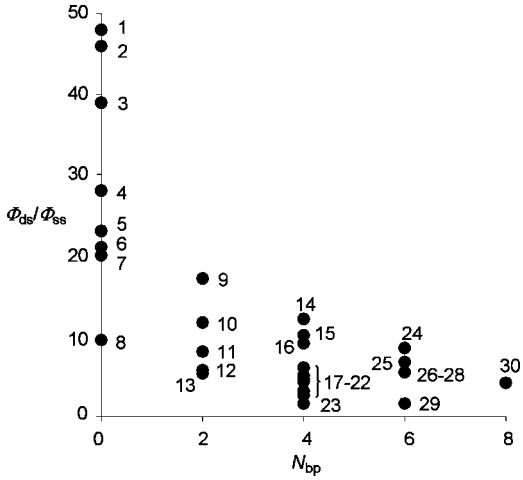

Figure 5. Relationship between the ratio of the quantum yields of the double- and single-stranded states (Φ_{ds}/Φ_{ss}) and the number of possible Watson−Crick base pairs formed within two bases from **X** (N_{bp}). 1, CCCCCC**X**CCCCCC; 2, TTTTTT**X**TTTTTT; 3, TTTTTC**X**CTTTTT; 4, TTTTTG**X**GTTTTT; 5, TTGTTT**X**TTTGTT; 6, TTTTGT**X**TGTTTT; 7, TTTGTT**X**TTGTTT; 8, AAAAAA**X**AAAAAA; 9, CGCAAA**X**AAACGC; 10, CGCAAC**X**CAACGC; 11, GTCCTC**X**TCGGCA; 12, TTTTAG**X**GTTGCG; 13, AGAAGA**X**GGTGGC; 14, TACCAG**X**CACCAT; 15, TATGCG**X**GATTTT; 16, TTTTTA**X**ATTTTT; 17, ACCTGCAC**X**ATAAGCAC; 18, ACAGTTCT**X**CAACTGGC; 19, CGCAAT**X**TAACGC, 20, ACAAACCA**X**TATGTGCT; 21, TGAAGGGCTT**X**TGAACTCTG; 22, GCCAAG**X**GAACCG; 23, CGCAAG**X**GAACGC; 24, CACCAG**X**CACTAC; 25, CAAGTGCC**X**TCACTGCA; 26, CACCAG**X**CACTGC; 27, TGCAAACA**X**CCGACTGA; 28, CCGCTTAA**X**ACTGA; 29, AGATCC**X**GACAGA; 30, CGCCAATA**X**TTACGTGC.

TGCG)-3′. The duplex structure neighboring **X** plays an important role for fluorescence emission, and the lack of duplex structure at one side of **X**, i.e., reduction in the dye-bindable region, resulted in a decrease in the fluorescence intensity of the hybrid. When *N* was C, G, or T, the fluorescence intensity of the hybrid became approximately half of that of the hybrid with *N* = A. The decrement in the fluorescence intensity by mismatched base pair formation at **X** was larger than was the case when **X** was put on the inside of the sequence. This is probably because the structural flexibility for **X** located at the end of the probe loosened the binding of dyes to the DNA structure.

Table 3. Photophysical Properties of Hybrids with Mismatched Base Pairs[a]

sequences (5′ → 3′) hybridized with CGCAAT**X**TAACGC	λ_{max}/nm (ε)	λ_{em}/nm[b]	Φ_f[c]	$\Phi_{mismatch}/\Phi_{match}$[d]
GCGTTAAATTGCG (Matched)	509 (89000)	528	0.272	-
GCGTTA**C**ATTGCG	509 (73000)	529	0.164	0.60
GCGTTA**G**ATTGCG	507 (72000)	531	0.194	0.71
GCGTTA**T**ATTGCG	510 (75000)	530	0.231	0.85
GCGTT**C**AATTGCG	510 (69000)	530	0.147	0.54
GCGTTAA**C**TTGCG	510 (50000)	528	0.120	0.44
GCGTT**C**A**C**TTGCG	512 (61000)	533	0.081	0.30
GCGTT**G**A**G**TTGCG	511 (75000)	528	0.239	0.88
GCGTTT**T**A**T**TTGCG	511 (74000)	530	0.122	0.45

[a] 0.4 μM DNA, 50 mM sodium phosphate buffer (pH = 7.0), 100 mM sodium chloride. [b] Excited at 488 nm. [c] Excited at λ_{max} (longer wavelength when there are two λ_{max}). [d] The ratio of the quantum yields of mismatched and matched duplexes.

Points for Probe Design. The fluorescence behavior described above facilitates the design of probes for effective DNA detection. The keys for probe design are as follows: (i) Avoid sequences that form self-dimers to induce effective quenching of the single-stranded probe. In particular, the self-dimer capable of the formation of a G/C base pair neighboring **X** should be avoided. (ii) Mismatched base pairs of the hybrid are acceptable. However, the mismatched base pair neighboring **X** is unfavorable because the **X**-neighboring region is a dye-binding site and the mismatched base pair decreases dye-binding affinity and fluorescence intensity of the dye. (iii) The probe with **X** at a strand end may be used for detection of the difference of one base such as single nucleotide polymorphism. However, the fluorescence change is limited to approximately 50%, and the target is also confined to the sequence concerned with adenine.

The most important key is (i). Unless one takes care of this issue, the activity of a probe as a hybridization-sensitive DNA detector may be lost. A typical example is the design of a probe for detection of the 50-mer DNA strand 5′-d(ACTTGAGCGGTCCTTCGAAAGGCGAAGACCAATGAT-CAATTATGGACCTA)-3′. When we require a probe binding to a 5′-d(GGCGAAGACCAATGATCAAT)-3′ region of the 50-mer DNA strand, we can design several probes that contain **X** at different sites, such as 5′-d(ATTGATCATTGGTCT**X**CGCC)-

Table 4. Photophysical Properties of 5′-End-Labeled Probes[a]

sequences (5′ → 3′) hybridized with **X**TAACGCCAAGTG	λ_{max}/nm (ε)	λ_{em}/nm[b]	Φ_f[c]	$\Phi_{mismatch}/\Phi_{match}$[d]
before hybridization	479 (88000) 507 (55000)	538	0.039	-
CACTTGGCGTTAAATTGCGGTTCAC	510 (99000)	533	0.155	-
CACTTGGCGTTA**C**ATTGCGGTTCAC	509 (89000)	534	0.085	0.55
CACTTGGCGTTA**G**ATTGCGGTTCAC	509 (87000)	533	0.082	0.53
CACTTGGCGTTA**T**ATTGCGGTTCAC	509 (89000)	530	0.094	0.61

[a] 0.4 μM DNA, 50 mM sodium phosphate buffer (pH = 7.0), 100 mM sodium chloride. [b] Excited at 488 nm. [c] Excited at λ_{max} (longer wavelength when there are two λ_{max}). [d] The ratio of the quantum yields of mismatched and matched duplexes.

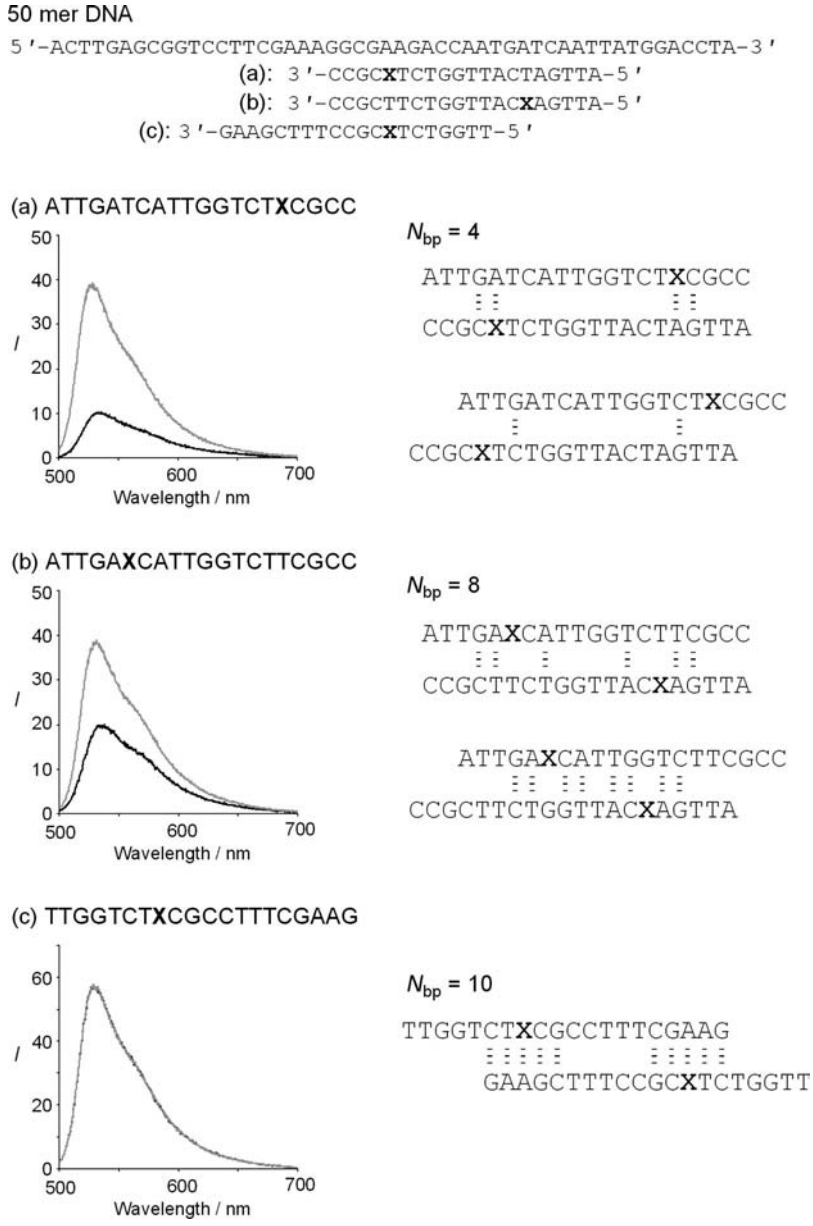

Figure 6. Probe design. Emission spectra of three designed probes were measured in 50 mM sodium phosphate buffer (pH = 7.0) containing 100 mM sodium chloride at 25 °C. Black, spectra before hybridization; gray, spectra after hybridization with the corresponding cDNA. Emission spectra were recorded with excitation at 488 nm. The two spectra in (c) almost exactly overlap each other. Watson−Crick base pairs formed within two bases from **X** are drawn by hashed lines.

3′ and 5′-d(ATTGA**X**CATTGGTCTTCGCC)-3′. The strand 5′-d(ATTGATCATTGGTCT**X**CGCC)-3′ exhibited relatively high Φ_{ds}/Φ_{ss} (Figure 6a), whereas the Φ_{ds}/Φ_{ss} value of the probe 5′-d(ATTGA**X**CATTGGTCTTCGCC)-3′ was lower (Figure 6b) because of the high fluorescence intensity of the single-stranded state. The N_{bp} values showing the possibility of self-dimer formation were 4 for the former probe and 8 for the latter probe. Therefore, N_{bp} values can inform us in advance that the former probe is a favorable sequence to be synthesized. The probe design is also similar when the site recognized by **X** is fixed and the hybridization region is selectable flexibly. For example, strands 5′-d(ATTGATCATTGGTCT**X**CGCC)-3′ and 5′-d(TTGGTCT**X**CGCCTTTCGAAG)-3′ have an **X** recognizing the same adenine base in the target DNA, and they were hybridized

with different regions of the 50-mer DNA strand. The former probe showed a high Φ_{ds}/Φ_{ss} value as describe above, whereas the fluorescence intensity observed for the latter probe before hybridization was almost the same as that of the hybrid with the target strand (Figure 6c). The N_{bp} value of the latter probe is 10, suggesting that the probe sequence is hopeless for working as a hybridization probe. Therefore, we must pay attention to the choice of the location of **X** and the recognition sequence to produce probes that are more effective.

In conclusion, the fluorescence emission and quenching of doubly thiazole orange labeled DNA probes are influenced strongly by the probe sequence. A variety of probe sequences including mismatched hybrids and end-labeled probes demonstrated how much the fluorescence emission and quenching of these probes depend on probe sequence and why such a sequence dependence is produced. The photophysical data organized in the present study make it possible to estimate the fluorescence ability of probes before synthesis and help the rational design of hybridization-sensitive probes to detect effectively the target DNA using on−off switching of fluorescence depending on hybridization.

ACKNOWLEDGMENT

We thank Dr. Takehiro Suzuki (Biomolecular Characterization Team, RIKEN) for the MALDI-TOF mass spectrometry.

LITERATURE CITED

(1) Paillasson, S., van de Corput, M., Dirks, R. W., Tanke, H. J., Robert-Nicoud, M., and Ronot, X. (1997) In situ hybridization in living cells: Detection of RNA molecules. *Exp. Cell Res. 231*, 226–233.

(2) Asseline, U. (2006) Development and applications of fluorescent oligonucleotides. *Curr. Org. Chem. 10*, 491–518.

(3) Marti, A. A., Jockusch, S., Stevens, N., Ju, J., and Turro, N. J. (2007) Fluorescent hybridization probes for sensitive and selective DNA and RNA detection. *Acc. Chem. Res. 40*, 402–409.

(4) Tyagi, S., and Kramer, F. R. (1996) Molecular beacons: Probes that fluoresce upon hybridization. *Nat. Biotechnol. 14*, 303–308.

(5) Lartia, R., and Asseline, U. (2006) New cyanine-oligonucleotide conjugates: Relationships between chemical structures and properties. *Chem. Eur. J. 12*, 2270–2281.

(6) Jarikote, D. V., Köhler, O., Socher, E., and Seitz, O. (2005) Divergent and linear solid-phase synthesis of PNA containing thiazole orange as artificial base. *Eur. J. Org. Chem. 15*, 3187–3195.

(7) Marin, V. L., and Armitage, B. A. (2006) Hybridization of complementary and homologous peptide nucleic acid oligomers to a guanine quadruplex-forming RNA. *Biochemistry 45*, 1745–1754.

(8) Kerr, C. E., Mitchell, C. D., Ying, Y. M., Eaton, B. E., and Netzel, T. L. (2000) Synthesis and photophysics of a 1-pyrenylmethyl-substituted 2′-deoxyuridine-5-carboxamide nucleoside: Electron-transfer product lifetimes and energies. *J. Phys. Chem. B 104*, 2166–2175.

(9) Okamoto, A., Tainaka, K., and Saito, I. (2003) Clear distinction of purine bases on the complementary strand by a fluorescence change of a novel fluorescent nucleoside. *J. Am. Chem. Soc. 125*, 4972–4973.

(10) Okamoto, A., Tanaka, K., Fukuta, T., and Saito, I. (2003) Design of base-discriminating fluorescent nucleoside and its application to T/C SNP typing. *J. Am. Chem. Soc. 125*, 9296–9297.

(11) Ikeda, S., and Okamoto, A. (2008) Hybridization-sensitive on-off DNA probe: Application of the exciton coupling effect to effective fluorescence quenching. *Chem. Asian J. 3*, 958–968.

(12) Khairutdinov, R. F., and Serpone, N. (1997) Photophysics of cyanine dyes: Subnanosecond relaxation dynamics in monomers, dimers, and H- and J-aggregates in solution. *J. Phys. Chem. B 101*, 2602–2610.

(13) Sagawa, T., Tobata, H., and Ihara, H. (2004) Exciton interactions in cyanine dye-hyaluronic acid (HA) complex: reversible and biphasic molecular switching of chromophores induced by random coil-to-double-helix phase transition of HA. *Chem. Commun.* 2–4.

(14) Fürstenberg, A., Julliard, M. D., Deligeorgiev, T. G., Gadjev, N. I., Vasilev, A. A., and Vauthey, E. (2006) Ultrafast excited-state dynamics of DNA fluorescent intercalators: New insight into the fluorescence enhancement mechanism. *J. Am. Chem. Soc. 128*, 7661–7669.

(15) Kasha, M. (1963) Energy transfer mechanisms and molecular exciton model for molecular aggregates. *Radiat. Res. 20*, 55–70.

(16) Kalnik, M. W., Kouchakdjian, M., Li, B. F. L., Swann, P. F., and Patel, D. J. (1988) Base pair mismatches and carcinogen-modified bases in DNA: An NMR study of G·T and G·O^{4}meT pairing in dodecanucleotide duplexes. *Biochemistry 27*, 108–115.

(17) Hunter, W. N., Kneale, G., Brown, T., Rabinovich, D., and Kennard, O. (1986) Refined crystal structure of an octanucleotide duplex with G·T mismatched base-pairs. *J. Mol. Biol. 190*, 605–618.

(18) Hare, D., Shapiro, L., and Patel, D. J. (1988) Wobble dG·dT pairing in right-handed DNA: Solution conformation of the d(CGTGAATTCGCG) duplex deduced from distance geometry analysis of nuclear Overhauser effect spectra. *Biochemistry 25*, 7445–7456.

BC800201M

Utilization of Intrachain 4′-*C*-Azidomethylthymidine for Preparation of Oligodeoxyribonucleotide Conjugates by Click Chemistry in Solution and on a Solid Support

Anu Kiviniemi,* Pasi Virta, and Harri Lönnberg

Department of Chemistry, University of Turku, FIN-20014 Turku, Finland. Received May 29, 2008; Revised Manuscript Received June 24, 2008

4′-*C*-Azidomethylthymidine 3′-(H-phosphonate) monomer (**10**) was synthesized in high yield and three such monomers were incorporated by the H-phosphonate coupling into a 15-mer oligodeoxyribonucleotide. The unmodified 2′-deoxynucleosides could be coupled by either the H-phosphonate or phosphoramidite chemistry, indicating that the Staudinger reaction between the azido group and the phosphoramidite reagent severely hampered the coupling only when it took place intramolecularly. After chain assembly, three alkynyl group bearing ligands, viz., propargyl 2,3,4,6-tetra-*O*-acetyl-α-D-mannopyranoside (**2**), *N*-{4-[*N*-(trifluoroacetyl)aminomethyl]benzyl}-4-pentynamide (**3**) and N^1,N^3,$N^{2'}$-tris(trifluoroacetyl)-$N^{6'}$-(4-pentynoyl)neamine (**4**), were conjugated to the azido groups of the oligonucleotide by click chemistry both on a solid support and in solution. The products were deprotected by conventional ammonolysis and purified by HPLC chromatography. Melting temperature studies revealed that the mannose conjugated oligonucleotides formed more stable duplexes with 2′-*O*-methyl RNA than with DNA strand. With 2′-*O*-methyl RNA, a slight destabilization compared to an unmodified sequence was observed at low ionic strength, while at high salt content, the manno-conjugation was stabilizing.

INTRODUCTION

Selective inhibition of gene expression by oligonucleotides, either by single stranded antisense oligonucleotides (*1*−*4*) or by double stranded siRNAs (*5*−*7*), has become a routine technique for mechanistic studies of gene expression. Both approaches also show promise as a novel form of chemotherapy, but several thresholds must still be overcome on the way to oligonucleotide drugs (*8*−*13*). Among the existing problems, inefficient cellular uptake appears to be the most severe one. A possible way to enhance the cell penetration and to provide the oligonucleotide with cell-type or organ selectivity is to conjugate the oligonucleotide with an agent known to be actively transported into the cell (*14, 15*). Cell-penetrating peptides have been extensively used for this purpose, but the results have been somewhat disappointing (*16, 17*). These conjugates tend to remain trapped in endosomes, without any marked increase of concentration in cytoplasm or nucleus, as far as delivery of polyanionic phosphodiester-like antisense oligonucleotides is concerned. Conjugation with cholesterol (*18*) or aptamers (*19*) has, in turn, clearly increased the efficiency of siRNA-induced gene-silencing *in vivo*. Among glycoconjugates, conjugation with galactose has been shown to direct the delivery of oligonucleotides to hepatocytes, probably by recognition of a membrane bound lectin, the asialoglycoprotein receptor (*20, 21*), and lactosylated PEG-siRNA conjugates have been reported to exhibit enhanced gene silencing in hepatoma cells (*22*). High affinity binding to lectins depends on several simultaneous interactions of monomeric sugar units with the protein, a phenomenon known as a glyco-cluster effect (*23*−*25*).

A possible way to target an antisense oligonucleotide to a membrane-anchored lectin is to use a complementary sugar decorated oligonucleotide as a carrier. This carrier oligonucleotide is aimed at serving as a scaffold to which the lecting-binding sugar ligands are tethered at appropriate distances. Since the carrier is simultaneously able to hybridize with the actual antisense oligomer, the latter becomes enriched at the cell surface and, hence, internalizated by receptor-mediated endocytosis. Accordingly, the site of attachment of the sugar ligands to the carrier should be such that the duplex formation is not severely retarded.

Chart 1

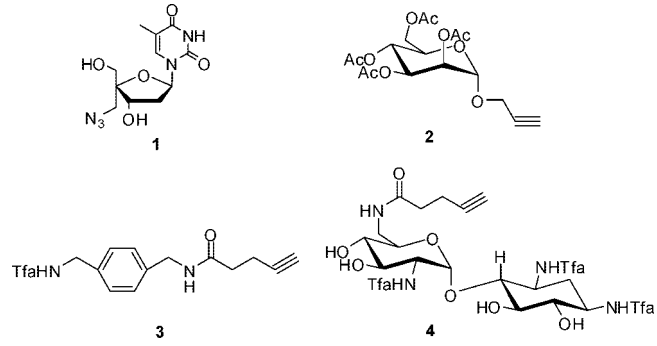

Previous studies show that 4′-modified oligonucleotides, in which the 4′-branch is facing the minor groove upon hybridization, form rather stable double helices with unmodified complementary sequences and, additionally, they are less prone to enzymatic degradation than their unmodified counterparts (*26*−*33*). Accordingly, relatively straightforward synthesis of 4′-*C*-azidomethylthymidine (**1**) (Chart 1) together with the efficient postsynthetic derivatization of the azido function by the click chemistry (*34*−*40*) makes this monomer particularly appealing for the purpose. Previously, an azido group had been introduced into nucelosides by enzymatic means and used for Staudinger ligation, but all these derivatives bear the modification on the base moiety (*41*−*44*).

Unfortunately, the azido group is not compatible with standard phosphoramidite chemistry, because of the Staudinger reaction

* Corresponding author. Phone +358-2-333 6786, Fax +358-2-333 6700, E-mail: ankaka@utu.fi.

10.1021/bc800221p CCC: $40.75 © 2008 American Chemical Society
Published on Web 08/01/2008

between azides and phosphines (*45*). This shortcoming may, however, be avoided by using H-phosphonate chemistry for the chain assembly. After the synthesis of the modified oligonucleotide, click reaction between the 4′-azidomethyl group and an alkyne functionalized conjugate group may then be performed, either on support or in solution after release and HPLC purification of the oligonucleotide. To test the applicability of the synthesis protocol and to learn more about the effects of C4′-conjugation on duplex stability, three different ligands have been used for the conjugation, viz. alkyne derivatives of mannose (**2**), *p*-aminomethylbenzene (**3**) and neamine (**4**). Mannose is a model of a neutral sugar ligand. The *p*-aminomethylbenzene-derived ligand, in turn, elucidates the effects that electrostatic interactions between the positively charged ammonium groups and negatively charged phosphate groups have on the duplex stability, and neamine serves as an example of a sugar-type ligand bearing amino groups in addition to hydroxyl functions.

EXPERIMENTAL PROCEDURES

General Remarks. The NMR spectra were recorded at 500 MHz. The chemical shifts are given in ppm from internal TMS. The mass spectra were recorded using EI, FAB, or ESI ionization methods. RP HPLC analysis of oligonucleotide conjugates were performed using Supelco Ascentis C18 (150 × 4.6 mm, 5 μm) analytical column, a gradient elution from 0.05 mol L^{-1} NH_4OAc (aq) to 30% MeCN in 0.05 mmol L^{-1} NH_4OAc (aq) buffer over 60 min, flow rate 1 mL min^{-1}, and detection at 260 nm. For semipreparative purifications, Thermo ODS Hypersil (250 × 10 mm, 5 μm) column and flow rate 3 mL min^{-1} were used. Electropherograms were obtained by capillary zone electrophoresis using a fused silica capillary (75 μm, 50 cm), inverted polarity, citrate buffer (0.2 mol L^{-1}, pH 3.1), −30 kV voltage, and detection wavelength of 254 nm.

3′-*O*-(4,4′-Dimethoxytrityl)-5′-*O*-trifluoromethylsulfonyl-4′-*C*-(trifluoromethylsulfonyl)-oxymethylthymidine (6). 3′-*O*-(4,4′-Dimethoxytrityl)-4′-*C*-hydroxymethylthymidine (2.84 g, 4.9 mmol, **5**) was dissolved in a mixture of dry CH_2Cl_2 (30 mL) and dry pyridine (10 mL). Trifluoromethanesulfonyl anhydride (2.06 mL, 12.4 mmol) was added dropwise on an ice bath. After 20 min, the ice bath was removed and the reaction mixture was stirred at rt for 1 h. The reaction mixture was then partitioned between ethyl acetate (200 mL) and water (40 mL). The organic phase was separated, dried with Na_2SO_4, and evaporated to dryness. The residue was purified by silica gel choromatography (40−100% ethyl acetate in hexane + 0.1% triethylamine) yielding product **6** (3.63 g, 87%) as a yellowish foam. ^{1}H NMR (500 MHz, $CDCl_3$) δ_{ppm} 8.24 (br s, 1H), 7.45−7.43 (m, 2H), 7.37−7.27 (m, 7H), 6.93 (br d, 1H), 6.91−6.88 (m, 4H), 5.82 (dd, 1H, J = 8.8 Hz, 3.3 Hz), 4.79 (d, 1H, J = 10.5 Hz), 4.76 (dd, 1H, J = 7.0 Hz, 2.0 Hz), 4.53 (d, 1H, J = 11.0 Hz), 4.04 (d, 1H, J = 11.0 Hz), 3.83 (s, 3H), 3.83 (s, 3H), 3.45 (d, 1H, J = 11.5 Hz), 2.64 (m, 1H), 2.29 (ddd, 1H, J = 14.0 Hz, 9.0 Hz, 3.5 Hz), 1.91 (s, 3H); ^{13}C NMR (125 MHz, $CDCl_3$) δ_{ppm} 163.3, 159.2, 159.2, 149.4, 144.4, 138.4, 135.3, 135.0, 130.4, 130.3, 128.3, 128.0, 127.6, 113.7, 111.3, 89.4, 88.4, 85.1, 74.3, 74.2, 74.1, 55.3, 39.5, 12.2 (Tf related peaks not listed); HRMS (FAB): M^+ calcd 838.1301, obsd 838.1327.

4′-*C*-Azidomethyl-3′-*O*-(4,4′-dimethoxytrityl)-O^2,5′-anhydrothymidine (7). Compound **6** (1.26 g, 1.5 mmol) was dissolved in a mixture of dry DMF (17 mL) and dry pyridine (3 mL). Sodium hydride (63 mg of 60% dispersion, 1.6 mmol) was added and the reaction was allowed to proceed for 20 min. Sodium azide (0.14 g, 2.2 mmol) was then added and the mixture was heated to 60 °C. To ensure the completeness of the reaction, another portion of sodium azide (0.10 g, 1.5 mmol) was added after 1 h. After 5.5 h from the beginning of the reaction, the mixture was evaporated and purified by silica gel choromatography (from ethyl acetate to 5−10% MeOH in ethyl acetate + 0.1% triethylamine). The yield was 0.80 g (91%) as a yellowish oil. ^{1}H NMR (500 MHz, $CDCl_3$) δ_{ppm} 7.38−7.26 (m, 9H), 7.09 (br d, 1H), 6.88−6.84 (m, 4H), 5.52 (d, 1H, J = 7.5 Hz), 4.65 (dd, 1H, J = 7.3 Hz, 2.3 Hz), 4.14 (d, 1H, J = 13.0 Hz), 4.08 (d, 1H, J = 12.5 Hz), 3.93 (d, 1H, J = 13.5 Hz), 3.81 (s, 3H), 3.81 (s, 3H), 2.78 (d, 1H, J = 13.5 Hz), 2.25 (ddd, 1H, J = 15.3 Hz, 8.0 Hz, 2.5 Hz), 2.12 (m, 1H), 1.95 (br d, 3H); ^{13}C NMR (125 MHz, $CDCl_3$) δ_{ppm} 171.8, 159.1, 159.1, 156.3, 144.6, 137.3, 135.5, 135.4, 130.5, 130.5, 128.3, 128.2, 127.5, 119.8, 113.5, 113.5, 92.7, 89.4, 88.0, 77.1, 75.5, 55.3, 52.1, 44.1, 13.4; HRMS (EI): M^+ calcd 581.2274, obsd 581.2275.

4′-*C*-Azidomethyl-3′-*O*-(4,4′-dimethoxytrityl)thymidine (8). To a solution of compound **7** (1.90 g, 3.3 mmol) in 33 mL of dioxane, aqueous NaOH (10 mL, 2 mol L^{-1}, 20 mmol) was added and the mixture was stirred for 3 h. The reaction mixture was partitioned between ethyl acetate (200 mL) and water (40 mL) and the organic phase was separated, dried with Na_2SO_4, and evaporated to dryness. Compound **8** (1.87 g) was received as yellowish solid foam in 95% yield. ^{1}H NMR (500 MHz, $CDCl_3$) δ_{ppm} 8.45 (br s, 1H), 7.44−7.42 (m, 2H), 7.35−7.23 (m, 7H), 7.07 (br. d, 1H), 6.86−6.83 (m, 4H), 6.04 (dd, 1H, J = 8.0 Hz, 4.0 Hz), 4.54 (t, 1H, J = 7.8 Hz), 3.83 (d, 1H, J = 13.0 Hz), 3.79 (s, 3H), 3.79 (s, 3H), 3.60 (d, 1H, J = 11.5 Hz), 3.37 (d, 1H, J = 13.0 Hz), 3.14 (d, 1H, J = 12.0 Hz), 2.25 (m, 1H), 1.84 (br s, 3H), 1.67 (m, 1H); ^{13}C NMR (125 MHz, $CDCl_3$) δ_{ppm} 163.5, 158.9, 158.9, 150.0, 150.0, 144.9, 137.0, 136.0, 135.9, 130.4, 130.4, 128.3, 128.0, 127.3, 113.3, 110.9, 88.9, 87.5, 86.0, 72.4, 63.2, 55.3, 53.3, 39.3, 12.4; HRMS (EI): M^+ calcd 599.2380, obsd 599.2404.

4′-*C*-Azidomethyl-5′-*O*-(4,4′-dimethoxytrityl)thymidine (9). Compound **8** (0.92 g, 1.5 mmol) was dissolved in 80% aq acetic acid (100 mL) and the mixture was stirred for 1 h. After evaporation, the residue was dried over P_2O_5 in vacuum, evaporated twice from dry pyridine, and finally dissolved in dry pyridine (20 mL). 4,4′-Dimethoxytrityl chloride (0.52 g, 1.5 mmol) was added and the mixture was stirred overnight at room temperature. After evaporation, the residue was purified by silica gel chromatography (5−20% ethyl acetate in CH_2Cl_2 + 0.1% triethylamine). This afforded compound **9** (0.81 g, 88%) as a white solid foam. ^{1}H NMR (500 MHz, $CDCl_3$) δ_{ppm} 8.92 (br s, 1H), 7.40−7.38 (m, 3H), 7.31−7.23 (m, 7H), 6.86−6.82 (m, 4H), 6.41 (∼t, 1H, J = 6.8 Hz), 4.55 (m, 1H), 3.79 (s, 6H), 3.59 (d, 1H, J = 12.5 Hz), 3.55 (d, 1H, J = 12.5 Hz), 3.40 (d, 1H, J = 10.0 Hz), 3.27 (d, 1H, J = 10.0 Hz), 2.75 (d, 1H, J = 5.0 Hz), 2.49−2.38 (m, 2H), 1.52 (br d, 3H); ^{13}C NMR (125 MHz, $CDCl_3$) δ_{ppm} 163.7, 158.8, 158.8, 150.3, 144.1, 135.7, 135.2, 135.0, 130.2, 130.1, 128.1, 128.1, 127.3, 113.3, 111.4, 88.0, 87.3, 84.9, 73.6, 65.8, 55.3, 52.9, 40.9, 11.9; HRMS (EI): M^+ calcd 599.2380, obsd 599.2369.

Triethylammonium 4′-*C*-Azidomethyl-5′-*O*-(4,4′-dimethoxytrityl)thymidine 3′-(*H*-phosphonate) (10). To the solution of compound **9** (0.31 g, 0.5 mmol) in dry pyridine (2 mL), diphenyl *H*-phosphonate (0.7 mL, 3.6 mmol) was added. After 45 min, water (0.6 mL) and triethylamine (0.6 mL) were added and the mixture was stirred for additional 15 min before evaporation. The residue was dissolved in CH_2Cl_2 (20 mL) and extracted with 5% aq $NaHCO_3$ (20 mL). The organic fraction was dried with Na_2SO_4 and, after evaporation, the compound was purified by silica gel chromatography (0−20% MeOH in CH_2Cl_2 + 0.1% triethylamine). The product (**10**, 0.34 g) was isolated as with powder in 86% yield. ^{1}H NMR (500 MHz, $CDCl_3$) δ_{ppm} 7.49 (s, 0.5 H), 7.40−7.39 (m, 3H), 7.30−7.22 (m, 7H), 6.84−6.83 (m, 4H), 6.46 (t, 1H, J = 7.0 Hz), 6.25 (s,

0.5 H), 5.02 (m, 1H), 3.79 (s, 6H), 3.70 (d, 1H, $J = 13.0$ Hz), 3.49 (d, 1H, $J = 13.0$ Hz), 3.37 (d, 1H, $J = 10.0$ Hz), 3.32 (d, 1H, $J = 10.0$ Hz), 2.83 (br q, 6H, $J = 6.5$ Hz; CH_2-triethylamine), 2.66 (m, 1H), 2.42 (m, 1H), 1.41 (s, 3H), 1.21 (t, 9H, $J = 7.3$ Hz; CH_3-triethylamine); ^{13}C NMR (125 MHz, $CDCl_3$) δ_{ppm} 163.5, 158.8, 158.7, 150.2, 144.1, 135.5, 135.1, 135.1, 130.3, 130.2, 128.3, 128.0, 127.2, 113.3, 111.2, 87.5, 87.3, 84.2, 74.3, 65.1, 55.3, 53.2, 40.1, 11.7. In addition, signals of triethylammonium ion at 45.9 and 10.0. ^{31}P NMR (200 MHz, $CDCl_3$) δ_{ppm} 3.71; HRMS(ESI): $[M + 2Na]^+$ calcd 708.1806, obsd 708.1802.

Propargyl 2,3,4,6-Tetra-*O*-acetyl-α-D-mannopyranoside (2). α-D-Mannopyranosyl pentaacetate (**13**, 2.32 g, 5.9 mmol) was dried over P_2O_5 in vacuum overnight, dissolved in dry CH_2Cl_2 (10 mL) under N_2, and boron trifluoride etherate (0.83 mL, 6.6 mmol) was added. The mixture was stirred at room temperature for 1 h before addition of propargyl alcohol (0.52 mL, 8.9 mmol), and the reaction was then allowed to proceed overnight. The mixture was transferred onto an ice bath and aq $NaHCO_3$ was added. The mixture was extracted with diethyl ether and the organic phase was washed once with water. The diethyl ether phase was dried with Na_2SO_4 and evaporated. The residue was purified by silica gel chromatography (50% ethyl acetate in petroleum ether). The yield of white amorphous solid **2** (1.76 g) was 76%. ^{1}H NMR (500 MHz, $CDCl_3$) δ_{ppm} 5.36−5.28 (m, 3H), 5.04 (d, 1H, $J = 1.5$ Hz), 4.31−4.28 (m, 3H), 4.12 (m, 1H), 4.03 (m, 1H), 2.48 (t, 1H, $J = 2.5$ Hz), 2.17 (s, 3H), 2.11 (s, 3H), 2.05 (s, 3H), 2.00 (s, 3H); ^{13}C NMR (125 MHz, $CDCl_3$) δ_{ppm} 170.7, 170.0, 169.9, 169.7, 96.3, 77.9, 75.6, 69.4, 69.0, 68.9, 66.0, 62.3, 55.0, 20.9, 20.8, 20.7, 20.7; HRMS(ESI): $[M + Na]^+$ calcd 409.1105, obsd 409.1085.

***N*-(4-Methoxytrityl)-1,4-phenylenedimethanamine (15).** 1,4-Phenylenedimethanamine (**14**, 4.00 g, 29.4 mmol) was dissolved in dry dioxane (80 mL) and 4-methoxytrityl chloride (6.30 g, 20.4 mmol) was added within 1 h. The reaction was stirred overnight at room temperature and 10% aq NaOH was added to convert the product to a free amine. The mixture was extracted with CH_2Cl_2 and the organic phase was dried with Na_2SO_4 and evaporated. The residue was purified by silica gel chromatography (5−30% MeOH in CH_2Cl_2 + 0.1% triethylamine) yielding product **15** (2.73 g, 32%) as a white solid foam. ^{1}H NMR (500 MHz, $CDCl_3$) δ_{ppm} 7.54−7.52 (m, 4H), 7.45−7.42 (m, 2H), 7.37−7.17 (m, 10H), 6.83−6.80 (m, 2H), 3.86 (s, 2H), 3.77 (s, 3H), 3.30 (s, 2H); ^{13}C NMR (125 MHz, $CDCl_3$) δ_{ppm} 157.9, 146.2, 140.9, 138.1, 129.8, 128.5, 128.4, 128.2, 127.9, 126.3, 113.2, 70.5, 55.2, 47.5, 44.8; HRMS (EI): M^+ calcd 408.2202, obsd 408.2201.

***N*-{4-[*N*-(4-Methoxytrityl)aminomethyl]benzyl}-4-pentynamide (16).** 4-Pentynoic anhyride was prepared by dissolving 4-pentynoic acid (1.31 g, 13.4 mmol) in dry dioxane (20 mL) and adding DCC (1.37 g, 6.6 mmol) into this solution on an ice bath. After 20 min, the ice bath was removed and the reaction was allowed to proceed for 4 h. Precipitated DCU was removed by filtration and the filtrate was added to a solution of **15** (2.72 g, 6.7 mmol) in dry pyridine (20 mL). A catalytic amount of 4-dimethylaminopyridine was added and the reaction was stirred at room temperature overnight. The reaction was evaporated and purified by silica gel chromatography (3−20% MeOH in CH_2Cl_2 + 0.1% triethylamine). Yield was 2.90 g (89%) as yellowish oil. ^{1}H NMR (500 MHz, $CDCl_3$) δ_{ppm} 7.55−7.53 (m, 4H), 7.46−7.43 (m, 2H), 7.37−7.18 (m, 10 H), 6.84−6.81 (m, 2H), 5.90 (br s, 1H), 4.45 (d, 2H, $J = 5.5$ Hz), 3.79 (s, 3H), 3.32 (s, 2H), 2.56 (td, 2H, $J = 7.0$ Hz, 2.5 Hz), 2.43 (t, 2H, $J = 7.3$ Hz), 2.00 (t, 1H, $J = 2.5$ Hz); ^{13}C NMR (125 MHz, $CDCl_3$) δ_{ppm} 170.7, 157.9, 146.2, 140.6, 138.1, 136.6, 129.8, 128.5, 128.3, 127.9, 126.3, 113.2, 83.0, 70.5, 69.5, 55.2, 47.6, 43.5, 35.4, 14.9; HRMS (EI): M^+ calcd 488.2464, obsd 488.2468.

***N*-{4-[*N*-(Trifluoroacetyl)aminomethyl]benzyl}-4-pentynamide (3).** To the solution of **16** (2.90 g, 5.9 mmol) in CH_2Cl_2 (20 mL), trifluoroacetic acid (0.93 mL, 12.1 mmol) in MeOH was added. TLC monitoring showed that the reaction had proceeded to completion in 20 min. After evaporation, the residue was dissolved in MeOH (25 mL) and triethylamine (4.5 mL) and methyl trifluoroacetate (3.87 g, 30.2 mmol) were added. After 1 h, the reaction was evaporated and purified by silica gel chromatography (3−10% MeOH in CH_2Cl_2). The product (**3**, 1.36 g) was obtained as a white powder in 73% yield; ^{1}H NMR (500 MHz, $CDCl_3$ + drop of MeOD) δ_{ppm} 7.27−7.23 (m, 4H), 4.45−4.44 (m, 2H), 4.39 (d, 2H, $J = 5.5$ Hz), 2.54−2.51 (m, 2H), 2.44 (t, 2H, $J = 7.0$ Hz), 2.03 (t, 1H, $J = 2.8$ Hz); ^{13}C NMR (125 MHz, $CDCl_3$ + drop of MeOD) δ_{ppm} 171.9, 157.5, 137.8, 135.6, 127.9, 127.9, 117.1, 82.7, 69.3, 43.1, 35.0, 14.8; HRMS (EI): M^+ calcd 312.1086, obsd 312.1098.

***N*^{1},*N*^{3},*N*$^{2'}$-Tris(trifluoroacetyl)-*N*$^{6'}$-(4-pentynoyl)neamine (4).** Succinimidyl 4-pentynoate was obtained by dissolving 4-pentynoic acid (0.40 g, 4.1 mmol) and *N*-hydroxysuccinimide (0.48 g, 4.2 mmol) into dry dioxane (6 mL) and adding DCC (0.84 g, 4.1 mmol) on an ice bath. After 2 h stirring at room temperature, precipitated DCU was removed by filtration and the filtrate was added in portions to the solution of neamine tetrahydrochloride (**17**, 1.91 g, 4.1 mmol) in a mixture of water (4 mL), dioxane (15 mL), and triethylamine (8.6 mL) during 1 h. The mixture was stirred at room temperature overnight and evaporated. The residue was dried over P_2O_5 in vacuo and subjected without further purification to trifluoroacetylation with methyl trifluoroacetate (5.22 g, 40.8 mmol) in a mixture of triethylamine (8.5 mL) and MeOH (35 mL). After 3 h, the mixture was evaporated and the residue was partitioned between ethyl acetate and water. The organic phase was dried with Na_2SO_4 and evaporated. To facilitate purification of the *N*^{1},*N*^{3},*N*$^{2'}$-triacylated product, the major part of the crude product (75%) was subjected to acetylation with acetic anhydride (1.5 mL, 15.9 mmol) in dry pyridine (25 mL). The reaction was allowed to proceed overnight, and after evaporation, the fully protected product was purified by silica gel chromatography (50−100% ethyl acetate in petroleum ether), giving a mixture of 6,3′,4′-tri-*O*-acetylated (**18**) and 5,6,3′,4′-tetra-*O*-acetylated (**19**) products as a white solid powder. Once the chromatographic purification on a silica gel column was accomplished, the O-acetyl groups were removed with methanolic sodium methoxide (0.15 mmol NaOMe in 14 mL MeOH). After 2.5 h, the mixture was neutralized with a strong cation-exchange resin (Dowex 50WX8−200, H^+-form) and filtered. The solution was evaporated yielding pure product **4** as a white solid powder. The overall yield, when taking into account that only 75% of the crude material was subjected to acetylation and subsequent purification, was 0.43 g (20%). ^{1}H NMR (500 MHz, MeOD) δ_{ppm} 5.25 (d, 1H, $J = 3.5$ Hz), 4.09 (m, 1H), 3.98 (dd, 1H, $J = 10.8$ Hz, 3.3 Hz), 3.86 (m, 1H), 3.75−3.68 (m, 2H), 3.62−3.58 (m, 2H), 3.52 (t, 1H, $J = 9.0$ Hz), 3.45−3.37 (m, 2H), 3.29 (t, 1H, $J = 9.5$ Hz), 2.55−2.47 (m, 4H), 2.32 (br s, 1H), 1.98 (ddd, 1H, $J = 12.5$ Hz, 4.3 Hz, 4.3 Hz), 1.72 (ddd, 1H, $J = 12.7$ Hz, 12.7 Hz, 12.7 Hz); ^{13}C NMR (125 MHz, MeOD) δ_{ppm} 173.7, 98.5, 82.2, 80.9, 76.6, 74.0, 71.7, 70.9, 70.3, 69.1, 54.8, 50.1, 49.4, 39.3, 34.4, 31.7, 14.4 (Tfa related peaks not listed); HRMS(ESI): $[M + Na]^+$ calcd 713.1476, obsd 713.1469.

Synthesis of Oligodeoxyribonucleotides. The oligodeoxyribonucleotides were synthesized on an Applied Biosystems 392 DNA synthesizer in a 1.0 μmol scale using commercial 1000 Å CPG-succinyl-nucleoside supports. Two coupling chemistry methods were applied: either the oligonucleotide was assembled using solely the H-phosphonate chemistry (Method A) or the H-phosphonate chemistry was combined with the phosphoramidite chemistry so that only modified nucleotide **10** was

Scheme 1[a]

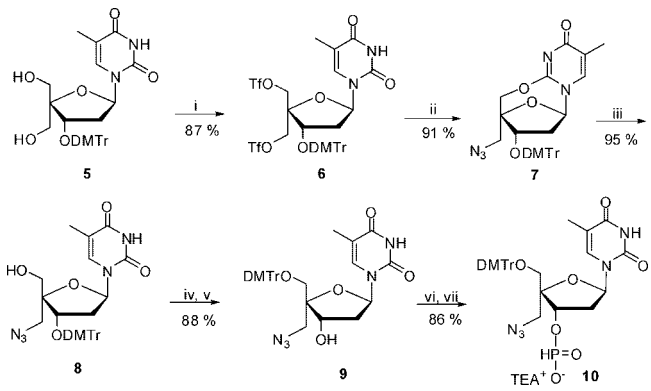

[a] Reagents: (i) Tf_2O, CH_2Cl_2, pyridine; (ii) NaH, NaN_3, DMF, pyridine; (iii) aq NaOH (2.0 mol L^{-1}), dioxane; (iv) 80% AcOH; (v) DMTrCl, pyridine; (vi) diphenyl *H*-phosphonate, pyridine; (vii) TEA, H_2O.

Scheme 2. Easy Formation of an Oxetane Byproduct

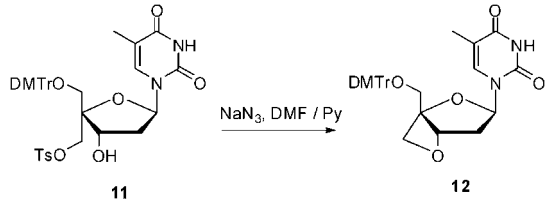

Scheme 3[a]

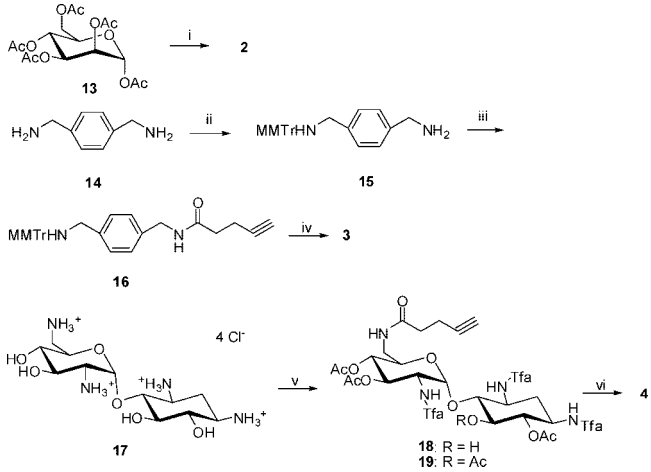

[a] Reagents: (i) propargyl alcohol, $BF_3 \cdot Et_2O$, CH_2Cl_2; (ii) (1) MMTrCl, dioxane, (2) aq NaOH (10% m/v); (iii) (1) 4-pentynoic acid, DCC, dioxane, (2) **15** in pyridine, DMAP; (iv) (1) TFA, CH_2Cl_2, MeOH, (2) TfaOMe, MeOH, TEA; (v) (1) 4-pentynoic acid, *N*-hydroxysuccinimide, DCC, dioxane, (2) **17** in water, dioxane, TEA, (3) TfaOMe, MeOH, TEA, (4) Ac_2O, pyridine; (vi) NaOMe, MeOH.

coupled as a H-phosphonate and commercial dA, dG, dC, and dT building blocks were used as phosphoramidites (Method B). Both approaches gave the same coupling effiency (DMTr-cation assay) and yields (RP HPLC chromatogram).

Method A. Nucleoside 3′-(H-phosphonates) (TEA salts) were dissolved in a mixture of dry MeCN and pyridine (1:1, v/v) to give a final concentration of 30 mmol L^{-1} for the commercial nucleoside phosphonates and 35 mmol L^{-1} for the 4′-modified phosphonate (**10**). Pivaloyl chloride and adamantane carbonyl chloride were tested as a condensing agent. Both of them were dissolved in a 1:1 mixture of MeCN and pyridine to obtain a concentration of 100 mmol L^{-1}. Both agents gave similar results. The H-phosphonate protocol was generated for the

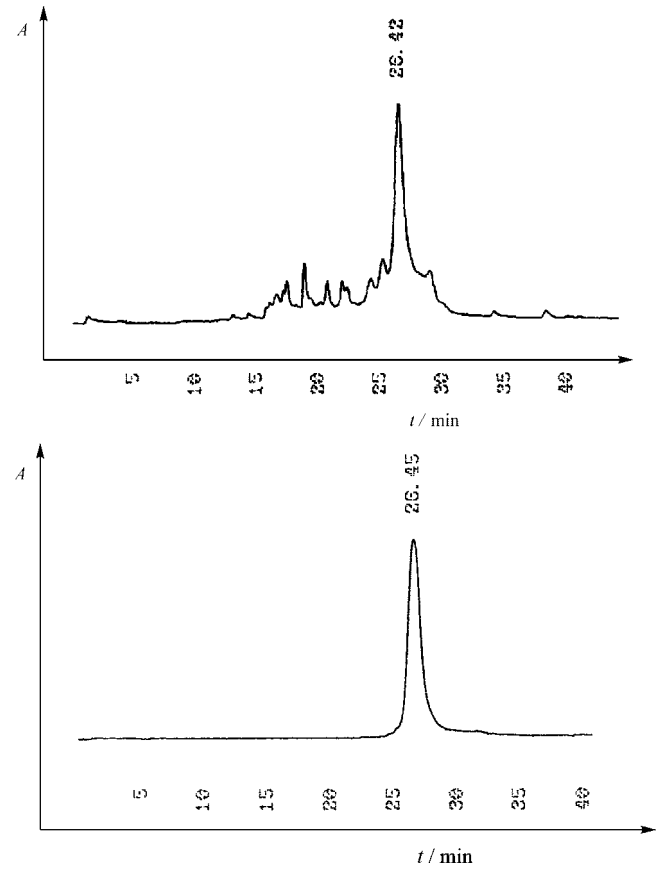

Figure 1. RP HPLC traces of the crude and purified oligonucleotide **21**.

synthesizer on the basis of previous reports (*46*, *47*). According to the DMTr-cation assay, the coupling yield for the 4′-modified H-phosphonate building block was 90% using a prolonged coupling time of 550−750 s. The coupling conditions were not optimized further. After the oligonucleotide assembly, the support-bound material was removed from the synthesizer, oxidized with iodine (0.1 mol L^{-1}) in wet pyridine (98:2, v/v) at rt for 1 h, washed with MeCN and MeOH, and dried in vacuum.

Method B. A protocol including both phosphoramidite and H-phosphonate couplings was generated for the synthesizer. No capping step was performed, but otherwise, standard phosphoramidite protocol was applied for commercial dA, dG, dC, and dT monomers and H-phosphonate protocol (as described in method A) was used for the modified monomer **10**. After completion of the chain assembly, oxidation of H-phosphonates was performed according to method A.

Oligonucleotides were released from the support with concentrated ammonia (33% aqueous NH_3) at 55 °C overnight. It should be noted that ammonolysis did not result in displacement of the azido groups. This was clearly seen by HPLC and ESI-MS characterization of the azido-functionalized oligonucleotides **20** and **21**.

Click Conjugation. Alkynyl-functionalized ligands **2**−**4** were conjugated to the azido groups of oligonucleotides **20** and **21**, containing one and three 4′-azidomethylthymidine units, respectively. The conjugation was carried out both on a solid support and in solution phase.

Conjugation on support. To the support-bound oligonucleotide, **20** or **21**, 15 or 30 equiv of the ligand in MeOH was added. With ligands **2** and **3**, the concentration was 50 mmol L^{-1}. With **4**, the concentration was 25 mmol L^{-1} and, owing to solubility problems, a mixture of MeOH, water, and DMSO

Scheme 4. Derivatization of Oligonucleotides 20 and 21 by Click Chemistry

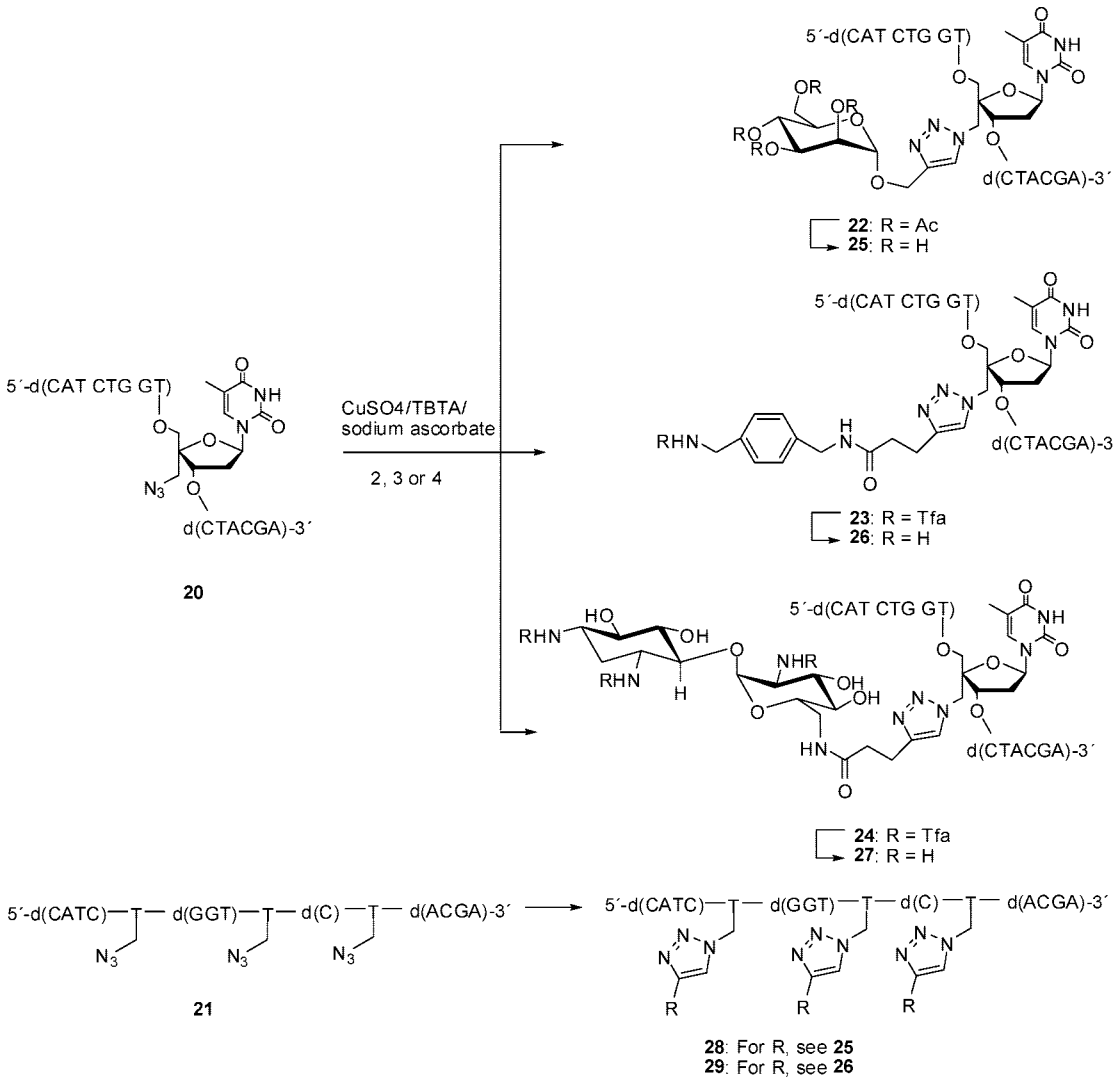

Table 1. ESI-MS Data of Oligonucleotides 20 and 21 and Their Conjugates 25−29

oligonucleotide	observed mass (g mol^{-1})	required mass (g mol^{-1})
20	4597.3	4598.1
21	4707.1	4708.1
25	4815.6	4816.3
26	4813.8	4814.3
27	4999.9	5000.5
28	5364.1	5362.7
29	5356.3	5357.0

(15:4:1 v/v/v) was used as a solvent. After that, $CuSO_4$ and tris[(1-benzyl-1,2,3-triazol-4-yl)methyl]amine (TBTA-ligand; 7.5 and 15 equiv with **20** and **21**, respectively) were added as a 25 mmol L^{-1} solution in a 12:3:1 mixture of water, DMSO, and 2-butanol. Finally, sodium ascorbate (15 and 30 equiv with **20** and **21**, respectively) as 0.1 mol L^{-1} aqueous solution was added. The mixture was efficiently stirred and allowed to stand overnight at 55 °C. The support was collected by filtration and washed with water, DMF, MeOH, aq EDTA (0.1 mol L^{-1}), water, DMF, MeOH, CH_2Cl_2, MeOH, and MeCN and finally dried in vacuum before ammonolytic release of the oligonucleotide conjugate from the support. The reason for the extensive washing was the attempt to remove as quantitatively as possible the copper salt and TBTA ligand used in the click reaction. After evaporation, the conjugate was purified by RP HPLC.

Conjugation in Solution. To an aqueous solution of the purified oligonucleotide (**20** or **21**, 0.6 mmol L^{-1}), methanolic solution of the ligand (**2** or **3**, 50 mmol L^{-1}, 50 equiv) was added. Ligand **4** was, however, added in a 15:4:1 mixture of MeOH, H_2O, and DMSO (25 mmol L^{-1}), because of its low solubility in MeOH. After that, $CuSO_4$ and TBTA-ligand (20 equiv) were added as a 25 mmol L^{-1} solution in a 12:3:1

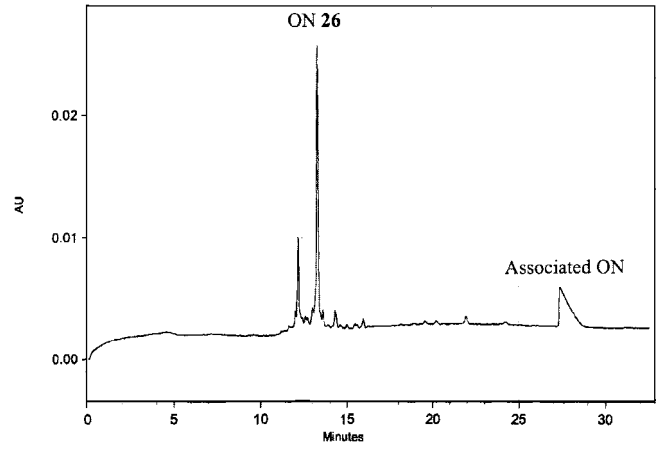

Figure 2. Electropherogram of the crude product (**26**) of the click reaction of oligonucleotide **20** with ligand **3** in solution.

Table 2. Melting Experiments of the Oligonucleotide Conjugates and Their Complementary DNA or 2′-*O*-Methyl-RNA Sequences[a]

	complementary DNA T_m/°C and (Δ T_m/°C)		complementary 2′-*O*-methyl RNA T_m/°C and (Δ T_m/°C)	
	0.1 mol L^{-1} NaCl	1.0 mol L^{-1} NaCl	0.1 mol L^{-1} NaCl	1.0 mol L^{-1} NaCl
5′-CAT CTG GTT CTA CGA	55.4	65.0	57.0	68.0
5′-CAT CTG GT**X**CTA CGA (**20**)	53.8 (−1.6)	63.3 (−1.7)	56.5 (−0.5)	67.4 (−0.6)
5′-CAT C**X**G GT**X** C**X**A CGA (**21**)	51.5 (−3.9)	62.3 (−2.7)	55.8 (−1.2)	67.4 (−0.6)
5′-CAT CTG GT**Y** CTA CGA (**25**)	53.0 (−2.4)	63.0 (−2.0)	56.8 (−0.2)	68.0 (0)
5′-CAT C**Y**G GT**Y** C**Y**A CGA (**28**)	50.3 (−5.1)	61.3 (−3.7)	56.2 (−0.8)	69.5 (+1.5)
5′-CAT CTG GT**Z** CTA CGA (**26**)	55.6 (+0.2)	64.7 (−0.3)	56.2 (−0.8)	67.6 (−0.4)
5′-CAT C**Z**G GT**Z** C**Z**A CGA (**29**)	56.4 (+1.0)	63.9 (−1.1)	55.6 (−1.4)	n. m.
5′-CAT CTG GT**W** CTA CGA (**27**)	55.8 (+0.4)	63.8 (−1.2)	55.3 (−1.7)	67.3 (−0.7)

[a] In 10 mmol L^{-1} potassium phosphate buffer (pH 7) containing 0.1 mol L^{-1} or 1.0 mol L^{-1} NaCl. The oligonucleotide conjugates and their cDNA or 2′-*O*-methyl RNA targets were used at a concentration of 2 μmol L^{-1}. **X** = 4′-*C*-azidomethylthymidine unit; **Y** = thymidine conjugate of deprotected **2**; **Z** = thymidine conjugate of deprotected **3**; **W** = thymidine conjugate of deprotected **4**; n.m. = not measured.

mixture of water, DMSO, and 2-butanol. Finally, aqueous sodium ascorbate (40 equiv, 0.1 mol L^{-1}) was added. The mixture was shaken overnight at room temperature. The resulting oligonucleotide conjugates were precipitated with EtOH. The precipitate was subjected to ammonolysis (overnight 55 °C) and then evaporated to dryness and purified by RP HPLC.

Melting Temperature Studies. The melting curves (absorbance versus temperature) were measured at 260 nm on a Perkin-Elmer Lambda 2 UV−vis spectrometer equipped with a Peltier Temperature contoller. The temperature was changed at a rate of 0.5 °C/min (from 20 to 90 °C). The measurements were performed in 10 mmol L^{-1} potassium phosphate buffer (pH 7) containing 0.1 or 1.0 mol L^{-1} NaCl. The oligonucleotide conjugates and their cDNA or 2′-*O*-methyl RNA targets were used at a concentration of 2 μmol L^{-1}. The T_m values were determined as the maximum of the first derivate of the melting curve.

RESULTS AND DISUCSSION

Synthesis of 4′-*C*-Azidothymidine 3′-(*H*-phosphonate) (10). 4′-*C*-Azidothymidine has been previously synthesized (*48*), but only in low yield via mesylation of 4′-*C*-hydroxymethyl-3′-*O*-TBDMS-thymidine and subsequent treatment of the mixture of the mono- and dimesylated products with LiN_3. Since this route includes tricky chromatographic separations of regioisomers, we decided to make use of O^2,5′-anhydronucleoside formation in making a difference between the two primary hydroxyl functions. Accordingly, 3′-*O*-(4,4′-dimethoxytrityl)-4′-*C*-hydroxymethylthymidine (**5**) was prepared as previously reported (*30, 49, 50*) and the primary hydroxyl groups were converted to their triflates to obtain **6** (Scheme 1). Deprotonation of the thymine base resulted in cyclization to O^2,5′-anhydro nucleoside (*51*), from which the remaining triflate group could be displaced with an azide ion, giving the desired 4′-*C*-azidomethyl group (**7**). The O^2,5′-anhydro linkage was hydrolyzed with sodium hydroxide and the resulting nucleoside 4′-*C*-azidomethyl-3′-*O*-DMTr-thymidine (**8**) was converted to its 5′-*O*-DMTr-isomer (**9**) and finally to the corresponding 3′-(H-phosphonate) (**10**). Altogether, the synthesis of building block **10** is efficient and the overall yield from compound **5** to **10** is 56%.

It should be noted that the 3′-hydroxy group must be masked before conversion of the hydroxyl function of the 4′-*C*-hydroxymethyl group to a better leaving group. The carbon atom of this group is surprisingly prone to nucleophilic attack of a neighboring hydroxyl group: a four-membered ring is easily formed by an attack of either the 5′- or 3′-OH. For example, the oxetane product **12** was the only product obtained when displacement of the tosyl group from 5′-*O*-(4,4′-dimethotrityl)-4′-*C*-tosyloxymethylthymidine (**11**) with azide ion was attempted (Scheme 2).

Synthesis of Ligands 2−4. The alkyne-derivatized ligands (**2**−**4**) used in the click conjugation were synthesized as outlined in Scheme 3. Fully acetylated propargyl α-D-mannopyranoside (**2**) was prepared from the commercially available peracetylated α-D-mannopyranose (**13**) by boron trifluoride etherate promoted glycosidation with propargyl alcohol (*52*). Trifluoroacetylated *N*-[4-(aminomethyl)benzyl]-4-pentynamide (**3**) was synthesized starting from the commercially available 1,4-phenylenedimethanamine (**14**). One of the two amino groups was protected with a 4-monomethoxytrityl group and the other one was acylated with 4-pentynoic acid by DCC activation. The acid-labile trityl protection was finally changed to a base-labile trifluoroacetyl protection, removable by the conventional ammonolysis used for release and deprotection of the oligonucleotide conjugate. Neamine tetrahydrochloride (**17**) was obtained by methanolysis of commercially available neomycin B trisulfate (*53*). The primary 6′-amino group of neamine (**17**) was selectively acylated with succinimidyl 4-pentynoate. To make this neamine derivative easier to handle and purify, the amino groups were trifluoroacetylated and the hydroxyl groups acetylated, and the product was purified at this stage. Owing to exceptionally difficult acetylation of the 5-hydroxy of neamine, a mixture of compounds **18** and **19** was obtained. Product **4** was received after removal of acetyl-protecting groups with methoxide ion catalyzed transesterification in MeOH.

Oligonucleotide Synthesis and Click Conjugation. Two 15-mer oligodeoxyribonucleotides containing either one or three 4′-*C*-azidomethylthymidine monomers were synthesized using H-phosphonate coupling chemistry: 5′-d(CAT CTG GT***T*** CTA CGA)-3′ (**20**) and 5′-d(CAT C***T***G GT***T*** C***T***A CGA)-3′ (**21**). The coupling yield for the 4′-*C*-azidomethylthymidine 3′-(H-phosphonate) monomer was 90%. The phosphoramidite coupling could not be applied, since intramolecular Staudinger reaction between the azido and phosphoramidite groups made the phosphoramidite building block highly unstable. Unmodified dA, dG, dC, and dT monomers could, however, be coupled as phosphoramidites. In other words, a mixed H-phosphonate and phosphoramidite method could be applied instead of mere H-phosphonate coupling. The yields of both approaches were comparable. This observation implies that the Staudinger reaction between the incoming phosphoramidite reagent and the support bound azide does not disturb the phosphoramidite coupling. Problems arise only when a genuine intramolecular reaction may take place. Figure 1 shows the HPLC traces of the crude oligonucleotide **21**, containing three azido-functionalized thymidine units and the product after purification.

After chain assembly, click chemistry was applied to attach alkyne-derivatized ligands **2**−**4** to the oligonucleotide backbone. To minimize radical induced modifications within the oligonucleotide chain, tris[(1-benzyl-1,2,3-triazol-4-yl)methyl]amine (TBTA) was used as a Cu(I)-stabilizing agent (*54*). Conjugation was performed either on the CPG support or in solution. Scheme 4

outlines the procedure in solution. Essentially the same chemistry was applied on a solid support. During the click reaction, the base moieties bore conventional acyl protections and the internucleosidic linkages were present as 2-cyanoethyl triesters. In both cases, the click reaction proceeded virtually quantitatively, as also reported previously for derivatization of alkyne-functionalized oligonucleotides with azides either on a solid support (*38*) or in solution (*36*). The advantage of the solid-supported synthesis is that only one HPLC purification is needed after ligation and release of the oligonucleotide from the support. By contrast, when the conjugation is carried out in solution, the oligonucleotide product must be purified both before and after conjugation. In addition, deprotection of the conjugate groups introduced requires a second ammonolysis after the click reaction. In principle, unprotected conjugate groups could have been used in the click reaction, but we felt that with amino groups containing ligands, in particular, it is safer to use protections to minimize the interactions with copper ion.

Standard ammonolysis (33% aq NH_3, 55 °C, overnight) was carried out to release oligonucleotides from the support and to remove the protections from base moieties, phosphodiester linkages, and conjugate groups. The conjugates (**25**−**29**) were then purified by RP-HPLC and their identity was verified by ESI-MS. The data are given in Table 1. The purity of the crude product mixtures were additionally checked by capillary electrophoresis. These studies quite unexpectedly revealed the existence of an additional conjugate or complex that is not seen by HPLC. In electropherograms, this species appeared as a wide peak after the signal of the oligonucleotide conjugate (Figure 2). Possibly the oligonucleotide conjugate remained partly associated with the TBTA ligand or its Cu(I) complex, albeit the solid support was thoroughly washed after the click reaction. Although this marked impurity could not be detected by HPLC, RP HPLC purification entirely removed it. After HPLC purification, no extra signals appeared any more in the electropherogram.

When the click reaction was carried out in solution, the elctropherogram of the crude product showed only the broad signal of the unidentified associate discussed above. After precipitation of the oligonucleotide conjugate from EtOH, the signals of both the desired conjugate (**26** in Figure 2) and the unidentified associate appeared, but again RP HPLC purification was needed to obtain a pure conjugate.

Capillary electrophoretic studies also revealed another peculiarity related to the click procedure. When amino group containing ligands (**3**, **4**) were conjugated on a solid support and the conjugates obtained were purified by HPLC, they still gave two peaks in electropherograms. In addition, their melting temperature curves were slightly biphasic, lending further support for the occurrence of the conjugates as two isomers that had the same molecular mass (in ESI-MS only one set of signals, *m*/*z*, was detected) and could not be separated by HPLC. When the conjugation was carried out in solution and the product was precipitated with EtOH, this anomality in behavior disappeared: the product was elecrophoretically homogeneous and exhibited normal sigmoid melting curves. Accordingly, some caution seems to be needed when applying click conjugation to ligands that offer good coordination sites, such as amino groups, for copper ions, in spite of fact that the groups are kept protected during the actual cycloaddition reaction.

Melting Temperature Studies. Melting temperatures (T_m) for the duplexes of oligonucleotides **20**, **21** and their conjugates **25**−**29** with the cDNA and 2′-*O*-methyl RNA sequences were measured at pH 7 at the ionic strength of 0.1 and 1.0 mol L^{-1} (Table 2).

When one or three 4′-*C*-azidomethylthymidine monomers were incorporated into an oligonucleotide (**20**, **21**), the melting temperature of the heteroduplexes with cDNA and 2′-*O*-methyl RNA sequences dropped, but less with 2′-*O*-methyl RNA (ΔT_m/modification ≈ −0.5 °C) than with DNA (ΔT_m/modification ≈ −1.5 °C). Conjugation of the 4′-*C*-azidomethylthymidine units with mannopyranoside (**25**, **28**) slightly increased the destabilization of the DNA-hybrid (ΔT_m/modification ≈ − 2 °C), but, interestingly, hybridization with 2′-*O*-methyl RNA was even slightly enhanced, in particular at high ionic strength.

In contrast to these results, conjugates **26**, **27**, and **29** bearing free amino group(s) formed more stable duplexes with cDNA than with 2′-*O*-methyl RNA. The difference in the behavior is, however, small. Now at low salt concentration, the modifications slightly increased the melting temperature of the hybrid complex with DNA, but at high salt concentration, T_m was decreased. This implies that the amino groups, being positively charged at neutral pH, reduce the electrostatic repulsion between negatively charged sugar−phosphate backbones, the influence playing a more important role at low ionic strength. With complementary 2′-*O*-methyl RNA strand, the melting temperatures, however, dropped more at low than at high salt concentration.

According to previous studies (*26*, *28*−*32*), oligonucleotides containing 4′-*C*-modified DNA monomers generally prefer hybridization toward cDNA over RNA. 4′-*C*-acylthymidines (*55*), for example, adopt a C(2′)-endo-like conformation found typically in B-type DNA-DNA duplex. 4′-*C*-Me, 4′-*C*-Et, and 4′-*C*-iPr groups are all, however, slightly destabilizing toward DNA (*56*). With conjugates **26**, **27**, and **29**, a similar preference for the cDNA is found. However, an opposite behavior occurs with oligonucleotides containing azido or mannose groups. The results with mannose derivatives (**25**, **28**) toward the complementary 2′-*O*-methyl RNA strand are encouraging, since they lend support for the feasibility of sugar-coated oligonucleotides as carriers of RNA-type oligonucleotides.

CONCLUSION

A novel high yielding synthesis has been developed for 4′-*C*-azidomethylthymidine 3′-(*H*-phophonate) (**10**). One or three such monomers have been incorporated into a 15-mer oligodeoxyribonucleotide using H-phosphonate coupling. Standard deoxynucleotide (dA, dG, dC, and dT) monomers have been coupled either with H-phosphonate or phosphoramidite chemistry. This suggests that the Staudinger reaction between the azido group and the phosphoramidite reagent severely hampers the coupling only when the reaction is intramolecular. Ligands bearing an alkynyl tail may be highly efficiently conjugated to the azido groups by click chemistry. This can be done both on a solid support and in solution. As far as neutral sugar ligands, such as mannose, are concerned, conjugation on support appears to be the method of choice, owing to easy removal of auxiliaries of the click reaction by washing. By contrast, for ligand containing amino groups, conjugation in solution followed by precipitation from EtOH and HPLC purification is recommended. With such ligands, washing of the solid support is not adequate to remove all impurities and these tend to comigrate with the product.

The melting temperature studies reveal that the mannose conjugates form more stable duplexes with 2′-*O*-methyl RNA than with DNA strand. With 2′-*O*-methyl RNA, a slight destabilization compared to an unmodified sequence is observed at low ionic strength, while at high salt content, the manno-conjugation is even stabilizing. With the conjugates derived from 1,4-phenylenedimethanamine or neamine, i.e., ligands containing amino groups, the situation is the opposite: compared to unmodified sequences, the 2′-*O*-methyl RNA hybrid is destabilized more markedly than the DNA hybrid, and the destabilization is more marked at high than low salt content. Evidently, the amino groups, being positively charged at neutral pH, reduce the electrostatic repulsion between negatively charged sugar−phosphate backbones, the influence playing a more important role at low ionic strength. The high stability of the duplex of 4′-mannosylated oligonucleotide with 2′-*O*-methyl RNA lends support for the feasibility of the use of such

oligonucleotide conjugates as carriers of RNA-type antisense oligonucleotides. A proper sugar coating may possibly have positive effects on the pharmacokinetics of the duplex and provide it with cell-type specificity. While coating with monosaccharide ligands may well be insufficient to warrant high affinity binding, it is worth noting that the procedure developed in the present study allows conjugation of more complicated oligosaccharide ligands, as long as they bear an alkynyl tail.

Supporting Information Available: NMR spectral data for **2**−**4**, **6**−**10**, **15**, and **16**. ESI-MS and RP HPLC chromatographic data for purified oligonucleotides **20**, **21**, and **25**−**29**. Additionally, example melting temperature curves for **20**, **21**, and **25**−**29** are presented. This material is available free of charge via the Internet at http://pubs.acs.org.

LITERATURE CITED

(1) Sasaki, S., and Nagatsuki, F. (2006) Application of unnatural oligonucleotides to chemical modification of gene expression. *Curr. Opin. Chem. Biol. 10*, 615–621.

(2) Aboul-Fadl, T. (2005) Antisense oligonucleotides: The state of the art. *Curr. Med. Chem. 12*, 2193–2214.

(3) Crooke, S. T. (2004) Progress in antisense technology. *Annu. Rev. Med. 55*, 61–95.

(4) Uhlmann, E., and Peyman, A. (1990) Antisense oligonucleotides: a new therapeutic principle. *Chem. Rev. 90*, 543–584.

(5) Grosshans, H., and Filipowicz, W. (2008) Molecular biology: The expanding world of small RNAs. *Nature 451,* 414–416.

(6) Corey, D. R. (2007) RNA learns from antisense. *Nat. Chem. Biol. 3*, 8–11.

(7) Mittal, V. (2004) Improving the efficiency of RNA interference in mammals. *Nat. Rev. Genet. 5*, 355–365.

(8) Wilson, C., and Keefe, A. D. (2006) Building oligonucleotide therapeutics using non-natural chemistries. *Curr. Opin. Chem. Biol. 10*, 607–614.

(9) Kim, D. H., and Rossi, J. J. (2007) Strategies for silencing human disease using RNA interference. *Nat. Rev. Genet. 8*, 173–184.

(10) Bumcrot, D., Manoharan, M., Koteliansky, V., and Sah, D. W. Y. (2006) RNAi therapeutics: a potential new class of pharmaceutical drugs. *Nat. Chem. Biol. 2*, 711–719.

(11) Dykxhoorn, D. M., Palliser, D., and Lieberman, J. (2006) The silent treatment: siRNAs as small molecule drugs. *Gene Ther. 13*, 541–552.

(12) Leung, R. K. M., and Whittaker, P. A. (2005) RNA interference: from gene silencing to gene-specific therapeutics. *Pharm. Ther. 107*, 222–239.

(13) Dorsett, Y., and Tuschl, T. (2004) siRNA: applications in functional genomics and potential as therapeutics. *Nat. Rev. Drug Discovery 3*, 318–329.

(14) Manoharan, M. (2002) Oligonucleotide conjugates as potential antisense drugs with improved uptake, biodistribution, targeted delivery, and mechanism of action. *Antisense Nucleic Acids Drug Dev. 12*, 103–108.

(15) de Fougerolles, A., Vornlocher, H.-P., Maraganore, J., and Lieberman, J. (2007) Interfering with disease: a progress report on siRNA-based therapeutics. *Nat. Rev. Drug Discovery 6*, 443–453.

(16) Gait, M. J. (2003) Peptide-mediated cellular delivery of antisense oligonucleotides and their analogues. *Cell. Mol. Life Sci. 60*, 844–853.

(17) Venkatesan, N., and Kim, B. H. (2006) Peptide conjugates of oligonucleotides: synthesis and applications. *Chem. Rev. 106*, 3712–3761.

(18) Soutschek, J., Akinc, A., Bramlage, B., Charisse, K., Constien, R., Donoghue, M., Elbashir, S., Geick, A., Hadwiger, P., Harborth, J., John, M., Kesavan, V., Lavine, G., Pandey, R. K., Racie, T., Rajeev, K. G., Röhl, I., Toudjarska, I., Wang, G., Wuschko, S., Bumcrot, D., Koteliansky, V., Limmer, S., Manoharan, M., and Vornlocher, H.-P. (2004) Therapeutic silencing of an endogenous gene by systemic administration of modified siRNAs. *Nature 432*, 173–178.

(19) McNamara, J. O., II, Andrechek, E. R., Wang, Y., Viles, K. D., Rempel, R. E., Gilboa, E., Sullenger, B. A., and Giangrande, P. H. (2006) Cell type-specific delivery of siRNAs with aptamer-siRNA chimeras. *Nat. Biotechnol. 24*, 1005–1015.

(20) Zhu, L., Ye, Z., Cheng, K., Miller, D. D., and Mahoto, R. I. (2008) Site-specific delivery of oligonucleotides to hapatocytes after systemic administration. *Bioconjugate Chem. 19*, 290–298.

(21) Biessen, E. A. L., Vietsch, H., Rump, E. T., Fluiter, K., Kuiper, J., Bijsterbosch, M. K., and Van Berkel, T. J. C. (1999) Targeted delivery of oligodeoxynucleotides to parenchymal liver cells *in vivo*. *Biochem. J. 340*, 783–792.

(22) Oishi, M., Nagasaki, Y., Itaka, K., Nishiyama, N., and Kataoka, K. (2005) Lactosylated poly(ethylene glycol)-siRNA conjugate through acid-labile β-thiopropionate linkage to construct pH-sensitive polyion complex micelles achieving enhanced gene silencing in hepatoma cells. *J. Am. Chem. Soc. 127*, 1624–1625.

(23) Yan, H., and Tram, K. (2007) Glycotargeting to improve cellular delivery efficiency of nucleic acids. *Glycoconj. J. 24*, 107–123.

(24) Ambrosi, M., Cameron, N. R., and Davis, B. G. (2005) Lectins: tools for the molecular understanding of the glycocode. *Org. Biomol. Chem. 3*, 1593–1608.

(25) Lundquist, J. J., and Toone, E. J. (2002) The cluster glycoside effect. *Chem. Rev. 102*, 555–578.

(26) Raunkjær, M., Bryld, T., and Wengel, J. (2003) N-Methylpiperazinocarbonyl-2′,3′-BcNA and 4′-*C*-(*N*-methylpiperazino)methyl-DNA: introduction of basic functionalities facing the major groove and the minor groove of a DNA:DNA duplex. *Chem. Commun.* 1604–1605.

(27) Wengel, J. (1999) Synthesis of 3′-*C*- and 4′-*C*-branched oligodeoxynucleotides and the development of locked nucleic acid (LNA). *Acc. Chem. Res. 32*, 301–310.

(28) Pfundheller, H. M., Bryld, T., Olsen, C. E., and Wengel, J. (2000) Oligonucleotides containing novel 4′-*C*- or 3′-*C*-(aminoalkyl)-branched thymidines. *Helv. Chim. Acta 83*, 128–151.

(29) Ueno, Y., Nagasawa, Y., Sugimoto, I., Kojima, N., Kanazaki, M., Shuto, S., and Matsuda, A. (1998) Nucleosides and nucleotides. 174. Synthesis of oligodeoxynucleotides containing 4′-C-[2[[*N*-(2-aminoethyl)carbamoyl]oxy]ethyl]thymidine and their thermal stability and nuclease-resistance properties. *J. Org. Chem. 63*, 1660–1667.

(30) Wang, G., and Seifert, W. E. (1996) Synthesis and evaluation of oligodeoxynucleotides containing 4′-*C*-substituted thymidines. *Tetrahedron Lett. 37*, 6515–6518.

(31) Fensholdt, J., Thrane, H., and Wengel, J. (1995) Synthesis of oligodeoxynucleotides containing 4′-*C*-(hydroxymethyl)thymidine: Novel promising antisense molecules. *Tetrahedron Lett. 36*, 2535–2538.

(32) Thrane, H., Fensholdt, J., Regner, M., and Wengel, J. (1995) Novel linear and branched oligodeoxynucleotide analogues containing 4′-*C*-(hydroxymethyl)thymidine. *Tetrahedron 51*, 10389–10402.

(33) Maag, H., Schmidt, B., and Rose, S. J. (1994) Oligodeoxynucleotide probes with multiple labels linked to the 4′-position of thymidine monomers: Excellent duplex stability and detection sensitivity. *Tetrahedron Lett. 35*, 6449–6452.

(34) Rostovtsev, V. V., Green, L. G., Fokin, V. V., and Sharpless, K. B. (2002) A stepwise Huisgen cycloaddition process: Copper(I)-catalyzed regioselective "ligation" of azides and terminal alkynes. *Angew. Chem., Int. Ed. 41*, 2596−2599.

(35) Tornoe, C. W., Christensen, C., and Meldal, M. (2002) Peptidotriazoles on solid phase: [1,2,3]-triazoles by regiospecific copper(I)-catalyzed 1,3-dipolar cycloadditions of terminal alkynes to azides. *J. Org. Chem. 67*, 3057–3064.

(36) Gierlich, J., Burley, G. A., Gramlich, P. M. E., Hammond, D. M., and Carell, T. (2006) Click chemistry as a reliable method for the high-density postsynthetic functionalization of alkyne-modified DNA. *Org. Lett. 8*, 3639–3642.

(37) Kumar, R., El-Sagheer, A., Tumpane, J., Lincoln, P., Wilhelmsson, L. M., and Brown, T. (2007) Template-directed oligonucleotide strand ligation, covalent intramolecular DNA circularization and catenation using click chemistry. *J. Am. Chem. Soc. 129*, 6859–6864.

(38) Seela, F., and Sirivolu, V. R. (2007) Nucleosides and oligonucleotides with diynyl side chains: base pairing and functionalization of 2′-deoxyuridine derivatives by the copper(I)-catalyzed alkyne-azide 'click'cycloaddition. *Helv. Chim. Acta 90*, 535–552.

(39) Wirges, C. T., Gramlich, P. M. E., Gutsmiedl, K., Gierlich, J., Burley, G. A., and Carell, T. (2007) Pronounced effect of DNA hybridization on click reaction efficiency. *QSAR Comb. Sci. 26*, 1159–1164.

(40) Jawalekar, A. M., Meeuwenoord, N., Cremers, J. G. O., Overkleeft, H. S., van der Marel, G. A., Rutjes, F. P. J. T., and van Delft, F. L. (2008) Conjugation of nucleosides and oligonucleotides by [3 + 2] cycloaddition. *J. Org. Chem. 73*, 287–290.

(41) Comstock, L. R., and Rajski, S. R. (2005) Conversion of DNA methyltransferases into azidonucleosidyl transferases via synthetic cofactors. *Nucleic Acids Res. 33*, 1644–1652.

(42) Comstock, L. R., and Rajski, S. R. (2005) Methyltransferase-directed DNA strand scission. *J. Am. Chem. Soc. 127*, 14136–14137.

(43) Weisbrod, S. H., and Marx, A. (2007) A nucleoside triphosphate for site-specific labelling of DNA by the Staudinger ligation. *Chem. Commun.* 1828–1830.

(44) Baccaro, A., Weisbrod, S. H., and Marx, A. (2007) DNA conjugation by the Staudinger ligation: New thymidine analogues. *Synthesis* 1949–1945.

(45) Wada, T., Mochizuki, A., Higashiya, S., Tsuruoka, H., Kawahara, S., Ishikawa, M., and Sekine, M. (2001) Synthesis and properties of 2-azidodeoxyadenosine and its incorporation into oligodeoxynucleotides. *Tetrahedron Lett. 42*, 9215–9219.

(46) Garegg, P. J., Lindh, I., Regberg, T., Stawinski, J., and Strömberg, R. (1986) Nucleoside H-phosphonates. III. Chemical synthesis of oligodeoxyribonucleotides by the hydrogenphosphonate approach. *Tetrahedron Lett. 27*, 4051–4054.

(47) Garegg, P. J., Lindh, I., Regberg, T., Stawinski, J., and Strömberg, R. (1986) Nucleoside H-phosphonates. IV. Automated solid-phase synthesis of oligodeoxyribonucleotides by the hydrogenphosphonate approach. *Tetrahedron Lett. 27*, 4055–4058.

(48) O-Yang, C., Kurz, W., Eugui, E. M., McRoberts, M. J., Verheyden, J. P. H., Kurz, L. J., and Walker, K. A. M. (1992) 4′-Substituted nucleosides as inhibitors of HIV: an unusual oxetane derivative. *Tetrahedron Lett. 33*, 41–44.

(49) Jones, G. H., Taniguchi, M., Tegg, D., and Moffatt, J. G. (1979) 4′-Substituted nucleosides. 5. Hydroxymethylation of nucleoside 5′-aldehydes. *J. Org. Chem. 44*, 1309–1317.

(50) Jung, K.-H., and Marx, A. (2008) Synthesis of 4′-*C*-modified 2′-deoxyribonucleoside analogues and oligonucleotides. *Curr. Org. Chem. 12*, 343–354.

(51) Wu, T., Nauwelaerts, K., Van Aerschot, A., Froeyen, M., Lescrinier, E., and Herdewijn, P. (2006) Base-base interactions in the minor groove of double-stranded DNA. *J. Org. Chem. 71*, 5423–5431.

(52) Schmidt, M., Chatterjee, S. K., Dobner, B., and Nuhn, P. (2002) New modified single chained glycolipids. Part 1: synthesis of deoxy and partially O-methylated glycolipids with or without a sulfur containing spacer. *Chem. Phys. Lip. 114*, 139–147.

(53) Park, W. K. C., Auer, M., Jaksche, H., and Wong, C.-H. (1996) Rapid combinatorial synthesis of aminoglycoside antibiotic mimetics: Use of a polyethylene glycol-linked amine and a neamine-derived aldehyde in multiple component condensation as a strategy for the discovery of new inhibitors of the HIV RNA rev response element. *J. Am. Chem. Soc. 118*, 10150–10155.

(54) Chan, T. R., Hilgraf, R., Sharpless, K. B., and Fokin, V. V. (2004) Polytriazoles as copper(I)-stabilizing ligands in catalysis. *Org. Lett. 6*, 2853–2855.

(55) Marx, A., Erdmann, P., Senn, M., Körner, S., Jungo, T., Petretta, M., Imwinkelried, P., Dussy, A., Kulicke, K. J., Macko, L., Zehnder, M., and Giese, B. (1996) 165. Synthesis of 4′-C-acylated thymidines. *Helv. Chim. Acta 79*, 1980–1994.

(56) Detmer, I., Summerer, D., and Marx, A. (2002) DNA minor groove hydration probed with 4′-alkylated thymidines. *Chem. Commun.* 2314–2315.

BC800221P

Utilization of Intrachain 4´-*C*-Azidomethylthymidine for Preparation of Oligodeoxyribonucleotide Conjugates by Click Chemistry in Solution and on a Solid Support

Anu Kiviniemi, * Pasi Virta and Harri Lönnberg

Department of Chemistry, University of Turku, FIN-20014 Turku, Finland

ankaka@utu.fi

SUPPORTING INFORMATION

Table of Contents

General procedures S2

Figure S1. ^{1}H NMR ($CDCl_3$, 500 MHz) spectrum of **2** S3

Figure S2. ^{1}H NMR ($CDCl_3$ + drop of MeOD, 500 MHz) spectrum of **3** S4

Figure S3. ^{1}H NMR (MeOD, 500 MHz) spectrum of **4** S5

Figure S4. ^{1}H NMR ($CDCl_3$, 500 MHz) spectrum of **6** S6

Figure S5. ^{1}H NMR ($CDCl_3$, 500 MHz) spectrum of **7** S7

Figure S6. ^{1}H NMR ($CDCl_3$, 500 MHz) spectrum of **8** S8

Figure S7. ^{1}H NMR ($CDCl_3$, 500 MHz) spectrum of **9** S9

Figure S8. ^{1}H NMR ($CDCl_3$, 500 MHz) spectrum of **10** S10

Figure S9. ^{31}P NMR ($CDCl_3$, 200 MHz) spectrum of **10** S10

Figure S10. ^{1}H NMR ($CDCl_3$, 500 MHz) spectrum of **15** S11

Figure S11. ^{1}H NMR ($CDCl_3$, 500 MHz) spectrum of **16** S12

Figure S12. MS(ESI) spectrum and HPLC chromatograph of pure **20** S13

Figure S13. MS(ESI) spectrum and HPLC chromatograph of pure **21** S14

Figure S14. MS(ESI) spectrum and HPLC chromatograph of pure **25** S15

Figure S15. MS(ESI) spectrum and HPLC chromatograph of pure **26** S16

Figure S16. MS(ESI) spectrum and HPLC chromatograph of pure **27** S17

Figure S17. MS(ESI) spectrum and HPLC chromatograph of pure **28** S18

Figure S18. MS(ESI) spectrum and HPLC chromatograph of pure **29** S19

Figure S19. T_m curve of 2´-*O*-methyl RNA : **20** duplex S20

Figure S20. T_m curve of 2´-*O*-methyl RNA : **21** duplex S20

Figure S21. T_m curve of 2´-*O*-methyl RNA : **25** duplex S21
Figure S22. T_m curve of DNA : **26** duplex S21
Figure S23. T_m curve of DNA : **27** duplex S22
Figure S24. T_m curve of 2´-*O*-methyl RNA : **28** duplex S22
Figure S25. T_m curve of DNA : **29** duplex S23

General procedures

The NMR spectra of **2-4, 6-10, 15** and **16** were recorded at 500 MHz. The chemical shifts are given in ppm from internal TMS. The mass spectra of **20, 21** and **25-29** were recorded by ESI ionization method. RP HPLC chromatographs of pure **20, 21** and **25-29** were performed using Supelco Ascentis C18 (150 × 4.6 mm, 5 μm) analytical column. The melting curves (absorbance versus temperature) were measured at 260 nm in Perkin-Elmer Lambda 2 UV-vis spectrometer equipped with Peltier Temperature contoller by using a rate of 0.5 ºC / min (from 20 to 90 ºC). The oligonucleotide conjugate and its complementary target DNA or 2´-*O*-methyl RNA were used in concentration of 2 μmol L^{-1}.

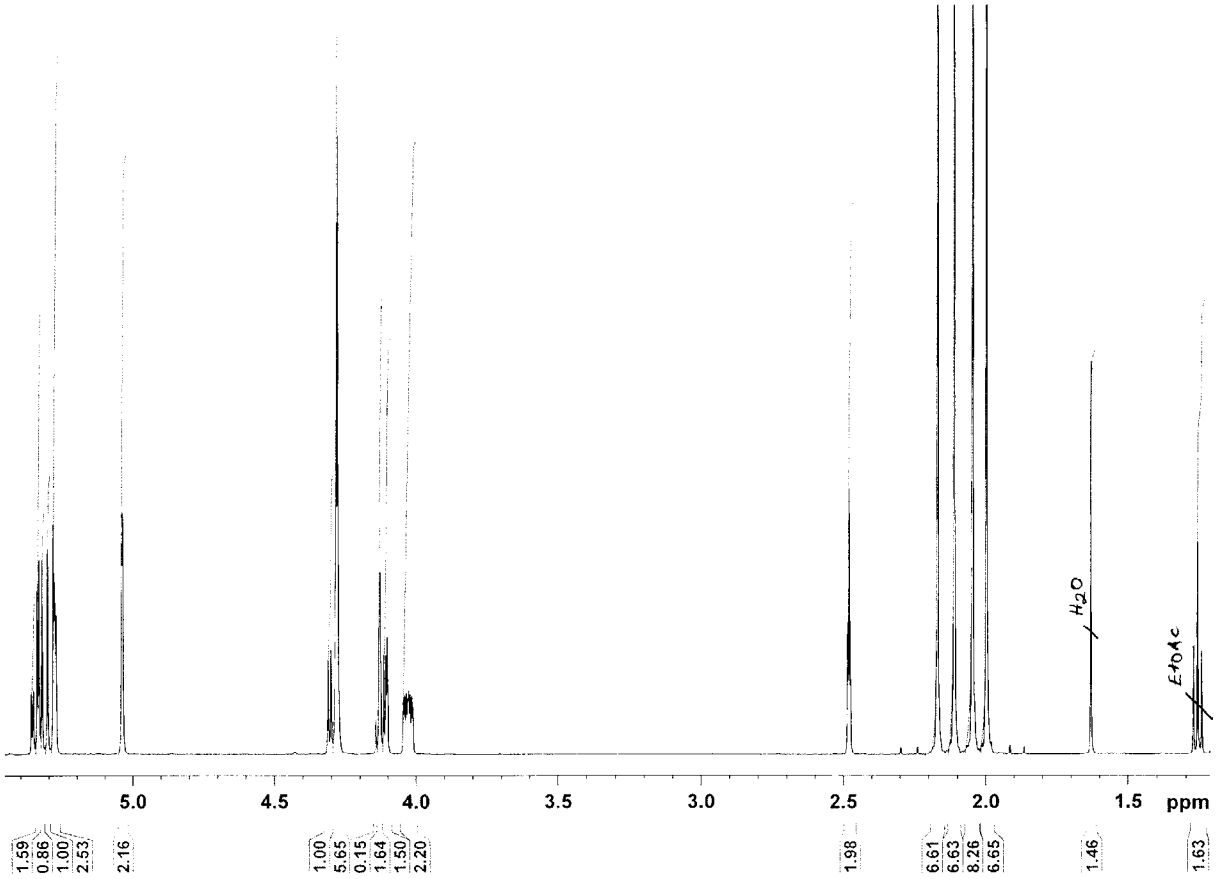

Figure S1. ^{1}H NMR ($CDCl_3$, 500 MHz) spectrum of **2**

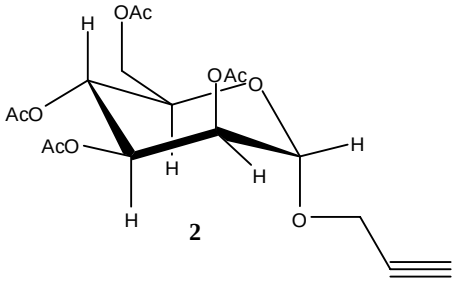

2

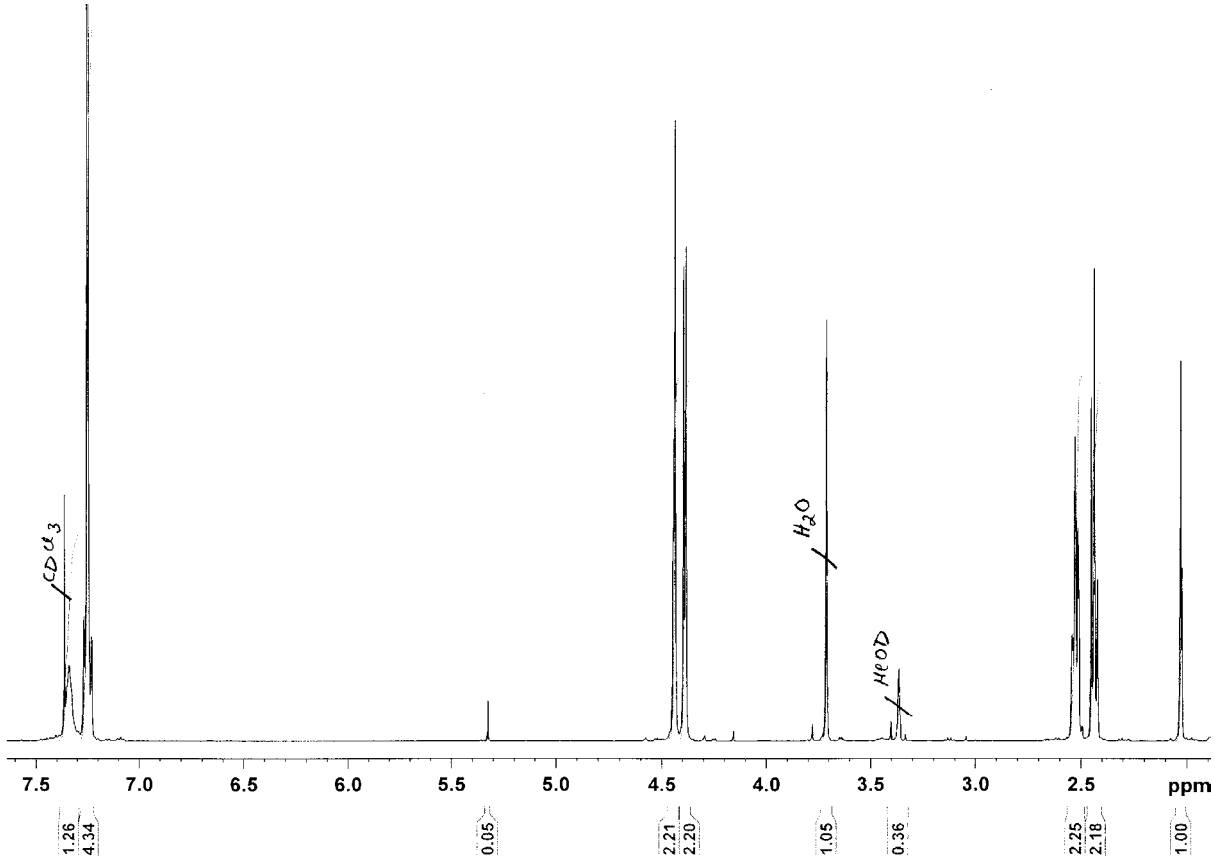

Figure S2. ^{1}H NMR ($CDCl_3$ + drop of MeOD, 500 MHz) spectrum of **3**

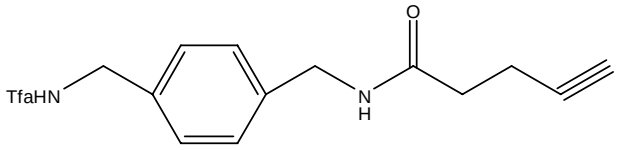

3

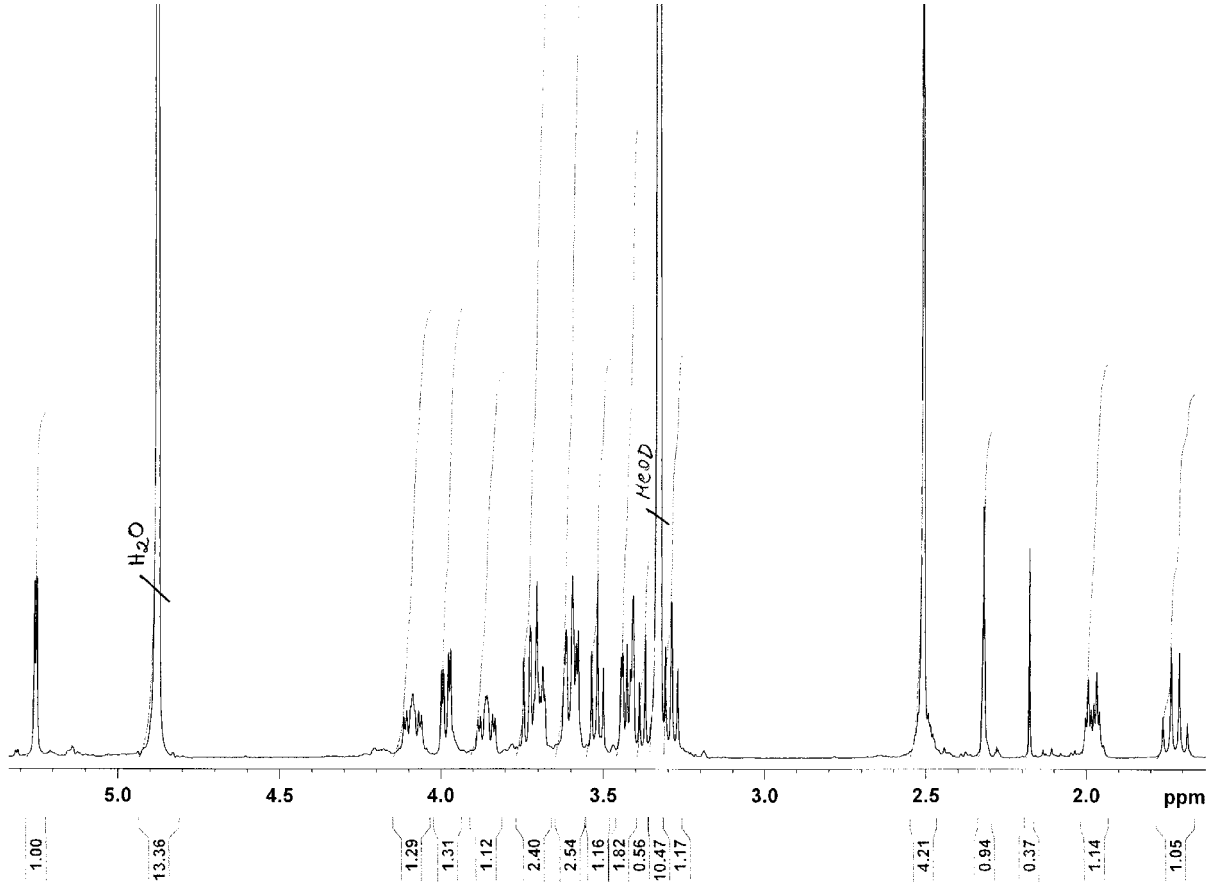

Figure S3. ^{1}H NMR (MeOD, 500 MHz) spectrum of **4**

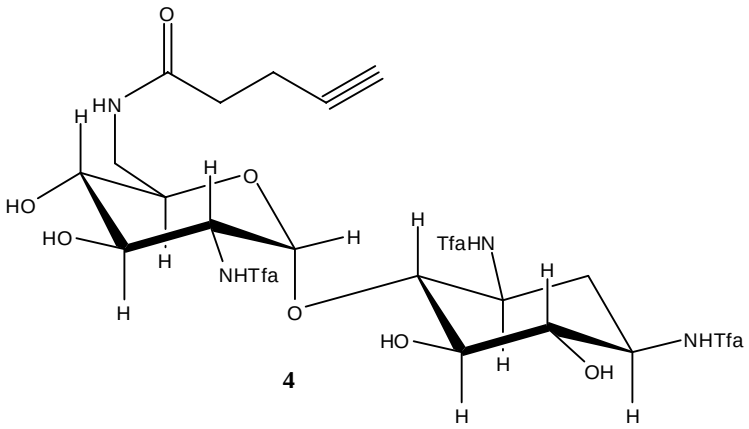

4

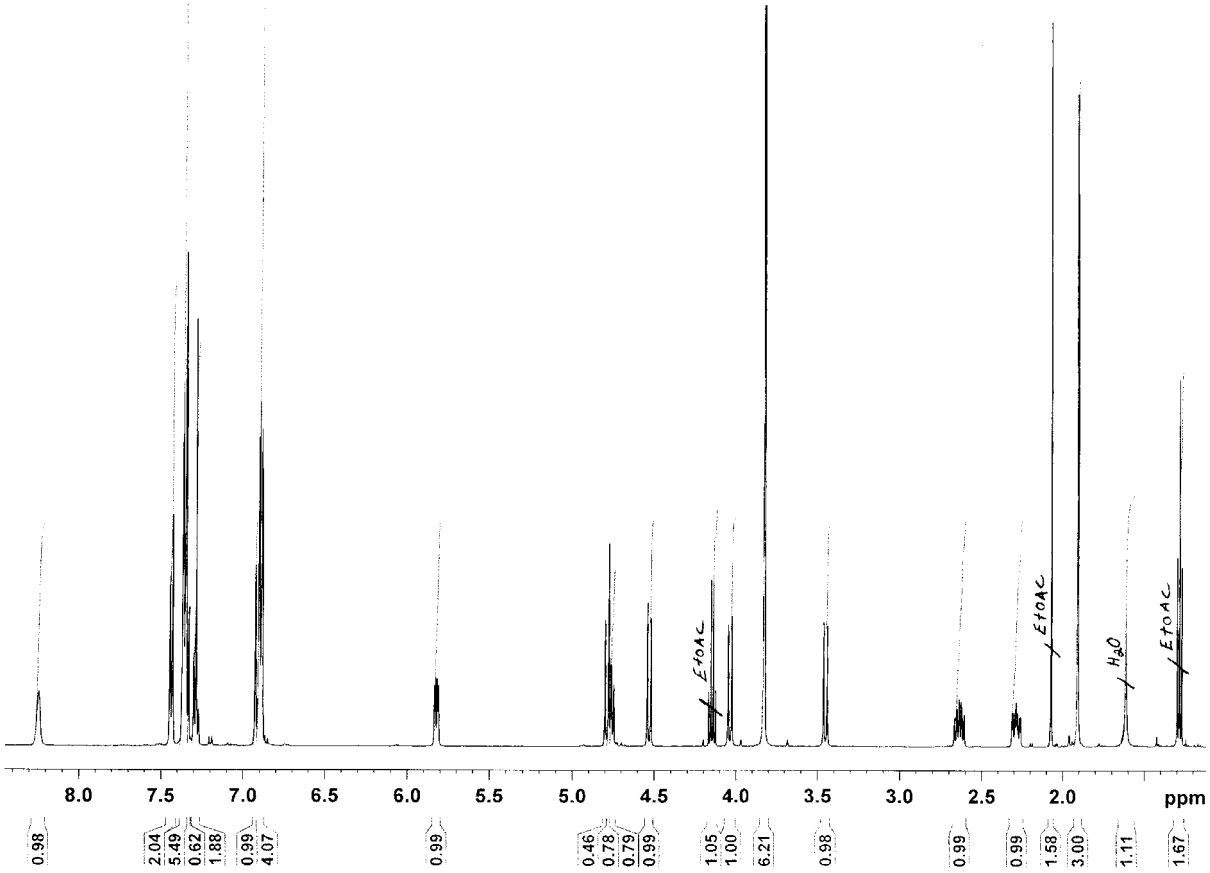

Figure S4. ^{1}H NMR ($CDCl_3$, 500 MHz) spectrum of **6**

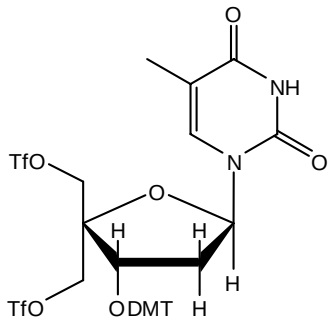

6

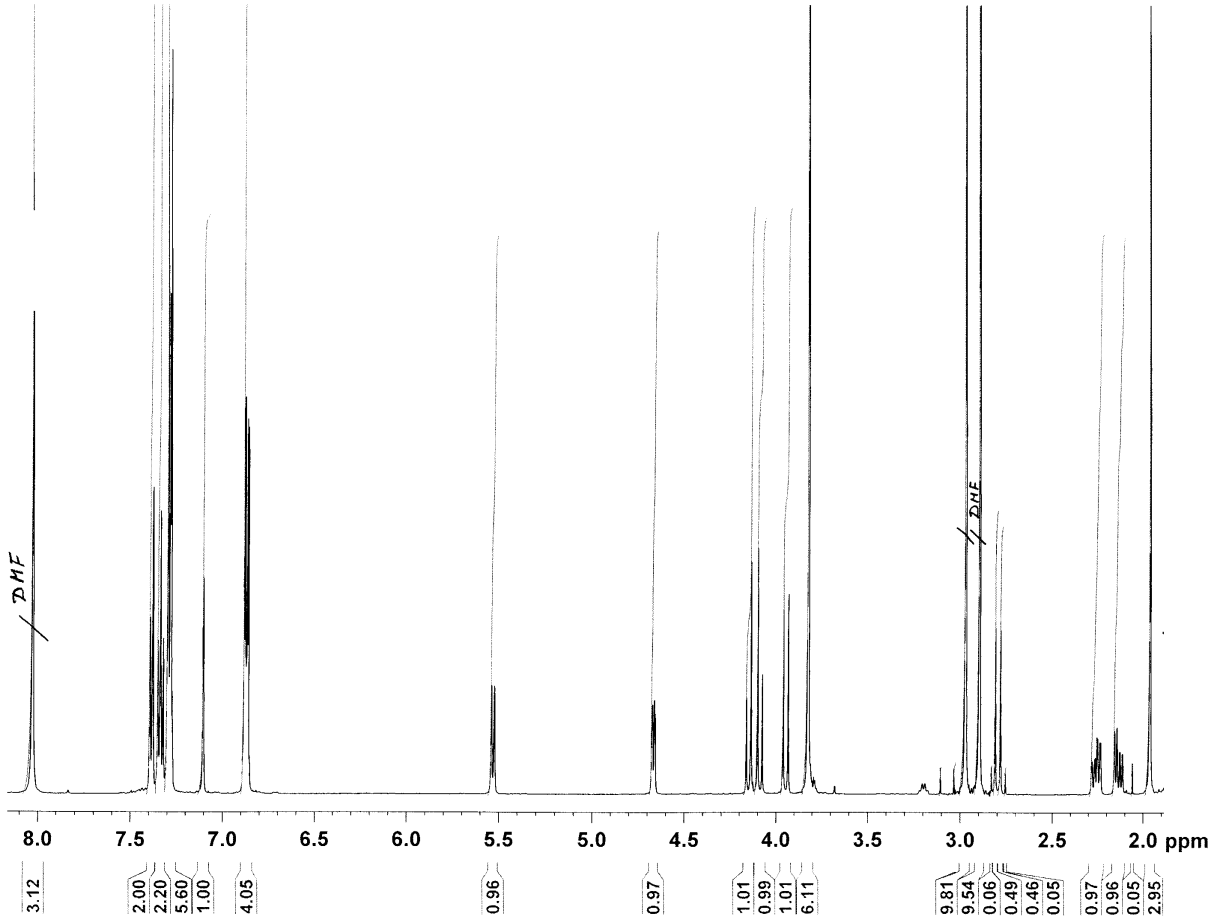

Figure S5. ^{1}H NMR ($CDCl_3$, 500 MHz) spectrum of **7**

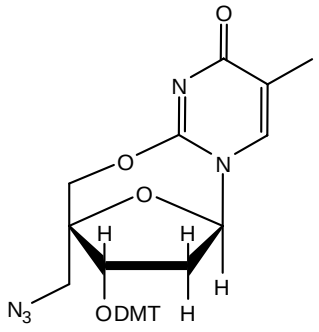

7

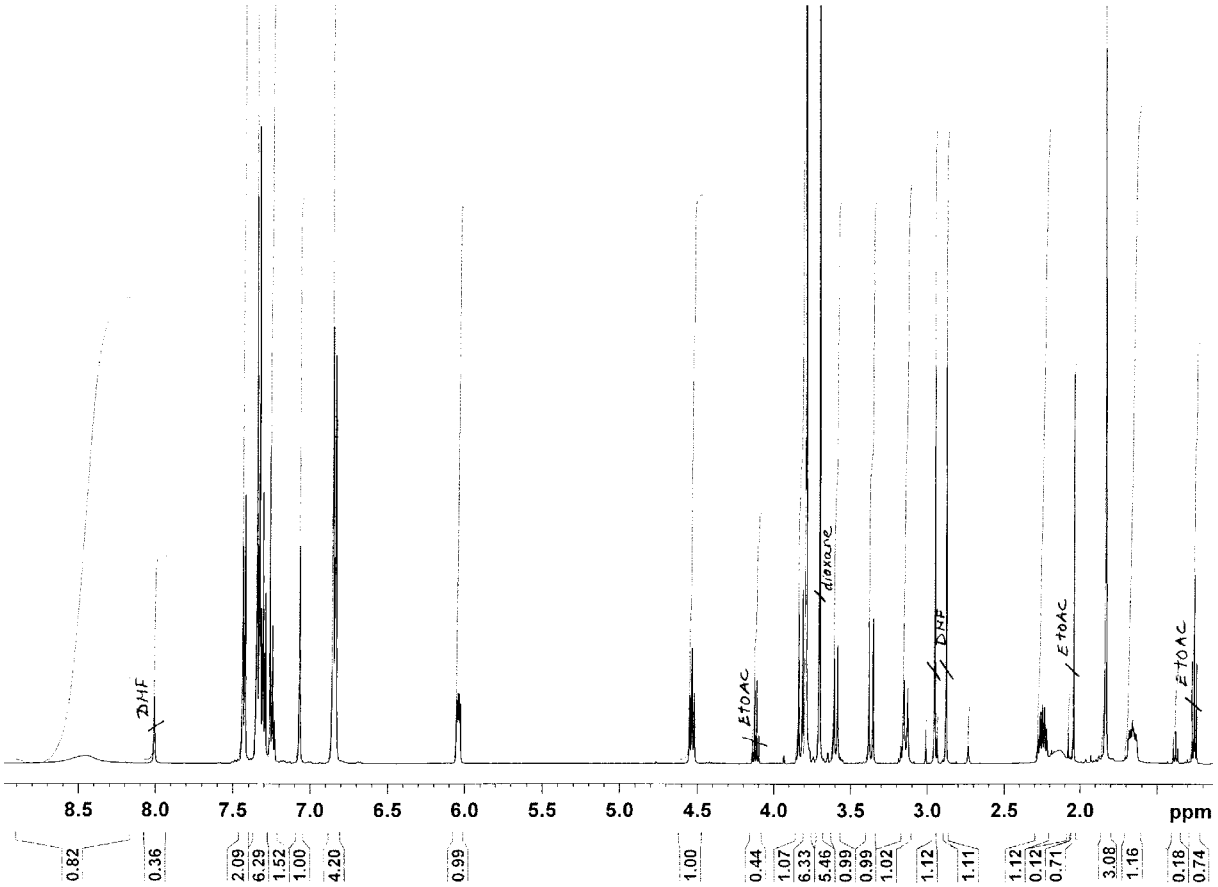

Figure S6. ^{1}H NMR ($CDCl_3$, 500 MHz) spectrum of **8**

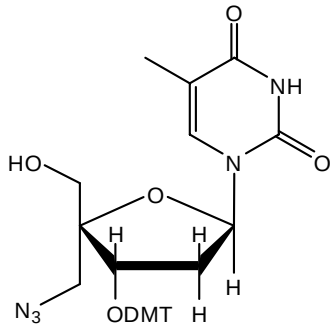

8

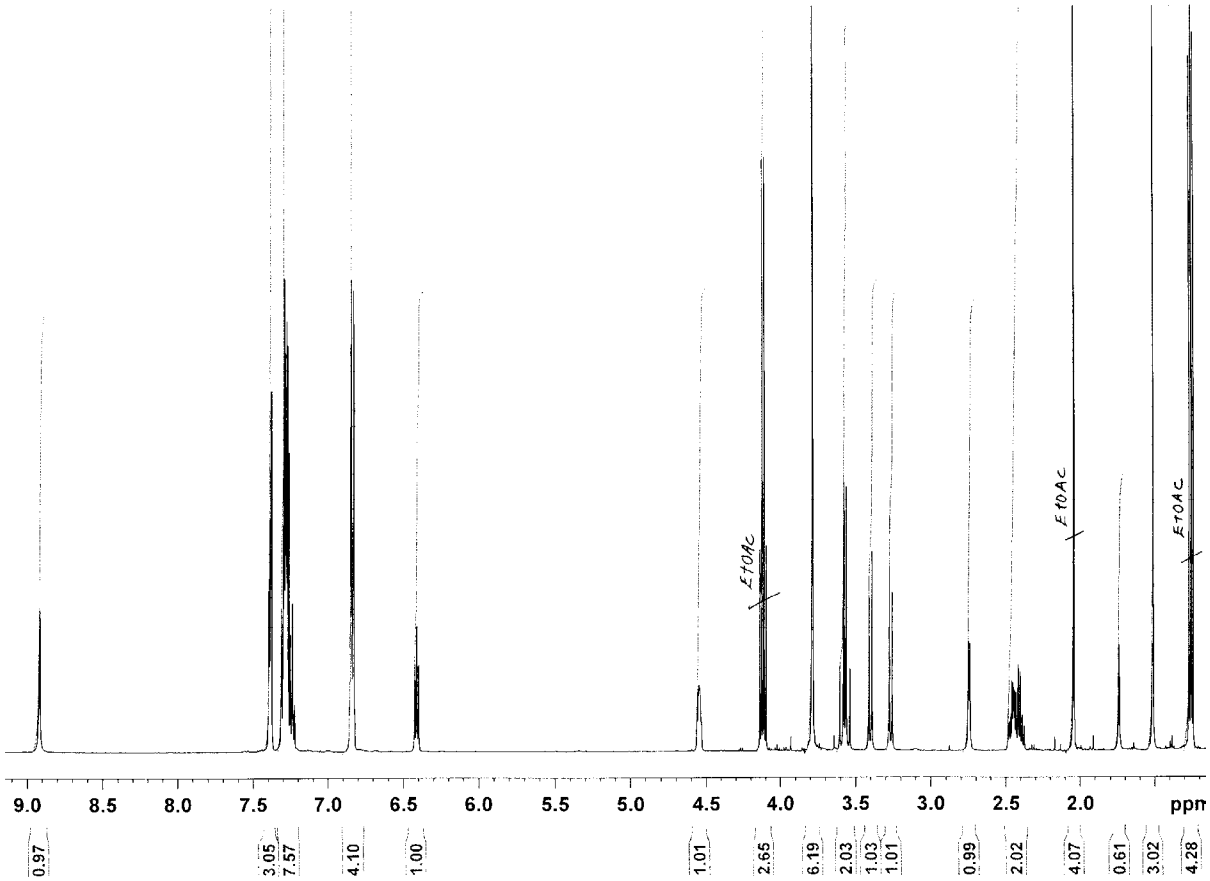

Figure S7. ^{1}H NMR ($CDCl_3$, 500 MHz) spectrum of **9**

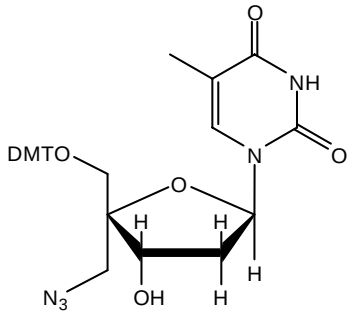

9

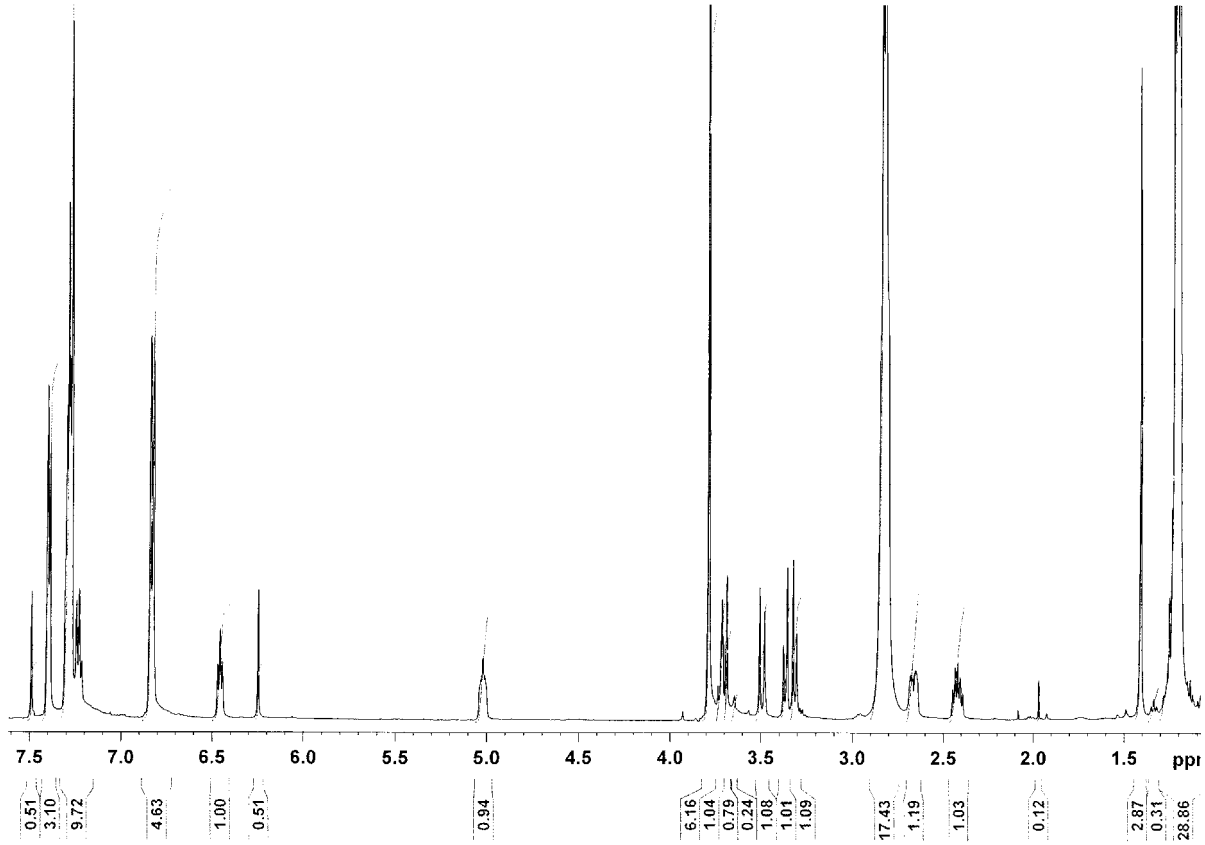

Figure S8. ^{1}H NMR ($CDCl_3$, 500 MHz) spectrum of **10**

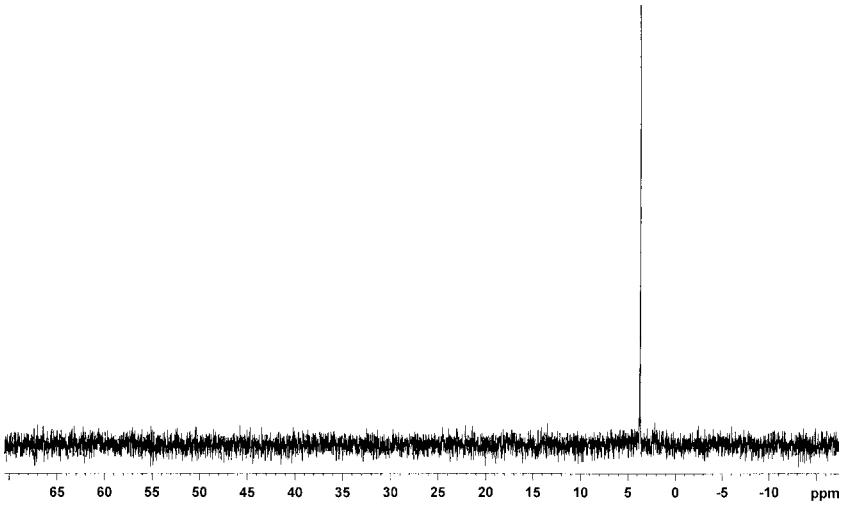

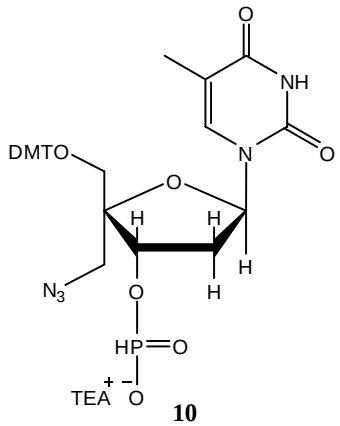

10

Figure S9. ^{31}P NMR ($CDCl_3$, 200 MHz) spectrum of **10**

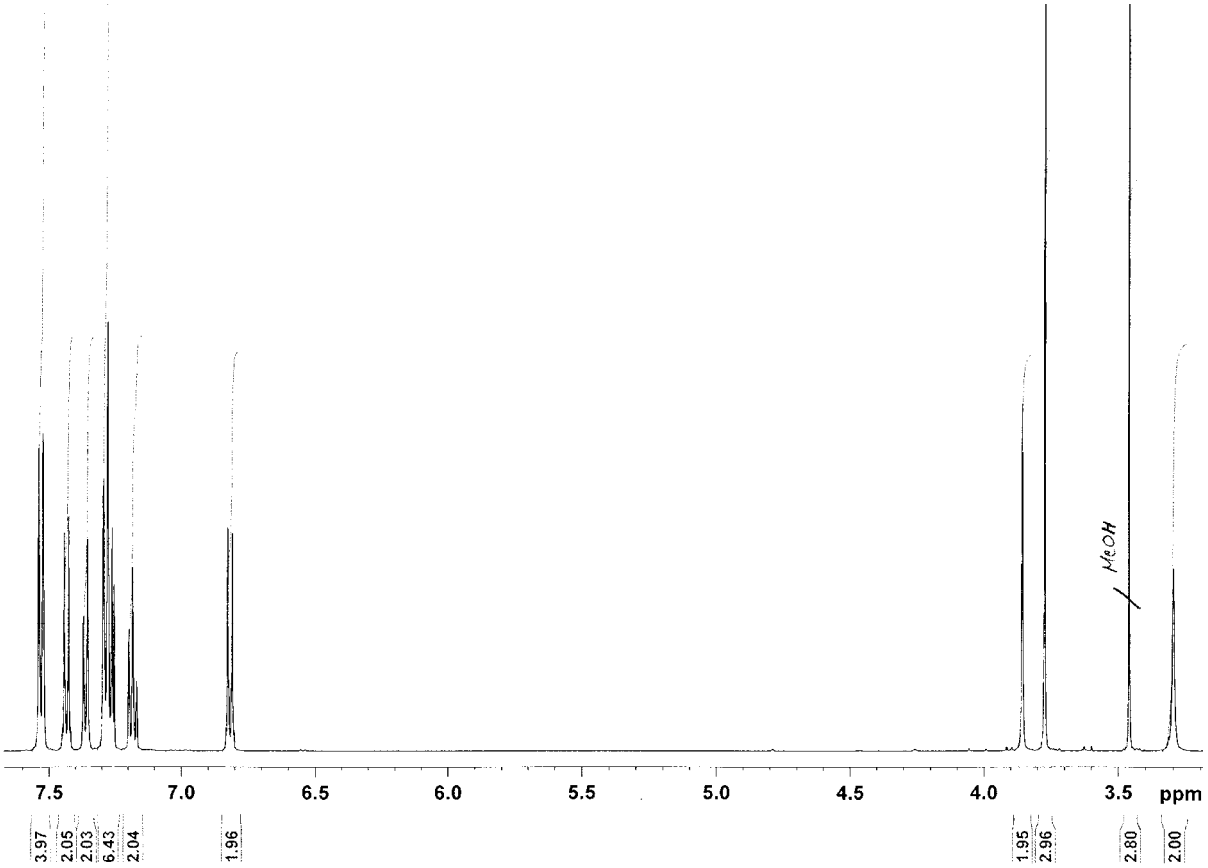

Figure S10. ^{1}H NMR ($CDCl_3$, 500 MHz) spectrum of **15**

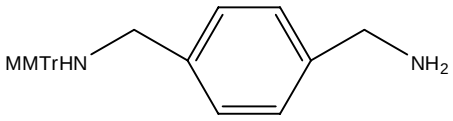

15

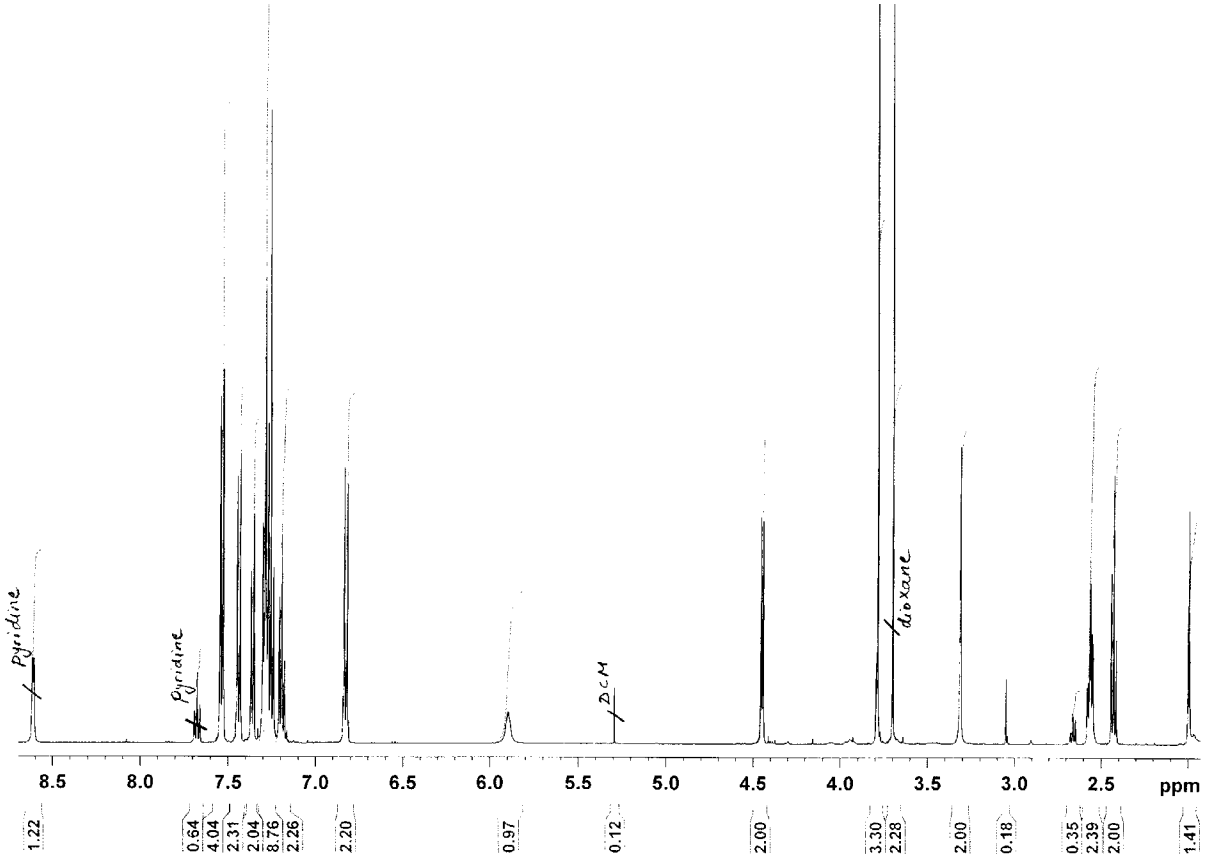

Figure S11. ^{1}H NMR ($CDCl_3$, 500 MHz) spectrum of **16**

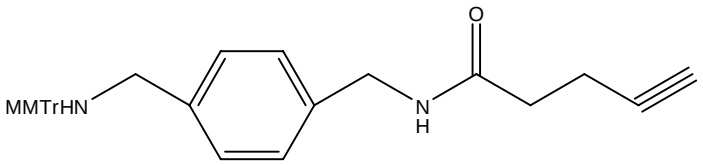

16

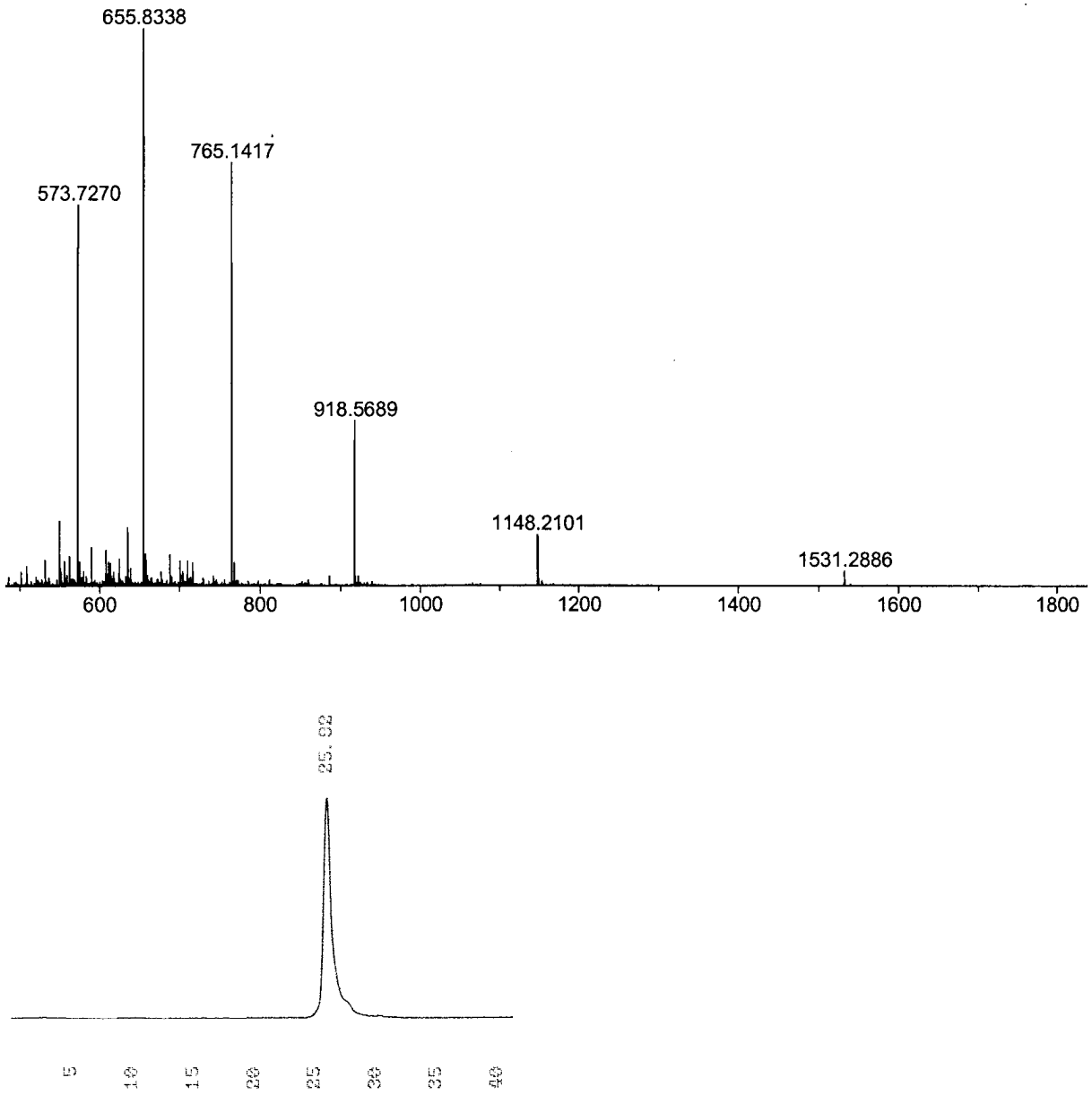

Figure S12. MS(ESI) spectrum and HPLC chromatograph of pure **20**

(RP HPLC conditions: gradient elution 0-30 % MeCN in 50 mmol L^{-1} NH_4OAc buffer over 60 min, flow rate 1 mL min^{-1})

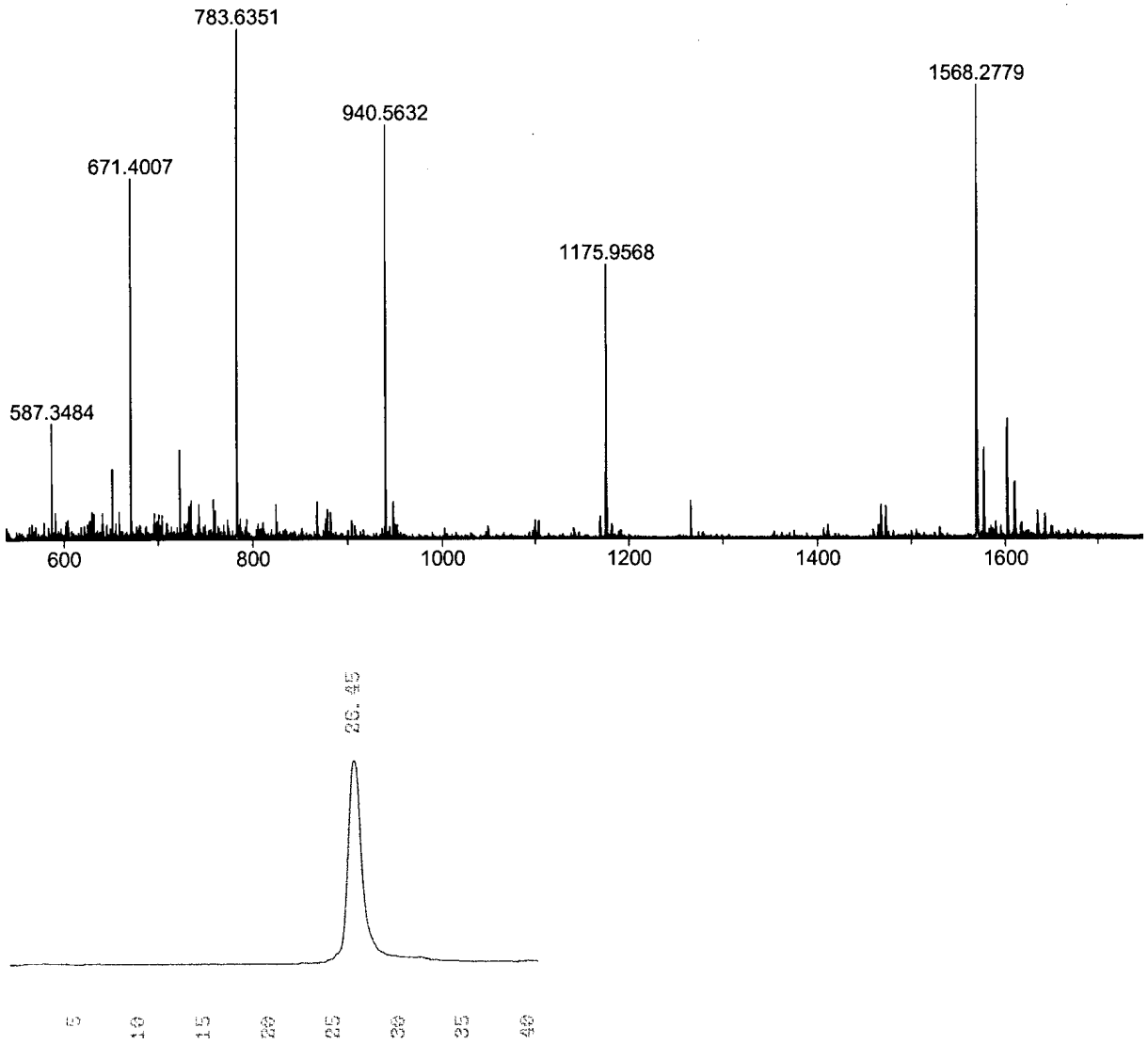

Figure S13. MS(ESI) spectrum and HPLC chromatograph of pure **21**

(RP HPLC conditions: gradient elution 0-30 % MeCN in 50 mmol L^{-1} NH_4OAc buffer over 60 min, flow rate 1 mL min^{-1})

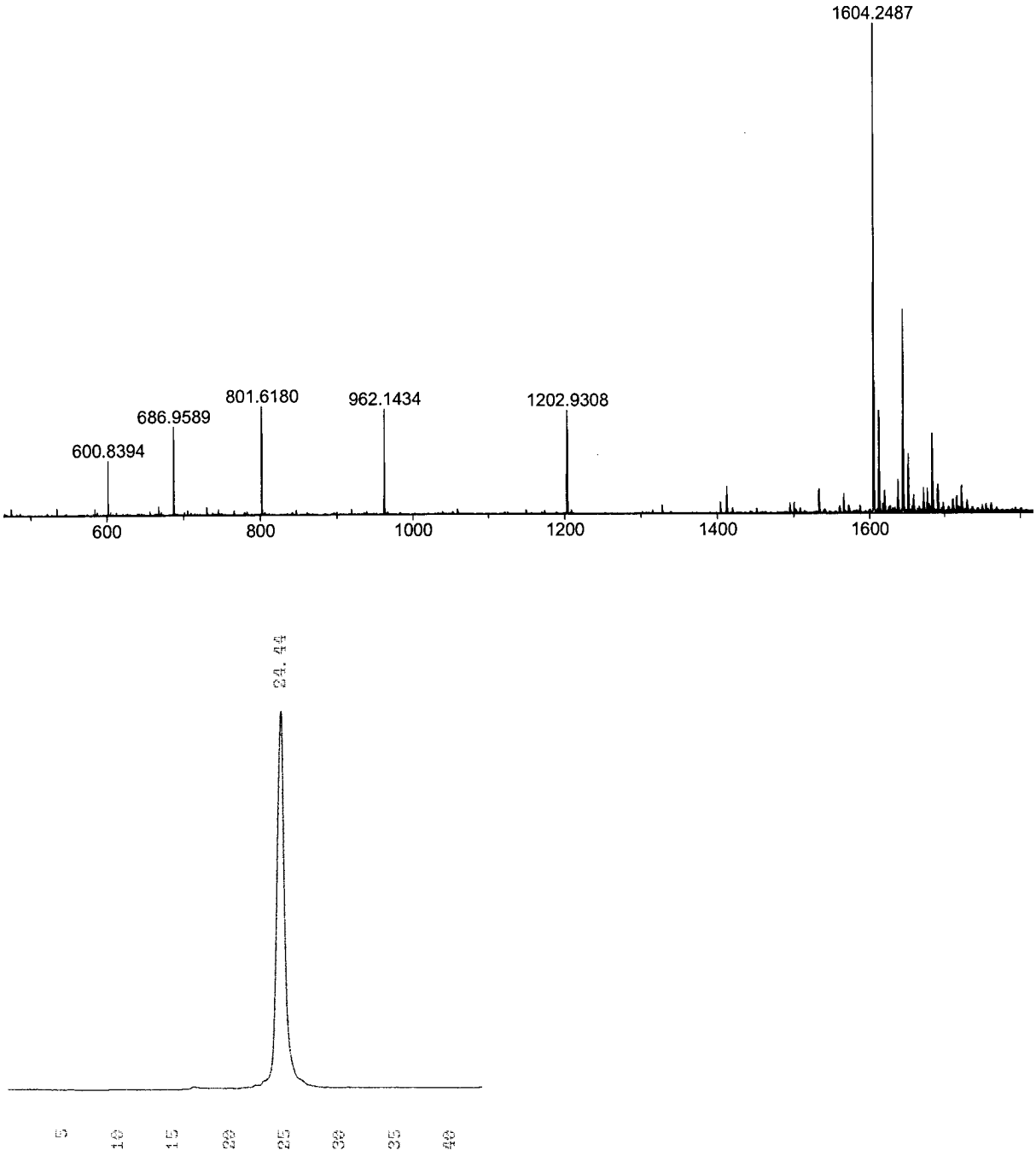

Figure S14. MS(ESI) spectrum and HPLC chromatograph of pure **25**

(RP HPLC conditions: gradient elution 0-30 % MeCN in 50 mmol L^{-1} NH_4OAc buffer over 60 min, flow rate 1 mL min^{-1})

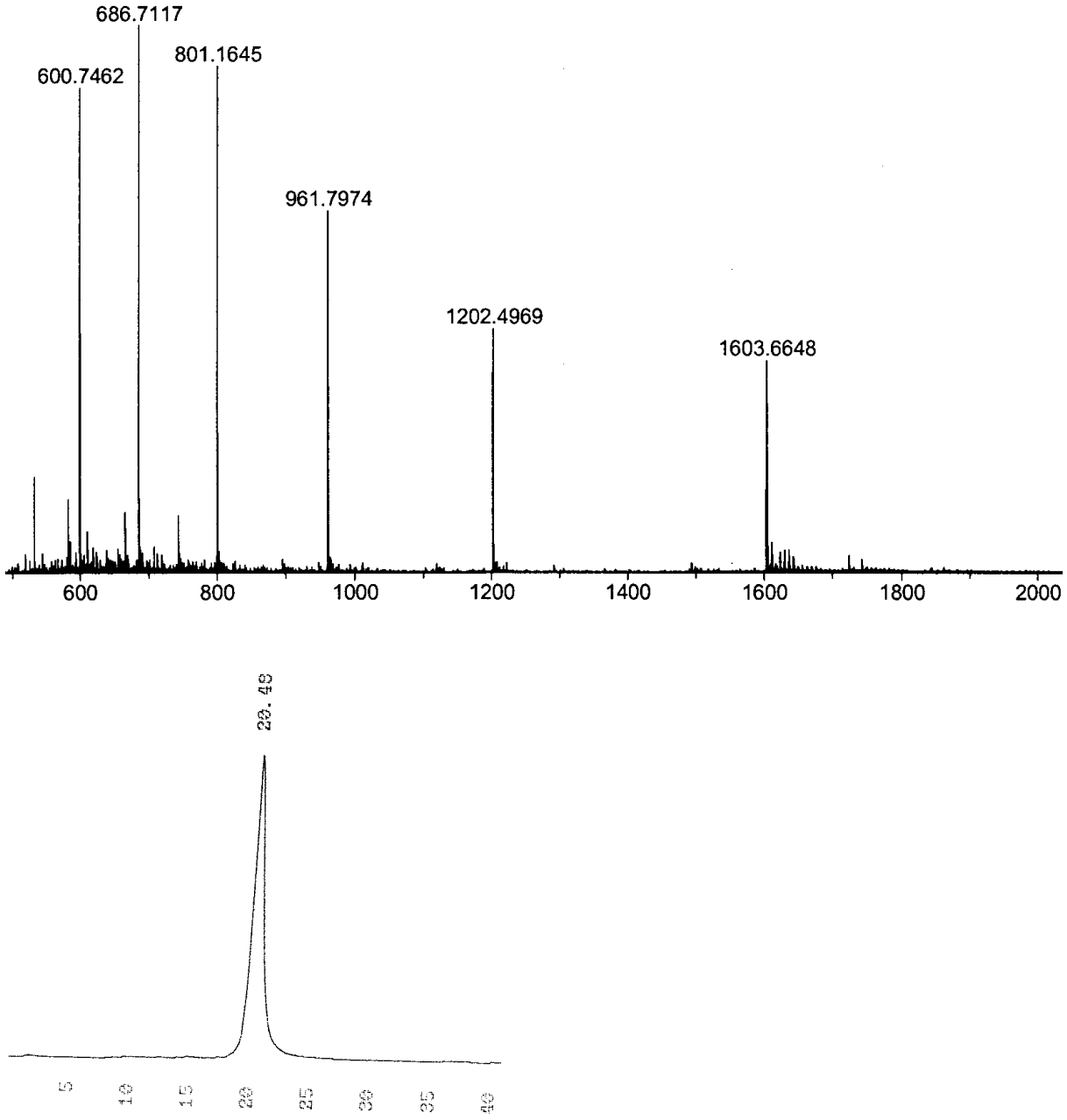

Figure S15. MS(ESI) spectrum and HPLC chromatograph of pure **26**

(RP HPLC conditions: gradient elution 0-40 % MeCN in 50 mmol L^{-1} NH_4OAc buffer over 60 min, flow rate 1 mL min^{-1})

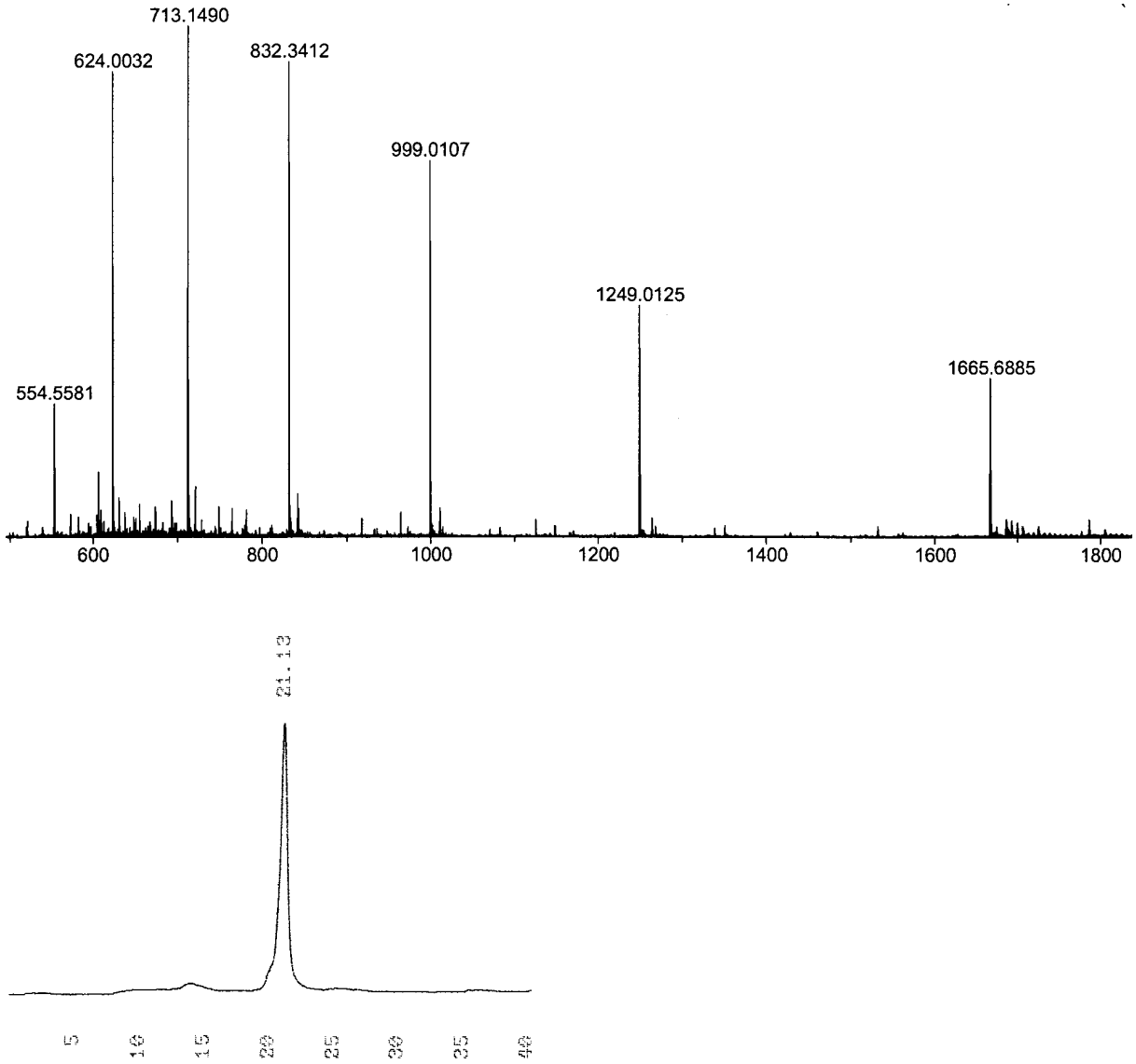

Figure S16. MS(ESI) spectrum and HPLC chromatograph of pure **27**

(RP HPLC conditions: gradient elution 0-40 % MeCN in 50 mmol L^{-1} NH_4OAc buffer over 60 min, flow rate 1 mL min^{-1})

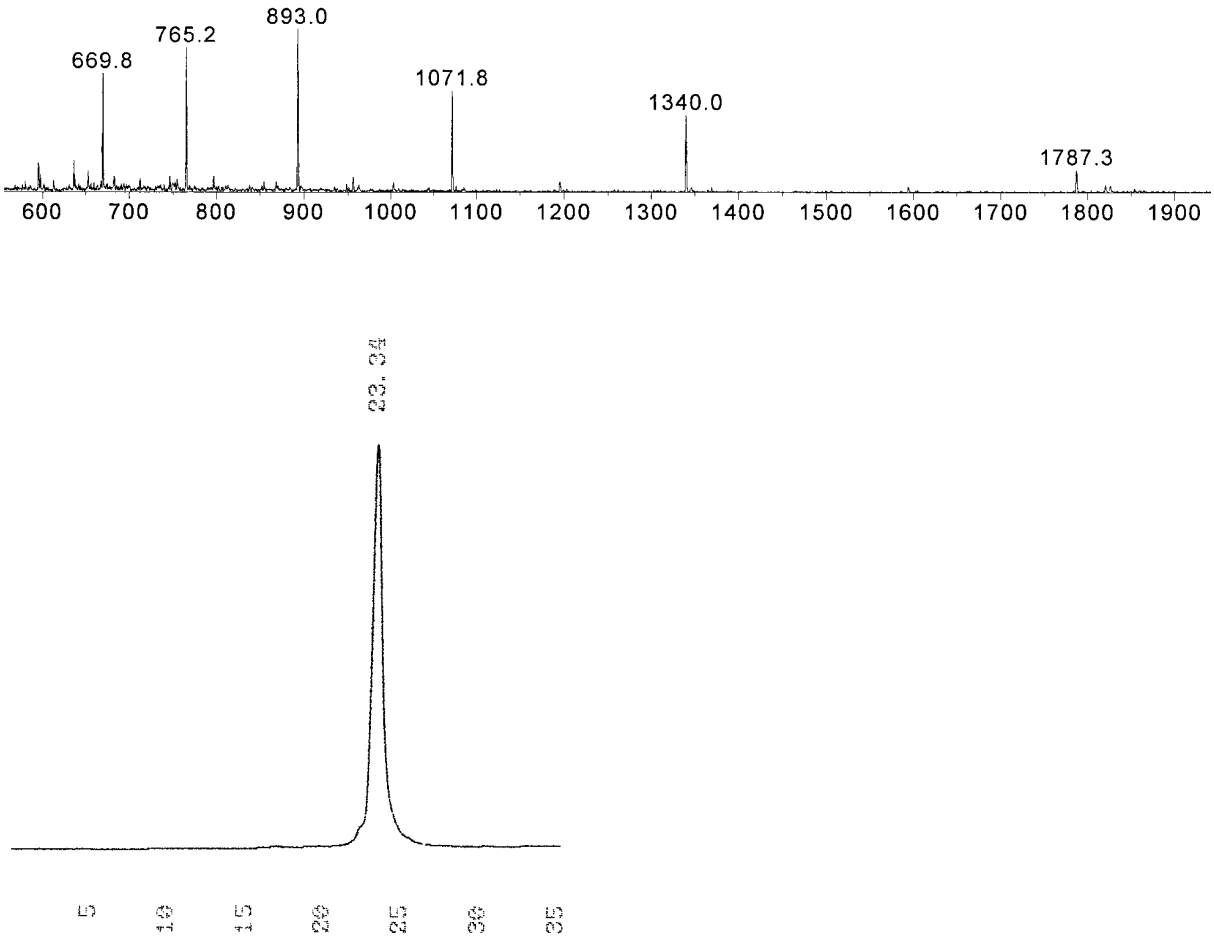

Figure S17. MS(ESI) spectrum and HPLC chromatograph of pure **28**

(RP HPLC conditions: gradient elution 0-30 % MeCN in 50 mmol L^{-1} NH_4OAc buffer over 60 min, flow rate 1 mL min^{-1})

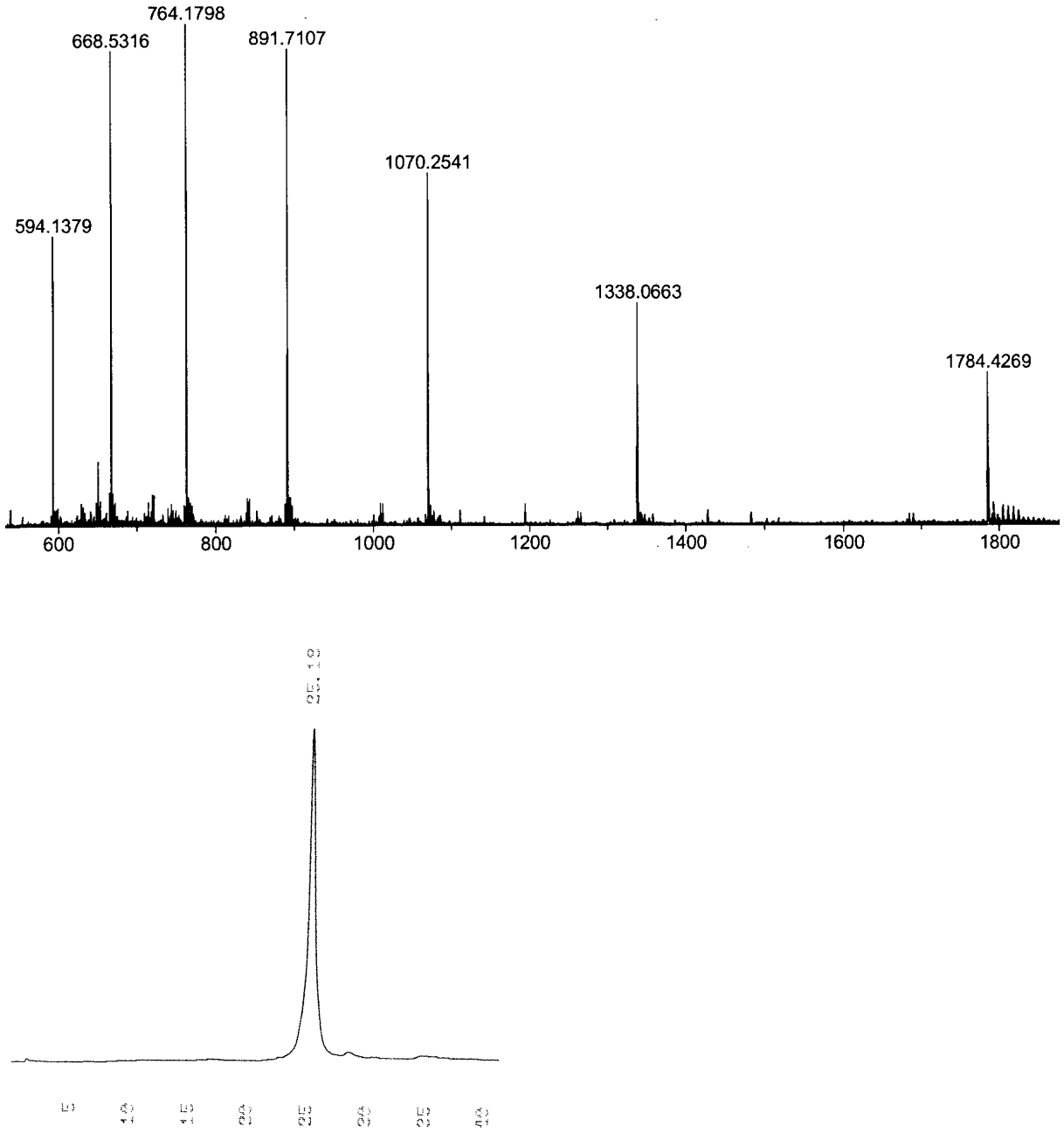

Figure S18. MS(ESI) spectrum and HPLC chromatograph of pure **29**

(RP HPLC conditions: gradient elution 0-30 % MeCN in 50 mmol L^{-1} NH_4OAc buffer over 60 min, flow rate 1 mL min^{-1})

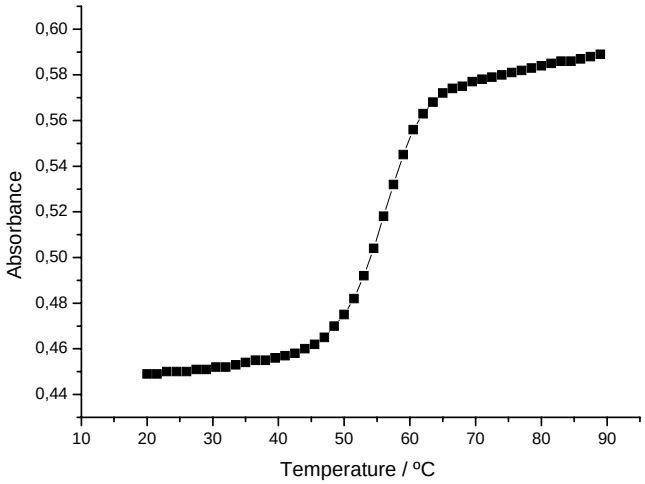

Figure S19. T_m curve of 2´-*O*-methyl RNA : **20** duplex (10 mM potassium phosphate buffer (pH 7), 0.1 mol L^{-1} NaCl)

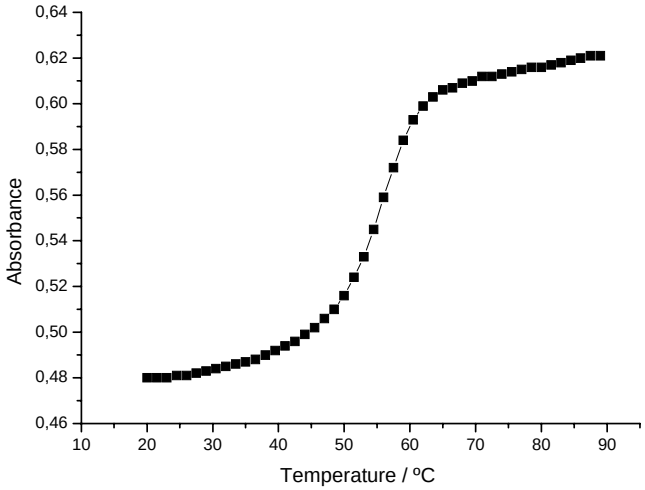

Figure S20. T_m curve of 2´-*O*-methyl RNA : **21** duplex (10 mM potassium phosphate buffer (pH 7), 0.1 mol L^{-1} NaCl)

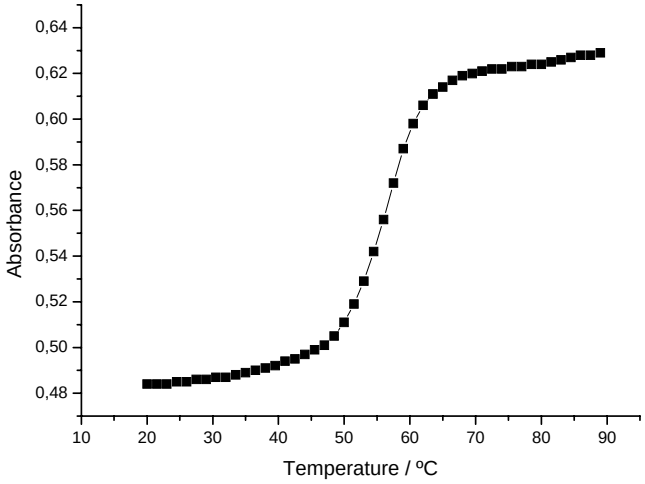

Figure S21. T_m curve of 2´-*O*-methyl RNA : **25** duplex (10 mM potassium phosphate buffer (pH 7), 0.1 mol L^{-1} NaCl)

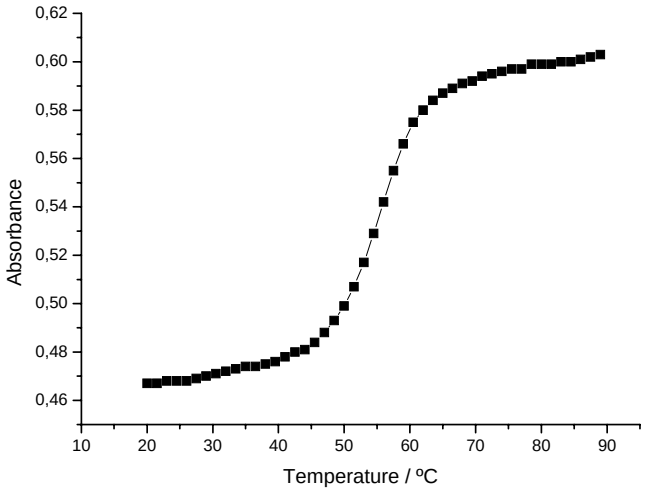

Figure S22. T_m curve of DNA : **26** duplex (10 mM potassium phosphate buffer (pH 7), 0.1 mol L^{-1} NaCl)

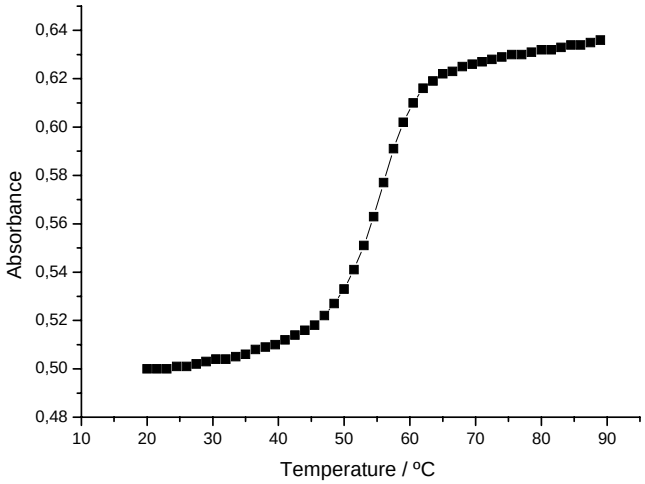

Figure S23. T_m curve of DNA : **27** duplex (10 mM potassium phosphate buffer (pH 7), 0.1 mol L^{-1} NaCl)

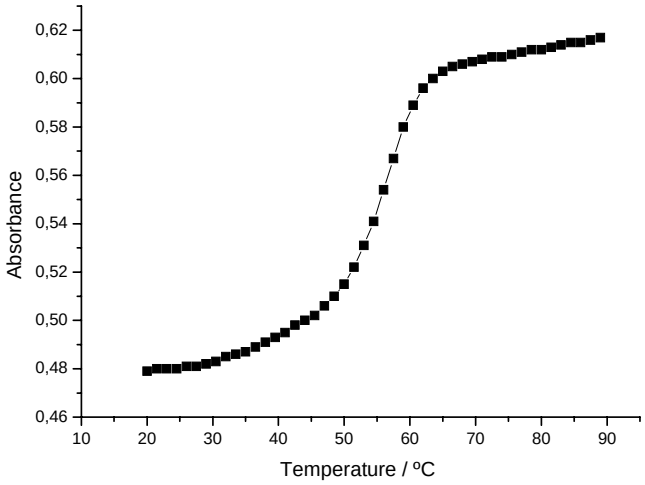

Figure S24. T_m curve of 2´-*O*-methyl RNA : **28** duplex (10 mM potassium phosphate buffer (pH 7), 0.1 mol L^{-1} NaCl)

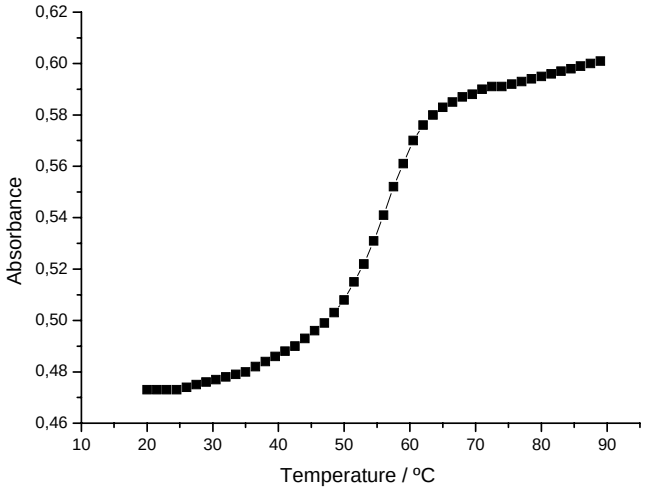

Figure S25. T_m curve of DNA : **29** duplex (10 mM potassium phosphate buffer (pH 7), 0.1 mol L^{-1} NaCl)

TECHNICAL NOTES

Determination of Optimal Rhodamine Fluorophore for *in Vivo* Optical Imaging

Michelle R. Longmire, Mikako Ogawa, Yukihiro Hama, Nobuyuki Kosaka, Celeste A. S. Regino, Peter L. Choyke, and Hisataka Kobayashi*

Molecular Imaging Program, Center for Cancer Research, National Cancer Institute, National Institutes of Health, Bethesda, Maryland 20892-1088. Received April 3, 2008; Revised Manuscript Received May 8, 2008

Optical imaging has the potential to improve the efficacy of surgical and endoscopic approaches to cancer treatment; however, the optimal type of fluorescent probe has not yet been established. It is well-known that rhodamine-core-derived fluorophores offer a combination of desirable properties such as good photostability, high extinction coefficient, and high fluorescence quantum yield. However, despite the ubiquitous use of rhodamine fluorophores for *in vivo* optical imaging, it remains to be determined if unique chemical properties among individual rhodamine core family members affect fluorophore parameters critical to *in vivo* optical imaging applications. These parameters include preserved fluorescence intensity in low pH environments, similar to that of the endolysosome; efficient fluorescence signal despite conformational changes to targeting proteins as may occur in harsh subcellular environments; persistence of fluorescence after cellular internalization; and sufficient signal-to-background ratios to permit the identification of fluorophore-targeted tumors. In the present study, we conjugated 4 common rhodamine-core based fluorescent dyes to a clinically feasible and quickly internalizing D-galactose receptor targeting reagent, galactosamine serum albumin (GmSA), and conducted a series of *in vitro* and *in vivo* experiments using a metastatic ovarian cancer mouse model to determine if differences in optical imaging properties exist among rhodamine fluorophores and if so, which rhodamine core possesses optimal characteristics for *in vivo* imaging applications. Herein, we demonstrate that the rhodamine-fluorophore, TAMRA, is the most robust of the 4 common rhodamine fluorophores for *in vivo* optical imaging of ovarian cancer metastases to the peritoneum.

INTRODUCTION

The application of targeted optical imaging probes as an aid to surgical or endoscopic procedures offers the potential for the identification and treatment of malignancies, such as ovarian and colon cancer, at subvisible volumes when the opportunity for cure is the greatest. However, maximal clinical benefit requires probes with high target-to-background ratios which are sufficient to permit identification and detection of cancer tissues in the human body. In addition, optical imaging probe selection must take into consideration imaging application-specific parameters. For example, in applications permitting access to superficial surfaces of targeted tissues, green dyes such as rhodamine core fluorophores are well-suited because of their high emission efficiency and high target-to-background ratios. In comparison, applications where greater depth of penetration is required, as occurs in submucosal lesions, near-infrared (NIR) probes are generally preferred (*1–5*). Another important consideration in the selection of an optimal fluorophore is the effect that internalization and subsequent entry into the endolysosome, with its harsh acidic microenvironment, has on the fluorescence of molecular probes (*6*).

Rhodamine core optical fluorophores are widely utilized in biomedical research, and among the green fluorescent dyes, Rhodamine Green has been shown to possess the highest emission efficiency and the longest sustained fluorescence even after cellular internalization (*6*). It remains to be determined, however, if unique chemical properties among individual rhodamine core family members affect fluorophore parameters critical to *in vivo* optical imaging. These parameters include preserved fluorescence intensity in low pH environments, similar to that of the endolysosome; efficient fluorescence signal despite possible conformational changes of targeting proteins, as may occur in harsh subcellular environments; persistence of fluorescence after cellular internalization; and sufficient target-to-background ratios of fluorophore-targeted tumors to permit identification of subvisible disease.

In the present study, we conjugated 4 common rhodamine-core based fluorescent dyes to a clinically feasible and quickly internalizing D-galactose receptor targeting reagent, galactosamine serum albumin (GmSA) (*7–9*), and conducted a series of *in vitro* and *in vivo* experiments using a mouse model of metastatic ovarian cancer to determine if differences in optical imaging properties exist among rhodamine fluorophores and if so, which rhodamine core derivative possesses optimal characteristics for *in vivo* imaging.

EXPERIMENTAL PROCEDURES

Selection of Rhodamine Fluorophores. Four fluorophores within the rhodamine fluorophore family, which differed with regard to structure of the amine side chains, were selected for this study: Rhodamine Green (RG; 9-[2-Carboxy-4(or 5)-[[(2,5-

* Correspondence to Hisataka Kobayashi, MD, PhD,Molecular Imaging Program, Center for Cancer for Cancer Research, National Cancer Institute, NIH, Bethesda, Maryland 20892-1088, USA; Phone: 301-435-4086; Fax: 301-402-3191; E-mail: Kobayash@mail.nih.gov.

10.1021/bc800140c This article not subject to U.S. Copyright. Published 2008 by the American Chemical Society
Published on Web 07/09/2008

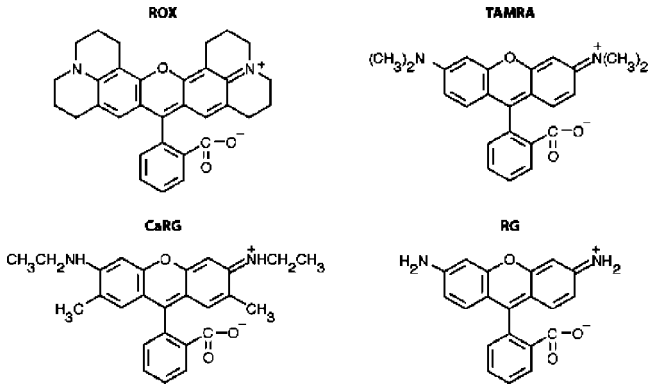

Figure 1. The chemical structures of the four rhodamine core fluorophores compared in this study. Note that all dyes possess a xanthen ring but each is unique in the structure of flanking amine side chains.

dioxo-1-pyrrolidinyl)oxy]carbonyl]phenyl]-3,6-bisamino-xanthylium); Carboxyrhodamine 6G (CaRG; 9-[2-carboxy-4-[[(2,5-dioxo-1-pyrrolidinyl)oxy]carbonyl]phenyl]-3,6-bis(ethylamino)-2,7-dimethyl-xanthylium); Carboxytetramethylrhodamine (TAMRA; 5-[[(2,5-dioxo-1-pyrrolidinyl)oxy]carbonyl]phenyl]-3,6-bis(dimethylamino)-xanthylium); and Carboxy-X-Rhodamine (ROX; 1-[[[2′,3′,6′,7′,12′,13′,16′,17′-octahydro-3-oxospiro[isobenzofuran-1(3*H*),9′-[1*H*,5*H*,9*H*,11*H*,15*H*]xantheno[2,3,4-ij:5,6,7-i′j′]diquinolizin]-5(or 6)-yl]carbonyl]oxy]-2,5-pyrrolidinedione). Each of these 4 dyes—RG, CaRG, TAMRA, and ROX—possessed distinct side chains with primary, secondary, tertiary, or cyclic amines, respectively (Figure 1).

Synthesis of Galactosamine Serum Albumin-Rhodamine Fluorophore Conjugates. Galactosamine serum albumin (GmSA), which has approximately 23 galactosamine residues per bovine serum albumin (BSA), was purchased from Sigma Chemical (St. Louis, MO, USA) and amino-reactive RG, CaRG, TAMRA, and ROX were purchased from Molecular Probes (Eugene, OR, USA). At room temperature, 400 μg of GmSA in 196 μL Na_2HPO_4 was incubated with 4 μL of a 6 mM solution (24 nmol) of each one of 4 amino-reactive rhodamine dyes in dimethyl sulfoxide for 15 min. The mixture was then purified with a Sephadex G-50 Gel Filtration System (PD-10; GE Healthcare, Milwaukee, WI, USA). GmSA-rhodamine conjugate samples were then kept at 4 °C as stock solutions.

Comparison of Fluorescence Intensity at Various pH Values. To compare the fluorescence capability of the 4 fluorophore conjugates, fluorescence intensity and emission spectra were measured in arbitrary units using the Maestro In-Vivo Imaging System (CRi Inc., Woburn, MA, USA). 5 μg of GmSA-RG, GmSA-CaRG, GmSA-TAMRA, and GmSA-ROX were pipetted into a nonfluorescent 96-well plate and diluted in 390 μL of a buffer solution containing appropriate ratios of sodium dihydrogen phosphate and phosphate to obtain pH values of 2.3, 3.3, 5.2, 6.4, or 7.4, and spectral fluorescence imaging was performed. The ratio of RG, CaRG, TAMRA, and ROX was ~3 molecules per albumin molecule. Appropriate band-pass and long pass filter sets (445 to 490 nm/515 nm for RG; 480 to 520 nm/550 nm for CaRG; 503 to 555 nm/580 nm for both TAMRA and ROX) were used for emission and excitation light, respectively. The tunable filter was automatically stepped in 10 nm increments from 500 to 800 nm while the camera captured images at each wavelength interval with constant exposure times. Spectral unmixing algorithms that subtracted any background autoflourescence were applied to create an unmixed image for each of the 4 dye conjugates, permitting accurate evaluation of the fluorescence intensity of each conjugate. A region of interest (ROI) was drawn over the entirety of each well to determine the fluorescence intensity and emission spectra for each of the 4 GmSA-dye conjugates.

Effect of Target Protein Unfolding on Fluorescence Intensity of GmSA-Rhodamine Fluorophore Conjugates. To evaluate the effect of target protein unfolding on the fluorescence characteristics of GmSA-fluorophore conjugates, each of the 4 conjugates was incubated with 5% SDS in PBS for 10 min at room temperature. Experimental controls were established by incubating each conjugate in normal PBS without SDS. The fluorescence signal intensity of each sample and control was measured using both a fluorescence spectrometer (Perkin-Elmer LS55, Perkin-Elmer, Shelton, CT, USA) and the Maestro In-Vivo Imaging System (CRi Inc., Woburn, MA, USA). The excited wavelengths were 505, 524, 555, and 576 nm for GmSA-RG, GmSA-CaRG, GmSA-TAMRA, and GmSA-ROX, respectively. To investigate the effect of target protein unfolding on the energy absorbance of each protein-fluorophore conjugate, the number of fluorophore molecules per GmSA was calculated. The GmSA concentration was determined by Coomassie Plus protein assay kit (Pierce Biotechnology) by measuring the absorption at 595 nm using a UV−vis system (8453 Value UV−vis system, Agilent Technologies, Santa Clara, CA, USA). The fluorophore concentration was then determined by measuring the absorbance at the maximum absorption wavelength of each fluorophore to confirm the number of rhodamine fluorophore molecules conjugated to each GmSA molecule.

Cell Culture. An established ovarian cancer cell line, SHIN3, was used for *in vitro* fluorescence microscopy, flow cytometry, and intraperitoneal ovarian cancer mouse models (*10*). The cell lines were grown in RPMI 1640 medium (Gibco, Gaithersburg, MD) containing 10% fetal bovine serum (FBS) (Gibco, Gaithersburg, MD), 0.03% L-glutamine at 37 °C, 100 units/mL penicillin, and 100 μg/mL streptomycin in 5% CO_2.

Fluorescence Microscopy. SHIN3 cells (1×10^4) were plated on a cover glass bottom culture well and incubated for 16 h, after which either GmSA-RG, GmSA-CaRG, and GmSA-TAMRA or GmSA-ROX was added to the medium (3 μg/mL), and the cells were incubated with conjugates for 0, 6, or 24 h. After the respective incubation period, cells were washed five times with PBS and fluorescence microscopy was performed using an Olympus BX51 microscope (Olympus America Inc., Melville, NY) equipped with excitation filters (470−490 nm) and emission filters (515 nm long pass). Fluorescence microscopy images of cells treated with each conjugate for each incubation period were obtained.

Flow Cytometry. One-color flow cytometry was performed to evaluate the fluorescing capability of GmSA-fluorophore conjugates in SHIN3 cancer cells. SHIN3 cells (1×10^4) were plated on a 12-chamber culture well and incubated for 16 h, after which, GmSA-RG, GmSA-CaRG, GmSA-TAMRA, or GmSA-ROX was added to the medium (30 μg/mL), and the cells were incubated with fluorophore conjugates for 3 h. Cells were washed twice with PBS and incubated in RPMI 1640 medium without fluorophore conjugates for 0, 6, or 24 h. Cells were then washed once with PBS, trypsinized, and flow cytometry was performed at each incubation time point 0, 6, and 24, after transfer to conjugate-free media. The argon ion 488 nm laser was employed for excitation. Signals from cells were collected using a 530/30 nm band-pass filter. Cells were analyzed in a FACScan cytometer (Becton Dickinson, Franklin Lakes, NJ) and all data were analyzed using *CellQuest* software (Becton Dickinson, Franklin Lakes, NJ). The fluorescing capability of each fluorophore conjugate was referred to as the mean fluorescence index (MFI).

Tumor Model. All procedures were carried out in compliance with the Guide for the Care and Use of Laboratory Animal Resources (1996), National Research Council, and approved by

Table 1. Fluorescence Intensity Ratios of GmSA-Rhodamine with and without SDS Treatment

	fluorescence intensity ratio (spectrometer)	fluorescence intensity ratio (multispectral camera)
GmSA-RG	6.9	6.6
GmSA-CaRG	11.3	5.0
GmSA-TAMRA	34.3	18.1
GmSA-ROX	3.3	4.1

the local Animal Care and Use Committee. The intraperitoneal tumor implants were established by intraperitoneal (i.p.) injection of 2×10^6 cells suspended in 200 μL of PBS in female nude mice (National Cancer Institute Animal Production Facility, Frederick, MD). Experiments with tumor-bearing mice were performed at 21 days after injection of the cells.

***In Vivo* Spectral Fluorescence Imaging.** 12.5 μg each of GmSA-RhodG, GmSA-CaRG, GmSA-TAMRA, and GmSA-ROX were diluted in 300 μL PBS and injected into the peritoneal cavities of mice bearing disseminated peritoneal SHIN3 ovarian cancer implants. Three hours after injection of the fluorophore conjugate, each mouse was sacrificed individually with carbon dioxide. Immediately after sacrifice, the abdominal cavity was exposed. Mice were placed on nonfluorescent black plates and whole abdominal multispectral fluorescence images were obtained using the Maestro In-Vivo Imaging System (CRi, Inc., Woburn, MA). A band-pass filter from 445 to 490 nm and a long-pass filter over 515 nm were used for emission and excitation light, respectively. The tunable filter was automatically stepped in 10 nm increments from 500 to 800 nm, while the camera captured images at each wavelength interval with constant exposure time. The spectral fluorescence images consisting of autofluorescence spectra, and the spectra for the specific GmSA-fluorophore conjugate were obtained and then unmixed on the basis of their spectral patterns using commercial software (*Maestro* software, CRi, Inc., Woburn, MA). The experiment was repeated three times ($n = 3$ mice per fluorophore). Spectral fluorescence images were obtained for the purpose of determining the target-to-background ratios of tumor implants versus normal anatomy (see discussion below).

Determination of Target-to-Background Ratios of Tumors Compared to Normal Tissue. Spectral fluorescence images of the whole abdominal cavity were obtained as previously described. Monochromatic images corresponding to the peak emission wavelength for each fluorophore conjugate were then generated from multispectral whole abdominal images using the Maestro In-Vivo Imaging System (CRi Inc., Woburn, MA, USA) software single wavelength channel extraction function. The target-to-background ratios of tumor implants compared to surrounding normal tissue were determined by placing an ROI over tumors and ROIs over the normal tissue of the liver, intestines, and skin. Intestinal tissue without substantial fluorescence due to food was chosen for intestinal ROI placement to establish target-to-background ratios indicative of normal intestinal autofluorescence with minimal fluorescence contribution due to feed, which often varies between research centers and investigative end points. ROI average signal intensity for tumors was then compared to the versus ROI average signal intensity of the liver, intestines, and skin, respectively, were determined for each animal (Table 2). In addition, to approximate tumor-to-background ratios of tumor implants to normal tissue in general, ROI average signal intensity of tumors was compared to a calculated average ROI signal intensity that combined the signal intensity measurements of all normal anatomic features (liver, intestines, and skin combined) for each animal.

Table 2. Signal-to-Backround Ratios of GmSA-Rhodamine Congujate Targeted Tumors versus Surrounding Normal Anatomy[a]

conjugate	tumor vs normal tissue	tumor vs intestines	tumor vs liver	tumor vs skin
GmSA-RG	7.5 (2)	6.4 (1)	10.5 (2)	4.5 (4)
GmSA-CaRG	7.2 (3)	4.9 (3)	10.4 (3)	7.3 (2)
GmSA-TAMRA	11.0 (1)	6.0 (2)	15.1 (1)	9.1 (1)
GmSA-ROX	5.9 (4)	3.8 (4)	7.6 (4)	6.1 (3)

[a] Fluorophore-conjugate rank in each category is shown in parenthesis.

RESULTS AND DISCUSSION

Comparison of Fluorescence Intensity at Various pH Values. After cellular internalization, the GmSA-flourophore probe enters the highly acidic lysosomal vesicle. This isolated low pH environment may affect fluorophore chemical composition and therefore has the potential to alter fluorescence. To evaluate the effect of pH on GmSA-fluorophore probe fluorescence, fluorescence intensity and emission spectra were measured under the same conditions: total dose, concentration of solution, number of fluorophores per GmSA, and exposure time. Excitation/emission filters varied according to which filter set was optimal for each dye. The effect of pH on fluorescence intensity was determined by measuring the fluorescence intensity for each dye at pH values 2.3, 3.3, 5.2, 6.4, and 7.4 (Figure 2). Measurements of the fluorescence intensities at neutral pH (7.4) for the four conjugates, GmSA-RG, GmSA-CaRG, GmSA-TAMRA, and GmSA-ROX, demonstrated that GmSA-CaRG had the highest signal intensity while GmSA-RG had the lowest. All of the conjugates with the exception of GmSA-TAMRA demonstrated a decrease in fluorescence intensity value when comparing values obtained at pH 7.4 to pH 2.3 (Figure 2). At pH 2.3, fluorescence intensity was reduced for all dyes with the exception of GmSA-TAMRA, which demonstrated an increase in fluorescence intensity with decreasing pH (Figure 2). Both GmSA-RG and GmSA-CaRG retained nearly optimal fluorescence at pH values as low as 3.3, after which lowering pH to 2.3 resulted in an approximately 20% reduction in fluorescence intensity (Figure 2). GmSA-ROX retained near optimal fluorescence at pH 7.4 and 6.4 but reduction in pH to 5.2 resulted in decrease in fluorescence intensity. At every pH value tested, GmSA-CaRG demonstrated the highest fluorescence intensity (Figure 2).

These results demonstrate that GmSA-RG, GmSA-CaRG, and GmSA-TAMRA retain fluorescence in low pH environments. Interestingly, only GmSA-TAMRA displayed increasing fluorescence signal with decreasing pH, although none of the conjugates demonstrated substantial changes. The ability of GmSA-RG, GmSA-CaRG, and GmSA-TAMRA to retain fluorescence at low pH suggests that these agents may be preferred for *in vivo* imaging if the molecular probe is internalized within the lysosome.

Effect of Target Protein Unfolding on Fluorescence Intensity of GmSA-Rhodamine Fluorophore Conjugates. The harsh chemical environment of the endolysosomal system may potentially alter the tertiary structure of the targeting protein. To evaluate the effect of structural changes of targeting proteins on the fluorescence properties of GmSA-fluorophore conjugates, fluorescence intensity values were measured for each of the 4 conjugates in a control solution of PBS as well as after treatment with a detergent solution containing SDS, and ratios comparing fluorescence with and without SDS treatment were generated. Treatment with SDS demonstrated higher fluorescence intensity

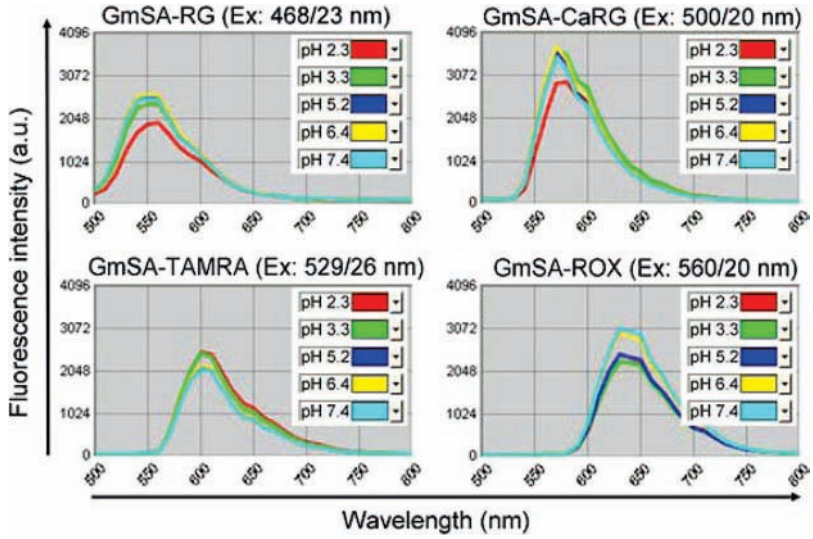

Figure 2. Fluorescence intensity of GmSA-rhodamine conjugates at neutral and acidic pH values. 5 μg of GmSA-RG, GmSA-CaRG, GmSA-TAMRA, or GmSA-ROX was placed in 390 μL PBS (pH 7.4) or in a mixture of sodium dihydrogen phosphate (pH 6.4, 5.2, 3.3, or 2.3) and then placed in a nonfluorescent 96-well plate and emission spectra and fluorescence intensity was measured. The ratio of RG, CaRG, TAMRA, and ROX molecules to GSA was approximately 3 in all cases. All four dyes possessed distinct emission peak spectra. At neutral pH (7.4), GmSA-CaRG had the highest signal intensity, whereas GmSA-RG had the lowest. With the exception of GmSA-TAMRA, all other conjugates demonstrated a decrease in fluorescence intensity value when comparing values obtained at pH 7.4 to the lowest pH value tested, pH 2.3. At pH 2.3, fluorescence intensity was substantially reduced for all GmSA-rhodamine conjugates with the exception of GmSA-TAMRA, which demonstrated an increase in fluorescence intensity with decreasing pH at all values tested.

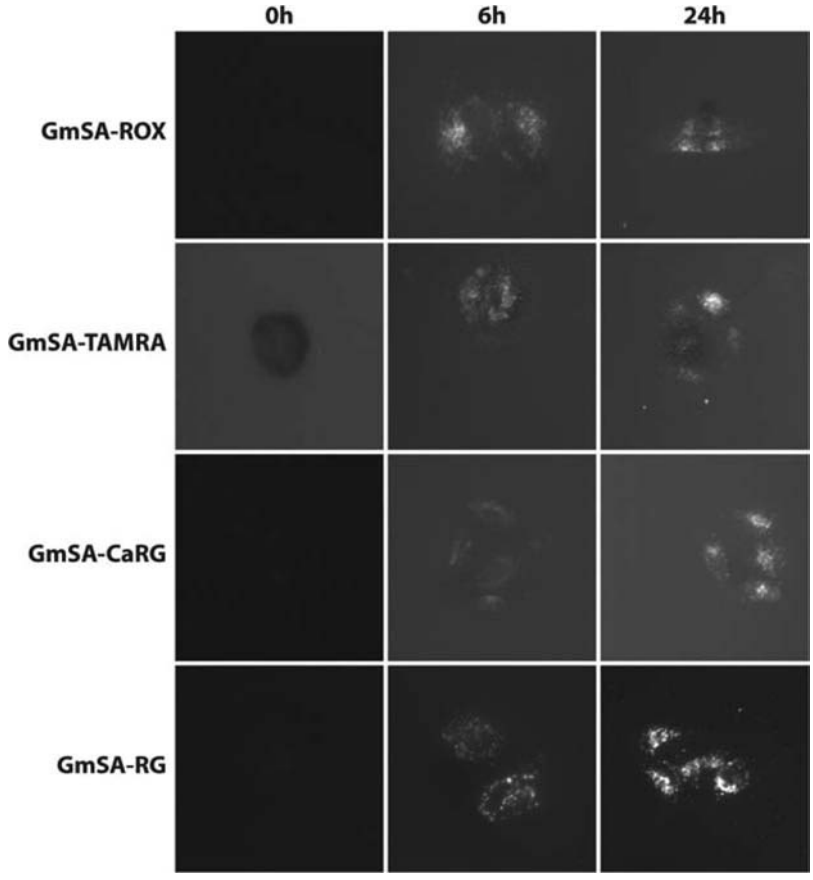

Figure 3. Serial fluorescence microscopy images of SHIN3 ovarian cancer cells treated with 3 μg/mL of GmSA-RG, GmSA-CaRG, GmSA-TAMRA, or GmSA-ROX. SHIN3 cells were incubated with each of the four GmSA-rhodamine fluorophore conjugates for 0, 6, or 24 h and fluorescence microscopy was then performed after washing with PBS. No fluorescence was detected in cells imaged immediately after treatment with GmSA-rhodamine fluorophore conjugates (at the incubation time point of 0 h) suggesting that optical probes had not yet undergone cellular internalization. Intracellular fluorescence was detected for all conjugates at the 6 h and 24 h incubation time points.

in all four GmSA-rhodamine conjugates compared to controls (Table 1). When measured using a fluorescence spectrometer (Perkin-Elmer LS55, Perkin-Elmer, Shelton, CT, USA), ratios for GmSA-RG, GmSA-CaRG, GmSA-TAMRA, and GmSA-ROX with and without SDS treatment were 6.9, 11.3, 34.3, and 3.3, respectively (Table 1). When measured with a multispectral

camera (Maestro In-Vivo Imaging System CRi Inc., Woburn, MA, USA), fluorescence intensity ratios for GmSA-RG, GmSA-CaRG, GmSA-TAMRA, and GmSA-ROX with and without SDS treatment were 6.6, 5.0, 18.1, and 4.1 (Table 1). Unfortunately, due to limitations in excitation filters available for the multispectral camera, excitation wavelengths were closer to optimal for some dyes than for others, and therefore comparison of ratios obtained with the two measurement techniques is not valid.

Although an important characteristic of xanthene ring fluorophores is their ability to undergo a synthesis reaction through the amino-reactive form by adding a succinimidyl ester, ultimately permitting conjugation with virtually any protein or peptide via the branched amine-residues on the lysine or the N-terminal anime, when the amino-reactive forms of fluorescence dyes are conjugated with proteins or peptides, it is well-known that the emission efficacy (extinction coefficient) of fluorophores is generally decreased depending on the distinct couplings of fluorescence dyes and proteins. However, our data suggest that fluorescence intensity losses due to conjugation may be minimized by exposure of conjugates to lysosomal microenvironments (*6*).

After cellular internalization, probes encounter isolated chemical environments that may alter targeting protein conformation and possibly protein−fluorophore interactions. We attempted to simulate these changes with SDS treatment. Interestingly, we have found that fluorophore-conjugated proteins can emit more light than the original conjugates after either treatment with SDS, or after lysosomal catabolism, as previously demonstrated (*6*). Among the 4 conjugates tested here, GmSA-TAMRA showed the largest increase in fluorescence after SDS-induced protein unfolding (Table 1). This feature is important for imaging applications as it enables target cells to have "activatable" potential, allowing successfully targeted probes to emit more light than the unbound agent. We have previously reported several conjugates, NuAv-BODIPY-FL and Avidin/GSA-ROX, which demonstrate such activatable characteristics and are capable of highly specific tumor targeted imaging (*9, 11*). Although we have observed this to be a general property of the rhodamine family of dyes, the data presented here suggest that the rhodamine family of dyes possess an inherent activatable characteristic. This "rhodamine effect" is most notably demonstrated by TAMRA.

Activation strategies are often independent and may have an additive effect when combined. Therefore, utilization of the rhodamine fluorescence characteristic in conjunction with other activation approaches, such as photon electron transfer, may aid in the development of fully activatable probes that exhibit fluorescence only after cellular internalization (*12*). Such probes represent an important goal in optical probe development as fluorescence due to nonspecific binding would be substantially reduced, providing maximum contrast of targeted tumors.

Intracellular Fluorescence Evaluation. To confirm fluorescence retention after cellular internalization, SHIN3 cells were incubated with each of the 4 fluorophore conjugates for 0, 6, or 24 h, and then imaged using fluorescence microscopy (Figure 3). Fluorescence microscopy revealed that all four GmSA-rhodamine conjugates demonstrated fluorescence after cellular internalization and that longer incubation resulted in increased brightness, likely due to increased intracellular accumulation of the respective fluorophore conjugate (Figure 3). However, the excitation filters were not optimized equally for all four conjugates. For instance, the excitation of ROX was not optimized in comparison to the other three conjugates.

Flow Cytometry. Not only do targeting probes need to remain fluorescent immediately after cellular internalization, but probes must also retain fluorescence for prolonged periods to be used clinically. To evaluate fluorescence longevity, one-color flow cytometry was performed using fluorophore conjugates in SHIN3 cancer cells. SHIN3 cells (1×10^4) were plated on a 12-chamber culture well and incubated for 16 h. GmSA-RG, GmSA-CaRG, GmSA-TAMRA, or GmSA-ROX was added to the medium (3 μg/mL), and the cells were incubated for 3 h to ensure dye internalization and then rinsed and placed in conjugate-free media. Flow cytometry was performed at 0, 6, and 24 h after transfer to conjugate-free media. Flow cytometry data for GmSA-RG, GmSA-CaRG, GmSA-TAMRA, and GmSA-ROX confirmed the presence of the 4 fluorophore conjugate treated cell populations (Figure 4, upper) and revealed that over time, the mean fluorescence index (MFI) decreased for each dye by 41.7%, 40.3%, 23.1%, and 5.0%, respectively, at 24 h. The rate of reduction in MFI was comparable for GmSA-RG and GmSA-CaRG (Figure 4, lower). Although the green excitation laser excited ROX less efficiently than the other 3 fluorophores, which may result in a slight underestimation of relative decrease of fluorescence intensity, GmSA-ROX dem-

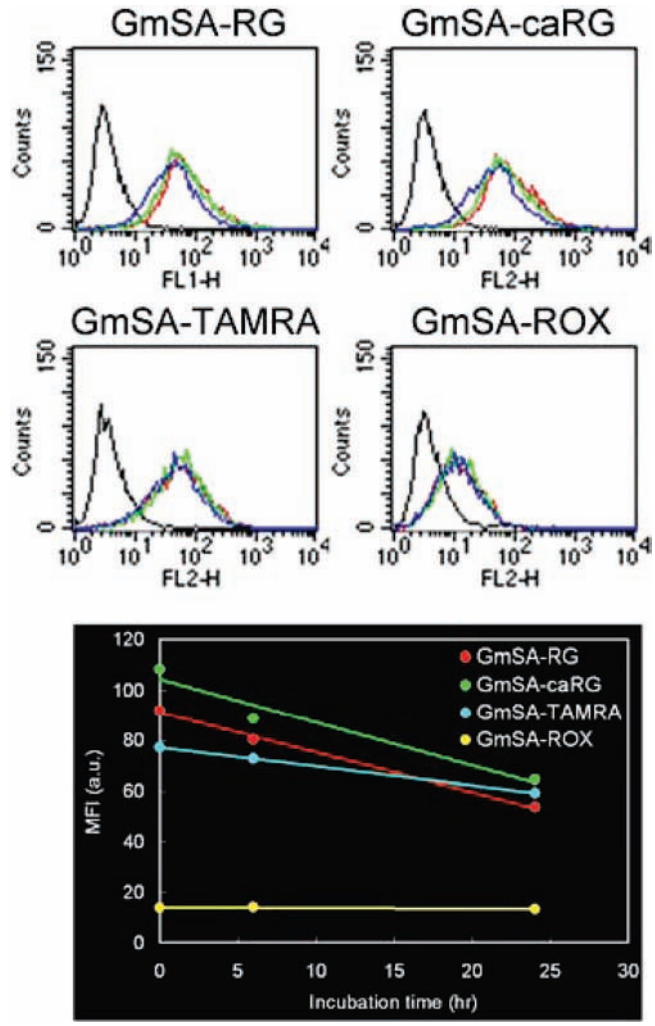

Figure 4. Change in fluorescence intensity over time. SHIN3 cancer cells treated with 30 μg/mL of GmSA-RG, GmSA-CaRG, GmSA-TAMRA, or GmSA-ROX for 3 h then rinsed and placed in dye-free media. One-color flow cytometry was performed after 0, 6, or 24 h incubation in dye-free media. (Upper) One-color flow data confirmed the presence of the 4 GmSA-rhodmamine conjugate treated cell populations. (Lower) Graphical depiction of flow data for GmSA-RG, GmSA-CaRG, GmSA-TAMRA, and GmSA-ROX. The rate of reduction in mean fluorescence index (MFI) was comparable for GmSA-RG and GmSA-CaRG, while GmSA-ROX demonstrated the lowest reduction in MFI over the 24 h time period and GmSA-TAMRA demonstrated the second lowest decrease in MFI over 24 h.

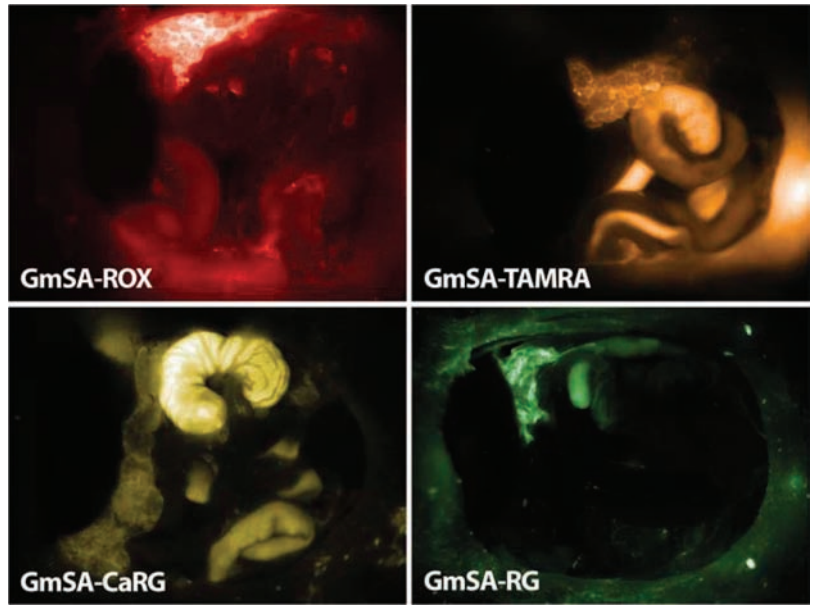

Figure 5. Representative monochromatic whole abdominal images of four mice with intraperitoneally disseminated SHIN3 ovarian cancer obtained 3 h after intraperitoneal injection of 12.5 μg of GmSA-RG, GmSA-CaRG, GmSA-TAMRA, or GmSA-ROX. Image wavelength corresponded to the peak emission-spectra wavelength for each GmSA-rhodamine conjugate. These images demonstrate that rhodamine optical probes effectively target SHIN3 cell tumors and result in tumor enhancement over background normal tissue. Images are depicted in the monochromatic color that corresponds to the fluorescence of each probe for presentation value only. Gray-scale monochromatic images similar to those shown here were used to calculate signal-to-background ratios of rhodamine fluorophore-targeted tumors.

Table 3. Summary of Fluorophore Performance in Parameters Critical to *in Vivo* Optical Imaging

in vivo imaging criteria	fluorophore performance	impact on images
fluorescence intensity at low ph	CarRhodG> TAMRA > RhodG > ROX	minor
fluorescence intensity after targeting protein unfolding	TAMRA > CarRhodG or RhodG > ROX	major
fluorescence-persistence after cellular internalization	ROX > TAMRA > CarRhodG > RhodG	minor
target-to-background ratio	TAMRA > RhodG > CarRhodG > ROX	moderate

onstrated the lowest reduction in MFI over the 24 h time period and GmSA-TAMRA demonstrated the second lowest decrease in MFI over 24 h (Figure 4).

Many *in vivo* applications of optical imaging agents involve administration of the targeted fluorophores before surgical or endoscopic procedures. It is therefore necessary for targeted imaging probes to have prolonged fluorescence half-lives to permit the completion of endoscopic or surgical procedures. Fluorescence longevity, which would derive from chemical, biological, and photophysical properties of a dye, is an important parameter to consider in probe selection. Unlike radionuclide counterparts, optical probes are prone to chemical degradation that cannot be "decay adjusted." Among the four conjugates, GmSA-ROX and GmSA-TAMRA demonstrated the lowest decrease in MFI 24 h after probe administration and therefore had the most persistent fluorescence. However, when considering multimodality and/or multiple color imaging (*13*), optical probes may not be the time-determining agent in the cocktail and therefore fluorescence longevity becomes an increasingly important parameter.

Target-to-Background Ratio of Fluorophore Targeted Tumors versus Normal Tissue. Ultimately, the goal of *in vivo* optical imaging, as applied to the detection of cancer, is to enable effective identification and removal of targeted tissues. This requires targeting probes that are easily recognized among a complex anatomic background, which often possess autofluorescent properties. To evaluate which GmSA-rhodamine probe offered the highest fluorescence signal over normal surrounding anatomic features, each of the 4 GmSA-fluorophore conjugates was injected into the peritoneal cavities of mice with disseminated peritoneal SHIN3 ovarian cancer implants ($n = 3$ for each fluorophore conjugate) and multispectral fluorescence images of the whole abdominal cavity were obtained 3 h later. Monochromatic images corresponding to the wavelength of the emission spectra peak for each fluorophore conjugate (Figure 5) were created from whole abdominal multispectral images and signal-to-background ratios of targeted tumors were determined by placing an ROI over tumors and ROIs over the surrounding normal tissues (skin, intestines, and liver) and a ratio of ROI average signal intensity value of targeted tumors versus selected anatomic features was generated. The average signal-to-background ratios of tumors targeted with GmSA-RG, GmSA-CaRG, GmSA-TAMRA, or GmSA-ROX to normal tissue was 7.5, 7.2, 11.0, and 5.9, respectively (Table 2). Thus, GmSA-TAMRA demonstrated the highest target-to-background ratio, while GmSA-ROX demonstrated the lowest ratio. In addition, when comparing target-to-background values, GmSA-TAMRA demonstrated the highest signal-to-background ratio in each case with the exception of the intestines, in which GmSA-RG was slightly better (Table 2).

The clinical application of optical imaging to surgical and endoscopic procedures requires optical probes that permit *in vivo* identification of targeted tissues. Optimal visualization of optical probes *in vivo* relies upon both probe fluorescence intensity and the level of contrast of tumor targeted fluorophores compared to the naturally occurring autofluorescence of skin and visceral organs. GmSA-TAMRA and GmSA-RG demonstrated the highest signal-to-background ratios, implying that these probes may permit the best visualization of targeted tissues *in vivo*.

Optical imaging represents a powerful technology for cancer research. Currently, *in vivo* imaging applications include: (1) the study of cancer biology *in vivo* through expression and imaging of endogenously expressed fluores-

cent proteins and (2) the development of clinical approaches for the treatment of cancer with disease-specific fluorescent probes. Early studies involving imaging of fluorescent proteins revealed the power of optical imaging in cancer biology, such as for the repeated imaging of cancer invasion and metastasis in longitudinal studies (*14–16*). One limitation to the use of fluorescence proteins for cell labeling in humans is that this process necessitates gene transfection, which is typically achieved in animal models with use of viral infection. Small fluorescent molecules such as organic fluorophores, however, may be used similarly to conventional contrast agents and are therefore more well-suited for development of optical probes for clinical applications as they do not require manipulation of the host genome. Additionally, fluorophores are small and easily conjugated to targeting proteins such as antibodies.

Rhodamine core-based fluorophores are characterized by a xanthene ring core with flanking amine residues (Figure 1). However, the structure of the amine side chains varies among core constructs (Figure 1), which results in distinct energy differences between basic and excited states and the characteristic fluorescence emission wavelengths of each dye. It is possible that variation in amine residues affects fluorescence properties of rhodamine-targeting protein conjugates *in vitro* and *in vivo*. In this study, we chose 4 well-known rhodamine fluorescent dyes with xanthene ring cores and distinct flanking amine residues: RG with primary amines, CaRG with secondary amines, and TAMRA and ROX with tertiary amines (Figure 1). In addition, variation exists within the chemical structure of the tertiary amine-containing rhodamine dyes as ROX possesses cyclic tertiary amines while TAMRA possess dimethyl amines (Figure 1). These structural differences likely affect fluorescence behavior *in vitro* and *in vivo*. For example, the bis-primary amine of RG may permit effective hydrogen bonding and the stereochemistry enables increased accessibility of the electron pair, likely enhancing basicity compared to secondary or tertiary amines. Differences in emission wavelength due to distinct side chains also affect the signal-to-background ratios of targeted tissue for *in vivo* imaging.

It is well-known that rhodamine core derived fluorophores offer a combination of desirable properties for optical imaging, including good photostability, high extinction coefficient, and high fluorescence quantum yield. Herein, we demonstrated that the rhodamine-fluorophores, CaRG and TAMRA, may represent superior probes for *in vivo* optical imaging applications (Table 3). Advantages to the use of CaRG include high fluorescence intensity at low pH and increased fluorescence intensity of fluorophore-targeting protein constructs in low pH environments. Advantages of TAMRA include superior fluorescence in low pH, persistent fluorescence after internalization and, importantly, superior *in vivo* signal-to-background ratios compared to other rhodamine core fluorophores. In addition, the data presented here suggest that rhodamine dyes possess an inherent activatable characteristic that is most markedly demonstrated by the TAMRA fluorophore. This is an important finding as creation of activatable probes would be of significant development for *in vivo* optical imaging.

Optical imaging represents an important technological advance that has the potential to improve the efficacy of surgical and endoscopic approaches to cancer treatment (*17, 18*). The physical accessibility of tumor implants has been shown to be an important criterion for optical probe selection. However, an equally important consideration is the effect of *in vivo* specific conditions on optical probe function. It was previously shown that RG possesses the highest emission efficiency after cellular internalization (*6*). With this in mind, we evaluated rhodamine core fluorophores with the following parameters critical to the *in vivo* application of optical imaging probes: probe function at low pH and protein-denaturing chemical environments, fluorescence persistence after internalization, and ultimately target-to-background ratios of fluorophore-targeted tissues. Using *in vivo* assays directly and *in vitro* assays aimed to simulate living cell conditions we demonstrated that members of the rhodamine core fluorophore family differ with regard to *in vivo* imaging functionality.

CONCLUSION

The rhodamine-core fluorophores represent a widely used group of fluorescent dyes for *in vivo* optical imaging. However, despite their ubiquitous use, a direct comparison of the performance of the rhodamine probes was previously lacking. Herein, we presented a comparison of 4 rhodamine-core fluorophores and determined that the TAMRA fluorophore represents a superior probe for *in vivo* optical imaging applications. Advantages to use of TAMRA include superior fluorescence in low pH and protein-denaturing environments, preserved fluorescence longevity postcellular internalization, and importantly, superior *in vivo* signal-to-background ratios compared to other rhodamine core fluorophores.

ACKNOWLEDGMENT

This research was supported by the Intramural Research Program of the NIH, National Cancer Institute, Center for Cancer Research.

Supporting Information Available: Additional figures. This material is available free of charge via the Internet at http://pubs.acs.org.

LITERATURE CITED

(1) Ntziachristos, V., Ripoll, J., and Weissleder, R. (2002) Would near-infrared fluorescence signals propagate through large human organs for clinical studies? Errata. *Opt. Lett. 27*, 1652.

(2) Frangioni, J. V. (2003) In vivo near-infrared fluorescence imaging. *Curr. Opin. Chem. Biol. 7*, 626–34.

(3) Ntziachristos, V., Bremer, C., and Weissleder, R. (2003) Fluorescence imaging with near-infrared light: new technological advances that enable in vivo molecular imaging. *Eur. Radiol. 13*, 195–208.

(4) Kiyose, K., Kojima, H., and Nagano, T. (2008) Functional near-infrared fluorescent probes. *Chem. Asian J. 3*, 506–15.

(5) Jin, Z. H., Josserand, V., Razkin, J., Garanger, E., Boturyn, D., Favrot, M. C., Dumy, P., and Coll, J. L. (2006) Noninvasive optical imaging of ovarian metastases using Cy5-labeled RAFT-c(-RGDfK-)4. *Mol. Imaging 5*, 188–97.

(6) Hama, Y., Urano, Y., Koyama, Y., Bernardo, M., Choyke, P. L., and Kobayashi, H. (2006) A comparison of the emission efficiency of four common green fluorescence dyes after internalization into cancer cells. *Bioconjugate Chem. 17*, 1426–31.

(7) Hama, Y., Urano, Y., Koyama, Y., Choyke, P. L., and Kobayashi, H. (2007) D-Galactose receptor-targeted in vivo spectral fluorescence imaging of peritoneal metastasis using galactosamin-conjugated serum albumin-rhodamine green. *J. Biomed. Opt. 12*, 051501.

(8) Hama, Y., Urano, Y., Koyama, Y., Gunn, A. J., Choyke, P. L., and Kobayashi, H. (2007) A self-quenched galactosamine-serum albumin-rhodamineX conjugate: a "smart" fluorescent molecular imaging probe synthesized with clinically applicable material for detecting peritoneal ovarian cancer metastases. *Clin. Cancer Res. 13*, 6335–43.

(9) Gunn, A. J., Hama, Y., Koyama, Y., Kohn, E. C., Choyke, P. L., and Kobayashi, H. (2007) Targeted optical fluorescence imaging of human ovarian adenocarcinoma using a galactosyl serum albumin-conjugated fluorophore. *Cancer Sci. 98*, 1727–33.

(10) Imai, S., Kiyozuka, Y., Maeda, H., Noda, T., and Hosick, H. L. (1990) Establishment and characterization of a human ovarian serous cystadenocarcinoma cell line that produces the tumor markers CA-125 and tissue polypeptide antigen. *Oncology 47*, 177–84.

(11) Hama, Y., Urano, Y., Koyama, Y., Choyke, P. L., and Kobayashi, H. (2007) Activatable fluorescent molecular imaging of peritoneal metastases following pretargeting with a biotinylated monoclonal antibody. *Cancer Res. 67*, 3809–17.

(12) Urano, Y., Kamiya, M., Kanda, K., Ueno, T., Hirose, K., and Nagano, T. (2005) Evolution of fluorescein as a platform for finely tunable fluorescence probes. *J. Am. Chem. Soc. 127*, 4888–94.

(13) Hoffman, R. M. (2005) The multiple uses of fluorescent proteins to visualize cancer in vivo. *Nat. Rev. Cancer 5*, 796–806.

(14) Hoffman, R. M. (2008) Imaging in mice with fluorescent proteins: from macro to subcellular. *Sensors 8*, 1157–73.

(15) Chishima, T., Miyagi, Y., Wang, X., Yamaoka, H., Shimada, H., Moossa, A. R., and Hoffman, R. M. (1997) Cancer invasion and micrometastasis visualized in live tissue by green fluorescent protein expression. *Cancer Res. 57*, 2042–7.

(16) Hoffman, R. M. (2008) A better fluorescent protein for whole-body imaging. *Trends Biotechnol. 26*, 1–4.

(17) Grimm, J., Kirsch, D. G., Windsor, S. D., Kim, C. F., Santiago, P. M., Ntziachristos, V., Jacks, T., and Weissleder, R. (2005) Use of gene expression profiling to direct in vivo molecular imaging of lung cancer. *Proc. Natl. Acad. Sci. U.S.A. 102*, 14404–9.

(18) Bremer, C., Ntziachristos, V., Weitkamp, B., Theilmeier, G., Heindel, W., and Weissleder, R. (2005) Optical imaging of spontaneous breast tumors using protease sensing 'smart' optical probes. *Invest. Radiol. 40*, 321–7.

BC800140C

Supplemental Figures

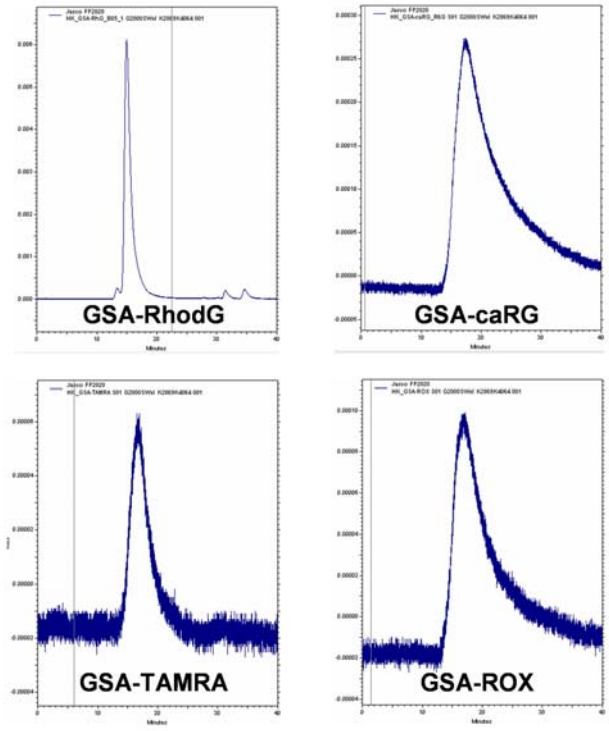

Supplemental Figure 1. High Performance Liquid Chromatography (HPLC). HPLC was conducted to verify that each dye was conjugated to galactosamine serum albumin (GmSA). It is notable that all conjugates showed slightly different retention profiles. This is most likely due to changes of hydrophobicity and/or adherence to the column. This data verifies that all dyes (> 97%) were associated with macromolecule (GmSA) and small molecules with fluorescence are minimal after gel-filtration with PBS.

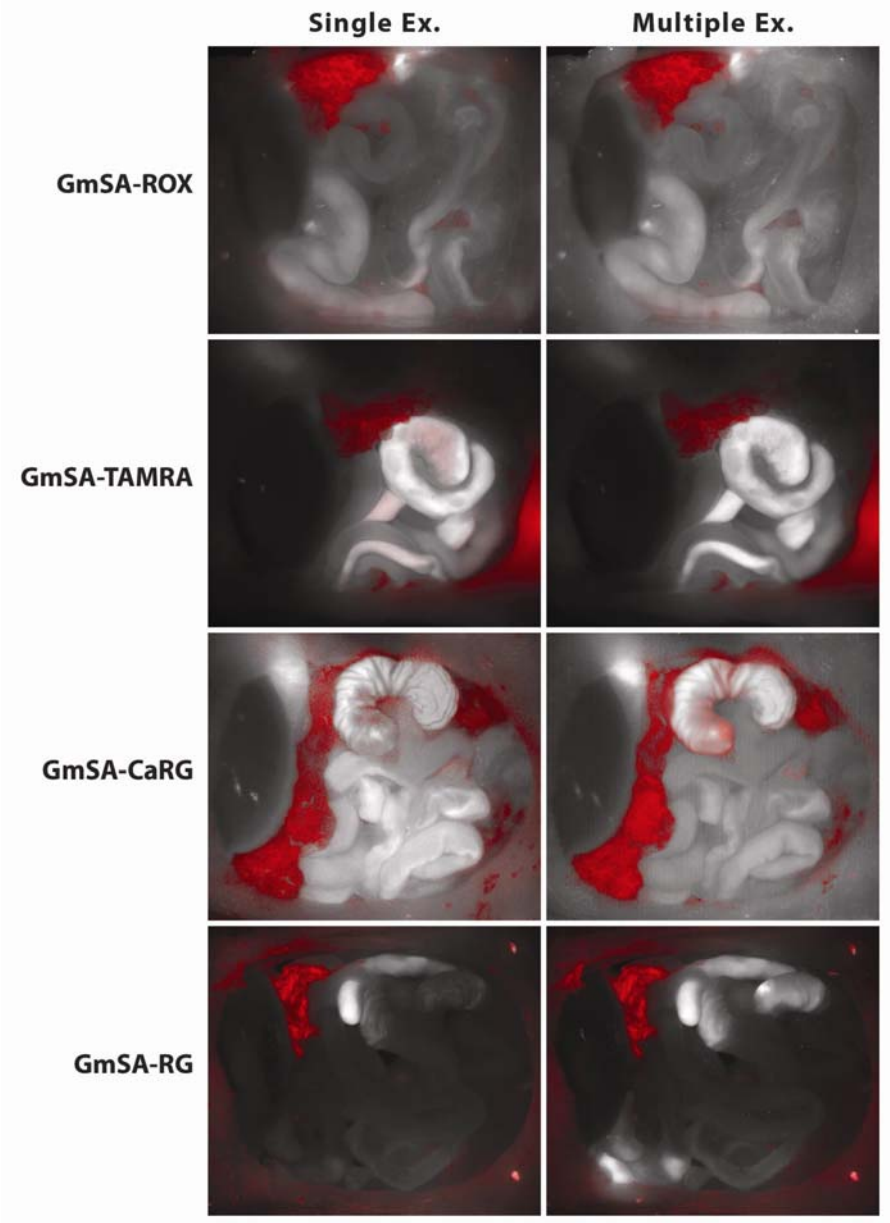

Supplemental Figure 2. Unmixed whole abdominal images of GmSA-rhodamine targeted tumor implants. Spectral fluorescence imaged of the whole abdominal cavity as well obtained. Using spectral unmixed algorithm, the fluorescence of tumors were clearly distinguished from autofluorescence of the intestines and other organs. Unmixed images of the peritoneal cavities demonstrated that GmSA-RG, GmSA-CaRG, GmSA-TAMRA, and GmSA-ROX depicted the tumor foci.

SEPTEMBER 2008
Volume 19, Number 9

© *Copyright 2008 by the American Chemical Society*

Bioconjugate Chemistry

COMMUNICATIONS

Dark Quenched Matrix Metalloproteinase Fluorogenic Probe for Imaging Osteoarthritis Development *in Vivo*

Seulki Lee,[†,§] Kyeongsoon Park,[†,§] Seung-Young Lee,[†] Ju Hee Ryu,[†] Jong Woong Park,[‡] Hyung Jun Ahn,[†] Ick Chan Kwon,[†] In-Chan Youn,[†] Kwangmeyung Kim,[†,*] and Kuiwon Choi[†,*]

Biomedical Research Center, Korea Institute of Science and Technology, Seongbuk-Gu, Seoul, South Korea, Department of Orthopaedic Surgery, College of Medicine, Korea University, Danwon-Gu, Ansan, Gyeonggi, South Korea.
Received June 30, 2008; Revised Manuscript Received July 24, 2008

The early detection of osteoarthritis (OA) is currently a key challenge in the field of rheumatology. Biochemical studies of OA have indicated that matrix metalloproteinase-13 (MMP-13) plays a central role in cartilage degradation. In this study, we describe the potential use of a dark-quenched fluorogenic MMP-13 probe to image MMP-13 in both *in vitro* and rat models. The imaging technique involved using a MMP-13 peptide substrate, near-infrared (NIR) dye, and a NIR dark quencher. The results from this study demonstrate that the use of a dark-quenched fluorogenic probe allows for the visual detection of MMP-13 *in vitro* and in OA-induced rat models. In particular, by targeting this OA biomarker, the symptoms of the early and late stages of OA can be readily monitored, imaged, and analyzed in a rapid and efficient fashion. We anticipate that this simple and highly efficient fluorogenic probe will assist in the clinical management of patients with OA, not only for early diagnosis but also to assess individual patient responses to new drug treatments.

Degenerative joint diseases including osteoarthritis (OA) are common, particularly in the elderly. General awareness of OA is low because this condition is typically considered to be an effect of aging. The initial stages of OA are clinically silent. Therefore, people may have the disease for years with no symptoms, and when symptoms do occur, the disease has often already reached an advanced stage. However, if it was possible to monitor and assess the disease states of OA, treatment could begin before significant damage occurs. For these reasons, early detection of OA is a key challenge in the field of rheumatology. The challenges posed in identifying OA are the detection of both early and subtle changes of joint and articular cartilage. Early signs of OA are characterized by the progressive loss of proteoglycan aggrecan, which is reflected by excessive damage to type II collagen. A decrease in proteoglycan aggrecan ultimately results in the loss of articular cartilage (*1*). X-rays and computed tomography (CT) can show large changes in a joint based on bone density; however, these techniques do not reveal detailed surface information (*2*). Although magnetic resonance imaging (MRI) (*3*) and ultrasound (US) (*4*) techniques recently provided both surface and internal details of articular

[†] Biomedical Research Center, Korea Institute of Science and Technology, Seongbuk-Gu, Seoul, South Korea.
[‡] Department of Orthopaedic Surgery, College of Medicine, Korea University, Danwon-Gu, Ansan, Gyeonggi, South Korea.
[§] These authors contributed equally to this work.
* To whom correspondence should be addressed. Korea Institute of Science and Technology, 39-1 Hawolgok-dong, Seongbuk-gu, Seoul 136-791, Korea. Tel: +82-2-958-5912. Fax: +82-2-958-5909. E-mail: kim@kist.re.kr and choi@kist.re.kr.

10.1021/bc800264z CCC: $40.75 © 2008 American Chemical Society
Published on Web 08/26/2008

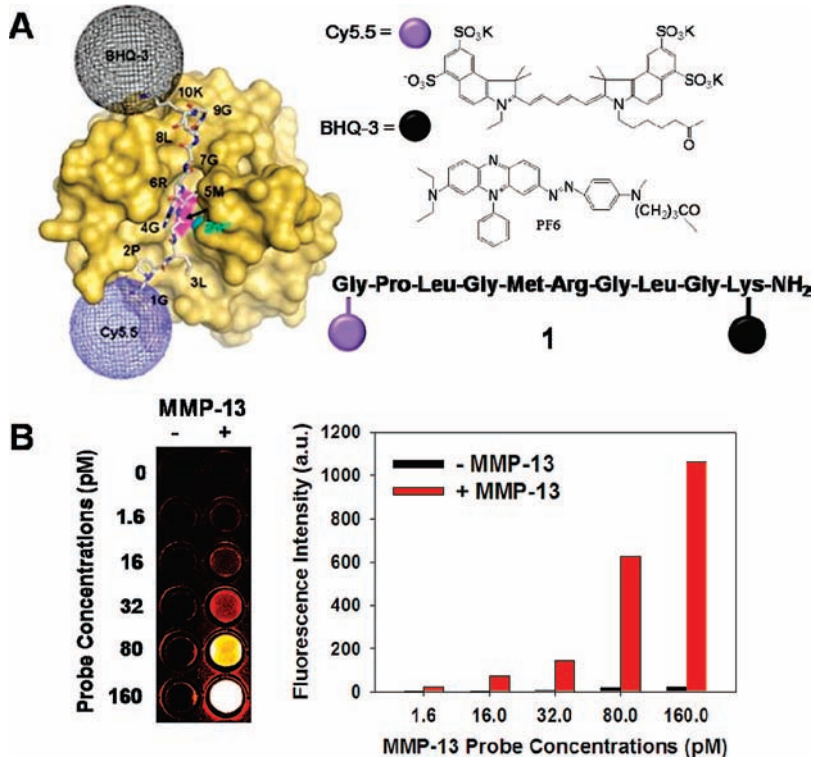

Figure 1. (A) Structure-based probe design. The molecular surface of hMMP-13 and the modeled binding pockets of the MMP-13 imaging probe **1**. Arrow and italics indicate the cleavage site. (B) Quenching properties and recovery of NIR fluorescence intensities in various concentrations of **1** with or without the addition of activated MMP-13. Left, fluorescence imaging sections of 96-well microplate; right, recovery of fluorescence emission intensity (695 nm).

cartilage, the limited resolution of these techniques prevent them from being able to detect small differences in the early stages of OA.

Recent progress in fluorescence-based optical imaging is paving the way for the development of novel methods in many biomedical areas, ranging from the detection of pathologies to biomolecular targets, i.e., biomarkers (*5, 6*). Biomarkers are molecules that reflect a specific pathological process or a response to therapeutic intervention. Biochemical studies in OA have indicated that there are various kinds of accessible biomarkers in OA, including matrix metalloproteinase (MMP), hyaluronic acid, osteocalcin, etc. (*7*). Therefore, the development of new technologies for the rapid, sensitive, and accurate optical imaging of specific biomarkers in OA would provide a method to diagnose OA early on and to assess the severity of the disease. One of the fundamental pathways in cartilage degradation is the up-regulation of expression of the MMP genes. Several lines of evidence have suggested that matrix metalloproteinase-13 (called MMP-13 or collagenase 3) promotes degradation of the cartilage extracellular matrix (*8, 9*). It was reported that MMP-13 expression occurred at very low levels in normal cartilage but was particularly upregulated in degenerating cartilage (*7*). The presence of excess MMP-13 in OA offers the possibility for successful MMP-13 targeted OA imaging and also for detecting MMP-13 inhibition (*10*) for OA treatment.

Conventional fluorogenic peptide kits for MMPs are available; however, they have had limited use *in vitro*. We have previously reported on the use of target biomolecules that are activated by fluorescence probes based on a FRET mechanism and the self-quenching properties of NIRF. However, these targets provided insufficient resolution for *in vitro* imaging (*11*−*13*). The limited resolution in this study was mainly attributed to a low signal-to-noise (S/N) ratio. Therefore, high quenching efficiency and specific recognition properties by target biomolecules that have improved S/N ratio are essential for the development of sensitive *in vitro* biomolecular probes. In this study, we describe the potential use of MMP-13 activatable near-infrared fluorescence (NIRF) dark-quenched fluorogenic probe for early OA diagnosis *in vitro* and in MMP-13 inhibitor screening.

On the basis of the known MMP-13 substrate, PLGMRG (*14*), we first designed different probes using a combination of the linker peptide and two bulky chemicals, Cy5.5 and the black hole quencher-3 (BHQ-3) (*15*). By modeling the X-ray crystal structure of hMMP-13, **1** was synthesized using standard solid-phase Fmoc peptide chemistry as an MMP-13 imaging probe (see Supporting Information, Figures 1S and 2S). As shown in Figure 1A, **1** is composed of (i) Cy5.5, which was used as the near-infrared (NIR) dye (ex/em; 675/695) and is adequate for *in vitro* imaging since it emits fluorescence above 650 nm where autofluorescence is minimal, (ii) a short peptide sequence, G*PLGMRG*LGK, which was used as the MMP-13 cleavable substrate (the recognition site indicated by italics with the cleavage site between G and L; see SI for details), and (iii) (BHQ-3), which was used as the NIR dark-quencher specific for Cy5.5 (abs. 650 nm). As a control, a probe containing a noncleavable linker **2**, which was composed of the scramble peptide sequence GRMGLPLGK was also prepared. There are two basic concepts of fluorogenic peptides when used for NIR imaging, which depends on the type of quencher used. In one case, the fluorescent pairs are composed of the dye-based donor and acceptor (fluorescence dye−dye quenching system), and in the second case, the acceptor is chemically different from the dye and does not fluoresce. Dark-quenched fluorogenic peptides have distinct advantages over conventional dye−dye quenched peptides. BHQ-3 is a dark quencher that has no native fluorescence and has maximal absorption in the 620 to 730 nm range, which can efficiently quenching fluorophores that emit in this range, i.e., Cy5.5. Therefore, Cy5.5 is spectrally matched with a BHQ-3, and FRET quenching can be maximized. The quenching properties of the probe were analyzed and visualized

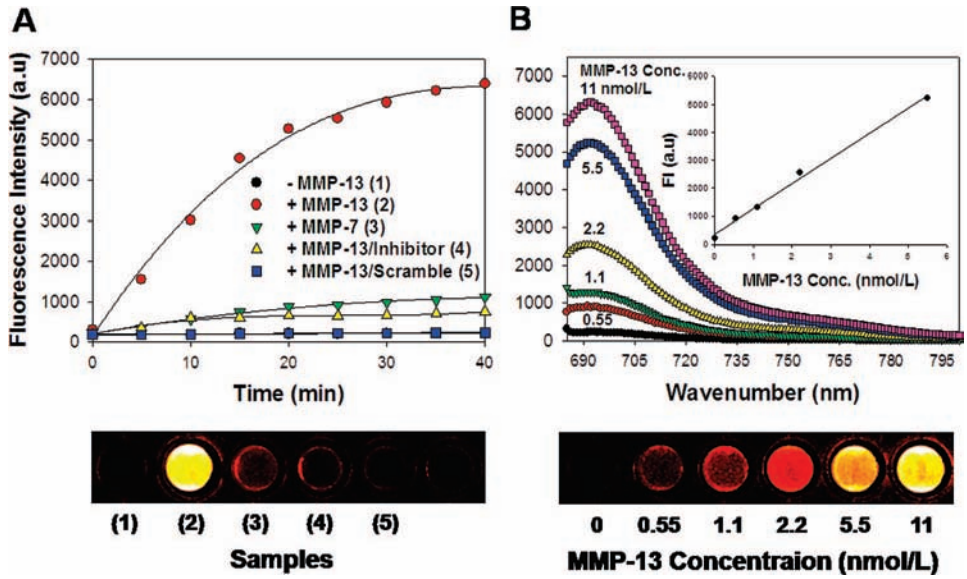

Figure 2. MMP-13 specificity of **1** in solution. (A) Fluorescence emission kinetic spectra of **1** (80 pM) in the presence of various stimuli (MMP-13 and MMP-7, 11 nmol/L; MMP-13 inhibitor) after a 40 min incubation at 37 °C. Below, fluorescence image sections of the 96-well microplate containing different combinations. (B) Fluorescence emission spectra of **1** in the presence of various concentrations of MMP-13 after a 40 min incubation at 37 °C; inset, MMP-13 standard curve; below, corresponding fluorescence image sections of a 96-well microplate.

using a spectrofluorometer with a fixed excitation wavelength of 675 nm and a Kodak Image Station 4000MM equipped with filter for Cy5.5. As shown in Figure 1B, increased concentrations of **1** in the 96-wells microplate did not affect the background NIR fluorescence signal. To determine the effect of activated MMP-13 on the NIR fluorescent signal, 11 nmol/L MMP-13 was activated by incubation with 2.5 mmol/L of *p*-aminophenyl mercuric acid in the reaction buffer (100 mM of Tris, 5 mM of calcium chloride, 200 mM of NaCl, and 0.1% of Brij) for 1 h at 37 °C. MMP-13 treatment resulted in an increased recovery of the NIR fluorescence signal, which depended on probe concentration (approximately 9, 22, 26, 37, 48-fold for 1.6, 16, 32, 80, 160 pM of the probe vs without MMP-13). The use of cleavable, dark-quenched NIR fluorescent probes resulted in significantly lower fluorescent backgrounds, which were amplified by the addition of MMP-13, thereby resulting in a highly sensitive visual detection method.

The selectivity of the MMP-13 probe was examined *in vitro* by incubating **1** (80 pM) in a cuvette containing the reaction buffer and 11 nmol/L activated MMP-13, MMP-7, MMP-13 with the MMP-13 inhibitor (pyrimidine-4,6-dicarboxylic acid, bis-(4-fluoro-3-methyl-benzylamide)) (*16*), or MMP-13 with **1**. After incubation in the reaction buffer at 37 °C for 40 min with the respective enzymes and inhibitor, the NIR fluorescence emission signals of the samples were measured using a spectrofluorometer. Simultaneously, each sample was moved into a 96-well microplate and imaged using a Kodak Image Station 4000MM. As shown in Figure 2A, the kinetics of the enzyme was evaluated and visualized through fluorescence images. The spectrofluometry plots clearly demonstrate that significant recovery of the NIR fluorescent signals only occurred in the samples containing MMP-13 (approximately 32-fold over that without MMP-13). The fluorescent signal recovery of **1** was inhibited in the presence of the MMP-13 inhibitor, thus providing clear evidence for the selectivity of **1**. Measurements were then performed under the same experimental conditions at different concentrations of activated MMP-13 (0, 0.55, 1.1, 2.2, 5.5, and 11 nmol/L; Figure 2B) in the presence of a fixed concentration of **1** (80 pM). In these experiments, there was a linear relationship between the recovered NIR fluorescent signals and MMP-13 concentrations up to 5.5 nmol/L ($r^2 = 0.995$) when **1** was used. This was further confirmed by the fluorescence images. Taken together, these results indicate that **1** could be used for quantitative and visual analysis of MMP-13 activity.

After the systematic validation of the utility of **1**, *in vitro*, its use *in vivo* was demonstrated using *in vivo* fluorescence tomography (*16*) (Kodak Image Station and eXplore Optix; see Supporting Information) in an experimental rat model of intermediate (six week OA-induced rats) and late-stage OA (eight week OA-induced rats; see Supporting Information) (*17*). Representative images are depicted in Figure 3. NIR fluorescence signals were monitored using the Kodak Image Station 1 h after intracartilage injection of **1** (10 μg/100 μL saline/cartilage, 4 nM) into OA-induced and normal cartilage rats. When **1** was injected into the normal side, NIR fluorescence signal intensity did not substantially increase. In contrast, **1** in OA-induced cartilage produced strong NIR fluorescence signals that were clearly visualized in the fluorescent images (1.3 ± 0.2, 3.3 ± 0.7, and 7.4 ± 1.4-fold vs normal side for 0, 6, and 8 weeks, respectively; $n = 3$). NIR fluorescence signals in the eight-week OA rat had a 2.2-fold increase relative to the six-week OA rat. Furthermore, the histological section of the normal cartilage showed a smooth articular surface with clear demarcation between the cartilage and subchondral bone. In contrast to the control, the images of the six and eight week OA-induced rats show a distinct erosion of the cartilage and a significant alteration in the bone−cartilage interface. These results confirm the feasibility of using **1** for the detection and visualization of upregulated MMP13 in relation to determining the stage of OA development *in vivo*.

For quantitative image analysis of the upregulation of MMP-13 in the OA rat model, similar *in vivo* imaging of OA was conducted 1 h after the injection of **1** with or without the MMP-13 inhibitor in the eight week OA rat model using a preclinical optical imaging system, eXplore Optix (ART Advanced Research Technologies Inc., Montreal, Canada) configured for NIR fluorescence detection (see Supporting Information). Figure 4A shows typical NIR fluorescence images of normal and OA cartilage obtained during the 1 h time period after the intracartilage injection of **1**. The total photon counts in normal and OA cartilage, which were quantified using Analysis Workstation Software (ART Advanced Research Technologies Inc.), were $(3.6 \pm 0.2) \times 10^6$ and $(11.5 \pm 1.73) \times 10^6$, respectively, and the NIR fluorescence intensity ratio between OA and normal

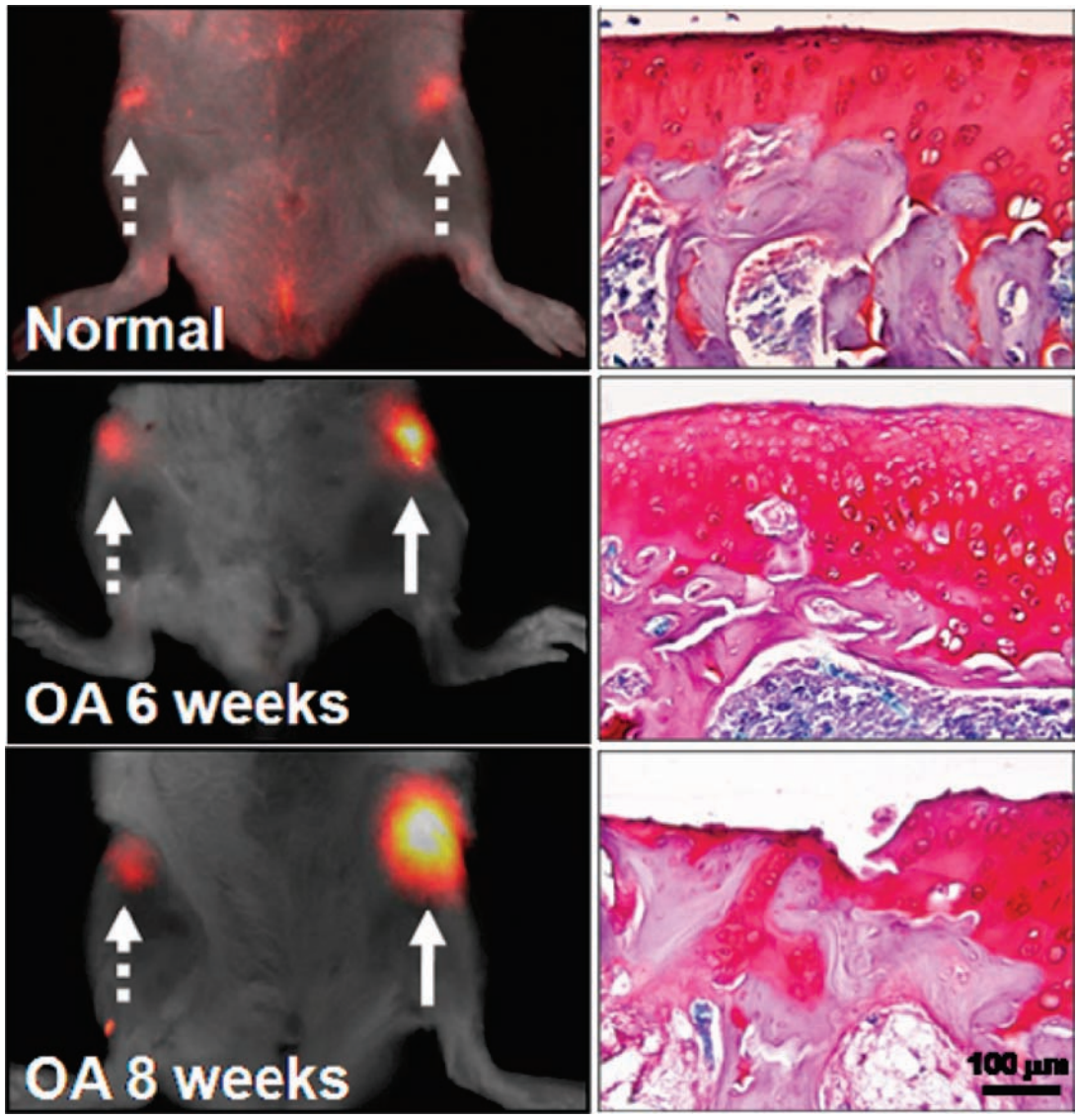

Figure 3. *In vivo* imaging of upregulated MMP-13 in normal, six, and eight week OA-induced cartilages 1 h after intracartilage-injection of **1** (4 nM). Left: NIR fluorescence reflectance imaging of normal and OA cartilage after local injection of **1**. Right: Histological evaluation of normal, six, and eight week OA joints by Safranin-O staining. Arrows: dotted line (normal) and solid line (OA).

cartilage (O/N) was approximately 3.2-fold ($p < 0.001$) (Figure 4B). However, fluorescence contrast was significantly reduced ($(4.7 \pm 0.8) \times 10^6$) when the MMP-13 inhibitor was administered 30 min before the injection of **1**. To analyze the depth profiles from the fluorescence images, the three-dimensional (3D) images were constructed by examining the intensity in slices cut along the Z-axis, which represented the two-dimensional (2D) slices, starting at $Z = 2$ to 7 mm deep (Figure 4C). The images from the OA-induced rats displayed a strong fluorescence signal between the depths of 3 to 5 mm, whereas normal and inhibitor treated cartilage displayed significantly low signals. Displaying the images in 2D allowed for the visualization of the expression and distribution of MMP-13 in OA cartilage. This may be useful for the longitudinal monitoring of the OA response in diagnosis and therapy. Overall, these data show that **1** is activated by MMP-13 and could produce strong NIR fluorescence signals, which enables OA imaging *in vivo*.

In summary, this study clearly demonstrates the potential use of the dark-quenched fluorogenic MMP-13 probe for the facile visual detection of MMP-13 *in vitro* and *in vivo*. In particular, by targeting a specific OA biomarker, the symptoms and development stages of OA can be readily and easily monitored, imaged, and analyzed in a rapid and efficient fashion. In addition, this technique can be widely applied to any target protease-based disease diagnosis and high-throughput drug screening simply by changing the specific peptide−substrate linker between the fluorophores and quenchers. Recently, the development of optical imaging instruments and sophisticated imaging probes have allowed researchers to detect and monitor molecular targets in live cells and in *in vivo* in real-time. However, because of the depth limitation of current optical imaging instruments, these techniques are only applicable to small animal models and superficial human tissues. Therefore, in order to translate dark-quenched imaging probes from preclinical studies to patients, the problems associated with interrogating fluorescence in deep tissue need to be addressed. We can envision improvements in imaging technologies that will allow optical probes to be used in larger subjects, and we anticipate that this simple and highly efficient fluorogenic probe will assist in the clinical management of patients with OA in the near future, not only for early diagnosis but also for assessing the response to treatment.

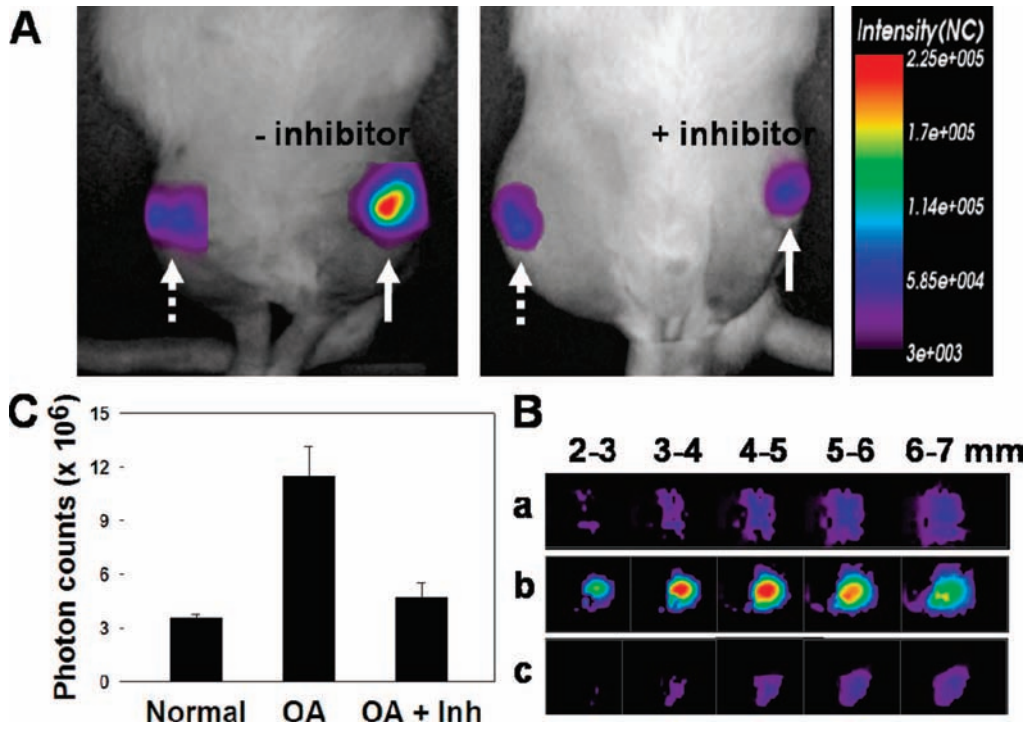

Figure 4. (A) *In vivo* NIR fluorescence tomographic images of normal and OA cartilage after local injection of **1** with or without the addition of the MMP-13 inhibitor in eight week OA-induced rat model. Left: **1** without MMP-13 inhibitor. Right: **1** with inhibitor in OA-induced cartilage. (B) Total photon counts in cartilage calculated from A. (C) 2D slices of the image from A and reconstruction in the Z direction. (a) Normal; (b) without or (c) with the addition of MMP-13 inhibitor. Arrows: dotted line (normal) and solid line (OA).

ACKNOWLEDGMENT

This work was supported by the Seoul R&BD Program and the GLR and Real-Time Molecular Imaging Project of MEST, and Intramural Research Program of the KIST.

Supporting Information Available: Synthetic, physicochemical properties, and experimental details. This material is available free of charge via the Internet at http://pubs.acs.org.

LITERATURE CITED

(1) Poole, A. R., Alini, M., and Hollander A. (1995) Chondrocytes and Cartilage Destruction. *Mechanisms and Models in Rheumatoid Arthritis* (Henderson, B., Edwards, J., and Pettipher, R., Eds.) pp 163−204, Academic Press, San Diego, CA.

(2) Blackburn, W. D., Chivers, S., and Bernreuter, W. (1996) Cartilage imaging in osteoarthritis. *Semin. Arthritis Rheum. 25*, 273–281.

(3) Eckstein, F., Cicuttini, F., Raynauld, J. P., Waterton, J. C., and Peterfy, C. (2006) Magnetic resonance imaging (MRI) of articular cartilage in knee osteoarthritis (OA): morphological assessment. *Osteoarthritis Cartilage 14*, A46−A75.

(4) Meenagh, G., Filippucci, E., Iagnocco, A., Delle, S. A., Riente, L., Bombardieri, S., Valesini, G., and Grassi, W. (2007) Ultrasound imaging for the rheumatologist VII. Ultrasound imaging in rheumatoid arthritis. *Clin. Exp. Rheumatol. 25*, 5–10.

(5) Weissleder, R. (2001) A clearer vision for in vivo imaging. *Nat. Biotechnol. 4*, 316–317.

(6) Ntziachristos, V. (2006) Fluorescence molecular imaging. *Annu. Rev. Biomed. Eng. 8*, 1–33.

(7) Rousseau, J. C., and Delmas, P. D. (2007) Biological markers in osteoarthritis. *Nat. Clin. Pract. Rheumatol. 3*, 346–356.

(8) Neuhold, L. A., Killar, L., Zhao, W., Sung, M. L., Warner, L., Kulik, J., Turner, J., Wu, W., Billinghurst, C., Meijers, T., Poole, A. R., Babij, P., and DeGennaro, L. J. (2001) Postnatal expression in hyaline cartilage of constitutively active human collagenase-3 (MMP-13) induces osteoarthritis in mice. *J. Clin. Invest. 107*, 35–44.

(9) Bau, B., Gebhard, P. M., Haag, J., Knorr, T., Bartnik, E., and Aigner, T. (2002) Relative messenger RNA expression profiling of collagenases and aggrecanases in human articular chondrocytes in vivo and in vitro. *Arthritis Rheum. 46*, 2648–2657.

(10) Close, D. R. (2001) Matrix metalloproteinase inhibitors in rheumatic diseases. *Ann. Rheum. Dis. 60* (Suppl 3), iii62−67.

(11) Kim, K., Lee, M., Park, H., Kim, J. H., Kim, S., Chung, H., Choi, K., Kim, I. S., Seong, B. L., and Kwon, I. C. (2006) Cell-permeable and biocompatible polymeric nanoparticles for apoptosis imaging. *J. Am. Chem. Soc. 128*, 3490–3491.

(12) Kim, J. H., Lee, S., Kim, K., Jeon, H., Park, R. W., Kim, I. S., Choi, I., and Kwon, I. C. (2007) Polymeric nanoparticles for protein kinase activity. *Chem. Comm. 13*, 1346–1348.

(13) Kim, J. H., Lee, S., Park, K., Nam, H. Y., Jang, S. Y., Young, I., Kim, K., Jeon, H., Park, R. W., Kim, I. S., Choi, K., and Kwon, I. C. (2007) Protein-phosphorylation-responsive polymeric nanoparticles for imaging protein kinase activities in single living cells. *Angew. Chem., Int. Ed. 46*, 5779–5782.

(14) Deng, S. J., Bickett, D. M., Mitchell, J. L., Lambert, M. H., Blackburn, R. K., Carter 3rd, H. L., Neugebauer, J., Pahel, G., Weiner, M. P., and Moss, M. L. (2000) Substrate specificity of human collagenase 3 assessed using a phage-displayed peptide library. *J. Biol. Chem. 275*, 31422–31427.

(15) Johansson, M. K., and Cook, R. M. (2003) Intramolecular dimers: a new design strategy for fluorescence-quenched probes. *Chemistry 9*, 3466–3471.

(16) Park, K., Kim, J. H., Nam, Y. S., Lee, S., Nam, H. Y., Kim, K., Park, J. H., Kim, I. S., Choi, K., Kim, S. Y., and Kwon, I. C. (2007) *J. Controlled Release 122*, 305–314.

(17) Engel, C. K., Pirard, B., Schimanski, S., Kirsch, R., Habermann, J., Klingler, O., Schlotte, V., Weithmann, K. U., and Wendt, K. U. (2005) Structural basis for the highly selective inhibition of MMP-13. *Chem. Biol. 12*, 181–191.

BC800264Z

Supporting Information

Dark Quenched Matrix Metalloproteinase Fluorogenic Probe for Imaging Osteoarthritis Development *In Vivo*

Seulki Lee[1], Kyeongsoon Park[1], Seung-Young Lee[1], Ju Hee Ryu[1], Jong Woong Park[2], Hyung Jun Ahn[1], Kuiwon Choi[1], Ick Chan Kwon[1], In-Chan Youn[1], Kwangmeyung Kim[1,*]

[1]Biomedical Research Center, Korea Institute of Science and Technology, Seongbuk-Gu, Seoul, South Korea; [2]Department of Orthopaedic Surgery, College of Medicine, Korea University, Danwon-Gu, Ansan, Gyeonggi, South Korea

Structure-based probe design.

MMP family proteins have highly conserved sequences and these proteins share a conserved substrate binding pocket and cleavage mechanism. From the peptide-bound structures (PDB accession code: 2OY2, 1JAP), we built a model of peptide-bound MMP-13 using the program O (ref 1). Based on the known MMP-13 substrate, PLGMRG, we designed different probes by combining the linker peptide and two bulky chemicals, Cy5.5 and BHQ-3. First the shortest fluorogenic probe was prepared labeling the N-terminus and C-terminus with Cy5.5 and BHQ-3, respectively, Cy5.5-GPLGMRGK(BHQ-3)amide. Glycine and lysine were incorporated at both termini to provide the chemical conjugation sites for the Cy5.5 dyes and BHQ-3. However, the narrow binding pocket did not allow for the bulky dye and quencher, therefore, the short peptide, GPLGMRGK, failed to access the binding pocket. The short peptide inhibited accesses to the binding pocket because the bulky quencher clashed with the narrow binding pocket through steric hindrance between MMP-13 and BHQ-3 (Fig. 1SA). By considering the quenching of Cy5.5 by BHQ-3, we found that a peptide containing at least two amino acid sequences was required for effective binding to MMP-13.

Therefore, to achieve an efficient quenching and affinity to MMP-13, we chose the glycine and leucine-glycine-lysine incorporated peptide substrate, Cy5.5-GPLGMRGLGK(BHQ-3), as the fluorogenic probe for MMP-13 (Fig. S1B).

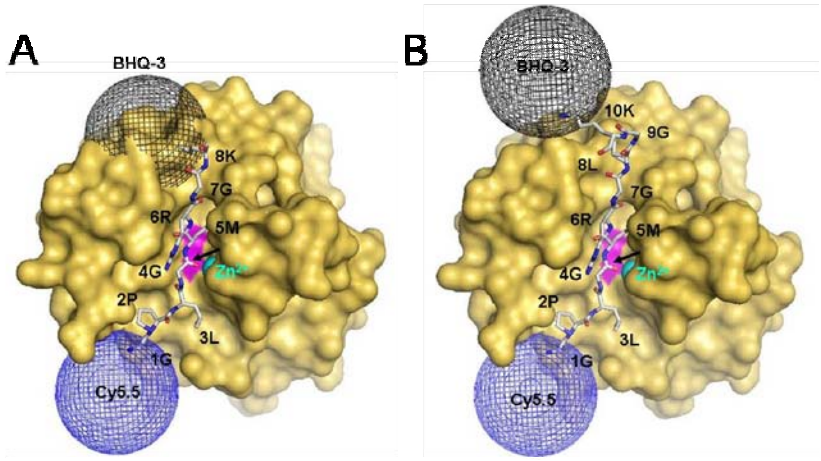

Fig. S1. Steric hindrance predicted by modeling. The molecular surface of Human MMP-13 and the peptide probes, GPLGMRGK and GPLGMRGLGK, which has Cy5.5 and BHQ-3 at both ends, are modeled in the binding pocket. Glutamic acid and Zn ion are colored by magenta and cyan. Arrow indicates the cleavage site. The short linker peptide, GPLGMRGK, results in a steric hindrance between MMP-13 and BHQ-3, thus, this substrate peptide does not have access to the binding pocket. Figures were drawn by the program Pymol (DeLano, W.L. The PyMOL Molecular Graphics System (2002) on World Wide Web [http://www.pymol.org]).

Ref 1. T. A. Jones, J.-Y. Zou, S. W. Cowan, M. Kjeldgaard, *Acta Crystallogr. Sect. A Biol. Crystallogr.*, **1991**, 47, 110-119.

Synthesis of the probe

The peptide sequence of 1 was synthesized using standard sold-phase Fmoc peptide chemistry. For site-specific conjugation of BHQ-3 to the primary amine of the lysine adjacent to the cleavable sequence, the Dde protecting group was selectively removed by addition of 2% hydrazine in DMF. After selective lysine deprotection, BHQ-3 succinimide ester in anhydrous DMF was added and

reacted overnight followed by extensive washes of the peptide resin. Subsequently, the last Fmoc group was removed from the peptide resin and Cy5.5 succinimide ester was coupled to the N-terminal glycine. After deprotecting and cleaving the peptide from the resin using trifluoroactic acid, resulting 1 was further purified by semi-preparative reversed-phase high liquid chromatography (RP-HPLC) and characterized by analytical RP-HPLC, MALDI-TOF mass spectrometry (m/z: calculated: 2476.1).

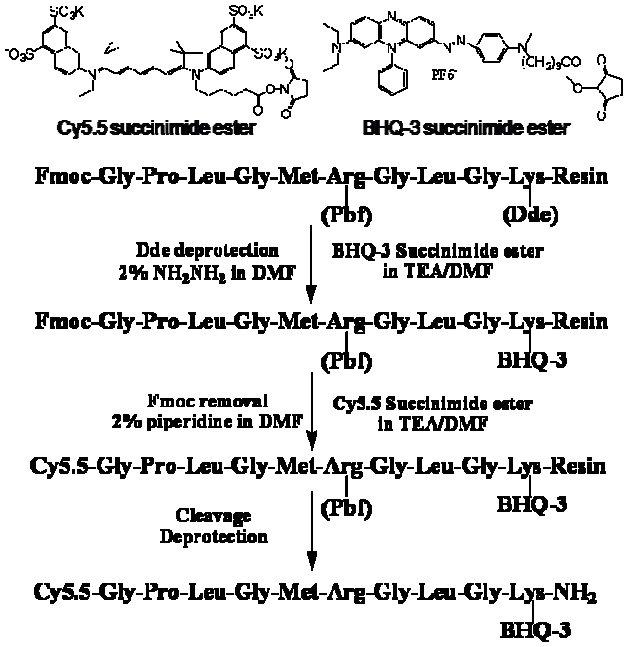

Fig. 2S. Synthetic scheme of **1**

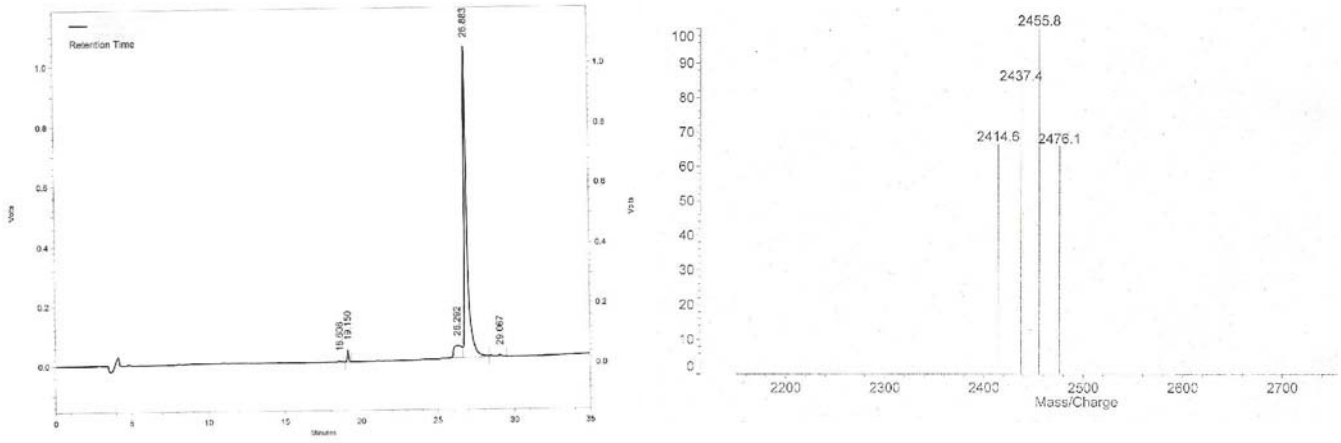

Fig. 3S. RP-HPLC and Maldi-tof spectra of **1**

Experimental animals and surgical procedures.

Sprague-Dawley rats (250~300g) were anesthetized with an intramuscular injection of ketamine (90mg/kg) and xylazine (10mg/kg). The right lower extremity was shaved and draped for aseptic surgery. After squeezing the leg, a sterile rubber tourniquet was applied for avascular filed during surgery. Under the operating microscope (Leica, M650, USA), the right knee joint was exposed using the anteromedial parapatellar approach. The patellar tendon was transected. Then, the anterior, posterior cruciate ligaments and the medial, lateral collateral ligaments were transected. The medial and lateral meniscuses were totally menisectomized. After copious irrigation with saline, the knee joint capsule was repaired with an absorbable suture and the skin was closed with a 4-0 monofilament nylon. The animals were allowed unrestricted activity, food, and water ad libitum.

Ref 2. S. Kamekura, L. Hoshi, T. Shimoaka, U. Chung, H. Chikuda, T. Yamada, M. Uchida, M. Ogada, A. Seichi, K. Nakamura, H. Kawaguchi, Osteoarthritis and Cartilage, 2005, 13, 632-641.

In vivo NIRF imaging.

After intracartilage-injection of 1 (10 μg/100 μl/cartilage, 4 nM) in OA and normal cartilages, fluorescence signals in OA and normal cartilage were imaged using an in vivo fluorescence imaging systems (Kodak Image Station 4000MM Digital Imaging System and eXplore OptixTM). 1 h after MMP-13 probe injection, NIR fluorescence images of animals were obtained with a 12-bit CCD camera (Kodak Image Station 4000MM, New Haven, CT) equipped with a special C-mount lens and CY5.5 bandpass emission filter (680 nm to 720 nm; Omega Optical) to visualize and compare the expression of MMP-13 in OA and normal cartilage. The tomographic NIRF images to detect the action of MMP-13 in OA and normal cartilage, were taken by positioning the rats on an animal plate heated to 36°C in the eXplore Optix System (ART Advanced Research Technologies Inc., Montreal, Canada, ref 3). The animal was automatically moved to the imaging chamber for scanning. Laser power and count time settings were optimized 13 μW and 0.3 s per point.

Excitation and emission spots were raster-scanned in 1 mm steps over the selected region of interest to generate emission wavelength scans. A 670 nm pulsed laser diode was used to excite Cy5.5 molecules. NIR fluorescence emission at 700 nm was collected and detected with a fast photomultiplier tube (Hamamatsu, Japan) and a time-correlated single photon counting system (Becker and Hickl GmbH, Berlin, Germany). To establish the time-dependent excretion profile, the total NIR fluorescence intensity per selected region (100 mm2) in the cartilage was calculated. Quantitative data are calculated using the region of interest (ROS) function of Analysis Workstation software (ART Advanced Research Technologies Inc., Montreal, Canada), and values are presented as means ± SE for groups of three animals.

Ref 3. S. Bloch, F. Lesage, L. Mclntosh, A. Gandjbakhche, K. Liang, S. Achilefu, J. Biomed. Opt. 2005, 13, 632-641.

Histological analysis.

To compare the destruction of OA and normal cartilage, the whole knee joints were dissected, and fixed in 4% paraformaldehde buffered with PBS (pH 7.4) for 4 h at 4°C. After dehydration with an increasing concentration of ethanol and embedding in paraffin, 5 μm sagittal sections were cut from the joints. Sections were stained with Safranin-O-fast green (ref 2).

The Implications of Stochastic Synthesis for the Conjugation of Functional Groups to Nanoparticles

Douglas G. Mullen,[†,‡] Ankur M. Desai,[‡] Jack N. Waddell,[§] Xue-min Cheng,[‡] Christopher V. Kelly,[‡,||] Daniel Q. McNerny,[‡,⊥] István J. Majoros,[‡] James R. Baker, Jr.,[‡] Leonard M. Sander,[∞] Bradford G. Orr,*[,‡,||,∞] and Mark M. Banaszak Holl*[,†,‡,||,#]

Program in Macromolecular Science and Engineering, Michigan Nanotechnology Institute for Medicine and Biological Sciences, Department of Mathematics, Program in Applied Physics, Department of Chemical Engineering, Department of Physics, and Department of Chemistry, University of Michigan, Ann Arbor, Michigan 48109. Received May 21, 2008; Revised Manuscript Received July 29, 2008

Stochastic synthesis of a ligand coupled to a nanoparticle results in a distribution of populations with different numbers of ligands per nanoparticle. This distribution was resolved and quantified using HPLC and is in excellent agreement with the ligand/nanoparticle average measured by ^{1}H NMR, gel permeation chromatography (GPC), and potentiometric titration, and yet significantly more disperse than commonly held perceptions of monodispersity. Two statistical models were employed to confirm that the observed heterogeneity is consistent with theoretical expectations.

Stochastic ligand conjugation is a common strategy to produce practical quantities of functionalized nanoparticles. Analytical methods used to quantify the average nanoparticle to ligand ratio, such as NMR, UV/visible spectroscopy, and elemental analysis, provide no information about the distribution of ligands bound to each particle. In this study, we quantitatively analyze the HPLC trace of the conjugated nanoparticle, including "tailing" effects, and show that the heterogeneity implied by the *entire* trace is consistent with theoretical expectations regarding the dispersity of the sample. The width of the distribution exceeds typical community expectations regarding sample homogeneity and is not well represented by a conjugated nanoparticle showing the average number of conjugated ligands. Given the importance of nanoparticle conjugates for applications such as drug delivery (*1*−*5*), biomedical diagnostics (*6*, *7*), and sensing (*8*, *9*), it is paramount that a detailed understanding of the product distribution resulting from a stochastic synthesis process be gained.

A number of groups have endeavored to characterize the distribution of ligands on nanoparticles. A variety of methods have been employed including gel electrophesis (*10*), anion-exchange HPLC (*11*), ultra performance liquid chromatography (*12*), mass spectrometry (*13*), and fluorescence quenching (*14*). In addition, synthetic efforts have focused on making particles with controlled 1:1 ligand/particle ratios (*15*−*18*). If a stochastic synthesis process is used to generate a 1:1 ratio, what percentage of the sample will be functional? In this study, we focus on the distribution that exists for ensembles with approximately one ligand per particle. This study employs partially acetylated dendrimers because these materials have been shown to be most effective for targeted drug delivery applications (*19*, *20*). The parent amine-terminated materials have been shown to nonselectively cause cell membrane permeability and are not suited for targeted drug delivery applications (*21*−*23*).

A series of reactions were conducted to conjugate varying amounts of 3-(4-(prop-2-ynyloxy)phenyl)propanoic acid to the surface primary amines of a partially acetylated generation 5 poly(amidoamine) dendrimer (G5 PAMAM; $G5(Ac)_{78}(NH_2)_{34}$) (Figure 1). Note that this ligand is suitable for "click" chemistry applications. These products were analyzed by ^{1}H NMR spectroscopy and HPLC. The ^{1}H NMR analysis, when combined with gel permeation chromatography (GPC) and potentiometic titration data, gives information about the average number of ligands bound per particle. The HPLC data, when combined with a peak fitting analysis, provide both the distribution of ligands per dendrimer and the average number of ligands per dendrimer.

The ligand−dendrimer conjugates (samples A−D) were determined to have an average of 0.20, 0.60, 1.04, and 1.47 ligands per dendrimer by comparing the integration of the methyl protons in the terminal acetyl groups to the aromatic protons on the conjugated ligand (Figure 2). The number of acetyl groups per dendrimer was independently determined by first computing the total number of end groups from the number average molecular weight (GPC) and potentiometric titration data for $G5\text{-}NH_2$(100%) as previously described (*24*). This value for the total number of end groups was applied to the ratio of primary amines to acetyl groups, obtained from the ^{1}H NMR of the partially acetylated dendrimer, to compute the average number of acetyl groups per dendrimer. This determination is sensitive to both the total number of particle functional groups and the number that have been acetylated. The excellent dispersity characteristics of PAMAM dendrimers (PDI = 1.01) greatly facilitates this analysis.

The HPLC elution profiles obtained at 210 nm for samples A−D are illustrated in Figure 3a, solid traces. The 210 nm

* To whom correspondence should be addressed. For B.G.O.: (e-mail) orr@umich.edu; (address) 450 Church Street, Ann Arbor, Michigan 48109-1040; (phone) (734) 764-4437; (fax) (734) 763-9694. For M.M.B.H: (e-mail) mbanasza@umich.edu; (address) 930 N. University Avenue, Ann Arbor, MI 48109-1055; (phone) 734-763-2283; (fax) 734-936-2307.

† Program in Macromolecular Science and Engineering.

‡ Michigan Nanotechnology Institute for Medicine and Biological Sciences.

§ Department of Mathematics.

|| Program in Applied Physics.

⊥ Department of Chemical Engineering.

∞ Department of Physics.

Department of Chemistry.

10.1021/bc8002106 CCC: $40.75 © 2008 American Chemical Society
Published on Web 08/26/2008

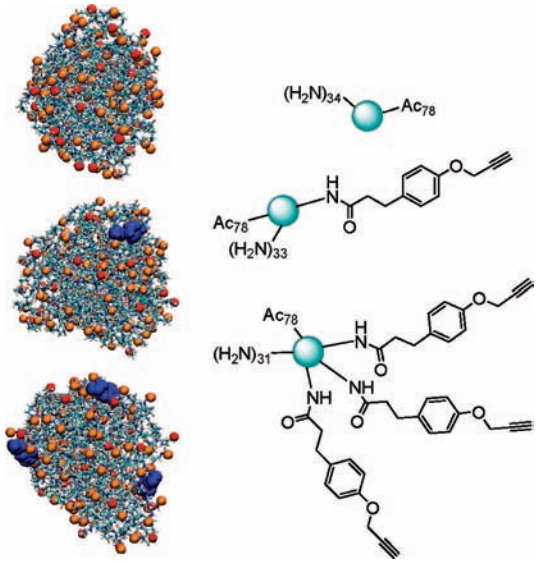

Figure 1. Equilibrated molecular dynamics models and schematics of G5 PAMAM dendrimers with different numbers of ligands. Terminal amines (red), acetyl groups (orange), and ligands (blue) are depicted in the models. Corresponding schematic representations show the dendrimer in teal with terminal groups. PAMAM dendrimers are monodisperse, highly ordered, water soluble, polymeric nanoparticles (~4.5 nm diameter). Terminal amines can be used as coupling points to attach different ligands.

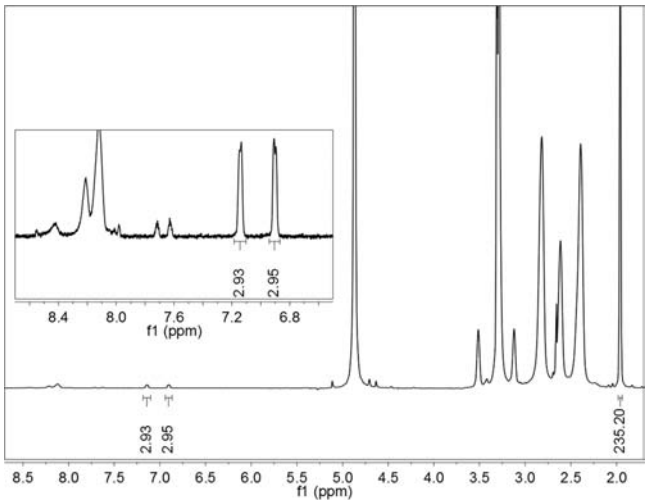

Figure 2. ^{1}H NMR spectrum for sample D. The average number of ligands per dendrimer was determined by comparison of the aromatic protons on the ligand vs the methyl protons in the acetyl group of the dendrimer. The number of acetyl groups was determined independently by GPC and potentiometric titration.

wavelength was selected because it is convenient for monitoring the PAMAM dendrimers and is not significantly affected by varying amounts of conjugated ligands (*25*). The first large peak (0) appears at an elution time consistent with unmodified $G5(Ac)_{78}(NH_2)_{34}$. The small peaks preceding peak 0 are also present in the original $G5(Ac)_{78}(NH_2)_{34}$ sample and likely result from a small amount of lower generation dendrimer (*26*). The second large peak (1) was preliminarily assigned as $G5(Ac)_{78}(NH_2)_{33}(L)_1$ (L= $NHCO(CH_2)_2C_6H_4OCH_2C_2H$) based upon elution order (Figure 3a, solid traces A−D). Additional data supporting this assignment were obtained from the elution profile monitored at 276 nm (sample D, dashed trace). At 276 nm, an absorbance maximum for the ligand with minimal contribution from the dendrimer, peak 0 ($G5(Ac)_{78}(NH_2)_{34}$), largely disappears as anticipated for dendrimer with no ligand

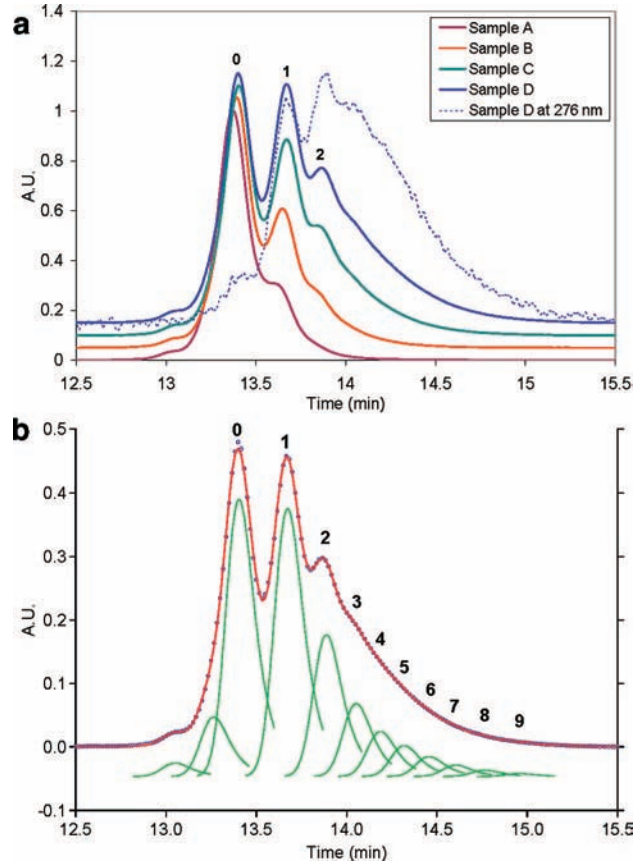

Figure 3. HPLC elution data for dendrimer−ligand conjugates. (a) Dendrimer concentration monitored at 210 nm for samples A−D are shown with solid lines. The elution profile of sample D at 276 nm, which is the maximum absorbance for the ligand, is displayed with a dashed line. Absorbance is normalized to the peak maximum. (b) The elution profile at 210 nm for sample D is shown in blue. Individual fitted peaks are presented in green, and the summation of the fitted peaks are in red.

conjugated. In this case, the first major feature observed (peak 1) was assigned as dendrimer containing one conjugated ligand ($G5(Ac)_{78}(NH_2)_{33}(L)_1$). Note that this is consistent with the assignment obtained based on monitoring dendrimer at 210 nm.

For the HPLC traces monitoring concentration of dendrimer at 210 nm, up to three distinct species are clearly resolved with a fourth apparent as an inflection point in trace D. Since the absorbance at 210 nm scales linearly with dendrimer concentration, we can use the area of each absorbance peak to obtain the relative concentration of each different dendrimer−ligand conjugate. Dilution studies of the conjugates demonstrate that Beer's law is followed and that each of the fitted peaks has the same extinction coefficient (see Supporting Information). The data taken at 276 nm are useful in helping to confirm the HPLC peak assignments but cannot be used quantitatively for concentration determinations because each dendrimer−ligand conjugate generates a dramatically different local concentration of ligand, thus causing a deviation from Beer's law.

In order to quantitatively assess the relative concentration of each dendrimer−ligand conjugate present, it was necessary to apply a peak fitting procedure to the HPLC traces. The functional form of the dendrimer peaks was determined by fitting the elution profile of acylated dendrimer ($G5(Ac)_{78}(NH_2)_{34}$) using Igor Pro 6.01. The peak shape, a Gaussian with an exponential decay tail to the right side of the elution peak, was then applied uniformly to all fitted peaks. The position and area of peaks 0−9 and the two lower generation impurity peaks at ~13 min were not constrained. The fit for sample D, which

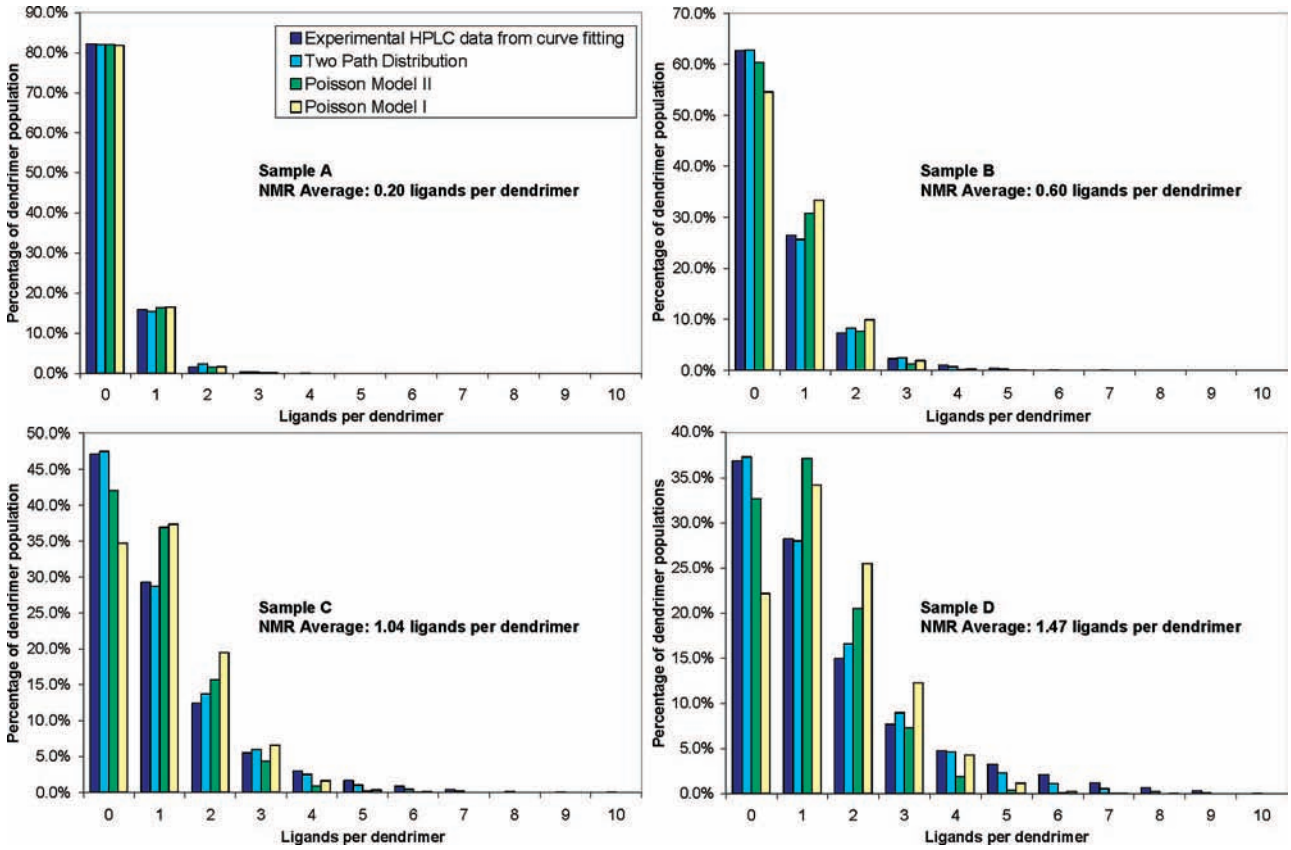

Figure 4. Experimental and statistical distributions of ligand−dendrimer conjugates A−D. Experimental distribution is calculated from fitted peaks to the HPLC elution profiles.

Table 1. Comparison of the Average Number of Ligands per Dendrimer Independently Computed by NMR and HPLC Techniques with the Three Statistical Models

	NMR average	HPLC average[a]	Poisson I ($\chi^2 = 66$)[b]	Poisson II ($\chi^2 = 47$)	two-path ($\chi^2 = 9$)
sample A	0.20 ± 0.02	0.20 ± 0.01	0.20	0.21	0.21
sample B	0.60 ± 0.06	0.54 ± 0.02	0.60	0.53	0.54
sample C	1.04 ± 0.10	0.98 ± 0.04	1.04	0.91	0.93
sample D	1.47 ± 0.15	1.45 ± 0.06	1.47	1.17	1.32

[a] Determination of HPLC error is discussed in the Experimental Methods section of the Supporting Information. [b] The Poisson I model uses the experimental NMR averages as input parameters.

has a 1.47 ligand/dendrimer ratio measured by ^{1}H NMR spectroscopy, is illustrated in Figure 3b. From these fits, the relative concentration of each dendrimer/ligand conjugate was determined (Figure 4) as well as the average ligand/dendrimer ratio (Table 1).

The relative proportions of dendrimer species, resolved by HPLC and quantified through fitted peaks, were used to calculate a weighted average number of ligands per dendrimer. Table 1 displays this for each of the dendrimer−ligand conjugates. This weighted average is in excellent agreement with the average determined independently by the combined NMR/GPC/titration analysis. Indeed, it is this comparison that gives confidence in the physical meaning of the peak fitting procedure. Significantly, the HPLC data produce additional distribution information that could not be extracted from the combined NMR/GPC/titration analysis.

The resolution of the various conjugated species by HPLC stands in stark contrast to the results obtained by NMR (Figure 2) in which no resolution of the various numbers of ligands conjugated is obtained. Gel permeation chromatography (GPC) exhibits a trend toward longer retention time but does not resolve the components (Figure 5a). Note that the longer retention time indicates that the conjugates are effectively smaller, as measured by GPC, although the light scattering and refractive index detectors verify that the mass has increased upon conjugation. MALDI-TOF MS also exhibits a trend to higher mass, but once again, the individual components are not resolved (Figure 5b).

Three statistical models were employed for comparison with the experimentally determined distributions (Figure 4, Table 1). Poisson model I assumed that ligand conjugation with the nanoparticle proceeds in a stochastic fashion. The total number of available attachment points on the dendrimer surface (34) and the average ligand/dendrimer ratio determined by NMR were used as input. This fit gave a χ^2 per degree of freedom of 66. In Poisson model II, the ligand/dendrimer ratios were allowed to vary as fitting parameters in a simultaneous χ^2 minimization using all four data sets. This fit gave a χ^2 per degree of freedom of 47. Both Poisson models match the 0.20 and 0.60 ligand/dendrimer distributions quite well but begin to deviate from the experimental data as the ligand/dendrimer ratio increases.

In order to better reproduce the experimental ligand distributions, a two-path kinetic model was used (see Supporting Information). It allowed for deviations from the Poisson distribution by varying the activation energy of the reaction as a function of n ligands on the nanoparticle (eq 1). This two-path model was also motivated by previous publications that

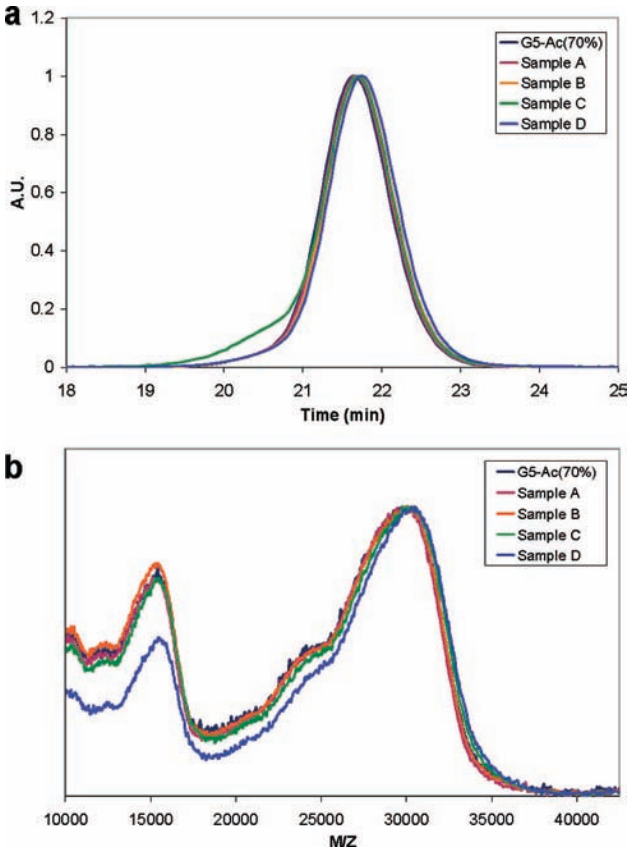

Figure 5. Standard analytical techniques that are commonly utilized to characterize nanoparticle conjugates fail to detect the different dendrimer−ligand populations. (a) The light scattering data of four dendrimer−ligand samples and partially acetylated dendrimer starting material, as separated by gel permeation chromatography (GPC), clearly demonstrate the challenges in detecting the different populations based on differences in size. The single peak resolution achieved by GPC is in stark contrast to the multiple peak resolution achieved by HPLC (see Supporting Information for GPC conditions). (b) Similarly, molecular weight analysis of the same material by matrix-assisted laser-desorption time-of-flight mass spectrometry (MALDI-TOF MS) cannot detect significant differences between the five samples (see Supporting Information for MALDI-TOF conditions).

indicate product amide autocatalysis should be expected for this reaction (*27*−*29*).

$$R_n = A_1 e^{-E_{a1}/(RT)} + nA_2 e^{-E_{a2}/(RT)} \quad (1)$$

The two paths correspond to attaching a ligand far from other ligands or near enough to previously attached ligands so that the barrier for attachment is reduced. These rates are fed into a master equation for the concentrations, c_n, of dendrimers with n ligands attached: $\dot{c}_n = R_{n-1}c_{n-1} - R_n c_n$. $A_{1,2}$ were adjusted to account for the number of available sites for the two paths. The solutions of the master equations were fit to all four data sets simultaneously using five independent parameters (E_{a1}−E_{a2}, and four independent values for the A parameters), resulting in a χ^2 per degree of freedom of 9. The best fit reproduced the experimental changes in concentration, which is a strong confirmation that the approach had physical meaning for this system. The difference in activation barrier between the two paths could be extracted from the fit and was determined to be $E_{a1} - E_{a2} = 6.2 \pm 1.5$ kJ/mol or 0.064 ± 0.016 eV.

Typically, analyses of functionalized nanoparticles only determine the average number of ligands per nanoparticle. In most cases, even HPLC does not resolve the distribution. Indeed, the "tailing" observed in the plots (Figure 3) is frequently ascribed to nonideal interaction between the analyte and the chromatography support. In this instance, we provide qualitative and quantitative data to demonstrate that tailing results from the distribution of ligands bound to dendrimers. This claim is supported by the following pieces of information: (1) no tailing is observed for the partially acetylated sample (see Figure S3); (2) the lower conversion samples (A, B) exhibit well-defined peaks; (3) dendrimers with a large number of conjugated ligands appear in "tail" region (see Figure S3); (4) the HPLC fits quantitatively agree with the NMR spectra in terms of the assessment of the average number of conjugated ligands.

The resolution of the distribution provides insight into the meaning of average ligand/dendrimer ratios. For the average of 0.20 ligands/dendrimer, the distribution comprises over 81% unmodified dendrimer, about 16% dendrimer with one ligand attached and less than 3% dendrimer with two ligands in fairly good accord with common expectations. However, the dendrimer−ligand conjugate with an average of 1.47 contains 0−9 ligands per dendrimer with the largest population of dendrimers actually containing no ligands. Note that both the random distribution and the two-path kinetic model accurately predict the breadth of the population. These experimentally measured breadths modeled herein challenge the commonly held perceptions that such a sample would comprise a narrower distribution predominantly containing dendrimers with one or two ligands attached. Furthermore, the average number misrepresents the functionally active portion of the dendrimer sample and does not make it apparent that the most common species contains no ligands and would therefore be inactive.

The deviation at larger ligand/dendrimers ratios of the experimental distribution from a Poisson analysis is quite interesting. The conjugation probability would be expected to *decrease* because of site blocking effects. Thus, the observation of an *increased* probability is particularly intriguing. A straightforward explanation of the activation energy barrier difference of ∼6 kJ/mol is product amide autocatalysis. This has the interesting implication of creating nonrandom spatial distribution of ligands on the polymer surface. These observations are of general interest, since amide/ester couplings are broadly used for conjugation reactions by the nanoparticle community.

In this paper, we have quantitatively analyzed the ligand/dendrimer distributions arising from conjugation of approximately one ligand on average to a spherical nanoparticle with excellent agreement between experimental measurements and theoretical analysis. Accurate understanding of these distributions for functional nanomaterials can lead to more informed applications and predictions of nanoparticle structure, function, and activity. It is expected that the details of the conjugation chemistry, site saturation effects, and steric blocking caused by the conjugated ligand can all affect the distributions obtained. Studies more closely examining these parameters will be the subject of future reports.

ACKNOWLEDGMENT

This project has been funded in part with Federal funds from the National Cancer Institute, National Institutes of Health, under Award 1 R01 CA119409, and with Federal funds from the National Science Foundation under Award DMS 0554587.

Supporting Information Available: Experimental methods, Beer's law analysis of dendrimer absorbance at 210 nm, GPC and MALDI-TOF analysis, additional HPLC profiles for the partially acetylated dendrimer starting material and a dendrimer-ligand conjugate with an average of 3.1 ligands, and detailed description of the two path kinetic model. This material is available free of charge via the Internet at http://pubs.acs.org.

LITERATURE CITED

(1) Tong, R., and Cheng, J. J. (2007) Anticancer polymeric nanomedicines. *Polym. Rev. 47*, 345–381.
(2) Gu, F. X., Karnik, R., Wang, A. Z., Alexis, F., Levy-Nissenbaum, E., Hong, S., Langer, R. S., and Farokhzad, O. C. (2007) Targeted nanoparticles for cancer therapy. *Nano Today 2*, 14–21.
(3) Rawat, M., Singh, D., Saraf, S., and Saraf, S. (2006) Nanocarriers: promising vehicle for bioactive drugs. *Biol. Pharm. Bull. 29*, 1790–1798.
(4) Patri, A. K., Majoros, I. J., and Baker, J. R. (2002) Dendritic polymer macromolecular carriers for drug delivery. *Curr. Opin. Chem. Biol. 6*, 466–471.
(5) Peer, D., Karp, J. M., Hong, S., Farokhzad, O. C., Margalit, R., and Langer, R. (2007) Nanocarriers as an emerging platform for cancer therapy. *Nat. Nanotechnol. 2*, 751–760.
(6) Nie, S. M., Xing, Y., Kim, G. J., and Simons, J. W. (2007) Nanotechnology applications in cancer. *Annu. Rev. Biomed. Eng. 9*, 257–288.
(7) Jain, K. K. (2005) Nanotechnology in clinical laboratory diagnostics. *Clin. Chim. Acta 358*, 37–54.
(8) Rossi, L. M., Quach, A. D., and Rosenzweig, Z. (2004) Glucose oxidase-magnetite nanoparticle bioconjugate for glucose sensing. *Anal. Bioanal. Chem. 380*, 606–613.
(9) Park, S. J., Taton, T. A., and Mirkin, C. A. (2002) Array-based electrical detection of DNA with nanoparticle probes. *Science 295*, 1503–1506.
(10) Sperling, R. A., Pellegrino, T., Li, J. K., Chang, W. H., and Parak, W. J. (2006) Electrophoretic separation of nanoparticles with a discrete number of functional groups. *Adv. Funct. Mater. 16*, 943–948.
(11) Claridge, S. A., Liang, H. Y. W., Basu, S. R., Frechet, J. M. J., and Alivisatos, A. P. (2008) Isolation of discrete nanoparticle−DNA conjugates for plasmonic applications. *Nano Lett. 8*, 1202–1206.
(12) Cason, C. A., Oehrle, S. A., Fabre, T. A., Girten, C. D., Walters, K. A., Tomalia, D. A., Haik, K. L., and Bullen, H. A. (2008) Improved methodology for monitoring poly(amidoamine) dendrimers surface transformations and product quality by ultra performance liquid chromatography. *J. Nanomater.* doi:10.1155/2008/456082.
(13) Tracy, J. B., Kalyuzhny, G., Crowe, M. C., Balasubramanian, R., Choi, J. P., and Murray, R. W. (2007) Poly(ethylene glycol) ligands for high-resolution nanoparticle mass spectrometry. *J. Am. Chem. Soc. 129*, 6706–6707.
(14) Casanova, D., Giaume, D., Moreau, M., Martin, J. L., Gacoin, T., Boilot, J. P., and Alexandrou, A. (2007) Counting the number of proteins coupled to single nanoparticles. *J. Am. Chem. Soc. 129*, 12592–12593.
(15) Huo, Q., and Worden, J. G. (2007) Monofunctional gold nanoparticles: synthesis and applications. *J. Nanopart. Res. 9*, 1013–1025.
(16) Fu, A. H., Micheel, C. M., Cha, J., Chang, H., Yang, H., and Alivisatos, A. P. (2004) Discrete nanostructures of quantum dots/Au with DNA. *J. Am. Chem. Soc. 126*, 10832–10833.
(17) Derfus, A. M., Chen, A. A., Min, D. H., Ruoslahti, E., and Bhatia, S. N. (2007) Targeted quantum dot conjugates for siRNA delivery. *Bioconjugate Chem. 18*, 1391–1396.
(18) Ackerson, C. J., Jadzinsky, P. D., Jensen, G. J., and Kornberg, R. D. (2006) Rigid, specific, and discrete gold nanoparticle/antibody conjugates. *J. Am. Chem. Soc. 128*, 2635–2640.
(19) Kukowska-Latallo, J. F., Candido, K. A., Cao, Z. Y., Nigavekar, S. S., Majoros, I. J., Thomas, T. P., Balogh, L. P., Khan, M. K., and Baker, J. R. (2005) Nanoparticle targeting of anticancer drug improves therapeutic response in animal model of human epithelial cancer. *Cancer Res. 65*, 5317–5324.
(20) Thomas, T. P., Majoros, I. J., Kotlyar, A., Kukowska-Latallo, J. F., Bielinska, A., Myc, A., and Baker, J. R. (2005) Targeting and inhibition of cell growth by an engineered dendritic nanodevice. *J. Med. Chem. 48*, 3729–3735.
(21) Hong, S. P., Bielinska, A. U., Mecke, A., Keszler, B., Beals, J. L., Shi, X. Y., Balogh, L., Orr, B. G., Baker, J. R., and Holl, M. M. B. (2004) Interaction of poly(amidoamine) dendrimers with supported lipid bilayers and cells: hole formation and the relation to transport. *Bioconjugate Chem. 15*, 774–782.
(22) Hong, S. P., Leroueil, P. R., Janus, E. K., Peters, J. L., Kober, M. M., Islam, M. T., Orr, B. G., Baker, J. R., and Holl, M. M. B. (2006) Interaction of polycationic polymers with supported lipid bilayers and cells: nanoscale hole formation and enhanced membrane permeability. *Bioconjugate Chem. 17*, 728–734.
(23) Leroueil, P. R., Hong, S. Y., Mecke, A., Baker, J. R., Orr, B. G., and Holl, M. M. B. (2007) Nanoparticle interaction with biological membranes: Does nanotechnology present a janus face? *Acc. Chem. Res. 40*, 335–342.
(24) Majoros, I. J., Thomas, T. P., Mehta, C. B., and Baker, J. R. (2005) Poly(amidoamine) dendrimer-based multifunctional engineered nanodevice for cancer therapy. *J. Med. Chem. 48*, 5892–5899.
(25) Islam, M. T., Majoros, I. J., and Baker, J. R. (2005) HPLC analysis of PAMAM dendrimer based multifunctional devices. *J. Chromatogr., B: Anal. Technol. Biomed. Life Sci. 822*, 21–26.
(26) Shi, X. Y., Bi, X. D., Ganser, T. R., Hong, S. P., Myc, L. A., Desai, A., Holl, M. M. B., and Baker, J. R. (2006) HPLC analysis of functionalized poly(amidoamine) dendrimers and the interaction between a folate−dendrimer conjugate and folate binding protein. *Analyst 131*, 842–848.
(27) Menger, F. M., Eliseev, A. V., and Khanjin, N. A. (1994) A self-replicating system—new experimental data and a new mechanistic interpretation. *J. Am. Chem. Soc. 116*, 3613–3614.
(28) Menger, F. M., Eliseev, A. V., Khanjin, N. A., and Sherrod, M. J. (1995) Evidence for an alternative mechanism to a previously proposed self-replicating system. *J. Org. Chem. 60*, 2870–2878.
(29) Titskii, G. D., and Litvinen, L. M. (1970) Nucleophilic catalysis of carboxamides and related compounds in acylation. *Zh. Obshch. Khim. 40*, 2680–2688.

BC8002106

The Implications of Stochastic Synthesis for the Conjugation of Functional Groups to Nanoparticles

Supporting Information

Douglas G. Mullen, Ankur M. Desai, Jack N. Waddell, Xue-min Cheng, Christopher V. Kelly, Daniel Q. McNerny, István J. Majoros, James R. Baker Jr., Leonard M. Sander, Bradford G. Orr*, and Mark M. Banaszak Holl*

Program in Macromolecular Science and Engineering, Michigan Nanotechnology Institute for Medicine and Biological Sciences, Department of Mathematics, Program in Applied Physics, Department of Chemical Engineering, Department of Physics, Department of Chemistry, University of Michigan, Ann Arbor, MI 48109

I. Experimental Methods:

Dendrimer Purification

Generation 5 PAMAM dendrimer was purchased from Dendritech Inc. To remove lower molecular weight impurities and trailing generations the dendrimer was dialysed with a 10,000 MWCO membrane against DI water for three days, exchanging washes every 4 hours. The number average molecular weight (27,336 g/mol) and PDI (1.018 +/- 0.014) was determined by GPC. Potentiometric titration was conducted to determine the average number of primary amines (112).

Partial Acetylation

Purified Generation 5 PAMAM dendrimer (133.7 mg, 4.89 μmole) was dissolved in anhydrous methanol (21 mL). Triethylamine (68.5 μL, 0.491 mmole) was added to this mixture and stirred for 30 minutes. Acetic anhydride (37.1 μL, 0.393 mmole) was added to anhydrous methanol (4 mL) and the resulting mixture was added in a dropwise manner to the dendrimer solution. The reaction was carried out in a glass flask, under nitrogen, at room temperature for 24 hours. Methanol was evaporated from the resulting solution and the product was purified using 10,000 MWCO centrifugal filtration devices. Purification consisted of five cycles (30 minutes at 5,000 rpm) using 1x PBS and five cycles using DI water. The purified dendrimer was lyophilized for three days to yield a white solid (138.4 mg, 92%). Number average molecular weight (30,660 g/mol) and PDI (1.026 +/- 0.015) were determined by GPC. ^{1}H NMR integration determined the degree of acetylation to be 70%.

Ligand Synthesis (3-(4-(prop-2-ynyloxy)phenyl)propanoic acid)

To a solution of methyl 3-(4-hydroxyphenyl)propanoate (2.18 g, 0.0121 mol) in dry acetone (56 mL) was added anhydrous K_2CO_3 (4.60 g, 0.0333 mol) followed by propargyl bromide (80% solution in toluene, 1.88 mL, 0.0126 mol). The resulting suspension was refluxed for 24 h with vigorous stirring. The reaction mixture was cooled to room temperature and the salt was removed by filtration followed by washing with portions of EtOAc. The filtrate was evaporated under vacuum to give the desired product as an oil (2.43g, 92%).

The crude product from above was dissolved in MeOH (60 mL). KOH (8 M, 5.0 mL, 0.040 mol) was added and the resulting mixture was heated at 70 °C for 1.5 h. The solution was cooled to room temperature and condensed under reduced pressure. The residue was dissolved in water (30 mL) and was acidified by addition of 1N HCl to pH 1. The white cloudy solution was diluted with EtOAc. Layers were separated and the aqueous layer was extracted with EtOAc (2 x 70 mL). The combined organic extracts were washed with a saturated NaCl solution and dried over $MgSO_4$. Solvent was evaporated under reduced pressure to give the desired product as a yellowish solid. (2.21 g, 97%).

^{1}H NMR (500 MHz, $CDCl_3$) δ 7.12, (d, 2H, J = 8.74 Hz), 6.89 (d, 2H, J = 8.71 Hz), 6.89 (d, 2H, J = 8.71 Hz), 4.65 (d, 2H, J = 2.40 Hz), 2.89 (t, 2H, J = 7.74 Hz), 2.64 (t, 2H, J = 7.75 Hz), 2.49 (t, 1H, J = 2.40 Hz)

Ligand Conjugation to Dendrimer

The ligand was conjugated to the partially acetylated dendrimer in two consecutive reactions. First, a stock solution of the ligand 3-(4-(prop-2-ynyloxy)phenyl)propanoic acid (9.4 mg, 0.046 mmole) was generated with a mixture of DMF (6.899 mL) and DMSO (2.300 mL). To this mixture was added 1-Ethyl-3-[3-dimethylaminopropyl]carbodiimide hydrochloride (EDC) (123.5 mg, 0.644 mmole). The resulting solution was stirred for 4 h at room temperature to create the active ester form of the ligand.

A stock solution of partially acetylated dendrimer (77.1 mg, 2.51 μmole) was made with DI water (17.190 mL). This solution was partitioned into four aliquots, A-D (15.0 mg, 0.489 μmole each). Additional DI water (2.520 mL, 2.016 mL, 1.512 mL) was added to the first three aliquots (A-C). The active ester form of the ligand (0.504 mL, 2.521 μmole) in DMF/DMSO was added in a dropwise manner (0.1 mL/min) to the first aliquot (A) of dendrimer-water solution. Similarly, the activated ester form of the ligand was added to the second, third, and fourth aliquots (5.043 μmole, 7.565 μmole, and 10.087 μmole respectively). The resulting mixtures were stirred for 2.5 days. All reaction steps were carried out in glass flasks at room temperature under nitrogen. The four reaction mixtures were purified using 10,000 MWCO centrifugal filtration devices. Purification consisted of five cycles using 1x PBS and six cycles using DI water. All cycles were 30 minutes at 5,000 rpm. The resulting products (A-D) were lyophilized for three days to yield a white solid (14.6 mg, 16.5 mg, 15.7 mg, and 15.5 mg respectively).

HPLC Characterization

HPLC analysis was carried out on a Waters Delta 600 HPLC system equipped with a Waters 2996 photodiode array detector, a Waters 717 Plus auto sampler, and Waters Fraction collector III. The instrument was controlled by Empower 2 software. For analysis of the conjugates, a C5 silica-based RP-HPLC column (250 x 4.6 mm, 300 Å) connected to a C5 guard column (4 x 3 mm) was used. The mobile phase for elution of the conjugates was a linear gradient beginning with 90:10 (v/v) water/acetonitrile and ending with 10:90 (v/v) water/acetonitrile over 25 min at a flow rate of 1 mL/min. Trifluoroacetic acid (TFA) at 0.14 wt % concentration in water as well as in acetonitrile was used as a counter ion to make the dendrimer surfaces hydrophobic.

To determine the experimental error associated with the HPLC characterization, Sample D was injected five times over two days under identical conditions. The absorbance data was normalized against the major peak for each injection and standard deviations were computed at each time point. The standard deviations were normalized against absorbance and the average error in the range between 12.5 and 15.5 minutes was computed to be 4%.

II. Beer's Law: Dilution Study

A dilution study of Sample D was performed to demonstrate that the dendrimer conjugates follow Beer's Law at 210 nm. Solutions of Sample D with different concentrations were injected on the HPLC using the conditions detailed in the Methods

section of this publication. The elution profile at 210 nm of Sample D at varying concentrations can be found in Figure S1.

Figure S1: HPLC profile of Sample D injected at varying concentrations

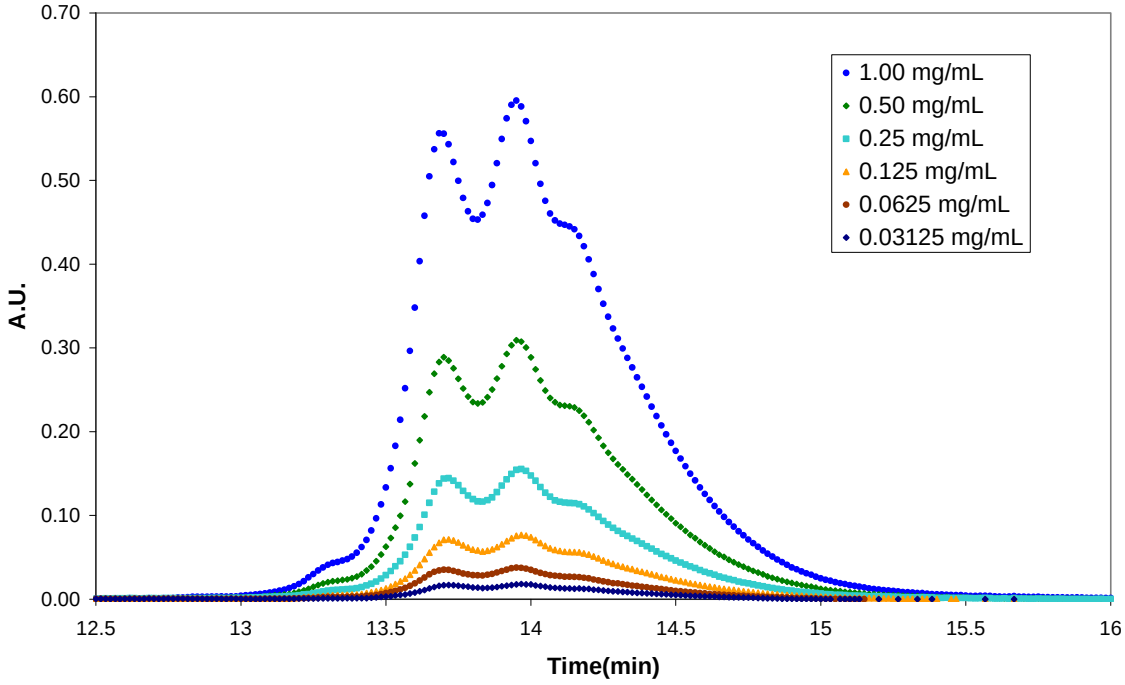

Using the fitting procedure described earlier in this publication, peaks were fit to each of the elution profiles in Figure S1. Peak concentration was calculated as the product of the Peak Area Fraction and the Sample Concentration. The linear relationship found in Figure S2 between Peak Area and Peak concentration clearly demonstrates that Beer's Law is followed at 210 nm for the dendrimer conjugates in this study.

Figure S2: Peak Area vs. Peak Concentration

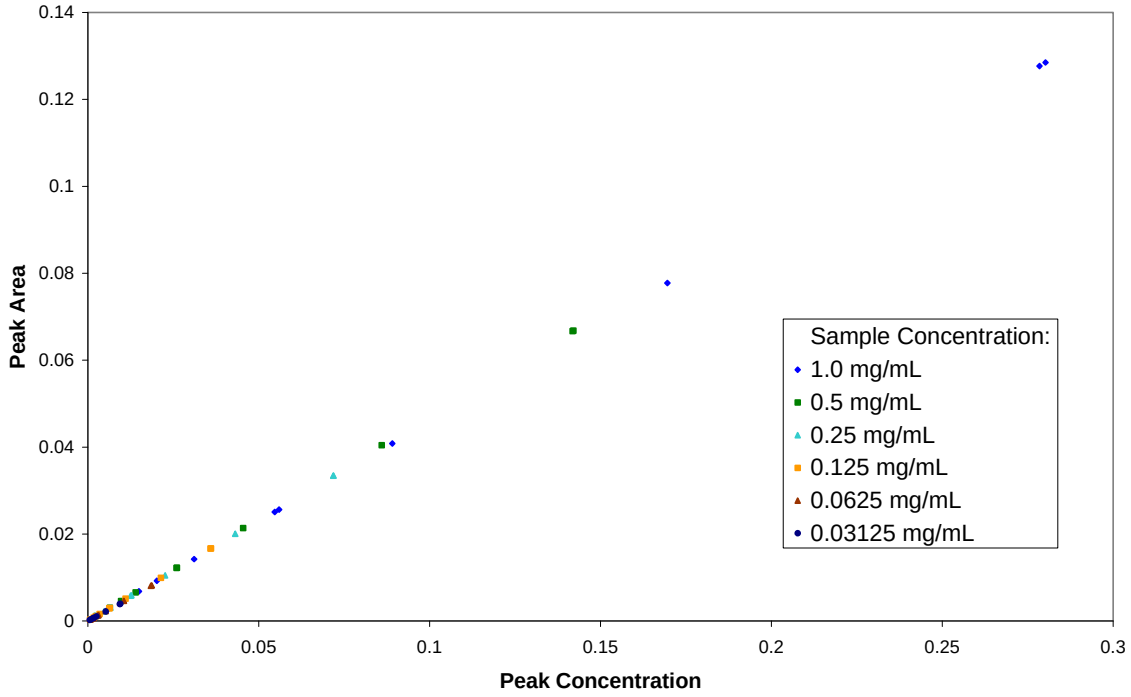

III. Characterization by Gel Permeation Chromatography (GPC)

GPC analysis was performed on the four dendrimer-ligand samples and the partially acetylated dendrimer using an Alliance Waters 2690/2695separations module (Waters Corp., Milford, MA) equipped with a Waters 2487 UV absorbance detector (Waters Corp.), a Wyatt Dawn DSP laser photometer (Wyatt Technology Corp., Santa Barbara, CA), an Optilab DSP interferometric refractometer (Wyatt Technology Corp.), and TosoHaas TSK-Gel Guard PHW 06762 (75 x 7.5 mm, 12 µm), G 2000 PW 05761 (300 x 7.5 mm, 10 µm), G 3000 PW 05762 (300 x 7.5 mm, 10 µm), and G 4000 PW (300 x7.5 mm, 17 µm) columns. Citric acid buffer (0.1 M concentration) with 0.025% sodium azide in water was used as a mobile phase, pH 2.74, using NaOH. Number Average Molecular Weight (Mn) and the Poly Dispersity Index (PDI) for each of the samples was calculated by using Astra software (version 4.9) (Wyatt Technology Corp.) and reported in Table S1. The general trend of increasing molecular weight is consistent with samples of increasingly higher averages of conjugated ligands.

Table S1: Number Average Molecular Weight and PDI calculated from GPC for the Dendrimer-Ligand conjugates

	Mn	PDI
G5Ac(70%)	30,660	1.026±0.015
Sample A	32,560	1.026±0.012
Sample B	33,200	1.025±0.012
Sample C	33,960	1.034±0.012
Sample D	35,080	1.024±0.012

IV. Molecular Weight Characterization of the Dendrimer-Ligand Conjugates and Starting Material by MALDI-TOF

The four dendrimer-ligand samples and the partially acetylated dendrimer were characterized with a Micromass TofSpec-2E Matrix-Assisted, Laser-Desorption Time-of-Flight Mass Spectrometer. Spectra were acquired in Linear mode. The MALDI-TOF sample mixtures were prepared using 5 μL of the matrix trihydroxyacetophenone in equal amounts of water and acetonitrile (10 mg/mL), and 5 μL of the dendrimer in equal amounts of water and methanol (1 mg/mL). Each spot volume was 1 μL. Data summing and smoothing was applied post acquisition to each set of spectra. All processed spectra were normalized to the peak maximum.

V. Additional HPLC Profiles

The HPLC profiles for partially acetylated dendrimer and a dendrimer-ligand conjugate with an average of 3.1 can be found in Figure S3. Synthesis of the partially acetylated dendrimer is described in the Experimental Methods section of this paper. The dendrimer-ligand conjugate with an average of 3.1 ligands was synthesized following the procedure described for the four dendrimer-ligand samples investigated in this publication. Partially acetylated dendrimer for this dendrimer-ligand conjugate was 74% acetylated. A linear baseline subtraction was applied to both data sets and peak maxima were normalized.

Figure S3: HPLC profiles for partially acetylated dendrimer (blue) and partially acetylated dendrimer with an average of 3.1 ligands (orange).

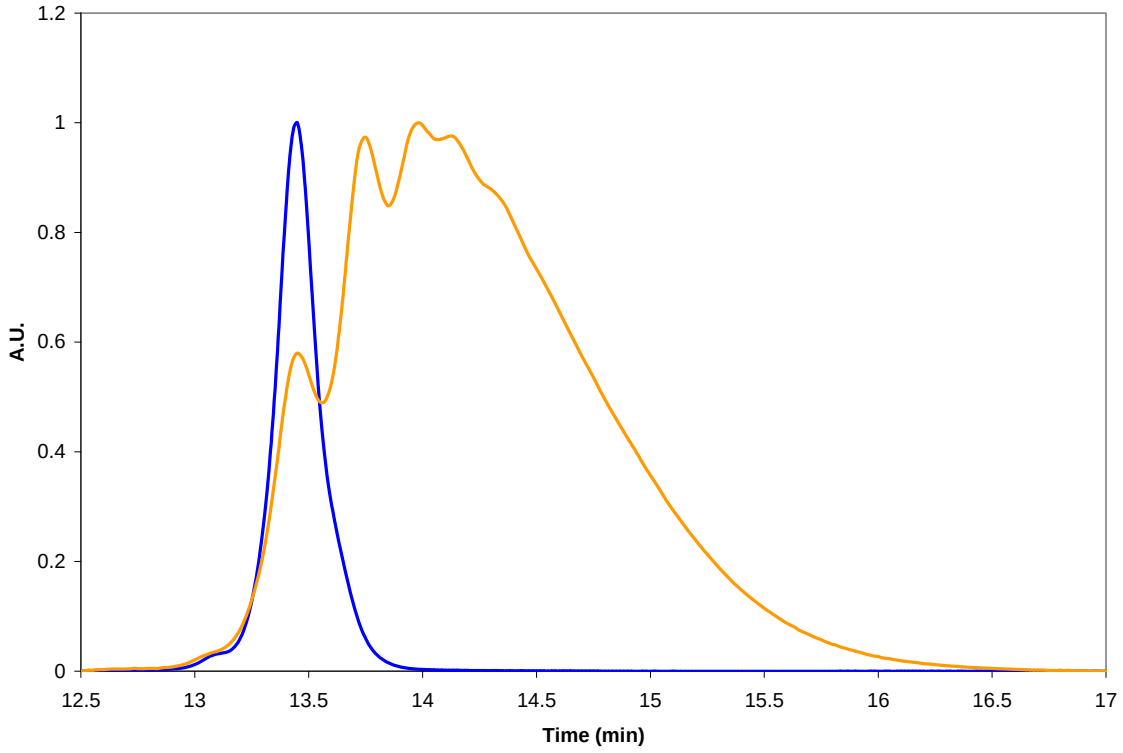

VI. The Two Path Kinetic Model

Suppose a dendrimer has *n* ligands bound, but where *n* is small compared to the total number of dendrimer branches $M = 112$. Should another ligand encounter this dendrimer, there are two most probable avenues, that the ligand attaches to an available branch far from the influence of already-attached ligands, and that the ligand binds near a previously attached ligand. Given the low occupancy, we discount the possibility of a ligand binding near more than one other ligand.

Each avenue has an associated rate of attachment depending upon the probability of encountering such a site, the activation energy barrier, and an underlying collision frequency ω that is assumed to be the same for the two paths. The two parallel paths give two rate contributions, R_{n1} and R_{n2}, such that the total rate $R_n = R_{n1} + R_{n2}$.

The probability p_2 of a ligand binding at a site near a previously bound ligand is given by $p_2 = nze^{-E_{a2}/RT}$, where z is the effective coordination number, the number of sites

a bonded ligand influences, and E_{a2} is the activation energy barrier for this pathway, a value influenced by the proximity to the bound ligand. This leads to the rate $R_{n2} = nA_2 e^{-E_{a2}/RT}$ by multiplying with ω, giving the association of $A_2 = z\omega$.

The probability p_1 of a ligand binding to one of the other available sites is the probability of encountering an open site that doesn't belong to the other pathway. That is, $p_1 = [m - n(z+1)]e^{-E_{a1}/RT}$, where m = 34 is the number of non-acetylated sites, and E_{a1} is the activation energy barrier for this unassisted pathway. The term $n(z+1)=nz + n$ has a contribution from discounting sites under the influence of a bound ligard, nz, and the sites at which the previously bound ligands are bound, giving the n term. This leads to the rate $R_{n1} = A_1 e^{-E_{a1}/RT}$ with the association $A_1 = [m - n(z+1)]\omega$.

The effective coordination number z depends on the arrangement of the dendrimer branches and the number of those branches which are not acetylated. If we consider first nearest neighbor interactions the end of a given branch may be near a handful of others, say between four and six. We expect that m/M = 30% of these branches are ligated or open to ligation. Therefore, the effective coordination number is a number of order unity, say between one and two.

A numerical estimate of the effective coordination results in z = 0.9. This estimate was generated by randomly populating a 10x10 triangular (close-packed) lattice with 30 sites, then counting the number of neighbors each site had. This process was sampled 10 000 times, giving a low-skewed distribution of numbers of neighbors with the average being 0.9. This results in a range of values for A_2/A_1 from 0.0025 to 0.1 for n between 1 and 10, with an average value of 0.04.

Fitting the Model

The Master equation $\dot{c}_n = R_{n-1}c_{n-1} - R_n c_n$ was numerically integrated using an Euler method for 1000 steps. The time step is arbitrary, since the time derivative in the equation is only known to a constant of proportionality that is absorbed into A_1 and A_2 for each data set. Integrating for 10 000 steps instead of 1000 does not significantly change the result. A non-linear least-squares fit was conducted simultaneously for the four data sets, resulting in the following fitted values for the parameters.

	Fitted Value
$\frac{A_2}{A_1}e^{-(E_{a2}-E_{a1})/RT}$	0.58
L_1	2.0 E-5
L_2	4.7 E-5
L_3	7.4 E-5
L_4	9.8 E-5

A significant confirmation of the model is the recovery of the ligand concentration ratios. The constants L_1, L_2, L_3, L_4 are proportional to the ligand concentrations, though the constant of proportionality is not independently recoverable. Therefore, normalizing each by L_4, and normalizing the ligand concentrations by the amount used in the most concentrated data set allow comparable values.

	Fitted Values	Actual Values
L_1/L_4	0.20	0.25
L_2/L_4	0.47	0.5
L_3/L_4	0.75	0.75

The prediction for this method is a difference between the activation energy barriers of the two paths in the model. From the fit $\frac{A_2}{A_1} e^{-(E_{a2}-E_{a1})/RT} = 0.58$, we can solve for the energy difference $(E_{a1} - E_{a2}) = RT \log(0.58 \frac{A_1}{A_2})$. After finding an estimate for $A_1/A_2 = 10$, we find the energy difference E_{a1}-E_{a2} = 6.2 ± 1.5 kJ/mol.

A Designed Protein for the Specific and Covalent Heteroconjugation of Biomolecules

Christopher Chidley, Katarzyna Mosiewicz, and Kai Johnsson*

Ecole Polytechnique Fédérale de Lausanne (EPFL), Institute of Chemical Sciences and Engineering, CH-1015 Lausanne, Switzerland. Received July 1, 2008; Revised Manuscript Received August 12, 2008

Bioconjugations often rely on adaptor molecules to cross-link different biomolecules. In this work, we introduce the molecular adaptor covalin, which is a protein chimera of two self-labeling proteins with nonoverlapping substrate specificity. Covalin permits a selective and covalent heteroconjugation of biomolecules displaying appropriate functional groups. Examples for the use of covalin include the specific heteroconjugation of a reporter enzyme to an antibody and of molecular probes to the surface of living cells. The efficiency and specificity of covalin-based bioconjugations together with the availability of a large variety of substrates create immediate and ubiquitous applications for covalin in bioconjugate chemistry.

The specific heteroconjugation of two different biomolecules generally relies on cross-linkers with two independent reactive groups or binding sites. Examples of cross-linkers include bifunctional synthetic molecules, oligonucleotides, and proteins (*1*−*3*). Streptavidin is the most widely used protein in bioconjugations, as it can stably conjugate biotinylated molecules with high efficiency (*3*, *4*). However, for the specific heteroconjugation of two different molecules the streptavidin−biotin technology has the limitation that streptavidin possesses four identical binding sites and that its simultaneous incubation with two different biotinylated molecules therefore leads to a heterogeneous mixture of conjugates. Mutants of streptavidin with a reduced number of binding sites have been described (*5*), but these mutants also do not allow a specific heteroconjugation of two different biotinylated molecules. Here, we introduce a designed protein for the specific and covalent heteroconjugation of two different (bio)molecules displaying appropriate functional groups. Using an antibody or cell surface proteins as examples, we demonstrate how this protein, named covalin, can be used to specifically conjugate proteins to other proteins or to synthetic probes. The simplicity, efficiency, and general applicability of the method should allow it to become an important tool for heteroconjugations in bioconjugate chemistry.

To achieve covalent and specific bioconjugations, covalin was designed as a fusion protein of two monomeric, self-labeling proteins with nonoverlapping substrate specificity (Figure 1). The first protein is a mutant of human O^6-alkylguanine-DNA alkyltransferase (known as SNAP-tag; 182 residues) that reacts with benzylguanine (BG) derivatives (*6*). The second protein is a mutant of a bacterial dehalogenase (known as HaloTag; 293 residues) that reacts with primary chloroalkanes (*7*). The rate constants of the reactions of both proteins with their substrates are high (10^4 s^{-1} M^{-1} for SNAP-tag and 10^6 s^{-1} M^{-1} for HaloTag). This makes them well-suited for bioconjugations, especially when compared to typical bioorthogonal reactions such as copper-free click chemistry or the Staudinger ligation, which are at least 10^4-fold slower (*8*, *9*). Numerous substrates are available for SNAP-tag and HaloTag (Figure 1b) and both tags have proven their versatility in vitro and in vivo (*6*, *7*). Covalin possesses an N-terminal His-tag for purification and a human rhinovirus 3C protease (PreScission protease) cleavage site between SNAP-tag and HaloTag for an optional separation of covalently conjugated biomolecules. Its size (55 kDa) is comparable to that of streptavidin (54 kDa). Although covalin is currently not commercially available, it can be readily produced through overexpression in *E. coli* (Supporting Information).

We first characterized the reactivity of covalin toward simple SNAP-tag and HaloTag substrates. Incubation of covalin with BG-547 and Halo-DAF, substrates for the labeling of SNAP-tag and HaloTag with the fluorescent dyes DY-547 and fluorescein, respectively, resulted in the labeling of covalin with both fluorophores (Figure 1c). Digestion of the labeled protein with PreScission protease yielded DY-547-labeled SNAP-tag and fluorescein-labeled HaloTag (Figure 1c), showing that covalin has two independent self-labeling sites. Incubation of covalin with either BG-DAF or Halo-DAF, substrates for the labeling of SNAP-tag and HaloTag with fluorescein, yielded fluorescein-labeled covalins with almost identical fluorescence intensities (±5%; Figure 1c, lane 1 and 2), indicating that in covalin SNAP-tag and HaloTag are active to the same extent.

We then used covalin in a series of proof-of-principle experiments for the conjugation of an antibody to a synthetic fluorophore, a reporter enzyme and magnetic beads (Figure 2a). In a first step, this requires a chemical labeling of the antibody with one of the two covalin substrates. Subsequently, the antibody can be functionalized through simultaneous incubation with covalin and the (bio)molecule of interest displaying the other covalin substrate. The first step of the procedure is similar to a chemical biotinylation of an antibody for subsequent bioconjugations with streptavidin. However, a subsequent simultaneous incubation of a biotinylated antibody with streptavidin and other biotinylated objects would inevitably lead to a complex mixture of different products.

The commonly used monoclonal antibody 12CA5 that recognizes the HA epitope tag was chosen as the antibody for the bioconjugation experiments. 12CA5 was labeled with primary chloroalkane through incubation of the antibody with a commercially available *N*-hydroxysuccinimide (NHS) ester (Figure 1b), a labeling strategy that should result in antibodies displaying varying amounts of the HaloTag substrate (*1*). Derivatized 12CA5 was stored for weeks at 4 °C without

* Corresponding author. E-mail: kai.johnsson@epfl.ch. Phone: +41−21−6939356. Fax: +41−21−6939365.

10.1021/bc800268j CCC: $40.75 © 2008 American Chemical Society
Published on Web 08/28/2008

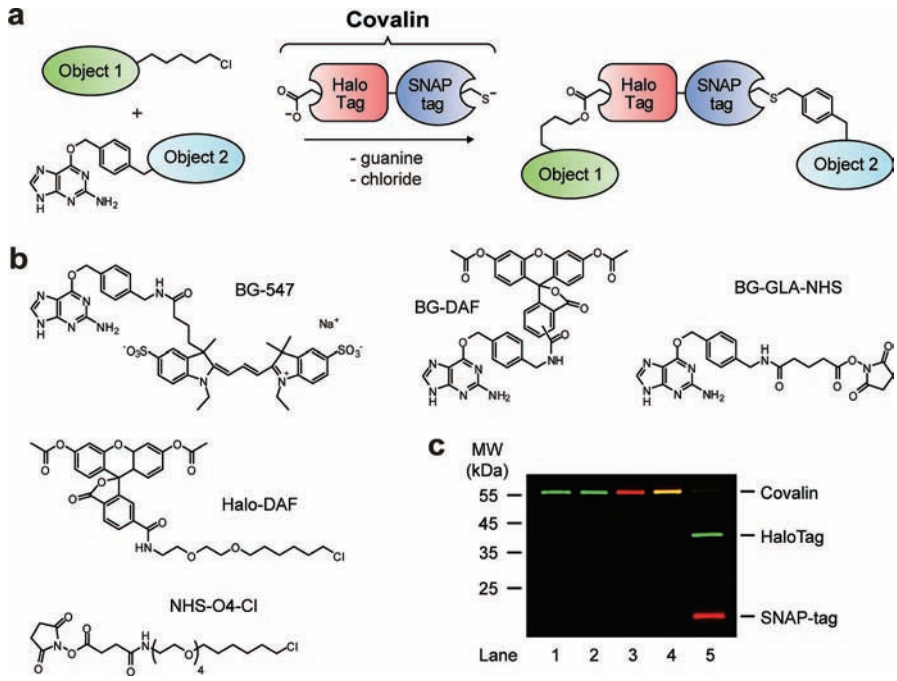

Figure 1. Covalin-dependent bioconjugations. (a) General scheme for covalin-dependent bioconjugations. An object represents synthetic probes, biomolecules, beads, or cells. (b) Covalin substrates used in this study. (c) SDS-PAGE and laser-based in-gel fluorescence scanning of covalin incubated with: BG-DAF (lane 1); Halo-DAF (lane 2); BG-547 (lane 3); Halo-DAF and BG-547 (lane 4); Halo-DAF, BG-547, and PreScission protease (lane 5). DY-547 and fluorescein fluorescence are shown in red and green, respectively.

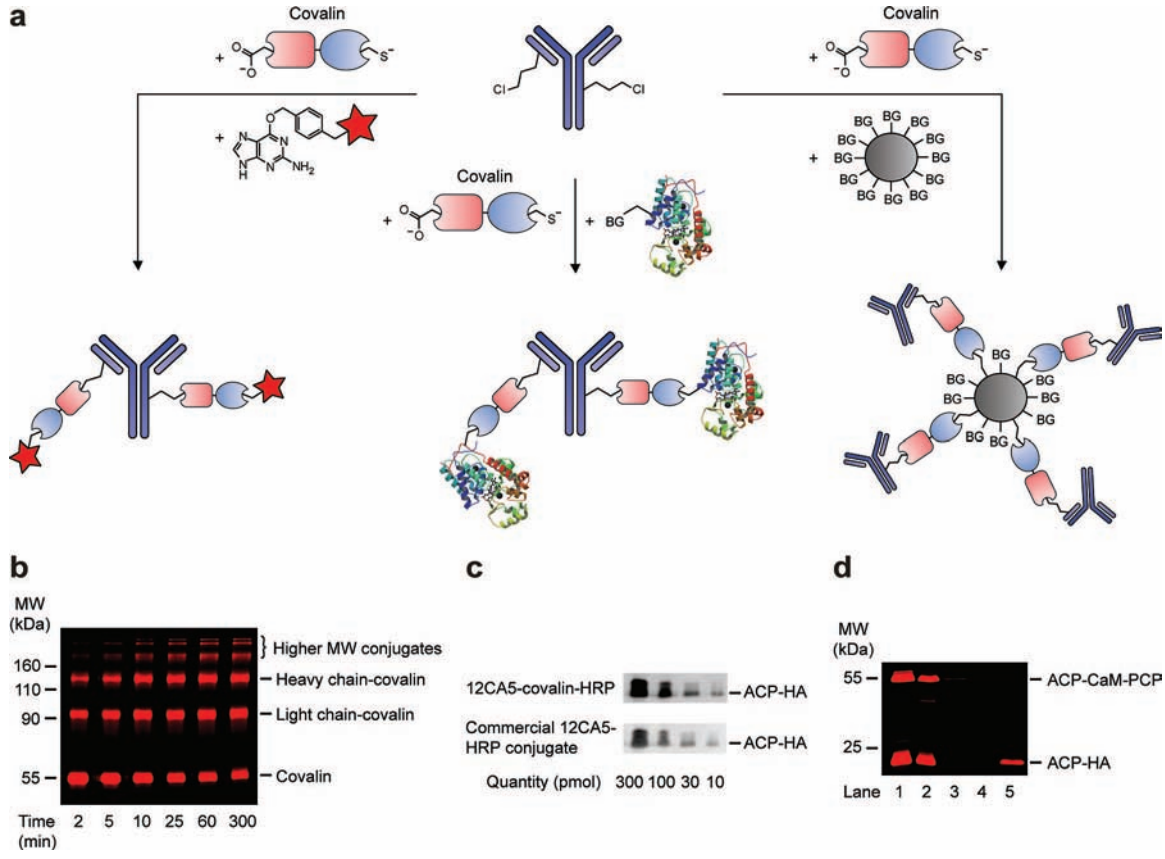

Figure 2. Covalin-dependent derivatization of an anti-HA antibody. (a) General scheme for the covalin-dependent conjugation of an antibody to a fluorophore (b), to a reporter protein (c), and to magnetic beads (d). (b) Derivatized anti-HA antibody 12CA5 (3 μM) was incubated with covalin (10 μM) and BG-547 (15 μM). Aliquots of the reaction mixture drawn at indicated time points were analyzed by SDS-PAGE and laser-based in-gel fluorescence scanning. (c) Detection of different dilutions of ACP-HA by Western blotting using 12CA5-covalin-HRP (0.17 μg/mL in 12CA5) or a commercially available 12CA5-HRP conjugate (0.15 μg/mL). (d) Analysis of the pulldown experiment using 12CA5 immobilized on magnetic beads via covalin and incubated with an equimolar mixture of Cy3-labeled ACP-HA and ACP-CaM-PCP. Samples of the pulldown were analyzed as in (b). Lane 1, sample before pulldown; lane 2, flowthrough of pulldown; lanes 3 and 4, wash fractions; lane 5, elution of captured proteins from beads.

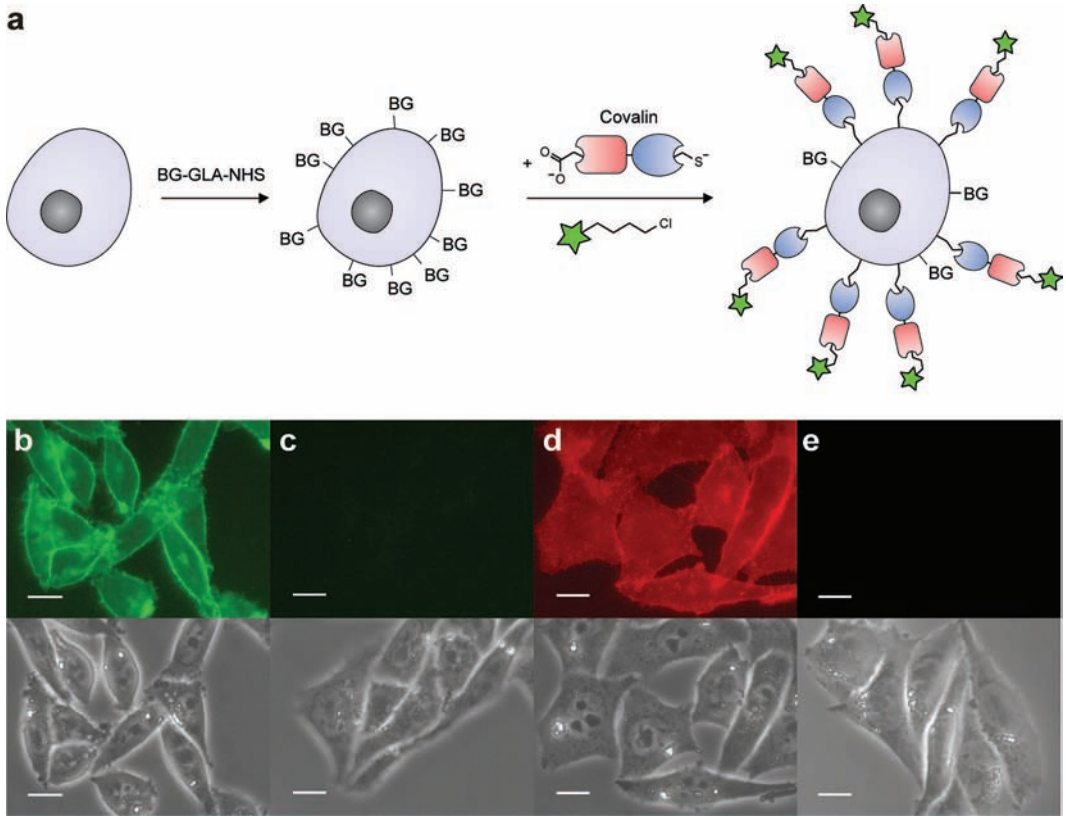

Figure 3. Use of covalin for the bioconjugation of molecular probes to cell surfaces. (a) General scheme for the bioconjugation of molecular probes via covalin to cell surfaces. In the first step, cell surfaces could either be derivatized with the SNAP-tag substrate or with the HaloTag substrate, but for reasons of clarity only one of the two orientations is shown. (b−e) Micrographs of derivatized and nonderivatized CHO cells incubated with covalin and a fluorescent covalin substrate. (b) CHO cells derivatized with BG and first incubated with covalin (10 μM) and then with Halo-DAF (2 μM). (c) CHO cells not derivatized with BG and first incubated with covalin (10 μM) and then with Halo-DAF (2 μM). (d) CHO cells derivatized with primary chloroalkane and first incubated with covalin (10 μM) and then with BG-547 (2 μM). (e) CHO cells not derivatized with primary chloroalkane and first incubated with covalin (10 μM) and then with BG-547 (2 μM). Scale bar, 10 μm.

decrease in reactivity toward covalin. To label 12CA5 with a fluorophore, the derivatized antibody (3 μM) was incubated with covalin (10 μM) and BG-547 (15 μM). Aliquots of the reaction mixture drawn at different time points were then analyzed by SDS-PAGE and in-gel fluorescence scanning (Figure 2b). Under these conditions, the fluorescence labeling of 12CA5 with covalin-DY-547 is near completion after one hour and heavy and light chains conjugated to one or multiple covalin-DY-547 could be detected. On average, approximately 2.5 covalin-DY-547 were bound per anti-HA antibody (Supporting Information; Figure S1a). This set of experiments serves as a first example to illustrate how covalin can be used for the straightforward conjugation of molecular probes to a derivatized protein. It should be noted that the covalent cross-linking of fluorescent probes to derivatized biomolecules such as 12CA5 allows the quantification of the initial derivatization step before use of the same derivatized biomolecule in further applications (vide infra).

One of the main applications that we foresee for the use of covalin is in the selective conjugation of two different proteins to each other, as it resolves the problem to derivatize one of the two proteins with a reactive group that specifically reacts only with the other protein. To demonstrate the potential of covalin for such applications, we attempted to conjugate 12CA5 via covalin to horseradish peroxidase (HRP) and to use the resulting conjugate in Western blotting. HRP is commonly used as a reporter enzyme in immunodetection experiments and HRP-antibody conjugates are therefore widely used. Toward this end, HRP was incubated with a BG-NHS ester. Derivatized HRP (3 μM) was incubated with covalin (3 μM) and Halo-DAF (4 μM) to verify that BG-labeled HRP is a substrate of covalin and to determine the degree of labeling of HRP with BG. In these experiments, 40% of HRP was derivatized with one covalin (Supporting Information; Figure S1b,c). The derivatization of HRP with NHS esters is known to be inefficient due to the low number of amino groups available (*1*), and no attempts were made to improve the labeling of HRP with BG. To conjugate HRP to the anti-HA antibody, derivatized 12CA5 (3 μM) was incubated with covalin (15 μM) and derivatized HRP (30 μM total HRP) for 5 h and then stored at 4 °C for later use. To evaluate the activity of the self-assembled 12CA5-covalin-HRP, we compared it to a commercially available 12CA5-HRP conjugate (Roche Molecular Biochemicals) optimized for applications in Western blotting. Using recombinant acyl carrier protein with a C-terminal HA tag (ACP-HA) as an arbitrary test antigen, 12CA5-covalin-HRP and the commercially available 12CA5-HRP permitted the detection of similar amounts of ACP-HA in Western blotting (Figure 2c). This demonstrates that the conjugation of HRP to 12CA5 via covalin does neither impede the antibody−antigen interaction nor the HRP activity. While the specific heteroconjugation of antibodies to HRP can be achieved via a number of different procedures using synthetic bifunctional cross-linkers (*1*), these procedures are not generally applicable to heteroconjugations of proteins, as they chemically exploit the fact that antibodies and HRP are glycosylated and/or that both proteins in their native form do not possess any free cysteines. This is in contrast to covalin-mediated heteroconjugations of proteins as the SNAP-tag and HaloTag substrates are chemically inert toward the functional groups found in proteins and other biomolecules.

Covalin should furthermore allow a selective immobilization of biomolecules on surfaces such as polymer beads as both SNAP-tag (*10*) and HaloTag (*7*) have already been successfully

used for this purpose. We therefore attempted the immobilization of the anti-HA antibody 12CA5 on magnetic beads for pulldown experiments. Primary chloroalkane-derivatized 12CA5 (6 μM) was incubated with covalin (9 μM) and magnetic beads displaying BG. For a mock pulldown experiment, derivatized beads were incubated with an equimolar mixture of ACP-HA and of a similar protein without HA-tag (a fusion protein of ACP with calmodulin and peptidyl carrier protein (ACP-CaM-PCP)) which was diluted into a crude cell lysate. For detection, ACP-HA and ACP-CaM-PCP were both labeled via ACP with Cy3 (*11*) before dilution into the cell lysate. After several washing steps, protein bound to the beads was eluted with SDS sample buffer and samples of different steps of the pulldown were analyzed (Figure 2d). The enrichment of ACP-HA over ACP-CaM-PCP in the pulldown was 80-fold and no enrichment was observed when either derivatized 12CA5 was replaced by original 12CA5 or when covalin was omitted (Supporting Information; Figure S1d). The different experiments with antibody 12CA5 show that once an antibody is derivatized with a covalin substrate it can be either conjugated to various probes or immobilized, providing the approach with a high degree of flexibility.

A further application for covalin is the conjugation of (bio)molecules to the surfaces of cells or viruses previously derivatized with appropriate substrates (Figure 3a). For a proof-of-principle experiment, we used covalin to conjugate fluorophores to the surface of CHO cells. CHO cells were first derivatized either with primary chloroalkane or with BG by a brief incubation of the cells with the corresponding NHS ester. Both NHS esters were utilized in order to test covalin in both orientations. The derivatized CHO cells were subsequently incubated first with covalin (10 μM) and then with either BG-547 or Halo-DAF (each 2 μM) for visualization. Labeling of derivatized cells with either DY-547 or fluorescein was detectable by fluorescence microscopy, whereas no labeling could be detected when nonderivatized CHO cells were incubated with covalin and either BG-547 or Halo-DAF (Figure 3b−e). The synthetic fluorophores used here could be easily exchanged for more complex (bio)molecules, thereby allowing a stepwise assembly of synthetic structures on cells and viruses.

In conclusion, covalin is a versatile and easy to use fusion protein for the specific conjugation of different molecules or objects displaying appropriate functional groups. In contrast to the popular adaptor protein streptavidin, it has two binding sites with nonoverlapping substrate specificity, ensuring the formation of complexes with defined composition and stoichiometry. Just as for streptavidin, covalin substrates are available for a large variety of applications, allowing the immediate and ubiquitous use of covalin in bioconjugate chemistry. Furthermore, the orthogonal substrate specificities of streptavidin and covalin should permit their simultaneous use in bioconjugations. Finally, the existence of other self-labeling proteins with nonoverlapping substrate specificities should allow the generation of a family of orthogonal covalins as well as covalins with different valencies (*12, 13*).

ACKNOWLEDGMENT

This work was supported by the Swiss National Science Foundation. We thank Marlon Hinner for valuable comments.

Supporting Information Available: Detailed procedures for all experiments are available. This material is available free of charge via the Internet at http://pubs.acs.org.

LITERATURE CITED

(1) Hermanson, G. T. (1996) *Bioconjugation Techniques*, Academic Press, London, UK.
(2) Niemeyer, C. M. (2002) The developments of semisynthetic DNA-protein conjugates. *Trends Biotechnol. 20*, 395–401.
(3) Laitinen, O. H., Nordlund, H. R., Hytonen, V. P., and Kulomaa, M. S. (2007) Brave new (strept)avidins in biotechnology. *Trends Biotechnol. 25*, 269–277.
(4) Astier, Y., Bayley, H., and Howorka, S. (2005) Protein components for nanodevices. *Curr. Opin. Chem. Biol. 9*, 576–584.
(5) Howarth, M., Chinnapen, D. J., Gerrow, K., Dorrestein, P. C., Grandy, M. R., Kelleher, N. L., El-Husseini, A., and Ting, A. Y. (2006) A monovalent streptavidin with a single femtomolar biotin binding site. *Nat. Methods 3*, 267–273.
(6) Keppler, A., Gendreizig, S., Gronemeyer, T., Pick, H., Vogel, H., and Johnsson, K. (2003) A general method for the covalent labeling of fusion proteins with small molecules in vivo. *Nat. Biotechnol. 21*, 86–89.
(7) Los, G. V., Encell, L. P., McDougall, M. G., Hartzell, D. D., Karassina, N., Zimprich, C., Wood, M. G., Learish, R., Ohana, R. F., Urh, M., Simpson, D., Mendez, J., Zimmerman, K., Otto, P., Vidugiris, G., Zhu, J., Darzins, A., Klaubert, D. H., Bulleit, R. F., and Wood, K. V. (2008) HaloTag: A novel protein labeling technology for cell imaging and protein analysis. *ACS Chem. Biol. 3*, 373–382.
(8) Baskin, J. M., Prescher, J. A., Laughlin, S. T., Agard, N. J., Chang, P. V., Miller, I. A., Lo, A., Codelli, J. A., and Bertozzi, C. R. (2007) Copper-free click chemistry for dynamic in vivo imaging. *Proc. Natl. Acad. Sci. U.S.A. 104*, 16793–16797.
(9) Agard, N. J., Baskin, J. M., Prescher, J. A., Lo, A., and Bertozzi, C. R. (2006) A comparative study of bioorthogonal reactions with azides. *ACS Chem. Biol. 1*, 644–648.
(10) Sielaff, I., Arnold, A., Godin, G., Tugulu, S., Klok, H. A., and Johnsson, K. (2006) Protein function microarrays based on self-immobilizing and self-labeling fusion proteins. *ChemBioChem 7*, 194–202.
(11) George, N., Pick, H., Vogel, H., Johnsson, N., and Johnsson, K. (2004) Specific labeling of cell surface proteins with chemically diverse compounds. *J. Am. Chem. Soc. 126*, 8896–8897.
(12) Griffin, B. A., Adams, S. R., and Tsien, R. Y. (1998) Specific covalent labeling of recombinant protein molecules inside live cells. *Science 281*, 269–272.
(13) Gautier, A., Juillerat, A., Heinis, C., Correa, I. R., Jr., Kindermann, M., Beaufils, F., and Johnsson, K. (2008) An engineered protein tag for multiprotein labeling in living cells. *Chem. Biol. 15*, 128–136.

BC800268J

Supporting Information

A designed protein for the specific and covalent hetero-conjugation of biomolecules

Christopher Chidley, Katarzyna Mosiewicz, Kai Johnsson
Ecole Polytechnique Fédérale de Lausanne (EPFL), Institute of Chemical Sciences and Engineering, CH-1015 Lausanne, Switzerland.

General

Substrates for the labeling of SNAP-tag were from Covalys Biosciences. Substrates for the labeling of HaloTag were from Promega.

Sequence of covalin

Covalin is composed of a fusion of HaloTag (HaloTag open reading frame from vector pHT2, Promega) (in blue) and SNAP-tag (182 amino acid mutant of the wild-type human AGT in which the last 25 amino acids were deleted and the following mutations were introduced: K32I, L33F, C62A, Q115S, Q116H, K125A, A127T, R128A, G131K, G132T, M134L, R135S, C150Q, S151G, S152D, G153L, A154D, N157G and S159E (in red).[1] The fusion has an N-terminal 6x His-tag and the linker between the two tags contains a *PreScission* protease cleavage site.

MGSSHHHHHHSSGLVPRGSHMGSEIGTGFPFDPHYVEVLGERMHYVDVGPRDGTPVLFLHGNPTS
SYLWRNIIPHVAPSHRCIAPDLIGMGKSDKPDLDYFFDDHVRYLDAFIEALGLEEVVLVIHDWGSALGF
HWAKRNPERVKGIACMEFIRPIPTWDEWPEFARETFQAFRTADVGRELIIDQNAFIEGALPMGVVRPL
TEVEMDHYREPFLKPVDREPLWRFPNELPIAGEPANIVALVEAYMNWLHQSPVPKLLFWGTPGVLIPP
AEAARLAESLPNCKTVDIGPGLFLLQEDNPDLIGSEIARWLPGLAG*LEVLFQGP*LEMDKDCEMKRTTL
DSPLGKLELSGCEQGLHEIIFLGKGTSAADAVEVPAPAAVLGGPEPLMQATAWLNAYFHQPEAIEEFP
VPALHHPVFQQESFTRQVLWKLLKVVKFGEVISYSHLAALAGNPAATAAVKTALSGNPVPILIPCHRVV
QGDLDVGGYEGGLAVKEWLLAHEGHRLGKPGLG

Expression of covalin

The sequence encoding covalin was inserted into pET-15b and the resulting plasmid was transformed by electroporation into the *E. coli* strain Rosetta-gami (DE3) (Novagen). A bacterial culture was grown at 37 °C in LB medium to an OD_{600nm} of 1.0 and expression of covalin was induced by the addition of 1 mM isopropyl-β-D-thiogalactopyranoside (IPTG). The bacteria were grown for an additional 21 hours at 16 °C and then were harvested by centrifugation. The bacteria were lysed by sonication and insoluble protein and cell debris were removed by centrifugation. For the purification of covalin, Ni-NTA (Qiagen) was used according to the instructions of the supplier. Eluted protein was further purified by gel filtration on a Superdex 200 column (GE Healthcare Life Sciences) using 20 mM Tris·Cl pH 8.0, 200 mM NaCl, 4 mM DTT. Glycerol was added to a final concentration of 30% (v/v) and the protein was stored at -80 °C. The concentration of the protein was determined using a Bradford assay with BSA as a standard.

Labeling of Anti-HA (12CA5) with primary alkyl chloride

HaloTag Succinimidyl ester (O4) ligand (NHS-O4-Cl; Promega) was added to a final concentration of 1 mM (from a 100 mM stock solution in anhydrous DMF) to a solution of 7 μM of 12CA5 antibody (Protein expression core facility, EPFL) in PBS pH 7.3 (137 mM NaCl, 2.7 mM KCl, 4.3 mM Na_2HPO_4, 1.4 mM KH_2PO_4). After 30 minutes at 25 °C, the excess N-hydroxysuccinimide ester was quenched for 10 minutes by adjusting the reaction mixture to 10 mM Tris·Cl pH 7.4. The labeled antibody was purified from excess HaloTag substrate by using a centrifugal filter device (Microcon YM-30, Millipore). Five washing cycles with 50 mM HEPES pH 7.4 were used to concentrate each time the sample from 500 μl to 20 μl. The derivatized antibody was stored at 4 °C until further use. The concentration of the 12CA5 antibody was determined prior to derivatization by UV spectrophotometry using an extinction coefficient for IgGs of 1.37 $ml \cdot mg^{-1} \cdot cm^{-1}$. After derivatization and purification, the concentration was set by using an estimated 90% recovery yield.

Labeling of Anti-HA (12CA5) with DY-547 via covalin

A solution of covalin and BG-547 (1.5 equivalents) was prepared and then mixed with primary alkyl chloride-derivatized 12CA5 to a final concentration of 3 μM 12CA5 and of 10 μM covalin in 50 mM HEPES pH 7.4. The kinetics of the reaction was monitored by taking samples of the reaction mixture after 2, 5, 10, 25, 60 and 300 minutes. After drawing the samples from the reaction tube, they were immediately mixed with one volume of 2x SDS sample buffer and heated to 95 °C for 5 minutes. The samples were then analyzed by SDS-PAGE and subsequent in-gel fluorescence scanning (Figure 2b).

Labeling of horseradish peroxidase with BG

Commercial horseradish peroxidase (HRP type VIA, Sigma) was dialyzed against PBS pH 7.3. BG-GLA-NHS (Covalys Biosciences) was added to a final concentration of 3 mM (from a 100 mM stock solution in anhydrous DMF) to a solution of 100 μM of HRP in PBS pH 7.3. After 90 minutes at 25 °C, the excess N-hydroxysuccinimide ester was quenched for 10 minutes by adjusting the reaction mixture to 10 mM Tris·Cl pH 7.4. The labeled HRP was purified from excess BG by using a centrifugal filter device (Microcon YM-30, Millipore). Five washing cycles with 50 mM HEPES pH 7.4 were used to concentrate each time the sample from 500 μl to 20 μl. After elution from the column, the derivatized HRP was stored at 4 °C until further use.

Labeling of horseradish peroxidase with fluorescein via covalin

A solution of covalin and Halo-DAF (HaloTag diAcFAM ligand, Promega) (1.3 equivalents) was prepared and then mixed with BG-derivatized HRP to a final concentration of 3 μM of HRP and covalin each in 50 mM HEPES pH 7.4, 1 mM PMSF and 2 μg/ml aprotinin. Kinetics of the reaction was monitored by taking samples of the reaction mixture after 5, 15, 60 and 300 minutes. After drawing the samples from the reaction tube, they were immediately mixed with 2x SDS sample buffer and heated to 95°C for 5 minutes. The samples were then analyzed by SDS-PAGE and subsequent in-gel fluorescence scanning (Figure S1b).

Procedure for Western blotting

The antibody-peroxidase conjugate was constructed with primary alkyl chloride-labeled 12CA5 and BG-labeled HRP (both prepared as described above) crosslinked via covalin. The crosslinking reaction was carried out by incubating 3 μM derivatized 12CA5, 15 μM covalin and 30 μM derivatized HRP in 50 mM HEPES pH 7.4 with 1 mM PMSF, 2 μg/ml aprotinin, 1 mM DTT and 0.1% BSA for 5 h at 25 °C. The reaction mixture was stored at 4 °C until final use. An HA-tagged recombinant acyl carrier protein (ACP-HA) was serially diluted and loaded in duplicate on a single SDS polyacrylamide gel. The proteins were then transferred to a PVDF membrane (Immobilon-P, Millipore) according to the supplier's instructions. After blocking with skim milk (3% in TBS (20 mM Tris·Cl, 500 mM NaCl) pH 7.5) for 90 minutes, the membrane was cut into two halves each composed of an identical serial dilution of ACP-HA. The first part of the membrane was incubated with 1.5 μl of the reaction mixture described above diluted in 4 ml PBS pH 7.3 + 0.05% Tween-20. This corresponds to a final concentration of 1.1 nM of 12CA5. The second part of the membrane was incubated with 6 μl of commercially available 12CA5-HRP conjugate (100 ng/μl, Roche) in 4 ml PBS pH 7.3 + 0.05% Tween-20, corresponding to a concentration of 0.15 μg/ml. Assuming a mono-derivatized antibody-HRP conjugate (MW of 12CA5-HRP: 200 kDa), the final concentration would be 0.8 nM. After 90 minutes at 25 °C, the incubation was prolonged 12 hours at 4 °C. The membranes were washed four times with PBS pH 7.3 + 0.1% Tween-20 and then detected using commercial chemiluminescent reagents (Western Lightning Chemiluminescence reagents, PerkinElmer Life Sciences) on a Kodak Image Station 440 (Eastman Kodak).

Pull-down experiments

Magnetic beads displaying BG (SNAP-capture magnetic beads, Covalys Biosciences) were washed twice with immobilization buffer (50 mM HEPES, 100 mM NaCl, 0.1% Tween-20, pH 7.4) + 1 mM DTT. In a first step, the beads were blocked with bovine serum albumin (BSA) at a final concentration of 3 μg/μl for 30 minutes at 25 °C on a tube rotator. Then, covalin was added to a final concentration of 9 μM for an additional 90 minutes. Finally, primary alkyl chloride-derivatized 12CA5 antibody was added to a final concentration of 6 μM. The reaction suspension was incubated

at 25 °C on the rotator for an additional 13 hours. The beads were then washed five times with immobilization buffer. Two recombinant proteins both containing acyl carrier protein (ACP-HA and ACP-CaM-PCP) were labeled via ACP with Cy3 according to published procedures.[2] A bacterial protein extract was prepared from *E. coli* JM83 according to standard procedures. The magnetic bead suspension in immobilization buffer was adjusted to a final concentration of 5 μM of both Cy3-ACP-HA and Cy3-ACP-CaM-PCP and to a final concentration of 10 μg/μl of bacterial protein extract. This suspension was incubated at 25 °C for 75 minutes on a tube rotator. The beads were then washed five times with immobilization buffer. Elution of the immobilized proteins was performed by adding 2x SDS loading buffer and heating the bead suspension for 5 minutes at 95 °C. In parallel to the experiment described above, two control reactions were performed. Both controls were performed in the same way as described for the experiment above except for the following: in control 1 the primary alkyl chloride derivatized antibody was replaced by original 12CA5 antibody, in control 2 covalin was replaced by a buffer load.

Labeling of CHO cells

Chinese hamster ovary cells (CHO-9-neo-C5) were grown in DMEM/F12 (Cambrex) supplemented with 10% fetal bovine serum (Cambrex) and antibiotics (Gibco, Invitrogen) (penicillin 100 U/ml and streptomycin 100 μg/ml final concentrations) in humidified atmosphere at 37 °C under 5% CO_2. Thirty-six hours before the derivatization reaction, cells were seeded on ibiTreat μ-Dishes (Ibidi) to a density of 80,000 cells per dish. Just before derivatization, the cells were washed three times with HBSS buffer (Lonza). The cells were either derivatized with BG by adjusting BG-GLA-NHS to a final concentration of 100 μM in HBSS or derivatized with primary alkyl chloride by adjusting NHS-O4-Cl to a final concentration of 500 μM in HBSS. Two control experiments were performed in which the activated ester solutions were replaced by a solvent load. The derivatization step was carried out for 30 minutes at 25 °C. The reaction was quenched for 15 minutes by adjusting to 50 mM Tris·Cl pH 7.4. The cells were washed three times with HBSS, then twice with HBSS + 0.1% BSA. Covalin was added to each plate to a final concentration of 10 μM in HBSS + 0.1% BSA and incubated at 25 °C under gentle rocking for 90 minutes. The cells were washed twice with HBSS, then once with HBSS + 0.1% BSA. The BG-

derivatized cells (and the corresponding control) were incubated with 2 μM Halo-Fl (Halo-DAF deacetylated in 25 mM K_2CO_3, 50% DMSO) in HBSS/0.1% BSA, whereas the primary alkyl chloride-derivatized cells (and the corresponding control) were incubated with 2 μM BG-547 in HBSS/0.1% BSA. After 15 minutes at 25 °C, the cells were washed three times with HBSS. The cells were then imaged in HBSS using a Zeiss Axiovert 200 inverted microscope, equipped with an LD “Plan Neofluar” 63×/0.75 corr Ph2 objective and an AxioCam MR digital camera (Zeiss). Zeiss filter sets 10 (excitation 450-490 nm; emission 515-565 nm) and 43 (excitation 545-625 nm; emission 605-670 nm) were used for fluorescence microscopy. Image analysis was performed with the AxioVision 4.0 software (Zeiss).

Figure S1

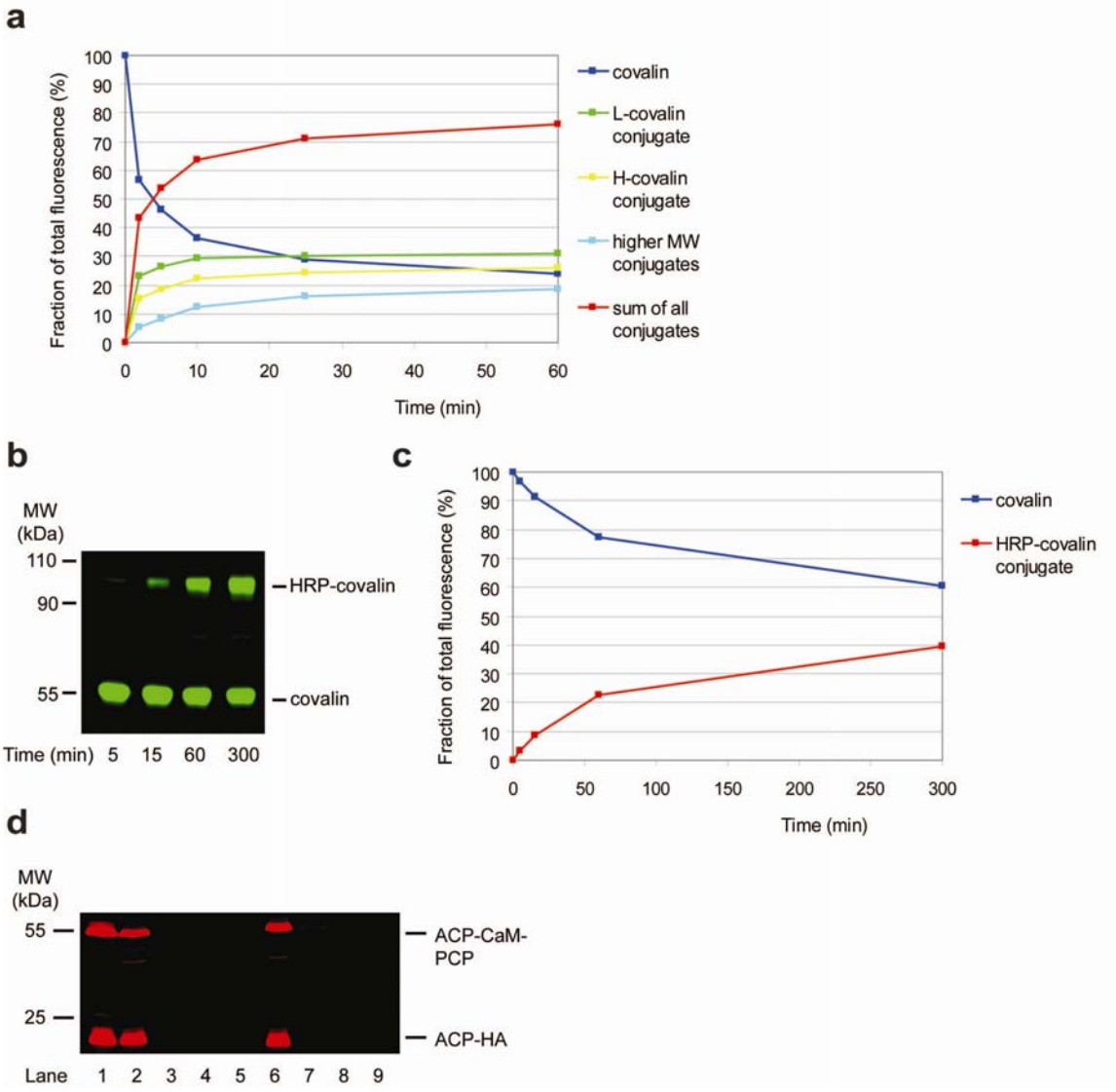

Figure S1**.** (**a**) Quantification of the fluorescence bands for Figure 2b. The four bands corresponding to covalin, Light chain-covalin conjugate, Heavy chain-covalin conjugate and higher molecular weight conjugates (Light and Heavy chains conjugated to 2 or more covalins) were quantified for each time point. Each of the four species was then represented as a percentage of the sum of the four values for each time point in the graphic representation. The sum of Light chain-covalin, Heavy chain-covalin and higher molecular weight conjugates was also represented in the graph (Sum of all conjugates). The time point 300 minutes was not included in the graph for a better visualization of the curves. The values after 300 minutes were very

close to those of the 60 minutes time point (<5% difference for the sum of all conjugates). The average number of covalin-DY-547 per anti-HA antibody was determined as follows: after 1 hour, 76% of the fluorescence signal of covalin-DY-547 is represented by antibody-covalin conjugates. This represents 7.6 μM of the initial 10 μM covalin. Using a 12CA5 concentration of 3 μM, an average number of 2.5 covalin per 12CA5 can be calculated. (**b**) Horseradish peroxidase (HRP) was derivatized with BG by incubation with the corresponding NHS ester. The derivatized HRP was then incubated with Covalin labeled with Halo-DAF. Aliquots of the reaction mixture drawn at different time points were analyzed by SDS-PAGE and in-gel fluorescence scanning. (**c**) Quantification of the fluorescence bands for Figure S1b. The two bands corresponding to covalin and HRP-covalin conjugate were quantified for each time point. Both species were represented as a percentage of the sum of the two bands in the graphic representation. (**d**) Control experiments for the pull-down experiment (Figure 2d). In control 1 (lanes 2-5) the primary alkyl chloride-derivatized 12CA5 was replaced by original 12CA5 and in control 2 (lanes 6-9) covalin was not added. Lane 1: before incubation with derivatized beads; lane 2: after incubation with derivatized beads; lanes 3 and 4: wash fractions; lane 5: elution of captured proteins from the beads; lane 6: after incubation with derivatized beads; lanes 7 and 8: wash fractions; lane 9: elution of captured proteins from the beads.

References

[1] T. Gronemeyer, C. Chidley, A. Juillerat et al., *Protein Eng Des Sel* **19** (7), 309 (2006).

[2] N. George, H. Pick, H. Vogel et al., *J Am Chem Soc* **126** (29), 8896 (2004).

ARTICLES

A Novel Synthetic Peptide Polymer with Cyclic RGD Motifs Supports Serum-Free Attachment of Anchorage-Dependent Cells

K. Markó,*[,†,‡] M. Ligeti,[†,§] G. Mező,[§] N. Mihala,[§] E. Kutnyánszky,[||] É. Kiss,[||] F. Hudecz,[§,⊥] and E. Madarász[‡]

Institute of Experimental Medicine, Hungarian Academy of Sciences, Szigony u. 43. 1083, Budapest, Research Group of Peptide Chemistry, Hungarian Academy of Sciences; Laboratory of Interfaces and Nanostructures, Institute of Chemistry; and Department of Organic Chemistry, Eötvös Loránd University, P.O. Box 32, Budapest 112 H-1518, Hungary. Received January 10, 2008; Revised Manuscript Received June 21, 2008

Cell adhesivity is a basic biological principle, which provides mechanisms for construction of multicellular organisms, tissue genesis, migration and individual cell survival. *In vivo*, the cell adhesive environment is provided by extracellular matrix molecules, neighboring cell surfaces and soluble factors delivered either by tissue cells or by blood circulation. The exact molecular composition of the microenvironment of a cell is not properly understood. The nondefined molecular composition of "native" adhesive components hinders their application when defined culture conditions are necessary, as, for an example, growing human cells for further clinical application. Applying large, substrate-coating molecules as backbones for carrying specific adhesive peptide motifs provides a relatively cheap, reproducible, and chemically defined group of synthetic adhesion molecules. Here, we report on the design, synthesis, and testing of a novel cyclic RGD-containing coating material, which promotes initial attachment, spreading, survival, and proliferation of a number of different cell types. The potent adhesive polypeptide-brush, composed of poly[Lys(DL-Ala_m)] branched chain polypeptide (AK) and multiple copies of cyclic(arginyl-glycyl-aspartyl-D-phenylalanyl-cysteine) pentapeptide prevents anoikis and supports cell attachment in the absence of serum or other biological additives. The defined conditions for cell maintenance make this material a promising candidate for coating artificial cell substrates even for therapeutic applications.

1. INTRODUCTION

Cell−extracellular matrix (ECM) interactions are pivotal for survival of adherent cells both *in vivo* and *in vitro*. Without proper attachment, cells adopt a special apoptotic fate, termed "anoikis" (homelessness in Greek) (*1*). For *in vitro* maintenance of adherent cells, artificial substrates should provide appropriate surfaces for rapid attachment.

In traditional cell culture techniques, sera of various origins, containing different attachment and spreading factors, are included in the culture medium. While serum application greatly helps cell culturing, its nondefined nature makes it ineligible when defined culture conditions are required, such as for growing human cells for clinical applications. Its high price, the risk of contamination, and the animal welfare considerations also hinder the use of sera (*2*).

Serum-free, chemically defined media are available for a wide variety of cell types (*3*), but most of them impair cell attachment. Coating the culture surfaces with native extracellular matrix molecules derived from either human/animal tissues or recombinant bacteria may overcome this difficulty but brings back the uncertainty in molecular composition and the risk of contamination. Synthetic, polycationic peptides/proteins, such as poly(L/D-lysine) (PLL, PDL) or polyornithine, are widely used for coating cell culture dishes. Such nonspecific adhesive coatings, however, promote initial cell adhesion with moderate efficiency, may cause abnormal cell-spreading, and might be cytotoxic (*4*). Applying such large, substrate-coating molecules as backbones for carrying specific adhesive peptide motifs, however, may provide a relatively cheap, reproducible, and chemically defined group of efficient synthetic adhesion molecules (*5*).

Cell−ECM adhesion is performed predominantly by integrins which serve as receptors for several ECM components (*6*). Besides anchoring the cells, signaling through the integrins can regulate the survival, proliferation, and differentiation of cells (*7*).

Various scaffold substrates had been modified with RGD motifs (*5*, *8*−*16*), a tripeptide sequence recognized by most integrins. The RGD (arginyl-glycyl-aspartic acid) sequence can be found in many extracellular matrix proteins (fibronectin, vitronectin, tenascin-C, etc.) and is responsible for the binding of these ECM proteins to their receptors (*17*) on the cell surfaces. In soluble form, RGD-containing oligopeptides can inhibit cell adhesion, by antagonizing the integrin−matrix interaction (*18*). The immobilized RGD sequence, on the other hand, is generally acknowledged as a promising biomaterial for promoting cell adhesion to artificial substrates and it is the most commonly

* Corresponding author. E-mail: marko@koki.hu. Fax: 36 1 2109966. Address: Szigony u. 43. 1083, Budapest, Hungary.

† These authors contributed equally to this work.

‡ Institute of Experimental Medicine, Hungarian Academy of Sciences.

§ Research Group of Peptide Chemistry, Hungarian Academy of Sciences, Eötvös Loránd University.

|| Laboratory of Interfaces and Nanostructures, Institute of Chemistry, Eötvös Loránd University.

⊥ Department of Organic Chemistry, Eötvös Loránd University.

10.1021/bc8000134 CCC: $40.75 © 2008 American Chemical Society
Published on Web 08/13/2008

applied protein motif on synthetic surfaces (*5*). Because of the uncovered carboxyl terminus of the aspartate residue, the RGD tripeptide, in itself, has no biological activity. In the active RGD motif, this C-terminus should be masked by addition of another amino acid (*18*). RGD-containing cyclic pentapeptides, such as cyclo[RGDfV], were originally described as potent inhibitors of cell adhesion to vitronectin and laminin fragment P1 (*19*). Cyclic (RGDfV) (*20*), (RGDfK) (*21*), and (RGDfC) peptides have the highest affinity and selectivity toward $\alpha_v\beta_3$ and bind strongly to $\alpha_v\beta_5$, $\alpha_v\beta_6$ (*22*) integrins and with lower affinity to other integrins (such as $\alpha_{IIb}\beta_3$ and $\alpha_5\beta_1$), as well (*20*).

In order to obtain an integrin-binding macromolecule, we designed a poly[Lys(DL-Ala_m)] (AK) branched polypeptide, carrying multiple copies of cyclic(arginyl-glycyl-aspartyl-D-phenylalanyl-cysteine) pentapeptide on the N-terminal positions of the oligoalanine branches (AK-cyclo[RGDfC]). The novel synthetic polypeptide readily adsorbed to various solid substrates and provided a strongly adhesive coating for cell attachment. In order to evaluate selective versus general adhesiveness of the polymer, the attachment of a number of different anchorage-dependent cells was investigated. AK-cyclo[RGDfC]-coated surfaces promoted adhesion and spreading of almost all investigated cell types in the absence of serum or any other adhesion or spreading factors. As AK-cyclo[RGDfC]-coating supported serum-free survival of several cell types in the critical, 24−48 h initial attachment period, it has been proven to be a tool for initiating cell cultures under strictly defined conditions.

2. EXPERIMENTAL PROCEDURES

2.1. Materials. All amino acid derivatives and Rink-Amide MBHA resin were purchased from Novabiochem (Läufelfingen, Switzerland). Scavengers, coupling agents, and cleavage reagents were Fluka products (Buchs, Switzerland). Solvents for synthesis and 2-Cl-trityl chloride resin were obtained from Reanal (Budapest, Hungary). Acetonitrile for HPLC was delivered by Sigma-Aldrich (Budapest, Hungary).

Cell culture media and chemicals for cell culturing were purchased from Sigma-Aldrich (Budapest, Hungary). Fetal calf serum (FCS; Gibco) was purchased from Csertex (Budapest, Hungary). Tissue culture plates and dishes were Greiner or Falcon, purchased from Dialab (Budapest, Hungary) and Softflow (Pécs, Hungary), respectively, and the glass coverslips were obtained from Erie Scientific (Budaörs, Hungary).

2.2. Synthesis of Cyclo[Arg-X-Asp-D-Phe-Cys]. Linear side chain protected precursor peptides H-Asp(O^{t}Bu)-D-Phe-Cys(Trt)-Arg(Pbf)-X-OH (where X is Gly or Ala) were synthesized manually by solid-phase peptide synthetic method according to Fmoc/^{t}Bu strategy using 2-Cl-trityl chloride resin as a support (*23*). The attachment of the C-terminal amino acid to the resin was carried out as follows: (i) prior to use, the resin was dried overnight over solid KOH in a desiccator; (ii) swelling of the resin in dichloromethane (DCM) for half an hour, then washing with *N*,*N*-dimethylformamide (DMF); (iii) coupling of the C-terminal amino acid to the resin using 2.5 equiv of Fmoc-Gly-OH or Fmoc-Ala-OH dissolved in DMF and 2.5 equiv of *N*-ethyldiisopropylamine (DIEA) (1 + 1.5 equiv added in two portions) for 1 h, then capping with methanol (0.8 mL/g resin) for 10 min; (iv) washing with DMF (5 × 0.5 min); (v) removal of Fmoc protecting group in three steps: 5% piperidine in DMF for 10 min, 30% piperidine in DMF for 15 min, 50% piperidine in DMF for 30 min; (vi) DMF washing (6 × 1 min). The Fmoc resin loading was determined by Gude's method and resulted in 0.6 mmol/g resin capacity in both cases (*24*).

After this procedure, the further amino acid derivatives were coupled according to the following protocol: (i) coupling of Fmoc-amino acid derivative with 1-hydroxybenzotriazole (HOBt) and *N*,*N*′-diisopropylcarbodiimide (DIC) (3 equiv each) in DMF (the efficacy of the coupling reaction was monitored by ninhydrin assay (*25*)); (ii) DMF washing (5 × 0.5 min); (iii) deprotection in two steps with 30% piperidine in DMF for 3 and 17 min; (iv) DMF washing (6 × 1 min). After washing the peptide-resins with DMF, DCM, methanol, and diethyl ether, the side chain protected peptides were cleaved from the dried resins using a mixture of DCM/methanol/acetic acid = 8:1:1 (v/v/v) for 2 h at room temperature. The cleavage step was repeated, then the cleavage mixtures were combined and the solution was concentrated *in vacuo*. The intermediate crude product was precipitated with cold diethyl ether, filtered, and washed three times with ether afterward. The solid material was dissolved in 5% acetic acid prior to freeze-drying. The purification of the linear side chain protected peptides was not necessary due to their high purity determined by RP-HPLC (over 90%). To change the acetate counterion to chloride, the linear peptide derivatives were dissolved in methanol in the presence of 10 equiv of pyridinium hydrochloride and then the solvent was evaporated.

The dried linear peptides were dissolved in DMF (1 mg/mL), then 3−3 equiv of (benzotriazol-1-yloxy)tris(dimethylamino)-phosphonium hexafluorophosphate (BOP) and HOBt coupling agents in the presence of 6 equiv of DIEA were added to both peptide solutions. The pH of the reaction mixtures was slightly alkaline (pH 7.5−8). Each reaction was followed by RP-HPLC. After 24 h, the reactions were completed; then, the solvent was evaporated *in vacuo*, and the crude products were precipitated with 5% $NaHCO_3$ (aqueous solution), filtered off, and washed with d.i. water until the filtrate was neutral. The cleavage of the side chain protecting groups of the dried cyclic peptides was performed by using modified Reagent-K cleavage mixture: trifluoroacetic acid (9.75 mL), water (0.25 mL), phenol (0.75 g), thioanisole (0.25 mL), ethane-1,2-dithiol (0.25 mL), and triisopropyl silane (0.125 mL) at room temperature for 3.5 h. After cleavage, the crude products were precipitated with cold diethyl ether, washed with ether three times, filtered off, and dried *in vacuo* over P_2O_5, followed by purification using semipreparative RP-HPLC. The pure cyclic peptides were characterized by analytical RP-HPLC and ESI-MS (Table 1). The racemization of Ala-containing peptide under cyclization conditions was determined by using Marfey's reagent (*26, 27*). The D-Ala content of the cyclic peptide was less than 1%.

Table 1. Characteristics of Derivatives

peptides	R_T [min][a]	calculated mass [M]	$[M + H]^{+b}$
cyclo[Arg-Gly-Asp-D-Phe-Cys]	9.0	578.2	578.9
cyclo[Arg-Ala-Asp-D-Phe-Cys]	9.6	592.2	593.0
cyclo[Arg-Gly-Asp-D-Phe-Cys(Cmc)]	7.7	635.3	636.0
H-Arg-Gly-Asp-D-Phe-Cys-NH_2	6.5	595.3	596.2

[a] Column, Vydac 218TP C_{18} (250 × 4.6 mm, 5 μm, 300 Å); eluents, 0.045% TFA/H_2O (A) and 0.036% TFA/acetonitrile (B); gradient, 5−95% B in 30 min; flow rate, 1 mL/min; detection λ = 220 nm. [b] ESI-MS

2.3. Preparation of Cyclo[Arg-Gly-Asp-D-Phe-Cys(Cmc)]. The carboxamidation of the thiol group of the cyclic peptide was carried out as follows: 1 equiv of iodoacetamide to the cyclic peptide was dissolved in 0.1 M Tris buffer (pH 8.1) and the cyclic peptide was added to the solution at a peptide concentration of 1 mg/mL. The reaction was monitored by RP-HPLC. In half an hour, the reaction was completed, the mixture was acidified by addition of a few drops of TFA, and then it was purified by semipreparative RP-HPLC. Pooled fractions were freeze-dried and the purified product was characterized by analytical RP-HPLC and ESI-MS (Table 1).

2.4. Synthesis of H-Arg-Gly-Asp-D-Phe-Cys-OH. In the case of synthesis of the linear RGD peptide, it was cleaved from the 2-ClTrt resin directly by modified Reagent-K mixture and

Table 2. Amino Acid Composition of Conjugates

conjugate	Asp	Gly	Ala	Phe	Lys	Arg
AK-cyclo[RGDfC]	0.33	0.34	4.64	0.34	1.00	0.31
AK-cyclo[RADfC]	0.32	-	5.00	0.33	1.00	0.32
AK-RGDfC	0.34	0.35	4.62	0.33	1.00	0.32

the pure linear peptide was isolated by RP-HPLC purification followed by lyophilization. The purified product was characterized by analytical RP-HPLC and ESI-MS, similarly to the cyclic versions (Table 1).

2.5. Conjugation of Peptides to Chloroacetylated Branched Chain Polymeric Polypeptide. Branched chain polymeric polypeptide (poly[Lys(DL-Ala_m)]; AK) was prepared according to the method previously described (*28*). Chloroacetylation of AK polymer was performed as described before (*29*). Briefly, for the preparation of conjugate, AK ($DP_n = 60$, Ala/Lys= 4.6:1, $M_w = 19\,600$) was reacted with chloroacetic acid pentachlorophenyl ester in DMF/water solution (9/1, v/v): first, 20 mg AK was dissolved in 1 mL water, and then the solution was diluted with 4 mL DMF; after that, 0.5 equiv chloroacetic acid pentachlorophenyl ester (ClAc-OPcp) calculated to the branches (8.2 mg) dissolved in 5 mL DMF was added. The reaction was carried out overnight, and then the mixture was dialyzed against 1% acetic acid for two days. The precipitate (pentachlorophenol) was filtered off and the filtrate was freeze-dried. According to the organic chlorine determination, the molar ratio of chlorine and lysine in polypeptide was 0.4:1 (*30*).

The conjugation reaction of multivalent chloroacetyl-AK polymer and cyclo[RXDfC] peptides or linear H-RGDfC-NH_2 peptide resulting in a thioether linkage was carried out in 0.1 M Tris buffer, pH 8.0. To avoid significant dimerization of RGD peptide derivatives *via* disulfide bond formation, the cysteine containing peptides (2 equiv altogether to the Cl content of the polymer) were added in solid form to the solution of the chloroacetylated polypeptide (1 mg/mL) from time to time during 3 h. In all cases, the reaction was terminated after 24 h by adding an excess of cysteine to block the unreacted chloroacetyl groups. The crude products were dialyzed against d.i. water to remove the unreacted RGD peptides and cyst(e)ine, then freeze-dried. The efficacy of the conjugation was calculated from the amino acid composition of the conjugates using amino acid analysis (Table 2).

2.6. Analysis and Purification by RP-HPLC. Analytical RP-HPLC measurements for the determination of the purity of intermediate peptide derivatives (for cyclization or conjugation) were carried out on Vydac 218TP C_{18} column, 250 × 4.6 mm, particle size 5 μm, pore size 300 Å (Vydac, Hesperia, CA) using Shimadzu HPLC system (two LC-6A pump, SPD-6AV UV-detector, SIL-6B auto injector, SCL-6B system controller; (Shimadzu Corporation, Kyoto, Japan)) with eluent A: 0.045% TFA in H_2O and eluent B: 0.036% TFA in acetonitrile. Linear gradient of 5−95% eluent B was developed with 1 mL/min flow rate, during 30 min. Peaks were detected at $\lambda = 220$ nm.

Purification of peptides was performed using Phenomenex Jupiter C_{18} column (250 × 10 mm, 10 μm, 300 Å) on a Knauer laboratory assembled semipreparative HPLC system (Knauer Pump type 120, Dynamic Mixing Chamber Analytical, Spectro Photometer K-2501; (Knauer, Berlin, Germany)); with eluent A: 0.1% TFA in H_2O and eluent B: 0.1% TFA in acetonitrile−H_2O (80:20, v/v). An isocratic elution with 10% of eluent B was applied from 0 to 5 min, then 5−28 min a gradient elution of 10−33% of eluent B was used with 4 mL/min flow rate. Peaks were detected at $\lambda = 220$ nm.

2.7. ESI Mass Spectrometry Analysis. The identification of the products was achieved by mass spectrometry. Electrospray ionization mass spectrometry was performed with a Bruker Daltonics Esquire 3000 Plus (Bremen, Germany) ion trap mass spectrometer, operating in continuous sample injection at 4 μL/min flow rate. The peptides were dissolved in 50% acetonitrile−water mixture. Mass spectra were recorded in positive ion mode in the *m/z* 200−1500 range.

2.8. Amino Acid Analysis. The amino acid composition of conjugates was determined by amino acid analysis using SYKAM S-433 amino acid analyzer (SYKAM GmbH, Eresing, Germany) equipped for the determination of amino acids with postcolumn reaction with ninhydrin. Prior to analysis, the samples were hydrolyzed in 6 M HCl in sealed and evacuated tubes at 110 °C for 24 h.

2.9. Surface Coatings. For cell-attachment analyses, polystyrene or glass surfaces were coated with the AK-cyclo[RGDfC] or with one of the control peptides (PLL, AK, AK-cyclo[RADfC], AK-RGDfC). The peptides were dissolved in distilled water in concentrations of 0.002−20 μg/mL. The solutions were left on the surfaces for 30 min, then aspirated, and the surfaces were allowed to dry at room temperature. Estimated surface densities—pretending that all molecules were deposited to the surface—were calculated between 0.00025 and 2.5 $\mu g/cm^2$. Coated surfaces could be stored for up to 4 months at 4 °C.

2.10. Atomic Force Microscopy. The morphology of the AK-cyclo[RGDfC] polypeptide layer after drying for at least 24 h was studied with an atomic force microscope (Park Syst. XE-100, South Korea). We used a cantilever NSC15 (Park Syst.) made of Si_3N_4. The tip curvature radius was less than 10 nm and the reflective side was coated with Al. The AFM scans were conducted at 0.3−0.5 Hz scanning rate taken at scan window of 2 × 2 μm. Several randomly selected locations with at least 8−10 different images were collected for each specimen. Observation was carried out at noncontact mode in air. The image analysis was performed using the XIE 1.6 progam (Park Syst.).

The morphology of the protein layers on the glass substrate was characterized by average roughness values (R_a) determined for the whole images.

2.11. Cell Cultures. Cell lines (MDCK, GENC, A431, A7r5, NE-4C, MC3T3-E1 sc4) and HUVEC cells were maintained

Table 3. Investigated Cell Types

name	cell type	origin	maintaining medium	reference
MDCK (madine darby canine kidney)	cloned kidney epithelial	canine	DMEM, 10% FCS	ATCC No.: CCL-34
GENC (glomerular endothelial cell)	cloned glomerular endothelial	mouse	DMEM, 10% FCS	31
A431	cloned epidermal epithelial	human	DMEM, 10% FCS	ATCC No.: CRL-2592
A7r5	cloned aorta smooth muscle	rat	DMEM, 10% FCS	ATCC No.: CRL-1444
NE-4C	cloned neuroepithelial stem cell	mouse	MEM, 4 mM glutamine, 5% FCS	32
MC3T3-E1 sc4	cloned osteoblast	mouse	αMEM, 10% FCS	ATCC No.: CRL-2593
HUVEC (human umbilical vein endothelial cell)	umbilical endothelial	human	M199, 15% FCS	ATCC No.: CRL-1730
primary neurons	neuron	mouse	MEM, 4 mM glutamine, 10% FCS	33
primary astrocytes	astrocyte	mouse	MEM, 10% FCS	34
primary fibroblast	fibroblast	mouse	DMEM, 10% FCS	35
bone marrow mesenchyme	mesenchyme	mouse	DMEM/F12 1/1 (v/v), 10% FCS + 5% HS	36

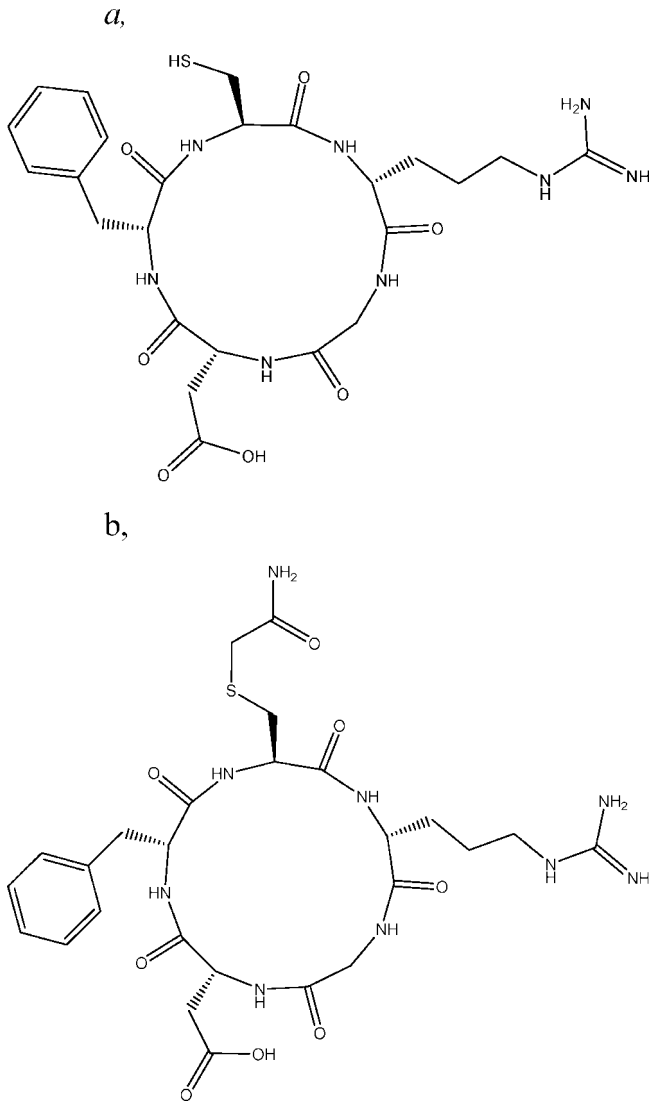

Figure 1. Structure of cyclo[RGDfC] (a) and cyclo[RGDfC(Cmc)] (b).

under standard culture conditions described for the particular cell type (Table 3). Primary cell cultures of neurons (*33*) and astrocytes (*34*) and maintained preparations of fibroblasts (*35*) and bone marrow mesenchymal cells (*36*) were established from mouse tissues and were maintained according to well established protocols, in serum-containing media (Table 3).

For cell-attachment assays, the cells were harvested by trypsinization (0.05 w/v % trypsin, in phosphate buffered saline [PBS] containing 5 mM EDTA). After inhibiting the enzyme activity and washing, the cells were collected in the maintaining media, but without serum. The cells were reseeded onto coated surfaces and were allowed to attach for no longer than 3 h (see below).

For analyzing the 48 h survival, harvested glomerular endothelial cells (GENC) were collected, seeded, and maintained in defined medium composed of DMEM/F12 3/1 (v/v) and supplemented with 1% ITS (ITS-G, GIBCO, Invitrogen) providing a final concentration of 10 μg/mL insulin, 5.5 μg/mL transferrin, and 6.7 ng/mL sodium selenite.

2.12. Microscopic Observations on Initial Cell Adhesion. 35 mm tissue culture dishes precoated with various peptides were placed into a thermo-stabilized (37 °C) chamber on the stand of a Zeiss Axiovert 200 M microscope. 1.5 mL suspensions of cells (5×10^5 cells/mL) in serum-free media were seeded and phase-contrast pictures ($10 \times$ objective) were taken at various time-points after seeding.

Time-lapse microscopic comparison of the initial attachment of MDCK cells on AK- cyclo[RGDfC] and on PLL is available in the Supporting Information. Videomicroscopic analysis was carried out similarly as described above, with a Zeiss Axiovert 200 M microscope. Photographs were taken at every 5 s.

2.13. Quantitative Cell Adhesion Assay. Cells were harvested by trypsinization, centrifuged, and washed with PBS to eliminate trypsin and EDTA and were collected in serum-free media. In some experiments (see the text), the media were supplemented with 5% (v/v) FCS. Cells were seeded into 96-well plates at densities of $(1-5) \times 10^4$ cells/well and were allowed to attach for a time-point, when the majority of cells ($\geq$75%) had adopted a spread-out, flattened shape on AK-cyclo[RGDfC] (1−3 h, depending on the cell type). Cultures were washed with PBS to eliminate nonattached cells and then fixed with 4% paraformaldehyde (w/v in PBS) for 20 min at room temperature. Attached cells were stained with 0.25% methylene blue, for 30 min (*37*). Stained cell mass was dissolved in acidic (0.05 M HCl) ethanol and light absorbance was measured at $\lambda = 650$ nm with a Bio-Rad 450 ELISA reader. For each condition, eight parallel wells were measured. Data were expressed as means and standard deviations.

2.14. Cell Viability Assay. Viability of GENC cells cultured in defined medium was determined by measuring reductive capacity according to Mosmann et al. (*38*). Briefly, cells were grown for 48 h in 96-well plates coated with different peptides and then treated with 3-(4,5-dimethylthiazol-2-yl)-2,5-diphenyltetrazolium bromide (MTT) for two hours at a final concentration of 250 μg/mL. After a 2 h incubation, cells and formazan crystals were dissolved in acidic (0.08 M HCl) isopropanol. Optical density was determined at a measuring wavelength of $\lambda = 570$ nm against $\lambda = 630$ nm as reference with a Bio-Rad

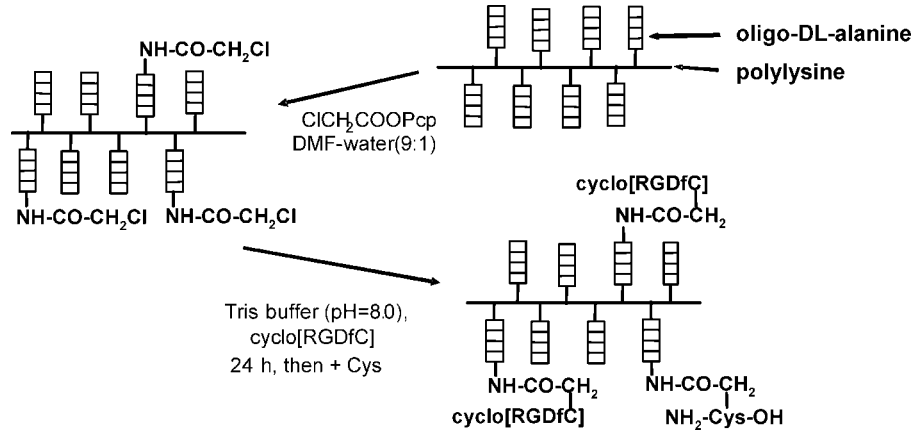

Figure 2. Conjugation of cyclo[Arg-Gly-Asp-D-Phe-Cys] to AK carrier molecule.

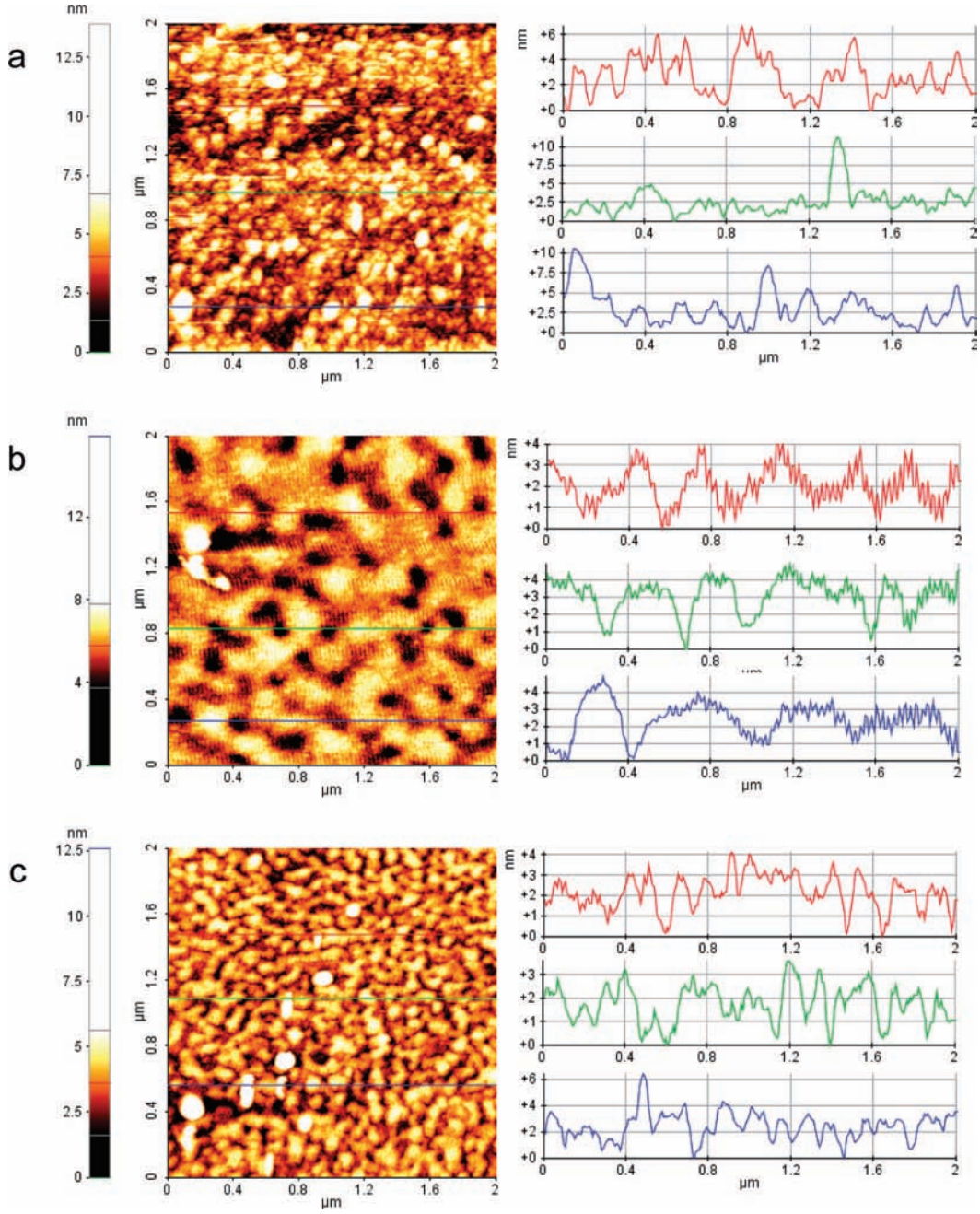

Figure 3. AFM topographic images (2 × 2 μm) of protein films formed from solution with a concentration of 2.5 (a), 0.25 (b), and 0.025 (c) μg/mL. Three selected profile lines are displayed for each image to present typical vertical cross sections of the protein films.

450 ELISA reader. Assays were carried out on 8 parallel wells. The viability data were expressed as means and standard deviations.

2.15. Visualization of Actin Cytoskeleton with Rhodamine-Conjugated Phalloidin. MDCK cells were plated onto AK-cyclo[RGDfC] coated glass coverslips in serum-free medium. They were fixed after 1.5 or 24 h with 4% paraformaldehyde for 20 min. The cell membranes were permeabilized by 5 min treatment with 0.1% Triton-X 100 (in PBS). Actin cytoskeleton was labeled with rhodamine-conjugated phalloidin according to the manufacturer's instruction (Invitrogen) and analyzed with a Zeiss Axiovert 200 M fluorescent microscope.

2.16. Statistical Analysis. All data were expressed as means and standard deviations. Statistical significance was determined by Student's *t* test. Differences were considered significant at $p < 0.05$.

3. RESULTS

3.1. Synthesis and Characterization of Cyclic RGD Conjugated AK Polymer. The aim of the present study was the development of cell adhesive conjugates carrying the biologically active integrin ligand, cyclic RGD peptide (cyclo-[RGDfC]) (Figure 1a) to provide potent adhesive surfaces for a wide range of cell types. As macromolecules with polycationic property bind readily to negatively charged tissue culture dishes and metal oxide surfaces, a polycationic branched polypeptide AK (Figure 2) with polylysine backbone was selected, in which oligo-DL-alanine moieties were introduced as branching side chains (poly[Lys(DL-Ala)$_m$]). The resulting AK (Figure 2) was used as polymeric carrier. The cyclic peptide cyclo[RGDfC] and also its cyclic and linear control derivatives (cyclo[RADfC] and H-RGDfC-NH_2)—which served as control peptides—were coupled to the AK polymer *via* thioether bonds. The thioether

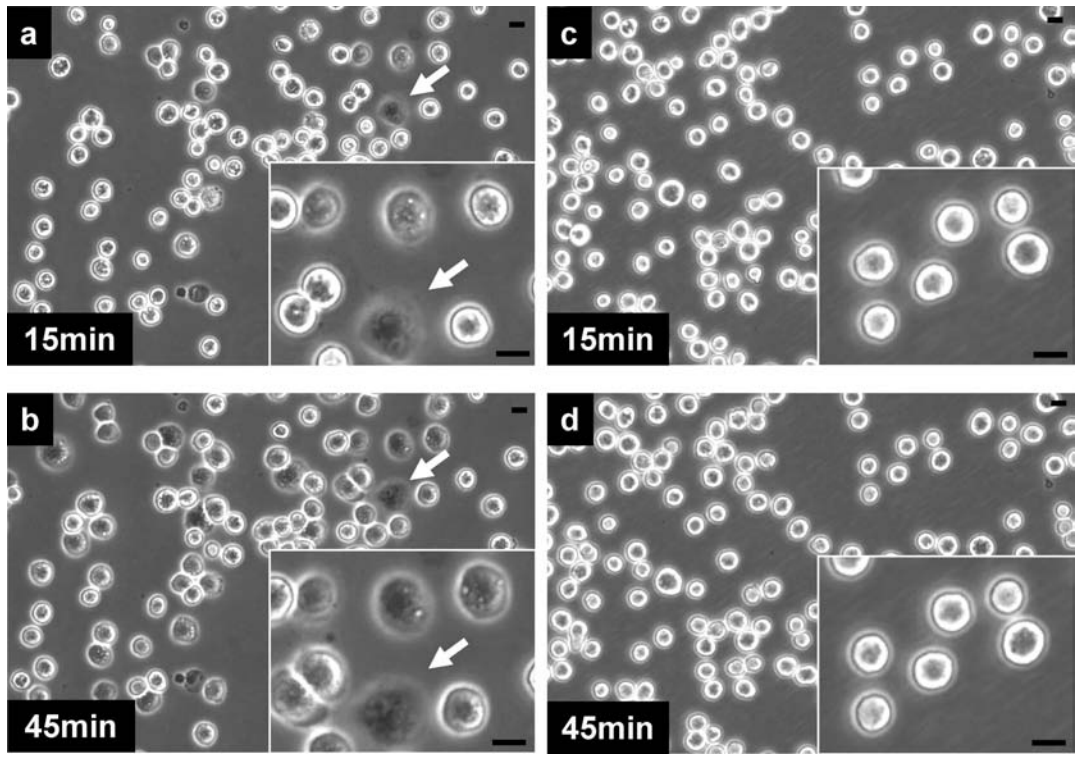

Figure 4. Initial attachment of MDCK cells on AK-cyclo[RGDfC] (a,b) and PLL (c,d) coated plastic surfaces. Pictures were taken at 15 and 45 min after plating. Note spreading cells (arrows) on the enlarged inserts on the left panels. Bars represent 10 μm.

linkage has several advantages such as easy and selective formation and high stability under the conditions of the chemical synthesis, purification, and biological measurements. For the formation of the thioether bond, the AK polymer was chloroacetylated using ClAc-OPcp, and a cysteine residue was incorporated into the sequence of the RGD peptides. To avoid the racemization during the "head-to-tail" cyclization step, glycine or alanine were the C-terminal amino acid residues. In this way, a linear, side chain protected precursor peptide with a sequence of DfCRX (X = Gly or Ala) was built up on solid phase. The peptide was prepared on 2-Cl-trityl chloride resin by Fmoc/^{t}Bu strategy. The side chain protected linear precursor peptide with free N- and C-termini (H-D(O^{t}Bu)fC(Trt)R(Pbf)X-OH) was produced by cleavage using a mixture of DCM/MeOH/AcOH = 8:1:1 (v/v/v). The purity of the crude products was over 90%; therefore, they were applied for cyclization without further purification. The "head-to-tail" cyclization was performed in a diluted DMF solution in the presence of BOP and HOBt coupling reagents and DIEA base to provide slightly alkaline conditions. The side chain protecting groups were removed from the cyclic peptides with a modified Reagent-K cleavage mixture. For a comparative study, a thiol-protected form of the cyclic peptide was also produced by carboxamidation of the Cys side chain (c[RGDfC(Cmc)]) (Figure 1b) using iodoacetamide. In order to analyze the importance of the RGD sequence and the cyclic form of the peptide, two further compounds were prepared (cyclo[RADfC] and H-RGDfC-NH_2) for conjugation. The peptides were characterized by RP-HPLC and ESI-MS (Table 1). Racemization study of cyclo[RADfC] showed no significant epimerization of Ala under cyclization conditions.

Prior to conjugation, the AK polymer was "activated" by chloroacetylation of the amino groups of the polypeptide using ClAc-OPcp at a molar ratio that resulted in about 40% substitution of the side chains of the polymer. The incorporated chlorine atoms could be exchanged for thiol-containing cyclic peptides in a nucleophile substitution reaction under slightly alkaline conditions. To avoid significant dimerization of the cysteine containing cyclic peptides by disulfide bond formation, the cyclic peptides were added in solid form to the solution of the choloracetylated polypeptide and the concentration of the peptide was kept low in the reaction mixture. After the conjugation reaction, unreacted chloroacetyl groups were blocked by the addition of an excess of cysteine to prevent alkylation during the biological experiments. The amount of the attached RGD peptides was calculated by the results of amino acid analysis (Table 2). In all three cases, 32−33% substitution of the branches of the polypeptide carrier was observed.

3.2. Coverage of the Substrate by the Deposited Peptide−Conjugates. Topographic AFM images (Figure 3) on peptide-coated glass substrates showed that the AK-cyclo[RGDfC] polypeptide conjugate formed continuous layers on the substrate. The roughness values of peptide-covered surfaces highly exceeded the values obtained for the pure glass (R_a < 0.1 nm) substrate. The surface roughness increased with the increasing peptide concentrations (0.025−2.5 μg/mL) with the average roughness values of 1.056, 0.777, and 0.729 nm for films prepared from solutions with concentrations of 2.5, 0.25, and 0.025 μg/mL, respectively. Sectional analyses on the structural details showed aggregates extending from the layer. The peak values of emerging aggregates reached about 10 nm on surfaces deposited from 2.5 μg/mL peptide solution.

3.3. Cell Adhesion. The initial attachment, spreading, and short-term (24−48 h) survival of different types of cells (Table 3) were investigated on surfaces coated with AK-[cRGDfC] polymer and were compared to the cell behavior on plastic or glass surfaces coated with control peptides. The cell types involved in the studies included cloned cell lines, long-term maintained tissue-derived cells (HUVEC, mouse bone marrow mesenchyme cells, and fibroblasts), and primary tissue cells (neurons, astrocytes) directly isolated by tissue dissociation (Table 3). The control substrates included tissue-culture treated polystyrene, poly(L-lysine) (PLL), the poly(L-lysine-alanine) (AK) carrier polypeptide, the AK-cyclo[RADfC] conjugate with

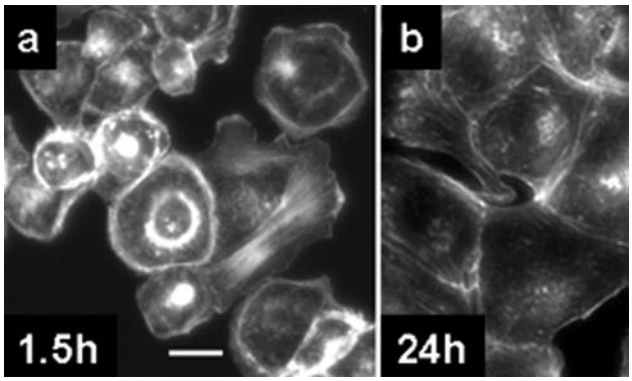

Figure 5. The rearrangement of actin fibers in MDCK cells attaching to (a) and spreading on (b) AK-cyclo[RGDfC] coated glass surfaces were visualized by rhodamine-conjugated phalloidin staining. Pictures were taken 1.5 (a) and 24 h (b) after plating. Bars represent 10 μm.

a corrupted RGD motive, and the AK-RGDfC conjugate containing the linear form of the pentapeptide. Cell attachment was assayed in serum-free environment.

The morphological observations on the cell shape during initial attachment and spreading followed with videomicroscopy (see Supporting Information) and conventional microscopy (Figure 4) indicated a rapid initial attachment to AK-cyclo-[RGDfC] coated surfaces. In the initiation of flattening, however, cell type dependent differences were observed. MDCK, GENC, or NE-4C cells were flattening against the AK-cyclo[RGDfC] coated surface within 10−15 min (Figure 4a), while spreading of MC 3T3 osteoblasts, HUVECs, or astroglial cells was observed no sooner than 40−60 min after plating. In comparison to control surfaces (bare polystyrene, PLL or AK, AK-cyclo[RADfC], AK-RGDfC), however, all cells developed filopodia and lamellipodia earlier on AK-cyclo[RGDfC] and cells flattened in a significantly shorter period (Figure 4).

The rearrangement of actin fibers during attachment to AK-cyclo[RGDfC] was visualized by rhodamine-conjugated phalloidin (Figure 5). In MDCK cells adhering to AK-cyclo[RGDfC] coated surface, spreading cells with actin stress fibers were observed within 1−1.5 h, among cells with an actin arrangement characteristic of initial attachment (*39*), namely, the inner actin ring and the outer actin zone at the actively palpating filopodia (Figure 5a). The cells kept on spreading until settling in a flattened monolayer arrangement (24 h), with stress fibers oriented toward the cell periphery and distributed almost evenly (Figure 5b). The morphological changes indicated that the contact with AK-cyclo[RGDfC] coated surface initiated a normal schedule of attachment, at least as it was judged by the rearrangement of the actin filaments.

Cell attachment was measured by colorimetric cell adhesion assay, modified after Oliver et al. (*37*). Evaluation of the attached cell mass after a period of initial attachment (see Experimental Procedures) revealed that AK-cyclo[RGDfC] promoted the initial attachment of all investigated cells, except freshly isolated neurons.

AK-cyclo[RGDfC] improved attachment if it was deposited from solutions containing 0.025−2.5 μg peptide per cm^2. The sufficient coating density, however, was cell type dependent. MDCK or NE-4C cells needed less dense (0.025 μg/cm^2 or 0.25 μg/cm^2, respectively) coating (Figure 6a), while MC 3T3 osteoblasts, astroglia, or fibroblast cells demanded higher density (2.5 μg/cm^2) for robust attachment (Figure 6b). The adhering cell mass increased with increasing AK-cyclo[RGDfC] density up to an "upper threshold". In the case of MDCK or GENC cells, adhesivity did not increase above the coating density of 0.25 μg/cm^2, while in the case of weakly adhering cells, an "upper threshold" was not reached even at the highest applied (2.5 μg/cm^2) density (Figure 6b). With changing concentration of AK-cyclo[RGDfC] solution, e.g., increasing the density of the coating molecules at the surface, the optimum coats for particular cells could be determined. Addition of fetal bovine serum (5%) to the medium could improve the attachment at low AK-cyclo[RGDfC] surface densities in the initial (1.5−3 h) period, but failed to influence cell attachment at or above the optimum coating density (Figure 7).

To test the specific adhesive effects of the cyclo[RGDfC] containing polymer, two different control motifs—a linear pentapeptide RGDfC and a cyclic pentapeptide (cyclo[RADfC])

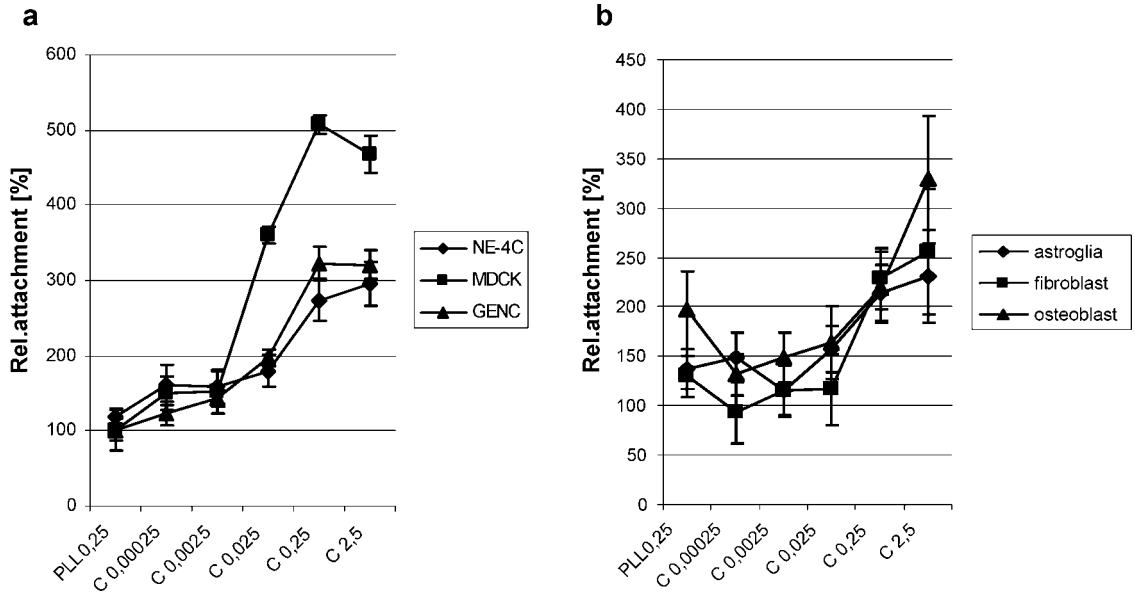

Figure 6. The attachment of different types of cells to AK-cyclo[RGDfC] deposited from coating solutions containing 0.00025−2.5 μg peptide−conjugate/cm^2. Attachment was determined by photometric evaluation of methylene-blue staining after washing off the unattached cells. The data are presented as the percentages of attachment on polystyrene (100%). Note the cell type dependent differences in the "threshold coating density" for attachment. Attachment of MDCK, GENC, and NE-4C cells (a); attachment of astrocytes, fibroblasts, and osteoblasts (b). (Abbreviations: PLL, poly(L-lysine); C, AK-cyclo[RGDfC]; the numbers indicate the peptide content [μg] in the coating solution calculated for 1 cm^2 surface area). Averages and standard deviations were calculated from 8 identical preparations.

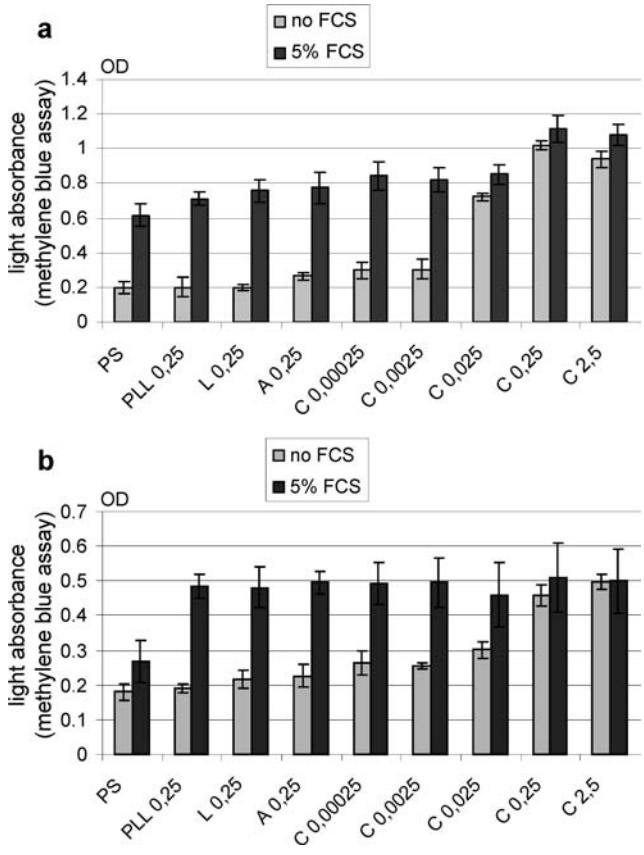

Figure 7. The effect of serum on the attachment of MDCK (a) and NE-4C (b) cells to AK-cyclo[RGDfC], AK-c[RADfC], AK-RGDfC, and poly(L-lysine) coated or bare, tissue culture treated polystyrene surfaces. Attachment was determined by photometric evaluation of methylene blue staining after washing off the unattached cells. The data are shown as averages and standard deviations of optical densities measured in 8 parallel preparations. Note that, above an "upper threshold density" of AK-cyclo[RGDfC], the presence of 5% FCS did not significantly improve the attachment. (Abbreviations: OD, optical density; PS, polystyrene; PLL, poly(L-lysine); A, AK-c[RADfC]; L, AK-RGDfC; C, AK-cyclo[RGDfC]; the numbers represent estimated surface densities of the coating peptides in $\mu g/cm^2$).

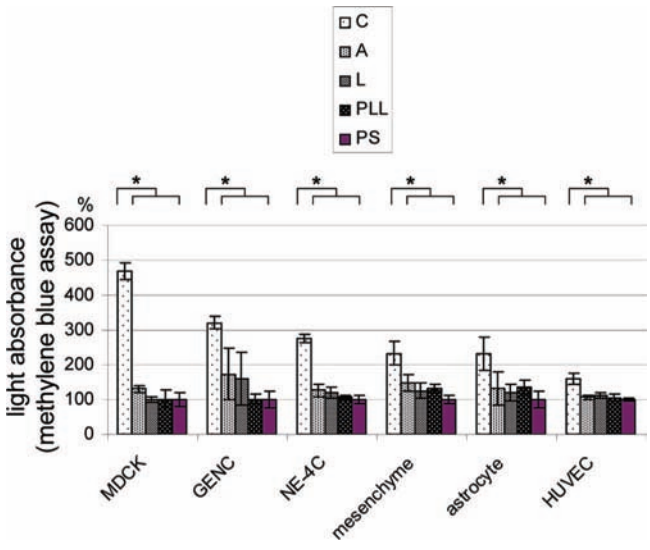

Figure 8. Comparison of initial attachment of various cell types (MDCK, GENC, NE-4C, mesenchyme, astrocyte, and HUVEC) on different substrates. The data are presented as the percentages of attachment on polystyrene (100%). (Abbreviations: PS, polystyrene; PLL, poly(L-lysine); A, AK-c[RADfC; L, AK-RGDfC; C, AK-cyclo[RGDfC]).

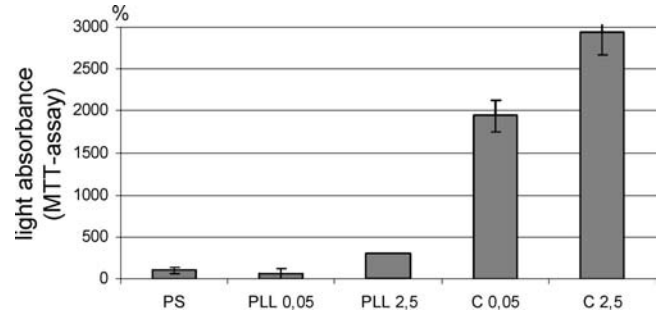

Figure 9. Serum-free survival of glomerular endothelial cells (GENC) on AK-cyclo[RGDfC] coated surfaces. MTT-assay revealed an almost 30-fold increase in viability on AK-cyclo[RGDfC] compared to polystyrene (PS) surface after 48 h. The data are presented as the percentages and standard deviations of viability on polystyrene. (Abbreviations: PS, polystyrene; PLL, poly(L-lysine); C, AK-cyclo-[RGDfC]; numbers represent the estimated surface densities of the coating peptides in $\mu g/cm^2$; 100% represents the OD value of the MTT assay on polystyrene).

with a corrupted RGD-motive—were designed and bound to the AK carrier. Neither the AK-RGDfC nor the AK-cyclo[RADfC] could support the attachment of the investigated cell types (Figure 8). On these substrates, both the morphology of the cells and the rate of attachment were indistinguishable from those observed on PLL or on the pure AK carrier peptide. The data support the importance of the stereochemical structure of the cyclo[RGDfC] motif in mediating cell adhesion.

3.4. Serum-Free Conditions for Growth of Cells. While cell type dependent growth factors have to be provided for long-term culturing of a number of cells, the application of AK-cyclo[RGDfC] surface could prevent anoikis (cell death initiated by lack of adhesion) in the case of anchorage-dependent cells. The AK-cyclo[RGDfC] surface supported a 48 h survival of several (tested for NE-4C, MDCK, GENC) types of cells in defined media (GENC; Figure 9) a "long-term" period if rapid anoikis is regarded. Moreover, serum-free cultures of selected neural stem-like cells were grown on AK-cyclo[RGDfC], in defined media supplemented with epithelial growth factor (EGF), for several weeks (personal communication; Marko et al.; manuscript in preparation). The use of the adhesive peptide conjugate provided strictly defined, serum-free conditions for initiation of cell cultures, and also for long-term growth of selected cell types.

4. DISCUSSION

In the present study, we report on the development of a novel, synthetic cell adhesion polypeptide. The conjugate contains a poly(L-lysine) backbone with oligo-DL-alanine side chains carrying biologically active cyclo[RGDfC] integrin ligand motifs at the N-termini of the oligo-alanine chains. The poly(L-lysine) backbone was chosen for promoting binding to a number of different substrates including tissue culture dishes, glass, and metal oxide surfaces. As was expected, AK-cyclo[RGDfC] bound readily to SiO_2 or metal oxide surfaces as was demonstrated by our previous studies (*40*) using the label-free OWLS technique (*41*).

To increase the accessibility of the attached cyclopeptide, a spacer was built from raceme alanine residues resulting in flexible, unstructured peptide side chains as was confirmed by previous CD analysis on AK polypeptide and related peptides (*42*, *43*). The random incorporation of 3 to 5 raceme alanine residues was shown to increase the flexibility of the spacer as well as the solubility of the carrier (*44*). The raceme oligo-alanine side chains increased the steric flexibility of the cyclo[RGDfC] end motif and improved the water solubility of the conjugate by preventing helix formation.

As a biologically active, cell-adhesive moiety, the cyclo-[RGDfC] cyclic pentapeptide was chosen due to the strong affinity of cyclic RGD pentapeptides to cell surface integrins (*19*) and the availability for conjugation through the Cys residue. The introduction of a D-enantiomer phenyalanine into the peptide ring was thought to result in a rigid RGD motif, easily recognized by integrins (*19*). The fact that AK conjugates carrying either the linear RGDfC pentapeptide or the cyclic cyclo[RADfC] peptide (with corrupted integrin binding motif) failed to support cell adhesion suggests that a precise positioning of the RGD sequence plays a crucial role in the enhanced cell-adhesive effect of the cyclo[RGDfC] conjugate. Cyclic RGD-containing peptides were reported to be potent ligands for a series of different integrin receptors, with a predominant selectivity to $\alpha_v\beta_3$, $\alpha_v\beta_5$, and $\alpha_v\beta_6$ (*22*). The specificity of the cyclic pentapeptide for integrin receptors, however, might have been modified as a consequence of coupling to the carrier polymer and also by introducing the Cys amino acid. Our previous observations demonstrated that—at least in the case of the investigated cell types—the soluble cyclo[RGDfC] and cyclo[RGDfV] pentapeptides exerted almost the same effect in cell detachment assays (Marko et al., personal observation).

While the exact amount of molecules for unit areas could not be determined, the density of the RGD-containing motifs on the surface seemed to play a crucial role in adhesivity. We think that with increasing local density of the ligand motifs, integrins displaying lower affinity to the specified ligand will also be implicated in binding, and therefore, the peptide will initiate cell adhesion above a defined "threshold density". Atomic force microscopic studies showed increasing surface roughness and aggregate formation with increasing concentration of the peptide−conjugate in the coating solution. The changing surface topography might contribute to the concentration-dependent adhesion preferences displayed by different cell types.

The AK-cyclo[RGDfC] polymer provided adequate adhesive coating for many different types of cells including cloned cells of epithelial, endothelial, or smooth muscle origin, and tissue-derived astrocytes, fibroblasts, mesenchymal, and neural stem cells.

We found that, below a "threshold" of deposited AK-cyclo[RGDfC], cell adhesion was improved by addition of serum, while at high surface densities of the conjugate, the serum did not affect adhesion. The observation indicates a synergistic action of the AK-cyclo[RGDfC] peptide with some serum components in initial cell adhesion. As fibronectin and vitronectin are the most abundant cell adhesive components in sera (*45*), the findings are in accordance with the notion that cyclic RGD pentapeptides are predominantly fibronectin- and/or vitronectin-mimetic integrin ligands.

As an exception, primary neurons could not adhere to AK-cyclo[RGDfC]. Neurons are known to adhere preferentially to the surface of glial cells or to laminin coatings *in vitro* (*46*), and—in the absence of adequate substrates—they form aggregates. As a consequence and for further application, AK-cyclo[RGDfC] may provide a "panning" surface to sort out non-attaching neurons from readily adhering non-neuronal cells.

For the anchoring of a wide variety of cells, AK-cyclo-[RGDfC] provides a chemically defined adhesive surface coating which supports serum-free cell attachment and survival in the most critical initial period of cell propagation on artificial surfaces. The defined adhesive layer, together with serum-free culture initiation, opens the way for strictly controlled cell cultivation and improves the conditions for growing human cells for therapeutic purposes. Degradation and *in vivo* stability studies should determine whether AK-cyclo[RGDfC] may serve also for coating implant surfaces, especially in cases when rapid attachment of the host cells is required.

ACKNOWLEDGMENT

This work was supported by the Hungarian National Science Fund (OTKA T 049814), Ministry of Health (ETT 202/2006), GVOP-3.2.1.-2004-04-0005/3.0, GVOP-3.2.1-2004-99/3.0., Natl. Science & Devl. Prog. NKFP 1A-060/2004, and NKFP 3A-058/2004. The authors are grateful for Zsuzsanna Környei and Bálint Szabó for their help in videomicroscopy.

Supporting Information Available: Time-lapse microscopic comparison of the attachment of MDCK cells on AK-cyclo-[RGDfC] and PLL substrares. This material is available free of charge via the Internet at http://pubs.acs.org.

LITERATURE CITED

(1) Howe, A. K., Aplin, A. E., and Juliano, R. L. (2002) Anchorage-dependent ERK signaling-mechanisms and consequences. *Curr. Opin. Genet. Devel. 12*, 30–35.
(2) Newman, C. (2003) Serum-free cell culture - the ethical, scientific and economic choice. *Biomed. Sci.* 940–941.
(3) www.focusonalternatives.org.uk.
(4) Bershadsky, A., Chausovsky, A., Becker, E., Lyubimova, A., and Geiger, B. (1996) Involvement of microtubules in the control of adhesion-dependent signal transduction. *Curr. Biol. 6*, 1279–1289.
(5) Hersel, U., Dahmen, C., and Kessler, H. (2003) RGD modified polymers: biomaterials for stimulated cell adhesion and beyond. *Biomaterials 24*, 4385–4415.
(6) Hynes, R. O. (2002) Integrins: bidirectional, allosteric signaling machines. *Cell 110*, 673–687.
(7) ffrench-Constant, C., and Colognato, H. (2004) Integrins: versatile integrators of extracellular signals. *Trends Cell Biol. 14*, 678–686.
(8) Biesalski, M. A., Knaebel, A., Tu, R., and Tirrell, M. (2006) Cell adhesion on a polymerized peptide-amphiphile monolayer. *Biomaterials 27*, 1259–1269.
(9) Comisar, W. A., Kazmers, N. H., Mooney, D. J., and Linderman, J. J. (2007) Engineering RGD nanopatterned hydrogels to control preosteoblast behavior: a combined computational and experimental approach. *Biomaterials 28*, 4409–4417.
(10) Connelly, J. T., Garcia, A. J., and Levenston, M. E. (2007) Inhibition of in vitro chondrogenesis in RGD-modified three-dimensional alginate gels. *Biomaterials 28*, 1071–1083.
(11) Hwang, D. S., Sim, S. B., and Cha, H. J. (2007) Cell adhesion biomaterial based on mussel adhesive protein fused with RGD peptide. *Biomaterials 28*, 4039–4046.
(12) Larsen, C. C., Kligman, F., Kottke-Marchant, K., and Marchant, R. E. (2006) The effect of RGD fluorosurfactant polymer modification of ePTFE on endothelial cell adhesion, growth, and function. *Biomaterials 27*, 4846–4855.
(13) Schuler, M., Owen, G. R., Hamilton, D. W., de Wild, M., Textor, M., Brunette, D. M., and Tosatti, S. G. (2006) Biomimetic modification of titanium dental implant model surfaces using the RGDSP-peptide sequence: a cell morphology study. *Biomaterials 27*, 4003–4015.
(14) Storrie, H., Guler, M. O., Abu-Amara, S. N., Volberg, T., Rao, M., Geiger, B., and Stupp, S. I. (2007) Supramolecular crafting of cell adhesion. *Biomaterials 28*, 4608–4618.
(15) Tugulu, S., Silacci, P., Stergiopulos, N., and Klok, H. A. (2007) RGD-Functionalized polymer brushes as substrates for the integrin specific adhesion of human umbilical vein endothelial cells. *Biomaterials 28*, 2536–2546.
(16) Weber, L. M., Hayda, K. N., Haskins, K., and Anseth, K. S. (2007) The effects of cell-matrix interactions on encapsulated beta-cell function within hydrogels functionalized with matrix-derived adhesive peptides. *Biomaterials 28*, 3004–3011.
(17) Pierschbacher, M. D., and Ruoslahti, E. (1984) Cell attachment activity of fibronectin can be duplicated by small synthetic fragments of the molecule. *Nature 309*, 30–33.

(18) Pierschbacher, M. D., and Ruoslahti, E. (1987) Influence of stereochemistry of the sequence Arg-Gly-Asp-Xaa on binding specificity in cell adhesion. *J. Biol. Chem. 262*, 17294–17298.
(19) Aumailley, M., Gurrath, M., Muller, G., Calvete, J., Timpl, R., and Kessler, H. (1991) Arg-Gly-Asp constrained within cyclic pentapeptides. Strong and selective inhibitors of cell adhesion to vitronectin and laminin fragment P1. *FEBS Lett. 291*, 50–54.
(20) Pfaff, M., Tangemann, K., Muller, B., Gurrath, M., Muller, G., Kessler, H., Timpl, R., and Engel, J. (1994) Selective recognition of cyclic RGD peptides of NMR defined conformation by alpha IIb beta 3, alpha V beta 3, and alpha 5 beta 1 integrins. *J. Biol. Chem. 269*, 20233–20238.
(21) Haubner, R., Gratias, R., Diefenbach, B., Goodman, S. L., Jonczyk, L., and Kessler, H. (1996) Structural and functional aspects of RGD-containing cyclic pentapeptides as highly potent and selective integrin alphaV beta3 antagonists. *J. Am. Chem. Soc. 118*, 7461–7472.
(22) Goodman, S. L., Holzemann, G., Sulyok, G. A., and Kessler, H. (2002) Nanomolar small molecule inhibitors for alphav(beta)6, alphav(beta)5, and alphav(beta)3 integrins. *J. Med. Chem. 45*, 1045–1051.
(23) Barlos, K., Chatzi, O., Gatos, D., and Stavropoulos, G. (1991) 2-Chlorotrityl chloride resin. Studies on anchoring of Fmoc-amino acids and peptide cleavage. *Int. J. Pept. Protein Res. 37*, 513–520.
(24) Gude, M., Ryf, M., and White, P. D. (2002) An accurate method for the quantitation of Fmoc-derivatized solid phase supports. *LIPS 9*, 203–206.
(25) Kaiser, E., Colescott, R. L., Bossinger, C. D., and Cook, P. I. (1970) Color test for detection of free terminal amino groups in the solid-phase synthesis of peptides. *Anal. Biochem. 34*, 595–598.
(26) Szokan, G., Mezo, G., and Hudecz, F. (1988) Application of Marfey's reagent in racemization studies of amino acids and peptides. *J. Chromatogr. 444*, 115–122.
(27) Marfey, P. (1984) Determination of D-amino acids. II. Use of a bifunctional reagent, 1,5-difluoro-2,4-dinitrobenzene. *Carlsberg Res. Commun. 49*, 591–596.
(28) Hudecz, F. (1995) Design of synthetic branched-chain polypeptides as carriers for bioactive molecules. *Anti-cancer Drugs 6*, 171–193.
(29) Mezo, G., de Oliveira, E., Krikorian, D., Feijlbrief, M., Jakab, A., Tsikaris, V., Sakarellos, C., Welling-Wester, S., Andreu, D., and Hudecz, F. (2003) Synthesis and comparison of antibody recognition of conjugates containing herpes simplex virus type 1 glycoprotein D epitope VII. *Bioconjugate Chem. 14*, 1260–1269.
(30) Schoniger, W. (1955) Eine mikroanalytische schnellbesimmung von halogenen in organischen substanzen. *Microchim. Acta 1*, 123–129.
(31) Akis, N., and Madaio, M. P. (2004) Isolation, culture, and characterization of endothelial cells from mouse glomeruli. *Kidney Int. 65*, 2223–2227.
(32) Schlett, K., and Madarasz, E. (1997) Retinoic acid induced neural differentiation in a neuroectodermal cell line immortalized by p53 deficiency. *J. Neurosci. Res. 47*, 405–415.
(33) Madarász, E., Kiss, J., and Bartók, I. (1984) Cell production and morphological pattern formation in primary brain cell cultures. I. Pattern formation within the basal layer(s). *Brain Res. 304*, 339–349.
(34) Környei, Z., Szlávik, V., Szabó, B., Gócza, E., Czirók, A., and Madarász, E. (2005) Humoral and contact interactions in astroglia/stem cell co-cultures in the course of glia-induced neurogenesis. *Glia 49*, 430–444.
(35) Nagy, A., Gertsenstein, M., Vintersten, K., and Behringer, R. (2003) Preparing Mouse Embryo Fibroblast. In *Manipulating the mouse embryo: a laboratory manual* (Nagy, A., Vintersten, K., and Behringer, R., Eds.) pp 371−373, Cold Spring Harbor Press, Cold Spring Harbor.
(36) Urbán, V. S., Kiss, J., Kovács, J., Gócza, E., Vas, V., Monostori, É., and Uher, F. (2008) Mesenchymal stem cells cooperate with bone marrow cells in therapy of diabetes. *Stem Cells 26* (1), 244–253.
(37) Oliver, M. H., Harrison, N. K., Bishop, J. E., Cole, P. J., and Laurent, G. J. (1989) A rapid and convenient assay for counting cells cultured in microwell plates: application for assessment of growth factors. *J. Cell Sci. 92*, 513–518.
(38) Mosmann, T. (1983) Rapid colorimetric assay for cellular growth and survival: application to proliferation and cytotoxicity assays. *J. Immunol. Methods 65*, 55–63.
(39) Defilippi, P., Olivo, C., Venturino, M., Dolce, L., Silengo, L., and Tarone, G. (1999) Actin cytoskeleton organization in response to integrin-mediated adhesion. *Microsc. Res. Technique 47*, 67–78.
(40) Madarász, E., Lefkovets, I., Erdélyi, K., and Szendro, I. (2006) Label-free OWLS assays on the kinetics of cell-attachment: quantification of cell adhesivity. *Progress on post-genome technologies - Proceeding of the 4th International Forum of Post-genome Technologies*, 7
(41) Vörös, J., Ramsden, J. J., Csúcs, G., Szendro, I., De Paul, S. M., Textor, M., and Spencer, N. D. (2002) Optical grating coupler biosensors. *Biomaterials 23*, 3699–3710.
(42) Votavova, H., Hudecz, F., Kajtár, J., Szekerke, M., Sponar, J., and Blaha, K. (1980) Conformation of branched polypeptides based on poly(L-lysine) - Circular-dichroism study. *Collect. Czech. Chem. Commun. 45*, 941–949.
(43) Mezo, G., Hudecz, F., Kajtár, J., and Szekerke, M. (1990) Synthesis and chiroptical properties of model peptides suitable for the immunological characterization of branched polypeptides with the general formula poly[Lys(Xi-DL-Alam)]. *Acta Chim. Hung. 127*, 803–812.
(44) Szokan, G., Mezo, G., Hudecz, F., Majer, Z., Schön, I., Nyeki, O., Szirtes, T., and Dölling, R. (1989) Racemization analysis of peptides and amino acid derivatives by chromatography with pre-column derivatization. *J. Liquid Chromatogr. 12*, 2855–2875.
(45) Underwood, P. A., Bean, P. A., Mitchell, S. M., and Whitelock, J. M. (2001) Specific affinity depletion of cell adhesion molecules and growth factors from serum. *J. Immunol. Methods 247*, 217–224.
(46) Ventimiglia, R., and Lindsay, R. M. (1998) Rat striatal neurons in low-density, serum-free culture, in *Culturing nerve cells*, 2nd ed. (Banker, G., and Goslin, K., Eds.) pp 371−393, MIT Press, Cambridge, Massachusetts.

BC8000134

Hyaluronan-Tethered Opioid Depots: Synthetic Strategies and Release Kinetics *In Vitro* and *In Vivo*

Diego A. Gianolio, Michael Philbrook, Luis Z. Avila, Lauren E. Young, Lars Plate, Michael R. Santos, Richard Bernasconi, Hanlan Liu, Sujin Ahn, Wei Sun, Peter K. Jarrett, and Robert J. Miller*

Drug and Biomaterial Research and Development, Genzyme Corporation, 153 Second Avenue, Waltham, Massachusetts 02451.
Received February 4, 2008; Revised Manuscript Received July 14, 2008

We proposed the use of opioid drug bound covalently to hyaluronan (HA) via ester linkages as a method to prolong drug delivery and to possibly increase the quality of perioperative pain management. The *in vitro* release profile of morphine conjugated to HA (1.3 million MW) was studied. The influence of parameters such as conjugation site and steric protection of the labile ester bonds was investigated in phosphate buffered saline (PBS) medium. HA−codeine and HA−naloxone conjugates were used as structural controls. Codeine and morphine conjugated via the allylic hydroxyl group had a release half-life of 14.0 days in PBS. Naloxone conjugated via the phenolic hydroxyl group showed a half-life of 0.3 days, and all drugs admixed in HA showed half-lives of 0.1 days. Methyl, ethyl, or *n*-propyl introduced in vicinal position to the ester bond prolonged release of naloxone with half-lives of 0.5, 4.0, and 4.0 days in PBS, respectively. Incorporation of a methyl group prolonged codeine release with a half-life of 55.0 days in PBS. Drugs were released chemically unaltered from the conjugates as confirmed by LC-MS/MS. Further, morphine was conjugated to divinylsulfone cross-linked HA (Hylan B) particles and the release profiles in rat plasma were studied *in vitro* and *in vivo*. Release in rat plasma was faster than in PBS with a half-life of 2.5 days, but the release was similar (ca. 12 days) when a cocktail of protease inhibitors was added to the plasma. Sustained release of morphine was observed in a rat surgical model over 30 h. Morphine was released chemically unaltered from the conjugate and morphine intermediates were not detected in significant amounts as confirmed by LC-MS/MS. These results suggest that the morphine release profile from the HA conjugates depends on the alkyl groups vicinal to the ester and the nature of the leaving group. In rat plasma, hydrolysis seems to be controlled by esterase activity.

INTRODUCTION

Perioperative pain management has been shown to maintain the patient's functional abilities, reduce hospital costs due to faster recovery times, and improve patient well-being due to decreased incidence of adverse events (*1*−*3*). Pain control may have a further benefit of improving clinical outcome by reducing postoperative complications such as myocardial infarction or ischemia, risk of tachycardia and dysrhythmia impaired wound healing, risk of atelectasis, thromboembolic events, peripheral vasoconstriction, and metabolic acidosis (*4*−*9*).

Techniques used by anesthesiologists for perioperative pain control include epidural or intrathecal opioid analgesia, patient-controlled analgesia with systemic opioids, and regional analgesic techniques, including but not limited to intercostal blocks, plexus blocks, and local anesthetic infiltration of incisions (*10*). Many hydrophilic opioids, such as morphine, have very short half-lives in the body (i.e., 2−3 h), and therefore require frequent bolus injections or continuous pump infusion to maintain therapeutic levels in the target tissues over time (*11*). Problems, however, remain in the modalities necessary to administer them. Frequent injections are inconvenient for patients and potentially expose the patient to inconsistent drug levels and an increased risk of infections (*12*). Issues associated with in-dwelling catheters providing continuous infusion include catheter dislodgment, infections, pump failure, fibrosis, and increased costs due to physician and nursing time (*13*, *14*).

To overcome the many challenges associated with the current modes of analgesic delivery, manipulation of the pharmacokinetic properties of the drug, more specifically, the absorption of the opioid, may help to expand the management of perioperative pain. Extended-release formulations may reduce analgesic gaps associated with intermittent delivery, decrease the risk associated with repeated injections and in-dwelling catheters, as well as reduce the burden of frequent dose administration placed on health care providers. In addition, the use of extended delivery systems has demonstrated shorter lengths of hospital stay and enhanced patient functionality (*15*). Currently, there are extended-delivery systems for oral administration of the opioids morphine, oxycodone, and oxymorphone that are used for treating postoperative pain. In addition, a parenteral delivery system, DepoDur, uses a liposomal formulation of morphine that, when delivered by single epidural injection, provides superior pain control during the first 1−2 postoperative days compared with epidural or intravenous administration of unencapsulated morphine (*16*).

Hyaluronan (HA) is a naturally occurring linear polysaccharide of alternating β-1,3-D-glucuronic acid and β-1,4-*N*-acetyl-D-glucosamine units found in the extracellular matrix and synovial fluid (*17*). HA is hydrophilic and forms gels of varying viscosity depending on its molecular weight and concentration. In addition, HA can be modified using a variety of cross-linkers generating materials with a range of biophysical properties (*18*−*20*).

Prolonging morphine's effect by delivering from viscous HA formulations was observed in rabbits whereby the duration of action depended directly on the HA formulation viscosity (*21*). In other studies, HA was used to control morphine delivery by ionic complexation with multivalent cations. A morphine−HA complex was prepared using calcium as the divalent cation (*22*). This complex was injected into rats and the morphine concen-

* Corresponding author. Tel: + 781-434-3645. Fax: + 781-672-5823. E-mail: Bob.Miller@genzyme.com.

10.1021/bc8000479 CCC: $40.75 © 2008 American Chemical Society
Published on Web 08/22/2008

tration in blood was monitored over time. The results showed that the HA−morphine complexation decreased the peak systemic drug concentration and prolonged the time of systemic exposure when compared to aqueous morphine sulfate control. In addition, increasing the calcium content was directly related to duration of pain control as measured by paw withdrawal response time in a rat incision pain model.

We previously reported a method to prolong the release of the local anesthetic bupivacaine by conjugating to HA via a hydrolytically labile imide linkage (*23*). The aim of the current study was to investigate the release rate of morphine conjugated to insoluble cross-linked HA (hylan B gel particles) via a hydrolytically labile ester linkage. The morphine-conjugated gel particles would serve as a drug depot that could be administered to local tissues or spaces (e.g., intra-articular space (*24*)) and would release the drug slowly to provide prolonged, local analgesia. The morphine-conjugated gel particles could also be administered via intrathecal, subcutaneous, or intramuscular routes to provide prolonged exposure of morphine above its minimum effective analgesic concentration to the systemic circulation. We hypothesized that a reversible covalent bond may more effectively maintain the drug in the carrier for a longer period of time relative to a physical admixture. Thus, ester conjugates (**1**) of morphine (**2**) as well as its structural controls naloxone and codeine (**3**, **4**) with HA were prepared. The conjugates of naloxone and codeine were prepared to evaluate relative stabilities of phenolic ester and alkyl ester groups, respectively.

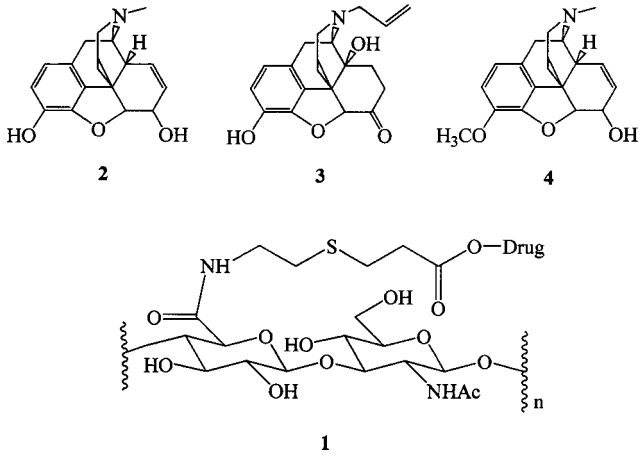

Our study included a divinylsulfone (DVS) cross-linked form of HA, hylan B, that shows longer residence time at the implantation site compared to non-cross-linked HA (*25*). This report describes a method to prepare morphine tethered to HA and hylan B particles. The rate of release of morphine from the conjugates was determined in phosphate buffered saline (PBS) and plasma. The rate of absorption of locally administered hylan B−morphine conjugate was compared against free morphine and morphine/hylan B particles admixture formulations by measuring morphine concentrations in plasma following subcutaneous administration in a rat model.

EXPERIMENTAL PROCEDURES

Materials and Methods. Morphine free base was a generous gift from Mallinckrodt Inc. (St. Louis, MO). Hyaluronan (1.3 MDa) was obtained by bacterial fermentation (Genzyme Corporation) and cross-linked with DVS (hylan B particles) following a previously published method (*26*). Anhydrous solvents and starting materials were purchased from Sigma-Aldrich Co. and used without further purification. Rat plasma was purchased from GeneTex, Inc. Protease inhibitor cocktail was purchased from Sigma-Aldrich Co. ^{1}H and ^{13}C NMR spectra were collected on a Varian spectrometer (400 MHz) against an internal standard of tetramethylsilane ($\delta = 0.0$ ppm). Mass spectra and high resolution mass spectrometry (HRMS) was performed on Applied Biosystems Qstar XL spectrometer with Turbolonspray source. Thin layer chromatography (TLC) was performed on Silica Gel 60 F_{254} precoated on aluminum sheets (EM Separation Technology) using CH_3OH/CH_2Cl_2 (1:4 and 1:9). Flash chromatography was carried out using silica gel (60 Å, 35−70 μ, 230−400 mesh, Teledyne Isco) using a gradient of 5% methanol in dichloromethane. Phosphate buffered saline (PBS) containing 137 mM NaCl, 2.7 mM KCl, 10 mM phosphate buffer, pH = 7.3−7.5 was purchased as a 10-fold concentrate (EMD Chemicals, Inc.) and diluted to a working concentration with deionized water. HA−drug conjugates were purified by dialysis in PBS using membrane tubing (7 kDa MWCO, Spectrum). *In vitro* release experiments in PBS were based on methodology reported in the literature (*27*, *28*) using tangential flow dialysis cassettes (Slide-A-Lyzer, 10 kDa MWCO, Pierce). UV/visible measurements were obtained using a Varian Cary 50 Probe spectrometer. The molecular weight and degree of molar modification of HA conjugates were determined using size exclusion chromatography and a multi-angle laser light scattering (SEC-MALLS) analyzer (model DAWN-EOS, Wyatt Technology). The SEC-MALLS analyzer was connected to refractive index and UV/visible (model UVIS-205, Perkin-Elmer) detectors. Separation was performed using a size exclusion column (300 Å, 7.5 × 300 mm, Macrosphere, Alltech) and a mobile phase of 0.05 M Na_2SO_4 solution. HA degree of molar modification was defined as the molar percentage of conjugated repeating dimeric units in HA. The quantitation of drug purity and release rate *in vitro* in PBS was determined by high performance liquid chromatography (HPLC model Waters 600) connected to a photodiode array detector (Waters 996 PDA) reading at 214 nm using a C18 reverse-phase column (80 Å, 4.6 × 150 mm, W Phenomenex Synergi 4 μm Max-RP) and mobile phase consisting of 90% 10 mM KH_2PO_4, 8% acetonitrile, and 2% methanol. The separation was performed at a column temperature of 25 °C ± 2 °C, flow rate of 1 mL/min, and under isocratic conditions. The quantification of morphine and morphine derivatives *in vitro* in PBS and plasma was determined by liquid chromatography tandem mass spectrometry (LC-MS/MS). The separation was performed at 25 °C ± 2 °C using a C18 reverse-phase column (80 Å, 2.0 × 50 mm, Phenomenex Synergi 4 μm Hydro RP). Mobile phases (A = 0.1% formic acid in water, B = 0.1% formic acid in acetonitrile) were delivered with a binary pump (series 1100, Agilent Technologies) using a flow rate of 0.5 mL/min. A gradient was used: 5−15% B over 1 min, 15−50% B over 1 min, 50−90% B over 0.5 min, and 90% B for 0.5 min. The effluent was monitored by tandem mass spectrometry (MS/MS) using a mass spectrometer (API4000, Applied Biosystems/MDS Sciex) with an electrospray ionization (ESI) interface in positive multiple reaction monitoring (MRM) mode.

Synthesis of Drugs Intermediates and HA Conjugates. *Synthesis of Acryl Naloxone (***5***).* Naloxone free base (800 mg, 2.44 mmol) was placed in a 250 mL round-bottom flask and anhydrous toluene (100 mL) was added under a nitrogen atmosphere. Triethylamine (408 μL, 2.93 mmol) was added and the solution was allowed to stir for 30 min at 50 °C. Acryloyl chloride (340 μL, 4.15 mmol) was added subsequently and the reaction mixture was allowed to stir at 50 °C overnight under nitrogen. Upon completion of reaction, as monitored by TLC, the mixture was cooled to room temperature and the excess reagent was quenched by the addition of MeOH (1 mL). The solvents were removed under reduced pressure and the crude product was dissolved in dichloromethane (100 mL), transferred

into a separatory funnel, and washed with water (150 mL). The organic phase was collected, dried with Na_2SO_4, hydroquinone (60 ppm) was added, and concentrated under reduced pressure. Acryl naloxone (**5**, 790 mg, 85% yield) was isolated by silica gel flash-chromatography (5% MeOH in CH_2Cl_2) to give a white solid. R_f (methanol/dichloromethane, 1/9): 0.68. mp: 85−87 °C. ^{1}H NMR (DMSO$_{d6}$): δ = 1.3 (d, 1H, J = 10.4 Hz, CH), 1.4 (dt, 1H, J = 3.3 Hz, 14.0 Hz, CH), 1.8 (d, 1H, J = 12.0 Hz, CH), 2.0 (t, 1H, J = 10.4 Hz, CH), 2.1 (td, 1H, J = 3.2, 14 Hz, CH), 2.4 (dt, 1H, J = 4.8 Hz, 12.6 Hz, CH), 2.6 (dt, 2H, J = 4.7 Hz, 16.0 Hz, CH_2), 2.9 (dt, 1H, J = 5.2 Hz, 14.4 Hz, CH), 3.0 (d, 1H, J = 4.2 Hz, CH), 3.1 (m, 1H, CH), 3.2 (s, 2H, CH_2), 4.9 (s, 1H, CH), 5.2 (d, 1H, J = 10.4 Hz, CH), 5.3 (d, 1H, J = 17.2 Hz, CH), 5.9 (m, 1H, CH), 6.2 (d, 1H, J = 10.0 Hz, CH acryl), 6.4 (m, 1H, CH acryl), 6.5 (dd, 1H, J = 1.2 Hz, 17.2 Hz, CH acryl), 6.8 (d, 1H, J = 8.4 Hz, CH aromatic), 6.9 (d, 1H, J = 8.4 Hz, CH aromatic) ppm. ^{13}C NMR (DMSO$_{d6}$): δ = 22.7, 29.8, 31.1, 35.6, 42.9, 50.2, 56.9, 61.4, 69.7, 90.2, 119.3, 122.5, 127.1, 130.3, 131.3, 131.4, 133.9, 147.2, 163.0, 207.5 ppm. HRMS calculated for $C_{22}H_{23}NO_5$ (M + H^+): 382.1649; found: 382.1584.

*Synthesis of Methacryl Naloxone (**6**).* Compound **6** was prepared as described above using naloxone free base (800 mg, 2.44 mmol), triethylamine (408 μL, 2.93 mmol), and methacryloyl chloride (405 μL, 4.15 mmol). Methacryl naloxone (**6**, 790 mg, 82% yield) was isolated by silica gel flash chromatography (5% MeOH in CH_2Cl_2) to give a white solid. R_f (methanol/dichloromethane, 1/9): 0.68. mp: 164−166 °C. ^{1}H NMR (DMSO$_{d6}$): δ = 1.3 (d, 1H, J = 11.2 Hz, CH), 1.5 (dt, 1H, J = 3.2 Hz, 14.0 Hz, CH), 1.6 (m, 1H, CH), 1.8 (d, 1H, J = 12.4 Hz, CH), 2.0 (s, 3H, CH_3), 2.1 (d, 1H, J = 14.0 Hz, CH), 2.4 (dt, 1H, J = 5.0 Hz, 13.2 Hz, CH), 2.6 (dt, 2H, J = 4.6 Hz, 16.4 Hz, CH_2), 2.9 (dt, 1H, J = 3.4 Hz, 14.2 Hz, CH), 3.0 (d, 1H, J = 4.4 Hz, CH), 3.1 (m, 1H, CH), 3.2 (s, 2H, CH_2), 4.9 (s, 1H, CH), 5.2 (d, 1H, J = 10.0 Hz, CH), 5.3 (d, 1H, J = 17.2 Hz, CH), 5.8 (m, 1H, CH), 5.9 (s, 1H, CH acryl), 6.3 (s, 1H, CH acryl), 6.8 (d, 1H, J = 8.0 Hz, CH aromatic), 6.9 (d, 1H, J = 8.4 Hz, CH aromatic) ppm. ^{13}C NMR (DMSO$_{d6}$): δ = 18.0, 22.7, 29.8, 31.1, 35.6, 42.9, 50.1, 56.9, 61.4, 69.7, 90.1, 119.3, 122.5, 125.3, 128.2, 128.9, 130.2, 131.1, 131.7, 134.8, 147.3, 164.1, 207.5 ppm. HRMS calculated for $C_{23}H_{25}NO_5$ (M + H^+): 396.1806; found: 396.1801.

*Synthesis of Ethylacryl Naloxone (**7**).* Compound **7** was prepared using the same method as compound **5** starting with naloxone free base (800 mg, 2.44 mmol), triethylamine (408 μL, 2.93 mmol), and ethylacryloyl chloride (440 μL, 4.15 mmol). Ethylacryl naloxone (**7**, 883 mg, 89% yield) was isolated by silica gel flash chromatography (5% MeOH in CH_2Cl_2) to give a white solid. R_f (methanol/dichloromethane, 1/9): 0.72. mp: 93−95 °C. ^{1}H NMR (DMSO$_{d6}$): δ = 1.1 (t, 3H, J = 7.4 Hz, CH_3), 1.3 (d, 1H, J = 12.0 Hz, CH), 1.5 (dt, 1H, J = 3.3 Hz, 14.0 Hz, CH), 1.8 (m, 1H, CH), 2.0 (m, 1H, CH), 2.1 (d, 1H, J = 14.8 Hz, CH), 2.3 (d, 1H, J = 14.4 Hz, CH), 2.4 (q, 2H, J = 7.4 Hz, CH_2), 2.6 (m, 2H, CH_2), 2.9 (dt, 1H, J = 4.9 Hz, 14.6 Hz, CH), 3.0 (s, 1H, CH), 3.1 (m, 1H, CH), 3.2 (s, 2H, CH_2), 4.9 (s, 1H, CH), 5.2 (d, 1H, J = 9.2 Hz, CH), 5.3 (d, 1H, J = 17.2 Hz, CH), 5.8 (s, 1H, CH acryl), 5.9 (m, 1H, CH), 6.3 (s, 1H, CH acryl), 6.8 (d, 1H, J = 8.0 Hz, CH aromatic), 6.9 (d, 1H, J = 8.0 Hz, CH aromatic) ppm. ^{13}C NMR (DMSO$_{d6}$): δ = 12.6, 22.7, 24.5, 29.7, 31.0, 35.6, 42.9, 50.1, 56.8, 61.4, 69.7, 90.1, 119.3, 122.5, 126.2, 128.1, 128.8, 130.2, 131.0, 131.7, 140.6, 147.4, 164.0, 207.4 ppm. HRMS calculated for $C_{24}H_{27}NO_5$ (M + H^+): 410.1962; found: 410.1935.

*Synthesis of Propylacryl Naloxone (**8**).* The preparation was identical to the method described for compound **5** using naloxone free base (800 mg, 2.44 mmol), triethylamine (408 μL, 2.93 mmol), and propylacryloyl chloride (493 μL, 3.78 mmol). Propylacryl naloxone (**8**, 876 mg, 85% yield) was isolated by silica gel flash chromatography (5% MeOH in CH_2Cl_2) to give a white solid. R_f (methanol/dichloromethane, 1/9): 0.72. mp: 89−91 °C. ^{1}H NMR (DMSO$_{d6}$): δ = 0.9 (t, 3H, CH_3), 1.3 (d, 1H, J = 10.8 Hz, CH), 1.4 (m, 1H, CH), 1.5 (sexlet, 2H, J = 7.2 Hz, CH_2), 1.8 (d, 1H, J = 8.0 Hz, CH), 2.0 (t, 1H, J = 10.8 Hz, CH), 2.1 (td, 1H, J = 2.8 Hz, 14.0 Hz, CH), 2.3 (t, 1H, J = 7.4 Hz, CH), 2.4 (dt, 1H, J = 5.0 Hz, 12.4 Hz, CH), 2.6 (dt, 2H, J = 5.0 Hz, 19.4 Hz, CH_2), 2.9 (dt, 1H, J = 5.1 Hz, 14.2 Hz, CH), 3.0 (d, 1H, J = 4.0 Hz, CH), 3.1 (m, 1H, CH), 3.2 (s, 2H, CH_2), 4.9 (s, 1H, CH), 5.2 (d, 1H, J = 10.4 Hz, CH), 5.3 (d, 1H, J = 17.2 Hz, CH), 5.8 (s, 1H, CH acryl), 5.9 (m, 1H, CH), 6.3 (s, 1H, CH acryl), 6.8 (d, 1H, J = 8.0 Hz, CH aromatic), 6.9 (d, 1H, J = 8.4 Hz, CH aromatic) ppm. ^{13}C NMR (DMSO$_{d6}$): δ = 13.5, 21.0, 22.7, 29.8, 31.1, 33.4, 35.6, 42.9, 50.1, 56.9, 61.4, 69.7, 90.2, 119.2, 122.5, 127.3, 130.3, 131.2, 131.7, 139.0, 147.3, 164.0, 207.5 ppm. HRMS calculated for $C_{25}H_{29}NO_5$ (M + H^+): 424.2119; found: 424.2089.

*Synthesis of Acryl Codeine (**9**).* Compound **9** was prepared using the method for compound **5** using codeine free base (800 mg, 2.67 mmol), triethylamine (895 μL, 6.41 mmol), dimethylaminopyridine (33 mg, 0.27 mmol), and acryloyl chloride (477 μL, 5.87 mmol). Acryl codeine (**9**, 504 mg, 54% yield) was obtained as an oily substance and used without further purification. Reversed-phase HPLC analysis: 97% AUC at t_R = 7.25 min. TLC R_f (methanol/dichloromethane, 1/9): 0.40. ^{1}H NMR (DMSO$_{d6}$): δ = 1.6 (d, 1H, J = 11.6 Hz, CH), 2.0 (dt, 1H, J = 5.1 Hz, 12.4 Hz, CH), 2.2 (m, 2H, CH_2), 2.3 (s, 3H, CH_3), 2.5 (dd, 1H, J = 4.0 Hz, 12.0 Hz, CH), 2.7 (s, 1H, CH), 2.9 (d, 1H, J = 18.8 Hz, CH), 3.3 (m, 1H, CH), 3.7 (s, 3H, -OCH_3), 5.0 (d, 1H, J = 6.8 Hz, CH), 5.2 (m, 1H, CH), 5.5 (d, 1H, J = 10.0 Hz, CH), 5.6 (d, 1H, J = 9.6 Hz, CH), 6.0 (d, 1H, J = 10.4 Hz, CH acryl), 6.2 (m, 1H, CH acryl), 6.4 (d, 1H, J = 16.4 Hz, CH acryl), 6.5 (d, 1H, J = 8.0 Hz, CH aromatic), 6.6 (d, 1H, J = 8.4 Hz, CH aromatic) ppm. ^{13}C NMR (DMSO$_{d6}$): δ = 19.9, 34.7, 42.1, 42.6, 46.0, 56.3, 58.0, 68.3, 87.6, 114.1, 119.0, 127.2, 127.9, 128.1, 130.1, 130.7, 131.9, 141.4, 146.2, 164.8 ppm. HRMS calculated for $C_{21}H_{23}NO_4$ (M + H^+): 354.1700; found: 354.1631.

*Synthesis of Methacryl Codeine (**10**).* Compound **10** was prepared as described for compound **5** using codeine free base (800 mg, 2.67 mmol), triethylamine (895 μL, 6.41 mmol), dimethylaminopyridine (33 mg, 0.27 mmol), and methacryloyl chloride (573 μL, 5.87 mmol). Methacryl codeine (**10**, 627 mg, 64% yield) was obtained as an oily substance and used without further purification. Reversed-phase HPLC analysis: 94% AUC at t_R = 7.35 min. TLC R_f (methanol/dichloromethane, 1/9): 0.40. ^{1}H NMR (DMSO$_{d6}$): δ = 1.5 (d, 1H, J = 19.2 Hz, CH), 1.9 (s, 3H, CH_3), 2.0 (dt, 1H, J = 4.8 Hz, 12.4 Hz, CH), 2.2 (m, 2H, CH_2), 2.3 (s, 3H, CH_3), 2.4 (m, 1H, CH), 2.7 (t, 1H, J = 2.4 Hz, CH), 2.9 (d, 1H, J = 18.8 Hz, CH), 3.3 (q, 1H, J = 2.9 Hz, CH), 3.7 (s, 3H, -OCH_3), 5.0 (d, 1H, J = 6.4 Hz, CH), 5.2 (m, 1H, CH), 5.5 (d, 1H, J = 9.6 Hz, CH), 5.6 (d, 1H, J = 11.6 Hz, CH), 5.7 (s, 1H, CH acryl), 6.0 (s, 1H, CH acryl), 6.5 (d, 1H, J = 8.0 Hz, CH aromatic), 6.6 (d, 1H, J = 8.4 Hz, CH aromatic) ppm. ^{13}C NMR (DMSO$_{d6}$): δ = 17.9, 20.9, 32.9, 37.7, 41.3, 43.5, 46.0, 56.4, 58.6, 67.7, 87.0, 114.6, 119.5, 124.7, 125.7, 126.1, 128.5, 128.8, 135.7, 137.1, 141.8, 146.1, 165.9 ppm. HRMS calculated for $C_{22}H_{25}NO_4$ (M + H^+): 368.1857; found: 368.1795.

*Synthesis of Mono-Acryl Morphine (**11**).* Morphine free base (100 mg, 0.35 mmol) was placed in a 50 mL round-bottom flask and anhydrous pyridine (5 mL) was added under a nitrogen atmosphere and allowed to stir for 15 min. Acrylic anhydride (85 μL, 0.74 mmol) was added and the reaction mixture was stirred at room temperature overnight under nitrogen. After completion of the reaction, as monitored by TLC, MeOH (100

μL) with hydroquinone (60 ppm) was added. The crude product was obtained by azeotropic removal of pyridine with toluene under reduced pressure. The desired product was subsequently purified by silica gel flash chromatography, using a gradient of methanol in dichloromethane (5%). Monoacryl morphine (**11**, 67 mg, 57% yield) was obtained as a white waxy solid. Reversed-phase HPLC analysis: 90% AUC at $t_R = 6.54$ min. TLC R_f (methanol/dichloromethane, 1/4): 0.56. ^{1}H NMR ($DMSO_{d6} + D_2O$): = 1.5 (d, 1H, $J = 12.0$ Hz, CH), 1.9 (dt, 1H, $J = 4.3$ Hz, 12.4 Hz, CH), 2.1 (m, 2H, CH_2), 2.2 (s, 3H, CH_3), 2.3 (s, 1H, CH), 2.5 (dd, 1H, $J = 4.2$ Hz, 12 Hz, CH), 2.8 (d, 1H, $J = 17.6$ Hz, CH), 3.3 (s, 1H, CH), 4.0 (s, 1H, CH), 4.6 (d, 1H, $J = 6.0$ Hz, CH), 5.1 (d, 1H, $J = 9.6$ Hz, CH), 5.4 (d, 1H, $J = 9.6$ Hz, CH), 5.6 (d, 1H, $J = 10.4$ Hz, CH acryl), 6.0 (m, 1H, CH acryl), 6.3 (m, 1H, CH acryl), 6.4 (d, 1H, $J = 8.4$ Hz, CH aromatic), 6.6 (d, 1H, $J = 8.0$ Hz, CH aromatic) ppm. ^{13}C NMR ($DMSO_{d6}$): = 21.2, 34.7, 42.4, 43.0, 46.0, 58.3, 66.4, 92.9, 119.4, 121.8, 127.6, 128.3, 130.9, 131.1, 132.2, 132.9, 133.8, 150.1, 163.9 ppm. HRMS calculated for $C_{20}H_{21}NO_4$ ($M + H^+$): 340.1544; found: 340.1535.

*Synthesis of Di-Acryl Morphine (***12***).* Compound **12** was prepared as described for compound **11** using morphine free base (1 g, 3.51 mmol), and acrylic anhydride (2.02 mL, 17.55 mmol). Diacryl morphine (**12**, 887 mg, 64% yield) was obtained as a white waxy solid. Reversed-phase HPLC analysis: 95% AUC at $t_R = 8.55$ min. TLC R_f (methanol/dichloromethane, 1/4): 0.73. ^{1}H NMR ($DMSO_{d6}$): $\delta = 1.6$ (d, 1H, $J = 11.6$ Hz, CH), 2.1 (dt, 1H, $J = 4.5$ Hz, 12.4 Hz, CH), 2.2 (t, 1H, $J = 12.0$ Hz, CH), 2.3 (m, 1H, CH), 2.34 (s, 3H, CH_3), 2.5 (m, 1H, CH), 2.8 (s, 1H, CH), 3.0 (d, 1H, $J = 18.8$ Hz, CH), 3.3 (s, 1H, CH), 5.1 (d, 1H, $J = 6.8$ Hz, CH), 5.2 (s, 1H, CH), 5.5 (d, 1H, $J = 10.0$ Hz, CH), 5.6 (d, 1H, $J = 10.4$ Hz, CH), 5.8 (d, 1H, $J = 9.6$ Hz, CH acryl), 6.0 (d, 1H, $J = 10.4$ Hz, CH acryl), 6.1 (m, 1H, CH acryl), 6.3 (m, 2H, CH acryl), 6.5 (d, 1H, $J = 17.2$ Hz, CH acryl), 6.6 (d, 1H, $J = 8.0$ Hz, CH aromatic), 6.8 (d, 1H, $J = 8.0$ Hz, CH aromatic) ppm. ^{13}C NMR ($DMSO_{d6}$): $\delta = 20.3$, 34.3, 42.0, 42.5, 46.0, 58.0, 67.7, 88.1, 115.6, 119.3, 121.6, 127.2, 127.9, 129.8, 130.9, 131.5, 131.8, 132.7, 133.6, 148.8, 163.1, 164.7 ppm. HRMS calculated for $C_{23}H_{23}NO_5$ ($M + H^+$): 394.1649; found: 394.1632.

*Synthesis of HA−Drug Conjugates (***14***).* The HA conjugates with naloxone, codeine, and morphine were prepared following a procedure described previously (*23*). The carboxyl group of HA (1.3 million MW) was reacted with 3-nitro-2-pyridinesulfenylethylamine (NEA) (*29, 30*) using carbodiimide-mediated coupling to provide HA−NEA with 10% degree of molar modification. To a solution of HA (1.5 g, 3.74 mmol) in water (375 mL) was added 1-hydroxybenzotriazole (1.0 g, 7.48 mmol) followed by NEA (1.5 g, 5.61 mmol). The pH of the reaction mixture was adjusted to 4.5 using 2 N HCl. Subsequently, 1-ethyl-3-(3-dimethylaminopropyl) carbodiimide hydrochloride (2.15 g, 11.22 mmol) was added, and the reaction was allowed to stir at room temperature for 2 h. The resulting HA−NEA was purified by exhaustive dialysis using a 7 kDa MWCO membrane against PBS, followed by dialysis against water overnight. HA−NEA was recovered by lyophilization as yellow foam (95% yield). Molecular weight and degree of modification of carboxy-modified HA−NEA were determined by SEC-MALLS analysis with detection at 350 nm. HA carrying a free sulfhydryl (**13**, HA-SH) was obtained after dissolving HA−NEA (1.5 g, 3.54 mmol) in a 25 mM solution of tris-2-(carboxyethyl)phosphine hydrochloride (375 mL) followed by stirring at 4 °C for 4 h. The free sulfhydryl was purified by dialysis against succinate buffer at pH 4 followed by water. The retentate was lyophilized to give a white solid (80% yield). Each HA−drug conjugate was assembled by reacting **13** with the corresponding drug intermediate (**5**−**12**) illustrated in Figure 1. Thus, aliquots of **13** (1.0 g, 2.50 mmol) were dissolved in water (250 mL) followed by pH adjustment to 8 using triethanolamine. One molar equivalent of each intermediate **5**−**12**, per molar equivalent of free sulfhydryl (0.25 mmol), dissolved in dimethylformamide was added and the reaction solution was allowed to stir at 4 °C overnight. The consumption of the free sulfhydryl groups was monitored colorimetrically (Ellman's reagent) (*31, 32*). The HA−drug conjugates were isolated after dialysis (7 kDa MWCO membrane) against PBS followed by water, lyophilized, and recovered as white foam (95% yield). MW (1.3 million) and degree of molar modification (10%) was consistent for all conjugates. Degree of molar modification was determined by UV/visible spectroscopy with detection at 280 nm, using naloxone, codeine, and morphine, respectively, as standards.

*Synthesis of Hylan B−Morphine (***15***).* Morphine was conjugated to hylan B as described above. The synthesis was performed starting from sterile hylan B particles and conducted under aseptic conditions. hylan B particles (371 mL, 5.4 mg/mL in 0.9% NaCl solution) were functionalized with NEA, and reduced to the free sulfhydryl form. Degree of molar modification was 8% as determined colorimetrically using Ellman's reagent (*31, 32*). Hylan B particles carrying free sulfhydryl groups were reacted with a half-molar equivalent of **12** per free sulfhydryl molar equivalent. The hylan B−morphine conjugate particles (**15**) were transferred into a 7 kDa MWCO membrane and dialyzed at 4 °C against PBS overnight, followed by dialysis against water for 6 h. The retentate was lyophilized to give a white solid product (2.0 g, 98% yield). Degree of molar modification was 8% as determined by UV/visible spectroscopy with detection at 280 nm, using morphine as a standard.

In Vitro Studies, Release Rate of Drugs in PBS. The *in vitro* release rates of drugs (infinite sink) from compounds **14** and **15** incubated in PBS were compared to admixtures of free drugs in a HA and hylan B solution, respectively. To prepare the test samples, compounds **14** and **15** were dissolved at 5% w/w in distilled water. The admixed control samples were prepared by dissolving one part naloxone, codeine, and morphine, respectively, in 99 parts of a 5% aqueous solution of HA (1.3 million MW) and Hylan B. Aliquots (approximately 1 to 1.5 g) of each solution were injected in triplicate into tangential flow dialysis cassettes (10 kDa MWCO). The cassettes were placed into separate screw-cap jars containing PBS (250 mL) at 37 °C with stirring. Samples of the receptor phase (1 mL of the elution medium) were removed over time and analyzed by HPLC.

Release Rate of Morphine in Rat Plasma. The *in vitro* release rate of morphine from compound **15** incubated in rat plasma was compared to the release rate in plasma in the presence of a cocktail of protease inhibitors with broad specificity for the inhibition of serine, cysteine, aspartic proteases, and aminopeptidases. To prepare the test samples, compound **15** was dissolved at 0.024% w/w in rat plasma, together with sodium azide (0.06% w/w). Protease inhibitors were added to an aliquot of the mixture and samples were incubated at 37 °C with gentle mixing. Fifty microliter aliquots were collected over time, 200 μL of acetonitrile containing 100 ng/mL naloxone as the internal standard were added, and samples were centrifuged. The supernatant was subjected to LC-MS/MS analysis of morphine, monoacryl morphine, and diacryl morphine.

Pharmacokinetic (PK) Profile of Morphine in a Rat Surgical Model. A total of 32 male Sprague−Dawley rats weighing 250 to 300 g were acclimated with free access to food and water for a minimum of one week prior to the performance of the experimental procedures. Deionized water was available *ad libitum* throughout the study period. Rats were allocated to treatment groups (Table 1), 8 rats per group, based on body weights taken during the acclimation period. The mean weights for each group were matched to ensure that the mean values

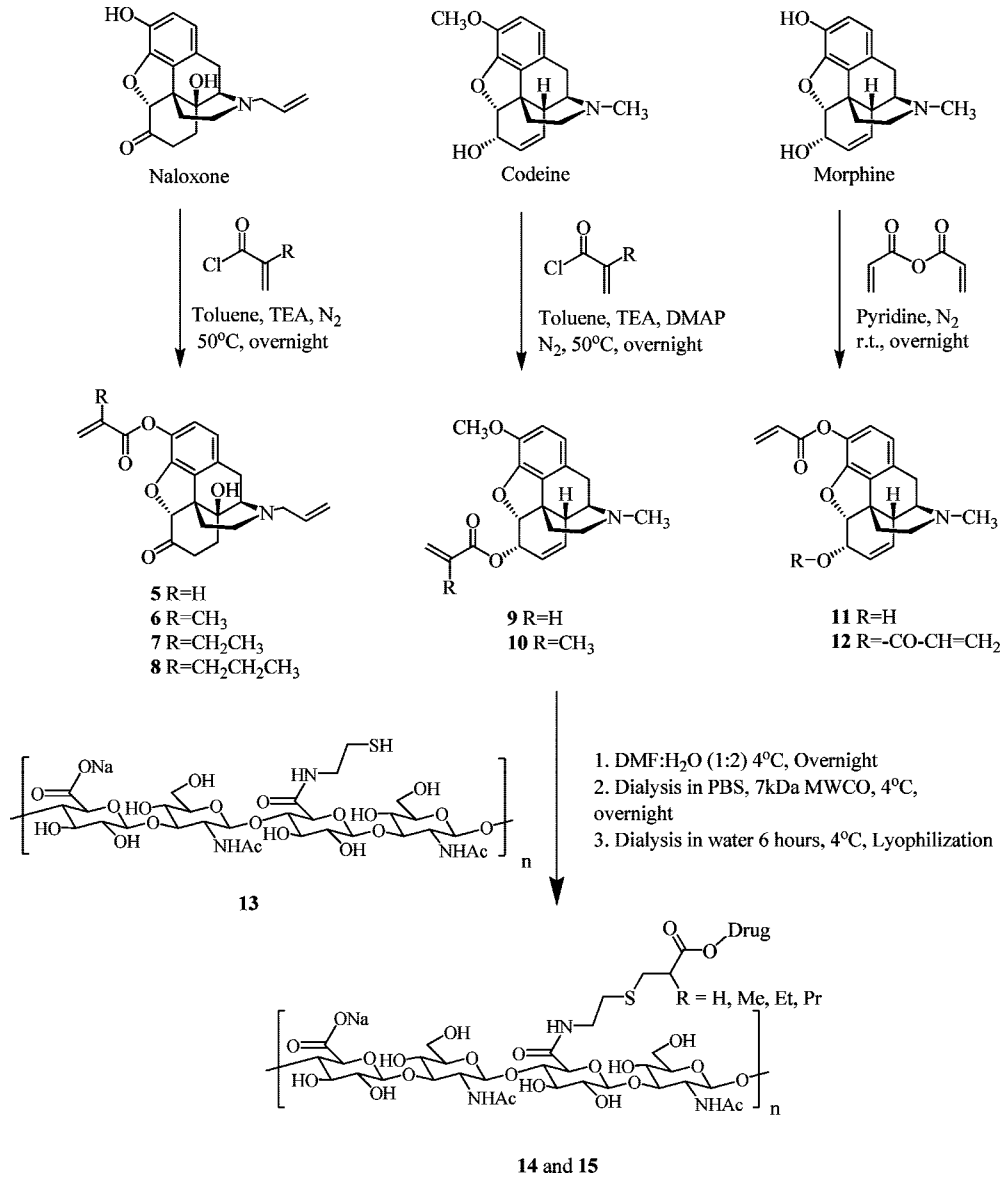

Figure 1. Synthesis of drug intermediates (**5**−**12**), HA−SH intermediate (**13**), HA−drug conjugates (**14**), and hylan B−morphine conjugate (**15**).

Table 1. Amounts of Free Morphine and Morphine from Conjugate 15 Injected Subcutaneously in Each Rat[a]

group	sample	dose	dose volume
1	morphine	5 mg/kg	5 mL
2	saline vehicle control	0 mg/kg	5 mL
3	Hylan B morphine/admix (nonconjugated)	5 mg/kg	5 mL
4	Hylan B−morphine conjugate (**15**)	146 mg/kg	5 mL

[a] $N = 8$ for each group. Morphine amounts are expressed as morphine sulfate pentahydrate (FW = 758.83).

and standard deviation satisfy the assumption of homogeneity. At time point 0, the animals were briefly sedated under inhalation anesthesia induced with 2−3% isoflurane in 100% oxygen, the dorsal area was shaved, a small skin incision was made, and blunt scissors were used to create a subcutaneous pocket. Five milliliters of either a control solution or a test formulation was injected into two sites (caudal and rostral from the incision), and the incision was closed with a wound clip. The experimenter was blinded as to which formulation was injected. At time points 1, 4, 8, 24, and 30 h, the animals were briefly anesthetized with inhalation anesthetic and approximately 250 μL of blood was collected via the retro-orbital sinus. The blood was collected into tubes containing EDTA as anticoagulant and centrifuged. Following centrifugation, the plasma was collected and transferred into separate tubes. The concentration of morphine in the plasma over time was analyzed by LC-MS/MS. Control animals were injected with 5 mg/kg morphine (i.e., morphine sulfate pentahydrate) either as a solution of free morphine or as an admixture of Hylan B gel particles and free morphine. This dose was based on previous experience that showed adequate levels of analgesia in this model without general sedation (*33*−*35*). The treatment group (Hylan B-morphine conjugate) used a ca. 30-fold higher morphine loading (146 mg/kg) compared to the controls. Samples were analyzed by LC-MS/MS as described above.

RESULTS AND DISCUSSION

Synthesis of HA−Drug Conjugates. Morphine possesses two functional groups (i.e., allylic and phenolic hydroxyl groups) that can be acrylated to form an ester. The hydrolytic cleavage of the ester bonds in the resulting HA−morphine conjugate (**14**) regenerates authentic morphine and releases it from the polymer at a slower rate compared to morphine admixed in HA. Further, it may be possible to modulate the rate of hydrolysis by

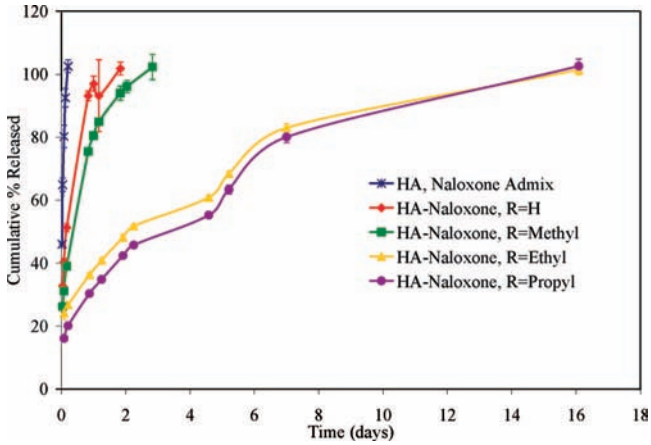

Figure 2. Release profiles of free and HA-conjugated naloxone (**14**) into receptor phase. $N = 3$, bars are SD. Receptor phase is defined as the elution medium (PBS) that is sampled to quantify the drug released. Conjugates were prepared using intermediates **5**−**8**. Increasing size of the R group (H, Me, Et, Pr) vicinal to the ester bond resulted in slower release rates.

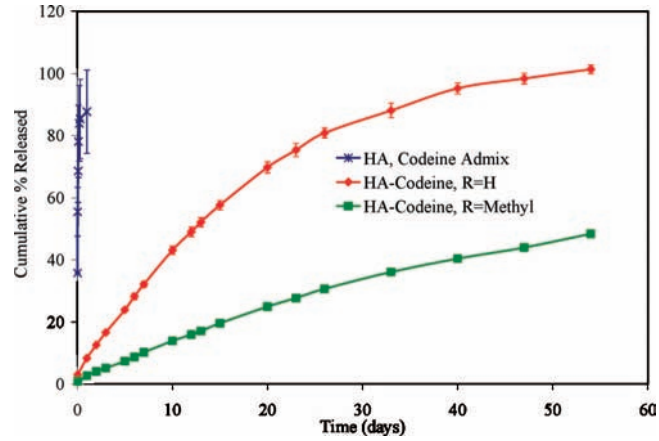

Figure 3. Release profiles of free and HA-conjugated codeine (**14**) into receptor phase. $N = 3$, bars are SD. Conjugates were prepared using intermediates **9** and **10**. Increasing size of the R group (H, Me) vicinal to the ester bond resulted in slower release rates.

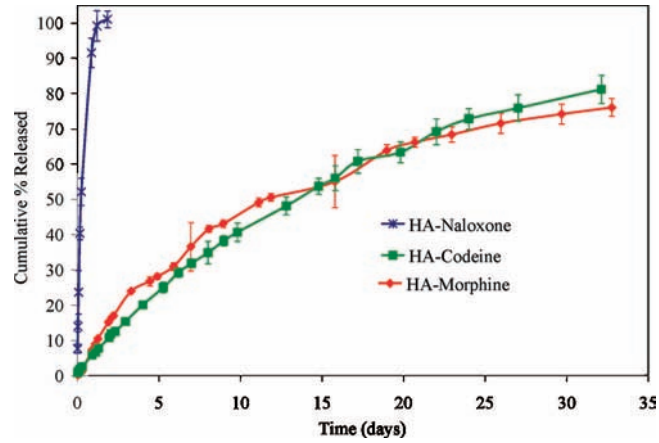

Figure 4. Release profiles of HA conjugated naloxone, codeine, and morphine (**14**) into receptor phase. $N = 3$, bars are SD. Conjugates were prepared using intermediates **5**, **9**, and **12**, respectively. Allylic leaving group (codeine and morphine) resulted in a slower release rate relative to phenolic leaving group (naloxone).

increasing the size of the alkyl functional groups (i.e., R = Me, Et, and Pr) in vicinal position to the ester bond. With these possibilities in mind, we studied the effects of acylation site and vicinal R group on the rate of hydrolysis using HA−naloxone and HA−codeine conjugates as structural controls. Using the approach described in Figure 1, naloxone, codeine, and morphine were conjugated to HA (**14**) with a 10% degree of molar modification and an overall mass recovery ranging between 80% and 90%. To avoid premature hydrolysis during workup and consequent loss of naloxone, codeine, and morphine from the conjugates, PBS and water used for dialysis were chilled to 4 °C (±2 °C).

Release Rate of Drugs in PBS. Figure 2 shows the *in vitro* release profiles obtained from the naloxone conjugates. Naloxone hydrochloride admixed in HA quickly eluted into the receptor phase, with 100% of the drug eluting within 5 h. In contrast, the HA−naloxone R = H conjugate (**14**), obtained using intermediate **5**, showed more prolonged release with 100% of the naloxone eluting within 2 days. In agreement with our expectations, delivery of naloxone was prolonged even further when R = Me, obtained using intermediate **6**, with half of the drug eluting within 12 h and 100% of the drug eluting within 3 days. For R = Et, obtained using intermediate **7**, half of the drug eluted within 3−4 days and 100% of the drug eluted within 16 days. A parallel release profile was observed for R = Pr, obtained using intermediate **8**, indicative of comparable steric protection of the ester bond by Et and Pr groups. It is known that steric hindrance of the substituents around the tetrahedral transition state influence the rate of ester hydrolysis (*36*). In particular, less sterically hindered putative tetrahedral intermediates are more stable. This greater stability leads to a higher equilibrium concentration and, in turn, a faster hydrolysis rate. The release profiles followed approximately a first-order rate consistent with the expected pseudo-first-order hydrolysis reaction.

Similar results were observed for the HA−codeine conjugates (see Figure 3). Codeine admixed in HA eluted into the receptor phase, with 100% of the drug eluting within 5 h. HA−codeine R = H conjugate, obtained using intermediate **9**, showed prolonged delivery with half the drug eluting within 14 days and 100% of the drug eluting within 55 days. Codeine delivery was significantly slower for R = Me, obtained using intermediate **10**, with only half of the drug eluted within 55 days.

Figure 4 shows a comparison of the release profiles for the HA−naloxone and codeine conjugates described above and HA−morphine conjugate obtained using intermediates **5**, **9**, and **12**, respectively. The naloxone phenolic was a much better leaving group than the codeine allylic group. HA−morphine conjugate possessed both phenolic and allylic ester groups, functioning also as HA cross-linker. However, the release profile of morphine approximately overlapped with the release profile of codeine, indicating that the rate-limiting step was the hydrolysis of the allylic ester. Half-life values in days observed for all HA conjugates are summarized in Table 2.

Table 2. Half-Lives (days) for HA−Naloxone, Codeine, and Morphine Conjugates (14) in PBS Determined by HPLC Using an Infinite Sink

sample	naloxone	codeine	morphine
HA admixture	0.1	0.1	0.1
conjugate (**14**), R = H	0.3	14.0	14.0
conjugate (**14**), R = Me	0.5	55.0	-
conjugate (**14**), R = Et	4.0	-	-
conjugate (**14**), R = Pr	4.0	-	-

PK Profile of Morphine in a Rat Surgical Model. Enzymatic and nonenzymatic release of steroid drugs conjugated through ester bonds to HA were reported in the literature (*37, 38*). Release rates *in vivo* using healthy animals, and in biological fluids obtained from healthy humans, were reported to be consistent with the release rates observed in aqueous buffered

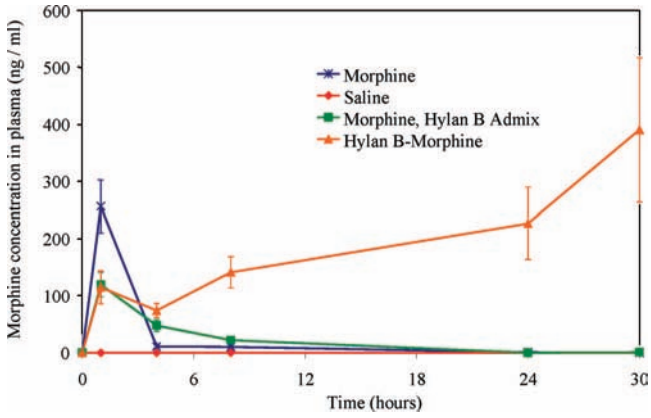

Figure 5. Pharmacokinetics in a rat surgical model. $N = 8$, bars are SD. Conjugation resulted in prolonged release relative to free morphine and morphine hylan B admix. Group 1 = free morphine (5 mg/kg), group 2 = saline, group 3 = morphine (5 mg/kg) and hylan B admix, group 4 = morphine (146 mg/kg) conjugated to hylan B (**15**).

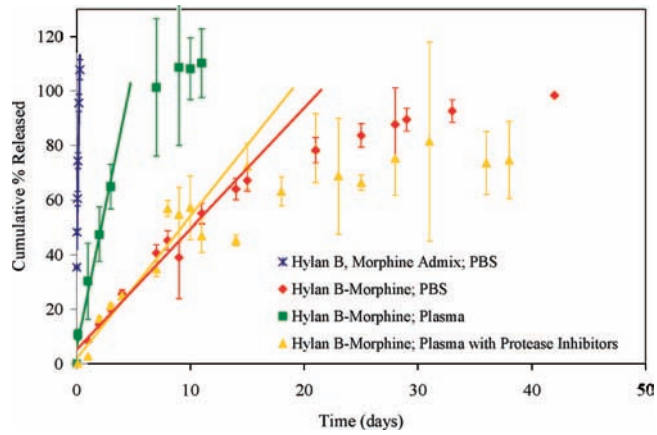

Figure 6. Comparison of release profiles of free and hylan B conjugated morphine (**15**) into receptor phase (PBS and in the presence of plasma). $N = 3$, bars are SD. Solid lines are the calculated slopes based on early data points. Conjugate was prepared using intermediate **12**. Faster release rate of morphine was observed in the presence of plasma without protease inhibitors. Release rate in plasma in the presence of protease inhibitors is similar to the release rate observed in PBS only.

solutions. With this in mind, we performed an *in vivo* study using a rat surgical model and the hylan B−morphine conjugate (**15**). Release rate of morphine from compound **15** was determined in plasma by LC-MS/MS after subcutaneous administration. The release rate was compared to a physical admixture of morphine in hylan B and bolus injection of morphine. The treatment group (compound **15**) used a ca. 30-fold higher morphine loading compared to the controls as the conjugate exhibited sustained release of morphine; a higher loading would be required to maintain the plasma morphine concentrations within the therapeutic window over time. The loading of morphine in the treatment group would also ensure that the plasma drug concentrations would be detectable by LC-MS/MS over the course of the study. Figure 5 shows the release profiles obtained from this experiment. Rapid clearance from the rats was observed for morphine sulfate admixed with hylan B and bolus injection of morphine sulfate with minimal to no detectable levels of the drug within 5 h. In agreement with our expectations, compound **15** resulted in sustained release of morphine with a significant level of morphine (ca. 400 ng/mL) detected after 30 h.

The rats were observed during the course of the PK study. Approximately 4 h post-dosing animals injected with compound **15** were hypothermic with body temperature of ca. 30 °C, and showed nonlocomotor, catatonic behavior. Heating pads were used to warm up the animals, and within one hour, their body temperature returned to normal (37.5 °C), and normal locomotor activity was observed. Twenty-four hours post-dosing, the rats performed continuous grooming activity and repetitive jaw movements. These observations were consistent with the effects of high-dose narcotic anesthesia reported in the literature (*39*−*42*).

Enzymatic and Non-Enzymatic Release Rates of Morphine. Morphine overdosing was unexpected according to our calculations based on the release profiles obtained in PBS. An additional *in vitro* study in enzymatic and non-enzymatic conditions was conducted to study the potential for nonspecific esterases to increase the release rate of morphine *in vivo* from the hylan B−morphine conjugate (**15**) obtained using intermediate **12**. Figure 6 shows a comparison of the release profiles for compound **15**, in PBS as determined by HPLC and in rat plasma as determined by LC-MS/MS. Morphine was the only species detected in the plasma samples confirming that there was no monoacryl morphine (**11**) and diacryl morphine (**12**) remaining from the conjugation reaction. Morphine admixed in hylan B eluted into the receptor phase, with 100% of the drug eluting within 5 h. hylan B−morphine conjugate eluted in PBS showed prolonged delivery with half the drug eluting within 14 days and 100% of the drug eluting within 45 days. These release profiles were consistent with those observed for compound **14**, obtained using intermediate **12**. Interestingly, the release of morphine from the same conjugate was faster in plasma than in PBS with half the drug eluting within 2.5 days and 100% of the drug eluting within 10 days. However, the release profile of morphine from the hylan B conjugate in plasma in the presence of protease inhibitors approximately overlapped with the release profile in PBS (see Figure 6), indicating that, in rat plasma samples, morphine release could be influenced by nonspecific esterase activity.

The release rates of morphine observed from hylan B conjugate in plasma *in vitro*, and during a pharmacokinetic study using rats, indicated that the system may be capable of providing sustained delivery of the drug *in vivo*. However, after observing the behavior of the animals consistent with narcotic overdosing, it will be necessary to take into account the nonspecific esterase activity of biological fluids together with the optimum dosing range to conceive of a new drug conjugate formulation. The ability to obtain sustained release of morphine *in vitro* and *in vivo* shown in this work is encouraging. This study identified a potential additional utility of HA as a drug carrier and deserves further investigation.

LITERATURE CITED

(1) Joshi, G. P., and Ogunnaike, B. O. (2005) Consequences of inadequate postoperative pain relief and chronic persistent postoperative pain. *Anesthesiol. Clin. North Am. 23*, 21–36.

(2) Jin, F., and Chung, F. (2001) Minimizing perioperative adverse events in the elderly. *Br. J. Anaesth. 87*, 608–24.

(3) Sinatra, R. S., Torres, J., and Bustos, A. M. (2002) Pain management after major orthopaedic surgery: current strategies and new concepts. *J. Am. Acad. Orthop. Surg. 10*, 117–29.

(4) Beattie, W. S., Badner, N. H., and Choi, P. (2001) Epidural analgesia reduces postoperative myocardial infarction: a meta-analysis. *Anesth. Analg. (Hagerstown, MD, U. S.) 93*, 853–8.

(5) Freedman, G., Entero, H., and Brem, H. (2004) Practical treatment of pain in patients with chronic wounds: pathogenesis-guided management. *Am. J. Surg. 188*, 31–5.

(6) Gust, R., Pecher, S., Gust, A., Hoffmann, V., Bohrer, H., and Martin, E. (1999) Effect of patient-controlled analgesia on pulmonary complications after coronary artery bypass grafting. *Crit. Care Med. 27*, 2218–23.

(7) Ragucci, M. V., Leali, A., Moroz, A., and Fetto, J. (2003) Comprehensive deep venous thrombosis prevention strategy after total-knee arthroplasty. *Am. J. Phys. Med. Rehabil. 82*, 164–8.
(8) Kabon, B., Fleischmann, E., Treschan, T., Taguchi, A., Kapral, S., and Kurz, A. (2003) Thoracic epidural anesthesia increases tissue oxygenation during major abdominal surgery. *Anesth. Analg. (Hagerstown, MD, U. S.) 97*, 1812–7.
(9) Demirag, A., Pastor, C. M., Morel, P., Jean-Christophe, C., Sielenkamper, A. W., Guvener, N., Mai, G., Berney, T., Frossard, J. L., and Buhler, L. H. (2006) Epidural anaesthesia restores pancreatic microcirculation and decreases the severity of acute pancreatitis. *World J. Gastroenterol. 12*, 915–20.
(10) Burton, A. W., and Eappen, S. (1999) Regional anesthesia techniques for pain control in the intensive care unit. *Crit. Care Clin. 15*, 77–88, vi.
(11) *Physicians' Desk Reference* (2004) Thomson, Montvale, NJ.
(12) Puehler, W., Brack, A., and Kopf, A. (2005) Extensive abscess formation after repeated paravertebral injections for the treatment of chronic back pain. *Pain 113*, 427–9.
(13) Tolomeo, C., and Mackey, W. (2003) Peripherally inserted central catheters (PICCs) in the CF population: one center's experience. *Pediatr. Nurs. 29*, 355–9.
(14) Nousia-Arvanitakis, S., Angelopoulou-Sakadami, N., and Metroliou, K. (1992) Complications associated with total parenteral nutrition in infants with short bowel syndrome. *Hepatogastroenterology 39*, 169–72.
(15) Domb, A., Amselem, S., Shah, J., and and Maniar, M (1992) Degradable polymers for site-specific drug delivery. *Polym. Adv. Technol. 3*, 279–92.
(16) Angst, M. S., and Drover, D. R. (2006) Pharmacology of drugs formulated with DepoFoam: a sustained release drug delivery system for parenteral administration using multivesicular liposome technology. *Clin. Pharmacokinet. 45*, 1153–76.
(17) Patti, A. M., Gabriele, A., Vulcano, A., Ramieri, M. T., and Della Rocca, C. (2001) Effect of hyaluronic acid on human chondrocyte cell lines from articular cartilage. *Tiss. Cell 33*, 294–300.
(18) Shu, X. Z., Liu, Y., Luo, Y., Roberts, M. C., and Prestwich, G. D. (2002) Disulfide cross-linked hyaluronan hydrogels. *Biomacromolecules 3*, 1304–11.
(19) Prestwich, G. D., Marecak, D. M., Marecek, J. F., Vercruysse, K. P., and Ziebell, M. R. (1998) Controlled chemical modification of hyaluronic acid: synthesis, applications, and biodegradation of hydrazide derivatives. *J. Controlled Release 53*, 93–103.
(20) Cai, S., Liu, Y., Zheng Shu, X., and Prestwich, G. D. (2005) Injectable glycosaminoglycan hydrogels for controlled release of human basic fibroblast growth factor. *Biomaterials 26*, 6054–67.
(21) Matsumoto, Y., Yamamoto, I., Watanabe, Y., and Matsumoto, M. (1995) Enhancing effect of viscous sodium hyaluronate solution on the rectal absorption of morphine. *Biol. Pharm. Bull. 18*, 1744–9.
(22) Prescott, A., Kislauskis, E., and Guberski, D. L. U. S. Patent 6,939,538, 2005.
(23) Gianolio, D. A., Philbrook, M., Avila, L. Z., MacGregor, H., Duan, S. X., Bernasconi, R., Slavsky, M., Dethlefsen, S., Jarrett, P. K., and Miller, R. J. (2005) Synthesis and evaluation of hydrolyzable hyaluronan-tethered bupivacaine delivery systems. *Bioconjugate Chem. 16*, 1512–8.
(24) Axelsson, K., Gupta, A., Johanzon, E., Berg, E., Ekback, G., Rawal, N., Enstrom, P., and Nordensson, U. (2008) Intraarticular administration of ketorolac, morphine, and ropivacaine combined with intraarticular patient-controlled regional analgesia for pain relief after shoulder surgery: a randomized, double-blind study. *Anesth. Analg. 106*, 328–33.
(25) Larsen, N. E., Leshchiner, E. A., Pollak, C., Balazs, E. A., and Piacquadio, D. (1995) Evaluation of Hylan B (Hylan gel) as soft tissue dermal implants. *Mater. Res. Soc. Symp. Proc. 394*, 193–7.
(26) Balazs, E., and Leshchiner, A. U. S. Patent 4,605,691, 1986.
(27) Forrest, M. L., Won, C. Y., Malick, A. W., and Kwon, G. S. (2006) In vitro release of the mTOR inhibitor rapamycin from poly(ethylene glycol)-b-poly(epsilon-caprolactone) micelles. *J. Controlled Release 110*, 370–7.
(28) Kimura, M., Takai, M., and Ishihara, K. (2007) Biocompatibility and drug release behavior of spontaneously formed phospholipid polymer hydrogels. *J. Biomed. Mater. Res. A 80*, 45–54.
(29) Vyas, D. M., Benigni, D., Rose, W. C., Bradner, W. T., and Doyle, T. W. (1989) Synthesis and in vivo antitumor activity of novel mitomycin A disulfide analogs. *J. Antibiot. (Tokyo) 42*, 1199–201.
(30) Calias, P., and Miller, R. U. S. Patent 6,749,865, 2004.
(31) Ellman, G. L. (1959) Tissue sulfhydryl groups. *Arch. Biochem. Biophys. 82*, 70–7.
(32) Riddles, P. W., Blakeley, R. L., and Zerner, B. (1983) Reassessment of Ellman's reagent. *Methods Enzymol. 91*, 49–60.
(33) Cicero, T. J., Nock, B., and Meyer, E. R. (1997) Sex-related differences in morphine's antinociceptive activity: relationship to serum and brain morphine concentrations. *J. Pharmacol. Exp. Ther. 282*, 939–44.
(34) Gleeson, R. M., and Atrens, D. M. (1982) Chlorpromazine hyperalgesia antagonizes clonidine analgesia, but enhances morphine analgesia in rats tested in a hot-water tail-flick paradigm. *Psychopharmacology (Berl.) 78*, 141–6.
(35) Stain, F., Barjavel, M. J., Sandouk, P., Plotkine, M., Scherrmann, J. M., and Bhargava, H. N. (1995) Analgesic response and plasma and brain extracellular fluid pharmacokinetics of morphine and morphine-6-β-D-glucuronide in the rat. *J. Pharmacol. Exp. Ther. 274*, 852–7.
(36) McCoy, C. P., Morrow, R. J., Edwards, C. R., Jones, D. S., and Gorman, S. P. (2007) Neighboring group-controlled hydrolysis: towards "designer" drug release biomaterials. *Bioconjugate Chem. 18*, 209–15.
(37) Rajewski, L., Stinnett, A., Stella, V., and Topp, E. (1992) Enzymic and non-enzymic hydrolysis of a polymeric prodrug: Hydrocortisone esters of hyaluronic acid. *Int. J. Pharm. 82*, 205–13.
(38) Payan, E., Jouzeau, J. Y., Lapicque, F., Bordji, K., Simon, G., Gillet, P., O'Regan, M., and Netter, P. (1995) In vitro drug release from HYC 141, a corticosteroid eseter of high molecular weight hyaluronan. *J. Controlled Release 34*, 145–53.
(39) Kolasiewicz, W., Baran, J., and Wolfarth, S. (1987) Mechanographic analysis of muscle rigidity after morphine and haloperidol: a new methodological approach. *Naunyn Schmiedebergs Arch. Pharmacol. 335*, 449–53.
(40) Powell-Jones, K., Saunders, W. S., St. Onge, R. D., and Thornill, J. A. (1987) Skeletal muscle thermogenesis: its role in the hyperthermia of conscious rats given morphine or β-endorphin. *J. Pharmacol. Exp. Ther. 243*, 322–32.
(41) Blasco, T. A., Lee, D., Amalric, M., Swerdlow, N. R., Smith, N. T., and Koob, G. F. (1986) The role of the nucleus raphe pontis and the caudate nucleus in alfentanil rigidity in the rat. *Brain Res. 386*, 280–6.
(42) Ferger, B., and Kuschinsky, K. (1995) Effects of morphine on EEG in rats and their possible relations to hypo- and hyperkinesia. *Psychopharmacology (Berl.) 117*, 200–7.

BC8000479

Identification of 14−3−3ζ by Chemical Affinity with Salicylanilide Inhibitors of Interleukin-12p40 Production

Jim P. Boyce,*,† Michael E. Brown,† Wilson Chin,‡ Jeffrey N. Fitzner,† Raymond J. Paxton,§ Min Shen,§ Tracey Stevens,‡ Martin F. Wolfson,§ and Clifford D. Wright‡

Amgen Incorporated, 1201 Amgen Court West, Seattle, Washington 98119. Received February 28, 2008; Revised Manuscript Received June 30, 2008

Salicylanilides were found as selective inhibitors of interleukin-12p40 production in stimulated dendritic cells. The conversion of one of these bioactive salicylanilides into a comparably bioactive, chemically labeled derivative was achieved using a facile and systematic functional group derivatization strategy. This resulted in a tool reagent that was then employed in an affinity chromatography approach that resulted in the identification of the protein 14−3−3ζ as having selective affinity for the chromatography matrix that was derivatized with a salicylanilide that inhibited IL-12p40 production.

INTRODUCTION

The interleukin (IL)-12 family of cytokines, including IL-12 and IL-23, play important roles in the effector functions of lymphocytes (*1*). IL-12 is involved in type 1 helper T cell (Th1) mediated inflammation in both normal host defense as well as inflammatory sequelae associated with elevated production of IL-12 such as in rheumatoid arthritis, asthma (*2*), psoriasis (*3*), and Crohn's disease (*4*, *5*). IL-23 has a divergent immunological role in regulating T cells that produce pro-inflammatory cytokines. IL-12p40 is a subunit component of both of these cytokines. Additionally, IL-12p40 may exist in monomeric or homodimeric (IL-12p80) forms that more recently have been recognized to possess their own bioactivities, independent of IL-12 and IL-23, that include chemoattraction of macrophages and stimulated dendritic cells (*6*).

As a class, salicylanilides have been reported with a wide variety of intriguing biological properties but in many cases the mechanism of action and specifically the target biomolecule(s) that these compounds interact with is not well understood. For example, niclosamide, **1**, originally discovered as a molluscicidal, is an orally administered, broad spectrum anthelmintic (*7*). Efuamide, **2a**, has been reported to be immunosuppressive in experimental allergic encephalomyelitis models in animals (*8*) and to inhibit phosphorylation and signaling of erbB-2 resulting in cell cycle arrest (*9*), and **2b** has been reported as an antimycobacterial (*10*).

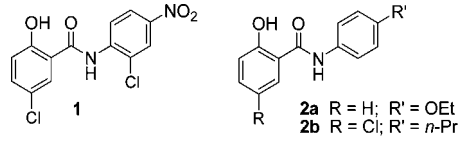

Figure 1. Examples of bioactive salicylanilides.

In the course of cell-based screening and directed analoging campaigns, we discovered certain other salicylanilides which potently and selectively inhibited IL-12p40 and IL-6 production in stimulated primary human dendritic cells. These salicylanilides were not found to be generally cytotoxic and did not show inhibition against any of the panels of recombinant proteins that we routinely screen against.

We describe here the structure−activity relationship guided conversion of these bioactive salicylanilides into a comparably bioactive derivative which was utilized as a tool for protein identification. This was accomplished using an affinity chromatography based approach to interrogate a cytosolic protein mixture which was derived from dendritic cells that were stimulated to produce IL-12p40. This approach, in conjunction with mass spectrometry, provided a method for biochemical target identification resulting in the discovery of the protein 14−3−3ζ as having selective affinity for specific salicylanilides.

EXPERIMENTAL PROCEDURES

General Synthesis Methods. Unless stated otherwise, hydrogenations were performed using a Parr 3911 hydrogenation apparatus and microwave irradiations were conducted with a CEM Explorer microwave apparatus with auto sampler. Chromatography-grade, anhydrous solvents were used without further purification. Concentration refers to distillation using a rotary evaporator (Buchi R-124). Flash chromatography was performed on E. Merck #60, 230−400 mesh silica gel. TLC analyses were performed using E. Merck glass backed silica gel #60 plates, 0.25 mm thickness, with 254 nm fluorescent indicator with visualization by UV absorption, iodine chamber, or solutions of $KMnO_4$ or other common staining technique. NMR spectra were collected with a Varian Inova AS500 equipped with a Zymark auto sampler, and spectral resonance shifts are reported after internal standardization to a characteristic resonance shift of the solvent. Coupling constants refer to apparent peak multiplicities and abbreviations used are as follows: s = singlet, d = doublet, t = triplet, q= quartet, br = broad. HPLC analyses were performed on an Agilent 1100 Series HPLC (binary pump) equipped with a reverse phase column (Zorbax Rx-C8, 9.4 mm ID × 25 cm) using an elution gradient composed of increasing ratios of 0.1% v/v TFA in CH_3CN/0.1% v/v TFA in H_2O and monitoring of analytes by UV absorption, evaporative light scattering (SEDEX ELSD), and mass spec detection (ESI/CI). Mass spectra were collected on an Agilent 1100 MSD and are reported as percent (%) relative intensity to the base peak.

* Author correspondence: Tel. 425.736.4463; Fax: 425.450.7300; E-mail: jboyce2000@aol.com, boycej@amgen.com.
† Medicinal Chemistry, Amgen Inc.
‡ Protein Chemistry, Amgen Inc.
§ Inflammation, Amgen Inc.

10.1021/bc800078q CCC: $40.75 © 2008 American Chemical Society
Published on Web 09/03/2008

Except where otherwise stated, all reagents including compounds **25** [21615−34−9] were purchased from Sigma-Aldrich Chemical Co. Compound **21** [3107−19−5] was purchased from ChemPacific (www.chempacific.com). Compounds **3** [439145−04−7], **4** [78154−58−2], and **7** [882158−06−7] were purchased from Maybridge/Thermo Fisher Scientific Inc. Compounds **8** [439145−07−0], **16** [55411−43−3], and **22** [145881−74−9] are previously known in the chemical literature but our preparation of each is described in the following section along with new compounds **5**, **6**, **9**−**15**, **17**, **18**, **23**, and relevant nonnumbered intermediates. Compound preparation and characterization follows.

Scheme 1. Preparation of Salicylanilides Listed in Table 1[a]

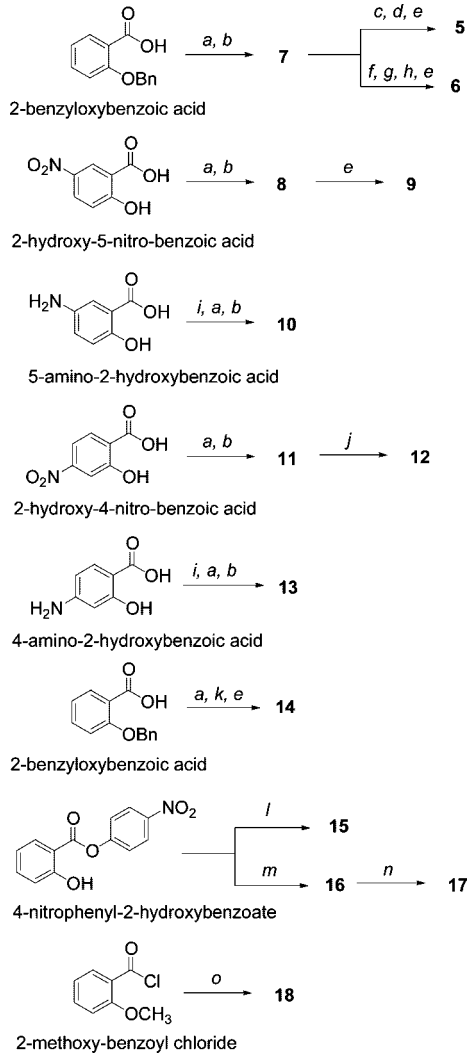

[a] Reagents: (a) DCC, *N*-hydroxysuccinimide, THF; (b) 3,5-dichloroaniline; (c) NaH, THF; (d) CH_3I; (e) Pd/C, H_2; (f) NaO-*t*-Bu, 1,2-dimethoxyethane; (g) *t*-butylbromoacetate; (h) TFA, CH_2Cl_2; (i) Ac_2O; (j) $SnCl_2$, HCl, EtOH; (k) *N*-(3-amino-5-chlorophenyl)acetamide, 140 °C; (l) *N*-(4-amino-2,6-dichlorophenyl)acetamide, NMP, 225 °C; (m) 3,5-dichloro-4-methoxyaniline, NMP, reflux; (n) benzyl bromide, K_2CO_3, DMF, 150 °C; (o) 2,5-dichloro-4-methoxybenzenamine, EtN(*i*-Pr)$_2$, toluene.

N-(3,5-Dichlorophenyl)-2-hydroxy-N-methylbenzamide (**5**). A solution of 2-benzyloxybenzoic acid (2.00 g, 8.76 mmol), *N*-hydroxysuccinimide (1.21 g, 10.5 mmol), and *N*,*N*′-dicyclohexylcarbodiimide (1.99 g, 9.64 mmol) in anhydrous THF (30 mL) was stirred (rt, 4 h). The resulting precipitant was filtered and the filtrate was concentrated *in vacuo* to afford *N*-hydroxysuccinyl 2-(benzyloxy)benzoate as a crude intermediate that was used without further purification (3.39 g): ^{1}H NMR (500 MHz, d_6-DMSO) δ 7.93 (d, J = 7.5, 1H), 7.73 (m, 1H), 7.50 (d, J = 7.5 Hz, 2H), 7.38 (m, 3H), 7.32 (d, J = 7.0 Hz, 1H), 7.16 (m, 1H), 5.30 (s, 2H), 2.89 (s, 4H); ^{13}C NMR (125 MHz, d_6-DMSO) δ 170.4, 160.2, 158.8, 136.4, 136.4, 131.7, 128.4, 127.7, 127.0, 120.8, 114.5, 113.9, 69.8, 25.5. An aliquot of this crude succinate ester (1.00 g, 3.07 mmol) and 3,5-dichloroaniline (1.50 g, 9.23 mmol) was briefly warmed as a melt (10 min, 140 °C, internal). The resulting yellow solution was allowed to cool (rt). The residue was diluted with EtOAc (100 mL), and after aqueous washing (3 N HCl, brine), the organic layer was dried ($MgSO_4$) and concentrated *in vacuo* to afford a tan solid which after crystallization (EtOAc) afforded 2-(benzyloxy)-*N*-(3,5-dichlorophenyl)benzamide (**7**), CAS Registry [882158−06−7], as a white crystalline solid (0.67 g, 1.80 mmol): ^{1}H NMR (500 MHz, $CDCl_3$) δ 10.09 (br s, 1H), 8.29 (d, J = 7.5 Hz, 1H), 7.54−7.52 (m, 6H), 7.15−7.12 (m, 2H), 7.08 (s, 2H), 7.97 (s, 1H), 5.19 (s, 2H); ^{13}C NMR (125 MHz, $CDCl_3$) δ 163.0, 156.7, 140.2, 134.9, 134.8, 133.8, 132.6, 129.8, 129.3, 129.0, 123.5, 122.0, 120.9, 117.6, 112.5, 72.0; MS (+EI) *m*/*z* 374 (MH+, 70), 372 (MH+, 100). To a cold (0 °C bath) suspension of **7** (100 mg, 0.269 mmol) and NaH (60% w/w oil disp., 16 mg, theor. 0.4 mmol) in anhydrous THF (2 mL) was added neat methyl iodide (0.2 mL, 3 mmol) and the resulting mixture was allowed to warm (rt, 30 min) with stirring. The resulting mixture was carefully quenched with methanol (0.5 mL), filtered through a plug of silica gel (hexanes/EtOAc, 5:1), and concentrated *in vacuo* to afford 2-(benzyloxy)-*N*-(3,5-dichlorophenyl)-*N*-methylbenzamide as a colorless oil (91 mg, 0.24 mmol) which was used without further purification: MS (+EI) *m*/*z* 388 (MH+, 70), 386 (MH+, 100). A suspension of 2-(benzyloxy)-*N*-(3,5-dichlorophenyl)-*N*-methylbenzamide (72 mg, 0.19 mmol) and 5% Pd/C (wet Degussa-type E101, 12 mg, theor. 0.0029 mmol Pd) in EtOAc (2 mL) was shaken under a hydrogen atmosphere (60 psi, rt, 1 h). The resulting mixture was filtered (diatomaceous earth) and the filtrate was concentrated *in vacuo* to afford a light orange oil which after flash chromatography afforded **5** (44 mg, 0.15 mmol) as a colorless oil: ^{1}H NMR (500 MHz, $CDCl_3$) δ 7.25−7.24 (m, 2H), 7.03 (s, 2H), 6.97 (d, J = 8.5 Hz, 1H), 7.39 (d, J = 8.5 Hz, 1H), 6.54 (m, 1H), 3.46 (s, 3H); ^{13}C NMR (125 MHz, $CDCl_3$) δ 171.5, 160.5, 147.0, 135.6, 133.5, 130.0, 127.2, 125.2, 125.2, 118.2, 115.2, 39.1; MS (+EI) *m*/*z* 298 (MH+, 70), 296 (MH+, 100).

2-(N-(3,5-Dichlorophenyl)-2-hydroxybenzamido)acetic acid (**6**). To a stirred solution of **7** (0.250 g, 0.672 mmol), prepared according to the method described in the preceding section, and sodium *tert*-butoxide (0.130 g, 1.34 mmol) in anhydrous 1,2-dimethoxyethane (7 mL) was added (rt, 5 min) neat *tert*-butylbromoacetate (0.22 mL, 1.3 mmol) and the resulting solution was stirred (rt, 90 min). After aqueous workup (EtOAc, H_2O), the organic layer was dried ($MgSO_4$) and concentrated *in vacuo* and filtered through a plug of silica gel (hexanes/EtOAc, 5:1) to afford *tert*-butyl 2-(2-(benzyloxy)-*N*-(3,5-dichlorophenyl)benzamido)acetate as a crude colorless oil (0.285 g) which was used without further purification: MS (+EI) *m*/*z* 510 (MNa+, 20), 508 (MNa+, 30), 432 ((M-56)H+, 70), 430 ((M-56)H+, 100). A suspension of this intermediate oil (0.285 g, theor. 0.586 mmol) and 5% Pd/C (wet Degussa-type E101, 22 mg, theor. 0.0053 mmol Pd) in EtOAc (3 mL) was shaken under a hydrogen atmosphere (60 psi, rt, 3 h). The resulting mixture was filtered (diatomaceous earth) and the filtrate was concentrated *in vacuo*. The crystalline solid that was obtained was triturated (hexanes) to afford *tert*-butyl 2-(*N*-(3,5-dichlorophenyl)-2-hydroxybenzamido)acetate as a white crystalline solid (0.148 g, 0.373 mmol): ^{1}H NMR (500 MHz, $CDCl_3$) δ 10.2 (br s, 1H), 7.27−7.24 (m with $CHCl_3$, ∼2H), 7.09 (s, 2H), 6.96 (d,

J = 8.0 Hz, 1H), 6.79 (d, J = 8.5 Hz, 1H), 6.55 (m, 1H), 4.41 (s, 2H), 1.50 (s, 9H); ^{13}C NMR (125 MHz, $CDCl_3$) δ 171.3, 167.5, 160.1, 145.9, 135.5, 133.7, 129.9, 127.6, 125.6, 118.4, 118.2, 115.2, 82.9, 53.6, 28.0; MS (+EI) *m/z* 396 (MH+, 70), 394 (MH+, 100). A solution of *tert*-butyl 2-(*N*-(3,5-dichlorophenyl)-2-hydroxybenzamido)acetate (109 mg, 0.275 mmol) in CH_2Cl_2/TFA (1:1 v/v, 4 mL) was stirred (rt, 1 h) and then concentrated *in vacuo*. The resulting solid was crystallized (hexanes/EtOAc) to afford **6** as a white crystalline solid (50 mg, 0.15 mmol): ^{1}H NMR (500 MHz, d_6-DMSO) δ 12.89 (br s, 1H), 9.87 (br s, 1H), 7.39 (m, 1H), 7.25 (s, 2H), 7.13 (m, 1H), 7.06 (d, J = 7.5 Hz, 1H), 6.74−6.71 (m, 2H), 4.51 (s, 2H); ^{13}C NMR (125 MHz, d_6-DMSO) δ 170.4, 168.6, 153.5, 145.0, 133.1, 130.9, 128.4, 126.1, 125.9, 123.3, 118.8, 115.6, 50.5; MS (+EI) *m/z* 340 (MH+, 70), 338 (MH+, 100).

*5-Amino-N-(3,5-dichlorophenyl)-2-hydroxybenzamide (***9***).* A solution of 2-hydroxy-5-nitrobenzoic acid (2.02 g, 11.0 mmol), *N*-hydroxysuccinimide (1.28 g, 11.1 mmol), and *N,N′*-dicyclohexylcarbodiimide (2.30 g, 11.1 mmol) in THF (47 mL) was stirred (rt, 4 h) and the resulting precipitant filtered and the filtrate was concentrated *in vacuo* to afford a crude intermediate succinate ester which was used without further purification (3.08 g): MS (-EI) *m/z* 279 (M-, 100). An aliquot of this crude intermediate succinate (1.17 g, theor. 4.18 mmol) was dissolved in toluene (10 mL) and to this solution was added neat 3,5-dichloroaniline (0.694 g, 4.28 mmol) and diisopropylethylamine (1.8 mL, 14 mmol). This mixture was warmed to reflux and stirred for 6 h and then allowed to cool to ambient temperature. After addition of aqueous HCl (10% v/v, 10 mL), the resulting precipitate was collected, dissolved into ethyl acetate, washed (H_2O) and dried ($MgSO_4$), and concentrated *in vacuo* to afford the known compound *N*-(3,5-dichlorophenyl)-2-hydroxy-5-nitrobenzamide [439145−07−0] (0.610 g, 1.86 mmol): ^{1}H NMR (500 MHz, d_6-acetone) δ 10.42 (br s, 1H), 8.94 (d, J = 3.0 Hz, 1H), 8.39 (dd, J = 9.0, 3.0 Hz, 1H), 7.88 (d, J = 2.0 Hz, 2H), 7.34 (s, 1H), 7.23 (d, J = 9.0 Hz, 1H); MS (+EI) *m/z* 327 (MH+, 70), 325 (MH+, 100). A suspension of *N*-(3,5-dichlorophenyl)-2-hydroxy-5-nitrobenzamide (0.594 g, 1.82 mmol) and 5% Pd/C (wet Degussa-type E101, 53 mg, theor. 0.013 mmol Pd) in ethanol (20 mL) was stirred under hydrogen atmosphere (1 atm., 4 h, rt). The mixture was filtered and the filtrate was concentrated *in vacuo* to afford a crude solid of which an aliquot was purified by flash chromatography (hexanes/ethyl acetate, 4:1) to afford an analytical sample of **9** (6 mg, 0.02 mmol): ^{1}H NMR (500 MHz, d_6-acetone) δ 10.62 (br s, 1H), 10.00 (br s, 1H), 7.94 (s, 1H), 7.39 (m, 2H), 6.88 (d, J = 9.0 Hz, 2H), 6.82 (d, J = 9.0 Hz, 1H), 3.39 (br s, 2H); MS (+EI) *m/z* 297 (MH+, 70), 295 (MH+, 100).

*5-Acetamido-N-(3,5-dichlorophenyl)-2-hydroxybenzamide (***10***).* A suspension of 5-amino-2-hydroxybenzoic acid (3.45 g, 22.5 mmol) in ethanol (800 mL) and acetic anhydride (2.56 g, 25.1 mmol) was stirred with warming (50 °C, 3 h) and then allowed to cool (rt). The mixture was then concentrated *in vacuo* and crystallization was induced by the addition of water. The crystals were collected and dried *in vacuo* to afford 5-acetamido-2-hydroxybenzoic acid (1.96 g, 10.0 mmol): ^{1}H NMR (500 MHz, d_6-acetone) δ 9.22 (br. s, 1H), 8.21 (d, J = 2.5 Hz, 1H), 7.70 (app t, J = 2.5 Hz, 1H), 6.86 (d, J = 2.5 Hz, 1H), 1.95 (s, 3H); MS (+EI) *m/z* 196 (MH+, 100). A solution of 5-acetamido-2-hydroxybenzoic acid (1.85 g, 9.48 mmol), *N*-hydroxysuccinimide (1.21 g, 10.5 mmol), and *N,N′*-dicyclohexylcarbodiimide (2.20 g, 10.6 mmol) in THF (100 mL) was stirred (rt, 4 h), then filtered, and the filtrate was dried *in vacuo* to afford a crude intermediate succinate ester that was used without further purification: MS (-EI) *m/z* 291 (M-, 100). To a portion of this crude intermediate (24.3 mg, theor. 0.0832 mmol) dissolved in NMP (1.5 mL) was added 3,5-dichloroaniline (63 mg, 0.39 mmol). The resulting solution was warmed with microwave irradiation (225 °C, 10 min.) then allowed to cool (rt). After aqueous workup (EtOAc/10% aq HCl), the organic layer was dried ($MgSO_4$), filtered, and concentrated *in vacuo*. The resulting brown oil was triturated (EtOAc) and the remaining crude solid was purified by flash chromatography (hexanes/ethyl acetate, 4:1) to afford an analytical sample of **10** (14 mg, 0.041 mmol): ^{1}H NMR (500 MHz, d_6-DMSO) δ 9.82 (br s, 1H), 7.92 (br s, 1H), 7.82 (s, 2H), 7.58 (br m, 1H), 7.30 (s, 1H), 6.89 (br m, 1H), 1.99 (s, 3H); MS (-EI) *m/z* 339 ((M-, 70), 337 (M-, 100).

*N-(3,5-Dichlorophenyl)-2-hydroxy-4-nitrobenzamide (***11***).* A solution of 2-hydroxy-4-nitrobenzoic acid (2.34 g, 12.8 mmol), *N*-hydroxysuccinimide (1.48 g, 12.8 mmol), and *N,N′*-dicyclohexylcarbodiimide (2.68 g, 13.0 mmol) in THF (25 mL) was stirred (rt, 3 h), and the resulting precipitate was filtered and the filtrate concentrated *in vacuo* to afford a crude succinate ester (2.97 g) which was used without further purification: MS (-EI) *m/z* 279 (M-, 100). A portion of this material (1.52 g, theor. 6.44 mmol) and 3,5-dichloroaniline (2.06 g, 12.7 mmol) was briefly warmed (140 °C, internal, 10 min) as a melt, with stirring, then allowed to cool (rt). After aqueous workup (EtOAc/10% aq HCl), the organic layer was dried ($MgSO_4$), filtered, and concentrated *in vacuo* to afford a crude solid from which an analytical sample of **11** (130 mg, 0.397 mmol) was prepared by flash chromatography (hexanes/ethyl acetate, 17:3). ^{1}H NMR (500 MHz, d_6-DMSO) δ 11.71 (br s, 1H), 10.75 (br s, 1H), 7.89 (d, J = 10.0 Hz, 1H), 7.84 (s, 2H), 7.77 (d, J = 10.0 Hz, 2H), 7.37 (s, 1H); MS (-EI) *m/z* 327 ((M-, 70), 325 (M-, 100).

*4-Amino-N-(3,5-dichlorophenyl)-2-hydroxybenzamide (***12***).* To a suspension of **11** (0.492 g, 1.50 mmol) in ethanol (9.0 mL) and HCl (12 N aq, 1.0 mL) was added neat stannous chloride (1.72 g, 9.09 mmol). The resulting suspension was heated with microwave irradiation (120 °C internal, 10 min). The resulting brown solution was allowed cool (rt) and the solvent removed *in vacuo*. The resulting solid was dissolved in ethyl acetate, washed (10% aq NaOH; brine), dried (Na_2CO_3), and concentrated *in vacuo* to afford a yellow solid (0.414 g) from which an analytical sample of **12** (12 mg, 0.040 mmol) was prepared by flash chromatography (hexanes/ethyl acetate, 4:1) to afford a crystalline white solid. ^{1}H NMR (500 MHz, d_6-acetone) δ 12.11 (br s, 1H), 9.45 (br s, 1H), 7.85 (s, 2H), 7.68 (d, J = 8.8 Hz, 1H), 7.19 (s, 1H), 6.24 (d, J = 8.8 Hz, 1H), 6.17 (s, 1H), 5.50 (s, 2H); MS (-EI) *m/z* 297 (MH+, 70), 295 (MH+, 100).

*4-Acetamido-N-(3,5-dichlorophenyl)-2-hydroxybenzamide (***13***).* A suspension of 4-amino-2-hydroxybenzoic acid (4.65 g, 30.3 mmol) in ethanol (400 mL) and acetic anhydride (3.10 g, 30.4 mmol) was stirred with warming (40 °C, 10 min) and then allowed to cool (rt). The mixture was then concentrated *in vacuo* and crystallization was induced by the addition of water. The crystals were collected and dried *in vacuo* to afford a crude sample of 4-acetamido-2-hydroxybenzoic acid (1.78 g, theor. 9.12 mmol) which was used without further purification: MS (+EI) *m/z* 196 (MH+, 100). A solution of crude 5-acetamido-2-hydroxybenzoic acid (1.66 g, theor. 8.52 mmol), *N*-hydroxysuccinimide (1.09 g, 9.49 mmol), and *N,N′*-dicyclohexylcarbodiimide (1.99 g, 9.66 mmol) in THF (100 mL) was stirred (rt, 4 h), then filtered, and the filtrate was dried *in vacuo* to afford a crude intermediate succinate ester that was used without further purification: MS (-EI) *m/z* 291 (M-, 100). To a portion of this crude intermediate (368 mg, theor. 1.26 mmol) dissolved in NMP (4.5 mL) was added 3,5-dichloroaniline (640 mg, 3.95 mmol). The resulting solution was warmed with microwave irradiation (225 °C, 10 min), then allowed to cool (rt). The resulting crystals that formed overnight were collected by filtration, washed with ethyl acetate, and dried *in vacuo* to afford

13 (0.369 g, 1.09 mmol) as white needles: ^{1}H NMR (500 MHz, d_6-DMSO) δ 11.40 (s, 1H), 10.58 (s, 1H), 9.78 (s, 1H), 7.93 (s, 2H), 7.89 (d, J = 8.0 Hz, 1H), 7.47 (app t, J = 8.0, 1H), 7.05−6.95 (m, 2H), 2.02 (s, 3H); MS (+EI) *m*/*z* 341 (MH+, 70), 339 (MH+, 100).

*N-(3-Acetamido-5-chlorophenyl)-2-hydroxybenzamide (***14***).* To a stirred solution of 3-amino-5-chloroaniline (1.00 g, 7.01 mmol) in anhydrous THF (200 mL) at room temperature was added (rt, over 90 min) a solution of acetic anhydride (0.663 mL, 7.01 mmol) in anhydrous THF (200 mL). After stirring overnight, the resulting solution was concentrated *in vacuo* to afford a dark oil which after flash chromatography (hexanes/EtOAc, 1:2) afforded *N*-(3-amino-5-chlorophenyl)acetamide as a tan solid (0.916 g, 5.00 mmol) which was used without further purification: MS (+EI) *m*/*z* 185 (MH+, 100). A solution of 2-benzyloxybenzoic acid (2.00 g, 8.76 mmol), *N*-hydroxysuccinimide (1.21 g, 10.5 mmol), and *N*,*N*′-dicyclohexylcarbodiimide (1.99 g, 9.64 mmol) in anhydrous THF (30 mL) was stirred (rt, 4 h). The resulting precipitant was filtered and the filtrate was concentrated *in vacuo* to afford a crude intermediate succinate ester that was used without further purification (3.30 g): ^{1}H NMR (500 MHz, d_6-DMSO) δ 7.94 (d, J = 7.5, 1H), 7.73 (m, 1H), 7.50 (d, J = 7.5 Hz, 2H), 7.38 (m, 3H), 7.32 (d, J = 7.0 Hz, 1H), 7.16 (m, 1H), 5.30 (s, 2H), 2.89 (s, 4H); ^{13}C NMR (125 MHz, d_6-DMSO) δ 170.4, 160.2, 158.8, 136.4, 136.4, 131.7, 128.4, 127.7, 127.0, 120.8, 114.5, 113.9, 69.8, 25.5. An aliquot of this crude succinate ester (0.286 g, theor. 0.880 mmol) and *N*-(3-amino-5-chlorophenyl)acetamide (0.650 g, 3.52 mmol) was briefly warmed as a melt (10 min, 140 °C, internal). The resulting brown solution was allowed to cool (rt). The residue was diluted with EtOAc (30 mL), and after aqueous washes (3 N HCl, brine), the organic layer was dried ($MgSO_4$) and concentrated *in vacuo* to afford a tan solid which after flash column chromatography (hexanes/EtOAc, 1:1) afforded *N*-(3-acetamido-5-chlorophenyl)-2-(benzyloxy)benzamide as a white crystalline solid (0.211 g, 0.535 mmol): ^{1}H NMR (500 MHz, d_6-DMSO) δ 10.33 (br s, 1H), 10.16 (br s, 1H), 7.95 (s, 1H), 7.65−7.51 (m, 5H), 7.37−7.27 (m, 4H), 7.17 (s, 1H), 7.09 (app t, J = 8.0 Hz, 1H), 5.23 (s, 2H), 2.05 (s, 3H); ^{13}C NMR (125 MHz, d_6-DMSO) δ 168.9, 164.8, 155.6, 140.8, 140.4, 136.5, 132.9, 132.1, 129.7, 128.4, 128.0, 127.8, 125.1, 120.8, 113.5, 113.4, 113.3, 108.2, 70.0, 24.0; MS (+EI) *m*/*z* 397 (MH+, 70), 395 (MH+, 100). A suspension of *N*-(3-acetamido-5-chlorophenyl)-2-(benzyloxy)benzamide (146 mg, 0.370 mmol) and 5% Pd/C (wet Degussa-type E101, 50 mg, theor. 0.012 mmol Pd) in MeOH (40 mL) was shaken under a hydrogen atmosphere (60 psi, rt, 1 h). The resulting mixture was filtered (diatomaceous earth) and the filtrate was concentrated *in vacuo*. This afforded a mixture consisting of approximately equal amounts of two products (fully resolved by silica gel TLC, hexanes/EtOAc, 1:1) that were separated by flash column chromatography (hexanes/EtOAc, 1:1). One white crystalline product appears to result from reductive dehalogenation and was isolated (39 mg) and found to be identical by HPLC, MS, ^{1}H NMR, and ^{13}C NMR to a previously prepared authentic sample of *N*-(3-acetamidophenyl)-2-hydroxybenzamide (analytical data not reported here). The other component, **14**, was isolated as a white crystalline solid (25 mg, 0.082 mmol): ^{1}H NMR (500 MHz, d_6-DMSO) δ 11.55 (br s, 1H), 10.47 (br s, 1H), 10.17 (br s, 1H), 7.90 (m, 2H), 7.53 (d, J = 12.5 Hz, 2H), 7.44 (m, 1H), 6.98 (m, 2H), 2.06 (s, 3H); ^{13}C NMR (125 MHz, d_6-DMSO) δ 168.7, 166.5, 157.9, 140.8, 139.8, 133.7, 132.9, 129.3, 119.1, 118.0, 117.1, 114.7, 114.0, 109.3, 24.0; MS (-EI) *m*/*z* 305 (M-, 70), 303 (M-, 100).

*N-(4-Acetamido-3,5-dichlorophenyl)-2-hydroxybenzamide (***15***).* To a solution of 4-nitrophenyl 2-hydroxybenzoate (0.494 g, 1.91 mmol) in NMP (15 mL) was added *N*-(4-amino-2,6-dichlorophenyl)acetamide (1.26 g, 5.75 mmol). The resulting solution was briefly warmed with microwave irradiation (225 °C internal, 10 min) then allowed to cool (rt). After aqueous workup (EtOAc/10% aq HCl), the combined organic layer was dried ($MgSO_4$), and concentrated *in vacuo* to afford a crude solid from which an analytical sample of **15** (12 mg, 0.035 mmol) was prepared by flash chromatography (hexanes/ethyl acetate, 55:45): ^{1}H NMR (500 MHz, d_6-DMSO) δ 11.39 (s, 1H), 10.52 (s, 1H), 9.74 (s, 1H), 7.93 (s, 2H), 7.86 (dd, J = 7.5, 1.5 Hz, 1H), 7.44 (app t, J = 7.5, 1H), 7.00−6.96 (m, 2H), 2.05 (s, 3H); MS (-EI) *m*/*z* 339 (M-, 70), 337 (M-, 100).

*2-(Benzyloxy)-N-(3,5-dichloro-4-methoxyphenyl)benzamide (***17***).* To a solution of 4-nitrophenyl-2-hydroxybenzoate (0.717 g, 2.76 mmol) in NMP (3 mL) was added 3,5-dichloro-4-methoxyaniline (1.51 g, 7.88 mmol). The resulting solution was briefly refluxed with stirring (15 min) and then allowed to cool (rt). After aqueous workup (EtOAc/10% aq HCl), the organic layer was washed (brine), dried ($MgSO_4$), and the solvent removed *in vacuo* followed by purification of the crude solid by flash chromatography (hexanes/ethyl acetate, 4:1) to afford known compound **16** (125 mg, 0.311 mmol), [55411−43−3]: ^{1}H NMR (500 MHz, d_6-DMSO) δ 11.41 (s, 1H), 10.45 (s, 1H), 7.89 (s, 2H), 7.85 (dd, J = 8.0, 1.0 Hz, 1H), 7.43 (app t, J = 7.5, 1H), 7.00−6.94 (m, 2H), 3.81 (s, 3H); MS (-EI) *m*/*z* 312 (M-, 70), 310 (M-, 100). To a suspension of **16** (25.1 mg, 0.0804 mmol) and K_2CO_3 (26 mg, 0.19 mmol) in DMF (0.5 mL) at room temperature was added neat benzyl bromide (20 uL, 0.17 mmol). The resulting mixture was briefly warmed by microwave irradiation (150 °C internal, 10 min.) and then allowed to cool (rt). The resulting mixture was filtered. The filtrate, after aqueous workup (EtOAc/10% aq HCl) and concentration *in vacuo*, afforded an analytical sample **17** (7.6 mg, 0.019 mmol). ^{1}H NMR (500 MHz, d_6-DMSO) δ 10.35 (s, 1H), 7.67−7.65 (m, 3H), 7.54−7.52 (m, 3H), 7.38−7.36 (m, 3H), 7.28 (d, J = 8.5 Hz, 1H), 7.10 (app t, J = 8.5 Hz, 1H), 5.23 (s, 2H), 3.78 (s, 3H); MS (-EI) *m*/*z* 404 (MH+, 70), 402 (MH+, 100).

*N-(3,5-Dichloro-4-methoxyphenyl)-2-methoxybenzamide (***18***).* A mixture of 2,5-dichloro-4-nitroanisole (5.47 g, 24.6 mmol) and 5% Pd/C (wet Degussa-type E101, 175 mg, theor. 0.0422 mmol Pd) in ethanol (200 mL) and acetic acid (10 mL) was stirred under hydrogen gas (1 atm, 4 h, rt). After filtration (diatomaceous earth), the bulk of the solvent was removed *in vacuo*, the residue was partitioned (ethyl acetate/1 N NaOH), and the organic layer dried ($NaSO_4$), and concentrated *in vacuo* to afford 2,5-dichloro-4-methoxybenzenamine (824 mg, 4.29 mmol [101251−23−4]) which was used without further purification. To a solution of 2,5-dichloro-4-methoxybenzenamine (0.341 g, 1.77 mmol) and diisopropylethylamine (0.5 mL, 4 mmol) in toluene (9.0 mL) was added 2-methoxybenzoyl chloride (0.489 g, 2.87 mmol) and the resulting solution was stirred (rt, 2 h). Addition of methanol (5.0 mL) resulted in a precipitate that was removed by filtration and the filtrate was concentrated *in vacuo* to afford a crude solid from which an aliquot was purified by flash chromatography (hexanes/ethyl acetate, 9.5:1 to 4:1) to afford an analytical sample of **18** (125 mg, 0.383 mmol).^{1}H NMR (500 MHz, d_6-acetone w/∼10% d_6-DMSO) δ 10.29 (s, 1H), 7.89 (s, 2H), 7.61 (dd, J = 7.5, 2.0 Hz, 1H), 7.52 (app t, J = 8.0 Hz, 1H), 7.18 (d, J = 8.5 Hz, 1H), 7.06 (app t, J = 7.5 Hz, 1H), 3.88 (s, 3H), 3.79 (s, 3H); MS (+EI) *m*/*z* 328 (MH+, 70), 326 (MH+, 100).

*Benzyl 2-(2-(4-amino-2,6-dichlorophenoxy)ethoxy)ethylcarbamate (***23***).* To a solution of 2-(2-aminoethoxy)ethanol (6.22 g, 59.2 mmol) in aq NaOH (0.8 M, 150 mL) at 0 °C (bath) was dropwise added (over 15 min) a solution of benzoyl chloroformate (13.0 g, 76.0 mmol) in THF (16 mL). The resulting solution was stirred (0 °C, 2 h) and then aqueous HCl (1.0 N, 50 mL) was added and the resulting mixture was allowed to

warm (rt). After aqueous workup (EtOAc/H_2O), the organic layer was dried ($MgSO_4$), filtered, and concentrated *in vacuo* to afford a crude solid that was purified by flash chromatography (EtOAc/CH_2Cl_2, 1:1) to afford **22** (9.2 g, 38 mmol) [145881−74−9]): ^{1}H NMR (500 MHz, $CDCl_3$) δ 7.35−7.30 (m, 5H), 5.25 (br s, 1H), 5.11 (s, 2H), 3.74−3.73 (m, 2H), 3.57−3.55 (m, 4H), 3.42−3.40 (m, 2H); MS (+EI) *m/z* 262 (MNa+, 20), 240 (MH+, 50), 196 (M-44/H+, 100). To a solution of **22** (9.2 g, 38 mmol) and 1,3-dichloro-2-fluoro-5-nitrobenzene, **21**, (7.33 g, 34.9 mmol) in THF (160 mL) was added sodium hydride (60% w/w disp. in mineral oil, 1.54 g, theor. 38.5 mmol) under a nitrogen atmosphere. The resulting suspension was stirred under reflux (6 h) then allowed to cool (rt) and concentrated *in vacuo*. After aqueous workup (EtOAc/H_2O), the organic layer was dried ($MgSO_4$) and concentrated *in vacuo* to afford benzyl 2-(2-(2,6-dichloro-4-nitrophenoxy)ethoxy)ethylcarbamate (13.8 g, 32.1 mmol) which was used without further purification: ^{1}H NMR (500 MHz, $CDCl_3$) δ 8.20 (s, 2H), 7.37−7.30 (m, 5H), 5.10 (s, 2H), 5.06 (br s, 1H), 4.33 (app t, J = 4.5 Hz, 2H), 3.86 (app t, J = 4.5 Hz, 2H), 3.62 (app t, J = 5.0 Hz, 2H), 3.40 (app t, J = 5.0 Hz, 2H); MS (+EI) *m/z* 431 (MH+, 70), 429 (MH+, 100). A suspension of benzyl 2-(2-(2,6-dichloro-4-nitrophenoxy)ethoxy)ethylcarbamate (12.7 g, 29.6 mmol) and stannous chloride (41.2 g, 182 mmol) in HCl (12 N, 50 mL) and ethanol (460 mL) was stirred at reflux (2 h) and then allowed to cool (rt). The bulk of the solvent was removed *in vacuo* and the pH was adjusted (to pH 8) by cautious addition (vigorous gas evolved) of aqueous $NaHCO_3$. After aqueous workup (EtOAc/H_2O), the organic layer was dried (Na_2SO_4), and concentrated *in vacuo* to afford a crude oil from which an aliquot was removed for purification by flash chromatography (hexanes/ethyl acetate, 3:1) to afford **23** (9.89 g, 24.8 mmol) as a colorless oil: ^{1}H NMR (500 MHz, $CDCl_3$ w/ ∼5% CD_3CO_2D) δ 7.36−7.30 (m, 5H), 6.77 (s, 2H), 5.11 (s, 2H), 4.11 (app t, J = 4.5 Hz, 2H), 3.81 (app t, J = 4.5 Hz, 2H), 3.62 (app t, J = 5.0 Hz, 2H), 3.41 (app t, J = 5.0 Hz, 2H); MS (+EI) *m/z* 401 (MH+, 70), 399 (MH+, 100).

*IL-12p40 Inhibitor-Modified AffiGel-15 (***19***).* A mixture of **23** (727 mg, 1.82 mmol) and phenyl salicylate, **24**, (537 mg, 2.50 mmol) was briefly warmed (melt) by microwave irradiation (200 °C internal, 10 min) and then allowed to cool (rt) and the resulting crude oil was purified by flash chromatography (hexanes/ethyl acetate, 7:3) to afford benzyl 2-(2-(2,6-dichloro-4-(2-hydroxybenzamido)phenoxy)ethoxy)ethylcarbamate (689 mg, 1.33 mmol) as a colorless oil: ^{1}H NMR (500 MHz, d_6-DMSO) δ 11.41 (d, J = 4.5 Hz, 1H), 10.43 (d, J = 7.0 Hz, 1H), 7.87−7.84 (m, 3H), 7.43 (app t, J = 7.8 Hz, 1H), 7.35−7.28 (m, 5H), 7.00−6.94 (m, 2H), 5.00 (s, 2H), 4.09 (t, J = 5.0 Hz, 2H), 3.74 (t, J = 5.0 Hz, 2H), 3.50 (t, J = 6.0 Hz, 2H), 3.16 (t, J = 6.0 Hz, 2H); MS (-EI) *m/z* 519 (M-, 70), 517 (M-, 100). A suspension of benzyl 2-(2-(2,6-dichloro-4-(2-hydroxybenzamido)phenoxy)ethoxy)ethylcarbamate (285 mg, 0.549 mmol), 5% Pd/C (wet Degussa-type E101, 22 mg, theor. 0.0053 mmol Pd), and acetic acid (0.2 mL) in chloroform/methanol (2:1, 15 mL) was shaken under hydrogen gas (25 psi, rt, 2 h). The resulting mixture was filtered (diatomaceous earth) and the filtrate concentrated *in vacuo* to afford *N*-(4-(2-(2-aminoethoxy)ethoxy)-3,5-dichlorophenyl)-2-hydroxybenzamide as a colorless oil (0.213 g, 0.534 mmol) that was used without further purification: ^{1}H NMR (500 MHz, d_6 DMSO) δ 11.41 (s, 1H), 10.43 (s, 1H), 7.90−7.86 (m, 3H), 7.43 (app t, J = 8.5 Hz, 1H), 7.01−6.94 (m, 2H), 4.14 (t, J = 5.0 Hz, 2H), 3.82 (t, J = 5.0 Hz, 2H), 3.70 (t, J = 5.5 Hz, 2H), 3.01 (t, J = 5.5 Hz, 2H); MS (+EI) *m/z* 387 (MH+, 70), 385 (MH+, 100). A solution of *N*-(4-(2-(2-aminoethoxy)ethoxy)-3,5-dichlorophenyl)-2-hydroxybenzamide (8.4 mM in DMSO/isopropanol, 1:20 v/v, 0.40 mL per column) was then nutated (24 h, 4 °C) with a portion of Affi-Gel-15 resin (reactive load level = 1.5 umol/mL, 0.3 mL) that had been washed and swelled with isopropanol (0.5 mL resin/slurry working volume per column). The postloading filtrate was collected and determined by LC-UV absorption (254 nm) to be 11% depleted in *N*-(4-(2-(2-aminoethoxy)ethoxy)-3,5-dichlorophenyl)-2-hydroxybenzamide relative to the solution that was introduced to the Affi-Gel 15 resin. The resulting loaded resin (load ∼1.3 umol/mL) was then quenched/capped by washing with an aqueous solution of 2-aminoethanol (1.0 M, 1 mL).

*IL-12p40 Non-Inhibitor-Modified Affigel-15 (***20***).* A solution of **23** (795 mg, 1.99 mmol), 2-methoxybenzoyl chloride (623 mg, 3.65 mmol) and diisopropylethylamine (829 mg, 6.41 mmol) in toluene (10 mL) was stirred under nitrogen (rt, 1 h). After aqueous workup (EtOAc, H_2O followed by aq. $NaHCO_3$, then 5% aq. HCl and last brine), the organic layer was dried ($MgSO_4$) and concentrated *in vacuo* to afford a crude solid that after purification by flash chromatography (hexanes/ethyl acetate, 3.5:1.5) afforded benzyl-2-(2-(2,6-dichloro-4-(2-methoxybenzamido)phenoxy)ethoxy)ethylcarbamate (1.04 g, 1.95 mmol) as a colorless oil: ^{1}H NMR (500 MHz, $CDCl_3$) δ 9.78 (br s, 1H), 8.27 (d, J = 7.5 Hz, 1H), 7.53 (app t, J = 7.5 Hz, 1H), 7.36−7.27 (m, 5H), 7.15 (app t, J = 7.5 Hz, 1H), 7.05 (d, J = 7.5 Hz, 1H), 5.11 (s, 2H), 4.18 (t, J = 5.0 Hz, 2H), 4.07 (s, 3H), 3.85 (t, J = 5.0 Hz, 2H), 3.66 (t, J = 5.0 Hz, 2H), 3.44 (t, J = 5.0 Hz, 2H); MS (+EI) *m/z* 535 (MH+, 70), 533 (MH+, 100). To a stirred solution of benzyl-2-(2-(2,6-dichloro-4-(2-methoxybenzamido)phenoxy)ethoxy)ethylcarbamate (120 mg, theor. 0.230 mmol) in $CHCl_3$ (5.0 mL) under argon (rt) was added neat trimethylsilyl iodide (153 mg, 0.765 mmol) in portions over 4 h. The resulting solution was diluted with MeOH (1 mL), 10% aq HCl (5 mL), CH_2Cl_2 (50 mL), and water (50 mL) resulting in a milky white suspension which was clarified by further addition of aqueous NaOH (10% w/w, 50 mL) and CH_2Cl_2 (50 mL). The aqueous layer was washed with CH_2Cl_2, and the combined organic layer was dried (Na_2SO_4) and concentrated *in vacuo* to afford a crude solid which after purification by flash chromatography ($CHCl_3$: methanol/triethyl amine, 100:10:0.1) afforded *N*-(4-(2-(2-aminoethoxy)ethoxy)-3,5-dichlorophenyl)-2-methoxybenzamide as a colorless oil (26 mg, 0.065 mmol) that was used without further purification: ^{1}H NMR (500 MHz, d_6-DMSO) δ 10.28 (s, 1H), 7.90 (s, 2H), 7.60 (d, J = 7.5 Hz, 1H), 7.52 (app t, J = 7.5 Hz, 1H), 7.15 (d, J = 7.5 Hz, 1H), 7.05 (app t, J = 7.5 Hz, 1H), 4.14 (t, J = 5.0 Hz, 2H), 3.94 (s, 3H), 3.82 (t, J = 5.0 Hz, 2H), 3.70 (t, J = 5.5 Hz, 2H), 3.01 (t, J = 5.5 Hz, 2H); MS (+EI) *m/z* 401 (MH+, 70), 399 (MH+, 100). A solution of *N*-(4-(2-(2-aminoethoxy)ethoxy)-3,5-dichlorophenyl)-2-methoxybenzamide (8.4 mM in DMSO: isopropanol, 1:20 v/v, 0.40 mL per column) was then nutated (24 h, 4 °C) with a portion of Affi-Gel-15 resin (0.3 mL) that had been washed and swelled with isopropanol (0.5 mL resin/slurry working volume per column). The postloading filtrate was collected and determined by LC-UV absorption (254 nm) to be 10% depleted in *N*-(4-(2-(2-aminoethoxy)ethoxy)-3,5-dichlorophenyl)-2-methoxybenzamide relative to the solution that was introduced to the Affi-Gel 15 resin. The resulting loaded resin (load ∼1.3 umol/mL) was then quenched/capped by washing with an aqueous solution of 2-aminoethanol (1.0 M, 1 mL).

General Bioassay Methods. All cell culture manipulations were performed in a biological safety cabinet, unless otherwise indicated. Media and additives were prepared and maintained under aseptic conditions with storage in the refrigerator up to one month. DC-B cell growth medium was prepared by combining Hepes buffer (1 M, 10 mL, pH = 7.4), Minimum Essential Medium (MEM) 100×x with sodium pyruvate (10 mL, Gibco catalog, #11360−070), MEM Vitamin Solution

(100×) (4 mL, Gibco catalog #1120−0511), MEM Essential Amino Acids 50× without Glutamine (8 mL, Gibco catalog #11130−051), MEM 100× Non-Essential Amino Acids (4 mL, Gibco catalog #11140−050), Penicillin-Streptomycin-Glutamine (10 mL, Gibco catalog #10378−016), and 2-mercaptoethanol (1 mM, 1 mL). The resulting solution was diluted (to 1 L) with aqueous sodium bicarbonate. To this solution was added heat inactivated fetal bovine serum (FBS) and murine granulocyte-macrophage colony stimulating factor (GM-CSF) to afford a final concentration of 10% v/v FBS and 20 ng/mL for GM-CSF. Assay medium for DC-B cells was prepared by combining MEM 100× Non-Essential Amino Acids (10 mL, Gibco catalog #11140−050), sodium pyruvate (100 mM, 10 mL), Hepes buffer (10 mM, 10 mL), and 2-mercaptoethanol (1 mM, 1 mL) and diluting this to a final volume of one liter with Iscove's Modified Dulbecco's Medium (Hyclone). To this solution was added heat inactivated fetal bovine serum (FBS) and murine granulocyte-macrophage colony stimulating factor (GM-CSF) to afford a final concentration of 1% v/v FBS and 20 ng/mL for GM-CSF. ELISA antibody pairs included purified rat antimouse IL-6 monoclonal antibody (PharMingen catalog #554400), biotinylated rat antimouse IL-6 monoclonal antibody (PharMingen catalog #554402), purified rat antimouse IL-12p40/p70 monoclonal antibody (PharMingen catalog #551219), biotinylated rat antimouse IL-12p40/p70 monoclonal antibody (PharMingen catalog #554476), DELFIA Assay Buffer (Wallac catalog #1244−111), europium-labeled streptavidin, (Wallac catalog #1244−360,) and Enhancement Solution (Wallac catalog #1244−105). Assay plates were high-binding 384-well plates (Greiner Catalog #781077) and cell culture plates were black wall/clear bottom 384-well plates (Costar Catalog #3712).

Fluorescence Immunoassay Protocol. A murine dendritic cell line (DC-B cells) was cultured in growth medium (60 mL total volume) in T-175 tissue culture flasks maintained in a 37 ± 2 °C, 5 ± 1% CO_2 high humidity incubator. Nonadherent cells were collected and diluted with growth medium (1:3 v/v) every 48 h. To the test compounds (40 uM in assay media containing 0.4% v/v DMSO, 12.5 uL per well), in 384-well in cell culture plates, were added DC-B cells in DELFIA assay buffer (27.5 uL/well, cell concentration of 7.27×10^5/mL) followed by the cytokine stimulatory mixture (or assay media if a control well; 10 uL/well) in order to induce IL-12p40 and IL-6 secretion by the DC-B cells (*11, 12*). The stimulatory mixture consisted of a solution of *mu*CD40L, *mu*IL-18, and *mu*IFNgamma in assay media resulting in final concentrations of 2 ng/mL, 40 ng/mL, and 20 ng/mL, respectively. The resulting assay plates containing test compounds at a concentration of 10 uM (50 uL volume per well) were incubated (18−24 h, 37 °C incubator with 5% CO_2). After incubation, the supernatant was transferred to 384 well assay plates that were precoated at 4 °C with either anti-IL-12p40 or anti-IL-6 capture antibodies. After incubation (2 h, rt), the assay plates were washed with Tween 20 (0.05% v/v in PBS) and a solution of the secondary antibody (20 uL/well in PBS containing 10% v/v heat inactivated FBS). The secondary antibody was either biotinylated rat antimouse IL-12p40 or biotinylated rat antimouse IL-6 depending upon the assay. After incubation (1 h, rt), the plates were washed with Tween 20 (0.05% v/v in PBS) and europium-labeled streptavidin (0.60 ug/mL in Delfia Assay Buffer, 20 uL/well) was added. After incubation (0.5 h, rt), the plates were washed with Tween 20 (0.05% v/v in PBS) and then the Enhancement Solution was added (40 uL/well). After incubation (5 min, rt), the plates were analyzed using a Victor^2 plate reader (Wallac) and measuring at 615 nm. Assay experimental data points were calculated as percentage of control (POC) and plotted vs concentration. Each concentration in the dose−response plots was composed of three assay experimental data points. The concentrations tested were over a range of ten values from 0.5 nM to 10 uM (i.e., 0.0005, 0.0015, 0.0046, 0.014, 0.041, 0.12, 0.37, 1.11, 3.33, 10.0 uM). From these plots, the IC50 ± SEM is reported (Table 1) and this represents the mean of at least two (and as many as eleven) separate determinations. Assay data analysis was performed using Spotfire Decision Site 8.1 (www.Tibco.com) and Activity Base 5.0 queried with SARgen (www.idbs.com).

Cytotoxicity and Recombinant Protein Profiling Assays. Cytotoxicity was assessed in our dendritic cell line by using the Cell Titer-GLO cell viability protocol (www.promega.com). The dendritic cells, treated with test compound, were then stimulated according to the same protocol described in the preceding section for the IL-12p40 assay protocol (i.e., incubated 18 h with murine CD40L, murine IL-18, and murine IFN-gamma). The Cell Titer-GLO reagent was then added in equal volume to culture volume and incubated (i.e., 2 min with orbital shaking to induce cell lysis followed by 10 min of incubation without shaking). Luminescence was then read (Victor^2 Microplate reader, Wallac). No cytotoxicity (POC <10%) was observed over a range of nine values from 1.5 nM to 10 uM (i.e., 0.0015, 0.0046, 0.014, 0.041, 0.12, 0.37, 1.11, 3.33, 10.0 uM) for any compound with IL-12p40 activity (i.e., IC50 < 10 uM). Routine counter-screening included 75× receptor binding and 71× enzyme inhibition assays performed at Cerep (www.cerep.com).

Affinity Chromatography Columns. Two columns, containing **19** or **20**, respectively, were prepared using Affi-Gel-15 resin (Bio-Rad Laboratories, www.biorad.com) which is composed of primary/secondary amine reactive succinate ester groups on an agarose matrix (load level = 15 μmol per mL as determined by vendor). The column containing agarose labeled salicylanilide **19** we refer to as the "specific" column and the column containing agarose labeled salicylanilide **20** we refer to as the "non-specific" column.

DC-B Cell Derived Cytosolic Preparation. The same murine dendritic cell line (~100×10^6 cells) that was stimulated and used for the IL-12p40 assay (i.e., incubated 18 h with murine CD40L, murine IL-18, and murine IFNgamma) was subjected to three sequential freeze and thaw cycles (dry ice, ethanol) in order to lyse the cells. Then, buffer A (1 mL) was added. Buffer A is composed of HEPES buffer (20 mM, pH 7.1), NaCl (50 mM), β-glycerophosphate (25 mM), sodium vanidate (2.5 mM), sodium fluoride (5 mM), and Protease Inhibitor (1 tab, Sigma-Aldrich catalog #P8340). The mixture was agitated (~3× stroke cycles through a 25 gauge needle equipped with a 3 mL syringe) and centrifuged. To the DC derived cytosolic protein mixture (750 uL per column) was added quenched Affi-Gel-15 (150 uL packed) and this was nutated (overnight, 4 °C). This step was envisioned as a further control for non-specific interactions with the unmodified Affi-Gel-15 resin. The resulting material was centrifuged and the supernatant collected and introduced to each chromatography column (i.e., **19** or **20**; see preceding section) followed by nutation (2 h, 4 °C). The columns were then centrifuged, washed with buffer A (4 mL per column, pH = 7.1, see preceding description), and the supernatant layers were removed.

Competitive Elution of Affinity Columns and Postelution Analysis by SDS-PAGE. Each of the above columns, **19** or **20**, was loaded with a cytosolic protein mixture and then eluted with a solution of **16** (0.06 mM in buffer A) with ten separate fractions collected from each column. Each column fraction (200 uL) was diluted with DMSO (200 uL) and nutated (rt, 3 min) with SDS-Page Sample Prep. Kit Binding Resin (www.piercenet.com) followed by centrifugation (1400 rpm, 3 min.) using the filter cup provided with the Prep. Kit to recover supernatant fractions containing protein material. The resin was

then washed (200 uL of 50% aq DMSO) according to the general vendor protocol and then nutated (60 °C, 5 min) with SDS-Page Sample Prep. Kit Elution buffer (40 uL per column fraction) before collecting filtrate. Each filtrate (~40 uL) was diluted with a solution of 2-mercaptoethanol in SDS-Page Sample Prep. Kit Sample Buffer (15 uL, 25% v/v) and warmed (100 °C, 5 min).

In-Gel Digestion. Protein bands of interest from SDS-PAGE gels were excised and the gel pieces were processed using an automated protein digestion station (Genomic Solutions, Ann Arbor, MI) that performed the tasks of reduction and alkylation of cysteines, tryptic digestion, and extraction of the peptides.

Mass Spectrometry. According to the general method of Johnson and Davis et al. (*13*), a fully automated mass spectrometry analysis of the trypsin proteinase treated peptides was performed on a Micromass QTOF instrument (Waters Corporation, Milford, MA) and a NanoLC-2D system (Eksigent, Dublin, CA). One self-packed 75 um i.d. × 15 cm Vydac C18 columns and one 200 μm i.d. × 5 mm Monolithic trap column were attached to a 10 port switching valve (Valco Instruments Co. Inc.) which allowed sample fast loaded in the trap column to be analyzed and LC/MS/MS data to be collected through the C18 capillary column. Total run time was 65 min. Peptides were identified by searching the IPI-mouse protein sequence database (http://www.ebi.ac.uk/IPI/IPImouse.html) using the search tool MASCOT (http://www.matrixscience.com).

Molecular Docking and Minimization Methods. For compound **16** and 14−3−3ζ: Five structures of human 14−3−3ζ were downloaded from the RCSB Protein Data Bank: 1IB1, 1QJA, 1QJB, 2C1J, and 2C1N. For evaluation purposes, bound molecules, waters, and equivalent protein molecules were deleted from each structure, and the five remaining proteins were superimposed using MOE 2006.08 software (Chemical Computing Group Inc., Montreal, CN). Upon evaluation of the overlaid active sites it was found that LYS 49 was the only highly variable residue and structure 2C1J (*14*) was deemed representative of the series and thus used for the following calculations. The heavy atoms on the protein were fixed, hydrogen atoms were added, partial charges for all the atoms were calculated and the protein was minimized using Amber 99 in MOE. The small molecule was constructed and partial charges were calculated using MMFF94 in MOE. The small molecule was docked into the fixed protein's active site using MOE Dock in MOE. The top results were minimized (using Amber 99 in MOE) in a partially fixed protein (residues LYS 49, ARG 56, ARG 127, TYR 128 were free).

Calculated Physical Properties. The calculated physical properties including cLogD and pK_a were determined using ACD/LogD Suite 9.0, Advanced Chemistry Development, Inc., (ACD/Laboratories, Toronto ON, Canada, www.acdlabs.com).

RESULTS AND DISCUSSION

In the course of cell-based screening campaigns, we discovered salicylanilide **3** which inhibited IL-12p40 and IL-6 production in stimulated primary human dendritic cells as well as behaving similarly in a dendritic cell line assay (Table 1). Compounds **1** and **2a**,**b** were unfortunately not included among the original compounds that we evaluated for inhibition of IL-12p40 production. On the basis of a hypothesis that a desirable therapeutic profile is one that could block IL-12p40 but not IL-6 production, we engaged in directed analoging and developed analogue **4**, in which there is a hydrogen in place of the bromine on the salicyl-ring (i.e., ring "A"). Compound **4** was found in our assays to behave similarly to compound **3** with respect to inhibition of IL-12p40 production but to be much more selective against inhibition of IL-6 production (Table 1). The correlation between IL-6 activity and halogenation of the salicyl-ring demonstrated by these two analogues was generally observed in other analogues (*15*) and could be hypothesized to be due to some variation in interactions with different target protein(s).

We were interested in understanding the mechanism of action of these salicylanilides, and as a first step, we undertook broad counter-screening of **4** against a diverse collection of recombinantly expressed proteins but this resulted in no significant inhibition being observed versus any of more than 150 known targets (*15*). We also assessed general cytotoxicity in our dendritic cell line, and for example, **3** and **4** were each determined to have cytotoxic thresholds above 10 uM.

Focusing on **4** as an IL-12p40 inhibitor that might lend itself to chemical labeling, we chose to use affinity chromatography as a technique for protein target identification. As a preliminary step to developing chromatography matrices containing salicylanilides, we utilized a prospecting strategy in which we systematically introduced (i.e., highlighted boxes in Table 1) a limited array of functional groups around the periphery of a salicylanilide pharmacophore as a means to identify a site that might tolerate chemical labeling with agarose in a manner that would not significantly alter the bioactivity relative to the unlabeled analogue (i.e., **4**). Experience has shown us, as may be expected, that not all molecules lend themselves to chemical labeling without changes in bioactivity and this cannot be predicted *a priori* without the benefit of sufficient analogues and/or target protein structural information. For this study, we favored simple functional groups (i.e., amide, ether, alkyl) that would offer tractable syntheses and result in analogues with reasonable expectations of stability in our cellular assays, as a way to rapidly identify pharmacophore positions that might tolerate further chemical labeling.

Beginning with the possibility of tethering through the central amide moiety, it was found that simple tertiary amides are not tolerated as replacements for the secondary amide group in **4** as evidenced by analogues **5** and **6**. Next, we explored the possibility of tethering through the phenol group, and various ethers such as analogue **7**, with an *O*-benzyl ether group, were prepared. However, masking the phenol group as an ether resulted in a dramatic loss of inhibition of IL-12p40 production at our highest assay concentration (i.e., 10 μM). A possible alternative strategy that may allow for tethering through the salicyl-ring (*15*) is the replacement of the phenol group on the salicyl-ring with an aryl-sulfonamide group possessing a comparable pK_a.

Continuing with positions *para* to the critical phenol group of the salicyl ring, we prepared amino- and *N*-acetyl analogues **9** and **10**, respectively. Neither of these analogues demonstrated any measurable IL-12p40 activity. Similarly, we explored the position *para* to the amide substituents on ring "A" and likewise found a dramatic loss of bioactivity in our assays with analogues **12** and **13**. Notably, synthetic intermediates **8** and **11** were identified as possessing moderate inhibition of IL-12p40 production; however, we viewed a nitro group as not being as readily useful as an amide/amine functional group for attachment to an agarose resin and thus we continued the study, orienting next on the "B" ring. We prioritized the atom positions *meta* and *para* to the critical *N*-(salicyl)-substituent of the "B" ring, since we were concerned about the stereoelectronic consequences of chemical labeling *ortho* to this critical group.

Early in our directed analoging of **3**, it was observed that the *meta*-chloro substituents as featured in **4** are important for IL-12p40 activity and neither one nor both chloro groups could be replaced with simple alkyl groups, such as isosteric methyl groups, without complete loss of inhibitory activity in the IL-12p40 assay (*15*). Thus, we looked at heteroatom replacements for the *meta*-chloro groups on ring "B" but we found that, for example, *N*-acetyl analogue **14** lacked activity in the IL-12p40

assay. However, analogue **15** with halogen substitution similar to **4** but featuring an *N*-acetyl group *para* to the *N*-(salicyl)-substituent retained some moderate activity in the IL-12p40 assay. Despite the ~50-fold lower activity of **15** relative to **4**, we were encouraged enough by this result to next examine ether functional groups at this same *para* position of ring "B". We were pleased to find that the methyl ether modification in analogue **16** resulted in comparable activity to analogue **4** with respect to inhibition of IL-12p40 production in stimulated dendritic cells.

Table 1. Salicylanilides: Survey for Tethering Site

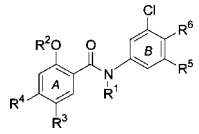

Entry	R1	R2	R3	R4	R5	R6	IC_{50} (μM)[a] IL-12p40	IL-6
3	H	H	Br	H	Cl	H	0.017 ± 0.012	0.24 ± 0.06
4	H	H	H	H	Cl	H	0.018 ± 0.017	>10
5	CH_3	H	H	H	Cl	H	>10	>10
6	CH_2CO_2H	H	H	H	Cl	H	>10	>10
7	H	Bn	H	H	Cl	H	>10	>10
8	H	H	NO_2	H	Cl	H	0.40 ± 0.01	0.38 ± 0.25
9	H	H	NH_2	H	Cl	H	>10	>10
10	H	H	NHAc	H	Cl	H	>10	>10
11	H	H	H	NO_2	Cl	H	0.27 ± 0.06	0.28 ± 0.04
12	H	H	H	NH_2	Cl	H	>10	>10
13	H	H	H	NHAc	Cl	H	>10	>10
14	H	H	H	H	NHAc	H	>10	>10
15	H	H	H	H	Cl	NHAc	0.65 ± 0.04	>10
16	H	H	H	H	Cl	OCH_3	0.017 ± 0.002	>10
17	H	Bn	H	H	Cl	OCH_3	>10	>10
18	H	CH_3	H	H	Cl	OCH_3	>10	>10

[a] Data reported here is for a murine dendritic cell line stimulated with a mixture of CD40L, IFNγ and IL-18. IL-12p40 and IL-6 detection by fluorescence immunoassay.

The affinity chromatography approach that we favored for subsequent protein target identification features two separate columns (Figure 2), each containing a differently modified agarose gel. One of these gels was derivatized using a bioactive small molecule and which we will refer to here as the "specific column" and the other, referred to as the "non-specific column", does not feature a bioactive compound attached to it (i.e., Scheme 2 describes structures **19** and **20**).

In order to make the non-specific column as similar as possible to the specific column, with respect to hydrophobicity and other bulk physical properties related to the structure of the salicylanilide-modified chromatography matrix, we required a salicylanilide analogue with no inhibitory activity toward IL-12p40 production and which would be attached in a similar manner to the agarose gel of the non-specific column. On the basis of the importance of the phenol group of salicylanilides, as seen earlier by comparing **4** with **7**, we prepared compounds **17** and **18** in which the phenol group is masked as an *O*-benzyl or *O*-methyl ether, respectively, and confirmed that these analogues had no activity in our IL-12p40 assay (Table 1). We felt that salicylanilide **16** (cLogD = 5.2, at pH 6.5 or 7.4) and its analogue **18** (cLogD = 4.3, at pH 6.5 or 7.4), which have similar structures and physical properties but very different IL-12p40 assay activities, constituted a suitable pair of candidate molecules for attachment to agarose gels for use as "specific" and "non-specific" chromatography columns, respectively.

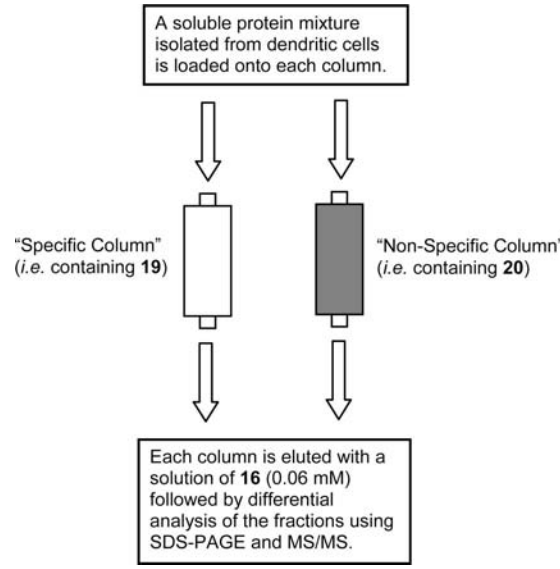

Figure 2. Chromatography: "specific" and "non-specific" agarose gels.

The preparation of agarose labeled salicylanilides **19** and **20** began (Scheme 2) with nucleophilic aromatic substitution of **21** with **22** followed by reduction of the product with stannous chloride to afford **23**. Acylation of **23**, using either **24** or **25** followed by removal of the CBZ-protecting group and reaction of the resulting primary amine with an *N*-(hydroxy)succinimide derivatized agarose gel, afforded **19** or **20**, respectively.

Scheme 2. Salicylanilide-Modified Agarose Gels[a]

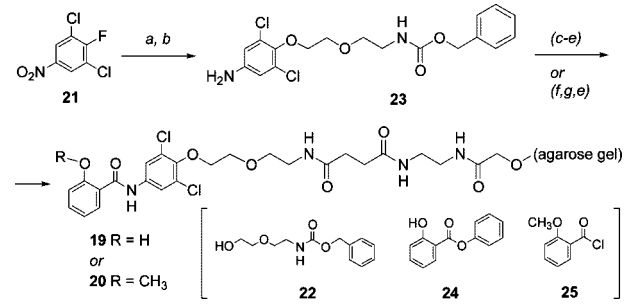

[a] Reagents: (a) **22**, NaH, THF, reflux; (b) $SnCl_2$, HCl aq., EtOH (71% from **21**); (c) **24**, melt at 200 °C; (d) H_2, Pd/C cat. (73% from **23**); (e) *N*-(hydroxy)succinimide derivatized agarose gel, aq. buffer (load level ~1.5 umol/mL); (f) **25**, ethyl-di(isopropyl)-amine, toluene; (g) TMSI, $CHCl_3$ (28% from **23**).

Protein target identification was accomplished by loading a mixture of proteins, prepared from lysis of the stimulated dendritic cell line used in the IL-12p40 assay, onto each column. Each column, in parallel, was washed and specific vs non-specific signal detection was enhanced in this experiment by competitive elution with the solution phase inhibitor **16** (0.06 mM). The fractions from each column were compared by SDS-PAGE analysis, after elution and concentration, in order to identify any specifically absorbed proteins (i.e., from column **19** not **20**). Characterization of protein bands was accomplished by cut-out of the gels, digestion with trypsin, and identification by MS/MS analysis. Reported here is a specifically retained 28 kDa protein, 14−3−3ζ (*16*, *17*) that was eluted from the "specific" column and not detected in the analysis of fractions eluted from the "non-specific" column. Interestingly, 14−3−3

```
1   mdknelvqka klaeqaeryd dmaacmksvt eqgaelsnee rnllsvaykn
    vvgarrsswr
61  vvssieqkte gaekkqqmar eyrekietel rdicndvlsl lekflipnas
    qpeskvfylk
121 mkgdyyryla evaagddkkg ivdqsqqayq eafeiskkem qpthpirlgl
    alnfsvfyye
181 ilnspekacs laktafdeai aeldtlsees ykdstlimql lrdnltlwts
    dtqgdeaeag
241 eggen

    Legend:   Underlined text: peptide fragments identified here by MS/MS
              Bold text: close contact residues defining a hydrophobic pocket
```

Figure 3. Consensus protein sequence of 14−3−3ζ of *Mus musculus.*

proteins have also recently been detected in immunostimulatory exosomes secreted by murine derived dendritic cells (*18*).

The 14−3−3 gene products are a large family of dimeric phosphoserine binding proteins with many reported biological functions (*19*). Of the seven isoforms known in mammals, the two peptide fragments that we found (i.e., "FLIPNASQPESK" and "DSTLIMQLLR", underlined in Figure 3) by MS/MS match only the phosphorylated and nonphosphorylated 14−3−3ζ/δ isoform of *Mus musculus* and do not match the ζ, φ/τ, ε, γ, β, or σ isoforms in *Mus musculus*. There are other human proteins that have homology with 14−3−3ζ proteins but none of these homologous proteins contain the two peptide sequences that we identified from our murine protein mixture. Murine and human 14−3−3ζ proteins share the same sequence except in one of the peptide sequences that we detected by MS/MS, PRO-112 in *Mus musculus* is an alanine in *Homo sapiens*. Serine-58, is highly conserved and, upon phosphorylation, by a number of different kinases has been shown to favor the monomeric form of the 14−3−3ζ proteins. Structurally, 14−3−3 proteins feature a bundle of nine antiparallel α-helices defining a large, concave hydrophobic pocket (*19*). Close contact amino acids are indicated (bold, Figure 3) and define a pocket where we hypothesize the small molecule (ex. "**16**") binds to 14−3−3ζ.

In a preliminary attempt to understand the binding of salicylanilides like **16** with 14−3−3ζ, we docked **16** into a solved X-ray structure (*14*) of human 14−3−3ζ in which the cocrystallized substrate peptide was first removed *in silico* and then minimization was conducted with the resulting apo-14−3−3ζ structure and **16** (Figure 4). We found that **16** prefers to bind such that its *para O*-methyl ether group accepts a hydrogen bond from ARG-56 with the methyl group (i.e., the same position that was chemically labeled to prepare target identifying gel **19**) extended away from the binding pocket. Such a binding feature would clearly be required for the affinity chromatography approach to succeed.

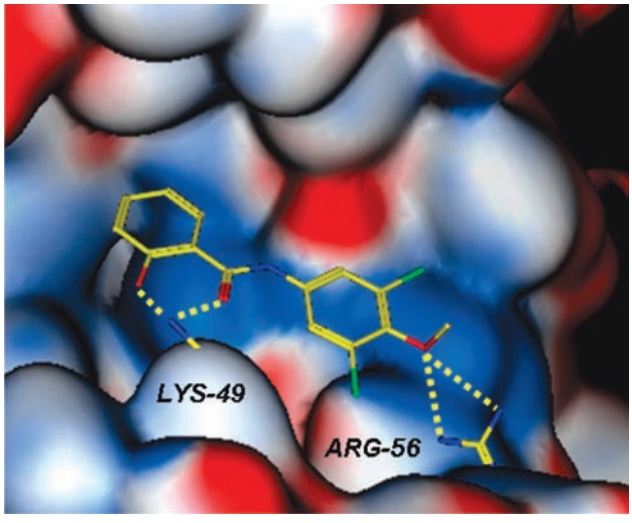

Figure 4. Molecular model of **16** docked in an apo-14−3−3, cocrystal. Surfaces are electrostatic renderings (i.e., red = positive, white = neutral, blue = negative charges).

It was also observed that the hydroxybenzamide system of **16** is preferred to be coplanar in this binding model which allows for a very favorable charge−charge interaction between the ε-amino side-chain (LYS-49) of 14−3−3ζ and both the phenolic hydroxyl group and the adjacent amide carbonyl group of **16.** This observation may explain why masking this key phenolic group as an ether, such as found in inactive analogues **7**, **17**, or **18**, and the non-specific resin **20**, would be expected to greatly diminish these salicylanilides' affinities for 14−3−3ζ. Much of the rest of the "A" ring and the N-H of the amide group are closely bound in proximity to hydrophobic residues (e.g., ILE-217, LEU-220) that define the interior of this pocket and which may explain why the chemical labeling survey (Table 1) disfavored all but certain "B" ring modifications of these salicylanilides with respect to retention of IL-12p40 activity.

In conclusion, we have demonstrated that example salicylanilides can functionally inhibit IL-12p40 production. The conversion of one of these bioactive salicylanilides into a comparably bioactive, chemically labeled derivative was achieved through a systematic synthesis strategy using readily tractable modifications around the periphery of a salicylanilide pharmacophore. This strategy provided a tool reagent for protein identification based upon selective biochemical affinity. Having demonstrated selective biochemical affinity, further experiments to address the functional role of 14−3−3ζ in IL-12p40 production, in stimulated dendritic cells, will be reported.

Supporting Information Available: NMR and mass spectral data for characterization of the novel salicylanilides. This material is available free of charge via the Internet at http://pubs.acs.org.

LITERATURE CITED

(1) Trinchieri, G., Pflanz, S., and Kastelein, R. A. (2003) The IL-12 family of heterodimeric cytokines: new players in the regulation of T cell responses. *Immunity 19*, 641–644.

(2) Gately, M. K., Renzetti, L. M., Magram, J., Stern, A. S., Adorini, L., Gubler, U., and Presky, D. H. (1998) The Interleukine-12/interleukine-12-receptor system: role in normal and pathologic immune responses. *Annu. Rev. Immunol. 16*, 495–521.

(3) Toichi, E., Torres, G., McCormick, T. S., Chang, T., Mascelli, M. A., Kauffman, C. L., Aria, N., Gottlieb, A. B., Everitt, D. E., Frederick, B., Pendley, C. E., and Cooper, K. D. (2006) An Anti-IL-12p40 antibody down-regulates type 1 cytokines, chemokines, and IL-12/IL-23 in psoriasis. *J. Immunol. 177* (7), 4917–4926.

(4) Mannon, P. J., Fuss, I. J., Mayer, L., Elson, C. O., Sandborn, W. J., Present, D., Dolin, B., Goodman, N., Groden, C., Hornung,

R. L., Quezado, M., Neurath, M. F., Salfeld, J., Veldman, G. M., Schwertschlag, U., and Strober, W. (2004) Anti-interleukin-12 antibody for active Crohn's disease. *New Engl. J. Med. 351*, 2069–2079.

(5) Burakoff, R., Barish, C. F., Riff, D., Pruitt, R., Chey, W. Y., Farraye, F. A., Shafran, I., Katz, S., Krone, C. L., Vander, V. M., Stevens, C., Sherman, M. L., Jacobson, E., and Bleday, R. (2006) A phase 1/2A trial of STA 5326, an oral interleukin-12/23 inhibitor, in patients with active moderate to severe Crohn's disease. *Inflammatory Bowel Diseases 12* (7), 558–565.

(6) Coopera, A. M., and Khader, S. A. (2007) IL-12p40: an inherently agonistic cytokine. *Trends Immunol. 28* (1), 33–38.

(7) Agrawal, V. K., and Sharma, S. (1984) Salicylanilides in the treatment of helminth diseases. *Pharmazie 39* (6), 373–378.

(8) Kasckow, J. W., Tabira, T., Itoyama, Y., Kuroiwa, Y., Takenaka, A., and Nagai, Y. (1981) Experimental allergic encephalomyelitis: suppression with SD-170, a new synthetic drug. *Jpn. J. Exp. Med. 51* (5), 293–298.

(9) Zhu, X.-F., Wang, J.-S., Cai, L.-L., Zeng, Y.-X., and Yang, D. (2006) SUCI-02 inhibits the ErbB-2 tyrosine kinase receptor signaling pathway and arrests the cell cycle in G1 phase in breast cancer cells. *Cancer Sci. 97* (1), 84–89.

(10) Waisser, K., Matyk, J., Divišová, H., Husáková, P., Kuneš, J., Klimešová, V., Kaustová, J., Möllmann, U., Dahse, H.-M., and Miko, M. (2006) The oriented development of antituberculotics: salicylanilides. *Arch. Pharm 339* (11), 616–620.

(11) Eriksson, U., Kurrer, M. O., Sonderegger, I., Iezzi, G., Tafuri, A., Hunziker, L., Suzuki, S., Bachmaier, K., Bingisser, R. M., Penninger, J. M., and Kopf, M. (2003) Activation of dendritic cells through the interleukin 1 receptor 1 is critical for the induction of autoimmune myocarditis. *J. Exp. Med. 197* (3), 323–331.

(12) Pasare, C., and Medzhitov, R. (2003) Toll pathway-dependent blockade of CD4+CD25+ T cell-mediated suppression by dendritic cells. *Science 299* (5609), 1033–1036.

(13) Johnson, R. S., Davis, M. T., Taylor, J. A., and Patterson, S. D. (2005) *Methods 35* (3), 223–236.

(14) Macdonald, N., Welburn, J. P. I., Noble, M. E. M., Nguyen, A., Yaffe, M. B., Clynes, D., Moggs, J. G., Orphanides, G., Thomson, S., Edmunds, J. W., Clayton, A. L., Endicott, J. A., and Mahadevan, L. C. (2005) Molecular basis for the recognition of phosphorylated and phosphoacetylated histone H3 by 14-3-3. *Mol. Cell 20* (2), 199–211.

(15) Unpublished results.

(16) Thomas, D., Guthridge, M., Woodcock, J., and Lopez, A. (2005) 14-3-3 protein signaling in development and growth factor responses. *Curr. Top. Dev. Biol. 67*, 285–303.

(17) Aitken, A. (2006) 14-3-3 proteins: A historic overview. *Semin. Cancer Biol. 16* (3), 162–172.

(18) Thery, C., Boussac, M., Veron, P., Ricciardi-Castagnoli, P., Raposo, G., Garin, J., and Amigorena, S. (2001) Proteomic analysis of dendritic cell-derived exosomes: a secreted subcellular compartment distinct from apoptotic vesicles. *J. Immunol. 166* (12), 7309–7318.

(19) Fu, H., Subramanian, R. R., and Masters, S. C. (2000) 14-3-3 proteins: structure, function, and regulation. *Annu. Rev. Pharmacol. Toxicol. 40*, 617–647.

BC800078Q

Identification of 14-3-3ζ by Chemical Affinity with Salicylanilide Inhibitors of Interleukin-12p40 Production.

Jim P. Boyce,* Michael E. Brown, Wilson Chin, Jeffrey N. Fitzner, Raymond J. Paxton, Min Shen, Tracey Stevens, Martin F. Wolfson, Clifford D. Wright

Amgen Inc., 1201 Amgen Court West, Seattle, WA 98119

E-mail: boycej@amgen.com

Supporting Information

Table of Contents: **Pages**

^{1}H NMR spectrum of *N*-(3,5-dichlorophenyl)-2-hydroxy-*N*-methylbenzamide (**5**) S4

^{13}C NMR spectrum of *N*-(3,5-dichlorophenyl)-2-hydroxy-*N*-methylbenzamide (**5**) S4

MS spectrum for *N*-(3,5-dichlorophenyl)-2-hydroxy-*N*-methylbenzamide (**5**) S5

^{1}H NMR spectrum of 2-(*N*-(3,5-dichlorophenyl)-2-hydroxybenzamido)acetic acid (**6**) S6

^{13}C NMR spectrum of 2-(*N*-(3,5-dichlorophenyl)-2-hydroxybenzamido)acetic acid (**6**) S6

MS spectrum for 2-(*N*-(3,5-dichlorophenyl)-2-hydroxybenzamido)acetic acid (**6**) S7

^{1}H NMR spectrum of 2-(benzyloxy)-*N*-(3,5-dichlorophenyl)benzamide (**7**) S8

^{13}C NMR spectrum of 2-(benzyloxy)-*N*-(3,5-dichlorophenyl)benzamide (**7**) S8

MS spectrum for 2-(benzyloxy)-*N*-(3,5-dichlorophenyl)benzamide (**7**) S9

MS spectrum for 2-(benzyloxy)-*N*-(3,5-dichlorophenyl)-*N*-methylbenzamide S10

^{1}H NMR spectrum of *tert*-butyl 2-(*N*-(3,5-dichlorophenyl)-2--hydroxybenzamido)acetate S11

^{13}C NMR spectrum of *tert*-butyl 2-(*N*-(3,5-dichlorophenyl)-2--hydroxybenzamido)acetate S11

MS spectrum for intermediate *tert*-butyl 2-(*N*-(3,5-dichlorophenyl)-2--hydroxybenzamido)acetate S12

^{1}H NMR spectrum of *N*-(3,5-dichlorophenyl)-2-hydroxy-5-nitrobenzamide (**8**) S13

MS spectrum for *N*-(3,5-dichlorophenyl)-2-hydroxy-5-nitrobenzamide (**8**) S14

^{1}H NMR spectrum of 5-amino-*N*-(3,5-dichlorophenyl)-2-hydroxybenzamide (**9**) S15

MS spectrum for 5-amino-*N*-(3,5-dichlorophenyl)-2-hydroxybenzamide (**9**) S16

^{1}H NMR spectrum of 5-acetamido-*N*-(3,5-dichlorophenyl)-2-hydroxybenzamide (**10**) S17

MS spectrum for 5-acetamido-*N*-(3,5-dichlorophenyl)-2-hydroxybenzamide (**10**) S18

^{1}H NMR spectrum of *N*-(3,5-dichlorophenyl)-2-hydroxy-4-nitrobenzamide (**1**) S19

MS spectrum for *N*-(3,5-dichlorophenyl)-2-hydroxy-4-nitrobenzamide (**11**) S20

^{1}H NMR spectrum of 4-amino-*N*-(3,5-dichlorophenyl)-2-hydroxybenzamide (**12**) S21

MS spectrum for 4-amino-*N*-(3,5-dichlorophenyl)-2-hydroxybenzamide (**12**) S22

^{1}H NMR spectrum of 4-acetamido-*N*-(3,5-dichlorophenyl)-2-hydroxybenzamide (**13**) S23

MS spectrum for 4-acetamido-*N*-(3,5-dichlorophenyl)-2-hydroxybenzamide (**13**) S24

^{1}H NMR spectrum of *N*-(3-acetamido-5-chlorophenyl)-2-hydroxybenzamide (**14**) S25

^{13}C NMR spectrum of *N*-(3-acetamido-5-chlorophenyl)-2-hydroxybenzamide (**14**) S25

MS spectrum for *N*-(3-acetamido-5-chlorophenyl)-2-hydroxybenzamide (**14**) S26

^{1}H NMR spectrum of *N*-(4-acetamido-3,5-dichlorophenyl)-2-hydroxybenzamide (**15**) S27

MS spectrum for *N*-(4-acetamido-3,5-dichlorophenyl)-2-hydroxybenzamide (**15**) S28

^{1}H NMR spectrum of *N*-(3,5-dichloro-4-methoxyphenyl)-2-hydroxybenzamide (**16**) S29

MS spectrum for *N*-(3,5-dichloro-4-methoxyphenyl)-2-hydroxybenzamide (**16**) S30

^{1}H NMR spectrum of 2-(benzyloxy)-*N*-(3,5-dichloro-4-methoxyphenyl)benzamide (**17**) S31

MS spectrum for 2-(benzyloxy)-*N*-(3,5-dichloro-4-methoxyphenyl)benzamide (**17**) S32

^{1}H NMR spectrum of *N*-(3,5-dichloro-4-methoxyphenyl)-2-methoxybenzamide (**18**) S33

MS spectrum for *N*-(3,5-dichloro-4-methoxyphenyl)-2-methoxybenzamide (**18**) S34

^{1}H NMR spectrum of benzyl 2-(2-hydroxyethoxy)ethylcarbamate (**22**) S35

MS spectrum for benzyl 2-(2-hydroxyethoxy)ethylcarbamate (**22**) S36

^{1}H NMR spectrum of benzyl 2-(2-(2,6-dichloro-4-nitrophenoxy)-
-ethoxy)ethylcarbamate S37

MS spectrum for benzyl 2-(2-(2,6-dichloro-4-nitrophenoxy)-
-ethoxy)ethylcarbamate S38

^{1}H NMR spectrum of benzyl 2-(2-(4-amino-2,6-dichlorophenoxy)ethoxy)-
-ethylcarbamate (**23**) S39

MS spectrum for benzyl 2-(2-(4-amino-2,6-dichlorophenoxy)ethoxy)-
-ethylcarbamate (**23**) S40

^{1}H NMR spectrum of benzyl 2-(2-(2,6-dichloro-4-(2--hydroxybenzamido)phenoxy)ethoxy)ethylcarbamate S41

MS spectrum for benzyl 2-(2-(2,6-dichloro-4-(2--hydroxybenzamido)phenoxy)ethoxy)ethylcarbamate S42

^{1}H NMR spectrum of *N*-(4-(2-(2-aminoethoxy)ethoxy)--3,5-dichlorophenyl)-2-hydroxybenzamide S43

MS spectrum for *N*-(4-(2-(2-aminoethoxy)ethoxy)--3,5-dichlorophenyl)-2-hydroxybenzamide S44

^{1}H NMR spectrum of benzyl 2-(2-(2,6-dichloro-4--(2-methoxybenzamido)phenoxy)ethoxy)ethylcarbamate S45

MS, spectrum for benzyl 2-(2-(2,6-dichloro-4--(2-methoxybenzamido)phenoxy)ethoxy)ethylcarbamate S46

^{1}H NMR spectrum of *N*-(4-(2-(2-aminoethoxy)ethoxy)--3,5-dichlorophenyl)-2-methoxybenzamide S47

MS spectrum for *N*-(4-(2-(2-aminoethoxy)ethoxy)--3,5-dichlorophenyl)-2-methoxybenzamide S48

SDS-PAGE gel stained to show band (28 kDA) corresponding to 14-3-3ζ S49

^{1}H NMR, Compound **5**

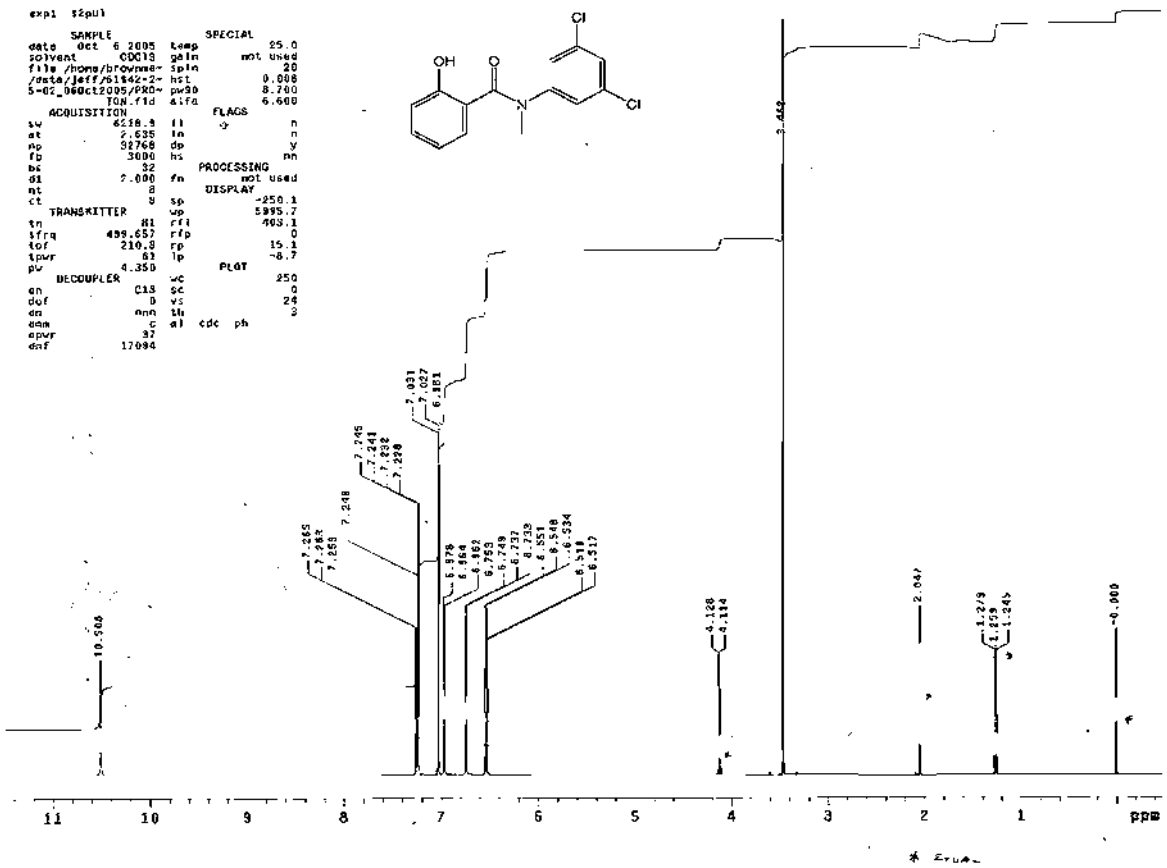

^{13}C NMR, Compound **5**

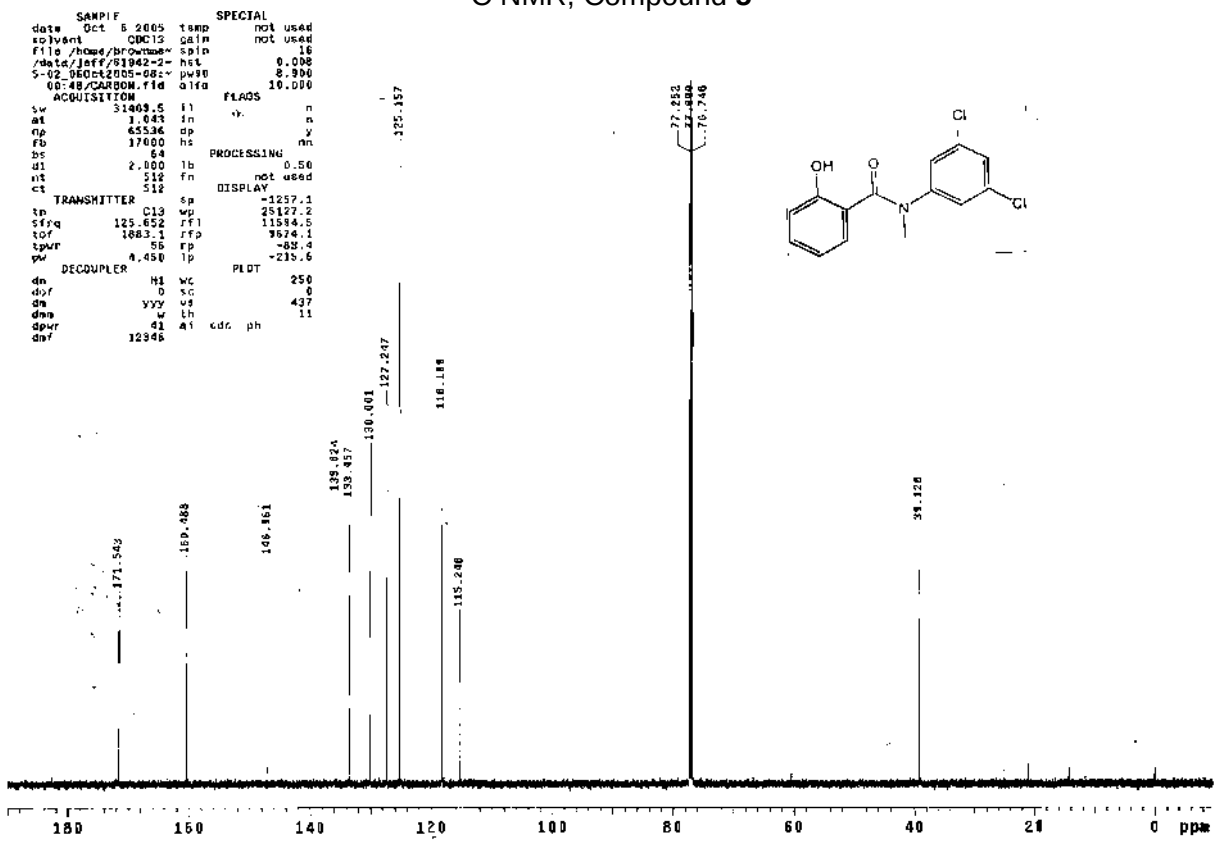

MS, Compound **5**

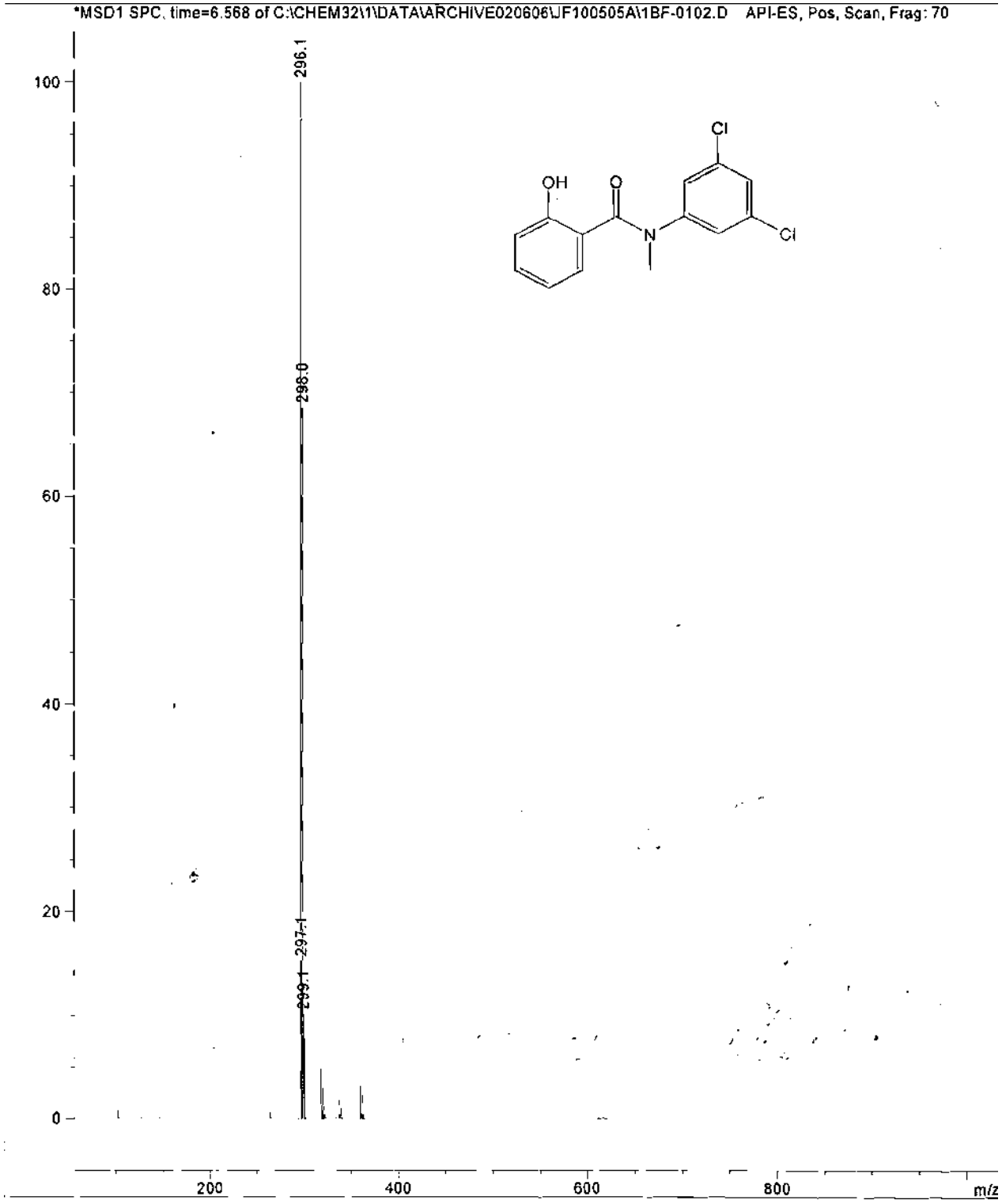

^{1}H NMR, Compound **6**

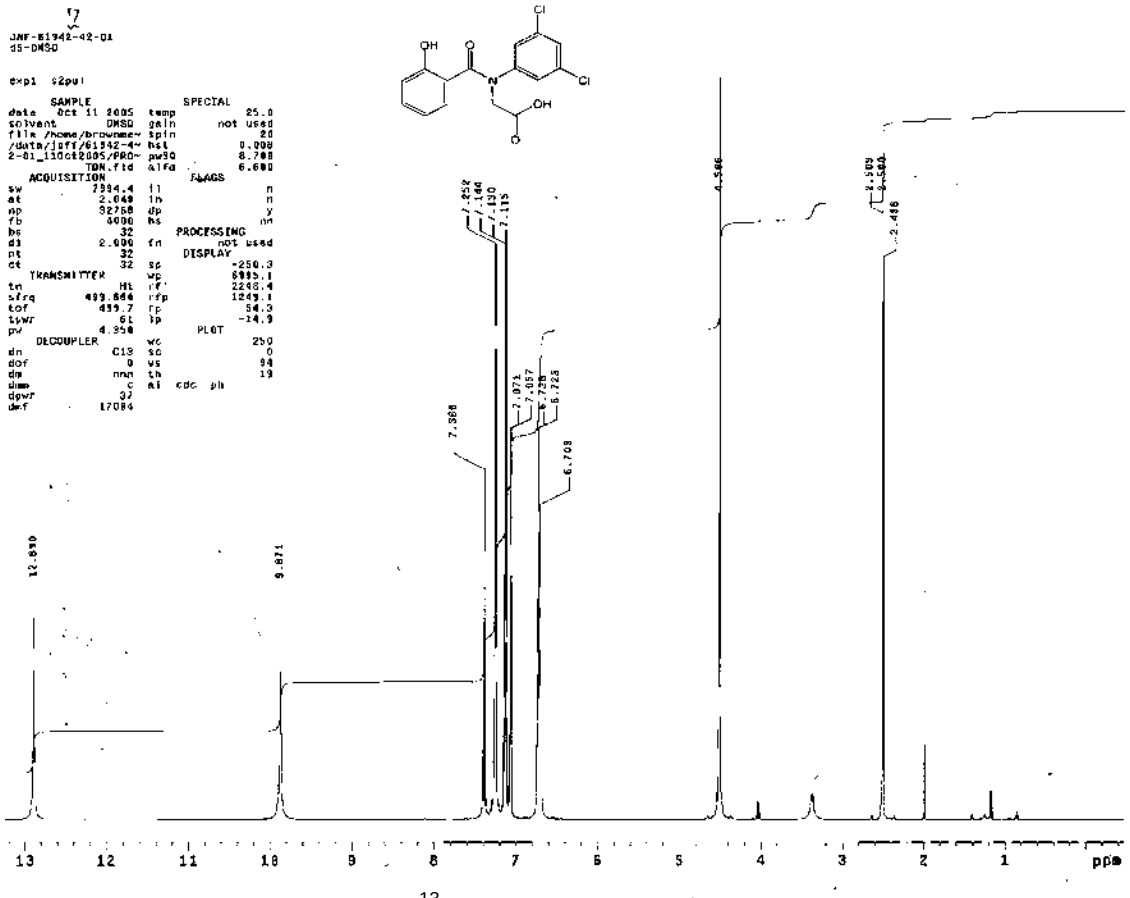

^{13}C NMR, Compound **6**

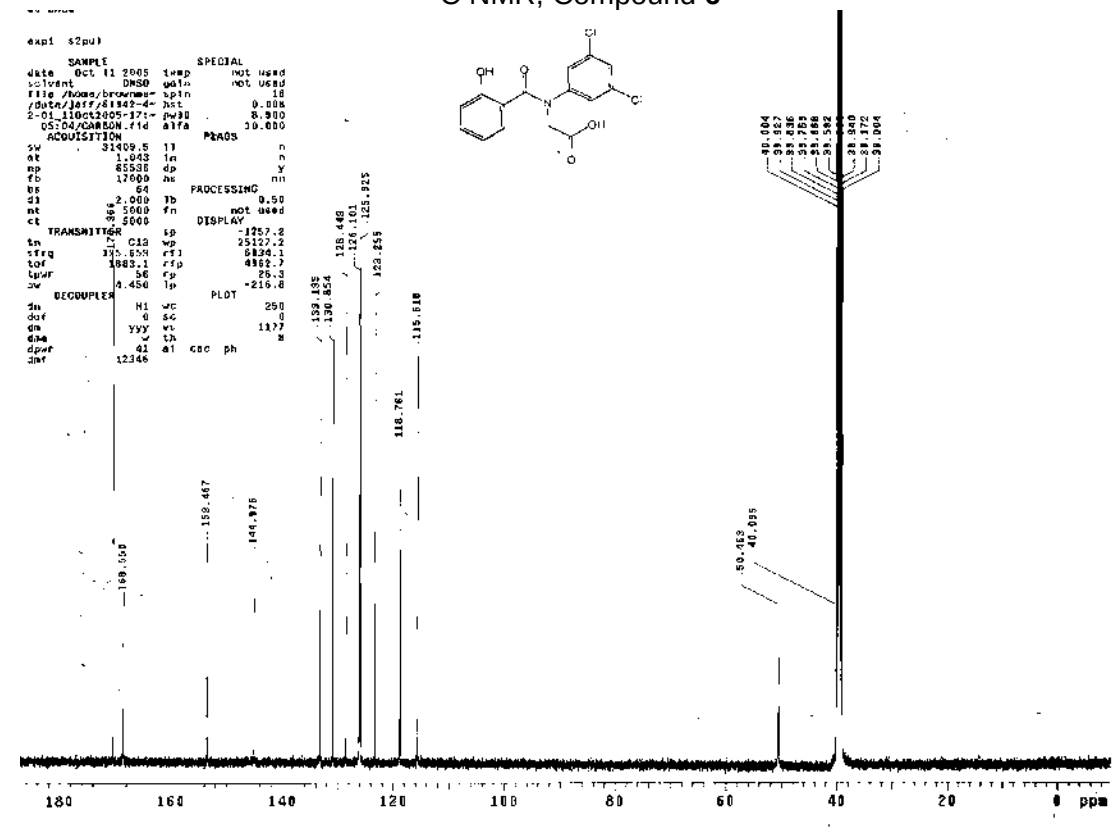

MS, Compound **6**

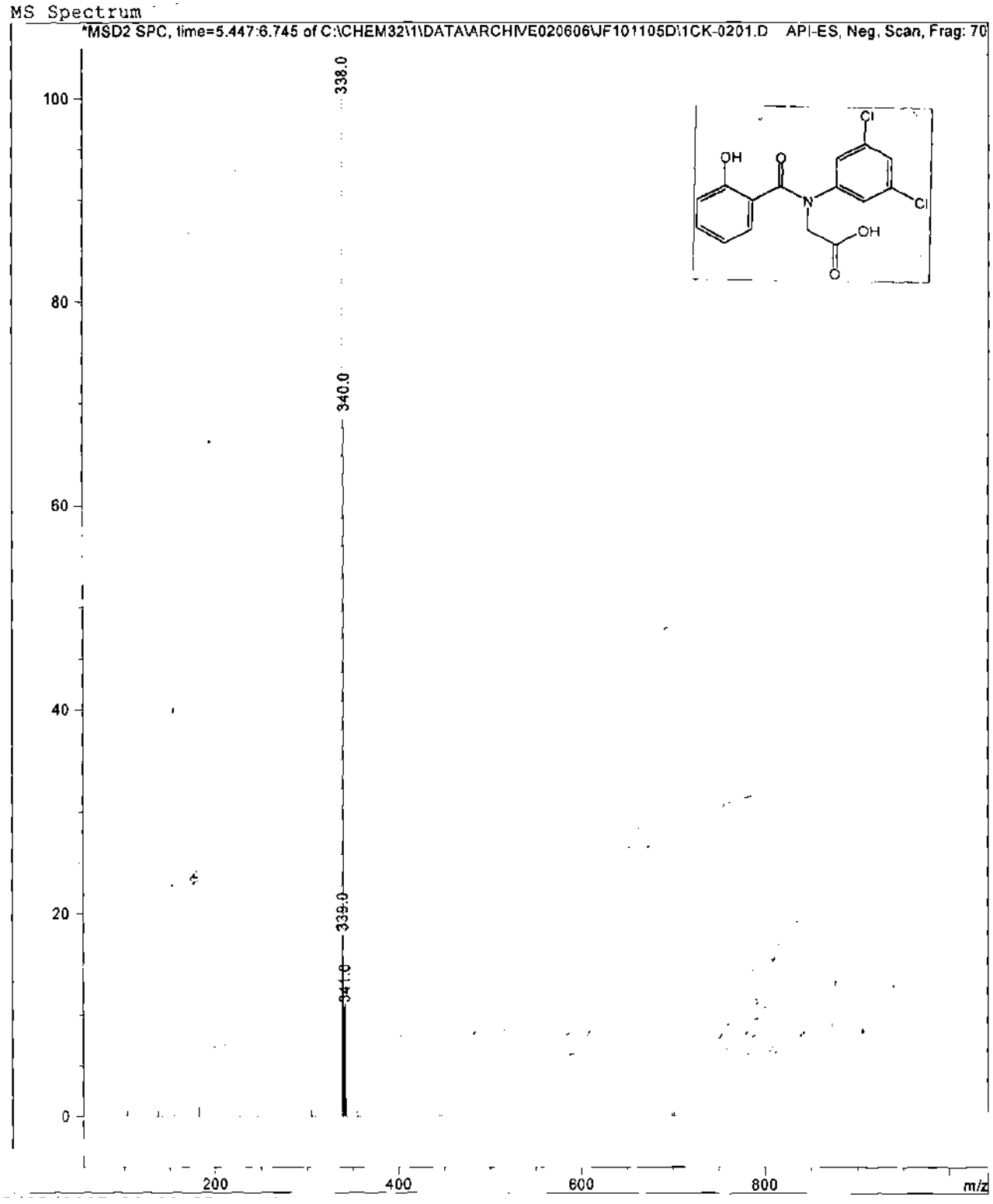

^{1}H NMR, Compound **7**

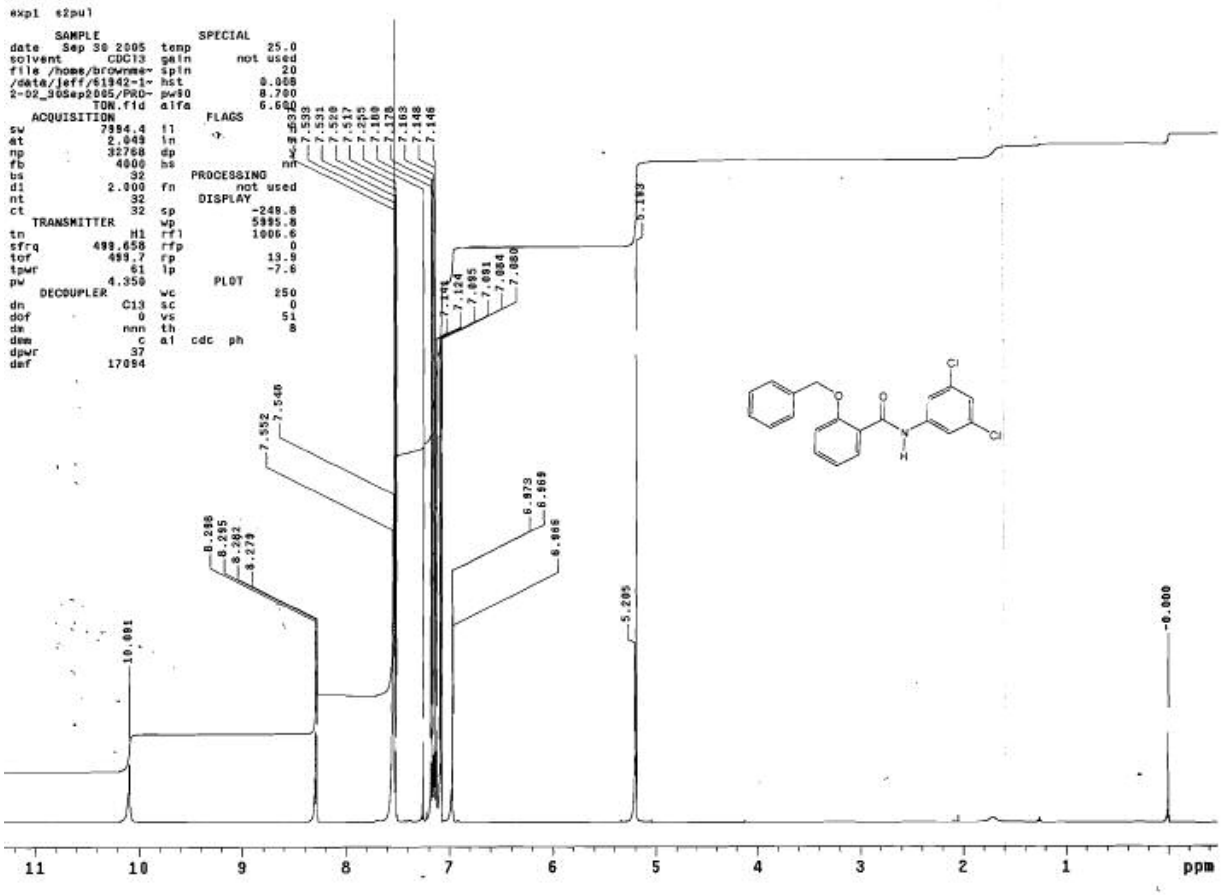

^{13}C NMR, Compound **7**

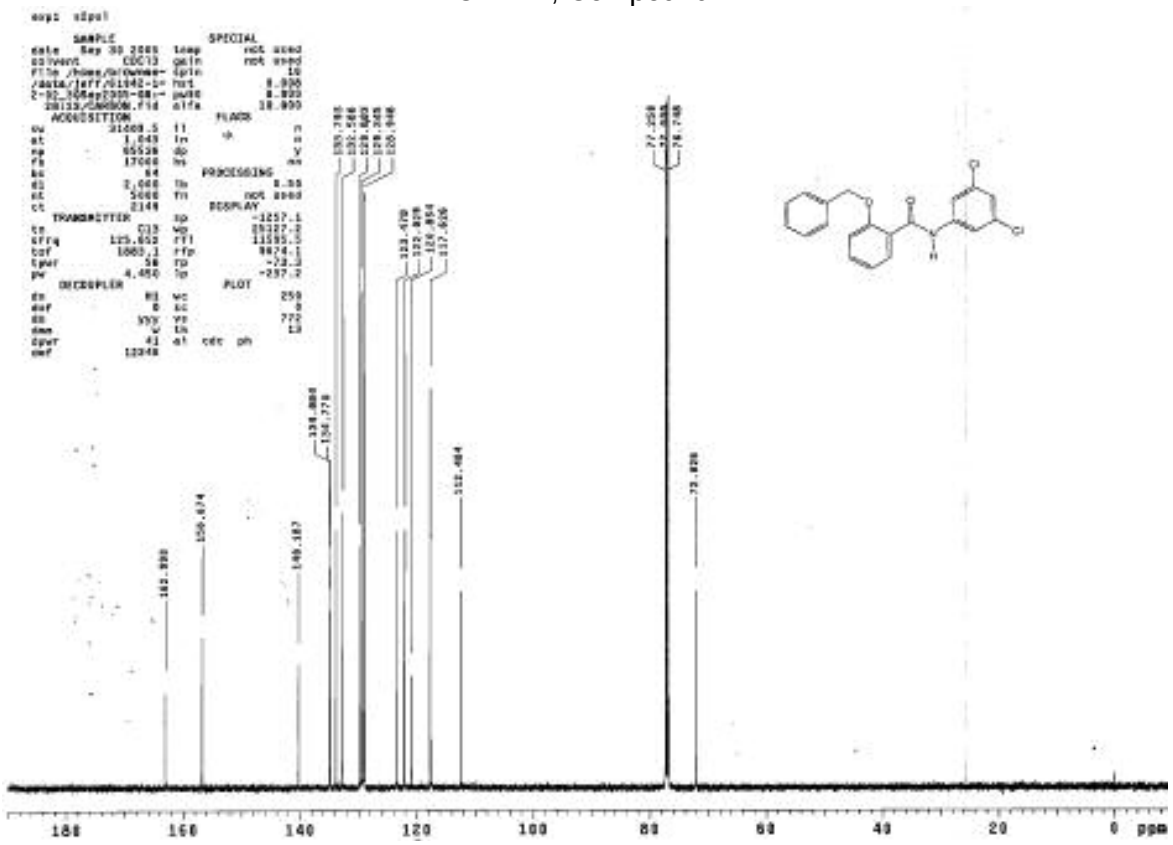

MS, Compound **7**

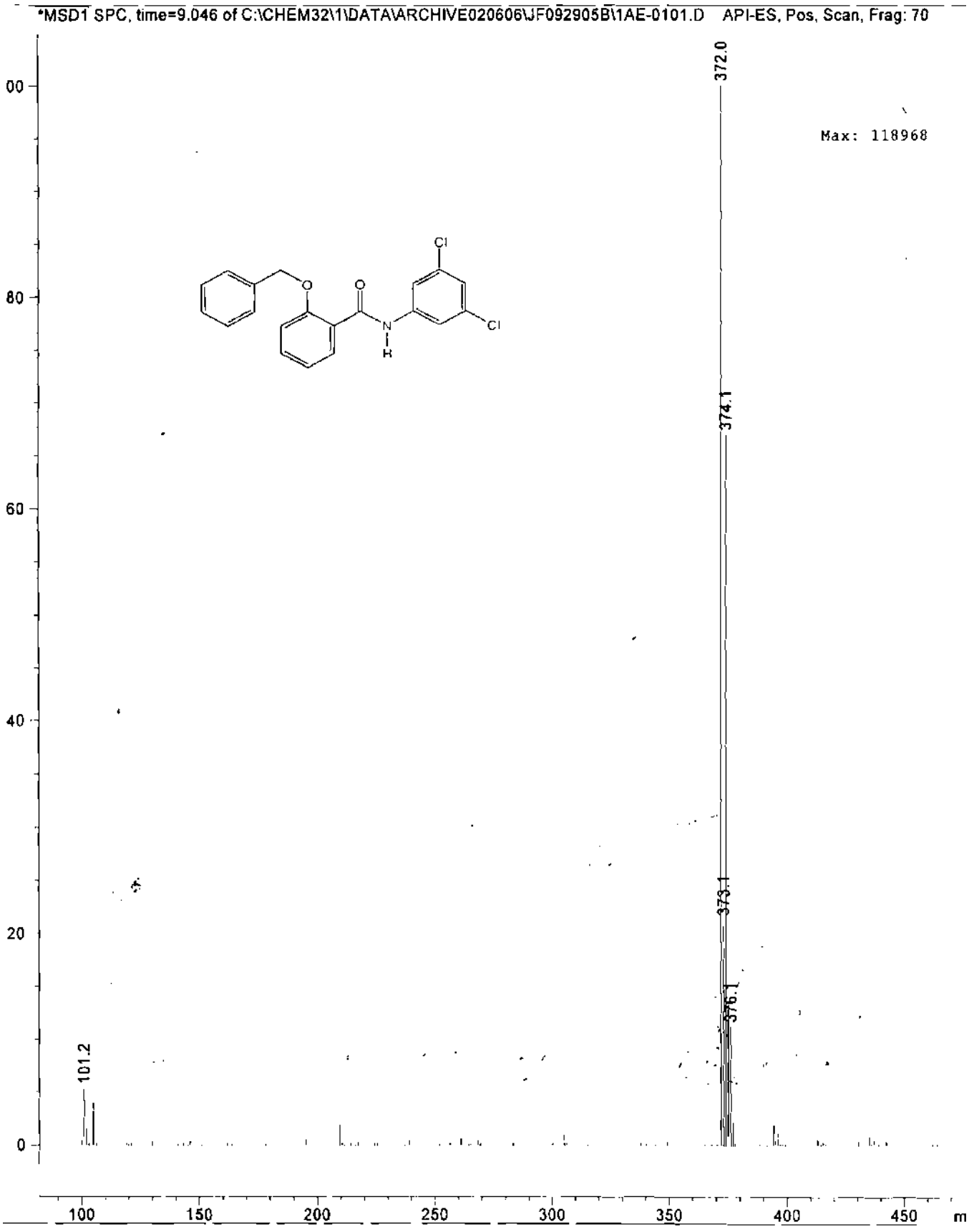

MS, intermediate material: 2-(benzyloxy)-*N*-(3,5-dichlorophenyl)-*N*-methylbenzamide

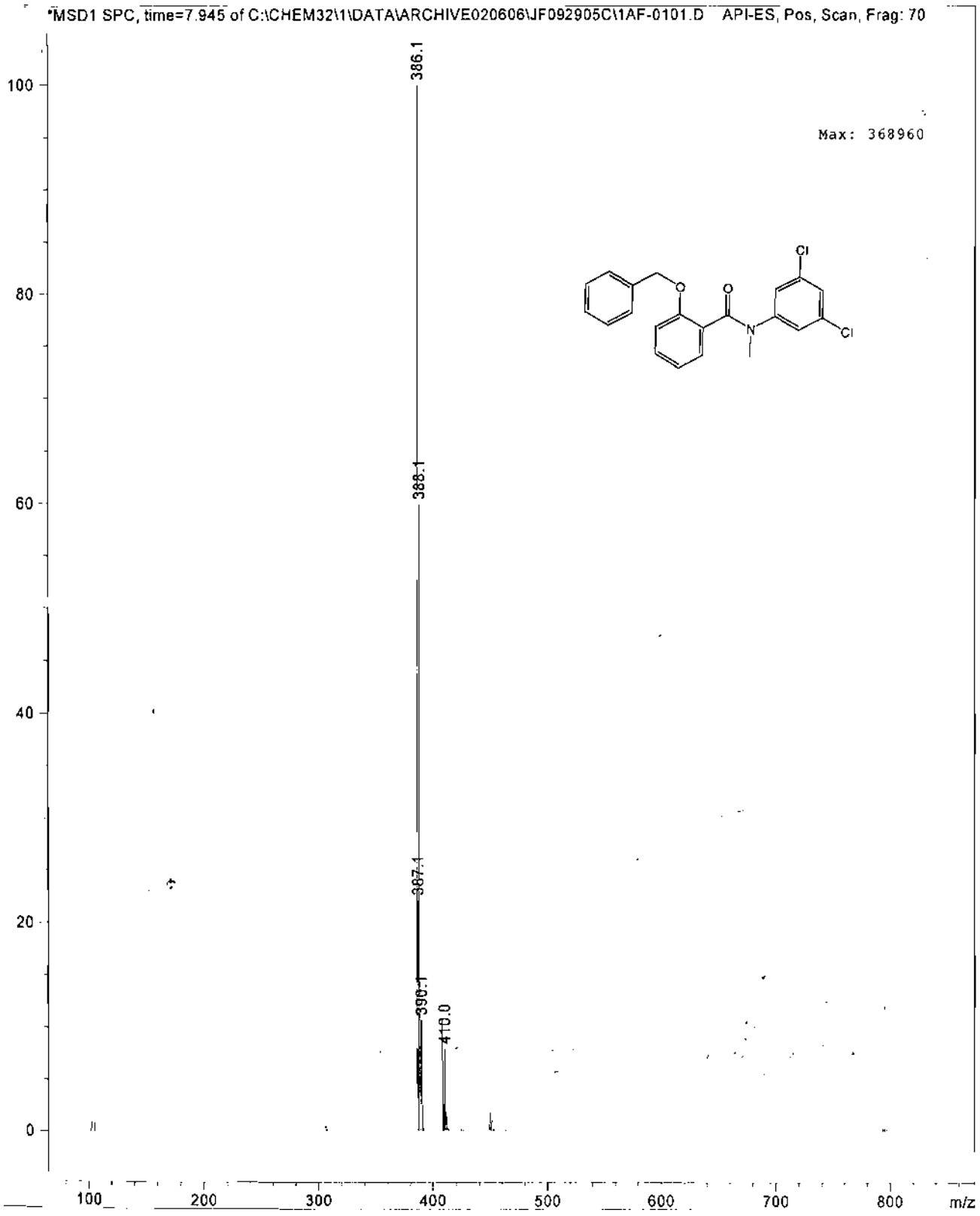

^{1}H NMR, intermediate material: *tert*-butyl 2-(*N*-(3,5-dichlorophenyl)-2-hydroxybenzamido)acetate

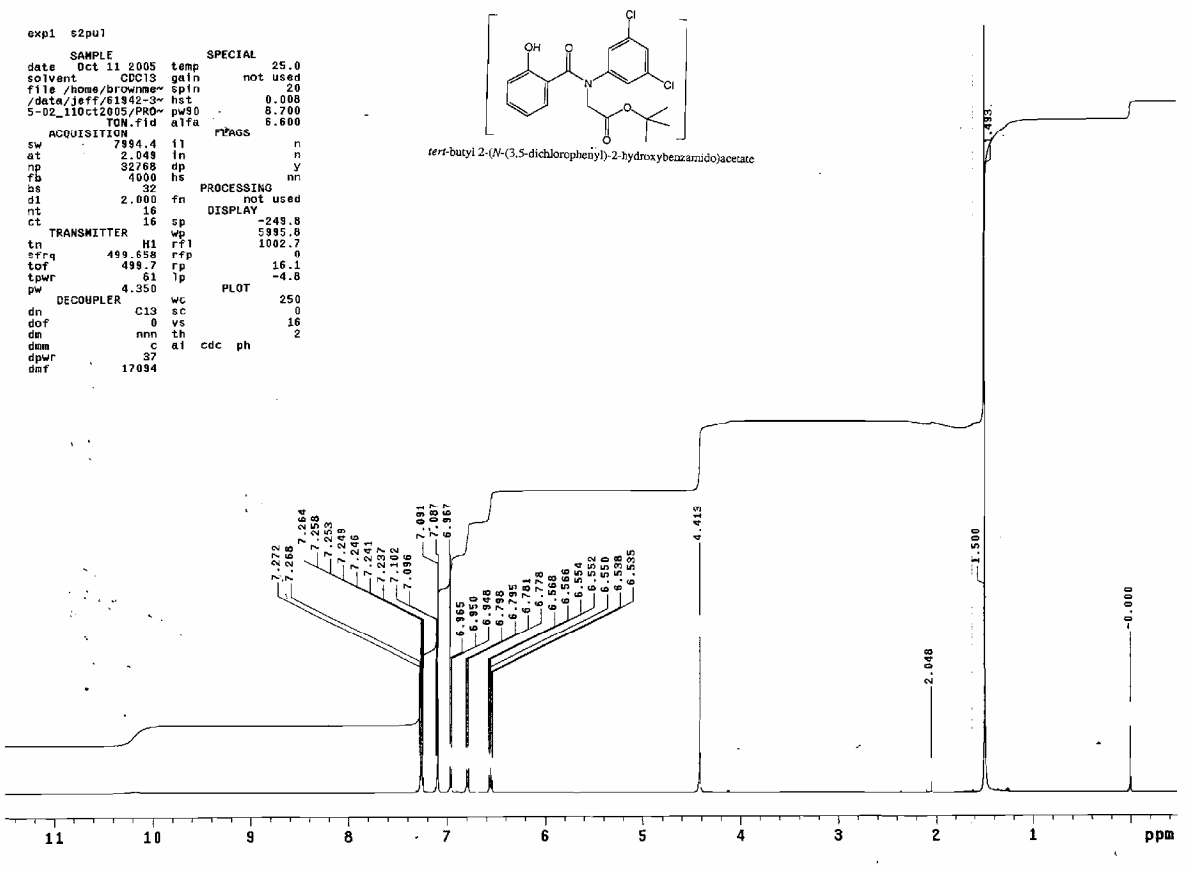

^{13}C NMR, intermediate material: *tert*-butyl 2-(*N*-(3,5-dichlorophenyl)-2-hydroxybenzamido)acetate

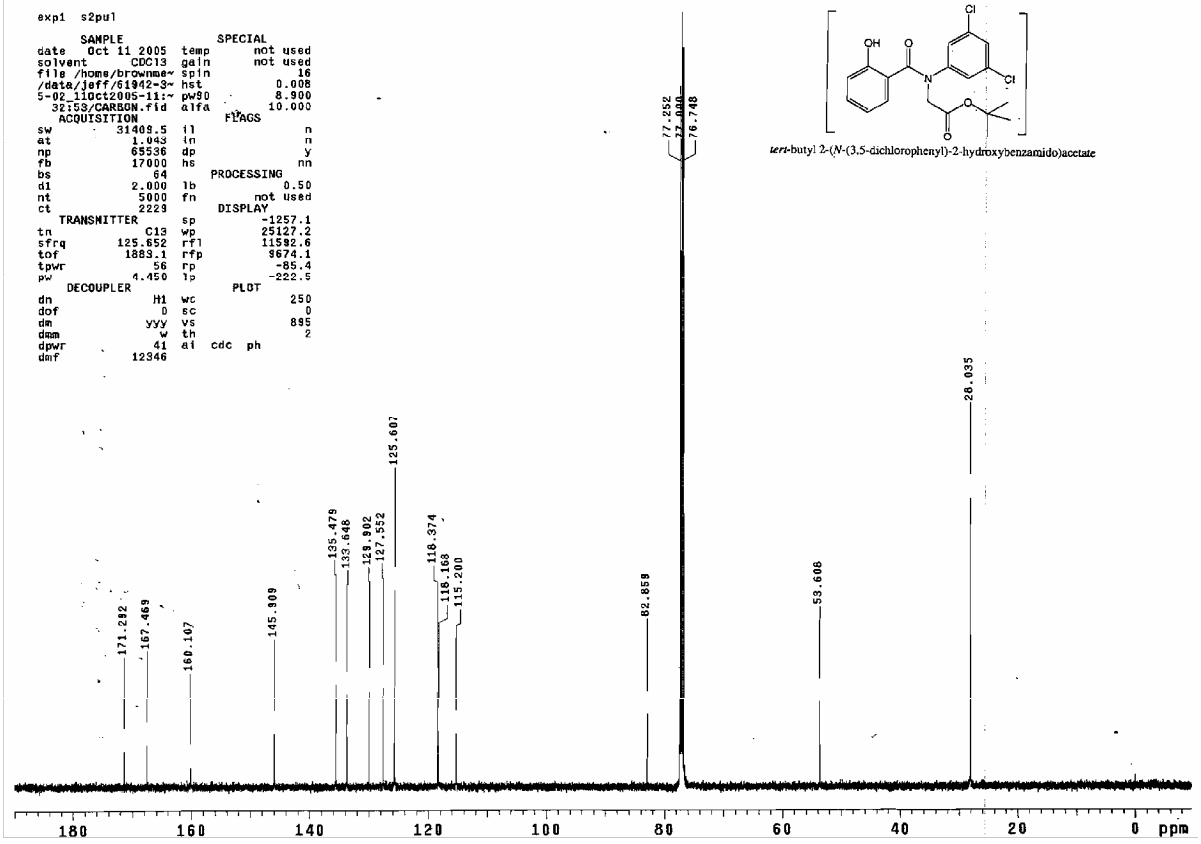

MS, intermediate material: *tert*-butyl 2-(*N*-(3,5-dichlorophenyl)-2-hydroxybenzamido)acetate

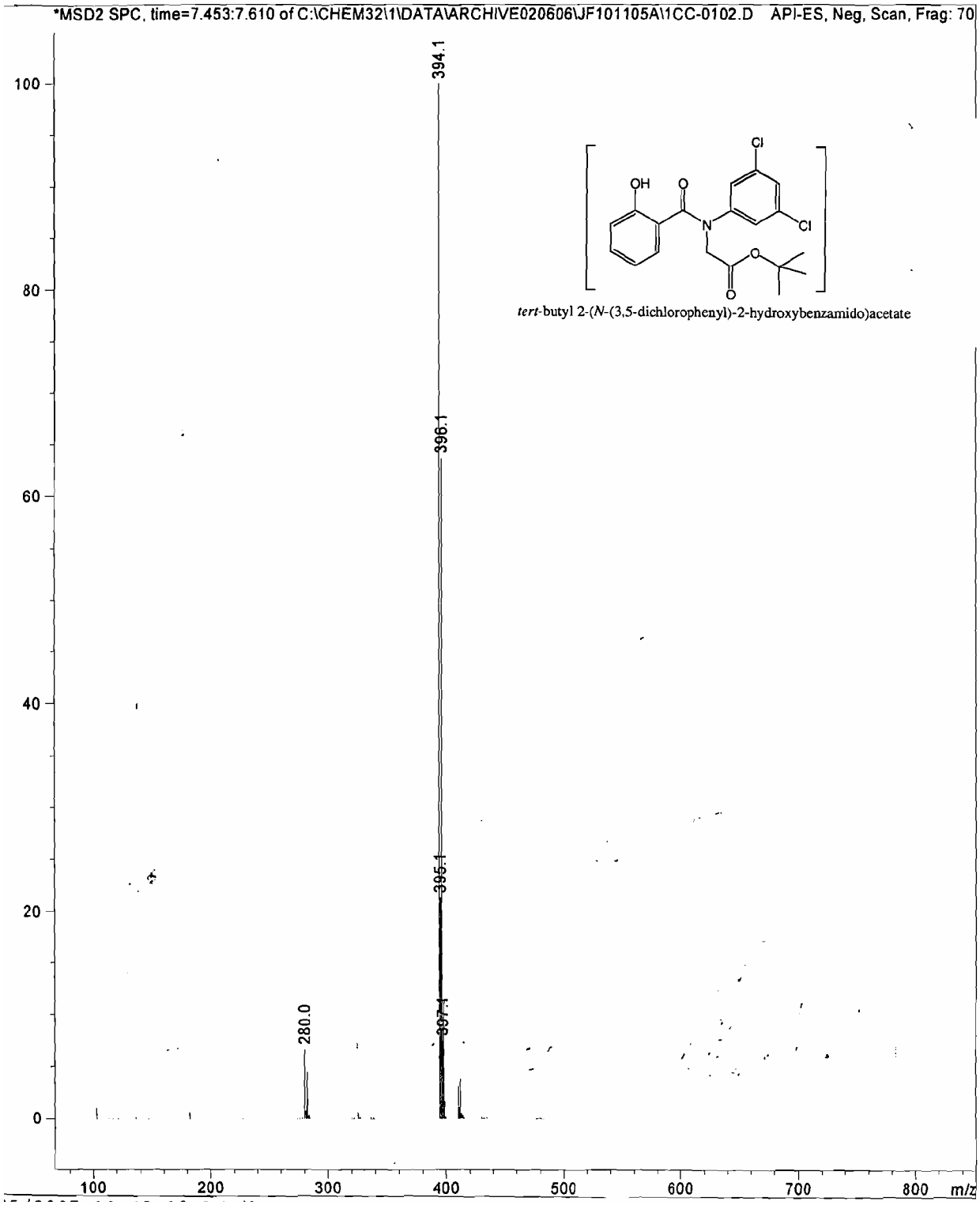

^{1}H NMR, Compound **8**

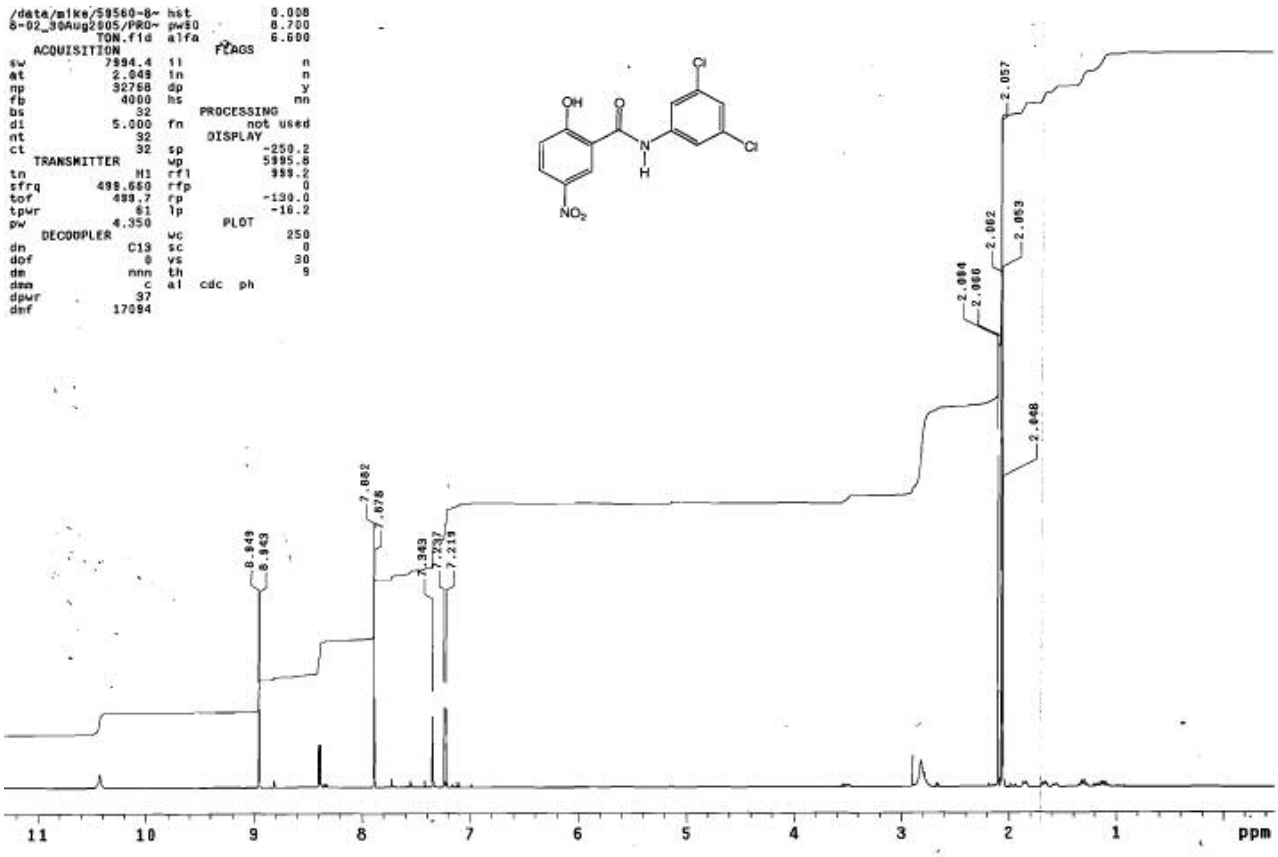

MS Compound **8**

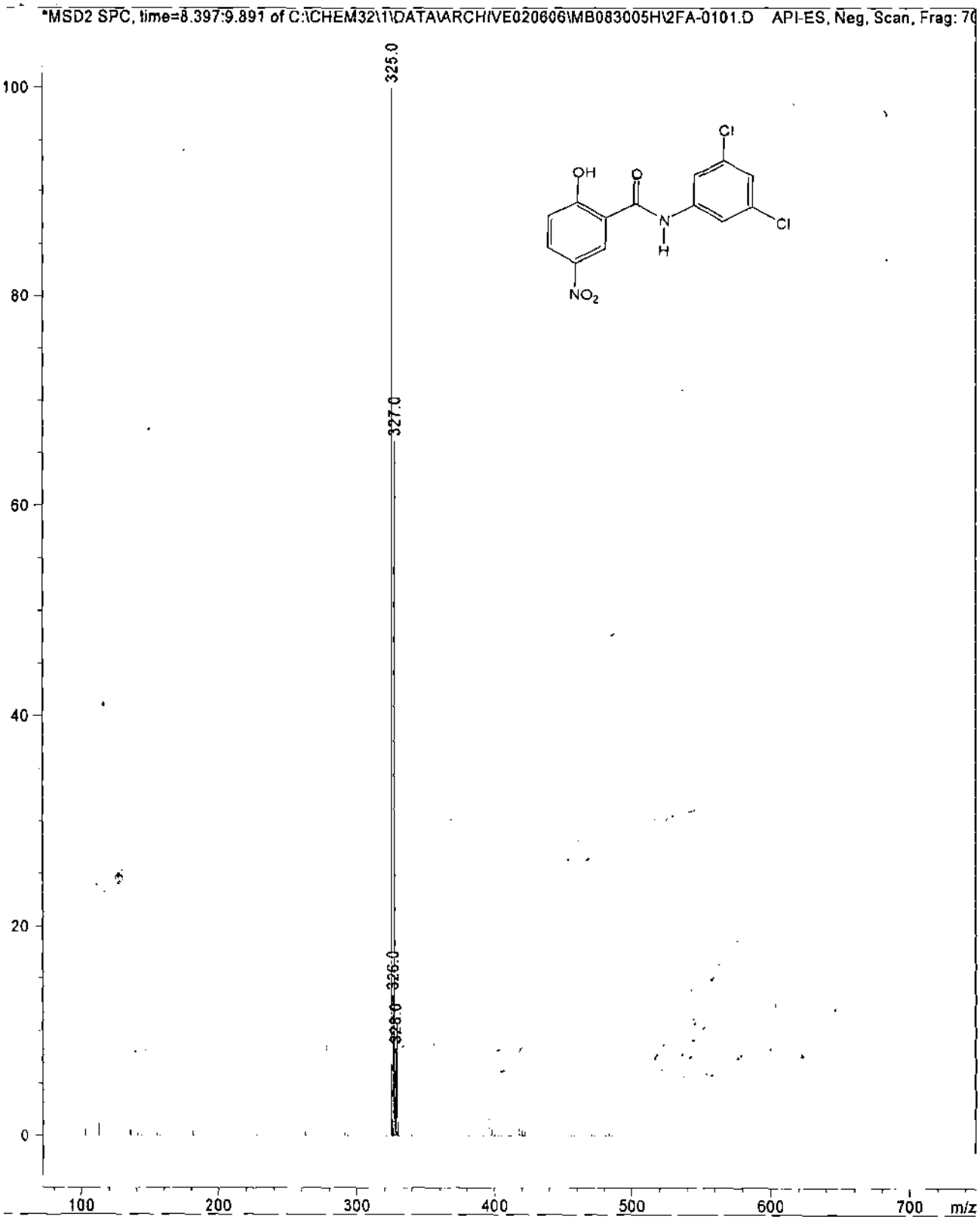

^{1}H NMR, Compound **9**

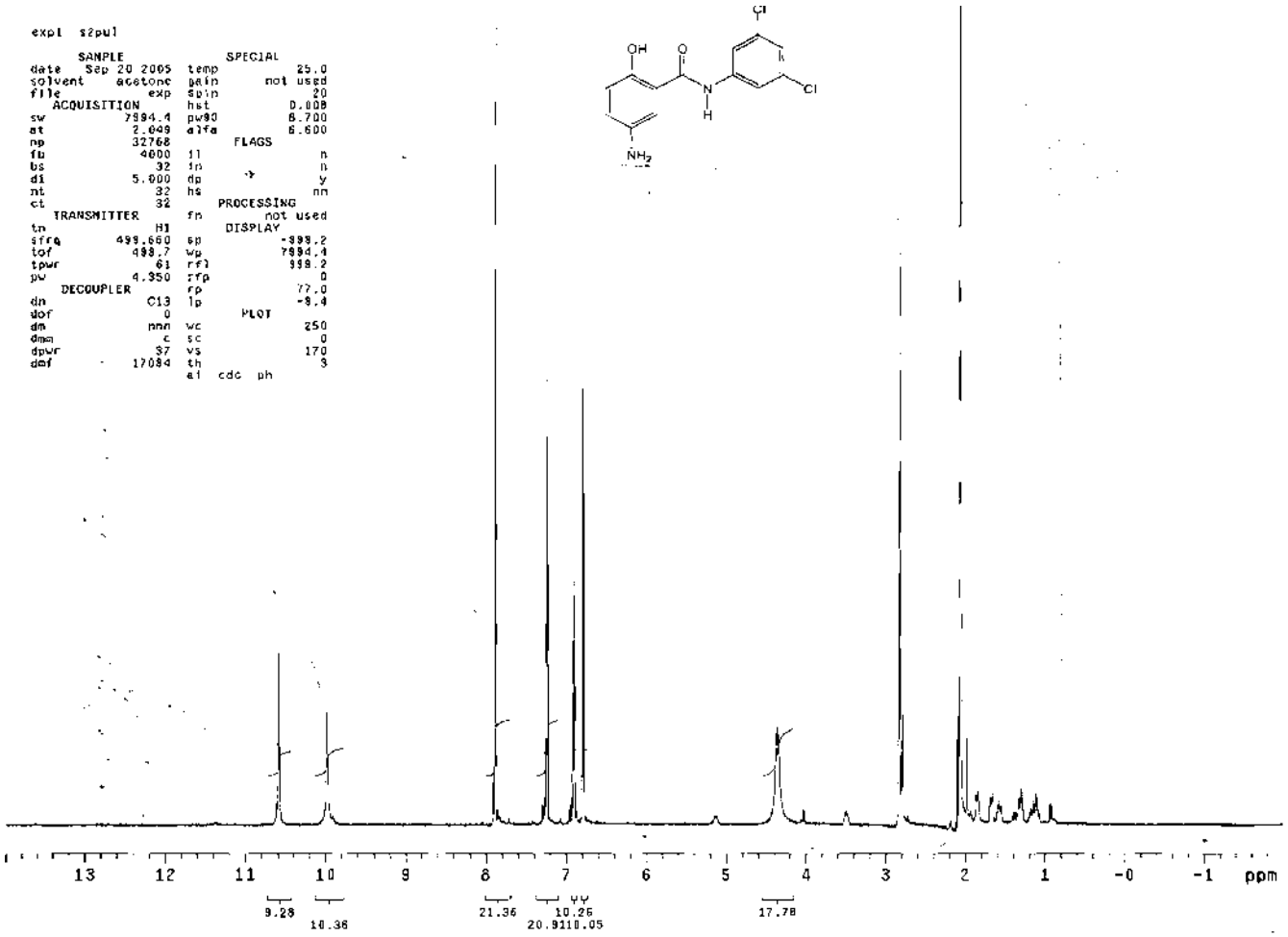

MS, Compound **9**

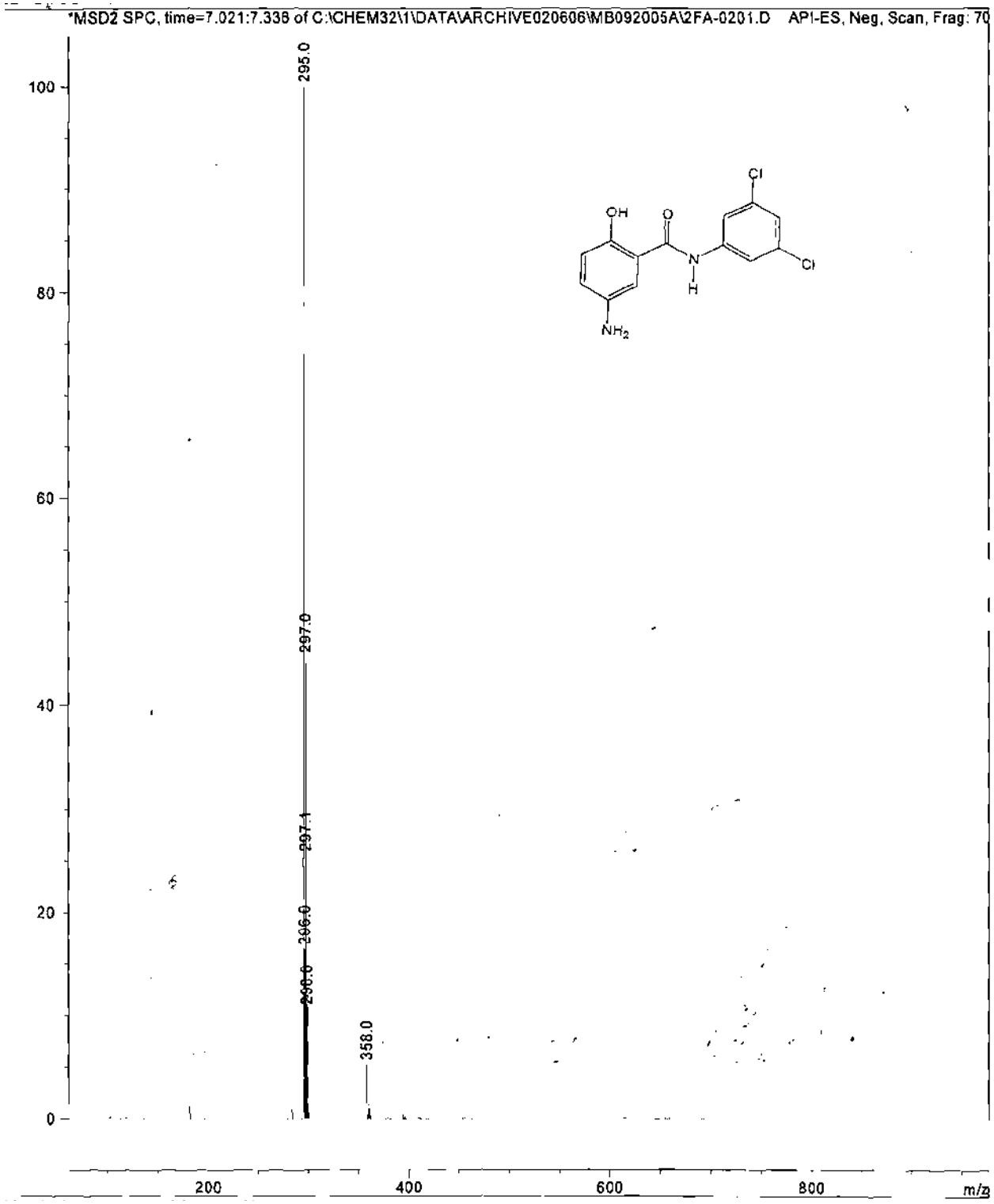

^{1}H NMR, Compound **10**

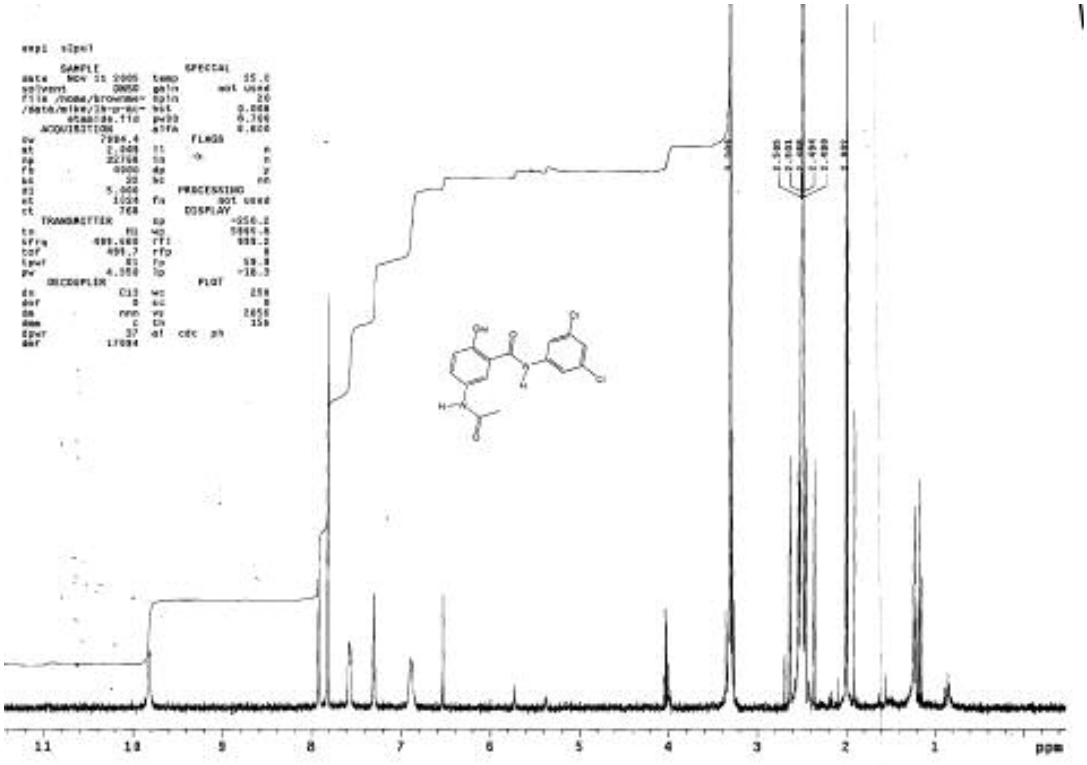

MS, Compound **10**

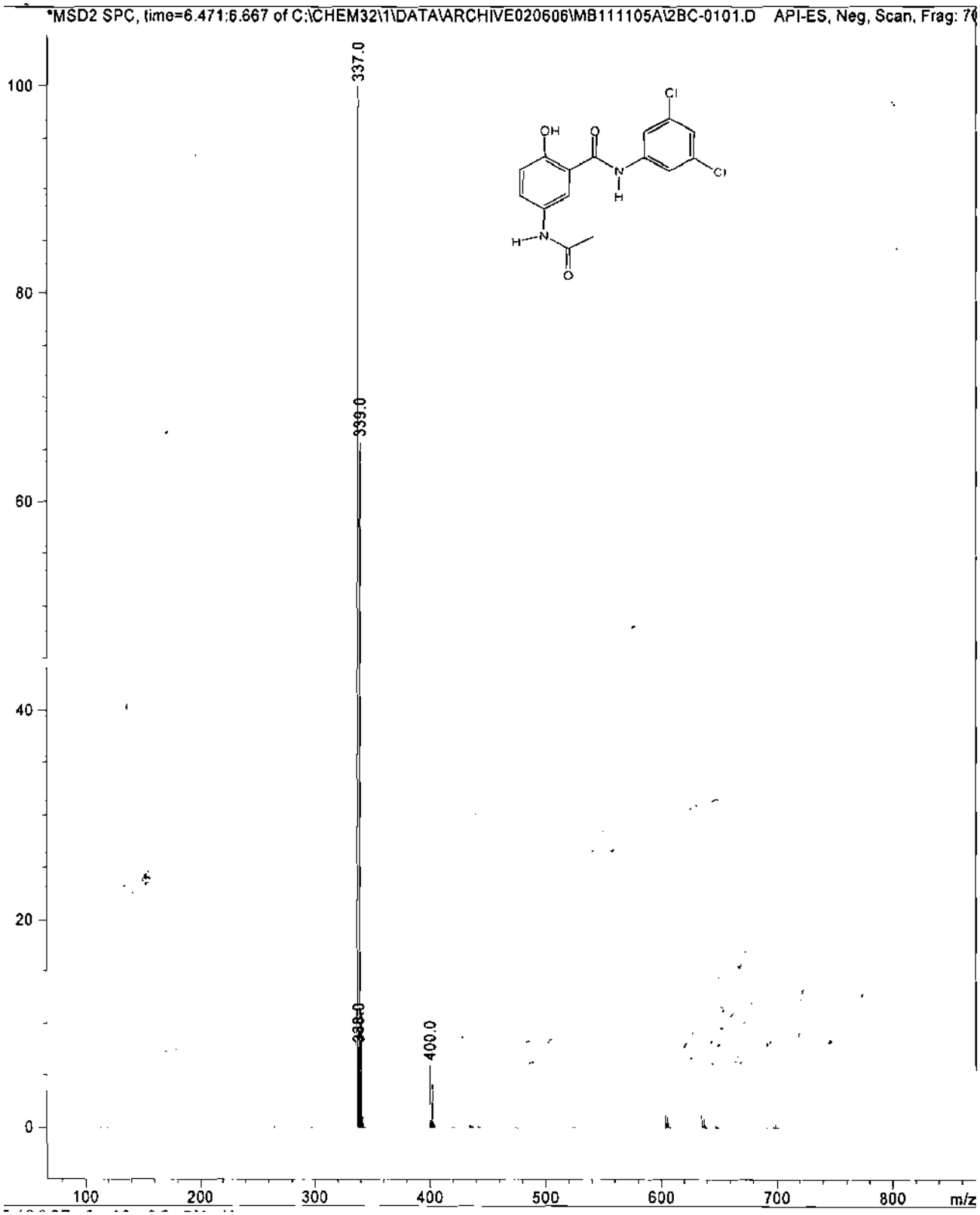

^{1}H NMR, Compound **11**

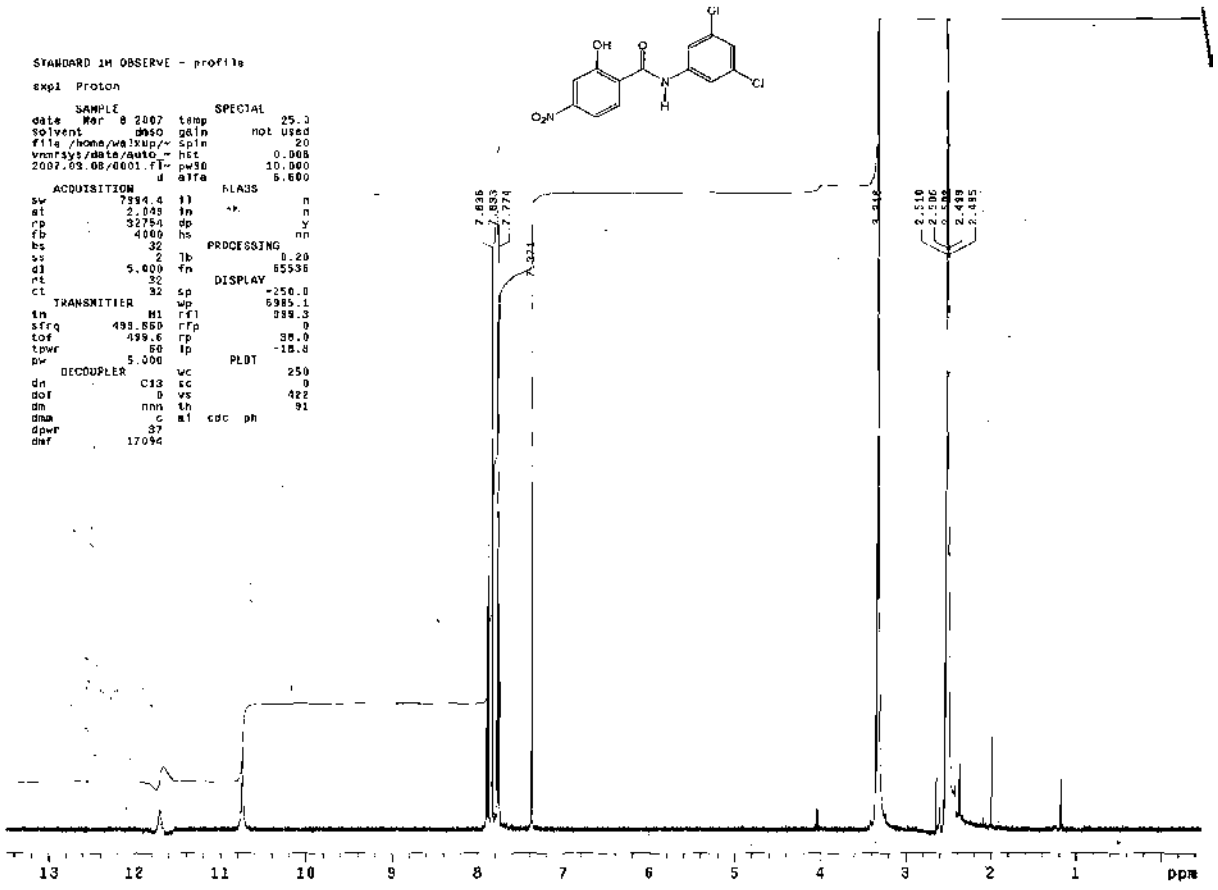

MS, Compound **11**

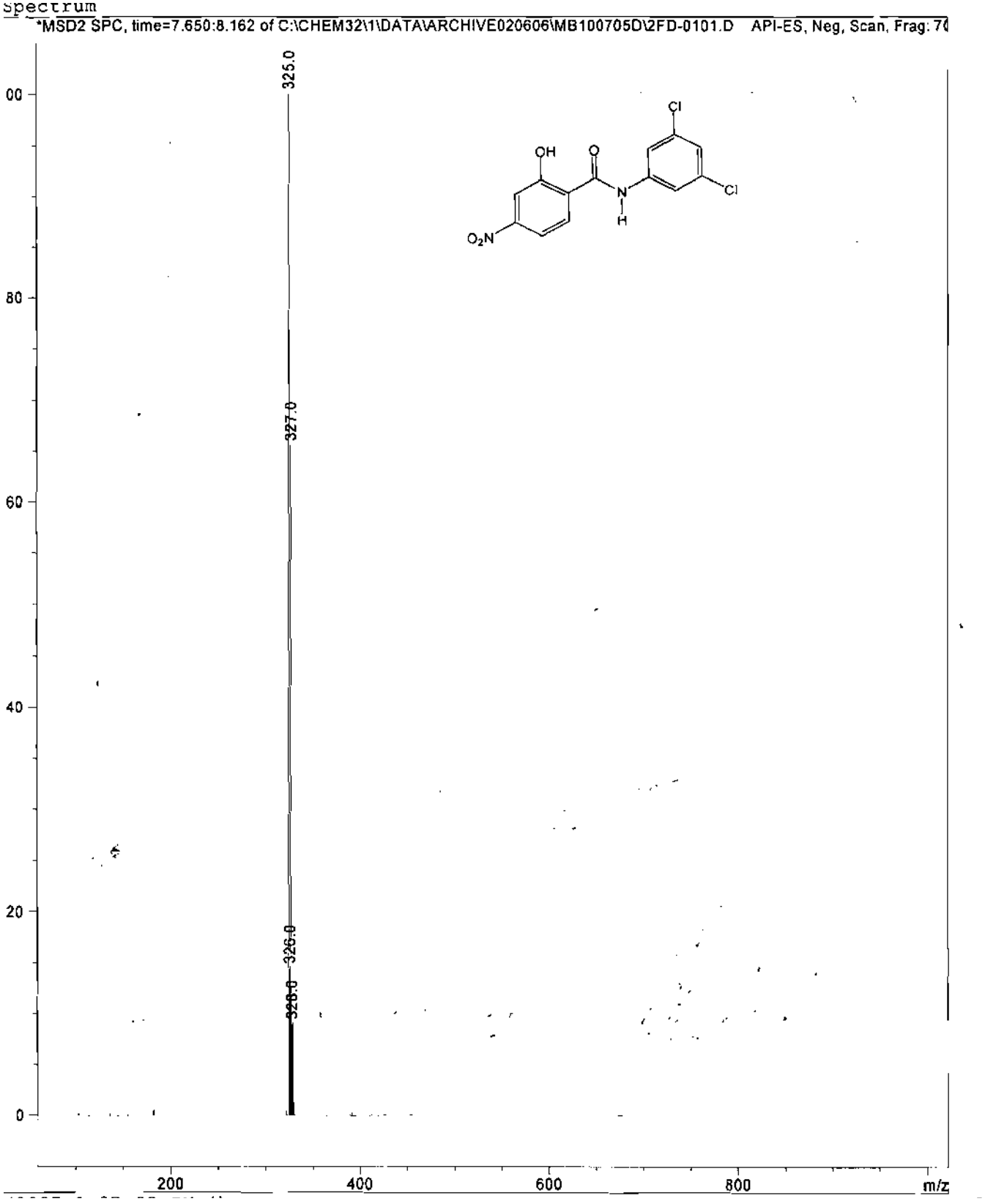

^{1}H NMR, Compound **12**

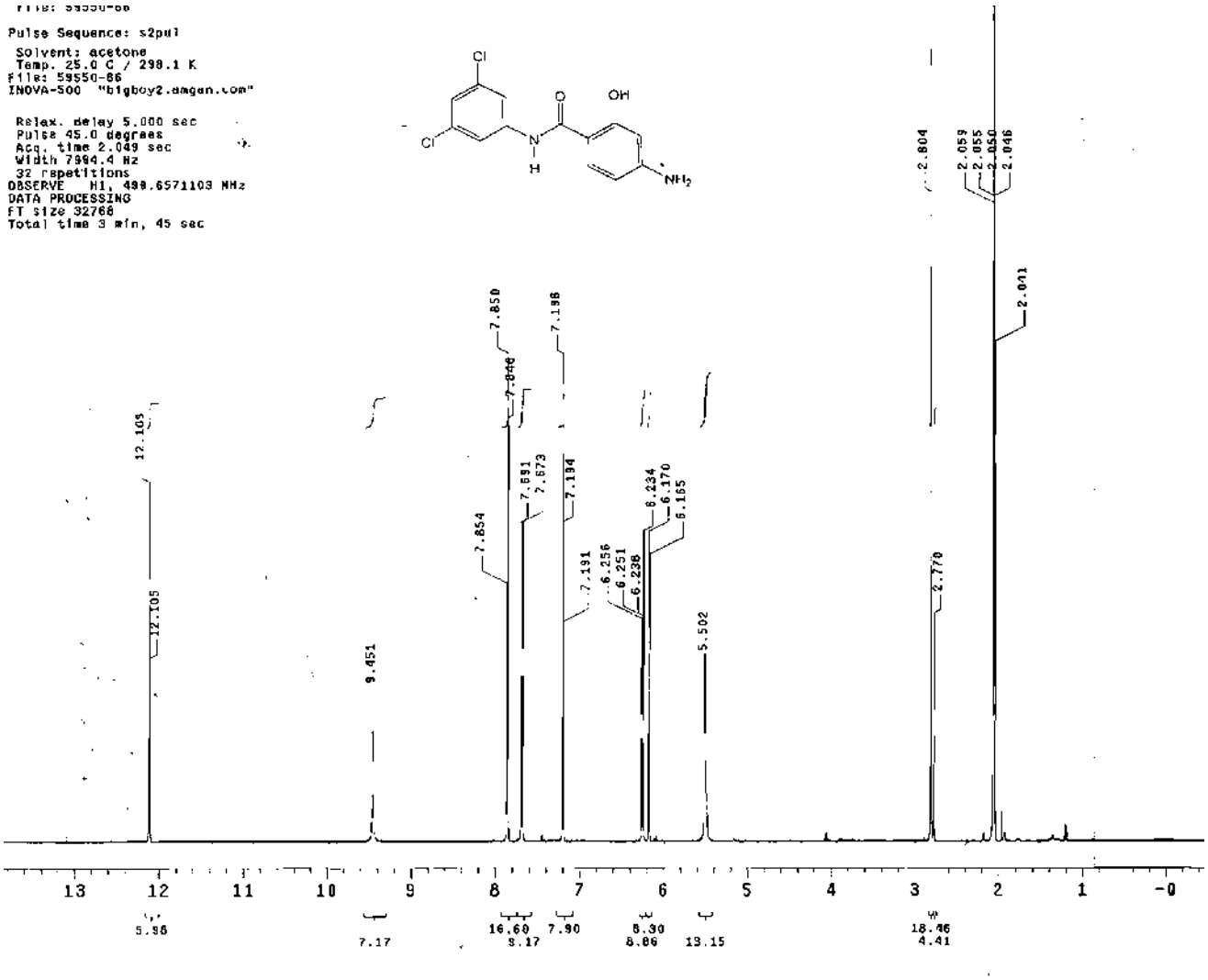

MS, Compound **12**

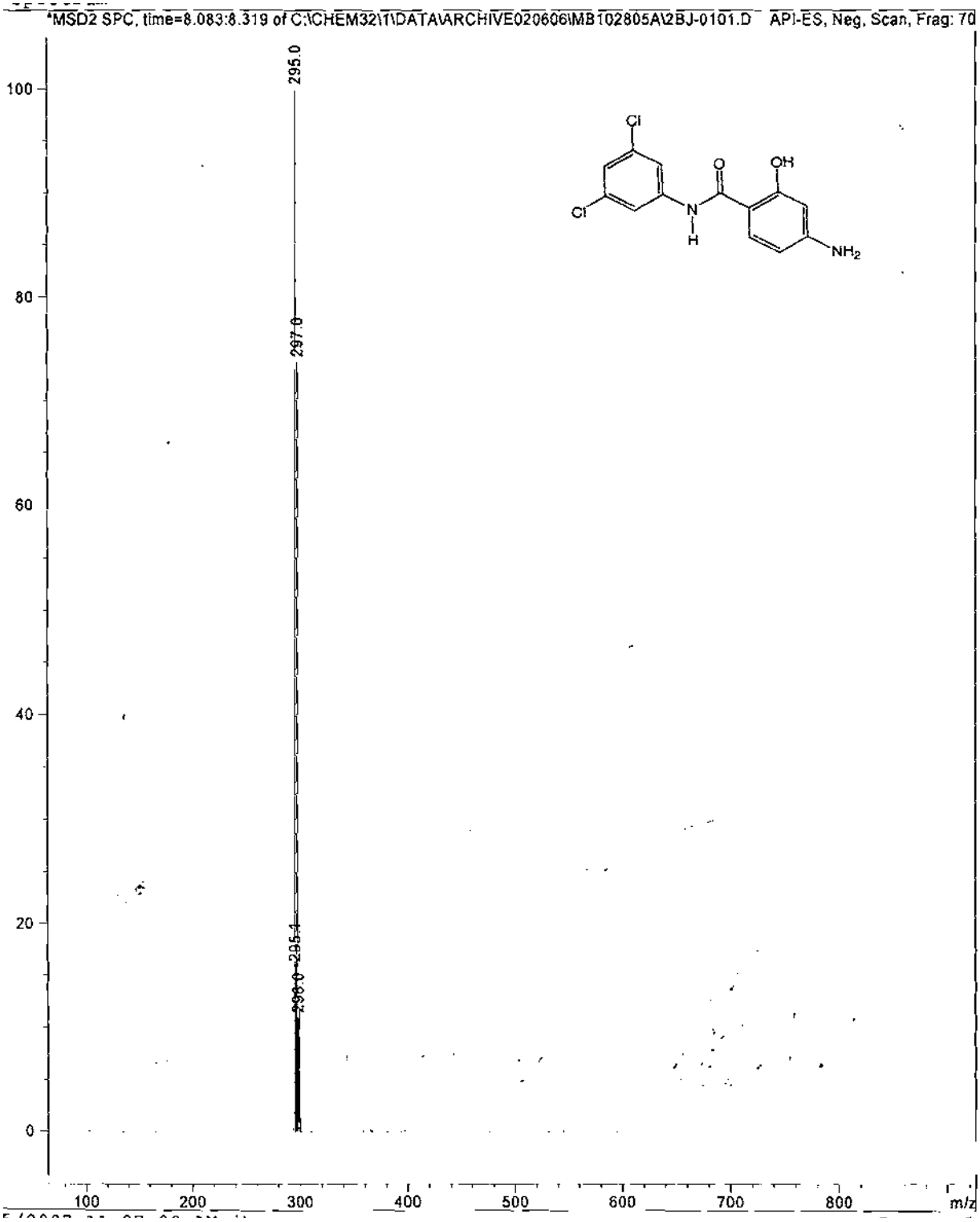

^{1}H NMR, Compound **13**

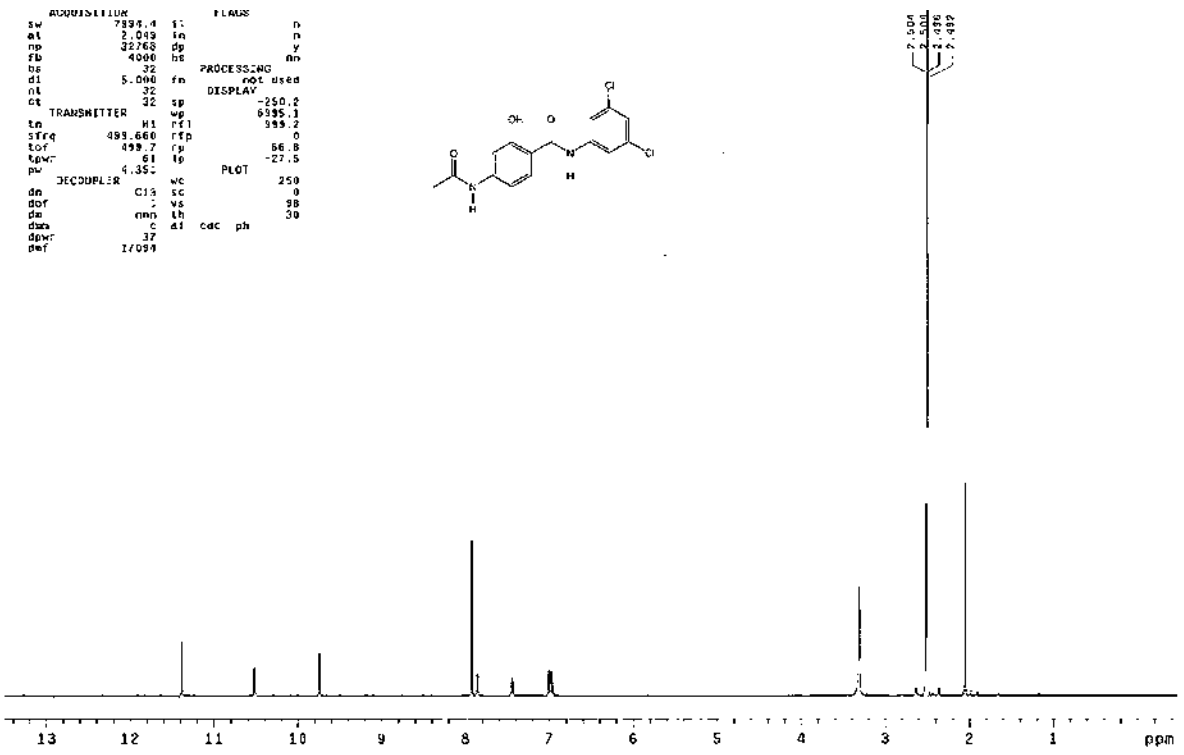

MS, Compound **13**

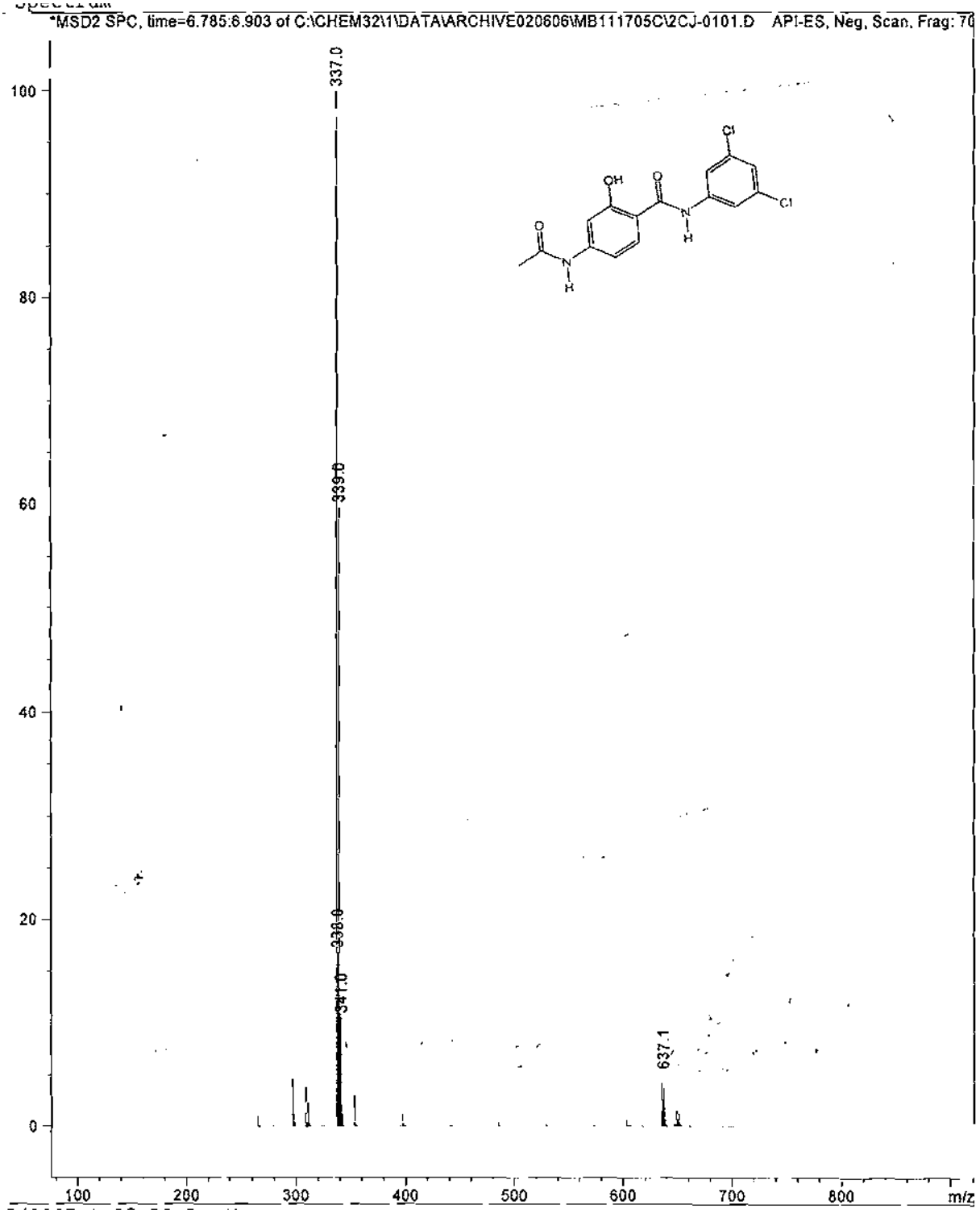

^{1}H NMR, Compound **14**

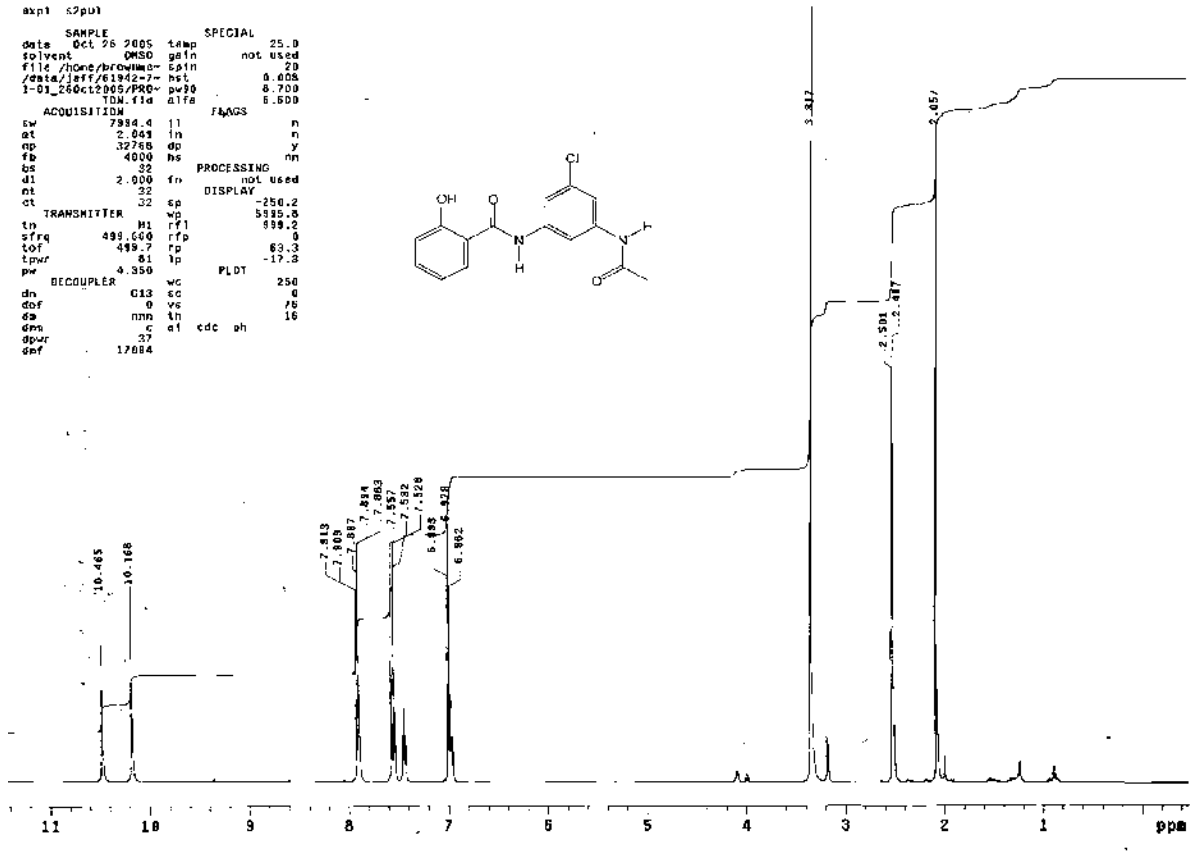

^{13}C NMR, Compound **14**

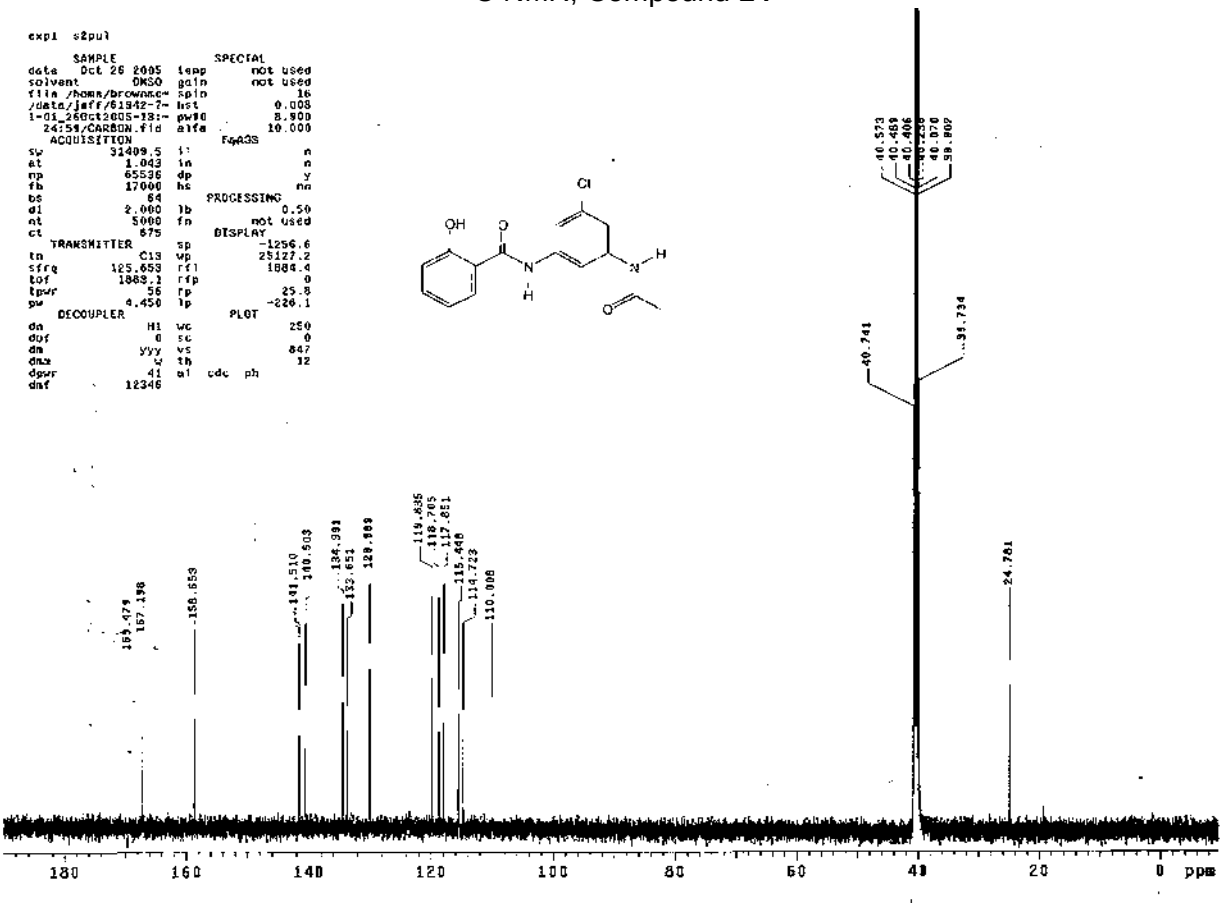

MS, Compound **14**

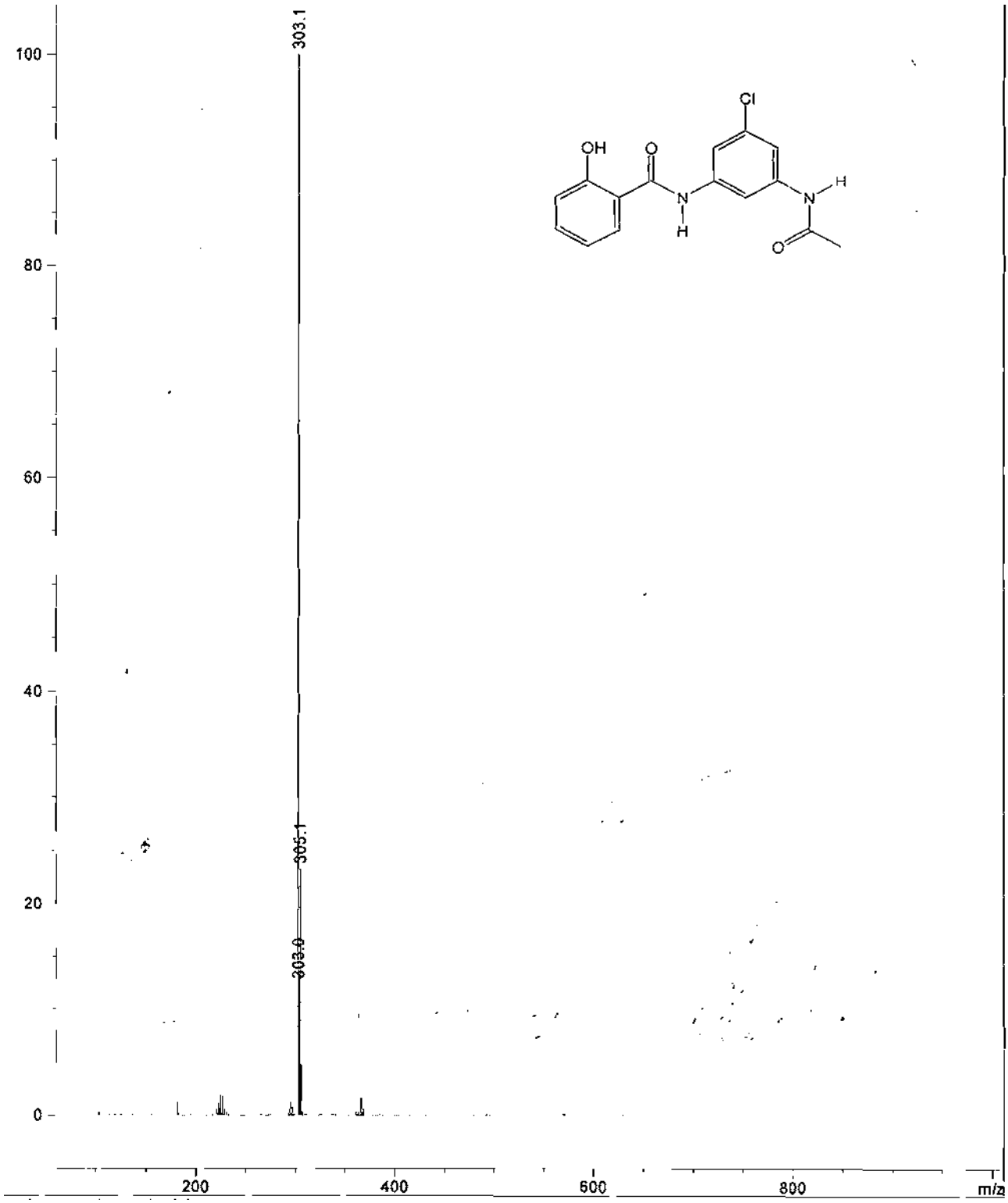

^{1}H NMR, Compound **15**

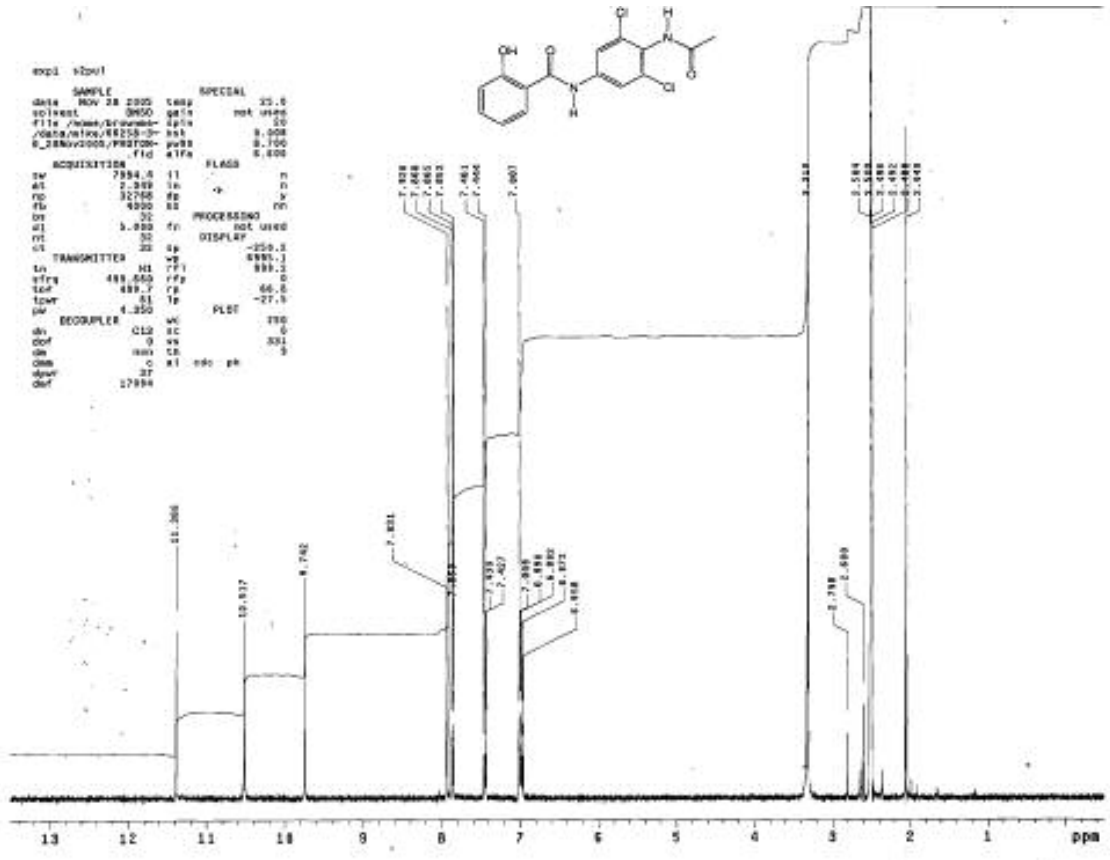

MS, Compound **15**

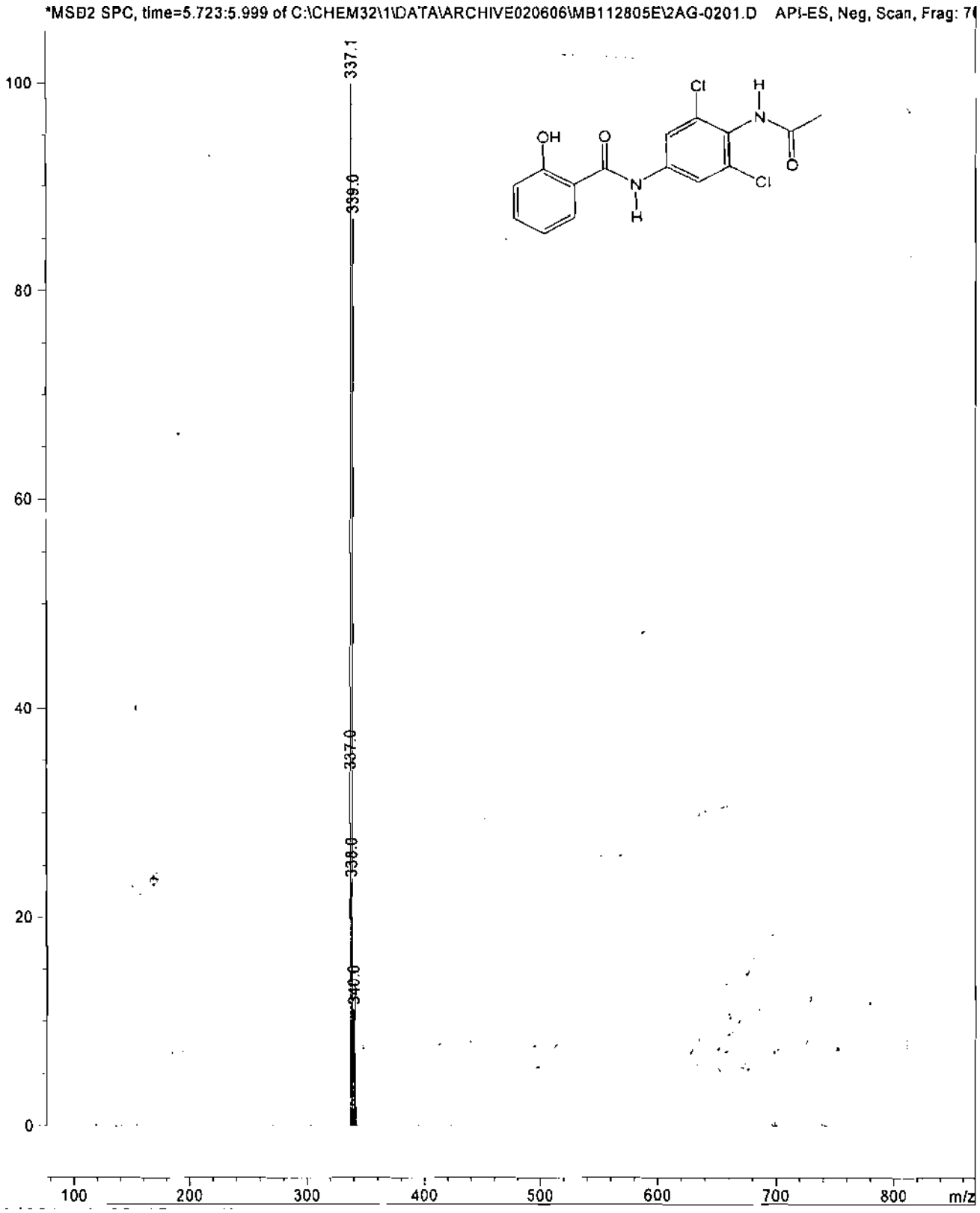

^{1}H NMR, Compound **16**

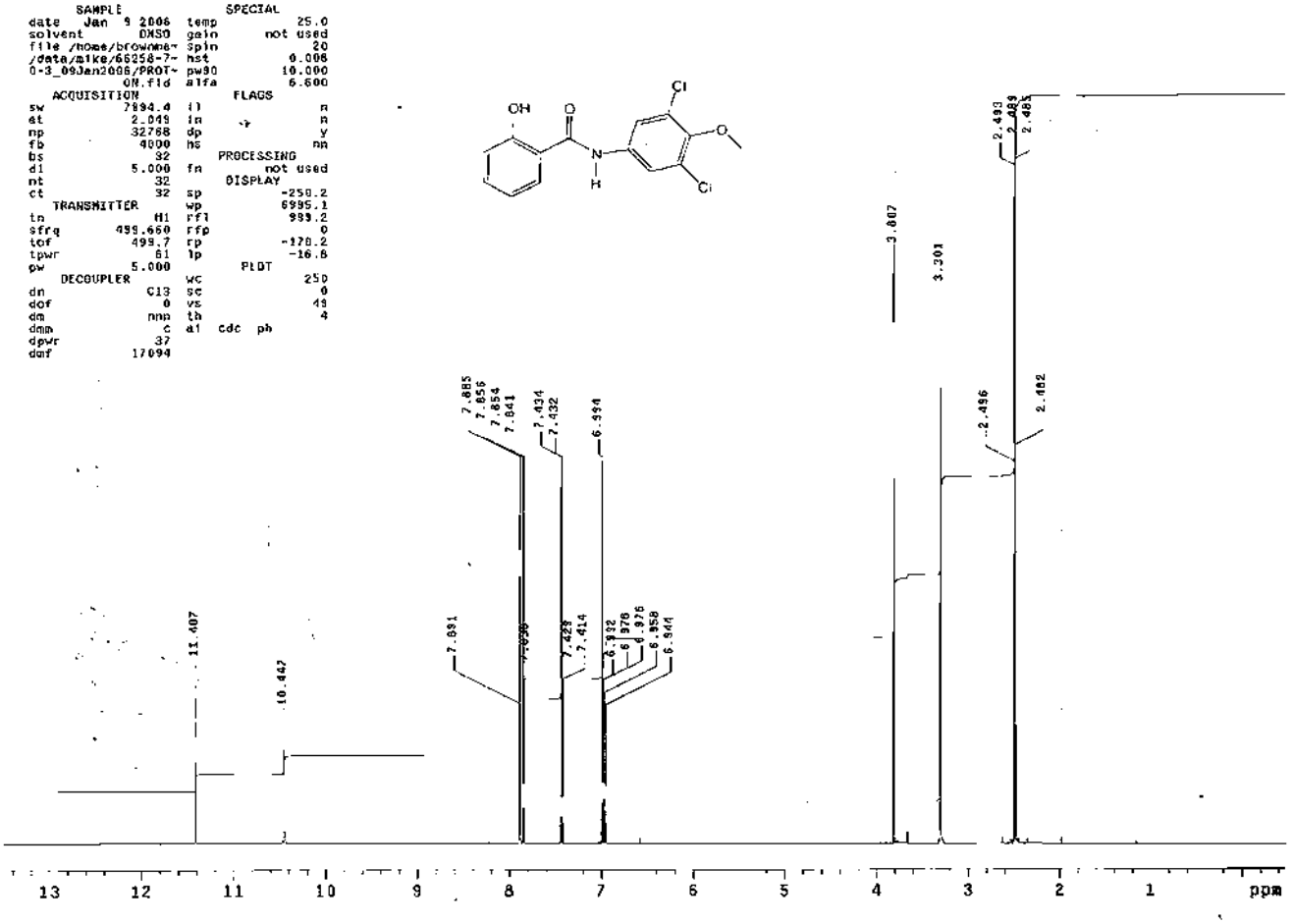

MS, Compound **16**

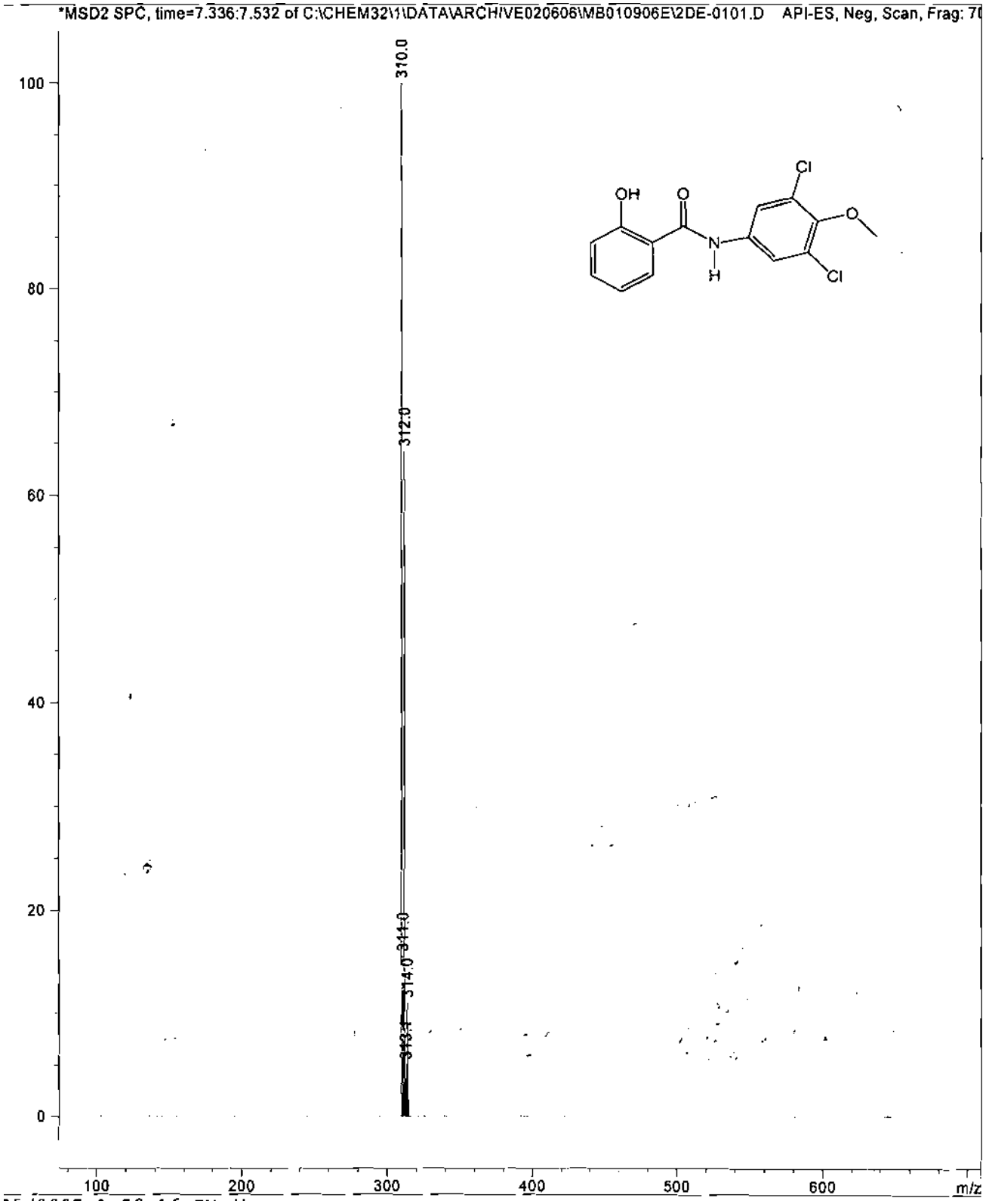

^{1}H NMR, Compound **17**

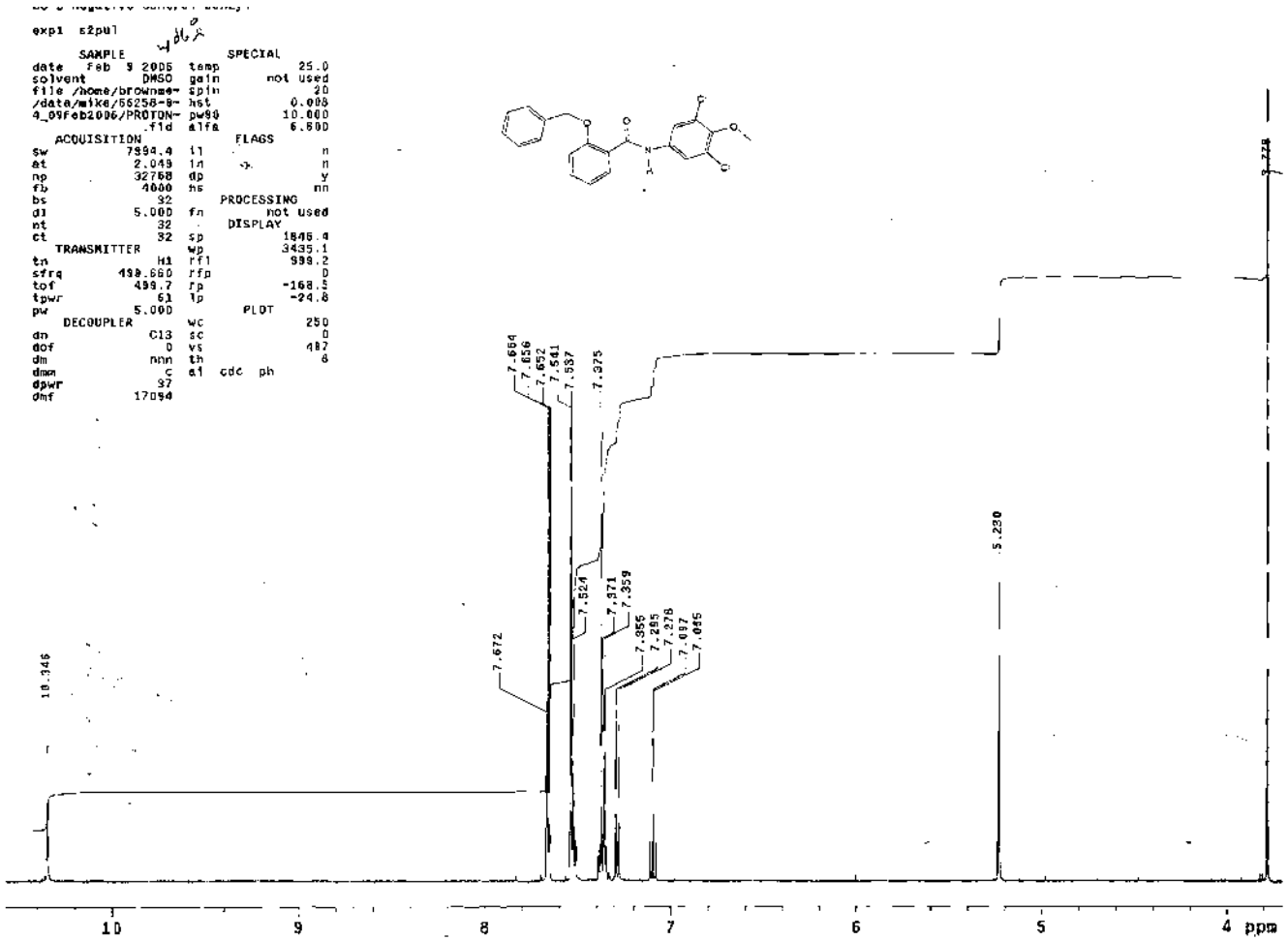

MS, Compound **17**

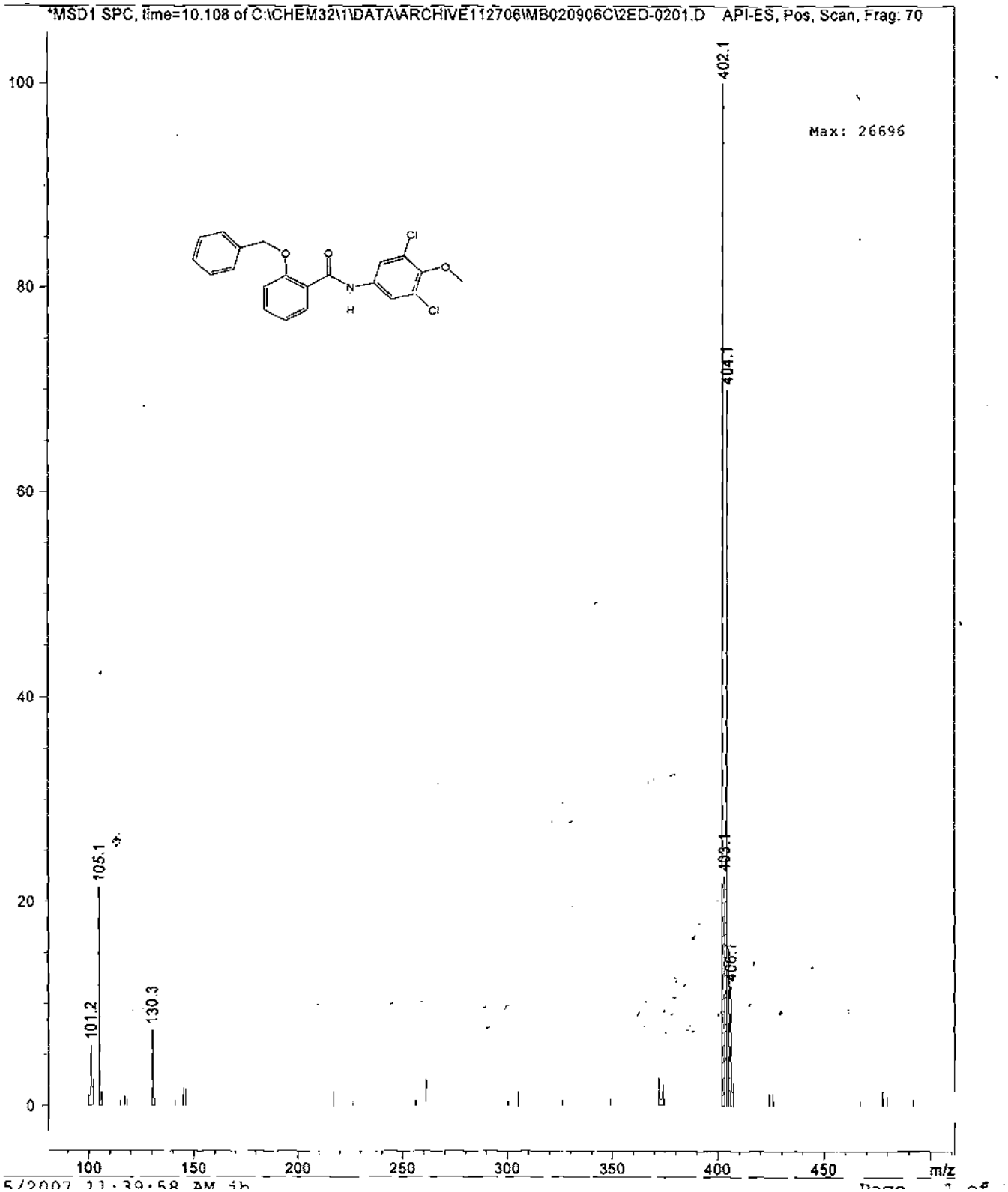

^{1}H NMR, Compound **18**

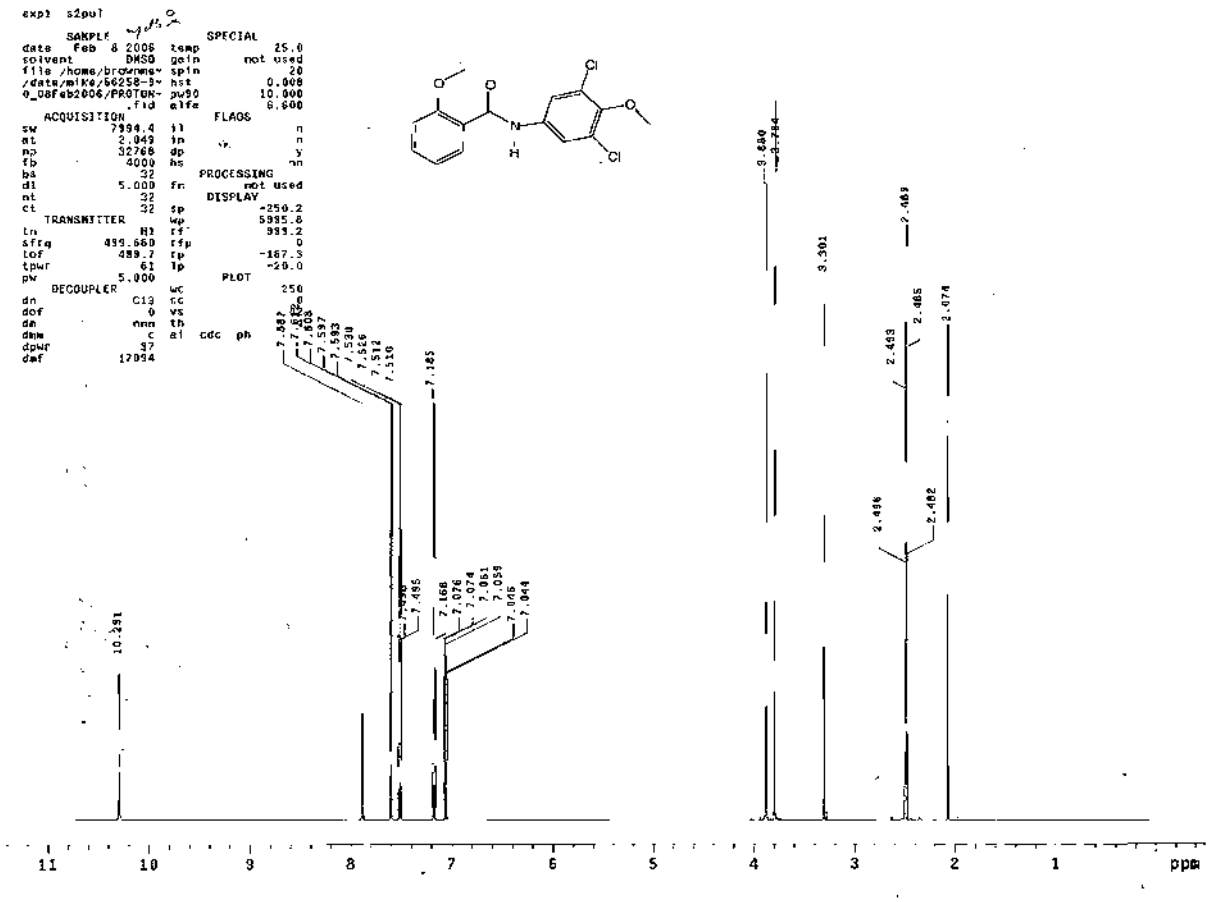

MS, Compound **18**

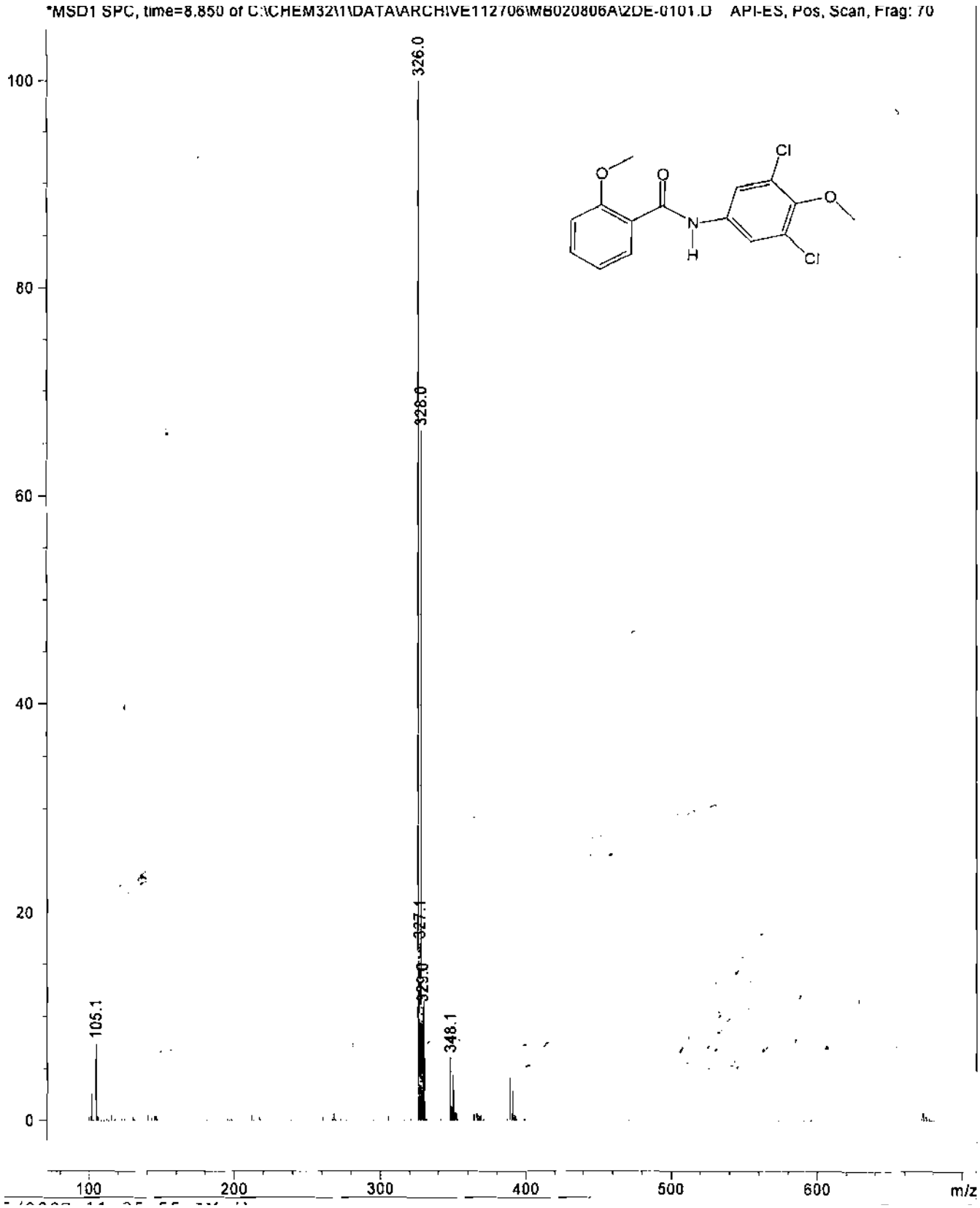
*MSD1 SPC, time=8.850 of C:\CHEM32\1\DATA\ARCHIVE112706\MB020806A\ZDE-0101.D API-ES, Pos, Scan, Frag: 70
326.0
326.0
327.1
329.0
105.1
348.1
Cl
O
O
N
H
O
Cl
100
80
60
40
20
0
100
200
300
400
500
600
m/z

^{1}H NMR, Compound **22**

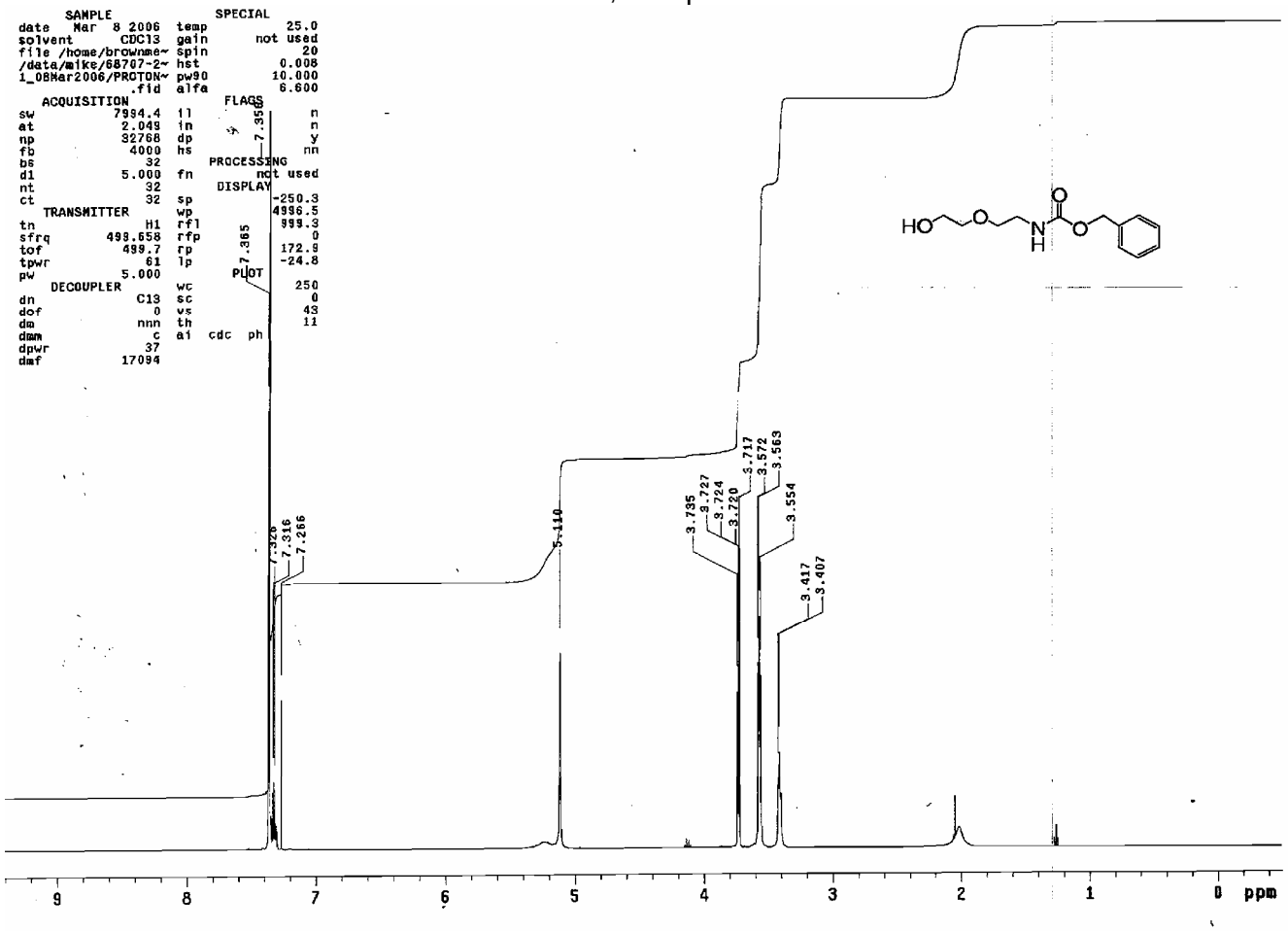

MS Compound **22**

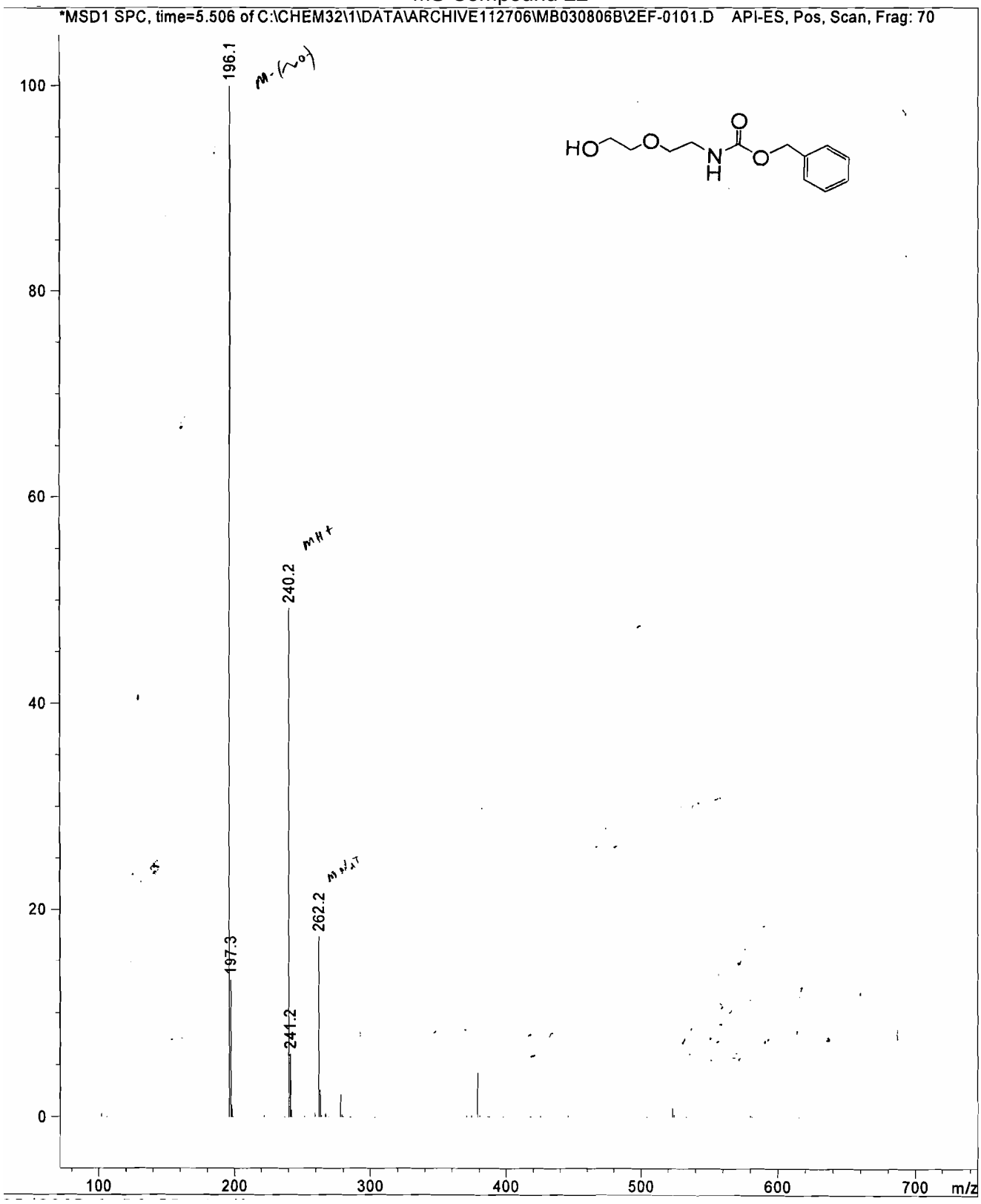

^{1}H NMR, intermediate material: benzyl 2-(2-(2,6-dichloro-4-nitrophenoxy)ethoxy)ethylcarbamate

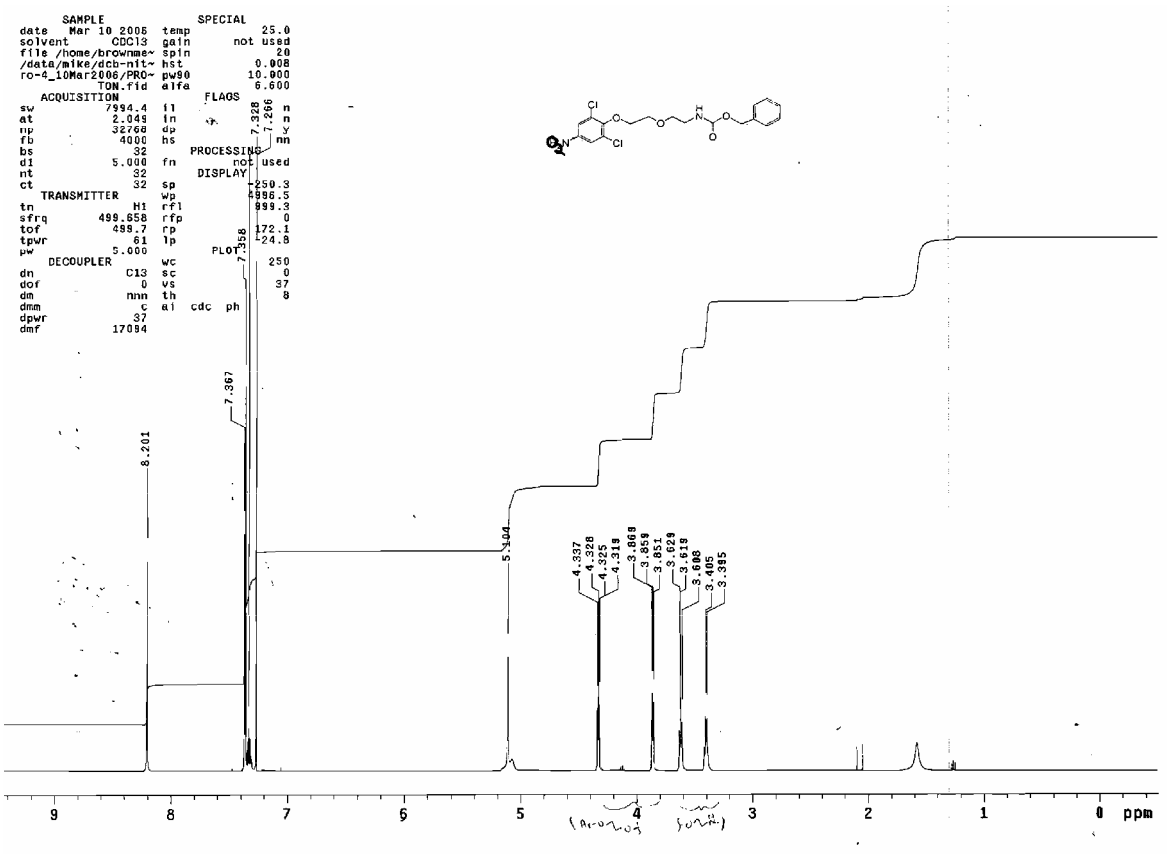

MS, intermediate material: benzyl 2-(2-(2,6-dichloro-4-nitrophenoxy)ethoxy)ethylcarbamate

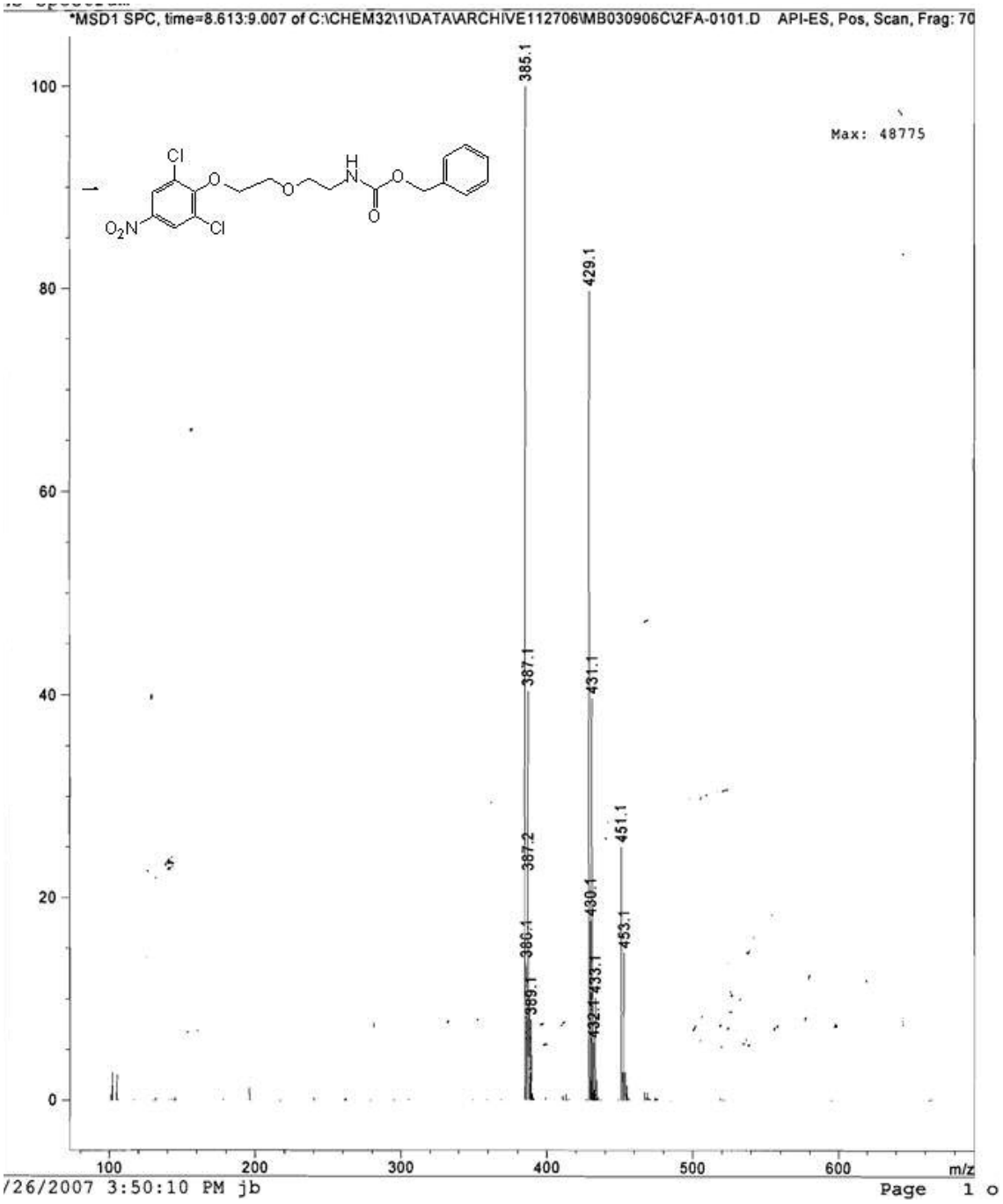

^{1}H NMR, Compound **23**

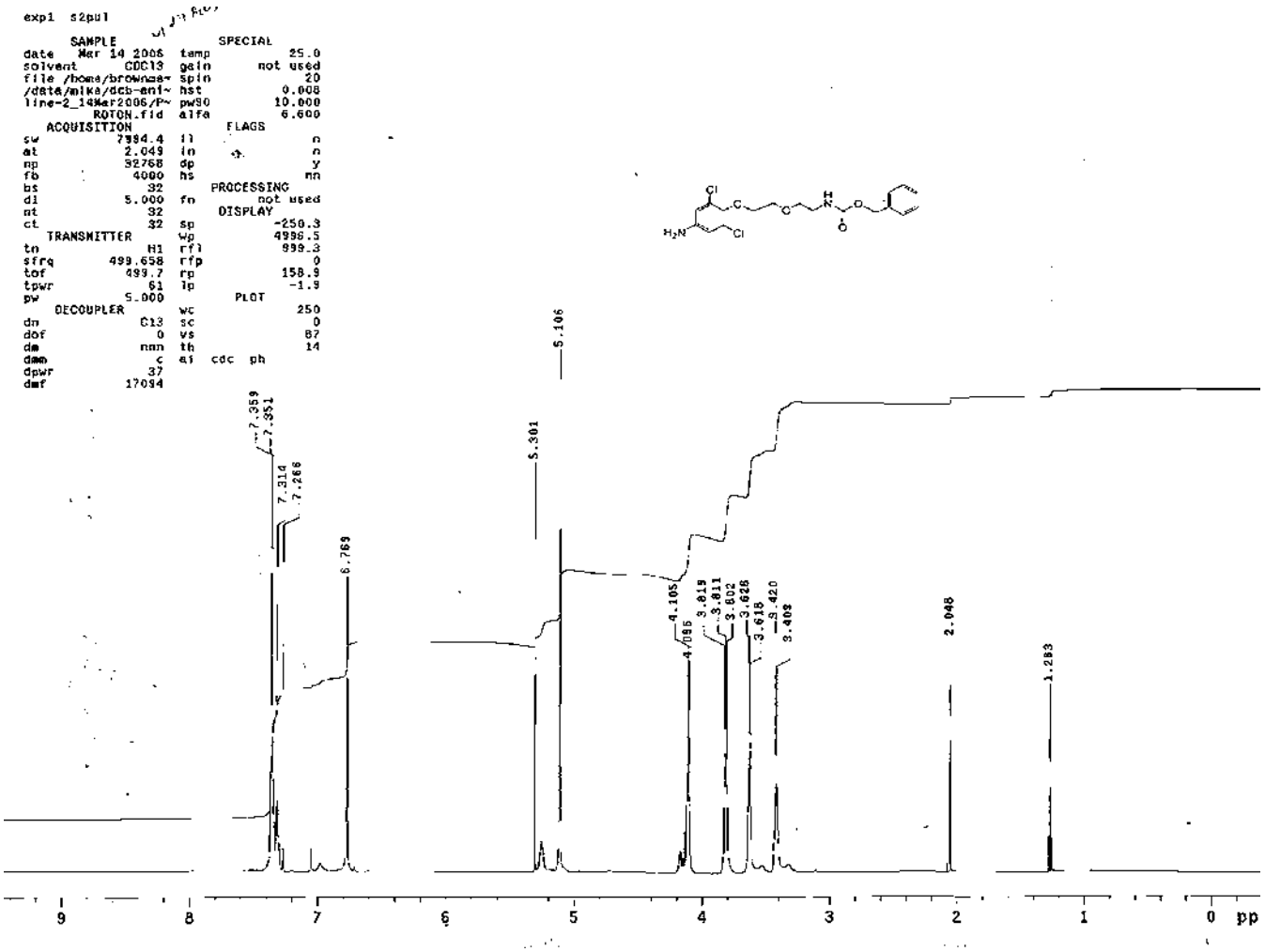

MS, Compound **23**

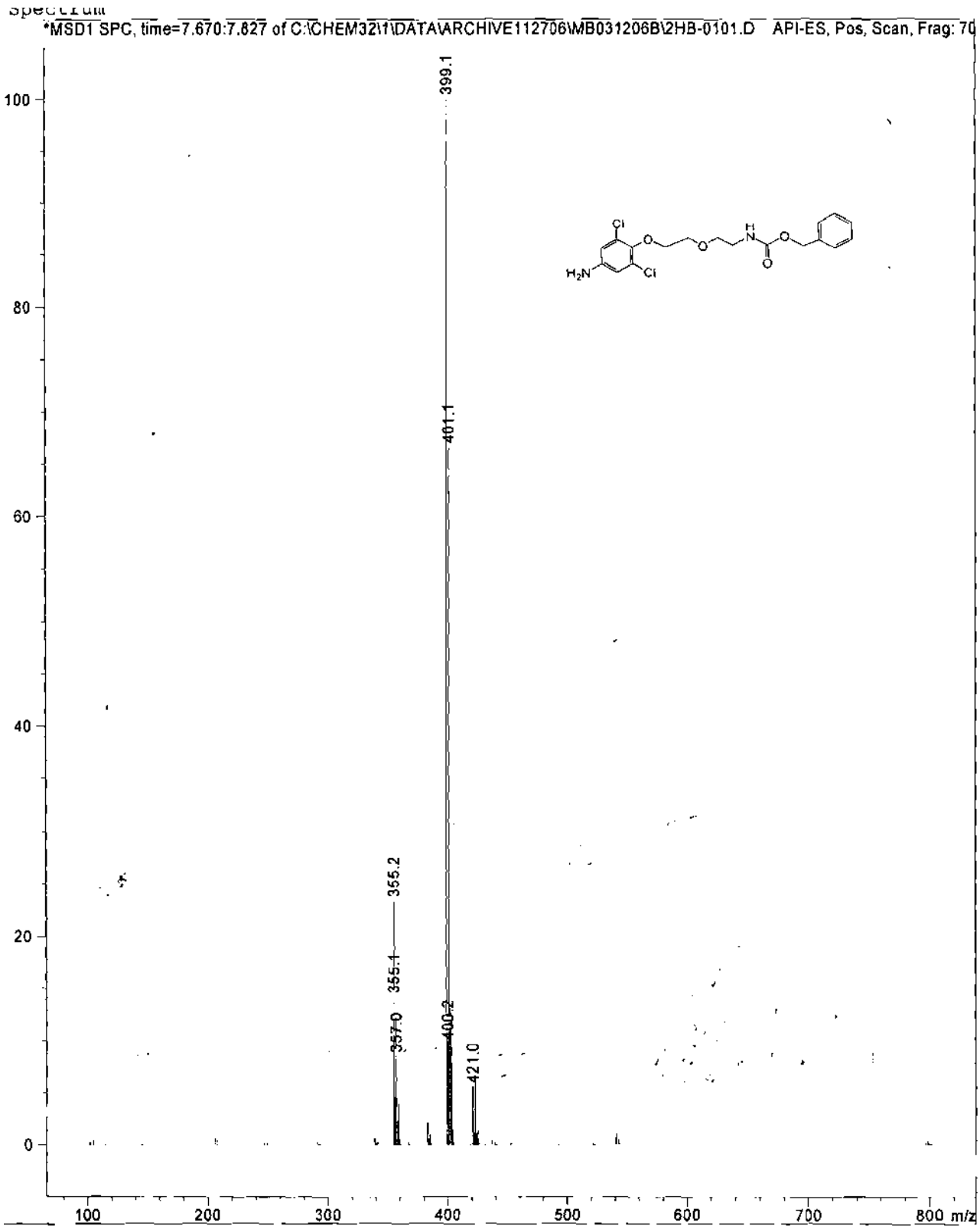
Spectrum
*MSD1 SPC, time=7.670:7.827 of C:\CHEM32\1\DATA\ARCHIVE112706\MB031206B\2HB-0101.D API-ES, Pos, Scan, Frag: 70
399.1
401.1
355.2
355.1
357.0
400.2
421.0
100
80
60
40
20
0
100
200
300
400
500
600
700
800 m/z
Cl
O
O
H
N
O
O
Cl
H2N

^{1}H NMR, intermediate material: benzyl 2-(2-(2,6-dichloro-4-(2-hydroxybenzamido)phenoxy)ethoxy)ethylcarbamate

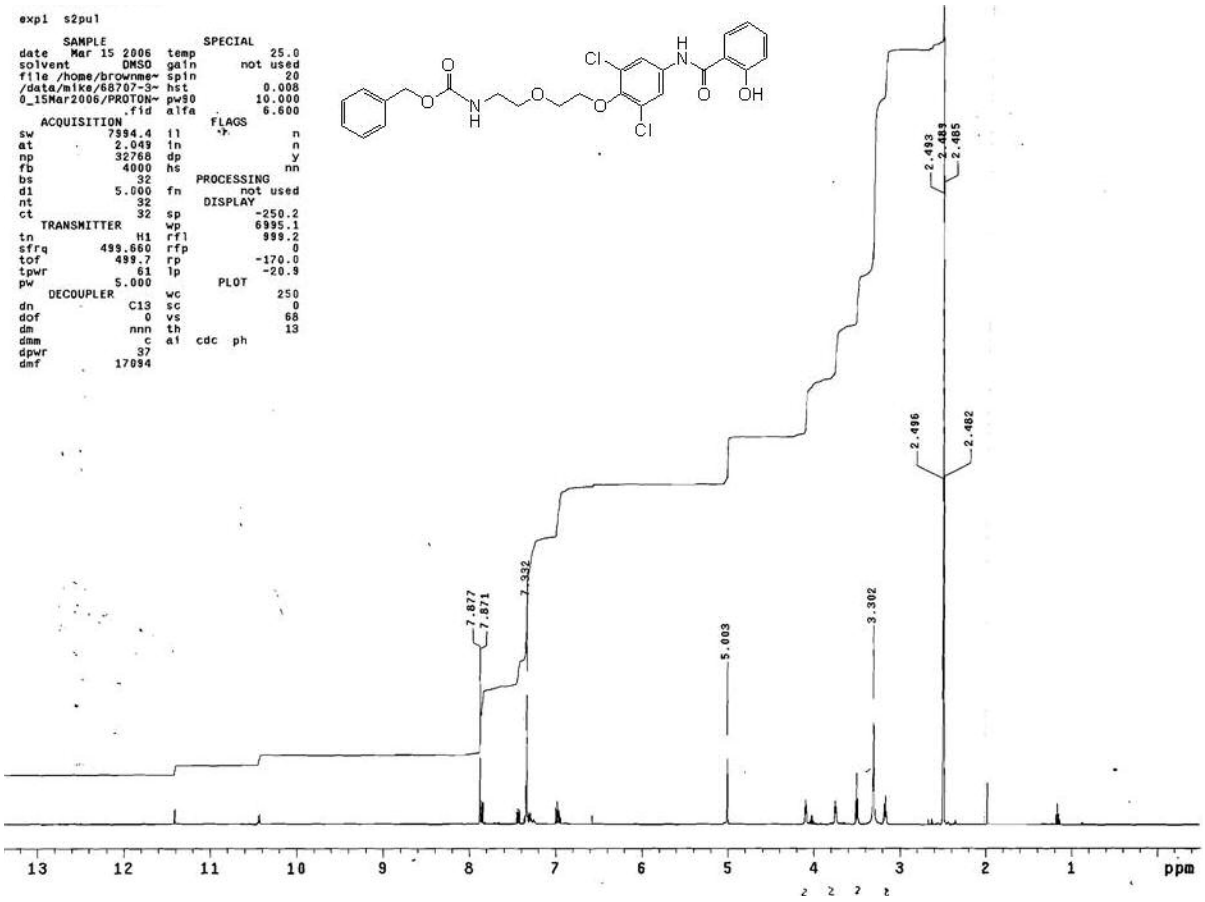

MS, intermediate material: benzyl 2-(2-(2,6-dichloro-4-(2-hydroxybenzamido)phenoxy)ethoxy)ethylcarbamate

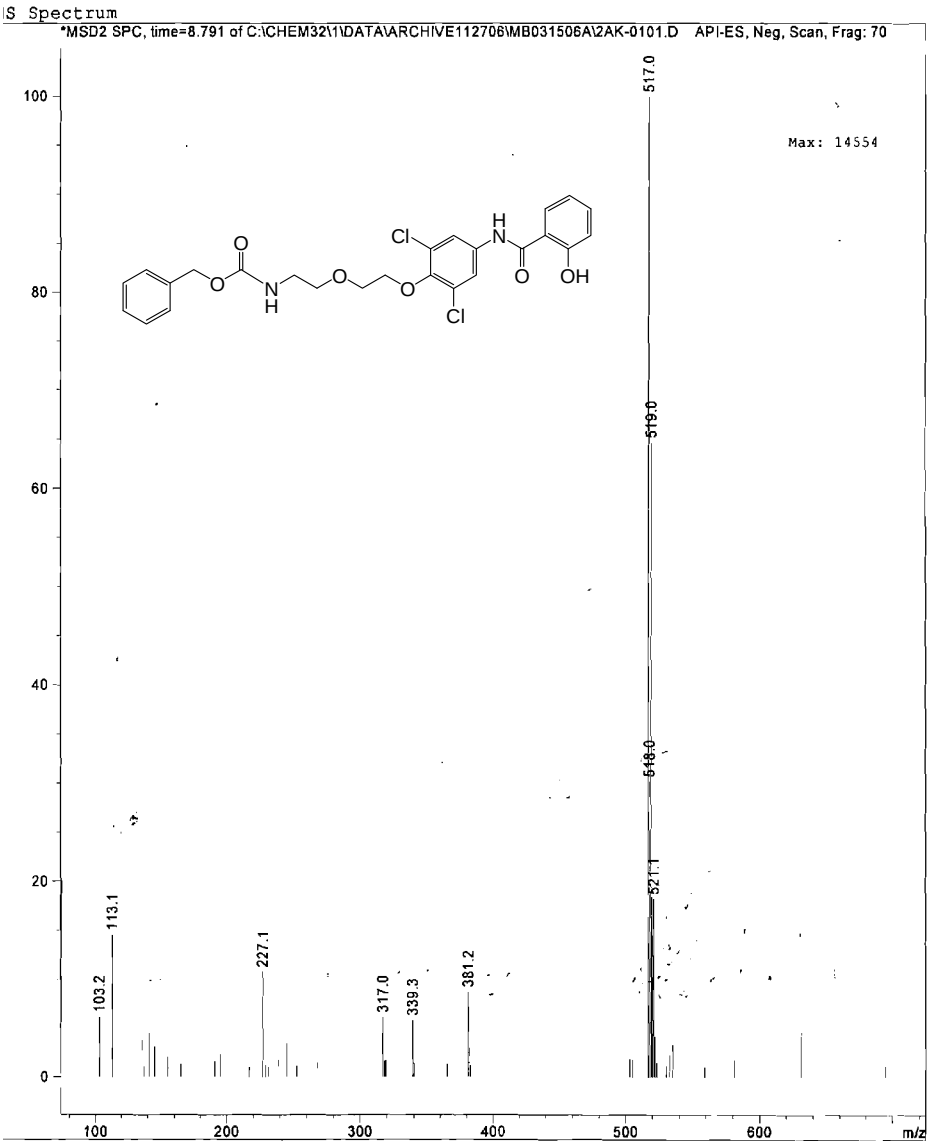

^{1}H NMR, intermediate material: *N*-(4-(2-(2-aminoethoxy)ethoxy)-3,5-dichlorophenyl)-2-hydroxybenzamide

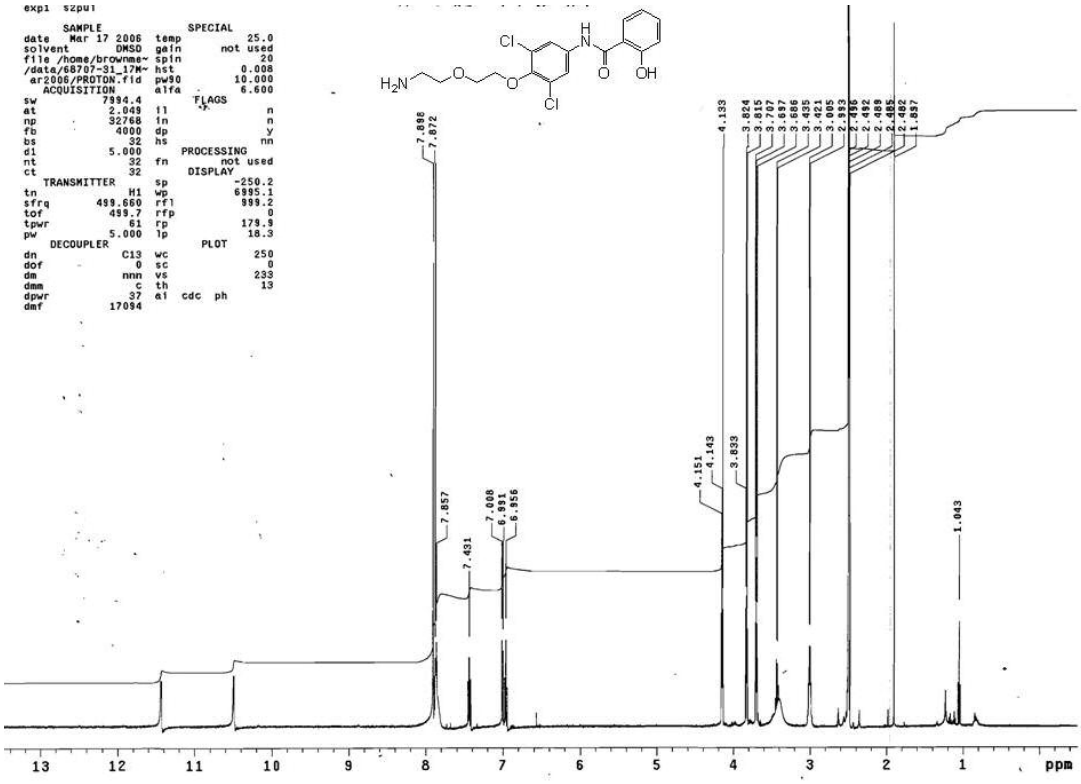

MS, intermediate material: *N*-(4-(2-(2-aminoethoxy)ethoxy)-3,5-dichlorophenyl)-2-hydroxybenzamide

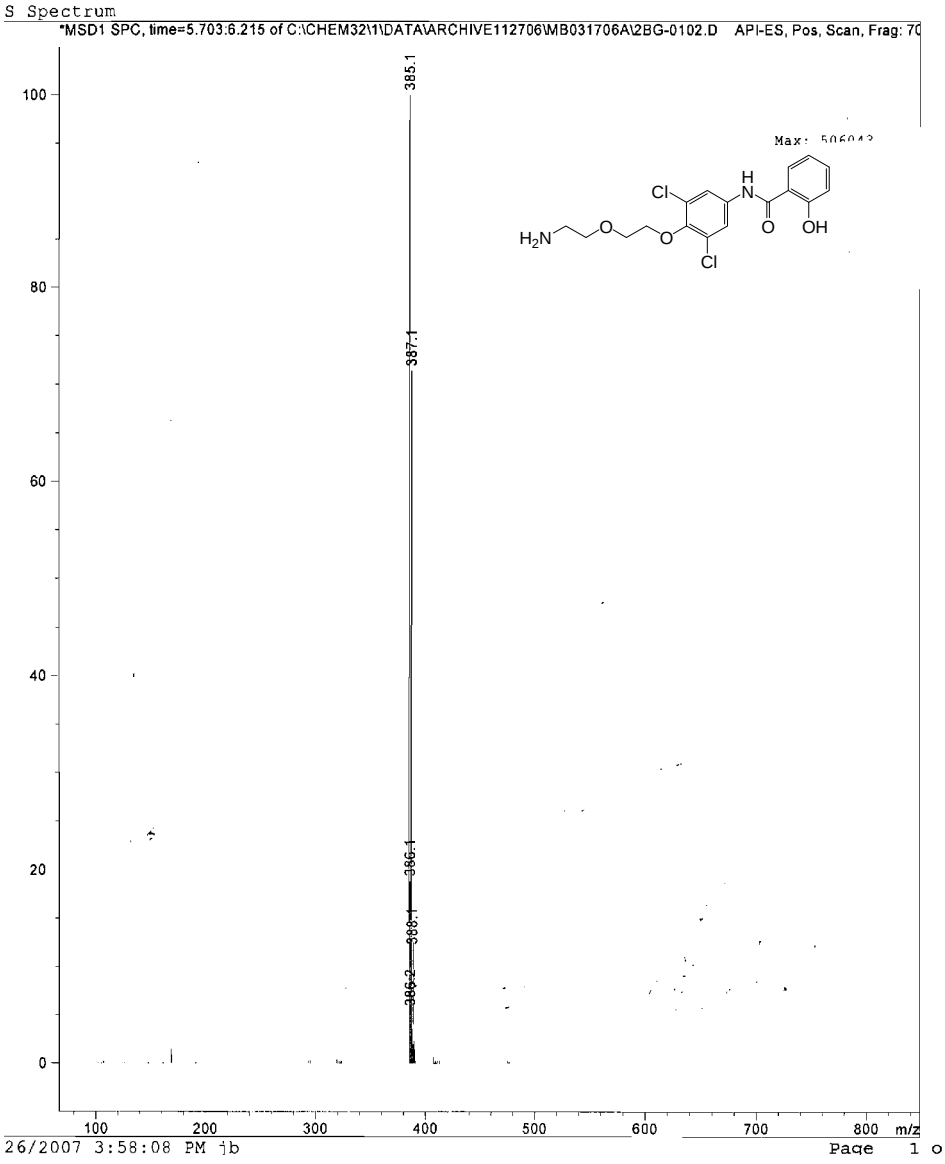

^{1}H NMR, intermediate material: benzyl 2-(2-(2,6-dichloro-4-(2-methoxybenzamido)phenoxy)ethoxy)ethylcarbamate

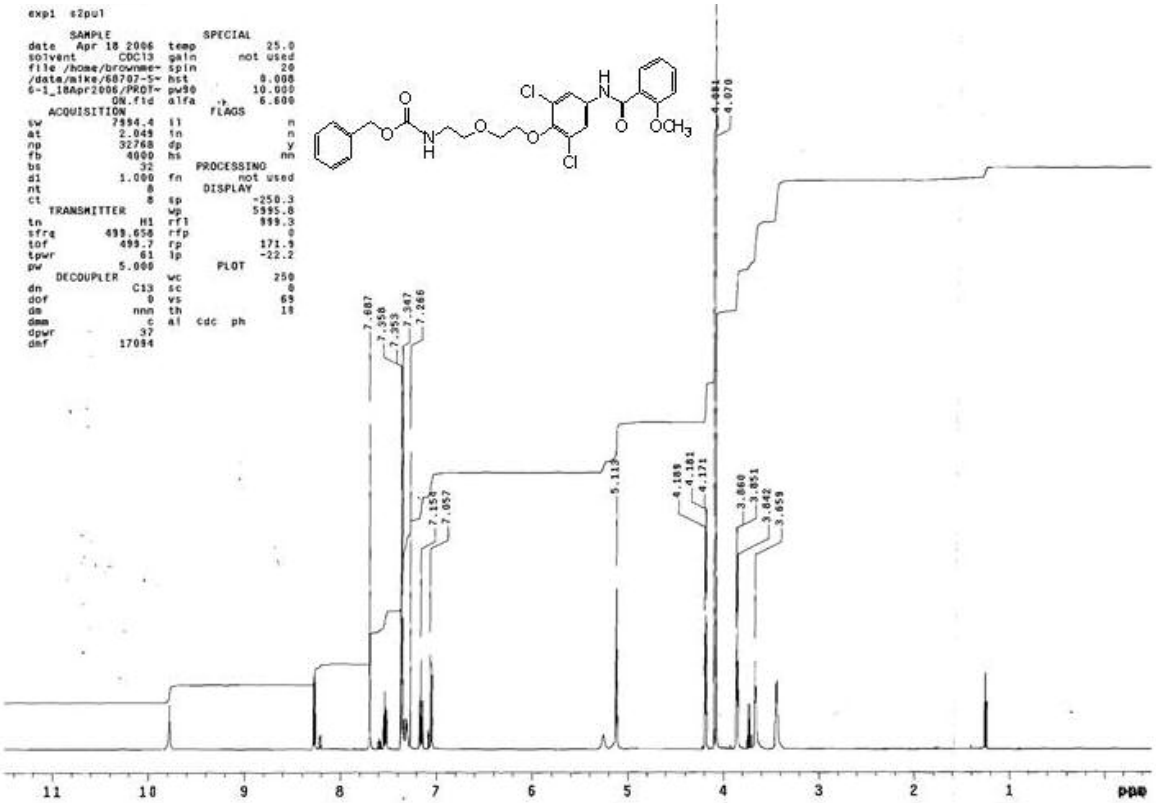

MS, intermediate material: benzyl 2-(2-(2,6-dichloro-4-(2-methoxybenzamido)phenoxy)ethoxy)ethylcarbamate

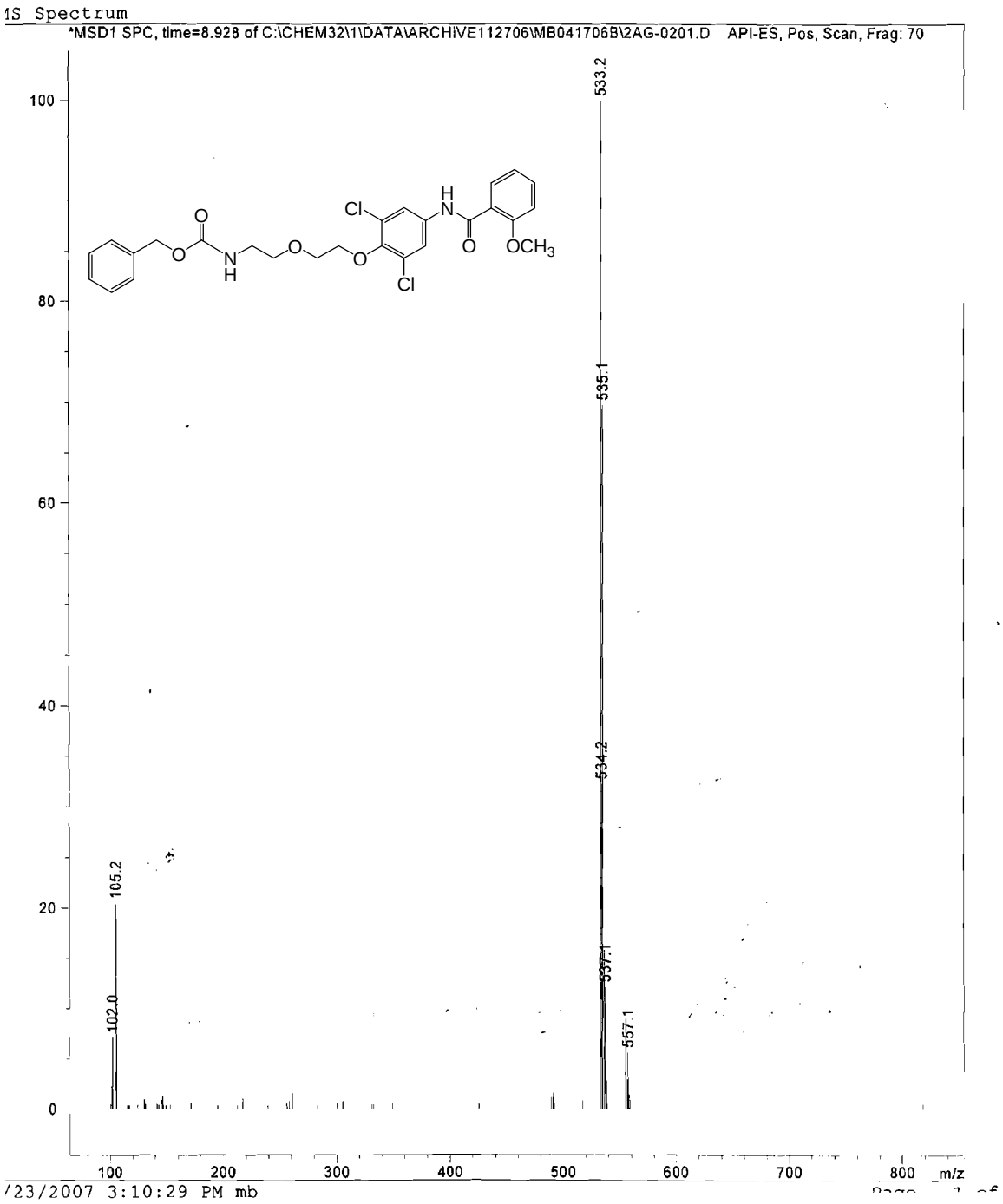

^{1}H NMR, intermediate material: *N*-(4-(2-(2-aminoethoxy)ethoxy)-3,5-dichlorophenyl)-2-methoxybenzamide

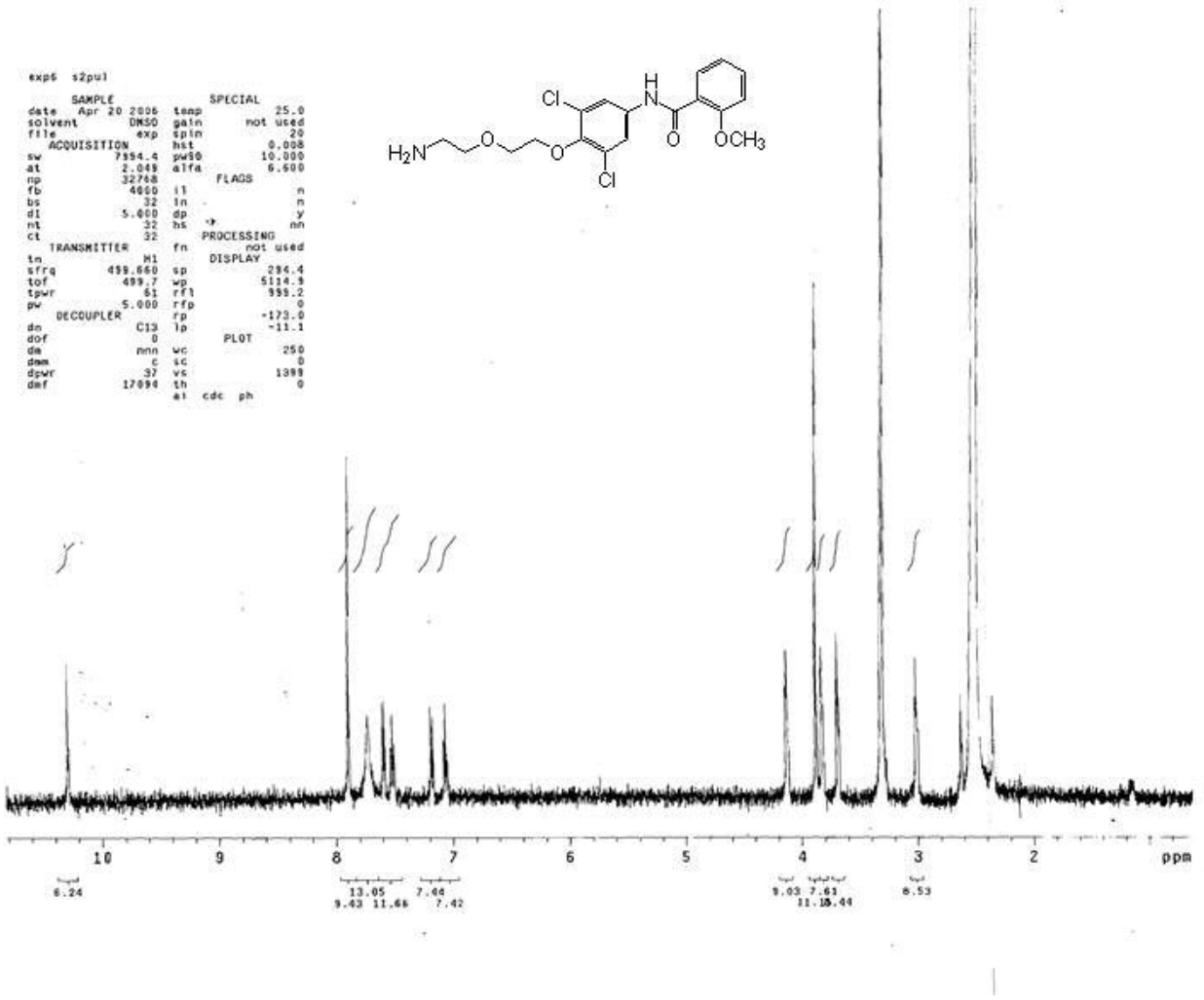

MS, intermediate material: *N*-(4-(2-(2-aminoethoxy)ethoxy)-3,5-dichlorophenyl)-2-methoxybenzamide

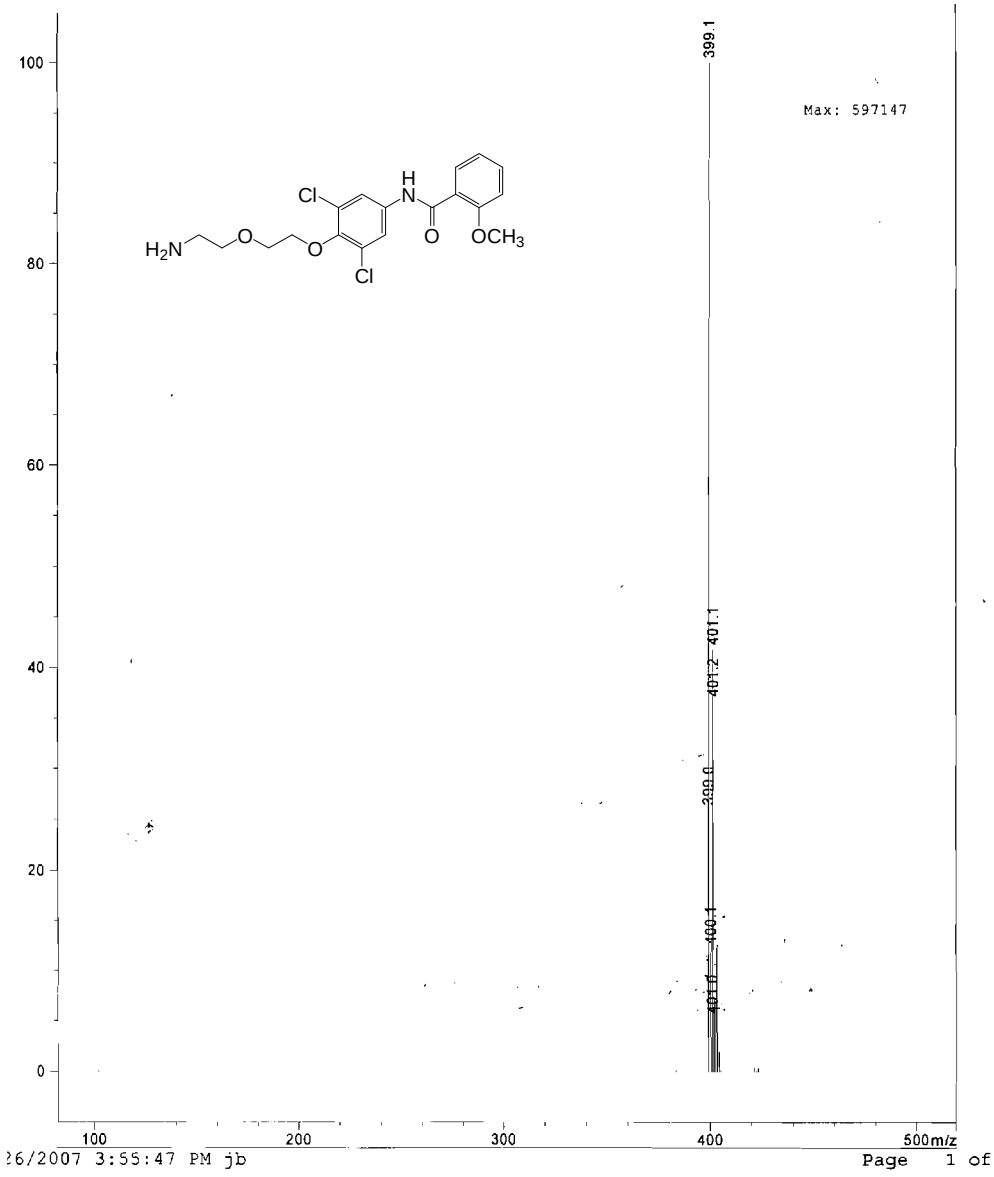

SDS-PAGE Gel stained to show band (28 kDA) corresponding to 14-3-3ζ

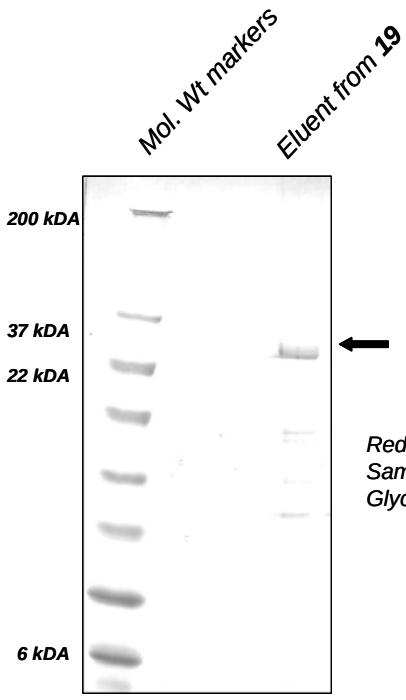

Reduced with 2-mercaptoethanol (0.25M in Sample Buffer™, 100ºC, 5 min). 4-20% Tris-Glycine Gel™ visualized with GelCode Blue™

Intracellular Delivery of Quantum Dot−Protein Cargos Mediated by Cell Penetrating Peptides

Igor L. Medintz,*[,†] Thomas Pons,[‡,#] James B. Delehanty,[†] Kimihiro Susumu,[‡] Florence M. Brunel,[§] Philip E. Dawson,[§] and Hedi Mattoussi*[,‡]

Center for Bio/Molecular Science and Engineering, Code 6900, and Division of Optical Sciences, Code 5611, U.S. Naval Research Laboratory, Washington, DC 20375, and Departments of Cell Biology and Chemistry and the Skaggs Institute for Chemical Biology, The Scripps Research Institute, La Jolla, California 92037. Received March 5, 2008; Revised Manuscript Received June 19, 2008

We utilize cell penetrating peptide functionalized QDs as specific vectors for the intracellular delivery of model fluorescent protein cargos. Multiple copies of two structurally diverse fluorescent proteins, the 27 kDa monomeric yellow fluorescent protein and the 240 kDa multichromophore b-phycoerythrin complex, were attached to QDs using either metal-affinity driven self-assembly or biotin−Streptavidin binding, respectively. Cellular uptake of these complexes was found to depend on the additional presence of cell-penetrating peptides within the QD−protein conjugates. Once inside the cells, the QD conjugates were mostly distributed within endolysosomal compartments, indicating that intracellular delivery of both QD assemblies was primarily driven by endocytotic uptake. Cellular microinjection of QD-fluorescent protein assemblies was also utilized as an alternate delivery strategy that could bypass the endocytic pathway. Simultaneous signals from both the QDs and the fluorescent proteins allowed verification of their colocalization and conjugate integrity upon delivery inside live cells. Due to their intrinsic fluorescence properties, this class of proteins provides a unique tool to test the ability of QDs functionalized with cell penetrating peptides to mediate the intracellular delivery of both small and large size protein cargos. Use of QD−peptide/fluorescent protein vectors may make powerful tools for understanding the mechanisms of nanoparticle-mediated drug delivery.

INTRODUCTION

Developing nanoparticles as delivery vehicles for drugs, genes, and contrast/imaging agents to live cells, tissues, and tumors has stimulated much interest recently (*1*−*5*). Among an array of available nanoparticles, luminescent semiconductor nanocrystals or quantum dots (QDs) provide a powerful prototypical example with many demonstrated applications in biological imaging and sensing (*6*−*9*). Their utility is derived from the combination of unique photophysical characteristics and sizes comparable to that of a large protein. The hydrodynamic radius of hydrophilic CdSe-ZnS QDs varies from ∼5 nm, for nanocrystals cap exchanged with molecular ligands, to ∼20 nm for nanocrystals encapsulated within block copolymers (*10*). A single QD can be conjugated to several biomolecules (such as antibodies, peptides, DNA) to provide multifunctional QD bioconjugates with enhanced avidity. In addition, their strong resistance to chemical and photodegradation can potentially allow long-term fluorescent monitoring of specific biological processes (*6*−*9, 11*).

Several methods have been investigated to achieve the efficient intracellular delivery of various nanoparticles, including QDs. They include electroporation (*12*), lipid-based transfection reagents (*13, 14*), and microinjection (*13*), as well as receptor-mediated endocytosis (*11, 15*). Use of cell-penetrating peptides (CPP) conjugated to hydrophilic QDs as an alternate strategy to facilitate their intracellular uptake has also been reported by several groups, and results suggest that delivery was primarily driven by endocytotic uptake (*13, 16*−*23*). Although a wide range of cell penetrating peptides exist, they are most often functional analogues of the canonical HIV-derived TAT sequence and usually consist of 8−10 sequentially repeated polyarginine residues (*24*). We have recently explored the use of CPP-mediated delivery of QD−peptide conjugates to eukaryotic HEK-293 and COS-1 cells (*25*). The peptide sequence used was modular and consisted of a C-terminal 8 arginine repeat-block for mediating cellular uptake, a short linker/spacer, and a N-terminal 8 histidine tract that promoted peptide self-assembly onto CdSe-ZnS core−shell QDs (*25, 26*). Efficiency of the CPP-facilitated delivery was found to depend on both peptide-to-QD ratio and overall QD conjugate concentration. CPP-mediated uptake required short incubation times of less than 1 h compared to 2−4 h or longer incubation time for passive uptake; it was also both selective and specific even when cells were incubated with mixtures of CPP and *other* nonpeptide functionalized QDs. Nanocrystals delivered via this approach did not exhibit any discernible toxic effects to the cells, and intracellular localization was again confirmed to be primarily endosomal (*25*). The intracellular delivery and stability of nanocrystals conjugated to a mixture of His-terminated CPP and dye-labeled peptides was further verified by multiphoton fluorescence resonance energy transfer imaging (FRET between QDs and proximal dyes) of intracellular compartments several hours post-uptake (*27*).

In this report, we build upon our previous results and demonstrate that cell penetrating peptides can further promote the effective intracellular delivery of QD cargos made of

* Email: hedi.mattoussi@nrl.navy.mil; igor.medintz@nrl.navy.mil.
† Center for Bio/Molecular Science and Engineering, Code 6900, U.S. Naval Research Laboratory.
‡ Division of Optical Sciences, Code 5611, U.S. Naval Research Laboratory.
§ The Scripps Research Institute.
# Present address: Institut National de la Santé et de la Recherche Médicale, Laboratoire Photons et Matière, CNRS UPRA0005, ESPCI, 10 Rue Vauquelin, 75005 Paris, France.

10.1021/bc800089r CCC: $40.75 © 2008 American Chemical Society
Published on Web 08/06/2008

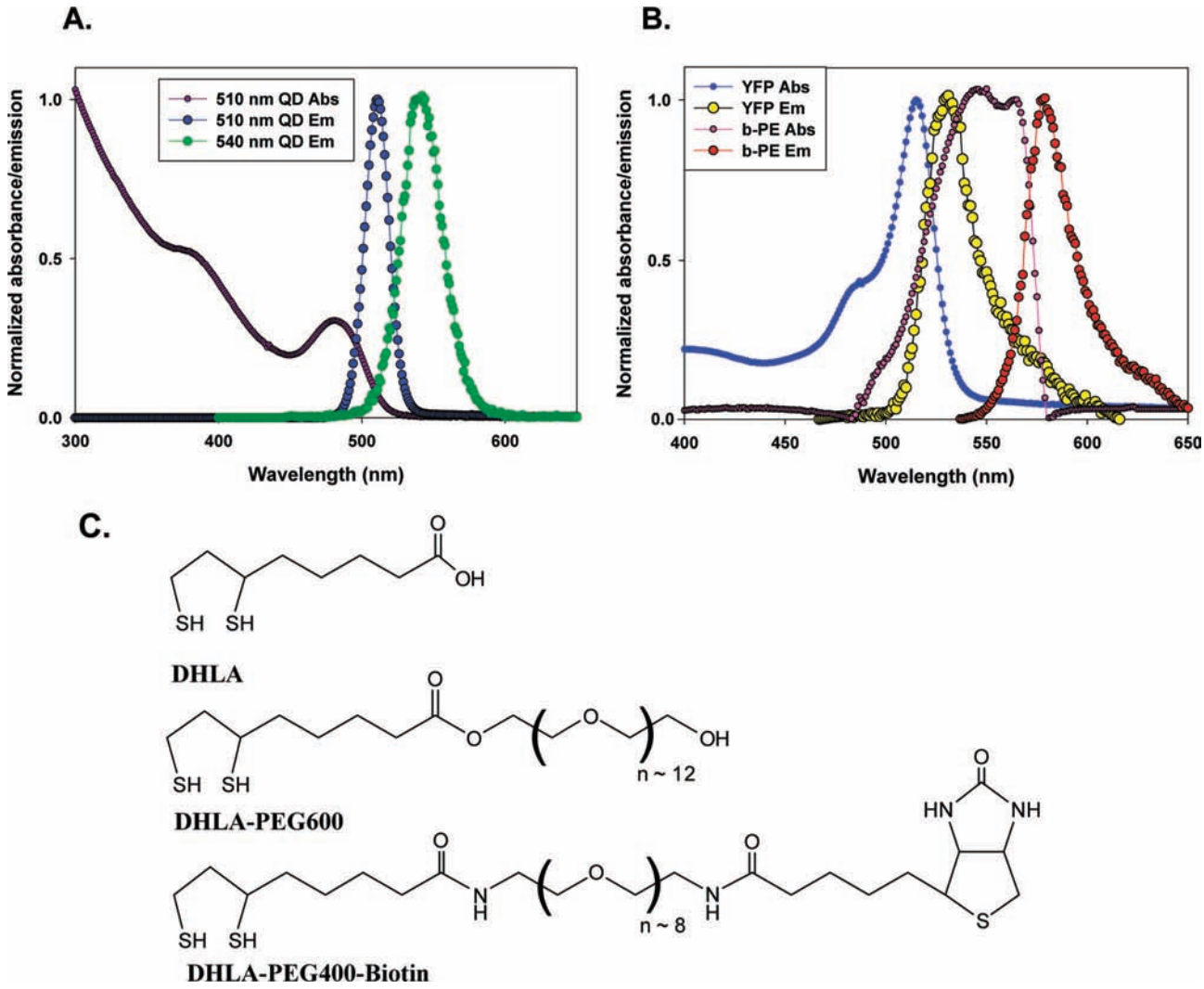

Figure 1. Absorption and emission spectra of QDs and fluorescent proteins used. (A) Normalized absorption spectrum of 510 nm emitting QDs along with the normalized PL spectra of 510 and 540 nm emitting QDs. (B) Normalized absorption and emission spectra of yellow fluorescent protein (YFP) and b-phycoerythrin (b-PE). (C) Structure of the DHLA, DHLA-PEG600, and DHLA-PEG400-biotin ligands used to provide aqueous compatibility of the QDs.

nanocrystals self-assembled with additional small or large fluorescent proteins. The QD serves as a central nanoscaffold for immobilizing proteins and peptides, while the CPPs promote conjugate internalization by eukaryotic cells. This class of proteins was specifically selected as they allow fluorescence monitoring of intracellular distribution as well as testing of the stability of QD−protein assemblies. Proteins, including yellow fluorescent protein (YFP) and the multichromophore b-phycoerythrin complex (b-PE), were conjugated to QDs, via a combination of metal-affinity interactions and biotin−avidin binding. We found that intracellular delivery of these conjugates strongly depended on CPP presence, while colocalization studies indicated that the mixed surface QD−peptide/protein assemblies were distributed within the endosomal compartments. In comparison, direct microinjection of QD−protein cargos into live cells bypassed the endolysosomal system and resulted in more homogeneous distribution of conjugates throughout the cytosol.

EXPERIMENTAL PROCEDURES

QD Synthesis. CdSe-ZnS core−shell QDs with emission maxima centered at 510 and 540 nm were synthesized using stepwise reactions of organometallic precursors in hot coordinating solvent mixtures following the procedures described in refs (*28*−*31*); absorption and emission spectra are provided in Figure 1A. The nanocrystals were made hydrophilic by exchanging the native capping shell, composed primarily of trioctyl phosphine and trioctyl phosphine oxide (TOP/TOPO), with bifunctional ligands as described in refs (*32*−*34*). We used two sets of hydrophilic QDs: (1) nanocrystals capped with only dihydrolipoic acid, and (2) nanocrystals capped with a mixture of poly(ethylene glycol)-appended dihydrolipoic acid (PEG Mw ≃ 600, DHLA-PEG) and biotin-terminated DHLA-poly(ethylene glycol) (PEG Mw ≃ 400, DHLA-PEG-biotin) with a 9:1 molar ratio of the ligands; these are referred to as DHLA-QDs and DHLA-PEG-biotin-QDs, respectively. Ligand structures are provided in Figure 1C (*32*−*34*).

Proteins and Peptides. The yellow fluorescent protein was generously provided by W. Frommer (Carnegie Institute, Stanford, CA) on plasmid pRSET B (Invitrogen, Carlsbad, CA) within a gene fusion encoding a blue fluorescent protein−glucose binding protein−yellow fluorescent protein sensor construct inserted between *Bam*HI and *Hind*III of the multiple cloning site (*35*). The blue fluorescent protein−glucose binding protein portion was excised by digestion with *Kpn*I and *Bam*HI and an insert encoding for a hexa-histidine $(His)_6$ sequence followed by a unique *Xho*I site (Asp-Gln) was ligated into the *Kpn*I and *Bam*HI restriction sites. Transformants were screened by *Xho*I digestion and confirmed with DNA sequencing. The final YFP

gene construct sequentially encodes a His_6 sequence after the start methionine, Asp-Gln, an Xpress Epitope (Asp-Leu-Tyr-Asp-Asp-Asp-Asp-Lys) and another His_6 sequence at the immediate N-terminus of the YFP coding sequence. This plasmid was introduced into BL21(DE3) *E. coli* cells (Invitrogen) and expression induced with 1 mM isopropyl-β-D-thiogalactopyranoside (IPTG, Sigma, St Louis, MO) for 3 days at 30 °C in the dark to allow for full maturation of the chromophore, before harvesting the cells by centrifugation at 4 °C. His-appended YFP was purified from soluble cell lysate using Ni-NTA Resin (Qiagen, Valencia, CA), as described in refs (*35, 36*). The absorption and emission spectra of the purified YFP are shown in Figure 1B. One-to-one b-phycoerythrin−Streptavidin conjugate solution at 1 mg/mL (referred to as b-PE) and AlexaFluor 647 dye-labeled Transferrin (AF647-TF, $\lambda_{abs\ max.} = 647$ nm, $\lambda_{em\ max.} = 670$ nm) were obtained from Invitrogen. Cell penetrating peptide (CPP) with the sequence $(His)_8$-Trp-Leu-Ala-Aib-Ser-Gly-$(Arg)_8$-amide, where Aib is α-aminoisobutyric acid and the c-terminus is blocked with an amide, was synthesized and purified as described in ref (*25*).

Self-Assembly of Quantum Dot Bioconjugates. To self-assemble QD−YFP conjugates at the desired valence, His-appended proteins at the appropriate molar ratios were added to 0.3 μM of 510-nm emitting DHLA-capped QDs in 10 mM Tris-Cl pH 8 buffer and incubated at room temp for ∼30 min. Similarly, b-PE-Streptavidin was added to 0.3 μM of 540-nm emitting QDs (capped with DHLA-PEG:DHLA-PEG-biotin 9:1 ratio) in phosphate buffered saline (137 mM NaCl, 10 mM phosphate, 2.7 mM KCl, pH 7.4, PBS) and incubated at 4 °C overnight; conjugate formation in this case is driven by Streptavidin−biotin interactions. Conjugates were characterized using gel electrophoresis, where changes in the electrophoretic mobility of QDs assembled with either His-appended YFP or Streptavidin-labeled b-PE were monitored (*10*). Samples were diluted in 1 × TBE buffer (0.09 M Tris, 0.002 M Na_2-EDTA 0.09 M Boric acid pH ∼8.3) and run on 1% or 2% agarose gels for QD−b-PE and YFP conjugates, respectively. In particular, the effects of varying the number of proteins per QD bioconjugate were monitored. Gel images were collected by exciting the QD and/or protein and capturing fluorescence images of the separated bands within the gels using a Kodak 440 Digital Image Station (Rochester, NY). Conjugate formation was also confirmed by monitoring changes in the energy transfer between the QDs and fluorescent proteins upon self-assembly. Fluorescent spectra were collected on a Tecan Safire Dual Monochromator Multifunction Microtiter Plate Reader (Tecan, Research Triangle Park, NC) using 325 nm excitation. For intracellular delivery and imaging experiments, QDs were self-assembled with a mixture of the protein and CPP at a nominal CPP:QD molar ratio of 50:1.

Intracellular Uptake of Quantum Dot−Fluorescent Protein Conjugates. HEK 293T/17 and COS-1 cell lines (ATCC, Manassas, VA) were cultured in complete growth medium (Dulbecco's Modified Eagle's Medium (DMEM) supplemented with 4 mM L-glutamine, 1 mM sodium pyruvate, 1% (v/v) penicillin/streptomycin/actinomycin D antibiotic/antimycotic, and 10% (v/v) heat-inactivated fetal bovine serum (FBS). Cells were incubated at 37 °C under 5% CO_2 atmosphere and a subculture was performed every 3 days (*25*). Cellular internalization experiments were performed in sterile Laboratory-Tek chambered coverglass wells (Nunc, Rochester, NY). The chambers were initially coated with 50 μg/mL fibronectin (Sigma-Aldrich, St Louis, MO) in sodium bicarbonate buffer pH 8.5. Approximately 2×10^4 cells were seeded into the wells and cultured overnight. QD bioconjugates were diluted into complete culture medium and added to the cell culture and incubated at 37 °C for 1 h. AF647-TF (at 40 μg/mL) was also added to the culture to specifically colabel the endosomal vesicles as described previously (*25*). Mixed surface QD conjugates consisting of either 1:5 or 1:10 QD/YFP and QD/b-PE with assembly valence of 1:1 to 1:2.5, together with CPP at ∼50 CPPs per QD, were incubated with the cell cultures at different QD conjugate concentrations. Excess unbound QD conjugates were removed by washing the culture at least 3 times with PBS. Cells were then fixed in 3.7% paraformaldehyde for 10 min at room temperature, washed twice with PBS, and mounted in ProLong Antifade mounting media containing DAPI dye (Invitrogen) for nuclear staining. Epifluorescence image collection was carried out using an Olympus IX-71 microscope. Side-by-side split fluorescence images were collected and quantitated using a DualView system (Optical Insights, Tucson, AZ) equipped with a 565 nm dichroic filter. For 510 nm QD−YFP cellular imaging, samples were excited at 488 nm and emissions were collected/separated with the 565 nm dichroic and deconvoluted. QD fluorescence was collected at $\lambda < 565$ nm and the YFP fluorescent tail collected at $\lambda > 565$ nm. YFP leakage into the QD window was subtracted as part of the deconvolution. The 540 nm QDs and b-PE were excited at 488 nm and their respective emissions were separated with the 565 nm dichroic filter and deconvoluted. DAPI fluorescence was excited using a Xe lamp and emission collected using a DAPI cube (D350/50× for excitation, dichroic 400DCLP, D460/50m for detection). AF647-TF was excited using the Xe lamp and fluorescence detected using a Cy5 cube (excitation HQ620/60×, dichroic Q660LP, emission HQ700/75m). Both excitation/detection cubes were provided by Chroma Technology (Rockingham, VT). Differential interference contrast (DIC) images were collected using a bright light source. For microinjection, the QD−YFP and QD−b-PE conjugates described above were diluted in PBS. Conjugates were directly injected into adherent COS-1 or HEK 293T/17 cells using an InjectMan NI2 micromanipulator equipped with a FemtoJet programmable microinjector (Eppendorf, Westbury, NY). This instrumental setup allows the injection of femtoliter aliquots of conjugate solution into individual cells (*37*).

RESULTS

Fluorescent Proteins and Self-Assembly of Quantum Dot Bioconjugates. Yellow fluorescent protein (YFP) is a slightly longer wavelength emitting variant of the green fluorescent protein (GFP), and is derived from the jellyfish *Aequorea*, as described in the work of Tsien (*38*). It consists of 11 β-strands which form a hollow β-barrel or cylinder, and the chromophore, located at the center of a threaded helix, is formed by a cyclic rearrangement of three central residues (Gly_{65}, Tyr_{66}, Gly_{67}) during maturation (*38*). This relatively small protein (Mw ∼27 kDa) is easily expressed in bacteria from a plasmid, has a short maturation time, and has been used in a variety of FRET-based intracellular sensing studies (*39−41*). The second fluorescent protein we used, b-phycoerythrin (b-PE), is a member of the phycobiliprotein family of light harvesting protein complexes known as phycobilisomes found in red algae and cyanobacteria (*42, 43*). b-PE differs photophysically and structurally from YFP in many respects; see Table 1. It consists of α/β monomers associated into a symmetrical $(\alpha/\beta)_6$ hexameric structure and has ca. 34−38 covalently attached bilins (open chain tatrapyrrole chromophores) per functional moiety. It has a large molecular weight, ∼10 times that of YFP, a very large extinction coefficient, ∼100 times higher than that of YFP, and has been widely used as a highly sensitive fluorescent probe (*42, 43*).

We utilize two self-assembly approaches to form our QD bioconjugates: metal-affinity interactions and biotin−avidin binding. When used for nanoparticle conjugation, metal affinity

Table 1. Properties of the Fluorescent Protein Assemblies Tested[a]

protein	structure	molecular weight (kDa)	extinction coefficient (M^{-1} cm^{-1})	quantum yield (QY)	quantum dot	method of QD attachment
YFP	11-stranded β-barrel	~27 000	20 200	0.60	510 nm QDs (QY ~ 12%)	metal-affinity coordination
b-PE	multi-subunit multichromophore protein assembly	~240 000 Streptavidin ~64 000	2 410 000	0.98	540 nm QDs (QY ~ 19%)	biotin-streptavidin

[a] b-PE utilized as a 1:1 Streptavidin conjugate (*38*, *42*, *43*).

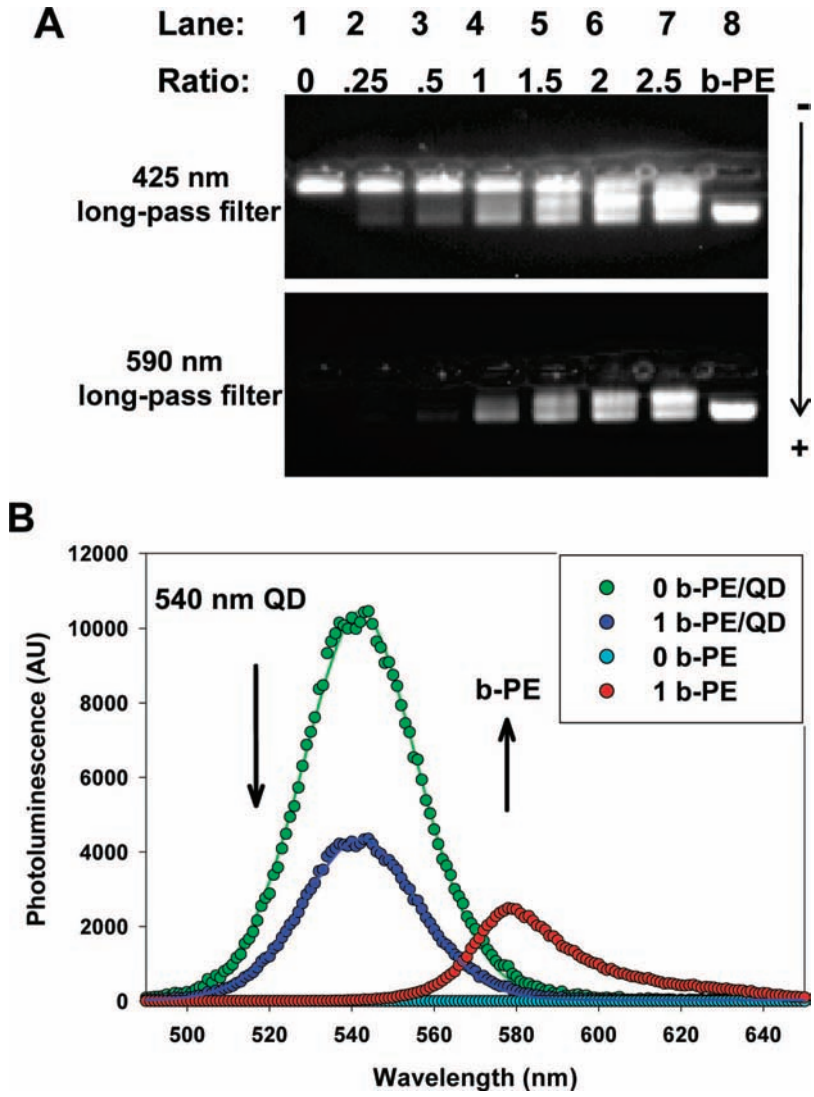

Figure 2. Agarose gel electrophoresis and FRET data. (A) Electrophoretic mobility bands captured from self-assembled QD−Streptavidin−b-PE conjugates; the corresponding average conjugate valences (ratio of b-PE per QD) are listed on top of each lane. Lane 8 has the equivalent amount of 2.5 b-PE alone. The gel was imaged with the indicated filters to isolate QD and protein emissions. QD−b-PE conjugates were separated on 1% agarose gels. (B) Deconvoluted PL spectra of 540 nm DHLA-PEG-biotin-QDs in the absence and presence of ~1 b-PE/QD along with b-PE FRET-sensitized emission. QD PL was fit to a Gaussian profile.

driven self-assembly can be versatile and easy to implement. We and other groups have shown that polyhistidine (His_n) sequences facilitate self-assembly of both proteins and peptides onto ZnS-overcoated CdSe QDs (*6*, *44*−*46*). More recently, we elucidated the kinetics of metal-His driven self-assembly between QDs and both proteins and peptides and showed that high affinity/low dissociation constants drive the interactions ($K_D \sim 10^{-9}$−10^{-8} M) (*26*). This study further showed that His interactions occur directly with the Zn-rich inorganic surface of the nanocrystals. Engineering YFP with an N-terminus bearing two-$(His)_6$ sequences separated by a small spacer and CPP having an N-terminal $(His)_8$ sequence permit the formation of tight QD−protein/peptide complexes driven by this self-assembly. Biotin−avidin binding is a ubiquitous bioconjugation strategy in biology, known for its strong interaction ($K_D \sim 10^{-15}$ M) (*47*). Using QDs surface-capped with a mixture of hydroxyl- and biotin-terminated PEG (DHLA-PEG-biotin-QDs) allowed easy conjugation to commercially available b-PE−Streptavidin.

The first characterization technique of these QD bioconjugates relied on agarose gel electrophoresis (no SDS present), where changes in the mobility shift were measured for QDs alone and QDs conjugated to increasing number of proteins. For QD−b-PE conjugates, since the emissions of the QDs and protein are spectrally distinguishable, gels were imaged with 425 and 590

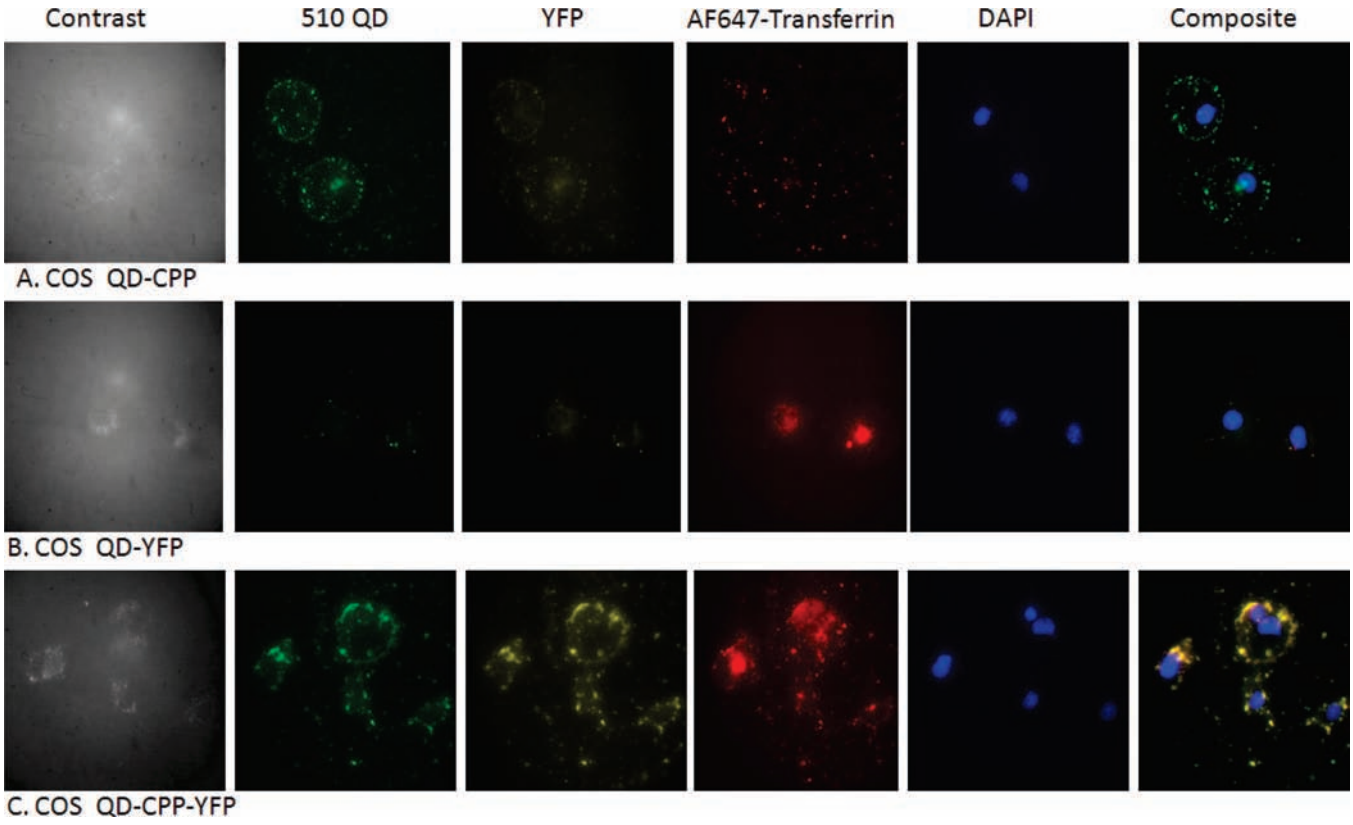

Figure 3. Cellular uptake of QD−YFP bioconjugates. Images collected from COS-1 cells incubated with (A) QD−CPP, (B) QD−YFP, and (C) QD−CPP−YFP assemblies; QD conjugate solutions at 75 nM concentration were used. For each series (left to right) the contrast, fluorescence images for 510-nm QD, YFP, AF647-Transferrin, DAPI, together with the merged fluorescence composite images are shown. Scale bar is 10 μm.

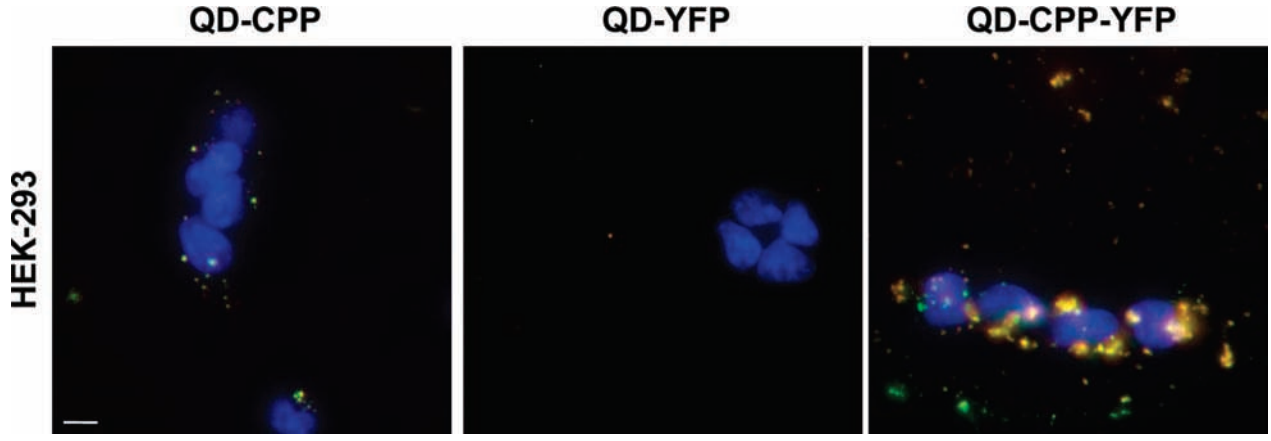

Figure 4. Cellular uptake of QD−YFP bioconjugates. HEK293/T17 cells were incubated with QD−CPP, QD−YFP, and CD−CPP−YFP assemblies as shown in Figure 2. Only merged representative fluorescent images compiled from the DAPI, QD, and YFP emissions are shown for each conjugate. Scale bar is 10 μm.

nm long-pass filters to allow visualization of either the simultaneous QD and b-PE emissions or only the emission of b-PE (see Figure 2A for representative images). The mobility of the unconjugated QDs capped with DHLA-PEG600/DHLA-PEG400-biotin mixture was essentially zero, as these ligands do not impart a net charge to the QDs. In comparison, a finite mobility shift was measured for b-PE alone. For solutions of conjugates at increasing b-PE-to-QD ratio, one can easily discern a discrete band with mobility intermediate between those of the QDs and b-PE (lanes 1 and 8, respectively). A concomitant decrease in the PL of the QD band is also noted as the ratio of b-PE and conjugate formation increases, which can be attributed to FRET interactions (see below). Furthermore, when the mobility bands corresponding to the various b-PE-to-QD ratios (lanes 2−7) and that of b-PE (control in lane 8) are compared, it appears that in addition to the main QD−b-PE conjugates, bands corresponding to the QDs and b-PE alone can also be visualized. The distribution in mobility bands for the conjugate solution is attributed to a distribution of conjugate valences varying between zero and the maximum expected, as previously observed for self-assembled bioconjugates (*10, 48*). The valence of QD conjugates is described by Poisson statistics and its effects are usually more visible at low protein-to-QD ratio as is the case in the present samples. Further, it is quite possible that not all the b-PE is conjugated to Streptavidin. Similarly, we carried out a side-by-side comparison of the mobility band shifts of solutions of QD−YFP conjugates at increasing YFP-to-QD ratios together with that of unconjugated QDs (data not shown).

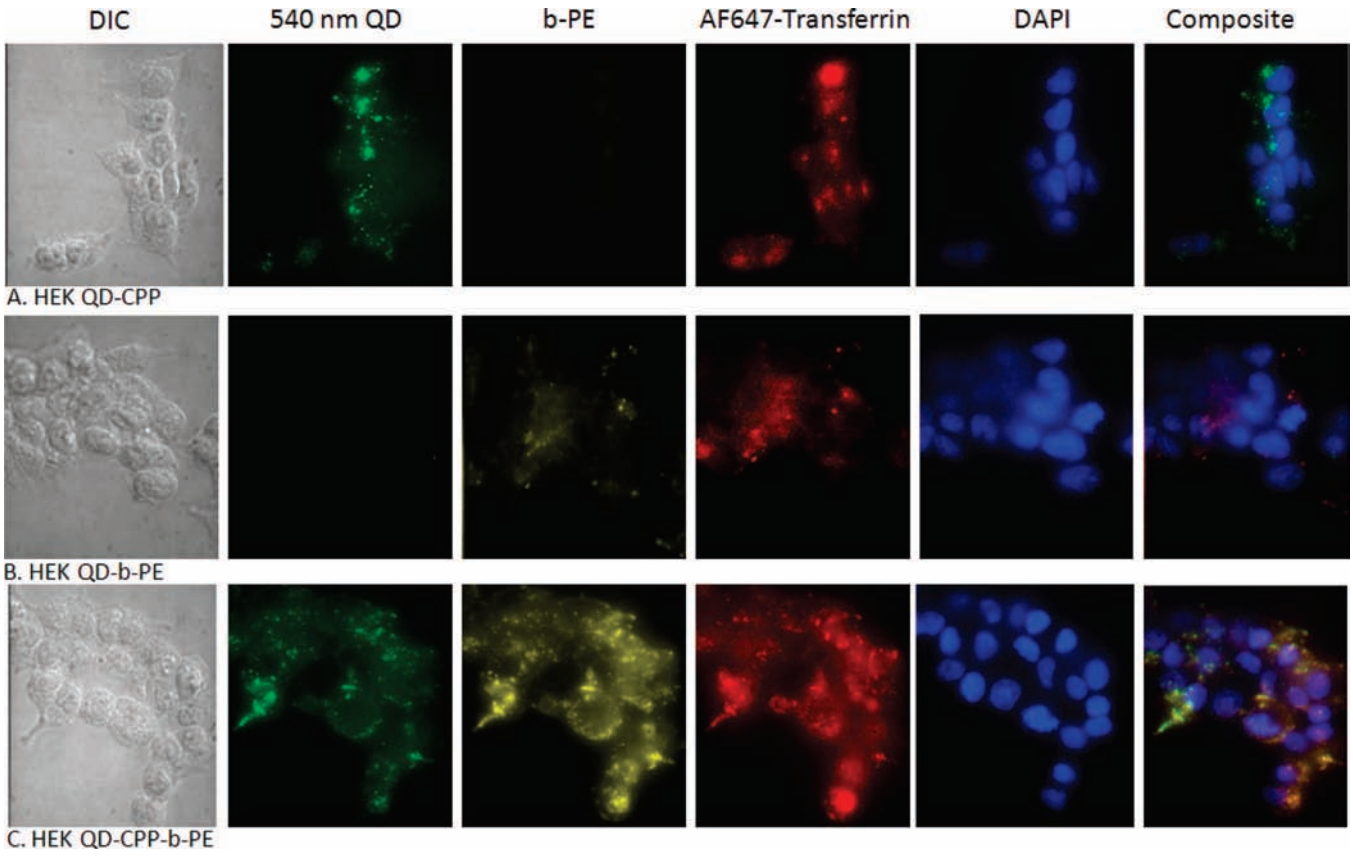

Figure 5. Cellular uptake of QD−b-phycoerythrin conjugates. Representative images of HEK293/T17 cells incubated with (A) QD−CPP, (B) QD−b-PE, (C) QD−CPP−b-PE. 540 nm emitting QD conjugates at 75 nM concentration were used. For each set of conjugates, the corresponding contrast, fluorescence images of 540-nm QD, b-PE, AF647-Transferrin, DAPI, along with the merged composite fluorescence images are shown. Due to overlap between the QD and b-PE emissions, spectral leakage between the QD and b-PE fluorescence can be seen along with some b-PE adherence to the cell membrane. Scale bar is 10 μm.

QDs exhibited the highest mobility shift due to the presence of negative surface charges (deprotonated carboxyl groups on the DHLA ligands), while a decrease in mobility shift with increasing conjugate valence was measured, which we attributed to an increase in conjugate size, i.e., YFP retards QD migration as more proteins are attached to the QD.

Assembly of both sets of QD−YFP and QD−b-PE conjugates were further confirmed by "visualizing" FRET between the central QD and proximal fluorescent proteins within the conjugates. The favorable spectral overlap between the nanocrystal emissions and either of the fluorescent proteins should result in a significant FRET interaction; see Figure 1. Representative deconvoluted spectra are shown in Figure 2B for QD−b-PE conjugates, where a loss in QD PL is measured along with a concomitant increase in acceptor PL upon conjugate, in agreement with previous results collected from solutions of QD−protein/peptide−dye conjugates (*10, 48−50*). Monitoring the relative QD donor and fluorescent protein acceptor emissions at different acceptor ratios allowed us to choose optimal assembly ratios for cellular uptake experiments. For imaging, significant emission from both the QD donor and the FRET-sensitized acceptor protein were desired. A detailed description and analysis of the FRET interactions will be presented elsewhere.

Intracellular Delivery of QD−YFP Conjugates. To verify that uptake of QDs surface functionalized with YFP cargo is mediated by the presence of CPP on the nanocrystal surface, two different cell lines, COS-1 and HEK293/T17, were separately incubated with 3 types of conjugate: QD−CPP conjugates (∼50 CPP per QD), QD−YFP conjugates (10 YFP per QD in the absence of CPP), and QDs assembled with a mixture of YFP and CPP (QD−YFP−CPP with ∼10 YFP and 50 CPP per conjugate). Cells were incubated with solutions of 510-nm emitting QD conjugates (at ∼75 nM concentration), rinsed to remove any unbound materials, and subsequently imaged using epifluorescence microscopy. Cells were also counter-stained with DAPI and AF647-transferrin to allow visualization of the nuclei and endosomes, respectively. Figure 3 shows images collected for COS-1 cells incubated with the indicated QD bioconjugates. Each row of panels shows representative DIC, 510-nm emitting QDs (green), YFP (yellow), AF647-TF (red), DAPI (blue), and the merged fluorescent composite images (right). Figure 4 shows only the merged images collected for the HEK cells similarly incubated with the three types of QD bioconjugates. The images collected for both types of cells indicate that in the absence of CPP there is essentially no intracellular uptake of QDs or QD−YFP conjugates during the incubation times used; the weak fluorescence measured in a few of the cells is attributed to nonspecific binding to the cell surfaces. When additional CPP is presented on the QD surface (mixed surface QD−protein−CPP conjugates), a substantial intracellular uptake of conjugates takes place as indicated by the pronounced fluorescence intensity measured for both sets of cells. Furthermore, images collected for both cultures showed that there is a nearly complete overlap between the fluorescence patterns of the QD and YFP; see last column of images in Figure 3 for COS-1 and merged images in Figure 4 for HEK293. Overlap between emissions of the QDs ($\lambda_{em} \sim 510$ nm) and YFP ($\lambda_{em} \sim 530$ nm) results in a small, non-negligible leakage of fluorescence signals between the respective images, as complete spectral separation is not possible with the dichroic filters used (see QD and YFP images in Figure 3). Evaluation of the staining patterns and colocalization with

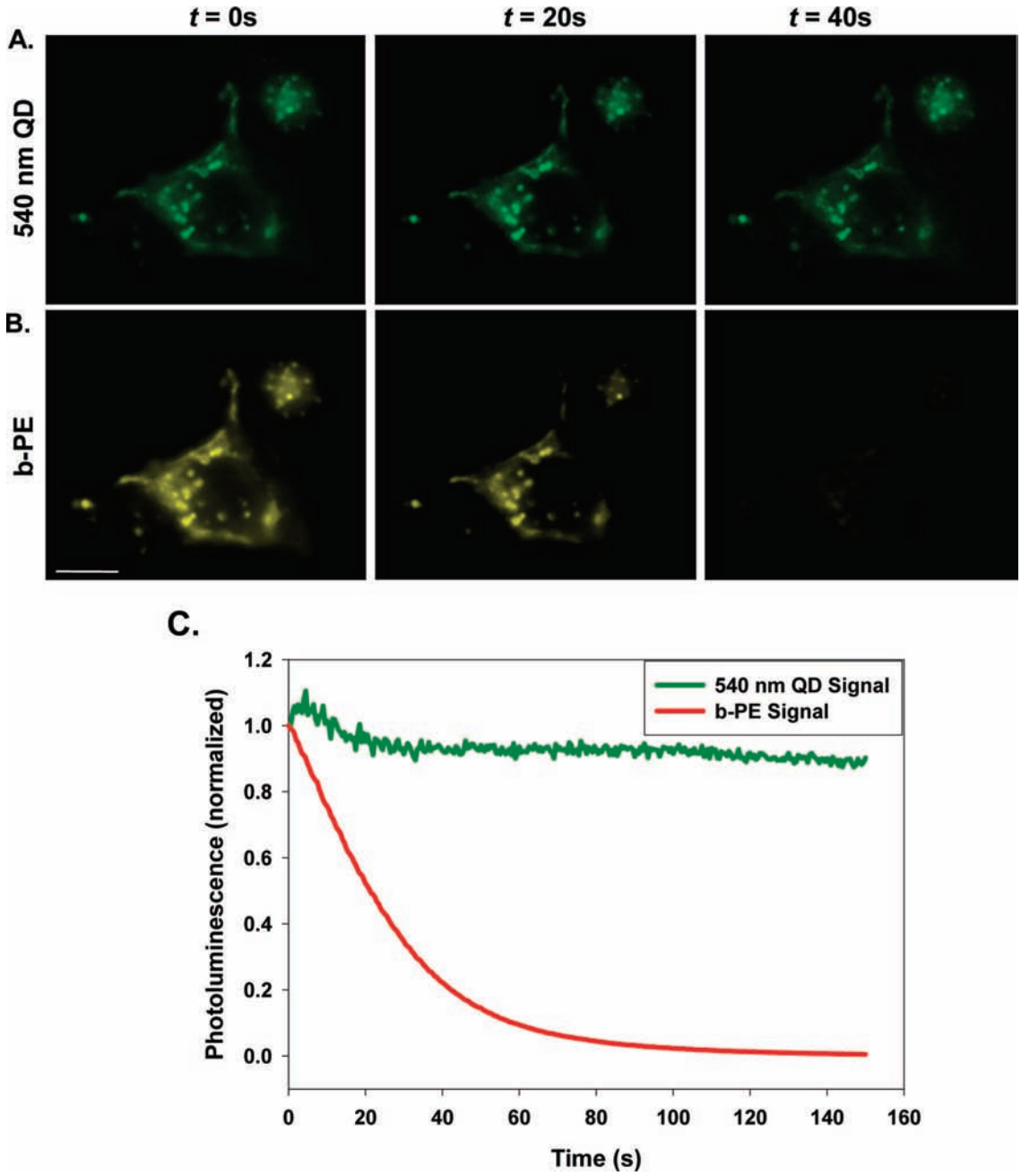

Figure 6. Photobleaching of intracellular QD−b-phycoerythrin conjugates. HEK293/T17 cells incubated with QD−CPP−b-PE conjugates and continuously illuminated with 488 nm laser excitation. (A) 540 nm QD and (B) b-PE fluorescence signals were separated using the Dualview imaging system and monitored over time; images shown were collected at the indicated time intervals. Scale bar is 10 μm. (C) Progression of integrated fluorescence intensity with time collected from the QD and protein emission channels.

the endosome-specific AF647-TF marker indicate that QD−protein/peptide conjugates remain intact after uptake, have a perinuclear distribution, and are predominantly confined within endosomal compartments. The efficient internalization of QD conjugates by both cell lines only in the presence of CPP again demonstrates that CPP facilitates the specific intracellular uptake of QDs surface-functionalized with fluorescent protein cargos and uptake is driven mainly by endocytosis. This result complements and supports our previous findings using QD−CPP conjugates, reported in ref (*25*).

Delivery of QD−b-Phycoerthrin Conjugates. Confident in the ability of CPP to promote the cellular uptake of QD bioconjugates carrying multiple copies of a relatively small protein, we next challenged this delivery mechanism with a far larger protein complex. Streptavidin conjugated b-PE (total estimated Mw ~300 kDa) were attached to DHLA-PEG-biotin-QDs with emission centered at 540 nm and, as done above, three variations of QD conjugates were incubated with HEK293/T17 cells: QD−CPP conjugates (no b-PE), QD−b-PE conjugates (no CPP), and QD−CPP−b-PE assemblies (protein and peptide both present). Average ratios of ~1 and 2.5 b-PE per QD conjugate were used. Each row of images displayed in Figure 5A−C shows representative DIC, 540 nm QD emission (green), b-PE (yellow), AF647-TF (red), DAPI (blue), and merged composite fluorescence images (right) for each of the three QD conjugates tested. Data are shown for QD−b-PE with valence of 1, but similar results were collected for conjugates having 2.5 b-PE per QD conjugate (not shown). As found above with YFP, CPP is the key mediator of cellular uptake. The strong fluorescence of b-PE is a clear reflection of the natural brightness of these proteins. The pattern of staining from the QD, b-PE, and Transferrin-marker channels in cells exposed to the

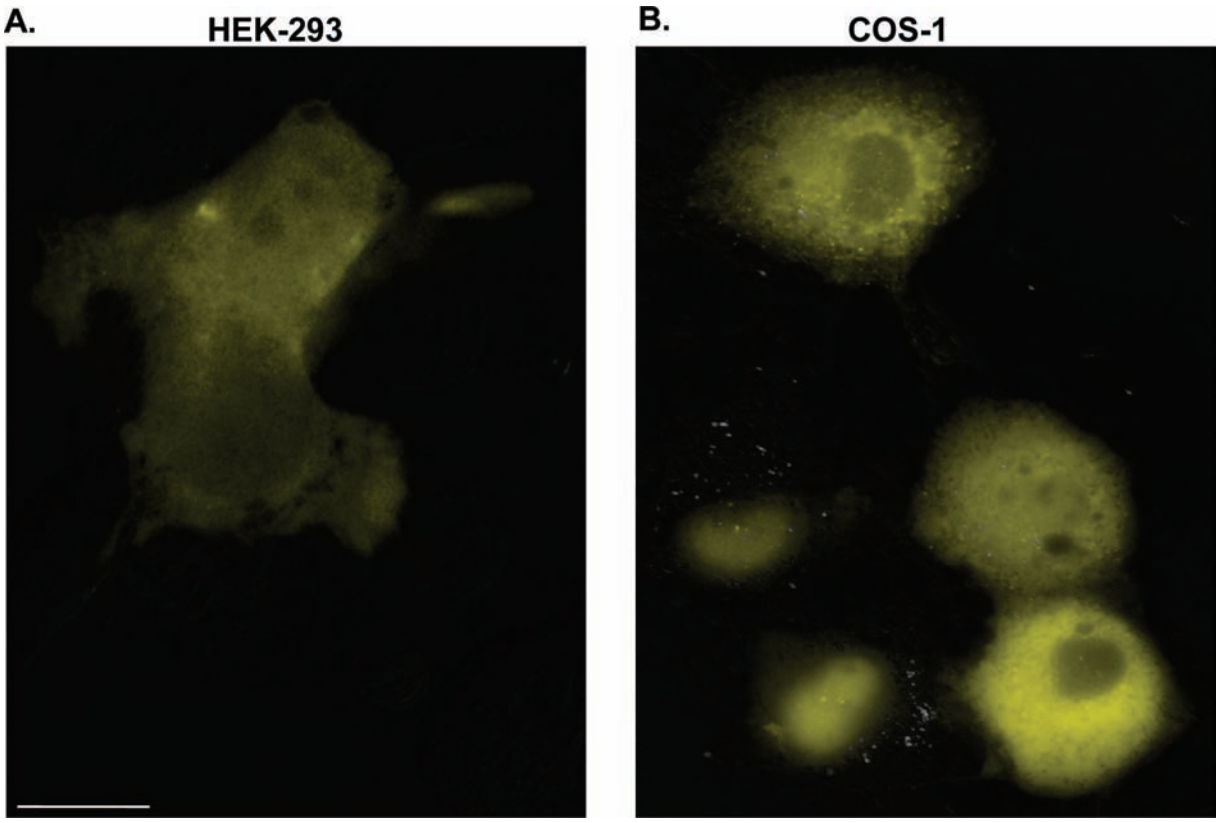

Figure 7. Cellular microinjection. 1:1 540 nm DHLA-PEG-biotin/QD−b-PE conjugates were microinjected directly into the cytosol of HEK293/T17 and COS-1 cells. Representative merged DIC and fluorescence images are shown. Note the clearly distinguishable nuclei in some of the COS-1 cells. Scale bar is 10 μm.

QD−CPP−b-PE assemblies are fully superimposable, which again strongly suggests that the b-PE remains attached to the nanocrystal and primarily localized within the endosomes. Similar results were also obtained with COS-1 cells (data not shown).

One of the unique features of luminescent QDs with direct relevance to biological imaging is their strong resistance to degradation combined with high photobleaching thresholds as compared to conventional dyes (*11, 51*). For example, Wu and co-workers compared the fluorescence decay of AlexaFluor 488 and CdSe-ZnS QDs in fixed 3T3 cells under continuous illumination and found that, while the dye fluorescence is essentially bleached after ~60 s, the QD signal persists for orders of magnitude longer exposure times (*51*). Our QD−YFP and QD−b-PE conjugates stay assembled after uptake and they thus offer an easy side-by-side comparison of QD and fluorescence protein signals for colocalization and stability studies. COS-1 cells incubated with 540 nm QD−CPP−b-PE bioconjugates were continuously excited at 488 nm for extended periods of time and the fluorescence signals of the QD and b-PE were separated using the DualView imaging system equipped with a 565 nm dichroic filter. The representative images shown in Figure 6A,B together with the plot of integrated PL intensities from each channel (Figure 6C) indicate that the b-PE signal decays to ~50% of its initial value in ca. 20 s and to less than 5% within 90 s. In comparison, the QD signal remains essentially unperturbed. The present comparison using fluorescent proteins extends and confirms prior findings on the pronounced QD resistance to photobleaching, using intracellular side-by-side comparisons between QDs and fluorescent dyes (*51*). This result also confirms the intracellular colocalization of the assembled conjugates, as the pattern of the rapidly bleached b-PE fluorescence is completely superimposed over the QD fluorescence pattern. Furthermore, by direct inference this also proves the structural and functional integrity of the QD−fluorescent protein cargos after delivery inside live cells.

DISCUSSION

Our results clearly show that cell-penetrating peptides can mediate the intracellular delivery of QDs conjugated to additional proteins of substantially larger size and molecular weight. This expands our previous results, where CPP was found to facilitate uptake of QD−CPP conjugates by eukaryotic cells (*25*). It also expands the findings by Torchilin and co-workers, where TAT peptide on the surface of liposomes allowed their intracellular delivery, even at low temperature and in the presence of metabolic inhibitors (*52*). In our case, CPP allows the QD−CPP conjugates to function as nanoscale vectors for the intracellular delivery of model fluorescent proteins cargos. Further, the conjugates essentially constitute multifunctional platforms, where the nanocrystals provide a fluorophore for visualization and scaffolds for immobilizing proteins and CPP, two biologically active "receptors" with different functions and spatial extensions. As YFP and b-PE are fluorescent, they also provide an additional means for conjugate visualization, and verification of both colocalization and delivered protein cargo integrity. The successful delivery of QD-CPP-YFP/b-PE conjugates into both HEK-293 and COS-1 cell lines proves that assembling additional larger size proteins on the nanocrystal surface does not interfere with the ability of CPP to mediate intracellular uptake of QD assemblies, a result that is *a priori* unexpected. Our results also show that multiple noncovalent conjugation schemes based on metal affinity self-assembly and biotin−avidin binding can be simultaneously applied within the same complex, without requiring further purification, to produce multifunctional QD bioconjugates that are stable even in intracellular environments. We found that the labeled cells displayed similar viability as that noted in our previous study

where little to no cytotoxicity was noted in cells exposed to QD bioconjugates for short 1 h incubations. We have also followed QD−CPP bioconjugates from 3−7 days following uptake and 1−3 days after microinjection with no apparent cytotoxicity noted (data not shown).

Although fluorescent proteins have become ubiquitous in biological research (*53*), there has not been much work aimed at exploiting hybrid dual fluorescent QD−protein conjugates beyond two preliminary studies investigating resonance energy transfer between QDs and fluorescent proteins (*54*, *55*). Our study shows the potential of such conjugates to explore specific issues such as intracellular delivery and conjugate distribution inside live cells. The ability of the relatively small cell penetrating peptide to facilitate the intracellular delivery of large protein cargos is rather remarkable. Our data suggest that by utilizing an average of ∼10 YFPs plus a nominal 50 CPP per QD, intracellular delivery of protein cargos with molecular weights of at least ∼300 kDa and a spatial extension of ∼150 Å can be achieved; the size estimate takes into account the nanocrystal and protein/peptide dimensions. The delivered cargos for QD−b-PE conjugates have much larger size and molecular weight. For instance, with an average of 2.5 Streptavidin−b-PE per conjugate, the delivered assemblies have a molecular weight that potentially exceeds $\sim 10^3$ kDa and overall dimensions approaching ∼500 Å. Molecular weight and size can increase quite substantially if conjugates with higher b-PE valences are used.

This study also provides further insight into CPP-mediated capabilities and confirms our earlier findings that nanoparticle conjugates taken up via this method are primarily distributed within endolysosomal compartments (*25*). Although CPP-mediated delivery is an efficient method of intracellular delivery and labeling of many different types of cells, a variety of cellular biosensing and translocation assays will ultimately require cytosolic distribution rather than endosomal confinement of the QD conjugates. Some techniques are available for nucleic acid transfection through endosomes; however, consistent and efficient endosomal escape methodologies, especially for functionalized nanoparticles, have yet to be developed (*56*, *57*). As such, cellular microinjection was evaluated as an alternate technique for delivering the QD−FP conjugates. Although a physical technique usually requiring manual operation, cellular microinjection is one of the few methods that can allow direct and consistent access to the cytosol of different cell types (*58*). The same 1:1 540 nm QD−b-PE bioconjugates utilized above, without additional CPP, were microinjected directly into the cytosol of both HEK293/T17 and COS-1 cells. Figure 7 show representative micrographs where the superimposed DIC and fluorescent images demonstrate a well-dispersed conjugate distribution across the entire cytoplasm, as opposed to the more localized and punctuate staining typically observed with CPP-mediated delivery. Though this delivery route is less efficient, since cells must be individually injected, it offers an alternative approach for targeted delivery of controlled cargo materials (such as drugs) directly into the cytoplasm of an array of live cells. This could potentially allow subsequent cellular effects to be intimately studied along with the tracking of other intracellular markers.

In summary, we have shown the remarkable ability of CPP to function as a simple and effective peptidic tool that can facilitate intracellular delivery of luminescent QDs decorated with both small and large protein cargos. Based on the multifunctional architecture demonstrated here, these hybrid nanostructures provide ideal tools for investigating intracellular tracking of proteins, protein−protein interactions, and potentially drug delivery (*2*, *8*, *9*, *59*, *60*). Such multifunctional QD conjugates could allow the evaluation of critical issues such as efficiency of cellular uptake, endosomal escape, intracellular conjugate stability, and intracellular fate through the simultaneous monitoring of QD and fluorescent protein emissions. Other recently described strategies aiming to address these questions necessitated multiple, complex synthetic steps to prepare the probe and rely on multiple metabolic processes and inference for results (*61*). Self-assembly of probes with control over their structures and direct monitoring of fluorescent signals potentially offers a much simpler approach. Including additional functionalities in the QD cargo such as FRET-based sensors (*50*, *62*), for example, could report on cellular physiology and responses to environmental or drug-induced challenges. Furthermore, substituting or simply adding other targeting peptides within the conjugate could also provide the means to evaluate the delivery efficacy of such cargos to particular cellular organelles. Future experiments will focus on studying QD−fluorescent protein FRET interactions intracellularly as a means of monitoring both conjugate fate and integrity over time. Lastly, it is worth noting that it is exactly these types of multifunctional nanoparticle assemblies that are projected to form the basis of next-generation nanomedicine and diagnostics (*1*−*5*, *8*, *9*, *59*, *60*, *63*) and it is clear that semiconductor quantum dots may play an important tole in their development.

ACKNOWLEDGMENT

The authors acknowledge Stephen Lee and Ilya Elashvilli of the CB Directorate/Physical S&T Division (DTRA), ONR, NRL, and the NRL-NSI for financial support. T.P. acknowledges a postdoctoral fellowship from the Fondation pour la Recherche Medicale (France).

LITERATURE CITED

(1) Luccardini, C., Yakovlev, A., Gaillard, S., van't Hoff, M., Alberola, A. P., Mallet, J.-M., Parak, W. J., Feltz, A., and Oheim, M. J. (2007) Getting across the plasma membrane and beyond: Intracellular uses of colloidal semiconductor nanocrystals. *Biomed. Biotechnol.* Article ID 68963.

(2) Ozkan, M. (2004) Quantum dots and other nanoparticles: what can they offer to drug discovery?". *Drug Discovery Today 9*, 1065–1071.

(3) Emerich, D. F., and Thanos, C. G. (2006) The pinpoint promise of nanoparticle-based drug delivery and molecular diagnosis. *Biomol. Eng. 23*, 171–184.

(4) Hilda, W. A., Breuniga, M., and Goepferich, A. (2007) Quantum dots - Nano-sized probes for the exploration of cellular and intracellular targeting. *Eur. J. Pharm. Biopharm. 68*, 153–168.

(5) Sukhorukov, G. B., and Mohwald, H. (2007) Multifunctional cargo systems for biotechnology. *TRENDS Biotechnol. 25*, 93–98.

(6) Medintz, I., Uyeda, H., Goldman, E., and Mattoussi, H. (2005) Quantum dot bioconjugates for imaging, labeling and sensing. *Nat. Mater. 4*, 435–446.

(7) Michalet, X., Pinaud, F. F., Bentolila, L. A., Tsay, J. M., Doose, S., Li, J. J., Sundaresan, G., Wu, A. M., Gambhir, S. S., and Weiss, S. (2005) Quantum dots for live cells, in vivo imaging, and diagnostics. *Science 307*, 538–544.

(8) Azzazy, H. M. E., Mansour, M. M.H., and Kazinierczak, S. C. (2007) From diagnostics to therapy: Prospects of quantum dots. *Clin. Biochem. 40*, 917–927.

(9) Hild, W. A., Breunig, M., and Goepferich, A. (2008) Quantum dots - Nano-sized probes for the exploration of cellular and intracellular targeting. *Eur. J. Pharm. Biopharm. 68*, 153–68.

(10) Pons, T., Uyeda, H. T., Medintz, I. L., and Mattoussi, H. (2006) Hydrodynamic dimensions, electrophoretic mobility and stability of hydrophilic quantum dots. *J. Phys. Chem. B 110*, 20308–20316.

(11) Jaiswal, J. K., Mattoussi, H., Mauro, J. M., and Simon, S. M. (2003) Long-term multiple color imaging of live cells using quantum dot bioconjugates. *Nat. Biotechnol. 21*, 47–51.

(12) Chen, F. Q., and Gerion, D. (2004) Fluorescent CdSe/ZnS nanocrystal-peptide conjugates for long-term, nontoxic imaging and nuclear targeting in living cells. *Nano Lett. 4*, 1827–1832.

(13) Derfus, A. M., Chan, W. C. W., and Bhatia, S. N. (2004) Intracellular delivery of quantum dots for live cell labeling and organelle tracking. *Adv. Mater. 16*, 961–966.

(14) Voura, E., B., Jaiswal, J. K., Mattoussi, H., and Simon S. M. (2004) Tracking early metastatic progression with quantum dots and emission scanning microscopy. *Nat. Med. 10*.

(15) Chan, W. C. W., and Nie, S. (1998) Quantum dot bioconjugates for ultrasensitive nonisotopic Detection. *Science 281*, 2016–2018.

(16) Hoshino, A., Fujioka, K., Oku, T., Nakamura, S., Suga, M., Yamaguchi, Y., Suzuki, K., Yasuhara, M., and Yamamoto, K. (2004) Quantum dots targeted to the assigned organelle in living cells. *Microbiol. Immunol. 48*, 985–994.

(17) Lagerholm, B. C., Weinreb, G. E., Thompson, N. L., and Jacobson, K. (2004) Probing membrane heterogeneity with quantum dots. *Mol. Biol. Cell 15*, 317A.

(18) Rozenzhak, S. M., Kadakia, M. P., Caserta, T. M., Westbrook, T. R., Stone, M. O., and Naik, R. R. (2005) Cellular internalization and targeting of semiconductor quantum dots. *Chem. Commun. 17*, 2217–2219.

(19) Silver, J., and Ou, W. (2005) Photoactivation of quantum dot fluorescence following endocytosis. *Nano Lett. 5*, 1445–1449.

(20) Biju, V., Muraleedharan, D., Nakayama, K., Shinohara, Y., Itoh, T., Baba, Y., and Ishikawa, M. (2007) Quantum dot-insect neuropeptide conjugates for fluorescence imaging, transfection, and nucleus targeting of living cells. *Langmuir 23*, 10254–10261.

(21) Chang, J. C., Su, H. L., and Hsu, S. H. (2007) The use of peptide-delivery to protect human adipose-derived adult stem cells from damage caused by the internalization of quantum dots. *Biomaterials 29*, 925–936.

(22) Lei, Y., Tang, H., Yao, L., Yu, R., Feng, M., and Zou, B. (2008) Applications of mesenchymal stem cells labeled with Tat peptide conjugated quantum dots to cell tracking in mouse body. *Bioconjugate Chem. 19*, 421–427.

(23) Ruan, G., Agrawal, A., Marcus, A. I., and Nie, S. (2007) Imaging and tracking of Tat peptide- conjugated quantum dots in living cells: New insights into nanoparticle uptake, intracellular transport, and vesicle shedding. *J. Am. Chem. Soc. 129*, 14759–14766.

(24) El-Andaloussi, S., Holm, T., and Langel, U. (2005) Cell-penetrating peptides: Mechanisms and applications. *Curr. Pharm. Des. 11*, 3597–3611.

(25) Delehanty, J. B., Medintz, I. L., Pons, T., Brunel, F. M., Dawson, P. E., and Mattoussi, H. (2006) Self-assembled quantum dot-peptide bioconjugates for selective intracellular delivery. *Bioconjugate Chem. 17*, 920–927.

(26) Sapsford, K. E., Pons, T., Medintz, I. L., Higashiya, S., Brunel, F. M., Dawson, P. E., and Mattoussi, H. (2007) Kinetics of metal-affinity driven self-assembly between proteins or peptides and CdSe-ZnS quantum dots. *J. Phys. Chem. C 111*, 11528–11538.

(27) Clapp, A. R., Pons, T., Medintz, I. L., Delehanty, J. B., Melinger, J. S., Tiefenbrunn, T., Dawson, P. E., Fisher, B. R., O'Rourke, B., and Mattoussi, H. (2007) Two-photon excitation of quantum dot-based fluorescence resonance energy transfer and its applications. *Adv. Mater. I19*, 1921–1926.

(28) Murray, C. B., Norris, D. J., and Bawendi, M. G. (1993) Synthesis and characterization of nearly monodisperse CdE (*E* = sulfur, selenium, tellurium) semiconductor nanocrystallites. *J. Am. Chem. Soc. 115*, 8706–15.

(29) Qu, L., Peng, Z. A., and Peng, X. (2001) Alternative routes toward high quality CdSe nanocrystals. *Nano Lett. 1*, 333–337.

(30) Dabbousi, B. O., Rodriguez-Viejo, J., Mikulec, F. V., Heine, J. R., Mattoussi, H., Ober, R., Jensen, K. F., and Bawendi, M. G. (1997) (CdSe)ZnS core-shell quantum dots: synthesis and optical and structural characterization of a size series of highly luminescent materials. *J. Phys. Chem. B 101*, 9463–9475.

(31) Clapp, A. R., Goldman, E. R., and Mattoussi, H. (2006) Capping of CdSe-ZnS quantum dots with DHLA and subsequent conjugation with proteins. *Nat. Protocols 1*, 1258–66.

(32) Mattoussi, H., Mauro, J. M., Goldman, E. R., Anderson, G. P., Sundar, V. C., Mikulec, F. V., and Bawendi, M. G. (2000) Self-assembly of CdSe-ZnS quantum dot bioconjugates using an engineered recombinant protein. *J. Am. Chem. Soc. 122*, 12142–12150.

(33) Uyeda, H. T., Medintz, I. L., Jaiswal, J. K., Simon, S. M., and Mattoussi, H. (2005) Synthesis of compact multidentate ligands to prepare stable hydrophilic quantum dot fluorophores. *J. Am. Chem. Soc. 127*, 3870–3878.

(34) Susumu, K., Uyeda, H. T., Medintz, I. L., Pons, T., Delehanty, J. B., and Mattoussi, H. (2007) Enhancing the stability and biological functionalities of quantum dots via compact multifunctional ligands. *J. Am. Chem. Soc. 129*, 13987–96.

(35) Deuschle, K., Okumoto, S., Fehr, M., Looger, L. L., Kozhukh, L., and Frommer, W. B. (2005) Construction and optimization of a family of genetically encoded metabolite sensors by semirational protein engineering. *Protein Sci. 14*, 2304–2314.

(36) Medintz, I. L., Goldman, E. R., Lassman, M. E., and Mauro, J. M. (2003) A fluorescence resonance energy transfer sensor based on maltose binding protein. *Bioconjugate Chem. 14*, 909–918.

(37) Minaschek, G., Bereiterhahn, J., and Bertholdt, G. (1989) Quantitation of the volume of liquid injected into cells by means of pressure. *Exp. Cell Res. 183*, 434–442.

(38) Tsien, R. Y. (1998) The green fluorescent protein. *Annu. Rev. Biochem. 67*, 509–544.

(39) Nguyen, A. W., and Daugherty, P. S. (2005) Evolutionary optimization of fluorescent proteins for intracellular FRET. *Nat. Biotechnol. 23*, 355–360.

(40) Schmid, J. A., and Neumeier, H. (2005) Evolutions in science triggered by green fluorescent protein (GFP). *ChemBioChem 6*, 1149–1156.

(41) Shaner, N. C., Campbell, R. E., Steinbach, P. A., Giepmans, B. N. G., Palmer, A. E., and Tsien, R. Y. (2004) Improved monomeric red, orange and yellow fluorescent proteins derived from *Discosoma* sp red fluorescent protein. *Nat. Biotechnol. 22*, 1567–1572.

(42) Glazer, A. N. (1985) Light harvesting by phycobilisomes. *Annu. Rev. Biophys. Biophys. Chem. 14*, 47–77.

(43) Glazer, A. N. (1994) Phycobiliproteins - a family of valuable, widely used fluorophores. *J. Appl. Phycol. 6*, 105–112.

(44) Sandros, M. G., Gao, D., and Benson, D. E. (2005) A modular nanoparticle-based system for reagentless small molecule biosensing. *J. Am. Chem. Soc. 127*, 12198–12199.

(45) Ipe, B. I., Shukla, A., Lu, H., Zou, B., Rehage, H., and Niemeyer, C. M. (2006) Dynamic light- scattering analysis of the electrostatic interaction of hexahistidine-tagged cytochrome P450 enzyme with semiconductor quantum dots. *ChemPhysChem 7*, 1112–1118.

(46) Liu, W., Howarth, M., Greytak, A. B., Zheng, Y., Nocera, D. G., Ting, A. Y., and Bawendi, M. G. (2008) Compact biocompatible quantum dots functionalized for cellular imaging. *J. Am. Chem. Soc. 130*, 1274–84.

(47) Hermanson, G. T. (1996) *Bioconjugate Techniques*, Academic Press, San Diego.

(48) Pons, T., Medintz, I. L., Wang, X., English, D. S., and Mattoussi, H. (2006) Solution-phase single quantum dot fluorescence resonant energy transfer sensing. *J. Am. Chem. Soc. 128*, 15324–15331.

(49) Clapp, A. R., Medintz, I. L., Mauro, J. M., Fisher, B. R., Bawendi, M. G., and Mattoussi, H. (2004) Fluorescence resonance energy transfer between quantum dot donors and dye-labeled protein acceptors. *J. Am. Chem. Soc. 126*, 301–310.

(50) Medintz, I. L., Clapp, A. R., Brunel, F. M., Tiefenbrunn, T., Uyeda, H. T., Chang, E. L., Deschamps, J. R., Dawson, P. E.,

and Mattoussi, H. (2006) Proteolytic activity monitored by fluorescence resonance energy transfer through quantum-dot-peptide conjugates. *Nat. Mater. 5*, 581–589.
(51) Wu, X., Liu, H., Liu, J., Haley, K. N., Treadway, J. A., Larson, J. P., Ge, N., Peale, F., and Bruchez, M. P. (2003) Immunofluorescent labeling of cancer marker Her2 and other cellular targets with semiconductor quantum dots. *Nat. Biotechnol. 21*, 41–46.
(52) Torchilin, V. P., Rammohan, R., Weissig, V., and Levchenko, T. S. (2001) TAT peptide on the surface of liposomes affords their efficient intracellular delivery even at low temperature and in the presence of metabolic inhibitors. *Proc. Natl. Acad. Sci. U.S.A. 98*, 8786–8791.
(53) Shaner, N. C., Steinbach, P. A., and Tsien, R. Y. (2005) A guide to choosing fluorescent proteins. *Nat. Methods 2*, 905–909.
(54) Geissbuehler, I., Hovius, R., Martinez, K. L., Adrian, M., Thampi, K. R., and Vogel, H. (2005) Lipid-coated nanocrystals as multifunctionalized luminescent scaffolds for supramolecular biological assemblies. *Angew. Chem., Int. Ed. 44*, 1388–1392.
(55) Hering, V. R., Gibson, G., Schumacher, R. I., Faljoni-Alario, A., and Politi, M. J. (2007) Energy transfer between CdSe/ZnS Core/Shell quantum dots and fluorescent proteins. *Bioconjugate Chem. 18*, 1705–1708.
(56) Yessine, M. A., and Leroux, J. C. (2004) Membrane-destabilizing polyanions:interaction with lipid bilayers and endosomal escape of biomacromolecules. *Adv. Drug Delivery Rev. 56*, 999–1021.
(57) Luo, D. (2005) Nanotechnology and DNA delivery. *MRS Bull. 30*, 654–658.
(58) Petit, A. C., Legue, E., and Nicolas, J. F. (2005) Methods in clonal analysis and applications. *Reprod. Nutr. Dev. 45*, 321–339.
(59) Sukhorukov, G. B., Rogach, A. L., Zebli, B., Liedl, T., Skirtach, A. G., Kohler, K., Antipov, A. A., Gaponik, N., Susha, A. S., Winterhalter, M., and Parak, W. J. (2005) Nanoengineered polymer capsules: Tools for detection, controlled delivery, and site-specific manipulation. *Small 1*, 194–200.
(60) Conti, M., Tazzari, V., Baccini, C., Pertici, G., Serino, L. P., and De Giorgi, U. (2006) Anticancer drug delivery with nanoparticles. *In Vivo 20*, 697–701.
(61) Lee, Y. J., Datta, S., and Pellois, J. P. (2008) Real-time fluorescence detection of protein transduction into live cells. *J. Am. Chem. Soc. 130*, 2398–2399.
(62) Medintz, I. L., Clapp, A. R., Mattoussi, H., Goldman, E. R., Fisher, B., and Mauro, J. M. (2003) Self-assembled nanoscale biosensors based on quantum dot FRET donors. *Nat. Mater. 2*, 630–638.
(63) Bakalova, R., Zhelev, Z., Aoki, I., and Kanno, I. (2007) Designing quantum-dot probes. *Nat. Photon. 1*, 487–489.

BC800089R

closo-Borane Conjugated Regulatory Peptides Retain High Biological Affinity: Synthesis of *closo*-Borane Conjugated Tyr^3-Octreotate Derivatives for BNCT

Thomas Betzel,[§] Tobias Heß,[§] Beatrice Waser,[‡] Jean-C. Reubi,[‡] and Frank Roesch*

Institute of Nuclear Chemistry, University of Mainz, Fritz-Strassmann-Weg 2, 55128 Mainz, Germany. Received April 1, 2008; Revised Manuscript Received July 1, 2008

Despite the improvements in cancer therapy during the past years, high-grade gliomas and many other types of cancer are still extremely resistant to current forms of therapy. Boron neutron capture therapy (BNCT) provides a promising way to destroy cancer cells without damaging healthy tissue. However, BNCT in practice is still limited due to the lack of boron-containing compounds that selectively deliver boron to cancer cells. Since many neuroendocrine tumors show an overexpression of the somatostatin receptor, it was our aim to synthesize compounds that contain a large number of boron atoms and still show high affinity toward this transmembrane receptor. The synthetic peptide Tyr^3-octreotate (TATE) was chosen as a high-affinity and internalizing tumor targeting vector (TTV). Novel boron cluster compounds, containing 10 or 20 boron atoms, were coupled to the N-terminus of TATE. The obtained affinity data demonstrate that the use of a spacer between TATE and the *closo*-borane moiety is the option to avoid a loss of biological affinity of *closo*-borane conjugated TATE. For the first time, it was shown that *closo*-borane conjugated regulatory peptides retain high biological affinity and selectivity toward their transmembrane tumor receptors. The results obtained and the improvement of spacer and boron building block chemistry may stimulate new directions for BNCT.

INTRODUCTION

In 1932, Chadwick (*1*) discovered the neutron (Nobel Prize in Physics in 1935); four years later, Locher (*2*) proposed boron neutron capture therapy (BNCT) as a potential strategy to treat cancer. It is based on the high cross section of ^{10}B (3838 barn) with thermal neutrons and the resulting nuclear processes. This reaction generates two charged particles, an α-particle and a ^{7}Li nucleus, having a range of about 10 μm, which is approximately one cell diameter. If ^{10}B could be accumulated selectively in tumor tissue, which subsequently could be irradiated with thermal neutrons, the nuclear reaction products would specifically damage tumor DNA due to their high linear energy transfer and would finally destroy tumor tissue selectively (cf. Figure 1).

However, there are adequate nontoxic and high-affinity boron-containing tumor targeting vectors (TTV) required, which deliver the necessary amount of boron to tumor cells (*3*). BPA (*p*-borophenylalanine) and BSH (sodium borocaptate), the only BNCT agents approved clinically, have been shown in many cases to exhibit insufficient selectivity and efficiency for BNCT.

In order to design better boron-containing candidates for BNCT, different targeting approaches have been described utilizing various properties of proliferating tumor cells, such as boronated nucleosides and nucleotides (*4, 5*), sugars (*6*), amino acids (*7*−*10*), and cytostatic target components (*11*).

Many neuroendocrine tumors overexpress somatostatin receptors (sst) that represent the molecular basis for the use of radiolabeled somatostatin analogues as tools for diagnostic and therapeutic applications in oncology (*12*). Due to the short plasma stability of the natural peptides somatostatin 14 (SRIF-14) and somatostatin 28 (SRIF-28) of approximately three minutes (*13*), they cannot be used directly as targeting vectors for these transmembrane receptors. The syntheses of octreotides—synthetic octapeptides containing the pharmacophoric part of somatostatin and threoninol at the C-terminus—provided derivatives with extended half-lives while even further increasing the affinity toward the sst. More recently, octreotate derivatives bearing a threonine instead of a threoninol moiety at the C-terminus have been investigated, such as D-Phe^1-c[Cys^2-Tyr^3-D-Trp^4-Lys^5-Thr^6-Cys^7]-Thr^8-OH (TATE). Compared to octreotide analogues, they show higher binding affinity and internalization rate (*14*−*16*).

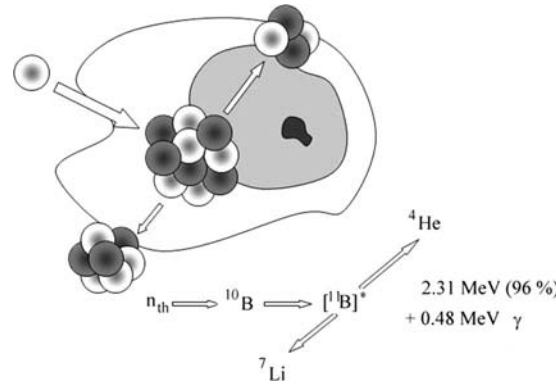

Figure 1. Simplified scheme of the BNCT reaction inside a cell.

Consequently, it was the concept of the present work to synthesize TATE based compounds that carry one, two, or more *closo*-borane units, i.e., a large number of boron atoms. Octreotate was selected as TTV instead of octreotide because its high internalization rate would allow an increased "shuttle"-type delivery of the boronated TTV. In this case, the cellular uptake is not necessarily limited by the initial number of

* Phone (+49)-6131-39-25302, Fax (+49)-6131-39-24692, e-mail: frank.roesch@unimainz.de.

[§] Equally contributing authors.

[‡] University of Bern, Institute of Pathology, Murtenstrasse 31, P.O. Box 62, 3010 Bern, Switzerland.

10.1021/bc800101h CCC: $40.75 © 2008 American Chemical Society
Published on Web 08/20/2008

Scheme 1. Synthesis of Mono- and Di-*closo*-Borane Building Blocks BBB1 and BBB2[a]

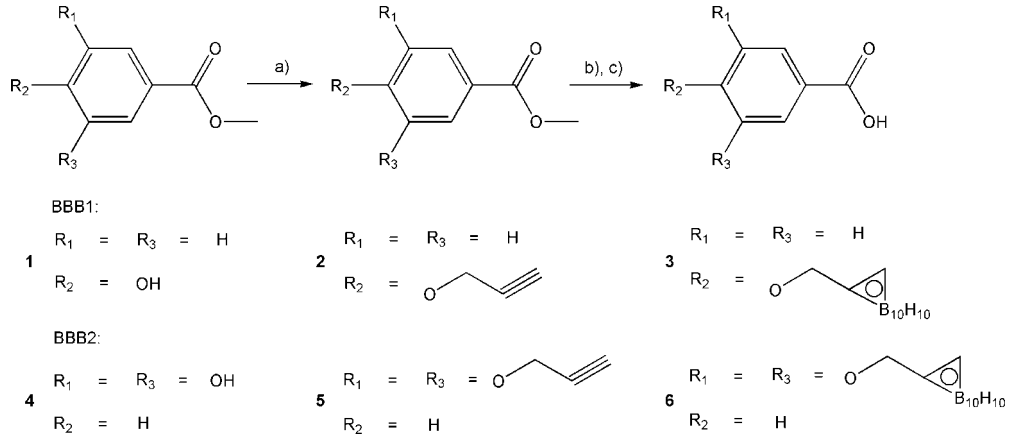

[a] (a) 3-bromopropyne/K_2CO_3, acetone; (b) 1. decaborane, MeCN, 2. methyl prop-2-ynyloxybenzoate, toluene; (c) LiOH, THF/H_2O.

somatostatin receptors expressed at the tumor cell membrane. Syntheses of other octreotate derivatives, coupled with borane clusters, have recently been published; however, affinity studies were not performed (*17*). Prior results on our new compounds with one and two *closo*-boranes directly attached to the N-terminus of the TTV, i.e., TATE-5,6-dicarba-*closo*-dodecaboranyl hexynoic acid (*18*) and TATE-4-amino-bis-(propane-2,3-dicarba-*closo*-dodecaboranyl)-butynoic acid, showed 16 nM and >1000 nM binding affinity to sst_2, respectively. These initial results indicated for the first time that *closo*-borane conjugation to TATE may not annihilate the biological affinity of the peptide, if appropriate coupling chemistry between the borane and the peptide compartments is applied. In contrast, an inadequate design of conjugation may yield new *closo*-borane containing peptides, which are, however, not useful because of a dramatic loss of affinity. This led to the intention of inventing a conjugation chemistry that offers the possibility to obtain a variety of peptide conjugates within a modular system, useful both for octreotides or for any other peptidic TTV. We report the syntheses and characterization of a series of novel *closo*-borane conjugated octreotate derivatives as potential compounds for BNCT. We demonstrate that the introduction of spacers between *closo*-borane cluster(s) and peptide increases receptor binding affinities and leads to nanomolar IC_{50} values for the most relevant subtype sst_2.

EXPERIMENTAL PROCEDURES

Materials and Instrumentation. Wang (*p*-benzyloxybenzyl alcohol) resin, Fmoc, and other amino acids were supplied by Novabiochem (Darmstadt, Germany). All other starting materials and (dehydrated) solvents were purchased from Acros Organics (Geel, Belgium), VWR (Darmstadt, Germany), Fluka, and Sigma-Aldrich (Seelze, Germany) and were used without further purification. Decaborane was purchased from Katchem (Prague, Czech Republic). The silica gel SiO_2 (0.060−0.200 mm) used for column chromatography was purchased from Acros Organics. Thin-layer chromatography was performed using silica gel 60 F_{254} aluminum backed TLC plates, purchased from VWR.

The NMR spectra were taken on a 300 MHz FT-NMR spectrometer, AC 300 (Bruker Analytik GmbH), operating at 300 MHz for ^1H and 75.5 MHz for ^{13}C. ^{11}B-spectra were taken on a 400 MHz FT-NMR spectrometer, DIX 400 (Bruker Analytik GmbH), operating at 128.4 MHz.

The electron spray ionization mass spectra (ESI-MS) were recorded using a QTOF Ultima 3 system (Micromass/Waters). FD mass spectra were recorded using a MAT90 spectrometer (Finnigan). The matrix-assisted laser desorption-ionization time-of-flight mass spectra (MALDI-TOF-MS) were measured on an Axima-CFR (Shimadzu) spectrometer.

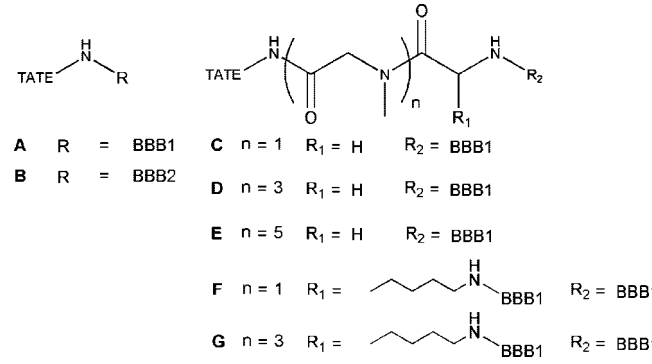

Figure 2. Overview on synthesized compounds.

Purification of the peptides was performed on a semipreparative Dionex HPLC system (P680 HPLC pump) equipped with a UV detector (UVD 170U) using a LiChroCART250 10 HPLC column LiChrosorbRP-select B (10 μ, 250 × 10 mm). The peptides were eluted applying various gradients of 0.1% TFA in 95% H_2O and 5% ACN (solvent A) and 0.1% TFA in 10% H_2O and 90% ACN (solvent B) at different flow rates. All solvent gradient programs are provided in Supporting Information. Effluent was monitored by detection of its optical absorption at 254 and 280 nm.

The synthetic chemistry was divided into three parts: the syntheses of boronated building blocks (BBB) which carry the necessary boron amount, the synthesis of the TTV using solid-phase chemistry including the conjugation with spacer units, and the coupling of various BBBs to the synthesized peptides.

***closo*-Borane Building Block Chemistry.** A hydroxybenzoate backbone was used as a linker molecule, which was conjugated with a triple bond. The introduction of a *closo*-borane cluster was achieved by coupling of decaborane to the triple bond (*19*). Due to promising experiences on the reaction of decaborane-acetonitrile adducts and triple bonds, this synthetic method was chosen for all BBBs. Two compounds, namely, *p*-(*O*-methylencarboranyl)-benzoic acid (BBB1) and 3,5-bis-(*O*-methylencarboranyl)-benzoic acid (BBB2), were synthesized starting from methyl 4-hydroxybenzoate or methyl 3,5-dihydroxybenzoate (cf. Scheme 1). The first step was the introduction of the essential triple bond via nucleophilic substitution with 3-bromopropyne, followed by the coupling with *closo*-borane cluster(s) in up to 70% yield (*20*). The use of equimolar amounts of LiOH in THF/H_2O gave the desired pure boronated benzoic

Table 1. Binding Affinities of the *closo*-Borane Conjugated Octreotates to the hsst Subtypes Expressed As IC_{50} in nM (Mean ± SEM; $n \geq 2$) with SRIF-28 as Reference

compound	boron atoms	$hsst_1$	$hsst_2$	$hsst_3$	$hsst_4$	$hsst_5$
SRIF-28	0	2.3 ± 0.2	2.6 ± 0.3	3.9 ± 0.3	4.0 ± 1.1	3.0 ± 0.3
A	10	>1000	19 ± 1.8	>1000	172 ± 3	975 ± 182
B	20	>1000	>1000	>1000	>1000	>1000
C	10	>1000	2.6 ± 0.2	>1000	82 ± 24	148 ± 30
D	10	>1000	2.6 ± 0.7	62 ± 9.3	33 ± 11	12 ± 2.4
E	10	>1000	1.8 ± 0.3	22 ± 1.2	8.6 ± 2	7.6 ± 1.2
F	20	>1000	415 ± 53	>1000	>1000	>1000
G	20	>1000	20 ± 5.8	89 ± 13	258 ± 33	146 ± 22

acids in yields of up to 92%. The overall yield of this three-step synthesis was up to 43%.

*Methyl-4-prop-2-ynyloxy-benzoate (***1***).* To a solution of methyl 4-hydroxybenzoate (9.12 g, 60 mmol) in acetone (100 mL), K_2CO_3 (11.58 g, 84 mmol) was added and the solution stirred for 30 min at room temperature under argon atmosphere. Propargylbromide (80% in toluene, 12.9 mL, 120 mmol) was added and the reaction mixture kept at 80 °C for 3 h. After cooling to room temperature, most of the solvent was removed in vacuo, and the residue was taken up in water (100 mL) and extracted with ethyl acetate (3 × 70 mL). The combined organic phases were successively washed with 10% NaOH, H_2O, and brine (3 × 75 mL) and dried over Na_2SO_4. The solvent was removed in vacuo and the pure product was obtained as pale yellow crystals (9.70 g, 85%). R_f = 0.75 (petrol ether/ethyl acetate, 2/1). ^{1}H NMR (300 MHz, $CDCl_3$, 298 K) δ: 7.99 (dd, ^3J(H,H) = 8.7 Hz, ^5J(H,H) = 1.2 Hz, 2 H, ArH), 6.98 (dd, ^3J(H,H) = 8.7 Hz, ^5J(H,H) = 1.2 Hz, 2 H, ArH), 4.73 (d, ^4J(H,H) = 2.4 Hz, 2 H, CH_2), 3.87 (s, 3 H, CH_3), 2.53 (tr, ^4J = 2,4 Hz, 1 H, C≡CH). ^{13}C NMR (75.5 MHz, $CDCl_3$, 298 K) δ: 165.90, 161.11, 131.25, 122.64, 114.95, 78.83, 78.75, 55.80, 51.97. MS (FD) *m/z*: calcd for $C_{11}H_{10}O_3$, 190.2; found, 190.3 $(M + H)^+$. Anal. ($C_{11}H_{10}O_3$) C, H.

*Methyl-4-(O-methylencarboranyl)-benzoate (***2***).* Decaborane (2.57 g, 23 mmol) was dissolved in dry acetonitrile (40 mL) and refluxed for 30 min. A solution of compound **1** (3.12 g, 16.5 mmol) in toluene (33 mL) was added to the yellow solution and the mixture was heated to reflux for a further 20 h. Methanol (5 mL) was added carefully, and the resulting mixture was refluxed for 30 min and afterward cooled to room temperature. The solvent was removed in vacuo, the crude product was purified by column chromatography (petrol ether/ethyl acetate, 4/1), and the pure product was obtained as a colorless solid (3.11 g, 61%). R_f = 0.33 (petrol ether/ethyl acetate, 4/1). ^{1}H NMR (300 MHz, $CDCl_3$, 298 K) δ: 7.99 (dd, ^3J(H,H) = 8.7 Hz, ^5J(H,H) = 1.2 Hz, 2 H, ArH), 6.85 (dd, ^3J(H,H) = 8.7 Hz, ^5J(H,H) = 1.2 Hz, 2 H, ArH), 4.45 (s, 2 H, CH_2), 4.05 (s, 1 H, CH), 3.88 (s, 3 H, CH_3), 1.25−3.1 (bm, 10 H, $B_{10}H_{10}$). ^{13}C NMR (75.5 MHz, $CDCl_3$, 298 K) δ: 165.78, 160.87, 131.35, 123.25, 114.98, 73.29, 68.59, 62.00, 52.01. ^{11}B-NMR (128.4 MHz, $CDCl_3$, 298 K) δ: −2.67 (bs, 1B), −4.47 (bs, 1B), −9.03 (bs, 2B), −11.59 (bs), −13.01 (bs, 6B). MS (FD) *m/z*: calcd for $C_{11}H_{20}B_{10}O_3$, 308.4; found, 308.6 $(M + H)^+$. Anal. ($C_{11}H_{20}B_{10}O_3$) C, H.

*4-(O-Methylencarboranyl)-benzoic Acid (***3** = *BBB1).* LiOH (60 mg, 2.5 mmol) was added in 4 portions to a solution of compound **2** (300 mg, 0.97 mmol) in THF/H_2O (36 mL, 2/1). The mixture was stirred for 22 h at room temperature. H_2O (25 mL) was added and most of the THF was removed in vacuo. The aqueous phase was washed with Et_2O (2 × 30 mL), adjusted to pH 2 with 1 M HCl, and extracted with ethyl acetate (3 × 30 mL), and the combined organic phases were dried over Na_2SO_4. Removal of the solvent in vacuo yielded the crude product which was purified by column chromatography (petrol ether/ethyl acetate, 2/1 + 3% formic acid). The pure product was obtained as a colorless solid (0.243 g, 82%). R_f = 0.55 (petrol ether/ethyl acetate, 2/1 + 3% formic acid). ^{1}H NMR (300 MHz, DMSO-d_6, 298 K) δ: 12.75 (s, 1 H, COOH), 7.89 (d, ^3J(H,H) = 9.0 Hz, 2 H, ArH), 7.07 (d, ^3J(H,H) = 9.0 Hz, 2 H, ArH), 5.34 (s, 1 H, CH), 4.69 (s, 2 H, CH_2), 1.25−3.1 (bm, 10 H, $B_{10}H_{10}$). ^{13}C NMR (75.5 MHz, DMSO-d_6, 298 K) δ: 166.89, 160.62, 131.47, 124.42, 114.79, 73.35, 68.60, 61.98. ^{11}B-NMR (128.4 MHz, DMSO-d_6, 298 K) δ: −2.60 (bs, 1B), −4.50 (bs, 1B), −9.12 (bs, 2B), −11.62 (bs), −13.12 (bs, 6B). MS (FD) *m/z*: calcd for $C_{10}H_{18}B_{10}O_3$, 294.4; found, 294.3 $(M + H)^+$. Anal. ($C_{10}H_{18}B_{10}O_3$) C, H.

*Methyl-3,5-bis(prop-2-ynyloxy)-benzoate (***4***).* To a solution of methyl 3,5-dihydroxybenzoate (1.68 g, 10 mmol) in acetone (15 mL), K_2CO_3 (3.86 g, 28 mmol) was added and the solution was stirred for 30 min at room temperature under argon atmosphere. Propargylbromide (80% in toluene, 4.3 mL, 40 mmol) was added and the reaction mixture kept at 80 °C for 3 h. After cooling to room temperature, most of the solvent was removed in vacuo. The residue was taken up in water (50 mL) and extracted with ethyl acetate (3 × 50 mL). The combined organic phases were successively washed with 10% NaOH, H_2O, and brine (3 × 50 mL) and dried over Na_2SO_4. The solvent was removed in vacuo and the pure product was obtained as pale yellow crystals (2.28 g, 93%). R_f = 0.51 (petrol ether/ethyl acetate, 4/1). ^{1}H NMR (300 MHz, $CDCl_3$, 298 K) δ: 7.26 (d, ^4J(H,H) = 2.7 Hz, 2 H, ArH), 6.78 (tr, ^4J(H,H) = 2.7 Hz, ArH), 4.68 (d, ^4J(H,H) = 2.1 Hz, 4 H, CH_2), 3.88 (s, 3 H, CH_3), 2.53 (tr, ^4J(H,H) = 2,1 Hz, 2 H, C≡CH). ^{13}C NMR (75.5 MHz, $CDCl_3$, 298 K) δ: 165.92, 158.82, 158.39, 131.68, 109.97, 107.12, 106.24, 73.45, 68.67, 61.95, 52.33. MS (FD) *m/z*: calcd for $C_{14}H_{12}O_4$, 244.2; found, 244.2 $(M + H)^+$. Anal. ($C_{14}H_{12}O_4$) C, H.

*Methyl-3,5-bis-(O-methylencarboranyl)-benzoate (***5***).* Decaborane (1.57 g, 14 mmol) was dissolved in dry acetonitrile (20 mL) and refluxed for 30 min. A solution of compound **4** (1.22 g, 5 mmol) in toluene (10 mL) was added to the yellow solution and the mixture was heated to reflux for a further 20 h. Methanol (2.5 mL) was added carefully and the resulting mixture was refluxed for 30 min and afterward cooled to room temperature. The solvent was removed in vacuo. The crude product was purified by column chromatography (petrol ether/ethyl acetate, 4/1) and the pure product was obtained as a colorless solid (0.957 g, 40%). R_f = 0.49 (petrol ether/ethyl acetate, 4/1). ^{1}H NMR (300 MHz, DMSO-d_6, 298 K) δ: 7.17 (d, ^4J(H,H) = 1.8 Hz, 2 H, ArH), 6.96 (d, ^4J(H,H) = 1.8 Hz, 1 H, ArH), 5.35 (s, 2 H, CH), 4.67 (s, 4 H, CH_2), 3.84 (s, 3 H, CH_3), 0.8−3.05 (bm, 20 H, $B_{10}H_{10}$). ^{13}C NMR (75.5 MHz, DMSO-d_6, 298 K) δ: 165.49, 158.31, 131.92, 109.21, 106.86, 73.29, 68.84, 61.86, 52.53. ^{11}B-NMR (128.4 MHz, $CDCl_3$, 298 K) δ: −3.47 (bs, 3 B), −9.64 (bs, 6 B), −11.31 to −15.30 (bm, 11 B). MS (FD) *m/z*: calcd for $C_{14}H_{32}B_{20}O_4$, 480.6; found, 480.7 $(M + H)^+$. Anal. ($C_{14}H_{32}B_{20}O_4$) C, H: calcd, 34.99, 6.71; found, 35.66, 6.64.

*3,5-Bis-(O-methylencarboranyl)-benzoic Acid (***6** = *BBB2).* LiOH (38.3 mg, 1.6 mmol) was added in 4 portions to a solution of compound **5** (300 mg, 0.62 mmol) in THF/H_2O (36 mL, 2/1). The mixture was stirred for 22 h at room temperature and the

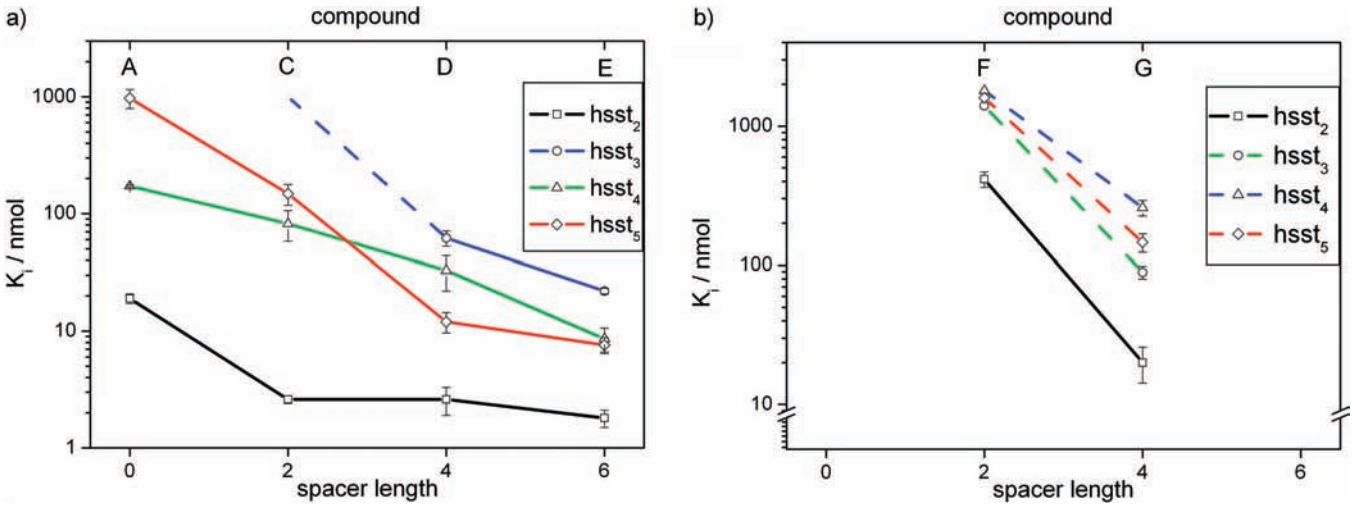

Figure 3. Structure−affinity correlation of (a) mono- and (b) di-*closo*-borane conjugated TATE-derivatives to hsst$_2$-hsst$_5$ subtypes.

solvent was removed in vacuo. Column chromatography (petrol ether/ethyl acetate, 2/1 + 3% formic acid) yielded the pure product as a colorless solid (0.215 g, 74%). R_f = 0.43 (petrol ether/ethyl acetate, 2/1 + 3% formic acid). ^{1}H NMR (300 MHz, DMSO-d_6, 298 K) δ: 7.15 (d, ^4J(H,H) = 2.1 Hz, 2 H, ArH), 6.91 (d, ^4J(H,H) = 2.1 Hz, 1 H, ArH), 5.34 (s, 2 H, CH), 4.66 (s, 4 H, CH_2), 0.8−3.05 (bm, 20 H, $B_{10}H_{10}$). ^{13}C NMR (75.5 MHz, DMSO-d_6, 298 K) δ: 166.56, 158.24, 133.22, 109.30, 106.53, 73.30, 68.81, 61.89. ^{11}B-NMR (128.4 MHz, DMSO-d_6, 298 K) δ: −3.47 (bs, 3 B), −4.47 (bs, 1B), −9.64 (bs, 6B), −11.60 (bs), −15.37 (bm, 11 B). MS (FD) *m/z*: calcd for $C_{13}H_{30}O_4$, 466.6; found, 466.5 $(M + H)^+$. Anal. ($C_{13}H_{30}O_4$) C, H: calcd, 33.46, 6.48; found, 35.25, 6.48.

Peptide Synthesis. The octapeptide TATE was synthesized manually via solid-phase reaction on a Wang resin (loading capacity 0.59 mmol/g) using standard Fmoc-strategy, HOBt/HBTU as coupling reagents, and DMF as solvent. The following N-protected and side chain protected amino acids were used: Fmoc-Thr(tBu)-OH, Fmoc-Cys(Acm)-OH, Fmoc-Lys(Boc)-OH, Fmoc-D-Trp(Boc)-OH, Fmoc-Tyr(tBu)-OH, and Fmoc-D-Phe-OH. Cyclization was achieved with Tl(III)$(CF_3COO)_3$ in DMF.

Different spacer units were coupled successively to the N-terminus of TATE on the solid phase using Fmoc-Sar-OH, Fmoc-Gly-OH, and Fmoc-Lys(Fmoc)-OH.

The following general procedures have been applied to all synthesized compounds unless otherwise noted. All methods are given for batches of 0.1 mmol. After swelling of the resin (*A1*), the Fmoc-group was removed by method *A2*. The amino acids were attached subsequently using coupling procedure *A3*. Cyclization was performed after the addition and Fmoc-deprotection of D-Phe^1 using procedure *A4*. Additional amino acids for the spacer were coupled successively to TATE on the solid phase.

Swelling of the Wang Resin (A1). The N-α-Fmoc-O-tBu-threonine Wang resin (168 mg, 0.1 mmol) was treated with DCM (2 mL) in a 5 mL syringe equipped with a frit and soaked for 3 h using a shaker and washed with DMF (6 × 1 mL).

Deprotecting Procedure (A2). The attached Fmoc-protected amino acids were treated three times successively: 1, 3, and 5 min with piperidine (20% in DMF, 1 mL). After each treatment, the resin was washed three times with DMF (1 mL).

Coupling Procedure (A3). The amino acid (4 equiv) and HOBt-hydrate (4 equiv) were dissolved in DMF (1 mL). HBTU (4 equiv) was added and the resulting solution was kept for 5 min in an ultrasonic bath. Finally, DIPEA (8 equiv) was added to the clear solution. The reaction mixture was vortexed, centrifuged, incubated for 1 min, added to the resin, and shaken for 30 min. After complete reaction, the reaction mixture was removed and the resin was washed with DMF (6 × 1 mL).

Cyclization (A4). Thallium(III)-trifluoroacetate (400 μL, 0.4 M in DMF) was added to the resin and the mixture kept for 1 h on the shaker and washed afterward successively with DMF, CCl_4, DCM, and MeOH.

Cleavage from the Resin (A5). The resin was suspended with the cleavage solution (100 μL/mg resin; 95% TFA, 2.5% H_2O, 2.5% TIS (triisopropylsilane)) and kept for 1.5 h at room temperature. Afterward the mixture was filtered over a glass frit and the remaining solid was washed with TFA (4 mL). The filtrate was evaporated in vacuo to give the crude product.

Coupling. The peptide conjugate was coupled with the boronated linker molecule (4 equiv) using HOBt/HBTU (4 equiv) in DMF as coupling reagents on the solid phase. Reaction time was extended to 4 h. After coupling, the final compounds were cleaved from the resin using TFA/H_2O/TIS (*A5*). Purification and analysis was performed on a semipreparative HPLC system to give the final products as colorless solids. All final compounds were characterized by ESI mass spectrometry. Compounds **A**, **C**, **D**, and **E** were additionally characterized by MALDI-TOF mass spectrometry.

*TATE-(BBB1)$_1$ (***A***).* 4-(*O*-Methylencarboranyl)-benzoic acid (**3**) was attached to TATE on the solid phase using *A3* with 4 h reaction time. The product was cleaved using *A5*. The pure product was obtained by HPLC purification (23.7 mg, 36%). t_R = 11.6 min. MS (MALDI-TOF) *m/z*: calcd for $C_{59}H_{80}B_{10}N_{10}O_{14}S_2$, 1325.6; found, 1326.1 $(M + H)^+$, 1348.5 $(M + Na)^+$. MS (ESI) *m/z*: found, 1326.6 $(M + H)^+$, 1348.5 $(M + Na)^+$, 1364.5 $(M + K)^+$.

*TATE-(BBB2)$_1$ (***B***).* 3,5-Bis-(*O*-methylencarboranyl)-benzoic acid (**6**) was attached to TATE on the solid phase using *A3* with 4 h reaction time. The product was cleaved using *A5*. The pure product was obtained by HPLC purification (6.9 mg, 9%). t_R = 13.2 min. MS (ESI) *m/z*: calcd for $C_{62}H_{92}B_{20}N_{10}O_{15}S_2$, 1497.8; found, 1498.9 $(M + H)^+$, 1520.9 $(M + Na)^+$, 1536.9 $(M + K)^+$.

*TATE-(sarcosine)$_n$-glycine-(BBB1)$_1$ (***C**, **D**, **E***).* The single sarcosine units (4 equiv/unit) and the glycine unit (4 equiv) were attached stepwise to TATE using *A1*−*A3*, the reaction time/unit was 30 min. After attachment of glycine, 4 equiv of compound **3** (59 mg, 0.2 mmol) were coupled to the resulting TATE derivative using *A3* with 4 h reaction time. The products were cleaved by using *A5*.

*TATE-(sarcosine)$_1$-glycine-(BBB1)$_1$ (***C***).* The pure product was obtained by HPLC purification (30.4 mg, 21%). t_R = 11.5 min. MS (MALDI-TOF) *m/z*: calcd for $C_{64}H_{88}B_{10}N_{12}O_{16}S_2$,

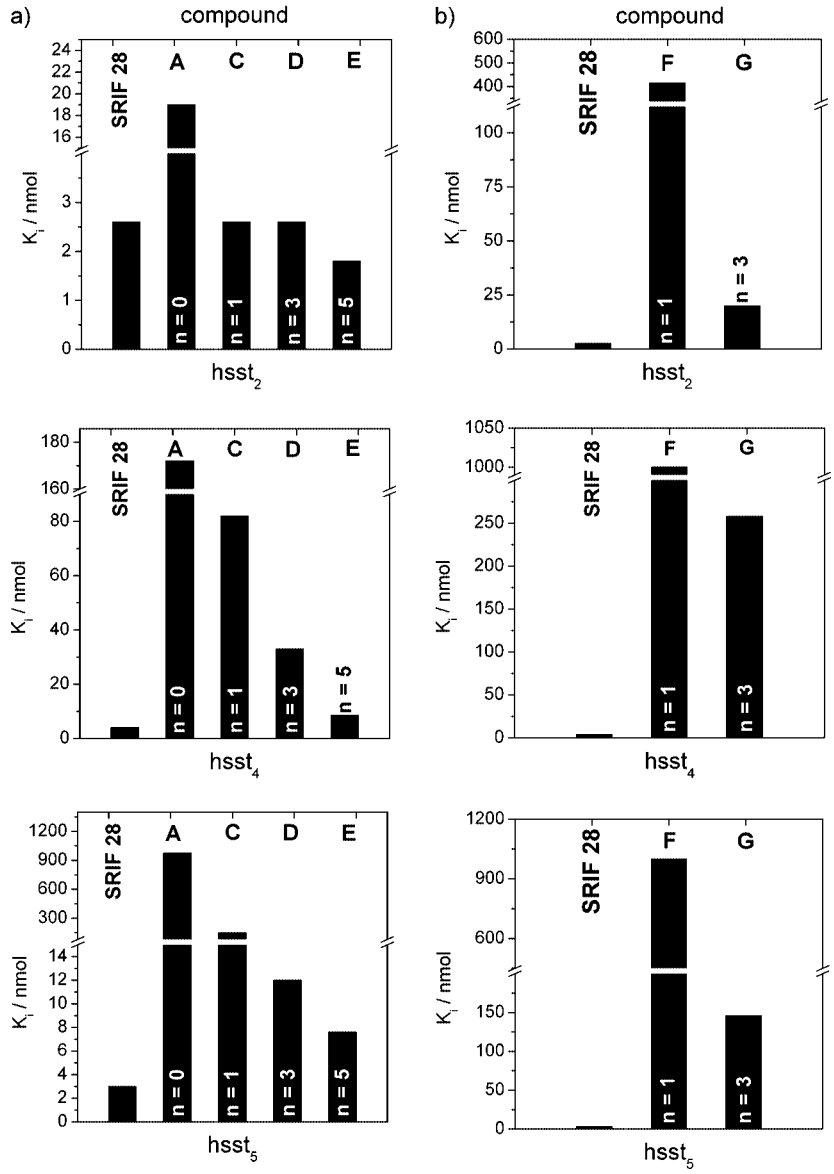

Figure 4. Structure−affinity correlation of compounds with (a) one unit of BBB1 and (b) two units of BBB1 toward $hsst_2$, $hsst_4$, and $hsst_5$.

1453.7; found, 1454.4 $(M + H)^+$, 1476.4 $(M + Na)^+$. MS (ESI) *m/z*: found, 1454.7 $(M + H)^+$, 1476.73 $(M + Na)^+$, 1492 $(M + K)^+$, 738.9 $(M + Na)^{2+}$, 746.9 $(M + K)^{2+}$.

*TATE-(sarcosine)$_3$-glycine-(BBB1)$_1$ (***D***).* The pure product was obtained by HPLC purification (17.5 mg, 22%). $t_R = 11.7$ min. MS (MALDI-TOF) *m/z*: calcd for $C_{70}H_{98}B_{10}N_{14}O_{18}S_2$, 1595.9; found, 1596.1 $(M + H)^+$, 1618.2 $(M + Na)^+$, 1634.2 $(M + K)^+$. MS (ESI) *m/z*: found, 1596.9 $(M + H)^+$, 1618.8 $(M + Na)^+$, 1634.8 $(M + K)^+$, 809.9 $(M + Na)^{2+}$, 817.9 $(M + K)^{2+}$.

*TATE-(sarcosine)$_5$-glycine-(BBB1)$_1$ (***E***).* The pure product was obtained by HPLC purification, (32.5 mg; 18%). $t_R = 11.7$ min. MS (MALDI-TOF) *m/z*: calcd for $C_{76}H_{108}B_{10}N_{16}O_{20}S_2$, 1738.0; found, 1739.4 $(M + H)^+$, 1761.4 $(M + Na)^+$, 1777.4 $(M + K)^+$. MS (ESI) *m/z*: found, 1738.9 $(M + H)^+$, 1760.9 $(M + Na)^+$, 1776.9 $(M + K)^+$, 880.4 $(M + Na)^{2+}$, 888.4 $(M + K)^{2+}$.

*TATE-(sarcosine)$_n$-lysine-(BBB1)$_2$ (***F**, **G***).* The single sarcosine units (4 equiv/unit) and the lysine unit (4 equiv) were attached stepwise to TATE using *A1*−*A3*, the reaction time/unit was 30 min. After attachment of lysine, compound **3** (4 equiv) was coupled to the resulting TATE derivative using *A3* with 4 h reaction time. The products were cleaved by using *A5*.

*TATE-(sarcosine)$_1$-lysine-(BBB1)$_2$ (***F***).* The pure product was obtained by HPLC purification (4.0 mg, 4%). $t_R = 13.6$ min. MS (ESI) *m/z*: calcd for $C_{78}H_{113}B_{20}N_{13}O_{18}S_2$, 1801.1; found, 1802.2 $(M + H)^+$, 1824.2 $(M + Na)^+$, 1840.1 $(M + K)^+$, 912.6 $(M + Na)^{2+}$.

*TATE-(sarcosine)$_3$-lysine-(BBB1)$_2$ (***G***).* The pure product was obtained by HPLC purification (2.7 mg, 3%). $t_R = 14.1$ min. MS (ESI) *m/z*: calcd for $C_{84}H_{123}B_{20}N_{15}O_{20}S_2$, 1943.3; found, 1943.2 $(M + H)^+$, 1966.2 $(M + Na)^+$, 1982.2 $(M + K)^+$, 983.6 $(M + Na)^{2+}$, 995.1 $(M + K)^{2+}$.

Binding Assay. All compounds were tested for their ability to bind to the five human sst receptor subtypes in complete displacement experiments using the universal SRIF radioligand [^{125}I]-[Leu^8, D-Trp^{22}, Tyr^{25}]-SRIF-28. CHO-K1 and CCL39 cells stably expressing the human sst_1−sst_5 receptors were grown as described previously (*14*). Cell membrane pellets were prepared and receptor autoradiography was done as described in detail previously (*14*). SRIF-28 was run in parallel as control. IC_{50} values were calculated after quantification of the data using

a computer-assisted image processing system and are given as a mean of 2 to 3 measurements.

RESULTS

***closo*-Borane Building Block Chemistry.** The first two steps of the reactions shown in Scheme 1 were accomplished in a fast and easy way and gave the desired compounds in high yields. In the final reaction, the methyl ester had to be cleaved. Here, a decomposition of the borane cluster under basic conditions was observed. Common ways of saponification of methyl esters, e.g., NaOH (0.005−5 N) as well as LiI/pyridine, were not successful. However, the use of equimolar amounts of LiOH in a mixture of THF and H_2O resulted in excellent yields. Therefore, this reaction scheme allows a practicable and sufficient synthesis of *closo*-borane conjugated linker molecules, containing 10 or 20 boron atoms.

Peptide Synthesis. The syntheses of the target compounds were performed on the solid phase, including cyclization, conjugation with spacer units, and coupling with linker molecules.

Coupling. In a first experiment, BBB1 was to be coupled to the TTV, which was conjugated with two, four, and six sarcosine units as spacer. In this trial, no coupling of the peptide conjugate and BBB1 was achieved. A possible explanation for this result is the importance of a primary amino group to couple the BBB. This led to the change of the spacer structure. Consequently, the final sarcosine unit was replaced by glycine to give conjugates with one, three, and five sarcosine units, followed by one glycine unit. The coupling of these compounds with the BBB was successful, which demonstrates the requirement of a primary amino function of the final amino acid. Alternatively, lysine was used as final amino acid to provide the possibility to connect two BBBs to one TTV by coupling a boron cluster to the N-terminus and to the ε-amino function in the side chain of lysine. Here, the final target compounds could be isolated as well. Figure 2 summarizes the derivatives synthesized.

Binding Assay. The data of the *in vitro* study prove that appropriate conjugation of TATE with a *closo*-borane compound provides derivatives still retaining biological affinity. Table 1 summarizes the results of the *in vitro* assays on the binding affinity of the derivatives to the five subtypes of the human somatostatin receptor. Furthermore, these data demonstrate a correlation between biological affinity and length of the inserted spacer.

There is almost any affinity if the boronated linker BBB1 or BBB2 is coupled to TATE directly (compound **A** and **B**). Except for sst_1 (there is no affinity toward the sst_1 subtype for almost all the octreotide and octreotate derivatives known in the literature), the affinities improve with an increase of spacer length. Similarly, the affinity increases by the use of spacer units even when two units of BBB1 are coupled to the same TATE molecule. However, a higher number of *closo*-borane clusters attached to the TTV has a negative influence on the affinity of the peptide. These findings are illustrated in Figure 3. Nevertheless, there are three compounds (**C**, **D**, **E**) that show equal or better affinity toward $hsst_2$, the most frequently overexpressed sst (*21*), than endogenous SRIF-28. Therefore, these three boronated compounds are extremely promising candidates for tumor targeting. The impact of the spacer is most obvious for $hsst_4$ for derivatives containing one or two units of BBB1.

DISCUSSION

We established a synthesis route directed to different *closo*-borane linker compounds in high yields, which contain 10 and 20 boron atoms per *closo*-borane building block. Saponification of the methyl esters could be performed by the use of LiOH in THF/water without decomposition of the borane clusters, which is essential for the synthesis of the *closo*-borane building blocks *p*-(*O*-methylencarboranyl)-benzoic acid (BBB1) and 3,5-bis-(*O*-methylencarboranyl)-benzoic acid (BBB2). These BBBs can directly be coupled to the N-terminus of TATE or to the N-terminus of other peptides. Furthermore, the BBB can be coupled to a primary amino function in the side chain of a peptide, e.g., to the ε-amino function of lysine.

Obviously, the introduction of a spacer is necessary to retain the high affinity of the peptidic targeting vector to the receptor. In the case of a directly coupled *closo*-borane building block to the TTV (e.g., compound **B**), the affinity to the somatostatin receptor may be lost completely. In contrast, various spacer units containing sarcosine, glycine, and lysine guarantee retaining affinity. This indicates a structure−affinity relation in a way that with increasing chain length of the spacer unit ($n = 1$, 3, 5 for compounds **C**, **D**, **E**) the affinities of the peptidic targeting vector to the transmembrane tumor receptor are being improved. These relationships of type affinity versus spacer length can be identified both for mono-*closo*-borane (Figure 3a) as well as di-*closo*-borane (Figure 3b) conjugated compounds for the four relevant human somatostatin receptor subtypes 2, 3, 4, and 5. In the case of the human sst_4 and sst_5 subtypes, the binding affinities of compounds **C**, **D**, and **E** successively improve by about 1 order of magnitude. This is graphically illustrated for $hsst_2$, $hsst_4$, and $hsst_5$ in Figure 4.

The affinity data demonstrate that the use of an appropriate spacer is the option to avoid a loss of biological affinity of *closo*-borane conjugated regulatory peptides. In fact, potentially useful affinities have been obtained for mono- and di-*closo*-borane linkers with 10 or 20 boron atoms per building block.

The use of amino acids with a primary amino group, such as glycine or lysine, is essential as final spacer units in the coupling step with the BBB. In the case of the N-methylated amino acid sarcosine, coupling was not successful.

The introduction of lysine as terminal spacer unit, in addition, allows the coupling of two BBBs to one TATE molecule. Even in the case of 20 boron atoms per TATE (cf. compound **G**), the binding affinities of the conjugates are still in the 20 nM range for sst_2. Continuing this concept, compounds with up to 60 boron atoms per peptide may be synthesized in the case of two tri-*closo*-borane building blocks. The approach of introducing one or two mono- or di-*closo*-borane building blocks into various candidates for BNCT by realizing the potential of appropriate spacer units may be directly converted to other relevant regulatory peptides.

There are many modified octreotide derivatives, such as ^{111}In-labeled DTPA-octreotide (OctreoScan), which is used as the gold standard for scintigraphic imaging of neuroendocrine tumors. This compound and alternative octreotide-based radioligands for PET/CT or radionuclide therapy, such as ^{68}Ga-DOTA-TOC and ^{90}Y-DOTA-TOC, show affinities to the somatostatin receptor in the ranges 2.5−22 nM for $hsst_2$ and 57−37 nM for $hsst_5$ (*14*). The best *closo*-borane conjugated TATE derivatives described in this study offer high affinities toward their transmembrane tumor receptor in the ranges 1.8−20 nM for $hsst_2$ and 7.6−146 nM for $hsst_5$. This justifies the assumption that these new *closo*-borane conjugated TATE derivatives could be potentially useful and may stimulate new directions for BNCT.

ACKNOWLEDGMENT

This work was supported by the Deutsche Forschungsgemeinschaft (RO985/22-1). We thank the group of Prof. Dr. H. Frey, especially Dr. E. Berger-Nicoletti, for measuring the MALDI-TOF spectra.

Supporting Information Available: Solvent gradients for HPLC. This material is available free of charge via the Internet at http://pubs.acs.org.

LITERATURE CITED

(1) Chadwick, J. (1932) Possible existence of a neutron. *Nature* 312.

(2) Locher, G. L. (1936) Biological effects and therapeutic possibility of neutrons. *Am. J. Roentgenol. Radium Ther. 36*, 1–13.

(3) Hawthorne, M. F. (1998) New horizons for therapy based on the boron neutron capture reaction. *Mol. Med. Today 4*, 174–181.

(4) Al-Madhoun, A. S., Johnsamuel, J., Barth, R. F., Tjarks, W., and Eriksson, S. (2004) Evaluation of human thymidine kinase 1 substrates as new candidates for boron neutron capture therapy. *Cancer Res. 64*, 6280–6286.

(5) Barth, R. F., Yang, W., Al-Madhoun, A. S., Johnsamuel, J., Byun, Y., Chandra, S., Smith, D. R., Tjarks, W., and Eriksson, S. (2004) Boron-containing nucleosides as potential delivery agents for neutron capture therapy of brain. *Cancer Res. 64*, 6287–6295.

(6) Bertozzi, C. R., and Kiessling, L. L. (2001) Chemical glycobiology. *Science 291*, 2357–2364.

(7) Mishima, Y., Honda, C., Ichihashi, M., Obara, H., Hiratsuka, J., Fukuda, H., Karashima, H., Kobayashi, T., Kanda, K., and Yoshino, K. (1989) Treatment of malignant melanoma by single thermal neutron capture therapy with melanoma-seeking ^{10}B-compound. *Lancet 8659*, 388–389.

(8) Kabalka, G. W., and Yao, M.-L. (2004) Synthesis of 1-amino-3-[(dihydroxyboryl)methyl]-cyclobutanecarboxylic acid as a potential therapy agent. *J. Org. Chem. 69*, 8280–8286.

(9) Kabalka, G. W., Wu, Z. Z., Yao, M.-L., and Natarajan, N. (2004) The syntheses and in vivo biodistribution of novel boronated unnatural amino acids. *Appl. Radiat. Isot. 61*, 1111–1115.

(10) Wyzlic, I. M., and Soloway, A. H. (1992) A general, convenient way to carborane-containing amino acids for boron neutron capture therapy. *Tetrahedr. Lett. 33*, 7489–7490.

(11) Soloway, A. H. (1964) Boron compounds in cancer therapy. *Progress in Cancer Therapy. Volume 1* (McCloskey, A. L., and Steinberg, H., Eds.) pp 203−234, Pergamon Press, New York.

(12) Reubi, J. C. (2003) Peptide receptors as molecular targets for cancer diagnosis and therapy. *Endocr. Rev. 24*, 389–427.

(13) Marks, N., and Stern, F. (1975) Inactivation of somatostatin (GH-RIH) and its analogs by crude and partially purified rat brain extracts. *FEBS Lett. 55*, 220–224.

(14) Reubi, J. C., Schaer, J. C., Waser, B., Wenger, S., Heppeler, A., Schmitt, J. S., and Maecke, H. R. (2000) Affinity profiles for human somatostatin receptor subtypes SST1-SST5 of somatostatin radiotracers selected for scintigraphic and radiotherapeutic use. *Eur. J. Nucl. Med. 27*, 273–282.

(15) de Jong, M., Breeman, B. F., Bakker, W. H., Schaar, M., van Gameren, A., Bugaj, J. E., Erion, J., Schmidt, M., Srinivasan, A., and Krenning, E. P. (2001) [^{177}Lu-DOTA°,Tyr^3]octreotate for somatostatin receptor-targeted radionuclide therapy. *Int. J. Cancer 92*, 628–633.

(16) de Jong, M., Breeman, W. A. P., Bakker, W. H., Kooij, P. P. M., Bernhard, B. F., Hofland, L. J., Visser, T. J., Srinivasan, A., Schmidt, M. A., Erion, J. L., Bugaj, J. E., Mäcke, H. R., and Krenning, E. P. (1998) Comparison of ^{111}In-labeled somatostatin analogues for tumor scintigraphy and radionuclide therapy. *Cancer Res. 58*, 437–441.

(17) Mier, W., Gabel, D., Haberkorn, U., and Eisenhut, M. (2004) Conjugation of the *closo*-borane mercaptoundecahydrododecaborate (BSH) to a tumour selective peptide. *Z. Anorg. Chem. 630*, 1258–1262.

(18) Schirrmacher, E., Schirrmacher, R., Beck, C., Mier, W., Trautmann, N., and Roesch, F. (2003) Synthesis of a Tyr^3-octreotate conjugated *closo*-carborane [$HC_2B_{10}H_{10}$]: a potential compound for boron neutron capture therapy. *Tetrahedr. Lett. 44*, 9143–9145.

(19) Heying, T. L., Jr., Clark, S. L., Mangold, D. J., Goldstein, H. L., Hillman, M., Polak, R. J., and Szymanski, J. W. (1963) A new series of organoboranes. I. Carboranes from the reaction of decaborane with acetylenic compounds. *Inorg. Chem. 2*, 1089–1092.

(20) Tietze, L. F., Bothe, U., Griesbach, U., Nakaichi, M., Hasegawa, T., Nakamura, H., and Yamamoto, Y. (2001) Carboranyl bisglycosides for the treatment of cancer by boron neutron capture therapy. *ChemBioChem 2*, 326–334.

(21) Reubi, J. C., Waser, B., Schaer, J. C., and Laissue, J. A. (2001) Somatostatin receptor sst1-sst5 expression in normal and neoplastic human tissues using receptor autoradiography with subtype-selective ligands. *Eur. J. Nucl. Med. 28*, 836–846.

BC800101H

Supporting Information for

closo-Borane Conjugated Regulatory Peptides Retain High Biological Affinity: Synthesis of *closo*-Borane Conjugated Tyr^3-Octreotate Derivatives for BNCT

Thomas Betzel,[§] Tobias Heß,[§] Beatrice Waser,[‡] Jean-C. Reubi[‡] and Frank Roesch*

Table S1. Semipreparative HPLC gradient systems

TATE-$(BBB1)_1$ (**A**)	time (min)	0	12	15	20	5.0 mL/min
	B (%)	0	80	80	0	
TATE-$(BBB2)_1$ (**B**)	time (min)	0	12	15	20	5.0 mL/min
	B (%)	0	80	80	0	
TATE-$(sarcosine)_1$-glycine-$(BBB1)_1$ (**C**)	time (min)	0	12	15	27	5.0 mL/min
	B (%)	0	80	80	0	
TATE-$(sarcosine)_3$-glycine-$(BBB1)_1$ (**D**)	time (min)	0	12	15	27	5.0 mL/min
	B (%)	0	80	80	0	
TATE-$(sarcosine)_5$-glycin-$(BBB1)_1$ (**E**)	time (min)	0	12	13	25	5.0 mL/min
	B (%)	0	80	80	0	
TATE-$(sarcosine)_1$-lysine-$(BBB1)_2$ (**F**)	time (min)	0	15	22	27	4.5 mL/min
	B (%)	0	80	80	0	
TATE-$(sarcosine)_3$-lysine-$(BBB1)_2$ (**G**)	time (min)	0	15	22	27	4.5 mL/min
	B (%)	0	80	80	0	

Evaluation of the Pharmacokinetic Effects of Various Linking Group Using the ^{111}In-DOTA-X-BBN(7−14)NH_2 Structural Paradigm in a Prostate Cancer Model

Jered C. Garrison,[†] Tammy L. Rold,[†] Gary L. Sieckman,[‡] Farah Naz,[†] Samantha V. Sublett,[‡] Said Daibes Figueroa,[‡,§] Wynn A. Volkert,[§] and Timothy J. Hoffman*[,†,‡,⊥]

Research Services, Harry S. Truman Memorial Veterans' Hospital, 800 Hospital Drive, Columbia, Missouri 65201, Department of Internal Medicine, MA408 Medical Science Building, and Department of Radiology, One Hospital Drive, University of Missouri-Columbia School of Medicine, Columbia, Missouri 65212, and Department of Chemistry, University of Missouri-Columbia, 601 South College Avenue, Columbia, Missouri 65211. Received April 2, 2008; Revised Manuscript Received July 3, 2008

The high incidence of BB2 receptor (BB2r) expression in various cancers has prompted investigators to pursue the development of BB2r-targeted agents for diagnostic imaging, chemotherapy, and radiotherapy. Development of BB2r-targeted agents, based on the bombesin (BBN) peptide, has largely involved the use of the bifunctional chelate approach in which the linking group serves several key roles including pharmacokinetic modification. Understanding the in vivo properties of the various pharmacokinetic modifying linking groups is crucial for developing BB2r-targeted agents with improved targeting and clearance characteristics. The goal of this study was to systematically evaluate the pharmacokinetic profile of aliphatic hydrocarbon, aromatic, and poly(ethylene glycol) (ether) functional groups in order to obtain a better understanding of the in vivo properties of these pharmacokinetic modifiers. Specifically, we synthesized six radioconjugates with the structure ^{111}In-DOTA-**X**-BBN(7−14)NH_2, where **X** = 8-aminooctanoic acid (8-AOC), 5-amino-3-oxapentyl-succinamic acid (5-ADS), 8-amino-3,6-dioxaoctyl-succinamic acid (8-AOS), *p*-aminobenzoic acid (AMBA), Gly-AMBA, and Gly-*p*-aminomethylbenzoic acid (Gly-AM2BA). All of the ^{nat}In-conjugates demonstrated nanomolar binding affinities to the BB2r. In CF-1 mice, the BB2r uptake in the pancreas of radioconjugates containing aromatic linking groups was found to be significantly higher at 1 h postinjection than the radioconjugates with ether linker moieties. For PC-3 tumor-bearing SCID mice, the tumor uptake was found to be 6.66 ± 2.00, 6.21 ± 1.57, 6.36 ± 1.60, 4.46 ± 0.81, and 7.76 ± 1.19 %ID/g for the 8-AOC, 8-ADS, AMBA, Gly-AMBA, and Gly-AM2BA radioconjugates, respectively, at 15 min postinjection. By 24 h postinjection, the radioconjugates containing aromatic groups exhibited the highest percentage tumor retention with 11.4%, 19.8%, 26.6%, 25.8%, and 25.5% relative to the 15 min values remaining in the tumor tissue for the 8-AOC, 8-ADS, AMBA, Gly-AMBA, and Gly-AM2BA radioconjugates, respectively. Fused Micro-SPECT/CT imaging studies performed at 24 h postinjection revealed substantial accumulation of radioactivity in the tumor tissue for all radioconjugates. In both biodistribution and Micro-SPECT/CT imaging studies, the radioconjugates containing aromatic linking groups typically exhibited significantly higher G.I. tract retention than the hydrocarbon or ether linking moieties. In conclusion, our studies indicate that radioconjugates incorporating aromatic linking groups, of the type investigated, generally demonstrated enhanced retention in BB2r expressing tissues in comparison to either the hydrocarbon or ether linking moieties. Furthermore, this investigation clearly demonstrates the significance of the linking group upon not only the in vivo clearance of the radiopharmaceutical, but also on the in vivo uptake and retention of the BB2r-targeted agent in tumor tissue. Future designs of BB2r-targeted agents should include a careful consideration of the effect linking group functionality has upon tumor targeting and retention.

INTRODUCTION

The bombesin family of receptors currently consists of four known receptor subtypes: BB1r[1], neuromedin B receptor; BB2r, gastrin-releasing peptide receptor; BB3r, orphan receptor; and BB4r, bombesin receptor (*1*, *2*). Of these four receptors, three (BB1r, BB2r, and BB3r) have been shown to be expressed in varying degrees in a variety of human tumors and human cancer cell lines (*3*, *4*). For prostate and breast carcinomas, the BB2r subtype has received the most attention from the research community due to the high expression density of the receptor relative to the BB1r and BB3r subtypes (*4*−*6*). In normal human tissues, the pancreas has been shown to have the highest degree of BB2r gene expression with significantly lower levels in the stomach, brain, and adrenal glands (*7*). The low expression of

* To whom correspondence should be addressed. Telephone: (573) 814-6000. Ext. 52593. Fax: (573) 882-1663. E-mail: HoffmanT@health.missouri.edu.

[†] Department of Internal Medicine, MU.

[‡] Research Services; HSTVA.

[§] Department of Radiology, MU.

[⊥] Department of Chemistry, MU.

[1]Abbreviations used: BB1r, Neuromedin B receptor; BB2r, gastrin-releasing peptide receptor; BB3r, orphan receptor; BB4r, Bombesin receptor; DOTA, 1,4,7,10-tetraazacyclododecane-*N*,*N*′,*N*″,*N*‴-tetraacetic acid; BBN, Bombesin peptide; SPECT, single photon emission computed tomography; PET, positron emission tomography; 8-AOC, 8-aminooctanoic acid; 5-ADS, 5-amino-3-oxapentyl-succinamic acid; 8-AOS, 8-amino-3,6-dioxaoctyl-succinamic acid; AMBA, *p*-aminobenzoic acid; Gly-AMBA, glycine-*p*-aminobenzoic acid; Gly-AM2BA, glycine-*p*-aminomethylbenzoic acid; NONSENSE, H-M-G-W-L-A-Q-V-NH_2.

10.1021/bc8001375 CCC: $40.75 © 2008 American Chemical Society
Published on Web 08/20/2008

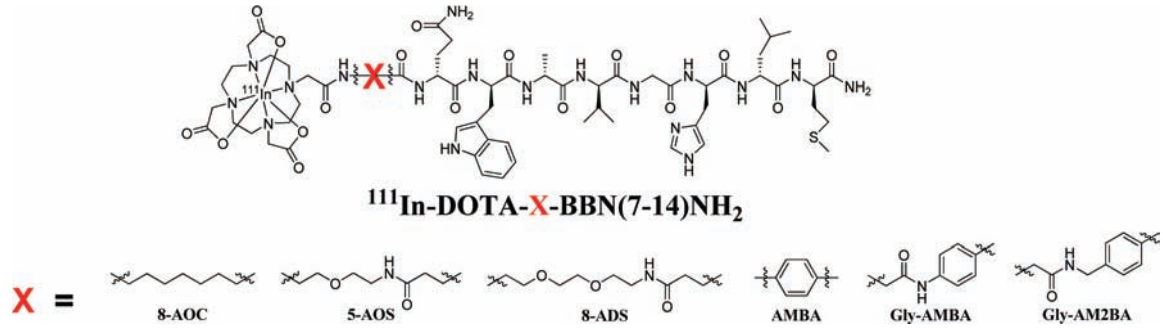

Figure 1. Structure of ^{111}In-Labeled BBN Analogues.

the BB2r in normal tissue relative to the increased expression in many cancers has validated the BB2r as a target for cancer detection and treatment. This has prompted the development of a wide variety of BB2r-targeted diagnostic imaging, chemotherapy, and radiotherapy agents. The majority of these agents have been based on bombesin, a 14 amino acid peptide. The BB2r binding region of the bombesin (BBN) peptide (Trp-Ala-Val-Gly-His-Leu-Met-NH_2, BBN(8−14)NH_2) shares a sequence homology with the gastrin-releasing peptide, the native ligand to the BB2r. Upon binding of the agonist bombesin analogue to the BB2r, the peptide and the attached chemotherapy agent and/or radionuclide are internalized and thereby retained in the cell.

The bifunctional chelate design has primarily been used in the development of BB2r-targeted BBN analogues for nuclear diagnostic imaging and radiotherapy. This approach has four distinctive components: a targeting vector, a radiometal, a chelation system, and a linking group. The choice of targeting vectors for the bombesin analogues have varied from the use of the entire 14 amino acid bombesin peptide to truncated portions of the peptide, with the latter being most prevalent in the literature. In any event, the targeting vector must employ the BBN(8−14)NH_2 or a BB2r-targeted derivative of this amino acid sequence in order to achieve uptake in BB2r expressing tissues. To date, a wide variety of radionuclides (e.g., ^{99m}Tc, ^{188}Re, ^{90}Y, ^{111}In, ^{18}F, ^{64}Cu, ^{177}Lu, ^{149}Pm, ^{68}Ga) have been used in the development of BB2-targeting peptides (*8*−*16*). The selection of the radionuclide for the BB2r-targeted BBN analogue is largely influenced by the desired function of the radiopharmaceutical. Diagnostic nuclear imaging agents employ radionuclides with gamma and positron emission properties that are appropriate for single photon emission computed tomography (SPECT) or positron emission tomography (PET), respectively. For targeted radiotherapy, radionuclides are selected to deliver a maximum radiation dose to the cancerous tissue based on tumor residence time, while at the same time attempting to ensure minimal damage to nontarget tissues (*17*). The chelation system, in general, is responsible for the binding of the radiometal and preventing transchelation throughout the in vivo lifetime of the radiopharmaceutical. The selection of the chelation system is largely dependent on the chemical nature of the radionuclide; however, an assortment of chelation systems (e.g., DOTA, TETA, DTPA) have been shown to be effective in stabilizing a variety of radionuclides in vivo (*8, 18*−*20*).

The linking group serves several crucial roles in the bifunctional chelate design of BB2r-targeted BBN analogues. The most obvious role of the linking group is to chemically connect the radiometal−chelation complex to the bombesin targeting vector. The linking group is also responsible for preventing the radiometal−chelation complex from interfering with the binding of the bombesin targeting vector to the BB2r. Our laboratory has demonstrated, using hydrocarbon-based linking groups, that the length of the linking group being employed directly impacts in vitro and in vivo BB2r targeting (*9*). These studies demonstrated that a linker length of >6 carbon atoms long, which corresponds to ∼6.5 Å, is needed to ensure optimal in vivo binding of the bombesin targeting vector to the BB2r. Finally, the linking group serves as a convenient chemical handle in which to modify the pharmacokinetics of the radiopharmaceutical. By altering the hydrophilic or hydrophobic properties of the linking group, the in vivo properties of the BB2r-targeted BBN analogue can often be tailored without altering the structure of the targeting vector and/or the radiometal−chelation complex, thereby avoiding changes that may have negative impacts on in vivo BB2r binding and/or radiometal-chelate stability.

Targeted diagnostic and radiotherapy agents based on small peptides and antibodies have employed an assortment of natural and non-natural cationic, anionic, and neutral amino acids in constructing the linker framework (*19*). Additionally, metabolically active linking groups based on esters, disulfides, protease active amino acid sequences, and other cleavable functional groups have been explored (*21, 22*). For BB2r-targeted BBN based radiopharmaceuticals, a variety of aliphatic hydrocarbons, amino acids, aromatic derivatives, and poly(ethylene glycol) units have been utilized in the design of linking groups (*1,2,14,23*−*25*). The in vivo effect of these different functional linking groups is challenging to assess because of difficulty in comparing BB2r-targeted BBN analogues that employ different components (i.e., targeting vectors, radionuclides, and chelation systems). In order to systematically determine the pharmacokinetic profile of some commonly used functional groups, we decided to synthesize and evaluate BB2r-targeted BBN analogues containing an aliphatic hydrocarbon, aromatic derivatives, and poly(ethylene glycol) derivatives. Specifically, six radioconjugates were synthesized and evaluated using the ^{111}In-DOTA-**X**-BBN(7−14)NH_2 (Figure 1) structural paradigm where **X** = 8-aminooctanoic acid (8-AOC), 5-amino-3-oxapentyl-succinamic acid (5-ADS), 8-amino-3,6-dioxaoctyl-succinamic acid (8-AOS), *p*-aminobenzoic acid (AMBA), Gly-AMBA, and Gly-*p*-aminomethylbenzoic acid (Gly-AM2BA). The synthesis and in vitro and in vivo evaluation of the radioconjugates in a PC-3 prostate cancer model is presented below.

MATERIALS AND METHODS

Unless otherwise noted, all chemicals and reagents were used as received. Indium-111 was purchased from Mallinckrodt (Maryland Heights, MO). Fmoc-protected natural amino acids, Fmoc-*p*-aminobenzoic acid, Fmoc-*p*-aminomethylbenzoic acid, and Rink Amide resins were purchased from EMD Biosciences Inc. (San Diego, CA). Tris(1,1-dimethylethyl)-1,4,7,10-tetraazacyclododecane-1,4,7,10-tetraacetic acid was purchased from Macrocyclics (Dallas, TX). *N*-(Fmoc-5-amino-3-oxapentyl)-succinamic acid and *N*-(Fmoc-8-amino-3,6-dioxaoctyl)-succinamic acid were purchased from NeoMPS (San Diegeo, CA). Fmoc-8-aminooctanoic acid was purchased from Advanced ChemTech (Louisville, KY). Naturally abundant indium chloride

was purchased from Strem Chemicals Inc. (Newburyport, MA). HPLC grade acetonitrile and trifluoroacetic acid were purchased from Fischer Scientific (Pittsburgh, PA). Deionized water used for HPLC analyses and all other chemical applications in this work was obtained from an in-house Millipore (Billerica, MA) Milli-Q Biocel water purification system. Roswell Park Memorial Institute (RPMI) 1640 media was purchased from Invitrogen/GIBCO (Carlsbad, CA). 4-(2-Hydroxyethyl)-1-piperazineethanesulfonic acid (HEPES) and bovine serum albumin (BSA) were purchased from Fisher Scientific (Fisher Bioreagents, Fisher Chemical, Fairlawn, NJ). [^{125}I-Tyr^4]BN (10 μCi, 370 kBq) was purchased from Perkin-Elmer (Wellesley, MA). Isoflurane was purchased from Baxter Healthcare Corp. (Deerfield, IL).

Solid-phase peptide Synthesis (SPPS) was performed using an Applied Biosystems (Foster City, CA) model 432 automated peptide synthesizer using standard Fmoc chemistry. RP-HPLC purification of the conjugates, ^{nat}In-conjugates, and ^{111}In-radioconjugates was accomplished using a Waters (Milford, MA) 600E controller equipped with an Eppendorf (Westbury, NY) TC-50 column heater. A Phenomenex (Torrance, CA) Jupiter 5u C_{18} 300 Å 250 × 10 mm semiprep column was used for the purification of bulk amounts of peptides. For the purification of conjugates, ^{nat}In-conjugates, and ^{111}In-radioconjugates used for mass spectrometric and in vitro and in vivo studies, a Phenomenex Jupiter 5u C_{18} 300 Å 250 × 4.60 mm analytical column was employed. Detection of the conjugates and ^{nat}In-conjugates during HPLC purification was accomplished using a JASCO (Easton, MD) UV 975 absorbance detector. The radioconjugates were detected during HPLC purification using a JASCO UV 1575 absorbance detector and an ORTEC (Oak Ridge, TN) NaI(Tl) scintillation detector. During the preparation of the radioconjugates, 3 M (St. Paul, MN) Empore high performance extraction disk cartridges 4215(HD) were employed. Mass spectrometric determination of the conjugates and ^{nat}In-conjugates was achieved using electrospray ionization with a Thermo-Finnigan TSQ7000 triple-quadrupole mass spectrometer equipped with an API2 source and performance pack. Gamma decay detection of ^{111}In for the in vitro binding studies was accomplished using the Packard Riastar (Downers Grove, IL) gamma counter. Pharmacokinetic gamma decay measurements were made using a well counter equipped with a NaI(Tl) scintillation detector.

Carworth Farms No. 1 (CF-1) mice were purchased from Charles Rivers Laboratories (Wilmington, MA). Four- to five-week-old Institute of Cancer Research severely combined immunodeficient (ICR SCID) mice were obtained from Taconic Farms (Germantown, NY). The mice were supplied with acidified water and irradiated rodent chow (Ralston Purina Co.) ad libitum. Five mice were housed per cage (Alternative Design) in a humidity- and temperature-controlled room with a 12 h light/dark cycle. The human prostate cancer PC-3 cell line was purchased from the American type Culture Collection (ATCC, Rockville, MD). The PC-3 cell line was grown and maintained by the University of Missouri Cell and Immunobiology Core Facility. PC-3 cells were grown in Custom RPMI Medium 1640 supplemented with 10% fetal bovine serum (FBS) (U.S. BioTechnologies Inc., Pottstown, PA) and Gentamicin (American Pharmaceutical Partners, Inc., Schaumburg, IL). To prepare the cells for inoculation, the PC-3 cells with media were centrifuged, the media decanted, and the cell pellet combined with Dulbecco's phosphate-buffered saline (Invitrogen Corporation, Carlsbad, CA) to reach a concentration of 5 million cells/100 μL. Under gas anesthesia, each SCID mouse was subcutaneously inoculated (bilateral flank) with 5 million PC-3 tumor cells in each flank. Using a nonrebreathing apparatus (Summit Medical Equipment Company, Bend, OR), gas anesthesia was administered at a vaporizer setting of ~3.5% isoflurane (Baxter Healthcare Corp., Deerfield, IL) with ~1 L/min oxygen. The flank tumors were allowed to grow for 2−3 weeks before studies were performed. All studies involving animals were conducted in accordance with protocols approved by both the Harry S. Truman Veterans' Hospital and the University of Missouri − Columbia Institutional Animal Care and Use Committees.

Solid-Phase Peptide Synthesis (SPPS). The conjugates were assembled using automated peptide synthesis. Briefly, the resin (25 μmol of the resin substituted peptide anchors) was deprotected using piperidine, resulting in the formation of a primary amine from which the C-terminus of the growing peptide was anchored. The Fmoc protected amino acids (75 μmol) with appropriate orthogonal protection were activated using HBTU and sequentially added to the resin. The resulting peptide was orthogonally deprotected and cleaved from the resin using a cocktail consisting of a 2:1:1:36 ratio of thioanisol, water, 1,2-ethanedithiol, and trifluoroacetic acid, respectively. The cleaved peptide was then precipitated and washed using cold (0 °C) methyl-*tert*-butyl ether. The crude conjugate was dried by vacuum, weighed, and analyzed by RP-HPLC. Purity of the crude peptides, as determined by RP-HPLC, varied depending on the peptide. The DOTA-8-AOC-BBN(7−14)NH_2, DOTA-8-AOC-NONSENSE, DOTA-5-AOS-BBN(7−14)NH_2, and DOTA-8-ADS-BBN(7−14)NH_2 conjugates ranged from 55% to 76% purity by RP-HPLC. The DOTA-Gly-AM2BA-BBN-(7−14)NH_2 conjugate was synthesized in a modest 47% yield. The DOTA-AMBA-BBN(7−14)NH_2 and DOTA-Gly-AMBA-BBN(7−14)NH_2 conjugates yielded crude products that were found to be 21% and 12%, respectively, by RP-HPLC. For the DOTA-AMBA-BBN(7−14)NH_2, DOTA-Gly-AMBA-BBN(7−14)NH_2, and DOTA-Gly-AM2BA-BBN(7−14)NH_2 conjugates, these peptides were purified using semipreparative RP-HPLC before studies were performed. All conjugates were peak purified to ≥93% purity and quantified by analytical RP-HPLC prior to mass spectrometric determination and in vitro cell binding assays. Confirmation of the constitution of the desired conjugates was provided by mass spectrometry.

Syntheses of ^{nat}In Conjugates. A 1 mg sample of the conjugate was dissolved in 500 μL of a 0.1 M ammonium acetate, 1.82 mM indium trichloride solution (pH = 5.5). The solution was heated at 60 °C for 30 min. In order to achieve sufficient separation (~2 min) of the ^{111}In-labeled conjugate from the unlabeled conjugate, solid $^{nat}CuSO_4 \cdot 5H_2O$ was added to the solution. The solution was heated for 5 min at 65 °C and allowed to cool to room temperature. ^{nat}In-conjugates were then peak purified and quantified by RP-HPLC. All ^{nat}In-conjugates were determined to be ≥93% pure by RP-HPLC analyses before mass spectrometric characterization and in vitro binding studies were performed.

Radiolabeling of Conjugates with $^{111}InCl_3$. A 100 μg sample of the conjugate and ~20 mg of L-ascorbic acid (radiolysis prevention reagent) was dissolved in 200 μL of a 0.4 M ammonium acetate (pH = 7.0) solution. An aliquot of $^{111}InCl_3$ (18.5−92.5 MBq) was added to the vial containing the conjugate and the solution was heated for 30−40 min at 65−75 °C. In order to achieve adequate peak separation (~2 min), solid $^{nat}CuSO_4 \cdot 5H_2O$ was added to the solution. The solution was heated for 5 min at 65 °C and allowed to cool to room temperature. The resulting ^{111}In-radioconjugate was peak purified using reverse-phase HPLC. The peak purified ^{111}In-radioconjugate was concentrated using a prepared C_{18} extraction disk and eluted with 400 μL of a 6:4 ethanol/sterile saline solution. For pharmacokinetic studies, the purified ^{111}In-radioconjugates were diluted with sterile saline to 185 kBq/100 μL. The purification of the radioconjugate and the use of carrier-free ^{111}In yielded the purified ^{111}In-radioconjugates with a specific activity on the order of the theoretical maximum

(Theo. Max: 1722 GBq/μmol). Preclinical SPECT imaging studies required 27.8−55.5 MBq/mouse necessitating the evaporation of the ethanol from the ethanic ^{111}In-radioconjugate solution under a stream of nitrogen and dilution to the appropriate volume with sterile saline solution. In all cases, the concentration of ethanol in solution was <8% by volume prior to administration. Overall radiochemical yields typically ranged from 35% to 89%. The radiochemical purity of all ^{111}In-radioconjugates for pharmacokinetic and imaging studies were reassessed prior to administration and found to be ≥93% pure.

HPLC Purification and Analyses. When necessary, bulk sample purification was performed using a semipreparative C_{18} column with a flow rate of 5.0 mL/min. Sample purification for mass spectrometric, in vitro, and in vivo studies was performed on an analytical C_{18} column with a flow rate of 1.5 mL/min. For all HPLC experiments, the mobile phase consisted of solvent A (99.9% H_2O and 0.1% TFA) and solvent B (99.9% CH_3CN and 0.1% TFA). For all conjugates, ^{nat}In-conjugates and ^{111}In-radioconjugates, the gradient was initiated at 80% A/20% B and over a period of 15 min linearly decreased to a gradient of 70% A/30% B. At the end of the 15 min run time for all HPLC experiments, the column was flushed with the gradient 5% A/95% B and re-equilibrated at the starting gradient.

In Vitro Competitive Cell Binding Studies. IC_{50} binding studies for all conjugates and ^{nat}In-conjugates were performed using PC-3 human prostate cancer cells. ^{nat}In-conjugates were used to determine the specific binding affinities for the corresponding ^{111}In-radioconjugates. Cell media consisted of Roswell Park Memorial Institute (RPMI) medium at pH 7.4, 4.8 mg/mL HEPES, and 2 mg/mL BSA. For binding assays, the cells ($\sim 3 \times 10^4$ PC-3 cells) were suspended in media and incubated at 37 °C for 40 min in the presence of radiolabeled [^{125}I-Tyr^4]BN, a known BB2r agonist, and a range of molar concentrations (10^{-6}−10^{-12} M) of the conjugate or ^{nat}In-conjugate. At the end of the incubation period, the cells were aspirated and washed 4× with media. The cell-associated activity was measured and the binding affinity determined.

In Vitro Internalization and Efflux Assays. Internalization and efflux studies were performed by incubating 3×10^4 PC-3 human cancer cells in cell media. The cell media consisted of RPMI medium with 2 mg/mL BSA and 2.8 mg/mL HEPES at a pH of 7.4. For the internalization studies, the cells were incubated at 37 °C with 20 000 cpm of the desired ^{111}In-radioconjugate in the presence of 5% CO_2 for 15, 30, 45, 60, 90, and 120 min time points. At the end of the time point, binding was halted by aspiration of the cell medium and washing of the cells (3×) with ice−cold cell culture medium. Surface-bound radioactivity was removed from the cellular membrane surface by addition of ice−cold pH 2.5 saline buffer (0.2 M acetic acid and 0.5 M NaCl). The cells were vortexed and incubated in the medium for 5 min, followed by the removal of the radioactivity in the supernatant by aspiration and washing the cells (2×) with pH 2.5 saline buffer. The radioactivity as a function of time was determined for the supernatant and the cells, which yielded the percent radioactivity surface-bound and internalized, respectively.

Efflux assays were performed by incubating the PC-3 cells with the desired ^{111}In-radioconjugate for 45 min. After this time, the cellular medium was aspirated and washed with 37 °C cell medium (3×). At 15, 30, 45, 60, and 90 min time points postincubation, samples of the incubated cellular medium were collected and the cellular media was aspirated and washed with ice−cold culture medium. This was followed by aspiration and washing of the cells with ice−cold pH 2.5 saline buffer. The radioactivity as a function of time was determined for the supernatant and the cells, which yielded the percent radioactivity effluxed from the cell and the percent remaining internalized, respectively.

Pharmacokinetic Studies of ^{111}In-Radioconjugates in normal CF-1 and PC-3 Xenograft SCID Mice. Pharmacokinetic studies were carried out using age-matched normal CF-1 and PC-3 tumor bearing SCID mice. For pharmacokinetic studies involving PC-3 xenograft SCID mice, the mice were inoculated with PC-3 cells, and the tumors, ranging from 0.1 to 1.0 g (2−3 weeks post-inoculation), were allowed to develop before the mice were utilized in pharmacokinetic studies. Each mouse (average weight, 25 g) received an intravenous bolus via the tail vein of 185 kBq of the radio-RP-HPLC peak purified ^{111}In-radioconjugate in 100 μL of saline. The mice were sacrificed and their tissues and organs excised at 0.25, 1, 4, and 24 h time points postinjection. The excised tissues were weighed, the ^{111}In activity in each tissue was measured, and the %ID and %ID/g were determined for each tissue. Whole blood %ID and %ID/g were determined under the assumption that the weight of the blood accounted for 6.5% of the body weight of the mouse.

Small Animal SPECT/CT Imaging Studies. The Micro-SPECT/CT is a combined modality unit (microCAT II, Siemens Medical Solutions) equipped with dual pixelated SPECT detectors each coupled to a square 3 × 3 array of position sensitive photomultiplier tubes. The CT component consists of a CCD X-ray detector and an 80 kVp microfocus X-ray source (40 μm focal spot). The mice were administered 27.8−55.5 MBq of the desired BB2r-targeted peptide in 150−200 μL of saline via tail vein injection. At 24 h postinjection, the mice were sacrificed and Micro-SPECT/CT imaging was performed. Micro-SPECT data were collected using a symmetrical 20% photopeak discriminating window and employing a 360° rotation, 60 step acquisition with a 2 mm pinhole collimator. Pinhole tomographic reconstruction of the generated Micro-SPECT data was performed using a 3D-OSEM algorithm with software corrections applied for pinhole misalignments. Micro-CT data acquisition proceeded immediately prior to Micro-SPECT data acquisition. Concurrent image reconstruction was achieved using a Fanbeam (Feldkamp) filtered back projection algorithm. Micro-SPECT data were fused with anatomical data from Micro-CT in order to accurately determine spatial location of radionuclide uptake within the three-dimensional volume. Whole body and axial images were normalized to the highest-intensity pixel for each image.

Statistical Analysis. A Student's *t* test was utilized to determine statistical significance. A confidence level of 95% was employed in the statistical analysis of this data and $P \leq 0.05$ was considered statistically significant.

RESULTS

Conjugate Synthesis and Radiolabeling. The conjugates were synthesized using standard solid-phase peptide synthesis techniques. Typical yields for the 8-AOC, 5-AOS, 8-ADS, and Gly-AM2BA peptide conjugates ranged from 47% to 76% as determined by RP-HPLC. Relatively poor yields (12−21%) were obtained from the AMBA and Gly-AMBA conjugates. Analysis of the crude product for the AMBA and Gly-AMBA conjugates by RP-HPLC and mass spectrometry revealed that a significant portion of the growing peptides had prematurely terminated. In the syntheses of both the AMBA and Gly-AMBA peptides, ∼45% of the crude material was attributed to the AMBA-Gln-Trp-Ala-Val-Gly-His-Leu-Met-NH_2 peptide ($[M + H]^+_{calc} = 1059.5$; $[M + H]^+_{obs} = 1059.5$). Attempts to increase the overall yield of the AMBA and Gly-AMBA conjugates by extending the coupling time and increasing the amount of the amino acids used per coupling cycle were unsuccessful. Mass spectrometric characterization of all conjugates is provided in Table 1.

Table 1. Mass Spectrometric Values, HPLC Retention Times, and IC_{50} Concentrations for the Conjugates Investigated

analogue	molecular formula	MS calculated	MS observed	RP-HPLC t_r (min)[b]	IC_{50} (nM)[c]
DOTA-8-AOC-NONSENSE[a]	$C_{67}H_{106}N_{18}O_{17}S$	1467.8	1468.0	16.4	>10,000
DOTA-8-AOC-BBN(7−14)NH_2	$C_{67}H_{106}N_{18}O_{17}S$	1467.8	1468.0	13.6	—
DOTA-5-AOS-BBN(7−14)NH_2	$C_{67}H_{105}N_{19}O_{19}S$	1512.8	1512.8	11.3	5.3 ± 0.7
DOTA-8-ADS-BBN(7−14)NH_2	$C_{69}H_{109}N_{19}O_{20}S$	1556.8	1556.8	11.3	11 ± 1
DOTA-AMBA-BBN(7−14)NH_2	$C_{66}H_{96}N_{18}O_{17}S$	1445.7	1445.7	13.2	3.3 ± 0.5
DOTA-Gly-AMBA-BBN(7−14)NH_2	$C_{68}H_{99}N_{19}O_{18}S$	1502.7	1502.7	12.5	2.4 ± 0.2
DOTA-AM2BA-BBN(7−14)NH_2	$C_{69}H_{101}N_{19}O_{18}S$	1516.7	1516.5	13.2	1.4 ± 0.2
In-DOTA-8-AOC-NONSENSE[a]	$C_{67}H_{103}N_{18}O_{17}SIn$	1579.6	1579.9	17.0	>10,000
In-DOTA-8-AOC-BBN(7−14)NH_2	$C_{67}H_{103}N_{18}O_{17}SIn$	1579.6	1579.7	13.5	0.51 ± 0.05
In-DOTA-5-AOS-BBN(7−14)NH_2	$C_{67}H_{102}N_{19}O_{19}SIn$	1624.6	1624.4	10.8	6.2 ± 0.3
In-DOTA-8-ADS-BBN(7−14)NH_2	$C_{69}H_{106}N_{19}O_{20}SIn$	1668.7	1668.7	11.6	3.2 ± 0.3
In-DOTA-AMBA-BBN(7−14)NH_2	$C_{66}H_{93}N_{18}O_{17}SIn$	1557.6	1557.6	12.6	1.13 ± 0.07
In-DOTA-Gly-AMBA-BBN(7−14)NH_2	$C_{68}H_{96}N_{19}O_{18}SIn$	1614.6	1614.4	12.2	1.88 ± 0.06
In-DOTA-Gly-AM2BA-BBN(7−14)NH_2	$C_{69}H_{98}N_{19}O_{18}SIn$	1628.6	1628.8	13.0	0.7 ± 0.1

[a] Non-Sense peptide sequence: H-M-G-W-L-A-Q-V-NH_2. [b] RP-HPLC methods described in Materials and Methods section. [c] In vitro binding assays were performed in triplicate.

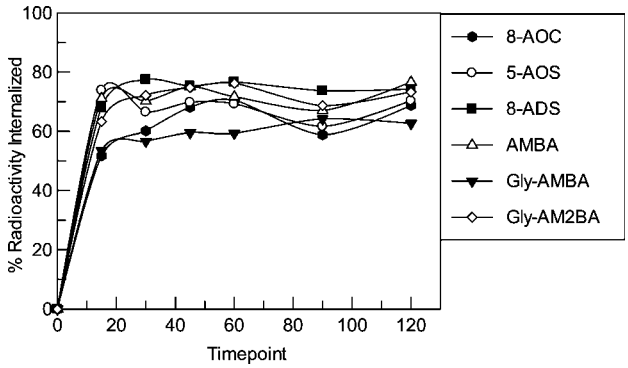

Figure 2. Internalization assays in PC-3 cells using the ^{111}In-BBN radioconjugates ($n = 4$ for each radioconjugate).

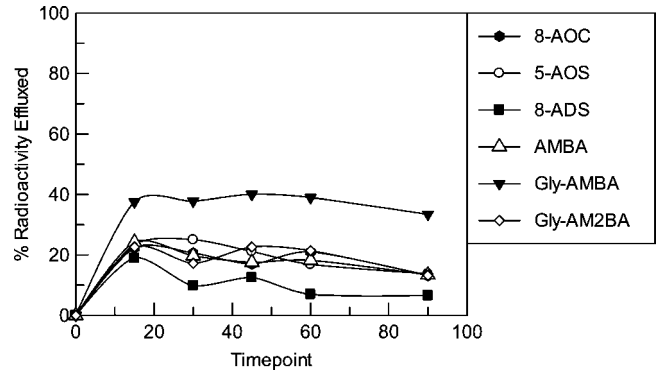

Figure 3. Efflux assays in PC-3 cells using the ^{111}In-BBN radioconjugates ($n = 4$ for each radioconjugate).

Labeling and purification of the conjugates with ^{nat}In and ^{111}In were carried out under similar conditions. Retention times for all conjugates and $^{nat/111}$In-conjugates are given in Table 1. The retention times of the unlabeled conjugates and $^{nat/111}$In-conjugates were similar (<1 min separation) and therefore were difficult to resolve due to peak overlap. Addition of excess $^{nat}CuSO_4 \cdot 5H_2O$ to the reaction vial after incubation of the peptide with $^{nat/111}$In resulted in complexation of the ^{nat}Cu with any available unlabeled conjugate. The ^{nat}Cu-conjugates typically had retention times that were ∼2 min longer relative to the $^{nat/111}$In-labeled conjugate. This allowed the $^{nat/111}$In-conjugate to be easily isolated without concern of collection overlap with the unlabeled conjugate.

In Vitro Cell Binding and Internalization Studies. The BB2r binding affinity of the conjugates and ^{nat}In-conjugates was investigated using in vitro PC-3 cell binding studies (Table 1). The scrambled peptide ^{111}In-DOTA-8-AOC-NONSENSE underwent in vitro and in vivo studies to assist in contrasting specific vs nonspecific binding. With the exception of the scrambled peptide, all of the conjugates and ^{nat}In-conjugates demonstrated nanomolar binding affinities with minimal (<10%) nonspecific binding. The ^{nat}In-labeled conjugates had IC_{50} values of 0.51 ± 0.05, 0.7 ± 0.1, 1.13 ± 0.07, 1.88 ± 0.06, 3.2 ± 0.3, and 6.2 ± 0.3 nM for the 8-AOC, Gly-AM2BA, AMBA, Gly-AMBA, 8-ADS, and 5-AOS, respectively. In general, the ^{nat}In-conjugates containing aromatic linking groups possessed higher binding affinities for the BB2r than ^{nat}In-conjugates with ether linking groups.

Internalization and efflux of the radioconjugates in PC-3 cells are depicted in Figures 2 and 3, respectively. At 15 min postincubation, the 8-AOC and Gly-AMBA radioconjugates demonstrated on average the lowest initial percent internalization. The radioconjugates demonstrated little, if any, increase in internalization after the initial 15 min incubation time point. With the exception of the Gly-AMBA radioconjugate, the radioconjugates demonstrated similar efflux of activity from the PC-3 cells. The Gly-AMBA radioconjugate exhibited an approximate 2-fold increase in efflux of the radioactivity from the cell relative to the other radioconjugates.

Biodistribution Studies. With the exception of the 8-AOC radioconjugate, the in vivo pharmacokinetic properties of the ^{111}In-radioconjugates were initially investigated in normal CF-1 mice. We have previously reported the pharmacokinetic profile of the ^{111}In-DOTA-8-AOC-BBN(7−14)NH_2 radioconjugate in normal CF-1 mice (*9*). Results from the in vivo pharmacokinetic studies in normal CF-1 mice at the 1 h p.i. time point are summarized in Table 2 (*26*). All of the investigated ^{111}In-radioconjugates demonstrated efficient blood clearance at 1 h postinjection. Biological clearance of all radioconjugates proceeded primarily through the renal/urinary system with the remaining radioactivity being secreted through the hepatobiliary pathway. At 1 h postinjection, the kidney retention of the radioconjugates was significantly higher ($P \leq 0.0003$) for the Gly-AMBA (10.60 ± 1.57%ID/g) and Gly-AM2BA (5.60 ± 2.12%ID/g) than the other derivatives (2.40 ± 0.40 to 2.51 ± 0.51). Interestingly, though, the Gly-AMBA and Gly-AM2BA radioconjugates demonstrated the highest clearance of kidney-associated activity over time with 0.70 ± 0.08 and 0.67 ± 0.08, respectively, at the 24 h p.i. time point. Even though the 5-AOS, 8-ADS, and AMBA radioconjugates had significantly less kidney-associated activity at 1 h postinjection, these radioconjugates did not clear as well with 1.29 ± 0.20, 1.30 ± 0.32, and 1.19 ± 0.18, respectively, remaining associated with the kidneys at 24 h postinjection. The rodent pancreas is known to express high densities of the BB2r and therefore provides a convenient in vivo target in which to gauge the efficacy of our

Table 2. Biodistribution Studies of ^{111}In-DOTA-5-AOS-BBN(7-14)NH_2, ^{111}In-DOTA-8-ADS-BBN(7-14)NH_2, ^{111}In-DOTA-AMBA-BBN(7-14)NH_2, ^{111}In-DOTA-Gly-AMBA-BBN(7-14)NH_2, ^{111}In-DOTA-Gly-AM2BA-BBN(7-14)NH_2, and ^{111}In-DOTA-8-AOC-NONSENSE at 1 h Postinjection in CF-1 Mice[a]

tissue	5-AOS	8-ADS	AMBA	Gly-AMBA	Gly-AM2BA	Nonsense
blood	0.16 ± 0.06	0.10 ± 0.01	0.16 ± 0.03	0.19 ± 0.04	0.10 ± 0.03	0.23 ± 0.02
heart	0.04 ± 0.06	0.07 ± 0.02	0.10 ± 0.02	0.18 ± 0.04	0.08 ± 0.02	0.13 ± 0.02
lung	0.24 ± 0.07	0.21 ± 0.09	0.25 ± 0.07	0.57 ± 0.25	0.32 ± 0.11	0.23 ± 0.03
liver	0.16 ± 0.01	0.10 ± 0.01	0.14 ± 0.03	0.19 ± 0.02	0.14 ± 0.01	0.42 ± 0.03
stomach	0.68 ± 0.16	0.44 ± 0.09	0.74 ± 0.11	2.27 ± 0.52	0.92 ± 0.17	0.27 ± 0.21
small intestines (%ID)	4.90 ± 0.33	7.44 ± 0.98	12.49 ± 1.21	10.33 ± 1.36	8.93 ± 1.18	1.04 ± 0.29
large intestines (%ID)	1.79 ± 0.29	2.34 ± 0.50	4.57 ± 1.19	6.18 ± 0.44	4.00 ± 0.44	0.19 ± 0.08
kidney	2.44 ± 0.34	2.51 ± 0.51	2.40 ± 0.40	10.60 ± 1.57	5.60 ± 2.12	1.92 ± 0.60
spleen	0.86 ± 0.17	0.96 ± 0.33	1.50 ± 0.19	2.90 ± 0.54	1.99 ± 0.78	0.14 ± 0.02
brain	0.02 ± 0.02	0.01 ± 0.01	0.02 ± 0.00	0.04 ± 0.01	0.02 ± 0.01	0.02 ± 0.00
pancreas	14.04 ± 2.24	18.85 ± 2.25	28.85 ± 2.73	63.35 ± 5.91	36.58 ± 5.27	0.09 ± 0.03
muscle	0.07 ± 0.02	0.05 ± 0.01	0.07 ± 0.01	0.13 ± 0.02	0.06 ± 0.02	0.05 ± 0.01
bone	0.28 ± 0.09	0.14 ± 0.04	0.18 ± 0.07	0.83 ± 0.04	0.34 ± 0.07	0.09 ± 0.04
excretion (%ID)[b]	83.57 ± 2.83	82.24 ± 1.31	68.43 ± 2.15	58.17 ± 2.22	72.27 ± 1.87	94.13 ± 0.45

[a] Organ uptake values expressed as %ID/g and $n = 5$ unless otherwise noted. [b] Excretion values were calculated using the activity values associated with the excreted urine and bladder contents at the time of sacrifice.

radioconjugates (*27*). The pancreatic uptake of radioconjugates containing aromatic linking groups was found to be significantly higher ($P \leq 0.0002$) than the radioconjugates with ether linker moieties. The Gly-AMBA radioconjugate demonstrated significantly higher pancreatic uptake (63.35 ± 5.91) than any other radioconjugate studied in CF-1 mice ($P \leq 0.0001$). As expected, the scrambled peptide demonstrated no BB2r specific binding and cleared effectively from the mice with 94.13 ± 0.45%ID being excreted at 1 h postinjection. The clearance of the ^{111}In-radioconjugates through the G.I. tract was not surprisingly found to be dependent upon the linker functional group of the radioconjugate. Radioconjugates containing aromatic linking groups had the highest intestinal uptake at 1 h postinjection ($P \leq 0.003$). Due to the relatively low in vivo BB2r targeting properties of the ^{111}In-DOTA-5-AOS-BBN(7−14)NH_2 radioconjugate, further investigation of this radioconjugate in the PC-3 tumor mouse model was not performed.

The pharmacokinetic profiles of the 8-AOC, 8-ADS, AMBA, Gly-AMBA, and Gly-AM2BA radioconjugates were examined in the SCID mouse model bearing PC-3 tumor xenografts. In vivo nonspecific interactions were investigated in the PC-3 tumor-bearing mouse model by performing biodistribution studies using the scrambled peptide at 1 h postinjection. The 1, 4, and 24 h time points from these studies are summarized in Table 3 (*26*). At 15 min postinjection, tumor uptake was found to be 6.66 ± 2.00, 6.21 ± 1.57, 6.36 ± 1.60, 4.46 ± 0.81, and 7.76 ± 1.19 %ID/g for the 8-AOC, 8-ADS, AMBA, Gly-AMBA, and Gly-AM2BA radioconjugates, respectively. At 24 h postinjection, 11.4%, 19.8%, 26.6%, 25.8%, and 25.5% of the initial uptake was retained in the tumor tissue corresponding, respectively, to the 8-AOC, 8-ADS, AMBA, Gly-AMBA, and Gly-AM2BA radioconjugates. At 1 h postinjection, the tumor uptake of the targeted radioconjugates was a factor of 3.4−5.8 greater than the nonspecific binding of the scrambled radioconjugate (0.58 ± 0.20%ID/g). All of the radioconjugates investigated cleared efficiently from the blood. Clearance of the radioconjugates proceeded largely through the renal/urinary system. Kidney retention was found to be dependent upon the radioconjugate used. The Gly-AMBA and 8-ADS radioconjugates had the largest kidney retention values with 3.71 ± 2.37 and 2.36 ± 0.66 %ID/g, respectively, at 24 h postinjection. The hepatobiliary retention at 24 h p.i. ranged from 8% to 15% ID depending on the radioconjugate. The most striking difference in G.I. tract retention was observed with the aromatic containing radioconjugates having 2−4-fold more radioactivity than the 8-AOC and 8-ADS radioconjugates.

Small Animal SPECT/CT Imaging Studies. Micro-SPECT/CT studies were performed in SCID mice bearing bilateral flank PC-3 tumors using the ^{111}In-DOTA-8-AOC-BBN(7−14)NH_2, ^{111}In-DOTA-AMBA-BBN(7−14)NH_2, ^{111}In-DOTA-Gly-AMBA-BBN(7−14)NH_2, and ^{111}In-DOTA-Gly-AM2BA-BBN(7−14)NH_2 radioconjugates. The whole body images and the respective axial slices of the PC-3 tumors are depicted in Figure 4 and were acquired at 24 h postinjection of the radioconjugates. In the fused Micro-SPECT/CT images, visual inspection of the normalized whole body images indicates a substantially smaller tumor-to-background ratio for the AMBA radioconjugate relative to the 8-AOC, Gly-AMBA, and Gly-AM2BA images. However, axial slices of the PC-3 tumor for all the radioconjugates investigated demonstrated substantial accumulation of radioactivity in the tumor tissue with excellent tumor-to-background ratios. For the AMBA and Gly-AMBA radioconjugates, significant abdominal accumulation is observed likely, as established in the pharmacokinetic studies, due to the retention of radioactivity in the G.I. tract and pancreas. The majority of the nontarget retention for the 8-AOC and Gly-AM2BA radioconjugates was located predominantly in the kidneys.

DISCUSSION

The conjugates were synthesized in moderate yields with the exception of the AMBA (yield: 21% by RP-HPLC) and Gly-AMBA (yield: 12% by RP-HPLC) conjugates. Analysis of the AMBA and Gly-AMBA conjugates by RP-HPLC and mass spectrometry revealed that the majority of the crude material prematurely terminated. The major source of peptide termination was found to occur after the *p*-aminobenzoic acid was coupled to the growing peptide during peptide synthesis. The early termination of the peptide is likely attributed to the significantly reduced nucleophilicity of the primary amine of the *p*-aminobenzoic acid due to the lone pair of the 1° amine being tied up in resonance with the aromatic ring. Whereas the linking group of the Gly-AM2BA conjugate employs *p*-aminomethylbenzoic acid in which the capability of p-orbital conjugation between the amine and the aromatic ring is eliminated by the presence of the benzylmethyl group. Yields for the Gly-AM2BA (yield: 47% by RP-HPLC) conjugate were significantly higher than either the AMBA or Gly-AMBA conjugates.

In our experiments, the addition of $^{nat}Cu(II)SO_4 \cdot 5H_2O$ to the reaction mixture after the radioconjugates were labeled significantly aided in the separation of the ^{111}In-labeled radioconjugate from the unlabeled conjugate. Biological evaluation of the radioconjugate containing a significant amount of unlabeled BBN conjugate in solution would result in significantly reduced uptake of the ^{111}In-BBN analogue in BB2r-expressing tissues due to the blocking of available BB2rs by the unlabeled BBN analogue. However, Lantry and co-workers recently reported

Table 3. Biodistribution Studies of ^{111}In-DOTA-8-AOC-BBN(7-14)NH$_2$, ^{111}In-DOTA-8-ADS-BBN(7-14)NH$_2$, ^{111}In-DOTA-AMBA-BBN(7-14)NH$_2$, ^{111}In-DOTA-Gly-AMBA-BBN(7-14)NH$_2$, and ^{111}In-DOTA-Gly-AM2BA-BBN(7-14)NH$_2$ at 1, 4, and 24 h Postinjection in PC-3 Tumor-Bearing SCID Mice[a]

tissue	8-AOC	8-ADS	AMBA	Gly-AMBA	Gly-AM2BA	Nonsense
			1 h p.i.			
blood	0.24 ± 0.03	0.28 ± 0.17	0.33 ±0.23	0.64 ± 0.25	0.15 ± 0.07[c]	0.35 ± 0.08
heart	0.19 ± 0.20	0.10 ± 0.03	0.26 ± 0.21	0.38 ± 0.11	0.11 ± 0.05[c]	0.19 ± 0.09
lung	0.40 ± 0.09	0.36 ± 0.21	0.59 ± 0.40	0.72 ± 0.26	0.39 ± 0.21[c]	0.44 ± 0.12
liver	0.54 ± 0.09	0.17 ± 0.03	0.31 ± 0.05	0.40 ± 0.13	0.23 ± 0.11[c]	0.70 ± 0.08
stomach	0.89 ± 0.40	0.73 ± 0.26	0.91 ± 0.18	2.25 ± 1.04	1.20 ± 0.33[c]	0.20 ± 0.18
small intestines (%ID)	9.95 ± 0.58	5.59 ± 0.88	6.43 ± 0.98	9.95 ± 1.82	9.52 ± 1.65[c]	1.04 ± 0.25
large intestines (%ID)	1.65 ± 0.14	2.34 ± 0.67	2.29 ± 0.20	5.22 ± 0.49	4.07 ± 0.53[c]	0.28 ± 0.17
kidney	4.41 ± 1.16	3.54 ± 0.36	5.69 ± 1.51	17.34 ± 7.45	6.00 ± 3.05[c]	3.10 ± 0.37
spleen	0.54 ± 0.25	0.43 ± 0.14	0.90 ± 0.26	1.97 ± 0.63	0.65 ± 0.23[c]	0.22 ± 0.06
brain	0.02 ± 0.01	0.02 ± 0.01	0.02 ± 0.01	0.05 ± 0.03	0.03 ± 0.02[c]	0.03 ± 0.02
pancreas	30.85 ± 5.07	19.22 ± 1.89	30.15 ± 5.90	46.85 ± 6.13	28.55 ± 1.46[c]	0.12 ± 0.02
muscle	0.06 ± 0.01	0.06 ± 0.01	0.09 ± 0.04	0.21 ± 0.05	0.09 ± 0.03[c]	0.12 ± 0.02
bone	0.26 ± 0.20	0.12 ± 0.07	0.26 ± 0.11	0.93 ± 0.34	0.63 ± 0.35[c]	0.22 ± 0.11
tumor	1.95 ± 1.07	2.53 ± 0.78	3.34 ± 0.70	2.97 ± 0.88	2.68 ± 0.62[c]	0.58 ± 0.20
excretion (%ID)[b]	72.54 ± 0.96	80.67 ± 0.74	78.69 ± 2.53	54.64 ± 4.43	67.23 ± 1.02[c]	90.85 ± 3.78
			4 h p.i.			
blood	0.03± 0.01	0.02 ± 0.01	0.06 ± 0.02	0.19 ± 0.04	0.02 ± 0.01	
heart	0.03 ± 0.02	0.04 ± 0.01	0.06 ± 0.03	0.21 ± 0.16	0.03 ± 0.03	
lung	0.14 ± 0.06	0.13 ± 0.09	0.16 ± 0.08	0.24 ± 0.15	0.11 ± 0.03	
liver	0.15 ± 0.02	0.13 ± 0.03	0.28 ± 0.08	0.25 ± 0.04	0.19 ± 0.08	
stomach	0.44 ± 0.31	0.42 ± 0.11	0.41 ± 0.15	1.09 ± 0.40	0.76± 0.21	
small intestines (%ID)	3.06 ± 1.00	2.01 ± 0.38	4.59 ± 0.88	6.94 ±1.17	4.04 ± 0.94	
large intestines (%ID)	8.67 ± 2.96	7.13 ± 1.75	4.05 ± 0.80	5.79 ± 1.27	6.22 ± 1.16	
kidney	2.15± 0.32	3.92 ± 0.86	4.28 ± 1.10	7.22 ± 2.67	3.24 ± 1.18	
spleen	0.34 ± 0.09	0.33 ± 0.09	0.60± 0.23	1.76 ± 0.91	1.98 ± 2.40	
brain	0.01 ± 0.00	0.01 ± 0.00	0.01 ± 0.01	0.04 ± 0.02	0.01 ± 0.01	
pancreas	21.51 ± 3.45	18.04 ± 1.47	30.53 ± 5.35	38.95 ± 6.32	35.12 ± 8.20	
muscle	0.02 ± 0.01	0.03 ± 0.02	0.04 ± 0.02	0.03 ± 0.05	0.04 ± 0.01	
bone	0.12 ± 0.03	0.14 ± 0.02	0.33 ± 0.21	0.65 ± 0.44	0.29 ± 0.10	
tumor	1.10 ± 0.23	1.61 ± 0.57	2.42 ± 0.81	2.46 ± 0.90	2.81 ± 0.56	
excretion (%ID)[b]	78.27 ± 4.22	84.82 ± 2.31	81.42 ± 2.85	68.74 ± 2.35	78.40 ± 2.48	
			24 h p.i.			
blood	0.01 ± 0.00	0.01 ± 0.00	0.02 ± 0.00	0.08 ± 0.04	0.01 ± 0.01	
heart	0.02 ± 0.02	0.02 ± 0.01	0.04 ± 0.01	0.14 ± 0.09	0.02 ± 0.02	
lung	0.07 ± 0.03	0.06 ± 0.01	0.08 ± 0.02	0.15 ± 0.06	0.10± 0.04	
liver	0.06 ± 0.01	0.07 ± 0.01	0.21 ± 0.03	0.26 ± 0.09	0.11 ± 0.06	
stomach	0.11 ± 0.04	0.17 ± 0.03	0.20 ± 0.08	1.33 ± 0.39	0.63 ± 0.28	
small intestines (%ID)	1.30 ± 0.30	1.23 ± 0.23	3.43 ± 0.56	5.33 ±0.64	2.13 ± 0.34	
large intestines (%ID)	0.93 ± 0.13	0.86 ± 0.14	1.59 ± 0.11	2.84 ± 0.41	2.69 ± 1.19	
kidney	0.72± 0.09	2.36 ± 0.66	1.90 ± 0.47	3.71 ± 2.37	1.40 ± 0.85	
spleen	0.28 ± 0.36	0.33 ± 0.08	0.45 ± 0.09	1.28 ± 0.77	0.97 ±0.73	
brain	0.00 ± 0.00	0.01 ± 0.00	0.01 ± 0.00	0.04 ± 0.04	0.01 ± 0.00	
pancreas	10.70 ± 2.40	17.04 ± 1.65	23.84 ± 2.97	28.19 ± 4.88	13.39 ± 3.20	
muscle	0.01 ± 0.01	0.02 ± 0.01	0.02 ± 0.01	0.11 ± 0.07	0.02 ± 0.02	
bone	0.12 ± 0.04	0.09 ± 0.02	0.15 ± 0.03	0.75 ± 0.33	0.23± 0.13	
tumor	0.76 ± 0.21	1.23 ± 0.30	1.69 ± 0.34	1.15 ± 0.57	1.96 ± 0.72	
excretion (%ID)[b]	93.72 ± 0.65	91.71 ± 0.89	87.35 ± 1.06	78.62 ± 1.88	89.61 ± 1.32	

[a] The biodistribution study of ^{111}In-DOTA-8-AOC-NONSENSE was performed at 1 hr postinjection in PC-3 tumor-bearing SCID mice. Organ uptake values expressed as %ID/g and $n = 5$ unless otherwise noted. [b] Excretion values at 1, 4, and 24 h time points were calculated using the activity values associated with the excreted urine and bladder contents at the time of sacrifice; at the 24 h time point, excretion values also included the activity associated with fecal material. [c] $n = 4$.

that predose administration of a small amount (83.2 μg/m^2) of a BB2r agonist prior to administration of a radiolabeled BB2r agonist (^{177}Lu-DOTA-Gly-AMBA-BBN(7−14)NH$_2$) reduced the uptake in the BB2r-rich mouse pancreas, while maintaining the same tumor uptake and retention as studies with no predose (*23*). This study suggests that there may be a beneficial effect of having a minimal concentration of unlabeled BB2r-targeting bombesin analogues in administered doses. Further studies are required to determine if such an optimum window of concentration for nonlabeled BB2r specific peptides exists.

In vitro competitive BB2r binding assays of the ^{nat}In-BBN analogues and unlabeled BBN analogues were performed using [^{125}I-Tyr^4]BBN in PC-3 cells. All ^{nat}In-BBN conjugates demonstrated nanomolar binding affinity for the BB2r. The binding affinities followed the trend: alkyl linker > aromatic linkers > ether linkers. All radioconjugates exhibited receptor-mediated internalization and retention of the radioactivity.

In vivo biodistribution studies for each radioconjugate with exception of the 8-AOC radioconjugate were performed using healthy CF-1 mice. Of the five radioconjugates investigated, the radioconjugates containing aromatic linking groups had significantly higher pancreatic retention at 1 h postinjection ($P \leq 0.0002$). Impressively, the pancreatic retention of the Gly-AMBA radioconjugate (63.35 ± 5.91%ID/g) was nearly twice that of any of the other radioconjugates investigated. The rationale for the increased in vivo BB2r uptake of Gly-AMBA over the structurally very similar analogue Gly-AM2BA is unclear. Kidney retention is an important factor when considering the development of therapeutic radiopharmaceuticals due to potential nephrotoxicity (*28*). Even though the Gly-AMBA

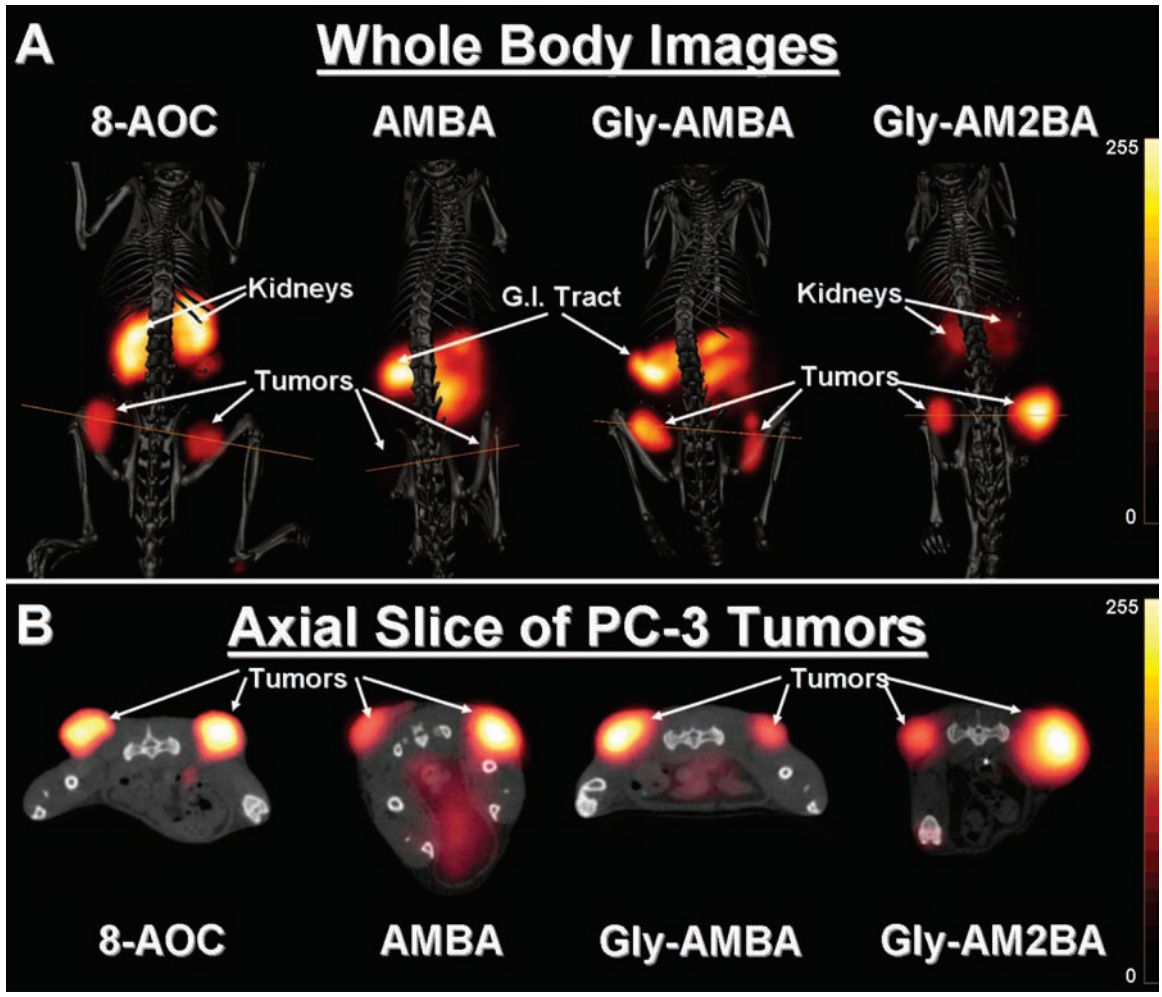

Figure 4. Small animal SPECT/CT imaging performed 24 h postinjection in PC-3 tumor-bearing SCID mice using ^{111}In-DOTA-8-AOC-BBN(7−14)NH_2, ^{111}In-DOTA-AMBA-BBN(7−14)NH_2, ^{111}In-DOTA-Gly-AMBA-BBN(7−14)NH_2, and ^{111}In-DOTA-Gly-AM2BA-BBN(7−14)NH_2. (A) Whole body images. (B) Axial slices of the PC-3 tumors corresponding to the respective transverse plane depicted in the whole body images. Each whole body and axial image was normalized to the highest-intensity pixel for each image.

and Gly-AM2BA radioconjugates initially demonstrated significantly higher kidney retention at 1 h p.i. compared to the 5-AOS, 8-ADS, and AMBA radioconjugates, all of the radioconjugates investigated demonstrated efficient clearance from the kidneys by 24 h postinjection. The hepatobiliary clearance of the radioconjugates containing ether-derived linking groups was significantly greater than radioconjugates containing aromatic linking groups ($P \leq 0.0003$). For diagnostic radiopharmaceuticals, obtaining a good target-to-nontarget ratio is crucial for the generation of easily interpretable clinical diagnostic images. The increased hepatobiliary retention of the radioconjugates with aromatic derivatives is clearly detrimental to obtaining high target-to-nontarget ratios with minimal abdominal background.

Taking the results from the CF-1 pharmacokinetic studies into account, the 8-AOC, 8-ADS, AMBA, Gly-AMBA, and Gly-AM2BA radioconjugates were further investigated in a PC-3 tumor-bearing mouse model. All of the radioconjugates cleared well from the blood, but the blood-associated activities were on average higher for the SCID mice compared to the CF-1 mice at 1 h postinjection. Like the CF-1 mice, the primary route of clearance of ^{111}In radioactivity from the SCID mice was the renal system. Renal retention of the radioconjugates at 1 h postinjection was higher in the SCID mouse model relative to what was observed with CF-1 mice. However, the overall trend in renal retention among the radioconjugates was largely unchanged. At 1 h postinjection, tumor retention followed the trend 8-AOC < 8-ADS < Gly-AM2BA < Gly-AMBA < AMBA. The AMBA radioconjugate had the highest accumulation in the tumors at the 1 h time point and was significantly greater than 8-AOC, 8-ADS, and Gly-AM2BA ($P = 0.0029$, 0.0251, and 0.0386, respectively). No statistically significant differences in tumor uptake were observed using the AMBA and Gly-AM2BA radioconjugates. The radioconjugates containing aromatic groups clearly demonstrate significantly higher retention ($P \leq 0.0213$) in the PC-3 tumor tissue at the 4 h postinjection time point when compared to the radioconjugates containing hydrocarbon or ether linking moieties. At 24 h postinjection, the trend in tumor retention was 8-AOC < Gly-AMBA < 8-ADS < AMBA < Gly-AM2BA. Statistical differences among individual radioconjugates were found, but no statistical significance was found in relating the retention of the radioconjugates in the PC-3 tumors to the linking group functionality. Comparison of the ^{111}In-labeled 8-AOC and Gly-AMBA radioconjugates with identical ^{177}Lu-labeled analogues reported by our laboratory and Lantry and co-workers revealed interesting trends in tumor retention with respect to the radionuclide employed (*23*, *29*). The ^{177}Lu-labeled 8-AOC and Gly-AMBA radioconjugates demonstrated tumor retention values at each time point that were ∼1.7−2.8 times greater relative to the ^{111}In-labeled 8-AOC and Gly-AMBA radioconjugates, suggesting that the choice of radionuclide can have a substantial impact on tumor retention. The pancreatic uptake of the ^{111}In-labeled radioconjugates was consistent in both the

CF-1 and SCID mouse models. However, it is noteworthy that the in vivo pancreatic uptake of the radioconjugates in both mouse models did not correlate strongly with the in vivo tumor uptake of the radioconjugates. The differences in pancreatic and tumor retention could possibly be accounted for by factors such as differences in the tumor vascular systems and/or differences between murine (pancreas) and human (PC-3 tumor) BB2r homology. From these studies, it appears that the methodology that employs normal mouse models (e.g., CF-1) as the sole screening tool for potential BB2r targeting radiopharmaceuticals may be inadequate in predicting the in vivo uptake in BB2r positive human tumors.

Micro-SPECT/CT imaging studies of the 8-AOC, AMBA Gly-AMBA, and Gly-AM2BA radioconjugates predominantly correlated well with the respective biodistribution studies. Visual inspection of the whole body images clearly illustrates superior tumor visualization with the Gly-AMBA and Gly-AM2BA radioconjugates. Examination of the normalized images also indicated significant abdominal accumulation for AMBA and Gly-AMBA radioconjugates, whereas the 8-AOC and Gly-AM2BA exhibited primarily renal retention as the major source of nontarget retention. Comparison of the 8-AOC and Gly-AM2BA radioconjugates reveals considerably higher tumor-to-kidney ratios for the Gly-AM2BA. The higher tumor-to-kidney ratios could be potentially significant if a radiotherapeutic derivative of the Gly-AM2BA radioconjugate were investigated. For the 8-AOC and Gly-AM2BA radioconjugates, the whole body images deviate somewhat from the corresponding biodistribution studies in which the retention of activity in both the G.I. tract and pancreas are an order of magnitude greater than the kidneys at the analogous time point. One possible explanation for the deviations between the biodistribution studies and the imaging data could be due to the fact that the preclinical SPECT/CT studies required the ^{111}In-radioconjugates to be administered in a quantity that was approximately 3 orders of magnitude greater than the biodistribution studies. The disparity in the quantity of the ^{111}In-radioconjugate employed in the studies may affect the pharmacokinetics of the radioconjugates in vivo.

In conclusion, we have systematically evaluated the pharmacokinetic profile of several diverse linking groups based upon hydrocarbon, ether, and aromatic moieties using in vitro studies and in vivo pharmacokinetic and SPECT/CT imaging studies. Our studies indicate that radioconjugates incorporating aromatic linking groups of the type investigated generally demonstrate significantly higher hepatobiliary retention when compared with either the hydrocarbon or ether linking groups. However, we found that radioconjugates containing aromatic linking groups typically exhibited higher in vivo uptake and retention in the murine pancreas, a BB2r rich tissue, than radioconjugates composed of ether linking groups. Similarly, in BB2r-positive human PC-3 tumors, the radioconjugates incorporating aromatic linking groups on average generally demonstrated higher PC-3 tumor retention. The role of linking groups in small peptide receptor-targeted radiopharmaceutical design has largely been viewed as merely a convenient way to adjust the blood retention and overall clearance of the radiopharmaceutical without making substantial alterations to the targeting vector. This study clearly demonstrates the significance of the linking group upon not only the in vivo clearance of the radiopharmaceutical, but also on the in vivo uptake and retention of the BB2r-targeted agent in tumor tissue. The design of future BB2r-targeted agents should include a careful consideration of the effect linking group functionality has upon tumor targeting and retention. Furthermore, in evaluating the uptake and retention of the radioconjugates in mouse and human BB2r expressing tissues, we find that the uptake and retention of the radioconjugates in human PC-3 tumors did not correlate strongly with the pharmacokinetic profiles obtained from the murine pancreas. This indicates that relying solely on BB2r expression in the murine pancreas to optimize or screen BB2r-targeted agents for human BB2r expressing tumors may not be appropriate. Future work will focus on evaluating and optimizing the pharmacokinetic profile of cleavable linking groups and linking groups composed of other nonstandard amino acids using the BBN paradigm.

ACKNOWLEDGMENT

The authors gratefully acknowledge the support of postdoctoral fellowship (PFTED-07-267-01-SIED) (J.C.G.) awarded by the Canary Foundation and the American Cancer Society and additional funding from the National Cancer Institute DHHS-R01-CA72942 (T.J.H.), DHHS-1P50-CA13013 (W.A.V.), the American Cancer Society RSG-99-331-04-CDD (T.J.H.) and the Department of Veterans Affairs MERIT award (T.J.H.). The authors would further like to acknowledge Dr. Nathan D. Leigh and the Mass Spectrometry Facility in the Department of Chemistry at the University of Missouri-Columbia for the collection and assistance in interpretation of the mass spectra in this manuscript. This work was supported with the resources and the use of facilities at the Harry S. Truman Memorial VA Hospital.

Supporting Information Available: Complete biodistribution data for the radioconjugates in CF-1 (1, 4, and 24 h time points) and PC-3 tumor bearing SCID mice (0.25, 1, 4, and 24 h time points) are given in tabular form. This material is available free of charge via the Internet at http://pubs.acs.org.

LITERATURE CITED

(1) Smith, C. J., Volkert, W. A., and Hoffman, T. J. (2005) Radiolabeled peptide conjugates for targeting of the bombesin receptor superfamily subtypes. *Nucl. Med. Biol. 32*, 733–740.

(2) Smith, C. J., Volkert, W. A., and Hoffman, T. J. (2003) Gastrin releasing peptide (GRP) receptor targeted radiopharmaceuticals: A concise update. *Nucl. Med. Biol. 30*, 861–868.

(3) Cornelio, D. B., Roesler, R., and Schwartsmann, G. (2007) Gastrin-releasing peptide receptor as a molecular target in experimental anticancer therapy. *Ann. Oncol. 18*, 1457–1466.

(4) Reubi, J. C., Wenger, S., Schmuckli-Maurer, J., Schaer, J.-C., and Gugger, M. (2002) Bombesin receptor subtypes in human cancers: Detection with the universal radioligand ^{125}I-[D-TYR^{6}, β-ALA^{11}, PHE^{13}, NLE^{14}] bombesin(6−14). *Clin. Cancer Res. 8*, 1139–1146.

(5) Gugger, M., and Reubi, J. C. (1999) Gastrin-releasing peptide receptors in non-neoplastic and neoplastic human breast. *Am. J. Pathol. 155*, 2067–2076.

(6) Markwalder, R., and Reubi, J. C. (1999) Gastrin-releasing peptide receptors in the human prostate: Relation to neoplastic transformation. *Cancer Res. 59*, 1152–1159.

(7) Jensen, R. T., Battey, J. F., Spindel, E. R., and Benya, R. V. (2008) International union of pharmacology. LXVIII. Mammalian bombesin receptors: Nomenclature, distribution, pharmacology, signaling, and functions in normal and disease states. *Pharmacol. Rev. 60*, 1–42.

(8) Garrison, J. C., Rold, T. L., Sieckman, G. L., Figueroa, S. D., Volkert, W. A., Jurisson, S. S., and Hoffman, T. J. (2007) In vivo evaluation and small-animal PET/CT of a prostate cancer mouse model using ^{64}Cu bombesin analogs: Side-by-side comparison of the CB-TE2A and DOTA chelation systems. *J. Nucl. Med. 48*, 1327–1337.

(9) Hoffman, T. J., Gali, H., Smith, C. J., Sieckman, G. L., Hayes, D. L., Owen, N. K., and Volkert, W. A. (2003) Novel series of ^{111}In-labeled bombesin analogs as potential radiopharmaceuticals for specific targeting of gastrin-releasing peptide receptors

expressed on human prostate cancer cells. *J. Nucl. Med. 44*, 823–831.

(10) Smith, C. J., Gali, H., Sieckman, G. L., Hayes, D. L., Owen, N. K., Mazuru, D. G., Volkert, W. A., and Hoffman, T. J. (2003) Radiochemical investigations of ^{177}Lu-DOTA-8-Aoc-BBN$^{7-14}$NH$_2$: An in vitro/in vivo assessment of the targeting ability of this new radiopharmaceutical for PC-3 human prostate cancer cells. *Nucl. Med. Biol. 30*, 101–109.

(11) Smith, C. J., Gali, H., Sieckman, G. L., Higginbotham, C., Volkert, W. A., and Hoffman, T. J. (2003) Radiochemical investigations of ^{99}mTc-N$_3$S-X-BBN$^{7-14}$NH$_2$: An in vitro/in vivo structure-activity relationship study where X = 0-, 3-, 5-, 8-, and 11-carbon tethering moieties. *Bioconjugate Chem. 14*, 93–102.

(12) Moustapha, M. E., Ehrhardt, G. J., Smith, C. J., Szajek, L. P., Eckelman, W. C., and Jurisson, S. S. (2006) Preparation of cyclotron-produced ^{186}Re and comparison with reactor-produced ^{186}Re and generator-produced ^{188}Re for the labeling of bombesin. *Nucl. Med. Biol. 33*, 81–89.

(13) Hu, F., Cutler, C. S., Hoffman, T., Sieckman, G., Volkert, W. A., and Jurisson, S. S. (2002) Pm-149 DOTA bombesin analogs for potential radiotherapy - In vivo comparison with Sm-153 and Lu-177 labeled DO3A-amide-βAla-BBN(7−14)NH$_2$. *Nucl. Med. Biol. 29*, 423–430.

(14) Zhang, H. W., Schuhmacher, J., Waser, B., Wild, D., Eisenhut, M., Reubi, J. C., and Maecke, H. R. (2007) DOTA-PESIN, a DOTA-conjugated bombesin derivative designed for the imaging and targeted radionuclide treatment of bombesin receptor-positive tumours. *Eur. J. Nucl. Med. Mol. Imaging 34*, 1198–1208.

(15) Zhang, X., Cai, W., Cao, F., Schreibmann, E., Wu, Y., Wu, J. C., Xing, L., and Chen, X. (2006) ^{18}F-labeled bombesin analogs for targeting GRP receptor-expressing prostate cancer. *J. Nucl. Med. 47*, 492–501.

(16) Zhang, H., Chen, J., Waldherr, C., Hinni, K., Waser, B., Reubi, J. C., and Maecke, H. R. (2004) Synthesis and evaluation of bombesin derivatives on the basis of pan-bombesin peptides labeled with indium-111, lutetium-177, and yttrium-90 for targeting bombesin receptor-expressing tumors. *Cancer Res. 64*, 6707–6715.

(17) Volkert, W. A., and Hoffman, T. J. (1999) Therapeutic radiopharmaceuticals. *Chem. Rev. 99*, 2269–2292.

(18) Prasanphanich, A. F., Nanda, P. K., Rold, T. L., Ma, L. X., Lewis, M. R., Garrison, J. C., Hoffman, T. J., Sieckman, G. L., Figueroa, S. D., and Smith, C. J. (2007) [^{64}Cu-NOTA-8-Aoc-BBN(7−14)NH$_2$] targeting vector for positron-emission tomography imaging of gastrin-releasing peptide receptor-expressing tissues. *Proc. Natl. Acad. Sci. U.S.A. 104*, 12462–12467.

(19) Liu, S., and Edwards, D. S. (2001) Bifunctional chelators for therapeutic lanthanide radiopharmaceuticals. *Bioconjugate Chem. 12*, 734.

(20) Anderson, C. J., and Welch, M. J. (1999) Radiometal labeled agents (non-technetium) for diagnostic imaging. *Chem. Rev. 99*, 2219–2234.

(21) Trail, P. A., King, H. D., and Dubowchik, G. M. (2003) Monoclonal antibody drug immunoconjugates for targeted treatment of cancer. *Cancer Immunol. Immun. 52*, 328–337.

(22) Smith-Jones, P. M., Stolz, B., Albert, R., Knecht, H., and Bruns, C. (1997) Synthesis, biodistribution and renal handling of various chelate-somatostatin conjugates with metabolizable linking groups. *Nucl. Med. Biol. 24*, 761–769.

(23) Lantry, L. E., Cappelletti, E., Maddalena, M. E., Fox, J. S., Feng, W., Chen, J., Thomas, R., Eaton, S. M., Bogdan, N. J., Arunachalam, T., Reubi, J. C., Raju, N., Metcalfe, E. C., Lattuada, L., Linder, K. E., Swenson, R. E., Tweedle, M. F., and Nunn, A. D. (2006) ^{177}Lu-AMBA: synthesis and characterization of a selective ^{177}Lu-labeled GRP-R agonist for systemic radiotherapy of prostate cancer. *J. Nucl. Med. 47*, 1144–52.

(24) Maina, T., Nock, B. A., Zhang, H., Nikolopoulou, A., Waser, B., Reubi, J.-C., and Maecke, H. R. (2005) Species differences of bombesin analog interactions with GRP-R define the choice of animal models in the development of GRP-R-targeting drugs. *J. Nucl. Med. 46*, 823–830.

(25) Prasanphanich, A. F., Lane, S. R., Figueroa, S. D., Ma, L. X., Rold, T. L., Sieckman, G. L., Hoffman, T. J., McCrate, J. M., and Smith, C. J. (2007) The effects of linking substituents on the in vivo behavior of site-directed, peptide-based, diagnostic radiopharmaceuticals. *In Vivo 21*, 1–16.

(26) Please see the supporting information for a complete listing of the biodistribution time points for the radioconjugates in CF-1 mice (1, 4, and 24 hr) and PC-3 tumor bearing SCID mice (0.25, 1, 4, and 24 h).

(27) Waser, B., Eltschinger, V., Linder, K., Nunn, A., and Reubi, J. C. (2007) Selective in vitro targeting of GRP and NMB receptors in human tumours with the new bombesin tracer ^{177}Lu-AMBA. *Eur. J. Nucl. Med. Mol. Imaging 34*, 95–100.

(28) Lambert, B., Cybulla, M., Weiner, S. M., Van De Wiele, C., Ham, H., Dierckx, R. A., and Otte, A. (2004) Renal toxicity after radionuclide therapy. *Radiat. Res. 161*, 607–611.

(29) Johnson, C. V., Shelton, T., Smith, C. J., Ma, L., Perry, M. C., Volkert, W. A., and Hoffman, T. J. (2006) Evaluation of combined Lu-177-DOTA-8-AOC-BBN (7−14)NH2 GRP receptor-targeted radiotherapy and chemotherapy in PC-3 human prostate tumor cell xenografted SCID mice. *Cancer Biother. Radiopharm. 21*, 155–166.

BC8001375

Evaluation of the Pharmacokinetic Effects of Various Linking Group Using the ^{111}In-DOTA-**X**-BBN(7-14)NH_2 Structural Paradigm in a Prostate Cancer Model

Jered C. Garrison[†], Tammy L. Rold[†], Gary L. Sieckman[‡], Farah Naz[†], Samantha Sublett[‡], Said Daibes Figueroa[‡,§], Wynn A. Volkert[§] and Timothy J. Hoffman[*,†,‡,∞]

Supporting Information

List of Contents

Table 1 - Biodistribution Studies in Normal CF-1 Mice 2

Table 2 - Biodistribution Studies in PC-3 Tumor Bearing SCID Mice.....3

Table 1 Biodistribution studies of ^{111}In-DOTA-5-AOS-BBN(7-14)NH_2, ^{111}In-DOTA-8-ADS-BBN(7-14)NH_2, ^{111}In-DOTA-AMBA-BBN(7-14)NH_2, ^{111}In-DOTA-Gly-AMBA-BBN(7-14)NH_2 and ^{111}In-DOTA-Gly-AM2BA-BBN(7-14)NH_2 at 1, 4 and 24 hr post-injection in CF-1 mice. The biodistribution study of ^{111}In-DOTA-8-AOC-NONSENSE was performed at 1 hr post-injection in CF-1 mice.

Tissue	5-AOS	8-ADS	AMBA	Gly-AMBA	Gly-AM2BA	Nonsense
1 hr p.i						
Blood	0.16 ± 0.06	0.10 ± 0.01	0.16 ± 0.03	0.19 ± 0.04	0.10 ± 0.03	0.23 ± 0.02
Heart	0.04 ± 0.06	0.07 ± 0.02	0.10 ± 0.02	0.18 ± 0.04	0.08 ± 0.02	0.13 ± 0.02
Lung	0.24 ± 0.07	0.21 ± 0.09	0.25 ± 0.07	0.57 ± 0.25	0.32 ± 0.11	0.23 ± 0.03
Liver	0.16 ± 0.01	0.10 ± 0.01	0.14 ± 0.03	0.19 ± 0.02	0.14 ± 0.01	0.42 ± 0.03
Stomach	0.68 ± 0.16	0.44 ± 0.09	0.74 ± 0.11	2.27 ± 0.52	0.92 ± 0.17	0.27 ± 0.21
Small Intestines (%ID)	4.90 ± 0.33	7.44 ± 0.98	12.49 ± 1.21	10.33 ± 1.36	8.93 ± 1.18	1.04 ± 0.29
Large Intestines (%ID)	1.79 ± 0.29	2.34 ± 0.50	4.57 ± 1.19	6.18 ± 0.44	4.00 ± 0.44	0.19 ± 0.08
Kidney	2.44 ± 0.34	2.51 ± 0.51	2.40 ± 0.40	10.60 ± 1.57	5.60 ± 2.12	1.92 ± 0.60
Spleen	0.86 ± 0.17	0.96 ± 0.33	1.50 ± 0.19	2.90 ± 0.54	1.99 ± 0.78	0.14 ± 0.02
Brain	0.02 ± 0.02	0.01 ± 0.01	0.02 ± 0.00	0.04 ± 0.01	0.02 ± 0.01	0.02 ± 0.00
Pancreas	14.04 ± 2.24	18.85 ± 2.25	28.85 ± 2.73	63.35 ± 5.91	36.58 ± 5.27	0.09 ± 0.03
Muscle	0.07 ± 0.02	0.05 ± 0.01	0.07 ± 0.01	0.13 ± 0.02	0.06 ± 0.02	0.05 ± 0.01
Bone	0.28 ± 0.09	0.14 ± 0.04	0.18 ± 0.07	0.83 ± 0.04	0.34 ± 0.07	0.09 ± 0.04
Excretion (%ID)[a]	83.57 ± 2.83	82.24 ± 1.31	68.43 ± 2.15	58.17 ± 2.22	72.27 ± 1.87	94.13 ± 0.45
4 hr p.i.						
Blood	0.01 ± 0.01	0.01 ± 0.00	0.01 ± 0.00	0.02 ± 0.01	0.01 ± 0.00	-----
Heart	0.03 ± 0.02	0.03 ± 0.01	0.02 ± 0.01	0.07 ± 0.02	0.03 ± 0.02	-----
Lung	0.11 ± 0.05	0.08 ± 0.02	0.05 ± 0.02	0.30 ± 0.10	0.16 ± 0.09	-----
Liver	0.10 ± 0.01	0.08 ± 0.01	0.08 ± 0.01	0.14 ± 0.02	0.11 ± 0.02	-----
Stomach	0.31 ± 0.14	0.72 ± 0.86	1.53 ± 0.97	2.00 ± 0.91	0.58 ± 0.25	-----
Small Intestines (%ID)	2.23 ± 0.25	2.88 ± 0.53	5.85 ± 0.86	9.30 ± 0.28	4.53 ± 0.81	-----
Large Intestines (%ID)	3.17 ± 0.74	6.88 ± 1.87	8.16 ± 1.60	7.47 ± 0.48	6.16 ± 0.57	-----
Kidney	2.02 ± 0.10	2.10 ± 0.39	1.70 ± 0.24	6.70 ± 1.66	1.86 ± 0.34	-----
Spleen	0.66 ± 0.27	1.02 ± 0.27	1.70 ± 0.55	2.77 ± 0.58	1.66 ± 0.57	-----
Brain	0.01 ± 0.01	0.01 ± 0.00	0.01 ± 0.00	0.03 ± 0.01	0.01 ± 0.00	-----
Pancreas	11.79 ± 2.39	15.98 ± 2.53	24.52 ± 4.11	53.63 ± 7.42	26.59 ± 3.54	-----
Muscle	0.03 ± 0.03	0.02 ± 0.02	0.01 ± 0.01	0.04 ± 0.02	0.04 ± 0.02	-----
Bone	0.24 ± 0.08	0.14 ± 0.12	0.11 ± 0.04	0.82 ± 0.28	0.23 ± 0.08	-----
Excretion (%ID)[a]	89.92 ± 0.73	82.99 ± 3.09	75.88 ± 2.05	64.98 ± 1.29	78.96 ± 1.06	-----
24 hr p.i.						
Blood	0.01 ± 0.00	0.00 ± 0.00	0.00 ± 0.00	0.01 ± 0.00	0.00 ± 0.00	-----
Heart	0.01 ± 0.02	0.02 ± 0.01	0.02 ± 0.02	0.04 ± 0.01	0.02 ± 0.01	-----
Lung	0.12 ± 0.12	0.04 ± 0.01	0.05 ± 0.03	0.14 ± 0.02	0.06 ± 0.02	-----
Liver	0.05 ± 0.01	0.05 ± 0.01	0.06 ± 0.01	0.14 ± 0.07	0.06 ± 0.01	-----
Stomach	0.12 v 0.02	0.09 ± 0.03	0.24 ± 0.08	0.86 ± 0.22	0.25 ± 0.11	-----
Small Intestines (%ID)	1.17 ± 0.07	1.27 ± 0.25	3.77 ± 0.71	4.89 ± 0.94	1.52 ± 0.35	-----
Large Intestines (%ID)	1.05 ± 0.23	1.04 ± 0.13	2.33 ± 0.40	3.73 ± 0.48	2.69 ± 1.19	-----
Kidney	1.29 ± 0.20	1.30 ± 0.32	1.19 ± 0.18	2.08 ± 0.20	0.67 ± 0.08	-----
Spleen	0.36 ± 0.13	0.79 ± 0.23	1.45 ± 0.53	1.58 ± 0.29	1.23 ± 0.24	-----
Brain	0.00 ± 0.00	0.00 ± 0.00	0.01 ± 0.01	0.03 ± 0.00	0.01 ± 0.01	-----
Pancreas	10.01 ± 2.84	11.52 ± 1.03	20.47 ± 2.27	46.27 ± 4.51	10.05 ± 1.53	-----
Muscle	0.01 ± 0.01	0.01 ± 0.00	0.02 ± 0.01	0.04 ± 0.01	0.02 ± 0.01	-----
Bone	0.26 ± 0.06	0.09 ± 0.02	0.11 ± 0.02	0.73 ± 0.28	0.14 ± 0.06	-----
Excretion (%ID)[a]	94.35 ± 0.26	93.25 ± 0.25	85.73 ± 1.80	75.27 ± 4.10	92.68 ± 0.15	-----

Organ uptake values expressed as %ID/g and n = 5 unless otherwise noted.

[a]Excretion values at 1, 4 and 24 hr time points were calculated using the activity values associated with the excreted urine and bladder contents at the time of sacrifice; at the 24 hr time point, excretion values also included the activity associated with fecal material.

Table 2 Biodistribution studies of ^{111}In-DOTA-8-AOC-BBN(7-14)NH_2, ^{111}In-DOTA-8-ADS-BBN(7-14)NH_2, ^{111}In-DOTA-AMBA-BBN(7-14)NH_2, ^{111}In-DOTA-Gly-AMBA-BBN(7-14)NH_2 and ^{111}In-DOTA-Gly-AM2BA-BBN(7-14)NH_2 at 0.25, 1, 4 and 24hr post-injection in PC-3 tumor bearing SCID mice. The biodistribution study of ^{111}In-DOTA-8-AOC-NONSENSE was performed at 1 hr post-injection in PC-3 tumor bearing SCID mice.

Tissue	8-AOC	8-ADS	AMBA	Gly-AMBA	Gly-AM2BA	Nonsense
15 min p.i.						
Blood	4.95 ± 2.54	3.09 ± 0.89	2.68 ± 0.54	3.29 ± 0.66 [b]	4.45 ± 0.66	-----
Heart	1.93 ± 0.64	1.44 ± 0.55	1.40 ± 0.50	1.29 ± 0.46 [b]	1.64 ± 0.63	-----
Lung	4.25 ± 1.82	2.40 ± 0.90	2.41 ± 0.41	2.93 ± 0.57 [b]	3.27 ± 0.90	-----
Liver	2.30 ± 0.87	1.13 ± 0.28	1.14 ± 0.18	1.32 ± 0.10 [b]	1.83 ± 0.31	-----
Stomach	1.62 ± 0.27	1.70 ± 0.32	1.87 ± 0.85	4.25 ± 1.82 [b]	2.83 ± 0.74	-----
Small Intestines (%ID)	9.59 ± 1.83	7.72 ± 0.89	7.45 ± 0.97	12.25 ± 1.38 [b]	9.26 ± 1.27	-----
Large Intestines (%ID)	2.65 ± 0.22	2.65 ± 0.24	2.81 ± 0.27	5.43 ± 0.27 [b]	4.95 ± 0.97	-----
Kidney	22.70 ± 11.96	11.77 ± 1.64	10.09 ± 1.62	18.97 ± 5.85 [b]	19.73 ± 3.66	-----
Spleen	2.20 ± 1.41	1.19 ± 0.46	1.31 ± 0.53	2.96 ± 2.60 [b]	5.16 ± 2.66	-----
Brain	0.19 ± 0.10	0.14 ± 0.08	0.12 ± 0.04	0.13 ± 0.08 [b]	0.17 ± 0.06	-----
Pancreas	47.96 ± 6.53	35.04 ± 7.33	33.27 ± 3.00	41.05 ± 6.17 [b]	43.59 ± 8.03	-----
Muscle	1.24 ± 0.60	0.80 ± 0.23	0.90 ± 0.39	0.86 ± 0.09 [b]	0.97 ± 0.58	-----
Bone	1.94 ± 0.69	1.39 ± 0.67	1.40 ± 0.64	1.99 ± 0.20 [b]	2.32 ± 0.66	-----
Tumor	6.66 ± 2.00	6.21 ± 1.57	6.36 ± 1.60	4.46 ± 0.81 [b]	7.76 ± 1.19	-----
Excretion (%ID)[a]	20.14 ± 12.63	44.03 ± 5.56	49.00 ± 9.30	26.36 ± 6.86 [b]	28.83 ± 4.83	-----
1 hr p.i.						
Blood	0.24 ± 0.03	0.28 ± 0.17	0.33 ± 0.23	0.64 ± 0.25	0.15 ± 0.07 [b]	0.35 ± 0.08
Heart	0.19 ± 0.20	0.10 ± 0.03	0.26 ± 0.21	0.38 ± 0.11	0.11 ± 0.05 [b]	0.19 ± 0.09
Lung	0.40 ± 0.09	0.36 ± 0.21	0.59 ± 0.40	0.72 ± 0.26	0.39 ± 0.21 [b]	0.44 ± 0.12
Liver	0.54 ± 0.09	0.17 ± 0.03	0.31 ± 0.05	0.40 ± 0.13	0.23 ± 0.11 [b]	0.70 ± 0.08
Stomach	0.89 ± 0.40	0.73 ± 0.26	0.91 ± 0.18	2.25 ± 1.04	1.20 ± 0.33 [b]	0.20 ± 0.18
Small Intestines (%ID)	9.95 ± 0.58	5.59 ± 0.88	6.43 ± 0.98	9.95 ± 1.82	9.52 ± 1.65 [b]	1.04 ± 0.25
Large Intestines (%ID)	1.65 ± 0.14	2.34 ± 0.67	2.29 ± 0.20	5.22 ± 0.49	4.07 ± 0.53 [b]	0.28 ± 0.17
Kidney	4.41 ± 1.16	3.54 ± 0.36	5.69 ± 1.51	17.34 ± 7.45	6.00 ± 3.05 [b]	3.10 ± 0.37
Spleen	0.54 ± 0.25	0.43 ± 0.14	0.90 ± 0.26	1.97 ± 0.63	0.65 ± 0.23 [b]	0.22 ± 0.06
Brain	0.02 ± 0.01	0.02 ± 0.01	0.02 ± 0.01	0.05 ± 0.03	0.03 ± 0.02 [b]	0.03 ± 0.02
Pancreas	30.85 ± 5.07	19.22 ± 1.89	30.15 ± 5.90	46.85 ± 6.13	28.55 ± 1.46 [b]	0.12 ± 0.02
Muscle	0.06 ± 0.01	0.06 ± 0.01	0.09 ± 0.04	0.21 ± 0.05	0.09 ± 0.03 [b]	0.12 ± 0.02
Bone	0.26 ± 0.20	0.12 ± 0.07	0.26 ± 0.11	0.93 ± 0.34	0.63 ± 0.35 [b]	0.22 ± 0.11
Tumor	1.95 ± 1.07	2.53 ± 0.78	3.34 ± 0.70	2.97 ± 0.88	2.68 ± 0.62 [b]	0.58 ± 0.20
Excretion (%ID)[a]	72.54 ± 0.96	80.67 ± 0.74	78.69 ± 2.53	54.64 ± 4.43	67.23 ± 1.02 [b]	90.85 ± 3.78
4 hr p.i.						
Blood	0.03 ± 0.01	0.02 ± 0.01	0.06 ± 0.02	0.19 ± 0.04	0.02 ± 0.01	-----
Heart	0.03 ± 0.02	0.04 ± 0.01	0.06 ± 0.03	0.21 ± 0.16	0.03 ± 0.03	-----
Lung	0.14 ± 0.06	0.13 ± 0.09	0.16 ± 0.08	0.24 ± 0.15	0.11 ± 0.03	-----
Liver	0.15 ± 0.02	0.13 ± 0.03	0.28 ± 0.08	0.25 ± 0.04	0.19 ± 0.08	-----
Stomach	0.44 ± 0.31	0.42 ± 0.11	0.41 ± 0.15	1.09 ± 0.40	0.76 ± 0.21	-----
Small Intestines (%ID)	3.06 ± 1.00	2.01 ± 0.38	4.59 ± 0.88	6.94 ± 1.17	4.04 ± 0.94	-----
Large Intestines (%ID)	8.67 ± 2.96	7.13 ± 1.75	4.05 ± 0.80	5.79 ± 1.27	6.22 ± 1.16	-----
Kidney	2.15 ± 0.32	3.92 ± 0.86	4.28 ± 1.10	7.22 ± 2.67	3.24 ± 1.18	-----
Spleen	0.34 ± 0.09	0.33 ± 0.09	0.60 ± 0.23	1.76 ± 0.91	1.98 ± 2.40	-----
Brain	0.01 ± 0.00	0.01 ± 0.00	0.01 ± 0.01	0.04 ± 0.02	0.01 ± 0.01	-----
Pancreas	21.51 ± 3.45	18.04 ± 1.47	30.53 ± 5.35	38.95 ± 6.32	35.12 ± 8.20	-----
Muscle	0.02 ± 0.01	0.03 ± 0.02	0.04 ± 0.02	0.03 ± 0.05	0.04 ± 0.01	-----
Bone	0.12 ± 0.03	0.14 ± 0.02	0.33 ± 0.21	0.65 ± 0.44	0.29 ± 0.10	-----
Tumor	1.10 ± 0.23	1.61 ± 0.57	2.42 ± 0.81	2.46 ± 0.90	2.81 ± 0.56	-----
Excretion (%ID)[a]	78.27 ± 4.22	84.82 ± 2.31	81.42 ± 2.85	68.74 ± 2.35	78.40 ± 2.48	-----
24 hr p.i.						
Blood	0.01 ± 0.00	0.01 ± 0.00	0.02 ± 0.00	0.08 ± 0.04	0.01 ± 0.01	-----
Heart	0.02 ± 0.02	0.02 ± 0.01	0.04 ± 0.01	0.14 ± 0.09	0.02 ± 0.02	-----
Lung	0.07 ± 0.03	0.06 ± 0.01	0.08 ± 0.02	0.15 ± 0.06	0.10 ± 0.04	-----
Liver	0.06 ± 0.01	0.07 ± 0.01	0.21 ± 0.03	0.26 ± 0.09	0.11 ± 0.06	-----
Stomach	0.11 ± 0.04	0.17 ± 0.03	0.20 ± 0.08	1.33 ± 0.39	0.63 ± 0.28	-----
Small Intestines (%ID)	1.30 ± 0.30	1.23 ± 0.23	3.43 ± 0.56	5.33 ± 0.64	2.13 ± 0.34	-----
Large Intestines (%ID)	0.93 ± 0.13	0.86 ± 0.14	1.59 ± 0.11	2.84 ± 0.41	2.69 ± 1.19	-----
Kidney	0.72 ± 0.09	2.36 ± 0.66	1.90 ± 0.47	3.71 ± 2.37	1.40 ± 0.85	-----
Spleen	0.28 ± 0.36	0.33 ± 0.08	0.45 ± 0.09	1.28 ± 0.77	0.97 ± 0.73	-----
Brain	0.00 ± 0.00	0.01 ± 0.00	0.01 ± 0.00	0.04 ± 0.04	0.01 ± 0.00	-----
Pancreas	10.70 ± 2.40	17.04 ± 1.65	23.84 ± 2.97	28.19 ± 4.88	13.39 ± 3.20	-----
Muscle	0.01 ± 0.01	0.02 ± 0.01	0.02 ± 0.01	0.11 ± 0.07	0.02 ± 0.02	-----
Bone	0.12 ± 0.04	0.09 ± 0.02	0.15 ± 0.03	0.75 ± 0.33	0.23 ± 0.13	-----
Tumor	0.76 ± 0.21	1.23 ± 0.30	1.69 ± 0.34	1.15 ± 0.57	1.96 ± 0.72	-----
Excretion (%ID)[a]	93.72 ± 0.65	91.71 ± 0.89	87.35 ± 1.06	78.62 ± 1.88	89.61 ± 1.32	-----

Organ uptake values expressed as %ID/g and n = 5 unless otherwise noted.

[a]Excretion values at 0.25, 1, 4 and 24 hr time points were calculated using the activity values associated with the excreted urine and bladder contents at the time of sacrifice; at the 24 hr time point, excretion values also included the activity associated with fecal material.

[b]n = 4

Peptide-Targeted Polyglutamic Acid Doxorubicin Conjugates for the Treatment of $\alpha_v\beta_6$-Positive Cancers

Huili Guan,[§] Michael J. McGuire,[§] Shunzi Li, and Kathlynn C. Brown*

Division of Translational Research, Department of Internal Medicine and The Simmons Comprehensive Cancer Center, University of Texas Southwestern Medical Center, Dallas, Texas 75390. Received April 14, 2008; Revised Manuscript Received July 8, 2008

Most chemotherapeutics exert their effects on tumor cells as well as their healthy counterparts, resulting in dose limiting side effects. Cell-specific delivery of therapeutics can increase the therapeutic window for treatment by maintaining the therapeutic efficacy while decreasing the untoward side effects. We have previously identified a peptide, named H2009.1, which binds to the integrin $\alpha_v\beta_6$. Here, we report the synthesis of a peptide targeted polyglutamic acid polymer in which the high affinity $\alpha_v\beta_6$-specific tetrameric H2009.1 peptide is incorporated via a thioether at the N-terminus of a 15 amino acid polymer of glutamic acid. Doxorubicin is incorporated into the polymer via an acid-labile hydrazone bond. Payloads of four doxorubicin molecules per targeting agent are achieved. The drug is released at pH 4.0 and 5.6 but the conjugate is stable at pH 7.0. The conjugate is selectively internalized into $\alpha_v\beta_6$ positive cells as witnessed by flow cytometric analysis and fluorescent microscopy. Cellular uptake is mediated by the H2009.1 peptide, as no internalization of the doxorubicin-PG polymer is observed when it is conjugated to a scrambled sequence control peptide. Importantly, the conjugate is more cytotoxic toward a targeted cell than a cell line that does not express the integrin.

INTRODUCTION

Most chemotherapeutics exert their effects on tumor cells as well as their healthy counterparts, resulting in dose limiting side effects. Cell-specific delivery of therapeutics can increase the efficacy of the drug while decreasing its side effects, thus opening the therapeutic window for treatment. Despite its advantages, tumor targeting of therapeutic molecules remains a major challenge in biomedicine. The challenges in developing targeted drug delivery systems can be broken into three main areas. First, cell specific binding reagents that display high affinity and specificity for the desired cell type must be identified. Additionally, if the drug mediates its cytotoxic effect by an intracellular activity, the ligand must mediate both binding and uptake by the targeted cell. Second, these targeting moieties must be incorporated into drug systems that allow delivery of molecular cargo specifically to the tumor. This takes into account factors such as size, vascular permeability, tissue retention, and stability. Third, the cargo needs to be released in an active form within the desired cellular compartment.

Toward the goal of targeted therapies for non-small cell lung carcinoma (NSCLC), we have isolated a peptide, named H2009.1, which binds to a large number of adenocarcinoma (AD) lung cancer cell lines (*1*). When placed on a tetrameric trilysine scaffold, this peptide has half-maximal binding affinity of 40−60 pM for its target cell. Additionally, the peptide can mediate cellular uptake (*2*). The cellular receptor for the H2009.1 peptide is the restrictively expressed integrin, $\alpha_v\beta_6$ (*3*). Expression of $\alpha_v\beta_6$ is widespread in early stage NSCLC, and it is associated with poor patient survival. Furthermore, this integrin is up-regulated in NSCLC tumors compared to normal lung tissue. The restricted expression suggests that it may be a good receptor for targeted therapies for lung cancer.

We have previously demonstrated that the H2009.1 peptide can be conjugated to doxorubicin to affect cell-specific death (*2*). While this experiment established proof-of-concept, only one molecule of doxorubicin was delivered per molecule of peptide. Increasing the drug load is expected to improve the efficacy. Polyglutamic acid (PG) has recently been used as a polymeric drug carrier (*4*). This water soluble biopolymer is biodegradable and is well tolerated at high doses. The pendant carboxyl groups of the glutamic acid provide a reactive moiety to which chemotherapeutics can be conjugated. As such, greater drug loads can be achieved based on a per molecule basis. This carrier has been used for doxorubicin (*5*−*7*), paclitaxel (*8*−*11*), camptothecin (*12, 13*), and retinoids (*14, 15*). In addition, MRI contrast reagents have been coupled to PG for tumor imaging (*16*−*18*). The PG-paclitaxel conjugate, XYOTAX (CT-2103, Cell Therapeutics Inc.) is in clinical trials for NSCLC and ovarian cancer (*19*−*21*).

Most of the PG-drug conjugates are large molecular weight polymers, which increase the circulation time of the drug when compared to free drug. Accumulation in the tumor is the result of passive targeting due to the enhanced permeability and retention (EPR) effect which results from the disordered, leaky vasculature of the tumor coupled with a dysfunctional lymphatic system (*22*). Active targeting of the PG-drug conjugates can be achieved by the incorporation of a targeting moiety. To date, few reports of targeted-PG conjugates have been reported, and they have relied on antibody-based targeting reagents (*5*).

Here, we report the synthesis of a peptide targeted polyglutamic acid polymer in which the high affinity $\alpha_v\beta_6$-specific tetrameric H2009.1 peptide is incorporated via a thioether at the N-terminus of a 15 amino acid polymer of glutamic acid. Doxorubicin is incorporated into the polymer via an acid-labile hydrazone bond. Payloads of four doxorubicin molecules per targeting agent are achieved and the drug is released in acidic conditions. The conjugate is selectively internalized into $\alpha_v\beta_6$ positive cells as witnessed by flow cytometric analysis and fluorescent microscopy. Cellular uptake is mediated by the

* Corresponding author. Kathlynn C. Brown, 5323 Harry Hines Blvd, Dallas, TX 75390. Kathlynn.Brown@UTSouthwestern.edu, 214-645-6348 (Office), 214-648-4156 (Fax).

[§] These authors contributed equally to this manuscript.

10.1021/bc800154f CCC: $40.75 © 2008 American Chemical Society
Published on Web 08/19/2008

H2009.1 peptide, as minimal internalization of the doxorubicin-PG polymer is observed when it is conjugated to a scramble sequence control peptide. Importantly, the conjugate is preferentially cytotoxic toward a targeted cell when compared to a cell line that does not express the $\alpha_v\beta_6$ integrin.

EXPERIMENTAL SECTION

General Peptide Synthesis and Characterization. All peptides were synthesized on a Symphony Peptide Synthesizer (Rainin Instruments, Protein Technologies, Inc. Woburn, MA) using standard Fmoc chemistry. All Fmoc-protected amino acids, 2-(1*H*-benzotriazole-l-yl)-1,1,3,3-tetramethyluronium hexafluorophosphate (HBTU), were purchased from EMD Biosciences Inc. (San Diego, CA), anhydrous 1-hydroxybenzotriazole (HOBt) was purchased from SynBioSci (Livermore, CA), *N*-methylmorpholine (NMM) was purchased from Acros Organics (Geel, Belgium), and piperidine was purchased from Sigma-Aldrich Inc. (St. Louis, MO). The crude peptides were dissolved in 20% methanol/8 M guanidinium hydrochloride and purified with RP-HPLC using eluents of H_2O/0.1% TFA (eluent A) and acetonitrile/0.1% TFA (eluent B). The programmed elution profile 0−1 min, 100% A; 1−80 min, B is increased from 0−75% at a flow rate of 10 mL/min on preparative column (Spirit Peptide C18, 5 μm column, 25 × 2.12) (referred to as method A) or 0−1 min, 100% A; 1−70 min, B is increased from 0−75% at a flow rate of 1 mL/min on analytical column (Spirit Peptide C18, 5 μm column, 15 × 0.4) (referred to as method B). Peptide purity was determined by analytical HPLC monitoring peptide elution by absorbance at 220 nm. The peptide mass was characterized by matrix assisted laser desorption/ionization (MALDI) on a Voyager DE Pro (Applied Biosystems Inc., Foster City, CA) using α-cyano-4-hydroxycinnamic acid as matrix in the reflector mode or in linear mode using sinapinic acid as matrix, respectively. N-terminal sequence analysis of peptide was carried out by Edman protein sequencers (Applied Biosystems 494) in the Protein Chemistry Technology Center of University of Texas Southwestern Medical Center.

Cell Lines. Human lung cancer cell lines were obtained from the Hamon Center for Therapeutic Oncology Research (UTSW) and were maintained according to standard protocols (*23*). RPMI1640 was purchased from Mediatech (Herndon, VA). Fetal bovine serum (FBS) was purchased from Gemini Bioproducts (Woodland, CA).

Synthesis of Tetrameric-10mer H2009.1 and a Corresponding Scrambled Sequence Peptide. The peptides were synthesized by standard Fmoc chemistry using the $Fmoc_4$-Lys_2-Lys-Cys(Acm)-β-Ala-CLEAR Acid Resin (loading 0.21 mmol/g, Peptides International, Louisville, KY). Fmoc-protected amino acids were doubly coupled at 5-fold molar excess using HBTU/HOBt/NMM (5/5/10) as an activator system. Coupling times of 40−50 min were employed. A single coupling of Fmoc-NH-$(PEG)_{11}$-COOH ($C_{42}H_{65}NO_{16}$, Polypure, Oslo, Norway) was performed overnight. The removal of the Fmoc group was carried out with 20% piperidine in DMF. The peptide was cleaved by treating the final resin with a cocktail of TFA/TIS/H_2O (95%/2.5%/2.5%) for 3 h. The cleavage solution was concentrated by passing Ar into the solution and the peptide was subsequently precipitated by addition of cold ether. The crude peptide was purified with HPLC using method A. The purified product was analyzed by method B. MALDI mass spectra were obtained in linear mode using sinapinic acid as matrix. N-terminal sequence was analyzed by Edman protein sequencer. Tetramer-10mer-H2009.1 (RGDLATLRQL; $C_{327}H_{606}N_{82}O_{114}S$): MALDI MH^+ (average mass calculated/found: 7543.86/7544.20), purity >98.4%, (RP-HPLC, retention time of 34.37 min using method B). Scramble Tetramer-10mer-H2009.1 (DALRLQGTLR; $C_{327}H_{606}N_{82}O_{114}S$): MALDI MH^+ (average mass calculated/found: 7543.86/7544.83), purity >98.1% (RP-HPLC, retention time of 34.58 min using method B).

Deprotection of the Acetamidomethyl-Cysteine To Reveal a Free Thiol on the Tetrameric Peptides. The tetrameric-10mer H2009.1 peptide with the acetamidomethyl-cysteine (22 mg, 3 μmol) was dissolved in TFA (1.5 mL) containing 1% anisole to which silver acetate (80 mg, 480 μmol) was added. The solution was stirred for 2 h at 4 °C and then concentrated under Ar to 0.5 mL. The peptide was precipitated by the addition of 5 mL of cold ether and collected by centrifugation, and then treated with dithiothreitol (1 mL, 0.2 M in 1 M acetic acid) at RT for 3 h. The solution was filtered and purified with HPLC using method A. The purified product was analyzed by method B. MALDI mass spectra were obtained in linear mode using sinapinic acid as matrix. The same reaction and characterization conditions were employed on scrambled sequence tetrameric peptide. Tetrameric-10mer-H2009.1 ($C_{324}H_{601}N_{81}O_{113}S$): MALDI MH^+ (average mass calculated/found: 7472.78/7473.99), purity >98.4% (RP-HPLC, retention time of 34.71 min using method B). Scramble tetrameric-10mer-H2009.1 ($C_{324}H_{601}N_{81}O_{113}S$): MALDI MH^+ (average mass calculated/found: 7472.78/7473.84), purity >98.1% (RP-HPLC, retention time of 33.55 min using method B).

Synthesis of Maleimido-PEG-polyGlu$_{15}$. Synthesis of maleimido-PEG-$polyGlu_{15}$ was performed by sequential coupling of Fmoc-Glu(O-*t*-Bu)-OH (5-fold molar excess) on Rink Amide AM resin (200−400 mesh, 0.43 mmol/g, EMD Biosciences Inc.). A double coupling was performed for each addition of glutamic acid to the growing peptide chain. A PEG moiety was incorporated by a single coupling of Fmoc-NH-$(PEG)_{11}$-COOH (5-fold molar excess). The peptide was capped with maleimide functionality at the amino terminus by the reaction of *N*-β-maleimidopropionic acid (BMPA, 5-fold molar excess) for 4 h. HBTU/HOBt/NMM (5/5/10) was employed as an activator system for all couplings. The removal of the Fmoc groups was performed in 20% piperidine with DMF. The linear peptide was cleaved from the final resin in a cocktail of TFA/TIS/H_2O (95%/2.5%/2.5%) for 3 h. Upon concentrating the cleavage cocktail by passing Ar into the solution, the peptide was precipitated in cold ether. The crude product was purified with HPLC using method A. The final product was analyzed by method B. The MALDI mass spectrum was obtained in reflector mode using α-cyano-4-hydroxycinnamic acid as matrix. Maleimido-PEG-$polyGlu_{15}$ (compound 1, $C_{109}H_{166}N_{18}O_{61}$): MALDI MNa^+ (monoisotopic mass calculated/found: 2726.487/2726.46), purity >98.3% (RP-HPLC, retention time of 27.95 min using method B).

Incorporation of H_2NNHBoc to Pendant Carboxyl Group of Maleimido-PEG-polyGlu$_{15}$. The hydrazide groups were conjugated to the pendant carboxyl groups of compound 1 via acid anhydride reaction. Triethylamine (TEA, 0.2 mL) was added to maliemido-PEG-$polyGlu_{15}$ (20 mg, 7.4 μmol polymer, 111 μmol COOH groups) dissolved in anhydrous DMF (1.5 mL), followed by dropwise addition of isobutyl chloroformate (0.2 mL, 1.5 mmol) under an Ar atmosphere at 4 °C. After 5 min, *tert*-butyl carbazate (H_2NNHBoc, 1.5 mmol in 0.8 mL DMF) was added. The reaction was performed for 30 min at 4 °C and then continued for 3 more hours at RT. The resultant salts were removed by filtration and low molecular weight impurities were removed by dialysis in DMF using a dialysis membrane with a molecular weight cutoff (MWCO) of 1 kDa. The final product was precipitated from cold ether and dried in vacuum. The number of carboxylate groups converted to CONHNHBoc was calculated by comparing intensity of characteristic resonance of the Boc protecting group at 1.41 ppm and maleimide resonance at 6.93 ppm (CH=CH) by ^{1}H NMR in DMSO-d_6. The results showed that 71% of the COOH groups

were converted to CONHNHBoc groups. This corresponds to an average of 10−11 hydrazide moieties per polymer molecule. MALDI mass spectrometry of the resultant maleimido-PEG-polyGlu(NHNHBoc)$_{15}$ (compound 2) showed a broad mass distribution centered around 4400 Da (α-cyano-4-hydroxycinnamic acid as matrix). This is consistent with a distribution of products due to incomplete modification of the carboxylate.

Removal of the Boc Protecting Group from Maleimido-PEG-polyGlu(NHNHBoc)$_{15}$. Compound 2 (15 mg) was treated by TFA (1 mL) to remove protective BOC groups. The resultant maleimido-PEG-polyGlu(NHNH$_2$) was purified with HPLC using method A. The removal of Boc groups is indicated by the complete disappearance of methyl proton at 1.41 ppm in ^{1}H NMR. MALDI mass spectrometry of the deprotected product maleimido-PEG-polyGlu(NHNH$_2$)$_{15}$ (compound 3) showed a broad mass distribution centered around 3288 Da (α-cyano-4-hydroxycinnamic acid as matrix). This is consistent with the removal of approximately 10−11 Boc protecting groups.

Conjugation of Peptides to Maleimido-PEG-polyGlu(NHNH$_2$)$_{15}$. A typical protocol for the reaction of thiol group of the peptide with maleimide is described below. Compound 3 (3.8 mg) was dissolved in PBS (0.5 mL, pH 7.0) containing EDTA (0.1 M) degassed by passing Ar into the solution for 5 min. The tetrameric 10mer H2009.1 peptide (9.6 mg, 1.3 μmol) was added, and the reaction was carried out at RT for 3 h. The product was isolated with HPLC using method A. The purified product was analyzed by method B and found to be a single peak with a retention time of 33.48 min for the tetrameric 10-mer H2009.1-PEG-PolyGlu(NHNH$_2$)$_{15}$ (compound 4). A retention time of 33.55 min was observed for the corresponding product coupled to the sequence scrambled version of the peptide. MALDI mass spectra were obtained in linear mode using sinapinic acid as matrix. A major product was observed with a MH$^+$ of 10 389.9 (compound 4).

Synthesis of Tetrameric 10mer H2009.1-PEG-polyGlu-(NHN=Dox). Compound 4 (5 mg, 0.48 μmol) and doxorubicin HCl (15 mg, 26 μmol, Shanco International, Inc., South Plainfield, NJ) were dissolved in anhydrous methanol (1.5 mL) with TFA as an acid catalyst. The reaction solution was stirred at RT in the dark for 48 h. After removal of the solvent, the resultant solid was dried overnight under vacuum. The crude product was purified by size exclusion chromatography (Ultrahydrogel 500, 7.8 × 300 mm) in PBS/CH$_3$CN (70/30). The proper fraction was collected and lyophilized to yield final product as wine red powder. The product was evaluated by HPLC (elution profile of 0−1 min, eluent B is increased from 0−15%; 1−40 min, B is increased from 15−80% at a flow rate of 1 mL/min using the Spirit Peptide C18 column) monitoring the presence of doxorubicin at 485 nm to confirm the absence of unbound free doxorubicin. The conjugate has a retention time of 17.8 min and is well separated from the free drug which elutes at 16.3 min. The loading percentage of doxorubicin in the conjugates was 24% as determined by comparing the concentration of Dox obtained by absorption at 481 nm (ε = 10 410 M^{-1} cm^{-1}) (*24*) and the concentration of peptide moiety obtained by Edman sequencing analysis.

Evaluation of pH Dependent Drug Release. Tetrameric 10mer H2009.1-M-PEG-polyGlu(NHN=Dox) (50 μM Dox equivalents) was dissolved in phosphate buffered saline (pH 7.0, 0.1 mL) or acetate buffer (pH 4.0, 0.1 mL and pH 5.6, 0.1 mL). The samples were incubated at 37 °C for the indicated times. The release of free doxorubicin was determined by RP-HPLC using a C18 column and monitoring doxorubicin absorbance at 485 nm.

Flow Cytometric Analysis. Integrin $\alpha_V\beta_6$-positive H2009 cells and $\alpha_V\beta_6$-negative H1299 cells (*3*) were seeded in 12 well culture plates at approximately 100 000 cells/well in a volume of 1 mL RPMI-1640 supplemented with 5% bovine serum (R5 medium) and allowed to adhere overnight. Cells were incubated for 120 min with 30 μM unconjugated doxorubicin, tetrameric scrambled peptide- or tetrameric 10mer-H2009.1-PEG-polyGlu(NHN=Dox). Cells were washed four times with PBS$^+$ containing 0.1% BSA, followed by 2 brief rinses with 20 mM HCl-glycine, pH 2.2 containing 150 mM NaCl. Following the washes, the cells were rinsed with PBS and 1 mL/well of enzyme-free cell dissociation buffer (Invitrogen, Grand Island, NY) was added. Cells were incubated for 30 min on ice in cell dissociation buffer, scraped from the plate, and prepared as a single cell suspension by passage through a 27 gauge needle. Doxorubicin uptake was assessed for 10 000 cells per treatment group by flow cytometry in a CellQuanta flow cytometer. Cells were gated by size and side scatter properties and doxorubicin assayed by fluorescence in channel 2 (excitation 488 nm, emission 550−600 nm).

Cell Viability Assay. Integrin $\alpha_v\beta_6$-positive H2009 cells and $\alpha_v\beta_6$-negative H1299 cells were seeded in 96 well culture plates at 1000 cells/well in a volume of 50 μL R5 medium and allowed to adhere overnight. Unconjugated doxorubicin or tetrameric 10mer H2009.1-M-PEG-polyGlu(NHN=Dox) was added to quadruplicate wells in 50 μL R5 media to produce the final concentrations indicated (ranging from 200 nM to 5 μM, all based on total doxorubicin concentration). Untreated control cells received 50 μL R5 only and were cultured as a set of eight replicate wells per plate. After 24 h of exposure to the drug, media was aspirated from all wells, and the wells were washed four times with 200 μL R5 before continuing culture in 100 μL R5 for 72 h. At the end of the post-treatment incubation, cell viability was assessed using CellTiter Glo reagent (Promega, Madison, WI). Luminescence was detected using a plate reader 30−60 min after the addition of the CellTiter Glo reagent.

Fluorescent Microscopy. Images of individual cells were captured from wells of 96 well plates from the viability assays detailed above. Cells were observed 2 h after removal of the drug and addition of fresh media using an inverted Leica 6500 microscope. Cell images were captured with phase contrast illumination to visualize the cells and fluorescence in the red channel to visualize doxorubicin uptake. Untreated control cells had no detectable intrinsic fluorescence under these conditions. Figures are displayed as overlays of the phase contrast and fluorescence microscopy. Images in an individual experiment were captured under the same settings (gain, time of exposure, contrast) so that fluorescence intensity is proportional to drug accumulation by the cells.

RESULTS

Synthesis of Tetrameric 10mer H2009.1-PEG-polyGlu-(NHN=Dox) (Compound 5). We sought to develop a targeted-doxorubicin conjugate that met three requirements. First, it must contain a high affinity targeting reagent that can be incorporated in a chemospecific fashion that allows for the targeting moiety to retain its activity. Second, the ratio of targeting reagent to drug must exceed the 1:1 ratio that can be achieved by direct conjugation. Third, the doxorubicin linker must be labile once the conjugate is internalized into the target cell so that doxorubicin can exert its cellular affects.

Toward these objectives, we synthesized the tetrameric 10mer H2009.1-polyGlu(NHN=Dox) (compound 5) according to Scheme 1. A defined length PG polymer serves as the drug carrier. Synthesis of the polyglutamic acid was accomplished by linear Fmoc peptide chemistry. A PEG moiety was incorporated at the amino terminus of the peptide to improve solubility and provide a flexible linker between the drug carrier and the targeting moiety. The amino terminus was capped with a maleimide so that the targeting reagent could be introduced by a chemoselective reaction with a free thiol.

While doxorubicin can be conjugated directly to the carboxylic acid of glutamic acid via an amide (*5*), we wished to incorporate the drug through an acid labile functionality. We and others have conjugated doxorubicin to a carrier by the formation of a hydrazone utilizing the ketone of 2-hydroxyacetyl group of doxorubicin (*2, 25*−*28*). To accomplish this, the carboxylic acid functionalities of the glutamic acid side chains were converted to hydrazide groups by treatment with *tert*-butyl carbazate (*25*). The number of converted carboxylate groups was determined using ^{1}H NMR by integrating the characteristic resonance of the Boc protecting group (9 protons per modification) at 1.41 ppm and maleimide resonance at 6.93 ppm (2 protons per polymer chain). Accordingly, 71% of the COOH groups were converted to CONHNHBoc groups, corresponding to 10−11 modified side chains. The Boc group was removed by treatment with trifluoroacetic acid to reveal the hydrazide.

The targeting reagent chosen was the peptide H2009.1 which binds specifically to the uniquely expressed integrin, $\alpha_v\beta_6$. This peptide was synthesized on a trilysine scaffold, as tetramerization has been demonstrated to increase affinity of this peptide for its cellular receptor (*2*). Although this peptide was originally selected as a 20 amino acid peptide, only the 10 N-terminal amino acids are necessary for binding to the integrin (S.L., M.J.M., and K.C.B., unpublished results). As such, we chose to focus on the smaller peptide to ease the difficulty of the peptide synthesis. Importantly, in this format, the peptide can mediate cellular uptake. Synthesis was performed using linear Fmoc chemistry using $Fmoc_4$-Lys_2-Lys-Cys(Acm)-β-Ala-CLEAR Acid Resin. An acetamidomethyl (Acm) protected cysteine was incorporated before the branch point. This allows for a reactive thiol to be revealed upon treatment with Ag(I). Additionally, a PEG linker was placed between the core and the peptide to improve solubility, increase flexibility between the peptide branches, and prevent peptide aggregation. As a control, a peptide that contains the same amino acid composition but a different sequence was synthesized as well. This scrambled sequence peptide has been shown to have no binding affinity for $\alpha_v\beta_6$ (data not shown). These peptides were integrated into the polyGlu($NHNH_2$) by reaction of the unique thiol of the peptide with the maleimide at the N-terminus of the polyGlu peptide.

The final step of the synthesis is the coupling of doxorubicin to the hydrazide to form the hydrazone linkage between the side chain of the glutamic acid and the ketone of doxorubicin. As the ketone functionality is chemically orthogonal to reactive groups found in naturally occurring amino acids, there was no need to protect the peptide side chains. Free drug was removed from the polymer by size exclusion chromatography under neutral pH conditions. The mole amount of doxorubicin in the conjugate was determined by UV absorbance at 481 nm. The concentration of compound 5 was determined by Edman sequencing analysis. The average drug loading is found to be 25% based on the number of glutamates or approximately 4 doxorubicin molecules per polymer unit.

Doxorubicin Is Released from the Carrier at Low pH. For the doxorubicin to be active, it must be released from the carrier so that it can exert its cellular effects within the nucleus. However, premature release of the drug will result in a decrease of the efficacy of the targeted therapeutic and will have similar side effects observed with the free drug. Internalization via a clatherin mediated endocytosis results in peptides entering the endosomal pathway with eventual localization in the lysosome (*29*−*31*). As the vesicles involved in this pathway have an acidic pH, pH sensitive linkers can be used for drug release. It is important to note that the pH drops at each sequential step of the internalization process, with early endosomes having a pH of 5.5−6.0; late endosomes exhibit a pH of approximately 5.0, whereas the lysosome's pH can drop to as low as 4.5. As such, if the drug conjugate becomes stalled at any one of these stages, drug release must occur at that pH. For this reason, the doxorubicin was coupled to the polyglutamic acid polymer via an acid labile hydrazone. To ensure that the drug conjugate is stable at the neutral pH but is released at the pH found within the lysosomal compartment of the cells, compound 5 was incubated at pH 7.0, pH 5.6, and pH 4.0 for defined times. Aliquots were removed and the release of doxorubicin was determined by HPLC. As shown in Figure 1, minimal drug was released at pH 7.0, even after 48 h. However, at pH 4.0, free doxorubicin was observed at 2 h. By 4 h, 25% of the drug has been released. This increases to 75% drug release at 51 h. As pH 4.5 is believed to be the minimum pH that would be reached in the cell, we also determined doxorubicin release at pH 5.6. The kinetics of drug release at pH 5.6 and pH 4.0 are the same (Figure 1). These results suggest that the drug will remain conjugated to the carrier in an inactive form in the serum but will be released intracellularly due to the low pH environment found in the endosome or lysosome.

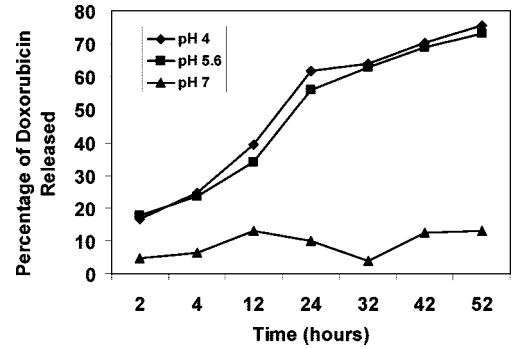

Figure 1. pH dependent release of doxorubicin from the polyglutamic acid-H2009.1 peptide conjugate. Polyglutamic acid-H2009.1-doxorubicin conjugate was dissolved in aqueous buffer at pH 7.0, pH 5.6, or pH 4.0 and incubated at 37 °C. At the indicated times, aliquots were removed and the ratio of unconjugated to conjugated doxorubicin was assessed by reverse phase HPLC on an analytical C18 column.

Tetrameric 10mer H2009.1-PEG-polyGlu(NHN=Dox) Selectivity Binds to $\alpha_v\beta_6$ Expressing Cells. Taking advantage of doxorubicin's fluorescence, the association of the conjugate with an $\alpha_v\beta_6$ expressing cell line was determined by flow cytometric analysis. Specifically, the conjugate was incubated with the human adenocarcinoma cell line H2009, which expresses $\alpha_v\beta_6$, or with H1299 cells, a human large cell lung cancer cell line which does not express the cellular receptor. As observed in Figure 2, the H2009 cells demonstrate 2-fold greater binding of targeted conjugate than the H1299 cells which do not bind the peptide. This binding is sequence specific, as the compound conjugated to the scrambled sequence peptide does not demonstrate significant binding to either cell line. Free doxorubicin internalizes into both cell lines equally. It should be noted that more doxorubicin is seen associated with the cells when they are treated with free drug versus the same concentration of targeted drug (based on total moles of doxorubicin). This phenomenon is not uncommon for drug conjugates and is most likely the result of receptor based transport of the drug versus the inherent cell permeability of the free drug (*32, 33*).

Of note, the fluorescence of doxorubicin is approximately 2-fold less when conjugated to the polymer compared to free doxorubicin (data not shown). As these studies were performed at 2 h of exposure to the polymer conjugate, in which time little doxorubicin is released from the polymer, the total uptake of the polymer conjugated drug is going to be underestimated by fluorescence experiments when compared to the free drug. However, the mean fluorescence intensity (MFI) determined by

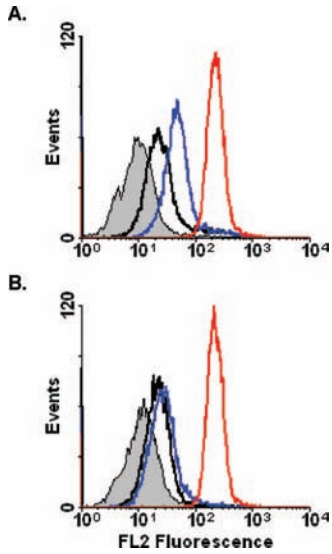

Figure 2. Cell targeted delivery of doxorubicin mediated by a cell-specific peptide. H2009 (panel A) and H1299 (panel B) cells were incubated for 2 h in the presence of 30 μM unconjugated doxorubicin (red line) or doxorubicin linked to the poly glutamic acid-H2009.1 (blue line) peptide conjugate or scrambled peptide conjugate (black line). At the end of this incubation period, the drug was removed; cells were washed with PBS^+/0.1% BSA 4 times as well as twice with 20 mM HCl-glycine, pH 2.2. Uptake of doxorubicin into cells was assessed by flow cytometry, counting 10 000 events per sample. Results obtained with untreated cells are shown in gray shaded area.

flow cytometry is greater than 4-fold higher for free doxorubicin than the conjugate on H2009 cells (Figure 2, panel A). As such, the data suggest that less drug is being delivered to the cells when conjugated to the polymer than when free doxorubicin is employed. Nonetheless, the differential binding of compound 5 to its target cell type compared to a nontargeted cell type is anticipated to reduce side effects, thus expanding the therapeutic window.

Tetrameric 10mer H2009.1-PEG-polyGlu(NHN=Dox) Is More Cytotoxic toward $\alpha_v\beta_6$ Expressing Cells. To determine if compound 5 could deliver doxorubicin selectivity to $\alpha_v\beta_6$ positive cells, H1299 and H2009 cells were incubated in the presence of varying concentrations (200 nM to 5 μM) of unconjugated doxorubicin or doxorubicin linked to the poly-glutamic acid-H2009.1 peptide conjugate. After 24 h, the drug was removed. Cells were incubated in fresh complete media for 72 h, after which the cell viability was determined. The results are shown in Figure 3. Both cell types are sensitive to free doxorubicin; pairwise comparison of cell viability after free doxorubicin treatment of both cell types did not demonstrate any statistical difference in the viability of these two cell types. However, after treatment with compound 5, more cell death was observed for the $\alpha_v\beta_6$ positive H2009 cells when compared to the $\alpha_v\beta_6$ negative H1299 cells at all concentrations ($p = 0.033$). Comparing the viability after treatment at 2 μM with the doxorubicin−peptide conjugate, the difference in viability of the two cell types is 2-fold ($p = 0.024$).

There is a significant reduction in the potency of the doxorubicin when it is conjugated to the polymer. This could be due to reduced uptake of the drug and/or inefficient release of the drug from its carrier. H1299 and H2009 cells were incubated in the presence of 5 μM unconjugated doxorubicin or doxorubicin linked to the polyglutamic acid-H2009.1 peptide conjugate. After 24 h, the drug was removed from the cells. Cells were then observed by phase contrast and fluorescence microscopy. Overlays of the resulting images are shown in Figure 4. Similar levels of unconjugated doxorubicin accumulate in the nuclei of both cell types (panel A and panel C). In

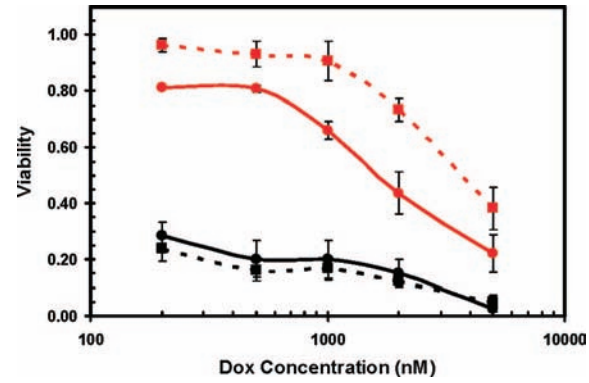

Figure 3. Cell targeted delivery of doxorubicin preferentially kills $\alpha_v\beta_6$-integrin positive tumor cells. H1299 (■ - black, red) and H2009 (● - black, red) cells were incubated in the presence of varying concentrations (200 nM to 5 μM) unconjugated doxorubicin (black lines) or doxorubicin linked to the polyglutamic acid-H2009.1 peptide conjugate (red lines). After 24 h, the drug was removed; cells were washed and incubated in fresh complete media for 72 h. Cell viability was determined using the Cell Titer-Glo assay (Promega Corp). The results shown are an average of 3 independent experiments. Pairwise comparison of cell viability after free dox treatment of both cell types did not demonstrate any statistical difference whereas the difference in the viability of these two cell types after poly-glu-dox-H2009.1 conjugate treatment was statistically significant ($p = 0.033$).

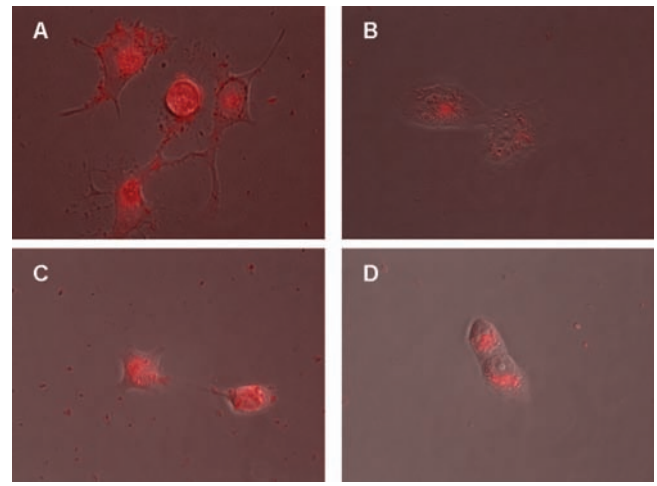

Figure 4. Cell targeted delivery of doxorubicin mediated by a cell-specific peptide. H1299 (A and B) and H2009 (C and D) cells were incubated in the presence of 5 μM unconjugated doxorubicin (A and C) or doxorubicin linked to the polyglutamic acid-H2009.1 peptide conjugate (B and D). After 24 h, the drug was removed; cells were washed and incubated in fresh complete media for 2 h. Cells were observed by phase contrast and fluorescence microscopy at 400× magnification. Overlays of the resulting images are shown.

contrast, higher levels of doxorubicin accumulate in $\alpha_v\beta_6$-integrin positive H2009 cells (panel D) than in H1299 cells (panel B) when treated with compound 5. However, most of the drug appears to be perinuclear in the H2009 cells, suggesting that the release kinetics of the drug from the conjugate may be slower in living cells than expected from the *in vitro* incubation at pH 4.0 and 5.6.

DISCUSSION

Targeted therapeutic strategies for the treatment of solid tumors are dependent on the availability of high affinity and specificity ligands for cell surface cancer biomarkers as well as appropriate drug carriers which can deliver potent therapeutics in an active form. Toward this goal, we have synthesized a targeted polyglutamic acid-doxorubicin conjugate. This com-

Scheme 1. Synthesis of Targeted PG-Doxorubicin Conjugate[a]

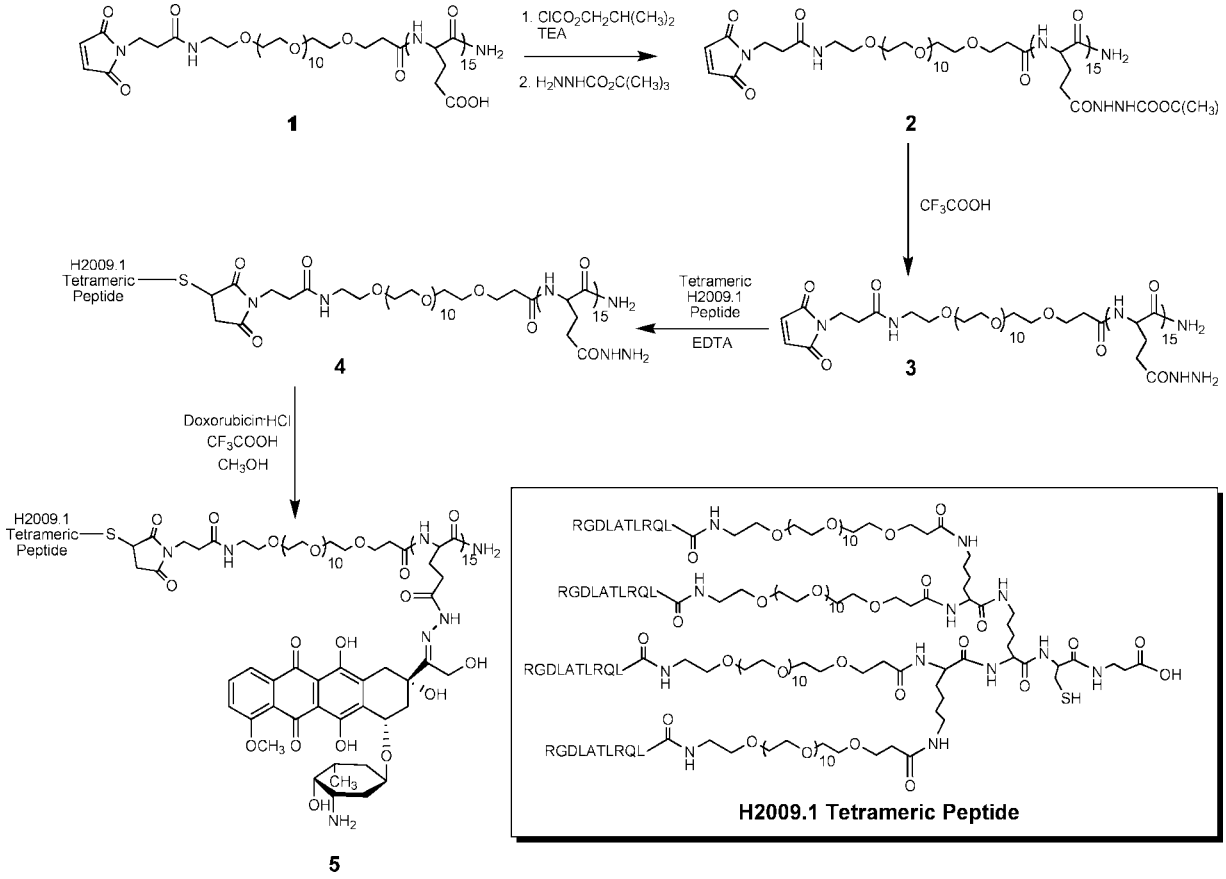

[a] The structure of the tetrameric H2009.1 peptide is shown in the inset.

pound incorporated the high affinity $\alpha_v\beta_6$-specific tetrameric H2009.1 peptide at the N-terminus of a 15 amino acid polymer of glutamic acid. Four doxorubicin molecules per peptidic targeting reagent are attached via an acid labile hydrazone. The conjugate is preferentially internalized into $\alpha_v\beta_6$ positive cells as witnessed by flow cytometric analysis and fluorescent microscopy. Cellular uptake is mediated by the H2009.1 peptide as less internalization of the doxorubicin-PG polymer is observed when it is conjugated to a scrambled sequence control peptide. Importantly, the conjugate is 2-fold more cytotoxic toward a targeted cell than a cell line that does not express the integrin.

Water soluble polymers as drug carriers have received much attention for the treatment of solid tumors (*34, 35*). These large molecular weight polymers offer several advantages over the use of nonconjugated therapeutics. First, the polymers can overcome the poor solubility associated with hydrophobic compounds. Second, the blood half-life of the drugs is often extended from minutes to hours or days, allowing the compound time to reach its target. Last, the polymer accumulates preferentially in the tumor because of the inherent leakiness of the tumor vasculature and is retained at this site because of the lack of a functional lymphatic system within the tumor. Passive targeting as a result of EPR effect increases the drug concentration in the tumor relative to other tissues.

Several different polymers have been explored as drug carriers (*34, 35*). Most prevalent are poly(ethylene glycol) (PEG), *N*-(2-hydroxypropylmethacrylamide) (HPMA) (*36*−*38*), and polyglutamic acid (PG) (*4*). Of these, only PG is biodegradable. As such, PEG and HPMA polymers must be kept under the size required for renal clearance. A variety of polymer−drug conjugates are in different stages of clinical trials (*35*). In addition to the nature of the polymer, the linkage between the drug and polymer plays an important role in the efficacy of the treatment (*28, 37*). Typically, one of three approaches have been employed: conjugation of the drug through a peptide linkage that is cleaved by endosomal and lysosomal proteases such as cathepsin-B (*37, 39*), attachment via an acid labile hydrazone that is cleaved in the acidic environment of the endosome and lysosome (*28, 37*), or by esterification (*4*). In the case of the hydrazone or peptidyl linkers, release of the drug requires cellular uptake of the polymer. However, in the case of the ester conjugate found in XYOTAX, release of the drug occurs in the extracellular space; the antitumor efficacy is greater due to the long dwell time of the polymer within the tumor (*4*).

Toward the goal of cell-targeted therapeutics, cell-specific targeting agents have been incorporated into polymeric drug carrier compounds (*5, 33, 40*−*43*). Most have conjugated an antibody to a tumor associated biomarker into the polymer itself. Increased efficacy is observed for the targeted polymeric carrier when compared to the corresponding nontargeted polymers. In some cases, extended survival is observed in animal models, albeit with nonsolid tumor models (*37, 42*). However, conjugation of antibodies or other targeting agents such as peptides or small molecules through the side chains of the polymers can be problematic; it is difficult to control the coupling efficiency of the antibody, it reduces the total drug load by using available coupling sites, and aggregation can occur. To address these problems, Li and co-workers attached an antibody to the epidermal growth factor receptor (EGFR) to the N-terminus of a PG-doxorubicin polymer (*5*). A PEG moiety was placed between the PG and the antibody. As such, a single targeting agent was incorporated in a chemospecific fashion. Uptake of the drug carrier was observed in an EGFR positive cell line, while minimal internalization was observed in NIH3T3 fibroblasts. Importantly, the construct was able to affect cell death.

It should be noted that doxorubicin was conjugated via an amide in this PG polymer, yet nuclear localization of doxorubicin was observed. The mechanism for the nuclear accumulation is unknown, but because of the rapid time frame in which it occurs, it is unlikely to be due to hydrolysis from the polymer.

While the larger polyglutamic acid polymers are often retained in tumors due to the EPR effect and have potentially higher drug capacity, we chose to focus on a defined 15 amino acid polymer. Smaller conjugates are expected to demonstrate better tumor penetration. Additionally, the smaller peptide is easier to modify in a regiospecific fashion. However, the tradeoff is lower drug loading capacities. Additionally, the tumor accumulation due to EPR may be less. On the other hand, the ease in which a tumor targeting agent can be incorporated into the polymer is a benefit, and active targeting can potentially be enhanced by more efficient escape from the vasculature and increased diffusion into the core of the tumor. Further *in vivo* experiments will be required to address the role of passive versus active targeting and tumor penetration of the smaller polymers.

The tumor targeting agent employed in this case is the tetrameric peptide H2009.1 which displays high affinity for $\alpha_v\beta_6$ (*2, 3*). This peptide does not bind to other RGD-binding integrins and has a half-maximal cell binding affinity in the 40−60 pM range. The integrin $\alpha_v\beta_6$ is emerging as an appealing cancer biomarker for targeted therapy. Expression of the β_6 subunit is restricted to epithelial cells, and its expression is low or undetectable in most normal adult primate tissues (*44*). This integrin is up-regulated in a variety of epithelial derived malignancies, including lung, oral, colon, breast, and ovarian cancers (*3, 45*−*49*). Expression of $\alpha_v\beta_6$ correlates with features found in more aggressive tumors, such as enhanced cell migration and invasion (*50*−*53*). β_6 expression is predictive of reduced survival time for patients with nonsmall cell lung carcinoma (*3*) and colorectal cancer (*54*). Thus, this targeting peptide is anticipated to have utility in molecular guided therapies for these aggressive tumor types.

While uptake of compound 5 is greater for cell line expressing $\alpha_v\beta_6$, the difference is only 2-fold, as observed by flow cytometry. Additionally, the conjugate is only 2-fold more cytotoxic toward H2009 cells compared to H1299 cells. However, it should be noted that there is a 60 fold difference in binding of the H2009.1 peptide for H2009 cells compared to the H1299 cells, when comparing binding of the individual peptide-displayed phage clones (*1*). This suggests that the polyGlu-doxorubicin portion of the molecule may dampen the selective uptake of the peptide by contributing to non-$\alpha_v\beta_6$ dependent cellular uptake. The flow cytometry data supports this, as some uptake of the conjugate containing the scramble control peptide is observed for both H1299 and H2009 cells. However, the cellular uptake of the nontargeted conjugate is substantially less than the freely cell permeable doxorubicin, and as such, there is a widening of the therapeutic index.

The cytotoxicity of compound 5 is less than that of free doxorubicin. The reduced efficacy of the conjugate is most likely due to a combination of reduced uptake of the conjugate compared to a cell permeable small molecule and poor release of the drug from the polymer scaffold. Flow cytometry shows that uptake of the conjugate is less than that of the free drug for the targeted cells. This is not uncommon for targeted drug conjugates. This limitation can be overcome by increasing the drug loads further or by moving to more cytotoxic agents. For example, the first line treatment of NSCLC usually employs paclitaxel whose IC_{50} is 40-fold lower than that of doxorubicin for H2009 cells (personal communication, Drs. John D. Minna and Michael Peyton). However, it should also be noted that the fluorescence of doxorubicin is 2-fold less when conjugated to the polymer compared to free doxorubicin (data not shown). As these studies were performed at 2 h, in which time little doxorubicin is released from the polymer, the total uptake of the polymer conjugated drug will be underestimated by fluorescence experiments. However, the differences in MFI cannot be accounted for by this effect alone, suggesting that the targeted polymer cannot deliver as much doxorubicin to H2009 cells as when the cells are treated with free drug.

Perhaps more importantly, microscopy reveals that the drug is perinuclear. This suggests that the drug is not being efficiently released from the conjugate and moving into the nucleus where it exerts its primary effect. While others have shown that doxorubicin hydrazones are hydrolyzed within the cell (*28, 37, 55*), hydrolysis from this conjugate may not occur within the appropriate time frame. The linker type, linker length, and mechanism of cellular uptake have been shown to influence the release of the drugs from polymeric carriers (*28*). This suggests that further optimization of the drug tether is required before progressing to *in vivo* experiments.

In summary, we have completed the synthesis of an integrin targeted polyglutamic acid-doxorubicin conjugate using a peptide that is highly specific for the tumor biomarker, $\alpha_v\beta_6$. To our knowledge, this is the first targeted polyglutamic acid drug conjugate which employs a peptidic targeting agent, and the only one that utilizes an acid labile linker between the therapeutic and polymer. This compound exhibits integrin specific cytotoxicity. Future work in lowering the background uptake of the polyglutamic acid-doxorubicin conjugates and improvement of the drug release by optimizing the linker will be required to improve the therapeutic properties of this compound.

ACKNOWLEDGMENT

We thank Bethany Gray for insightful discussions and critical reading of the manuscript. This work was supported by the NIH (1RO1CA106646) and the Welch Foundation (I1622). This paper represents publication # CSCN034 from the Cell Stress and Cancer Nanomedicine Program of the Simmons Comprehensive Cancer Center.

LITERATURE CITED

(1) Oyama, T., Sykes, K. F., Samli, K. N., Minna, J. D., Johnston, S. A., and Brown, K. C. (2003) Isolation of lung tumor specific peptides from a random peptide library: generation of diagnostic and cell-targeting reagents. *Cancer Lett. 202*, 219–230.

(2) Zhou, X., Chang, Y., Oyama, T., McGuire, M. J., and Brown, K. C. (2004) Cell-specific delivery of a chemotherapeutic to lung cancer cells. *J. Am. Chem. Soc. 129*, 15656–15657.

(3) Elayadi, A. N., Samli, K. N., Prudkin, L., Liu, Y. H., Bian, A., Xie, X. J., Roth, J. A., Wistuba, I. I., McGuire, M. J., and Brown, K. C. (2007) A peptide selected by biopanning identifies the integrin $\alpha_v\beta_6$ as a prognostic biomarker for non-small cell lung cancer. *Cancer Res. 67*, 5889–5895.

(4) Li, C. (2002) Poly(L-glutamic acid)-anticancer drug conjugates. *Adv. Drug Delivery Rev. 54*, 695–713.

(5) Vega, J., Ke, S., Fan, Z., Wallace, S., Charsangavej, C., and Li, C. (2003) Targeting doxorubicin to epidermal growth factor receptors by site-specific conjugation of C225 to poly(L-glutamic acid) through a polyethylene glycol spacer. *Pharm. Res. 20*, 826–832.

(6) Zunino, F., Pratesi, A., and Micheloni, A. (1989) Poly(carboxylic acid) polymers as carriers for anthracyclines. *J. Controlled Release 10*, 65–73.

(7) Hoes, C. J. T., Potman, W., van Heeswijk, W. A. R., Mud, J., de Grooth, B. G., Greve, J., and Feijen, J. (1985) Optimization of macromolecular prodrugs of the antitumor antibiotic adriamycin. *J. Controlled Release 2*, 205–213.

(8) Li, C., Yu, F. F., Newman, R. A., Cabral, F., Stephens, L. C., Hunter, N., Milas, L., and Wallace, S. (1998) Regression of well-established tumors using a novel water-soluble poly(L-glutamic acid)-paclitaxel conjugate. *Cancer Res. 58*, 2404–2409.

(9) Li, C., Price, J. E., Milas, L., Hunter, N. R., Ke, S., Yu, D. F., Charnsangavej, C., and Wallace, S. (1999) Antitumor activity of poly(L-glutamic acid)-paclitaxel on syngeneic and xenografted tumors. *Clin. Cancer Res. 5*, 891–897.

(10) Milas, L., Mason, K. A., Hunter, N., Li, C., and Wallace, S. (2003) Poly(L-glutamic acid)-paclitaxel conjugate is a potent enhancer of tumor radiocurability. *Int. J. Rad. Oncol. Biol. Phys. 55*, 707–712.

(11) Auzenne, E., Donato, N. J., Li, C., Leroux, E., Price, R. E., Farquhar, D., and Klostergaard, J. (2002) Superior therapeutic profile of poly-L-glutamic acid-paclitaxel copolymer compared with taxol in xenogeneic compartmental models of human ovarian carcinoma. *Clin. Cancer Res. 8*, 573–581.

(12) Singer, J. W., de Vries, P., Bhatt, R., Tulinsky, J., Klein, P., Li, C., Milas, L., Lewis, R. A., and Wallace, S. (2000) Conjugation of camptothecins to poly-(L-glutamic acid). *Ann. N.Y. Acad. Sci. 922*, 136–150.

(13) Zou, Y., Wu, Q. P., Tansy, D., Chow, M. C., Hung, C., Charnsangavej, C., and Wallace, S. (2001) Effectiveness of water soluble poly(L-glutamic acid)-camptothecin conjugate against resistant human lung cancer xenografted in nude mice. *Int. J. Oncol. 18*, 331–336.

(14) Zou, C., Brewer, M., Cao, X., Zang, R., Lin, J., Deng, Y., and Li, C. (2007) Antitumor activity of 4-(N-hydroxyphenyl) - retinamide conjugated with poly(L-glutamic acid) against ovarian cancer xenografts. *Gynecol. Oncol. 107*, 441–449.

(15) Zhu, G., Cao, X., Chang, J. Y., Milas, L., and Li, C. (2007) Polymeric retinoid prodrug PG-4HPR enhances the radiation response of lung cancer. *Oncol. Rep. 18*, 645–651.

(16) Wen, X., Jackson, E. F., Price, R. E., Kim, E., Wu, Q., Wallace, S., Charsangavej, C., Gelovani, J. G., and Li, C. (2004) Synthesis and characterization of poly(L-glutamic acid) gadolinium chelate: A new biodegradable MRI contrast reagent. *Bioconjugate Chem. 15*, 1408–1415.

(17) Melacon, M. P., Wang, Y., Wen, X., Bankson, J. A., Stephens, L. C., Jasser, S., Gelovani, J. G., Myers, J. N., and Li, C. (2007) Development of macromolecular dual-modality MR-optical imaging for sentinel lymph node mapping. *Invest. Rad. 42*, 569–578.

(18) Jackson, E. F., Esparza-Coss, E., Wen, X., Ng, C. S., Daniel, S. L., Price, R. E., Rivera, B., Charnsangavej, C., Gelovani, J. G., and Li, C. (2007) Magnetic resonance imaging of therapy-induced necrosis using gadolinium-chelated polyglutamic acids. *Int. J. Rad. Oncol. Biol. Phys. 68*, 830–838.

(19) Singer, J. W. (2005) Paclitaxel poliglumex (XYOTAX™, CT-2103): A macromolecular taxane. *J. Controlled Release 109*, 120–126.

(20) Nemunaitis, J., Cunningham, C., Senzer, N. S., Gray, M., Oldham, F., Pippen, J., Mennel, R., and Eisenfeld, A. (2005) Phase I study of CT-2103, a polymer-conjugated paclitaxel, and carboplatin in patients with advanced solid tumors. *Cancer Invest. 23*, 671–676.

(21) Bonomi, P. (2007) Paclitaxel poliglumex (PPX, CT-2103): macromolecular medicine for advanced non-small-cell lung cancer. *Expert Rev. Anticancer Ther. 74*, 415–422.

(22) Jain, R. K. (2001) Delivery of molecular and cellular medicine to solid tumors. *Adv. Drug Delivery Rev. 46*, 149–168.

(23) Phelps, R. M., Johnson, B. E., Ihde, D. C., Gazdar, A. F., Carbone, D. P., Linnoila, P., Matthews, M. J., Bunn, P. A., Carney, D., Minna, J. D., and Mulshine, J. L. (1996) NCI-Navy medical oncology branch cell line database. *J. Cell. Biochem.* 32–91.

(24) Tian, Y., Bromberg, L., Lin, S. N., Hatton, T. A., and Tam, K. C. (2007) Complexation and release of doxorubicin from its complexes with pluronic P85-*b*-poly(acrylic acid) block copolymers. *J. Controlled Release 121*, 137–145.

(25) Bae, Y., Fukushima, S., Harada, A., and Kataoka, K. (2003) Design of environment-sensitive supramolecular assemblies for intracellular drug delivery: Polymeric micelles that are responsive to intracellular pH change. *Angew. Chem., Int. Ed. 42*, 4640–4643.

(26) Ulbrich, K., and Subr, V. (2004) Polymeric anticancer drugs with pH-controlled activation. *Adv. Drug Delivery Rev. 56*, 1023–1050.

(27) Lee, C. C., Gillies, E. R., Fox, M. E., Guillaudeu, S. J., Frechet, J. M. J., Dy, E. E., and Szoka, F. C. (2006) A single dose of doxorubicin-functionalized bow-tie dendrimer cures mice bearing C-26 colon carcinomas. *Proc. Natl. Acad. Sci. U.S.A. 103*, 16649–16654.

(28) Hovorka, O., Etrych, T., Subr, V., Strohalm, J., Ulbrich, K., and Rihova, B. (2006) HPMA based macromolecular therapeutics: Internalization, intracellular pathway and cell death depend on the character of covalent bond between the drug and the peptide spacer and alos on spacer composition. *J Drug Targeting 14*, 391–403.

(29) Feener, E. P., and King, G. L. (1998) The biochemical and physiological characteristics of receptors. *Adv. Drug Delivery Rev. 29*, 197–213.

(30) Bareford, L., and Swaan, P. (2007) Endocytotic mechanisms for targeted drug delivery. *Adv. Drug Delivery Rev. 59*, 748–758.

(31) Conner, S., and Schmid, S. (2003) Regulated portals of entry into the cell. *Nature 422*, 37–44.

(32) Rodrigues, P. C., Beyer, U., Schumacher, P., Roth, T., Fiebig, H. H., Unger, C., Messori, L., Orioli, P., Paper, D. H., Mulhaupt, R., and Kratz, F. (1999) Acid-sensitive polyethylene glycol conjugates of doxorubicin: preparation, in vitro efficacy and intracellular distribution. *Bioorg. Med. Chem. 7*, 2517–24.

(33) Luo, Y., Bernshaw, N. J., Lu, Z.-R., Kopecek, J., and Prestwich, G. D. (2002) Targeted delivery of doxorubicin by HMPA copolymers-hyaluronan bioconjugates. *Pharm. Res. 19*, 396–402.

(34) Vicent, M. J., and Duncan, R. (2006) Polymer conjugates: nanosized medicines for treating cancer. *Trends Biotechnol. 24*, 39–47.

(35) Duncan, R. (2006) Polymer conjugates as anticancer nanomedicines. *Nat. Rev. Cancer* 688–701.

(36) Satchi-Fainaro, R., Puder, M., Davies, J. W., Tran, H. T., Sampson, D. A., Greene, A. K., Corfas, G., and Folkman, J. (2004) Targeting angiogenesis with a conjugate of HPMA copolymer and TNP-470. *Nat. Med. 10*, 255–261.

(37) Kovar, M., Kovar, L., Subr, V., Etrych, T., Ulbrich, K., Mrkvan, T., Loucka, J., and Rihova, B. (2004) HPMA copolymers containing doxorubicin bound by a proteolytically or hydrolytically cleavable bond: comparison of biological properties in vitro. *J. Controlled Release 99*, 301–314.

(38) Kopecek, J., Kopeckova, P., Minko, T., and Lu, Z. (2000) HPMA copolymer-anticancer drug conjugates: design, activity, and mechanism of action. *Eur. J. Pharm. Biopharm. 50*, 61–81.

(39) Dubowchik, G. M., Firestone, R. A., Padilla, L., Willner, D., Hofstead, S. J., Mosure, K., Knipe, J. O., Lasch, S. J., and Trail, P. A. (2002) Cathepsin B-labile dipeptide linkers for lysosomal release of doxorubicin from internalizing immunoconjugates: Model studies of enzymatic drug release and antigen-specific in vitro anticancer activity. *Bioconjugate Chem. 13*, 855–869.

(40) Tang, A., Kopeckova, P., and Kopecek, J. (2003) Binding and cytotoxicity of copolymer conjuagtes to lymphocytes mediated by receptor-binding epitopes. *Pharm. Res. 20*, 360–367.

(41) Kovar, M., Mrkvan, T., Strohalm, J., Etrych, T., Ulbrich, K., Stastny, M., and Rihova, B. (2003) HPMA copolymer-bound doxorubicin targeted to tumor-specific antigen of BCL1 mouse B cell leukemia. *J. Controlled Release 92*, 315–330.

(42) Ulbrich, K., Etrych, T., Chytil, P., Jelinkova, M., and Rihova, B. (2004) Antibody-targeted polymer-doxorubicin conjugates with pH-controlled activation. *J. Drug Targeting 12*, 477–489.

(43) Nan, A., Ghandehari, H., Hebert, C., Siavash, H., Nititakis, N., Reynolds, M., and Sauk, J. J. (2005) Water-soluble polymers for targeted drug delivery to human squamous carcinoma of head and neck. *J. Drug Targeting 13*, 189–197.

(44) Breuss, J. M., Gillette, M., Lu, L., Sheppard, D., and Pytela, R. (1993) Restricted distribution of integrin β_6 mRNA in primate epithelial tissues. *J. Histochem.Cytochem.* 41.

(45) Ahmed, N., Riley, C., Rice, G. E., Quinn, M. A., and Baker, M. S. (2002) $\alpha_v\beta_6$ Integrin- A marker for the malignant potential of epithelial ovarian cancer. *J. Histochem. Cytochem. 50*, 1371–1379.

(46) Arihiro, K., Kaneko, M., Fujii, S., Inai, K., and Yokosaki, Y. (2000) Significance of $\alpha_9\beta_1$ and $\alpha_v\beta_6$ integrin expression in breast carcinoma. *Breast Cancer 7*, 19–26.

(47) Jones, J., Sugiyama, M., Watt, F. M., and Speight, P. M. (1993) Integrin expression in normal, hyperplastic, dysplastic, and malignant oral epithelium. *J. Pathol. 169*, 235–243.

(48) Kawashima, A., Tsugawa, S., Boku, A., Kobayashi, M., Minamoto, T., Nakanishi, I., and Oda, Y. (2003) Expression of α_v integrin family in gastric carcinomas: Increased $\alpha_v\beta_6$ is associated with lymph node metastasis. *Pathol. Res. Pract. 199*, 57–64.

(49) Breuss, J. M., Gallo, J., DeLisser, H. M., Klimanskaya, I. V., Folkesson, H. G., Pittet, J. F., Nishimura, S. L., Aldape, K., Landers, D. V., Carpenter, W., Gillette, M., Sheppard, D., Matthay, M. A., Albelda, S. M., Kramer, R. H., and Pytela, R. (1995) Expression of the β_6 integrin in development, neoplasia, and tissue repair suggests a role in epithelial remodeling. *J. Cell Sci. 108*, 2241–2251.

(50) Thomas, G. J., Poomsawat, S., Lewis, M. P., Hart, I. R., Speight, P. M., and Marshall, J. F. (2001) $\alpha_v\beta_6$ Integrin upregulates matrix metalloproteinase 9 and promotes migration of normal oral keratinocytes. *J. Invest. Derm. 116*, 898–904.

(51) Thomas, G. J., Lewis, M. P., Whawell, S. A., Russell, A., Sheppard, D., Hart, I. R., Speight, P. M., and Marshall, J. F. (2001) Expression of the $\alpha_v\beta_6$ integrin promotes migration and invasion in squamous carcinoma cells. *J. Invest. Derm. 117*, 67–73.

(52) Thomas, G. J., Lewis, M. P., Hart, I. R., Marshall, J. F., and Speight, P. M. (2001) $\alpha_v\beta_6$ integrin promotes invasion of squamous carcinoma cells through up-regulation of matrix metalloproteinase-9. *Int. J. Cancer 92*, 641–650.

(53) Agrez, M., Gu, X., Turton, J., Meldrum, C., Niu, J., Antalis, T., and Howard, E. W. (1999) The $\alpha_v\beta_6$ integrin induces gelatinase secretion in colon cancer cells. *Int. J. Cancer 81*, 90–97.

(54) Bates, R. C., Bellovin, D. I., Brown, C., Maynard, E., Wu, B., Kawakatsu, H., Sheppard, D., Oettgen, P., and Mercurio, A. M. (2005) Transcriptional activation of integrin β_6 during the epithelial-mesenchymal transition defines a novel prognostic indicator of aggressive colon cancer. *J. Clin. Invest. 115*, 339–347.

(55) Kovar, L., Strohalm, J., Chytil, P., Mrkvan, T., Kovar, M., Hovorka, O., Ulbrich, K., and Rihova, B. (2007) The same drug but a different mechanism of action: Comparison of free doxorubicin with two different N-(2-hydroxypropyl)methacrylamide copolymer-bound doxorubicin conjugates in EL-4 cancer cell line. *Bioconjugate Chem. 18*, 894–902.

BC800154F

Characterization of and Mechanism for Copper-Induced Thioureation of Serum Albumin

Yu-Wei Wu[†] and Yu-Hui Tsai*[,†,‡]

Graduate Institute of Pharmacy and Graduate Institute of Medical Sciences, Taipei Medical University, Taipei, Taiwan. Received November 10, 2007; Revised Manuscript Received July 30, 2008

Thioureas (Tus) are widely used in chemical and pharmaceutical industries. This study demonstrated that copper induced the disulfide-linkage between Tus, such as α-naphthylthiourea (ANTU) and fluorescein-5-isothiocyanate cadaverine (FTC), with albumin (Alb), a major carrier protein in plasma with multiple functions. This reaction was absolutely copper-dependent, whereas cobalt, nickel, calcium, magnesium, zinc, iron, and manganese ions could not induce the same reaction. The reaction was substrate dose-dependent, and occurred optimally at pH 6.5. The resulting conjugated product was heat-labile, but stable in pH 6.0−8.0 buffer at 25 °C. The linkage could be reduced by Cu(I) (in acidic pH) and thiol-reducing agents. The mechanism of albumin thioureation was concluded: (i) the binding of Cu(II) with albumin is not necessary for the reaction, while the formation of Tus-Cu(II) complex is essential; (ii) thioureation resulted from the attack of Tus-Cu(II) at Alb-Cys^{34}-SH to form the Alb-Cys^{34}-S-S-Tus complex accompanied by the release of Cu(I); (iii) the released Cu(I) would back inhibit the reaction because of its competition with Cu(II) for Tus binding. These phenomenons may have important implications for the pharmacokinetics of thiourea-based drugs in plasma.

INTRODUCTION

Thiourea (Tu[1]) and its derivatives are widely used in chemical, agricultural, metallurgical, and pharmaceutical industries (*1*). Exposure of human and animals to Tu-containing compounds has been considered as an environmental risk factor that may cause various illnesses such as thyroid hyperplasia, pulmonary edema, pleural effusion, tumors, and so forth (*1*−*3*). Physiologically, Tu is absorbed from the gastrointestinal tract in humans and animals and is mostly excreted unchanged in urine (*1*, *4*). The accumulation of radiolabeled Tu in rats was found mainly in thyroid tissue and to a lesser degree in the kidney, blood cells, lung, and liver (*4*, *5*). The metabolism of Tu in the thyroid gland and liver is quite different. In the thyroid gland, Tu is oxidized by thyroid peroxidase to form dithioformamidine (Tu-S-S-Tu), which is later decomposed to cyanamide, sulfur, and Tu. Both Tu and cyanamide are inhibitors of thyroid peroxidase and finally lead the dysfunction of the thyroid gland (*6*). In the liver, Tu is metabolized to formamidine sulfenate and formamidine sulfinate by microsomal flavin-containing monooxygenase (FMO)-catalyzed S-oxygenation (*7*). In addition, radiolabeled Tu was found covalently and nonenzymatically binding to thyroid and lung proteins (*8*, *9*). The binding of Tu to thyroid proteins resulted from thiol−disulfide exchange between the thiol of Tu with the intramolecular disulfide bridge of proteins to form the protein−S-S-Tu complex. The complex was finally hydrolyzed to protein−S-SH and urea (*8*).

Tu is known to interact with sulfhydryl-containing compounds such as cysteine or glutathione in vitro (*10*, *11*). The oxidation of cysteine catalyzed by Tu in the presence of hydrogen peroxide in acid solution was illustrated in reactions A and B. The formation of the Cys-S-S-Tu complex was found in the reaction of cysteine with equimolar or excess amount of dithioformamidine (Tu-S-S-Tu) (reaction C). Cys-S-S-Tu was also produced by reacting cysteine with Tu (reaction D). Finally, the Cys-S-S-Tu formed in reactions C and D was spontaneously hydrolyzed (reaction E).

$$2\text{Tu} + \text{H}_2\text{O}_2 \rightarrow \text{Tu-S-S-Tu} + 2\text{H}_2\text{O} \quad \text{(A)}$$

$$2\text{Cys-SH} + \text{Tu-S-S-Tu} \rightarrow \text{Cys-S-S-Cys} + 2\text{Tu} \quad \text{(B)}$$

$$\text{Cys-SH} + \text{Tu-S-S-Tu} \rightarrow \text{Cys-S-S-Tu} + \text{Tu} \quad (\text{Tu-S-S-Tu} \geq \text{Cys-SH}) \quad \text{(C)}$$

$$\text{Cys-S-S-Cys} + \text{Tu} \rightarrow \text{Cys-S-S-Tu} + \text{Cys-SH} \quad \text{(D)}$$

$$\text{Cys-S-S-Tu} + \text{H}_2\text{O} \rightarrow \text{Cys-SOH} + \text{Tu} \quad \text{(E)}$$

The protective role of thioureas (Tus) was found in the clearance of free radicals (*12*−*14*). In addition, Tus were known to interact with miscellaneous metal ions including copper (*15*−*17*). It was speculated that the binding of copper with Tu may protect cells from copper-induced oxidative damage (*18*). In pharmaceutical applications, Tu-containing compounds are designed as anti-HIV drugs (*19*), high-density lipoprotein (HDL)-elevating agents (*20*), appetite suppressants (*21*), and so forth. Some of these compounds were found to hydrophobically interact with albumin (*22*, *23*).

Albumin is the most abundant protein in blood plasma with miscellaneous functions. Human serum albumin (HSA) itself is a 67 KD single chain protein with 35 cysteine residues; however, it has only one free thiol group of cysteine residues at position 34 (Cys^{34}); the other 34 cysteine residues form 17 disulfide bridges for its tertiary structure. HSA with the free thiol in Cys^{34}, known as mercaptoalbumin, is capable of

* To whom correspondence should be addressed. Graduate Institute of Medical Sciences, Taipei Medical University, 250 Wu-Hsing Street, Taipei, Taiwan 110. Tel: 886-2-2736-1661ext. 3417 and 3411. Fax: 886-2-2377-8620. E-mail: cmbyht18@tmu.edu.tw.

† Graduate Institute of Pharmacy.

‡ Graduate Institute of Medical Sciences.

[1]Abbreviations: Alb, albumin; HSA, human serum albumin; Tus, thioureas; Tu, thiourea; FTC, fluorescein-5-isothiocyanate cadaverine; FCC, fluorescein-5-carboxamide cadaverine; DC, dansylcadaverine; ANTU, α-naphthylthiourea; EDTA, ethylenediaminetetraacetic acid; DTT, dithiothreitol; SDS, sodium dodecyl sulfate; NCP, neocuproine; NAC, *N*-acetyl-L-cysteine; GSSG, oxidized glutathione; MD-Charcoal, magnetic dextran-coated charcoal; CFA, charcoal-based fluorescence assay.

10.1021/bc7004158 CCC: $40.75 © 2008 American Chemical Society
Published on Web 08/20/2008

participating in numerous redox reactions. Albumin is known to bind small molecules of many types. Metal ions such as copper, nickel, cobalt, zinc, and so forth are carried by albumin. Endogenous and exogenous ligands, metabolites, and drugs are generally bound to Sudlow's site-I or site-II of albumin, with some exceptions (*24*−*26*). In addition, covalent interactions with albumin including glycosylation (*27*), acylation (*28*), thiolation (*29*, *30*), S-nitrosation (*31*, *32*), and N-homocysteinylation (*33*) are also found. Thiolation of HSA (HSA-S-R) occurs at Cys^{34} with low molecular weight thiol-containing substances (e.g., cysteine, homocysteine, glutathione, and drugs such as cisplatin, D-penicillamine, and *N*-acetyl-cysteine) via disulfide bridge formation (*24*−*26*). Thiolation of albumin has not been previously reported as a copper-dependent reaction; however, a fast S-nitrosation of albumin was mediated by copper (*32*).

In our previous study, a charcoal-based fluorescence assay (CFA) was developed to rapidly analyze the incorporation of small fluorescent molecules into large protein molecules (*34*). By using the method, a copper-dependent FITC-binding protein was found in human plasma. This protein was subsequently purified and identified as albumin (*35*). The mechanism of copper-induced albumin thioureation was proposed, evaluated, and established in this study. Furthermore, the importance of this finding is discussed.

EXPERIMENTAL PROCEDURES

Materials. Essentially fatty acid free, globulin free albumin with 99% in purity from human (HSA; A3782), bovine (BSA; A0281), and porcine (PSA; A1173) sera were purchased from Sigma-Aldrich (St. Louis, MO, USA). Recombinant human serum albumin (rHSA), containing 584 amino acid residues with a single deletion at Asp^1 residue that reduces its binding affinity for copper and nickel, was from United States Biological (Swampscott, MA, USA). Fluorescein-5-isothiocyanate cadaverine (FTC) and fluorescein-5-carboxamide cadaverine (FCC) were from AnaSpec, Inc. (San Jose, CA, USA). BioMag magnetic dextran-coated charcoal (MD-Charcoal) concentrate (40 mg/mL, approximately 1.5 μm particle size) was supplied by Bangs Laboratories, Inc. (Fishers, IN, USA). Other chemicals used were of analytical grade from either Sigma-Aldrich, or Merck (Darmstadt, Germany), unless otherwise stated.

NHS-activated Sepharose 4 Fast Flow media were from Amersham Biosciences AB (Uppsala, Sweden). The ultrafiltration unit was from Millipore (Bedford, MA, USA). V96 microwell plate (#249945) was from Nalge Nunc International (Rochester, NY, USA). Slot blot manifold (Hoefer PR648) was from Hoefer, Inc. (San Francisco, CA, USA).

Stocks of 1 mM FTC, FCC, and dansylcadaverine (DC) were dissolved in 20% dimethyl sulfoxide and stored at 4 °C till use. Cuprous chloride (CuCl) of 10 mM was freshly prepared in 50 mM HCl. L-Cystine was prepared as 1 mM stock solution in 50 mM HCl. Solution of 50 mM neocuproine (NCP) was dissolved in 50% methanol. MD-Charcoal concentrate was 5-fold diluted with water and stored at 4 °C for subsequent application. The water used in this study was prepared by the Milli-Q system (Millipore, Bedford, MA, USA).

Modification of Albumin. Albumin used in this study was mercaptoalbumin (Alb-Cys^{34}-SH) unless otherwise stated. Mercaptoalbumin preparation was modified from a previous publication (*36*). Briefly, 1 mM HSA (or BSA, PSA, and rHSA) in sodium phosphate buffer (0.1 M Na_2PO_4, pH 6.86, 0.3 M NaCl, and 1 mM EDTA) was treated with 5 mM DTT at 25 °C for 45 min. The phosphate buffer of the specimen was then changed to HBS buffer (10 mM Hepes-pH 7.0, 0.15 M NaCl) by dialysis at 4 °C. One mole of albumin was confirmed to contain 1 mol of free thiol by Ellman's method (*37*).

Alkylation of albumin (Alk-HSA) was performed according to Glowacki et al. with modification (*33*). Briefly, 1 mM iodoacetamide was incubated with 0.1 mM human mercaptoalbumin containing 0.1 M Hepes-pH 7.5 and 0.2 mM EDTA at 37 °C for 2 h. The buffer of resulting products was changed to HBS buffer by dialysis at 4 °C. Free thiol content of Alk-HSA was calculated to be 0.13 (M/M).

For cysteinylation, human mercaptoalbumin (50 μM) was treated with 1 mM L-cystine in 0.1 M Hepes-pH 7.5 buffer containing 0.1 mM EDTA at 37 °C for 21 h. The mixture was subject to HBS buffer exchange by using a 30 K ultrafiltration unit (Amicon Ultra-15). This protein product (50 μM) was further treated with 1 mM IAN in 0.1 M Hepes-pH 7.5 buffer containing 0.1 mM EDTA at 37 °C for 3 h. The buffer of the protein was changed to HBS buffer as described above. This protein product was termed Cys-HSA. To determine the extent of albumin cysteinylation, Cys-HSA (165 μM) was treated with 5 mM DTT at room temperature for 45 min. The buffer of the reduced protein was changed to HBS buffer again as described above. The product from this step was termed r-Cys-HSA (thiol-reduced Cys-HSA). Free thiol content for Cys-HSA and r-Cys-HSA was calculated to be 0.08 and 0.50 (M/M), respectively. The contents of r-Cys-HSA and Cys-HSA were thus estimated as follows: r-Cys-HSA contained Alb-SH (∼50%) and Alk-HSA (∼50%); Cys-HSA contained Alb-SH (∼8%), Alb-S-S-Cys (∼42%), and Alk-HSA (∼50%).

Analysis of Ligand-Binding by CFA. A high-throughput CFA method modified from our previous publication was used to analyze the binding capacity of albumin for fluorescent dyes (see Supporting Information, Figure 1) (*34*). Typically, 30 μL per well of protein samples (2 μM HSA, unless otherwise stated) dissolved in HBS buffer (10 mM Hepes-pH 7.0, 0.15 M NaCl) were added to microplates at 4 °C. After 30 μL of freshly prepared reagent-A (100 mM Hepes-pH 7.0, 0.2 mM $CuCl_2$, and 6 μM FTC) was added into each well, the reaction was initiated by incubating the microplate in a 37 °C humidified incubator for 10 min and terminated by adding 60 μL of reagent-B (2 mM EDTA, 0.5 M Hepes-pH 8.0; 4 °C). Suspended MD-Charcoal (200 μL per well) was then added and incubated at room temperature for 5 min to remove all of the free fluorescent dyes. After precipitating MD-Charcoal by magnet for 1 min, the fluorescence intensity in each well was measured by a microplate reader (Plate Chameleon, Hidex Oy, Finland) with excitation wavelength setting at 485 nm and emission wavelength at 535 nm (Ex485/Em535); gain 35. Transfer of supernatant to a new plate for fluorescence counting is not necessary because the precipitated MD-Charcoal did not influence the fluorescence in the supernatant. Background level of fluorescence intensities were measured by replacing protein samples with HBS buffer. The binding capacity of albumin for fluorescent dye was expressed as net or relative fluorescence (fluo.) intensity per reaction. All experiments were performed in triplicate for each datum point, and the data were presented as the means ± SD.

In addition, supplementation of metal ions or small molecules such as cysteine, NCP, and so forth in the reaction mixture did not influence fluorescence counting by using our assay system (see Supporting Information Figures 2 and 3).

Beads Preparation. Tu- and Cys-beads were prepared by coupling each ligand with NHS-activated Sepharose 4 matrix. In detail, Tu (0.1 M) or cysteine (0.1 M) dissolved in PBS buffer (137 mM NaCl, 2.7 mM KCl, 10 mM Na_2HPO_4, and 2 mM KH_2PO_4, pH 7.4) was mixed with equal volume of the drained NHS-activated Sepharose 4 Fast Flow media at 25 °C for 2 h with constant shaking. The resulting matrix was washed with basic buffer (0.5 M Tris, pH 9.0, and 0.5 M NaCl) and then with acidic buffer (0.1 M acetate and 0.5 M NaCl, pH 4.0) for 3 cycles. Finally, these beads were washed with HBS buffer

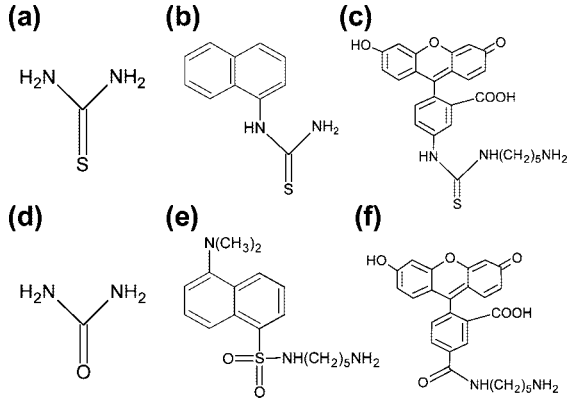

Figure 1. Chemical structures of Tu derivatives and analogues. (a) Tu; (b) ANTU; (c) FTC; (d) urea; (e) DC; (f) FCC.

and stored at 4 °C. The Cys-bead was treated with 10 mM DTT at 25 °C for 30 min before use.

Alkylation of the Cys-bead (Alk-Cys-bead) was performed by incubating the bead with an equal volume of 10 mM iodoacetamide at 37 °C for an hour with shaking. The bead was then washed with HBS buffer and stored at 4 °C.

Copper pretreated Tu- or Cys-beads were produced by mixing the Tu- or Cys-beads with an equal volume of 5 mM $CuCl_2$ at 25 °C for 15 min with constant shaking. After supplementation with 20 mM EDTA, the beads were then washed with HBS buffer and then stored at 4 °C till use.

Formation and Purification of the HSA−FTC Complex. The HSA−FTC complex was produced by reacting 2 μM human mercaptoalbumin with an equal volume of reagent-A (100 mM Hepes-pH 7.0, 0.2 mM $CuCl_2$, and 6 μM FTC) at 37 °C for an hour. After supplementation with 2 mM EDTA, the protein fraction was concentrated, and the buffer was changed to HBS buffer by ultrafiltration using a 10 kDa cutoff filter device. The resulting product (0.72 mg/mL) was stored at 4 °C till use within 24 h.

RESULTS

Copper-Induced Specific Binding of Tus to HSA. The analysis of albumin-bound fluorescent dyes was performed by CFA. As shown in Figure 2, no dyes bound to HSA unless copper was added. By comparing the structural analogues (ANTU versus DC, and FTC versus FCC), HSA-bound fluorescent dyes, either ANTU or FTC, have similar Tu functional groups (Figure 1). Thus, the Tu group is speculated to interact with albumin upon copper induction. FTC was selected for subsequent HSA binding analyses. The coupling reaction showed a positive dose-dependence on HSA, FTC, and copper contents (Figure 3).

Disulfide Bridge Formation between Tus and Cysteine. To identify the type of linkage between HSA and FTC, the purified HSA−FTC complexes were treated with/without NaCl, urea, DTT, or SDS (Figure 4a). While urea- or SDS-treatment damaged up to 40% of complexes, DTT-treatment almost eliminated the fluorescence signal of protein fractions (>90%). This indicates that the linkage between HSA and FTC is a disulfide bond. In addition, a high concentration of salt (1 M NaCl) did not significantly influence the stability of HSA−FTC complexes.

To confirm that thioureation occurred at the Cys^{34} residue of albumin, Cys^{34}-modified albumins, Cys-HSA, r-Cys-HSA, or Alk-HSA, were employed in the reaction (Figure 5). The binding capacity of FTC with Cys-HSA, r-Cys-HSA, or Alk-HSA corresponded to their free thiol content, as compared to that with HSA. In addition, the interaction of cysteine with FTC

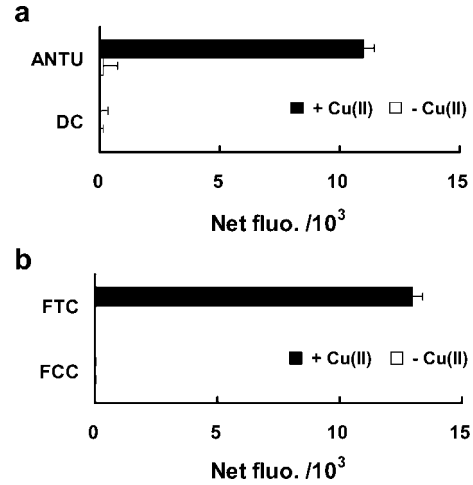

Figure 2. Analysis of copper-induced binding using the CFA method. Aliquots of 60 μL of reaction mixture containing (a) 7.52 μM HSA, 30 μM ANTU (or dansyl-cad), 50 mM Hepes-pH 7.0, with/without 0.1 mM $CuCl_2$, or (b) 1 μM HSA, 3 μM FTC (or FCC), 50 mM Hepes-pH 7.0, with/without 0.1 mM $CuCl_2$, were incubated at 37 °C for 30 or 10 min, respectively. After the addition of equal volume reagent-B (2 mM EDTA, 0.5 M Hepes-pH 8.0), unbound fluorescent dyes were removed by MD-Charcoal (0.2 mL/well). MD-Charcoal was precipitated, and the fluorescence intensities were measured at Ex340/Em460 for ANTU, Ex340/Em353 for dansyl-cad, and Ex485/Em535 for FTC and FCC. Gain value was set at 35. Data presented are the means ± SD ($n = 3$).

was also further confirmed by using the Cys-bead and Alk-Cys-bead in copper-induced reaction (Figure 4b). Similar to albumin, the Cys-bead interacts with FTC through the disulfide bond, as compared to that with Alk-Cys-bead (as control).

Furthermore, the Tu-bead was also used to confirm the participation of the Tu group of FTC in disulfide bridge formation, and the Cys-bead was used as the control (Figure 4c). In the presence of copper, HSA was also found to form a disulfide bond with the Tu-bead. The same phenomenon was also observed for Cys-beads. In the absence of copper, however, only the Cys-bead that was pretreated with copper could bind HSA. The mechanism of copper-induced cysteinylation appears different from that of copper-dependent thioureation of HSA.

The Influence of Ligand-Binding for Albumin Thioureation. Various reagents were evaluated for their effects on the formation of the HSA−FTC complex by the CFA method (Table 1). It was found that free thiol-containing molecules, such as NAC and cysteine, greatly reduced the binding of HSA with FTC, while cystine and GSSG had no significant effect. Because cysteine was also observed to interact with FTC under copper treatment (Figure 4b), the inhibitory effects of free thiol-containing molecules are speculated to compete with HSA for interacting with the Tu-Cu(II) complex. As expected, Tu and ANTU competed with FTC for HSA-binding as compared to the Tu analogue, urea. The competition of Tu was not as effective as ANTU. In addition, dansylglutamine and dansylglycine, the site I and II binding probes of albumin (*25*), respectively, did not affect the interaction of FTC with HSA.

The Effect of pH on Thioureation. Copper-induced HSA−FTC complex formation was greatly influenced by the pH of the reaction solution (Figure 6a). The optimal pH for the reaction was pH 6.5. Above pH 6.5, the reaction was gradually reduced with increasing pH and is completely abolished at pH above 8.0. The relative initial reaction rate constants of reactions at various pH values were also calculated (Figure 6b), and the kinetic data did support the observations shown in Figure 6a. In the absence of albumin, the interaction between FTC and Cu(II) was also influenced by pH (Figure 6c). Upon Cu(II) supplementation, the fluorescence intensity of FTC is severely

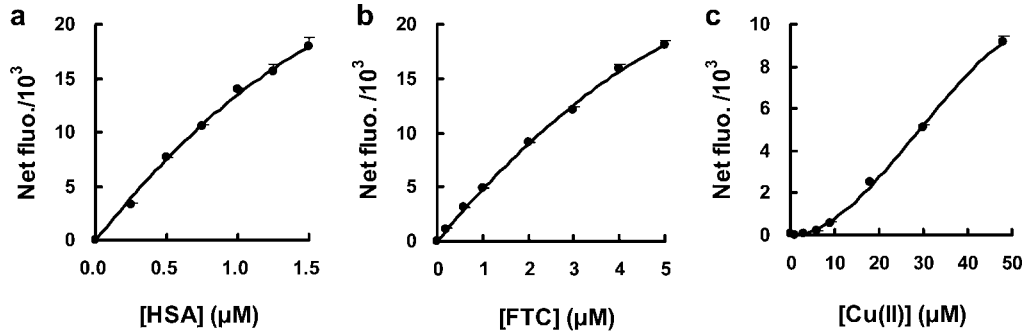

Figure 3. Dose dependence of HSA, FTC, and $CuCl_2$ for albumin thioureation. Reaction mixtures containing (a) HSA (0−1.5 μM), 3 μM FTC, 0.1 mM $CuCl_2$, and 50 mM Hepes-pH 7.0; (b) FTC (0−5.0 μM), 1 μM HSA, 0.1 mM $CuCl_2$, and 50 mM Hepes-pH 7.0; or (c) $CuCl_2$ (0−48 μM), 1 μM HSA, 3 μM FTC, and 50 mM Hepes-pH 7.0 were incubated at 37 °C for 10 min and analyzed by the CFA method as described in Experimental Procedures. Data presented are the means ± SD (n = 3).

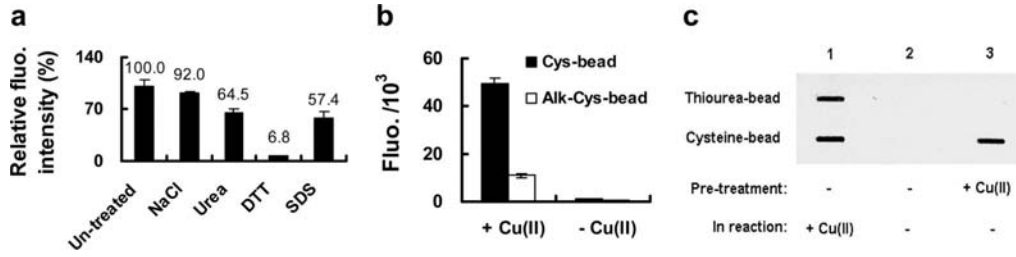

Figure 4. Disulfide bridge formation between (a) HSA and FTC; (b) cysteine and FTC; and (c) HSA and Tu. In (a), 28 μg of HSA−FTC complex in HBS buffer was treated with 1 M NaCl, 3 M urea, 5 mM DTT, or 0.1% SDS, separately, at 37 °C for 15 min. The mixtures were then ultrafiltrated using Microcon YM-30 tubes. Protein fractions were collected in microplates and adjusted to pH 8.0 for fluorescence counting. In (b), Cys-beads or Alk-Cys-beads (drained volume = 30 μL/reaction) after reaction with 3 μM FTC (in 50 mM Hepes-pH 7.0) in the presence or absence of $CuCl_2$ (0.1 mM) at 37 °C for 30 min were washed with 0.5 M NaCl (in 10 mM Hepes-pH 7.0) and then treated with 5 mM DTT at 25 °C for 15 min. The supernatants supplemented with 50 mM Hepes-pH 8.0 were measured for fluorescent intensities to assess the bound FTC molecules. In (c), reaction mixtures containing HSA (0.5 mg) and Tu- or Cys-beads (0.1 mL drain matrix) with/without 2 mM $CuCl_2$ were incubated at 25 °C for 30 min. Copper-pretreated Tu- or Cys-beads were also tested for HSA binding in the absence of copper. The copper-containing reaction was terminated by adding 2 mM EDTA. After washing with 0.5 M NaCl (in 10 mM Hepes-pH 7.0), the bead-bound proteins were eluted with DTT followed by slot blotting the eluted proteins onto nitrocellulose membranes. The existence of protein on the membrane was visualized by a MemCode reversible protein stain kit (Pierce Biotechnology, Rockford, IL, USA).

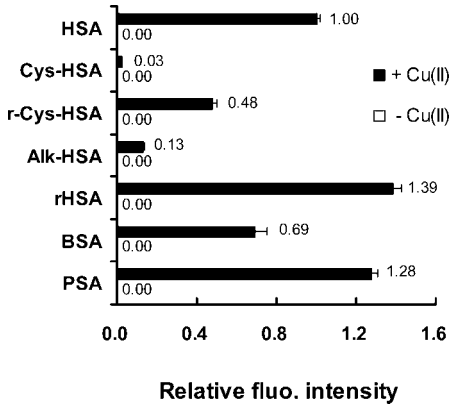

Figure 5. Evaluation of FTC binding capacity by various albumins. Various albumins (1 μM) were incubated with 3 μM FTC, 0.1 mM $CuCl_2$, and 50 mM Hepes-pH 7.0 at 37 °C for 10 min. The copper-induced coupling reactions were assessed by the CFA method as described in Experimental Procedures. The fluorescence intensity of each was calculated relative to that of HSA. Data presented are the means ± SD (n = 3). The calculated free thiol content for mercaptoalbumin (HSA, rHSA, BSA, or PSA), Cys-HSA, r-Cys-HSA (thiol-reduced Cys-HSA), and Alk-HSA were 1.00, 0.08, 0.50, and 0.13 (M/M), respectively.

Table 1. Influence of Thiol-Containing Agents, Tu Analogues, Ligands, and Cu(I) on HSA−FTC Complex Formation[a]

reagents	relative fluorescence intensity (%)
control	100.0 ± 3.4
thiol-containing molecules:	
DTT, 10 μM	7.4 ± 0.9
NAC, 10 μM	5.6 ± 0.3
Cys-SH 10 μM	5.6 ± 0.5
cystine, 10 μM	98.2 ± 2.6
GSSG, 10 μM	96.2 ± 1.9
Tu and Tu analogues:	
Tu, 10 μM	79.1 ± 0.9
Tu, 100 μM	33.5 ± 2.0
ANTU, 10 μM	31.3 ± 0.9
Urea, 100 μM	99.0 ± 1.4
ligands:	
dansylglutamine, 10 μM	98.7 ± 1.5
dansylglycine, 10 μM	99.8 ± 3.2
Cu(I):	
CuCl, 10 μM	83.0 ± 1.5
CuCl, 100 μM	34.9 ± 0.6

[a] Various reagents were included in the reaction of 1 μM HSA, 3 μM FTC, 0.1 mM $CuCl_2$, and 50 mM Hepes-pH 7.0. The complex formation of HSA−FTC was analyzed by the CFA method, and shown as relative fluorescence intensities comparing to control (no reagents added). Data represents the means ± SD (n = 3).

quenched (ΔQ). However, the fluorescence of the FTC−Cu(II) mixture is greatly enhanced (ΔH_1) with increasing pH above 7.5, as compared to that observed in the absence of copper (ΔH_2). The increased fluorescence intensity (ΔH_1) at high pH was speculated to be the result of the dissociation of FTC from Cu(II) ions.

Participation of Metal Ions in Thioureation. Various metal ions (0.1 mM in reaction), including CuCl, $CuCl_2$, $CoCl_2$, $NiCl_2$, $CaCl_2$, $MgCl_2$, $ZnCl_2$, $MnCl_2$, $FeCl_2$, and $FeCl_3$, were tested for Alb−FTC complex formation by using the CFA method. As shown in Figure 7, only Cu(II) induced the thioureation reaction among various metal ions; the small amplitude of the

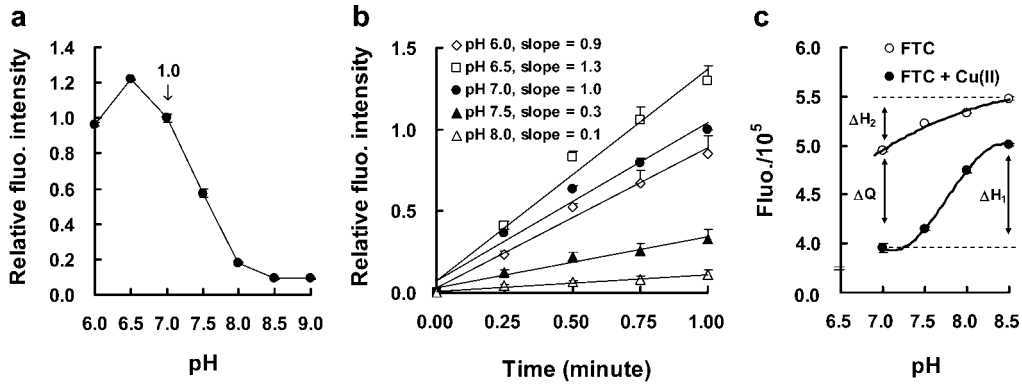

Figure 6. pH effect on Alb−FTC complex formation. (a) Reaction mixtures as described in Figure 5 were incubated at various pH values at 37 °C for 10 min to evaluate the influence of pH on the formation of the Alb−FTC complex. (b) The kinetics of the reaction at various pH values. Reactions at various pH values (pH 6.0−8.0) were performed at 37 °C for designated time intervals (0−60 s). The fluorescence intensity of the reaction at pH 7.0 for 1 min was set as 1.0, and the relative initial rate was calculated. The slopes of the trend lines of the reaction data points at various pH values correspond to the relative rate constants for the reactions. (c) The effect of pH on the interaction between Cu(II) and FTC. The fluorescence intensities of 3 μM FTC with/without 0.1 mM $CuCl_2$, in 50 mM Hepes at various pH values, were measured to assess the interaction between FTC and Cu(II). Data presented are the means ± SD ($n = 3$). ΔQ: quenched fluorescence intensity of FTC upon the addition of Cu(II). ΔH_1: increased fluorescence intensity of the FTC−$CuCl_2$ mixture with increasing pH. ΔH_2: increased fluorescence intensity of FTC with increasing pH.

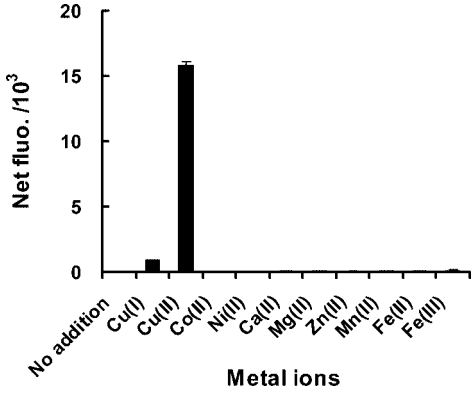

Figure 7. Necessity of metal ions for thioureation. Various metal ions (0.1 mM) incubated with 1 μM HSA, 3 μM FTC, and 50 mM Hepes-pH 7.0 at 37 °C for 10 min were analyzed by the CFA method as described in Experimental Procedures. Data presented are the means ± SD ($n = 3$).

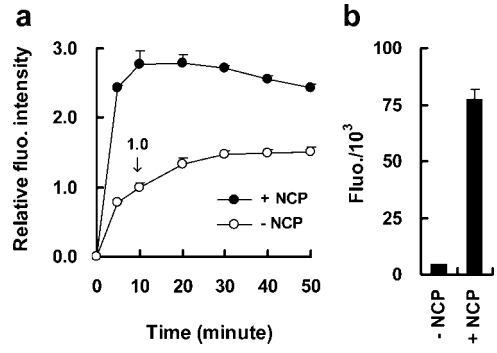

Figure 8. Effect of NCP on thioureation of HSA. (a) Reaction mixtures as described in Figure 5 were incubated at 37 °C in the presence or absence of NCP for indicated time-intervals. The relative fluorescent intensities were calculated relative to that of the 10-min reaction without NCP treatment. (b) Drained Cys-beads (30 μL) supplemented with 30 μL of HBS buffer and 30 μL of reagent-A (100 mM Hepes-pH 7.0, 0.2 mM $CuCl_2$, and 6 μM FTC), with/without 0.1 mM NCP, were incubated at 37 °C for 15 min. After the addition of 2 mM EDTA, the beads were washed with HBS buffer. Bead-bound FTC was finally eluted with 5 mM DTT (dissolved in 0.1 M Hepes-pH 8.0) and subjected to fluorescence measurement. Data presented are the means ± SD ($n = 3$).

Cu(I)-induced reaction may result from the oxidation of Cu(I) to Cu(II) during material preparation. The necessity of Cu(II) for thioureation was demonstrated by the dose-dependent reaction (Figure 3c), and the reduction of Cu(II) to Cu(I) during thioureation processes was speculated. NCP, a specific Cu(I) chelator, was used to confirm the formation of Cu(I). In the presence of NCP, the formation of HSA−FTC is greatly enhanced and reaches its plateau within 10 min as compared to that observed in the absence of NCP (Figure 8a). Similarly, the cross-linking of FTC with cysteine (which was evaluated by Cys-beads) was also elevated by NCP treatment (Figure 8b). In addition, the supplement of Cu(I) did decrease the Cu(II)-induced formation of HSA−FTC complexes (Table 1). These results implied that Cu(I) was a byproduct associated with the Cu(II)-induced thioureation of Cys^{34} of albumin and that the released Cu(I) would back inhibit thioureation.

Stability of Thioureated Products. The purified HSA−FTC complex was used for stability evaluation (Figure 9). This product appears stable at 25 °C, pH 7.0, within an hour but is unstable with increasing temperature (Figure 9a). As to the pH effect, the HSA−FTC complex was stable at pH 6−8 at 25 °C but degraded significantly in acidic (pH < 6.0) or basic (pH > 8.0) conditions (Figure 9b). In acidic conditions, Cu(I) was capable of reducing the Alb−FTC complex (Figure 9c). The presence of thiol-containing agents, including DTT, NAC, cysteine, and Tu, ANTU caused the release of FTC from the HSA−FTC complex (Figure 9d). However, cystine and GSSG did not reduce the linkage of Alb−FTC.

DISCUSSION

This study demonstrated the essential role of copper in the cross-linking of albumin with Tus, such as ANTU or FTC (Figure 2). To facilitate the assessment of the albumin−Tus interaction, FTC was chosen for subsequent analyses in this study. It was found that the level of HSA−FTC complex formation depends on the amount of HSA, FTC, and copper included in the reaction (Figure 3). As few as 6 μM Cu(II) could induce a detectable HSA−FTC complex reaction in vitro (Figure 3c). The copper concentration in blood plasma was about 15 μM (*38*); thus, the thioureation of albumin may actually occur in physiological conditions.

Our data show that the linkage between HSA and FTC is a disulfide bridge (Figure 4a). Because there is only one reactive thiol group in the Cys^{34} residue of albumin (*26*), FTC was

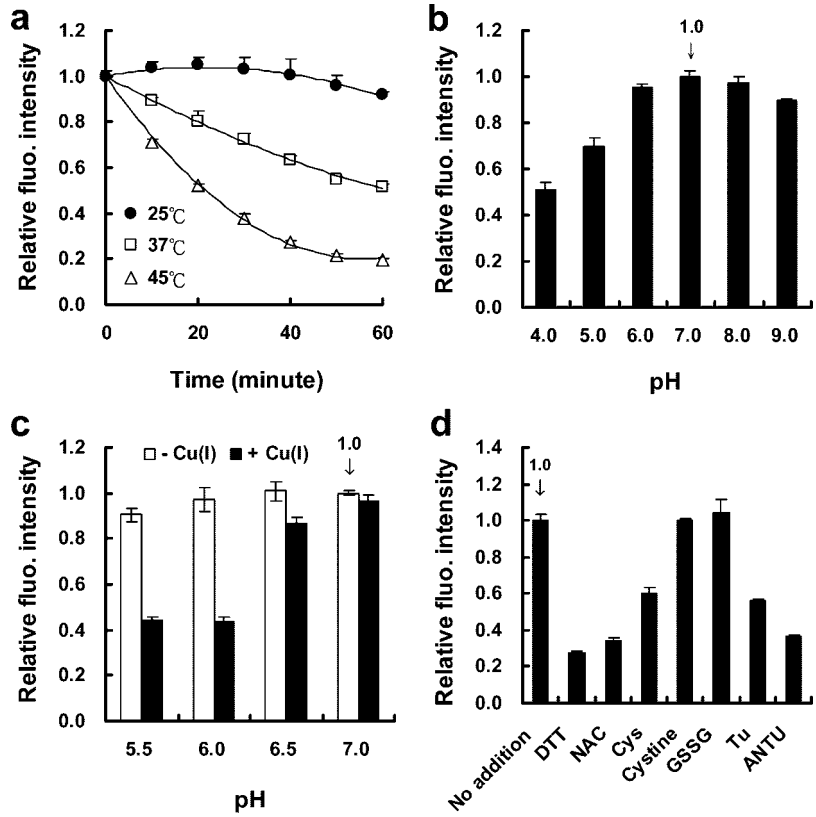

Figure 9. Stability of the thioureated complex. The influence of (a) temperature, (b) pH, (c) Cu(I), or (d) thiol-containing molecules on the stability of Alb−FTC was evaluated by using a modified CFA method (see Supporting Information, Figure 1). Aliquots of purified HSA−FTC (3 μg/well) were (a) incubated at the indicated temperature in 50 mM Hepes-pH 7.0 for designated time intervals; (b) incubated in various pH (in 50 mM sodium acetate-pH 4.0−5.0; 50 mM Hepes-pH 6.0−9.0) at 25 °C for an hour; (c) mixed with 0.1 mM Cu(I) in 50 mM Hepes-pH 5.5−7.0, at 25 °C for an hour; (d) mixed with 0.1 mM thiol-containing agents in 50 mM Hepes-pH 7.0 at 25 °C for 3 h. Reagent-B (60 μL/well) and MD-Charcoal (200 μL/well) were then added to adjust pH and remove the released FTC, respectively. After magnetic precipitation with MD-Charcoal, the fluorescent intensities were measured. Data presented are the means ± SD ($n = 3$).

speculated to cross-link with cysteine at this site. This notion was further confirmed by using Cys^{34}-modified albumin (Cys-HSA, r-Cys-HSA, and Alk-HSA) and the fact that FTC did not interact with cysteinylated or alkylated albumin (Figure 5). Furthermore, copper-induced cross-linking was also demonstrated for the interaction of FTC with cysteine (Figure 4b) and that of Tu with HSA (Figure 4c). The difference between albumin thioureation and cysteinylation could be distinguished by comparing the interaction of HSA with Tu-beads and HSA with Cys-beads. As shown in Figure 4c, both Tu- and Cys-beads were found to conjugate with HSA in the presence of copper. In the absence of copper, however, only Cys-beads that were pretreated with copper could react with HSA. As reported by other investigators (*29, 32, 39*), the binding of HSA with Cys-beads in this study is probably caused by the copper-catalyzed autoxidation of cysteine to cystine, followed by the interaction of cystine with HSA through thiol−disulfide exchange. However, copper-pretreated Tu-beads did not induce the same reaction as did Cys-beads. We speculate that the pretreatment with copper did not form dithioformamidine (Tu-S-S-Tu) in Tu-beads; instead, the Tu-Cu(II) complex was formed as described by Doona and Stanbury (*15*).

The thioureation reaction is highly sensitive to pH changes (Figure 6a and b). The decreased thioureation reaction at low pH may be due to the instability of the resulting product (Alb−FTC) in acidic conditions (Figure 9b). However, in basic conditions, the thioureation reaction is greatly reduced although the thioureated product is stable (at pH 8.0, Figure 9b). Such decreased thioureation reaction at high pH is likely due to the insolubility of copper in basic buffers, thus leading to the decomposition of the FTC-Cu(II) complex (Figure 6c). This observation implicates the importance of Tus-Cu(II) complex formation in the process of albumin thioureation.

Other metal ions tested in this study, including ferric ion, did not induce the same reaction as copper did, indicating the specific nature of copper in the reaction (Figure 7). It is difficult to clarify the role of copper in Alb-S-S-Tus complex formation since both albumin and Tus were known to interact with copper (*15, 16, 26*). The interaction site of copper with HSA was at its N-terminal copper-binding site (N-Asp-Ala-His-Lys-) and the Cys^{34} residue (*26, 40*). However, the truncated rHSA, which has a single deletion at Asp^1 and exhibits a reduced copper-binding affinity, did not reduce the binding of FTC, as compared to intact HSA (Figure 5). It appears that the binding of copper at the N-terminal copper-binding site appears unnecessary for the thioureation of HSA. Similarly, PSA, which exhibits low-affinity for copper (there is a single residue change in PSA, $His^3 \rightarrow Tyr^3$, as compared to BSA at the N-terminal Asp-Thr-His-Lys- sequence), interacted more efficiently with FTC than did BSA. We thus exclude the N-terminal copper-binding site of albumin from the reaction.

The possible interaction of Cu(II) with Cys^{34} of albumin was considered. In copper-induced S-nitrosation of albumin (*32*), it was suggested that the interaction of Cu(II) with Cys^{34} of albumin leads to the formation of a copper−thiol complex, which could further react with NO to form BSA-SNO. According to Zhang et al., Cu(II) bound with high affinity to Cys^{34} of albumin at higher pH (approximately 9) (*41*). If the formation of HSA-Cys^{34}-Cu(II) is essential for thioureation, more HSA−FTC would be formed at high pH. However, our data show that the incorporation of FTC to HSA was greatly reduced with increasing pH, and the conjugation was abolished com-

pletely above pH 8.5 (Figure 6a). Although the interaction of Cu(II) with Cys^{34} may occur, it was not essential for the incorporation of FTC into albumin. Consequently, a mechanism similar to S-nitrosation is not suitable for albumin thioureation.

Because Tus were known to form complexes with copper (*15*−*17*), we suggest that the formation of the Tus-Cu(II) complex is essential for the reaction. In copper-induced reactions, Tus including FTC, ANTU, and Tu-beads, which were in their copper-bound form would further interact with albumin (Figures 2 and 4c). There are two possible reaction mechanisms for the thioureation of cysteine or Cys^{34} of albumin: (a) Cys-SH or Alb-Cys^{34}-SH attacked by Tus-Cu(II) as shown in reactions F and G, respectively (the release of Cu(I) will be discussed later); (b) Cys-S-S-Cys or dimerized albumin (Alb-Cys^{34}-S-S-Cys^{34}-Alb) reacting with Tus by thiol−disulfide exchange as described in reaction D (see Introduction).

$$\text{Cys-SH} + \text{Tus-Cu(II)} \rightarrow \text{Cys-S-S-Tus} + \text{Cu(I)} + 2H^+ \quad \text{(F)}$$

$$\text{Alb-Cys}^{34}\text{-SH} + \text{Tus-Cu(II)} \rightarrow \text{Alb-Cys}^{34}\text{-S-S-Tus} + \text{Cu(I)} + 2H^+ \quad \text{(G)}$$

The scheme b described above was probably excluded from the copper-induced fast coupling reaction because (i) copper may not participate in the formation of dimerized albumin. In fact, the treatment of albumin with Cu(II) did not lead to the oxidation of Cys^{34} and the dimerization of BSA (*32*). (ii) Cys-HSA (Alb-Cys^{34}-S-S-Cys) could not complex with FTC in a 10-min reaction without copper (Figure 5). Therefore, it is not the major mechanism in the copper-induced reaction, although thiol−disulfide exchange described in reaction D may occur.

According to Stubauer et al., Cu(II)-induced albumin S-nitrosation accompanied the release of Cu(I) as judged by using NCP, a Cu(I) specific chelator (*32*). Similarly, by using NCP, the formation of HSA-S-S-FTC and Cys-S-S-FTC is predominantly increased (Figure 8). Thus, we speculate that the release of Cu(I) is involved in reactions F−G. There are two possible mechanisms for the Cu(I)-inhibited formation of Alb-Tus at neutral pH: (i) the Cu(I) decomposes the disulfide bridge of Alb-S-S-Tus; and (ii) the competition of Cu(I) with Cu(II) for Tus. The former is suggested by the report of Kato et al. that oxidized D-penicillamine (PSSP) and glutathione (GSSG) were reduced by Cu(I) with the release of Cu(II) (*42*). Stubauer et al. also described that the decomposition of BSA-SNO by Cu(I) reduced the S-nitrosation reaction (*32*). At neutral pH in this study, Cu(I) did decrease the formation of Alb−FTC (Table 1). However, once Alb−FTC formed, Cu(I) did not significantly decompose the complex at pH 7.0 (Figure 9c), indicating that the first scheme is not likely to occur at neutral pH. Alternatively, the second scheme that Cu(I) competes with Cu(II) for Tu is, thus, a more feasible model at neutral pH because Tu was also known to form a complex with Cu(I). It was also reported that the formation of a redox-inactive Tu-Cu(I) complex prevents copper-mediated protein oxidation (*18*). Therefore, we speculate that the Cu(II) bound Tus is active for the progression of thioureation while Cu(I)-bound Tus is inactive.

The stability of thioureated albumin, Alb−FTC, was also assessed. As shown in Figure 9a and b, Alb−FTC was unstable at high temperature (37 °C and 45 °C), under acidic (pH < 6.0) or basic conditions (pH > 8.0). Although the breakdown of the disulfide bond is considered, other possibilities may not be excluded: (i) Cys-S-S-Tu was hydrolyzed to Cys-SOH and Tu in reaction E (*10, 11*); (ii) thioureated protein (protein−S-S-Tu) in thyroid tissue was hydrolyzed to thiosulfenic acid (protein−S-SH) and urea (*8*). The latter implied that the decomposition of cross-linked product may be influenced by surrounding amino acids near the binding site. The hydrolytic products may vary among various Tu derivatives. Further experiments are required to establish the hydrolytic mechanism.

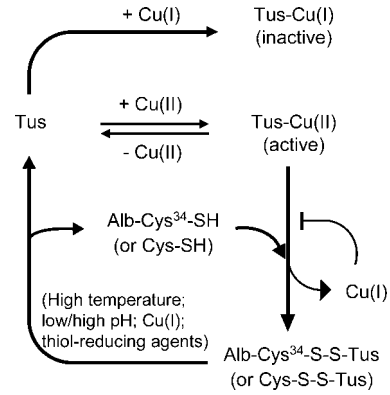

Figure 10. Schematic mechanism of copper-induced thioureation. The complex of Tus-Cu(II) is actively catalyzing the thioureation between Tus and cysteine or Cys^{34} residue of mercaptoalbumin (Alb-Cys^{34}-SH) at weak acidic or physiological pH. The resulting product is thioureated cysteine (Cys-S-S-Tus) or albumin (Alb-Cys^{34}-S-S-Tus) with the formation of a disulfide bridge and the release of Cu(I). The released Cu(I) is speculated to compete with Cu(II) for Tus, thus inhibiting the progress of thioureation. The complex, Alb-Cys^{34}-S-S-Tus, was unstable at high temperature (>25 °C) and either acidic (<pH 6.0) or basic pH (>pH 8.0). Both Cu(I) (at acidic pH only) and thiol-reducing agents degraded the Alb-Cys^{34}-S-S-Tus complex.

In addition, Cu(I) was found to reduce the linkage between albumin and FTC in acidic conditions (Figure 9c). The diminished reduction effect of Cu(I) with increasing pH may be due to the decreased solubility of Cu(I) in basic conditions (considering that CuCl must be prepared in 50 mM HCl). Finally, because of the formation of disulfide linkage between thiourea and albumin, the produced thioureated albumin could also be reduced or modified by thiol-containing compounds presented in blood plasma, such as cysteine (but not cystine) as demonstrated in Figure 9d. The mechanism of copper-induced thioureation is summarized and illustrated in Figure 10.

Tus were considered as hydroxyl radical scavengers and may help to suppress metal-induced protein damage (*12*−*14*). However, high levels of Tus are intrinsically toxic physiologically (*1*−*3*). It is noteworthy that the combination of copper with Tus (e.g., phenylthiourea, ANTU, and pyrrolidine dithiocarbamate) was much more toxic than copper or Tus alone for cultured cells (*43, 44*). The treatment of these cells with copper-binding protein such as albumin would decrease the cytotoxic effect (*44*). In our opinion, the decreased cytotoxicity in these cases may be due to the dysfunction of some important cellular proteins or enzymes that were thioureated by Tus-Cu(II) and finally resulted in cell death. Although the diminished cytotoxicity by albumin-treatment may be due to the competition of albumin with Tus for copper, the possible contribution of sacrificial albumin for Tu-binding (that forms Alb-Tus to prevent thioureation of important cellular proteins) should not be ignored. We therefore speculate that albumin may play a role in the clearance of Tus in the presence of copper. This may be important for reducing the toxicity of these compounds in circulation. In today's pharmaceutical industry, many drugs are developed in the form of Tus (*19*−*21*). Since albumin is the major thiol-containing protein in plasma, the pharmacokinetics of these Tu-based drugs may require special evaluation for patients with copper metabolism disorders such as Wilson's disease (*45*).

ACKNOWLEDGMENT

The study was supported by NSC 94-2314-B-038-034 (ROC) and NSC 96-2314-B-038-015 (ROC).

Supporting Information Available: Schemes of the CFA method and the influence of metal ions and small molecules on fluorescence intensity by using the CFA method. This material is available free of charge via the Internet at http://pubs.acs.org.

LITERATURE CITED

(1) IPCS (2003) Thiourea, in *CICADs 49* (2003 IPCS, Ed.) WHO, Geneva, Switzerland.

(2) Scott, A. M., Powell, G. M., Upshall, D. G., and Curtis, C. G. (1990) Pulmonary toxicity of thioureas in the rat. *Environ. Health Perspect. 85*, 43–50.

(3) Onderwater, R. C., Commandeur, J. N., and Vermeulen, N. P. (2004) Comparative cytotoxicity of N-substituted N′-(4-imidazole-ethyl)thiourea in precision-cut rat liver slices. *Toxicology 197*, 81–91.

(4) Schulman, J., Jr., and and Keating, R. P. (1950) Studies on the metabolism of thiourea. I. Distribution and excretion in the rat of thiourea labeled with radioactive sulfur. *J. Biol. Chem. 183*, 215–221.

(5) Hollinger, M. A., Giri, S. N., Alley, M., Budd, E. R., and Hwang, F. (1974) Tissue distribution and binding of radioactivity from 14C-thiourea in the rat. *Drug Metab. Dispos. 2*, 521–525.

(6) Davidson, B., Soodak, M., Strout, H. V., Neary, J. T., Nakamura, C., and Maloof, F. (1979) Thiourea and cyanamide as inhibitors of thyroid peroxidase: the role of iodide. *Endocrinology 104*, 919–924.

(7) Ziegler, D. M. (1978) Intermediate metabolites of thiocarbamides, thioureylenes and thioamides: mechanism of formation and reactivity. *Biochem. Soc. Trans. 6*, 94–96.

(8) Maloof, F., and Soodak, M. (1961) Cleavage of disulfide bonds in thyroid tissue by thiourea. *J. Biol. Chem. 236*, 1689–1692.

(9) Hollinger, M. A., and Giri, S. N. (1990) Non-enzymatic covalent binding of radioactivity from [14C]thiourea to rat lung protein. *Toxicol. Lett. 52*, 1–5.

(10) Pirie, N. W. (1933) The oxidation of sulphydryl compounds by hydrogen peroxide: Catalysis of oxidation of cysteine by thiocarbamides and thiolglyoxalines. *Biochem. J. 27*, 1181–1188.

(11) Toennies, G. (1937) Relations of thiourea, cysteine, and the corresponding disulfides. *J. Biol. Chem. 120*, 297–313.

(12) Ziegelstein, R. C., Zweier, J. L., Mellits, E. D., Younes, A., Lakatta, E. G., Stern, M. D., and Silverman, H. S. (1992) Dimethylthiourea, an oxygen radical scavenger, protects isolated cardiac myocytes from hypoxic injury by inhibition of Na(+)-Ca2+ exchange and not by its antioxidant effects. *Circ. Res. 70*, 804–811.

(13) Kelner, M. J., Bagnell, R., and Welch, K. J. (1990) Thioureas react with superoxide radicals to yield a sulfhydryl compound. Explanation for protective effect against paraquat. *J. Biol. Chem. 265*, 1306–1311.

(14) Wasil, M., Halliwell, B., Grootveld, M., Moorhouse, C. P., Hutchison, D. C., and Baum, H. (1987) The specificity of thiourea, dimethylthiourea and dimethyl sulphoxide as scavengers of hydroxyl radicals. Their protection of alpha 1-antiproteinase against inactivation by hypochlorous acid. *Biochem. J. 243*, 867–870.

(15) Doona, C. J., and Stanbury, D. M. (1996) Equilibrium and redox kinetics of copper(II)-thiourea complexes. *Inorg. Chem. 35*, 3210–3216.

(16) Foye, W. O., and Chao, C. C. (1984) Antiradiation compounds XIX: metal-binding abilities of thioureas. *J. Pharm. Sci. 73*, 1284–1286.

(17) Piro, O. E., Piatti, R. C., Bolzan, A. E., Salvarezza, R. C., and Arvia, A. J. (2000) X-ray diffraction study of copper(I) thiourea complexes formed in sulfate-containing acid solutions. *Acta Crystallogr., Sect. B 56*, 993–997.

(18) Zhu, B. Z., Antholine, W. E., and Frei, B. (2002) Thiourea protects against copper-induced oxidative damage by formation of a redox-inactive thiourea-copper complex. *Free Radical Biol. Med. 32*, 1333–1338.

(19) Tsogoeva, S. B., Hateley, M. J., Yalalov, D. A., Meindl, K., Weckbecker, C., and Huthmacher, K. (2005) Thiourea-based nonnucleoside inhibitors of HIV reverse transcriptase as bifunctional organocatalysts in the asymmetric Strecker synthesis. *Bioorg. Med. Chem. 13*, 5680–5685.

(20) Coppola, G. M., Damon, R. E., Eskesen, J. B., France, D. S., and Paterniti, J. R., Jr. (2002) Thiourea-based gemfibrozil analogues as HDL-elevating agents. *Bioorg. Med. Chem. Lett. 12*, 2439–2442.

(21) Bhandari, K., Srivastava, S., and Shankar, G. (2004) Synthesis of tetrahydronaphthyl thioureas as potent appetite suppressants. *Bioorg. Med. Chem. 12*, 4189–4196.

(22) Cui, F., Cui, Y., Luo, H., Yao, X., Fan, J., and Lu, Y. (2006) The interaction between N-n-undecyl-N′-(sodium p-aminobenzenesulfonate) thiourea and serum albumin studied using various spectroscopies and the molecular modeling method. *Biopolymers 83*, 170–181.

(23) Cui, F., Wang, J., Cui, Y., Li, J., Lu, Y., Fan, J., and Yao, X. (2007) Binding of human serum albumin to N-(p-ethoxy-phenyl)-N′-(1-naphthyl)thiourea and synchronous fluorescence determination of human serum albumin. *Anal. Sci. 23*, 719–725.

(24) Peters Jr., T. (1996) Ligand Binding by Albumin, in *All About Albumin: Biochemistry, Genetics, and Medical Applications* pp 76−132, Academic Press, San Diego, CA.

(25) Kragh-Hansen, U., Chuang, V. T., and Otagiri, M. (2002) Practical aspects of the ligand-binding and enzymatic properties of human serum albumin. *Biol. Pharm. Bull. 25*, 695–704.

(26) Quinlan, G. J., Martin, G. S., and Evans, T. W. (2005) Albumin: biochemical properties and therapeutic potential. *Hepatology 41*, 1211–1219.

(27) Iberg, N., and Fluckiger, R. (1986) Nonenzymatic glycosylation of albumin in vivo. Identification of multiple glycosylated sites. *J. Biol. Chem. 261*, 13542–13545.

(28) van Breemen, R. B., and Fenselau, C. (1985) Acylation of albumin by 1-O-acyl glucuronides. *Drug Metab. Dispos. 13*, 318–320.

(29) Sengupta, S., Wehbe, C., Majors, A. K., Ketterer, M. E., DiBello, P. M., and Jacobsen, D. W. (2001) Relative roles of albumin and ceruloplasmin in the formation of homocystine, homocysteine-cysteine-mixed disulfide, and cystine in circulation. *J. Biol. Chem. 276*, 46896–46904.

(30) Sengupta, S., Chen, H., Togawa, T., DiBello, P. M., Majors, A. K., Budy, B., Ketterer, M. E., and Jacobsen, D. W. (2001) Albumin thiolate anion is an intermediate in the formation of albumin-S-S-homocysteine. *J. Biol. Chem. 276*, 30111–30117.

(31) Zhang, H., and Means, G. E. (1996) S-nitrosation of serum albumin: spectrophotometric determination of its nitrosation by simple S-nitrosothiols. *Anal. Biochem. 237*, 141–144.

(32) Stubauer, G., Giuffre, A., and Sarti, P. (1999) Mechanism of S-nitrosothiol formation and degradation mediated by copper ions. *J. Biol. Chem. 274*, 28128–28133.

(33) Glowacki, R., and Jakubowski, H. (2004) Cross-talk between Cys34 and lysine residues in human serum albumin revealed by N-homocysteinylation. *J. Biol. Chem. 279*, 10864–10871.

(34) Wu, Y. W., and Tsai, Y. H. (2006) A rapid transglutaminase assay for high-throughput screening applications. *J. Biomol. Screen. 11*, 836–843.

(35) Wu, Y. W., Chen, S. F., Yang, C. B., and Tsai, Y. H. (2008) Screening, purification, and identification of a copper-dependent FITC-binding protein in human plasma: albumin. *J. Chromatogr., B 863*, 187–191.

(36) Sogami, M., Nagoka, S., Era, S., Honda, M., and Noguchi, K. (1984) Resolution of human mercapt- and nonmercaptalbumin by high-performance liquid chromatography. *Int. J. Pept. Protein Res. 24*, 96–103.

(37) Ellman, G. L. (1959) Tissue sulfhydryl groups. *Arch. Biochem. Biophys. 82*, 70–77.

(38) Samman, S. (2002) Trace elements, in *Essentials of Human Nutrition* (Mann, J., and Truswell, A. S., Eds.) 2nd ed., pp 164−166, Oxford University Press Inc., New York.

(39) Kachur, A. V., Koch, C. J., and Biaglow, J. E. (1999) Mechanism of copper-catalyzed autoxidation of cysteine. *Free Radical Res. 31*, 23–34.

(40) Suzuki, K. T., Karasawa, A., and Yamanaka, K. (1989) Binding of copper to albumin and participation of cysteine in vivo and in vitro. *Arch. Biochem. Biophys. 273*, 572–577.

(41) Zhang, Y., and Wilcox, D. E. (2002) Thermodynamic and spectroscopic study of Cu(II) and Ni(II) binding to bovine serum albumin. *J. Biol. Inorg. Chem. 7*, 327–337.

(42) Kato, N., Nakamura, M., and Uchiyama, T. (1999) 1H NMR studies of the reactions of copper(I) and copper(II) with D-penicillamine and glutathione. *J. Inorg. Biochem. 75*, 117–121.

(43) Masuda, A., and Eguchi, G. (1984) Phenylthiourea enhances Cu cytotoxicity in cell cultures: its mode of action. *Cell Struct. Funct. 9*, 25–35.

(44) Chen, S. H., Liu, S. H., Liang, Y. C., Lin, J. K., and Lin-Shiau, S. Y. (2000) Death signaling pathway induced by pyrrolidine dithiocarbamate-Cu(2+) complex in the cultured rat cortical astrocytes. *Glia 31*, 249–261.

(45) Ala, A., Walker, A. P., Ashkan, K., Dooley, J. S., and Schilsky, M. L. (2007) Wilson's disease. *Lancet 369*, 397–408.

BC7004158

Supporting information

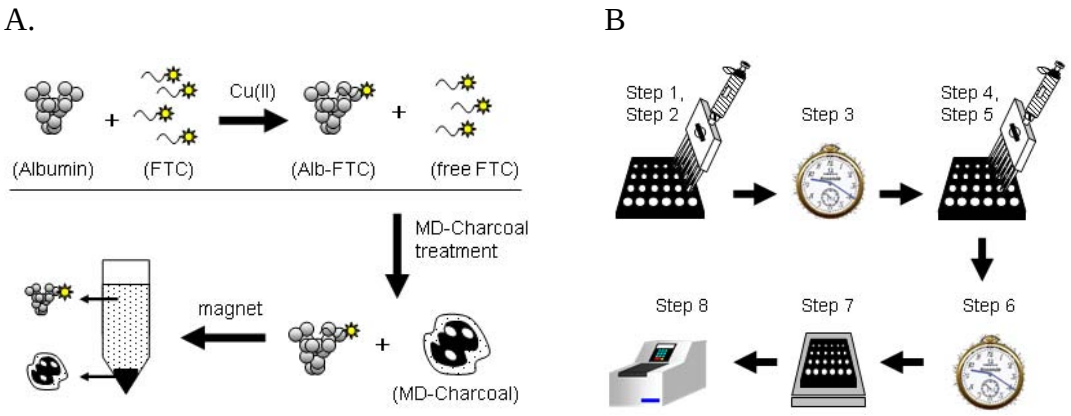

Figure 1 The schemes of CFA method. (A) The combination of albumin with FTC was initiated by the addition of copper. After reaction, the free FTC was rapidly removed from the reaction mixture by MD-Charcoal treatment. MD-Charcoal was then magnetically precipitated to separate from the Alb-FTC complex. (B) Basic protocol of CFA. To evaluate the formation of Alb-FTC complex, albumin samples (30 μl/well) are added in the wells of a microplate at 4℃ (Step 1). Upon the addition of 30 μl/well reagent-A (Step 2) (final concentration in reaction: 1 μM HSA, 3 μM FTC, 0.1 mM CuCl2, in 50 mM Hepes-pH 7.0), the reaction is immediately initiated by incubating the plate at 37℃ for 10 minutes (Step 3), and terminated by adding 60 μl reagent-B (2 mM EDTA in 0.5 M Hepes-pH 8.0) (Step 4). After addition of 200 μl MD-Charcoal (Step 5), the plate is kept at room temperature for 5 minutes to remove all of the free FTC and other small molecules (Step 6). Finally, the MD-Charcoal is precipitated by magnet (Step 7), and the fluorescence is measured by microplate reader (Step 8). Transfer of supernatant to another plate for fluorescence measurement is unnecessary due to the precipitated MD-Charcoal that had captured FTC does not exhibit fluorescent properties. In addition, a **modified CFA method** was used to evaluate the stability of Alb-FTC complex: in Step 1 & 2,

the purified Alb-FTC complex was incubated (i) at designated temperature, (ii) in various pH, (iii) with Cu(I), or (iv) with thiol-containing agents, for designated periods of time (Step 3). Reagent-B (Step 4) and MD-Charcoal (Step 5) were then added to adjust the final pH to pH 8.0 and to remove the released FTC molecules, respectively. Steps 6 ~ 8 were as described above. The measured fluorescence intensities reflect the remaining Alb-bound FTC molecules.

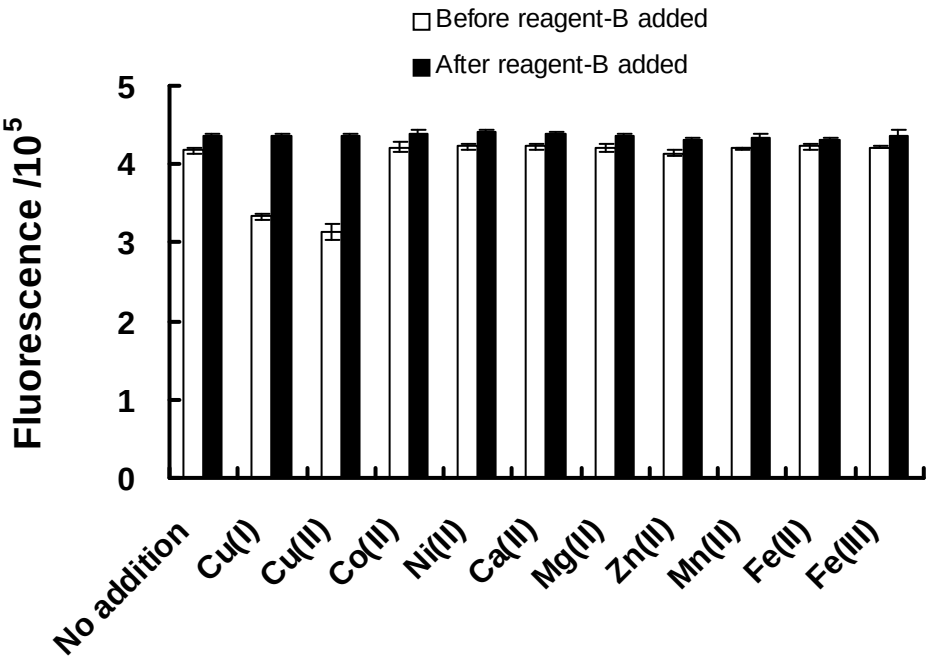

Figure 2 Metal ions did not influence the fluorescence intensity by using CFA method. The fluorescence intensities of reaction mixtures (60 μl; 50 mM Hepes-pH 7.0, 3 μM FTC, and 100 μM of various metal ions) was measured before and after reagent-B (60 μl; 2 mM EDTA, 0.5 M Hepes-pH 8.0) added. Before reagent-B added, only Cu(I) and Cu(II) found to reduce the fluorescence intensity of FTC. This effect, however, was completely eliminated after addition of reagent-B. Other metal ions did not influence the fluorescence intensity even without reagent-B added. The data presented are means ± SD (n = 3).

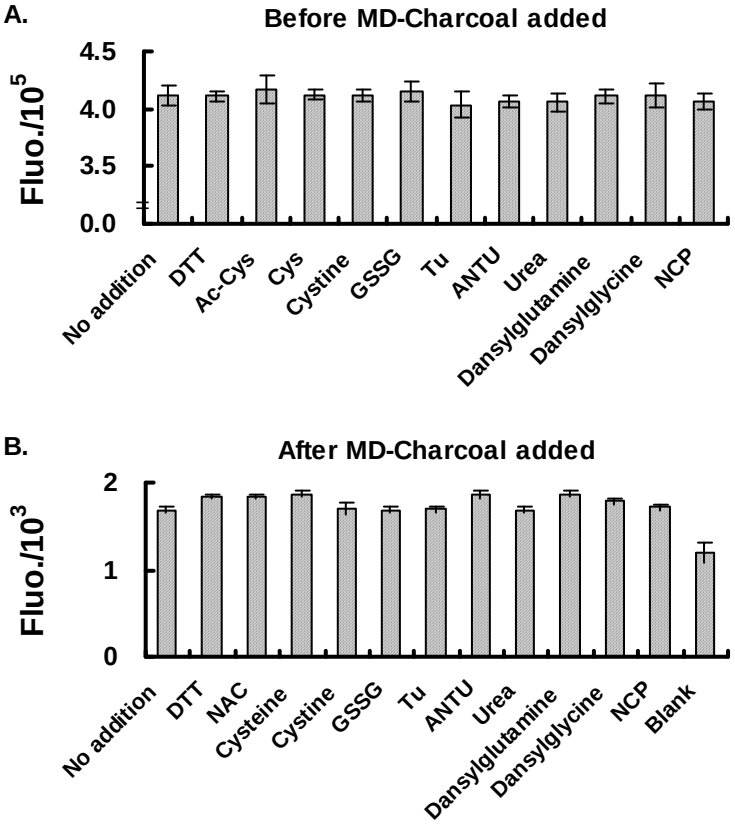

Figure 3 Small molecules analyzed by CFA did not influence the fluorescence counting. Various small molecules used in this study (Table I & Fig. 8) including thiol-containing molecules, Tu analogues, ligands, and NCP were tested for possible influence on fluorescence intensity of FTC. The reaction mixtures (60 μl; 50 mM Hepes-pH 7.0, 3 μM FTC, and 100 μM of various tested agents) was mixed with equal volume of reagent-B (2 mM EDTA, 0.5 M Hepes-pH 8.0), and the fluorescence intensities were measured before (A) or after (B) MD-Charcoal (200 μl) treatment. Before MD-Charcoal treatment (A), these molecules did not influence the fluorescence intensity of FTC. After MD-Charcoal treatment (B), the fluorescence intensities of each group were nearly the same as blank (empty well). This indicate CFA molecules were nearly completely removed by MD-Charcoal. The data presented are means ± SD (n = 3).

Nanoparticulate Glutathione Peroxidase Mimics Based on Selenocystine−Pullulan Conjugates

Mamoru Haratake,* Shinya Matsumoto, Masahiro Ono, and Morio Nakayama*

Graduate School of Biomedical Sciences, Nagasaki University, 1-14, Bunkyo-machi, Nagasaki 852-8521, Japan. Received January 4, 2008; Revised Manuscript Received June 23, 2008

We synthesized nanoparticulate glutathione peroxidase (GPx) mimics in which selenocystine (SeCyst) was conjugated to a hydrophilic linear polysaccharide, pullulan (Pul). The SeCyst ester-conjugated Pul derivatives (SeCyst-Pul) in phosphate buffer (pH 7) were treated with a sonicator to spontaneously form particulate materials. Dynamic light scattering measurements revealed that the SeCyst-Pul conjugates could form particulate materials with diameters between 100 and 300 nm. Distinctive endothermic peaks were observed for the SeCyst-Pul aggregate solutions based on a differential scanning calorimetric analysis. The tryptophan (Trp) fluorescence intensity of SeCyst benzyl ester-tryptophanyl-Pul (SeCyst-Bz-Trp-Pul) mostly decreased in comparison to those of the Trp-Pul (its precursor) and free Trp, which indicates that the Trp residues come close to each other during the aggregation of the conjugates. Formation of SeCyst-Pul aggregates could be induced by the hydrophobic interactions between the SeCyst esters and the amino acid residues on Pul. The GPx-like activity of SeCyst-Bz-Trp-Pul aggregates for the reduction of H_2O_2 was enhanced nearly 20-fold higher than that of free SeCyst. The double-reciprocal plots of the SeCyst-Bz-Trp-Pul aggregate-catalyzed reduction yielded parallel lines by varying the substrate concentrations, indicating a "ping-pong" mechanism that is similar to those of the natural GPxs. The enhanced GPx activity of the SeCyst-Bz-Trp-Pul aggregate was also supported by higher kinetic parameters, k_{cat}/K_m^{GSH} and $k_{cat}/K_m^{H_2O_2}$. Overall, the enhanced activity of the SeCyst-Bz-Trp-Pul aggregate would be attributed to a hydrophobic environment that was formed at the vicinity of the SeCyst.

INTRODUCTION

Glutathione peroxidases (GPxs) are the major antioxidant defense in living systems, which catalyze the reduction of hydrogen peroxide and phospholipid hydroperoxides using reduced glutathione (GSH) ($2GSH + R\text{-}OOH \rightarrow GSSG + R\text{-}OH + H_2O$) (*1*). Selenium-dependent GPxs (GPx-1, GPx-2, GPx-3, GPx-4, and GPx-6), except for GPx-5, contain the selenocysteine (Sec) residue in their catalytic centers (*2–4*). The Sec residue, which is called the twenty-first amino acid, is encoded by the UGA stop codon that normally functions as a stop codon. The biosynthesis of Sec incorporated in response to the UGA codon is distinctive from the twenty standard amino acids. Translation of the Sec residue is a complicated mechanism which is controlled by the specific stem-loop Sec insertion sequence (SECIS) located in the downstream of the UGA codon and four execution elements [Sec synthase (*selA*), an elongation factor (*selB*), seryl-$tRNA^{sec}$ (*selC*), and selenophosphate synthase (*selD*)] (*5–9*). As the Sec insertion into the selenoproteins occurs by such a specific translational control process, at present, it is still quite difficult to express the Sec-containing proteins by the state-of-the-art genetic engineering techniques (*10*).[1]

In the X-ray crystal structures of the GPxs, the residues that could be functionally important in the vicinity of the catalytic Sec are some aromatic amino acids [tryptophan (Trp), phenylalanine and tyrosine] and glutamine (Gln) and arginine presumably forming salt bridges and/or hydrogen bonding to the glutathione molecule (*11, 12*). A common structure around the catalytic center, i.e., the "catalytic triad", was also found in the X-ray crystal structures of the GPxs, which involves Sec and the adjacent Gln and Trp residues. The reactive selenol group of the Sec residue is thought to be stabilized by the formation of the hydrogen-bonding with the imino group of Trp and/or the carbamoyl group of Gln, and the catalytic triad of these three residues represent a catalytic center, whose integrity is essential for the full catalytic function of the GPxs (*13*).

To explore the catalytic mechanism of natural GPxs and/or apply it to medicine, low mass GPx mimics, such as Ebselen, have been synthesized (*14–21*). A report by Wilson et al. described that an improved GPx-like activity of diselenide compounds (R-Se-Se-R) resulted from intramolecular interactions of the selenium atom with the nitrogen atom that stabilizes the reaction intermediates (*18*). Some researchers also suggested that noncovalent interactions between selenium and nitrogen or oxygen atoms increase the GPx-like activity (*19, 20*). Natural GPxs, except for GPx-4, comprise four identical subunits of 21 kDa that contains one Sec residue as the active center, while most of the GPx mimics previously known was low mass compounds and not yet comparable with the natural GPxs regarding the GPx-like activity. The binding affinity of the substrates in the vicinity of the selenium atom must also be an important element for improving the GPx-like activity. Ren et al. reported that the selenocystine (SeCyst)-conjugated β-cyclodextrin provided the GPx-like activity for the organic cumene hydroperoxide that can be included in the hydrophobic cavity of β-cyclodextrin (*16*). Sun et al. developed the diselenide-linked 15-mer selenopeptide with a high GPx-like activity by incorporating a specific amino acid sequence for the binding of glutathione (*21*). However, there are only a few reports on the

* To whom correspondence should be addressed. E-mail: haratake@nagasaki-u.ac.jp for M. Haratake; morio@nagasaki-u.ac.jp for M. Nakayama.

[1]Abbreviations: GPx, glutathione peroxidase; GSH, reduced glutathione; Sec, selenocysteine; SeCyst, D,L-selenocystine; Pul, pullulan; DAN, 2,3-diaminonaphtharene; EEDQ, *N*-ethoxycarbonyl-2-ethoxy-1, 2-dihydroquinoline; DMF, *N,N*-dimethylformamide; NADPH, nicotinamide adenine dinucleotide phosphate in reduced form; GR, glutathione reductase.

10.1021/bc800086z CCC: $40.75 © 2008 American Chemical Society
Published on Web 08/16/2008

GPx mimics that are designed from the viewpoint of the substrate binding.

In this study, we synthesized nanosized particulate GPx mimics based on the conjugates of which the selenocystine (SeCyst) as a functional element was attached to the hydrophilic linear polysaccharide, pullulan (Pul). The structural features of the particulate GPx mimics formed by the self-aggregation of the SeCyst-Pul conjugates were characterized by the dynamic light scattering, differential scanning calorimetric, and fluorescence spectroscopic techniques. Their GPx-like activity and steady state kinetics were further examined.

EXPERIMENTAL PROCEDURES

Materials. Pullulan (average Mw 73000, $M_w/M_n = 1.54$, Pul) used as a conjugate polymer was purchased from Nacalai Tesque, Inc. (Kyoto, Japan). Seleno-D,L-cystine (SeCyst) was obtained from Sigma Co., Ltd. (St. Louis, MO) The amino acid derivatives were from either Merck Biosciences AG Novabiochem (Läufelfingen, Switzerland) or Kanto Chemical Co., Inc. (Tokyo, Japan). 2,3-Diaminonaphtharene (DAN) and reduced glutathione (GSH) were obtained from Tokyo Chemical Ind. Co., Ltd. (Tokyo, Japan). Nicotinamide adenine dinucleotide phosphate in the reduced form (NADPH) and glutathione reductase (GR) were from Wako Pure Chemical Ind., Ltd. (Osaka, Japan). H_2O_2, used for the substrate to determine GPx-like activity, was obtained from Nacalai Tesque, Inc. (Kyoto, Japan). An Ultrafree-MC (Millipore Corp., nominal molecular weight cutoff: 5000) was used for ultracentrifugation of the polymer solutions. Water, used for the preparations of the SeCyst-Pul aggregates and their GPx-like activity measurements, was generated by a Milli-Q Biocel system (Millipore Corp., Billerica, MA). All other chemicals were of commercial reagent grade and used as received.

Synthesis of Carboxymethylated Pullulan (CM-Pul) (*22*). Pul (1.5 g) dissolved in a 6 M sodium hydroxide aqueous solution (25 mL) and chloroacetic acid (0.375, 0.75, 1.5, 3, or 4.5 g) were combined at 70 °C, and allowed to react for 2 h with stirring. The reaction mixture was neutralized with a 1 M acetic acid aqueous solution, and then dialyzed against deionized water for 24 h. The dialysate was poured into strong cation-exchange resins (DIAION SK1B, Mitsubishi Chemical Co., Tokyo, Japan) in the free form to transform it from sodium form to free form, and then were subjected to lyophilization (CM-Pul, yield: 57.5%). CM-Pul (DS = 0.44) − IR (ATR, cm^{-1}): 3354 (O−H stretching), 1734 (C═O stretching), 1026 (C−O−C bending). ^{1}H NMR (DMSO-d_6): δ 4.42 (carboxymethyl *H*), 2.56−4.58 (glucose 2*H*, 3*H*, 4*H*, 5*H*, and 6*H*), 4.62 (glucose 1*H* (1→4)), 5.12 (glucose 1*H* (1→6)).

The degree of substitution of the carboxymethyl group in CM-Pul (DS) was estimated by pH titration; an appropriate amount of CM-Pul in free form (50−100 mg, Pul-CH_2COOH) dissolved in 10 mL of a 0.1 M sodium hydroxide aqueous solution was titrated with a 0.1 M HCl aqueous solution. The temperature of the titration vessels was maintained at 30 °C throughout each titration by a circulator RTE-111 (NESLAB Instruments, Inc., Newington, NH). The pH-metric titrations were performed on a titrator DL25 (Mettler-Toledo, Inc., Columbus, OH). The DS values were calculated from the difference between V_S and V_B using the following equation (eq 1); where F is the titer of the 0.1 M HCl, V_B is the volume of the titrant consumed for the sample-free blank (mL), V_S is the volume of the titrant consumed for the samples (mL), W is the sample weight used for the titration (mg), 162 is the molar mass of a glucose unit in Pul ($C_6H_{10}O_5$), and 59 is the molar mass of carboxymethyl group ($C_2H_3O_2$). One milliliter of 0.1 M sodium hydroxide corresponds to 0.1 mmol carboxymethyl group in this titration.

$$\mathrm{DS} = 162 \times 0.1 \times F \times (V_B - V_S)/[W - 58 \times 0.1 \times F \times (V_B - V_S)] \quad (1)$$

Synthesis of SeCyst Esters. The SeCyst esters were synthesized according to the procedures reported by Bondanszky (*23*) as follows: For the SeCyst alkyl esters, a mixture of SeCyst (30 mg) and *p*-toluenesulfonic acid (300 mg) dissolved in 10 mL of absolute methanol (ethanol or isopropanol) was refluxed for 40 h. After the removal of the alcohol, the resultant was left for 24 h in diethyl ether. The obtained solid materials were washed several times with diethyl ether, and dried *in vacuo*. For the synthesis of the SeCyst benzyl ester (SeCyst-Bz), SeCyst (30 mg), *p*-toluenesulfonic acid (300 mg) and benzyl alcohol (7.5 mL) were mixed in benzene (15 mL), and refluxed for 3 h. After removal of the benzene, the residual material was left in a 1:1 mixture of petroleum ether and diethyl ether (100 mL) for 24 h. The obtained solid material was left in diethyl ether for another 24 h (yield: 75.3%). IR (ATR, cm^{-1}): SeCyst-Me 1702 (ester C═O stretching), SeCyst-Et 1712 (ester C═O stretching), SeCyst-*i*Pro 1710 (ester C═O stretching), SeCyst-Bz 1716 (ester C═O stretching). ^{1}H NMR (CD_3OD): SeCyst-Me; δ 2.37 (s, 3H), 3.29 (s, 3H), 3.30−3.31 (m, 2H), 3.85 (s, 3H), 4.40 (m, 1H), 7.22−7.25 (d, 2H), 7.69−7.72 (d, 2H), SeCyst-Et; δ 1.30 (m, 3H), 2.37 (s, 3H), 3.40 (m, 2H), 4.29 (q, 2H), 4.32 (m, 1H), 7.25 (d, 2H), 7.70 (d, 2H), SeCyst-*i*Pro; δ 1.32 (d, 6H), 2.37 (s, 3H), 3.20−3.31 (m, 2H), 4.35 (m, 1H), 5.08−5.19 (q, 1H), 7.23 (d, 2H), 7.70 (d, 2H). SeCyst-Bz; δ 2.36 (s, 3H), 3.29 (m, 1H), 4.46 (m, 1H), 5.27 (s, 2H), 7.22 (d, 2H), 7.36 (m, 5H), 7.70 (d, 2H).

Conjugation of SeCyst Esters and Amino Acids to CM-Puls. CM-Pul (50 mg) and amino acid methyl ester (50 mg) were dissolved in 10 mL of deionized water. Triethylamine and *N*-ethoxycarbonyl-2-ethoxy-1,2-dihydroquinoline (EEDQ, 100 mg) dissolved in *N,N*-dimethylformamide (DMF, 10 mL) were sequentially added to the mixture, and stirred for 2 h at room temperature. After the dialysis against deionized water for 24 h, an equal volume mixture of the dialysate and a 2 M sodium hydroxide aqueous solution was stirred for another 24 h at room temperature to remove any of the unreacted amino acid esters. The resulting solution was dialyzed against deionized water, followed by lyophilization (white powder, yield: 55.1%). The degree of introduction of the Trp and Tyr residues in Pul was estimated by measuring the intrinsic absorbance at 280 nm. His residue (*24*) was also spectrophotometrically estimated by measuring the absorbance at 240 nm using diethyl bicarbonate.

CM-Pul or Trp-Pul was combined with the SeCyst esters in 10 mL deionized water in a flask, and then an appropriate amount of triethylamine and EEDQ dissolved in 10 mL DMF was added to the flask. The mixture was allowed to react for 2 h with stirring at room temperature. The resultant material was dialyzed against deionized water for 24 h, and then subjected to lyophilization (pale yellow powder, yield: 69.3%). All the SeCyst-Pul conjugates were stored in a desiccator at ambient temperature until use. SeCyst-Me-Pul (DS = 0.44) − IR (ATR, cm^{-1}): 3341 (O−H stretching), 1715 (ester C═O stretching), 1650 (amide C═O stretching), 1522 (amide N−H bending), 1038 (C−O−C bending). ^{1}H NMR (DMSO-d_6): δ 2.37−2.58, 7.30−7.72 (SeCyst-Me *H*), 2.60−4.60 (glucose 2*H*, 3*H*, 4*H*, 5*H*, and 6*H*), 4.62 (glucose 1*H* (1→4)), 5.10 (glucose 1*H* (1→6)). SeCyst-Me-Trp-Pul (DS = 0.44) − IR (ATR, cm^{-1}): 3353 (O−H stretching), 1706 (ester C═O stretching), 1642 (amide C═O stretching), 1541 (amide N−H bending), 1050 (C−O−C bending). ^{1}H NMR (DMSO-d_6): δ 2.37−2.58, 7.30−7.72 (SeCyst-Me *H*), 2.60−4.60 (glucose 2*H*, 3*H*, 4*H*, 5*H*, and 6*H*), 4.62 (glucose 1*H* (1→4)), 5.10 (glucose 1*H* (1→6)), 6.80−7.23 (tryptophan imidazole *H*). SeCyst-Bz-Trp-Pul (DS = 0.36) − IR (ATR, cm^{-1}): 3350 (O−H stretching), 1716 (ester C═O stretching), 1650 (amide C═O stretching),

1540 (amide N−H bending), 1030 (C−O−C bending), ^{1}H NMR (DMSO-d_6): δ 2.37−2.58, 7.30−7.72 (SeCyst-Bz *H*), 2.58−4.60 (glucose 2*H*, 3*H*, 4*H*, 5*H*, and 6*H*), 4.52 (glucose 1*H* (1→4)), 5.12 (glucose 1*H* (1→6)), 6.71−7.30 (tryptophan imidazole *H*).

Determination of Selenium Concentration. The selenium concentrations in the sample solutions were fluorometrically determined using DAN after digestion using a 1:4 mixture of $HClO_4$ and HNO_3 (*25*).

Dynamic Light Scattering (DLS) Measurements. The particle diameter and distribution of the SeCyst-Pul aggregates were measured by a DLS technique. The DLS measurements were carried out at 25 °C using a Zetasizer Nano ZS (Malvern Instruments, Worcs, UK) at 90° to the incident beam (a wavelength 633 nm from a 4 mW He−Ne laser tube) in a 1 cm length quartz cuvette. The SeCyst-Pul conjugates dispersed in 0.05 M phosphate buffer (pH 7) (0.2 mg/mL) were treated by a Sonifier 250D probe-type sonicator (Branson Danburg, CT) at 120 W for 5 min in an ice bath 24 h before the measurements. Data fitting was performed using a multimodal algorithm supplied by Malvern Instruments. The collected correlelograms were fitted to diffusion coefficients and converted to a hydrodynamic diameter using the Einstein-Stokes equation.

Differential Scanning Calorimetry. Differential scanning calorimetry (DSC) was performed using an MC-2 ultrasensitive scanning calorimeter (Microcal, Inc., Amherst, MA). The MC-2 contains a fixed pair of matched tantalum cells (cell volume 1.2 mL), which are separately filled with the sample and the reference solution. The SeCyst-Pul aggregate solution samples (0.01 wt %) were injected into the sample cell and the reference cell was filled with 0.05 M phosphate buffer (pH 7). A nitrogen cylinder normally set at 4 kg/cm maintained pressure in the cells to suppress the formation of air bubbles during scanning. Temperature scans were performed at the rate of 1 °C/min and in the range 30−100 °C. The baseline was drawn with the help of *ORIGIN* software supplied by Microcal, Inc. The DSC thermograms of the pullulan in 0.05 M phosphate buffer (pH 7) were subtracted from those of the SeCyst-Pul aggregates.

Determination of GPx-Like Activity (*18, 26*). The SeCyst-Pul aggregate solution (final selenium concentration: 6.25 μM) was sequentially combined with ethylenediaminetetraacetic acid (EDTA, 0.63 mM), sodium azide (0.63 mM), glutathione reductase solution (0.63 unit), reduced glutathione solution (0.63 mM), and NADPH solution (2.34 mM) in 0.05 M phosphate buffer (pH 7). The reaction was initiated by the addition of H_2O_2 solutions (3.14 mM). Absorbance at 340 nm due to the NADPH was recorded every 10 s just after mixing by inversion. The GPx-like activity was calculated using the following equation (eq 2) as μmoles NADPH oxidized per minute, where ΔA_{SMP} is the decrease in absorbance at 340 nm of sample solutions between 10 and 70 s after addition of the substrates, ΔA_{BLK} is the decrease in absorbance at 340 nm per minute of the solutions without the SeCyst-Pul conjugates, ε_{mM} is the extinction coefficient for 1 mM NADPH solution [6.22/(mM·cm)], and c is final selenium concentration (μM).

$$\text{GPx-like activity} = (\Delta A_{SMP} - \Delta A_{BLK}) \times 1000/\varepsilon_{mM}/c \quad (2)$$

Kinetic Study of SeCyst-Pul Aggregate-Catalyzed Reduction. The initial reaction rate of the SeCyst-Pul aggregates was determined by varying the H_2O_2 and GSH concentrations: at several concentrations of one substrate while the concentration of the other substrate remained the same (H_2O_2 concentrations, 0.25, 0.5, and 1.0 mM; GSH concentrations, 0.2, 0.4, 0.6, and 1.0 mM). The other reaction conditions and operating procedures were the same as those described above. By the double-reciprocal plotting (1/[GSH] versus 1/v), the kinetic parameters were calculated from the following equation (eq 3) (*27*).

$$\frac{1}{v} = \frac{1}{[GSH]}\frac{K_m^{GSH}}{V_{max}} + \frac{1}{V_{max}}\left(\frac{[H_2O_2] + K_m^{H_2O_2}}{[H_2O_2]}\right) \quad (3)$$

where $[H_2O_2]$ and [GSH] are the concentrations of hydrogen peroxide and glutathione, respectively, K_m^S is the Michaelis constant for substrate S, $V_{max} = k_{cat}[E_0]$, k_{cat}, and $[E_0]$ are a general rate constant and a total concentration of selenium, respectively.

Statistical Analysis. All data were presented as mean ± standard deviation ($n = 5$ or more). Statistical analyses were performed using *PRISM 4* (GraphPad Software Inc., San Diego, CA). Multiple mean values were compared by a two-way ANOVA with a Bonferroni posthoc test with the treatment and selenium concentration in the diets as factors. Comparisons were considered statistically significant at $P < 0.05$.

RESULTS AND DISCUSSION

Synthesis of SeCyst-Pul Conjugates (Scheme 1). Natural GPxs have a Sec residue in their active center. The direct Sec introduction to polymers is quite difficult, because of its poor chemical stability. In this study, SeCyst (Sec-Se-Se-Sec) was used as a catalytic site to be attached to the polymers. Pullulan (Pul, average Mw 73 000) was employed as a polymer material to improve the chemical stability and the solubility of SeCyst in an aqueous medium. The Pul molecule is a hydrophilic linear polysaccharide consisting of a maltotriose repeating unit in which three glucose molecules are connected by an α-1,4 glycosidic bond. Pul molecule was first carboxymethylated in order to sequentially attach the SeCyst ester moieties through an amide linkage (CM-Pul). As the highly substituted SeCyst-Pul conjugates were thought to become water-insoluble due to the poor solubility of SeCyst, the CM-Pul derivatives with less than a 0.5 substitution degree of the carboxymethyl group per glucose unit of Pul were employed for the further chemical modifications. We tried to examine the substituent distribution of the carboxymethyl group in the CM-Pul by NMR spectroscopy, but it could not be clearly detected probably due to the low degree of substitution. It seems common knowledge that the primary alcohol at C-6 (OH-6) is the most reactive hydroxyl group of glucose in most substitution reactions. However, Glinel et al. recently reported that the reactivity order of hydroxyl groups in the carboxymethylation of Pul was found to be OH-2 > OH-4 > OH-6 > OH-3 using the hydrolyzed pullulan fragment (*28*). As the CM-Pul used in this study was also thought to be substituted by carboxymethyl groups at several positions of the hydroxyl groups, the same batches of the CM-Pul were used for the subsequent conjugation reactions.

The free SeCyst was decomposed to the red elemental selenium in both the solid and aqueous solution states. However, the conjugation of the SeCyst esters to Pul fairly improved their stability; when they were exposed to sonication and/or heating, no elemental selenium was observed throughout the experiments and during storage. The selenium contents of the SeCyst-Pul conjugates increased with an increase in the degree of substitution of the carboxymethyl group (Table 1). When the SeCyst-Pul conjugate ethanolic aqueous solutions were ultrafiltered through a 5000 molecular weight cutoff filter, the selenium amount in the filtrates was less than 1% of the total selenium amount listed in Table 1. Thus, the SeCyst esters noncovalently attached to Pul were thought to be a negligible amount in the conjugates. In addition, the residual carboxymethyl groups in the SeCyst-Pul conjugates could hardly be detected. The selenium contents of SeCyst-Me-His-Pul, SeCyst-Me-Tyr-Pul, SeCyst-Me-Trp-Pul, and SeCyst-Bz-Trp-Pul conjugates were almost consistent with those that were calculated from the contents of the amino acids in the respective precursors (97−105%), indicating that SeCyst and these amino acids were introduced into these conjugates in equal molar ratios.

Scheme 1. Synthetic Route of SeCyst-Pul Conjugates

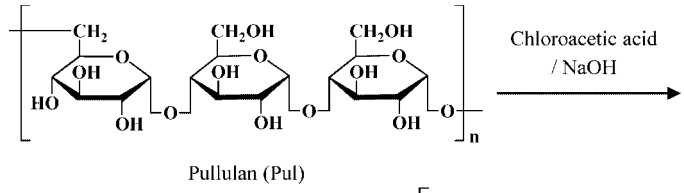

Pullulan (Pul)

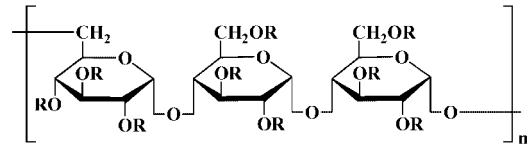

Carboxymethylated Pul (CM-Pul, R: carboxymethyl)

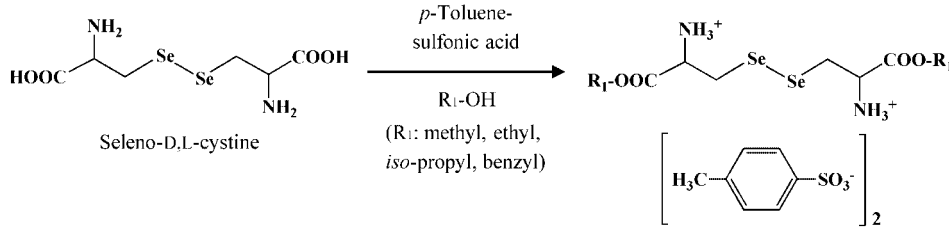

Seleno-D,L-cystine

SeCyst ester

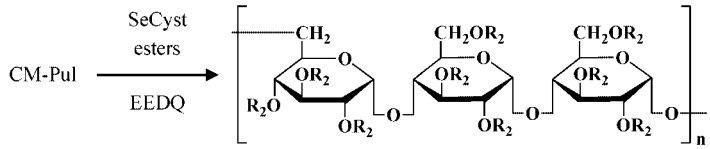

- SeCyst-Me-Pul (R2: CH_2CO-SeCyst methyl ester)
- SeCyst-Et-Pul (R2: CH_2CO-SeCyst ethyl ester)
- SeCyst-*i*Pr-Pul (R2: CH_2CO-SeCyst *iso*-propyl ester)
- SeCyst-Bz-Pul (R2: CH_2CO-SeCyst benzyl ester)

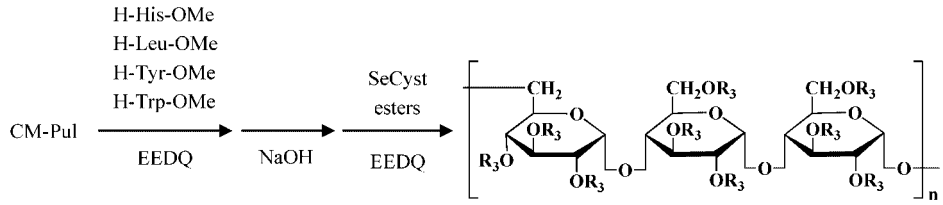

- SeCyst-Me-His-Pul (R3: CH_2CO-L-histidyl-SeCyst methyl ester)
- SeCyst-Me-Leu-Pul (R3: CH_2CO-L-leucyl-SeCyst methyl ester)
- SeCyst-Me-Tyr-Pul (R3: CH_2CO- L-tyrosyl-SeCyst methyl ester)
- SeCyst-Me-Trp-Pul (R3: CH_2CO-L-tryptophyl-SeCyst methyl ester)
- SeCyst-Bz-Trp-Pul (R3: CH_2CO-L-tryptophyl-SeCyst benzyl ester)

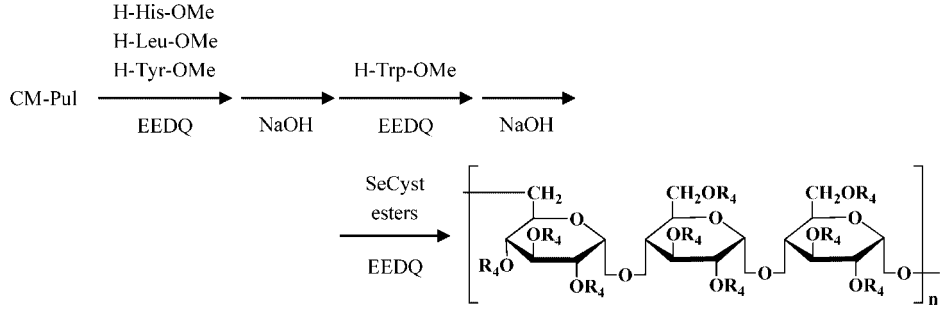

- SeCyst-Me-His-Trp-Pul (R4: CH_2CO-L-histidyl-L-tryptophyl-SeCyst methyl ester)
- SeCyst-Me-Leu -Trp-Pul (R4: CH_2CO-L-leucyl-L-tryptophyl-SeCyst methyl ester)
- SeCyst-Me-Tyr -Trp-Pul (R4: CH_2CO- L-tyrosyl-L-tryptophyl-SeCyst methyl ester)

Table 1. Degree of Substitution of Carboxymethyl Group in CM-Pul and Selenium Content of SeCyst-Pul Conjugates

Conjugate	Degree of substitution of CM group (/glucose unit of Pul)	Selenium content (mg/g conjugate)
SeCyst-Me-Pul	0.06	12.4 ± 0.3
	0.21	45.4 ± 0.7
	0.44	79.7 ± 0.5
SeCyst-Et-Pul	0.44	82.2 ± 1.8
SeCyst-*i*Pr-Pul	0.44	70.9 ± 0.9
SeCyst-Bz-Pul	0.44	79.1 ± 1.1
SeCyst-Me-His-Pul	0.44	44.1 ± 0.3
SeCyst-Me-Leu-Pul	0.44	57.9 ± 1.1
SeCyst-Me-Tyr-Pul	0.44	56.4 ± 1.9
SeCyst-Me-Trp-Pul	0.44	49.7 ± 0.7
SeCyst-Bz-Trp-Pul	0.36	56.6 ± 0.7
SeCyst-Me-His-Trp-Pul	0.36	49.9 ± 1.5
SeCyst-Me-Leu-Trp-Pul	0.36	56.2 ± 0.7
SeCyst-Me-Tyr-Trp-Pul	0.36	45.2 ± 2.7

The SeCyst esters have two chemically equivalent primary amino groups at both ends. Both amino groups could be possibly reacted intra- and/or intermolecularly with the carboxymethyl groups of the CM-Puls. To obtain structural information on the SeCyst-Pul conjugates, the particle diameters of the SeCyst-Pul conjugates were measured by the DLS technique. The mean particle diameters of SeCyst-Me-Pul (DS = 0.44), SeCyst-Me-Trp-Pul, and SeCyst-Bz-Trp-Pul conjugates were almost comparable to each other, and were close to that of Pul (Table 2 and Figure 1). The particle diameter distributions of these conjugates were also similar to that of Pul. The diselenide linkage (R-Se-Se-R) can react with free thiol compounds (R′-SH) to form selenosulfide (R-Se-S-R′). When the SeCyst-Pul conjugates are treated with an excess molar amount of glutathione (GSH), the Sec fragment (Sec-Se-SG) could be released from the SeCyst esters bound to Pul through its one end amino group. Practically, such low molecular mass selenium-containing fragments were not released from the SeCyst-Pul conjugates. Overall, the reaction of the CM-Pul with the bifunctional SeCyst esters appears to mainly result in intramolecular substitution rather than intermolecular linkage.

Aggregation of SeCyst-Pul Conjugates. The SeCyst esters have hydrophobic characteristics, and hydrophobic amino acids were also introduced to a hydrophilic Pul molecule. As the SeCyst-Pul conjugates have amphiphilic structure elements within the molecules, these conjugates could possibly form self-

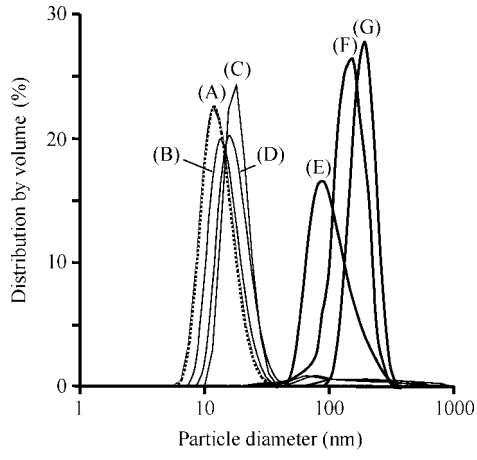

Figure 1. Particle diameter distribution of Pul (A), SeCyst-Me-Pul conjugate (B), SeCyst-Me-Trp-Pul conjugate (C), SeCyst-Bz-Trp-Pul conjugate (D), SeCyst-Me-Pul aggregate (E), SeCyst-Me-Trp-Pul aggregate (F), and SeCyst-Bz-Trp-Pul aggregate (G). Degree of substitution of carboxymethyl group for SeCyst-Me-Pul conjugate: 0.44.

Table 2. Particle Diameter of SeCyst-Pul Aggregates and Conjugates

Aggregate/conjugate	Degree of substitution of CM group (/glucose unit of Pul)	Particle diameter (nm)
SeCyst-Me-Pul aggregate	0.06	446.0 ± 25.6
	0.21	602.4 ± 16.8
	0.44	106.5 ± 0.9
SeCyst-Et-Pul aggregate	0.44	211.1 ± 5.7
SeCyst-*i*Pr-Pul aggregate	0.44	118.9 ± 1.2
SeCyst-Bz-Pul aggregate	0.44	175.8 ± 0.9
SeCyst-Me-His-Pul aggregate	0.44	151.1 ± 2.2
SeCyst-Me-Leu-Pul aggregate	0.44	240.9 ± 3.0
SeCyst-Me-Tyr-Pul aggregate	0.44	189.9 ± 3.5
SeCyst-Me-Trp-Pul aggregate	0.44	162.8 ± 1.3
SeCyst-Bz-Trp-Pul aggregate	0.36	253.1 ± 1.6
SeCyst-Me-His-Trp-Pul aggregate	0.36	194.2 ± 18.4
SeCyst-Me-Leu-Trp-Pul aggregate	0.36	185.7 ± 0.7
SeCyst-Me-Tyr-Trp-Pul aggregate	0.36	128.5 ± 3.6
SeCyst-Me-Pul conjugate	0.44	18.9 ± 0.8
SeCyst-Me-Trp-Pul conjugate	0.44	15.8 ± 2.8
SeCyst-Bz-Trp-Pul conjugate	0.36	15.6 ± 1.2
Pul	0.00	13.3 ± 1.0

aggregates. The aggregation behavior of the SeCyst-Pul conjugates in an aqueous medium was preliminarily checked by the static light scattering method (Supporting Information Figure S1). Scattered lights were observed from all the tested SeCyst-Pul conjugate solutions, and their intensities were apparently greater than that from the unmodified Pul solution. In comparison to the SeCyst-Me-Pul conjugates with different selenium contents, the scattered light intensity increased with the increasing selenium content (≈ degree of substitution of SeCyst ester moiety). The SeCyst-Me-Trp-Pul and SeCyst-Bz-Trp-Pul conjugates provided higher scattered light intensities than the SeCyst-Me-Pul conjugate. These facts suggest the presence of particulate materials that were formed by the self-aggregation of the SeCyst-Pul conjugates.

The SeCyst-Pul aggregates were characterized by the DLS technique (Table 2). Pul used as the starting material had a mean diameter of 13.3 nm, which indicates that Pul without any chemical modifications does not form self-aggregates. The mean particle diameters of the SeCyst-Pul aggregates were in the range from 100 to 300 nm, which were apparently greater than that of Pul. The particle diameters of the SeCyst-Me-Pul conjugates tended to decrease with an increase in the degree of substitution of the SeCyst ester moiety. The mean particle diameters of the SeCyst-Me-Pul, SeCyst-Me-Trp-Pul, and SeCyst-Bz-Trp-Pul aggregates also became greater than those of the corresponding conjugates that are dissolved in a molecularly dispersed state. The particle diameter distributions of the SeCyst-Me-Pul, SeCyst-Me-Trp-Pul, and SeCyst-Bz-Trp-Pul aggregates were evidently shifted to larger diameter ranges than those of Pul and these conjugates (Figure 1). In general, the morphology of the stable aggregate of the amphiphiles depends on their molecular orientation and freedom; the key factors are to control the hydrophile−lipophile balance, the hydrophobic interactions and dispersion of the hydrophilic moiety in the aqueous medium for formation of the structured self-aggregates (*29, 30*). The SeCyst-Me-Pul conjugates with a low DS produced larger aggregates with diameters of 400−600 nm, while the SeCyst-Bz-Pul conjugate with a high DS and benzyl group and amino acid residue produced smaller aggregate diameters (100−300 nm). Self-aggregation of the SeCyst-Pul conjugates is dependent on the degree of introduction of the SeCyst and its chemical structures, although no unambiguous relation between the hydrophobicity of the substituents and the size of the formed aggregates was found.

Since an intramolecular linkage of Pul molecules through the SeCyst esters could be cleaved by GSH treatment, the treatment of the SeCyst-Pul aggregates with GSH may give rise to

Table 3. Changes in Particle Diameter of SeCyst-Puls Aggregates after the Glutathione Treatment[a]

Aggregate	Degree of substitution of CM group (/glucose unit of Pul)	Particle diameter (nm)	
		Before	After
SeCyst-Me-Pul	0.44	106.5 ± 0.9	108.6 ± 0.4
SeCyst-Bz-Pul	0.44	175.8 ± 0.9	184.8 ± 8.8
SeCyst-Me-Trp-Pul	0.44	162.8 ± 1.3	154.2 ± 1.9
SeCyst-Bz-Trp-Pul	0.36	253.1 ± 1.6	272.1 ± 3.8

[a] Aggregate solutions were treated with 2 mM GSH at 37 °C for 30 min.

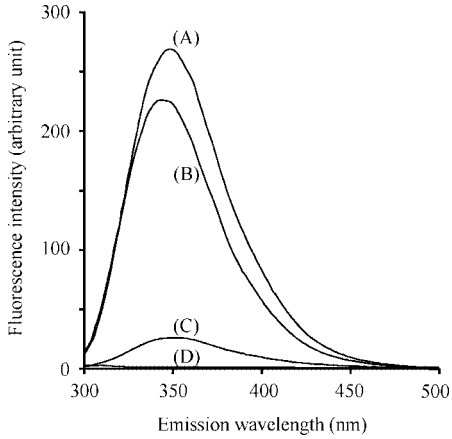

Figure 2. Tryptophan fluorescence spectra of free Trp (A), Trp-Pul (B), SeCyst-Me-Trp-Pul aggregate (C), and SeCyst-Bz-Trp-Pul aggregate (D). Trp concentration: 60 μM (*Trp concentrations were adjusted by UV absorbance at 280 nm). Excitation wavelength: 280 nm.

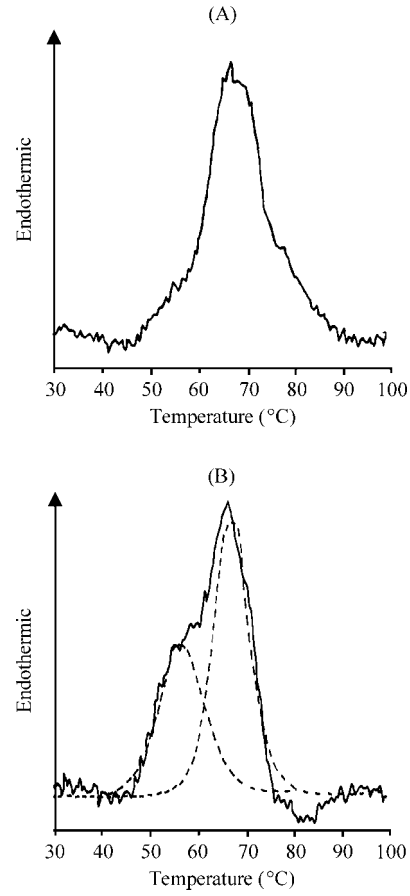

Figure 3. DSC thermograms of SeCyst-Me-Pul aggregate (A) and SeCyst-Bz-Trp-Pul aggregate (B). *Degree of substitution of carboxymethyl group for SeCyst-Me-Pul conjugate: 0.44. Heating rate: 1 °C/min. The broken lines in panel (B) were drawn by *ORIGIN* software.

structural changes in the SeCyst-Pul aggregates. The particle diameters of the SeCyst-Pul aggregates were compared before and after the treatment with an excess amount of GSH. No remarkable changes in the particle diameters were found for the SeCyst-Me-Pul, SeCyst-Bz-Pul, SeCyst-Me-Trp-Pul, and SeCyst-Bz-Trp-Pul aggregates after the GSH treatment (Table 3). Therefore, the intramolecular linkage of Pul through amino groups at both ends of the SeCyst esters does not appear to be a dominant structural element for formation of the nanosized aggregates. Consequently, the structures of the SeCyst-Pul aggregates are likely to involve noncovalent interactions such as the hydrophobic interactions between the SeCyst esters and amino acid residues rather than the diselenide linkage.

To obtain information on the structures of the SeCyst-Pul aggregates from another viewpoint, the Trp intrinsic fluorescence spectra of the SeCyst-Trp-Pul conjugates were compared to the free Trp and their precursor (Trp-Pul). Self-aggregation in aqueous medium would transfer Trp and SeCyst moieties to a hydrophobic environment. The fluorescence intensity of the SeCyst-Me-Trp-Pul aggregate mostly decreased as compared to those of the free Trp and its precursor, Trp-Pul (Figure 2). Furthermore, aggregation of SeCyst-Bz-Trp-Pul almost quenched its Trp fluorescence, demonstrating that the SeCyst-Bz-Trp moieties in Pul are associated with each other in the formed aggregates. Independently, the SeCyst-Me-Pul, SeCyst-Me-Trp-Pul, and SeCyst-Bz-Trp-Pul aggregates were prepared in the presence of a fluorescent 8-anilino-1-naphthalene sulfonic acid (ANS), and the fluorescence spectra of ANS were measured at the excitation wavelength of 380 nm. The Trp-containing SeCyst-Me-Trp-Pul and SeCyst-Bz-Trp-Pul aggregates provided a 60 nm blue shift in their fluorescence spectra (Supporting Information Figure S2). Consequently, self-aggregation of the SeCyst-Pul conjugates appears to be driven by both intramolecular chemical linking of Pul with SeCyst and the hydrophobic interactions that occur between the SeCyst side groups and amino acid residues.

The SeCyst-Pul aggregates were further characterized by a DSC analysis. When supplying heat energy to the aggregates or assemblies (e.g., lipid membranes) that are formed by noncovalent interactions, an enthalpy change due to the decomposition (disassembly) of the aggregates would be observed. Cholesterol-conjugated pullulan (CHP) can spontaneously form hydrogel aggregates in an aqueous medium with diameters ranging between 20 and 30 nm (*31–34*). The CHP self-aggregates contain hydrophobic domains that are formed by the noncovalent hydrophobic interactions among the cholesterol moieties. When the CHP aggregates were subjected to the DSC analysis, a characteristic endothermic peak was observed in the temperature range between 60 and 80 °C (Supporting Information Figure S3). This is due to the dissociation of the cholesterol hydrophobic domains in the CHP hydrogel aggregates. SeCyst-Me-Pul and SeCyst-Bz-Trp-Pul (DS of carboxymethyl group: 43.78%) also gave similar endothermic peaks at 60−80 °C (Figure 3). The observed thermal behavior resulted from the hydrophobic domains structured in the SeCyst-Pul aggregates. The Trp-containing SeCyst-Pul aggregates such as SeCyst-Me-Trp-Pul and SeCyst-Bz-Trp-Pul also produced other endothermic peaks at different temperature ranging from 50 to 70 °C. The appearance of these endothermic peaks suggests that Trp residue-associated hydrophobic interactions occur in the Trp-containing SeCyst-Pul aggregates.

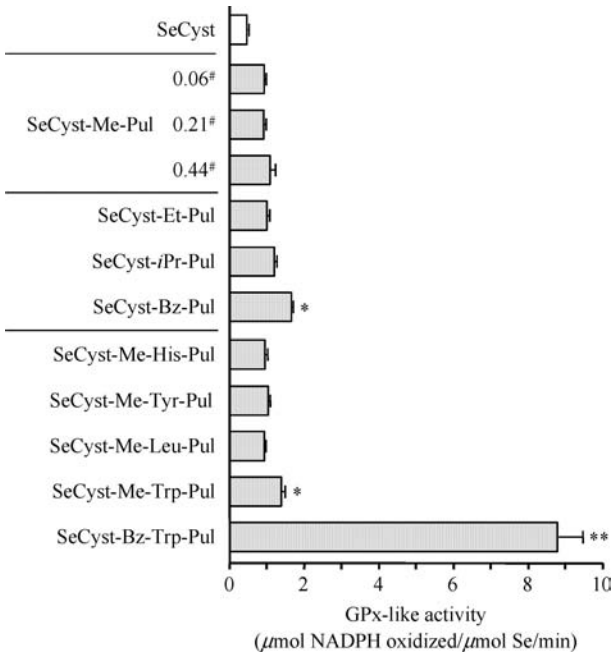

Figure 4. GPx-like activity of SeCyst-Pul aggregates for hydrogen peroxide. #: Degree of substitution of carboxymethyl group. * and **: significantly different from SeCyst at $P < 0.05$ and $P < 0.01$, respectively.

GPx-like Activity and Steady State Kinetics of SeCyst-Pul Aggregates. The GPx-like activity of the SeCyst-Pul aggregates was determined according to the conventional procedure, in which oxidation of NADPH is spectrophotometrically monitored by coupling to the reduction of the oxidized glutathione (GSSG) catalyzed by glutathione reductase. The GPx-like activity was compared among three SeCyst-Me-Pul aggregates with different degrees of SeCyst methyl ester loading. There was no significant difference in the activity among the three aggregates, and their activities were almost comparable to that of the free SeCyst (Figure 4). The SeCyst-Me-Pul, SeCyst-Et-Pul, and SeCyst-*i*Pr-Pul aggregates showed 2-fold higher activities than the free SeCyst, while the SeCyst-Bz-Pul aggregate provided 3-fold higher activity. The activities of the amino acid-inserted SeCyst-Me-His-Pul, SeCyst-Me-Tyr-Pul, and SeCyst-Me-Leu-Pul aggregates were almost twice that of the free SeCyst, whereas the Trp-containing SeCyst-Me-Trp-Pul aggregate was more effective than the other three. When SeCyst was attached to Pul through a dipeptide linkage consisting of Trp and His, Tyr, or Leu, no remarkable enhancement in the activity was also observed for SeCyst-Me-His-Trp-Pul, SeCyst-Me-Tyr-Trp-Pul, and SeCyst-Me-Leu-Trp-Pul. On the basis of these results, the benzyl side groups of the SeCyst and Trp residue appear to be good substituents for enhancing the GPx-like activity in our system. The SeCyst benzyl ester and Trp residue were, therefore, introduced to Pul. The SeCyst-Bz-Trp-Pul aggregate synergistically exhibited nearly a 20-fold higher GPx-like activity than the free SeCyst. The enhanced activity of the SeCyst-Bz-Trp-Pul aggregate was not inhibited by the radical trap 2,6-di-*tert*-butyl-4-methylphenol, which suggests that this aggregate catalyzes the reduction of H_2O_2 by the SeCyst moiety via a nonradical mechanism (*35*).

The steady state kinetics of the SeCyst-Bz-Trp-Pul aggregate-catalyzed reduction was analyzed using the double-reciprocal equation with varying concentrations of both H_2O_2 and GSH (Figure 5). The double-reciprocal plots (1/[GSH] versus 1/v) of the SeCyst-Bz-Trp-Pul aggregate-catalyzed reduction yielded parallel straight lines for three different H_2O_2 concentrations, suggesting that its reaction pathway is a "ping-pong" (double-displacement) reaction pathway analogous to those of the natural GPxs. A similar result was also obtained for the SeCyst-Me-Pul aggregate. The kinetic parameters of the two aggregates were calculated from the slope and *Y*-axis intercept of the double-reciprocal plots. The apparent reduction rate constant, k_{cat}, for the SeCyst-Bz-Trp-Pul was greater than that for SeCyst-Me-Pul (Table 4). This kinetic advantage can be supportive evidence for the enhanced GPx-like activity of the SeCyst-Bz-Trp-Pul aggregate in comparison to that of the SeCyst-Me-Pul aggregate. In addition, the SeCyst-Bz-Trp-Pul aggregate provided a higher binding affinity for GSH (K_m^{GSH}) and H_2O_2 ($K_m^{H_2O_2}$), as compared to the SeCyst-Me-Pul aggregate. Taken together with the characterization data of the SeCyst-Bz-Trp-Pul aggregate, its activity enhancement would be attributed to the hydrophobic environments that were formed together with the benzyl group and Trp residue in the vicinity of the SeCyst moiety.

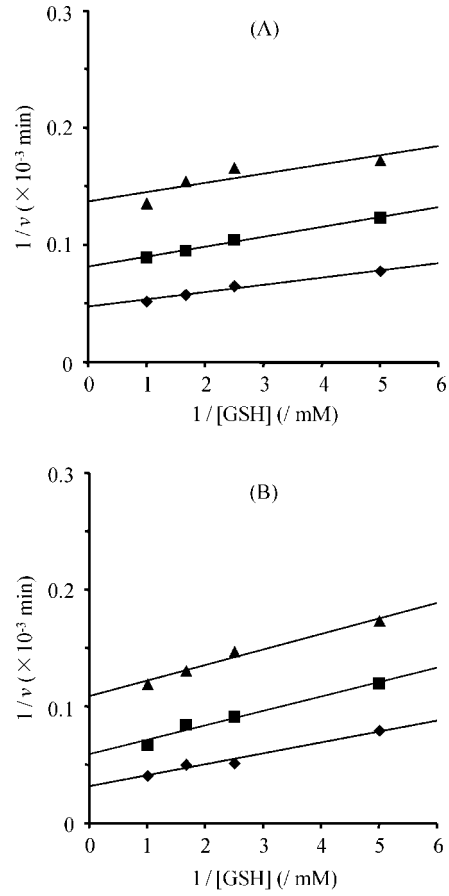

Figure 5. Double-reciprocal plots for SeCyst-Me-Pul (A) and SeCyst-Bz-Trp-Pul (B) aggregate-catalyzed H_2O_2 reduction. Selenium concentrations in SeCyst-Me-Pul and SeCyst-Bz-Trp-Pul aggregate samples: 43.6 and 2.1 μM. $[H_2O_2] = 0.25$ (▲), 0.5 (■), and 1 mM (◆).

Table 4. Kinetic Parameters of SeCyst-Me-Pul and SeCyst-Bz-Trp-Pul Aggregate-Catalyzed H_2O_2 Reduction

		K_m (mM)		k_{cat}/K_m [1/(mM·min)]	
Aggregate	k_{cat}(/min)	GSH	H_2O_2	GSH	H_2O_2
SeCyst-Me-Pul[a]	4.12	2.04	4.64	2.02	0.82
SeCyst-Bz-Trp-Pul	49.26	0.76	3.76	64.82	13.10

[a] Degree of substitution of carboxymethyl group for SeCyst-Me-Pul conjugate: 0.44.

The GPx-like activity of SeCyst-Bz-Trp-Pul aggregate for organic *tert*-butylhydroperoxide (*t*-BuOOH) as a substrate was also examined (Supporting Information Figure S4). SeCyst-Bz-Trp-Pul aggregate did not provide enhancements in the activity

for this substrate as much as that for hydrogen peroxide (nearly a 4-fold increase). A previous paper by Ren et al. (*16*) reported that SeCyst bound to the primary side of β-cyclodextrin (β-CD) via the two amino groups resulted in enhanced GPx-like activity for *t*-BuOOH and cumene hydroperoxide (CuOOH), which is ascribed to the inclusion interactions of these substrates into the hydrophobic cavity of β-CD. Although the SeCyst moieties in SeCyst-Bz-Trp-Pul aggregate exist in hydrophobic environments, *t*-BuOOH may be less accessible to the SeCyst moieties than hydrogen peroxide due to hydrophilic surrounds by Pul molecules. Consequently, the hydrophobic regions that are formed in the SeCyst-Bz-Trp-Pul aggregate do not seem to provide binding sites for such an organic substrate. Actually, selenium-dependent native GPxs possess the substrate specificity; GPx-1 is active for inorganic hydrogen peroxide, but not for organic phospholipid hydroperoxides that are substrates of GPx-4 (*36*).

In conclusion, we synthesized nanoparticulate glutathione peroxidase mimics based on the SeCyst esters-attached Pul conjugates. The chemical stability of SeCyst in an aqueous medium was somewhat improved by attachment to the Pul polymer. SeCyst-Pul conjugates were spontaneously formed into self-aggregates with diameters of several hundred nanometers. The results of the physicochemical characterization suggest the formation of hydrophobic microenvironments in the vicinity of SeCyst in the SeCyst-Pul aggregates. In comparison to the free SeCyst, improvements in the activity of the H_2O_2 reduction were observed for all the SeCyst-Pul aggregates. Even better, the most effective SeCyst-Bz-Trp-Pul aggregate produced a nearly 20-fold activity enhancement. The double-reciprocal plot analysis of the SeCyst-Bz-Trp-Pul aggregate-catalyzed reduction revealed that the catalytic mechanism of SeCyst-Bz-Trp-Pul aggregate was analogous to those of the natural GPxs (a "ping-pong" reaction pathway), and the kinetic parameters of the SeCyst-Bz-Trp-Pul aggregate were improved. Consequently, several features of our nanosized aggregate system were found to be different from the low mass GPx-mimics: (i) to improve the water solubility and stability of the liable selenium compounds in order to function as the active site; (ii) to be capable of forming a hydrophobic environment in the vicinity of the selenium compound; and (iii) to concentrate the local selenium compound in the self-aggregates. We are now designing more efficacious SeCyst-Pul aggregates with GPx-like activity. In addition, we will try to apply these aggregates to medicine as a particulate antioxidant material.

Supporting Information Available: Scattered light intensity of SeCyst-Pul conjugates (Figure S1), fluorescence spectra of SeCyst-Bz-Trp-Pul and cholesterol-conjugated Pul aggregates prepared in the presence of ANS and ANS alone (Figure S2), DSC thermogram of cholesterol-conjugated Pul self-aggregate (Figure S3), GPx-like activity of SeCyst-Pul aggregates for *tert*-butylhydroperoxide (*t*-BuOOH) (Figure S4). This material is available free of charge via the Internet at http://pubs.acs.org.

LITERATURE CITED

(1) Rayman, M. R. (2000) The importance of selenium to human health. *Lancet 356*, 233–241.

(2) Chu, F. F. (1994) The human glutathione peroxidase genes GPX2, GPX3, and GPX4 map to chromosomes 14, 5 and 19, respectively. *Cytogenet. Cell Genet. 66*, 96–98.

(3) Drevet, J. R. (2006) The antioxidant peroxidase family and spermatozoa: A complex story. *Mol. Cell. Endoclinol. 250*, 70–79.

(4) Singh, A. K., and Shichi, H. (1998) A novel glutathione peroxidase in bovine eye. *J. Biol. Chem. 273*, 26171–26178.

(5) Berry, M. J., Banu, L., Chen, Y., Mandel, S. K., Kieffer, J. D., Harney, J. W., and Larsen, P. R. (1991) Recognition of UGA as a Sec codon in Type I deiodinase requires sequences in the 3′ untranslated region. *Nature 353*, 273–276.

(6) Bock, A. (2000) Biocynthesis of selenoproteins. *BioFactors 11*, 77–78.

(7) Atokins, F. J., and Gesteland, F. R. (2000) The twenty-first amino acid. *Nature 407*, 463–464.

(8) Hatfield, L. D., and Gradyshev, N. V. (2002) How selenium has altered our understanding of the genetic code. *Mol. Cell. Biol. 22*, 3565–3576.

(9) Mizutani, T., and Fujiwara, T. (2000) SBP, SECIS binding protein, binds to the RNA fragment upstream of the Sec UGA codon in glutathione peroxidase mRNA. *Mol. Cell. Reports 27*, 99–105.

(10) Hendrickson, T. L. (2007) Easing selenocysteine into proteins. *Nat. Struct. Mol. Biol. 14*, 100–101.

(11) Epp, O., Ladenstein, R., and Wendel, A. (1983) The refined structure of the seleno-enzyme glutathione peroxidase at 0.2-nm resolution. *Eur. J. Biochem. 133*, 51–69.

(12) Ren, B., Huang, W., Akesson, B., and Ladenstein, R. (1997) The crystal structure of seleno- glutathione peroxidase from human plasma at 2.9-angstrom resolution. *J. Mol. Biol. 268*, 869–885.

(13) Maiorino, M., Aumann, D. K., Flohe, B. R., Doria, D., McCarthy, J., Roveri, A., Ursini, F., and Flohe, L. (1995) Probing the presumed catalytic triad of selenium-containing peroxidases by mutational analysis of phospholipid hydroperoxide glutathione peroxidase (PHGPx). *Biol. Chem. Hoppe-Seyler 376*, 651–660.

(14) Klayman, D. L., and Griffin, S. T. (1973) Reaction of selenium with sodium borohydride in protic solvents. A facile method for the introduction of selenium into organic molecules. *J. Am. Chem. Soc. 95*, 197–199.

(15) Luo, G., Ren, J., Liu, J., Mu, Y., and Shen, J. (2003) Towards more efficient glutathione peroxidase mimics: Substrate recognition and catalytic group assembly. *Curr. Med. Chem. 10*, 1151–1183.

(16) Ren, X., Liu, J. Q., Luo, G. M., Zhang, Y., Luo, Y., Yan, G., and Shen, J. (2000) A novel selenocystine-β-cyclodextrin conjugate that acts as a glutathione peroxidase mimic. *Bioconjugate Chem. 11*, 682–687.

(17) Liu, J., Gao, S., Luo, G., Yan, G., and Shen, J. C. (1998) Artificial imitation of glutathione peroxidase with 6-selenium-bridged β-cyclodextrin. *Biochem. Biophys. Res. Commun. 247*, 397–400.

(18) Wilson, S. R., Zucker, A. P., Huang, R. C., and Spector, A. (1989) Development of synthetic compounds with glutathione peroxidase activity. *J. Am. Chem. Soc. 111*, 5936–5939.

(19) Iwaoka, M., and Tomoda, S. (1994) A model study on the effect of an amino group on the antioxidant activity of glutathione peroxidase. *J. Am. Chem. Soc. 116*, 2557–2561.

(20) Zade, S.S., Sighn, B. H., and Butcher, J. B. (2004) The isolation and crystal structure of a cyclic selenenate este derived from bis(2,6-diformyl-4-tert-butylphenyl) diselenide and its glutathione peroxidase-like activity. *Angew. Chem., Int. Ed. 43*, 4513–4515.

(21) Sun, Y., Li, T., Chen, H., Zhang, K., Zheng, K., Mu, Y., Yan, G., Li, W., Shen, J., and Luo, G. (2004) Selenium-containing 15-mer peptides with high glutathione peroxidase-like activity. *J. Biol. Chem. 279*, 37235–37240.

(22) Nogusa, H., Yano, T., Okuno, S., Hamana, H., and Inoue, K. (1995) Synthesis of carboxymethylpullulan-peptide-doxorubicin conjugates and their properties. *Chem. Pharm. Bull. 43*, 1931–1936.

(23) Bondanszky, M. (1984) Alkyl esters of amino acids. *Int. J. Pept. Protein Res. 23*, 111.

(24) Burstein, Y., Walsh, K. A., and Neurath, H. (1974) Evidence of an essential histidine residue in thermolysin. *Biochemistry 13*, 205–210.

(25) Watkinson, J. H. (1966) Fluorometric determination of selenium in biological material with 2,3-diaminonaphtalene. *Anal. Chem. 38*, 92–97.

(26) Mannervik, B. (1985) Glutathione peroxidase. *Methods Enzymol. 133*, 490–495.

(27) Cleland, W. W. (2002)Enzyme kinetics: steady state, In *Nature Encyclopedia of Life Sciences*, Vol. 6, pp 421−425.

(28) Glinel, K., Sauvage, J. P., Oulyadi, H., and Huguet, J. (2000) Determination of substituents distribution in carboxymethylpullulans by NMR spectroscopy. *Carbohydr. Res. 382*, 343–354.

(29) Kunitake, T., Okahata, Y., Shmomura, M., Yasunami, S., and Takarabe, K. (1981) Fomation of stable bilayer assemblies in water from single-chain amphiphiles. Relationship between the amphiphile structure and the aggregate morphology. *J. Am. Chem. Soc. 103*, 5401–5413.

(30) Park, S. J., Han, H. T., Lee, Y. K., Han, S. S., Hwang, J. J., Moon, H. D., Kim, Y. S., and Cho, W. Y. (2006) N-acetyl histidine-conjugated glycol chitosan self-assembled nanoparticles for intracytoplasmic delivery of drugs: Endocytosis, exocytosis and drug release. *J. Controlled Release 115*, 37–45.

(31) Akiyoshi, K., Yamaguchi, S., and Sunamoto, J. (1991) Self-aggregates of hydrophobic polysaccharide derivatives. *Chem. Lett. 20*, 1263–1266.

(32) Akiyoshi, K., Deguchi, S., Moriguchi, N., Yamaguchi, S., and Sunamoto, J. (1993) Self-aggregates of hydrophobized polysaccharides in water. Fomation and characteristics of nanoparticles. *Macromolecules 26*, 3062–3068.

(33) Akiyoshi, K., Deguchi, S., Tajima, H., Nishikawa, T., and Sunamoto, J. (1995) Self-assembly of hydrophobized polysaccharide. *Proc. Jpn. Acad. 71*, 15–19.

(34) Akiyoshi, K., Deguchi, S., Tajima, H., Nishikawa, T., and Sunamoto, J. (1997) Microscopic structure and thermoresponsiveness of a hydrogel nanoparticle by self-assembly of a hydrophobized polysaccharide. *Macromolecules 30*, 857–861.

(35) Bell, I. M., and Hilvert, D. (1993) Peroxide dependence of the semisynthetic enzyme selenosubtilisin. *Biochemistry 32*, 13969–13973.

(36) Brigelius-Flohé, R. (1999) Tissue-specific functions of individual glutathione peroxidases. *Free Radic. Biol. Med. 27*, 951–965.

BC800086Z

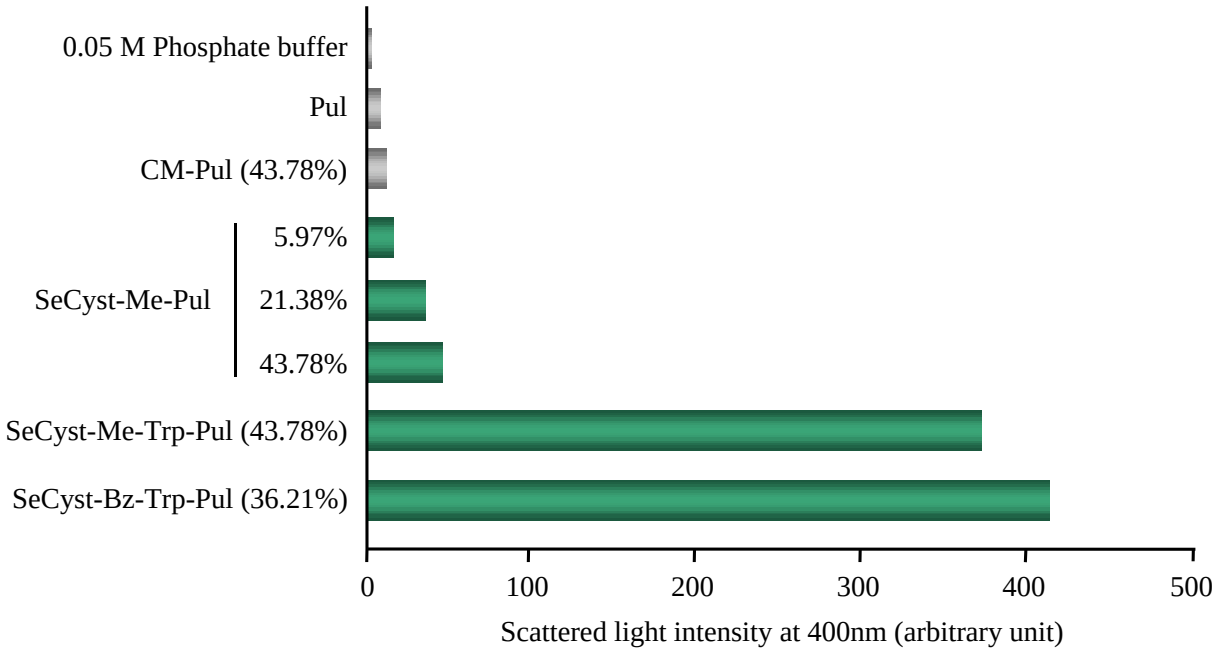

Figure S1. Scattered light intensity of SeCyst-Pul conjugates. SeCyst-Pul conjugate solutions dissolved in 0.05 M phosphate buffer (pH 7) (conjugate concn: 0.1 mg/mL, selenium concn: 15–126 μM) were passed through a surfactant-free cellulose acetate membrane filter (pore size 0.45 μm, ADVANTEC, Tokyo, Japan) to remove particulate materials. The resulting solutions were transferred to a quartz cuvette (1-cm length) and placed in a FP-6600 spectrofluorometer (JASCO, Tokyo, Japan) with both excitation and emission monochrometers set at 400 nm. The intensity of scattered light due to the aggregation at 90 ° to the incident beam was measure at 25 ℃.

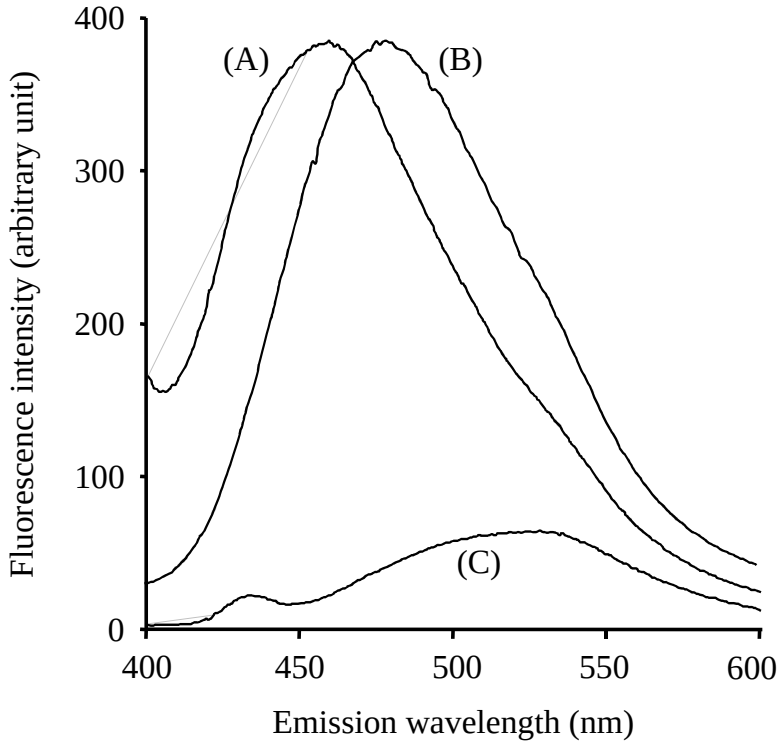

Figure S2. Fluorescence spectra of SeCyst-Bz-Trp-Pul (A) and cholesterol-conjugated Pul (B) aggregates prepared in the presence of ANS and ANS alone (C). ANS concentration: 20 μM, Conjugate concn: 2 mg/mL, Medium: 0.05 M phosphate buffer (pH 7), Excitation wavelength: 380 nm.

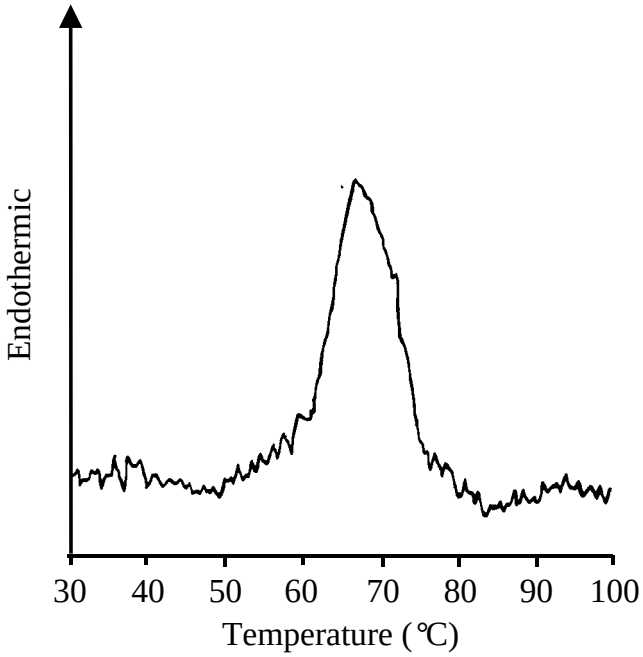

Figure S3. DSC thermogram of cholesterol-conjugated Pul self-aggregate. Heating rate: 1 ℃/min.

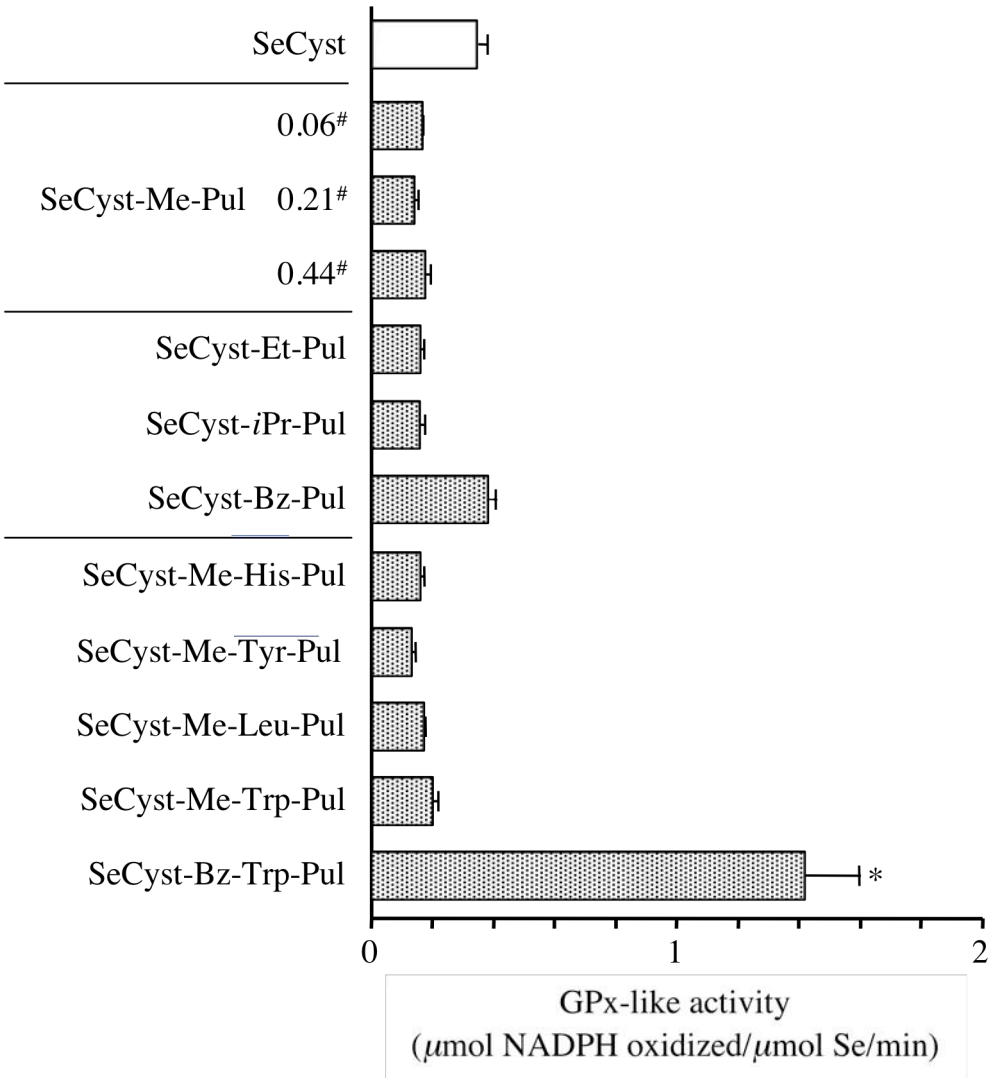

Figure S4. GPx-like activity of SeCyst-Pul aggregates for *tert*-butylhydroperoxide (*t*-BuOOH). #: Degree of substitution of carboxymethyl group. *: Significantly different from SeCyst at $P < 0.05$. The assay was carried out at 37℃ in 0.05 M phosphate buffer (pH 7) containing 1 mM EDTA, 1 mM sodium azide, 1 mM GSH, 0.5 mM *t*-BuOOH, 0.25 mM NADPH, 1 unit of GSH reductase and 10 μmol Se/L samples.

DNA Binding and Cleaving Activity of the New Cleft Molecule *N,N′*-Bis(guanidinoethyl)-2,6-pyridinedicarboxamide in the Absence or in the Presence of Copper(II)

Ying Shao, Xin Sheng, Ying Li, Zhao-Li Jia, Jing-Jing Zhang, Fang Liu,* and Guo-Yuan Lu*

Department of Chemistry, State Key Laboratory of Coordination Chemistry, Nanjing University, Nanjing 210093, People's Republic of China. Received February 15, 2008; Revised Manuscript Received July 2, 2008

Novel cleft molecule pyridine-2,6-dicarboxamide appending two guanidinoethyl group side arms (**Gua**) was synthesized. The interactions of the cleft molecule in the absence of copper(II) (**Gua**) or in the presence of copper(II) (Cu^{2+}-**Gua**) with calf thymus DNA were studied by fluorescence and CD spectroscopy. The results indicate that the DNA binding affinity of Cu^{2+}-**Gua** is stronger than that of **Gua**, and the binding constants of Cu^{2+}-**Gua** and **Gua** are 1.61×10^6 M^{-1} and 2.86×10^5 M^{-1}, respectively. Agarose gel electrophoresis was used to assess the plasmid pUC 19 DNA cleavage activities in the presence of **Gua** and Cu^{2+}-**Gua**. Kinetic data of DNA cleavage promoted by Cu^{2+}-**Gua** under physiological conditions fit a saturation kinetic profile with k_{max} of 0.0173 ± 0.0011 h^{-1}, which gave a $\sim 10^6$-fold rate acceleration over uncatalyzed supercoiled DNA, while the catalyst concentration is lower than 0.0625 mM. The hydrolysis pathway was proposed as the possible mechanism for DNA cleavage promoted by Cu^{2+}-**Gua**. The acceleration is due to efficient cooperative catalysis of the copper cation center and the functional groups (bis(guanidinium) groups).

INTRODUCTION

Some small organic molecules and metal complexes as binding and cleaving agents for phosphodiester bonding of nucleic acids have widely been investigated due to their potential applications in the fields of molecular biological technology and drug development (*1*−*21*). However, their binding and cleaving efficiencies are still far from that of natural nuclease. In Nature, the cleavage rate of the phosphodiesters of DNA and RNA via a hydrolytic pathway is 10^{15}−10^{16}-fold accelerated by the metalloenzymes, such as staphylococcal nuclease (SNase) from *Staphylococcus aureus* (*22*−*26*). At the active site of SNase, calcium(II) ion and two guanidinium groups of arginine residues (Arg-35 and Arg-87) cooperate to activate the substrate and stabilize phosphorate-like transition states by electrostatic interaction, hydrogen bonding, and/or proton transfer (*22*−*29*). Hence, one of the basic principles of the enormous catalytic efficiency for phosphodiester cleavage of DNA and RNA by natural nucleases has been well-established as the efficient cooperation of metal ions and such functional groups at the active site.

Recently, several interesting studies (*30*−*34*) using synthetic models resembling the active site of natural nucleases, i.e., cleft molecule with amino (or ammonium) or guanidine (or guanidinium) functional groups in the presence of metal ions, have demonstrated that the reactivity toward phosphodiester cleavage can be greatly increased. The bipy unit with two ammonium groups in the presence of copper(II) designed by Krämer and Kövari (*30, 31*) can increase the hydrolytic rate of phosphodiester of bis(*p*-nitrophenyl) phosphate (BNPP). Similarly, a rigid cleft in the presence of zinc(II), reported by Anslyn and co-workers (*32*), has two guanidinium or ammonium groups proximal to the metal ion, which leads to a 3.3×10^3 enhancement of the rate of hydrolysis of the RNA dimer adenylyl phosphoadenine (ApA) compared to a corresponding complex lacking the guanidinium or ammonium group. Quite recently, Williams and co-workers (*33*) designed the Zn^{2+} complex of tetradentate tripodal ligand with aminopyridyl hydrogen bond donors that was found to be 1.5×10^3 times more reactive in promoting the cleavage of phosphodiesters of 2-hydroxypropyl 4-nitrophenyl phosphate (HPNPP) via intramolecular transesterification than the corresponding structure missing the two amino groups. These groups' outstanding work has successfully modeled the efficient catalytic cooperativity of a metal ion and functional groups and resulted in considerable increase of the cleavage rate of active phosphodiesters, e.g., BNPP, HPNPP (RNA model), and ApA. As is well known, the phosphodiester bonds of DNA are extremely stable under uncatalyzed physiological conditions and the half-life of DNA for hydrolysis is estimated to be about 200 million years (*35*−*37*). Thus, DNA cleavage via the hydrolytic pathway by artificial synthetic nuclease is a major challenge. The strategy of introduction of the functional groups proximal to the metal ion may reveal a way to cleave the DNA phosphodiester backbone effectively via a nonoxidative pathway.

Compounds with guanidium groups have attracted extensive attention due to their powerful binding ability to negative moieties as SNase (*22*−*26*) and Ptilomycalin A (*38*−*40*). With the knowledge of intermolecular recognition, the guanidium group is always used for identifying negative groups through hydrogen bonding and electrostatic interaction (*41*−*46*) in biological molecules just as the phosphate of DNA or RNA (*41, 47*−*54*). This interaction helps compounds with guanidium groups to be useful agents in phosphodiester cleaving promoters (*55*−*66*) which have been reported by several groups (e.g., Anslyn (*11, 55*−*58*), Göbel (*59*−*62*), Hamilton (*63*−*66*), and their co-workers), and a few of them were identified as powerful cleavers of RNA. Furthermore, as the guanidium group is positively charged, the corresponding compounds might also have reasonable aqueous solubility which could be used to leach toward cell wells at physiological conditions. Therefore, to mimic efficient DNA nuclease models, cleft molecule pyridine-

* Correspondence to Guo-Yuan Lu, Department of Chemistry, State Key Laboratory of Coordination Chemistry, Nanjing University, Nanjing 210093, P.R. China. Fax: +86-25-83321884. Tel:+86-25-83685613. E-mail: lugyuan@nju.edu.cn.

10.1021/bc800062g CCC: $40.75 © 2008 American Chemical Society
Published on Web 08/23/2008

Scheme 1. Synthesis of the Compound Gua

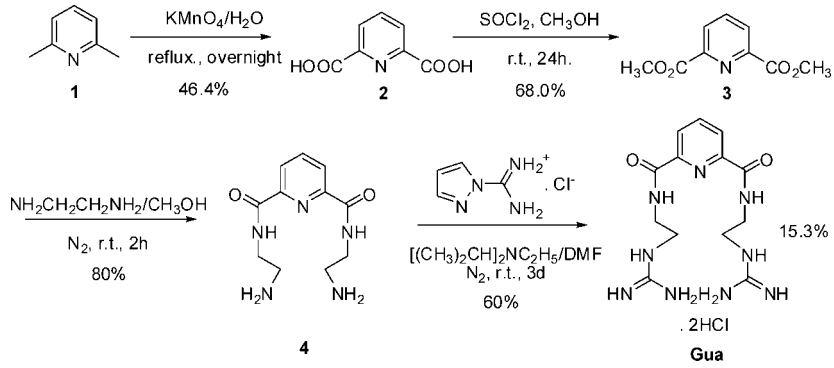

2,6-dicarboxamide appending two guanidinoethyl group side arms (**Gua**) as hydrogen bond donors combined with strong Lewis acid copper(II) was designed as the "cooperative catalyst" promoting DNA cleavage.

In this paper, we report the synthesis (Scheme 1) of *N*,*N*′-bis(guanidinoethyl)-2,6-pyridinedicarboxamide (**Gua**), the interactions of **Gua** in the absence (**Gua**) or in the presence of copper(II) (Cu^{2+}-**Gua**) with calf thymus DNA through the spectroscopic techniques including fluorescence and circular dichroism (CD) spectroscopy, the plasmid pUC 19 DNA cleavage activities in the presence of **Gua** and Cu^{2+}-**Gua** via agarose gel electrophoresis assays, and the possible mechanism of the DNA cleavage promoted by Cu^{2+}-**Gua**.

EXPERIMENTAL PROCEDURES

Materials. All reagents, purchased from commercial sources, were of analytical grade and used without further purification. pUC 19 plasmid DNA was purchased from TaKaRa Biotechnology Co. Ltd., and the purity was checked by agarose gel electrophoresis; concentrations were determined by UV spectroscopy using the extinction coefficient appropriate for double-stranded DNA (1.0 OD_{260} = 50 μg/mL). Agarose was from Oxoid Limited (Basingstoke, UK). Ethidium bromide (EB) was from Amresco Inc. Tris(hydroxymethyl)aminomethane (Tris-Base) was from Robiot Co. Ltd. Bromophenol blue, glycerol, and ethyldiaminetetraacetic acid (EDTA) were commercially available. Deionized water was obtained from an ionized column from doubly distilled water. All solvents were purified by the standard procedure. All aqueous solutions were prepared from deionized water.

The stock solution of CT-DNA (stored at 4 °C and used for not more than 2 days) was prepared in 5 mM Tris-HCl/10 mM NaCl, pH 7.0, and the concentration of the CT-DNA was determined according to its absorption intensity at 260 nm with a molar extinction coefficient value of 6600 M^{-1} cm^{-1}, and the ratio of UV absorbance at 260 and 280 nm, A_{260}/A_{280} = 1.8−1.9, indicating that the DNA was sufficiently free of protein (*67, 68*).

Apparatus. ^{1}H NMR and ^{13}C NMR spectra were recorded on a Brucker AM 300 spectrometer. Mass spectra were obtained on an electrospray mass spectrometer (LCQ, Finnigan or TSQ 7000, Finnigan) in positive or negative mode. IR spectra were recorded in the 4000−400 cm^{-1} region (KBr discs) on a VEVTOR 22 FT-IR spectrometer. The pH value was confirmed with an ORION868 pH meter with an Ag/AgCl electrode as the reference electrode in a saturated KCl solution at room temperature. Agarose gel electrophoresis was conducted with a DYY−5 electrophoresis apparatus. Bands were visualized by UV light and photographed using a DigiDoc-It gel imaging and documentation system (version 1.1.23, UVP, Inc., Unpland, CA). The intensity of the DNA bands was estimated by *TotalLab* image analysis software (version 2.01).

UV−vis Spectral Measurements. UV−visible spectra were measured on Perkin-Elmer Lambda 25 UV−vis Spectrometer using a 1 cm path length UV cell at room temperature. An anhydrous MeCN solution in a final volume of 3 mL consisted of 12.8 μM $CuCl_2$ and the incremental addition of **Gua** from 0 to 54.6 μM in MeCN at room temperature was prepared and subjected to spectral analysis.

Fluorescence Measurements. The fluorescent spectral studies were carried out through the detection of the emission intensity of ethidium bromide (EB) on an AMINCO Bowman Series 2 luminescence spectrometer. The experiments were carried out by adding 0 to 46 μM **Gua** or Cu^{2+}-**Gua** into the EB bound CT-DNA (0.046 mM) solution in 5 mM Tris-HCl buffer (pH 7.0), and the fluorescence was measured and normalized to 100% relative fluorescence.

Circular Dichroism Measurements. All CD spectroscopic studies were carried out with a continuous flow of nitrogen purging the polarimeter by using a Jasco J−810 automatic recording spectropolarimeter, and the measurements were performed at room temperature with 1 cm pathway cells. The CD spectra were run from 320 to 220 nm at a speed of 20 nm/min and the buffer background was automatically subtracted. Data were recorded at an interval of 0.1 nm. The CD spectrum of CT-DNA alone (116 μM) was recorded as the control experiment.

Gel Electrophoresis Assays. Cleavage reactions of supercoiled pUC 19 DNA (0.025 mM bp) were carried out at 37 °C in 50 mM Tris-HCl/10 mM NaCl buffer in a total volume of 15 μL. The results of cleavage reactions were monitored by agarose gel electrophoresis (80 V for 2 h), and the supercoiled pUC 19 DNA values were corrected by a factor of 1.3 on the basis of average literature estimates of the weakened binding of EB to this structure (*69*−*71*).

Synthesis of 2,6-Pyridinedicarboxic Acid (2). (*72*) 2,6-Dimethylpyridine (2.5 g, 23.3 mmol) was stirred with potassium permanganate (8 g, 50.6 mmol) in water (150 mL) under refluxing. When the color of the mixture turned dark without any purple for nearly 2 h, another amount of potassium permanganate (8 g, 50.6 mmol) in 30 mL of water was added dropwise. The reaction then stood overnight under reflux. The precipitate was filtered off immediately without cooling. The filtrate was condensed to about 80 mL, followed by addition of concentrated hydrochloric acid (15 mL). After cooling, acicular crystal (1.81 g, 10.8 mmol) was obtained from the solution. Yield 46.4%. m.p. 196−200 °C. ^{1}H NMR (300 MHz, D_2O) δ 8.18 (t, J = 9.0 Hz, 1H, Ar−H), 8.29 (d, J = 9.0 Hz, 2H, 2 × Ar−H).

Synthesis of 2,6-Pyridinedicarboxate Dimethyl Ester (3). (*73*) Thionyl chloride (1.9 g, 16.0 mmol) was added dropwise to a solution of 2,6-pyridinedicarboxic acid (2.5 g, 15.0 mmol) in methanol (30 mL) while stirring at room temperature. The mixture was then stirred for another 24 h.

Table 1. Selected IR Spectral Data of Gua and Cu^{2+}-Gua (cm^{-1})[a]

compound	ν_{N-H}	$\nu_{C=O}$ [amide I]	amide II	amide III	pyridine ring streching	pyridine ring C−H deformation
Gua	3302m, 3163m	1651b	1543s	1286w	(n. o.), 1446s	723m
Cu^{2+}-**Gua**	3328m, 3269m, 3203w	1651s	1548w	1288w	1624s, 1458w, 1431w	726m

[a] IR spectra of **Gua** and (b) Cu^{2+}-**Gua** (Figure S09, Supporting Information). m = medium, b = broad, s = strong, w = weak, n. o. = not observed distinctly, might have merged with the amide I band.

Filtered and washed with cold methanol, white powder (2 g, 10.2 mmol) was obtained after evaporating to dryness. Yield 68.0%. m.p. 130−132 °C. ^{1}H NMR (300 MHz, $CDCl_3$) δ 4.02 (s, 2H, 2 × CH_3), 8.04 (t, J = 7.8 Hz, 1H, Ar−H), 8.33 (d, J = 7.8 Hz, 2H, 2 × Ar−H).

Synthesis of *N,N′*-Bis(2-aminoethyl)-2,6-pyridinedicarboxamide (4). (*74*) A mixture of **3** (2 g, 0.010 mol) and 1,2-diaminoethane (4.5 g, 0.075 mol) in anhydrous methanol (150 mL) was stirred under the protection of dry nitrogen at room temperature for 2 h. The solution was filtered and evaporated under vacuum followed by azeotropy with dichloromethane (2 × 50 mL) to remove the superfluous diaminoethane. The residue was further distilled in vacuum to afford a colorless oil (2 g, 0.008 mol) at 70 °C (20 mmHg): Yield 80%. ^{1}H NMR (300 MHz, D_2O) δ 2.76 (t, J = 6.3 Hz, 4H, $2NCH_2$), 3.37 (t, J = 6.3 Hz, 4H, $2CONCH_2$), 7.86−7.94 (m, 3H, 3Ar−H). ^{1}H NMR (300 MHz, $CDCl_3$) δ 1.91 (sb, 4H, $2NH_2$), 2.98−3.07 (m, 4H, $2NCH_2$), 3.55−3.61 (m, 4H, $2CONCH_2$), 8.03 (t, J = 7.8 Hz, 2H, 2Ar−H), 8.37 (d, J = 7.8 Hz, 1H, Ar−H), 8.59 (sb, 2H, 2CONH). ESI-MS m/z $[M + H]^+$ calcd 252.1, found 252.2.

Synthesis of *N,N′*-Bis(guanidinoethyl)-2,6-pyridinedicarboxamide (Gua). (*75*). Compound **4** (550 mg, 2.2 mmol), 1*H*-pyzazole-carboxamidine hydrochloride (710 mg, 6.4 mmol), and *N,N*-diisopropyl ethylamine (DIEA, 620 mg, 4.8 mmol) were dissolved in anhydrous DMF (30 mL) and stirred under dry nitrogen at room temperature for 3 days. Then, diethyl ether (100 mL) was poured into the mixture to quench the reaction with an appearance of precipitation. Frozen in the refrigerator for 24 h, followed by filtration and washing with diethyl ether (2 × 20 mL), the solid was dried under vacuum to get a pale yellow powder (440 mg, 1.3 mmol). Yield 60%, m.p. 262−264 °C. ^{1}H NMR (300 MHz, D_2O) δ 3.41(t, J = 6.0 Hz, 4H, $2NCH_2$), 3.59 (t, J = 6.0 Hz, 4H, $2CONCH_2$), 8.01−8.16 (m, 3H, 3Ar−H). ^{13}C NMR (75 MHz, D_2O) δ 38.6 (NCH_2), 41.0 (NCH_2), 125.4 (Ar−C), 147.9 (Ar−C), 140.2 (Ar−C), 157.4 (guanidino-C), 166.2 (C=O). ESI-MS m/z $[M - 2Cl^-]^{2+}$ calcd 168.6, found 168.7; $[M - 2Cl^- - H^+]^+$ calcd 336.2, found 336.3; $[M - Cl^-]^+$ calcd 372.2, found 372.0.

Preparation of Cu^{2+}-Gua Storage Solution. A mixture of dried $CuCl_2$ (0.013 g, 0.10 mmol) and **Gua** (0.041 g, 0.10 mmol) in methanol (10 mL) was stirred for 1 h at room temperature and then evaporated to remove the solvent. The residue was dissolved in 10 mL deionized water as the Cu^{2+}-**Gua** storage solution (10 mM). ESI-MS m/z $[\mathbf{Gua} + Cu^{2+} - Cl^-]^{3+}$ calcd 145.03, found 145.00.

RESULTS AND DISCUSSION

General Aspects. The synthesis of the target compound **Gua** (Scheme 1) was achieved via a four-step reaction sequence of oxidation, esterification, nucleophilic substitution, and guanylation, starting from 2,6-dimethylpyridine **1**. Guanylation (*75*) of the primary amino group was carried out by using the guanylating reagent 1*H*-pyrazole-1-carboxamidine hydrochloride to give **Gua** in good yield. The compound **Gua** was characterized by ^{1}H NMR, ^{13}C NMR, and ESI-MS spectra (Supporting Information, S5−6). In ^{13}C NMR spectrum, the signal at δ157.4 ppm consists of the chemical shift of the guanidinium group, and in the ESI-MS spectrum, the signals at m/z 168.7, 336.2, and 372.0 correspond to $[\mathbf{Gua} - 2Cl]^{2+}$ (calcd. 168.6), $[\mathbf{Gua} - Cl^- - HCl]^+$ (calcd 336.2), and $[M - Cl^-]^+$ (calcd 372.2), respectively. The main signal at m/z 145.0 (Supporting Information, S6) in ESI-MS spectrum of Cu^{2+}-**Gua** corresponds to $[Cu^{2+} - \mathbf{Gua} - Cl^-]^{3+}$, indicating binding of **Gua** with Cu^{2+} (with an uncharged amide functional group), and the binding constants (K_{ML}) were determined to be (1.20 ± 0.09) × 10^6 M^{-1} (Figure S01, Supporting Information) by spectrophotometric titration at room temperature according to the literature (*76*−*78*). Kalagouda and co-workers reported that a pyridinedicarboxamide derivative with an uncharged amide functional group can coordinate metal ions through either the O or N and the coordination modes of several metal complexes using infrared spectrum analysis (*101*). In the IR spectra of Cu^{2+}-**Gua** (Figure S09, Supporting Information; selected data shown in Table 1), compared with that of **Gua**, the band of ν(N−H) is split into multisignals, indicating the involvement of nitrogen in coordination with either amide or guanidino, while the band of ν(C=O) (1651 cm^{-1}) does not show any considerable shift, indicating the noninvolvement of oxygen in coordination (*102*). The amide II and amide III bands show a small shift of 2−5 cm^{-1} suggesting the coordination of amide nitrogen. The pyridine band was shifted to a lower wavenumber in the Cu^{2+}-**Gua** by about 20 cm^{-1}. The band at 1446 cm^{-1} is split into two components, 1458 cm^{-1} and 1431 cm^{-1}, and indicates clearly the coordination of pyridine nitrogen to the metal. The changes in the C−H deformation mode in all of the complexes indicate the coordination of pyridine nitrogen (*102*).

DNA Binding Assays. DNA binding is the critical step for DNA cleavage in most cases. Therefore, the binding of **Gua** and Cu^{2+}-**Gua** to CT-DNA has been studied by using fluorescence and CD spectroscopy. UV−vis absorption spectroscopy is also one of the convenient tools for examining the interaction between small molecule and nucleic acids (*79*−*81*), but their UV absorbances to calf thymus (CT-DNA) were disturbed by absorbances of CT-DNA itself, and thus the DNA binding studies were not carried out by using UV−vis absorption spectroscopy.

Fluorescence Spectroscopic Studies. The binding of the compounds to CT-DNA was studied by evaluating the fluorescence emission intensity of the ethidium bromide (EB)-DNA system upon the addition of the two compounds. If these compounds added to the EB-DNA system replace the bound EB, the emission intensity will be reduced. The fluorescence quenching of EB bound to DNA by **Gua** and Cu^{2+}-**Gua** is shown in Figure S02 (Supporting Information), in which the fluorescence intensity at 600 nm (λ_{ex} = 526 nm) of EB in the bound form was plotted against the compound concentration. The relative binding propensity of the compounds to CT-DNA was determined by the classical Stern-Volmer equation I_0/I = 1 + Kr (*82*, *83*), where I_0 and I are the fluorescence intensities in the absence and the presence of the quencher, respectively. K is the linear Stern-Volmer quenching constant dependent on the ratio of r_{bE} (the ratio of the bound concentration of EB to the concentration of DNA). r is the ratio of total concentration of the quencher to that of DNA (*82*−*84*). Figure 1a is the plot of I_0/I versus [quencher]/[DNA]; the quenching constant K is given by the ratio of the slope to the intercept. The quenching constant K values obtained for **Gua** and Cu^{2+}-**Gua** are 0.045 ± 0.001 and 0.807 ± 0.020, respectively. These results demonstrate that Cu^{2+}-**Gua** has stronger affinity to DNA than **Gua**. The apparent binding constant (K_{app}) is also calculated

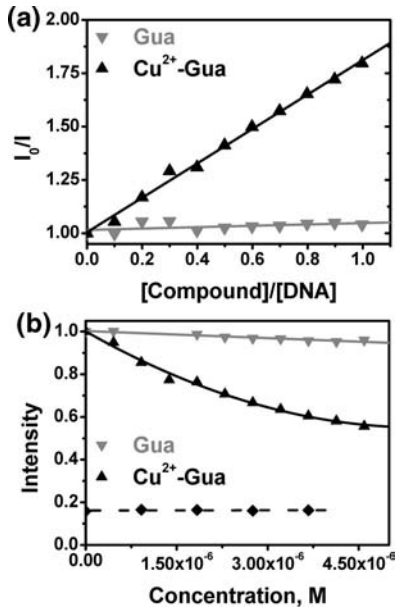

Figure 1. (a) Emission profiles of 0.046 mM CT-DNA-bound EB in a 5 mM Tris-HCl buffer (pH 7.0) upon the addition of (▼) **Gua** and (▲) Cu^{2+}-**Gua** at 25 °C. (b) The Stern-Volmer quenching plots of EB bound to DNA by (▲) **Gua** and (▼) Cu^{2+}-**Gua**, which give the quenching constants K (◆, the emission intensity of EB without CT DNA in the presence of different concentrations of Cu^{2+}-**Gua**).

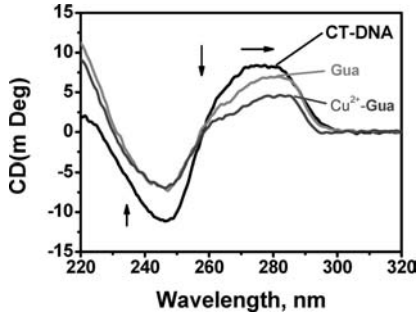

Figure 2. CD spectra of CT-DNA (0.116 mM) in black and the interaction with Cu^{2+}, **Gua**, and Cu^{2+}-**Gua** at ratio of [compound]/[DNA] = 0.4. All the spectra were recorded in Tris-HCl buffer pH 7.0.

from the equation K_{EB}[EB] = K_{app}[complex], where the complex concentration is the value at a 50% reduction of the fluorescence intensity of EB and $K_{EB} = 1.0 \times 10^7$ M^{-1} ([EB] = 1.3 μM) (*84*). The K_{app} values are $(2.86 \pm 0.29) \times 10^5$ M^{-1} for **Gua** and $(1.61 \pm 0.11) \times 10^6$ M^{-1} Cu^{2+}-**Gua** (Figure 1b). It is noticeable that the binding constant of Cu^{2+}-**Gua** is about 5-fold greater than that of **Gua**.

Circular Dichroism Studies. Circular dichroism is a powerful technique to diagnose changes in DNA morphology during drug−DNA interactions, as the band due to base stacking (275 nm) and that due to right-handed helicity (248 nm) are quite sensitive to the mode of DNA interactions with small molecules (*85*, *86*). The changes in CD signals of DNA observed on interaction with drugs may often be assigned to the corresponding changes in DNA structure (*87*). Thus, simple groove binding and electrostatic interaction of small molecules show little or no perturbation on the base-stacking and helicity bands, while intercalation enhances the intensities of both the bands stabilizing the right-handed B conformation of CT-DNA as observed for the classical intercalator methylene blue (*88*). Figure 2 displays the CD spectra of CT-DNA treated with **Gua** and Cu^{2+}-**Gua** with the ratio of 0.4 ([Compound]/[DNA]). The positive (∼275 nm) band decreased in intensity with a concomitant red shift to 280 nm (*89*) with the addition of the compound, while the negative (∼247 nm) band increased in intensity. This suggests that **Gua** and Cu^{2+}-**Gua** can unwind the DNA helix and lead to the loss of helicity (*90*, *91*). The largest decrease in the CD band intensity caused by Cu^{2+}-**Gua** larger than **Gua** at the same concentration implies that Cu^{2+}-**Gua** is more effective than **Gua** in perturbing the secondary structure of DNA.

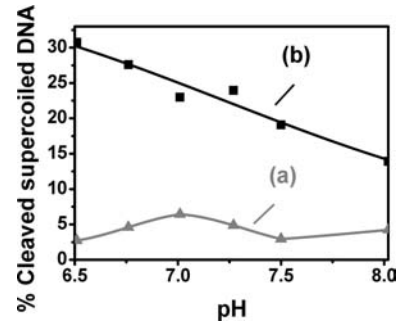

Figure 3. pH-dependent profile for pUC DNA (0.025 mM bp) cleavage promoted by 0.0375 mM (a) **Gua** and (b) Cu^{2+}-**Gua**. (The agarose gel (Figure S03, Supporting Information) of pUC 19 DNA (0.025 mM bp) incubated for 30 h in different pH buffer (50 mM Tris-HCl/10 mM NaCl) at 37 °C.)

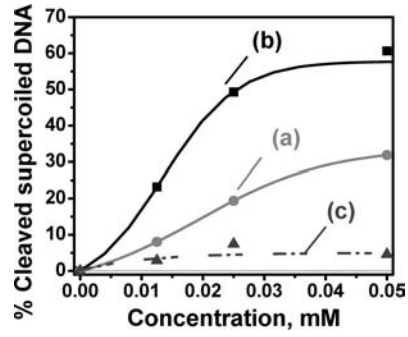

Figure 4. Plot of % cleaved DNA vs different concentrations of (a) **Gua** (b) Cu^{2+}-**Gua** and (c) Cu^{2+} control. (The agarose gel (Figure S04, Supporting Information) of pUC 19 DNA (0.025 mM bp) incubated for 48.0 h at 37 °C with different concentrations of (a) Cu^{2+}-**Gua** and (b) **Gua** in pH 7.0 buffer (50 mM Tris-HCl/10 mM NaCl).)

From the results of fluorescence and CD spectroscopic studies, it is concluded that Cu^{2+}-**Gua** binds more strongly to DNA than **Gua**.

DNA Cleavage Activity. *pH Dependence of DNA Cleavage Promoted by* **Gua** *and* Cu^{2+}-**Gua.** Figure 3 presents the pH-dependence profile which indicates that the optimal pH in physiological condition for DNA cleavage in the presence of **Gua** is pH 7.0, while the cleaving ability of Cu^{2+}-**Gua** was decreasing with the increase of pH from 6.5 to 8.0 at the same condition (the agarose gel is shown in Figure S03, Supporting Information). Therefore, pH 7.0 was chosen for the following agarose gel electrophoresis assays.

Concentration Dependence Assays of DNA Cleavage Promoted by **Gua** *and* Cu^{2+}-**Gua.** Figure 4 shows the plots of % cleaved DNA vs different concentrations of **Gua**, Cu^{2+}, and Cu^{2+}-**Gua** (the agarose gel is shown in Figure S04, Supporting Information), which represents the saturation profiles and indicates that the DNA cleavage activities of **Gua** and Cu^{2+}-**Gua** are increased with the increase of their concentrations. The further increase of concentrations of **Gua** and Cu^{2+}-**Gua** (larger than 0.05 mM) results in further fragmentation and DNA smearing on the electrophoresis gel (the agarose gel is shown in Figure S05, Supporting Information). In order to further

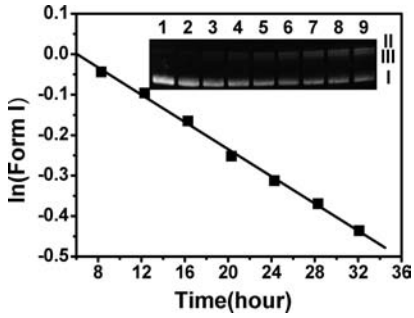

Figure 5. Time course of pUC19 DNA (0.025 mM bp) cleavage promoted by Cu^{2+}-**Gua** (0.0375 mM). Inset is agarose gel (1%) of the time-variable reaction products. Lanes 1−9: reaction times of 0, 4.27, 8.3, 12.3, 16.3, 20.3, 24.27, 28.3, and 32.10 h, respectively.

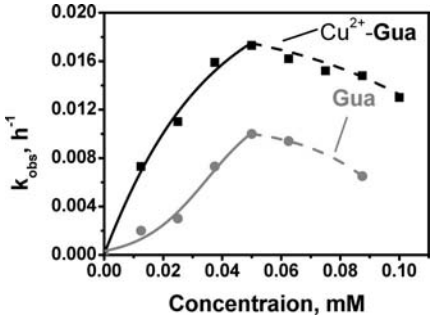

Figure 6. Kinetics plot of k_{obs} vs various concentrations of Cu^{2+}-**Gua** (■) and **Gua** (•).

understand that whether the copper ions alone are able to cleave DNA, control assays were carried out under the same conditions by the metal ions alone. Figure S04c (Supporting Information) shows the results of pUC 19 DNA cleavage in the presence of different concentrations of copper ions. Little cleavage was found and the same result was reported by Barton (*92*).

Kinetic Assays. Kinetics of pUC 19 DNA degradation has been studied. Figure 5 shows the supercoiled plasmid DNA cleavage in nicked and linear form with further reaction, promoted by Cu^{2+}-**Gua** (0.0375 mM) in Tris-HCl/NaCl buffer (pH 7.0) at 37 °C. The time course plot indicates that the extension of supercoiled DNA cleavage varies exponentially with the reaction time giving pseudo first-order kinetics with an apparent initial first-order rate constant (k_{obs}) of 0.0159 ± 0.0006 h^{-1}. Then, the apparent initial first-order rate constants of DNA cleavage reactions promoted by a series of various concentrations of **Gua** and Cu^{2+}-**Gua** under the similar conditions as described above are summarized in Table S01 (Supporting Information). Figure 6 shows the kinetics profile of the supercoiled DNA cleavage at various concentrations of **Gua** and Cu^{2+}-**Gua**. Data of Cu^{2+}-**Gua** give the first-order rate constant k_{max} of 0.0173 ± 0.0011 h^{-1} (Table S01, Supporting Information). The activity increases with the concentration of **Gua** and Cu^{2+}-**Gua** up to a maximum at approximately 0.0500 mM. When the concentration is further increased, the bands corresponding to form II and III are ill-defined due to the appearance of DNA smearing on gel, resulting in the decrease of k_{obs}, and the binding of **Gua** and Cu^{2+}-**Gua** to smaller fragments of DNA could reduce the obvious catalytic efficency for cleaving supercoiled DNA.

DNA Cleavage Mechanism. Copper(II) complexes can cleave DNA by both hydrolytic (*92*−*96*) and oxidative (*97*−*99*) pathways. In the second case, they have been shown to react with molecular oxygen or hydrogen peroxide to produce a variety of reactive oxygen species (ROS) (*100*). Normally, a reducing agent (a thiol or ascorbic acid) is required to initiate

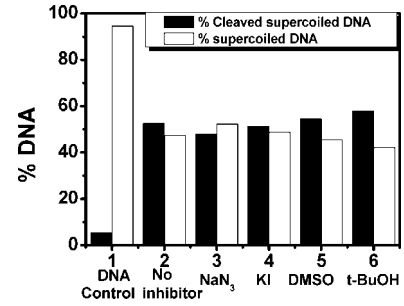

Figure 7. Histogram representing of pUC19 plasmid DNA (0.025 mM bp) cleaved by Cu^{2+}-**Gua** (0.05 mM) in the presence of standard radical scavengers incubated for 33 h at 37 °C in pH 7.0 buffer (50 mM Tris-HCl/10 mM NaCl) (the agarose gel is shown in Figure S06, Supporting Information).

and sustain the radical reaction, but particularly with the employment of DNA derived from biological sources, the presence of adventitious reducing agent is always possible (*93*). To verify whether ROS are, at least in part, responsible for the cleavage of DNA promoted by Cu^{2+}-**Gua**, reactions were carried out in the presence of typical scavengers for singlet oxygen (NaN_3, 10 mM), for superoxide (KI, 10 mM), and for hydroxyl radical (1 mM DMSO and 1 mM *t*-BuOH) (Figure 7). For Cu^{2+}-**Gua**, there is no evident inhibition effect on the DNA cleavage in the presence of all scavengers (NaN_3, DMSO, *t*-BuOH, and KI), which rules out the involvement of these reactive oxygen species, at least in a free and diffusible form, and suggests a nonoxidative pathway.

Generally, the oxidative DNA cleavage process is due to the oxidation of the ribose or base group of DNA by the reactive oxygen species (*97*−*99*). Thus, the DNA samples containing Cu^{2+}-**Gua** were incubated in the presence of nucleosides (adenosine, guanosine, and cytidine, respectively) with the ratio of [nucleoside]/[DNA bp] = 1:1, followed by electrophoresis and quantitation (Figure S07, Supporting Information). No inhibition in the amount of cleaved DNA was detected after the treatment with Cu^{2+}-**Gua** in the presence of all of the nucleosides, which proves the nonoxidative process and/or the competitive binding ability with the nucleosides (Table S03, Supporting Information). On the other hand, in the DNA cleavage reactions promoted by Cu^{2+}-**Gua**, when the active phosphates bis(2,4-dinitrophenyl) phosphate (BDNPP) or bis(*p*-nitrophenyl) phosphate (BNPP) without the pentose and the pyrimidine or purine base was added, the reactions were partially inhibited (Table S03, Supporting Information). The inhibition can be ascribed to the preferentially hydrolyzed phosphodiester of BDNPP or BNPP. It implies that the hydrolysis pathway for the DNA cleavage process is possible. All these results suggest that the DNA cleavage promoted by Cu^{2+}-**Gua** is mainly through the hydrolysis pathway.

In order to further prove the hydrolysis pathway, a small dinucleotide model system adenylyl(3′−5′)phosphoadenine (ApA) was used as the nucleic acid mimics. ApA (0.05 mM) and Cu^{2+}-**Gua** (0.0375 mM) were dissolved in deionized water (1:1), and after 8 h equilibration time at 37 °C, ESI-MS analysis was carried out. In the ESI-MS spectrum (Figure S08b, Supporting Information), the signals at *m*/*z* 267.9 and 346.2 show the ApA cleavage products $[A+H]^+$ (adenosine) (calc 268.1) and $[AMP-H]^-$ (adenosine monophosphate) (calc 346.1), and no sign of ApA was found. While at the same condition, ESI-MS spectra of ApA alone show only the signal of ApA; no sign of A and AMP (Figure S08c, Supporting Information). The generation of the A and AMP indicates that the phosphodiester bond of ApA would be cleaved by Cu^{2+}-**Gua** via the hydrolysis pathway (*47, 103*). As a comparison, ESI-MS analysis of ApA treated with **Gua** alone was also

carried out under the same conditions (Figure S08a, Supporting Information), and there were weaker signals of cleavage products A and AMP, as well as the obvious signal of ApA (Figure S08b, Supporting Information). Therefore, similar to ApA, the hydrolysis pathway should be the possible mechanism for DNA cleavage promoted by Cu^{2+}-**Gua** and the phosphodiester bond hydrolysis ability of Cu^{2+}-**Gua** is stronger than that of **Gua**.

CONCLUSION

In conclusion, novel cleft molecule, pyridine-2,6-dicarboxamide appending two guanidinoethyl group side arms (**Gua**), was synthesized. The interactions of the interactions of **Gua** in the absence or in the presence of copper(II) (Cu^{2+}-**Gua**) with calf thymus DNA were studied by spectroscopic techniques (fluorescence and CD spectroscopy). The results indicate that the DNA binding affinity of Cu^{2+}-**Gua** is stronger than that of **Gua**. Agarose gel electrophoresis was used to assess the plasmid pUC 19 DNA cleavage activities in the presence of **Gua** and Cu^{2+}-**Gua**. Kinetic data of DNA cleavage promoted by Cu^{2+}-**Gua** under the physiological conditions give the maximal initial rate constant k_{max} of 0.0173 h^{-1}, which shows about 10^6-fold rate acceleration over uncatalyzed supercoiled DNA (*35*−*37*). The acceleration is due to the efficient cooperative catalysis of the copper(II) cation center and the functional groups (bisguanidinium groups). The hydrolysis pathway should be the possible mechanism for DNA cleavage promoted by Cu^{2+}-**Gua**.

ACKNOWLEDGMENT

This work was supported by the National Basic Research (grant no. 2007CB925103) and National Science Foundation (grant no. 20774039) of China. We acknowledge gratefully Prof. Chen-Yu Zhang and Li-Qing Qiang for the assistance with the electrophoresis assays.

Supporting Information Available: Spectra for all new compounds, fluorescence and UV−vis spectroscopy, photographs of the agarose gels, and kinetic data. This material is available free of charge via the Internet at http://pubs.acs.org.

LITERATURE CITED

(1) Erkkila, K. E., Odom, D. T., and Barton, J. K. (1999) Recognition and reaction of metallointercalators with DNA. *Chem. Rev. 99*, 2777–2795.

(2) Rajski, S. R., and Williams, R. M. (1998) DNA cross-linking agents as antitumor drugs. *Chem. Rev. 98*, 2723–2795.

(3) Burger, R. M. (1998) Cleavage of nucleic acids by bleomycin. *Chem. Rev. 98*, 1153–1169.

(4) Sherman, S. E., and Lippard, S. J. (1987) Structural aspects of platinum anticancer drug interactions with DNA. *Chem. Rev. 87*, 1153–1181.

(5) Cowan, J. A. (2001) Chemical nucleases. *Curr. Opin. Chem. Biol. 5*, 634–642.

(6) Morrow, J. R., and Iranzo, O. (2004) Synthetic metallonucleases for RNA cleavage. *Curr. Opin. Chem. Biol. 8*, 192–200.

(7) Baker, B. F., Lot, S. S., Kringel, J., Cheng-Flournoy, S., Villiet, P., Sasmor, H. M., Siwkowski, A. M., Chappell, L. L., and Morrow, J. R. (1999) Oligonucleotide-europium complex conjugate designed to cleave the 5′ cap structure of the ICAM-1 transcript potentiates antisense activity in cells. *Nucleic Acids Res. 27*, 1547–1551.

(8) Perreault, D. M., and Anslyn, E. V. (1997) Unifying the current data on the mechanism of cleavage-transesterification of RNA. *Angew. Chem., Int. Ed. 36*, 432–450.

(9) Cheng, C. C., Rokita, S. E., and Burrows, C. J. (1993) Nickel (III)-promoted DNA cleavage with ambient dioxygen. *Angew. Chem. 105*, 290–292; *Angew. Chem., Int. Ed. 32*, 277−278.

(10) Friedel, M. G., Pieck, J. C., Klages, J., Dauth, C., Kessler, H., and Carell, T. (2006) Synthesis and stereochemical assignment of DNA spore photoproduct analogues. *Chem. Eur. J. 12*, 6081–6094.

(11) Mancina, F., and Tecilla, P. (2007) Zinc(II) complexes as hydrolytic catalysts of phosphate diester cleavage: from model substrates to nucleic acids. *New J. Chem. 31*, 800–817.

(12) Noll, D. M., Mason, T. M., and Miller, P. S. (2006) Formation and repair of interstrand cross-links in DNA. *Chem. Rev. 106*, 277–301.

(13) Hettich, R., and Schneider, H.-J. (1997) Cobalt(III) polyamine complexes as catalysts for the hydrolysis of phosphate esters and of DNA. A measurable 10 million-fold rate increase. *J. Am. Chem. Soc. 119*, 5638–5647.

(14) Ren, R., Yang, P., Zheng, W., and Hua, Z. (2000) A simple copper(II)-L-histidine system for efficient hydrolytic cleavage of DNA. *Inorg. Chem. 39*, 5454–5463.

(15) Komiyama, M., Kina, S., Matsumura, K., Sumaoka, J., Tobey, S., Lynch, V. M., and Anslyn, E. (2002) Trinuclear copper(II) complex showing high selectivity for the hydrolysis of 2′−5′ over 3′−5′ for UpU and 3′−5′ over 2′−5′ for ApA ribonucleotides. *J. Am. Chem. Soc. 124*, 13731–13736.

(16) Yang, M.-Y., Richard, J. P., and Morrow, J. R. (2003) Substrate specificity for catalysis of phosphodiester cleavage by a dinuclear Zn(II) complex. *Chem. Commun.* 2832–2833.

(17) Worm, K., Chu, F., Matsumoto, K., Best, M. D., Lynch, V., and Anslyn, E. V. (2003) Preorganized bis-zinc phosphodiester cleavage catalysts possessing natural ligands: A lesson pertinent to bimetallic artificial enzymes. *Chem. Eur. J. 9*, 741–747.

(18) Jin, Y., and Cowan, J. A. (2005) DNA cleavage by copper-ATCUN complexes. Factors influencing cleavage mechanism and linearization of dsDNA. *J. Am. Chem. Soc. 127*, 8408–8415.

(19) An, Y., Tong, M.-L., Ji, L.-N., and Mao, Z.-W. (2006) Double-strand DNA cleavage by copper complexes of 2,2′-dipyridyl with electropositive pendants. *Dalton Trans.* 2071.

(20) Corneillie, T. M., Whetstone, P. A., Lee, K. C., Wong, J. P., and Meares, C. F. (2004) Converting weak binders into infinite binders. *Bioconjugate Chem. 15*, 1389–1391.

(21) Qian, J., Gu, W., Liu, H., Gao, F., Feng, L., Yan, S., Liao, D., and Cheng, P. (2007) The first dinuclear copper(II) and zinc(II) complexes containing novel Bis-TACN: syntheses, structures, and DNA cleavage activities. *Dalton Trans.* 1060–1066.

(22) Cotton, F. A., Hazen, E. J., and Legg, M. J. (1979) Staphylococcal nuclease: proposed mechanism of action based on structure of enzyme-thymidine 3′,5′-bisphosphate-calcium ion complex at 1.5-.ANG. resolution. *Proc. Natl. Acad. Sci. U.S.A. 76*, 2551–2555.

(23) Weber, D. J., Meeker, A. K., and Mildvan, A. S. (1991) Interactions of the acid and base catalysts on staphylococcal nuclease as studied in a double mutant. *Biochemistry 30*, 6103–6114.

(24) Judice, T. R., Gamble, T. R., Murphy, E. C., de Vos, A. M., and Schultz, P. G. (1993) Probing the mechanism of staphylococcal nuclease with unnatural amino acids: kinetic and structural studies. *Science 261*, 1578–1581.

(25) Hale, S. P., Poole, L. B., and Gerlt, J. A. (1993) Mechanism of the reaction catalyzed by staphylococcal nuclease. *Biochemistry 29*, 7479–7487.

(26) Friedhoff, P., Meiss, G., Kolmes, B., Pieper, U., Gimadutdinow, O., Urbanke, C., and Pingoud, A. (1996) Kinetic analysis of the cleavage of natural and synthetic substrates by the Serratia nuclease. *Eur. J. Biochem. 241*, 572–580.

(27) Schug, K. A., and Lindner, W. (2005) Noncovalent binding between guanidinium and anionic groups: focus on biological- and synthetic-based arginine/guanidinium interactions with phosph[on]ate and sulf[on]ate residues. *Chem. Rev. 105*, 67–113.

(28) Oost, T., and Kalesse, M. (1997) Synthesis of RNAse active site model systems using a steroid template. *Tetrahedron 53*, 8421–8438.

(29) Kato, T., Takeuchi, T., and Karube, I. (1996) Bis-imidazolyl cleft-shaped mimic of the active site of ribonuclease A. *Chem. Commun.* 953–954.

(30) Kövari, E., and Krämer, R. (1996) Rapid phosphodiester hydrolysis by an ammonium-functionalized copper(II) complex. A model for the cooperativity of metal ions and NH-acidic groups in phosphoryl transfer enzymes. *J. Am. Chem. Soc. 118*, 12704–12709.

(31) Kövari, E., Heitker, J., and Krämer, R. (1995) Metal-ammonium cooperativity in phosphodiester hydrolysis. *J. Chem. Soc., Chem. Commun.* 1205–1206.

(32) Aït-Haddou, H., Sumaoka, J., Wiskur, S. L., Folmer-Andersen, J. F., and Anslyn, E. V. (2002) Remarkable cooperativity between a Zn^{II} ion and guanidinium/ammonium groups in the hydrolysis of RNA. *Angew. Chem., Int. Ed. 41*, 4014–4016; *Angew. Chem. 114*, 4185−4188.

(33) Feng, G., Mareque-Rivas, J. C., Martin de Rosales, R. T., and Williams, N. H. (2005) A highly reactive mononuclear Zn(II) complex for phosphodiester cleavage. *J. Am. Chem. Soc. 127*, 13470–13471.

(34) Feng, G., Mareque-Rivas, J. C., and Williams, N. H. (2006) Comparing a mononuclear Zn(II) complex with hydrogen bond donors with a dinuclear Zn(II) complex for catalysing phosphate ester cleavage. *Chem. Commun.* 1845–1847.

(35) Westheimer, F. H. (1987) Why nature chose phosphates. *Science 235*, 1173–1178.

(36) Williams, N. H., Takasaki, B., Wall, M., and Chin, J. (1999) Structure and nuclease activity of simple dinuclear metal complexes: quantitative dissection of the role of metal ions. *Acc. Chem. Res. 32*, 485–493.

(37) Sigman, D. S., Mazumder, A., and Perrin, D. M. (1993) Chemical nucleases. *Chem. Rev. 93*, 2295–2316.

(38) Anderson, G. Y., Alexander, M. D., Taylor, S. D., Smithrud, D. B., Benkovic, S. J., and Weinreb, S. M. (1996) Catalytic antibodies in synthesis: design and synthesis of a hapten for application to the preparation of a scalemic pyrrolidine ring synthon for ptilomycalin A. *J. Org. Chem. 61*, 125–132.

(39) Kashman, Y., Hirsh, S., McConnell, O. J., Ohtani, I., Kusumi, T., and Kakisawa, H. (1989) Ptilomycalin A: a novel polycyclic guanidine alkaloid of marine origin. *J. Am. Chem. Soc. 111*, 8925–8926.

(40) Palagiano, E., De Marino, S., Minale, L., Riccio, R., Zollo, F., Iorizzi, M., Carré, J. B., Debitus, C., Lucarain, L., and Provost, J. (1995) Ptilomycalin A, crambescidin 800 and related new highly cytotoxic guanidine alkaloids from the starfishes *Fromia monilis* and *Celerina heffernani*. *Tetrahedron 51*, 3675–3682.

(41) Schmidtchen, F. P., and Berger, M. (1997) Artificial organic host molecules for anions. *Chem. Rev. 97*, 1609–1646.

(42) Zafar, A., Melendez, R., Geib, S. J., and Hamilton, A. D. (2002) Hydrogen bond controlled aggregation of guanidinium-carboxylate derivatives in the solid state. *Tetrahedron 58*, 683–690.

(43) Schmuck, C., and Geiger, L. (2004) Dipeptide binding in water by a de novo designed guanidiniocarbonylpyrrole receptor. *J. Am. Chem. Soc. 126*, 8898–8899.

(44) Zepik, H. H., and Benner, S. A. (1999) Catalysts, anticatalysts, and receptors for unactivated phosphate diesters in water. *J. Org. Chem. 64*, 8080–8083.

(45) Liu, F., Lu, G.-Y., He, W.-J., Liu, M.-H., Zhu, L.-G., and Wu, H.-M. (2002) Molecular recognition of nucleotides by a calix[4]arene derivative with two alkyl guanidinium groups at the air-water interface. *New J. Chem. 26*, 601–606.

(46) Blondeau, P., Segura, M., Perez-Fernandez, R., and de Mendoza, J. (2007) Molecular recognition of oxoanions based on guanidinium receptors. *Chem. Soc. Rev. 36*, 198–210.

(47) Sheng, X., Lu, X.-M., Chen, Y.-T., Lu, G.-Y., Zhang, J.-J., Shao, Y., Liu, F., and Xu, Q. (2007) Synthesis, DNA-binding, cleavage and cytotoxic activity of new artificial receptors 1,7-dioxa-4,10-diazacyclododecane containing bisguanidinoethyl or diaminoethyl double side arms. *Chem. Eur. J. 13*, 9703–9712.

(48) Sheng, X., Lu, X.-M., Zhang, J.-J., Chen, Y.-T., Lu, G.-Y., Shao, Y., Liu, F., and Xu, Q. (2007) Synthesis and DNA cleavage activity of artificial receptor 1,4,7-triazacyclononane containing guanidinoethyl and hydroxyethyl side arms. *J. Org. Chem. 72*, 1799–1802.

(49) Peczuh, M. W., and Hamilton, A. D. (2000) Peptide and protein recognition by designed molecules. *Chem. Rev. 100*, 2479–2494.

(50) Montero, A., Goya, P., Jagerovic, N., Callado, L. F., Meana, J. J., Giron, R., Goicoechea, C., and Martin, M. I. (2002) Guanidinium and aminoimidazolinium derivatives of N-(4-piperidyl)propanamides as potential ligands for μ opioid and I2-imidazoline receptors: synthesis and pharmacological screening. *Bioorg. Med. Chem. 10*, 1009–1018.

(51) Rothbard, J. B., Kreider, E., VanDeusen, C. L., Wright, L., Wylie, B. L., and Wender, P. A. (2002) Arginine-rich molecular transporters for drug delivery: role of backbone spacing in cellular uptake. *J. Med. Chem. 45*, 3612–3618.

(52) Van Hecke, K., Nam, P. C., Nguyen, M. T., and Van Meervelt, L. (2005) Netropsin interactions in the minor groove of d(G-GCCAATTGG) studied by a combination of resolution enhancement and ab initio calculations. *FEBS J. 272*, 3531–3541.

(53) Murchie, A. I. H, Davis, B., Isel, C., Afshar, M., Drysdale, M. J., Bower, J., Potter, A. J., Starkey, I. D., Swarbrick, T. M., Mirza, S., Prescott, C. D., Vaglio, P., Aboul-ela, F., and Karn, J. (2004) Structure-based drug design targeting an inactive RNA conformation: exploiting the flexibility of HIV-1 TAR RNA. *J. Med. Biol. 336*, 625–638.

(54) Goodwin, K. D., Long, E. C., and Georgiadis, M. M. (2005) A host-guest approach for determining drug-DNA interactions: an example using netropsin. *Nucleic Acids Res. 33*, 4106–4116.

(55) Hannon, C. L., and Anslyn, E. V. (1993) The guanidinium group: its biological role and synthetic analogs. *Bioorg. Chem. Front. 3*, 193–255.

(56) Smith, J., Ariga, K., and Anslyn, E. V. (1993) Enhanced imidazole-catalyzed RNA cleavage induced by a bis-alkylguanidinium receptor. *J. Am. Chem. Soc. 115*, 362–364.

(57) Perreault, D. M., Cabell, L. A., and Anslyn, E. V. (1997) Using guanidinium groups for the recognition of RNA and as catalysts for the hydrolysis of RNA. *Bioorg. Med. Chem. 5*, 1209–1220.

(58) Piatek, A. M., Gray, M., and Anslyn, E. V. (2004) Guanidinium groups act as general-acid catalysts in phosphoryl transfer reactions: a two-proton inventory on a model system. *J. Am. Chem. Soc. 126*, 9878–9879.

(59) Muche, M.-S., and Göbel, M. W. (1996) Bis(guanidinium) alcohols as models of staphylococcal nuclease: substrate binding through ion pair complexes and fast phosphoryl transfer reactions. *Angew. Chem. 108*, 2263–2265; *Angew. Chem., Int. Ed. 35*, 2126−2129.

(60) Gnaccarini, C., Peter, S., Scheffer, U., Vonhoff, S., Klussmann, S., and Göbel, M. W. (2006) Site-specific cleavage of RNA by a metal-free artificial nuclease attached to antisense oligonucleotides. *J. Am. Chem. Soc. 128*, 8063–8067.

(61) Scheffer, U., Strick, A., Ludwig, V., Peter, S., Kalden, E., and Göbel, M. W. (2005) Metal-free catalysts for the hydrolysis of RNA derived from guanidines, 2-aminopyridines, and 2-aminobenzimidazoles. *J. Am. Chem. Soc. 127*, 2211–2217.

(62) Göbel, M. W., Bats, J. W., and Duerner, G. (1992) Approaches to synthetic phosphodiesterases: supramolecular phosphoryl transfer mediated by amidinium phosphate contact ion pairs. *Angew. Chem. 104*, 217–218; *Angew. Chem. Int. Ed. 31*, 207−209.

(63) Jubian, V., Dixon, R. P., and Hamilton, A. D. (1992) Molecular recognition and catalysis. Acceleration of phosphodiester cleavage by a simple hydrogen-bonding receptor. *J. Am. Chem. Soc. 114*, 1120–1121.

(64) Jubian, V., Veronese, A., Dixon, R. P., and Hamilton, A. D. (1995) Acceleration of a phosphate diester transesterification reaction by bis(alkylguanidinium) receptors containing an appended general base. *Angew. Chem., Int. Ed. 34*, 1237–1239.

(65) Jubian, V., Veronese, A., Dixon, R. P., and Hamilton, A. D. (1995) Acceleration of a phosphate diester transesterification reaction by bis(alkylguanidinium) receptors containing an appended general base. *Angew. Chem. 107*, 1343–1345; *Angew. Chem. Int. Ed. 34*, 1237−1239.

(66) Linton, B. R., Goodman, M. S., Fan, E., van Arman, S. A., and Hamilton, A. D. (2001) Thermodynamic aspects of dicarboxylate recognition by simple artificial receptors. *J. Org. Chem. 66*, 7313–7319.

(67) Zhao, Y., Zhu, J., He, W., Yang, Z., Zhu, Y., Li, Y., Zhang, J., and Guo, Z. (2006) Oxidative DNA cleavage promoted by multinuclear copper complexes: activity dependence on the complex structure. *Chem. Eur. J. 12*, 6621–6629.

(68) Marmur, J. (1961) A procedure for the isolation of deoxyribonucleic acid from microorganisms. *J. Mol. Biol. 3*, 208–218.

(69) Gonzalez-Alvarez, M., Alzuet, G., Borras, J., Macias, B., and Castineiras, A. (2003) Oxidative cleavage of DNA by a new ferromagnetic linear trinuclear copper(II) complex in the presence of H_2O_2/sodium ascorbate. *Inorg. Chem. 42*, 2992–2998.

(70) Detmer, C. A., III., Pamatong, F. V., and Bocarsly, J. R. (1996) Nonrandom double strand cleavage of DNA by a monofunctional metal complex: mechanistic studies. *Inorg. Chem. 35*, 6292–6298.

(71) Rammo, J., Hettich, R., Roigk, A., and Schneider, H.-J. (1996) Catalysis of DNA cleavage by lanthanide complexes with nucleophilic or intercalating ligands and their kinetic characterization. *Chem. Commun.* 105–107.

(72) Black, G., Depp, E., and Corson, B. B. (1949) Oxidation of certain methylpyridines to pyridinecarboxylic acids. *J. Org. Chem. 14*, 14–21.

(73) Jew, S., Park, B., Lim, D., Kim, M. G., Chung, I. K., Kim, J. H., Hong, C. II, Kim, J.-K., Park, H.-J., Lee, J.-H., and Park, H. (2003) Synthesis of 6-formyl-pyridine-2-carboxylate derivatives and their telomerase inhibitory activities. *Bioorg. Med. Chem. Lett. 13*, 609–612.

(74) Motekaitis, R. J., and Martell, A. E. (1988) Potentiometric determination of the stabilities of cobalt(II) complexes of polyamine Schiff bases and their dioxygen adducts. *Inorg. Chem. 27*, 2718–2724.

(75) Bernatowicz, M. S., Wu, Y., and Matsueda, G. R. (1992) 1H-Pyrazole-1-carboxamidine hydrochloride an attractive reagent for guanylation of amines and its application to peptide synthesis. *J. Org. Chem. 57*, 2497–2502.

(76) Fukuhara, K., Nagakawa, M., Nakanishi, I., Ohkubo, K., Imai, K., Urano, S., Fukuzumi, S., Ozawa, T., Ikota, N., Mochizuki, M., Miyata, N., and Okuda, H. (2006) Structural basis for DNA-cleaving activity of resveratrol in the presence of Cu(II). *Bioorg. Med. Chem. 14*, 1437–1443.

(77) Itoh, S., Taniguchi, M., Takada, N., Nagatomo, S., Kitagawa, T., and Fukuzumi, S. (2000) Effects of metal ions on the electronic, redox, and catalytic properties of cofactor TTQ of quinoprotein amine dehydrogenases. *J. Am. Chem. Soc. 122*, 12087–12097.

(78) Itoh, S., Kawakami, H., and Fukuzumi, S. (1998) Model studies on calcium-containing quinoprotein alcohol dehydrogenases. Catalytic role of Ca^{2+} for the oxidation of alcohols by coenzyme 4,5-dihydro-4,5-dioxo-1H-pyrrolo[2,3-f]quinoline-2,7,9-tricarboxylic acid. *Biochemistry 37*, 6562–6571.

(79) 71 Yellappa, S., Seetharamappa, J., Rogers, L. M., Chitta, R., Singhal, R. P., and D'Souza, F. (2006) Binding, electrochemical activation, and cleavage of DNA by cobalt(II) tetrakis-N-methylpyridyl porphyrin and its β-pyrrole brominated derivative. *Bioconjugate Chem. 17*, 1418–1425.

(80) Benesi, H. A., and Hildebrand, J. H. (1949) A spectrophotometric investigation of the interaction of iodine with aromatic hydrocarbons. *J. Am. Chem. Soc. 71*, 2703–2707.

(81) Liu, J., Zhang, T., Lu, T., Qu, L., Zhou, H., Zhang, Q., and Ji, L. (2002) DNA-binding and cleavage studies of macrocyclic copper(II) complexes. *J. Inorg. Biochem. 91*, 269–276.

(82) Lakowicz, J. R., and Webber, G. (1973) Quenching of fluorescence by oxygen. Probe for structural fluctuations in macromolecules. *Biochemistry 12*, 4161–4170.

(83) Lee, M., Rhodes, A. L., Wyatt, M. D., Forrow, S., and Hartley, J. A. (1993) GC base sequence recognition by oligoimidazolecarboxamide and C-terminus-modified analogs of distamycin deduced from circular dichroism, proton nuclear magnetic resonance, and methidiumpropylethylenediaminetetraacetate-iron(II) footprinting studies. *Biochemistry 32*, 4237–4245.

(84) Dhar, S., Nethaji, M., and Chakravarty, A. R. (2005) Steric protection of a photosensitizer in a N,N-bis[2-(2-pyridyl)ethyl]-2-phenylethylamine-copper(II) bowl that enhances red light-induced DNA cleavage activity. *Inorg. Chem. 44*, 8876–8883.

(85) Ivanov, V. I., Minchenkova, L. E., Schyolkina, A. K., and Poletayer, A. I. (1973) Different conformations of double-stranded nucleic acid in solution as revealed by circular dichroism. *Biopolymers 12*, 89–110.

(86) Maheswari, P. U., and Palaniandavar, M. (2004) DNA binding and cleavage properties of certain tetrammine ruthenium(II) complexes of modified 1,10-phenanthrolines - effect of hydrogen-bonding on DNA-binding affinity. *J. Inorg. Biochem. 98*, 219–230.

(87) Lincoln, P., Tuite, E., and Norden, B. (1997) Short-circuiting the molecular wire: cooperative binding of Δ-$[Ru(phen)_2dppz]^{2+}$ and Δ-$[Rh(phi)_2bipy]^{3+}$ to DNA. *J. Am. Chem. Soc. 119*, 1454–1455.

(88) Norden, B., and Tjerneld, F. (1982) Structure of methylene blue-DNA complexes studied by linear and circular dichroism spectroscopy. *Biopolymers 21*, 1713–1734.

(89) Robinson, H., and Wang, A. H.-J. (1996) Neomycin, spermine and hexaamminecobalt(III) share common structural motifs in converting B- to A-DNA. *Nucleic Acids Res. 24*, 676–682.

(90) Pasternack, R. F. (2003) Circular dichroism and the interactions of water soluble porphyrins with DNA -a minireview. *Chirality 15*, 329–332.

(91) Karidi, K., Garoufis, A., Hadjiliadis, N., and Reedijk, J. (2005) Solid-phase synthesis, characterization and DNA binding properties of the first chloro(polypyridyl)ruthenium conjugated peptide complex. *Dalton Trans.* 728–734.

(92) Basile, L. A., Raphael, A. L., and Barton, J. K. (1987) Metal-activated hydrolytic cleavage of DNA. *J. Am. Chem. Soc. 109*, 7550–7551.

(93) Sissi, C., Mancin, F., Gatos, M., Palumbo, M., Tecilla, P., and Tonellato, U. (2005) Efficient plasmid DNA cleavage by a mononuclear copper(II) complex. *Inorg. Chem. 44*, 2310–2317.

(94) Gupta, T., Dhar, S., Nethaji, M., and Chakravarty, A. R. (2004) Bis(dipyridophenazine)copper(II) complex as major groove directing synthetic hydrolase. *Dalton Trans.* 1896–1900.

(95) Kirin, S. I., Happel, C. M., Hrubanova, S., Weyhermueller, T., Klein, C., and Metzler-Nolte, N. (2004) Synthesis, structure and comparison of the DNA cleavage ability of metal complexes M(II)L with the N-(2-hydroxyethoxyethyl)-bis(2-picolyl)amine ligand L (M = Co, Ni, Cu and Zn). *Dalton Trans.* 1201–1207.

(96) Zhu, L., dos Santos, O., Koo, C. W., Rybstein, M., Pape, L., and Canary, J. W. (2003) Geometry-dependent phosphodiester hydrolysis catalyzed by binuclear copper complexes. *Inorg. Chem. 42*, 7912–7920.

(97) Singh, U. S., Scannell, R. T., An, H., Carter, B. J., and Hecht, S. M. (1995) DNA cleavage by di- and trihydroxyalkylbenzenes. Characterization of products and the roles of O_2, Cu(II), and alkali. *J. Am. Chem. Soc. 117*, 12691–12699.

(98) Abraham, A. T., Zhou, X., and Hecht, S. M. (2001) Metallobleomycin-mediated cleavage of DNA not involving a threading-intercalation mechanism. *J. Am. Chem. Soc. 123*, 5167–5175.

(99) Wagner, C., and Wagenknecht, H.-A. (2005) Reductive electron transfer in phenothiazine-modified DNA is dependent on the base sequence. *Chem. Eur. J. 11*, 1871–1876.

(100) Pogozelski, W. K., and Tullius, T. D. (1998) Oxidative strand scission of nucleic acids: routes initiated by hydrogen abstraction from the sugar moiety. *Chem. Rev. 98*, 1089–1108.

(101) Kalagouda, B., Gudasi, K. B., Vadavi, R. S., Shenoy, R. V., Patil, M. S., and Patil, S. A. (2005) Ambidentate behavior of pentadentate N,N′-bis(2-hydroxyphenyl)-pyridine-2,6-dicarboxamide towards transition metal(II) salts. *Transit. Metal Chem. 30*, 569–574.

(102) Bellamy, L. J. (1975) *The Infrared Spectra of Complex Molecules*, Halsted, New York.

(103) Sheng, X., Guo, X., Lu, X.-M., Lu, G.-Y, Shao, Y., Liu, F., and Xu, Q. (2008) DNA binding, cleavage, and cytotoxic activity of the preorganized dinuclear zinc(II) complex of triazacyclononane derivatives. *Bioconjugate Chem. 19*, 490–498.

BC800062G

DNA Binding and Cleaving Activity of the New Cleft Molecule N,N'-Bis(guanidinoethyl)-2,6-pyridinedicarboxamide in the Absence or in the Presence of Copper(Ⅱ)

Ying Shao, Xin Sheng, Ying Li, Zhao-Li Jia, Jing-Jing Zhang, Fang Liu* and Guo-Yuan Lu*

Department of Chemistry, State Key Laboratory of Coordination Chemistry, Nanjing University, Nanjing, P.R. China

lugyuan@nju.edu.cn

Table of content

1. NMR , ESI-MS spectra P2-P6
2. UV-Visible spectra (Figure S01) P7
3. Fluorescent spectra (Figure S02) P8-P9
4. Agarose gel of pH dependence (Figure S03) P10
5. Agarose gel of Concentration dependence (Figure S04-05) P11-12
6. Kinetic data (Table S01) P13-P27
7. Figure S06 and Table S02 P28
8. Figure S07 and Table S03 P29
9. ESI-MS spectra of ApA (Figure S08) P30-P32
10. IR spectra (Figure S09) P33-P34

NMR and ESI-MS spectra

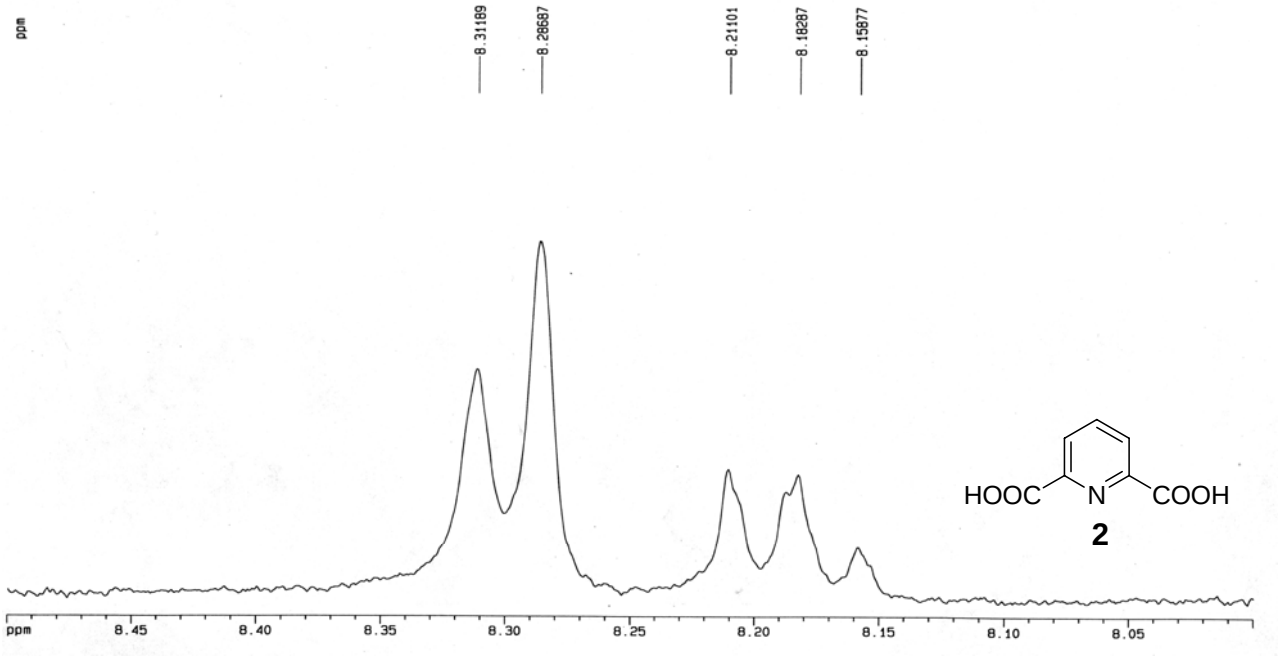

^{1}H NMR (300 MHz, D_2O) spectrum of **2**.

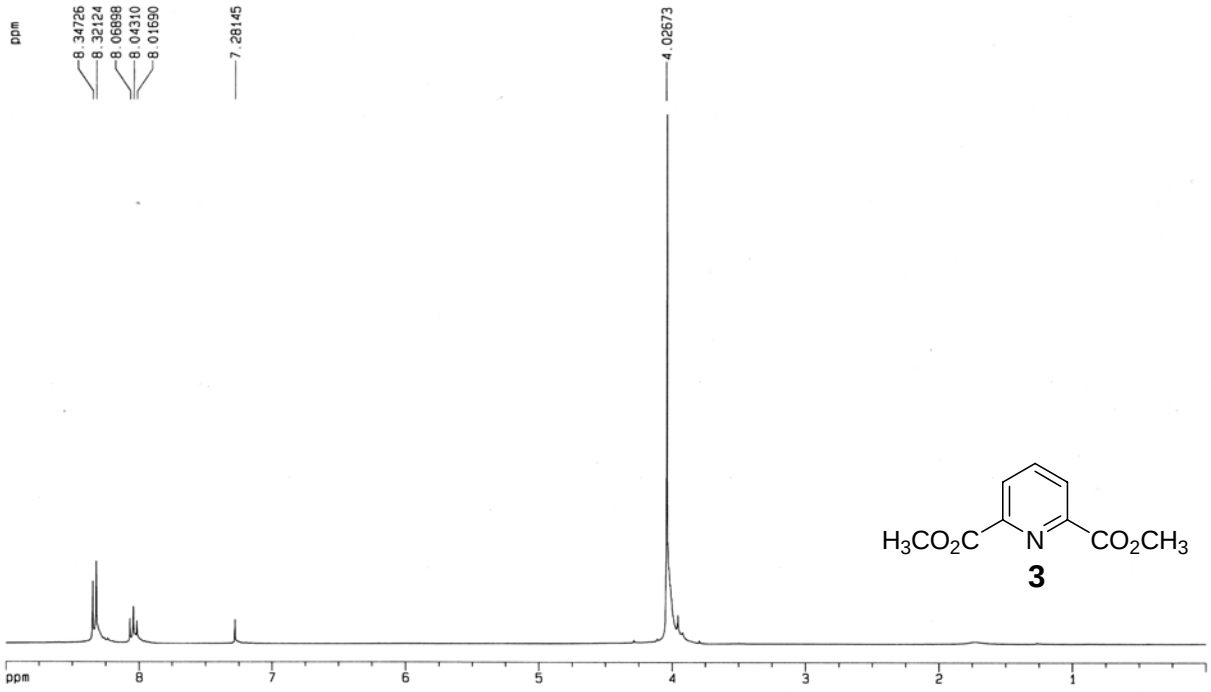

^{1}H NMR (300 MHz, $CDCl_3$) spectrum of **3**.

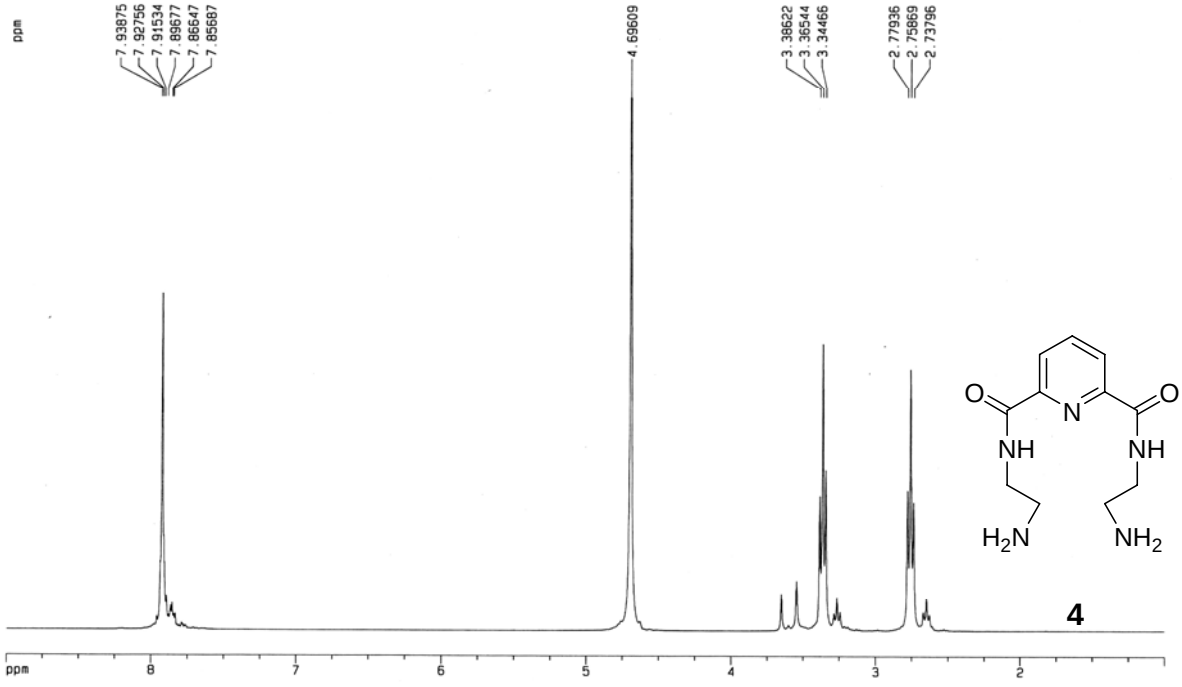

^{1}H NMR (300 MHz, D_2O) of **4**.

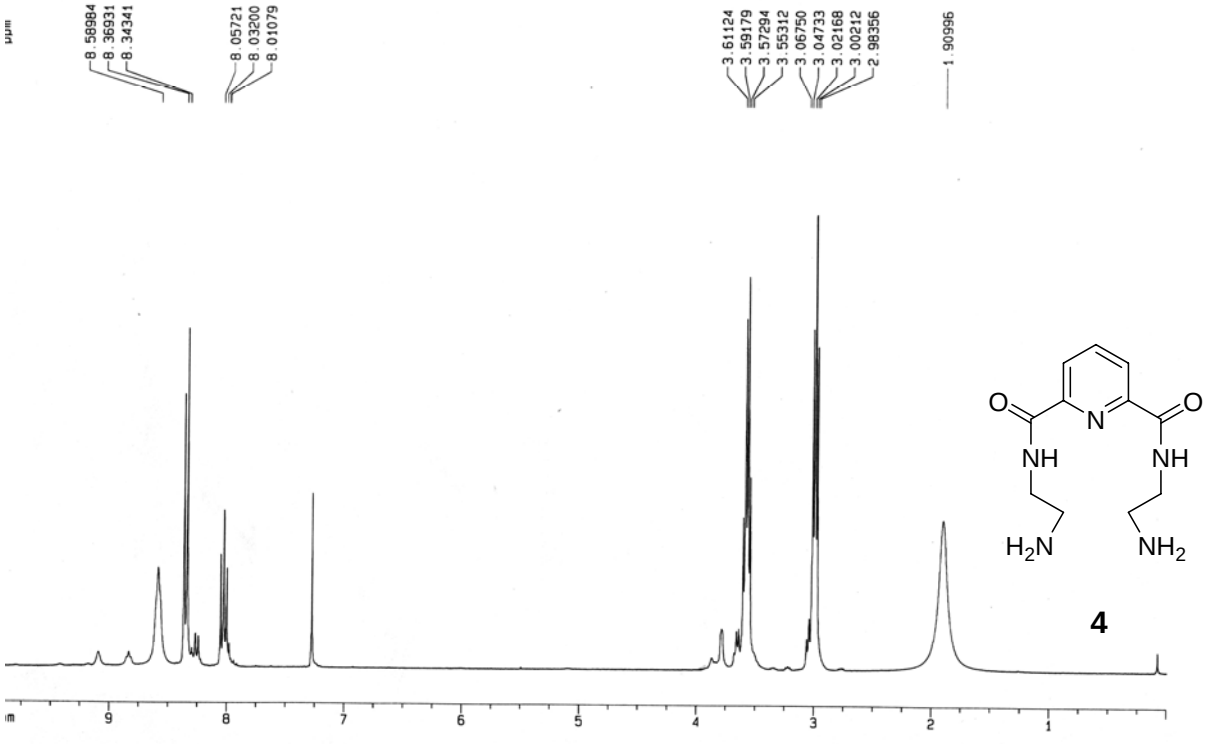

^{1}H NMR (300 MHz, $CDCl_3$) of **4**.

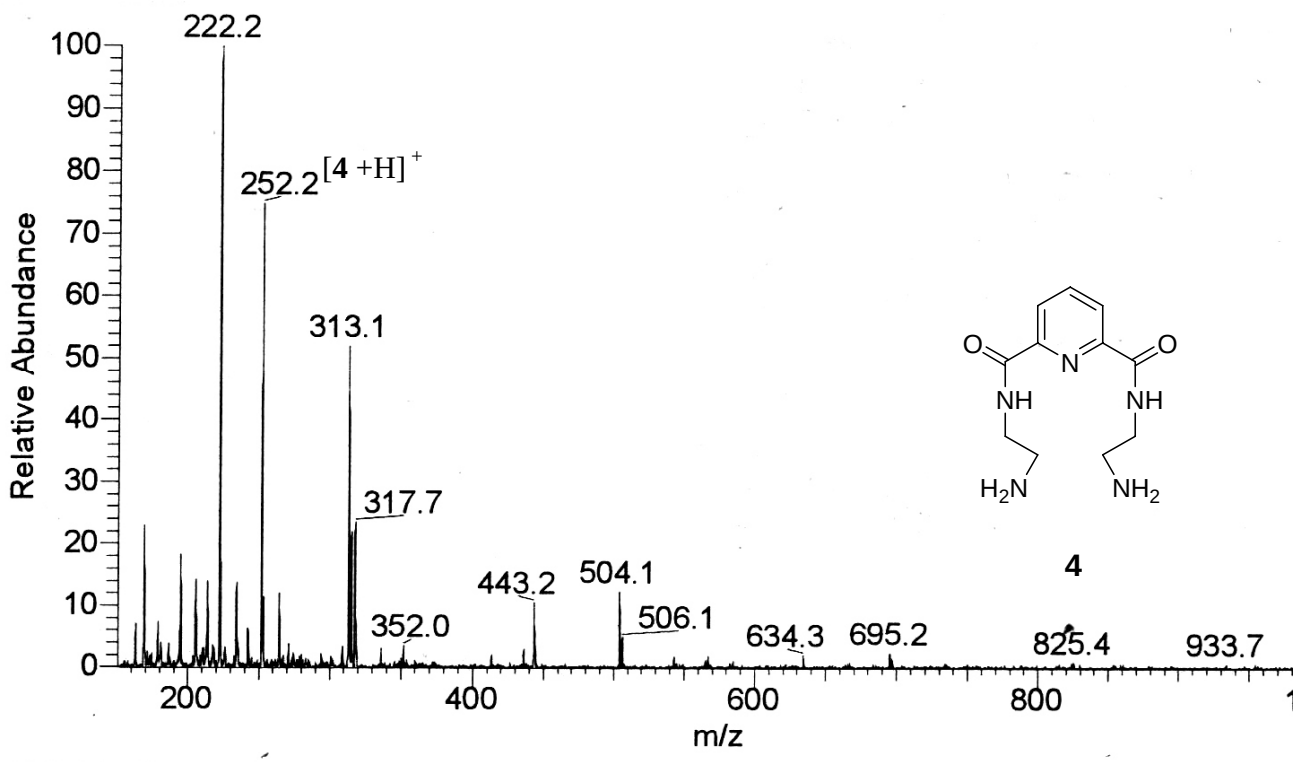

ESI–MS spectra of **4**.

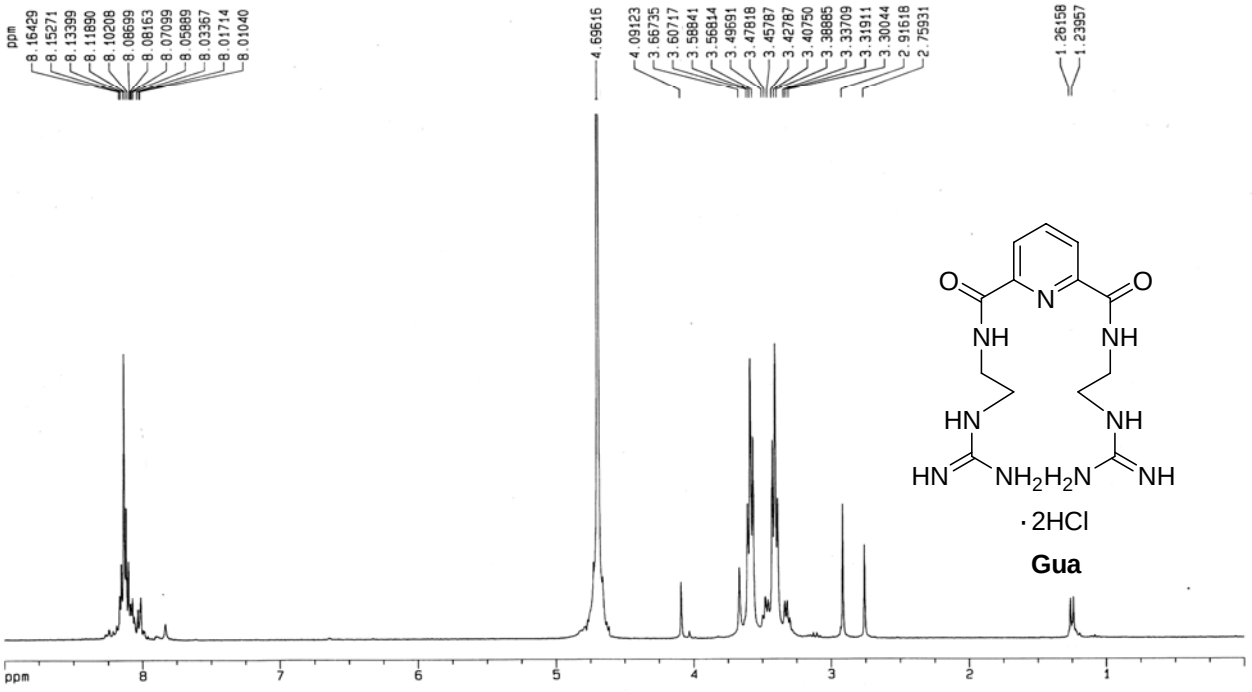

^{1}H NMR (300 MHz, D_2O) of **Gua**.

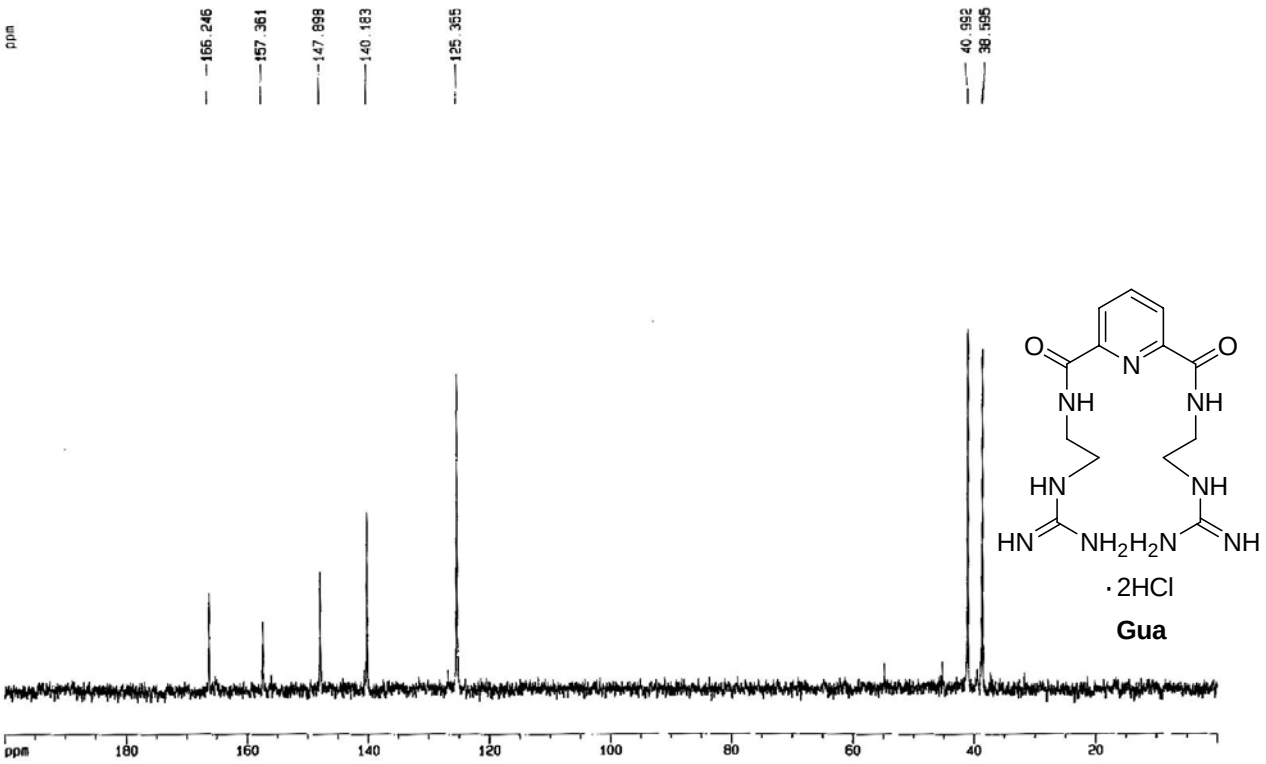

^{13}C NMR (75 MHz, D_2O) of **Gua**.

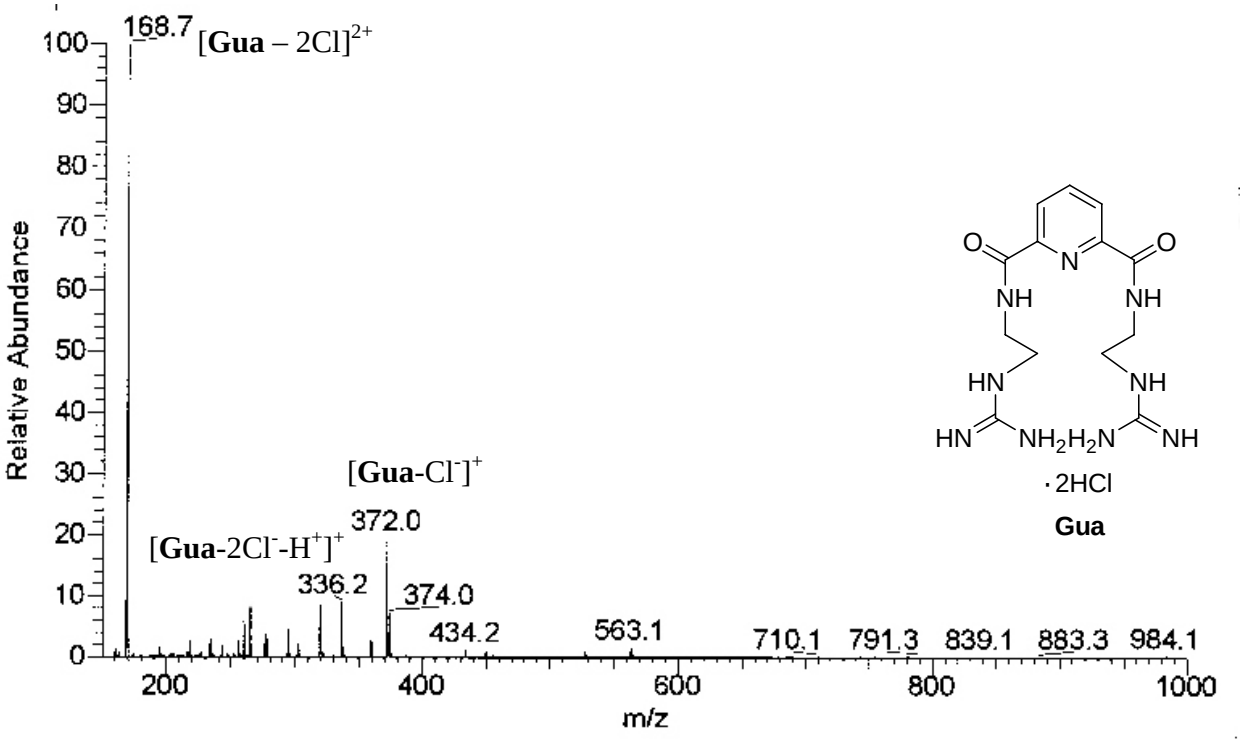

ESI–MS spectra of **Gua**.

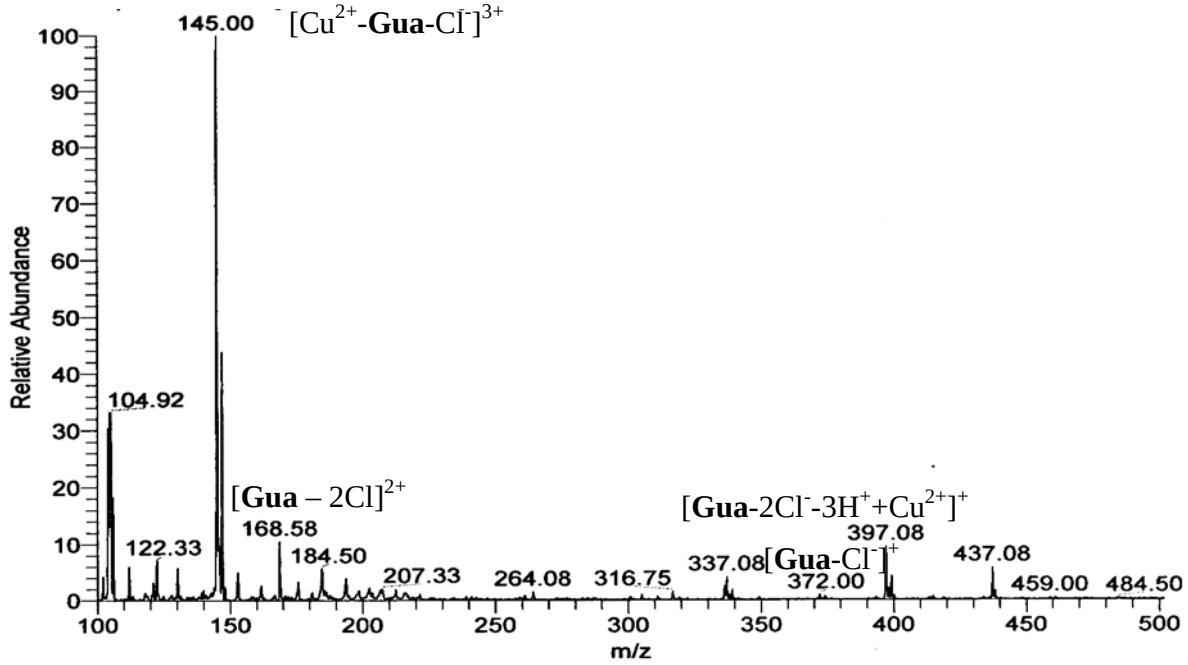

ESI–MS spectra of Cu^{2+}-**Gua**.

UV-Visible spectra

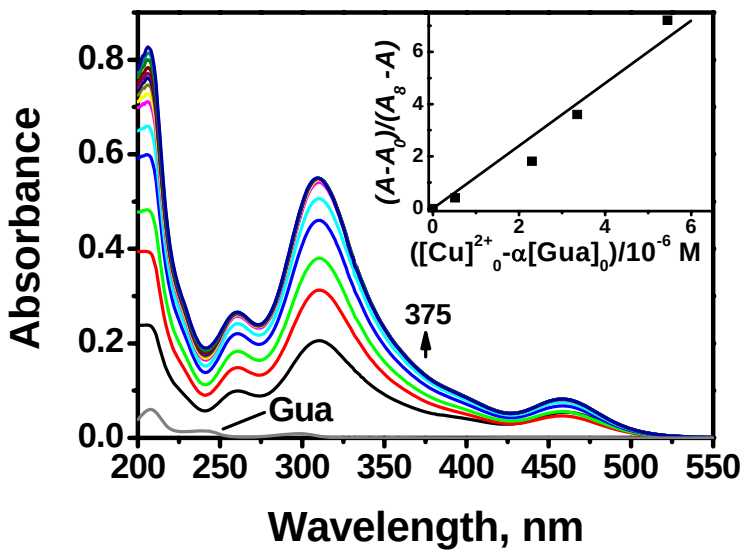

Figure S01. UV-Visible spectral changes observed upon addition of **Gua** (0 ~ 5.46×10^{-5} M) to an aqueous solution of $CuCl_2$ (1.28×10^{-5} M) at 25 °C. Insets: Plot of $(A - A_0)/(A_\infty - A)$ versus ($[Cu^{2+}]$-α[**Gua**]$_0$), $\alpha=(A - A_0)/(A_\infty - A_0)$.

Fluorescence spectra

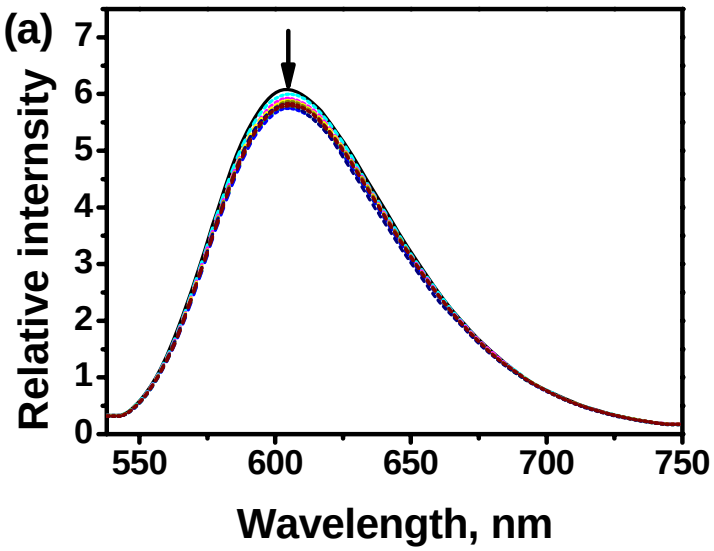

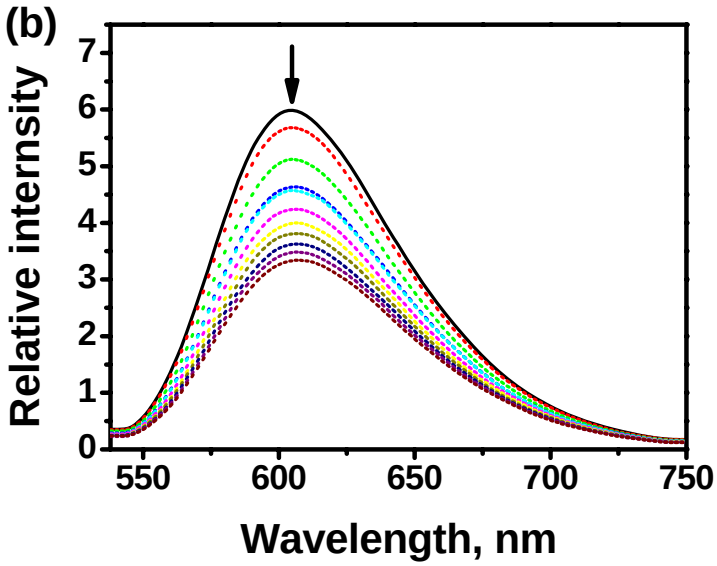

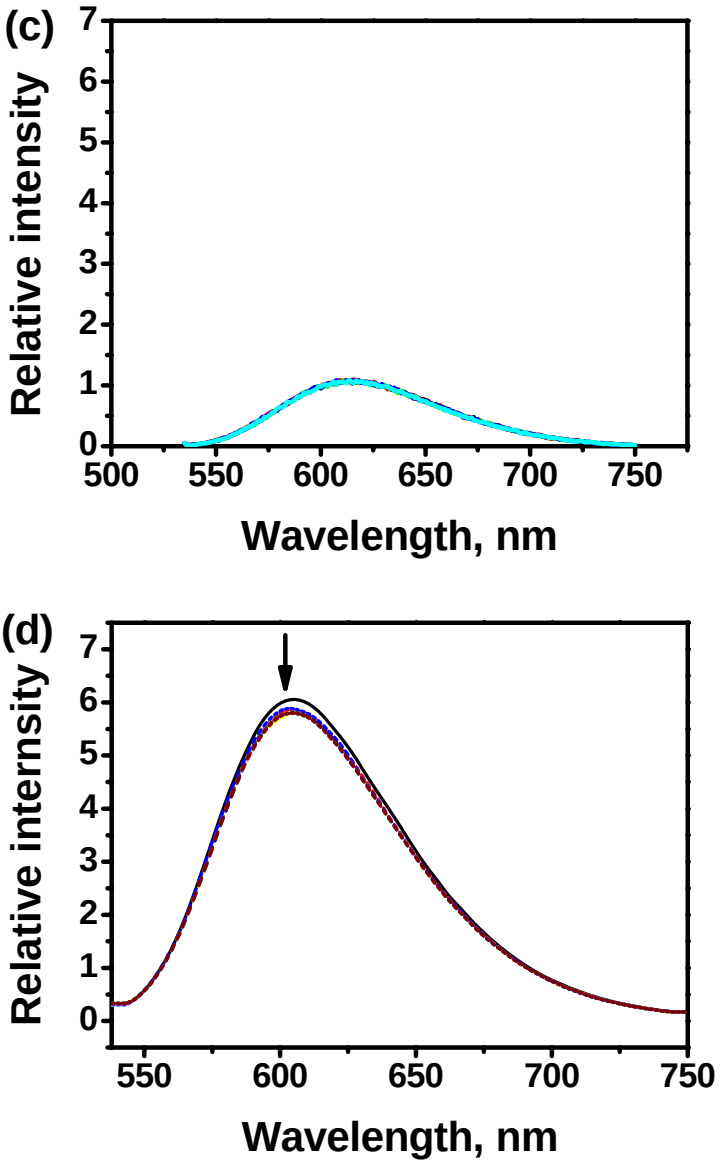

Figure S02. Emission spectra of EB bound to DNA in the absence (—) and presence (---) of (a) **Gua** (*r* = 0, 0.1, 0.2, 0.3, 0.4, 0.5, 0.6, 0.7, 0.8, 0.9, 1) (b) Cu^{2+}-**Gua** (*r* = 0, 0.1, 0.2, 0.3, 0.4, 0.5, 0.6, 0.7, 0.8, 0.9, 1) and (d) Zn^{2+}-**Gua** (*r* = 0, 0.1, 0.2, 0.3, 0.4, 0.5, 0.6, 0.7, 0.8, 0.9, 1). (c) Emission spectra of EB in presence of Cu^{2+}-**Gua** (*r* = 0, 0.1, 0.2, 0.3, 0.4, 0.5, 0.6, 0.7, 0.8, 0.9, 1). [CT–DNA] = 0.046 mM. Arrows show the intensity changes upon the addition of increasing concentration of **Gua** and Cu^{2+}-**Gua**, respectively. λ_{ex} = 526 nm.

Agarose gel

pH dependence

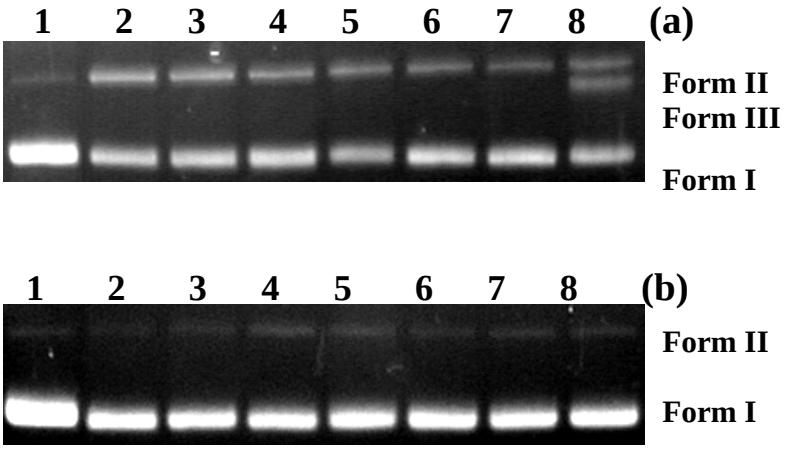

Figure S03. Agarose gel (1%) of pUC 19 DNA (0.025 mM bp) incubated for 30 h at 37°C with 0.0375 mM (a) Cu^{2+}–**Gua** and (b) **Gua** in different pH buffer (50 mM Tris–HCl / 10 mM NaCl). Lane 1, DNA control; Lanes 2–8, pH 6.51, 6.76, 7.01, 7.27, 7.50, 8.02 and 8.52, respectively.

Concentration dependence

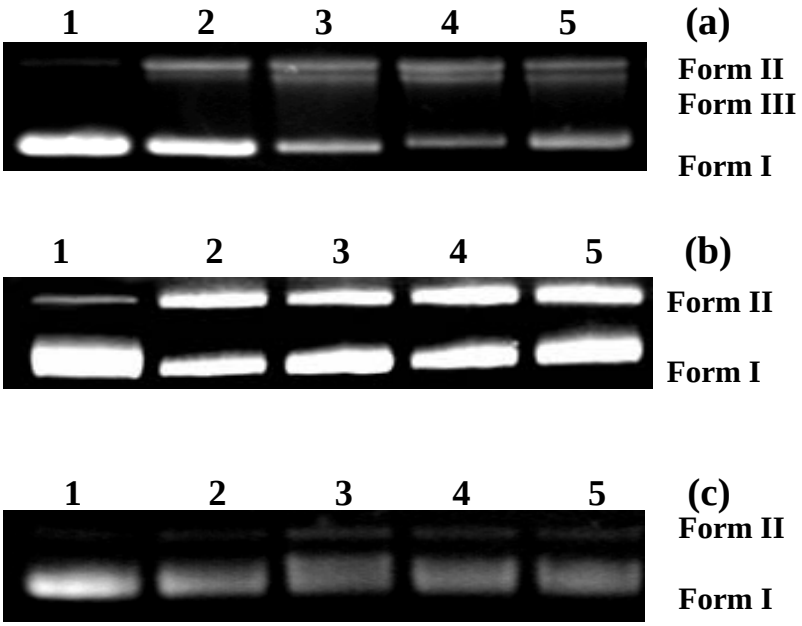

Figure S04. Agarose gel (1%) of pUC 19 DNA (0.025 mM bp) incubated for 48.0 h at 37°C with different concentrations of (a) Cu^{2+}–**Gua**, (b) **Gua** and (c) Cu^{2+} in pH 7.0 buffer (50 mM Tris–HCl / 10 mM NaCl). (a) Lanes 1-5, 0, 0.0125, 0.0250, 0.0375 and 0.0500 mM Cu^{2+}–**Gua**, respectively. (b) Lanes 1-5, 0, 0.0125, 0.0250, 0.0375 and 0.0500 mM **Gua**, respectively. (c) Lanes 1-5, 0, 0.0125, 0.0250, 0.0375 and 0.0500 mM $CuCl_2$, respectively.

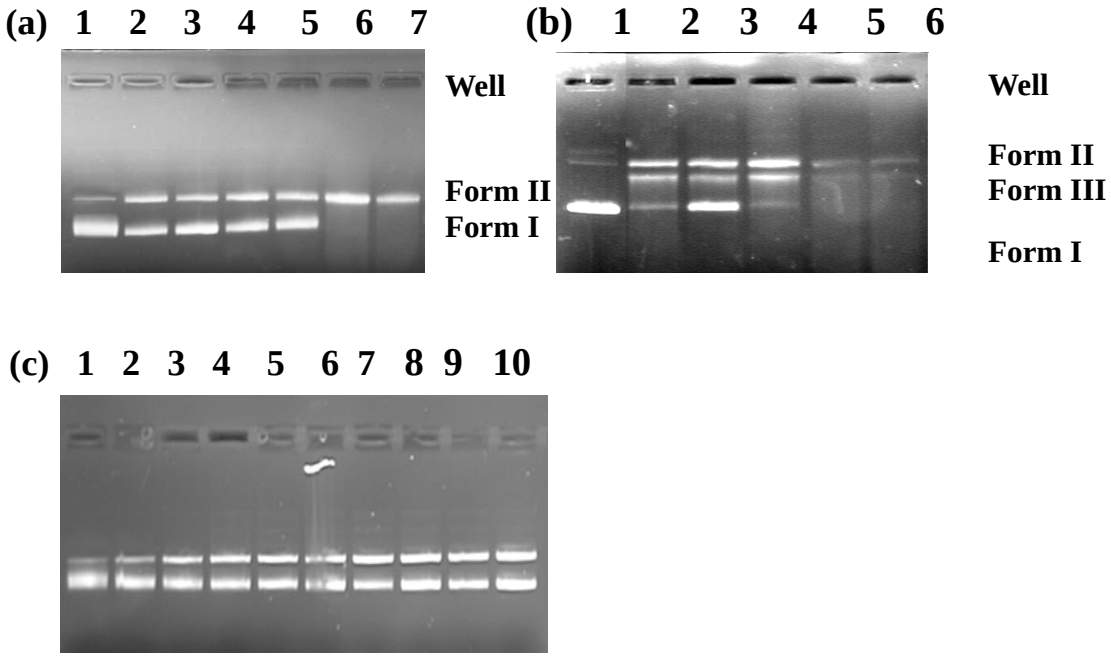

Figure S05. (a) Agarose gel (1%) of pUC 19 DNA (0.025 mM bp) incubated for 48.0 h at 37°C in pH 7.0 buffer (50 mM Tris–HCl / 10 mM NaCl) with different concentrations of **Gua**. Lanes 1-7, 0, 0.0125, 0.0250, 0.0500, 0.0625, 0.1000 and 0.1250 mM Cu^{2+}–**Gua**, respectively.

(b) Agarose gel (1%) of pUC 19 DNA (0.025 mM bp) incubated for 48.0 h at 37°C in pH 7.0 buffer (50 mM Tris–HCl / 10 mM NaCl) with different concentrations of Cu^{2+}–**Gua**. Lanes 1-6, 0, 0.0375, 0.0500, 0.0625, 0.0750 and 0.100 mM **Gua**, respectively.

(c) Agarose gel (1%) of pUC 19 DNA (0.025 mM bp) incubated for 48.0 h at 37°C in pH 7.0 buffer (50 mM Tris–HCl / 10 mM NaCl) with different concentrations of Zn^{2+}–**Gua**. Lanes 1-10, 0, 0.025, 0.050, 0.10, 0.015, 0.2, 0.25, 0.3, 0.4 and 0.5 mM **Gua**, respectively.

Kinetic Data

Table S01. Apparent initial first-order rate constants of DNA cleavage reactions at various concentrations of compound Cu^{2+}–**Gua** and **Gua**. The reactions were carried out at 37 °C in 50 mM Tris-HCl/10 mM NaCl buffer (pH 7.0).

	Cu^{2+}–**Gua**		**Gua**	
	Concentration (mM)	k_{obs} (h^{-1})	Concentration (mM)	k_{obs} (h^{-1})
1	0.0125	0.0073 ± 0.0002	0.0125	0.0020 ± 0.0002
2	0.0250	0.0110 ± 0.0002	0.0250	0.0030 ± 0.0002
3	0.0375	0.0159 ± 0.0006	0.0375	0.0073 ± 0.0004
4	0.0500	0.0173 ± 0.0011	0.0500	0.0103 ± 0.0004
5	0.0625	0.0162 ± 0.0009	0.0625	0.0094 ± 0.0005
6	0.0750	0.0152 ± 0.0006	0.0875	0.0065 ± 0.0004
7	0.0875	0.0148 ± 0.0014		
8	0.1	0.0130 ± 0.0007		

Time course of pUC 19 DNA (0.025 mM bp) cleavage promoted by Cu^{2+}–**Gua** (0.0125 mM)**.** The reactions were carried out at 37 °C in 50 mM Tris-HCl/10 mM NaCl buffer (pH 7.0).

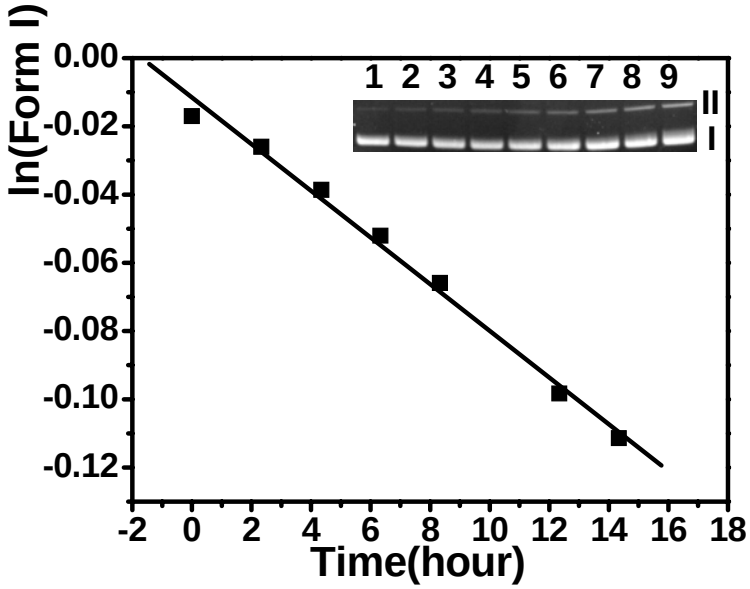

Lane	Time (h)	Ln (Form I)	% DNA	
			Form I	Form II
1	0	0.02	98.31	1.69
2	2.33	0.03	97.43	2.57
3	4.35	0.04	96.21	3.79
4	6.33	0.05	94.93	5.07
5	8.33	0.07	93.62	6.38
6	10.35	0.07	93.31	6.69
7	12.33	0.10	90.64	9.36
8	14.33	0.11	89.46	10.54
9	16.17	0.11	89.27	10.73

Time course of pUC 19 DNA (0.025 mM bp) cleavage promoted by Cu^{2+}–**Gua** (0.0250 mM)**.** The reactions were carried out at 37 °C in 50 mM Tris-HCl/10 mM NaCl buffer (pH 7.0).

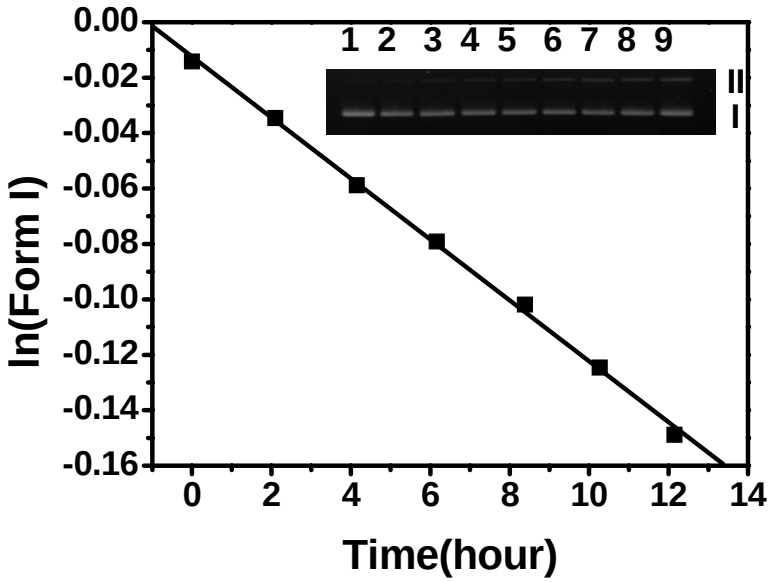

Lane	Time (h)	Ln (Form I)	% DNA	
			Form I	Form II
1	0.00	-0.01	98.59	1.41
2	2.10	-0.03	96.60	3.40
3	4.15	-0.06	94.29	5.71
4	6.17	-0.08	92.39	7.61
5	8.38	-0.10	90.31	9.69
6	10.27	-0.12	88.29	11.71
7	12.15	-0.15	86.17	13.83
8	14.22	-0.14	87.03	12.97
9	16.00	-0.15	85.80	14.20

Time course of pUC 19 DNA (0.025 mM bp) cleavage promoted by Cu^{2+}–**Gua** (0.0375 mM)**.** The reactions were carried out at 37 °C in 50 mM Tris-HCl/10 mM NaCl buffer (pH 7.0).

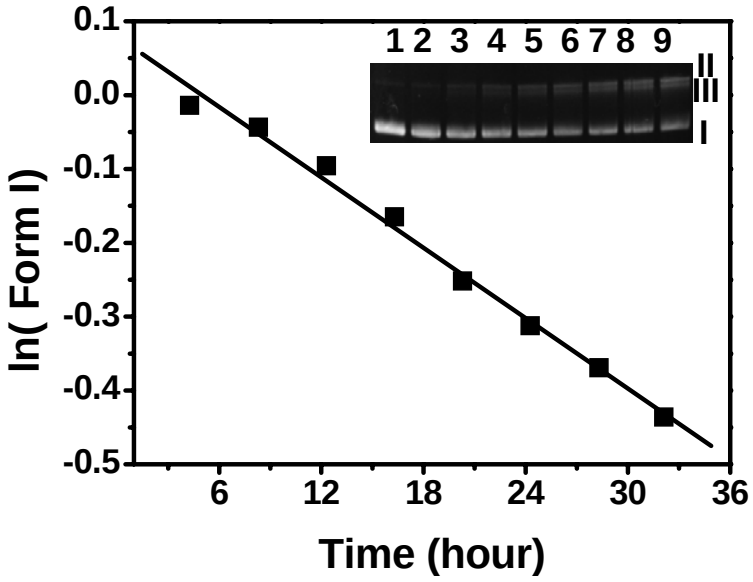

Lane	Time (h)	Ln (Form I)	% DNA	
			Form I	Form II + Form III
1	0.00	-0.01	99.15	0.85
2	4.27	-0.01	98.61	1.39
3	8.30	-0.04	95.75	4.25
4	12.30	-0.10	90.86	9.14
5	16.30	-0.16	84.82	15.18
6	20.30	-0.25	77.75	22.25
7	24.27	-0.31	73.16	26.84
8	28.30	-0.37	69.11	30.89
9	32.10	-0.44	64.66	35.34

Time course of pUC 19 DNA (0.025 mM bp) cleavage promoted by Cu^{2+}–**Gua** (0.0500 mM)**.** The reactions were carried out at 37 °C in 50 mM Tris-HCl/10 mM NaCl buffer (pH 7.0).

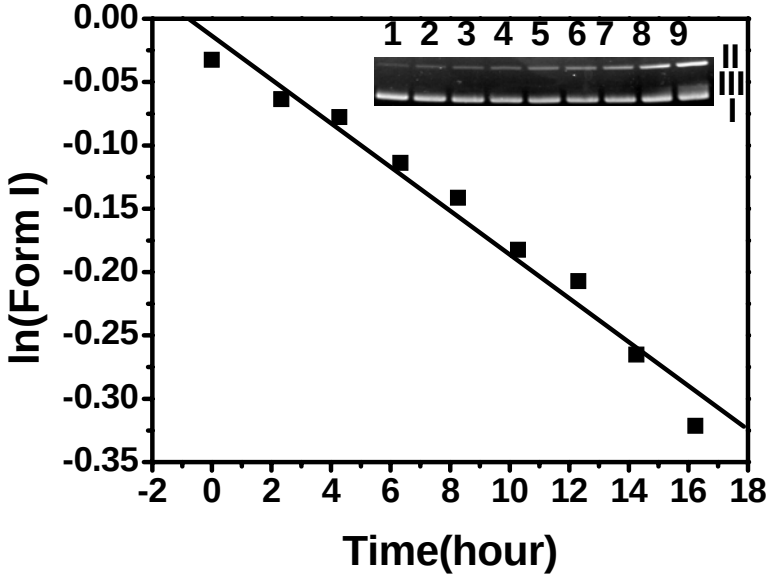

			% DNA	
Lane	Time (h)	Ln (Form I)	Form I	Form II + Form III
1	0.00	-0.03	96.80	3.20
2	2.33	-0.06	93.84	6.16
3	4.28	-0.08	92.54	7.46
4	6.33	-0.11	89.25	10.75
5	8.27	-0.14	86.83	13.17
6	10.28	-0.18	83.34	16.66
7	12.30	-0.21	81.30	18.70
8	14.25	-0.27	76.71	23.29
9	16.23	-0.32	72.52	27.48

Time course of pUC 19 DNA (0.025 mM bp) cleavage promoted by Cu^{2+}–**Gua** (0.0625 mM)**.** The reactions were carried out at 37 °C in 50 mM Tris-HCl/10 mM NaCl buffer (pH 7.0).

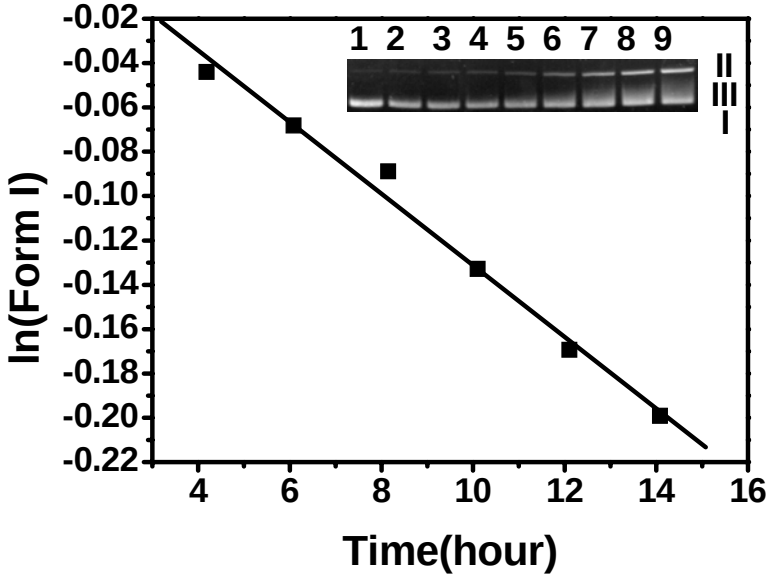

Lane	Time (h)	Ln (Form I)	% DNA	
			Form I	Form II + Form III
1	0.00	-0.02	98.31	1.69
2	2.30	-0.04	96.08	3.92
3	4.18	-0.04	95.69	4.31
4	6.08	-0.07	93.41	6.59
5	8.15	-0.09	91.50	8.50
6	10.10	-0.13	87.56	12.44
7	12.10	-0.17	84.42	15.58
8	14.08	-0.20	81.95	18.05
9	15.98	-0.27	76.68	23.32

Time course of pUC 19 DNA (0.025 mM bp) cleavage promoted by Cu^{2+}–**Gua** (0.0750 mM)**.** The reactions were carried out at 37 °C in 50 mM Tris-HCl/10 mM NaCl buffer (pH 7.0).

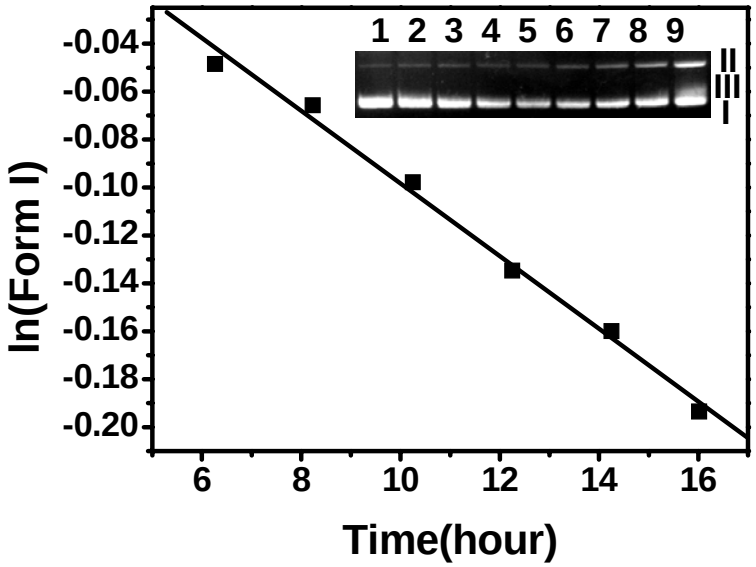

Lane	Time (h)	Ln (Form I)	% DNA	
			Form I	Form II + Form III
1	0.00	-0.02	98.06	1.94
2	2.25	-0.03	96.97	3.03
3	4.25	-0.04	95.79	4.21
4	6.27	-0.05	95.27	4.73
5	8.23	-0.07	93.63	6.37
6	10.25	-0.10	90.68	9.32
7	12.25	-0.13	87.40	12.60
8	14.25	-0.16	85.22	14.78
9	16.02	-0.19	82.41	17.59

Time course of pUC 19 DNA (0.025 mM bp) cleavage promoted by Cu^{2+}–**Gua** (0.0875 mM)**.** The reactions were carried out at 37 °C in 50 mM Tris-HCl/10 mM NaCl buffer (pH 7.0).

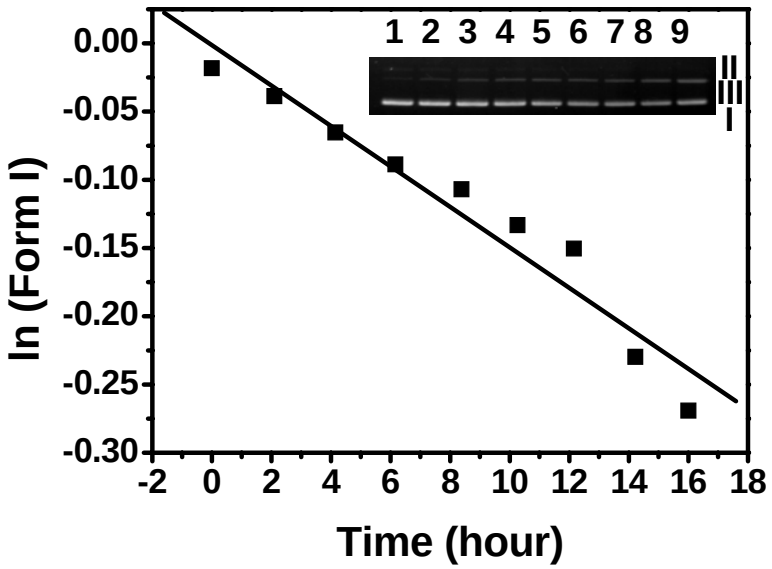

Lane	Time (h)	Ln (Form I)	% DNA	
			Form I	Form II + Form III
1	0.00	-0.02	98.20	1.80
2	2.10	-0.04	96.20	3.80
3	4.15	-0.07	93.68	6.32
4	6.17	-0.09	91.51	8.49
5	8.38	-0.11	89.86	10.14
6	10.27	-0.13	87.54	12.46
7	12.15	-0.15	86.04	13.96
8	14.22	-0.23	79.47	20.53
9	16.00	-0.27	76.40	23.60

Time course of pUC 19 DNA (0.025 mM bp) cleavage promoted by Cu^{2+}–**Gua** (0.1000 mM)**.** The reactions were carried out at 37 °C in 50 mM Tris-HCl/10 mM NaCl buffer (pH 7.0).

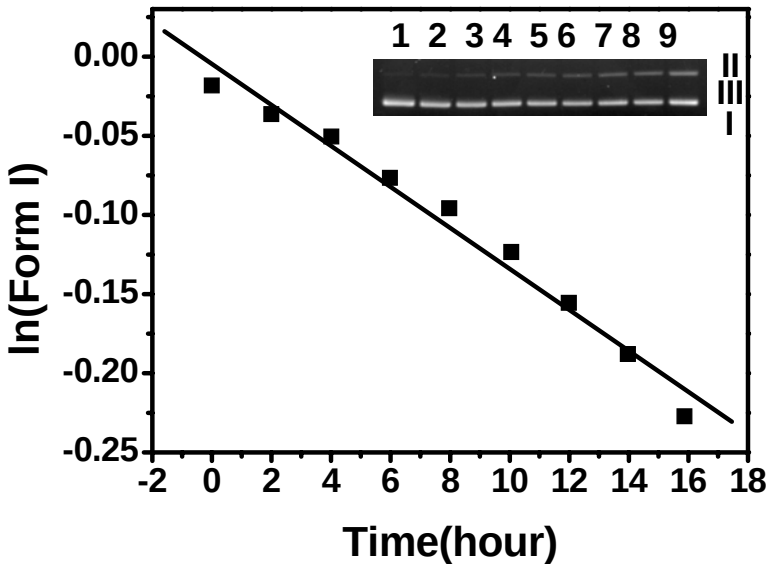

Lane	Time (h)	Ln (Form I)	% DNA	
			Form I	Form II + Form III
1	0.00	-0.02	98.20	1.80
2	2.10	-0.04	96.20	3.80
3	4.15	-0.07	93.68	6.32
4	6.17	-0.09	91.51	8.49
5	8.38	-0.11	89.86	10.14
6	10.27	-0.13	87.54	12.46
7	12.15	-0.15	86.04	13.96
8	14.22	-0.23	79.47	20.53
9	16.00	-0.27	76.40	23.60

Time course of pUC 19 DNA (0.025 mM bp) cleavage promoted by **Gua** (0.0125 mM)**.** The reactions were carried out at 37 °C in 50 mM Tris-HCl/10 mM NaCl buffer (pH 7.0).

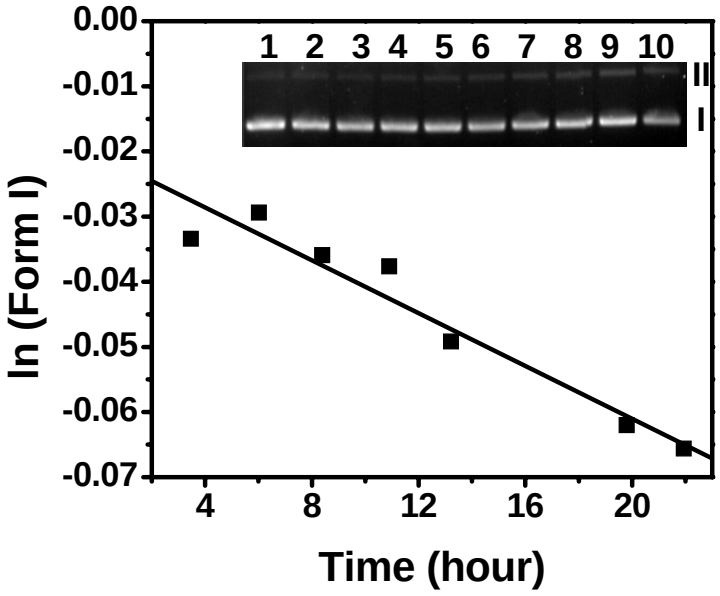

Lane	Time (h)	Ln (Form I)	% DNA	
			Form I	Form II
1	3.47	-0.03	96.71	3.29
2	6.02	-0.03	97.11	2.89
3	8.38	-0.04	96.47	3.53
4	10.90	-0.04	96.31	3.69
5	13.22	-0.05	95.20	4.80
6	19.80	-0.06	93.99	6.01
7	21.93	-0.07	93.65	6.35
8	24.40	-0.09	91.48	8.52
9	26.93	-0.10	90.60	9.40
10	29.35	-0.11	90.03	9.97

Time course of pUC 19 DNA (0.025 mM bp) cleavage promoted by **Gua** (0.025 mM)**.** The reactions were carried out at 37 °C in 50 mM Tris-HCl/10 mM NaCl buffer (pH 7.0).

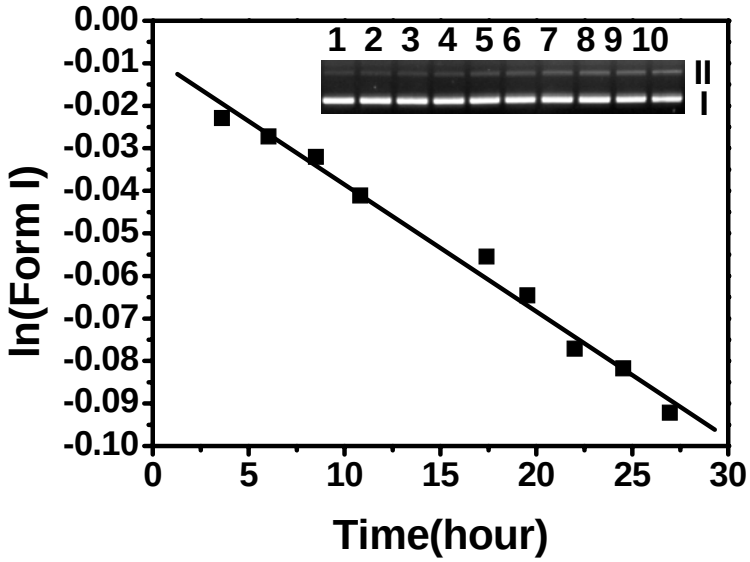

Lane	Time (h)	Ln (Form I)	% DNA	
			Form I	Form II
1	3.62	-0.02	97.74	2.26
2	6.03	-0.03	97.32	2.68
3	8.50	-0.03	96.85	3.15
4	10.82	-0.04	95.98	4.02
5	17.40	-0.06	94.61	5.39
6	19.53	-0.06	93.75	6.25
7	22.00	-0.08	92.58	7.42
8	24.53	-0.08	92.15	7.85
9	26.97	-0.09	91.20	8.80
10	29.48	-0.11	89.17	10.83

Time course of pUC 19 DNA (0.025 mM bp) cleavage promoted by **Gua** (0.0375 mM)**.** The reactions were carried out at 37 °C in 50 mM Tris-HCl/10 mM NaCl buffer (pH 7.0).

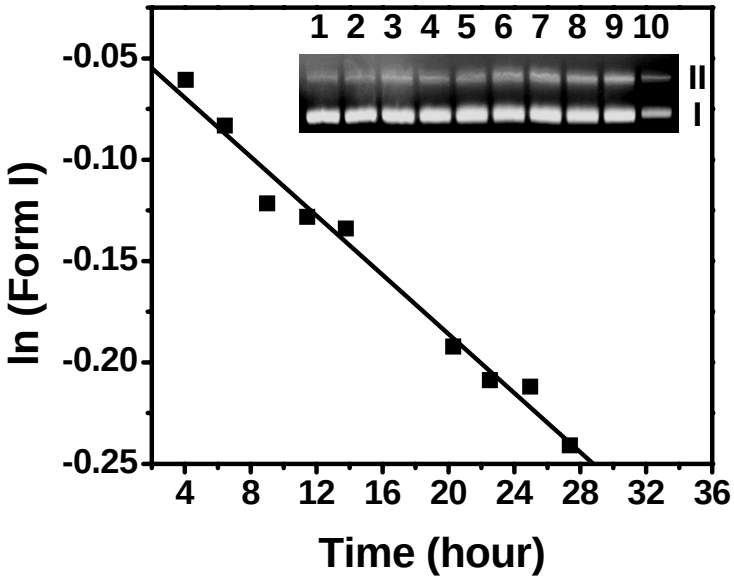

Lane	Time (h)	Ln (Form I)	% DNA	
			Form I	Form II
1	3.43	-0.06	94.24	5.76
2	6.03	-0.08	92.37	7.63
3	8.38	-0.11	89.77	10.23
4	10.90	-0.12	88.68	11.32
5	13.35	-0.12	88.72	11.28
6	15.72	-0.13	87.89	12.11
7	22.18	-0.18	83.38	16.62
8	24.37	-0.20	82.04	17.96
9	26.85	-0.27	76.67	23.33
10	29.53	-0.24	78.77	21.23

Time course of pUC 19 DNA (0.025 mM bp) cleavage promoted by **Gua** (0.050 mM)**.** The reactions were carried out at 37 °C in 50 mM Tris-HCl/10 mM NaCl buffer (pH 7.0).

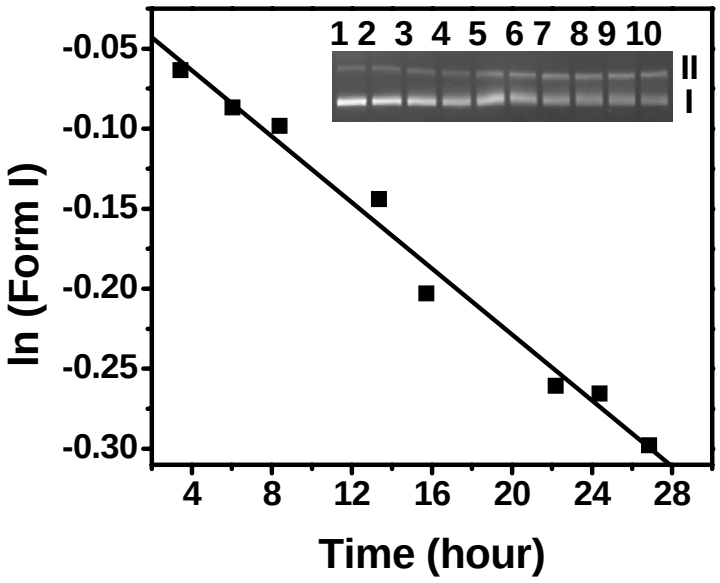

			% DNA	
Lane	Time (h)	Ln (Form I)	Form I	Form II
1	3.43	-0.06	93.85	6.15
2	6.03	-0.09	91.69	8.31
3	8.38	-0.10	90.64	9.36
4	10.90	-0.10	90.77	9.23
5	13.35	-0.14	86.59	13.41
6	15.72	-0.20	81.63	18.37
7	22.18	-0.26	77.05	22.95
8	24.37	-0.27	76.68	23.32
9	26.85	-0.30	74.25	25.75
10	29.52	-0.37	69.38	30.62

Time course of pUC 19 DNA (0.025 mM bp) cleavage promoted by **Gua** (0.0625 mM)**.** The reactions were carried out at 37 °C in 50 mM Tris-HCl/10 mM NaCl buffer (pH 7.0).

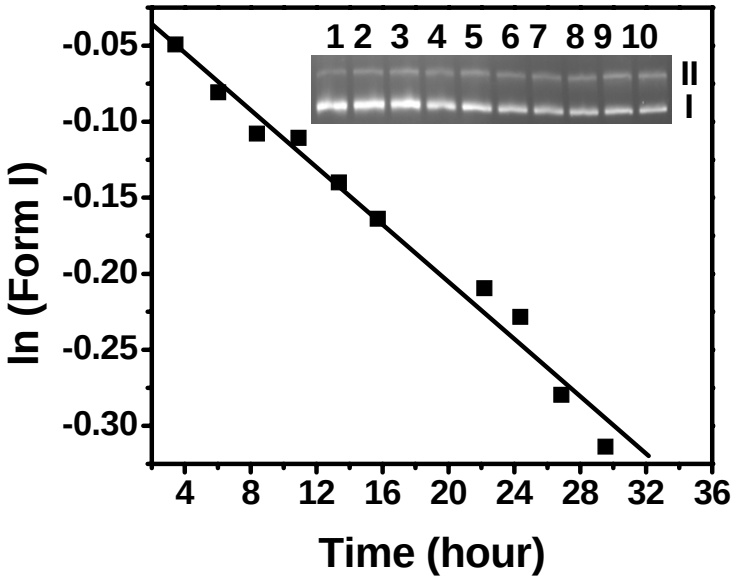

Lane	Time (h)	Ln (Form I)	% DNA	
			Form I	Form II
1	3.43	-0.05	95.20	4.80
2	6.03	-0.08	92.25	7.75
3	8.38	-0.11	89.78	10.22
4	10.90	-0.11	89.53	10.47
5	13.35	-0.14	86.95	13.05
6	15.72	-0.16	84.88	15.12
7	22.18	-0.21	81.09	18.91
8	24.37	-0.23	79.58	20.42
9	26.85	-0.28	75.61	24.39
10	29.53	-0.31	73.07	26.93

Time course of pUC 19 DNA (0.025 mM bp) cleavage promoted by **Gua** (0.0875 mM)**.** The reactions were carried out at 37 °C in 50 mM Tris-HCl/10 mM NaCl buffer (pH 7.0).

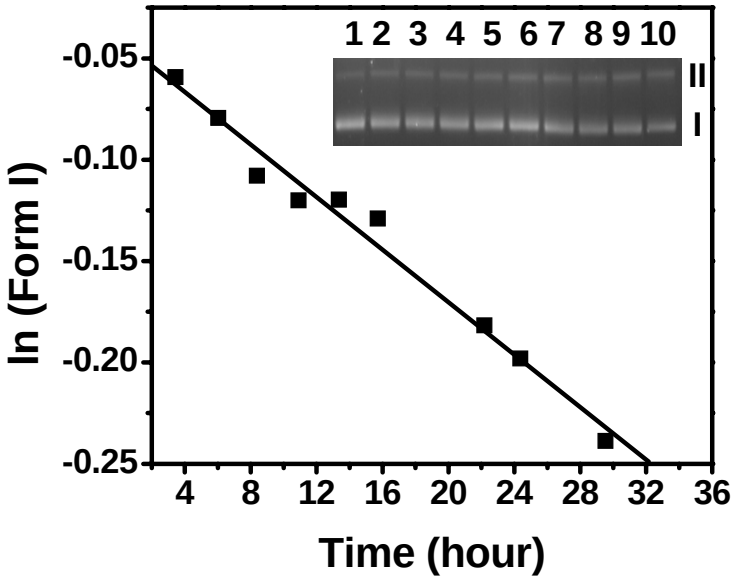

Lane	Time (h)	Ln (Form I)	% DNA	
			Form I	Form II
1	4.05	-0.06	94.11	5.89
2	6.43	-0.08	92.01	7.99
3	9.00	-0.12	88.56	11.44
4	11.43	-0.13	87.97	12.03
5	13.78	-0.13	87.47	12.53
6	20.30	-0.19	82.52	17.48
7	22.52	-0.21	81.16	18.84
8	24.97	-0.21	80.90	19.10
9	27.37	-0.24	78.59	21.41
10	29.78	-0.24	79.30	20.70

Agarose gel for mechanism study

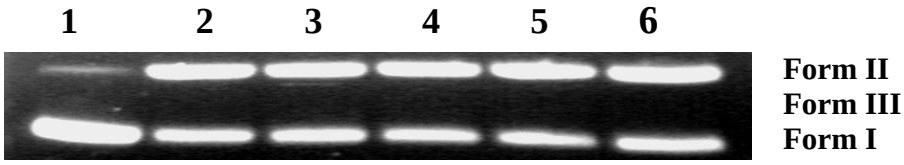

Figure S06. Agarose gel (1%) of pUC19 plasmid DNA (0.025 mM bp) cleaved by (a) Cu^{2+}–**Gua** (0.05 mM) in the presence of standard radical scavengers incubated for 48 h at 37°C in pH 7.0 buffer (50 mM Tris–HCl / 10 mM NaCl). Lanes 1–6, DNA control, DNA + Cu^{2+}–**Gua**, DNA + Cu^{2+}–**Gua** + NaN_3 (1mM), DNA + Cu^{2+}–**Gua** + KI (1mM), DNA + Cu^{2+}–**Gua** + DMSO (1mM) and DNA + Cu^{2+}–**Gua** + t-BuOH (1mM) , respectively.

Table S02. DNA cleavage promoted by Cu^{2+}–**Gua** in the presence of standard radical scavengers.

Scavengers	DNA %	
	Form I	Form II + Form III
DNA control (Lane 1)	94.53	5.47
No scavenger (Lane 2)	47.38	52.62
NaN_3	52.21	47.79
KI	48.72	51.28
DMSO	45.44	54.56
t-BuOH	42.12	57.88

Agarose gel for mechanism study

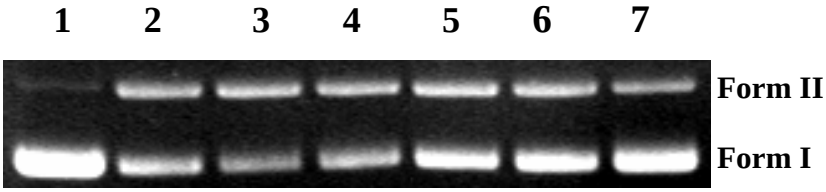

Figure S07. Agarose gel (1%) of pUC 19 DNA (0.025 mM bp) cleavage promoted by 0.05 mM Cu^{2+}–**Gua** (incubated for 30 h at 37 °C in pH 7.0 buffer). Lane 1, DNA control; Lane 2, DNA + Cu^{2+}–**Gua**; Lane 3, DNA + Cu^{2+}–**Gua** + 0.025 mM adenosine; Lane 4, DNA + Cu^{2+}–**4** + 0.025 mM guanosine; Lane 5, DNA + Cu^{2+}–**4** + 0.025 mM cytidine; Lane 6, DNA + Cu^{2+}–**4** + 0.20 mM BNPP; Lane 7, DNA + Cu^{2+}–**4** + 0.20 mM BDNPP

Table S03. DNA cleavage promoted by Cu^{2+}–**4** in the presence of nucleosides monophosphates.

added metal ion	DNA %	
	Form I	Form II + Form III
DNA control	97.34	2.66
Cu^{2+}–**Gua** only	64.22	35.78
Adenosine	55.37	44.63
Guanosine	63.37	36.63
Cytidine	a69.68	30.32
BNPP (0.20 mM)	73.48	26.52
BDNPP (0.20 mM)	83.35	16.65

ESI-MS spectra of ApA

(a)

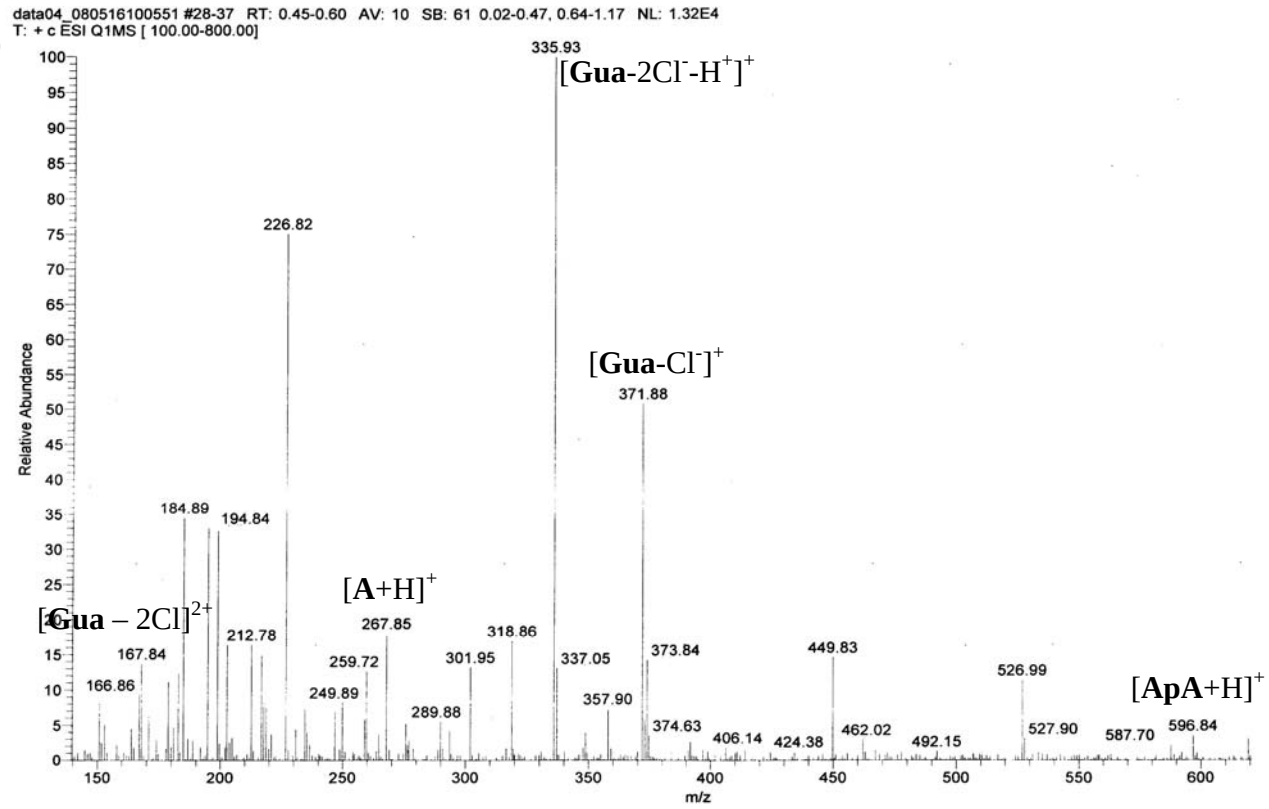

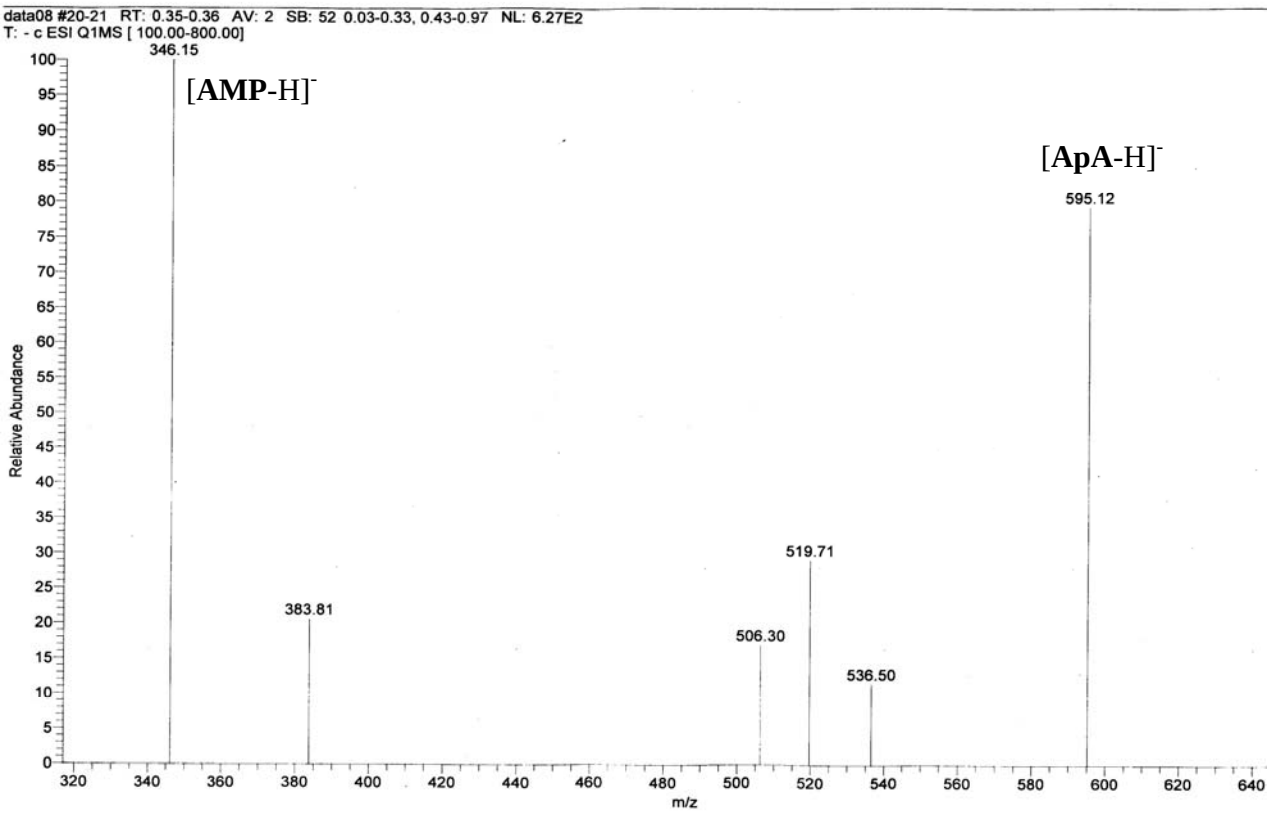

(b)

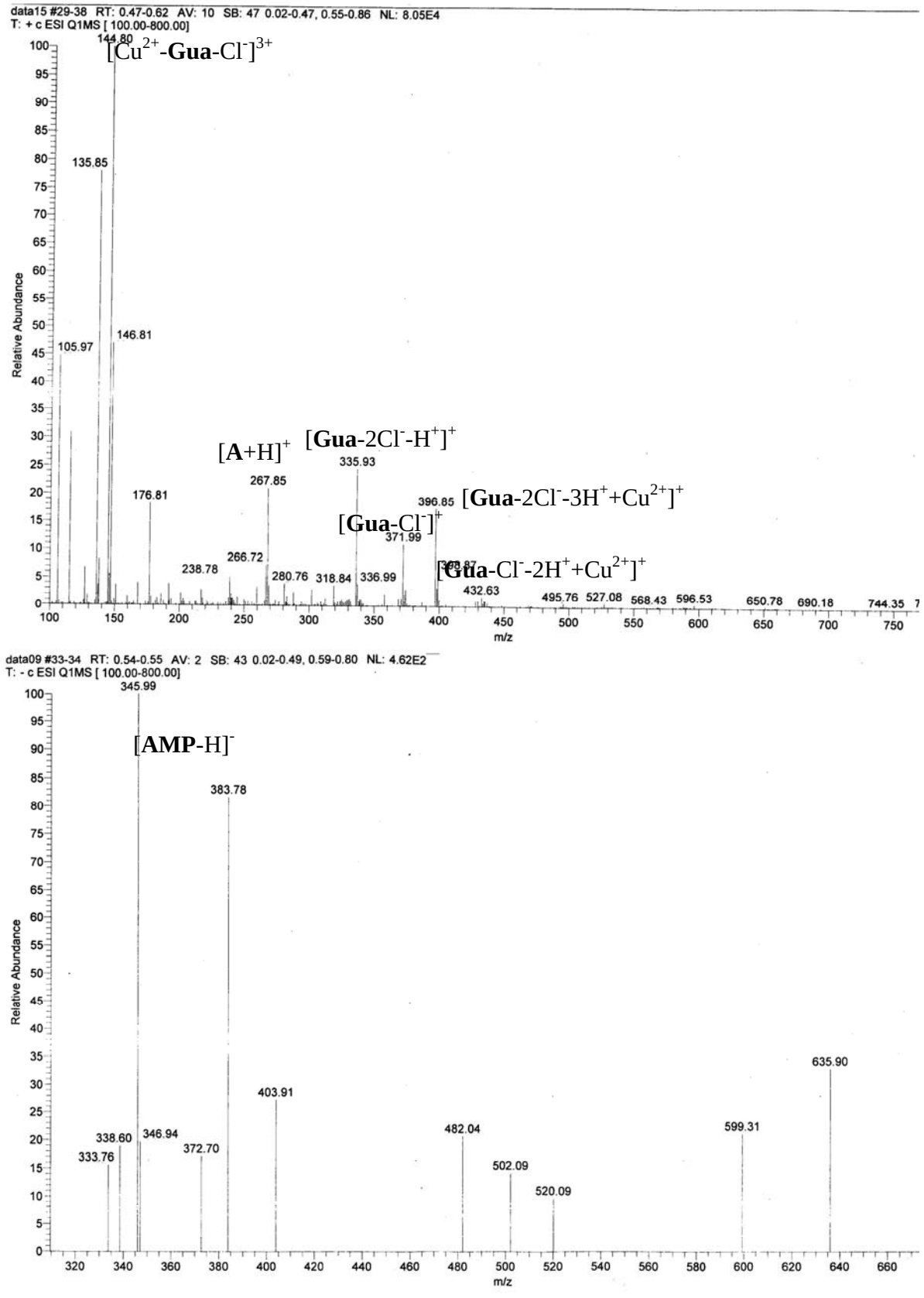
data15 #29-38 RT: 0.47-0.62 AV: 10 SB: 47 0.02-0.47, 0.55-0.86 NL: 8.05E4
T: + c ESI Q1MS [100.00-800.00]
[Cu2+-Gua-Cl-]3+
144.80
135.85
105.97
146.81
[A+H]+
[Gua-2Cl--H+]+
335.93
267.85
176.81
396.85
[Gua-2Cl--3H++Cu2+]+
[Gua-Cl-]+
371.99
266.72
238.78
280.76
318.84
336.99
[Gua-Cl--2H++Cu2+]+
432.63
495.76
527.08
568.43
596.53
650.78
690.18
744.35
Relative Abundance
m/z
data09 #33-34 RT: 0.54-0.55 AV: 2 SB: 43 0.02-0.49, 0.59-0.80 NL: 4.62E2
T: - c ESI Q1MS [100.00-800.00]
345.99
[AMP-H]-
383.78
403.91
635.90
482.04
599.31
338.60
346.94
333.76
372.70
502.09
520.09
Relative Abundance
m/z

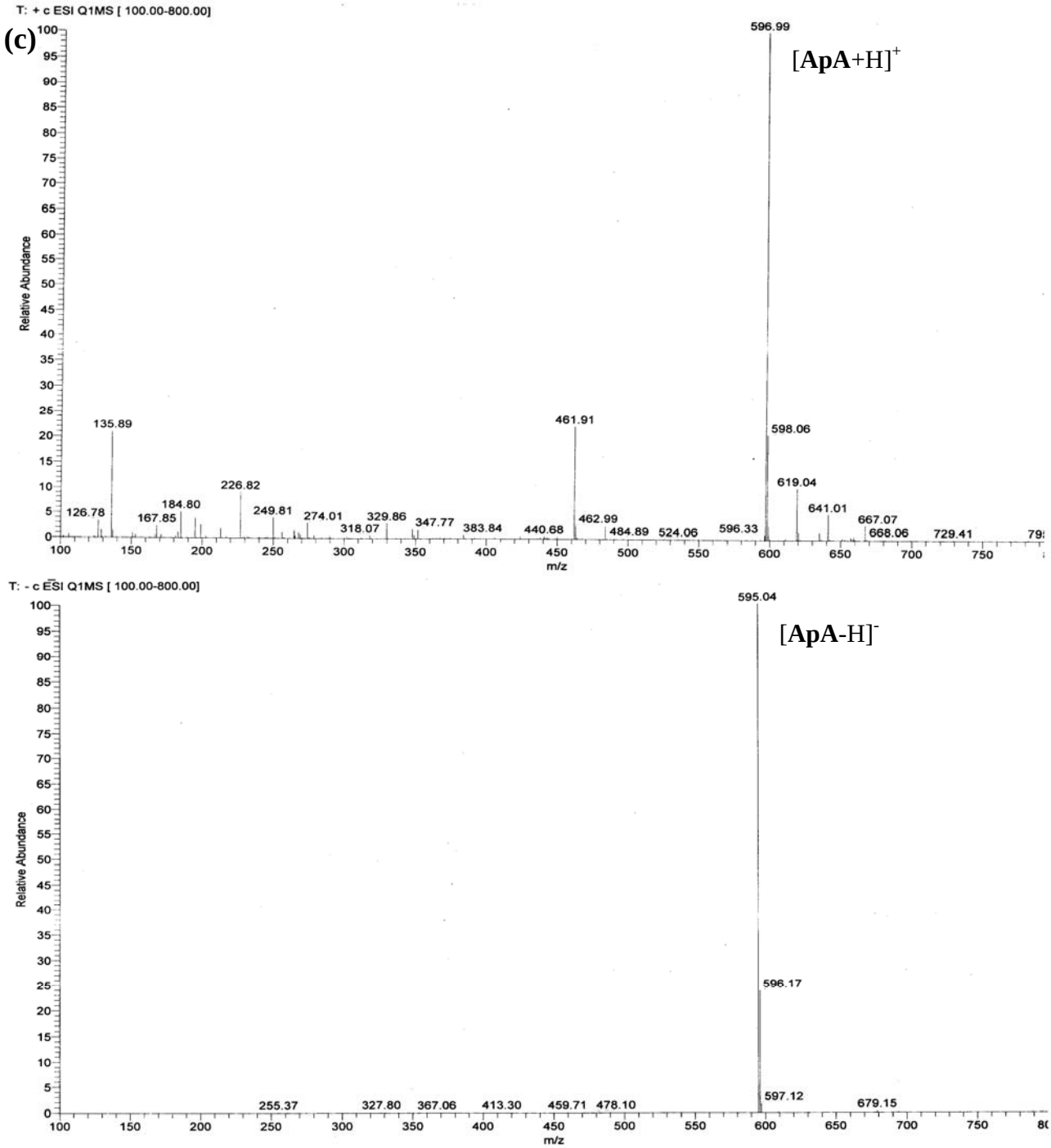

Figure S08. ESI–MS analysis of ApA after treatment with (a) **Gua**, (b) Cu^{2+}–**Gua** and (c) alone for 8 h at 37 °C.

IR spectra

(a)

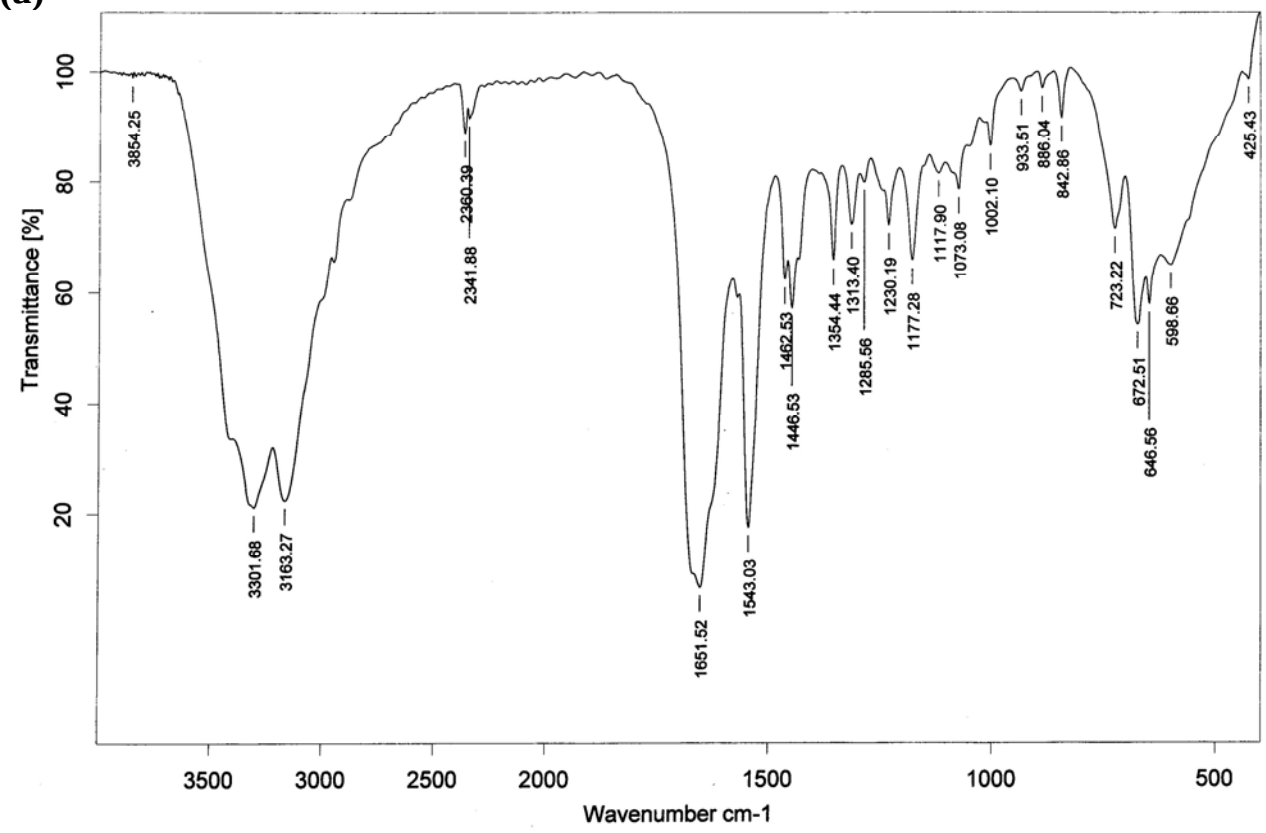
Transmittance [%]
100
80
60
40
20
3854.25
3301.68
3163.27
2360.39
2341.88
1651.52
1543.03
1462.53
1446.53
1354.44
1313.40
1285.56
1230.19
1177.28
1117.90
1073.08
1002.10
933.51
886.04
842.86
723.22
672.51
646.56
598.66
425.43
3500
3000
2500
2000
1500
1000
500
Wavenumber cm-1

(b)

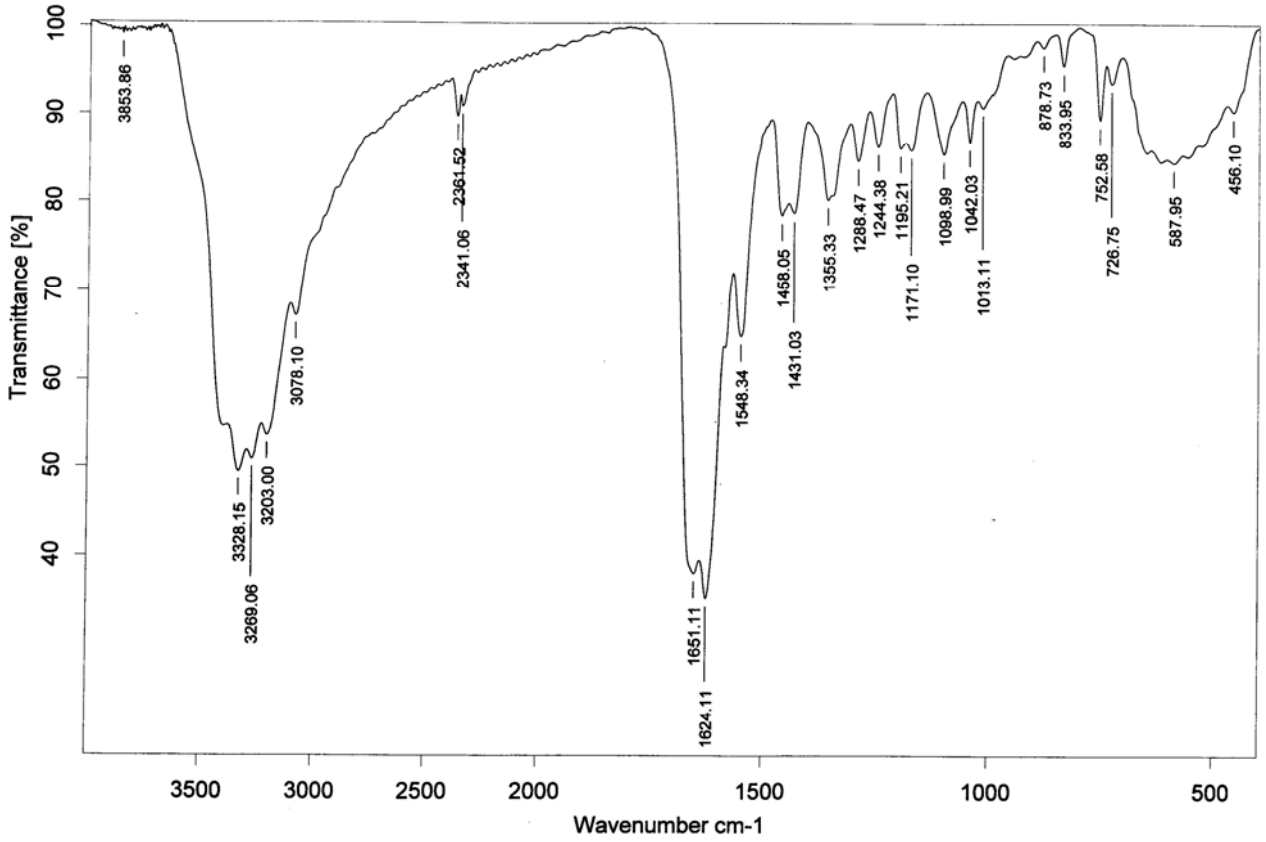

Figure S09. IR spectra of (a) **Gua** and (b) Cu^{2+}–**Gua**.

Tyrosinase-Catalyzed Synthesis of a Universal Coil-Chitosan Bioconjugate for Protein Immobilization

Antoine Demolliens,[†] Cyril Boucher,[†,‡] Yves Durocher,[‡] Mario Jolicoeur,[†] Michael D. Buschmann,[†] and Gregory De Crescenzo*[,†]

Department of Chemical Engineering, Institute of Biomedical Engineering, Ecole Polytechnique de Montréal, P.O. Box 6079, Station Centre-ville, Montréal, Québec, Canada H3C 3A7, and Animal Cell Technology Group, Bioprocess Sector, Biotechnology Research Institute, National Research Council Canada. 6100 Royalmount Avenue, Montréal, Quebec, Canada H4P 2R2. Received February 19, 2008; Revised Manuscript Received June 16, 2008

Chitosan has been reported as a promising material for gene and drug delivery as well as for tissue engineering and regenerative medicine. We report here the conjugation of a *de novo* designed coil peptide (Kcoil) to chitosan (M_n = 200 kDa) to achieve a universal Kcoil-chitosan scaffold for subsequent immobilization of proteins tagged with the Kcoil partner, i.e., the Ecoil peptide. Kcoil-chitosan conjugate was synthesized using a tyrosinase-catalyzed protocol. Extensive UV/vis and IR characterization demonstrated that Kcoil peptide was covalently grafted to amines of chitosan. The ability of Kcoil-chitosan conjugate to recruit Ecoil tagged epidermal growth factor (EGF) was assessed by surface plasmon resonance measurements (SPR). Despite nonspecific interactions between chitosan and EGF, the specific formation of an E/K coiled coil complex was observed at slightly acidic pH and high salt concentration conditions, demonstrating that grafting to chitosan did not negatively impact binding characteristics of Kcoil peptide. Finally, the benefits of such bioconjugates for biomedical applications are discussed.

INTRODUCTION

Within the past decades, natural polysaccharides have emerged as attractive biomaterials for the development of scaffolds in the domain of tissue regeneration as well as for the production of nanoparticles to replace classical viral gene delivery vehicles (*1*). Among them, chitosan has been demonstrated to be especially promising (*2*). More specifically, its availability as a medical grade polymer combined with its gelation properties when mixed with glycerol phosphate makes it an interesting cell carrier (*3, 4*). A novel hybrid biomaterial, produced by combining chitosan with freshly drawn autologous blood, has also demonstrated beneficial wound healing properties for cartilage repair (*3–5*). The use of chitosan as a drug carrier/delivery system (*6–9*) as well as a nonviral vector for gene delivery has also led to the development of innovative therapeutic treatments (*10*).

Chitosan is a linear polysaccharide of β (1−4) linked glucosamine and N-acetyl glucosamine units obtained through N-deacetylation of chitin, which is extracted from insect and crustacean shells (*11*). The presence of primary amino groups on most of the chitosan monomeric units confers crucial chemical properties such as nucleophilicity and solubility at low pH (pH < 6.5) (*12, 13*). Several studies suggest that intrinsic properties of chitosan that are currently exploited may be further enhanced by tailored chitosan functionalization, thereby augmenting its potential applications to gene delivery and regenerative medicine. For example, the conjugation of macromolecules interacting with cell surface receptors to chitosan-based nanoparticles may enable the specific targeting of cell populations to which a gene has to be delivered. Also, specific growth factors stably immobilized onto chitosan three-dimensional scaffolds may control and modulate cell survival, growth, and differentiation. The potential advantages of immobilized growth factor versus soluble growth factor supply were recently highlighted by Fan et al. The latter demonstrated that covalent tethering of epidermal growth factor (EGF) on poly(methyl methacrylate)-based polymers and exposure to mesenchymal stem cells provided a survival advantage when compared to soluble EGF (*14*) or to adsorbed EGF (*15*).

Although unambiguous effects of tethered EGF have been reported by Fan et al., there is still a crucial need for a universal and flexible protocol that would allow any growth factor or any other desired protein to be easily and specifically captured on scaffolds. With this in view, we have developed a novel approach based on the use of *de novo* designed peptides, namely, the Ecoil and Kcoil that heterodimerize in a highly specific and stable fashion to adopt a coiled-coil structure (*16, 17*) (Figure 1). This Ecoil/Kcoil capture/delivery system has also been recently reported to be useful for adenoviral vector retargeting (*18*). Also, previous studies have demonstrated that the Ecoil/Kcoil system can be used as a versatile domain for capturing proteins onto surfaces without any loss of bioactivity (*19–21*). In the present approach, ligand tethering is achieved by incubating coil-tagged ligands with surfaces or scaffolds on which the other coil partner has been covalently attached (Figure 1).

The purpose of the present study was to examine the applicability of our coil-based approach for modification of chitosan scaffolds and nanoparticles. To achieve this, we explored the use of an enzymatic protocol (*22, 23*) in which tyrosinase-catalyzed oxidation of a tyrosine-containing Kcoil peptide is followed by its condensation onto chitosan in a nonenzymatic step (Figure 2). Peptide functionalized chitosan was then characterized by UV−vis and FT-IR spectroscopies. Additional surface plasmon resonance (SPR) assays confirmed that Kcoil-functionalized chitosan was able to recruit the Ecoil-tagged epidermal growth factor (E-EGF) *via* coiled-coil interac-

* Corresponding author. Tel: +1 514 340 4711 x7428; fax: 1 (514) 340 2990. E-mail address: gregory.decrescenzo@polymtl.ca.
[†] Institute of Biomedical Engineering.
[‡] Biotechnology Research Institute.

10.1021/bc800066b CCC: $40.75 © 2008 American Chemical Society
Published on Web 08/14/2008

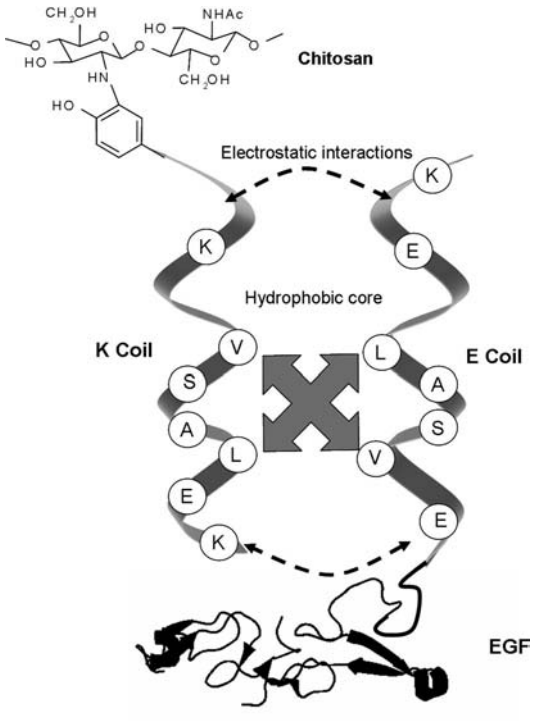

Figure 1. Schematic representation of the heterodimeric E/K coiled-coil domain and its application as a universal capture/delivery system. Each heptad, K-V-S-A-L-K-E for the Kcoil and E-V-S-A-L-E-K for the Ecoil, is repeated five times in each peptide. The stability of the coiled-coil complex is primarily due to the formation of a hydrophobic core involving leucine and valine residues of each coil, while electrostatic interactions provide additional stability as well as high specificity. This universal system enables the immobilization of coil tagged proteins (e.g., EGF as shown) on chitosan conjugated with its partner coil.

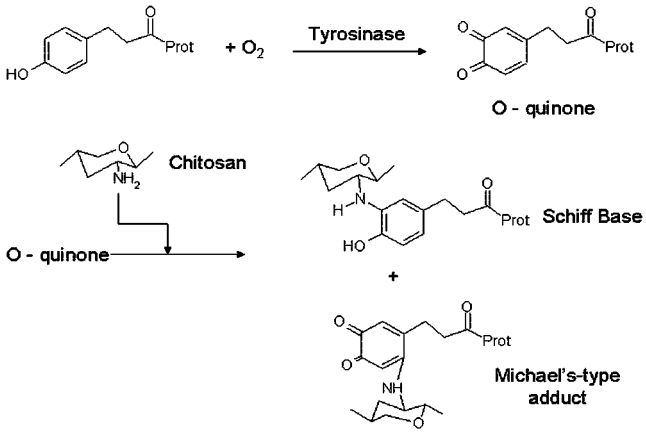

Figure 2. Chemical and tyrosinase-catalyzed reactions for the conjugation of a tyrosine-containing peptide to chitosan. Tyrosinase catalyzes the formation of an O-quinone derivative that undergoes a nonenzymatic reaction with chitosan to form two types of products, i.e., a Schiff base and a Michael's type adduct.

tions, hence validating our procedure that produces chitosan functionalized with a universal coil peptide capture/delivery system.

MATERIALS AND METHODS

High molecular weight chitosan (number average molecular mass M_n = 200 000 Da with degree of deacetylation that is % of monomers that are deacetylated called DDA = 80%) was supplied by Biosyntech (Laval, QC, Canada). 1% (w/v) chitosan solution was obtained by dissolving 500 mg of chitosan powder in 50 mL of water acidified with 20 mM HCl. After continuous overnight stirring, the pH of the solution was 4.5. Mushroom tyrosinase (EC 1.14.18.1, specific activity of 5370 U/mg according to the manufacturer) was purchased from Sigma Chemical Co. (St. Louis, MO). The enzyme was dissolved in PBS (150 mM NaCl, 50 mM potassium phosphate, pH 6.5) up to 308 U/mL, aliquoted and stored at −20 °C according to the manufacturer recommendations. Kcoil peptide (primary sequence: YGG(KVSALKE)$_5$GGC, > 80% purity) was synthesized by BioSynthesis (Lewisville, TX). 21.2 mg of Kcoil peptide was dissolved in 4 mL of distilled water, aliquoted, and stored at −20 °C before use. The K-EGF and E-EGF coding for Kcoil or Ecoil tag, (His)$_8$ tag, and EGF cDNA were produced using HEK-293 cells and purified by immobilized metal affinity chromatography (IMAC) as previously described in Boucher and al. (in press).

Synthesis of Kcoil-Chitosan Bioconjugate. Chitosan was diluted in distilled water to a final concentration of 0.1% (w/v) and 1 M NaOH was slowly added to reach a pH of 6.0, which is the highest pH that maintains solubility for this chitosan (*24, 25*). A high pH is desirable since tyrosinase only reacts with deprotonated amine groups and tyrosinase has a maximal effectiveness at pH between 6 and 7. Tyrosinase was diluted in PBS (pH 6.5) to achieve a specific activity of 120 U/mL. Equal volume of tyrosinase and chitosan solutions were then mixed and the pH was adjusted to 6.0. Kcoil peptide was then added to the mixture (4 mg of Kcoil peptide per 100 mg of chitosan, corresponding to 2 mmol of peptide per mole of chitosan glucosamine units). After overnight stirring at room temperature, the pH of the mixture was slowly increased to 11−12 by dropwise addition of NaOH, 1 M. Precipitated chitosan was separated by centrifugation (2 × 250 g for 10 min at room temperature). The pellet was extensively washed by rinsing with water and NaOH precipitation (at least twice). The washed pellet was then dissolved in water and the pH of the solution was adjusted to 5.5 for maximal product solubility. The product was aliquoted and stored at 4 °C before analysis.

UV Measurements. UV measurements (230−600 nm scans, 2 nm resolution) for pure chitosan, controls, and conjugated chitosan were carried out on a UNICO S 2100 UV spectrophotometer (UNICO, Dayton, NJ).

IR Measurements. Functionalized chitosan and control samples were first lyophilized (Benchtop 3 L freeze-Dryer, VirTis, Warminster, PA) for 24 h and used directly thereafter. Pure chitosan powder was desiccated for 24 h and used directly thereafter as control. FT-IR measurements were performed in duplicate using an FTIR 6000 StingRay instrument (Bio Rad, Hercules, CA) equipped with a photoacoustic cell (PAS) maintained in a helium atmosphere. Spectra were recorded from 500 to 4000 cm^{-1} with resolution set to 2 cm^{-1} and measurement frequency of 5 kHz. Approximately 8 mg of each sample was introduced into the PAS.

Surface Plasmon Resonance (SPR)-Based Assays. Coiled-coil mediated interactions between Kcoil conjugated chitosan and Ecoil tagged EGF were monitored using an SPR-based optical biosensor (Biacore 3000, GE Healthcare, Piscataway, NJ). HBS-EP (10 mM Hepes, pH 6.0, 150 mM NaCl, 3.0 mM EDTA, 0.05% P20 surfactant) was chosen as running buffer and for diluting all injected species. For all experiments, the flow rate was set at 10 μL.min^{-1}.

Chitosan Surface Preparation. Kcoil conjugated chitosan was adsorbed to the surface of a C1 sensorchip flowcell by manual injection of 10 mg/L Kcoil chitosan dissolved in running buffer (approximately 12 μL). Guanidium-HCl (5M) was then injected (20 μL at 100 μL.min^{-1} flow rate) to remove unbound material. After baseline stabilization, the resulting mass ac-

cumulation was of ~82 resonance units (1000 RUs corresponds to 1 ng of proteins bound to the surface). The control surface was then generated by manual injection of pure chitosan (0.1 mg.L^{-1} in running buffer) for subsequent monitoring of nonspecific protein adsorption on the chitosan-only surface without any coil. The amount of bound chitosan was adjusted to the level of the test surface. After the guanidium−HCl washing procedure (see above), chitosan mass accumulation was ~79 RUs. Control-corrected sensorgrams thus correspond to the subtraction of the chitosan-only sensorgrams from those obtained with Kcoil conjugated chitosan surface.

Monitoring of Coiled-Coil Mediated Interaction between Kcoil-Conjugated Chitosan and Ecoil Tagged EGF. Various samples (Buffer, Kcoil tagged EGF for negative control and Ecoil tagged EGF both at a concentration of 5 μg/mL) were injected for 120 s at a flow rate of 50 μL.min^{-1} over both surfaces. This was followed by buffer injection for 180 s in order to monitor complex dissociation. In between sample injections, regeneration of the surface was achieved by 5 M guanidium-HCl injection (20 μL at a flow rate of 100 μL.min^{-1}) in addition to 1 M NaCl injection (pulse of 6 s at the same flow rate). Sensorgrams were then control-corrected as described in the previous section using *Biaevaluation 3.1* software package enclosed with the Biacore 3000 instrument.

RESULTS AND DISCUSSION

Tyrosinase-Mediated Grafting of Kcoil Peptide onto Chitosan. Three different products were prepared and tested in order to provide chemical evidence for conjugation of Kcoil peptide to chitosan. The first product was generated as described in section 2.1 and corresponded to the test sample while the two others were used as controls. Specifically, the first control (referred to as Control #1 below) was prepared with tyrosinase but without Kcoil peptide added to the mixture and the second control (referred to as Control #2 below) was prepared with Kcoil peptide but without tyrosinase added to the mixture. After incubation, washing and extraction procedures were performed for each sample as described in section 2.1. Chitosan was also used as a negative control baseline in spectroscopic assays.

UV−vis Spectroscopic Characterization. Figure 3a shows UV/vis spectra (230 to 470 nm) for Control #1, pure and grafted chitosan. The spectrum of Control #2 was superimposable on that of chitosan (data not shown). Of interest, the absorbance between 230 and 350 nm was found to be considerably greater for the bioconjugate than for the other samples (Figure 3a). The conjugated chitosan showed characteristic features of proteins, i.e., a peak near 280 nm due to the presence of a tyrosine residue in the peptide chain, as well as chitosan features for wavelengths higher than 350 nm, i.e., in the region where the peptide moiety does not absorb and where all spectra superpose. When the blank chitosan spectrum was subtracted from that of modified chitosan, its high similarity with the spectrum of the pure peptide (Figure 3b) affirms that the increase in absorbance near 280 nm observed for bioconjugate was from the covalent attachment of the Kcoil peptide on chitosan. A slight shift of the peak could be observed, from 270 to 274 nm. This bathochrome effect was attributed to the disturbance of electronic distribution near the aromatic ring where glucosamine is grafted.

These UV/vis spectroscopic assays also permit an estimation of the degree of peptide grafting to chitosan. By assuming that the extinction coefficient of the conjugated peptide remained the same as that of original Kcoil peptide only (i.e., 1490 $M^{-1}.cm^{-1}$ due to the presence of one tyrosine), one can estimate the conjugation degree as follows. The absorbance at 280 nm of 0.028 A provides a peptide concentration of 0.028/1490 = 18.8 μM while the concentration of monomers (glucosamines and N-acetylated glucosamines) of chitosan in solution is 0.5 g/L ÷ 169.4 g/mol = 2.95 mM (where 169.4 g/mol is the average molecular mass of a monomer of 80% DDA chitosan (*24*)) resulting in 1 peptide conjugated per 157 monomers. A 200 kDa 80% DDA chitosan contains (200,000 ÷ 169.4 g/mol)*0.8 = 947 glucosamine monomers, thus resulting in an average of 7 peptides per chitosan chain. This level of conjugation corresponds to a modification of less than one percent of total glucosamine units and a near-complete grafting of the peptide added in the original reaction solution.

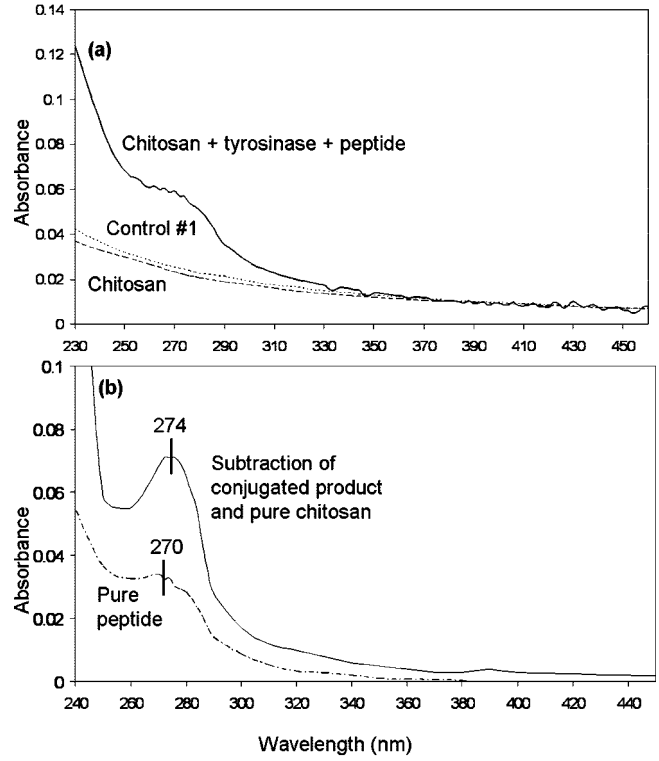

Figure 3. UV/vis spectrophotometric measurements demonstrate that both peptide and tyrosinase are necessary for bioconjugation on chitosan. (a) Each chitosan sample was incubated overnight in buffered solution with either tyrosinase (Control #1) or peptide (Control #2, not shown), or both and then washed following the procedure described in section 2.1. (b) The spectrum of the peptide-conjugated chitosan after subtraction of the chitosan-only spectrum is compared to that of the pure peptide.

Taken together, UV−vis spectroscopic results indicated that, even when working with low amounts of Kcoil peptide (4% w/w), conjugation was successfully achieved, and required the presence of both tyrosinase and peptide.

FT-IR Characterization of the Compounds. The IR spectra of blank chitosan (1), Control #1 (2), Control #2 (3), and conjugated chitosan (4) are shown in Figure 4a,b,c (corresponding to 700−1100 cm^{-1}, 1500−2000 cm^{-1}, and 3100−3650 cm^{-1} ranges, respectively). All observed spectra displayed peaks characteristic of chitosan including the imine stretch νC═N (1663 cm^{-1}, Figure 4b) and the amide II band (1559 cm^{-1}, Figure 4b), both arising from N-acetyl groups of chitosan (*26*). The intense band at 1076 cm^{-1} (Figure 4a) is likely the result of several overlapping vibrations (νCO, νCN, νCC) and has been previously reported as a spectral feature of chitosan (*22*, *27*). Of interest, its intensity was observed to increase for Kcoil conjugated chitosan (Figure 4a), which is likely due to peptidic bonds of the Kcoil peptide conjugated to chitosan.

In the case of the bioconjugate, new peaks and shifts were observed over the whole range of scanned wavenumbers. More specifically, peaks of medium intensity falling at 832 cm^{-1} (νC═C bending), 1600 cm^{-1} (νC═C stretching in aromatic

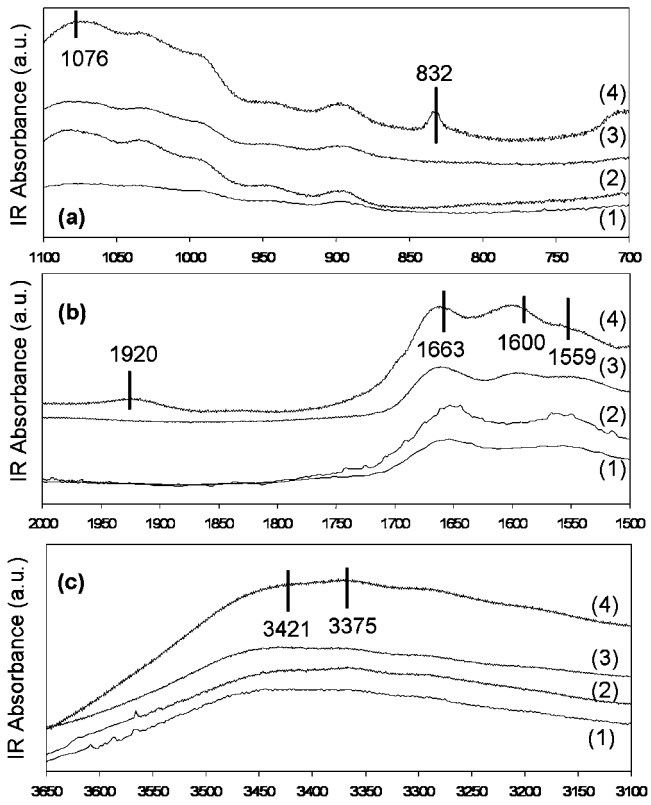

Figure 4. FT-IR characterization of the Kcoil-chitosan bioconjugate. FT-IR spectra of (1) pure chitosan, (2) Control #1 (no peptide), (3) Control #2 (no tyrosinase), and (4) Kcoil conjugated to chitosan. The products were prepared as described in section 2.1 of Materials and Methods. The resolution was set to 2 cm^{-1} and the measurement frequency was 5 kHz. The ranges of wavelengths shown are (a) 700−1100 cm^{-1}, (b) 1500−2000 cm^{-1}, and (c) 3100−3650 cm^{-1}.

rings), and 1920 cm^{-1} (νC−H out-of-plane deformation) only appeared on the spectrum of conjugated chitosan (Figure 4a,b) and are characteristic of the phenyl-group of tyrosine (*28–30*). No additional intense IR bands were observed, which can be attributed to the lack of strong IR features assigned to the aromatic ring of tyrosine (*22, 26*). Also, as can be seen in the 3100−3650 cm^{-1} range (Figure 4c) which displays the νNH bands, the primary amine band of the unmodified chitosan sample at 3421 cm^{-1} remained unchanged in both controls, whereas the bioconjugate displayed a shoulder at 3375 cm^{-1}. This additional shoulder is consistent with the modification of some primary amine groups of chitosan into secondary amino groups, as a consequence of the chemical conjugation of a peptide onto a glucosamine unit as previously observed (*23*).

Altogether, UV/vis and FT-IR measurements unambiguously demonstrated that tyrosinase was able to oxidize the tyrosyl residue of the Kcoil peptide, since subsequent covalent grafting to chitosan was achieved. Indeed, tyrosinase-modified Kcoil was shown to undergo a nonenzymatic grafting onto chitosan, whereas in the absence of tyrosinase, no grafting was observed (Figures 3 and 4). These results are in agreement with previously reported work by Lenhart and colleagues (*31*). Although quinones are able to react with several nucleophiles, the low pK_a of chitosan amino groups favored grafting as compared to lysyl or sulfydryl groups of Kcoil whose p*K*as are higher (10 for lysine, 8 for cysteine) (*22, 32*). The addition of a tyrosine at the N-terminus of the Kcoil peptide thus provided a means for controllable and oriented grafting of the Kcoil peptide.

Surface Plasmon Resonance (SPR) Characterization of Ecoil Tagged EGF Binding to Kcoil-Conjugated Chitosan. The ability of Kcoil-chitosan to recruit and bind to Ecoil tagged EGF *via* specific E/K coiled-coil interaction was tested using an SPR-based optical biosensor. Briefly, pure chitosan was immobilized on the control flowcell and grafted chitosan on the test flowcell. Buffer, Kcoil tagged EGF (negative control) and Ecoil tagged EGF were then injected over both surfaces. Preliminary experiments performed in running buffer (HBS-EP) at pH 7.4 led to high nonspecific binding of Kcoil tagged EGF to Kcoil chitosan surface (data not shown). This observation led us to hypothesize that this binding was attributable to nonspecific chitosan-protein interactions, i.e., between chitosan itself and EGF, since neither Kcoil/Kcoil nor Kcoil/chitosan interactions are likely to occur due to electrostatic repulsion between cationic chitosan and the cationic Kcoil (*19*). The pI of Ecoil tagged EGF was computed on Clone Manager (Sci-ED Software, Cary, NC) and found to be around 5.2, which indicates that the protein bears a negative charge for pH > 5.2. These nonspecific interactions are thus more likely to be due to EGF interacting with the positively charged NH_3^+ groups of chitosan (*33*). The use of HBS EP at a lower pH of 6.0 as running buffer allowed chitosan and Kcoil chitosan to remain soluble during deposition on the surface, resulting in very stable surfaces that were not modified by 5 M guanidinium-HCl injections. At this pH, chitosan and Kcoil chitosan were observed to have a high affinity for the dextran surface of the biosensor ((*34*) and results not shown). However, nonspecific interactions between injected EGF and deposited chitosan were still observed in this configuration ((*33*) and data not shown). In order to limit these nonspecific chitosan-protein interactions, NaCl pulse injections were added during the regeneration step, just after the 5 M guanidinium-HCl injection. Note that this salt injection is only required to demonstrate specific coiled-coil interactions by SPR and does not need to be applied in general to achieve coupling.

Raw data and control-corrected results corresponding to buffer, Kcoil tagged EGF (negative control) and Ecoil tagged EGF injections over Kcoil conjugated chitosan and pure chitosan surfaces, following the above-described optimized protocol, are shown in Figure 5a,b, respectively. In contrast to previous experiments performed at pH 7.4 or in the absence of NaCl pulses, Kcoil tagged EGF showed little interaction with the Kcoil chitosan surface since the raw signal monitored on test cell for Kcoil tagged EGF injection was very similar to that of buffer-only injection (only 15 RUs of accumulated material were observed, Figure 5a). In contrast, Ecoil tagged EGF injection over Kcoil chitosan surface led to approximately 75 RUs of accumulated material at the end of the injection (Figure 5a). Taken together, these results indicated that Ecoil tagged EGF capture on Kcoil-chitosan was mediated by the Ecoil moiety of Ecoil tagged EGF. However, this result did not distinguish whether the mode of interaction was between Ecoil tagged EGF and Kcoil chitosan *via* an E/K coiled-coil interaction versus Ecoil interacting directly with chitosan chains adsorbed to the test surface. To further address this issue, the sensorgrams corresponding to Kcoil tagged and Ecoil tagged EGF injections over the pure chitosan surface were subtracted from the sensorgrams obtained by injections over the surface coated with Kcoil conjugated chitosan (Figure 5b). The control-corrected sensorgram corresponding to the injection of Kcoil tagged EGF was characterized by rapid transition (less than 2 s) to equilibrium (25 RUs) during injection and by the absence of dissociation of bound material during subsequent buffer injection. In contrast, injection of Ecoil tagged EGF resulted in a kinetic profile characterized by a 5-fold higher mass accumulation during injection and dissociation of Ecoil tagged EGF/Kcoil chitosan complexes during subsequent buffer injection. Of interest, the same level of permanent accumulation of EGF after buffer injection was observed as in the case of Kcoil tagged EGF (25 RUs). These observations are thus consistent with a

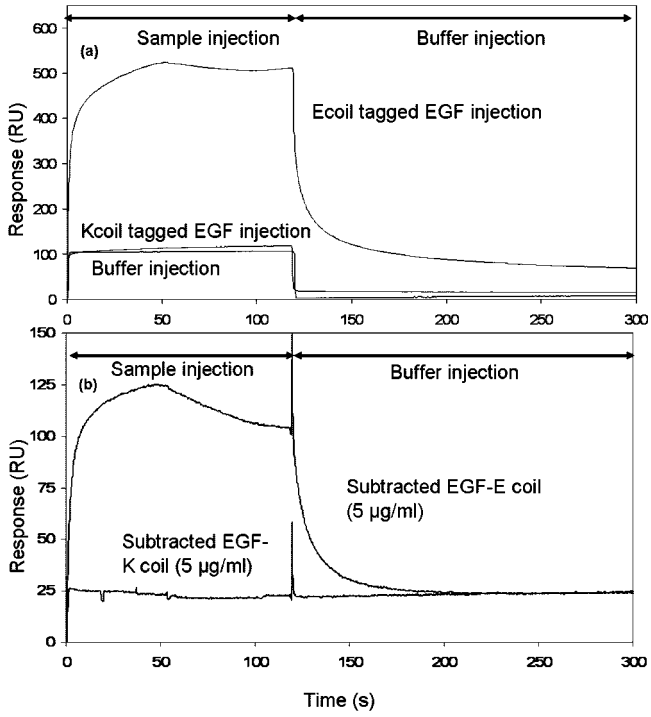

Figure 5. SPR investigation of coil tagged EGF/Kcoil chitosan interactions. (a) Raw and (b) control-corrected SPR sensorgrams corresponding to the injections of buffer, Kcoil tagged EGF (5 μg/mL) and Ecoil tagged EGF (5 μg/mL) over Kcoil chitosan bioconjugate coated surface. HBS-EP (pH 6.0) was chosen as running buffer. 1 M NaCl and 5 M guanidium-HCl injections were used to regenerate the surface.

specific E/K coiled-coil mediated interaction between Ecoil tagged EGF and Kcoil conjugated chitosan, in addition to a smaller nonspecific interaction between EGF and chitosan that is present for both E and Kcoil tagged proteins.

One limitation of the current approach and in particular of the conditions used for SPR tests is the limited stability of the coiled-coil complex composed of Ecoil tagged EGF and Kcoil chitosan that was observed to dissociate within 100 s (Figure 5b). Such instability was due to stringent experimental conditions, i.e., acidic pH in combination with injection of high concentration of salt, which we used to highlight the coiled-coil specific interactions. Indeed, maintaining chitosan solubility and simultaneously screening nonspecific interactions negatively impacted coiled-coil stability since hydrophobic cores within coiled-coil complexes are less stable at pH 6.0 than at physiological pH and since the presence of salt will mask electrostatic interactions that allow further stabilization of the complex. Thus, the hydrophobic core was formed, which created the increase of SPR signal, but the domain could not be maintained because of the lack of stabilizing electrostatic interactions consistent with previous work (*19, 20*). One remaining challenge in future work is to limit nonspecific binding of proteins to chitosan and thus achieve stable and, most of all, monitorable coiled-coil interactions at physiological pH. Indeed, the E/K coiled-coil system used in this study has already been demonstrated to be extremely stable ($k_d \sim 10^{-4}$ s^{-1}) in a physiological context (*16, 17, 19–21*), affirming the promising nature of coil-chitosan conjugates as biocompatible substrates for oriented immobilization of proteins. This may be achieved by appropriate mixing and buffer exchange systems where conditions appropriate for specificity of coiled-coil formation are followed by those required for stability of the established coiled-coil complex.

CONCLUSION

Chitosan has been reported as a promising material for gene and drug delivery as well as in tissue engineering and regenerative medicine. This report demonstrates that enzymatic covalent grafting of a *de novo* designed coil peptide to chitosan can be achieved by exploiting the high chemoselectivity of tyrosinase. A particular advantage of the current approach is the absence of tedious and time-consuming purification steps making this enzymatic process very promising to obtain easily a pure and safe product for biomedical applications. This study also demonstrates the ability of coil-chitosan conjugate to specifically capture proteins tagged with the partner coil peptide, for example, the growth factor EGF. The well-known beneficial properties of chitosan (biocompatibility, degradability, bioadhesion, antimicrobial activity) can thus be complemented with a procedure allowing flexible and oriented protein conjugation to chitosan *via* coiled-coil interactions, providing multiple additional functionalities in applications such as gene delivery and regenerative medicine.

ACKNOWLEDGMENT

This work was supported by the Canada Research Chairs on Protein-enhanced Biomaterials (G.D.C.), on the Development of Metabolic Tools as well as the Canadian Institutes of Health Research (M.D.B.) and the Natural Sciences and Engineering Research Council of Canada (M.D.B., G.D.C., M.J.).

LITERATURE CITED

(1) Dang, J. M., and Leong, K. W. (2006) Natural polymers for gene delivery and tissue engineering. *Adv. Drug Delivery Rev. 58*, 487–499.

(2) Kim, I.-Y., Seo, S.-J., Moon, H.-S., Yoo, M.-K., Park, I.-Y., Kim, B.-C., and Cho, C.-S. (2008) Chitosan and its derivatives for tissue engineering applications. *Biotechnol. Adv. 26*, 1–21.

(3) Hoemann, C. D., Chenite, A., Sun, J., Hurtig, M., Serreqi, A., Lu, Z., Rossomacha, E., and Buschmann, M. D. (2007) Cytocompatible gel formation of chitosan-glycerol phosphate solutions supplemented with hydroxyl ethyl cellulose is due to the presence of glyoxal. *J. Biomed. Mater. Res. A 83*, 521–9.

(4) Hoemann, C. D., Hurtig, M., Rossomacha, E., Sun, J., Chevrier, A., Shive, M. S., and Buschmann, M. D. (2005) Chitosan-glycerol phosphate/blood implants improve hyaline cartilage repair in ovine microfracture defects. *J. Bone Joint Surg. Am. 87*, 2671–86.

(5) Chevrier, A., Hoemann, C. D., Sun, J., and Buschmann, M. D. (2007) Chitosan-glycerol phosphate/blood implants increase cell recruitment, transient vascularization and subchondral bone remodeling in drilled cartilage defects. *Osteoarthritis Cartilage 15*, 316–27.

(6) Denkbas, E., and Odabas, M. (2000) Chitosan microspheres and sponges: Preparation and characterization. *J. Appl. Polym. Sci. 76*, 1637–1643.

(7) Dodane, V., Amin Khan, M., and Merwin, J. R. (1999) Effect of chitosan on epithelial permeability and structure. *Int. J. Pharm. 182*, 21–32.

(8) Lee, J. E., Kim, K. E., Kwon, I. C., Ahn, H. J., Lee, S.-H., Cho, H., Kim, H. J., Seong, S. C., and Lee, M. C. (2004) Effects of the controlled-released TGF-[beta]1 from chitosan microspheres on chondrocytes cultured in a collagen/chitosan/glycosaminoglycan scaffold. *Biomaterials 25*, 4163–4173.

(9) Mattioli-Belmonte, M., Gigante, A., Muzzarelli, R. A., Politano, R., De Benedittis, A., Specchia, N., Buffa, A., Biagini, G., and Greco, F. (1999) N,N-dicarboxymethyl chitosan as delivery agent for bone morphogenetic protein in the repair of articular cartilage. *Med. Biol. Eng. Comput. 37*, 130–4.

(10) Lavertu, M., Methot, S., Tran-Khanh, N., and Buschmann, M. D. (2006) High efficiency gene transfer using chitosan/DNA nanoparticles with specific combinations of molecular weight and degree of deacetylation. *Biomaterials 27*, 4815–24.

(11) Muzzarelli, R. A., Jeuniaux, C., and Gooday, G. W. (1986) *Chitin in nature and technology*, Plenum Press, New York.

(12) Kumar, M. N., Muzzarelli, R. A., Muzzarelli, C., Sashiwa, H., and Domb, A. J. (2004) Chitosan chemistry and pharmaceutical perspectives. *Chem. Rev. 104*, 6017–84.

(13) VandeVord, P. J., Matthew, H. W., DeSilva, S. P., Mayton, L., Wu, B., and Wooley, P. H. (2002) Evaluation of the biocompatibility of a chitosan scaffold in mice. *J. Biomed. Mater. Res. 59*, 585–90.

(14) Fan, V. H., Tamama, K., Au, A., Littrell, R., Richardson, L. B., Wright, J. W., Wells, A., and Griffith, L. G. (2007) Tethered epidermal growth factor provides a survival advantage to mesenchymal stem cells. *Stem Cells 25*, 1241–51.

(15) Kuhl, P. R., and Griffith-Cima, L. G. (1996) Tethered epidermal growth factor as a paradigm for growth factor-induced stimulation from the solid phase. *Nat. Med. 2*, 1022–7.

(16) De Crescenzo, G., Pham, P. L., Durocher, Y., and O'Connor-McCourt, M. D. (2003) Transforming growth factor-beta (TGF-beta) binding to the extracellular domain of the type II TGF-beta receptor: receptor capture on a biosensor surface using a new coiled-coil capture system demonstrates that avidity contributes significantly to high affinity binding. *J. Mol. Biol. 328*, 1173–83.

(17) Litowski, J. R., and Hodges, R. S. (2002) Designing heterodimeric two-stranded α-helical coiled-coils. Effects of hydrophobicity and α-helical propensity on protein folding, stability, and specificity. *J. Biol. Chem. 277*, 37272–37279.

(18) Zeng, Y., Pinard, M., Jaime, J., Bourget, L., Uyen Le, P., O'Connor-McCourt, M. D., Gilbert, R., and Massie, B. (2008) A ligand-pseudoreceptor system based on de novo designed peptides for the generation of adenoviral vectors with altered tropism. *J. Gene Med. 14*, 14.

(19) De Crescenzo, G., Litowski, J. R., Hodges, R. S., and O'Connor-McCourt, M. D. (2003) Real-time monitoring of the interactions of two-stranded de novo designed coiled-coils: Effect of chain length on the kinetic and thermodynamic constants of binding. *Biochemistry 42*, 1754–1763.

(20) Tripet, B., De Crescenzo, G., Grothe, S., O'Connor-McCourt, M., and Hodges, R. S. (2002) Kinetic analysis of the interactions between troponin C and the C-terminal troponin I regulatory region and validation of a new peptide delivery/capture system used for surface plasmon resonance. *J. Mol. Biol. 323*, 345–62.

(21) Tripet, B., De Crescenzo, G., Grothe, S., O'Connor-McCourt, M., and Hodges, R. S. (2003) Kinetic analysis of the interactions between troponin C (TnC) and troponin I (TnI) binding peptides: evidence for separate binding sites for the 'structural' N-terminus and the 'regulatory' C-terminus of TnI on TnC. *J. Mol. Recognit. 16*, 37–53.

(22) Anghileri, A., Lantto, R., Kruus, K., Arosio, C., and Freddi, G. (2007) Tyrosinase-catalyzed grafting of sericin peptides onto chitosan and production of protein-polysaccharide bioconjugates. *J. Biotechnol. 127*, 508–519.

(23) Kumar, G., Smith, P. J., and Payne, G. F. (1999) Enzymatic grafting of a natural product onto chitosan to confer water solubility under basic conditions. *Biotechnol. Bioeng. 63*, 154–165.

(24) Filion, D., Lavertu, M., and Buschmann, M. D. (2007) Ionization and solubility of chitosan solutions related to thermosensitive chitosan/glycerol-phosphate systems. *Biomacromolecules 8*, 3224–34.

(25) Lavertu, M., Filion, D., and Buschmann, M. D. (2008) Heat-induced transfer of protons from chitosan to glycerol phosphate produces chitosan precipitation and gelation. *Biomacromolecules 9*, 640–50.

(26) Sampaio, S., Taddei, P., Monti, P., Buchert, J., and Freddi, G. (2005) Enzymatic grafting of chitosan onto Bombyx mori silk fibroin: Kinetic and IR vibrational studies. *J. Biotechnol. 116*, 21–33.

(27) Gupta, A., Tandon, P., Gupta, V. D., and Rastogi, S. (1997) Vibrational dynamics and heat capacity of β-poly(L-serine). *Polymer 38*, 2389–2397.

(28) Arp, Z., Autrey, D., Laane, J., Overman, S. A., and Thomas, G. J. (2001) Tyrosine Raman signatures of the filamentous virus Ff are diagnostic of non-hydrogen-bonded phenoxyls: demonstration by raman and infrared spectroscopy of p-cresol vapor. *Biochemistry 40*, 2522–2529.

(29) Socrates, G. (1995) Infrared characteristic group frequencies, second edition. Tables and charts. *J. Am. Chem. Soc. 117*, 1671.

(30) Freddi, G., Anghileri, A., Sampaio, S., Buchert, J., Monti, P., and Taddei, P. (2006) Tyrosinase-catalyzed modification of *Bombyx mori* silk fibroin: Grafting of chitosan under heterogeneous reaction conditions. *J. Biotechnol. 125*, 281–294.

(31) Lenhart, J. L., Chaubal, M. V., Payne, G. F., and Barbari, T. A. (1998) Enzymatic modification of chitosan by tyrosinase. *ACS Symp. Ser. 684*, 188–198.

(32) Chen, T., Embree, H. D., Wu, L.-Q., and Payne, G. F. (2002) In vitro protein-polysaccharide conjugation: Tyrosinase-catalyzed conjugation of gelatin and chitosan. *Biopolymers 64*, 292–302.

(33) Aguilar, M. R., Gallardo, A., Lechuga, L. M., Calle, A., and San Roman, J. (2004) Modulation of proteins adsorption onto the surface of chitosan complexed with anionic copolymers. Real time analysis by surface plasmon resonance. *Macromol. Biosci. 4*, 631–638.

(34) Serizawa, T., Yamaguchi, M., Matsuyama, T., and Akashi, M. (2000) Alternating bioactivity of polymeric layer-by-layer assemblies: Anti-vs procoagulation of human blood on chitosan and dextran sulfate layers. *Biomacromolecules 1*, 306–309.

BC800066B

Synthesis and Convenient Functionalization of Azide-Labeled Diacylglycerol Analogues for Modular Access to Biologically Active Lipid Probes

Matthew D. Smith,[†] Denghuang Gong,[†] Christopher G. Sudhahar,[‡] Justin C. Reno,[†] Robert V. Stahelin,[‡] and Michael D. Best*,[†]

Department of Chemistry, The University of Tennessee, Knoxville, Tennessee 37996, and Department of Biochemistry and Molecular Biology, Indiana University School of Medicine—South Bend, and Department of Chemistry and Biochemistry and The Walther Center for Cancer Research, University of Notre Dame, South Bend, Indiana 46617. Received March 10, 2008; Revised Manuscript Received July 2, 2008

Cell membrane lipids have been identified as key participants in cell signaling activities. One important role is their involvement as site-specific ligands in protein—membrane binding interactions, which result in the anchoring of peripheral proteins onto cellular membranes. These events generally regulate protein function and localization and have been implicated in both normal physiological processes and those pertaining to disease state onset. Thus, it is important to elucidate the details of interactions at the molecular level, such as lipid-binding specificities and affinities, the location of receptor binding domains and multivalency in binding. For this purpose, we have designed and developed azido-tagged lipid analogues as conveniently functionalizable lipid probe scaffolds. Herein, we report the design and synthesis of the initial structure of this type, diacylglycerol analogue **2**, which contains an azide tag at the *sn*-1 position of the lipid headgroup. Direct functionalization of this compound with a range of reporter groups has been performed to illustrate the facile access to probes of use for characterizing binding. Quantitative lipid-binding studies using protein kinase C, a known DAG-binding receptor, demonstrate that these probes are active mimetics of natural DAG. Thus, these DAG probes will serve as robust sensors for studies aimed at understanding binding interactions and as precursors for the development of analogous probes of more complex phospholipids and glycolipids.

INTRODUCTION

Signaling lipids present at low percentages in cellular membranes, such as diacylglycerol (DAG) (*1, 2*), phosphatidic acid (PA) (*3, 4*), and the phosphoinositides (PIP_ns) (*5*—*9*), have emerged as vital regulators in a wide array of crucial physiological and pathophysiological events. A prominent role involves the targeting and docking of peripheral proteins onto the membrane surface through site-specific lipid binding, a process that generally regulates protein function and subcellular localization (*1, 2, 10, 11*). Elucidation of the details of protein—lipid binding is necessary, as many of these interactions have been directly implicated in disease state onset. For instance, despite the simplicity of its structure, DAG has been connected to several high-profile pathophysiological events including cancer (*12, 13*) and diabetes (*14*).

The best studied DAG-responsive receptors reside in the protein kinase C (PKC) family, which consists of at least eleven known isozymes categorized into conventional (calcium, DAG, and phospholipid-dependent), novel (calcium-independent, but DAG and phospholipid-dependent), and atypical (calcium and DAG-independent) subgroups (*1, 2, 15*—*17*). PKCs have long been known to be directly involved in tumorigenesis, which is not surprising due to the various and often opposing roles of PKC isozymes in cell-cycle processes such as proliferation, differentiation, and apoptosis (*12, 13, 18*). Furthermore, compounds that compete for the DAG-binding domains of PKCs, such as the bryostatins (*19*), have shown great promise as agents for cancer therapy. However, despite a vast amount of research, the exact links between PKC activity and carcinogenesis remain unknown, primarily due to complications in elucidating the specific activities and localization of the different isozymes. Understanding the lipid-binding specificities of these isozymes is thus crucial, since these properties control both protein function and localization.

Phospholipids derived from the core diacylglycerol scaffold are also important ligands in biological processes, as evidenced by the interaction of PA with Raf-1 kinase. Binding of Raf-1 kinase to PA results in membrane association, at which point this enzyme is then activated by a protooncogene, Ras GTPase, when the two proteins are in proximity at the membrane surface (*20*—*27*). This system is crucial, as point mutations in Ras have been detected in 20% to 30% of all human tumors and carcinogenesis is known to propagate through activation of effector kinases by Ras enzymes (*28, 29*). Finally, the PIP_n family represents a highly complex series of seven phospholipids composed of phosphodiester-linked *myo*-inositol headgroups containing anywhere from one to three phosphate groups at every combination of the 3-, 4-, and 5-positions. The PIP_ns have been implicated in a litany of crucial physiological processes (*5*—*8, 30, 31*) as well as the onset of disease states including cancer, leukemia, and diabetes (*32*).

The development of lipid probes is highly beneficial for understanding the details of membrane-binding interactions at the molecular level, as these compounds can be implemented for efficient strategies aimed at the characterization of these recognition events. The synthesis of probes from scratch provides the ability to generate pure samples of a single lipid structure and the freedom to explore a wide variety of modification approaches. For instance, access to analogues through enzymatic or synthetic conversion of natural lipids limits the scope of probes that can be obtained, involves high costs, and

* mdbest@utk.edu.
[†] The University of Tennessee.
[‡] Indiana University School of Medicine-South Bend and University of Notre Dame.

10.1021/bc8001002 CCC: $40.75 © 2008 American Chemical Society
Published on Web 08/07/2008

often precludes the production of pure samples of one specific lipid structure. Furthermore, functionalization at different positions, such as through replacement of a hydrogen at the *sn*-1 position, which has been rarely pursued due to the required synthesis (*33*), may be beneficial for presenting a reporter at the headgroup yet as far away from the *sn*-3 position, the point of lipid variation and primary recognition site, as possible.

In the end, access to an arsenal of probes with different structural modifications would be beneficial, as each compound may be particularly suited to a given study. For this purpose, a modular approach to probe development involving late-stage functionalization is beneficial to facilitate access to a range of target probe structures. Herein, we report the culmination of our initial approach to the development of diverse probes that are effective as functional derivatives of DAG as they are able to recruit DAG effector protein to lipid vesicles with similar affinities to the natural lipid. As a result, these derivatives offer a viable means of assaying complex binding mechanisms of DAG effectors *in vitro* and in cell based assays.

EXPERIMENTAL PROCEDURES

General. All reagents were purchased from Aldrich or Acros and used as received. Dry solvents were obtained from a Pure Solv solvent delivery system purchased from Innovative Technology, Inc. Column chromatography was performed using 230−400 mesh silica gel purchased from Sorbent Technologies. NMR spectra were obtained using a Bruker AC250 spectrometer updated with a TecMag data collection system, a Varian Mercury 300 spectrometer, and a Bruker Avance 400 spectrometer. Mass spectra were obtained with a JEOL DART-AccuTOF spectrometer with high resolution capabilities. Optical rotation values were obtained using a Perkin-Elmer 241 polarimeter. HPLC data was obtained using an HP series 1100 HPLC with an Alltech Lichrosphere SI 60 50U column with HPLC grade solvents purchased from Fischer. 1-Palmitoyl-2-oleoyl-*sn*-glycero-3-phosphocholine (POPC), 1-palmitoyl-2-oleoyl-*sn*-glycero-3-phosphoserine (POPS), and *sn*-1,2-dioleoylglycerol (DiC_{18}) were purchased from Avanti Polar Lipids, Inc. (Alabaster, AL).

((4*S*,5*S*)-2,2-Dimethyl-1,3- dioxolane-4,5-diyl) dimethanol (5). A solution of diethyl-L-tartrate (6.76 mL, 39.5 mmol) and *p*-toluenesulfonic acid (128 mg, 0.672 mmol) in benzene (80 mL) was prepared in a flame-dried round-bottom flask. To the solution was added with stirring 2,2-dimethoxypropane (6.03 mL, 48.6 mmol). The solution was heated to 80 °C for 3 h and the azeotrope was collected in a Dean−Stark trap. The solution was allowed to cool to room temperature, at which point sodium carbonate (200 mg, 1.89 mmol) was added and stirring was continued for 2 h. The solution was filtered, concentrated on a rotary evaporator, and moved to the next step without further purification.

A solution of lithium aluminum hydride (3.0 g, 79 mmol) in anhydrous THF (70 mL) was prepared in a flame-dried, three-neck round-bottom flask. The suspension was cooled to 0 °C and kept under nitrogen. The crude mixture from above was dissolved in anhydrous THF (20 mL) and added dropwise to the reaction over 30 min. The reaction mixture was stirred at 0 °C for 1 h, then at room temperature for 1 h, and was then cooled back to 0 °C. The reaction was quenched by the dropwise addition of 3 mL water, 3 mL of 10% NaOH, and 9 mL more of water. Vigorous stirring was continued for 20 min while the mixture returned to room temperature. Anhydrous magnesium sulfate was added with stirring for 1 h to dry the reaction. The reaction was filtered and the solvent was removed by rotary evaporation. Column chromatography with silica gel and a gradient solvent system of 3% to 5% methanol/dichloromethane afforded **5** as a clear oil (4.5 g, 70% over 2 steps).

Characterizations matched previous reports (*34*). ^{1}H NMR (250 MHz, $CDCl_3$) δ 4.02−4.00 (m, 2H), 3.83−3.71 (m, 4H), 2.49−2.45 (m, 2H), 1.44 (s, 6H); ^{13}C NMR (62.9 MHz, $CDCl_3$) δ 109.3, 78.3, 62.1, 27.0; HRMS $[M + H]^+$ calcd: 163.09703, found: 163.09705.

((4*S*,5*S*)-5-(Azidomethyl)-2,2-dimethyl-1,3-dioxolan-4-yl)-methanol (7). Compound **5** (990 mg, 6.10 mmol) was suspended in anhydrous dichloromethane (36 mL). With stirring was added silver (I) oxide (2.12 g, 9.15 mmol), tosyl chloride (1.28 g, 6.71 mmol), and crushed potassium iodide (203 mg, 1.22 mmol). The reaction was stirred at room temperature for 2 h at which point it was filtered through a short plug of silica using ethyl acetate as an eluent and concentrated under reduced pressure to afford crude **6**. This was passed on without further purification.

To the crude solution of **6** dissolved in anhydrous DMF (60 mL) was added sodium azide (1.19 g, 18.3 mmol). The reaction was heated to 85 °C and stirred overnight. The crude mixture was extracted with ethyl acetate, dried with magnesium sulfate, and concentrated under reduced pressure. Column chromatography with silica gel and a gradient solvent system of 20−60% ethyl acetate/hexanes afforded **7** as a colorless oil (934 mg, 82% over 2 steps).

Characterizations matched previous reports (*35*). ^{1}H NMR (300 MHz, $CDCl_3$) δ 4.12−3.97 (m, 2H), 3.84−3.78 (m, 1H), 3.69−3.55 (m, 2H), 3.37−3.31 (m, 1H), 2.39 (t, J = 6 MHz, 1H), 1.47 (s, 1H), 1.44 (s, 1H).

(2*S*,3*S*)-4-Azidobutane-1,2,3-triol (8). Alcohol **7** was dissolved in 10 mL of 90% acetic acid. The solution was heated to reflux for 10 min and then slowly cooled to room temperature. Solvent was removed under reduced pressure and column chromatography with silica gel and 10% methanol/dichloromethane afforded compound **8** as a yellow syrup (232 mg, 92%).

^{1}H NMR (300 MHz, CD_3OD) showed removal of the acetonide protecting group and, along with the R_f value by TLC analysis, matched previous characterizations (*36*). Compound **8** was thus used without any further characterization.

(2*S*,3*S*)-1-Azido-4-((4,4′-dimethoxytrityl)methoxy)butane-2,3-diol (9). Triol **8** (75.3 mg, 0.512 mmol) was dissolved in pyridine (5 mL) and a small amount of 4 Å MS was added to the reaction flask. With stirring, 4,4′-dimethoxytrityl chloride (260 mg, 0.768 mmol) was added. The reaction was placed under nitrogen and stirred at room temperature overnight. The reaction was then filtered with dichloromethane and the solvent was removed under reduced pressure at low temperature (45 °C). Column chromatography with silica gel and a gradient solvent system of 30−80% ethyl acetate/hexanes afforded **9** as a yellow oil (143 mg, 62%).

$[\alpha]_D^{296K}$ − 5.53 (c = 1.428, $CHCl_3$); ^{1}H NMR (300 MHz, $CDCl_3$) δ 7.42−7.18 (m, 9H), 6.82 (d, J = 8.7 Hz, 4H), 3.82−3.64 (m, 8H ($OC\underline{H}_3$ + 2C$\underline{H}$OH)), 3.38−3.18 (m, 4H), 2.98 (d, J = 4.8 Hz, 1H), 2.82 (d, J = 6 Hz, 1H); ^{13}C NMR (100.6 MHz, $CDCl_3$) δ 158.6, 144.5, 135.7, 135.5, 130.0, 128.02, 127.97, 127.0, 113.3, 86.7, 71.3, 70.7, 65.2, 55.2, 53.6; HRMS $[M + Cl^-]^-$ calcd: 484.16392, found: 484.16204.

(2*S*,3*S*)-1-Azido-4-((4,4′-dimethoxytrityl)methoxy)butane-2,3-diyl distearate (10d). Diol **9** (289 mg, 0.643 mmol), stearic acid (549 mg, 1.93 mmol), 4-dimethylaminopyridine (79 mg, 0.643 mmol), and dicyclohexylcarbodiimide (398 mg, 1.93 mmol) were combined in dichloromethane (7 mL). The reaction was stirred at room temperature for 7 h, at which point it was filtered with ethyl acetate. Column chromatography with silica gel and 10% ethyl acetate/hexanes afforded **10d** as a white solid (546 mg, 86%).

$[\alpha]_D^{296K}$ + 3.10 (c = 0.967, $CHCl_3$); ^{1}H NMR (300 MHz, $CDCl_3$) δ 7.42−7.18 (m, 9H), 6.82 (d, J = 8.7 Hz, 4H),

5.45−5.40 (m, 1H), 5.27−5.23 (m, 1H), 3.78 (s, 6H), 3.45−3.39 (m, 1H), 3.31−3.19 (m, 2H), 3.11−3.06 (m, 1H), 2.39−2.22 (m, 4H), 1.67−1.54 (m, 4H), 1.26 (bs, 56H), 0.88 (t, $J = 6.6$ Hz, 6H); ^{13}C NMR (100.6 MHz, $CDCl_3$) δ 172.8, 172.7, 158.6, 144.3, 135.6, 135.4, 129.96, 129.90, 128.0, 127.9, 126.9, 113.2, 86.3, 71.2, 70.7, 61.7, 55.2, 50.9, 34.4, 34.1, 32.0, 29.73, 29.69, 29.68, 29.67, 29.5, 29.4, 29.3, 29.28, 29.2, 25.0, 24.8, 22.7, 14.1; $[M + O_2]$[9] calcd: 1013.70683, found: 1013.71083.

(2*S*,3*S*)-1-Azido-4-hydroxybutane-2,3-diyl distearate (2). Compound **10d** (35 mg, 0.036 mmol) and *p*-aminobenzoic acid (49 mg, 0.360 mmol) were combined in 2 mL of solvent in a ratio of 1 dichloromethane/8.5 acetic acid/0.5 water. The solution was stirred at room temperature for 12.5 h. The reaction was extracted with dichloromethane (50 mL) and dried with magnesium sulfate. The solvent was removed under reduced pressure. Column chromatography was carried out on a short plug of silica gel using 30% ethyl acetate/hexanes. Because compound **2** is known to undergo acyl chain migration on silica, purification was performed rapidly. As a result of not being able to carefully purify the reaction, **2** was not obtained in pure form, but the trityl adduct impurities did not affect the next reaction and were easily removed during purification of the subsequent DAG analogues.

^{1}H NMR (300 MHz, $CDCl_3$) δ 5.33−5.30 (m, 1H), 5.12−5.07 (m, 1H), 3.68−3.61 (m, 2H), 3.49−3.46 (m, 2H), 2.44−2.33 (m, 5H, OH buried), 1.66−1.60 (m, 4H), 1.26 (b s, 56H), 0.88 (t, $J = 6.3$ Hz, 6H); ^{13}C NMR (62.9 MHz, $CDCl_3$) δ 173.7, 173.2, 72.5, 70.5, 60.8, 51.1, 34.2, 32.0, 29.7, 29.5, 29.4, 29.3, 29.2, 25.0, 24.9, 22.7, 14.1; HRMS $[M - H_2O + H]^+$ calcd: 662.58358, found: 662.58257.

General Procedure for Obtaining DAG Analogues Modified by "Click" Chemistry. Compound **10d** (1 equiv) and pyrrole (2.05 equiv) or *p*-ABA (10 equiv) were dissolved in 2 mL of solvent in a ratio of 1 dichloromethane/8.5 AcOH/0.5 H_2O. The solution was stirred at room temperature for 6 h if using pyrrole or 12.5 h if using *p*-ABA. The reaction was extracted with dichloromethane (2 × 25 mL) and dried with magnesium sulfate. The solvent was removed under reduced pressure. The crude residue was then dried under high vacuum for 1−3 h and used directly in the click reactions as described below.

(2*S*,3*S*)-1-Hydroxy-4-(4-((2-(naphthalen-2-yl)acetamido)-methyl-1*H*-1,2,3-triazol-1-yl)butane-2,3-diyl distearate (11a). Alkyne **12a** (14.3 mg, 0.064 mmol) and **2** (0.064 mmol) were dissolved in dry THF (0.5 mL). Copper sulfate pentahydrate (16 mg, 0.064 mmol) and sodium ascorbate (12.7 mg, 0.064 mmol) were added along with water (0.5 mL). The reaction was stirred in the dark at room temperature overnight. The reaction was extracted with dichloromethane (2 × 50 mL) from water, and the organic phase was dried with magnesium sulfate, filtered, and the solvent removed by rotary evaporation. Column chromatography on a short plug of silica gel and a gradient solvent system of 50% to 100% ethyl acetate/hexanes afforded **11a** as a white solid (29 mg, 50% (2 steps)).

$[\alpha]_D^{296K}$ − 11.0 ($c = 0.963$, $CHCl_3$); ^{1}H NMR (300 MHz, $CDCl_3$) δ 7.82−7.77 (m, 3H), 7.69 (s, 1H), 7.57 (s, 1H), 7.51−7.45 (m, 2H),7.36−7.33 (m, 1H), 6.30 (t, $J = 5.7$ Hz, 1H), 5.55−5.50 (m, 1H), 5.02−4.97 (m, 1H), 4.54 (d, $J = 6$ Hz, 2H), 4.42 (d, $J = 5.7$ Hz, 2H), 3.79−3.56 (m and s overlapped, 4H), 2.71 (b s, 1H), 2.38−2.24 (m, 4H), 1.64−1.51 (m, 4H), 1.25 (b s, 56H), 0.88 (t, $J = 6.2$ Hz, 6H); ^{13}C NMR (75 MHz, $CDCl_3$) δ 173.4, 173.1, 171.1, 144.9, 133.5, 132.5, 131.9, 128.9, 128.3, 127.71, 127.65, 127.2, 126.4, 126.1, 123.3, 72.0, 70.0, 60.5, 50.3, 43.8, 35.0, 34.1, 33.9, 29.72, 29.68, 29.5, 29.4, 29.3, 29.2, 29.1, 24.9, 24.8, 22.7, 14.1; HRMS $[M + H]^+$ calcd: 903.69386, found: 903.68995.

(2*S*,3*S*)-1-(4-((5-(Dimethylamino)naphthalene-1-sulfonamido)methyl-1*H*-1,2,3-triazol-1-yl)-4-hydroxybutane-2,3-diyl distearate (11b). Alkyne **12b** (16.4 mg, 0.057 mmol) and **2** (0.057 mmol) were dissolved in dry THF (0.5 mL). Copper sulfate pentahydrate (14.2 mg, 0.057 mmol) and sodium ascorbate (11.3 mg, 0.057 mmol) were added along with water (0.5 mL). The reaction mixture was stirred in the dark at room temperature overnight. The reaction was extracted with dichloromethane (2 × 50 mL) from water, and the organic phase was dried with magnesium sulfate, filtered, and the solvent removed by rotary evaporation. Column chromatography on a short plug of silica gel and a gradient solvent system of 50% to 100% ethyl acetate/hexanes afforded **11b** as a greenish solid (30 mg, 55% (2 steps)).

$[\alpha]_D^{296K}$ − 12.2 ($c = 1.01$, $CHCl_3$); ^{1}H NMR (300 MHz, $CDCl_3$) δ 8.55 (d, $J = 8.7$ Hz, 1H), 8.27−8.24 (m, 2H), 7.58−7.50 (m, 2H), 7.43 (s, 1H), 7.19 (d, $J = 7.5$ Hz, 1H), 5.51−5.44 (m, 2H, NH buried), 4.98−4.93 (m, 1H), 4.48 (d, $J = 6$ Hz, 2H), 4.18 (d, $J = 6$ Hz, 2H), 3.79−3.58 (m, 2H), 2.89 (s, 6H), 2.64 (b s, 1H), 2.39−2.27 (m, 4H), 1.66−1.53 (m, 4H), 1.25 (b s, 56H), 0.88 (t, $J = 6.5$ Hz, 6H); ^{13}C NMR (75 MHz, $CDCl_3$) δ 173.4, 173.2, 151.9, 144.4, 134.4, 130.6, 129.8, 129.6, 129.5, 128.6, 123.3, 123.2, 118.7, 115.3, 72.0, 69.8, 60.5, 50.2, 45.4, 38.7, 34.1, 33.9, 31.9, 29.72, 29.68, 29.5, 29.4, 29.3, 29.26, 29.2, 29.1, 24.9, 24.8, 22.7, 14.1; HRMS $[M + H]^+$ calcd: 968.68739, found: 968.68743.

(2*S*,3*S*)-1-Hydroxy-4-(4-((2-oxo-2*H*-chromene-3-carboxamido)methyl)-1*H*-1,2,3-triazol-1-yl)butane-2,3-diyl distearate (11c). Alkyne **12c** (12.7 mg, 0.056 mmol) and **2** (0.056 mmol) were dissolved in dry THF (0.5 mL). Copper sulfate pentahydrate (14 mg, 0.056 mmol) and sodium ascorbate (11.1 mg, 0.056 mmol) were added along with water (0.5 mL). The reaction mixture was stirred in the dark at room temperature overnight. Solvent was removed, and column chromatography on a short plug of silica gel and a gradient solvent system of 20% to 100% acetone/chloroform afforded **11c** as a tan solid (31 mg, 60% (2 steps)).

$[\alpha]_D^{296K}$ − 14.6 ($c = 1.224$, $CHCl_3$); ^{1}H NMR (300 MHz, $CDCl_3$) δ 9.29 (bs, 1H), 8.91 (s, 1H), 7.71−7.65 (m, 3H), 7.42−7.36 (m, 2H), 5.60−5.55 (m, 1H), 5.07−5.02 (m, 1H), 4.73 (b s, 2H), 4.61−4.60 (m, 2H), 3.80−3.59 (m, 2H), 2.64−2.62 (m, 1H), 2.39−2.28 (m, 4H), 1.65−1.53 (m, 4H), 1.25 (b s, 56H), 0.88 (t, $J = 6.6$ Hz, 6H); ^{13}C NMR (75 MHz, $CDCl_3$) δ 173.4, 173.1, 161.8, 161.2, 154.5, 148.5, 144.8, 134.3, 129.8, 125.3, 123.3, 118.5, 118.1, 116.7, 72.1, 70.0, 60.5, 50.3, 35.4, 34.1, 33.9, 31.9. 29.72, 29.67, 29.5, 29.4, 29.3, 29.2, 29.1, 24.9, 24.8, 22.7, 14.2; HRMS $[M + H]^+$ calcd: 907.65239, found: 907.65176.

(2*S*,3*S*)-1-Hydroxy-4-(4-((5(6)-fluoresceinamido)methyl)-1*H*-1,2,3-triazol-1-yl)butane-2,3-diyl distearate (11d). Alkyne **12d** (19.8 mg, 0.048 mmol) and **2** (0.048 mmol) were dissolved in dry THF (0.5 mL). Copper sulfate pentahydrate (12 mg, 0.048 mmol) and sodium ascorbate (9.5 mg, 0.048 mmol) were added along with water (0.5 mL). The reaction was stirred in the dark at room temperature overnight. Solvent was removed and column chromatography on a short plug of silica gel and a gradient solvent system of 30% to 100% acetone/chloroform afforded **11d** as an orange solid (25 mg, 47% (2 steps)). Note: since both fluorescein isomers (5- and 6-carboxy) were present in the ^{1}H NMR spectra for compounds **12d** and **11d**, and the ratio of each isomer is unknown in the commercially available acid, integration values are not reported. ^{13}C NMR data for compounds **12d** and **11d** are not reported due to poor solubility of the compounds and the complex nature of the spectra due to the isomeric mixture.

$[\alpha]_D^{296K}$ − 8.5($c = 0.823$, 1 acetone/1 $CHCl_3$); ^{1}H NMR (300 MHz, $CDCl_3$/$(CD_3)_2CO$ (1:1)) δ 9.05 (b s), 8.60 (b s), 8.50 (b s), 8.33−8.30 (m), 8.24−8.21 (m), 8.04−8.01 (m) 7.91 (b s), 7.81−7.78 (m), 7.74 (s), 7.31−7.28 (m), 6.77−6.56 (m), 5.61−5.51 (m), 5.04−4.99 (m), 4.72−4.59 (m) 4.30−4.17 (m),

3.83−3.65 (m), 2. 39−2.18 (m), 1.62−1.43 (m), 1.27 (b s), 0.88 (t, $J = 6.3$ Hz); HRMS $[M + H]^+$ calcd: 1093.68408, found: 1093.68461.

(2*S*,3*S*)-1-(4-((4-Benzoylbenzamido)methyl-1*H*-1,2,3-triazol-1-yl)-4-hydroxybutane-2,3-diyl distearate (11e). Alkyne **12e** (13.6 mg, 0.052 mmol) and **2** (0.052 mmol) were dissolved in dry THF (0.5 mL). Copper sulfate pentahydrate (13 mg, 0.052 mmol) and sodium ascorbate (10 mg, 0.052 mmol) were added along with water (0.5 mL). The reaction was stirred in the dark at room temperature overnight. The reaction was extracted with dichloromethane (2 × 50 mL) from water, and the organic phase was dried with magnesium sulfate, filtered, and the solvent removed by rotary evaporation. Column chromatography on a short plug of silica gel and a gradient solvent system of 50% to 100% ethyl acetate/hexanes afforded **11e** as a white solid (34 mg, 69% (2 steps)).

$[\alpha]_D^{296K} - 11.4$ ($c = 1.127$, $CHCl_3$); ^{1}H NMR (300 MHz, $CDCl_3$) δ 7.92 (d, $J = 8.1$ Hz, 2H), 7.84−7.73 (m, 5H), 7.61 (t, $J = 7.4$ Hz, 1H), 7.49 (m, 2H), 7.33 (b s, 1H), 5.61−5.57 (m, 1H), 5.06−5.01 (m, 1H), 4.77−4.71 (m, 2H), 4.62−4.59 (m, 2H), 3.81−3.75 (m, 1H), 3.67−3.60 (m, 1H), 2.39−2.27 (m, 4H), 1.64−1.49 (m, 4H), 1.25 (b s, 56H), 0.88 (t, $J = 6.6$ Hz, 6H); ^{13}C NMR (100.6 MHz, $CDCl_3$) δ 195.9, 173.3, 173.2, 166.6, 144.7, 140.2, 137.2, 137.0, 132.9, 130.1, 128.4, 127.1, 123.6, 72.1, 70.0, 60.6, 50.4, 35.4, 34.2, 34.0, 31.9, 29.7, 29.5, 29.4, 29.3, 29.2, 29.1, 24.9, 24.8, 22.1, 14.1; HRMS $[M + H]^+$ calcd: 943.68877, found: 943.68741.

Protein Binding Analysis. The DAG binding protein PKCδ was purified from Sf9 cells as previously described (*37*). Lipid vesicles were prepared as previously described (*37*) and consisted of POPC/POPS/DAG (78:20:2 where DAG is any synthetic DAG tested). POPC vesicles were prepared for the control surface. All surface plasmon resonance (SPR) experiments were performed at 25 °C using a Biacore X as described previously (*38*). Equilibrium SPR measurements were carried out at the flow rate of 5 μL/min with coating of the L1 sensor chip (GE Healthcare) done as previously reported (*38*). After injecting 85 μL of PKCδ, the protein−lipid association and dissociation were measured for 1020 and 500 s, respectively. The sensorgrams were obtained using five or more different concentrations of the protein (within a 10-fold range of K_d) for each condition tested. The sensorgrams were corrected for refractive index change by subtracting the control surface response. The maximal response (R_{eq}, saturation value) was determined from the plots and then plotted versus protein concentrations (C). The K_d value was determined by a nonlinear least-squares analysis of the binding isotherm using the equation $R_{eq} = R_{max}/(1 + K_d/C)$ (*39*).

RESULTS AND DISCUSSION

While recent advances have yielded progress in understanding protein−lipid association, these studies are complicated by the membrane environment in which they occur, and results often reveal the complex nature of these events and raise further questions for scrutiny. One of the best-studied families of peripheral proteins are the PKCs, which contain tandem C1 domains and one C2 domain, which each form specific interactions with lipids such as DAG, PS, and PA, depending on the specific domain and isoform (*1, 2*). The presence of multiple lipid-binding domains indicates multivalency in binding, a common cell-surface motif in which multiple ligands are simultaneously bound by a protein receptor (*40, 41*). Furthermore, subtle differences in lipid-binding specificities and affinities have been discerned among the eleven known PKC isoforms (*1, 2*). Differential binding properties have also been observed in the interaction of PKC isozymes with phorbol esters, which occurs at the same site as DAG recognition (*42*). In addition, variation exists in the subcellular localization of the different PKC isoforms, which often occurs in a cell-type specific manner that has represented a formidable obstacle to elucidating the roles of the different isozymes in biological processes including tumorigenesis (*12*). A current hypothesis is that the subtle differences in binding patterns between isozymes result in the variation in their distinct cellular localization, which in turn controls their involvement in specific physiological processes (*2, 11*). Due to these ramifications, it is necessary to fully characterize the multivalent lipid-binding specificities of peripheral proteins, the patterns of affinities among domains, and the role this has in controlling distribution and function.

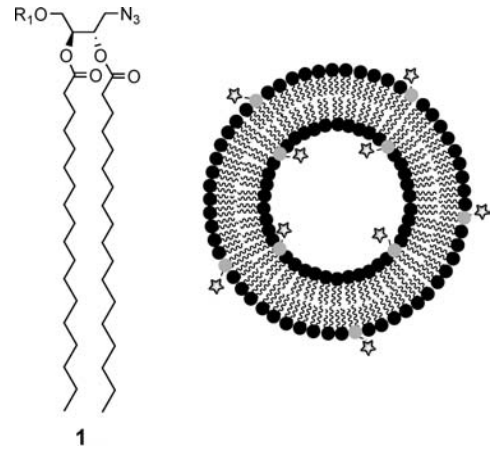

Figure 1. General design for headgroup azide-tagged lipid analogues and tag presentation in a membrane environment.

Fully synthetic lipid probes have previously proven effective for scrutinizing binding events (*7, 33, 43−49*). However, the scope of studies is often limited by the complexity of synthesis required for each distinct reporter-functionalized probe. An effective lipid probe design involves the incorporation of a versatile reactive tag into the lipid structure. This provides a common modular intermediate that can be specifically modified to introduce a variety of reporter groups or for direct functionalization within the context of a study. However, the choice of functionality for lipid derivatization is crucial, as the diversity of functional groups in these structures complicates modification. For this purpose, we have designed versatile lipid core structures, described generically by **1** (Figure 1), containing an azide-reactive tag in the form of an azidomethyl group at the *sn*-1 position. The azide group is specifically chosen due to its diminutive size, robust properties, and bio-orthogonal reactivity through the 1,3-dipolar cycloaddition (click chemistry) (*50−52*) and Staudinger ligation (*53−55*) reactions. The azide can also be reduced to an amine for functionalization (*56*). Thus, multiple pathways exist for direct modification of the tagged lipid analogue to produce a wide array of probes.

The initial modular glycerolipid probe structure of type **1** that we have developed is DAG analogue **2**. This compound can be implemented both to study the involvement of DAG in important recognition events and as the scaffold for the synthesis of probes of more complex phospholipids and glycolipids. The synthetic route that has been developed for DAG derivative **2**, indicated in Scheme 1, begins with commercially available diethyl L-tartrate (**3**). This C_2 symmetric precursor is employed to avoid mixtures of enantiomeric products during synthesis (*33*). Precursor **3** was converted to synthetic intermediate **7** via modified literature procedures (*34, 35*). Here, the diol of **3** is first protected via acetonide formation to provide fully protected tartrate analogue **4**, which is followed by ester reduction to bis-hydroxymethyl compound **5**. Next, monotosylation produces **6**,

Scheme 1. Synthetic Route to Head Group Azide-Tagged Diacylglycerol Scaffold 2

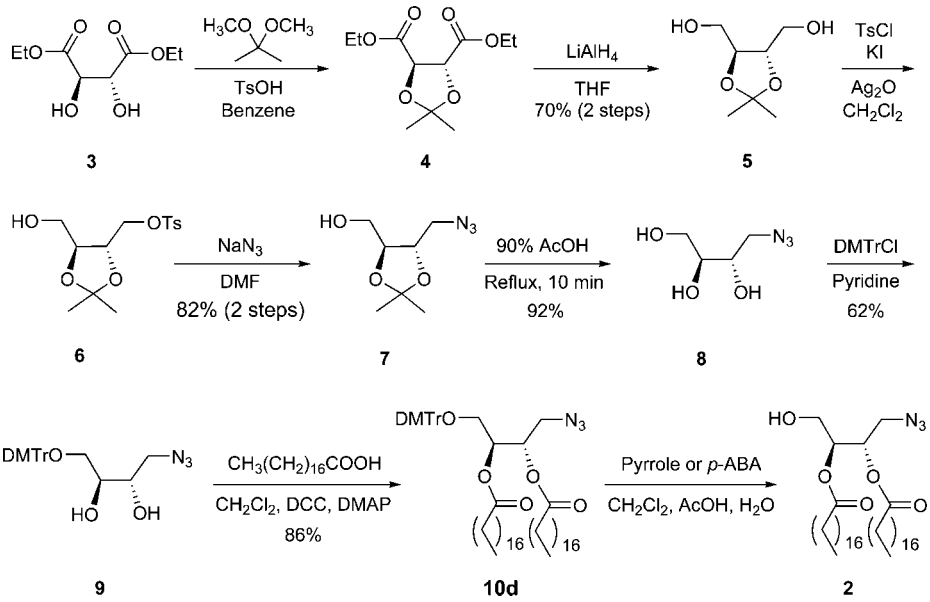

Scheme 2. Products Obtained from Deprotection and Acyl Migration of DAG analogues

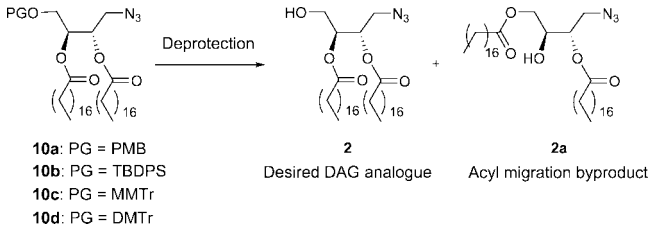

which is then substituted with azide to **7**. The final synthetic route to azido-DAG analogue **2** employs a dimethoxytrityl (DMTr) group to protect the primary hydroxyl group in the corresponding product (see discussion in the following paragraphs). However, the DMTr group would not survive the subsequent acetonide deprotection under acidic conditions, which is necessary to introduce the acyl chains of the lipid. However, an advantage of the DMTr group is that it can be selectively installed onto a primary over a secondary hydroxyl group (*57*). Thus, our synthetic route employs acetonide deprotection of **7** to triol **8** in acid followed by selective DMTr introduction to **9**. Next, the acyl chains are introduced using standard coupling conditions with stearic acid to **10d**. Finally, the DMTr group is removed under mild conditions to access azido-DAG analogue **2**.

A significant issue in the synthesis of **2** involved acyl group migration upon deprotection of intermediates of type **10** (Scheme 2). Here, byproduct **2a** arose from *sn*-2 to *sn*-3 migration in amounts that were dependent upon the protecting group that was employed as well as the reaction conditions. Such migrations in acylglycerols, which can occur in both acidic and basic conditions, complicate the synthesis and biological analysis of these compounds (*58*). We pursued a range of different protecting groups and deprotection conditions to determine the most effective approach. The first attempt employed a *para*-methoxybenzyl (PMB)-protected DAG analogue (**10a**). Deprotection was performed under typical oxidative conditions using DDQ and yielded **2a** as a byproduct (Table 1). Next, we switched to the *tert*-butyldiphenylsilyl (TBDPS) group of **10b** following previous reports of this group for successfully avoiding acyl migration (*59*). Initial deprotection using just TBAF yielded quantitative migration product (**2a**). While this

Table 1. Protecting Groups and Deprotection Conditions Employed to Avoid Acyl Migration

protecting group (PG)	deprotection conditions	% **2**[a]	% **2a**[a]
PMB (**10a**)	DDQ	85%	15%
TBDPS (**10b**)	TBAF	0%	100%
TBDPS (**10b**)	TBAF/AcOH	83%	17%
MMTr (**10c**)	*p*-TsOH	0%	100%
DMTr (**10d**)	$Cl_2HCCOOH$	0%	100%
DMTr (**10d**)	AcOH/*p*-ABA or pyrrole	98%	2%
DMTr (**10d**)	AcOH/pyrrole or *p*-ABA/direct click	>99.5%	<0.5%

[a] Approximate percentages of **2** and **2a** were determined by analysis of ^{1}H NMR spectra.

was minimized through TBAF deprotection in the presence of acetic acid (*59, 60*), the migration product still appeared in an amount similar to that of PMB deprotection. Modification to install the monomethoxytrityl (MMT) of **10c** unfortunately once again led to quantitvative migration product upon deprotection using acids such as *para*-toluenesulfonic acid.

Failure of each of these approaches indicated that the described system is particularly prone to undergoing migration. This is likely attributable to the increased steric bulk in the form of the added azidomethyl group, which could increase the driving force for migration of the neighboring *sn*-2 acyl chain to the less substituted *sn*-3 position. Finally, the DMTr protecting group was pursued, producing protected DAG **10d**, as it can be removed under mildly acidic conditions (*57*) and has been used in *sn*-3 hydroxyl protection (*61*). Here, deprotection using acetic acid was quite effective in reducing migration to essentially trace amounts. We initially employed traditional DMTr removal conditions, including the use of pyrrole to scavenge the intermediate dimethoxytrityl cation (*62*). However, the resulting DMTr-pyrrole adduct was found to complicate purification due to chromatographic overlap with **2**. This was especially the case because rapid chromatographic separation of all DAG analogues containing the unprotected *sn*-3 hydroxyl group was necessary to avoid on-column acyl migration, which has been previously documented (*58*). As a result, we instead employed *para*-aminobenzoic acid (*p*-ABA) for cation scavenging as the pendant carboxylic acid decreases the chromatographic mobility of the resulting DMTr-adduct. While this decreased the amount of trityl adduct impurity present following fast chromatography, it could not be completely removed. However, the trityl byproduct could be easily purified out

Scheme 3. Direct Derivatization of Azido-DAG Core 2 for Convenient Incorporation of Reporter Groups

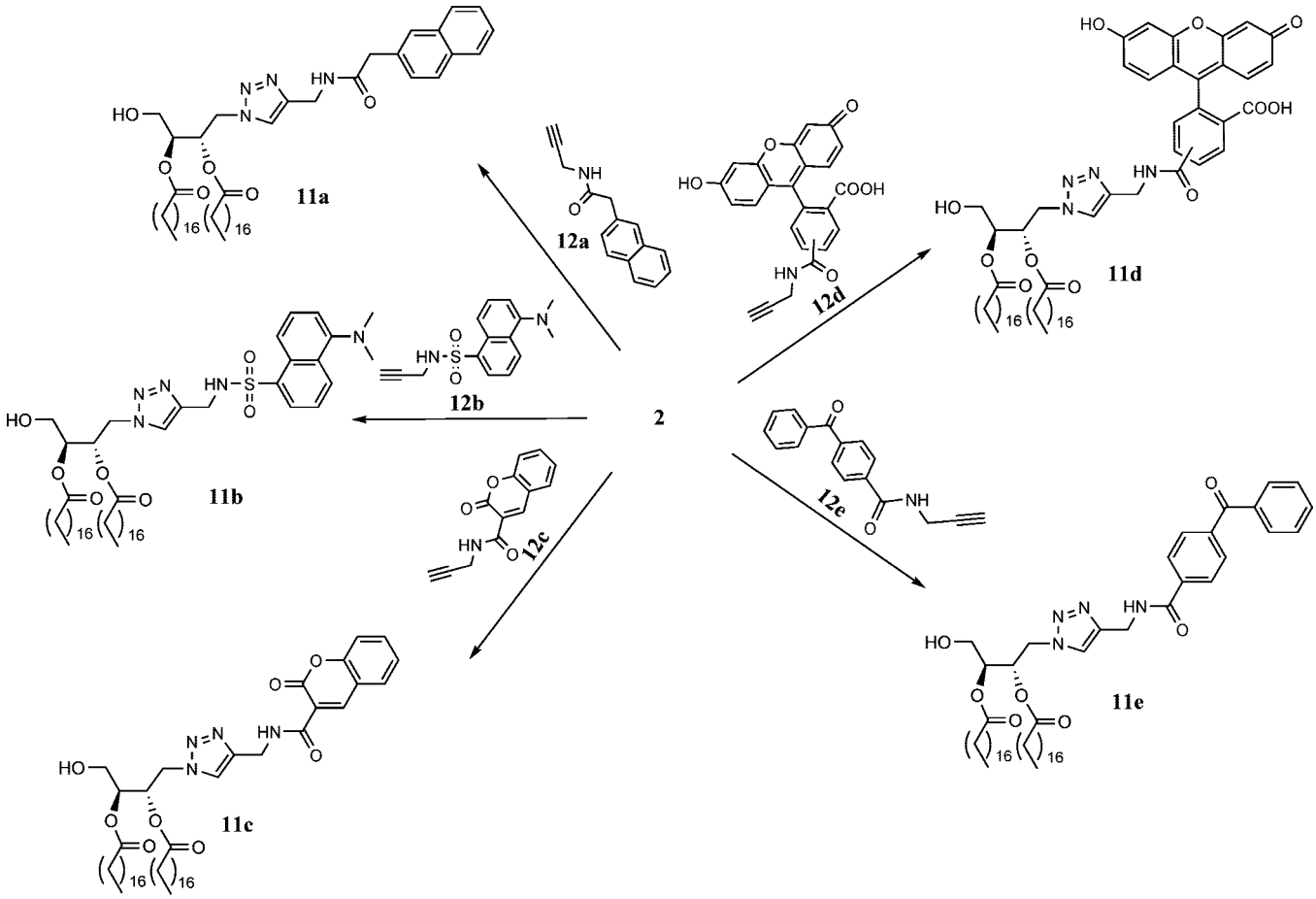

following subsequent azido-DAG functionalization, and thus compound **2** was directly used for the next step with some trityl adduct impurity.

Following the synthesis of DAG scaffold **2**, we have extended efforts to derivatization of this core structure to showcase the ability to produce a variety of probes in a single convenient step. Here, we have utilized the 1,3-dipolar cycloaddition reaction to incorporate fluorescent (**11a**−**d**) and photoaffinity (**11e**) groups onto **2** through reaction with alkyne reagents **12a**−**e**, which were accessed in one step from propargylamine (Scheme 3). The mild conditions of the azide−alkyne cycloaddition are particularly beneficial for producing functionalized DAGs by avoiding the aforementioned acyl migration byproducts. Among the fluorophores that have been incorporated are multiple Förster resonance energy transfer (FRET) pairs. Probes labeled with FRET pairs are useful for the direct detection of changes in proximity of ligands during various processes due to the sensitivity of energy transfer to distance (*63*−*65*). Installation of a photoaffinity tag is advantageous for performing photo-cross-linking studies to characterize protein binding, such as for the mapping of the location of binding domains on receptor proteins (*66*). Functionalization at the headgroup *sn*-1 position is particularly beneficial for these studies in order to present the tag in close proximity to the bound protein and thus maximize fluorescent signal transduction or cross-linking efficiency. This strategy for probe development is beneficial, as it allows for direct access to a range of functionalized lipids in a single step. Thus, a panel of compounds can be efficiently accessed and implemented for studies to determine those that are particularly suited to a given investigation.

Having developed a series of functionalized DAG derivatives, we next sought to analyze their efficacy as probes for characterizing DAG-binding interactions. In order to demonstrate that the newly synthesized DAG probes retain the typical binding properties of DAG effectors, we monitored the binding of a well-known DAG receptor, PKCδ, to lipid vesicles containing the different analogues. To do so, we performed SPR equilibrium binding analysis using POPC vesicles as a control and POPC/POPS/DAG (78:20:2 containing varying DAG probes) as an active surface. We first performed binding experiments with DiC_{18} since the binding of PKCδ to vesicles containing this ligand has been well-documented (*47*). PKCδ bound with 24 nM affinity to these vesicles as shown in Table 2. Next, we systematically analyzed the binding efficacy of each of the described DAG reporters. As shown by the equilibrium binding constants (or K_d values) in Table 2 and binding isotherms in Figure 2, all DAG reporters displayed analogous properties to DiC_{18} for PKCδ recruitment with K_d values ranging from 16 to 28 nM.

Table 2. Binding properties of PKCδ with different DAG analogues

lipid	K_d (nM) using POPC/POPS/DAG (78:20:2)
DiC_{18}	24 ± 4
Synthetic DiC_{18}	19 ± 2
Naphthyl-DAG (11a)	16 ± 3
Dansyl-DAG (11b)	20 ± 3
Coumarin-DAG (11c)	18 ± 2
5(6)-CBF DAG (11d)	28 ± 5
Benzophenone-DAG (11e)	21 ± 3

The first quantitative analysis of these DAG derivatives illustrates their ability to mimic DAG despite the fact that each compound contains a bulky reporter appended at the headgroup. Thus, these results validate the synthetic introduction of

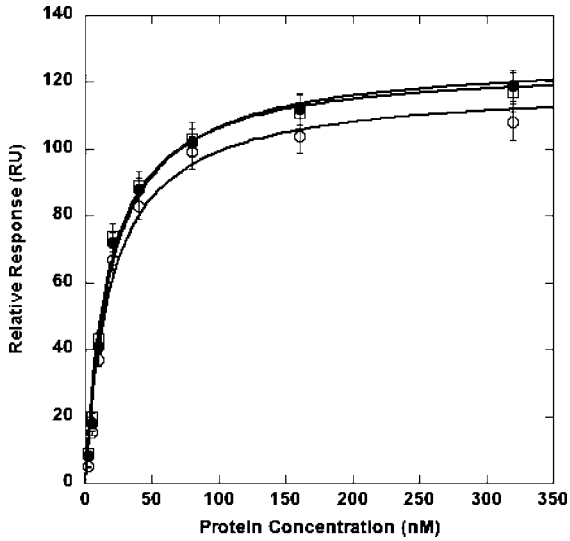

Figure 2. Affinity of PKCδ for DAG-containing membranes determined by SPR analysis. SPR measurements were used to determine K_ds of PKCδ for POPC/POPS/DAG (78:20:2) vesicles where DAG represents synthetic DAGs reported in this manuscript (see Table 2 or Scheme 3). PKCδ was injected at varying concentrations at a flow rate of 5 μL/min and the subsequent association and dissociation were monitored. From these plots, the saturation response (R_{eq}, equilibrium value) was determined. In order to calculate the K_d of PKCδ for the DAG containing vesicles, the equilibrium value (saturating response (R_{eq}) of protein bound) determined from each sensorgram was then plotted versus respective protein concentration (2, 5, 10, 20, 40, 80, 160, and 320 nM).The solid lines represent theoretical curves constructed from R_{max} and K_d values determined by nonlinear least-squares analysis of the isotherms using $R_{eq} = R_{max}/(1 + K_d/C)$. Representative curves are shown for three different DAGs tested, synthetic-DAG (•), dansyl-DAG (○), and coumarin-DAG (□).

functionality at the *sn*-1 position as an advantageous approach for obtaining effective headgroup-derivatized glycerolipid probes. These data also demonstrate the relevance of these novel probes for use as robust reporters of important biological interactions. We are currently pursuing multiple avenues for extending these investigations. First, we are implementing these compounds for the characterization of protein−membrane binding events at the molecular level. Second, we are building upon the DAG core of these structures to access probes for more structurally complex glycerolipids such as PA, PS, and the PIP_ns.

ACKNOWLEDGMENT

M.D.B. acknowledges bioorganic colleagues at UTK, Drs. David Baker, Shane Foister, and Shawn Campagna, as well as a collaborator, Dr. Wonhwa Cho, for beneficial discussions. M.D.B. also thanks the University of Tennessee for funding, and J.C.R. acknowledges a Summer Undergraduate Research Fellowship from Pfizer Global Research. R.V.S. acknowledges a Biomedical Research Grant from Indiana University School of Medicine and a grant from the American Cancer Society (IRG-84-002-22).

Supporting Information Available: Further synthetic procedures and characterizations are included. This material is available free of charge via the Internet at http://pubs.acs.org.

LITERATURE CITED

(1) Cho, W. H., and Stahelin, R. V. (2005) Membrane-protein interactions in cell signaling and membrane trafficking. *Annu. Rev. Biophys. Biomol. Struct. 34*, 119–151.
(2) Colon-Gonzalez, F., and Kazanietz, M. G. (2006) C1 domains exposed: From diacylglycerol binding to protein-protein interactions. *Biochim. Biophys. Acta 1761*, 827–837.
(3) Testerink, C., and Munnik, T. (2005) Phosphatidic acid: a multifunctional stress signaling lipid in plants. *Trends Plant Sci. 10*, 368–375.
(4) Stace, C. L., and Ktistakis, N. T. (2006) Phosphatidic acid- and phosphatidylserine-binding proteins. *Biochim. Biophys. Acta 1761*, 913–926.
(5) McLaughlin, S., Wang, J. Y., Gambhir, A., and Murray, D. (2002) PIP2 and proteins: Interactions, organization, and information flow. *Annu. Rev. Biophys. Biomol. Struct. 31*, 151–175.
(6) Lemmon, M. A. (2003) Phosphoinositide recognition domains. *Traffic 4*, 201–213.
(7) Prestwich, G. D. (2004) Phosphoinositide signaling: From affinity probes to pharmaceutical targets. *Chem. Biol. 11*, 619–637.
(8) Di Paolo, G., and De Camilli, P. (2006) Phosphoinositides in cell regulation and membrane dynamics. *Nature 443*, 651–657.
(9) Lemmon, M. A. (2008) Membrane recognition by phospholipid-binding domains. *Nature Rev. Mol. Cell Biol. 9*, 99–111.
(10) Hurley, J. H. (2006) Membrane binding domains. *Biochim. Biophys. Acta 1761*, 805–811.
(11) Schultz, A., Ling, M., and Larsson, C. (2004) Identification of an amino acid residue in the protein kinase CC1b domain crucial for its localization to the Golgi network. *J. Biol. Chem. 279*, 31750–31760.
(12) Griner, E. M., and Kazanietz, M. G. (2007) Protein kinase C and other diacylglycerol effectors in cancer. *Nat. Rev. Cancer 7*, 281–294.
(13) Mackay, H. J., and Twelves, C. J. (2007) Targeting the protein kinase C family: are we there yet? *Nat. Rev. Cancer 7*, 554–562.
(14) Sampson, S. R., and Cooper, D. R. (2006) Specific protein kinase C isoforms as transducers and modulators of insulin signaling. *Mol. Genet. Metab. 89*, 32–47.
(15) Carrasco, S., and Merida, I. (2007) Diacylglycerol, when simplicity becomes complex. *Trends Biochem. Sci. 32*, 27–36.
(16) Gomez-Fernandez, J. C., and Corbalan-Garcia, S. (2007) Diacylglycerols, multivalent membrane modulators. *Chem. Phys. Lipids 148*, 1–25.
(17) Spitaler, M., and Cantrell, D. A. (2004) Protein kinase C and beyond. *Nat. Immunol. 5*, 785–790.
(18) Gutcher, I., Webb, P. R., and Anderson, N. G. (2003) The isoform-specific regulation of apoptosis by protein kinase C. *Cell. Mol. Life Sci. 60*, 1061–1070.
(19) Wender, P. A., DeBrabander, J., Harran, P. G., Jimenez, J. M., Koehler, M. F. T., Lippa, B., Park, C. M., Siedenbiedel, C., and Pettit, G. R. (1998) The design, computer modeling, solution structure, and biological evaluation of synthetic analogs of bryostatin 1. *Proc. Natl. Acad. Sci. U.S.A. 95*, 6624–6629.
(20) Ghosh, S., Strum, J. C., Sciorra, V. A., Daniel, L., and Bell, R. M. (1996) Raf-1 kinase possesses distinct binding domains for phosphatidylserine and phosphatidic acid - Phosphatidic acid regulates the translocation of Raf-1 in 12-*O*-tetradecanoylphorbol-13-acetate-stimulated Madin-Darby canine kidney cells. *J. Biol. Chem. 271*, 8472–8480.
(21) Mott, H. R., Carpenter, J. W., Zhong, S., Ghosh, S., Bell, R. M., and Campbell, S. L. (1996) The solution structure of the Raf-1 cysteine-rich domain: A novel Ras and phospholipid binding site. *Proc. Natl. Acad. Sci. U.S.A. 93*, 8312–8317.
(22) Improta-Brears, T., Ghosh, S., and Bell, R. M. (1999) Mutational analysis of Raf-1 cysteine rich domain: Requirement for a cluster of basic aminoacids for interaction with phosphatidylserine. *Mol. Cell. Biochem. 198*, 171–178.
(23) Rizzo, M. A., Shome, K., Vasudevan, C., Stolz, D. B., Sung, T. C., Frohman, M. A., Watkins, S. C., and Romero, G. (1999) Phospholipase D and its product, phosphatidic acid, mediate agonist-dependent Raf-1 translocation to the plasma membrane and the activation of the mitogen-activated protein kinase pathway. *J. Biol. Chem. 274*, 1131–1139.
(24) Rizzo, M. A., Shome, K., Watkins, S. C., and Romero, G. (2000) The recruitment of Raf-1 to membranes is mediated by direct interaction with phosphatidic acid and is independent of association with Ras. *J. Biol. Chem. 275*, 23911–23918.

(25) Andresen, B. T., Rizzo, M. A., Shome, K., and Romero, G. (2002) The role of phosphatidic acid in the regulation of the Ras/MEK/Erk signaling cascade. *FEBS Lett. 531*, 65–68.

(26) Hekman, M., Hamm, H., Villar, A. V., Bader, B., Kuhlmann, J., Nickel, J., and Rapp, U. R. (2002) Associations of B- and C-raf with cholesterol, phosphatidylserine, and lipid second messengers - Preferential binding of Raf to artificial lipid rafts. *J. Biol. Chem. 277*, 24090–24102.

(27) Ghosh, S., Moore, S., Bell, R. M., and Dush, M. (2003) Functional analysis of a phosphatidic acid binding domain in human Raf-1 kinase - Mutations in the phosphatidate binding domain lead to tail and trunk abnormalities in developing zebrafish embryos. *J. Biol. Chem. 278*, 45690–45696.

(28) Wittinghofer, A., and Waldmann, H. (2000) Ras - A molecular switch involved in tumor formation. *Angew. Chem., Int. Ed. 39*, 4193–4214.

(29) Gupta, S., Ramjaun, A. R., Haiko, P., Wang, J., Warne, P. H., Nicke, B., Nye, E., Stamp, G., Alitalo, K., and Downward, J. (2007) Binding of Ras to phosphoinositide 3-kinase p110α is required for Ras-driven tumorigenesis in mice. *Cell 129*, 957–968.

(30) Overduin, M., and Cheever, M. L. (2001) Signaling with phosphoinositides: better than binary. *Mol. Intervent. 1*, 150–159.

(31) Misra, S., Miller, G. J., and Hurley, J. H. (2001) Recognizing phosphatidylinositol 3-phosphate. *Cell 107*, 559–562.

(32) Pendaries, C., Tronchere, H., Plantavid, M., and Payrastre, B. (2003) Phosphoinositide signaling disorders in human diseases. *FEBS Lett. 546*, 25–31.

(33) Rzepecki, P. W., and Prestwich, G. D. (2002) Synthesis of hybrid lipid probes: Derivatives of phosphatidylethanolamine-extended phosphatidylinositol 4,5-bisphosphate (Pea-PIP2). *J. Org. Chem. 67*, 5454–5460.

(34) Fernandes, R. A. (2007) An efficient synthesis of (-)-posticlure: The sex pheromone of Orgyia postica. *Eur. J. Org. Chem.* 5064–5070.

(35) Wroblewski, A. E., and Glowacka, I. E. (2005) Enantiomerically pure 4-amino-1,2,3-trihydroxybutylphosphonic acids. *Tetrahedron 61*, 11930–11938.

(36) Glacon, V., Benazza, M., El Anzi, A., Beaupere, D., and Demailly, G. (2004) Synthesis of alpha,omega-diazidoalditol derivatives via both bis- or tris-cyclic sulfites and peracetylated alpha,omega-dibromoalditols as bielectrophilic intermediates. *J. Carbohydr. Chem. 23*, 95–110.

(37) Stahelin, R. V., Digman, M. A., Medkova, M., Ananthanarayanan, B., Rafter, J. D., Melowic, H. R., and Cho, W. H. (2004) Mechanism of diacylglycerol-induced membrane targeting and activation of protein kinase C delta. *J. Biol. Chem. 279*, 29501–29512.

(38) Stahelin, R. V., and Cho, W. H. (2001) Differential roles of ionic, aliphatic, and aromatic residues in membrane-protein interactions: A surface plasmon resonance study on phospholipases A(2). *Biochemistry 40*, 4672–4678.

(39) Stahelin, R. V., Long, F., Diraviyam, K., Bruzik, K. S., Murray, D., and Cho, W. H. (2002) Phosphatidylinositol 3-phosphate induces the membrane penetration of the FYVE domains of Vps27p and Hrs. *J. Biol. Chem. 277*, 26379–26388.

(40) Mammen, M., Choi, S. K., and Whitesides, G. M. (1998) Polyvalent interactions in biological systems: Implications for design and use of multivalent ligands and inhibitors. *Angew. Chem., Int. Ed. 37*, 2755–2794.

(41) Kiessling, L. L., Gestwicki, J. E., and Strong, L. E. (2006) Synthetic multivalent ligands as probes of signal transduction. *Angew. Chem., Int. Ed. 45*, 2348–2368.

(42) Irie, K., Oie, K., Nakahara, A., Yanai, Y., Ohigashi, H., Wender, P. A., Fukuda, H., Konishi, H., and Kikkawa, U. (1998) Molecular basis for protein kinase C isozyme-selective binding: The synthesis, folding, and phorbol ester binding of the cysteine-rich domains of all protein kinase C isozymes. *J. Am. Chem. Soc. 120*, 9159–9167.

(43) Prestwich, G. D. (1996) Touching all the bases: Synthesis of inositol polyphosphate and phosphoinositide affinity probes from glucose. *Acc. Chem. Res. 29*, 503–513.

(44) Thum, O., Chen, J., and Prestwich, G. D. (1996) Synthesis of a photoaffinity analogue of phosphatidylinositol 3,4-bisphosphate, an effector in the phosphoinositide 3-kinase signaling pathway. *Tetrahedron Lett. 37*, 9017–9020.

(45) Chaudhary, A., Chen, J., Gu, Q. M., Witke, W., Kwiatkowski, D. J., and Prestwich, G. D. (1998) Probing the phosphoinositide 4,5-bisphosphate binding site of human profilin I. *Chem. Biol. 5*, 273–281.

(46) Manifava, M., Thuring, J., Lim, Z. Y., Packman, L., Holmes, A. B., and Ktistakis, N. T. (2001) Differential binding of traffic-related proteins to phosphatidic acid- or phosphatidylinositol (4,5)-bisphosphate-coupled affinity reagents. *J. Biol. Chem. 276*, 8987–8994.

(47) Lim, Z. Y., Thuring, J. W., Holmes, A. B., Manifava, M., and Ktistakis, N. T. (2002) Synthesis and biological evaluation of a PtdIns(4,5)P-2 and a phosphatidic acid affinity matrix. *J. Chem. Soc., Perkin Trans. 1*, 1067–1075.

(48) Picq, M., Huang, Y., Lagarde, M., Doutheau, A., and Nemoz, G. (2002) Synthesis of photoreactive phosphatidic acid analogues displaying activatory properties on cyclic AMP-phosphodiesterases. Photoaffinity labeling of an isoform of phosphodiesterase. *J. Med. Chem. 45*, 1678–1685.

(49) Chen, J., Profit, A. A., and Prestwich, G. D. (1996) Synthesis of photoactivatable 1,2-*O*-diacyl-*sn*-glycerol derivatives of L-phosphatidyl-D-*myo*-inositol 4,5-bisphosphate (PtdInsP(2)) and 3,4,5-trisphosphate (PtdInsP(3)). *J. Org. Chem. 61*, 6305–6312.

(50) Lewis, W. G., Green, L. G., Grynszpan, F., Radic, Z., Carlier, P. R., Taylor, P., Finn, M. G., and Sharpless, K. B. (2002) Click chemistry in situ: Acetylcholinesterase as a reaction vessel for the selective assembly of a femtomolar inhibitor from an array of building blocks. *Angew. Chem., Int. Ed. 41*, 1053–1057.

(51) Kolb, H. C., Finn, M. G., and Sharpless, K. B. (2001) Click chemistry: Diverse chemical function from a few good reactions. *Angew. Chem., Int. Ed. 40*, 2004–2021.

(52) Rostovtsev, V. V., Green, L. G., Fokin, V. V., and Sharpless, K. B. (2002) A stepwise Huisgen cycloaddition process: Copper(I)-catalyzed regioselective "ligation" of azides and terminal alkynes. *Angew. Chem., Int. Ed. 41*, 2596–2599.

(53) Saxon, E., Armstrong, J. I., and Bertozzi, C. R. (2000) A "traceless" Staudinger ligation for the chemoselective synthesis of amide bonds. *Org. Lett. 2*, 2141–2143.

(54) Saxon, E., and Bertozzi, C. R. (2000) Cell surface engineering by a modified Staudinger reaction. *Science 287*, 2007–2010.

(55) Kohn, M., and Breinbauer, R. (2004) The Staudinger ligation-A gift to chemical biology. *Angew. Chem., Int. Ed. 43*, 3106–3116.

(56) Spencer, T. A., Wang, P. Z., Li, D. S., Russel, J. S., Blank, D. H., Huuskonen, J., Fielding, P. E., and Fielding, C. J. (2004) Benzophenone-containing cholesterol surrogates: synthesis and biological evaluation. *J. Lipid Res. 45*, 1510–1518.

(57) Smith, M., Khorana, H. G., Rammler, D. H., and Goldberg, I. H. (1962) Studies on polynucleotides 0.14. Specific synthesis of C3′-C5′ interrribonucleotide linkage - syntheses of uridylyl-(3′-5′)-uridine and uridylyl-(3′-5′)-adenosine. *J. Am. Chem. Soc. 84*, 430.

(58) Kodali, D. R., Tercyak, A., Fahey, D. A., and Small, D. M. (1990) Acyl migration in 1,2-dipalmitoyl-*sn*-glycerol. *Chem. Phys. Lipids 52*, 163–170.

(59) Jiang, G. W., Xu, Y., and Prestwich, G. D. (2006) Practical enantiospecific syntheses of lysobisphosphatidic acid and its analogues. *J. Org. Chem. 71*, 934–939.

(60) Baker, D. C., Haskell, T. H., Putt, S. R., and Sloan, B. J. (1979) Prodrugs of 9-(beta-D-arabinofuranosyl)adenine 0.2. Synthesis and evaluation of a number of 2′,3′-di-*O*-acyl derivatives and 3′,5′-di-*O*-acyl derivatives. *J. Med. Chem. 22*, 273–279.

(61) Kubiak, R. J., and Bruzik, K. S. (2003) Comprehensive and uniform synthesis of all naturally occurring phosphorylated phosphatidylinositols. *J. Org. Chem. 68*, 960–968.
(62) Reese, C. B., and Yan, H. B. (2002) Solution phase synthesis of ISIS 2922 (Vitravene) by the modified H-phosphonate approach. *J. Chem. Soc., Perkin Trans. 1*, 2619–2633.
(63) Wu, P., and Brand, L. (1994) Resonance energy transfer: methods and applications. *Anal. Biochem. 218*, 1–13.
(64) Clegg, R. M. (1995) Fluorescence resonance energy transfer. *Curr. Opin. Biotechnol. 6*, 103–110.
(65) Sapsford, K. E., Berti, L., and Medintz, I. L. (2006) Materials for fluorescence resonance energy transfer analysis: Beyond traditional donor-acceptor combinations. *Angew. Chem., Int. Ed. 45*, 4562–4588.
(66) Hatanaka, Y., and Sadakane, Y. (2002) Photoaffinity labeling in drug discovery and developments: Chemical gateway for entering proteomic frontier. *Curr. Top. Med. Chem. 2*, 271–288.

BC8001002

Supporting Information

1) Original synthetic route to PMB-protected DAG analog (**10a**): Azido-DAG analog **2** was first pursued through PMB- and TBDPS-protection as shown in the scheme below. A modified literature procedure [1] was followed to convert diethyl L-tartrate (**3**) to intermediate **13a**.

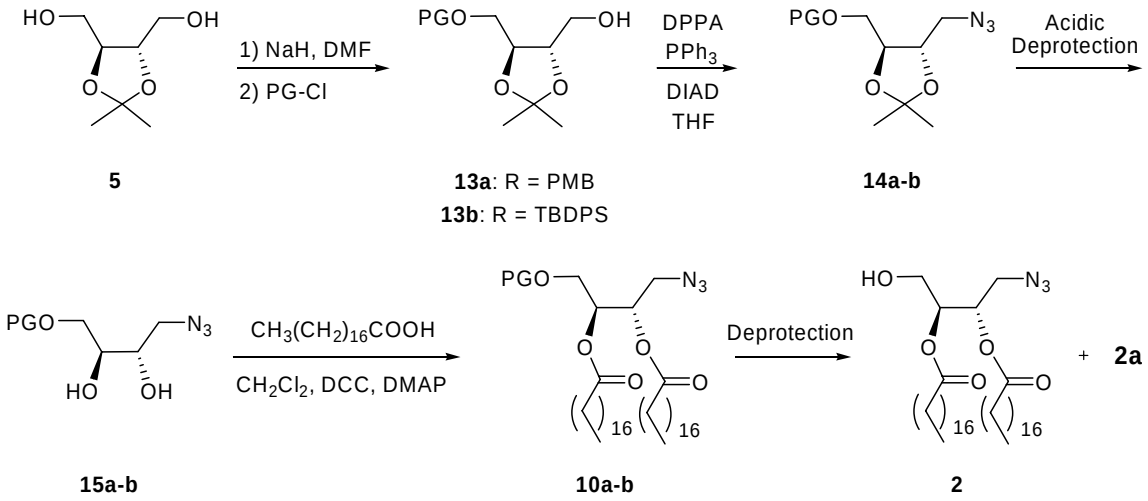

1A) PMB-protection experimental procedures:

((4S,5S)-5-((4-Methoxybenzyloxy)methyl-2,2-dimethyl-1,3-dioxolan-4-yl)methanol (13a). A solution of sodium hydride (162 mg, 4.06 mmol, 60% purity) in anhydrous DMF (20 mL) was prepared in a flame-dried round-bottom flask under nitrogen and cooled to 0 °C with stirring. Diol **5** (658 mg, 4.06 mmol) was dissolved in anhydrous DMF (20 mL) and added dropwise. Stirring was continued at 0 °C for 10 min and then at room temperature for 20 min. At this point the reaction mixture was cooled to 0 °C and 4-methoxybenzyl chloride (606 µL, 4.47 mmol) was added dropwise. The mixture was then stirred at room temperature overnight. The reaction was quenched with ~50 mL water, and the mixture was extracted with dichloromethane (2 x 50 mL). The organic layer was then dried with magnesium sulfate and filtered, and the solvent was removed by rotary evaporation. Column chromatography with silica gel and a gradient solvent system of 20 to 60% ethyl acetate/hexanes afforded **13a** as a clear oil (908 mg, 79%).

^{1}H NMR (300MHz, $CDCl_3$) δ 7.24 (d, *J* = 8.7 Hz, 2H), 6.87 (d, *J* = 8.7 Hz, 2H), 4.56-4.47 (m, 2H), 4.05-3.99 (m, 1H), 3.94-3.88 (m, 1H), 3.79 (s, 3H), 3.78-3.63 (m, 3H), 3.54-3.49 (m, 1H), 2.56-2.52 (m, 1H), 1.41 (s, 6H); ^{13}C NMR (62.9 MHz, $CDCl_3$) δ 159.4, 129.6, 129.5, 113.9, 109.3, 79.8, 76.5, 73.4, 70.1, 62.5, 55.2, 27.0; HRMS $[M-H]^+$ cacld: 281.13890, found: 281.13718

(4S,5S)-4-(Azidomethyl)-5-((4-methoxybenzyloxy)methyl)-2,2-dimethyl-1,3-dioxolane (14a). Alcohol **13a** (589 mg, 2.09 mmol) was dissolved in dry THF (15 mL) along with triphenylphosphine (1.096 g, 4.18 mmol). The solution was placed under nitrogen and diisopropyl azodicarboxylate (810 µL, 4.18 mmol) was added with stirring. Diphenylphosphoryl azide (901 µL, 4.18 mmol) was dissolved in dry THF (5 mL) and added to the reaction, which was then stirred overnight at room temperature. The solvent was removed with a rotary evaporator, and column chromatography with silica

gel and a gradient solvent system of 10 to 20% ethyl acetate/hexanes afforded **14** as a clear oil (507 mg, 79%).

^{1}H NMR (300 MHz, $CDCl_3$) δ 7.23 (d, *J* = 8.6 Hz, 2H), 6.87 (d, *J* = 8.6 Hz, 2H), 4.53-4.45 (m, 2H), 4.06-3.96 (m, 2H), 3.79 (s, 3H), 3.63-3.47 (m, 3H), 3.30-3.24 (m, 1H), 1.45 (s, 3H), 1.41 (s, 3H); ^{13}C NMR (75 MHz, $CDCl_3$) δ 159.4, 129.8, 129.3, 113.8, 109.9, 78.1, 76.5, 73.2, 69.9, 55.2, 52.0, 27.0, 26.8; HRMS $[M\text{-}N_2+H]^+$ calcd: 280.15488, found: 280.15483

(2S,3S)-1-Azido-4-(4-methoxybenzyloxy)butane-2,3-diol (15a). Compound **14a** (820 mg, 2.67 mmol) was dissolved in THF (14 mL) and 1 N HCl (14 mL) was added. The reaction was stirred at room temperature for 48 h and was then quenched with saturated sodium bicarbonate. The mixture was then diluted with water (50 mL) and extracted with dichloromethane (2 x 50 mL). The organic layer was then dried with magnesium sulfate and filtered, and the solvent was removed by rotary evaporation. Column chromatography with silica gel and a gradient solvent system of 50 to 90% ethyl acetate/hexanes afforded **15a** as a clear oil (627 mg, 88%).

^{1}H NMR (250 MHz, $CDCl_3$) δ 7.23 (d, *J* = 8.5 Hz, 2H), 6.88 (d, *J* = 8.5 Hz, 2H), 4.50-4.40 (m, 2H), 3.79 (s, 3H) 3.79-3.72 (m, 2H), 3.55-3.53 (m, 2H), 3.37-3.33 (m, 2H), 3.19 (*b* s, 1H), 3.06 (*b* s, 1H); ^{13}C NMR (62.9 MHz, $CDCl_3$) δ 159.5, 129.6, 129.5, 114.0, 73.3, 71.7, 71.3, 70.2, 55.3, 53.6; HRMS $[M\text{-}N_2+H]^+$ calcd: 240.12358, found: 240.12340

(2S,3S)-1-Azido-4-(4-methoxybenzyloxy)butane-2,3-diyl distearate (10a). Diol **15a** (375.2 mg, 1.40 mmol) was dissolved in anhydrous dichloromethane (15 mL). With stirring was added stearic acid (1.194 g, 4.2 mmol), 4-dimethylaminopyridine (188 mg, 1.54 mmol), and *N,N*-dicyclohexylcarbodiimide (866 mg, 4.2 mmol). The reaction was stirred at room temperature for 3 h at which point it was filtered. Column chromatography with silica gel and a gradient solvent system of 0 to 10% ethyl acetate/hexanes afforded **10a** as a white solid (1 g, 89%).

^{1}H NMR (300 MHz, $CDCl_3$) δ 7.22 (d, *J* = 8.7 Hz, 2H), 6.87 (d, *J* = 8.7 Hz, 2H), 5.34-5.29 (m, 1H), 5.25-5.20 (m, 1H), 4.49-4.37 (m, 2H), 3.80 (s, 3H), 3.52-3.44 (m, 3H), 3.37-3.31 (m, 1H), 2.34-2.29 (m, 4H), 1.63-1.58 (m, 4H), 1.25 (*b* s, 56H), 0.88 (t, *J* = 6.8 Hz, 6H); ^{13}C NMR (75 MHz, $CDCl_3$) δ 172.9, 172.8, 159.4, 129.5, 129.46, 113.9, 73.0, 70.59, 70.55, 67.5, 55.2, 51.0, 34.3, 34.2, 32.0, 29.73, 29.69, 29.5, 29.4, 29.3, 29.2, 25.0, 24.9, 22.7, 14.1; HRMS $[M\text{-}N_2+H]^+$ calcd: 772.64551, found: 772.64821

(2S,3S)-1-Azido-4-hydroxybutane-2,3-diyl distearate (2). Compound **10a** (592 mg, 0.740 mmol) was dissolved in dichloromethane (7 mL) and 2,3-dichloro-5,6-dicyano-1,4-benzoquinone (DDQ) (410 mg, 1.81 mmol) and water (700 µL, 10%) were added with stirring. Stirring was continued at room temperature for 6 h at which point the reaction was quenched with saturated sodium bicarbonate. The reaction mixture was extracted with dichloromethane (2 x 50 mL), and the organic layer was dried with magnesium sulfate and filtered. The solvent was then removed by rotary evaporation. The crude product was placed on a high vacuum line overnight to assist in the removal of volatile side products. Column chromatography with silica gel and a gradient solvent system of 0 to 20% ethyl acetate/hexanes afforded **2** as a white solid (426 mg, 85%). See paper for characterizations.

1B) TBDPS-protection experimental procedures:

((4S,5S)-5-((*tert*-butyldiphenylsilyloxy)methyl-2,2-dimethyl-1,3-dioxolan-4-yl)methanol (13b). Compound (**13b**) was prepared following published literature procedure [2] (80%).

(4S,5S)-4-(Azidomethyl)-5-((*tert*-butyldiphenylsilyloxy)methyl)-2,2-dimethyl-1,3-dioxolane (14b). To a solution of alcohol **13b** (440 mg, 1.1 mmol) in anhydrous THF (12 mL) at room temperature was added diisopropyl azodicarboxylate (426 µL, 2.2 mmol) and triphenylphosphine (577 mg, 2.2 mmol). Diphenylphosphoryl azide (474 µL, 2.2 mmol) was dissolved in dry THF (3 mL) and added to the reaction which was stirred overnight at room temperature. After the reaction was complete the mixture was concentrated under reduced pressure and column chromatography with silica gel and a gradient solvent system of 0 to 10% ethyl acetate/hexanes afforded **14b** as a pale yellow oil (380 mg, 81%).

$[\alpha]_D^{296K}$ -25.97 (c = 1.155, $CHCl_3$); ^{1}H NMR (300 MHz, $CDCl_3$) δ 7.71-7.66 (m, 4H), 7.49-7.39 (m, 6H), 4.20-4.15 (m, 1H), 4.02-3.96 (m, 1H), 3.87-3.73 (m, 2H), 3.63-3.57 (m, 1H), 3.33-3.27 (m, 1H), 1.48 (s, 3H), 1.42 (s, 3H), 1.09 (s, 9H); ^{13}C NMR (75 MHz, $CDCl_3$) δ 135.5, 132.9, 132.8, 129.9, 129.8, 127.8, 109.7, 78.0, 77.6, 64.0, 52.2, 27.0, 26.9, 26.8, 19.2; HRMS [M-N_2+H]+ calcd: 398.21514, found: 398.21530

(2S,3S)-1-Azido-4-(*tert*-butyldiphenylsilyloxy)butane-2,3-diol (15b). Azide **14b** (350 mg, 0.822 mmol) was dissolved in 8 mL 90% acetic acid and heated at reflux for 10 minutes. The reaction was then slowly cooled to room temperature and concentrated under reduced pressure and purified via column chromatography with silica gel and a gradient solvent system of 10 to 50% ethyl acetate/hexanes to afford **15b** as a pale yellow oil (235 mg, 74%).

$[\alpha]_D^{296K}$ +5.21 (c = 0.845, $CHCl_3$); ^{1}H NMR (300 MHz, $CDCl_3$) δ 7.69-7.65 (m, 4H), 7.47-7.39 (m, 6H), 3.88-3.66 (m, 4H), 3.44-3.32 (m, 2H), 2.89-2.87 (m, 1H), 2.72-2.70 (m, 1H), 1.09 (s, 9H); ^{13}C NMR (75 MHz, $CDCl_3$) δ 135.49, 135.45, 132.5, 132.4, 130.0, 127.9, 71.1, 70.9, 65.6, 53.6, 26.8, 19.1; HRMS [M+NH4]+ calcd: 403.21654, found: 403.21717

(2S,3S)-1-Azido-4-(*tert*-butyldiphenylsilyloxy)butane-2,3-diyl distearate (10b). Diol **15b** (220 mg, 0.571 mmol), stearic acid (487 mg, 1.71 mmol), 4-dimethylaminopyridine (209 mg, 1.71 mmol), and dicyclohexylcarbodiimide (353 mg, 1.71 mmol) were combined in dichloromethane (8 mL). The reaction was stirred at room temperature overnight at which point it was filtered. Column chromatography with silica gel and a gradient solvent system of 0 to 10% ethyl acetate/hexanes afforded **10b** as a white solid (524 mg, 100%).

$[\alpha]_D^{296K}$ -2.78 (c = 0.360, $CHCl_3$); ^{1}H NMR (300 MHz, $CDCl_3$) δ 7.66-7.63 (m, 4H), 7.47-7.36 (m, 6H), 5.43-5.38 (m, 1H), 5.23-5.18 (m, 1H), 3.78-3.67 (m, 2H), 3.55-3.39 (m, 2H), 2.34-2.26 (m, 4H), 1.62-1.61 (m, 4H), 1.27 (bs, 56H), 1.06 (s, 9H), 0.89 (t, J = 6.0 Hz); ^{13}C NMR (75 MHz, $CDCl_3$) δ 172.8, 172.7, 135.6, 135.5, 132.8, 132.7, 129.9, 127.8, 127.7, 72.0, 70.3, 62.0, 51.0, 34.2, 34.1, 31.9, 29.7, 29.65, 29.62, 29.5, 29.35, 29.28, 29.26, 29.2, 29.1, 26.7, 24.84, 24.70, 22.7, 19.1, 14.1

(2S,3S)-1-Azido-4-hydroxybutane-2,3-diyl distearate (2). Compound **10b** (57 mg, 0.062 mmol) was dissolved in THF (2 mL). Acetic acid (3.5 µL, 0.062 mmol) and TBAF·3 H_2O were each dissolved in THF (2 mL) and added successively to the reaction. The reaction was stirred at room temperature for 80 minutes and the solvent was removed with reduced pressure. The product was extracted using a solution of 30 mL $CHCl_3$, 20 mL MeOH, and 10 mL H_20. The bottom layer was kept and concentrated. Quick chromatography with a short column of silica gel and a gradient solvent system of 10 to 100% ethyl acetate/hexanes afforded **2** as a white solid (31.3 mg, 74%, 11% TBDPS by-product that was not separable). See paper for characterizations.

2) Synthetic Procedures for Alkyne-Functionalized reagents 12a-e: Standard amide bond-forming coupling conditions were employed to obtain alkyne-functionalized fluorescent and cross-linking groups. Generally, the coupling reagent *N,N*-dicyclohexylcarbodiimide (DCC) was used to produce the highly non-polar alkyne conjugates. For the more polar alkyne conjugates, such as fluorescein, other coupling reagents, exemplified by 1-Ethyl-3-(3-dimethylaminopropyl)carbodiimide hydrochloride (EDC), were used to avoid problems with separating the products from the urea byproduct of DCC.

2-(Naphthalene-2-yl)-*N*-(prop-2-ynyl)acetamide (12a). 2-Naphthylacetic acid (100 mg, 0.537 mmol), *N,N*-dicyclohexylcarbodiimide (166.2 mg, 0.806 mmol), 4-dimethylaminopyridine, (32.8 mg, 0.269 mmol) and propargylamine (44 µL, 0.644 mmol) were dissolved in dichloromethane (6 mL). The reaction was stirred at room temperature in the dark overnight. The reaction was extracted with dichloromethane (2 x 50 mL) from water (50 mL) and the organic layer was dried with magnesium sulfate and filtered, and the solvent was removed by rotary evaporation. Column chromatography with silica gel and a gradient solvent system of 25 to 50% ethyl acetate/hexanes afforded **12a** as a white solid (95 mg, 79%).

^{1}H NMR (300 MHz, $CDCl_3$) δ 7.87-7.81 (m, 3H), 7.73 (s, 1H), 7.54-7.47 (m, 2H), 7.39-7.36 (m, 1H), 5.58, (*b* s, 1H), 4.02 (dd, *J* = 5.3, 2.6 Hz, 2H), 3.77 (s, 2H), 2.16 (t, *J* = 2.6 Hz, 1H); ^{13}C NMR (62.9 MHz, $CDCl_3$) δ 170.5, 133.5, 132.6, 131.9, 128.8, 128.3, 127.7, 127.7, 127.3, 126.4, 126.1, 79.4, 71.5, 43.6, 29.3; HRMS $[M+H]^+$ calcd: 224.10754, found: 224.10790

5-(Dimethylamino)-*N*-(prop-2-ynyl)naphthalene-1-sulfonamide (12b). Compound **11b** was synthesized according to a literature procedure[3] using Dansyl chloride (100 mg, 0.371 mmol), propargylamine (31 µL, 0.445 mmol), and triethylamine (62 µL, 0.445 mmol). The reaction mixture was extracted with dichloromethane (2 x 50 mL) from water (50 mL), and the organic phase was then dried with magnesium sulfate and filtered. Next, the solvent was removed by rotary evaporation. Column chromatography with silica gel and a gradient solvent system of 25 to 50% ethyl acetate/hexanes afforded **12b** as a yellow solid (97 mg, 90%). Characterization agreed with previous literature reports. HRMS $[M+H]^+$ calcd: 289.10107, found: 289.10202

2-Oxo-*N*-(prop-2-ynyl)-2*H*-chromene-3-carboxamide (12c). Coumarin-3-carboxylic acid (191 mg, 1 mmol) was dissolved in dry DMF (10 mL) and HBTU (455 mg, 1.2 mmol) and hydroxybenzotriazole (162 mg, 1.2 mmol) were added. The sides of the reaction flask were rinsed with dry DMF (1 mL), and diisopropylethylamine (198 µL, 1.2 mmol) was added and stirred for 5 min. Propargylamine (82 µL, 1.2 mmol) was dissolved in DMF (1 mL) and added to the reaction mixture, which was then allowed to stir in the dark

at room temperature overnight. After the reaction was complete, DMF was removed on a rotary evaporator and the residue was extracted with ethyl acetate (2 x 50 mL) from 10% sodium bicarbonate (50 mL). The organic phase was then dried with magnesium sulfate and filtered, and the solvent was removed by rotary evaporation. Column chromatography with silica gel and a gradient solvent system of 20 to 70% ethyl acetate/hexanes afforded **12c** as a pale yellow solid (161 mg, 71%).

^{1}H NMR (300 MHz, $CDCl_3$) δ 9.01 (*b* s, 1H), 8.29 (s, 1H), 7.72-7.66 (m, 2H), 7.43-7.39 (m, 2H), 4.26 (dd, *J* = 5.1, 2.4 Hz, 2H), 2.28 (t, *J* = 2.4 Hz, 1H); ^{13}C NMR (69.2 MHz, $CDCl_3$) δ 161.4, 154.6, 148.8, 134.3, 129.9, 125.4, 118.6, 118.0, 116.7, 79.1, 71.6, 29.5; HRMS $[M+H]^+$ calcd: 228.06607, found: 228.06633

2-Oxo-*N*-(prop-2-ynyl)-5(6)-carboxyfluoresceinamide (12d). Propargylamine (34.3 µL, 0.5 mmol), 4-dimethylaminopyridine (61.1 mg, 0.5 mmol), *N*-methylmorpholine (82.5 µL, 0.75 mmol), and 5(6)-carboxyfluorescein (226 mg, 0.6 mmol) were dissolved in a 1:1 mixture of dry DMF and dichloromethane (4 mL) at room temperature. 1-Ethyl-3-(3-dimethylaminopropyl)carbodiimide hydrochloride (EDC, 115 mg, 0.6 mmol) was added. The reaction mixture was stirred at room temperature overnight in the dark. After the reaction was complete, the mixture was extracted with ethyl acetate (2 x 50 mL) from 2 N HCl (50 mL), and the organic layer was dried with magnesium sulfate and filtered. The solvent was then removed by rotary evaporation. Column chromatography with silica gel and a gradient solvent system of 5 to 15% methanol/chloroform with 0.1% acetic acid afforded **12d** as an orange solid (140 mg, 68%). Note: Since both isomers were present in the ^{1}H NMR spectra for compounds **12d** and **11d** and the ratio of each isomer is unknown in the commercially available acid, integration values are not reported. ^{13}C NMR data for compounds **12d** and **11d** are not reported due to poor solubility of the compounds and the complex nature of the spectra due to the isomeric mixture.

^{1}H NMR (300 MHz, CD_3OD), δ 8.75 (*b* s), 8.52-8.43 (m), 8.22-8.07 (m), 7.93 (*b* s), 7.62 (s), 7.32-7.30 (m), 6.69-6.52 (m), 4.21 (d, *J* = 2.4 Hz), 4.08 (d, *J* = 4.08 Hz), 2.66 (t, *J* = 2.3 Hz), 2.56 (t, J = 2.3 Hz); HRMS $[M+H]^+$ calcd: 414.09776, found: 414.09632

4-Benzoyl-*N*-(prop-2-ynyl)benzamide (12e). A solution of 4-benzoylbenzoic acid (200 mg, 0.884 mmol), *N,N'*-dicyclohexylcarbodiimide (273.5 mg, 1.33 mmol), and 4-dimethylaminopyridine (54 mg, 0.442 mmol) was prepared in dry dichloromethane and allowed to react for 30 min. Propargylamine (72.8 µL, 1.06 mmol) was added, and the reaction mixture was stirred at room temperature overnight in the dark. After the reaction was complete, the mixture was extracted with dichloromethane (2 x 50 mL) from water (50 mL), and the organic layer was dried with magnesium sulfate and filtered, followed by solvent removal. Column chromatography with silica gel and a gradient solvent system of 20 to 70% ethyl acetate/hexanes afforded **12e** as a white solid (145 mg, 62%).

^{1}H NMR (300 MHz, $CDCl_3$) δ 7.92-7.84 (m, 4H), 7.82-7.78 (m, 2H), 7.65-7.60 (m, 1H), 7.53-7.48 (m, 2H), 6.37 (*b* s, 1H), 4.30 (dd, *J* = 2.6, 5.25 Hz, 2H), 2.32 (t, *J* = 2.6 Hz, 1H); ^{13}C NMR (62.9 MHz, $CDCl_3$) δ 196.0, 166.4, 140.3, 137.0, 136.9, 132.9, 130.1, 128.5, 127.1, 79.3, 72.0, 29.9; HRMS $[M+H]^+$ calcd: 264.10245, found: 264.10361

2) HPLC trace for functionalized DAG Probe 11b.

As discussed in the paper, the acyl chains of diacylglycerols are known to migrate in the presence of silica. NMR analysis of analogs obtained via removal of the PMB protecting group indicated that migration was occurring. Removal of the DMT group and direct modification via "click" chemistry followed by purification produced compounds with NMRs that showed virtually no migration (see subsequent NMR spectra). However, upon HPLC analysis, two peaks appeared (chromatogram for **11b** shown below), one for the migrated product and one for the unmigrated product. The same sample was reanalyzed by NMR after HPLC analysis and only trace migration was detected, leading to the conclusion that the migration observed in the HPLC occurred on the column.

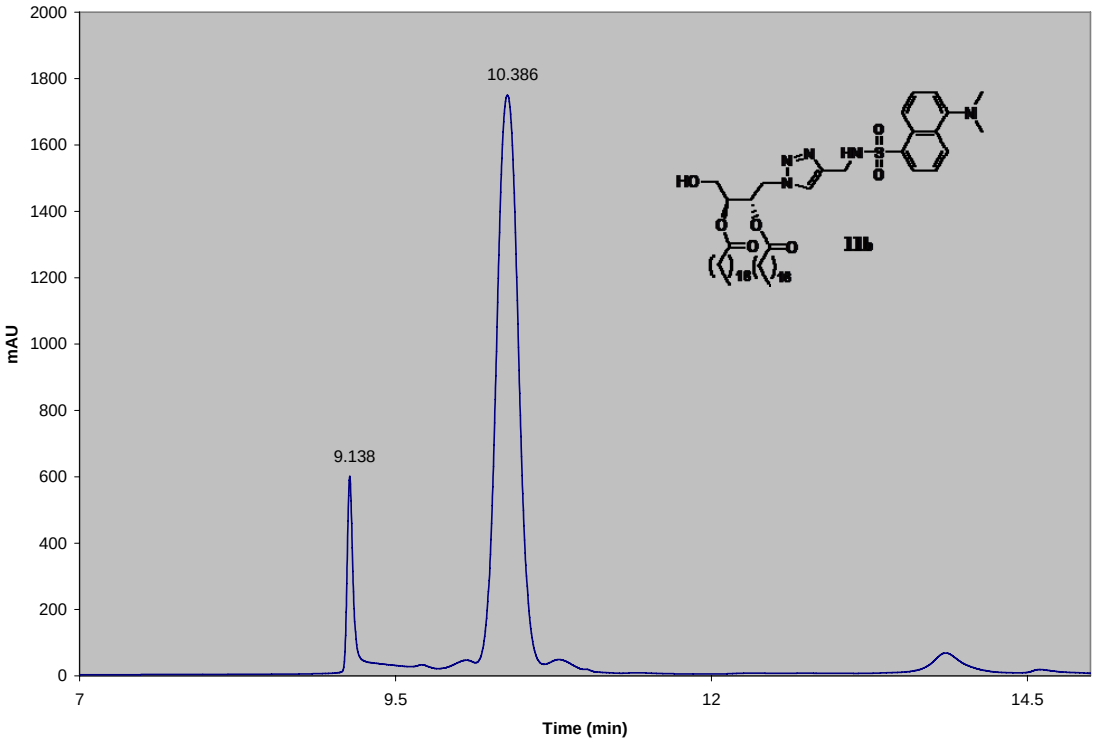

(1) Rzepecki, P. W., and Prestwich, G. D. (2002) Synthesis of hybrid lipid probes: Derivatives of phosphatidylethanolamine-extended phosphatidylinositol 4,5-bisphosphate (Pea-PIP2). *J. Org. Chem. 67*, 5454-5460.

(2) Uchida, K., Kato, K., and Akita, H. (1999) A convenient synthesis of a *N*-protected L-carbamoylpolyoxamic acid derivative: Total synthesis of (+)-polyoxin J and (+)-polyoxin L. *Synthesis*, 1678-1686.

(3) Bolletta, F., Fabbri, D., Lombardo, M., Prodi, L., Trombini, C., and Zaccheroni, N. (1996) Synthesis and photophysical properties of fluorescent derivatives of methylmercury. *Organometallics 15*, 2415-2417.

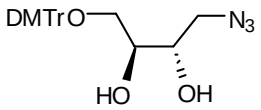

9

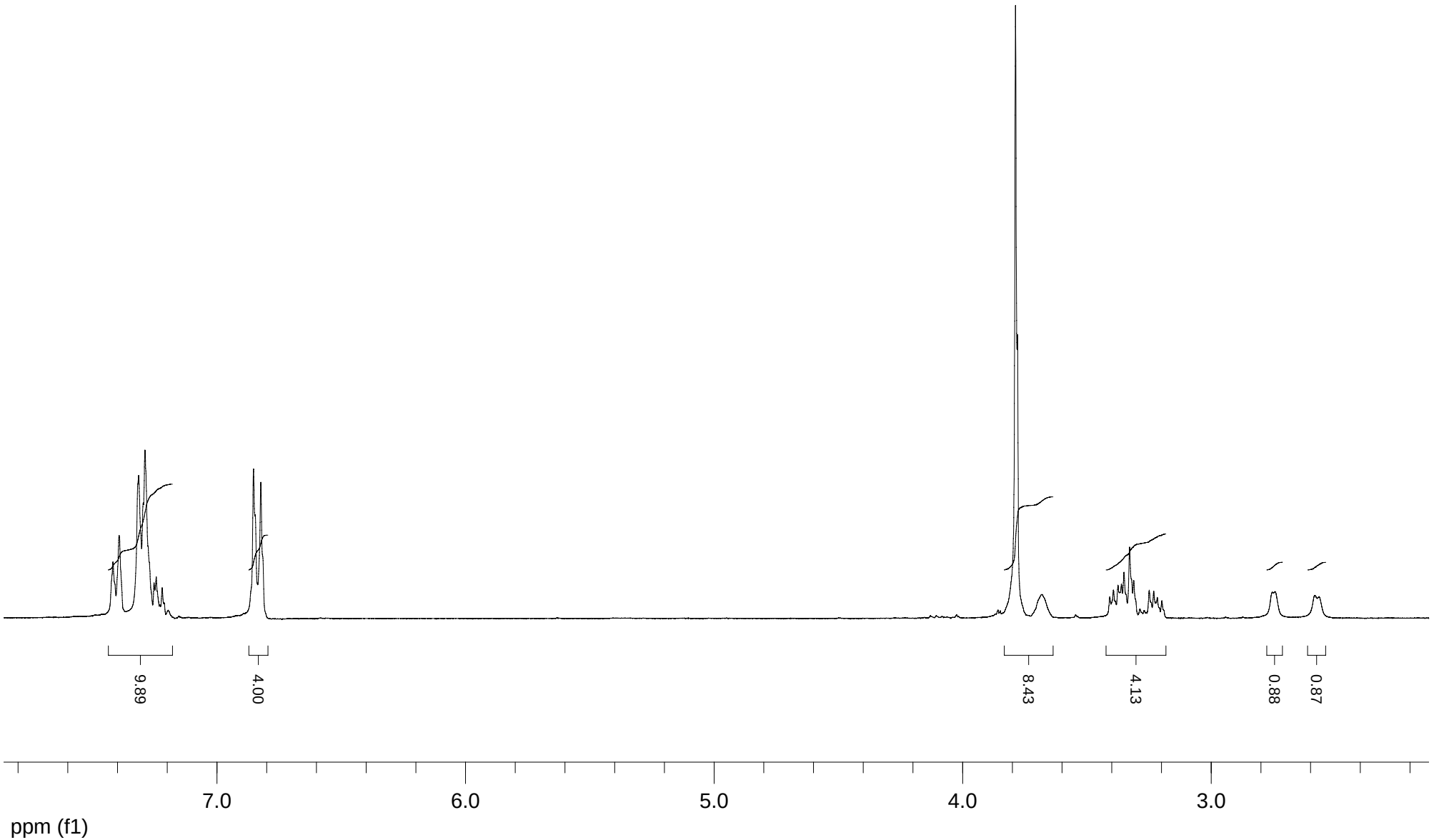

DMTrO
N3
O
O
O
O
16
16

10d

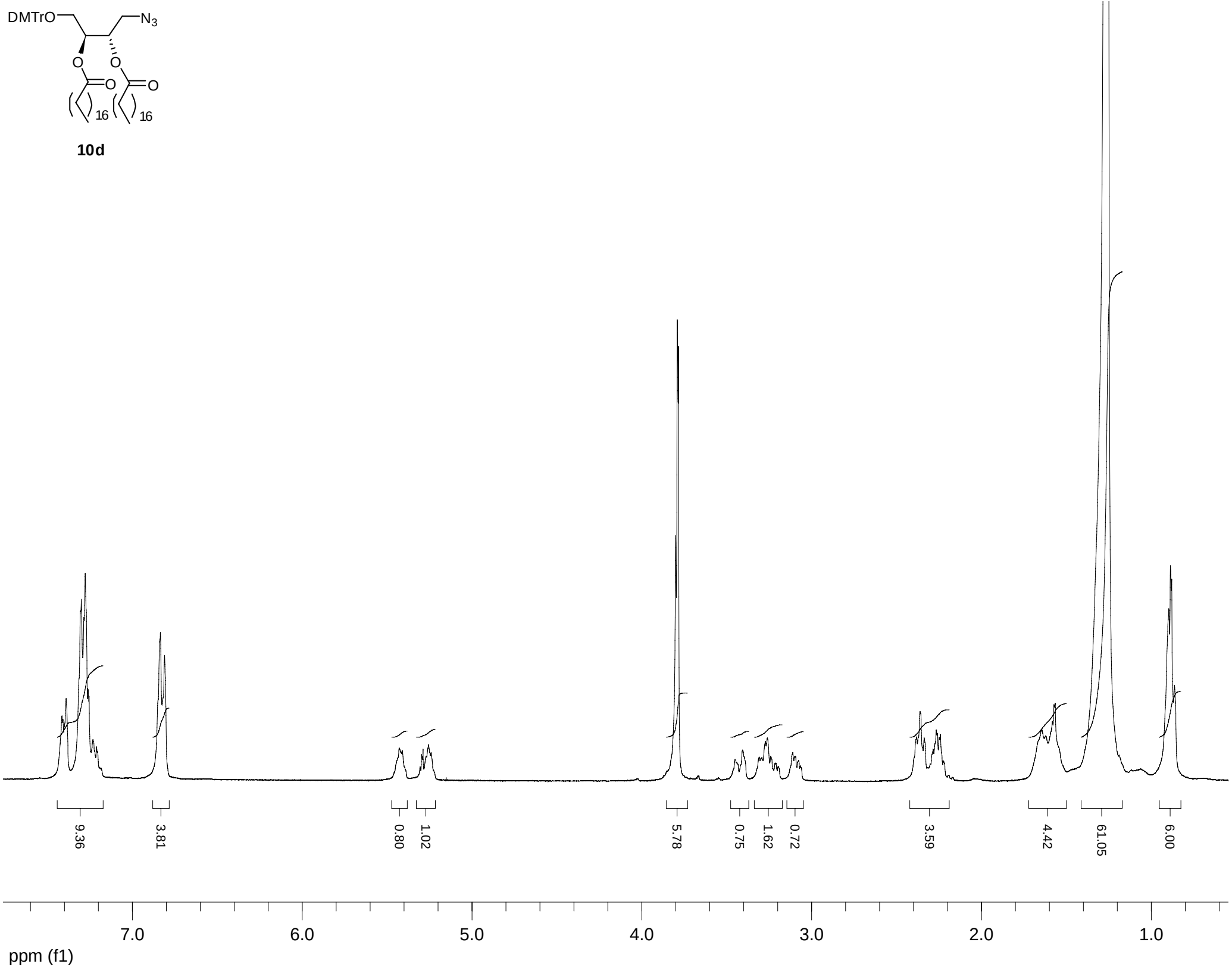
9.36
3.81
0.80
1.02
5.78
0.75
1.62
0.72
3.59
4.42
61.05
6.00
7.0
6.0
5.0
4.0
3.0
2.0
1.0
ppm (f1)

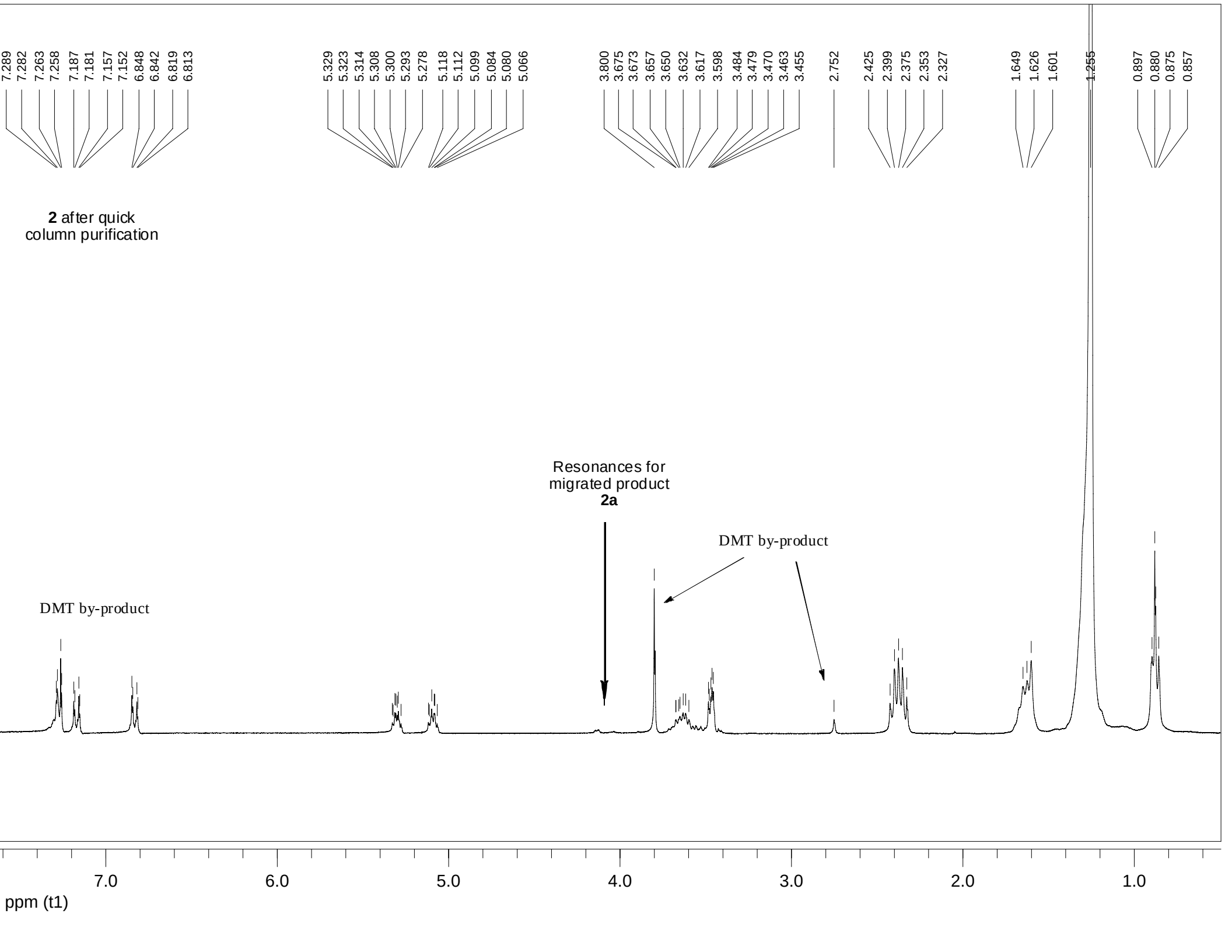
7.289
7.282
7.263
7.258
7.187
7.181
7.157
7.152
6.848
6.842
6.819
6.813
5.329
5.323
5.314
5.308
5.300
5.293
5.278
5.118
5.112
5.099
5.084
5.080
5.066
3.800
3.675
3.673
3.657
3.650
3.632
3.617
3.598
3.484
3.479
3.470
3.463
3.455
2.752
2.425
2.399
2.375
2.353
2.327
1.649
1.626
1.601
1.255
0.897
0.880
0.875
0.857
2 after quick column purification
Resonances for migrated product 2a
DMT by-product
DMT by-product
7.0
6.0
5.0
4.0
3.0
2.0
1.0
ppm (t1)

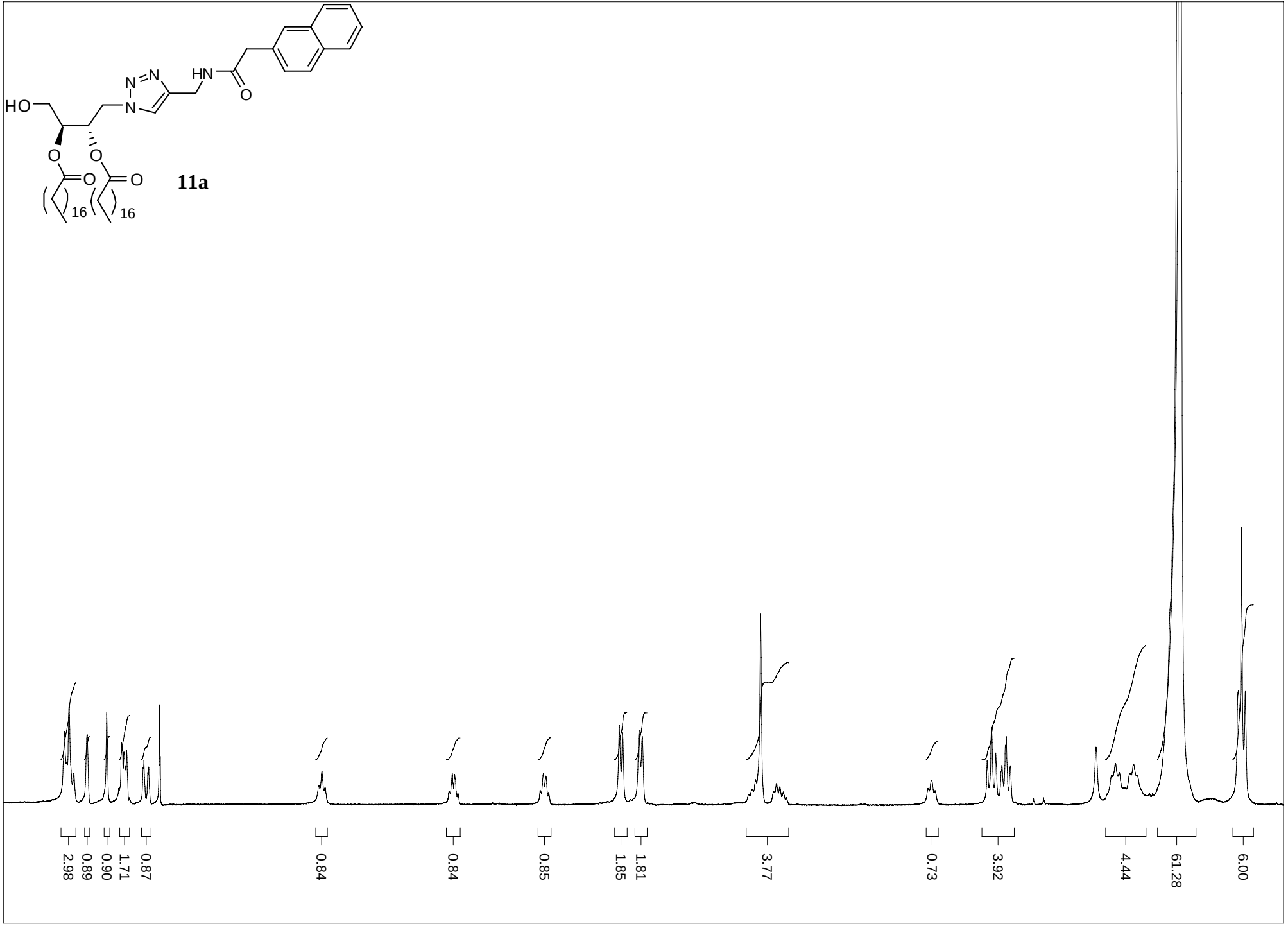
HO
N
N
N
HN
O
O
O
O
O
16
16
11a
2.98
0.89
0.90
1.71
0.87
0.84
0.84
0.85
1.85
1.81
3.77
0.73
3.92
4.44
61.28
6.00
8.0
7.0
6.0
5.0
4.0
3.0
2.0
1.0
ppm (t1)

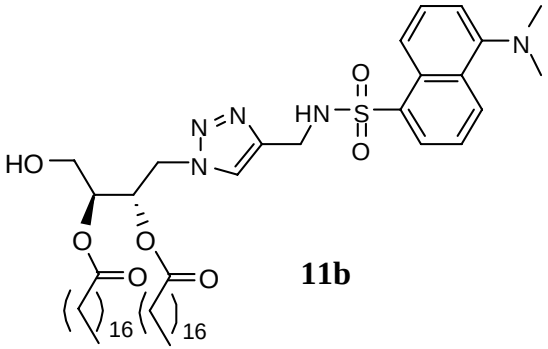
HO
N
N
N
HN
S
O
O
O
O
O
O
16
16

11b

1.01
1.96
2.07
0.83
0.90
1.82
0.81
1.75
1.88
1.73
6.10
0.69
3.97
5.41
61.50
6.00
8.0
7.0
6.0
5.0
4.0
3.0
2.0
1.0
ppm (t1)

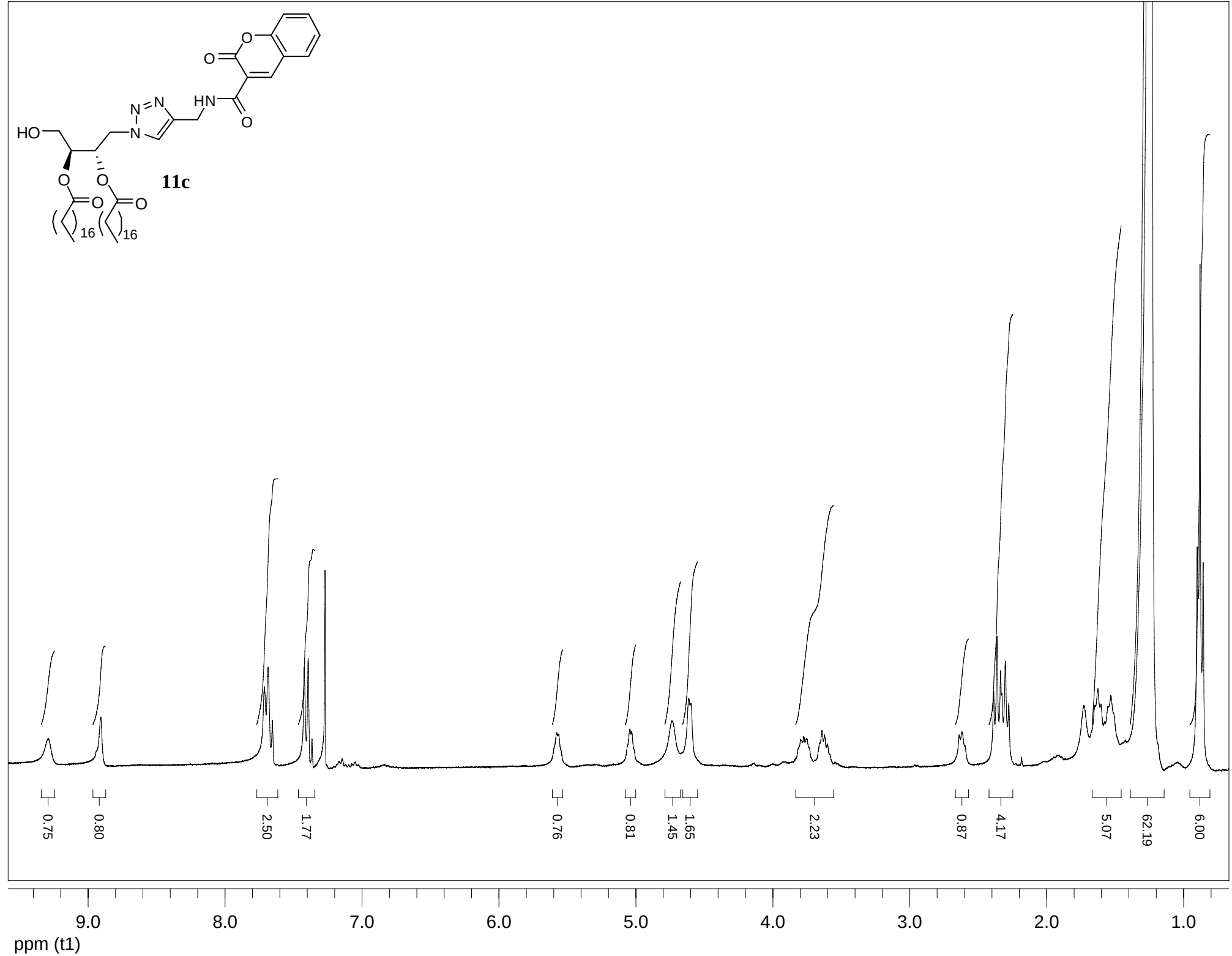
HO
O
O
HN
N
N
N
O
O
O
O
16
16
11c
0.75
0.80
2.50
1.77
0.76
0.81
1.45
1.65
2.23
0.87
4.17
5.07
62.19
6.00
9.0
8.0
7.0
6.0
5.0
4.0
3.0
2.0
1.0
ppm (t1)

11d

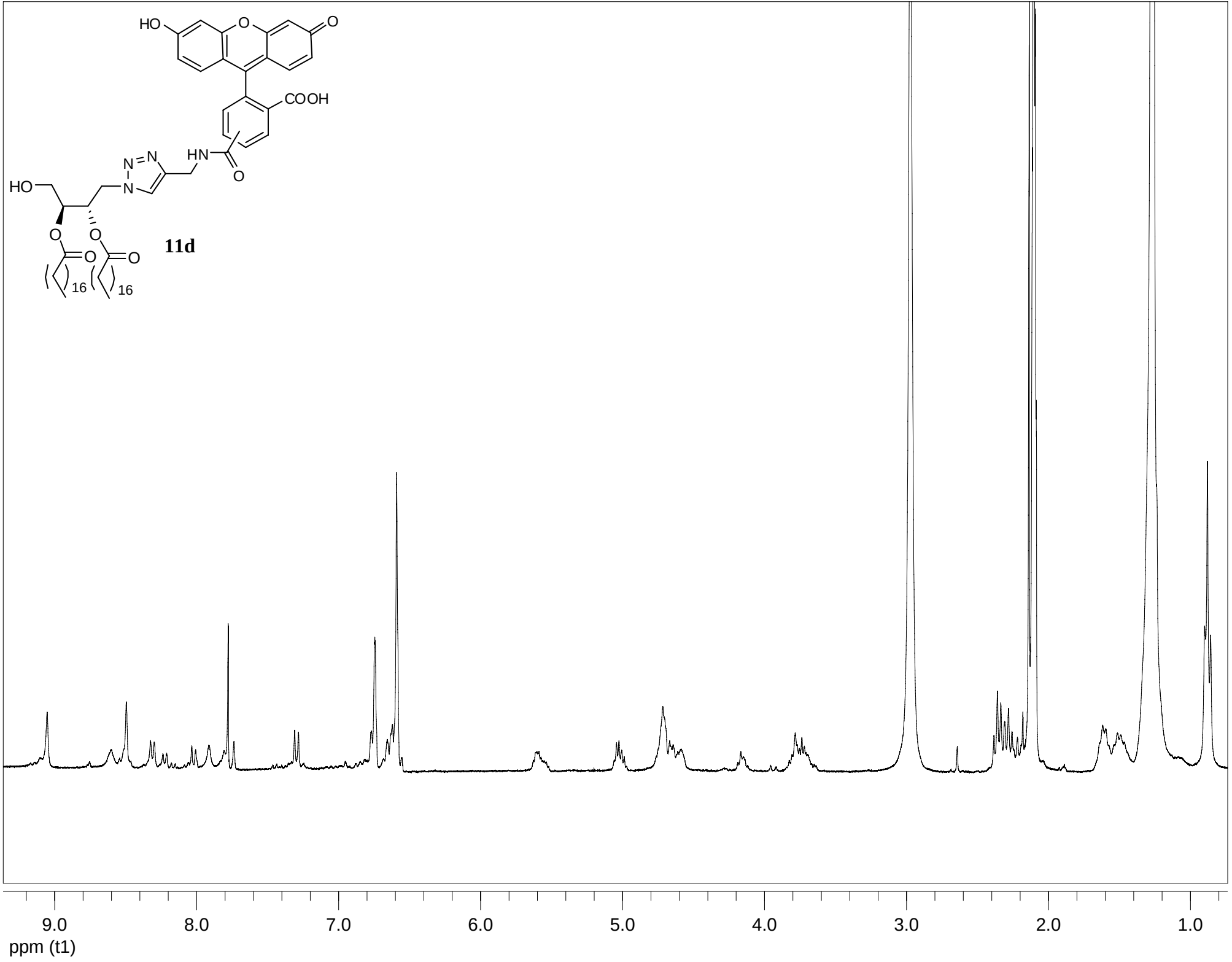

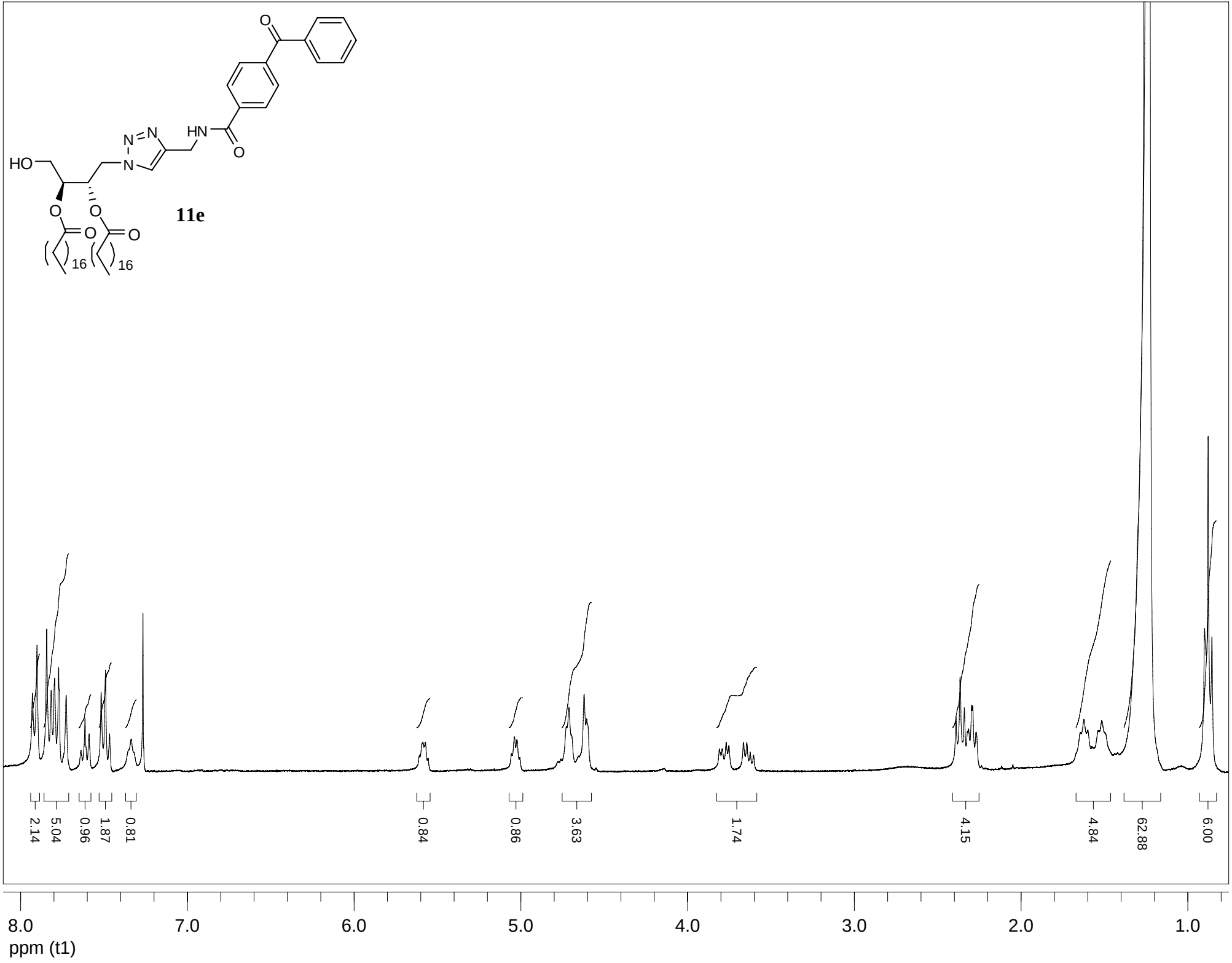
HO
HN
O
N
N
O
O
O
O
16
16
11e
2.14
5.04
0.96
1.87
0.81
0.84
0.86
3.63
1.74
4.15
4.84
62.88
6.00
8.0
7.0
6.0
5.0
4.0
3.0
2.0
1.0
ppm (t1)

A Peptide-Based, Ratiometric Biosensor Construct for Direct Fluorescence Detection of a Protein Analyte

Karin Enander,*[,†] Laurence Choulier,[‡] A. Linnéa Olsson,[†,⊥] Dmytro A. Yushchenko,[§,¶] Daniel Kanmert,[†] Andrey S. Klymchenko,[§] Alexander P. Demchenko,[||] Yves Mély,[§] and Danièle Altschuh[‡]

Division of Molecular Physics, Department of Physics, Chemistry and Biology, Linköping University, 581 83 Linköping, Sweden, Institut Gilbert Laustriat, University Strasbourg 1, CNRS - UMR 7175, ESBS, Bld Sébastien Brant, BP 10413, 67412 Illkirch, France, Photophysique des Interactions Biomoléculaires, UMR 7175-LC1 du CNRS, Institut Gilbert Laustriat, Faculté de Pharmacie, Université Louis Pasteur, 67401 Illkirch, France, and A. V. Palladin Institute of Biochemistry, Leontovicha 9, Kiev 01030, Ukraine.
Received April 17, 2008; Revised Manuscript Received June 23, 2008

We present the design, synthesis, and functional evaluation of peptide-based fluorescent constructs for wavelength-ratiometric biosensing of a protein analyte. The concept was shown using the high-affinity model interaction between the 18 amino acid peptide pTMVP and a recombinant antibody fragment, Fab57P. pTMVP was functionalized in two different positions with 6-bromomethyl-2-(2-furanyl)-3-hydroxychromone, an environmentally sensitive fluorophore with a two-band emission. The equilibrium dissociation constant of the interaction between pTMVP and Fab57P was largely preserved upon labeling. The biosensor ability of the labeled peptide constructs was evaluated in terms of the relative intensity change of the emission bands from the normal (N*) and tautomer (T*) excited-state species of the fluorophore (I_{N*}/I_{T*}) upon binding of Fab57P. When the peptide was labeled in the C terminus, the I_{N*}/I_{T*} ratio changed by 40% upon analyte binding, while labeling close to the residues most important for binding resulted in a construct that completely lacked ratiometric biosensor ability. Integrated biosensor elements for reagentless detection, where peptides and ratiometric fluorophores are combined to ensure robustness in both recognition and signaling, are expected to become an important contribution to the design of future protein quantification assays in immobilized formats.

INTRODUCTION

The availability of sensitive, specific, and robust biomolecular quantification assays is crucial for fundamental characterization of biomolecular interactions as well as for disease diagnostics, environmental monitoring, and quality control in food production. In assay design, strategies for both biospecific recognition and detection have to be carefully considered. Proteins are attractive candidates as recognition elements, since they have evolved to specifically bind a wide variety of targets. In particular, antibodies and antibody fragments are preferred because of their target binding diversity, high affinity, and high specificity. For detection, fluorescence-based strategies are safe, inexpensive, and well-established, and offer a level of sensitivity still unrivalled by other methods. The accessibility of the technique is further expanded through a wide range of commercially available fluorophores that allow for labeling using a variety of coupling chemistries.

Today, many protein quantification systems rely on a traditional immunoassay-type of detection, involving either a multistep sandwich analysis or sample labeling. An interesting alternative is based on the design of so-called molecular (bio)sensors, where the recognition and signaling events have been molecularly integrated by the attachment of one or more fluorescent reporter probe(s) to the recognition element in a fashion that allows the probe(s) to respond to analyte binding (Figure 1) (*1*). The basis of detection is typically fluorescence resonance energy transfer (FRET) (*2*, *3*), the formation of a nonfluorescent complex (*4*), fluorescence anisotropy (*5*), or, more relevant to the present work, the change of emission intensity of a single environmentally sensitive fluorophore in the presence of the analyte. Reagentless molecular sensing methods based on singly labeled proteins or peptides and capable of direct analyte detection have mainly been demonstrated for probing of ions and small molecules (*6*–*9*), but there are also examples where fluorophores have been conjugated to streptococcal protein G (*10*), antibodies (*11*), or synthetic peptides (*12*) for the detection of protein analytes.

The construction of protein-based molecular biosensors, which requires the large-scale production and purification of recombinant proteins and their derivatization with a fluorescent dye, represents a labor-intensive task with unpredictable success. Full-length proteins are susceptible to denaturation, a problem that is especially relevant if the biosensor concept should be applied in a microarray format where the immobilization of sensor molecules would be necessary. Moreover, the only current solution to the problem of site-specific fluorophore labeling of proteins in arbitrary positions is the production of single-cysteine mutants, which is difficult to implement on a general basis, since some proteins contain crucial cysteine residues in the wild-type sequence. Also, side reactions between thiol-reactive fluorophores and lysine side chains have been observed (*13*, *14*). Synthetic binders such as peptide or nucleic acid aptamers (*15*) offer a promising alternative to recombinant proteins in molecular biosensor applications. In particular,

* Corresponding author. E-mail: karen@ifm.liu.se. Phone: +46-13-282359. Fax: +46-13-288969.
† Linköping University.
‡ University Strasbourg.
§ Université Louis Pasteur.
|| A. V. Palladin Institute of Biochemistry.
⊥ Present address: Division of Molecular Surface Physics and Nanoscience, Department of Physics, Chemistry and Biology, Linköping University, 581 83 Linköping, Sweden.
¶ Present address: MPI for Biophysical Chemistry, Department of Molecular Biology, Am Fassberg 11, 370 77 Göttingen, Germany.

10.1021/bc800159d CCC: $40.75 © 2008 American Chemical Society
Published on Web 08/12/2008

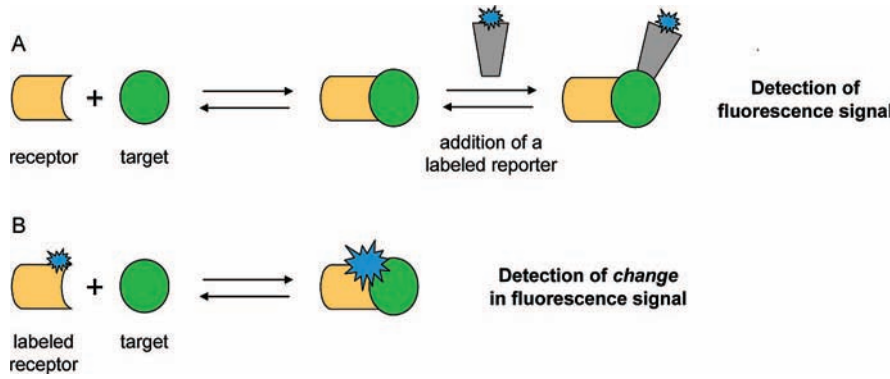

Figure 1. (a) A conventional sandwich assay for protein quantification relies on a labeled reporter molecule for detection. With this multistep approach, the target molecule must provide two distinct binding sites, and separation of free and bound molecules is required after each step. (b) If the recognition and reporting functions can be molecularly integrated, detection can be obtained in a homogeneous assay. This requires a fluorophore the emission properties of which are sensitive to changes in the local environment induced by binding to the target molecule.

synthetic peptides are ideal for molecular biosensor design since they can be straightforwardly produced at a low price, offer functional robustness superior to most proteins, and are well suited for long-term storage in dry, dissolved, and immobilized states (*16*). Also, site-specific functionalization is readily obtained.

In this work, we present the design and functional evaluation of synthetic, singly labeled peptide constructs as a promising alternative to recombinant protein-based conjugates for biosensing of a protein target. The concept was shown with an antibody fragment serving as the analyte. We further provide the first demonstration of the applicability of 3-hydroxychromone (3-HC) derivatives for wavelength-ratiometric biosensing of proteins, as an alternative to conventional dyes, which typically offer changes in absolute steady-state fluorescence intensities upon analyte binding. When relying on relative fluorescence signals for quantification, interpretation problems related to instrument parameters, photobleaching, and concentration variations of the fluorophore between samples can be avoided (*17*).

EXPERIMENTAL SECTION

Peptide Synthesis and Modification. Fluorophores 2-(2-furanyl)-3-hydroxychromone (FC) (*18*) and 6-bromomethyl-2-(2-furanyl)-3-hydroxychromone (BMFC) (*19*) were synthesized as described. The peptides pTMVP, corresponding to amino acids 134−151 of the tobacco mosaic virus coat protein (sequence: H_2N-RGTGSYNRSSFESSSGLV-$CONH_2$), C-pTMVP (H_2N-CRGTGSYNRSSFESSSGLV-$CONH_2$), R134K (H_2N-KGTGSYNRSSFESSSGLV-$CONH_2$), S146C (CH_3CO-KRGTGSYNRSSFECSSGLV-$CONH_2$), and V151C (CH_3CO-KRGTGSYNRSSFESSSGLC-$CONH_2$) were synthesized on a Pioneer automated peptide synthesizer (Applied Biosystems) using standard fluorenylmethoxycarbonyl (Fmoc) chemistry. The synthesis of each peptide was performed on a 0.1 mmol scale using an Fmoc-PAL-PEG-PS polymer (Applied Biosystems). Before each coupling, the Fmoc group was removed by treatment with 20% piperidine in *N*,*N*-dimethylformamide (DMF). Each amino acid, used at 4-fold excess, was activated with a mixture of *O*-(7-benzotriazole-1-yl)-1,1,3,3-tetramethyluronium tetrafluoroborate (TBTU, 0.5 M in DMF; Alexis Biochemicals) and diisopropylethylamine (DIPEA, 1 M in DMF). Coupling times were 60−120 min. In the synthesis of pTMVP, S146C, and V151C, a pseudoproline dipeptide, Fmoc-Ser(tBu)-Ser($\Psi^{Me,Me}$pro)-OH (Calbiochem-Novabiochem AG), was used in two positions instead of the amino acid form of Ser in order to improve yields.

To allow for site-specific labeling of S146C and V151C, the side chain of Cys was protected by 4-methoxytrityl, which can be selectively removed by treatment with 1% trifluoroacetic acid (TFA). The final N termini of the peptides were capped with 0.3 M acetic anhydride in DMF. Cys was orthogonally deprotected by treatment with TFA, triisopropylsilane (TIS), and dichloromethane (DCM) (1:2:97 v/v), and the process was visually monitored by the yellow color of the detached trityl ion. For fluorophore coupling, the resins were mixed with 1.2 equiv of BMFC and 6 equiv of DIPEA in DMF (6 mL per gram of polymer) and were left at room temperature in the dark with careful swirling for 48−72 h to yield S146C-FC and V151C-FC.

Resins were rinsed in DCM and dried. Peptides were cleaved from the solid phase by treatment with 95% TFA for 2 h at room temperature (TMVP, R134K: TFA/TIS/H_2O 95:2.5:2.5 v/v; C-pTMVP, S146C, V151C: TFA/TIS/H_2O/ethanedithiol 94:2.5:2.5:1 v/v). After filtration, TFA was evaporated and peptides were precipitated by the addition of cold diethyl ether, washed, and lyophilized. They were then purified by reversed-phase HPLC on a semipreparative C-8 column with aqueous acetonitrile (ACN) containing 0.1% TFA as the mobile phase and at a flow rate of 8−10 mL/min. Elution conditions were 20−40% ACN; 40 min gradient (pTMVP), 18% ACN (C-pTMVP and R134K), and 10−50% ACN; 30 min gradient (S146C and V151C). Purified peptides were identified by MALDI-TOF mass spectrometry.

Expression and Purification of Fab57P. Cloning and expression of recombinant Fab57P in *Escherichia coli* was performed as described (*20*) with some modifications. Cells were grown in 30 × 500 mL of LB medium containing 0.3 mM ampicillin. After induction at OD_{600nm} ~0.9 with 1 mM isopropyl thiogalactoside (IPTG; final concentration), Fab57P was expressed at 30 °C for 15 h. Cells were harvested by centrifugation and treated with 0.6 M sucrose in 30 mM Tris-HCl pH 8.0 containing 1 mM ethylenediaminetetraacetic acid (EDTA) and 0.15 mg/mL lysozyme for 3.5 h on ice. The supernatant (600 mL) was dialyzed twice against HEPES-buffered saline (10 mM HEPES, 150 mM NaCl, 3 mM EDTA, pH 7.4) containing 0.2 mM phenylmethanesulfonyl fluoride. Dialyzed samples were filtered (0.22 μm) and stored at 4 °C. Presence of Fab57P was confirmed by Western blotting using a rat anti(mouse κ light chain) antibody conjugated to alkaline phosphatase for revelation.

Fab57P was affinity purified using CNBr-activated Sepharose 4B (Amersham Biosciences) and R134K as the specific capture molecule. R134K (22 mg, 12 μmoles) dissolved in 0.1 M $NaHCO_3$, 0.5 M NaCl, pH 8.3 (5 mL) was added to 4 mL washed gel and coupling was allowed for 2 h at room temperature. Blocking of unreacted CNBr groups was performed in 0.1 M Tris-HCl pH 8.0 (15 mL) for 2 h at room temperature.

The gel was then washed according to the manufacturer's instructions. The peptide coupling reaction was monitored by dot blotting of coupling and washing solutions, followed by incubation with mAb174P (*21*), which binds to TMVP and pTMVP. For revelation, a secondary goat antimouse antibody conjugated to alkaline phosphatase was used.

Filtered cell extracts containing Fab57P were applied to the gel column following equilibration at pH 7.4. The protein was eluted with 10 mM glycine pH 2.2 in 2 mL fractions. A small amount of 1 M Tris-HCl pH 8.0 was added promptly to the eluate to give a final pH of 7.2−7.5. With this protocol, 90−95% of the protein eluted within the first 8 mL. The purified protein was stored in aliquots at −20 °C until use.

Analysis of Binding Kinetics. Kinetic analysis was performed with a Biacore 2000 instrument (Biacore AB) at 25 °C using using HEPES-buffered saline (HBS-EP: 10 mM HEPES, 0.15 M NaCl, 3 mM EDTA, 0.005% polysorbate 20, pH 7.4) as the running buffer. S146C-FC and V151C-FC were immobilized in separate flow channels of a CM5 sensor chip at low (90 or 120 RU) or medium (190 or 340 RU) levels. pTMVP was immobilized to yield 10 and 20 RU. Immobilization levels were defined as the baseline difference before and promptly after the injection of the peptide. A reference flow cell without immobilized peptide was included for analysis. A detailed coupling protocol can be found in Supporting Information.

The experimental conditions were checked for mass transport limitations through variation of the analyte flow rate (30, 50, and 70 μL/min) at a constant Fab57P concentration (25 nM). For kinetic analysis, sensorgrams were collected for six analyte concentrations between 1.6 nM and 50 nM, at a flow rate of 50 μL/min. Samples were diluted in HBS-EP. One of the samples was run in duplicate to check the stability of the sensor surface. Regeneration was efficiently achieved with 50 mM HCl (30 s) after each protein injection. Reference subtraction and kinetic evaluation of the sensorgrams were performed with the *BIAevaluation 4.1* software, fitting data from the entire injection phase and the first 100 s of the postinjection (dissociation) phase in each concentration series using the Langmuir bimolecular binding model in a global fit algorithm.

Fluorescence Biosensor Experiments. Fluorescence biosensor experiments were performed in a Safire2 microplate detection system (Tecan Trading AG) using 96-well plates (Corning) at 23 °C. The sample volume in each well was 75 μL. The excitation wavelength was 365 nm and emission was monitored in the range 400−700 nm. Excitation and emission slits were 10 nm. All measurements were done in HEPES-buffered saline (10 mM HEPES, 150 mM NaCl, pH 7.4). For each peptide, three samples were measured in duplicate: 5 μM peptide, 5 μM peptide + 5 μM Fab57P, and 5 μM peptide + 2.5 μM goat antirabbit F(ab′)$_2$ (Sigma-Aldrich; product number R9130). F(ab′)$_2$ was used as a negative control. As it contains two Fab units, it was added at half the concentration relative to Fab57P. With V151C-FC, a measurement series of 10 μM peptide, 10 μM peptide + 10 μM Fab57P, and 10 μM peptide + 5 μM F(ab′)$_2$ was performed as well. At the excitation wavelength used, Fab57P and F(ab′)$_2$ did not give rise to any background fluorescence. The ratio of the maximum intensity values of the N* band (at 432 nm) and the T* band (at 520 nm), I_{N*}/I_{T*}, was calculated for each sample and the fractional signal change upon introduction of Fab57P or F(ab′)$_2$ was obtained from

$$C = \frac{|(I_{N*}/I_{T*})_{-\mathrm{Fab}} - (I_{N*}/I_{T*})_{+\mathrm{Fab}}|}{(I_{N*}/I_{T*})_{-\mathrm{Fab}}} \cdot 100\%$$

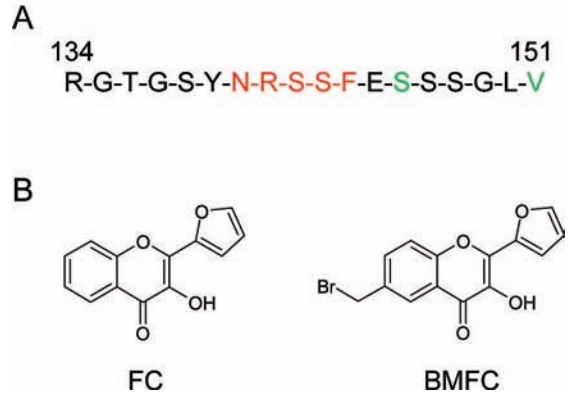

Figure 2. (a) Sequence of pTMVP, corresponding to amino acids 134−151 in TMVP and comprising the residues most important for binding of Fab57P (red). Positions targeted for fluorophore labeling are shown in green. (b) Structure of the ratiometric fluorophore 2-(2-furanyl)-3-hydroxychromone (FC) and its thiol-reactive derivative, 6-bromomethyl-2-(2-furanyl)-3-hydroxychromone (BMFC).

where the subscripts +Fab and −Fab refer to the samples with and without added Fab, respectively.

RESULTS

Design of Molecular Biosensor Constructs. A biomolecular model system with a mapped binding site and well-characterized interaction kinetics was selected to demonstrate the design of a robust molecular biosensor for ratiometric detection of a protein analyte. The 18 kDa four-helix bundle tobacco mosaic virus coat protein (TMVP) is recognized by Fab57P, a recombinant antibody fragment (*20*), and essential residues of the epitope have been mapped to positions 140−144 (*22*). In earlier studies, Fab57P has been found to bind TMVP and a synthetic peptide derivative, pTMVP, with similar affinities (*23*). pTMVP consists of eighteen amino acids, corresponding to TMVP residues 134−151, thus comprising the epitope (Figure 2a). The fact that the affinity of the protein toward Fab57P is retained in the peptide makes pTMVP an ideal recognition element for the further design into a robust molecular biosensor. In order to obtain peptide constructs for ratiometric sensing, the recently developed thiol-reactive dye 6-bromomethyl-2-(2-furanyl)-3-hydroxychromone (BMFC; Figure 2b), which has been successfully used for protein functionalization earlier (*19*), was chosen for labeling of pTMVP. BMFC is a derivative of the 3-HC fluorophore 2-(2-furanyl)-3-hydroxychromone (FC; Figure 2b) (*18*, *24*). These dyes undergo excited-state intramolecular proton transfer (ESIPT) between the normal (N*) and a phototautomer (T*) excited-state species, which are both highly emissive and give rise to a two-band fluorescence spectrum. The intensity ratio of the high energy band from the N* state and the low energy band from the T* state, I_{N*}/I_{T*}, is a very sensitive indicator of solvent polarity and hydrogen bonding ability (*25*–*27*). In aprotic solvents such as acetonitrile, FC exhibits emission predominantly from the T* state, which gives a low value of the I_{N*}/I_{T*} ratio (Figure 3). In protic media, when increasing solvent polarity in the line octanol−ethanol−methanol−water, FC exhibits a gradual increase in the I_{N*}/I_{T*} ratio until almost complete disappearance of the T* emission (Figure 3). The I_{N*}/I_{T*} ratio of an FC derivative attached to the peptide recognition element was expected to be useful as a signal for analyte binding in the molecular biosensor context explored here, where the local probe environment was expected to change upon interaction.

In a design where the biosensor response should be based on spectral changes induced by direct contact of the probe with the analyte upon binding, the position of labeling has to be

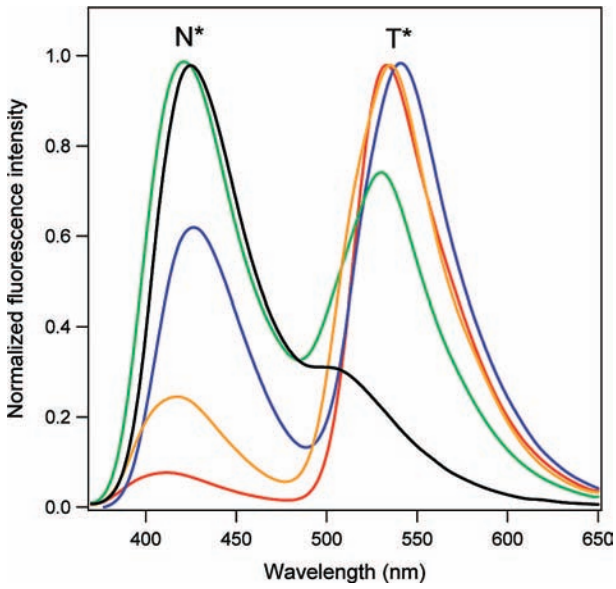

Figure 3. Normalized fluorescence spectra of FC in acetonitrile (red), octanol (orange), ethanol (blue), methanol (green), and water (black). The excitation wavelength was 350 nm. Positions of N* and T* bands are indicated.

chosen close to the binding site. However, it is important that the probe does not interfere with the interaction, thus reducing affinity. Although structural data are helpful in the selection of suitable sites, it is very difficult to rationally predict the optimal position for labeling. Here, in the absence of structural data, two positions were targeted: Ser146 in the immediate vicinity of positions mapped as essential for binding, and Val151 in the peptide C terminus. The numbering of the amino acid positions from TMVP was used also for pTMVP. Labeling in position 146 was assumed not to dramatically reduce the high affinity between Fab57P and pTMVP, as the interaction is tolerant to amino acid substitutions in this position (*22*). Both sites were assumed to allow for spectral changes of the attached probe upon peptide−protein interaction, but the local peptide flexibility was thought to be more pronounced in position 151 than in position 146.

Peptide Synthesis and Functionalization. Two variants of pTMVP were produced, where either Ser146 or Val151 was changed into a cysteine to allow for probe coupling. The peptides S146C and V151C were synthesized on the solid phase. To avoid labeling of the N terminal amine group, the peptide N termini were acetylated. BMFC was introduced after selective deprotection of the thiol at the side chain of Cys146 or Cys151 to form S146C-FC and V151C-FC. The peptides were cleaved from the resin by 95% trifluoroacetic acid to yield a C terminal amide, purified by reversed phase HPLC, and identified from their MALDI-TOF mass spectra. Yields of labeled peptides were very low, possibly due to poor accessibility of the coupling sites caused by the peptide forming secondary structure on the polymer.

Expression, Purification, and Concentration Determination of Fab57P. Fab57P was expressed in *E. coli* and identified by Western blotting. Affinity purification was performed with a lysine-containing derivative of pTMVP, R134K, as the capture molecule. The concentration of native Fab57P in cell extracts and after purification was determined in a surface plasmon resonance (SPR) assay. A pTMVP-derived peptide with an additional N terminal cysteine, C-pTMVP, was synthesized and immobilized to a Biacore CM5 sensor chip at high concentration, and Fab57P samples were introduced in solution. From the slopes of the binding curves, it was found that the production protocol resulted in approximately 0.3 mg native Fab57P per liter of culture. The purification yield was 74%. Experimental details for the concentration determination assay can be found in Supporting Information.

Kinetic Analysis. The association rate constant k_a and the dissociation rate constant k_d describing the interaction between C-pTMVP and nonpurified Fab57P have been determined by SPR (*22*). It was found that $k_a = 7.8 \times 10^5\ M^{-1}\ s^{-1}$ and $k_d = 1.4 \times 10^{-3}\ s^{-1}$, resulting in a equilibrium dissociation constant $K_d = 1.8$ nM. Here, the kinetic analysis was repeated using immobilized pTMVP and purified Fab57P. The average kinetic parameters were $k_a = 5.8 \times 10^5\ M^{-1}\ s^{-1}$ and $k_d = 0.93 \times 10^{-3}\ s^{-1}$, resulting in $K_d = 1.6$ nM (Table 1).

The kinetics of the interaction between Fab57P and the functionalized pTMVP derivatives S146C-FC and V151C-FC were analyzed in order to evaluate the effects on the interaction from labeling. The values of the kinetic parameters obtained at two different levels of peptide immobilization are summarized in Table 1. Affinities were only slightly decreased compared to that of the unlabeled peptide. In the case of S146C-FC, labeling in the immediate vicinity of residues important for binding resulted in a 2-fold decrease in the association rate and a 2-fold increase in the dissociation rate (average $K_d = 6.3$ nM). The goodness of fit was assessed by inspection of the residual plots and by relating the average squared residuals, χ^2, to the experimental value of the maximum SPR response ($R_{max,\ exp}$). The fitted curves ran closely to the experimental data and statistical parameters were good with a $\chi^2/R_{max,\ exp}$ ratio lower than 0.05.

In order to show that the equilibrium dissociation constants obtained for the labeled peptides were reasonable and that the peptide molecules were available for binding Fab57P in solution, an SPR experiment was performed where the ability of S146C-FC and V151C-FC to inhibit the interaction between Fab57P and immobilized C-pTMVP was analyzed. Fab57P was mixed with peptides at a range of concentrations and introduced to a sensor surface where C-pTMVP was immobilized at high density. The concentration of unbound Fab57P in the mixture was calculated under the assumption of K_d values obtained from the kinetic analysis and the expected slope of a binding curve from Fab57P at this concentration was compared to the experimental data. Experimental details can be found in Supporting Information. It was found that the inhibition ability of both pTMVP and the labeled peptides corresponded reasonably well with calculated values (Table S-1, Supporting Information). Consequently, the inhibition experiment showed that the kinetic data of the labeled peptides are reliable, and thus justified the conclusion that labeling did not dramatically reduce the affinity of the functionalized peptides toward Fab57P compared to that of pTMVP.

Fluorescence Biosensor Analysis. Fluorescence quantum yields Φ of 3-HC dyes are rather low in water and other polar solvents (*27*). Using quinine sulfate as a reference, it was found that Φ of S146C-FC and V151C-FC in HEPES-buffered saline pH 7.4 was 0.061 and 0.046, respectively (average of two measurements; experimental details can be found in Supporting Information). These values are in very good agreement with what could be expected, considering that Φ of FC in water is 0.05 (*27*). Moreover, they are sufficiently large to record useful fluorescence signals from the peptide constructs in a biosensor analysis.

Incorporating BMFC in a peptide or a protein can change its emission profile substantially. The I_{N*}/I_{T*} ratio of FC in water is >3.2 (Figure 3) but when attached to the αA subunit of bovine α-crystallin the ratio drops below 0.3 (*19*). Such differences could reflect a decrease in the local polarity and hydrogen-bonding ability experienced by the fluorophore due to the

Table 1. Kinetic Parameters Obtained for the Interactions Between Fab57P and TMVP-Derived Peptides[a]

peptide	level of immob.[b] (RU)	$R_{max,\ exp}$[c] (RU)	$R_{max,\ theor}$[d] (RU)	k_a (10^5 M^{-1} s^{-1})	k_d (10^{-4} s^{-1})	K_d (10^{-9} M)	χ^2 (RU^2)	$\chi^2/R_{max,\ exp}$ (RU)
pTMVP	20	323	529	5.94	8.65	1.46	2.93	0.0091
	10	106	265	5.57	9.87	1.77	0.343	0.0032
				5.76	**9.26**	**1.61**		
S146C-FC	190	190	4107	3.72	21.7	5.84	0.640	0.0034
	190	180	4107	3.70	21.6	5.84	0.775	0.0043
	90	15	1945	2.82	19.3	6.83	0.274	0.018
				3.27[e]	**20.5**[e]	**6.27**[e]		
V151C-FC	340	130	7388	4.87	9.08	1.86	3.47	0.027
	340	134	7388	5.01	9.68	1.93	4.95	0.037
	120	45	2608	3.97	11.9	2.99	0.539	0.012
				4.42[e]	**10.49**[e]	**2.37**[e]		

[a] Numbers in bold refer to average values. [b] The level of immobilization was defined as the baseline difference before and promptly after the injection of the peptide. [c] Experimental R_{max} obtained from the global fit. [d] Theoretical R_{max} obtained from the immobilization level and the molecular weight of Fab57P (~50 kDa). [e] Average of the first measurement at the higher immobilization level and the single measurement at the lower immobilization level.

Table 2. Ratiometric Response from Biosensor Constructs upon Binding of Analyte[a]

		I_{N*}/I_{T*}			change in I_{N*}/I_{T*} (%)	
peptide	measurement	peptide	peptide + Fab57P	peptide + $F(ab')_2$	Fab57P	$F(ab')_2$
S146C-FC[b]	1	0.70	0.69	0.69	1.4	1.4
	2	0.73	0.70	0.74	4.1	1.4
		0.72	**0.70**	**0.71**	**2.8**	**1.4**
V151C-FC[b]	1	0.94	0.60	0.92	36	2.1
	2	0.95	0.56	0.86	41	9.5
		0.95	**0.58**	**0.89**	**39**	**5.8**
V151C-FC[c]	1	0.91	0.52	0.91	43	0

[a] Numbers in bold refer to average values. [b] Measurements at 5 μM of peptide. [c] Measurements at 10 μM of peptide.

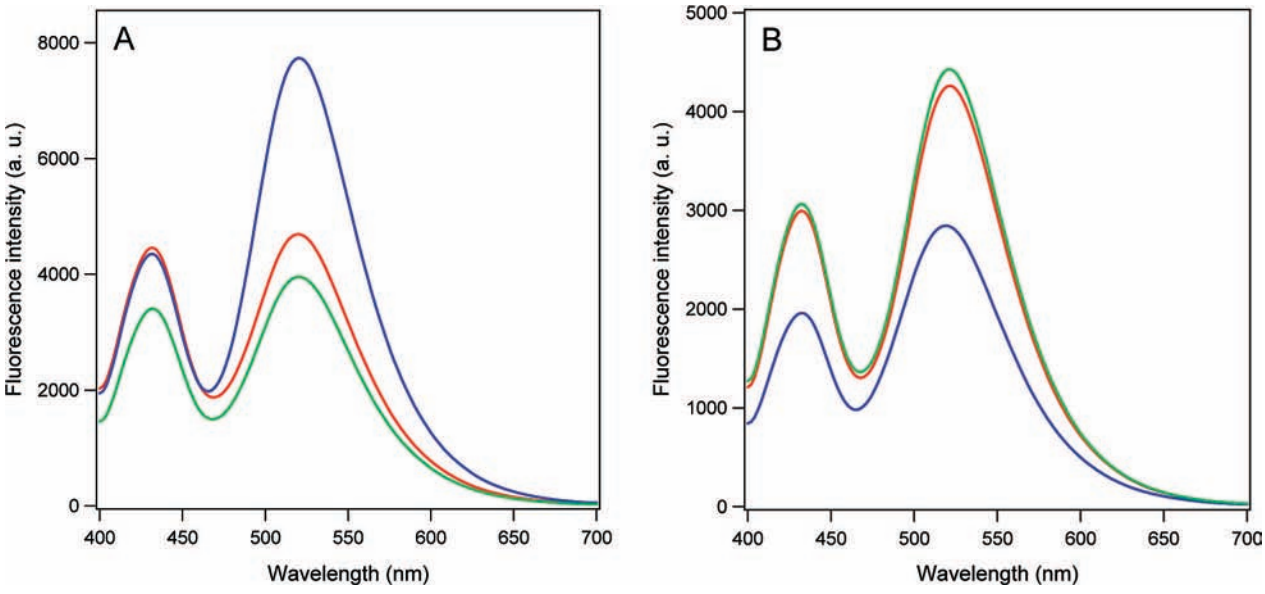

Figure 4. Fluorescence spectra of (a) V151C-FC and (b) S146C-FC in the absence (red) and presence (blue) of saturating amounts of Fab57P. A $F(ab')_2$ fragment with unrelated specificity was used as a negative control (green).

adjacent peptide chain screening it from bulk water. However, attaching BMFC to a polypeptide chain *per se* should not change the emission properties of the fluorophore, since the conjunction is realized through the formation of a thiomethylene group, which should not allow the electronic structure of FC to be modified to any significant extent.

Like in the case of labeling of α-crystallin, the I_{N*}/I_{T*} ratios of S146C-FC (I_{N*}/I_{T*} ~0.7) and V151C-FC (I_{N*}/I_{T*} ~0.9) are dramatically reduced compared to the corresponding value of FC in water (Table 2, Figure 3, Figure 4). The difference in the I_{N*}/I_{T*} value between the two constructs indicates that the choice of labeling site is important, since it can substantially influence the original signal of the molecular biosensor and thus probably the fractional change that can be obtained upon binding of the analyte. The observed spectral difference could reflect the hydrogen-bonding ability of the fluorophore being different in the two positions, as a result of screening from bulk water being less efficient in the case where the probe is attached in the peptide C terminus. However, it is also possible that specific intramolecular interactions between the probe moiety and amino acid residues are responsible for this effect. As confirmed by circular dichroism spectroscopy (data not shown), the peptide constructs do not form any well-defined secondary structure that can aid in determining which of these phenomena are primarily responsible for the spectral differences of S146C-FC and V151C-FC.

For the biosensor evaluation, the fluorescence signal from each peptide construct alone was compared to that where a fraction of >96% of the peptide molecules were bound to Fab57P, according to affinities obtained from the SPR study.

Equimolar amounts of peptide and Fab57P (5 μM or 10 μM) were used. Addition of the analyte to V151C-FC caused a pronounced change in the I_{N*}/I_{T*} ratio, from >0.9 to <0.6 (~40% decrease; Table 2, Figure 4a), without affecting the positions of the N* and T* bands (at 432 and 520 nm, respectively). The most immediate interpretation of this observation is that binding of Fab57P results in a decrease of hydrogen-bonding ability of the probe due to exclusion of water molecules from the interaction site. In contrast, the introduction of a negative control antirabbit $F(ab')_2$ did not have any significant impact on the ratiometric emission profile. V151C-FC thus demonstrates the ratiometric biosensor concept, where the two emission bands are differently affected by the binding of a protein analyte.

In contrast to V151C-FC, S146C-FC did not show any significant change in the I_{N*}/I_{T*} ratio when binding the analyte (Table 2, Figure 4b). This result was rather unexpected taking into account that the fluorophore in S146C-FC is situated very close to the residues most important for binding and should not be less shielded from buffer upon introduction of Fab57P than when attached in the C terminus. It can be speculated that if the spectral differences of the peptide constructs observed in the absence of the analyte can be attributed to specific intramolecular interactions between the peptide and the probe, upon binding of the analyte, these interactions in S146C-FC might be preserved or substituted for similar interactions with residues of Fab57P. However, without any structural data of the binding complex, it is difficult to deduce the detailed biosensor mechanism of V151C-FC and the reason for the insensitivity of S146C-FC to Fab57P binding.

DISCUSSION

Current assays for biomolecular quantification are based on a vast number of different strategies, many of them typically involving a multistep procedure where color reagents or labeled secondary antibodies are used. In contrast, we have focused on the concept of reagentless biosensing, where a single molecular construct integrates recognition specificity and reporting ability (*1*).

The key criterion for a useful fluorescent biosensor construct — attaching the fluorophore in a position where it experiences large environmental differences upon analyte binding but does not interfere with the interaction — was met in a design where the peptide recognition element was labeled seven amino acids away from the residues most important for binding. Interestingly, labeling in the immediate vicinity of the epitope core was not a sufficient condition for the realization of a ratiometric biosensor. The significance of the choice of labeling position when designing a molecular biosensor has also been thoroughly demonstrated on a larger scale by others (*28*, *11*). De Lorimier et al. attached eight environmentally sensitive fluorophores in different amino acid positions of eleven bacterial periplasmic binding proteins. The choice of positions for labeling was based on structural considerations and both allosteric and peristeric sites were addressed. A minority of the resulting 320 constructs were judged as being useful for sensing purposes and in only five protein mutants, there was a biosensor signal above the criterion level from all the analyzed fluorophores (*28*). This shows that rational prediction of a labeling site from where a probe will emit a useful signal is very difficult also when structural data is available, and that the choice of fluorophore may critically influence the biosensor performance. The studies referred to above were focused on the labeling of full-length proteins. Our results indicate that finding a suitable labeling position may require some effort also when targeting peptides. However, the number of candidate positions is more limited, which in combination with straightforward peptide synthesis procedures facilitates screening for the optimal site.

Limited reproducibility in biosensor results sometimes observed for protein constructs labeled with conventional single-band fluorophores (*11*, *29*) may very well be due to batch-to-batch variations in the degree of labeling and in the extent of photobleaching of the fluorophore. Due to the ratiometric nature of detection, the influence of such factors is minimized in the molecular biosensor design reported here. Also, ratiometric signaling will be highly interesting in future microarray applications with immobilized biosensor constructs, since the surface density of immobilized molecules is generally more difficult to control than the concentration in corresponding solution assays.

A challenging issue for the implementation of synthetic molecular biosensors on a more general level is related to binding specificity. Antibodies are highly attractive providers of specific binding, since their recognition ability is extremely versatile with respect to the nature of the analyte. In order to constitute a competitive alternative, synthetic binders displaying high-affinity, specific interactions toward virtually any target are needed. Examples of such classes of molecules are nucleic acid aptamers selected from large combinatorial libraries by selective evolution of ligands by exponential enrichment (SELEX) (*30*, *31*) and affibodies based on a robust, 58 amino acid scaffold protein derived from staphylococcal protein A (*32*–*34*). The combination of such libraries with ratiometric fluorophores attached at carefully selected positions should eventually surpass conventionally labeled protein-based biosensor molecules as components in, e.g., immobilized protein detection platforms, where robustness of the biosensor element with respect to both recognition and signaling is imperative for reliable results.

In conclusion, we have expanded the repertoire of fluorescence strategies available for protein detection assays by demonstrating the concept of wavelength-ratiometric biosensing in solution based on straightforwardly obtained steady-state emission spectra from a two-band fluorophore. Optimization of the labeling position of the recognition element will require some work in future constructs, especially in cases where the recognition site might not be as well-characterized. However, the prospect of reagentless, robust sensing should be a strong motive for investing this effort.

ACKNOWLEDGMENT

This project was supported by Délégation Générale pour l'Armement (DGA; contract number 05 34 013), Carl Tryggers Stiftelse (CTS; contract numbers 05:106 and 06:120), Magn. Bergvalls Stiftelse (MBS), Centre National de la Recherche Scientifique (CNRS), and the European Commission through the Integrated Project Targeting Replication and Integration of HIV (TRIoH).

Supporting Information Available: Additional information on experimental procedures; results from SPR inhibition study. This material is available free of charge via the Internet at http://pubs.acs.org.

LITERATURE CITED

(1) Altschuh, D., Oncul, S., and Demchenko, A. P. (2006) Fluorescence sensing of intermolecular interactions and development of direct molecular biosensors. *J. Mol. Recognit. 19*, 459–477.

(2) Miyawaki, A., Llopis, J., Heim, R., McCaffery, J. M., Adams, J. A., Ikura, M., and Tsien, R. Y. (1997) Fluorescent indicators for Ca^{2+} based on green fluorescent proteins and calmodulin. *Nature 388*, 882–887.

(3) Karlström, A., and Nygren, P. Å. (2001) Dual labeling of a binding protein allows for specific fluorescence detection of native protein. *Anal. Biochem. 295*, 22–30.

(4) Wei, A. P., Blumenthal, D. K., and Herron, J. N. (1994) Antibody-mediated fluorescence enhancement based on shifting the intramolecular dimer-monomer equilibrium of fluorescent dyes. *Anal. Chem. 66*, 1500–1506.

(5) Jiskoot, W., Hoogerhout, P., Beuvery, E. C., Herron, J. N., and Crommelin, D. J. A. (1991) Preparation and application of a fluorescein-labeled peptide for determining the affinity constant of a monoclonal antibody hapten complex by fluorescence polarization. *Anal. Biochem. 196*, 421–426.

(6) Walkup, G. K., and Imperiali, B. (1996) Design and evaluation of a peptidyl fluorescent chemosensor for divalent zinc. *J. Am. Chem. Soc. 118*, 3053–3054.

(7) Hamachi, I., Nagase, T., and Shinkai, S. (2000) A general semisynthetic method for fluorescent saccharide-biosensors based on a lectin. *J. Am. Chem. Soc. 122*, 12065–12066.

(8) Morii, T., Sugimoto, K., Makino, K., Otsuka, M., Imoto, K., and Mori, Y. (2002) A new fluorescent biosensor for inositol trisphosphate. *J. Am. Chem. Soc. 124*, 1138–1139.

(9) Zheng, Y. J., Gattas-Asfura, K. M., Konka, V., and Leblanc, R. M. (2002) A dansylated peptide for the selective detection of copper ions. *Chem. Commun.* 2350–2351.

(10) Sloan, D. J., and Hellinga, H. W. (1998) Structure-based engineering of environmentally sensitive fluorophores for monitoring protein-protein interactions. *Protein Eng. 11*, 819–823.

(11) Renard, M., Belkadi, L., Hugo, N., England, P., Altschuh, D., and Bedouelle, H. (2002) Knowledge-based design of reagentless fluorescent biosensors from recombinant antibodies. *J. Mol. Biol. 318*, 429–442.

(12) Enander, K., Dolphin, G. T., Andersson, L. K., Liedberg, B., Lundström, I., and Baltzer, L. (2002) Designed, folded polypeptide scaffolds that combine key biosensing events of recognition and reporting. *J. Org. Chem. 67*, 3120–3123.

(13) Yem, A. W., Epps, D. E., Mathews, W. R., Guido, D. M., Richard, K. A., Staite, N. D., and Deibel, M. R. (1992) Site-specific chemical modification of interleukin-1-beta by acrylodan at cysteine-8 and lysine-103. *J. Biol. Chem. 267*, 3122–3128.

(14) Mims, M. P., Sturgis, C. B., Sparrow, J. T., and Morrisett, J. D. (1993) Acrylodan can label amino as well as sulfhydryl-groups - results with low-density lipoprotein, lipoprotein a, and lipid-free proteins. *Biochemistry 32*, 9215–9220.

(15) Cho, E. J., Collett, J. R., Szafranska, A. E., and Ellington, A. D. (2006) Optimization of aptamer microarray technology for multiple protein targets. *Anal. Chim. Acta 564*, 82–90.

(16) Kodadek, T. (2002) Development of protein-detecting microarrays and related devices. *Trends Biochem. Sci. 27*, 295–300.

(17) Demchenko, A. P. (2005) The problem of self-calibration of fluorescence signal in microscale sensor systems. *Lab Chip 5*, 1210–1223.

(18) Klymchenko, A. S., Pivovarenko, V. G., and Demchenko, A. P. (2003) Perturbation of planarity as the possible mechanism of solvent-dependent variations of fluorescence quantum yield in 2-aryl-3-hydroxychromones. *Spectrochim. Acta, Part A 59*, 787–792.

(19) Avilov, S. V., Bode, C., Tolgyesi, F. G., Klymchenko, A. S., Fidy, J., and Demchenko, A. P. (2005) Temperature effects on alpha-crystallin structure probed by 6-bromomethyl-2-(2-furanyl)-3-hydroxychromone, an environmentally sensitive two-wavelength fluorescent dye covalently attached to the single Cys residue. *Int. J. Biol. Macromol. 36*, 290–298.

(20) Chatellier, J., Rauffer-Bruyère, N., van Regenmortel, M. H. V., Altschuh, D., and Weiss, E. (1996) Comparative interaction kinetics of two recombinant Fabs and of the corresponding antibodies directed to the coat protein of tobacco mosaic virus. *J. Mol. Recognit. 9*, 39–51.

(21) Al Moudallal, Z., Briand, J. P., and van Regenmortel, M. H. V. (1985) A major part of the polypeptide chain of tobacco mosaic virus protein is antigenic. *EMBO J. 4*, 1231–1235.

(22) Choulier, L., Laune, D., Orfanoudakis, G., Wlad, H., Janson, J. C., Granier, C., and Altschuh, D. (2001) Delineation of a linear epitope by multiple peptide synthesis and phage display. *J. Immunol. Methods 249*, 253–264.

(23) Choulier, L., Rauffer-Bruyère, N., Ben Khalifa, M., Martin, F., Vernet, T., and Altschuh, D. (1999) Kinetic analysis of the effect on Fab binding of identical substitutions in a peptide and its parent protein. *Biochemistry 38*, 3530–3537.

(24) Klymchenko, A. S., Kenfack, C., Duportail, G., and Mély, Y. (2007) Effects of polar protic solvents on dual emissions of 3-hydroxychromones. *J. Chem. Sci. 119*, 83–89.

(25) Ercelen, S., Klymchenko, A. S., and Demchenko, A. P. (2002) Ultrasensitive fluorescent probe for the hydrophobic range of solvent polarities. *Anal. Chim. Acta 464*, 273–287.

(26) Klymchenko, A. S., and Demchenko, A. P. (2003) Multiparametric probing of intermolecular interactions with fluorescent dye exhibiting excited state intramolecular proton transfer. *Phys. Chem. Chem. Phys. 5*, 461–468.

(27) Klymchenko, A. S., and Demchenko, A. P. (2004) 3-Hydroxychromone dyes exhibiting excited-state intramolecular proton transfer in water with efficient two-band fluorescence. *New J. Chem. 28*, 687–692.

(28) De Lorimier, R. M., Smith, J. J., Dwyer, M. A., Looger, L. L., Sali, K. M., Paavola, C. D., Rizk, S. S., Sadigov, S., Conrad, D. W., Loew, L., and Hellinga, H. W. (2002) Construction of a fluorescent biosensor family. *Protein Sci. 11*, 2655–2675.

(29) Renard, M., and Bedouelle, H. (2004) Improving the sensitivity and dynamic range of reagentless fluorescent immunosensors by knowledge-based design. *Biochemistry 43*, 15453–15462.

(30) Ellington, A. D., and Szostak, J. W. (1990) In vitro selection of RNA molecules that bind specific ligands. *Nature 346*, 818–822.

(31) Tuerk, C., and Gold, L. (1990) Systematic evolution of ligands by exponential enrichment - RNA ligands to bacteriophage T4 DNA-polymerase. *Science 249*, 505–510.

(32) Nilsson, B., Moks, T., Jansson, B., Abrahmsen, L., Elmblad, A., Holmgren, E., Henrichson, C., Jones, T. A., and Uhlén, M. (1987) A synthetic IgG-binding domain based on staphylococcal protein A. *Protein Eng. 1*, 107–113.

(33) Nord, K., Nilsson, J., Nilsson, B., Uhlén, M., and Nygren, P.Å. (1995) A combinatorial library of an α-helical bacterial receptor domain. *Protein Eng. 8*, 601–608.

(34) Nord, K., Gunneriusson, E., Ringdahl, J., Ståhl, S., Uhlén, M., and Nygren, P. Å. (1997) Binding proteins selected from combinatorial libraries of an α-helical bacterial receptor domain. *Nat. Biotechnol. 15*, 772–777.

BC800159D

SUPPORTING INFORMATION

A peptide-based, ratiometric biosensor construct for direct fluorescence detection of a protein analyte

Karin Enander,[†]* Laurence Choulier,[‡] A. Linnéa Olsson,[†],[1] Dmytro A. Yushchenko,[§],[2] Daniel Kanmert,[†] Andrey S. Klymchenko,[§] Alexander P. Demchenko,[#] Yves Mély,[§] and Danièle Altschuh[‡]

[†] Dr. K. Enander, A. L. Olsson, D. Kanmert

Division of Molecular Physics, Department of Physics, Chemistry and Biology, Linköping University, 581 83 Linköping, Sweden

[‡] Dr. L. Choulier, Dr. D. Altschuh

Institut Gilbert Laustriat, University Strasbourg 1, CNRS - UMR 7175, ESBS, Bld Sébastien Brant, BP 10413, 67412 Illkirch, France

[§] Dr. D. A. Yushchenko, Dr. A. S. Klymchenko, Prof. Y. Mély

Photophysique des Interactions Biomoléculaires, UMR 7175-LC1 du CNRS, Institut Gilbert Laustriat, Faculté de Pharmacie, Université Louis Pasteur, 67401 Illkirch, France

[#] Dr. A. P. Demchenko

A. V. Palladin Institute of Biochemistry, Leontovicha 9, Kiev 01030, Ukraine

* Corresponding author. E-mail: karen@ifm.liu.se. Phone: +46-13-282359. Fax: +46-13-288969.

[1] Present address: Division of Molecular Surface Physics and Nanoscience, Department of Physics, Chemistry and Biology, Linköping University, 581 83 Linköping, Sweden.

[2] Present address: MPI for Biophysical Chemistry, Department of Molecular Biology, Am Fassberg 11, 370 77 Göttingen, Germany

TABLE OF CONTENTS

EXPERIMENTAL DETAILS

Determination of Fab57P Concentrations……. S3

Immobilization of pTMVP, S146C-FC, and V151-FC for Analysis of Binding Kinetics ……...S3

Inhibition Study……. S4

Determination of Fluorescence Quantum Yields…….. S5

RESULTS

Table S-1. Inhibition Study……S6

REFERENCES…….S6

EXPERIMENTAL DETAILS

Determination of Fab57P Concentrations. The native concentration of Fab57P was determined with a Biacore 2000 instrument (Biacore AB) at 25°C using HEPES-buffered saline (HBS-EP: 10 mM HEPES, 0.15 M NaCl, 3 mM EDTA, 0.005% polysorbate 20, pH 7.4) as the running buffer. C-pTMVP was immobilized to the dextran hydrogel of a Biacore CM5 sensor chip at a flow rate of 10 μl/min using a modified variant of the "ligand thiol" method with 2-(2-pyridinyldithio)ethaneamine (PDEA), described in the BIAapplications Handbook (version AB 1998, Biacore AB). Conventional carbodiimide activation (with a mixture of 250 mM ethyldimethylaminopropylcarbodiimide (EDC) and 50 mM N-hydroxysuccinimide (NHS) during 10 min) was followed by derivatization with PDEA (100 mM in 100 mM sodium borate, pH 8.5, 3.5 min) and deactivation of excess active esters with ethanolamine (1 M, pH 8.5, 3.5 min). After the injection of the peptide (50 μM in 10 mM sodium formate, pH 3.0, 10 min), excess PDEA groups were eliminated by the introduction of cysteine (50 mM in 100 mM sodium formate, 1 M NaCl, pH 4.3, 3.5 min). A high surface concentration of the peptide (~1400 RU) was obtained with this protocol, which allowed for mass-transport limited binding of Fab57P independent of interaction kinetics *(1)*. Purified Fab57P was diluted in HBS-EP prior to analysis, while non-purified, dialyzed protein was introduced without dilution. Fab57P was injected over the sensor chip at a low flow rate (10 μl/min, 1 min) and for each sample the slope of the linear interaction phase was related to a standard curve of Fab57P response vs concentration. Introduction of 50 mM HCl (30 s) between Fab57P injections fully regenerated the sensor surface.

Immobilization of pTMVP, S146C-FC, and V151-FC for Analysis of Binding Kinetics. Coupling to the dextran hydrogel of a Biacore CM5 sensor chip was performed at a flow rate of 10 μl/min. Carbodiimide

activation of carboxylic acid groups with a mixture of 250 mM EDC and 50 mM NHS (4 min) was followed by the introduction of S146C-FC or V151C-FC (2-10 μM in 10 mM sodium acetate pH 4.0, diluted from a 90 μM stock in water) in several short pulses (30-60 s). Deactivation was achieved with 1 M ethanolamine, pH 8.5 (4 min). pTMVP (20 μM in 10 mM sodium acetate pH 5.5, diluted from a 90 μM stock in water) was immobilized with a similar protocol. A reference flow cell was prepared by deactivation with ethanolamine promptly after the EDC/NHS activation.

Inhibition Study. A binding inhibition study was performed with a Biacore 2000 instrument at 25°C with HBS-EP as the running buffer and at a flow rate of 10 μl/min. The sensor chip was the same as that used for the determination of Fab57P concentrations described above, with C-pTMVP immobilized to a level of 1400 RU to allow for mass-transport limited binding profiles. Fab57P was introduced to the surface (20 nM in HBS-EP; 1 min) and the slope of the linear binding curve was compared to slopes obtained when Fab57P (20 nM) was premixed with different concentrations (5, 10, 20 or 50 nM) of pTMVP, S146C-FC, or V151C-FC. Regeneration was achieved with 50 mM HCl between each analyte injection (30 s). Measurements were performed in duplicates. The concentration of unbound Fab57P, [Fab], when mixed with a peptide at total concentration $[P]_{tot}$ is given by

$$[Fab] = -\frac{[P]_{tot} - [Fab]_{tot} + [K_d]}{2} + \sqrt{\left(\frac{[P]_{tot} - [Fab]_{tot} + [K_d]}{2}\right)^2 + [Fab]_{tot} \cdot [K_d]} \qquad \text{(e1)}$$

where $[Fab]_{tot}$ is the total concentration of Fab57P and K_d is the equilibrium dissociation constant describing the interaction. As the slope of the SPR binding curve is directly proportional to the concentration of available Fab57P, expected slopes from Fab57P concentrations calculated from (e1) were obtained from the

binding curve in the case where no peptide was present in the analyte sample. These values were then compared to the experimental data.

Determination of Fluorescence Quantum Yields. Fluorescence quantum yields (Φ) of S146C-FC and V151C-FC were measured in a safire2 microplate detection system (Tecan Trading AG) according to a well-established method *(2)*. Quinine sulfate in 0.1 M H_2SO_4 was used as a reference. Each peptide and quinine sulfate were diluted in HEPES-buffered saline (10 mM HEPES, 150 mM NaCl, pH 7.4) and 0.1 M aqueous H_2SO_4, respectively, to concentrations where their absorbances (A) at 350 nm were close to 0.1. The integrated emission spectra (I) between 382 and 698 nm (λ_{exc} = 350 nm) were recorded and the quantum yield of the peptide (Φ_P) was calculated from

$$\Phi_P = \frac{A_{QS}}{A_P} \cdot \frac{I_P}{I_{QS}} \cdot \Phi_{QS} \qquad \text{(e2)}$$

where the subscripts P and QS refer to peptide and quinine sulfate, respectively. Φ_{QS} = 0.58 *(3)*.

RESULTS

Table S-1. Normalized slopes of SPR binding curves upon interaction between immobilized C-pTMVP and Fab57P mixed with peptides at different concentrations.[a]

[peptide] (nM)		pTMVP	S146C-FC	V151C-FC
5	Calc.	77	82	78
	Exp.	75	85	96
10	Calc.	56	66	58
	Exp.	55	73	72
20	Calc.	25	42	29
	Exp.	14	42	62
50	Calc.	5	16	7
	Exp.	1	5	6

[a]A slope of 100 corresponds to the experimental value obtained in the case where no peptide was present in the analyte sample. Calculated slopes were based on values of K_d obtained in the kinetic analysis. [Fab57P] = 20 nM. Average values from two measurements are shown.

REFERENCES

(1) Karlsson, R., Roos, H., Fägerstam, L., and Persson, B. (1994) Kinetic and concentration analysis using BIA technology. *Methods: Companion Methods Enzymol. 6*, 99-110.

(2) Demas, J. N., and Crosby, G. A. (1971) The measurement of photoluminescence quantum yields. A review. *J. Phys. Chem. 75*, 991-1024.

(3) Eastman, J. W. (1967) Quantitative spectrofluorimetry - the fluorescence quantum yield of quinine sulfate. *Photochem. Photobiol. 6*, 55-72.

Synthesis, ^{18}F-Labeling, and *in Vitro* and *in Vivo* Studies of Bombesin Peptides Modified with Silicon-Based Building Blocks

Aileen Höhne,[†] Linjing Mu,[†] Michael Honer,[†] P. August Schubiger,[†] Simon M. Ametamey,*[,†] Keith Graham,[‡] Timo Stellfeld,[‡] Sandra Borkowski,[‡] Dietmar Berndorff,[‡] Ulrich Klar,[‡] Ulrike Voigtmann,[‡] John E. Cyr,[‡] Matthias Friebe,[‡] Ludger Dinkelborg,[‡] and Ananth Srinivasan[‡]

Center for Radiopharmaceutical Science of ETH, PSI and USZ, Department of Chemistry and Applied Biosciences, ETH Zurich, CH-8093 Zurich, Switzerland, and Bayer Schering Pharma AG, Global Drug Discovery, D-13342 Berlin, Germany.
Received April 17, 2008; Revised Manuscript Received July 11, 2008

The gastrin-releasing peptide receptor (GRPr) is overexpressed on various human tumors. The goal of our study was the synthesis of new ^{18}F-labeled bombesin analogues for the PET imaging of GRPr expression in prostate tumor using a silicon-based one-step n. c. a. radiolabeling method. The silicon-containing building blocks were efficiently coupled to the *N*-terminus of the peptides via solid-phase synthesis. Radiolabeling of the obtained peptide precursors proceeded smoothly under acidic conditions (34−85% conversion). Using the di-*tert*-butyl silyl building block as labeling moiety, products containing a hydrolytically stable ^{18}F-label were obtained. In *in vitro* receptor binding experiments 2-(4-(di-*tert*-butylfluorosilyl)phenyl)acetyl-Arg-Ava-Gln-Trp-Ala-Val-NMeGly-His-Sta-Leu-NH_2 (**4b**, IC_{50} = 22.9 nM) displayed a 12-fold higher binding affinity than 2-(4-(di-*tert*-butylfluorosilyl)phenyl)acetyl-Arg-Ava-Gln-Trp-Ala-Val-Gly-His(3Me)-Sta-Leu-NH_2 (**3b**, IC_{50} = 276.6 nM), and **4b** was therefore chosen for further evaluation. *In vitro* and *ex vivo* metabolite studies of **[^{18}F]4b** showed no significant degradation. In biodistribution experiments, tumor uptake of **[^{18}F]4b** was low and unspecific, whereas the GRPr-rich pancreas revealed a high and specific accumulation of the radiotracer. This study demonstrates the applicability of our silicon-based one-step n. c. a. radiolabeling method for the synthesis of new ^{18}F-labeled bombesin derivatives. This innovative approach represents a general, straightforward access to radiolabeled peptides as PET imaging probes.

INTRODUCTION

Radiolabeled peptides have been the focus of research over the past decades due to their potential as molecular imaging probes and therapeutic agents (*1, 2*). Among the peptides for tumor targeting, bombesin (BBN) and bombesin derivatives have received significant interest as they exhibit high affinity and selectivity for the gastrin-releasing peptide receptor (GRPr) (*3, 4*). The GRPr is overexpressed on various human tumors including prostate, breast, pancreatic, and small cell lung cancers (*5*). With respect to prostate cancer, a high incidence of GRP receptors was found in human normal prostate tissues, in contrast to their very low abundance in non-neoplastic prostatic tissues (*6*). Thus, radiolabeled bombesin peptides are potentially valuable tools for the discrimination of prostate cancers from prostate hyperplasia and prostatitis.

Accordingly, a lot of research has gone into the development of optimized BBN derivatives for imaging and therapy involving a wide range of peptide sequences, labeling moieties, and radionuclides. Research efforts have been devoted in particular to the optimization of peptide sequences leading to improved binding affinity and metabolic stability. The C-terminus of bombesin is required for high-affinity binding and biological potency (*7*); therefore, usually the N-terminus of bombesin is modified in order to allow labeling with radioisotopes. A number of ^{99m}Tc- and ^{111}In-labeled BBN analogues have been developed as diagnostic probes for single-photon emission computed tomography (SPECT) (*8*). For potential peptide receptor radiotherapy applications, ^{90}Y-, ^{177}Lu-, and ^{188}Re-labeled BBN conjugates have been evaluated (*9, 10*).

Despite the obvious advantage of being a more quantitative imaging method with better spatial resolution and image contrast compared to SPECT, PET imaging of GRPr expression has been less studied and labeling of bombesin conjugates has been limited to metallic PET nuclides such as ^{64}Cu, ^{68}Ga, and ^{86}Y (*11, 12*). Among the available PET nuclides, ^{18}F has ideal characteristics for peptide receptor imaging studies regarding its half-life (109.7 min) and low β^+ energy (0.64 MeV) (*13*). However, so far only one report on the ^{18}F-labeling of bombesin analogues including their *in vitro* and *in vivo* evaluation has been published (*14*). ^{18}F has been introduced into two bombesin derivates through the prosthetic labeling group *N*-succinimidyl-4-[^{18}F]fluorobenzoate (^{18}F-SFB). This approach, however, requires a multistep reaction sequence and is therefore laborious. Very recently, Schirrmacher et al. described the two-step radiolabeling of a N-amino-oxy derivatized bombesin peptide using the labeling synthon *p*-(di-*tert*-butylfluorosilyl)benzaldehyde ([^{18}F]SiFA-A) (*15*). Due to low precursor amounts, high specific activities could be obtained (225−680 GBq/μmol for [^{18}F]SiFA-A), although the ^{18}F-fluorination was achieved *via* isotopic exchange. Data from the biological evaluation of this bombesin derivative are currently not available.

We have developed new silicon-based building blocks for the one-step n. c. a. ^{18}F-labeling of biomolecules by nucleophilic displacement of an alkoxy, hydroxy, or hydride leaving group (*16, 17*). These building blocks can be efficiently coupled to the N-terminus of peptides during solid-phase synthesis.

* To whom correspondence should be addressed. (S.M.A.) Center for Radiopharmaceutical Science of ETH, PSI and USZ, ETH Hönggerberg D-CHAB IPW HCI H427, Wolfgang-Pauli-Strasse 10, CH-8093 Zurich, Switzerland. Tel.: +41 44 633 74 63. Fax: +41 44 633 13 67. E-mail address: simon.ametamey@pharma.ethz.ch.

[†] ETH Zurich.

[‡] Bayer Schering Pharma AG.

10.1021/bc800157h CCC: $40.75 © 2008 American Chemical Society
Published on Web 08/28/2008

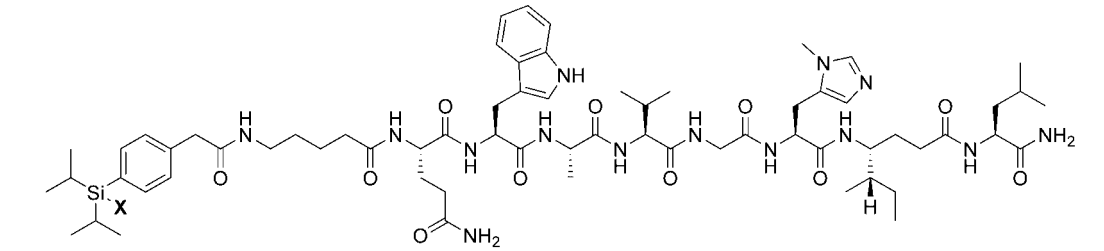

1a: X = OH; **1b**: X = F; **[^{18}F]1b**: X = ^{18}F

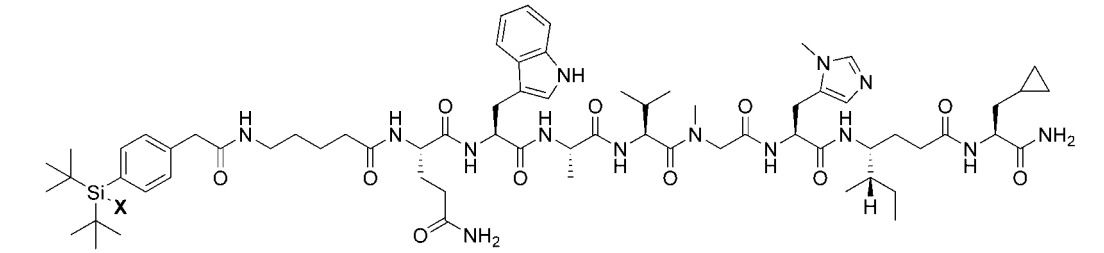

2a: X = H; **2b**: X = F; **[^{18}F]2b**: X = ^{18}F

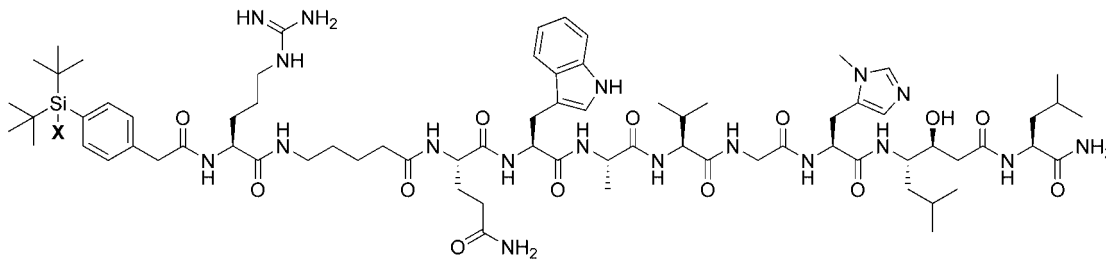

3a: X = H; **3b**: X = F; **[^{18}F]3b**: X = ^{18}F

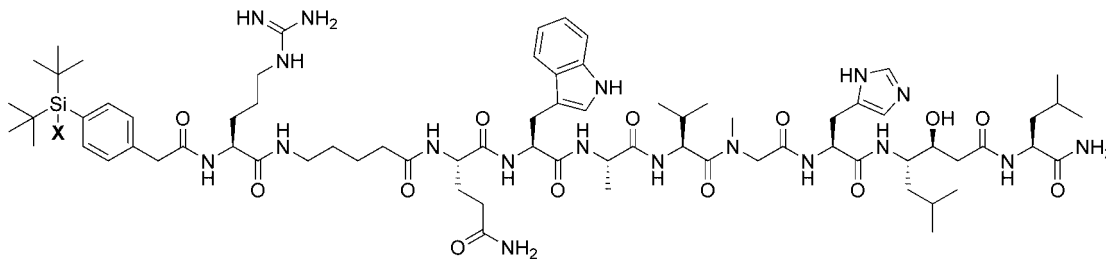

4a: X = H; **4b**: X = F; **[^{18}F]4b**: X = ^{18}F

Figure 1. Structures of bombesin derivatives.

Facile one-step radiolabeling of model compounds and tetrapeptides containing these building blocks could be demonstrated. An ^{18}F-labeled di-*tert*-butyl silyl based tetrapeptide has been shown to be stable against defluorination under physiological conditions (*17*). Here, we report on the application of this one-step labeling protocol to the radiosynthesis of a series of ^{18}F-labeled bombesin analogues (Figure 1). Moreover, we evaluated the analogue with the best *in vitro* binding affinity for its metabolic stability and *in vivo* distribution.

EXPERIMENTAL SECTION

General. All chemicals unless otherwise stated were purchased from Sigma-Aldrich or Merck and used without further purification. The syntheses of 2,5-dioxopyrrolidin-1-yl 2-(4-(hydroxydi-*iso*-propylsilyl)phenyl)acetate and 2-(4-(di-*tert*-butylsilyl)phenyl)acetic acid were previously reported (*17*). Peptide synthesis was carried out using Rink-Amide resin (0.68 mmol/g) following standard 9-fluorenylmethyloxycarbonyl (Fmoc) strategy (*18*). All amino acid residues were, if not further specified, L-amino acid residues. FA01010 is (4*R*,5*S*)-4-amino-5-methylheptanoic acid, Statine (Sta) is (3*S*,4*S*)-4-amino-3-hydroxy-6-methylheptanoic acid, and Ava is 5-aminopentanoic acid.

High-performance liquid chromatography (HPLC) analyses were performed using either a Hamilton PRP-1 (250 × 4.1 mm, 7 μm) or an ACE C18 column (50 × 4.6 mm, 3 μm) and the indicated conditions. Analytical HPLC systems used were Agilent 1100 systems with Gina or Agilent software and a Merck-Hitachi L6200A system, equipped with UV multiwavelength and Raytest Gabi Star detectors. Semipreparative HPLC purifications were carried out using a semipreparative ACE C18 column (250 × 10 mm, 5 μm) and the indicated conditions. Semipreparative HPLC systems used were an Agilent 1100 system equipped with UV multiwavelength and Raytest Gabi Star detector and a Merck-Hitachi L6200A system equipped with Knauer variable wavelength detector and Eberline radiation monitor. UV chromatograms were recorded at 218 or 230 nm. For the *ex vivo* metabolite studies, an Ultraperformance liquid chromatography (UPLC) system from Waters with a Waters

Acquity UPLC BEH C18 column (2.1 × 50 mm, 1.7 μm) and an attached Berthold coincidence detector (FlowStar LB513) was used.

All animal experiments were performed in compliance with the current version of the German law on the Protection of Animals.

Peptide Synthesis. *Fmoc-Deprotection (General Procedure).* The resin-bound Fmoc peptide was treated with 20% piperidine in DMF (v/v) for 5 min. This step was repeated with a reaction time of 20 min. The resin was washed with DMF (2×), CH_2Cl_2 (2×), and DMF (2×).

HBTU/HOBT Coupling (General Procedure). A solution of Fmoc-Xaa-OH (Xaa = amino acid, 4 equiv), HBTU (*O*-(benzotriazol-1-yl)-*N*,*N*,*N*,*N*-tetramethyluronium hexafluorophosphate, 4 equiv), HOBT (1-hydroxybenzotriazole, 4 equiv), DIPEA (*N*,*N*′-di-*iso*-propylethylamine, 4 equiv) in DMF was added to the resin-bound, free amine peptide and shaken for 90 min at room temperature. This step was repeated with a reaction time of 60 min. The resin was washed with DMF (2×), CH_2Cl_2 (2×), and DMF (2×). The peptides were typically prepared starting with 147 mg (100 μmol) of the resin. The amounts of reagents and building blocks in all subsequent reactions were calculated based on this amount.

Synthesis of 3-(3-(Di-iso-propylhydroxysilyl)phenyl)acetyl-Ava-Gln-Trp-Ala-Val-Gly-His(3Me)-FA01010-Leu-NH$_2$ (Precursor Compound **1a***).* The resin-bound, side chain protected peptide was prepared according to the general procedures described above. 2,5-Dioxopyrrolidin-1-yl 2-(4-(hydroxydi-*iso*-propylsilyl)phenyl)acetate (54.5 mg, 150 μmol) was dissolved in DMF (1 mL). The resin-bound peptide (100 μmol) was suspended in this solution and the suspension was shaken for 12 h at ambient temperature. The resin was then filtered, washed with DMF (3 × 3 mL) and CH_2Cl_2 (3 × 3 mL), and dried *in vacuo*. Subsequent treatment of the resin with 2 mL TFA/water/tri-*iso*-propylsilane/phenol (85:5:5:5) afforded the crude, fully deprotected peptide, which was precipitated and washed with cold methyl *tert*-butyl ether. The crude peptide was dried *in vacuo*, purified by preparative RP-HPLC, and lyophilized. The purified peptide (42 mg, 32%) was analyzed by HPLC-MS (*m*/*z* $[M + H]^+$ calcd.: 1311.8, found: 1311.7).

Procedure for the Syntheses of Di-tert-butylsilyl-Functionalized Peptides (Precursor Compounds **2a**−**4a***).* Representative procedure: The resin-bound, side chain protected peptide was prepared according to the general procedures described above. 2-(4-(Di-*tert*-butylsilyl)phenyl)acetic acid (55.7 mg, 200 μmol), HBTU (75.8 mg, 200 μmol), and HOBt (30.6 mg, 200 μmol) were dissolved in DMF (1.5 mL) and DIPEA (68 μL, 400 μmol) was added. The resin-bound peptide (100 μmol) was suspended in this solution and the suspension was shaken for 12 h at ambient temperature. The resin was then filtered, washed with DMF (3 × 3 mL) and CH_2Cl_2 (3 × 3 mL), and dried *in vacuo*. Subsequent treatment of the resin with 2 mL TFA/water/tri-*iso*-propylsilane/phenol (85:5:5:5) afforded the crude, fully deprotected peptide, which was precipitated and washed with cold methyl *tert*-butyl ether. The crude peptide was dried *in vacuo*, purified by preparative RP-HPLC, and lyophilized. The products were analyzed by HPLC-MS:

2-(4-(Di-*tert*-butylsilyl)phenyl)acetyl-Ava-Gln-Trp-Ala-Val-NMeGly-His(3Me)-FA01010-Cpa-NH$_2$ (**2a**, 10 mg, 7.5%): *m*/*z* $[M + H]^+$ calcd.: 1335.8 found: 1335.9.

2-(4-(Di-*tert*-butylsilyl)phenyl)acetyl-Arg-Ava-Gln-Trp-Ala-Val-Gly-His(3Me)-Sta-Leu-NH$_2$ (**3a**, 18.5 mg, 12%): *m*/*z* $[(M + 2H)/2]^+$ calcd.: 748.5, found: 749.0.

2-(4-(Di-*tert*-butylsilyl)phenyl)acetyl-Arg-Ava-Gln-Trp-Ala-Val-NMeGly-His-Sta-Leu-NH$_2$ (**4a**, 33 mg, 22%): *m*/*z* $[(M + 2H)/2]^+$ calcd.: 748.5, found: 749.0.

Synthesis of Fluorinated Peptides (Reference Compounds **1b**−**4b***).* Representative procedure: The silane- or hydroxysilane-functionalized peptide (**1a**−**4a**, 3.3 μmol) was dissolved in THF (0.5 mL). This solution was added to a mixture of KF (0.8 mg, 13.1 μmol), K2.2.2. (Kryptofix 2.2.2., 4.9 mg, 13.1 μmol), and K_2CO_3 (0.9 mg, 6.6 μmol). Glacial acetic acid (2.2 μL, 39 μmol) was added and the resulting suspension was heated at 60 °C for 30 min. The crude mixture was directly subjected to preparative RP-HPLC, and the purified product was lyophilized. The products were analyzed by HPLC-MS:

3-(3-(Di-*iso*-propylfluorosilyl)phenyl)acetyl-Ava-Gln-Trp-Ala-Val-Gly-His(3Me)-FA01010-Leu-NH$_2$ (**1b**, 2 mg, 40%): *m*/*z* $[M + H]^+$ calcd.: 1313.8, found: 1313.5.

2-(4-(Di-*tert*-butylfluorosilyl)phenyl)acetyl-Ava-Gln-Trp-Ala-Val-NMeGly-His(3Me)-FA01010-Cpa-NH$_2$ (**2b**, 2.5 mg, 50%): *m*/*z* $[M + H]^+$ calcd.: 1353.8 found: 1353.8.

2-(4-(Di-*tert*-butylfluorosilyl)phenyl)acetyl-Arg-Ava-Gln-Trp-Ala-Val-Gly-His(3Me)-Sta-Leu-NH$_2$ (**3b**, 3 mg, 59%): *m*/*z* $[(M + 2H)/2]^+$ calcd.: 757.5, found: 758.0.

2-(4-(Di-*tert*-butylfluorosilyl)phenyl)acetyl-Arg-Ava-Gln-Trp-Ala-Val-NMeGly-His-Sta-Leu-NH$_2$ (**4b**, 2 mg, 40%): *m*/*z* $[(M + 2H)/2]^+$ calcd.: 757.5, found: 758.0.

Radiolabeling and Stability Studies. No-carrier-added $[^{18}F]$fluoride was produced via the $^{18}O(p,n)^{18}F$ nuclear reaction by irradiation of enriched $[^{18}O]H_2O$. $[^{18}F]$Fluoride was trapped on an anion-exchange resin cartridge (Sep-Pak QMA light, Waters). The cartridge was eluted with a solution of Kryptofix (K2.2.2., 5 mg) and potassium carbonate (1 mg) in H_2O (0.5 mL) and CH_3CN (1.0−1.5 mL). Solvents were removed by heating at 100−140 °C for 20−30 min applying a gentle stream of nitrogen. During this time, CH_3CN (3 × 1 mL) was added and evaporated to give the dry K$[^{18}F]$F/K2.2.2. complex. The peak of the ^{18}F-labeled products was confirmed by comparison with the HPLC retention time of their nonradioactive reference molecule or by coinjection.

*3-(3-(Di-iso-propyl[^{18}F]fluorosilyl)phenyl)acetyl-Ava-Gln-Trp-Ala-Val-Gly-His(3Me)-FA01010-Leu-NH$_2$ (***[^{18}F]1b***).* A solution of **1a** (2.0 mg) and glacial acetic acid (3 μL) in anhydrous DMSO (150 μL) was added to the dry K$[^{18}F]$F/K2.2.2. complex. After heating at 90 °C for 15−30 min, an aliquot of the reaction mixture was diluted with CH_3CN (1 mL). The crude reaction mixture was analyzed using an analytical HPLC (PRP-1; isocratic 10 mM K_2HPO_4 in CH_3CN/H_2O (7:3)/10 mM K_2HPO_4 in H_2O 55:45, 1.0 mL/min). Hydrolytic stability of the ^{18}F-label was tested by addition of water (9 mL) to the CH_3CN-diluted aliquot of the reaction mixture and analysis of this mixture by HPLC at different time points.

*2-(4-(Di-tert-butyl[^{18}F]fluorosilyl)phenyl)acetyl-Ava-Gln-Trp-Ala-Val-NMeGly-His(3Me)-FA01010-Cpa-NH$_2$ (***[^{18}F]2b***).* A solution of **2a** (1.0−1.5 mg) in anhydrous DMSO (150 μL) was added to the dry K$[^{18}F]$F/K2.2.2. complex. After heating at 70 °C for 30 min or 90 °C for 15 min, an aliquot of the reaction mixture was diluted with CH_3CN (1 mL). The crude reaction mixture was analyzed using an analytical HPLC (PRP-1; isocratic 10 mM K_2HPO_4 in CH_3CN/H_2O (7:3)/10 mM K_2HPO_4 in H_2O 70:30, 0.8 mL/min). The reaction mixture was diluted with H_2O (8−9 mL) and slowly eluted through a Chromafix C18 (s) cartridge. The product was eluted with ethanol (1.5−2 mL) and analyzed by HPLC. Hydrolytic stability of **[^{18}F]2b** was tested by addition of PBS to the ethanolic solution of the product and analyses of this mixture by HPLC at different time points.

*2-(4-(Di-tert-butyl[^{18}F]fluorosilyl)phenyl)acetyl-Arg-Ava-Gln-Trp-Ala-Val-Gly-His(3Me)-Sta-Leu-NH$_2$ (***[^{18}F]3b***).* A solution of **3a** (2.0 mg) and glacial acetic acid (5 μL) in anhydrous DMSO (150 μL) was added to the dry K$[^{18}F]$F/K2.2.2. complex. After heating at 110 °C for 20 min, an aliquot of the reaction

mixture was diluted with CH_3CN (1 mL). The crude reaction mixture was analyzed using an analytical HPLC (ACE C18; gradient 10 mM K_2HPO_4 in CH_3CN/H_2O (7:3)/10 mM K_2HPO_4 in H_2O 5:95−95:5 in 7 min, 2.0 mL/min). The reaction mixture was diluted with HPLC eluent (CH_3CN/H_2O + 0.1% TFA 45:55, 4.0 mL). This solution was injected into a semipreparative HPLC (ACE C18; isocratic CH_3CN/H_2O + 0.1% TFA 45:55, 3.0 mL/min) and the product peak was collected.

2-(4-(Di-tert-butyl[^{18}F]fluorosilyl)phenyl)acetyl-Arg-Ava-Gln-Trp-Ala-Val-NMeGly-His-Sta-Leu-NH$_2$ (**[^{18}F]4b**). A solution of **4a** (2.0 mg) and glacial acetic acid (5 μL) in anhydrous DMSO (150 μL) was added to the dry K[^{18}F]F/K2.2.2. complex and heated at 110 °C for 20 min. An aliquot of the crude reaction mixture was analyzed using an analytical HPLC (ACE C18; gradient CH_3CN/H_2O + 0.1% TFA 5:95−95:5 in 10 min, 1.0 mL/min) either before or after addition of 4.0−4.5 mL HPLC eluent (CH_3CN/H_2O + 0.1% TFA 42:58) into the reaction vial. The diluted reaction mixture was injected into a semipreparative HPLC (ACE C18; isocratic CH_3CN/H_2O + 0.1% TFA 42:58, 3.0 mL/min) and the product peak was collected. The product fraction was diluted with water (20−45 mL) and immobilized on a C18 cartridge (Sep-Pak light C18, Waters, or Chromafix C18 (s), Machery-Nagel). After washing with water (2 × 10 mL), **[^{18}F]4b** was eluted with ethanol or 5% 0.1 N HCl in ethanol (2 mL). The solvent was evaporated at 90 °C. For *in vitro* applications, **[^{18}F]4b** was reconstituted in 0.02 M phosphate buffer or phosphate buffered saline (PBS) containing max. 5% ethanol. For *ex vivo* biodistribution experiments, the radiotracer was reconstituted in 0.9% NaCl containing max 5% ethanol; for *ex vivo* metabolite studies, dried **[^{18}F]4b** was dissolved in PEG-200/H_2O (1:1).

Log *D* Measurement. The experimental determination of distribution coefficient of **[^{18}F]4b** was performed in 1-octanol and 0.06 M phosphate buffer at a pH of 7.4. The two phases were presaturated with each other. 1-Octanol (0.5 mL) and phosphate buffer (0.5 mL) were pipetted into five tubes (1.5 mL) containing of **[^{18}F]4b** (5 μL). The tubes were shaken for 15 min at room temperature and centrifuged (3 min, 5000 U/min). From each tube, 50 μL of each phase was transferred into an empty tube for counting in a γ-counter.

***In Vitro* Receptor Binding Assay.** The receptor affinity of two BBN analogues, **3b** and **4b**, was determined in quadruplicate in a scintillation proximity assay (SPA) using human bombesin 2 receptor membranes (PerkinElmer). The membranes were suspended in 20 mM HEPES, 3 mM $MgCl_2$, 1 mM EDTA, and 10% sucrose (pH 7.4) and kept on ice until use. Assay buffer was 50 mM Tris (pH 7.2, HCl, Roth), 5 mM $MgCl_2$, 1 mM EGTA, 0.3% polyethylenemine solution, protease inhibitor (Roche Diagnostics GmbH, 1 tablet/50 mL). For competition binding studies, membranes solution (106 μg/ml, 10 μL, 1.1 μg protein per well), suspended beads (agglutinin coupled SPA beads, Amersham Bioscience, 40 mg/mL, 10 μL), [^{125}I]-Tyr^4-bombesin (PerkinElmer, specific activity: 81.4 TBq/mmol, 0.50 nM, 20 μL), and increasing concentrations of test compounds (8 pM-1500 nM, 10 μL) were added to well plates to give a final volume of 50 μL. For determination of the total binding, the compound was replaced by the corresponding volume of assay buffer. Unspecific binding was measured using 1000× excess of bombesin. After incubation for 2 h at room temperature, 50 μL of assay buffer was added to the wells. The plates were centrifuged (1700 rpm) and counted in a Top-counter (PerkinElmer). IC_{50} values were calculated using GraFit 5 software (Erithacus software, version 5.0.6). K_i values were calculated using the Cheng-Prusoff equation $\{K_i = IC_{50}/(1 + [L]/K_d)\}$.

***In Vitro* Plasma Stability.** The degradation of **[^{18}F]4b** was investigated in mouse and human plasma from healthy donors. PBS was used as a control. **[^{18}F]4b** was incubated for different time periods (from 0 to 2 h) at 37 °C in PBS, and human and mouse plasma. After incubation, plasma proteins were precipitated with CH_3CN + 0.1% TFA and samples were centrifuged (10 min, 13 000 rpm) at 4 °C. The PBS controls were diluted with the same volume of CH_3CN + 0.1% TFA. The supernatants and PBS controls were analyzed by HPLC (ACE C18; gradient CH_3CN/H_2O + 0.1% TFA 5:95−95:5 in 10 min, 1.0 mL/min). The percentage of intact peptide was determined at different incubation times.

***Ex Vivo* Metabolite Studies.** Mice were injected intravenously with 120−200 MBq of **[^{18}F]4b**). Animals were sacrificed at 10 and 30 min p.i. (one animal per time point), and blood and urine were collected. An aliquot of plasma and urine was mixed with CH_3CN for protein precipitation. The samples were centrifuged (5000 rpm, Megafuge R, Heraeus) and the supernatants were analyzed by UPLC (Waters Acquity UPLC BEH C18; gradient CH_3CN/H_2O + 0.1% TFA 5:95−95:5 in 3 min, 0.8 mL/min).

Biodistribution. The biodistribution experiments were performed using nude mice bearing a human prostate tumor (PC-3). For the induction of tumor xenografts, PC-3 cells (2 × 10^6 cells/mouse) were injected subcutaneously and allowed to grow for four weeks. Animals were injected intravenously with 150 kBq of **[^{18}F]4b** (100 μL, 2.4 fmol). The animals were sacrificed at different postinjection times (from 0.5 to 4 h, $n = 3$ for each time point). Organs and tissues of interest were collected and weighed. The amount of radioactivity was determined in the γ-counter to calculate the uptake (% injected dose per g tissue). In addition, a group of 3 mice received 100 μg of GRP coinjected with the radiolabeled compound and was sacrificed at 1 h postinjection to determine unspecific uptake.

RESULTS

Peptide Synthesis. Peptide synthesis was carried out using Rink Amide resin following standard Fmoc strategy (*18*). Coupling of the resin-bound peptide with the activated ester of 2-(4-(hydroxydi-*iso*-propylsilyl)phenyl)acetic acid was achieved directly in DMF at room temperature, whereas the conjugation with 2-(4-(di-*tert*-butylsilyl)phenyl)acetic acid required the use of a coupling reagent system (HBTU/HOBt/DIPEA). The ^{19}F-reference compounds were obtained by direct fluorination of the appropriate precusors with KF in the presence of Kryptofix K2.2.2. and glacial acetic acid. Representative HPLC-MS chromatograms of a peptide precusor and reference are shown in Figure 2.

Radiolabeling and Hydrolytic Stability Studies. The direct ^{18}F-fluorination protocol developed previously in our laboratory for the radiolabeling of model compounds and tetrapeptides was tested on a series of BBN peptide precursors. To demonstrate the general applicability of the method on targeting peptides, the radiolabeling of a di-*iso*-propylsilyl building block containing a BBN derivative was investigated. A reaction time of 15 min at 90 °C led to an ^{18}F-incorporation of 4% (Table 1, entry 1). However, after heating for another 15 min at the same temperature,^{18}F-incorporation increased to 34% (entry 2). We verified the hydrolytic stability of the ^{18}F-label after the addition of water to an aliquot of the reaction mixture followed by HPLC analysis at different time points. Defluorination of the di-*iso*-propylsilyl building block was observed: the percentage of **[^{18}F]1b** in radiochromatograms decreased to 37% and 13% of the original value within 0.5 and 1 h, respectively.

Subsequently, the radiolabeling of a BBN analogue containing the most stable di-*tert*-butylsilyl building block was studied. The applied nonacidic conditions gave a rather poor ^{18}F-incorporation (entries 3 and 4, Table 1). As the radiolabel was expected to be stable under aqueous conditions, the product was

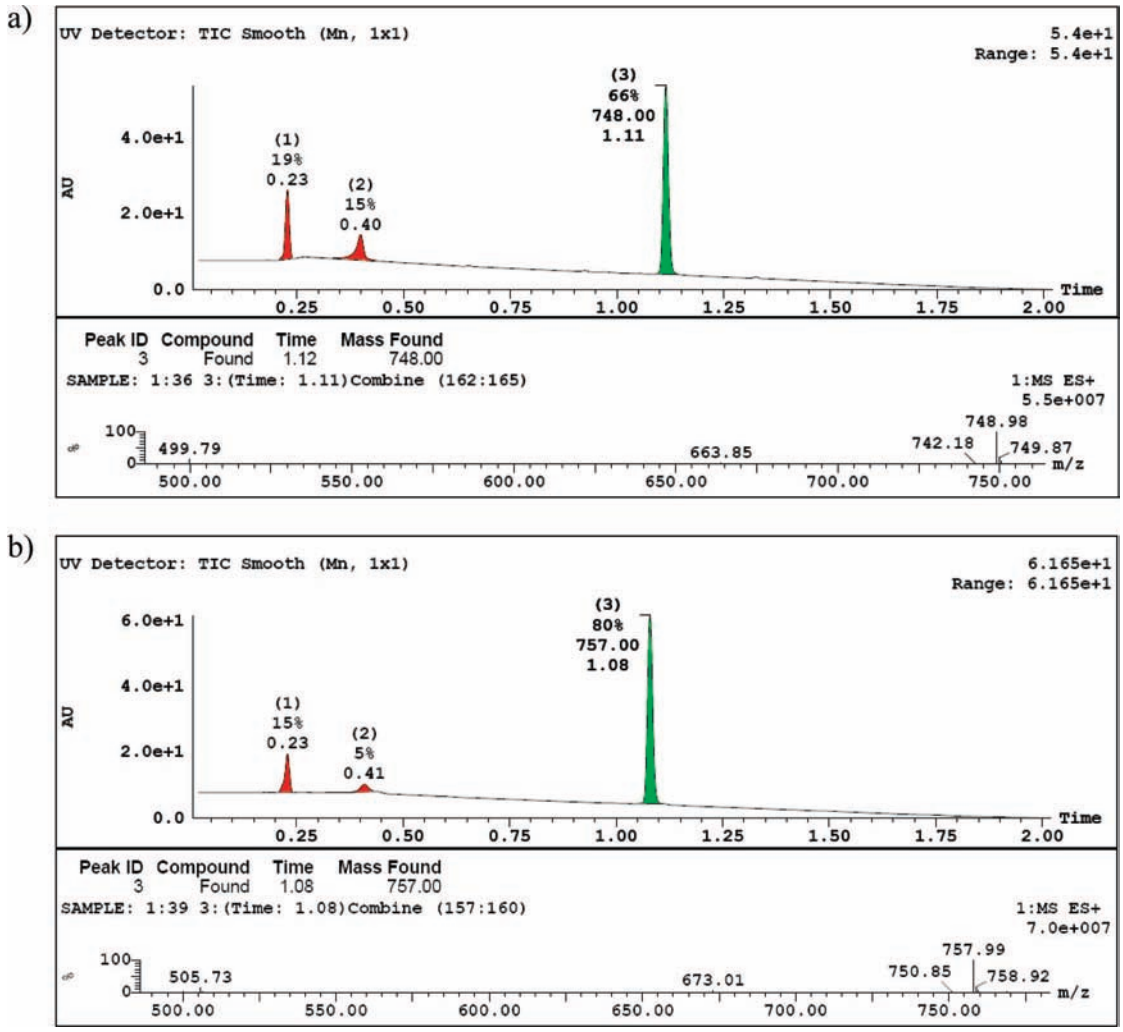

Figure 2. Representative HPLC-MS chromatograms of silyl-functionalized peptides: (a) 2-(4-(di-*tert*-butylsilyl)phenyl)acetyl-Arg-Ava-Gln-Trp-Ala-Val-NMeGly-His-Sta-Leu-NH_2 (**4a**, peak 3 at 1.1 min; peak 1 and 2: system peaks) and (b) 2-(4-(di-*tert*-butylfluorosilyl)phenyl)acetyl-Arg-Ava-Gln-Trp-Ala-Val-NMeGly-His-Sta-Leu-NH_2 (**4b**, peak 3 at 1.08 min; peak 1 and 2: system peaks).

Table 1. Radiolabeling of Bombesin Derivatives

entry	precursor	precursor amount (mg)	acetic acid (μL)	T (°C)	t (min)	^{18}F-incorporation (% HPLC)
1	**1a**	2.0	3	90	15	4
2	**1a**	2.0	3	90	30	34
3	**2a**	1.0	0	70	30	15
4	**2a**	1.5	0	90	15	19
5	**3a**	2.0	5	110	20	85
6	**4a**	2.0	5	110	20	73.5 ± 1.8% [a] ($n = 2$)
7	**4a**	2.0	5	110	20	31.0 ± 2.0% [b] ($n = 2$)

[a] Aliquot directly removed from the reaction mixture. [b] Aliquot taken after dilution of the reaction mixture with HPLC eluent.

purified by solid-phase extraction (SPE) to avoid any influence of the other components in the reaction mixture during the hydrolytic stability study. **[^{18}F]2b** was obtained in 69% radiochemical purity. A minor amount of ^{18}F (6%) and side products (25%) could not be removed by this simple purification method. The stability test of **[^{18}F]2b** in PBS showed that no defluorination occurred within 2 h.

Radiolabeling of **3a** was achieved under acidic conditions (entry 5, Table 1). Starting from 257 MBq ^{18}F, 55 MBq of **[^{18}F]3b** (radiochemical purity >99%) was obtained by semi-preparative HPLC (30% d. c. RCY). **4a** was labeled under the same conditions. If an aliquot was removed from the reaction mixture directly and analyzed by HPLC, the radiochromatograms showed 73.5 ± 1.8% product (entry 6). If an aliquot of the reaction mixture was taken after dilution with HPLC eluent, the percentage of **[^{18}F]4b** measured by HPLC was 31.0 ± 2.0% (entry 7). This is probably an indication that not all of the K[^{18}F]F/K2.2.2. complex was dissolved from the vessel walls into the reaction mixture, and therefore only a certain amount of the K[^{18}F]F/K2.2.2. complex was available for the nucleophilic substitution reaction. HPLC purification and formulation gave **[^{18}F]4b** in 13.1 ± 3.3% radiochemical yield (decay-corrected, $n = 4$) and >95% radiochemical purity (Figure 4a) within 115−155 min. In a typical experiment, 2.78 GBq ^{18}F provided 191 MBq of **[^{18}F]4b** with a specific activity of 62 GBq/μmol (EOS). The distribution coefficient was determined in an equal volume mixture of 1-octanol and 0.06 M phosphate buffer (pH = 7.4). The log D value was 1.3 ± 0.1 ($n = 5$).

In Vitro Receptor Binding Assay. The IC_{50} (K_i) values determined for **3** and **4** were 267.7 (69.7) and 22.9 (5.76) nM, respectively (Figure 3). Due to the higher binding affinity, **[^{18}F]4b** was further evaluated *in vitro* and *in vivo*.

In Vitro and ex Vivo Stability Studies. Metabolite studies did not show any significant degradation of **[^{18}F]4b** in PBS or in mouse or human plasma within 2 h (Figure 4b−d). Also, after injection into mice, no degradation products of **[^{18}F]4b** were observed in blood at 10 and 30 min postinjection. (Figure 5a−c). Metabolite analyses of urine revealed intact labeled peptide and [^{18}F]-fluoride as a metabolite.

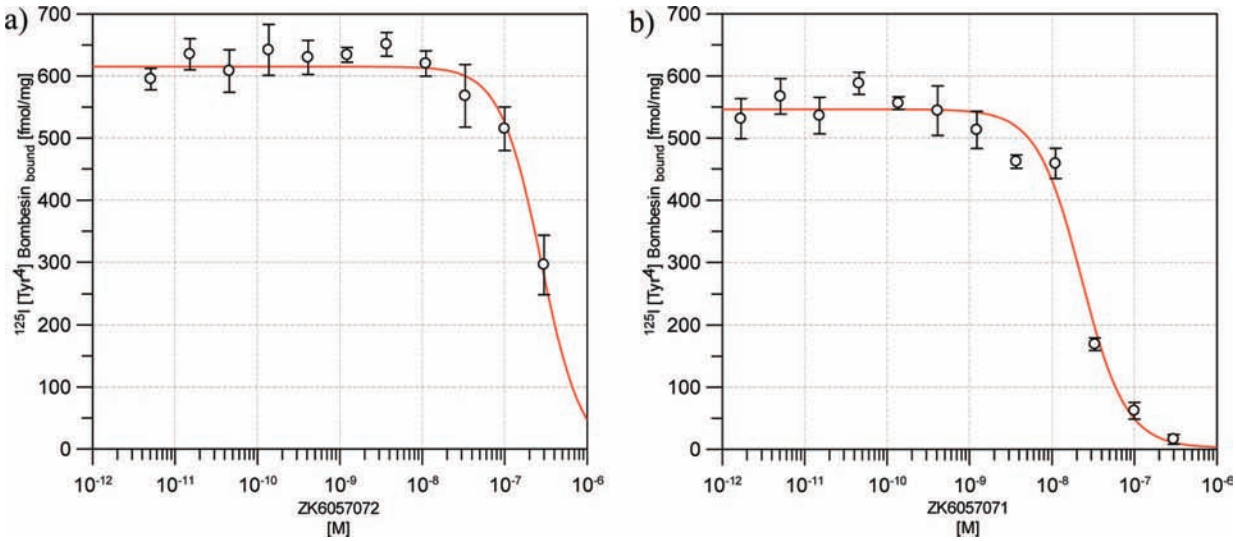

Figure 3. Competitive binding assays of (a) 2-(4-(di-*tert*-butylfluorosilyl)phenyl)acetyl-Arg-Ava-Gln-Trp-Ala-Val-Gly-His(3Me)-Sta-Leu-NH_2 (**3b**) and (b) 2-(4-(di-*tert*-butylfluorosilyl)phenyl)acetyl-Arg-Ava-Gln-Trp-Ala-Val-NMeGly-His-Sta-Leu-NH_2 (**4b**) versus [^{125}I]-Tyr 4-bombesin on human bombesin 2 receptor membranes in a scintillation proximity assay.

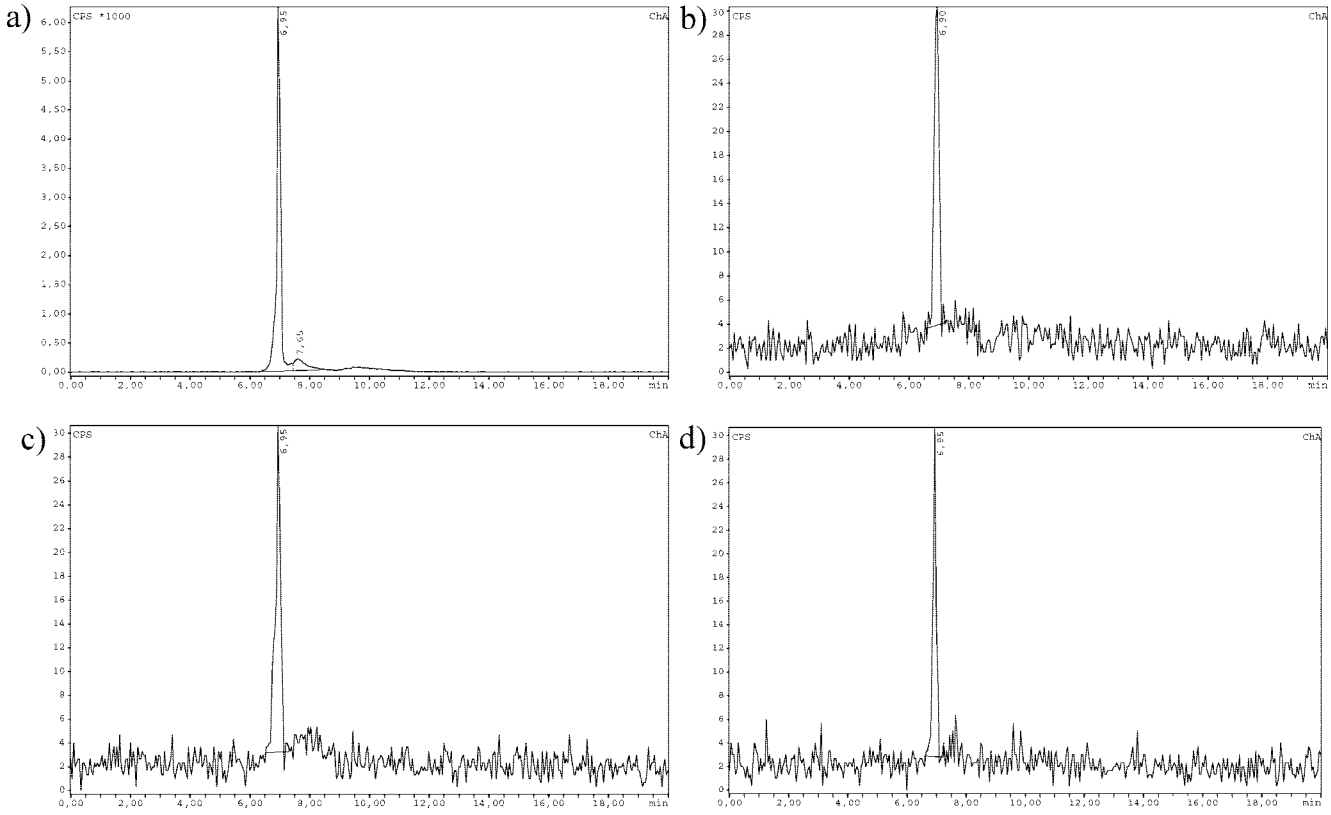

Figure 4. Radio-HPLC profiles of 2-(4-(di-*tert*-butyl[^{18}F]fluorosilyl)phenyl)acetyl-Arg-Ava-Gln-Trp-Ala-Val-NMeGly-His-Sta-Leu-NH_2 (**[^{18}F]4b**): (a) purified compound; (b) after 2 h in PBS; (c) after 2 h in human plasma; and (d) after 2 h in mouse plasma.

Biodistribution. The biodistribution of **[^{18}F]4b** was evaluated in nude mice bearing subcutaneous PC-3 tumors. The results are shown in Table 2. Thirty minutes after injection, tumor uptake was 0.63 ± 0.13%ID/g. It essentially remained steady over the measured period of time and was not reduced by a blocking dose of bombesin. In contrast, uptake in the GRPr-rich pancreas was high (between 5.41 ± 0.12%ID/g 0.5 h p.i. and 3.93 ± 1.11%ID/g 4 h p.i.) and specific (73% uptake reduction in the blocking group). Bone uptake increased from 1.35 ± 0.47%ID/g 0.5 h p.i. to 5.14 ± 2.71%ID/g 4 h p.i. High accumulation of the radiotracer was found in liver, gallbladder, and intestine.

DISCUSSION

Prostate tumors are characterized by low metabolic activity, which impairs the use of the most common, unspecific accumulating PET agents (e.g., FDG, ^{18}F/^{11}C-choline, ^{11}C-acetate) for the imaging of prostate cancer (*19*). A PET tracer with high sensitivity and specificity is needed for the reliable diagnosis of lymph node involvement of prostate cancer at an early stage (first diagnosis) and for the clear discrimination between local

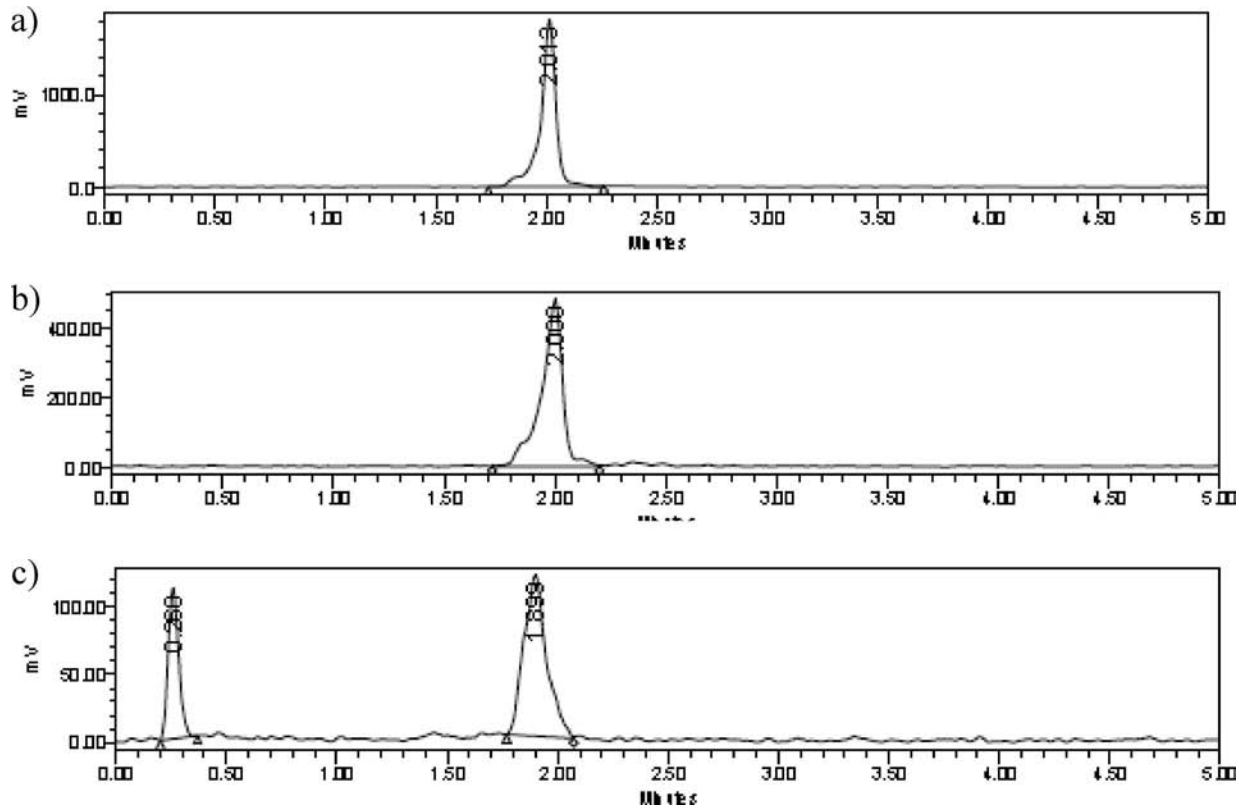

Figure 5. Radio-UPLC profiles of 2-(4-(di-*tert*-butyl[^{18}F]fluorosilyl)phenyl)acetyl-Arg-Ava-Gln-Trp-Ala-Val-NMeGly-His-Sta-Leu-NH_2 (**[^{18}F]4b**): (a) purified compound; (b) in blood 30 min postinjection into mouse; (c) in urine 30 min postinjection into mouse.

Table 2. Biodistribution of 2-(4-(Di-*tert*-butyl[^{18}F]fluorosilyl)phenyl)acetyl-Arg-Ava-Gln-Trp-Ala-Val-NMeGly-His-Sta-Leu-NH_2 ([^{18}F]4b) in Nude Mice with PC-3 Xenografts at Different Times p.i.[a]

tissue	0.5 h	1.0 h	1.0 h[b]	2.0 h	4.0 h
blood	0.95 ± 0.06	0.48 ± 0.01	1.04 ± 0.14	0.42 ± 0.04	0.37 ± 0.11
kidney	2.76 ± 0.27	1.96 ± 0.08	2.18 ± 0.36	1.73 ± 0.24	1.36 ± 0.19
liver	13.56 ± 0.43	7.03 ± 1.69	22.30 ± 2.85	4.40 ± 1.04	3.55 ± 0.83
spleen	1.48 ± 1.50	0.71 ± 0.24	4.38 ± 1.44	0.46 ± 0.06	0.81 ± 0.13
gallbladder	177.65 ± 21.60	259.02 ± 129.67	118.89 ± 161.64	146.40 ± 126.00	146.43 ± 117.44
intestine	12.79 ± 2.96	18.94 ± 6.12	9.05 ± 0.44	15.74 ± 3.78	14.57 ± 2.89
bone	1.35 ± 0.47	2.49 ± 0.08	2.58 ± 0.32	2.67 ± 0.09	5.14 ± 2.71
pancreas	5.41 ± 0.12	4.67 ± 0.71	1.25 ± 0.55	4.08 ± 0.67	3.93 ± 1.11
tumor	0.63 ± 0.13	0.63 ± 0.03	0.61 ± 0.45	0.40 ± 0.05	0.58 ± 0.18

[a] Results are expressed as %ID/g ± SD ($n = 3$). [b] Blockade study: animals received 100 μg of GRP coinjected with the radiolabeled compound.

recurrence and distant metastases in the case of prostate-specific antigen (PSA) level increase after radical prostectomy, since both cases have different therapeutic implications.

Peptides provide excellent characteristics for PET imaging, as they have fast and specific targeting features. They are rapidly cleared from the body, usually mainly via the urinary pathway (*1*). In particular, peptides targeting G-protein coupled receptors are effective in tumor accumulation because the cells internalize them. The gastrin-releasing peptide receptor (GRPr), which is overexpressed on prostatic tumors, belongs to this class of receptors.

We have synthesized new BBN analogues (Figure 1) based on the amino acid sequence 7−14 (Gln^7-Trp^8-Ala^9-Val^{10}-Gly^{11}-His^{12}-Leu^{13}-Met^{14}-NH_2). In order to increase the metabolic stability of this fragment and to allow the attachment of the labeling moiety while retaining the binding affinity, a number of changes were introduced into the molecule. Met^{14} was replaced by Leu for stabilization against aminopeptidase 3.4.11.1, and Leu^{13} was replaced by a non-natural amino acid (FA01010 or Sta) to prevent cleavage by neutral endopeptidase 3.4.24.11 (*20*). Further modifications were the introduction of the methylated versions of His^{12} and/or Gly^{11} and the insertion of a spacer, -Ava- or -Ava-Arg-, between the silicon-based building block and the binding sequence in order to avoid interference of the labeling moiety with the receptor binding C-terminus of the peptide. The new BBN analogues contained either a di-*iso*-propyl or di-*tert*-butyl silyl building block as labeling moiety.

The applicability of the direct labeling method for targeting peptides was successfully demonstrated on a di-*iso*-propyl silyl building block containing BBN derivative **1a**. As expected from previous studies (*17*), defluorination of **[^{18}F]1b** was observed under aqueous conditions. The radiolabeling of BBN analogues modified with the di-*tert*-butyl silyl building block proceeded smoothly under acidic conditions (72−85% conversion), whereas nonacidic conditions gave relatively low yields of ^{18}F-incorporation (15−19%). A preliminary study of the hydrolytic stability of one of the di-*tert*-butyl silyl substituted ^{18}F-labeled peptides showed no defluorination under aqueous conditions.

In vitro receptor binding studies verified a rather poor binding affinity for peptide **3b** (Figure 3, $IC_{50} = 276.6$ nM). Peptide **4b**, however, displayed a 12-fold higher affinity ($IC_{50} = 22.9$ nM) which is in the same range as the affinities of previously reported ^{18}F-labeled bombesin analogues ($IC_{50} = 5.3$ nM for FB-[Lys^3]BBN and $IC_{50} = 48.7$ nM for FB-Aca-BBN(7−14))

(*14*). **[^{18}F]4b** was therefore chosen for *in vitro* and *ex vivo* stability tests. No significant degradation products of **[^{18}F]4b** were detected in PBS, or mouse or human plasma within 2 h (Figure 4b−d). Compound **[^{18}F]4b** also showed high *in vivo* stability in the blood of mice (Figure 5b) demonstrating successful stabilization of the peptide sequence against degradation by endogenous enzymes.

Biodistribution experiments of **[^{18}F]4b** showed low and unspecific tumor uptake. In contrast, the GRPr-rich mouse pancreas revealed a high and specific accumulation of the radiotracer. This result may be explained by the higher receptor densities in pancreas compared to tumor and/or by the better accessibility of the GRPr-expressing pancreatic acini cells in comparison to the weakly vascularized and potentially necrotic PC-3 tumors. Bone uptake gradually increased over time, suggesting a slow defluorination (i.e., silanol formation) of the radiotracer. Due to the lipophilic character of **[^{18}F]4b**, it exhibited a mainly hepatobiliary clearance as suggested by very strong signals in the liver, gallbladder, and intestine.

Significant accumulation of radioactivity in the abdominal region can impair the effective imaging of tumors or metastatic lesions in this area of the body. Assuming that the lipophilicity of the entire molecule is decisive for its *in vivo* behavior (*21*), a reduction of the overall lipophilicity of the radiolabeled peptide may lead to new bombesin derivatives with improved pharmacokinetic profile. An indication of the superiority of less lipophilic peptides is also the prolonged retention of radiometal-labeled BBNs in PC-3 cells, which is most likely due to the lack of cell permeability of the hydrophilic macrocyclic conjugate (*9*, *22*, *23*). Furthermore, intracellular cleavage of the hydrophilic macrocycle from the peptide might lead to trapping of the radiometal inside the cells. On the opposite, ^{18}F-labeled peptides contain inherently a lipophilic labeling moiety. Consequently, ^{18}F-labeled BBNs, after GRPr-mediated internalization, are more amenable to penetration in and out of the cells due to the relatively lipophilic character of both the intact peptide and its radioactive metabolites.

Zhang et al. found in biodistribution studies that the tumor uptake of ^{18}F-FB-[Lys^3]BBN (IC_{50} = 5.3 nM) is relatively high (5.94 ± 0.78%ID/g at 60 min p.i.) compared to another derivative with lower binding affinity (^{18}F-FB-Aca-BBN(7−14), IC_{50} = 48.7 nM, 0.43 ± 0.18%ID/g at 60 min p.i.) (*14*). Hence, a high affinity may partly compensate for the comparatively high lipophilicity of ^{18}F-labeled BBNs. Besides their hydrophilicity, the subnanomolar IC_{50} values of some of the radiometal-labeled BBN derivatives known in the literature (*3*, *4*) are probably another factor for their favorable *in vivo* characteristics. Thus, our future efforts will be directed toward the synthesis of both more potent and more hydrophilic ^{18}F-silyl bombesin peptides for GRPr-targeted PET imaging.

CONCLUSION

This study demonstrates the applicability of our silicon-based one-step n. c. a. radiolabeling method for the synthesis of ^{18}F-labeled bombesin derivatives. Using the di-*tert*-butyl silyl building block as labeling moiety, products containing a hydrolytically stable ^{18}F label were obtained. Biodistribution experiments of a di-*tert*-butyl silyl substituted ^{18}F-labeled bombesin peptide revealed, besides substantial hepatobiliary clearance, low and unspecific uptake in GRPr-positive tumors. To enhance their suitability for the imaging of prostate tumors, optimization efforts toward a reduced overall lipophilicity and higher potency of our ^{18}F-silyl BBNs will be made. In conclusion, we believe that our direct labeling method is transferable to targeting peptides in general and will allow straightforward access to novel PET imaging probes.

ACKNOWLEDGMENT

We gratefully acknowledge Cindy Fischer and Claudia Keller for some experimental support, Dr. Thomas Nauser and Mathias Nobst for technical support, and Marion Kuzora, Bodo Röhr, and Frank Kuczynski for technical assistance.

LITERATURE CITED

(1) Okarvi, S. M. (2004) Peptide-based radiopharmaceuticals: future tools for diagnostic imaging of cancers and other diseases. *Med. Chem. Rev. 24*, 357–397.
(2) Reubi, J. C. (2003) Peptide receptors as molecular targets for cancer diagnosis and therapy. *Endocr. Rev. 24*, 389–427.
(3) Smith, C. J., Volkert, W. A., and Hoffman, T. J. (2005) Radiolabeled peptide conjugates for targeting of the bombesin receptor superfamily subtypes. *Nucl. Med. Biol. 32*, 733–740.
(4) Smith, C. J., Volkert, W. A., and Hoffman, T. J. (2003) Gastrin releasing peptide (GRP) receptor targeted radiopharmaceuticals: a concise update. *Nucl. Med. Biol. 30*, 861–868.
(5) Patel, O., Shulkes, A., and Baldwin, G. S. (2006) Gastrin-releasing peptide and cancer. *Biochim. Biophys. Acta 1766*, 23–41.
(6) Markwalder, R., and Reubi, J. C. (1999) Gastrin-releasing peptide receptors in the human prostate: relation to neoplastic transformation. *Cancer Res. 59*, 1152–1159.
(7) Moody, T. W., Crawley, J. N., and Jensen, R. T. (1982) Pharmacology and neurochemistry of bombesin-like peptides. *Peptides 3*, 559–563.
(8) Varvarigou, A., Bouziotis, P., Zikos, C., Scopinaro, F., and De Vincentis, G. (2004) Gastrin-releasing peptide (GRP) analogues for cancer imaging. *Cancer Biother. Radiopharm. 19*, 219–229.
(9) Zhang, H., Chen, J., Waldherr, C., Hinni, K., Waser, B., Reubi, J. C., and Mäcke, H. R. (2004) Synthesis and evaluation of bombesin derivatives on the basis of pan-bombesin peptides labeled with indium-111, lutetium-177, and yttrium-90 for targeting bombesin receptor-expressing tumors. *Cancer Res. 64*, 6707–6715.
(10) Smith, C. J., Sieckman, G. L., Owen, N. K., Hayes, D. L., Mazuru, D. G., Volkert, W. A., and Hoffman, T. J. (2003) Radiochemical investigation of [^{188}Re(H_2O)(CO)$_3$-diaminopropionic acid-SSS-bombesin(7−14)NH_2]: synthesis, radiolabeling and in vitro/in vivo GRP receptor targeting studies. *Anticancer Res. 23*, 63–70.
(11) Biddlecombe, G. B., Rogers, B. E., de Visser, M., Parry, J. J., de Jong, M., Erion, J. L., and Lewis, J. S. (2007) Molecular imaging of gastrin-releasing peptide receptor-positive tumors in mice using ^{64}Cu- and ^{86}Y-DOTA-(Pro 1,Tyr 4)-bombesin(1−14). *Bioconjugate Chem. 18*, 724–730.
(12) Schuhmacher, J., Zhang, H., Doll, J., Mäcke, H. R., Matys, R., Hauser, H., Henze, M., Haberkorn, U., and Eisenhut, M. (2005) GRP receptor-targeted PET of a rat pancreas carcinoma xenograft in nude mice with a ^{68}Ga-labeled bombesin(6−14) analog. *J. Nucl. Med. 46*, 691–699.
(13) Okarvi, S. M. (2001) Recent progress in fluorine-18 labelled peptide radiopharmaceuticals. *Eur. J. Nucl. Med. 28*, 929–938.
(14) Zhang, X., Cai, W., Cao, F., Schreibmann, E., Wu, Y., Wu, J. C., Xing, L., and Chen, X. (2006) ^{18}F-labeled bombesin analogs for tageting GRP receptor-expressing prostate cancer. *J. Nucl. Med. 47*, 492–501.
(15) Schirrmacher, E., Wängler, B., Cypryk, M., Bradtmöller, G., Schäfer, M., Eisenhut, M., Jurkschat, K., and Schirrmacher, R. (2007) Synthesis of p-(di-tert-butyl[^{18}F]fluorosilyl)benzaldehyde ([^{18}F]SiFA-A) with high specific activity by isotopic exchange: a convenient labeling synthon for the ^{18}F-labeling of N-aminooxy derivatized peptides. *Bioconjugate Chem. 18*, 2085–2089.
(16) Höhne, A., Mu, L., Schubiger, P. A., Ametamey, S. M., Graham, K., Cyr, J. E., Dinkelborg, L., Stellfeld, T., Srinivasan, A., Voigtmann, U., and Klar, U. (2007) Development of new silicon-based building blocks ^{18}F-labeling of biomolecules. *J. Labelled Compd. Radiopharm. 50*, S6.

(17) Mu, L., Höhne, A., Schubiger, P. A., Ametamey, S. M., Graham, K., Cyr, J. E., Dinkelborg, L., Stellfeld, T., Srinivasan, A., Voigtmann, U., Klar, U. (2008) Silicon-based building blocks for one-step ^{18}F-radiolabeling of peptides for PET imaging. *Angew Chem., Int. Ed. 47*, 4922–4925.

(18) Fields, G. B., and Noble, R. L. (1990) Solid phase peptide synthesis utilizing 9- fluorenylmethoxycarbonyl amino acids. *Int. J. Pept. Protein Res. 35*, 161–214.

(19) Fanti, S., Nanni, C., Ambrosini, V., Gross, M. D., Rubello, D., and Farsad, M. (2007) PET in genitourinary tract cancers. *Q. J. Nucl. Med. Mol. Imaging 51*, 260–271.

(20) Davis, T. P., Crowell, S., Taylor, J., Clark, D. L., Coy, D., Staley, J., and Moody, T. W. (1992) Metabolic stability and tumor inhibition of bombesin/GRP receptor antagonists. *Peptides 13*, 401–407.

(21) Smith, C. J., Gali, H., Sieckman, G. L., Higginbotham, C., Volkert, W. A., and Hoffman, T. J. (2003) Radiochemical investigations of ^{99m}Tc-N_3S-X-BBN 7−14 NH_2: An in vitro/in vivo structure-activity relationship study where X = 0-, 3-, 5-, 8-, and 11-carbon tethering moieties. *Bioconjugate Chem. 14*, 93–102.

(22) Rogers, B. E., Bigott, H. M., McCarthy, D. W., Della Manna, D., Kim, J., Sharp, T. L., and Welch, M. J. (2003) MicroPET imaging of a gastrin-releasing peptide receptor-positive tumor in a mouse model of human prostate cancer using a ^{64}Cu-labeled bombesin analogue. *Bioconjugate Chem. 14*, 756–763.

(23) Scopinaro, F., De Vincentis, G., Corazziari, E., Massa, R., Osti, M., Pallotta, N., Covotta, A., Remediani, S., Di Paolo, M., Monteleone, F., and Varvarigou, A. (2004) Detection of colon cancer with ^{99m} Tc-labeled bombesin derivative (^{99m}Tc-leu13-BN1). *Cancer Biother. Radiopharm. 19*, 245–252.

BC800157H

Shape Effects of Nanoparticles Conjugated with Cell-Penetrating Peptides (HIV Tat PTD) on CHO Cell Uptake

Ke Zhang,[†,‡] Huafeng Fang,[†] Zhiyun Chen,[†] John-Stephen A. Taylor,[†] and Karen L. Wooley*[,†,‡]

Department of Chemistry, Washington University School of Arts and Sciences, 1 Brookings Drive, Saint Louis, Missouri 63130, and Department of Radiology, Washington University School of Medicine, 510 South Kingshighway Boulevard, Saint Louis, Missouri 63110. Received April 18, 2008; Revised Manuscript Received May 30, 2008

In order to probe the nanoparticle shape/size effect on cellular uptake, a spherical and two cylindrical nanoparticles, whose lengths were distinctively varied, were constructed by the selective cross-linking of amphiphilic block copolymer micelles. Herein, we demonstrate that, when the nanoparticles were functionalized with the protein transduction domain of human immunodeficiency virus type 1 Tat protein (HIV Tat PTD), the smaller, spherical nanoparticles had a higher rate of cell entry into Chinese hamster ovary (CHO) cells than did the larger, cylindrical nanoparticles. It was also found that nanoparticles were released after internalization and that the rate of cell exit was dependent on both the nanoparticle shape and the amount of surface-bound PTD.

INTRODUCTION

The plasma membrane of a cell serves as one of the major barriers against inward transportation of extraneous materials, such as a gene and/or a nanoscale synthetic delivery system. Modern synthetic designs have incorporated various cell-penetrating peptides (CPPs), borrowed initially from virus particles, to facilitate their uptake by cells through a receptor-independent pathway (*1*), whose mechanism is not yet completely understood. The ability of a nanostructure to translocate across the cell plasma membrane is of fundamental and practical interest, and will determine the possible outcomes of the nanomaterial in a biological context. Nanostructures of various sizes, shapes, and chemical compositions have gained access to the cell's interior with or without the assistance of CPPs, including metal nanoparticles (*2*), dendrimers (*3*), liposomes (*4*), single-walled carbon nanotubes (*5*), virus mimics (*6*), and so forth. However, the amount of assistance provided by the CPPs for the nanoparticles to be internalized by a cell may be limited (*7*); eventually, the influence of the size and geometric features of the cargo will become increasingly important. Recently, Chan et al. (*2, 8*) probed the effects of size and shape, for penetratin-coated gold nanoparticles within the 10−100 nm range, on the endo- and exocytosis by mammalian cells. A nonlinear relationship between size and uptake was found, and 50 nm spherical particles were identified as having the highest cell uptake. On the micrometer scale, Mitragotri et al. investigated the shape effect by synthesizing a variety of geometrically anisotropic polystyrene particles, whose phagocytosis rates were found to be strongly dependent on the shape of the microparticle (*9*). However, a study to compare across the 10−1000 nm region using particles of similar chemical nature is still unavailable. The mechanism of CPP-assisted cell internalization of the cylindrical structure (several μm in length), which was recently discovered to enhance *in vivo* circulation times much beyond that which can be achieved by other morphologies (*10*), remains largely unknown. It is, therefore, of interest to bridge the gap between nanoscale and microscale structures, in terms of comparing and understanding their CPP-assisted cell uptake and release.

Advances in the design and synthesis of well-controlled block copolymers have given rise to the rapid growth of a new class of complex nanostructures having various compositions, morphologies, sizes, and physical and biological properties (*11*−*13*), which can serve as the primary materials for examination of the effects of nano- to microstructure size and shape on cell internalization. For example, shell-cross-linked assemblies of amphiphilic block copolymers have in recent years attracted researchers to explore their biological and medicinal uses (*14*−*17*). These shell-cross-linked nanoparticles have enhanced stability compared to micelles and are capable of carrying biologically active molecules, which drastically change the biological behavior of the nanoparticles (*15, 18*). In this work, we take advantage of the vast array of morphologies available to polymer micelle-based nanoparticles (*19*−*23*) and their ability to allow for chemical modifications (*24, 25*) in order to study the shape and size effects of a nanoscopic particle in a cellular system.

Herein, we report a method to create spherical and cylindrical nanostructures, of different lengths, from self-assembly of block copolymers. After functionalizing the nanostructures with the protein transduction domain of human immunodeficiency virus type 1 Tat protein (HIV Tat PTD, one commonly used CPP, having the sequence GYGRKKRRQRRR), we demonstrate that the smaller spherical particles (on the 10 nm scale) are internalized by CHO cells more rapidly than are the larger cylindrical particles (20 or 30 nm diameters and larger than 200 nm in one dimension). It is also shown that, upon cellular uptake, the spherical particles are released from the cell, and the rate of release is also dependent on the amount of PTD loading.

EXPERIMENTAL PROCEDURES

Polymer Synthesis. All polymers used in this study were synthesized by atom transfer radical polymerization, according to literature procedures (*26*).

Peptide Synthesis. The ivDde-protected HIV Tat PTD peptide (sequence: GGYGRK(ivDde)K(ivDde)RRQRRR) was synthesized manually by standard Fmoc solid-phase chemistry. The two ivDde protecting groups for lysine were intentionally left on the peptide prior to and following cleavage from the

* klwooley@artsci.wustl.edu.
† Department of Chemistry.
‡ Department of Radiology.

10.1021/bc800160b CCC: $40.75 © 2008 American Chemical Society
Published on Web 08/09/2008

solid support, using 95% trifluoroacetic acid/2.5% triisopropylsilane/2.5% water solution (volume fractions) for 90 min. The beads were treated with cleavage solution 3 times total, and the solutions were combined and concentrated *in vacuo*. The concentrate was precipitated into cold ether, and the precipitates were centrifuged at 3500 rpm for 10 min. The supernatant was decanted, the pellet was resuspended in cold ether, and the centrifugation process was repeated. The pellet was purified by reversed-phase HPLC. MS (MALDI-ToF): 2087.532 $[M + H]^+$ (calcd: 2087.529).

Spherical Micelle Formation. Spherical polymer micelles of narrow size distribution were obtained by dissolving the block copolymer PAA_{128}-*b*-PS_{40} (32.5 mg) in DMF (35 mL) followed by gradual addition (4 mL/h) of an equal volume of nonsolvent (H_2O) for the hydrophobic polystyrene to induce micellization. The micelles were stirred for 4 h before being transferred to presoaked and rinsed dialysis bags (MWCO 6−8 kDa) and dialyzed against nanopure water (18.0 M·cm) for 3 days to remove the organic solvent. The final volume was 115 mL of aqueous micelle solution for a final concentration of 0.28 mg/mL. TEM: 11 ± 2 nm (diameter).

Short Cylindrical Micelle Formation. PAA_{96}-*b*-PS_{48} block copolymer (10 mg) was dissolved in THF (50 mL) and was dried in a round-bottom flask *in vacuo*, leaving a thin membrane of the polymer in the flask. To the flask, nanopure water (58.8 mL) was added and then sonicated while rotating in an aqueous sonicator (VMR Aquasonic 75T) for 40 min. The resulting solution contained short cylindrical micelles, which gave a light-blue color to the solution, a characteristic of the light scattering caused by the cylindrical micelle assemblies. The final concentration was 0.17 mg/mL. TEM: 180 ± 120 nm (length) and 20 ± 2 nm (cross-sectional diameter).

Shell-Cross-Linked Spherical and Short Cylindrical Nanoparticle Formation. The aqueous solutions of spherical and short cylindrical micellar assemblies of PAA_{128}-*b*-PS_{40} and PAA_{96}-*b*-PS_{48}, respectively, were individually mixed with *O*-bis-(aminoethyl)ethylene glycol (0.15 equiv, relative to the molar number of available COOH groups) and allowed to stir at room temperature. After 30 min, an aqueous solution of 1-[3′-(dimethylamino)propyl]-3-ethylcarbodiimide hydrochloride (EDCI) (1 equiv, relative to the molar number of available COOH groups) was added. The reaction mixture was allowed to stir overnight before being transferred to presoaked and rinsed dialysis tubing (MWCO 3 kDa) and dialyzed against nanopure water (18.0 M·cm) for 3 days.

Long Cylindrical Shell-Cross-Linked Nanoparticle formation. To a solution of triblock copolymer PAA_{94}-*b*-PMA_{103}-*b*-PS_{28} (8.4 mg) in THF (8.00 mL) with stirring was added a solution of THF (2.0 mL) containing *O*-bis-(aminoethyl)ethylene glycol (0.93 mg, 0.15 equiv, relative to COOH groups). The mixture was allowed to stir overnight at room temperature, and then H_2O (40 mL) was added at a rate of 7.50 mL/h to induce micellization. To this water−THF mixture, EDCI (5.6 mg) was added to cross-link the shell domain of the micelle and to lock the morphology (*27*). The premixing of the diamine cross-linker with the triblock copolymer is essential to the formation of the desired morphology (*19*). After stirring overnight, the reaction mixture was transferred to presoaked and rinsed dialysis tubing (MWCO 6−8 kDa) and dialyzed against nanopure water (18.0 M·cm) for 3 days to remove the organic solvent. The final volume was 61.3 mL of aqueous cross-linked long, cylindrical micelle solution for a final concentration of 0.14 mg/mL. TEM: 970 ± 900 nm (length) and 30 ± 2 nm (cross-sectional diameter).

Functionalization with Fluorescent Tag. The respective shell-cross-linked nanoparticle solutions were diluted to the same molar concentration (7.5 μM polymer) and each was placed into a round-bottom flask and cooled to 0 °C using an ice bath. A mixed solution of 1:1 EDCI/*N*-hydroxysulfosuccinimide (sulfo-NHS) was added to each nanoparticle solution (1.2:1 molar ratio, relative to the available COOH groups) to activate the acrylic acid residues. After 30 min, aliquots of Alexa Fluor 594 cadaverine stock solution were added to each flask and the mixtures were allowed to react overnight. The solutions were then transferred to presoaked dialysis tubing (MWCO 6−8 kDa) and allowed to dialyze for 5 days against nanopure water.

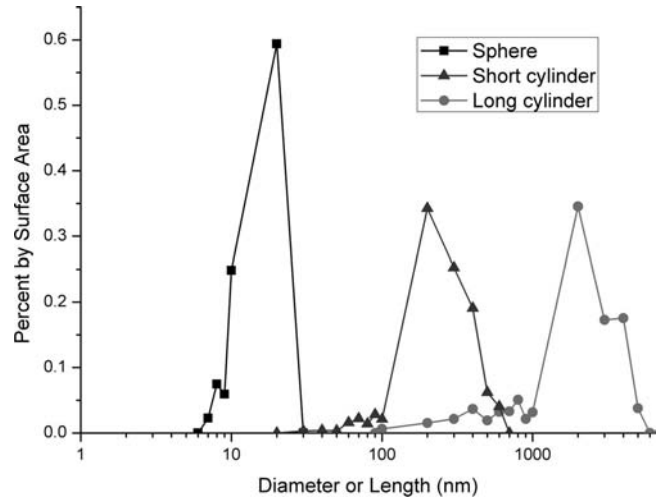

Figure 1. Size distribution by surface area. The size of the three nanostructures is each separated by an order of magnitude.

Functionalization with PTD. Shell-cross-linked nanoparticle solutions prefunctionalized with Alexa Fluor 594 were each placed into a 25 mL round-bottom flask. Sodium chloride was placed into each flask to give a concentration of 5.0 mg/mL, to minimize particle−particle aggregation. The flask was then placed in an ice bath. A mixed solution of 1:1 EDCI/sulfo-NHS was added to each nanoparticle solution (1.2:1 molar ratio, relative to the available COOH groups) to activate the acrylic acid residues. A stock solution (18.21 mg/mL) of the ivDde-protected PTD peptide was made in nanopure water, and aliquots of the solution were added to the respective flasks 30 min after the addition of EDCI/NHS. The pH of each reaction mixture was adjusted to 7.40 using pH = 8.00 sodium phosphate buffer. The mixtures were allowed to react overnight. The solutions were then transferred to presoaked dialysis tubings (MWCO 12 kDa) and allowed to dialyze for 5 days against nanopure water. At the end of dialysis, the nanoparticle solutions were treated with 2.0% hydrazine for 20 min to remove the ivDde protecting groups, and then the pH was adjusted to 6.50 using pH = 6.34 sodium phosphate buffer. The solutions were then transferred to presoaked dialysis tubings (MWCO 100 kDa) for a second-stage dialysis over a period of 15 days. UV−vis measurements confirmed coupling of the PTD peptide to the shell-cross-linked nanostructures (*18*). Removal of the ivDde protecting groups under these reaction conditions was confirmed by MALDI-ToF mass spectrometry for a model reaction performed upon nonconjugated PTD peptide (Figure 3).

Cell Line and Fluorescence Confocal Microscopy. Chinese hamster ovary cells (CHO-K1) were incubated in Ham's F-12K containing 10% FBS and 1% antibiotics (penicillin−streptomycin, 10 000 U/mL) at 37 °C in a humidified atmosphere containing 5% CO_2. 5×10^5 CHO cells were plated at 35 mm MatTek glass-bottom microwell dishes (MatTek Co.). After 24 h, the medium was replaced with 1.0 mL of fresh medium containing no FBS and combined with the respective nanoparticle solutions (100 μL each, at 7.5 μM). The plates were then returned to the incubator to incubate at 37 or 0 °C. Following desired incubation

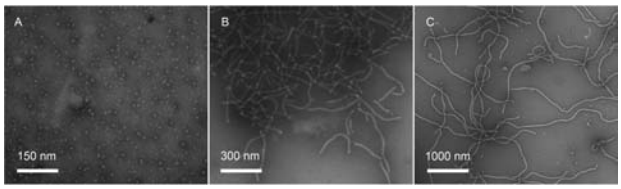

Figure 2. TEM of PAA_{128}-*b*-PS_{40} (A), PAA_{98}-*b*-PS_{48} (B), and PAA_{94}-*b*-PMA_{103}-*b*-PS_{28} (C) micelles in nanopure water.

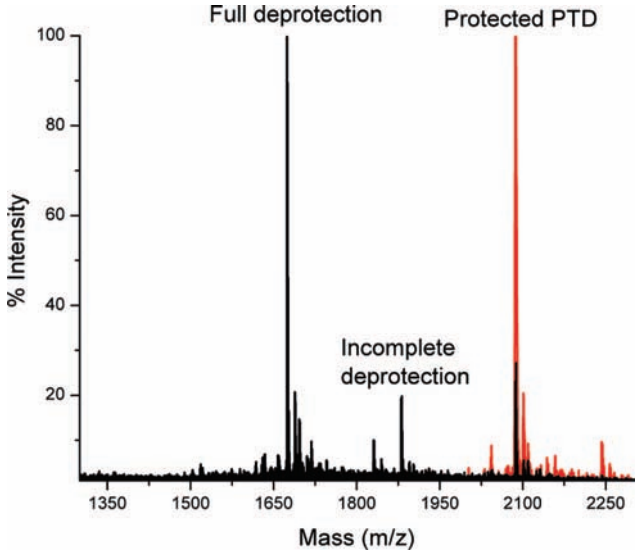

Figure 3. Overlaid MALDI-ToF spectra of ivDde-protected PTD before and after treatment with 2.0% hydrazine for 20 min in water. Adequate removal of ivDde (>70%) was achieved, despite the deprotection reaction being less efficient in water than in organic solvent.

times, the nanoparticles were removed, and each well was washed with Hanks Balanced Salt Solution (HBSS) (3 × 5.00 mL) and viewed under bright field and fluorescent conditions using a Leica TCS SP2 inverted microscope.

Quantitative Analysis of Confocal Images. The background levels of the red channel containing the signal of Alexa Fluor-labeled nanoparticles for each image were determined and subtracted from the original image. Then, individual cells in that image were manually selected and measured. A minimum of 120 cells were measured for each time point of each sample, and 10 cells with highest intensities and 10 cells with lowest intensities were removed. The mean intensity values and standard deviation values were calculated. The background levels were determined using the following method: (1) Binary masks corresponding to nanoparticles-associated fluorescence were generated ($Mask_{NP0}$). Threshold levels were determined by visual inspection. (2) $Mask_{NP0}$ was inverted by applying a NOT operation to generate a binary mask for the background ($Mask_{bg}$). (3) The inverted mask $Mask_{bg}$ was multiplied with the original red channel, Red_0, and the mean value of the resulting image, containing only the signals of the background, was determined as the background level. Cell fluorescence intensities were determined by the following method: (1) Background noise was subtracted from the original signal, Red_0, giving Red_1. (2) Binary masks were generated ($Mask_{NP1}$) for Red_1. Threshold levels were determined by visual inspection. (3) $Mask_{NP1}$ was multiplied by Red_1. (4) Over the resulting image, individual cells were manually selected as regions of interest (ROI), and mean intensities were recorded for each cell.

Cytotoxicity Assay. The cytotoxicity of PTD−nanoparticle conjugates was examined by CellTiter-GloLuminescent Cell Viability Assay (Promega Co.). The CHO-K1 (ATCC) cells were seeded in the 96-well plate at a density of 1×10^4 cells/well and cultured for 24 h in 100 μL Ham's F-12K containing 10% FBS. Thereafter, the medium was replaced with 100 μL of fresh medium containing various concentrations of nanoparticles. After 24 h incubation at 37 °C, 100 μL CellTiter-Gloreagent was added. Contents were mixed and the plate was allowed to incubate at room temperature for 10 min to stabilize luminescence signals. Luminescence intensities were recorded on a Luminoskan Ascentluminometer (Thermo Scientific) with an integration time of 1 s per well. The relative cell viability was calculated by the following equation:

$$\text{Cell viability (\%)} = (\text{luminescence}_{(\text{sample})} / \text{luminescence}_{(\text{control})}) \times 100$$

where $\text{luminescence}_{(\text{control})}$ was obtained in the absence of particles and $\text{luminescence}_{(\text{sample})}$ was obtained in the presence of particles. Polyfect dendrimer (Qiagen, Inc.), a known toxic compound, was used as a positive control. Data are shown as mean ± SD ($n = 6$).

RESULTS AND DISCUSSION

In order to validate size/shape effects of the nanoparticle carrier in their cell internalization characteristics, mediated by PTD peptide, two series of nanoparticle solutions were prepared. The first series included the same spherical structures with increasing loadings of PTD; the second series contained particles having the same amount of PTD but increasing particle length in one dimension (from 10 nm to several μm). The first series was used to probe the effectiveness of PTD on cell internalization, while the second series was used to probe the size/shape effect.

We designed and synthesized shell-cross-linked nanoparticles of different sizes and spherical or cylindrical shapes and then performed further functionalization for fluorescent labeling and PTD attachment to afford the two series of materials (Scheme 1). The spherical nanoparticle was assembled from a diblock copolymer (poly(acrylic acid)$_{128}$-*b*-polystyrene$_{40}$, PAA_{128}-*b*-PS_{40}). The short and long cylindrical nanoparticles were assembled from a diblock and a triblock copolymer, PAA_{98}-*b*-PS_{48} and poly(acrylic acid)-*b*-poly(methyl acrylate)-*b*-polystyrene (PAA_{94}-*b*-PMA_{103}-*b*-PS_{28}), respectively. All three particles were nominally 30% cross-linked in the shell domain, using standard procedures (*28*). The spherical particle had an average diameter of 11 ± 2 nm, as evidenced by transmission electron microscopy (TEM). The short cylinder had an average cross-sectional diameter of 20 ± 2 nm, and an average length of 180 ± 120 nm. The long cylinder had an average cross-sectional diameter of 30 ± 2 nm, and an average length of 970 ± 900 nm (Table 1). TEM images (Figure 1) show the morphologies of the three nanostructures.

Functionalization of the nanostructures with both the fluorescent tag (Alexa Fluor 594 cadaverine) for confocal microscopy and the Tat PTD peptide was achieved by using carbodiimide chemistry. Attachment of the Alexa Fluor 594 to the nanostructures was performed first. To ensure that all final solutions had the same amount of total fluorescence, the solution of spherical particles was then split for further labeling with different amounts of PTD (at levels of 0.5%, 1%, and 2% consumption of total COOH groups of the PAA_{128}-*b*-PS_{40}), while the solutions of cylindrical nanostructures were functionalized at a level that coincided with the 1% labeling of the spheres. Higher loadings of PTD (up to 6%, which correlates to several hundred peptides per nanoparticle) for the spherical particles were possible, although the particle dispersions appeared to become unstable, leading to aggregation observed as solution cloudiness. In addition, in our trial of 2.0% loading for the long cylindrical particles, precipitation was observed.

Scheme 1. Block Copolymers (PAA_{128}-*b*-PS_{40}, PAA_{98}-*b*-PS_{48}, and PAA_{94}-*b*-PMA_{103}-*b*-PS_{28}) Were Micellized by Different Procedures, To Afford Spherical and Cylindrical Nanoparticles of Different Cross-Sectional Diameters and Lengths

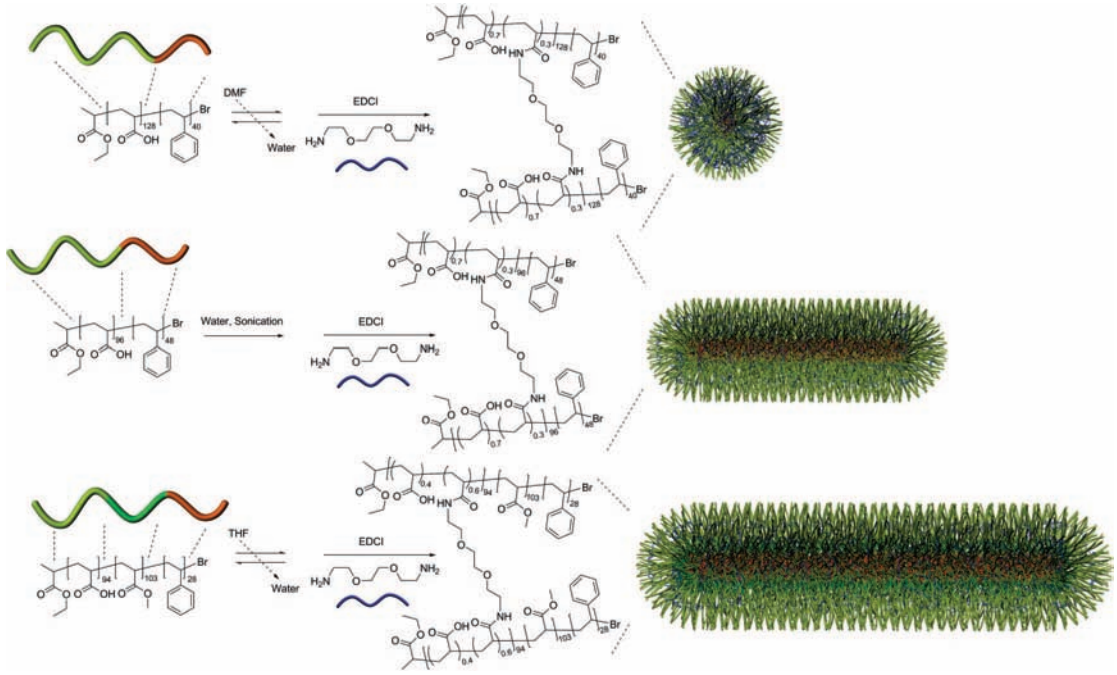

Table 1. Dimensions of the Nanostructures Evaluated

sample	cross-sectional diameter (nm)	length (nm)
sphere	11 ± 2	n. a.
short cylinder	20 ± 2	180 ± 120
long cylinder	30 ± 2	970 ± 900

Therefore, to ensure comparison of all three sizes, 1.0% PTD loading was used for both cylindrical nanoparticles. Because the Tat PTD has two lysine residues, whose side chain amine could compete with the terminal amine for the activated carboxylic acid on the nanoparticle, ivDde protecting groups were used to cap the lysine residues and were subsequently removed, after the Tat PTD was coupled to the nanoparticle (Scheme 2). A model study on aqueous ivDde removal by matrix-assisted laser desorption ionization-time of flight (MALDI-ToF) mass spectrometry demonstrated adequate removal under reaction with 2% hydrazine in water (Figure 3). These reaction conditions were fairly mild to the nanoparticle framework, although some amount of the AlexaFluor 594 cadaverine was cleaved. Therefore, all samples, even the control particles without PTD, were treated to these deprotection reaction conditions. Extensive dialysis was used to remove unbound peptide, which previously had been reported to be effective (*18*). Both the fluorescent dye and the Tat PTD were loaded successfully within the nanoparticles, as evidenced by UV−vis spectroscopy (Figure 4), although it is not clear whether all detected peptide was covalently bound or electrostatically adsorbed onto or absorbed into the nanoparticles, due to their oppositely and highly positively charged characteristics. The UV absorbances of the nanoparticles at 263 and 300 nm correspond with the absorbances of tyrosine in the PTD peptide. Although the cylinder samples were both nominally labeled with 1% PTD, the short cylinder appeared to have slightly more than 1% PTD and the long cylinder less than 1% PTD. This result may be due to some extent of light scattering that occurred for the relatively large nanostructures (Figure 5). After functionalization, the morphologies of each nanostructure did not undergo discernible changes, as confirmed by TEM (images not shown).

Because the PTD peptides were conjugated after the micellization and cross-linking and should be present on the particles' surfaces, the surface areas of the nanostructures determine the number of peptides loaded onto each particle given the total amount of PTD peptide, assuming the particles' densities are similar (*29*). The three nanostructures each represented a unique size distribution, with the greatest percentage surface area for each morphology being separated by an order of magnitude (Figure 1).

Biocompatibility is a major concern when external substances are introduced to a living organism. In the current work, cytotoxicity is of particular importance because disruption of cellular uptake behavior due to toxicity can lead to a false understanding of the relationship between particle shape/size and cellular uptake. Low toxicity has been observed for shell-cross-linked nanoparticles comprising poly(acrylic acid) shells, even after conjugation of the PTD peptide sequence. As had been determined for spheres of similar composition to those studied here, loss in mouse myeloma B cell viability occurred only at concentrations above 500 mg/L (*30*). We considered it important to determine the cytotoxicity for the uniquely shaped structures against the CHO cells employed for the cell uptake experiments, and therefore, we further assessed the cytotoxicity of 1% PTD-functionalized spheres and cylinders. The CellTiter-Glo Luminescent cell viability assay (Promega Co.) was used to examine the cell viability of CHO-K1 cells, following exposure to PTD-shell-cross-linked nanoparticle conjugates. In the concentration range and time period over which the cell uptake experiments were performed, no adverse effects to cell viability were observed by this assay (Figure 9), thus confirming the general understanding that poly(acrylic acid)-shell particles are of low cytotoxicity, even when 1% PTD is conjugated (Figure 2).

To verify the effectiveness of CPP, spherical particles of the same size loaded with different amounts of CPP (series 1) were incubated with CHO cells at a concentration of 0.68 μM (polymer) at 37 and 0 °C for 1 h. Confocal microscopy imaging of nonfixed, live cells suggests that CPP had a pronounced enhancement in the uptake of the nanoparticles by the CHO cells (Figure 6). The highest amount of PTD loading, 2.0%,

Scheme 2[a]

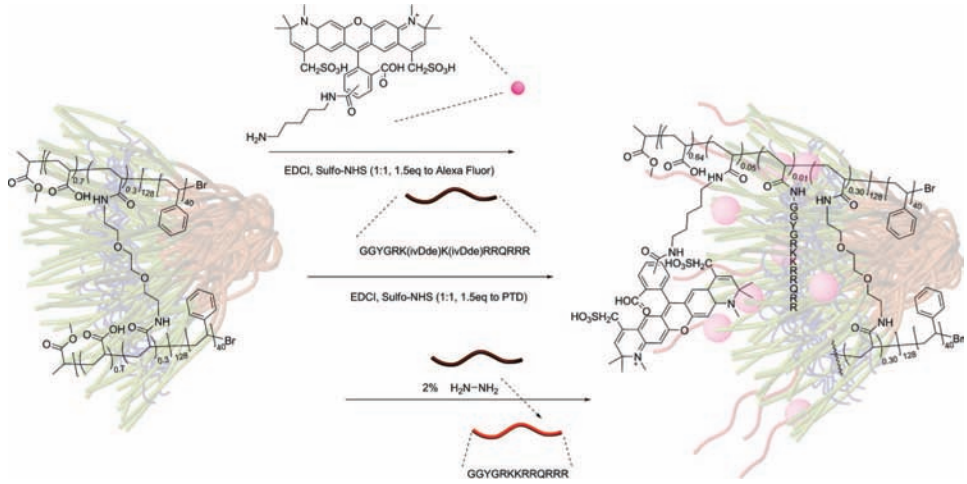

[a] Functionalization of the spherical nanoparticle sample was achieved through a three-step synthesis. Alexa Fluor 594 and protected PTD were respectively coupled to the nanoparticle via carbodiimide chemistry. The ivDde protecting groups were removed by treatment with a 2.0% hydrazine solution in water.

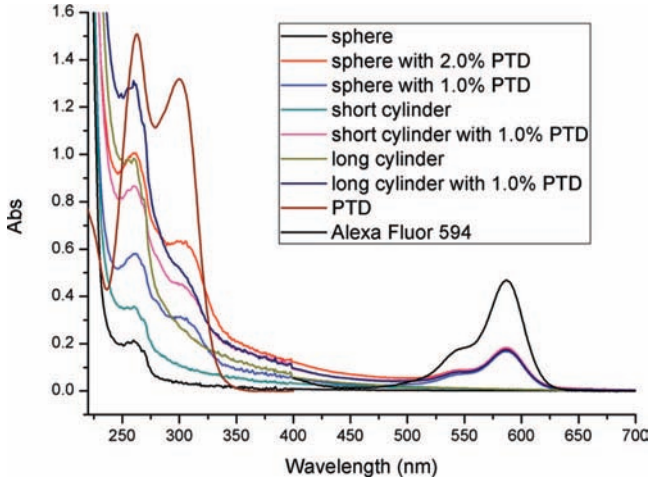

Figure 4. UV−vis spectra of spheres and cylinders labeled with Alexa Fluor 594 cadaverine and PTD peptide. The absorbances at 263 and 300 nm for the nanoparticle solutions correlate with the absorbances of the PTD peptide, and the absorption at 594 nm correlate with the absorbance of the fluorescent tag, Alexa Fluor 594.

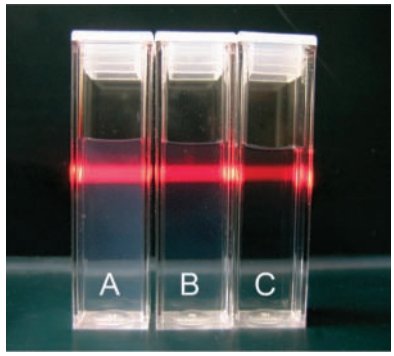

Figure 5. Light scattering of the long cylinders complicates accurate UV−vis measurement. A: Long cylinders. B: Short cylinders. C: Spheres.

gave nanoparticles that exhibited nearly a 5-fold increase in cell uptake at 37 °C than the nanoparticles without PTD. Incubation at 0 °C, under otherwise identical conditions, resulted in little cell uptake. The difference in cell uptake at different temperatures can be due to reduced membrane permeability at low temperatures, to the energy dependency of the uptake process, or to both. An interesting phenomenon we noticed is that the PTD−nanoparticle conjugates were both contained within cellular vesicles and partly spread into the cytoplasm, with exclusion from the nucleus, whereas PTD alone has been reported to accumulate selectively in the cell nucleus (*31, 32*). This observation is possibly due to the overall negatively charged nature of the PTD−particle conjugate or may be due to comparisons among different cell lines.

To probe the size/shape effect, we loaded the three differently shaped particles with a fixed amount of PTD (equivalent to 1% of the carboxylates of PAA_{128}-*b*-PS_{40}) and incubated CHO cells in their solutions (0.68 μM polymer) at 37 °C for 1 h. It was found that the smaller, spherical particle had higher cell uptake than the larger, cylindrical nanoparticles (Figure 7). In other words, a higher molar amount of polymer was internalized by the cell, through the spherical particles, relative to the cylindrical nanostructures, when both forms had the same molar concentration of polymers. On the basis of these results, we can speculate on the general mechanisms that govern the transduction of the PTD-functionalized nanomaterials. Many variables determine the uptake rate, including adhesion rate and receptor diffusion kinetics. Freund et al. (*33*) and Bao et al. (*34*) have modeled these factors and developed a hypothesis involving "wrapping time" of the membrane: the shorter the wrapping time, the faster the uptake. It has been predicted theoretically by this model that, through the competition between thermodynamic driving force and diffusion kinetics, there is an optimum radius for efficient "wrapping", which is 27−30 nm. Because the early endocytic vesicles are usually less than 100 nm in diameter (*6*), most short cylindrical particles (average length = 170 nm) would have to be curved or bent to be internalized, which requires additional energy. Therefore, although the cylindrical particles have higher surface area and hence more membrane−particle interaction (less diffusion), the system is not able to either overcome the overall lack of thermodynamic driving force caused by having to bend the cylinders to "fit" in the endosomes or create larger endocytic vesicles to contain the cylindrical nanostructures. Another factor, for the higher uptake of the small, spherical particle by the cell at a given time, is the higher particle molar concentration for the spheres, which is the result of the lower aggregation numbers of polymer chains to form the spherical particles, compared with the cylindrical particles. For example, the average long cylinder occupies ca. 1000 times as much volume as does the sphere, based on calculations from

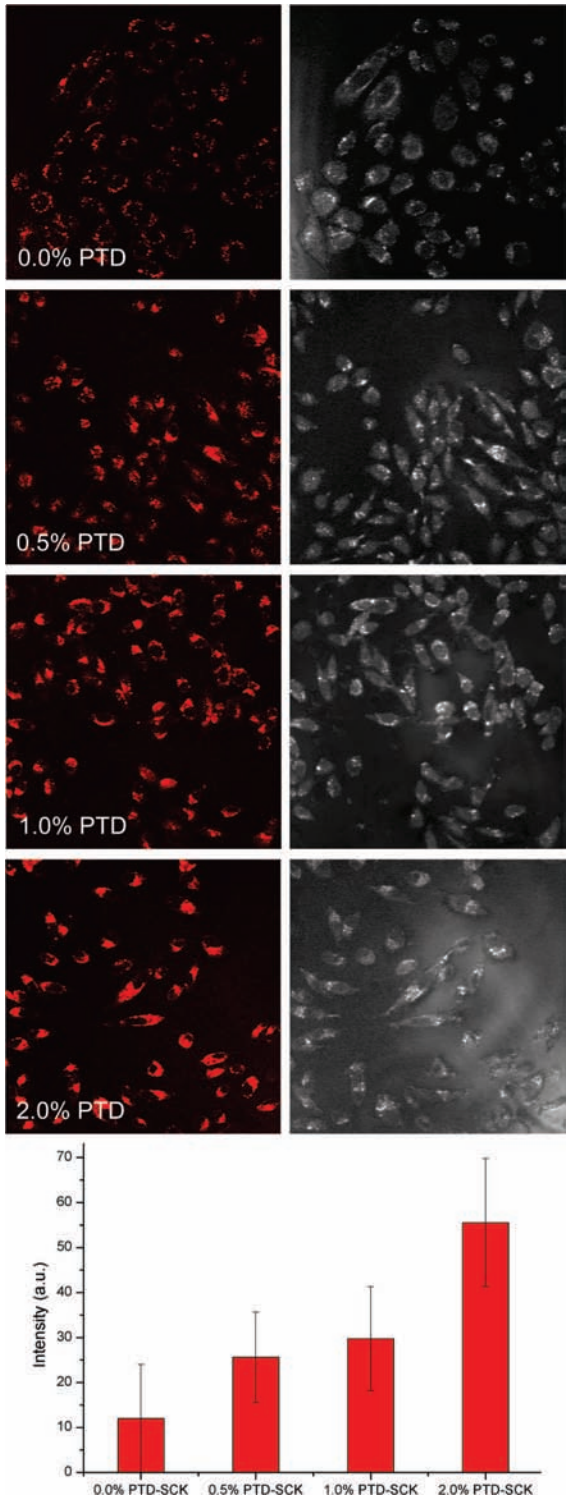

Figure 6. Confocal images of CHO cells incubated with the spherical nanoparticles having different amounts of PTD for 1 h. Cell uptake of PTD−sphere conjugates increased by the action of increasing loadings of surface-bound PTD peptide, as shown in the bar graph.

TEM cross-sectional and longitudinal measurements. It would be extremely difficult, or perhaps impossible, to investigate these materials at the same molar concentration of particles and allow for their observation in cell assays at a usable concentration range (i.e., to compare one of our micrometer-length cylinders vs one of the 10 nm particle requires a difference in material mass and number of chromophores by several orders of magnitude). Therefore, the experiments were performed at the same molar concentration of polymer (vide supra), which

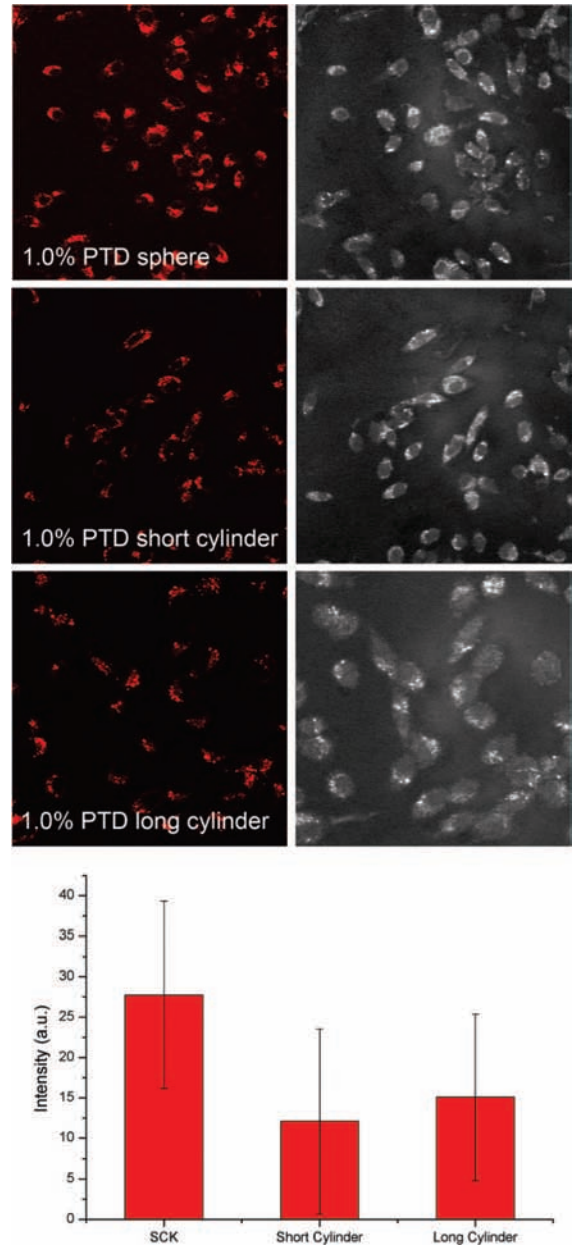

Figure 7. When conjugated with the same amount of PTD peptide, greater amounts of the smaller, spherical nanoparticles were internalized than were the larger, cylindrical nanoparticles as shown in the bar graph. Images were taken after 1 h of incubation.

corresponded to higher molar concentrations of spherical vs cylindrical nanostructures.

Last, we investigated the release of the PTD−nanoparticle conjugates from CHO cells. CHO cells were incubated with 0.68 μM particle solutions for 1 h at 37 °C. Following the incubation period, the nanoparticle-containing solutions were removed, the cells were washed with PBS, and serum-free RPMI 1640 media was introduced, followed by further incubation. Fluorescence monitoring of CHO cells immediately after buffer change and at 2, 4, and 8 h time points revealed that fluorescence intensity decreased over time for spherical nanoparticles labeled with 2%, 1%, and 0.5% PTD, suggesting particles being released from the cell (Figure 8). The rates of release of spherical particles appeared to be dependent on the amount of PTD loaded on the nanoparticle, for which the highest loading (2%) led to the fastest release. This result could suggest that PTD-assisted particle transduction works in a two-way fashion: both entry and exit seem to be facilitated by PTD (*35*). The cells that had

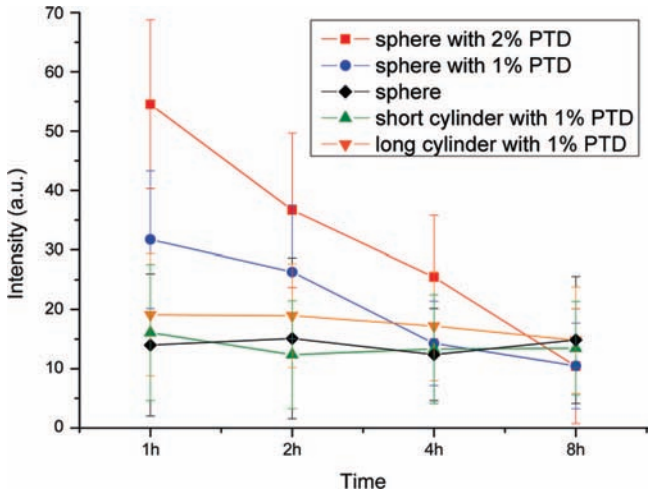

Figure 8. Release profile of series 1 nanoparticles (spherical in shape; different amounts of PTD peptide) and series 2 nanoparticles (different shapes; each with 1.0% PTD peptide conjugation).

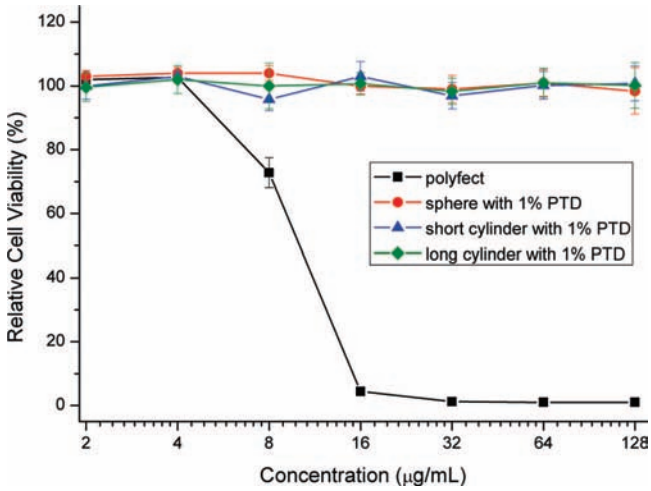

Figure 9. Relative cell viability of CHO-K1 cells in the presence of PTD-functionalized nanoparticles and polyfect dendrimer (Qiagen Inc.). Data are shown as mean ± SD ($n = 6$).

been incubated with spheres having no PTD did not show apparent decrease of fluorescence over 8 h. Both the long and short cylinders behaved similarly to the spheres without the PTD peptide, showing little uptake and no measurable release. Other PTD-independent processes, such as peptide degradation, are possible, and thus more detailed studies on cell uptake and release of differently shaped nanostructures are needed to reveal a fuller picture of the mechanisms involved.

CONCLUSIONS

The self-assembly of block copolymers afforded spherical nanostructures and cylindrical nanostructures having distinctive lengths required to investigate the effects of different particle sizes and shapes, across a wide size range (10−1000 nm), upon cell transduction. Attachment of the Tat cell penetration peptide of HIV-1 improved cell internalization of the spheres. The amount of cell uptake was a function of PTD loading, with increasing amounts of PTD providing for increasing levels of cell internalization at a given time point. Attachment of PTD to the small cylinders (∼200 nm) and long cylinders (∼1000 nm) did not produce a detectable increase in cell uptake. Once internalized, the PTD−spherical nanoparticle conjugates escaped from the cell at a rate that was a function of PTD loading. The observation of reversible cell transduction will become important, as these nanostructures are functionalized also with ligands that are designed to probe intracellular targets, so that escape from cells lacking the target can be facilitated to allow for the nanostructures to accumulate in the designated cells.

The polymer micelle-based nanoparticles in this study have enabled comparison of size and shape on cellular uptake, for materials that have the same surface chemistry, differing only in their core composition, size, and shape. Further studies are required to understand fully the mechanisms by which the particle characteristics lead to the observed differences in cellular uptake and release. Moreover, the particles and the methodologies for functionalization described herein can be employed for fundamental studies that extend to systems involving ligand−receptor interactions to promote endocytosis, which will be important to gain new insights into the interface of biological systems with synthetic nanostructures. These results also serve as a guideline in engineering artificial nanoscale carrier particles for drug delivery, where the control of size/shape is of significance.

ACKNOWLEDGMENT

The authors gratefully acknowledge support from the National Heart Lung and Blood Institute of the National Institutes of Health as a Program of Excellence in Nanotechnology (NHLBI-PEN HL080729). The authors also thank senior microscopist G. Michael Veith of the Washington University Department of Biology Microscopy Facility for providing technical support with TEM and fluorescence confocal microscopy.

LITERATURE CITED

(1) Duchardt, F., Fotin-Mleczek, M., Schwarz, H., Fischer, R., and Brock, R. (2007) A comprehensive model for the cellular uptake of cationic cell-penetrating peptides. *Traffic 8*, 848–866.
(2) Chithrani, B. D., and Chan, W. C. W. (2007) Elucidating the mechanism of cellular uptake and removal of protein-coated gold nanoparticles of different sizes and shapes. *Nano Lett. 7*, 1542–1550.
(3) Kang, H., DeLong, R., Fisher, M. H., and Juliano, R. L. (2005) Tat-conjugated PAMAM dendrimers as delivery agents for antisense and siRNA oligonucleotides. *Pharm. Res. 22*, 2099–2106.
(4) Matthaeus, C., Kale, A., Chernenko, T., Torchilin, V., and Diem, M. (2008) New ways of imaging uptake and intracellular fate of liposomal drug carrier systems inside individual cells, based on Raman microscopy, *Mol. Pharmaceutics* [Online early access].
(5) Kam, N. W. S., and Dai, H. (2005) Carbon nanotubes as intracellular protein transporters: Generality and biological funcitonality. *J. Am. Chem. Soc. 127*, 6021–6026.
(6) Osaki, F., Kannamori, T., Sando, S., Sera, T., and Aoyama, Y. (2004) A quantum dot conjugated sugar ball and its cellular uptake. On the size effects of endocytosis in the subviral region. *J. Am. Chem. Soc. 126*, 6520–6521.
(7) Foerg, C., and Merkle, H. P. (2007) On the biomedical promise of cell penetrating peptides: limits *versus* prospects. *J. Pharm. Sci. 97*, 144–162.
(8) Chithrani, B. D., Chazani, A. A., and Chan, W. C. W. (2006) Determining the size and shape dependence of gold nanoparticle uptake into mammalian cells. *Nano Lett. 6*, 662–668.
(9) Champion, J. A., and Mitragotri, S. (2006) Role of target geometry in phargocytosis. *Proc. Natl. Acad. Sci. U.S.A. 103*, 4930–4934.
(10) Geng, Y., Dalhaimer, P., Cai, S., Tsai, R., Tewari, M., Miniko, T., and Discher, D. E. (2007) Shape effects of filaments *versus* spherical particles in flow and drug delivery. *Nat. Nanotechnol. 2*, 249–255.
(11) Read, E. S., and Armes, S. P. (2007) Recent advances in shell cross-linked micelles. *Chem. Commun.* 3021–3035.

(12) Krikorian, V., Kang, Y., and Thomas, E. L. (2007) Self-assembly and morphology diagrams for solution and bulk materials: Experimental aspects, In *Macromolecular Engineering* (Matyjaszewski, K., Gnanou, Y., and Leibler, L., Eds.) pp 1387−1430, Wiley-VCH Verlag GmbH & Co. KGaA, Weinheim, Germany.

(13) Hamley, I. (2005) Nanoshells and nanotubes from block copolymers. *Soft Matter 1*, 36–43.

(14) Sun, G., Xu, J., Hagooly, A., Rossin, R., Li, Z., Moore, D. A., Hawker, C. J., Welch, M. J., and Wooley, K. L. (2007) Strategies for optimized radiolabeling of nanoparticles for in vivo PET imaging, *Adv. Mater.* [Online early access].

(15) Rossin, R., Pan, D., Qi, K., Turner, J. L., Sun, X., Wooley, K. L., and Welch, M. J. (2005) ^{64}Cu-labeled folate-conjugated shell cross-linked nanoparticles for tumor imaging and radiotherapy: Synthesis, radiolabeling, and biologic evaluation. *J. Nucl. Med. 46*, 1210–1218.

(16) Yang, T.-F., Chen, C.-N., Chen, M.-C., Lai, C.-H., Liang, H.-F., and Sung, H.-W. (2006) Shell-crosslinked Pluronic L121 micelles as a drug delivery vehicle. *Biomaterials 28*, 725–734.

(17) Lazzari, M., Liu, G., and Lecommandoux, S. (2006) *Block Copolymers in Nanoscience*, Wiley-VCH Verlag GmbH & Co. KGaA, Weinheim, Germany.

(18) Becker, M. L., Remsen, E. E., Pan, D., and Wooley, K. L. (2004) Peptide-derivatized shell-cross-linked nanoparticles. 1. Synthesis and characterization. *Bioconjugate Chem. 15*, 699–709.

(19) Cui, H., Chen, Z., Wooley, K. L., and Pochan, D. J. (2006) Controlling micellar structure of amphiphilic charged triblock copolymers in dilute solution *via* coassembly with organic counterions of different spacer lengths. *Macromolecules 39*, 6599–6607.

(20) Cui, H., Chen, Z., Zhong, S., Wooley, K. L., and Pochan, D. J. (2007) Block copolymer assembly *via* kinetic control. *Science 317*, 647–650.

(21) Discher, D. E., and Eisenberg, A. (2002) Polymer vesicles. *Science 297*, 967–973.

(22) Pressly, E. D., Rossin, R., Hagooly, A., Fukukawa, K.-I., Messmore, B. W., Welch, M. J., Wooley, K. L., Lamm, M. S., Hule, R. A., Pochan, D. J., and Hawker, C. J. (2007) Structural effects on the biodistribution and positron emission tomography (PET) imaging of well-defined (64)Cu-labeled nanoparticles comprised of amphiphilic block graft copolymers. *Biomacromolecules 8*, 3126–3134.

(23) Pochan, D. J., Chen, Z., Cui, H., Hales, K., Qi, K., and Wooley, K. L. (2004) Toroidal triblock copolymer assemblies. *Science 306*, 94–97.

(24) Turner, J. L., Pan, D., Plummer, R., Chen, Z., Whittaker, A. K., and Wooley, K. L. (2005) Synthesis of gadolinium-labeled shell-crosslinked nanoparticles for magnetic resonance imaging applications. *Adv. Funct. Mater. 15*, 1248–1254.

(25) Pan, D., Turner, J. L., and Wooley, K. L. (2004) Shell cross-linked nanoparticles designed to target angiogenic blood vessels *via* $\alpha_v\beta_3$ receptor-ligand interactions. *Macromolecules 37*, 7109–7115.

(26) Ma, Q., and Wooley, K. L. (2000) The preparation of tbutyl acrylate, methyl acrylate, and styrene block copolymers by atom transfer radical polymerization: precursors to amphiphilic and hydrophilic block copolymers and conversion to complex nanostructured materials. *J. Polym. Sci., Part A: Polym. Chem. 38*, 4805–4820.

(27) Ma, Q., Remsen, E. E., Clark, C. G. Jr., Kowalewski, T., and Wooley, K. L. (2002) Chemically induced supramolecular reorganization of triblock copolymer assemblies: trapping of intermediate states a shellcrosslinking methodology. *Proc. Natl. Acad. Sci. U.S.A. 99*, 5058–5063.

(28) Huang, H., Remsen, E. E., and Wooley, K. L. (1998) Amphiphilic core-shell nanospheres obtained by intramicellar shell crosslinking of polymer micelles with poly(ethylene oxide) linkers. *Chem. Commun.* 1415–1416.

(29) Remsen, E. E., Thurmond, K. B., II, and Wooley, K. L. (1999) Solution and surface charge properties of shell-crosslinked knedel nanoparticles. *Macromolecules 32*, 3685–3689.

(30) Becker, M. L., Bailey, L. O., and Wooley, K. L. (2004) Peptide-derivatized shell cross-linked nanoparticles. 2. Biocompatibility evaluation. *Bioconjugate Chem. 15*, 710–717.

(31) Ziegler, A., Nervi, P., Durrenberger, M., and Seelig, J. (2005) The cationic cell-penetrating peptide CPP(TAT) derived from the HIV-1 protein TAT is rapidly transported into living fibroblasts: Optical, biophysical, and metabolic evidence. *Biochemistry 44*, 138–148.

(32) Ziegler, A., and Seelig, J. (2007) High affinity of the cell-penetrating peptide HIV-1 Tat-PTD for DNA. *Biochemistry 46*, 8138–8145.

(33) Gao, H., Shi, W., and Freund, L. B. (2005) Mechanics of receptor-mediated endocytosis. *Proc. Natl. Acad. Sci. U.S.A. 102*, 9469–9474.

(34) Bao, G., and Bao, X. R. (2005) Shedding light on the dynamics of endocytosis and viral budding. *Proc. Natl. Acad. Sci. U.S.A. 102*, 9997–9998.

(35) Hirano, K., Hirano, M., Nishimura, J., and Kanaide, H. (2004) A critical period requiring Rho proteins for cell cycle progression uncovered by reversible protein transduction in endothelial cells. *FEBS Lett. 570*, 149–154.

BC800160B

A Surface Active Benzodiazepine Receptor Ligand for Potential Probing Membrane Order of $GABA_A$-Receptor Surroundings

Anahí V. Turina,[†] Benjamín Caruso,[†] Gloria I. Yranzo,[‡] Elizabeth L. Moyano,[‡] and María A. Perillo*[,†]

Biofísica-Química, Cátedra de Química Biológica, Departamento de Química, Facultad de Ciencias Exactas, Físicas y Naturales, and INFIQC-Departamento de Química Orgánica, Facultad de Ciencias Químicas, Universidad Nacional de Córdoba. Av. Vélez Sarsfield 1611, 5016 Córdoba, Argentina. Received April 28, 2008; Revised Manuscript Received July 17, 2008

A conjugable analogue of the benzodiazepine 5-(2-hydroxiphenyl)-7-nitro-benzo[*e*][1,4]diazepin-2(3*H*)-one N_1-substituted with an aliphatic chain (CNZ acyl derivative, CAd) was synthesized. CAd inhibited FNZ binding to $GABA_A$-R with an inhibition binding constant $K_i = 176$ nM and expanded a model membrane packed up to 13 mN/m when penetrating from the aqueous phase. CAd exhibited surface activity with a collapse pressure $\pi = 18.8$ mN/m and minimal molecular area $A_{min} = 49$ Å^2/molecule at the closest molecular packing, resulting in full and nonideal mixing with a phospholipid in a monolayer up to a molar fraction $x \cong 0.1$, decreasing its surface potential and contributing with a dipole that pointed its positive end toward the air and reoriented at the interface upon compression. These findings suggested that CAd could be stabilized at the membrane−water interface with its CNZ moiety stacked at the $GABA_A$-R while its acyl chain can be inserted into the membrane depth.

1. INTRODUCTION

The 1,4-benzodiazepin-2-ones (BZDs)[1] are drugs widely used as anxiolytics, hypnotics, and anticonvulsants. They act by enhancing the activity of the neurotransmitter γ-amino butyric acid (GABA) through an allosteric binding site at the integral membrane receptor $GABA_A$ ($GABA_A$-R) (*1*). This is a pentameric protein that acts as a ligand-gated chloride channel and is the site of action of a variety of pharmacologically important drugs including benzodiazepines (BZDs) (*2*).

Several nonspecific mechanisms are known to affect the conformation and activity of membrane-bound protein receptors, such as (i) the coupling between hydrophobic mismatch and curvature stress (*3*), (ii) changes in the lateral stresses profile (the depth-dependent distribution of lateral stresses within the membrane) which affect the conformation equilibrium and the activity of intrinsic proteins, the function of which involves a structural change accompanied by a depth-dependent variation in its cross-sectional area within the transmembrane domain (*4*), and (iii) the dipolar arrangement of the membrane which was shown to affect significantly the insertion, folding, conformation, and activity of membrane proteins (*5, 6*). With GABA-R as an example, studies on natural membranes support the hypothesis that the allosteric modulation of monoterpenes (*6, 7*) and detergents (*8*) on this receptor comprise effects caused by drug insertion or other sources of mechanical tension on the supramolecular organization of the receptor environment, through the mechanisms described above. Electrophysiological (*9*) and binding (*10*) experiments showed that the cholesterol content, a known buffering mechanism of membrane microsviscosity, affected the coupling between the binding sites for BZDs and the other drugs that interact with $GABA_A$-R. Moreover, temperature-induced variations in membrane microviscosity also modulated the ligand binding to $GABA_A$-R ((*11*) and refs therein).

Membrane microviscosity is considered the main modulatory mechanism of membrane protein function. Changes in this general membrane property are accompanied by modifications in the hydrophobic thickness or in the lateral pressure profile of bilayers, which, as stated above, are indirect ways of connecting the protein structure with its function (*12*−*17*). It is known that the plasma membrane of cells is substantially ordered (e.g., RBL-2H3 cells (*18*)). It exhibits a limiting anisotropy (0.225 ± 0.005) significantly higher than that observed in the fluid phase of liposome bilayers. This indicates that, on average, a considerable amount of order exists in plasma membrane (*19*). However, far from homogeneous, many types of experiments have shown that, at the mesoscopic level, the plasma membranes of cells are patchy and locally differentiated into domains of different degrees of molecular order, some of which arise through lipid−lipid interactions (*20*). For this reason, typical evaluation of microviscosity through the analysis of general anisotropy is not enough to understand the $GABA_A$-R sensitivity to membrane mechanical properties. The latter should include a scan of $GABA_A$-R closest membrane surroundings and may be achieved by the use of molecular probes that can remain close to the protein and, at the same time, allow the scanning of the local molecular organization within the membrane depth. Hence, we propose to use a probe bearing, at one end, a $GABA_A$-R ligand that will make the whole probe capable of stacking at the receptor and, at the other end, a hydrophobic tail with a fluorescent or spin label moiety covalently attached. The latter, once inserted in the membrane, would provide spectroscopic information about the molecular order within the membrane depth where it is located. This approach is based on similar studies on the nicotinic acetylcholine receptor (*21*). In our laboratory, we have tackled this challenge in two stages.

* Corresponding author. Biofísica-Química, Departamento de Química, Facultad de Ciencias Exactas, Físicas y Naturales, Universidad Nacional de Córdoba, Av. Vélez Sarsfield 1611, 5016 Córdoba, Argentina. E-mail: mperillo@efn.uncor.edu. Phone: +54-351-4344983 int 5. FAX: +54-351-4334139.

[†] Departamento de Química.

[‡] INFIQC-Departamento de Química Orgánica.

[1] Abbreviations: BZD, benzodiazepines; CAd, clonazepam acyl derivative; CNZ, clonazepam; dpPC, dipalmitoylphosphatidylcholine; DZ, diazepam; FNZ, flunitrazepam; GABA, gamma aminobutyric acid; $GABA_A$-R, $GABA_A$ receptor; MGd, methyl glycinate derivative; NMR, nuclear magnetic resonance spectroscopy; sem, standard error of the mean; SM, synaptosomal membranes; TLC, thin layer chromatography; TMS, tetramethyl silane.

10.1021/bc800175z CCC: $40.75 © 2008 American Chemical Society
Published on Web 08/13/2008

Scheme 1. Synthesis of the CNZ−Acyl Derivative (CAd)

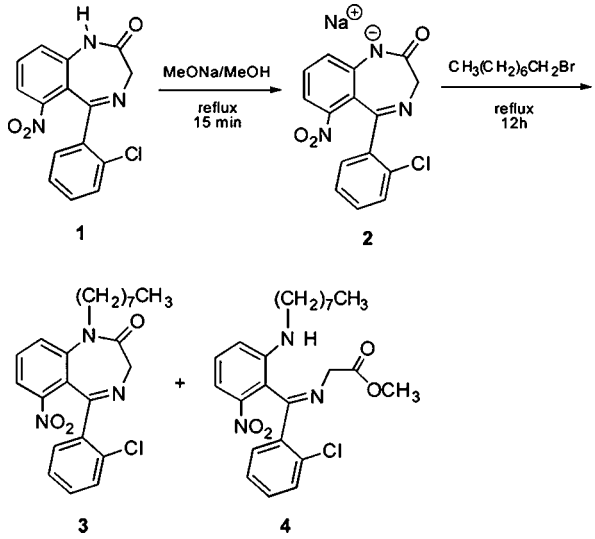

The first stage, consisting of the synthesis of a surface active GABA$_A$-R ligand, will be followed by the addition of the sensing group in a second stage.

In the present paper, we describe the synthesis, the GABA$_A$-R binding kinetics, and the biophysical properties of a 5-(2-hydroxiphenyl)-7-nitro-benzo[*e*][1,4]diazepin-2(3*H*)-one (clonazepam, CNZ) substituted at the N_1 position with an aliphatic chain which was named CNZ acyl derivative (CAd). The ability of this compound to interact and stabilize at the membrane−water interface was studied in monomolecular layers at the air−water interface by the Wilhelmy plate method. Molecular parameters determined from surface pressure−area isotherms were used to predict not only the type of self-assembled structures that CAd would be able to form in aqueous dispersions, but also the molecular features that would contribute to enhancing the stability of this compound in the typical planar configuration that characterizes a membrane bilayer.

2. EXPERIMENTAL PROCEDURES

2.1. Materials. BZDs diazepam and clonazepam (DZ and CNZ) were kindly supplied by Products La Roche (Córdoba, Argentina). [^{3}H]-FNZ was purchased from New England Nuclear Chemistry (E.I. DuPont de Nemours & Co. Inc., Boston, MA). Dipalmitoylphosphatidylcholine was obtained from Avanti Polar Lipids (Alabaster, AL). Other drugs and solvents were of analytical grade. Merck silica gel 60 was used for filtration and Aldrich silica gel 60 F254 was used for preparative TLC.

2.2. Procedure for Preparation of CNZ Derivative. A methanolic solution of sodium methoxide (1.85 mmol/mL methanol) was added to a solution of CNZ (1.52 mmol) in 25 mL of anhydrous methanol as described in ref *22*. The mixture was refluxed for a period of 15 min. After this time, 2.26 mmol of 1-bromooctane was added and subsequently refluxed for 12 h. After cooling, methanol was evaporated and the crude was filtered using silica gel. This mixture was then purified by preparative TLC using hexane/ethyl acetate (80:20) and petroleum ether/ethyl acetate/ethanol (95:4:1) as eluents. The reaction yield was 50% compound **3** and 30% compound **4** as main products. These derivatives will be named CAd and MGd, respectively (see Scheme 1).

*5-(2-Chlorophenyl)-6-nitro-1-octyl-1,3-dihydro-2H-1,4-benzodiazepin-2-one (***3***, CAd).* ^{1}H NMR (200 MHz, CDl$_3$): δ 0.85 (t, J = 6.6 Hz, 3H), 1.24 (s, 10H), 1.60 (m, 2H), 4.31 (m, 2H), 4.37 (dd, J = 11 and 228 Hz, 2H), 7.30−7.50 (m, 4H), 7.55 (d, J = 9.1 Hz, 1H), 7.62−7.70 (m, 1H), 7.93 (d, J = 2.6 Hz, 1H), 8.35 (dd, J = 2.6 and 9.1 Hz, 1H). ^{13}C (50.33 MHz, CDCl$_3$): δ = 14.7, 23.2, 27.6, 29.1, 29.8, 29.8, 32.4, 48.2, 57.8, 123.2, 125.3, 126.6, 128.1, 131.0, 131.8, 132.4, 133.7, 137.8, 143.9, 147.8, 168.6, 169.2.

*Methyl-N-{(2-chlorophenyl)-[2-nitro-6-(octylamino)phenyl]-methylene}glycinate (***4***, MGd).* ^{1}H NMR (200 MHz, CDCl$_3$): δ 0.89 (t, J = 6.6 Hz, 3H), 1.30 (s, 10H), 1.84 (q, J = 7.3 Hz, 2H), 3.37 (m, 2H), 3.76 (s, 3H), 4.04 (q, J = 19 and 47 Hz, 2H), 6.72 (d, J = 9 Hz, 1H), 7.09−7.14 (m, 1H), 7.35−7.60 (m, 4H), 7.71 (d, J = 2.6 Hz, 1H), 8.11 (dd, J = 4 and 10 Hz), 11.08 (s, 1H). ^{13}C (50.33 MHz, CDCl$_3$): δ = 14.1, 22.6, 27.3, 29.2, 29.3, 31.8, 43.5, 51.9, 54.2, 110.4, 115.9, 127.6, 128.6, 129.8, 130.3, 131.4, 133.8, 135.1, 154.4, 170.2, 170.6.

2.3. NMR Spectroscopy. All starting materials were commercially available and solvents were distilled and dried before use. ^{1}H and ^{13}C NMR spectra were recorded on a Bruker FT-200 (^{1}H at 200 MHz and ^{13}C at 50.33 Hz) spectrometer using CDCl$_3$. Chemical shifts are reported in parts per million (ppm) downfield from TMS.

2.4. Monolayer Studies. *2.4.1. Surface Pressure−Area and Surface Potential−Area Compression Isotherms.* Monomolecular layers were prepared and monitored essentially according to Perillo et al. (*23*). Experiments were performed at room temperature. The surface pressure (π, Wilhelmy plate method via a platinized-Pt plate), surface potential (ΔV, vibrating plate method), and the area enclosing the monolayer (A) were automatically measured with a Minitrough II (KSV, Helsinki, Finland). The Teflon trough used had 24 075 mm^2 total area. Bidistilled water (230 mL total volume) was used as subphase. Lipid monolayers were formed by spreading, on the air−water interface, between 30 and 80 μL of 1 mg/mL chloroform−methanol 2:1 of (a) the newly synthesized CNZ acyl derivative (CAd), (b) a pure saturated phospholipid (dipalmitoylphosphatidylcholine, dpPC), or (c) a binary mixture dpPC-CAd at a molar fraction (x) varying between 0 and 1. The $\pi-A$ and $\Delta V-A$ compression isotherms were recorded continuously, at a compression rate of 5 mm/min. Isotherms shown resulted from typical experiments repeated at least twice.

2.4.2. Compressional Modulus and Critical Packing Parameter Calculation. The compressional modulus (K) was calculated according to eq 1.

$$K = -(A_\pi)\left(\frac{\delta\pi}{\delta A}\right)_\pi \tag{1}$$

The critical packing parameter (P_C) was calculated according to the Israelachvili theory (*24*) by eq 2.

$$P_c = \frac{v}{a_0 \cdot l_c} \tag{2}$$

The average molecular area (a_0) was experimentally determined from $\pi-A$ isotherms, and optimal values for the hydrocarbon volume (v) and chain length (l_c) were calculated from eqs 3 and 4, according to Perillo et al. ((*23*) and refs therein):

$$v \cong (27.4 + 26.9n)n_{ch} \tag{3}$$

$$l_c \cong 1.5 + 1.265n \tag{4}$$

where n and n_{ch} are the number of methylene groups in the hydrocarbon chain and the number of chains per molecule, respectively. The molecular area (a_0) is a function of the interfacial free energy; hence, it was assigned the actual mean molecular areas (Mma) at specific values of surface pressure taken from the $\pi-A$ isotherm of each monolayer at the different compositions studied. P_c values for the binary dpPC-CAd mixtures were calculated from the weighted mean values of (v) and (l_c) of individual components.

2.4.3. Penetration of CAd in Monomolecular Layers of dpPC at the Air−Water Interface. The aim of this experiment was to determine the maximum value of π that allowed drug penetration in the monolayer (π_{cutoff}). These experiments were done in a circular Teflon trough (4.5 cm diameter and 0.5 cm depth). Between 5 and 30 μL of a chloroform−methanol 2:1 solution of phospholipid were spread on an aqueous surface (bidistilled water) and about 5 min were allowed for solvent evaporation. Monolayers were prepared at constant surface area but at different initial surface pressures (π_i). The temporal variation of π induced by the CAd penetration into the monolayer after the injection of an ethanolic solution of the derivative in the subphase was measured until reaching a plateau (π_{max}). The values of $\Delta\pi = \pi_{max} - \pi_i$ were plotted against π_i and a straight line was fitted to them. The π_{cutoff} was determined from the intersection of the regression line with the abscissa axis.

2.5. Synaptosomal Membrane Preparations. Synaptosomal membranes (SM) were obtained from bovine brain cerebral cortex. Meninges were eliminated, the cortex dissected, and the SM were purified essentially according to the method of Enna and Snyder, modified by Perillo and Arce (*25*), lyophilized and stored at −20 °C. Immediately before use, membranes were resuspended in 50 mM pH 7 Hepes buffer containing 100 mM NaCl at a final protein concentration of 0.25 mg/mL. This SM suspension was used as membrane receptor preparation and $GABA_A$-R source in the experiments that followed.

2.6. Competition Binding Experiments. The aim of this experiment was to assess the ability of the newly synthesized CAd to displace [^{3}H]-FNZ from its binding site at the $GABA_A$-R in SM.

Binding was performed essentially as described previously (*26*). The whole procedure was carried out at 4 °C. The incubation system contained, in a final volume of 230 μL, the SM suspension at a final protein concentration of 0.25 mg/mL, 3 nM (minimum specific activity 74.1 Ci/mmol) [^{3}H]-FNZ, 100 mM NaCl−50 mM Tris−HCl pH 7.4 buffer containing 9.4 μM DZ or 10 μM CAd (final concentrations). Samples were incubated at 4 °C in the dark for 1 h and then filtered through SS filters (Whatman GF/B type) with a Brandel automatic filtration apparatus (Brandel, Gaithersburg, MD). After filters were rinsed and dried in the air, they were placed in vials containing 2.5 mL of scintillation liquid (25% v/v Triton X-100, 0.3% w/v diphenyloxazole in toluene). The retained radioactivity was measured with a scintillation spectrometer Rackbeta 1214 (Pharmacia-LKB, Finland) at 60% efficiency for tritium. Specific binding (*B*) was calculated as the difference between total binding (TB) and nonspecific binding (NB) determined in the absence and in the presence of 9 nM DZ, respectively. Protein concentration was determined by the method of Lowry (*27*).

2.7. Statistical Analysis. Binding data were statistically analyzed using a two-tailed Student's *t*-test for independent samples. $p < 0.05$ was considered to be statistically significant. Regression analysis was done by the least-squares method (*28*).

3. RESULTS AND DISCUSSION

3.1. Synthesis of the Probe Precursor. The probe precursor (**3**, CAd) was synthesized from the sodium salt (**2**) of 5-(2-chlorophenyl)-7-nitro-1,3-dihydro-2*H*-1,4-benzodiazepin-2-one (CNZ) (**1**) and 1-bromooctane (Scheme 1). The salt (**2**) was obtained by the treatment of CNZ with sodium methoxide according to the literature (*22*). The reaction of the BZD **1** and the bromoderivative was carried out *in situ* without isolation of the salt intermediate. The methyl *N*-methylene glycinate **4** (MGd) was also obtained in this reaction by the hydrolysis reaction of the benzodiazepinone ring in the presence of methanol. The formation of compound **4** could not be avoided even when the reaction times and temperatures were modified. Therefore, compound **3** was purified as described in section 2.2 (purity was higher than 95%). Detailed spectra are provided as Supporting Information.

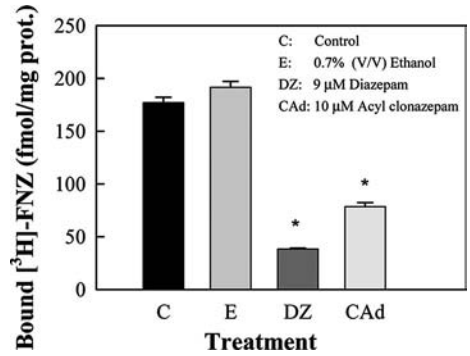

Figure 1. Displacement of the [^{3}H]-FNZ bound at synaptosomal membranes from bovine cortex induced by CAd and DZ at similar concentrations. The [^{3}H]-FNZ and protein concentration used were 3 nM and 0.25 mg prot/mL, respectively. Other details were described in the Experimental Procedures section. Data shown are the mean ± sem of triplicates. *, significantly different with respect to *E* ($p < 0.01$, Student's *t* test).

3.2. [^{3}H]-FNZ Displacement Experiments. The ability of CAd to displace [^{3}H]FNZ was evaluated by means of a radioreceptor binding assay. Results were analyzed in comparison with the well-known competitive inhibitor DZ. The results, depicted in Figure 1, show that DZ as well as CAd at similar concentrations (9 and 10 μM, respectively) were able to displace 80% and 59% of the total [^{3}H]FNZ bound to SM, respectively. According to the denifition given in the Experimental Procedures section, the 20% residual binding in the presence of 9 nM DZ corresponded to nonspecific binding. Furthermore, CAd at the concentration assayed left a 21% undisplaced binding over the nonspecific indicating a lower affinity for the $GABA_A$-R with respect to DZ.

Assuming that CAd induces a competitive inhibition of [^{3}H]FNZ binding, the inhibition binding constant (K_i) of this displacement agent can be calculated from eq 5 as follows:

$$B = \frac{B_{max} L}{K_d\left(1 + \frac{[I]}{K_i}\right) + L} \quad (5)$$

where L is the free radioligand concentration (3 nM), B and B_{max} are the specific activities of bound radioligand (expressed in moles per protein mass units) at L or at saturating radioligand concentration, respectively, and K_d is the dissociation binding constant of the radioligand−receptor interaction.

With B_{max} = 1404 fmol/mg protein and K_d = 2.28 nM for [^{3}H]FNZ binding to SM (*26*) and the experimental data shown in Figure 1, the K_i values for CAd were 176 nM. This value was similar to previously reported data (*29*) for other BZDs. This was a strong indication that the CNZ acyl derivative not only could interact with the BZD binding site at $GABA_A$-R, but also that it was bound with an affinity comparable with that of a typical BZD.

3.3. Monomolecular Layers at the Air−Water Interface. *3.3.1. Surface Pressure−Molecular Area Isotherms.* Surface pressure−area isotherms are shown in Figure 2. In Figure 2a, an isotherm of pure dpPC is shown as a reference. Dashed lines indicate the determination of the collapse pressure (π_c = 55.5 mN/m), the molecular area at the closest packing also known as minimal molecular area (A_{min} = 40 Å^2), and the transition surface pressure (π_T = 6 mN/m) corresponding to the bidimensional phase transition characteristic of dpPC.

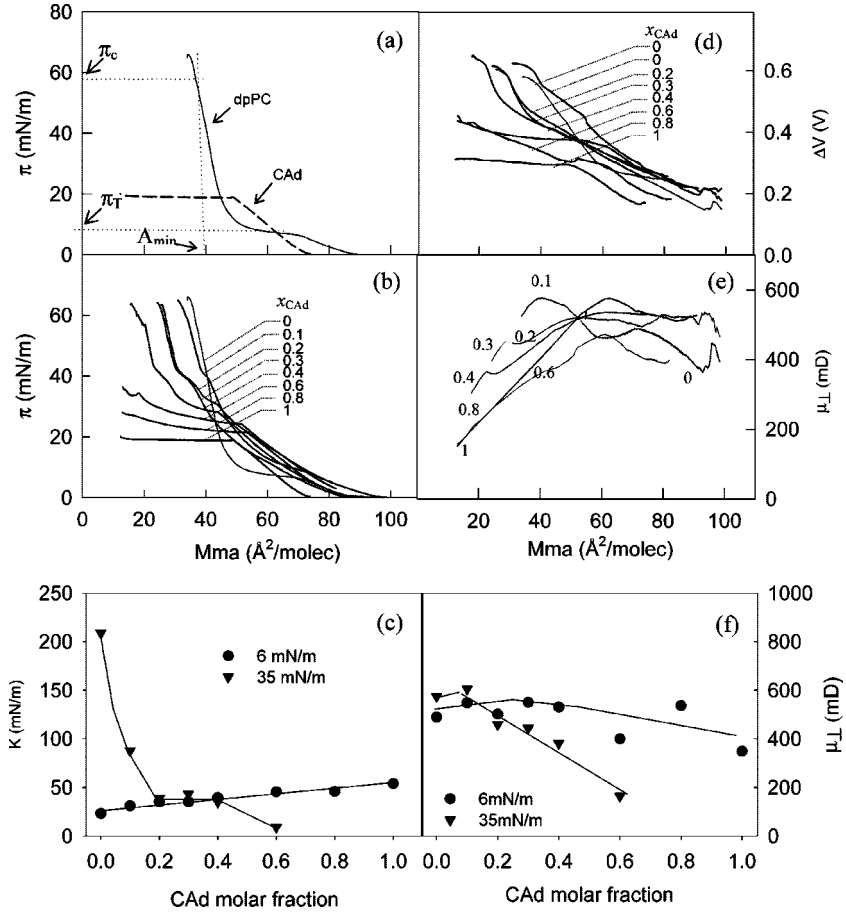

Figure 2. Behavior of dpPC/CAd binary mixtures at the air−water interface. (a) Collapse pressure (π_c), transition pressure (π_T), and minimal molecular area (A_{min}) determination exemplified over a dpPC $\pi-A$ compression isotherm. (b) Surface pressure−Mma isotherms of dpPC-CAd binary mixtures. (c) Compressional modulus at 6 and 35 mN/m, as a function of monolayer composition. (d) Surface potential−Mma and (e) $\mu_\perp$−Mma compression isotherms of dpPC-CAd binary mixtures. Dipole moments ($\mu_\perp$) calculated according to eq 6 from ΔV values taken from panel (d) depicted as a function of Mma (f) Resultant dipolar modulus at 6 and 35 mN/m, as a function of monolayer composition. Numbers in panel (e) indicate the CAd molar fraction.

CAd was able to form monomolecular layers at the air−water interface both alone (Figure 2a) as well as in mixtures with dpPC at various molar fractions (x) (Figure 2b). From the analysis of the $\pi-A$ compression isotherm of CAd (Figure 2a), a collapse pressure $\pi_c = 18.8$ mN/m and $A_{min} = 49$ Å^2 were determined and no bidimensional transitions were observed. In comparison with dpPC, CAd exhibited lower stability as reflected by its lower π_c value, which may be due to the shorter length of its hydrocarbon chain. This provides a low London dispersion energy stabilizing the aggregate, which is not enough to counterbalance the repulsive interactions between the polar head groups. This leads to an inefficient molecular packing explaining the fact that, in spite of having only one hydrocarbon chain and not two as in the case of dpPC, CAd exhibits a minimal molecular area substantially higher than that of the phospholipid.

The CAd/dpPC mixtures exhibited full miscibility up to $x_{CAd} \cong 0.1$. Above $x_{CAd} = 0.1$, mixtures showed several bidimensional reorganizations indicating the occurrence of partial collapse processes of different bidimensional phases (enriched in dpPC, within the range $0.1 < x_{CAd} < 0.4$, or in CAd, within the range $0.4 < x_{CAd} = 1$) coexisting in the monolayer. This indicated a partial miscibility of both components (Figure 2b). Further analysis was done through a phase diagram (see Figure 3 below).

The effect of the proportion of CAd in the mixtures with dpPC on the monolayer elasticity was analyzed through the compressibility modulus K (Figure 2c) in the conditions of full miscibility at all compositions (6 mN/m) or compositionally dependent miscibility (35 mN/m). At 6 mN/m, K increased continuously as a function of x_{CAd} reflecting both the higher coherence of CAd films with respect to the liquid expanded phase of dpPC (corresponding to $x_{CAd} = 0$) as well as full miscibility of both compounds at this lateral pressure. At 35 mN/m, K decreased as a function of x_{CAd} showing discontinuities that reinforced the different miscibility regimes exhibited by the phase diagram (miscibility of CAd in dpPC which is lost at $x_{CAd} \leq 0.1$) and suggested a partial miscibility of dpPC in a continuous CAd phase within the range $0.4 < x_{dpPC} < 0.6$).

3.3.2. Surface Electrostatics. The surface potential $\Delta V-$area isotherms (Figure 2d) showed that ΔV increased upon compression and decreased as a function of CAd in the mixtures. At the closest packing, $\Delta V_{dpPC} = 530$ mV and $\Delta V_{CAd} = 296$ mV, while the mixtures showed intermediate values. Surface potential is a measure of the electrostatic field gradient perpendicular to the membrane interface and thus varies considerably with the molecular surface density and with changes in orientation accompanying the monolayer compression. Taking the dielectric constant of the medium (water) as unity, the molecular dipole moment can be calculated according to eq 6

$$\Delta V = 12 \times \frac{\pi}{A} \mu_\perp + \psi_0 \qquad (6)$$

where $\pi = 3.1416$, A (molecular area), and V (surface potential) are expressed in Å^2.molecule^{-1} and mV, respectively, $\mu_\perp$ (expressed in Debye units, mD) is the apparent (resultant) perpendicular dipole moment of the molecule, and ψ_0 is the

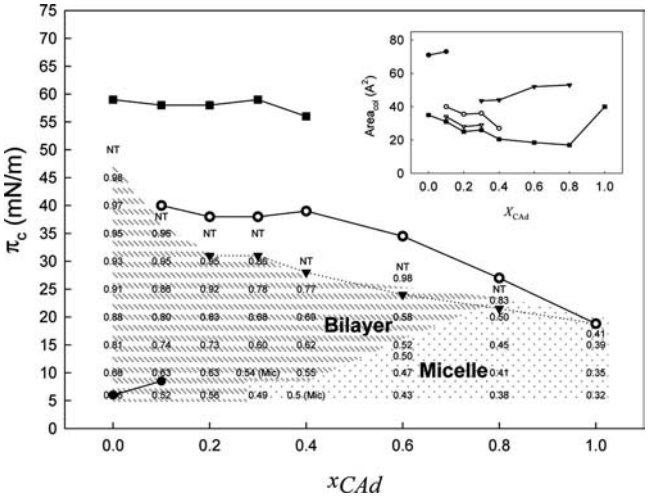

Figure 3. Surface pressure−composition phase diagram overlapped with critical packing parameter (P_c) for dpPC-CAd mixtures. Numbers on the graph refer to P_c values calculated for each mixture at the specified surface pressure. NT: no structure predicted in the theory ($P_c > 1$). The phase diagram ($\pi - x_{CAd}$) was constructed using π_c values (■), typical pure dpPC bidimensional phase transition pressure (●), and phase transitions pressures in the mixtures (▼ and ○), taken from Figure 2. The inset shows the Mma corresponding to those surface pressures at which bidimensional phase transitions and collapses occur, at each of the CAd molar fractions studied. (●) bidimensional phase transition characteristic of the pure dpPC, (○ and ▼) other bidimensional phase transitions observed in mixtures, and (■) Mma at the monolayer collapse point. Note that P_c values above the line joining the phase transition points, particularly in the range $0.2 < x_{CAd} < 0.4$, might be meaningless due to possible immiscibility.

electrostatic potential difference at the interface caused by the ionic double layer in ionized monolayers (for uncharged molecules $\psi_0 = 0$) (*23, 30*). The parameter $\mu_\perp$ contains different electrostatic contributions. In the case of uncharged molecules such as dpPC (a zwitterionic phospholipid) and CAd (uncharged at the pH assayed), main contributions arise from the resultant dipole moments of the monolayer components and those of the water hydration network (water molecules oriented at the polar headgroup). In turn, contributions from monolayer components include the polar headgroup and hydrocarbon chain contributions. An initial increase in the magnitude of $\mu_\perp$ was observed upon compression due to molecular reorientations at the surface (Figure 2e). Beyond a maximum, all $\mu_\perp$ vs Mma plots showed a decreasing trend which, in conjunction with the information taken from the π−Mma curves, can be interpreted as an indication of a monolayer compositional change due to instability occurring at high surface pressures. Figure 2f shows that, at π low enough to allow total mixing between dpPC and CAd, $\mu_\perp$ decreased upon an increase in x_{CAd}. At a high surface pressure (35 mN/m), (a) within the x_{CAd} range that allowed miscibility, $\mu_\perp$ was higher than at 6 mN/m, and (b) at $x_{CAd} > 0.1$, $\mu_\perp$ values exhibited a decreasing tendency even more noticeable than at 6 mN/m which, in this case, would be reflecting the partial collapse of the monolayer (see phase diagram in Figure 3).

3.3.3. dpPC-CAd Binary Mixtures: Phase Diagram and Prediction of Their Self-Assembling Structures in Water. From data shown in Figure 2b, the $\pi - x$ phase diagram was constructed (Figure 3). Lines in Figure 3 indicate the presence of $\pi - x$ states at which phase transitions occur and delimit regions of single bidimensional phases that may coexist with an already collapsed phase. A single monolayer phase can be found at low pressures within the whole compositional range. This monolayer shows a π_T that varies continuously with x_{CAd} (triangles joint by a dotted line). This π_T might be associated either with a bidimensional phase transition or with a partial collapse of the monolayer. The second hypothesis is supported by the shape inspection of $\pi - A$ isotherms at the high x_{CAd} (e.g., above 0.6) which suggests that after a collapse point monolayers go through overcompression states. At higher pressures, another partial collapse is observed at a π_c that remains invariant up to $x_{CAd} = 0.4$ and then, at $x_{CAd} > 0.4$, it decreases continuously with x_{CAd} (hollow circles) up to the point where π_c equaled the π_c value of pure CAd. Hence, CAd seems totally miscible in dpPC up to $x_{CAd} = 0.1$, exhibiting a bidimensional phase transition between 6 and 8 mN/m. Within the x_{CAd} range 0.1−0.2, the solubility of CAd in dpPC would be reached. This is based on the fact that, upon compression, the collapse pressure of mixtures with $0.1 < x_{CAd} < 0.2$ decreased from 39 to 37 mN/m, while at $0.1 < x_{CAd} < 0.4$, the π_c value remained constant at $\pi_c = 37$ mN/m. Within this compositional range, there was a remaining monolayer that would be composed of a dpPC excess as indicated by a third collapse point which had the typical value of 55 mN/m. The interfacial stability of mixtures with $x_{CAd} < 0.4$ decreased continuously as a function of the x_{CAd} as indicated by the decreasing π_c. Moreover, within this compositional range, after the monolayer collapsed no excess of dpPC remained stable at the air−water interface.

Critical packing parameter values (P_c) allow the prediction of the type of self-assembling structures that would be formed when an amphipathic substance is dispersed in water. P_c values for the binary dpPC-CAd mixtures were calculated by eqs 2, 3, and 4 using values of mean molecular area which were taken from the isotherms shown in Figure 2b. Those P_c values were superimposed on the phase diagram (Figure 3). $P_c < 0.5$ predicts the self-assembling into micelles, $0.5 < P_c < 1$ predicts the self-association into bilayer phases which would lead to the formation of vesicles, and $P_c > 1$ would correspond to phases with negative curvature. Although the latter are not predicted in Israelachvili's theory, those phases are compatible with inverted vesicles, as well as with hexagonal II and cubic phases (*23, 31*). According to this interpretation in Figure 3, within the region located at the bottom-left corner of the $\pi - x_{CAd}$ phase space (at low x_{CAd} and π), the resulting P_c values were compatible with the formation of bilayers. At the bottom-right corner (high x_{CAd} and low π), P_c values predicted the formation of micelles. At the top of the $\pi - x_{CAd}$ phase space, in the region located above a line crossing the plane approximately along the diagonal from 45 mN/m at $x_{CAd} = 0$ through 28 mN/m at $x_{CAd} = 0.4$ to 18.8 at $x_{CAd} = 1$, P_c values were all above 1. In conditions of total miscibility, this may be interpreted as an indication of a tendency to form negative curvature phases when the mixture is dispersed in water. However, within regions of the phase diagram where components are partially miscible with one another, these calculated P_c values become meaningless. Hence, to obtain stable planar membranes at a π compatible with the equilibrium surface pressure of biomembranes (near 30−35 mN/m) the molar faction of CAd should not be higher than 0.2.

The analysis of the variation of the Mma (mean molecular area) or the $\Delta V.A$ (surface potential per unit of molecular surface density) with the mole fraction (x_{CAd}) at constant packing conditions ($\pi = 6$, 18.5, or 35 mN/m) is shown in Figure 4. Straight dotted lines joined the values corresponding to the molecular parameters of pure dpPC and pure CAd. Experimental points lying on this line would represent either ideal mixing or immiscibility behavior of components in the monolayer. The compositional dependence or independence, respectively, of the collapse pressure might help to discriminate between both behaviors. At 6 mN/m, Mma (Figure 4a) as well as $\Delta V.A$ (Figure 4b) decreased as a function of x_{CAd}. At this lateral pressure, these parameters showed positive deviations from ideality, suggesting repulsive interactions or other steric restrictions to

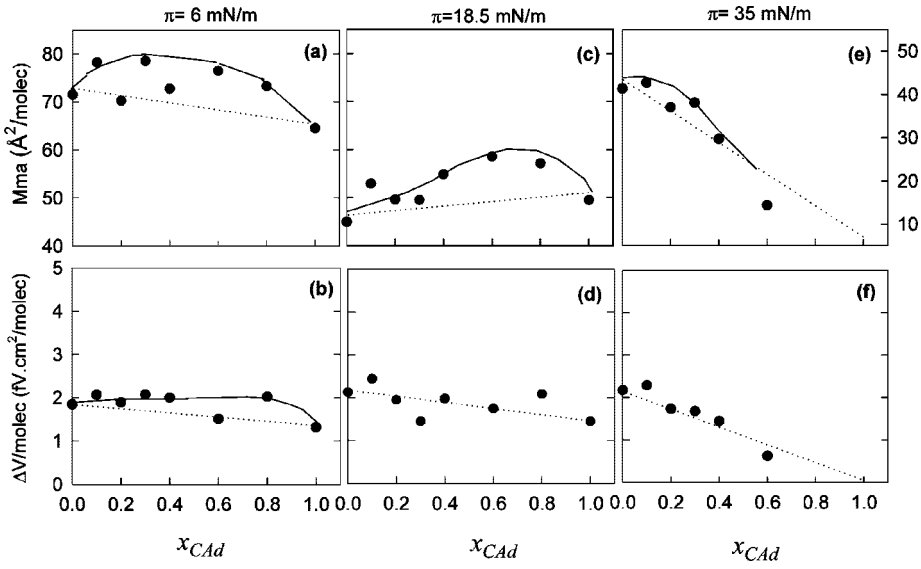

Figure 4. Mean molecular area (a, c, and e) and surface potential per unit of molecular surface density (b, d, and f) vs composition plots at constant surface pressures. $\pi = 6$ (a,b), 18.5 (c,d), or 35 mN/m (e,f). Straight lines represent the behavior expected for ideal mixing or complete segregation of the components. Deviations from this behavior, particularly at 6 mN/m, are more clearly reflected in Mma$-x$ plots.

the ideal molecular packing between the monolayer components. While the expansion observed in Mma was very important, in the case of $\Delta V.A$ the expansion was less significant. These results indicate that the permanence of CAd at high proportions in the monolayer at low π disrupts the organization of the phospholipids (Mma is highly expanded) without acquiring a coherent organization (changes in $\Delta V.A$ were small). A similar behavior was in the Mma$-x_{CAd}$ plot at 18.5 mN/m (surface pressure higher but still within the miscibility region according to the phase diagram); however, no deviation from ideality was observed in $\Delta V.A$ (Figure 4c,d). At 35 mN/m, the monolayer phase exists up to $x_{CAd} = 0.6$ and at higher proportions of CAd a discontinuity was shown in Mma (there are no data at these π and x_{CAd}, as shown in Figure 2b). Hence, at 35 mN/m, Mma and $\Delta V.A$ vs x_{CAd} plots decreased up to the ordinate axis and reach zero. Negligible x_{CAd}-dependent expansions were observed with respect to the ideality line not only in $\Delta V.A$ but also in Mma (Figure 4e,f). Either ideal mixing or total immiscibility may have exhibited this behavior. The inspection of the phase diagram suggested immiscibility within the range $0.2 < x_{CAd} < 0.4$ and partial miscibility within $0.4 < x_{CAd} < 0.6$ due to the compositional constancy and dependency of π_c, respectively. Contrary to what happened within $0 < x_{CAd} < 0.1$, where we found CAd solubility in dpPC, the latter should be ascribed to dpPC mixed within a continuous CAd phase. Beyond $x_{CAd} = 0.6$, this miscibility continued with π_c decreasing up to 18.8 mN/m at $x_{CAd} = 1$.

3.3.4. CAd Penetration in Phospholipid Monolayers. The ability of CAd to penetrate in the monomolecular layers of dpPC from the aqueous subphase was evidenced by the π increase at constant area at different initial surface pressures up to a $\pi_{cutoff} = 13.08 \pm 4.6$ mN/m. This value was determined by extrapolating the plot of $\Delta\pi$ versus π_i to $\Delta\pi = 0$ (Figure 5). On the other hand, the smooth variation of the monolayer compressibility (K) with the x_{CAd} also showed that CAd was stable in the film at low molecular packings (low π). Above 13 mN/m, not only did CAd not penetrate in the film from the subphase ($\Delta\pi = 0$), but also K at high π (Figure 2c) suffered a discontinuous variation with x_{CAd} at $x_{CAd} > 0.2$. Taken together, these results suggest that it was not possible to stabilize high amounts of CAd in highly packed monolayers independently of the direction from which the drug got access to the model membrane. However, small amounts of CAd can remain in the monolayer

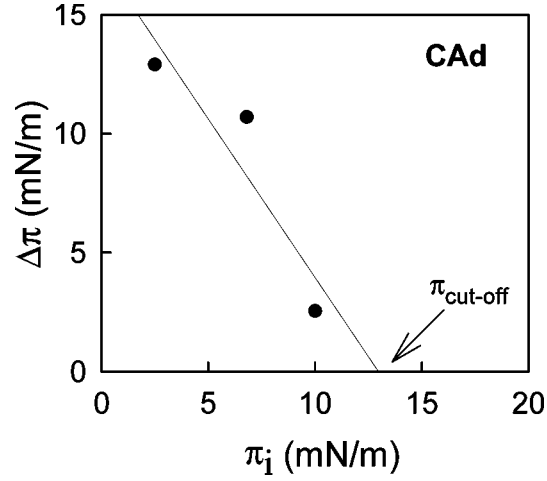

Figure 5. Penetration of CAd in monomolecular layers of dpPC at different initial molecular packings. The line represents the fitness of a straight line to the experimental points by regression analysis by the least-squares method. The π_{cutoff} value, indicated by the arrow, represents the maximum π allowing drug penetration and monolayer deformation. The regression line is defined by the equation $\Delta\pi = a + b \times \pi_i$, where a is the ordinate (17 ± 4 mN/m) and b the slope (-1.3 ± 0.6 mN/m). At $\Delta\pi = 0$, π_i equals the $\pi_{cutoff} = 13.08 \pm 4.6$ mN/m.

at lateral surface pressures compatible with the equilibrium pressure of bilayers—ca. 30−35 mN/m (*32*)—as shown in the phase diagram (Figure 3) as well as by the resultant dipolar contributions at $x_{CAd} < 0.2$ (Figure 2f).

CAd was unstable at intermediate x_{CAd} (0.2−0.4) leading to immiscibility behavior with dpPC, which at high x_{CAd} (>0.4) became a phase inversion with dpPC partially miscible in a continuous CAd phase. This interpretation was strongly suggested by the linear $A-x_{CAd}$ and $\Delta V.A-x_{CAd}$ plots (Figure 4e,f) in conjunction with π_c independence (within $0.2 < x_{CAd} < 0.4$) or dependence (within $0.4 < x_{CAd} \leq 1$) on x_{CAd}, respectively (Figure 3).

4. CONCLUSIONS

The CAd synthesized in the present work was an amphipathic CNZ derivative capable of binding at the BZD site of the GABA$_A$-R by means of its hydrophilic end and anchoring in a

Table 1. Physicochemical Characteristics of CAd Compared with dpPC, Both at Their Respective Collapse Points

property (units)	dpPC	CAd
π_c (mN/m)	55.5	18.8
Mma (Å^2/molec)	40	49
$\Delta V_{\pi c}$ (V)	0.530	0.296
$\mu_\perp$ (mD) [a]	562	385
K_c (mN/m)	198	55
P_c^c	0.86	0.41
predicted self-organization	bilayer	micelle
x_{max} for $0.5 < P_c < 1$ at $\pi = 30$ mN/m[b]	-	0.3
π_{cutoff} (mN/m)	-	13

[a] Calculated as indicated in section 3.3.2. [b] Molar fraction to allow self-assembly into bilayers at a surface pressure of 30 mN/m. [c] Calculated at the π_c of CAd.

biomembrane through the hydrophobic end represented by a hydrocarbon chain attached at the N_1 position. The design of the BZD derivate was supported by theoretical studies about the BZD structure−activity relationship where high-affinity analogues interacted with three $GABA_A$-R electrophilic groups located at C_7, C_2, and the iminic nitrogen N_4. It is known that the N_4 interaction is facilitated by the presence of halogens in C_2 and when the phenyl ring is rotated in the greater coplanarity direction between the phenyl and the plane $C'1 - C5 = N4$ (*33*). Consequently, some chemical alteration in the N_1 position was not expected to affect (at least chemically) the BZD capacity to interact with the receptor binding site, and our results confirmed this hypothesis.

Molecular parameters as well as conditions for self-assembly in water determined for CAd were summarized in Table 1 together with those of dpPC, which was taken as a reference.

CAd as a Precursor to Obtain a Probe to Evaluate the Molecular Organization of Synaptosomal Membranes, In the Vicinity of $GABA_A$-R. The present findings suggested that CAd could be stabilized at the membrane−water interface with its CNZ moiety stacked at the $GABA_A$-R, while its methylene end inserted within the membrane depth may be useful for sensing the molecular order in the receptor surroundings provided a hydrophobic label is attached to it. Hence, such a chemical modification would make CAd a suitable molecular probe. The longer the hydrocarbon chain attached at N_1 position of CNZ, the deeper the membrane regions that could be sensed would be. It is important to recall that a probe should provide information about the system properties without affecting them. That is why they are used at proportions sufficiently low (e.g., 0.5 mol % representing a $x_{probe} = 0.005$). Our results indicate that this condition would be satisfied with CAd in bilayers which have an equilibrium surface pressure centered at 35 mN/m (*32*).

CAd as a Precursor of an Affinity-Based Purification System for $GABA_A$-R. Both the surface activity of CAd and its ability to interact with the BZD binding site at $GABA_A$-R are equally important characteristics that would make CAd an appropriate molecule to develop an affinity-based precipitation method to purify $GABA_A$-R based on CAd coated microparticles. The latter may be proposed as a useful substitute of traditional inmunoprecipitation procedures to avoid the requirement of monoclonal antibodies against specific epitopes of $GABA_A$-R subunits (*34*).

ACKNOWLEDGMENT

The present work was partially financed by grants from CONICET, SECyT-Universidad Nacional de Córdoba and ANPCyT from Argentina. B.C. is a Ph.D. student of the Doctorado en Ciencias Biológicas of the Universidad Nacional de Córdoba. A.V.T. and B.C. are fellowship holders and E.L.M, G.I.Y., and M.A.P are Career Investigators from CONICET.

Supporting Information Available: All figures as well as ^{1}H NMR and ^{13}C NMR spectra. This material is available free of charge via the Internet at http://pubs.acs.org.

LITERATURE CITED

(1) Mehta, A. K., and Ticku, M. K. (1999) An update on GABAA receptors. *Brain Res. Rev. 29*, 196–217.

(2) Sieghart, W. (1992) GABAA receptors: ligand-gated Cl- ion channels modulated by multiple drug-binding sites. *Trends Pharmacol. Sci. 13*, 446–450.

(3) Nielsen, C., Goulian, M., and Andersen, O. S. (1998) Energetics of inclusion-induced bilayer deformations. *Biophys. J. 74*, 1966–1983.

(4) Cantor, R. S. (1999) Lipid composition and the lateral pressure profile in bilayers. *Biophys. J. 76*, 2625–2639.

(5) Honig, B. H., Hubbell, W. L., and Flewelling, R. F. (1986) Electrostatic interactions in membranes and proteins. *Annu. Rev. Biophys. Biophys. Chem. 15*, 163–193.

(6) Perillo, M. A., Guidotti, A., Costa, E., Yu, R. K., and Maggio, B. (1994) Modulation of phospholipases A2 and C activities against dilauroylphosphorylcholine in mixed monolayers with semisynthetic derivatives of ganglioside and sphingosine. *Molec. Membr. Biol. 11*, 119–126.

(7) Sanchez, M. E., Turina Adel, V., Garcia, D. A., Nolan, M. V., and Perillo, M. A. (2004) Surface activity of thymol: implications for an eventual pharmacological activity. *Colloids Surf., B 34*, 77–86.

(8) Sogaard, R., Werge, T. M., Bertelsen, C., Lundbye, C., Madsen, K. L., Nielsen, C. H., and Lundbaek, J. A. (2006) GABA(A) receptor function is regulated by lipid bilayer elasticity. *Biochemistry 45*, 13118–13129.

(9) Sooksawate, T., and Simmonds, M. A. (2001) Influence of membrane cholesterol on modulation of the GABA(A) receptor by neuroactive steroids and other potentiators. *Br. J. Pharmacol. 134*, 1303–1311.

(10) Turina, A. d. V., Schreier, S., and Perillo, M. A. (2008) Coupling between R-GABAA activity and membrane organization in cholesterol depleted synaptosomal membranes from bovine brain cortex. New insights from EPR experiments. *Mol. Membr. Biol.*

(11) Garcia, D. A., and Perillo, M. A. (2002) Flunitrazepam-membrane non-specific binding and unbinding: two pathways with different energy barriers. *Biophys. Chem. 95*, 157–164.

(12) Biaggi, M. H., Schreier, S., Castrucci, A. M., and Lamy-Freund, M. T. (1993) Interaction of melanotropic peptides with lipid membranes. *Ann. N.Y. Acad. Sci. 680*, 459–461.

(13) Biaggi, M. H., Pinheiro, T. J., Watts, A., and Lamy-Freund, M. T. (1996) Spin label and 2H-NMR studies on the interaction of melanotropic peptides with lipid bilayers. *Eur. Biophys. J. 24*, 251–259.

(14) Gonzalez, M., Lezcano, N., Celis, M. E., and Fidelio, G. D. (1996) Interaction of alpha-MSH and substance P with interfaces containing gangliosides. *Peptides 17*, 269–274.

(15) Cantor, R. S. (1997) The lateral pressure profile in membranes: a physical mechanism of general anesthesia. *Biochemistry 36*, 2339–2344.

(16) Perozo, E., Kloda, A., Cortes, D. M., and Martinac, B. (2002) Physical principles underlying the transduction of bilayer deformation forces during mechanosensitive channel gating. *Nat. Struct. Biol. 9*, 696–703.

(17) Goforth, R. L., Chi, A. K., Greathouse, D. V., Providence, L. L., Koeppe, R. E., 2nd, and Andersen, O. S. (2003) Hydrophobic coupling of lipid bilayer energetics to channel function. *J. Gen. Physiol. 121*, 477–493.

(18) Gidwani, A., Holowka, D., and Baird, B. (2001) Fluorescence anisotropy measurements of lipid order in plasma membranes and lipid rafts from RBL-2H3 mast cells. *Biochemistry 40*, 12422–12429.

(19) Sinha, M., Mishra, S., and Joshi, P. G. (2003) Liquid-ordered microdomains in lipid rafts and plasma membrane of U-87 MG cells: a time-resolved fluorescence study. *Eur. Biophys. J. 32*, 381–391.

(20) Edidin, M. (2001) Shrinking patches and slippery rafts: scales of domains in the plasma membrane. *Trends Cell Biol. 11*, 492–496.

(21) Bienvenüe, A., Rousselet, A., Kato, G., and Devaux, P. F. (1977) Fluidity of the lipids next to the acetylcholine receptor protein of torpedo membrane fragments. Use of amphiphilic reversible spin-labels. *Biochemistry 16*, 841–848.

(22) Sternbach, L. H., Kaiser, S., and Reeder, E. (1960) Quinazoline 3-Oxide Structure of Compounds Previously Described in the Literature as 3.1.4-Benzoxadiazepines. *J. Am. Chem. Soc. 82*, 475–480.

(23) Perillo, M. A., Polo, A., Guidotti, A., Costa, E., and Maggio, B. (1993) Molecular parameters of semisynthetic derivatives of gangliosides and sphingosine in monolayers at the air-water interface. *Chem. Phys. Lipids 65*, 225–238.

(24) Israelachvili, J. N. (1989) *Intermolecular and Surface Forces*, Academic Press, New York.

(25) Perillo, M. A., and Arce, A. (1991) Determination of the membrane-buffer partition coefficient of flunitrazepam, a lipophilic drug. *J. Neurosci. Methods 36*, 203–208.

(26) Perillo, M. A., Garcia, D. A., Marin, R. H., and Zygadlo, J. A. (1999) Tagetone modulates the coupling of flunitrazepam and GABA binding sites at GABAA receptor from chick brain membranes. *Mol. Membr. Biol. 16*, 189–194.

(27) Lowry, O. H., Rosebrough, N. J., Farr, A. L., and Randall, R. J. (1951) Protein measurement with the Folin phenol reagent. *J. Biol. Chem. 193*, 265–275.

(28) Sokal, R., and Rohlf, F. (1987) *Introduction to biostatistics*, W. H. Freeman & Company, New York.

(29) Perillo, M. A., Marianacci, I. A., Ruiz, L., and Arce, A. (1986) Un nuevo método radioreceptor para la cuantificación de benzodiazepinas en fluidos biológicos. *Acta Bioquim. Clin. Lat. 20*, 559–572.

(30) Gaines, G. (1966) *Insoluble Monolayers at Liquids-Gas Interfaces*, Interscience Publishers, New York.

(31) Perillo, M. A., Scarsdale, N. J., Yu, R. K., and Maggio, B. (1994) Modulation by gangliosides of the lamellar-inverted micelle (hexagonal II) phase transition in mixtures containing phosphatidylethanolamine and dioleoylglycerol. *Proc. Natl. Acad. Sci. U.S.A. 91*, 10019–10023.

(32) Marsh, D. (1996) Lateral pressure in membranes. *Biochim. Biophys. Acta 1286*, 183–223.

(33) Loew, G. H., Nienow, J. R., and Poulsen, M. (1984) Theoretical structure-activity studies of benzodiazepine analogues. Requirements for receptor affinity and activity. *Mol. Pharmacol. 26*, 19–34.

(34) Duggan, M. J., Pollard, S., and Stephenson, F. A. (1991) Immunoaffinity purification of GABAA receptor alpha-subunit iso-oligomers. Demonstration of receptor populations containing alpha 1 alpha 2, alpha 1 alpha 3, and alpha 2 alpha 3 subunit pairs. *J. Biol. Chem. 266*, 24778–24784.

BC800175Z

SUPPORTING INFORMATION

Manuscript title: A surface active benzodiazepine receptor targeted agent for potential probing membrane order of $GABA_A$-receptor surroundings.

Authors: *Turina A. V. , Moyano E. L., Caruso B., Yranzo G. I. and Perillo M. A.*

Contents

S 2 - Scheme 1

S 3 - Figure 1

S 4 - Figure 2

S 5 - Figure 3

S 6 – Figure 4

S 7 – Figure 5

S 8 - Characterization of 5-(2-chlorophenyl)-6-nitro-1,3-dihydro-2*H*-1,4-benzodiazepin-2-one (Clonazepam) (1).

S10- Characterization of 5-(2-Chlorophenyl)-6-nitro-1-octyl-1,3-dihydro-2*H*-1,4-benzodiazepin-2-one (3, CAd).

S13- Characterization of Methyl-*N*-{(2-chlorophenyl)[2-nitro-6-(octylamino)phenyl] methylene}glycinate (4, MGd)

Scheme 1.

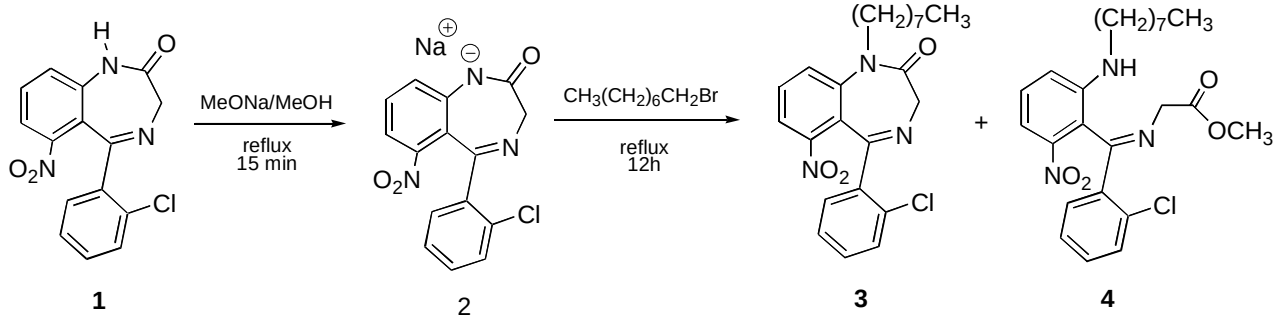

1 2 **3** **4**

Fig. 1

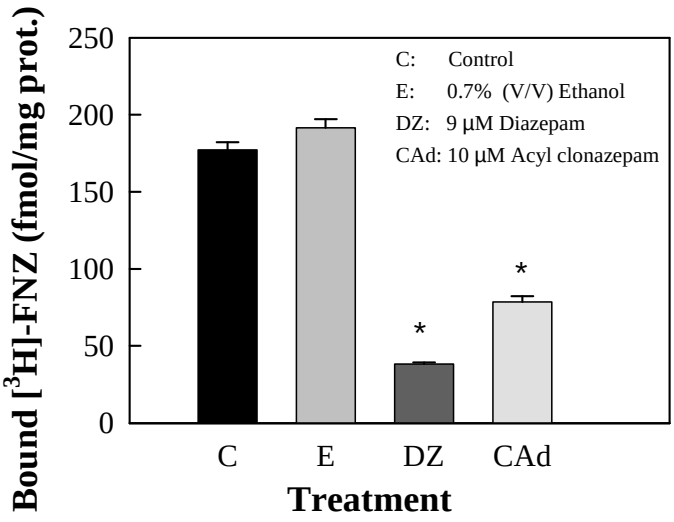
Bound [3H]-FNZ (fmol/mg prot.)
250
200
150
100
50
0
C: Control
E: 0.7% (V/V) Ethanol
DZ: 9 µM Diazepam
CAd: 10 µM Acyl clonazepam
*
*
C
E
DZ
CAd
Treatment

Fig. 2

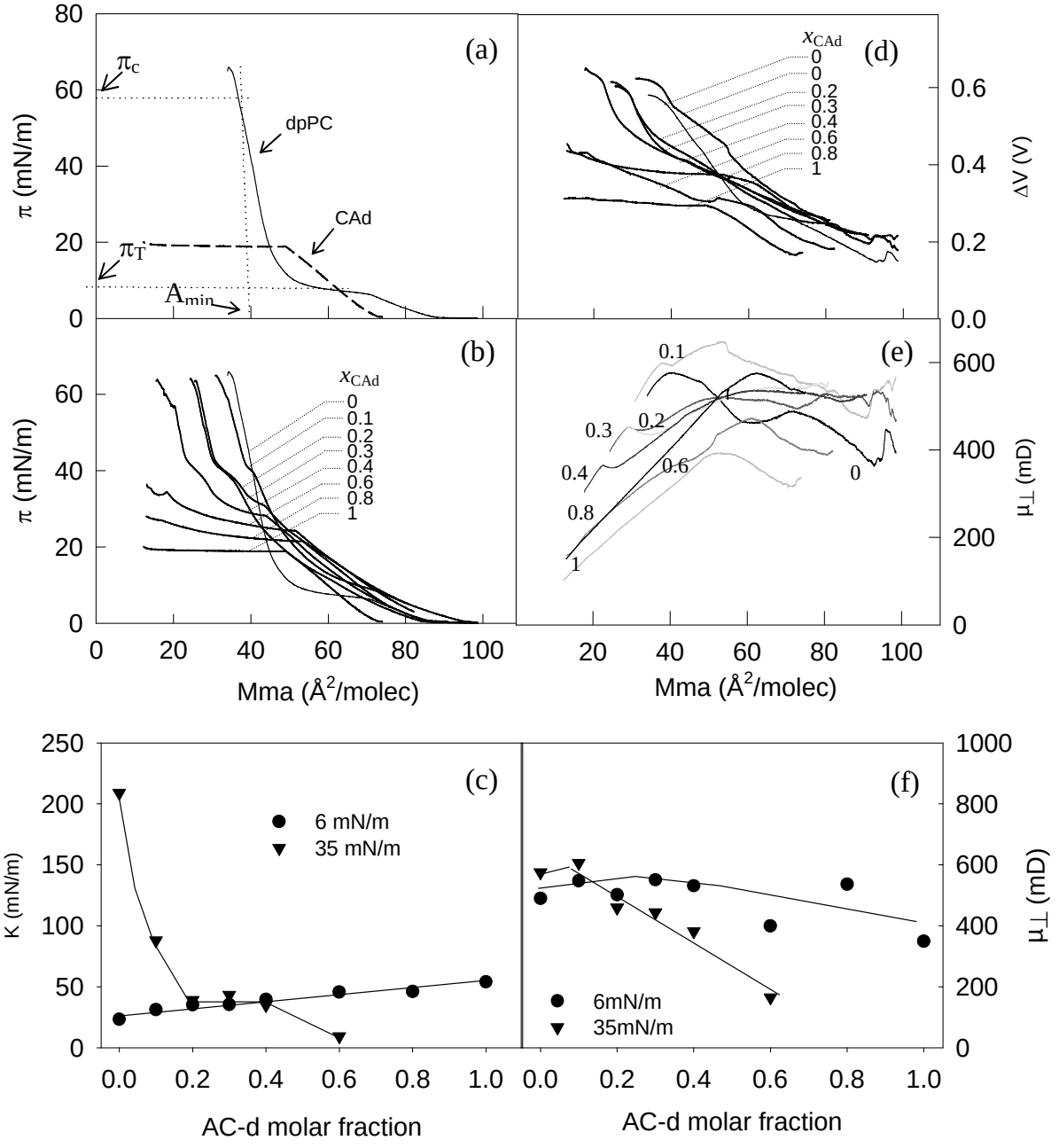
(a)
(b)
(c)
(d)
(e)
(f)
π (mN/m)
Mma (Å²/molec)
ΔV (V)
μ⊥ (mD)
K (mN/m)
AC-d molar fraction
dpPC
CAd
6 mN/m
35 mN/m
6mN/m
35mN/m

Fig. 3

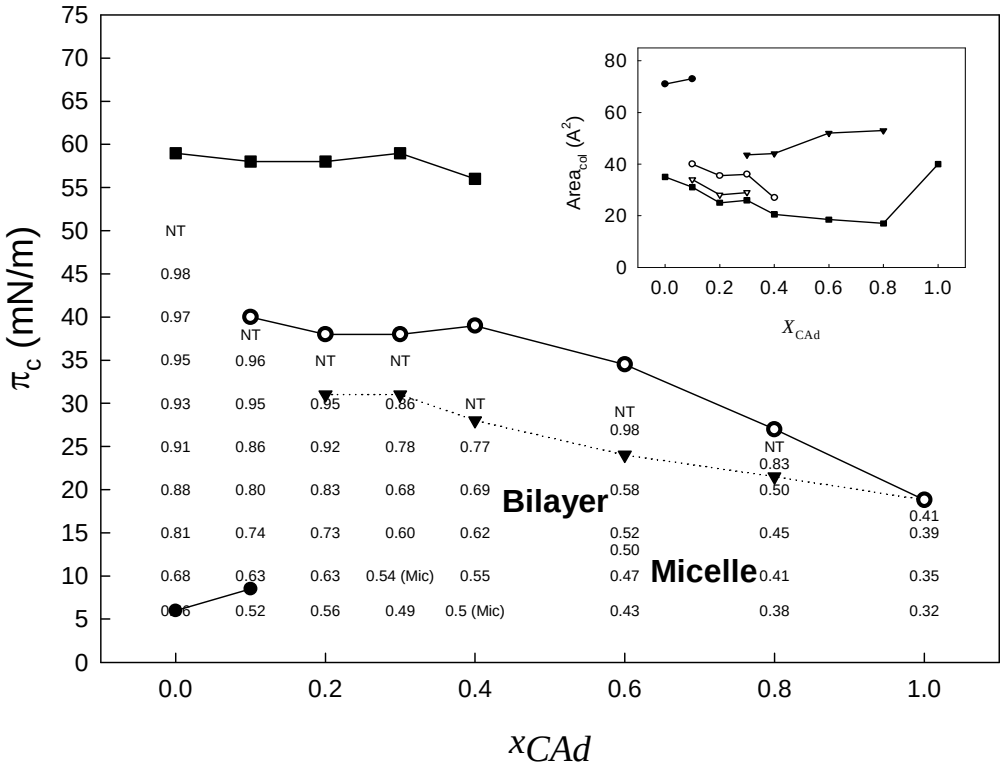
π_c (mN/m)
x_{CAd}
Bilayer
Micelle
$Area_{col}$ (A^2)
X_{CAd}
NT
0.98
0.97
NT
0.95
0.96
NT
NT
0.93
0.95
0.95
0.86
NT
NT
0.98
0.91
0.86
0.92
0.78
0.77
NT
0.83
0.88
0.80
0.83
0.68
0.69
0.58
0.50
0.41
0.81
0.74
0.73
0.60
0.62
0.52
0.45
0.39
0.50
0.68
0.63
0.63
0.54 (Mic)
0.55
0.47
0.41
0.35
0.56
0.52
0.56
0.49
0.5 (Mic)
0.43
0.38
0.32

Fig. 4

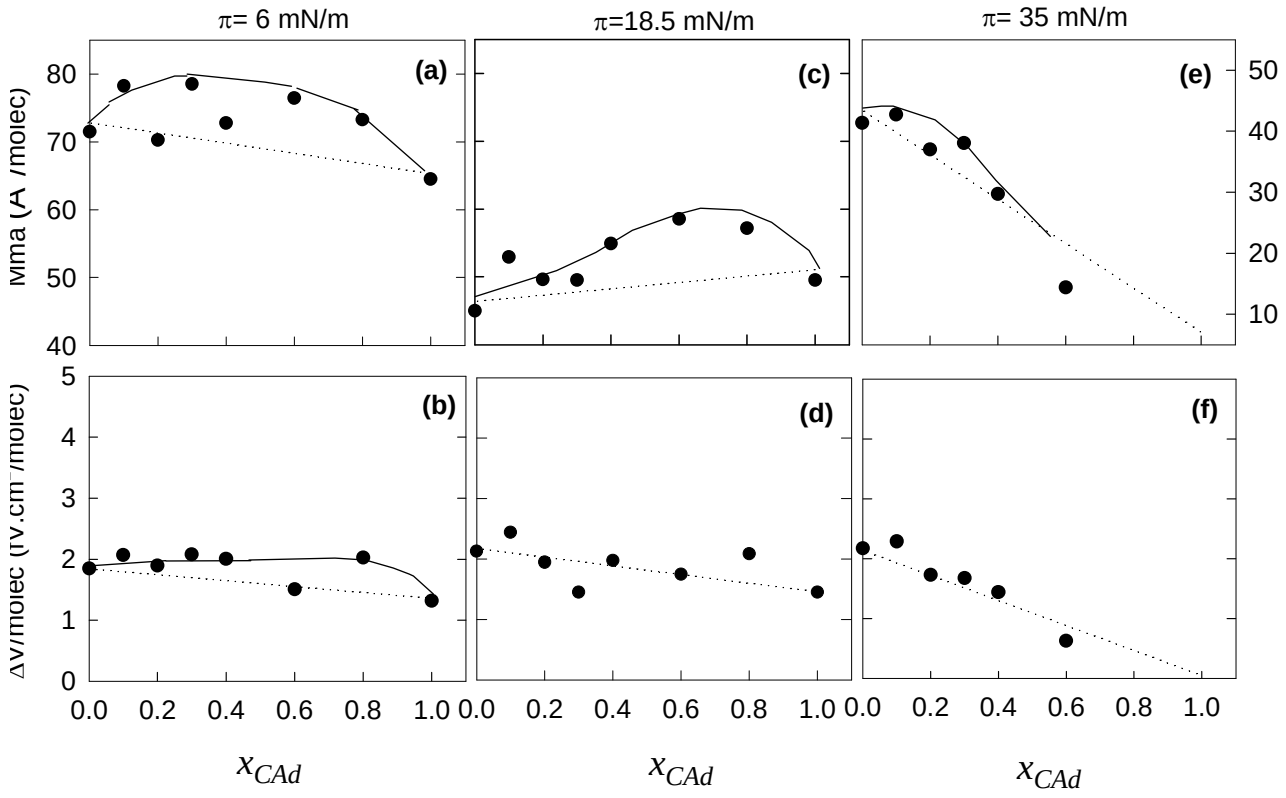
π= 6 mN/m
π=18.5 mN/m
π= 35 mN/m
(a)
(b)
(c)
(d)
(e)
(f)
Mma (Å /moiec)
ΔV/moiec (IV.cm⁻/moiec)
x_{CAd}
x_{CAd}
x_{CAd}

Fig. 5

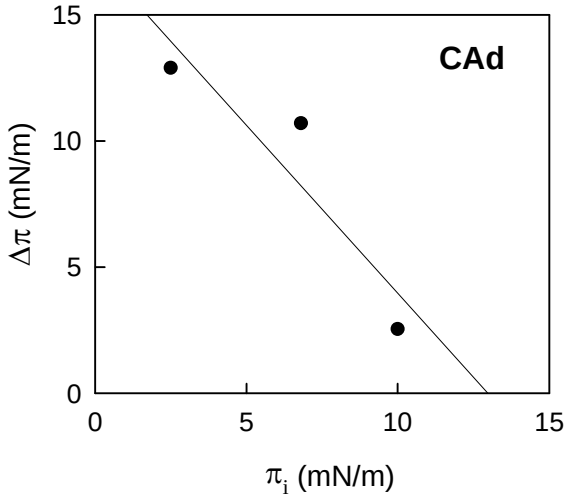

Characterization of 5-(2-chlorophenyl)-6-nitro-1,3-dihydro-2*H*-1,4-benzodiazepin-2-one (Clonazepam) (1).

^{1}H NMR (200 MHz, $CDCl_3$): δ (ppm) 4.46 (s, 2H); 7.30 -7.50 (m, 4H); 7.56 -7.70 (m, 1H); 7.98 (d, *J* = 2.6Hz, 1H); 8.32 (dd, J = 26 and 8 Hz, 1H), 9.70 (s, 1H, *NH*).

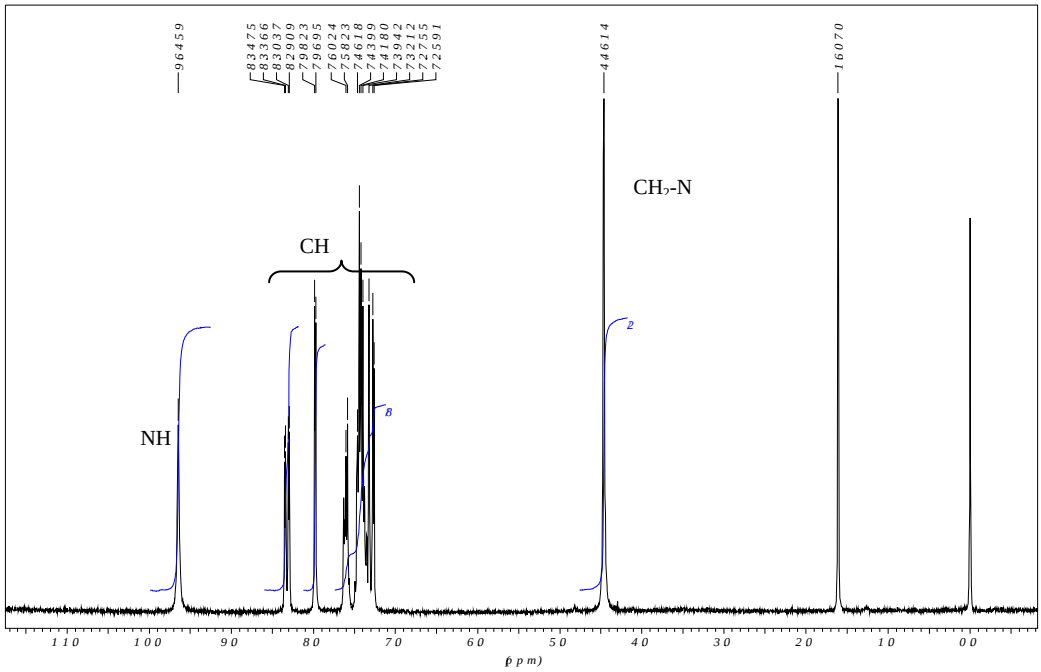

^{13}C-RMN (50.3 MHz, $CDCl_3$): δ (ppm) 56.60, 121.80, 125.78, 126.62, 127.35, 128.11, 130.37, 131.20, 131.61, 133.12, 137.75, 142.74, 143.28, 169.23, 170.88.

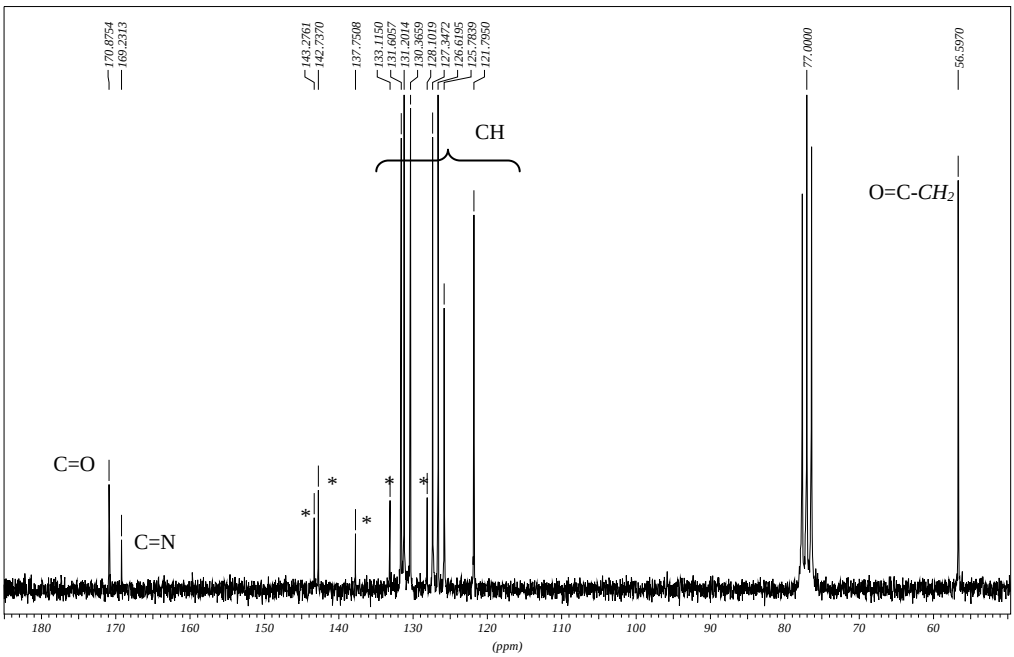

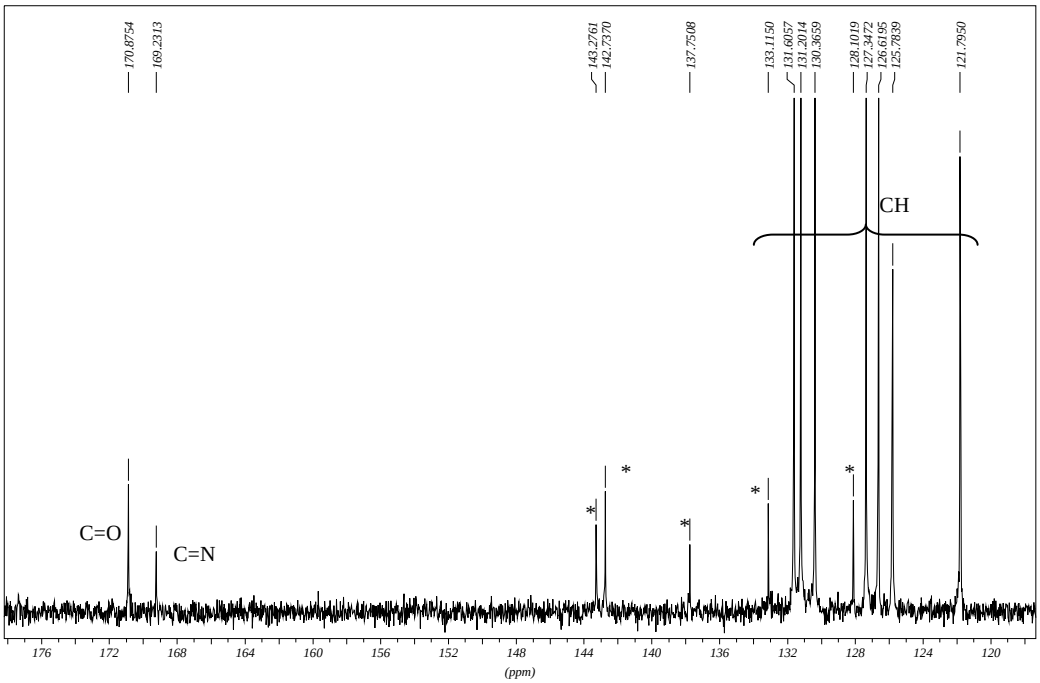
170.8754
169.2313
143.2761
142.7370
137.7508
133.1150
131.6057
131.2014
130.3659
128.1019
127.3472
126.6195
125.7839
121.7950
CH
C=O
C=N
*
176
172
168
164
160
156
152
148
144
140
136
132
128
124
120
(ppm)

Characterization of 5-(2-Chlorophenyl)-6-nitro-1-octyl-1,3-dihydro-2*H*-1,4-benzodiazepin-2-one (3, CAd).

^{1}H NMR (200 MHz, $CDCl_3$): δ (ppm) 0.85 (t, *J* = 6.6 Hz, 3H), 1.24 (s, 10H), 1.60 (m, 2H), 4.31 (m, 2H), 4.37 (dd, *J* = 11 and 228 Hz, 2H), 7.30-7.50 (m, 4H), 7.55 (d, *J* = 9.1 Hz, 1H), 7.62-7.70 (m, 1H), 7.93 (d, *J* = 2.6 Hz, 1H), 8.35 (dd, J = 2.6 and 9.1 Hz, 1H).

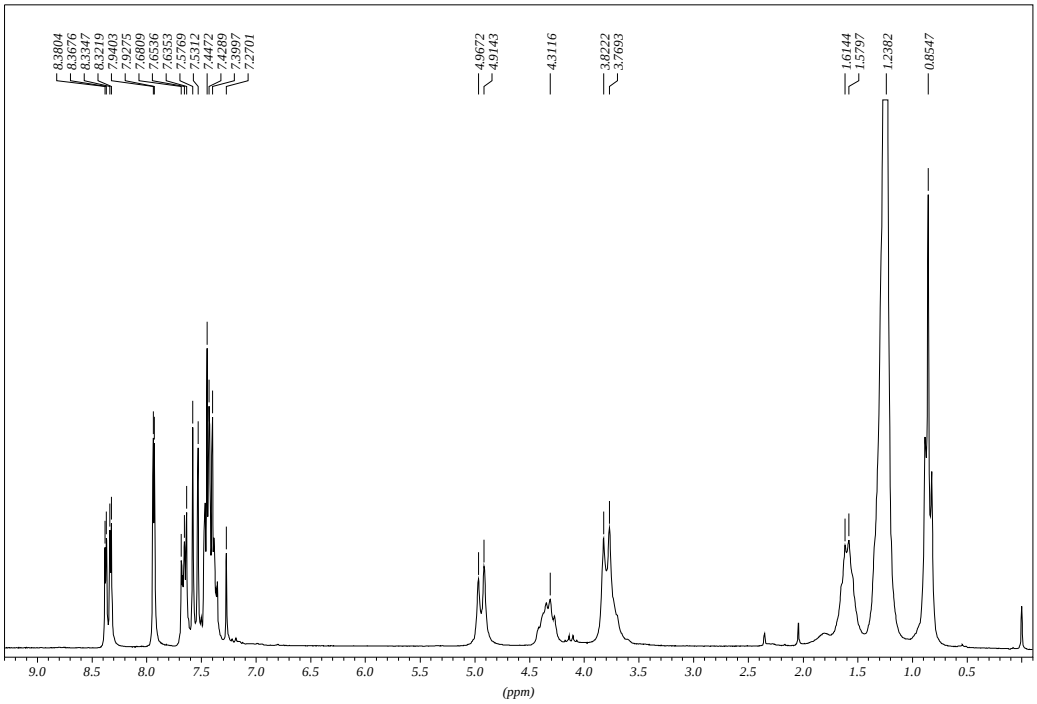

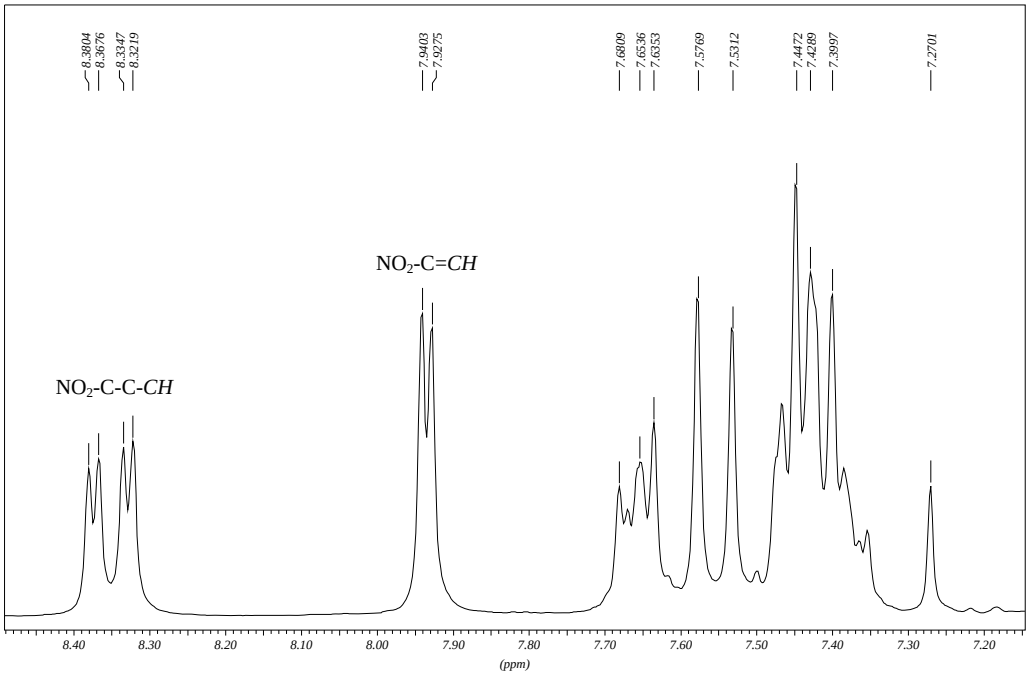

^{13}C NMR (50.33 MHz, $CDCl_3$): δ (ppm) 14.69, 23.23, 27.60, 29.11, 29.75, 29.81, 32.37, 48.19, 57.84, 123.22, 125.32, 126.65, 128.07, 131.04, 131.85, 132.41, 133.65, 137.80, 143.95, 147.80, 168.64, 169.18.

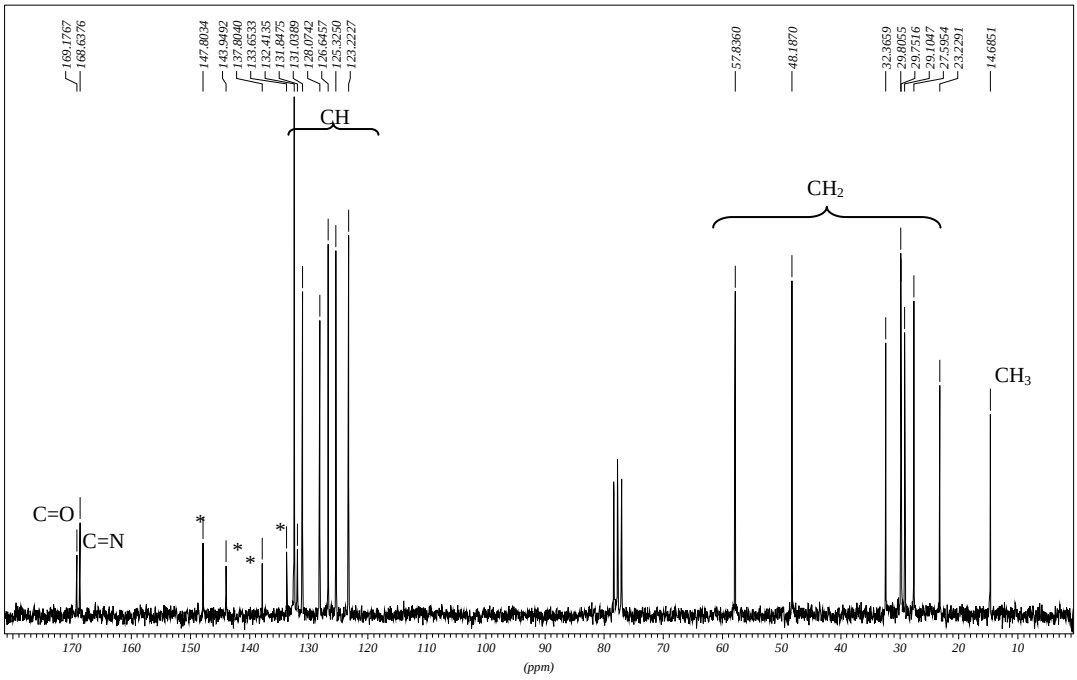

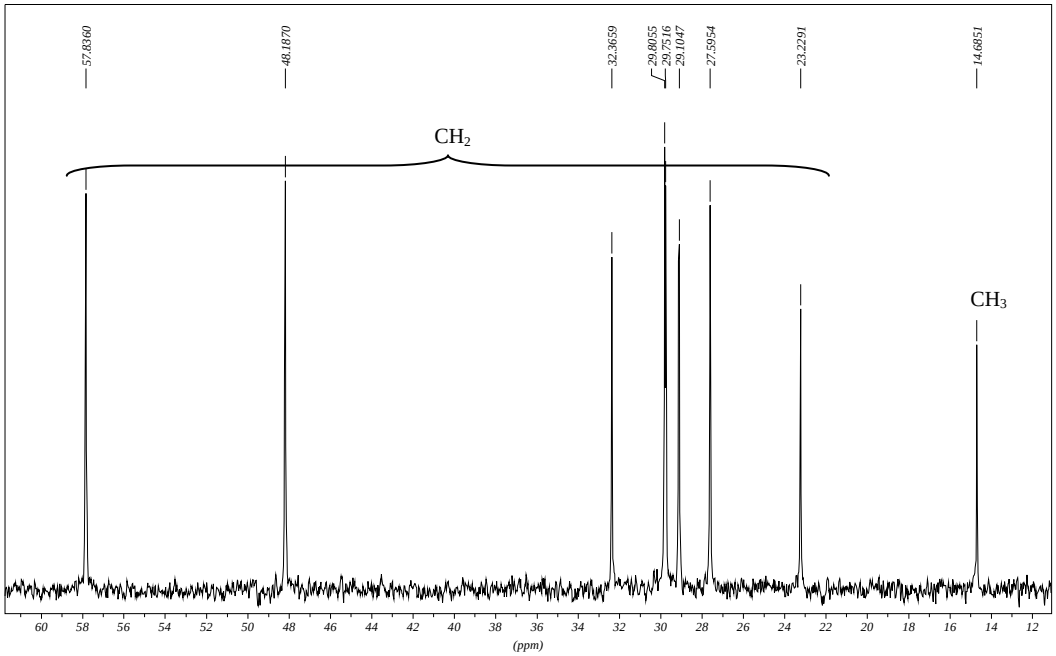

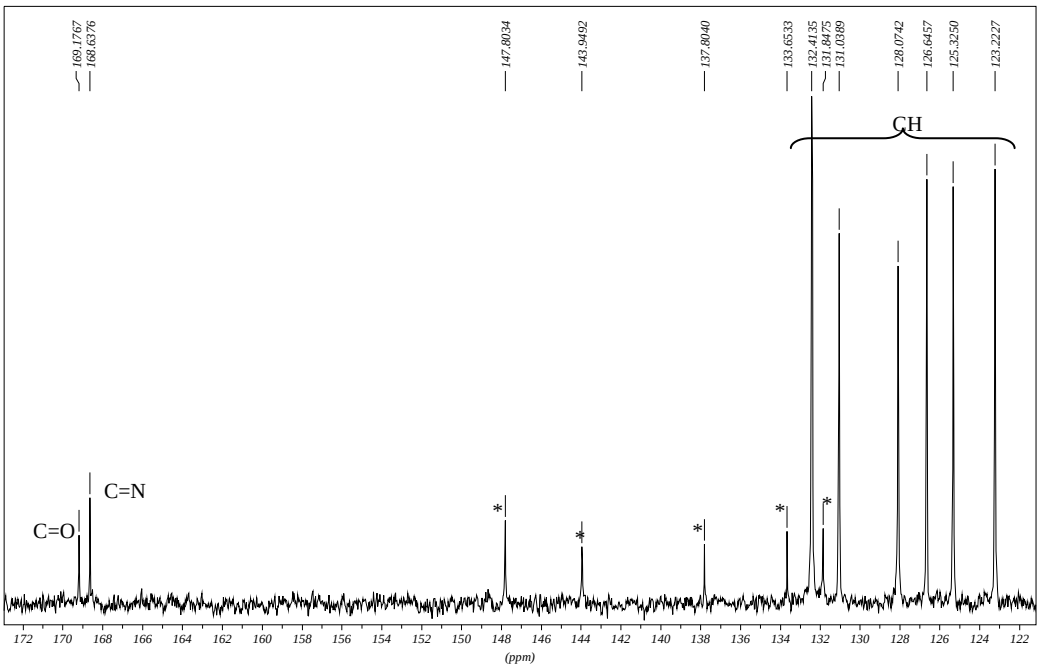
169.1767
168.6376
147.8034
143.9492
137.8040
133.6533
132.4135
131.8475
131.0389
128.0742
126.6457
125.3250
123.2227
CH
C=N
C=O
*
172 170 168 166 164 162 160 158 156 154 152 150 148 146 144 142 140 138 136 134 132 130 128 126 124 122
(ppm)

Characterization of Methyl-*N*-{(2-chlorophenyl)[2-nitro-6-(octylamino)phenyl] methylene}glycinate (4, MGd).

^{1}H NMR (200 MHz, $CDCl_3$): δ (ppm) 0.89 (t, *J* = 6.6Hz, 3H), 1.30 (s, 10H), 1.84 (q, *J* = 7.3 Hz, 2H), 3.37 (m, 2H), 3.76 (s, 3H), 4.04 (q, *J* = 19 y 47 Hz, 2H), 6.72 (d, *J* = 9 Hz, 1H), 7.09-7.14 (m, 1H), 7.35-7.60 (m, 4H), 7.71 (d, *J* = 2.6 Hz, 1H), 8.11 (dd, *J* = 4 and 10 Hz), 11.08 (s, 1H).

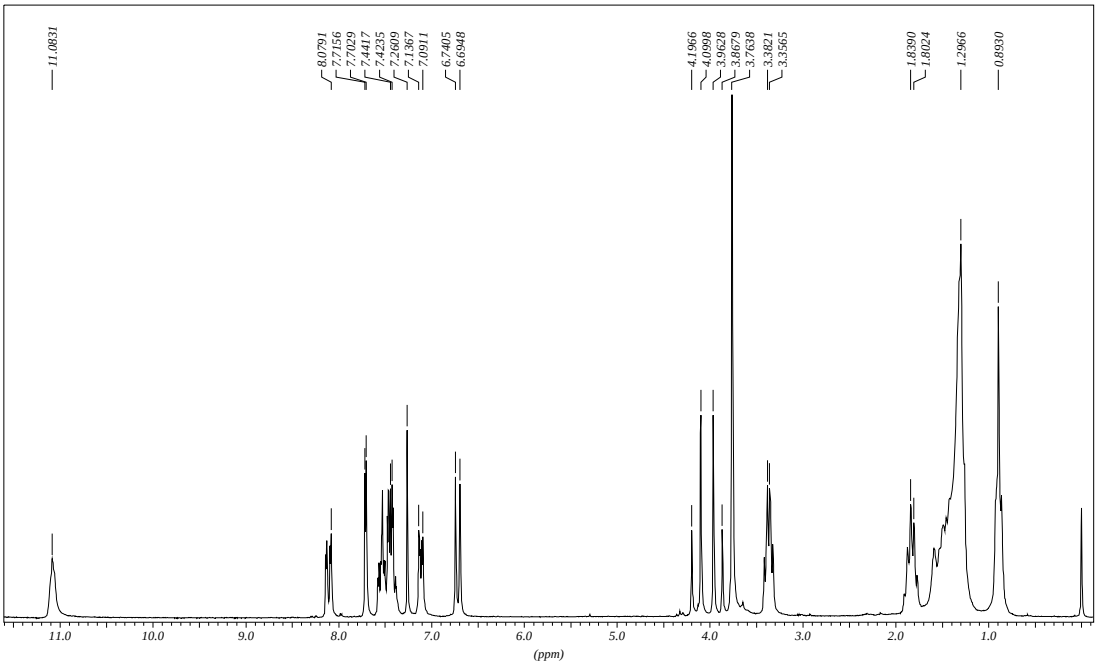

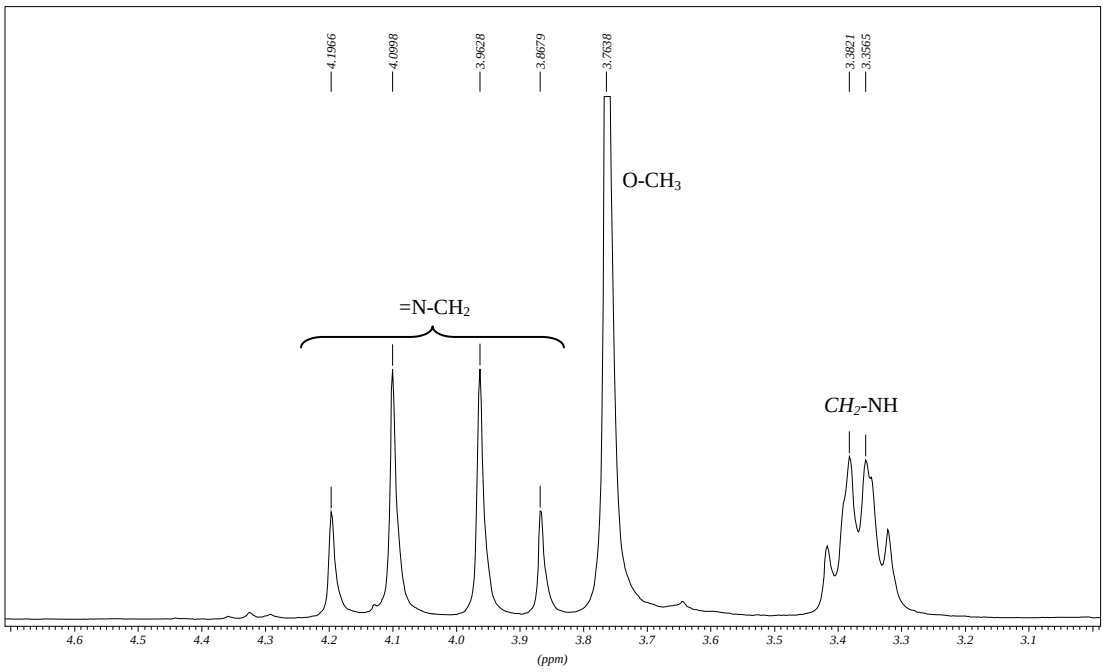

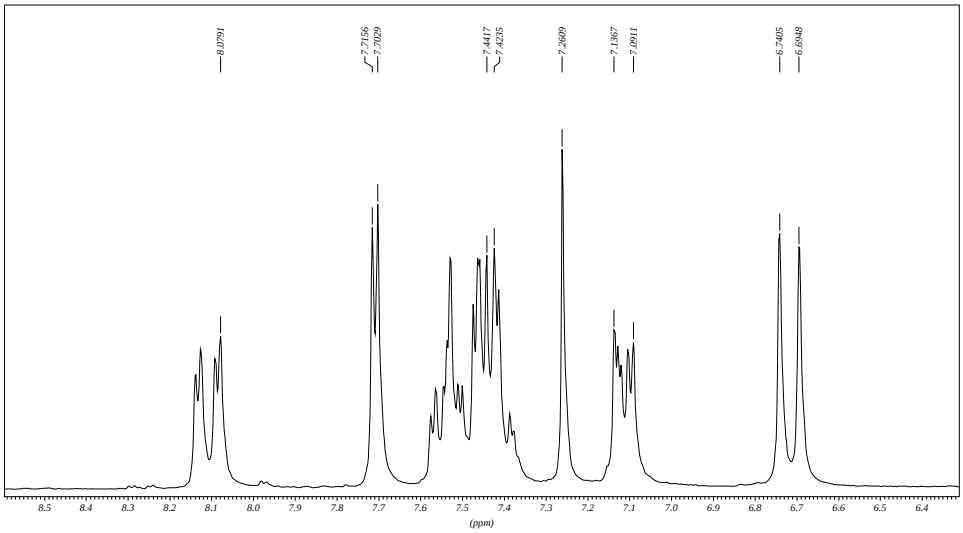

^{13}C NMR (50.33 MHz, $CDCl_3$): δ (ppm) 14.07, 22.64, 27.30, 29.24, 29.32, 31.83, 43.52, 51.99, 54.17, 110.39, 115.89, 127.64, 128.59, 129.80, 130.33, 131.42, 133.76, 135.14, 154.43, 170.20, 170.66.

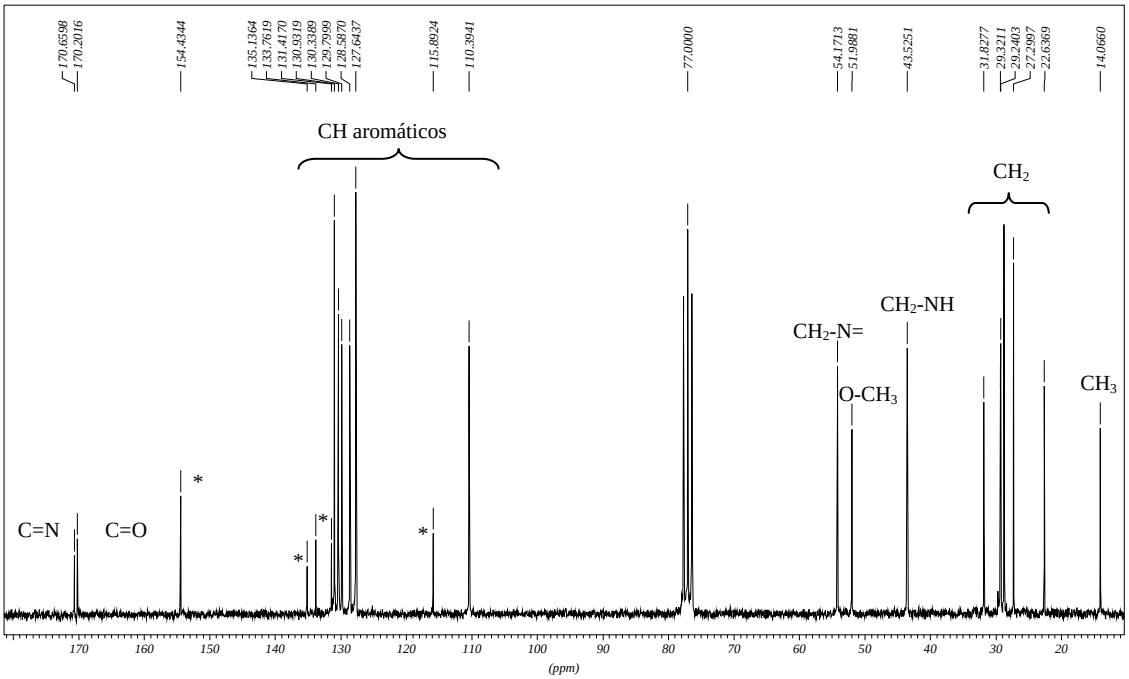

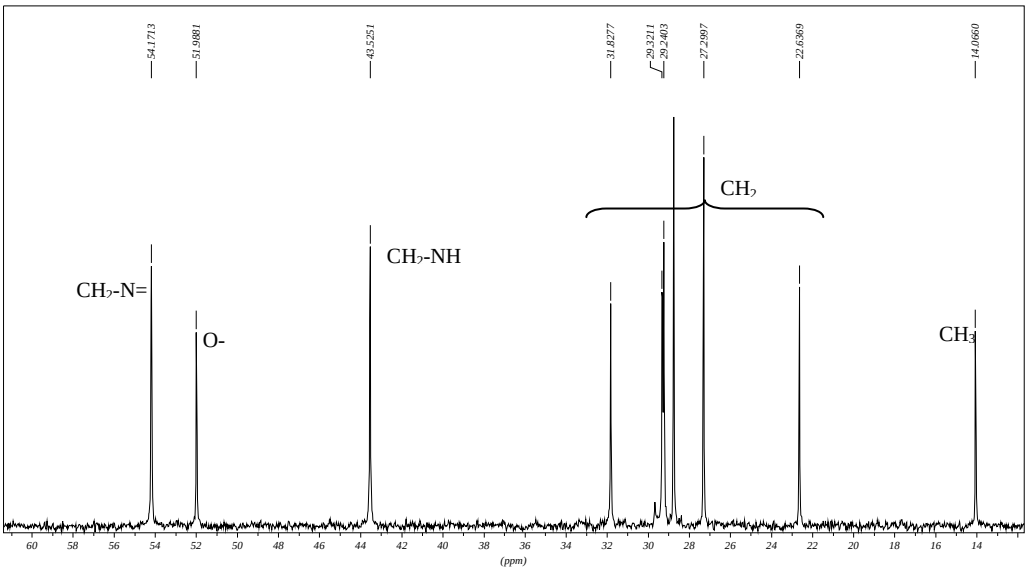
54.1713
51.9881
43.5251
31.8277
29.3211
29.2403
27.2997
22.6369
14.0660
CH2
CH2-NH
CH2-N=
O-
CH3
60 58 56 54 52 50 48 46 44 42 40 38 36 34 32 30 28 26 24 22 20 18 16 14
(ppm)

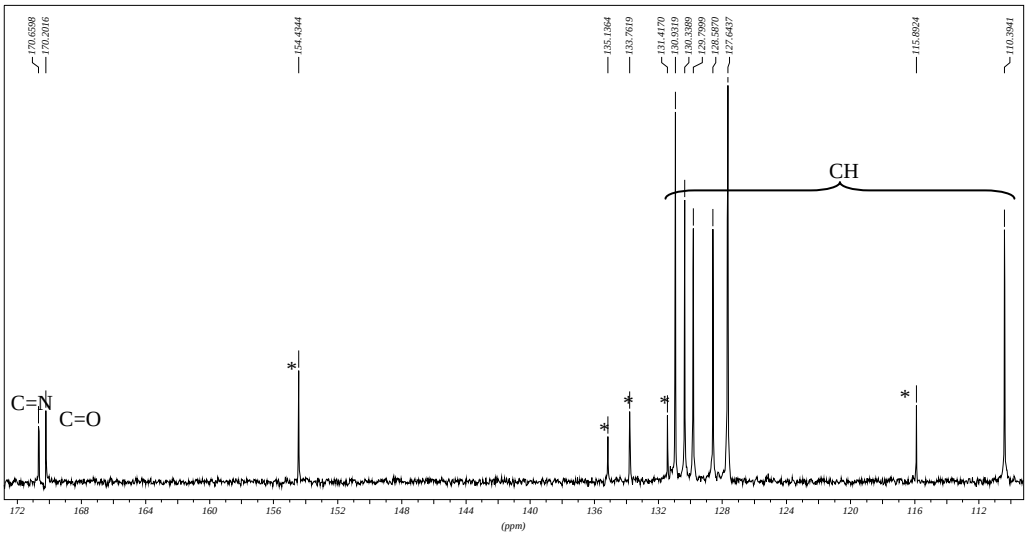
170.6598
170.2016
154.4344
135.1364
133.7619
131.4170
130.9319
130.3389
129.7999
128.5870
127.6437
115.8924
110.3941
CH
C=N
C=O
*
172 168 164 160 156 152 148 144 140 136 132 128 124 120 116 112
(ppm)

DEPT NMR (50.33 MHz, $CDCl_3$): δ (ppm) 14.7 (CH_3); 23.2, 27.6, 29.1, 29.7, 32.4, 48.2 and 57.8 (CH_2); 123.2, 125.3, 126.6, 128.1, 131 and 132.4 (CH).

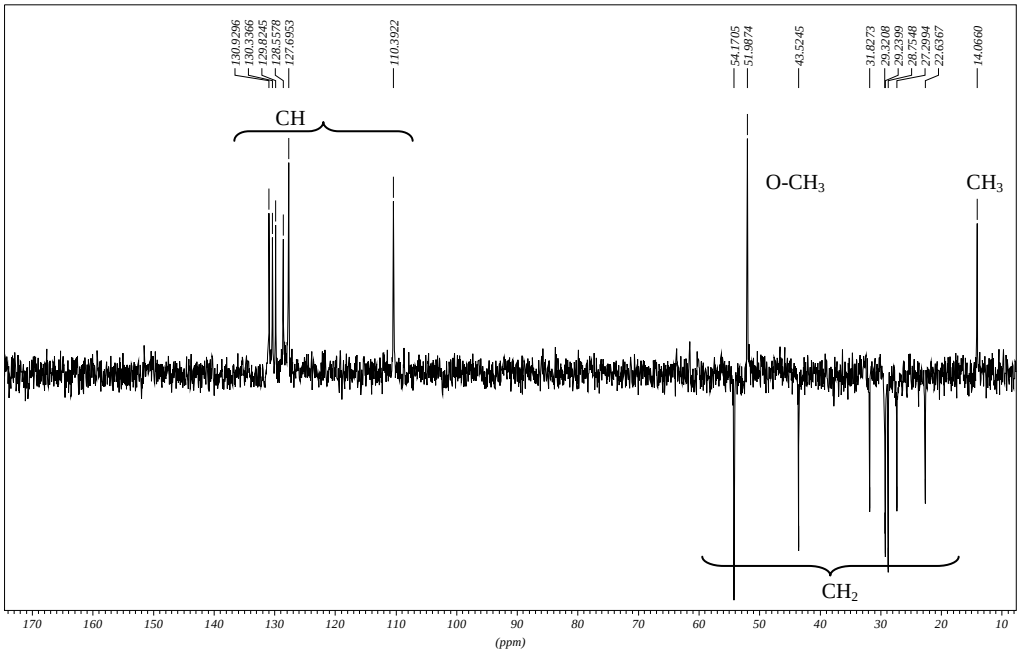

Bacterial RNase P RNA Is a Drug Target for Aminoglycoside−Arginine Conjugates

Alexander Berchanski and Aviva Lapidot*

Department of Organic Chemistry, The Weizmann Institute of Science, Rehovot 76100, Israel. Received May 14, 2008; Revised Manuscript Received July 29, 2008

The ribonuclease P (RNase P) holoenzymes are RNPs composed of RNase P RNA (PRNA) and a variable number of P protein subunits. Primary differences in structure and function between bacterial and eukaryotic RNase P and its indispensability for cell viability make the bacterial enzyme an attractive drug target. On the basis of our previous studies, aminoglycoside−arginine conjugates (AACs) bind to HIV-1 TAR and Rev responsive element (RRE) RNAs significantly more efficiently than neomycin B. Their specific inhibition of bacterial rRNA as well as the findings that the hexa-arginine neomycin derivative (NeoR6) is 500-fold more potent than neomycin B in inhibiting bacterial RNase P, led us to explore the structure−function relationships of AACs in comparison to a new set of aminoglycoside−polyarginine conjugates (APACs). We here present predicted binding modes of AACs and APACs to PRNA. We used a multistep docking approach comprising rigid docking full scans and final refinement of the obtained complexes. Our docking results suggest three possible mechanisms of RNase P inhibition by AACs and APACs: competition with the P protein and pre-tRNA on binding to P1−P4 multihelix junction and to J19/4 region (probably including displacement of Mg^{2+} ions from the P4 helix) of PRNA; competition with Mg^{2+} ions near the P15 loop; and competition with the P protein and/or pre-tRNA near the P15 helix and interfering with interactions between the P protein and pre-tRNA at this region. The APACs revealed about 10-fold lower intermolecular energy than AACs, indicating stronger interactions of APACs than AACs with PRNA.

INTRODUCTION

The complexity and diversity of RNA structures offer targets for small molecule ligands to be used as pharmacological agents (*1*). Ribonucleoprotein complexes (RNPs) are ubiquitous and essential components of all cells and appealing targets for new drugs due to their diverse functional roles in various cellular processes (*2, 3*). The ribonuclease P (RNase P) holoenzymes are RNPs composed of RNase P RNA (PRNA) and a variable number of P protein subunits: at least 1, 4, and 9 in Bacteria, Archaea and Eukarya, respectively (*4, 5*). Fundamental differences in structure and function between bacterial and eukaryotic RNase P and its indispensability for cell viability make the bacterial enzyme an attractive drug target candidate (*6*−*10*). Bacterial RNase P is composed of one RNA (∼400 nucleotides) and one small P protein (∼120 amino acids). Although the PRNA can catalyze the pre-tRNA-processing reaction *in vitro* in the absence of P protein at high salt concentrations (*11*), the P protein significantly influences multiple aspects of catalysis and is required for function *in vivo* (*12*). P protein plays a central role in RNase P function: it interacts with the 5′ leader of pre-tRNA substrates, leading to enhanced affinity for substrates (*13, 14*). In addition, P protein increases metal ion affinity (*15*) and pre-tRNA cleavage rate constants (*16*). Cross-linking studies have suggested that the central cleft of the P protein interacts with pre-tRNA 5′ leaders of at least 4 nucleotides in length, which locates the protein in close proximity to the active site (*14*). Crystal structures (*13, 17*) and the NMR structures (*18*) of P proteins reveal a remarkably similar overall topology for P proteins from different bacteria. It was suggested that three regions of the P protein interact with the RNA: the RNR motif, the central cleft, and the metal binding loop. The RNR motif is a highly basic region (K52 to R68, *Bacillus subtilis*) abundantly conserved among all bacterial P proteins, suggesting that this region is functionally important (*19*−*21*). Therefore, inhibition of bacterial RNase P activity could be accomplished with a compound that either interacts directly with the catalytic core in the PRNA or disrupts RNP interactions essential for the assembly of a functional RNase P holoenzyme.

Aminoglycosides (e.g., neomycin, neamine, paromomycin, and gentamicin) are small, polycationic molecules. These compounds are used clinically as antibacterial agents because of their ability to specifically bind prokaryotic rRNA and to inhibit bacterial protein synthesis (*22*). It has become apparent that aminoglycosides as well as their derivatives bind mRNAs (*23*), tRNAs (*24*), viral RNAs (*25*−*27*), and catalytic (*28, 29*) RNAs and that the binding of these ligands could alter the function of the RNA target. Aminoglycosides also interact with two essential elements of the human immunodeficiency virus type 1 (HIV-1) genome, Rev responsive element (RRE) and the transactivation responsive element (TAR) (*26*). Lapidot and co-workers have shown that arginine−aminoglycoside conjugates (AACs, Figure 1) are significantly more efficient anti-HIV-1 agents than aminoglycosides, as these conjugates comprise the RNA binding ability of aminoglycosides and the specific binding of arginine moieties to HIV-1 TAR and RRE RNAs (*30*−*36*). Significantly, AACs specifically inhibit bacterial rRNA (*37*). For example, the binding constants (K_D) of hexa-arginine neomycin B (NeoR6) for TAR and RRE RNAs were 5 and 23 nM, respectively (*35*). AACs (especially NeoR6) inhibit the binding of *trans*-activator protein (Tat) to various RNAs by mimicking the conserved binding arginine/lysine-rich motif of the Tat protein (*35*). Thus, we here propose that AACs, with their multiple arginine moieties, could also mimic the conserved arginine/lysine residues in the RNR motif of the bacterial RNase P protein and disrupt bacterial RNase P

* Corresponding author. Tel: 972-8-9343413. Fax: 972-8-9344142. E-mail: aviva.lapidot@weizmann.ac.il.

10.1021/bc800191u CCC: $40.75 © 2008 American Chemical Society
Published on Web 08/20/2008

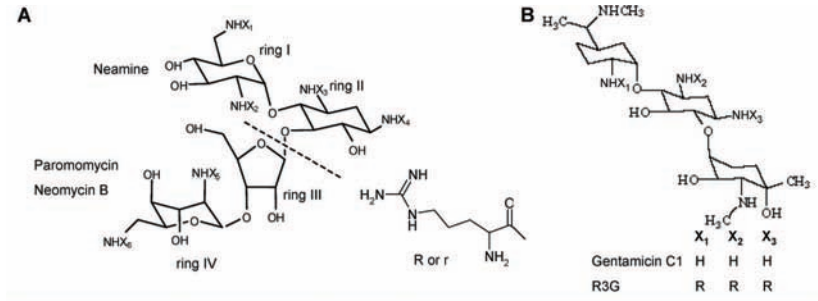

Compound	X_1	X_2	X_3	X_4	X_5	X_6
Neamine	H	H	H	H	-	-
Neam-r9	r9	H	H	H	-	-
Neomycin B	H	H	H	H	H	H
Neo-r9	r9	H	H	H	H	H
Neo-r6	r6	H	H	H	H	H
NeoR6	R	R	R	R	R	R
NeoR5	R	R	H	R	R	R
NeoR1	R	H	H	H	H	H
Paromomycin	OH*	H	H	H	H	H
ParomoR5	OH*	R	R	R	R	R

* OH group instead of NH_2; R = L-arginine; r = D-arginine

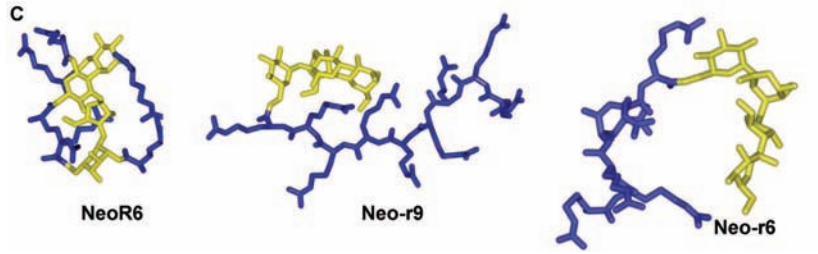

Figure 1. (A and B) Schematic representation of AACs, APACs, and aminoglycosides used in this study. R, L-arginine; r, D-arginine. (C) PRNA-bound conformations of NeoR6, Neo-r9, and Neo-r6. The aminoglycoside cores of the compounds are colored in yellow and the arginine moieties in blue.

holoenzyme assembly. Already in their report regarding the high potency of NeoR6 and triarginine−gentamicin C conjugate (R3G), Gopalan and Lapidot (*7*) showed that AACs act as potent and selective peptidomimetics that could prevent RNP assembly. For example, NeoR6 revealed nearly 500-fold higher potency than neomycin B in inhibiting bacterial RNase P (*7*).

Peptides carrying an arginine-rich sequence of Tat and a nona-D-arginine peptide, bind TAR RNA with high affinity and specificity (e.g. ref *38* and *39*). Arginine-rich peptides comprise a common motif of RNA recognition by proteins (*39*). Although the dominant contributions of the arginine side-chains may differ between complexes, the ability of the arginine side chains to be involved in electrostatic interactions, hydrogen bond formation, and stacking interactions makes arginine an important moiety for RNA recognition (*39*). Attempts to mimic the arginine-rich peptides led to the development of novel RNA ligands (e.g., tetra-arginine kanamycin (R4K) and R3G (*30*), and NeoR6 (*32*). Recently, we synthesized a novel set of poly arginine (hexa- and nona-arginines) aminoglycoside conjugates (APACs, Figure 1). Their anti-HIV-1 activities revealed high potency for the hexa-D-arginine-neomycin conjugate (Neo-r6), nona-D-arginine-neomycin conjugate (Neo-r9), and nona-D-arginine-neamine conjugate (Neam-r9) (*40, 41*). Thus, we anticipate that, as well as NeoR6, ParomoR5, and NeoR5, they may also bind PRNA (and other RNAs) and inhibit RNase P activity.

Westhof and co-workers (*42, 43*) succeeded in making an RNase P model with the aid of computer programs and data from physical−chemical experiments on the P protein (*44*). Their RNA model is in good agreement with most of the crystallography results (*45, 46*) including the core of the catalytic site. Thus, we, as well as Fierke and co-workers (*47*), utilize the whole modeled PRNA molecule for further investigation. This approach avoids complications introduced by unresolved regions and the effects of crystal packing contacts (*47*). These advances in our understanding of RNase P provide insight into the interface between the RNA and protein worlds. The development of many drugs (e.g., HIV-1 protease inhibitors) was heavily influenced by or based on structure-based design and screening strategies (*48*). Computational methodologies have become a crucial component of many drug discovery programs (*48*).

The main aim of our present study is predicting the binding modes of AACs and APACs to PRNA. The model presented by Westhof, Gopalan, and co-workers (*43*) was utilized in this study for docking AACs and APACs. We used a multistep docking approach (Figure 2) containing (i) geometric, geometric-electrostatic, and geometric-hydrophobic docking full scans by MolFit; (ii) intersecting of the lists of predictions from geometric-electrostatic-hydrophobic docking scans for identify-

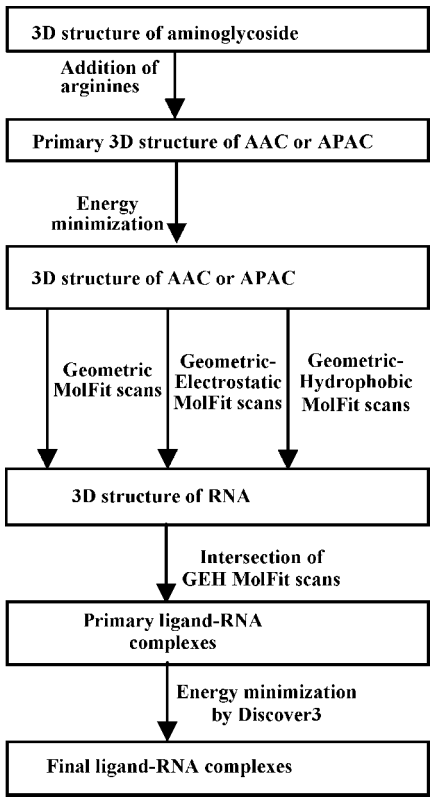

Figure 2. Schematic representation of the molecular modeling and multistep docking procedure followed in this study.

ing putative geometrically and chemically suitable binding sites; and (iii) final refinement of the obtained complexes by Discover3.

Several preferred AACs and APACs binding positions were highlighted by this approach. On the basis of these models, we here propose that AACs and APACs can inhibit RNase P activity by (i) interacting with the P protein/pre-tRNA binding site of PRNA; (ii) competing with the P protein for binding PRNA; and/or by (iii) displacing Mg^{2+} ions near the PRNA P15 loop leading to interference with RNase P catalysis. This molecular docking approach may be useful in drug design.

EXPERIMENTAL PROCEDURES

AACs and APACs. The synthesis, purification, and analysis of the following compounds NeoR6, ParomoR5, R3G, hexa-D-arginine-neomycin conjugate (Neo-r6), nona-D-arginine-neomycin conjugate (Neo-r9), and nona-D-arginine-neamine conjugate (Neam-r9) (biologically stable enantiomers) (Figure 1) were previously described (*30*−*36*, *41*).

General Procedure of Docking. We docked aminoglycosides and their arginine conjugates as well as RNase P protein to the three-dimensional (3D) model structure of the PRNA. A multistep docking procedure was used: exhaustive rotation−translation docking scans by MolFit, followed by intersecting lists of predictions and flexible ligand docking by Discover3 (Figure 2). We used the model coordinates of bacterial RNase P holoenzyme of *B. subtilis* described by Westhof and coworkers (*43*). This RNA−protein complex consists of RNA component (nucleotides 4−395), pre-tRNA molecule (includes nucleotides −9 to 72), and P protein. Molecular docking was performed with free PRNA (without P protein and pre-tRNA).

Models of NeoR6, ParomoR5, NeoR5, Neo-r9, and Neo-r6 were constructed by addition of arginines to neomycin B (its 3D coordinates were taken from PDB entry 1qd3 (*49*)) using the Biopolymer module of InsightII. We used the first NMR structure (out of 17) from 1qd3. Neam-r9 was built by trimming aminoglycoside rings III and IV of the Neo-r9 model. All these modeled structures were solvated in water and energy minimized (Figure 2). In general, all the energy minimizations in this study were performed for molecules immersed in a layer of 5 Å of water until the maximum derivative was less than 0.001 using the Discover 3 module of InsightII (Accelrys, Inc., San Diego, CA, USA) and the CVFF force field.

Full Rigid-Body Docking of Ligands to PRNA. AACs (NeoR6, NeoR5, and ParomoR5), APACs (Neo-r9, Neo-r6, and Neam-r9), neomycin B (PDB entry 1qd3 (*49*)), and P protein were docked to PRNA using the program MolFit (*50*). MolFit treats the molecules as rigid bodies. They are represented by 3D grids in which each grid point carries information concerning its position with respect to the surface/interior of the molecule. The surface grid points carry chemical information such as the electrostatic potential or the hydrophobicity of the surface. MolFit performs an exhaustive scan of the relative rotations and translations of the molecules and produces a list of models. Since PRNA consists of many negative charges, while AACs and APACs are highly positively charged compounds, at first we performed full geometric-electrostatic scans (*51*) of these ligands against PRNA. The electrostatic potential of each molecule was calculated using the program Delphi as implemented in the InsightII package. Each full docking scan tested 8760 relative orientations (angular grid interval of 12°), and for each orientation, one best scoring solution was saved. These solutions were further sorted by their geometric-electrostatic complementarity score.

Geometric, geometric-hydrophobic (*50*), and geometric-electrostatic docking scans were performed for all ligands. Geometric-electrostatic-hydrophobic (GEH) complementarity scores were obtained by intersecting the lists of predictions from geometric, geometric-electrostatic, and geometric-hydrophobic docking scans, as described previously (*50*) (Figure 2). The nearly correct solutions are likely to be included in each of the three lists, that is, in a subset of common solutions. For this subset of solutions, it is possible to combine the geometric, electrostatic, and hydrophobic scores to obtain a combined geometric-electrostatic-hydrophobic score, $S_{geo+elec+hydro} = S_{geo} + e \cdot S_{elec} + h \cdot S_{hydro}$, where S_{elec} is the difference between the geometric-electrostatic and the geometric scores, and S_{hydro} is the difference between the geometric-hydrophobic and geometric scores for a given solution. The combination of electrostatic and hydrophobic complementarity with geometric complementarity improves the docking results for complexes of proteins. This improvement is due, in some cases, to the higher combined score for the nearly correct solution. Some of the improvement in rank is also due to the elimination of false solutions, which are found in only one of the 3 lists (geometric, geometric-electrostatic, or geometric-hydrophobic) and are eliminated in the intersection process (*50*).

Flexible Docking of Ligands to PRNA. The top-ranked GEH MolFit scan solutions were used for input to the flexible ligand docking performed by the program Discover3 (Figure 2). We added the hydrogens to PRNA by using the Biopolymer module of InsightII. The PRNA was immersed in a layer of 5 Å of water and energy minimized in complex with each ligand represented by its top-ranked GEH MolFit scan solution using the Discover 3 module of InsightII. We tested several possible binding sites of each ligand to PRNA formed by GEH MolFit clusters. The intermolecular energy of the finally refined complexes was measured by the Docking module of InsightII

according to maximal radii of ligands. The best models were selected by the lowest intermolecular energy.

RESULTS

Rationale. The increased (i) affinity of AACs to HIV-1 TAR and RRE (*35*), and (ii) potency in disrupting RNP interactions and inhibiting bacterial RNase P, compared to aminoglycosides (*7*), led us to hypothesize that NeoR6 and other structurally similar AACs and APACs may inhibit RNase P activity by interacting with PRNA. Therefore, our main objective was deciphering the structure−function relationships of the two families of aminoglycoside−arginine conjugates (AACs and APACs) in the context of their interactions with PRNA, with the aim of developing effective novel antimicrobial drugs. A structural model proposed for *Bacillus subtilis* holoenzyme−substrate complex (*43*) was employed. The predicted binding sites of AACs and APACs to several regions of PRNA obtained by docking as well as their interference with the holoenzyme−pre-tRNA interaction for the cleavage process of pre-tRNA are described below.

Rigid-Body Docking of P Protein, APACs, and AACs to PRNA. We assume that AACs and APACs structurally mimic arginine/lysine-rich P protein (*19*−*21*) and may disrupt the formation of the RNase P holoenzyme complex by preventing binding of the P protein to the RNA moiety. Thus, the most potent compounds of AACs and APACs were docked to the naked PRNA molecular model. Geometric, geometric-hydrophobic, and geometric-electrostatic docking scans were performed for P protein, APACs, and AACs to PRNA using the program MolFit (see Experimental Procedures and Figure 2). Each predicted MolFit solution is a plausible position of ligand on PRNA. Since geometric-electrostatic docking does not always suggest the nearly correct solution at the first ranked position, the intersection of the lists of predictions from geometric, geometric-electrostatic, and geometric-hydrophobic docking scans was also performed according to a procedure previously described (*50*). The use of this procedure (i) improves the rank of solutions, which not only have good electrostatic contacts with macromolecule but also increase the significance of geometric and hydrophobic contacts (in case they exist); (ii) drastically reduces the number of putative solutions; and (iii) forms clusters. After intersecting GEH MolFit scans of several top-ranked solutions for each cluster, optimal matches with PRNA are obtained, which are very useful for following analysis and final refinement.

We docked the P protein to PRNA (GEH MolFit scans with intersection of the results). We obtained a cluster of putative MolFit solutions (which includes the top ranked ones) exactly at the site that was predicted by Westhof and co-workers (*43*) and confirmed by Fierke and co-workers (*47*) (Figure 3 B). Our top ranked solution was slightly rotated relative to the predicted position of the P protein within the RNase P holoenzyme structure (*43*) since the P protein consists of many arginines and lysines, not only at the RNR motif but also at other regions.

(a) Docking of APACs. The geometric-electrostatic docking scans of APACs (Neo-r9, Neam-r9, and Neo-r6) revealed two very large clusters and several smaller ones (Figure 3 C, E and G). The 60 top ranked solutions were within these two clusters. The first cluster was situated at the region of PRNA (P4, P3, P2, and J19/4, Figure 3 C); this region interacts with P protein and pre-tRNA (*43*, *47*). The second cluster was located proximal to the PRNA P15 helix. The intersection of the lists of predictions from GEH MolFit docking scans drastically reduced the number of putative solutions (from 8760 to 32 for Neo-r9 and from 8760 to 43 for Neam-r9). The first ranked solutions of Neo-r9, Neam-r9, and Neo-r6 were within cluster 1 (PRNA region of P4, P3, P2, and J19/4; Figure 3 D, F, and H). This PRNA region contacts RNR and neighboring motifs of P protein and pre-tRNA (*43*, *47*). Therefore, our suggestion, that APACs structurally mimic an RNR motif of the P protein, is supported. Cluster 2 (proximal to P15), which also consists of several high ranked docking solutions, must also be considered for a binding site.

(b) Docking of AACs. The full geometric-electrostatic docking scans of AACs (NeoR6, ParomoR5, NeoR5, and R3G) and neomycin B (Figure 4A, C, E, G, and I) revealed more disperse patterns (there are many more clusters of the putative solutions) than for APACs; however, cluster 1 at the region P4, P3, P2, J19/4, and cluster 2 near P15, which include the 10−20 high ranked solutions, are also present for NeoR6, ParomoR5, and NeoR5 (but not for neomycin B and R3G), similar to that for APACs (Figure 3). The intersection of the lists of predictions from GEH MolFit docking scans reduced the number of putative solutions, but not as markedly as for the APACs (Figure 4B, D, F, H, and J). The first ranked solution of all AACs is within cluster 1 (PRNA region P4, P3, P2, and J19/4). Cluster 2 (near P15) also consists of several high ranked solutions. In contrast to APACs, there are many additional clusters for AACs. In general, these clusters that are not situated near PRNA regions P4, P3, P2, and J19/4 or P15 helices consist of solutions with lower MolFit GEH scores. Therfore, the preference of AACs to bind PRNA at the regions P4, P3, P2, and J19/4 or P15 is significantly weaker than that of APACs. The pattern of neomycin B binding is even more disperse than for the arginine conjugates, suggesting lower binding specificity (Figure 4B). The top ranked MolFit solutions of neomycin B are not at P4, P3, P2, and J19/4 or P15 helices, and it is difficult to prefer one cluster over the others.

Refinement of APACs−PRNA Complexes. The best-scoring representatives of several predicted MolFit clusters were used for final the refinement by Discover3 (see Experimental Procedures and Figure 2). The PRNA and ligands were immersed in water, and the complex was energy minimized. Therefore, both PRNA and ligand were hydrated and flexible. The nucleotides of PRNA regions that were distant from a ligand were fixed. The ranges of intermolecular docked energies (kcal/mol) measured according to maximal radii of the ligands for Neo-r9−PRNA complexes are from −15283 to −14386 at cluster 1, from −14441 to −12645 at cluster 2, and from −13211 to −12354 at other clusters (Table 1). Similar values were found for Neam-r9−PRNA complexes from −15897 to −13988, −14331 to −12645, and −13047 to −12211, respectively. The average values of intermolecular docked energies for Neo-r9−PRNA and Neam-r9−PRNA complexes at cluster 1 are almost the same (Table 1). To determine the PRNA nucleotides that interact with the P protein and pre-tRNA, we calculated the distances between the P protein or pre-tRNA and the PRNA atoms in the RNase P holoenzyme−pre-tRNA complex (*43*). The distances between all docked ligands and PRNA were also calculated. We took into consideration intermolecular distances within 4 Å between heavy atoms. The results of comparisons between binding sites of our docked ligands and those of P protein and pre-tRNA are summarized in Tables 2 and 3. The Neo-r9−PRNA complex with the lowest energy (−15283 kcal/mol) refers to the PRNA region, which binds protein P and pre-tRNA (P2, P3, P4, J18/2, and J19/4) (Figure 5A and B, and Table 2). The best Neam-r9−PRNA complex is situated exactly at this site with some different contacts. All arginine residues of Neo-r9 and Neam-r9 have electrostatic interactions with the PRNA nucleotides. Already, the MolFit scans highlighted that rings I and II of Neo-r9 neomycin core have more contacts with PRNA in comparison to rings III and IV (Figure 1). The final refinement by Discover 3 strengthens this observation. Our results reveal similar ranges

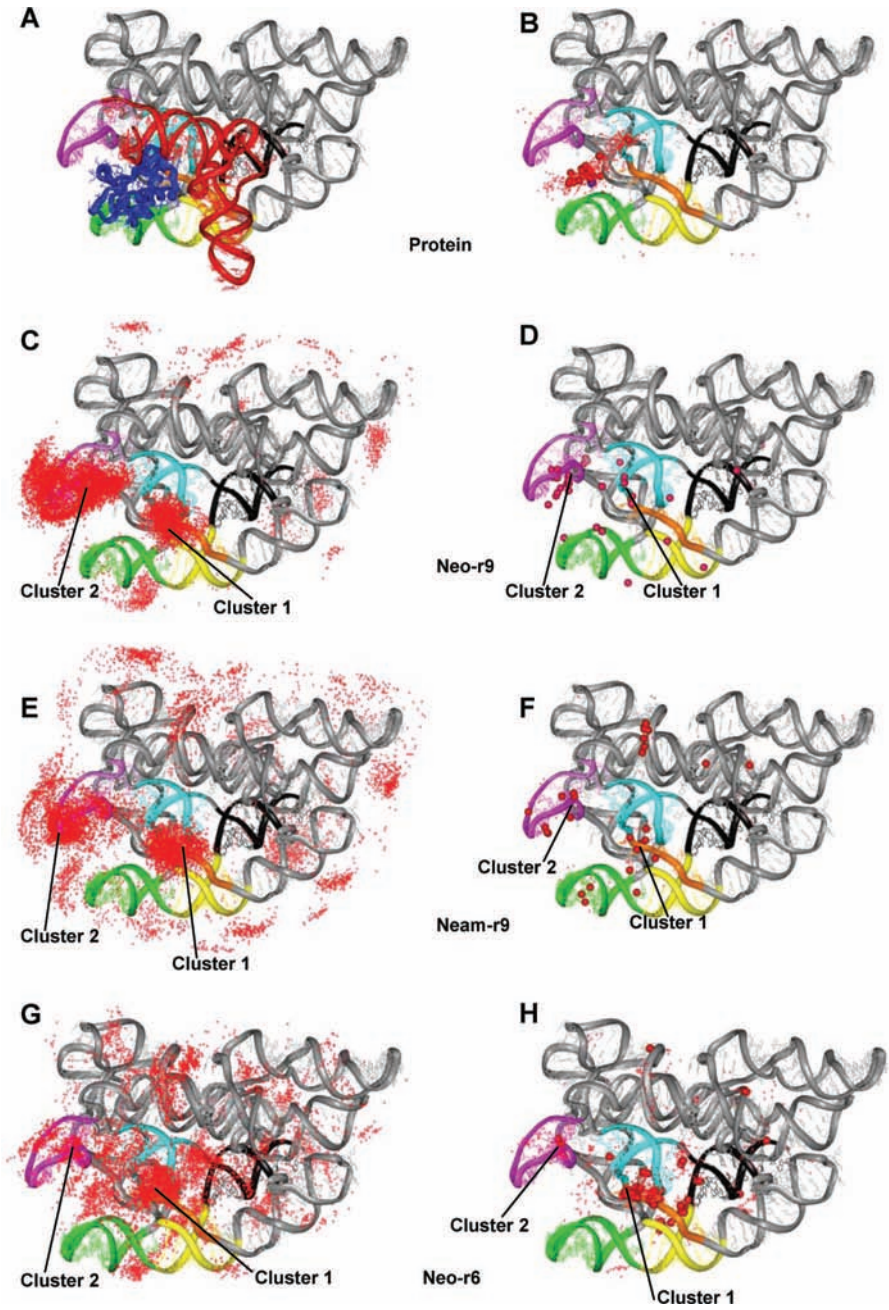

Figure 3. (A) Structural model of *B. subtilis* RNase P holoenzyme−pre-tRNA complex (*43*). The PRNA is shown as a ribbon. The important PRNA regions for interactions with pre-tRNA or P protein (according to Westhof and co-workers (*43*) and Fierke and co-workers (*47*)) are colored: P1 (black), P2 (yellow), P3 (green), P4 (cyan), and J19/4 (orange). P15 is colored magenta. P protein (dark blue) and pre-tRNA (red) are shown as ribbons. The colors and representation of PRNA, PRNA regions, pre-tRNA, and P protein are the same in Figures 4 and 5. (B) Results of P protein-PRNA GEH MolFit scans with intersection of the prediction lists. Each solution is the plausible position of ligand on PRNA, represented by the center of ligand mass (colored red). The top ranked solutions are shown in CPK representation. The colors and representation of MolFit solutions are the same for all ligands in this figure and Figure 4. (C−H) Results of MolFit geometric-electrostatic scans (C, E, and G) and GEH MolFit scans with intersection of the prediction lists (D, F, and H) for APACs (Neo-r9, Neam-r9, and Neo - r6, respectively).

of intermolecular energy for Neo-r9 and Neam-r9 (Table 1), which may be due to the fact that the number of contacts for common neomycin and neamine rings (I and II) is approximately equivalent.

The refined complexes between Neo-r9 (Figure 5D) or Neam-r9 with PRNA near the P15 region (cluster 2) reveal ranges of intermolecular energy similar to those of cluster 1 representatives. The complexes between Neo-r9 or Neam-r9 with PRNA had significantly higher interaction energy within clusters other than 1 and 2, indicating that the interactions of these ligands at other sites are less favorable than with the P2, P3, P4, J18/2, and J19/4 or P15. Therefore, all the docking results point that Neo-r9 and Neam-r9 bind PRNA preferably at the protein/pre-tRNA binding site (or at P15) than at the other possible sites.

Refinement of AACs−PRNA complexes. The ranges of intermolecular docked energies (kcal/mol) for NeoR6−PRNA complexes were from −1457 to −1403 at cluster 1, from −1427 to −1358 at cluster 2, and from −1394 to −1179 at the other clusters (Table 1). The ranges of these values for complexes of ParomoR5 and NeoR5 with PRNA were relatively similar. Figure 5C depicts the NeoR6−PRNA complex with the lowest energy (−1457 kcal/mol). For all three AACs, NeoR6, ParomoR5, and NeoR5, as well as for APACs, the complex with the lowest energy was derived from cluster 1 (P2, P3, P4, J18/

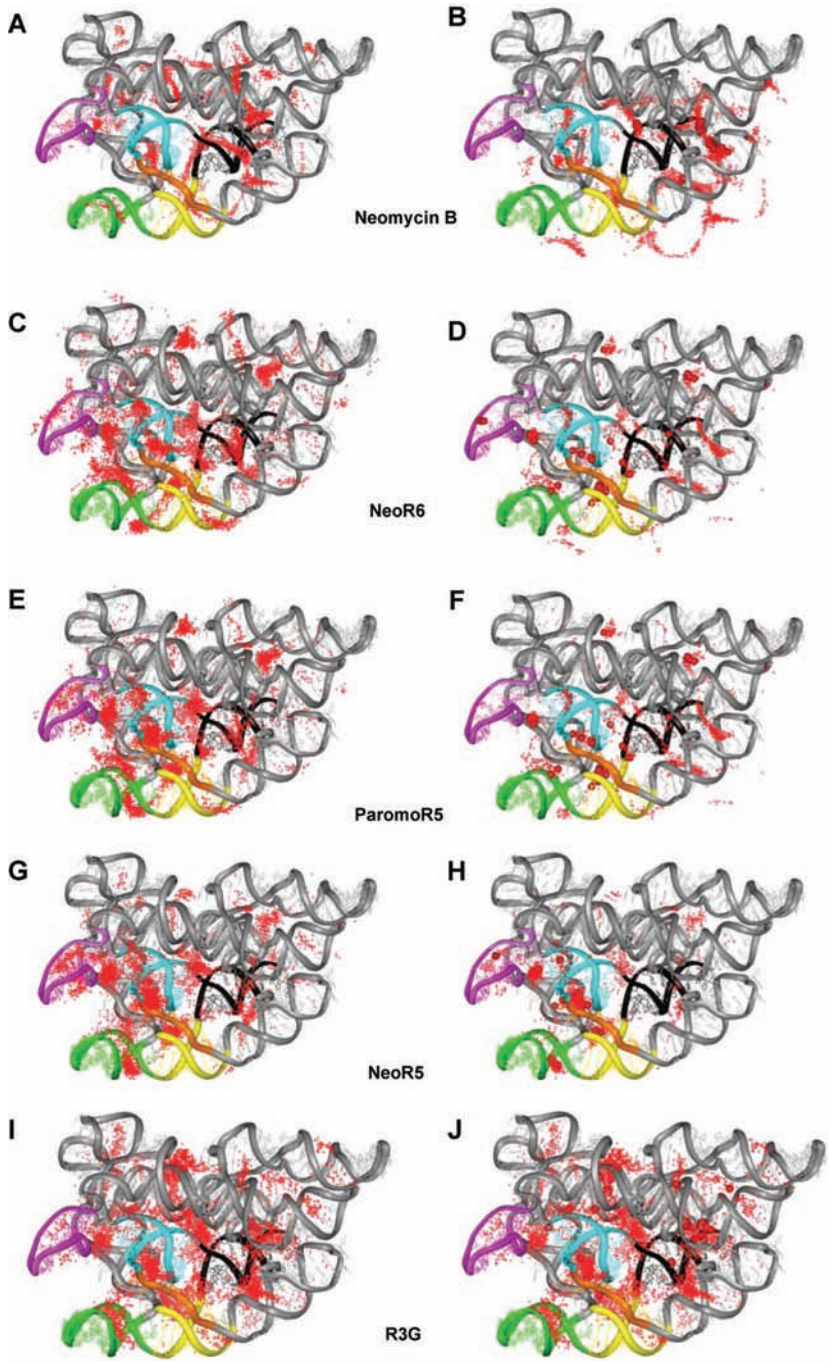

Figure 4. Results of MolFit geometric-electrostatic scans (A, C, E, and G) and GEH MolFit scans with intersection of the prediction lists (B, D, F, and H) for neomycin B and AACs (NeoR6, ParomoR5, and NeoR5, respectively). The colors and representation of PRNA and MolFit solutions are as described in Figure 3.

Table 1. Intermolecular Binding Energies (kcal/mol) for Final Ligand−PRNA Complexes

	clusters		
compounds	cluster 1	cluster 2	other clusters
Neo-r9	from −15283 to −14386	from −14431 to −12837	from −13211 to −12354
Neam-r9	from −15897 to −13988	from −14331 to −12645	from −13047 to −12211
NeoR6	from −1457 to −1403	from −1427 to −1358	from −1394 to −1179
ParomR5	from −1327 to −1278	from −1285 to −1211	from −1156 to −1096
NeoR5	from −1346 to −1304	from −1301 to −1167	from −1177 to −1078
Neomycin B	from −501 to −435	from −489 to −439	from −526 to −486

2, and J19/4). However, the other complexes with low energy were situated near P15 (cluster 2, e.g., Figure 5E). ParomoR5 and NeoR5 consistently showed somewhat higher ranges of intermolecular energies.

In contrast to the aminoglycoside−arginine conjugates (AACs and APACs), the value of intermolecular energy of the best neomycin−B-PRNA complex was −525 kcal/mol. We did not obtain significant differences in intermolecular

Table 2. Putative Ligand Interaction Sites on PRNA Based on Structural Analysis of Refined PRNA−Ligand Complexes at the P1−P4 multi-helix Junction

	PRNA regions											
	C[a]											
	P3				P4							
compounds	33	34	35	36	49	50	51	52	53	54	55	56
P protein	R/K[b]	R/K	R/K	R/K			+					
Pre-tRNA						+	+	+	+			
Neo-r9				+		+	+	+	+		+	
Neam-r9						+	+	+	+	+	+	+
NeoR6					+	+	+					
ParomoR5					+	+	+					
NeoR5					+	+	+					

	S[c]								C			
	J11/12					P11			P15			
	185	186	188	189	191	227	230	231	246	247	258	259
Pre-tRNA	+	+	+	+	+	+	+	+	+	+	+	+
Neomycin B							+	+	+	+		

	C											
	P15		J18/2				P2	P19				
	260	261	318	319	320	321	322	354	357	366	367	368
P protein			+									
Pre-tRNA	+	+						+	+	+	+	+
Neo-r9						+	+					
Neam-r9			+	+			+					
NeoR6			+		+							
ParomoR5			+		+							
NeoR5			+	+	+							

	C						
	P19	J19/4				P4	
	369	371	372	373	374	375	376
P protein				R/K	+		
Pre-tRNA	+		+				
Neo-r9			+	+	+	+	
Neam-r9				+	+	+	+
NeoR6		+	+	+	+	+	
ParomoR5			+	+	+	+	
NeoR5		+	+	+	+		

[a] C: catalytic domain of PRNA. [b] R/K: P protein arginine or lysine interact with PRNA. [c] S: specificity domain of PRNA.

energy between neomycin−B-PRNA complexes in the different tested regions.

DISCUSSION

Validation of the RNase P Holoenzyme Model. A previously published model of the PRNA from the PRNA−protein−pre-tRNA complex, based on biochemical, phylogenetic, and biophysical studies (*43*), was employed in this study. In addition, data obtained from a recent RNase P holoenzyme model (*47*) were also considered. The constructed model of PRNA by Westhof and co-workers (*43*) from the RNase P holoenzyme−substrate complex (Figure 3A) of *B. subtilis* was significantly modified without drastically altering the overall architecture of their previous model of the PRNA (*42*), especially the positioning of various highly conserved nucleotides proximal to the cleavage site. Moreover, the resulting enzyme−substrate complex model is in excellent agreement with various biochemical and biophysical studies (*43*).

The recent findings regarding detailed distance constraints within the holoenzyme−substrate complex (*47*) are also in accordance with the complex of Westhof/Gopalan and co-workers (*43*). These groups (*43*, *47*) applied a large amount of data from previous biochemical investigations of RNase P structure in solution to construct their models. Although Fierke and co-workers (*47*) claim that the biochemical model differs in details from recently published crystal structures of PRNA, the topology and relative orientations of PRNA helices of interest for our docking study (P1−P4) are similar. Fierke and co-workers (*47*) mapped their affinity cleavage data from *B. subtilis* RNase P onto the crystal structure of PRNA from *B. stearothermophilus* (*47*) and compared the relevant parts (P1−P4, J18/2, and J19/4) of these two RNA structures. This comparison suggests that, within the resolution of their model (∼10 Å), the structural model and crystal structure yield comparable results. The final model of Fierke and co-workers (*47*) is generally in accordance with the RNase P holoenzyme−substrate complex (*43*), and it is consistent with all their cleavage results, except those observed in P19.

Interference of AACs and APACs with the Binding of P Protein and/or Pre-tRNA to the PRNA P1−P4 Region. It has been proposed that the PRNA catalytic domain recognizes the pre-tRNA acceptor stem, cleavage site, and the conserved CCA sequence on the 3 end of the pre-tRNA (*52*). Furthermore, Pan and co-workers demonstrated that the PRNA specificity domain interacts with the T-stem loop of pre-tRNA (*53*). RNase P needs Mg^{2+} ions for many functions including folding, substrate binding, and catalysis (*15*). The Mg^{2+} ions binding sites have not yet been clearly defined, although several sites,

Table 3. Putative Ligand Interaction Sites on PRNA Based on Structural Analysis of Refined PRNA−Ligand Complexes at the P15 Region

	PRNA regions								
	C								
	P15								
compounds	255	256	257	258	259	261	262	263	264
Pre-tRNA				+	+	+			
Neo-r9	+	+	+	+	+				
NeoR6						+	+	+	+
NeoR5						+	+	+	

	C				
	P15.1		P18		
	266	268	314	315	316
NeoR6	+	+	+	+	+
NeoR5	+		+	+	

Table 4. IC_{50} Values (nM) for the Inhibition of RNase P Holoenzyme by Neomycin B and AACs

	IC_{50} (nM)	
compound	*E. coli*	*N. gonorrheoae*
Neomycin B	6×10^4 [a]	
NeoR1	4×10^3 [b]	
NeoR5	500 [c]	
NeoR6	125 [d]	1 [e]
Paromomycin	19×10^4 [a]	
R3G	300 [d]	

[a] Ref *28*. [b] Lapidot and Gopalan, unpublished results. [c] Ref *10*. [d] Ref *7*. [e] Lapidot and Eder, unpublished results.

including positions in helix P4, have been implicated in metal binding (*54*). It was suggested that Mg^{2+} ion specifically binds to a site in helix P4, at the same region of PRNA that cross-links to the P protein, and where the putative catalytic site of the enzyme is located (*47*). It was reported that the formation of the P1−P4 multihelix junction is dependent on a cluster of metal ions and that this structure contributes to catalysis (*55*). Further corroboration for metal binding in P4 comes from NMR studies that demonstrate specific Mg^{2+} binding sites in a stem-loop that serves as a model for the P4 helix (*56*). The experimental data (*47, 57*) and structural holoenzyme models placing the P protein near PRNA helix P4 suggest that the P protein could stabilize the PRNA structure to enhance the affinity of one or more metal ions binding to helix P4 and to facilitate catalysis (*47*). Therefore, the P1−P4 multihelix junction and J19/4 are the most important regions for catalytic activity of PRNA because both P protein and pre-tRNA bind to this region. Our docking studies reveal that cluster 1 of geometric-electrostatic and intersection of GEH MolFit predictions lists for all tested AACs and APACs is situated near the P1−P4 multihelix junction and J19/4 region (Figures 3−4). Cluster 1 consists of the top ranked solutions, including the first one, indicating that all tested AACs and APACs prefer binding to this region and compete with the P protein and/or pre-tRNA. Moreover, the final refined complexes with lowest energy are also derived from this cluster (Tables 1 and 2).

Interference of AACs and APACs with RNase P Activity near P15. It was reported that inhibition of *E. coli* PRNA by neomycin B was partially attributed to its capability to displace Mg^{2+} ions from P15 loop (L15); this inference was based on the moderately decreased susceptibility of P15 loop mutants to inhibition by neomycin B (*28*). P15 loop in the bacterial PRNA plays a role in substrate recognition, cleavage site selection, and metal ion binding (*58*). Biochemical data support that P15 loop is an autonomous metal (Mg^{2+}) ion-binding domain (*59*). Our results reported here suggest that AACs can inhibit RNase P primarily by binding to P4, J18/2, and J19/4 (near the protein/pre-tRNA binding); although AACs can also interfere with RNase P function by binding to P15, all our docking results (rigid body docking by MolFit and final refinement by Discover3) show consistent preference of AACs to bind P4, J18/2, and J19/4 somewhat stronger than to P15, and binding to both of these sites is much stronger than that to all other tested putative sites (other clusters). The pattern of APACs binding is generally similar to that of AACs, but with stronger preference to interact with the protein/pre-tRNA binding site (P3, P4, J18/2, P2, J19/4). Although recent findings (*10*) suggest that NeoR5 could inhibit wild-type *E. coli* RNase P holoenzyme by binding to the P15 loop, the *E. coli* RNase P ΔL15/P16/P17 mutant must offer an alternative binding site for NeoR5 that still permits its interference with RNase P function.

Our docking results suggest that AACs and APACs may also competitively interfere with the interactions between PRNA and pre-tRNA (and/or P protein) near the helix P15 (Figure 5).

The holoenzyme preference for binding pre-tRNA over mature tRNA by *B. subtilis* RNase P holoenzyme suggests the formation of a direct contact between the pre-tRNA 5′ leader and P protein in the holoenzyme (*14*). This interaction is confirmed by photo-crosslinking and affinity cleavage studies demonstrating that the 5′ leader of pre-tRNA is in close proximity to the central cleft, but not to the RNR motif or metal binding loop of the P protein (*47*). Time-resolved fluorescence resonance energy transfer studies show that the 5′ leader contacts the P protein in *B. subtilis* RNase P holoenzyme (*60*). Thus, it was suggested (*47*) that interactions between the P protein and pre-tRNAs contribute to the uniformity of the binding affinity for RNase P for pre-tRNAs. According to our docking results AACs and APACs can interact with PRNA at the region of P15 and therefore interrupt interactions between P protein and pre-tRNA at this region (Figure 5 and Table 3).

Structure−activity Relationships of AACs in Comparison to APACs. The structure−function relationship of AACs and APACs with respect to RNA binding is important for their development as possible drugs. Previously, we designed and synthesized a set of different conjugates of neomycin B, paromomycin, neamine, and gentamicin with different numbers (1−6) of arginines (*31−34*). We also reported the ability of AACs to inhibit RNA translation in direct relation to the number of arginine groups linked to the aminoglycoside backbone and on the nature of the aminoglycoside (*37*). The strong interaction between the α-amino of the arginine moiety of NeoR6 and the TAR RNA phosphate group was a modeling prediction, which was experimentally supported (*30, 31*). Indeed, the affinity of tetra-γ-guanidinobutyrate kanamycin A derivative (GB4K), lacking an α-amino acid group in the linker, to TAR RNA was very low compared to that of the tetra-arginine derivative, R4K (*30, 31*). Also, the anti-HIV activity of GB4K in cell culture (*61*) and antiequine infectious anemia virus (EIAV) activity in equine dermal fibroblasts (ED) (*31*) were very low. Thus, all of the above may explain the very low antiviral activities and affinity of GB4K and other guanidino conjugates for HIV-1 TAR RNA (*30*) and for HIV-1 RRE RNA (e.g., ref *62*). Neomycin B that binds RRE IIB with the highest affinity (K_D of 1.18 μM (*63*)) among the aminoglycosides is about 240 times weaker than NeoR6 and 6−7 times weaker than monoarginine derivative (NeoR1) (*35*). These results indicate that even one arginine conjugated to neomycin B already significantly increases its binding affinity to HIV-1 regulatory RNAs. Other aminoglycoside conjugates, e.g., guanylated aminoglycosides (e.g., ref *62*), bind TAR or RRE RNAs much weaker than AACs. Similarly, their anti-HIV-1 activities are much lower than the respective AACs (*31−34*). Thus, the recent finding (*10*) of low inhibition of RNase P catalytic activity

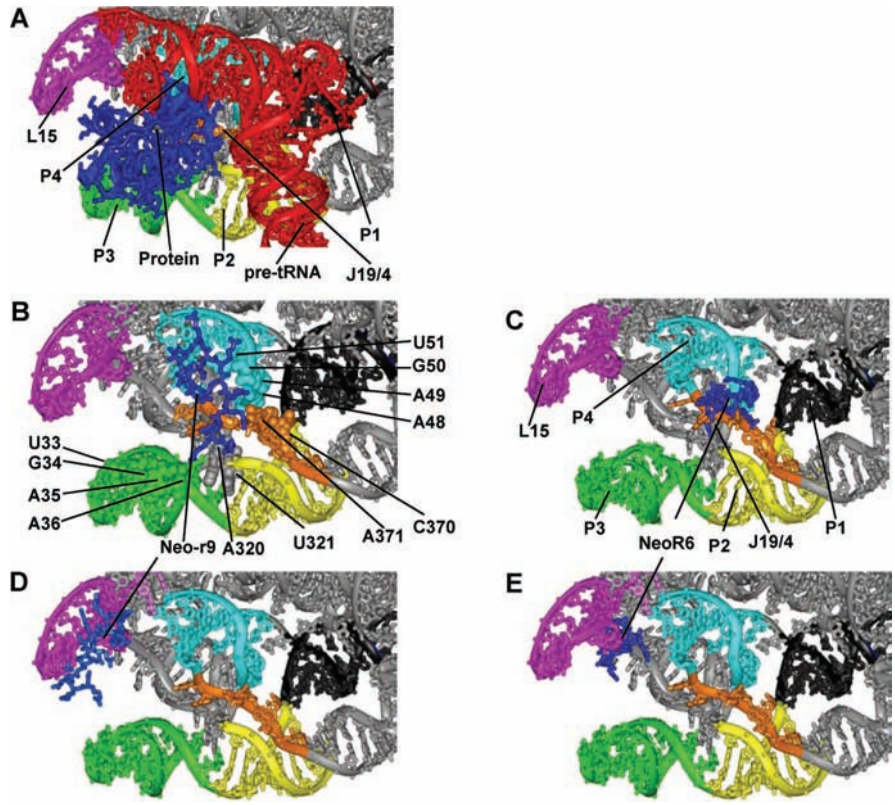

Figure 5. (A) Extended view of the catalytic domain of the structural model of *B. subtilis* RNase P holoenzyme−pre-tRNA complex (*43*). (B) Final Neo-r9−PRNA complex near the P1−P4 multihelix junction. (C) Final NeoR6−PRNA complex near the P1−P4 multihelix junction. (D) Final Neo-r9−PRNA complex near the P15 helix. (E) Final NeoR6−PRNA complex near the P15 helix. The colors and representation of PRNA and PRNA regions are as decribed in Figures 3 and 4. Neor9 and NeoR6 are shown in stick representation and colored blue.

by guanidino conjugates of neomycin (hexa-guanidinium−neomycin B conjugate) in comparison to that of arginines conjugated to neomycin (e.g., NeoR5 and NeoR6), supporting our previous reports, is not surprising. To determine the importance of the number of arginines conjugated to neomycin B, we compared anti-RNase P activities of NeoR1 with NeoR6 to free neomycin B. The findings that *E. coli* RNase P activity is inhibited with IC_{50} values of 60 μM (*28*), 4 μM, and 125 nM (*7*) by neomycin B, NeoR1, and NeoR6, respectively (Table 4), suggest that the number of conjugated arginine residues to neomycin B is important. Of note, using RNase P of *Neisseria gonorrheae* revealed the specifically high potency of NeoR6 (IC_{50} of 1 nM), (Table 4). The differences in IC_{50} observed for the two bacterial RNase P holoenzymes indicate the susceptibility of this inhibitor. Thus, NeoR6 is a more efficient inhibitor against RNase P of *Neisseria gonorrheae*. In accordance with our previous results, NeoR6 does not inhibit eukaryotic translation initiation, indicating its ability to discriminate between the eukaryotic and the bacterial translational machinery (*37*). Similarly, NeoR6 inhibits bacterial RNase P activity significantly (about 10-fold) more effectively than human RNase P activity (*7*). The sphere-like NeoR6−PRNA binding conformer reveals different structure in comparison to the extended structure of Neo-r9, Neam-r9, and Neo-r6 in complex with PRNA, as depicted in Figure 5. The APACs revealed about 10-fold lower intermolecular energy than AACs, indicating stronger interactions of APACs than AACs with PRNA (Table 1). Interestingly, no significant differences in intermolecular energy between Neo-r9 and Neam-r9 complexes with PRNA were found. The docking results point to the fact that only rings I and II of the neomycin core of Neo-r9 interact with PRNA, similar to neamine rings I and II of Neam-r9.

Additional studies are needed to correlate our docking results of AACs and APACs to their inhibition of bacterial RNase P activity. Our preliminary results regarding antimicrobial activity of AACs and APACs against a variety of Gram-positive and Gram-negative bacterial strains, including clinical and gentamicin-resistant isolates, indicate that most of these compounds are active, but not the free nona-D-arginine (*64*).

CONCLUSIONS

Our docking results suggest three possible mechanisms of action of AAC and APAC inhibition of RNase P: (i) the most likely mechanism of RNase P inhibition is AAC and APAC competition with the P protein and pre-tRNA on the P1−P4 multihelix junction and J19/4 region (probably including displacement of Mg^{2+} ions from P4 helix); (ii) competition with Mg^{2+} ions near the P15 loop; and (iii) competition with the P protein and/or pre-tRNA near the P15 helix and interference with interactions between the P protein and pre-tRNA at this region are also considered.

Structure−function relationships of the molecules described above with respect to PRNA binding is important for further drug design. Indeed, while the free neomycin B showed very low anti-RNase P activity (IC_{50} 60 μM (*28*)), already one arginine conjugated to neomycin B revealed much stronger activity (~15-fold) and was extremely better when 6 arginines conjugated to each amino group of neomycin−NeoR6 (~500-fold) (*7*). Notably, guanidinium or lysyl conjugates of neomycin showed significantly weaker potency against RNase P (*10*) in comparison to that of AACs (*7*). Our rigid-body docking results suggest that the binding pattern of aminoglycoside conjugates with short arginine peptide chains (APACs) to the P protein/pre-tRNA binding site (P1−P4 and J19/4) and near the P15 loop is generally similar to that of the sphere-like AACs (e.g., NeoR6). Importantly, APACs prefer to interact with the P protein/pre-tRNA binding site (Figures 3 and 4). The ranges of

intermolecular energy of APACs (after refinement) are about 10-fold lower than those of AACs, especially at the P protein/pre-tRNA binding site (Table 1), indicating stronger interactions of APACs than AACs with PRNA. Thus, the novel compounds, APACs, can be predicted as more potent RNase P inhibitors than AACs, by preventing P protein binding with PRNA (probably including displacement of Mg^{2+} ions from P4 helix). AACs interact with these two PRNA binding sites approximately with comparable potency. The competition of AACs with Mg^{2+} ions near the P15 loop is also important, almost as competition with P protein binding on PRNA. The ranges of intermolecular energy of AACs and APACs are considerably better than those of neomycin B (Table 1). Thus, arginines conjugated to aminoglycosides extremely improved their interaction with PRNA. All of the above designate that the affinity of a ligand for a target PRNA can be enhanced synergistically by fusing two different functionalities capable of RNA-binding (i.e., aminoglycosides and arginine-rich peptides). Our docking approach described in this article, in combination with RNase P holoenzyme models of Westhof and co-workers (*43*) and Fierke and co-workers (*47*), may be used for predicting the binding modes of AACs and APACs in different specific sites of PRNA and for ligand interference with RNase P activity. This approach also can be extended for the future design of new molecules.

ACKNOWLEDGMENT

We thank Dr. G. Borkow and Dr. M. Eisenstein for critical remarks and discussions. The docking program MolFit was downloaded from http://www.weizmann.ac.il/Chemical_Research_Support/molfit.

LITERATURE CITED

(1) Ecker, D. J., and Griffey, J. (1999) RNA as a small-molecule drug target: doubling the value of genomics. *Drug Discovery Today 4*, 420–429.

(2) Gallego, J., and Varani, G. (2001) Targeting RNA with small-molecule drugs: Therapeutic promise and chemical challenges. *Acc. Chem. Res. 34*, 836–843.

(3) Hermann, T. (2003) Chemical and functional diversity of small molecule ligands for RNA. *Biopolymers 70*, 4–18.

(4) Altman, S., and Kirsebom, L. (1999) Ribonuclease P, in *The RNA World* (Gesteland, R. F., Cech, T., and Atkins, J. F., Eds.), pp 351−380, CSH Laboratory Press, Cold Spring Harbor, NY.

(5) Walker, S. C., and Engelke, D. R. (2006) Ribonuclease P; the evolution of an ancient RNA enzyme. *Crit. Rev. Biochem. Mol. Biol. 41*, 77–102.

(6) Hall, T. A., and Brown, J. W. (2001) The ribonuclease P family. *Methods Enzymol. 341*, 56–77.

(7) Eubank, T. D., Biswas, R., Jovanovic, M., Litovchick, A., Lapidot, A., and Gopalan, V. (2002) Inhibition of bacterial RNase P by aminoglycoside−arginine conjugates. *FEBS Lett. 511*, 107–112.

(8) Willkomm, D. K., Gruegelsiepe, H., Goudinakis, O., Kretschmer-Kazemi Far, R., Bald, R., Erdmann, V. A., and Hartmann, R. K. (2003) Evaluation of bacterial RNase P RNA as a drug target. *ChemBioChem 4*, 1041–1048.

(9) Walker, S. C., and Engelke, D. R. (2006) Ribonuclease P; the evolution of an ancient RNA enzyme. *Crit. Rev. Biochem. Mol. Biol. 41*, 77–102.

(10) Kawamoto, S. A., Sudhahar, C. G., Hatfield, C. L., Sun, J., Behrman, E. J., and Gopalan, V. (2008) Studies on the mechanism of inhibition of bacterial ribonuclease P by aminoglycoside derivatives. *Nucleic Acids Res. 36*, 697–704.

(11) Guerrier-Takada, C., Gardiner, K., Marsh, T., Pace, N. R., and Altman, S. (1983) The RNA moiety of ribonuclease P is the catalytic subunit of the enzyme. *Cell 35*, 849–857.

(12) Hsieh, J., Andrews, A. J., and Fierke, C. A. (2004) Roles of protein subunits in RNA-protein complexes: Lessons from ribonuclease P. *Biopolymers 73*, 79–89.

(13) Stams, T., Niranjanakumari, S., Fierke, C. A., and Christianson, D. W. (1998) Ribonuclease P protein structure: Evolutionary origins in the translational apparatus. *Science 280*, 752–755.

(14) Kurz, J. C., Niranjanakumari, S., and Fierke, C. A. (1998) Protein component of *Bacillus subtilis* RNase P specifically enhances the affinity for precursor-$tRNA^{Asp}$. *Biochemistry 37*, 2393–2400.

(15) Kurz, J. C., and Fierke, C. A. (2002) The affinity of magnesium binding sites in the *Bacillus subtilis* RNase Pxpre-tRNA complex is enhanced by the protein subunit. *Biochemistry 41*, 9545–9558.

(16) Sun, L., Campbell, F. E., Zahler, N. H., and Harris, M. E. (2006) Evidence that substrate-specific effects of C5 protein lead to uniformity in binding and catalysis by RNase P. *EMBO J. 25*, 3998–4007.

(17) Kazantsev, A. V., Krivenko, A. A., Harrington, D. J., Carter, R. J., Holbrook, S. R., Adams, P. D., and Pace, N. R. (2003) High-resolution structure of RNase P protein from Thermotoga maritime. *Proc. Natl. Acad. Sci. U.S.A. 100*, 7497–7502.

(18) Spitzfaden, C., Nicholson, N., Jones, J. J., Guth, S., Lehr, R., Prescott, C. D., Hegg, L. A., and Eggleston, D. S. (2000) The structure of ribonuclease P protein from *Staphylococcus aureus* reveals a unique binding site for single-stranded RNA. *J. Mol. Biol. 295*, 105–115.

(19) Altman, S. (1989) Ribonuclease P: An enzyme with a catalytic RNA subunit. *Adv. Enzymol. Relat. Areas Mol. Biol. 62*, 1–36.

(20) Gopalan, V., Baxevanis, A. D., Landsman, D., and Altman, S. (1997) Analysis of the functional role of conserved residues in the protein subunit of ribonuclease P from *Escherichia coli*. *J. Mol. Biol. 267*, 818–829.

(21) Jovanovic, M., Sanchez, R., Altman, S., and Gopalan, V. (2002) Elucidation of structure−function relationships in the protein subunit of bacterial RNase P using a genetic complementation approach. *Nucleic Acids Res. 30*, 5065–5073.

(22) Silva, J. G., and Carvalho, I. (2007) New insights into aminoglycoside antibiotics and derivatives. *Curr. Med. Chem. 14*, 1101–1119.

(23) Tok, J. B., Cho, J., and Rando, R. R. (1999) Aminoglycoside antibiotics are able to specifically bind the 5′- untranslated region of thymidylate synthase messenger RNA. *Biochemistry 38*, 199–206.

(24) Mikkelsen, N. E., Johansson, K., Virtanen, A., and Kirsebom, L. A. (2001) Aminoglycoside binding displaces a divalent metal ion in a tRNA-neomycin B complex. *Nat. Struct. Biol. 8*, 510–514.

(25) Delling, U., Roy, S., Sumner-Smith, M., Barnett, R., Reid, L., Rosen, C. A., and Sonenberg, N. (1991) The number of positively charged amino acids in the basic domain of Tat is critical for trans-activation and complex formation with TAR RNA. *Proc. Natl. Acad. Sci. U.S.A. 88*, 6234–6238.

(26) Zapp, M. L., Stern, S., and Green, M. R. (1993) Small molecules that selectively block RNA binding of HIV-1 Rev protein inhibit Rev function and viral production. *Cell 74*, 969–978.

(27) Wang, S., Huber, P. W., Cui, M., Czarnik, A. W., and Mei, H. Y. (1998) Binding of neomycin to the TAR element of HIV-1 RNA induces dissociation of Tat protein by an allosteric mechanism. *Biochemistry 37*, 5549–5557.

(28) Mikkelsen, N. E., Brannvall, M., Virtanen, A., and Kirsebom, L. A. (1999) Inhibition of RNase P RNA cleavage by aminoglycosides. *Proc. Natl. Acad. Sci. U.S.A. 96*, 6155–6160.

(29) Puglisi, J. D., Chen, L., Frankel, A. D., and Williamson, J. R. (1993) Role of RNA structure in arginine recognition of TAR RNA. *Proc. Natl. Acad. Sci. U.S.A. 90*, 3680–3684.

(30) Litovchick, A., Evdokimov, A. G., and Lapidot, A. (1999) Arginine-aminoglycoside conjugates that bind to HIV transactivation responsive element RNA in vitro. *FEBS Lett. 445*, 73–79.

(31) Litovchick, A., Evdokimov, A. G., and Lapidot, A. (2000) Aminoglycoside-arginine conjugates that bind TAR RNA: Synthesis, characterization, and antiviral activity. *Biochemistry 39*, 2838–2852.
(32) Litovchick, A., Lapidot, A., Eisenstein, M., Kalinkovich, A., and Borkow, G. (2001) Neomycin B-arginine conjugate, a novel HIV-1 Tat antagonist: Synthesis and anti-HIV activities. *Biochemistry 40*, 15612–15623.
(33) Borkow, G., Vijayabaskar, V., Lara, H. H., Kalinkovich, A., and Lapidot, A. (2003) Structure-activity relationship of neomycin, paromomycin, and neamine-arginine conjugates, targeting HIV-1 gp120-CXCR4 binding step. *Antiviral Res. 60*, 181–192.
(34) Borkow, G., Lara, H. H., and Lapidot, A. (2003) Mutations in gp41 and gp120 of HIV-1 isolates resistant to hexa-arginine neomycin B conjugate. *Biochem. Biophys. Res. Commun. 312*, 1047–1052.
(35) Lapidot, A., Vijayabaskar, V., Litovchick, A., Yu, J., and James, T. L. (2004) Structure−activity relationships of aminoglycoside−arginine conjugates that bind HIV-1 RNAs as determined by fluorescence and NMR spectroscopy. *FEBS Lett. 577*, 415–421.
(36) Borkow, G., and Lapidot, A. (2005) Multi-targeting the entrance door to block HIV-1. *Curr. Drug Targets: Infect. Disord. 5*, 3–15.
(37) Carriere, M., Vijayabaskar, V., Applefield, D., Harvey, I., Garneau, P., Lorsch, J., Lapidot, A., and Pelletier, J. (2002) Inhibition of protein synthesis by aminoglycoside−arginine conjugates. *RNA 8*, 1267–1279.
(38) Weeks, K. M., Ampe, C., Schultz, S. C., Steitz, T. A., and Crothers, D. M. (1990) Fragments of the HIV-1 Tat protein specifically bind TAR RNA. *Science 249*, 1281–1285.
(39) Cheng, A. C., Calabro, V., and Frankel, A. D. (2001) Design of RNA-binding proteins and ligands. *Curr. Opin. Struct. Biol. 11*, 478–484.
(40) Berchanski, A., and Lapidot, A. (2007) Prediction of HIV-1 entry inhibitors neomycin−arginine conjugates interaction with the CD4-gp120 binding site by molecular modeling and multistep docking procedure. *BBA-Biomembranes 1768*, 2107–2119.
(41) Hegde, R., Borkow, G., Berchanski, A., and Lapidot, A. (2007) Structure-function relationship of novel X4 HIV-1 entry inhibitors: L- and D-arginine peptides-aminoglycoside conjugates. *FEBS J. 274*, 6523–6536.
(42) Massire, C., Jaeger, L., and Westhof, E. (1998) Derivation of the three-dimensional architecture of bacterial ribonuclease P RNAs from comparative sequence analysis. *J. Mol. Biol. 279*, 773–793.
(43) Tsai, H. Y., Masquida, B., Biswas, R., Westhof, E., and Gopalan, V. (2003) Molecular modeling of the three-dimensional structure of the bacterial RNase P holoenzyme. *J. Mol. Biol. 325*, 661–675.
(44) Altman, S. (2007) A view of RNase P. *Mol. BioSyst. 3*, 604–607.
(45) Kazantsev, A. V., Krivenko, A. A., Harrington, D. J., Holbrook, S. R., Adams, P. D., and Pace, N. R. (2005) Crystal structure of a bacterial ribonuclease P RNA. *Proc. Natl. Acad. Sci. U.S.A. 102*, 13392–13397.
(46) Torres-Larios, A., Swinger, K. K., Krasilnikov, A. S., Pan, T., and Mondragon, A. (2005) Crystal structure of the RNA component of bacterial ribonuclease P. *Nature 437*, 584–587.
(47) Niranjanakumari, S., Day-Storms, J. J., Ahmed, M., Hsieh, J., Zahler, N. H., Venters, R. A., and Fierke, C. A. (2007) Probing the architecture of the *B. subtilis* RNase P holoenzyme active site by cross-linking and affinity cleavage. *RNA 13*, 521–535.
(48) Kitchen, D. B., Decornez, H., and Bajorath, J. (2004) Docking and scoring in virtual screening for drug discovery: methods and applications. *Nature Rev. 3*, 935–949.
(49) Faber, C., Sticht, H., Schweimer, K., and Rosch, P. (2000) Structural rearrangements of HIV-1 Tat-responsive RNA upon binding of neomycin B. *J. Biol. Chem. 275*, 20660–20666.
(50) Berchanski, A., Shapira, B., and Eisenstein, M. (2004) Hydrophobic complementarity in protein-protein docking. *Proteins 56*, 130–142.
(51) Heifetz, A., Katchalski-Katzir, E., and Eisenstein, M. (2002) Electrostatics in protein-protein docking. *Protein Sci. 11*, 571–587.
(52) Zahler, N. H., Sun, L., Christian, E. L., and Harris, M. E. (2005) The Pre-tRNA Nucleotide Base and 2′-Hydroxyl at N(−1) Contribute to Fidelity in tRNA Processing by RNase P. *J. Mol. Bio.l 345*, 969–985.
(53) Pan, T., Loria, A., and Zhong, K. (1995) Probing of tertiary interactions in RNA: 2′-Hydroxyl-base contacts between the RNase P RNA and pre-tRNA. *Proc. Natl. Acad. Sci. U.S.A. 92*, 12510–12514.
(54) Christian, E. L., Smith, K. M., Perera, N., and Harris, M. E. (2006) The P4 metal binding site in RNase P RNA affects active site metal affinity through substrate positioning. *RNA 12*, 1463–1467.
(55) Kaye, N. M., Christian, E. L., and Harris, M. E. (2002) NAIM and site-specific functional group modification analysis of RNase P RNA: magnesium dependent structure within the conserved P1-P4 multihelix junction contributes to catalysis. *Biochemistry 41*, 4533–4545.
(56) Getz, M. M., Andrews, A. J., Fierke, C. A., and Al-Hashimi, H. M. (2007) Structural plasticity and Mg2+ binding properties of RNase P P4 from combined analysis of NMR residual dipolar couplings and motionally decoupled spin relaxation. *RNA 13*, 251–266.
(57) Buck, A. H., Dalby, A. B., Poole, A. W., Kazantsev, A. V., and Pace, N. R. (2005) Protein activation of a ribozyme: the role of bacterial RNase P protein. *EMBO J. 24*, 3360–3368.
(58) Kirsebom, L. A. (2007) RNase P RNA mediated cleavage: substrate recognition and catalysis. *Biochimie 89*, 1183–1194.
(59) Kufel, J., and Kirsebom, L. A. (1998) The P15-loop of *Escherichia coli* RNase P RNA is an autonomous divalent metal ion binding domain. *RNA 4*, 777–788.
(60) Rueda, D., Hsieh, J., Day-Storms, J. J., Fierke, C. A., and Walter, N. G. (2005) The 5′ leader of precursor tRNAAsp bound to the *Bacillus subtilis* RNase P holoenzyme has an extended conformation. *Biochemistry 44*, 16130–16139.
(61) Cabrera, C., Gutierrez, A., Blanco, J., Barretina, J., Litovchick, A., Lapidot, A., Evdokimov, A. G., Clotet, B., and Este, J. A. (2000) Anti-human immunodeficiency virus activity of novel aminoglycoside−arginine conjugates at early stages of infection. *AIDS Res. Hum. Retroviruses 16*, 627–634.
(62) Baker, T. J., Luedtke, N. W., Tor, Y., and Goodman, M. (2000) Synthesis and anti-HIV activity of guanidinoglycosides. *J. Org. Chem. 65*, 9054–9058.
(63) Wang, Y., Hamasaki, K., and Rando, R. R. (1997) Specificity of aminoglycoside binding to RNA constructs derived from the 16S rRNA decoding region and the HIV-RRE activator region. *Biochemistry 36*, 768–779.
(64) Lapidot, A., Vijayabaskar, V., and Borkow, G. (2004) Amino-Modified Polysaccharides and Methods of Generating and Using Same, US Patent 10/831,224[PCT 2003027-00-01].

BC800191U

Cellular Uptake and Intracellular Pathways of PLL-g-PEG-DNA Nanoparticles

Tessa Lühmann,[†,‡] Markus Rimann,[†,‡] Anne Greet Bittermann,[§] and Heike Hall*[,‡]

Department of Materials, ETH Zurich, Zurich, Switzerland, and ZMB, Center for Microscopy and Image Analysis, University of Zurich, Switzerland. Received May 20, 2008; Revised Manuscript Received July 23, 2008

Polycationic molecules form condensates with DNA and are used for gene therapy as an alternative to viral vectors. As clinical efficacy corresponds to cellular uptake, intracellular stability of the condensates, and bioavailability of the DNA, it is crucial to analyze uptake mechanisms and trafficking pathways. Here, a detailed study of uptake, stability, and localization of PLL-g-PEG-DNA nanoparticles within COS-7 cells is presented, using FACS analysis to assess the involvement of different uptake mechanisms, colocalization studies with markers indicative for different endocytotic pathways, and immunofluorescence staining to analyze colocalization with intracellular compartments. PLL-g-PEG-DNA nanoparticles were internalized in an energy-dependent manner after 2 h and accumulated in the perinuclear region after >6 h. The nanoparticles were found to be stable within the cytoplasm for at least 24 h and did not colocalize with the endosomal pathway. Nanoparticle uptake was ~50% inhibited by genistein, an inhibitor of the caveolae-mediated pathway. However, genistein did not inhibit gene expression, and PLL-g-PEG-DNA nanoparticles were not colocalized with caveolin-1 indicating that caveolae-mediated endocytosis is not decisive for DNA delivery. Clathrin-mediated endocytosis and macropinocytosis pathways were reduced by 17 and 24%, respectively, in the presence of the respective inhibitors. When cells were transfected in the presence of double and triple inhibitors, transfection efficiencies were increasingly reduced by 40 and 70%, respectively; however, no differences were found between the different uptake mechanisms. These findings suggest that PLL-g-PEG-DNA nanoparticles enter by several pathways and might therefore be an efficient and versatile tool to deliver therapeutic DNA.

INTRODUCTION

Gene therapy has gained a lot of attention for the treatment of chronic diseases, cancer, and genetic disorders (*1*−*4*). It is also considered as a valuable alternative for conventional protein therapy since it overcomes inherent problems that are associated with the administration of protein drugs in terms of bioavailability, systemic toxicity, *in vivo* clearance rate, and manufacturing costs (*2, 4, 5*). For this reason, safe and efficient delivery systems for therapeutic DNA are developed. Polycationic substances such as poly-L-lysine (PLL), poly-L-ornithine, or polyethylenimine (PEI) alone or as graft- and copolymers with different amounts of poly(ethylene glycol) (PEG) have been shown to form complexes with DNA and are widely used as an attractive alternative to viral vectors in gene therapy (*2, 6*−*11*). However, not only the DNA-delivery vehicle itself but also cellular uptake, intracellular stability, and bioavailability of the therapeutic DNA within the cell are crucial for clinical relevance. Therefore, uptake mechanisms of DNA-containing vehicles and trafficking pathways within the cells were analyzed (*3, 12*−*14*). Unfortunately, (nano)-particle uptake and intracellular pathways seem to be dependent on the analyzed cell type (*15*) as well as on the particular size, shape, charge, and chemistry of the delivery vehicle (*16, 17*). Especially, when certain cell types or specific uptake pathways are targeted, the uptake mechanism(s) and intracellular pathways need to be analyzed carefully (*1, 3, 4, 17*). Therefore, rational design of PLL-g-PEG-DNA nanoparticles might benefit from the knowledge raised about the uptake pathways involved and the release mechanisms of therapeutic DNA in order to optimize their performance.

The analysis of gene delivery vehicles is still a complex challenge, as endocytosis may involve several pathways (*3, 18*−*21*). The first barrier is to overcome the plasma membrane, followed by cytoplasmatic pathways prior to DNA delivery into the nucleus where gene expression takes place. So far, five major uptake mechanisms are distinguished (*14, 18, 21, 22*) including phagocytosis that is performed only by specialized cells such as macrophages, neutrophils, or monocytes to eliminate debris and pathogens. In this study, four pinocytotic pathways are studied to assess cellular uptake and intracellular pathway(s) of PLL-g-PEG-DNA nanoparticles: (i) macropinocytosis that is stimulated by growth factors or phorbol esters, which cause actin-driven formation of membrane ruffles that fuse with the plasma membrane forming large endocytotic vesicles known as macropinosomes (*14, 23*). They either fuse with lysosomes or are recycled back to the cell surface. Large particles up to 1−5 μm in diameter can be internalized by macropinocytosis (*14, 22*). (ii) Clathrin-mediated endocytosis is a process involving specific receptors that recognize and internalize cargo (*24*). Ligand-bound receptors are internalized via clathrin-coated vesicles involving GTPase activity and are transformed to early endosomes. Receptor−ligand complexes are separated by low pH generated by vacuolar proton ATPases (*25*). The ligands are transferred into late endosomes for potential degradation in lysosomes, whereas the receptors are recycled and transported back to the plasma membrane (*19*). (iii) Caveolae-mediated endocytosis is characterized by the evolution of caveolae, which

* Corresponding author. ETH Zurich, Department of Materials, HCI E415, Cells and BioMaterials, Wolfgang-Pauli-Strasse 10, CH-8093 Zürich, Switzerland Phone: +41 44 633 69 75. Fax: +41 44 632 10 73. E-mail: heike.hall@mat.ethz.ch.

† These authors contributed equally to this work and should be regarded as first authors.

‡ ETH Zurich.

§ University of Zurich, Switzerland.

10.1021/bc800206r CCC: $40.75 © 2008 American Chemical Society
Published on Web 08/22/2008

are associated with caveolin-1/caveolin-2 (or caveolin-3 in the muscle) (*26*). Caveolae derive from subdomains of sphingolipid- and cholesterol-rich cell membrane fractions called lipid rafts (*27*). Caveolae are considered to be static organelles, whose internalization is induced by specific ligands such as simian virus-40 (SV40) or cholera toxin (*18, 28, 29*). After internalization, those ligands are either transferred into caveosomes having neutral pH that translocate to the endoplasmic reticulum or the Golgi complex (*30*) or they enter the endosomal pathway (*31*). (iv) This pathway is described as clathrin- and caveolae-independent, transporting cargo to the GPI-anchored protein-enriched early endosomal compartment (GEEC) and ending in the Golgi complex or in recycling endosomes (*18*). Glycosylphophatidylinositol-anchored proteins (GPI-AP) can be internalized via 40−50 nm lipid rafts (*18*). But regulatory mechanisms for this pathway are still unknown.

A recent report from our group showed evidence that PLL-g-PEG-DNA nanoparticles are a promising tool for effective transport and delivery of therapeutic DNA as they show long-term stability, a hydrodynamic diameter of 80−90 nm, and high transfection efficiency at a N/P ratio 3.125 of ∼40% combined with low cytotoxicity (>95% of cell viability) in COS-7 cells (*11*). In order to understand the uptake mechanism(s) and intracellular pathway(s) of PLL-g-PEG-DNA nanoparticles, PLL-g-PEG and plasmid DNA were differentially fluorescently labeled, and uptake into COS-7 cells was determined by uptake-inhibition analysis. Furthermore, transfected COS-7 cells were analyzed after different time points for colocalization with markers for individual uptake mechanisms, and immunofluorescence staining of cellular compartments was performed. This study may be helpful in the future design of PEGylated PLL-polymers for gene delivery approaches to identify the most efficient uptake and delivery mechanisms.

MATERIALS AND METHODS

Polymer Synthesis. The polymers were synthesized using poly-L-lysine hydrobromide with a molecular weight of 20 kDa (Sigma), referred to as PLL_{20} and an *N*-hydroxysuccinimidyl ester of methoxy-terminated poly(ethylene glycol) (Nektar, USA, MW 5 kDa) as described previously (*11, 32*). FITC-labeled PLL-g-PEG polymer was synthesized in an analogous manner, using 20% FITC-terminated poly(ethylene glycol) *N*-hydroxy succinimidyl ester (Nektar, USA, MW 5 kDa) and 80% *N*-hydroxysuccinimidyl ester of methoxy-terminated poly-(ethylene glycol). Grafting (g) was calculated using the absolute number of PEG-moieties per lysine of the PLL backbone and was about 5% for all the polymers. PLL_{20}-g_5-PEG_5 or PLL_{20}-g_5-PEG_5-FITC was used for all experiments and is referred to as PLL-g-PEG or PLL-g-PEG-FITC, respectively. Reaction rates were determined by ^{1}H NMR (D_2O) (β, γ, and δ CH_2 peaks of lysine at 1−2 ppm, CH_2CH_2O of PEG at 3.3−3.9 ppm, and the FITC-group at 6.9−7.2 ppm). The polymers were stored in PBS at −20 °C until further use.

Formulation of PLL-g-PEG-DNA Condensates. PLL-g-PEG-DNA condensates were formed using a plasmid expressing enhanced green fluorescent protein (pEGFP-N1, Clontech) at a final DNA concentration of 1 μg/150 μL (= 6.7 μg/mL) in PBS (0.01 M phosphate buffered saline, pH 7.4, Sigma) and a PLL-g-PEG concentration according to the NH_4^+/PO_4^{3-} (amino group in PLL/phosphate group in DNA; N/P) charge ratio of 3.125. For a 24-well plate, PLL-g-PEG was provided in 75 μL of PBS, and the DNA dissolved in 75 μL of PBS was added dropwise into the polymer solution. The complexes were equilibrated for 30 min at room temperature (RT) and were always freshly prepared prior to use.

Plasmid Propagation. The vector pEGFP-N1 used in this study was transformed into *E. coli* strain Top10 (Invitrogen) and grown in LB medium supplemented with 30 μg/mL kanamycin. The plasmid DNA was purified using a Maxiprep kit (Qiagen), and the concentration was determined spectrophotometrically at 260 nm.

DNA Labeling. Plasmid DNA pEGFP-N1 was covalently labeled using *Label*IT nucleic acid labeling kits (Mirus, Cat. No.: MIR3100 (CX-rhodamine) and MIR3700 (Cy5), respectively) according to the manufacturer's protocol. For colocalization studies, the DNA was labeled with CX-rhodamine (DNA-CX-rh), and for flow cytometry analysis, the plasmid was labeled with Cy5 (DNA-Cy5).

Cells and Cell Culture. COS-7 (SV 40 transformed kidney cells of African green monkey, ATCC CRL 1651, ATCC Rocksville, MA) cells were cultured as exponentially growing subconfluent monolayers at 37 °C and 5% CO_2. The cell culture was kept in 25 cm^2 culture flasks in DMEM (Cat. No.: 21885, low glucose, Glutamax I, GibcoBRL) supplemented with 10% heat inactivated FBS (Cat. No.: F7524, Sigma) and 1% ABAM (Cat. No.: 15240, GibcoBRL). For experiments, cells were used 24 h post seeding.

Temperature-Dependent Nanoparticle Uptake. In order to determine energy-dependency of nanoparticle uptake, COS-7 cells were transfected with DNA nanoparticles at either 37 or 4 °C. COS-7 cells were seeded 24 h prior to transfection in 24 well plates (10,000 cells/well). The growth medium then was replaced with 150 μL of PLL-g-PEG-DNA nanoparticles in PBS (per well: 1 μg plasmid pEGFP-N1, N/P ratio = 3.125), and the cells were incubated for 30 min, either at 37 °C or at 4 °C (here, in all the subsequent steps, the solutions were prechilled to 4 °C). Then, 400 μL of 2% serum-containing DMEM was added, and the cells were again incubated at either 37 or 4 °C for an additional 3 h. Finally, the cells were extensively washed 3× with PBS at the corresponding temperatures before DMEM supplemented with 10% FBS at 37 °C was added. After 48 h of incubation at 37 °C for both conditions, the cells were analyzed for GFP expression. To identify the total cell number, Hoechst 33342 nuclear stain (Invitrogen) was used, and ethidium bromide (AppliChem) visualized potential cytotoxicity. Briefly, the cells were incubated for 2 min in PBS containing 4 μg/mL Hoechst 33342 and 10 μg/mL ethidium bromide. After rinsing the cells three times with PBS, the transfection efficiency was analyzed by counting the GFP-expressing cells in 3 nonoverlapping areas of 500 μm^2 in relation to the total cell number as determined by the Hoechst nuclear stain. In order to analyze the data, ImageJ 1.38 was used.

In order to visualize nanoparticle uptake at 4 and 37 °C, 8000 COS-7 cells were seeded in 4 well chamber slides (Lab-Tek Chambered #1.0 Borosilicate Cover glass System, Nunc) and cultured for 16 h in DMEM containing 10% FBS. Complexes were formed by using PLL-g-PEG-FITC and DNA-CX-rh (1 μg/well) at N/P ratio 3.125 and were incubated with the cells for 3.5 h at either 4 °C or 37 °C as mentioned above. After 3× PBS washing, the cells were Hoechst-stained. Finally, cells were fixed with 1% (w/v) paraformaldehyde (PFA, Sigma) in PBS for 30 min at RT and analyzed using a high-resolution TCS-SP5 laser scanning confocal microscope (Leica Microsystems, Mannheim, Germany). To avoid cross talk, emission signals were collected independently. Image processing was performed using IMARIS software, version 6.0.0 (Bitplane AG, Zurich, Switzerland).

Colocalization Studies of Nanoparticles Formed by PLL-g-PEG-FITC Polymer and DNA-CX-rh. PLL-g-PEG-FITC was first confirmed to have transfection efficiency similar to that of nonlabeled PLL-g-PEG. Eight thousand COS-7 cells were seeded in 4 well chamber slides and cultured for 16 h in DMEM containing 10% FBS as indicated above. Complexes were formed by using PLL-g-PEG-FITC and DNA-CX-rh (1 μg/well)

at N/P ratio 3.125 as described above and were applied on the cells for 30 min and 2, 6, and 24 h. DMEM with 2% FBS was added 30 min after nanoparticle addition to guarantee cell viability. After the indicated time points, noninternalized nanoparticles were removed by rinsing the cells with PBS. Hoechst 33342 nuclear stain was performed and cells were rinsed 3× with PBS. Finally, cells were fixed with 1% (w/v) paraformaldehyde (PFA, Sigma) in PBS for 30 min at RT and analyzed by CLSM.

Optimization of Endocytosis Inhibitor Concentrations. In order to determine the most efficient concentrations of several endocytosis inhibitors without decreasing cell viability, a WST-1 proliferation assay (Roche) was performed in 48 well plates (TPP, Switzerland). The following inhibitors have been used: 150 μM−10 mM methyl-β-cyclodextrin (Sigma, Cat. No.: C4555), 200 μM genistein (Sigma Cat. No.: 91955), 2 μM−60 μM chlorpromazine (Sigma, Cat. No.: C8138), and 50 nM−20 μM wortmannin (Sigma, Cat. No.: 95455). As positive control, cells were treated with PLL-g-PEG-DNA nanoparticles in the absence of any inhibitors. Eight thousand COS-7 cells/48 well were seeded 24 h prior to the addition of inhibitors. Afterwards, the cell culture medium was replaced with 270 μL of serum free DMEM containing the different inhibitors, and the cells were incubated at 37 °C for 1 h. Then, freshly prepared 30 μL PLL-g-PEG-DNA nanoparticles in PBS (per well: 0.4 μg plasmid DNA; N/P ratio = 3.125) were added and incubated for another 3 h. Finally, the cells were washed 3× with PBS before they were incubated in 300 μL of growth medium for 48 h. Subsequently, 30 μL of WST-1 reagent was applied to each well, and the cells were incubated for another hour at 37 °C and 5% CO_2. Absorption at 440 nm was measured using a microplate reader Infinite M200 (Tecan). Each condition was performed in quadruple and repeated three times.

DNA Nanoparticle Uptake in the Presence of Endocytosis Inhibitors (FACS Analysis). Twenty-four hours prior to the experiment, 50,000 COS-7 cells were seeded into a 6 well plate and cultured as describes above. The growth medium was replaced with 1 mL of serum free medium containing the different inhibitors using the optimized concentrations. The cells were incubated for 1 h. Subsequently, the medium was replaced with 500 μL of PBS containing PLL-g-PEG-DNA-Cy5 nanoparticles (per well: 1 μg DNA-Cy5; N/P ratio = 3.125) in addition to the inhibitors as described above. The cells were incubated for 30 min, and then an additional 1.5 mL serum free DMEM medium containing the inhibitors was added. After a total inhibitor incubation time of 4 h, the cells were rinsed twice with PBS before they were detached with 500 μL of trypsin-EDTA (0.25%, GibcoBRL), resuspended, and incubated for 10 min in PBS containing 10 mg of heparin (H9399, Sigma) at RT to detach cell-surface-bound DNA-containing nanoparticles. Subsequently, the cells were washed twice with PBS before they were transferred into tubes (REF 352054, Falcon) for flow cytometry analysis. The analysis was carried out with a FACSCalibur instrument and CellGate software (BD Biosciences). Dead cells and debris were gated out by forward and side scatter spectra. The mean fluorescence intensity of 10,000 individual cells was determined. All experiments have been performed in duplicate and were repeated three times. As controls, COS-7 cells were transfected with DNA-Cy5-nanoparticles in the absence of inhibitors, and naked DNA-Cy5 was used.

Transfection Studies with Endocytosis Inhibitors. Eight thousand COS-7 cells were seeded for 24 h in 24 well plates and incubated for 1 h with inhibitors dissolved in 200 μL of serum free DMEM. The optimized inhibitor concentrations were used as follows: methyl-β-cyclodextrin (5 mM), genistein (200 μM), chlorpromazine (10 μM), and wortmannin (10 μM). Later, the inhibitor solutions were removed, and 150 μL of freshly prepared PLL-g-PEG-DNA nanoparticles in PBS (per well: 1 μg pEGFP-N1; N/P ratio = 3.125) containing the same inhibitor concentrations as those mentioned above were added and further incubated for 30 min. Then, 400 μL of serum free medium supplemented with inhibitors was added and the incubation time extended for an additional 2.5 h. Subsequently, the cells were washed 3× with PBS before 10% serum-containing medium was added to further incubate the cells for 48 h. Double and triple inhibitor transfection experiments were performed in an analogous manner. In order to determine cell viability of the multiple inhibitors used, a WST-1 proliferation assay was carried out in parallel as described above. Finally, the cells were analyzed for GFP expression by fluorescence microscopy as mentioned before. As positive control, DNA nanoparticles without inhibitors were used to transfect the cells.

Nanoparticle Distribution in the Presence of Colocalization Markers. Eight thousand COS-7 cells were seeded in 4 well chamber slides (Lab-Tek Chambered #1.0 Borosilicate Cover glass System, Nunc) and cultured as described before. After washing the cells with PBS, the condensates, consisting of 1 μg of plasmid DNA (pEGFP-N1) complexed with PLL-g-PEG-FITC at N/P ratio 3.125, were coincubated with either cholera toxin subunit B (10 μg/mL) labeled with Alexa Fluor 594 (Molecular Probes, AF-ctB) or Texas Red-labeled transferrin (50 μg/mL: Molecular Probes, TR-tf) for 30 min. DMEM supplemented with 2% FBS was added to a final volume of 500 μL per chamber slide. Additionally, cells were first incubated with FITC-labeled condensates for 1.5 h before adding AF-ctB (10 μg/mL) or TR-tf (50 μg/mL). For both experimental setups, coincubation of the nanoparticles with the colocalization markers or when colocalization markers were added after 1.5 h, the nuclei were Hoechst-stained after 2 h total incubation time. Then, cells were washed 3× with PBS and fixed in 1% (w/v) PFA in PBS for 30 min at RT. Cells were washed again with PBS and analyzed by CLSM as described above.

Immunofluorescence of TFR, Caveolin-1, GM1, and EEA-1. Eight thousand COS-7 cells were seeded into 4 well chamber slides and cultured for 16 h prior to incubation with PLL-g-PEG-DNA-CX-rh (DNA-CX-rh = 1 μg/well) condensates at N/P = 3.125. Cells were stained with antibodies against transferrin receptor (TFR), caveolin-1, and GM1 after 30 min and 45 min, and 1 and 2 h. The cultures were stained against early endosome antigen-1 (EEA-1) after 1, 2, 4, and 6 h. After the indicated time points, the cell culture medium was removed, the cells were washed 3× with PBS and fixed in 1% (w/v) PFA in PBS for 30 min at RT followed by rinsing 3× with PBS. Cells were permeabilized with 0.1% Triton X-100 in PBS for 10 min and washed with PBS. Subsequently, the cells were blocked with 5% donkey serum (Chemicon) and 2% BSA (Sigma) in PBS for at least 1 h. Polyclonal rabbit antibodies against TFR (Chemicon), caveolin-1 (Upstate), ganglioside GM1 (Calbiochem), and mouse against EEA-1 (early endosome antigen-1, BD-Transduction Laboratories) were diluted 1:100 in 1% BSA in PBS and either incubated for 1 h at RT or overnight at 4 °C. Each well was washed intensively 3× with PBS, before secondary antibodies donkey antimouse-FITC and donkey anti-rabbit-FITC (both from Chemicon) were added for 1 h (dilution 1:200 in 5% donkey serum in PBS). Cell nuclei were stained with DAPI (1 mg/mL, dilution 1:1000, Molecular Probes) for 10 min. The cells were washed 3× with PBS and analyzed by CLSM as described above.

Statistical Analysis. The mean values were compared by one-way ANOVA analysis using Origin 7.5 software. Statistical

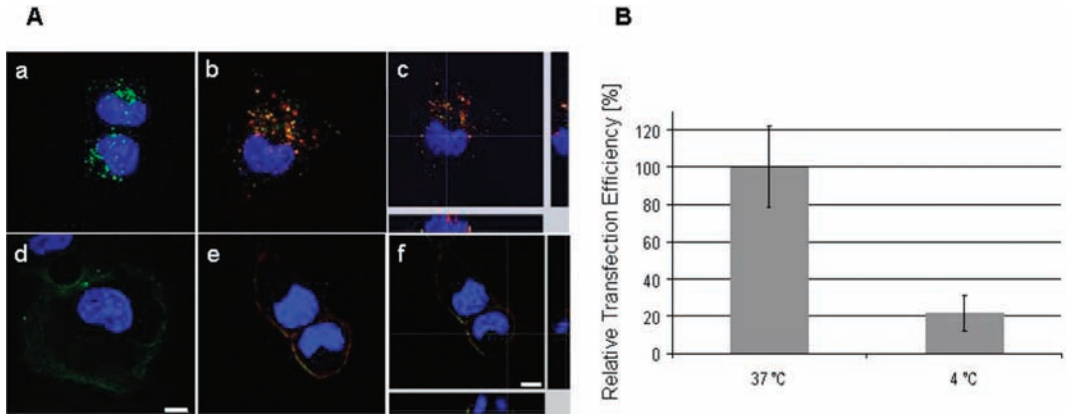

Figure 1. Temperature-dependent nanoparticle uptake into COS-7 cells. (A) Representative confocal images of COS-7 cells, which were transfected with PLL-g-PEG-FITC and CX-rhodamine-labeled pEGFP-N1 (DNA-CX-rh) nanoparticles for 3.5 h at 37 °C (a, b, and c) or 4 °C (d, e, and f). b and e display overlay images of all sections, and c and f show a section view. Uptake of PLL-g-PEG-FITC without DNA cargo at 37 and 4 °C, respectively, is demonstrated in a and d. Blue indicates Hoechst-stained nuclei, red shows CX-rhodamine-labeled DNA, and green displays PLL-g-PEG-FITC polymer. Scale bar is 10 μm. (B) PLL-g-PEG-DNA (plasmid DNA: pEGFP-N1) nanoparticles were applied on COS-7 cells and incubated for 3.5 h at either 37 or 4 °C. Transfection efficiency was analyzed after 48 h by counting transfected cells in relation to the total number of cells. The experiments indicate mean values ± standard deviation of three independent experiments carried out in triplicate. The values are normalized to particle uptake at 37 °C.

significance was accepted for $p < 0.05$ after comparing the mean values by Bonferroni test.

RESULTS

PLL-g-PEG-DNA Nanoparticles are Internalized by Endocytosis and Remain Stable within the Cytoplasm. As nonviral gene delivery systems are promising tools for gene therapy approaches, it is important to analyze nanoparticle internalization and trafficking pathways within the cell. This is especially important when comparing to viral gene delivery systems that benefit from their inherent high cell transduction efficiency. Information on particle uptake mechanisms and intracellular pathways will lead to improved design of PLL-g-PEG-DNA nanoparticles for further applications.

As PLL-g-PEG-DNA nanoparticle stability is maintained by ionic interactions between the PLL backbone of positively charged amines in PLL-g-PEG to negatively charged phosphate groups of the DNA, it is crucial to gain insight into nanoparticle uptake kinetics and intracellular stability. Therefore, PLL-g-PEG and DNA were covalently labeled with two different fluorescent labels. An FITC-labeled PEG-moiety was incorporated during PLL-g-PEG synthesis to obtain PLL-g-PEG-FITC. As determined by NMR, 1 FITC per PLL-g-PEG polymer was attached per PLL-g-PEG-FITC (data not shown). The plasmid DNA harboring the sequence of green fluorescent protein (pEGFP-N1) was covalently labeled at amino groups with CX-rhodamine to maintain condensate formation. PLL-g-PEG-FITC-DNA-CX-rh nanoparticles that were transfected into COS-7 cells showed similar transfection efficiency compared to that of the unlabeled condensates (data not shown).

Initial experiments were performed to determine the energy-dependent dependency of PLL-g-PEG-DNA nanoparticle uptake as endocytosis can be strongly inhibited by lowering the temperature (*19*). For this purpose, fluorescent PLL-g-PEG-DNA nanoparticles were prepared, and COS-7 cells were transfected at 4 and 37 °C (Figure 1). Representative confocal images taken 3.5 h after nanoparticle exposure at 4 and 37 °C show that at 37 °C nanoparticles were found in the cytoplasm of the cell (Figure 1A, b and c). In c, an optical cross section indicated that the nanoparticles were indeed found within the cytoplasm. When only fluorescently labeled PLL-g-PEG was incubated with the cells (Figure 1A, a), it was also found within the cytoplasm close to the nucleus. In contrast, lowering the temperature strongly reduced nanoparticle uptake as they remained at the cell membrane (Figure 1A, e and f). This behavior was also seen for PLL-g-PEG-FITC (Figure 1A, d). These findings were quantified; at 4 °C, transfection efficiency was found to be only 25% as compared to transfection efficiency at 37 °C. These findings suggest that PLL-g-PEG enters the cytoplasm by energy-dependent uptake processes and that it enters independent of the DNA-cargo.

Close colocalization of PLL-g-PEG-FITC and DNA-CX-rh resulted in yellow nanoparticles that could be detected. Uptake studies were performed and COS-7 cells were analyzed after 30 min and 2, 6, and 24 h of nanoparticle incubation. Figure 2A−D shows representative confocal images of fluorescent-labeled nanoparticles (DNA-CX-rh, PLL-g-PEG-FITC). After 30 min of nanoparticle incubation, the condensates were poorly incorporated into COS-7 cells as only few fluorescent particles were observed in association with the plasma membrane. After 2 and 6 h, nanoparticle uptake was enhanced indicated by the increase in the number of yellow particles. Initially, the nanoparticles were homogenously distributed within the cytoplasm (2 h), whereas after more than 6 h, nanoparticles accumulated in the perinuclear region of the cell. Optical cross-sections of transfected cells (Figure 2E and F) show that after 2 h, the nanoparticles were clearly localized within the cytoplasm and remained closely associated with the nucleus for more than 24 h. When COS-7 cells were exposed to DNA-CX-rh or PLL-g-PEG-FITC for 2 h, DNA-CX-rh did not enter the cells, whereas PLL-g-PEG-FITC was found to be distributed within the entire cytoplasm (Figure 2G and H, respectively).

Analysis of PLL-g-PEG-DNA Nanoparticle Uptake into COS-7 Cells. Uptake of PLL-g-PEG-DNA nanoparticles was studied by using different endocytosis inhibitors. Figure 3A lists endocytosis inhibitors that were used to inhibit their respective target pathways. As the effective range of inhibitors is very narrow, cell viability assays were performed 48 h after inhibitor treatment to determine efficient but not toxic inhibitor concentrations (Figure 3C). The inhibitor concentrations used here showed more than 85% cell viability compared to untreated COS-7 cells. To quantify nanoparticle uptake into COS-7 cells, FACS analysis was carried out (Figure 3B). PLL-g-PEG-DNA-Cy5 nanoparticles were individually coincubated with different substances, and inhibition of nanoparticle uptake was determined. As controls, fluorescent-labeled nanoparticles and DNA-Cy5 in the absence of inhibitors were used. Genistein, an inhibitor of caveolae-mediated endocytosis, reduced nanoparticle

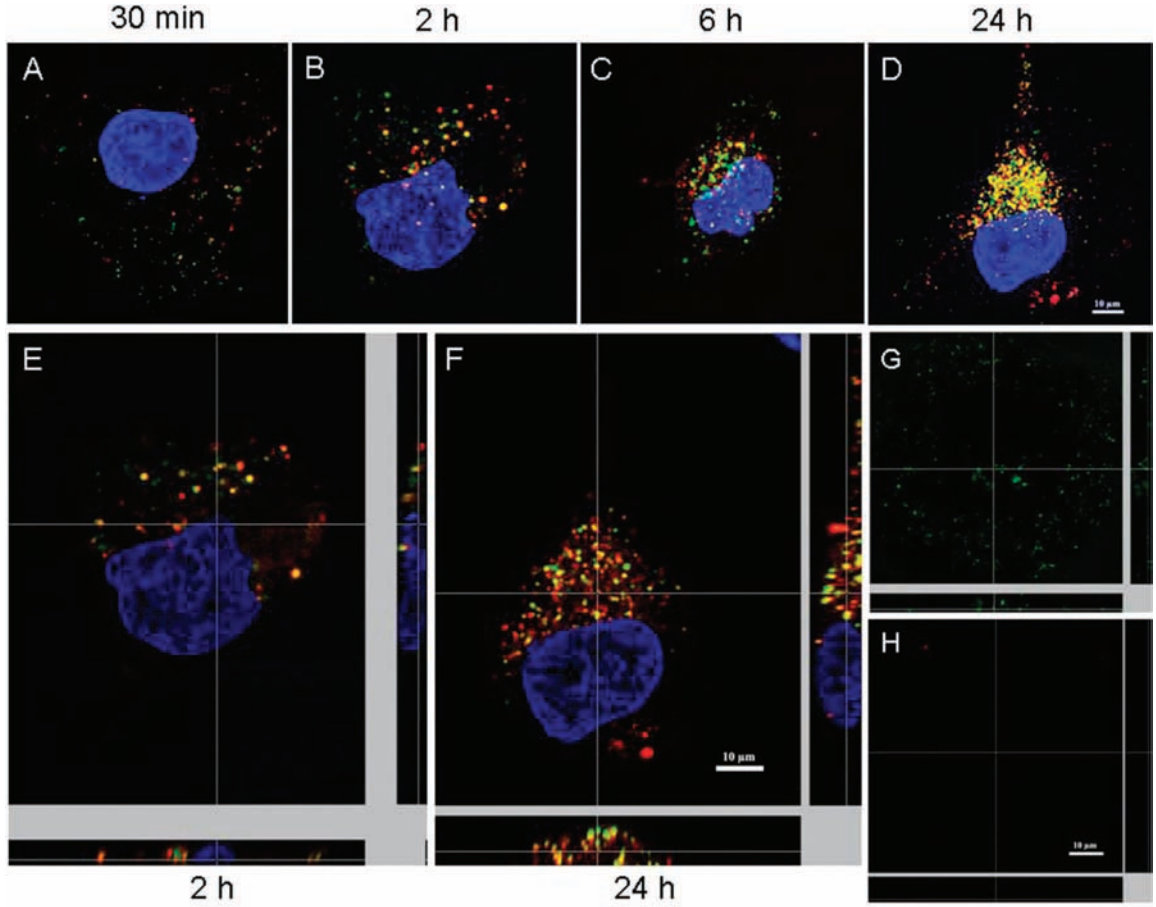

Figure 2. Colocalization of PLL-g-PEG-FITC and CX-rhodamine-labeled pEGFP-N1 (DNA-CX-rh) in COS-7 cells. Nanoparticles were prepared and applied on COS-7 cells for 30 min and 2, 6, and 24 h. After the indicated time points, cells were fixed and analyzed by confocal microscopy. Images A−D show COS-7 cells incubated with nanoparticles for the indicated times, whereas images E and F display section views of cells incubated for 2 and 24 h, respectively. G and H indicate uptake of PLL-g-PEG-FITC and DNA-CX-rh, respectively. Blue indicates Hoechst-stained nuclei, green shows PLL-g-PEG-FITC, red displays DNA-CX-rh, and yellow indicates tight association of labeled polymer and plasmid DNA. Scale bar is 10 μm.

uptake to 43 ± 5%. Whereas all other inhibitors reduced nanoparticle uptake only a little, wortmannin by 17 ± 3% and chlorpromazine by 3 ± 2%, indicating the involvement of several pathways, 74 ± 2% of the nanoparticles were internalized when methyl-β-cyclodextrin was applied.

As nanoparticle uptake is not indicative for gene expression, transfection experiments in the presence of single inhibitors were performed (Figure 3D). PLL-g-PEG-DNA nanoparticles were coincubated with the respective inhibitors, and GFP expression was analyzed. In the presence of wortmannin and methyl-β-cyclodextrin, transfection efficiency was reduced by 35 ± 18% and 30 ± 19%, respectively, whereas in the presence of genistein or chlorpromazine, transfection efficiency was not reduced significantly. In order to further analyze if multiple pathways are involved in PLL-g-PEG nanoparticle uptake, double and triple inhibitor experiments were performed. Cell viability with double inhibitors was found to be above 90% (Figure 3E), whereas triple inhibitors decreased cell viability by ∼20% (Figure 3G). Double inhibitors showed a reduction in transfection efficiency to ∼70% (Figure 3F). The transfection efficiency with triple inhibitors was reduced to ∼30% in comparison to that of control cells (Figure 3H). Interestingly, no inhibitor combination used was able to completely block nanoparticle uptake and gene expression, indicating that PLL-g-PEG-DNA nanoparticles might use several uptake mechanisms.

Analysis of PLL-g-PEG-DNA Nanoparticle Pathways within COS-7 Cells. To visualize intracellular pathways of the PLL-g-PEG-DNA nanoparticle within COS-7 cells, PLL-g-PEG-DNA nanoparticles were coincubated with known endocytosis ligands cholera toxin B and transferrin. The nontoxic subunit B of cholera toxin was used to study lipid raft-mediated endocytosis as cholera toxin B binds to membrane sphingolipid GM1 to enter a cell (*29*, *33*). Transferrin is internalized by receptor-mediated endocytosis forming clathrin-coated pits and is widely used as a tracker for clathrin-mediated endocytosis. COS-7 cells were incubated for 2 h with PLL-g-PEG-FITC-DNA nanoparticles and endocytosis markers Alexa Fluor-594-labeled cholera toxin B (AF-ctB) and Texas Red-labeled transferrin (TR-tf) were either coincubated with nanoparticles for 2 h or COS-7 cells were preincubated for 1.5 h with nanoparticles prior to the addition of transferrin or cholera toxin B for 30 min (Figure 4). When COS-7 cells were preincubated for 1.5 h with the nanoparticles prior to the addition of cholera toxin B or transferrin (Figure 4A and C), cholera toxin B was found attached to the plasma membrane, whereas transferrin was already internalized and localized close to the nucleus. PLL-g-PEG-FITC-DNA nanoparticles were internalized, but only few particles colocalized with the endocytosis markers as indicated by a few yellow particles. When COS-7 cells were coincubated with PLL-g-PEG-FITC-DNA nanoparticles and endocytosis markers for 2 h (Figure 4B and D), cholera toxin B was found in the nucleus not colocalized with PLL-g-PEG-FITC-DNA nanoparticles. Also transferrin and PLL-g-PEG-FITC-DNA nanoparticles were not colocated within COS-7 cells.

To support the findings obtained with colocalization studies, immunofluorescence stainings with endocytosis markers GM1,

A

Inhibitor	Macro-pinocytosis	Clathrin-Mediated Endocytosis	Caveolae-Mediated Endocytosis	Caveolae- and Clathrin-independent Endocytosis
Wortmannin	x			
Chlorpromazine		x		
Genistein			x	
Methyl-β-cyclodextrin			x	x

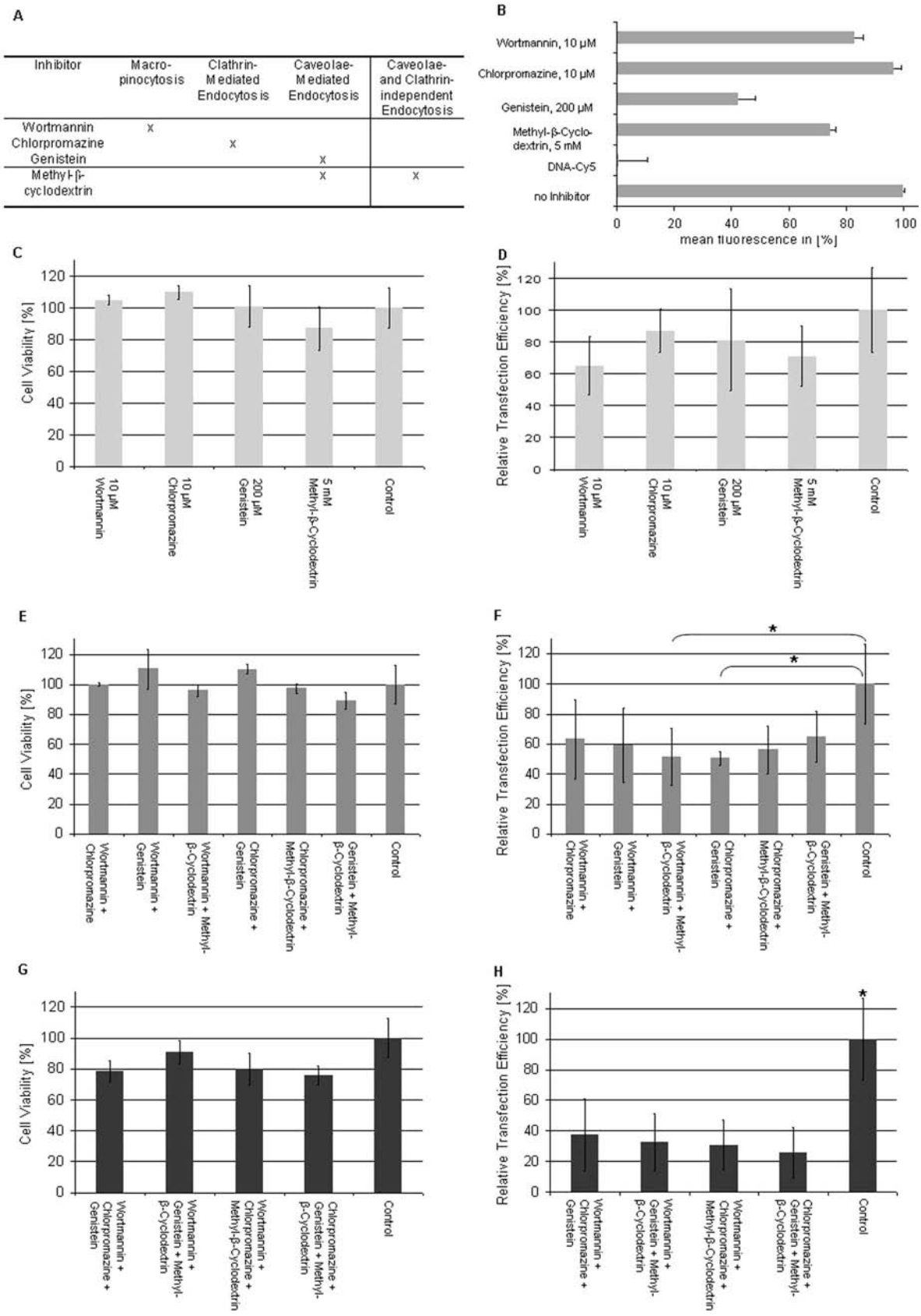

Figure 3. Inhibition of PLL-g-PEG-DNA nanoparticle uptake. (A) Endocytosis inhibitors and their targets used. (B) FACS analysis of COS-7 cells incubated with nanoparticles in the presence of four different endocytosis inhibitors. The graph displays mean fluorescence intensities of one of three independent experiments performed in duplicate. As controls, PLL-g-PEG-DNA-Cy5 without inhibitors, plasmid DNA only, and untreated COS-7 cells were used (not shown). Cell viability as determined by the WST-1 proliferation assay performed in the presence of single (C), double (E), and triple (G) endocytosis inhibitors. Transfection efficiencies after coincubation with single (D), double (F), and triple (H) endocytosis inhibitors. In D, F, and H, unlabeled pEGFP-N1 was used for nanoparticle production. The values were normalized to transfection efficiencies in the absence of any inhibitor (control). The values shown here represent mean values ± standard deviation from two to five independent experiments performed in duplicate. * refers to values that are statistically different from the control ($p < 0.05$).

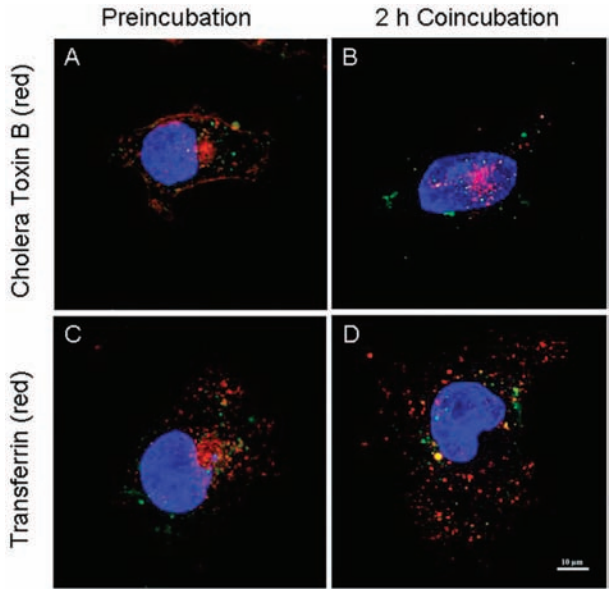

Figure 4. Colocalization studies with PLL-g-PEG-FITC-DNA nanoparticles and endocytosis markers Alexa Fluor-594-labeled cholera toxin B (AF-ctB) and Texas Red-labeled transferrin (TR-tf). In A and C, COS-7 cells were preincubated with PLL-g-PEG-FITC-DNA nanoparticles for 1.5 h, before cholera toxin B or transferrin was added for 30 min. After a total of 2 h, the cells were analyzed. In B and D, cholera toxin B and transferrin were coapplied with the nanoparticles for an entire 2 h prior to analysis. The cells were analyzed by CLSM. Blue indicates Hoechst-stained nuclei, green shows PLL-g-PEG-FITC, and red displays colocalization markers for cholera toxin B (in A and B) and transferrin (in C and D). Scale bar is 10 μm.

transferrin receptor (TFR), and caveolin-1 were performed. Ganglioside GM1, is mainly found in lipid rafts indicative for clathrin-independent pathways, TFR is involved in clathrin-mediated endocytosis, and caveolin-1 represents the main component in caveolae-mediated endocytosis. As shown in Figure 2, the majority of nanoparticles were located within the cytoplasm after 2 h; therefore, colocalization of PLL-g-PEG-DNA nanoparticles with GM1, TFR, and caveolin-1 was analyzed after 30 and 45 min, and 1 and 2 h. In addition, it was important to find out whether PLL-g-PEG-DNA nanoparticles would enter the lysosomal pathway. Therefore, colocalization with EEA-1 (early endosome antigen-1) was analyzed after 1, 2, 4, and 6 h to guarantee sufficient time for sorting into the endosomal pathway. Most PLL-g-PEG-DNA nanoparticles visualized by DNA-CX-rh did not colocalize with GM1 (Figure 5A−D). They also did not colocalize with transferrin receptors (Figure 5E−H) nor with caveolin-1 (Figure 5I−L). Moreover, PLL-g-PEG-DNA nanoparticles were not localized in early endosomal compartments (Figure 5M−P). These findings essentially confirm the inhibition of uptake and colocalization experiments in that internalized PLL-g-PEG-DNA nanoparticles do not strictly follow one of the main uptake mechanisms. Moreover, they avoid endosomal degradation within COS-7 cells that might lead to fast clearance and inefficient transfection.

DISCUSSION

Knowledge about uptake mechanisms and intracellular pathways of nonviral gene delivery vehicles is of great interest for the design of high performance delivery systems for therapeutic DNA. As PLL-g-PEG-DNA nanoparticles were previously identified as potent gene delivery vehicles in COS-7 cells that combine small size (80−90 nm), long storage stability, and low cytotoxicity with high transfection rates (*11*), this study aimed at elucidating the uptake mechanisms and intracellular pathways of these particles. Cargo uptake is usually energy-dependent and leads to the formation of membranous vesicles (*3, 4, 14, 18, 22*). PLL-g-PEG-DNA nanoparticles were shown to enter COS-7 cells by energy-dependent mechanisms as reduction of the temperature to 4 °C reduced nanoparticle uptake as shown by confocal imaging. Consequently, transfection efficiency was decreased by 75% at 4 °C. The nanoparticles were shown to enter the cytoplasm within the first 2 h of transfection; later, PLL-g-PEG-DNA nanoparticles accumulate in the perinuclear region preceding nuclear uptake. Furthermore, PLL-g-PEG-DNA nanoparticles were found within the cytoplasm at least for 24 h, and no colocalization with endosomal compartments, as indicated by fluorescence staining against early endosome antigen-1, was observed. These experiments indicate that PLL-g-PEG-DNA nanoparticles translocate efficiently to the nucleus and eventually enter the nucleus, e.g., during mitosis, to express the gene of interest. Most studies in the field of particle uptake focused on pathways via caveolin- or clathrin-coated vesicles and cholesterol- and ganglioside GM1-enriched microdomain-mediated endocytosis (*14, 34−36*). Therefore, our studies were based on such methodology to classify the intracellular fate of PLL-g-PEG-DNA nanoparticles. Inhibition of uptake experiments were performed in the presence of optimized single inhibitor concentrations of wortmannin (macropinocytosis), chlorpromazine (clathrin-mediated), genistein (caveolae-mediated), and methyl-β-cyclodextrin (caveolae-mediated and caveolae- and clathrin- independent pathways) and with double and triple inhibitor combinations. These experiments revealed that only genistein was able to substantially inhibit (∼55%) PLL-g-PEG-DNA nanoparticle uptake into COS-7 cells. However, transfection efficiency performed in the presence of genistein did not show any reduction. Also, colocalization studies with antibodies against caveolin-1 indicate no correlation between caveolin-1 and PLL-g-PEG-DNA nanoparticles. In addition, caveolae-mediated endocytosis was described to be very fast (>20 min), and the vesicles produced are usually smaller (50−80 nm diameter) (*22*) than the diameter of PLL-g-PEG-DNA nanoparticles. Therefore, all findings suggest that these nanoparticels do not follow caveolae-mediated pathways and that the inhibitory effects of genistein might be the result of genistein side reactions. It is known that genistein acts as an ATPase inhibitor (*37*) as well as a hormone analogue (*38*) that might affect nanoparticle uptake in one way or another. Similar findings with respect to genistein activity were shown when COS-7 cells were transfected with cationic polymer pDMAEMA and PEI nanoparticles (*21*).

Clathrin-mediated pathways might also be an option for PLL-g-PEG-DNA nanoparticle uptake as particles up to 120 nm in diameter can be internalized (*22*). Here, no correlation between nanoparticle uptake and markers indicative for clathrin-mediated pathways could be demonstrated. Nanoparticle uptake was not inhibited in the presence of chlorpromazine, nor was transfection efficiency in the presence of chlorpromazine impaired. Moreover, no colocalization was found for PLL-g-PEG-DNA nanoparticles with transferrin, transferrin receptors, and EEA-1.

Also macropinocytotic and caveolae- and clathrin-independent uptake mechanisms could not be assigned as primary uptake pathways for PLL-g-PEG-DNA nanoparticles. Particle uptake and transfection could be inhibited in the presence of wortmannin or methyl-β-cyclodextrin by 17 and 24%, respectively, whereas colocalization between cholera toxin subunit B and PLL-g-PEG-DNA nanoparticles as well as the membrane ganglioside GM1 with the nanoparticles failed.

The conclusion is that these PLL-g-PEG-DNA nanoparticles do not strictly follow one of the classical endocytotic pathways, although some inhibition of endocytosis can be observed for several pathways, and transfection efficiencies were reduced when combinations of inhibitors were used (Figure 6). These

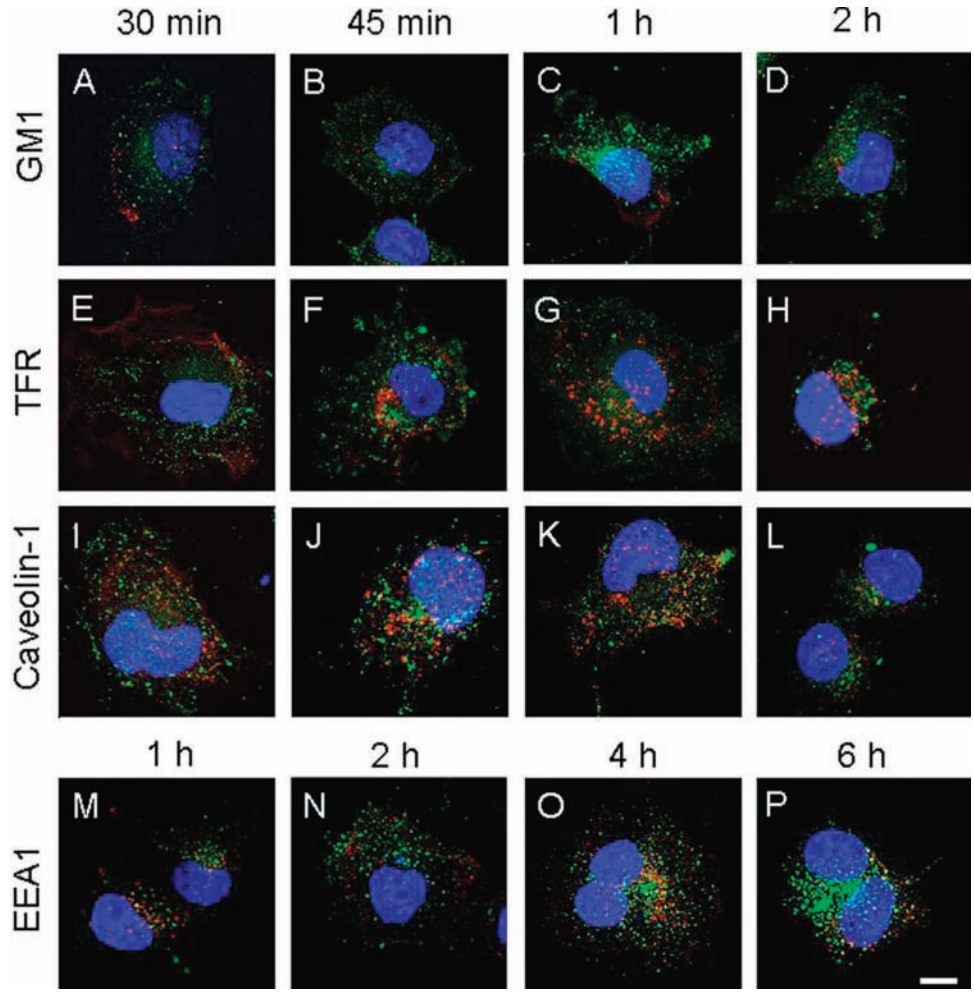

Figure 5. Colocalization studies with PLL-g-PEG-DNA-CX-rh-labeled nanoparticles and markers indicative for different endocytosis pathways. PLL-g-PEG-DNA-CX-rh nanoparticles were added to COS-7 cells, and at indicated time points, cells were fixed and immunostained against GM1 (ganglioside GM1, A-D), transferrin receptor (TFR, E-H), caveolin-1 (I-L), and early endosome antigen-1 (M-P). The cells were analyzed by CLSM. Blue indicates Hoechst-stained nuclei, red shows CX-rhodamine-labeled DNA, and green displays different endocytosis markers. Scale bar is 10 μm.

Energy-dependency	yes
Intracellular localization	< 2 h
Nuclear localization	< 24 h
Stability of nanoparticles within the cytoplasm	> 24 h
Endosomal localization	no

1) Macropinocytosis (> 1 µm)
2) Clathrin-mediated endocytosis (~ 120 nm):
a) invagination
b) early endosome
3) Caveolae-mediated endocytosis (~ 60 nm)
4) Clathrin- and caveolae-independent endocytosis (90 nm)
5) PLL_{20}-g_5-PEG_3-DNA nanoparticles (Ø 100 nm)
6) Nucleus

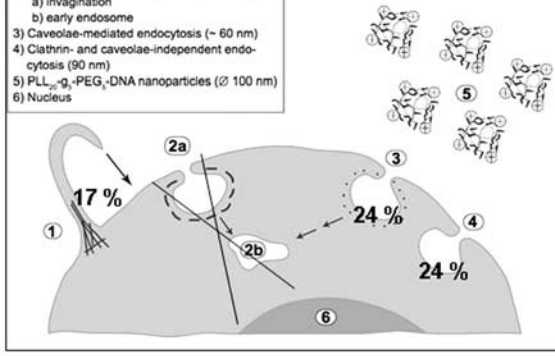

1) Macropinocytosis	
- uptake inhibition with wortmannin	~17 %
- colocalization with cholera toxin B	no
- colocalization with GM1 in lipid rafts	no
2) Clathrin-mediated endocytosis	
- uptake inhibition with chlorpromazine	no
- colocalization with transferrin receptor	no
- colocalization with transferrin	no
3) Caveolae-mediated endocytosis	
- uptake inhibition with genistein	~50 %
- inhibition with Methyl-β-Cyclodextrin	~24 %
- colocalization with cholera toxin B	no
- colocalization with GM1 in lipid rafts	no
4) Clathrin- and caveolae-independent endocytosis	
- inhibition with Methyl-β-Cyclodextrin	~24 %
- colocalization with cholera toxin B	no
- colocalization with GM1 in lipid rafts	no
5) Reduction in gene expression with single, double and triple inhibitor combinations	
- single inhibitors	~20 %
- double inhibitor combinations	~40 %
- triple inhibitor combinations	~70 %

Figure 6. Summary of PLL-g-PEG-DNA nanoparticle uptake mechanisms and trafficking pathways. The schematic summarizes endocytosis pathways that have been investigated. The numbers in brackets in the figure represent the diameters of particles that have been found to be internalized through that pathway.

findings might have been due to a general cellular inhibition, although overall cell viability was not impaired. Nanoparticle uptake has been described for pDMAEMA and PEI nanoparticles to follow the clathrin- and caveolae-dependent pathways

in COS-7 cells, respectively (*21*). Another study pointed out that COS-7 cells were very efficiently transfected with alginate−chitosan nanoparticles that were internalized predominantly by caveolae-mediated endocytosis (*15*). Pegylated poly-L-lysine (C_1K_{30}-PEG) compacted DNA transfected into COS-7 cells also did not show colocalization with early endosome antigen-1 (EEA-1) or transferrin receptor (TFR), indicating cytosomal stability and no involvement of clathrin-mediated uptake pathways (*3*). As C_1K_{30}-PEG-DNA condensates displayed a rod-like shape with a length of up to 300 nm, involvement of macropinocytotic uptake could clearly be identified (*3*). However, in our study the PLL-g-PEG-DNA nanoparticles display a spherical shape with homogeneous hydrodynamic diameter of 80−90 nm (*11*). One explanation for the failure to assign one prominent uptake pathway into COS-7 cells might be that PLL-g-PEG-DNA nanoparticles are formed by noncovalent bonds between the amino groups of poly-L-lysine and phosphate groups of the plasmid DNA. As the structure of such condensates is not known and might also be flexible in watery solution, it might well be that dangling ends of poly-L-lysine extend to the surface of the condensates and serve as cell-penetrating peptide sequences helping to internalize PLL-g-PEG-DNA nanoparticles (Figure 6). Cell-penetrating peptides cross biological membranes in a nondisruptive way without apparent toxicity and can therefore deliver macromolecular cargo into target cells via endocytotic-dependent and -independent ways (*14, 17, 39, 40*). They form stable complexes with proteins and nucleic acids, and the interaction is either covalent or noncovalent (*40, 41*). Cell-penetrating peptides may consist of Pep and MPG families that are short amphipathic peptides consisting of three domains: a variable N-terminal hydrophobic motif, responsible for membrane fusion; a hydrophilic lysine-rich domain, which is required for the interactions with DNA, intracellular trafficking of the cargo, and solubility of the peptide vector; and a linker domain separating the two domains (*40, 42, 43*). Structural and mechanistic investigations have revealed that the flexibility between the two domains, which is maintained by the linker sequence between the fusion and the DNA-binding motifs, is crucial for macromolecule delivery (*42*−*45*). Uptake mechanisms of condensates formed between cell penetration peptides and their cargo are usually energy-dependent, independent of the endosomal pathway, and are directly correlated to the size of particles and the nature of cargoes (*46, 47*). Here, PLL-g-PEG-DNA nanoparticles might function as cell-penetrating condensates where surface-exposed lysines in combination with flexible, noncharged PEG moieties are able to deliver plasmid DNA into the cytoplasm (*14*) and thereby circumvent the endocytotic machinery. In favor of such a hypothesis might be the fact that PLL-g-PEG enters into the cytoplasm of COS-7 cells independently of the presence of plasmid DNA (Figures 1A, a and 2G). This hypothesis might also be an explanation for the fast and efficient delivery of plasmid DNA combined with the low cytotoxicity of PLL-g-PEG-DNA nanoparticles used in this study. In future studies, this feature needs to be explored for the delivery of therapeutic DNA in the context of gene therapy.

ACKNOWLEDGMENT

This study was supported by Gebert Rüf Foundation (GRS-053/05), Switzerland and by CCMX, Competence Center for Materials Science and Technology, Switzerland. We thank Annina Maria Hafner for the introduction in the FACSCalibur system.

LITERATURE CITED

(1) Benns, J. M., and Kim, S. W. (2000) Tailoring new gene delivery designs for specific targets. *J. Drug Targetting 8*, 1–12.
(2) Park, T. G., Jeong, J. H., and Kim, S. W. (2006) Current status of polymeric gene delivery systems. *Adv. Drug Delivery Rev. 58*, 467–486.
(3) Walsh, M., Tangney, M., O′Neill, M. J., Larkin, J. O., Soden, D. M., McKenna, S. L., Darcy, R., O'Sullivan, G. C., and O′Driscoll, C. M. (2006) Evaluation of cellular uptake and gene transfer efficiency of pegylated poly-L-lysine compacted DNA: implications for cancer gene therapy. *Mol. Pharmaceutics 3*, 644–653.
(4) Torchilin, V. P. (2006) Recent approaches to intracellular delivery of drugs and DNA and organelle targeting. *Annu. Rev. Biomed. Eng. 8*, 1.11.33.
(5) Ledley, F. D. (1996) Pharmaceutical approach to somatic gene therapy. *Pharm. Res. 13*, 1595–1614.
(6) Dincer, S., Turk, M., and Piskin, E. (2005) Intelligent polymers as nonviral vectors. *Gene Ther. 12* (Suppl 1), S139–S45.
(7) Lee, M., and Kim, S. W. (2005) Polyethylene glycol-conjugated copolymers for plasmid DNA delivery. *Pharm. Res. 22*, 1–10.
(8) Rosenecker, J., Huth, S., and Rudolph, C. (2006) Gene therapy for cystic fibrosis lung disease: current status and future perspectives. *Curr. Opin. Mol. Ther. 8*, 439–445.
(9) Pietersz, G. A., Tang, C. K., and Apostolopoulos, V. (2006) Structure and design of polycationic carriers for gene delivery. *Mini Rev. Med. Chem. 6*, 1285–1298.
(10) Romano, G. (2007) Current development of nonviral-mediated gene transfer. *Drug News Perspect. 20*, 227–231.
(11) Rimann, M., Lühmann, T., Textor, M., Guerino, B., Ogier, J., and Hall, H. (2008) Characterization of PLL-g-PEG-DNA nanoparticles for the delivery of therapeutic DNA. *Bioconjugate Chem. 19*, 548–557.
(12) Panyam, J., Sahoo, S. K., Prabha, S., Bargar, T., and Labhasetwar, V. (2003) Fluorescence and electron microscopy probes for cellular and tissue uptake of poly(D,L-lactide-co-glycolide) nanoparticles. *Int. J. Pharm. 262*, 1–11.
(13) Feng, M., Lee, D., and Li, P. (2006) Intracellular uptake and release of poly(ethyleneimine)-co-poly(methyl methacrylate) nanoparticle/pDNA complexes for gene delivery. *Int. J. Pharm. 311*, 209–214.
(14) Patel, L. N., Zaro, J. L., and Shen, W. C. (2007) Cell penetrating peptides: Intracellular pathways and pharmaceutical perspectives. *Pharm. Res. 24*, 1977–1992.
(15) Douglas, K. L., Piccirillo, C. A., and Tabrizian, M. (2008) Cell line-dependent internalization pathways and intracellular trafficking determine transfection efficiency of nanoparticle vectors. *Eur. J. Pharm. Biopharm. 68*, 676–687.
(16) Chithrami, B. D., and Chan, W. C. W. (2007) Elucidating the mechanism of cellular uptake and the removal of protein-coated gold nanoparticles of different sizes and shapes. *Nano Letters 7*, 1542–1550.
(17) Harush-Frenkel, O., Debotton, N., Benita, S., and Altschuler, Y. (2007) Targetting nanoparticles to the clathrin-mediated endocytotic pathway. *BBRC 353*, 26–32.
(18) Perret, E., Lakkaraju, A., Deborde, S., Schreiner, R., and Rodriguez-Boulan, E. (2005) Evolving endosomes: how many varieties and why? *Curr. Opin. Cell Biol. 17*, 423–434.
(19) Khalil, I. A., Kogure, K., Akita, H., and Harashima, H. (2006) Uptake pathways and subsequent intracellular trafficking in nonviral gene delivery. *Pharmacol. Rev. 58*, 32–45.
(20) van der Aa, M. A., Huth, U. S., Häfele, S. Y., Schubert, R., Oosting, R. S., Mastrobattista, E., Hennink, W. E., Peschka-Suss, R., Koning, G. A., and Crommelin, D. J. (2007) Cellular uptake of cationic polymer-DNA complexes via caveolin plays a pivotal role in gene transfection in COS-7 cells. *Pharm. Res. 24*, 1590–1598.
(21) van der Aa, M. A., Huth, U. S., Hafele, S. Y., Schubert, R., Oosting, R. S., Mastrobattista, E., Hennink, W. E., Peschka-Suss,

R., Koning, G. A., and Crommelin, D. J. (2007) Cellular uptake of cationic polymer-DNA complexes via caveolae plays a pivotal role in gene transfection in COS-7 cells. *Pharm. Res. 24*, 1590–1598.

(22) Conner, S. D., and Schmid, S. L. (2003) Regulated portals of entry into the cell. *Nature 422*, 37–44.

(23) Swanson, J. A., and Watts, C. (1995) Macropinocytosis. *Trends Cell Biol. 5*, 424–428.

(24) Takei, K., and Haucke, V. (2001) Clathrin-mediated endocytosis: membrane factors pull the trigger. *Trends Cell Biol. 11*, 385–391.

(25) Maxfield, F. R., and McGraw, T. E. (2004) Endocytic recycling. *Nat. Rev. Mol. Cell Biol. 5*, 121–32.

(26) Thomsen, P., Roepstorff, K., Stahlhut, M., and van Deurs, B. (2002) Caveolae are highly immobile plasma membrane microdomains, which are not involved in constitutive endocytic trafficking. *Mol. Biol. Cell 13*, 238–250.

(27) Parton, R. G., and Richards, A. A. (2003) Lipid rafts and caveolae as portals for endocytosis: new insights and common mechanisms. *Traffic 4*, 724–738.

(28) Pelkmans, L., and Helenius, A. (2002) Endocytosis via caveolae. *Traffic 3*, 311–320.

(29) Neu, U., Woellner, K., Gauglitz, G., and Stehle, T. (2008) Structural basis of GM1 ganglioside recognition by simian virus 40. *PNAS 105*, 5219–5224.

(30) Pelkmans, L., Kartenbeck, J., and Helenius, A. (2001) Caveolar endocytosis of simian virus 40 reveals a new two-step vesicular-transport pathway to the ER. *Nat. Cell Biol. 3*, 473–483.

(31) Parton, R. G., and Simons, K. (2007) The multiple faces of caveolae. *Nat. Rev. Mol. Cell Biol. 8*, 185–94.

(32) Pasche, S., Textor, M., Meagher, L., Spencer, N. D., and Griesser, H. J. (2005) Relationship between interfacial forces measured by colloid-probe atomic force microscopy and protein resistance of poly(ethylene glycol)-grafted poly(L-lysine) adlayers on niobia surfaces. *Langmuir 21*, 6508–6520.

(33) Saslowski, D. E., and Lancer, W. I. (2008) Conversion of apical plasma membrane sphingomyelin to ceramide attenuates the intoxication of host cells by cholera toxin. *Cell Microbiol. 10*, 67–80.

(34) Foerg, C., Ziegler, U., Fernandez-Carneado, J., Giralt, E., Rennert, R., Beck-Sickinger, A. G., and Merkle, H. P. (2005) Decoding the entry of two novel cell-penetrating peptides in HeLa cells: lipid raft-mediated endocytosis and endosomal escape. *Biochemistry 44*, 72–81.

(35) Vendeville, A., Rayne, F., Bonhoure, A., Bettache, N., Montcourrier, P., and Beaumelle, B. (2004) HIV-1 Tat enters T cells using coated pits before translocating from acidified endosomes and eliciting biological responses. *Mol. Biol. Cell 15*, 2347–2360.

(36) Schmid, S. L. (1997) Clathrin-coated vesicle formation and protein sorting: an integrated process. *Annu. Rev. Biochem. 66*, 511–548.

(37) Zheng, J., and Ramirez, V. D. (2000) Inhibition of mitochondrial proton F0F1-ATPase/ATP synthase by polyphenolic phytochemicals. *Br. J. Pharmacol. 130*, 1115–1123.

(38) Kuiper, G. G. J. M., Lemmen, J. G., Carlsson, B., Corton, J. C., Safe, S. H., Van der Saag, P. T., Van der Burg, B., and Gustavsson, J. A. (1998) Interaction of estrogenic chemicals and phytoestrogens with estrogen receptor β. *Biotechnology 139*, 4252–4263.

(39) Amand, H. L., Fant, K., Norden, B., and Esbjörner, E. K. (2008) Stimulated endocytosis in penetratin uptake: effect of arginine and lysine. *Biochem. Biophys. Res. Commun. 371*, 621–625.

(40) Morris, M. C., Deshayes, S., Heitz, F., and Divita, G. (2008) Cell-penetrating peptides: from molecular mechanisms to therapeutics. *Biol. Cell 100*, 201–217.

(41) Foged, C., and Nielsen, H. M. (2008) Cell-penetrating peptides for drug delivery across membrane barriers. *Expert Opin. Drug Delivery 5*, 105–117.

(42) Morris, M. C., Chaloin, L., Méry, J., Heitz, F., and Divita, G. 1999a A novel potent strategy for gene delivery using a single peptide vector as a carrier. *Nucleic Acids Res. 27*, 3510–3517.

(43) Simeoni, F., Morris, M. C., Heitz, F., and Divita, G. (2003) Insight into the mechanism of the peptide-based gene delivery system MPG: implications for delivery of siRNA into mammalian cells. *Nucleic Acids Res. 31*, 2717–2724.

(44) Deshayes, S., Gerbal-Chaloin, S., Morris, M. C., Aldrian-Herrada, G., Charnet, P., Divita, G., and Heitz, F. (2004) On the mechanism of non-endosomal peptide-mediated cellular delivery of nucleic acids. *Biochim. Biophys. Acta 1667*, 141–147.

(45) Simeoni, F., Morris, M. C., Heitz, F., and Divita, G. (2005) Peptide-based strategy for siRNA delivery into mammalian cells. *Methods Mol. Biol. 309*, 251–260.

(46) Gros, E., Deshayes, S., Morris, M. C., Aldrian-Herrada, G., Depollier, J., F., H., and Divita, G. (2006) A non-covalent peptide-based strategy for protein and peptide nucleic acid transduction. *Biochim. Biophys. Acta 1758*, 384–393.

(47) Muñoz-Morris, M. A., Heitz, F., Divita, G., and Morris, M. C. (2007) The ep-1 forms biologically efficient nanoparticle complexes. *Biochem. Biophys. Res. Commun. 355*, 877–882.

BC800206R

Fluorophore Labeling Enables Imaging and Evaluation of Specific CXCR4−Ligand Interaction at the Cell Membrane for Fluorescence-Based Screening

Wataru Nomura,[†] Yasuaki Tanabe,[†] Hiroshi Tsutsumi,[†] Tomohiro Tanaka,[†] Kenji Ohba,[‡] Naoki Yamamoto,[‡] and Hirokazu Tamamura*[,†]

Institute of Biomaterials and Bioengineering, Tokyo Medical and Dental University, Chiyoda-ku, Tokyo 101-0062, Japan, and AIDS Research Center, National Institute of Infectious Diseases, Shinjuku-ku, Tokyo 162-8640, Japan. Received May 24, 2008; Revised Manuscript Received July 23, 2008

Development of CXCR4-specific ligands is an important issue in chemotherapy of HIV infection, cancer metastasis, and rheumatoid arthritis, and numerous potential ligands have been developed to date. However, it is difficult to assess their binding mode and specificity because of uncertainties in the structure of the CXCR4−ligand complexes. To address this problem, we have synthesized fluorophore labeled Ac-TZ14011, which is derived from T140, a powerful CXCR4 antagonist. Binding of Ac-TZ14011 to CXCR4 on the cell membrane was observed by fluorescence microscope, and analysis of the binding data produced IC_{50} values of several ligands comparable to those obtained in RI-based assays. This fluorescence-based assay is applicable to explore new pharmacophores of CXCR4-specific ligands with high-throughput screening and also to screening of the other GPCR binding ligands.

The interaction of CXCR4 with ligands causes diverse effects on cellular functions such as metastasis of progenitor cells (*1*−*3*), and a major role of CXCR4 is as the receptor of the chemokine, CXCL12. The interaction of CXCL12 with CXCR4 has been shown to be correlated with cancer progression (*4*) and $CD4^+$ T cell accumulation in the rheumatoid arthritis synovium (*5*). CXCR4 is also known as the second receptor of X4-type HIV-1 (*6*), and numerous ligands for CXCR4 derived from natural and synthetic compounds have been identified as inhibitors of HIV infection and cancer metastasis. [^{125}I]-CXCL12 has been utilized as a competitor in the assays to evaluate the CXCR4-binding activity of synthetic compounds such as T140 (*7*), its derivatives (*8*), KRH-1636 (*9*), and AMD3100 (*10*). Experimental methods utilizing radioisotopes (RI[1]) have advantages in the high resolution of the assays. Recently, molecular probes and fluorescent labeling, an emergent technology in chemical biology, have proved to be very useful for the evaluation in vivo of the functions of proteins and of the biological effect of changing concentrations of Ca^{2+} (*11*), Zn^{2+} (*12*), and NO (*13*), enzyme activity (*14*), and protein phosphorylation (*15*) in cells. Moreover, imaging of living cells by fluorescent probes can be utilized to estimate the accuracy of binding assays under statistically identical conditions. This article describes the synthesis and use of fluorophore labeled Ac-TZ14011 to analyze the CXCR4 binding of ligands at the cell membrane and to determine the IC_{50} values of ligands.

Ac-TZ14011, a derivative of T140 optimized for CXCR4 binding and stability in vivo by functional group substitutions, was synthesized as described previously (*16*, *17*). The D-lysine at position 8 was selectively labeled with TAMRA or fluorescein (Figure 1). A hexamethylene group was incorporated into the TAMRA or fluorescein derivative to maintain an appropriate distance between T140 residues and the fluorophore. Residues critical to the CXCR4 binding activity of TZ14011 are Arg2, Nal3, Tyr5, and Arg14, and were assessed by screening of amino acid substitution of T140 (*16*). On the basis of the previously determined interaction between Ac-TZ14011 and CXCR4 (*18*), the fluorophores labeled at D-lysine 8 were assumed not to inhibit binding of fluorescent-Ac-TZ14011 to CXCR4. To investigate if fluorescent labeled Ac-TZ14011 maintains binding activity against CXCR4, the IC_{50} values of peptides were estimated by competitive assays against [^{125}I]-CXCL12 binding. In this assay, the IC_{50} of T140 was 3.7 nM. The IC_{50} values for fluorescein- or TAMRA-labeled Ac-TZ14011 were 11 and 14 nM, respectively. These values indicated that fluorophore labeling does not inhibit binding of Ac-TZ14011 as reported elsewhere about binding of TAMRA-Ac-TZ14011 (*19*).

The binding of TAMRA-Ac-TZ14011 to a cell membrane was observed with a laser-scanning confocal microscope to determine the specific binding of Ac-TZ14011 to CXCR4. The CXCR4-GFP fusion protein was stably expressed in the NP-2 cell line (*20*), and TAMRA-Ac-TZ14011 binding to CXCR4 was clearly observed at the membrane in the absence of competitors (Figure 2A). To assess the specific binding of ligands, excess unlabeled Ac-TZ14011 was added to the medium with TAMRA-Ac-TZ14011. Upon addition of Ac-TZ14011, weak fluorescence intensity was observed on the cell membrane or cytoplasm (Figure 2B). Vesicles observed in the cytoplasm show internalization of CXCR4 receptors induced by binding of the ligands, and signals from GFP and TAMRA showed colocalization in the cytoplasm. These results indicate the specific binding of TAMRA-Ac-TZ14011 to CXCR4. To evaluate the binding specificity for CXCR4 across the different kinds of GPCRs, HeLa cells, which stably express CD4-CCR5, were utilized for microscopy assays. The binding of TAMRA-Ac-TZ14011 was observed as for the NP-2 CXCR4-GFP cell line (Figure 2C). With the addition of excess CXCL12 (Figure

* To whom correspondence should be addressed. E-mail: tamamura.mr@tmd.ac.jp.

[†] Tokyo Medical and Dental University.

[‡] National Institute of Infectious Diseases.

[1]Abbreviations: Ac, acetyl; Cit, L-citrulline; DIC, differential interference contrast; ESI-MS, electron spray ionization-mass spectrometry; FBS, fetal bovine serum; Fmoc, 9-fluorenylmethoxycarbonyl; GPCR, G-protein-coupled receptor; HEPES, 4-(2-hydroxyethyl)-1-piperazineethanesulfonic acid; Nal, L-3-(2-naphthyl)alanine; Nal(1), L-3-(1-naphthyl)alanine; RI, radioisotope; RP-HPLC, reverse-phase HPLC; TAMRA, tetramethylrhodamine; TFA, trifluoroacetic acid.

10.1021/bc800216p CCC: $40.75 © 2008 American Chemical Society
Published on Web 08/16/2008

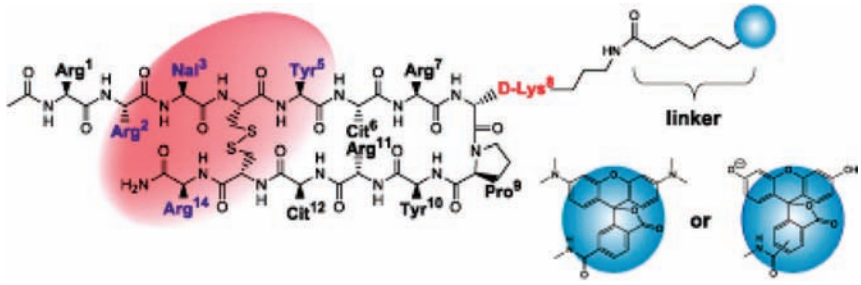

Figure 1. Design of fluorophore-labeled Ac-TZ14011. The amino acid residues in the red area are critical to CXCR4 binding activity. Fluorophores are shown as blue spheres.

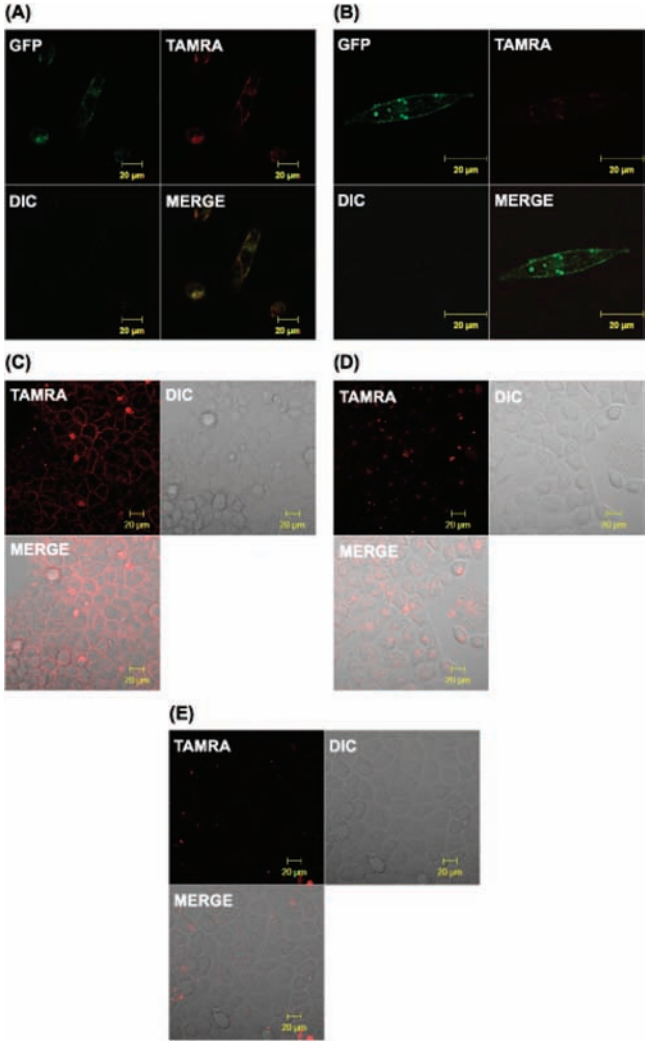

Figure 2. Confocal microscopy assays of TAMRA-Ac-TZ14011 binding to CXCR4. The signals of GFP and TAMRA are displayed in green and red, respectively. (A) Binding to NP2-GFP-CXCR4 cells. (B) Competitive binding to NP2 cells with excess amount of Ac-TZ14011. (C) Binding to HeLa-CD4-CCR5 cells. (D) Competitive binding to HeLa-CD4-CCR5 cells with excess CXCL12. (E) Competitive binding to HeLa-CD4-CCR5 cells with excess Ac-TZ14011. Descriptions of images are indicated in the pictures.

2D) or Ac-TZ14011 (Figure 2E), the fluorescence intensity on the cell membrane was decreased. These results show that TAMRA-Ac-TZ14011 binds specifically to CXCR4 but not to CCR5.

To investigate the utility of fluorescein-labeled Ac-TZ14011, cell-based binding assays were performed. In this binding assay, fluorescein-Ac-TZ14011 was utilized as a competitor to derivatives of FC131 (*8*) and the dipicolylamine-*p*-xylene Zn(II) complex [Zn^{2+}-(Dpa)-*p*-Xyl] that were developed as CXCR4 antagonists (Figure 3) (*21*). The binding constants of these compounds were previously estimated by competitive assays with [^{125}I]-CXCL12. As a result, larger values of IC_{50} than those in the previous assays were observed (Table 1). The difference of the binding constants of competitors was assumed to be a reflection of the difference of IC_{50} values in the assays. It is especially interesting that the values of IC_{50} as determined by fluorescent- and RI-competition assays are clearly correlated. It was clearly indicated that binding activity of compounds can be estimated by binding inhibition assays conducted at a constant concentration of compounds. Indeed, in the detailed binding assays, a significant correlation was observed in IC_{50} values measured by both methods for T140, TC13, and TC22.

Table 1. K_d Values Determined by RI-Competition and Fluorescent Probe Competition Assays

	IC_{50} (nM)		
	[^{125}I]-CXCL12 competition (IC_{50}C)	fluorescein-Ac-TZ14011 competition (IC_{50}F)	IC_{50}F/IC_{50}C
T140	3.93	24.7	6.3
Zn^{2+}-(Dpa)-*p*-Xyl	47[a]	291	6.2
FC131	14.6	109	7.5

[a] This value is derived from ref *18*.

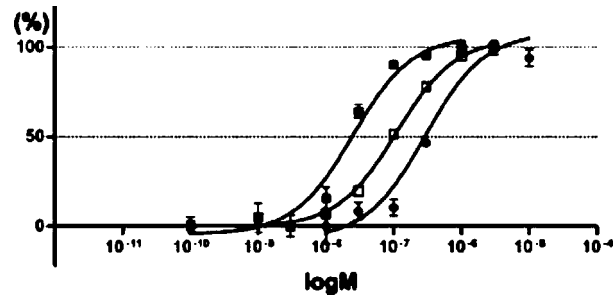

Figure 3. Curve fitting for CXCR4 binding of T140 (■), Zn^{2+}-(Dpa)-*p*-Xyl (●), and FC131 (□) in competitive assays by fluorescein-Ac-TZ14011. The *x* and *y* axes show concentrations and inhibition percentages of the binding of test compounds, respectively.

In the application of high-throughput screening for pharmacophores of CXCR4 ligands, it is important to be able to rapidly determine IC_{50} values. To test whether fluorescein-Ac-TZ14011 could be useful as a ligand in high-throughput screening, binding inhibition analyses at constant compound concentrations were performed. Twenty-four derivatives of a cyclic pentapeptide, FC131, were prepared for the analyses as described previously (Figure 4A) (*8*). The conditions used were the same as in the binding experiments shown in Figure 3 except that the compound concentration was kept constant at 2 μM. Nine compounds were found to induce >75% inhibition at this concentration (Figure 4B). The IC_{50} values of compounds that showed high inhibitory scores in the screening analyses were examined

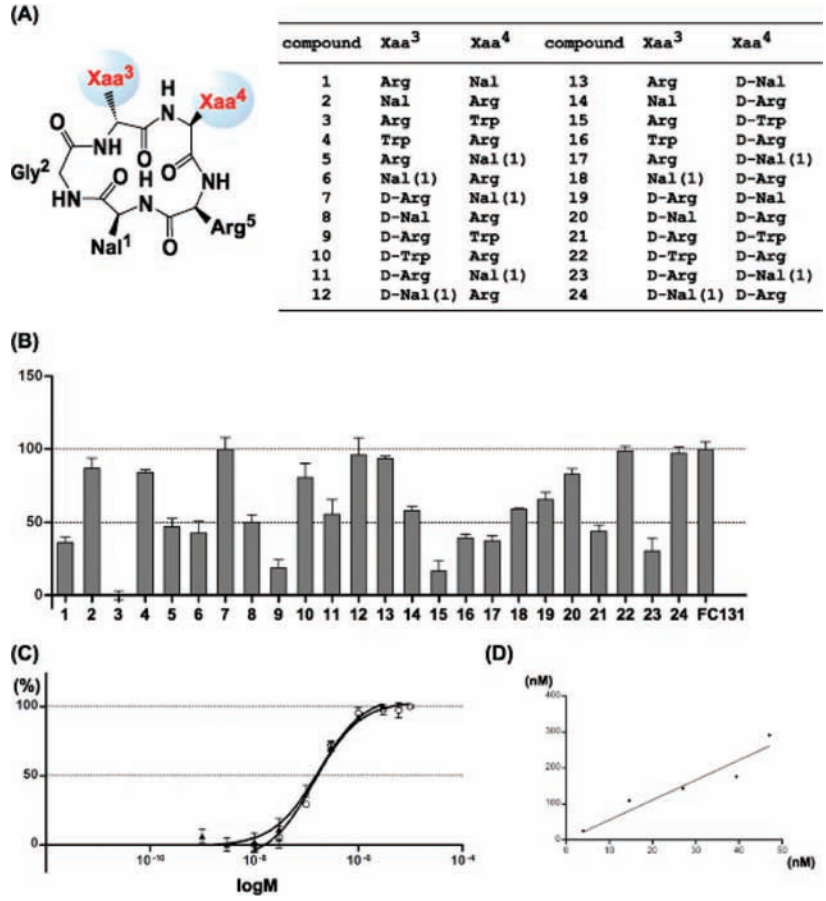

compound	Xaa^3	Xaa^4	compound	Xaa^3	Xaa^4
1	Arg	Nal	13	Arg	D-Nal
2	Nal	Arg	14	Nal	D-Arg
3	Arg	Trp	15	Arg	D-Trp
4	Trp	Arg	16	Trp	D-Arg
5	Arg	Nal(1)	17	Arg	D-Nal(1)
6	Nal(1)	Arg	18	Nal(1)	D-Arg
7	D-Arg	Nal(1)	19	D-Arg	D-Nal
8	D-Nal	Arg	20	D-Nal	D-Arg
9	D-Arg	Trp	21	D-Arg	D-Trp
10	D-Trp	Arg	22	D-Trp	D-Arg
11	D-Arg	Nal(1)	23	D-Arg	D-Nal(1)
12	D-Nal(1)	Arg	24	D-Nal(1)	D-Arg

Figure 4. (A) Design of cyclic pentapeptides. Xaa^3 and Xaa^4 (red area) were manually randomized. (B) Results of single concentration point assays for determination of the binding activity of library compounds at one time. The *x* and *y* axes show concentrations and inhibition percentages of binding of test compounds, respectively. Data were measured in triplicate, and error bars show the SEM. (C) Curve fitting for CXCR4 binding of TC13 (○) and TC22 (▲) in competitive assays by fluorescein-Ac-TZ14011. The *x* and *y* axes show concentrations and inhibition percentages of binding of test compounds, respectively. (D) Correlation between IC_{50} values determined by RI-competition assays (*x*-axis) and fluorescein-Ac-TZ14011 competition assays (*y*-axis). The compound and IC_{50} values are shown in Tables 1 and 2. The *P* value determined from correlation analysis was 0.012.

Table 2. K_d Values Determined by RI-Competition and Fluorescent Probe Competition Assays

	IC_{50} (nM)		
	[^{125}I]-CXCL12 competition (IC_{50}C)	fluorescein-Ac-TZ14011 competition (IC_{50}F)	$IC_{50}F/IC_{50}C$
T140	3.93	24.7	6.3
TC13	27.0	143	5.3
TC22	39.4	176	4.5

further (Table 2). The IC_{50} values of TC13 and TC22 were determined to be 143 and 176 nM, respectively (Figure 4C). The IC_{50} values determined in this assay showed a clear correlation with those in RI-competition assays (Figure 4D, manuscript in preparation).

Advantages of the fluorescence-based analyses include their utility in high-throughput screening and direct observation of the binding state on cell membrane by fluorescence microscope; binding assays and confocal microscopy study were performed to evaluate these advantages. The binding of T140 was previously assessed with site-directed mutagenesis of CXCR4, which indicated that the extracellular loop 2 of the receptor is the main target for this peptide (*22*). The observation of Ac-TZ14011 binding to cell membranes provided convincing evidence of specificity for the target receptor. Competition with excess unlabeled Ac-TZ14011 and CXCL12 showed clear inhibition of TAMRA-Ac-TZ14011 binding. There has been concern that CXCR4 ligands could bind nonspecifically to other GPCRs. A binding study utilizing CCR5-CD4-HeLa cells showed evidence of a high degree of specificity of the ligands. HeLa cells naturally express CXCR4 (*23*), and in the event of overexpression of CCR5-CD4 on the membrane, the binding of TAMRA-Ac-TZ14011 was prevented by the addition of competitors. These results indicate that these peptides bind to the same target site on the cell membrane, CXCR4. Internalization of CXCR4 stimulated by binding of ligands was clearly observed, particularly in the presence of competitors indicating that ligands bound to CXCR4 are simultaneously incorporated in the cytoplasm. Interestingly, on the basis of the numbers and size of vesicles observed, CXCL12 showed stronger induction of CXCR4 internalization than Ac-TZ14011. Promotion of CXCR4 internalization is one of the important mechanisms for inhibition of HIV entry (*24*). The difference of ligand-dependent effects on CXCR4 internalization will be studied further in our laboratory.

In conclusion, the structure−activity relationships of ligands for CXCR4 have been well studied, but relatively few known ligand pharmacophores have been studied because of the difficulty associated with the analysis of receptor−ligand interactions. Our results strongly indicate that fluorescence-based ligand binding assays could be useful in the exploration of novel pharmacophores for CXCR4 ligands and that such compounds have promise as therapeutic agents for AIDS, breast cancer metastasis, and rheumatoid arthritis. Furthermore, this methodology is applicable to the design of ligands for other GPCRs.

ACKNOWLEDGMENT

We are grateful to Professor Kazunari Akiyoshi for his generous cooperation in experiments. This research was supported in part by a Grant-in-Aid for Scientific Research from the Ministry of Education, Culture, Sports, Science and Technology, Japan, and Health and Labour Sciences Research Grants.

Supporting Information Available: Detailed materials and methods. This material is available free of charge via the Internet at http://pubs.acs.org.

LITERATURE CITED

(1) Oberlin, E., Amara, A., Bachelerie, F., Bessia, C., Virelizier, J. L., Arenzana-Seisdedos, F., Schwartz, O., Heard, J. M., Clark-Lewis, I., Legler, D. F., Loetscher, M., Baggiolini, M., and Moser, B. (1996) The CXC chemokine SDF-1 is the ligand for LESTR/fusin and prevents infection by T-cell-line-adapted HIV-1. *Nature 382*, 833–835.

(2) Bleul, C. C., Farzan, M., Choe, H., Parolin, C., Clark-Lewis, I., Sodroski, J., and Springer, T. A. (1996) The lymphocyte chemoattractant SDF-1 is a ligand for LESTR/fusin and blocks HIV-1 entry. *Nature 382*, 829–833.

(3) Baird, A. M., Gerstein, R. M., and Berg, L. J. (1999) The role of cytokine receptor signaling in lymphocyte development. *Curr. Opin. Immunol. 11*, 157–166.

(4) Koshiba, T., Hosotani, R., Miyamoto, Y., Ida, J., Tsuji, S., Nakajima, S., Kawaguchi, M., Kobayashi, H., Doi, R., Hori, T., Fujii, N., and Imamura, M. (2000) Expression of stromal cell-derived factor 1 and CXCR4 ligand receptor system in pancreatic cancer: a possible role for tumor progression. *Clin. Cancer Res. 6*, 3530–3535.

(5) Nanki, T., Hayashida, K., El-Gabalawy, H. S., Suson, S., Shi, K., Girschick, H. J., Yavuz, S., and Lipsky, P. E. (2000) Stromal cell-derived factor-1-CXC chemokine receptor 4 interactions play a central role in $CD4^+$ T cell accumulation in rheumatoid arthritis synovium. *J. Immunol. 165*, 6590–6598.

(6) Feng, Y., Broder, C. C., Kennedy, P. E., and Berger, E. A. (1996) HIV-1 entry cofactor: functional cDNA cloning of a seven-transmembrane, G protein-coupled receptor. *Science 272*, 872–7.

(7) Tamamura, H., Xu, Y., Hattori, T., Zhang, X., Arakaki, R., Kanbara, K., Omagari, A., Otaka, A., Ibuka, T., Yamamoto, N., Nakashima, H., and Fujii, N. (1998) A low-molecular-weight inhibitor against the chemokine receptor CXCR4: a strong anti-HIV peptide T140. *Biochem. Biophys. Res. Commun. 25*, 877–882.

(8) Fujii, N., Oishi, S., Hiramatsu, K., Araki, T., Ueda, S., Tamamura, H., Otaka, A., Kusano, S., Terakubo, S., Nakanishi, H., Broach, J. A., Trent, J. O., Wang, Z., and Peiper, S. C. (2003) Molecular-size reduction of a potent CXCR4-chemokine antagonist using orthogonal combination of conformation- and sequence-based libraries. *Angew. Chem., Int. Ed. 42*, 3251–3.

(9) Ichiyama, K., Yokoyama-Kumakura, S., Tanaka, Y., Tanaka, R., Hirose, K., Bannai, K., Edamatsu, T., Yanaka, M., Niitani, Y., Miyano-Kurosaki, N., Takaku, H., Koyanagi, Y., and Yamamoto, N. (2003) A duodenally absorbable CXC chemokine receptor 4 antagonist, KRH-1636, exhibits a potent and selective anti-HIV-1 activity. *Proc. Natl. Acad. Sci. U.S.A. 100*, 4185–4190.

(10) Donzella, G. A., Schols, D., Lin, S. W., Esté, J. A., Nagashima, K. A., Allaway, G. P., Sakmar, T. P., Henson, G., De Clercq, E., and Moore, J. P. (1998) AMD3100, a small molecule inhibitor of HIV-1 entry via the CXCR4 co-receptor. *Nat. Med. 4*, 72–77.

(11) Grynkiewicz, G., Poenie, M., and Tsien, R. Y. (1985) A new generation of Ca^{2+} indicators with greatly improved fluorescence properties. *J. Biol. Chem. 260*, 3440–3450.

(12) Kiyose, K., Kojima, H., Urano, Y., and Nagano, T. (2006) Development of a ratiometric fluorescent zinc ion probe in near-infrared region, based on tricarbocyanine chromophore. *J. Am. Chem. Soc. 128*, 6548–6549.

(13) Takakusa, H., Kikuchi, K., Urano, Y., Sakamoto, S., Yamaguchi, K., and Nagano, T. (2002) Design and synthesis of an enzyme-cleavable sensor molecule for phosphodiesterase activity based on fluorescence resonance energy transfer. *J. Am. Chem. Soc. 124*, 1653–1657.

(14) Kojima, H., Urano, Y., Kikuchi, K., Higuchi, T., Hirata, Y., and Nagano, T. (1999) Fluorescent indicators for imaging nitric oxide production. *Angew. Chem., Int. Ed. 38*, 3209–3212.

(15) Ojida, A., Mito-oka, Y., Sada, K., and Hamachi, I. (2004) Molecular recognition and fluorescence sensing of monophosphorylated peptides in aqueous solution by bis(zinc(II)-dipicolylamine)-based artificial receptors. *J. Am. Chem. Soc. 126*, 2454–2463.

(16) Tamamura, H., Omagari, A., Oishi, S., Kanamoto, T., Yamamoto, N., Peiper, S. C., Nakashima, H., Otaka, A., and Fujii, N. (2000) Pharmacophore identification of a specific CXCR4 inhibitor, T140, leads to development of effective anti-HIV agents with very high selectivity indexes. *Bioorg. Med. Chem. Lett. 10*, 2633–2637.

(17) Tamamura, H., Hiramatsu, K., Mizumoto, M., Ueda, S., Kusano, S., Terakubo, S., Akamatsu, M., Yamamoto, N., Trent, J. O., Wang, Z., Peiper, S. C., Nakashima, H., Otaka, A., and Fujii, N. (2003) Enhancement of the T140-based pharmacophores leads to the development of more potent and bio-stable CXCR4 antagonists. *Org. Biomol. Chem. 1*, 3663–3669.

(18) Hanaoka, H., Mukai, T., Tamamura, H., Mori, T., Ishinoa, S., Ogawa, K., Iida, Y., Doi, R., Fujii, N., and Saji, H. (2006) Development of a 111In-labeled peptide derivative targeting a chemokine receptor, CXCR4, for imaging tumors. *Nucl. Med. Biol. 33*, 489–494.

(19) Oishi, S., Masuda, R., Evans, B., Ueda, S., Goto, Y., Ohno, H., Hirasawa, A., Tsujimoto, G., Wang, Z., Peiper, S. C., Naito, T., Kodama, E., Matsuoka, M., and Fujii, N. (2008) Synthesis and application of fluorescein- and biotin-labeled molecular probes for the chemokine receptor CXCR4. *ChemBioChem 9*, 1154–1158.

(20) Futahashi, Y., Komano, J., Urano, E., Aoki, T., Hamatake, M., Yoshida, T., Koyanagi, Y., Matsuda, Z., and Yamamoto, N. (2007) Separate elements are required for ligand-dependent and -independent internalization of metastatic potentiator CXCR4. *Cancer Sci. 98*, 373–379.

(21) Tamamura, H., Ojida, A., Ogawa, T., Tsutsumi, H., Masuno, H., Nakashima, H., Yamamoto, N., Hamachi, I., and Fujii, N. (2006) Identification of a new class of low molecular weight antagonists against the chemokine receptor CXCR4 having the dipicolylamine-zinc(II) complex structure. *J. Med. Chem. 49*, 3412–3415.

(22) Trent, J. O., Wang, Z., Murray, J. L., Shao, W., Tamamura, H., Fujii, N., and Peiper, S. C. (2003) Lipid bilayer simulations of CXCR4 with inverse agonists and weak partial agonists. *J. Biol. Chem. 278*, 47136–47144.

(23) Valente, S. T., Chanel, C., Dumonceaux, J., Olivier, R., Marullo, S., Briand, P., and Hazan, U. (2001) CXCR4 is down-regulated in cells infected with the CD4-independent X4 human immunodeficiency virus type 1 isolate m7NDK. *J. Virol. 75*, 439–447.

(24) Orsini, M. J., Parent, J. L., Mundell, S. J., Marchese, A., and Benovic, J. L. (1999) Trafficking of the HIV coreceptor CXCR4. Role of arrestins and identification of residues in the C-terminal tail that mediate receptor internalization. *J. Biol. Chem. 274*, 31076–31086.

BC800216P

SUPPORTING INFORMATION

Fluorophore labeling Enables Imaging and Evaluation of Specific CXCR4-Ligand Interaction at the Cell Membrane for Fluorescence-Based Screening

Wataru Nomura[a], Yasuaki Tanabe[a], Hiroshi Tsutsumi[a], Tomohiro Tanaka[a], Kenji Ohba[b], Naoki Yamamoto[b], and Hirokazu Tamamura[a,*]

[a]*Department of Molecular Recognition, Institute of Biomaterials and Bioengineering, Tokyo Medical and Dental University, Chiyoda-ku, Tokyo 101-0062, Japan*

[b]*AIDS Research Center, National Institute of Infectious Diseases, Shinjuku-ku, Tokyo 162-8640, Japan*

*correspondence should be addressed; tamamura.mr@tmd.ac.jp

MATERIALS AND METHODS

Reagents and chemicals

NP-2 cells with or without stable expression of CXCR4 and green fluorescent protein (GFP) fusion were kindly donated by Dr. Jun Komano. All chemicals were purchased from Wako Chemicals (Tokyo, Japan), unless otherwise indicated.

Synthesis of fluorescent Ac-TZ14011

Protected peptide resin of Ac-TZ14011 was constructed using the Fmoc-based solid-phase synthesis on Rink Amide MBHA resin, and its N-terminus was acetylated. After being treated with thioanisole/TFA in the presence of triisopropylsilane, H_2O and 1,2-ethanedithiol, the crude peptide was air-oxidized to cause disulfide bond formation and then purified by RP-HPLC. ESI-MS: calcd. for $C_{92}H_{143}N_{35}O_{19}S_2$ $[M+H^+]$; m/z 2108.47, found: m/z 2108.96.

TAMRA-Ac-TZ14011 was prepared by condensation of Ac-TZ14011 with TAMRA. N-Hydroxysuccinimide (2.22 mg, 19.3 μmol) and 1-ethyl-3-(3-dimethylaminopropyl) carbodiimide hydrochloride (3.98 mg, 19.3 μmol) were added to a solution of 6-(TAMRA-5-(and-6)-carboxami)hexanoic acid (TAMRA-COOH, 10 mg, 18.4 μmol) in CH_3CN (500 μL) at 0°C, and the mixture was left overnight at room temperature. After cooling to 0°C again, 200 μL of the reaction mixture was added to 200 μL of Ac-TZ14011 (7.64 mg, 2.86 μmol) in a 1:1 mixture of acetonitrile and phosphate buffer (pH 7.4) and incubated overnight at room

temperature. The crude peptide was purified by RP-HPLC. ESI-MS: calcd. for $C_{123}H_{174}N_{38}O_{24}S_2$ [M+H^+]; m/z 2632.38, found: m/z 2632.49.

Fluorescein-Ac-TZ14011 was prepared by fluorescein conjugation. Ac-TZ14011 (14 mg, 3.4 μmol) in a phosphate buffer (pH 7.4) (130 μL), was added to a solution of 6-(fluorescein-5-(and-6)-carboxamido)hexanoic acid succinimidyl ester (Fluorescein-OSu) in CH_3CN (130 μL) and the mixture was allowed to stand overnight at room temperature. The crude peptide was purified by RP-HPLC. ESI-MS: calcd. for $C_{119}H_{164}N_{36}O_{26}S_2$ [M+H^+]; m/z 2577.28, found: m/z 2578.23.

Imaging analysis using a confocal microscope system

The binding of TAMRA-Ac-TZ14011 to CXCR4 on the cell surface was investigated using an LSM 510 laser-scanning confocal microscope (Zeiss GmbH, Oberkochen, Germany). NP-2 cells with or without a stable expression of CXCR4-GFP fusion [18] were seeded in a 1.4 cm diameter glass-bottom-dish containing RPMI1640 supplemented with 10% fetal bovine serum (FBS) (1×10^5 cells per dish). After 2 days incubation at 37°C under 5% CO_2, the medium was removed, and the cells were washed three times with RPMI 1640 containing 20 mM HEPES (pH 7.4). CXCR4 ligands were added to each well, and the mixture was incubated for 15 min at room temperature. The medium was then removed, and the cells were washed three times with phenol red-free RPMI 1640 medium. The concentrations of TAMRA-Ac-TZ14011

and Ac-TZ14011 that were used were 25 nM and 2.5 μM, respectively.

Cell-based binding assay

Jurkat cells were harvested and resuspended in binding buffer (RPMI 1640 medium containing 20 mM HEPES, pH 7.4). Binding experiments were performed in the presence of 10 nM Fluorescein-Ac-TZ14011 and various concentrations of test compounds. After 30 min incubation at 0°C, cells were washed with PBS, and cell-associated fluorescence intensity was counted by Wallac 1420 ARVO MX (Ex/Em = 485/535 nm). The degree of inhibition was calculated with equation (1),

$$\text{Inhibition}(\%) = (Et - Ea)/(Et - Ec) \times 100 \quad (1)$$

where Et, Ea and Ec respectively, represent the fluorescence intensity without test compounds, fluorescence intensity with addition of test compounds, and fluorescence intensity with excess amount of Ac-TZ14011 as a competitor. The inhibition values were derived by non-linear regression, and IC_{50} values were calculated by Prism 5 software.

Fluorine-18-Labeled Phospholipid Quantum Dot Micelles for *in Vivo* Multimodal Imaging from Whole Body to Cellular Scales

Frédéric Ducongé,[†,‡] Thomas Pons,[§] Carine Pestourie,[†,‡] Laurence Hérin,[†,‡] Benoît Thézé,[†,‡] Karine Gombert,[†,‡] Benoît Mahler,[§] Françoise Hinnen,[†] Bertrand Kühnast,[†] Frédéric Dollé,[†] Benoît Dubertret,*[,§] and Bertrand Tavitian*[,†,‡]

CEA, DSV, I^{2}BM, SHFJ, Laboratoire d'Imagerie Moléculaire Expérimentale, and Inserm U803, 4 place du général Leclerc, 91401 Orsay Cedex, France, and Laboratoire Photons et Matière, CNRS UPRA0005, ESPCI, 10 rue Vauquelin, 75005 Paris, France. Received May 6, 2008; Revised Manuscript Received June 16, 2008

We have designed new nanoprobes applicable for both positron emission tomography (PET) and optical fluorescence *in vivo* imaging. Fluorine-18, which is commonly used for clinical imaging, has been coupled to phospholipid quantum dot (QD) micelles. This probe was injected in mice and we demonstrated that its dynamic quantitative whole body biodistribution and pharmacokinetics could be monitored using PET as well as the kinetics of their cellular uptake using *in vivo* fibered confocal fluorescence imaging. Phospholipid micelle encapsulation of QDs provides a highly versatile surface chemistry to conjugate multiple chemicals and biomolecules with controlled QD:molecule valency. Here, we show that, in contrast with several previous studies using other QD polymer coatings, these phospholipid QD micelles exhibit long circulation half-time in the bloodstream (on the order of 2 h) and slow uptake by reticulo-endothelial system.

INTRODUCTION

Molecular imaging revolutionizes the way biomedical research is performed by looking at molecular events in the living organism without destroying it. Molecular meaningful images can be captured at different levels of spatial resolution and depth using different imaging modalities. For example, fluorescence imaging allows functional multiplexed imaging with submicrometer resolution, but is inherently restricted to biological objects not thicker than a few millimeters or centimeters, and does not provide quantitative concentration measurements. In contrast, nuclear imaging techniques, such as positron emission tomography (PET), allow quantitative whole body imaging, albeit with a low (a few mm) spatial resolution. Tools for combining the different levels of observation are required to reconcile molecular images into a global picture. One of nanotechnology's most promising aspects lies in the ability to design multifunctional platforms including several contrast agents for multimodal imaging. Here, we explore new multifunctional nanoparticles containing both fluorescence and nuclear contrast agents and show that they allow multimodal *in vivo* imaging from the whole body to the subcellular scale.

Semiconductor nanocrystals, or "quantum dots" (*1, 2*), are potentially excellent fluorescent probes for *in vivo* imaging due to their intrinsic optical properties, such as high quantum yields, excellent resistance to photobleaching, broad excitation spectra, and narrow emission bands tunable from the UV to the NIR regions (*3, 4*). QDs have been used in laboratory animals for optical imaging of blood vessels (*5*) and lymph nodes (*6*), for cell tracking (*7, 8*), and for specific targeting of peptides and antibodies (*9, 10*). Yet their use has been limited by concerns about their *in vivo* targeting, biocompatibility, and toxicity, which are mainly determined by nanoparticle size and surface chemistry. While fluorescence imaging offers a rapid tool to qualitatively assess the final QD biodistribution, combining optical and nuclear imaging techniques will provide a more quantitative tool to characterize the dynamics of these nanoparticle biodistribution. A recent report by Schipper et al. utilized copper-64-labeled/polymer-coated commercially available QDs to follow their biodistribution in mice using PET (*11*). Consistent with previous reports (*12, 13*), this study demonstrated QD uptake by the liver and the spleen within a few minutes, without evidence of clearance from these organs. However, the authors did not use fluorescence imaging to investigate their cellular distribution. Furthermore, even if the long half-life of ^{64}Cu is attractive for preclinical PET applications, it is not widely used in humans where ^{18}F labeling is preferred for PET radiopharmacy.

Here, we report a novel bifunctional probe for fluorescence and nuclear imaging based on QDs encapsulated in functionalized phospholipid micelles and covalently labeled with fluorine-18, the most popular positron-emitting isotope. We demonstrate that a combination of PET and fluorescence imaging can be used to monitor quantitatively and dynamically the *in vivo* distribution of these probes, from the whole body to cellular scales, and we report for the first time the major pharmacokinetics parameters of nontargeted micelle-encapsulated QDs. These probes exhibit a long circulation time in the blood, before their uptake by the reticulo-endothelial system.

EXPERIMENTAL PROCEDURES

CdSe/CdZnS Core−Shell Synthesis. CdSe nanocrystal cores were synthesized using slight variations of previously published protocols (*14, 15*). Briefly, a solution of Se in trioctylphosphine (TOP) and oleylamine was swiftly injected in a three-neck flask containing octadecene, trioctylphosphine oxide, and Cd-oleate precursors at 300 °C. The temperature was lowered to 250 °C for 10 min for nanocrystal growth. The CdSe cores were isolated by precipitation and resuspended in hexane. CdZnS shell growth was performed using dropwise injection of TOP-S solution in a three-neck flask containing CdSe cores, Cd-oleate, and Zn-

* Corresponding authors. Benoît Dubertret, +33 1 40 79 45 92, benoit.dubertret@espci.fr; and Bertrand Tavitian, +33 1 69 86 77 79, bertrand.tavitian@cea.fr.

† Laboratoire d'Imagerie Moléculaire Expérimentale.

‡ Inserm U803.

§ Laboratoire Photons et Matière.

10.1021/bc800179j CCC: $40.75 © 2008 American Chemical Society
Published on Web 08/28/2008

Scheme 1. [^{18}F]-Labeled PEG-Phospholipid QD Micelle

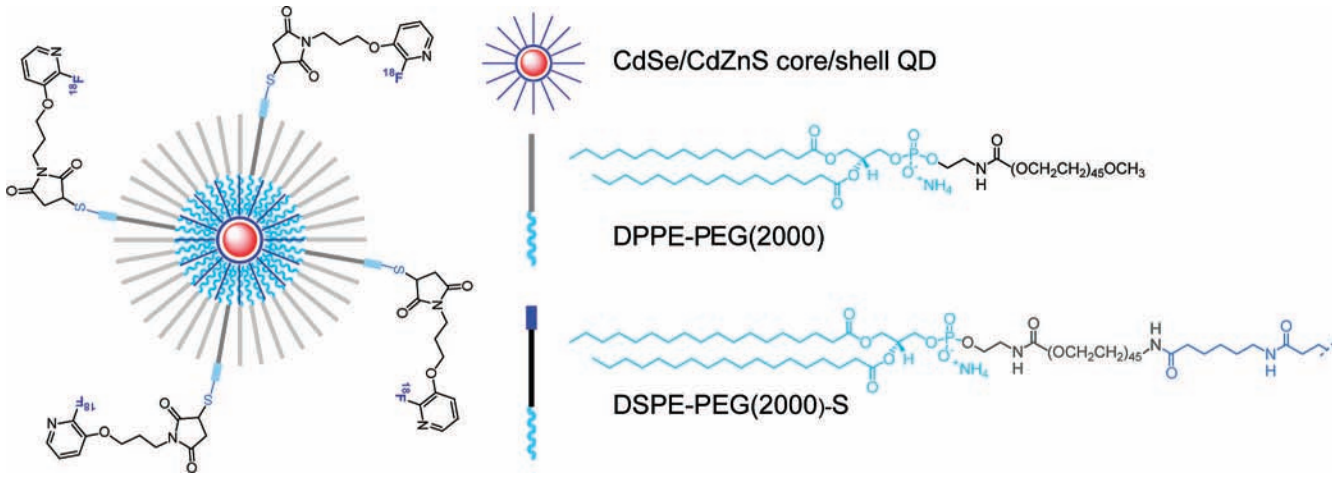

oleate precursors dissolved in trioctylamine at 300 °C under argon. Supporting Information Figure S1A shows the resulting QD absorption and emission spectra. The diameter of the obtained QDs is typically 6−8 nm, as measured by transmission electron microscopy (*15*).

QD Encapsulation and Functionalization with Thiol Groups. QDs were encapsulated in PEG-phospholipid micelles as previously described (*7, 15*). QDs were dissolved in $CHCl_3$ with a mixture of 1,2-dipalmitoyl-*sn*-glycero-3-phosphoethanolamine-*N*-[methoxy(poly(ethylene glycol))-2000] (DPPE-PEG2000) and DSPE-PEG2000-NH_2 (Avanti Polar Lipids) at the desired ratio. The total number of lipids per QD in the encapsulation solution was kept constant at ∼700. Distilled water was added and the solution was heated to 70−80 °C until the chloroform was evaporated. Encapsulated QDs were purified from aggregates and empty micelles by ultracentrifugation at 300 000 *g* in 30% sucrose solution, sucrose was eliminated by ultrafiltration (Vivaspin 500 10 kDa VS0102, Sartorius), and the encapsulated QDs were resuspended in PBS buffer. The resulting QD micelles have typical hydrodynamic sizes ∼20−25 nm as measured by dynamic light scattering (*15*). The amine groups at the extremity of the DSPE-PEG2000-NH_2 were converted into thiols using standard bioconjugation schemes (*16*) (Supporting Information Figure S1). Heterobifunctional linker sulfo-lc-SPDP (Pierce) was added to the QD solution with 100 sulfo-lc-SPDP per QD. The pyridine disulfide thiol group was reduced using dithiothreitol (DTT, Fluka) and the solution was purified with a desalting column (NAP-5, Amersham GE Health Care) and ultrafiltration in PBS.

Functional Group Titration. The number of functional thiol groups per QD was estimated from the absorbance of the QDs and a conjugated organic dye. Fluorescein-5-maleimide was added to the QD solution at a 40:1 fluorescein/QD ratio, and the QDs were purified with a desalting column and ultrafiltration in PBS. The absorbance of the purified QD-dye conjugates were compared to the absorbance of QD only and dye only solutions of known concentrations, and a ratio of dye per QD was calculated (Supporting Information Figure S2B). This ratio provides an estimate for the number of thiol groups per QD. As shown in Supporting Information Figure S2C, the number

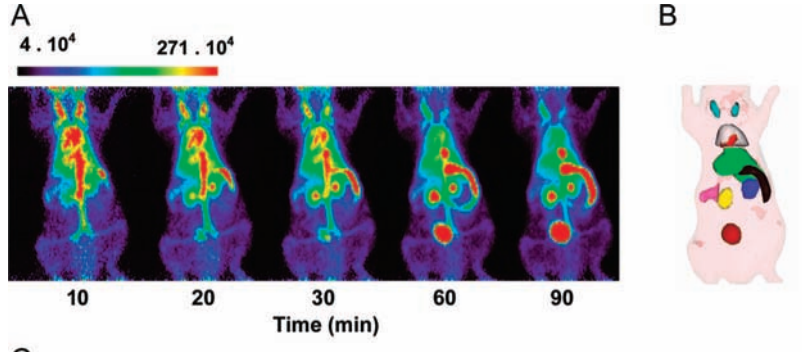

C

Time (min)	Heart	Duodenum	Liver	Kidneys	Spleen	Bladder	Lung
0-1	19.1 ± 2.0	3.9 ± 1.4	10.4 ± 1.1	6.4 ± 2.7	4.4 ± 0.4	0.8 ± 0.4	12.8 ± 1.0
1-2	18.4 ± 2.1	4.1 ± 1.3	10.5 ± 1.0	6.7 ± 2.8	4.7 ± 0.7	0.9 ± 0.1	12.4 ± 1.3
4-5	17.3 ± 2.2	5.0 ± 1.0	10.7 ± 0.9	7.4 ± 2.8	5.2 ± 0.8	2.2 ± 2.4	11.7 ± 1.4
13-15	15.3 ± 1.9	7.3 ± 0.7	10.5 ± 1.1	6.5 ± 3.2	6.0 ± 0.6	7.0 ± 11.2	10.4 ± 1.0
15-20	14.9 ± 1.8	7.9 ± 0.8	10.4 ± 1.0	6.7 ± 3.3	6.0 ± 0.7	8.5 ± 13.1	10.2 ± 1.0
30-40	13.0 ± 1.2	10.2 ± 1.8	10.2 ± 0.9	6.6 ± 3.7	6.2 ± 0.5	15.2 ± 20.6	9.1 ± 0.7
50-60	11.5 ± 0.5	12.3 ± 2.1	10.0 ± 0.8	6.6 ± 2.9	6.0 ± 0.8	29.4 ± 7.2	8.0 ± 0.2
60-75	10.7 ± 0.3	13.3 ± 2.4	9.8 ± 0.7	6.9 ± 3.2	5.8 ± 0.9	34.2 ± 7.0	7.5 ± 0.1
75-90	10.0 ± 0.2	13.7 ± 3.2	9.6 ± 0.7	6.8 ± 3.8	5.6 ± 0.8	37.8 ± 11.2	7.0 ± 0.1

Figure 1. *In vivo* imaging of [^{18}F]-QDs with PET. (A) Whole-body PET projection images acquired after intravenous injection of 200 μCi (7.4 MBq, 1 nmol) of [^{18F}]-QDs, in a nude mouse. Each image corresponds to a 10 min acquisition time interval ending at the indicated time. (B) 3D reconstruction of mouse body with the ROI of organs that were used for PET data quantification: Heart in red, lungs in gray, liver in green, spleen in pink, duodenum in black, left kidney in yellow, right kidney in blue, bladder in brown. (C) Biodistribution of [^{18F}]-QDs (%ID/g) obtained by semiautomatic quantification of PET data. Mean ± SD of three independent experiments.

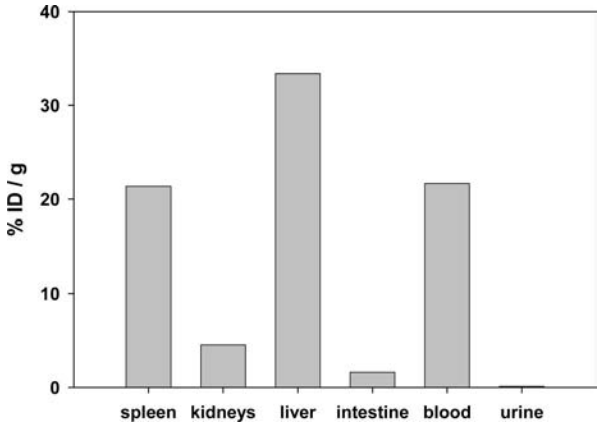

Figure 2. Elemental analysis of dissected organs. Cadmium amount measured in organs dissected 90 min postinjection. Measurements were made by inductively coupled plasma-mass spectrometry (ICP-MS).

of available thiol groups per QD is proportional to the initial percentage of DSPE-PEG2000-NH_2 phospholipids used for encapsulation. This linear dependence corresponds to ~110 phospholipids per QD micelle, consistent with a measured aggregation number of ~75 for empty DPPE-PEG2000 micelles (*17*). This allows easy control on the number of conjugated molecules per QD simply by varying the composition of the initial encapsulation solution.

Fluorine-18-Labeling of QDs. A maleimido [^{18}F]reagent, coded [^{18}F]FPyME (1-[3-(2-fluoropyridin-3-yloxy)propyl]pyrrole-2,5-dione) (*18*), was recently developed for the fluorine-18-labeling of peptides and proteins. In this reagent, the pyridinyl moiety carries the radioactive fluorine which can be efficiently incorporated *via* a nucleophilic *hetero*aromatic substitution, and the maleimido function ensures that the efficient alkylation of a sulfhydryl function borne by the macromolecules. QDs were fluorine-18-labeled using [^{18}F]FPyME, which represents the first labeling of this class of nanoobjets with such a short-lived radioactive isotope. 740−1850 MBq (20−50 mCi) of [^{18}F]-QDs (SRA: 370−740 GBq/μmol @ EOB), ready-to-use (555−1110 MBq/mL in aq. 0.9% NaCl), could be obtained starting from 37 GBq of cyclotron-produced [^{18}F]fluoride in 145 min of radiosynthesis (automation in place on a Zymate XP (Zymark) robotic system).

Step 1. Synthesis of [3-(3-*tert*-butoxycarbonylamino-propoxy)-pyridin-2-yl]-trimethyl-ammonium trifluoromethanesulfonate as precursor for fluorine-18-labeling. 3-(3-*tert*-Butoxycarbonylaminopropoxy)-pyridin-2-yl]-trimethylammonium trifluoromethanesulfonate was synthesized in two steps from commercially available (3-hydroxypropyl)-carbamic acid *tert*-butyl ester and 2-dimethylamino-3-hydroxypyridine as previously described (*18*). ^{1}H NMR (CD_2Cl_2, 298K): δ 8.10 (bd, J = 3.3 Hz, 1H); 7.66 (d, J = 8.1 Hz, 1H); 7.60 (dd, J = 6.1 and 4.2 Hz, 1H); 4.31 (t, J = 6.3 Hz, 2H); 3.71 (s, 9H); 3.31 (q, J = 6.3 Hz, 2H); 2.12 (q^5, J = 6.3 Hz, 2H); 1.38 (s, 9H).^{13}C NMR (CD_2Cl_2, 298 K): δ 156.6 [C]; 147.7 [C]; 142.6 [C]; 139.0 [CH]; 129.0 [CH]; 124.6 [CH]; 121.2 [q, J = 319 Hz, CF_3]; 79.3 [C]; 68.1 [CH_2]; 54.8 [3 × CH_3]; 37.5 [CH_2]; 30.0 [CH_2]; 28.4 [3 × CH_3].

Step 2. Radiosynthesis of 1-[3-(2-[^{18}F]fluoropyridin-3-yloxy)-propyl]pyrrole-2,5-dione as fluorine-18-labeled reagent. 1-[3-(2-[^{18}F]-Fluoropyridin-3-yloxy)propyl]pyrrole-2,5-dione ([^{18}F]FPyME, HPLC-purified) was prepared from [3-(3-*tert*-butoxycarbonylamino-propoxy)-pyridin-2-yl]-trimethylammonium trifluoromethanesulfonate according to slightly modified published procedure (*18*) in 17−20% non-decay-corrected yield (based on starting [^{18}F]fluoride) using a three-step radiochemical pathway in 110 min.

Step 3. Conjugation of QDs with 1-[3-(2-[^{18}F]fluoropyridin-3-yloxy)propyl]pyrrole-2,5-dione. [^{18}F]-QDs were prepared as following: To 100 μL of DMSO containing HPLC-purified [^{18}F]FPyME (freed from HPLC-solvents by concentration to dryness at 65−75 °C under a gentle nitrogen stream) was added ca. 4.75−6.25 nmol of QDs dissolved in PBS (0.1 M, pH 8.0, 900 μL). The reaction mixture was gently vortexed for 15 min and then purified by gel filtration on a NAP-10 G25 Sephadex cartridge (Amersham Pharmacia Biotech). The labeled conjugated [^{18}F]-QDs was eluted in 1.5 mL of aq. 0.9% NaCl according to manufacturer's instructions.

PET Imaging. After i.v. injection of the [^{18}F]-QDs in athymic nude mice (25−30 g body weight) under isoflurane anesthesia, dynamic PET images were acquired in 3D mode in a small animal dedicated PET scanner (Siemens-Concorde Microsystems Focus 220) continuously during 90 min. The time−activity curves of [^{18}F]-QDs in the mouse organs were calculated from regions of interest placed at the center of the organs delineated by a semiautomatic segmentation method (*19*).

Metabolism Analysis. 200 μL of blood were collected from 30 g nude mice at 1 and 3 h after i.v. injection of 37 × 10^6 Bq of [^{18}F]-QDs. Blood samples were centrifuged at 3000 rpm for 5 min at 4 °C. Plasma was filtrated on a Microcon YM-10 tube (Millipore). Radioactivity from the filtrate and retentate recovery were measured by a beta counter (Cobra II Auto gamma, Packard Bioscience Company) to quantify [^{18}F]-QDs degradation. Urine was directly filtrated on a Microcon tube.

Elemental Analysis of Dissected Organs. Liver, spleen, kidneys, and intestine were dissected and blood and urine samples were taken 90 min postinjection. Samples were weighted, then diluted in 2−10 mL concentrated sulfuric acid and heated at 60 °C for 4 h for complete dissolution. Cadmium doses in each sample were then measured by ICP-MS at the Service Central d'Analyse du CNRS, Vernaison, France.

***In Vivo* Fibered Confocal Fluorescence Microscopy.** The CellVizio(R) 488, from Mauna Kea Technologies (MKT), France, consists in a flexible submillimetric probe containing *ca.* 30 000 optical fibers that carry light from a continuous laser source at 488 nm to the living tissue. Fluorescence emitted after excitation of the QDs present in the tissue is sent back to the apparatus where a dedicated set of algorithms reconstructs images in real time at a rate of acquisition of 12 frames per second. In the experiments reported here, we used a MiniO/30 probe (lateral resolution 1.8 μm, axial resolution 5 μm at 37 μm) over a field of view of 175 μm × 125 μm, corresponding in that case to 12218 fibers only. After injection of 5 nanomoles of QDs in athymic nude mice (25−30 g body weight) under isoflurane anesthesia, microsurgery in the abdominal part was performed in order to access the liver and the spleen with the probe. Both organs were scanned regularly at selected time intervals.

QD Cellular Uptake Quantification from Fibered Confocal Fluorescence. Using the data acquisition software *ICviewer* (MKT, France) and *Image J*, we constructed fluorescence intensity histograms for 30 independent pictures acquired from film scans of the liver at selected time intervals. In the first films acquired immediately after QDs administration (i.e., at a time when tissue fluorescence corresponds to the QDs present in the blood pool), values never exceeded 220 fluorescent CellVizio(R) arbitrary units (AU). Choosing this value as a threshold, we quantified the cellular uptake of QDs in the liver identifying pixels above this threshold with QDs captured by cells.

***Ex Vivo* Fluorescence Microscopy.** For microscopic analyses, tissues were recovered 90 min after QDs injection, fixed overnight in 4% paraformaldehyde, incubated overnight in 20% sucrose, snap frozen in cold isopentane, and sectioned at a thickness of 5 μm. Slides were mounted with Prolong antifade reagent with DAPI (Invitrogen). Micrographs were obtained with a wide-field fluorescence microscope (Provis AX70, Olympus) equipped with the excitation filter BP 330−385 nm, the dichroic

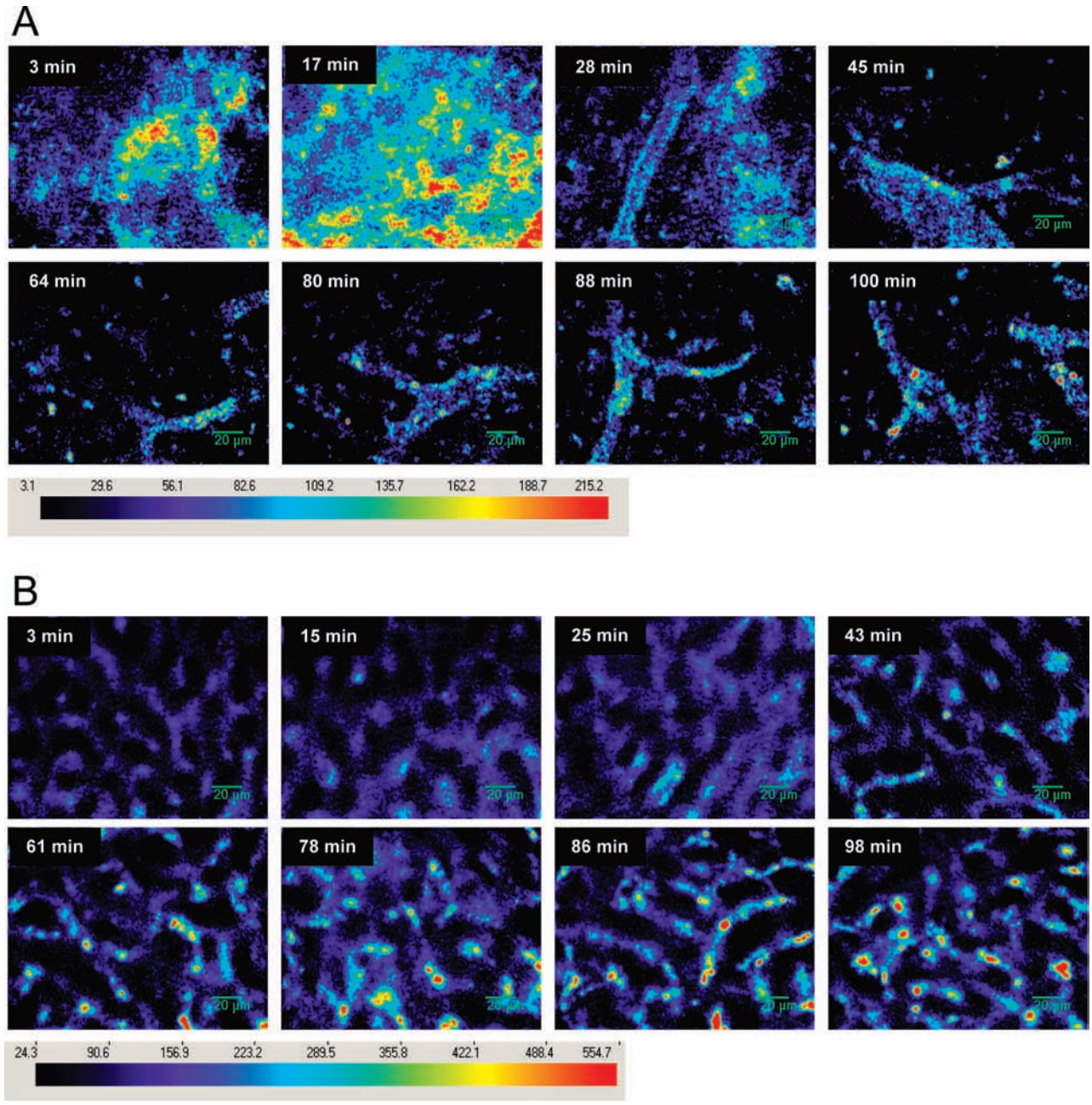

Figure 3. *In vivo* fluorescence imaging of QDs. (A) Representative *in vivo* fluorescence images of the spleen at the indicated times postinjection using the fibered confocal microscope. (B) Same as A in the liver.

mirror DM 400 nm, the barrier filter BA420 nm, and a digital color camera.

***Ex Vivo* Fluorescence Confocal Microscopy.** Tissue sections were processed as above and observed in a Leica confocal microscope SP2. 3D rendering was obtained with the *ImageJ* plugin VolumeJ from a Z-stack captured with the Leica confocal microscope SP2.

RESULTS

Core/shell CdSe/CdZnS nanocrystals were synthesized using standard organometallic procedures and encapsulated into poly(ethylene glycol) (PEG)-phospholipid micelles. The resulting nanoparticles exhibit small hydrodynamic sizes and high stability. While PEG moieties efficiently envelop the nanoparticles and limit nonspecific interactions with their environment, introduction of functionalized phospholipids bearing chemical functional groups allows fine-tuning of the QD surface chemistry and easy covalent coupling to a wide variety of molecules (*7, 15*) with a controlled molecule-per-QD ratio (see Supporting Information Figures S1−S2). Here, we conjugated PEG-phospholipid QD micelles displaying thiol groups with [^{18}F]F-PyME, a fluorine-18-containing (positron-emitter, half-life = 109.8 min) maleimide reagent (*18, 20*) (Scheme 1). Efficient coupling of [^{18}F]FPyME with the nanoparticle was confirmed by the high radioactivity observed for the purified QDs (37−75 $\times$ 10^7 Bq/QD nmol). The coupling was stable *ex vivo*, as no radioactive elements smaller than 10 kDa could be separated from the QDs by membrane separation, even six hours after coupling. The biodistribution of the [^{18}F]-QDs was then followed *in vivo* in mice using both PET and CellVizio(R) imaging, and *ex vivo* using fluorescence microscopy.

Dynamic PET imaging was recorded in a small animal dedicated PET scanner up to 90 min after i.v. injection of 1 nanomole of [^{18}F]-QDs (Figure 1). [^{18}F]-QDs were rapidly taken

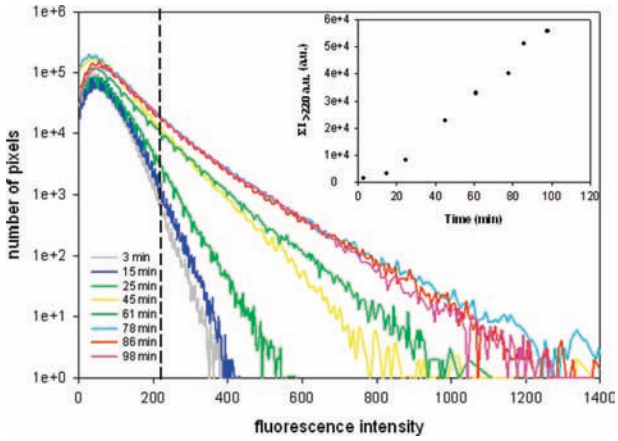

Figure 4. Quantification at the cellular scale of *in vivo* biodistribution of QDs in the liver. Distribution of the fluorescence intensities (a.u.) measured in the liver by the fibered confocal microscope in series of images corresponding to different time postinjection. QDs in the blood are predominantly detected in pixels with fluorescence intensities >220 au (dotted line). Inset: The kinetics of QD cellular uptake is estimated by plotting the sum of fluorescence intensity values above this threshold as a function of time.

up in highly vascularized organs such as the heart, the lungs, the kidneys, the liver, and the spleen. The labeled QDs were found essentially stable in plasma (less than 3% degradation three hours postinjection). The small amount of fluorine-18-labeled degradation products were readily excreted through the kidney (87% of the radioactivity recovered in urine 90 min postinjection corresponded to >10 kDa products). Taken together, these results indicate that the radioactivity concentrations measured in organs other than kidney and bladder reflect predominantly intact [^{18}F]-QDs.

Washout from the heart and lungs was slow; however, *ex vivo* fluorescence microscopy of the lungs and heart showed the absence of uptake of QDs in these organs (see Supporting Information Figure S3). This indicates that the PET signal in these two organs is essentially contributed by QDs from the blood pool. Therefore, the cardiac time−activity curve was used to calculate blood pharmacokinetics parameters of the [^{18}F]-QDs (Supporting Information Table 1). QDs exhibit a long circulation time in blood with a $T_{1/2}$ of approximately 2 h. In the liver and the spleen, radioactivity concentrations at 90 min postinjection were, respectively, 10% and 6% of the injected dose per gram tissue (Figure 1C). This major difference with polymer-coated QDs that have been shown to accumulate very rapidly at high levels in the liver (*11–13*) (ca. 30−50%ID/g, 10 min after injection), is likely a consequence of the PEG coating of our PEG phospholipid micelle QDs. Accordingly, significant amounts (ca. 10%ID/g) of QDs were detected in the blood 90 min after injection, confirming the long circulation time of PEG phospholipid micelle QDs in the bloodstream, before getting cleared from the circulation by the reticulo-endothelial system.

The biodistribution data obtained with PET were correlated by dosing cadmium using elemental analysis at 90 min postinjection. Major organs such as liver, spleen, kidney, and intestine, and blood and urine were dissolved in concentrated sulfuric acid and analyzed by ICP-MS. Concentration measurements confirmed the absence of cadmium in the bladder, urine, or intestine 90 min after injection, whereas a high concentration of cadmium could be measured in the blood, liver, and spleen (see Figure 2). These results are consistent with radioactive metabolite analysis indicating that the radioactivity detected in the urinary tract corresponded to degradation products and confirm the biodistribution of the [^{18}F]-conjugated QDs measured by PET in the other organs.

In vivo fiber confocal fluorescence imaging was used to further explore the QD biodistribution at the cellular level in the organs showing prolonged high levels of uptake, i.e., the liver and the spleen. In the spleen, QD distribution was initially very heterogeneous and particularly elevated in regions that correspond to leaky venous sinuses of the red pulp. After ~25 min, the QDs were progressively washed from these zones while uptake by macrophages sheathing small capillaries could be observed (Figure 3A). In the liver, fluorescence originated predominantly from the blood pool in agreement with PET data. A progressive uptake by cells located inside the hepatic tissue could be observed 30 min after injection (Figure 3B). These individual cells are uniformly distributed around the centrolobular vessels, a distribution suggestive of Kuppfer cells, the tissular macrophages lining the hepatic sinusoids. High resolution confocal microscopy of *ex vivo* liver sections demonstrated that QDs were internalized in these cells 90 min postinjection (Supporting Information Figures S3F and S3G). The kinetics of QD uptake by Kupffer cells was quantified and showed a constant increase between 15 and 90 min, consistent with a slow reticulo-endothelial uptake (Figure 4 and Supporting Information video).

DISCUSSION

We have designed a novel multimodal imaging probe based on a [^{18}F]-labeled QD phospholipid micelle. This QD conjugate provides a strong radioactive signal for high-sensitivity PET imaging, along with bright and stable fluorescence for *in vivo* and *ex vivo* cellular imaging. We have demonstrated the potential of this multimodal imaging probe by investigating the dynamics of the *in vivo* biodistribution of nontargeted [^{18}F]-QDs. These QD micelles do not show renal clearance, which, as suggested by the recent studies of Choi et al. (*21*), could be the result of their large diameter (>20 nm). Interestingly, these phospholipid micelle QDs exhibited prolonged circulation in the blood, with a $T_{1/2}$ on the order of 2 h. This relatively long circulation time is due to a complete coverage of the nanoparticle with PEG. In comparison, QDs coated with amphiphilic polymers containing PEG chains of similar molecular weights exhibited much faster uptake by the reticuloendothelial system, probably due to its different surface chemistry. We assume that the capacity of our QDs to evade opsonization and capture by reticuloendothelial sytem for a relatively long period of time could allow more efficient delivery to specific tissular and/or endothelial targets. On the other hand, long circulating QDs could provide higher background, and more specific studies on targeted QDs are required to optimize both delivery efficiency and signal-to-background ratios.

In vivo targeting of QDs or nanoparticles has been previously demonstrated, e.g., using peptides or antibodies (*9, 10*). In this respect, the versatility of phospholipid micelle surface chemistry is an advantage, as different functionalized phospholipids are readily commercially available. Therefore, micelles with mixed surface composition can easily be obtained without *de novo* synthesis, in contrast to polymer encapsulation. We have shown that tuning the composition of the phospholipid micelle can further provide a variety of functional end groups for easy covalent conjugation of QDs with multiple chemicals and biomolecules with controlled QD:molecule valency (*7, 15*). In that respect, it is noteworthy that our radiolabeling method does not preclude further conjugation of [^{18}F]-QDs to targeting moieties. Finally, we note that phospholipid micelle encapsulation is a general principle that has been demonstrated with various nanoparticles such as gold or iron oxide particles (see, e.g., refs *22, 23*). As a consequence, conjugation techniques using phospholipid micelles and optimization of the micelle surface chemistry for *in vivo* imaging could benefit a wide array of biomedical applications.

In conclusion, this work represents the first report of a fluorine-18-labeling and quantitative whole body imaging study of PEG-phospholipid QD micelles with PET. The results differ noticeably from previous reports on *in vivo* biodistribution using QDs (*11–13*, *24*). The results presented here show that these phospholipids QD micelles are well distributed throughout the body and exhibit long circulation times and, as expected for nanoparticles, slow uptake by the reticulo-endothelial system. These properties could stand in favor of the further development of QDs for some *in vivo* imaging applications. Furthermore, bimodal [^{18}F]-QDs are appealing nanoprobes because they make the best of two *in vivo* molecular imaging systems: PET imaging for whole body imaging and fluorescence imaging for subcellular localization, and therefore allow multiscale imaging of biomarkers of interest.

ACKNOWLEDGMENT

This work was supported by grants from the European Molecular Imaging Laboratory (EMIL) network (EU contract LSH-2004-503569), l'Agence Nationale pour la Recherche (ANR TechSan Dot-Imager and ANR Emergence ARTIC), and the Association pour la Recherche sur le Cancer (3527) and ANR-INCA programme FLUOR-C. We are grateful to Olivier Carion for discussions, Yohan Fontyn for PET experiments, Renaud Maroy for help with Semi Automatic quantification of PET data, Susanne Bolte and Marie-Noelle Soler for help in confocal microscopy at the plate-forme Imagerie et Biologie Cellulaire of Gif sur Yvette and to Arnaud Le Nevez, Tom Vercauteren and Aymeric Perchant from Mauna Kea Technologies for technical assistance with the CellVizio(R).

Supporting Information Available: The pharmacokinetics parameters of QDs, their photophysical properties and functional group titration, a chemical scheme of phospholipid QD micelle conjugation with fluorescein and fluorine-18, *ex vivo* fluorescence imaging of QD in different organs by histology, and video showing *in vivo* imaging of QD uptake in the Kuppfer cells. This material is available free of charge via the Internet at http://pubs.acs.org.

Note Added after ASAP Publication: This paper published ASAP on August 28, 2008 with errors in Figure 1 and in the DISCUSSION and the ACKNOWLEDGMENT sections. The correct version was published on September 4, 2008.

LITERATURE CITED

(1) Efros, A. L., and Rosen, M. (2000) The electronic structure of semiconductor nanocrystals. *Annu. Rev. Mater. Sci. 30*, 475–521.

(2) Murray, C. B., Kagan, C. R., and Bawendi, M. G. (2000) Synthesis and characterization of monodisperse nanocrystals and close-packed nanocrystal assemblies. *Annu. Rev. Mater. Sci. 30*, 545–610.

(3) Medintz, I. L., Uyeda, H. T., Goldman, E. R., and Mattoussi, H. (2005) Quantum dot bioconjugates for imaging, labelling and sensing. *Nat. Mater. 4*, 435–446.

(4) Michalet, X., Pinaud, F. F., Bentolila, L. A., Tsay, J. M., Doose, S., Li, J. J., Sundaresan, G., Wu, A. M., Gambhir, S. S., and Weiss, S. (2005) Quantum dots for live cells, in vivo imaging, and diagnostics. *Science 307*, 538–544.

(5) Larson, D. R., Zipfel, W. R., Williams, R. M., Clark, S. W., Bruchez, M. P., Wise, F. W., and Webb, W. W. (2003) Water-soluble quantum dots for multiphoton fluorescence imaging in vivo. *Science 300*, 1434–1436.

(6) Kim, S., Lim, Y. T., Soltesz, E. G., De Grand, A. M., Lee, J., Nakayama, A., Parker, J. A., Mihaljevic, T., Laurence, R. G., Dor, D. M., Cohn, L. H., Bawendi, M. G., and Frangioni, J. V. (2004) Near-infrared fluorescent type II quantum dots for sentinel lymph node mapping. *Nat. Biotechnol. 22*, 93–97.

(7) Dubertret, B., Skourides, P., Norris, D. J., Noireaux, V., Brivanlou, A. H., and Libchaber, A. (2002) In vivo imaging of quantum dots encapsulated in phospholipid micelles. *Science 298*, 1759–1762.

(8) Voura, E. B., Jaiswal, J. K., Mattoussi, H., and Simon, S. M. (2004) Tracking metastatic tumor cell extravasation with quantum dot nanocrystals and fluorescence emission-scanning microscopy. *Nat. Med. 10*, 993–998.

(9) Akerman, M. E., Chan, W. C. W., Laakkonen, P., Bhatia, S. N., and Ruoslahti, E. (2002) Nanocrystal targeting in vivo. *Proc. Nat. Acad. Sci. U.S.A. 99*, 12617–12621.

(10) Gao, X. H., Cui, Y. Y., Levenson, R. M., Chung, L. W. K., and Nie, S. M. (2004) In vivo cancer targeting and imaging with semiconductor quantum dots. *Nat. Biotechnol. 22*, 969–976.

(11) Schipper, M. L., Cheng, Z., Lee, S.-W., A., B. L., Iyer, G., Rao, J., Chen, X., Wu, A. M., Weiss, S., and Gambhir, S. S. (2007) microPET-based biodistribution of quantum dots in living mice, *J. Nucl. Med.*

(12) Ballou, B., Lagerholm, B. C., Ernst, L. A., Bruchez, M. P., and Waggoner, A. S. (2004) Noninvasive imaging of quantum dots in mice. *Bioconjugate Chem. 15*, 79–86.

(13) Morgan, N. Y., English, S., Chen, W., Chernomordik, V., Russo, A., Smith, P. D., and Gandjbakhche, A. (2005) Real time in vivo non-invasive optical imaging using near-infrared fluorescent quantum dots. *Acad. Radiol. 12*, 313–323.

(14) Qu, L. H., Peng, Z. A., and Peng, X. G. (2001) Alternative routes toward high quality CdSe nanocrystals. *Nano Lett. 1*, 333–337.

(15) Carion, O., Mahler, B., Pons, T., and Dubertret, B. (2007) Synthesis, encapsulation, purification and coupling of single quantum dots in phospholipid micelles for their use in in vivo imaging. *Nat. Prot. 2*, 2383–2390.

(16) Hermanson, G. T. (1996) *Bioconjugate Techniques*, Academic Press, London,

(17) Johnsson, M., Hansson, P., and Edwards, K. (2001) Spherical micelles and other self-assembled structures in dilute aqueous mixtures of poly(ethylene glycol) lipids. *J. Phys. Chem. B 105*, 8420–8430.

(18) de Bruin, B., Kuhnast, B., Hinnen, F., Yaouancq, L., Amessou, M., Johannes, L., Samson, A., Boisgard, R., Tavitian, B., and Dolle, F. (2005) 1-[3-(2-[^{18}F]fluoropyridin-3-yloxy)propyl]pyrrole-2,5-dione: design, synthesis, and radiosynthesis of a new [^{18}F]fluoropyridine-based maleimide reagent for the labeling of peptides and proteins. *Bioconjugate Chem. 16*, 406–420.

(19) Maroy, R., Boisgard, R., Comtat, C., Frouin, V., Cathier, P., Duchesnay, E., Dolle, F., Nielsen, P. E., Trebossen, R., and Tavitian, B. (2008) Segmentation of rodent whole-body dynamic PET images: an unsupervised method based on voxel dynamics. *IEEE Trans. Med. Imaging 27*, 342–354.

(20) Dollé, F. (2004) Preparation of [^{18}F] labeled maleimides, their use for marking macromolecules for medical imaging. PCT Int. Appl. WO2004002984 (58 pp).

(21) Choi, H. S., Liu, W., Misra, P., Tanaka, E., Zimmer, J. P., Ipe, B. I., Bawendi, M. G., and Frangioni, J. V. (2007) Renal clearance of quantum dots. *Nat. Biotechnol. 25*, 1165–1170.

(22) Fan, H. Y., Yang, K., Boye, D. M., Sigmon, T., Malloy, K. J., Xu, H. F., Lopez, G. P., and Brinker, C. J. (2004) Self-assembly of ordered, robust, three-dimensional gold nanocrystal/silica arrays. *Science 304*, 567–571.

(23) Nitin, N., LaConte, L. E. W., Zurkiya, O., Hu, X., and Bao, G. (2004) Functionalization and peptide-based delivery of magnetic nanoparticles as an intracellular MRI contrast agent. *J. Biol. Inorg. Chem. 9*, 706–712.

(24) Hardman, R. (2006) A toxicologic review of quantum dots: toxicity depends on physicochemical and environmental factors. *Environ. Health Perspect. 114*, 165–172.

BC800179J

SUPPORTING INFORMATION

Fluorine 18-labeled phospholipid quantum dot micelles for *in vivo* multimodal imaging from whole body to cellular scales.

Frédéric Ducongé †‡, Thomas Pons §, Carine Pestourie †‡, Laurence Hérin †‡, Benoît Thézé †‡, Karine Gombert †‡, Benoit Mahler §, Françoise Hinnen †, Bertrand Kuhnast †, Frédéric Dollé †, Benoît Dubertret § and Bertrand Tavitian †‡*.*

† CEA, DSV, I^2BM, SHFJ, Laboratoire d'Imagerie Moléculaire Expérimentale, 4 place du général Leclerc, 91401 Orsay Cedex, France.

‡ Inserm U803, 4 place du général Leclerc, 91401 Orsay Cedex, France.

§ Laboratoire Photons et Matière, CNRS UPRA0005, ESPCI, 10 rue Vauquelin, 75005 Paris, France.

CORRESPONDING AUTHORS:

*Benoît Dubertret
+33 1 40 79 45 92
benoit.dubertret@espci.fr

and

*Bertrand Tavitian
+33 1 69 86 77 66
bertrand.tavitian@cea.fr.

RUNNING TITLE: Radioactive Quantum Dots for *in vivo* multi-scale imaging.

LIST OF CONTENTS **Pages**

Table 1: Pharmacokinetic parameters of QDs. **3**

Figure S2: QD photophysical properties and functional group titration. **4**

Figure S1: Phospholipid QD micelle conjugation with fluorescein and fluorine-18. **5**

Figure S3: *Ex vivo* fluorescence imaging of QD biodistribution. **6**

Video 1 legend: *In vivo* imaging of QD uptake in the Kuppfer cells. **7**

Injected dose *(10^6 Bq)*	**7.3 ± 0.6**
$AUC_{0\rightarrow\infty}$ *(10^6 Bq $_x$ min/mL)*	**124 ± 41**
Half-life ($T_{1/2}$) *(min)*	**111 ± 28**
Volume of distribution at steady state *(mL)*	**5.8 ± 0.8**
Elimination rate constant *(min^{-1})*	**$1.1\ 10^{-4} \pm 0.3\ 10^{-4}$**
Clearance *(mL/min)*	**$6.2\ 10^{-4} \pm 1.1\ 10^{-4}$**
Mean residence time *(min)*	**159 ± 39**

Table 1: Pharmacokinetic parameters of QDs.

Pharmacokinetic parameters were obtained from the time-activity curves of [^{18}F]-QDs in the heart using a noncompartmental approach and Trapezoid calculation with Kinetica software (Thermo Scientific).

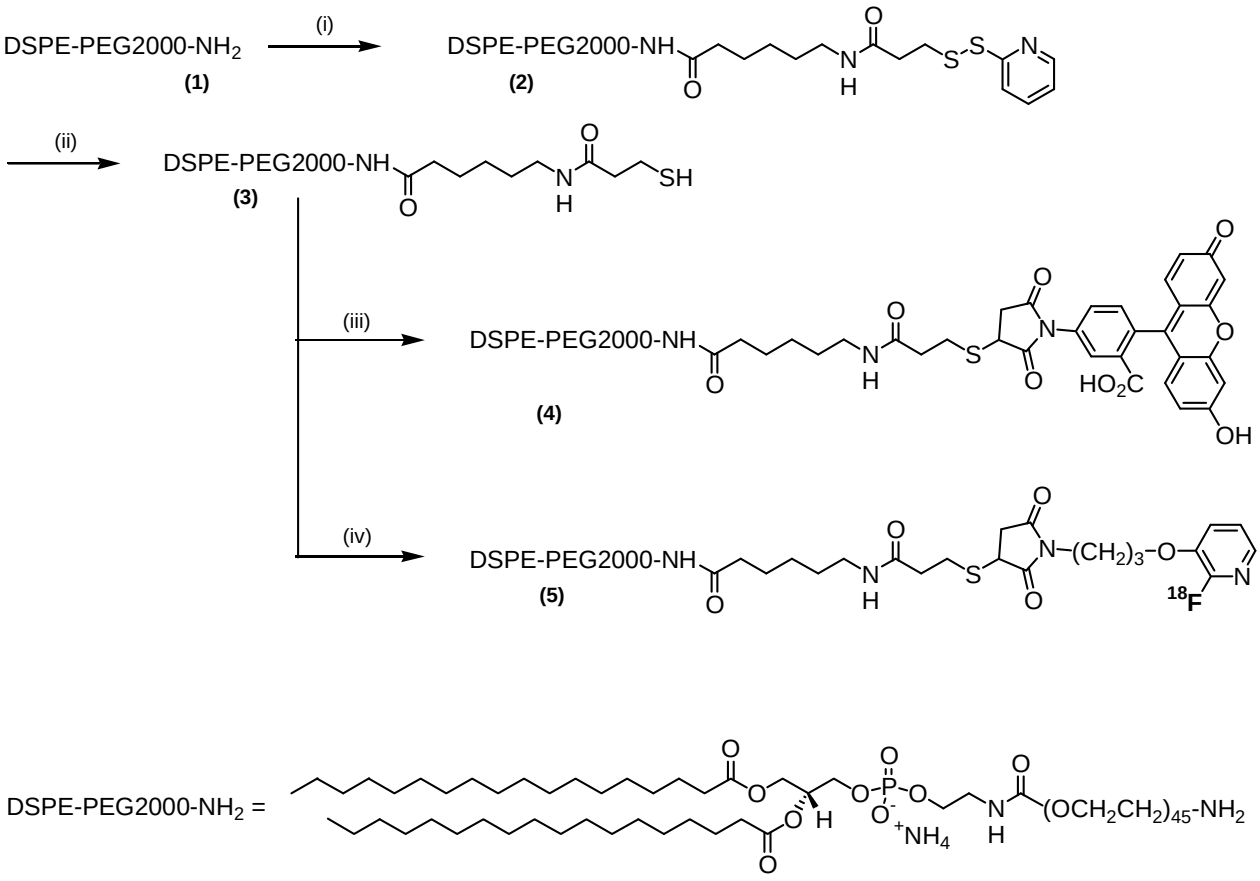

Figure S1: Phospholipid QD micelle conjugation with fluorescein and fluorine-18.

Chemical modification and conjugation of DSPE-PEG(2000)-NH_2 occurs directly on the QD-micelle. (i) sulfo-lc-SPDP; (ii) DTT; (iii) Fluorescein-5-maleimide; (iv) [^{18}F]FPyME.

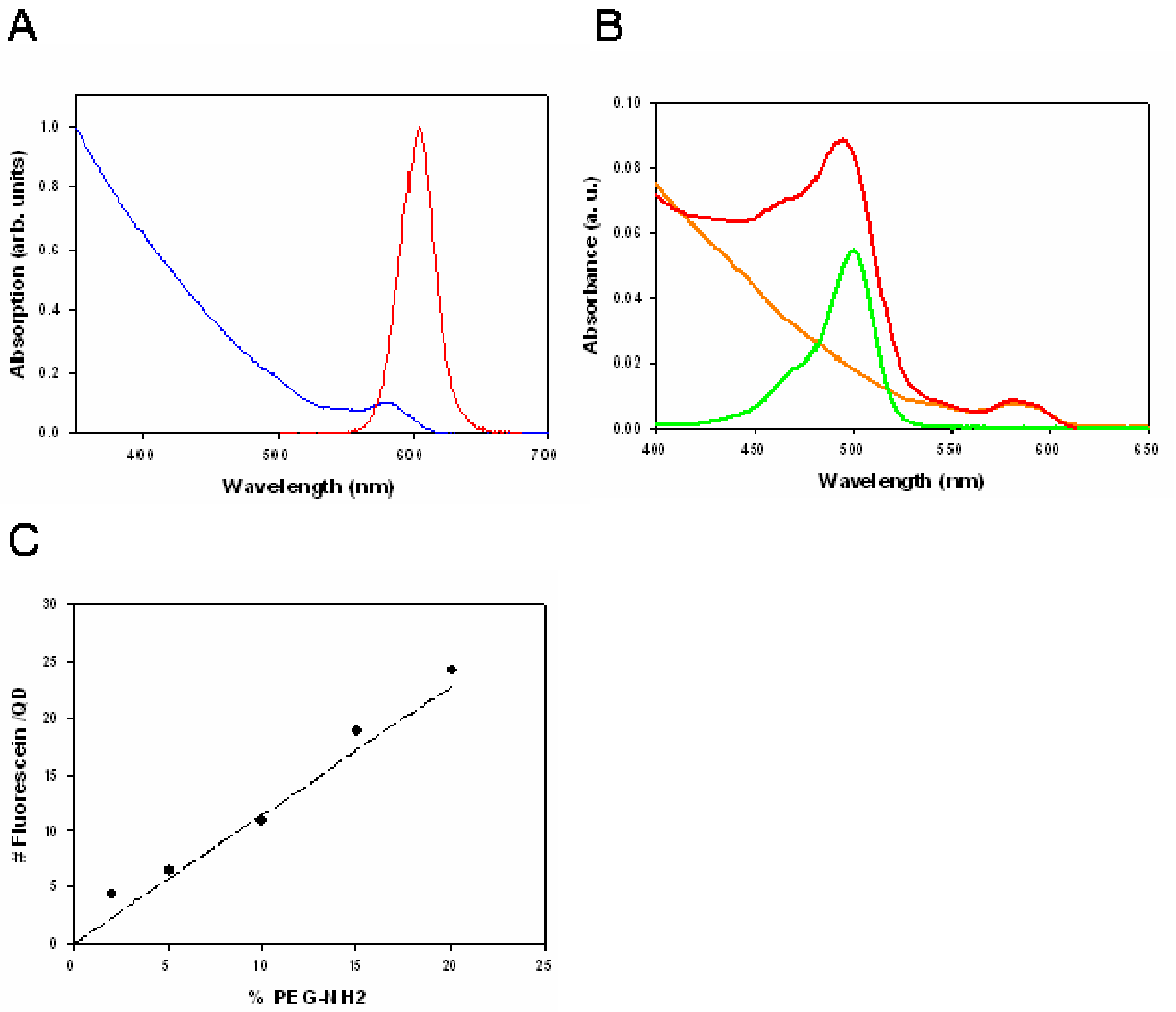

Figure S2: QD photophysical properties and functional group titration.

A: Absorption and photoluminescence spectra of CdSe/CdZnS QDs.

B: Absorption spectra of fluorescein only (green), QD only (orange) and purified QD-fluorescein conjugate (red) solutions.

C: Number of conjugated fluorescein molecules per QD as a function of DSPE-PEG-NH_2 proportion used during encapsulation.

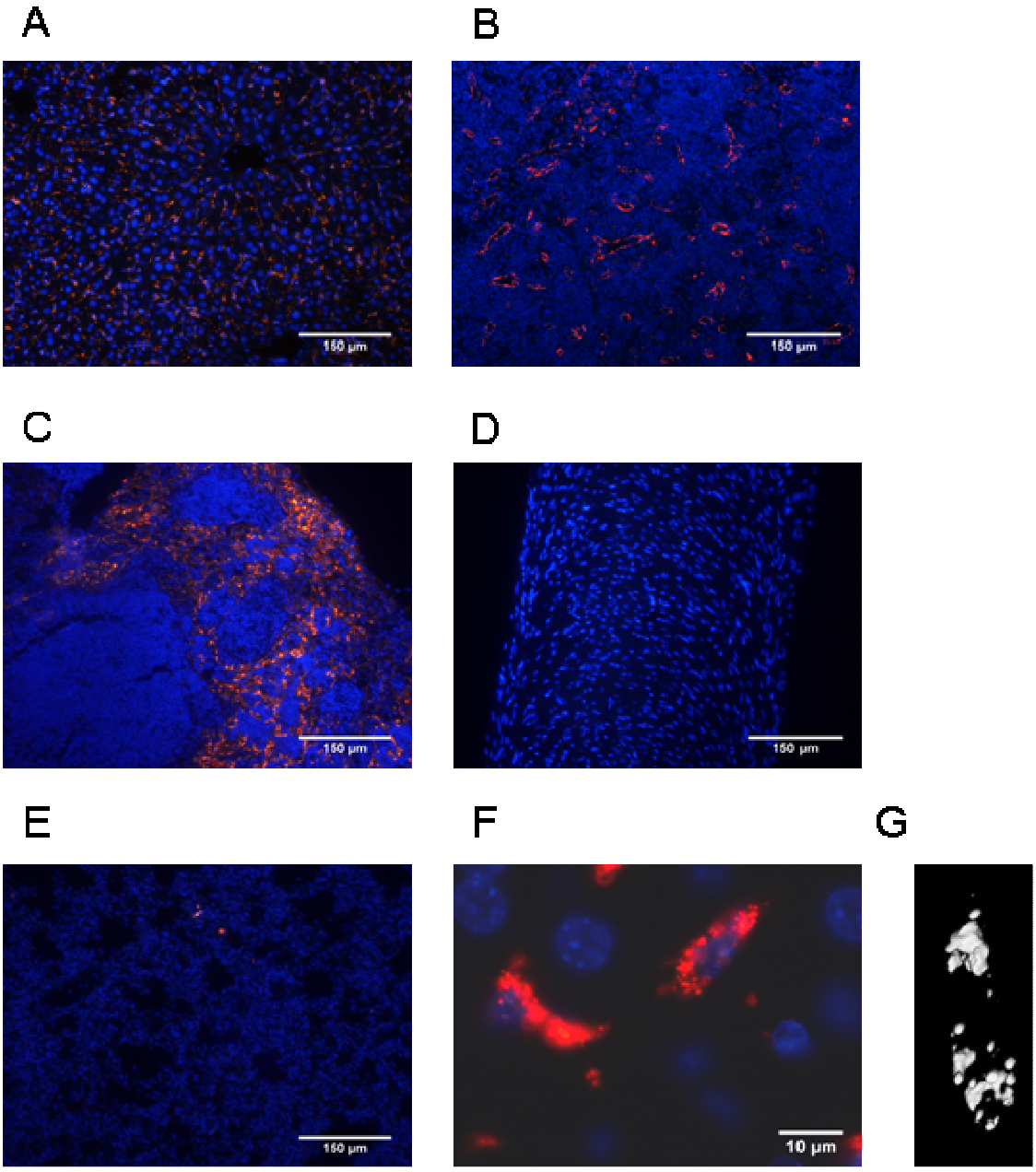

Figure S3: *Ex vivo* fluorescence imaging of QD biodistribution.

Ex vivo fluorescence micrograph of tissues section snap-frozen 90 min after QD administration A and F: liver; B: spleen; C: lymph node; D: heart and E: Lungs. Cell nuclei are stained with DAPI (blue), QDs appear in red. G: 3D rendering of a Z-stack of confocal images of a liver section.

Video 1 legend: *In vivo* imaging of QD uptake in the Kuppfer cells.

In vivo fluorescence imaging of the liver at the indicated times post-injection using the fibered confocal microscope. QDs fluorescence is found predominantly in the blood and never exceeds 220 AU (blue), whereas fluorescence uptake by the Kuppfer cells increases overtime is depicted from green to red.

Rapid and Efficient Production of Radiolabeled Antibody Conjugates Using Vacuum Diafiltration Guided by Mathematical Modeling

Derek W. Bartlett, David Colcher, and Andrew A. Raubitschek*

Division of Cancer Immunotherapeutics & Tumor Immunology, Beckman Research Institute and City of Hope National Medical Center, Duarte, California 91010. Received May 30, 2008; Revised Manuscript Received July 28, 2008

Increasing interest in the use of radiolabeled antibodies for cancer imaging and therapy drives the need for more efficient production of the antibody conjugates. Here, we illustrate a method for rapid and efficient production of radiolabeled antibody conjugates using vacuum diafiltration guided by mathematical modeling. We apply this technique to the production of 1,4,7,10-tetraazacyclododecane-1,4,7,10-tetraacetic acid (DOTA)-conjugated antibodies at the milligram and gram production scale and achieve radiolabeling efficiencies >95% using In-111. Using vacuum diafiltration, antibody−chelate conjugation and purification can be accomplished within the same vessel, and the entire process can be completed in <24 h. Vacuum diafiltration also offers safer and gentler processing conditions by eliminating the need to keep the retentate vessel under positive pressure through applied gas pressure or shear-inducing restriction points in the retentate flow path. Experimental data and mathematical model calculations suggest there exists a weak binding affinity ($\sim 10^4\ M^{-1}$) between the charged chelate molecules (e.g., DOTA) and the antibodies that slows the removal of excess chelate during purification. By analyzing the radiolabeling efficiency as a function of the number of diavolumes, we demonstrate the importance of balancing the removal of free chelate with the introduction of metal contaminants from the diafiltration buffer and also illustrate how to optimize radiolabeling of antibody conjugates under a variety of operating conditions. This methodology is applicable to the production of antibody conjugates in general.

INTRODUCTION

Radiolabeled antibodies have been used for therapy and imaging of cancer for over two decades (*1*). Radioimmunotherapy has been particularly effective in the treatment of hematologic malignancies (lymphomas), evidenced by the two FDA-approved radiolabeled anti-CD20 antibodies, Zevalin and Bexxar (*2*). The use of antibodies to achieve targeted delivery of radiation provides benefits not achievable by monoclonal antibodies or external beam radiation alone. Metal chelators, such as DOTA, can be covalently attached to antibodies and subsequently used to bind radioisotopes (*3, 4*). However, antibody-conjugated chelators can be hampered by slow radiolabeling kinetics and poor radiolabeling efficiencies (*5*). While functionalization of the chelate, as in the conjugation to lysines on a protein, has been shown to slow the metal loading rate and lower the overall thermodynamic stability of the metal complex (*4, 6, 7*), other factors such as metal contamination or unconjugated free chelate also contribute significantly to the low radiolabeling efficiencies.

Several techniques have been proposed to address the issues of metal contamination and removal of unconjugated chelate. Besides minimizing contact with metal containing materials, buffers can be processed with chelating resins such as Chelex 100 to reduce the metal burden (*8*−*12*). Care must be taken when using chelating resins, such as iminodiacetate (IDA), whose metal binding affinity may be orders of magnitude lower than chelators such as DOTA or diethylenetriaminepentaacetic acid (DTPA). If the resin is allowed to equilibrate with a solution containing the chelate (e.g., DOTA−antibody conjugate), then the metal can be thermodynamically driven to bind to DOTA instead of the chelating resin depending on the relative concentrations. Pretreatment of the buffers using a column of the chelating resin can avoid such complications, and previous reports have demonstrated >99% removal of trace metal contaminants by column operation of the Chelex 100 resin (*12*).

Dialysis is a commonly used method for purification because of its ease of scalability and gentle conditions. Each dialysis-based buffer exchange or purification step is time-intensive and can require multiple days depending on the number of buffer changes required. Furthermore, dialysis can require a large amount of buffer volume that can also increase the risk of introducing metal contaminants. Other membrane-based purification strategies, such as ultrafiltration, can offer faster processing times with reduced buffer volumes. Application of ultrafiltration requires convecting the fluid toward the membrane, and the membrane can be designed to retain larger molecules, such as antibodies, while allowing low molecular weight impurities to penetrate through the membrane. If repeated cycles of ultrafiltration are used to remove impurity-containing fluid by replacing the fluid removed with impurity-free fluid, the process is called diafiltration. Rapid changes in antibody concentration resulting from the cycles of ultrafiltration and buffer replacement can negatively impact antibody stability. This problem is avoided by using constant-volume diafiltration, where the impurity-free buffer is added to the retentate at the same rate as the fluid is removed. Previous studies have demonstrated the feasibility of constant-volume diafiltration for the preparation of radiolabeled antibody conjugates (*13, 14*).

Here, we describe the use of a constant-volume, vacuum-driven diafiltration process for the rapid buffer exchange and purification of conjugated antibodies in preparation for radiolabeling. A mathematical model of the diafiltration and radiolabeling steps is used to predict optimum operating conditions and elucidate possible mechanisms to explain experimental observations. We demonstrate the utility of this technique

* Corresponding author. Division of Cancer Immunotherapeutics & Tumor Immunology, Beckman Research Institute, City of Hope, 1500 East Duarte Road, Duarte, CA 91010. Tel: 626-256-4673 × 62451. Fax: 626-301-8817. E-mail: araubitschek@coh.org.

10.1021/bc800223x CCC: $40.75 © 2008 American Chemical Society
Published on Web 08/23/2008

through production of DOTA-conjugated monoclonal antibodies at the milligram and gram production scales. Observed radiolabeling efficiencies with In-111 exceeded 95%, and model calculations are used to specifically illustrate how metal contamination and excess chelate can both contribute to low radiolabeling efficiencies. Using vacuum diafiltration, the entire conjugation and radiolabeling procedure can be accomplished within 24 h. Besides expediting the conjugation and purification process, the use of vacuum diafiltration avoids risks associated with membrane-based processing strategies that employ positive pressure gradients as the driving force. When the retentate vessel is under positive pressure, the potential for catastrophic leakage and loss of material is greater since fluid in the retentate will be driven out under pressure through any leak in the system; such a problem is avoided under vacuum diafiltration since the retentate vessel remains near atmospheric pressure. In certain embodiments of ultrafiltration or diafiltration processes, the positive pressure gradient is created by applying a restriction in the retentate flow path. This restriction creates a region of increased shear stress that can exacerbate protein degradation. Vacuum diafiltration provides more gentle processing conditions, and the stability of the applied vacuum enables strict control of the pressure differential across the membrane for the duration of the diafiltration process. The prevalence of small vacuum pumps or house vacuum systems make vacuum diafiltration widely applicable and easily scalable from the laboratory to clinical production, and we have used this technique for the conjugation of a variety of molecules (e.g., biotin and fluorochromes) with antibodies, thereby making it generally applicable to bioconjugations.

MATERIALS AND METHODS

Proteins. Rituximab (Rituxan), a chimeric monoclonal IgG1 against the CD20 antigen, was purchased from Genentech (South San Francisco, CA). Albuminar-25, a 25% w/w human serum albumin preparation with 0.02 M sodium *N*-acetyl-DL-tryptophan and 0.02 M sodium caprylate, was purchased from Aventis Behring (King of Prussia, PA).

Radioisotope. High-purity indium-111 (indium chloride) was obtained in 0.05 M HCl from Trace LifeSciences (Denton, TX).

Buffers. Dulbecco's phosphate-buffered saline without calcium and magnesium was purchased from Mediatech (21−031-CV, Herndon, VA). Sodium bicarbonate buffer was prepared using sodium bicarbonate (7412, Mallinckrodt Baker, Phillipsburg, NJ) and plasma grade water (W9, Fisher Chemical, Fairlawn, NJ). Ammonium acetate buffer was prepared using ammonium acetate (372331, Aldrich, St. Louis, MO) and plasma grade water (W9, Fisher Chemical). Sodium acetate buffer was prepared using sodium acetate (3462-01, Mallinckrodt Baker, Phillipsburg, NJ) and plasma grade water (W9, Fisher Chemical).

Chelex 100 Trace Metal Removal. Biotechnology grade Chelex 100 chelating resin (Bio-Rad, 100−200 mesh, 143−2832) was used in column mode for trace metal removal from the ammonium acetate buffer. The Chelex 100 resin (100 g) was initially washed with ∼400 mL of 0.1 N NaOH and allowed to stand for 18 h for depyrogenation. Following depyrogenation, the liquid was removed by vacuum filtration, and the resin was rinsed with 500 mL of plasma grade water. Subsequently, the resin was washed with ∼400 mL of 0.1 N HCl followed by ∼750 mL of plasma grade water. The resin was then washed twice with 0.25 M ammonium acetate buffer (pH 7) and poured into a 5-cm diameter XK50 column (GE Healthcare, Chalfont St. Giles, United Kingdom) connected to an AKTA FPLC (GE Healthcare). In the column mode, the resin was further rinsed with ∼600 mL of 0.25 M ammonium acetate buffer (pH 7) such that the measured pH and conductivity of the effluent from the column matched that of the inlet ammonium acetate buffer. The final bed volume of the Chelex 100 resin in the ammonium form was ∼150 mL. Ammonium acetate buffer (0.25 M, pH 7) was pumped through the equilibrated Chelex 100 column at a flow rate of 5 mL/min, and the effluent was collected directly from the outlet of the column into a sterile 2-L Stedim Flexboy Bag (Stedim Biosystems, Aubagne, France).

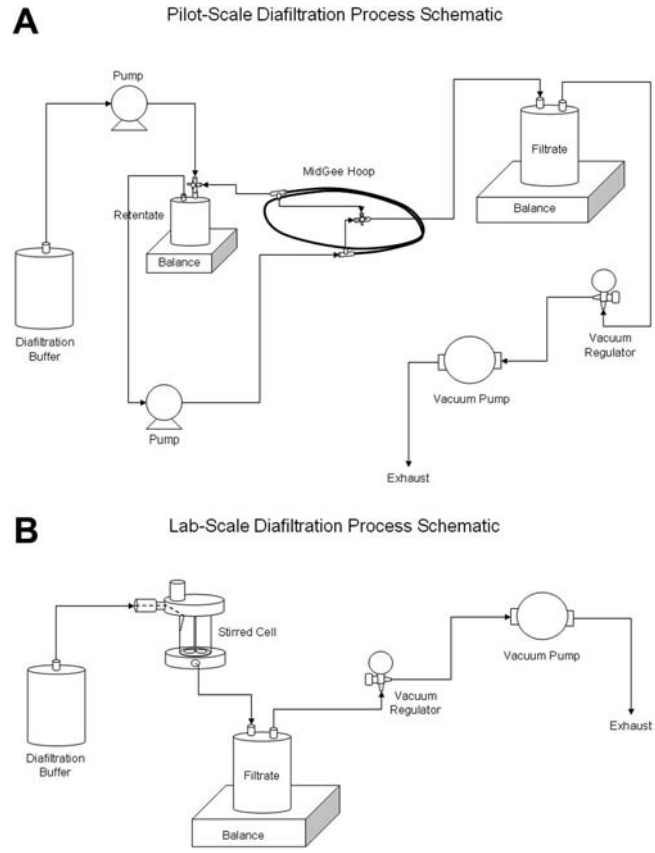

Figure 1. Schematic for vacuum diafiltration at the pilot-scale (A) and laboratory-scale (B).

Pilot-Scale Vacuum Diafiltration. A schematic of the pilot-scale vacuum diafiltration setup is shown in Figure 1A. Vacuum diafiltration was performed at room temperature using a MidGee Hoop (GE Healthcare) cross-flow hollow fiber filter with a 30 kDa MWCO polysulfone membrane, two 1-mm inner diameter fibers, and a membrane area of 73 cm^2. The retentate solution (containing the protein to be diafiltered) was circulated through the hollow fibers at a flow rate of 25−50 mL/min using a peristaltic pump. A vacuum pump was used to apply vacuum to the filtrate side of the membrane to achieve a net transmembrane pressure (TMP) of approximately 8 psi. Under these operating conditions, the flux was 20−25 L/m^2/h (LMH) during diafiltration of the antibody solutions. A weighing balance was used on both the filtrate and retentate vessels to monitor changes in mass (i.e., volume). The diafiltration buffer was pumped into the retentate vessel by a peristaltic pump at a flow rate equal to the flow rate of the filtrate to achieve constant-volume diafiltration.

Laboratory-Scale Vacuum Diafiltration. A schematic of the laboratory-scale vacuum diafiltration setup is shown in Figure 1B. By using the inlet port, normally utilized for the attachment of a gas pressure line, to introduce additional diafiltration buffer under a closed-system operation using HPLC tubing and fittings, constant-volume diafiltration could be achieved. This apparatus requires no additional equipment to achieve constant-volume diafiltration, and it can be operated under vacuum generated from a house vacuum line or a small vacuum pump. If desired, multiple diafiltration devices could

be run in parallel using a common vacuum line, offering flexibility that would facilitate screening multiple variations of an antibody conjugate during the development stage.

Laboratory-scale diafiltration experiments were performed at room temperature using an Amicon Stirred Cell Model 8010 (10-mL sample volume, 4.1 cm^2 effective membrane area) with a Biomax ultrafiltration membrane (PBQK, Millipore, Billerica, MA) with a 50 kDa MWCO. The stirring rate was adjusted such that the vortex created was approximately one-third the depth of the liquid in the stirred cell. Vacuum was applied to the filtrate side of the membrane using a vacuum pump to achieve a net TMP of approximately 8.5 psi. Under these operating conditions, the flux was typically 25−35 LMH during diafiltration of the antibody solutions. The diafiltration buffer reservoir was connected to the stirred cell using 1/16 inch i.d. HPLC tubing connected by HPLC fittings so that the outlet for the diafiltration buffer tubing dripped onto the wall of the stirred cell as shown in Figure 1B (to minimize bubble formation and to prevent contact with any other parts of the stirred cell device). Because the diafiltration setup was operated as a closed system, the diafiltration buffer was pulled into the stirred cell at the same rate as the filtrate flowed out of the stirred cell.

Removal of Acetyltryptophanate (AT) in the Presence of Human Serum Albumin (HSA) or Rituxan by Vacuum Diafiltration. The removal of AT in the presence of both HSA and Rituxan by vacuum diafiltration was studied using the pilot-scale diafiltration setup with a MidGee Hoop cross-flow hollow fiber filter and a retentate flow rate of 25 mL/min. The HSA was used at a concentration of 7 mg/mL, diluted in PBS from Albuminar-25 (which contains 0.02 M AT). Rituxan was used at a concentration of 8.3 mg/mL along with *N*-acetyl-L-tryptophan at a concentration of 4×10^{-4} M^{-1}. The HSA was initially at a concentration of 7 mg/mL in PBS, and it was diafiltered with approximately 6 diavolumes of 0.1 M bicarbonate buffer (pH 8.3). Rituxan was initially at a concentration of 8.3 mg/mL in PBS, and it was first diafiltered with 5 diavolumes of 0.1 M bicarbonate buffer (pH 8.3). Subsequently, the *N*-acetyl-L-tryptophan was added to the Rituxan solution, and the mixture was diafiltered with 7 diavolumes of 0.25 M sodium acetate buffer (pH 7.2). Samples (∼100 μL) were removed from the retentate vessel during diafiltration. The concentration of HSA/Rituxan and AT in each sample was determined by integrating the A280 peak area of the trace from a Superdex 200 column (30 cm x 10 mm i.d.; GE Healthcare) using an AKTA purifier HPLC (GE Healthcare).

Removal of DOTA or DTPA in the Presence of Rituxan by Vacuum Diafiltration. The removal of DOTA or DTPA in the presence of Rituxan by vacuum diafiltration was studied using both the pilot-scale and laboratory-scale diafiltration setup. For the pilot-scale diafiltration, Rituxan was initially at a concentration of 8.3 mg/mL in PBS, and it was buffer-exchanged by diafiltration with 5 diavolumes of 0.1 M bicarbonate buffer (pH 8.3). Subsequently, 1 mM DOTA (Parish Chemical Company, Orem, UT) was added to the Rituxan solution, and the mixture was diafiltered with 7 diavolumes of 0.25 M sodium acetate buffer (pH 7.2). For the laboratory-scale diafiltration, Rituxan was initially at a concentration of 7 mg/mL in PBS, and it was buffer-exchanged into 0.1 M bicarbonate buffer (pH 8.3). After the addition of either 1 mM DOTA or 1 mM DTPA, the mixture was diafiltered with 7 diavolumes of 0.25 M ammonium acetate buffer (pH 7). Samples (∼50−100 μL) were removed from the retentate vessel during the diafiltration. Each experiment was also repeated in the absence of Rituxan.

The concentration of DOTA or DTPA in each sample was determined by a colorimetric assay using arsenazo III. Arsenazo III exhibits a bathochromic shift from 548 to 660 nm upon binding to free gadolinium. To the DOTA- or DTPA-containing samples in microcentrifuge tubes were added 20 nmol of gadolinium chloride in 0.1 M ammonium acetate buffer (pH 6). The reaction mixture was allowed to incubate for 15 min at 75 °C to enable complex formation between the gadolinium and chelate. Using the elevated temperature also helps to minimize interference in the assay from the potential binding between IgG and arsenazo III since IgG molecules show rapid denaturation and aggregation at these temperatures (*15*). Subsequently, the reaction mixture was combined with an equal volume of 1 mM arsenazo III, and the absorbance at 655 nm was measured with a Bio-Rad 680 microplate reader (Bio-Rad, Hercules, CA) to determine the amount of free gadolinium remaining. The relative concentration of DOTA or DTPA was calculated from the change in the level of gadolinium−arsenazo III complexes formed (as indicated by absorbance at 655 nm) since the chelated gadolinium cannot interact with arsenazo III.

Pilot-Scale Production of Radiolabeled Antibodies Using Vacuum Diafiltration. Buffer exchanges and purification required in the preparation of DOTA-conjugated Rituxan were performed using the pilot-scale diafiltration setup with a MidGee Hoop cross-flow hollow fiber filter and a retentate flow rate of 50 mL/min. Rituxan was conjugated with the NHS-activated form of the macrocyclic chelator, DOTA, which reacts with exposed amine groups on the antibody. Rituxan was processed at a concentration of 7 mg/mL in a volume of 50 mL. It was initially exchanged into 0.1 M bicarbonate buffer (pH 8.3) with 1 mM DTPA (metal scavenger) for conjugation. This was achieved with 5 diavolumes and was performed in ∼2 h, after which a 19.5-molar excess of DOTA−NHS (Macrocyclics, Dallas, TX) was added and allowed to react with Rituxan for 2 h at room temperature. Dissolving the DOTA−NHS in water instead of the pH 8.3 buffer can help to reduce unwanted NHS hydrolysis prior to addition to the reaction vessel due to the low pH of the DOTA−NHS solution. Subsequently, the unreacted DOTA−NHS was removed and the conjugate exchanged into 0.25 M sodium acetate buffer (pH 7.2) with 10 diavolumes, and this diafiltration was performed in ∼4 h. Diafiltration with an additional 5 diavolumes of 0.25 M sodium acetate buffer was performed 5 days later. After each diavolume during the postconjugation diafiltration, a 100 μL sample was removed and subjected to radiolabeling with In-111. Additionally, each sample was subjected to HPLC analysis on a Superdex 200 column (30 cm x 10 mm i.d.; GE Healthcare) to analyze antibody concentration and aggregate formation by following absorbance at 280 nm.

Laboratory-Scale Production of Radiolabeled Antibodies Using Vacuum Diafiltration. For preparation of DOTA-conjugated antibodies with the laboratory-scale vacuum diafiltration setup, diafiltration was performed using an Amicon stirred cell and a Biomax ultrafiltration membrane with a 50 kDa MWCO. Rituxan was processed at a concentration of 7 mg/mL in a volume of 5 mL. The initial exchange into the 0.1 M bicarbonate buffer (pH 8.3) with 1 mM DTPA was achieved with 5 diavolumes and was performed in ∼2 h, after which a 15-molar excess of DOTA−NHS (Macrocyclics, Dallas, TX) dissolved in water was added and allowed to react with the antibody inside the stirred cell for 1 h at room temperature. Subsequently, the unreacted chelate was removed and the conjugate exchanged into 0.25 M ammonium acetate buffer (pH 7, processed with Chelex 100 as described previously) with 18 diavolumes (still using the same stirred cell device) in ∼8 h. During the postconjugation diafiltration, samples (∼75 μL each) were removed at specified diavolumes and subjected to radiolabeling with In-111. Each sample was also subjected to HPLC analysis on a Superdex 200 column (30 cm x 10 mm i.d.; GE Healthcare) to analyze antibody concentration and aggregate formation by following absorbance at 280 nm.

Radiolabeling Efficiency. Radiolabeling reactions were performed at a ratio of 5 mCi/mg antibody conjugate in acetate buffer (pH 5.5), and the reaction was allowed to proceed for 45 min at 43 °C. Radiolabeling efficiency was measured by instant thin layer chromatography (ITLC). Two equal aliquots of the reaction mixture were withdrawn, and 10 mM DTPA solution (pH 6) was added to one aliquot to give a final concentration of 1 mM DTPA. This was incubated for 10 min at room temperature. Samples from the radiolabeling reaction with and without the DTPA chase were then analyzed on 2.25 inches × 0.5 inches Tec-Control ITLC strips (Cat. # 151-020, Biodex Medical Systems, Shirley, NY) using 0.9% saline as the mobile phase. Each strip was cut into 0.5-cm segments, and each segment was counted in a Cobra Autogamma counter. The ratio of radioactivity at the origin (In-111 bound to the DOTA−antibody conjugate or free, hydrolyzed In-111) to the radioactivity near the solvent front (DOTA- or DTPA-chelated radioisotope) was calculated. An estimate of the amount of free radioisotope remaining was obtained from the difference between the fraction of the radioactivity measured at the origin (bottom half) for ITLC strips run with or without the DTPA chase.

Mathematical Model Calculations. Model calculations were performed using MATLAB 7 (The MathWorks, Inc., Natick, MA). The differential equations governing the clearance of solutes during diafiltration were solved numerically using the forward Euler method with a step size equal to 1/1000 the total number of diavolumes analyzed. Chelate−metal complex formation is assumed to reach equilibrium (both during diafiltration and during the radiolabeling reaction) to simplify calculation of metal loading and overall radiolabeling efficiency.

RESULTS

Theoretical Development. *Impurity Removal by Vacuum Diafiltration.* Removal of low molecular weight impurities during constant-volume diafiltration can be calculated from a mass balance on the impurity in the retentate. If the impurity exhibits a reversible binding affinity interaction with the retained molecule, such as an antibody, then impurity removal will proceed more slowly as a result of the binding interaction. The impact of protein binding during diafiltration has been previously analyzed using D-tryptophan and bovine serum albumin as a model system (*16*). The change in the concentration of impurity, C_i, during constant-volume diafiltration is given by the following equation:

$$V\frac{dC_i}{dt} = -f_i C_i S_i J_v A \tag{1}$$

where V is the constant retentate volume, f_i is the unbound fraction of impurity i, S_i is the sieving coefficient of impurity i, J_v is the filtrate flux through the membrane, and A is the membrane area. The binding interaction between the impurity and a retained protein can be expressed in terms of an equilibrium binding constant, K_a, which is defined as

$$K_a = \frac{[C_{i,b}]}{[C_{i,f}][C_{p,f}]} \tag{2}$$

where $C_{i,b}$ is the bound concentration of impurity i, $C_{i,f}$ is the free concentration of impurity i, and $C_{p,f}$ is the free concentration of the protein that interacts with the impurity. This expression can be used to derive an expression for f_i, the unbound fraction of impurity i, given by the following equation:

$$f_i = \frac{-nC_p + C_i - \frac{1}{K_a} + \sqrt{\left(nC_p - C_i + \frac{1}{K_a}\right)^2 + \frac{4C_i}{K_a}}}{2C_i} \tag{3}$$

where n is the number of binding sites per protein for impurity i. For an impurity that has no protein binding ($f_i = 1$), the concentration of impurity remaining after a given number of diavolumes, N_D, is equal to

$$C_i = C_{i,0}e^{-N_D S_i} \tag{4}$$

where $C_{i,0}$ is the initial impurity concentration, and the concentration of remaining impurity decays exponentially with the number of diavolumes.

Chelate−Metal Complex Formation. Chelation of metal species by compounds such as DOTA can be approximated as an association reaction between the metal species, *M*, and the chelate, *C*, to form a metal−chelate complex, *M-C*. This equilibrium binding can be described by

$$K_f = \frac{[M-C]}{[M][C]} \tag{5}$$

where K_f is the stability constant of the metal−chelate complex. This equation can be used to estimate the equilibrium metal loading into the chelate molecules given the stability constant and the initial concentrations of *M* and *C* (*17*). Metal loading is calculated for both free chelate (not protein-bound), C_f, and chelate molecules covalently coupled to the antibody molecule, *C-Ab*. For example, separate equilibrium relationships can be written for the free and conjugated chelate,

$$K_{f1} = \frac{[M-C_f]}{[M][C_f]} \tag{6}$$

$$K_{f2} = \frac{[M-C-Ab]}{[M][C-Ab]} \tag{7}$$

where K_{f1} is the free chelate−metal stability constant, and K_{f2} is the antibody−chelate−metal stability constant.

For the model calculations, any nonradioactive metal present in the buffer during diafiltration or the radiolabeling reaction is also allowed to form complexes with either free chelate or antibody−chelate according to the equilibrium relationships described by eqs 6 and 7. Chelate (remaining after diafiltration) or chelate−antibody conjugate that binds metal during the diafiltration stage is no longer available for binding to additional metal species (radioactive or nonradioactive) during the radiolabeling reaction. Since the thermodynamic stability for the DOTA−metal or DTPA−metal complexes is generally characterized by high log K_f values, a log K_f value of 23 was used for all calculations regardless of the metal species (*18*). This is justified for these calculations since the equilibrium is essentially shifted completely in favor of the complex formation for such large log K_f values. More complicated model calculations could incorporate the relative formation rate constants for DOTA or DTPA binding to the metal species, but such equations were not incorporated into the model used here. The model calculations used here also restrict nonspecific antibody binding (eq 3) to the metal-free chelate, meaning any chelate that has formed a metal complex is no longer available for antibody binding.

Since the fraction of the radiolabeled metal, *M**, that is bound to free chelate or chelate−antibody conjugates is equal to the fraction of total metal bound by each (under the assumption of equivalent chelation of all metal species), the radiolabeling efficiency is calculated as

$$RE = \frac{[M-C-Ab]}{[M]_{tot}} = \frac{[M^*-C-Ab]}{[M^*]_{tot}} \tag{8}$$

where M_{tot} is the total concentration of all metal species present, *M*-C-Ab* is the concentration of radioisotope-labeled chelate−antibody conjugates, and M^*_{tot} is the total concentration of radioisotope added to the radiolabeling reaction.

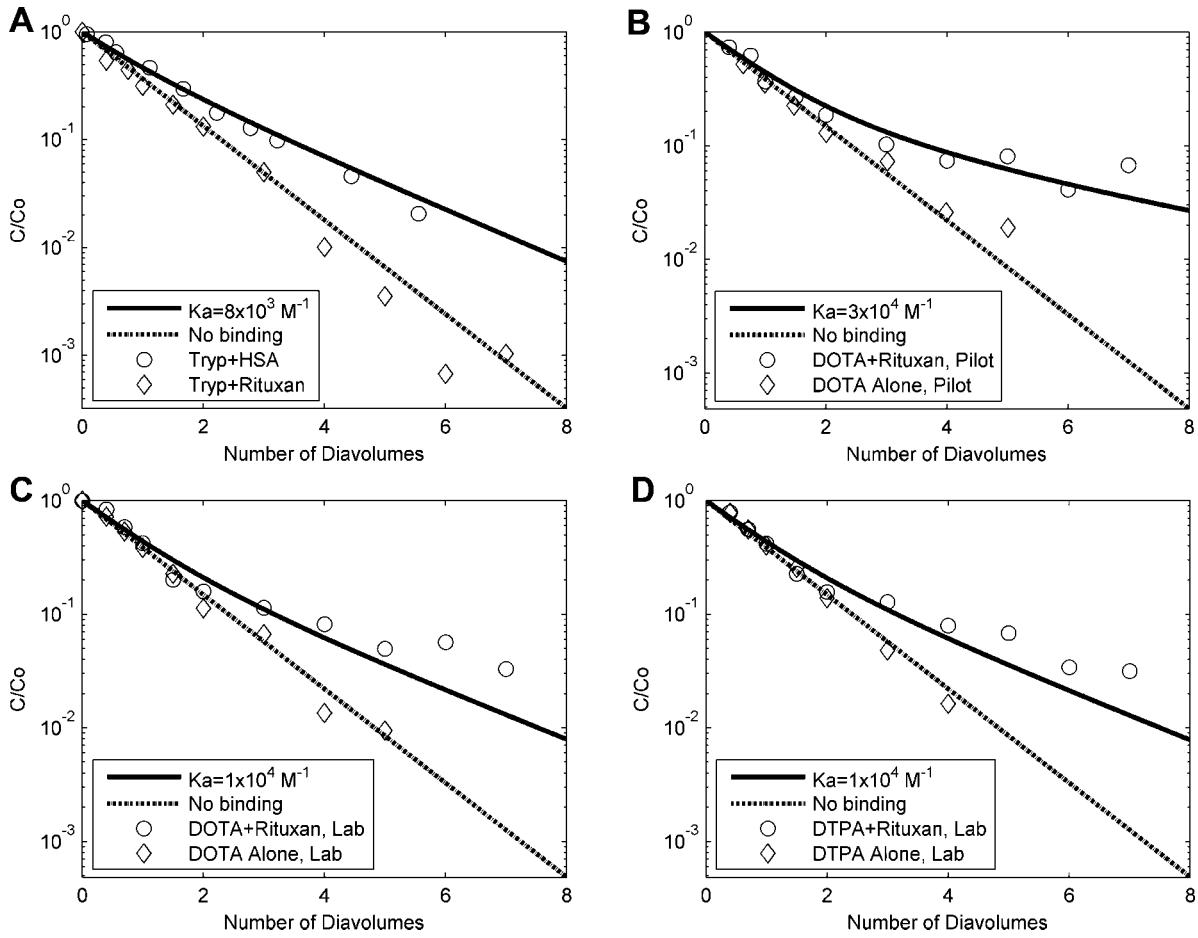

Figure 2. Effect of protein binding on the removal of acetyltryptophanate, DOTA, or DTPA by vacuum diafiltration. (A) Experimentally determined removal of acetyltryptophan by pilot-scale vacuum diafiltration in the presence of 7 mg/mL HSA (○) or 8.3 mg/mL Rituxan (◊). (B) Experimentally determined removal of DOTA by pilot-scale vacuum diafiltration in the presence of 8.3 mg/mL Rituxan (○) or no protein (◊). (C) Experimentally determined removal of DOTA by laboratory-scale vacuum diafiltration in the presence of 7 mg/mL Rituxan (○) or no protein (◊). (D) Experimentally determined removal of DTPA by laboratory-scale vacuum diafiltration in the presence of 7 mg/mL Rituxan (○) or no protein (◊). Predicted clearances are shown for protein binding (—) and no protein binding (---).

Solute Removal by Vacuum Diafiltration. It has been previously established that tryptophan and its derivative acetyltryptophan reversibly bind human serum albumin with a stoichiometry of approximately 1:1, and this interaction can be characterized by affinity constants of 10^4-10^5 M^{-1} for L-tryptophan and 10^3-10^4 M^{-1} for D-tryptophan (*19*). Furthermore, Klotz et al. estimated the binding affinity between *N*-acetyl-DL-tryptophan (acetyltryptophanate) and bovine serum albumin to be $\sim 4 \times 10^3$ M^{-1} (*20*). Using eq 1, the concentration of acetyltryptophanate (AT) can be predicted during diafiltration in the presence of human serum albumin. The predicted removal of AT was compared to experimentally determined values obtained by sampling the retentate during vacuum diafiltration. The results shown in Figure 2A reveal that the experimental data closely match the predicted removal of a solute with a sieving coefficient of 1 and an affinity constant for human serum albumin of approximately 8×10^3 M^{-1}, within the same order of magnitude as those binding constants reported previously for the interaction between tryptophan and albumin. No such binding was observed between *N*-acetyl-L-tryptophan and the monoclonal antibody, Rituxan, however (Figure 2A).

We extended this analysis to the interaction between the metal chelators, DOTA or DTPA, and the monoclonal antibody, Rituxan. Because each Rituxan molecule contains >100 negatively or positively charged amino acids, we hypothesized that it would potentially act as an ion exchanger with a weak affinity for charged molecules such as DOTA or DTPA, which contain multiple amine and carboxylate groups. Least squares regression was first used to estimate the sieving coefficient of the chelate in the absence of Rituxan from the data in Figure 2, yielding an average value of $S = 0.95$. Although the Biomax (polyethersulfone) and polysulfone membranes do exhibit a negative surface charge density at the pH values used in these studies, the negatively charged DOTA or DTPA molecules still exhibit a sieving coefficient of near unity, as indicated by the observed clearance of each chelator in the absence of Rituxan (Figure 2). Shao et al. determined that small charged impurities can be strongly rejected by charged membranes (including Biomax) at low flux or low ionic strength (*21*). Because the buffers used in our experiments had relatively high ionic strengths, these charge interactions were minimal. Subsequently, the affinity constant characterizing the binding between DOTA or DTPA and Rituxan was estimated using the data for their clearance in the presence of Rituxan (Figure 2). Assuming two binding sites per antibody ($n = 2$) on the basis of the symmetrical IgG1 structure containing two identical heavy chains and two identical light chains, the magnitude of the affinity constant, $K_a \sim 1 \times 10^4-3 \times 10^4$ M^{-1}, is similar to the weak binding observed between AT and HSA. Since the magnitude of this affinity constant will vary with the exact antibody or buffer used during diafiltration, the slightly lower affinity constant observed at the laboratory-scale relative to the pilot-scale may be the result of using ammonium acetate instead of sodium acetate buffer. The ammonium ions, more than sodium ions, may compete with the amines on the antibody for binding with the chelate carboxylates. Such a hypothesis is supported by the observation

that ammonium ions have a greater affinity toward cation exchangers than sodium ions (*22*). Future studies must be done to more precisely examine the impact that different processing conditions can have on the interaction between the chelate and antibody molecules. Comparison can also be made between the affinity constants measured using antibodies with or without prior chelate modification, as the presence of covalently conjugated chelate may impact the binding affinity toward nonspecifically bound chelate.

Production of Radiolabeled Antibodies Using Vacuum Diafiltration. During the production of radiolabeled antibodies, DOTA is first conjugated to the antibody at a molar excess of DOTA−NHS/antibody. The unreacted DOTA−NHS must be removed since it will directly compete with the conjugated DOTA−Ab for binding to the radioactive isotope during the radiolabeling reaction. The chelate−antibody nonspecific affinity constant estimated from the data in Figure 2 can be combined with eqs 1−3 to estimate the number of diavolumes needed to reduce the free chelate concentration below a desired threshold. Furthermore, the use of eqs 6−8 can allow estimation of the predicted radiolabeling efficiency, which depends on the amount of free chelate remaining as well as the total metal contaminants introduced during diafiltration. Such information allows the rational design of DOTA−Ab production to yield high radiolabeling efficiencies. To demonstrate such a procedure, a DOTA−Rituxan conjugate was synthesized and purified using both pilot-scale and laboratory-scale vacuum diafiltration and subsequently radiolabeled with In-111. The results of radiolabeling efficiency versus number of diavolumes are shown graphically in Figure 3A and provided in tabular format in the Supporting Information. Each sample was also subjected to gel filtration chromatography on a Superdex 200 column to analyze relative antibody concentration as well as the formation of any aggregates. At all diavolumes tested, there was negligible fluctuation in the measured antibody concentration (Figure 3B), and the aggregate formation remained <1.5%.

Theoretical Considerations for Maximizing Radiolabeling Efficiencies. Because variability in radiolabeling efficiencies has often plagued the production of radiolabeled antibodies, we sought to elucidate key parameters controlling the radiolabeling efficiency using a mathematical model of the vacuum diafiltration and radiolabeling processes. Additional parameters for the model calculations are given in Table 1. The solid lines in Figure 4A and B show the good fit that can be achieved between the predicted and experimentally determined radiolabeling efficiencies under the conditions used at both the pilot and laboratory scales, respectively. The dashed lines show the radiolabeling efficiency predicted if the chelate molecules exhibited no antibody binding. In the absence of antibody binding, significant radiolabeling efficiency should begin to appear as early as 4 diavolumes. Instead, measurable radiolabeling began to appear after >6 diavolumes had been processed, indicating hindered removal of the free chelate. This hindered removal can be accounted for by a weak binding affinity ($\sim 10^4$ M^{-1}) between the free chelate and the antibody molecules (Figure 2). The rapid sigmoidal rise in radiolabeling efficiency between diavolumes 6 and 10 would be expected if the free chelate (DOTA or DTPA) was able to bind the metal more readily than the DOTA−antibody conjugate. Previous studies have demonstrated that the stability constant for metals binding to monofunctionalized DOTA molecules (such as those containing amide bond linkages to the lysines on proteins) are approximately 2 orders of magnitude lower than the stability constant for metals binding to free DOTA (*7, 23*). Furthermore, there is a decreased metal loading rate when DOTA is conjugated to protein (*6*). Consistent with these observations, the model predictions closely matched the experimental data

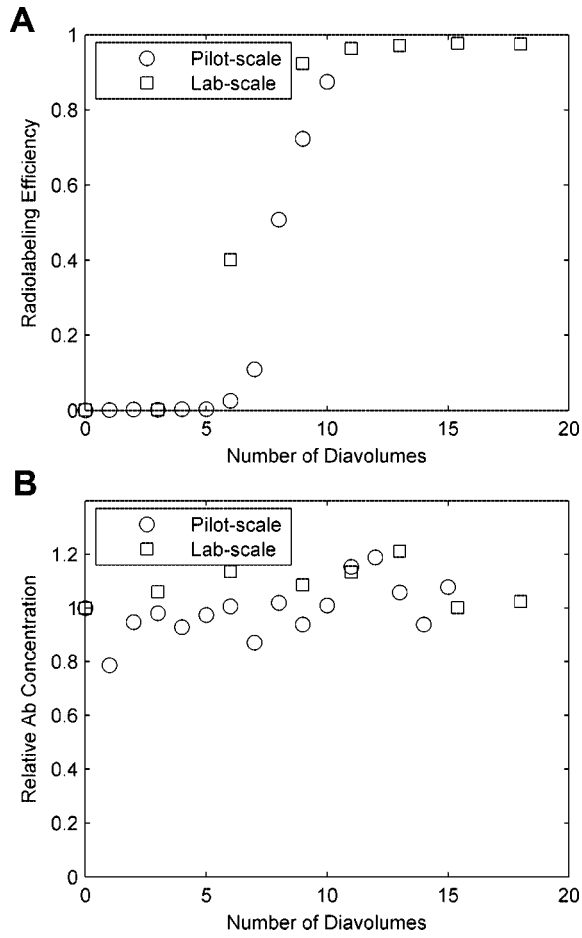

Figure 3. Production of radiolabeled Rituxan using vacuum diafiltration. (A) Experimentally determined radiolabeling efficiency as a function of the number of diavolumes by pilot-scale and laboratory-scale vacuum diafiltration. (B) Relative Rituxan concentration determined by HPLC (Superdex 200, 280 nm) as a function of the number of diavolumes during vacuum diafiltration.

observed here if the metal preferentially loaded into the free chelate relative to the DOTA−Ab conjugate. This was implemented in the model by setting the actual metal loading as a fraction of the maximum equilibrium loading value (eqs 6 and 7) depending on the relative concentrations of the two species. The preferential binding by free chelate was realized by multiplying the free chelate concentration by 100 (higher effective concentration) to enhance the relative fraction of metal bound by free chelate. Such a preferential binding by free chelate enhances the sigmoidal shape of the curve and inhibits radiolabeling at low diavolumes when there is still sufficient free chelate (DOTA or DTPA) to compete with the DOTA−Ab for metal binding. However, after approximately 6 diavolumes, the free chelate is predicted to be at a low enough concentration that it no longer can bind to all of the metal present in the radiolabeling reaction, and the radiolabeling efficiency rapidly increases with additional diavolumes. When the radiolabeling efficiency begins to plateau after ∼10 diavolumes, there is a negligible amount remaining of free chelate available for radioisotope binding (it has either been removed in the filtrate or already occupied with nonradioactive metal); therefore, all of the subsequent radioactive or nonradioactive metal in the radiolabeling reaction will bind to the DOTA−Ab conjugate. Once there is no longer any additional free chelate to be removed, then additional diavolumes will potentially add metal contaminants (depending on the metal content of the diafiltration buffer) to the DOTA−Ab conjugate until a point is reached when enough of the DOTA−Ab conjugate has been occupied

Table 1. Additional Parameters Used for Model Calculations to Predict Chelate Clearance and Radiolabeling Efficiency

parameter description	value	determination
impurity sieving coefficient (DOTA, DTPA)	0.95	least squares regression of experimental data in Figure 2
relative chelating ability (free vs conjugated chelate)	100	estimated from experimental data, supported by literature (*7*, *23*)
K_{f1}, free chelate-metal association constant (M^{-1})	1×10^{23}	literature (*17*, *18*)
K_{f2}, antibody-chelate-metal association constant (M^{-1})	1×10^{21}	calculated from K_{f1} and the relative chelating ability of free vs conjugated chelate
K_a, chelate−antibody nonspecific binding association constant (M^{-1})	3×10^4 = pilot 1×10^4 = laboratory	least squares regression of experimental data in Figure 2
n, number of nonspecific binding sites per antibody	2	estimated from experimental data and the symmetry of IgG molecules
number of conjugated DOTA per antibody	2	literature (*4*)
buffer metal concentration (M)	4×10^{-6} = pilot 2×10^{-7} = laboratory	estimated from max specifications from certificate of analysis (sodium acetate, pilot-scale) and an estimated 90−95% reduction from max specifications by Chelex 100 treatment (ammonium acetate, laboratory-scale)
radioisotope purity at calibration time and after 5-day decay	0.025 = day 0 0.008 = day 5	estimated from certificate of analysis; decayed value calculated using In-111 half-life of 67 h

by metal contaminants that it no longer can bind all of the radioactive isotope during radiolabeling, thus decreasing the radiolabeling efficiency. However, the model predicts that addition of metal can enhance radiolabeling efficiencies if there is substantial free chelate remaining in the radiolabeling reaction since the free chelate would otherwise be able to bind the majority of both the radioactive and nonradioactive metal present. Only after this extra free chelate is saturated with bound metal will the DOTA−Ab be able to bind a significant portion of the radioactive metal, meaning higher radiolabeling efficiencies can be achieved by addition of nonradioactive metal even when free chelate remains at low diavolumes.

To test this hypothesis experimentally, the same batch of In-111 that was used for the pilot-scale radiolabeling reactions shown in Figure 3 was again used to radiolabel the samples from diavolumes 8−10 of the pilot-scale diafiltration, although the In-111 had decayed for an additional 5 days before these labelings were performed. The DOTA−Ab conjugate was also subjected to an additional 5 diavolumes by pilot-scale diafiltration, and samples were removed at each diavolume for radiolabeling with this same batch of decayed In-111. The samples from diavolumes 8−10 and the new samples from diavolumes 11−15 were radiolabeled under the same reaction conditions that were used 5 days previously, and the radiolabeled samples were subjected to ITLC. The ITLC analysis was performed with and without a DTPA chase to differentiate between radioisotope that had been bound by free chelate remaining in the DOTA−Ab preparation versus free radioisotope that was still available to bind to the DTPA chase. Under the ITLC conditions without the DTPA chase, both free radioisotope and radioisotope bound to DOTA−Ab will remain at the origin, while radioisotope bound by any residual free chelate (DOTA or DTPA not removed during diafiltration) will migrate with the solvent. However, if an additional DTPA chase is included during ITLC, then any free radioisotope that would have remained at the origin will bind to DTPA and migrate with the solvent. The difference between the radioactive concentrations at the origin can thus be used to indicate the presence of free radioisotope remaining after the radiolabeling reaction. An overview of the experimental procedure is depicted in Figure 5A, while the experimental data and model calculations are summarized in Figure 5B and C, respectively. Figure 5B depicts the results of the ITLC measurements with and without a DTPA chase. The radiolabeling efficiencies are provided in tabular format in Supporting Information. Free radioisotope began to appear after 12−13 diavolumes, and the model calculations offer a possible explanation for these observations, as shown in Figure 5C. As hypothesized, the use of the decayed In-111 (which contains a higher relative amount of nonradioactive metal contaminants and thus a lower radioisotope purity) enhances the observed radiolabeling efficiency at low diavolumes because the additional nonradioactive metal saturates the remaining free chelate and thereby allows the remaining radioactive metal to be bound by the DOTA−Ab conjugate. However, at higher diavolumes, the level of free chelate has been reduced to low levels and instead of helping the radiolabeling efficiency, the additional nonradioactive metal from the diafiltration buffer (in this case, sodium acetate buffer that was not pretreated with the Chelex 100 resin) and the decayed In-111 preparation now saturates the available DOTA−Ab binding sites and prevents the conjugate from being able to bind all of the radioactive metal. This is indicated by the detection of free radioactive isotope by ITLC performed with and without the DTPA chase. However, no free radioactive isotope was detected by ITLC for samples even out to 18 diavolumes when using the Chelex 100-treated ammonium acetate buffer, which should have reduced metal contamination (Supporting Information). Previous studies have shown that the complexes formed between antibody-conjugated DOTA and metals are extremely stable, with total release of bound In-111 of ∼3% after 240 h in the presence of 1 mM DTPA (*23*). Such observations suggest that most of the bound metal is stably coordinated by the DOTA conjugates and that the contribution of metal binding to other sites on the antibody is likely to be minimal. Furthermore, this stability of the metal within the DOTA complexes enables the use of a DTPA chase to probe for the presence of free remaining radiometal after the labeling reaction is completed. The data shown in Figure 5 therefore corroborate the predictions made with the model calculations and also offer important insights into potential mechanisms for the variability in radiolabeling efficiencies.

As described earlier, the model calculations assume equilibrium binding between the chelate and metal, although the residence time during the constant diafiltration process may limit the accuracy of such an assumption. The assumption of equilibrium therefore represents a worst-case scenario for metal

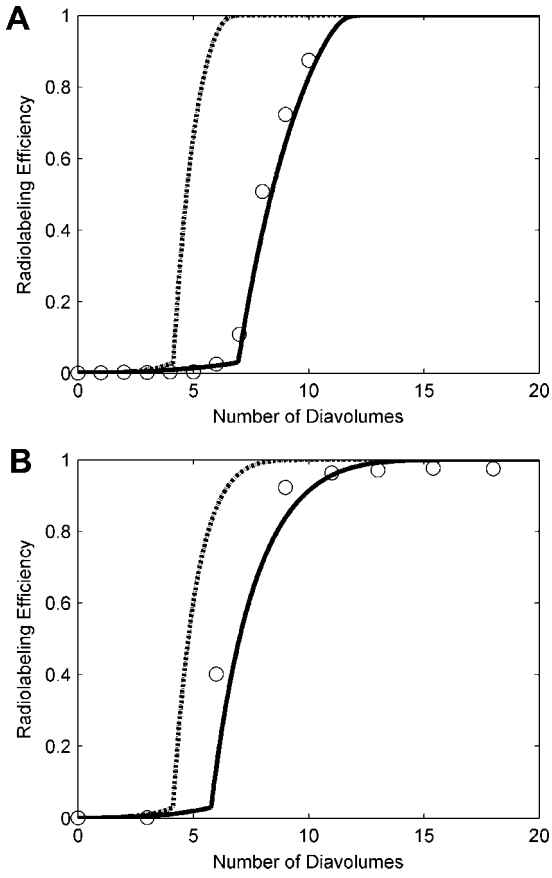

Figure 4. Comparison of predicted and experimentally determined radiolabeling efficiency as a function of the number of diavolumes. (A) Model calculations are shown for the pilot-scale diafiltration when a 19.5-molar excess of DOTA−NHS is reacted with Rituxan and the excess free chelate exhibits either a weak affinity for Rituxan of $3 \times 10^4\ M^{-1}$ (—) or no affinity for Rituxan (---). The pilot-scale diafiltration data from Figure 3A are shown for comparison (○). (B) Model calculations are shown for the laboratory-scale diafiltration when a 15-molar excess of DOTA−NHS is reacted with Rituxan and the excess free chelate exhibits either a weak affinity for Rituxan of $1 \times 10^4\ M^{-1}$ (—) or no affinity for Rituxan (---). The laboratory-scale diafiltration data from Figure 3A are shown for comparison (○). Additional model parameters are given in Table 1.

contamination from the diafiltration buffers. Notwithstanding, there is likely an optimum number of diavolumes that will achieve the highest radiolabeling efficiency, representing a balance between removal of free chelate and introduction of nonradioactive metal with the diafiltration buffer or the radioisotope preparation. The plots in Figure 6 illustrate the impact of different operating parameters (antibody concentration during diafiltration, radioisotope purity, diafiltration buffer metal concentration, and the radiolabeling reaction ratio) on the predicted radiolabeling efficiency for the pilot-scale diafiltration parameters. Similar analyses were performed for the laboratory-scale diafiltration parameters as well as for antibody conjugates containing a higher conjugation efficiency with 5 DOTA per antibody (Supporting Information). While these plots apply to the specific operating conditions used in this study, the observed trends are generally applicable for the production of radiolabeled antibodies using diafiltration.

DISCUSSION

In this article, we describe the use of constant-volume vacuum diafiltration for the production of radiolabeled antibodies. The method is a modification of standard diafiltration techniques whereby the transmembrane pressure is created by applying a vacuum to the filtrate side of the membrane as opposed to using positive pressure on the retentate side of the membrane. Vacuum diafiltration can be quickly and easily implemented with minimal equipment requirements since a house vacuum line is sufficient to generate the transmembrane pressure required for filtration. Furthermore, the use of vacuum as the driving force minimizes the risk for leakage or loss of expensive antibody materials since the membrane interface is the only region of significant pressure differential that makes contact with the antibody, thereby meaning recoverable loss into the filtrate is the most likely failure. In contrast, applying a positive pressure to the retentate (antibody) side of the membrane creates the potential for catastrophic leakage out of the retentate vessel if any of the seals were to fail under the applied pressure differential. Such safety precautions become especially important at the clinical production scale. Vacuum diafiltration is easily scalable, as we have demonstrated here on both the milligram and gram production scales, and overall processing times and buffer volumes required can be drastically reduced relative to other purification strategies such as dialysis. While we illustrate the use of the method in the production of radiolabeled antibodies, vacuum diafiltration offers an easily accessible strategy for preparing any antibody conjugate. Besides using vacuum diafiltration to achieve high radiolabeling efficiencies (>90%) for several different antibodies in addition to Rituxan, we also have used it for labeling antibodies with fluorochromes and biotin.

Through the use of mathematical modeling combined with experimental data, we also elucidate several factors that can contribute to variable radiolabeling efficiencies. Since excess free chelate can directly compete with chelate−antibody conjugates for radiolabeling, it must be stringently removed prior to radiolabeling to ensure maximum yield. The experimental data presented here suggest a weak binding affinity between DOTA or DTPA and antibodies, further complicating the removal of excess chelate. Notwithstanding, free chelate can be reduced to acceptably low levels through extensive purification, as illustrated here by the high radiolabeling efficiencies achieved at diavolumes greater than approximately 10. An interesting result of following the radiolabeling efficiency as a function of the number of diavolumes was the observation that there can be an optimum number of diavolumes for maximizing radiolabeling efficiency, beyond which point the yield will decrease if metal contaminants from the buffers outweigh the benefit derived from removing additional free chelate. Controlling the level of metal contaminants therefore emerged as one of the most important factors influencing the consistency of the radiolabeling efficiency.

The influence of metal contamination becomes most significant with respect to the purity of the radioisotope used for radiolabeling. Metal contamination during the initial conjugation and diafiltration steps can be minimized by including metal scavengers (e.g., DTPA) in the buffers used for washing or diafiltration (although one must then also ensure that sufficient diavolumes are processed during diafiltration to reduce the free DTPA concentration to levels that will not interfere with radiolabeling). Additionally, treatment of the diafiltration buffers with chelating resins, such as Chelex 100, can significantly reduce the potential burden of metal contamination (*8*−*12*). In our experience, high radiolabeling efficiencies (>95%) are achieved using Chelex 100-treated ammonium acetate buffer even out to 18 diavolumes. Removal of trace metal contaminants in the diafiltration buffer by chelating resins helps to minimize variability that could be introduced by fluctuations in buffer metal content, thereby widening the range of diavolumes that can achieve high radiolabeling efficiencies and yielding a more robust process (Figure 6 and Supporting Information).

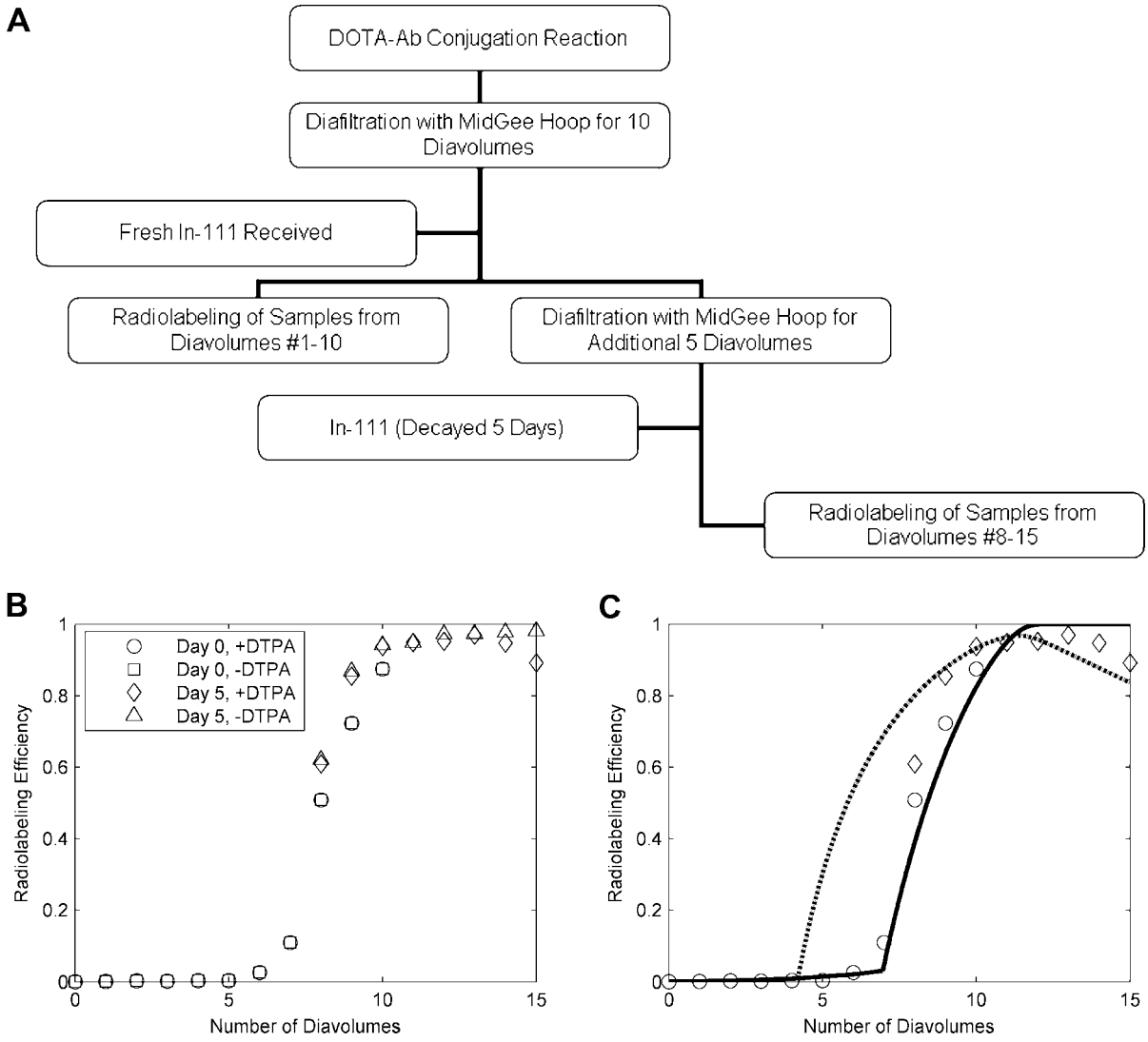

Figure 5. Effect of metal contamination on radiolabeling efficiency. (A) Flowchart depicting the experimental procedure. (B) Radiolabeling efficiency as a function of the number of diavolumes on day 0 (fresh radioisotope) and on day 5 (decayed radioisotope). ITLC was performed with or without a DTPA chase to detect the presence of free metal remaining after the radiolabeling reaction. The day 0 data points with DTPA (○) are the same data shown in Figure 3; additionally, the ITLC samples without DTPA (□) are shown for comparison, demonstrating the absence of any free metal. The day 5 data points represent samples taken from diavolumes 8−10 from the initial diafiltration and samples taken from an additional 5 diavolumes of the same DOTA−antibody conjugate preparation (diavolumes 11−15). Data are shown for ITLC samples with DTPA (◊) or without DTPA (△), demonstrating the appearance of free metal beginning at diavolumes 12−13. (C) The predicted radiolabeling efficiency as a function of the number of diavolumes was calculated for a radioisotope purity of 0.025 (day 0, solid line) and 0.008 (day 5, dashed line). Experimental data of the ITLC samples with DTPA from day 0 (○) and day 5 (◊) are shown for comparison.

Unfortunately, neither of these methods is feasible for separation of the radioactive metal from nonradioactive metal in the radioisotope preparation. Evaluation of the certificate of analysis provided by several vendors of radioisotope preparations reveals that even though the radionuclide purity may be >99.9%, there can be sufficient metal contaminants to impact radiolabeling efficiencies. For example, the specifications for In-111 (Trace LifeSciences) require the metal contaminants (including Cd, Cu, Fe, Ni, Pb, and Zn) to be at a level below 0.1 μg/mCi. Given the specific activity of In-111 (4.7×10^7 Ci/mol), then the In-111 can represent <1 mol% of the total metal contaminants and meet specifications. A typical radiolabeling reaction might be performed at a concentration of 5 mCi/mg antibody conjugate, meaning there is ∼100-fold molar excess of Ab-conjugated DOTA molecules relative to the moles of In-111 in 5 mCi. The resulting radiolabeling efficiency represents the fraction of the total In-111 atoms that will be bound by the Ab-conjugated DOTA molecules. If the In-111 represents 0.5% of the total metal atoms present in the radioisotope preparation, for example, then a 200-fold excess of available Ab-conjugated DOTA molecules would be required for all of the In-111 to be bound (assuming, for simplicity, that all of the metal atoms can bind to DOTA with equal efficiency). If the radiolabeling ratio results in only a 100-fold excess of Ab-conjugated DOTA molecules present (as described above), then the maximum theoretical radiolabeling efficiency would be 50%. These calculations illustrate the ease with which variations in radioisotope purity can alter the radiolabeling efficiencies under typical reaction conditions, even when the radioisotope is within the manufacturer's specification limits for metal contaminants.

To facilitate more consistent radiolabeling efficiencies, the metal contaminants in radioisotope preparations must be stringently controlled. The specifications for current preparations make radiolabeling reactions inherently subject to variability. Regardless of any changes made in the production of radioisotopes, several steps can be taken toward achieving more consistent radiolabeling efficiencies. First, metal contaminants must be reduced in the steps prior to the radiolabeling reaction. By minimizing the amount of metal contaminants in the buffers

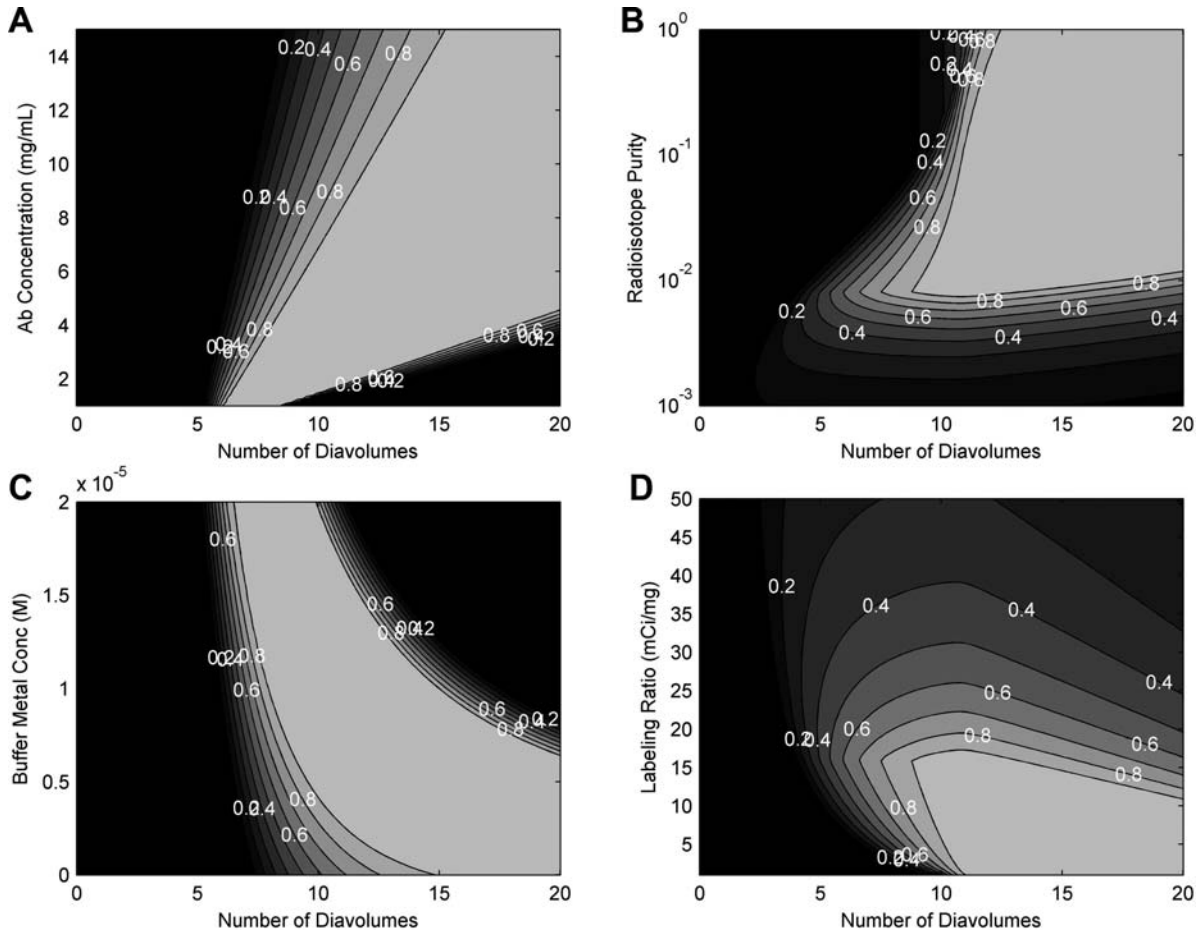

Figure 6. Contour plots showing the impact of different operating parameters on the predicted radiolabeling efficiency as a function of the number of diavolumes for pilot-scale diafiltration. Model calculations are used to estimate the predicted radiolabeling efficiency for a range of (A) antibody concentrations, (B) radioisotope purities, (C) metal concentrations in the diafiltration buffer, and (D) radiolabeling reaction ratios given as the amount of radioactivity per mass of antibody. Fixed parameter values were chosen to match those of the pilot-scale diafiltration experiment as given in Table 1. Lighter color represents higher radiolabeling efficiencies, and labels indicate the radiolabeling efficiency of a given contour line.

through the use of metal scavengers or chelating resins, it is possible to more accurately predict the ratio of available antibody-conjugated DOTA molecules to the total metal in the radiolabeling reaction. Otherwise, metal contamination prior to the radiolabeling reaction can lead to a significant fraction of the antibody-conjugated DOTA molecules already being occupied by metals, making them unavailable for radiolabeling. Second, it is important to analyze the certificate of analysis provided with the radioisotope preparation and estimate its purity (moles radioisotope relative to total moles of metal present). This purity can then be used to predict the radiolabeling reaction ratio (mCi/mg antibody conjugate) needed to ensure that there is sufficient capacity to bind all of the radioisotope during the radiolabeling reaction. Third, care must be taken to account for the decay of the radioisotope preparation, meaning the purity of the radioisotope will decrease with time as the radioisotope decays. As illustrated in Figure 5, this change in purity can either increase or decrease the radiolabeling efficiency depending on the presence of additional free chelate (which can be estimated from the number of diavolumes processed) and the ratio of radioisotope to antibody-conjugated DOTA molecules (mCi/mg antibody conjugate) used during the radiolabeling reaction.

In summary, vacuum diafiltration offers a convenient and scalable method that can be easily implemented for the production of radiolabeled antibody conjugates. Mathematical models enable a rational approach for optimizing operating conditions for the production of radiolabeled antibodies, including controlling metal contamination and free chelate removal. Several suggestions to improve overall radiolabeling efficiencies were offered according to model predictions and experimental observations. The study presented here facilitates production of radiolabeled antibodies with increased consistency and higher efficiency, offering benefits for patient safety, therapeutic efficacy, and cost minimization in the clinical application of radioimmunotherapeutics.

ACKNOWLEDGMENT

We are especially grateful to Anne-Line Anderson for performing the radiolabeling reactions, Militza Bocic for running HPLC samples, Barbara Szpikowska for preparing the Chelex 100-treated ammonium acetate buffer, Agnes Gardner for helpful discussions regarding pilot-scale diafiltration, and Nicole Skidmore for helping to assemble the laboratory-scale diafiltration apparatus. D.W.B. is a W.M. Keck Fellow. This publication was made possible in part by the W.M. Keck Foundation and program project grant P01 CA043904 and SPORE grant P50 CA107399 from the National Cancer Institute.

Supporting Information Available: Tabular presentation of the experimentally determined radiolabeling efficiencies and additional contour plots showing the impact of different operating parameters on the predicted radiolabeling efficiency as a function of the number of diavolumes. This material is available free of charge via the Internet at http://pubs.acs.org.

LITERATURE CITED

(1) Goldenberg, D. M. (2002) Targeted therapy of cancer with radiolabeled antibodies. *J. Nucl. Med. 43*, 693–713.

(2) Macklis, R. M. (2007) Radioimmunotherapy as a therapeutic option for non-Hodgkin's lymphoma. *Semin. Radiat. Oncol. 17*, 176.

(3) Liu, Y., and Wu, C. (1991) Radiolabeling of monoclonal antibodies with metal chelates. *Pure Appl. Chem. 63*, 427–463.

(4) Lewis, M. R., Kao, J. Y., Anderson, A. L. J., Shively, J. E., and Raubitschek, A. (2001) An improved method for conjugating monoclonal antibodies with N-hydroxysulfosuccinimidyl DOTA. *Bioconjugate Chem. 12*, 320–324.

(5) Liu, S. (2004) The role of coordination chemistry in the development of target-specific radiopharmaceuticals. *Chem. Soc. Rev. 33*, 445–461.

(6) Keire, D. A., and Kobayashi, M. (1999) NMR studies of the metal-loading kinetics and acid-base chemistry of DOTA and butylamide-DOTA. *Bioconjugate Chem. 10*, 454–463.

(7) Sherry, A. D., Brown, R. D., Geraldes, C. F. G. C., Koenig, S. H., Kuan, K.-T., and Spiller, M. (1989) Synthesis and characterization of the gadolinium(3+) complex of DOTA-propylamide: a model DOTA-protein conjugate. *Inorg. Chem. 28*, 620–622.

(8) Gode, F., and Pehlivan, E. (2003) A comparative study of two chelating ion-exchange resins for the removal of chromium(III) from aqueous solution. *J. Hazard. Mater. 100*, 231.

(9) Leinonen, H., and Lehto, J. (2000) Ion-exchange of nickel by iminodiacetic acid chelating resin Chelex 100. *React. Funct. Polym. 43*, 1.

(10) Lin, L.-C., and Juang, R.-S. (2007) Ion-exchange kinetics of Cu(II) and Zn(II) from aqueous solutions with two chelating resins. *Chem. Eng. J. 132*, 205.

(11) Lin, L.-C., and Juang, R.-S. (2005) Ion-exchange equilibria of Cu(II) and Zn(II) from aqueous solutions with Chelex 100 and Amberlite IRC 748 resins. *Chem. Eng. J. 112*, 211.

(12) Davey, E. W., Gentile, J. H., Erickson, S. J., and Betzer, P. (1970) Removal of trace metals from marine culture media. *Limnol. Oceanogr. 15*, 486–488.

(13) Nikula, T. K., Curcio, M. J., Brechbiel, M. W., Gansow, O. A., Finn, R. D., and Scheinberg, D. A. (1995) A rapid, single vessel method for preparation of clinical grade ligand conjugated monoclonal antibodies. *Nucl. Med. Biol. 22*, 387.

(14) Wu, C., Gansow, O. A., and Brechbiel, M. W. (1999) Evaluation of methods for large scale preparation of antibody ligand conjugates. *Nucl. Med. Biol. 26*, 339.

(15) Vermeer, A. W. P., and Norde, W. (2000) The thermal stability of immunoglobulin: unfolding and aggregation of a multi-domain protein. *Biophys. J. 78*, 394–404.

(16) Shao, J., and Zydney, A. L. (2004) Optimization of ultrafiltration/diafiltration processes for partially bound impurities. *Biotechnol. Bioeng. 87*, 286–292.

(17) Zhu, X., and Lever, S. Z. (2002) Formation kinetics and stability studies on the lanthanide complexes of 1,4,7,10-tetraazacyclododecane-N-N′-N″-N‴-tetraacetic acid by capillary electrophoresis. *Electrophoresis 23*, 1348–1356.

(18) Byegard, J., Skarnemark, G., and Skalberg, M. (1999) The stability of some metal EDTA, DTPA, and DOTA complexes: application as tracers in groundwater studies. *J. Radioanal. Nucl. Chem. 241*, 281–290.

(19) McMenamy, R. H., and Oncley, J. L. (1958) The specific binding of L-tryptophan to serum albumin. *J. Biol. Chem. 233*, 1436–1447.

(20) Klotz, I. M., Triwush, H., and Walker, F. M. (1948) The binding of organic ions by proteins. Competition phenomena and denaturation effects. *J. Am. Chem. Soc. 70*, 2935–2941.

(21) Shao, J., and Zydney, A. L. (2004) Retention of small charged impurities during ultrafiltration. *Biotechnol. Bioeng. 87*, 7–13.

(22) Dufresne, C. (1998) Isolation by Ion-Exchange Methods, in *Natural Products Isolation*, pp 141−164, Humana Press Inc., Totowa, New Jersey.

(23) Lewis, M. R., Raubitschek, A., and Shively, J. E. (1994) A facile, water-soluble method for modification of proteins with DOTA. Use of elevated temperature and optimized pH to achieve high specific activity and high chelate stability in radiolabeled immunoconjugates. *Bioconjugate Chem. 5*, 565–576.

BC800223X

SUPPORTING INFORMATION

Rapid and Efficient Production of Radiolabeled Antibody Conjugates Using Vacuum Diafiltration Guided by Mathematical Modeling

Derek W. Bartlett, David Colcher, Andrew A. Raubitschek*
Division of Cancer Immunotherapeutics & Tumor Immunology, Beckman Research Institute and City of Hope National Medical Center, Duarte, California 91010

List of Contents

Table S1. Observed radiolabeling efficiencies for the pilot-scale and lab-scale diafiltration experiments.

Figure S1. Contour plots showing the impact of different operating parameters on the predicted radiolabeling efficiency as a function of the number of diavolumes using the fixed parameter values for lab-scale diafiltration given in Table 1.

Figure S2. Contour plots showing the impact of different operating parameters on the predicted radiolabeling efficiency as a function of the number of diavolumes using the fixed parameter values for pilot-scale diafiltration given in Table 1 (with the exception that the number of DOTA conjugated per antibody is 5 instead of 2).

Figure S3. Contour plots showing the impact of different operating parameters on the predicted radiolabeling efficiency as a function of the number of diavolumes using the fixed parameter values for lab-scale diafiltration given in Table 1 (with the exception that the number of DOTA conjugated per antibody is 5 instead of 2).

Table S1. Observed radiolabeling efficiencies for the pilot-scale and lab-scale diafiltration experiments. Radiolabeling efficiency is calculated as the fraction of total radioactivity present at the origin (bottom half) of the ITLC strips (see Materials and Methods).

# DV	*Pilot-Scale Diafiltration (In-111, Fresh)*		*Pilot-Scale Diafiltration (In-111, 5-d Decay)*		*Lab-Scale Diafiltration (In-111)*	
	- DTPA	*+ DTPA*	*- DTPA*	*+ DTPA*	*- DTPA*	*+ DTPA*
0	0%	0%			0%	0%
1	0%	0%				
2	0%	0%				
3	0%	0%			0%	0%
4	0%	0%				
5	0%	0%				
6	3%	3%			43%	40%
7	11%	11%				
8	51%	51%	62%	61%		
9	72%	72%	87%	85%	92%	92%
10	87%	87%	94%	94%		
11			95%	95%	96%	96%
12			97%	95%		
13			97%	97%	97%	97%
14			98%	95%		
15			98%	89%	98%	98%
16						
17						
18					98%	98%

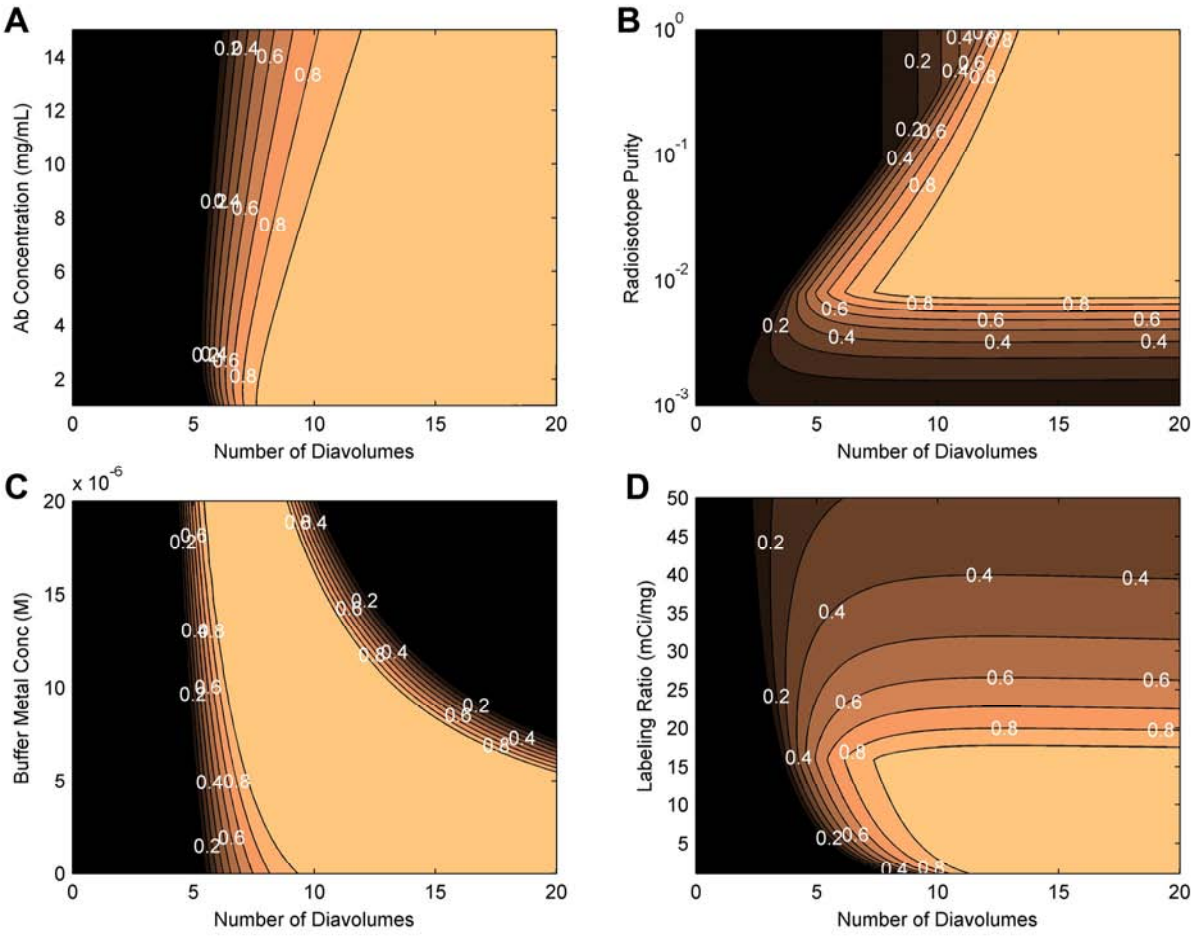

Figure S1. Contour plots showing the impact of different operating parameters on the predicted radiolabeling efficiency as a function of the number of diavolumes for lab-scale diafiltration. Model calculations are used to estimate the predicted radiolabeling efficiency for a range of **(A)** antibody concentrations, **(B)** radioisotope purities, **(C)** metal concentrations in the diafiltration buffer, and **(D)** radiolabeling reaction ratios given as the amount of radioactivity per mass of antibody. Fixed parameter values were chosen to match those of the lab-scale diafiltration experiment as given in Table 1. Lighter color represents higher radiolabeling efficiencies, and labels indicate the radiolabeling efficiency of a given contour line.

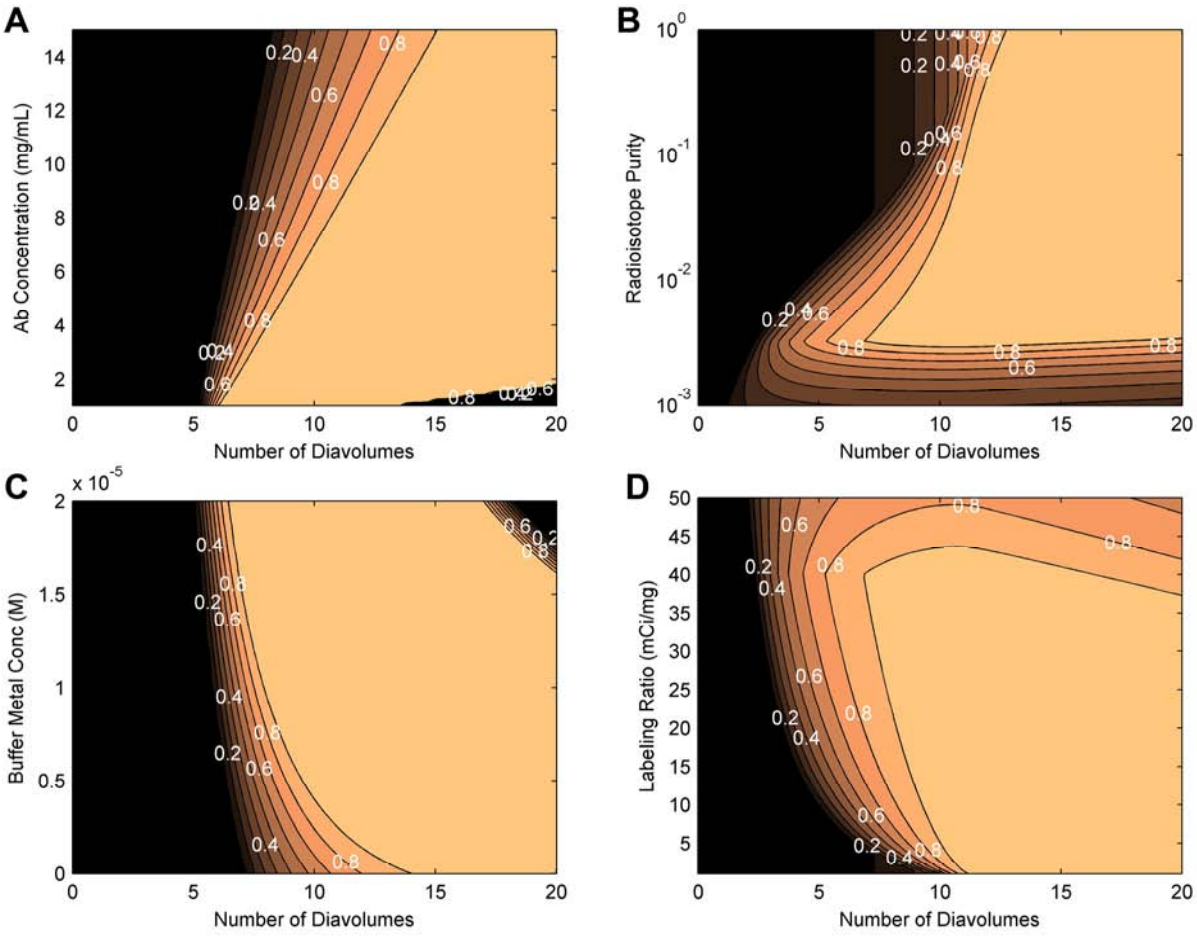

Figure S2. Contour plot showing the impact of different operating parameters on the predicted radiolabeling efficiency as a function of the number of diavolumes for pilot-scale diafiltration – same as Figure 6 except the number of DOTA conjugates per antibody is 5 instead of 2. Model calculations are used to estimate the predicted radiolabeling efficiency for a range of **(A)** antibody concentrations, **(B)** radioisotope purities, **(C)** metal concentrations in the diafiltration buffer, and **(D)** radiolabeling reaction ratios given as the amount of radioactivity per mass of antibody. Fixed parameter values were chosen to match those of the pilot-scale diafiltration experiment as given in Table 1, except the number of DOTA conjugates per antibody is 5 instead of 2. Lighter color represents higher radiolabeling efficiencies, and labels indicate the radiolabeling efficiency of a given contour line.

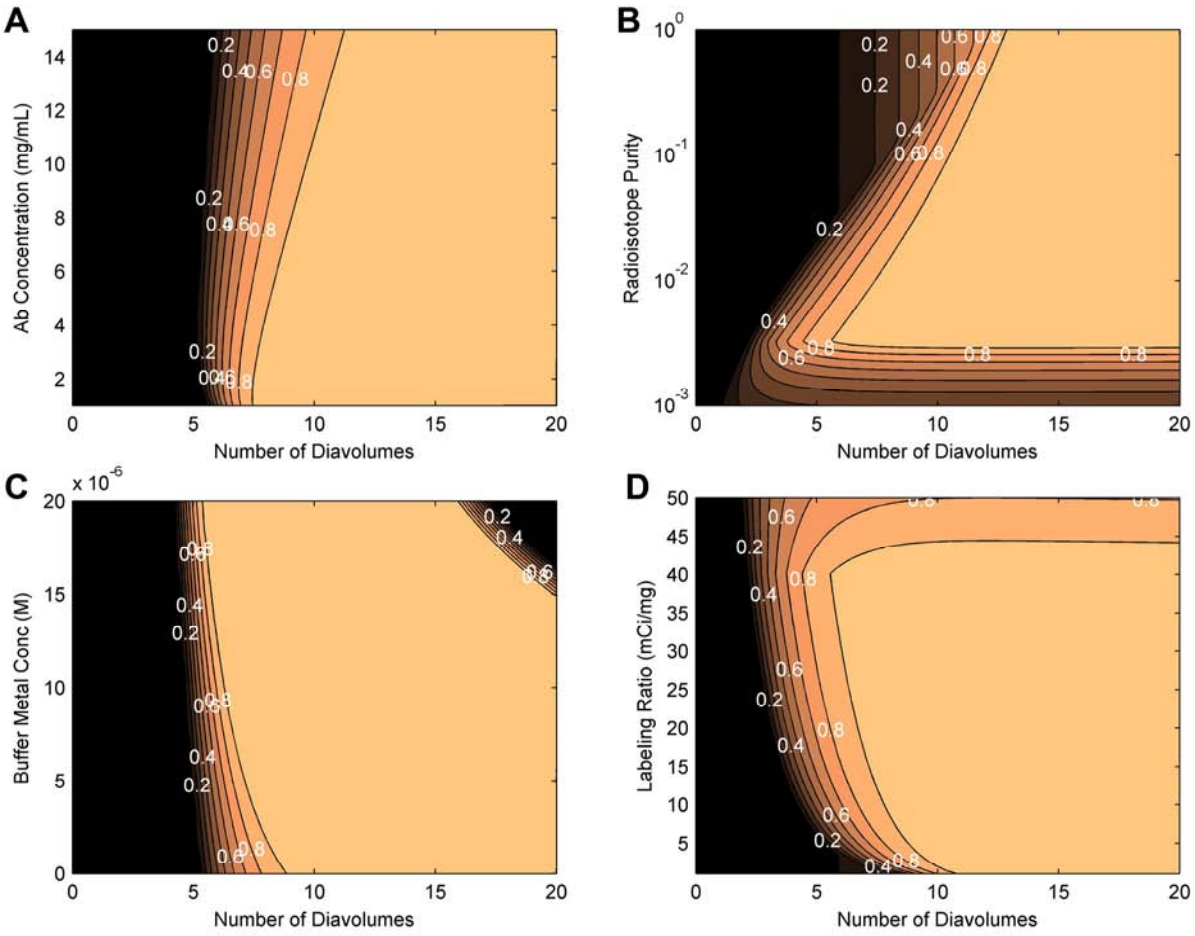

Figure S3. Contour plot showing the impact of different operating parameters on the predicted radiolabeling efficiency as a function of the number of diavolumes for lab-scale diafiltration – same as Figure S1 except the number of DOTA conjugates per antibody is 5 instead of 2. Model calculations are used to estimate the predicted radiolabeling efficiency for a range of **(A)** antibody concentrations, **(B)** radioisotope purities, **(C)** metal concentrations in the diafiltration buffer, and **(D)** radiolabeling reaction ratios given as the amount of radioactivity per mass of antibody. Fixed parameter values were chosen to match those of the lab-scale diafiltration experiment as given in Table 1, except the number of DOTA conjugates per antibody is 5 instead of 2. Lighter color represents higher radiolabeling efficiencies, and labels indicate the radiolabeling efficiency of a given contour line.

TECHNICAL NOTES

Probing Ras Effector Interactions on Nanoparticle Supported Lipid Bilayers

Daniel Filchtinski,[†] Christine Bee,[†] Tudor Savopol,[‡] Martin Engelhard,[‡] Christian F. W. Becker,[‡,§] and Christian Herrmann*[,†]

Physikalische Chemie 1, Ruhr-Universität-Bochum, Fakultät für Chemie and Biochemie, Universitätsstr. 150, 44780 Bochum, Germany, and Max-Planck Institut für Molekulare Physiologie, Abt. Physikalische Biochemie, Otto-Hahn-Str. 11, 44227 Dortmund, Germany. Received March 10, 2008; Revised Manuscript Received July 28, 2008

Many biological processes take place in close proximity to lipid membranes. For a detailed understanding of the underlying mechanisms, tools are needed for the quantitative characterization of such biomolecular interactions. In this work, we describe the development of methods addressing the dynamics and affinities of protein complexes attached to an artificial membrane system. A semisynthetic approach provides the Ras protein with palmitoyl anchors, which allow stable membrane insertion, as a paradigm for membrane associated proteins that interact with multiple effectors. An artificial membrane system is constituted by nanoparticles covered with a lipid bilayer. Such a stable suspension allows for the characterization of the interaction between membrane-bound Ras and effector proteins using conventional fluorescence-based methods.

INTRODUCTION

Many biological processes mediated by the specific interaction between proteins take place in close proximity to the plasma membrane or intracellular compartments. In particular, small GTP binding proteins such as members of the Ras, Rho, and Rab protein families are attached to membranes by insertion of hydrophobic anchor molecules covalently attached to their C-terminal region (*1*−*3*). These proteins interact with various proteins such as regulator and effector proteins, respectively, in order to further propagate the desired biological signal.

Ras is a small GTP binding protein playing a central role in cellular signal transduction. It interacts in a nucleotide dependent manner with downstream effectors such as Raf kinase (*4*), RalGDS (*5*), and Nore1A (*6*), while its activity is regulated by extra- and intracellular inputs through nucleotide exchange factors and GTPase activating proteins (*7*). In all these respects, Ras is the prototype for a large number of GTP binding proteins from various subfamilies (*8*). Crucial for function of Ras is its attachment to the inner leaflet of the plasma membrane achieved through hydrophobic anchors at its C-terminus. For example, one farnesyl group and two palmitoyl groups are linked to the isoform H-Ras by post-translational processing (*1*). The distinct roles of those modifications were investigated in great detail (*1, 9*−*11*). The farnesyl anchor alone is not able to stably attach Ras to the membrane (*1*). Therefore, H-Ras is further modified with the two palmitoyl groups. Importantly, the plasma membrane attachment of Ras correlates with its biological function. Only properly bound to the plasma membrane can H-Ras trigger cell signaling via the activation of the mitogen-activated protein kinase. The nonpalmitoylated H-Ras mislocalizes to the cytosol and fails to promote cell signaling (*10*). In contrast, constructs of H-Ras allowing for palmitoylation but not farnesylation suggested that the membrane attachment can be provided without the farnesyl group (*11*). Nevertheless, most of the biochemical studies on Ras activity and activity of many other proteins lack these modifications neglecting their potential impact and the influence of the membrane surface on interactions with effector proteins. An important issue for understanding the complex network of Ras signaling is its interaction with a defined but varying set of effector proteins depending on the particular task of Ras, such as initiating cell division, contributing to morphology changes, or leading to apoptosis (*12*). In this work, we establish a general method for analyzing protein−protein interactions at membrane surfaces using the interaction between Ras proteins and effectors as a paradigm for such processes. In order to develop a widely usable experimental setup, readily available fluorescence based methods should be used that allow the quantification of both Ras/effector affinities as well as dynamics. The artificial membrane system devised for this purpose is based on lipid coated nanoparticles with a defined size. Using a suspension of such lipidated nanoparticles allows the application of fluorescence assays previously developed in our laboratory in order to characterize Ras/effector interactions. The necessary membrane anchor is incorporated into Ras by expressed protein ligation (EPL) (*13*) where a chemically synthesized peptide carrying two palmitoyl groups is ligated to the C-terminus of Ras (*14*).

EXPERIMENTAL METHODS

Peptide Synthesis. Solid phase peptide synthesis was performed manually using Fmoc-chemistry (*15*). Cleavage of ivDde-protecting groups was achieved with 3% hydrazine in DMF. Subsequent palmitoylation was carried out with 20 equiv of palmitoylchloride, 20 equiv of *N*-hydroxybenzotriazole, and

* Corresponding author. Tel: +49 234 3224173. Fax: +49 234 3214785. E-mail: chr.herrmann@rub.de.

[†] Ruhr-Universität-Bochum.

[‡] Max-Planck Institut für Molekulare Physiologie.

[§] Current address: Technische Universität München, Department Chemie, Lichtenbergstr. 4, 85747 Garching and Center for Integrated Protein Science Munich.

10.1021/bc800099p CCC: $40.75 © 2008 American Chemical Society
Published on Web 08/20/2008

22 equiv of triethylamine in dichlormethane/dimethylformamide (3:1) for 4 h. Cleavage was achieved by 2.5% H_2O and 5% triisopropylsilane in trifluoracetic acid (TFA). The crude product was precipitated with diethyl ether, dissolved in 50% aqueous acetonitrile (0.1% TFA), and lyophilized. Purification was carried out by RP-HPLC on C4-columns from Vydac using linear gradients of acetonitrile with 0.08% TFA in water.

Bacterial expression and purification of the effector RBDs was described earlier (*16*). Briefly, the resuspended bacterial cell pellet was sonicated, the cell lysate was cleared by centrifugation, and the GST fusion proteins were purified by glutathione sepharose affinity chromatography followed by size exclusion chromatography.

Preparation of Double Palmitoylated Ras. The DNA insert coding for C-terminally truncated H-Ras (1−180) was subcloned into the multiple cloning site of a pTXB1 vector (New England Biolabs) to express H-Ras (1−180) as fusion protein with a C-terminal intein from *M. xenopi* and the chitin binding domain from *B. circulans*. The vector was transformed into the *E. coli* BL21(DE3) strain. For protein expression, the 50 mL starting culture in LB containing 100 μg/mL Ampicillin was transferred to 10 L of the same media, and the media were incubated at 37 °C until an OD_{600} of 0.6 was reached. Expression of the fusion protein was induced by addition of 100 μM IPTG, and the culture was incubated at 37 °C overnight. The bacteria were harvested by centrifugation, and the cell pellet was resuspended in buffer A (25 mM Tris (pH 7.9), 100 mM NaCl, and 5 mM $MgCl_2$) and 1 mM PMSF. Cell lysis was achieved by 10 min of sonication (Bendelin), and the lysate was centrifuged to remove insoluble cell material. The supernatant was applied to a 40 mL chitin column (New England Biolabs) equilibrated with buffer A. The chitin material loaded with fusion protein was washed with 5 column volumes of buffer A and incubated for three days in buffer A containing 250 mM MESNA (sodium 2-mercaptoethane sulfonate) at 4 °C in order to form the H-Ras(1−180)-thioester. The cleaved protein was separated from the chitin beads, concentrated by ultrafiltration (Vivaspin) to a volume of 5 mL and further purified by size exclusion chromatography (Superdex 75 26/60, Pharmacia). The fractions containing H-Ras-thioester were pooled and concentrated using ultrafiltration (Vivaspin) to a final concentration of 70 mg/mL. The protein was shock frozen in liquid nitrogen and stored at −80 °C.

Three hundred micromolars of the protein were incubated with 5.4 molar excess of the double palmitoylated 2Palm-3PPO-peptide in the presence of 200 mM MESNA for 4 days. The ligation product was selectively precipitated from the reaction mixture by the addition of 400 mM ammonium sulfate, redissolved in buffer A, shock frozen in liquid nitrogen, and stored at −80 °C.

Peptide and protein masses were determined by electrospray ionization mass spectrometry on an LCQ Advantage Max (Finnigan) operating in positive ion mode. The molecular masses were deconvoluted from the ion spectra.

Preparation of Lipidated Nanoparticles. The amount of 1,2-dioleoyl-*sn*-glycero-3-phosphocholine (DOPC, Sigma) required in order to achieve a 40-fold excess of lipid surface over the nanoparticle surface (26 mg of DOPC) was dissolved in 2 mL of chloroform, dried under a stream of nitrogen, and subsequently dried for 2 h in vacuum. The lipid film was rehydrated in 2−4 mL of buffer A flushed with argon. The suspension was then sonicated and cooled on ice (Brenson Sonifier 250 Cup Horn) until it was clear and then ultracentrifuged (Beckman) at 100,000*g*. The clear supernatant containing small unilamellar vesicles (SUV) was used for nanoparticle preparation.

Then, 100 μL of a 50 mg/mL stock solution of silica nanoparticles (Micromod, Germany) was washed with 1 mL methanol, 1 mL 1 M KOH, and five times with buffer A, respectively. Separation of nanoparticles from supernatant was achieved by centrifugation (table top centrifuge, 5000 rpm). After washing, the nanoparticle suspension was mixed with the supernatant of the lipid preparation, flushed with argon, and incubated under gentle rotation for 2 h at room temperature. After lipidation, 1 mL of the nanoparticle suspension was washed twice to remove excess DOPC and mixed with 144 μg of the double palmitoylated H-Ras to cover (calculated) 20% of the nanoparticle surface. For this calculation, a particle radius of 130 nm, a particle concentration of 2.5 mg/mL, a particle density of 2 g/cm^3, and a footprint of Ras of 9 nm^2 were assumed. The suspension was incubated at room temperature overnight under gentle rotation, washed twice to remove the nonmembrane bound protein, and used for the GDI-assay and stopped flow experiments in concentrations of 0.05 μM and 0.25 μM, respectively. The characterization of particle size distribution was achieved by the dynamic light scattering technique. Samples of DOPC small unilamellar vesicles and lipidated nanoparticles were filtered using 0.45 μm filters, whereas blank nanoparticles were sonicated prior to addition into the cuvette. For the measurement, a He-Ne-Laser (633 nm) with a power of 35 mW was used, and the signal was collected at 90° using a four-quadrant detector (ALV 5001, Langen, Germany). The autocorrelation traces were fitted using the ALV software package, calculating the weight averaged particle size (*17*).

Measurement of Interactions. In order to detect the interaction between Ras proteins and effectors in solution, various fluorescence based methods were developed previously. The *N*-methyl-anthraniloyl (mant) group attached to the guanine nucleotide serves as a fluorescence label in these experiments. Ras, which is tightly bound to GDP after the purification, is loaded with mantGppNHp by addition of a 5-fold excess of this nucleotide and 10 mM EDTA, and overnight incubation at 4 °C. The nucleotide excess was removed by Zeba Desalt Spin Columns (Pierce) following the desalting instructions of the manufacturer. Loading was examined by C18 reversed phase HPLC. The so-called GDI-assay (*g*uanine nucleotide *d*issociation *i*nhibitor) takes advantage of a large fluorescence change upon dissociation of the mant-nucleotide after addition of a large excess (1000-fold) of nonfluorescent GppNHp. The time course of the decrease in fluorescence is measured by a Perkin-Elmer LS 55 fluorescence spectrometer with an excitation wavelength of 360 nm and an emission wavelength of 450 nm at 37 °C using buffer A. A single exponential function is fitted to the fluorescence traces yielding the observed rate constant k_{obs} representing the rate of the dissociation of mantGppNHp and Ras. Dependent on the binding of Ras effectors such as Raf, RalGDS, and Nore1A, the nucleotide dissociation rate is decreased. The observed rate constants are plotted against the concentration of the effector, and a quadratic function is fitted to the data in order to yield the K_D values of the Ras/effector interaction as described earlier (*16*, *18*).

In order to obtain, in addition to the K_D values, the individual rate constants for the Ras/effector association and dissociation, the stopped flow method was used (*19*, *20*). Again, this is a well established method for dynamic measurements of Ras/effector interactions in solution. Using a stopped flow apparatus (Biologic, Grenoble, France), Ras loaded with mantGppNHp and effector solutions were rapidly mixed and the fluorescence traces recorded. A 10-fold excess of the effector ensures pseudo-first-order conditions. To improve the fluorescence signal-to-noise ratio, fluorescence resonance energy transfer (FRET) was employed by the use of Ras·mantGppNHp and the tryptophan mutant Nore1A M305W. The largest fluorescence changes were observed at low temperatures, and therefore, kinetic measurements were performed at 10 °C in buffer A using an excitation

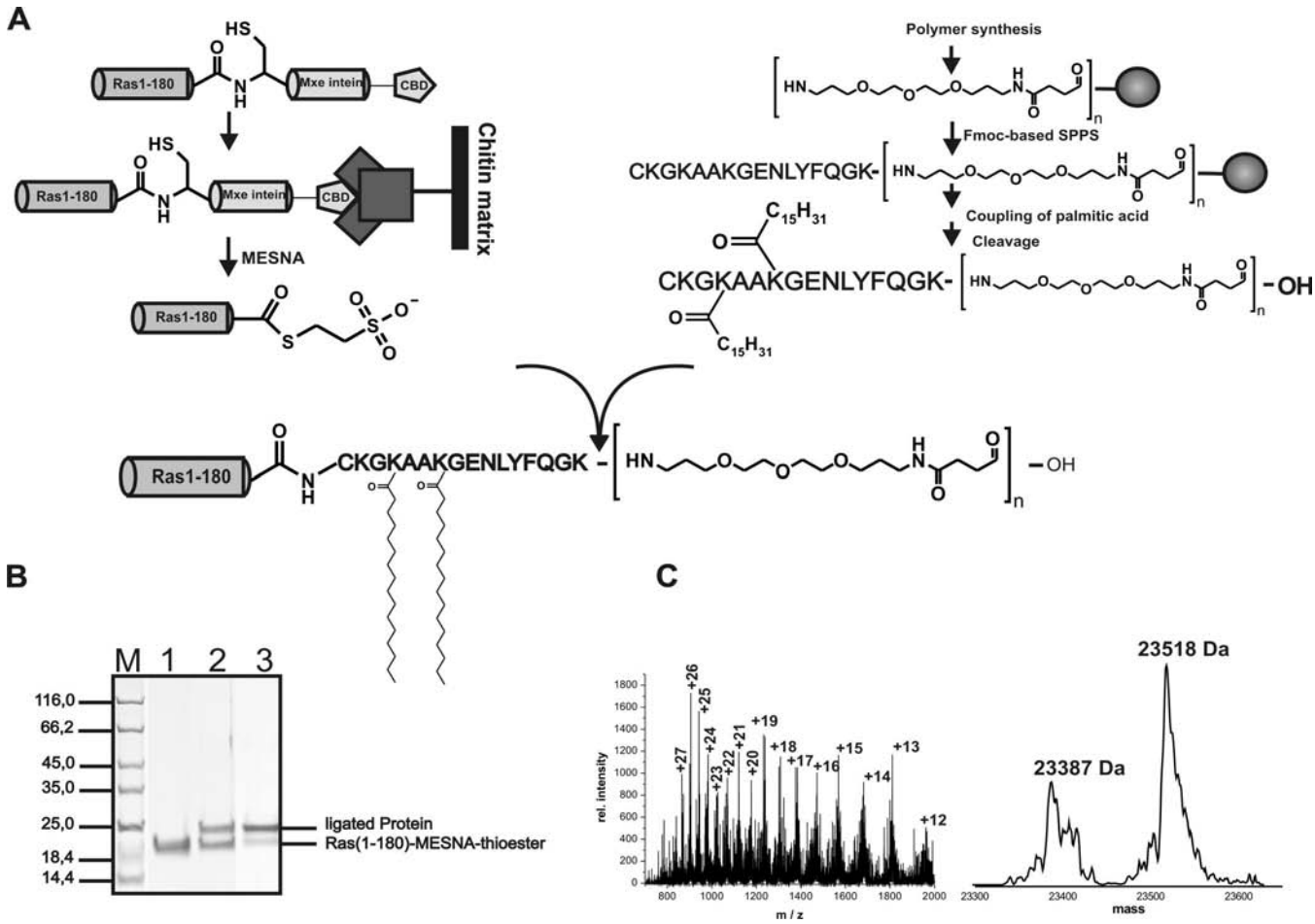

Figure 1. Synthesis of a double palmitoylated Ras variant. (A) Solid phase synthesis of a polymer-modified palmitoylated peptide (2Palm-3PPO peptide with $n = 3$; mass, 3196.1 Da) and native chemical ligation of Ras1−180 thioester with this peptide. (B) SDS−PAGE of the ligation mixture. Lane 1, Ras-MESNA thioester; lane 2, ligation mixture after one day; lane 3, ligation mixture after four days. (C) ESI-MS of the purified ligation product Ras2Palm-3PPO. The deconvoluted spectrum is shown on the right and contains 2 peaks corresponding to Ras-2Palm-3PPO with a theoretical mass of 23519.3 Da and missing its N-terminal methionine with a theoretical mass of 23388.1 Da.

wavelength of 290 nm and a fluorescence light cut off filter of 420 nm. To determine the dissociation rate constant, the double palmitoylated Ras immobilized on lipidated nanoparticles was incubated with Nore1A M305W at a concentration of 2 μM and rapidly mixed in the stopped flow apparatus with Ras loaded with the nonfluorescent GppNHp to displace the effector.

RESULTS

Palmitoylated Ras by Expressed Protein Ligation. In order to study Ras/effector interactions under conditions close to their native environment, Ras was equipped with an artificial membrane anchor. Figure 1A summarizes the strategy for the synthesis of double palmitoylated Ras. H-Ras encompassing residues 1−180 is expressed as a fusion construct with an intein and a chitin binding domain in *E. coli* and purified by affinity chromatography. By incubation with MESNA, H-Ras (1−180) is cleaved off harboring a reactive thioester at its C-terminus (*21*). In parallel, a peptide is synthesized with a cysteine at the N-terminus and two palmitoyl groups coupled to lysine side chains according to Figure 1A. In order to improve handling properties and solubility of this peptide, a polyethylene glycol polyamide oligomer (PPO) comprising three PPO subunits was introduced at the C-terminus without affecting the membrane binding properties (Figure 1A) (*22, 23*). Peptides containing shorter PPOs comprising two or only one subunit have been prepared, but these shorter PPOs do not efficiently solubilize the lipidated peptide in aqueous buffers during purification and ligation. This water-soluble 2Palm-3PPO-peptide is ligated to Ras using a large excess of MESNA as ligation mediator (Figure 1A). The ligation reaction proceeds slowly but reaches a yield of 90% after four days (Figure 1B). LC-MS analysis and deconvolution of the resulting ESI spectrum shows two mass peaks that correspond to the ligation product Ras-2Palm-3PPO (calculated mass: 23519.3 Da) with and without the N-terminal methionine (Δmass: 131.2 Da, Figure 1C). The product was precipitated by the addition of 400 mM ammonium sulfate and separated from unligated Ras protein that remained soluble. The redissolved ligation product was loaded with the fluorescent GTP analogue mantGppNHp by incubation with a 5-fold excess of this nucleotide in the presence of 10 mM EDTA.

Ras Attached to Nanoparticle Supported Lipid Bilayers. As a membrane mimic, we chose nanoparticle supported lipid bilayers that were prepared using a procedure similar to that described by Richter et al. (*24*). Small unilamellar vesicles (SUV) made of DOPC by sonication collapse onto silica beads. The size and integrity of the particles were characterized by dynamic light scattering studies and autocorrelation analysis (Figure 2A). The polydispersity index of 0.10 and 0.08, for blank and lipidated nanoparticles, respectively, indicates a narrow distribution of the particle size before and after lipidation. The hydrodynamic radius of the lipidated particles was measured to 130 nm (Figure 2B). This nanoparticle supported lipid bilayer system should be well suited for membrane anchor insertion of Ras and other proteins carrying palmitoyl groups as these

anchors are shorter than half the bilayer thickness. A high mechanical stability without loss of fluidity is provided (*25*), and these particles are easy to handle, e.g., for changing buffers or concentrating the particles by gentle centrifugation and resuspension. A large, defined surface area can be offered with varying lipid composition. Double palmitoylated Ras was inserted into this artificial membrane by the addition of the protein amount required for covering of the desired fraction of lipid surface. A reasonable upper limit of coverage seemed to be 20%, and the required protein concentration [Ras] was calculated according to eq 1

$$[\mathrm{Ras}] = \frac{[\mathrm{nanoparticle}] \cdot A_{\mathrm{nanoparticle}}}{\rho \cdot V_{\mathrm{nanoparticle}} \cdot A_{\mathrm{Ras}} \cdot N_{\mathrm{A}}} \cdot 20\% \qquad (1)$$

where A_{Ras} is the footprint of the Ras-protein estimated from its structure to be 9 nm^2 and N_{A} the Avogadro constant. [nanoparticle] is the concentration of nanoparticles in mg/mL, ρ is the density of the nanoparticles taken from the manufacturer information, which is 2 $\mathrm{g/cm}^3$. $V_{\mathrm{nanoparticle}}$ and $A_{\mathrm{nanoparticle}}$ are the volume and the surface area of the single nanoparticle, respectively, that were determined from the radius. After incubation overnight, 25% of added Ras (1 μM) was immobilized as judged by SDS−polyacrylamide electrophoresis of samples from the separated phases. This corresponds to the amount of ca. 1000 molecules of Ras per lipidated nanoparticle. Noninserted Ras was removed by two washing cycles.

Affinity of Ras/Effector Interactions at Artificial Membranes. In order to characterize the interaction of Ras immobilized on the lipidated particles with other proteins, we employed fluorescence based methods previously established for studying Ras/effector binding in solution. In order to perform the GDI assay (*16*, *18*), Ras immobilized on lipidated nanoparticles and loaded with *N*-methyl-anthraniloyl-GppNHp (mantGppNHp) is incubated with effector proteins at defined concentrations. The mant-nucleotide is excited at 360 nm, and fluorescence is detected at 450 nm. The particle suspension shows no detectable sedimentation even after 1 h, and therefore, continuous stirring is not required. Intriguingly, light scattering of the milky particle suspension only weakly interferes with fluorescence excitation and emission. Compared to fluorescence measurements in solution with approximately 50% fluorescence decrease after mantGppNHp dissociation, the scattering background in the presence of lipidated particles still gives rise to ca. 20% change of the initial signal. From this, approximately equal contributions to the signal by light scattering and fluorescence can be estimated (Figure 3A).

The affinity of three different effector proteins was titrated with help of the GDI assay. This assay relies on the inhibition of the dissociation of the guanine nucleotide by effector binding, and an increasing Ras/effector complex concentration is reported by a decreasing dissociation rate of the nucleotide (*26*). A single exponential fit (Figure 3B) yields the observed rate constant, which is plotted versus effector concentration in Figure 3C and D. From this, the K_{D} value of the Ras/effector complex is obtained by fitting a quadratic equation. An overall error on the K_{D} values of 30% is estimated from the experimental errors on the kinetic data and the measurements of the protein concentrations. The results are listed in Table 1 together with the data obtained in solution. Only an increase by a factor of 1.5 to 3 is observed for the K_{D} values of all three effectors when measuring membrane bound Ras. It should be stressed here that only the Ras binding domain of the effectors was used in these studies. Other domains of the effector adjacent to the RBD as the cysteine rich region in Raf and Nore1A may contribute to membrane interaction as well (*27*, *28*).

Dynamics of Ras/Effector Interactions at Artificial Membranes. For measuring the dynamics of the interaction between effector protein and Ras attached to an artificial membrane through its C-terminal palmitoyl anchors we used a stopped flow apparatus (biologic, France). Again, the presence of lipid bilayer covered nanoparticles does not pose any technical problems. But, as in solution, the relative change of mant-fluorescence upon formation of the Ras/effector complex is much smaller compared to the mant-nucleotide dissociation measured in the GDI-assay. It is less than 10% even in the absence of particles and decreases to 3% in the presence of our nanoparticle preparations. Therefore, we used a FRET couple based on a Trp residue introduced at position 305 of Nore1A (donor) and the mant-nucleotide (acceptor) bound to Ras in order to obtain a clear fluorescence readout for complex formation. Fluorescence was excited at 290 nm and detected through a 420 nm cutoff filter. Fluorescence changes were much larger at lower temperatures, and therefore, we measured at 10 °C. The fit to the fluorescence time course by a single exponential equation did not yield satisfying residuals. Therefore, a double exponential function was used, and the observed rate constant of the faster phase was plotted against effector concentration (Figure 4A). The linear plot of the observed rate constants versus Nore1A concentration yields a value of 1.5 $\mu\mathrm{M}^{-1}\ \mathrm{s}^{-1}$ for the apparent association rate constant k_{on} (Figure 4B), which compares to 8.9 $\mu\mathrm{M}^{-1}\ \mathrm{s}^{-1}$ for Nore1A wild type in solution in the absence of NaCl (*29*). Notably, the second phase is almost as large in amplitude as the first one, and it is 15−20-fold slower than the fast reaction. In control stopped flow experiments using the same buffer, the same Nore1A mutant and Ras loaded with mantGppNHp but without the palmitoyl modification, we observed single exponential fluorescence changes yielding a k_{on} value of 3.3 $\mu\mathrm{M}^{-1}\ \mathrm{s}^{-1}$. There is no slow phase of association of Ras/Nore1A in solution.

The dissociation rate constant k_{off} can be obtained from the intercept of the plot in Figure 4B, and it is obvious from this that the k_{off} value is close to zero and therefore not well defined

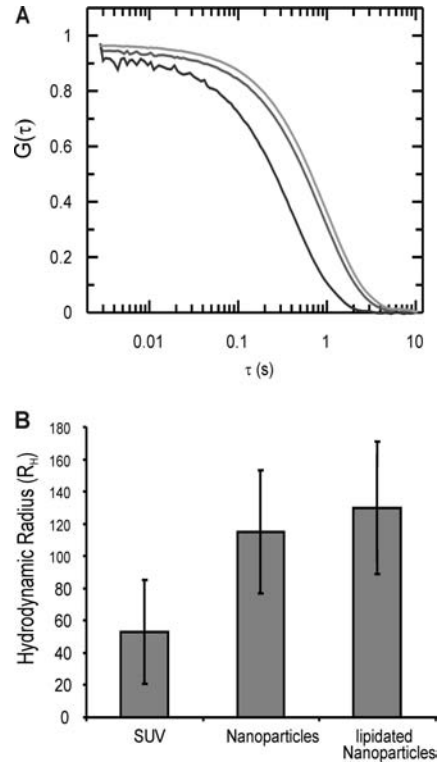

Figure 2. Dynamic light scattering and particle size distribution. (A) Autocorrelation curves of small unilamellar vesicles, naked nanoparticles, and lipidated particles (from left to right). (B) The histogram shows the hydrodynamic radii of these three species where the width of the size distribution (at half-maximum value) is indicated by the vertical lines at the top of the bars.

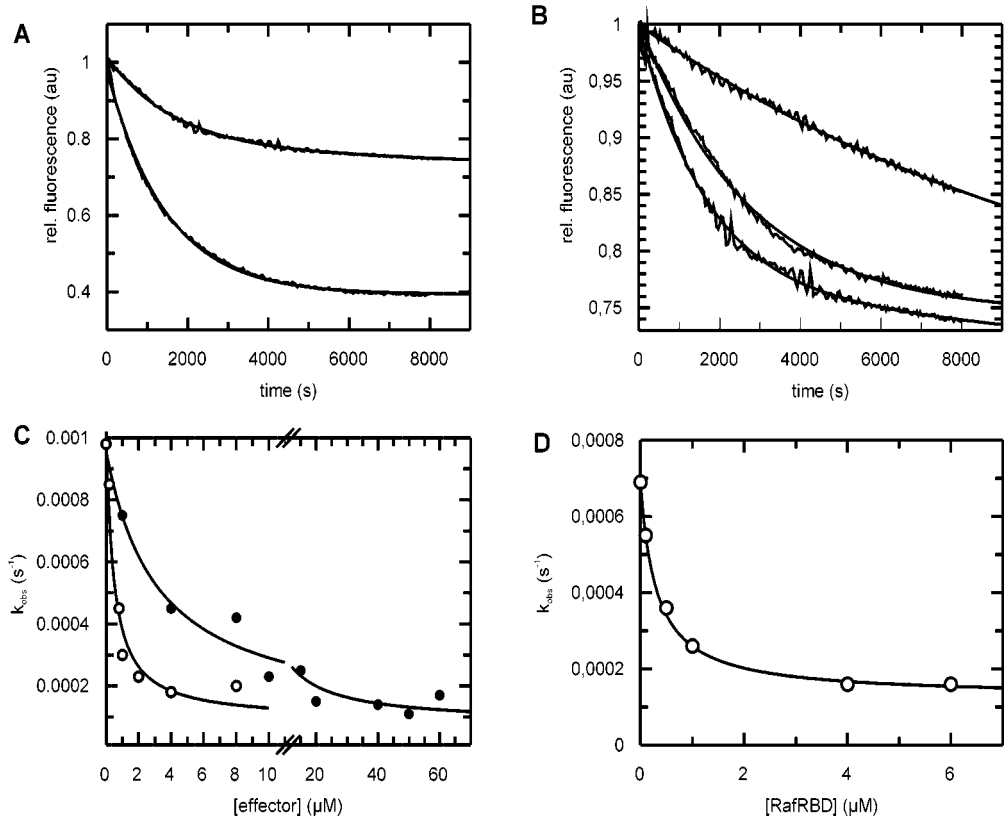

Figure 3. Ras/effector affinity measured by GDI-assay. The basis of the GDI assay is the dissociation of mantGppNHp from Ras achieved by the addition of an excess of nonfluorescent nucleotide and indicated by the strong decrease of fluorescence in buffer. (A) Ras-2Palm-3PPO bound to lipidated nanoparticles with a decay amplitude of 24% (upper curve) and in solution (lower curve) with a decay amplitude of 60%. (B) Fluorescence traces of the GDI-assay with the double palmitoylated Ras immobilized on lipidated nanoparticles in the presence of 0 μM, 0.5 μM, and 2.0 μM Raf-RBD (from bottom to top). (C) GDI plot for Ras-2Palm-3PPO with Nore1A (○) and RalGDS (●) as effectors, and (D) with Raf on lipidated nanoparticles each, fitted with a quadratic equation yielding the K_D values given in Table 1.

Table 1. Ras/Effector Affinity[a]

effector	K_D (μM) in solution	K_D (μM) on lipid. part.
Nore1A M305W	0.3	0.45
RalGDS	3.5	3.2
Raf	0.13	0.3

[a] K_D values for Ras·mantGppNHp/effector complexes in solution (*28, 30*−*32*) and on lipidated nanoparticles, respectively, obtained from GDI experiments at 37 °C, with an overall error of 30%. The solutions in all experiments contained 100 mM NaCl and were buffered with 25 mM Tris at pH 7.9 and 5 mM $MgCl_2$.

by this experiment. Nevertheless, this rate constant can be determined with high precision by a displacement experiment. The preformed complex of Ras·mantGppNHp and Nore1A-(M305W) is mixed with an excess of nonfluorescent Ras. The overall rate of the formation of the nonfluorescent complex is controlled by the dissociation of the preformed complex. In Figure 4C, the observed fluorescence time course is shown representing the dissociation of the Ras·mantGppNHp/Nore1A M305W complex. A single exponential equation plus linear slope is fitted to this curve, which yields a value of $k_{off} = 0.15$ s^{-1} (0.18 s^{-1} in solution) (*30*) for the dissociation of the complex. The slower linear decrease of fluorescence can be attributed to photo bleaching as demonstrated in control experiments. Together, from these stopped flow experiments, a K_D value of 0.10 μM is calculated that fits well to the GDI results above when taking the temperature difference into account.

DISCUSSION

Many biochemical studies report on the characterization of protein/protein interactions, but most of them ignore the membranous environment in the case when one of the partner proteins is usually bound to a membrane and neglect the possible implications for binding affinity and dynamics. With the present work, we provide a versatile method that allows one to take into account the effect of membranes on interactions between proteins of which one is attached to the membrane. We show here that conventional fluorescence techniques developed for studies in solution are also applicable for measurements of Ras/effector interactions on nanoparticle supported lipid bilayers.

An efficient synthesis of native-like small GTP binding proteins is the crucial requirement for investigations of protein interactions at membrane, if possible with the option to vary the composition of the hydrophobic anchorage. Here, expressed protein ligation was successfully employed in order to link a small synthetic peptide equipped with the desired hydrophobic anchor moieties to the Ras protein synthesized in bacteria. The Ras protein carrying two palmitoyl groups at the C-terminus was obtained in high yield, was easy to purify, and was shown to be intact in terms of nucleotide and effector binding, respectively.

As an artificial membrane system, we selected nanoparticles covered with DOPC lipids. As shown by others, such particles are straightforward to prepare, and they are covered homogenously by a lipid double layer. Incubation with palmitoylated Ras leads to attachment of the protein to the lipid surface by insertion of the hydrophobic moieties into the bilayer. Control experiments with unmodified Ras and other proteins such as the effectors clearly prove that there is no tendency of these

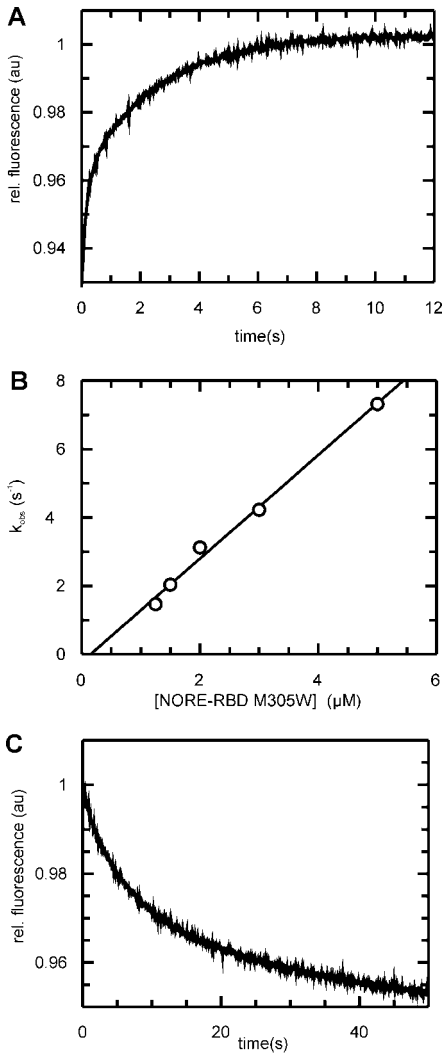

Figure 4. Interaction dynamics characterized by stopped flow. (A) Ras-2Palm-3PPO in complex with mantGppNHp and bound to lipidated nanoparticles was mixed with varying concentrations of Nore1A M305W in a stopped flow apparatus. Double exponential equations were fitted to the fluorescence traces recorded. (B) The observed rate constants of the fast phase are plotted versus the concentration. The slope of the linear fit yields the k_{on} value of 1.5 μM^{-1} s^{-1}. (C) Dissociation of the complex between double palmitoylated Ras·mantGppNHp on nanoparticles and Nore1A M305W. For displacement, an excess of GppNHp loaded Ras was mixed with the preformed complex. The exponential part of the curve yields the k_{off} value of 0.15 s^{-1}.

proteins to stick to the lipidated particles. The particles can be spun down and resuspended, which facilitates separation of bilayer-bound protein from soluble proteins as well as changing buffer conditions, e.g., during nucleotide exchange in Ras. The suspension of these particles with and without Ras attached is stable for hours as no sedimentation or coagulation is observed, and moreover, dynamic light scattering demonstrates a low degree of polydispersity and indicates an average particle radius of 130 nm. Thus, a robust and versatile protein/membrane system is provided, suitable for investigations with various biophysical techniques including spectroscopy.

We aimed at a quantitative characterization of Ras/effector interactions beyond their qualitative verification by experiments such as cosedimentation. Surprisingly, we found that conventional fluorescence spectroscopy is only perturbed a little by interference of light scattering originating from the nanoparticle suspension. Therefore, we were able to employ fluorescence assays previously established for studies on Ras/effector complexes in solution. For three different effector proteins, the GDI assay with Ras attached to lipidated particles yielded values of the equilibrium dissociation constant (K_D) that are similar to the respective values obtained in solution (Table 1). These results demonstrate on the one hand that the Ras binding domains of the effectors used in these studies do not contribute to membrane binding and on the other hand that the membrane environment does not change the ability of Ras to bind to the effector. There is no significant interference and no enhancement either. The GDI assay used in this pilot study is an indirect method as it reports the increasing saturation of Ras/effector binding through a decreased rate of nucleotide exchange. This is a big advantage here since artifacts such as unspecific effector binding to the particles can be excluded. The GDI effect most clearly indicates a specific interaction between Ras and effector protein showing the same characteristics as those in solution and emphasizing the full integrity of our Ras/membrane system.

We utilized stopped flow with fluorescence detection in order to determine the rate constants of Ras/effector interactions. After mixing Ras·mantGppNHp attached to nanoparticle supported lipid bilayers and the Trp mutant of Nore1A (M305W), the observed fluorescence traces were analyzed. There is a biphasic behavior with two rate constants, which are different by more than a factor of 10. The concentration dependence of the faster phase yields a k_{on} value comparable to Ras/Nore1A association in solution where the value for nonmodified Ras is two times larger. The slow phase of the association suggests the presence of another species of Ras immobilized on the lipidated nanoparticles, which seems to be not directly accessible for Nore1A binding. Notably, the dissociation is a single exponential and indicates a homogeneous Ras/Nore1A complex population. The k_{off} value extracted from the single exponential fit to the displacement experiment is almost identical to the value obtained for the complex in solution. Similar to the equilibrium data, we can conclude that the results on the rate constants for association and dissociation of the Ras/Nore1A complex are not significantly different when soluble and membrane bound Ras are compared apart from an unknown fraction of Ras binding Nore1A 10 times more slowly.

In summary, we demonstrated the application of readily available fluorescence techniques for the investigation of protein/protein interactions at the surface of an artificial membrane system based on nanoparticle supported lipid bilayers. Not only protein complex affinity but also binding dynamics can be quantified. The interaction of double palmitoylated, membrane bound Ras with the RBD of three different effectors does not show significant differences to the results obtained from studies in solution. In a next step, this experimental setup can be used in order to address the role of other protein domains located next to the RBD of the respective effector proteins. To this end, we provide a widely usable assay that will allow the determination of the influence of membrane composition one the one hand and lipid binding domains such as C1 and PH domains on the other hand on the overall interaction of protein complexes located at lipid membranes.

ACKNOWLEDGMENT

We are grateful for financial support by Gerhard C. Starck Stiftung (grant to D.F.), Deutsche Forschungsgemeinschaft (SFB 642), and Fonds der chemischen Industrie.

LITERATURE CITED

(1) Hancock, J. F., Magee, A. I., Childs, J. E., and Marshall, C. J. (1989) All ras proteins are polyisoprenylated but only some are palmitoylated. *Cell 57*, 1167–1177.

(2) Hori, Y., Kikuchi, A., Isomura, M., Katayama, M., Miura, Y., Fujioka, H., Kaibuchi, K., and Takai, Y. (1991) Post-translational

modifications of the C-terminal region of the rho protein are important for its interaction with membranes and the stimulatory and inhibitory GDP/GTP exchange proteins. *Oncogene 6*, 515–522.

(3) Khosravi-Far, R., Lutz, R. J., Cox, A. D., Conroy, L., Bourne, J. R., Sinensky, M., Balch, W. E., Buss, J. E., and Der, C. J. (1991) Isoprenoid modification of rab proteins terminating in CC or CXC motifs. *Proc. Natl. Acad. Sci. U.S.A. 88*, 6264–6268.

(4) Koide, H., Satoh, T., Nakafuku, M., and Kaziro, Y. (1993) GTP-dependent association of Raf-1 with Ha-Ras: identification of Raf as a target downstream of Ras in mammalian cells. *Proc. Natl. Acad. Sci. U.S.A. 90*, 8683–8686.

(5) Spaargaren, M., and Bischoff, J. R. (1994) Identification of the guanine nucleotide dissociation stimulator for Ral as a putative effector molecule of R-ras, H-ras, K-ras, and Rap. *Proc. Natl. Acad. Sci. U.S.A. 91*, 12609–12613.

(6) Vavvas, D., Li, X., Avruch, J., and Zhang, X. F. (1998) Identification of Nore1 as a potential Ras effector. *J. Biol. Chem. 273*, 5439–5442.

(7) Vetter, I. R., and Wittinghofer, A. (2001) The guanine nucleotide-binding switch in three dimensions. *Science 294*, 1299–1304.

(8) Wennerberg, K., Rossman, K. L., and Der, C. J. (2005) The Ras superfamily at a glance. *J. Cell Sci. 118*, 843–846.

(9) Hancock, J. F., Paterson, H., and Marshall, C. J. (1990) A polybasic domain or palmitoylation is required in addition to the CAAX motif to localize p21ras to the plasma membrane. *Cell 63*, 133–139.

(10) Dudler, T., and Gelb, M. H. (1996) Palmitoylation of Ha-Ras facilitates membrane binding, activation of downstream effectors, and meiotic maturation in Xenopus oocytes. *J. Biol. Chem. 271*, 11541–11547.

(11) Booden, M. A., Baker, T. L., Solski, P. A., Der, C. J., Punke, S. G., and Buss, J. E. (1999) A non-farnesylated Ha-Ras protein can be palmitoylated and trigger potent differentiation and transformation. *J. Biol. Chem. 274*, 1423–1431.

(12) Cox, A. D., and Der, C. J. (2003) The dark side of Ras: regulation of apoptosis. *Oncogene 22*, 8999–9006.

(13) Muir, T. W. (2003) Semisynthesis of proteins by expressed protein ligation. *Annu. Rev. Biochem. 72*, 249–289.

(14) Olschewski, D., Seidel, R., Miesbauer, M., Rambold, A. S., Oesterhelt, D., Winklhofer, K. F., Tatzelt, J., Engelhard, M., and Becker, C. F. (2007) Semisynthetic murine prion protein equipped with a GPI anchor mimic incorporates into cellular membranes. *Chem. Biol. 14*, 994–1006.

(15) Atherton, E. and Sheppard, R. C. (1989) *Solid Phase Peptide Synthesis: A Practical Approach*, The Practical Approach Series, pp 1−216, Oxford University Press, New York.

(16) Herrmann, C., Horn, G., Spaargaren, M., and Wittinghofer, A. (1996) Differential interaction of the ras family GTP-binding proteins H-Ras, Rap1A, and R-Ras with the putative effector molecules Raf kinase and Ral-guanine nucleotide exchange factor. *J. Biol. Chem. 271*, 6794–6800.

(17) Koppel, D. E. (1972) Analysis of macromolecular polydispersity in intensity corrleation spectroscopy: The method of cumulants. *J. Chem. Phys. 57*, 4814–4820.

(18) Herrmann, C., and Nassar, N. (1996) Ras and its effectors. *Prog. Biophys. Mol. Biol. 66*, 1–41.

(19) Linnemann, T., Kiel, C., Herter, P., and Herrmann, C. (2002) The activation of RalGDS can be achieved independently of its Ras binding domain. Implications of an activation mechanism in Ras effector specificity and signal distribution. *J. Biol. Chem. 277*, 7831–7837.

(20) Sydor, J. R., Engelhard, M., Wittinghofer, A., Goody, R. S., and Herrmann, C. (1998) Transient kinetic studies on the interaction of Ras and the Ras-binding domain of c-Raf-1 reveal rapid equilibration of the complex. *Biochemistry 37*, 14292–14299.

(21) Becker, C. F., Seidel, R., Jahnz, M., Bacia, K., Niederhausen, T., Alexandrov, K., Schwille, P., Goody, R. S., and Engelhard, M. (2006) C-terminal fluorescence labeling of proteins for interaction studies on the single-molecule level. *ChemBioChem 7*, 891–895.

(22) Becker, C. F., Oblatt-Montal, M., Kochendoerfer, G. G., and Montal, M. (2004) Chemical synthesis and single channel properties of tetrameric and pentameric TASPs (template-assembled synthetic proteins) derived from the transmembrane domain of HIV virus protein u (Vpu). *J. Biol. Chem. 279*, 17483–17489.

(23) Rose, K., and Vizzanova, J. (1999) Stepwise solid-phase synthesis of polyamides as linkers. *J. Am. Chem. Soc. 121*, 7034–7038.

(24) Richter, R. P., Berat, R., and Brisson, A. R. (2006) Formation of solid-supported lipid bilayers: an integrated view. *Langmuir 22*, 3497–3505.

(25) Sackmann, E. (1996) Supported membranes: scientific and practical applications. *Science 271*, 43–48.

(26) Linnemann, T., Geyer, M., Jaitner, B. K., Block, C., Kalbitzer, H. R., Wittinghofer, A., and Herrmann, C. (1999) Thermodynamic and kinetic characterization of the interaction between the Ras binding domain of AF6 and members of the Ras subfamily. *J. Biol. Chem. 274*, 13556–13562.

(27) Eing, A., Janshoff, A., Galla, H. J., Block, C., and Steinem, C. (2002) Quantification of the Raf-C1 interaction with solid-supported bilayers. *ChemBioChem 3*, 190–197.

(28) Harjes, E., Harjes, S., Wohlgemuth, S., Muller, K. H., Krieger, E., Herrmann, C., and Bayer, P. (2006) GTP-Ras disrupts the intramolecular complex of C1 and RA domains of Nore1. *Structure 14*, 881–888.

(29) Kiel, C., Selzer, T., Shaul, Y., Schreiber, G., and Herrmann, C. (2004) Electrostatically optimized Ras-binding Ral guanine dissociation stimulator mutants increase the rate of association by stabilizing the encounter complex. *Proc. Natl. Acad. Sci. U.S.A. 101*, 9223–9228.

(30) Wohlgemuth, S., Kiel, C., Kramer, A., Serrano, L., Wittinghofer, F., and Herrmann, C. (2005) Recognizing and defining true Ras binding domains I: biochemical analysis. *J. Mol. Biol. 348*, 741–758.

(31) Block, C., Janknecht, R., Herrmann, C., Nassar, N., and Wittinghofer, A. (1996) Quantitative structure-activity analysis correlating Ras/Raf interaction in vitro to Raf activation in vivo. *Nat. Struct. Biol. 3*, 244–251.

(32) Vetter, I. R., Linnemann, T., Wohlgemuth, S., Geyer, M., Kalbitzer, H. R., Herrmann, C., and Wittinghofer, A. (1999) Structural and biochemical analysis of Ras-effector signaling via RalGDS. *FEBS Lett. 451*, 175–180.

BC800099P

OCTOBER 2008
Volume 19, Number 10

© *Copyright 2008 by the American Chemical Society*

Bioconjugate Chemistry

TEACHING EDITORIAL

Covalent Immobilization of Proteins on Carbon Nanotubes Using the Cross-Linker 1-Ethyl-3-(3-dimethylaminopropyl)carbodiimide—a Critical Assessment

Yuan Gao* and Ilias Kyratzis

Materials Science and Engineering, Commonwealth Scientific and Industrial Research Organization (CSIRO), Bayview Ave, Clayton 3168, Australia. Received February 5, 2008; Revised Manuscript Received May 29, 2008

Functionalization of carbon nanotubes (CNTs) with proteins is often a key step in their biological applications, particularly in biosensing. One popular method has used the cross-linker 1-ethyl-3-(3-dimethylaminopropyl)carbodiimide (EDC) to covalently conjugate proteins onto carboxylated CNTs. In this article, we critically assess the evidence presented in these conjugation studies in the literature. As CNTs have a natural affinity for diverse proteins through hydrophobic and electrostatic interactions, it is therefore important to differentiate protein covalent attachment from adsorption in the immobilization mechanism. Unfortunately, many studies of conjugating proteins onto CNTs using EDC lacked essential controls to eliminate the possibility of protein adsorption. In studies where the attachment was claimed to be covalent, discrepancies existed and the observed immobilization appeared to be due to adsorption. So far, bond analysis has been lacking to ascertain the nature of the attachment using EDC. We recommend that this approach of covalent immobilization of proteins on CNTs be re-evaluated and treated with caution.

1. INTRODUCTION

The discovery and subsequent large-scale production of carbon nanotubes (CNTs) have opened a new door in nanotechnology (*1*). Due to their nanosize, exceptional physical strength, chemical stability, and conductive properties, CNTs are being explored for a wide range of applications (*2*). Among these, CNT-based biosensing has drawn particular interest with some extensive reviews published recently (*3*−*7*).

A key step in CNT-based biosensing is the immobilization of a biomolecule on the surface of the CNTs in devices such as electrodes and field effect transistors. The biomolecules are often proteins such as an antibody (*8*), antigen (*9*), or enzyme (*10*). They typically bind to, catalyze a reaction of, or are inhibited by the target molecule. The nanostructure of CNTs, together with their conducting properties, enables tiny signals to be detected and transmitted, leading to the detection of target molecules at extremely low levels. Noncovalent (e.g., adsorption) and covalent conjugation have been reported for the immobilization of various proteins. Noncovalent attachment preserves the unique properties of the CNTs, but the immobilized protein is in equilibrium in a solution and can therefore be gradually lost during the use of the CNT biosensor. On the other hand, covalent conjugation provides durable attachment, but the harsh oxidation step (e.g., with strong acids) disrupts the π-networks on the CNT surfaces and may diminish their mechanical and electronic properties (*11*). Covalent

* Corresponding author. Phone: (61)-3-9545 2104. Fax: (61)-3-9545 2363. E-mail: yuan.gao@csiro.au (Y. Gao).

10.1021/bc800051c CCC: $40.75 Published 2008 by the American Chemical Society
Published on Web 08/29/2008

Table 1. Some Proteins That Have Been Adsorbed or Claimed to Be Covalently Attached onto CNTs[a]

protein	adsorption (ref)	covalent attachment (ref)
AChE	(*56*)	(*51*)
Antibody		(*17, 18, 20, 21*)
Avidin	(*9*)	(*57*)
BSA	(*9, 32, 33*)	(*12, 13, 53*)
Chymotrypsin	(*30*)	
Cytochrome C	(*23, 24, 26, 58*)	(*26*)
Ferritin	(*26, 27*)	(*13, 26, 27, 52*)
Fibrinogen	(*59*)	
Glucose oxidase	(*26, 34, 60, 61*)	(*15, 26*)
α-glucosidase	(*9*)	
β-glucosidase	(*62*)	
Hemoglobin	(*28, 63*)	
HRP		(*16, 17, 19*)
HupR	(*25*)	
Hydrogenase	(*64*)	(*22*)
β-lactamase	(*23*)	
Lipase	(*32*)	(*50*)
Lysozyme	(*33*)	
Metallothionein	(*23, 24*)	
Myoglobin	(*64*)	(*16*)
OPH	(*65*)	
SBP	(*30*)	(*50*)
Streptavidin	(*9, 25, 29, 66−68*)	(*14*)

[a] AChE, acetylcholinesterase; OPH, organophosphorus hydrolase.

attachment of proteins on carboxylated CNTs using the popular cross-linker 1-ethyl-3-(3-dimethylaminopropyl)carbodiimide (EDC) was first reported by Huang et al. (*12*) and Jiang et al. (*13*). Since then, it has been widely used in the covalent immobilization of proteins on carboxylated CNTs in biosensing studies (*14*−*22*).

The validity of covalent conjugation of proteins onto carboxylated CNTs using EDC appears to have been accepted without due scrutiny. In this article, we critically examine the evidence presented in the conjugation studies in the literature. We find that conclusive evidence for covalent immobilization is lacking, and that the protein immobilization in most of these studies may be largely due to adsorption.

2. ADSORPTION OF PROTEINS ONTO CNTS

Before we proceed to consider EDC-mediated covalent attachment of proteins on CNTs, it is necessary to briefly look at protein adsorption first.

Tsang and colleagues first reported that small proteins such as metallothionein, cytochrome C, and *β*-lactamase were able to adsorb on the internal as well as outer walls of CNTs after the ends were opened by treatment with concentrated nitric acid (*23, 24*). Since then, both multiwalled (MWCNT) and single-walled CNTs (SWCNT), whether dispersed or oxidized, have been demonstrated to have the ability to adsorb diverse proteins (Table 1). The adsorbed proteins form a coat on the CNT surface when visualized by atomic force microscopy (AFM) or electron microscopy (*25*−*28*). Streptavidin can almost completely cover the surface of MWCNT where it forms a highly ordered helical structure (*25, 29*). Some proteins, such as *β*-glucosidase, chymotrypsin, and soybean peroxidase (SBP), are adsorbed at very large quantities, i.e., at 630, 670, and 575 *μ*g protein per mg of CNTs, respectively (*30, 31*). Bovine serum albumin (BSA) is also adsorbed well and has been reported as an effective agent in dispersing CNTs (*9, 32, 33*).

The adsorption is spontaneous when the protein comes in contact with CNTs in a solution, and follows a pseudosaturation behavior (*30, 31, 34*). The interaction between the CNTs and the protein can be very strong. Using techniques such as FT-IR and AFM, the conformation of the adsorbed protein is observed to be distorted or partially unfolded due to the strong interaction with the CNTs (*23, 30*). As a result of such structural perturbations and other mechanisms, the activities of adsorbed enzymes are reduced by 70−99% for *β*-lactamase, *β*-glucosidase, chymotrypsin, and SBP as compared with the free enzyme in solution (*23, 30, 31*).

The interacting force between CNTs and a protein is predominantly hydrophobic interaction (*25, 29, 33*), although electrostatic interaction and hydrogen bonding can also play a role in some situations (*31, 35*). The relationship between the structure of a protein and its binding to CNTs has been further studied using peptides. Ring structures in aromatic amino acids (e.g., phenylalanine and tryptophan) are important for the interaction between the peptide and CNTs through *π*-stacking (*35*−*37*). However, due to protein folding, the binding ability of a protein to CNTs cannot be predicted by its number of hydrophobic or aromatic residues in the primary structure (*33*).

3. COVALENT IMMOBILIZATION OF PROTEINS ON CNTS USING EDC

3.1. Chemistry of EDC Conjugation. In order to better understand the studies in which EDC is used to covalently attach proteins onto CNTs, it is helpful to look at the conjugation mechanism. EDC is a zero-length cross-linker widely used in protein conjugations (*38*). The conjugation reactions occur in two sequential steps (Figure 1). EDC first reacts with a carboxyl group, forming an amine-reactive *O*-acylisourea intermediate which subsequently reacts with an amine group to produce a stable amide bond. However, the *O*-acylisourea intermediate is very unstable and susceptible to hydrolysis. Such instability results in low coupling efficiency. The addition of NHS (*N*-hydroxysuccinimide or its more water soluble analogue Sulfo-NHS) stabilizes the intermediate by converting it to a semistable amine-reactive NHS ester, thus increasing the coupling efficiency by 10−20 fold (*39, 40*).

The coupling of a protein onto carboxylated CNTs can be achieved in a single-step or a two-step procedure. In the former case, the protein, CNTs, and EDC are mixed in a single tube. The use of NHS is conceptually not essential but will greatly improve the coupling efficiency. In this single-step procedure, interprotein conjugation also takes place and can lead to protein supramolecules or even aggregates. To overcome this problem, a two-step conjugation procedure can be used. The carboxylated CNTs are first reacted with EDC in the presence of NHS (or sulfo-NHS) to yield a semistable amine-reactive NHS-ester. After excess EDC is washed off or deactivated by the addition of *β*-mercaptoethanol (*41*), the activated CNTs are then reacted with a protein. In this case, interprotein conjugation is eliminated because only the CNTs are exposed to the cross-linker. The only covalent bond formed is between the solid CNT support and the protein.

The buffer used in EDC coupling is also an important consideration. The coupling is typically performed at slightly acidic pH in MES buffer (2-morpholinoethanesulfonic acid). The use of phosphate buffer should be avoided, as phosphate reacts with EDC and reduces its stability from a $t_{1/2}$ of 20 h in MES buffer to 0.4 h at pH 6.0 (*42*). If phosphate buffer has to be used, a large excess of EDC can be used to compensate for the instability.

3.2. Conjugation of Proteins onto Carboxylated CNTs Using EDC. Due to the chemical inertness of CNTs, any covalent immobilization of molecules will require chemical modifications to create reactive groups on the surface first. Popular methods include sonicating CNTs in a mixture of sulfuric acid and nitric acid (typically 3:1 v/v) or refluxing in concentrated nitric acid. Such oxidative treatments create carboxylic groups, among others, at the ends and defect sites

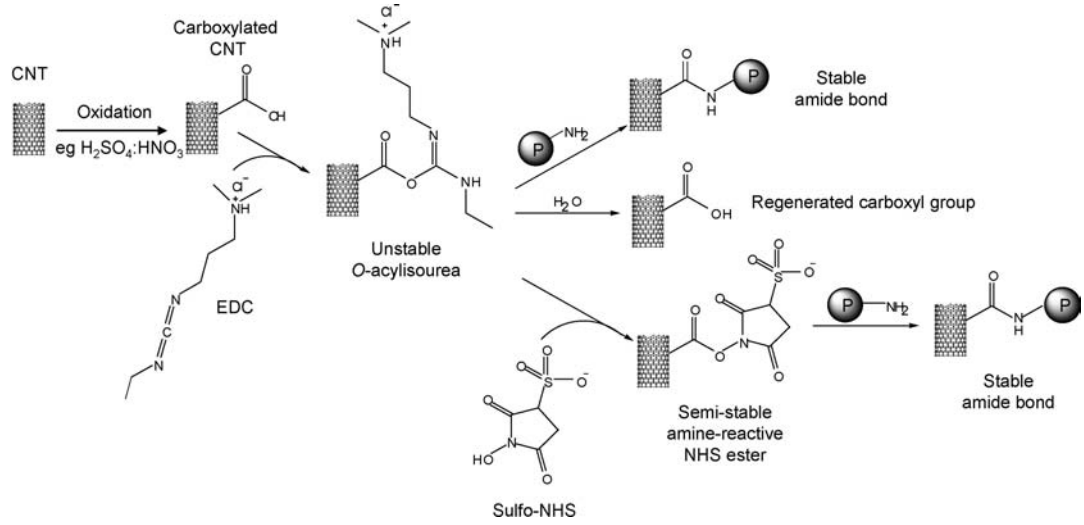

Figure 1. Theoretical conjugation of proteins to carboxylated CNTs using EDC in the presence or absence of sulfo-NHS.

on the sidewalls of the CNTs (*43*, *44*). The presence of carboxylic groups has been verified by titration experiments (*45*−*47*) and IR spectroscopy (*48*, *49*).

The carboxylic groups on the CNTs provide, in theory, ideal anchoring points for the covalent attachment of proteins using the cross-linker EDC. Indeed, this has been the method of choice by many researchers in recent years, although other cross-linkers have been occasionally used. Table 1 lists proteins that have been claimed to be covalently coupled onto CNTs using EDC. However, many of these proteins can also be adsorbed onto CNTs. This raises a question whether the observed protein immobilization in the coupling studies is actually due to covalent attachment or due to adsorption.

Huang et al. (*12*) were the first to specifically report the covalent coupling of a protein onto CNTs using EDC. In their work, acid-treated SWCNTs were sonicated for two hours in phosphate buffer containing 50 mM EDC but in the absence of NHS. BSA was then added to the solution and the coupling was allowed to proceed for 24 h at room temperature. BSA immobilization was observed by AFM to be at various points on the CNTs, which seemed to be consistent with the notion that carboxylic groups are at defect sites on the sidewall. However, the evidence presented to support the claim that BSA was covalently attached to the CNTs was inconclusive, for the following reasons. First, the comparison of CNT-conjugated BSA with free BSA on a SDS-polyacrylamide gel actually showed that the two behaved similarly (Figure 5 in (*12*)). This indicated that the CNT−BSA complex was dissociated under the denaturing electrophoretic conditions, revealing their non-covalent association nature. Second, the study lacked essential controls. As various studies have demonstrated that CNTs have great affinity for BSA, it is imperative that negative controls, i.e., reactions in the absence of the cross-linker, be incorporated to determine whether the immobilization is due to protein adsorption. Third, very unfavorable coupling conditions were used in this study. The omission of NHS in the reaction, the use of phosphate buffer, and the two hour time delay before BSA was added to the reaction would have collectively resulted in very low conjugation efficiency in a coupling reaction.

Jiang et al. (*13*) also specifically studied covalent coupling of proteins onto CNTs using EDC but using a two-step procedure. Acid-treated MWCNTs were first activated with EDC/NHS and then reacted with BSA or ferritin. Under TEM, the immobilized ferritin was observed to distribute relatively evenly on the sidewalls of the CNTs (Figure 2 in (*13*)). The authors claimed, but without presenting the data, that ferritin did not bind to the CNTs when EDC or NHS was omitted in the reactions. For BSA conjugation, the only evidence presented was two AFM images showing BSA on the CNTs. These results led to the conclusion that the attachment of ferritin and BSA onto the CNTs was mediated by EDC/NHS. This conclusion is open for further discussion. First, the uniform distribution of ferritin on the side wall may be inconsistent with carboxylic groups which are only located at the tips and defect sites on the sidewall of the oxidized CNTs. Second, it is unclear whether or not ferritin adsorbs onto CNTs. Azamian et al. and Lin et al. have shown that ferritin adsorbs efficiently to oxidized SWCNT, and that adding EDC to the binding solution does not alter the immobilization (*26*, *27*). Third, proper controls, which were not reported in the study, were needed to eliminate that the observed BSA immobilization was not due to physical adsorption.

A few other studies have used EDC to conjugate other proteins onto CNTs. Lee et al. observed that horseradish peroxidase (HRP) could be adsorbed on MWCNT and the use of EDC increased its immobilization by up to 20% (*19*). It was unknown, however, whether this small increase was significant because no statistical analysis could be performed. It is interesting to note that this increase occurred only at 10−40 mM but not at 60−100 mM of EDC. As unfavorable coupling conditions were employed in this study, (i.e., the use of phosphate buffer in the absence of NHS), one would expect that covalent conjugation should have increased with increasing EDC concentration. Asuri et al. reported that 170 μg of SBP could be coupled to 1 mg CNTs, and a control reaction in the absence of EDC/NHS showed that nonspecific binding accounted for less than 5% of total immobilized activity (*50*). Similarly, Wohlstadter et al. reported, without presenting the data, that EDC/NHS coupling tripled the amount of streptavidin immobilized on the CNTs (*14*). However, as both SBP and streptavidin can adsorb to CNTs spontaneously in large quantities resulting in complete coverage of the CNT surface, it is difficult to imagine how these proteins could still be conjugated by the much slower covalent process. More studies are needed to reconcile these studies. Some of these studies have used a two-step conjugating procedure where the only amide bonds formed would have been between the protein and the CNT surface. Functional group analysis by techniques such as FT-IR or Raman could potentially assist in determining the nature of the attachment.

EDC has been used to immobilize a number of enzymes and antibodies on CNTs using diverse conditions in biosensing studies (*15*−*18*, *20*, *21*, *51*−*53*). These studies generally did not include any necessary control reactions to differentiate adsorption from covalent conjugation and did not characterize

the immobilization. Protein immobilization on the CNTs in these studies was simply assumed to be due to the action of EDC.

Therefore, no conclusive evidence so far exists to show that proteins have been covalently conjugated onto carboxylated CNTs by the use of carbodiimide chemistry. Given the affinity of CNTs for many proteins including those used in the conjugating studies, proteins immobilization observed using EDC may be predominantly due to adsorption. If this is true, it is necessary to rethink the value of this "covalent" approach. If it does not significantly contribute to the amount of protein immobilization, the drawback would be, apart from labor and chemical cost, the likely loss of protein activity resulting from the many steps of handling in the conjugation process and the formation of cross-linked protein aggregates (if a one-step conjugation protocol is used). For many applications, it may make little difference whether the protein is adsorbed or covalently bound as long as adequate activity is maintained.

In contrast to proteins, small molecules such as short peptide nucleic acid (*54*) and amine-containing quantum dots (*55*) have been conjugated to acid-oxidized CNTs by EDC/NHS chemistry. Through the use of proper negative controls, FT-IR analysis, and localization by SEM imaging, the immobilization of these substances appears to be covalent. The difficulty with covalent protein coupling may be due to a number of factors. First, for many proteins, there is a competition between adsorption and covalent conjugation for surfaces of the CNTs. Adsorption, due to its strong affinity and spontaneity, is probably the dominating process over the much slower covalent reactions. Once occurred, the adsorbed protein may shield adjacent carboxylic groups from reacting with other protein molecules. Second, the carboxylic groups on oxidized CNTs are directly associated with the CNTs (i.e., without a spacer arm); this may lead to steric hindrance in the reactions between a soluble protein and the solid surface of CNTs, resulting in low conjugation efficiency.

4. CONCLUSIONS

Covalent conjugation of proteins on carboxylated CNTs using the coupling agent EDC has been widely used in recent years. However, many proteins used in such conjugation studies have also been shown to adsorb onto CNTs. So far, conclusive evidence is lacking to show that EDC could significantly improve protein immobilization on CNTs above the level of adsorption. It is necessary to re-evaluate this approach of protein conjugation onto CNTs. The unnecessary use of EDC chemistry will not only increase the cost of the work, but also may lead to some loss of protein activity resulting from the handling in the process and the possible formation of cross-linked protein aggregates. We recommend that this approach be treated with caution.

LITERATURE CITED

(1) Iijima, S. (1991) Helical microtubules of graphitic carbon. *Nature 354*, 56–58.

(2) Polizu, S., Savadogo, O., Poulin, P., and Yahia, L. (2006) Applications of carbon nanotubes-based biomaterials in biomedical nanotechnology. *J. Nanosci. Nanotechnol. 6*, 1883–1904.

(3) Moulton, S. E., Minett, A. I., and Wallace, G. G. (2005) Carbon nanotube based electronic and electrochemical sensors. *Sens. Lett. 3*, 183–193.

(4) Wang, J. (2005) Carbon-nanotube based electrochemical biosensors: a review. *Electroanalysis 17*, 7–14.

(5) Gruner, G. (2006) Carbon nanotube transistors for biosensing applications. *Anal. Bioanal. Chem. 384*, 322–335.

(6) Allen, B. L., Kichambare, P. D., and Star, A. (2007) Carbon nanotube field-effect-transistor-based biosensors. *Adv. Mater. 19*, 1439–1451.

(7) Veetil, J. V., and Ye, K. M. (2007) Development of immunosensors using carbon nanotubes. *Biotechnol. Prog. 23*, 517–531.

(8) Li, C., Curreli, M., Lin, H., Lei, B., Ishikawa, F. N., Datar, R., Cote, R. J., Thompson, M. E., and Zhou, C. W. (2005) Complementary detection of prostate-specific antigen using Ln(2)O(3) nanowires and carbon nanotubes. *J. Am. Chem. Soc. 127*, 12484–12485.

(9) Chen, R. J., Bangsaruntip, S., Drouvalakis, K. A., Kam, N. W. S., Shim, M., Li, Y. M., Kim, W., Utz, P. J., and Dai, H. J. (2003) Noncovalent functionalization of carbon nanotubes for highly specific electronic biosensors. *Proc. Natl. Acad. Sci. U.S.A. 100*, 4984–4989.

(10) Patolsky, F., Weizmann, Y., and Willner, I. (2004) Long-range electrical contacting of redox enzymes by swcnt connectors. *Angew. Chem., Int. Ed. 43*, 2113–2117.

(11) Star, A., Liu, Y., Grant, K., Ridvan, L., Stoddart, J. F., Steuerman, D. W., Diehl, M. R., Boukai, A., and Heath, J. R. (2003) Noncovalent side-wall functionalization of single-walled carbon nanotubes. *Macromolecules 36*, 553–560.

(12) Huang, W. J., Taylor, S., Fu, K. F., Lin, Y., Zhang, D. H., Hanks, T. W., Rao, A. M., and Sun, Y. P. (2002) Attaching proteins to carbon nanotubes via diimide-activated amidation. *Nano Lett. 2*, 311–314.

(13) Jiang, K. Y., Schadler, L. S., Siegel, R. W., Zhang, X. J., Zhang, H. F., and Terrones, M. (2004) Protein immobilization on carbon nanotubes via a two-step process of diimide-activated amidation. *J. Mater. Chem. 14*, 37–39.

(14) Wohlstadter, J. N., Wilbur, J. L., Sigal, G. B., Biebuyck, H. A., Billadeau, M. A., Dong, L. W., Fischer, A. B., Gudibande, S. R., Jamieson, S. H., Kenten, J. H., Leginus, J., Leland, J. K., Massey, R. J., and Wohlstadter, S. J. (2003) Carbon nanotube-based biosensor. *Adv. Mater. 15*, 1184.

(15) Lin, Y. H., Lu, F., Tu, Y., and Ren, Z. F. (2004) Glucose biosensors based on carbon nanotube nanoelectrode ensembles. *Nano Lett. 4*, 191–195.

(16) Yu, X., Chattopadhyay, D., Galeska, I., Papadimitrakopoulos, F., and Rusling, J. F. (2003) Peroxidase activity of enzymes bound to the ends of single-wall carbon nanotube forest electrodes. *Electrochem. Commun. 5*, 408–411.

(17) Yu, X., Kim, S. N., Papadimitrakopoulos, F., and Rusling, J. F. (2005) Protein immunosensor using single-wall carbon nanotube forests with electrochemical detection of enzyme labels. *Mol. Biosyst.* 70–78.

(18) Yu, X., Munge, B., Patel, V., Jensen, G., Bhirde, A., Gong, J. D., Kim, S. N., Gillespie, J., Gutkind, J. S., Papadimitrakopoulos, F., and Rusling, J. F. (2006) Carbon nanotube amplification strategies for highly sensitive immunodetection of cancer biomarkers. *J. Am. Chem. Soc. 128*, 11199–11205.

(19) Lee, Y. M., Kwon, O. Y., Yoon, Y. J., and Ryu, K. (2006) Immobilization of horseradish peroxidase on multi-wall carbon nanotubes and its electrochemical properties. *Biotechnol. Lett. 28*, 39–43.

(20) Hu, P., Tanii, T., Zhang, G. J., Hosaka, T., and Ohdomari, I. (2007) Ultrasensitive detection of biomolecules using functionalized multi-walled carbon nanotubes. *Sens. Actuators, B: Chem. 124*, 161–166.

(21) Yun, Y., Bange, A., Heineman, W. R., Halsall, H. B., Shanov, V. N., Dong, Z. Y., Pixley, S., Behbehani, M., Jazieh, A., Tu, Y., Wong, D. K. Y., Bhattacharya, A., and Schulz, M. J. (2007) A nanotube array immunosensor for direct electrochemical detection of antigen-antibody binding. *Sens. Actuators, B: Chem. 123*, 177–182.

(22) Alonso-Lomillo, M. A., Rudiger, O., Maroto-Valiente, A., Velez, M., Rodriguez-Ramos, I., Munoz, F. J., Fernandez, V. M., and De Lacey, A. L. (2007) Hydrogenase-coated carbon nanotubes for efficient H-2 oxidation. *Nano Lett. 7*, 1603–1608.

(23) Davis, J. J., Green, M. L. H., Hill, H. A. O., Leung, Y. C., Sadler, P. J., Sloan, J., Xavier, A. V., and Tsang, S. C. (1998) The immobilisation of proteins in carbon nanotubes. *Inorg. Chim. Acta 272*, 261–266.

(24) Guo, Z. J., Sadler, P. J., and Tsang, S. C. (1998) Immobilization and visualization of DNA and proteins on carbon nanotubes. *Adv. Mater. 10*, 701–703.
(25) Balavoine, F., Schultz, P., Richard, C., Mallouh, V., Ebbesen, T. W., and Mioskowski, C. (1999) Helical crystallization of proteins on carbon nanotubes: a first step towards the development of new biosensors. *Angew. Chem., Int. Ed. 38*, 1912–1915.
(26) Azamian, B. R., Davis, J. J., Coleman, K. S., Bagshaw, C. B., and Green, M. L. H. (2002) Bioelectrochemical single-walled carbon nanotubes. *J. Am. Chem. Soc. 124*, 12664–12665.
(27) Lin, Y., Allard, L. F., and Sun, Y. P. (2004) Protein-affinity of single-walled carbon nanotubes in water. *J. Phys. Chem. B 108*, 3760–3764.
(28) Jia, N. Q., Wang, L. J., Liu, L., Zhou, Q., and Jiang, Z. Y. (2005) Bamboo-like CNX nanotubes for the immobilization of hemoglobin and its bioelectrochemistry. *Electrochem. Commun. 7*, 349–354.
(29) Shim, M., Kam, N. W. S., Chen, R. J., Li, Y. M., and Dai, H. J. (2002) Functionalization of carbon nanotubes for biocompatibility and biomolecular recognition. *Nano Lett. 2*, 285–288.
(30) Karajanagi, S. S., Vertegel, A. A., Kane, R. S., and Dordick, J. S. (2004) Structure and function of enzymes adsorbed onto single-walled carbon nanotubes. *Langmuir 20*, 11594–11599.
(31) Gomez, J. M., Romero, M. D., and Fernandez, T. M. (2005) Immobilization of beta-glucosidase on carbon nanotubes. *Catal. Lett. 101*, 275–278.
(32) Karajanagi, S. S., Yang, H. C., Asuri, P., Sellitto, E., Dordick, J. S., and Kane, R. S. (2006) Protein-assisted solubilization of single-walled carbon nanotubes. *Langmuir 22*, 1392–1395.
(33) Matsuura, K., Saito, T., Okazaki, T., Ohshima, S., Yumura, M., and Iijima, S. (2006) Selectivity of water-soluble proteins in single-walled carbon nanotube dispersions. *Chem. Phys. Lett. 429*, 497–502.
(34) Guiseppi-Elie, A., Lei, C. H., and Baughman, R. H. (2002) Direct electron transfer of glucose oxidase on carbon nanotubes. *Nanotechnology 13*, 559–564.
(35) Li, X. J., Chen, W., Zhan, Q. W., Dai, L. M., Sowards, L., Pender, M., and Naik, R. R. (2006) Direct measurements of interactions between polypeptides and carbon nanotubes. *J. Phys. Chem. B 110*, 12621–12625.
(36) Wang, S. Q., Humphreys, E. S., Chung, S. Y., Delduco, D. F., Lustig, S. R., Wang, H., Parker, K. N., Rizzo, N. W., Subramoney, S., Chiang, Y. M., and Jagota, A. (2003) Peptides with selective affinity for carbon nanotubes. *Nat. Mater. 2*, 196–200.
(37) Zorbas, V., Smith, A. L., Xie, H., Ortiz-Acevedo, A., Dalton, A. B., Dieckmann, G. R., Draper, R. K., Baughman, R. H., and Musselman, I. H. (2005) Importance of aromatic content for peptide/single-walled carbon nanotube interactions. *J. Am. Chem. Soc. 127*, 12323–12328.
(38) Hermanson, G. T. (1996) *Bioconjugate Techniques*. Academic Press, San Diego.
(39) Staros, J. V., Wright, R. W., and Swingle, D. M. (1986) Enhancement by N-hydroxysulfosuccinimide of water-soluble carbodiimide-mediated coupling reactions. *Anal. Biochem. 156*, 220–222.
(40) Sehgal, D., and Vijay, I. K. (1994) A method for the high-efficiency of water-soluble carbodiimide-mediated amidation. *Anal. Biochem. 218*, 87–91.
(41) Grabarek, Z., and Gergely, J. (1990) Zero-length crosslinking procedure with the use of active esters. *Anal. Biochem. 185*, 131–135.
(42) Gilles, M. A., Hudson, A. Q., and Borders, C. L. (1990) Stability of water-soluble carbodiimides in aqueous-solution. *Anal. Biochem. 184*, 244–248.
(43) Wong, S. S., Joselevich, E., Woolley, A. T., Cheung, C. L., and Lieber, C. M. (1998) Covalently functionalized nanotubes as nanometre-sized probes in chemistry and biology. *Nature 394*, 52–55.
(44) Hamon, M. A., Hu, H., Bhowmik, P., Niyogi, S., Zhao, B., Itkis, M. E., and Haddon, R. C. (2001) End-group and defect analysis of soluble single-walled carbon nanotubes. *Chem. Phys. Lett. 347*, 8–12.
(45) Marshall, M. W., Popa-Nita, S., and Shapter, J. G. (2006) Measurement of functionalised carbon nanotube carboxylic acid groups using a simple chemical process. *Carbon 44*, 1137–1141.
(46) Mawhinney, D. B., Naumenko, V., Kuznetsova, A., Yates, J. T., Liu, J., and Smalley, R. E. (2000) Surface defect site density on single walled carbon nanotubes by titration. *Chem. Phys. Lett. 324*, 213–216.
(47) Hu, H., Bhowmik, P., Zhao, B., Hamon, M. A., Itkis, M. E., and Haddon, R. C. (2001) Determination of the acidic sites of purified single-walled carbon nanotubes by acid-base titration. *Chem. Phys. Lett. 345*, 25–28.
(48) Kuznetsova, A., Mawhinney, D. B., Naumenko, V., Yates, J. T., Liu, J., and Smalley, R. E. (2000) Enhancement of adsorption inside of single-walled nanotubes: opening the entry ports. *Chem. Phys. Lett. 321*, 292–296.
(49) Kim, U. J., Furtado, C. A., Liu, X. M., Chen, G. G., and Eklund, P. C. (2005) Raman and IR spectroscopy of chemically processed single-walled carbon nanotubes. *J. Am. Chem. Soc. 127*, 15437–15445.
(50) Asuri, P., Karajanagi, S. S., Sellitto, E., Kim, D. Y., Kane, R. S., and Dordick, J. S. (2006) Water-soluble carbon nanotube-enzyme conjugates as functional biocatalytic formulations. *Biotechnol. Bioeng. 95*, 804–811.
(51) Lin, Y. H., Lu, F., and Wang, J. (2004) Disposable carbon nanotube modified screen-printed biosensor for amperometric detection of organophosphorus pesticides and nerve agents. *Electroanalysis 16*, 145–149.
(52) Bhattacharyya, S., Sinturel, C., Salvetat, J. P., and Saboungi, M. L. (2005) Protein-functionalized carbon nanotube-polymer composites. *Appl. Phys. Lett.* 86.
(53) Elkin, T., Jiang, X. P., Taylor, S., Lin, Y., Gu, L. R., Yang, H., Brown, J., Collins, S., and Sun, Y. P. (2005) Immuno-carbon nanotubes and recognition of pathogens. *ChemBioChem 6*, 640–643.
(54) Singh, K. V., Pandey, R. R., Wang, X., Lake, R., Ozkan, C. S., Wang, K., and Ozkan, M. (2006) Covalent functionalization of single walled carbon nanotubes with peptide nucleic acid: nanocomponents for molecular level electronics. *Carbon 44*, 1730–1739.
(55) Ravindran, S., Chaudhary, S., Colburn, B., Ozkan, M., and Ozkan, C. S. (2003) Covalent coupling of quantum dots to multiwalled carbon nanotubes for electronic device applications. *Nano Lett. 3*, 447–453.
(56) Joshi, K. A., Tang, J., Haddon, R., Wang, J., Chen, W., and Mulchandani, A. (2005) A disposable biosensor for organophosphorus nerve agents based on carbon nanotubes modified thick film strip electrode. *Electroanalysis 17*, 54–58.
(57) Kim, Y. S., Cho, J. H., Ansari, S. G., Kim, H. I., Dar, M. A., Seo, H. K., Kim, G. S., Lee, D. S., Khang, G., and Shin, H. S. (2006) Immobilization of avidin on the functionalized carbon nanotubes. *Synth. Met. 156*, 938–943.
(58) Boussaad, S., Tao, N. J., Zhang, R., Hopson, T., and Nagahara, L. A. (2003) In situ detection of cytochrome c adsorption with single walled carbon nanotube device. *Chem. Commun.* 1502–1503.
(59) Song, L., Meng, J., Zhong, J., Liu, L. F., Dou, X. Y., Liu, D. F., Zhao, X. W., Luo, S. D., Zhang, Z. X., Xiang, Y. J., Xu, H. Y., Zhou, W. Y., Wu, Z. Y., and Xie, S. S. (2006) Human fibrinogen adsorption onto single-walled carbon nanotube films. *Colloids Surf. B: Biointerf. 49*, 66–70.
(60) Wang, S. G., Zhang, Q., Wang, R. L., Yoon, S. F., Ahn, J., Yang, D. J., Tian, J. Z., Li, J. Q., and Zhou, Q. (2003) Multi-walled carbon nanotubes for the immobilization of enzyme in glucose biosensors. *Electrochem. Com. 5*, 800–803.
(61) Sotiropoulou, S., and Chaniotakis, N. A. (2003) Carbon nanotube array-based biosensor. *Anal. Bioanal. Chem. 375*, 103–105.
(62) Chen, S. H., Yuan, R., Chai, Y. Q., Zhang, L. Y., Wang, N., and Li, X. L. (2007) Amperometric third-generation hydrogen

peroxide biosensor based on the immobilization of hemoglobin on multiwall carbon nanotubes and gold colloidal nanoparticles. *Biosens. Bioelectron. 22*, 1268–1274.

(63) Liu, A. R., Wakayama, T., Nakamura, C., Miyake, J., Zorin, N. A., and Qian, D. J. (2007) Electrochemical properties of carbon nanotubes-hydrogenase conjugates Langmuir-Blodgett films. *Electrochim. Acta 52*, 3222–3228.

(64) Zhang, L., Zhao, G. C., Wei, X. W., and Yang, Z. S. (2005) A nitric oxide biosensor based on myoglobin adsorbed on multi-walled carbon nanotubes. *Electroanal. 17*, 630–634.

(65) Liu, N. Y., Cai, X. P., Lei, Y., Zhang, Q., Chan-Park, M. B., Li, C. M., Chen, W., and Mulchandani, A. (2007) Single-walled carbon nanotube based real-time organophosphate detector. *Electroanalysis 19*, 616–619.

(66) Bottini, M., Cerignoli, F., Tautz, L., Rosato, N., Bergamaschi, A., and Mustelin, T. (2006) Adsorption of streptavidin onto single-walled carbon nanotubes: application in fluorescent supramolecular nanoassemblies. *J. Nanosci. Nanotechnol. 6*, 3693–3698.

(67) Lenihan, J. S., Gavalas, V. G., Wang, J. Q., Andrews, R., and Bachas, L. G. (2004) Protein immobilization on carbon nanotubes through a molecular adapter. *J. Nanosci. Nanotechnol. 4*, 600–604.

(68) Goux-Capes, L., Filoramo, A., Cote, D., Bourgoin, J. P., and Patillon, J. N. (2006) Coupling carbon nanotubes through DNA linker using a biological recognition complex. *Phys. Stat. Solidi A: Appl. Mater. Sci. 203*, 1132–1136.

BC800051C

REVIEWS

3-D Tissue Culture Systems for the Evaluation and Optimization of Nanoparticle-Based Drug Carriers

Thomas Tyrel Goodman,† Chee Ping Ng,† and Suzie Hwang Pun*

Department of Bioengineering, University of Washington, 1705 NE Pacific Street, Seattle, Washington 98195. Received June 7, 2008; Revised Manuscript Received August 18, 2008

Nanoparticle carriers are attractive vehicles for a variety of drug delivery applications. In order to evaluate nanoparticle formulations for biological efficacy, monolayer cell cultures are typically used as *in vitro* testing platforms. However, these studies sometimes poorly predict the efficacy of the drug *in vivo*. The poor *in vitro* and *in vivo* correlation may be attributed in part to the inability of two-dimensional cultures to reproduce extracellular barriers, and may also be due to differences in cell phenotype between cells cultured as monolayers and cells in native tissue. In order to more accurately predict *in vivo* results, it is desirable to test nanoparticle therapeutics in cells cultured in three-dimensional (3-D) models that mimic *in vivo* conditions. In this review, we discuss some 3-D culture systems that have been used to assess nanoparticle delivery and highlight several implications for nanoparticle design garnered from studies using these systems. While our focus will be on nanoparticle drug formulations, many of the systems discussed here could, or have been, used for the assessment of small molecule or peptide/protein drugs. We also offer some examples of advancements in 3-D culture that could provide even more highly predictive data for designing nanoparticle therapeutics for *in vivo* applications.

INTRODUCTION

The delivery of therapeutic agents using nanoparticulate formulations offers a number of advantages over delivery of the agents alone. For this reason, both small and macromolecular drugs are often incorporated into nanoparticle vehicles. These vehicles can potentially enhance drug efficacy by incorporating adjuvants, targeting agents, and multiple therapeutics within one carrier. The nanoparticles can also offer protection against degradation of therapeutic agents as well as facilitate the delivery of otherwise insoluble agents. An additional advantage is that the pharmacokinetic profile of drugs can be favorably altered by controlling the size and surface chemistry of the nanoparticle delivery vehicles. However, the significantly increased size of nanoparticle carriers compared to their therapeutic payload generally results in reduced tissue distribution after extravasation from the circulation. There are several therapeutic applications that benefit from efficient tissue penetration of the delivery vector. For example, some vectors, such as nonviral nucleic acid delivery vehicles that assist in intracellular trafficking, would ideally remain intact until internalization by the maximum number of target cells. For such systems, a key criterion for *in vivo* efficacy is that nanoparticle carriers must be able to overcome the various extracellular barriers encountered after extravasation to reach target cells.

Currently, initial evaluations of nanoparticulate delivery formulations are usually completed in monolayer, or 2-D, cell culture systems. Oftentimes, successful nanoparticle delivery observed in 2-D cell culture studies does not translate to similar results *in vivo*. This is in part due to limitations in monolayer cultures that fail to account for extracellular barriers that are present *in vivo* (*1*−*3*) (Figure 1). While monolayer cultures produce extracellular matrix materials, they are less dense on the monolayer apical side compared to cells in a 3-D environment (*4*−*7*) and thus present a less-significant barrier for transport and cell-binding of delivered agents compared to cells in 3-D. Thus, whereas nanoparticles delivered in a bulk solution to a 2-D cell culture typically reach and bind to cells relatively unimpeded, the same nanoparticles delivered *in vivo* will be hindered by extracellular factors such as the relatively small pore sizes within the extracellular matrix (ECM) (*8*) and the tortuosity of the interstitium. The surface properties of the nanoparticles can also lead to interactions with charged ECM components, such as proteoglycans, thereby affecting the fate and stability of nanoparticles (*9, 10*). In addition, cell monolayer

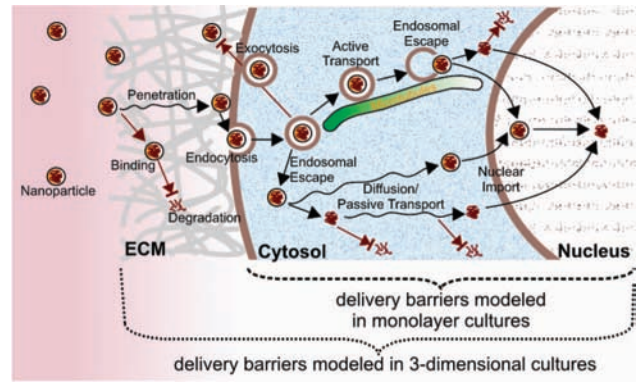

Figure 1. 3-D culture systems include additional extracellular barriers encountered by delivery vehicles that are not accounted for in 2-D monolayer cultures.

* Corresponding author. Tel. 1 206 685 3488; Fax. 1 206 616 3928; E-mail: spun@u.washington.edu.

† Equally contributing authors.

10.1021/bc800233a CCC: $40.75 © 2008 American Chemical Society
Published on Web 09/13/2008

studies are typically performed under static culturing conditions, whereas living tissues are mechanically dynamic systems and are constantly subjected to mechanical forces such as tension, compression, and interstitial fluid flow. The direction and magnitude of fluid flow can alter the bioavailability of the delivery vehicle by redirecting nanoparticles in the direction of flow and potentially away from the target sites.

Cell culture conditions also affect the phenotype of cells and thereby affect the cellular response to delivered drugs. For example, hepatocytes lose some liver-specific functions, such as albumin production, when maintained under monolayer single cell-type conditions, but retain the functions when cultured in 3-D perfusion models (*11, 12*) or when co-cultured with supporting cell types such as fibroblasts (*13*−*15*) or epithelial cells (*16, 17*). These phenotypic differences may be due in part to cells residing in materials that are more compliant than on 2-D plastic substrates typically used for monolayer cultures (*18*−*21*). Cell phenotype is also determined by interactions between cells and the supporting extracellular matrix (ECM), as well as cell−cell communication that results in changes in biological activities, including gene and protein expression, proliferation, migration, remodeling, and signal transduction (*13, 22*−*25*). Cells in 2-D monolayer cultures are generally exposed to a uniform environment under culture medium, whereas cells in tissues, particularly in solid tumors, are exposed to gradients of pH, nutrients, and waste products that exert both stimulatory and inhibitory influences on proliferation and malignant properties of the cells (*26*). Furthermore, multicellular drug resistances can result from conditions in the 3-D tissue microenvironment that may not be present in monolayer cultures, such as the occurrence of hypoxic tissue regions, altered cell proliferation, and poor availability of delivered drugs in deeper tissue layers (*27*).

For these reasons, researchers are utilizing and developing 3-D culture systems with the goal of more closely mimicking the human clinical setting. Realistic and controllable *in vitro* 3-D tissue culture systems that more closely mimic *in vivo* human tissues in terms of functionality, morphological, and mechanical architecture could be applied during the development and evaluation of delivery vehicles to offer a more predictive platform for assessing *in vivo* delivery efficiencies. Such systems can serve to bridge the considerable gap between traditional 2-D monolayer experiments, animal studies, and clinical trials, since nanoparticle formulations can be more effectively optimized in these 3-D *in vitro* models (*28*).

In this review, we will summarize the evaluation of nanoparticle carriers in several prevalent 3-D cell culture models currently used in nanoparticle delivery studies. In addition, we will highlight several advanced 3-D systems designed to account for additional factors in the complex biochemical and biomechanical environment that cells experience *in vivo*. Finally, we will discuss existing challenges in the adoption of such systems and some future directions in the development of 3-D systems for the assessment of nanoparticle delivery to tissues.

3-D CULTURE SYSTEMS

Hydrogels. Acellular hydrogels have been used to study nanoparticle diffusion in a tissue-like environment. These systems offer perhaps the simplest model of a "tissue" for assessing nanoparticle behavior. Although these models lack cells and generally employ simplified ECM compositions, they offer a practical method for probing the stability, diffusion rates, and binding interactions of nanoparticle carriers in cross-linked networks. For example, investigations using iron oxide particles have shown that diffusion through isolated ECM is highly restricted even for particles as small as 130 nm in diameter (*29*). The importance of particle surface chemistry was highlighted by Valentine and co-workers who demonstrated that the addition of the hydrophilic polymer poly(ethylene glycol) (PEG) to the nanoparticle surface, an approach known as PEGylation, led to significant reductions in particle binding to fibrin networks and subsequently increased diffusion rates compared to unmodified particles (*30*). Other studies have confirmed that the PEGylation of particles can increase movement through hydrogels, but the rate of movement is still size-dependent (*29*). The effectiveness of PEGylation is highly dependent on the type of matrix and the composition of nanoparticle formulations. For example, charged matrixes can lead to the aggregation or unpackaging of polyplexes (polymer/DNA complexes) even after PEGylation (*31*). The implications of particle shape have also been probed in hydrogels with results suggesting that extending nanoparticles into a flexible wormlike structure may allow for more effective tissue penetration compared to the traditional spherical carrier (*32*). To partially alleviate the restricted movement of particles, covalent conjugation of an ECM disrupting enzyme, collagenase, to nanoparticles has been carried out, which led to significant improvements in magnetically driven nanoparticle movement through isolated ECM (*33*).

In summary, evaluations of delivery vehicles in acellular constructs have provided valuable insight into the stability of carriers in the presence of ECM components as well as the effect of size, shape, and surface chemistry on the mobility of vectors through the ECM. Still, the usefulness of such systems is limited by their inability to offer information about the interactions of carriers with cells and the efficacy of therapeutics on the target cells.

Multicellular Spheroids. Perhaps the most widely used 3-D tissue model for the assessment of nanoparticle delivery is the multicellular spheroid. Multicellular spheroids are formed by culturing cells in spinner flasks or agar-coated culture plates (*34*). Under these conditions, cells form spherical clusters that can survive for weeks and can reach sizes of up to several millimeters in diameter. Multicellular spheroids offer a simple and highly reproducible model that contains many of the features of natural tissue *in vivo* including some patterns of protein production (*35*) and the production of an ECM (*36*). In the later stages of growth, larger spheroids mimic properties of avascular regions of solid tumors including regions of differential growth such as a proliferating region, a quiescent region, and a necrotic core (*35*). As spheroids are relatively easy to handle, they are amenable to confocal analysis, cryosectioning, and commonly used fixing and tissue processing methods. They can also be dissagregated by trypsin treatment and individual cells collected for analysis by flow cytometry. Exposure of the spheroids to a cell-permeable dye prior to flow cytometry allows for determination of the original radial location of the cells within the spheroid (*37*). These properties make spheroids a very useful and widely used model for investigating nanoparticle−tissue interactions.

Multicellular spheroids have been used to probe some of the major barriers to effective drug delivery to solid tumors, including the effect of hindered vehicle diffusion in the ECM and the effect of nonspecific binding between nanoparticles and tissue components. The heterogeneous nature of the spheroids has also allowed for the study of the effect of the proliferative state of cells on delivery efficacy.

Hindered diffusion of delivery vehicles due to restrictive pore sizes and high tortuosity in the interstitial space was demonstrated in experiments that highlight the correlation between nanoparticle carrier size and tissue penetration into multicellular spheroids. Studies investigating the penetration of carboxylated polystyrene beads in spheroids showed that particles with diameters less than 100 nm can infiltrate spheroids more effectively than particles $\geq$100 nm, but that particle penetration

for all tested sizes (20−200 nm) was significantly hindered (*3*). Enger and co-workers demonstrated that adeno-associated virus (AAV), with effective diameters of ∼25 nm, can more effectively penetrate multicellular spheroids compared to adenovirus with average diameters of 100 nm (*38*). Differences in viral penetration were attributed at least in part to these differences in particle size.

In addition to size, vector surface charge affects distribution in multicellular spheroids. The penetration of liposomes with different surface charges was analyzed in this model, and liposomes with neutral or low surface charge were shown to penetrate to the central regions of the spheroids while liposomes with higher surface charge were confined to the outer cell layers of the spheroid, demonstrating an example of a binding site barrier (*39*). One approach to reduce strong binding interactions is PEGylation. Indeed, PEGylation of polyplexes results in a reduction in toxicity and improved penetration of polyplexes in multicellular spheroids (*40, 41*). Interestingly, in studies by Han et al., toxicity profiles of PEGylated polyplexes differed for spheroid cultures compared to monolayer cultures, with spheroids exhibiting an increased sensitivity to non-PEGylated polyplexes. Oishi et al. have also demonstrated that the effectiveness of siRNA delivery using lipoplexes and PEGylated polyplexes is affected by the method of cell culture, with cells in a monolayer showing increased sensitivity to therapy compared to spheroid cultures (*42*). These studies further demonstrate the importance of 3-D screening for nanoparticle carriers, as important toxicological data could be missed with only monolayer screening (Table 1).

Multicellular spheroids that reach a certain size contain different regions that are also present in solid tumors, including an outer proliferating region, an intermediate quiescent region, and a central necrotic core. For certain carriers, such as nonviral gene delivery vectors, cells must be dividing in order to observe effective therapy; therefore, quiescent regions of spheroids are not efficiently transfected even if vectors reach these target cells (*43*). The effect of cell proliferation on cell killing by antineoplastic agents has also been well-documented in the literature (*44*).

The limitations in nanoparticle penetration due to some of the aforementioned physiochemical properties of the nanoparticles can be partially overcome by modulation of the ECM. Several studies have demonstrated the potential of this approach for improving delivery efficiency. Addition of the matrix metalloproteinase (MMP), collagenase, either in solution or immobilized on the surface of nanoparticles, increases the penetration of vectors up to 100 nm in size (*3*) (Figure 2). Improved viral particle penetration has also been accomplished in spheroids through the use of the peptide hormone, relaxin (*45*). Relaxin, which can down-regulate collagen production and increase collagenase production (*46*), was engineered into an oncolytic adenovirus and delivered to multicellular spheroids. Viruses that included the relaxin gene were able to transduce almost all areas of spheroids, while control virus transduction was confined to the outer few cell layers. The ability to incorporate these penetration enhancers into nanoparticle drug carriers offers a promising method for improving treatments, such as gene therapy for solid tumors, which rely on effective access to the majority of the target tissue.

From these studies, it is clear that the 3-D tissue environment affects the mobility of nanoparticles through tissue, which in turn affects therapeutic efficacy of delivered nanoparticles. These factors also affect the sensitivity of tissues to cytotoxic therapeutics. Studies using multicellular spheroids have been used to understand key challenges for *in vivo* delivery to tissue and to demonstrate the importance of 3-D screening for nanoparticle carriers.

Table 1. Examples of Differences in Nanoparticle-Based Drug Delivery Observed in 2-D versus 3-D Cell Culture Systems

deliverable	difference between 2-D and 3-D systems	ref
cytotoxic small molecules drugs	multicellular resistance (lower cytotoxicity) observed in spheroid cultures and polystyrene scaffolds compared to monolayer cultures.	*23, 83, 84*
PEI polyplex delivery of plasmid DNA	PEI-mediated transfection was limited to cells at the spheroid periphery, even with electroporation. This spatially dependent transgene expression is not observable with monolayer cultures.	*38*
P[Asp(DET)] polyplex delivery of plasmid DNA	difference in cytotoxicity of PEGylated compared to non-PEGylated polyplexes observed in spheroids but not detected with the conventional monolayer cultures. Specifically, PEG-*b*-P[Asp(DET)] polyplex micelles did not induce the destruction of spheroids even at N/P = 40, where the MCTS structures were destroyed by the transfection with P[Asp(DET)] polyplexes. Difference in the timecourse of transgene expression observed in 3-D spheroid cultures vs monolayer cultures. Peak transgene expression occurred at 6 days after transfection in spheroids whereas difficulties were encountered in maintaining viable monolayer cultures beyond 4 days.	*36*
lipoplex delivery of siRNA	differences in growth-inhibitory effect between spheroid and monolayer cultures. OligofectAMINE-siRNA lipoplexes had no inhibitory effect on HuH-7 spheroids compared to strong effects on HuH-7 monolayer culture.	*42*
poly(glycerol-adipate) nanoparticle delivery of DNA	differences in cellular uptake of nanoparticles in cocultures. Nanoparticles were predominantly taken up by cancerous cells rather than normal cells in 3-D cocultures whereas nanoparticles were taken up more readily by normal cells in monolayer cultures.	*45*
adeno-associated vectors (AAV) and adenovirus vector (ADV)	differences in penetration efficiencies between AAV vs ADV vectors. AAV penetrated glioblastoma spheroids and xenografts more efficiently compared to ADV vectors; biodistribution not observable with monolayer cultures.	*34*
lentivirus	enhanced transduction of epithelial cells and underlying fibroblasts compared to static coculture controls in airway wall model; this transgene expression profile was not observable with monolayer cultures.	*49*

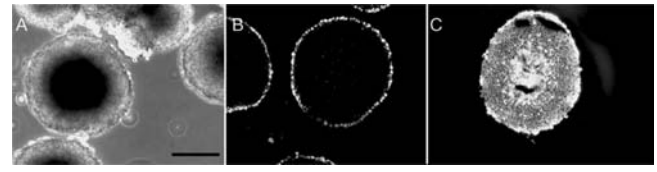

Figure 2. Penetration of model nanoparticles into multicellular spheroids. Phase contrast of multicellular spheroids shows intact spheroids prior to treatment with 40 nm fluorescent polystyrene nanoparticles (A). Cryosections of untreated spheroids (B) showed poor particle association compared to spheroids coincubated with collagenase (C). Scale bar is 200 μm.

Multilayer Cell Cultures. Multilayer cell cultures have been used for the assessment of small molecule drug delivery (*47*), and even though they have not been used extensively for nanoparticle delivery applications, they merit brief mention because they have potential use in assessing nanoparticle delivery across tissue layers. Multilayer cultures are most commonly formed by allowing monolayer cultures to continue to grow beyond confluence in Transwell cell culture dishes. The

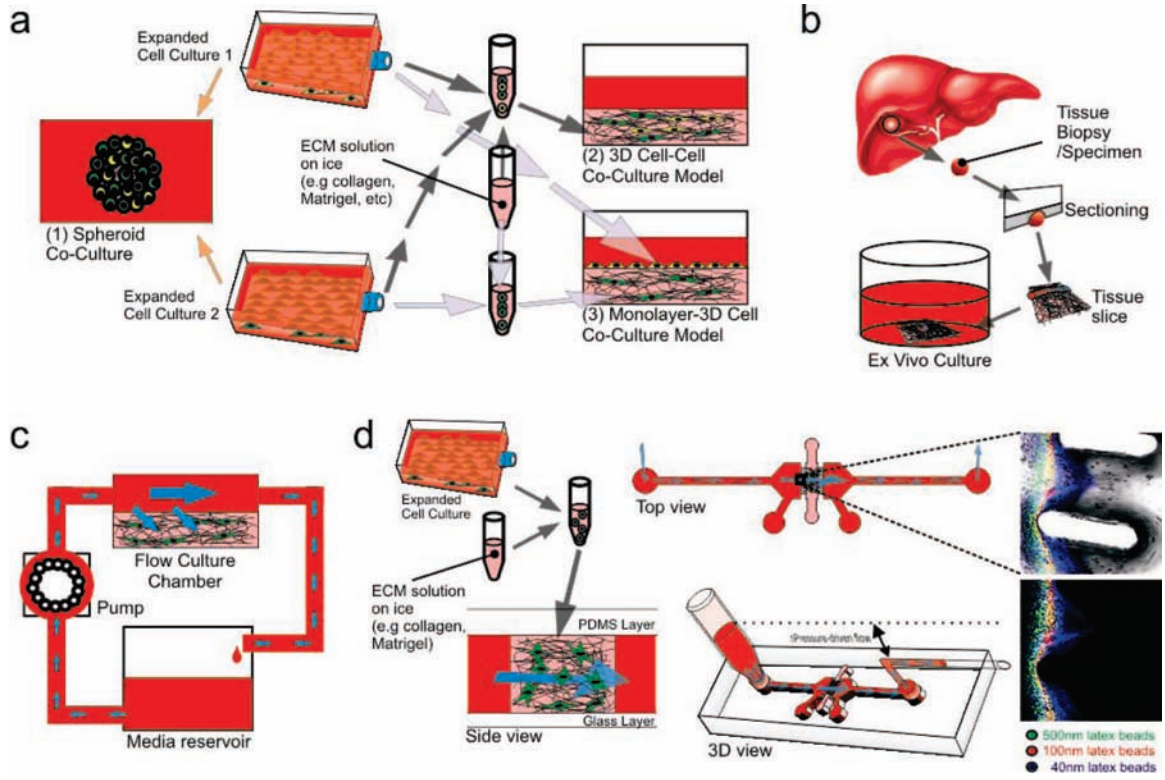

Figure 3. Examples of advanced 3-D models. (a) Some variations of co-culture models: (1) spheroid co-culture models, (2) cell−cell coculture in ECM, and (3) cell-monolayer on 3-D cell−ECM co-culture model; (b) *ex vivo* models: one version where samples of tissues such as the liver are harvested, sectioned, and cultured on 2-D substrates for screening; (c) a typical setup of 3-D perfusion cell−ECM culture models where media flow is driven over the cell−ECM by a pump from a reservoir; and (d) a short-term perfusion system developed by Ng and Pun for nanoparticle penetration studies.

Transwell dishes allow isolation between the apical and basal layer of the multilayer cell growth so that any compound delivered to one side must pass through the cell layers to reach the opposing side. This allows for easy assessment of transcellular drug delivery by incubation of drugs on one side of the growing culture followed by collection of media on the opposite side to assess the concentration of drug that has passed through the cell layer. Studies have been carried out to assess the diffusion of anticancer drugs through multilayer cultures (*47*), and could easily be extended to nanoparticulate drug carriers.

Limitations of Aforementioned Culture Systems. Despite the valuable information that can be gained from the 3-D culture systems mentioned above, deficiencies remain in the systems that limit their *in vivo* predictive power. These weaknesses include, in the case of acellular models, the inability to predict how interactions with cells affect nanoparticle distribution and therapeutic efficacy, and, in the case of the other models, an inability to recreate outside forces such as mechanical stress and convective flow. These forces could dramatically affect nanoparticle distributions. Therefore, advanced 3-D systems that incorporate mechanical forces and multiple cell types and that more closely mimic the *in vivo* architecture are desirable. In order to address the limitations of the previously described 3-D systems, more advanced 3-D models have been developed that mimic physiological conditions even more realistically. These include (a) co-culturing of 2 or more cell types in a biological matrix to mimic the complex cell−cell communications in addition to cell−ECM interactions, (b) using tissue explants, and (c) incorporating mechanical forces such as fluid flow into culture platforms to mimic the mechanical environments that cells experience *in vivo*, or combinations of these methods.

Co-Culture Models. Co-culture models, wherein two or more different cell types are grown together (Figure 3a), are useful as *in vitro* models, because tissues *in vivo* consist of more than a single cell type, and cell−cell interactions are important in determining and maintaining the normal cell function and phenotype (*14*, *16*, *17*, *48*, *49*). Applications of co-culture models are useful for investigating of the specificity of nanoparticle carriers. For example, Garnett and co-workers developed a brain tumor co-culture model consisting of cancerous cell aggregates and organotypic brain slices (*50*). Evaluation of the uptake of poly(glycerol−adipate) nanoparticles revealed that, in 3-D co-cultures, nanoparticles were predominantly taken up by cancerous cells rather than normal cells. In contrast, in monolayer cultures, nanoparticles were taken up more readily by normal cells. This conditional specificity of the nanoparticle uptake suggests that the nanoparticles may be useful for anticancer formulations with reduced toxicity to normal cells, an observation apparent only through studies with 3-D co-culture. A multicellular spheroid co-culture was also successfully used to demonstrate the specificity of a viral vector targeted toward cancer cells (*51*).

Co-culture models are particularly important when attempting to mimic a tissue containing many types of specialized cells whose function determines the tissue microenvironment. Along these lines, a 3-D co-culture that contains differentiated cells that are similar to *in vivo* lung tissue has been constructed (*52*, *53*). The co-culture of bronchial epithelial cells seeded on a human lung fibroblast-embedded collagen matrix contained a pseudostratified epithelium consisting of basal cells, mucus-secreting cells, and ciliated columnar cells with beating cilia. The cilia and mucus are important *in vivo* barriers to nanoparticle delivery to airway cells as they are specifically adapted to resist and remove foreign particles. Only in the 3-D co-cultures are well-differentiated ciliated epithelial cells observed *in vitro*; cells in monolayer culture do not express these cilia. Furthermore, the airway wall co-culture model was placed in a dynamic cyclic strain device to mimic the compressive effect observed

during bronchoconstriction in asthma in order to study the rate of viral infection of the epithelial and subepithelial cells (*54*). Previous studies with cyclic stretch in monolayer culture have suggested that intracellular processes are affected that in turn affect transfection, (*55*) and in the bronchial 3-D culture model, dynamic compression substantially increased lentiviral transduction of epithelial cells and underlying fibroblasts compared to static coculture controls (*54*). This increased transduction was attributed, in part, to enhanced transport through the matrix due to the mechanical compression. This finding, not observable in 2-D static monolayer cultures, may be useful for asthma pathophysiology as well as for designing delivery strategies of viral gene therapies to the airway.

From these studies, it can be concluded that co-culture models can promote differentiation and cell behavior of the cultured cells that resembles *in vivo* conditions more realistically than single-cell type culture models. Co-culture models thus offer a better predictive platform for nanoparticle uptake and therapeutic efficacy in complex tissue with specialized cells. An additional attribute of these models is the ability to evaluate the cell specificity of nanoparticle formulations, an important parameter for applications that must target diseased tissue while sparing surrounding healthy tissue.

***Ex Vivo* Models.** *Ex vivo* models involve harvesting tissue from human or animal sources followed by culturing on substrates such as culture wells and coverslips (*56*−*59*). Although *ex vivo* models require the use of animals, multiple data points may be obtained from a single animal source in most cases. The main advantage of *ex vivo* models is that they generally preserve the native complex and differentiated 3-D cell−matrix architecture, cell phenotype, and cell−cell interactions of the tissue of interest, thus providing a more accurate mimic of cell behavior and transport of particles to these primary cells. The *ex vivo* model also allows for direct delivery of nanoparticle formulations to target tissue along with the ability to more easily process tissues for analysis after exposure. Near real-time monitoring through confocal microscopy is also possible. *Ex vivo* models are especially beneficial if human tissue can be obtained. For example, human tissue slices have been used to screen adenoviral gene therapy agents for specificity and efficiency. In these studies, vectors were identified that effectively transduced cancerous cells while sparing normal cells (*60, 61*). For specificity studies such as this, the maintenance of cell phenotype, which is facilitated by the *ex vivo* model, is necessary for results that are likely to be predictive of *in vivo* results.

Ex vivo studies have also been used to demonstrate the possibility of gene delivery to fetal somatic cells for the treatment of monogenic disorders such as cystic fibrosis. Human fetal tracheas, maintained in *ex vivo* cultures, were shown to be highly susceptible to adeno-associated virus transduction (*62*). The high efficiency of transduction was attributed to reduced physical barriers to target cells in the prenatal tissue compared to developed tissue, which is resistant to transduction (*63, 64*). Again, preservation of the tissue in its near-native state during these studies may result in a higher probability of predicting *in vivo* efficacy and specificity.

Other *ex vivo* studies have been useful in developing methods to overcome physical barriers to therapeutic nanoparticle penetration. Quinlan et al. developed an embryonic mouse intestinal epithelium model that permits the maintenance of the gut tube and enables the introduction of exogenous genes to study the normal development of the intestinal epithelium and pathogenesis of intestinal neoplasia (*58*). These researchers found that high-efficiency adenoviral vector transduction of the intact mesenchymal and epithelial layers required the addition of an ECM modulating agent for effective adenoviral transduction.

As with other static models, results from *ex vivo* studies may not reflect the actual biodistribution of the delivery vehicles *in vivo*, because some of these studies involve incubating the explanted tissue in a bulk solution with media containing the nanoparticles of interest (Figure 3b), while *in vivo* delivery is typically administered intravenously or injected at a specific site. Furthermore, mechanical forces are typically absent during static *ex vivo* culturing, and a lack of mechanical forces, perfusion, and surrounding tissue results in remodeling and changes in cell behavior compared to the original *in vivo* environment. Long-term studies with *ex vivo* models may, therefore, be difficult, as the tissue may exhibit significant changes over the course of the experiment. Another major drawback of the *ex vivo* cultures is that they require harvesting of tissue from animal or human subjects. However, the advantage of maintaining native tissue structure makes *ex vivo* models unique.

Perfusion Models. The majority of the studies discussed to this point have been carried out under static culture conditions. As mentioned previously, cells in tissues are typically subject to fluid flow, which can be an important determinant of nanoparticle distribution in tissues as convective transport can often dominate diffusion. Nanoparticles diffuse very slowly in biological tissues and may take several months to diffuse a millimeter's distance, whereas the time to cover the same distance aided by convective transport can be much shorter. Therefore, convective transport can either greatly aid or greatly hamper the delivery of nanoparticles depending on the direction of fluid flow. In addition, it has also been shown that fluid flow can influence cellular functions. For example, under long-term culture, perfused hepatocytes maintained their liver-specific functions such as albumin secretion substantially closer to native liver compared to single monolayer or 3-D static cultures (*12, 65, 66*). Finally, static cultures can result in gradients of waste and nutrients within larger tissue constructs. Although this may be useful in studies of tissues like avascular regions of solid tumors, it can be detrimental to the preservation of larger 3-D cultures designed to model normally vascularized tissue. Thus, a model incorporating fluid flow may be beneficial for the optimization of delivery vehicles that encounter convective forces that influence their interstitial distributions.

There have been many recent advances toward the development of 3-D culture systems (Figure 3c) that allow for perfusion of tissue cultures, with particularly useful contributions from the fields of microfluidics and microfabrication (*67*−*74*). Some of these systems have the potential for higher-throughput screening due to the ability to simultaneously establish various conditions such as pH, flow rate, or drug formulation concentrations on different portions of the array. Many of the systems also allow for *in situ* visualization of the cultures and, therefore, potential real-time imaging of nanoparticle delivery. One such promising perfusion system has been developed by Griffith and co-workers, who have constructed a microfabricated multiwell chamber that allows for growth of isolated hepatocyte cultures in wells under flow conditions (*65*). A broad comparison to other standard *in vitro* models, including static ones, revealed that the perfusable system more closely mirrored *in vivo* liver function with respect to gene and protein expression as well as the ability of the cultured cells to metabolize delivered drugs (*11*). Although perfusable systems are apparently useful for nanoparticle delivery studies, there are limited examples, as many of the systems are relatively new or their development has focused primarily on cellular and tissue engineering applications rather than gene/drug delivery applications.

We have recently developed a perfusable 3-D cell-matrix gel culture model and demonstrated its applicability for *in situ* observation of nanoparticle transport in cell−gel matrixes (*75*). In this model (Figure 3d), a cell−matrix culture is loaded and

immobilized in a PDMS-glass chamber which allows for real-time imaging of particles in the 3-D structure over time. This potentially avoids any artifacts that would occur if tissue processing was necessary for visualization. Nanoparticles can be introduced laterally to media compartments situated in each side of the gel. We found size-dependent penetration of model fluorescent polystyrene nanoparticles similar to that observed in other 3-D systems such as multicellular spheroids (*3*). In addition, we observed deeper penetration of nanoparticles under interstitial flow compared to static controls using the same chamber. Currently, we are applying this simplified perfusion model to evaluate the penetration and cellular uptake of therapeutic nanoparticles, such as polyplexes, under various flow conditions. Besides the ability for real-time imaging, other advantages of this system include ease of manufacture, control over components of the initial cell−gel composition, and an ability to recover cells for flow cytometry analysis. The system can also be used for calculating the permeability of different cell−gel matrix compositions.

In summary, perfusion systems provide an additional advancement over static cultures by mimicking flow conditions in vascularized tissues. These perfusion chambers also offer the ability to recreate *in vivo* situations where convective flow is a driving force in determining nanoparticle distributions.

IMPLICATIONS FOR NANOPARTICLE CARRIER DESIGN

The results from previous studies of nanoparticle delivery to *in vitro* 3-D tissue models offer insight into a number of parameters that need to be considered during nanoparticle design. In particular, they highlight the importance of nanoparticle size, charge, surface chemistry, and stability when designing a drug delivery vehicle that can efficiently penetrate tissue. The effect of these design parameters on delivery may be understated or even ignored when nanoparticle vehicles are simply analyzed in monolayer cultures. The *in vitro* 3-D models also offer a more favorable platform for optimization compared to *in vivo* studies in terms of cost, ease of use, and time requirements.

First, and perhaps foremost, the nanoparticle carrier size must be considered. This is important for nanoparticle therapeutics that rely on transport through interstitial spaces in order to reach cells in the tissue interior. A key consideration is that particle size should be smaller than the characteristic pore size of the extracellular space. Because tissue architecture varies greatly depending on tissue type, it is impossible to determine a global cutoff diameter for tissue penetration, but the results from the studies summarized here suggest that nanoparticles with sizes less than 150 nm experience less-hindered transport.

Nanoparticle surface charge and chemistry provide an example of the balancing act that must often be played when designing a nanoparticle carrier. For charge-mediated uptake of nanoparticles, effective cell surface binding is necessary for uptake of therapeutics, but if the charge density is too high, then the carrier may experience hindered diffusion due to nonspecific interactions en route to target cells (*76*). Addition of steric shielding molecules, such as PEG, have in several instances proven to increase particle penetration in tissue (*29, 40, 41*), but can also hinder cellular uptake of particles, thus decreasing delivery efficacy (*77, 78*). The use of cleavable shielding molecules or shielding molecules with terminal targeting groups may provide a method for overcoming this reduced cell uptake (*31, 79, 80*). It is also important that targeted nanoparticles are assessed in culture models where phenotypes of cells are similar to *in vivo* situations in order to more accurately predict specificity.

Three-dimensional culture models have also helped demonstrate the usefulness of including components in nanoparticle carriers that can disrupt or digest ECM components in order to improve particle penetration. Similar to strategies employed by some pathogens to increase tissue distributions by stimulation of MMPs production to locally degrade tissue, nanoparticles that incorporate such enzymes could lead to much more favorable distributions of therapeutics in tissues (*81*).

It is important to keep in mind the high degree of variability in tissue architecture and composition. The results from studies in these 3-D tissue models offer insight into the most important parameters to consider when designing nanoparticle carriers, but specific nanoparticle behavior will vary greatly depending on the type of target tissue under consideration as well as vehicle administration method. However, 3-D models, overall, will provide a more accurate prediction of *in vivo* outcome compared to simple monolayer cultures.

CHALLENGES AND FUTURE DIRECTIONS

While researchers are increasingly turning to 3-D cell−matrix cultures for studying gene expression and other biological activities (*82*), the use of these cultures in the nanoparticle delivery field has not been widespread. This could be due, in part, to the higher degree of difficulty for setup and use compared to 2-D systems. In addition, many advanced systems are not as appealing because they are still in prototypical stages and could benefit from improvements in ease of manufacture and use. Also, the exact determinants of cell differentiation, such as cell−cell signaling, cell−ECM signaling, tissue architecture, and mechanical forces are different for each tissue and are often not well-elucidated. Therefore, accurate advanced 3-D models will have to be refined on a tissue-to-tissue basis. Despite the difficulties associated with the use of 3-D culture, many of the studies reviewed here have reinforced the need to move from 2-D to 3-D culture in order to more accurately predict the *in vivo* efficacy of drug delivery with nanoparticle formulations.

Refinement of advanced systems will most likely result through combinations of elements from many of the models discussed here. An ideal 3-D culture would allow for the introduction of multiple cell types grown in a chamber that allows for recreation of as many *in vivo* forces that act on the cells as possible, including mechanical forces that affect cell behavior. To accomplish this, current systems may need to be modified to include (i) surface modification of cell chambers to allow for long-term perfusion culture without matrix detachment due to cell contraction, (ii) more precise characterization of flow rates and profiles, (ii) the incorporation of appropriate cell types and extracellular materials to better mimic the heterotypic cell interactions, tissue architecture, and fluid flow stresses to obtain the full possible spectrum of tissue-specific functions, and, for some applications, (iv) chamber flexibility to allow for the application of mechanical forces to the tissue. With the addition of high-throughput capabilities, such systems could lead to improved screening and evaluation of nanoparticle formulations, resulting in more accurate predictions of *in vivo* outcomes and a smoother transition into clinical trials.

ACKNOWLEDGMENT

This work was supported by NIH/NCI grant 1R21CA114141-02, the Alliance for Cancer Gene Therapy (Patricia Zoch Tate Young Investigator Award), and the National Science Foundation (Graduate Fellowship to TTG).

LITERATURE CITED

(1) Netti, P., Berk, D., Swartz, M., Grodzinsky, A., and Jain, R. (2000) Role of extracellular matrix assembly in interstitial transport in solid tumors. *Cancer Res. 60,* 2497–2503.

(2) Pluen, A., Boucher, Y., Ramanujan, S., McKee, T., Gohongi, T., di Tomaso, E., Brown, E., Izumi, Y., Campbell, R., Berk, D., and Jain, R. (2001) Role of tumor-host interactions in interstitial diffusion of macromolecules: Cranial vs. subcutaneous tumors. *Proc. Natl. Acad. Sci. U.S.A. 98*, 4628–4633.
(3) Goodman, T. T., Olive, P. L., and Pun, S. H. (2007) Increased nanoparticle penetration in collagenase-treated multicellullar spheroids. *Int. J. Nanomed. 2*, 265–274.
(4) Grayson, W. L., Ma, T., and Bunnell, B. (2004) Human mesenchymal stem cells tissue development in 3D PET matrices. *Biotechnol. Prog. 20*, 905–912.
(5) Mao, Y., and Schwarzbauer, J. E. (2005) Stimulatory effects of a three-dimensional microenvironment on cell-mediated fibronectin fibrillogenesis. *J. Cell Sci. 118*, 4427–4436.
(6) Gruber, H. E., Jr. (2000) Human disc cells in monolayer vs 3D culture: cell shape, division and matrix formation. *BMC Musculoskel. Dis. 1*, 1.
(7) Garbi, C., Zurzolo, C., Bifulco, M., and Nitsch, L. (1988) Synthesis of extracellular matrix glycoproteins by a differentiated thyroid epithelial cell line. *J. Cell. Physiol. 135*, 39–46.
(8) Thorne, R. G., and Nicholson, C. (2006) In vivo diffusion analysis with quantum dots and dextrans predicts the width of brain extracellular space. *Proc. Natl. Acad. Sci. U.S.A. 103*, 5567–72.
(9) Burke, R. S., and Pun, S. H. (2008) Extracellular barriers to in vivo PEI and PEGylated PEI polyplex-mediated gene delivery to the liver. *Bioconjugate Chem. 19*, 693–704.
(10) Ruponen, M., Yla-Herttuala, S., and Urtti, A. (1999) Interactions of polymeric and liposomal gene delivery systems with extracellular glycosaminoglycans: physicochemical and transfection studies. *Biochim. Biophys. Acta, Biomembr. 1415*, 331–341.
(11) Sivaraman, A., Leach, J., Townsend, S., Iida, T., Hogan, B., Stolz, D., Fry, R., Samson, L., Tannenbaum, S., and Griffith, L. (2005) A microscale in vitro physiological model of the liver: Predictive screens for drug metabolism and enzyme induction. *Curr. Drug Metab. 6*, 569–591.
(12) Ostrovidov, S., Jiang, J., Sakai, Y., and Fujii, T. (2004) Membrane-based PDMS microbioreactor for perfused 3D primary rat hepatocyte cultures. *Biomed. Microdevices 6*, 279–87.
(13) Bhatia, S., Balis, U., Yarmush, M., and Toner, M. (1998) Microfabrication of hepatocyte/fibroblast co-cultures: Role of homotypic cell interactions. *Biotechnol. Prog. 14*, 378–387.
(14) Bhandari, R. N., Riccalton, L. A., Lewis, A. L., Fry, J. R., Hammond, A. H., Tendler, S. J., and Shakesheff, K. M. (2001) Liver tissue engineering: a role for co-culture systems in modifying hepatocyte function and viability. *Tissue Eng. 7*, 345–57.
(15) Lu, H. F., Chua, K. N., Zhang, P. C., Lim, W. S., Ramakrishna, S., Leong, K. W., and Mao, H. Q. (2005) Three-dimensional co-culture of rat hepatocyte spheroids and NIH/3T3 fibroblasts enhances hepatocyte functional maintenance. *Acta Biomater. 1*, 399–410.
(16) Agius, L. (1988) Metabolic interactions of parenchymal hepatocytes and dividing epithelial-cells in co-culture. *Biochem. J. 252*, 23–28.
(17) Auth, M. K., Okamato, M., Ishida, Y., Keogh, A., Auth, S. H. G., Gerlach, J., Encke, A., McMaster, P., and Strain, A. J. (1998) Maintained function of primary human hepatocytes by cellular interactions in coculture: implications for liver support systems. *Transpl. Int. 11*, S439−S443.
(18) Discher, D., Janmey, P., and Wang, Y. (2005) Tissue cells feel and respond to the stiffness of their substrate. *Science 310*, 1139–1143.
(19) Georges, P., and Janmey, P. (2005) Cell type-specific response to growth on soft materials. *J. Appl. Phys. 98*, 1547–1553.
(20) Yeung, T., Georges, P. C., Flanagan, L. A., Marg, B., Ortiz, M., Funaki, M., Zahir, N., Ming, W. Y., Weaver, V., and Janmey, P. A. (2005) Effects of substrate stiffness on cell morphology, cytoskeletal structure, and adhesion. *Cell Motil. Cytoskelet. 60*, 24–34.
(21) Kong, H. J., Liu, J., Riddle, K., Matsumoto, T., Leach, K., and Mooney, D. J. (2005) Non-viral gene delivery regulated by stiffness of cell adhesion substrates. *Nat. Mater. 4*, 460–4.
(22) Cukierman, E., Pankov, R., Stevens, D., and Yamada, K. (2001) Taking cell-matrix adhesions to the third dimension. *Science 294*, 1708–1712.
(23) Albrecht, D., Underhill, G., Wassermann, T., Sah, R., and Bhatia, S. (2006) Probing the role of multicellular organization in three-dimensional microenvironments. *Nat. Methods 3*, 369–375.
(24) Liu, V., and Bhatia, S. (2002) Three-dimensional photopatterning of hydrogels containing living cells. *Biomed. Microdevices 4*, 257–266.
(25) Griffith, L., and Swartz, M. (2006) Capturing complex 3D tissue physiology in vitro. *Nat. Rev. Mol. Cell Biol. 7*, 211–224.
(26) Heldin, C., Rubin, K., Pietras, K., and Ostman, A. (2004) High interstitial fluid pressure - An obstacle in cancer therapy. *Nat. Rev. Cancer 4*, 806–813.
(27) Desoize, B., and Jardillier, J. (2000) Multicellular resistance: a paradigm for clinical resistance? *Crit. Rev. Oncol. Hematol. 36*, 193–207.
(28) Pampaloni, F., Reynaud, E., and Stelzer, E. (2007) The third dimension bridges the gap between cell culture and live tissue. *Nat. Rev. Mol. Cell Biol. 8*, 839–845.
(29) Kuhn, S. J., Hallahan, D. E., and Giorgio, T. D. (2006) Characterization of superparamagnetic nanoparticle interactions with extracellular matrix in an in vitro system. *Ann. Biomed. Eng. 34*, 51–8.
(30) Valentine, M. T., Perlman, Z. E., Gardel, M. L., Shin, J. H., Matsudaira, P., Mitchison, T. J., and Weitz, D. A. (2004) Colloid surface chemistry critically affects multiple particle tracking measurements of biomaterials. *Biophys. J. 86*, 4004–14.
(31) DeRouchey, J., Schmidt, C., Walker, G. F., Koch, C., Plank, C., Wagner, E., and Radler, J. O. (2008) Monomolecular assembly of siRNA and poly(ethylene glycol)-peptide copolymers. *Biomacromolecules 9*, 724–32.
(32) Kim, Y., Dalhaimer, P., Christian, D. A., and Discher, D. E. (2005) Polymeric worm micelles as nano-carriers for drug delivery. *Nanotechnology 16*, S484−S491.
(33) Kuhn, S. J., Finch, S. K., Hallahan, D. E., and Giorgio, T. D. (2006) Proteolytic surface functionalization enhances in vitro magnetic nanoparticle mobility through extracellular matrix. *Nano Lett. 6*, 306–312.
(34) Nederman, T., and Twentyman, P. (1984) Spheroids for studies of drug effects. *Recent Results Cancer Res. 95*, 84–102.
(35) Waleh, N. S., Gallo, J., Grant, T. D., Murphy, B. J., Kramer, R. H., and Sutherland, R. M. (1994) Selective down-regulation of integrin receptors in spheroids of squamous cell carcinoma. *Cancer Res. 54*, 838–43.
(36) Nederman, T., Norling, B., Glimelius, B., Carlsson, J., and Brunk, U. (1984) Demonstration of an extracellular matrix in multicellular tumor spheroids. *Cancer Res. 44*, 3090–7.
(37) Durand, R. E., Chaplin, D. J., and Olive, P. L. (1990) Cell sorting with Hoechst or carbocyanine dyes as perfusion probes in spheroids and tumors. *Methods Cell Biol. 33*, 509–18.
(38) Enger, P. O., Thorsen, F., Lonning, P. E., Bjerkvig, R., and Hoover, F. (2002) Adeno-associated viral vectors penetrate human solid tumor tissue in vivo more effectively than adenoviral vectors. *Hum. Gene Ther. 13*, 1115–25.
(39) Saga, T., Neumann, R. D., Heya, T., Sato, J., Kinuya, S., Le, N., Paik, C. H., and Weinstein, J. N. (1995) Targeting cancer micrometastases with monoclonal antibodies: a binding-site barrier. *Proc. Natl. Acad. Sci. U.S.A. 92*, 8999–9003.
(40) Han, M., Bae, Y., Nishiyama, N., Miyata, K., Oba, M., and Kataoka, K. (2007) Transfection study using multicellular tumor spheroids for screening non-viral polymeric gene vectors with low cytotoxicity and high transfection efficiencies. *J. Controlled Release 121*, 38–48.
(41) Oishi, M., Kataoka, K., and Nagasaki, Y. (2006) pH-responsive three-layered PEGylated polyplex micelle based on a lactosylated ABC triblock copolymer as a targetable and

endosome-disruptive nonviral gene vector. *Bioconjugate Chem. 17*, 677–88.
(42) Oishi, M., Nagasaki, Y., Nishiyama, N., Itaka, K., Takagi, M., Shimamoto, A., Furuichi, Y., and Kataoka, K. (2007) Enhanced growth inhibition of hepatic multicellular tumor spheroids by lactosylated poly(ethylene glycol)-siRNA conjugate formulated in PEGylated polyplexes. *ChemMedChem 2*, 1290–97.
(43) Mellor, H. R., Davies, L. A., Caspar, H., Pringle, C. R., Hyde, S. C., Gill, D. R., and Callaghan, R. (2006) Optimising non-viral gene delivery in a tumour spheroid model. *J. Gene Med. 8*, 1160–70.
(44) Hochhauser, D. (1997) Modulation of chemosensitivity through altered expression of cell cycle regulatory genes in cancer. *Anti-Cancer Drugs 8*, 903–910.
(45) Kim, J. H., Lee, Y. S., Kim, H., Huang, J. H., Yoon, A. R., and Yun, C. O. (2006) Relaxin expression from tumor-targeting adenoviruses and its intratumoral spread, apoptosis induction, and efficacy. *J. Natl. Cancer Inst. 98*, 1482–93.
(46) Unemori, E. N., Pickford, L. B., Salles, A. L., Piercy, C. E., Grove, B. H., Erikson, M. E., and Amento, E. P. (1996) Relaxin induces an extracellular matrix-degrading phenotype in human lung fibroblasts in vitro and inhibits lung fibrosis in a murine model in vivo. *J. Clin. Invest. 98*, 2739–45.
(47) Padron, J. M., van der Wilt, C. L., Smid, K., Smitskamp-Wilms, E., Backus, H. H., Pizao, P. E., Giaccone, G., and Peters, G. J. (2000) The multilayered postconfluent cell culture as a model for drug screening. *Crit. Rev. Oncol. Hematol. 36*, 141–57.
(48) Hwa, A., Fry, R., Sivaraman, A., So, P., Samson, L., Stolz, D., and Griffith, L. (2007) Rat liver sinusoidal endothelial cells survive without exogenous VEGF in 3D perfused co-cultures with hepatocytes. *FASEB J. 21*, 2564–2579.
(49) Villaschi, S., and Nicosia, R. (1994) Paracrine interactions between fibroblasts and endothelial-cells in a serum-free coculture model - modulation of angiogenesis and collagen gel contraction. *Lab. Invest. 71*, 291–299.
(50) Meng, W., Kallinteri, P., Walker, D., Parker, T., and Garnett, M. (2007) Evaluation of poly (glycerol-adipate) nanoparticle uptake in an in vitro 3-D brain tumor co-culture model. *Exp. Biol. Med. 232*, 1100–1108.
(51) Kilani, R., Tamimi, Y., Hanel, E., Wong, K., Karmali, S., Lee, P., and Moore, R. (2003) Selective reovirus killing of bladder cancer in a co-culture spheroid model. *Virus Res. 93*, 1–12.
(52) Choe, M., Sporn, P., and Swartz, M. (2003) An in vitro airway wall model of remodeling. *Am. J. Physiol. 285*, L427−L433.
(53) Choe, M., Tomei, A., and Swartz, M. (2006) Physiological 3D tissue model of the airway wall and mucosa. *Nat. Protoc. 1*, 357–362.
(54) Tomei, A., Choe, M., and Swartz, M. (2008) Effects of dynamic compression on lentiviral transduction in an in vitro airway wall model. *Am. J. Physiol. 294*, L79−L86.
(55) Taylor, W., Gokay, K. E., Capaccio, C., Davis, E., Glucksberg, M., and Dean, D. A. (2003) The effects of cyclic stretch on gene transfer in alveolar epithelial cells. *Mol. Ther. 7*, 542–9.
(56) Huang, L., Reebye, S., Yeung, A., Jia, W., and Skarsgard, E. (2006) Lentiviral-mediated fetal gene therapy for monogenic disorders: Development of an in vitro rabbit model. *Fetal Diagn. Ther. 21*, 241–245.
(57) Lang, D., Droemann, D., Schultz, H., Branscheid, D., Martin, C., Ressmeyer, A., Zabel, P., Vollmer, E., and Goldmann, T. (2007) A novel human ex vivo model for the analysis of molecular events during lung cancer chemotherapy. *Respiratory Res. 8*, 43.
(58) Quinlan, J., Yu, W., Hornsey, M., Tosh, D., and Slack, J. (2006) In vitro culture of embryonic mouse intestinal epithelium: cell differentiation and introduction of reporter genes. *BMC Dev. Biol. 6*, 24.
(59) Torche, A., Jouan, H., Le Corre, P., Albina, E., Primault, R., Jestin, A., and Le Verge, R. (2000) Ex vivo and in situ PLGA microspheres uptake by pig ileal Peyer's patch segment. *Int. J. Pharm. 201*, 15–27.
(60) Rots, M., Elferink, M., Gommans, W., Oosterhuis, D., Schalk, J., Curiel, D., Olinga, P., Haisma, H., and Groothuis, G. (2006) An ex vivo human model system to evaluate specificity of replicating and non-replicating gene therapy agents. *J. Gene Med. 8*, 35–41.
(61) Kirby, T., Rivera, A., Rein, D., Wang, M., Ulasov, I., Breidenbach, M., Kataram, M., Contreras, J., Krumdieck, C., Yamamoto, M., Rots, M., Haisma, H., Alvarez, R., Mahasreshti, P., and Curiel, D. (2004) A novel ex vivo model system for evaluation of conditionally replicative adenoviruses therapeutic efficacy and toxicity. *Clin. Cancer Res. 10*, 8697–8703.
(62) Lim, F. Y., Martin, B. G., SenaEsteves, M., Radu, A., and Crombleholme, T. M. (2002) Adeno-associated virus (AAV)-mediated gene transfer in respiratory epithelium and submucosal gland cells in human fetal tracheal organ culture. *J Pediatr. Surg. 37*, 1051–7, discussion 1051−7.
(63) Halbert, C. L., Alexander, I. E., Wolgamot, G. M., and Miller, A. D. (1995) Adeno-associated virus vectors transduce primary cells much less efficiently than immortalized cells. *J. Virol. 69*, 1473–9.
(64) Bals, R., Xiao, W., Sang, N., Weiner, D. J., Meegalla, R. L., and Wilson, J. M. (1999) Transduction of well-differentiated airway epithelium by recombinant adeno-associated virus is limited by vector entry. *J. Virol. 73*, 6085–8.
(65) Powers, M. J., Domansky, K., Kaazempur-Mofrad, M. R., Kalezi, A., Capitano, A., Upadhyaya, A., Kurzawski, P., Wack, K. E., Stolz, D. B., Kamm, R., and Griffith, L. G. (2002) A microfabricated array bioreactor for perfused 3D liver culture. *Biotechnol. Bioeng. 78*, 257–69.
(66) Chen, J. P., and Lin, T. C. (2006) High-density culture of hepatocytes in a packed-bed bioreactor using a fibrous scaffold from plant. *Biochem. Eng. J. 30*, 192–198.
(67) Jang, K., Sato, K., Igawa, K., Chung, U., and Kitamori, T. (2008) Development of an osteoblast-based 3D continuous-perfusion microfluidic system for drug screening. *Anal. Bioanal. Chem. 390*, 825–832.
(68) Kim, M., Yeon, J., and Park, J. (2007) A microfluidic platform for 3-dimensional cell culture and cell-based assays. *Biomed. Microdevices 9*, 25–34.
(69) Lee, P., Gaige, T., Ghorashian, N., and Hung, P. (2007) Microfluidic tissue model for live cell screening. *Biotechnol. Prog. 23*, 946–951.
(70) Toh, Y., Zhang, C., Zhang, J., Khong, Y., Chang, S., Samper, V., van Noort, D., Hutmacher, D., and Yu, H. (2007) A novel 3D mammalian cell perfusion-culture system in microfluidic channels. *Lab Chip 7*, 302–309.
(71) Torisawa, Y., Shiku, H., Yasukawa, T., Nishizawa, M., and Matsue, T. (2005) Three-dimensional micro-culture system with a silicon-based cell array device for multi-channel drug sensitivity test. *Sens. Actuators, B 108*, 654–659.
(72) Wu, M., Huang, S., Cui, Z., Cui, Z., and Lee, G. (2008) A high throughput perfusion-based microbioreactor platform integrated with pneumatic micropumps for three-dimensional cell culture. *Biomed. Microdevices 10*, 309–319.
(73) Tan, W., and Desai, T. A. (2003) Microfluidic patterning of cells in extracellular matrix biopolymers: effects of channel size, cell type, and matrix composition on pattern integrity. *Tissue Eng. 9*, 255–67.
(74) Khong, Y. M., Zhang, J., Zhou, S., Cheung, C., Doberstein, K., Samper, V., and Yu, H. (2007) Novel intra-tissue perfusion system for culturing thick liver tissue. *Tissue Eng. 13*, 2345–2356.
(75) Ng, C. P., and Pun, S. H. (2008) A perfusable 3D cell-matrix tissue culture chamber for in situ evaluation of nanoparticle vehicle penetration and transport. *Biotechnol. Bioeng. 99*, 1490–1501.
(76) Jain, R. K. (1999) Transport of molecules, particles, and cells in solid tumors. *Annu. Rev. Biomed. Eng. 1*, 241–263.

(77) Kostarelos, K., Emfietzoglou, D., Papakostas, A., Yang, W. H., Ballangrud, A., and Sgouros, G. (2004) Binding and interstitial penetration of liposomes within avascular tumor spheroids. *Int. J. Cancer. 112*, 713–721.

(78) Mishra, S., Webster, P., and Davis, M. E. (2004) PEGylation significantly affects cellular uptake and intracellular trafficking of non-viral gene delivery particles. *Eur. J. Cell. Biol. 83*, 97–111.

(79) Luten, J., van Steenbergen, M. J., Lok, M. C., de Graaff, A. M., van Nostrum, C. F., Talsma, H., and Hennink, W. E. (2008) Degradable PEG-folate coated poly(DMAEA-co-BA)phosphazene-based polyplexes exhibit receptor-specific gene expression. *Eur. J. Pharm. Sci. 33*, 241–251.

(80) Wagner, E. (2007) Programmed drug delivery: nanosystems for tumor targeting. *Expert Opin. Biol. Ther. 7*, 587–593.

(81) Watanabe, K. (2004) Collagenolytic proteases from bacteria. *Appl. Microbiol. Biotechnol. 63*, 520–526.

(82) Abbott, A. (2003) Cell culture: Biology's new dimension. *Nature 424*, 870–872.

(83) Finocchiaro, L. M., Bumaschny, V. F., Karara, A. L., Fiszman, G. L., Casais, C. C., and Glikin, G. C. (2004) Herpes simplex virus thymidine kinase/ganciclovir system in multicellular tumor spheroids. *Cancer Gene Ther. 11*, 333–45.

(84) Bokhari, M., Carnachan, R. J., Cameron, N. R., and Przyborski, S. A. (2007) Culture of HepG2 liver cells on three dimensional polystyrene scaffolds enhances cell structure and function during toxicological challenge. *J. Anat. 211*, 567–76.

BC800233A

COMMUNICATIONS

Novel Peptide Linkers for Highly Potent Antibody−Auristatin Conjugate

Svetlana O. Doronina,* Tim D. Bovee, David W. Meyer, Jamie B. Miyamoto, Martha E. Anderson, Carol A. Morris-Tilden, and Peter D. Senter

Seattle Genetics, Incorporated, 21823 30th Drive SE, Bothell, Washington 98021. Received July 10, 2008; Revised Manuscript Received August 18, 2008

Auristatins are highly potent antimitotic agents that have received considerable attention because of their activities when targeted to tumor cells in the form of antibody−drug conjugates (ADCs). Our lead agent, SGN-35, consists of the cAC10 antibody linked to the N-terminal amino acid of monomethylauristatin E (MMAE) via a valine-citrulline *p*-aminobenzylcarbamate (val-cit-PABC) linker that is cleaved by intracellular proteases such as cathepsin B. More recently, we developed an auristatin F (AF) derivative monomethylauristatin F (MMAF), which unlike MMAE contains the amino acid phenylalanine at the C-terminal position. Because of the negatively charged C-terminal residue, the potency of AF and MMAF is impaired. However, their ability to kill target cells is greatly enhanced through facilitated cellular uptake by internalizing mAbs. Here, we explore the effects of linker technology on AF-based ADC potency, activity, and tolerability by generating a diverse set of dipeptide linkers between the C-terminal residue and the mAb carrier. The resulting ADCs differed widely in activity, with some having significantly improved therapeutic indices compared to the original mAb-Val-Cit-PABC-MMAF conjugate. The therapeutic index was increased yet further by generating dipeptide-based ADCs utilizing new auristatins with methionine or tryptophan as the C-terminal drug residue. These results demonstrate that manipulation of the C-terminal peptide sequence used to attach auristatins to the mAb carrier can lead to highly potent and specific conjugates with greatly improved therapeutic windows.

INTRODUCTION

The use of monoclonal antibodies (mAbs) for the delivery of anticancer drugs to tumor cells has been the subject of a great deal of investigation (*1, 2*). In the past year, the field has advanced significantly, based on clinical studies with SGN-35, an anti-CD30-auristatin conjugate used to treat patients with Hodgkin's lymphoma and anaplastic large cell lymphoma, and trastuzumab-DM1, an anti-Her2/neu-maytansine conjugate for patients with breast cancer (*1, 3*−*6*). Both antibody−drug conjugates (ADCs) have led to many objective responses at well-tolerated doses.

There are several aspects of ADC design that can markedly influence activity, safety, and specificity. We and others have previously shown that highly potent drugs, stable linker technologies, carefully controlled conjugation processes, and restricted antigen expression contribute to ADC activity and tolerability (*1, 2*). Our most advanced ADC is SGN-35, which consists of the potent antimitotic agent monomethylauristatin E (MMAE), linked via the N-terminal monomethylvaline unit to the anti-CD30 AC10 mAb through a valine-citrulline (Val-Cit) dipeptide linker (*7*). ADCs containing the Val-Cit linker have been shown to be much more stable in vivo ($t_{1/2}$ for drug release ∼7 days) than previously described hydrazone and disulfide-based linkers (*7, 8*). Dipeptide linkers used for the attachment of such drugs as MMAE (*7, 9*) as well as MMAF (*10*) (Figure 1), high-potency doxorubicin derivatives (*11*), and DNA minor groove binders (*12*) to mAbs result in conjugates having pronounced and potent activities against an array of tumor types.

One of the noteworthy aspects of auristatin-based ADCs is that the drug component is synthetic, allowing for linker attachment sites to be incorporated at various positions within the molecule. This has allowed us to produce ADCs from auristatin E and MMAE involving acid-labile C-terminal hydrazones and protease-sensitive N-terminal peptides as the cleavable groups for drug release (*7*). Similarly, while MMAF was designed for linker attachment to the N-terminal monomethylvaline, the C-terminal carboxyl group could also be used as a point of linker attachment (Figure 1). Since the C-terminal residue together with the appended dipeptide would be within the binding site, it is expected that the sequence would dictate the repertoire of enzymes capable of catalyzing drug release, and would also affect the kinetics of hydrolysis. Thus, it was envisioned that dipeptide linkers attached to auristatins with various C-terminal amino acids would modulate efficacy, potency, and tolerability. In this report, we describe the design, preparation, and in vitro and in vivo properties of C-terminal linked auristatin ADCs. This work has led to the identification of new highly active conjugates with greatly improved therapeutic indices.

RESULTS AND DISCUSSION

To test the hypothesis that the dipeptide linker could influence the therapeutic window of auristatin conjugates when linked through the C-terminus, we generated a library of 29 dipeptide derivatives attached directly to the phenylalanine carboxyl group of AF (representative molecules are shown in Figure 1, Table

* sdoronina@seagen.com.

10.1021/bc800289a CCC: $40.75 © 2008 American Chemical Society
Published on Web 09/20/2008

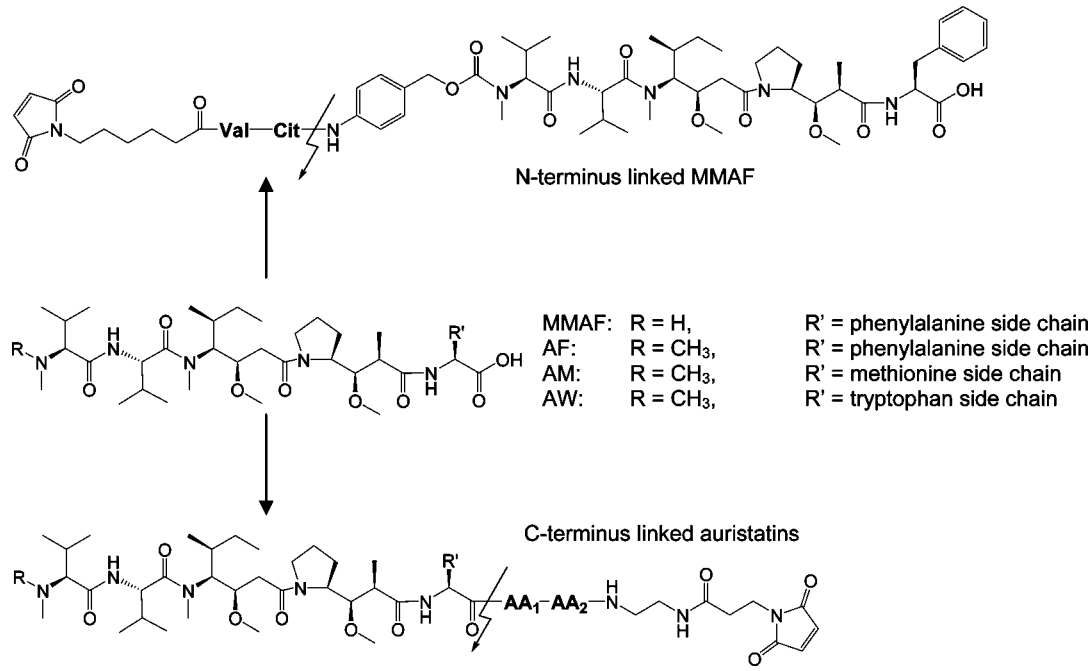

Figure 1. Structures of drugs and linkers. The arrows indicate the intended sites of enzymatic hydrolysis. For the N-terminal Val-Cit-PABC-MMAF derivative, hydrolysis is followed by spontaneous [1,6]-fragmentation of the *p*-aminobenzylcarbamate group (*7, 10*).

Table 1. In Vitro Cytotoxicity and Mouse Tolerability of ADCs Generated by Attaching Auristatin Peptide Derivatives to the 1F6 mAb

		IC_{50} (ng/mL)[a]			
Auristatin	AA_1-AA_2	786-O (RCC)	Caki-1 (RCC)	L428 (HD)	MTD (mg/kg)[b]
AF	Ile-Val	3	4	3	<50[c]
	Asp-Val	18	25	18	<50[c]
	His-Val	6	11	6	<50[c]
	NorVal-(D)Asp	28	12	24	50
	β-Ala-(D)Asp	525	1585	1096	50
	Met-Lys	7	4	3	50
	Asn-Lys	9	8	8	50
	Ile-Pro	10	9	5	75
	Me_3Lys-Pro	20	11	24	75
	PhenylGly-(D)Lys	339	44	275	75
	Met-(D)Lys	12	9	168	100
	Asn-(D)Lys	10	6	9	100
	Pro-(D)Lys	>10 000	>10 000	>10 000	>100[d]
MMAF	Met-(D)Lys	10	8	123	<100[d]
	Asn-(D)Lys	9	7	7	<100[d]
AM	Met-(D)Lys	56	39	1000	150
	Asn-(D)Lys	20	20	28	>150[d]
AW	Met-(D)Lys	16	15	19	>150[d]
	Asn-(D)Lys	20	22	>1000	<150[d]
Val-Cit-PABC-MMAF		9.1 ± 3.6[e]	6.1 ± 2.7[e]	5.9 ± 2.0[e]	50

[a] Cells were exposed to the drugs for 96 h. The cytotoxic effects were determined using Alamar Blue dye conversion as a measure of cell viability. Concentrations are represented by the mAb component. The cell lines are CD70 antigen positive. The cytotoxicity assay used for these measurements has shown a 40% coefficient of variability in over 20 repeat measurements of h1F6-Val-Cit-PABC-MMAF. A select number of compounds in this table were assayed 4 times and gave IC_{50} values with a coefficient of variability of 13−27%; we therefore expect all compounds to show comparable variance. [b] MTD is defined as the highest dose not inducing >20% weight loss and overt toxicities. Concentrations are represented by the mAb component of the ADCs. [c] Lowest concentration tested. [d] Only concentration tested. [e] IC_{50} values are the mean and SD of 21 independent experimental titrations, each performed at least in duplicate.

1). The library was biased with D-amino acids or prolines at AA_2 in order to block potential hydrolysis between AA_1-AA_2 sequences and to increase the stringency of free drug release through proteolysis. Conjugates of these modified auristatins were generated by reacting the maleimide present on the drug linker with hinge cysteine thiol groups on the 1F6 antibody, forming ADCs that bound to the CD70 antigen on hematologic malignancies and renal cell carcinoma (*13*). After separating any unconjugated drugs (*10*), the purified ADCs contained an average of 4 drugs/mAb, according to previously published reversed-phase HPLC methods (*14*). The use of AF in this series, rather than MMAF, simplified the chemistry, as no N-terminal protecting groups were required during the synthesis, and based on previous work (*7, 10*), it was expected that there would be no loss in drug potency.

With few exceptions, the C-terminal dipeptide AF ADCs were active against the CD70 positive cell line panel (Table 1). The maximum tolerated doses (MTDs) as defined by the highest dose not inducing >20% weight loss, and overt toxicities varied from <50 mg/kg for some of the ADC constructs to 100 mg/kg for AF-Met-(D)Lys-1F6 and AF-Asn-(D)Lys-1F6. Notably, corresponding conjugates with natural L-amino acid at AA_2 position, AF-Met-Lys-1F6 and AF-Asn-Lys-1F6, were less tolerated with MTDs 50 mg/kg. These results indicated that the

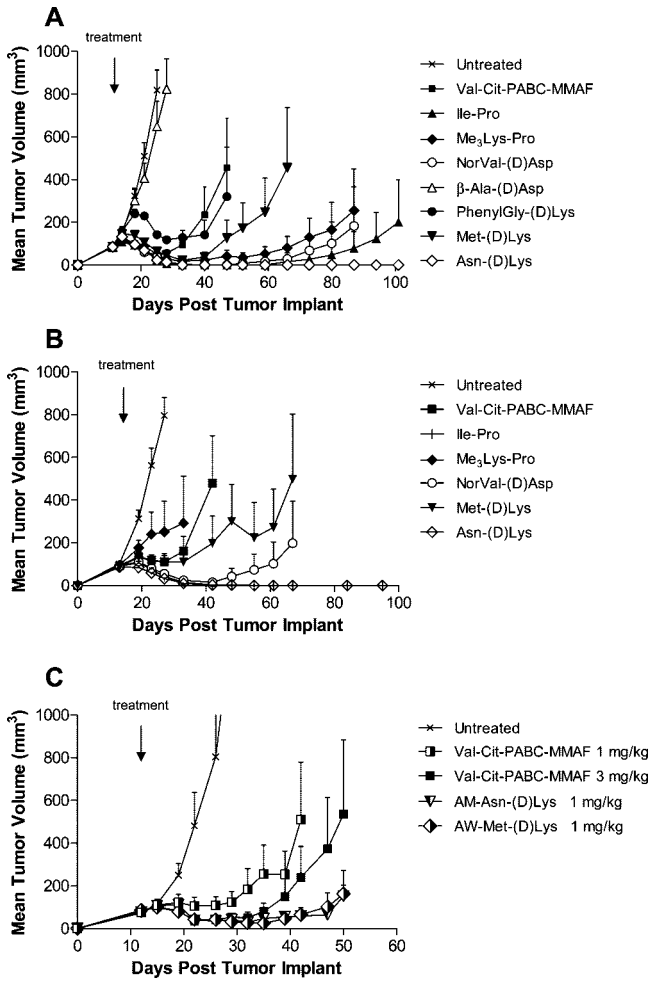

Figure 2. In vivo therapeutic efficacy of the conjugates in nude mice (5 animals/group). ADCs were delivered via intraperitoneal injections. Groups of mice with (A) subcutaneous 786-O human RCC tumors or (B) DBTRG-05MG glioblastoma tumors were treated with 1F6-Val-Cit-PABC-MMAF or AF-AA_1-AA_2-1F6 ADCs at 3 mg mAb component/kg. (C) Groups of mice with subcutaneous 786-O human RCC tumors were treated with 1F6-Val-Cit-PABC-MMAF at 1 mg or 3 mg mAb component/kg, or with AM-Asn-(D)Lys-1F6 and AW-Met-(D)Lys-1F6 at 1 mg mAb component/kg.

tolerability profiles of auristatin-based ADCs could be modulated through direct dipeptide attachment to the C-terminal residue of AF.

Several of the ADCs were tested in vivo in mice bearing subcutaneous CD70 positive 786-O RCC tumor xenografts (Figure 2A). This tumor model has been shown in previous studies to be sensitive to the 1F6-Val-Cit-PABC-MMAF (Figure 1), in which the auristatin component was linked through the N-terminal monomethylvaline residue (*13*, *15*). Treatment was initiated once the tumors were staged ($\sim$100 mm^3) and growing with a single ADC dose of 3 mg 1F6 component/kg body weight. As expected, the dose and dosing schedule of 1F6-Val-Cit-PABC-MMAF used resulted in activity against 786-O RCC tumors, but did not induce cures or durable regressions. All other C-terminal dipeptide ADCs were as potent as or more potent than 1F6-Val-Cit-PABC-MMAF, with the exception of AF-β-Ala-(D)Asp, which was inactive on cancer cell lines (Table 1). Of particular note were the activities of the most highly tolerated and active ADCs (Table 1), AF-Asn-(D)Lys-1F6 ($P = 0.0018$ by Log-rank test), which displayed greater potency than 1F6-Val-Cit-PABC-MMAF, and AF-Met-(D)Lys-1F6, which had similar potency. In addition, AF-Ile-Pro-1F6 was more potent than 1F6-Val-Cit-PABC-MMAF in this model ($P = 0.0064$), but was slightly more toxic than AF-Asn-(D)Lys-1F6 and AF-Met-(D)Lys-1F6 (Table 1).

Selected ADCs from the 786-O study were then tested for activity against subcutaneous CD70 positive DBTRG-05MG glioblastoma tumors using the previously described dosing scheme of a single treatment at 3 mg mAb component/kg (Figure 2B). The results were consistent with those obtained in the 786-O study, in that the Met-(D)Lys conjugate had comparable potency, and the Asn-(D)Lys conjugate was more potent than 1F6-Val-Cit-PABC-MMAF ($P = 0.0018$). These in vivo therapy results, taken together with the tolerability studies shown in Table 1, demonstrate that alterations in the mode of drug attachment can have a pronounced effect on ADC potency, activity, and tolerability.

We next extended the findings to include a set of auristatins in which the C-terminal phenylalanine residue was replaced with methionine or tryptophan (AM and AW, respectively; Figure 1). These molecules were identified in an independent SAR screen of auristatin analogues as drugs retaining high activity yet providing increased tolerability in mice. The new tripeptide sequences presented for protease-mediated drug release were expected to alter the spectrum of activating enzymes and potentially the therapeutic window of the ADCs as well. Mouse tolerability studies were undertaken at 150 mg/kg, since the goal of this work was to identify new ADCs that were tolerated at doses significantly higher than those reported up to this point.

In vitro cytotoxicity experiments with four of the phenylalanine replacement ADCs are shown in Table 1. Of them, AM-Asn-(D)Lys-1F6 and AW-Met-(D)Lys-1F6 were approximately as potent on all three cell lines tested as 1F6-Val-Cit-PABC-MMAF. Both AM-Asn-(D)Lys-1F6 and AW-Met-(D)Lys-1F6 were distinguished from other ADCs tested in this series, since they were tolerated at $>$150 mg/kg and had comparable in vitro potencies to 1F6-Val-Cit-PABC-MMAF. These ADCs were then tested for therapeutic efficacy in mice with 786-O RCC xenografts (Figure 2C) and were at least 3-fold more potent than 1F6-Val-Cit-PABC-MMAF. The results extend the findings with AF-dipeptide based ADCs to include new auristatin forms, providing evidence that both the peptide linker and the released drug can impact ADC therapeutic index.

CONCLUSIONS

We have demonstrated that it is possible to alter the therapeutic window of auristatin-based ADCs by changing the peptide linker between the drug and the mAb carrier protein. Attaching the dipeptide linkers directly to the C-terminal residue on the auristatin rather than to the PABC group on the amino terminus of the drug (*7*, *10*, *17*−*19*) places greater stringency on enzymatic hydrolysis. This was deemed important in the design of the drug linker, since both the site and the rate of drug release would be expected to impact ADC efficacy and tolerability. Indeed, the AF-Asn-(D)Lys and AF-Met-(D)Lys ADCs were not only more potent than 1F6-Val-Cit-PABC-MMAF (Figure 2A,B), but were also tolerated at higher doses (Table 1). This work was extended to include new auristatins (AW and AM), leading to ADCs with $>$3-fold increased potency compared to 1F6-Val-Cit-PABC-MMAF (Figure 2C), and $>$3-fold increased tolerability as determined by weight loss in mice (Table 1). Thus, the approach of optimizing both the dipeptide linker and the C-terminal residue of the auristatins leads to new generation ADCs with very promising biological properties. Currently, we are extending these findings to include mAbs with different specificities, assessing the activities of these altered auristatin linker derivatives in several in vivo models for efficacy and tolerability, and identifying the enzymes required for active drug release.

Supporting Information Available: Experimental procedures and synthetic schemes for drug linkers. This material is available free of charge via the Internet at http://pubs.acs.org.

LITERATURE CITED

(1) Carter, P. J., and Senter, P. D. (2008) Antibody-drug conjugates for cancer therapy. *Cancer J. 14*, 154–69.

(2) Chari, R. V. (2008) Targeted cancer therapy: conferring specificity to cytotoxic drugs. *Acc. Chem. Res. 41*, 98–107.

(3) Beeram, M., Krop, I., Modi, S., Tolcher, A., Rabbee, N., Girish, S., Tibbitts, J., Holden, S., Lutzker, S., and Burris, H. (2007) A phase I study of trastuzumab-MCC-DM1 (T-DM1), a first-in-class HER2 antibody-drug conjugate (ADC), in patients (pts) with HER2+ metastatic breast cancer (BC). *J. Clin. Oncol. 25*, Abstract 1042.

(4) Krop, I. E., Beeram, M., Modi, S., Rabbee, N., Girish, S., Tibbitts, J., Holden, S. N., Lutzker, S. G., and Burris, H. A. (2007) A phase I study of trastuzumab-DM1, a first-in-class HER2 antibody-drug conjugate, in patients with advanced HER2+ breast cancer, In *30th Annual San Antonio Breast Cancer Symposium*, Abstract 310.

(5) Younes, A., Forero-Torres, A., Bartlett, N., Leonard, J. P., Rege, B., Kennedy, D. A., Lorenz, J., and Sievers, E. L. (2007) A novel antibody-drug conjugate, SGN-35, (anti-CD30-auristatin), induces objective responses in patients with relapsed or refractory Hodgkin lymphoma, preliminary results of a phase I tolerability study, In *7th International Symposium on Hodgkin Lymphoma*.

(6) Younes, A., Forero-Torres, A., Bartlett, N. L., Leonard, J. P., Rege, B., Kennedy, D. A., Lorenz, J. M., and Sievers, E. L. (2008) Objective responses in a phase I dose-escalation study of SGN-35, a novel antibody-drug conjugate (ADC) targeting CD30, in patients with relapsed or refractory hodgkin lymphoma. *Am. Soc. Clin. Oncol.*

(7) Doronina, S. O., Toki, B. E., Torgov, M. Y., Mendelsohn, B. A., Cerveny, C. G., Chace, D. F., DeBlanc, R. L., Gearing, R. P., Bovee, T. D., Siegall, C. B., Francisco, J. A., Wahl, A. F., Meyer, D. L., and Senter, P. D. (2003) Development of potent monoclonal antibody auristatin conjugates for cancer therapy. *Nat. Biotechnol. 21*, 778–84.

(8) Sanderson, R. J., Hering, M. A., James, S. F., Sun, M. M., Doronina, S. O., Siadak, A. W., Senter, P. D., and Wahl, A. F. (2005) In vivo drug-linker stability of an anti-CD30 dipeptide-linked auristatin immunoconjugate. *Clin. Cancer Res. 11*, 843–52.

(9) Francisco, J. A., Cerveny, C. G., Meyer, D. L., Mixan, B. J., Klussman, K., Chace, D. F., Rejniak, S. X., Gordon, K. A., DeBlanc, R., Toki, B. E., Law, C. L., Doronina, S. O., Siegall, C. B., Senter, P. D., and Wahl, A. F. (2003) cAC10-vcMMAE, an anti-CD30-monomethyl auristatin E conjugate with potent and selective antitumor activity. *Blood 102*, 1458–65.

(10) Doronina, S. O., Mendelsohn, B. A., Bovee, T. D., Cerveny, C. G., Alley, S. C., Meyer, D. L., Oflazoglu, E., Toki, B. E., Sanderson, R. J., Zabinski, R. F., Wahl, A. F., and Senter, P. D. (2006) Enhanced activity of monomethylauristatin F through monoclonal antibody delivery: effects of linker technology on efficacy and toxicity. *Bioconjugate Chem. 17*, 114–24.

(11) Jeffrey, S. C., Nguyen, M. T., Andreyka, J. B., Meyer, D. L., Doronina, S. O., and Senter, P. D. (2006) Dipeptide-based highly potent doxorubicin antibody conjugates. *Bioorg. Med. Chem. Lett. 16*, 358–62.

(12) Jeffrey, S. C., Nguyen, M. T., Moser, R. F., Meyer, D. L., Miyamoto, J. B., and Senter, P. D. (2007) Minor groove binder antibody conjugates employing a water soluble beta-glucuronide linker. *Bioorg. Med. Chem. Lett. 17*, 2278–80.

(13) Law, C. L., Gordon, K. A., Toki, B. E., Yamane, A. K., Hering, M. A., Cerveny, C. G., Petroziello, J. M., Ryan, M. C., Smith, L., Simon, R., Sauter, G., Oflazoglu, E., Doronina, S. O., Meyer, D. L., Francisco, J. A., Carter, P., Senter, P. D., Copland, J. A., Wood, C. G., and Wahl, A. F. (2006) Lymphocyte activation antigen CD70 expressed by renal cell carcinoma is a potential therapeutic target for anti-CD70 antibody-drug conjugates. *Cancer Res. 66*, 2328–37.

(14) Sun, M. M., Beam, K. S., Cerveny, C. G., Hamblett, K. J., Blackmore, R. S., Torgov, M. Y., Handley, F. G., Ihle, N. C., Senter, P. D., and Alley, S. C. (2005) Reduction-alkylation strategies for the modification of specific monoclonal antibody disulfides. *Bioconjugate Chem. 16*, 1282–90.

(15) Alley, S. C., Benjamin, D. R., Jeffrey, S. C., Okeley, N. M., Meyer, D. L., Sanderson, R. J., and Senter, P. D. (2008) Contribution of linker stability to the activities of anticancer immunoconjugates. *Bioconjugate Chem. 19*, 759–65.

(16) Shnyder, S. D., Cooper, P. A., Millington, N. J., Pettit, G. R., and Bibby, M. C. (2007) Auristatin PYE, a novel synthetic derivative of dolastatin 10, is highly effective in human colon tumour models. *Int. J. Oncol. 31*, 353–60.

(17) Dubowchik, G. M., and Firestone, R. A. (1998) Cathepsin B-sensitive dipeptide prodrugs. 1. A model study of structural requirements for efficient release of doxorubicin. *Bioorg. Med. Chem. Lett. 8*, 3341–6.

(18) Dubowchik, G. M., Mosure, K., Knipe, J. O., and Firestone, R. A. (1998) Cathepsin B-sensitive dipeptide prodrugs. 2. Models of anticancer drugs paclitaxel (Taxol), mitomycin C and doxorubicin. *Bioorg. Med. Chem. Lett. 8*, 3347–52.

(19) Dubowchik, G. M., and Walker, M. A. (1999) Receptor-mediated and enzyme-dependent targeting of cytotoxic anticancer drugs. *Pharmacol. Ther. 83*, 67–123.

BC800289A

EXPERIMENTAL PROCEDURES

General. Unless otherwise noted, materials were obtained from commercial suppliers in the highest purity grade available and used without further purifications. Anhydrous DMF and CH_2Cl_2 were purchased from Aldrich. Fmoc-Dap-OH and Fmoc-MeVal-Val-Dil-OH were custom synthesized by Albany Molecular Research, Inc. (Albany, NY). 3-Maleimidopropionic acid NHS ester was obtained from Molecular Biosciences, Inc. (Boulder, CO). 1,2-Diaminoethane trityl resin was purchased from Novabiochem (substitution 0.9 mmol/gram). Solid phase synthesis was performed in plastic syringes (National Scientific Company) fitted with a filter cut out of fritware PE medium grade porous sheet (Scienceware). Burrell wrist action® shaker (Burrell Scientific, Pittsburg, PA) was used for agitation. All solid-phase yields reported are based upon the initial substitution level of the resin and constitute a mass balance of isolated pure material, unless otherwise stated.

Preparative HPLC purifications were performed on Varian instrument equipped with C12 Phenomenex Synergy MAX-RP 4μ reversed phase column, 250 × 21.2 mm, eluting with 0.1% TFA in a water-acetonitrile gradient.

Low resolution mass spectra (LCMS) were recorded on a ZMD-Micromass Single Quadrupole Mass Spectrometer equipped with an electrospray ion source (45 eV) coupled with HP1100 HPLC system (reverse phase C12 Phenomenex column, 4 μ, 100 Å, 150 × 2.0 mm. The eluent was a linear gradient of acetonitrile from 5% to 95% in water in the presence of 0.1% formic acid in 10 min, then 95% acetonitrile for 5 min, flow rate 400 μL/min).

The humanized h1F6 recognizes the CD70 antigen (*13*). Human renal cell carcinoma cell lines 786-O and Caki-1, and the glioblastoma DBTRG05-MG line were purchased from the ATCC (Manassas, Virginia). Hodgkin's disease cell line L428 was obtained from the DSMZ (Braunschweig, Germany). All cell lines were grown according to the manufacturers' recommendations and routinely checked for mycoplasma contamination.

General procedures for auristatin-AA_1-AA_2-diaminoethane-propionyl-maleimide synthesis.

Resin loading. In a 5 ml solid phase reaction vessel (plastic syringe with PET frit) was added 200 mg of 1,2-diaminoethane trityl resin (0.18 mmol based on the manufacturer's label), followed by a solution of Fmoc-AA_2-OH (0.36 mmol, 2 equiv), HATU (0.36 mmol, 2 equiv), and DIEA (0.90 mmol, 5 equiv) in 2 ml of dry DMF. The vessel was shaken for 18 h, and then the resin was washed with DMF (6 × 3 mL), CH_2Cl_2 (6 × 3 mL), ethyl ether (6 × 3 mL), and dried *in vacuo*. Complete reaction was confirmed by a negative Kaiser test.

Fmoc removal. Resin containing Fmoc-protected peptide was treated with 20% piperidine in DMF for 2 h at room temperature. Then the resin was washed with DMF (6 × 3 mL), CH_2Cl_2 (6 × 3 mL), ethyl ether (6 × 3 mL), and dried *in vacuo*.

Peptide coupling. To the resin (0.18 mmol) containing deprotected N-terminus amino acid, a solution of Fmoc-AA-OH (0.36 mmol, 2 equiv), HATU (0.36 mmol, 2 equiv), and DIEA (0.72 mmol, 4 equiv) in DMF (2 mL) was added. The reaction vessel was agitated for 2 h. Then the resin was washed with DMF (6 × 3 mL), CH_2Cl_2 (6 × 3 mL), ethyl ether (6 × 3 mL), and dried *in vacuo*.

Maleimide stretcher attachment. Penultimate diaminoethane-peptide was cleaved off the resin by treatment with 20% hexafluoroisopropanol in CH_2Cl_2 (4 mL) for 5 min, and then purified by preparative HPLC. Thus isolated diaminoethane-peptide and maleimidopropionic acid NHS ester (0.36 mmol, 2 equiv) were dissolved in CH_2Cl_2 (1 mL) with DIEA (0.72 mmol, 4 equiv) and stirred at room temp for 4 h. Solvent was removed *in vacuo.* After final deprotection with 20% TFA/CH_2Cl_2 (4 mL) for 2 h at room temperature, the product was purified by reverse phase preparative HPLC.

Drug-linker	Yield (%)	HPLC-based purity (215 nm)	Exact mass calc.	ESMS m/z found
AF-Asp-Val	26	>90%	1152.68	1153.50
AF-Ile-Val	33	>95%	1150.74	1151.68
AF-Asn-Val	63	>95%	1151.70	1152.96
AF-Tyr-Val	68	>95%	1200.72	1201.67
AF-Me_3Lys-Pro	21	>90%	1206.79	1207.03
AF-Ile-Pro	19	>95%	1148.72	1149.38
AF-Asn-Pro	19	>95%	1149.68	1150.32
AF-Met-Pro	18	>95%	1166.68	1167.05
AF-Tyr-(D)Asp	11	>90%	1216.67	1217.79

AF-Norval-(D)Asp	6	>95%	1152.68	1153.96
AF-β-Ala-(D)Asp	8	>95%	1124.65	1125.71
AF-Met-(D)Asp	25	>95%	1184.65	1185.20
AF-Pro-(D)Lys	40	>95%	1163.73	1164.72
AF-PhenylGly-(D)Lys	11	>90%	1199.73	1200.66
AF-Met-(D)Lys	49	>90%	1197.72	1198.80
AF-Asn-(D)Lys	62	>95%	1180.72	1181.70
AF-Gln-(D)Lys	20	>90%	1194.74	1195.81
AF-Arg-(D)Lys	18	>95%	1222.76	1223.91
AF-Cit-(D)Lys	33	>95%	1223.76	1223.93
AF-Tyr-(D)Lys	34	>95%	1229.74	1230.71
MMAF-Met-(D)Lys	22	>90%	1183.70	1184.55
MMAF-Asn-(D)Lys	16	>90%	1166.71	1167.17
AF-Met-(D)Met	7	>90%	1200.67	1201.17
AF-Met-(D)Val	13	>90%	1168.69	1169.52
AF-Met-Lys	15	>90%	1197.72	1198.99
AF-Asn-Lys	16	>90%	1180.72	1181.85
AM-Met-(D)Lys	25	>90%	1181.69	1182.56

AM-Asn-(D)Lys	24	>95%	1164.59	1165.82
AW-Met-(D)Lys	37	>97%	1236.73	1238.00
AW-Asn-(D)Lys	26	>97%	1219.73	1220.69

Preparation of Antibody-Drug Conjugates.

h1F6 antibody-drug conjugates with four drugs per antibody were prepared by partial reduction of the mAb followed by reaction with the desired drug-linker. The antibody h1F6 (23 mg/mL) was partially reduced by addition of 2.1 molar equivalents of tris(2-carboxyethyl)phosphine (TCEP) in phosphate buffered saline (PBS) pH 7.4 (Invitrogen, Carlsbad, CA) with 1 mM diethylenetriaminepentaacetic acid (DTPA), followed by incubation at 37^{o}C for ~1 h. The unpurified reaction mixture was aliquoted and frozen at -80°C for future use. The thiol content of the partially reduced h1F6 mAb was determined by alkylating a small fraction with Val-Cit-PABC-MMAF drug-linker and analyzing it by hydrophobic interaction chromatography (HIC). The average loading of Val-Cit-PABC-MMAF drug linker was determined to be 3.9 drugs/Ab. For conjugation of novel drug-linkers, a suitable quantity of partially reduced Ab was warmed to room temperature. The drug-linker was then added to a drug-linker /thiol molar ratio of ~1.5. The conjugation reaction was carried out in the presence of 10% v/v of DMSO for approximately 60 min. After conjugation, excess free N-acetyl-cysteine (4 mM final) was used to quench any unreacted, excess drug-linker. The reaction mixture was purified and buffer-exchanged into PBS using PD-10 desalting columns (GE Healthcare, Piscataway, NJ) to obtain the partially loaded h1F6-linker-drug$_4$ conjugate.

The drug/Ab ratio was estimated by HIC analysis and ranged from 3.8 – 4.2 drugs/Ab. In addition, each ADC was analyzed by size exclusion chromatography. No aggregation was observed.

In Vitro Growth Inhibition. Log phase cultures of cells were collected and cells plated at seeding densities ranging from 500 – 10,000 cells/well according to pre-determined conditions. After incubating 24 h to allow surface protein reconstitution, serial dilutions of test molecules were added and cultures incubated further for 4 days. Assessment of cellular growth and data reduction to generate IC_{50} values was done using Alamar Blue (Biosource International, Camarillo, CA) dye reduction assay. Briefly, a 40% solution (wt/vol) of Alamar Blue was freshly prepared in complete media just before cultures were added. Ninety-two hours after drug exposure, Alamar Blue solution was added to cells to constitute 10% culture volume. Cells were incubated for 4 h, and dye reduction was measured on a Fusion HT fluorescent plate reader (Packard Instruments, Meriden, CT).

In Vivo Therapy Experiments. 786-O and DBTRG05-MG cells were obtained from American Type Culture Collection (ATCC, Manassas, VA) and propagated in culture conditions recommended by ATCC. To establish 786-O, DBTRG05-MG tumors, 5×10^6 cells were implanted into the right flank of athymic nu/nu female donor mice (Harlan, Indianapolis, IN). When donor tumors were approximately 500 mm^3, mice were euthanized and tumors were aseptically excised and ~0.5 x 0.5 mm fragments were loaded into a sterilized 13-gauge trocar for implantation into nu/nu mice. When tumors reached ~100 mm^3, mice were randomly allocated to treatment groups. Experimental groups were treated via intraperitoneal injection with compounds at the dose and

schedule indicated or alternatively left untreated. Tumors were measured periodically and volumes were calculated using the formula $V= ((L \times W^2)/2)$. Animals were euthanized when tumors reached the volume of 1000 mm^3 or at the end of the study, whichever came first.

Tumor quadrupling times were chosen as time to endpoint (TTE), which was determined by using the non-liner regression analysis for exponential growth of each individual tumor growth data sets from each experimental animal. The median tumor quadrupling time was calculated based on the tumor volume at the beginning of treatment. Animals that did not reach the endpoint were assigned a TTE value equal to the last day of the study.

Statistical analysis was conducted using Prism (GraphPad) software for Windows. The Logrank test of the TTE was used to analyze the significance of the differences between the two groups, with differences deemed significant at $0.01 \leq P \leq 0.05$, and highly significant at $P \leq 0.01$.

Synthesis of auristatin-AA_1-AA_2-diaminoethane-propionyl-maleimide drug-linkers

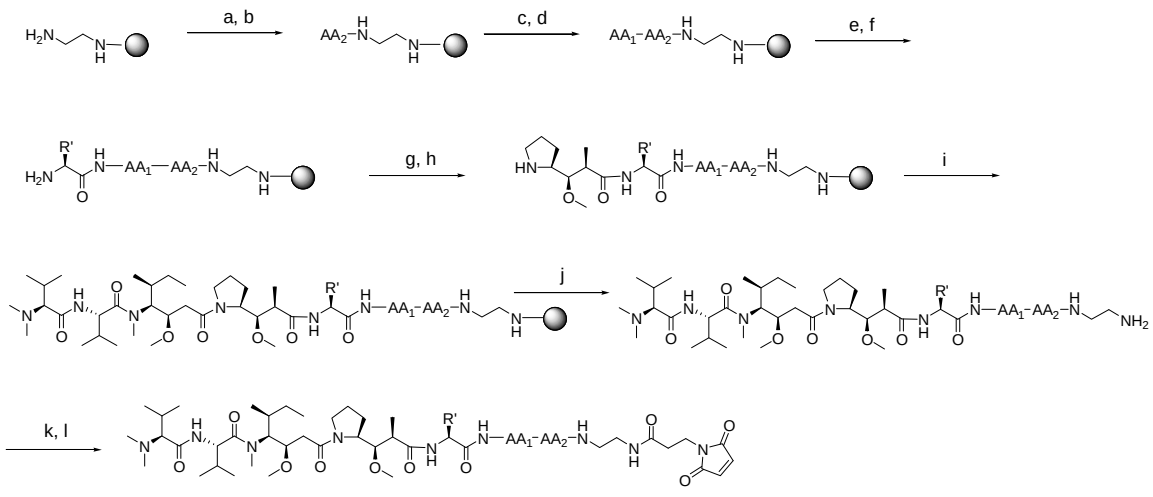

Reaction conditions: (a) Fmoc-AA_2-OH (2-5 equiv), HATU (2-5 equiv), and DIEA (4-10 equiv), DMF, 18h; (b) 20% piperidine/DMF, 2h: (c) Fmoc- AA_1-OH (2 equiv), HATU (2 equiv), and DIEA (4 equiv), DMF, 2h (d) 20% piperidine/DMF, 2h; (e) Fmoc-Phe-OH, or Fmoc-Met-OH, or Fmoc-Trp(Boc)-OH (2 equiv), HATU (2 equiv), and DIEA (4 equiv), DMF, 2h: (f): 20% piperidine/DMF, 2h; (g): Fmoc-Dap-OH (2 equiv), HATU (2 equiv), and DIEA (4 equiv), DMF, 2h; (h) 20% piperidine/DMF, 2h; (i) Dov-Val-Dil-OH (2 equiv), HATU (2 equiv), and DIEA (4 equiv), DMF, 2h; (j) 20% hexafluoroisopropanol/CH_2Cl_2, 10 min; (k) 3-Maleimidopropionic acid NHS ester (2 equiv), DIEA (4 equiv), CH_2Cl_2, 1h; (l) 40% TFA/CH_2Cl_2, 1h.

Synthesis of MMAF-AA_1-AA_2-diaminoethane-propionyl-maleimide drug-linkers

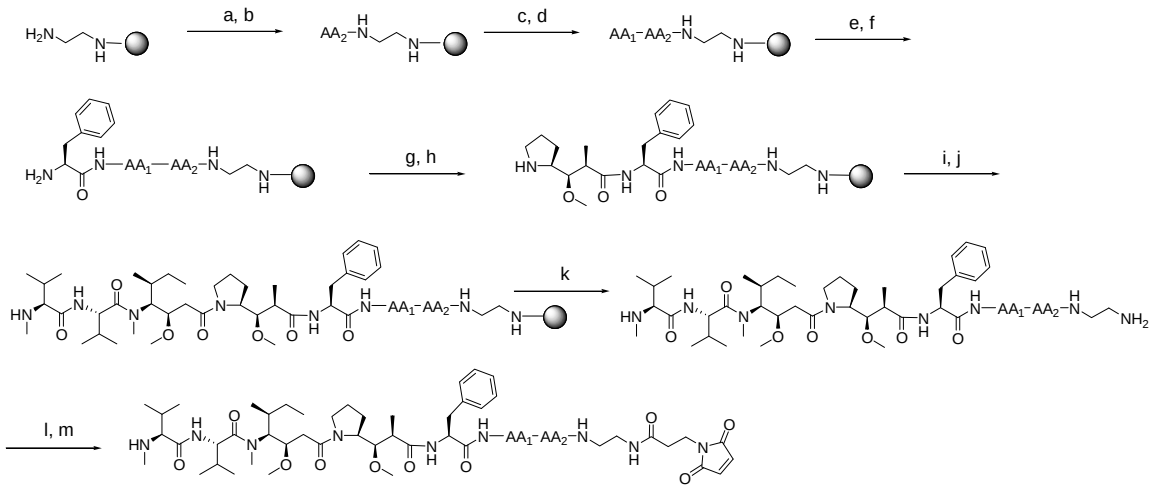

Reaction conditions: (a) Fmoc-AA_2-OH (2-5 equiv), HATU (2-5 equiv), and DIEA (4-10 equiv), DMF, 18h; (b) 20% piperidine/DMF, 2h: (c) Fmoc- AA_1-OH (2 equiv), HATU (2 equiv), and DIEA (4 equiv), DMF, 2h (d) 20% piperidine/DMF, 2h; (e) Fmoc-Phe-OH (2 equiv), HATU (2 equiv), and DIEA (4 equiv), DMF, 2h: (f): 20% piperidine/DMF, 2h; (g): Fmoc-Dap-OH (2 equiv), HATU (2 equiv), and DIEA (4 equiv), DMF, 2h; (h) 20% piperidine/DMF, 2h; (i) Fmoc-MeVal-Val-Dil-OH (2 equiv), HATU (2 equiv), and DIEA (4 equiv), DMF, 2h; (j) 20% piperidine/DMF, 2h; (k) 20% hexafluoroisopropanol/CH_2Cl_2, 10 min; (l) 3-Maleimidopropionic acid NHS ester (2 equiv), DIEA (4 equiv), CH_2Cl_2, 1h; (m) 40% TFA/CH_2Cl_2, 1h.

Nitrilotriacetic Acid-Derivatized Quantum Dots for Simple Purification and Site-Selective Fluorescent Labeling of Active Proteins in a Single Step

Manish Gupta, Anne Caniard, Ángeles Touceda-Varela, Dominic J. Campopiano, and Juan C. Mareque-Rivas*

Received July 3, 2008; Revised Manuscript Received August 16, 2008

We demonstrate that QDs coated with nitrilotriacetic acid (NTA) bound to Ni^{2+} can be used to reversibly and selectively bind, purify, and fluorescently label His_6-tagged (N-terminal) glutathione S-transferase (GST) in one step with retention of enzymatic activity. We find binding to be less effective in the absence of the His_6-tag or Ni^{2+} ions.

Colloidal semiconductor nanocrystals (quantum dots, QDs) have emerged as powerful fluorescent probes for biological imaging applications (*1*−*5*). QDs have several advantages over small organic dyes and fluorescent proteins such as size-tuneable photoluminescence, wide excitation−narrow emission properties, improved brightness, and high resistance to photobleaching and degradation. To conjugate QDs to biomolecules, the QD surface is derivatized in such a way as to allow the attachment of the biomolecule through a covalent bond, electrostatic, or hydrophobic interactions. A typical biomolecule contains many residues capable of forming covalent and noncovalent linkages with the QD. The ability to control the site of attachment is important to ensure that the biomolecule bound to the QD is still active. Site-specific noncovalent binding of QDs to biomolecules has been achieved by exploiting carbohydrate−lectin and streptavidin−biotin interactions (*6, 7*).

A common approach to facilitate protein purification involves the use of genetically encoded oligohistidine (His_n) tags (*8*−*10*). Since His_n-tags are recognized by nitrilotriacetic acid (NTA) complexes of nickel(II) (Scheme 1), purification of these proteins is achieved by passing the protein mixture through chromatography columns containing Ni-NTA resins (*11*−*13*). Given the widespread use of His_n-tags and the fact that they can be introduced into regions of peptides where they do not disturb protein structure and function such as at the termini or in loops, they provide a convenient way to achieve site-specific binding for many applications (*14*−*18*). Hence, the fluorescent labeling of specific proteins by encoding His_n-tags on them coupled to the recognition of these tags by Ni-NTA has become popular. Initially, this was done using organic dye−NTA conjugates (*19, 20*), but very recently it has been extended to QDs. Thus, during the final stages of preparation of this manuscript the first study showing that Ni-NTA-containing QDs that can be applied to imaging His_6-tagged proteins in live cells has appeared (*21*). This is interesting because it has been shown that His_n-tags can also bind with very high affinity ($K_d \approx 1$ nM) to QDs with carboxylic acid functionalities requiring fewer synthetic steps and cheaper reagents (*22*). In another study, however, it was reported that QDs with carboxylic acids presented at the surface bind His-tagged proteins only in the presence of Ni^{2+} cations (*23*). Thus, it is interesting to investigate the advantages, disadvantages and applicability of each of these functionalities for the formation of QD−protein conjugates.

Here, we investigate binding of His_6-tagged and untagged GST as model protein to CdSe-ZnS core−shell nanoparticles with carboxylates, NTA, and Ni^{2+}-bound NTA at the surface.

Scheme 1[a]

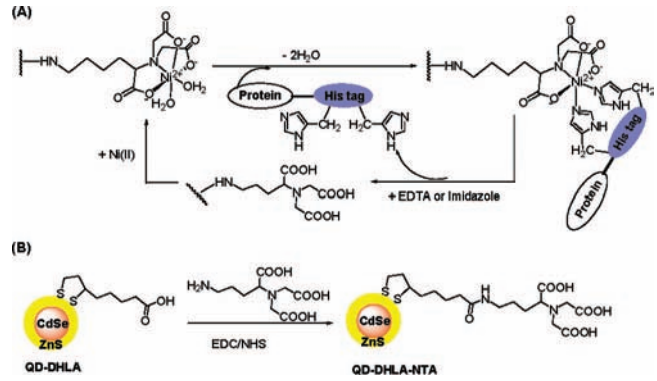

[a] (A) Reversible binding between a His-tagged protein and Ni(NTA). (B) Synthesis of the QD functionalized with NTA.

QDs−GST conjugates are interesting because GSTs catalyze the nucleophilic addition of GSH to the electrophilic center of a range of nonpolar substrates as a way of detoxifying a wide range of harmful endogenous and xenobiotic compounds (*24*), and in drug resistance mechanisms (*25*). Since GST activity requires not only the formation of a dimeric structure (i.e., protein−protein interactions) but also binding of both GSH and an acceptor substrate (i.e., protein−substrate interactions), it is a good enzyme to investigate the effect of specific and nonspecific binding of QDs on enzymatic activity. We report that the combination of His_6-tagged GST with CdSe-ZnS core−shell nanoparticles coated with Ni^{2+}-bound NTA gives the best results. The resulting QD−protein conjugate is strongly fluorescent and readily purified by filtration or ultracentrifugation, which should enable widespread use of these QDs as a "two-in-one" purification−fluorescence labeling tool. Moreover, the QD binds the His_6-tagged GST with little disruption of its enzymatic activity, whereas QD binding is weaker and disrupts enzymatic activity when GST lacks a His-tag or when Ni^{2+} is unavailable. This is a significant result in that it shows that by using this simple construct protein purification, fluorescent tagging, and precise positioning of the fluorescent probe to preserve structural/functional properties are all accomplished in a single, inexpensive step. It shows also that QDs presenting Ni-NTA at the surface provide a good alternative to site-specifically binding His-tagged proteins if, like in this case, the easier-to-make QDs with carboxylic acids at the surface fail to do so (*vide infra*).

The QDs decorated with NTA were easily prepared from the reaction of CdSe-ZnS core−shell dihydrolipoic acid (DHLA)-

* Corresponding author. E-mail: juan.mareque@ed.ac.uk.

10.1021/bc800273j CCC: $40.75 © 2008 American Chemical Society
Published on Web 09/19/2008

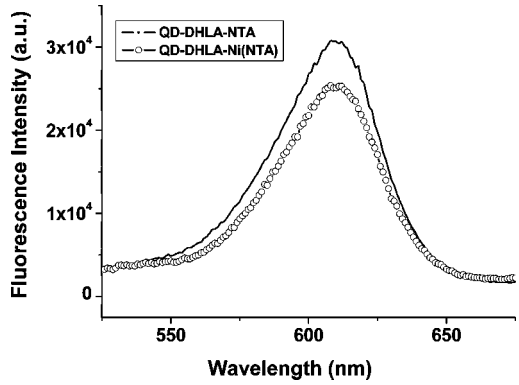

Figure 1. Photoluminescence spectra for CdSe-ZnS core−shell QDs coated with DHLA-NTA and DHLA-Ni(NTA) (spectra were acquired in 20 mM PBS pH 6.7, excitation at 350 nm; $T = 293$ K). The integrated emission decreases 15% upon Ni^{2+} addition.

capped QDs (*26*) with commercially available *N,N*-bis(carboxymethyl)-L-lysine hydrate using EDC and *N*-hydroxysuccinimide as coupling agents in phosphate buffer solution (Scheme 1). The product is purified by filtration with a Nanosep 100K centrifugal device (Pall Corporation). The composition of the QDs was examined by X-ray photoelectron spectroscopy (XPS). The XPS spectra showed the main diagnostic peaks of the product QDs: a 2s peak at 400.1 eV due to N, and 2p3 and 2p1 peaks at 857.1 and 874.1 eV, respectively, due to Ni^{2+} (Supporting Information).

The photoluminescence intensity of the Ni-NTA-capped QD is ca. 85% that of the NTA-capped QD (Figure 1). This is important because the paramagnetic Ni^{2+} was found to strongly quench the photoluminescence of some organic dyes, limiting their applications (*19*).

We selected GST from the helminth worm *Schistosoma japonica* (SjGST, 26 kDa monomer) as our target enzyme because it is amenable to recombinant overexpression in *E. coli* as a His_6-tagged construct and has been well-characterized (*9*). It is important to note that the His_6-tag was genetically fused at the N-terminus. The noncovalent attachment of His_6-tagged and untagged GST to the QD surface before and after derivatization with Ni-NTA was analyzed by SDS-PAGE. A solution of the QD or PBS (as control) was incubated with the corresponding enzyme for 2 h and passed through a Nanosep 300K centrifugal device. The retenate was redissolved in PBS buffer, and both retenate and filtrate were analyzed by SDS-PAGE. In the absence of the QD, His_6-tagged and untagged GST were found only in the filtrate. Several reports have shown that the DHLA-coated CdSe-ZnS core−shell QDs are capable of binding His-tagged proteins by coordination to Zn^{2+} ions at the nanocrystal surface (*22, 26*−*28*). Our SDS-PAGE studies, however, did not find protein in the retenate (Figure 2). Lack of binding could be due to steric hindrance at the N-terminus location of the His_6-tag preventing access to the Zn^{2+} atoms of the nanoparticle. It is also possible that the different synthetic procedures used to prepare QDs lead to subtle changes at the QD surface which affect binding of biomolecules. However, it is worth noting that it is not rare for His-tagged proteins to exhibit different properties depending on whether the His-tag is at the N- or C-terminus, and that in the studies reporting direct His-tag binding to carboxylate-coated QDs the His-tag was located at the C-terminus (*22, 26*−*28*). In contrast, using the same experimental conditions the Ni-NTA-capped QDs immobilized both enzymes. Moreover, we found more His_6-tagged than untagged GST in the retenate. Binding was also investigated in the presence of high salt concentrations. His_6-GST binding to Ni-NTA-capped QDs was not affected by 1 M NaCl. In contrast, untagged GST did not bind to the QDs under these conditions,

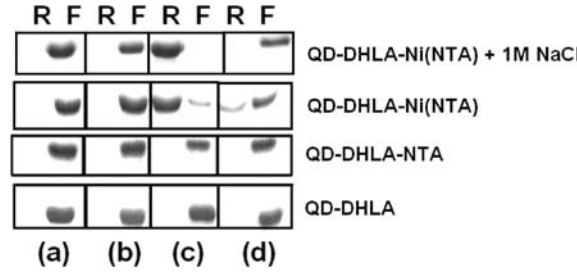

Figure 2. SDS-PAGE of the retenate (R) and filtrate (F) after ultrafiltration through a Nanosep 300K filter of His_6-GST (a), untagged GST (b), His_6-GST incubated with QD (c), and untagged GST incubated with QD (d). In each case, the enzyme and QD concentrations were 16.5 μM and 9.0 μM, respectively.

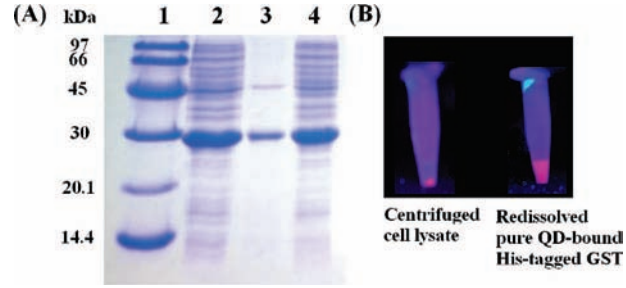

Figure 3. (A) SDS-PAGE studies of the cell lysate containing His_6-tagged GST (lane 2) and proteins released from the Ni-NTA-coated QDs treated with PBS containing 0.5 M imidazole (lane 3) and supernatant (lane 4) after ultracentrifugation. Lane 1 is the molecular weight marker. (B) Images of the cell lysate after ultracentrifugation and of the pure QD-bound His_6-tagged GST.

which suggests it is predominantly electrostatic. Thus, high salt concentrations can be used to avoid binding of untagged proteins while ensuring binding of the desired His_6-tagged target. The enzyme was easily released from the QD surface upon addition of 0.5 M imidazole, which competes for the Ni^{2+} binding sites. Thus, decorating the surface of the QD with Ni^{2+} complexes of NTA seems a good approach for noncovalent site-specific fluorescent labeling of proteins, which can be used for instance if carboxylate-functionalized QDs lacking Ni^{2+} ions fail. Potential advantages of attaching Ni-NTA units to QDs could be stronger interactions with the His-tag ($K_d \approx 10^{-13}$ M) (*18*) and less sensitivity to steric hindrance and surface properties by being further away from the nanocrystal surface.

Recently, the value of magnetic nanoparticles as affinity probes to selectively trap and separate His-tagged proteins from cell lysates has been elegantly demonstrated (*29*−*32*). The protein purification efficiency of the Ni-NTA-capped QDs was investigated by incubating cell lysates containing His_6-tagged GST for 2 h. Remarkably, pure fluorescently labeled GST was obtained simply by ultracentrifugaton of this mixture (Figure 3). Thus, by using the Ni-NTA-capped QDs it is possible to purify and fluorescently label His-tagged proteins in a single step. Current methods for efficiently purifying and fluorescently labeling His-tagged proteins need various labor-intensive and expensive steps, such as conjugation of NTA derivatives on support materials or the preparation of suitable magnetic nanoparticles for purification purposes, followed by the attachment of fluorescent tags. Another construct suitable for one-step protein purification and site-specific labeling was recently developed and involves organic fluorophore-doped Ni-NTA-modified silica nanoparticles (*33*).

In order to obtain information about the effect of QD binding on the catalytic activity of GST, we have used 1-chloro-2,4-dinitrobenzene (CDNB) as substrate. The GST-catalyzed reaction of GSH with CDNB produces a dinitrophenyl thioether

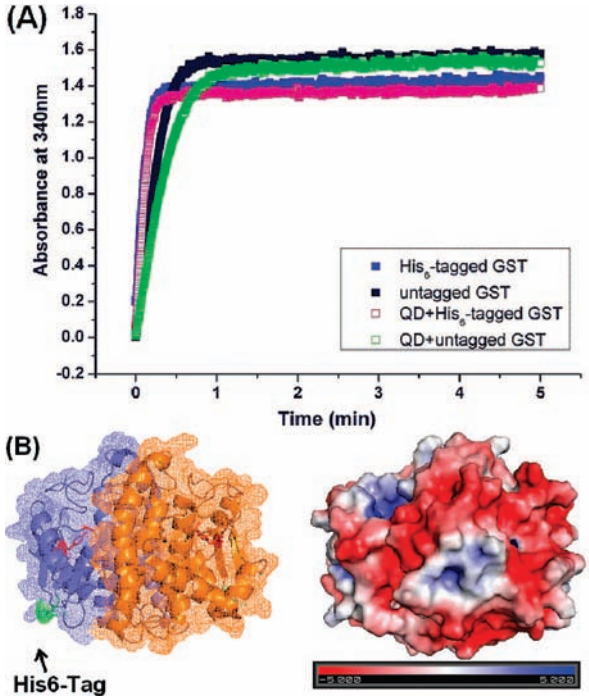

Figure 4. (A) Activity of His_6-tagged (N-terminal) and untagged GST in the presence of Ni-NTA coated QDs. Conditions: [GSH] = 8 mM, [CDNB] = 2 mM in PBS (pH 6.7), T = 298 K. The QD alone did not have any activity. (B) X-ray crystal structure of the SjGST homodimer highlighting the catalytically crucial Tyr7 residue in red, and the N-terminus site for the His_6-tag in green (left); surface charge distributions (right).

which can be conveniently detected spectrophotometrically at 340 nm (*34*). His_6-tagged GST and untagged GST were incubated with the same concentration of Ni-NTA-capped QD. We have found that His_6-tagged GST retains its activity after binding to the QD, whereas the untagged GST loses activity (Figure 4). We suggest that the ability of the His_6-tag to control the position of the Ni-NTA-capped QD relative to the GST active site is responsible for preserving the activity of the enzyme. The X-ray crystal structure of SjGST (*35*) shows that the N terminus, which is where the His_6 tag was placed, is ca. 25 Å away from the essential catalytic residue Tyr7 (Figure 4). We have examined the distribution of positively and negatively charged residues and found that there are positive and negative regions close to the active site. These are sites where in the absence of the His_6 tag nonspecific electrostatic binding could occur, disrupting the enzyme activity. By comparing the activity of the enzyme which did not bind to the QD with that of the enzyme before incubation with QD, we estimated the protein binding capacity and number of His_6-GST molecules immobilized on each QD (~16). This surface coverage correlates well with that found for QDs and proteins of similar size (*26, 27*).

In summary, we have shown that Ni-NTA-coated QDs provide a straightforward method to, in one step, purify and fluorescently reversibly label proteins. By using these QDs, we have selectively purified and labeled an N-terminal His_6-tagged GST, which was not possible using QDs with carboxylates at the surface. Moreover, we have found that Ni^{2+} provides a docking site which helps to precisely orient the fluorescent nanoparticle on the protein surface and that, as a result, GST retained its activity. The use of His-tags has been broadly adopted in the molecular biology and biochemistry communities, and therefore this specific conjugation strategy should enable widespread use of these QDs for a broad range of biological applications.

ACKNOWLEDGMENT

We are grateful to EaStCHEM for a PhD studentship to M.G. A.T.V. acknowledges the Xunta de Galicia (Spain) for a postdoctoral fellowship. A.C. is funded by a Marie Curie Fellowship. We acknowledge support from the EPSRC to purchase the XPS. We would like to thank Dr. Wuzong Zhou and Ross Blackley at EaStCHEM-St. Andrews for the HRTEM studies.

Supporting Information Available: Details on experimental procedures and characterization data. This material is available free of charge via the Internet at http://pubs.acs.org.

LITERATURE CITED

(1) Medintz, I. L., Uyeda, H. T., Goldman, E. R., and Mattoussi, H. (2005) Quantum dot bioconjugates for imaging, labelling and sensing. *Nat. Mater. 4*, 435–446.
(2) Gao, X., Yang, L., Petros, J. A., Marshall, F. F., Simons, J. W., and Nie, S. (2005) In vivo molecular and cellular imaging with quantum dots. *Curr. Opin. Biotechnol. 16*, 63–72.
(3) Alivisatos, A. P., Gu, W., and Larabell, C. (2005) Quantum dots as cellular probes. *Annu. Rev. Biomed. Eng. 7*, 55–76.
(4) Michalet, X., Pinaud, F. F., Bentolila, L. A., Tsay, J. M., Doose, S., Li, J. J., Sundaresan, G., Wu, A. M., Gambhir, S. S., and Weiss, S. (2005) Quantum dots for live cells, in vivo imaging, and diagnostics. *Science 307*, 538–544.
(5) Klostranec, J. M., and Chan, W. C. (2006) Quantum dots in biological research: recent progress and present challenges. *Adv. Mater. 18*, 1953–1964.
(6) Babu, P., Sinha, S., and Surolia, A. (2007) Sugar-quantum dot conjugates for a selective and sensitive detection of lectins. *Bioconjugate Chem. 18* (1), 146–151.
(7) Howarth, M., Takao, K., Hayashi, Y., and Ting, A. Y. (2005) Targeting quantum dots to surface proteins in living cells with biotin ligase. *Proc. Natl. Acad. Sci. U.S.A. 102*, 7583–7588.
(8) Waugh, D. S. (2005) Making the most of affinity tags. *Trends Biotechnol. 23*, 316–320.
(9) Esposito, D., and Chatterjee, D. K. (2006) Enhancement of soluble protein expression through the use of fusion tags. *Curr. Opin. Biotechnol. 17*, 353–358.
(10) Terpe, K. (2003) Overview of tag protein fusions: from molecular and biochemical fundamentals to commercial systems. *Appl. Microbiol. Biotechnol. 60*, 523–533.
(11) Porath, J., Carlsson, J., Olsson, I., and Belfrage, G. (1975) Metal chelate affinity chromatography, a new approach to protein fractionation. *Nature 258*, 598–599.
(12) Bornhorst, J. A., and Falke, J. J. (2000) Purification of proteins using polyhistidine affinity tags. *Methods Enzymol. 326*, 245–254.
(13) Guignet, E. G., Hovius, R., and Vogel, H. (2004) Reversible site-selective labeling of membrane proteins in live cells. *Nat. Biotechnol. 22*, 440–444.
(14) Lata, S., Reichel, A., Brock, R., Tampé, R., and Piehler, J. (2005) High-affinity adaptors for switchable recognition of histidine-tagged proteins. *J. Am. Chem. Soc. 127*, 10205–10215.
(15) Abad, J. M., Mertens, S. F. L., Pita, M., Fernandez, V. M., and Schiffrin, D. J. (2005) Functionalization of thioctic acid-capped gold nanoparticles for specific immobilization of histidine-tagged proteins. *J. Am. Chem. Soc. 127*, 5689–5694.
(16) Sigal, G. B., Bamdad, C., Barberis, A., Strominger, J., and Whitesides, G. M. (1996) A self-assembled monolayer for the binding and study of histidine-tagged proteins by surface plasmon resonance. *Anal. Chem. 68*, 490–497.
(17) Cho, M., Lee, S., Han, S.-Y., Park, J.-Y., Rahman, M. A., Shim, Y.-B., and Ban, C. (2006) Electrochemical detection of mismatched DNA using a MutS probe. *Nucleic Acids Res. 34*, e75/1–e75/10.
(18) Hainfeld, J. F., Liu, W., Halsey, C. M. R., Freimuth, P., and Powell, R. D. (1999) Ni-NTA-gold clusters target His-tagged proteins. *J. Struct. Biol. 127*, 185–198.

(19) Kapanidis, A. N., Ebright, Y. W., and Ebright, R. H. (2001) Site-specific incorporation of fluorescent probes into protein: hexahistidine-tag-mediated fluorescent labeling with (Ni^{2+}: nitrilotriacetic Acid)$_n$-fluorochrome conjugates. *J. Am. Chem. Soc. 123*, 12123–12125.

(20) Goldsmith, C. R., Jaworski, J., Sheng, M., and Lippard, S. J. (2006) Selective labeling of extracellular proteins containing polyhistidine sequences by a fluorescein-nitrilotriacetic acid conjugate. *J. Am. Chem. Soc. 128*, 418–419.

(21) Kim, J., Park, H. Y., Kim, J., Ryu, J., Kwon, do. Y., Grailhe, R., and Song, R. (2008) Ni-nitrilotriacetic acid-modified quantum dots as a site-specific labeling agent of histidine-tagged proteins in live cells. *Chem. Commun. 16*, 1910–1912.

(22) Sapsford, K. S., Pons, T., Medintz, I. L., Higashiya, S., Brunel, F. M., Dawson, P. E., and Mattoussi, H. (2007) Kinetics of metal-affinity driven self-assembly between proteins or peptides and CdSe-ZnS Quantum dots. *J. Phys. Chem. C 111*, 11528–11538.

(23) Yao, H., Zhang, Y., Xiao, F., Xia, F., and Rao, J. (2007) Quantum dot/bioluminescence resonance energy transfer based highly sensitive detection of proteases. *Angew. Chem., Int. Ed. 46*, 4346–4349.

(24) Mahajan, S., and Atkins, W. M. (2005) The chemistry and biology of inhibitors and pro-drugs targeted to glutathione S-transferases. *Cell. Mol. Life Sci. 62*, 1221–33.

(25) Shi, B., Stevenson, R., Campopiano, D. J., and Greaney, M. F. (2006) Discovery of glutathione S-transferase inhibitors using dynamic combinatorial chemistry. *J. Am. Chem. Soc. 128*, 8459–8467.

(26) Mattoussi, H., Mauro, J. M., Goldman, E. R., Anderson, G. P., Sundar, V. C., Mikulec, F. V., and Bawendi, M. G. (2000) Self-assembly of CdSe-ZnS quantum dot bioconjugates using an engineered recombinant protein. *J. Am. Chem. Soc. 122*, 12142–12150.

(27) Medintz, I. L., Clapp, A. R., Mattoussi, H., Goldman, E. R., Fisher, B., and Mauro, J. M. (2003) Self-assembled nanoscale biosensors based on quantum dot FRET donors. *Nat. Mater. 2*, 630–638.

(28) Ipe, B. I., and Niemeyer, C. M. (2006) Nanohybrids composed of quantum dots and cytochrome P450 as photocatalysts. *Angew. Chem., Int. Ed. 45*, 504–507.

(29) Lee, I. S., Lee, N., Park, J., Kim, B. H., Yi, Y. W., Kim, T., Kim, T. K., Lee, I. H., Paik, S. R., and Hyeon, T. (2006) Ni/NiO core/shell nanoparticles for selective binding and magnetic separation of histidine-tagged proteins. *J. Am. Chem. Soc. 128*, 10658–10659.

(30) Xu, C., Xu, K., Gu, H., Zhong, X., Guo, Z., Zheng, R., Zhang, X., and Xu, B. (2004) Nitrilotriacetic acid-modified magnetic nanoparticles as a general agent to bind histidine-tagged proteins. *J. Am. Chem. Soc. 126*, 3392–3393.

(31) Lee, K. B., Park, S., and Mirkin, C. A. (2004) Multicomponent magnetic nanorods for biomolecular separations. *Angew. Chem., Int. Ed. 43*, 3048–3050.

(32) Lee, K. S., and Lee, I. S. (2008) Decoration of superparamagnetic iron oxide nanoparticles with Ni^{2+}: agent to bind and separate histidine-tagged proteins. *Chem. Commun. 6*, 709–711.

(33) Kim, S. H., Jeyakumar, M., and Katzenellenbogen, J. A. (2007) Dual-mode fluorophore-doped nickel nitrilotriacetic acid-modified silica nanoparticles combine histidine-tagged protein purification with site-specific fluorophore labeling. *J. Am. Chem. Soc. 129*, 13254–13264.

(34) Habig, W. H., Pabst, M. J., and Jakoby, W. B. (1974) Glutathione S-transferases. The first enzymatic step in mercapturic acid formation. *J. Biol. Chem. 249*, 7130–7139.

(35) McTigue, M. A., Williams, D. R., and Tainer, J. A. (1995) Crystal structures of a schistosomal drug and vaccine target: glutathione S-transferase from *Schistosoma japonica* and its complex with the leading antischistosomal drug praziquantel. *J. Mol. Biol. 246*, 21–27.

BC800273J

SUPPORTING INFORMATION FOR:

Nitrilotriacetic acid-derivatized quantum dots for simple purification and site-selective fluorescent labelling of active proteins in a single step

Manish Gupta, Anne Caniard, Angeles Touceda-Varela, Dominic Campopiano and Juan C. Mareque-Rivas*

School of Chemistry, University of Edinburgh,

Joseph Black Building, King's Buildings,

West Mains Road, Edinburgh, EH9 3JJ, UK

Tel:44-(0)131-650-4761

Fax:44-(0)131-650-4743

Contents:

Materials and Methods
QD Synthesis
Expression and Purification of His_6-SjGST and untagged GST
Protein Binding Studies
GST Activity Assay

Fig. S1 TEM and HRTEM images of the hydrophobic ((a) and (b)) and hydrophilic ((c) and (d)) CdSe-ZnS core-shell nanocrystals.

Fig. S2 X-ray photoelectron spectra highlighting the (A) N 1s and (B) Ni 2p transitions of the DHLA-Ni(NTA) coated CdSe-ZnS core-shell QDs.

Materials and Methods. All chemicals were obtained from commercial sources and used as received. Cadmium oxide (CdO, 99.5%), tri-*n*-octylphosphine oxide (TOPO, 99%), tri-*n*-butylphosphine (TBP, 97%), hexadecylamine (HDA, 98%), diethylzinc ($ZnEt_2$,1M in hexane), hexametyldisilathiane [$(TMS)_2S$ 98%], nickel (II) chloride, *N*-hydroxysuccinimide (NHS, 98%) and *N*-*N*-bis(carboxymethyl)-L-lysine hydrate were purchased from Sigma Aldrich. 1-Ethyl-3-[3'-(dimethylamino)propyl]carbodiimide was purchased from Ademtech. Stearic acid (≥98.5) was purchased from Fluka. Selenium powder (Se, 99.999%) was obtained from Alfa Aesar.

Fluorescence studies were carried out with an Edinburgh Instruments FS900 fluorimeter. Excitation was at 350 nm with bandwidths of 2 nm for excitation (unpolarised) and emission (unpolarised). Temperature was maintained at 25 °C.

X-ray photoelectron spectra were obtained with a VG Scientific Sigma Probe (UK) XPS system. The Al Kα anode X-ray source (hυ = 1486.6 eV) was operated at 200W and the take-off angle for photoelectrons was 37º. Samples were mounted with a spring clip. In a typical experiment, a few survey scans in the -10 to 1100 eV kinetic energy range were collected at a resolution of 1 eV. Then, detailed scans of 20-60 eV over a single feature were collected at a resolution of 0.2 eV. During the measurements the pressure was 10^{-9}-10^{-10} Torr.

High-resolution transmission electron microscopy (HRTEM) studies were conducted on a JEOL JEM-2011 electron microscope operating at 200 kV. The samples were prepared by depositing a drop of a solution of nanocrystals in pyridine onto a copper specimen grid coated with a holey carbon film and allowing it to dry.

Enzyme concentrations were determined by Bradford assay on a UNICAM UV-vis spectrometer with bovine serum albumin as a standard.[1] The QD concentration was determined by the method of Peng et al.[2] Enzyme activity assays were conducted on a CARY 300 SCAN UV-vis spectrometer.

QD Synthesis. Tri-*n*-butylphosphine selenide (TBP-Se, 1M) was prepared in a N_2-filled glove box by shaking 0.08 g of selenium powder in 1 mL of TBP. A ZnS stock solution was prepared in a N_2-filled glove box by reacting $(TMS)_2S$ (0.5 ml, 2.5 mmoles) with $ZnEt_2$ (3.5 ml, 3.5 mM in hexane) in TOP (6 ml).

TOPO-coated CdSe-ZnS QDs. The TOPO-coated core-shell CdSe-ZnS QDs were synthesised and purified according to previously reported procedures.[3] In a typical synthesis, CdO (0.013 g, 0.1mmol) and stearic acid (0.254 g, 0.89 mmol) were loaded into a three-neck flask and heated to 225 °C under N_2 flow and stirring. Once the

mixture was completely dissolved, it was allowed to cool to room temperature. Then, TOPO (3 g) and HDA (1 g) were added and the mixture was heated to 225 °C under N_2 flow and vigorous stirring. At this temperature, 1 mL of freshly prepared TPB-Se solution (1 M) was quickly injected into the flask. Following injection the temperature was adjusted to ~200 °C to promote nanocrystal growth. On reaching the desired nanoparticle size, as determined by UV/vis and fluorescence spectroscopy,[2] the temperature is lowered to ca. 100 °C to stop further growth. Then, the solution is heated to 210 °C. At this temperature, 0.5 ml of the ZnS stock solution was slowly injected in. The temperature of the mixture was set to 100 °C and stirred for 2 hr. After cooling to room temperature, the nanocrystals were dispersed in chloroform and precipitated by addition of methanol. After centrifugation the supernatant liquid phase was removed. This procedure was repeated at least three times. The precipitates were combined and air-dried at room temperature. The results reported in this study are for nanocrystals which had the first absorption band at 594 nm, and a maximum emission peak at 610 nm with excitation at 350 nm, but the same results were obtained with QDs of different sizes and emission maxima.

DHLA-coated CdSe-ZnS QDs. Dihydrolipoic acid (DHLA) was prepared according to the method given by Uyeda *et al.*[4] Thiotic acid (1.22 g) was dissolved in an aqueous solution of $NaHCO_3$ (25 ml, 0.25 M) and the resultant solution was cooled to 0 °C. $NaBH_4$ (0.9 g) was added and the temperature was maintained at ca. 5 °C with continuous stirring for about 2 hr in nitrogen. The reaction mixture was acidified with HCl (3.3 M) to pH 1. The product was extracted with toluene (~30 ml) dried by adding $MgSO_4$. The final product was isolated as colourless oil.

Then, the water-soluble DHLA-coated CdSe/ZnS QDs were prepared according to the method given by Mattousi *et al.*[5] In a typical reaction, TOPO-coated CdSe-ZnS QDs (50 mg) and DHLA (50 mg) were mixed in DMF (15 ml). The solution was heated to 60-70 °C and stirred overnight. Then, potassium-*tert*-butoxide (100 mg) was slowly added to deprotonate the terminal lipoic acid groups. The nanoparticles were separated by centrifugation and the supernatant liquid was discarded. The resulting quantum dots were dried under vacuum. The QDs were further purified by redissolving them in water and passing this solution through a 100K microsep filter.

NTA-coated CdSe/ZnS QDs. *N*-*N*-bis(carboxymethyl)-L-lysine hydrate (NTA) (5 mg, 0.0132 mmoles) was dissolved in 3 ml of HEPES (20 mM, pH 7.5). Activation of

carboxylate groups of the DHLA-coated QDs was performed by mixing the QDs (9 mg) in 1 ml of EDC (3 mM in HEPES) and 1ml of NHS (3 mM in HEPES) with stirring for 30 min. Then, 1ml of NTA (4.4 mM) was added and the solution was stirred for 24 hrs. The resulting NTA-modified nanocrystals were purified using a Nanosep 100k omega membrane filter (low protein-binding, modified polyethersulfone on polyethylene substrate). The Ni-NTA coated nanocrystals were prepared in the same way using the preformed complex, which was prepared by mixing of *N*,*N*-bis(carboxymethyl)-l-lysine hydrate (NTA) (5 mg, 0.0132 mmoles) and $NiCl_2$ (5 mg, 0.021 mmoles) in 3 ml of HEPES (20 mM) with stirring for 1 hr using. Alternatively, the NTA-coated nanocrystals (18 μM) were dissolved in water and reacted with $NiCl_2$ (200 μM) for 1 hr. The excess nickel was removed by passing the solution through a 100K microsep filter.

Expression and Purification of His_6-SjGST and untagged GST

Overexpression of *Schistosoma japonicum* His_6-GST and untagged GST were achieved as we described previously[6] with the following modifications. Fresh LB broth medium (3 L) were inoculated with 100 mL of seed culture and induced with isopropyl thio-β-D-galactoside (IPTG) (0.1 mM final concentration) when OD_{600} reached 0.6. The cell debris was removed by centrifugation at 15000 g for 1 h at 4 °C. Purification of *Schistosoma japonicum* His_6-GST was achieved as described previously.[6]

Purification of untagged GST. The cell lysate was applied to a GSTPrep FF 16/10 column (20 mL, GE Healthcare Life science) pre-equilibrated with 1x PBS binding buffer (140 mM NaCl, 2.7 mM KCl, 10 mM Na_2HPO_4, 1.8 mM KH_2PO_4). The column was then washed with 5 column volumes of binding buffer (100 mL) before bound material was eluted with an elution buffer (10 mM glutathione, 50 mM Tris/HCl, pH 8.0) over 5 column volumes (100 mL). Fractions were analysed by SDS-PAGE, and those containing GST were pooled and dialyzed overnight against 4 L of a 20 mM potassium phosphate buffer (pH 7.0) at 4 °C. Liquid chromatography mass spectrometry (LCMS) analysis of the pure enzyme gave the molecular mass of the SjGST as 28059 (± 0.9 Da), in good agreement with the predicted value of 28057 Da for the monomer. The final yield of untagged GST using this method was ~ 25 mg per L of bacterial culture.

Protein Binding Studies

Protein binding studies were carried out by incubating 100 µl of the corresponding QD (1.5×10^{-5} M) with 75 µl of His-GST and Untagged-GST (1.09 mg/ml) for 2 hr at room temperature. The enzyme-QDs complexes were separated from the unbound enzyme molecules by passing this solution through a Nanosep 300k Omega membrane filter (low protein-binding, modified polyethersulfone on polyethylene substrate). The retenate containing the QD-bound enzyme was treated with 175 µl of a PBS solution of imidazole (0.5 M) to release the enzyme. Retenate and filtrate fractions were analysed by SDS-PAGE. Incubation of QDs with cell lysates was carried out at 4 ^{o}C.

GST Activity Assay

The GST activity was determined spectrophotometrically by measuring the change in absorbance at 340 nm (ε = 9600 M^{-1} cm^{-1}).[7] The solution for the blank assay was composed of potassium phosphate buffer (850 µl, 0.1 M, pH 6.5), 1-chloro-2, 4-dinitrobenzene (50µl, 40 mM) and GSH (100 µl, 80 mM). The solution for sample assay was composed of potassium phosphate buffer (800 µl, 0.1 M, pH 6.5), 1-chloro-2,4-dinitrobenzene (50 µl, 40 mM), GSH (100 µl ,80 mM) and GST (His-GST 50 µl, 2.7 mg/ml; Untagged-GST 50 µL, 1.09 mg/ml free and immobilized on QD-NTA-Ni^{+2} (9 µM)). The absorbance was measured at 340 nm for five minutes (T = 25 °C).

References:

1. M. Bradford, *Anal. Biochem*. 1976, **72**, 248.

2. W. W. Yu, L. Qu, W. Guo and X. Peng, *Chem. Mater*., 2003, **15**, 2854.

3. (a) L. Qu and X. Peng, *J. Am. Chem. Soc*., 2002, **124**, 2049; (b) T. Jin, F. Fujii, E. Yamada, Y. Nodasaka and M. Kinjo, *J. Am. Chem. Soc*., 2006, **128**, 9288.

4. H. T. Uyeda, I. L. Medintz, J. K. Jaiswal, S. M. Simon and H. Mattoussi, *J. Am. Chem. Soc.*, 2005, **127**, 3870.

5. H. Mattoussi, J. M. Mauro, E. R. Goldman, G. P. Anderson, V. C. Sundar, F. V. Mikulec and M. G. Bawendi, *J. Am. Chem. Soc*., 2000, **122**, 12142.

6. B. Shi, R. Stevenson, D. J. Campopiano and M. F. Greaney, *J. Am. Chem. Soc*., 2006, **128**, 8459.

7. W. H. Habig, M. J. Pabst and W. B. Jakoby, *J. Biol. Chem*., 1974, **249**, 7130.

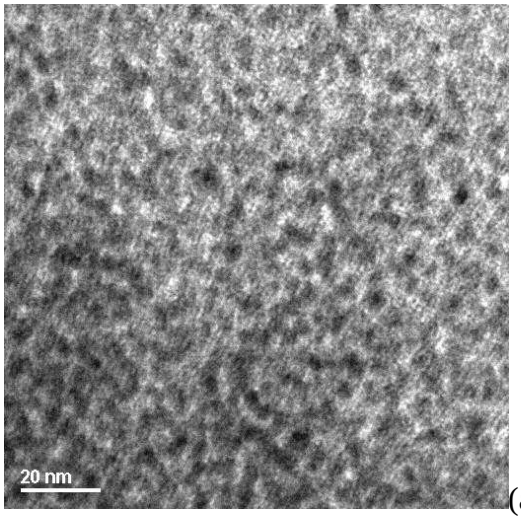

(a)

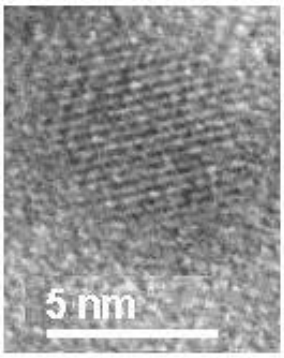

(b)

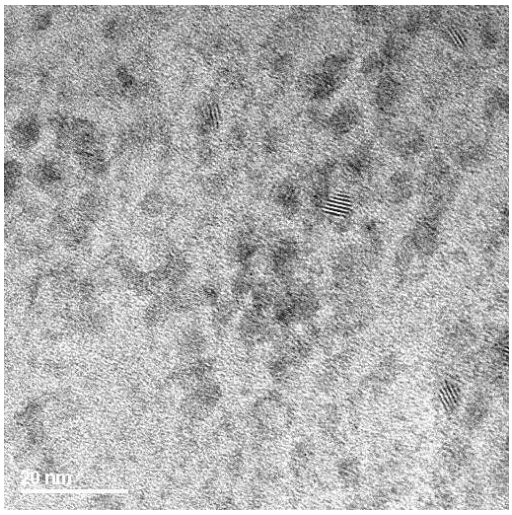

(c)

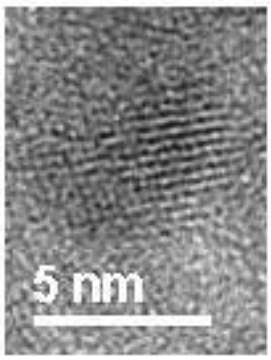

(d)

Fig. S1 TEM and HRTEM images of the hydrophobic ((a) and (b)) and hydrophilic ((c) and (d)) CdSe-ZnS core-shell nanocrystals.

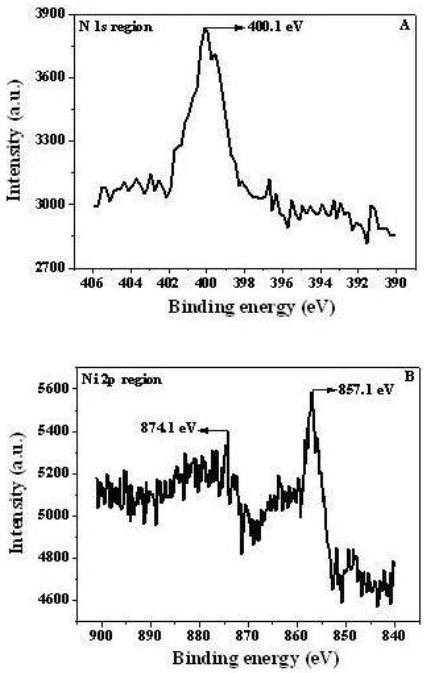

Fig. S2 X-ray photoelectron spectra highlighting the (A) N 1s and (B) Ni 2p transitions of the DHLA-Ni(NTA) coated CdSe-ZnS core-shell QDs.

N,N,N′,N′-Tetramethylchloroformamidinium Hexafluorophosphate (TCFH), a Powerful Coupling Reagent for Bioconjugation

Judit Tulla-Puche,[†,*] Ángela Torres,[‡] Pilar Calvo,[§] Miriam Royo,[‡] and Fernando Albericio*[,†,||,Δ]

Institute for Research in Biomedicine, Combinatorial Chemistry Unit, and CIBER-BBN, Networking Centre on Bioengineering, Biomaterials and Nanomedicine, Barcelona Science Park, 08028 Barcelona, Spain, PharmaMar, S.A., 28770-Colmenar Viejo, Spain, and Department of Organic Chemistry, University of Barcelona, 08028 Barcelona, Spain. Received June 14, 2008; Revised Manuscript Received August 29, 2008

Prodrugs are increasingly used as delivery vehicles for pharmaceutical agents that present solubility and/or pharmacokinetic/metabolic issues. In the course of the development of prodrugs for the antitumoral agent thiocoraline, standard coupling reagents and procedures failed to provide the desired target derivatives because of the lack of reactivity of its quinolinic alcohol. In contrast, the use of *N,N,N′,N′*-tetramethylchloroformamidinium hexafluorophosphate (TCFH) resulted in good yields of ester prodrugs of thiocoraline and could be applicable to other drugs with similar limitations.

The development of numerous drugs currently in the pipeline of pharmaceutical companies is being hampered by their poor solubility and/or pharmacokinetic/metabolic properties. A way to overcome this limitation is the use of prodrugs (*1*), which are chemically modified drugs that remain inactive while being delivered, but that, having reached the target site, release the active drug in response to a change in pH or to the presence of certain enzymes (*2*). The use of prodrugs has increased enormously over recent years, which is reflected by the fact that 15% of the pharmaceutical agents approved in 2001 and 2002 were prodrugs (*3*). The design of prodrugs is limited in each case by the functional groups amenable to derivatization in the parent drug. Thus, we can find hydroxyls, carboxylic acids, amines, phosphate, and carbonyl groups susceptible to modification to esters, carbonates, carbamates, amides, phosphates, and oximes (*4*). Of these, esters are the most common type of prodrug, because their synthesis is usually straightforward, and the presence of many types of esterases in the body makes the ester bond highly labile (*5*). This linkage is used, for instance, in PGA[1]-Paclitaxel (Xyotax), currently under phase III clinical trials (*6, 7*). PEGylation (*8, 9*) has also frequently been used for drug conjugation, since it greatly enhances water solubility and decreases immunogenicity (*10*). PEGs have been introduced into many drugs, such as paclitaxel, camptothecin, doxorubicin, or interferon, among others, which have undergone clinical trials or are on the market.

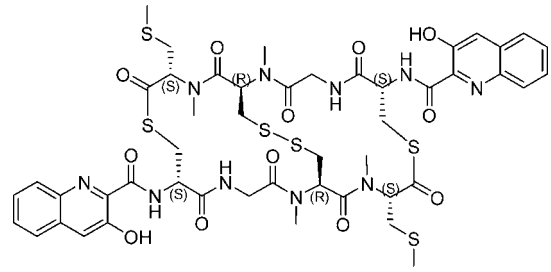

Figure 1. Structure of thiocoraline.

One drug that presents poor solubility is thiocoraline (Figure 1), a potent antitumoral agent (10^{-9} M) isolated from marine *Actynomycetes*.

Thiocoraline (*11, 12*) has a highly hydrophobic structure, where the only polar groups are the two quinolinic hydroxyls and a few amides. To develop prodrugs, we focused on anchoring solubilizing groups to the quinolinic hydroxyl group.

Nevertheless, this functionality proved to be unreactive, and esterification with common coupling reagents resulted in low yields or full recovery of starting material. To optimize conditions, we examined acetylation with several coupling systems (Table 1). For the first five entries, only the starting material was recovered. Thus, *in situ* activation of AcOH by formation of the corresponding fluoride (TFFH **1**, DAST **2**) (*13, 14*), "the mixed anhydride" (BOP-Cl, **3**) (*15*), or by using Ac_2O in the presence of pyridine (**4**), failed in rendering the desired derivative. The same results were obtained by previously activating resin-bound HOBt in polystyrene (*16, 17*) with Ac_2O and pyridine (**5**). Next, formation of the ester bond with carbodiimide/DMAP with and without activating agent (HOAt) was examined (**6**, **7**). In these conditions, some conversion was observed, although the recovery of starting material was considerable. Similar results were obtained when using a uronium salt such as TBTU (**8**) or the sulfonate MSNT (**9**) (*18*),

To whom correspondence should be addressed: E-mail: albericio@irbbarcelona.org; judit.tulla@irbbarcelona.org. Phone: +34 93 4037088. Fax: +34 93 4037126.

[†] Institute for Research in Biomedicine, Barcelona Science Park.

[‡] Combinatorial Chemistry Unit, Barcelona Science Park.

[§] PharmaMar, S.A.

[||] Department of Organic Chemistry, University of Barcelona.

[Δ] CIBER-BBN, Networking Centre on Bioengineering, Biomaterials and Nanomedicine, Barcelona Science Park.

[1]Abbreviations: BOP-Cl, bis(2-oxo-3-oxazolidinyl)phosphinic chloride; CTC, chlorotrityl chloride (Barlos) resin; DAST, (diethylamino) sulfur trifluoride; DIEA, *N,N*-diisopropylethylamine; DIPCDI, *N,N′*-diisopropylcarbodiimide; DMAP, 4-dimethylaminopyridine; HOBt, 1-hydroxybenzotriazole; HOAt, 1-hydroxy-7-azabenzotriazole(3-hydroxy-3*H*-1,2,3-triazolo-[4,5-*b*]pyridine); MSNT, 1-(2-mesitylenesulfonyl)-3-nitro-1*H*-1,2,4-triazole; NMI, *N*-methyl imidazole; PEG, poly(ethylene glycol); PGA, poly(glutamic acid); PS, polystyrene; TBTU, 1-[bis(dimethylamino)methylene]-1*H*-benzotriazolium tetrafluoroborate 3-oxide; TCFH, *N,N,N′,N′*-tetramethylchloroformamidinium hexafluorophosphate; TFFH, *N,N,N′,N′*-tetramethylfluoroformamidinium hexafluorophosphate; TFA, trifluoroacetic acid; TIS, triisopropylsilane; TMUC-Cl, *N*-[chloro(dimethylamino)methylene]-*N*-methylmethanaminium chloride; Trt, trityl.

10.1021/bc8002327 CCC: $40.75 © 2008 American Chemical Society
Published on Web 09/20/2008

Table 1. Coupling Systems

entry	coupling system
1	AcOH/TFFH/DMAP/Et_3N/CH_2Cl_2
2	AcOH/DAST/anh. CH_2Cl_2
3	AcOH/BOP-Cl/DIEA/CH_2Cl_2
4	Ac_2O/pyridine/CH_2Cl_2
5	Ac_2O/PS-HOBt/pyridine
6	AcOH/DIPCDI/DMAP/CH_2Cl_2
7	AcOH/DIPCDI/HOAt/DMAP/CH_2Cl_2
8	AcOH/TBTU/HOAt/DIEA/DMF
9	AcOH/MSNT/NMI/DIEA/CH_2Cl_2
10	AcOH/TMUC-Cl/DIEA/CH_2Cl_2
11	AcOH/TCFH/HOAt/DIEA/DMF
12	AcOH/TCFH/HOAt/DIEA/CH_2Cl_2

which is routinely used for esterification. In the latter case, the presence of several byproducts was observed, probably caused by the large excess of DIEA and NMI applied for this type of coupling. Reaction with AcCl (10 equiv), DIEA (10 equiv), and DMAP (0.1 equiv) in CH_2Cl_2 (**10**) gave good yields, thus obtaining only the bis derivative with 76% yield. In view of these results and to avoid the previous preparation of each single acid chloride, reagents that allow *in situ* formation of acid chlorides were studied. In the case of TMUC-Cl (*19*), no product was recovered. However, the use of *N*,*N*,*N*′,*N*′-tetramethylchloroformamidinium hexafluorophosphate (TCFH) resulted in high conversions to the bis and mono derivatives.

Here, we present TCFH (Figure 2) as a powerful derivatizing coupling reagent for the syntheses of ester prodrugs.

The best results for obtaining the bis derivative were achieved using AcOH/TCFH/HOAt/DIEA (10 equiv/10 equiv/10 equiv/30 equiv) in CH_2Cl_2, for 2 h at 25 °C (as the ester is not stable to basic treatment, products were directly purified by RP-HPLC). Under these conditions, a range of percentages of the mono and bis derivatives were obtained. Longer reaction times resulted in hydrolysis of the ester with more recovery of starting material.

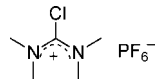

Figure 2. Structure of TCFH.

The application of microwave irradiation for this reaction was also studied in CH_2Cl_2 (MW 50) and DMF (MW 25). However, while in the first case no improvement was noticed, the use of DMF caused degradation of thiocoraline.

Another way to drive reactions to completion is the application of solid-phase synthesis, since large excesses of reagent can be used, which can later be washed away easily, thereby avoiding tedious purifications. Thus, thiocoraline was loaded on 2-CTC resin (*20*) through the quinolinic alcohol with DIEA in CH_2Cl_2 (Scheme 1). Next, the remaining free quinolinic alcohol was reacted with TCFH/HOAt/DIEA in CH_2Cl_2 for 2 h and then the resin was cleaved with TFA−CH_2Cl_2 (1:99). However, under these conditions, low yields of product were obtained. Thus, subsequent derivatizations were carried out in solution.

After optimization of the coupling conditions, a number of carboxylic acids were tested (Table 2). These included PEG acids of various sizes, protected amino acids, aliphatic acids, aliphatic acids with a protected thiol at the terminus, tertiary amine-containing acids, and diacids. For most of these, mixtures of bis and mono derivatives were obtained. The ratio of these two products depended on the acid used. Thus, in the case of octanoic acid (**11**), for instance, the bis derivative was obtained as a major product, while the mini PEG (**3**) gave mainly the mono derivative. For **14**−**16** (tertiary amines and protected Cys), thiocoraline degradation was observed, whereas for succinic acid (**17**), no reaction occurred. All products were purified by semipreparative HPLC.

Attempts to Cleave the Fmoc and Boc Groups from Protected Conjugates To improve solubility, compounds with free amino functionalities were pursued. Thus, coupling with protected amines was performed followed by deprotection of the corresponding Boc and Fmoc groups. In this regard, Boc-Lys(Boc)-OH (**8**) was coupled to thiocoraline, thus obtaining the corresponding mono and bis derivatives. Treatment of the products with 25% TFA in CH_2Cl_2 or 1 M HCl in dioxane/CH_2Cl_2 resulted in recovery of the starting thiocoraline. Under milder reaction conditions (AcCl, MeOH), monitoring of the reaction by HPLC showed the disappearance of the protected compound and appearance of plain thiocoraline. The same

Scheme 1. Esterification of Thiocoraline on Solid Phase

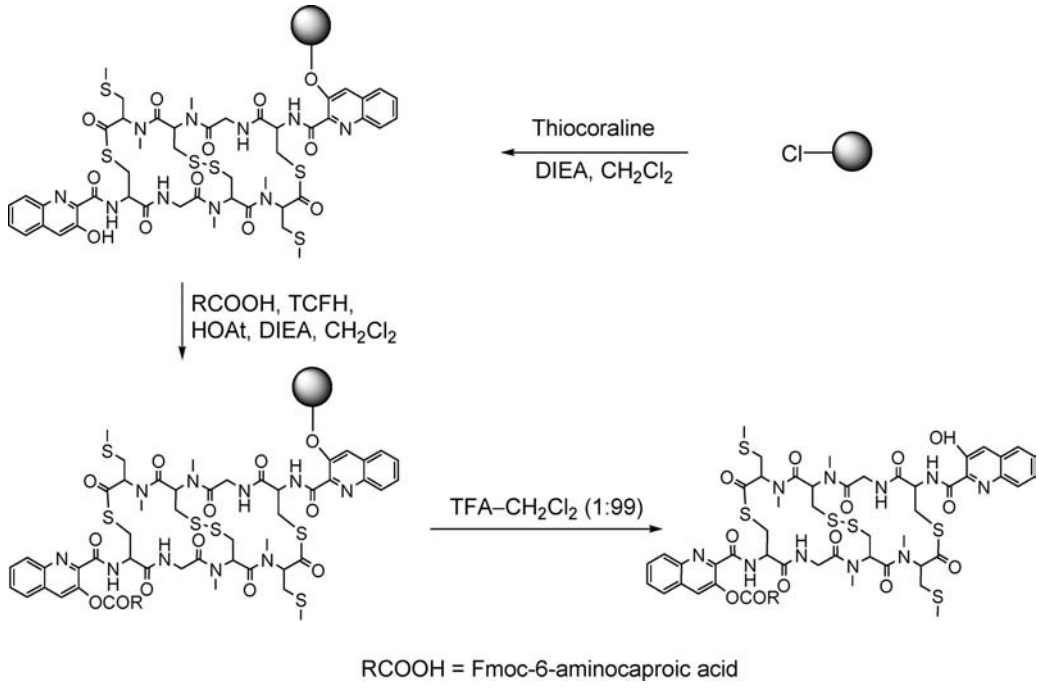

RCOOH = Fmoc-6-aminocaproic acid

Table 2. Derivatization of Thiocoraline Using TCFH/HOAt/DIEA

Entry	R-	%Mono	%Bis
1		20	79
2	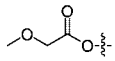	49	35
3	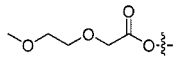	38	6
4	PEG 5000	87%*	
5	PEG 2000	57%	–
6	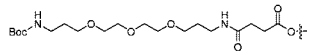	42	15
7	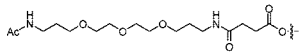	17	27
8	Boc-Lys(Boc)-O–	43	49
9	Boc-Glu(*t*-Bu)-O–	36	47
10	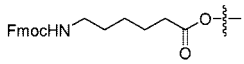	15	74
11	CH_3-$(CH_2)_6$-COOH	4	74
12	CH_3-$(CH_2)_{14}$-COOH	55	–
13	TrtS-$(CH_2)_{10}$-COOH	52	–
14		–	–
15	Boc-Cys(Npys)-OH	–	–
16	Boc-Cys(Trt)-OH	–	–
17	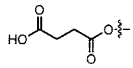	–	–

* Sum of PEGytaded products.

results were obtained with the derivative Boc-Glu(*t*Bu)-O-thiocoraline (**9**), and Boc-Lys(Boc)-Pro-O-thiocoraline (not shown), which was synthesized with the aim of keeping the free amino groups further away from thiocoraline. Attempts were also made to remove the Fmoc group of several conjugates both in solution (from **10**) and on solid-phase, since in the latter case, cleavage of the Fmoc group is easier. As explained, thiocoraline was loaded on 2-CTC resin, and Fmoc-β-Ala-OH or Fmoc-6-aminocaproic acid was coupled. The Fmoc group was then removed with piperidine−DMF (1:4), using only two treatments of 1 min. Under these conditions, only thiocoraline was recovered. These results suggest that free amino groups attack the newly formed ester bond, even when using longer chains.

To obtain free thiols that could be conjugated to gold nanoparticles, protected thiols were used and then deprotected. However, as described above, complex mixtures were obtained when using protected Cys (**15**−**16**). In contrast, when a long-chain aliphatic carboxylic acid bearing an S-Trt protected thiol

Table 3. *In Vitro* Results

R-			Breast MDA-MB-231	NSCLC A-549	Colon HT29
	Mono	GI50	1.25E-8	2.08E-8	2.50E-8
		TGI	5.00E-8	5.84E-8	6.84E-8
		LC50	1.83E-7	1.92E-7	5.42E-7
	Bis	GI50	3.95E-8	7.57E-8	7.89E-8
		TGI	1.37E-7	1.93E-7	2.09E-7
		LC50	4.11E-7	5.16E-7	n.d.
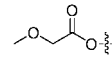	Mono	GI50	1.30E-8	2.03E-8	2.36E-8
		TGI	5.12E-8	5.53E-8	5.61E-8
		LC50	1.87E-7	1.71E-7	3.09E-7
	Bis	GI50	1.46E-8	2.31E-8	2.77E-8
		TGI	5.07E-8	5.61E-8	6.61E-8
		LC50	1.46E-7	1.46E-7	3.38E-7
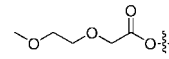	Mono	GI50	1.33E-8	2.12E-8	2.04E-8
		TGI	5.03E-8	5.26E-8	5.26E-8
		LC50	1.65E-7	1.41E-7	3.46E-7
	Bis	GI50	2.66E-8	4.46E-8	4.39E-8
		TGI	9.36E-8	1.08E-7	9.36E-8
		LC50	2.73E-7	2.52E-7	3.02E-7
PEG 2000		GI50	2.79E-7	3.0E-7	n.d.
		TGI	n.d.	n.d.	n.d.
		LC50	n.d.	n.d.	n.d.
PEG 5000		GI50	n.d.	n.d.	n.d.
		TGI	n.d.	n.d.	n.d.
		LC50	n.d.	n.d.	n.d.
		GI50	n.d.	n.d.	n.d.
		TGI	n.d.	n.d.	n.d.
		LC50	n.d.	n.d.	n.d.
		GI50	8.06E-7	4.53E-7	n.d.
		TGI	n.d.	n.d.	n.d.
		LC50	n.d.	n.d.	n.d.
		GI50	1.48E-7	2.47E-7	5.84E-7
		TGI	3.56E-7	6.14E-7	8.02E-7
		LC50	n.d.	n.d.	9.80E-7
Octanoic	Mono	GI50	7.79E-9	5.14E-9	1.01E-8
		TGI	3.51E-8	2.34E-8	3.27E-8
		LC50	1.87E-7	1.79E-7	n.d.
	Bis	GI50	9.93E-9	5.25E-9	3.90E-8
		TGI	3.26E-8	2.41E-8	7.80E-8
		LC50	9.93E-8	2.13E-7	n.d.
Palmitic	Mono	GI50	5.16E-8	2.15E-8	2.29E-7
		TGI	2.29E-7	1.00E-7	4.87E-7
		LC50	1.00E-6	1.07E-6	2.01E-6
HOOC-$(CH_2)_{10}$-SH	Mono	GI50	3.17E-8	1.40E-8	1.10E-7
		TGI	1.25E-7	5.38E-8	2.28E-7
		LC50	4.86E-7	5.01E-7	n.d.

group (**13**) was used, the reaction gave the mono derivative, and the Trt group was cleanly removed using TFA−TIS−CH_2Cl_2 (10:2.5:87.5). The final product was purified by reversed-phase HPLC, albeit purification proved difficult because of the hydrophobicity of the compound.

These results suggest that PEG and aliphatic chains can be used for thiocoraline prodrug formation, but that other functionalities such as free carboxylic acids, tertiary amines, free amines, or short thiol alkyl chains are not tolerated.

Biological Activity. The products obtained were tested in three cell lines: breast, nonsmall cell lung (NCSLC), and colon (Table 3). *In vitro* results showed that, for most of the derivatives, the activity is maintained, or decreases slightly, thereby suggesting that the ester bond is rapidly cleaved before bisintercalation to DNA. In the case of PEG 2000 and 5000, the decrease in activity can be attributed to the high increase in molecular weight of the resulting prodrug.

In conclusion, using TCFH as a coupling reagent for the esterification of thiocoraline, we prepared a number of conjugates including PEGylated compounds with higher solubility. These derivatives were assayed for biological activity in three cell lines and gave, in most cases, results comparable to the parent natural product. On the basis of our findings, we conclude that the coupling system TCFH/HOAt/DIEA could be applied

for the syntheses of ester prodrugs of molecules bearing groups of low reactivity.

ACKNOWLEDGMENT

This study was partially supported by CICYT (CTQ2006-03794/BQU), the ISCIII (CIBER, nanomedicine), CENIT (Nanomedicine), PharmaMar S. A., the Institute for Research in Biomedicine, and the Barcelona Science Park. J.T.-P. is a Juan de la Cierva fellow (MEC).

Supporting Information Available: Experimental procedures and characterization data. This material is available free of charge via the Internet at http://pubs.acs.org.

LITERATURE CITED

(1) Stella, V. J., and Nti-Addae, K. W. (2007) Prodrug strategies to overcome poor water solubility. *Adv. Drug Delivery Rev. 59*, 677–694.

(2) Liederer, B. M., and Borchardt, R. T. (2006) Enzymes involved in the bioconversion of ester-based prodrugs. *J. Pharm. Sci. 95*, 1177–1195.

(3) Stella, V. J. (2004) Prodrugs as therapeutics. *Expert Opin. Ther/ Pat. 14*, 277–280.

(4) Routio, J., Kumpulainen, H., Heimbach, T., Oliyai, R., Oh, D., Järvinen, T., and Savolainen, J. (2008) Prodrugs: design and clinical applications. *Nat. Rev. 7*, 255–270.

(5) Beaumont, K., Webster, R., Gardner, I., and Dack, K. (2003) Design of ester prodrugs to enhance oral absorption of poorly permeable compounds: challenges to the discovery scientist. *Curr. Drug Metab. 4*, 461–485.

(6) Li, C., Yu, D. F., Newman, R. A., Cabral, F., Stephens, L. C., Hunter, N., Milas, L., and Wallace, S. (1998) Complete regression well-established tumors using a novel water soluble poly(L-glutamic acid)-paclitaxel conjugate. *Cancer Res. 58*, 2404–2409.

(7) Greco, F., and Vicent, M. J. (2008) Polymer-drug conjugates: current status and future trends. *Front. Biosci. 13*, 2744–2756.

(8) Abuchowski, A., McCoy, J. R., Palczuk, N. C., van Es, T., and Davis, F. F. (1977) Effect of covalent attachment of polyethylene glycol on immunogenicity and circulating life of bovine liver catalase. *J. Biol. Chem. 252*, 3582–3586.

(9) Veronese, F. M., and Pasut, G. (2005) PEGylation, successful approach to drug delivery. *Drug Discovery Today 10*, 1451–1458.

(10) Greenwald, R. B., Choe, Y. H., McGuire, J., and Conover, C. D. (2003) Effective drug delivery by PEGylated drug conjugates. *Adv. Drug Deliveryv. 55*, 217–250.

(11) Romero, F., Espliego, F., Pérez Baz, J., García de Quesada, T., Gravalos, D., De la Calle, F., and Fernández-Puentes, J. L. (1997) Thiocoraline, a new depsipeptide with antitumor activity produced by a marine Micromonospora. I. Taxonomy, fermentation, isolation, and biological activities. *J. Antibiot. 50*, 734–737.

(12) Pérez Baz, J., Cañedo, L. M., Fernández Puentes, J. L., and Silva Elipe, M. V. (1997) Thiocoraline, a novel depsipeptide with antitumor activity produced by a marine Micromonospora. II. Physico-chemical properties and structure determination. *J. Antibiot. 50*, 738–741.

(13) Carpino, L. A., and El-Faham, A. (1995) Tetramethylfluoroformamidinium hexafluorophosphate: a rapid-acting peptide coupling reagent for solution and solid phase peptide synthesis. *J. Am. Chem. Soc. 117*, 5401–5402.

(14) Kaduk, C., Wenschuh, H., Beyerman, M., Forner, K., Carpino, L. A., and Bienert, M. (1996) Synthesis of Fmoc-amino acid fluorides via DAST, an alternative fluorinating agent. *Lett. Pept. Sci. 2*, 285–288.

(15) Diago-Meseguer, J., Palomo-Coll, A. L., Fernández-Lizarbe, J. R., and Zugaza-Bilbao, A. (1980) A new reagent for activating carboxyl groups: preparation and reactions of *N*,*N*-bis[2-oxo-3-oxazolidinyl]phosphorodiamidic chloride. *Synthesis* 547–551.

(16) (a) Kalir, R., Warshawsky, A., Fridkin, M., and Patchornik, A. (1975) New useful reagents for peptide synthesis. Insoluble active esters of polystyrene-bound 1-hydroxybenzotriazole. *Eur. J. Biochem. 59*, 55–61. (b) Mokotoff, M., and Patchornik, A. (1983) Synthesis of the *C*-terminal half of thymosin α1 by the polymeric reagent method. *Int. J. Pept. Protein Res. 21*, 145–154.

(17) Pop, I. E., Deprez, B. P., and Tartar, A. L. (1997) Versatile acylation of *N*-Nucleophiles using a new polymer-supported 1-hydroxybenzotriazole derivative. *J. Org. Chem. 62*, 2594–2603.

(18) Blankemeyer-Menge, B., Nimtz, M., and Frank, R. (1990) An efficient method for anchoring Fmoc-amino acids to hydroxyl-functionalized solid supports. *Tetrahedron Lett. 31*, 1701–1704.

(19) Vendrell, M., Ventura, R., Ewenson, A., Royo, M., and Albericio, F. (2005) *N*-[Chloro(dimethylamino)methylene]-*N*-methylmethanaminium chloride (TMUC Cl), the reagent of choice for the solid-phase synthesis of anilides. *Tetrahedron Lett. 46*, 5383–5386.

(20) Barlos, K., Gatos, D., Kallitsis, J., Papaphotiu, G., Sotiriu, P., Yao, W., and Schaefer, W. (1989) Preparation of protected peptide fragments using triphenylmethyl resins. *Tetrahedron Lett. 30*, 3943–3946.

BC8002327

N,N,N',N'-TETRAMETHYLCHLOROFORMAMIDIUM HEXAFLUOROPHOSPHATE (TCFH), A POWERFUL COUPLING REAGENT FOR BIOCONJUGATION

Judit Tulla-Puche, Ángela Torres, Pilar Calvo, Miriam Royo, and Fernando Albericio

Institute for Research in Biomedicine, Barcelona Science Park, Baldiri Reixac 10, 08028-Barcelona (Spain)

PharmaMar, S.A.U., 28770-Colmenar Viejo (Spain)

Combinatorial Chemistry Unit, Barcelona Science Park, University of Barcelona, Baldiri Reixac 10, 08028-Barcelona (Spain)

Department of Organic Chemistry, University of Barcelona, 08028 Barcelona (Spain)

CIBER-BBN, Networking Centre on Bioengineering, Biomaterials and Nanomedicine Barcelona Science Park, Baldiri Reixac 10, 08028-Barcelona (Spain)

SUPPLEMENTARY INFORMATION

Experimental procedures S2

GENERAL S2

Synthesis of thiocoraline conjugates in solution..... S3

Microwave-assisted synthesis S6

Synthesis using PS-HOBt S6

Solid-phase synthesis S7

Synthesis of Boc-protected 4,7,10-trioxa-1,13-tridecanediamine Succinimic Acid S7

Synthesis of Acetyl-protected 4,7,10-Trioxa-1,13-tridecanediamine Succinimic Acid S8

Cell growth inhibitory assays S8

Experimental Procedures

General

Protected and raw amino acid derivatives were obtained from Applied Biosystems (Framingham, MA), Bachem (Bubendorf, Switzerland), Albatross (Montreal, Canada), and NovaBiochem (Läufelfingen, Switzerland). DIEA, TFA, were obtained from Aldrich (Milwaukee, WI). DMF, CH_2Cl_2, TCFH was obtained from Iris Biotech GmbH (Marktredwitz, Germany). Acetonitrile (HPLC grade), methanol (HPLC grade), TBME (*t*-butyl methyl ether) and EtOAc (ethyl acetate) were obtained from SDS (Peypin, France). All commercial reagents and solvents were used as received with the exception of DMF and CH_2Cl_2 , which were bubbled with nitrogen to remove volatile contaminants (DMF) and stored over activated 4 Å molecular sieves (Merck, Darmstadt, Germany); and THF, which was distilled from sodium/benzophenone.

Solution reactions were performed in round-bottomed flasks. Organic solvent extracts were dried over anhydrous $MgSO_4$, followed by solvent removal under reduced pressure at temperatures below 40 ºC.

Solid-phase syntheses were performed in polypropylene syringes (2, 5 mL), each fitted with a polyethylene porous disc. Solvents and soluble reagents were removed by suction. The Fmoc group was removed with piperidine–DMF (1:4, v/v) (2 × 1 min, 2 × 5 min). Washings between reaction steps were carried out with DMF (5 × 1 min) and CH_2Cl_2 (5 × 1 min) using 5 mL solvent.g^{-1} resin for each wash. Peptide synthesis transformations and washes were performed at 25 ºC.

Microwave-assisted synthesis was performed on a CEM Discover® Labmate instrument equipped with an IntelliVent™ pressure control system in sealed tubes.

HPLC columns (Symmetry® C18 reversed-phase analytical column, 5.0 µm × 4.6 mm × 150 mm and Symmetry® C18 reversed-phase semi-preparative column, 5.0 µm × 7.8 mm × 100 mm) were obtained from Waters (Ireland). Analytical HPLC was performed on a Waters instrument comprising a separation module (Waters 2695), automatic injector, photodiode array detector (Waters 996), and system controller (Millenium^{32} login). UV detection was performed at 220 and 254 nm, and linear gradients of ACN (+0.036% TFA) into H_2O (+0.045% TFA) were run at 1.0 mL·min^{-1} flow rate for 15 min. Semi-preparative HPLC was carried out on a Waters instrument comprising a separation module (Waters 600), automatic injector, and a dual absorbance detector (Waters 2487). UV detection was performed at 220 and 254 nm, and linear gradients of ACN (+0.05% TFA) into H_2O (+0.1% TFA) were run under the conditions specified for each case.

MALDI-TOF and ES(+)-MS analyses of peptide samples were performed on an Applied Biosystems VoyagerDE RP, using a DHB matrix, in a Waters Micromass ZQ spectrometer and in an Agilent Ion Trap 1100 Series LC/MSDTrap.

General procedure for the synthesis of thiocoraline bioconjugates

Thio-O-Ac. Thiocoraline (10.0 mg, 0.0087 mmol) was dissolved in CH_2Cl_2. AcOH (5.0 µL, 0.087 mmol) and HOAt (10.9 mg, 0.087 mmol) were suspended in CH_2Cl_2. DIEA (44 µL, 0.26 mmol) was added, followed by TCFH (24.6 mg, 0.087 mmol), dissolved in CH_2Cl_2, and the mixture was added to the thiocoraline solution. The reaction mixture was stirred for 2 h at 25 °C, was then evaporated, and purified by RP-HPLC. Analytical HPLC (linear gradient: 50:50 to 100:0 (ACN/H_2O) in 15 min): t_R = 6.59 min (bis), t_R = 7.78 min (mono). HPLC-ESMS (mono): *m/z* calcd for $C_{50}H_{58}N_{10}O_{13}S_6$, 1198.25; found,

1199.50 $[M + H]^+$. HPLC-ESMS (bis): *m/z* calcd for $C_{52}H_{60}N_{10}O_{14}S_6$, 1240.26, found, 1241.10 $[M + H]^+$.

Thio-O-CO-CH_2-O-CH_3. Analytical HPLC (linear gradient: 50:50 to 100:0 (ACN/H_2O) in 15 min): t_R = 6.44 min (bis), t_R = 7.68 min (mono). HPLC-ESMS: *m/z* calcd for $C_{51}H_{60}N_{10}O_{14}S_6$ (mono) 1228.26; found, 1228.79 [M]•+. HPLC-ESMS: *m/z* calcd for $C_{54}H_{64}N_{10}O_{16}S_6$ (bis) 1300.28; found, 1300.84 [M]•+.

Thio-O-CO-CH_2-O-$(CH_2)_2$-O-CH_3. Analytical HPLC (linear gradient: 50:50 to 100:0 (ACN/H_2O) in 15 min): t_R = 6.32 min (bis), t_R = 7.61 min (mono). HPLC-ESMS: *m/z* calcd for $C_{53}H_{64}N_{10}O_{15}S_6$ (mono) 1272.29; found, 1272.98 [M]•+. HPLC-ESMS: *m/z* calcd for $C_{58}H_{72}N_{10}O_{18}S_6$ (bis) 1388.34; found, 1388.92 [M]•+.

Thio-O-(Boc)-Lys(Boc). Analytical HPLC (linear gradient: 50:50 to 100:0 (ACN/H_2O) in 15 min): t_R = 10.80 min (mono), t_R = 12.16 min (bis). HPLC-ESMS: *m/z* calcd for $C_{64}H_{84}N_{12}O_{17}S_6$ (mono) 1484.44; found 1485.18 $[M + H]^+$, 1508.11 $[M + Na]^+$. HPLC-ESMS: *m/z* calcd for $C_{80}H_{112}N_{14}O_{22}S_6$ (bis) 1812.64; found, 1813.44 $[M + H]^+$, 1835.45 $[M + Na]^+$.

Thio-O-(Boc)-Glu(*t*Bu). Analytical HPLC (linear gradient: 50:50 to 100:0 (ACN/H_2O) in 15 min): t_R = 11.47 min (mono), t_R = 13.19 min (bis). HPLC-ESMS: *m/z* calcd for $C_{62}H_{79}N_{11}O_{17}S_6$ (mono) 1441.40; found, 1442.21 $[M + H]^+$. HPLC-ESMS: *m/z* calcd for $C_{76}H_{102}N_{12}O_{22}S_6$ (bis) 1726.56; found, 1727.13 $[M + H]^+$.

Thio-O-(Fmoc)-6-aminocaproic. Analytical HPLC (linear gradient: 50:50 to 100:0 (ACN/H_2O) in 15 min): t_R = 11.95 min (mono), t_R = 13.88 min (bis). HPLC-ESMS: *m/z* calcd for $C_{69}H_{77}N_{11}O_{15}S_6$ (mono), 1491.39; found, 1492.04 $[M + H]^+$. HPLC-ESMS: *m/z* calcd for $C_{90}H_{98}N_{12}O_{18}S_6$ (bis), 1826.54; found, 1827.95 $[M + H]^+$.

Thio-O-(Fmoc)-β-Ala. Analytical HPLC (linear gradient: 50:50 to 100:0 (ACN/H_2O) in 15 min): t_R = 11.03 min (mono). MALDI-TOF: *m/z* calcd for $C_{66}H_{71}N_{11}O_{15}S_6$ (mono), 1449.35; found, 1472.52 $[M + Na]^+$.

Thio-O-PEG5000. Analytical HPLC (linear gradient: 50:50 to 100:0 (ACN/H_2O) in 15 min): t_R = 7.19, t_R = 7.73 min, t_R = 7.93 min, and t_R = 8.70 min. MALDI-TOF: average masses: 7582.70, 8653.57, 11043.24, 6993.97.

Thio-O-PEG2000. Analytical HPLC (linear gradient: 0:100 to 100:0 (ACN/H_2O) in 15 min): t_R = 9.25 min (mono); HPLC-ESMS: *m/z* calcd (mono) 3138.24; found, 1050.24 $[M + 3]^+/3$.

Thio-O-CO-$(CH_2)_2$-CONH-$(CH_2)_3$-O-$(CH_2)_2$-O-$(CH_2)_2$-O-$(CH_2)_3$-NHBoc. Analytical HPLC (linear gradient: 50:50 to 100:0 (ACN/H_2O) in 15 min): t_R = 7.19 (mono), t_R = 7.98 min (bis). HPLC-ESMS: *m/z* calcd for $C_{67}H_{90}N_{12}O_{19}S_6$ (mono) 1558.48; found 1559.25 $[M + H]^+$. HPLC-ESMS: *m/z* calcd for $C_{86}H_{124}N_{14}O_{26}S_6$ (bis) 1960.71; found 1961.54 $[M + H]^+$.

Thio-O-CO-$(CH_2)_2$-CONH-$(CH_2)_3$-O-$(CH_2)_2$-O-$(CH_2)_2$-O-$(CH_2)_3$-NHAc. Analytical HPLC (linear gradient: 0:100 to 100:0 (ACN/H_2O) in 15 min): t_R = 9.12 (bis), t_R = 11.21 min (mono). HPLC-ESMS: *m/z* calcd for $C_{64}H_{84}N_{12}O_{18}S_6$ (mono) 1500.44; found, 1501.38 $[M + H]^+$. HPLC-ESMS: *m/z* calcd for $C_{80}H_{112}N_{14}O_{24}S_6$ (bis) 1844.63; found, 1845.55 $[M + H]^+$.

Thio-O-octanoic. Analytical HPLC (linear gradient: 0:100 to 100:0 (ACN/H_2O) in 15 min): t_R = 16.34 min (mono), t_R = 17.63 min (bis). HPLC-ESMS: *m/z* calcd for $C_{56}H_{70}N_{10}O_{13}S_6$ (mono) 1282.34; found, 1283.00 [M]•+. HPLC-ESMS: *m/z* calcd for $C_{64}H_{84}N_{10}O_{14}S_6$ (bis) 1408.45; found, 1408.89 [M]•+.

Thio-O-palmitic. Analytical HPLC (linear gradient: 0:100 to 100:0 (ACN/H_2O) in 15 min): t_R = 20.56 min (mono), t_R = 21.15 min (bis). MALDI-TOF: *m/z* calcd for $C_{64}H_{86}N_{10}O_{13}S_6$ (mono) 1394.47; found, 1395.54 $[M + H]^+$, 1417.52 $[M + Na]^+$, 1433.50 $[M + K]^+$. MALDI-TOF: *m/z* calcd for $C_{80}H_{116}N_{10}O_{14}S_6$ (bis) 1632.70; found, 1657.83 $[M + 2H + Na]^+$, 1673.78 $[M + 2H + K]^+$.

Thio-O-CO-$(CH_2)_{10}$-SH. Analytical HPLC (linear gradient: 0:100 to 100:0 (ACN/H_2O) in 15 min): t_R = 16.75 min (mono), ESMS: *m/z* calcd for $C_{59}H_{76}N_{10}O_{13}S_7$ 1356.36; found, 1377.80 $[M + Na]^+$.

Microwave-assisted synthesis of thiocoraline conjugates: Thiocoraline (5.0 mg, 0.0043 mmol), CH_3-O-$(CH_2)_2$-O-CH_2COOH (4.9 µL, 0.043 mmol), TCFH (12.3 mg, 0.043 mmol), HOAt (5.9 mg, 0.043 mmol), and DIEA (22 µL, 0.13 mmol) were weighed in a microwave glass tube. CH_2Cl_2 or DMF (2 mL) was added, and the tube was sealed, and introduced into the microwave. Reactions with CH_2Cl_2 were performed at MW ~50, and up to 110 °C, whereas reactions with DMF were performed at MW ~25 and 100 °C.

Synthesis using PS-HOBt. PS-HOBt (100 mg, 1.05 mmol/g) was washed with CH_2Cl_2 and Ac_2O (75.5 µL, 0.8 mmol), pyridine (48.3 µL, 0.6 mmol) in CH_2Cl_2 (1 mL) was then added to the resin. After 1 h at 25 °C, the resin was washed with CH_2Cl_2. Thiocoraline (4.9 mg, 0.004 mmol) in CH_2Cl_2 was added to an aliquot of the resin (29 mg, 0.028 mmol), and the reaction was left for 3 h at 25 °C. The reaction mixture was filtered, and the filtrates were evaporated and analyzed by analytical HPLC.

Solid-phase synthesis. 2-CTC resin (10 mg, 1.5 mmol/g) was washed with DMF and CH_2Cl_2. Next, thiocoraline (11 mg, 0.01 mmol) and DIEA (11.3 μL, 0.07 mmol) in CH_2Cl_2 were added. After 5 min another portion of DIEA was added (5.6 μL, 0.03 mmol) and the resin was shaken for 45 min. After this period, MeOH (8 μL) was added to cap any unreacted site, and the resin was washed with DMF (3 × 1 min) and CH_2Cl_2 (3 × 1 min). Next, a solution of Fmoc-6-aminocaproic acid (35.4 mg, 0.10 mmol) and HOAt (13.6 mg, 0.10 mmol) in CH_2Cl_2 was added, followed by DIEA (51.0 μL, 0.30 mmol) and TCFH (28.0 mg, 0.10 mmol). The reaction was shaken for 1 h, washed with DMF and CH_2Cl_2. The Fmoc group was removed with piperidine–DMF (1:4) (2 × 1 min, 2 × 5 min). Cleavage of the resin was achieved by treatment with TFA–CH_2Cl_2 (1:99; 6 × 1 min).

Synthesis of Boc protected 4,7,10-Trioxa-1,13-tridecanediamine Succinimic Acid. 4,7,10-Trioxa-1,13-tridecanediamine (100 mg, 0.45 mmol) was dissolved in CH_3CN (10 mL) in a round-bottomed flask provided with magnetic stirring. Succinic anhydride (45.5 mg, 0.45 mmol, 1.0 equiv) was dissolved in CH_3CN (5 mL) and added dropwise over 20 min. The reaction was allowed to proceed for an additional 2 h at 25 °C. The organic solvent was decanted and discarded. The crude product (white oil) and triethylamine (94.2 μL, 0.68 mmol, 1.5 equiv) were dissolved in CH_2Cl_2 (20 mL) and placed in an ice bath for 15 min before Boc_2O (133.5 g, 0.58 mmol, 1.3 equiv) in CH_2Cl_2 (10 mL) was added dropwise over 15 min. After stirring overnight at 25 °C, the solvent was removed under vacuum. The resultant crude product (pale yellow oil) was dissolved in 5% $NaHCO_3$ (50 mL) and washed with EtOAc. The aqueous phase was then acidified with 1

N HCl to pH 4 and extracted with EtOAc (3 × 50 mL). The combined organic layers were washed with brine and dried over anhydrous $MgSO_4$. Evaporation of the organic solvent gave 128.6 mg of the desired product (68% yield). The final product was characterized by analytical RP-HPLC and HPLC-ESMS (linear gradient: 0:100 to 100:0 (ACN/H_2O) in 10 min): t_R: 5.38 min, purity: 90%, *m/z* calcd for $C_{19}H_{36}N_2O_8$ 420.25; found, 421.30 $[M + H]^+$.

Synthesis of Acetyl protected 4,7,10-Trioxa-1,13-tridecanediamine Succinimic Acid. Succinic anhydride (45.5 mg, 0.45 mmol, 1.0 equiv) dissolved in CH_3CN (5 mL) was added dropwise over 20 min to a solution of 4,7,10-Trioxa-1,13-tridecanediamine (100 mg, 0.45 mmol) in CH_3CN (10 mL). The reaction was stirred for 2 h at 25 °C. The organic solvent was decanted and discarded. The resultant product (white oil), triethylamine (94.2 L, 0.68 mmol, 1.5 equiv) and acetic anhydride (40 μL, 0.54 mmol, 1.2 equiv) were dissolved in CH_2Cl_2 (20 mL) and stirred for 3 h at at 25 °C. The mixture was evaporated under vacuum and the residue was dissolved in 5% $NaHCO_3$ (50 mL) and washed with EtOAc. The aqueous phase was then acidified with 1 N HCl to pH 2 and extracted with EtOAc (3 × 50 mL). The organic layer was washed with brine, dried over anhydrous $MgSO_4$ and evaporated to dryness to obtain 101.0 mg of the desired compound as a yellow oil (62% yield). The final product was characterized by analytical RP-HPLC and HPLC-ESMS (linear gradient: 0:100 to 100:0 (ACN/H_2O) in 10 min): t_R: 3.95 min, purity: 82%, *m/z* calcd for $C_{16}H_{30}N_2O_7$ 362.23; found, 363.50 $[M + H]^+$.

Cell growth inhibition assay

A colorimetric assay using sulforhodamine B (SRB) was adapted to perform a quantitative measurement of cell growth and viability, following a previously described method. The cells were seeded in 96-well microtiter plates at 5×10^3 cells/well in aliquots of 195 µL of RPMI medium and were left to grow in drug-free medium for 18 h to allow attachment to the plate surface. Samples were then added in aliquots of 5 µL (dissolved in DMSO–H_2O, 3:7). After 72 h of exposure, the antitumor effect was measured by the SRB methodology: cells were fixed by adding 50 µL of cold 50% (wt/vol) trichloroacetic acid (TCA) and were incubated for 60 min at 4 ˚C. Plates were washed with deionized H_2O, and dried, and 100 µL of SRB solution (0.4% wt/vol in 1% acetic acid) was added to each microtiter well and incubated for 10 min at room temperature. Unbound SRB was removed by washing with 1% acetic acid. Plates were air-dried, and the bound stain was dissolved with Tris buffer. Optical densities were read on an automated spectrophotometer plate reader at a single wavelength of 490 nm. Data analyses were automatically generated by LIMS implementation. Assays were done in a dose-response manner at 10 concentrations (from 10 µg/mL with 1:2.5 dilutions to 0.0026 µg/mL). Although concentrations were adjusted in mg/mL, GI_{50} values were calculated in molarity. All assays were run in triplicate, and the curves were automatically adjusted with 30 points by non-linear regression using "Prism 3.03" (GraphPad) software.

ARTICLES

Modularly Assembled Magnetite Nanoparticles Enhance in Vivo Targeting for Magnetic Resonance Cancer Imaging

Ping-Ching Wu, Chia-Hao Su, Fong-Yu Cheng, Jun-Cheng Weng, Jyh-Horng Chen, Tsung-Lin Tsai, Chen-Sheng Yeh, Wu-Chou Su, Jih Ru Hwu, Yonhua Tzeng, and Dar-Bin Shieh*

Institute of Basic Medical Sciences and Department of Chemistry, National Cheng Kung University, Tainan 701, Interdisciplinary MRI/MRS Laboratory, Department of Electrical Engineering, National Taiwan University, Taipei 112, Department of Internal Medicine, National Cheng Kung University Hospital, Tainan 704, Department of Chemistry, National Tsing Hua University, Hsinchu 30013, Department of Electrical Engineering and Institute of Innovation and Advanced Studies, National Cheng Kung University College of Electrical Engineering and Computer Science, Tainan 701, and Institute of Oral Medicine and Department of Stomatology and Institute of Innovation and Advanced Studies, National Cheng Kung University, Tainan 701, Taiwan. Received March 7, 2008; Revised Manuscript Received August 13, 2008

Modularly assembled targeting nanoparticles were synthesized through self-assembly of targeting moieties on surfaces of functional nanoparticles. Specific molecular recognition of nickel nitrilotriacetate on Fe_3O_4 nanoparticles with hexahistidine tag on RGD4C peptides results in precisely controlled orientation of the targeting peptides. Better selectivity of the self-assembled RGD4C-Fe_3O_4 nanoparticles targeting oral cancer cells than that achievable through a conventional chemical cross-link strategy was demonstrated by means of atomic absorption spectrometry (AAS). An oral cancer hamster model was applied to reveal specific in vivo targeting and MR molecular imaging contrast in cancer lesions expressing $\alpha v\beta 3$ integrin. Both AAS and MRI revealed that the self-assembled nanoparticles improved the targeting efficiency and reduced the hepatic uptake as compared with the conventional chemical cross-link particles. We investigated the biosafety, biodistribution, and kinetics of the nanoparticles and found that the nanoparticles were significantly cleared from the liver and kidneys after one week. By recombining the desired targeting moiety and various functional nanoparticles through self-assembly, this new modularly designed platform has the capability of enhancing the efficiency of targeted diagnosis and therapies for a wide spectrum of biomedical applications.

INTRODUCTION

Molecular imaging of cancers provides valuable information regarding the clinical behavior of a disease and treatment response to certain therapeutic modalities. Among various molecular imaging modalities under development, magnetic resonance imaging (MRI) provides high spatial resolution, excellent perception with tomographic capabilities, outstanding soft-tissue contrast, and good anatomical detail and orientation. Conventional MRI, however, has relatively low signal contrast because of partial volume dilution effects (*1*). Different image contrast agents have been developed for MRI by modulating proton-T1 or -T2 relaxations using contrast agents such as manganese (Mn^{2+}) (*2*), gadolinium ethoxybenzyl diethylenetriamine pentaacetic acid (Gd-EOB-DTPA) (*3*), and iron oxide nanoparticles (*4*). These contrast agents have been developed and evaluated in the past decades for their MRI applications in the laboratory and clinical use (*5*−*8*). However, in vivo molecular targeting imaging is still in the proof-of-concept stage (*9*). The major challenges for targeted MRI include effective bioconjugation and the in vivo dynamics and sensitivity of the detection. This is due to the limitations of functional groups on a given targeting antibody or peptide, which can be selected for bioconjugation without compromising binding affinity. Traditional direct chemical labeling has failed to provide homogeneous functional nanoparticles with sufficient affinity to generate high MR contrast (*10*). Recently, a study demonstrating a comprehensive artificial synthetic approach reported an optimal size (12 nm) and composition of magnetic nanoparticles ($MnFe_2O_4$) for in vivo targeting imaging of small tumors using trastuzumab (Herceptin) conjugation (*11*). However, all these efforts used to direct chemical conjugation require optimization based on each different targeting contrast agent synthesis and on the complicated combination of different targeting peptides, antibodies, and various types of functional nanoparticles, all with different surface chemistry.

Nitrilotriacetic acid (NTA) forms a stable complex with transitional metal ions such as Ni^{2+}, Zn^{2+}, and Co^{2+} (*12*). The 3D conformation of NTA enables stable and strong binding with polyhistidine sequences (*13*). Recently, NTA-modified magnetic nanoparticles attached to nickel ion (Ni^{2+}) can act as a general agent to separate, transport, and anchor a protein with an engineered arrangement of six consecutive histidine residues (*14*). This platform was capable of efficient purification of His 6-His tagged proteins that are expressed at low levels in mammalian cells (*15*). These studies revealed that Ni-NTA and 6-His have strong specific affinity to each other and potential application for self-assembling design.

Specific integrins, such as $\alpha v\beta 3$, have been highly expressed on the neoangiogenic endothelial cells of cancer lesions, for

* E-mail: dshieh@mail.ncku.edu.tw. Tel: 886-6-235-3535ext. 5377. Fax: 886-6-276-6626.

10.1021/bc800092w CCC: $40.75 © 2008 American Chemical Society
Published on Web 09/23/2008

example, glioblastoma, melanoma, breast, ovarian, and prostate tumors. Some of these cancers cells overexpress the specific integrins, while their healthy counterparts do not (*16*−*19*). Cyclic RGD4C (CDCRGDCFC) peptide is a potent but highly selective binder of $\alpha v\beta 3$ integrins and target tumors (*20, 21*). These peptides have been successfully used for tumor imaging, cancer gene therapy, and chemotherapy (*22*−*27*).

In this article, we report the concept of modularly designed nanoparticles that separate the functional part of the nanoparticle from the targeting biomolecules. Their self-assembly through molecular recognition between the Ni-NTA molecule and the 6-histidine peptide structure enabled improved in vivo targeting imaging, effective clearance from liver and kidney, and a versatible recombination of different functional nanoparticles and different targeting biomolecules in future development.

EXPERIMENTAL PROCEDURES

Preparation of Dispersed, Water-Soluble Fe_3O_4 Nanoparticles. For preparing water-soluble and dispersed Fe_3O_4 nanoparticles, two-stage additions of protective agent and chemical coprecipitation were employed in the process (*28, 29*). Briefly, 2 M Fe(II) and 1 M Fe(III) aqueous solutions were prepared by dissolving $FeCl_2$ and $FeCl_3$, respectively. To produce Fe_3O_4 nanoparticles, 1 mL of Fe(II) and 4 mL of Fe(III) aqueous solutions were mixed at room temperature, followed by the addition of 0.5 g organic acid as adherent. Subsequently, 0.5 M NaOH was dropwise added into the mixed solution to adjust the pH. The reaction was finished when the pH of the solution reached 11. The precipitates were collected by a magnet and washed with 50 mL of deionized water three times, followed by addition of another 3 g of organic acid to achieve complete coating of the particle surface that is required for their dispersion and surface functionalization with the $-NH_3^+$ group. The excess adherents were removed by centrifugation, and the precipitates were redispersed in deionized water. The amine functional group was a portion of the adherent used to coat the surface of the nanoparticles. The adherents are organic acids that have amine groups at the same time. The nanoparticle size was determined to be about 6.2 ± 2.1 nm by TEM.

Fe_3O_4 Nanoparticle Modification, Peptide Synthesis, and Conjugation to Nanoparticles. $Fe_3O_4-NH_3^+$ nanoparticles and NTA were conjugated as previously described (*30*). Briefly, 100 μL of 0.2 M Fe_3O_4 nanoparticles were added to 46 μL of 0.22 M N^{α},N^{α}-Bis(carboxymethyl)-L-lysine, 20 μL of 55% (w/w) glutaraldehyde, and 334 μL of H_2O; the mixture was then stirred at room temperature (approximately 25 °C) for 4 h. The Fe_3O_4 nanoparticle can conjugate with NTA when glutaraldehyde and $NaBH_3CN$ were added. The amine group can conjugate with the aldehyde group of glutaraldehyde to form the C═N form; then, the C═N form was reduced to the C−N form with $NaBH_3CN$. Therefore, glutaraldehyde was a linker between the nanoparticle and NTA. The resulting precipitate (Fe_3O_4−NTA) was resuspended in 1 mL of H_2O and then centrifuged at 13 000 rpm for 20 min to remove the excess NTA. After the precipitate had been washed three times with milliQ water, resuspended in 1 mL of 1.0 M $NiSO_4$, stirred at room temperature for 8 h, and then centrifuged again to obtain the $Fe_3O_4-NTA-Ni^{2+}$ complex, cyclic RGD4C with a 6-histidine peptide residue on the C-terminal (CDCRGDCFCGGGGGGH-HHHHH) was synthesized (Genesis Biotech Inc., Taipei, Taiwan) and evaluated for self-assembly on the nanoparticle surfaces. Twenty-three microliters of 8.9 mM RGD4C-6-histidine peptide was added to 1 mL of 20 μM aqueous Ni-NTA-modified Fe_3O_4 to obtain self-assembled Fe_3O_4−NTA-Ni-RGD4C nanoparticles. As a control, the original Fe_3O_4 nanoparticles, with an amine functional group on the surface, were conjugated with the same concentration of RGD4C peptide through a conventional chemical cross-linking strategy using glutaraldehyde (nanoparticles/peptides = 1:10). After the samples had been incubated at 4 °C overnight, they were centrifuged at 13 000 rpm for 10 min, and the supernatant discarded to obtain the targeting nanoparticles.

Cell Culture and Maintenance. The HCDB-1 is a hamster oral squamous cell carcinoma cell line previously isolated and characterized by Professor Lin of National Yang-Ming University, Taiwan (*31*). The NIH3T3 mouse fibroblast cell line and human oral squamous cell carcinoma line (SCC15) were purchased from the American type Culture Collection (ATCC). OEC-M1 was established by Dr. CL Meng from a Taiwanese male oral cancer patient with areca quid chewing history. HCDB-1 and OEC-M1 were maintained in RPMI 1640 medium (Invitrogen Corp., Carlsbad, CA). SCC15 cells were maintained in Dulbecco's Modified Eagle's medium (Invitrogen Corp., Carlsbad, CA). NIH3T3 cells were maintained in Dulbecco's Modified Eagle's medium (Invitrogen Corp., Carlsbad, CA). These media were supplemented with 10% fetal bovine serum (FBS; Invitrogen Corp., Carlsbad, CA) and 1% penicillin−streptomycin (Invitrogen Corp., Carlsbad, CA). Healthy oral mucosal epithelial cells were derived from excessive retromolar gingival tissue of healthy donors with consent during surgical extraction of the third molar teeth. The oral keratinocytes were purified using a previously described method (*32*). The culture was maintained in serum-free keratinocyte growth medium (Cascade Biologics, Inc., Portland, OR) with keratinocyte growth supplement. Passage-4 cultures were used in the analysis for all studies. All cell lines were incubated at 37 °C in an atmosphere with 5% CO_2.

Ligand Competition Assay. We did a ligand competition assay using free cyclic RGD4C peptide (Genesis Biotech Inc., Taipei, Taiwan) as a competitor for the RGD-4 conjugated magnetite particles. The free RGD4C (CDCRGDCFCGGGGGG) was added to the medium to a final concentration of 3 μM for 1 h to saturate the receptor molecules on the cell surface. After they had been washed with PBS, the cells were added to a different concentration of Fe_3O_4-NTA-Ni-RGD4C and analyzed using AAS.

Biocompatibility Assay for the Fe_3O_4-NTA-Ni-RGD4C. NIH3T3 and HCDB-1 cells were cultured in 96-well culture plates at a density of 5×10^3 cells/well. Fe_3O_4-NTA-Ni-RGD4C nanoparticles of different concentrations (0.003−9.4 mg/mL) were added to each culture well and incubated for 24 h. Cell viability was determined using a 5-dimethylthiazol-2-yl-2,5-diphenyl tetrazolium bromide (MTT) assay (*33*). The systemic toxicity of the Fe_3O_4-NTA-Ni-RGD4C nanoparticles were determined in vivo using 6-week-old BALB/c mice ($n = 36$) randomly assigned to three experimental groups with different dosages of nanoparticles (1, 2.5, and 5 mg/kg groups) and one PBS control group ($n = 9$ mice/group). The nanoparticles were injected into the tail vein of each mouse. The survival and pathological symptoms and signs of each mouse were monitored for a period of one month.

Animals and Tumor Model. The male Syrian gold hamsters were purchased from the National Laboratory Animal Center (Taipei, Taiwan) and BALB/c mice from the National Cheng Kung University Laboratory Animal Center (Tainan, Taiwan). All animals were given humane care in compliance with the institution's guidelines for maintenance and use of laboratory animals in research. All experimental protocols involving live animals were reviewed and approved by the Animal Experimentation Committee of Nation Cheng Kung University. HCDB1 tumor xenografts were established by injecting 10^7 tumor cells in 100 μL of normal saline into the right buccal pouch using a 27-gauge needle. Tumors were normally visible one week after the injection. For MRI experiments, the hamsters

were anesthetized with 2% isoflurane (Abbott Laboratories, Abbott Park, IL) mixed with 100% O_2 delivered using a veterinary anesthesia delivery system (ADS 1000; Engler Engineering Corp., Hialeah, FL). The animals were given an overdose of 2.5% pentothal (Abbott Laboratories, Abbott Park, IL). Their tumor and organ tissues were harvested in the following experiments.

Atomic Absorption Spectrometry Analysis. Cells (5×10^6 cells) in a 10 cm^2 culture dish were incubated with different concentrations of nanoparticles or PBS at 4 °C for 1 h. After the cells had been washed three times with cold PBS, 5 mL of nitric acid was added to dissolve the cells. The total lysate was subjected to atomic absorption spectroscopy (AAS) (Unicam Solaar M6 series) analysis. The tumor and organ tissues were surgically harvested from the hamsters, and then 1 g of the tumor and organ tissues were isolated from the harvested tissue. After they had been homogenized, they were placed into a centrifuge tube containing 30 mL of nitric acid (12 M), and incubated for 3 days to permit complete dissolution of the tissues. The obtained liquid was analyzed using AAS.

Magnetic Resonance Imaging. Sequential MRI acquisition was done in a 3T MR imager (Biospec System; Bruker BioSpin MRI GmbH, Ettlingen, Switzerland) equipped with a high-performance gradient coil (inner diameter = 12 cm; maximal gradient strength = 200 mT m^{-1}) and a quadrature coil (inner diameter = 10 cm) for RF transmission and reception. The hamsters were anesthetized using 2% isoflurane (Abbott Laboratories, Abbott Park, IL) mixed with 100% O_2 delivered using a veterinary anesthesia delivery system (ADS 1000; Engler). Fe_3O_4-NTA-Ni-RGD4C yielded signal contrast using a T2* pulse sequence (TR/TE, 743/5 ms; MTX, 256 × 256 × 25).

Measurements MR Image of Fe_3O_4 in Tumor Site with Matlab Workstation. Three sequential axial images (1.5 mm thickness, original magnification × 1.5) of each of the 75 potential implant sites were selected ($N = 225$) using *Matlab* software to analysis. The operator determined the red circle of the ROI in all sites. The spatial coordinate tool (x, y) was manually set to define a circular or oval ROI at the same anatomic location on each of the 3 axial images. The average signal intensity of each ROI relative to that of the control (fish oil capsule indicator) was calculated. The alterations in the MR signal of the tumor site in a time series (0, 24, and 48 h) were compared to that before injection. The same method was applied for the calculation of MR signal alterations in the liver.

Histological Examination. For Prussian blue, hematoxylin, and eosin staining (H&E), the tumor tissue was fixed with 4% paraformaldehyde and paraffin-sectioned. Tissue samples were sliced into 5-μm-thick sections and then incubated with 2% potassium ferrocyanide in 6% hydrochloric acid for 30 min. After they had been washed, they were counterstained with Giemsa solution. The specimens were then mounted and examined under a light microscope (BH-2; Olympus, Tokyo, Japan).

Statistical Analysis. All experiments were repeated at least three times and the values are means ± standard deviation. Statistical analyses were done using Student's *t*-test. Statistical significance was set at $p < 0.05$.

RESULT AND DISCUSSION

We previously demonstrated that self-assembly of 6-His tagged RGD4C peptide to nanoparticle surface improved molecular orientation control and cancer cell targeting in vitro (*30*). In this article, the strategy was evaluated for in vivo cancer imaging. The superparamagnetic Fe_3O_4 nanoparticles (6.2 ± 2.1 nm) in aqueous solution were conjugated with RGD4C peptide through traditional chemical conjugation (Fe_3O_4-RGD4C) or the self-assembly on the particle surface method (Fe_3O_4-NTA-Ni-RGD4C) (Scheme 1).

Scheme 1. Schematic Diagram Illustrating Two Different Bioconjugation Methods[a]

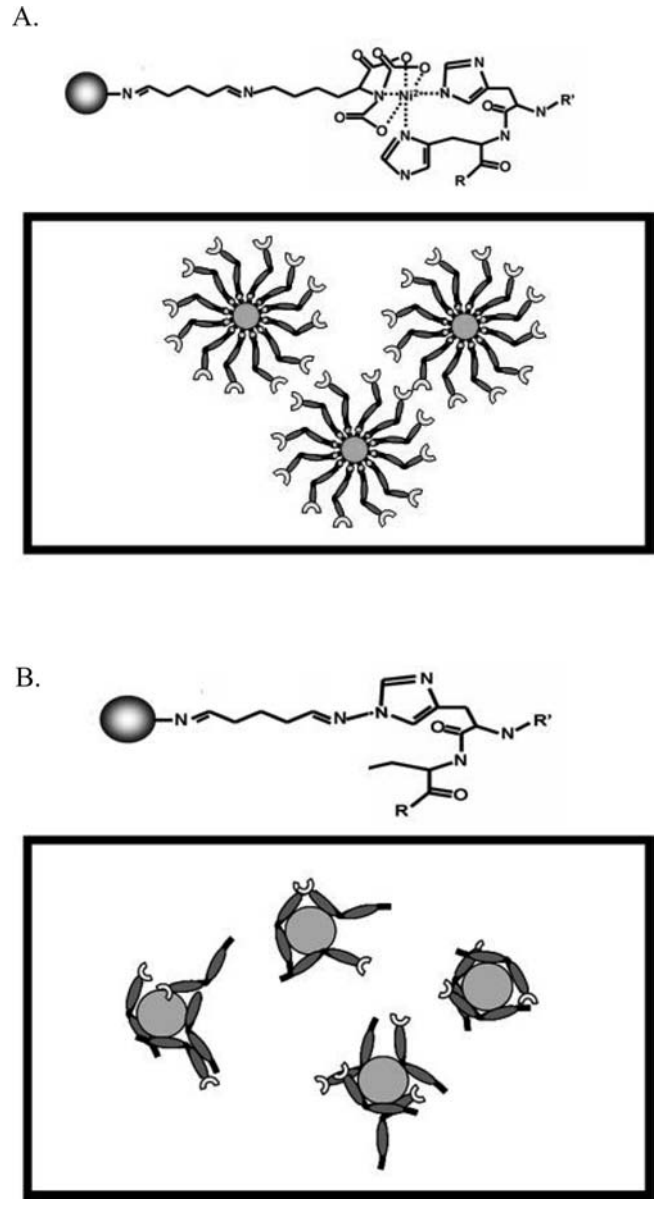

[a] (A) The modular-targeting nanoparticles with orientation control made through self-assembly of the molecular key (Ni^{2+}-NTA) on the particle and the molecular lock (6-His tag) on the peptide. (B) The traditional chemical cross-linking using glutaraldehyde usually derived a peptide−nanoparticle complex with random molecular orientation because multiple sites on the peptide are available for conjugation.

Cytotoxicity of Fe_3O_4-NTA-Ni-RGD4C Nanoparticles. The cytotoxicity of the nanoparticles was evaluated using both HCDB1 (Figure 1A) and NIH3T3 cells (seeSupporting Information S1) using MTT assay. The results showed satisfactory (>80%) biocompatibility at a particle concentration below 0.376 mg/mL (Figure 1A) in both cell lines. This particle concentration was sufficient to produce a significant MR contrast effect in vivo (*28*). The inhibition in cell growth at high dosages (1.88 and 9.4 mg/mL) may attribute to the interaction of the targeting peptide with the integrin signaling pathway. The nanoparticle concentrations were referenced to iron concentration determined from AA (atomic absorption) spectrometry. Selective binding of RGD-4C peptide to $\alpha v\beta 3$ and $\alpha v\beta 5$ integrins in human

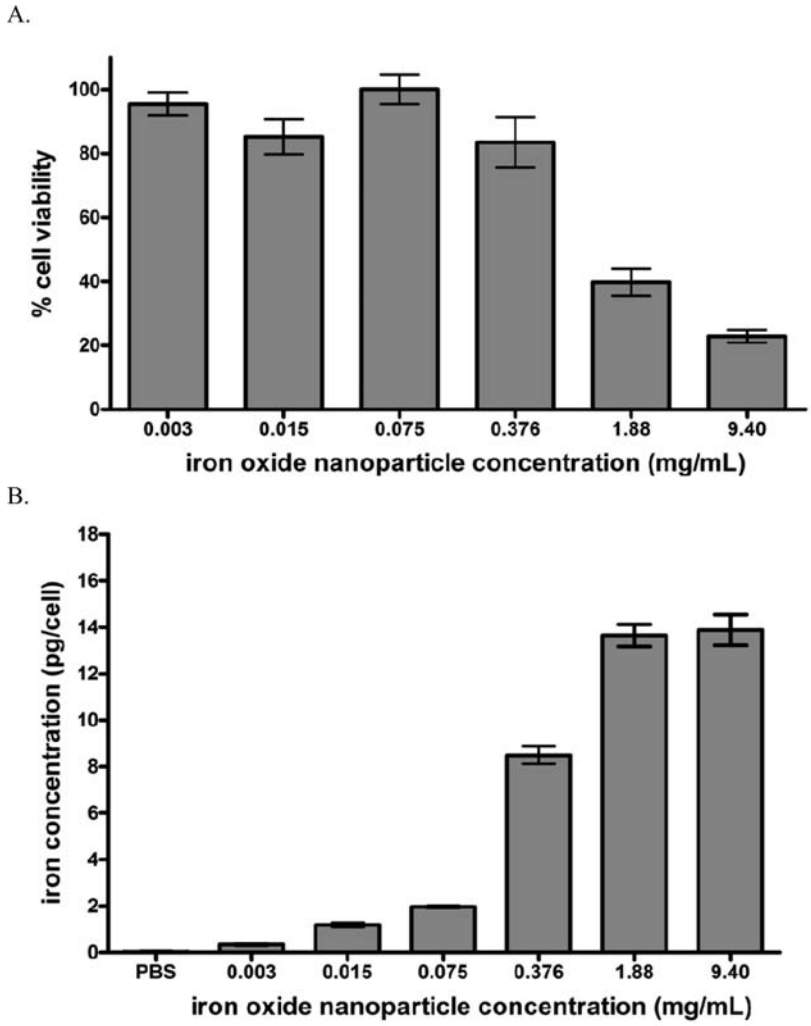

Figure 1. The biocompatibility of the nanoparticles was evaluated using MTT assay. (A) The cell viability of HCDB1 with different nanoparticle concentrations was analyzed. Biocompatibility was satisfactory at doses lower than 1.25 μM. Targeting of the self-assembled Fe_3O_4-NTA-Ni-RGD4C nanoparticles to HCDB1 cells as a function of the nanoparticle concentration was evaluated. (B) HCDB1 cells (5×10^6 cells/dish) were cultured in 10 cm^2 culture dishes and exposed to nanoparticles of different concentrations for 1 h before a quantitative atomic absorption spectroscopy analysis of the iron in the cells.

umbilical endothelial cells (HUVECs) have been reported to induce cellular detachment, caspase-8 activation, and apoptosis (*34*).

Dose-Dependent Affinity Targeting of Fe_3O_4-NTA-Ni-RGD4C Nanoparticles. The dosage-dependent affinity targeting of Fe_3O_4-NTA-Ni-RGD4C nanoparticles to HCDB1 cells that express $\alpha v\beta 3$ was analyzed in vitro by AAS quantification of total cell lysate. A dosage-dependent affinity targeting of HCDB-1 cells by the self-assembled nanoparticles was observed (Figure 1B). The targeting reached a plateau at 1.88 mg/mL concentration, while it was about 64% of the plateau at the biocompatible concentration of 0.376 mg/mL. We then evaluated the selectivity of the targeting nanoparticles toward cancerous oral epithelial cells at 0.376 mg/mL of nanoparticle concentration.

Selective Targeting of Fe_3O_4-NTA-Ni-RGD4C Nanoparticles. Three oral cancer cell lines (HCDB-1, OEC-M1, and SCC15) and one primary culture normal human oral keratinocytes (hNOK) were targeted by 0.376 mg/mL of Fe_3O_4-NTA-Ni-RGD4C or Fe_3O_4-RGD4C at 4 °C for 1 h to evaluate (1) whether Fe_3O_4-NTA-Ni-RGD4C self-assembled nanoparticles selectively bind to the selected cancer cells but not their normal counterpart healthy cells and (2) whether this modularly assembled complex exhibits at a higher targeting efficiency than that of the conventional direct chemical conjugation using the same total amount of targeting peptide for conjugation. The cells were processed for AAS analysis to calculate the total amount of the nanoparticles targeted onto the cells. The cancer cells showed a significantly ($P < 0.0001$) higher targeting efficiency than did the hNOK (range from 7.2:1 to 3.5:1). In all groups of the in vitro targeting analysis, the self-assembled Fe_3O_4-NTA-Ni- RGD4C nanoparticles outperformed the Fe_3O_4-RGD4C nanoparticles ($P < 0.001$) (Figure 2A).

To examine the specifics of the targeting, we did a ligand competition assay. The results indicated that free RGD4C peptide was highly specific and selective, as it significantly restricts the targeting efficiency in all groups with a range 23−33% for self-assembled Fe_3O_4-NTA-Ni-RGD4C nanoparticles and 40−53% for conventional Fe_3O_4-RGD4C nanoparticles (Figure 2B). It is well-known that cyclic RGD4C peptide has a specific affinity for $\alpha v\beta 3$ integrins that are selectively expressed in some tumor cells and their neoangiogenic tissue (*20, 21, 35*). An improved targeting efficiency may attribute to the increased molecular-orientation control through the on-particle self-assembly of the targeting peptide enabled by the engineered affinity peptide "lock" (6-histidine) for the Ni-NTA "key" on the nanoparticle surface (Scheme 1A).

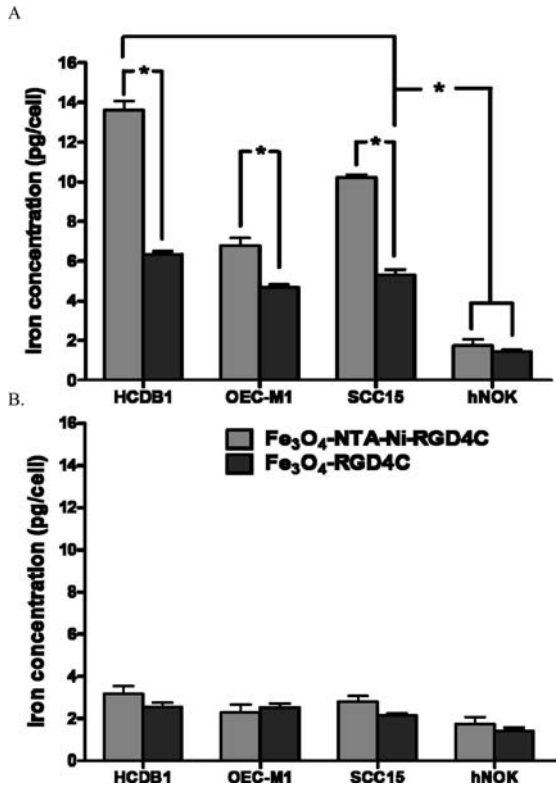

Figure 2. Atomic absorption spectroscopy analysis of the specificity and targeting efficiency for Fe_3O_4-RGD4C nanoparticles and self-assembled Fe_3O_4-NTA-Ni-RGD4C nanoparticles to oral cancer cells compared to their specificity and targeting efficiency for healthy oral keratinocytes (hNOK). (A) Both types of nanoparticles showed improved cancer cell targeting. Self-assembled targeting nanoparticles consistently outperformed the conventionally prepared nanoparticles. (B) A competition assay was done using RGD4C peptide. The affinity targeting of the nanoparticles was significantly inhibited in all groups. *, $P < 0.001$. The iron concentration for the untreated cells in all groups were between 0.06 and 0.09 pg/cell. The iron concentration of the nanoparticle treated cells presented in the chart has been subtracted from their baseline iron levels.

Biocompatibility of Fe_3O_4-NTA-Ni-RGD4C Nanoparticles in Vivo. To further explore in vivo use of the self-assembled Fe_3O_4-NTA-Ni-RGD4C nanoparticles, we analyzed their in vivo biocompatibility. The hemocompatibility of Fe_3O_4-NTA-Ni has been reported (*30*). To determine the in vivo systemic toxicity, the Fe_3O_4-NTA-Ni-RGD4C nanoparticles were injected into the tail vein of 36 6-week-old BALB/c mice with PBS as a control. We monitored the survival and pathological symptoms and signs of each mouse for one month. Only 2 mice died, 1 in the 2.5 mg/kg group on day 17, and 1 in the 5 mg/kg group on day 10. These results suggested that the RGD4C self-assembled Fe_3O_4 nanoparticles are safe for in vivo applications within the dosage range for effective MR contrast (Figure 3) (*28*).

Molecular MR Imaging of Oral Cancer Using Fe_3O_4-NTA-Ni-RGD4C Nanoparticles. We then evaluated the molecular imaging of cancer lesions for specific integrin membrane protein in orthotopic hamster buccal pouch oral cancer model. For the MRI of each tumor lesion, we injected Fe_3O_4-NTA-Ni-RGD4C or the control Fe_3O_4-Ni-NTA at a concentration of 5 mg/kg through the right jugular vein and then sequentially acquired images at 1, 6, 12, 24, and 48 h intervals in a 3T MR imager. Fe_3O_4-NTA-Ni-RGD4C yielded a specifically targeted negative contrast image of the oral cancer lesion within 24 h using a T2* pulse sequence (TR/TE, 743/5 ms; MTX, 256 × 256 × 25) (Figure 4A). The signal contrast persisted for at least 48 h after self-assembled Fe_3O_4-NTA-Ni-RGD4C nanoparticles had been intravenously injected. In order to evaluate whether the conjugation of RGD4C to iron oxide nanoparticles would affect its hepatic uptake, Fe_3O_4-NTA-Ni (5 mg/kg) with or without self-assembly with RGD4C-6-his were injected into each hamster's jugular vein, and then a series of MRI taken.

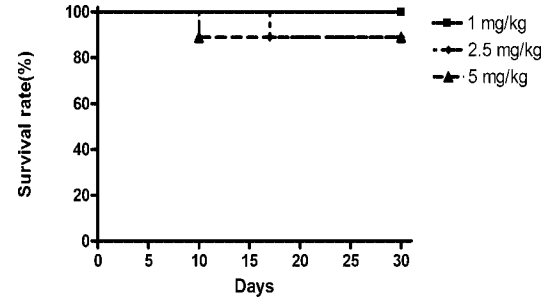

Figure 3. Survival analysis of BALB/c mice exposed to 1, 2.5, and 5 mg/kg of the self-assembled Fe_3O_4-NTA-Ni-RGD4C targeting nanoparticles ($n = 9$). In vivo biocompatibility was satisfactory.

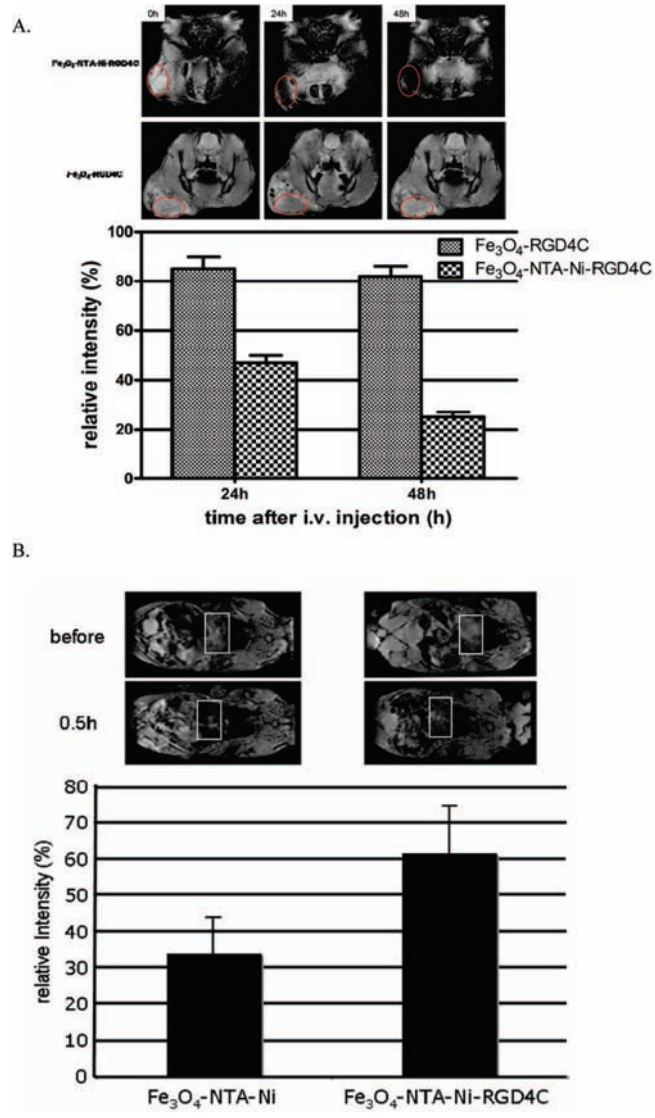

Figure 4. (A) In vivo molecular magnetic resonance imaging of oral cancer in a hamster model shows significant inverse contrast T2* images 24 and 48 h after i.v. injection of the Fe_3O_4-NTA-Ni-RGD4C and Fe_3O_4-RGD4C nanoparticles. (The red circled areas indicate the orthotopically induced tumor lesion). (B) Quantitative measurement (*Matlab* software) of tissue signal intensity showed that modifying the magnetite nanoparticles with the self-assembled targeting moiety (RGD4C) significantly decreased their absorption in the liver.

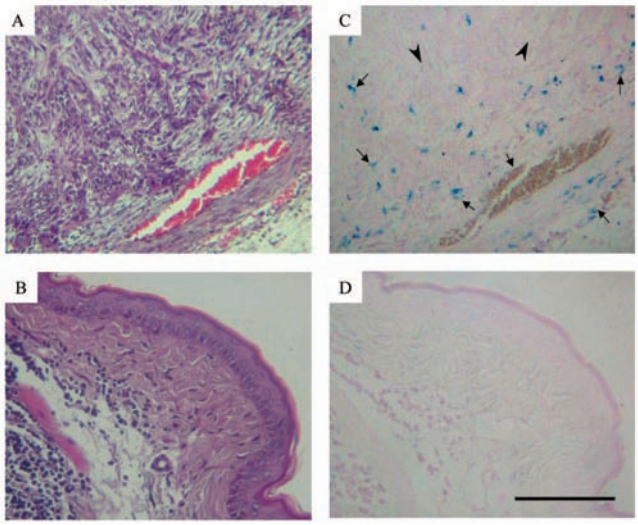

Figure 5. Oral cancer tissue and healthy oral mucosal tissue from the same hamster taken 24 h after i.v. injection of the Fe_3O_4-NTA-Ni-RGD4C nanoparticles was processed for histological and histochemical analysis. (A) Hematoxylin and eosin-stained cancer tissue showed that cancer cells had invaded through the connective tissue with numerous neoangiogenic blood vessels. (B) healthy oral mucosal tissue on the contralateral site. (C) Pearl's iron stain of the adjacent section showed a diffuse bluish-purple in the tumor tissue (arrowheads) with significant accumulation in the endothelial cells (arrows) and some macrophages. (D) Healthy oral mucosal tissue showed only pink background counterstain. (Scale bar: 100 μm.)

The signal intensity of the nanoparticles was quantified in 10 randomly selected areas of the liver. The self-assembled Fe_3O_4-NTA-Ni-RGD4C showed significantly lower hepatic uptake (39% reduction of signal intensity 30 min after i.v. injection) than the Fe_3O_4-NTA-Ni without a targeting peptide (66%) (Figure 4B).

Histological Analysis. To explore the distribution of Fe_3O_4-NTA-Ni-RGD4C nanoparticles in tumor and healthy oral mucosal tissue, a histological examination of formalin-fixed paraffin-embedded tumor and healthy tissue was performed on the surgically removed specimens 24 h after delivery of the nanoparticles. Tissue samples were analyzed for H&E (Figure 5A,B) or Pearl's iron stain (Figure 5C,D). Tumor cells (upper left region of Figure 5A) showed light bluish-purple Pearl's iron staining (Figure 5B, arrowheads) in contrast to healthy oral mucosal tissue (Figure 5C) that showed only pinkish background staining (Figure 5D). This indicates an increased uptake of the targeting iron oxide nanoparticles by the tumor cells. Some of the capillary structure of the tumor lesion and the surrounding neoangiogenic blood vessels showed a strong bluish staining (Figure 5B, arrows) from accumulated targeting nanoparticles, which was not present in healthy oral mucosal tissue (Figure 5D).

In Vivo Targeting Efficiency in the Tumor Lesions Quantified Using AAS. The in vivo targeting efficiency in the tumor lesions was quantified using AAS at a series of time points after Fe_3O_4-RGD4C nanoparticles or self-assembled Fe_3O_4-NTA-Ni-RGD4C nanoparticles had been intravenously injected. The Fe^{2+} concentration peaked 24 h after the injection for both types of nanoparticles and then decreased to the original background level after 72 h (Figure 6A). At all observation points, significantly higher Fe^{2+} concentration was detected in tumor tissue targeted by Fe_3O_4-NTA-Ni-RGD4C nanoparticles than in tumor tissue targeted by Fe_3O_4-RGD4C nanoparticles. The MR image analysis show significant decrease in the tumor signal intensity (47%) from 0 to 24 h (Figure 4A) followed by a decrease from 24 to 48 h (25%). Quantitative analysis of AA

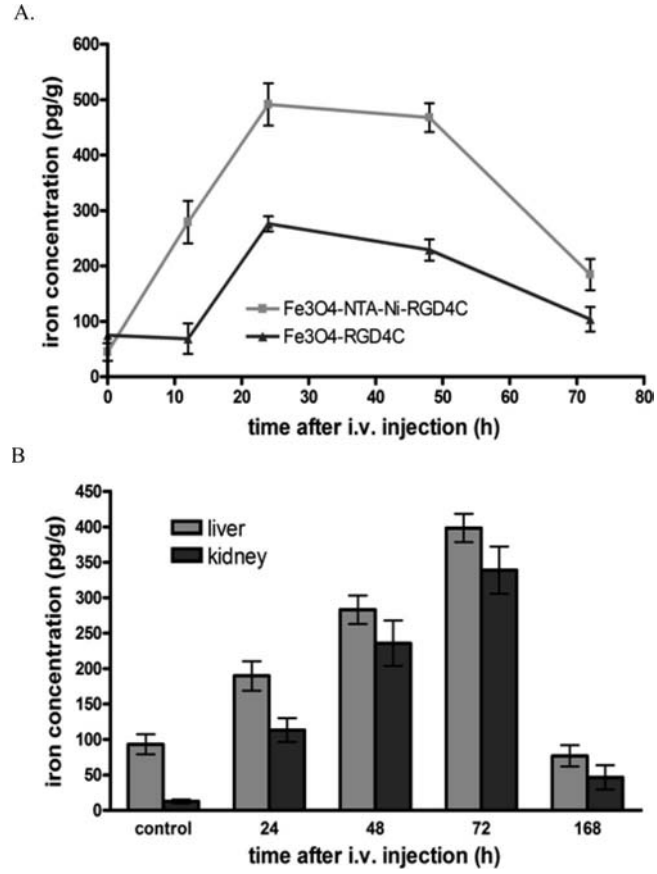

Figure 6. Hamster oral cancer lesions were surgically removed at each time point indicated and then evaluated, using atomic absorption spectroscopic quantitative analysis, for nanoparticle accumulation. (A) The accumulation of Fe_3O_4-NTA-Ni-RGD4C and Fe_3O_4-RGD4C nanoparticles (iron concentration). (B) The accumulation of Fe_3O_4-NTA-Ni-RGD4C in the liver and the kidneys was analyzed after i.v. injection of the nanoparticles.

revealed no statistical difference between iron oxide concentrations at 24 and 48 h ($p = 0.11$). The decrease in the MRI signal intensity at 48 h, while slightly decreasing the tissue iron concentration, could be explained by the aggregation of iron oxide nanoparticles in tissue or cells. A previous report demonstrated that the aggregation of magnetic particles can enhance the T2 or T2* volume in the magnetic field (*36, 37*). Nevertheless, all these data indicate that the self-assembled targeting iron oxide nanoparticles in the current report could be retained in the tumor site for at least 48 h for prolonged observation.

Biodistribution and Excretion of Iron Oxide Nanoparticles. The in vivo biodistribution of the Fe_3O_4-NTA-Ni-RGD4C nanoparticles in the liver and kidneys over time was evaluated using AAS analysis. The organs were processed for AAS analysis as described in the Experimental Procedures. The liver and kidneys were surgically removed from the hamsters at 24, 48, 72, and 168 h after injection with Fe_3O_4-NTA-Ni-RGD4C or PBS. Nanoparticles gradually accumulated in the liver and kidneys and peaked 72 h after injection (Figure 6B). The iron signal in the liver tissue returned to the normal level 168 h after i.v. injection, while decreasing to 8% of the peak level in kidney tissue at the same time point.

Using MRI to retrieve the information of molecular imaging and to track the progression of a certain disease targeting is highly valuable for disease management. A wide range of MR molecular imaging approaches for cancers have been extensively investigated (*38, 39*). However, the key has been the design of imaging probes that can sensitively relay

specific molecular recognition of certain components or pathways in cancer cells with high sensitivity. This allows for signal acquisition and image reconstruction. In vivo iron oxide-based molecular imaging modalities have also been recently reported (*40*, *41*). To the best of our knowledge, our findings here are the first to illustrate the concept of functional nanoparticles that are modularly assembled for in vivo targeted molecular imaging.

As stated above, integrin $\alpha v\beta 3$ is selectively overexpressed in the cancer and neoangiogenic blood vessels, but at a much lower level in mature quiescent cells (*42*). As a result of such expression specificity, it was chosen as the target for molecular imaging in the current study. We showed, both in vivo and in vitro, that the molecular self-assembled modular design performed better than the conventional direct chemical cross-link design in affinity targeting of cancer cells. MRI, using self-assembled nanoparticles, clearly demonstrated a cancer-specific image contrast and a relatively normal image contrast of liver tissue, superior to MRI using non-self-assembled nanoparticles. Nanoparticles are known to be easily trapped and absorbed by the RES system (*43*, *44*), especially in the liver, and normally required for special biological stealth modifications by the surface decoration of polymers such as poly(ethylene glycol) (PEG) before in vivo applications. In the present study, self-assembly of RGD4C on the nanoparticles also significantly decreased the nonspecific uptake of magnetite into the liver without additional surface modifications (Figure 4B). AAS spectroscopy also showed that nanoparticles were retained in tumor tissue for more than 48 h (Figure 6A), which allowed in vivo imaging tracking of the tumor. The results were consistent with those obtained from the iron-stained histological sections of cancer and normal mucosa tissues where only cancer tissues presented significant accumulation of the targeting nanoparticles. The nanoparticles went through metabolic clearance after about a week in the liver and the kidneys (Figure 6B), suggesting their safety as a targeting contrast agent with a traceable clearance mechanism.

CONCLUSION

The new concept of modular nanoparticle platform presented in this report enabled us to compile a library of targeting diagnostic and therapeutic agents (Supporting Information Figure S2). These agents could be sufficiently versatile for individual patient-based combinational assembly of the targeting moiety for a specific clinical need. They may meet the requirements of a variety of medial diagnostic and therapeutic purposes through selection of appropriate nanoparticle modules suitable for respective modalities, for example, magnetite nanoparticle for MRI in this report. This new concept may also fulfill the need of reduction in preparation time and transportation costs. It also allows prolonging of the half-life of the bionanoparticle-based agents, because the two modules can be stored separately in optimized environments before use. It is our goal to further enhance our current design so that it will make a significant contribution to advancement of translational applications using targeting nanoparticles in future medicine.

ACKNOWLEDGMENT

We thank the National Science Council of Taiwan for supporting this research with grants NSC95-95-2120-M-006-013, NSC-95-2120-M-006-006, NSC-95-2314-B-006-014, and NSC94-2120-M-006-004.

Supporting Information Available: Additional information for the cytotoxicity in NIH3T3 cells and an illustration for the concept of key and key lock modular design. This material is available free of charge via the Internet at http://pubs.acs.org.

LITERATURE CITED

(1) Shapiro, E. M., Sharer, K., Skrtic, S., and Koretsky, A. P. (2006) In vivo detection of single cells by MRI. *Magn. Reson. Med. 55*, 242–249.

(2) Lee, J. H., and Koretsky, A. P. (2004) Manganese enhanced magnetic resonance imaging. *Curr. Pharm. Biotechnol. 5*, 529–537.

(3) Bluemke, D. A., Sahani, D., Amendola, M., Balzer, T., Breuer, J., Brown, J. J., Casalino, D. D., Davis, P. L., Francis, I. R., Krinsky, G., Lee, F. T., Jr., Lu, D., Paulson, E. K., Schwartz, L. H., Siegelman, E. S., Small, W. C., Weber, T. M., Welber, A., and Shamsi, K. (2005) Efficacy and safety of MR imaging with liver-specific contrast agent: U.S. multicenter phase III study. *Radiology 237*, 89–98.

(4) Nishimura, H., Tanigawa, N., Hiramatsu, M., Tatsumi, Y., Matsuki, M., and Narabayashi, I. (2006) Preoperative esophageal cancer staging: magnetic resonance imaging of lymph node with ferumoxtran-10, an ultrasmall superparamagnetic iron oxide. *J. Am. Coll. Surg. 202*, 604–611.

(5) Cheng, F. Y., Su, C. H., Yang, Y. S., Yeh, C. S., Tsai, C. Y., Wu, C. L., Wu, M. T., and Shieh, D. B. (2005) Characterization of aqueous dispersions of Fe(3)O(4) nanoparticles and their biomedical applications. *Biomaterials 26*, 729–38.

(6) Lee, H., Lee, E., Kim do, K., Jang, N. K., Jeong, Y. Y., and Jon, S. (2006) Antibiofouling polymer-coated superparamagnetic iron oxide nanoparticles as potential magnetic resonance contrast agents for in vivo cancer imaging. *J. Am. Chem. Soc. 128*, 7383–7389.

(7) Muller, K., Skepper, J. N., Posfai, M., Trivedi, R., Howarth, S., Corot, C., Lancelot, E., Thompson, P. W., Brown, A. P., and Gillard, J. H. (2007) Effect of ultrasmall superparamagnetic iron oxide nanoparticles (Ferumoxtran-10) on human monocyte-macrophages in vitro. *Biomaterials 28*, 1629–1642.

(8) Lencioni, R., and Bartolozzi, C. (2004) Clinical impact of Resovist-enhanced MRI: results of an Italian multicenter trial. *Eur. Radiol.* 14 Suppl 1, C10.

(9) Corot, C., Robert, P., Idee, J. M., and Port, M. (2006) Recent advances in iron oxide nanocrystal technology for medical imaging. *Adv. Drug Delivery Rev. 58*, 1471–1504.

(10) Gohr-Rosenthal, S., Schmitt-Willich, H., Ebert, W., and Conrad, J. (1993) The demonstration of human tumors on nude mice using gadolinium-labelled monoclonal antibodies for magnetic resonance imaging. *Invest. Radiol. 28*, 789–795.

(11) Lee, J. H., Huh, Y. M., Jun, Y. W., Seo, J. W., Jang, J. T., Song, H. T., Kim, S., Cho, E. J., Yoon, H. G., Suh, J. S., and Cheon, J. (2007) Artificially engineered magnetic nanoparticles for ultra-sensitive molecular imaging. *Nat. Med. 13*, 95–99.

(12) Juang, R. S., and Wang, Y. C. (2003) Use of complexing agents for effective ion-exchange separation of Co(II)/Ni(II) from aqueous solutions. *Water Res. 37*, 845–852.

(13) Bhattacharyya, R., Saha, R. P., Samanta, U., and Chakrabarti, P. (2003) Geometry of interaction of the histidine ring with other planar and basic residues. *J. Proteome Res. 2*, 255–263.

(14) Xu, C., Xu, K., Gu, H., Zhong, X., Guo, Z., Zheng, R., Zhang, X., and Xu, B. (2004) Nitrilotriacetic acid-modified magnetic nanoparticles as a general agent to bind histidine-tagged proteins. *J. Am. Chem. Soc. 126*, 3392–3393.

(15) Kim, J. S., Valencia, C. A., Liu, R., and Lin, W. (2007) Highly-efficient purification of native polyhistidine-tagged proteins by multivalent NTA-modified magnetic nanoparticles. *Bioconjugate Chem. 18*, 333–341.

(16) Brooks, P. C., Clark, R. A., and Cheresh, D. A. (1994) Requirement of vascular integrin alpha v beta 3 for angiogenesis. *Science 264*, 569–571.

(17) Friedlander, M., Brooks, P. C., Shaffer, R. W., Kincaid, C. M., Varner, J. A., and Cheresh, D. A. (1995) Definition of two

angiogenic pathways by distinct alpha v integrins. *Science 270*, 1500–1502.

(18) Hood, J. D., and Cheresh, D. A. (2002) Role of integrins in cell invasion and migration. *Nat. Rev. Cancer 2*, 91–100.

(19) Jin, H., and Varner, J. (2004) Integrins: roles in cancer development and as treatment targets. *Br. J. Cancer 90*, 561–565.

(20) Koivunen, E., Wang, B., and Ruoslahti, E. (1995) Phage libraries displaying cyclic peptides with different ring sizes: ligand specificities of the RGD-directed integrins. *Biotechnology (N. Y.) 13*, 265–270.

(21) de Groot, F. M., Broxterman, H. J., Adams, H. P., van Vliet, A., Tesser, G. I., Elderkamp, Y. W., Schraa, A. J., Kok, R. J., Molema, G., Pinedo, H. M., and Scheeren, H. W. (2002) Design, synthesis, and biological evaluation of a dual tumor-specific motive containing integrin-targeted plasmin-cleavable doxorubicin prodrug. *Mol. Cancer Ther. 1*, 901–911.

(22) Pasqualini, R., and Ruoslahti, E. (1996) Organ targeting in vivo using phage display peptide libraries. *Nature 380*, 364–366.

(23) Arap, W., Pasqualini, R., and Ruoslahti, E. (1998) Cancer treatment by targeted drug delivery to tumor vasculature in a mouse model. *Science 279*, 377–80.

(24) Hong, F. D., and Clayman, G. L. (2000) Isolation of a peptide for targeted drug delivery into human head and neck solid tumors. *Cancer Res. 60*, 6551–6556.

(25) Wang, F., Malac, M., and Egerton, R. F. (2006) Energy-loss near-edge fine structures of iron nanoparticles. *Micron 37*, 316–323.

(26) Montet, X., Montet-Abou, K., Reynolds, F., Weissleder, R., and Josephson, L. (2006) Nanoparticle imaging of integrins on tumor cells. *Neoplasia 8*, 214–222.

(27) de la Fuente, J. M., Berry, C. C., Riehle, M. O., and Curtis, A. S. (2006) Nanoparticle targeting at cells. *Langmuir 22*, 3286–3293.

(28) Shieh, D. B., Cheng, F. Y., Su, C. H., Yeh, C. S., Wu, M. T., Wu, Y. N., Tsai, C. Y., Wu, C. L., Chen, D. H., and Chou, C. H. (2005) Aqueous dispersions of magnetite nanoparticles with NH3+ surfaces for magnetic manipulations of biomolecules and MRI contrast agents. *Biomaterials 26*, 7183–7191.

(29) R. O.C. Patent 202070; German Patent 102004035803.

(30) Shieh, D. B., C. H. Su, C. H., Chang, F. Y., Wu, Y. N., Su, W. C., Hwu, J. R., Chen, J. H., and Yeh, C. S. (2006) Aqueous nickel-nitrilotriacetate modified Fe_3O_4-NH^{+3} nanoparticles for protein purification and cell targeting. *Nanotechnology 17*, 4174–4182.

(31) Lin, S. C., Chang, K. W., Chang, C. S., Yu, S. Y., Chao, S. Y., and Wong, Y. K. (2000) Establishment and characterization of a cell line (HCDB-1) derived from a hamster buccal pouch carcinoma induced by DMBA and Taiwanese betel quid extract. *Proc. Natl. Sci. Counc., Repub. China, Part B: Basic Sci. 24*, 129–135.

(32) Kim, M. S., Li, S. L., Bertolami, C. N., Cherrick, H. M., and Park, N. H. (1993) State of p53, Rb and DCC tumor suppressor genes in human oral cancer cell lines. *Anticancer Res. 13*, 1405–1413.

(33) Mosmann, T. (1983) Rapid colorimetric assay for cellular growth and survival: application to proliferation and cytotoxicity assays. *J. Immunol. Methods 65*, 55–63.

(34) Lin, C. L., Lee, C. F., and Chiu, W. Y. (2005) Preparation and properties of poly(acrylic acid) oligomer stabilized super-paramagnetic ferrofluid. *J. Colloid Interface Sci. 291*, 411–420.

(35) Goede, V., Fleckenstein, G., Dietrich, M., Osmers, R. G., Kuhn, W., and Augustin, H. G. (1998) Prognostic value of angiogenesis in mammary tumors. *Anticancer Res. 18*, 2199–2202.

(36) Koh, I., Hong, R., Weissleder, R., and Josephson, L. (2008) Sensitive NMR sensors detect antibodies to influenza. *Angew. Chem., Int. Ed. 47*, 4119–4121.

(37) Perez, J. M., Josephson, L., O'Loughlin, T., Hogemann, D., and Weissleder, R. (2002) Magnetic relaxation switches capable of sensing molecular interactions. *Nat. Biotechnol. 20*, 816–820.

(38) Mulder, W. J., Koole, R., Brandwijk, R. J., Storm, G., Chin, P. T., Strijkers, G. J., de Mello Donega, C., Nicolay, K., and Griffioen, A. W. (2006) Quantum dots with a paramagnetic coating as a bimodal molecular imaging probe. *Nano Lett. 6*, 1–6.

(39) Saksena, M. A., Saokar, A., and Harisinghani, M. G. (2006) Lymphotropic nanoparticle enhanced MR imaging (LNMRI) technique for lymph node imaging. *Eur. J. Radiol. 58*, 367–374.

(40) Thorek, D. L., Chen, A. K., Czupryna, J., and Tsourkas, A. (2006) Superparamagnetic iron oxide nanoparticle probes for molecular imaging. *Ann. Biomed. Eng. 34*, 23–38.

(41) Medarova, Z., Pham, W., Kim, Y., Dai, G., and Moore, A. (2006) In vivo imaging of tumor response to therapy using a dual-modality imaging strategy. *Int. J. Cancer 118*, 2796–2802.

(42) Sipkins, D. A., Cheresh, D. A., Kazemi, M. R., Nevin, L. M., Bednarski, M. D., and Li, K. C. (1998) Detection of tumor angiogenesis in vivo by alphaVbeta3-targeted magnetic resonance imaging. *Nat. Med. 4*, 623–626.

(43) Kreuter, J. (1994) Drug targeting with nanoparticles. *Eur. J. Drug Metab. Pharmacokinet. 19*, 253–256.

(44) Araujo, L., Lobenberg, R., and Kreuter, J. (1999) Influence of the surfactant concentration on the body distribution of nanoparticles. *J. Drug Targeting 6*, 373–385.

BC800092W

Supporting information

Modularly Assembled Magnetite Nanoparticles Enhance in vivo Targeting for Magnetic Resonance Cancer Imaging

Ping-Ching Wu[†], Chia-Hao Su[‡], Fong-Yu Cheng[§], Jun-Cheng Weng[‡], Jyh-Horng Chen[‡], Tsung-Lin Tsai[†], Chen-Sheng Yeh[§], Wu-Chou Su[∥], Jih-Ru Hwu[⊥], Yonhua Tzeng[±], Dar-Bin Shieh[#,*]

[#]Institute of Oral Medicine and Department of Stomatology and Center for Micro/Nano Science and Technology, National Cheng Kung University, Tainan 701, Taiwan. email, dshieh@mail.ncku.edu.tw; Tel, 886-6-235-3535 ext. 5377; Fax, 886-6-276-6626

S1……Figure S1

S2……Figure S2

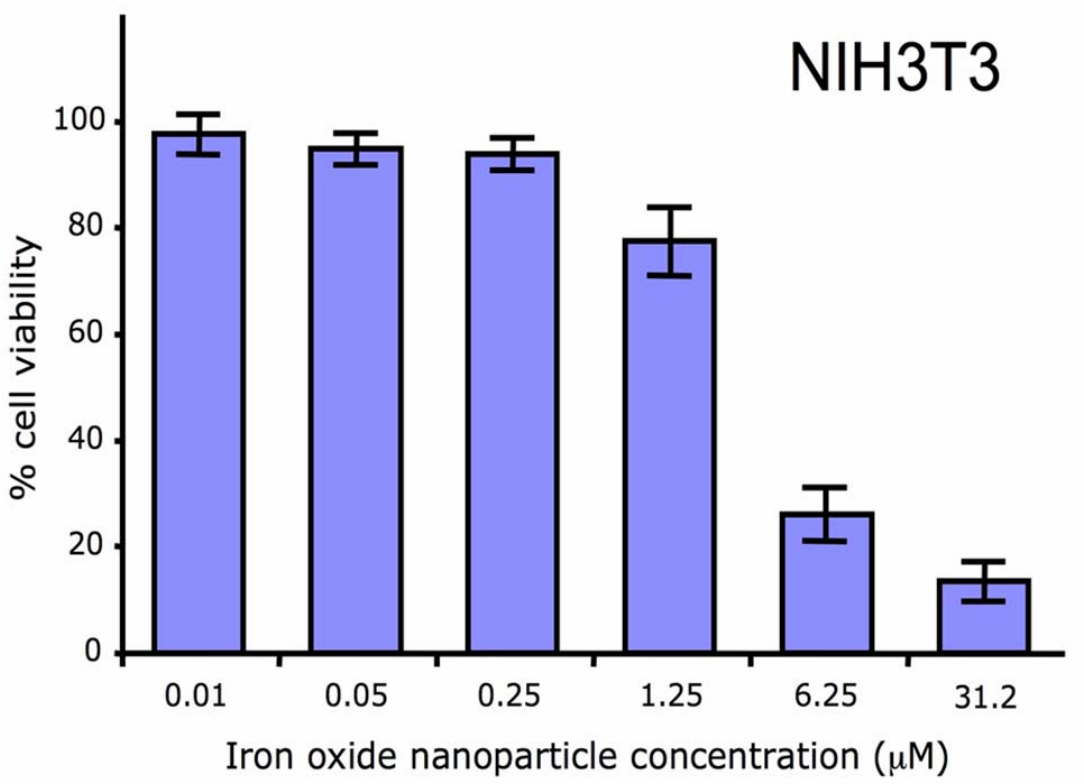

Figure S1. To evaluate the biocompatibility of the nanoparticles, NIH3T3 cells were cultured in 96-well plates. Fe_3O_4-NTA-Ni-RGD4C nanoparticles at different concentrations (range: 0.01-31 μM) were added to each culture well and incubated for an additional 24 h before the spectrophotometric quantification of cell viability using an MTT assay. Cell viability was satisfactory (> 80%) at a particle concentration below 1.25 μM.

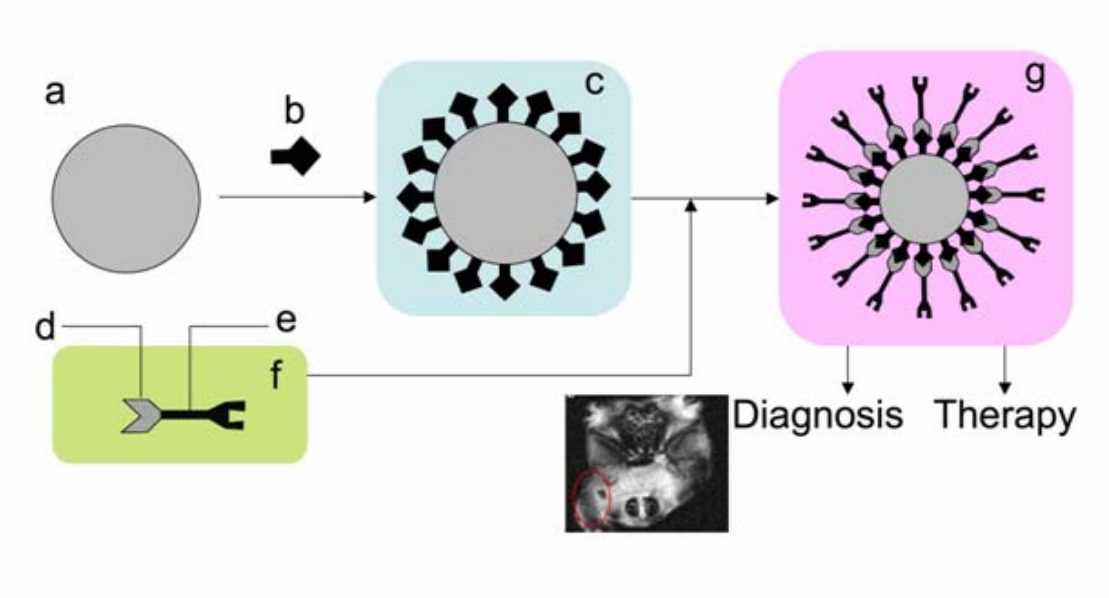

Figure S2. We developed a new concept of modular-targeting functional nanoparticles through self-assembly of the targeting moiety and the functional nanoparticles by modifying the nanoparticle surface with a small "key molecule" and the targeting peptide or recombinant antibody with an affinity peptide tag for the "lock molecule".

Schematic diagram illustrating the concept of modular-targeting functional nanoparticles for diagnostic imaging and therapeutic applications. Nanoparticle module (c) is composed of a functional nanoparticle (a) with a common surface "key molecule" (b), Ni-NTA for example, to self-assemble with targeting moieties in biomolecular module (d~f). Biomolecular module (f) is composed of a biomolecule (d) such as antibody or a peptide with a genetically engineered “lock molecule” (e) tag (6-his domain for example) for binding to "key molecules" on the nanoparticles. The two modules self-assembled to form functional targeting nanoparticles (g) that not only gives a versatile combination for biological end and the nanoparticle end based on clinical applications , but also may improve the targeting because of the orientation-control and enrichment of the effective targeting moiety through self-assembly.

An RGD-Modified Endostatin-Derived Synthetic Peptide Shows Antitumor Activity *in Vivo*

Han-Mei Xu,[†] Runting Yin,[†] Luosheng Chen,[†] Sami Siraj,[†] Xiaofeng Huang,[‡] Min Wang,[†] Huisheng Fang,[†] and Ying Wang*,[†]

Department of Life Science and Technology, China Pharmaceutical University, Nanjing, 210009, and Department of Oral Pathology, Nanjing Stamotology Hospital, Affiliated Medical School, Nanjing University, 210008, P. R. China. Received April 1, 2008; Revised Manuscript Received August 22, 2008

It has been reported that an endostatin-derived synthetic peptide, named ES-2, that contains the amino acids 60−70 of endostatin from its N terminus, efficiently inhibits basic fibroblast growth factor-induced directional migration and tubular morphogenesis of microvascular endothelial cells. We found that the peptide had no effects on tumor growth *in vivo*. However, when the peptide Arg-Gly-Asp (RGD) was introduced into ES-2, the modified ES-2 showed significant antitumor results in animal models. Histochemical and immunohistochemical analysis showed that RGD-modified ES-2 induced large areas of continuous necrosis within tumors and significantly reduced the vessel density compared to control. Furthermore, only the peptides with RGD were able to bind tumor cells *in vitro*, suggesting that additional RGD domains may help in improving the receptor-binding ability and pharmacokinetic properties of ES-2 and preventing organic clearance, as well as enzymatic degradation of the peptide, thus enabling a greater fraction of the administered dose to be biologically available.

INTRODUCTION

Endostatin, the C-terminal fragment of collagen XVIII with a molecular weight of 20 kDa, has been approved by the State Food and Drug Administration (SFDA[1]) of China for its antitumor activity. It specifically inhibits endothelial cell proliferation and migration and reduces vascularization and blood flow in gliosarcoma (*1*). It also dramatically inhibits growth of various primary tumors in mice. Integrins could be the potential targets for endostatin (*2, 3*). Endostatin binds one atom of zinc (Zn) per monomer via the three histidines in the amino terminus of the molecule (histidines 1, 3, and 11) and aspartic acid 76 (*4*−*6*). The crystal structure of mouse endostatin reveals a compact globular fold and a basic patch of 11 arginine residues, which have been suggested to act as binding sites for heparin (*7*).

Numerous attempts have been made to produce biologically active endostatin via recombinant DNA technology (*8*). However, when expressed in *Escherichia coli*, recombinant endostatin accumulated as inclusion bodies in the cytoplasm. During the *in vitro* renaturation or refolding process, the recovery of soluble and active endostatin was very low, and most of the protein precipitated during the refolding process owing to the renaturation of proteins containing multiple disulfide bonds (*9*−*11*). Further investigations are necessary to elucidate the structure−function relationship of endostatin to meet the urgent need for new antitumor drugs. To achieve this goal, several groups have synthesized and studied the peptides that correspond to the partial sequence of endostatin (*12*−*17*). One group has reported that an 11-amino-acid peptide (ES-2: IVRRADRAAVP) derived from the amino terminus of endostatin promoted endothelial cell adhesion, migration, and tube formation (*12*). However, another group obtained data indicating that a peptide containing the 11 amino acids failed to inhibit tumor growth (*13*).

In our previous study (*18*), we found that ES-2 dramatically inhibited angiogenesis on the chorioallantoic membrane of the chick embryo *in vivo*, but had no antitumor effect in tumor-bearing mice. We speculate that this difference might be caused by a lesser distribution of the drug in the mouse model than in the chick embryo. In order to validate this hypothesis, a new strategy that increases the targeted delivery of the peptide to tumors is needed. In the past decade, many molecules with the RGD peptide have been described that efficiently deliver drugs to tumor vasculature endothelium (*19, 20*). Therefore, in the present study, we examined whether the addition of RGD will also lead to the pronounced antitumor activity of the peptide.

MATERIALS AND METHODS

Cell Lines, Animals, And Peptides. B16F10 mouse melanoma cells (provided by Nanjing University), human hepatic carcinoma Bel-7402, human gastric cancer cell line MGC-803, and human hepatic carcinoma SMMC-7721 cell line were purchased from American type Cell Culture (ATCC, Shanghai, China) and maintained in Dulbecco's modified Eagle's medium (DMEM) with 10% fetal bovine serum and antibiotics. Human umbilical vein endothelial cells (HUVEC, provided by Nanjing Keygen Biotech Co. Ltd.) were routinely grown in DMEM, supplemented with 20% heat-inactivated fetal bovine serum (FBS) and 25 μg of endothelial cell growth factor. Mice were purchased from the Shanghai Laboratory Animal Center of the Chinese Academy of Sciences. Synthesis of the peptides was performed by GL Biochem (Shanghai) Ltd. All peptides are

* Corresponding author. Han-Mei Xu, Center of Biotechnology, Department of Life Science and Technology, China Pharmaceutical University, 24 Tongjiaxiang, Nanjing, 210009, P. R. China. Tel: 86-25-83271007. Fax: 86-25-85438355. E-mail: xuhanmei@yahoo.com.cn.

[†] China Pharmaceutical University.

[‡] Nanjing University.

[1]Abbreviations: Arg-Gly-Asp (RGD); Ala-Cys-Asp-Cys-Arg-Gly-Asp-Cys-Phe-Cys (RGD-4C); the State Food and Drug Administration (SFDA); American type Cell Culture (ATCC); Dulbecco's modified Eagle's medium (DMEM); human umbilical vein endothelial cells (HUVEC); fetal bovine serum (FBS); phosphate-buffered saline (PBS); fluorescein isothiocyanate (FITC); bovine serum albumin (BSA); diaminobenzidine (DAB); basic fibroblast growth factor (bFGF); subcutaneously (s.c.); hematoxylin and eosin (H&E).

10.1021/bc800132p CCC: $40.75 © 2008 American Chemical Society
Published on Web 09/19/2008

Table 1. Sequences of Synthetic Peptides

name of peptides	sequences
ES-2	IVRRADRAAVP
P1	IVRRADRAAVPGGGGRGD
P2	RGDGGGGIVRRADRAAVP
ES-2mut1	IVAAADRAAVP
P3	IVAAADRAAVPGGGGRGD

very soluble in water. The purity of the products was more than 99% by analytical high-performance liquid chromatography. Amino acid analysis and mass spectroscopy were conducted to confirm their compositions.

N-terminal amino-acid sequence analysis was performed at Fudan University (Shanghai, China). Endostatin was expressed in *E. coli* and purified by our laboratory. Antibodies were purchased from Boster Biological Company (Wuhan, P. R. China).

Preparation of Conditioned Medium. Confluent cells were washed and grown in serum-free DMEM. After 20 h of incubation, conditioned medium was collected and centrifuged at 500 × *g* for 10 min and then at 800 × *g* for 20 min to remove debris. The resultant conditioned medium was immediately used for migration and tube formation assays or stored at −70 °C until use.

Cell Migration Assay. To quantify cell migration, a modified Boyden chamber assay was used as described previously (*21*). Polycarbonate filters with 8 μm pores in a 24-well Transwell chamber (Costar, Shanghai, China) were coated with 15 μL Matrigel (Becton-dickinson, Shanghai, China, 50 μg/pore) and placed at 37 °C for 1 h. Cells (0.5 mL, 8×10^4) suspended in serum-free medium were placed in the upper compartment of the chambers. Six hundred microliters of conditioned medium was added to the lower compartment. Following 48 h incubation at 37 °C, cells in the upper chamber and the remaining cells on the upper surface of filters were mechanically removed. After washing with phosphate-buffered saline (PBS), the membranes were fixed in 30% methanol for 10 min and stained with 0.1% methyl violet, and the cells that migrated to the lower surface were counted under inverted microscope at 200× magnification. Five random fields from each well were counted, and values represent five independent experiments. Migration activity was assessed by the average number of cells that migrated to the lower surface of the filter.

Tumor Implantation. B16F10 mouse melanoma, human gastric cancer cell line MGC-803, and human hepatic carcinoma SMMC-7721 cell line were grown in culture. Cell lines were washed with PBS, dispersed in a 0.05% trypsin solution, and resuspended. After centrifugation at 800 × *g* for 5 min, the cell pellets were resuspended in PBS and adjusted to a concentration of 2.5×10^6 cells/mL. BALB/c nude female mice, 5−6 weeks old, were implanted subcutaneously (s.c.) on the midright side with 5×10^6 MGC-803, SMMC-7721 cells in 0.2 mL PBS. C57BL/6 female mice (5−6 weeks old) were implanted s.c on the midright side with 1×10^6 B16F10 cells in 0.2 mL PBS.

C57BL/6 Female Mouse Treatment. After the B16F10 mouse melanoma tumor mean volume reached 100−300 mm^3, mice were separated randomly into different groups with eight mice per group. Group 1 received recombinant human endostatin at a dose of 10 mg/kg in 0.1 mL PBS, and group 2 was injected with an equal volume of PBS. The other nine groups were treated with P1, P2, or ES-2 at doses of 5, 10, or 20 mg/kg in 0.1 mL PBS. All of the groups were injected s.c., at a site distant from the tumor, once daily for 10 d. After the first round of treatment, we carried out another round of treatment with P1 alone, at doses of 6, 3, and 1.5 mg/kg.

BALB/c Nude Mouse Treatment. After the mean SMMC-7721 tumor volume reached 100−300 mm^3, mice were randomly divided into four groups with eight mice per treatment group and twelve mice in the negative control group. Group 1 received paclitaxel (Taxol, provided by Tai ji Pharmaceutical Co. Ltd., Chendu in Sichuan province of China) at a dose of 10 mg/kg, group 2 received equal volume injections of PBS alone. Another group was treated with P1 at a dose of 3 mg/kg. All the nude mouse treatment groups were injected intravenously with 0.1 mL of the drug, once a day for 10 d. Mice implanted with MGC-803 tumor cells were injected with 3 mg/kg/d of P1 peptide. The duration of this treatment was also 10 d.

Measurement of Tumor Growth. Tumors were measured individually with a vernier caliper. Volumes were determined using the formula: tumor volume = length × width^2 × 0.52. Therapeutic effects on tumor growth were expressed as mean tumor volumes versus time, calculated as $(1 - T/C) \times 100\%$, where T = treated tumor volume and C = control tumor volume. For example, if treated tumors were 40% of the volume of control tumors on a given day, tumor suppression in the treated group was 60%.

Western Blot Analysis. Cells were harvested, centrifuged, and the protein fractions separated. The protein was analyzed by 10% SDS-PAGE and further identified by Western blot analysis with PVDF Western blotting membranes (Roche, Shanghai, China) and mouse polyclonal antibody.

Flow Cytometric Analysis of Peptide Binding. Cells were grown in a 24-well plate until 80% confluency, harvested, and washed twice with ice-cold PBS. Before labeling, cells were resuspended in PBS + 1% bovine serum albumin (BSA) for 30 min, then added with 1 μL fluorescein isothiocyanate (FITC)-labeled peptides (P1, P2, RGD, and ES-2) for an additional 25 min. After labeling, cells were collected and washed again with ice-cold PBS twice, resuspended in PBS at a volume of 400 μL, and analyzed with flow cytometry (Becton Dickinson, Shanghai, China). To exclude nonviable cells, 0.5 μM of each peptide was added immediately before analysis. FITC fluorescence was measured in FL1 channel. Cells with FITC emission were gated for further analysis.

Histochemistry and Immunohistochemistry. Mice were euthanized 2 weeks post-treatment, and tumor tissue was collected, fixed with 4% formaldehyde, embedded in paraffin, and sectioned for hematoxylin and eosin (H&E) staining and immunohistochemical staining for CD31. H&E staining was performed according to standard histological procedures. Necrosis and vascularization in tumor tissue were observed under a light microscope. Vascular structures in tumors were evaluated by immunohistochemical staining of CD31 with rabbit anti-CD31 polyclonal antibody (Boster Biological Company). Briefly, staining for CD31 was performed on sections using their specific primary antibodies and biotinylated goat antirabbit secondary antibody, incubated with horseradish peroxidase-labeled streptavidin, visualized with diaminobenzidine (DAB) chromogen, counterstained with hematoxylin, and observed with a microscope.

Three-Dimensional Modeling. Modeling of the composed peptides' structure was done by using the InsightII/CHARMm module (Accelrys Inc., USA). During the simulation, residues 1 to 11 of P1 and residues 8 to 18 of P2 were combined by template which is the structure of residues 50 to 60 in human endostatin (Protein Data Base, PDB ID: 1BNL). The modified protocol was performed by 500 steps of steepest descents (convergence is 0.1 kcal/mol) and 500 steps of conjugate gradients (convergence is 0.01 kcal/mol) under the CHARMm27 force field. Then, simulation of the three-dimensional structure was performed by molecule dynamics at 300 K.

Statistical Methods. Data are expressed as mean ± SD. Statistical significance was assessed using the Student *t* test. For all statistical comparisons, treated groups were compared

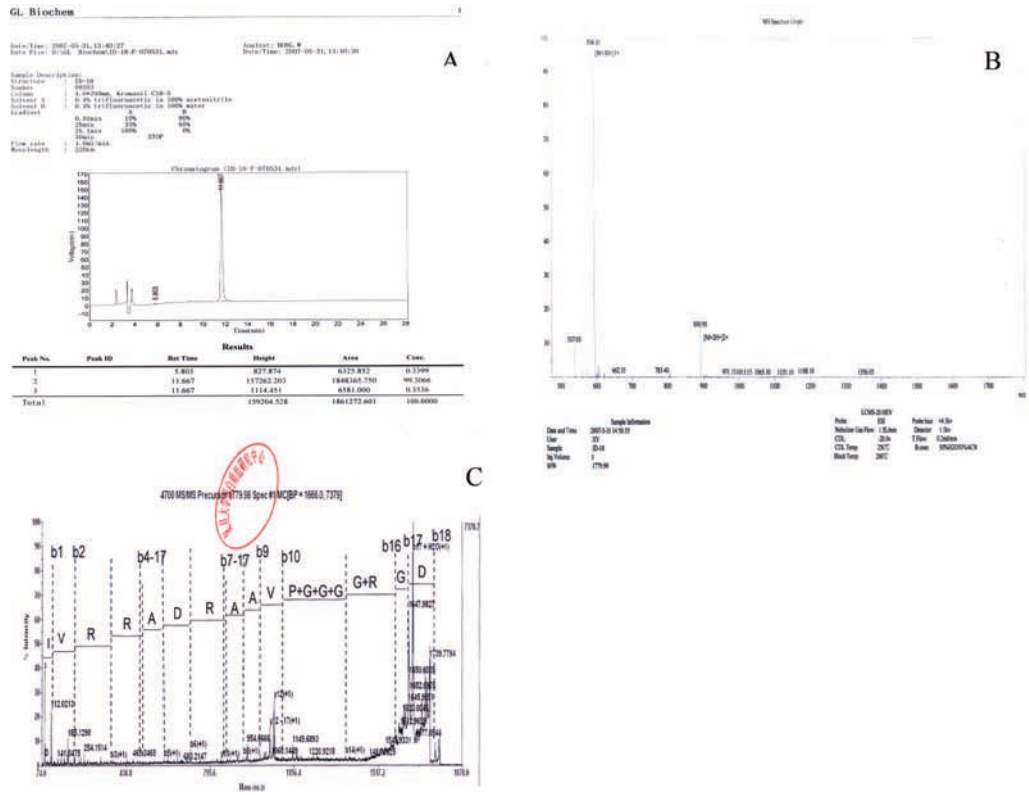

Figure 1. HPLC (A), mass spectroscopy (B), and amino acid sequencing (C) analyses of peptide P1.

with PBS-treated controls, and $P < 0.05$ was considered statistically significant.

RESULTS AND DISCUSSION

Endostatin, after its approval for clinical use, has given a new dimension to cancer treatment by targeting the tumor vasculature; however, the exact mechanism of endostatin remains unknown. Moreover, it is relatively expensive compared to other conventional antineoplastic drugs such as chemical antiangiogenic agents. These disadvantages limit its further use. Recently, evidence has outlined the role of integrin binding in the biological effects of endostatin in the cell (*22*−*24*). In another study, it was shown that an arginine-rich peptide, ES-2, in the soluble form inhibited basic fibroblast growth factor-induced directional migration and tubular morphogenesis of microvascular endothelial cells (*12*). The peptide induced the loss of focal adhesions and actin stress fibers in these cells. This activity was found to be lost in mutated peptides where arginine residues were substituted with alanine. This reflects some of the properties of endostatin that are associated with the heparin-binding characteristic of endostatin. However, in one study, an endostatin peptide (hP3) that contains ES-2 failed to inhibit tumor growth *in vivo* (*13*). The authors found that the entire antiangiogenic activity of endostatin was located in a 27-amino-acid peptide that binds Zn, and showed that Zn binding was required for antitumor and antimigration activities of endostatin. These results indicated that the mechanism of endostatin is complex and the unique chemical composition of each protein (or peptide) is important for its function. A change in just one amino acid can change the structure and function of a protein, so an endostatin-derived peptide could not reflect the true characteristic of endostatin.

Therefore, protein properties and activities relate to the number and type of factors. Although certain amino acid sequences can be identified as more likely to have activity *in vitro*, it is still not possible to completely predict whether the protein will be active *in vivo*. The *in vitro* antimigratory activity of ES-2 has been mapped to 60−70 amino acids of endostatin (*12*), but the *in vivo* inhibitory effect of this peptide remains poorly investigated. Peptides containing ES-2 (like hP3) cannot reflect the true characteristics of ES-2. However, ES-2 is the shortest active sequence derived from endostatin, and the results of antimigratory activity shed some light on reducing the cost of endostatin. The synthesis of a smaller peptide is much simpler and less expensive when compared to the expression and purification of endostatin, and its mechanism is clear. Still, it is necessary to identify the *in vivo* activity of ES-2.

We previously tested the antiangiogenic activity of ES-2 peptide. ES-2 at different concentrations was loaded onto chick embryos to validate the *in vivo* antiangiogenic activity, the results of which demonstrated that ES-2 dose-dependently suppressed the embryonic neovascularization and angiogenesis (*18*). Furthermore, ES-2 higher than 200 ng/mL almost completely prevented blood vessel formation and was lethal to the chicken embryo. These data indicate that the ES-2 peptide is a potent inhibitor of angiogenesis.

However, in a tumor-bearing mouse model, we found that ES-2 peptide did not show any significant antitumor activity (data not shown). We speculate that this inconsistency may be due to the lesser bioavailability and/or receptor binding by ES-2 peptide. A possible explanation could be that heparin may not be the only candidate for this peptide, which could mean it has to bind to another ligand and/or receptor *in vivo*. Additionally, direct administration of the peptide in chick embryo assay will lead to better bioavailability of the drug, but in an animal model, the drug is distributed to many compartments. Biotransformation of these drugs could lead to its inactivation because of the changes in the elimination after metabolism or the effects of other biomolecules. If ES-2 could be effectively transferred to tumor angiogenic endothelium, it may exhibit antitumor activity.

Recently, lines of evidence have shown that the addition of RGD, or RGD-4C short peptide, facilitates the molecular

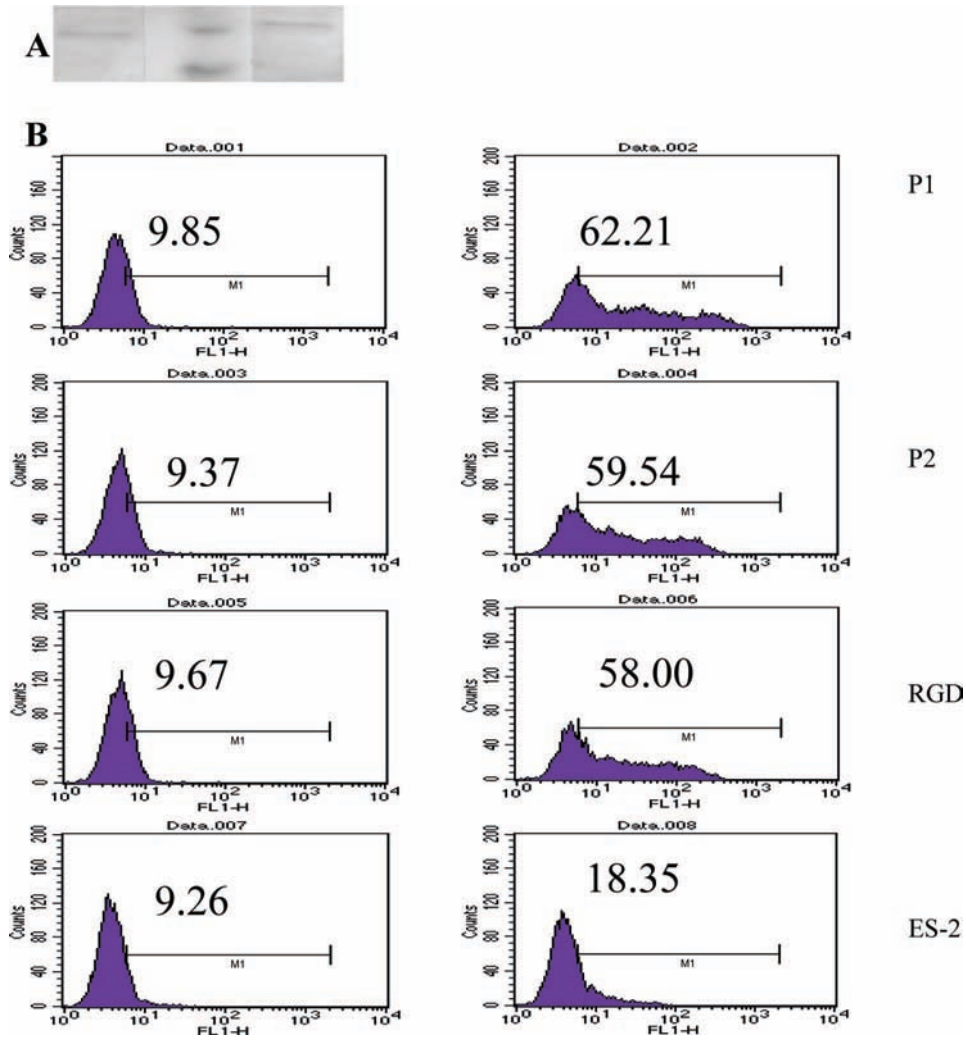

Figure 2. Western blot analysis of the expression of integrin αv and $\beta 3$ in human Bel-7402 cells using mouse antihuman integrin polyclonal antibody (A). Flow cytometry demonstrating the binding of RGD-FITC-labeled peptide to human Bel-7402 cells (B).

targeting of integrins on angiogenic endothelium, which has proven to be an effective strategy for delivering a drug to the tumor vasculature. The RGD sequence on ES-2 might have the ability to bind with the tumor endothelial cells. In view of this fact, we synthesized two peptides with RGD attached to the amino and carboxy terminals of ES-2. Four glycine residues were added between the RGD motif and ES-2 in an attempt to increase its flexibility (Table 1). The purity, molecular weight, and sequence of P1 were shown (Figure 1).

First, we wanted to know whether the modified peptides could efficiently bind integrins. Western blot analysis was performed on human hepatic carcinoma Bel-7402 whole-cell lysates using integrin αv and $\beta 3$ polyclonal antibody, and expression of both subunits was observed in Bel-7402 (Figure 2A).

A target analysis was performed on P1 and P2 coupled with FITC; RGD and ES-2 coupled with FITC were used as positive control and negative control, respectively. Bel-7402 cells were used as the target to determine the RGD-FITC-peptide binding with the cell surface receptors (integrins). Flow cytometric analysis of FITC-peptides binding to tumor cells was performed. A positive reaction was seen with P1, P2, and RGD, while ES-2 did not bind to cells (Figure 2B), which suggested that RGD-modified ES-2 could specifically bind to the receptor expressed by Bel-7402 tumor cells, resulting in efficient antitumor activity of P1 and P2 *in vivo*.

Reselection was performed with the mutant peptides. First of all, *in vitro* selection has been used to find the peptides with similar or better activity than ES-2. To investigate the role of the peptides for their antimigratory effect, transwell chamber migration assays were performed using the synthetic peptides. P1, P2, and ES-2 all displayed reduced HUVEC ability to migrate toward the basic fibroblast growth factor (bFGF) stimulus. At 1 μg/mL, P1 was most effective in inhibiting migration of HUVEC (Figure 3). Thus, P1 and P2 were used for further investigations.

For the *in vivo* assay, the mice (C57BL/6) implanted with B16F10 melanoma cells were injected s.c. with the peptides to perform the preliminary screening. According to published data, 5−20 mg/kg/d of endostatin has been reported to exert an antitumor effect; we used doses up to 20 mg/kg/d in the experiment. We assessed P1 and P2 at three doses of 20, 10, and 5 mg/kg/d and discovered that 5 mg/kg/d has the most effective cytostatic effect on the melanoma (data not shown). On the basis of this finding, we performed another experiment by testing three smaller doses, i.e., 6, 3, and 1.5 mg/kg/d, and found that 3 mg/kg/d of P1 or P2 was most effective in arresting the growth of the tumor (data not shown). Moreover, we also discovered that the administration of the drug twice a day had the most desirable effect. Adding RGD peptide sequences to any protein can cause its binding to antiangiogenic integrins. Hence, it is not clear that the biological effects are associated with ES-2 or RGD. It would be important to compare the active peptide with RGD and modified inactive endostatin sequence for reference. A mutated peptide, ES-2mut1, displayed reduced

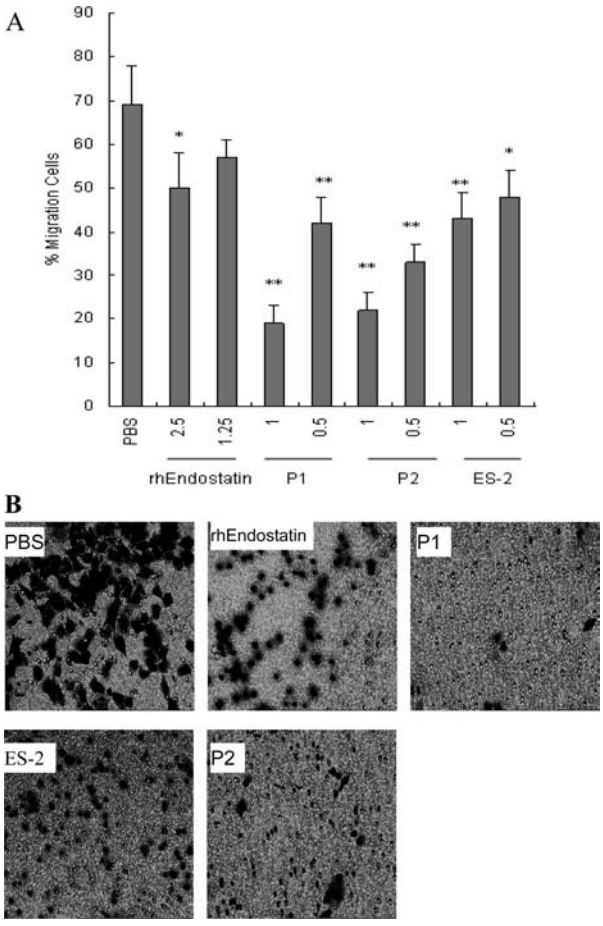

Figure 3. Inhibition of endothelial cell migration by synthetic peptides. The migration response of HUVEC was assayed by the Boyden chamber. Cells were treated with P1, P2, and ES-2. As controls, rhEndostatin and PBS were used. Columns represent mean ± SD of 5 experiments (*P < 0.05; **P < 0.01 vs control).

levels of activity compared with ES-2 (*12*). RGD was also introduced into the carboxy terminal of ES-2mut1 (i.e., P3). We found that P3 and RGD all exhibited moderate antitumor activity (compared with P1 and P2; data not shown), suggesting that the two domains were involved in the antitumor activity.

On the basis of these findings, we selected P1 to further examine their effects on tumor-bearing nude mice (P1 and P2 were all modified by RGD and P2 has antitumor effects similar to P1, so only P1 was selected). ES-2 did not show any activity *in vivo*, while endostatin expressed and purified by different laboratories had different antitumor effects because of the inclusion body's denaturation and renaturation, so for this paper, further experiments of ES-2 and endostatin were not conducted. Taxol is a standard drug for the treatment of advanced cancer, and in order to get a reliable and comparable result, we selected Taxol as a positive control. *In vivo*, the results show that intravenous injection of P1 at 3 mg/kg/d inhibited human SMMC-7721 hepatic carcinoma growth by 78% (Figure 4A). However, P1 displayed higher antitumor effects as compared to Taxol at 10 mg/kg/d, suggesting that P1 has significant antitumor effect at lower doses. We performed an additional series of experiments in a human gastric tumor model. The intravenous injection of P1 at 3 mg/kg/d inhibited human gastric cancer cell MGC-803 growth by 58% (Figure 4B).

We also examined the effect of the peptides on tumor tissue. P1 displayed more severe tissue necrosis than the control (Figure 5A,B). The control displayed necrosis interspersed with viable tumor cells, whereas P1 induced large areas of continuous necrosis within tumors. We then counted the number of visible

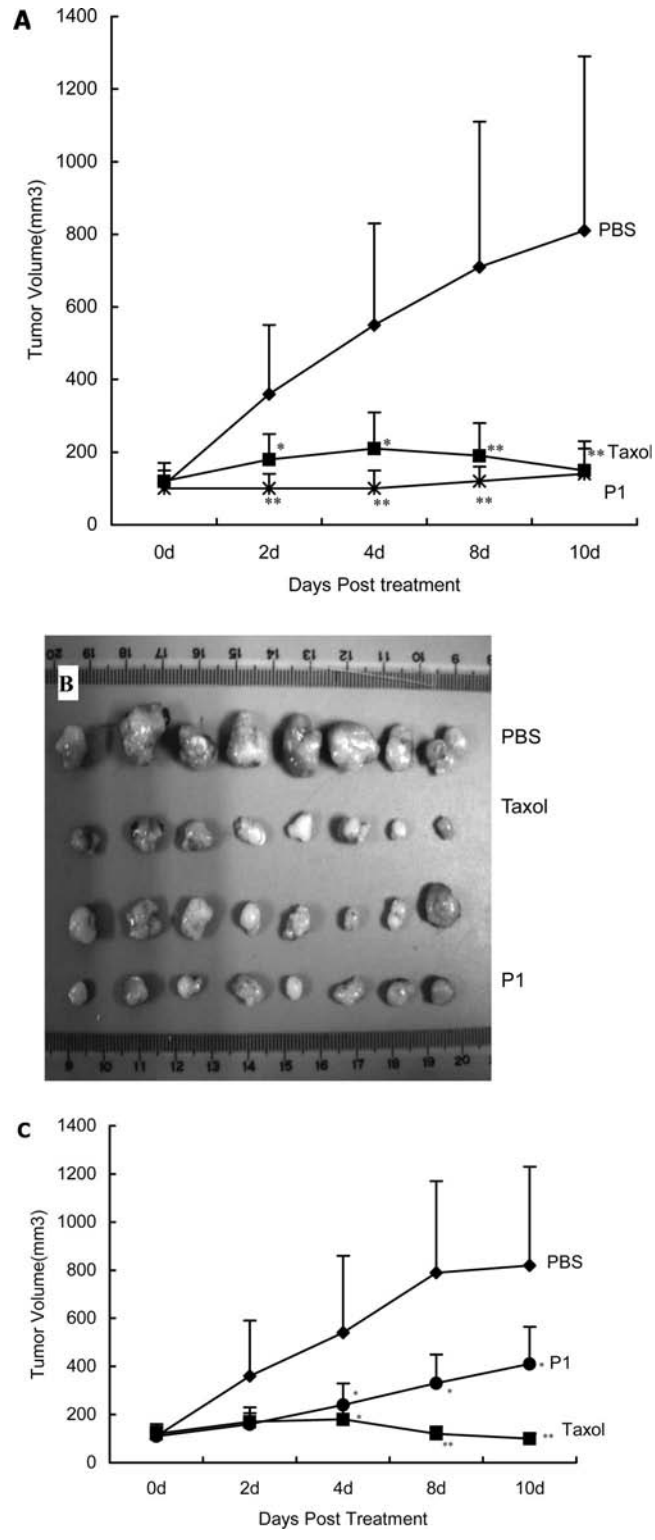

Figure 4. Therapeutic effects of peptides on the growth of tumor. (A) represents human SMMC-7721 hepatic carcinoma suppression mediated by 3 mg/kg P1 twice a day. (B) displays the tumor in different treatment groups. (C) MGC-803 human gastric cancer suppression by 3 mg/kg P1 twice a day. Each point represents mean ± SD of each group (*P < 0.05; **P < 0.01 vs control).

blood vessels in CD31 staining, and found that P1 significantly reduced the vessel density compared to control (Figure 5C,D,E) (P < 0.05).

The finding that the addition of RGD at amino and carboxy terminals has the same result calls for a justification. The peptides with an additional RGD sequence (P1, P2), regardless

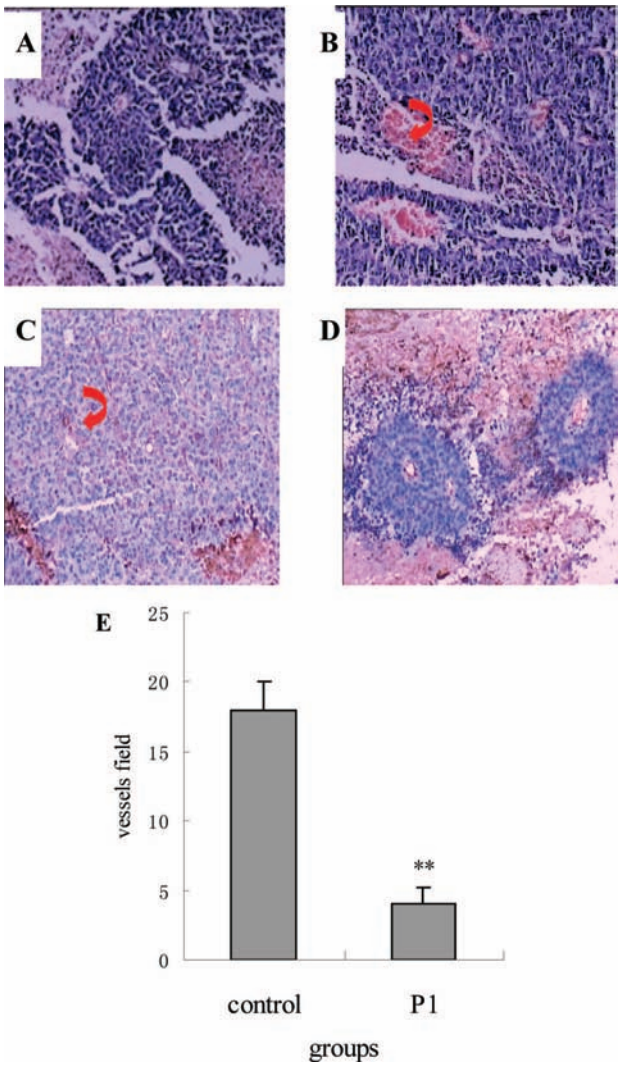

Figure 5. Necrosis areas within tumor and tumor blood vessel density. The figure shown by H&E staining observed with light microscope (40× original magnifications). PBS (A) treatment exibit incomplete tissue necrosis interspersed with viable tumor cells. (B) represents P1 treatment, showing continuously extensive necrosis area. (C, D, E) Tumor blood vessel density. (C) represents PBS, and (D) represents P1 treatment. Blood vessels in CD31 staining were indicated with arrows (40× original magnifications). Results were expressed as mean ± SD of nine regions of three sections per group (*P < 0.05; **P < 0.01 vs control).

of its location at either the amino or carboxy terminal, show an effective arrest of tumor growth. This may be due to the fact that the RGD peptide, the primary recognition sequence of some integrins, has less secondary structure (Figure 6A,B), thus P1 and P2 exhibited similar binding capability to integrins.

ES-2 is the smallest endostatin structure unit that has been discovered recently, but there is no further *in vivo* assessment to support its effectiveness. In this study, we evaluated the effectiveness of ES-2 *in vivo* for the first time, along with the determination of the most effective dosage range of modified ES-2, the most effective administration frequency, and the change in its *in vivo* activity after the addition of an RGD motif at different locations. We also performed the histochemical and immunohistochemical analysis of the tumor under investigation. Moreover, safety experiments were conducted to study the possible toxic effects of P1, and a tail vein injection of 1500 mg/kg/d P1 into Kunming strain mice revealed no evidence of toxicity in the treated animals (data not shown). These results show that P1 is an effective and safe peptide as an anticancer

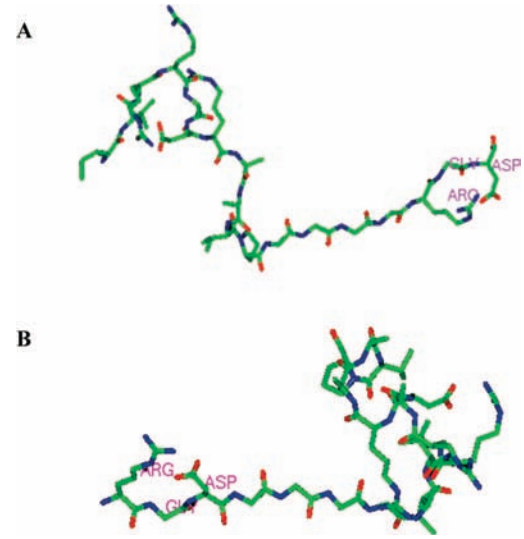

Figure 6. Modeling of the structures of the composed peptides was done by using the InsightII (Accelrys Inc.)/CHARMm module. Peptides 1 and 2 (A,B) have less secondary structure and fold in an extended manner.

drug. RGD modified ES-2 (P1 and P2) has only 18 amino acids and showed remarkable suppression of growth of human gastric and hepatic cancer at doses as small as 3 mg/kg/d. The study has proven that the addition of RGD motif to peptides is an effective strategy for the delivery of the peptide to the tumor vasculature.

During the past decade, RGD peptides have become a popular tool for the targeting of drugs and imaging agents to tumor vasculature expressing αv and β3 integrins. Some of these products show impressive results in preclinical animal models, and an RGD-targeted radiotracer has already successfully been tested in humans for the visualization of αv and β3 integrins, which demonstrates the feasibility of this approach (*25*−*27*).

The study on P1 and P2 has made it possible to develop a new drug to fight solid tumors. We are currently investigating the activity of P1 and P2 on another four types of human cancer. We also plan to study the pharmacokinetic and pharmacodynamic aspects of peptide P1, to ensure a better clinical application of it.

ACKNOWLEDGMENT

The authors are grateful to Zichun Hua (Department of Life Science, Nanjing University, 210008, P. R. China) for providing B16F10 mouse melanoma. We thank Dr. Yinwu (Department of Life Science, Nanjing University, P. R. China) for critical reading of the manuscript and Drs. Wanzhou Zhao, Yijun Sun, and Junshi Ma for assisting us to implant tumors.

LITERATURE CITED

(1) Sorensen, D. R., Read, T-A., and Porwol, T. (2002) Endostatin reduces vascularization, blood flow and growth in a rat gliosarcoma. *Neuro-Oncology (Durham, NC, U. S.) 4*, 1–8.

(2) Sudhakar, A., Sugimoto, H., Yang, C. Q., Lively, J., Zeisberg, M., and Kalluri, R. (2003) Human tumstatin and human endostatin exhibit distinct anti-angiogenic activities mediated by αvβ3 and α5β1 integrins. *Proc. Natl. Acad. Sci. U.S.A. 100*, 4766–71.

(3) Rehn, M., Veikkola, T., and Kukk-Valdre, E. (2001) Interaction of endostatin with integrins implicated in angiogenesis. *Proc. Natl. Acad. Sci. U.S.A. 98*, 1024–9.

(4) Ding, Y. H., Javaherian, K., and Lo, K. M. (1998) Zinc-dependent dimers observed in crystals of human endostatin. *Proc. Natl. Acad. Sci. U.S.A. 95*, 10443–8.

(5) Boehm, T., O'Reilly, M. S., Keough, K., Shiloach, J., Shapiro, R., and Folkman, J. (1998) Zinc-binding of endostatin is essential for its antiangiogenic activity. *Biochem. Biophys. Res. Commun. 252*, 190–4.

(6) Sasaki, T., Fukai, N., Mann, K., Göhring, W., Olsen, B. R., and Timpl, R. (1998) Structure, function and tissue forms of the C-terminal globular domain of collagen XVIII containing the angiogenesis inhibitor endostatin. *EMBO J. 17*, 4249–56.

(7) Sasaki, T., Larsson, H., and Kreuger, J. (1999) Structural basis and potential role of heparin/heparin sulfate binding to the angiogenesis inhibitor endostatin. *EMBO J. 18*, 6240–8.

(8) Dhanabal, M., Volk, R., Ramchandran, R., Simons, M., and Sukhatme, V. P. (1990) Cloning, expression, and in vitro activity of human endostatin. *Biochem. Biophys. Res. Commun. 258*, 345–52.

(9) O'Reilly, M. S., Boehm, T., and Folkman, J. (1997) Endostatin: an endogenous inhibitor of angiogenesis and tumor growth. *Cell 88*, 277–85.

(10) Dhanabal, M., Ramchandran, R., Volk, R., Stillman, E. I., Lombardo, M., Iruela-Arispe, M. L., Simons, M., and Sukhatme, P. V. (1999) Endostatin: yeast production, mutants, and anti-tumor effect in renal cell carcinoma. *Cancer Res. 59*, 189–97.

(11) You, W. K., So, S. H., Lee, H., Park, S. Y., Yoon, M. R., Chang, S. I., Kim, H. K., Joe, Y. A., Hong, Y. K., and Chung, S. I. (1999) Purification and characterization of recombinant murine endostatin in *E. coli*. *Exp. Mol. Med. 31*, 197–202.

(12) Wickstrom, S. A., Alitalo, K., and Keski-Oja, J. (2004) An endostatin-derived peptide interacts with integrins and regulates actin cytoskeleton and migration of endothelial cells. *J. Biol. Chem. 279*, 20178–85.

(13) Robert, M., Sjin, T. T., Satchi-Fainaro, R., Birsner, A. E., Sadagopa Ramanujam, V. M., Folkman, J., and Javaherian, K. (2005) A 27-amino-acid synthetic peptide corresponding to the NH_2-teminal zinc-binding domain of endostatin is responsible for its antitumor activity. *Cancer Res. 65*, 3656–63.

(14) Cattaneo, M. G., Pola, S., Francescato, P., Chillemi, F., and Vicentini, L. M. (2003) Human endostatin-derived synthetic peptides possess potent antiangiogenic properties in vitro and in vivo. *Exp. Cell Res. 283*, 230–6.

(15) Chillemi, F., Francescato, P., Ragg, E., Cattaneo, M. G., Pola, S., and Vicentini, L. (2003) Studies on the structure-activity relationship of endostatin: synthesis of human endostatin peptides exhibiting potent antiangiogenic activities. *J. Med. Chem. 46*, 4165–72.

(16) Morbidelli, L., Donnini, S., Chillemi, F., Giachetti, A., and Ziche, M. (2003) Angiosuppressive and angiostimulatory effects exerted by synthetic partial sequences of endostatin. *Clin. Cancer Res. 9*, 5358–69.

(17) Cho, H., Kim, W. J., Lee, Y. M., Kim, Y. M., Kwon, Y. G., Park, Y. S., Choi, E. Y., and Kim, K. W. (2004) N-/C-terminal deleted mutant of human endostatin efficiently acts as an anti-angiogenic and anti-tumorigenic agent. *Oncol. Rep. 11*, 191–5.

(18) Xu, H-M., Chen, L-S., Yin, R-T., and Xi, T. (2005) The study about biological activity of human endostatin-derived synthetic peptide—ES-2. *Journal of China Pharmaceutical University 37* (4), 346–8.

(19) Zitzmann, S., Ehemann, V., and Schwab, M. (2002) Arginine-glycine-aspartic acid (RGD)-peptide binds to both tumor and tumor-endothelial cells *in vivo*. *Cancer Res. 62*, 5139–43.

(20) Arap, W., Pasqualini, R., and Ruoslahti, E. (1998) Cancer treatment by targeted drug delivery to tumor vasculature in a mouse model. *Science 279*, 377–80.

(21) Attiga, F. A., Fernandez, P. M., Weeraratna, A. T., Manyak, M. J., and Patierno, S. R. (2000) Inhibitors of prostaglandin synthesis inhibit human prostate tumor cell invasiveness and reduce the release of matrix metalloproteinases. *Cancer Res. 60*, 4629–37.

(22) Wickström, S. A., Alitalo, K., and Keski-Oja, J. (2002) Endostatin associates with integrin alpha5beta1 and caveolin-1, and activates Src via a tyrosyl phosphatase-dependent pathway in human endothelial cells. *Cancer Res. 62*, 5580–9.

(23) Wickström, S. A., Alitalo, K., and Keski-Oja, J. (2003) Endostatin associates with lipid rafts and induces reorganization of the actin cytoskeleton via down-regulation of RhoA activity. *J. Biol. Chem. 278*, 37895–901.

(24) Sudhakar, A., Sugimoto, H., Yang, C., Lively, J., Zeisberg, M., and Kalluri, R. (2003) Human tumstatin and human endostatin exhibit distinct antiangiogenic activities mediated by $\alpha v\beta 3$ and $\alpha 5\beta 1$ integrins. *Proc. Natl. Acad. Sci. U.S.A. 100*, 4766–71.

(25) Temming, K., Schiffelers, R., Molema, G., and Kok, R. J. (2005) RGD-based strategies for selective delivery of therapeutics and imaging agents to the tumour vasculature. *Drug Resist. Updates. 8*, 381–402.

(26) Weide, T., Modlinger, A., and Kessler, H. (2007) Spatial screening for the identification of the bioactive conformation of integrin ligands. *Top. Curr. Chem. 272*, 1–50.

(27) Yokoyama, Y., and Ramakrishnan, S. (2004) Addition of integrin binding sequence to a mutant human endostatin improves inhibition of tumor growth. *Int. J. Cancer 111* (6), 839–48.

BC800132P

Amphiphilic Block Copolymers Enhance Cellular Uptake and Nuclear Entry of Polyplex-Delivered DNA

Zhihui Yang, Gaurav Sahay, Srikanth Sriadibhatla, and Alexander V. Kabanov*

Center for Drug Delivery and Nanomedicine and Department of Pharmaceutical Sciences, College of Pharmacy, University of Nebraska Medical Center, 985830 Nebraska Medical Center, Omaha, Nebraska 68198-5830, and Faculty of Chemistry, M.V. Lomonosov Moscow State University, 119899 Moscow, Russia. Received April 4, 2008; Revised Manuscript Received July 25, 2008

This work for the first time demonstrates that synthetic polymers enhance uptake and nuclear import of plasmid DNA (pDNA) through the activation of cellular trafficking machinery. Nonionic block copolymers of poly(ethylene oxide) and poly(propylene oxide), Pluronics, are widely used as excipients in pharmaceutics. We previously demonstrated that Pluronics increase the phosphorylation of IκB and subsequent NFκB nuclear localization as well as upregulate numerous NFκB-related genes. In this study, we show that Pluronics enhance gene transfer by pDNA/polycation complexes ("polyplexes") in a promoter-dependent fashion. Addition of Pluronic P123 or P85 to polyethyleneimine-based polyplexes had little effect on polyplex particle size but significantly enhanced pDNA cellular uptake, nuclear translocation, and gene expression in several cell lines. When added to polyplex-transfected cells after transfection, Pluronics enhanced nuclear import of pDNA containing NFκB binding sites, but have no effect on import of pDNA without these sites. Altogether, our studies suggest that Pluronics rapidly activate NFκB, which binds cytosolic pDNA that possesses promoters containing NFκB binding sites and consequently increase nuclear import of pDNA through NFκB nuclear translocation.

INTRODUCTION

Nonviral gene delivery systems, such as DNA incorporated in cationic lipids, polycations, or nanoparticles, are safer, cheaper, and easier to produce in comparison to viral vectors (*1*). Unfortunately, these systems are also much less efficient in delivering DNA and initiating gene expression than the viruses. This is due to low efficacy of the nonviral vectors in overcoming numerous barriers for gene delivery into a cell. These barriers include (i) cellular uptake by endocytosis, (ii) escape from endosomes prior to delivery to lysosomes, (iii) release to the cytoplasm, and (iv) transport to the nucleus. Nuclear delivery of the DNA is believed to be among the most challenging barriers for every type of nonviral vector (*2*). Its significance is evident from numerous studies showing that microinjection of plasmid DNA (pDNA) into the cytoplasm results in negligible expression compared to expression of the same pDNA injected directly in the nucleus (*3*−*7*). It is well-known that nuclear import substrates, such as transcription factors, contain nuclear localization signals (NLSs) that are recognized by nuclear import factors (*8*). Hence, NLS-containing peptides or proteins were coupled to pDNA to facilitate its nuclear delivery (*9*−*21*). As an alternative, we posit that some safe and nontoxic pharmaceutical excipients can activate selected cell signaling pathways (*22, 23*) and harness cell trafficking machinery to enhance nuclear transport of pDNA without DNA modification. In particular, a nonionic block copolymer of poly(ethylene oxide) and poly(propylene oxide), Pluronic, can activate a transcription factor, NFκB, in cells and enhance gene expression *in vitro* and *in vivo* without inducing a cytotoxic effect (*24, 25*). It is known that NFκB can bind pDNA in cytoplasm and transport it to the nucleus through nuclear transport machinery (*26*−*28*). In this study, we demonstrate for the first time that Pluronic enhances both cellular uptake and nuclear transport of pDNA delivered into cells with DNA/polycation complexes ("polyplexes") and suggest that by combining Pluronic with existing nonviral vectors the efficiency of gene delivery can be safely increased.

MATERIALS AND METHODS

Materials. Nonionic block copolymers Pluronic P123 and Pluronic P85 were kindly provided by BASF Corp (Parsippany, NJ). SP1017, a mixture of 0.25% Pluronic L61 and 2% Pluronic F127, was kindly provided by Supratek Pharma Inc. (Montreal, Canada). Exgen 500, a 22 kD linear PEI, was purchased from MBI Fermentas Inc. (Hanover, MD). The cyanine dimmer dye, YOYO-1, was purchased from Molecular Probes (Carlsbad, CA). Plasmid gWIZLuc (encoding luciferase, under control of CMV promoter) was purchased from Gene Therapy Systems, Inc. (San Diego, CA) and plasmid pEGFP-N1 (encoding enhanced green fluorescent protein (GFP)) was purchased from Clontech (palo Alto, CA). "PathDetect c*is*-Reporting Systems" containing luciferase reporter gene with NFκB and AP-1 response elements (pNFκB-luc and pAP-1-luc) were purchased from Stratagene (La Jolla, CA). All the plasmids were expanded in DH5α *E. coli* and isolated using Qiagen endotoxin-free plasmid giga-prep kits according to the supplier's protocol. TRIzol reagent was purchased from Invitrogen (Carlsbad, CA). Oligo GEArray Mouse NFκB Signaling Pathway Microarray was purchased from SuperArray Bioscience Corporation (Frederick, MD). Methyl-β-cyclodextrin (MBCD) and sucrose were purchased from Sigma Aldrich (St Loius, MO). Bovine serum albumin was purchased from Fischer Scientific (Waltham, MA).

Synthesis of PB25080 and P85PEI Conjugates. Cationic graft or block copolymers P85PEI and PB25080 were synthesized by Dr. Vinogradov at University of Nebraska Medical Center (UNMC). Briefly, in case of P85PEI (2 kDa) 20% of free terminal hydroxyl groups of Pluronics P85 were activated by 1,1′-carbonyldiimidazole (CDI) in anhydrous acetonitrile for 4 h at 20 °C and then reacted with equimolar quantity of branched PEI (MW 2 kDa) in 20% ethanol for 48 h at 20 °C.

* Corresponding author. Durham Research Center, Room 1036, 985830 Nebraska Medical Center, Omaha, NE 68198-5830. Tel.: +1 402 559 9364; Fax: +1 402 559 9365. E-mail: akabanov@unmc.edu.

10.1021/bc800144a CCC: $40.75 © 2008 American Chemical Society
Published on Web 08/27/2008

The conjugate was purified from free PEI by gel permeation chromatography on Sephadex G-25 using 20% ethanol as eluent (*29*). To obtain PB25080 PEG (MW 8 kDa) was modified by one terminal hydroxyl group with 4,4′-dimethoxytrityl (DMT) chloride to obtain DMT-PEG (*30*). DMT-PEG was activated with CDI in acetonitrile and reacted with ethylenediamne to obtain monoamino-PEG. Monoamino-PEG was treated with D-biotin *p*-nitrophenyl ester in 5 mL of dimethylformamide containing 1% (v/v) of triethylamine for 18 h at 40 °C to obtain biotin-PEG. Biotin-PEG was treated again with CDI and then reacted with PEI (25 kDa) to obtain PB25080 (*31*).

Labeling of Pluronic. Ahydrous Pluronic P123 (2 mg) was activated with CDI (213 mg) in 10 mL of acetonitrile for 2 h at 37 °C and reacted with ethylenediamine (313 mg) in 20 mL ethanol for 12 h at room temperature. The reaction mixture was dialyzed in a 2 kD cutoff membrane against 15% ethanol for 72 h (change ethanol twice) and lyophilized. Amino-Pluronic (0.4 mg) was dissolved in 2 mL acetonitrile, mixed with 2 mL 0.1 M NaH_2CO_3 buffer, and reacted with 25 mg of rhodamine B isothiocyanate (RITC) or fluorescein isothiocyanate (FITC) in 1 mL dimethylformamide added dropwise over 10 min with stirring. After 2 h incubation at room temperature RITC- or FITC-labeled Pluronic was dialyzed in a 2 kD cutoff membrane in 20% ethanol for 72 h at 4 °C in dark and then lyophilized. Similar procedure was used for Pluronic P85. For cell uptake studies, the labeled Pluronic 123 was mixed with the unlabeled copolymer at 1:10 ratio.

Cell Culture. Mouse fibroblasts NIH 3T3 cell line and human prostate cancer PC-3 cell line were cultured in Dulbecco's Modified Eagle's Medium **(**DMEM**)** and RPMI 1640, respectively, supplemented with 10% heat-inactivated fetal bovine serum (FBS), 100 U/mL penicillin/100 μg/mL streptomycin (complete media). All tissue material media was obtained from Gibco Life Technologies, Inc. (Grand Island, NY). Stable transfected C2C12-CMV^{luc} cells were generated as described previously (*24*). Cells were seeded at a density of 50 000 cells per well in 24 well plates and allowed to adhere for 24−48 h prior to transfection. For confocal microscopy, cells were seeded onto untreated glass coverslips at 50 000 cells per coverslip.

Formation of Polyplexes and Transfection. Transfection solutions were prepared in 1.5 mL Eppendorf tube by mixing (i) 45 μL of pDNA (0.1 mg/mL) or 90 μL of YOYO-1 labeled pDNA (0.05 mg/mL), (ii) 9 μL of Pluronic P123 solution (Pluronic P85 or SP1017 when indicated), (iii) 150 μL of DMEM, and (iv) polycations. For transfections, cell transport, and localization studies, the polycation nitrogen to pDNA phosphate ratios (N/P ratio) were kept constant N/P = 8 for PB25080 and P85PEI and N/P = 9 for Exgen 500. For physicochemical characterization, the N/P ratios were varied as indicated below. The solutions were vortexed for 30 s immediately after addition of polycation, incubated for 5 min at room temperature, and supplemented with 1270 μL of complete media. Cells were incubated with transfection solution (250 μL per well or 500 μL per coverslip) for 2 h at 37 °C (5% CO_2), rinsed with phosphate buffer saline (PBS), incubated for additional 24 h in complete media, and analyzed for luciferase or GFP expression as previously described (*24*).

Particle Size. Effective hydrodynamic diameters were measured by photon correlation spectroscopy using a ZetaPlus Zeta Potential Analyzer (Brookhaven Instrument) equipped with the Multi-Angle Option at 22 °C at an angle of 90°. Prior to particle formation, all reagents were filtered through a Whatman 200 nm polysulfone filter. Data represents average of five separate 3 min analyses. All systems exhibited stable effective diameters over the measurement time.

Transmission Electron Microscopy (TEM). Polyplexes were prepared in Eppendorf tube by first, mixing 100 μL of 0.1 M phosphate buffer (pH7.0), 120 μL of 0.1 mg/mL gWIZLuc, and 6 μL of 5% Pluronic P123, and second, adding polycation, vortexing for 30 s, and diluting with phosphate buffer to 500 μL. A drop of the sample solution was allowed to settle on a Formavar precoated grid for 1 min, the excess sample was wicked away with filter paper, and a drop of staining solution (1% uranyl acetate) was allowed to contact the sample for 1 min. The samples were analyzed using a Philips 410 TEM microscope.

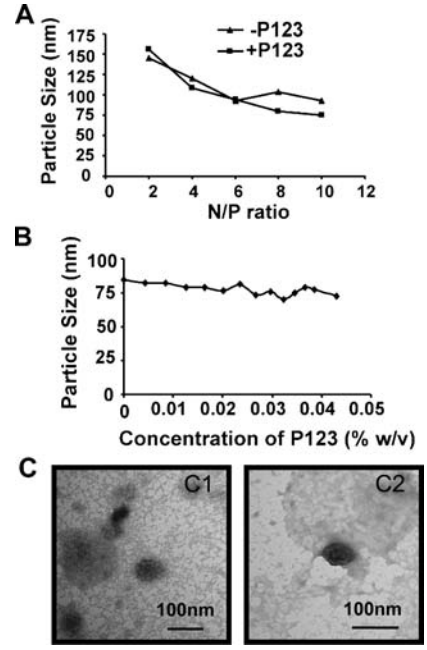

Figure 1. Effect of Pluronic P123 on the particle size and morphology of PB25080-based polyplex: (A−C) Particle effective diameters were measured at (A) various N/P ratios and (B) different Pluronic concentrations. (C) TEM images of PB25080-based polyplex without (C1) and with (C2) Pluronic P123. (B,C) Polyplexes were formed at N/P = 8. (A,C) Pluronic P123 concentration was 0.03% w/v. (A,B) All measurements were performed in phosphate buffer, pH 7.0.

Flow Cytometry Analysis. Polyplexes containing YOYO-1 labeled pDNA (*32*) with/without Pluronic were incubated with NIH 3T3 or PC-3 cells for 2 h at 37 °C (Figure 3). In select experiments, cells were pretreated for 30 min with inhibitors of endocytosis (2 mM MBCD or 0.25 M sucrose), and then, the same inhibitors were also present during subsequent incubation with the polyplex in presence or absence of the copolymer. Cells were washed by PBS, trypsinized, and suspended in 1% FBS. The mean fluorescence intensity was analyzed using Becton Dickinson FACStarPlus flow cytometer operating under Lysis II (San Jose, CA), equipped with an argon ion laser (excitation - 488 nm; emission filter - 530 ± 30 nm bandpass). Data were acquired in linear mode and visualized in logarithmic mode. Data from 10 000 events were gated using forward and side scatter parameters to exclude debris and dead cells. In a separate study, the flow cytometry analysis was performed to quantify the amount of DNA in nuclei isolated after transfection of the cells as described below.

Intracellular Trafficking. Cells were transfected with Exgen 500-based polyplex with/without RITC-labeled Pluronic P85. At the end of each time point, cells were washed, fixed (using 4% parafomaldehyde), labeled with ToPro-3 iodide, and examined under confocal microscope.

Nuclear Translocation. Cells were transfected for 2 h with YOYO labeled pAP-1-luc or pNFκB-luc using Exgen 500, washed twice with PBS, and then incubated in fresh medium with/without 0.03% Pluronic P123 for additional time points.

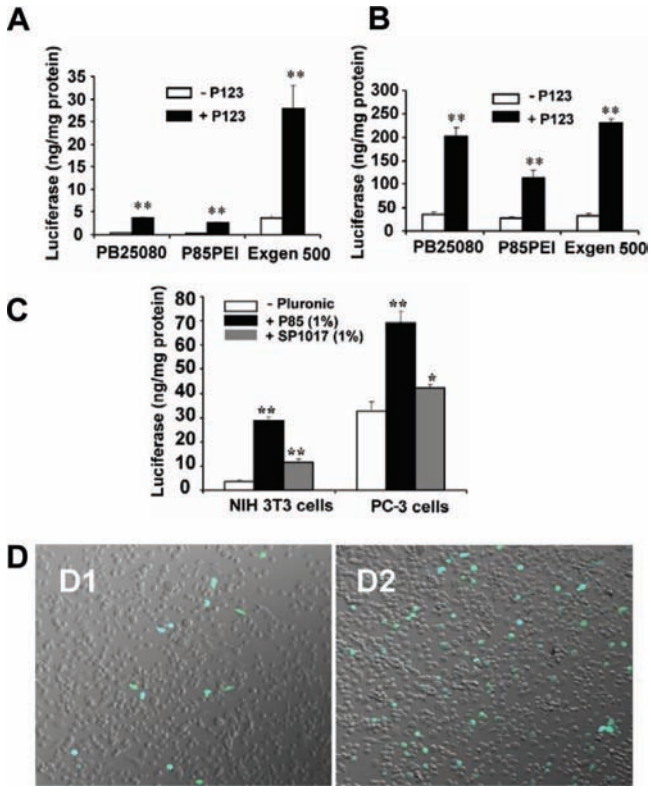

Figure 2. Enhancement of gene expression by Pluronic block copolymers in cells transfected with polyplexes. (A,B) Luciferase gene expression in NIH 3T3 (A) and PC-3 cells (B) transfected with different types of polyplexes containing gWIZLuc pDNA with/without 0.03% Pluronic P123 (** $p < 0.01$, $n = 3$). (C) Luciferase gene expression in NIH 3T3 and PC-3 cells transfected with Exgen 500-based polyplex with/without 1% Pluronic P85 or SP1017 (* $p < 0.05$, ** $p < 0.01$, $n = 3$). (D) Confocal microscopy images of GFP gene expression in PC-3 cells transfected with Exgen 500-based polyplex containing pEGFP-N1 pDNA without (D1) or with (D2) Pluronic P123.

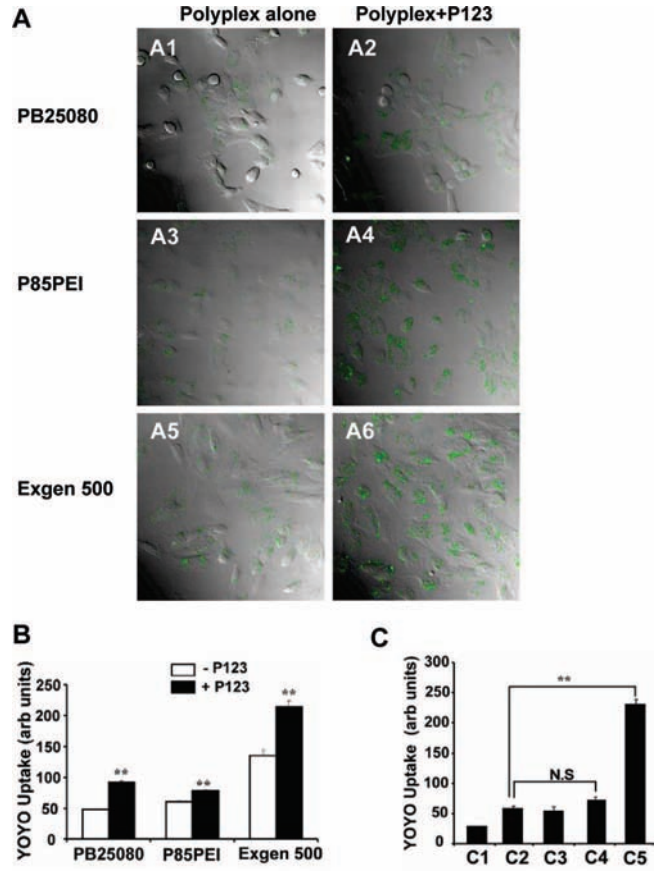

Figure 3. Effect of 0.03% w/v Pluronic P123 on uptake of the YOYO-1 labeled gWIZLuc pDNA in NIH 3T3 and PC-3 cells. (A) Confocal microscopy images of live cells 2 h after NIH 3T3 cells transfection with PB25080 (A1,A2), P85PEI (A3,A4), and Exgen 500 (A5,A6) based polyplexes without (A1,A3,A5) or with (A2,A4,A6) Pluronic P123. (B) Flow cytometry under the same transfection conditions as (A) comparing groups with/without Pluronic. (C) Flow cytometry of (C1) PC-3 cells alone and PC-3 cells transfected for 2 h with (C2) naked pDNA, (C3) naked pDNA with Pluronic P123, (C4) PB25080/pDNA polyplex, and (C5) PB25080/pDNA polyplex with Pluronic P123. (B,C) Statistical comparisons between (B) untreated and Pluronic P123 treated groups or (C) pDNA alone and polyplex-treated groups were made as follows ** $p < 0.01$, n.s., not significant ($n = 3$).

Localization of YOYO-1 labeled DNA was examined under the confocal microscope and flow cytometery was performed on nuclei isolated after transfection in these cells.

Nuclei Isolation. NIH 3T3 cells were plated in 100 × 20 mm^2 tissue culture plates (BD Biosciences, San Jose, CA) and grown overnight. Nuclei were isolated using Qproteome Nuclear Protien kit (Qiagen, Germantown, MD). Briefly, after transfection of YOYO-1 labeled DNA cells were washed twice with PBS, removed gently using a scraper, and centrifuged (12 000 rpm, 5 min, 4 °C). The pellets were lysed using the Qiagen lysis buffer supplemented with protease inhibitor solution and 0.1 M dithiothreitol, centrifuged, resuspended in the Qiagen detergent solution, centrifuged again, and then finally, the nuclei were resuspended in 1% bovine serum albumin in PBS.

Immunocytochemistry. Cells were pretreated with DMEM without FBS for 30 min and then treated with 0.03% FITC-labeled Pluronic P123 for 1 h, washed, and fixed with 4% paraformaldehyde. Rabbit anticaveolin-1-Cy3 antibody (1:100) (Sigma Aldrich, St Louis, MO) and mouse anticlathrin antibody (Affinity Bioreagents, Golden, CO) (1:10) were incubated in blocking buffer overnight at 4 °C. For detection of anticlathrin antibody specific IgG antibody conjugated to Alexa 568 (Invitrogen Inc., Carlsbad, CA) was added to cells for 1 h at 37 °C. After extensive washing, cells were labeled with ToPro-3 iodide, mounted with antifade reagent, and examined under confocal microscope.

NFκB Signaling Pathway Microarray. C2C12-CMV^{luc} cells were treated with 1% Pluronic P85 for 5 min, washed twice with PBS, and incubated for additional 3 h. Cells were collected and total RNA was isolated with TRIzol reagent, then quantified and qualified by UV spectrophotometry and gel electrophoresis, respectively. Oligo GEArray with 3 μg of total RNA of each sample was performed following the manufacture's protocol (cDNA synthesis; cRNA synthesis, labeling and amplification; cRNA cleanup; Oligo GEArray hybridization and detection). Statistical analysis was performed using the GEArray Expression Analysis Suite software.

Statistical Analysis. Unless indicated otherwise, statistical comparisons are made using Student's *t* test.

RESULTS

Polyplex Particle Size and Morphology. All polycations when mixed with the pDNA formed stable nanoparticles with effective diameters from approximately 85 nm for PB25080 to 180 nm for Exgen 500 (Table 1). Effective particle diameters were practically unchanged or changed slightly upon addition of Pluronic 123 using different orders of mixing (Table 1), N/P ratios (Figure 1A), or concentrations of the copolymer (Figure 1B). Similar results were observed with Pluronic P85 (not shown). Furthermore, the particle morphology as determined by TEM remained appear to be spherical (Figure 1C). Alto-

Table 1. Effect of Pluronic P123 on Particle Size for Different Polyplex Compositions and Component Mixing Orders

polyplex[a]	effective diameter (nm)[b]	polydispersity
DNA + P123	N/A	N/A
DNA + PB25080	85 ± 3	0.096
DNA + P123 + PB25080	76 ± 6	0.229
DNA + PB25080 + P123	72 ± 5	0.213
DNA + P85PEI	150 ± 2	0.155
DNA + P123 + P85PEI	120 ± 2	0.212
DNA + Exgen 500	180 ± 4	0.164
DNA + P123 + Exgen 500	160 ± 6	0.241

[a] Polyplexes were formed at N/P = 8 for PB25080 and P85PEI and N/P = 9 for Exgen 500. [b] Data are mean ± SEM (n = 5).

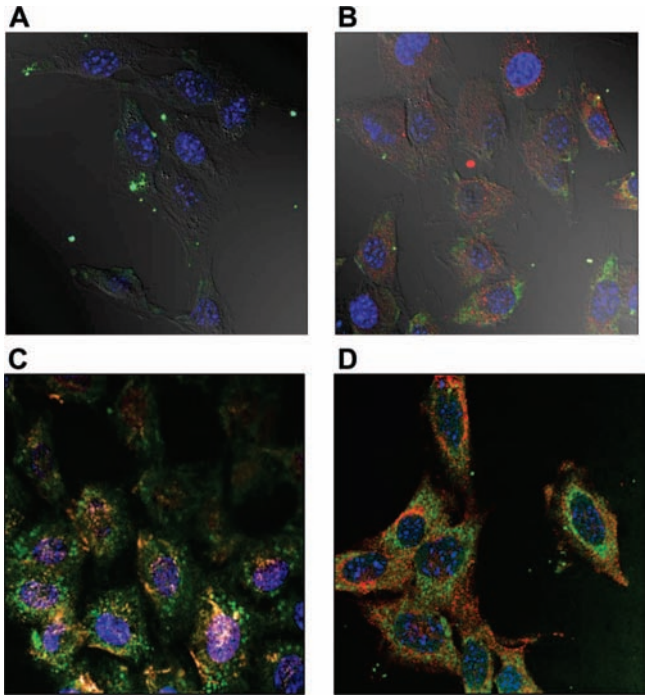

Figure 4. Cellular localization of fluorescently labeled DNA and/or Pluronic 123 examined by confocal microscopy on fixed NIH 3T3 cells. (A,B) Cells were transfected for 30 min with Exgen 500-based polyplex without (A) or with (B) 0.03% Pluronic P123. Signals correspond to YOYO-1 labeled gWIZLuc pDNA (green), RITC-labeled Pluronic P123 (red), and ToPro-3 stained nuclei (blue), respectively. (C,D) Cells were exposed to 0.03% Pluronic P123 alone for 60 min and then examined for colocalization of Pluronic P123 with caveolin-1 (C) and clathrin (D). Signals correspond to FITC-labeled Pluronic P123 (green), caveolin-1 (red), clathrin (red), and ToPro-3 stained nuclei (blue).

gether, these results demonstrate that addition of Pluronic results in little change in polyplex size or morphology.

Enhancement of Gene Expression with Pluronic. Significant enhancement of luciferase expression was observed upon addition of Pluronic P123, Pluronic P85, or SP1017 in both NIH 3T3 and PC-3 cells transfected with various polyplexes (Figure 2A−C). Overall protein levels in the cells treated with polyplexes were not affected by adding Pluronic (not shown) although the portion of cells expressing the transgene increased (Figure 2D). A similar enhancement was observed with several other polyplex types (Superfect, linear PEI) and in a different cell line (C2C12) (*24*). Thus, there is compelling evidence that Pluronic block copolymers enhance transfection by different polyplexes in numerous cell types.

Effect of Pluronic on DNA Uptake in Cells. Addition of Pluronic P123 considerably enhanced the uptake of polyplex-delivered DNA in NIH 3T3 cells (Figure 3A). The magnitude of the effect varied for each polyplex type (1.3, 1.6, and 1.9-fold for P85PEI, Exgen 500, and PB25080, respectively), but

Table 2. Effect of Endocytosis Inhibitors on Uptake of YOYO-Labeled gWIZLuc pDNA in NIH 3T3 Cells

	mean fluorescence (arb units)[a]	
polyplex	− P123	+ P123
DNA + PB25080	100 ± 3	158 ± 3
DNA + PB25080 + MBCD	75 ± 6**	111 ± 7**
DNA + PB25080 + sucrose	50 ± 1***	71 ± 1***

[a] Statistical comparisons were made for inhibitor treated and nontreated groups (** $p < 0.01$, *** $p < 0.001$, $n = 3$).

the differences in the presence of Pluronic were significant (Figure 3B). An even greater enhancement of uptake of polyplex-delivered DNA with Pluronic was observed in PC-3 cells (Figure 3C). In contrast, Pluronic did not affect uptake of the naked DNA. The effects of Pluronic on cell uptake were observed as early as 30 min after exposure (Figure 4A,B). Notably, Pluronic was internalized during the same period, but exhibited little if any colocalization with the DNA (Figure 4A,B). Interestingly, Pluronic exhibited greater colocalization with caveolin-1 compared to clathrin (Figure 4C,D). This is consistent with a recent study suggesting that caveolae-mediated endocytosis is a preferred pathway for cellular uptake of Pluronic individual molecules (*33*). At the same time, PEI-based polyplexes enter cells through both caveolae- and clathrin-mediated endocytosis (*34, 35*). Inhibitors of these pathways, MBCD for caveolae and hypertonic sucrose for clathrin, each significantly decreased uptake of pDNA delivered with polyplexes without and with Pluronic (Table 2). However, the effect of sucrose was much more pronounced than that of MBCD, suggesting clathrin-mediated endocytosis is a preferred route for the polyplex. Hence, Pluronic and polyplex are likely to have different internalization pathways, and the transport pathways of pDNA apparently did not change in the presence of Pluronic.

Enhancement of Nuclear Transport of DNA by Pluronic. Initial confocal microscopy of cellular localization of YOYO-1 labeled DNA suggested that the presence of Pluronic during transfection enhanced nuclear transport of the gWIZLuc plasmid at different time points (Figure 5). Specifically, in Pluronic treatment groups the DNA exhibited enhanced perinuclear localization 2 h after transfection and increased nuclear uptake 3 h after transfection. To exclude possible effects of the copolymer on the early stage of DNA internalization, the subsequent experiments first transfected cells with a polyplex without Pluronic (for 2 h) and then treated cells with Pluronic for different periods. In these experiments, along with the gWIZLuc plasmid we also used two other plasmids, pNFκB-luc and pAP-1-luc, containing NFκB and AP-1 response elements, respectively. Figure 6 presents the results both as quantification of the DNA in isolated nucleus as well as confocal images in live cells. The addition of Pluronic resulted in a quantitative increase in accumulation of the gWIZLuc and pNFκB-luc plasmids in isolated nuclei. The gWIZLuc is controlled by a CMV promoter, which also contains NFκB binding sites. In contrast, no increase in nuclei accumulation was observed with the pAP-1-luc, which does not contain NFκB binding sites. Altogether, these results suggest that Pluronic can enhance nuclear translocation of polyplex-delivered DNA in a promoter-dependent fashion.

Activation of NFκB Signaling Pathway by Pluronic. Pluronic was previously shown to activate the NFκB signaling pathway by inducing phosphorylation of IκB (*24*). Here, we examined the effect of Pluronic on NFκB-related genes using microarray (Figure 7). Pluronic P85 significantly upregulated

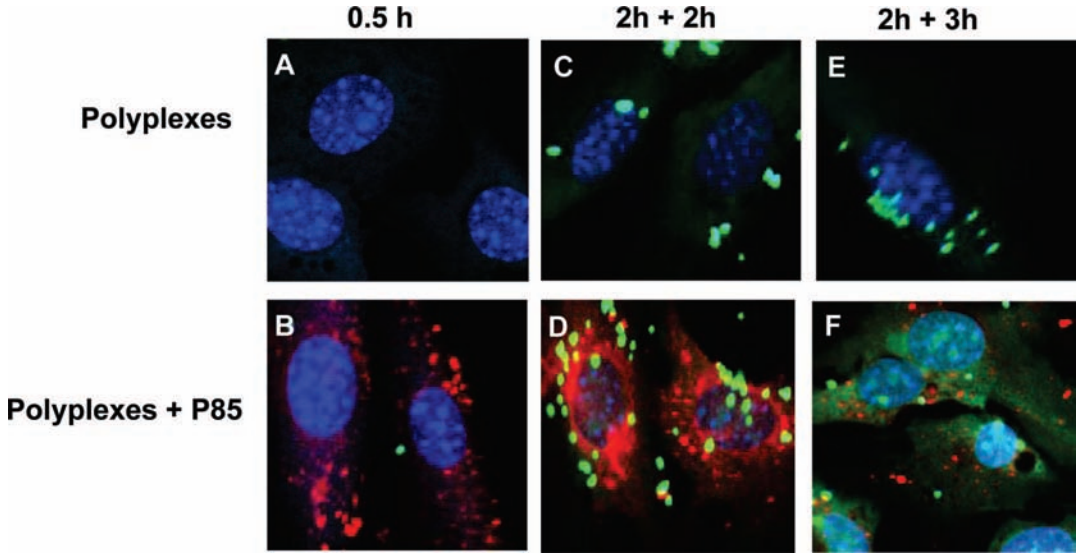

Figure 5. Effect of Pluronic on intracellular localization of DNA in NIH 3T3 cells. Confocal microscopy images of cells transfected with Exgen 500-based polyplexes with (B,D,F) or without (A,C,E) 1% Pluronic P85. Cells were exposed to polyplex for (A,B) 30 min or (C−F) 2 h and then incubated for additional 2 (C,D) or 3 h (E,F) in a fresh medium. Signals correspond to YOYO-labeled pDNA (green), RITC-labeled Pluronic P85 (red), and ToPro-3 stained nuclei (blue), respectively. This figure is representative of multiple areas in confocal images.

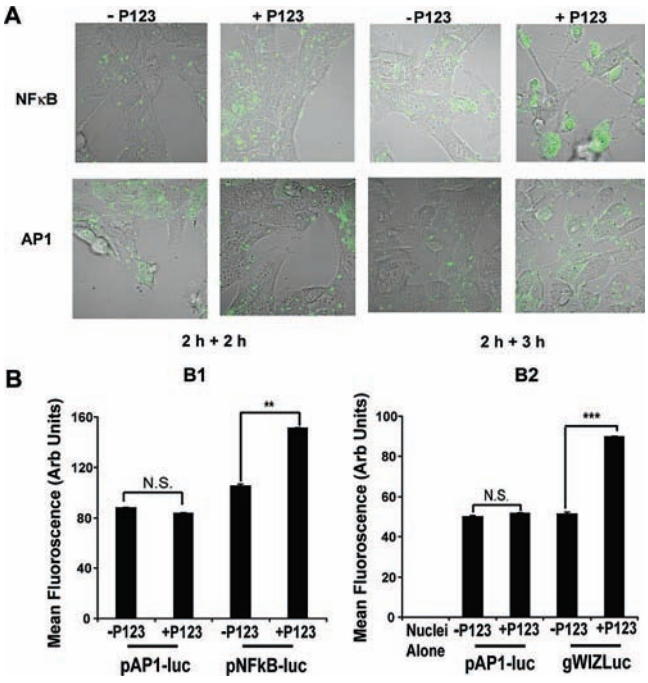

Figure 6. Promoter-dependent enhancement of nuclear transport of pDNA by Pluronic P123 in NIH 3T3 cells. (A) Confocal microscopy images of live cells transfected (2 h) with pNFκB-luc or pAP-1-luc using Exgen 500 polyplexes and then cultured for 2 or 3 h with or without 0.03% Pluronic P123. Signal corresponds to YOYO-1 labeled pDNA. (B) Flow cytometery of isolated nuclei of cells transfected with pAP-1-luc (as a control B1, B2) and either pNFκB-luc (B1) or gWIZLuc (B2). Cells were transfected using the same procedure as in (A) and then cultured for 3 h with or without 0.03% Pluronic P123. (B) ** $p < 0.01$, *** $p < 0.001$, n.s., not significant ($n = 3$).

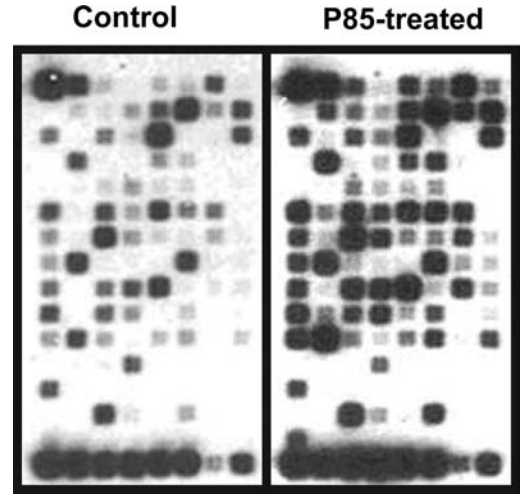

Figure 7. Effect of Pluronic on NFκB related genes expression in C2C12-CMV^{luc} cells. Cells were exposed to 1% Pluronic P85 for 5 min, washed by PBS, and incubated for additional 3 h. Total RNA was isolated and assayed using Oligo GEArray Mouse NFκB Signaling Pathway Microarray. A representative set of images is shown for control and Pluronic treated groups. The triplicate averaged data are presented in Supporting Information (Table S-1).

39 out of 113 genes related to NFκB-mediated signal transduction (Supporting Information Table S-1).

DISCUSSION

Inefficient nuclear translocation of DNA is believed to be the Achilles' heel of gene therapy (*36*). Coupling NLS peptides with pDNA to facilitate its nuclear import has been a major approach to address this problem (*9*−*21*). Our work demonstrates a simpler and potentially safer approach using a well-known pharmaceutical excipient, Pluronic block copolymer, to activate intrinsic nuclear translocation machinery and enhance nuclear gene transfer with polyplex-delivered pDNA. Pluronics are amphiphilic block copolymers that are widely used in pharmaceutical compositions and were evaluated successfully as intravenous agents in cancer therapy clinical trials (*37*). Astafieva et al. were the first to report that addition of Pluronic P85 can increase the uptake and expression of pDNA delivered by poly(*N*-ethyl-4-vinylpyridinium)-based polyplex (*38*). In this work, we demonstrate for the first time that Pluronics additionally increase nuclear transport of pDNA delivered with polyplexes in a promoter-dependent manner. To demonstrate the effects of Pluronics, we evaluated three representative polycations: (1) a linear PEI, Exgen 500; (2) biotin-modified graft copolymer of PEO and PEI, PB25080; and (3) a graft/block copolymer of Pluronic P85 and PEI, P85PEI. Among a variety

of polycations used in polyplexes, linear PEI is, perhaps, one of the most efficacious (*39, 40*). Two other PEI-based polycations evaluated in this work were developed in our laboratory to enhance polyplex stability in the body by grafting hydrophilic PEO chains to PEI (PB25080) (*30*) or enhance membrane interactions of polyplex by grafting amphiphilic Pluronic P85 to PEI (P85PEI) (*41*).

We previously suggested that Pluronic can increase gene transfer by binding with polyplexes and decreasing particle size (*32*). Since Pluronic is not charged, this interaction involves hydrophobic binding of poly(propylene oxide) chains of Pluronic with nonpolar sites in a polyplex. However, contrary to previously studied polyplex systems, which aggregated in the absence of Pluronic (*32*), the polycations used in this work each formed stable polyplexes with pDNA. Addition of Pluronic to these polyplexes resulted in little if any change in particle size. Furthermore, confocal microscopy suggested that Pluronic distribution within the cells was different from that of pDNA at each time point; i.e., Pluronic is not transported along with the DNA but may act independently, perhaps by affecting cell transport machinery, such as activating NFκB signaling pathway (as described later). Therefore, we propose that Pluronic acts as a biological response modifier, presumably by binding with cellular membranes and activating cell signaling pathways that enhance nuclear gene delivery (*22, 23*). This is supported by the observation that nuclear transport of the pDNA was enhanced when Pluronic was added to cells after polyplex transfection (Figure 6). The time course for the nuclear entry of pDNA, 4 to 5 h after beginning of transfection, is consistent with a previous report (*42*). Polyplexes formed by Exgen 500 rapidly escape the endosomes, spread into the cytoplasm, and then dissociate within 4 h, followed by the nuclear uptake of pDNA (*43, 44*). Previously, Pitard et al. reported that coinjection of pDNA and Pluronic L64 into the cytosol increased the percentage of cells expressing a reporter gene (*45*), suggesting that Pluronic may enhance transport of naked pDNA from the cytosol into the nucleus.

The involvement of the NFκB signaling pathway was directly demonstrated by the promoter dependence of Pluronic effect on pDNA nuclear uptake. The plasmids containing NFκB binding sites, gWIZLuc and pNFκB-luc, exhibited increased unclear uptake with Pluronic, while the pAP-1-luc plasmid, which lacks an NFκB binding, site did not. Evidence that supports the activation of the NFκB pathway by Pluronic was shown by phosphorylation of IκB within 5 min (*24*), increased NFκB nuclear localization (*25*), and upregulation of numerous NFκB-related genes. It has also been shown that NFκB can bind cytosolic DNA and transport it to the nucleus through nuclear import machinery (*27, 46, 47*). Furthermore, the NLS of NFκB alone can transport DNA across the plasma membrane and into the cytosol (*47*). Thus, the early stages of gene transfer may also be affected by the activation of NFκB, which would explain the increased cellular uptake of pDNA observed in this work. Altogether, we propose that Pluronics rapidly activate NFκB (*24*), and NFκB binds pDNA that contain NFκB-binding sites, then increases nuclear import of a pDNA through the NF-κB transport into the nucleus. Furthermore, following the delivery of pDNA to the nucleus, Pluronics increase transcriptional activation of genes through the NFκB signaling pathway (*24*). We present evidence here that Pluronic colocalizes in cells with caveolin-1, which regulates NFκB activation (*48*). In addition, an extensive study describing binding of Pluronic with caveolae and disruption of caveolae-mediated endocytosis has been recently published (*33*). Hence, there is a possibility that Pluronic activates NFκB through the disruption of caveolae.

The safety of Pluronic formulations may be an important advantage for their use in nonviral gene delivery. Even though NFκB was activated, inflammatory responses to Pluronics are mild and no cytotoxic effects are seen at their effective doses in many cell lines (*24*). More importantly, clinical trials in human subjects reinforce the safety of Pluronic formulations, such as SP1017 (*37*), which was also used in this study. This suggests a possibility of optimizing Pluronic formulations to safely enhance gene therapy. Pluronic may be delivered simultaneously with polyplexes or administered after polyplexes. For example, after intravenous administration Pluronic block copolymers were shown to accumulate in the tumors (data in preparation), which are same sites where polyplexes may be targeted. In addition, both polyplexes and Pluronic can be administered locally (*49*). Furthermore, the fact that the increased nuclear transfer was observed with Pluronic added after transfection introduces a possibility for consequent treatments with the polyplex and Pluronic. It is also important to note that Pluronics may not be the only polymers capable of affecting nuclear delivery of pDNA via modulation of cell signaling. Hence, it is advisable to evaluate the effects of all polymer transfection systems, especially those that produce very strong enhancements of gene expression and may have membrane-active hydrophobic moieties (*50*−*52*). It is noteworthy that most polyplex transfection systems require a considerable excess of polycation that cannot incorporate in the complex with DNA and may directly affect cell signaling machinery. Finally, this study underscores the need to match the polymeric formulation with pDNA structure to take full advantage of potential polymer effects on signal transduction.

ACKNOWLEDGMENT

This study was supported by Tobacco Settlement Funds awarded to University of Nebraska, and National Institutes of Health R01 CA116591 to A.V.K. We would like to thank Dr. Sergey Vinogradov for assistance in synthesizing PB25080 and P85PEI. We also thank UNMC Confocal and Flow Cytometery Core facilities for technical assistance. A.V.K. is a cofounder, shareholder and scientific advisor of Supratek Pharma Inc. (Montreal, Canada), which developed Pluronic-based SP1049C and SP1017 formulations for chemotherapy and gene delivery respectively.

Supporting Information Available: Additional data as described in the text. This material is available free of charge via the Internet at http://pubs.acs.org.

LITERATURE CITED

(1) Schaffer, D. V., and Lauffenburger, D. A. (2000) Targeted synthetic gene delivery vectors. *Curr. Opin. Mol. Ther. 2*, 155–61.

(2) Wiethoff, C. M., and Middaugh, C. R. (2003) Barriers to nonviral gene delivery. *J. Pharm. Sci. 92*, 203–17.

(3) Capecchi, M. R. (1980) High efficiency transformation by direct microinjection of DNA into cultured mammalian cells. *Cell 22*, 479–88.

(4) Graessmann, M., Menne, J., Liebler, M., Graeber, I., and Graessmann, A. (1989) Helper activity for gene expression, a novel function of the SV40 enhancer. *Nucleic Acids Res. 17*, 6603–12.

(5) Mirzayans, R., Aubin, R. A., and Paterson, M. C. (1992) Differential expression and stability of foreign genes introduced into human fibroblasts by nuclear versus cytoplasmic microinjection. *Mutat. Res. 281*, 115–22.

(6) Thorburn, A. M., and Alberts, A. S. (1993) Efficient expression of miniprep plasmid DNA after needle micro-injection into somatic cells. *Biotechniques 14*, 356–8.

(7) Dean, D. A., Dean, B. S., Muller, S., and Smith, L. C. (1999) Sequence requirements for plasmid nuclear import. *Exp. Cell Res. 253*, 713–22.

(8) Friedrich, B., Quensel, C., Sommer, T., Hartmann, E., and Kohler, M. (2006) Nuclear localization signal and protein context both mediate importin alpha specificity of nuclear import substrates. *Mol. Cell. Biol. 26*, 8697–709.

(9) Aronsohn, A. I., and Hughes, J. A. (1998) Nuclear localization signal peptides enhance cationic liposome-mediated gene therapy. *J. Drug Target. 5*, 163–9.

(10) Chan, C. K., and Jans, D. A. (1999) Enhancement of polylysine-mediated transferrinfection by nuclear localization sequences: polylysine does not function as a nuclear localization sequence. *Hum. Gene Ther. 10*, 1695–702.

(11) Kaneda, Y., Iwai, K., and Uchida, T. (1989) Increased expression of DNA cointroduced with nuclear protein in adult rat liver. *Science 243*, 375–8.

(12) Hagstrom, J. E., Ludtke, J. J., Bassik, M. C., Sebestyen, M. G., Adam, S. A., and Wolff, J. A. (1997) Nuclear import of DNA in digitonin-permeabilized cells. *J. Cell Sci. 110*, 2323–31, Pt 18.

(13) Ciolina, C., Byk, G., Blanche, F., Thuillier, V., Scherman, D., and Wils, P. (1999) Coupling of nuclear localization signals to plasmid DNA and specific interaction of the conjugates with importin alpha. *Bioconjugate Chem. 10*, 49–55.

(14) van der Aa, M. A., Koning, G. A., d'Oliveira, C., Oosting, R. S., Wilschut, K. J., Hennink, W. E., and Crommelin, D. J. (2005) An NLS peptide covalently linked to linear DNA does not enhance transfection efficiency of cationic polymer based gene delivery systems. *J. Gene Med. 7*, 208–17.

(15) Zanta, M. A., Belguise-Valladier, P., and Behr, J. P. (1999) Gene delivery: a single nuclear localization signal peptide is sufficient to carry DNA to the cell nucleus. *Proc. Natl. Acad. Sci. U.S.A. 96*, 91–6.

(16) Branden, L. J., Mohamed, A. J., and Smith, C. I. (1999) A peptide nucleic acid-nuclear localization signal fusion that mediates nuclear transport of DNA. *Nat. Biotechnol. 17*, 784–7.

(17) Branden, L. J., Christensson, B., and Smith, C. I. (2001) In vivo nuclear delivery of oligonucleotides via hybridizing bifunctional peptides. *Gene Ther. 8*, 84–7.

(18) Liang, K. W., Hoffman, E. P., and Huang, L. (2000) Targeted delivery of plasmid DNA to myogenic cells via transferrin-conjugated peptide nucleic acid. *Mol. Ther. 1*, 236–43.

(19) Morris, M. C., Chaloin, L., Choob, M., Archdeacon, J., Heitz, F., and Divita, G. (2004) Combination of a new generation of PNAs with a peptide-based carrier enables efficient targeting of cell cycle progression. *Gene Ther. 11*, 757–64.

(20) Dean, D. A., Strong, D. D., and Zimmer, W. E. (2005) Nuclear entry of nonviral vectors. *Gene Ther. 12*, 881–90.

(21) Cartier, R., and Reszka, R. (2002) Utilization of synthetic peptides containing nuclear localization signals for nonviral gene transfer systems. *Gene Ther. 9*, 157–67.

(22) Kabanov, A. V., Batrakova, E. V., Sriadibhatla, S., Yang, Z., Kelly, D. L., and Alakov, V. Y. (2005) Polymer genomics: shifting the gene and drug delivery paradigms. *J. Controlled Release 101*, 259–71.

(23) Kabanov, A. V. (2006) Polymer genomics: an insight into pharmacology and toxicology of nanomedicines. *Adv. Drug Delivery Rev. 58*, 1597–621.

(24) Sriadibhatla, S., Yang, Z., Gebhart, C., Alakhov, V. Y., and Kabanov, A. (2006) Transcriptional activation of gene expression by pluronic block copolymers in stably and transiently transfected cells. *Mol. Ther. 13*, 804–13.

(25) Yang, Z., Zhu, J., Sriadibhatla, S., Gebhart, C., Alakhov, V., and Kabanov, A. (2005) Promoter- and strain-selective enhancement of gene expression in a mouse skeletal muscle by a polymer excipient Pluronic P85. *J. Controlled Release 108*, 496–512.

(26) Muller, C. W., Rey, F. A., Sodeoka, M., Verdine, G. L., and Harrison, S. C. (1995) Structure of the NF-kappa B p50 homodimer bound to DNA. *Nature 373*, 311–7.

(27) Mesika, A., Grigoreva, I., Zohar, M., and Reich, Z. (2001) A regulated, NFkappaB-assisted import of plasmid DNA into mammalian cell nuclei. *Mol. Ther. 3*, 653–7.

(28) Mesika, A., Kiss, V., Brumfeld, V., Ghosh, G., and Reich, Z. (2005) Enhanced intracellular mobility and nuclear accumulation of DNA plasmids associated with a karyophilic protein. *Hum. Gene Ther. 16*, 200–8.

(29) Belenkov, A. I., Alakhov, V. Y., Kabanov, A. V., Vinogradov, S. V., Panasci, L. C., Monia, B. P., and Chow, T. Y. (2004) Polyethyleneimine grafted with pluronic P85 enhances Ku86 antisense delivery and the ionizing radiation treatment efficacy in vivo. *Gene Ther. 11*, 1665–72.

(30) Vinogradov, S. V., Bronich, T. K., and Kabanov, A. V. (1998) Self-assembly of polyamine-poly(ethylene glycol) copolymers with phosphorothioate oligonucleotides. *Bioconjugate Chem. 9*, 805–12.

(31) Vinogradov, S., Batrakova, E., Li, S., and Kabanov, A. (1999) Polyion complex micelles with protein-modified corona for receptor-mediated delivery of oligonucleotides into cells. *Bioconjugate Chem. 10*, 851–60.

(32) Gebhart, C. L., Sriadibhatla, S., Vinogradov, S., Lemieux, P., Alakhov, V., and Kabanov, A. V. (2002) Design and formulation of polyplexes based on pluronic-polyethyleneimine conjugates for gene transfer. *Bioconjugate Chem. 13*, 937–44.

(33) Sahay, G., Batrakova, E. V., and Kabanov, A. V. (2008) Different internalization pathways of polymeric micelles and unimers and their effects on vesicular transport. *Bioconjugate Chem.*, in press.

(34) Rejman, J., Bragonzi, A., and Conese, M. (2005) Role of clathrin- and caveolae-mediated endocytosis in gene transfer mediated by lipo- and polyplexes. *Mol. Ther. 12*, 468–74.

(35) Rejman, J., Conese, M., and Hoekstra, D. (2006) Gene transfer by means of lipo- and polyplexes: role of clathrin and caveolae-mediated endocytosis. *J. Liposome Res. 16*, 237–47.

(36) Verma, I. M., and Somia, N. (1997) Gene therapy - promises, problems and prospects. *Nature 389*, 239–42.

(37) Danson, S., Ferry, D., Alakhov, V., Margison, J., Kerr, D., Jowle, D., Brampton, M., Halbert, G., and Ranson, M. (2004) Phase I dose escalation and pharmacokinetic study of pluronic polymer-bound doxorubicin (SP1049C) in patients with advanced cancer. *Br. J. Cancer 90*, 2085–91.

(38) Astafieva, I., Maksimova, I., Lukanidin, E., Alakhov, V., and Kabanov, A. (1996) Enhancement of the polycation-mediated DNA uptake and cell transfection with Pluronic P85 block copolymer. *FEBS Lett. 389*, 278–80.

(39) Godbey, W. T., Wu, K. K., and Mikos, A. G. (1999) Poly(ethylenimine) and its role in gene delivery. *J. Controlled Release 60*, 149–60.

(40) Kichler, A., Chillon, M., Leborgne, C., Danos, O., and Frisch, B. (2002) Intranasal gene delivery with a polyethylenimine-PEG conjugate. *J. Controlled Release 81*, 379–88.

(41) Vinogradov, S. V., Batrakova, E. V., Li, S., and Kabanov, A. V. (2004) Mixed polymer micelles of amphiphilic and cationic copolymers for delivery of antisense oligonucleotides. *J. Drug Target. 12*, 517–26.

(42) Godbey, W. T., Wu, K. K., and Mikos, A. G. (1999) Tracking the intracellular path of poly(ethylenimine)/DNA complexes for gene delivery. *Proc. Natl. Acad. Sci. U.S.A. 96*, 5177–81.

(43) Brunner, S., Furtbauer, E., Sauer, T., Kursa, M., and Wagner, E. (2002) Overcoming the nuclear barrier: cell cycle independent nonviral gene transfer with linear polyethylenimine or electroporation. *Mol. Ther. 5*, 80–6.

(44) Itaka, K., Harada, A., Yamasaki, Y., Nakamura, K., Kawaguchi, H., and Kataoka, K. (2004) In situ single cell observation by fluorescence resonance energy transfer reveals fast intra-cytoplasmic delivery and easy release of plasmid

DNA complexed with linear polyethylenimine. *J. Gene Med. 6*, 76–84.
(45) Pitard, B., Pollard, H., Agbulut, O., Lambert, O., Vilquin, J.-T., Cherel, Y., Abadie, J., Samuel, J.-L., Rigaud, J.-L., Menoret, S., Anegon, I., and Escande, D. (2002) A nonionic amphiphile agent promotes gene delivery in vivo to skeletal and cardiac muscles. *Hum. Gene Ther. 13*, 1767–1775.
(46) Ragin, A. D., Morgan, R. A., and Chmielewski, J. (2002) Cellular import mediated by nuclear localization signal peptide sequences. *Chem. Biol. 9*, 943–8.
(47) Vacik, J., Dean, B. S., Zimmer, W. E., and Dean, D. A. (1999) Cell-specific nuclear import of plasmid DNA. *Gene Ther. 6*, 1006–14.
(48) Garrean, S., Gao, X. P., Brovkovych, V., Shimizu, J., Zhao, Y. Y., Vogel, S. M., and Malik, A. B. (2006) Caveolin-1 regulates NF-kappaB activation and lung inflammatory response to sepsis induced by lipopolysaccharide. *J. Immunol. 177*, 4853–60.
(49) Nguyen, H. K., Lemieux, P., Vinogradov, S. V., Gebhart, C. L., Guerin, N., Paradis, G., Bronich, T. K., Alakhov, V. Y., and Kabanov, A. V. (2000) Evaluation of polyether-polyethyleneimine graft copolymers as gene transfer agents. *Gene Ther. 7*, 126–38.
(50) Akinc, A., Anderson, D. G., Lynn, D. M., and Langer, R. (2003) Synthesis of poly(β-amino ester)s optimized for highly effective gene delivery. *Bioconjugate Chem. 14*, 979–88.
(51) Anderson, D. G., Peng, W., Akinc, A., Hossain, N., Kohn, A., Padera, R., Langer, R., and Sawicki, J. A. (2004) A polymer library approach to suicide gene therapy for cancer. *Proc. Natl. Acad. Sci. U.S.A. 101*, 16028–33.
(52) Anderson, D. G., Akinc, A., Hossain, N., and Langer, R. (2005) Structure/property studies of polymeric gene delivery using a library of poly(β-amino esters). *Mol. Ther. 11*, 426–34.

BC800144A

Supporting Information

Amphiphilic Block Copolymers Enhance Nuclear Entry of Polyplex-Delivered DNA

Zhihui Yang[*], *Gaurav Sahay*[*], *Srikanth Sriadibhatla*[*], *Alexander V. Kabanov*[*†]

[*]Center for Drug Delivery and Nanomedicine and Department of Pharmaceutical Sciences, College of Pharmacy, University of Nebraska Medical Center, 985830 Nebraska Medical center, Omaha, NE 68198-5830, United States and [†]Faculty of Chemistry, M.V. Lomonosov Moscow State University, 119899 Moscow, Russia

Position	Symbol	Refseq	Description	Folds increased
3	Atf1	NM_007497	Activating transcription factor 1	2.9
4	Atf2	NM_009715	Activating transcription factor 2	4.6
30	Hmgb1	NM_010439	High mobility group box 1	2.3
72	Polr2a	NM_009089	Polymerase (RNA) II (DNA directed) polypeptide A	2.9
77	Rel	NM_009044	Reticuloendotheliosis oncogene	4.5
78	Rela	NM_009045	V-rel reticuloendotheliosis viral oncogene homolog A	2.4
70	Pcaf	NM_020005	P300/CBP-associated factor	2.2
84	Smad4	NM_008540	MAD homolog 4 (Drosophila)	4.3
6	Bcl3	NM_033601	B-cell leukemia/lymphoma 3	3.3
10	Card14	NM_130886	Caspase recruitment domain family, member 14	2.2
11	Card4	NM_172729	Caspase recruitment domain 4	2.2
108	Tradd	NM_001033161	TNFRSF1A-associated via death domain	3.2
110	Traf3	NM_011632	Tnf receptor-associated factor 3	2.1
112	Traf6	NM_009424	Tnf receptor-associated factor 6	2.8
66	Nalp12	XM_355971	NACHT, LRR and PYD containing protein 12	2.0
74	Ppp5c	NM_011155	Protein phosphatase 5, catalytic subunit	3.6
53	Map2k6	NM_011943	Mitogen activated protein kinase kinase 6	2.6
54	Map3k1	NM_011945	Mitogen activated protein kinase kinase kinase 1	3.0
56	Map3k3	NM_011947	Mitogen activated protein kinase kinase kinase 3	4.4
60	Map4k2	NM_009006	Mitogen activated protein kinase kinase kinase kinase 2	4.4
61	Mapk11	NM_011161	Mitogen-activated protein kinase 11	4.4
64	Mapk8	NM_016700	Mitogen activated protein kinase 8	4.1
87	Tgfbr1	NM_009370	Transforming growth factor, beta receptor I	2.1
88	Tgfbr2	NM_009371	Transforming growth factor, beta receptor II	2.8
71	Plk2	NM_152804	Polo-like kinase 2 (Drosophila)	6.4
80	Ripk1	NM_009068	Receptor (TNFRSF)-interacting serine-threonine kinase 1	4.0
99	Tnfrsf10b	NM_020275	Tumor necrosis factor receptor superfamily, member 10b	2.7
103	Tnfrsf7	NM_001033126	Tumor necrosis factor receptor superfamily, member 7	4.4
100	Tnfrsf1a	NM_011609	Tumor necrosis factor receptor superfamily, member 1a	2.3
113	Vapa	NM_013933	Vesicle-associated membrane protein, associated protein A	2.2
8	Card10	NM_130859	Caspase recruitment domain family, member 10	5.1
105	Tnfsf14	NM_019418	Tumor necrosis factor (ligand) superfamily, member 14	3.6
35	Ikbkb	NM_010546	Inhibitor of KappaB Kinase beta	1.6
5	Bcl10	NM_009740	B-cell leukemia/lymphoma 10	2.9
22	Edaradd	NM_133643	EDAR (ectodysplasin-A receptor)-associated death domain	4.3
37	Ikbkg	NM_010547	Inhibitor of KappaB Kinase gamma	1.5
32	Icam1	NM_010493	Intercellular adhesion molecule	3.9
42	Il6	NM_031168	Interleukin 6	2.5
48	Lta	NM_010735	Lymphotoxin A	4.7

Table S-1. Effect of Pluronic P85 on the expression of NFκB related genes in C2C12-CMV^{luc} cells. Cells were exposed to 1% Pluronic P85 for 5 min, washed by PBS and incubated for additional 3 h. Total RNA was assayed using Oligo GEArray® Mouse NFκB Signaling Pathway Microarray (see **Figure 7** for a representative gene array) and gene expression was analyzed by GEArray Expression Analysis Suite software (see http://www.superarray.com/gene_array_product/HTML/OMM-025.html for detailed list of genes and layout). Only genes exhibiting at least 2-fold increase in expression are presented. (*i*) NFκB pathway: (**3, 4, 30, 72, 77, 78, 70, 84**) transcription factors; (**6, 10, 11, 108, 110, 112, 66, 74**) other factors; (**53, 54, 56, 60, 61, 64, 87, 88, 71, 80**) kinases; (**99, 103**) ligands and receptors; (**100, 113**) inflammatory response, extracellular or membrane molecules. (*ii*) activation of NFκB pathway: (**8, 105**) ligands and receptors; (**35, 5, 22**) IκB kinase/NFkB cascade; (**37**) transcription factor; (**32**) extracellular or membrane molecules; (*iii*) NFκB responsive genes: (**42, 48**) ligands and receptors, or cytokines.

Perylene Attached to 2′-Amino-LNA: Synthesis, Incorporation into Oligonucleotides, and Remarkable Fluorescence Properties *in Vitro* and in Cell Culture

Irina V. Astakhova,[†,‡] Vladimir A. Korshun,[‡] Kasper Jahn,[§] Jørgen Kjems,[§] and Jesper Wengel*[,†]

Nucleic Acid Center, Department of Physics and Chemistry, University of Southern Denmark, DK-5230 Odense M, Denmark, Shemyakin-Ovchinnikov Institute of Bioorganic Chemistry, Miklukho-Maklaya 16/10, 117997 Moscow, Russia, and Interdisciplinary Nanoscience Center, Department of Molecular Biology, University of Aarhus, DK-8000 Aarhus, Denmark.
Received May 19, 2008; Revised Manuscript Received July 8, 2008

During recent years, fluorescently labeled oligonucleotides have been extensively investigated within diagnostic approaches. Among a large variety of available fluorochromes, the polyaromatic hydrocarbon perylene is an object of increasing interest due to its high fluorescence quantum yield, long-wave emission compared to widely used pyrene, and photostability. These properties make perylene an attractive label for fluorescence-based detection *in vitro* and *in vivo*. Herein, the synthesis of 2′-*N*-(perylen-3-yl)carbonyl-2′-amino-LNA monomer **X** and its incorporation into oligonucleotides is described. Modification **X** induces high thermal stability of DNA:DNA and DNA:RNA duplexes, high Watson−Crick mismatch selectivity, red-shifted fluorescence emission compared to pyrene, and high fluorescence quantum yields. The thermal denaturation temperatures of duplexes involving two modified strands are remarkably higher than those for double-stranded DNAs containing modification **X** in only one strand, suggesting interstrand communication between perylene moieties in the studied 'zipper' motifs. Fluorescence of single-stranded oligonucleotides having three monomers **X** is quenched compared to modified monomer (quantum yields $\Phi_F = 0.03-0.04$ and 0.67, respectively). However, hybridization to DNA/RNA complements leads to Φ_F increase of up to 0.20−0.25. We explain it by orientation of the fluorochrome attached to the 2′-position of 2′-amino-LNA in the minor groove of the nucleic acid duplexes, thus protecting perylene fluorescence from quenching with nucleobases or from the environment. At the same time, the presence of a single mismatch in DNA or RNA targets results in up to 8-fold decreased fluorescence intensity of the duplex. Thus, distortion of the duplex geometry caused by even one mismatched nucleotide induces remarkable quenching of fluorescence. Additionally, a perylene-LNA probe is successfully applied for detection of mRNA *in vivo* providing excitation wavelength, which completely eliminates cell autofluorescence.

INTRODUCTION

During the past decade, there has been remarkable growth in the use of synthetic oligonucleotide analogues in nucleic acid research. Thus, fluorescently labeled oligonucleotides have now been introduced into a variety of studies within molecular biology and biochemistry (*1*−*3*). The sensitivity of fluorescence detection, its simplicity, and relative cheapness stimulate continuing development of medicinal tests based on fluorescence. Detection of nucleic acid hybridization is an important task in this area, which includes diagnostics of genetic and infectious diseases, discovery of gene-targeted drugs, and other biomedicinal studies (*1*−*5*). To become an effective tool for hybridization analysis, the labeled oligonucleotide has to display considerable change of fluorescence upon formation of complexes with complementary strands. Development of such detection methods has led to several formats of homogeneous fluorescence assays (*4*). For example, fluorescence polarization detection is based on the measurement of the increase in anisotropy when labeled DNA binds to the complementary strand (*5*). Fluorescence resonance energy transfer (FRET), another useful process for the above purposes that occurs in the excited state, is determined by the distance between the donor and acceptor of fluorescence (*1*, *3*, *4*). Taqman probes (also known as 5′-nuclease probes) (*7*), sunrise primers (*8*), molecular beacons (*3*, *9*), and duplex scorpion primers (*10*) utilize a distance-dependent fluorescence quenching mechanism. Labeling of oligonucleotide with a single kind of hybridization-sensitive substance is another promising paradigm for fluorescent probe design (*11*−*22*).

Chart 1. Structures of Pyrene and Perylene Fluorochromes

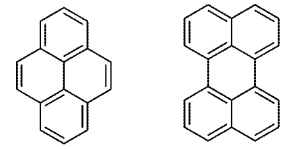

Among a wide variety of fluorochromes used to covalently label DNA, fluorescent dyes based on polyaromatic hydrocarbons (PAHs) have been extensively introduced in biochemical studies. The most common PAH in this area is pyrene (Chart 1). A long lifetime of the excited state (*23*), high fluorescence quantum yield (*24*), and the possibility to form noncovalent interactions with another PAH molecule (*25*−*37*) or nucleic acids (for example, by intercalation *38*−*41*) have inspired researchers to use pyrene for the design of many different detection systems. Thus, fluorescence of a single pyrene label linked to oligonucleotides was shown to be sensitive to duplex

* Corresponding author. E-mail: jwe@ifk.sdu.dk, Tel: +45-6550-2510, Fax: +45-6550-4385.
† University of Southern Denmark.
‡ Shemyakin-Ovchinnikov Institute of Bioorganic Chemistry.
§ University of Aarhus.

10.1021/bc800202v CCC: $40.75 © 2008 American Chemical Society
Published on Web 09/05/2008

Chart 2. Chemical Structures of LNA, 2′-Amino-LNA, and Its Pyrene and Perylene Derivatives

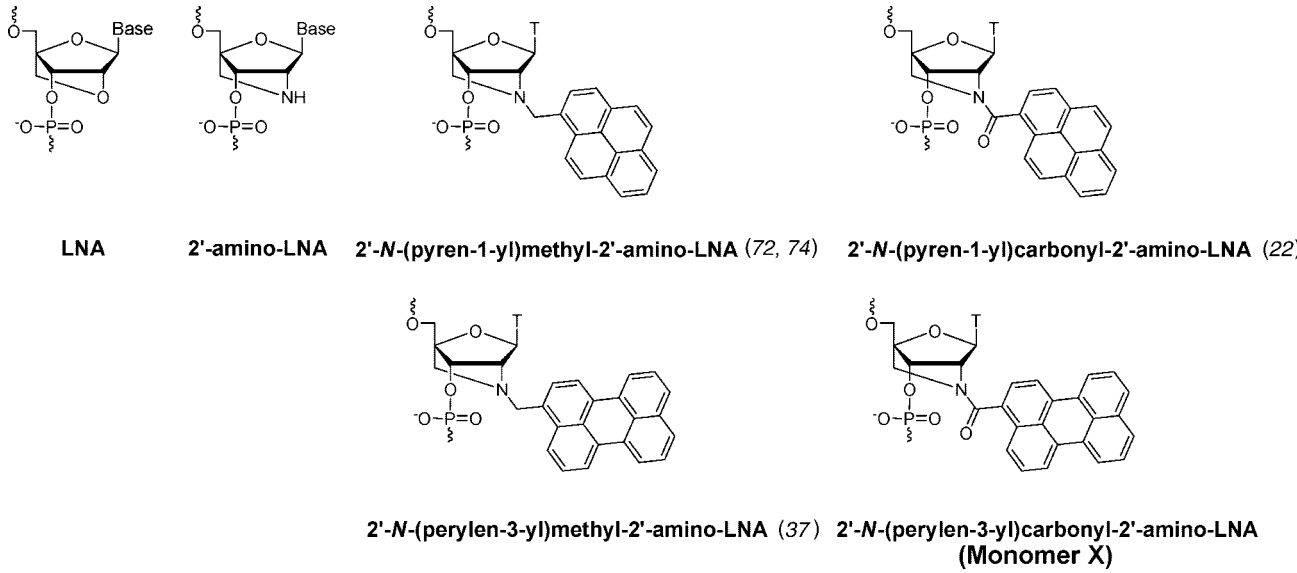

formation (*19, 21, 42*−*46*). It has also been pointed out that changes in the pyrene excimer-to-monomer fluorescence intensity ratio can be useful for detection of nucleic acid hybridization (*27*). More recently, Hrdlicka et al. investigated multilabeled pyrene-functionalized 2′-amino-LNA probes which exhibited high-affinity hybridization to DNA/RNA complements, quenched fluorescence of single-stranded probe, and large increase of the quantum yield and fluorescence brightness after hybridization (*22*). However, pyrene and its simple derivatives absorb at relatively short wavelengths (334 nm for pyrene in ethanol), which is likely to be unsatisfactory for experiments in living cells due to irradiation of several intrinsic fluorochromes at the same wavelengths (*47*). This limitation of pyrene can be overcome by its chemical functionalization (for example, introduction of phenylethynyl substituents *47*−*49*), or by choosing another fluorochrome with a long-wave emission spectrum relative to pyrene. Among PAHs, perylene is such a fluorochrome (Chart 1), which resembles pyrene in its chemical behavior, but has essentially different photochemical properties (*23*). Fluorescence of perylene is observed at 450−500 nm; its excited lifetime is relatively short (4−5 ns), while the fluorescence quantum yield is very high (0.5−1.0). Furthermore, perylene displays a strong fluorescence anisotropy effect (*24*). Unlike pyrene, perylene is not a common fluorescent dye for modification of oligonucleotides, whereas it is widely used in the field of lipids (*50*−*55*). Mostly, perylene attached to DNA was employed as an acceptor of fluorescence energy in FRET-studies (*27, 37, 56*−*59*), and only scarcely in nucleic acid hybridization assays (*60*−*65*).

Besides insertion of fluorescent dyes, chemical modification of oligonucleotides allows improvement of their binding affinity and selective recognition of cDNA and/or RNA. These properties have in particular been reported for locked nucleic acids (LNA (*66*−*70*), 2′-amino-LNA (*71*), and its *N*-functionalized derivatives *22, 40, 72*−*74*) (Chart 2), and have stimulated intensive investigations of LNA-modified oligonucleotides as diagnostic tools and therapeutic agents (*75, 76*). Moreover, affinity enhancing LNAs are interesting monomers within nucleic acid nanotechnology, including so-called Ångström-scale chemical engineering (*32, 77*).

Stimulated by the high-affinity hybridization of LNAs (*40, 66*−*74*), sensitivity of pyrene-functionalized 2′-amino-LNA probes to hybridization (*22*), and taking into account perylene's superiority in fluorescence quantum yield and emission wavelengths relative to pyrene, we have investigated perylene-modified 2′-amino-LNA. In this paper, we describe synthesis of 2′-*N*-(perylen-3-yl)carbonyl-2′-amino-LNA monomer **X**, its incorporation into synthetic oligonucleotides, thermal denaturation studies, and spectral properties of the conjugates containing perylene residue either in one or in two complementary strands of the duplexes (Chart 3).

EXPERIMENTAL PROCEDURES

General. Reagents obtained from commercial suppliers were used as received; 3-acetylperylene (*78*), diisopropylammonium tetrazolide (*79*), and nucleoside **1** (*71, 80, 81*) were synthesized as described. Perylene and 9,10-diphenylanthracene used as standards for emission quantum yield measurements were recrystallized. HPLC grade toluene and acetone were distilled and stored over activated 4 Å molecular sieves. DCM was always used freshly distilled over CaH_2. Other solvents were used as received. Photochemical studies were performed using spectral grade cyclohexane.

NMR spectra were recorded at 303 K on Varian Gemini 2000 300 MHz and Bruker DRX 500 MHz instruments. Chemical shifts are reported in ppm, relative to solvents peaks (DMSO-d_6, 2.50 ppm for ^{1}H and 39.5 ppm for ^{13}C; 85% aq H_3PO_4, 0.00 ppm for ^{31}P). ^{1}H NMR coupling constants are reported in Hz and refer to apparent multiplicities. High resolution mass spectra were recorded in positive ion mode using IonSpec Fourier Transform ICR mass spectrometer (MALDI) or PE SCIEX QSTAR pulsar mass spectrometer (ESI). Melting points were determined using a Boetius heating table and are uncorrected. Analytical thin-layer chromatography was performed on Kieselgel 60 F_{254} precoated aluminum plates (Merck). Silica gel column chromatography was performed using Merck Kieselgel 60 0.040−0.063 mm.

Oligonucleotide synthesis was carried out on a PerSpective Biosystems Expedite 8909 instrument in a 200 nmol scale using manufacturer's standard protocols. In the case of LNA phosphoramidites (monomers T^L and $^{Me}C^L$), the coupling step time was extended to 15 min. To accomplish incorporation of monomer **X**, a double hand-coupling procedure with extended coupling time (2 × 30 min) was performed. In the case of phosphoramidite **3** pyridine hydrochloride solution in CH_3CN was used as activator. 95−99% per step coupling yields of monomer **X** were obtained based on the absorbance of the dimethoxytrityl cation released after each coupling. The coupling efficiencies of standard DNA and LNA amidites varied between

Chart 3. Representative Structures of the Perylene Conjugates Prepared in This Study[a]

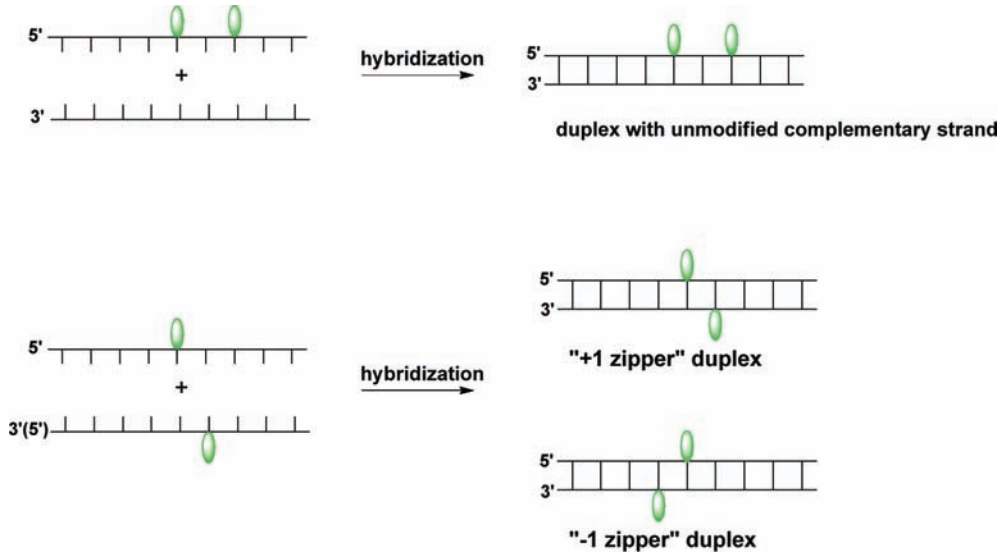

[a] Green droplets indicate monomer **X**.

98% and 100%. Cleavage from solid support and removal of nucleobase protecting groups was effected using standard conditions (32% aqueous ammonia for 12 h at 55 °C). Unmodified DNA/RNA strands were obtained from commercial suppliers and used without further purification, while all the modified oligonucleotides were purified by DMT-ON RP-HPLC using the Waters Prep LC 4000 equipped with Xterra MS C18-column (10 μM, 300 mm × 7.8 mm). Elution was performed starting with an isocratic hold of A-buffer for 5 min followed by a linear gradient to 55% B-buffer over 75 min at a flow rate of 1.0 mL/min (A-buffer: 95% 0.1 M NH_4HCO_3, 5% CH_3CN; B-buffer: 25% 0.1 M NH_4HCO_3, 75% CH_3CN). RP-purification was followed by detritylation (80% aq AcOH, 20 min), precipitation (abs EtOH, −18 °C, 12 h) and washing with abs EtOH three times. The identity of ONs was verified by MALDI-TOF mass spectrometry (Table S1, Supporting Information). UV−visible absorption spectra and thermal denaturation experiments were performed on a Perkin-Elmer Lambda 35 UV/vis spectrometer equipped with PTP 6 (Peltier Temperature Programmer) in a medium salt buffer (100 mM NaCl, 10 mM sodium phosphate, 0.1 mM EDTA, pH 7.0). Concentrations of ONs were calculated using the following extinction coefficients (OD_{260}/μmol): G, 10.5; A, 13.9; T/U, 7.9; C, 6.6; perylene, 33.2. ONs (1.0 μM each strand) were thoroughly mixed, denaturated by heating, and subsequently cooled to the starting temperature of the experiment. Thermal denaturation temperatures (T_m values, °C) were determined as the maximum of the first derivative of the thermal denaturation curve (A_{260} vs temperature). Reported T_m values are an average of two measurements within ±1.0 °C. Fluorescence spectra were obtained in a medium salt buffer using a PerkinElmer LS 55 luminescence spectrometer equipped with a Peltier temperature controller. For recording of fluorescence spectra, 0.1 μM concentrations of the single-stranded probe or corresponding duplex were used. For weakly fluorescent samples, concentration was increased to 0.5 μM. Excitation spectrum was obtained recording emission at 510 nm. The fluorescence quantum yields (Φ_F) were measured by the relative method using standards of highly diluted solutions of perylene (Φ_F 0.93 (*82*)) and 9,10-diphenylanthracene (Φ_F 0.95 (*83*)) in cyclohexane. CD spectra were recorded on a JASCO J-815 CD Spectrometer equipped with CDF 4265/15 temperature controller. In cell studies, fluorescence was visualized with a Ziess axiovert 200m microscope using excitation wavelengths of 360 nm (DAPI), 435 nm (perylene-LNA probe), and 570 nm (mCherry protein) and emission wavelengths of 460, 480, and 630 nm for DAPI, perylene-LNA, and mCherry protein, respectively (±15 nm).

3-Perylenecarboxylic Acid. To a precooled to 0 °C solution of sodium hydroxide (600 mg, 15 mmol) in water (12 mL), bromine (205 μL, 4 mmol) and 1,4-dioxane (12 mL) were subsequently added. The resulting mixture was stirred at 0 °C for 10 min, and 3-acetylperylene (294 mg, 1 mmol) was added in 5 portions, over 10 min. The solution was stirred at 0 °C for 3 h, then left at room temperature overnight. Saturated Na_2SO_3 (2 mL) was added, and the stirring was continued for 1 h; then, the reaction mixture was acidified with 1 M aq citric acid to pH 3 and extracted with $CHCl_3$ (3 × 100 mL). The combined organic phase was dried over Na_2SO_4 and evaporated. The product was recrystallized from 5% DMF in nitromethane (v/v) to give 250 mg (84%) of the desired product as a red solid. R_f 0.45 (silica gel, 30% EtOH in $CHCl_3$, v/v). Mp 331−334 °C (5% DMF in nitromethane, v/v) (lit *78*. 333−335 °C). MALDI-HRMS: *m/z* 319.0732 ($[M + Na]^+$, $C_{21}H_{12}O_2Na^+$ calcd. 319.0730). ^{1}H NMR (300 MHz, DMSO-d_6) δ 8.70 (d, J = 8.4 Hz, 1H), 8.29−8.24 (m, 4H), 8.01 (d, J = 8.1 Hz, 1H), 7.76−7.69 (m, 2H), 7.53 (dd, J = 8.1 Hz, 1H), 7.45−7.40 (m, 2H). Carboxylate proton signal was not observed. ^{13}C NMR (75.4 MHz, DMSO-d_6) δ 171.3, 168.4, 134.5, 134.0, 132.4, 130.7, 130.5, 130.2, 129.5, 129.2, 128.3, 128.2, 128.0, 127.1, 127.0, 126.9, 125.6, 122.3, 131.5, 121.0, 119.7.

(1*R*,3*R*,4*R*,7*S*)-1-(4,4′-Dimethoxytrityloxymethyl)-7-hydroxy-5-(perylen-3-ylcarbonyl)-3-(thymin-1-yl)-2-oxa-5-azabicyclo[2.2.1]heptane (2a). To a stirred solution of the 3-perylenecarboxylic acid (116 mg, 0.39 mmol) and HBTU (136 mg, 0.36 mmol) in DMF (2 mL), diisopropylethylamine (132 μL, 0.76 mmol) was added in one portion. The mixture was stirred for 15 min at room temperature and then added dropwise to a stirred solution of nucleoside **1** (200 mg, 0.35 mmol) in DMF (2 mL). After stirring for 40 min, the reaction mixture was diluted with DCM (100 mL) and washed with water (2 × 100 mL), 5% $NaHCO_3$ (2 × 100 mL), and water (3 × 100 mL). The organic layer was dried over Na_2SO_4 and evaporated. The residue was chromatographed on silica gel using gradient elution 10→20% acetone in toluene, containing 1% NEt_3 (v/v/v) to yield nucleoside **2a** (267 mg, 90%) a as an orange foam (rotameric mixture ∼ 1:2.4:1.2 by ^{1}H NMR). R_f 0.40 (50%

Scheme 1[a]

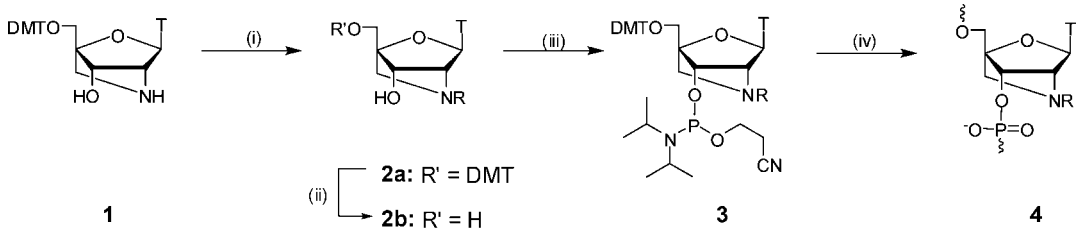

[a] Reagents and conditions: (i) 3-perylenecarboxylic acid, HBTU, EtN(i-Pr)$_2$, DMF (**2a**, 90%); (ii) dichloroacetic acid, Et$_3$SiH, DCM, 40 min (**2b**, 73%); (iii) NC(CH$_2$)$_2$OP(N(i-Pr)$_2$)$_2$, diisopropylammonium tetrazolide, DCM (**3**, 95%); (iv) DNA synthesizer. DMT = 4,4′-dimethoxytrityl. T = thymin-1-yl.

acetone, 1% NEt$_3$ in toluene, v/v/v). ESI-HRMS: m/z = 872.2927 [M + Na]$^+$, calc. for $C_{53}H_{43}N_3O_8Na^+$ 872.2943. ^{1}H NMR (500 MHz, DMSO-d_6; the signals are given for the major rotamer) δ 11.12 (br s, 1H), 8.42−8.32 (m, 4H), 7.87−7.46 (m, 10H), 7.38−7.17 (m, 7H), 6.98 (m, 4H), 6.03 (m, 1H), 5.79 (s, 1H), 4.18 (m, 1H), 4.07 (s, 1H), 3.80 (s, 6H), 3.76 (d, J = 12.0 Hz, 1H), 3.58 (m, 2H), 3.48 (d, J = 11.0 Hz, 1H), 1.45 (s, 3H). ^{13}C NMR (125.7 MHz, DMSO-d_6; the signals are given for the major rotamer) δ 169.5, 164.6, 159.2 (2C), 150.6, 145.6, 136.3, 136.1, 136.0, 135.8, 135.3, 135.2, 135.1, 135.0, 134.7, 132.6, 132.5, 131.9, 131.5, 131.2, 131.0, 130.8, 130.7, 130.6, 130.5, 129.8, 129.5, 129.1, 128.9 (2C), 128.7, 128.6 (2C), 128.4, 127.9, 127.8, 127.7, 126.4, 114 (4C), 109.3, 88.4, 87.5, 86.7, 69.8, 66.2, 60.2, 56.0 (2C), 52.2, 12.5.

(1*R*,3*R*,4*R*,7*S*)-1,7-Dihydroxy-5-(perylen-3-ylcarbonyl)-3-(thymin-1-yl)-2-oxa-5-azabicyclo[2.2.1]heptane (2b). To a stirred solution of **2a** (85 mg, 0.1 mmol) in DCM (0.5 mL), dichloroacetic acid (20% solution in DCM, 400 μL) and triethylsilane (200 μL, 1.0 mmol) were subsequently added. After 40 min at room temperature, TLC displayed the complete conversion of starting nucleoside. The reaction mixture was transferred on a column (silica gel, gradient elution 5→10% MeOH in CHCl$_3$, v/v) to give nucleoside **2b** (40 mg, 73%) as a yellow solid (rotameric mixture ~ 1:2.5 by ^{1}H NMR). R_f 0.52 (10% MeOH in CHCl$_3$, v/v). MALDI-HRMS: m/z = 570.1648 [M + Na]$^+$, calc. for $C_{32}H_{25}N_3O_6Na^+$ 570.1641. ^{1}H NMR (300 MHz, DMSO-d_6; the signals are given for the major rotamer) δ 11.03 (br s, 1H), 8.35−8.26 (m, 4H), 7.90−7.81 (m, 3H), 7.71−7.58 (m, 5H), 6.24 (br.s, 1H), 5.66 (m, 1H), 4.18 (br s, 1H), 4.00−3.43 (m, 6H, partial overlap with water), 1.45 (s, 3H). ^{13}C NMR (75.4 MHz, DMSO-d_6; the signals are given for the major rotamer) δ 169.6, 164.6, 150.7, 135.7, 135.2, 134.9, 134.2, 132.6, 132.5, 131.8, 131.6, 131.2, 130.9, 130.8, 129.5, 129.2, 128.9, 128.6, 128.4, 127.9, 127.8, 122.2, 122.0, 120.7, 109.0, 89.9, 87.2, 70.0, 66.2, 57.5, 51.8, 13.3.

(1*R*,3*R*,4*R*,7*S*)-7-(2-Cyanoethoxy(diisopropylamino)phosphinoxy)-1-(4,4′-dimethoxytrityloxymethyl)-7-hydroxy-5-(perylen-3-ylcarbonyl)-3-(thymin-1-yl)-2-oxa-5-azabicyclo[2.2.1]heptane (3). The LNA nucleoside derivative **2a** (170 mg, 0.2 mmol) was evaporated with dry DCM (2 × 30 mL), dissolved in anhydrous DCM (20 mL), diisopropylammonium tetrazolide (52 mg, 0.3 mmol), and bis(*N*,*N*-diisopropylamino)-2-cyanoethoxyphosphine (96 μL, 0.3 mmol) were added under argon, and the resulting mixture was stirred for 4 h. The mixture was diluted with DCM (100 mL) and washed with saturated solution of NaHCO$_3$ (2 × 100 mL) and brine (100 mL). The organic layer was dried over Na$_2$SO$_4$, evaporated, and the crude material purified by chromatography (silica gel, 30% acetone in toluene, containing 1% NEt$_3$, v/v/v). Yield 228 mg (95%). R_f 0.53, 0.50 (50% acetone, 1% NEt$_3$, toluene, v/v/v). ESI-HRMS: m/z = 1072.3985 [M + Na]$^+$, calc. for $C_{62}H_{60}N_5O_9PNa^+$ 1072.4020. ^{31}P NMR (121.4 MHz, DMSO-d_6) δ 149.22, 148.83 (1:1.7) (main conformer).

RESULTS AND DISCUSSION

Synthesis. Modified phosphoramidite was synthesized as shown in Scheme 1. The starting DMT-protected 2′-amino-LNA monomer **1** (*82, 83*) was coupled with 3-perylenecarboxylic acid, synthesized from 3-acetylperylene (*78*) under haloform oxidation conditions (*84, 85*). A small portion of perylene-modified 2′-amino-LNA **2a** was reacted with dichloroacetic acid in the presence of triethylsilane giving DMT-deprotected nucleoside **2b** required for spectroscopic and photophysical studies. The main portion of **2a** was converted to the phosphoramidite derivative **3** (in 86% overall yield), which was used in automated oligonucleotide synthesis to prepare a series of modified oligonucleotides (ONs). Sequences of ONs were similar to those designed for studies of pyrene-functionalized 2′-amino-LNA (*22*).

Synthesis of **X**-labeled ONs was performed following standard protocols, except for incorporation of monomer **X** for which a double coupling procedure with an extended coupling time (2 × 30 min) using pyridine hydrochloride as an activator was applied. This resulted in 95−99% stepwise coupling yields of monomer **X** based on the absorbance of the dimethoxytrityl cation released after each coupling. The coupling efficiencies of standard amidites varied between 98% and 100%. All synthesized conjugates were purified by RP-HPLC and their identity confirmed by MALDI-TOF mass spectrometry (Table S1, Supporting Information).

Spectral Properties of 2′-*N*-(Perylen-3-yl)carbonyl-2′-amino-LNA Monomer (2b). To get true solutions of nucleoside **2b** for recording of UV−vis absorption, steady-state fluorescence emission, and excitation spectra in aqueous media (Figure 1), it was dissolved in a medium salt buffer with 1% DMSO (v/v). Perylene absorbs with a maximum at 445 nm, an additional band at 419 nm, and a shoulder at 396 nm. Spectral broadening of the spectrum of **2b** compared to that of perylene (*23*) indicates increased ground-state interactions for the perylene attached to 2′-amino-LNA. These interactions are most likely caused by the nearby thymine, and less probably, by the sugar ring. Emission spectra of **2b** displays a broad, featureless peak near 480 nm corresponding to a Stokes shift of 35 nm. Compared to perylene, emission of **2b** is 30 nm red-shifted and significantly broadened.

Fluorescence emission quantum yield (Φ_F) of nucleoside **2b** was determined by the relative method using highly diluted solutions of perylene (Φ_F = 0.93 (*82*)) and 9,10-diphenylanthracene (Φ_F = 0.95 (*83*)) in cyclohexane as the reference standards. Optical densities of the solutions used for quantum yield measurements were kept between 0.1 and 0.01 to avoid

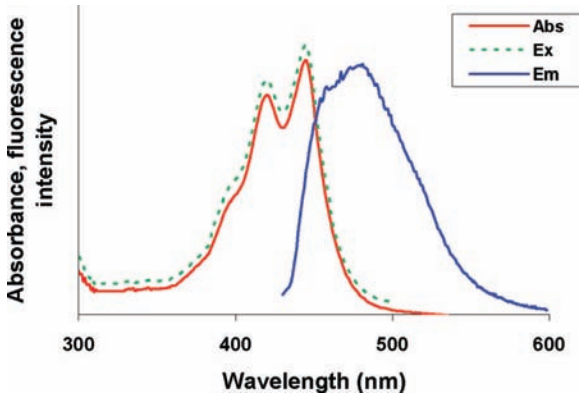

Figure 1. Normalized absorption, emission, and excitation spectra of nucleoside **2b** in a medium salt buffer containing 1% DMSO (v/v) recorded at 19 °C using an excitation wavelength of 425 nm, emission wavelength of 510 nm for excitation, 2 μM concentration of **2b** for the absorption spectrum, and 0.1 μM concentration for the excitation and emission fluorescence spectra.

Table 1. Thermal Denaturation Temperatures for Duplexes of Modified ONs and DNA/RNA Complements[a]

					duplex	
#	sequence, 5′→3′				with DNA T_m (ΔT_m/mod)/°C	with RNA T_m (ΔT_m/mod)/°C
ON1	GTG	A**X**A	TGC		31.0 (+3.0)	32.5 (+6.5)
ON2	GCA	**X**AT	CAC		35.0 (+7.0)	32.0 (+7.5)
ON3	GCA	TA**X**	CAC		34.5 (+6.0)	31.0 (+6.5)
ON4	GTG	A**X**A	**X**GC		43.5 (+7.8)	57.0 (+15.5)
ON5	GCA	**X**A**X**	CAC		42.0 (+7.0)	38.0 (+6.8)
ON6	GTG	**XX**T	TGC		32.5 (+0.5)	37.5 (+4.0)
ON7	G**X**G	A**X**A	**X**GC		43.0 (+5.0)	44.0 (+6.0)
ON8	G**X**G	**X**T**X**	TGC		38.5 (+2.3)	46.0 (+5.5)
ON9	TT**X**	A**X**A	**X**A**X**	CA^{Me}C^{L}G	37.5 (+0.5)[b]	42.0 (+2.0)
ON10	TT^{L}T	A**X**A	**X**A**X**	CA^{Me}C^{L}G	42.5 (+2.3)	47.0 (+4.3)

[a] Thermal denaturation temperatures T_m (°C) (change in T_m per modification relative to corresponding reference duplex, ΔT_m/mod (°C)). The melting temperatures of the unmodified duplexes or LNA-modified duplex (in the case of **ON9–ON10**) used as references were as follows: 28.0 °C for **ON1–ON5**,**ON7**:DNA, 26.0 °C for **ON1**,**ON4**,**ON7**:RNA, 24.5 °C for **ON2**,**ON3**,**ON5**:RNA, 31.5 °C for **ON6**,**ON8**:DNA, 29.5 °C for **ON6**,**ON8**:RNA, 35.5 °C for **ON9–ON10**:DNA, and 34.0 °C for **ON9–ON10**:RNA. T_m values measured as the maximum of the first derivatives of the melting curves (A_{260} vs temperature). Reported expected to be hybridized to its RNA target. T_m values are averages of at least two measurements. **X** = 2′-*N*-(perylen-3-yl)carbonyl-2′-amino-LNA monomer; TL and ^{Me}CL = thymin-1-yl and 5-methylcytosin-1-yl LNA monomers, respectively. All T_m values were recorded in medium salt buffer. [b] T_m value for **ON9**:DNA measured using perylene absorbance at 425 nm.

uncertainties. The Φ_F values were corrected with the refractive index of the solvents. Quantum yield of **2b** in aerated buffer solution containing 1% DMSO measured using these conditions was $\Phi_F = 0.67$, while Φ_F for the 2′-amino-LNA nucleoside functionalized with pyrene was $\Phi_F = 0.34$ (*22*). Superiority of perylene relative to pyrene with respect to quantum yield becomes clear if fluorescence rate constants are compared ($K_f = 0.25 \cdot 10^{-7}$ s^{-1} for pyrene and $14.62 \cdot 10^{-7}$ s^{-1} for perylene in cyclohexane, respectively) (*86*).

Labeled Oligonucleotides and Duplexes Having Monomer X in One Strand. *(a) Thermal Denaturation Studies.* Thermal denaturation temperatures were determined in medium salt buffer using 1.0 μM concentration of the two complementary strands, and were compared to the denaturation temperatures of the corresponding unmodified duplexes (Table 1). The perylene-modified ONs displayed higher affinity toward complementary RNA while exhibiting lower affinity toward DNA. Previously, it had been reported that conjugates containing functionalized 2′-amino-LNA monomers form stable complexes to both DNA and RNA complements, and that N2′-acylated 2′-amino-LNA derivatives exhibit higher thermal stabilities than N2′-alkylated (*22*, *72*). In agreement with these results, the thermal stabilities of duplexes involving singly labeled **ON1**–**ON3** were much higher than those of the corresponding unmodified duplexes and of duplexes involving a recently reported perylenemethyl-2′-amino-LNA monomer (*37*), but similar to those for N2′-pyrenecarbonyl-functionalized 2′-amino-LNAs (*22*). This implies that neither a perylene nor a pyrene moiety attached to LNA essentially distorts the structure of nucleic acid helixes. Incorporation of two monomers **X** separated by one base pair induces even larger increases in thermal stabilities, especially in the case of duplex **ON4**:RNA (ΔT_m/mod = +15.5 °C). On the contrary, insertion of modifications in the neighboring positions, as well as incorporation of an additional monomer **X**, results in lower melting temperatures compared to doubly labeled conjugates **ON4**–**ON5**:DNA/RNA (Table 1, T_m values for **ON6**–**ON8**:DNA/RNA), which again parallels the behavior of pyrene attached via an amide linkage to 2′-amino-LNA (*22*).

The thermal denaturation curves of all the above-mentioned duplexes displayed S-shaped monophasic transitions similar to those of the unmodified reference duplexes. Surprisingly, 13-mer **ON9** having four perylenes showed a sigmoidal melting curve only against its RNA complement, but not its DNA complement. Therefore, a thermal denaturation experiment was performed at perylene's absorbance at 425 nm (Supporting Information, Figure S1). The resulting melting curve displayed clear S-shaped perylene hypochromism similar to that previously reported for pyrene (*19*). In the case of duplex **ON9**:RNA, the melting temperature values determined using absorbance at 260 and 425 nm coincided precisely. The observed hypochromism can be explained by the increase of the distance between perylene residues in the more rigid duplex compared to the flexible single-stranded oligonucleotide. Upon incorporation of an additional number of fluorochromes, the total absorbance of perylene residues at 260 nm may become rather significant and, therefore, may affect the 'nucleotide' melting curve.

The Watson−Crick selectivity of the perylene-functionalized conjugate **ON7** was determined also for the duplexes containing single mismatched nucleotides at positions 4−6 (Table 2). The presence of mismatches in the DNA/RNA target resulted in significantly decreased thermostability of the complexes compared to the corresponding fully matched duplexes **ON7**:DNA/RNA (data presented in Table 2 compared to T_m values of **ON7**:DNA/RNA**)**. It was previously reported that mismatches opposite of LNA monomers are generally discriminated more strongly than opposite of unmodified nucleotides (*67*). However, in the case of monomer **X**, mismatches at position 6 of target DNA resulted in more remarkable destabilization of the complexes than at position 5.

(b) Spectral Properies. The UV−visible absorption and steady-state fluorescence emission spectra were obtained in medium salt buffer using 0.1−1.0 μM concentration of the single-stranded probe or the two complementary strands. For the recording of fluorescence spectra, an excitation wavelength of 425 nm was used. Table 3 lists the resulting spectral and photophysical properties of single-stranded ONs (SS**P**) and their duplexes with DNA and RNA complements.

The UV−visible spectra recorded of all the modified ONs and duplexes, as well as the spectrum of monomer **2b**, contain two main absorption bands in the visible region with $\lambda_{max} \approx$ 448−456 nm and $\lambda_{max} \approx$ 422−429 nm. Noteworthy, perylene longwave absorption maxima of the **X**-modified ONs and duplexes are red-shifted compared to those of the nucleoside **2b**. As a result of perylene−ON interactions, the UV−visible absorption spectrum of the perylene unit has lost many of its

Table 2. Thermal Denaturation Temperatures for Duplexes of ON7 and DNA/RNA Complements Containing Single Mismatches[a]

		T_m/°C							
		DNA target				RNA target			
ON7:TARGET	**B**:	**A**	**C**	**G**	**T**	**A**	**C**	**G**	**U**
5′-G**X**G A**X**A **X**GC[a] 3′-CAC T**B**T ACG		43.0	23.0	28.5	29.5	44.0	25.5	<10	24.0
5′-G**X**G A**X**A **X**GC 3′-CAC **B**AT ACG		25.5	29.0	32.5	43.0	30.5	29.0	30.5	44.0
5′-G**X**G A**X**A **X**GC 3′-CAC TA**B** ACG		<10	<10	28.5	43.0	36.5	28.0	30.0	44.0

[a] For conditions of thermal denaturation experiments see Table 1; the metling temperatures of the unmodified duplexes are 28.0 and 26.0 °C for double-stranded DNA and DNA:RNA, respectively.

Table 3. Spectroscopic and Photophysical Properties of Modified Oligonucleotides and Duplexes

	λmax^{abs}, bands I, II (nm)			λmax^{fls}, (nm)			Φ_F			FB[a]		
#	SSP	DNA	RNA	SSP	DNA	RNA	SSP	DNA	RNA	SSP	DNA	RNA
ON1	452,426	448, 422	449, 422	488	484	486	0.61	0.49	0.50	13.4	17.1	16.5
ON4	453,427	449, 423	449, 423	490	479	480	0.11	0.24	0.24	5.4	14.6	13.7
ON6	453,427	452, 427	452, 426	492	490	490	0.06	0.06	0.03	4.5	4.4	2.4
ON7	454,429	449, 423	449, 423	492	483	481	0.04	0.25	0.23	3.4	28.8	25.5
ON8	455,429	451, 425	448, 423	490	485	493	0.03	0.2	0.21	2.4	17.8	21.8
ON9	456,429	451, 425	451, 426	492	488	488	0.03	0.09	0.1	4.7	12.9	14.3

[a] Fluorescence brightness FB = $\varepsilon_{425} \times \Phi_F$ (*22*).

vibrational features compared to the spectra of perylene itself (*23*) and the monomer fluorochome **2b** (Supporting Information, Figure S2). The absorption maxima (λ_{max}) of the conjugates bathochromically shift 1−4 nm and absorption coefficients (ε) increase with increasing number of monomers **X** and, conversely, upon hybridization absorption maxima shift 1−8 nm to shorter wavelengths. The excitation spectra of ONs and duplexes containing one to three monomers **X** are of the same shape as the corresponding absorption spectra. The difference consists of the entire red shift 6−8 nm of the excitation spectra compared to the absorption spectra. No changes in the positioning of the excitation peaks for different emission wavelengths were observed. The peaks of the emission spectra of perylenecarbonyl-2′-amino-LNA conjugates lie within the 440−590 nm region, and none of the spectra exhibit significant vibrational features (Supporting Information, Figure S3). Singly labeled **ON1**–**ON3** revealed a broad unstructured band at fluorescence maximum $\lambda_{em} \approx 490$ nm, which is 100 nm red-shifted relative to the corresponding conjugates of pyrenecarbonyl-2′-amino-LNA (*22*). Upon duplex formation, λ_{em} slightly shifts (2−4 nm) to shorter wavelengths. No perceptible changes in the shape of the spectral curve or the fluorescence intensity were observed.

Fluorescence emission quantum yields (Φ_F) of perylene-modified ONs and the corresponding duplexes were determined by the method described in the section concerning spectral properties of fluorochrome monomer **2b**. The quantum yields of several samples were also measured in degassed buffer solutions, but no significant difference compared to nondegassed solutions was found. Thus, all Φ_F values collected in Table 3 are determined for air-saturated solutions. Fluorescence quantum yields of **ON1** and its duplexes are remarkably high (Table 3, Φ_F values for **ON1**, **ON1**:DNA/RNA). Usually, PAH molecules (for example, pyrene) incorporated into nucleic acids display low quantum yields due to interactions with the polar aqueous environment and the nucleobases (*87*). However, if the sequence can adopt a structure shielding the fluorochrome from the quenchers (i.e., nucleobases), quantum yields of ONs become very high. Direction of the fluorochrome into the groove upon hybridization can also reduce fluorescence quenching (*64*). Previously, it has been shown that the rigid bicyclic backbone of 2′-amino-LNA together with a short amide linkage direct the functionalities in the minor groove of a nucleic acid helix (*22, 40, 72*−*74, 88*). Thus, high fluorescent quantum yields of **ON1** and of its duplexes can be explained by reduced interactions of the perylene moiety with the nucleobases resulting from the above-mentioned particular features of N2′-acylated 2′-amino-LNA.

Single-stranded probe **ON4** having two incorporations of monomer **X** separated by one nucleotide exhibits significantly lower quantum yield compared to **ON1**. However, duplexes **ON4**:DNA and **ON4**:RNA display Φ_F values that are twice as high relative to **ON4** and fluorescence brightness values (FB = $\varepsilon_{425} \times \Phi_F$ (*22*)) that are almost the same as for duplexes involving **ON1**. Noteworthy, insertion of two monomers **X** in neighboring positions reduced the spectral effects observed for **ON4** (compare Φ_F and FB values for **ON4** and **ON6**). Previously, ONs with sequential incorporations of pyrene−LNA monomers exhibited very low quantum yields and FBs as well ($\Phi_F = 0.02-0.09$ (*22*)). This suggests that separation of fluorochromes by at least one base pair is an important structural requirement for this clan of probe ONs to achieve distinctly hybridization-modulated fluorescence and to generate brightly fluorescent duplexes. Thus, hybridization of **ON7** containing three separated monomers **X** results in a ∼14-fold increase of fluorescence intensity at $\lambda_{em} \approx 490$ nm (Figure 2). The quantum yield of **ON7** is $\Phi_F = 0.04$, whereas upon formation of the duplexes it increases up to $\Phi_F = 0.23-0.25$. The bright green fluorescence exhibited by the duplex **ON7**:DNA can be detected by the naked eye at concentrations less than 0.5 μM. Unlike pyrene-labeled ONs (*17, 22, 38*), perylene-functionalized **ON7** and **ON8** do not show any DNA/RNA discrimination in the fluorescence intensity response. However, in spite of this distinction, the basic spectral features (quenched fluorescence of multilabeled single-stranded probe and remarkable increase of fluorescence intensity upon hybridization) are, probably, general properties of such 2′-amino-LNA derivatives N2′-functionalized with amide-linked PAHs.

Interestingly, in contrast to pyrene-functionalized 2′-amino-LNAs, incorporation of four perylene modifications **X** into a T-rich 13-mer did not result in high values of the quantum yields for the duplexes (Table 3, Φ_F values for **ON9**:DNA/RNA compared with $\Phi_F = 0.99$ and 0.96 for pyrene-modified dsDNA and DNA:RNA, respectively) (*22*). Conjugate **ON9** does show a response in fluorescence intensity to hybridization, with ∼10×

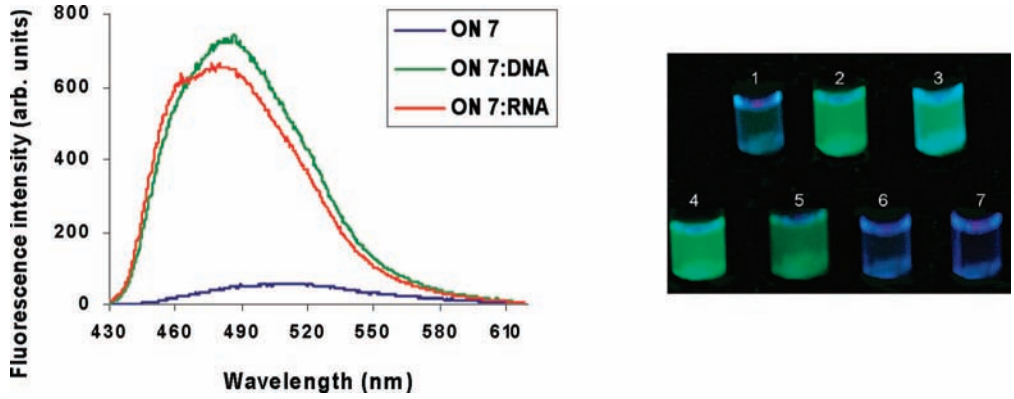

Figure 2. Left: steady-state fluorescence emission spectra of **ON7** (5′-G**X**G A**X**A **X**GC; **X** = 2′-*N*-(perylen-3-yl)carbonyl-2′-amino-LNA monomer) and the corresponding duplexes with cDNA/RNA. Spectra were obtained in a medium salt buffer at 19 °C using an excitation wavelength of 425 nm and 0.1 μM concentration of ONs. Right: photographs of the fluorescence emission in a medium salt buffer: single stranded **ON7** (vial 1, 1 μM concentration); **ON7**:DNA (vial 2, 1 μM concentration), **ON7**:RNA (vial 3, 1 μM concentration); **ON7**:DNA (vials 4−6, concentrations: 1 μM, 0.5 μM, and 0.1 μM, respectively); medium salt buffer (vial 7). Photographs were taken with a digital camera using a laboratory UV-lamp (λ_{ex} = 365 nm).

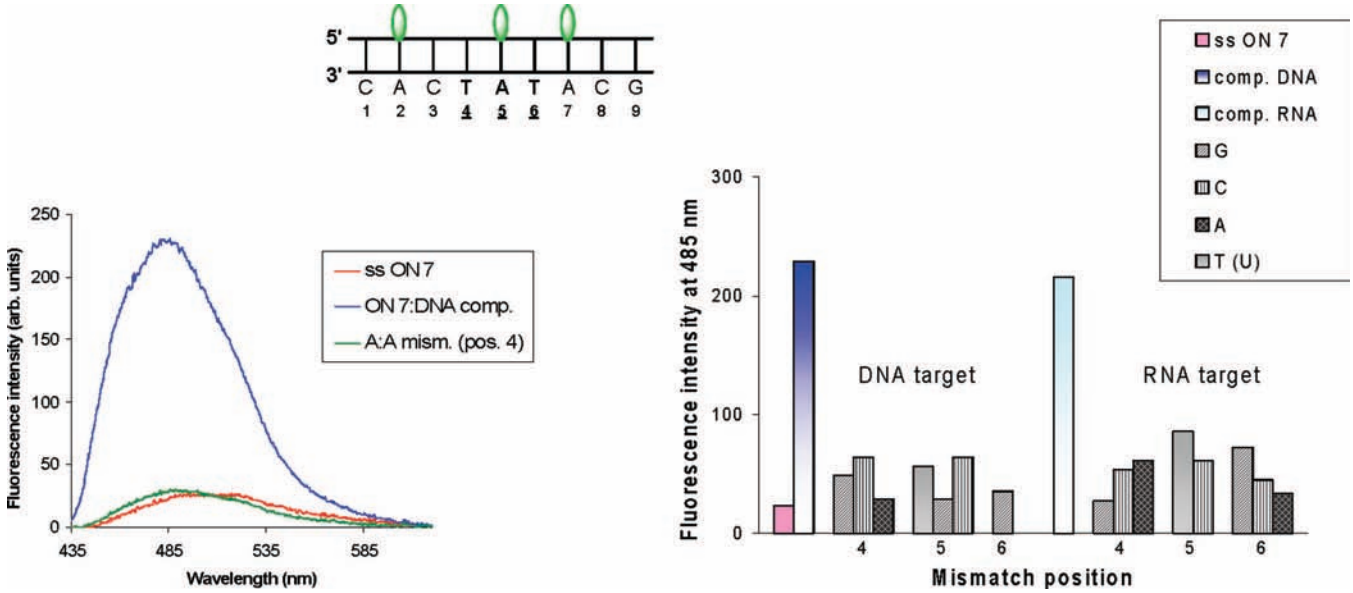

Figure 3. Left: steady-state fluorescence emission spectra of **ON7** and its duplexes with complementary and singly mismatched DNA. Right: fluorescence intensities of duplexes between **ON7** and complementary or singly mismatched DNA/RNA targets. Conditions are described in Figure 2. Green droplets indicate monomer **X**.

fluorescence intensity increase for both **ON9**:DNA and **ON9**:RNA (Supporting Information, Figure S3). However, due to decreased quantum yields the FB values of **ON9**:DNA/RNA are low (Table 3, compare FBs for **ON9**:DNA/RNA and **ON7**:DNA/RNA; also compare to FB = 51 and 52 for pyrene-modified dsDNA and DNA:RNA, respectively) (*22*).

Next, fluorescence properties of complexes formed by **ON7** and singly mismatched DNA/RNA targets were investigated. Mismatched duplexes displaying T_m values of more than 22 °C (Table 2) can be expected to be fully hybridized during steady-state fluorescence experiments performed at 19 °C. Thus, for these complexes, fluorescence emission spectra were recorded using the conditions described above. Resulting fluorescence intensities, as well as representative fluorescence spectra, are shown in Figure 3. Probe **ON7** was seen to be equally sensitive to the presence of mismatched nucleosides in DNA and RNA targets, and a decrease in fluorescence intensity of at least 60% for the all singly mismatched complexes was observed. The highest value of discrimination displayed by perylene-functionalized probe **ON7** is eight for single-base mismatches T/G, A/A, A/G in the case of the DNA target, and for A/G, A/A mismatches in the case of the RNA target. The observed significant level of discrimination is comparable with, if not better than, the discrimination previously reported for FRET-based biosensors (*89*), molecular beacons (*90*−*92*), and for other probes containing various fluorochromes (*41*, *93*−*98*). Thus, 2′-*N*-(perylen-3-yl)carbonyl-2′-amino-LNA monomer **X** may become a useful tool for homogeneous detection of genetic mutations.

To study structural features of the modified duplexes in detail, circular dichroism (CD) spectroscopy was employed (Supporting Information, Figure S4). All the modified dsDNA duplexes seem to be changed toward an intermediate A/B form, and as expected, deviations from the unmodified dsDNA clearly increase in the order **ON1** < **ON4** < **ON7** (with insertion of more RNA reminiscent monomers **X**) (*99*).

Fluorescence staining techniques and fluorescence microscopy constitute powerful tools for the biological investigations. Thus, we examined a 13-mer perylene−LNA probe for mRNA staining in cell culture, visualized by fluorescence microscopy. In doing that, a 13-mer probe **ON10** complementary to target mRNA was synthesized. For the investigation, a pCDNA5/FRT/

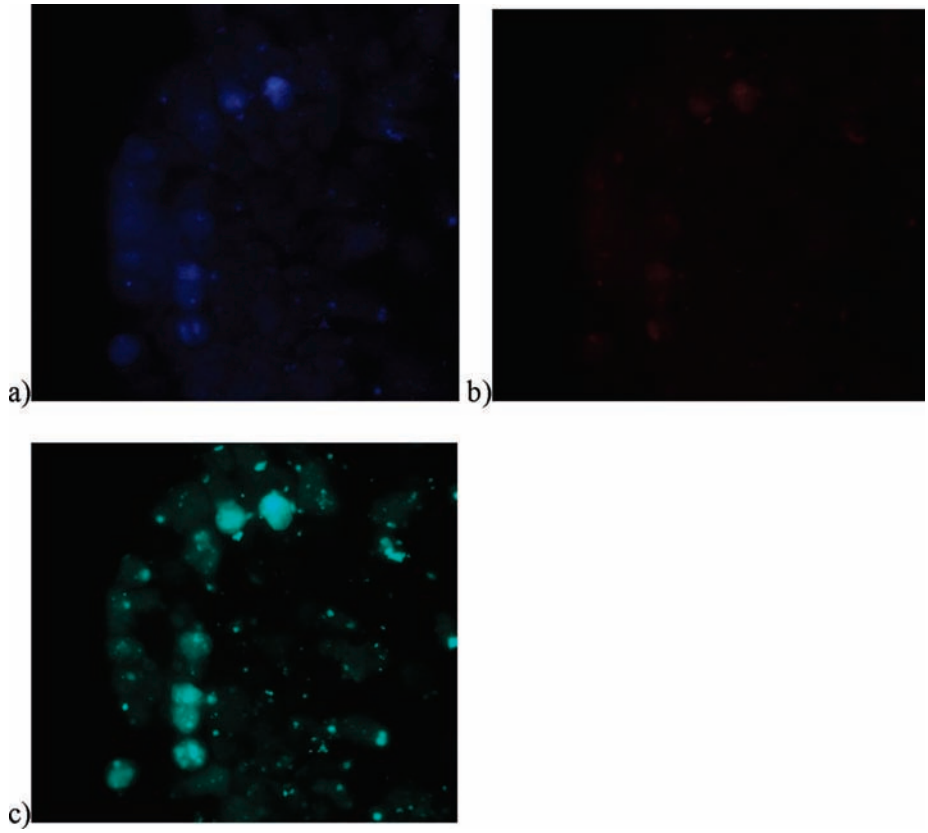

Figure 4. Images of cell culture observed using fluorescence microscopy. Cell nuclear DNA was stained with DAPI (blue signals in a, $\lambda_{em} = 460$ nm). (b) Fluorescence of mCherry protein ($\lambda_{em} = 630$ nm). (c) Fluorescence of the probe **ON10** ($\lambda_{em} = 480$ nm) expected to be hybridized to its RNA target.

Table 4. Thermal Denaturation Temperatures for Modified Duplexes Having Monomer X in Both Complementary Strands[a]

Complementary strands	3′→5′		
	ON2	**ON3**	**ON5**
5′→3′	Illustration/ $T_m(\Delta T_m/mod)/^oC$		
ON1	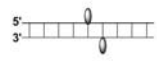 30.5 (+1.3)	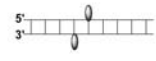 48.5 (+10.3)	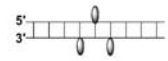 53.0 (+8.3)
ON4	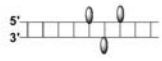 51.0 (+7.8)	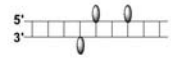 40.0 (+4.0)	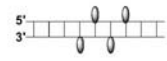 69.5 (+10.4)
ON7	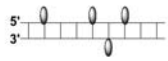 53.0 (+6.3)	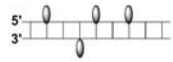 59.0 (+7.8)	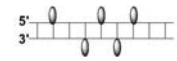 77.5 (+9.9)

[a] Thermal denaturation temperatures recorded using the same conditions as described in Table 1. The droplets represent monomer **X**.

TO vector containing cloned genetic code for mCherry protein (*100*) followed by four copies of the target sequence of the probe was transfected into HEK 293 cells. The perylene−LNA probe was transfected after 40 h and cells were fixated after an additional 6 h. To identify nuclei, DAPI staining was applied ($\lambda_{ex} = 350$ nm), while red fluorescence of the mCherry protein ($\lambda_{ex} = 570$ nm) confirmed presence of the mRNA of interest in the cells (Figure 4A,B). In turn, bright cyan fluorescence of the probe **ON10** under excitation at 435 nm is seen to be colocalized with red emission of the mCherry protein and DAPI signal suggesting successful uptake of the synthesized probe into the cells (Figure 4C). Next, fluorescence of **ON10** is more intensive in well-countered zones within the cells compared to the other areas. This is most likely due to localization of the probe around the synthesized target mRNA. An important observation is that the emission signal of perylene−LNA is not obscured by cell autofluorescence—upon excitation at 435 nm in the absence of **ON10**, there is no fluorescence signal detected. Furthermore, since fluorescence of single-stranded **ON10** is quenched and its remarkable enchancement observed only upon binding to

Table 5. Spectroscopic and Photophysical Properties of the Duplexes Containing Monomers X in '+1 zipper' and '−1 zipper' Constitutions

#	Illustration	λ_{max}^{abs}, bands I, II (nm)	λ_{max}^{fl} (nm)	Φ_F	FB[a]
ON1:ON2	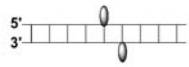	450, 424	488	0.26	15.8
ON1:ON3	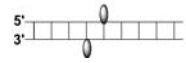	450, 424	491	0.13	7.3

[a] Fluorescence brightness FB = $\varepsilon_{425} \times \Phi_F$ (*22*).

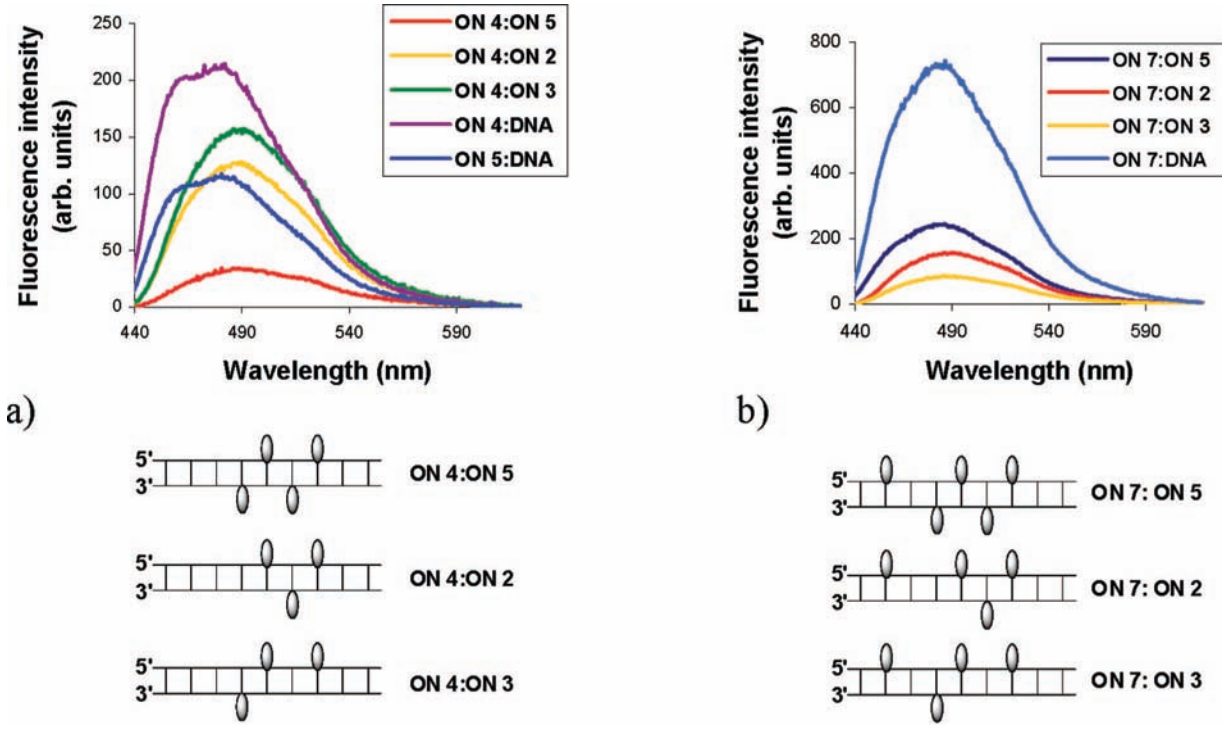

Figure 5. Steady-state fluorescence emission spectra of multilabeled duplexes formed by (a) **ON4** and (b) **ON7** (0.5 μM solutions). For conditions, see Figure 2.

nucleic acids, there should be little to no background signal of the probe. Thus, the results of this initial study suggest that probes containing introduced label **X** have a big potential to become useful for experiments in cell culture (e.g., mRNA-FISH analysis) with advantages of eliminated cell autofluorescence and low background signal.

Duplexes Containing Monomer X in Both Strands. *(a) Thermal Denaturation Studies.* Thermal denaturation temperatures of duplexes involving two strands each modified with a perylene-functionalized monomer **X** were determined as described before. The measured T_m values were compared to those of the corresponding unmodified dsDNA as shown in Table 4.

Positioning of two monomers **X** in a '+1 zipper' constitution does not significantly affect the thermal stability of the duplex, while two perylene−LNA residues placed in a '−1 zipper' result in remarkable stabilization (Table 4, data for **ON1**:**ON2** relative to **ON1**:**ON3**). Duplexes containing three modifications **X** in '1 + 2' and '2 + 1 zippers' exhibit higher T_m values relative to doubly modified analogues (Table 4, **ON1**:**ON5**, **ON4**:**ON2**, compared to **ON1**:**ON2**, **ON1**:**ON3**). However, incorporation of three monomers **X** in **ON4**:**ON3** decreases the thermal stability compared to other triply labeled duplexes (Table 4, T_m value for **ON4**:**ON3**, compared to **ON1**:**ON3**,**ON1**:**ON5**,**ON4**:**ON2**). Remarkably high thermal denaturation temperatures were observed for the duplexes with four insertions of the **X**-monomer (Table 4, **ON4**:**ON5**, **ON7**:**ON2**, **ON7**:**ON3**). As an illustration, **ON4**:**ON5** containing four modifications in a 'zipper' motif shows a T_m value of 69.5 °C, but incorporation of an additional fifth perylene monomer results in a T_m value of 77.5 °C, which is an extraordinary thermal stability of a 9-mer duplex containing only five modified nucleotides. Noteworthy, **X**-labeled duplexes in various 'zipper' constructions display thermal stabilities remarkably higher than those of parent dsDNAs labeled in one strand (data presented in Table 4 compared to data in Table 1). This suggests an effective and stabilizing interstrand communication between perylene functionalities in the engineered motifs.

To summarize the data listed in Table 4, the duplexes multilabeled with monomer **X** in general display remarkably high thermal stabilities, which are caused by the rigid bicyclic LNA skeleton, the short amide linkage of 2′-*N*-(perylen-3-yl)carbonyl-2′-amino-LNA monomer **X**, and consequential perylene−perylene stabilizing interactions existing in the engineered motifs.

(b) Spectral Properties. The UV−vis absorption and steady-state fluorescence emission spectra of the various interstrand 'zipper' arrangements of monomers **X** were obtained using the same conditions as described for the oligonucleotides and

duplexes containing **X**-monomer in only one strand. The spectroscopic and photophysical data evaluated for modified conjugates having monomers **X** in '+1 zipper' and '−1 zipper' constitutions are listed in Table 5. The fluorescence quantum yield for the '−1 zipper' is twice less than for the '+1 zipper', and both of them are much lower than measured for the parent duplex **ON1**:DNA (Table 3). However, the FB value for **ON1**:**ON2** is of the same magnitude as for **ON1**:DNA, as a result of an increased absorption coefficient (ε_{425}) for **ON1**:**ON2**.

All the duplexes having monomers **X** in both complementary strands displayed an unstructured emission band at $\lambda_{em} \approx 490$ nm (Figure 5) and no explicit perylene excimer signal, similar to base-coupled 1-ethynylpyrene in the RNA minor groove (*101*). The fluorescence intensity of the 'zippers' was lower than of the previously described duplexes having perylene residues in only one strand. Quenching of the fluorescence, together with increased thermal stability of these duplexes, points to electronic interstrand interaction between perylene residues taking place in the constructed duplexes and being responsible for the observed quenching effect. Alternatively, perylene↔perylene energy migration might be responsible for fluorescence quenching. In contrast, insertion of pyrene-functionalized LNAs in the 'zipper' motifs of such constitution was previously reported to result in effective excimer formation (*24*).

The CD spectra of the **ON1**:**ON2** verify the same intermediate A/B-type geometry as for duplexes involving **ON1** (Supporting Information, Figure S4). However, **ON1**:**ON3** containing perylene−LNAs in '−1 zipper' constitution exhibit significant deviation toward the A-type, which becomes apparent in disappearance of the negative bang at ~250 nm in the CD spectrum.

CONCLUSIONS

Herein, we have reported the synthesis of 2′-*N*-(perylen-3-yl)carbonyl-2′-amino-LNA monomer **X**, its incorporation into oligonucleotides, thermal denaturation studies, spectral and photophysical properties, and structural aspects for effective detection of nucleic acid hybridization. Oligonucleotides containing monomer **X** exhibit high-affinity hybridization toward complementary unmodified DNA, RNA, and monomer **X**-containing DNA, considerably quenched fluorescence of single-stranded multilabeled probes, and an evident increase of fluorescence intensity (up to 14-fold), brightness, and quantum yields upon hybridization. In the presence of single base-pair mismatches in DNA/RNA targets, perylene-functionalized probes display remarkably quenched fluorescence compared to fully matched duplexes. Thus, the executed replacement of the previously reported pyrene moiety attached via an amide group to 2′-amino-LNA (*22*) with perylene results in creation of very promising probes for homogeneous fluorescence assays. These probes display hybridization-increased fluorescence, but with an advantage of 100 nm red-shifted emission compared to pyrene and documented sensitivity of the fluorescence to single mismatches. Initial experiments in cell culture confirm that perylene-LNA ONs do provide a wavelength window which eliminates cell autofluorescence and makes them a promising tool to probe biological RNA specimens by fluorescence microscopy. Duplexes having monomer **X** in both complementary strands reveal remarkable thermal stabilities. This indicates interstrand communication between perylene functionalities, resulting in stabilizing effects and quenching of fluorescence but, however, not in the formation of perylene excimers. The attractive spectral characteristics reported herein, together with high-affinity binding to complementary targets, make probes containing 2′-*N*-(perylen-3-yl)carbonyl-2′-amino-LNA monomer potentially very useful within different fields of nucleic acid research, allowing accomplishment of experiments both *in vitro* and *in vivo*.

ACKNOWLEDGMENT

We greatly appreciate funding from The Sixth Framework Programme Marie Curie Host Fellowships for Early Stage Research Training under contract number MEST-CT-2004−504018 and The Danish National Research Foundation. I.V.A. and V.A.K. acknowledge support of RFBR grant 06−03−32426.

Supporting Information Available: MALDI-TOF MS of synthesized ODNs; fluorescence steady-state emission studies and quantum yield determination details; CD measurements; representative thermal denaturation curves, UV−visible absorption, excitation, fluorescence and CD spectra; cell transfection experiments and fluorescence microscopy details. This material is available free of charge via the Internet at http://pubs.acs.org.

LITERATURE CITED

(1) Didenko, V. V., Ed. (2006) *Methods in Molecular Biology. Vol. 335: Fluorescent Energy Transfer Nucleic Acid Probes*, Humana Press, Totowa, NJ.

(2) Hilario, E., and Mackay, J., Eds. (2007) *Methods in Molecular Biology. Vol. 353: Protocols for Nucleic Acid Analysis by Nonradioactive Probes*, Humana Press, Totowa, NJ.

(3) Marx, A. , and Seitz, O., Eds. (2008) *Methods in Molecular Biology. Vol. 429: Molecular Beacons: Signalling Nucleic Acid Probes*, Humana Press, Totowa, NJ.

(4) Marras, S. A. E., Tyagi, S., and Kramer, F. R. (2006) Real-time assays with molecular beacons and other fluorescent nucleic acid hybridization probes. *Clin. Chim. Acta 363*, 48–60.

(5) Latif, S., Bauer-Sardina, I., Ranade, K., Livak, K. Y., and Kwok, P.-Y. (2001) Fluorescence polarization in homogeneous nucleic acid analysis II: 5′-nuclease assay. *Genome Res. 11*, 436–440.

(6) Chen, X., and Kwok, P.-Y. (1997) Template-directed dye-terminator incorporation (TDI) assay: a homogeneous DNA diagnostic method based on fluorescence resonance energy transfer. *Nucleic Acid Res. 25*, 347–353.

(7) Whitcombe, D., Brownie, J., Gillard, H. L., McKechnie, D., Theaker, J., Newton, C. R., and Little, S. (1998) A homogeneous fluorescence assay for PCR amplicons: its application to real-time, single-tube genotyping. *Clin. Chem. 44*, 918–923.

(8) Nazarenko, I. A., Bhatnagar, S. K., and Hohman, R. J. (1997) A closed tube format for amplification and detection of DNA based on energy transfer. *Nucleic Asids Res. 25*, 2516–2521.

(9) Tyagi, S., and Kramer, F. R. (1996) Molecular beacons: probes that fluoresce upon hybridization. *Nat. Biotechnol. 14*, 303–308.

(10) Whitcombe, D., Theaker, J., Guy, S. P., Brown, T., and Little, S. (1999) Detection of PCR products using self-probing amplicons and fluorescence. *Nat. Biotechnol. 17*, 804–807.

(11) French, D. J., Archard, C. L., Brown, T., and McDowell, D. G. (2001) HyBeacon™ probes: a new tool for DNA sequence detection and allele discrimination. *Mol. Cell. Probes 15*, 363–374.

(12) French, D. J., Archard, C. L., Andersen, M. T., and McDowell, D. G. (2002) Ultra-rapid DNA analysis using HyBeacon™ probes and direct PCR amplification from saliva. *Mol. Cell. Probes 16*, 319–326.

(13) Dobson, N., McDowell, D. G., French, D. J., Brown, L. J., Mellor, J. M., and Brown, T. (2003) Synthesis of HyBeacons and dual-labelled probes containing 2′-fluorescent groups for use in genetic analysis. *Chem. Commun.* 1234–1235.

(14) Leijon, M., Mousavi-Jazi, M., and Kubista, M. (2006) LightUp® probes in clinical diagnostics. *Mol. Asp. Med. 27*, 160–175.

(15) Crockett, A. O., and Wittwer, C. T. (2001) Fluorescein-labeled oligonucleotides for real-time PCR: using the inherent quenching of deoxyguanosine nucleotides. *Anal. Biochem. 290*, 89–97.

(16) Vaughn, C. P., and Elenitoba-Johnson, K. S. J. (2003) Hybridization-induced dequenching of fluorescein-labeled oligonucleotides: a novel strategy for PCR detection and genotyping. *Am. J. Pathol. 163*, 29–35.
(17) Yamana, K., Zako, H., Asazuma, K., Iwase, R., Nakano, H., and Murakami, A. (2001) Fluorescence detection of specific RNA sequences using 2′-pyrene-modified oligoribonucleotides. *Angew. Chem., Int. Ed. Engl. 40*, 1104–1106.
(18) Yamana, K., Iwai, T., Ohtani, Y., Sato, S., Nakamura, M., and Nakano, H. (2002) Bis-pyrene-labeled oligonucleotides: sequence specificity of excimer and monomer fluorescence changes upon hybridization with DNA. *Bioconjugate Chem. 13*, 1266–1273.
(19) Korshun, V. A., Stetsenko, D. A., and Gait, M. J. (2002) Novel uridin-2′-yl carbamates: synthesis, incorporation into oligodeoxyribonucleotides, and remarkable fluorescence properties of 2′-pyren-1-ylmethylcarbamate. *J. Chem. Soc., Perkin. Trans 1* 1092–1104.
(20) Mahara, A., Iwase, R., Sakamoto, T., Yamana, K., Yamaoka, T., and Murakami, A. (2002) Bispyrene-conjugated 2′-O-methyloligonucleotide as a highly specific RNA-recognition probe. *Angew. Chem., Int. Ed. 41*, 3648–3650.
(21) Okamoto, A., Kanatani, K., and Saito, I. (2004) Pyrene-labeled base-discriminating fluorescent DNA probes for homogeneous SNP typing. *J. Am. Chem. Soc. 126*, 4820–4827.
(22) Hrdlicka, P. J., Babu, B. R., Sørensen, M. D., Harrit, N., and Wengel, J. (2005) Multilabeled pyrene-functionalized 2′-amino-LNA probes for nucleic acid detection in homogeneous fluorescence assays. *J. Am. Chem. Soc. 127*, 13293–13299.
(23) Berlman, I. B. (1971) *Handbook of Fluorescence Spectra of Aromatic Molecules*, Academic Press, New York.
(24) Lakowicz, J. R. (2006) *Principles of Fluorescence Spectroscopy*, 3rd ed., Springer, Singapore.
(25) Balakin, K. V., Korshun, V. A., Prokhorenko, I. A., Maleev, G. V., Kudelina, I. A., Gontarev, S. V., and Berlin, Y. A. (1997) A new reagent for labeling macromolecules: an activated derivative of the pyrene bichromophore with excimer fluorescence. *Russ. J. Bioorg. Chem. 23*, 28–36.
(26) Lewis, F. D., Zhang, Y., and Letsinger, R. L. (1997) Bispyrenyl excimer fluorescence: a sensitive oligonucleotide probe. *J. Am. Chem. Soc. 119*, 5451–5452.
(27) Balakin, K. V., Korshun, V. A., Mikhalev, I. I., Maleev, G. V., Malakhov, A. D., Prokhorenko, I. A., and Berlin, Y. A. (1998) Conjugates of oligonucleotides with polyaromatic fluorophores as promising DNA probes. *Biosens. Bioelectron. 13*, 771–778.
(28) Kostenko, E., Dobrikov, M., Pyshnyi, D., Petyuk, V., Komarova, N., Vlassov, V., and Zenkova, M. (2001) 5′-Bis-pyrenylated oligonucleotides displaying excimer fluorescence provide sensitive probes of RNA sequence and structure. *Nucleic Acids Res. 29*, 3611–3620.
(29) Yamana, K., Ohtani, Y., Nakano, H., and Saito, I. (2003) Bispyrene labeled DNA aptamer as an intelligent fluorescent biosensor. *Bioorg. Med. Chem. Lett. 13*, 3429–3431.
(30) Dioubankova, N. N., Malakhov, A. D., Stetsenko, D. A., Gait, M. J., Volynsky, P. E., Efremov, R. G., and Korshun, V. A. (2003) Pyrenemethyl *ara*-uridine-2′-carbamate: a strong interstrand excimer in the major groove of a DNA duplex. *ChemBioChem 4*, 841–847.
(31) Okamoto, A., Ichiba, T., and Saito, I. (2004) Pyrene-labeled oligodeoxynucleotide probe for detecting base insertion by excimer fluorescence emission. *J. Am. Chem. Soc. 126*, 8364–8365.
(32) Hrdlicka, P. J., Babu, B. R., Sørensen, M. D., and Wengel, J. (2004) Interstrand communication between 2′-*N*-(pyren-1-yl)-methyl-2′-amino-LNA monomers in nucleic acid duplexes: directional control and signalling of full complementarity. *Chem. Commun.* 1478–1479.
(33) Kawai, K., Yoshida, H., Takada, T., Tojo, S., and Majima, T. (2004) Formation of pyrene dimer radical cation at the internal site of oligodeoxynucleotides. *J. Phys. Chem. B108* 13547–13550.
(34) Novopashina, D. S., Stetsenko, D. A., Totskaya, O. S., Repkova, M. N., and Venyaminova, A. G. (2005) 2′-Bis-pyrene modified oligonucleotides: sensitive fluorescent probes of nucleic acids structure. *Nucleosides Nucleotides Nucleic Acids 24*, 729–734.
(35) Yamana, K., Fukunaga, Y., Ohtani, Y., Sato, S., Nakamura, M., Kim, W. J., Akaike, T., and Maruyama, A. (2005) DNA mismatch detection using a pyrene-excimer-forming probe. *Chem. Commun.* 2509–2511.
(36) Hrdlicka, P. J., Kumar, T. S., and Wengel, J. (2005) Targeting of mixed sequence double-stranded DNA using pyrene-functionalized 2′-amino-α-L-LNA. *Chem. Commun.* 4279–4281.
(37) Lindegaard, D., Madsen, A. S., Astakhova, I. V., Malakhov, A. D., Babu, B. R., Korshun, V. A., and Wengel, J. (2008) Pyrene-perylene as a FRET pair coupled to the N2′-functionality of 2′-amino-LNA. *Bioorg. Med. Chem. 16*, 94–99.
(38) Nakamura, M., Fukunaga, Y., Sasa, K., Ohtoshi, Y., Kanaori, K., Hayashi, H., Nakano, H., and Yamana, K. (2005) Pyrene is highly emissive when attached to the RNA duplex but not to the DNA duplex: the structural basis of this difference. *Nucleic Acid Res. 33*, 5887–5895.
(39) Yamana, K., Gokota, T., Ozaki, H., Nakono, H., Sangen, O., and Shimidzu, T. (1992) Enchanced fluorescence in the binding of oligonucleotides with a pyrene group in the sugar fragment to complementary polynucleotides. *Nucleosides Nucleotides 11*, 383–390.
(40) Honcharenko, D., Zhou, C., and Chattopadhyaya, J. (2008) Modulation of pyrene fluorescence in DNA probes depends upon the nature of the conformationally restricted nucleotide. *J. Org. Chem. 73*, 2829–2842.
(41) Dohno, C., and Saito, I. (2005) Discrimination of single-nucleotide alterations by G-specific fluorescence quenching. *ChemBioChem 6*, 1075–1081.
(42) Yamana, K., Nunota, K., Nakano, H., and Sangen, O. (1994) A new method for introduction of a pyrene group into a terminal position of an oligonucleotide. *Tetrahedron Lett. 35*, 2555–2558.
(43) Yamana, K., Takei, M., and Nakano, H. (1997) Synthesis of oligonucleotide derivatives containing pyrene labeled glycerol linkers: Enchanced excimer fluorescence on binding to a complementary DNA sequence. *Tetrahedron Lett. 38*, 6051–6054.
(44) Kierzek, R., Li, Y., Turner, D. H., and Bevilacqua, P. C. (1993) 5′-Amino pyrene provides a sensitive, nonperturbing fluorescent probe of RNA secondary and tertiary structure formation. *J. Am. Chem. Soc. 115*, 4985–4992.
(45) Li, Y., Bevilacqua, P. C., Mathews, D., and Turner, D. H. (1995) Thermodynamic and activation parameters for binding of a pyrene-labeled substrate by the *Tetrahymena* ribozyme: docking is not diffusion-controlled and is driven by a favorable entropy change. *Biochemistry 34*, 14394–14399.
(46) Mann, J. S., Shibata, Y., and Meehan, T. (1992) Synthesis and properties of an oligodeoxynucleotide modified with a pyrene derivative at the 5′-phosphate. *Bioconjugate Chem. 3*, 554–558.
(47) Maeda, H., Maeda, T., Mizuno, K., Fujimoto, K., Shimizu, H., and Inouye, M. (2006) Alkynylpyrenes as improved pyrene-based biomolecular probes with the advantages of high fluorescence quantum yields and long absorption/emission wavelengths. *Chem. Eur. J. 12*, 824–831.
(48) Malakhov, A. D., Skorobogatyi, M. V., Prokhorenko, I. A., Gontarev, S. V., Kozhich, D. T., Stetsenko, D. A., Stepanova, I. A., Shenkarev, Z. O., Berlin, Y. A., and Korshun, V. A. (2004) 1-(Phenylethynyl)pyrene and 9,10-bis(phenylethynyl)anthracene, useful fluorescent dyes for DNA labeling: Excimer formation and energy transfer. *Eur. J. Org. Chem.* 1298–1307.
(49) Dioubankova, N. N., Malakhov, A. D., Shenkarev, Z. O., and Korshun, V. A. (2004) Oligonucleotides containing new fluorescent 1-phenylethynylpyrene and 9,10-bis(phenylethynyl)anthracene uridine-2′-carbamates: synthesis and properties. *Tetrahedron 60*, 4617–4626.
(50) Lakowicz, J. R., and Knutson, J. R. (1980) Hindered depolarizing rotations of perylene in lipid bilayers. Detection by

lifetime-resolved fluorescence anisotropy measurements. *Biochemistry 19*, 905–911.

(51) Adler, M., and Tritton, T. R. (1988) Fluorescence depolarization measurements on oriented membranes. *Biophys. J. 53*, 989–1005.

(52) Khan, T. K., and Chong, P. L.-G. (2000) Studies of archaebacterial bipolar tetraether liposomes by perylene fluorescence. *Biophys. J. 78*, 1390–1399.

(53) Johansson, L. B.-Å., Molotkovsky, J. G., and Bergelson, L. D. (1987) Fluorescence and absorption properties of perylenyl and perylenoyl probe molecules in solvents and liquid crystals. *J. Am. Chem. Soc. 109*, 7374–7381.

(54) Klonis, N., Wang, H., Quazi, N. H., Casey, J. L., Neumann, G. M., Hewish, D. R., Hughes, A. B., Deady, L. W., and Tilley, L. (2001) Characterization of a series of far red absorbing perylene diones: A new class of fluorescent probes for biological applications. *J. Fluorescence 11*, 1–11.

(55) Chotimarkorn, C., Ohshima, T., and Ushio, H. (2006) Fluorescent image analysis of lipid hydroperoxides in fish muscle with 3-perylene diphenylphosphine. *Lipids 41*, 295–300.

(56) Skorobogatyi, M. V., Pchelintseva, A. A., Ustinov, A. V., Korshun, V. A., and Malakhov, A. D. (2005) Perylene attached to DNA through stiff or flexible linker: Duplex stability and FRET. *Nucleosides Nucleotides Nucleic Acids 24*, 931–934.

(57) Lewis, F. D., Zhang, L., Kelley, R. F., McCamant, D., and Wasielewski, M. R. (2007) A perylenedicarboxamide linker for DNA hairpins. *Tetrahedron 63*, 3457–3464.

(58) Masuko, M., Ohuchi, S., Sode, K., Ohtani, H., and Shimadzu, A. (2000) Fluorescence resonance energy transfer from pyrene to perylene labels for nucleic acid hybridization assays under homogeneous solution conditions. *Nucleic Acids Res. 28*, e34.

(59) Lewis, F. D., Zhang, L., and Zuo, X. (2005) Orientation control of fluorescence resonance energy transfer using DNA as a helical scaffold. *J. Am. Chem. Soc. 127*, 10002–10003.

(60) Asseline, U., and Cheng, E. (2001) Synthesis and binding properties of perylene-oligo-2′-deoxyribonucleotide conjugates. *Tetrahedron Lett. 42*, 9005–9010.

(61) Aubert, Y., and Asseline, U. (2004) Synthesis and hybridization properties of oligonucleotide–perylene conjugates: influence of the conjugation parameters on triplex and duplex stabilities. *Org. Biomol. Chem. 2*, 3496–3503.

(62) Zheng, Y., Long, H., Schatz, G. C., and Lewis, F. D. (2005) Duplex and hairpin dimer structures for perylene diimide–oligonucleotide conjugates. *Chem. Commun.* 4795–4797.

(63) Bevers, S., Schutte, S., and McLaughlin, L. W. (2000) Naphtalene- and perylene-based linkers for the stabilization of hairpin triplexes. *J. Am. Chem. Soc. 122*, 5905–5915.

(64) Skorobogatyi, M. V., Malakhov, A. D., Pchelintseva, A. A., Turban, A. A., Bondarev, S. L., and Korshun, V. A. (2006) Fluorescent 5-alkynyl-2′-deoxyuridines: high emission efficiency of a conjugated perylene nucleoside in a DNA duplex. *ChemBioChem 7*, 810–816.

(65) Kashida, H., Takatsu, T., and Asanuma, H. (2007) Detection of genetic polymorphisms with high sensitivity by DNA-perylene conjugate. *Tetrahedron Lett. 48*, 6759–6762.

(66) Singh, S. K., Nielsen, P., Koshkin, A. A., and Wengel, J. (1998) LNA (locked nucleic acids): synthesis and high-affinity nucleic acid recognition. *Chem. Commun.* 455–456.

(67) Koshkin, A. A., Singh, S. K., Nielsen, P., Rajwanshi, V. K., Kumar, R., Meldgaard, M., Olsen, C. E., and Wengel, J. (1998) LNA (Locked Nucleic Acids): Synthesis of the adenine, cytosine, guanine, 5-methylcytosine, thymine and uracil bicyclonucleoside monomers, oligomerisation, and unprecedented nucleic acid recognition. *Tetrahedron 54*, 3607–3630.

(68) Obika, S., Nanbu, D., Hari, Y., Andoh, J., Morio, K., Doi, T., and Imanishi, T. (1998) Stability and structural features of the duplexes containing nucleoside analogues with a fixed N-type conformation, 2′-*O*,4′-*C*-methyleneribonucleosides. *Tetrahedron Lett. 39*, 5401–5404.

(69) Koshkin, A. A., Nielsen, P., Meldgaard, M., Rajwanshi, V. K., Singh, S. K., and Wengel, J. (1998) LNA (Locked Nucleic Acid): An RNA mimic forming exceedingly stable LNA:LNA duplexes. *J. Am. Chem. Soc. 120*, 13252–13253.

(70) Bondensgaard, K., Petersen, M., Singh, S. K., Rajwanshi, V. K., Kumar, R., Wengel, J., and Jacobsen, J. P. (2000) Structural studies of LNA:RNA duplexes by NMR: conformations and implications for RNase H activity. *Chem. Eur. J. 6*, 2687–2695.

(71) Singh, S. K., Kumar, R., and Wengel, J. (1998) Synthesis of 2′-amino-LNA: A novel conformationally restricted high-affinity oligonucleotide analogue with a handle. *J. Org. Chem. 63*, 10035–10039.

(72) Sørensen, M. D., Petersen, M., and Wengel, J. (2003) Functionalized LNA (locked nucleic acid): high-affinity hybridization of oligonucleotides containing N-acylated and N-alkylated 2′-amino-LNA monomers. *Chem. Commun.* 2130–2131.

(73) Babu, B. R., Hrdlichka, P. J., McKenzie, C. J., and Wengel, J. (2005) Optimized DNA targeting using *N*,*N*-bis(2-pyridylmethyl)-β-alanyl-2′-amino-LNA. *Chem. Commun.* 1705–1707.

(74) Babu, B. R., Lindegaard, D., Kumar, T. S., Maity, J., Astakhova, I. V., Malakhov, A. D., Sørensen, M., Karla, N., Korshun, V. A., Hrdlichka, P. J., Prasad, A. K., Parmar, V. S., and Wengel, J. Manuscript in preparation.

(75) Petersen, M., and Wengel, J. (2003) LNA: a versatile tool for therapeutics and genomics. *Trends Biotechnol. 21*, 74–81.

(76) Vester, B., Lundberg, L. B., Sørensen, M. D., Babu, B. R., Douthwaite, S., and Wengel, J. (2002) LNA-zymes: incorporation of LNA-type monomers into DNAzymes markedly increases RNA cleavage. *J. Am. Chem. Soc. 124*, 13682–13683.

(77) Wengel, J. (2004) Nucleic acid nanotechnology – towards Ångström-scale engineering. *Org. Biomol. Chem. 2*, 277–280.

(78) Zieger, H. E. (1966) Alkylperylenes. The isomeric ethylperylenes. *J. Org. Chem. 31*, 2977–2981.

(79) Caruthers, M. H., Barone, A. D., Beaucage, S. L., Dodds, D. R., Fisher, E. F., McBride, L. J., Matteucci, M., Stabinsky, Z., and Tang, J.-Y. (1987) Chemial synthesis of deoxyoligonucleotides by the phosphoramidite method. *Methods Enzymol. 154*, 287–313.

(80) Rosenbohm, C., Christensen, S. M., Sørensen, M. D., Pedersen, D. S., Larsen, L.-E., Wengel, J., and Koch, T. (2003) Synthesis of 2′-amino-LNA: a new strategy. *Org. Biomol. Chem. 1*, 655–663.

(81) Christensen, S. M., Rosenbohm, C., Sørensen, M., Larsen, L.-E., Wengel, J., and Koch, T. (2003) Improved synthesis of 2′-amino-LNA. *Nucleotides Nucleotides Nucleic Acids 22*, 1131–1133.

(82) Nijegorodov, N., Mabbs, R., and Downey, W. S. (2001) Evolution of absorption, fluorescence, laser and chemical properties in the series of compounds perylene, benzo(ghi)perylene and coronene. *Spectrochim. Acta, Part A 57*, 2673–2685.

(83) Morris, J. V., Mahaney, M. A., and Huber, J. R. (1976) Fluorescence quantum yield determinations. 9,10-Diphenylanthracene as a reference standard in different solvents. *J. Phys. Chem. 80*, 969–974.

(84) Trahanovsky, W. S. (1978) *Oxidation in Organic Chemistry, Part C*, Chapter V, Academic Press, New York.

(85) Okamoto, A., Tainaka, K., Nishiza, K., and Saito, I. (2005) Monitoring DNA structures by dual fluorescence of pyrene derivatives. *J. Am. Chem. Soc. 127*, 13128–13129.

(86) Nijegorodov, N. I., and Downey, W. S. (1994) The influence of planarity and rigidity on the absorption and fluorescence parameters and intersystem crossing rate constant in aromatic molecules. *J. Phys. Chem. 98*, 5639–5643.

(87) Gaballah, S. T., Hussein, Y. H. A., Anderson, N., Lian, T. T., and Netzel, T. L. (2005) Comparison of $Py^{\cdot+}$ /$dU^{\cdot-}$ charge transfer state dynamics in 5-(1-pyrenyl)-2′-deoxyuridine nucleoside conjugates with amido-, ethylenyl-, and ethynyl linkers. *J. Phys. Chem. A 109*, 10832–10845.

(88) Auld, D., and Simeonov, A. (2005) Literature search and review. *Assay Drug Dev. Technol. 3*, 581–593.

(89) Massey, M., Algar, W. R., and Krull, U. J. (2006) Fluorescence resonance energy transfer (FRET) for DNA biosensors: FRET pairs and Förster distances for various dye–DNA conjugates. *Anal. Chim. Acta 568*, 181–189.

(90) Liu, X., and Tan, W. (1999) A fiber-optic evanescent wave DNA biosensor based on novel molecular beacons. *Anal. Chem. 71*, 5054–5059.

(91) Frutos, A. G., Pal, S., Quesada, M., and Lahiri, J. (2002) Method for detection of single-base mismatches using bimolecular beacons. *J. Am. Chem. Soc. 124*, 2396–2397.

(92) Hwang, G. T., Seo, Y. J., and Kim, B. H. (2004) A highly discriminating quencher-free molecular beacon for probing DNA. *J. Am. Chem. Soc. 126*, 6528–6529.

(93) Hwang, G. T., Seo, Y. J., Kim, S. J., and Kim, B. H. (2004) Fluorescent oligonucleotides incorporating 5-(1-ethynylpyrenyl)-2′-deoxyuridine: sequence-specific fluorescence changes upon duplex formation. *Tetrahedron Lett. 45*, 3543–3546.

(94) Brunner, J., and Kraemer, R. (2004) Copper(II)-quenched oligonucleotide probes for fluorescent DNA sensing. *J. Am. Chem. Soc. 126*, 13626–13627.

(95) Köhler, O., Jarikote, D. V., and Seitz, O. (2005) Forced intercalation probes (FIT Probes): thiazole orange as a fluorescent base in peptide nucleic acids for homogeneous single-nucleotide-polymorphism detection. *ChemBioChem 6*, 69–77.

(96) Valis, L., Amann, N., and Wagenknecht, H.-A. (2005) Detection of single-base mismatches and abasic sites using phenanthridinium as an artificial DNA base and charge donor. *Org. Biomol. Chem. 3*, 36–38.

(97) Bag, S. S., Suito, Y., Hanawa, K., Hayasi, K., Kodate, S., Suzuka, I., and Saito, I. (2006) Synthesis of perylene-labeled base-discriminating fluorescent (BDF) nucleoside and its fluorescence properties. *Nucleic Acids Symp. Ser. 50*, 179–180.

(98) Asseline, U., Chassignol, M., Aubert, Y., and Roig, V. (2006) (2006) Detection of terminal mismatches on DNA duplexes with fluorescent oligonucleotides. *Org. Biomol. Chem. 4*, 1949–1957.

(99) Nielsen, K. E., Singh, S. K., Wengel, J., and Jakobsen, J. P. (2000) Solution structure of an LNA hybridized to DNA: NMR study of the d($CT^{L}GCT^{L}T^{L}CT^{L}GC$):d(GCAGAAGCAG) duplex containing four locked nucleotides. *Bioconjugate Chem. 11*, 228–238.

(100) Shaner, N. C., Campbell, R. E., Steinbach, P. A., Giepmans, B. N. G., Palmer, A. E., and Tsien, R. Y. (2004) Improved monomeric red, orange and yellow fluorescent proteins derived from *Discosoma* sp. red fluorescent protein. *Nat. Biotechnol. 22*, 1567–1572.

(101) Grünewald, C., Kwon, T., Piton, N., Förster, U., Wachtveitl, J., and Engels, J. W. (2008) RNA as scaffold for pyrene excited complexes. *Bioorg. Med. Chem. 16*, 19–26.

BC800202V

Perylene Attached to 2´-Amino-LNA: Synthesis, Incorporation into Oligonucleotides and Remarkable Fluorescence Properties *In Vitro* and in Cell Culture

Irina V. Astakhova, Vladimir A. Korshun, Kasper Jahn, Jørgen Kjems and Jesper Wengel*

SUPPORTING INFORMATION

S2. MALDI-MS of synthesized oligonucleotides (Table S1).

S3. Thermal denaturation curves (Figure S1).

S4. UV-visible absorption and excitation spectra of **ON8** and its duplexes with DNA/RNA (Figure S2).

S5. Fluorescence steady-state emission studies and quantum yield determinations.

S7. Fluorescence steady-state emission spectra of modified ODNs and their duplexes with complementary DNA and RNA (Figure S3).

S8. CD measurements.

S8. CD spectra of modified duplexes containing modification in one and both complementary strands (Figure S4).

S9. Cell transfection experiments and visualization details.

S10. References.

Table S1. MALDI-MS of synthesized ONs.[a]

#	Sequence, 5′→3′	Found *m/z* $[M-H]^-$	Calc. *m/z* $[M-H]^-$
ON1	GTG A**X**A TGC	3059	3060
ON2	GCA **X**AT CAC	2988	2987
ON3	GCA TA**X** CAC	2988	2987
ON4	GTG A**X**A **X**GC	3365	3363
ON5	GCA **X**A**X** CAC	3293	3293
ON6	GTG **XX**T TGC	3348	3349
ON7	G**X**G A**X**A **X**GC	3669	3669
ON8	G**X**G **X**T**X** TGC	3654	3655
ON9	TT**X** A**X**A **X**A**X** CA^{Me}C^{L} G	5186	5183
ON10	TT^{L}T A**X**A **X**A**X** CA^{Me}C^{L} G	4911	4911

[a] **X** = 2′-*N*-(perylen-3-yl)carbonyl-2′-amino-LNA monomer; T^{L} and $^{Me}C^{L}$ = thymin-1-yl and 5-methylcytosin-1-yl LNA monomers, respectively.

A)

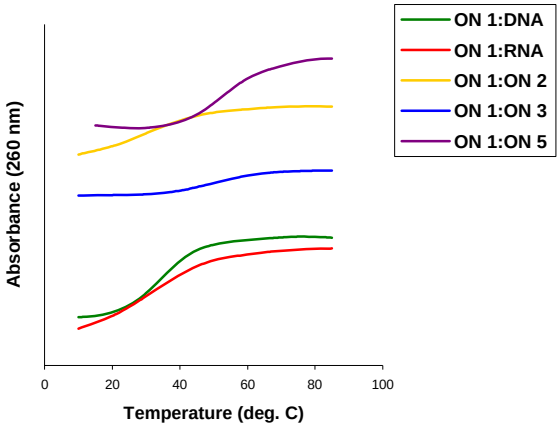

B)

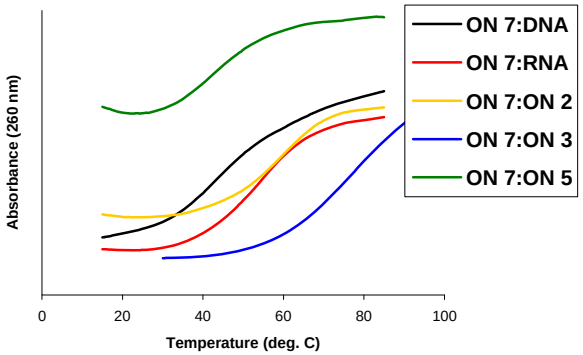

C)

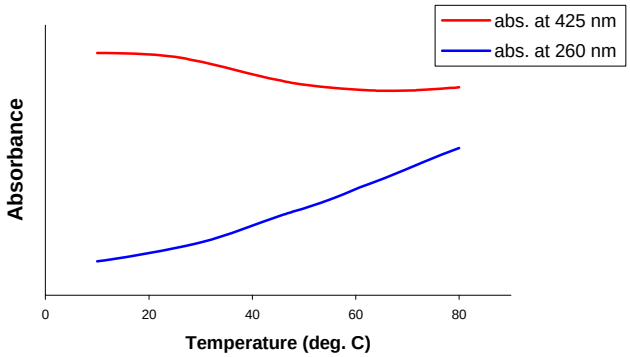

Figure S1. Thermal denaturation curves of A) singly modified **ON1**, and B) doubly modified **ON7** against DNA/RNA complements and DNAs containing monomers **X**. Recorded in medium salt buffer at 260 nm. C) Thermal denaturation curves of the duplex **ON9**:DNA detected at 260 nm and 425 nm. Spectra were obtained in medium salt buffer using 1.0 µM concentrations of the two complementary strands.

A)

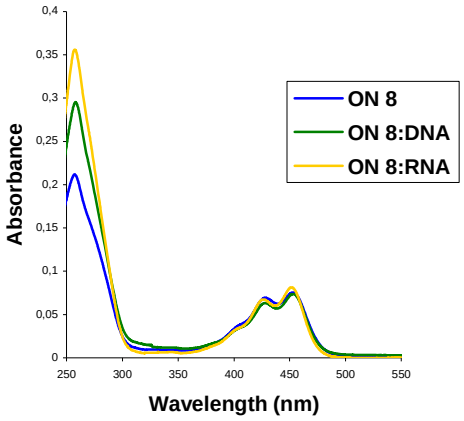

B)

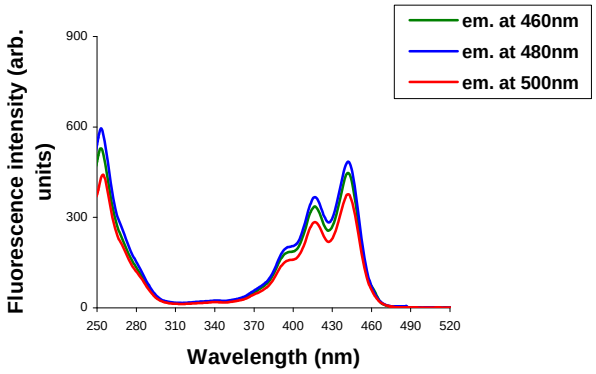

C)

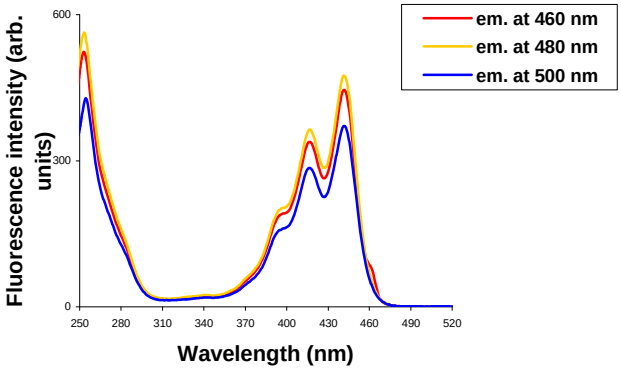

Figure S2. A) UV-visible absorption spectra of **ON8** and corresponding duplexes with DNA/RNA complements in a medium salt buffer. B) Excitation spectra of **ON8**:DNA, and C) excitation spectra of **ON8**:RNA in medium salt buffer recorded at different emission wavelengths (not normalized). Excitation spectra were obtained recording emission at 460 nm, 480 nm and 500 nm.

Fluorescence steady-state emission studies and quantum yield determinations

Fluorescence spectra were obtained in a medium salt buffer using a PerkinElmer LS 55 luminiscence spectrometer equipped with a Peltier temperature controller. For recording of fluorescence spectra 0.1 μM concentrations of the ss probe or corresponding duplex were used. For weakly fluorescent samples concentration was increased to 0.5 μM. Excitation spectra were obtained recording emission at 460 nm, 480 nm and 500 nm. The fluorescence quantum yields (Φ_F) were measured by the relative method using standards of highly diluted solutions of perylene (Φ_F 0.93 (*1*)) and 9,10-diphenylantracene (Φ_F 0.95 (*2*)) in cyclohexane. For fluorescence quantum yields determination concentration of 1 μM or 0.5 μM (for intensively fluorescent ONs or duplexes) of the solution was used. In all cases, absorption in the range 435-650 nm of the solutions used for quantum yield measurements did not exceed 0.1, and was not less than 0.01. Control experiments with an elimination of dissolved oxygen in the buffer solution did not show significant change of fluorescence intensity compared to non-degassed solutions. Thus, the samples used in quantum yield measurements were not degassed. Steady-state fluorescence emission spectra were obtained as an average of 5 scans using an excitation wavelength of 425 nm, excitation slit of 4.0 nm, emission slit of 2.5 nm and scan speed of 120 nm/min. The fluorescence quantum yield of perylene in cyclohexane in these experimental settings was measured to be 0.90 relative to 9,10-diphenylantracene in cyclohexane (lit. (*2*) Φ_F 0.95).

Emission quantum yields of perylene-labeled ODNs Φ_F *(ON)* were determined according to (*3*):

$$\Phi_F(ON) = \Phi_F(PerH) \times \frac{I(ON)}{I(PerH)} \times \frac{OD_{425}(PerH)}{OD_{425}(ON)} \times \frac{n^2_{buffer}}{n^2_{cyclohexane}}$$

where Φ_F (*PerH*) is the cross-calibrated (by using of 9,10-diphenylantracene in cyclohexane as a second standard) value of the fluorescence quantum yield of perylene in toluene, *I (ON)* is the area of the fluorescence emission spectra of the sample from 435 to 650 nm, *I (PerH)* is the area of the perylene's emission spectra at the same region, n_{buffer} and $n_{toluene}$ are the refractive indexes of the buffer (1.334) and cyclohexane (1.426), respectively. High quantum yields ($\Phi_F > 0.2$) were determined as the average

of two measurements within ±10%. Determinations of low quantum yields ($\Phi_F < 0.1$) may be associated with considerably larger error.

A)

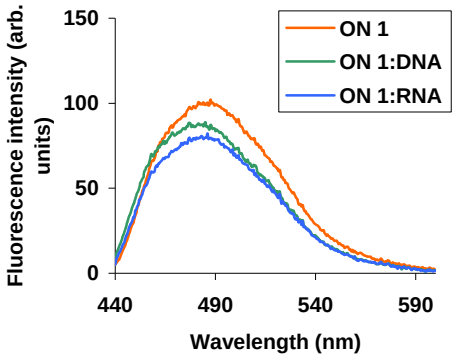

B)

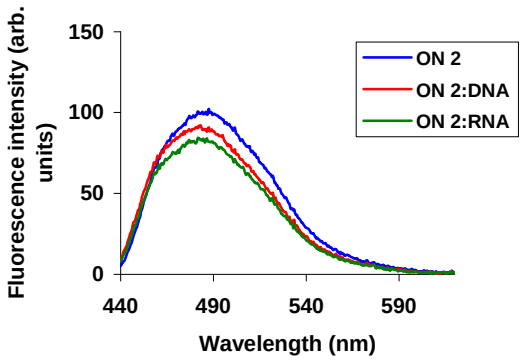

C)

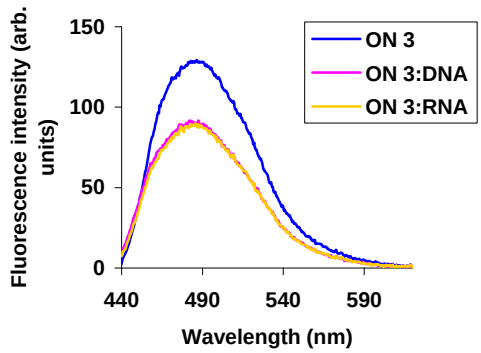

D)

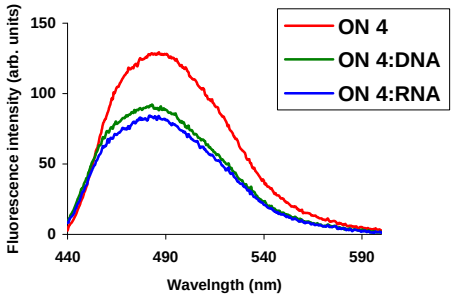

E)

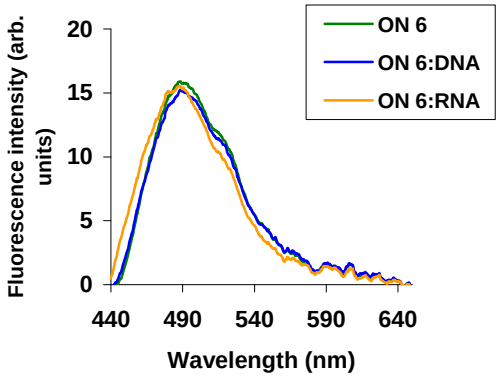

F)

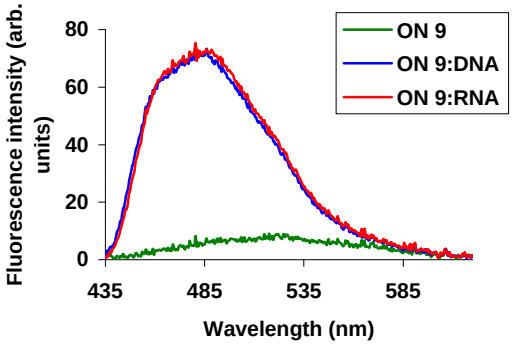

Figure S3. Steady-state fluorescence emission spectra of modified modified oligonucleotides and the corresponding duplexes with complementary DNA/RNA (0.5 μM solutions). For conditions see Figure 2.

CD measurements

CD spectra were recorded on JASCO J-815 CD Spectrometer equipped with CDF 4265/15 temperature controller. Samples for CD measurements were prepared as described in the thermal denaturation studies section except that a concentration of 2.0 µM of both the complementary strands was used. Quartz optical cells with a path-length of 0.5 cm were used.

A) B)

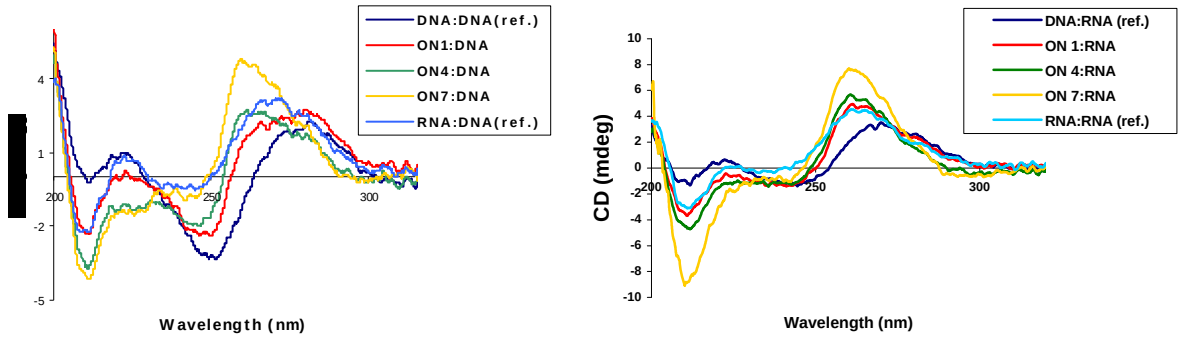

C) D)

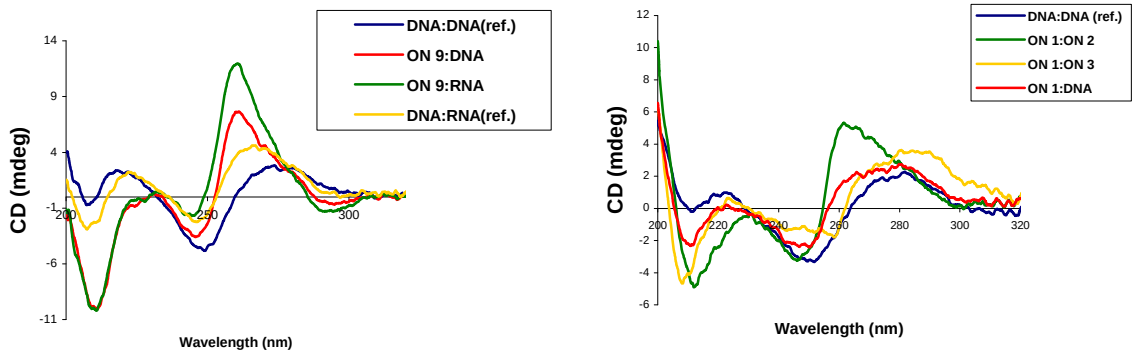

Figure S4. CD spectra of **ON1**,**ON4**, and **ON7** against A) DNA complement and B) complementary RNA; C) CD spectra of **ON9**:DNA and **ON9**:RNA. dsDNA, DNA:RNA and dsRNA. D) CD spectra of **ON1** towards **ON2** and **ON3** ("+1 zipper" and "-1 zipper" constitution, respectively) relative to **ON1**:DNA. The spectra were recorded in medium salt buffer at 19 ºC, using 2.0 µM concentration of complementary strands.

Cell transfection experiments

HEK 293 cells were grown in Gibco RPMI medium with 10% FBS. Experiments were performed on coverslips in 12 well plates coated with polyL lysine. The genetic code for mCherry protein followed by 4 x target sequence was cloned into a pCDNA5/FRT/TO vector which was transfected with Lipofectamine 2000 (LF-2000) transfection reagent using 4 µL LF-2000 and 1.6 µg DNA following the LF-2000 protocol. The medium was changed after 12 hours. The LNA probe **ON10** was transfected after 40 hours with LF-2000 using 40 pmol of the probe and 2 µL of LF-2000.

Protocol for the transfection of cloned DNA/probe **ON10**

1) Mix DNA/**ON10** with 100 µL Serum free medium. Let sit for 5 min.
2) Mix Lipofectamine-2000 transfection reagent with 100 µL Serum free medium in another tube. Let sit for 5 min.
3) Mix the contents of the two tubes and mix gently. Let it stand at room temperature for 25 min.
4) Pour the mixture over cells and rock 12-well plate gently to distribute the transfection reagent evenly.

Cells were fixated after 6 hours by washing with 2 x in PBS, incubated in 4% formaldehyde solution for 30 min, and washed with 3 x in PBS. Coverslips were mounted on objective slides with 3µL mounting media containing DAPI stain.

Visualization

Fluorescence was visualized with a Ziess axiovert 200m microscope using excitation wavelengths of 360 nm (DAPI), 435 nm (perylene-LNA probe) and 570 nm (mCherry protein) and emission wavelengths of 460 nm, 480 nm and 630 nm for DAPI, perylene-LNA and mCherry protein, respectively (±15 nm).

References

(1) Nijegorodov, N., Mabbs, R., Downey, W. S. (2001) Evolution of absorption, fluorescence, laser and chemical properties in the series of compounds perylene, benzo(ghi)perylene and coronene. *Spectrochim. Acta A 57*, 2673-2685.

(2) Morris, J. V., Mahaney, M. A., Huber, J. R. (1976) Fluorescence quantum yield determinations. 9,10-Diphenylantracene as a reference standard in different solvents. *J. Phys. Chem.* **1976**, *80*, 969-974.

(3) Lakowicz, J. R. (2006) Principles of Fluorescence Spectroscopy, 3th Ed., Springer, Singapore.

^{64}Cu-Labeled 2-(Diphenylphosphoryl)ethyldiphenylphosphonium Cations as Highly Selective Tumor Imaging Agents: Effects of Linkers and Chelates on Radiotracer Biodistribution Characteristics

Chang-Tong Yang,[†] Young-Seung Kim,[†] Jianjun Wang,[†] Lijun Wang,[†] Jiyun Shi,[†] Zi-Bo Li,[‡] Xiaoyuan Chen,[‡] Ming Fan,[†] Jian-Jian Li,[†] and Shuang Liu*,[†]

School of Health Sciences, Purdue University, West Lafayette, Indiana, and Molecular Imaging Program at Stanford, Department of Radiology and Bio-X, Stanford University, Stanford, California. Received May 21, 2008; Revised Manuscript Received July 28, 2008

Radiolabeled organic cations, such as triphenylphosphonium (TPP), represents a new class of radiotracers for imaging cancers and the transport function of multidrug resistance P-glycoproteins (particularly MDR1 Pgp) by single photon emission computed tomography (SPECT) or positron emission tomography (PET). This report presents the synthesis and biological evaluation of ^{64}Cu-labeled 2-(diphenylphosphoryl)ethyldiphenylphosphonium (TPEP) cations as novel PET radiotracers for tumor imaging. Biodistribution studies were performed using the athymic nude mice bearing subcutaneous U87MG human glioma xenografts to explore the impact of linkers, bifunctional chelators (BFCs), and chelates on biodistribution characteristics of the ^{64}Cu-labeled TPEP cations. Metabolism studies were carried out using normal athymic nude mice to determine the metabolic stability of four ^{64}Cu radiotracers. It was found that most ^{64}Cu radiotracers described in this study have significant advantages over ^{99m}Tc-Sestamibi for their high tumor/heart and tumor/muscle ratios. Both BFCs and linkers have significant impact on biological properties of ^{64}Cu-labeled TPEP cations. For example, ^{64}Cu(DO3A-xy-TPEP) has much lower liver uptake and better tumor/liver ratios than ^{64}Cu(DO3A-xy-TPP), suggesting that TPEP is a better mitochondrion-targeting molecule than TPP. Replacing DO3A with DO2A results in ^{64}Cu(DO2A-xy-TPEP)$^{+}$, which has a lower tumor uptake than ^{64}Cu(DO3A-xy-TPEP). Substitution of DO3A with NOTA-Bn leads to a significant decrease in tumor uptake for ^{64}Cu(NOTA-Bn-xy-TPEP). The use of DOTA-Bn to replace DO3A has little impact on the tumor uptake, but the tumor/liver ratio of ^{64}Cu(DOTA-Bn-xy-TPEP)$^{-}$ is not as good as that of ^{64}Cu(DO3A-xy-TPEP), probably due to the aromatic benzene ring in DOTA-Bn. Addition of an extra acetamido group in ^{64}Cu(DOTA-xy-TPEP) results in a lower liver uptake, but tumor/liver ratios of ^{64}Cu(DOTA-xy-TPEP) and ^{64}Cu(DO3A-xy-TPEP) are comparable due to a faster tumor washout of ^{64}Cu(DOTA-xy-TPEP). Substitution of xylene with the PEG_2 linker also leads to a significant reduction in both tumor and liver uptake. MicroPET imaging studies on ^{64}Cu(DO3A-xy-TPEP) in athymic nude mice bearing U87MG glioma xenografts showed that the tumor was clearly visualized as early as 1 h postinjection with very high T/B contrast. There was very little metabolite (<2%) detectable in the urine and feces samples for ^{64}Cu(DO3A-xy-TPEP), ^{64}Cu(DOTA-Bn-xy-TPEP)$^{-}$, and ^{64}Cu(NOTA-Bn-xy-TPEP). Considering both tumor uptake and T/B ratios (particularly tumor/heart, tumor/liver, and tumor/muscle), it was concluded that ^{64}Cu(DO3A-xy-TPEP) is a promising PET radiotracer for imaging the MDR-negative tumors.

INTRODUCTION

Alteration in the mitochondrial potential ($\Delta\Psi_m$) is an important characteristic of cancer (*1*−*4*). It has been demonstrated that the mitochondrial potential in carcinoma cells is significantly higher than that in normal epithelial cells (*5*−*9*). For example, the difference in $\Delta\Psi_m$ between the colon carcinoma cell line CX-1 and the control green monkey kidney epithelial cell line CV-1 was approximately 60 mV (163 mV in tumor cells versus 104 mV in normal cells). The observation that the enhanced mitochondrial potential is prevalent in tumor cell phenotype provides the conceptual basis for development of the mitochondrion-targeting pharmaceuticals and imaging probes (*1*−*3*, *10*−*13*).

Recently, we reported several ^{64}Cu-labeled triphenylphosphonium (TPP) cations as radiotracers for tumor imaging by positron emission tomography (PET) in athymic nude mice bearing U87MG human glioma xenografts (*14*−*16*). We found that that ^{64}Cu(DO3A-xy-TPP) and ^{64}Cu(DO2A-xy-TPP)$^{+}$ have relatively high tumor uptake with long tumor retention. The most striking difference between the ^{64}Cu-labeled TPP cations and ^{99m}Tc-Sestamibi, the most successful radiopharmaceutical currently available for both tumor and myocardial perfusion imaging, is that they all have much lower heart uptake (<0.6% ID/g) than ^{99m}Tc-Sestamibi (∼18% ID/g) at >30 min postinjection (p.i.). Their tumor/heart ratios are >40× better than that of ^{99m}Tc-Sestamibi at 120 min p.i. The muscle uptake of ^{64}Cu(DO3A-xy-TPP) was undetectable at >30 min p.i. while ^{99m}Tc-Sestamibi has very high muscle uptake (∼5% ID/g) over the 2 h study period. Despite their charge difference, ^{64}Cu(DO3A-xy-TPP) and ^{64}Cu(DO2A-xy-TPP)$^{+}$ share very similar lipophilicity, tumor uptake, tumor/heart, and tumor/lung ratios. However, the positive charge in ^{64}Cu(DO2A-xy-TPP)$^{+}$ results in a dramatic reduction in its liver uptake. As a result, its tumor/liver ratio is significantly better than that of ^{64}Cu(DO3A-xy-

* To whom correspondence should be addressed: School of Health Sciences, Purdue University, 550 Stadium Mall Drive, West Lafayette, IN 47907. Phone: 765-494-0236; Fax 765-496-1377; E-mail: lius@pharmacy.purdue.edu.

[†] Purdue University.

[‡] Stanford University.

10.1021/bc8002056 CCC: $40.75 © 2008 American Chemical Society
Published on Web 09/03/2008

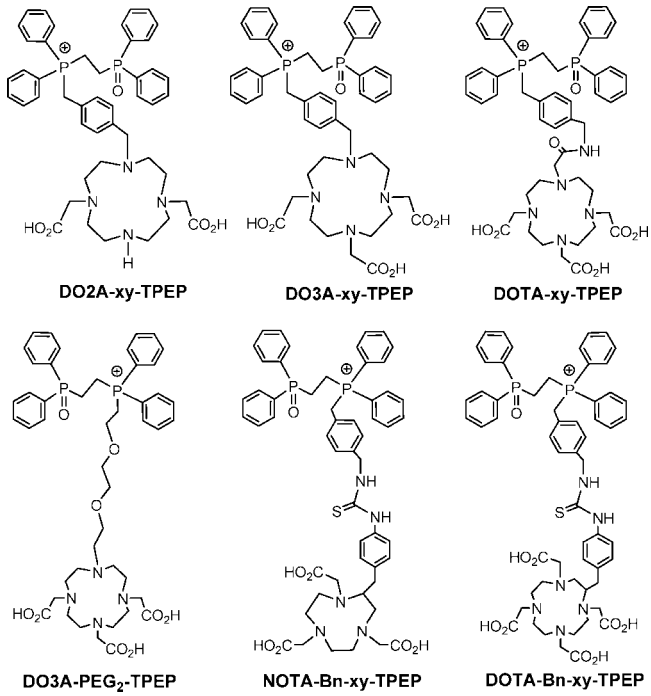

Figure 1. TPEP conjugates for preparation of the ^{64}Cu TPEP cations useful as radiotracers for imaging tumors by PET. The TPEP moiety is used as the "mitochondrion-targeting biomolecule" to carry ^{64}Cu into tumor cells that have higher mitochondrial potential than normal cells. DO3A, DO2A, DOTA, and NOTA are used as BFCs for ^{64}Cu chelation. Different linkers are used to modify pharmacokinetics and improve T/B ratios of ^{64}Cu radiotracers.

TPP) (*16*). Results from *in vitro* assays show that ^{64}Cu(DO3A-xy-TPP) is able to localize in mitochondria of glioma cells. MicroPET imaging data show that the tumor could be visualized as early as 30 min p.i. in the tumor-bearing mice administered with ^{64}Cu(DO3A-xy-TPP) (*14*). However, its high liver uptake remains a significant challenge for ^{64}Cu(DO3A-xy-TPP) to be clinically useful as a PET radiotracer.

To further improve the tumor uptake and tumor/background (T/B) ratios, we prepared several 2-(diphenylphosphoryl)ethyldiphenylphosphonium (TPEP) conjugates (Figure 1) and their ^{64}Cu complexes. We are particularly interested TPEP cation because of the phosphoryl group (P═O) that may help improve the radiotracer hydrophilicity and excretion kinetics from the liver. Biodistribution and imaging studies were performed using athymic nude mice bearing subcutaneous U87MG glioma xenografts. The U87MG glioma cell line was chosen because it has no expression of multidrug resistance P-glycoprotein (particularly MDR1 Pgp) (*17*−*20*). This tumor-bearing animal model would allow us to evaluate the intrinsic tumor-targeting capability of ^{64}Cu radiotracers and their excretion kinetics from noncancerous organs, such as heart, liver, lungs, and muscle. The main objective of this study is to explore the impact of linkers, bifunctional chelators (BFCs), and ^{64}Cu-chelates on biodistribution characteristics and excretion kinetics of the ^{64}Cu-labeled TPEP cations.

[1]ABBREVIATIONS: DO2A, 1,4,7,10-tetraazacyclododecane-1,7-diacetic acid; DO3A, 1,4,7,10-tetraazacyclododecane-4,7,10-triacetic acid; DOTA, 1,4,7,10-tetraazacyclododecane-1,4,7,10-tetraacetic acid; NOTA, 1,4,7-triaazacyclononane-1,4,7-triacetic acid; DO2A-xy-TPP,(4-((4,10-bis(carboxymethyl)-1,4,7,10-tetraazacyclododecan-1-yl)methyl) benzyl)triphenylphosphonium; DO3A-xy-TPP, triphenyl(4-((4,7,10-tris (carboxymethyl)-1,4,7,10-tetraazacyclododecan-1-yl)methyl)benzyl) phosphonium; DO2A-xy-TPEP, (4-((4,10-bis(carboxymethyl)-1,4,7,10-tetraazacyclododecan-1-yl)methyl)benzyl)(2-(diphenylphosphoryl)ethyl) diphenylphosphonium; DO3A-xy-TPEP, (2-(diphenylphosphoryl)ethyl)diphenyl(4-((4,7,10-tris(carboxymethyl)-1,4,7,10-tetraazacyclododecan-1-yl)methyl)benzyl)phosphonium; DO3A-PEG$_2$-TPEP, (2-(diphenylphosphoryl)ethyl)diphenyl(4-((2-(4,7,10-tris(carboxymethyl)-1,4,7,10-tetraazacyclododecan-1-yl)acetamido)methyl)benzyl)phosphonium; DOTA-Bn-xy-TPEP,(2-(Diphenylphosphoryl)ethyl)diphenyl(4-((3-(4-((1,4,7,10-tetrakis(carboxymethyl)-1,4,7,10-tetraazacyclododecan-2-yl)methyl)phenyl)thisoureido)methyl)benzyl)phosphonium; NOTA-Bn-xy-TPEP,(2-(Diphenylphosphoryl)ethyl)diphenyl(4-((3-(4-((1,4,7-tris(carboxymethyl)-1,4,7-triazonan-2-yl)methyl)phenyl)thioureido) methyl)benzyl)phosphonium.

EXPERIMENTAL SECTION

Materials and Instruments. Chemicals were purchased from Sigma/Aldrich (St. Louis, MO) and used as received. DO3A(OBu-t)$_3$ (1,4,7,10-tetraazacyclododecane-4,7,10-tris(*t*-butyl acetate)), DO2A(OBu-t)$_2$ (1,4,7,10-tetraazacyclododecane-4,7-bis(*t*-butyl acetate)), DOTA(OBu-t)$_3$-NHS (1,4,7,10-tetraazacyclododecane-1-(*N*-hydroxysuccinimide acetate)-4,7,10-tris(*t*-butyl acetate)), *p*-SCN-Bn-DOTA(2-(*p*-isothiocyanobenzyl)-1,4,7,10-tetraazacyclododecane-1,4,7,10-tetraacetic acid), and *p*-SCN-Bn-NOTA (2-(*p*-isothiocyanobenzyl)-1,4,7-triaazacyclononane-1,4,7-triacetic acid) were purchased from Macrocyclics Inc. (Dallas, TX). NMR (^{1}H, ^{13}C, and ^{31}P) data were obtained using a Bruker DRX 300 MHz FT NMR spectrometer. Chemical shifts are reported as δ in ppm relative to TMS. ESI mass spectral data were collected using positive mode on a Finnigan LCQ classic mass spectrometer, School of Pharmacy, Purdue University. Elemental analysis was performed by Dr. H. Daniel Lee using a Perkin-Elmer Series III analyzer, Department of Chemistry, Purdue University. ^{64}Cu was produced using a CS-15 biomedical cyclotron at Washington University School of Medicine by the ^{64}Ni(p,n)^{64}Cu nuclear reaction.

HPLC Methods. Method 1 used a LabAlliance semiprep HPLC system equipped with a UV/vis detector (λ = 254 nm) and Zorbax C_{18} semiprep column (9.4 mm × 250 mm, 100 Å pore size). The flow rate was 2.5 mL/min. The mobile phase was isocratic with 90% solvent A (0.1% acetic acid in water) and 10% solvent B (0.1% acetic acid in acetonitrile) at 0−5 min, followed by a gradient mobile phase going from 90% solvent A and 10% solvent B at 5 min to 60% solvent A and 40% solvent B at 20 min. Method 2 used the LabAlliance HPLC system equipped with a UV/vis detector (λ = 254 nm), a β-ram IN-US detector and Vydac C_{18} column (4.6 mm × 250 mm, 300 Å pore size). The flow rate was 1 mL/min with the mobile phase being isocratic with 90% solvent A (10 mM ammonium acetate) and 10% solvent B (acetonitrile) at 0−5 min, followed by a gradient mobile phase going from 10% B at 5 min to 60% B at 20 min.

(4-(Bromomethyl)benzyl)(2-(diphenylphosphoryl)ethyl)-diphenylphosphonium Bromide (TPEP-xy-Br). To a hot solution of α,α′-dibromo-*p*-xylene (528 mg, 2 mmol) in toluene (30 mL) was added slowly bis(diphenylphosphino)ethane monooxide (828 mg, 2 mmol). The mixture was heated to reflux for 20 h. The white solid was filtered, washed with toluene (20 mL) and diethyl ether (40 mL), and then dried under vacuum to give the expected intermediate product: 4-bromomethylbenzyl(diphenylphosphinoethane)phosphonium bromide (TPEP-xy-Br). The yield was 1.26 g (93%). ^{1}H NMR ($CDCl_3$, chemical shift δ in ppm relative to TMS): 2.78 (m, 2H, O═PCH_2); 3.05 (m, 2H, PCH_2); 4.23 (s, 2H, CH_2Br); 4.75 (d, 2H, PCH_2, J_{PH} = 13 Hz); 6.83 (d, 4H, C_6H_4); 7.52−7.91 (m, 20H, C_6H_5). ESI-MS: m/z = 598.5 for [M^+ + H] (calcd. 598 for $C_{34}H_{32}OP_2Br^+$). TPEP-xy-Br was isolated as the bromide salt, and was used for the next step reaction without further purification.

(2-(Diphenylphosphoryl)ethyl)diphenyl(4-((4,7,10-tris(carboxymethyl)-1,4,7,10-tetraazacyclododecan-1-yl)methyl)benzyl)phosphonium Acetate (DO3A-xy-TPEP). To a solution of TPEP-xy-Br (67.8 mg, 0.1 mmol) and DO3A(OBu-t)$_3$ (51.5

mg, 0.1 mmol) in dry DMF (3 mL) was added triethylamine (0.07 mL, 0.5 mmol). The reaction mixture was stirred at 50 °C overnight. After complete removal of volatiles, the residue was dissolved in 12 N HCl (2 mL). The resulting solution was stirred at room temperature for 30 min. Volatiles were completely removed under vacuum. The residue was then dissolved in water (3 mL) and subjected to HPLC purification (Method 1). The fractions at ~17.3 min were collected, combined, and lyophilized to give a white powder. The yield was 30.1 mg (33%). ^{1}H NMR (D_2O, chemical shift δ in ppm relative to TMS): 1.89 (s, 3H, CH_3COO^-); 2.80−3.7 (m, 26H); 3.67 (s, 2H); 4.29 (d, 2H, PCH_2, J_{PH} = 13 Hz); 6.71 (d, 2H, C_6H_4); 7.18 (d, 2H, C_6H_4); 7.38−7.67 (m, 20H, C_6H_5). ESI-MS: m/z = 863.2 for $[M + H]^+$ (calcd. 863 for $[C_{48}H_{57}N_4O_7P_2]^+$). Anal. Calcd. for $C_{48}H_{57}N_4O_7P_2 \cdot CH_3CO_2 \cdot 5H_2O$: C, 59.28; H, 6.96; N, 5.53. Found: C, 59.48; H, 6.85; N, 5.71.

(4-((4,10-Bis(carboxymethyl)-1,4,7,10-tetraazacyclododecan-1-yl)methyl)benzyl)(2-(diphenylphosphoryl)ethyl)diphenylphosphonium Acetate (DO2A-xy-TPEP). To a solution of TPEP-xy-Br (67.8 mg, 0.1 mmol) and DO2A(OBu-t)$_2$ (80 mg, 0.2 mmol) in dry DMF (3 mL) was added triethylamine (0.07 mL, 0.5 mmol). The mixture was stirred at room temperature overnight. After complete removal of volatiles, the residue was dissolved in 12 N HCl (3 mL). The solution was stirred at room temperature for 30 min. Volatiles were removed completely on a rotary evaporator. The residue was then dissolved in water (3 mL), and the product was separated from the mixture by HPLC purification (Method 1). The fractions at ~11.8 min were collected, combined, and lyophilized to give a white powder. The yield was 28.5 mg (33%). ^{1}H NMR (in $CDCl_3$): 1.89 (s, 3H, CH_3COO^-); 2.42 (m, 4H); 2.70−3.01 (m, 20H); 3.40 (s, NCH_2); 4.85 (d, 2H, PCH_2, J_{PH} = 13 Hz); 6.78 (d, 2H, C_6H_4); 7.30 (d, 2H, C_6H_4); 7.47−7.83 (m, 20H, C_6H_5). ESI-MS: m/z = 805.4 for $[M + H]^+$ (805 calcd. for $C_{46}H_{55}N_4O_5P_2^+$). Anal. Calcd. for $C_{46}H_{55}N_4O_5P_2 \cdot CH_3CO_2 \cdot 6.5H_2O$: C, 58.71; H, 7.29; N, 5.71. Found: C, 58.50; H, 6.89; N, 5.77.

(2-(Diphenylphosphoryl)ethyl)diphenyl(2-(2-(2-(tosyloxy)-ethoxy)ethoxy)ethyl) phosphonium Tosylate (TPEP-PEG$_2$-OTs). TsO-PEG2-OTs was prepared using the literature procedure (*16*). TPEP mono-oxide (104 mg, 0.25 mmol) and TsO-PEG$_2$-OTs (230 mg, 0.5 mmol) were suspended in dry toluene (10 mL). The mixture was heated to reflux for 20 h. Volatiles were removed under vacuum. The residue was dissolved in 50% DMF/H_2O mixture. The resulting solution was subject to HPLC purification (Method 1). The fractions at ~16.5 min were collected and lyophilized to give a white solid. The yield was 65.5 mg (30%). ^{1}H NMR (in $CDCl_3$): 2.33 (s, 3H, CH_3), 2.43 (s, 3H, CH_3), 2.75 (m, 2H, O=PCH_2), 3.17−3.71 (m, 12H), 4.09 (t, 2H, PCH_2), 7.12 (d, 2H, J = 7.8 Hz), 7.32−7.78 (m, 26H). ESI-MS: m/z = 701.17 for $[M]^+$ (calcd. 701 for $[C_{39}H_{43}O_6P_2S]^+$).

(2-(Diphenylphosphoryl)ethyl)diphenyl(2-(2-(2-(4,7,10-tris(carboxymethyl)-1,4,7,10-tetraazacyclododecan-1-yl)ethoxy)ethoxy)ethyl)phosphonium Tosylate (DO3A-PEG2-TPEP). TPEP-PEG$_2$-OTs (24 mg, 0.027 mmol) and DO3A(t-Bu)$_3$ (14 mg, 0.027 mmol) were dissolved in dry DMF (3 mL). After addition of Et_3N (30 μL, 0.20 mmol), the solution was stirred at room temperature for 20 h. After removal of volatiles, the residue was dissolved in 12 N HCl (3 mL). The solution was stirred for 2 h. After complete removal of volatiles under vacuum, the residue was dissolved in water (3 mL). The resulting solution was subjected to HPLC purification (Method 1). The fractions at ~10 min were collected, combined, and lyophilized to give a white powder. The yield was 8.5 mg (30%). ^{1}H NMR (in $CDCl_3$): 2.21 (s, 3H, CH_3), 2.39−3.63 (m, 38H), 7.19 (d, 2H), 7.35−7.72 (m, 22 H). ^{31}P NMR: 32.41 (d, J = 54.4 Hz), 42.84 (d, J = 54.4 Hz). ESI-MS: m/z = 875.01 for $[M]^+$ (calcd. 875 for $[C_{46}H_{61}N_4O_9P_2]^+$). Anal. Calcd. for $C_{46}H_{61}N_4O_9P_2 \cdot CH_3C_6H_4SO_3 \cdot H_2O$: C, 59.76; H, 6.62; N, 5.71. Found: C, 59.48; H, 6.85; N, 5.62.

(4-((1,3-Dioxoisoindolin-2-yl)methyl)benzyl)(2-(diphenylphosphoryl)ethyl)diphenyl-phosphonium Bromide (TPEP-xy-PA). TPEP-xy-Br (340 mg, 0.5 mmol) and potassium pthalimide (110 mg, 0.6 mmol) were suspended in acetonitrile (10 mL). The suspension was heated to reflux for 24 h. The solid was filtered and the filtrate was dried under vacuum to give a light-yellow solid (300 mg, 0.40 mmol, 80%). ^{1}H NMR (in $CDCl_3$): 2.83 (m, 2H), 3.14 (m, 2H), 4.66 (s, 2H, CH_2N), 5.14 (d, 2H, PCH_2, J_{PH} = 14.4 Hz), 6.80 (dd, 2H, J = 8.1, 2.7 Hz), 6.93 (d, 2H, J = 8.1 Hz), 7.45−7.90 (m, 20H), 8.05−8.18 (m, 4H). ^{31}P NMR: 28.9 (d, J = 53.1 Hz), 33.0 (d, J = 53.1 Hz). ESI-MS: m/z = 664.03 for $[M]^+$ (calcd. 664 for $[C_{42}H_{36}NO_3P_2]^+$).

(4-(Aminomethyl)benzyl)(2-(diphenylphosphoryl)ethyl)-diphenylphosphonium (TPEP-xy-NH$_2$). The TPEP-xy-PA intermediate (300 mg, 0.40 mmol) and 0.53 mL of aqueous hydrazine (55%, 88 mmol) were added into absolute ethanol (20 mL). The resulting solution was heated to reflux for 20 h. Volatiles were removed under vacuum. The light-yellow solid was dissolved in dichloromethane (20 mL). After filtration, the solvent was evaporated to get light-yellow solid. The yield was 230 mg (92%). ^{1}H NMR (in $CDCl_3$): 2.88 (m, 2H), 3.10 (m, 2H), 3.72 (s, 2H, CH_2N), 5.14 (d, 2H, PCH_2, J_{PH} = 14.4 Hz), 6.85 (m, 4H), 7.42−7.85 (m, 16H), 8.05−8.15 (m, 4H). ^{31}P NMR: 28.8 (d, J = 51.7 Hz), 33.1 (d, J = 51.7 Hz). ESI-MS: m/z = 534.11 for $[M]^+$ (calcd. 534 for $[C_{34}H_{34}NOP_2]^+$).

(2-(Diphenylphosphoryl)ethyl)diphenyl(4-((2-(4,7,10-tris(carboxymethyl)-1,4,7,10-tetraazacyclododecan-1-yl)acetamido)methyl)benzyl)phosphonium Acetate (DOTA-xy-TPEP). TPEP-xy-NH$_2$ (10 mg, 0.01 mmol) and PF_6 salt of DOTA(t-Bu)$_3$-NHS (6.7 mg, 0.01 mmol) were dissolved in dry DMF (3 mL). Upon addition of triethylamine (44 μL, 0.32 mmol), the resulting mixture was stirred at room temperature for 20 h. After removal of volatiles, the residue was dissolved in the concentrated HCl (3 mL). The solution was then stirred at room temperature for 2 h. Volatiles were completely removed under vacuum, and the residue was dissolved in water (3 mL). The product was separated from the mixture by HPLC (Method 1). The fractions at ~18 min were collected and lyophilized to give a white powder. The yield was 5.6 mg (56%). ^{1}H NMR (in D_2O): 1.88 (s, 3H, CH_3COO^-); 2.55−3.35 (m, 26H), 3.59 (d, 2H, NCH_2), 4.12 (s, 2H, CH_2NH), 4.21 (d, 2H, PCH_2, J = 14.7 Hz), 6.60 (dd, 2H, J = 7.8 and 2.2 Hz), 6.94 (d, 2H, J = 7.8), 7.32−7.75 (m, 20H). ^{31}P NMR: 30.64 (d, J = 53.0 Hz), 43.09 (d, J = 53.0 Hz). ESI-MS: m/z = 920.1 for $[M]^+$ (calcd. 920 for $[C_{50}H_{60}N_5O_8P_2]^+$). Anal. Calcd. for $C_{50}H_{60}N_5O_8P_2 \cdot CH_3CO_2 \cdot 2H_2O$: C, 61.47; H, 6.65; N, 6.89. Found: C, 61.11; H, 6.53; N, 6.96.

(2-(Diphenylphosphoryl)ethyl)diphenyl(4-((3-(4-((1,4,7,10-tetrakis(carboxymethyl)-1,4,7,10-tetraazacyclododecan-2-yl)-methyl)phenyl)thioureido)methyl)benzyl)phosphonium Acetate (DOTA-Bn-xy-TPEP). TPEP-xy-NH$_2$ (6 mg, 0.01 mmol) and p-SCN-Bn-DOTA (6.7 mg, 0.01 mmol) were dissolved in the equal volume mixture (2 mL) of DMF and water. The pH value in the mixture was adjusted to 8.5 with 1 N NaOH. The resulting mixture was stirred at room temperature overnight and then purified by HPLC (Method 1). The fractions at ~17.8 min were collected. Lyophilization of the collected fractions gave a white powder. The yield was 6.3 mg (56%). ^{1}H NMR (in D_2O): 1.90 (s, 3H, CH_3COO^-); 2.35−3.82 (m, 29 H); 4.22 (d, 2H, PCH_2, J_{PH} = 16.2 Hz); 4.49 (s, 2H, CH_2NH); 6.55 (dd, 2H); 6.78 (m, 2H); 7.16 (m, 2H); 7.32−7.53 (m, 20H); 7.69 (m, 3 H). ^{31}P NMR: 30.62 (d, J = 52.4 Hz) and 42.84 (d, J = 52.4 Hz). ESI-MS: m/z = 1085.22 for $[M]^+$ (calcd. 1085 for

Table 1. HPLC Retention Time and Log *P* Values for ^{64}Cu-Labeled TPEP Cations

compound	RCP (%)	retention time (min)	log *P* value
^{64}Cu(DO3A-xy-TPEP)	>95	17.5	−1.69 ± 0.11
^{64}Cu(DO3A-PEG$_2$-TPEP)	>95	17.7	−3.01 ± 0.09
^{64}Cu(DO2A-xy-TPEP)$^+$	>95	17.5	−1.90 ± 0.10
^{64}Cu(DOTA-xy-TPEP)	>90	19.9	−2.45 ± 0.02
^{64}Cu(DOTA-Bn-xy-TPEP)$^-$	>98	20.2	−1.92 ± 0.03
^{64}Cu(NOTA-Bn-xy-TPEP)	>98	20.2	−1.75 ± 0.03

$[C_{58}H_{67}N_6O_9P_2S]^+$). Anal. Calcd. for $C_{58}H_{67}N_6O_9P_2S\cdot CH_3CO_2$: C, 62.92; H, 6.16; N, 7.34. Found: C, 62.80; H, 6.46; N, 7.39.

(2-(Diphenylphosphoryl)ethyl)diphenyl(4-((3-(4-((1,4,7-tris(carboxymethyl)-1,4,7-triazonan-2-yl)methyl)phenyl)thioureido)methyl)benzyl)phosphonium Acetate (NOTA-Bn-xy-TPEP). NOTA-Bn-xy-TPEP was prepared according to the same procedure for DOTA-Bn-xy-TPEP using TPEP-xy-NH_2 (5 mg, 0.008 mmol) and p-SCN-Bn-NOTA (3.7 mg, 0.008 mmol). The fractions at ~15.1 min (Method 1) were collected, combined, and lyophilized to give a white powder. The yield was 4.6 mg (54%). ^{1}H NMR (in D_2O): 1.92 (s, 3H, CH_3COO^-); 2.35−3.70 (m, 23H), 4.47 (s, 2H, C*H*$_2$NH), 4.21 (d, 2H, PC*H*$_2$, J_{PH} = 14.1 Hz), 6.53 (d, 2H), 6.86 (d, 2H), 7.02−7.22 (m, 4H), 7.30−7.56 (m, 18H), 7.68 (m, 2H). ^{31}P NMR: 30.38 (d, J = 52.6 Hz), 42.66 (d, J = 52.6 Hz). ESI-MS: m/z = 984.06 for $[M]^+$ (calcd. 984 for $[C_{54}H_{60}N_5O_7P_2S]^+$). Anal. Calcd. for $C_{54}H_{60}N_5O_7P_2S\cdot CH_3CO_2$: C, 64.42; H, 6.08; N, 6.71. Found: C, 64.29; H, 6.00; N, 6.83.

^{64}Cu-Labeling. To a 5 mL vial were added 0.5 mL 0.1 M NaOAc buffer (pH = 6.9) containing 50 μg of the TPEP conjugate and 0.12 mL of $^{64}CuCl_2$ solution (1.0−2.0 mCi) in 0.05 N HCl. The final pH was 5.0−5.5. The mixture was heated at 100 °C for 30 min. After cooling to room temperature, a sample of resulting solution was analyzed by radio-HPLC (Method 2). The radiochemical purity (RCP) was >90% for all ^{64}Cu radiotracers with specific activity being ~50 Ci/mmol. RCP data and HPLC retention times of ^{64}Cu radiotracers are listed in Table 1.

Dose Preparation. All newly synthesized ^{64}Cu radiotracers were purified by HPLC before being used for biodistribution studies. Volatiles in the HPLC mobile phases were completely removed under vacuum (<10 mmHg) at 40−50 °C. The residue was dissolved in saline to ~25 μCi/mL. The resulting solution was filtered with a 0.20 μ syringe-driven filter unit to eliminate any particles. Each animal was administered intravenously with ~0.10 mL of the dose solution. For the imaging study, ^{64}Cu(DO3A-xy-TPEP) was prepared and the resulting mixture was used without purification. The reaction mixture was diluted to ~5 mCi/mL with saline. The injected dose for each tumor-bearing mouse was about 250 μCi of ^{64}Cu(DO3A-xy-TPEP).

Solution Stability. For solution stability, ^{64}Cu(DO3A-xy-TPEP), ^{64}Cu(DO2A-xy-TPEP), ^{64}Cu(NOTA-Bn-xy-TPEP), and ^{64}Cu(DOTA-Bn-xy-TPEP)$^-$ were prepared and purified by HPLC (Method 2). Volatiles in the HPLC mobile phase were removed under vacuum. The residue was dissolved in saline to ~1 mCi/mL. Samples were analyzed by HPLC (Method 2) at 0, 1, 2, 4, and 12 h post purification. In the EDTA challenge experiment, the HPLC purified ^{64}Cu radiotracers were dissolved in 25 mM phosphate buffer (pH = 7.4) containing EDTA (1 mg/mL) to 1 mCi/mL. Samples of the resulting solution were analyzed by radio-HPLC (Method 2) at 0, 1, 2, 4, and 12 h post purification.

Partition Coefficient. All new ^{64}Cu radiotracers were purified before being used for partition coefficient determination. HPLC purification is needed to eliminate potential interference from other radio-impurities. After complete removal of volatiles in the HPLC mobile phases under vacuum (<10 mmHg) at 40−50 °C, the residue was dissolved in a mixture of 3 mL 25 mM phosphate buffer (pH 7.4) and 3 mL *n*-octanol. The mixture was stirred vigorously for 20 min at room temperature, and was then transferred to an Eppendorf microcentrifuge tube. The tube was centrifuged at 12 500 rpm for 5 min. Samples in triplets from *n*-octanol, and aqueous layers were obtained and were counted a Perkin-Elmer Wizard 1480 automatic γ-counter (Shelton, CT). The log *P* value was reported as an average of the data obtained in three independent measurements.

Tumor-Bearing Animal Model. The ex vivo biodistribution studies were performed using athymic nude mice bearing U87MG human glioma xenografts in compliance the NIH animal experiment guidelines (Principles of Laboratory Animal Care, NIH Publication No. 86-23, revised 1985). The animal protocol has been approved by Purdue University Animal Care and Use Committee (PACUC). Female athymic nu/nu mice (4−5 weeks of age) were purchased from Harlan (Charles River, MA). Each mouse was implanted with 5×10^6 U87MG glioma cells into the upper shoulder flank. Three to four weeks after inoculation, the tumor size was in the range 0.3−0.6 g, and animals were used for both biodistribution and imaging studies.

Biodistribution Protocol. Twelve tumor-bearing mice (20−25 g) were randomly divided into four groups. The ^{64}Cu radiotracer (~2.5 μCi dissolved in 0.1 mL saline) was administered to each animal via tail vein. Three animals were sacrificed by sodium pentobarbital overdose (100 mg/kg) at 5, 30, 60, and 120 min p.i. The blood sample was withdrawn from the heart. Organs were excised, washed with saline, dried with absorbent tissue, weighed, and counted on a Perkin-Elmer Wizard 1480 γ-counter (Shelton, CT). Organs of interest included tumor, brain, heart, spleen, lungs, liver, kidneys, muscle, and intestine. The organ uptake was calculated as a percentage of the injected dose per organ (%ID/organ) and a percentage of the injected dose per gram of organ tissue (%ID/g).

Calibration of microPET. Scanner activity calibration was performed to map between microPET image units and units of activity concentration. A preweighed 50 mL centrifuge tube was filled with solution containing $^{64}CuCl_2$ (~9.3 MBq as determined by the dose calibrator) was used to simulate whole body of the mouse. This tube was weighed, centered in the scanner aperture, and imaged for 30 min static image. From the sample weight and the density of 1 g/mL, the activity concentration was calculated as μCi/mL. Eight planes were acquired in the coronal section. A rectangular region of interest (ROI) (counts/pixel/s) was drawn on the middle of 8 coronal planes. The calibration factor was obtained by dividing the known radioactivity in the cylinder (μCi/mL) by the image ROI. This calibration factor was determined periodically and did not vary significantly with time.

MicroPET Imaging. MicroPET imaging of the tumor-bearing mice was performed using a microPET R4 rodent model scanner (Concorde Microsystems, Knoxville, TN). The tumor-bearing mice (n = 3) were imaged in the prone position in the microPET scanner. Each tumor-bearing mouse was injected with ~250 μCi of ^{64}Cu(DO3A-xy-TPEP) via the tail vein, then anesthetized with 2% isoflurane and placed near the center of the FOV where the highest resolution and sensitivity are obtained. Multiple static scans were obtained at 0.5, 1.0, 2, and 20 h p.i. The images were reconstructed by a two-dimensional ordered subsets expectation maximum (OSEM) algorithm. No correction was necessary for attenuation or scatter. At each microPET scan, the ROIs were drawn over the tumor and major organs on decay-corrected whole-body coronal images. The average radioactivity concentration within the tumor or an organ was obtained from mean pixel values within the multiple ROI volume, which were converted to counts/mL/min by using the calibration constant *C*. Assuming that the tissue density is 1

Chart 1. Synthesis of TPEP and TPPP Conjugates

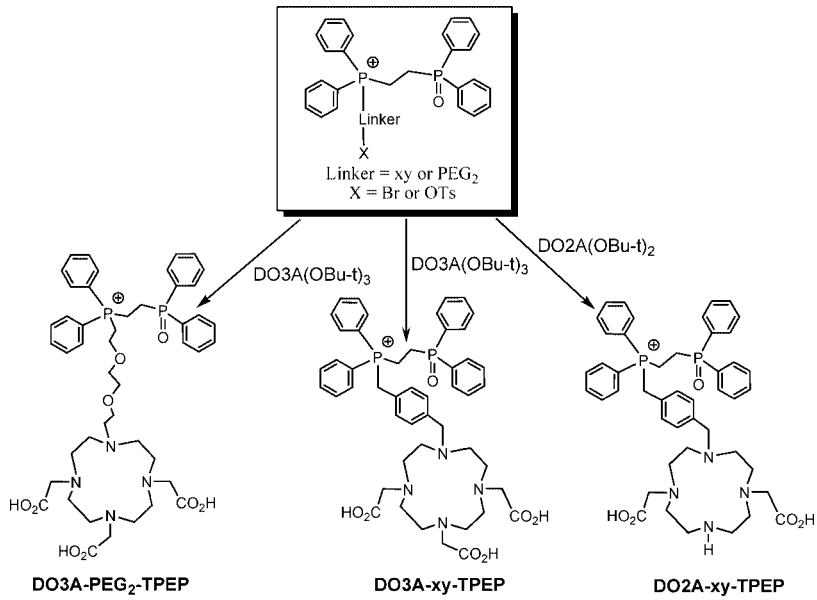

g/mL, the ROIs were converted to counts/g/min, and were then divided by the total administered activity to obtain an imaging ROI-derived percentage administered activity per gram of tissue (%ID/g).

Metabolism. Metabolic stability was evaluated in normal nude mice for ^{64}Cu(DO3A-xy-TPEP), ^{64}Cu(DOTA-xy-TPEP), ^{64}Cu(DOTA-Bn-xy-TPEP)$^-$, and ^{64}Cu(NOTA-Bn-xy-TPEP). Each mouse was administered with 100 μCi of ^{64}Cu radiotracer via tail vein. Urine samples were collected at 30 and 120 min p.i. by manual void, and were mixed with equal volume of acetonitrile. The mixture was centrifuged at 8000 rpm. The supernatant was collected and filtered through a 0.20 μm Millex-LG syringe-driven filter unit to remove the precipitate and large proteins. The filtrate was analyzed by radio-HPLC (Method 2). The feces samples were collected at ~120 min p.i., and were suspended in a mixture of 50% acetonitrile aqueous solution. The mixture was vortexed for 5−10 min. After centrifuging at 8000 rpm for 5 min, the supernatant was collected and passed through a 0.20 μm Millex-LG syringe-driven filter unit to remove the precipitate or particles. The filtrate was then analyzed by radio-HPLC (Method 2).

Stability of ^{64}Cu(DO3A-xy-TPEP) in Liver. The liver tissue was harvested at 120 min p.i. from the mouse administered with ^{64}Cu(DO3A-xy-TPEP) (~100 μCi), counted in a γ-counter (Perkin-Elmer Wizard 1480, Shelton, CT) for total liver radioactivity, and homogenized. The homogenate was mixed with 2 mL of saline. After centrifuging at 8000 rpm for 5 min, the supernatant was collected and counted on a γ-counter (Perkin-Elmer Wizard 1480, Shelton, CT) to determine the percentage of radioactivity recovery. After filtration through a 0.20 μm Millex-LG filter unit to remove foreign particles, the filtrate was then analyzed by radio-HPLC (Method 2).

Data and Statistical Analysis. The biodistribution data and T/B ratios are reported as an average plus the standard variation based on results from three tumor-bearing mice at each time point. Comparison between two different radiotracers was made using the two-way ANOVA test (GraphPad Prim 5.0, San Diego, CA). The level of significance was set at $p < 0.05$.

RESULTS

Synthesis of TPEP Conjugates. DO3A-xy-TPEP, DO2A-xy-TPEP, and DO3A-PEG$_2$-TPEP were prepared according to Chart 1. They were designed to examine the impact of linkers (xy vs PEG$_2$) and molecular charge (^{64}Cu-DO3A vs ^{64}Cu-DO2A) on organ uptake and excretion kinetics of the ^{64}Cu radiotracers. DOTA-xy-TPEP, DOTA-Bn-xy-TPEP, and NOTA-Bn-xy-TPEP were designed to examine the impact of BFCs (DO3A vs DOTA, DOTA-Bn, and NOTA-Bn) on biodistribution patterns of ^{64}Cu-labeled TPEP cations. DOTA-xy-TPEP was prepared from the reaction of DOTA(OBu-t)$_3$-NHS with TPEP-xy-NH$_2$ (Chart 2), followed by hydrolysis of DOTA(OBu-t)$_3$-xy-TPEP in 12 N HCl. DOTA-Bn-xy-TPEP and NOTA-Bn-xy-TPEP were prepared by reacting TPEP-xy-NH$_2$ with *p*-SCN-Bn-DOTA and *p*-SCN-Bn-NOTA (Chart 2), respectively. All the TPEP conjugates, except DO3A-PEG$_2$-TPEP, were obtained as acetate salts after lyophilization since the HPLC mobile phases contain 0.1% acetic acid. They all have been characterized by NMR, ESI-MS, and elemental analysis. The purity values of the TPEP conjugates were >95% before being used for ^{64}Cu-labeling. Both TPEP-PEG$_2$ and DO3A-PEG$_2$-TPEP were isolated as tosylate salts, as evidenced by the proton signals of tosylate anion in their ^{1}H NMR spectra and the molecular ion at $m/z = 171$ in their negative mode ESI-mass spectra. It is not clear why TPEP-PEG$_2$ and DO3A-PEG$_2$-TPEP were obtained as tosylate salts while other TPEP conjugates were isolated as acetate salts after HPLC purification and lyophilization.

Radiochemistry. All ^{64}Cu radiotracers were prepared by reacting ^{64}CuCl$_2$ with the TPEP conjugate in 0.1 M NaOAc buffer (pH = 5.0−5.5) at 100 °C for 30 min, and were analyzed using the same reversed-phase HPLC method (Method 2). The RCP for all new ^{64}Cu radiotracers was >95% with the specific activity being >50 Ci/mmol. Their partition coefficients were determined in a 50%/50% (v/v) mixture of *n*-octanol and 25 mM phosphate buffer (pH = 7.4). Their log *P* values and HPLC retention times are listed in Table 1. All new ^{64}Cu radiotracers are very hydrophilic with their log *P* values less than −1.50. BFCs and linkers have a significant impact on lipophilicity of the ^{64}Cu radiotracer. For example, ^{64}Cu(DOTA-xy-TPEP) (log $P = -2.45 \pm 0.02$) is more hydrophilic than ^{64}Cu(DO3A-xy-TPEP) (log $P = -1.69 \pm 0.11$) due to the replacement of DO3A with DOTA. Substitution of xylene with the PEG$_2$ linker made ^{64}Cu(DO3A-PEG$_2$-TPEP) (log $P = -3.01 \pm 0.09$) more hydrophilic than ^{64}Cu(DO3A-xy-TPEP). Despite their charge difference, the lipophilicity of ^{64}Cu(DO3A-xy-TPEP) (log $P = -1.69 \pm 0.11$) was close to that of ^{64}Cu(DO2A-xy-TPEP)$^+$ (log $P = -1.90 \pm 0.10$). ^{64}Cu(NOTA-Bn-xy-TPEP) (log $P = -1.75$

Chart 2. Synthesis of TPEP Conjugates

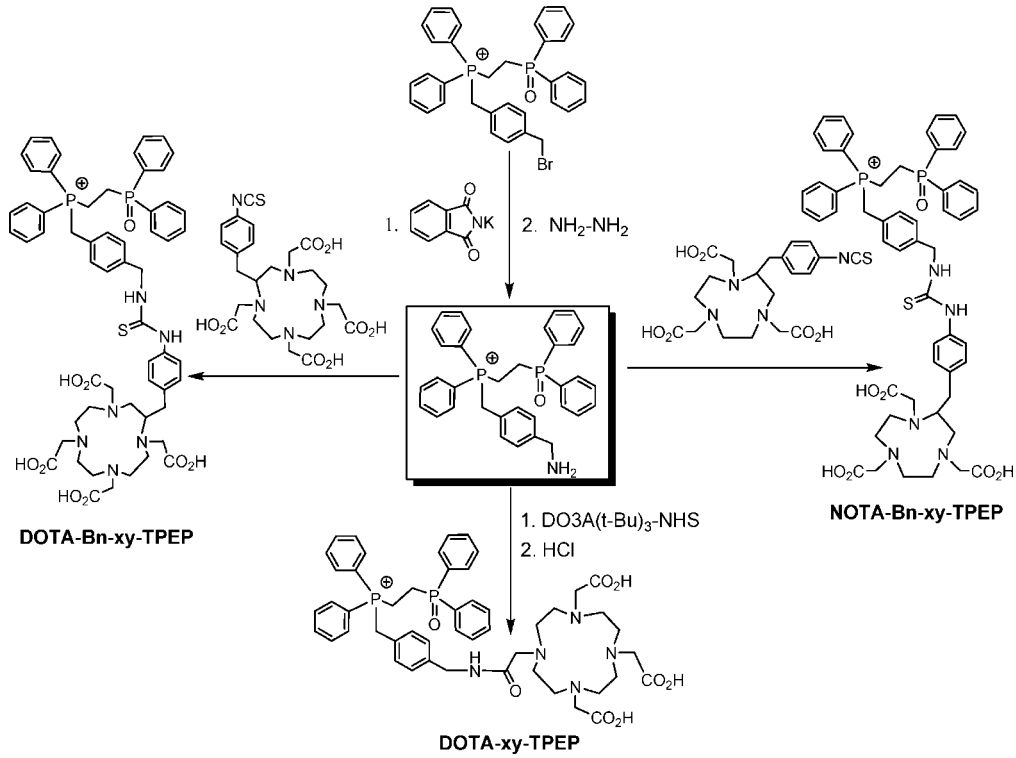

Table 2. Solution Stability Data for HPLC Purified ^{64}Cu-Labeled TPEP Cations in the Presence of Excess EDTA (1 mg/mL in 25 mM phosphate buffer, pH = 7.5)

time post-purification	0.5 h	1 h	2 h	4 h	12 h
^{64}Cu(DO3A-xy-TPEP)	99	99	98	98	97
^{64}Cu(DO2A-xy-TPEP)$^{+}$	99	98	98	97	95
^{64}Cu(DOTA-Bn-xy-TPEP)$^{-}$	99	98	99	98	97
^{64}Cu(NOTA-Bn-xy-TPEP)	99	98	99	98	97

$\pm$ 0.03) also shared similar lipophilicity with ^{64}Cu(DO3A-xy-TPEP) in spite of the extra aromatic phenyl group. Since NOTA-Bn has the same number of acetate chelating arms as DO3A, ^{64}Cu in ^{64}Cu-NOTA-Bn is most likely coordinated by six N_3O_3 donor atoms in the distorted-pseudoprismatic coordination geometry as observed in the solid-state structure of Na[Cu-(NOTA)]·0.2NaBr·0.8H_2O (*21*). Therefore, it is reasonable to believe that ^{64}Cu(NOTA-Bn-xy-TPEP) exists as its zwitterion form. In ^{64}Cu(DOTA-Bn-xy-TPEP)$^{-}$, however, ^{64}Cu is likely coordinated by only six (N_4O_2) of its eight donor atoms (N_4O_4) in the distorted octahedral coordination geometry, as observed in the solid-state structure of Cu(DOTA)$^{2-}$ with two acetate-O atoms remaining uncoordinated (*22, 23*). The extra acetate groups will results in the negative molecular charge under physiological conditions (pH = 7.4); ^{64}Cu(DOTA-Bn-xy-TPEP)$^{-}$ (log $P = -1.92 \pm 0.03$) is slightly more hydrophilic than ^{64}Cu(DO3A-xy-TPEP).

Solution Stability. The EDTA challenge experiment was used to study the solution stability of ^{64}Cu(DO3A-xy-TPEP), ^{64}Cu(DO2A-xy-TPEP)$^{+}$, ^{64}Cu(DOTA-Bn-xy-TPEP)$^{-}$, and ^{64}Cu(NOTA-Bn-xy-TPEP). These four ^{64}Cu radiotracers were selected because they represent four different types of BFCs (DO3A, DO2A, DOTA-Bn, and NOTA-Bn) for ^{64}Cu chelation. The purpose of these studies was to demonstrate that the ^{64}Cu radiotracer remains intact before being injected into the tumor-bearing mice. Table 2 summarizes their solution stability data in the presence of excess EDTA (3 mM, pH = 7.4). On the basis of these data, it becomes quite clear that all four ^{64}Cu-labeled TPEP cations are stable for >12 h in the presence of 3 mM EDTA (25 mM phosphate buffer, pH = 7.4).

Biodistribution Data. Biodistribution characteristics of six new ^{64}Cu radiotracers were evaluated in athymic nude mice bearing U87MG glioma xenografts. The Western Blot data (Supporting Information Figure SI) clearly demonstrated that there is no MDR1 Pgp expression on U87MG glioma xenografts. Selected biodistribution data and T/B ratios are listed in Tables 3 and 4, respectively. Detailed biodistribution data and T/B ratios are summarized in Supporting Information Tables SI−SVI. The main objective of these studies was to explore the impact of linkers and ^{64}Cu chelates on biodistribution characteristics and excretion kinetics of ^{64}Cu-labeled TPEP cations.

Comparison with ^{99m}Tc-Sestamibi and ^{64}Cu(DO3A-xy-TPP). Figure 2 compares the selected organ uptake and T/B ratios between ^{64}Cu(DO3A-xy-TPEP), ^{64}Cu(DO3A-xy-TPP), and ^{99m}Tc-Sestamibi. This comparison allows us to demonstrate advantages of the ^{64}Cu-labeled TPEP cations over ^{99m}Tc-Sestamibi with respect to tumor uptake and T/B ratios, and to assess the impact of "targeting moiety" (TPEP vs TPP) on biodistribution patterns of ^{64}Cu radiotracer. ^{99m}Tc-Sestamibi was used as the "control" since it has been clinically used for imaging tumors and monitoring the tumor MDR transport functions (*25*−*33*). Biodistribution data and T/B ratios for ^{64}Cu(DO3A-xy-TPP) and ^{99m}Tc-Sestamibi were obtained from our previous report (*14*).

The most striking differences between ^{64}Cu(DO3A-xy-TPEP) and ^{99m}Tc-Sestamibi are their uptake in the heart and muscle and their T/B (tumor/heart, tumor/liver, tumor/lung, and tumor/muscle) ratios. For example, the heart uptake of ^{64}Cu(DO3A-xy-TPEP) was <1% ID/g at >30 min p.i., while the heart uptake of ^{99m}Tc-Sestamibi was 19.22 $\pm$ 7.62 at 5 min p.i. and 19.19 $\pm$ 5.32% ID/g at 120 min p.i (*14*). The muscle uptake of ^{64}Cu(DO3A-xy-TPEP) was almost undetectable at $\geq$60 min p.i. while ^{99m}Tc-Sestamibi had a high muscle uptake (4.84 $\pm$ 1.22% and 5.45 $\pm$ 1.24% ID/g at 5 and 120 min p.i., respectively) over the 2 h period (Table 3). ^{64}Cu(DO3A-xy-TPEP) had the tumor uptake that is significantly ($p < 0.05$) higher than that of ^{99m}Tc-Sestamibi at all four time points. The tumor/heart ratio of ^{64}Cu(DO3A-xy-TPEP) at 120 min p.i. was more than 50×

Table 3. Selected Biodistribution Data for ^{64}Cu Radiotracers in Athymic Nude Mice ($n = 3$ unless specified) Bearing U87MG Glioma Xenografts[a]

time	tumor	blood	lungs	liver	kidneys	heart	muscle
			^{64}Cu(DO3A-xy-TPEP)				
5 min	5.27 ± 1.21	9.52 ± 1.27	7.72 ± 0.78	8.03 ± 1.41	31.79 ± 8.51	4.04 ± 0.75	3.07 ± 0.48
30 min	2.09 ± 0.53	1.68 ± 0.39	2.27 ± 0.48	6.48 ± 1.39	6.79 ± 0.97	0.94 ± 0.19	0.55 ± 0.17
60 min	2.58 ± 0.31	0.65 ± 0.12	1.84 ± 0.38	6.40 ± 1.94	4.24 ± 1.08	0.67 ± 0.17	0.22 ± 0.11
120 min[b]	2.35 ± 0.57	0.36 ± 0.07	1.51 ± 0.18	5.59 ± 1.39	2.98 ± 0.53	0.55 ± 0.09	0.10 ± 0.06
			^{64}Cu(DO3A-PEG$_2$-TPEP)				
5 min	5.06 ± 0.84	7.19 ± 1.40	6.08 ± 0.57	6.44 ± 1.29	29.11 ± 2.57	3.64 ± 0.25	2.45 ± 0.36
30 min	1.24 ± 0.31	1.03 ± 0.09	1.63 ± 0.27	3.76 ± 0.06	4.69 ± 0.19	0.71 ± 0.06	0.39 ± 0.13
60 min	1.41 ± 0.35	0.49 ± 0.11	1.08 ± 0.07	3.20 ± 0.56	2.70 ± 0.19	0.42 ± 0.03	0.17 ± 0.10
120 min	1.60 ± 0.45	0.33 ± 0.05	1.06 ± 0.08	2.91 ± 0.12	2.53 ± 0.44	0.44 ± 0.07	0.07 ± 0.02
			^{64}Cu(DO2A-xy-TPEP)$^+$				
5 min	5.06 ± 0.43	9.25 ± 0.84	7.51 ± 0.78	3.95 ± 0.16	25.60 ± 1.21	3.26 ± 0.24	2.81 ± 0.22
30 min	1.66 ± 0.21	2.13 ± 0.73	2.18 ± 0.43	2.18 ± 0.29	5.99 ± 1.85	0.78 ± 0.23	0.51 ± 0.25
60 min	0.78 ± 0.32	0.44 ± 0.17	0.89 ± 0.12	1.91 ± 0.02	2.44 ± 0.43	0.41 ± 0.26	0.25 ± 0.11
120 min	0.51 ± 0.08	0.24 ± 0.13	0.47 ± 0.06	1.49 ± 0.12	1.28 ± 0.10	0.10 ± 0.06	0.07 ± 0.03
			^{64}Cu(DOTA-xy-TPEP)				
5 min	4.84 ± 0.96	11.65 ± 1.62	7.27 ± 0.63	5.61 ± 0.37	21.61 ± 5.63	3.96 ± 0.91	2.65 ± 0.61
30 min	1.99 ± 0.41	2.99 ± 0.03	2.78 ± 0.32	4.47 ± 0.45	7.72 ± 0.76	1.14 ± 0.19	1.31 ± 0.65
60 min	1.78 ± 0.65	1.74 ± 0.51	2.00 ± 0.36	3.93 ± 0.84	5.53 ± 0.56	0.90 ± 0.23	0.31 ± 0.12
120 min	1.39 ± 0.59	0.33 ± 0.01	1.00 ± 0.28	2.99 ± 0.21	2.84 ± 0.50	0.30 ± 0.07	0.01 ± 0.01
			^{64}Cu(DOTA-Bn-xy-TPEP)				
5 min	3.03 ± 0.52	14.35 ± 2.38	7.25 ± 1.28	10.32 ± 2.02	18.07 ± 5.96	4.07 ± 0.66	2.65 ± 0.43
30 min	2.47 ± 0.09	4.45 ± 0.27	3.95 ± 0.14	9.24 ± 0.98	9.02 ± 0.13	1.86 ± 0.23	1.06 ± 0.04
60 min	2.68 ± 0.07	2.29 ± 0.58	3.48 ± 0.54	9.28 ± 0.91	7.72 ± 0.25	1.73 ± 0.43	0.56 ± 0.09
120 min	1.91 ± 0.30	1.14 ± 0.18	2.31 ± 0.16	8.66 ± 0.12	5.44 ± 0.40	1.03 ± 0.17	0.23 ± 0.03
			^{64}Cu(NOTA-Bn-xy-TPEP)				
5 min	2.74 ± 0.05	11.55 ± 1.93	8.39 ± 1.05	11.17 ± 1.63	13.52 ± 2.14	4.09 ± 0.96	1.83 ± 0.83
30 min	1.06 ± 0.23	2.58 ± 0.84	2.30 ± 0.61	5.86 ± 1.37	3.28 ± 0.68	0.80 ± 0.35	0.92 ± 0.42
60 min	0.47 ± 0.04	0.92 ± 0.04	0.81 ± 0.09	3.99 ± 0.93	1.37 ± 0.09	0.19 ± 0.00	0.10 ± 0.06
120 min	0.28 ± 0.04	0.30 ± 0.07	0.35 ± 0.08	2.20 ± 0.18	1.08 ± 0.06	0.04 ± 0.02	0.02 ± 0.03

[a] The organ uptake is expressed as %ID/gram. [b] $n = 6$ due to difficulty to determine the radiotracer uptake in muscle.

better than that of ^{99m}Tc-Sestamibi. Its tumor/lung and tumor/liver ratios were much better than those of ^{99m}Tc-Sestamibi (Figure 2). ^{64}Cu(DO3A-xy-TPEP) had a tumor uptake that is comparable to that of ^{64}Cu(DO3A-xy-TPP) at >30 min p.i., but its liver uptake was significantly lower ($p < 0.01$) than that of ^{64}Cu(DO3A-xy-TPP) at all four time points (Table 3). As a result, ^{64}Cu(DO3A-xy-TPEP) has tumor/liver ratios >3× better than those of ^{64}Cu(DO3A-xy-TPP). Thus, TPEP is better than TPP as a mitochondrion-targeting molecule.

Impact of BFCs. Figure 3 compares the organ uptake (heart, liver, and muscle) and T/B ratios of ^{64}Cu(DO3A-xy-TPEP), ^{64}Cu(DO2A-xy-TPEP)$^+$, ^{64}Cu(DOTA-Bn-xy-TPEP)−, and ^{64}Cu-(NOTA-Bn-xy-TPEP). This comparison allows us to assess the impact of BFCs on biological properties of ^{64}Cu radiotracers. ^{64}Cu(DO3A-xy-TPEP) has the lipophilicity (log $P = -1.69 \pm 0.11$) close to that of ^{64}Cu(DO2A-xy-TPEP)$^+$ (log $p = -1.90 \pm 0.10$) despite their different charges. While the tumor uptake of ^{64}Cu(DO3A-xy-TPEP) remained unchanged between 30 and 120 min p.i., there was a significant tumor washout for ^{64}Cu(DO2A-xy-TPEP)$^+$ over the 2 h period. The liver uptake of ^{64}Cu(DO2A-xy-TPEP)$^+$ was significantly lower ($p < 0.01$) than that of ^{64}Cu(DO3A-xy-TPEP) at all four time points. Its tumor/liver ratio at 120 min p.i. was also significantly ($p < 0.05$) lower. The lipophilicity of ^{64}Cu(DOTA-Bn-xy-TPEP)$^-$ (log $p = -1.92 \pm 0.03$) is close to that of ^{64}Cu(DO3A-xy-TPEP). Even though they share a similar tumor uptake, the uptake of ^{64}Cu(DOTA-Bn-xy-TPEP)$^-$ in the heart, liver, and muscle was higher at >30 min p.i. As a result, the T/B ratios of ^{64}Cu(DOTA-Bn-xy-TPEP)$^-$ were lower than that those of ^{64}Cu(DO3A-xy-TPEP). ^{64}Cu(NOTA-Bn-xy-TPEP) has the same overall charge as ^{64}Cu(DO3A-xy-TPEP); but its tumor uptake and tumor/heart ratios were much lower than those of ^{64}Cu(DO3A-xy-TPEP). Apparently, the BFCs and their ^{64}Cu chelates have a significant impact on both tumor uptake and T/B ratios of the radiotracer.

Linker Effects. Figure 4 illustrates a comparison of the tumor uptake and tumor/heart ratios among ^{64}Cu(DO3A-xy-TPEP), ^{64}Cu(DO3A-PEG$_2$-TPEP), and ^{64}Cu(DOTA-xy-TPEP). The addition of an extra acetamide group between DO3A and TPEP resulted in a significant reduction of liver uptake. However, the tumor/liver ratios (Table 4) of ^{64}Cu(DOTA-xy-TPEP) and ^{64}Cu(DO3A-xy-TPEP) were comparable within the experimental error, probably due to the faster tumor washout of ^{64}Cu(DOTA-xy-TPEP). Substitution of xylene with PEG$_2$ also leads to a significant reduction of the uptake in tumor and liver. As a result, ^{64}Cu(DO3A-PEG$_2$-TPEP) and ^{64}Cu(DO3A-xy-TPEP) shared very similar tumor/liver ratios.

PET Imaging. We performed a microPET imaging study on ^{64}Cu(DO3A-xy-TPEP) using the athymic nude mice bearing U87MG glioma xenografts. Figure 5 shows microPET images of the tumor-bearing mouse administered with ~250 μCi of ^{64}Cu(DO3A-xy-TPEP) at 1, 4, and 24 h p.i. The tumor was clearly visualized as early as 1 h p.i. with very high T/B contrast. No significant radioactivity accumulation was detected in the brain, heart, or muscle. After normalization, the tumor uptake of ^{64}Cu(DO3A-xy-TPEP) was 2.57 ± 0.41% ID/g, 3.51 ± 1.20% ID/g, and 3.11 ± 1.44% ID/g at 1, 4, and 24 h p.i., respectively. These data are completely consistent with that observed in the *ex vivo* biodistribution study (Table 3), and have clearly demonstrated that ^{64}Cu(DO3A-xy-TPEP) is useful for imaging the MDR-negative tumors.

Metabolic Properties. Metabolism studies were performed on ^{64}Cu(DO3A-xy-TPEP), ^{64}Cu(DOTA-xy-TPEP), ^{64}Cu(DOTA-Bn-xy-TPEP)$^-$, and ^{64}Cu(NOTA-Bn-xy-TPEP) using normal

Table 4. T/B Ratios for ^{64}Cu Radiotracers in Athymic Nude Mice ($n = 3$ unless specified) Bearing U87MG Human Glioma Xenografts

time	tumor/blood	tumor/heart	tumor/lung	tumor/muscle	tumor/liver
		^{64}Cu(DO3A-xy-TPEP)			
5 min	0.57 ± 0.13	1.26 ± 0.34	0.63 ± 0.15	1.57 ± 0.49	0.68 ± 0.27
30 min	1.48 ± 0.52	3.06 ± 0.82	1.11 ± 0.53	5.08 ± 4.37	0.43 ± 0.18
60 min	4.66 ± 0.65	4.73 ± 0.45	1.45 ± 0.56	17.96 ± 9.11	0.54 ± 0.10
120 min[a]	5.87 ± 1.91	5.42 ± 0.54	1.39 ± 0.39	20.42 ± 9.72	0.64 ± 0.15
		^{64}Cu(DO3A-PEG$_2$-TPEP)			
5 min	0.72 ± 0.15	1.38 ± 0.16	0.84 ± 0.17	2.09 ± 0.39	0.80 ± 0.13
30 min	1.21 ± 0.31	1.78 ± 0.54	0.77 ± 0.15	3.38 ± 0.96	0.33 ± 0.18
60 min	2.99 ± 1.03	3.40 ± 1.00	1.31 ± 0.37	9.99 ± 0.4.74	0.45 ± 0.15
120 min	4.83 ± 1.05	3.66 ± 0.77	1.51 ± 0.36	23.95 ± 9.63	0.55 ± 0.16
		^{64}Cu(DO2A-xy-TPEP)$^+$			
5 min	0.55 ± 0.06	1.55 ± 0.14	0.68 ± 0.08	1.81 ± 0.23	1.28 ± 0.12
30 min	0.87 ± 0.37	2.30 ± 0.83	0.79 ± 0.20	4.04 ± 2.24	0.78 ± 0.16
60 min	1.94 ± 0.84	2.26 ± 1.00	0.90 ± 0.44	3.64 ± 2.35	0.41 ± 0.17
120 min	2.63 ± 1.47	6.32 ± 2.92	1.09 ± 0.11	7.83 ± 3.05	0.34 ± 0.06
		^{64}Cu(DOTA-xy-TPEP)			
5 min	0.41 ± 0.04	1.24 ± 0.18	0.66 ± 0.07	1.86 ± 0.36	0.86 ± 0.12
30 min	0.67 ± 0.14	1.78 ± 0.51	0.71 ± 0.07	1.65 ± 0.39	0.45 ± 0.07
60 min	1.08 ± 0.46	2.05 ± 0.79	0.89 ± 0.21	5.18 ± 1.17	0.47 ± 0.22
120 min	4.21 ± 1.66	4.61 ± 1.90	1.36 ± 0.29	7.65 ± 1.04	0.47 ± 0.23
		^{64}Cu(DOTA-Bn-xy-TPEP)			
5 min	0.21 ± 0.04	0.75 ± 0.08	0.42 ± 0.06	1.15 ± 0.07	0.30 ± 0.07
30 min	0.56 ± 0.04	1.34 ± 0.17	0.63 ± 0.04	2.32 ± 0.07	0.27 ± 0.02
60 min	1.21 ± 0.26	1.61 ± 0.36	0.78 ± 0.11	4.92 ± 0.83	0.29 ± 0.02
120 min	1.69 ± 0.26	1.88 ± 0.43	0.83 ± 0.14	8.00 ± 1.54	0.22 ± 0.04
		^{64}Cu(NOTA-Bn-xy-TPEP)			
5 min	0.24 ± 0.03	0.69 ± 0.14	0.33 ± 0.04	1.68 ± 0.63	0.25 ± 0.03
30 min	0.42 ± 0.07	1.42 ± 0.47	0.46 ± 0.03	1.25 ± 0.36	0.18 ± 0.01
60 min	0.51 ± 0.03	2.42 ± 0.25	0.58 ± 0.07	5.59 ± 2.86	0.12 ± 0.02
120 min	0.94 ± 0.19	3.19 ± 1.12	0.80 ± 0.08	5.22 ± 0.40	0.13 ± 0.01

[a] $n = 6$ due to difficulty determining the tumor/muscle muscle ratios.

mice. These four ^{64}Cu radiotracers were selected because of their difference in ^{64}Cu chelate. Since they were excreted from the renal and hepatobiliary routes, we tried to collect both urine and feces samples from the normal mice administered with the ^{64}Cu radiotracer. A reversed-phase HPLC method (Method 2) was used to analyze the collected urine and feces samples. Figure 6 shows representative radio-HPLC chromatograms of ^{64}Cu(DO3A-xy-TPEP) (left) and ^{64}Cu(DOTA-xy-TPEP) (right) in saline before injection, in urine at 30 and 120 min p.i., and in feces at 120 min p.i. There was very little metabolite (<2%) detectable for ^{64}Cu(DO3A-xy-TPEP) in both urine and feces samples. Similar metabolic stability was also observed for ^{64}Cu(DOTA-Bn-xy-TPEP)$^-$ and ^{64}Cu(NOTA-Bn-xy-TPEP) (Supporting Information Figure SII). ^{64}Cu(DOTA-xy-TPEP) is excreted without significant metabolism via renal route (Figure 6). However, only 15% of it remained intact in feces, and 85% of radioactivity appeared at 4 min. Thus, the extra acetamido group has a significant impact on metabolic stability of ^{64}Cu(DOTA-xy-TPEP) during its hepatobiliary excretion while it had no effect on its metabolic stability during renal excretion.

Transchelation of ^{64}Cu(DO3A-xy-TPEP) in Liver. We examined the in vivo stability of ^{64}Cu(DO3A-xy-TPEP) in the liver. About 50% of total liver activity was recovered in the liver homogenate. The liver homogenate samples were analyzed using the reversed-phase and size-exclusion radio-HPLC methods. Figure SIII shows radio-HPLC chromatograms of the supernatant from liver homogenate. Using the size-exclusion HPLC method, we were able to identify four major radiometric peaks in its HPLC chromatogram (Figure SIII: bottom). While the identity of these radiometric peaks are not known, one thing is sure that ^{64}Cu(DO3A-xy-TPEP) underwent extensive tranchelation in the liver during the 2 h study period.

DISCUSSION

For the new radiotracer to be successful as a tumor imaging agent by PET or SPECT (single photon emission computed tomography), it must show a high tumor uptake. Since most of high-incidence tumors occur in torso (namely, lung, colorectal, and breast cancers metastatic to the lymphatic system), it is highly desirable for the radiotracer to clear from the liver and lungs so that the high T/B ratios can be achieved and clinically useful tumor images can be obtained in a short period of time. Cationic radiotracers, such as ^{99m}Tc-Sestamibi and ^{99m}Tc-Tetrofosmin, have been clinically used for imaging tumors of different origin and the transport function of MDR Pgp by SPECT (*25*−*33*). However, their cancer diagnostic values are often limited due to their insufficient tumor localization and high uptake in the noncancerous organs, such as heart, liver, and muscle, which makes it difficult to detect small lesions in the chest and abdominal regions. Radiolabeled lipophilic organic cations, such as 4-(^{18}F-benzyl)triphenylphosphonium (^{18}F-BzTPP), have also been proposed as radiotracers for tumor imaging by PET (*34*−*38*). Their high uptake in the heart and liver may also impose a significant challenge for early detection of small tumors in the chest and abdominal regions. Thus, there is an unmet need for radiotracers that have high tumor selectivity (high tumor uptake with little accumulation in noncancerous organs) and are sensitive to the mitochondrial potential changes at the early stage of tumor growth.

In our previous studies, we have demonstrated that the ^{64}Cu-labeled TPP cations, such as ^{64}Cu(DO3A-xy-TPP), are able to

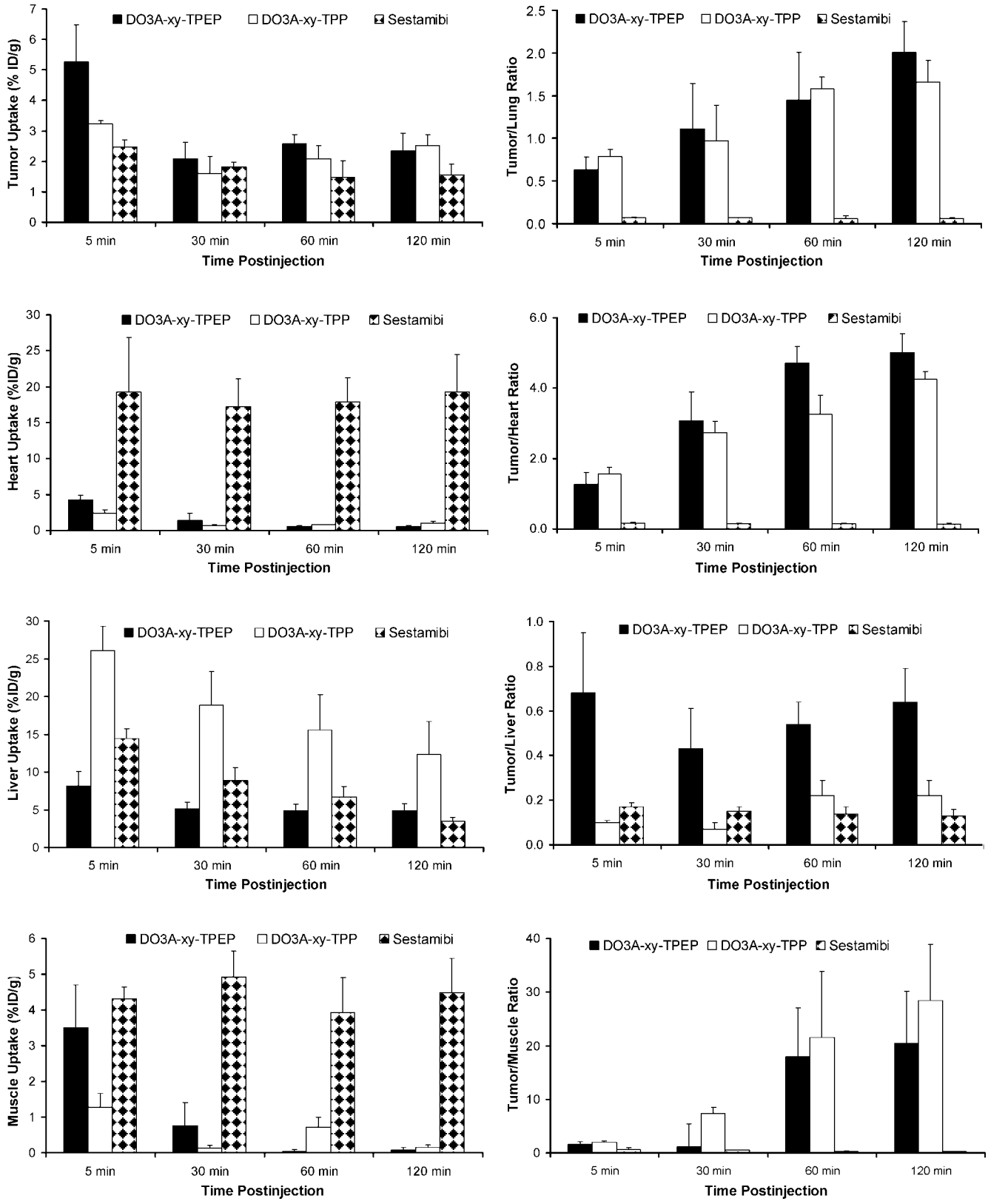

Figure 2. Direct comparison of organ uptake and T/B ratios between ^{64}Cu(DO3A-xy-TPEP), ^{64}Cu(DO3A-xy-TPP), and ^{99m}Tc-Sestamibi in the athymic nude mice bearing U87MG human glioma xenografts.

localize in the mitochondria of U87MG glioma cells. MicroPET imaging data also show that the tumor could be visualized clearly as early as 30 min p.i. (*14*). Considering the tumor uptake selectivity,^{64}Cu(DO3A-xy-TPP) has a significant advantage over ^{99m}Tc-Sestamibi, the radiopharmaceutical currently available for both myocardial perfusion and tumor imaging (*24*−*33*, *39*−*45*). However, the high liver uptake of ^{64}Cu(DO3A-xy-TPP) remains a challenge for its clinical application as a new PET radiotracer for imaging tumors.

In this study, we used TPEP as the mitochondrion-targeting molecule. We are interested in TPEP cation because of the phosphoryl group that may improve radiotracer excretion kinetics from the liver. As expected, the liver uptake of ^{64}Cu(DO3A-xy-TPEP) was lower ($p < 0.01$) than that of

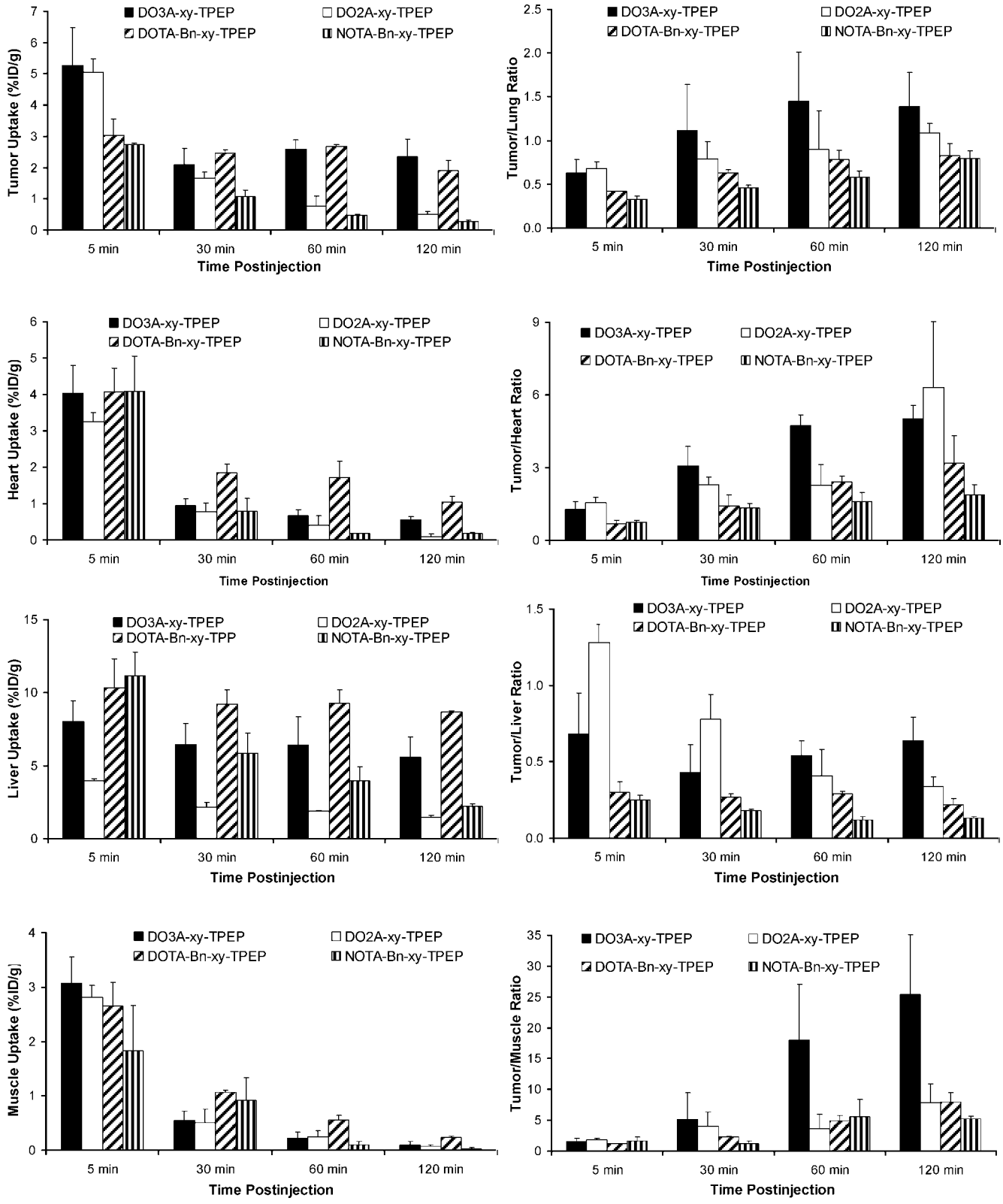

Figure 3. Impact of BFCs on organ uptake and T/B ratios of the ^{64}Cu-labeled TPEP cations.

^{64}Cu(DO3A-xy-TPP) (Figure 2), even though ^{64}Cu(DO3A-xy-TPEP) (log $P = -1.69 \pm 0.11$) is 10× more lipophilic than ^{64}Cu(DO3A-xy-TPP) (log $P = -2.67 \pm 0.21$). The tumor uptake of ^{64}Cu(DO3A-xy-TPEP) is comparable to that of ^{64}Cu(DO3A-xy-TPP) at >30 min p.i. (Figure 2). As a result, tumor/liver ratios of ^{64}Cu(DO3A-xy-TPEP) are >3× better than those of ^{64}Cu(DO3A-xy-TPP). On the basis of these results, we believe that ^{64}Cu(DO3A-xy-TPEP) is a better PET radiotracer than ^{64}Cu(DO3A-xy-TPP) for imaging the MDR-negative tumors. ^{64}Cu(DO3A-xy-TPEP) also has significant advantages over ^{99m}Tc-Sestamibi with respect to the tumor uptake and T/B (tumor/heart, tumor/liver, tumor/lung, and tumor/muscle) ratios.

The exact localization mechanism remains unknown even though the results from in vitro assays show that ^{64}Cu(DO3A-xy-TPP) is able to localize in mitochondria of glioma cells (*14*).

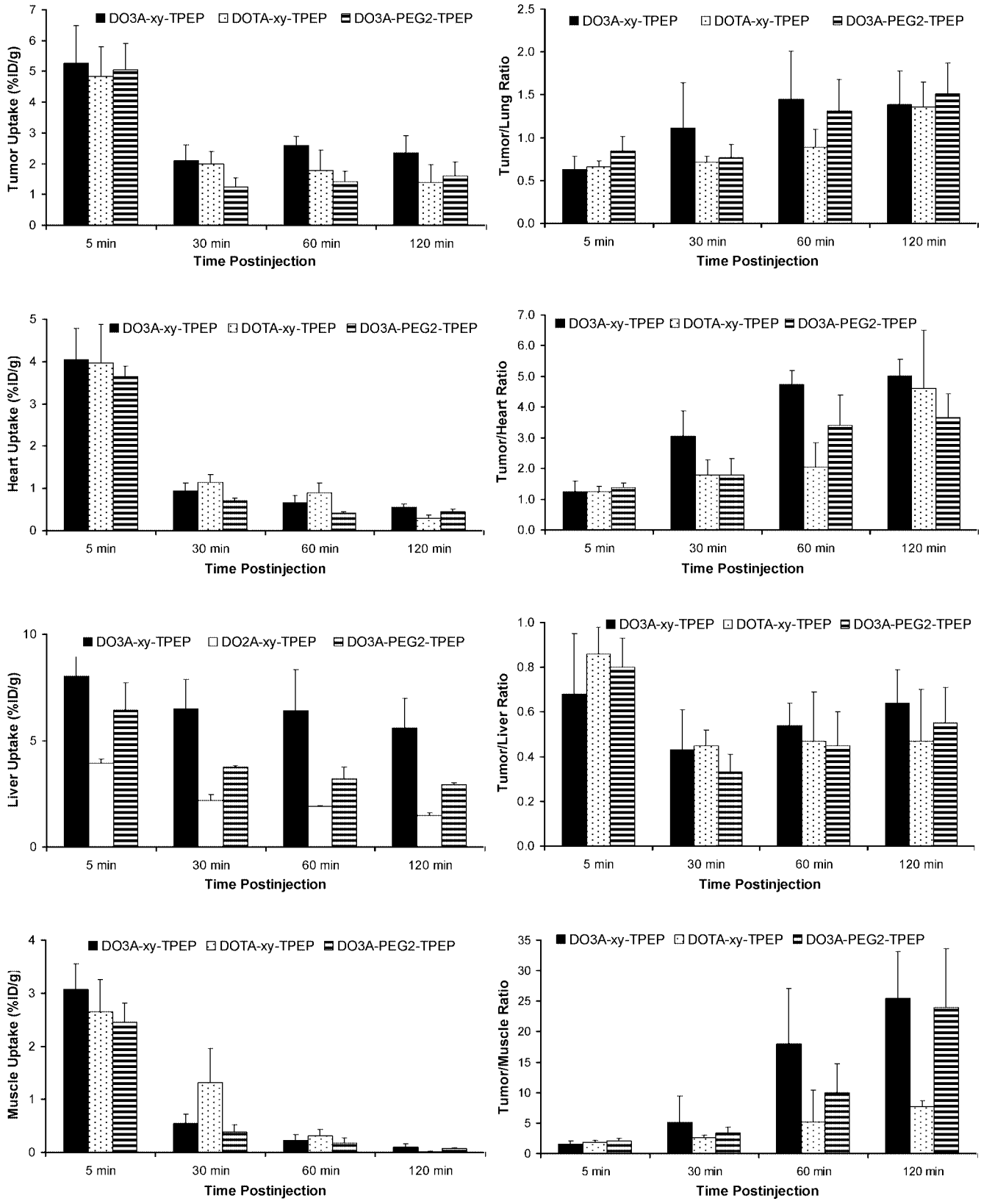

Figure 4. Impact of the linker on organ uptake and T/B ratios of the ^{64}Cu-labeled TPEP cations.

Many factors can influence biological properties of the ^{64}Cu-labeled TPEP cations. Previously, we found that replacing DO3A in ^{64}Cu(DO3A-xy-TPP) with DO2A leads to formation of ^{64}Cu(DO2A-xy-TPP)$^{+}$ and results in a dramatic reduction in liver uptake without altering its tumor uptake. In this study, a similar reduction in liver uptake was seen for ^{64}Cu(DO2A-xy-TPEP)$^{+}$ (Figure 3), but ^{64}Cu(DO2A-xy-TPEP)$^{+}$ had a rapid tumor washout over the 2 h study period. As a result, its tumor/liver ratio is significantly lower ($p < 0.01$) than that of ^{64}Cu(DO3A-xy-TPEP).

^{64}Cu(NOTA-Bn-xy-TPEP) has the same molecular charge as ^{64}Cu(DO3A-xy-TPEP). They also share almost identical lipophilicity with log P values being -1.69 ± 0.11 and -1.75 ± 0.03, respectively. However, the tumor uptake and T/B ratios

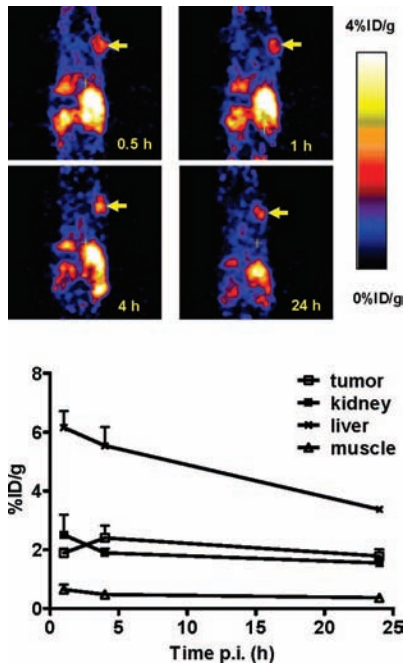

Figure 5. The decay-corrected whole-body coronal microPET images (top) and the radioactivity accumulation quantification ($n = 3$, mean ± SD) in selected organs (bottom) of athymic nude mice bearing U87MG tumor administered with ~250 μCi of ^{64}Cu(DO3A-xy-TPEP). Arrows indicate the presence of glioma tumors.

of ^{64}Cu(NOTA-Bn-xy-TPEP) are lower ($p < 0.01$) than those of ^{64}Cu(DO3A-xy-TPEP) (Figure 3). A similar adverse effect was also seen for the ^{64}Cu-labeled TPP analogues (*16*). Among six ^{64}Cu radiotracers evaluated in this study, ^{64}Cu(NOTA-Bn-xy-TPEP) has the lowest tumor uptake and poorest T/B ratios in noncancerous organs, such as the heart, liver, lungs, and muscle. Thus, it is reasonable to believe that the coordination geometry of the ^{64}Cu-DO3A chelates might play a significant role in tumor uptake and tumor retention of the ^{64}Cu-labeled TPP and TPEP cations.

The lipophilicity (log $p = -1.92 \pm 0.03$) of ^{64}Cu(DOTA-Bn-xy-TPEP)$^-$ is also close to that of ^{64}Cu(DO3A-xy-TPEP) (log $p = -1.69 \pm 0.11$) despite the difference in molecular charges. Their tumor uptake (Figure 3) is comparable within experimental error. It seems that the negative charge in ^{64}Cu(DOTA-Bn-xy-TPEP)$^-$ does not affect its capability to localize in tumor cells. However, the uptake of ^{64}Cu(DOTA-Bn-xy-TPEP)$^-$ in the heart, liver, and muscle was higher than that of ^{64}Cu(DO3A-xy-TPEP) at >30 min p.i. As a result, its T/B ratio was lower than that of ^{64}Cu(DO3A-xy-TPEP).

Linkers have a significant impact on tumor uptake and tumor/heart ratios of ^{64}Cu-labeled TPEP cations. For example, the extra acetamido group in ^{64}Cu(DOTA-xy-TPEP) results in a lower liver uptake than that of ^{64}Cu(DO3A-xy-TPEP). However, the tumor/liver ratios of ^{64}Cu(DOTA-xy-TPEP) and ^{64}Cu(DO3A-xy-TPEP) compare well within experimental error (Figure 4) due to a faster tumor washout of ^{64}Cu(DOTA-xy-TPEP). Substitution of xylene with PEG_2 leads to a significant reduction of the tumor and liver uptake. As a result, the tumor/liver ratios of ^{64}Cu(DO3A-PEG_2-TPEP) and ^{64}Cu(DO3A-xy-TPEP) are also comparable.

In addition, linkers also affect the metabolic stability of ^{64}Cu radiotracers. For example, ^{64}Cu(DO3A-xy-TPEP), ^{64}Cu(DOTA-Bn-xy-TPEP)$^-$, and ^{64}Cu(NOTA-Bn-xy-TPEP) have no metabolism during their excretion via renal and hepatobiliary routes as evidenced by the lack of metabolite(s) in urine and feces samples. ^{64}Cu(DOTA-xy-TPEP) remains intact during excretion via the kidney, but only ~15% of it remains intact in the feces sample (Figure 6). Since the only difference between ^{64}Cu(DO3A-xy-TPEP) and ^{64}Cu(DOTA-xy-TPEP) is the extra acetamido group, the metabolic instability of ^{64}Cu(DOTA-xy-TPEP) is most likely caused by the cleavage of CO−NH bond during hepatobiliary excretion.

The radioactivity detected in urine and feces samples represents only the portion excreted from the renal and hepatobiliary routes. The remaining activity is still "trapped" in organ tissues. We examined the stability of ^{64}Cu(DO3A-xy-TPEP) in the liver, and found that there was no intact ^{64}Cu(DO3A-xy-TPEP) in the liver homogenate (Supporting Information Figure SIII: top). While the identity of these four major radiometric peaks (Supporting Information Figure SIII: bottom) remains unknown, the size-exclusion HPLC chromatographic pattern of ^{64}Cu(DO3A-xy-TPEP) is very similar to that of the ^{64}Cu-labeled TETA-Octreotide in the rat liver homogenate (*46*). On the basis of the results from stability studies of ^{64}Cu complexes with tetraazamacrocycles (*46*−*50*), we believe that these radiometric peaks are likely caused by transchelation of ^{64}Cu to the proteins, such as superoxide dismutase (SOD) abundant in the liver and kidneys (*51*).

The metabolism of the ^{64}Cu-labeled biomolecules (antibodies and peptides) and ^{64}Cu complexes of tetraazamacrocycles has been investigated extensively (*46*−*59*). These studies clearly show that kinetic inertness of the ^{64}Cu chelate is particularly important for the *in vivo* stability of ^{64}Cu radiotracers, and their instability is often caused by transchelation of ^{64}Cu from the ^{64}Cu-BFC chelate to proteins (*46, 51*). For target-specific ^{64}Cu radiotracers, the tumor uptake is predominantly determined by receptor binding of targeting biomolecules (antibodies or peptides). The BFCs for ^{64}Cu chelation should be those which form the ^{64}Cu-BFC chelates with high kinetic inertness in order to minimize the liver radioactivity. For the ^{64}Cu-labeled TPEP cations, however, the BFC contributes greatly to the radiotracer tumor uptake and excretion kinetics from noncancerous organs, such as liver and lungs. The optimal BFCs should be those which result in the ^{64}Cu radiotracer with high tumor uptake and the best T/B, particularly tumor/heart and tumor/liver, ratios. From this point view, DO3A and DOTA are suitable BFCs for ^{64}Cu-labeling of TPEP cations. It must be noted that the radioactivity "trapped" inside the liver due to transchelation of ^{64}Cu is only a small portion of the injected radioactivity. Whenever possible, one has to consider the radioactivity excreted from renal and hepatobiliary routes (urine and feces samples), as well as the radioactivity "trapped" in various organ tissues.

CONCLUSIONS

In summary, we evaluated six new ^{64}Cu-labeled TPEP cations for their biodistribution properties and excretion kinetics using the athymic nude mice bearing U87MG human glioma xenografts. It was found that most of the ^{64}Cu radiotracers described in this study have significant advantages over ^{99m}Tc-Sestamibi with respect to their tumor/heart and tumor/muscle ratios. TPEP seems to be a better mitochondrion-targeting molecule than TPP because of the lower liver uptake and better tumor/liver ratios of ^{64}Cu(DO3A-xy-TPEP) than that of ^{64}Cu(DO3A-xy-TPP). BFCs and molecular charge also have significant impact on biological properties of ^{64}Cu-labeled TPEP cations. For example, replacing DO3A with DO2A results in ^{64}Cu(DO2A-xy-TPEP)$^+$, which has a lower tumor uptake and T/B ratios than ^{64}Cu(DO3A-xy-TPEP). Substitution of DO3A with NOTA-Bn has a significant adverse effect on tumor uptake of the ^{64}Cu radiotracer. However, the use of DOTA-Bn to replace DO3A has minimal impact on the radiotracer tumor uptake; but the tumor/liver ratio of ^{64}Cu(DOTA-Bn-xy-TPEP)$^-$ is not as good as that of ^{64}Cu(DO3A-xy-TPEP),

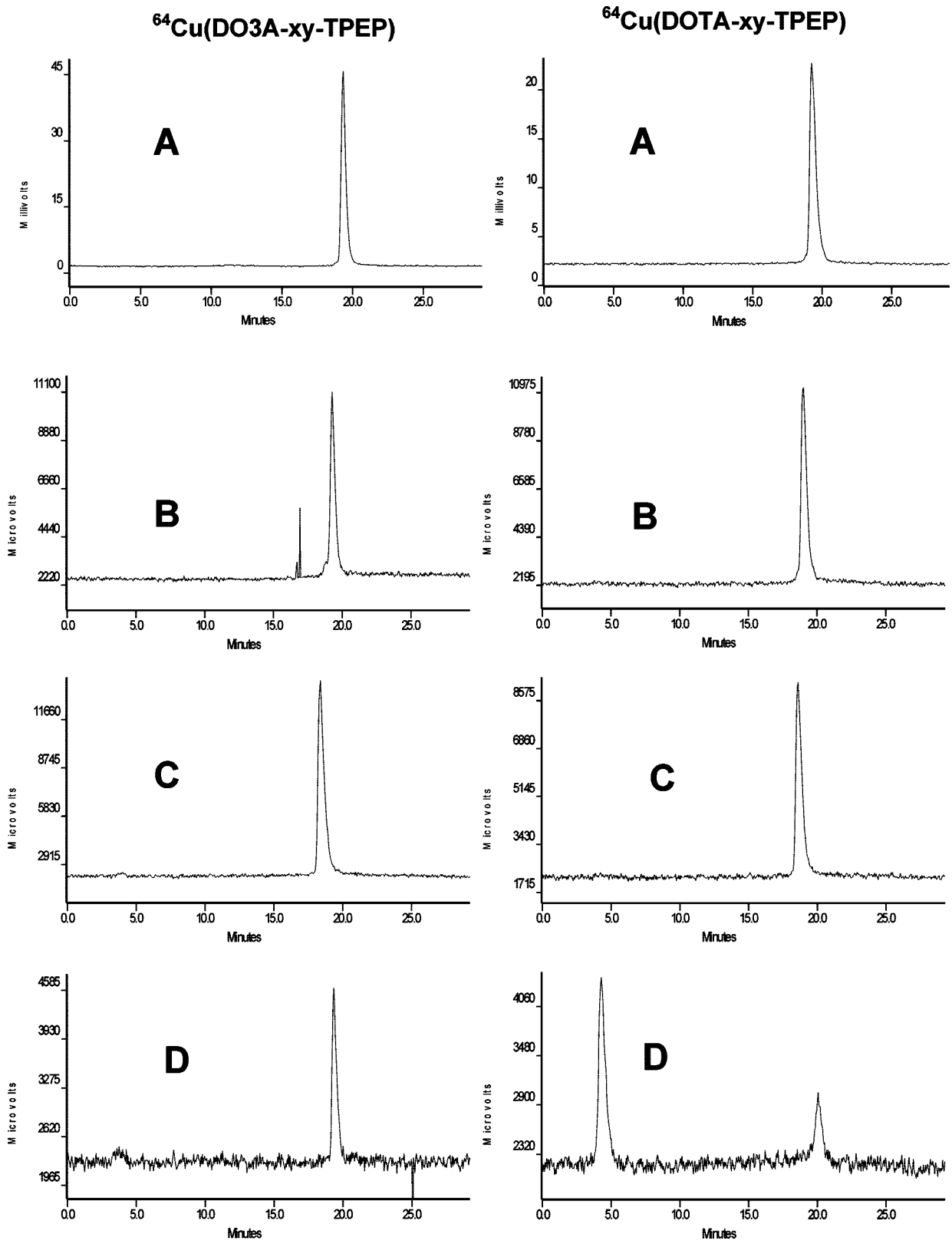

Figure 6. Typical reversed-phase radio-HPLC chromatograms (Method 3) of ^{64}Cu(DO3A-xy-TPEP) (left) and ^{64}Cu(DOTA-xy-TPEP) (right) in saline before injection (A), in the urine sample at 30 min p.i. (B), in the urine sample at 120 min p.i. (C), and in the feces sample (D) at 120 min p.i.

probably due to the aromatic benzene ring in DOTA-Bn. Addition of an extra acetamido group in ^{64}Cu(DOTA-xy-TPEP) results in a lower liver uptake, but the tumor/liver ratios of ^{64}Cu(DOTA-xy-TPEP) and ^{64}Cu(DO3A-xy-TPEP) are comparable, probably due to a faster tumor washout of ^{64}Cu(DOTA-xy-TPEP). Substitution of xylene with PEG_2 also leads to a significant reduction in both tumor and liver uptake. As a result, ^{64}Cu(DO3A-PEG_2-TPEP) and ^{64}Cu(DO3A-xy-TPEP) share very similar tumor/liver ratios. On the basis of both tumor uptake and T/B ratios of the ^{64}Cu radiotracers, we believe that both DO3A and DOTA are suitable BFCs for the ^{64}Cu-labeling of TPP cations. Among the six ^{64}Cu

radiotracers evaluated in this tumor-bearing animal model, ^{64}Cu(DO3A-xy-TPEP) is of particular interest due to its higher tumor uptake and better T/B ratios (particularly tumor/heart, tumor/liver, and tumor/muscle). ^{64}Cu(DO3A-xy-TPEP) will be further evaluated for its potential as a new PET radiotracer to monitor the MDR transport function in tumors of different origins.

ACKNOWLEDGMENT

Authors would like to thank Dr. Sulma I. Muhammed, the Director of Purdue Cancer Center Drug Discovery Shared Resource, Purdue University, for her assistance with the tumor-bearing model. This work is supported in part by research grants: R01 CA115883 A2 (S.L.) from National Cancer Institute (NCI), R21 EB003419-02 (S.L.) from National Institute of Biomedical Imaging and Bioengineering (NIBIB), and R21 HL083961-01 from National Heart, Lung, and Blood Institute (NHLBI).

Supporting Information Available: Detailed biodistribution data and T/B ratios for six ^{64}Cu-labeled TPEP cations are listed in Tables SI − SVI. Figure SI shows the Western blot data to demonstrate the absence of MDR1 expression in the U87MG human glioma xenografts. Figure SII shows radio-HPLC chromatograms of ^{64}Cu(NOTA-Bn-xy-TPEP) (left) and ^{64}Cu-(DOTA-Bn-xy-TPEP)- (right) in saline (A), in the urine at 30 min p.i. (B), in the urine at 120 min p.i. (C), and in the feces at 120 min p.i. (D). Figure SIII illustrates the radio-HPLC chromatograms of the liver homogenate at 120 min p.i. This material is available free of charge via the Internet at http://pubs.acs.org.

LITERATURE CITED

(1) Kroemer, G., Dallaporta, B., and Resche-Rigon, M. (1998) The mitochondrial death/life regulator in apoptosis and necrosis. *Annu. Rev. Physiol. 60*, 619–642.

(2) Modica-Napolitano, J. S., and Aprille, J. R. (2001) Delocalized lipophilic cations selectively target the mitochondria of carcinoma cells. *Adv. Drug Delivery Rev. 49*, 63–70.

(3) Duchen, M. R. (2004) Mitochondria in health and disease: perspectives on a new mitochondrial biology. *Mol. Aspects Med. 25*, 365–451.

(4) Modica-Napolitano, J. S., and Singh, K. K. (2002) Mitochondria as targets for detection and treatment of cancer *Expert Rev. Mol.ecular Med.*, http://www.ermm.cbcu.cam.ac.uk, (02)00445−3a (short code: txt001ksb).

(5) Johnson, L. V., Walsh, M. L., and Chen, L. B. (1980) Localization of mitochondria in liver cells with rhodamine 123. *Proc. Natl. Acad. Sci. U.S.A. 77*, 990–994.

(6) Summerhayes, I. C., Lampidis, T. J., Bernal, S. D., Nadakavukaren, J. J., Nadakavukaren, K. K., Shepard, E. L., and Chen, L. B. (1982) Unusual retention of rhodamine 123 by mitochondria in muscle and carcinoma cells. *Proc. Natl. Acad. Sci. U.S.A. 79*, 5292–5296.

(7) Modica-Napolitano, J. S., and Aprille, J. R. (1987) Basis for the selective cytotoxicity of rhodamine 123. *Cancer Res. 47*, 4361–4365.

(8) Davis, S., Weiss, M. J., Wong, J. R., Lampidis, T. J., and Chen, L. B. (1985) Mitochondrial and plasma membrane potentials cause unusual accumulation and retention of rhodamine 123 by human breast adenocarcinoma-derived MCF-7 cells. *J. Biol. Chem. 260*, 3844–3850.

(9) Dairkee, S. H., and Hackett, A. J. (1991) Differential retention of rhodamine 123 by breast carcinoma and normal human mammary tissue. *Breast Cancer Res. Treat. 18*, 57–61.

(10) Gottlieb, E., and Thompson, C. B. (2003) Targeting the mitochondria to enhance tumor suppression. *Methods Mol. Biol. 223*, 543–554.

(11) Mannella, C. A. (2006) The relevance of mitochondrial membrane topology to mitochondrial function. *Biochim. Biophys. Acta 1762*, 140–147.

(12) Ross, M. F., Kelso, G. F., Blaikie, F. H., James, A. M., Cocheme, H. M., Filipovska, A., Da Ros, T. D., Hurd, T. R., Smith, R. A. J., and Murphy, M. P. (2005) Lipophilic triphenylphosphonium cations as tools in mitochondrial bioenergetics and free radical biology. *Biochem. (Moscow) 70*, 222–230.

(13) Jakobs, S. (2006) High resolution imaging of living mitochondria. *Biochim. Biophys. Acta 1763*, 561–575.

(14) Wang, J., Yang, C., Kim, Y. S., Sreerama, S. G., Cao, Q., Li, Z., He, Z., Chen, X., and Liu, S. (2007) ^{64}Cu-Labeled triphenylphosphonium and triphenylarsonium cations as highly tumor-selective PET imaging agents. *J. Med. Chem. 50*, 5057–5069.

(15) Yang, C., Li, Y. X., and Liu, S. (2007) Synthesis and structural characterization of complexes of a DO3A-conjugated triphenylphosphonium cation with diagnostically important metal ions. *Inorg. Chem. 46*, 8988–8997.

(16) Kim, Y. S., Yang, C., Wang, J., Sreerama, S. G., Cao, Q., Li, Z., He, Z., Chen, X., and Liu, S. (2008) Radiolabeled triphenylphosphonium cations as highly tumor-selective imaging agents: Effects of radiometals, bifunctional chelators and molecular charge. *J. Med. Chem. 51*, 2971–2984.

(17) Bähr, O., Rieger, J., Duffner, F., Meyermann, R., Weller, M., and Wick, W. (2003) P-glycoprotein and multidrug resistance-associated protein mediate specific patterns of multidrug resistance in malignant glioma cell lines, but not in primary glioma cells. *Brain Pathol. 13*, 482–494.

(18) Le Jeune, N., Perek, N., Denoyer, D., and Dubois, F. (2004) Influence of glutathione depletion on plasma membrane cholesterol esterification and on Tc-99m-Sestamibi and Tc-99m-Tetrofosmin uptakes; a comparative study in sensitive U87MG and multidrug-resistant MRP1 human glioma cells. *Cancer Biother. Radiopharm. 19*, 411–421.

(19) Bähr, O., Wick, W., and Weller, M. (2001) Modulation of MDR/MRP by wild-type and mutant p53. *J. Clin. Invest. 107*, 643–645.

(20) Nakatsu, S., Kondo, S., Kondo, Y., Yin, D., Peterson, J. W., Kaakaji, R., Morimura, T., Kikuchi, H., Takeuchi, J., and Barnett, G. H. (1997) Induction of apoptosis in multi-drug resistant (MDR) human glioblastoma cells by SN38, a metabolite of the camptothecin derivative CPT. *Cancer Chemother. Pharmacol. 39*, 417–423.

(21) Wieghardt, K., Bossek, U., Chaudhuri, P., Herrmann, W., Menke, B. C., and Weiss, J. (1982) 1,4,7-Triazacyclononane-N,N′,N″-triacetate (TCTA), a hexadentate ligand for divalent and trivalent metal ions. Crystal structures of [Cr^{III}(TCTA)], [Fe^{III}(TCTA)], and Na[Cu^{II}(TCTA)] 0.2BaBr 0.8H_2O. *Inorg. Chem. 21*, 4308–4314.

(22) Riesen, A., Zehnder, M., and Kaden, T. A. (1986) Metal complexes of macrocyclic ligands Part XXIII. Synthesis, properties, and structures of mononuclear complexes with 12- and 14-membered tetraazamacrocycle-N,N′,N″,N‴-tetraacetic acids. *Helv. Chim. Acta 69*, 2067–2073.

(23) Riesen, A., Zehnder, M., and Kaden, T. A. (1986) Metal complexes of macrocyclic ligands. *Helv. Chim. Acta 69*, 2074–2080.

(24) Herman, L. W., Sharma, V., Kronauge, J. F., Barbarics, E., Herman, L. A., and Piwnica-Worms, D. (1995) Novel hexakis(areneisonitrile)technetium(I) complexes as radioligands targeted to the multidrug resistance P-glycoprotein. *J. Med. Chem. 38*, 2955–2963.

(25) Agrawal, M., Abraham, J., Balis, F. M., Edgerly, M., Stein, W. D., Bates, S., Fojo, T., and Chen, C. C. (2003) Increased ^{99m}Tc-Sestamibi accumulation in normal liver and drug resistant-tumors after the administration of the glycoprotein inhibitor, XR9576. *Clin. Cancer Res. 9*, 650–656.

(26) Luker, G. D., Francisco, P. M., Dobkin, J., and Piwbica-Worms, D. (1997) Modulation of the multidrug resistance P-glycoprotein: Detection with technetium-99m sestamibi in vivo. *J. Nucl. Med. 38*, 369–372.

(27) Liu, Z. L., Stevenson, G. D., Barrett, H. H., Kastis, G. A., Bettan, M., Furenlid, L. R., Wilson, D. W., and Woolfenden, J. M. (2004) Imaging recognition of multidrug resistance in human breast tumors using ^{99m}Tc-labeled monocationic agents and a high-resolution stationary SPECT system. *Nucl. Med. Biol. 31*, 53–65.

(28) Liu, Z. L., Stevenson, G. D., Barrett, H. H., Furenlid, L. R., Wilson, D. W., Kastis, G. A., Bettan, M., and Woolfenden, J. M. (2005) Imaging recognition of inhibition of multidrug resistance in human breast cancer xenografts using ^{99m}Tc-labeled sestamibi and tetrofosmin. *Nucl. Med. Biol. 32*, 573–583.

(29) Muzzammil, T., Ballinger, J. R., and Moore, M. J. (1999) ^{99m}Tc-sestamibi imaging of inhibition of the multidrug resistance transporter in a mouse xenograft model of human breast cancer. *Nucl. Med. Commun. 20*, 115–122.

(30) Sharma, V. (2004) Radiopharmaceuticals for assessment of multidrug resistance P-glycoprotein-mediated drug transport activity. *Bioconjugate Chem. 15*, 1464–1474.

(31) Vaidyanathan, G., and Zalutsky, M. R. (2004) Imaging drug resistance with radiolabeled molecules. *Curr. Pharm. Des. 10*, 2965–2979.

(32) Filippi, L., Santoni, R., Manni, C., Danieli, R., Floris, R., and Schillaci, O. (2005) Imaging primary brain tumor by single-photon emission computed tomography (SPECT) with technetium-99m Sestamibi (MIBI) and Tetrofosmin. *Curr. Med. Imaging Rev. 1*, 61–66.

(33) Sharma, V., and Piwnica-Worms, D. (1999) Metal complexes for therapy and diagnosis of drug resistance. *Chem. Rev. 99*, 2545–2560.

(34) Madar, I., Anderson, J. H., Szabo, Z., Scheffel, U., Kao, P. F., Ravert, H. T., and Dannals, R. F. (1999) Enhanced uptake of [^{11}C]TPMP in canine brain tumor: a PET study. *J. Nucl. Med. 40*, 1180–1185.

(35) Madar, I., Weiss, L., and Izbicki, G. (2002) Preferential accumulation of ^{3}H-tetraphenylphosphonium in non-small cell lung carcinoma in mice: comparison with ^{99m}Tc-MIBI. *J. Nucl. Med. 43*, 234–238.

(36) Min, J. J., Biswal, S., Deroose, C., and Gambhir, S. S. (2004) Tetraphenylphosphonium as a novel molecular probe for imaging tumors. *J. Nucl. Med. 45*, 636–643.

(37) Steichen, J. D., Weiss, M. J., Elmaleh, D. R., and Martuza, R. L. (1991) Enhanced in vitro uptake and retention of ^{3}H-tetraphenylphosphonium by nervous system tumor cells. *J. Neurosurg. 74*, 116–122.

(38) Cheng, Z., Winant, R. C., and Gambhir, S. S. (2005) A new strategy to screen molecular imaging probe uptake in cell culture without radiolabeling using matrix-assisted laser desorption/ionization time-of-flight mass spectrometry. *J. Nucl. Med. 46*, 878–886.

(39) Acampa, W., Di Benedetto, C., and Cuocolo, A. (2000) An overview of radiotracers in nuclear cardiology. *J. Nucl. Cardiol. 7*, 701–707.

(40) Dilsizian, V. (2000) The role of myocardial perfusion imaging in vascular endothelial dysfunction. *J. Nucl. Cardiol. 7*, 180–184.

(41) Schwaiger, M., and Melin, J. (1999) Cardiological applications of nuclear medicine. *Lancet 354*, 661–666.

(42) Beller, G. A., and Zaret, B. L. (2000) Contributions of nuclear cardiology to diagnosis and prognosis of patients with coronary artery disease. *Circulation 101*, 1468–1478.

(43) Parker, J. A. (2001) Cardiac nuclear medicine in monitoring patients with coronary heart disease. *Semin. Nucl. Med. 31*, 223–237.

(44) Saha, G. B., Go, R. T., and Macintyre, W. J. (1992) Radiopharmaceuticals for cardiovascular imaging. *Nucl. Med. Biol. 19*, 1–20.

(45) Jain, D. (1999) Technetium-99m labeled myocardial perfusion imaging agents. *Semin. Nucl. Med. 29*, 221–236.

(46) Bass, L. A., Wang, M., Welch, M. J., and Anderson, C. J. (2001) In vivo transchelation of copper-64 from TETA-Octreotide to superoxide dismutase in rat liver. *Bioconjugate Chem. 11*, 527–532.

(47) Boswell, C. A., Sun, X., Niu, W., Weisman, G. R., Wong, E. H., Rheingold, A. L., and Anderson, C. J. (2004) Comparative in vivo stability of copper-64-labeled cross-bridged and conventional tetraazamacrocyclic complexes. *J. Med. Chem. 47*, 1465–1474.

(48) Boswell, C. A., McQuade, P., Weisman, G. R., Wong, E. H., and Anderson, C. J. (2005) Optimization of labeling and metabolite analysis of copper-64-labeled azamacrocyclic chelators by radio-LC-MS. *Nucl. Med. Biol. 32*, 29–38.

(49) Anderson, C. J. (2001) Metabolism of radiometal labeled proteins and peptides: what are the real radiopharmaceuticals in vivo? *Cancer Biother. Radiopharm. 16*, 451–455.

(50) Sprague, J. E., Peng, Y., Fiamengo, A. L., Wooden, K. S., Southwick, E. A., Wiseman, G. R., Wong, E. H., Golden, J. A., Rhengold, A. L., and Anderson, C. J. (2007) Synthesis, characterization and in vivo studies of Cu(II)-64-labeled cross-bridges tetraazamacrocycle-amide complexes as models of peptide conjugate imaging agents. *J. Med. Chem. 50*, 311–318.

(51) Bartnikas, T. B., and Gitlin, J. D. (2003) Mechanisms of biosynthesis of mammalian copper/zinc superoxide dismutase. *J. Biol. Chem. 278*, 33602–33608.

(52) Deshpande, S. V., DeNardo, S. J., Meares, C. F., McCall, M. J., Adams, J. P., Moi, M. K., and DeNardo, G. L. (1988) Copper-67-labeled monoclonal antibody Lym-1, a potential radiopharmaceutical for cancer therapy: Labeling and biodistribution in RAJI tumored mice. *J. Nucl. Med. 29*, 217–225.

(53) Li, W. P., Lewis, J. S., Kim, J., Bugaj, J. E., Johnson, M. A., Erion, J. L., and Anderson, C. J. (2002) DOTA-D-Tyr^{1}-Octreotate: a somatostatin analogue for labeling with metal and halogen radionuclides for cancer imaging and therapy. *Bioconjugate Chem. 13*, 721–728.

(54) McQuade, P., Miao, Y., Yoo, J., Quinn, T. P., Welch, M. J., and Lewis, J. S. (2005) Imaging of melanoma using ^{64}Cu- and ^{86}Y-DOTA-ReCCMSH(Arg^{11}), a cyclized peptide analogue of α-MSH. *J. Med. Chem. 48*, 2985–2992.

(55) Biddlecombe, G. B., Rogers, B. E., de Visser, M., Parry, J. J., de Jong, M., Erion, J. L., and Lewis, J. S. (2007) Molecular imaging of gastrin-releasing peptide receptor-positive tumors in mice using ^{64}Cu- and ^{86}Y-DOTA-(Pro^{1}, Tyr^{4})-Bombesin(1−14). *Bioconjugate Chem. 18*, 724–730.

(56) Parry, J. J., Andrews, R., and Rogers, B. E. (2007) MicroPET imaging of breast cancer using radiolabeled bombesin analogs targeting the gastrin-releasing peptide receptor. Breast. *Cancer Res. Treat. 101*, 175–183.

(57) Parry, J. J., Kelly, T. S., Andrews, R., and Rogers, B. E. (2007) In vitro and in vivo evaluation of ^{64}Cu-labeled DOTA-Linker-Bombesin(7−14) analogues containing different amino acid linker moiety. *Bioconjugate Chem. 18*, 1110–1117.

(58) Chen, X., Liu, S., Hou, Y., M., Tohme, M., Park, R., Bading, J. R., and Conti, P. S. (2005) MicroPET imaging of breast cancer α_v-integrin expression with ^{64}Cu-labeled dimeric RGD peptides. *Mol. Imaging Biol. 6*, 350–359.

(59) Wu, Y., Zhang, X., Xiong, Z., Cheng, Z., Fisher, D. R., Liu, S., Gambhir, S. S., and Chen, X. (2005) MicroPET imaging of glioma $\alpha_v\beta_3$ integrin expression using ^{64}Cu-labeled tetrameric RGD peptide. *J. Nucl. Med. 46*, 1707–1718.

BC8002056

Supplementary Materials for the Manuscript Entitled

"^{64}Cu-Labeled 2-(Diphenylphosphoryl)ethyldiphenylphosphonium Cations as Highly Selective Tumor Imaging Agents: Effects of Linkers and Chelates on Radiotracer Biodistribution Characteristics"

by

Chang-Tong Yang,[1] Young-Seung Kim,[1] Jianjun Wang,[1] Lijun Wang,[1] Jiyun, Shi,[1] Zi-Bo Li,[2] Xiaoyuan Chen,[2] Ming Fan,[1] Jian-Jian Li,[1] and Shuang Liu[1]*

[1]School of Health Sciences, Purdue University, West Lafayette, Indiana, USA

[2]Molecular Imaging Program at Stanford, Department of Radiology & Bio-X, Stanford University, Stanford, California, USA

Running Title: ^{64}Cu-Labeled TPEP Cations for Tumor Imaging

---

[1]*To whom correspondence should be addressed. School of Health Sciences, Purdue University, 550 Stadium Mall Drive, West Lafayette, IN 47907. Phone: 765-494-0236; Fax 765-496-1377; Email: lius@pharmacy.purdue.edu

Contents of Supporting Information

Table SI. Biodistribution data and T/B ratios of ^{64}Cu(DO3A-xy-TPEP) in the athymic nude mice bearing U87MG human glioma xenografts. The organ uptake is expressed as %ID/g. Each data point represents an average of biodistribution data in three animals.

Table SII. Biodistribution data and T/B ratios of ^{64}Cu(DO3A-PEG$_2$-TPEP) in the athymic nude mice bearing U87MG human glioma xenografts. The organ uptake is expressed as %ID/g. Each data point represents an average of biodistribution data in three animals.

Table SIII. Biodistribution data and T/B ratios of ^{64}Cu(DO2A-xy-TPEP) in the athymic nude mice bearing U87MG human glioma xenografts. The organ uptake is expressed as %ID/g. Each data point represents an average of biodistribution data in three animals.

Table SIV. Biodistribution data and T/B ratios of ^{64}Cu(DOTA-xy-TPEP) in the athymic nude mice bearing U87MG human glioma xenografts. The organ uptake is expressed as %ID/g. Each data point represents an average of biodistribution data in three animals.

Table SV. Biodistribution data and T/B ratios of ^{64}Cu(DOTA-Bn-xy-TPEP) in the athymic nude mice bearing U87MG human glioma xenografts. The organ uptake is expressed as %ID/g. Each data point represents an average of biodistribution data in three animals.

Table SVI. Biodistribution data and T/B ratios of ^{64}Cu(NOTA-Bn-xy-TPEP) in the athymic nude mice bearing U87MG human glioma xenografts. The organ uptake is expressed as %ID/g. Each data point represents an average of biodistribution data in three animals.

Figure SI. Western blot experiment was performed to demonstrate the absence of MDR1 Pgp on U87MG glioma xenografts. Twenty micrograms of tissue lysate from each of the six tumor-bearing mice were analyzed by 5% SDS-PAGE and transferred to PVDF membranes, which were blocked with 5% nonfat milk in tris-buffered saline containing 0.1% Tween-20 for 1 h at 37 °C. MES-SA/Dx5 lysate (Santa Cruz, CA) was used as the positive control. Blots were immunostained with primary antibodies MDR1 (Santa Cruz, CA) at 4 °C overnight and probed with secondary antibodies conjugated to horseradish peroxidase. Specific bands were visualized by enhanced chemiluminescence kit from Pierce.

Figure SII. Typical reversed-phase radio-HPLC chromatograms of ^{64}Cu(NOTA-Bn-xy-TPEP) (left) and ^{64}Cu(DOTA-Bn-xy-TPEP)$^-$ (right) in saline before injection (A), in the urine at 30 min p.i. (B), in the urine at 120 min p.i. (C), and in the feces at 120 min p.i. (D). Each tumor-bearing mouse was administered with ~ 100 μCi of ^{64}Cu radiotracer.

Figure SIII. Radio-HPLC chromatograms of the liver homogenate at 120 min p.i. using the reversed-phase HPLC method (top) and size-exclusion HPLC method (bottom), which used the LabAlliance HPLC system equipped with a UV/vis detector (λ = 254 nm), a β-ram IN-US detector, a Superose™ 12 10/300 GL size-exclusion column, and the flow rate of 0.4 mL/min. The aqueous mobile phase was isocratic with 20 mM HEPES and 150 mM NaCl.

Table SI. Biodistribution data and T/B radios of ^{64}Cu(DO3A-xy-TPEP) in the athymic nude mice bearing U87MG human glioma xenografts. The organ uptake is expressed as %ID/g. Each data point represents an average of biodistribution data in three animals.

Organ (% ID/gram)	5 min	30 min	60 min	120 min
Blood	9.52 ± 1.27	1.68 ± 0.39	0.65 ± 0.12	0.36 ± 0.07
Brain	0.22 ± 0.06	0.06 ± 0.03	0.04 ± 0.02	0.02 ± 0.02
Heart	4.04 ± 0.75	0.94 ± 0.19	0.67 ± 0.17	0.55 ± 0.09
Intestine	4.06 ± 0.82	3.11 ± 0.99	3.39 ± 0.47	2.61 ± 1.26
Kidney	31.79 ± 8.51	6.79 ± 0.97	4.24 ± 1.08	2.98 ± 0.53
Liver	8.03 ± 1.41	6.48 ± 1.39	6.40 ± 1.94	5.59 ± 1.39
Lungs	7.72 ± 0.78	2.27 ± 0.48	1.84 ± 0.38	1.51 ± 0.18
Muscle	3.07 ± 0.48	0.55 ± 0.17	0.22 ± 0.11	0.10 ± 0.06
Spleen	2.73 ± 0.33	0.97 ± 0.32	0.63 ± 0.25	0.56 ± 0.17
Tumor	5.27 ± 1.21	2.09 ± 0.53	2.58 ± 0.31	2.15 ± 0.58
Tumor/Blood	0.57 ± 0.13	1.48 ± 0.52	4.66 ± 0.65	5.87 ± 1.91
Tumor/Brain	23.29 ± 4.58	34.59 ± 17.36	78.69 ± 15.13	57.47 ± 26.14
Tumor/Heart	1.26 ± 0.34	3.06 ± 0.82	4.73 ± 0.45	3.42 ± 1.05
Tumor/Liver	0.68 ± 0.27	0.43 ± 0.18	0.54 ± 0.10	0.54 ± 0.15
Tumor/Lungs	0.63 ± 0.15	1.11 ± 0.53	1.45 ± 0.56	1.39 ± 0.39
Tumor/Muscle	1.57 ± 0.49	5.08 ± 4.37	17.96 ± 9.11	25.42 ± 19.72

Table SII. Biodistribution data and T/B ratios of ^{64}Cu(DO3A-PEG$_2$-TPEP) in the athymic nude mice bearing U87MG human glioma xenografts. The organ uptake is expressed as %ID/g. Each data point represents an average of biodistribution data in three animals.

Organ (% ID/gram)	5 min	30 min	60 min	120 min
Blood	7.19 ± 1.40	1.03 ± 0.09	0.49 ± 0.11	0.33 ± 0.05
Brain	0.18 ± 0.07	0.05 ± 0.01	0.03 ± 0.01	0.02 ± 0.01
Heart	3.64 ± 0.25	0.71 ± 0.06	0.42 ± 0.03	0.44 ± 0.07
Intestine	4.05 ± 0.72	3.67 ± 2.13	2.15 ± 0.14	2.30 ± 1.29
Kidney	29.11 ± 2.57	4.69 ± 0.19	2.70 ± 0.19	2.53 ± 0.44
Liver	6.44 ± 1.29	3.76 ± 0.06	3.20 ± 0.56	2.91 ± 0.12
Lungs	6.08 ± 0.57	1.63 ± 0.27	1.08 ± 0.07	1.06 ± 0.08
Muscle	2.45 ± 0.36	0.39 ± 0.13	0.17 ± 0.10	0.07 ± 0.02
Spleen	2.18 ± 0.38	0.97 ± 0.27	1.31 ± 0.24	0.90 ± 0.35
Tumor	5.06 ± 0.84	1.24 ± 0.31	1.41 ± 0.35	1.60 ± 0.45
Tumor/Blood	0.72 ± 0.15	1.21 ± 0.31	2.99 ± 1.03	4.83 ± 1.05
Tumor/Brain	30.25 ± 11.33	27.39 ± 7.92	45.20 ± 16.50	67.53 ± 28.94
Tumor/Heart	1.38 ± 0.16	1.78 ± 0.54	3.40 ± 1.00	3.66 ± 0.77
Tumor/Liver	0.80 ± 0.13	0.33 ± 0.08	0.45 ± 0.15	0.55 ± 0.16
Tumor/Lung	0.84 ± 0.17	0.77 ± 0.15	1.31 ± 0.37	1.51 ± 0.36
Tumor/Muscle	2.09 ± 0.39	3.38 ± 0.96	9.99 ± 4.74	23.95 ± 9.63

Table SIII. Biodistribution data and T/B ratios of ^{64}Cu(DO2A-xy-TPEP) in the athymic nude mice bearing U87MG human glioma xenografts. The organ uptake is expressed as %ID/g. Each data point represents an average of biodistribution data in three animals.

Organ (% ID/gram)	5 min	30 min	60 min	120 min
Blood	9.25 ± 0.84	2.13 ± 0.73	0.44 ± 0.17	0.24 ± 0.13
Brain	0.26 ± 0.04	0.06 ± 0.03	0.02 ± 0.01	0.02 ± 0.01
Heart	3.26 ± 0.24	0.78 ± 0.23	0.41 ± 0.26	0.10 ± 0.06
Intestine	3.89 ± 0.29	1.65 ± 0.49	1.22 ± 0.53	0.52 ± 0.13
Kidney	25.60 ± 1.21	5.99 ± 1.85	2.44 ± 0.43	1.28 ± 0.10
Liver	3.95 ± 0.16	2.18 ± 0.29	1.91 ± 0.02	1.49 ± 0.12
Lungs	7.51 ± 0.78	2.18 ± 0.43	0.89 ± 0.12	0.47 ± 0.06
Muscle	2.81 ± 0.22	0.51 ± 0.25	0.25 ± 0.11	0.07 ± 0.03
Spleen	2.72 ± 0.16	1.26 ± 0.28	0.36 ± 0.02	0.51 ± 0.24
Tumor	5.06 ± 0.43	1.66 ± 0.21	0.78 ± 0.32	0.51 ± 0.08
Tumor/Blood	0.55 ± 0.06	0.87 ± 0.37	1.94 ± 0.84	2.63 ± 1.47
Tumor/Brain	19.81 ± 3.66	39.60 ± 29.76	33.25 ± 14.96	27.50 ± 13.03
Tumor/Heart	1.55 ± 0.14	2.30 ± 0.83	2.26 ± 1.00	6.32 ± 2.92
Tumor/Liver	1.28 ± 0.12	0.78 ± 0.16	0.41 ± 0.17	0.34 ± 0.06
Tumor/Lung	0.68 ± 0.08	0.79 ± 0.20	0.90 ± 0.44	1.09 ± 0.11
Tumor/Muscle	1.81 ± 0.23	4.04 ± 2.24	3.64 ± 2.35	7.83 ± 3.05

Table SIV. Biodistribution data and T/B ratios of ^{64}Cu(DOTA-xy-TPEP) in the athymic nude mice bearing U87MG human glioma xenografts. The organ uptake is expressed as %ID/g. Each data point represents an average of biodistribution data in three animals.

Organ (% ID/gram)	5 min	30 min	60 min	120 min
Blood	11.65 ± 1.62	2.99 ± 0.03	1.74 ± 0.51	0.33 ± 0.01
Brain	0.23 ± 0.04	0.09 ± 0.04	0.05 ± 0.01	0.03 ± 0.01
Heart	3.96 ± 0.91	1.14 ± 0.19	0.90 ± 0.23	0.30 ± 0.07
Intestine	5.25 ± 2.27	4.52 ± 1.47	4.05 ± 1.89	1.38 ± 0.43
Kidney	21.61 ± 5.63	7.72 ± 0.76	5.53 ± 0.56	2.84 ± 0.50
Liver	5.61 ± 0.37	4.47 ± 0.45	3.93 ± 0.84	2.99 ± 0.21
Lungs	7.27 ± 0.63	2.78 ± 0.32	2.00 ± 0.36	1.00 ± 0.28
Muscle	2.65 ± 0.61	1.31 ± 0.65	0.31 ± 0.12	0.01 ± 0.01
Spleen	2.69 ± 0.73	1.12 ± 0.24	0.95 ± 0.10	0.61 ± 0.16
Tumor	4.84 ± 0.96	1.99 ± 0.41	1.78 ± 0.65	1.39 ± 0.59
Tumor/Blood	0.41 ± 0.04	0.67 ± 0.14	1.08 ± 0.46	4.21 ± 1.66
Tumor/Brain	21.27 ± 1.00	31.31 ± 8.14	36.74 ± 19.55	59.62 ± 41.23
Tumor/Heart	1.24 ± 0.18	1.78 ± 0.51	2.05 ± 0.79	4.61 ± 1.90
Tumor/Liver	0.86 ± 0.12	0.45 ± 0.07	0.47 ± 0.22	0.47 ± 0.23
Tumor/Lung	0.66 ± 0.07	0.71 ± 0.07	0.89 ± 0.21	1.36 ± 0.29
Tumor/Muscle	1.86 ± 0.36	1.65 ± 0.39	5.18 ± 1.17	76.29 ± 8.84

Table SV. Biodistribution data and T/B ratios of ^{64}Cu(DOTA-Bn-xy-TPEP) in the athymic nude mice bearing U87MG human glioma xenografts. The organ uptake is expressed as %ID/g. Each data point represents an average of biodistribution data in three animals.

Organ (% ID/gram)	5 min	30 min	60 min	120 min
Blood	14.35 ± 2.38	4.45 ± 0.27	2.29 ± 0.58	1.14 ± 0.18
Brain	0.40 ± 0.01	0.17 ± 0.02	0.20 ± 0.10	0.10 ± 0.03
Heart	4.07 ± 0.66	1.86 ± 0.23	1.73 ± 0.43	1.03 ± 0.17
Intestine	4.03 ± 0.54	4.11 ± 0.92	4.69 ± 0.39	3.28 ± 0.50
Kidney	18.07 ± 5.96	9.02 ± 0.13	7.72 ± 0.25	5.44 ± 0.40
Liver	10.32 ± 2.02	9.24 ± 0.98	9.28 ± 0.91	8.66 ± 0.12
Lungs	7.25 ± 1.28	3.95 ± 0.14	3.48 ± 0.54	2.31 ± 0.16
Muscle	2.65 ± 0.43	1.06 ± 0.04	0.56 ± 0.09	0.23 ± 0.03
Spleen	3.11 ± 0.38	1.45± 0.07	1.57 ± 0.23	1.05 ± 0.16
Tumor	3.03 ± 0.52	2.47 ± 0.09	2.68 ± 0.07	1.91 ± 0.30
Tumor/Blood	0.21 ± 0.04	0.56 ± 0.04	1.21 ± 0.26	1.69 ± 0.26
Tumor/Brain	7.60 ± 1.09	14.50 ± 1.95	16.46 ± 8.66	21.00 ± 5.38
Tumor/Heart	0.75 ± 0.08	1.34 ± 0.17	1.61 ± 0.36	1.88 ± 0.43
Tumor/Liver	0.30 ± 0.07	0.27 ± 0.02	0.29 ± 0.02	0.22 ± 0.04
Tumor/Lung	0.42 ± 0.06	0.63 ± 0.04	0.78 ± 0.11	0.83 ± 0.14
Tumor/Muscle	1.15 ± 0.07	2.32 ± 0.07	4.92 ± 0.83	8.00 ± 1.54

Table SVI. Biodistribution data and T/B ratios of ^{64}Cu(NOTA-Bn-xy-TPEP) in the athymic nude mice bearing U87MG human glioma xenografts. The organ uptake is expressed as %ID/g. Each data point represents an average of biodistribution data in three animals.

Organ (% ID/gram)	5 min	30 min	60 min	120 min
Blood	11.55 ± 1.93	2.58 ± 0.84	0.92 ± 0.04	0.30 ± 0.07
Brain	0.39 ± 0.15	0.08 ± 0.05	0.01 ± 0.00	0.04 ± 0.02
Heart	4.09 ± 0.96	0.80 ± 0.35	0.19 ± 0.00	0.18 ± 0.03
Intestine	4.58 ± 0.62	10.25 ± 3.26	5.98 ± 1.09	1.36 ± 0.58
Kidney	13.52 ± 2.14	3.28 ± 0.68	1.37 ± 0.09	1.08 ± 0.06
Liver	11.17 ± 1.63	5.86 ± 1.37	3.99 ± 0.93	2.20 ± 0.18
Lungs	8.39 ± 1.05	2.30 ± 0.61	0.81 ± 0.09	0.35 ± 0.08
Muscle	1.83 ± 0.83	0.92 ± 0.42	0.10 ± 0.06	0.02 ± 0.03
Spleen	3.44 ± 0.86	1.25± 0.63	0.35 ± 0.17	0.42 ± 0.16
Tumor	2.74 ± 0.05	1.06 ± 0.23	0.47 ± 0.04	0.28 ± 0.04
Tumor/Blood	0.24 ± 0.03	0.42 ± 0.07	0.51 ± 0.03	0.94 ± 0.19
Tumor/Brain	7.56 ± 2.23	16.16 ± 7.87	50.96 ± 5.49	10.19 ± 6.67
Tumor/Heart	0.69 ± 0.14	1.42 ± 0.47	2.42 ± 0.25	3.19 ± 1.12
Tumor/Liver	0.25 ± 0.03	0.18 ± 0.01	0.12 ± 0.02	0.13 ± 0.01
Tumor/Lung	0.33 ± 0.04	0.46 ± 0.03	0.58 ± 0.07	0.80 ± 0.08
Tumor/Muscle	1.68 ± 0.63	1.25 ± 0.36	5.59 ± 2.86	5.22 ± 0.40

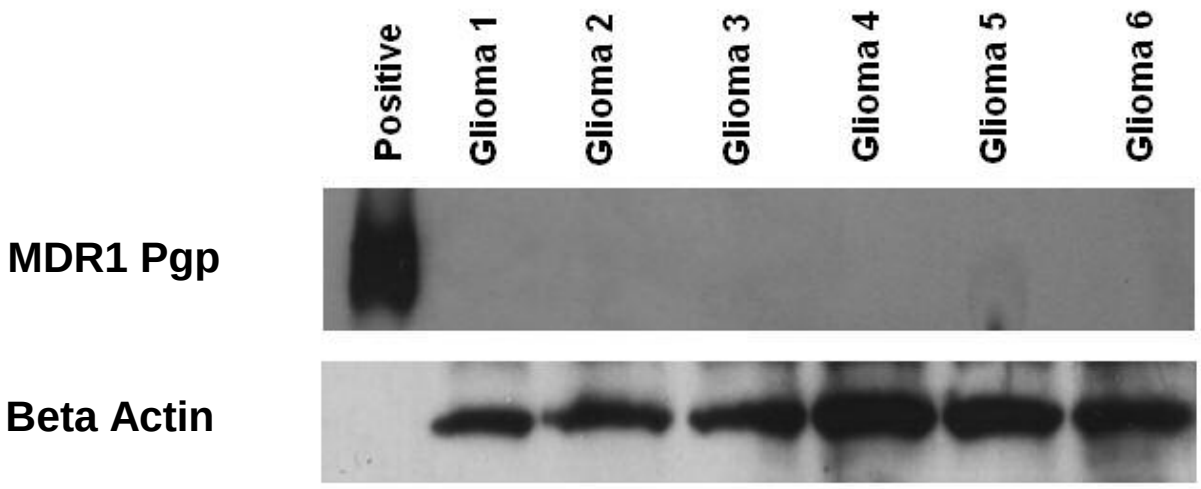

Figure 2. Western blot experiment was performed to demonstrate the absence of MDR1 Pgp on U87MG glioma xenografts. Twenty micrograms of tissue lysate from each of the six tumor-bearing mice were analyzed by 5% SDS-PAGE and transferred to PVDF membranes, which were blocked with 5% nonfat milk in tris-buffered saline containing 0.1% Tween-20 for 1 h at 37 °C. MES-SA/Dx5 lysate (Santa Cruz, CA) was used as the positive control. Blots were immunostained with primary antibodies MDR1 (Santa Cruz, CA) at 4 °C overnight and probed with secondary antibodies conjugated to horseradish peroxidase. Specific bands were visualized by enhanced chemiluminescence kit from Pierce.

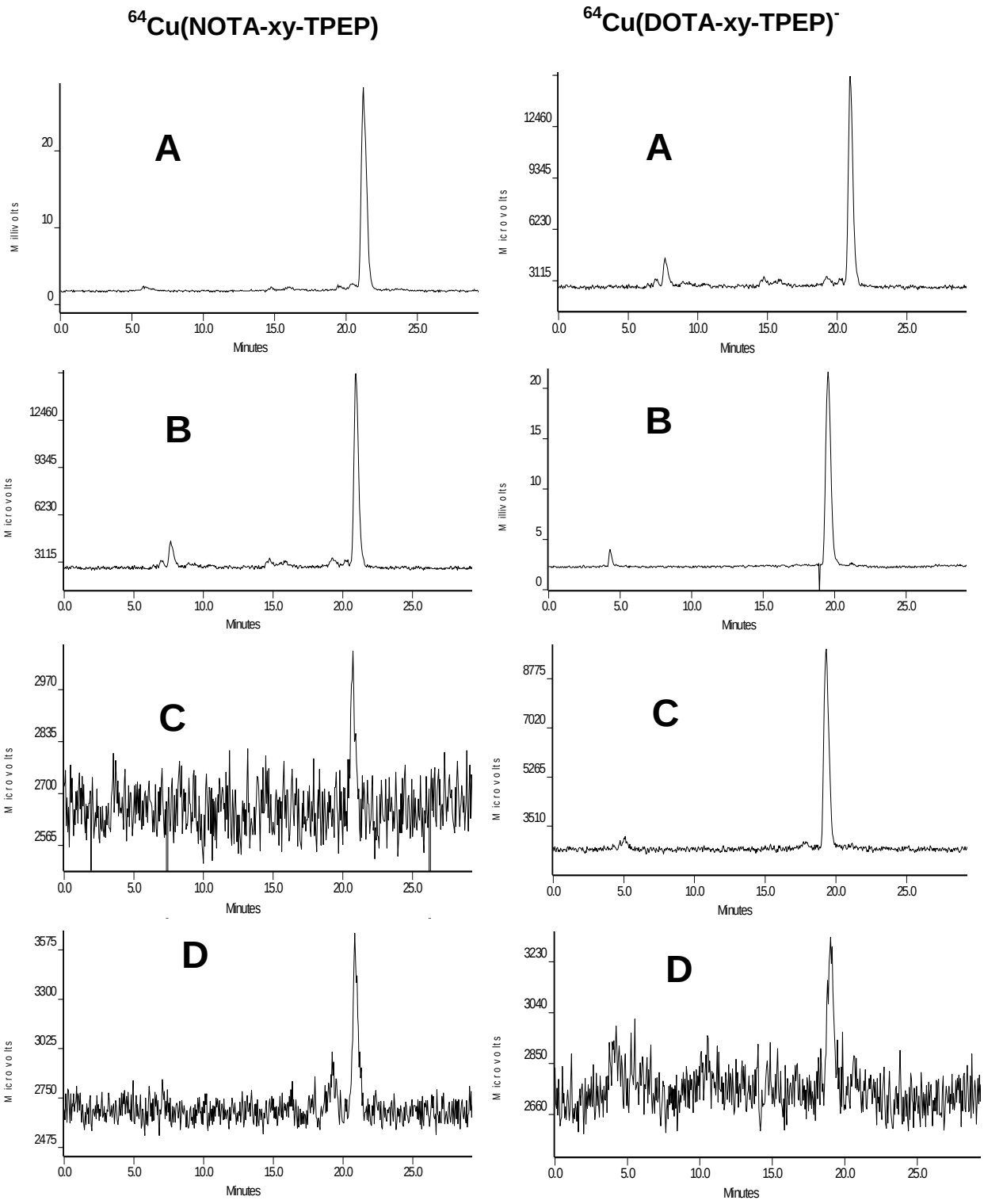

Figure SII. Radio-HPLC chromatograms of ^{64}Cu(NOTA-Bn-xy-TPEP) (left) and ^{64}Cu(DOTA-Bn-xy-TPEP)$^{-}$ (right) in saline before injection (A), in the urine at 30 min p.i. (B), in the urine at 120 min p.i. (C), and in the feces at 120 min p.i. (D). Each tumor-bearing mouse was administered with ~ 100 μCi of ^{64}Cu radiotracer.

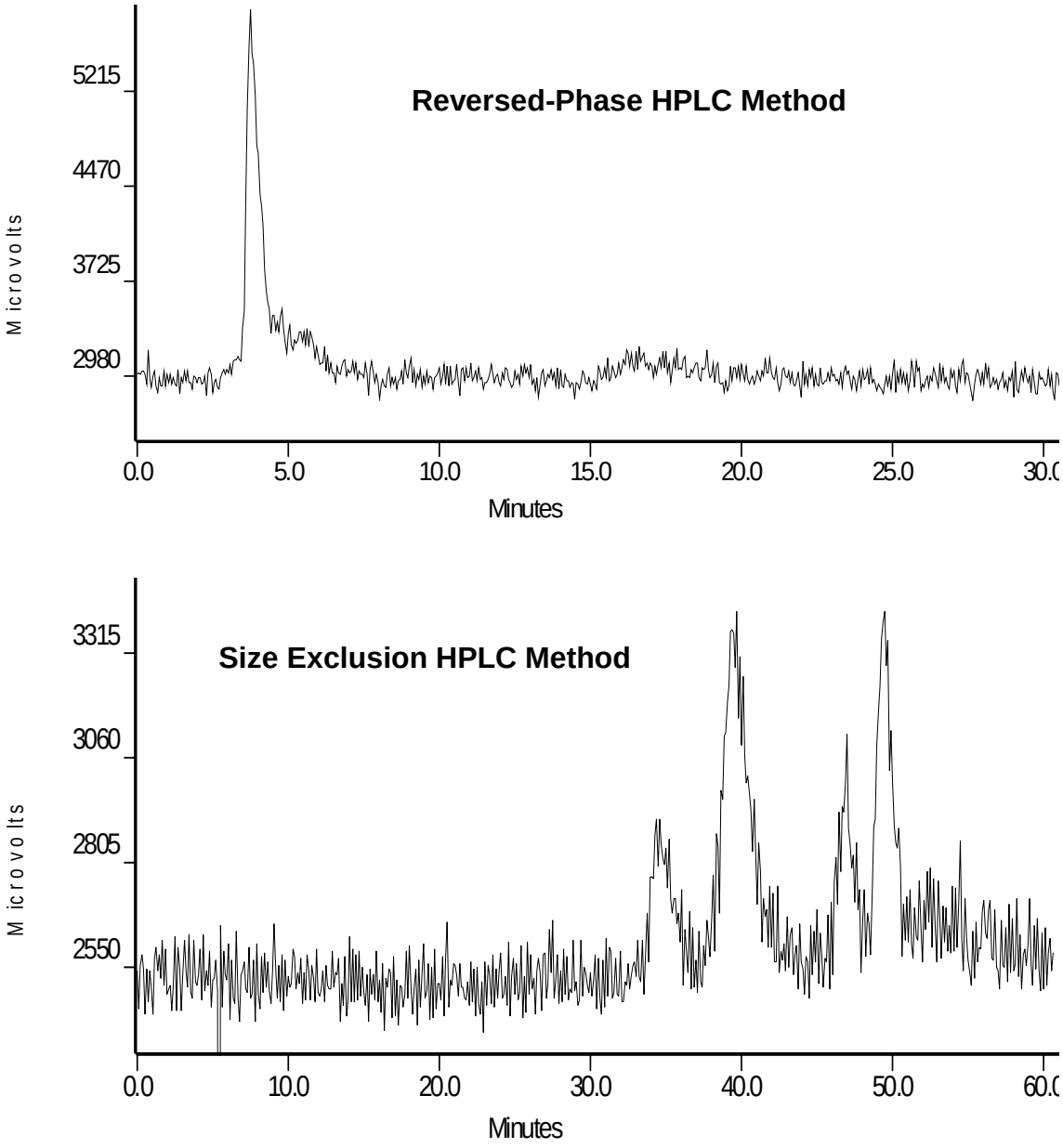

Figure SIII. Radio-HPLC chromatograms of the liver homogenate at 120 min p.i. using the reversed-phase HPLC method (top) and size-exclusion HPLC method (bottom), which used the LabAlliance HPLC system equipped with a UV/vis detector (λ = 254 nm), a β-ram IN-US detector, a Superose™ 12 10/300 GL size-exclusion column, and the flow rate of 0.4 mL/min. The aqueous mobile phase was isocratic with 20 mM HEPES and 150 mM NaCl.

Different Internalization Pathways of Polymeric Micelles and Unimers and Their Effects on Vesicular Transport

Gaurav Sahay, Elena V. Batrakova, and Alexander V. Kabanov*

Department of Pharmaceutical Sciences and Center for Drug Delivery and Nanomedicine, College of Pharmacy, University of Nebraska Medical Center, Omaha, Nebraska 68198-5830, and Faculty of Chemistry, M.V. Lomonosov Moscow State University, 119899 Moscow, Russia. Received June 5, 2008; Revised Manuscript Received July 29, 2008

Efficient entry of synthetic polymers inside cells is a central issue in polymeric drug delivery. Though polymers are widely believed to interact nonspecifically with plasma membrane, we present unexpected evidence that amphiphilic block copolymers, depending on their aggregation state, can distinguish between caveolae- and clathrin-mediated endocytosis. A block copolymer of poly(ethylene oxide) (PEO) and poly(propylene oxide) (PPO), Pluronic P85 (P85), below critical micelle concentration (CMC) exists as single molecule coils (unimers) and above CMC forms 14.6 nm aggregated micelles with a hydrophobic PPO core and hydrophilic PEO shell. The internalization pathways of P85 in mammalian cells were elucidated using endocytosis inhibitors and colocalization with endocytosis markers (clathrin-specific antibodies and transferrin for clathrin and caveolin-1-specific antibodies and cholera toxin B for caveolae). Altogether, our results indicate that P85 unimers internalize through caveolae-mediated endocytosis, while P85 micelles internalize through clathrin-mediated endocytosis. Furthermore, at concentrations above 0.01% P85 inhibits caveolae-mediated endocytosis (cholera toxin B), while having little or no effect on the clathrin-mediated endocytosis (transferrin). Selective interaction of Pluronic with caveolae may explain its striking pharmacological activities including inhibition of drug efflux transport, activation of gene expression, and dose-dependent hyperlipidemia.

INTRODUCTION

Amphiphilic triblock copolymers of poly(ethylene oxide)-*b*-poly(propylene oxide)-*b*-poly(ethylene oxide) (PEO-PPO-PEO), also known as Pluronic or poloxamers, have been evaluated extensively as carriers for delivery of drugs and diagnostic imaging agents (*1, 2*). In aqueous solutions above the critical micelle concentration (CMC), the PPO chains of these block copolymers spontaneously segregate into a hydrophobic core of a micelle with the PEO chains forming a hydrophilic shell (*1*). The diameters of Pluronic micelles usually vary from ca. 10 to 100 nm. The PPO core can incorporate considerable amounts (up to 20−30 wt %) of many water-insoluble drugs (*1*). The micelles can be targeted to a specific body compartment, such as brain, by conjugating with neurospecific antibodies or insulin as targeting moieties (*3*−*5*). In addition, below the CMC Pluronic exists in the form of "unimers", which, in case of relatively hydrophobic copolymers, can bind with cell membranes and transport into cells (*3, 6*−*9*). Such block copolymers were also shown to inhibit a drug efflux pump, P-glycoprotein, Pgp, expressed in the membranes of multidrug-resistant cells (*7, 10, 11*) and induce transcriptional activation of gene expression in cells through activation of certain cell signaling pathways (*12*−*14*). Finally, Pluronic block copolymers also can serve as synthetic polymer transduction domains and carry proteins as large as horseradish peroxidase (HRP) into cells and across the blood brain barrier (BBB) (*15*).

Pluronic unimers and micelles have been known to undergo internalization in cells (*7*), which can be abolished by metabolic inhibitors (*7, 9*). On this basis, a general endocytosis mechanism was suggested for cellular entry of Pluronic, although the specific pathways remained unknown. Endocytosis can be divided into two broad categories, phagocytosis (the uptake of large particles) and pinocytosis (the uptake of fluids and solutes) (*16*). Pinocytosis can be further classified on the basis of either the membrane interaction or the type of membrane structures involved in the initial stages of internalization. The first classification includes (i) fluid-phase endocytosis (e.g., HRP uptake); (ii) receptor-mediated endocytosis (e.g., transferrin (Tf) uptake *via* Tf receptor (TfR)); or (iii) adsorptive endocytosis (e.g., albumin or wheat germ agglutinin uptake) (*17*). The second classification includes (i) clathrin-mediated endocytosis and (ii) caveolae-mediated endocytosis (*16*).

Clathrin-mediated endocytosis involves polymerization of a cytosolic protein, clathrin, which binds to the cell plasma membrane and induces formation of a coated pit (*18*). After budding, the vesicle sheds its clathrin coat and then delivers its protein cargo to endosomes. The cargo can then be recycled or transported to lysosomes via late endosomes. Tf is commonly used as a marker for this pathway. Caveolae are cholesterol-rich "flask-shaped invaginations" in the plasma membrane formed due to the presence of a dimeric protein, caveolin (*19*). These vesicles travel to caveosomes, which prevents lysosomal degradation of the cargo. Cholera toxin B (CTB) or Simian Virus 40 (SV40) typically use the caveolae-mediated mechanism for cellular entry (*18, 20, 21*). Recent studies have also indicated the existence of clathrin- and caveolae-independent endocytosis, which still remains relatively poorly explored (*22*).

In this study, we hypothesize that Pluronic block copolymers can undergo endocytosis via a clathrin- or caveolae-mediated mechanism. We further posit that Pluronic can interfere with selected membrane trafficking mechanisms. The latter is based on the knowledge that Pluronic molecules (i) incorporate into membranes by inserting their hydrophobic PPO chains into lipid bilayers (*23, 24*), (ii) decrease membrane microviscosity (*7*), and (iii) inhibit selected membranes enzymes, such as Pgp ATPase, which may be associated with cholesterol-rich membrane microdomains (*25*). To test this hypothesis, we use

* Corresponding author. akabanov@unmc.edu, 402-559-9364 (Office), 402-559-9365 (Fax).

10.1021/bc8002315 CCC: $40.75 © 2008 American Chemical Society
Published on Web 08/27/2008

Pluronic P85 (P85) as a representative copolymer of the Pluronic series, which exhibits all of the above listed activities (*1, 3, 7, 26*). Our approach involves (1) evaluation of P85 internalization in the presence of chemical inhibitors of selected endocytosis pathways; (2) colocalization of P85 unimers (below CMC) and micelles (above CMC) with clathrin- and caveolin-specific antibodies and various endocytosis markers (Tf and CTB); and (3) evaluation of the effect of P85 on the internalization of the clathrin- and caveolae-mediated and fluid-phase endocytosis markers (Tf, CTB, and HRP). The MDCK cells are used as an *in vitro* model. Altogether, our results indicate that P85 unimers at concentrations below the CMC (0.03 wt %) internalize through caveolae-mediated endocytosis, while P85 micelles at higher concentrations internalize mainly through clathrin-mediated endocytosis. Furthermore, at high concentration above 0.1 wt %, P85 inhibits caveolae-mediated endocytosis, while having little or no effect on the clathrin-mediated endocytosis. For the first time, we demonstrate that binding of the amphiphilic block copolymer with the cells may be constrained to selected membrane domains. The results are significant for understanding the mechanisms of transport of the block copolymers into cells as well as for relating the block copolymer−membrane interactions to the biological activities of the block copolymers, which may be mediated by the specific membrane microdomains affected by these interactions.

MATERIALS AND METHODS

Materials. P85, EO_{26}-PO_{40}-EO_{26} (lot # WPAU-549B) was kindly provided by BASF Corp. Synthesis of FITC labeled Pluronic block copolymers was performed by Dr. Srikanth Sriadibhatala at the University of Nebraska Medical Center (UNMC) as previously reported (*9*). Alexa 594 labeled CTB (Alexa 594-CTB), unlabeled CTB antibody, and Alexa 647 labeled Tf (Alexa 647-Tf) were purchased from Invitrogen Inc. (Carlsbad, CA). FITC labeled CTB (FITC-CTB), methyl-β-cyclodextrin (MBCD), sucrose, sodium azide, cytochalasin D, and 2-deoxyglucose (2DG) were purchased from Sigma-Aldrich (St. Louis, MO). Bovine serum albumin (BSA) (Fischer Scientific, Waltham, MA) RITC-HRP was prepared by labeling HRP (2 mg/mL) Sigma-Aldrich (St. Louis, MO) in 0.1 M bicarbonate buffer with RITC. RITC-HRP was separated from the mixture using a Sephadex G-25 column Sigma-Aldrich (St. Louis, MO).

Cell Lines. Madin-Darby Canine Kidney **(**MDCK) cells were maintained in Dulbecco's Modified Eagle's Medium (DMEM), containing 10% heat inactivated fetal bovine serum (FBS) and penicillin/streptomycin as described elsewhere (*27*). All tissue material media was obtained from Gibco Life Technologies, Inc. (Grand Island, NY). MDCK cells were used after 48 h of plating.

FACS Analysis of FITC-P85 Uptake. MDCK cells (5×10^4 cell/well in 24 well plates) were exposed to 0.001% FITC-P85 alone or to 0.001% FITC-P85 mixed with different concentrations of unlabeled P85 for 1 h at 37 °C. Cells were then washed by phosphate-buffered saline (PBS), trypsinized, and resuspended in PBS. In select experiments, cells were pretreated for 30 min with inhibitors of endocytosis (5 mM MBCD, or 0.45 M sucrose, or 0.25 mM cytochalasin D), and then the same inhibitors were also present during subsequent incubation with the copolymer. The mean fluorescence intensity was analyzed using Becton Dickinson FACStarPlus flow cytometer operating under Lysis II (San Jose, CA) equipped with an argon ion laser. Data were acquired in linear mode and visualized in logarithmic mode. Data from 10 000 events were gated using forward and side scatter parameters to exclude debris and dead cells.

FACS Analysis. MDCK cells (5×10^4 cell/well in 24 well plates) were exposed to 5 μg/mL Alexa 647-Tf or 5 μg/mL FITC-CTB with/without P85 for 1 h at 37 °C. Cells were washed, trypsinized, resuspended, and analyzed by FACS as described above. In select experiments, cells were pretreated with inhibitors of endocytosis (5 mM MBCD, or 0.45 M sucrose, or 0.25 mM cytochalasin D), and then the same inhibitors were also present during incubation with the endocytosis markers. All experiments were conducted thrice and measurements were conducted in triplicate and data presented as means ± SEM. Statistical comparisons between groups were made using the Student's *t* test.

Confocal Analysis on Live Cells. Pulse-Chase experiments were conducted for FITC-P85 uptake using live cell confocal microscope (Carl Zeiss LSM 510 Meta, Peabody, MA). MDCK cells (1×10^6) were plated in Biotech dishes (Fischer Scientific, Waltham, MA) and after two days (37 °C, 5% CO_2) were exposed for 30 min to 0.001% FITC-P85 mixed with 0.01% unlabeled P85 followed by another 30 min exposure 0.01% unlabeled P85. In select experiments, 5 μg/mL Alexa 594-CTB for 30 min, cells were washed, followed by concurrent addition of unlabeled CTB antibody with the copolymer for 30 min. The exposures to the copolymer were carried out at either 4 or 37 °C. In other experiments, 5 μg/mL Alexa 647-Tf were added to cells for 30 min and concurrently incubated with unlabeled copolymer for additional 30 min. Cells were finally washed and kept in complete media for imaging using the confocal microscope. The live cell microscopy was also used to assess effects of P85 on uptake of RITC-HRP. In this case, cells were incubated with 0.01 mg/mL RITC-HRP with/without P85 for 60 min and then analyzed by confocal microscopy.

Immunocytochemistry on Fixed Cells. Cells were pretreated with DMEM without FBS for 30 min, and then treated with 0.001% FITC-P85 in the presence of 0.01% or 0.1% unlabeled P85 for 1 h, washed, and fixed with 4% paraformaldehyde. Rabbit anticaveolin-1-Cy3 antibody (Sigma Aldrich, St Louis, MO) (1:100) and mouse anticlathrin antibody (Affinity Bioreagents, Golden, CO) (1:10) were incubated in blocking buffer overnight at 4 °C. For detection of anticlathrin antibody, specific IgG antibody (1:100) conjugated to Alexa 568 (Invitrogen Inc., Carlsbad, CA.) was added to cells for 1 h at 37 °C. Cells were examined under confocal microscope.

HRP Assay. The enzymatic activity of HRP was assessed with *o*-phenylenediamine as described earlier (*15*). Briefly, cells were treated with HRP solution (0.1 mg/mL) with/without P85. In select experiments, before adding the copolymer the cells were preincubated with 25 mM 2DG and 5 mM sodium azide, which was then added also during the exposure to the copolymer. Cells were then lysed with 0.1% Triton X-100 (Sigma-Aldrich, St. Louis, MO) and the lysate was added to a 96-well plate with the solution of *o*-phenylenediamine (5 mg/mL) in 0.1 M citrate buffer (pH 5.0) containing 1 mg/mL BSA, 0.1% Triton X-100, and 0.02% hydrogen peroxide solution. After incubating the mixture for 5 min at 37 °C, the reaction was stopped by adding 0.5% sodium sulfite in 2 M sulfuric acid (Acros Organic, Waltham, MA), and absorbance was measured at 550 nm using the microplate reader Multiskan MCC/340. The amounts of HRP in the samples were determined using a standard calibration curve. All measurements were conducted in triplicate and data presented as means ± SEM. Statistical comparisons between groups were made using Student's *t* test.

RESULTS

Internalization Pathways of P85. The confocal analysis was indicative of the vesicular uptake of FITC-P85 at 37 °C (Figure 1A). The FACS analysis further demonstrated that the uptake of the block copolymer was temperature-dependent and was considerably inhibited at 4 °C compared to 37 °C (Figure 1B). On this basis, we posit that endocytosis is a prominent pathway for internalization of P85.

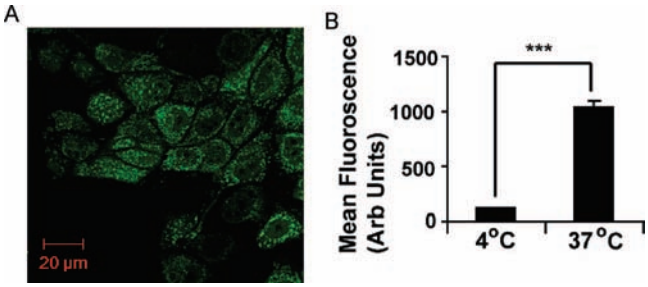

Figure 1. Uptake of FITC-P85 in MDCK cells: (A) confocal microscopy on live cells at 37 °C; (B) temperature dependence by FACS analysis. Cells were exposed to the copolymer at the corresponding temperatures for 60 min. The exposure solution contained 0.001% FITC-P85 mixed with 0.01% P85. (B) Data are means ± SEM (n = 3). Difference between 4 and 37 °C groups has a significance level of *** $p = 0.001$.

To further elucidate the specific internalization pathways of P85, we examined the effects of the endocytosis inhibitors on the uptake of this copolymer into the cells. This study used three different types of inhibitors: (1) MBCD, a cholesterol-depleting agent, for caveolae-mediated endocytosis (*28*), (2) hypertonic sucrose for clathrin-mediated endocytosis (*29, 30*), and (3) cytochalasin D, a potent inhibitor of actin polymerization, for both pathways as well as macropinocytosis (*31, 32*). To differentiate the transport of P85 unimers and micelles, the two concentrations of the copolymer were used. The first, 0.001 wt % FITC-P85, was below the CMC (~0.03% wt.) to examine the entry of the P85 unimers. The second, 0.001 wt % FITC-P85 (as a tracer) mixed with 0.1 wt % P85, was above the CMC, to characterize the entry of the micelles as well as unimers. At this high concentration, at least 70% of FITC-P85 was incorporated into the micelles, while the rest was in equilibrium in the unimer form (*33*). In each case, the FACS analysis was performed 1 h after exposure of the MDCK cells to the copolymer with or without the corresponding inhibitors. Since there is literature suggesting that various inhibitors may interfere with multiple endocytic pathways (*34*−*36*), we first demonstrated that MBCD inhibits CTB but not Tf uptake (i.e., is likely to be selective for caveolae) and sucrose inhibits Tf but not CTB uptake (i.e., is selective for clathrin) (data presented below in Figure 6).

As shown in Figure 2A, at the unimer concentration the FITC-P85 entry was blocked in the presence of MBCD but was not affected by the sucrose, suggesting that the unimers were entering cells via caveolae-mediated endocytosis. The situation was drastically changed at the higher P85 concentration (Figure 2B). In this case, the greatest inhibition of FITC-P85 entry was observed with sucrose, suggesting that the most prominent pathway for the micelle uptake was the clathrin-mediated endocytosis. Although MBCD had some effect on FITC-P85 uptake at this concentration, its effect was much less pronounced than that of the sucrose. It could be due to the presence of a smaller portion of FITC-P85 in the form of unimers, which were taken into cells by caveolae. Additionally, a minor portion of the micelles could be internalized through the caveolae-mediated pathway. Interestingly, cytochalasin D inhibited FITC-P85 uptake at both concentrations, although it was more pronounced at the unimer concentration.

To validate the conclusions of the inhibitor analysis, the cellular localization of FITC-P85 at different copolymer concentrations was examined by immunocytochemistry. In these studies following exposure to the copolymer for 60 min the cells were fixed and stained with antibodies against clathrin or caveolin-1 and examined by confocal microscope (Figure 3). Consistent with the inhibitor analysis, at the lowest concentration of the copolymer (0.001%) there was a significant colocalization of the unimers with caveolin-1, which considerably diminished as the concentration of the copolymer increased. In contrast, colocalization with clathrin was minimal if any at low concentration of the copolymer, but it greatly increased as the copolymer concentration increased. To further corroborate this result, we performed live cell microscopy on MDCK cells incubated with low concentration of labeled copolymer and either Alexa 594-CTB or Alexa 647-Tf. As shown in Figure 4, there was strong colocalization of the FITC-P85 and CTB. When the cells were exposed to the copolymer and CTB at 4 °C, the localization of both labels appeared to be mainly constrained to the plasma membrane areas. In contrast, at 37 °C the internalization and the colocalization of the labels were clearly evident. This suggests that FITC-P85 and Alexa 594-CTB are transported into cells through the same pathways. Conversely, there was little if any colocalization of FITC-P85 and Alexa 647-Tf (data not shown).

Effect of P85 on Endocytosis. To elucidate possible effects of P85 on different vesicular transport processes, we used HRP, CTB, and Tf as the markers of fluid-phase, caveolae-mediated, and clathrin-mediated endocytosis, respectively. The MDCK cells were exposed to the corresponding markers with/without P85 at different concentrations. As seen in Figure 5A, the uptake of HRP was practically unchanged at 0.001% P85, significantly decreased at 0.01% and 0.1% P85 and practically abolished at 1% P85. In the latter case, the inhibitory effect of the copolymer was practically the same as the effect of the metabolic inhibitor, 25 mM 2DG and 5 mM sodium azide. The inhibition of internalization of RITC-HRP by high concentrations of P85 was also evident in the live cell confocal microscopy experiment (Figure 5B). Altogether, these experiments demonstrate that at higher concentrations P85 inhibits nonspecific fluid-phase endocytosis of HRP.

In a separate experiment, the effects of various concentrations of P85 on the uptake of FITC-CTB and Alexa 647-Tf were evaluated using FACS analysis. At low concentrations, 0.0001% and 0.001%, the copolymer had no effect on the FITC-CTB uptake (Figure 6A). However, significant inhibition of the uptake of this marker was observed already at 0.1% P85, while at 1% and 5% P85, the uptake was completely abolished. Notably, the cytotoxicity analysis using MTT (3-(4,5-dimethylthiazol-2-yl)-2,5-diphenyltetrazolium bromide) assay (*14*) as well as FACS analysis of the cells showed that 60 min exposure of the MDCK cells to these concentrations of P85 did not produce cytotoxicity (data not shown). Therefore, the plausible explanation of the data is that at higher concentrations P85 inhibits FITC-CTB uptake via caveolae-mediated endocytosis. This was reinforced by the effects of the endocytosis inhibitors on the FITC-CTB uptake, suggesting that cholesterol depletion by MBCD practically abolished the internalization of this marker (Figure 6A). At the same time, inhibition of clathrin-mediated endocytosis by hypertonic sucrose had no effect of the FITC-CTB uptake. Finally, using Alexa 647-Tf as a clathrin-mediated endocytosis marker we demonstrated that P85 at any concentration did not inhibit this endocytosis pathway (Figure 6B). Notably, this may explain the lack of overall toxicity of the copolymer under the conditions studied. The Alexa 647-Tf was inhibited by the hypertonic sucrose but not by the MBCD.

DISCUSSION

Nanoscale-size drug delivery systems based on synthetic polymers have attracted significant attention in pharmaceutics and medicine (*37*−*39*). An important and promising example of such systems is Pluronic block copolymers, which have been evaluated as drug and gene delivery agents in numerous studies (*3, 4, 26, 40*−*42*). A characteristic of Pluronic molecules is the ability to self-assemble into micelles in aqueous solutions

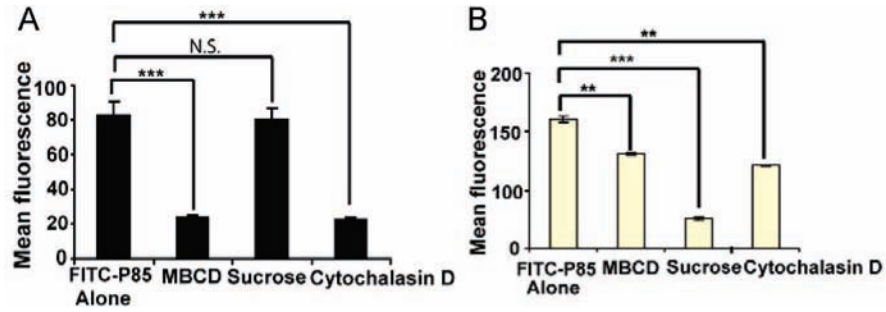

Figure 2. Effect of endocytosis inhibitors on the uptake of FITC-P85 in MDCK cells: (A) 0.001% FITC-P85 and (B) 0.001% FITC-P85 mixed with 0.1% P85. Cells were exposed to the copolymer that corresponding temperatures for 60 min at 37 °C. (A,B) Data are mean ± SEM ($n = 3$). Statistical comparisons between the control group (no inhibitor) and the corresponding inhibitor group are shown as follows: n.s. - not significant, ** $p = 0.01$ *** $p = 0.001$.

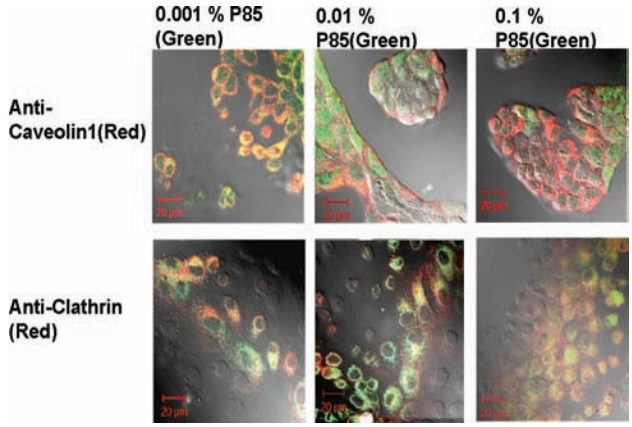

Figure 3. Colocalization of FITC-P85 with caveolin-1 and clathrin in fixed MDCK cells. Live cells were exposed for 60 min at 37 °C to 0.001% FITC-P85 alone, 0.001% FITC-P85 mixed with 0.01% P85, or 0.001% FITC-P85 mixed with 0.1% P85.

(*40*). The noncovalent incorporation of drugs into the hydrophobic PPO core of the Pluronic micelle increases (1) drug solubility, (2) drug metabolic stability, and (3) drug circulation time in the body. Furthermore, Pluronic unimers can also act as biological response modifiers: they can (1) bind with the cell membranes, (2) alter membrane microviscosity, and (3) inhibit selected membrane proteins, notably Pgp (*1, 7, 43*). This results in increased delivery of Pgp-dependent drugs in MDR tumors, as well as transport of such drugs across the BBB and intestinal epithelium, which are known to overexpress Pgp (*3, 7, 9, 10, 44*). Most recently, Pluronic block copolymers were shown to increase gene expression in stably and transiently transfected cells by activating pro-inflammatory (NFκB) cell signaling (*12, 14*) and to enhance drug-induced apoptosis in MDR cells (*45*). These multiple effects may result from interaction of block copolymers with the cellular membranes. Furthermore, the profound inhibition of Pgp in MDR cells (*10*) and, possibly, enhanced pro-apoptotic signaling in MDR cells (paper in preparation) appear to be related to the ability of Pluronic to transport inside the cells and interact with the mitochondrial membranes. Therefore, understanding of interaction of Pluronic block copolymer with cell membranes and the transport of these copolymers inside the cells is critically important for understanding their diverse biological response modifying activities. Furthermore, since Pluronic can exist in the form of (1) single chains (unimers), which exhibit the biological responses in cells, and (2) micelles, which can carry solubilized drugs inside the cells, it is essential to examine trafficking of these different aggregate forms of the copolymer. This study addresses such a need by evaluating the early stages of entry of Pluronic into cells.

Given a relative simplicity of the Pluronic block copolymer structure and apparent lack of sites for binding with specific cellular trafficking molecules, one could expect that the membrane interaction and cellular entry of this copolymer is quite unspecific. Surprisingly, to the contrary we demonstrate that Pluronic unimers appear to colocalize with markers of caveolae and enter cells rather selectively via caveolae-mediated endocytosis. Caveolae are subsets of specific cellular domains, often known as "lipid rafts", with which both the CTB and caveolin-1 are associated (*46*). Although this result appears to be paradoxical at first glance, its origin may be characteristic of interactions and self-assembly in polymeric systems. Such systems are known to exhibit highly cooperative behavior. For example, polyelectrolytes interacting with oppositely charged macromolecular species (other polyions, particles, etc.) can precisely "recognize" and "select" among different types of such species in the mixture (*47*). A recent example of this phenomenon is DNA topology recognition by synthetic polycations (*48*). This selectivity rises from small differences in the binding energy between polymers counted on a per-unit base, which is amplified on a scale of the entire polymer molecule. It is, therefore, possible that PPO blocks in Pluronic molecules may similarly recognize the cholesterol-rich microdomains in the cell membranes. To the best of our knowledge, this study is the first demonstration that amphiphilic block copolymers can interact selectively with membrane domains. One necessary factor for molecular recognition in polymeric systems is the reversibility of the binding and/or possibility of exchange between the bound polymeric species, so that the polymer can find the optimal partner by multiple trials (*13*). Such reversibility of binding with cellular membranes was previously shown for Pluronic molecules (*7*).

As the copolymer concentration in the media increases, the copolymer unimers self-assemble into polymeric micelles. In particular, P85 micelles are spherical core−shell structures of approximately 14.6 nm in diameter (*33*). They are composed of approximately 60 P85 molecules and have a PPO core of 5.4 nm in diameter surrounded by 3.7 nm PEO shell. The exterior surface of such micelles is hydrophilic and is unlikely to bind with the lipid portions of the cell membranes. For example, the lack of PEO interactions with lipid domains in cell membranes was apparent in studies using hydrophobic fluorescent probes embedded in the membranes (*9*). However, the same study also suggested that copolymers with high PEO content may adhere to the cellular surface and limit the lateral mobility of membrane lipids. It is not surprising, therefore, that micelles have different pathways of cellular uptake compared to unimers. Indeed, it was previously shown that drug solubilized in the micelles is transported into cells through a vesicular pathway rather than through trans-membrane diffusion (*49*). Furthermore, micelles can be conjugated with ligands, such as

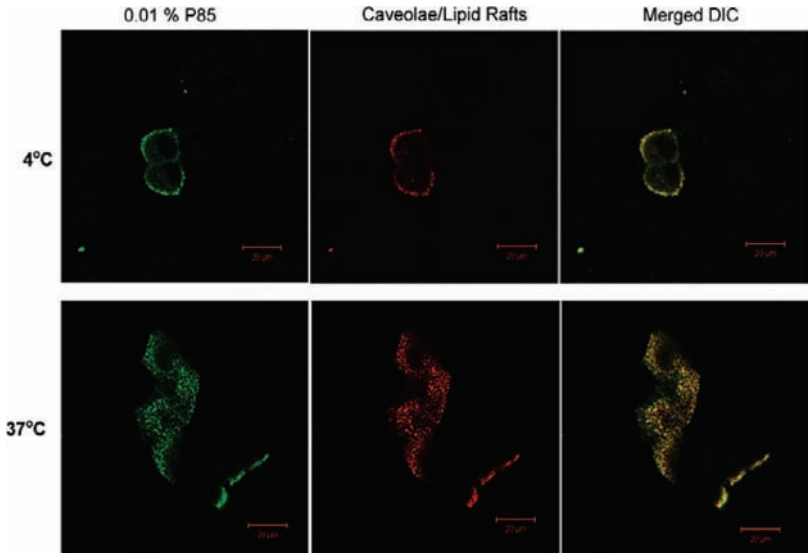

Figure 4. Colocalization of FITC-P85 and Alexa 594-CTB in live MDCK cells at 4 and 37 °C. Cells were exposed for 30 min. to 0.001% FITC-P85 mixed with 0.01% unlabeled P85 followed by another 30 min exposure 0.01% unlabeled P85 (see Materials and Methods). Some intracellular localization of the labels at 4 °C may be due to the increase of the temperature to r.t., during fluorescence observation, which could initiate endocytosis in live cells.

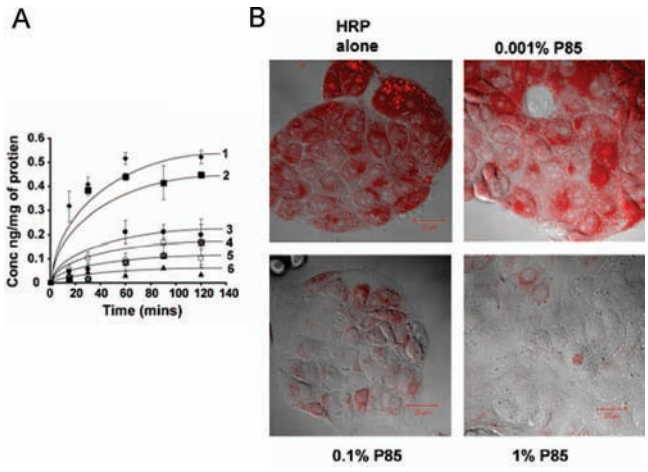

Figure 5. Effect of P85 (conc. reported as wt %) on uptake of HRP in MDCK cells: (A) cellular levels of HRP as determined by enzymatic activity in cell lyzates, cells were treated in the absence or presence of P85 and are grouped as 1, HRP alone; 2, 0.001 wt % P85; 3, 0.01% P85; 4, 0.1% P85; 5, 1% P85; 6, 2DG and sodium azide; (B) live cell confocal microscopy using RITC-HRP. (A) Data are mean ± SEM (n = 3).

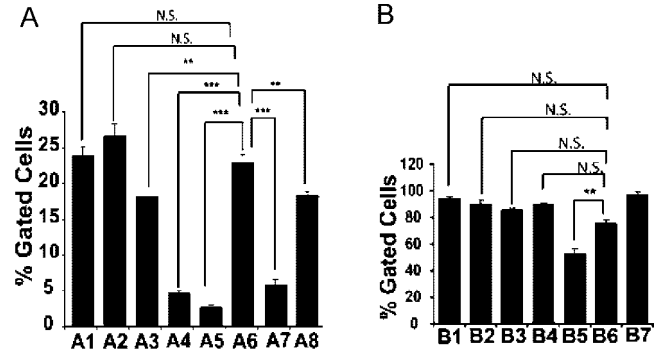

Figure 6. Effect of P85 (conc. reported as wt %) and various endocytosis inhibitors on the uptake of (A) FITC-CTB and (B) Alexa 647-Tf in MDCK cells. The experiments were grouped for (A) as A1 = 0.0001% P85, A2 = 0.001% P85, A3 = 0.1% P85, A4 = 1% P85, A5 = 5% P85, A6 = FITC-CTB, A7 = MBCD, and A8 = sucrose; and (B) as B1 = 0.0001% P85, B2 = 0.1% P85, B3 = 1% P85, B4 = 5% P85, B5 = sucrose, B6 = Alexa 647-Tf, and B7 = MBCD. (A, B) Data are mean ± SEM (n = 3). Statistical comparisons between the control group (no inhibitor) and the corresponding inhibitor group are shown as follows: n.s. - not significant, ** p = 0.05, *** p = 0.001.

insulin, and thus directed into cells via receptor-mediated endocytosis (*40, 50*). In this study, however, for the first time we can suggest with high likelihood that P85 micelles enter into cells via clathrin-mediated endocytosis.

The reasons for the apparent selectivity of the micelles with respect to the clathrin-mediated pathway as opposed to the caveolae-mediated pathway may lie in the ability of the block copolymer at relatively high concentration to inhibit caveolae-mediated endocytosis, which was also demonstrated here for the first time. The inhibition of the uptake of the fluid-phase endocytosis marker, HRP, and caveolae-mediated endocytosis marker, CTB, was already observed at 0.01% P85, which is below the CMC. (Although the mechanism of the fluid-phase endocytosis is still unclear, it was shown to be non-clathrin-mediated (*51*), and could be mediated through caveolae (manuscript in preparation)). Altogether, this indicates that the Pluronic unimers can somehow perturb the caveolae structure, with which they bind, possibly, by changing membrane micro-viscosity (*7*) or membrane curvature due to incorporation of bulky hydrophobic PPO chains in the membranes. Notably, the inhibition of caveolae cannot be linked to depletion of cellular ATP because at these concentrations no ATP depletion in MDCK cells is observed (*44*). (It is unlikely that P85 interacts directly with endocytic markers (HRP, CTB, and Tf) since, first, P85 copolymer has neutral charge and, second, all markers are hydrophilic in nature.) At higher concentrations of the copolymer, above the CMC, the unimers coexist with the micelles, and thus can inhibit the micelle transport through the caveolae pathway. Furthermore, as the concentration of P85 increases above the CMC even more copolymer can bind with membranes and further contribute to the disruption of caveolae. Under these conditions, the entry of the copolymer micelles can still proceed through the clathrin-mediated pathway, which is not inhibited. In addition, although there is no direct evidence of a specific receptor for micelles at clathrin microdomains one cannot exclude such a possibility. Moreover, nonspecific interaction of the micelle PEO corona with these domains is also possible.

As already mentioned, despite of the fact that PEO is often considered inert some surface interactions with cell membranes have been suggested (*9*). This may include one or a combination of hydrophobic and hydrogen binding interactions, for example, with membrane proteins. Interestingly, several studies suggest that either PEO alone or PEO-covered nanoparticles may induce complement activation (*52*). The structural similarity between the terminal region of the PEO chain and carbohydrates has also been noted, which may result in PEO binding with lectins (*53*) as well as carbohydrate receptors, which are endocytosed through a clathrin-mediated route (*54*).

Finally, selective interactions of P85 unimers via PPO blocks with caveolae may be also related to the copolymer's functional activities in cells. The ability of Pluronic to decrease microviscosity of some rigid membrane structures (membrane fluidization) was previously shown (*7*). It is possible that these structures are the same as or similar to the cholesterol-rich lipid rafts/caveolae. Furthermore, there are indications in literature that Pgp, also affected by Pluronic block copolymer, can colocalize with the lipid rafts/caveolae (*55*). Thus, the effects of Pluronic block copolymers on Pgp and caveolae-mediated endocytosis may be related to each other. We plan to determine this in our subsequent studies. In addition, one needs to take into account that caveolae regulate cellular signaling of cholesterol, as well as activity of various ion channels. It is known that one side effect of overexposure to Pluronic block copolymers is dose-dependent hyperlipidemia, in particular, a rise in the cholesterol and triglyceride levels in the plasma (*56*). This can be due to impairment of cholesterol trafficking and metabolism resulting from inhibition of the caveolae-mediated endocytosis. Notably, caveolae are known to cluster multiple receptors, such as EGF, CCK, Endothelin, Tyrosine Kinases, and so forth, which enable signal integration and amplification (*13*, *57*). They also host signal transducers, for example, PKC, MAPK, eNOS, and calmodulin, transporters (e.g., IP3 receptor and Porin) as well as structural molecules (e.g., actin and myosin). Therefore, detailed characterization of interactions of Pluronic block copolymers with cell membranes is likely to provide a foundation for future understanding of the diverse biological response modifying activities of these copolymers, including alteration of cell signaling, activation of transcription, and other processes.

ACKNOWLEDGMENT

This study was supported by National Institutes of Health grants RO1 NS36229, 2RO1 CA89225, and RO1 NS051334 awarded to A.V.K. We thank Dr. Srikanth Sriadibhatala for assistance in synthesizing FITC labeled P85. We would also like to thank the flow cytometery and confocal microscopy core facilities at UNMC. AVK is a cofounder, shareholder and chair of scientific advisory board of Supratek Pharma Inc. (Montreal, Canada), which developed Pluronic-based SP1049C and SP1017 formulations for chemotherapy and gene delivery, respectively.

LITERATURE CITED

(1) Kabanov, A. V., and Alakhov, V. Y. (2002) Pluronic block copolymers in drug delivery: from micellar nanocontainers to biological response modifiers. *Crit. Rev. Ther. Drug Carrier Syst. 19*, 1–72.

(2) Kabanov, A. V., Batrakova, E. V., and Alakhov, V. Y. (2002) Pluronic block copolymers as novel polymer therapeutics for drug and gene delivery. *J. Controlled Release 82*, 189–212.

(3) Batrakova, E. V., Li, S., Miller, D. W., and Kabanov, A. V. (1999) Pluronic P85 increases permeability of a broad spectrum of drugs in polarized BBMEC and Caco-2 cell monolayers. *Pharm. Res. 16*, 1366–72.

(4) Kabanov, A. V., Slepnev, V. I., Kuznetsova, L. E., Batrakova, E. V., Alakhov, V., Melik-Nubarov, N. S., Sveshnikov, P. G., and Kabanov, V. A. (1992) Pluronic micelles as a tool for low-molecular compound vector delivery into a cell: effect of Staphylococcus aureus enterotoxin B on cell loading with micelle incorporated fluorescent dye. *Biochem. Int. 26*, 1035–42.

(5) Chekhonin, V. P., Kabanov, A. V., Zhirkov, Y. A., and Morozov, G. V. (1991) Fatty acid acylated Fab-fragments of antibodies to neurospecific proteins as carriers for neuroleptic targeted delivery in brain. *FEBS Lett. 287*, 149–52.

(6) Alakhov, V., Klinski, E., Lemieux, P., Pietrzynski, G., and Kabanov, A. (2001) Block copolymeric biotransport carriers as versatile vehicles for drug delivery. *Expert Opin. Biol. Ther. 1*, 583–602.

(7) Batrakova, E. V., Li, S., Vinogradov, S. V., Alakhov, V. Y., Miller, D. W., and Kabanov, A. V. (2001) Mechanism of pluronic effect on P-glycoprotein efflux system in blood-brain barrier: contributions of energy depletion and membrane fluidization. *J. Pharmacol. Exp. Ther. 299*, 483–93.

(8) Kabanov, A. V., Lemieux, P., Vinogradov, S., and Alakhov, V. (2002) Pluronic block copolymers: novel functional molecules for gene therapy. *Adv. Drug Delivery Rev. 54*, 223–33.

(9) Batrakova, E. V., Li, S., Alakhov, V. Y., Miller, D. W., and Kabanov, A. V. (2003) Optimal structure requirements for pluronic block copolymers in modifying P-glycoprotein drug efflux transporter activity in bovine brain microvessel endothelial cells. *J. Pharmacol. Exp. Ther. 304*, 845–54.

(10) Batrakova, E. V., Li, S., Elmquist, W. F., Miller, D. W., Alakhov, V. Y., and Kabanov, A. V. (2001) Mechanism of sensitization of MDR cancer cells by Pluronic block copolymers: Selective energy depletion. *Br. J. Cancer 85*, 1987–97.

(11) Batrakova, E. V., Li, S., Li, Y., Alakhov, V. Y., and Kabanov, A. V. (2004) Effect of pluronic P85 on ATPase activity of drug efflux transporters. *Pharm. Res. 21*, 2226–33.

(12) Yang, Z., Zhu, J., Sriadibhatla, S., Gebhart, C., Alakhov, V., and Kabanov, A. (2005) Promoter- and strain-selective enhancement of gene expression in a mouse skeletal muscle by a polymer excipient Pluronic P85. *J. Controlled Release 108*, 496–512.

(13) Kabanov, A. V. (2006) Polymer genomics: an insight into pharmacology and toxicology of nanomedicines. *Adv. Drug Delivery Rev. 58*, 1597–621.

(14) Sriadibhatla, S., Yang, Z., Gebhart, C., Alakhov, V. Y., and Kabanov, A. (2006) Transcriptional activation of gene expression by pluronic block copolymers in stably and transiently transfected cells. *Mol. Ther. 13*, 804–13.

(15) Batrakova, E. V., Vinogradov, S. V., Robinson, S. M., Niehoff, M. L., Banks, W. A., and Kabanov, A. V. (2005) Polypeptide point modifications with fatty acid and amphiphilic block copolymers for enhanced brain delivery. *Bioconjugate Chem. 16*, 793–802.

(16) Conner, S. D., and Schmid, S. L. (2003) Regulated portals of entry into the cell. *Nature 422*, 37–44.

(17) Abbott, N. J., Ronnback, L., and Hansson, E. (2006) Astrocyte-endothelial interactions at the blood-brain barrier. *Nat. Rev. Neurosci. 7*, 41–53.

(18) Carver, L. A., and Schnitzer, J. E. (2003) Caveolae: mining little caves for new cancer targets. *Nat. Rev. Cancer 3*, 571–81.

(19) Rothberg, K. G., Heuser, J. E., Donzell, W. C., Ying, Y.-S., Glenney, J. R., and Anderson, R. G. W. (1992) Caveolin, a protein component of caveolae membrane coats. *Cell 68*, 673–682.

(20) Nichols, B. (2003) Caveosomes and endocytosis of lipid rafts. *J. Cell Sci. 116*, 4707–4714.

(21) Nabi, I. R., and Le, P. U. (2003) Caveolae/raft-dependent endocytosis. *J. Cell Biol. 161*, 673–677.

(22) Mayor, S., and Pagano, R. E. (2007) Pathways of clathrin-independent endocytosis. *Nat. Rev. Mol. Cell Biol. 8*, 603–612.

(23) Kabanov, A. V., Levashov, A. V., and Alakhov, V. (1989) Lipid modification of proteins and their membrane transport. *Protein Eng. 3*, 39–42.

(24) Kabanov, A. V., Levashov, A. V., Alakhov, V., Martinek, K., and Severin, E. S. (1990) Fatty acylation of proteins for translocation across cell membranes. *Biomed. Sci. 1*, 33–6.
(25) Barakat, S., Demeule, M., Pilorget, A., Regina, A., Gingras, D., Baggetto, L. G., and Beliveau, R. (2007) Modulation of p-glycoprotein function by caveolin-1 phosphorylation. *J. Neurochem. 101*, 1–8.
(26) Batrakova, E. V., Miller, D. W., Li, S., Alakhov, V. Y., Kabanov, A. V., and Elmquist, W. F. (2001) Pluronic P85 enhances the delivery of digoxin to the brain: in vitro and in vivo studies. *J. Pharmacol. Exp. Ther. 296*, 551–7.
(27) Herzlinger, D. A., Easton, T. G., and Ojakian, G. K. (1982) The MDCK epithelial cell line expresses a cell surface antigen of the kidney distal tubule. *J. Cell Biol. 93*, 269–277.
(28) Hailstones, D., Sleer, L. S., Parton, R. G., and Stanley, K. K. (1998) Regulation of caveolin and caveolae by cholesterol in MDCK cells. *J. Lipid Res. 39*, 369–379.
(29) Self, T. J., Oakley, S. M., and Hill, S. J. (2005) Clathrin-independent internalization of the human histamine H1-receptor in CHO-K1 cells. *Br. J. Pharmacol. 146*, 612–624.
(30) Heuser, J. E., and Anderson, R. G. (1989) Hypertonic media inhibit receptor-mediated endocytosis by blocking clathrin-coated pit formation. *J. Cell Biol. 108*, 389–400.
(31) Nakase, I., Niwa, M., Takeuchi, T., Sonomura, K., Kawabata, N., Koike, Y., Takehashi, M., Tanaka, S., Ueda, K., Simpson, J. C., Jones, A. T., Sugiura, Y., and Futaki, S. (2004) Cellular uptake of arginine-rich peptides: roles for macropinocytosis and actin rearrangement. *Mol. Ther. 10*, 1011–1022.
(32) Jones, A. T. (2007) Macropinocytosis: searching for an endocytic identity and role in the uptake of cell penetrating peptides. *J. Cell. Mol. Med. 11*, 670–684.
(33) Kabanov, A. V., Nazarova, I. R., Astafieva, I. V., Batrakova, E. V., Alakhov, V. Y., Yaroslavov, A. A., and Kabanov, V. A. (1995) Micelle formation and solubilization of fluorescent probes in poly(oxyethylene-*b*-oxypropylene-*b*-oxyethylene) solutions. *Macromolecules* 2303–2314.
(34) Ivanov, A. I. (2008) Pharmacological inhibition of endocytic pathways: Is it specific enough to be useful? *Methods Mol. Biol. 440*, 15−33.
(35) Rodal, S. K., Skretting, G., Garred, O., Vilhardt, F., van Deurs, B., and Sandvig, K. (1999) Extraction of cholesterol with methyl-beta-cyclodextrin perturbs formation of clathrin-coated endocytic vesicles. *Mol. Biol. Cell 10*, 961–74.
(36) Subtil, A., Gaidarov, I., Kobylarz, K., Lampson, M. A., Keen, J. H., and McGraw, T. E. (1999) Acute cholesterol depletion inhibits clathrin-coated pit budding. *Proc. Natl. Acad. Sci. U.S.A. 96*, 6775–80.
(37) Duncan, R. (2006) Polymer conjugates as anticancer nanomedicines. *Nat. Rev. Cancer 6*, 688–701.
(38) Torchilin, V. P. (2000) Polymeric contrast agents for medical imaging. *Curr. Pharm. Biotechnol. 1*, 183–215.
(39) Kopecek, J. (2002) Polymer chemistry: swell gels. *Nature 417*, 388−9–391.
(40) Batrakova, E. V., Han, H. Y., Miller, D. W., and Kabanov, A. V. (1998) Effects of pluronic P85 unimers and micelles on drug permeability in polarized BBMEC and Caco-2 cells. *Pharm. Res. 15*, 1525–32.
(41) Lemieux, P., Guerin, N., Paradis, G., Proulx, R., Chistyakova, L., Kabanov, A., and Alakhov, V. (2000) A combination of poloxamers increases gene expression of plasmid DNA in skeletal muscle. *Gene Ther. 7*, 986–91.
(42) Oh, K. T., Bronich, T. K., and Kabanov, A. V. (2004) Micellar formulations for drug delivery based on mixtures of hydrophobic and hydrophilic Pluronic block copolymers. *J. Controlled Release 94*, 411–22.
(43) Kabanov, A. V., Batrakova, E. V., and Miller, D. W. (2003) Pluronic block copolymers as modulators of drug efflux transporter activity in the blood-brain barrier. *Adv. Drug Delivery Rev. 55*, 151–64.
(44) Batrakova, E. V., Li, S., Alakhov, V. Y., Elmquist, W. F., Miller, D. W., and Kabanov, A. V. (2003) Sensitization of cells overexpressing multidrug-resistant proteins by pluronic P85. *Pharm. Res. 20*, 1581–90.
(45) Minko, T., Batrakova, E. V., Li, S., Li, Y., Pakunlu, R. I., Alakhov, V. Y., and Kabanov, A. V. (2005) Pluronic block copolymers alter apoptotic signal transduction of doxorubicin in drug-resistant cancer cells. *J. Controlled Release 105*, 269–78.
(46) Simons, K., and Toomre, D. (2000) Lipid rafts and signal transduction. *Nat. Rev. Mol. Cell Biol 1*, 31–39.
(47) Kabanov, A. V., and Kabanov, V. A. (1998) Interpolyelectrolyte and block ionomer complexes for gene delivery: physicochemical aspects. *Adv. Drug Delivery Rev. 30*, 49–60.
(48) Bronich, T. K., Nguyen, H. K., Eisenberg, A., and Kabanov, A. V. (2000) Recognition of DNA topology in reactions between plasmid DNA and cationic copolymers. *J. Am. Chem. Soc. 122*, 8339–8343.
(49) Miller, D. W., Batrakova, E. V., Waltner, T. O., Alakhov, V., and Kabanov, A. V. (1997) Interactions of pluronic block copolymers with brain microvessel endothelial cells: evidence of two potential pathways for drug absorption. *Bioconjugate Chem. 8*, 649–57.
(50) Batrakova, E. V., Han, H. Y., Alakhov, V., Miller, D. W., and Kabanov, A. V. (1998) Effects of pluronic block copolymers on drug absorption in Caco-2 cell monolayers. *Pharm. Res. 15*, 850–5.
(51) Damke, H., Baba, T., Warnock, D. E., and Schmid, S. L. (1994) Induction of mutant dynamin specifically blocks endocytic coated vesicle formation. *J. Cell Biol. 127*, 915–934.
(52) Reddy, S. T., van der Vlies, A. J., Simeoni, E., Angeli, V., Randolph, G. J., O'Neil, C. P., Lee, L. K., Swartz, M. A., and Hubbell, J. A. (2007) Exploiting lymphatic transport and complement activation in nanoparticle vaccines. *Nat. Biotechnol. 25*, 1159–1164.
(53) Moghimi, S. M., Hunter, A. C., Dadswell, C. M., Savay, S., Alving, C. R., and Szebeni, J. (2004) Causative factors behind poloxamer 188 (Pluronic F68, Flocor(TM))-induced complement activation in human sera: A protective role against poloxamer-mediated complement activation by elevated serum lipoprotein levels. *Biochim. Biophys. Acta 1689*, 103–113.
(54) Klink, D., Yu, Q.-C., Glick, M. C., and Scanlin, T. (2003) Lactosylated poly-L-lysine targets a potential lactose receptor in cystic fibrosis and non-cystic fibrosis airway epithelial cells. *Mol Ther 7*, 73–80.
(55) Jodoin, J., Demeule, M., Fenart, L., Cecchelli, R. o., Farmer, S., Linton, K. J., Higgins, C. F., and Béliveau, R, R. (2003) P-glycoprotein in blood brain barrier endothelial cells: interaction and oligomerization with caveolins. *J. Neurochem. 87*, 1010.
(56) Palmer, W. K., Emeson, E. E., and Johnston, T. P. (1998) Poloxamer 407-induced atherogenesis in the C57BL/6 mouse. *Atherosclerosis 136*, 115–123.
(57) Anderson, R. G. W. (1998) The caveolae membrane system. *Annu. Rev. Biochem. 67*, 199–225.

BC8002315

Selectins Ligand Decorated Drug Carriers for Activated Endothelial Cell Targeting

Xavier Banquy,[†] Grégoire Leclair,[†,‡] Jean-Michel Rabanel,[†] Anteneh Argaw,[§] Jean-François Bouchard,[§,||] Patrice Hildgen,*[,†,||] and Suzanne Giasson*[,†,||,⊥]

Faculté de Pharmacie, Ecole d'Optométrie, and Département de Chimie, Université de Montréal, and Groupe de Recherche Universitaire sur le Médicament de l'Université de Montréal, C.P. 6128, succursale Centre-Ville, Montréal, Québec, H3C 3J7, Canada, and Merck-Frosst Canada, Kirkland, Québec, Canada. Received June 25, 2008; Revised Manuscript Received August 14, 2008

New active particulate polymeric vectors based on branched polyester copolymers of hydroxy-acid and allyl glycidyl ether were developed to target drugs to the inflammatory endothelial cell surface. The hydroxyl and carboxyl derivatives of these polymers allow grafting of ligand molecules on the polyester backbones at different densities. A known potent nonselective selectin ligand was selected and synthesized using a new scheme. This synthesis allowed the grafting of the ligand to the polyester polymers, preserving its binding activity as assessed by docking simulations. Selectin expression on human umbilical cord vascular endothelial cells (HUVEC) was induced with the pro-inflammatory bacterial lipopolysaccharide (LPS) or with the nonselective inhibitor of nitric oxide synthase L-NAME. Strong adhesion of the ligand decorated nanoparticles was evidenced *in vitro* on activated HUVEC. Binding of nanoparticles bearing ligand molecules could be efficiently inhibited by prior incubation of cells with free ligand, demonstrating that adhesion of the nanoparticles is mediated by specific interaction between the ligand and the selectin receptors. These nanoparticles could be used for specific drug delivery to the activated vascular endothelium, suggesting their application in the treatment of diseases with an inflammatory component such as rheumatoid arthritis and cancer.

INTRODUCTION

Inflammation is a naturally occurring defense mechanism upon exposure to specific antigens, chemicals, infections, and physical stress. It is characterized by different events taking place at or near the injured area, including vascular endothelium cell (VEC) activation and leukocyte accumulation. VEC, upon activation by pro-inflammatory cytokines, increases the expression of cell adhesion molecules (CAMs) in a highly regulated and sequential process. This sequence involves expression of P-selectin followed by E-selectin, which promote rolling and tethering of leukocytes along the vessel wall (*1*). Exaggerated and/or prolonged inflammatory response is associated with a large number of acute and chronic disorders, including organ ischemia/reperfusion injury, allergic asthma, rheumatoid arthritis, inflammatory bowel disease, and atherosclerosis.

The selectin family has three members, namely, L-, E-, and P-Selectin. Their expression is restricted to circulating leukocytes (L-selectin) and VEC (P- and E-selectins). Upon inflammatory stimulation, P-selectin (CD62P) appears rapidly at the cell surface, owing to its intracellular storage in Weibel-Palade bodies. On the other hand, maximum levels of E-selectin (CD62E) are reached in 4−6 h after activation, due to *de novo* synthesis (*2*). Since E-selectin is expressed in both acute and chronic inflammation, it has been considered as a good candidate for drug targeting. In addition, the cytokines IL-1β and TNFα, as well as bacterial lipopolysaccharide (LPS), have been shown to stimulate the expression of E-selectin (*3*). Moreover, E-selectin is reported to exhibit a highly localized expression in neovasculature (*4*) and prostate cancer (*5*). The natural ligands of E- and P-selectin are either fucosylated glycoproteins (ESL-1, for E-selectin ligand) or sialomucin glycoproteins (PSGL-1 for P-selectin glycoprotein-1) presenting sialylated carbohydrate moieties (sialyl-Lewis x, sLe^x) epitopes. These selectin ligands are known to be present on circulating leukocytes plasmatic membrane (*6*, *7*). Synthetic analogues of the natural ligands have been investigated for their ability to block inflammation (*6*, *8*, *9*). Some of these analogues have been reported to have higher affinity to the target compared to the natural ligand, rendering them very attractive molecules for active drug targeting developments.

Among promising new therapeutic approaches, targeted drug carriers have received increasing interest during the past few decades (*10*). These carriers aim to release the drug close to the pathologic site, protecting the active substance from fast degradation and elimination leading to dose reduction and avoiding side effects. Several approaches such as drug immunoconjugation, bioconjugation, liposomes, dendrimers, micelles, or coated nanoparticles (NPs) have been proposed to achieve active or passive targeting of drug. However, compared to other delivery systems, polymeric NP drug carriers offer the possibility of encapsulating several types of molecules and protecting them from enzymatic degradation. The polymers forming the NP carriers are generally highly stable in physiological media and allow controlled release by matrix degradation.

A general approach to confer targeting capabilities to NPs is to functionalize their surface with a specific ligand. This approach is strongly limited by the stability of the link between the ligand and the NP surface. If this link is not stable enough in physiological media, release of the ligand (by hydrolysis, for example) from the NP surface could be rapid. To circumvent

* To whom correspondence should be addressed: patrice.hildgen@umontreal.ca; suzanne.giasson@umontreal.ca.
[†] Faculté de Pharmacie, Université de Montréal.
[‡] Merck-Frosst Canada.
[§] Ecole d'Optométrie, Université de Montréal.
[||] Groupe de Recherche Universitaire sur le Médicament de l'Université de Montréal.
[⊥] Département de Chimie, Université de Montréal.

10.1021/bc800257m CCC: $40.75 © 2008 American Chemical Society
Published on Web 09/20/2008

Scheme 1. Chemical Structure of the Synthetic Ligand of E- and P-Selectin

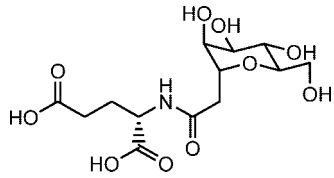

this severe drawback and to improve the binding properties of the NPs, new coupling strategies must be investigated.

Specific drug delivery to activated VECs to modulate the inflammation response have been shown to be a valid therapeutic strategy (*11*). Drug immunoconjugation (*12*, *13*) and immunoliposomes directed against E-selectin (*14*−*16*), as well as liposomes incorporating sLe^x as ligands (*17*−*19*), are among the most described methods. They all present the strong disadvantage of using natural ligands (as sLe^x) which are in competition with the free homologue in the bloodstream.

In this study, a ligand of E- and P-selectin was synthesized and conjugated to a poly-L,D-lactic acid polymer (PLA). The ligand is a nonselective selectin antagonist, which may be advantageous in pathological settings involving both P- and E-selectin activities. The conjugation was done using carboxylic acid functions introduced in the PLA backbone. This functionalized polymer was subsequently mixed with pure PLA to form the NPs. NPs formulated with ligand functionalized PLA (NP-L) present higher adhesive capabilities to HUVEC plasmatic membrane compared to nonfunctionalized PLA NPs. Inhibition of binding could be observed for NP-L when cells are incubated with free ligand prior to the NP introduction. This study provides strong evidence that NPs functionalized with the synthetic ligand can specifically bind to endothelial cells activated by pro-inflammatory molecules.

EXPERMENTAL PROCEDURES

Materials. Chemicals were purchased from Sigma-Aldrich (Oakville, ON, Canada). Solvents were from Laboratoire MAT (Québec, PQ, Canada). All media and reagents for cell culture were purchased from Gibco (Invitrogen, Burlington, ON, Canada). Human vascular endothelial cells (CRL 1730) were from ATCC; Raw 264.7 murine macrophage cell line was a gift from Pr. J. C. Leroux.

Ligand Docking Simulations. All simulations were performed with E-selectin receptor using GOLD (Genetic Optimisation for Ligand Docking) docking program (*20*) in order to identify the most probable conformation of the free and grafted ligand interacting with its receptor. The structure of the chosen ligand can be seen in Scheme 1. The protein data file was obtained from the structure published by Somers et al. (*21*). The protein was prepared as described by Jones et al. (*20*, *22*). The ligand and grafted ligand (Scheme 1 and compound (**9**)) were built using Material Studio software (Accelrys, San Diego, USA) and their structure was minimized using the Discover module assigning CFF force field to each atom. The grafted ligand consisted of a ligand molecule linked to a PLA chain (of 4 monomers) via a glycidyl linker. For the docking simulations, the binding pocket of E-selectin was defined using the conformation of the natural ligand sialyl Lewis acid X (sLe^x) given by Somers et al. The two equatorial hydroxyl groups of the mannose ring of the studied ligand were constrained to bind the calcium ion present in the binding pocket. In that way, the mannose ring of the ligand overlaid onto the L-fucose ring of the sLe^x and the glutamate side chain was free to bind to the protein amino acids. More than 30 genetic algorithm runs were performed in order to identify best fitting structures. The final optimized conformations were picked using GOLD scoring function.

Scheme 2. General Synthesis of the Selectin Ligand

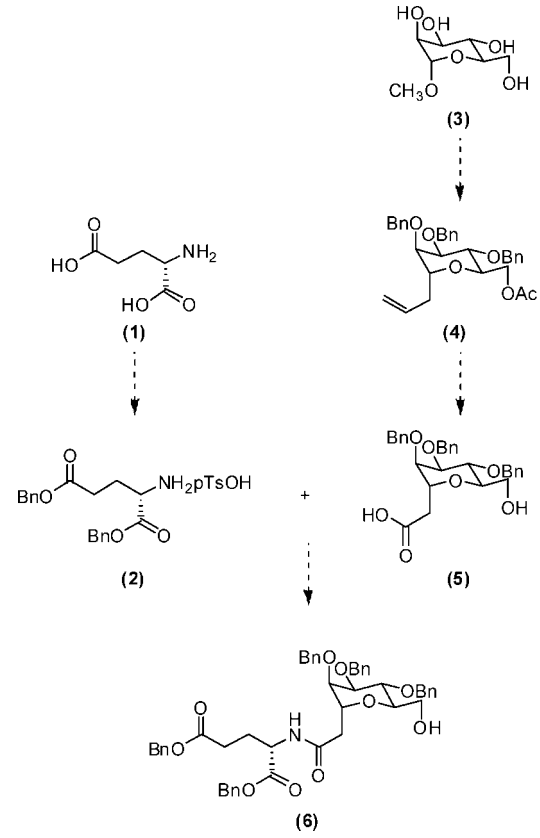

Ligand Synthesis. A general scheme of the ligand synthesis is represented in Scheme 2.

*Synthesis of Fragment **2**.* 25.5 g of *p*-toluene sulfonic acid (*p*TsOH) were added to a solution of 10 g glutamic acid **1** in 100 g of benzylic alcohol under N_2 atm. The mixture was heated at 80 °C for 24 h under stirring and subsequently poured onto 1 L aqueous solution of 1 M NaOH and extracted three times with diethyl ether (Et_2O). The organic phases were pooled and dried on Na_2SO_4. A solution of 10 g (*p*TsOH) sulfonic acid (*p*TsOH) in 100 mL Et_2O was added to the organic phase, which was kept at 4 °C for 24 h. The crystals obtained were filtered and washed with ether to yield 12.3 g of product **2** (36% yield).

^{1}H NMR (400 MHz, DMSO-d_6) δ 2.00−2.17 (m, 2 H, -CH_2−CH_2−CH-), 2.28 (s, 3 H, CH_3- (*p*TsO^-)), 2.43−2.66 (m, 2 H, -CH_2−CO_2Bn), 4.17 (t, 6.60 Hz, 1 H, -CH(NH_3^+)-CO_2-), 5.05−5.12 (m, 2 H, -CH_2−Ph), 5.17−5.26 (m, 2 H, -CH_2−Ph), 7.12 (d, 8.0 Hz, 2 H, aromatic *p*TsO^-), 7.31−7.43 (m, 10 H, aromatic -Bn), 7.51 (d, 8.0 Hz, 2 H, aromatic *p*TsO^-), 8.28−8.64 (m, 3 H, -NH_3^+). SM (FAB) *m*/*e* 328.5 (M + H-*p*TsOH, 100%), 192.3 (10%), 154.2 (32%).

*Synthesis of Fragment **4**.* 3.8 g of tetrabutyl ammonium iodide (TBAI) and 54 mL of bromobenzyl (BnBr) were added to a 10% (w/w) solution of α-methylmannoside **3** in dimethyl formamide (DMF) under N_2 atmosphere. The mixture was cooled down to 0 °C and 18.2 g of NaH was slowly added to avoid a temperature rise. The mixture was stirred for 16 h and cooled down to 0 °C. 100 mL of isopropanol was slowly added, followed by 20 g of salicylic acid. The solution was evaporated and redissolved in 500 mL of ethyl acetate (EtAc). The organic phase was washed three times successively with 100 mL NaOH 10%, 100 mL 1 N HCl, and 100 mL NaCl saturated salt solutions. The organic phase was dried on Na_2SO_4, filtered, and evaporated. The residual product was purified by flash chromatography on silica with an eluent mix 10:90 to 20:80 Et_2O and hexane (HEX) to yield 27.3 g (43%) of intermediate product.

^{1}H NMR (400 MHz, $CDCl_3$) δ 3.35 (s, 3 H, -OCH_3), 3.74−3.84 (m, 4 H), 3.90−3.93 (m, 1 H), 3.97−4.04 (m, 1 H), 4.51−4.82 (m, 8 H), 4.91 (d, 11.0 Hz, 1 H), 7.17−7.42 (m, 20 H, aromatic). ^{13}C NMR (400 MHz, $CDCl_3$) δ 54.7, 69.2, 71.6, 72.0, 72.5, 73.3, 74.4, 74.8, 75.0, 80.2, 98.9, 127.4−128.4 (m, 20 C), 138.2−138.4 (m, 4 C). SM (FAB) *m/e* 553.4 (M − H, 7%), 271.4 (10%), 181.3 (100%). SMHR Calculated for $C_{35}H_{37}O_6$ (M − H) 553.2590, found 553.2600 (−1.8 ppm).

Allyltrimethylsilane (14.3 mL) and trimethylsilyl triflate (4.1 mL) were added to a solution of 25 g of intermediate product in acetonitrile (ACN) at 0 °C under N_2 atmosphere. The mixture was maintained at 4 °C for 16 h, and then 65 mL of anhydrous acetic acid was added. Under stirring at room temperature, 600 mL of dichloromethane (DCM) and 60 mL of aqueous solution of $NaHCO_3$ were added to the mixture. The pH was adjusted to 12 with 10% w/v NaOH. After phase separation, the aqueous phase was extracted with 300 mL of DCM. The obtained organic phases were pooled, dried on Na_2SO_4, and filtered. The solvents were eliminated by distillation under vacuum. The residual product was purified by flash chromatography on silica, using a mix of Et_2O and HEX in proportion ranging from 25:75 to 100:0 to yield 18.5 g (79%) of product **4**.

^{1}H NMR (400 MHz, $CDCl_3$) δ 2.05 (s, 3 H, Ac-), 2.24−2.40 (m, 2 H), 3.61−3.64 (m, 1 H), 3.75−3.83 (m, 3 H), 4.05−4.10 (m, 1 H), 4.23−4.27 (m, 1 H), 4.37−4.42 (m, 1 H), 4.53−4.63 (m, 5 H), 4.74−4.77 (m, 1 H), 4.99−5.04 (m, 2 H), 5.67−5.77 (m, 1 H), 7.27−7.37 (m, 15 H, aromatic).

*Synthesis of Fragment **5***. 90 mL water and 4.5 mL of an aqueous solution of 50% (w/w) of 4-methylmorpholine *N*-oxide (NMO) were added to a solution of 9.00 g of compound **4** in 90 mL distilled acetone, followed by an addition of 2.25 mL of a 2.5% (w/w) solution of osmium tetraoxide in *t*-butanol. The solution was stirred for 3 h; then, 2.25 mL of an aqueous solution of 10% (w/w) $Na_2S_2O_3$, 9 g of Florisil, and 180 mL of water were added. The pH was adjusted to 1 with 1 M HCl. The aqueous phase was extracted three times with 500 mL of EtAc. The organic phases were pooled, dried on Na_2SO_4, and filtered. The solvent was eliminated by distillation under vacuum. The diol intermediate product was used in the next step without purification. 4.5 g of sodium periodate and 90 mL of water were added to a solution of 17.4 mM of the intermediate diol in 90 mL THF. The solution was stirred for 1 h and then 450 mL of water was added. The aqueous phase was extracted three times with 450 mL of EtAc. The organic phases were pooled, dried on Na_2SO_4, filtered, and the solvent eliminated by distillation under vacuum. The residual aldehyde product was used in the next step without further purification. 20.9 mM of CrO_3 from the Jones reagent (CrO_3:H_2SO_4:H_2O, 1:1:3) were added to a solution of 17.4 mM of aldehyde product in 90 mL of distilled acetone at 0 °C. After 15 min, reagent in excess was neutralized by the addition of 10 mL of isopropanol. The solution was poured on 900 mL of 1 M HCl and extracted three times with 400 mL of EtAc. The organic phases were pooled, and the remnant solvent was eliminated by distillation under vacuum. The aldehyde product was used in the next step without further purification. A solution of 4.0 g potassium hydroxyde was prepared with 20 mL water and 20 mL of MeOH. This solution was added to a solution of 17.4 mM of intermediate aldehyde compound in 100 mL MeOH. 100 mL of potassium hydroxyde 10% (w/v) was further added and the mixture poured into 1 L of 1 N HCl; then, the aqueous phase was extracted three times with 500 mL EtAc. The organic phases were pooled, dried on Na_2SO_4, filtered, and the solvent eliminated by distillation under vacuum. The residual product was purified by flash chromatography on silica using Et_2O as the eluent to obtain 7.56 g of acid alcohol **5**. The yield of the synthesis was 88%.

^{1}H NMR (400 MHz, $CDCl_3$) δ 2.54 (dd, 9.9 and 16.7 Hz, 1 H), 2.82 (dd, 3.3 and 16.8 Hz, 1 H), 3.45 (dd, 3.7 and 12.1 Hz, 1 H), 3.55 (dd, 3.6 and 5.0 Hz, 1 H), 3.62 (dd, 2.8 and 7.6 Hz, 1 H), 3.81 (dd, 3.0 and 5.0 Hz, 1 H), 3.84−3.92 (m, 1 H), 4.21 (dd, 9.1 and 12.2 Hz, 1 H), 4.39−4.59 (m, 7 H), 7.22−7.38 (m, 15 H), -OH and -COOH absent. SM (FAB) *m/e* 515.2 (M + Na, 4%), 271.1 (8%), 181.1 (100%), 132.9 (51%). SMHR Calculated for $C_{29}H_{32}O_7Na$ (M + Na) 515.2046, found 515.2032 (+2.7 ppm).

*Coupling **2** and **5**: Protected Ligand **6***. 9.5 g of amine tosylate **2** was solubilized in 200 mL of EtAc and mixed three times with the same volume of 1 N NaOH. The amine compound corresponding to **2** was obtained after drying the organic phase on Na_2SO_4 and filtration and elimination of the solvent by evaporation under vacuum. A 10% (w/w) solution of the acid alcohol **5** in DCM was added with a canula to a solution containing 2.4 g of ethyl-3-(3-dimethylaminopropyl)-carbodiimide (EDC). 1.7 g of 1-hydroxybenzotriazole hydrate (HOBt) and compound **2** were mixed in 31 mL DCM under N_2 atmosphere. The solution was stirred for 16 h. Solvents were eliminated by distillation under vacuum. The residual product was purified by flash chromatography on silica using 1:1 EtAc/HEX to get 3.17 g of the protected ligand **6** (yield of 63%).

^{1}H NMR (400 MHz, $CDCl_3$) δ 1.92−2.02 (m, 1 H), 2.14−2.23 (m, 1 H), 2.31−2.45 (m, 3 H), 2.69 (dd, 2.0 and 15.4 Hz, 1 H), 3.40 (dd, 3.0 and 12.3 Hz, 1 H), 3.50 (dd, 3.0 and 4.8 Hz, 1 H), 3.57 (dd, 2.6 and 8.2 Hz, 1 H), 3.78 (dd, 3.1 and 4.4 Hz, 1 H), 3.96−4.01 (m, 1 H), 4.26 (dd, 9.9 and 12.4 Hz, 1 H), 4.33−4.40 (m, 1 H), 4.43−4.61 (m, 6 H), 4.67−4.74 (m, 1 H), 5.05 (d, 12.3 Hz, 1 H), 5.09 (d, 12.4 Hz, 1 H), 5.14 (s, 2 H), 7.15−7.39 (m, 25 H), -OH and -CONH- absent. ^{13}C NMR (400 MHz, $CDCl_3$) δ 27.07, 30.28, 37.27, 51.49, 59.92, 66.51, 67.50, 71.52, 72.47, 72.83, 74.69, 75.72, 76.89, 127.76−128.60 (25 °C), 134.98, 135.66, 137.63, 137.68, 137.78, 171.20, 172.51, 172.70. SM (FAB) *m/e* 802.2 (M + H, 68%), 694.3 (10%), 418.2 (8%), 328.1 (12%), 271.1 (6%), 181.1 (100%), 136.0 (14%). SMHR Calculated for $C_{48}H_{52}NO_{10}$ (M + H) 802.3591, found 802.3554 (+4.6 ppm).

Polymer Synthesis and Subsequent Ligand Conjugation and Deprotection. Synthesis of PLA polymer bearing pendant carboxyl groups for ligand grafting has been described elsewhere (*23*). A solution of PLA 1 mg/mL with 1% (mol/mol) (relative to lactic monomer) acyl chloride pendant groups in chloroform was prepared (polymer **7**) and to this were added successively 1.5 equiv of **6** in chloroform at a concentration of 0.25 mM and a 10% (w/v) solution of dimethylamino propane (DMAP) in pyridine. The mixture was stirred for 3 h after which a 1 N HCl solution was added to neutralize the pyridine. Chloroform was evaporated and the aqueous phase was filtered to yield the protected ligand−PLA. Activated palladium (Pd−C 5%) was added to a solution of 0.8 mg/mL of protected ligand−polymer in glacial acetic acid at a ratio of 1 mg/mg. This mixture was placed under hydrogen (atmospheric pressure) for 16 h. Pd−C was eliminated by filtration on Celite (MeOH as eluent). Solvent was eliminated by evaporation, and the product dissolved in chloroform. Chloroform was eliminated by evaporation in the presence of an equivalent volume of water to yield the precipitated polymer in aqueous phase. This step was repeated twice to obtain PLA with 5 mol % of grafted selectin synthetic ligand (compound **9** or PLA-$SEL_{5\%}$) with a 70% yield for the two-step procedure after drying.

PLA polymer bearing hydroxyl groups was synthesized as described in Nadeau et al. (*23*). Rhodamine B was grafted to the PLA backbone using standard EDC/NHS coupling reaction. The obtained polymer (PLA-$Rhod_{5\%}$) was precipitated in water and dissolved in DCM after complete water removal. This

operation was repeated three times for complete elimination of remnant chemicals.

NP Preparation. NPs were prepared by the solvent evaporation method. Briefly, 500 mg of a 1:1 mixture of PLA-$Rhod_{5\%}$ and PLA (or PLA-$Sel_{5\%}$) were dissolved in 15 mL of DCM. The polymer solution was then gently injected into 100 mL of aqueous 15% (w/v) of sucrose solution containing a surfactant mixture (2.5% Tween 20, 0.5% PEG Laurate), while emulsification was being achieved by means of high-pressure homogenization (Emulsiflex C30, Avestin, Ottawa, ON, Canada) at 10 000 psi for 3 min in order to obtain the NP suspension. After collection of the NPs, the suspension was stirred for 5 h under reduced pressure to allow solvent evaporation and NP solidification. NP suspension was then lyophilized (Freeze-Dry System, Lyph.Lock 4.5, Labconco) and stored at 4 °C until further use.

NP Characterization. *Particle Size Distribution.* NP size distribution was measured by photon correlation spectroscopy (PCS) (N4 Plus, Coulter Electronics, Miami, FL) at 90° scattering angle for 180 s and at 25 °C. The mean particle diameter was calculated using differential size distribution processor (SDP) intensity analysis program.

Zeta Potential Measurements. NPs were suspended in 0.25% (w/v) saline solution filtered through 0.22 μm filter and zeta potential was measured at 25 °C on a Malvern ZetaSizer Nanoseries ZS (Malvern Instruments, Worcestershire, UK) in triplicate.

Time-of-Flight Secondary Ion Mass Spectrometry (TOF-SIMS). NP samples were analyzed using a TOF-SIMS IV (ION-TOF GmbH, Munster, Germany). The mass spectra were produced by irradiating the NPs with a 15 keV monoisotopic $^{69}Ga^+$ primary ion source with a target current of 1.02 pA in order to stay in static regime (ionic dose lower than 10^{13} ions/cm^2). Mass resolution was above 8200 μma for $^{29}Si^+$. The scanned surface area was 40 μm × 40 μm. Both positive and negative secondary ions were collected over a mass range 5−800 and analyzed.

Cytotoxicity Assay of NPs. Cytotoxicity assay was performed on two cell lines using MTT cell proliferation assays. RAW 264.7 murine macrophage cell line was cultured in Dulbecco's Modified Eagle Medium (DMEM) supplemented with 10% fetal bovine serum (FBS) and penicillin/streptomycin (Invitrogen Canada, Burlington, ON, Canada). Human vascular endothelium cells were cultivated in F12 Kaighn's modification medium, 10% FBS with penicillin/streptomycin supplemented with heparin, and endothelial growth supplement from neural bovine tissue (Sigma-Aldrich, Oakville, ON). Both cell lines were grown in tissue culture flasks and incubated at 37 °C in a 5% CO_2 atmosphere.

Raw 264.7 cells were diluted in complete medium at a final concentration of 5×10^5 cells/mL and plated (100 μL/well) on a 96 well flat-bottom microplate (Corning, NY). NPs suspended in 10 μL PBS sterile buffer were added in the wells in triplicate for each concentration. The plates were incubated for 24 h after which cellular proliferation was assessed by MTT assay. Cell medium was removed and cell monolayer washed with PBS. Complete medium was replaced and 10 μL of thiazolyl blue tetrazolium bromide (Sigma-Aldrich, Oakville, ON, Canada), dissolved in PBS (10 mM, pH 7.4) at a concentration of 5 mg/mL and filtered on 0.22 μm sterile filter (Millipore, Bedford, MA), was added to each well. After 3 h incubation time at 37 °C in 5% CO_2 atmosphere, 50 μL of solubilizing solution (Isopropanol, 10% Triton X100, 0.1 N HCl) was added to each well to dissolve the dark blue formazan crystals. Absorbance was read at a wavelength of 570 nm on a microplate reader (SAFIRE, Tecan, Austria). Procedures with HUVECs were similar, except for initial seeding densities of 2×10^4 cell/m were plated on 96 well flat-bottom microplate (treated with fibronectin) and extra incubation time of 6 h was used prior to addition of solubilizing solution.

***In Vitro* Binding Assays.** *Selectin Induction by Pro-Inflammatory Drugs.* HUVEC were plated on sterile round coverslips (Fisher Scientific, Ottawa, ON, Canada) treated with human fibronectin at a seeding density of 5×10^4 cells/wells and grow for 48 h prior to experiment in 24 well plates (Costar, Corning). Selectin expression on the cell surface was induced by LPS (5 μg/mL) or with L-NAME (3 mM) for 4 h. After repeated rinsing with cold PBS, the activated cells were fixed with a filtered 1% (w/w) formaldehyde PBS solution for 10 min. After addition of 250 μL of blocking solution (2% (w/v) BSA in PBS), cells were incubated overnight at 4 °C with mouse anti-E-Selectin (clone BBIG-E4 (5D11), R&D Systems, Minneapolis, MN) or P-Selectin (clone P8G8, Chemicon, Temecula, CA) antibodies. After washing with PBS, secondary goat antimouse Alexa546 antibody (Invitrogen) was added for 2 h. Cell nucleus staining was performed using Hoechst 33352. All micrographs were taken using an inverted Olympus IX71 microscope (Olympus Canada Inc., Markham, ON) and an Evolution VF camera (MediaCybernetics, Bethesda, MD) with the same 60× objective lens and exposure time to allow comparison of measurements. All images were processed with ImagePro software (MediaCybernetics, Bethesda, MD).

NP Binding Assays. HUVECs were activated as described above and cooled to 4 °C prior to incubation with cold NP suspension for 5 min (100 μg/wells) in serum-free medium. After repeated rinsing with cold PBS, cells were lysed for 2 h at 2 °C with a 0.2% (w/w) Triton X100 solution (1 N NaOH), and fluorescence intensity was read with a fluorescence plate reader (Ex., 550 nm; Em., 580 nm). A similar procedure was used for studies using the free ligand as an inhibitor. Activated HUVECs were incubated for 30 min at 37 °C with different concentrations of free ligand and cooled to 4 °C before incubation with NPs (50 μg/mL) in serum-free medium. After repeated rinsing with cold PBS, cells were lysed during 2 h and fluorescence was read at 25 °C.

Statistical Analysis. The data were calculated as means ± SE, where statistical significance was determined by Student's *t* test.

RESULTS

Ligand Docking Simulations. The synthetic ligand (see Scheme 1), an analogue of the sLe^x epitope, was selected in this study due to its high binding affinity for P- and E-selectin (*8*) compared to sLe^x (*9*). Ligand docking simulations were performed on E-selectin in order to confirm that grafted ligands still possess high binding affinity to receptors. The synthetic ligand is a mannose-based mimic of sLe^x, whose structure incorporates a carboxylate group which replaces the Gal residue. Interaction between sLe^x and E-selectin has been extensively described and is now well-understood. The binding site of E-selectin is known to be located on the lectin domain of the protein. The calcium ion present in this domain has two main functions: to maintain the structure of the binding site (the calcium ion interacts with 5 residues of the protein, namely, Glu80, Asn82, Asn83, Asn105, and Asp106) and to bind the two hydroxyl groups in the equatorial position of the l-fucose ring of the sLe^x ligand. This last function has been extensively used to develop ligands derived from mannose and having two hydroxyl functions in the equatorial position and another one in the radial position.

Results from docking simulations performed with the synthetic ligand showed that the mannose cycle fits in the binding site and interacts strongly with a large number of amino acids forming the binding pocket. One of the two equatorial hydroxyl functions of the mannose ring was able to bond strongly to the

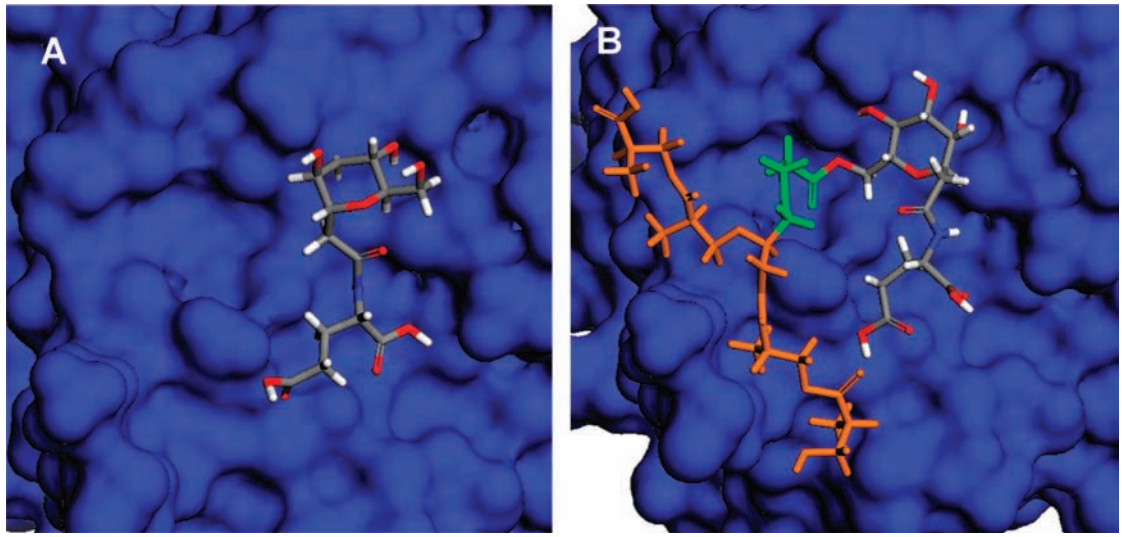

Figure 1. Conformation of the ligand in the bonded state obtained from docking experiments. (A,B) Top view of the binding pocket. Protein is represented by the Connelly surface in blue. The PLA is chain represented in orange. Linker monomer is represented in green.

Scheme 3. Grafting Reaction of the Synthetic Ligand on a PLA Chain and Deprotection

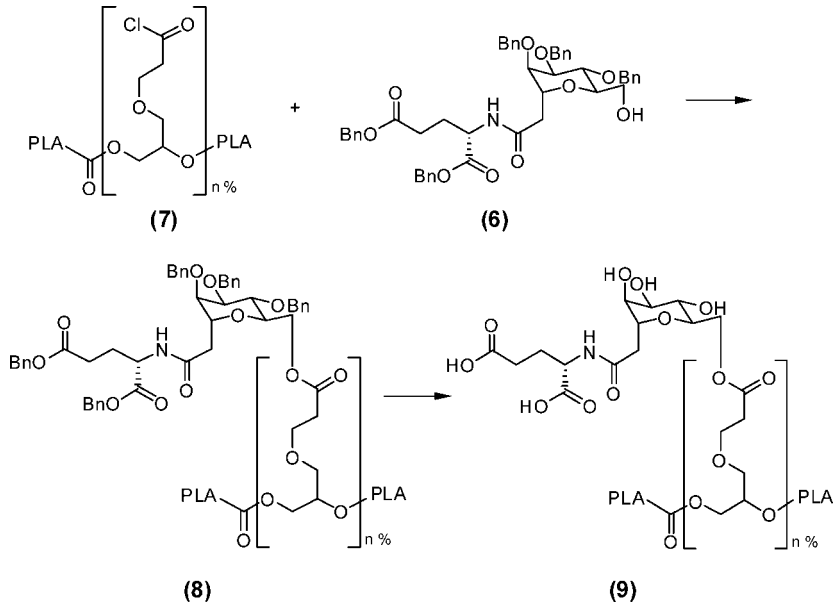

calcium ion of the lectin domain, while the other one interacted with Asp106 and Asn83 side chains. Moreover, one carboxylate of the glutamate moiety of the ligand binds strongly to Arg97 and to Tyr48. These interactions allow the ligand to be positioned in a similar direction to sLe^x. It is interesting to note that the synthetic ligand interacts with the same amino acid as sLe^x but with almost no steric constraint, which is certainly the cause of its potent inhibition capacity. Moreover, these docking simulations showed that one hydroxyl group of the mannose ring is not involved in the binding pattern and could be used as a coupling function with a macromolecule.

We performed another series of docking simulations using the synthetic ligand grafted to a PLA chain of 5 monomers. The interaction pattern of the grafted ligand was very similar to the original nongrafted ligand. We observed that the fitness index of the best structure was much higher for the grafted ligand than for the nongrafted ligand, indicating that the presence of the polymer chain favored binding of the ligand. The conformations of the free and grafted ligands in the binding pocket are slightly different. One remarkable difference is the position of the mannose ring, which is flipped in the case of the grafted ligand (Figure 1). This conformational change allows the polymer chain to lie aside from the binding pocket. Surprisingly, this conformation does not affect the interaction pattern of the ligand. The hydrogen bond network between the receptor and the grafted ligand was identical to that of the free ligand. The same amino acids from the receptor were involved in the interaction pattern as well as the same hydroxyl groups from the mannose ring and the carboxylate groups from the glutamate moiety of the ligand. The main difference between the two interaction patterns is located in the two hydroxyl groups of the mannose ring, which are inverted in the case of the grafted ligand compared to the free ligand configuration.

Table 1. Particle Size and Zeta Potential Measurements of the Different NPs Used in This Study

tested nanoparticles	particle size (nm)	zeta potential (mV)
PLA-Rhod/PLA-SEL5%	173 ± 23	−25.7
PLA-Rhod/PLA	168 ± 37	−19.2

Ligand and Polymer Synthesis. Protected ligand **6** was obtained from the coupling between the amine of the protected

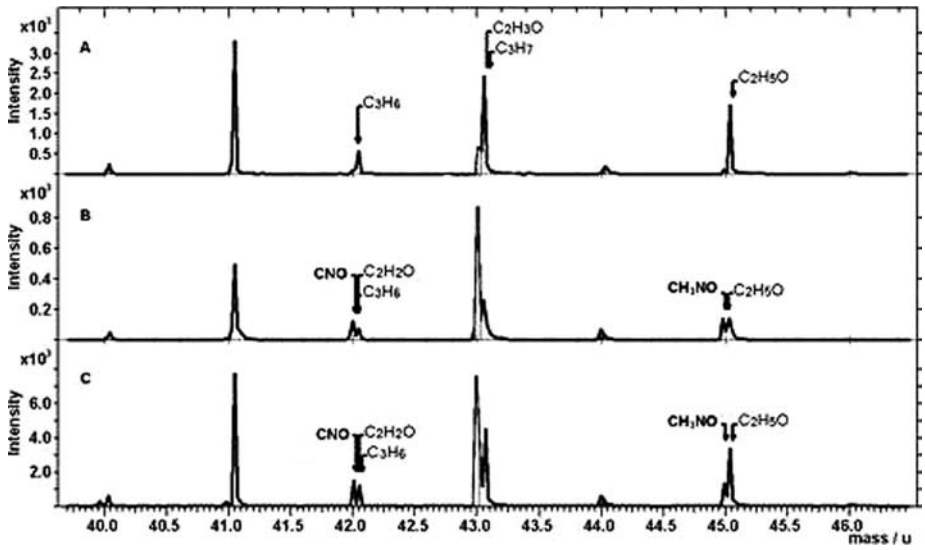

Figure 2. Partial TOF-SIMS spectrum (40−46 amu). (A) NPs made of PLA, (B) NPs made of PLA and PLA-SEL$_{5\%}$ (50:50), and (C) NPs made of PLA-SEL$_{5\%}$ alone. Significant peaks are identified by arrows.

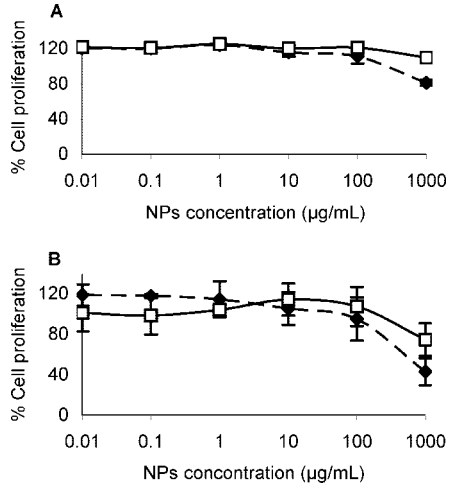

Figure 3. Cytotoxicity assays of NPs on endothelial cells and rat macrophages. (A) NPs suspended in PBS were incubated with Raw 264.7 murine macrophage cell line; (B) NPs were incubated with HUVEC. □, NPs bearing the synthetic ligand; ♦, NPs made of PLA only.

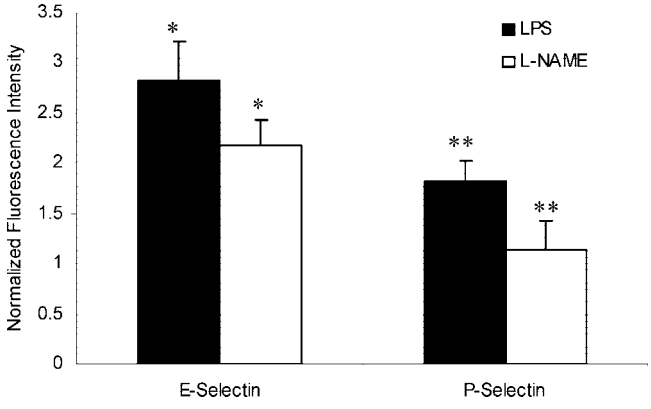

Figure 4. Normalized E- and P-selectin expression quantification from fluorescence microscopy in response to LPS and L-NAME activation ($p < 0.01$, $n = 3$). Fluorescence intensity per cell was quantified and normalized to basal expression.

amino acid **2** and the acid **5** (Scheme 2). A challenging aspect of this reaction was to realize the coupling in the presence of free hydroxyl functions on **5**. The reaction sequence was important in order to prevent oxidation of the primary hydroxyl groups into carboxylic acid. We used acetyl functions to protect the primary alcohol during the reaction. As illustrated in Scheme 3, the coupling reaction yielded the amide ligand **6** ready to be grafted to PLA. The grafting of the synthetic ligand to PLA was mediated by an ester linkage on pendant groups of a new family of polyester polymers developed in our laboratory (*23*). For this purpose, the ligand must present only one reactive hydroxyl group, which does not belong to the active part of the ligand. The use of a benzyl group to protect the other hydroxyl and carboxyl functions was guided by the ease of removal by hydrogenation in one step after polymer grafting. The presence and removal of the benzyl group before and after deprotection of the grafted ligand was confirmed by NMR (data not shown). The ligand grafting reaction takes place between the unprotected hydroxyl group on the ligand **6** and the acyl chloride groups present on the polymer pendant groups **7** in the presence of DMAP and pyridine (Scheme 3). Molecular weights of the synthesized polymers, determined by GPC, were found to be M_n 23 103, M_w 41 623 for PLA and M_n 16 412, M_w 34 868 for PLA-SEL$_{5\%}$. A small decrease of the molecular weight of PLA-SEL$_{5\%}$ could be due to partial hydrolysis of the polymer, as some reaction steps of the ligand grafting reaction involve acidic or basic treatments. The free ligand was obtained by catalytic hydrogenation of **6**, which removed the benzyl protecting groups and gave the ligand described by Wong et al. (*8, 24*). The structure of the free ligand was confirmed by mass spectrometry as well as ^{1}H and ^{13}C NMR.

Preparation and Characterization of NPs. Particle size and zeta potential measurements performed on the NPs used in this study are summarized in Table 1. As expected, no significant differences in zeta potential between bare PLA and PLA-SEL$_{5\%}$ NPs were observed due to the low concentration of synthetic ligand in the NPs. The negative surface charge of the NPs is mostly due to the remnant carboxylic groups of PLA.

NP Surface Characterization. We used TOF-SIMS to detect the presence of the ligand directly on the surface of the NPs. For these experiments, no fluorescently labeled polymers were used. Excipients coming from NP preparation and polymers used did not contain any nitrogen atoms. TOF-SIMS is a very surface-specific technique and sensitive to the outermost 10 Å of the NP surface. In Figure 2, the 40−46 amu region of the mass

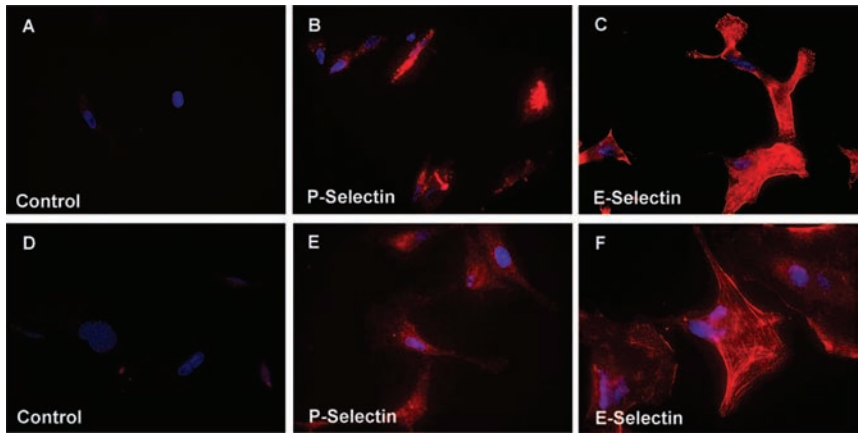

Figure 5. Fluorescent micrographs of HUVECs activated with LPS (B,C) and with L-NAME (E,F). Significant localization of fluorescence (red channel) was observed for E-selectin induced by L-NAME compared to LPS, while LPS-activated cells demonstrate higher levels of E- and P-selectin on their surfaces. Control experiments represent E-selectin (A) and P-selectin (D) expression under basal conditions. Blue channel represents nucleus staining.

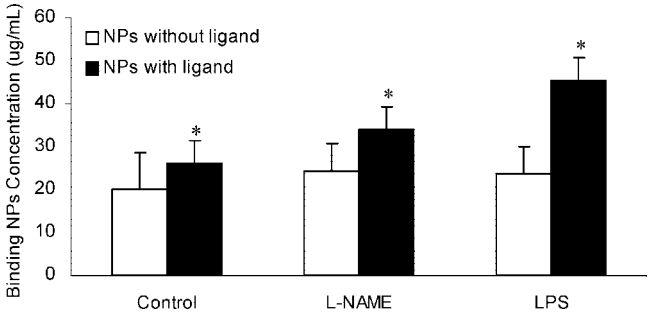

Figure 6. Fluorescence spectrophotometry demonstrates that binding of the NPs is regulated by receptor expression. The concentration of bound NPs on the cell surface was dependent on the activating molecule and was a maximum for LPS ($p < 0.01$, $n = 3$). NP binding time was 5 min at 4 °C, followed by extensive washing and cell lysis.

spectra is displayed, showing peak differences that can be attributed to nitrogen compounds found on ligand-functionalized NPs only.

NP Cytotoxicity Studies. Cytotoxicity of NPs made of PLA or PLA- $SEL_{5\%}$ was investigated *in vitro* on two different cell lines, namely, rat macrophages (Raw 264.7) and human vascular endothelial cells (Figure 3A,B). Blank experiments showed no significant polymer absorbance in the concentration range studied. Results of MTT assay demonstrated that the NPs are nontoxic in concentration lower than 100 μg/mL. Moreover, microscopic observations of the macrophage or human vascular endothelial monolayer during the study showed no changes in cell morphology or growing patterns (data not shown).

Binding Capacity of the NPs *in Vitro.* Selectin expression by HUVECs incubated with pro-inflammatory drugs was characterized by fluorescence microscopy. The relative concentration of E- and P-selectins on HUVEC surface was quantified using fluorescent anti-E-selectin and anti-P-selectins mAbs and normalized to basal concentrations on control cells (Figure 4). Upon incubation with LPS, E- and P-selectin concentrations could be enhanced 3- and 2-fold, respectively. Incubation of cells with the drug L-NAME leads to lower expression of the receptors but was still significantly higher than control cells. Fluorescence micrographs also evidenced differences in E-selectin distribution on the surface of activated cells dependently of the activating drug (Figure 5). P-selectin stained with anti-P-selectin mAbs appeared to be uniformly distributed around the cell nucleus independently of the activating drug (Figure 5B,E). E-Selectin exhibits a very different distribution pattern depending on the activating molecules. With LPS activation, a large fraction of the proteins are uniformly distributed on cell surfaces, (Figure 5C), while with L-NAME, a significant amount are clustered in filamentous structures (Figure 5F). Cytoskeletal staining with anti-F-actin mAbs was done to ensure that cell membrane permeability was not increased by formaldehyde treatment.

To determine the binding capacity of NPs to HUVECs expressing basal or high levels of selectin receptors, cells were treated with NPs for 5 min at 4 °C in order to decrease uptake by active endocytosis. After this short incubation, cells were abundantly washed and the concentration of bound NPs was quantified at 25 °C by fluorescence photospectrometry (Figure 6). For cells incubated with LPS, NPs formulated with PLA-$Sel_{5\%}$ present a 2-fold enhancement of bound concentration compared to nonactivated cells and a 30% enhancement for cells incubated with L-NAME. NPs formulated with PLA were not sensitive to expression levels of selectins and exhibit a constant but low bound NPs concentration independently of the experimental conditions. The level of NPs bearing the synthetic ligand corresponds well with the level of expression of E- and P-selectin induced by LPS and L-NAME, indicating that adhesion of these NPs is strongly dependent on selectin expression.

Fluorescent micrographs of cells activated with LPS confirmed this result. Strong fluorescence localized on the whole surface of the cell was observed after just 5 min of incubation with NPs bearing the synthetic ligand, while almost no fluorescence could be observed with the NPs formulated with PLA (Figure 7). Control experiments of F-actin staining on permeabilized and nonpermeabilized cells were also realized and confirmed that the observed fluorescence in micrographs came from cell surfaces and not from cytosol (data not shown).

Binding assay of NPs in the presence of free ligand was also realized. Free ligand was incubated for 30 min with HUVEC, which were activated with LPS or L-NAME. They were cooled to 4 °C prior to the introduction of the NPs. An increase of the free ligand concentration was followed by a decrease in the fluorescence intensity only for the NPs bearing the synthetic ligand (Figure 8). Fluorescence intensities similar to those of control cells, which were not activated or incubated with the free ligand, were obtained for free ligand concentrations higher

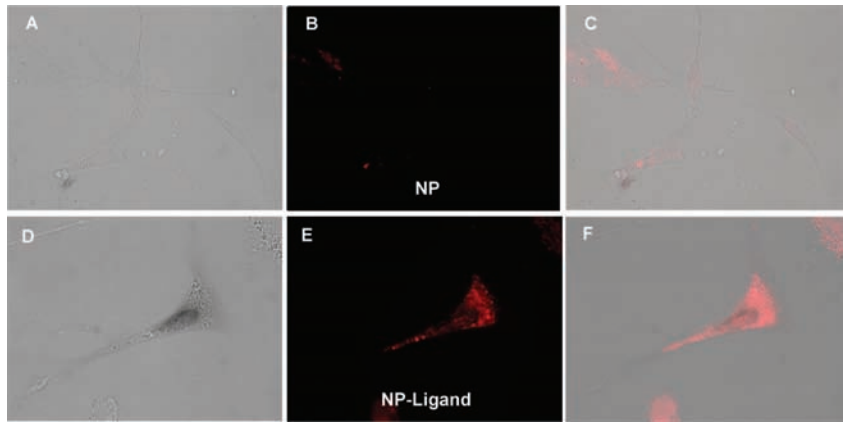

Figure 7. Fluorescent microscopy was used to assess localization of the NPs (red) on LPS activated cell surface. Images confirmed that NPs bearing ligand molecules rapidly adhere to the cell surface (E) compared to the bare NPs (B). NP binding time was 5 min at 4 °C and was followed by extensive washing and fixation of the cells. (A) and (D) are DIC images; (C) and (F) are merged images.

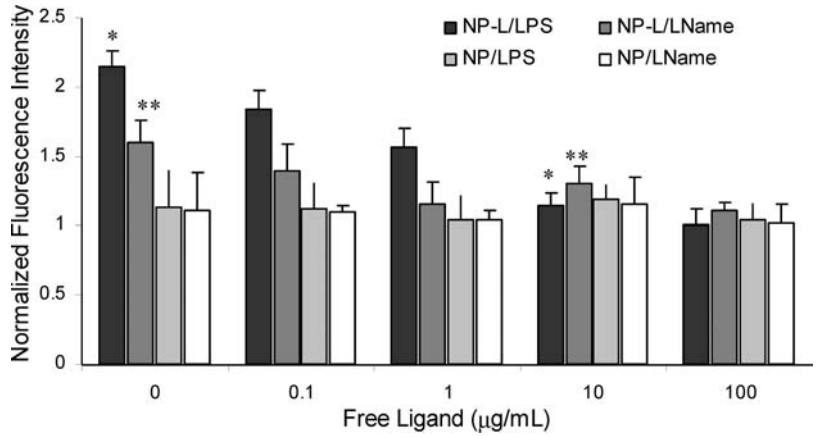

Figure 8. Fluorescence spectrophotometry demonstrated that free ligand can inhibit binding of NPs bearing ligand molecules ($p < 0.01$, $n = 3$). Binding of bare NPs was not affected. NP binding time was 5 min at 4 °C and was followed by extensive washing and cell lysis. Fluorescence intensities were normalized to control conditions (nonactivated cells treated with NPs).

than 10 μg/mL. NPs formulated with PLA were not sensitive to the presence of free ligand in the whole range of concentration studied.

DISCUSSION

The natural ligand of E- and P-selectin, the tetrasaccharide sialyl Lewis x (sLe^X), has a weak affinity (around 0.6 mM) for E-selectin as determined in cell-free assays (*25*). Development of synthetic carbohydrate ligands having higher affinities has been hindered by the fact that the synthesis of modified carbohydrate is complex and expensive. Moreover, most proteins bind carbohydrates with weak affinity. At a molecular level, X-ray diffraction analysis of E- and P-selectin (*21*) binding sites of natural ligand sLe^x had recently shown the essential chemical groups involved in the binding pocket. Consequently, several designs of antagonist ligands have been proposed (*8, 9*). Among them, carbohydrate mimetics of sLe^x based on a mannose ring have been extensively studied (*24, 26*). The advantage of these molecules is the relative ease of their synthesis and their high affinity toward E- and P-selectin. The binding pattern and conformation of the synthetic ligand grafted to a polymeric chain of PLA was evaluated and compared to the free synthetic ligand. Docking experiments performed on the free synthetic ligand showed that one of the anomeric hydroxyl functions present at the 6-O position of the α-D-mannopyranosyl ring is nonessential for the binding of the ligand. Thus, it could be possible to graft a polymeric chain at that position. The simulation results showed that grafting the synthetic ligand to a hydrophobic polymeric chain like PLA did not alter significantly the interaction pattern of the ligand with the protein. This is in agreement with previous experimental observations made by Wong et al. who showed that conjugation of hydrophobic groups like C_{16} alkyl chains on the nonessential hydroxyl group of the ligand strongly increased the affinity of the ligand to E- and P-selectin (*24*). The technique used to evaluate the NPs allows mixing of functionalized and nonfunctionalized PLA chains and offers the possibility of adjusting the concentration of ligand in the NPs. This versatility in the formulation has also allowed encapsulation of hydrophilic (*27*) or hydrophobic drugs (*28*) in PLA NPs and fine-tuning of the delivery kinetics of these drugs. An important advance of the present approach resides in the fact that, by mixing a ligand functionalized polymer with a nonfunctionalized homologue, a high concentration of ligand on the NP surface can be maintained during the whole lifetime of the NPs, contrary to NPs that are surface-functionalized only (*29*).

As already mentioned, the presence of the synthetic ligand on the NPs is a key factor to ensure strong affinity of the NPs to their target. TOF-SIMS results ensured that functionalized NPs really exposed the synthetic ligand on their surfaces. Cytotoxicity assays did not reveal any toxicity associated with NPs over a large range of NP concentrations, ensuring that binding of NPs was not affected by the chemical components of the polymers.

Under normal conditions, both E-selectin and P-selectin are present in low concentrations in vascular endothelial cells but can be induced by interleukins (IL), tumor necrosis factor-α

(TNF-α), lipopolysaccharides, endotoxins (*30*), and cytomegalovirus infection (*31*). Expression of E- and P-selectin by L-NAME has been used in model systems of ischemia or artherosclerosis, as it has been reported to inhibit the production of nitric oxide from endothelial cells. Our observation showed that the concentration and the distribution of E-selectin following L-NAME activation and LPS activation in HUVECs are very different. E- and P-selectin levels are higher on cells stimulated with LPS after 4 h of induction. Maximum expression of selectin on the cell surface has been reported to be at 4 h for both LPS and L-NAME activation (*32, 33*), suggesting that the differences observed in selectin concentration do not come from different expression kinetics. We observed marked differences in selectin distribution on endothelial cells activated by L-NAME or LPS. Scholz et al. reported a more diffuse pattern of E-selectin distribution on HUVEC cells activated by IL-β (*34*). This suggest that receptor distribution on the cell surface is strongly dependent on the stimulating molecule and therefore on the regulation process. More experiments are needed to truly characterize the effect of the protein distribution on the adhesive capacity of the NPs, but it can be advanced that this factor is expected to strongly affect the adhesive properties of the NPs as already suggested by other studies. Indeed, it has been reported that the location of the ligand−receptor bond relative to the endothelial or particle surface influences the adhesion of NPs to the endothelium (*35, 36*).

Results from *in vitro* adhesion tests demonstrated that the presence of the ligand was necessary to achieve strong adhesion between cells and NPs. Given that the NPs used in this study have the same particle size and similar zeta potentials, differences in binding properties of the NPs could be directly correlated with the presence of the ligand on NP surface. We observed that NP binding was modulated by selectin upregulation. Indeed, different levels of selectin expression could be achieved by incubating the cells with different pro-inflammatory drugs. These differences in receptor expression could be correlated with differences in binding concentrations for the NPs bearing the synthetic ligand.

In a nutshell, these results obtained *in vitro* confirm the adhesion capabilities of NPs functionalized with selectin ligand, which makes them good candidates for active targeting of the endothelium. Such findings provide important information regarding possible treatments of acute inflammation using drug delivery systems.

ACKNOWLEDGMENT

The authors want to thank NSERC and GRUM for financial support and Suzie Poulin (École Polytechnique, Université de Montréal) for TOF-SIMS analysis. J.-F. Bouchard is supported by Health Research Foundation R&D Canadian Institutes of Health Research Scholar.

LITERATURE CITED

(1) Simon, S. I., and Green, C. E. (2005) Molecular mechanics and dynamics of leukocyte recruitment during inflammation. *Annu. Rev. Biomed. Eng. 7*, 151–85.

(2) Colden-Stanfield, M., and Gallin, E. K. (1998) Modulation of K+ currents in monocytes by VCAM-1 and E-selectin on activated human endothelium. *Am. J. Physiol. 275* (1 Pt 1), C267–77.

(3) Ye, C., Kiriyama, K., Mistuoka, C., Kannagi, R., Ito, K., Watanabe, T., Kondo, K., Akiyama, S., and Takagi, H. (1995) Expression of E-selectin on endothelial cells of small veins in human colorectal cancer. *Int. J. Cancer 61* (4), 455–60.

(4) Vallien, G., Langley, R., Jennings, S., Specian, R., and Granger, D. N. (2000) Expression of endothelial cell adhesion molecules in neovascularized tissue. *Microcirculation 7* (4), 249–58.

(5) Bhaskar, V., Law, D. A., Ibsen, E., Breinberg, D., Cass, K. M., DuBridge, R. B., Evangelista, F., Henshall, S. M., Hevezi, P., Miller, J. C., Pong, M., Powers, R., Senter, P., Stockett, D., Sutherland, R. L., von Freeden-Jeffry, U., Willhite, D., Murray, R., Afar, D. E., and Ramakrishnan, V. (2003) E-selectin upregulation allows for targeted drug delivery in prostate cancer. *Cancer Res. 63* (19), 6387–94.

(6) Ehrhardt, C., Kneuer, C., and Bakowsky, U. (2004) Selectins-an emerging target for drug delivery. *Adv. Drug Delivery Rev. 56* (4), 527–49.

(7) Magnani, J. L. (2004) The discovery, biology, and drug development of sialyl Lea and sialyl Lex. *Arch. Biochem. Biophys. 426* (2), 122–31.

(8) Simanek, E. E., McGarvey, G. J., Jablonowski, J. A., and Wong, C. H. (1998) Selectin-carbohydrate interactions: from natural ligands to designed mimics. *Chem. Rev. 98*, 833–862.

(9) Kaila, N., and Thomas, B. E. t. (2002) Design and synthesis of sialyl Lewis(x) mimics as E- and P-selectin inhibitors. *Med. Res. Rev. 22* (6), 566–601.

(10) Allen, T. M., and Cullis, P. R. (2004) Drug delivery systems: entering the mainstream. *Science 303* (5665), 1818–22.

(11) Kuldo, J. M., Ogawara, K. I., Werner, N., Asgeirsdottir, S. A., Kamps, J. A., Kok, R. J., and Molema, G. (2005) Molecular pathways of endothelial cell activation for (targeted) pharmacological intervention of chronic inflammatory diseases. *Curr. Vasc. Pharmacol. 3* (1), 11–39.

(12) Everts, M., Kok, R. J., Asgeirsdottir, S. A., Melgert, B. N., Moolenaar, T. J., Koning, G. A., van Luyn, M. J., Meijer, D. K., and Molema, G. (2002) Selective intracellular delivery of dexamethasone into activated endothelial cells using an E-selectin-directed immunoconjugate. *J. Immunol. 168* (2), 883–9.

(13) Everts, M., Asgeirsdottir, S. A., Kok, R. J., Twisk, J., deVries, B., Lubberts, E., Bos, E. J., Werner, N., Mejer, D. K., and Molema, G. (2003) Comparison of E-selectin expression at mRNA and protein levels in murine models of inflammation. *Inflamm. Res. 52* (12), 512–8.

(14) Spragg, D. D., Alford, D. R., Greferath, R., Larsen, C. E., Lee, K. D., Gurtner, G. C., Cybulsky, M. I., Tosi, P. F., Nicolau, C., and Gimbrone, M. A., Jr. (1997) Immunotargeting of liposomes to activated vascular endothelial cells: a strategy for site-selective delivery in the cardiovascular system. *Proc. Nat. Acad. Sci. U.S.A. 94* (16), 8795–800.

(15) Bendas, G., Krause, A., Schmidt, R., Vogel, J., and Rothe, U. (1998) Selectins as new targets for immunoliposome-mediated drug delivery. A potential way of anti-inflammatory therapy. *Pharm. Acta Helv. 73* (1), 19–26.

(16) Kessner, S., Krause, A., Rothe, U., and Bendas, G. (2001) Investigation of the cellular uptake of E-Selectin-targeted immunoliposomes by activated human endothelial cells. *Biochim. Biophys. Acta 1514* (2), 177–90.

(17) Murohara, T., Margiotta, J., Phillips, L. M., Paulson, J. C., DeFrees, S., Zalipsky, S., Guo, L. S., and Lefer, A. M. (1995) Cardioprotection by liposome-conjugated sialyl Lewisx-oligosaccharide in myocardial ischaemia and reperfusion injury. *Cardiovasc. Res. 30* (6), 965–74.

(18) Vodovozova, E. L., Moiseeva, E. V., Grechko, G. K., Gayenko, G. P., Nifant'ev, N. E., Bovin, N. V., and Molotkovsky, J. G. (2000) Antitumour activity of cytotoxic liposomes equipped with selectin ligand SiaLe(X), in a mouse mammary adenocarcinoma model. *Eur. J. Cancer 36* (7), 942–9.

(19) DeFrees, S. A., Phillips, L., Guo, L., and Zalipsky, S. (1996) Sialyl Lewis x liposomes as a multivalent ligand and inhibitor of E-selectin mediated cellular adhesion. *J. Am. Chem. Soc. 118* (26), 6101–6104.

(20) Jones, G., Willett, P., and Glen, R. C. (1995) Molecular recognition of receptor-sites using a genetic algorithm with a description of desolvation. *J. Mol. Biol. 245* (1), 43–53.

(21) Somers, W. S., Tang, J., Shaw, G. D., and Camphausen, R. T. (2000) Insights into the molecular basis of leukocyte tethering and rolling revealed by structures of P- and E-selectin bound to SLe(X) and PSGL-1. *Cell 103* (3), 467–79.

(22) Jones, G., Willett, P., Glen, R. C., Leach, A. R., and Taylor, R. (1997) Development and validation of a genetic algorithm for flexible docking. *J. Mol. Biol. 267* (3), 727–748.

(23) Nadeau, V., Leclair, G., Sant, S., Rabanel, J. M., Quesnel, R., and Hildgen, P. (2005) Synthesis of new versatile functionalized polyesters for biomedical applications. *Polymer 46* (25), 11263–11272.

(24) Wong, C. H., MorisVara, F., Hung, S. C., Marron, T. G., Lin, C. C., Gong, K. W., and WeitzSchmidt, G. (1997) Small molecules as structural and functional mimics of sialyl Lewis X tetrasaccharide in selectin inhibition: A remarkable enhancement of inhibition by additional negative charge and/or hydrophobic group. *J. Am. Chem. Soc. 119* (35), 8152–8158.

(25) Weitz-Schmidt, G., Gong, K. W., and Wong, C. H. (1999) Selectin/glycoconjugate binding assays for the identification and optimization of selectin antagonists. *Anal. Biochem. 273* (1), 81–8.

(26) Marron, T. G., Woltering, T. J., WeitzSchmidt, G., and Wong, C. H. (1996) C-Mannose derivatives as potent mimics of sialyl Lewis X. *Tetrahedron Lett. 37* (50), 9037–9040.

(27) Hammady, T., Nadeau, V., and Hildgen, P. (2006) Microemulsion and diafiltration approaches: An attempt to maximize the global yield of DNA-loaded nanospheres. *Eur. J. Pharm. Biopharm. 62* (2), 143–154.

(28) Sant, S., Thommes, M., and Hildgen, P. (2008) Microporous structure and drug release kinetics of polymeric nanoparticles. *Langmuir 24* (1), 280–287.

(29) Eniola, A. O., and Hammer, D. A. (2005) Characterization of biodegradable drug delivery vehicles with the adhesive properties of leukocytes II: effect of degradation on targeting activity. *Biomaterials 26* (6), 661–70.

(30) Fries, J. W. U., Williams, A. J., Atkins, R. C., Newman, W., Lipscomb, M. F., and Collins, T. (1993) Expression of Vcam-1 and E-Selectin in an in-Vivo Model of Endothelial Activation. *Am. J. Pathol. 143* (3), 725–737.

(31) Scholz, M., Hamann, A., Blaheta, R. A., Auth, M. K. H., Encke, A., and Markus, B. H. (1992) Cytomegalovirus-related and interferon-related effects on human endothelial-cells - cytomegalovirus-infection reduces up-regulation of HLA class-II antigen expression after treatment with interferon-gamma. *Hum. Immunol. 35* (4), 230–238.

(32) Leeuwenberg, J. F. M., Smeets, E. F., Neefjes, J. J., Shaffer, M. A., Cinek, T., Jeunhomme, T., Ahern, T. J., and Buurman, W. A. (1992) E-Selectin and intercellular-adhesion molecule-1 are released by activated human endothelial-cells invitro. *Immunology 77* (4), 543–549.

(33) Armstead, V. E., Minchenko, A. G., Schuhl, R. A., Hayward, R., Nossuli, T. O., and Lefer, A. M. (1997) Regulation of P-selectin expression in human endothelial cells by nitric oxide. *Am. J. Physiol. 273* (2), H740–746.

(34) Scholz, D., Devaux, B., Hirche, A., Potzsch, B., Kropp, B., Schaper, W., and Schaper, J. (1996) Expression of adhesion molecules is specific and time-dependent in cytokine-stimulated endothelial cells in culture. *Cell Tissue Res. 284* (3), 415–23.

(35) Patel, K. D., Nollert, M. U., and McEver, R. P. (1995) P-selectin must extend a sufficient length from the plasma membrane to mediate rolling of neutrophils. *J. Cell Biol. 131*, 1893–1902.

(36) Schaffer, D. V., and Lauffenburger, D. A. (1998) Optimization of cell surface binding enhances efficiency and specificity of molecular conjugate gene delivery. *J. Biol. Chem. 273* (43), 28004–28009.

BC800257M

Design, Synthesis, and Biological Evaluation of an Antagonist−Bombesin Analogue as Targeting Vector

Wael R. Abd-Elgaliel,[†] Fabio Gallazzi,[‡] Jered C. Garrison,[§,#] Tammy L. Rold,[§,#] Gary L. Sieckman,[§,#] Said Daibes Figueroa,[||,#] Timothy J. Hoffman,[†,§,#] and Susan Z. Lever*[,†,⊥]

Department of Chemistry, Structural Biology Core, Department of Internal Medicine, Department of Radiology, and Research Reactor Center, University of Missouri—Columbia, and Harry S. Truman Memorial VA Hospital, Columbia Missouri. Received July 11, 2008; Revised Manuscript Received August 10, 2008

The gastrin releasing peptide receptor (GRP-R) is overexpressed on a number of tumors and cancer cell lines including pancreas, prostate, breast, gastrointestinal, and small cell lung cancer (SCLC). Radiolabeled bombesin (BBN) analogues have exhibited high binding affinity and specificity to the GRP-R. A bombesin analogue with an antagonist targeting vector at the C-terminus, DOTA-aminohexanoyl-[*D*-Phe^6, Leu-NHCH$_2$CH$_2$CH$_3$^{13}, des Met^{14}] BBN[6−14] (**1**, "Bomproamide"), has been synthesized and displays high binding affinity (IC_{50} = 1.36 ± 0.09 nM) against ^{125}I-Tyr^4-BBN in in vitro competitive assays using PC-3 cells. Maximum internalization of ^{111}In-**1** reached 14% in PC-3 cells after 45 min of incubation. Rapid (0.25 h PI) and high (12.21 ± 3.2%ID/g) pancreatic uptake of ^{111}In-**1** was observed in healthy CF-1 mice, and 90% of the activity was blocked by coinjection of 100 μg of BBN. Rapid (0.25 h PI) and high uptake (6.90 ± 1.06%ID/g) was observed in PC-3 prostate cancer xenografts in SCID mice, as well as visualized clearly in a SPECT/CT study. These results support the use of a bombesin construct with an antagonist C-terminal vector as a candidate of choice for specific in vivo imaging of tumors overexpressing GRP-receptors.

INTRODUCTION

Receptor-avid radiopharmaceuticals have attracted great attention as efficient biomarkers. Molecular selectivity is achieved with the appropriate choice of a biomolecule, whether it is a monoclonal antibody or fragment, small molecule, or peptide. For many imaging or radiotherapeutic applications, introduction of the radioactive nuclide is addressed through the bifunctional chelate approach. Regulatory peptides such as the bombesin (BBN), gastrin-releasing peptide (GRP), and neuromedin-B are a group of promising small biovectors. BBN contains 14 amino acid residues and is the amphibian analogue of the mammalian counterpart GRP which contains 27 amino acid residues (*1, 2*). BBN, originally isolated and purified from the skin of European frog *Bombina bombina*, shows marked binding affinity and specificity to the GRP receptor subtype BB2 (*3*). GRP receptors are normally expressed in the non-neurocrine tissues of the pancreas and breast as well as in neuroendocrine tissue of the prostate, lung, colon, and anterior pituitary cells, as well as central and peripheral nervous system (*4*−*6*). Overexpression of several regulatory peptide receptors, such as BB2, has been detected in various human neoplasia (*7*−*12*) and may act as a prognostic marker for prostate, breast, and lung carcinogenesis (*13*−*15*).

Agonist-based peptide constructs have been studied as receptor targeting agents (*16*−*21*) due to their ability to induce receptor-mediated internalization, most likely by endocytosis.

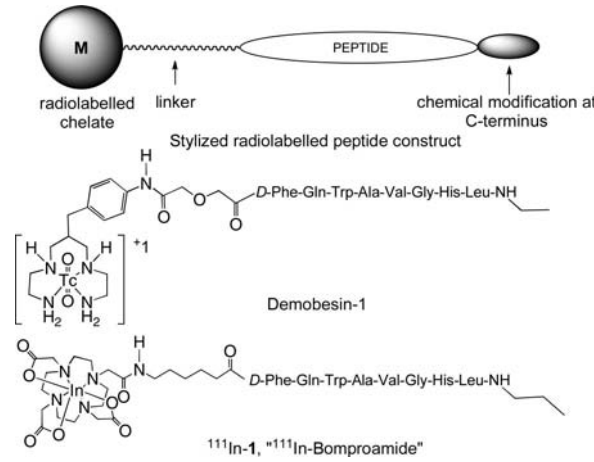

Figure 1. General structure for a radiolabeled peptide construct, structure of Demobesin-1 and ^{111}In-Bomproamide (^{111}In-**1**).

Accumulation of the radioconjugate within the targeted cells is a prerequisite to triggering efficient internalization. For therapeutic purposes, efficient internalization of the radioconjugate appears to be important in delivering the highest radioactivity dose to the targeted cells.

Structural modifications to these radiopharmaceuticals have included variation in the peptide sequence, the nature of the chelate and radiometal, and the length of the spacer attaching the two components (Figure 1). For example, an agonist BBN analogue, DO_3A-CH_2CO-G-4-aminobenzoyl-Q-W-A-V-G-H-L-M-NH_2 (AMBA), was synthesized and labeled with ^{177}Lu for prostate cancer targeting (*22*). ^{177}Lu-AMBA shows a high affinity for the GRP-R (IC_{50} = 2.50 ± 0.50 nM) and 76.8% internalization. The in vitro binding properties of ^{177}Lu-AMBA were subsequently investigated in human neoplastic and non-neoplastic tissues known for their expression of GRP-receptors

* Send all correspondence to Susan Z. Lever. Tel.: 573-882-8395. Facsimile: 573-882-2754. E-mail: levers@missouri.edu. 125 Chemistry Bldg., 601 S. College Ave., Columbia, MO 65211.
[†] Department of Chemistry.
[‡] Structural Biology Core.
[§] Department of Internal Medicine.
[#] Harry S. Truman Memorial VA Hospital.
[||] Department of Radiology.
[⊥] Research Reactor Center.

10.1021/bc800290c CCC: $40.75 © 2008 American Chemical Society
Published on Web 09/23/2008

(*16*). Interestingly, in contrast to the labeling observed in GRP-positive mouse pancreas, the authors reported that the human pancreas shows no labeling with ^{177}Lu-AMBA unless chronic pancreatitis was present.

A novel series of DTPA coupled BBN analogues with a shortened peptide sequence also containing non-natural amino acid residues was recently reported (*19*). Among this series, DTPA-ACMpip-Tha^{6}-BAla^{11}-Tha^{13}-Nle^{14}-BBN[6-14] showed two to three times higher uptake for CA20948 pancreas tumor and 1.3 times for PC-3 prostate tumors when compared to DTPA-BBN[1−14]. The authors concluded that shortening the amino acid sequence and replacing specific amino acids in the BBN sequence can improve the receptor binding affinity (*19*).

A method of radiolabeling with technetium or rhenium via the metal precursor $[M(H_2O)_3(CO)_3]^+$ was tested with an agonist BBN analogue containing an appended 2,3-diaminopropanoyl moiety. The radiolabeled construct, (DPr)-Ser-Ser-Ser-Gln-Trp-Ala-Val-Gly-His-Leu-Met-(NH_2), exhibits excellent binding affinity to the GRP-receptors in the human PC-3 cell line (IC_{50} $\sim$ 0.86 nM). In addition, high uptake (16 $\pm$ 1.3%ID/g) in normal pancreas and extensive internalization 80% after 90 min incubation with PC-3 cells was reported (*23*). Studies on compounds reported by Nock et al. in 2005 utilized the open chain tetraamine-functionalized BBN analogue based on the agonist sequence [Pro^{1}, Tyr^{4}, Nle^{14}] BBN, Demobesin-4 (*15*). Demobesin-4 has binding affinity for the GRP-receptors in the PC-3 cells with (IC_{50} $\sim$ 0.15 nM) (*15*). The number of receptors to which an agonist or antagonist binds may differ. For example, ^{125}I-[Tyr^{0}]rat urocortin, an agonist, was shown to bind to less corticotropin-releasing factor type 1 receptor sites than ^{125}I-[DTyr^{1}]astressin, an antagonist (*24*).

Two chelation systems, CB-TE2A (1,4,8,11-tetraazabicyclo[6.6.2]hexadecane-4,11-diacetic acid) and NOTA (1,4,7-triazacyclononane-1,4,7-triacetic acid), have been compared to DOTA (1,4,7,10-tetraazacyclododecane-1,4,7,10-tetraacetic acid) for the stable incorporation of ^{64}Cu for PET imaging of prostate cancer using the construct BBN[7−14]NH_2 (*18, 25*). The authors reported that the lack of retention of NOTA complex radioactivity in collateral tissues such as liver at 4 and 24 h time points suggests a high degree of in vivo stability of NOTA complex as compared with peptide conjugates comprising similar polyaminocarboxylate chelators such as DOTA (*25*). The images of the ^{64}Cu-CB-TE2A radioconjugate demonstrate considerably reduced activity in the kidneys and gastrointestinal tract compared to ^{64}Cu-DOTA radioconjugate. The authors reported that the high stability of ^{64}Cu-CB-TE2A radioconjugate in vivo contributes to less retention of the radioactivity as opposed to the ^{64}Cu-DOTA radioconjugate (*18*). Kidney uptake and retention of ^{64}Cu-NOTA conjugate was lower than the ^{64}Cu-DOTA-conjugate and very similar to ^{64}Cu-CB-TE2A-Y3-TATE at 1 h postinjection (*25*).

The effect of the length of the hydrocarbon spacer [0-carbon, β-Ala, 5-Ava, 8-Aoc, and 11-Aun] between the agonist BBN [7−14]NH_2 moiety and the radiochelate on the in vitro binding affinity toward GRP-Receptors was studied (*26*).The results illustrated that analogues containing either no spacer or the 11 carbon spacer (11-Aun) exhibited GRP-receptor specificity, but the measured affinity was less than 1% of the eight-carbon spacer analogue. The authors concluded that the length of the hydrocarbon spacer could be varied from three to eight carbon atoms without adversely affecting the resultant binding affinity.

Structural modifications at the C-terminus of bombesin yield peptides that retain their superb binding affinity for GRP-receptors, but also confer antagonist properties (*27, 28*). The rationale of developing antagonist agents is their capability of binding the receptors regardless of their limited capability to trigger internalization. The superb binding characteristics of antagonist radioconjugates may be due to their ability to bind a higher number of receptor binding sites than agonists (*24, 29*). These antagonist-based peptide constructs are now gaining attention as efficient targeting agents for diagnostic applications (*30, 31*). The in vitro biological results (*32*) as well as the solid-phase synthesis (*33*) of some of these parent peptides have been reported. One BBN analogue, [*D*-Phe^{6}, Leu-NHEt^{13}, des Met^{14}] BBN[6−14], was derivatized with a benzylaminodiglycolic acid linker and the open-chain tetraamine chelate to incorporate technetium to yield Demobesin-1 (Figure 1) (*33*). Results show that Demobesin-1 has a high binding affinity (IC_{50} = 0.7 nM) in human prostate PC-3 cancer cells. Pancreatic uptake of 58.7%ID/g at 30 min postinjection was also reported. Demobesin-1 internalized within the cells to approximately 25%. During the course of our work, Demobesin-1 was tested for its internalization properties using the intercellular calcium mobilization-based signaling assay in PC-3 and HEK-GRPR cells and an ELISA-based internalization assay in HEK-GRPR cells. On the basis of these results, the authors confirm that their construct was acting as an antagonist. In addition, Demobesin-1 exhibited a much higher in vivo uptake than the aforementioned Demobesin-4, an agonist; thus, the authors concluded that GRP-receptor antagonists may be preferable agents to GRP-receptor agonists for tumor targeting (*30*).

In this study, we report the solid-phase synthesis of an antagonist bombesin analogue, DOTA-aminohexanoyl-[*D*-Phe^{6}, Leu-NHCH$_2$CH$_2$CH$_3^{13}$, des Met^{14}] BBN [6−14] (**1**, "Bomproamide"; Figure 1), as a targeting vector for radioimaging human prostate cancer (PC-3) overexpressing GRP-receptors. This peptide was chosen because the reported IC_{50} of [*D*-Phe^{6}, Leu-NHCH$_2$CH$_2$CH$_3^{13}$, des Met^{14}] BBN [6−14] to guinea pig acini was higher (1.6 nM) than that observed for [*D*-Phe^{6}, Leu-NHCH$_2$CH$_3^{13}$, des Met^{14}] BBN [6−14] (7.0 nM) (*27*). The peptide is first synthesized and then equipped with a six-carbon linker to a DOTA chelate for the efficient incorporation of ^{111}In. The initial in vitro and in vivo evaluation of this radioconjugate in CF1 mice and those containing PC-3 prostate cancer xenografts in SCID mice are described.

MATERIALS AND METHODS

All reagents used were of analytical reagent or HPLC grade. All syntheses were conducted in a manual solid-phase peptide synthesis (SPPS) reaction vessel. HPLC analysis and separations were performed with a C-18 Kromosil column (5 μm, 100 Å, 150 mm $\times$ 4.5 mm, Keystone Scientific Inc.). HPLC solvents consisted of 0.1% aqueous trifluoroacetic acid (TFA) (solvent A) and acetonitrile (ACN) containing 0.1% TFA (solvent B) at a 1.0 mL/min flow rate and UV detection at 214 and 280 nm.

A TSQ700 mass spectrometer (Thermo Finnigan) was coupled to an HPLC equipped with a NovaPak C18 column (3.9 $\times$ 300 mm, Waters) for LC-MS analyses.

HPLC analysis and isolation of the ^{111}In-radiolabeled constructs were performed with a C-18 Jupiter (RP-18) HPLC analytical column, (5 μm, pore size 300 Å, 4.6 $\times$ 250 mm, Phenomenex). HPLC solvents consisted of water (H_2O) containing 0.1% TFA (solvent A) and ACN containing 0.1% TFA (solvent B). Elution system of 25% to 40% ACN in 60 min was used for purification. The flow rate was maintained at 1.5 mL/min for all the analytical and separation runs at 280 nm.

$^{111}InCl_3$ in 0.05 M HCl (pH $\sim$1.48) was obtained from Mallinckrodt Inc., St. Louis, MO. Radioactivity was counted using a well counter equipped with a sodium iodide (thallium), NaI(Tl), scintillation detector. Gamma ray radioactivity of the in vitro binding affinity (IC_{50}) studies was counted using a gamma counter.

All biodistribution studies performed during the course of this research were conducted using protocols approved by the

Institutional Animal Care and in accordance with U.S. Public Health Service Guidelines.

The micro single photon emission tomography (microSPECT) imaging was performed using a microCAT II SPECT/CT (Siemens Medical Solutions) small animal system composed of dual SPECT system. Each microSPECT detector contains 10 000 NaI(Tl) crystals (1.25 × 1.25 × 5 mm elements) with a detector pitch of 1.45 mm and a field of view of 145 mm × 145 mm. The detectors are coupled to a 3 × 3 array of position sensitive photomultiplier tubes (Hamamatsu H8500), each of which has a 49 × 49 mm^2 nominal active area and housing dimensions of 52 × 52 mm^2. The crystal arrays are separated by approximately 0.20 mm with the region between the crystals filled with an opaque white reflective compound material. The imaging was performed using dual pinhole collimators with interchangeable pinhole apertures of 2 mm in diameter. The pinhole focal length or detector-to-aperture distance was 90 mm. The pinhole apertures were fabricated as knife-edge apertures to minimize photon penetration and are fabricated of tungsten.

The micro computed tomography (CT) images were performed using Micro CT unit (microCAT II MicroCT scanner, CTI). The system consists of a fully shielded cabinet X-ray system with a maximum voltage of 80 kV, maximum current of 500 μA, and a tungsten anode. The X-ray detector has a 4096 × 4096 pixel charge-coupled device (CCD) array that is couple to a phosphor screen via a fiber-optic device. The scanner is a third-generation "step and shoot" system in which the low-power X-ray source and CCD array detector rotate about the specimen. Computer algorithms were use for reconstructing images of <50 μm isotropic voxel dimension using the *Cobra 4.1* reconstruction engine.

The human immortalized prostate PC-3 cancer cell lines (American type Culture Collection) used in the course of this study were grown in custom PRMI medium 1640 (Invitrogen Corp.) with 10% fetal bovine serum (US Bio-Technologies Inc.) and gentamicin (American Pharmaceutical Partners, Inc.). The PC-3 cell lines were grown and maintained by the University of Missouri Cell and Immunology Core Facility.

DOTA-Aminohexanoyl-[*D*-Phe^6, Leu-NHCH$_2$CH$_2$CH$_3^{13}$, des Met^{14}] BBN[6−14] (1), "Bomproamide.". The *D*-Phe^6, Leu-NHCH$_2$CH$_2$CH$_3^{13}$, des Met^{14} BBN[6−14]-HMBA resin precursor, **2,** was synthesized as previously described (*34*). Three equivalents, relative to the resin loading, of Fmoc-6-aminohexanoic acid (0.520 mmol, 183 mg) was dissolved in 9 mL NMP. HBTU (466 μmol, 177 mg) and HOBt (518 μmol, 79.0 mg) were dissolved in 3 mL DMF. These two solutions were mixed, and 3 equiv (518 μmol, 89 μL) of DIPEA were added and vortexed thoroughly for 10−15 min and added directly to **2** in a manual SPPS reaction vessel and agitated gently for 30 min under N_2 at rt. The Fmoc group was removed by adding 3−4 mL of 25% (v/v) piperidine/DMF to yield 6-aminohexanoyl-[*D*-Phe^6, Leu-NHCH$_2$CH$_2$CH$_3^{13}$, des Met^{14}] BBN [6−14]-HMBA resin, **3**. Three equivalents, relative to the resin loading, of DOTA *tris* (*t*-Bu ester) (0.520 mmol, 296 mg) were dissolved in 9 mL of NMP. The carboxylic acid moiety was activated as above and was mixed with **3** and agitated gently for 30 min under N_2 at rt to yield **4**. The acid-sensitive side chain protecting groups of histidine, tryptophan, and glutamine, as well as the three BOC protecting groups on DOTA, were removed by adding a deprotection−scavenger cocktail (10−20 mL cocktail per 1 g peptidyl resin) consisting of 95%TFA/2.5%H_2O/2.5%TIS for 3−4 h at rt with gentle agitation using a stream of N_2. DOTA-aminohexanoyl-[*D*-Phe^6, Leu-NHCH$_2$CH$_2$CH$_3^{13}$, des Met^{14}] BBN [6−14]-HMBA resin was separated by filtration, washed twice with TFA, then five times with NMP, and dried. Subsequently, a sample was swelled with THF (12 mL/g) for 1 h and a cleavage solution of TEA/propylamine/THF (1:5:5 v/v), 50 mL of cleavage cocktail/g peptidyl resin, was added to the mixture and stirred overnight (∼18 h) at 50 °C. The solution containing **1** was filtered and reduced in volume to ∼1 mL of yellowish oil. **1** was precipitated by the addition of cold diethyl ether to yield 180 mg (87.4% crude recovery) as white granules in 76% purity; $k' = 8.11$. Crude **1** was dissolved in 4 mL DMSO and 7 mL of ACN/H_2O (50:50 v/v) and purified by semi-preparative HPLC using 10% ACN/H_2O at starting flow rate of 4 mL/min with a gradient from 30% to 50% ACN in 60 min at a flow rate of 10 mL/minute. Fractions containing **1** with the same purity were collected and lyophilized to yield 23 mg (39.5%) as a white powder: $k' = 8.07$, >90% purity. ESI-MS showed the molecular ions (*m*/*z*): theoretical $C_{72}H_{108}O_{17}N_{18}$ = 1496.81; actual $(M + H)^+ = 1497.7$ and $(M + 2H)^{2+}/2 = 749.7$. The conjugate was stored at 4 °C.

In Vitro Competitive Cell Binding Affinity Assay. The binding affinity of **1** to immortalized human prostate carcinoma PC-3 cells was examined by competitive displacement of ^{125}I-Tyr^4 BBN. In brief, 22 000 cpm of ^{125}I-Tyr^4-BBN and eight increasing concentrations (from 3.33×10^{-13} to 3.33×10^{-6} M) of **1** were incubated for 30 min at 37 °C in humidified air containing 5% CO_2 with 3×10^4 PC-3 cells suspended at pH 7.4 in Roswell Park Memorial Institute (RPMI) medium 1640, containing 4.8 mg/mL *N*-(2-hydroxyethyl)piperazine-*N*′-(2-ethanesulfonic acid), HEPES, 0.1 μg/mL Bacitracin, and 2 mg/mL bovine serum albumin (BSA). At the end of the incubation period, the medium was aspirated and the cells were washed three times with fresh medium solution to remove any unbound radioactivity. The remaining cell-bound radioactivity was counted using a Packard Riastar gamma counter. The 50% inhibitory concentration (IC_{50}) value of was determined by plotting the percentage of the ^{125}I-Tyr^4-BBN radioactivity bound to the PC-3 cells surface receptors versus the concentration of **1**.

Labeling with ^{nat}In. A sample of **1** (1.5 mg, 1.0 μmol) was dissolved in NH_4OAc buffer (5 mg/mL, 65 mM, 200 μL) and mixed with a solution of $^{nat}InCl_3$ (2.2 mg, 10 μmol) in NH_4OAc buffer (200 μL). The pH of the NH_4OAc buffer solution was adjusted to ∼5.5−6.0 using 0.01 M aqueous HCl. The solution was incubated for 60 min at 80 °C. After cooling to rt, ^{nat}In-**1** was obtained as a white powder (1.3 mg, 81% crude recovery); $k' = 9.03$, 87.5% purity. ESI-MS showed the molecular ions (*m*/*z*): theoretical $C_{72}H_{105}InO_{17}N_{18}$ = 1608.69; actual $(M + H)^+$ = 1610.1, and $(M + 2H)^{2+}/2 = 805.5$.

Radiolabeling with ^{111}In. A sample of conjugate **1** (110 μg, 67.0 nmol) was dissolved in ammonium acetate (NH_4OAc) buffer (200 μL, 0.4 M, pH 7.0) and mixed with ascorbic acid (∼20 mg). $^{111}InCl_3$ (5.55 MBq, 150 μCi) as $^{111}InCl_3$ in 0.05 M HCl (pH ∼1.48) was added to the solution of **1** (resultant pH ∼5.5) and incubated for 60 min at 80 °C. Ammonium acetate buffer solution, pH 7.0, was used to adjust the pH of the radiolabeling mixture. EDTA (50 μL, 0.002 M) was added to chelate any remaining $^{111}In^{3+}$, and the reaction mixture was allowed cool to rt. A few crystals of $CuSO_4 \cdot 5H_2O$ were added to complex excess **1**. Aliquots (25 μL) of the radiolabeling mixture solution were subjected for HPLC analysis. The HPLC radiochromatogram indicates that 74% of the detected radioactivity was located at t_R = 18.86 min corresponding to ^{nat}In-**1**. The HPLC UV chromatogram indicates the absence of **1**, while the UV peak corresponding to ^{nat}Cu-DOTA−peptide conjugate retention time appeared (t_R = 20 min).

^{111}In-**1** was purified by RP-HPLC with a gradient consisting of 25% to 40% ACN in 60 min (1.0% ACN/4.0 min). The HPLC eluent containing pure ^{111}In-**1**, was diluted with 3 mL of water and concentrated on an Empore C18-High Performance Extraction Disk (C18-HD) Cartridge 4215. The retained radioactivity was eluted using a 400 μL of ethanol/saline (6:4 v/v)

mixture. A Capintec CRC-15W Dose Calibrator/well counter was used to measure the collected radioactivity of ^{111}In-**1** before and after concentration. Approximately 90−94% of the original radioactivity was recovered and the radiochemical purity of the formulated ^{111}In-DOTA−peptide conjugates was found to be ≥98% by HPLC.

For the in vitro internalization and efflux studies, as well as in vivo pharmacokinetic studies, ^{111}In-**1** was diluted with an adequate volume of sterile normal saline to achieve 0.148−0.185 MBq (4−5 μCi)/100 μL solution. For the SPECT/CT imaging studies, the ethanol concentration was reduced to <5% by evaporation under a stream of nitrogen. Quality control runs were performed using an HPLC separation gradient of 25% to 40% ACN in 60 min. Only samples with radiochemical purity of >99% were used for the subsequent in vivo and imaging studies.

In Vitro Internalization and Efflux Studies. The degree of residualization in the PC-3 human prostate cancer cells was tested by incubating ∼20 000 cpm of ^{111}In-**1** with 3×10^4 PC-3 cells at 37 °C in an environment of 5% CO_2 for various time periods. The PC-3 cells were suspended in an ice-cooled RPMI medium comprising 2.8 mg/mL HEPES and 2 mg/mL BSA (pH 7.4). After 15, 30, 45, 60, 90, and 120 min incubation periods, the interaction between ^{111}In-**1** and the PC-3 cells was stopped by aspiration of the incubation medium and washing the cells three times with fresh ice-cooled cell culture medium. The PC-3 cell-surface-bound radioactivity was removed by incubating the PC-3 cells with an acidic buffer solution (pH 2.5) comprising 0.2 M acetic acid and 0.5 M sodium chloride for 5 min. At the end of the incubation period, the PC-3 cells were precipitated from the buffer solution by centrifugation. The supernatant, containing the removed PC-3 cell-surface-bound radioactivity, was aspirated, and the precipitated PC-3 cells were washed two times with fresh pH 2.5 buffer solution. Both the supernatant and the PC-3 cells were counted for their associated radioactivity, and thereafter, the percentages of both the internalized and the cell-surface-bound radioactivity were calculated.

The efflux studies were performed using the PC-3 cells at the time identified above with the highest percentage of ^{111}In-**1** internalization. The PC-3 cells after 45 min incubation were allowed to efflux at 15, 30, 45, 60, and 90 min periods. The PC-3 cells were treated and counted for their associated radioactivity as described above. The percentages of both the cell-surface-bound and effluxed radioactivity were calculated.

Biodistribution Studies in Healthy CF-1 Mice. Twenty healthy CF-1 mice mice, with an average weight of 27 g (five mice per time point), were injected with 100 μL of 0.148 MBq (4 μCi) aliquots of ^{111}In-**1** via the tail vein. The mice were sacrificed by neck dislocation at 0.25, 1, 4, and 24 h postinjection. Blood and urine were collected immediately after the mice were sacrificed. The organs and tissues of interest were excised and weighed, and their associated radioactivity was counted using an NaI(Tl) well counter. The small and large intestines as well as the stomach were weighed and counted without evacuating their contents. The %ID of the whole blood weight and %ID/g blood were calculated assuming that the whole blood volume constituted 6.5% of the whole mouse body weight. The distribution of radioactivity was calculated as a percentage of the injected dose per organ (%ID/organ) and as a percentage of the injected dose per gram (%ID/g), using an in-house program.

Blocking Studies. Three mice were injected with ^{111}In-**1** (100 μL, 0.185 MBq, 5 μCi) aliquots via the tail vein. Three mice were injected with ^{111}In-**1** (100 μL, 0.185 MBq, 5 μCi) along with 100 μg BBN via the tail vein. The mice were sacrificed by neck dislocation 1 h postinjection. The organs and tissues of interest were excised and weighed, and their associated radioactivity was counted. Distribution of radioactivity was calculated as %ID/organ and %ID/g using an in-house program.

Pharmacokinetic Studies in PC-3 Tumor-Bearing SCID Mice. PC-3 cells were suspended in the culture media, centrifuged, and the culture media decanted. The resultant PC-3 cells pellets were suspended in Dulbecco's phosphate-buffered saline solution. The concentrations of the PC-3 cells were adjusted to approximately 5 million cells per 100 μL of Dulbecco's phosphate-buffered saline solution. Four-to-five-week-old ICR (Institute of Cancer Research) severely compromised immunodeficient (SCID) female mice were obtained from Taconic Farms. The mice were fed with the supplied irradiated rodent chow and water (Ralston Purina Corporation) ad libitum. Each group of five mice was housed in a sterile microisolator cage (Alternative Design) in temperature-and humidity-controlled rooms with alternating 12 h periods of light and darkness. The mice were anesthetized for PC-3 cells inoculation with a gas composed of ∼3.5% isoflurane (Baxter Healthcare Corp.) and ∼1 L/min oxygen. The gas anesthesia was administrated to SCID mice using a non-rebreathing multiterminal anesthesia vaporizer apparatus (Summit Medical Equipment Co.). Approximately five million PC-3 cells suspended in 100 μL of normal sterile saline were inoculated subcutaneously in the bilateral flank of each SCID mice under gas anesthesia. The tumors were allowed to grow (ranging from 0.2 to 1.0 g) in the flanks of the SCID mice for 3−4 weeks after inoculation. The biodistribution was studied by injecting twenty mice, of average weight of 23.4 g (five mice per time point), with 100 μL (0.185 MBq, 5 μCi) aliquots of ^{111}In-**1** via the tail vein. The mice were sacrificed by neck dislocation at 0.25, 0.5, 1, and 4 h postinjection. Blood and urine were collected immediately after the mice were sacrificed. The organs and tissues of interest were processed as described above.

MicroSPECT/MicroCT Imaging Studies. The microSPECT imaging was performed using a microCAT II SPECT/CT (Siemens Medical Solutions) small animal system composing of dual SPECT system. The microCT images performed using MicroCT unit (microCAT II MicroCT scanner, CTI, Knoxville, TN). The tomographic SPECT imaging of a PC-3 tumor-bearing SCID mouse was performed at 1 h postinjection with ^{111}In-**1** (11.1 MBq, 300 μCi). The mouse was sacrificed 1 h after administration of ^{111}In-**1**, and scanned for γ-ray acquisition. The mouse was aligned at the center of the scanner using a laser beam. The image was collected with the detectors fully calibrated and normalized for ^{111}In. The mouse was scanned for 60 projections (rotation steps) over 360°. Reconstructed SPECT mouse data generated with a 3D-OSEM algorithm with geometrical corrections. The reconstructed images were smoothed postreconstruction with a 3D Gaussian kernel. A concurrent microCT scan was performed on the same mouse for future anatomical coregistration of the SPECT data.

RESULTS AND DISCUSSION

Synthesis of Construct 1. Bombesin and GRP most likely exert their effects through binding to the membrane surface G-protein bound receptors characterized by their similar seven trans-membrane domains which cluster to form the peptide binding pocket (*2*). The bombesin analogue, [*D*-Phe^6, Leu-NHCH$_2$CH$_2$CH$_3$^{13}, des Met^{14}] BBN[6−14], was developed as a potential antagonist binding motif for targeting GRP receptors (*35, 36*). Placing *D*-Phe in position 6 was based on the reported results indicating that placing *D*- or an unnatural amino acid in the peptide increases the resistance to proteolysis (*35, 36*). The readily oxidized Met^{14} residue was removed so that leucine became the C-terminal residue in position 13. This terminus was derivatized upon cleavage from the resin with propylamine, resulting in a structural change that confers

Scheme 1

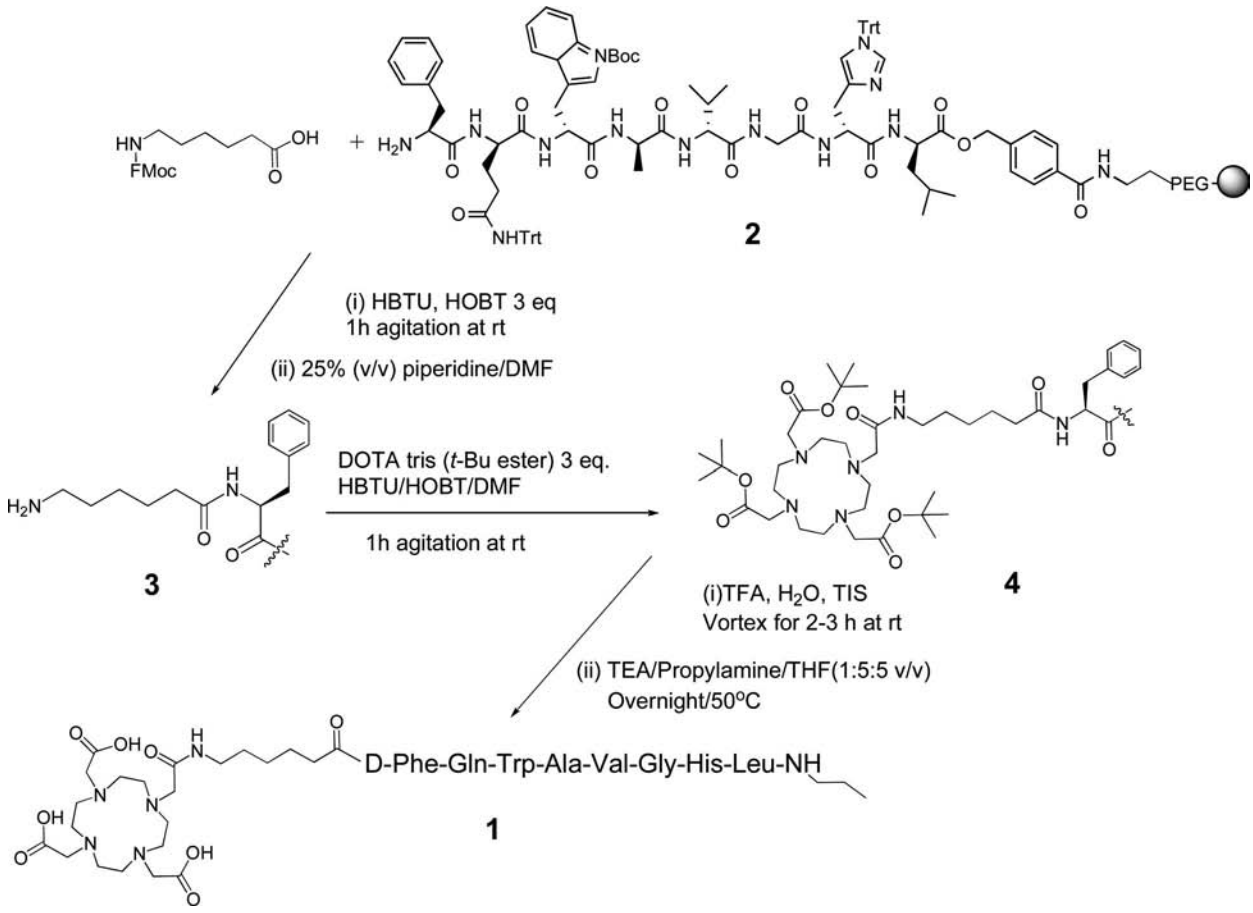

antagonist behavior on the peptide. DOTA was selected as a bifunctional chelating agent to confer high thermodynamic stability and kinetic inertness to the formed ^{111}In chelate. Since it is reported that the length of the hydrocarbon spacer could be varied from at least 3 to 8 carbon atoms without interrupting the binding affinity to the GRP receptors (*26*), we linked DOTA to the peptide through an aminohexanoyl moiety. The construct, DOTA-aminohexanoyl-[*D*-Phe^6, Leu-NHCH$_2$CH$_2$CH$_3$^{13}, des Met^{14}] BBN[6−14] (**1**), "Bomproamide", was synthesized on HMBA resin as shown in Scheme 1 using conventional solid-phase peptide synthesis strategies and our published protocols (*34*). Briefly, coupling of Fmoc-6-aminohexanoic acid and DOTA *tris*-(*t*-Bu ester) was performed sequentially by conventional in situ carboxy activation using HBTU and HOBT to afford **3** and **4**, respectively. Side chain deprotection using TFA yielded DOTA-hexanoyl-*D*-Phe^6-BBN [6−13]-HMBA resin. Treatment with TEA/propylamine/THF (1:5:5 v/v) overnight at 50 °C achieved cleavage of the peptide from the resin with concomitant formation of the C-terminal propylamide to afford **1**. After purification of **1** by RP-HPLC, 23 mg (∼13%) at >92% purity was recovered and characterized using ESI-MS.

In Vitro Competitive Cell Binding Affinity Assay. The in vitro competitive cell binding affinity experiments were performed with **1** against ^{125}I-Tyr^4-BBN as the GRP receptor radioligand. The experiments were performed with immortalized human androgen-insensitive prostate cancer PC-3 cells that are known to overexpress the GRP receptors predominantly. **1** retained high affinity (1.36 ± 0.09 nM) toward the GRP-receptor subtype.

Labeling with ^{nat}In and ^{111}In and Characterization. The metalation of **1** was performed under standard conditions and was analyzed by LC-MS. Results indicate that the HPLC peak at t_R = 23.5 min (k' = 8.7) corresponds to the ^{nat}In-DOTA−peptide, ^{nat}In-**1**, in 89% purity. The radiolabeling of **1** with ^{111}In was performed and the HPLC chromatograms show the coincidence of the major HPLC radio peak with the UV peak of ^{nat}In-**1**, offset only by the order of respective detectors of the HPLC. The isolation of pure ^{111}In-**1** was achieved by two modifications of a standard radiolabeling protocol prior to preparative HPLC. First, EDTA was added at the end of the radiolabeling period to chelate any remaining noncomplexed ("free") $^{111}In^{3+}$. In addition, a few crystals of $CuSO_4 \cdot 5H_2O$ were added to complex excess **1**. Aliquots (25 μL) of the radiolabeling mixture were analyzed by HPLC. The chromatogram depicts that most of the detected radioactivity was located at t_R = 18.86 min corresponding to ^{111}In-DOTA−peptide conjugate, ^{111}In-**1**, while the UV peak corresponding to the unlabeled DOTA−peptide conjugate, **1**, was absent. The UV peak at longer retention time (t_R = 20 min) is assigned as ^{nat}Cu-**1**. Pure ^{111}In-**1** was obtained through preparative HPLC in 75−80% radiochemical yield in high radiochemical purity. The corresponding UV chromatogram confirms the absence of **1** or ^{nat}Cu-**1**. This result is important, as the presence of excess **1** or ^{nat}Cu-**1** could saturate the receptors in vivo. Only samples with radiochemical purity of >99% were used for the subsequent in vivo studies. Concentration of the HPLC eluent containing ^{111}In-**1** was achieved through solid-phase extraction. Approximately 90−94% of the original radioactivity could be recovered after the formulation.

In Vitro Internalization and Efflux Studies. Internalization is the process of radioconjugate accumulation over time within the cells expressing the targeting receptors. The internalization behavior of ^{111}In-**1** in the human PC-3 prostate cancer cells was studied by incubation at 37 °C for 15, 30, 45, 60, 90, and 120

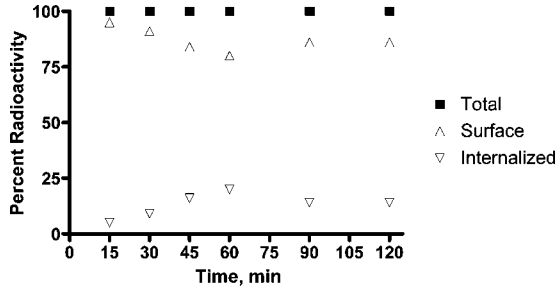

Figure 2. Internalization of ^{111}In-**1** in prostate cancer PC-3 cells as a function of time ($n = 2$; trials conducted in duplicate).

min. The percentage of ^{111}In-**1** trapping within the cells was characterized by a steady and gradually increasing rate of accumulation within the cells up to 45 min of incubation (Figure 2). Internalization reaches its maximum value, ~14%, after 45 min of incubation. The percentage of surface-bound radioactivity exceeded the percentage of the internalized activity over the entire investigated time points of incubation. The internalization does not increase by extending the incubation period beyond 45 min. The percentage of the internalized radioligand decreases to 12% at 60 min of incubation and then plateaus at 120 min of incubation. The level of internalization of ^{111}In-**1** is consistent with its antagonist-based structure.

Efflux, on the other hand, is the process of radioconjugate externalization over time from the cells expressing the targeted receptors. The externalization behavior of ^{111}In-**1** from the PC-3 cells was observed after a 45 min incubation, the time at which the highest internalization percentage (14%) had been noted. Efflux of radioactivity was studied over 15, 30, 45, 60, and 90 min. The internalized radioactivity remained almost constant over the investigated efflux time points (data not shown). This behavior is consistent with prior trapping of a small amount of ^{111}In-**1** within the cells, and a significantly slow washout.

In Vivo Biodistribution Studies. The usefulness of bombesin-based constructs for in vivo GRP receptor targeting has been primarily assessed using agonists. Very little is known about the potential of using antagonist-based constructs as suitable biomarkers for in vivo GRP receptor imaging (*33*). Thus, the in vivo targeting behavior of ^{111}In-**1** for GRP receptors was studied using healthy (CF-1) and tumor-bearing SCID mice.

Pharmacokinetic Studies in Healthy CF-1 Mice. The biodistribution behavior of ^{111}In-**1** in healthy CF-1 mice at 0.25, 1, 4, and 24 h postinjection is presented in Table 1. The pancreas is the primary nonmalignant tissue that normally expresses a high density of GRP cell-surface receptors (*37*). It is well-established that accumulation of the radioactivity in the pancreatic tissue in preference over other tissues is a direct reflection of the efficiency of the radioconjugate under evaluation for in vivo targeting of GRP cell surface receptors (*13, 26, 33*). The results indicate that ^{111}In-**1** demonstrates rapid (0.25 h PI) and high (12.21 ± 3.2% ID/g) uptake in the pancreatic tissue. This pancreatic uptake was reduced to 0.95 ± 0.26%ID/g at 1 h PI and diminished to 0.01 ± 0.01%ID/g at 4 h PI. The observed decrease of pancreatic uptake was consistent with the suspected uptake behavior of an antagonist-based construct that exhibits limited internalization. It has been reported that the pancreatic uptake of Demobesin-1 decreases from 33.13 ± 3.63%ID/g at 1 h PI to 4.59 ± 0.63%ID/g at 4 h PI (*33*). Marginal uptake was observed in the liver (1.33 ± 0.24%ID/g) and abdominal area at 0.25 h PI. The liver uptake diminishes significantly (0.18 ± 0.02%ID/g) at 1 h PI. Similarly, the abdominal uptake decreased markedly [small (0.35 ± 0.03%ID/g) and large (0.20 ± 0.05%ID/g) intestine] at 1 h PI. ^{111}In-**1** demonstrated rapid clearance from the blood (0.17 ± 0.05%ID/g at 1 h PI) mainly by renal extraction (1.74 ± 0.32%ID/g at 1 h PI) and urinary tract excretion (0.86 ± 0.46%ID/g at 1 h PI) into the urine (94.70 ± 0.62%ID/g at 1 h PI).

Table 1. Biodistribution of ^{111}In-1 in Healthy CF-1 Mice at 0.25, 1, 4, and 24 h PI ($n = 5$)[a]

organ/tissue	0.25 h PI	1 h PI	4 h PI	24 h PI
bladder	3.34 ± 0.59	0.86 ± 0.46	0.05 ± 0.06	0.04 ± 0.6
heart	1.52 ± 0.49	0.10 ± 0.06	0.03 ± 0.01	0.00 ± 0.01
lung	2.00 ± 0.50	0.30 ± 0.09	0.29 ± 0.19	0.08 ± 0.06
liver	1.33 ± 0.24	0.18 ± 0.02	0.07 ± 0.01	0.02 ± 0.01
kidneys	7.56 ± 0.89	1.74 ± 0.32	0.90 ± 0.11	0.09 ± 0.03
spleen	0.83 ± 0.27	0.10 ± 0.02	0.03 ± 0.01	0.01 ± 0.01
stomach	0.75 ± 0.13	0.17 ± 0.03	0.06 ± 0.02	0.00 ± 0.00
s. intestine	1.74 ± 0.30	0.35 ± 0.03	0.14 ± 0.05	0.01 ± 0.00
l. intestine	1.37 ± 0.41	0.20 ± 0.05	0.65 ± 0.08	0.04 ± 0.01
muscle	0.81 ± 0.19	0.07 ± 0.01	0.01 ± 0.01	0.00 ± 0.00
bone	1.07 ± 0.35	0.11 ± 0.08	0.02 ± 0.01	0.02 ± 0.02
brain	0.20 ± 0.04	0.02 ± 0.00	0.01 ± 0.00	0.00 ± 0.00
pancreas	12.21 ± 3.2	0.95 ± 0.26	0.31 ± 0.04	0.01 ± 0.01
blood	3.30 ± 2.98	0.17 ± 0.05	0.01 ± 0.00	0.00 ± 0.00
carcass	1.61 ± 0.11	0.17 ± 0.04	0.03 ± 0.00	0.00 ± 0.00
excretion (% ID ± SD)	52.65 ± 4.65	94.70 ± 0.62	97.96 ± 0.16	98.80 ± 0.05

[a] All data, except excretion, are presented as an average %ID/g ± SD.

Table 2. Biodistribution of ^{111}In-1 in Healthy CF-1 Mice at 1 h Postinjection in the Presence and Absence of 100 μg BBN ($n = 3$)[a]

organ/tissues	blocked	control
bladder	1.96 ± 1.39	0.99 ± 0.69
heart	0.13 ± 0.02	0.09 ± 0.04
lung	0.35 ± 0.05	1.37 ± 0.08
liver	0.24 ± 0.01	0.26 ± 0.07
kidneys	1.44 ± 0.26	1.54 ± 0.16
spleen	0.11 ± 0.04	0.17 ± 0.03
stomach	0.11 ± 0.03	0.38 ± 0.07
s. intestine	0.69 ± 0.11	0.90 ± 0.28
l. intestine	0.13 ± 0.03	0.44 ± 0.31
muscle	0.06 ± 0.01	0.04 ± 0.01
bone	0.09 ± 0.03	0.07 ± 0.01
brain	0.02 ± 0.00	0.01 ± 0.00
pancreas	0.20 ± 0.01	2.04 ± 0.17
blood	0.24 ± 0.02	0.16 ± 0.09
carcass	0.20 ± 0.02	0.16 ± 0.01
excretion (%ID ± SD)	91.25 ± 0.44	90.97 ± 1.08

[a] All data, except excretion, are presented as an average %ID/g ± SD.

Blocking Studies. The effect of blocking the GRP receptors on the pancreatic uptake of ^{111}In-**1** was investigated in CF-1 mice (Table 2). More than 90% of the GRP receptor-mediated radioconjugate uptake in the pancreatic tissue was blocked by coinjection of 100 μg of BBN. The pancreatic uptake in the control mice was 2.04 ± 0.17%ID/g at 1 h postinjection and was significantly decreased by a factor of 10 to 0.20 ± 0.01%ID/g by blocking the binding sites with BBN. The remaining activity in the pancreas may be a reflection of GRP receptor subtype-mediated trapping of ^{111}In-**1**. Uptake studies in healthy CF-1 mice at 1 h PI showed pancreatic uptake of 0.95 ± 0.26%ID/g and lung uptake of 0.30 ± 0.09%ID/g (Table 1). However, the blocking studies in healthy CF-1 control mice at 1 h postinjection showed pancreatic uptake of 2.04 ± 0.17%ID/g and lung uptake of 1.37 ± 0.08%ID/g (Table 2). The observed difference in the pancreas and lung uptakes between these two studies might be due to the differences in the density of normal GRP receptor expression. This expectation is strongly confirmed by the substantial decrease, ~75% less, in uptake (0.35 ± 0.05%ID/g) of the blocked lung tissue.

Pharmacokinetic Studies in PC-3 Tumor-Bearing SCID Mice. The pharmacokinetic studies in healthy CF-1 mice reflect a significant decrease of ^{111}In-**1** in the tissues with time. At 24 h PI, the investigated tissues retained insignificant radioactiv-

Table 3. Biodistribution of ^{111}In-1 in PC-3 Tumor-Bearing SCID Mice ($n = 5$)[a]

organ/tissue	0.25 h PI	0.5 h PI	1 h PI	4 h PI
bladder	14.09 ± 21.1	7.03 ± 8.68	1.67 ± 1.06	0.26 ± 0.14
heart	1.85 ± 0.27	1.00 ± 0.30	0.16 ± 0.06	0.03 ± 0.02
lung	4.45 ± 0.82	3.56 ± 1.72	1.78 ± 1.64	1.48 ± 2.54
liver	2.14 ± 0.14	0.88 ± 0.20	0.27 ± 0.07	0.12 ± 0.02
kidneys	11.84 ± 1.97	5.88 ± 1.91	3.06 ± 0.92	2.24 ± 1.02
spleen	0.98 ± 0.37	0.59 ± 0.27	0.15 ± 0.08	0.06 ± 0.02
stomach	1.91 ± 0.29	1.17 ± 0.37	0.34 ± 0.07	0.05 ± 0.03
s. intestine	3.41 ± 0.54	1.46 ± 0.35	0.62 ± 0.19	0.18 ± 0.11
l. intestine	1.64 ± 0.29	0.59 ± 0.07	0.54 ± 0.68	0.88 ± 0.39
muscle	1.00 ± 0.10	0.40 ± 0.13	0.07 ± 0.04	0.02 ± 0.01
bone	1.21 ± 0.42	0.78 ± 0.40	0.08 ± 0.02	0.05 ± 0.07
brain	0.17 ± 0.06	0.12 ± 0.04	0.02 ± 0.01	0.00 ± 0.00
pancreas	14.88 ± 1.86	3.99 ± 0.49	0.96 ± 0.18	0.41 ± 0.14
tumor #1	7.33 ± 1.18	5.41 ± 1.98	3.91 ± 0.46	2.02 ± 0.34
tumor #2	6.47 ± 0.82	6.11 ± 1.04	3.52 ± 0.70	2.29 ± 0.36
blood	4.28 ± 0.59	1.85 ± 0.47	0.33 ± 0.15	0.02 ± 0.02
carcass	2.26 ± 0.34	1.16 ± 0.41	0.39 ± 0.38	0.05 ± 0.03
excretion (% ID ± SD)	40.86 ± 4.60	68.70 ± 7.55	89.15 ± 7.11	96.16 ± 1.06
tumors	6.90 ± 1.06	5.76 ± 1.54	3.72 ± 0.60	2.15 ± 0.36

[a] All data, except excretion, are presented as an average %ID/g ± SD.

ity. Accordingly, 0.5 h PI was selected as a new time point for investigating the pharmacokinetic behavior of ^{111}In-**1** in PC-3 tumor-bearing SCID mice, and the 24 h time point was excluded. The biodistribution behavior of ^{111}In-**1** in immortalized prostate cancer PC-3 tumor-bearing mice at 0.25, 0.5, 1, and 4 h postinjection are presented in Table 3. Rapid (15 min postinjection) and significantly high uptake (6.90 ± 1.06%ID/g) as observed in the tumors. The tumor uptake decreased over time to a value at 4 h PI that was approximately 30% that found at 15 min (2.15 ± 0.36%ID/g). In contrast to the prolonged uptake of ^{111}In-**1** in the tumor tissue, fast clearance from the other tissues was observed. This behavior is consistent with the reported data of antagonist-based Demobesin 1 (*33*). In these animals, ^{111}In-**1** demonstrated rapid (0.25 h PI) and significantly high (14.88 ± 1.8%ID/g) uptake in the pancreatic tissue. This pancreatic uptake showed a steep reduction to 3.99 ± 0.49%ID/g at 0.5 h PI and 0.96 ± 0.18%ID/g at 1 h PI. The pancreatic uptake behavior in PC-3 tumor-bearing mice mirrored its behavior in healthy CF-1 mice. The pancreatic uptake of ^{111}In-**1** at 4 h PI decreased by ~57% of its uptake at 1 h PI. This behavior is comparable with the reported decrease (~65%) of Demobesin-1 (*33*). These results are consistent with the marked internalization behavior of the agonist-based constructs and the limited internalization capabilities of the antagonist-based constructs. The observed high retention of ^{111}In-**1** in the tumor tissue over the investigated time points may be due in part to the fact that the human tumor xenografts are supported by murine vasculature architecture (*26*). It is also reported that antagonists form slowly dissociating antagonist−receptor complexes that result in long-lasting in vivo receptor binding (*38*). On the other hand, the low retention of ^{111}In-**1** in the pancreatic tissue may be due to excessive enzymatic activity of the pancreatic tissue as well as the limited internalization capabilities of the antagonist-based constructs (*33*). The high uptake and retention in the tumors and pancreas cells over the entire investigated time points is a direct reflection of the efficiency of antagonist-based constructs for in vivo targeting of the GRP cell surface receptors. Therefore, antagonist-based constructs seem to be the candidates of choice for in vivo imaging purposes, while for in vivo therapy purposes, the agonist-based constructs (trigger the internalization process that confers the basis for an efficient accumulation of the radioconjugate within the cells over the time) seem to be the candidates of choice.

Table 4. Target-to-Nontumor Uptake Ratios of ^{111}In-1 in PC-3 Tumor-Bearing SCID Mice ($n = 5$)

tumor/nontumor tissue	0.25 h PI	0.5 h PI	1 h PI	4 h PI
tumor/blood	1.62	2.87	10.76	108.5
tumor/muscle	6.92	13.28	50.71	108.5
tumor/liver	3.23	6.03	13.15	18.08
tumor/kidneys	0.58	0.90	1.16	0.97
tumor/lung	1.56	1.49	1.99	1.47
tumor/bladder	0.49	0.76	2.13	8.35
tumor/spleen	7.06	9.00	23.67	36.17
tumor/stomach	3.62	4.54	10.44	43.4
tumor/l. intestine	4.33	9.00	6.57	2.47
tumor/s. intestine	2.03	3.64	5.73	12.06

Significant uptake of 4.45 ± 0.82%ID/g was observed in the lung tissue at 0.25 h PI and retained over the entire investigated time points. This lung uptake may be in part due to the normal expression of the GRP receptors in this tissue (*39*). Lung tissue is one of the gastro-entero-pancreatic-neuroendocrine tissues (GEP-NET) that is characterized by normal expression of GRP receptors in the interface between the endocrine hormonal cells and nervous cells (*37*). It is also reported that the three bombesin family receptors are expressed with various degrees in overlapping subsets of lung cancer cell lines (*40*, *41*). The committed lung uptake at the various investigated time points may act as a prognostic biomarker for early detection of small cell lung cancer (SCLC) and non-small lung cells (NSLC) carcinogenesis. More research would have to be conducted to explore this hypothesis further.

Low uptake of ^{111}In-**1** was observed in the liver (2.14 ± 0.14%ID/g) and abdominal area. The liver uptake decreased (0.88 ± 0.2%ID/g) at 0.5 h postinjection. Similarly, the abdominal uptake decreased markedly [small (1.46 ± 0.35%ID/g) and large (0.59 ± 0.07%ID/g) intestines] at 0.5 h PI. ^{111}In-**1** demonstrated rapid clearance from the blood (1.85 ± 0.47%ID/g at 0.5 h PI) mainly by renal extraction (5.88 ± 1.91%ID/g at 0.5 h PI) and urinary tract excretion (7.03 ± 8.68%ID/g at 0.5 h PI) into the urine (68.70 ± 7.55%ID at 0.5 h PI).

Tumor to Nontumor Uptake Ratios of ^{111}In-1. The main pharmacokinetic consideration in the development of peptide-based imaging agents is to achieve diagnostically useful tumor to nontumor uptake ratios (~5) with minimal time required to achieve them. Table 4 shows the tumor/nontumor uptake ratios of ^{111}In-**1** at 0.25, 0.5, 1, 4 h postinjection. At the same time, significantly high (>10) and diagnostically useful ratios were achieved in most of the tissues after 1 h postinjection. The tumor/nontumor uptake ratios in certain tissues (muscle, spleen) were significantly high, >20, at both 1 and 4 h PI. Comparable (difference less than five) target to nontarget uptake ratios were achieved at 1 and 4 h PI in certain tissues (liver and small intestine). Higher tumor/nontumor uptake ratios were achieved at 1 h PI, rather than 4 h, in certain tissues (kidneys, lung, and large intestine). For prostate cancer radioimaging, there is high demand for achieving minimal possible noise in the abdominal area (large intestine, small intestine, stomach, liver, kidneys, and bladder) in a minimal possible time. It is clear from the tumor/nontumor uptake ratios that diagnostically useful ratios in mice could be achieved in most of the abdominal tissues (except bladder) at 1 h PI. Accordingly, microSPECT imaging of PC-3 tumor xenografts in SCID mouse was performed at 1 h PI.

MicroSPECT/Micro CT Imaging Studies. MicroSPECT/CT images of immortalized prostate cancer-xenografts (Figure 3) were taken over 16 h after 1 h PI of 11.1 MBq (300 μCi) of ^{111}In-**1** in a PC-3 tumor-bearing SCID mouse. The camera head was positioned at multiple angles around the mouse body accumulating as many as 360° of views at specific angular intervals. The radioactivity associated with the images was acquired over time due to the rapid clearance properties of ^{111}In-

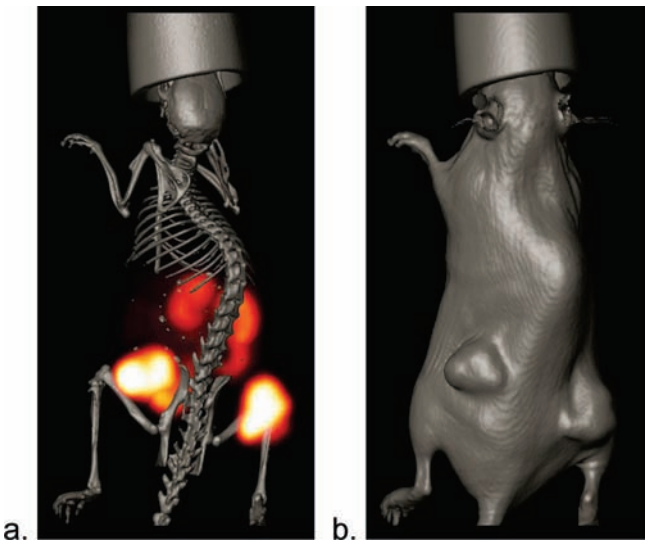

Figure 3. (a) Axial MicroSPECT/CT image of PC-3 xenografts in a SCID mouse after 1 h of ^{111}In-**1** administration. (b) Skin CT image. Details of acquisition are found in the Materials and Methods.

1. A reconstruction process was performed to retrieve the radiotracer spatial distribution from the projection data using a fully 3D OSEM algorithm. Regions where backprojection lines from different angles intersect represent areas that contain a higher concentration of radiopharmaceutical. The PC-3 tumor xenografts in the SCID mouse were visualized clearly in the images. Delineating the kidneys in the image is an indication of the radioconjugate clearance via renal excretion. The images revealed the absence of the liver's anatomical boundaries and delineated the insignificance of radioactivity uptake in the gastrointestinal tract. The radioactivity distribution and accumulation in the microSPECT/CT images are consistent with the biodistribution data obtained from the pharmacokinetic studies. The power of the presented diagnostic imaging lies in its external detection of the in vivo radioactivity delineating anatomical boundaries and having a clue to status of the organs being imaged.

CONCLUSION

The bombesin antagonist, [*D*-Phe^6, Leu-NHCH$_2$CH$_2$CH$_3$^{13}, des Met^{14}] BBN[6−14], was synthesized and developed into ^{111}In-DOTA-aminohexanoyl-[*D*-Phe^6, Leu-NHCH$_2$CH$_2$CH$_3$^{13}, des Met^{14}] BBN[6−14] (^{111}In-**1**), "Bomproamide", a high-affinity imaging agent targeting the GRP receptor. This study demonstrates the potential of using the bombesin analogues possessing antagonist C-terminal vectors as a diagnostic candidate of choice for specific in vivo targeting of the tumors overexpressing GRP receptors.

ACKNOWLEDGMENT

The authors acknowledge the National Cancer Institute (P50 CA 103130: Center for Single Photon-Emitting Cancer Imaging Agents, W.A. Volkert, PI) for partial support of this research. This work was supported with the resources and the use of facilities at the Chemistry Department, University of Missouri-Columbia and Harry S. Truman Memorial VA Hospital.

LITERATURE CITED

(1) Anastasi, A., Erspamer, V., and Bucci, M. (1971) Isolation and structure of bombesin and alytesin, 2 analogous active peptides from the skin of the European amphibians *Bombina* and *Alytes*. *Experientia 27*, 166–7.

(2) McDonald, T. J., Jornvall, H., Nilsson, G., Vag-Bloom, S. R., and Mutt, V. (1979) Characterization of a gastrin releasing peptide from porcine non-antral gastric tissue. *Biochem. Biophys. Commun. 90*, 227–233.

(3) Ohki-Hamazaki, H., Iwabuchi, M., and Maekawa, F. (2005) Development and function of bombesin-like peptides and their receptors. *Int. J. Dev. Biol. 49*, 293–300.

(4) Reubi, J. C., and Waser, B. (2003) Concomitant expression of several peptide receptors in neuroendocrine tumours: molecular basis for in vivo multireceptor tumour targeting. *Eur. J. Nucl. Med. Mol. Imaging 30*, 781–93.

(5) Reubi, J. C., Korner, M., Waser, B., Mazzucchelli, L., and Guillou, L. (2004) High expression of peptide receptors as a novel target in gastrointestinal stromal tumours. *Eur. J. Nucl. Med. Mol. Imaging 31*, 803–10.

(6) Reubi, J. C., Gugger, M., and Waser, B. (2002) Co-expressed peptide receptors in breast cancers as molecular basis for in vivo multireceptor tumor targeting. *Eur. J. Nucl. Med. Mol. Imaging 29*, 855–862.

(7) Darker, J. G., Brough, S. J., Heath, J., and Smart, D. (2001) Discovery of potent and selective peptide agonists at the GRP-preferring bombesin receptor (BB2). *J. Pept. Sci. 7*, 598–605.

(8) Fleischmann, A., Laderach, U., Friess, H., Buechler, M. W., and Reubi, J. C. (2000) Bombesin receptors in distinct tissue compartments of human pancreatic diseases. *Lab. Invest. 80*, 1807–1817.

(9) Reubi, J. C. (1995) In vitro identification of vasoactive intestinal peptide receptors in human tumors: implications for tumor imaging. *J. Nucl. Med. 36*, 1846–1853.

(10) Rogers, B. E., Parry, J. J., Andrews, R., Cordopatis, P., Nock, B. A., and Maina, T. (1889) (2005) MicroPET imaging of gene transfer with a somatostatin receptor-based reporter gene and (94m)Tc-Demotate 1. *J. Nucl. Med. 46* 97.

(11) Reubi, J. C. (1995) Neuropeptide receptors in health and disease: the molecular basis for in vivo imaging. *J. Nucl. Med. 36*, 1825–1835.

(12) Van de Wiele, C., Dumont, F., Vanden Broecke, R., Oosterlinck, W., Cocquyt, V., Serreyn, R., Peers, S., Thornback, J., Slegers, G., and Dierckx, R. A. (2000) Technetium-99m RP527, a GRP analogue for visualisation of GRP receptor-expressing malignancies: a feasibility study. *Eur. J. Nucl. Med. 27*, 1694–9.

(13) Zhang, H., Chen, J., Waldherr, C., Hinni, K., Waser, B., Reubi, J. C., and Maecke, H. R. (2004) Synthesis and evaluation of bombesin derivatives on the basis of pan-bombesin peptides labeled with indium-111, lutetium-177, and yttrium-90 for targeting bombesin receptor-expressing tumors. *Cancer Res. 64*, 6707–15.

(14) Lin, K. S., Luu, A., Baidoo, K. E., Hashemzadeh-Gargari, H., Chen, M. K., Brenneman, K., Pili, R., Pomper, M., Carducci, M. A., and Wagner, H. N., Jr. (2005) A new high affinity technetium-99m-bombesin analogue with low abdominal accumulation. *Bioconjugate Chem. 16*, 43–50.

(15) Nock, B. A., Nikolopoulou, A., Galanis, A., Cordopatis, P., Waser, B., Reubi, J. C., and Maina, T. (2005) Potent bombesin-like peptides for GRP-receptor targeting of tumors with 99mTc: a preclinical study. *J. Med. Chem. 48*, 100–10.

(16) Waser, B., Eltschinger, V., Linder, K., Nunn, A., and Reubi, J. C. (2007) Selective in vitro targeting of GRP and NMB receptors in human tumours with the new bombesin tracer ^{177}Lu-AMBA. *Eur. J. Nucl. Med. Mol. Imaging 34*, 95–100.

(17) Zhang, H., Schuhmacher, J., Waser, B., Wild, D., Eisenhut, M., Reubi, J. C., and Maecke, H. R. (2007) DOTA-PESIN, a DOTA-conjugated bombesin derivative designed for the imaging and targeted radionuclide treatment of bombesin receptor-positive tumours. *Eur. J. Nucl. Med. Mol. Imaging 34*, 1198–208.

(18) Garrison, J. C., Rold, T. L., Sieckman, G. L., Figueroa, S. D., Volkert, W. A., Jurisson, S. S., and Hoffman, T. J. (2007) In vivo evaluation and small-animal PET/CT of a prostate cancer mouse model using ^{64}Cu bombesin analogs: side-by-side

comparison of the CB-TE2A and DOTA chelation systems. *J. Nucl. Med. 48*, 1327–37.

(19) de Visser, M., Bernard, H. F., Erion, J. L., Schmidt, M. A., Srinivasan, A., Waser, B., Reubi, J. C., Krenning, E. P., and de Jong, M. (2007) Novel ^{111}In-labelled bombesin analogues for molecular imaging of prostate tumours. *Eur. J. Nucl. Med. Mol. Imaging 34*, 1228–38.

(20) Maina, T., Nock, B., and Mather, S. (2006) Targeting prostate cancer with radiolabelled bombesins. *Cancer Imaging 6*, 153–7.

(21) Ma, L., Yu, P., Veerendra, B., Rold, T. L., Retzloff, L., Prasanphanich, A., Sieckman, G., Hoffman, T. J., Volkert, W. A., and Smith, C. J. (2007) In vitro and in vivo evaluation of Alexa Fluor 680-bombesin[7−14]NH2 peptide conjugate, a high-affinity fluorescent probe with high selectivity for the gastrin-releasing peptide receptor. *Mol. Imaging 6*, 171–80.

(22) Lantry, L. E., Cappelletti, E., Maddalena, M. E., Fox, J. S., Feng, W., Chen, J., Thomas, R., Eaton, S. M., Bogdan, N. J., Arunachalam, T., Reubi, J. C., Raju, N., Metcalfe, E. C., Lattuada, L., Linder, K. E., Swenson, R. E., Tweedle, M. F., and Nunn, A. D. (2006) ^{177}Lu-AMBA: Synthesis and characterization of a selective ^{177}Lu-labeled GRP-R agonist for systemic radiotherapy of prostate cancer. *J. Nucl. Med. 47*, 1144–52.

(23) Smith, C. J., Sieckman, G. L., Owen, N. K., Hayes, D. L., Mazuru, D. G., Kannan, R., Volkert, W. A., and Hoffman, T. J. (2003) Radiochemical investigations of gastrin-releasing peptide receptor-specific [(99m)Tc(X)$(CO)_3$-Dpr-Ser-Ser-Ser-Gln-Trp-Ala-Val-Gly-His-Leu-Met-(NH_2)] in PC-3, tumor-bearing, rodent models: syntheses, radiolabeling, and in vitro/in vivo studies where Dpr = 2,3-diaminopropionic acid and $X = H_2O$ or $P(CH_2OH)_3$. *Cancer Res. 63*, 4082–8.

(24) Perrin, M. H., Sutton, S. W., Cervini, L. A., Rivier, J. E., and Vale, W. W. (1999) Comparison of an agonist, urocortin, and an antagonist, astressin, as radioligands for characterization of corticotropin-releasing factor receptors. *J. Pharmacol. Exp. Ther. 288*, 729–34.

(25) Prasanphanich, A. F., Nanda, P. K., Rold, T. L., Ma, L., Lewis, M. R., Garrison, J. C., Hoffman, T. J., Sieckman, G. L., Figueroa, S. D., and Smith, C. J. (2007) [^{64}Cu-NOTA-8-Aoc-BBN(7−14)NH_2] targeting vector for positron-emission tomography imaging of gastrin-releasing peptide receptor-expressing tissues. *Proc. Natl. Acad. Sci. U.S.A. 104*, 12462–7.

(26) Hoffman, T. J., Gali, H., Smith, C. J., Sieckman, G. L., Hayes, D. L., Owen, N. K., and Volkert, W. A. (2003) Novel series of^{111}In-labeled bombesin analogs as potential radiopharmaceuticals for specific targeting of gastrin-releasing peptide receptors expressed on human prostate cancer cells. *J. Nucl. Med. 44*, 823–31.

(27) Wang, L. H., Coy, D. H., Taylor, J. E., Jiang, N. Y., Moreau, J. P., Huang, S. C., Frucht, H., Haffar, B. M., and Jensen, R. T. (1990) des-Met carboxyl-terminally modified analogues of bombesin function as potent bombesin receptor antagonists, partial agonists, or agonists. *J. Biol. Chem. 265*, 15695–703.

(28) Coy, D. H., Taylor, J. E., Jiang, N. Y., Kim, S. H., Wang, L. H., Huang, S. C., Moreau, J. P., Gardner, J. D., and Jensen, R. T. (1989) Short-chain pseudopeptide bombesin receptor antagonists with enhanced binding affinities for pancreatic acinar and Swiss 3T3 cells display strong antimitotic activity. *J. Biol. Chem. 264*, 14691–7.

(29) Sleight, A. J., Stam, N. J., Mutel, V., and Vanderheyden, P. M. (1996) Radiolabelling of the human 5-HT2A receptor with an agonist, a partial agonist and an antagonist: effects on apparent agonist affinities. *Biochem. Pharmacol. 51*, 71–6.

(30) Cescato, R., Maina, T., Nock, B., Nikolopoulou, A., Charalambidis, D., Piccand, V., and Reubi, J. C. (2008) Bombesin receptor antagonists may be preferable to agonists for tumor targeting. *J. Nucl. Med. 49*, 318–26.

(31) Ginj, M., Zhang, H., Waser, B., Cescato, R., Wild, D., Wang, X., Erchegyi, J., Rivier, J., Macke, H. R., and Reubi, J. C. (2006) Radiolabeled somatostatin receptor antagonists are preferable to agonists for in vivo peptide receptor targeting of tumors. *Proc. Natl. Acad. Sci. U.S.A. 103*, 16436–41.

(32) Coy, D. H., Jensen, R. T., Jiang, N. Y., Lin, J. T., Bogden, A. E., and Moreau, J. P. (1992) Systematic development of bombesin/gastrin-releasing peptide antagonists. *J. Natl. Cancer Inst. Monogr.* 133–9.

(33) Nock, B., Nikolopoulou, A., Chiotellis, E., Loudos, G., Maintas, D., Reubi, J. C., and Maina, T. (2003) [^{99m}Tc]Demobesin 1, a novel potent bombesin analogue for GRP receptor-targeted tumour imaging. *Eur. J. Nucl. Med. Mol. Imaging 30*, 247–58.

(34) Abd-Elgaliel, W. R., Gallazzi, F., and Lever, S. Z. (2007) Total solid-phase synthesis of bombesin analogs with different functional groups at the C-terminus. *J. Pept. Sci. 13*, 487–92.

(35) Lister-James, J., Moyer, B. R., and Dean, R. T. (1997) Pharmacokinetic considerations in the development of peptide-based imaging agents. *Q. J. Nucl. Med. 41*, 111–8.

(36) Arano, Y. (1998) Strategies to reduce renal radioactivity levels of antibody fragments. *Q. J. Nucl. Med. 42*, 262–70.

(37) Gonzalez, N., Moody, T. W., Igarashi, H., Ito, T., and Jensen, R. T. (2007) Bombesin-related peptides and their receptors: recent advances in their role in physiology and disease states. *Curr. Opin. Endocrinol. Diabetes Obes. 15*, 58–64.

(38) Vauquelin, G., and Van Liefde, I. (2006) Slow antagonist dissociation and long-lasting in vivo receptor protection. *Trends Pharmacol. Sci. 27*, 356–9.

(39) Pelosi, G., Volante, M., Papotti, M., Sonzogni, A., Masullo, M., and Viale, G. (2006) Peptide receptors in neuroendocrine tumors of the lung as potential tools for radionuclide diagnosis and therapy. *Q. J. Nucl. Med. Mol. Imaging 50*, 272–87.

(40) Corjay, M. H., Dobrzanski, D. J., Way, J. M., Viallet, J., Shapira, H., Worland, P., Sausville, E. A., and Battey, J. F. (1991) Two distinct bombesin receptor subtypes are expressed and functional in human lung carcinoma cells. *Biol. Chem. 266*, 18771–18779.

(41) Hohla, F., Schally, A. V., Kanashiro, C. A., Buchholz, S., Baker, B., Kannadka, C., Moder, A., Aigner, E., Datz, C., and Halmos, G. (2007) Growth inhibition of non-small-cell lung carcinoma by BN/GRP antagonist is linked with suppression of K-Ras, COX-2, and pAkt. *Proc. Natl. Acad. Sci. U.S.A. 104*, 18671–6.

BC800290C

Cell-Permeable MR Contrast Agents with Increased Intracellular Retention

Paul J. Endres,[†] Keith W. MacRenaris,[†] Stefan Vogt,[‡] and Thomas J. Meade*[,†]

Departments of Chemistry, Biochemistry, and Molecular and Cell Biology, Neurobiology, and Physiology, and Radiology, Northwestern University, 2145 Sheridan Road, Evanston, Illinois 60208, and X-ray Science Division, Argonne National Laboratory, 9700 S. Cass Avenue, Argonne, Illinois 60439. Received July 11, 2008; Revised Manuscript Received August 26, 2008

Magnetic resonance imaging (MRI) is a technique used in both clinical and experimental settings to produce high-resolution images of opaque organisms without ionizing radiation. Currently, MR imaging is augmented by contrast agents, and the vast majority these small molecule Gd(III) chelates are confined to the extracellular regions. As a result, contrast agents are confined to vascular regions reducing their ability to provide information about cell physiology or molecular pathology. We have shown that polypeptides of arginine have the capacity to transport Gd(III) contrast agents across cell membranes. However, this transport is not unidirectional, and once inside the cell, the arginine-modified contrast agents efflux rapidly, decreasing the intracellular Gd(III) concentration and corresponding MR image intensity. By exploiting the inherent disulfide reducing environment of cells, thiol compounds, Gd(III)-DOTA-SS-Arg_8 and Gd(III)-DTPA-SS-Arg_8, are cleaved from their cell-penetrating peptide transduction domains upon cell internalization. This reaction prolongs the cell-associated lifetime of the chelated Gd(III) by cleaving it from the cell transduction domain.

INTRODUCTION

The advent of wide-bore, high-field instruments with improved coil designs and pulse sequences has made magnetic resonance imaging (MRI[1]) a powerful tool for observing developmental and physiological events (*1*−*4*). This versatile modality is noninvasive and allows 3D imaging of whole animals (*5*). This imaging technique is supplemented with an array of exogenous Gd(III) contrast agents conjugated to scaffolds (nanoparticles, antibodies, and proteins) that can detect physiological events (metal ion concentration, enzyme activation, and pH), and can be cell membrane permeable (via cell-penetrating peptides or receptor uptake) (*6*−*17*). The focus of this work is to develop cell-permeable contrast agents that can be trapped inside cells via a cleavable disulfide linkage between the agent and the transduction moiety.

The biological role of thiol-containing molecules has been actively explored, and a great deal is known about the active species and relative concentrations (*18*). The pseudotripeptide of glutathione (GSH) is recognized as the most abundant and subsequently most active thiol species in biological environments (*19, 20*). Previous work has shown that the intracellular GSH concentration of living cells (∼1−10 mM) is significantly higher than that of the surrounding extracellular plasma (∼2 μM). Therefore, thiols can be exploited as a selective chemical release switch for intracellular delivery of cargo (*21*−*23*). We have applied this strategy to our reported intracellular MR contrast agents in order to reduce cellular leaching (*24*). As a result, we have prepared a class of MR probes that are cell-permeable while displaying increased intracellular lifetimes. These probes provide a method to passively label and noninvasively track the fate of transplanted tissues and cells.

It has been shown that an octamer of arginine residues allows cell membrane transduction of various cargo molecules, including fluorophores and contrast agents (*25*−*27*). However, the ability of these probes to cross cell membranes is not unidirectional. Not surprisingly, arginine-modified agents are able to leach out of the cells displaying a concentration decay curve of intracellular contrast agent and consequently decreasing the observed MR signal over time (*28, 29*).

Therefore, contrast agents containing a disulfide bond between the Gd(III) chelate and the transduction moiety (e.g., an octamer of arginine residues) were synthesized to enhance cell-associated retention (Figure 1). Exploiting the inherent disulfide reducing environment of cells, these new agents are cleaved from the cellular transduction domains upon entrance into the cytoplasm. This cleavage of the arginine transport domain shows prolonged cellular lifetime of the MR probe by dissociation of the transport peptide.

EXPERIMENTAL PROCEDURES

All reagents and solvents were of the highest purity available from Sigma-Aldrich (Milwaukee, WI) and Fluka (Sigma-Aldrich Chemie; GmbH, Switzerland) unless otherwise noted. Modified Wang resin and amino acids were purchased from Novabiochem (San Diego, CA). DMEM (with 4 mM L-glutamine modified to contain 4.5 g/L glucose and 1.5 g/L sodium carbonate), EMEM

* Corresponding e-mail address: tmeade@northwestern.edu.

[†] Northwestern University, 2145 Sheridan Rd., Evanston, IL 60208, phone 847-491-2841.

[‡] X-ray Science Division, Argonne National Laboratory, 9700 S. Cass Ave., Argonne, IL 60439.

[1]Abbreviations: MRI (magnetic resonance imaging), GSH (glutathione), DOTA (1,4,7,10-tetraacetic acid-1,4,7,10-tetraazacyclododecane), DTPA (Diethylenetriaminepentaacetic acid), DMEM (Dulbecco's modified Eagle's medium), EMEM (Eagle's minimum essential medium), DPBS (Dulbecco's phosphate buffered saline), FBS (fetal bovine serum), CBS (calf bovine serum), EDTA (ethylenediaminetetraacetic acid), DOTA-tris-TB (1,4,7-tris(acetic acid-*tert*-butyl ester)-10-acetic acid-1,4,7,10-tetraazacyclododecane), MALDI-TOF (matrix assisted laser desorption ionization time-of-flight), ESI (electrospray ionization), RP (reverse-phase), MeCN (acetonitrile), ICP-MS (Inductively Coupled Plasma Mass Spectrometry), Fmoc (fluorenyl-methoxy-carbonyl), DMF (*N*,*N*- dimethylformamide), Pbf (pentamethyldihydrobenzofuran-5-sulfonyl), HATU (*N*,*N*,*N*′,*N*′-tetramethyl-*O*-(7-azabenzotriazol-1-yl)uraniumhexafluoro-phosphate), DIPEA (*N*,*N*-diisopropylethylamine), Trt (trityl), TFA (trifluoroacetic acid), EDT (1,2-ethanedithiol), TIS (triisopropylsilane), MTBE (methyl *tert*-butyl ether), AETP (*S*-(2-Aminoethylthio)-2-thiopyridine hydrochloride), DMSO (dimethylsulfoxide), SR-XRF (synchrotron radiation X-ray fluorescence).

10.1021/bc8002919 CCC: $40.75 © 2008 American Chemical Society
Published on Web 09/20/2008

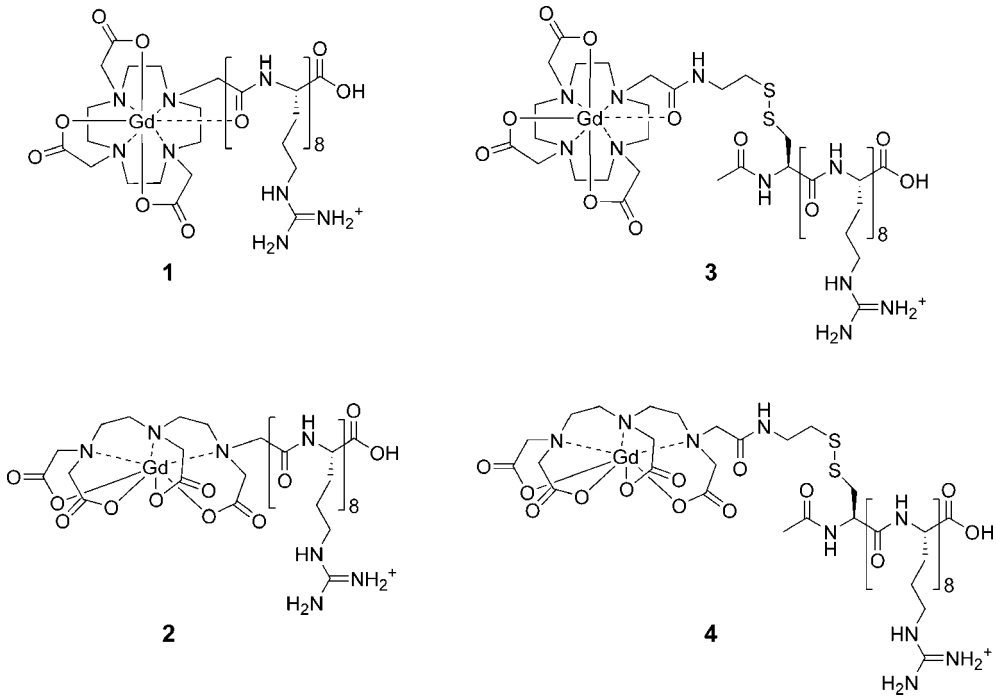

Figure 1. Structures of the arginine-modified (cell-permeable contrast agents) and disulfide-bridged (cell-permeable contrast agents), respectively. (**1**) Gd(III)-DOTA-Arg_8, (**2**) Gd(III)-DTPA-Arg_8, (**3**) Gd(III)-DOTA-SS-Arg_8, and (**4**) Gd(III)-DTPA-SS-Arg_8.

(with Earle's BSS and 2 mM L-glutamine modified to contain 1.0 mM sodium pyruvate, 0.1 mM nonessential amino acids, and 1.5 g/L sodium bicarbonate), NIH/3T3 cells, FBS, CBS, and 0.25% trypsin/EDTA solutions were purchased from the American Type Culture Collection (ATCC; Manassas, VA). Vent-cap flasks, multiwell plates, cell scrapers, and DPBS without calcium and magnesium were purchased from Fisher Scientific (Pittsburgh, PA).

^1H and ^{13}C NMR spectra were obtained on a Varian (Walnut Creek, CA) Inova spectrometer at 500 and 125 MHz, respectively. Compounds were dissolved in D_2O (4.80 ppm used as internal references for NMR spectra). Due to the minimal solubility associated with the peptide−chelate conjugates, ^{13}C NMR spectra were collected in D_2O, and the first carbon resonance was assigned a value of 24.42 ppm. Mass spectrometry samples were analyzed using ESI, single quadrupole mass spectrometry on a Varian 1200 L spectrometer, or MALDI-TOF mass spectrometry on an Applied Biosystems (Foster City, CA) Voyager-DE Pro. Results reported for *m*/*z* are for $[M + H^+]^+$ or $[M - H^+]^-$ unless stated otherwise. Elemental analyses were performed at Desert Analytics Laboratory (Tuscon, AZ).

ICP-MS was performed on a computer-controlled Thermo Elemental (Waltham, MA) PQ ExCell inductively coupled plasma mass spectrometer. All standards and samples contain 5 ng/mL of a multielement internal standard (Spex CertiPrep; Metuchen, NJ) consisting of Bi, Ho, In, Li, Sc, Tb, Y, and 3% nitric acid (v/v). Gadolinium standards were prepared in concentrations of 0.05, 0.10, 0.25, 0.50, 1.0, 5.0, 10, 25, and 50 ng/mL. Analysis was accomplished with 1 survey and 3 main scans (peak jumping, 100 sweeps per run) using ^{156}Gd and ^{157}Gd isotopes and interpolating through ^{209}Bi and ^{115}In internal standards.

HPLC-MS. Analytical reverse-phase HPLC-MS was performed on a computer-controlled Varian Prostar system consisting of a 410 autosampler equipped with a 100 μL sample loop, two 210 pumps with 5 mL/min heads, a 363 fluorescence detector, a 330 photodiode array (PDA) detector, and a 1200 L single quadrupole ESI-MS. All separations were executed with a 1.0 mL/min flow rate using a Waters 4.6 × 250 mm 5 μm Atlantis C18 column, with a 3.1:1 split directing one part to the MS and 3.1 parts to the series-connected light and fluorescence detectors. Mobile phases consisted of Millipore Synthesis grade water (solvent A) and HPLC-grade MeCN (solvent B). Preparative HPLC was accomplished using a Varian Prostar system. Two Prostar 210 pumps with 25 mL/min heads supplied a 5 mL manual inject sample loop. Detection was performed after a 20:1 split by a two-channel Prostar 325 UV−visible detector and, on the low-flow side, a HP 1046A fluorescence detector. The mobile phases were Millipore Synthesis grade water and HPLC-grade MeCN. Preparative runs were on a Waters 19 × 250 mm 10 μm Atlantis C18 column.

Relaxivity (r_1). A 2 mM stock solution of **1**−**4**, Gd(III)-DTPA, or Gd(III)-DOTA in 100 mM PBS buffer at pH 7.41 were serially diluted to give 500 μL of each of the five approximate concentrations for each compound: 0.15, 0.3, 0.5, 1.0, and 2.0 mM. The T_1 of each sample was determined at 60 MHz (1.5 T) and 37 °C using an inversion recovery pulse sequence on a Bruker mq60 minispec (Bruker Canada; Milton, Ontario, Canada) and at 600 MHz (14.1 T) and ambient temperature using a saturation recovery pulse sequence on a Bruker Omega 600WB spectrometer (Bruker BioSpin; Billerica, MA). Reproducibility of the T_1 data was ±0.3%. Ten microliters of each sample was analyzed for exact gadolinium concentration using ICP-MS. The inverse of the longitudinal relaxation time (T_1) was plotted against the concentration obtained from ICP-MS and fit to a straight line. Lines were fit with $R^2 > 0.998$, and each relaxivity was assessed in duplicate.

Determination of *q* by Luminescence Lifetime Measurements. Complexes (*10*−*13*) were dissolved in H_2O and D_2O. Emission was monitored at 544 nm with excitation at 229 nm on a Hitachi F4500 Fluorescence Spectrophotometer operating in phosphorescence lifetime mode. Twenty-five scans were averaged and fit to a monoexponential decay ($R^2 > 0.98$) to give the phosphorescent lifetimes which were entered into this equation (corrected for one amide oscillator, where k is given in ms^{-1}): $q = 5.0(k_{H2O} - k_{D2O} - 0.06)$ (*30*, *31*).

Determination of τ_m by ^{17}O Transverse Relaxation Rate Measurements. Samples of **1**−**4**were prepared at 15−20 mM concentrations in 1% ^{17}O enriched water (Medical Isotopes, Inc.; Pelham, NH) adjusted to pH 7.40. Lock was achieved by means of an external D_2O standard. ^{17}O spectra were obtained at 54 MHz (number of averaged transients was 160−320 and relaxation delay was 400 ms) at temperatures ranging from 1 to 86 °C in 5 °C increments. The ^{17}O transverse relaxation rate was determined by obtaining the line width (in Hz) at half of the peak height, $\Delta P_{1/2}$, of the ^{17}O water signal and later fitting the data (*32*−*34*). Using known sample concentrations and q values, the relaxation data were fit to these four parameters at 25 °C: τ_m (water exchange rate), $\Delta H^{\ddagger}$ (activation enthalpy), T_{1e} (electronic relaxation rate), and ΔE_{T1e} (activation energy of T_{1e}) (*35*).

Cell Culture Conditions. All cell lines, media, sera, buffers, and dissociation reagents were purchased from ATCC. NIH/3T3 cells (CRL-1658) were grown in DMEM (with 4 mM L-glutamine, 4.5 g/L glucose, 1.0 mM sodium pyruvate, 1.5 g/L sodium carbonate, and phenol red supplemented with 10% CBS). Cells were grown in a humidified incubator at 37 °C and 5% CO_2. Cells were washed with DPBS (without calcium and magnesium) and dissociated with a 0.25% trypsin−EDTA solution. All flasks and multiwell plates were Corning brand, tissue culture treated, and sterile. The studies for each contrast agent and time point were performed in triplicate.

Cells were counted and viability assessed using a Guava EasyCite Mini Personal Cell Analyzer (Guava Technologies; Hayward, CA). Cell samples were diluted 10-fold with Guava ViaCount reagent (total volume of 200 μL), allowed to stain at room temperature for at least 5 min (but no longer than 20 min), vortexed, and measured. Each sample was measured using the Guava ViaCount software module using 1000 trials per run doing 2 separate runs per sample. Instrument reproducibility was assessed daily following the manufacturer's suggested protocol using GuavaCheck reagent and the corresponding software module.

ICP-MS assessment of the cell-associated gadolinium was determined by collecting and processing all cell and media samples via this procedure: addition of 70% (v/v) nitric acid in water, vortexing (∼5 min), and digestion at 65 °C for at least 4 h. Samples were added to a 15 mL conical tube along with internal standard (5 ng/mL of indium and holmium) and water to give a final nitric acid concentration of 3% (v/v).

Synchrotron Radiation X-ray Fluorescence (SR-XRF) Analysis. NIH/3T3 cells were grown to 65% confluency on silicon nitride windows (membrane thickness of 500 nm and frame size of 5.0 mm × 5.0 mm, Silson Ltd.; Northampton, England) in Corning brand 24-well cell culture treated plates. Each well had two silicon nitride windows (one incubation sample and one leach sample). Cells were incubated with 3.0 mM of compounds **1**−**4** for 4 h. Samples were rinsed three times with DPBS and one window was removed for processing (time = 0, named *No leach* sample) while one window was allowed to incubate with fresh media for 4 more hours followed by processing (named *Leached* sample). Windows were processed by cell fixation in 3.7% formalin for 5 min at room temperature, rinsing with DPBS (1×), rinsing with Millipore water (1×), rinsing with 100% ethanol (1×), and drying overnight (18 h, room temperature). The silicon nitride windows were mounted onto a kinematic specimen holder for both visible light and X-ray fluorescence microscopy. The samples were examined on a light microscope (Leica DMXRE), and the cells to be scanned with SR-XRF were located on the window relative to a reference point (one of the four window corners) using a high spatial resolution motorized x/y stage (Ludl Bioprecision).

Scanning SR-XRF microscopy was carried out at the 2-ID-E beamline of the Advanced Photon Source at Argonne National Laboratory (IL, USA). Hard X-rays from an undulator source were monochromatized using a single bounce Si κ monochromator. The energy was selected to allow for efficient excitation of the Gd L-lines, and also to enable the detection of the P, S, Fe, and Zn K-lines. A Fresnel zone plate (320 μm diameter, focal length f = 250 mm, X-radia; Concord, CA) was used to focus the monochromatic X-ray beam to a spot size of∼0.4 × 0.3 μm^2 on the specimen. The sample was raster scanned through the beam at room temperature under a helium atmosphere. At each scan position, a full fluorescence spectrum was acquired using an energy-dispersive germanium detector (Ultra-LEGe detector, Canberra; Meriden, CT). Elemental content was determined by comparison of fitted sample spectra with NBS thin film standards 1832 and 1833 (NIST; Gaithersburg, MD) using MAPS software supplemented with fitting of fluorescence spectra at every pixel (*36*).

MR Imaging and T_1 Analysis. MR measurements were performed on a General Electric/Bruker Omega 600WB 14.1 T imaging spectrometer fitted with Accustar shielded gradient coils at ambient temperature (∼25 °C). Spin lattice relaxation times (T_1) were measured using a saturation recovery pulse sequence with static T_E (10.18 ms) and variable T_R (127.5, 165, 200, 300, 500, 1000, 2000, 5000, 7500, 10 000 ms) values. Two independent trials were run per sample and at least 5 slices were quantified per trial. Student's t-tests were calculated in Origin 7 SR2 (Origin Laboratory; Northampton, MA) at a 95% confidence level with 8 degrees of freedom and a null hypothesis value (minimum acceptable time difference) of 100 ms. Images were acquired using a T_1-weighted, spin−echo pulse sequence (T_E = 10.18, T_R = 750 ms) on freshly harvested cells that were spun down (at 250 g) within glass capillary tubes for 5 min prior to image acquisition. Total time from harvest to image acquisition was 1−2 h.

Synthesis. Complex Gd(III)-DOTA-Arg_8 (**1**), Gd(III)-DTPA-Arg_8 (**2**), and (*S*-(2-Aminoethylthio)-2-thiopyridine hydrochloride) (AETP) were synthesized following previously published procedures (*14*, *24*, *37*) and (1,4,7-tris(acetic acid-*tert*-butyl ester)-10-acetic acid-1,4,7,10-tetraazacyclododecane) (DOTA-tris-TB) was purchased from Macrocyclics (Dallas, TX).

Synthesis of End-Capped RRRRRRRRC (5). Polystyrene-based Wang resin containing an Fmoc-protected arginine residue (2.00 g, 0.580 mmol/g) was swelled in CH_2Cl_2 for 10 min (×3) and washed with peptide synthesis grade DMF (4 × 10 min). The resin was treated three times with a solution of 20% piperdine in DMF (10 min), and the deprotected resin was washed with DMF (4 × 10 min). In a separate vial, Fmoc-protected Pbf-arginine (1.51 g, 2.32 mmol), HATU (0.881 g, 2.32 mmol), and DIPEA (0.748 g, 5.80 mmol) were dissolved in approximately 3 mL of DMF. The resulting solution was added to the deprotected resin, and nitrogen was bubbled through the mixture for 6−8 h. The peptide solution was removed from the resin, which was subsequently rinsed with DMF (4 × 10 min). This procedure was repeated a total of seven times in order to achieve the synthesis of an eight-amino-acid polyarginine oligomer bound to the Wang resin (3.96 g).

The Arg_8 functionalized resin (2.00 g, 0.290 mmol/g, 0.580 mmol) was deprotected with the piperdine solution and washed with DMF as described above. In a separate vial, Fmoc-protected Trt-cysteine (0.725 g, 1.16 mmol) and 2,4,6-trimethylpyridine (0.154 g, 1.27 mmol) were dissolved in a minimal amount of DMF. The resulting solution was added to the deprotected resin, and nitrogen was bubbled through the mixture for 6−8 h. The peptide solution was removed, and the resin was washed with DMF (4 × 10 min each). The resin-bound Arg_8-Cys oligomer was deprotected with the piperdine solution and washed with

DMF. The resin was resuspended in a solution of acetic anhydride (0.118 g, 1.16 mmol), DIPEA (0.374 g, 2.90 mmol), and DMF (3 mL). Bubbling nitrogen through this mixture for 4 h effectively capped the peptide's N-terminus. Upon removal of the capping solution, the resin was washed with DMF, CH_2Cl_2, and MeOH (4 × 10 min each). Following the methanol washes, the resin was dried under vacuum. A solution of 95% TFA, 2.5% EDT, 1.5% H_2O, and 1.0% TIS (50 mL) was added to the resin, and nitrogen was bubbled through the mixture for 1 h. The resin was filtered, and to the filtrate was added MTBE (40 mL) to precipitate a white solid that was subsequently washed with MTBE (3×). The solid was dissolved in 30 mL of water and freeze−dried to yield white flaky crystals of the peptide, Arg_8-Cys (0.692 g, 84%). ^{1}H NMR spectrum (D_2O @ pH 1.0): δ = 1.22−1.40 (m, 16H), 1.50 (dd, J = 8.5, 5.5 Hz, 16H), 1.59−1.69 (m, 2H), 1.74 (d, J = 6.0 Hz, 3H), 2.89 (m, 16H), 3.95−4.10 (m, 8H). ^{13}C NMR (D_2O @ pH 1.0): δ = 24.42, 27.50, 28.03, 39.36, 40.52, 52.26, 53.25, 156.57, 172.61, 173.44, 174.84. With ESI-MS (*m*/*z*): 1413.58; calc. for $C_{53}H_{105}N_{33}O_{11}S + H^+$: 1413.68.

Synthesis of 1,4,7-Tris(carboxymethyl)-10-(*N*-[2-(pyridin-2-yldithio)ethyl]acetamide)-1,4,7,10-tetraazacyclododecane (6). DOTA-tris-TB (0.600 g, 1.05 mmol), HATU (1.20 g, 3.15 mmol), and anhydrous DIPEA (0.683 g, 5.25 mmol) were dissolved in 4.0 mL of anhydrous DMF and allowed to stir for 10 min under a nitrogen atmosphere while AETP (0.466 g, 2.10 mmol) was dissolved in 2.0 mL of anhydrous DMF. After a 10 min activation time, the AETP solution was added via syringe and the mixture was allowed to stir for 5 h while being monitored by TLC [KNO_3−H_2O−MeCN (1:9:90)]. Upon reaction completion, the solution was evaporated *in vacuo*. The resulting yellow residue was stirred overnight in 95% TFA, 2.5% TIS, and 2.5% H_2O (30 mL). The reaction mixture was concentrated to 10 mL by application of a steady stream of dry nitrogen across the top of the vessel. The crude product was precipitated by addition of MTBE (40 mL) and was subsequently washed with MTBE (3×). The yellow solid was dried *in vacuo* to yield 1.12 g of the crude product.

The crude mixture was submitted to preparatory HPLC using a Waters Atlantis column. The solid was brought up in H_2O and purified using the following method: begin at 0% B, ramp to 3% B over 1 min, hold at 3% B for 15 min, ramp to 20% B over 7 min, and hold for 8 min, followed by a wash to 100% B before returning to 0% B. The desired fractions (retention time: 32.20 min by UV spectroscopy at 235, 280 nm) were collected and freeze−dried to yield the product as a white solid (0.410 g, 68%). ^{1}H NMR spectrum (D_2O): δ = 2.96−3.10 (m, 11H), 3.41−3.51 (m, 13H), 3.79 (q, J = 16.5 Hz, 4H), 7.33 (t, J = 4.5 Hz, 1H), 7.88 (d, J = 3.5 Hz, 2H), 8.40 (d, J = 4.5 Hz, 1H). ^{13}C NMR spectrum (D_2O): δ = 37.05, 38.13, 48.22, 48.46, 50.94, 51.64, 53.73, 55.51, 56.59, 121.92, 122.26, 139.56, 148.50, 158.48, 170.02, 171.96, 175.07. ESI-MS (*m*/*z*): 573.26; calc. for $C_{23}H_{36}N_6O_7S_2 + H^+$: 573.70. with Anal. Calcd. for $C_{23}H_{36}N_6O_7S_2 \cdot Na \cdot 1.5\ H_2O$: C, 44.36; H, 6.31; N, 13.50; S, 10.30. Found: C, 44.20; H, 6.17; N, 13.38; S, 10.98.

Synthesis of [(2-{Carboxymethyl-[2-(carboxymethyl-{[2-(pyridin-2-yldisulfanyl)ethylcarbamoyl]methyl}amino)ethyl]-amino}ethyl)amino]acetic Acid (7). DTPA dianhydride (2.00 g, 5.60 mmol) was dissolved in 100 mL of anhydrous DMSO and allowed to stir under a nitrogen atmosphere, while AETP (0.672 g, 3.04 mmol) was dissolved in a stirring solution of anhydrous DMSO (25 mL) and anhydrous DIPEA (1.07 g, 8.21 mmol). The AETP solution was slowly added to the DTPA dianhydride solution via syringe pump over 5 h. Upon complete addition, the resulting solution was stirred for an additional hour before being quenched with H_2O (100 mL) and concentrated *in vacuo*. The resulting residue was brought up in H_2O and submitted to preparatory HPLC with the Waters Atlantis column using the following method: begin at 0% B, ramp to 100% B over 35 min, followed by a wash at 100% B for 5 min before returning to 0% B. The desired fractions (retention time: 10.28 min by UV at 235, 280 nm) were collected and freeze−dried to yield the product as a white solid (1.07 g, 63%). ^{1}H NMR (D_2O): δ = 3.04 (t, J = 5.5 Hz, 2H), 3.24−3.35 (m, 6H), 3.54 (t, J = 6.0 Hz, 2H), 3.59 (t, J = 6.0 Hz, 2H), 3.69 (s, 2H), 3.75−3.90 (m, 8H), 7.57 (t, J = 6.5 Hz, 1H), 8.05 (d, J = 8.5 Hz, 1H), 8.15 (t, J = 8.5 Hz, 1H), 8.53 (d, J = 5.5 Hz, 1H). ^{13}C NMR (D_2O): δ = 37.45, 37.94, 50.30, 51.24, 52.52, 52.09, 54.48, 56.52, 57.04, 57.21, 123.29, 123.95, 142.71, 145.62, 157.07, 168.74, 170.56, 172.17, 172.78. ESI-MS (*m*/*z*): 560.19; calc. for $C_{21}H_{31}N_5O_9S_2 - H^+$: 560.63. Anal. Calcd. for $C_{21}H_{31}N_5O_9S_2 \cdot Na$: C, 43.14; H, 5.34; N, 11.98; S, 10.97. Found: C, 42.70; H, 5.21; N, 12.02; S, 11.29.

Synthesis of DO3A-SS-Arg_8 (8). Compound **6** (0.160 g, 0.306 mmol) was added to end-modified Arg_8-Cys (**5**) (0.432 g, 0.306 mmol) dissolved in 30 mL of degassed phosphate buffer (10 mM, pH 8.0). The solution was stirred under nitrogen atmosphere at room temperature. The reaction was monitored by analytical HPLC and found to be complete after 72 h. An aliquot (2.5 mL) of the solution was removed for characterization, while the remaining material (27.5 mL) was carried onto the synthesis of Gd(III)-DOTA-SS-Arg_8 (**3**). Dialysis (MW cutoff 1000) against Millipore H_2O (4 L × 4 days) yielded 3 mL of a translucent liquid that was 0.2 μm syringe-filtered and freeze−dried to yield a white solid (0.389 g, 74%). ^{1}H NMR spectrum (D_2O) shows the disappearance of all aromatic protons. ^{13}C NMR spectrum (D_2O): δ = 24.42, 28.16, 28.88, 37.11, 38.17, 40.65, 40.79, 48.44, 50.71, 51.90, 53.59, 54.91, 55.52, 56.66, 156.86, 170.04, 172.19, 172.80, 173.75, 175.41. ESI-MS (*m*/*z*): 1875.31; calc. for $C_{70}H_{136}N_{38}O_{18}S_2 + H^+$: 1875.21.

Synthesis of DTPA-SS-Arg_8 (9). Compound **7** (0.175 g, 0.312 mmol) was added to end-modified Arg_8-Cys (**3**) (0.440 g, 0.312 mmol) dissolved in 30 mL of degassed phosphate buffer (10 mM, pH 8.0). The solution was stirred under a nitrogen atmosphere at room temperature. The reaction was monitored by analytical HPLC and found to be complete after 72 h. An aliquot (2.5 mL) of the solution was removed for characterization, while the remaining material (27.5 mL) was carried onto the synthesis of Gd(III)-DTPA-SS-Arg_8 (**4**). Dialysis (MW cutoff 1000) against Millipore H_2O (4 L × 4 days) yielded 4 mL of a translucent liquid that was 0.2 μm syringe-filtered and freeze−dried to yield a white solid (0.351 g, 66%). ^{1}H NMR (D_2O) shows the disappearance of all aromatic protons. ^{13}C NMR (D_2O): δ = 24.42, 28.20, 38.79, 40.66, 50.53, 52.19, 53.44, 53.53, 54.94, 55.19, 57.88, 58.91, 156.84, 172.70, 172.97, 173.60, 174.32, 178.33. ESI-MS (*m*/*z*): 1864.21; calc. for $C_{69}H_{131}N_{37}O_{20}S_2 + H^+$: 1864.14.

Synthesis of Gd(III)-DOTA-SS-Arg_8 (3). To an aliquot of DO3A-SS-Arg_8 (**8**) (27.5 mL, 0.285 mmol) was added $Gd(OH)_3$ (0.064 g, 0.314 mmol). All metalations were performed with a 1.1:1.0 molar excess of metal salt to unmetalated complex to minimize unmetalated final product. The reaction mixture was brought to pH 6.0 with 1.0 M NaOH and allowed to stir for 7 d at room temperature under a nitrogen atmosphere. Dialysis (MW cutoff 1000) against Millipore H_2O (4 L × 4 days) yielded 30 mL of a translucent liquid that was brought to pH 11.0 with concentrated NH_4OH to precipitate excess free gadolinium. This suspension was 0.2 μm syringe-filtered and freeze−dried to yield a white powder which was found to be (**3**) (0.453 g, 78%) by ESI-MS (*m*/*z*): 2029.44 (*m*/1), 1014.70 (*m*/2), 677.43 (*m*/3), 508.26 (*m*/4) with Gd isotope pattern; calc. for $C_{71}H_{133}GdN_{38}O_{18}S_2 + H^+$: 2029.44.

Synthesis of Gd(III)-DTPA-SS-Arg_8 (4). To an aliquot of DTPA-SS-Arg_8 (**9**) (27.5 mL, 0.286 mmol) was added $Gd(OH)_3$

Scheme 1. Synthesis of the Pyridyl-Activated Gd(III) Chelators[a]

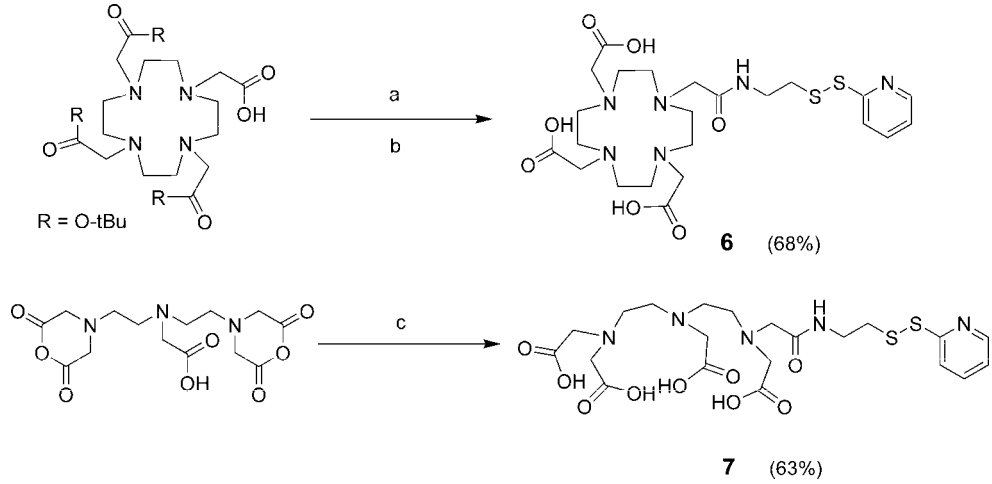

[a] Conditions: (a) AETP, HATU, DIPEA, DMF; (b) TFA/H_2O/TIS, followed by MTBE precipitation; (c) AETP, DMSO, and H_2O.

(0.064 g, 0.315 mmol). The reaction mixture was brought to pH 6.0 with 1.0 M NaOH and allowed to stir for 7 d at room temperature under a nitrogen atmosphere. Dialysis (MW cutoff 1000) against Millipore H_2O (4 L × 4 days), yielded 30 mL of a translucent liquid that was brought to pH 11.0 with concentrated NH_4OH to precipitate excess free gadolinium. This suspension was 0.2 μm syringe-filtered and freeze−dried to yield a white powder which was found to be (**4**) (0.484 g, 84%) by ESI-MS (*m*/*z*): 2017.30 (*m*/1), 1008.55 (*m*/2), 672.99 (*m*/3), 505.12 (*m*/4), 404.38 (*m*/5) with a Gd isotope pattern; calc. for $C_{69}H_{127}GdN_{37}O_{20}S_2 + H^+$: 2017.36.

Synthesis of Tb(III)-DOTA-Arg$_8$ (10). The Tb(III) analogue of **1** was synthesized using a previously outlined metalation procedure and substituting $Tb(OH)_3$ for $Gd(OH)_3$ (*14*). The resulting white solid was found to be **10** (45.7 mg, 42%) by ESI-MS (*m*/*z*): 1810.85 (*m*/1), 906.07 (*m*/2), 604.24 (*m*/3), 453.47 (*m*/4); calc. for $C_{64}H_{121}N_{36}O_{16}Tb + H^+$: 1810.80.

Synthesis of Tb(III)-DTPA-Arg$_8$ (11). The Tb(III) analogue of **2** was synthesized using a previously outlined metalation procedure and substituting $Tb(OH)_3$ for $Gd(OH)_3$ (*24*). The resulting white solid was found to be **11** (42.0 mg, 52%) by ESI-MS (*m*/*z*): 1798.63 (*m*/1), 899.91 (*m*/2), 600.26 (*m*/3), 450.47 (*m*/4); calc. for $C_{62}H_{115}N_{35}O_{18}Tb + H^+$: 1798.73.

Synthesis of Tb(III)-DOTA-SS-Arg$_8$ (12). The Tb(III) analogue of **3** was synthesized using compound **8** (10.0 mg, 0.005 mmol), $Tb(OH)_3$ (1.23 mg, 0.006 mmol), and the same metalation procedure previously described for **3** (6.0 mg, 60%). ESI-MS (*m*/*z*): 2031.01 (*m*/1), 1016.00 (*m*/2), 677.73 (*m*/3) 508.54 (*m*/4), 407.12 (*m*/5); calc. for $C_{71}H_{133}N_{38}O_{18}S_2Tb + H^+$: 2031.12.

Synthesis of Tb(III)-DTPA-SS-Arg$_8$ (13). The Tb(III) analogue of **4** was synthesized using compound **9** (10.0 mg, 0.005 mmol), $Tb(OH)_3$ (1.23 mg, 0.006 mmol), and the same metalation procedure described for **4** (5.9 mg, 55%). ESI-MS (*m*/*z*): 2019.02 (*m*/1), 1010.01 (*m*/2), 673.64 (*m*/3) 505.43 (*m*/4), 404.65 (*m*/5); calc. for $C_{69}H_{127}N_{37}O_{20}S_2Tb + H^+$: 2019.04.

RESULTS

Synthesis. The synthesis of the pyridyl-activated Gd(III) chelators was accomplished by coupling an amine-terminated AETP to an activated form of either the DTPA or DOTA chelate (Scheme 1). Commercially available DTPA-dianhydride is amidated forming amines, while the DOTA-tris-TB was activated *in situ* by the commonly used uranium salt, HATU. Both reactions required an excess of DIPEA in order to deprotonate the hydrochloride salt starting material (AETP) and to aid in amide bond formation (*24*). Upon purification via preparative RP-HPLC, compounds **4** and **5** were afforded with yields of 68% and 63%, respectively. The peptide RRRRRRRRC was synthesized without automation using standard Fmoc solid-phase synthesis methodology on preloaded Wang resin (*24*, *25*). After the addition of the cysteine residue, the resin was treated with acetic anhydride to end-cap the peptide's terminal amine. To prepare peptide sequences with minimal structural differences as compared to the previously published Arg$_8$-MR contrast agents (e.g., charge and no free terminal amine), this end-capping step was performed prior to cleavage and deprotection from the resin (*24*, *25*).

In order to optimize the thiol exchange reaction required to produce **8** and **9**, the pyridyl-activated chelates (**6** or **7**) were quickly added to stirring solutions of the end-capped Arg$_8$-Cys (**5**) oligomer under a nitrogen atmosphere in degassed phosphate buffer at pH 8.0 (Scheme 2). It was found that, when **6** and **7** were added in equimolar quantities to **5**, synthetic yields were maximized. We speculate that adding higher amounts of the free thiol (**5**) lowered the overall yield by increasing oxidation and disulfide exchange of the desired product. This effect has been observed in previous disulfide exchange reactions (*38*). Metalation of the cell-permeable contrast agents was achieved by adding $Gd(OH)_3$ to the phosphate buffered solutions of **8** and **9**. To ensure the complete insertion of Gd(III), the buffered solutions were lowered to pH 6.0 and allowed to stir for 7 days under a nitrogen atmosphere. The proposed structures of the peptide conjugates **5**, **8**, and **9** were confirmed by NMR spectroscopy, ESI-MS, and HPLC, while the unconjugated, small molecule chelates were characterized by NMR spectroscopy, ESI-MS, HPLC, and EA.

Relaxivity, q, and τ_M. The relaxivity measurements (r_1, $mM^{-1}\,s^{-1}$) provided in Table 1 show the relative enhancement of water proton relaxation rates per Gd(III) ion for complexes **1**−**4**. These rates were measured at 1.5 and 14.1 T in order to provide data at both clinical and research field strengths. As expected, the r_1 rates are strongly field dependent; however, **1**−**4** maintain higher relaxation rates than currently available contrast agents, Gd(III)-DOTA and Gd(III)-DTPA, at both 1.5 and 14.1 T. The relaxation rates of **1**−**4** were tested over a wide pH range (1.0−12.5) in order to determine the efficacy of these agents to relax water molecules at biologically relevant pH levels (Figure 3). At low pH (∼1−4), the relaxivity for **1**−**4** is consistent with Gd(III) diassociation from the chelating cage. Conversely, at high pH (∼9−13), the relaxivity shows a decrease that is most likely attributable to a structure that allows

Scheme 2. Synthesis of Disulfide Bridged, Intracellular Contrast Agents (3) Gd(III)-DOTA-SS-Arg$_8$ and (4) Gd(III)-DTPA-SS-Arg$_8$[a]

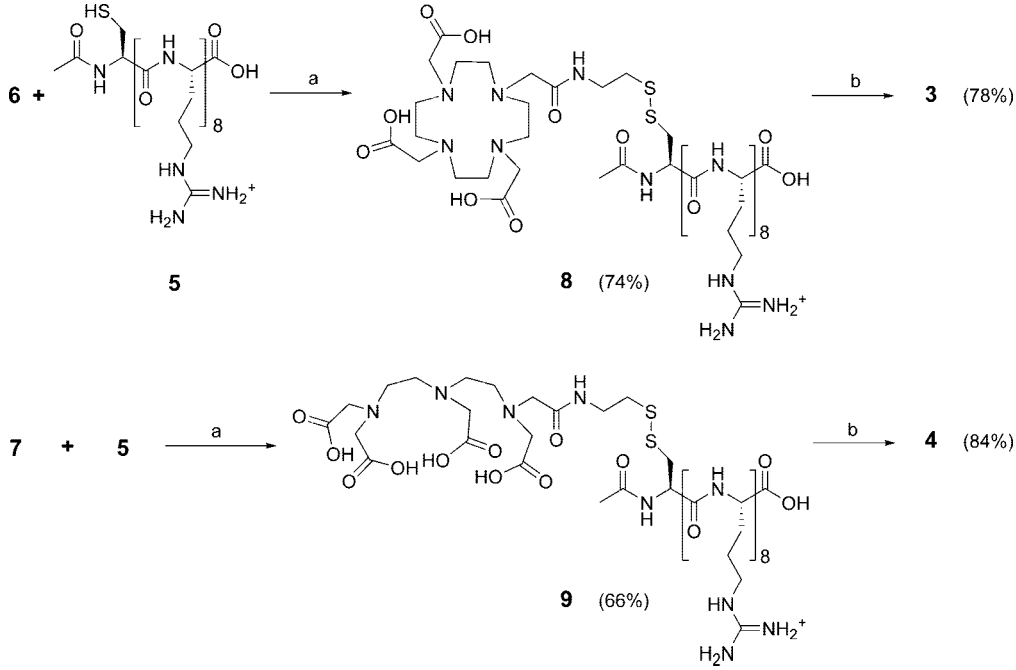

[a] Conditions: (a) stirring for 3 days under N_2 atmosphere in 10 mM phosphate buffer at pH 8.0; (b) $Gd(OH)_3$, 5 days, pH 6.0.

Table 1. Relaxometric Properties of Complexes 1−4 at pH 7.4 and 37 °C

	relaxivity (mM^{-1} s^{-1})[a]			
	60 MHz (1.5 T)	600 MHz (14.1 T)[b]	q	τ_m (ns)[c]
(Gd(III)-DOTA-Arg$_8$) **1**	6.8	3.50	1.0	916
(Gd(III)-DTPA-Arg$_8$) **2**	7.8	3.45	1.2	1105
(Gd(III)-DOTA-SS-Arg$_8$) **3**	6.9	3.52	0.9	840
(Gd(III)-DTPA-SS-Arg$_8$) **4**	7.4	3.46	1.1	1327
Gd(III)-DOTA	3.2	2.12	1.2[d]	243[e]
Gd(III)-DTPA	3.8	2.09	1.2[d]	303[e]

[a] Measured in 100 mM phosphate buffer. [b] Measured at ambient temperature (~25 °C). [c] Calculated at 25 °C. [d] Data from ref *51*. [e] Data from ref *52*.

carbonate ion binding or association of the metal center to the slowly exchanging hydroxyl ions (*23*, *39*, *40*). However, in the physiologically relevant range of pH 4−8, all four of the cell-permeable agents display constant relaxivity values.

The Tb(III) analogues of complexes **1**−**4** (complexes **10**−**13**) were subjected to fluorescence measurements so that the number of complex-associated water molecules could be determined. These measurements provided the following data (ms^{-1}): **10**, $k_{H2O} = 0.566$, $k_{D2O} = 0.315$; **11**, $k_{H2O} = 0.635$, $k_{D2O} = 0.331$; **12**, $k_{H2O} = 0.644$, $k_{D2O} = 0.397$; **13**, $k_{H2O} = 0.671$, $k_{D2O} = 0.390$. These values were inserted into the equation listed in the Experimental Procedures section, resulting in the q values shown in Table 1. Typical of most small molecule DOTA and DTPA-based contrast agents where one carboxylic acid arm has been replaced with an amide, these values reflect one bound water molecule within acceptable experimental error of ±0.5 (*41*, *42*).

To evaluate the mean residence lifetime (τ_m) of the water molecule coordinated to the metal center of complexes **1**−**4**, temperature-dependent ^{17}O NMR measurements were performed (*32*,*34*). Plotting the paramagnetic contribution of the observed ^{17}O NMR transverse relaxation rate of water gave the expected bell-shaped curves for each complex that were subjected to the fitting parameters outlined in the Experimental Procedures section

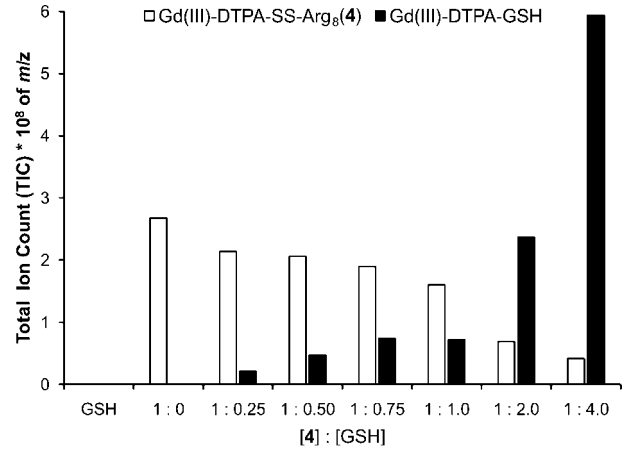

Figure 2. Quantification of *in vitro* cleavage of Gd(III)-DTPA-SS-Arg$_8$ (**4**) via disulfide exchange with GSH. **4** was incubated with increasing amounts of GSH for 4 h in 1.0 mM DPBS. The exchange was monitored by plotting the total ion count (TIC) of the desired product (Gd(III)-DTPA-GSH, $m/z = 912^+$amu, black bars) and the starting material (**4**, $m/z = 3, 673^+$ amu, white bars). The data represent the calculated total area under the curve of the integrated molecular ion chromatograms (912^+ and 673^+). **4** decreases with increasing amounts of GSH which corresponds to an increase in Gd(III)-DTPA-GSH representing*in vitro*disulfide exchange. GSH had no discernible peak to integrate.

(Supporting Information Figure S1) (*32*−*34*). The fitted ^{17}O vs temperature (T) profiles revealed the τ_m values displayed in Table 1.

The τ_m values for **1**−**4** are similar and decidedly higher than the previously reported optimal value of 10 ns for Gd(III) MR contrast agents (*41*). These bound-water lifetimes are substantially slower than those reported for DOTA and DTPA; however, this observation can be explained. Substitution of an acetate arm to an amide linkage (as in the case of **1**−**4**) decreases the steric crowding of the lanthanide and lowers the overall molecular charge of the metalated complexes (*1*, *43*). Both factors affect τ_m, and such values are similar to those obtained for other amidated DOTA and DTPA structures (*44*−*46*).

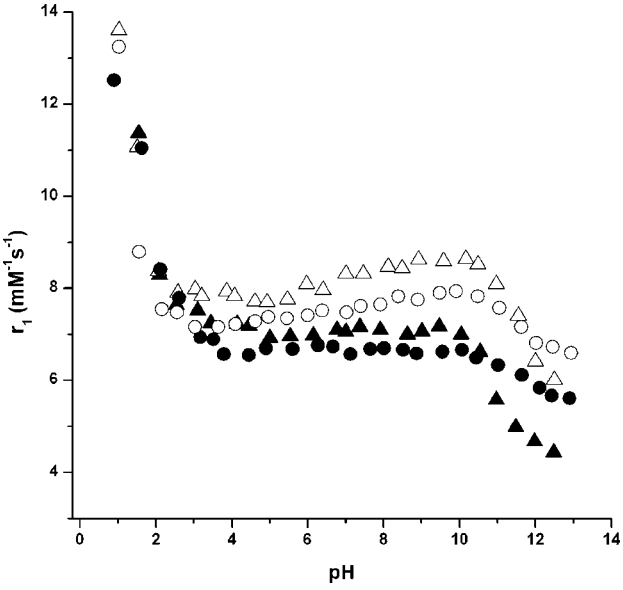

Figure 3. The millimolar relaxivities (r_1, mM^{-1} s^{-1}) of complexes **1**−**4** plotted against pH. Values were measured at 60 MHz and 37 °C. The contrast agents are represented as follows: **1** (closed triangles), **2** (open triangles), **3** (closed circles), and **4** (open circles). Comparison of the closed data points allows correlation of the two DOTA-based ligands. Comparison of the open data points allows correlation of the two DTPA-based ligands.

Typically, a structural modification that lengthens τ_m should be avoided, however, the relaxivity of these small molecule chelates at high fields (>20 MHz) is dominated by another parameter, the rotational correlation motion (τ_R) (*47*). Although the contrast agent is attached to the transport peptide via a flexible linker, τ_R for **1**−**4** must be substantially higher than Gd(III)-DOTA and Gd(III)-DTPA. **1**−**4** have the same q, T_{1e}, and less than optimal τ_m values compared to Gd(III)-DOTA and Gd(III)-DTPA, yet exhibit a 2.0−2.5-fold increase in overall relaxivity. Therefore, the increase is likely due to an increase in τ_R (through an increase in molecular weight). In summary, this system is highly dependent on τ_R, allowing relaxivity values to remain acceptable in spite of varying, less-than-optimal τ_m values (*1*).

In Vitro Cleavage. To assess thiol-mediated release of the chelated Gd(III) from the disulfide-linked arginine oligomer in solution, varying equivalents of GSH were added to a solution of **4** and the cleavage product was quantified via HPLC-MS. The samples were prepared by adding increasing amounts of GSH, from 0.25:1 to 4:1 (GSH/**4**), to a stock solution of **4** (1.0 mM in DPBS). These samples were combined with incrementally delayed starting times so that each could be incubated in a 37 °C water bath for 4 h prior to LC-MS analysis (this is consistent with the cell culture conditions). Separation was accomplished by a gradient ramp starting with 0% MeCN which reached 60% MeCN at 40 min before returning to 0% MeCN. The proposed cleavage reaction was followed by plotting the total ion count (TIC) of the desired product (Gd(III)-DTPA-GSH, $m/z = 912^+$ amu) and the starting material (**4**, $m/z = 3$, 673^+ amu), as their concentrations changed in response to GSH addition (Supporting Informatio Figure S2). The molecular ions chromatograms (912^+ and 673^+) were integrated so that the total area under the curve could be calculated (Figure 2).

Cellular Retention. To elucidate cellular uptake and retention of complexes **1**−**4**, 80% confluent cultures of NIH/3T3 cells were incubated with 0.10 mM of **1**−**4** for 4 h. After a 4 h incubation, the cells were washed three times with DPBS (time = 0, initial amount), placed in fresh media, and allowed to equilibrate for 1 h. Three cell samples and aliquots of the corresponding cell media were removed for analysis. This procedure was repeated 4 times for a total of 5 washes where the last wash was allowed to leach for 24 h.

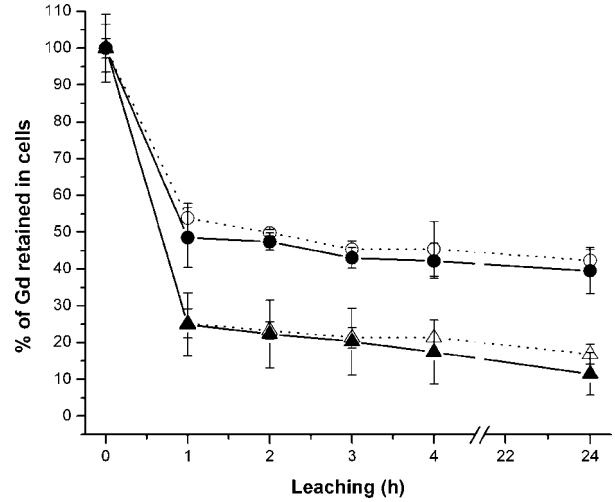

Figure 4. The percentage of Gd(III) associated with the NIH/3T3 cells as a function of the initial uptake concentration (data taken directly from Supporting Information Table S1). Cells were washed with DPBS at each time point displayed. The contrast agents are represented as follows: **1** (closed triangles), **2** (open triangles), **3** (closed circles), and **4** (open circles). Comparison of the closed data points allows correlation of the two DOTA-based ligands. Comparison of the open data points allows correlation of the two DTPA-based ligands.

Each cell culture well consists of two Gd(III)-containing phases: (i) the cells and (ii) the external media. ICP-MS provided absolute quantities of accumulated, retained, and leached Gd(III) for the cells at five time points. These data show that, prior to leaching of the agent, nondisulfide complexes **1** and **2** show increased uptake efficacy over **3** and **4** (Supporting Information Table S1). However, Figure 4 shows that, after washes, cells treated with **1** and **2** lose a more significant amount of the agent than those treated with **3** and **4**. The absolute quantities (Supporting Information Table S1) were divided by their respective initial concentrations (those collected at time = 0) in order to elucidate the relative amount of each agent retained within the cells. Incorporation of a disulfide linkage between the transduction moiety and Gd(III) chelate of these cell-permeable contrast agents drastically improves cellular retention (Figure 4; e.g., from 15% to 40% in the case of **1** vs **3** in the NIH/3T3 cell line).

SR-XRF Analysis. Synchrotron-based XRF analysis was performed to determine the cellular association of complexes **1**−**4**. For each sample, three to five randomly chosen areas were raster-scanned to acquire a multicell-containing image with high resolution (60 × 60 μm with 0.25 μm^2 pixel size). These high-resolution elemental maps provide pixel by pixel data sets that globally confirm, map, and quantify the Gd distribution within each sampled area (*24*). An example of these data is displayed in Figure 5 where the leaching and nonleaching data of **2** and **4** in the NIH/3T3 cell line is compared. Fluorescence maps of inherent biological elements (e.g., P and S) accompany each gadolinium image to prove cellular existence and provide boundaries. The overlay column combines the data from the three elemental maps (P, S, and Gd columns) to provide information on the areas of multielement overlap. Owing to the proximity of the Gd and Fe fluorescence energy levels, it is important to deconvolute potential peak overlap between Fe and Gd fluorescence. This was accomplished using modified Gaussian curves that were fitted at each scan position to the acquired X-ray fluorescence spectra (*36*). Supporting Information Figure S3 contains images of complexes **1** and **3**. The top two rows of images displayed in Figure 5 show the extent to which leaching

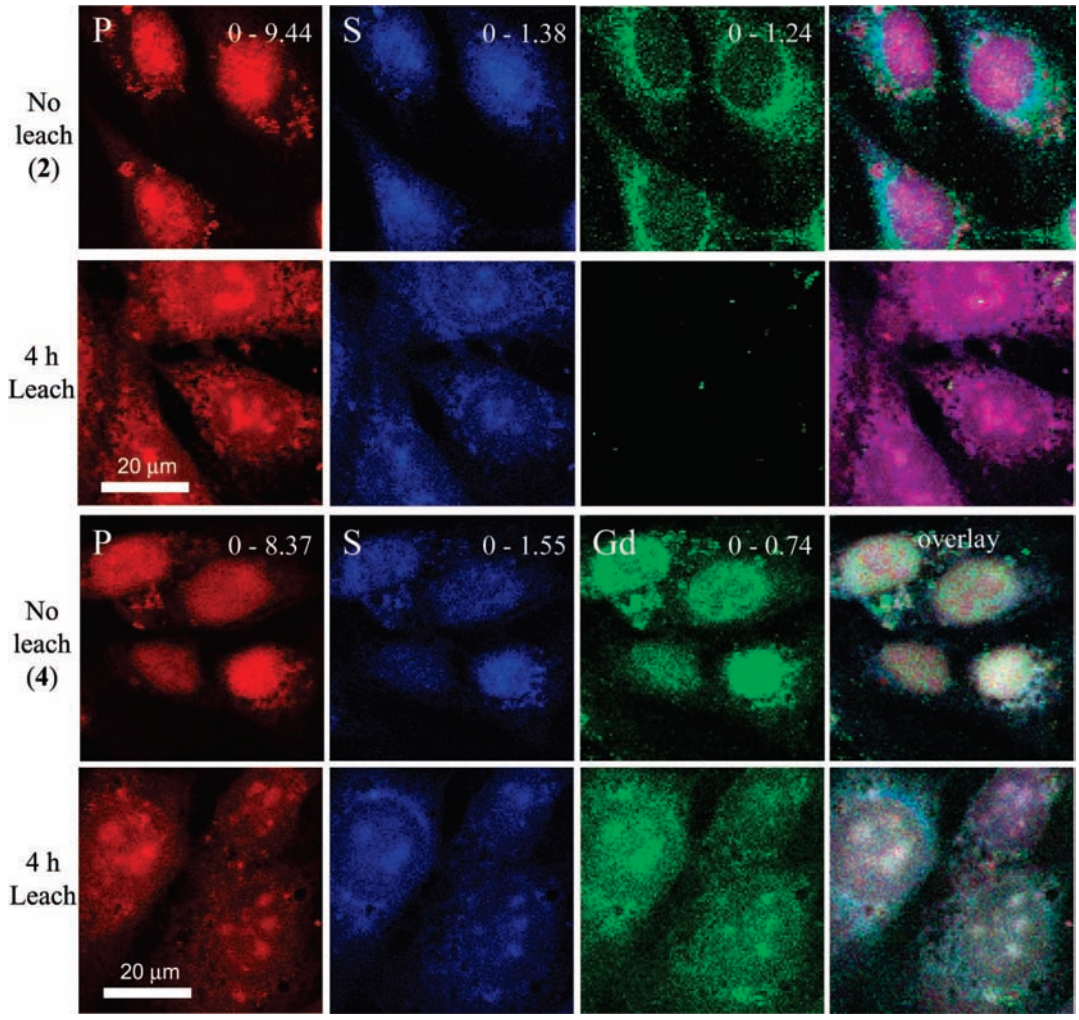

Figure 5. XRF images of NIH/3T3 cells treated with contrast agents **2** (top 8 images) and **4** (bottom 8 images) at time = 0 (No leach) and after 4 h (Leach). Phosphorus fluorescence is red, sulfur is blue, and gadolinium is green. Note that each column of images is scaled to its respective maximum value (displayed at the upper right corner and given in $\mu g/cm^2$).

has depleted the NIH/3T3 cells of associated gadolinium when treated with the nondisulfide contrast agent (**2**). Conversely, when the cells are treated with a disulfide linked contrast agent (**4**), they retain a large amount of gadolinium postleach (bottom 2 rows, Figure 5).

MR Imaging and T_1 Analysis. In order to assess the feasibility of the disulfide linkage to increase cell retention and maintain MR image contrast over an extended time period, NIH/3T3 cells were incubated with 1.0 mM of **1**−**4**. After the cells were harvested and placed in glass capillary tubes, MR images were acquired (Figure 6A). Cells incubated with complexes **1** and **2** exhibit a significantly brighter signal than control cells. However, after the washing procedure outlined for the SR-XRF and ICP-MS experiments (4 h, with washes at 1 h intervals), the cells incubated with **1** and **2** have a significantly lower intensity in the MR image. This loss of image contrast (due to leaching of the contrast agent) is much less in the case of the cells incubated with complexes **3** and **4** (Figure 6B). The signal intensities of the leached cells are similar to their respective nonleached samples, and show little loss of signal intensity (MR image intensity differences were mathematically confirmed via Student's *t*-tests of the corresponding T_1 values (Supporting Information Table S2).

DISCUSSION

Arginine-bound cell-permeable contrast agents **3** and **4** were prepared via thiol-activated pyridyl intermediates to create cell-permeable MR conjugates linked to cell transduction moieties via a disulfide bond. These agents (**3** and **4**), although structurally similar to **1** and **2**, must be coupled to their respective Gd(III) chelating moieties off-resin and under strict pH and equivalence control. Once conjugated to the end-capped Arg_8-Cys, compounds **8** and **9** are exposed to $Gd(OH)_3$ to provide cell-permeable MR contrast agents with antileaching properties (Scheme 2).

The structural changes made to **1** and **2** in order to incorporate the disulfide bond were tested to determine their affect on proton relaxation. As seen in Table 1, the coordination environment of the Gd(III) ion (expressed by the q, τ_m) and relaxivity measurements has not been significantly changed in spite of the structural differences between nondisulfide (**1** and **2**) and disulfide (**3** and **4**) agents. Even with varying pH, the observed relaxivities remain relatively constant (Figure 3). This structural stability and documented characterization make contrast agents **1**−**4** excellent choices for labeling cells cultured in a nonleaching environment (Supporting Information Table S1).

In order to quantify the efficiency of in vivo disulfide cleavage, we used a model disulfide exchange reaction in vitro. Disulfide-bridged complexes undergo exchange or reduction with endogenous thiols, especially GSH (*18*). As a result, the Gd(III) chelate will be cleaved from its cell-penetrating polyarginine oligomer and consequently prolong the intracellular lifetime of the chelated Gd(III). The lifetime of the disulfide linkage was assessed by incubating agent **4** at 37 °C in the

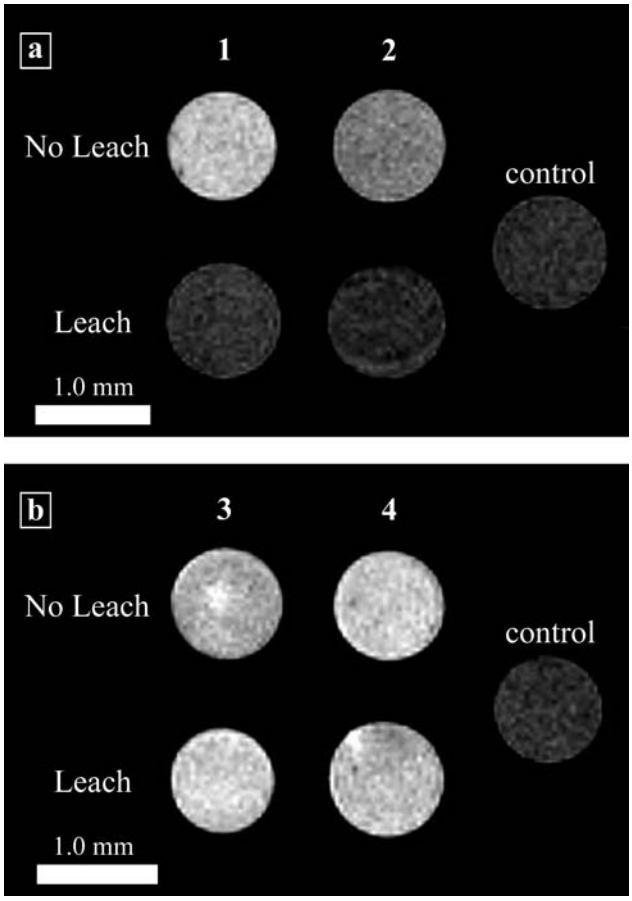

Figure 6. T_1-weighted MR images of NIH/3T3 cells incubated with complexes **1**−**4**. The No Leach rows are the cell populations that were not allowed to leach. The Leach rows are the cell populations that were allowed to leach for 4 h with washes of DPBS at the hours. The control cells were not incubated with contrast agent but were harvested and packed following the same procedure. (a) Cells incubated with Gd(III)-DOTA-Arg_8 or Gd(III)-DTPA-Arg_8 (**1** and **2**). (b) Cells incubated with Gd(III)-DOTA-SS-Arg_8 or Gd(III)-DTPA-SS-Arg_8 (**3** and **4**). Images were acquired at 14.1 T with a FOV of 10 × 10 mm^2 (matrix size 256 × 256) and a slice thickness of 1.0 mm. The scale bar represents 1.0 mm. T_1 values and Student's *t*-tests confirming statistically significant differences can be found in Supporting Information Table S2.

presence of increasing quantities of GSH (Figure 2). A qualitative depiction of these results is displayed in Supporting Information Figure S2. As the concentration of GSH is increased, the amount of desired product (Gd(III)DTPA-GSH) detected via quantitative HPLC-MS is increased. Conversely, as the concentration of GSH is increased, the amount of starting material (Gd(III)DTPA-SS-Arg_8, **4**) decreases. This trend continues through ratios of [GSH]:[**4**] that reach 4:1 and implies that, while disulfide cleavage begins at very low GSH concentrations (0.25 equiv), complete cleavage is not obtainable even at GSH concentrations that are 4 times that of the contrast agent.

When cells are incubated with the same initial concentration of agent, cell uptake of **1** and **2** is higher in NIH/3T3 cells than **3** and **4** (Initial Amount, Supporting Information Table S1). The initial uptake values of **1** and **2** show that NIH/3T3 cells prefer the negatively charged DTPA over the neutral DOTA chelate with the same transduction moiety. Conversely, with agents **3** and **4**, the neutral DOTA chelate is preferred over the charged DTPA. We have previously shown that small changes in structure or charge have significant effects on the uptake efficiency multiple contrast agents (*24*). In contrast to initial uptake, the percentage of Gd(III) retained in cells postleaching implies that incorporation of the disulfide bond into **3** and **4** has a positive effect on long-term contrast agent retention. Addition of the reactive disulfide linkage (**3** and **4**) increases cell retention of the Gd(III) chelate 3.5 and 2.5 more than their nondisulfide counterparts (**1** and **2**), respectively (Figure 4).

To covalidate ICP-MS measurements at the single cell level, cells incubated with **1**−**4** were evaluated by SR-XRF. SR-XRF microprobes alleviate the difficulties associated with visualizing intracellular lanthanides and allow direct gadolinium imaging without covalent attachment of organic fluorophores that alter cell transport properties. Additionally, SR-XRF offers submicrometer resolution and quantifiable elemental data of subcellular regions of interest that are displayed in two-dimensional, intensity-weighted images (*48*). As shown, cells labeled with **2** and **4** (fixed at time = 0) show a significant amount of associated gadolinium (No leach, rows 1 and 3, Figure 5). In contrast, rows 2 and 4 have significant differences in the amount of gadolinium (4 h Leach for **2** and **4**, respectively). The 4 h leach images for complex **2** show only trace amounts of gadolinium, while the corresponding images of cells treated with **4** display a relatively large amount of gadolinium comparable to nonleached cells. These results are in agreement with the ICP-MS measurements and can be attributed to the incorporation of the disulfide linkage between the Gd(III) chelate and the arginine transduction moiety.

The data from ICP-MS and SR-XRF images reveals that incorporation of the disulfide linkage increases the cell retention of contrast agents **3** and **4**. However, since ICP-MS and SR-XRF are highly sensitive toward gadolinium concentration, the utility of **1**−**4** to increase MR image intensity was examined (before and after the leaching). This assessment was accomplished by incubating **1**−**4** (1.0 mM) on 2 populations of NIH/3T3 cells, one subjected to the leaching protocol outlined in the Experimental Procedures section and one that was not. Visual comparison of the images in Figure 6A to those in B clearly show that cells incubated with **3** and **4** retain their image contrast enhancement to a greater extent than those incubated with **1** and **2** (e.g., 88% signal retention for complex **3** over the leaching period). These images show that the SR-XRF and ICP-MS data have translated to MRI whereby increased cell retention of the Gd(III)-based contrast agents prolongs image contrast. We performed T_1 analysis to validate that the image intensity changes are due to changes in T_1. As shown in Supporting Information Table S2, the shortest T_1 values correspond to the highest image intensities.

Complexes **1**−**4** undergo similar cell uptake; the disulfide exchange reactions possible for **3** and **4** must significantly alter their intracellular fate from **1** and **2**. If **1** and **2** are nonspecifically bound to the internal membrane or sequestered in lysosomes, the image intensity and resultant T_1 values will decrease due to reduced Gd(III) access to the bulk water. This explains the high T_1 values and reduced MR image intensity in Figure 6A (Leach) despite the Gd(III) measurements displayed in Supporting Information Table S1. Such encapsulation allows the contrast agent access to only a small number of rapidly exchanging inner sphere water molecules. This phenomenon has been observed within artificial systems such as those involving LIPOCEST contrast agents and, more importantly, within certain subcellular compartments (*49, 50*)

The SR-XRF images display a similar loss of gadolinium signal after the leaching process. We propose that **1** and **2** have been processed differently than **3** and **4**, leaving the Gd(III) chelate nonspecifically bound to the recycling membrane (either endosomal or lysosomal). Thus, nonspecific contrast agent binding was only removed when the cells were subjected to harsh conditions (i.e., the formaldehyde fixation and dehydration necessary for SR-XRF sample preparation). Therefore, the SR-XRF images supplement the MR images while supporting our current hypothesis of membrane internalization and nonspecific binding of complexes **1** and **2**.

In conclusion, we have synthesized Gd(III)-DOTA-SS-Arg_8 (**3**) and Gd(III)-DTPA-SS-Arg_8 (**4**), cell-permeable contrast agents that show increased cell retention via disulfide bond incorporation, which may be a result of intracellular thiol concentrations. The agents' relaxometric properties, pH stability, in vitro cleavage kinetics, and cell retention have been investigated. As expected, **3** and **4** show increased cell retention (ICP-MS), single cell association (SR-XRF), and viability as long-term MRI contrast agents (MR images). These agents could be used to ectopically label cell populations and provide long-term contrast enhancement for cell tracking and lineage analysis using MR imaging.

ACKNOWLEDGMENT

We thank Prof. Matthew J. Allen for helpful discussions. This research was supported by the National Institutes of Health under Grant Number 1 R01 EB005866-01, the Nanomaterials for Cancer Diagnostics and Therapeutics under 5 U54 CA1193 41-02, and the Center for Excellence in Transitional Human Stem Cell Research under 1 P50 NS0542 78-01. Use of the Advanced Photon Source was supported by the U.S. Department of Energy, Office of Science, Office of Basic Energy Sciences, under Contract Number W-31-109-ENG-38. MR images were acquired on a 14.1 T-WB imaging spectrometer operated by the CBMRR under NIH/NCRR Grant Number 1 S10 RR13880-01.

Supporting Information Available: The variable temperature ^{17}O data accompanied by the τ_m fitting curves, HPLC-MS ion count of disulfide exchange, quantitation of cell uptake and leaching, additional SR-XRF images, and MR image T_1 values and Student's *t*-test results for the MR images.This material is available free of charge via the Internet at http://pubs.acs.org.

LITERATURE CITED

(1) Merbach, A. E., and Toth, E. Eds. (2001) *The Chemistry of Contrast Agents in Medical Magnetic Resonance Imaging*, John Wiley and Sons, New York.

(2) Aime, S., Cabella, C., Colombatto, S., Geninatti Crich, S., Gianolio, E., and Maggioni, F. (2002) Insights into the use of paramagnetic Gd(III) complexes in MR-molecular imaging investigations. *J. Magn. Reson. Imaging 16*, 394–406.

(3) Hu, X., and Norris, D. G. (2004) Advances in high-field magnetic resonance imaging. *Annu. Rev. Biomed. Eng. 6*, 157–184.

(4) Collins, C. M., Wang, Z., Mao, W., Fang, J., Liu, W., and Smith, M. B. (2007) Array-optimized composite pulse for excellent whole-brain homogeneity in high-field MRI. *Magn. Reson. Med. 57*, 470–4.

(5) Winter, P. M., Caruthers, S. D., Wickline, S. A., and Lanza, G. M. (2006) Molecular imaging by MRI. *Curr. Cardiol. Rep. 8*, 65–9.

(6) Endres, P. J., Paunesku, T., Vogt, S., Meade, T. J., and Woloschak, G. E. (2007) DNA-TiO2 nanoconjugates labeled with magnetic resonance contrast agents. *J. Am. Chem. Soc. 129*, 15760–15761.

(7) Towner, R. A., Smith, N., Doblas, S., Tesiram, Y., Garteiser, P., Saunders, D., Cranford, R., Silasi-Mansat, R., Herlea, O., Ivanciu, L., Wu, D., and Lupu, F. (2008) In vivo detection of c-Met expression in a rat C6 glioma model. *J. Cell. Mol. Med. 12*, 174–186.

(8) Caravan, P., Cloutier, N. J., Greenfield, M. T., McDermid, S. A., Dunham, S. U., Bulte, J. W. M., Amedio, J. C., Jr., Looby, R. J., Supkowski, R. M., Horrocks, W. D., Jr., McMurry, T. J., and Lauffer, R. B. (2002) The interaction of MS-325 with human serum albumin and its effect on proton relaxation rates. *J. Am. Chem. Soc. 124*, 3152–3162.

(9) Major, J. L., Parigi, G., Luchinat, C., and Meade, T. J. (2007) The synthesis and in vitro testing of a zinc-activated MRI contrast agent. *Proc. Natl. Acad. Sci. U.S.A. 104*, 13881–13886, S13881/1-S13881/9.

(10) Louie, A. Y., Huber, M. M., Ahrens, E. T., Rothbacher, U., Moats, R., Jacobs, R. E., Fraser, S. E., and Meade, T. J. (2000) In vivo visualization of gene expression using magnetic resonance imaging. *Nat. Biotechnol. 18*, 321–5.

(11) Kalman, F. K., Woods, M., Caravan, P., Jurek, P., Spiller, M., Tircso, G., Kiraly, R., Bruecher, E., and Sherry, A. D. (2007) Potentiometric and relaxometric properties of a gadolinium-based MRI contrast agent for sensing tissue pH. *Inorg. Chem. 46*, 5260–5270.

(12) Saborowski, O., Simon, G. H., Raatschen, H.-J., Wendland, M. F., Fu, Y., Henning, T., Baehner, R., Corot, C., Chen, M.-H., and Daldrup-Link, H. E. (2007) MR imaging of antigen-induced arthritis with a new, folate receptor-targeted contrast agent. *Contrast Med. Mol. Imaging 2*, 72–81.

(13) Allen, M. J., and Meade, T. J. (2004) Magnetic Resonance Contrast Agents for Medical and Molecular Imaging, In *Metal Ions in Biological Systems*, (Sigel, A., and Sigel, H. Eds.) Marcel Dekker Inc., New York, pp 1−28.

(14) Allen, M. J., and Meade, T. J. (2003) Synthesis and visualization of a membrane-permeable MRI contrast agent. *J. Biol. Inorg. Chem. 8*, 746–750.

(15) Frullano, L., and Meade Thomas, J. (2007) Multimodal MRI contrast agents. *J. Biol. Inorg. Chem. 12*, 939–949.

(16) Datta, A., Hooker, J. M., Botta, M., Francis, M. B., Aime, S., and Raymond, K. N. (2008) High relaxivity gadolinium hydroxypyridonate-viral capsid conjugates: nanosized MRI contrast agents. *J. Am. Chem. Soc. 130*, 2546–2552.

(17) Aime, S., Castelli, D. D., Lawson, D., and Terreno, E. (2007) Gd-loaded liposomes as T1, susceptibility, and CEST agents, all in one. *J. Am. Chem. Soc. 129*, 2430–2431.

(18) Meister, A., and Anderson, M. E. (1983) Glutathione. *Annu. Rev. Biochem. 52*, 711–60.

(19) Franco, R., Schoneveld, O. J., Pappa, A., and Panayiotidis, M. I. (2007) The central role of glutathione in the pathophysiology of human diseases. *Arch. Physiol. Biochem. 113*, 234–258.

(20) Pastore, A., Federici, G., Bertini, E., and Piemonte, F. (2003) Analysis of glutathione: Implication in redox and detoxification. *Clin. Chim. Acta 333*, 19–39.

(21) Hong, R., Han, G., Fernandez, J. M., Kim, B.-j., Forbes, N. S., and Rotello, V. M. (2006) Glutathione-mediated delivery and release using monolayer protected nanoparticle carriers. *J. Am. Chem. Soc. 128*, 1078–1079.

(22) Han, G., Chari Nandini, S., Verma, A., Hong, R., Martin Craig, T., and Rotello Vincent, M. (2005) Controlled recovery of the transcription of nanoparticle-bound DNA by intracellular concentrations of glutathione. *Bioconjugate Chem. 16*, 1356–9.

(23) Carrera, C., Digilio, G., Baroni, S., Burgio, D., Consol, S., Fedeli, F., Longo, D., Mortillaro, A., and Aime, S. (2007) Synthesis and characterization of a Gd(III) based contrast agent responsive to thiol containing compounds. *Dalton Trans.* 4980–4987.

(24) Endres, P. J., MacRenaris, K. W., Vogt, S., Allen, M. J., and Meade, T. J. (2006) Quantitative imaging of cell-permeable magnetic resonance contrast agents using X-ray fluorescence. *Mol. Imaging 5*, 485–97.

(25) Allen, M. J., MacRenaris, K. W., Venkatasubramanian, P. N., and Meade, T. J. (2004) Cellular delivery of MRI contrast agents. *Chem. Biol. 11*, 301–307.

(26) Futaki, S. (2005) Membrane-permeable arginine-rich peptides and the translocation mechanisms. *Adv. Drug Delivery Rev. 57*, 547–558.

(27) Futaki, S., Suzuki, T., Ohashi, W., Yagami, T., Tanaka, S., Ueda, K., and Sugiura, Y. (2001) Arginine-rich peptides: An abundant source of membrane-permeable peptides having potential as carriers for intracellular protein delivery. *J. Biol. Chem. 276*, 5836–5840.

(28) Allen, M. J. (2004) *Department of Chemistry*, California Institute of Technology, Pasadena, CA, p 181.

(29) Endres, P. J. (2008) *Department of Chemistry*, Northwestern University, Evanston, IL, p 204.

(30) Beeby, A., Clarkson, I. M., Dickins, R. S., Faulkner, S., Parker, D., Royle, L., de Sousa, A. S., Williams, J. A. G., and Woods, M. (1999) Non-radiative deactivation of the excited states of europium, terbium and ytterbium complexes by proximate energy-matched OH, NH and CH oscillators: An improved luminescence method for establishing solution hydration states. *J. Chem. Soc., Perkin Trans. 2*, 493–504.

(31) Quici, S., Cavazzini, M., Marzanni, G., Accorsi, G., Armaroli, N., Ventura, B., and Barigelletti, F. (2005) Visible and near-infrared intense luminescence from water-soluble lanthanide [Tb(III), Eu(III), Sm(III), Dy(III), Pr(III), Ho(III), Yb(III), Nd(III), Er(III)] complexes. *Inorg. Chem. 44*, 529–537.

(32) Terreno, E., Botta, M., Boniforte, P., Bracco, C., Milone, L., Mondino, B., Uggeri, F., and Aime, S. (2005) A multinuclear NMR relaxometry study of ternary adducts formed between heptadentate Gd(III) chelates and L-lactate. *Chem.-Eur. J. 11*, 5531–5537.

(33) Aime, S., Botta, M., Crich, S. G., Giovenzana, G., Pagliarin, R., Sisti, M., and Terreno, E. (1998) NMR relaxometric studies of Gd(III) complexes with heptadentate macrocyclic ligands. *Magn. Reson. Chem. 36*, S200−S208.

(34) Swift, T. J., and Connick, R. E. (1962) NMR (nuclear magnetic resonance)-relaxation mechanisms of O17 in aqueous solutions of paramagnetic cations and the lifetime of water molecules in the first coordination sphere. *J. Chem. Phys. 37*, 307–20.

(35) Caravan, P., Parigi, G., Chasse, J. M., Cloutier, N. J., Ellison, J. J., Lauffer, R. B., Luchinat, C., McDermid, S. A., Spiller, M., and McMurry, T. J. (2007) Albumin binding, relaxivity, and water exchange kinetics of the diastereoisomers of MS-325, a Gadolinium(III)-based magnetic resonance angiography contrast agent. *Inorg. Chem. 46*, 6632–6639.

(36) Vogt, S. (2003) MAPS: A set of software tools for analysis and visualization of 3D X-ray fluorescence data sets. *J. Phys. IV 104*, 635–638.

(37) Ebright, Y. W., Chen, Y., Kim, Y., and Ebright, R. H. (1996) S-[2-(4-azidosalicylamido)ethylthio]-2-thiopyridine: Radioiodinatable, cleavable, photoactivatable crosslinking agent. *Bioconjugate Chem. 7*, 380–384.

(38) Glogard, C., Stensrud, G., and Aime, S. (2003) Novel radical-responsive MRI contrast agent based on paramagnetic liposomes. *Magn. Reson. Chem. 41*, 585–588.

(39) Botta, M., Aime, S., Barge, A., Bobba, G., Dickins, R. S., Parker, D., and Terreno, E. (2003) Ternary complexes between cationic Gd(III) chelates and anionic metabolites in aqueous solution: An NMR relaxometric study. *Chem.-Eur. J. 9*, 2102–2109.

(40) Urbanczyk-Pearson, L. M., Femia, F. J., Smith, J., Parigi, G., Duimstra, J. A., Eckermann, A. L., Luchinat, C., and Meade, T. J. (2008) Mechanistic investigation of b-galactosidase-activated MR contrast agents. *Inorg. Chem. 47*, 56–68.

(41) Caravan, P., Ellison, J. J., McMurry, T. J., and Lauffer, R. B. (1999) Gadolinium(III) chelates as MRI contrast agents: Structure, dynamics, and applications. *Chem. Rev. 99*, 2293–2352.

(42) Chan, K. W.-Y., and Wong, W.-T. (2007) Small molecular gadolinium(III) complexes as MRI contrast agents for diagnostic imaging. *Coord. Chem. Rev. 251*, 2428–2451.

(43) Jaszberenyi, Z., Moriggi, L., Schmidt, P., Weidensteiner, C., Kneuer, R., Merbach, A. E., Helm, L., and Toth, E. (2007) Physicochemical and MRI characterization of Gd3+-loaded polyamidoamine and hyperbranched dendrimers. *J. Biol. Inorg. Chem. 12*, 406–420.

(44) Kubicek, V., Rudovsky, J., Kotek, J., Hermann, P., Vander Elst, L., Muller, R. N., Kolar, Z. I., Wolterbeek, H. T., Peters, J. A., and Lukes, I. (2005) A bisphosphonate monoamide analogue of DOTA: A potential agent for bone targeting. *J. Am. Chem. Soc. 127*, 16477–16485.

(45) Laurent, S., Parac-Vogt, T. N., Kimpe, K., Thirifays, C., Binnemans, K., Muller, R. N., and Vander Elst, L. (2007) Bis(phenylethylamide) derivatives of Gd-DTPA as potential receptor-specific MRI contrast agents. *Eur. J. Inorg. Chem.* 2061–2067.

(46) Zhang, S., Jiang, X., and Sherry, A. D. (2005) Modulation of the lifetime of water bound to lanthanide metal ions in complexes with ligands derived from 1,4,7,10-tetraazacyclododecane tetraacetate (DOTA). *Helv. Chim. Acta 88*, 923–935.

(47) Lauffer, R. B. (1987) Paramagnetic metal complexes as water proton relaxation agents for NMR imaging: Theory and design. *Chem. Rev. 87*, 901–27.

(48) Twining, B. S., Baines, S. B., Fisher, N. S., Maser, J., Vogt, S., Jacobsen, C., Tovar-Sanchez, A., and Sanudo-Wilhelmy, S. A. (2003) Quantifying trace elements in individual aquatic protist cells with a synchrotron X-ray fluorescence microprobe. *Anal. Chem. 75*, 3806–3816.

(49) Aime, S., Castelli, D. D., and Terreno, E. (2005) Highly sensitive MRI chemical exchange saturation transfer agents using liposomes. *Angew. Chem., Int. Ed. 44*, 5513–5515.

(50) Bulte, J. W. M., Douglas, T., Witwer, B., Zhang, S.-C., Strable, E., Lewis, B. K., Zywicke, H., Miller, B., van Gelderen, P., Moskowitz, B. M., Duncan, L. D., and Frank, J. A. (2001) Magnetodendrimers allow endosomal magnetic labeling and in vivo tracking of stem cells. *Nat. Biotechnol. 19*, 1141–1147.

(51) Bryden, C. C., and Reilley, C. N. (1982) Europium luminescence lifetimes and spectra for evaluation of 11 europium complexes as aqueous shift reagents for nuclear magnetic resonance spectrometry. *Anal. Chem. 54*, 610–15.

(52) Powell, D. H., Ni Dhubhghaill, O. M., Pubanz, D., Helm, L., Lebedev, Y. S., Schlaepfer, W., and Merbach, A. E. (1996) High-pressure NMR kinetics. Part 74. Structural and dynamic parameters obtained from 17O NMR, EPR, and NMRD studies of monomeric and dimeric Gd3+ complexes of interest in magnetic resonance imaging: An integrated and theoretically self-consistent approach. *J. Am. Chem. Soc. 118*, 9333–9346.

BC8002919

Cell-Permeable MR Contrast Agents with Increased Intracellular Retention

Paul J. Endres,[†] Keith W. MacRenaris,[†] Stefan Vogt,[‡] and Thomas J. Meade[†*]

[†]*Departments of Chemistry, Biochemistry and Molecular and Cell Biology, Neurobiology and Physiology, and Radiology, Northwestern University, 2145 Sheridan Rd., Evanston, IL 60208;*
[‡]*Experimental Facilities Division, Argonne National Laboratory, 9700 S. Cass Ave., Argonne, IL 60439.*

Corresponding E-mail Address: tmeade@northwestern.edu

Page	**Contents**
S1	Table of Contents
S2	τ_m Measurements and Fittings (Supporting Figure S1)
S3	HPLC-MS Ion Count of Disulfide Exchange (Supporting Figure S2)
S4	Quantitation of Cell Uptake and Leaching (Supporting Table S1)
S5	Additional SR-XRF Images of NIH/3T3 Cells (Supporting Figure S3)
S6	T_1 values and Student *t*-Tests for MR Images (Supporting Table S2)

Determination of τ_m by ^{17}O Transverse Relaxation Rate Measurements. Samples of **1**-**4** were prepared at 15-20 mM concentrations in 1% ^{17}O enriched water (Medical Isotopes, Inc., Pelham, NH) adjusted to pH 7.40. Lock was achieved by means of an external D_2O standard. ^{17}O spectra were obtained at 54 MHz (number of averaged transients was 160 – 320 and relaxation delay was 400 ms) at temperatures ranging from 1 °C to 86 °C in 5 °C increments. The ^{17}O transverse relaxation rate was determined by obtaining the line width (in Hz) at half of the peak height, $\Delta\nu_{1/2}$, of the ^{17}O water signal and later fitting the data at 25 °C (references 22-24). This data and their respective fittings are shown below in Figure S1.

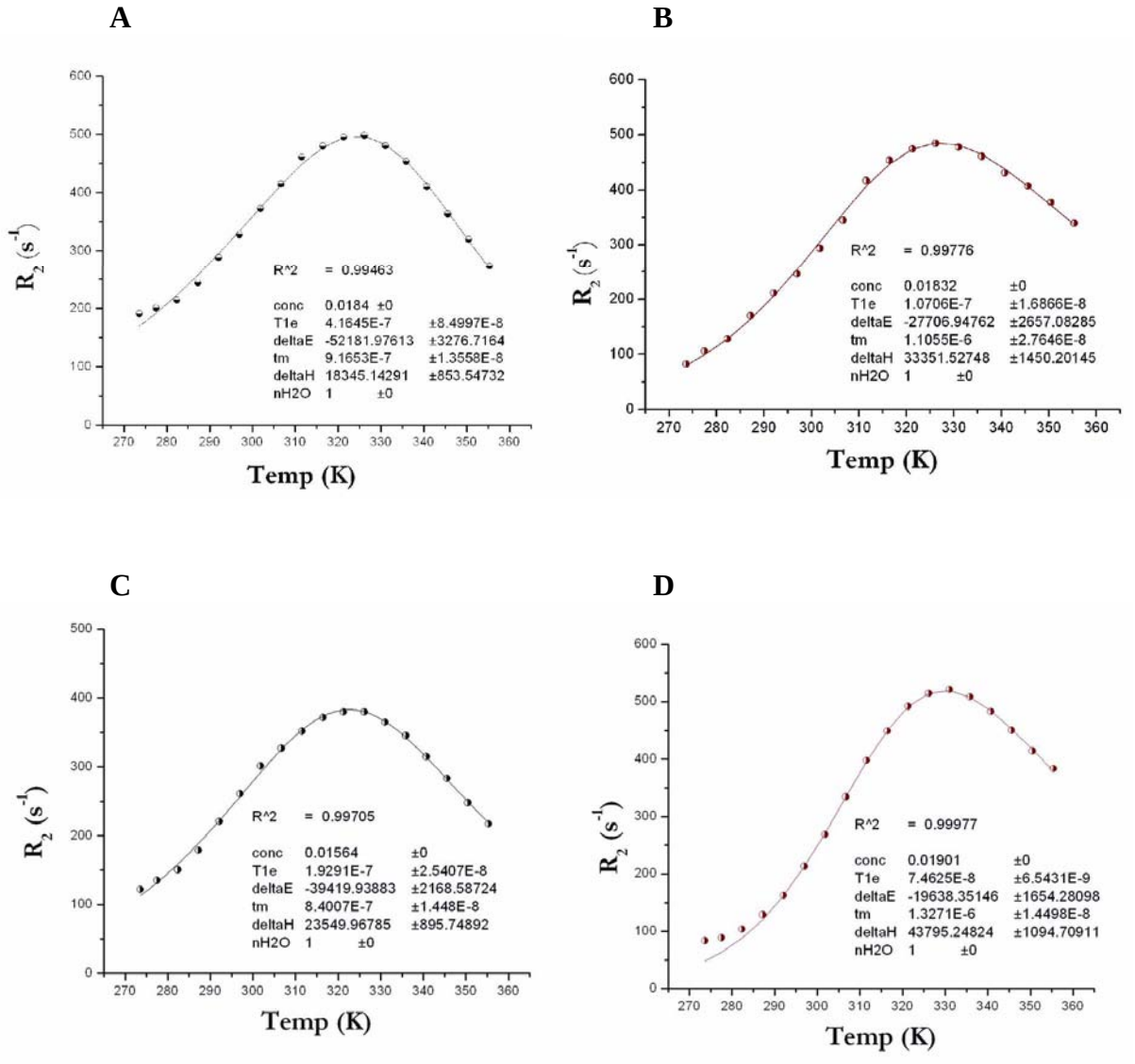

Supporting Figure S1. (A) Raw ^{17}O data and τ_m fitting of compound **1**. (B) Raw ^{17}O data and τ_m fitting of compound **2**. (C) Raw ^{17}O data and τ_m fitting of compound **3**. (D) Raw ^{17}O data and τ_m fitting of compound **4**. The relaxation data were fit to these four parameters: τ_m (water exchange rate), $\Delta H^{\ddagger}$ (activation enthalpy), T_{1e} (electronic relaxation rate), and ΔE_{T1e} (activation energy of T_{1e}).

In Vitro Cleavage. Determination of disulfide exchange using the total ion count (TIC) of **4** plus the addition of GSH with increasing amounts of GSH for 4 hours in PBS.

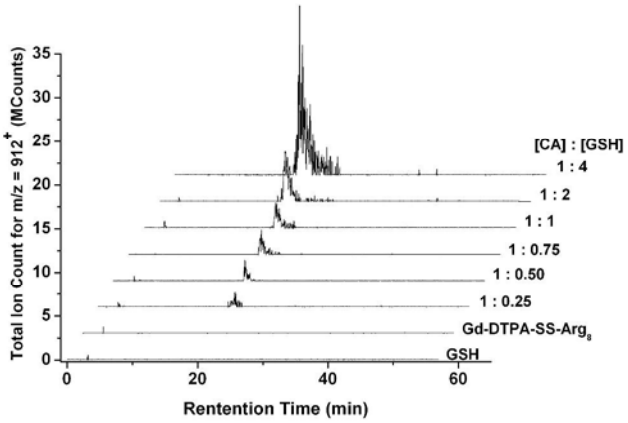

Supporting Figure S2. Treatment of **4** with increasing concentrations of GSH leads to disulfide exchange and subsequent product formation (Gd(III)-DTPA-GSH, $m/z = 912^{+}$).

Quantitation of Cell Uptake. Gadolinium ICP-MS data for complexes **1-4** associated with NIH/3T3 cells before (Initial Amt.) and after leaching. These data were used to produce Figure 3.

Complex	**1**	**2**	**3**	**4**
Initial Amt.(10^{-11} moles)	13.6 ±0.36[a]	15.3 ±1.0	2.45 ±0.22	2.23 ±0.04
Leach 1 (1 h)	3.39 ±0.03	3.87 ±0.15	1.18 ±0.09	1.12 ±0.16
Leach 2 (2 h)	3.04 ±0.21	3.58 ±0.03	1.16 ±0.02	1.06 ±0.02
Leach 3 (3 h)	2.77 ±0.26	3.27 ±0.10	1.05 ±0.02	0.97 ±0.07
Leach 4 (4 h)	3.56 ±0.22	3.26 ±0.24	1.03 ±0.05	0.94 ±0.04
Leach 5[b] (24 h)	2.35 ±0.08	2.59 ±0.06	0.97 ±0.06	0.92 ±0.03

Supporting Table S1. All values given in 10^{-11} moles. [a]Error is given as +/- one standard deviation of triplicate runs. [b]A single wash allowed to leach for 24 hours.

SR-XRF Analysis. Synchrotron XRF analysis was performed to determine the cellular association of complexes **1**-**4**. These images are representative of the NIH/3T3 cells following the image acquisition procedure reported in the Experimental Procedures section. From our previous report, these high-resolution elemental maps provide pixel by pixel data sets that globally confirm, map, and quantify the Gd distribution within each sampled area *(24)*.

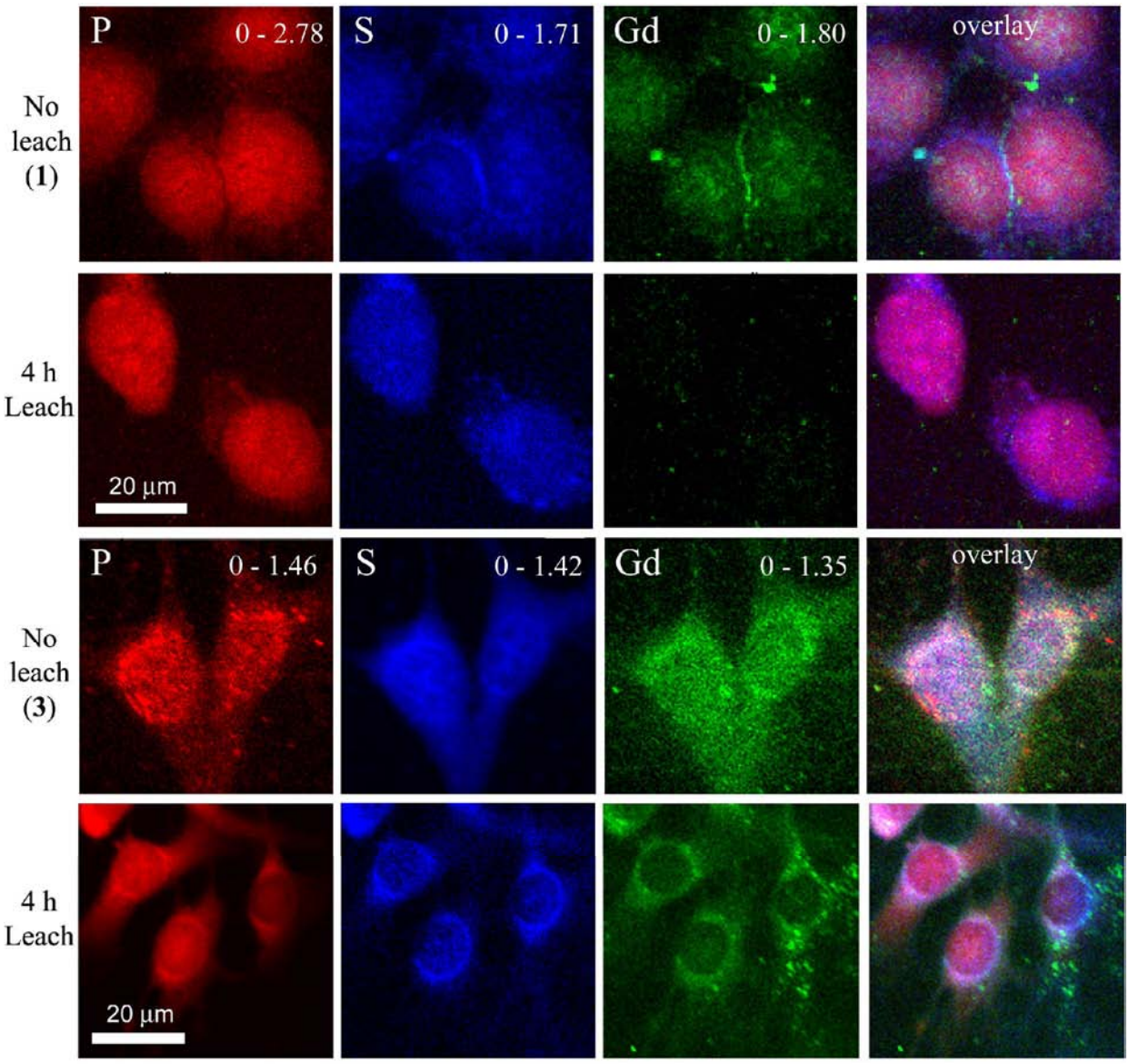

Supporting Figure S3. XRF images of NIH/3T3 cells treated with contrast agents **1** (top 8 images) and **3** (bottom 8 images) at time = 0 (No leach) and after 4 h (Leach). Phosphorus fluorescence is red, sulfur is blue, and gadolinium is green. Note that each column of images is scaled to its respective maximum value (displayed at the upper right corner and given in $\mu g/cm^2$).

MR Imaging and T_1 Analysis. To assess the feasibility of the disulfide linkage to increase cell retention and increase MR image contrast over an extended time period, NIH/3T3 cells were incubated with 1.0 mM of **1**-**4**. After the cells were harvested and placed in glass capillary tubes, they were visualized via MRI.

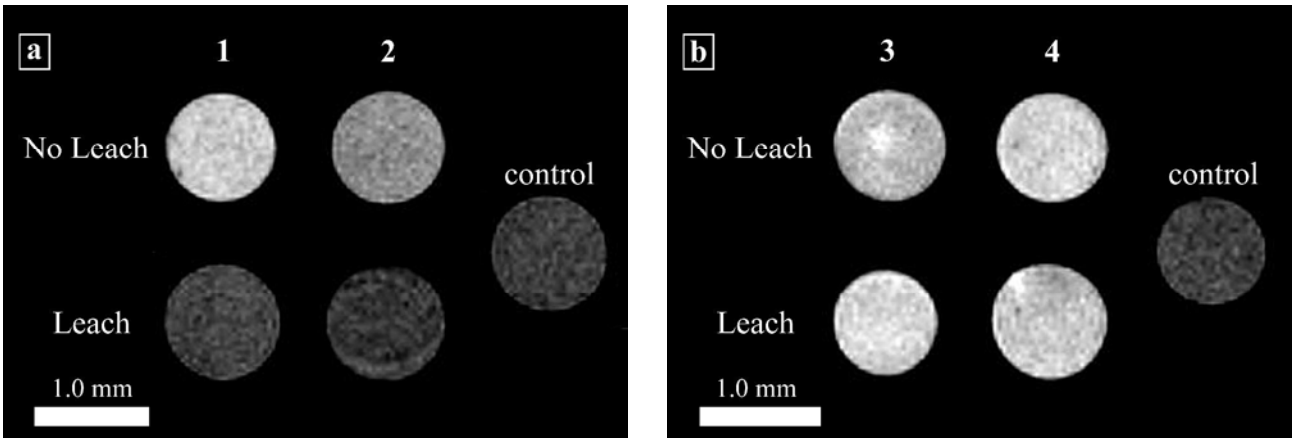

Sample name	Avg. T_1 time (ms)	Std. Dev. (ms)		*t* test comparison (value x *to* value y)	Meets 95% confidence level?
Fig. 7A: **1** *No Leach*	1847	94		contrast agent **1** No Leach *to* Leach	Yes
Fig. 7A: **1** *Leach*	2773	123		contrast agent **2** No Leach *to* Leach	Yes
Fig. 7A: **2** *No Leach*	2415	99		contrast agent **3** No Leach *to* Leach	No
Fig. 7A: **2** *Leach*	2824	138		contrast agent **4** No Leach *to* Leach	No
Fig. 7A: **control**	3017	111			
Fig. 7B: **3** *No Leach*	1687	63		contrast agent **1** Leach *to* Control	Yes
Fig. 7B: **3** *Leach*	1899	78		contrast agent **2** Leach *to* Control	Yes
Fig. 7B: **4** *No Leach*	1671	35		contrast agent **3** Leach *to* Control	Yes
Fig. 7B: **4** *Leach*	1834	59		contrast agent **4** Leach *to* Control	Yes
Fig. 7B: **control**	2912	72			

Figure 6 (in text) and accompanying table, **Supporting Table S2**. T_1 values and student *t*-tests confirming statistically significant differences. Student's *t*-tests were calculated in Origin 7 SR2 (Origin Lab, Northampton, MA) at a 95% confidence level with 8 degrees of freedom, independent testing, and a null hypothesis value (minimum acceptable time difference) of 100 ms. At least 5 slices per sample were averaged.

Synthetic and Immunological Studies of *5′-N*-Phenylacetyl sTn to Develop Carbohydrate-Based Cancer Vaccines and to Explore the Impacts of Linkage between Carbohydrate Antigens and Carrier Proteins

Qianli Wang, Sandamali Amarasingha Ekanayaka, Jian Wu, Junping Zhang, and Zhongwu Guo*

Department of Chemistry, Wayne State University, 5101 Cass Avenue, Detroit, Michigan 48202. Received June 17, 2008; Revised Manuscript Received September 3, 2008

5′-N-Phenylacetyl sTn (sTnNPhAc), an unnatural derivative of sTn antigen expressed by many tumors, and its α-linked protein conjugates were prepared and investigated to explore glycoconjugate cancer vaccines. sTnNPhAcα-KLH elicited a robust T cell dependent immunity. The antiserum derived from sTnNPhAcα- or sTnNPhAc*β*-KLH-inoculated mice was similarly reactive to sTnNPhAcα and sTnNPhAc*β* but showed very little reactivity to sTn, NeuNPhAcα(2,3)GalNAc—a regioisomer of sTnNPhAc, isolated phenylacetyl group, and the linker employed to conjugate sTnNPhAc and carrier protein. It was concluded that the sTnNPhAc-elicited immunity was specific for the whole antigen rather than the phenylacetyl group or other partial structures of sTnNPhAc and that the reducing end configuration or linkage of sTnNPhAc did not affect its immunological identity. It was also concluded that a new linker designed to conjugate carbohydrates and proteins did not provoke any immune reaction and that the linker, as well as the associated new and convenient coupling strategy, can be safely used for the development of glycoconjugate vaccines.

INTRODUCTION

Tumor-associated carbohydrate antigens (TACAs) are useful targets in the development of cancer vaccines (*1*−*3*). To form functional cancer vaccines, TACAs must be covalently conjugated to carrier proteins, because free carbohydrates only induce T cell independent immune responses (*4*), which are not particularly useful in the treatment of cancer. Therefore, different linkers or spacers and coupling methods have been developed to facilitate the conjugation between carbohydrates and proteins (*2, 5*). However, many linkers contain functionalities that are not compatible with the chemical synthesis of oligosaccharides, while late-stage installation of a linker to synthesized oligosaccharides can be difficult and usually needs multistep transformations. To address these issues, our group developed a novel strategy for coupling synthetic oligosaccharides to proteins, which employs a simple linker as shown in Scheme 1 (*6*). The azido group utilized to attach the linker is a widely adopted protecting group in oligosaccharide synthesis; thus, it can be installed as a protection of the oligosaccharide reducing end during the TACA synthesis. After oligosaccharides are accomplished, the azido group can be readily reduced to give a free amino group for introducing an unsaturated acyl linker, which in turn can be selectively oxidized to form an aldehyde functionality, enabling the reliable and effective coupling of synthetic TACAs to carrier proteins via reductive amination. This coupling strategy has been used to construct some hopeful conjugate vaccines (*7, 8*).

Because all synthetic glycoconjugate vaccines contain unnatural linkers or spacers, it is natural to inquire how these linkers may affect the immunological properties of resultant vaccines. It has been reported that some linkers themselves may provoke a strong immune response (*9, 10*), which is not only unhelpful but rather detrimental, and that some linkers may even suppress the immune system and decrease its response to TACAs (*9, 11*). Immunological studies of the synthetic glycoconjugates containing this new linker suggest that it is probably immunologically inert (*7, 8*), which is a useful property and needs to be investigated in detail.

In nature, TACAs are directly α- or *β*-linked to membrane proteins or lipids on the cell surfaces, while most synthetic cancer vaccines have TACAs coupled to carrier proteins via unnatural linkers or anomeric linkages. Consequently, another question about these vaccines is whether this would affect the immunological identity of TACAs or whether the provoked immune system can recognize and target cancer cells that bear differently configured TACAs. For example, sialyl Tn (sTn, Figure 1) is a disaccharide TACA α-linked to the polypeptide backbone of mucins on cancer cells and is richly expressed by numerous tumors including breast, prostate, colorectal, ovarian, pancreatic, and gastric cancer (*12*−*15*). Due to its unique expression on cancer cells and its relevance to tumor metastasis (*16*), sTn has become an attractive target in cancer vaccine development (*17*−*22*). Recently, we have shown that sTn derivatives containing unnatural *N*-acyl sialic acids, for instance, *N*-phenylacetyl sialic acid (NeuNPhAc), were much more immunogenic than the natural counterpart and that the sTn derivatives could elicit robust T cell dependent immune responses (*7*). However, the glycoconjugates employed there, such as the keyhole limpet hemocyanin (KLH) conjugate of unnatural 5′-*N*-phenylacetyl sTn (sTnNPhAc) (**1**), had the sTn derivatives *β*-linked to carrier proteins. It is therefore natural to inquire whether the provoked immune system would interact with the α-linked antigens expressed on cancer cells following metabolic engineering (*23, 24*).

An even more interesting question about glycoconjugate vaccines is whether the elicited immune reactions were mainly against the whole carbohydrate antigens or they also directed at partial structures of the antigen, such as a segment of an oligosaccharide or the unnatural functionality of a conjugate vaccine consisting of an unnatural TACA derivative. An answer to this question should be helpful for understanding the functions and functional mechanisms of carbohydrate-based vaccines. It

* To whom correspondence should be addressed. Tel. +1-313-577-2557; Fax. +1-313-577-8822; E-mail: zwguo@chem.wayne.edu.

10.1021/bc800243f CCC: $40.75 © 2008 American Chemical Society
Published on Web 09/25/2008

Scheme 1

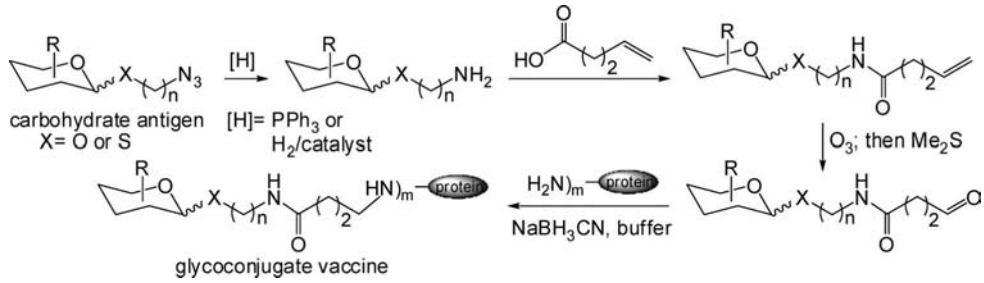

can also assist in addressing issues concerning the specificity of a novel strategy for cancer immunotherapy developed by our laboratory, where synthetic glycoconjugate vaccines consisting of unnatural TACA derivatives are combined with metabolic engineering of cancer cells for their expression of the unnatural TACA derivative (*7*, *8*, *25*−*27*).

To explore the problems mentioned above, we prepared glycoconjugate **3**, which has sTnNPhAc α-linked to KLH, and compared its immunological properties with that of the *β*-linked glycoconjugate **1**. The α-linked human serum albumin (HSA) conjugate of sTnNPhAc **4** was prepared and employed in assaying the immunological properties of **3**. Meanwhile, HSA conjugates **2**, **5**, **6**, and **7** containing sTnNPhAc*β*, natural sTn, the phenylacetylated linker, and NeuNPhAcα(2,3)GalNAcα—a regioisomer of sTnNPhAcα, respectively, were also prepared to check the reactivity of **1** and **3** provoked antisera to sTn, *β*-linked sTnNPhAc, the linker, NeuNPhAc, the phenylacetyl functionality, and other partial structures of sTnNPhAc.

EXPERIMENTAL PROCEDURES

General Methods. NMR spectra were recorded on a 400 MHz spectrometer with chemical shifts reported in ppm (*δ*) in reference to $SiMe_4$ if not specified otherwise. Coupling constants (*J*) are reported in hertz (Hz). High-resolution (HR) ESI MS was performed on a Micromass Autospec Ultima magnetic sector mass spectrometer or on Waters GCT time-of-flight mass spectrometers. MALDI TOFMS was obtained on a Bruker Ultraflex mass spectrometer. Thin layer chromatography (TLC) was performed on silica gel GF_{254} plates detected by charring with phosphomolybdic acid in EtOH or with 1% H_2SO_4/EtOH solution. Molecular sieves were dried under high vacuum at 170−180 °C for 6−10 h just before use. Glycoconjugates **1**, **2**, and **5** were prepared and reported previously (*7*), and glycoconjugate **7** was prepared for a different project and will be reported separately. Commercial anhydrous solvents and other reagents were used without further purification.

2-Azidoethyl 2-Acetamido-2-deoxy-α-D-galactopyranoside (10). To a solution of *N*-acetyl-D-galactosamine (**8**, 1.2 g, 5.42 mmol) in 2-chloroethanol (15 mL) at 0 °C was added dropwise acetyl chloride (0.47 g, 5.97 mmol), and the reaction mixture was heated at 70 °C for 4 h. The solution was concentrated, and the residue was coevaporated with toluene and then purified by flash column chromatography (CH_2Cl_2/MeOH 10:1) to yield **9** as a white solid (0.66 g, 45%). ^{1}H NMR (D_2O, 400 MHz): *δ* 4.95 (d, $J = 3.2$ Hz, 1H, H-1), 4.14 (dd, $J = 11.6$ and 4.0 Hz, 1H, H-2), 4.02 (t, $J = 6.8$ Hz, 1H, H-4), 3.97−3.90 (m, 3H), 3.79−3.72 (m, 5H), 2.02 (s, 3H, NHAc); ^{13}C NMR (D_2O, 100 MHz): *δ* 174.9, 97.5, 71.4, 68.7, 68.5, 67.8, 61.5, 50.1, 43.8, 22.2. The mixture of **9** (0.51 g, 1.80 mmol), NaN_3 (1.17 g, 18.0 mmol), and monobenzo-15-crown-5 (48 *μ*g, 0.18 mmol) in anhydrous DMF (5 mL) was stirred at 80 °C overnight. After cooling to rt, inorganic salts were removed by filtration and washed with CH_3CN. The filtrate and washings were combined and concentrated. The residue was purified by flash column chromatography (CH_2Cl_2/MeOH 10:1) to give **10** as a white solid (0.52 g, quantitative). Its spectroscopic data were consistent with that reported in the literature (*28*).

2-Azidoethyl 2-Acetamido-2-deoxy-3,4-*O*-(1-methylethylidene)-α-D-galactopyranoside (11). To a solution of **10** (0.45 g, 1.55 mmol) in a mixture of DMF (4.5 mL) and 2,2-dimethoxypropane (9.0 mL) was added *p*-toluenesulfonic acid monohydrate (0.029 mg, 0.155 mmol) at 65 °C. After the solution was stirred at 65 °C for 5 h, it was cooled to rt, and Et_3N (0.5 mL) was added. The mixture was stirred for another 15 min, and it was concentrated and coevaporated twice with toluene to remove traces of Et_3N. The residue was dissolved in MeOH/H_2O (10:1) (15 mL) and heated under reflux for 30 min until TLC (CH_2Cl_2/MeOH 16:1) showed the complete disappearance of the reaction intermediate. The solution was then concentrated and coevaporated with toluene. The residue was purified by flash column chromatography (CH_2Cl_2/MeOH 20:1) to give **11** as light yellow oil (0.47 g, 92%). $R_f = 0.20$ (CH_2Cl_2/MeOH 16:1). ^{1}H NMR ($CDCl_3$, 400 MHz): *δ* 5.62 (d, $J = 10.0$ Hz, 1H, NHAc), 4.87 (d, $J = 3.2$ Hz, 1H, H-1), 4.31 (dt, $J = 9.2$ and 3.6 Hz, 1H, H-2), 4.21 (dd, $J = 4.8$ and 2.4 Hz, 1H, H-4), 4.12−4.04 (m, 2H), 4.01−3.90 (m, 2H), 3.85 (dd, $J = 11.6$ and 4.0 Hz, 1H, H-3), 3.66−3.60 (m, 1H), 3.49−3.42 (dq, 1H), 3.36−3.29 (m, 1H, H-5), 2.03 (s, 3H, NHAc), 1.57, 1.34 (s, 2 × 3H, CH_3). ^{13}C NMR ($CDCl_3$, 100 MHz): *δ* 170.5, 110.3, 98.3, 74.6, 73.6, 68.2, 67.8, 62.9, 50.6, 50.5, 28.1, 26.8, 23.6. HR ESI MS (*m*/*z*) calcd. for $C_{13}H_{22}N_4NaO_6$ $(M + Na)^+$ 353.1437, found 353.1442.

Methyl (Ethyl 4,7,8,9-tetra-*O*-acetyl-3,5-dideoxy-2-thio-5-phenylacetamido-D-glycer-D-galacto-non-2-ulopyranosid)onate (15). A solution of **13** (4.0 g, 7.47 mmol) (*7*, *8*) and methanesulfonic acid (1.9 mL, 29.88 mmol) in anhydrous methanol (60 mL) was refluxed overnight. After the reaction was completed, the reaction mixture was neutralized with Et_3N to pH 8 and then concentrated under reduced pressure. The residue was dissolved again in methanol (60 mL) and Et_3N was added to adjust pH to 9. After the mixture was cooled to 0 °C, phenylacetic anhydride (3.8 g, 14.94 mmol) was added slowly and the mixture was stirred at rt for 1 h. The reaction mixture was concentrated under vacuum and the residue was purified by flash column chromatography (toluene/AcOEt/CH_3OH 5:5:1) to give **14** (2.47 g, 75%), which was dissolved in pyridine (12 mL) at 0 °C, followed by addition of DMAP (42 mg) and acetic anhydride (6 mL). After the mixture was stirred at 0 °C for 30 min and at rt for 5 h, it was diluted with ethyl acetate (100 mL); washed with 1 N HCl, brine, saturated $NaHCO_3$ aqueous solution, and brine; dried over anhydrous Na_2SO_4; and concentrated under vacuum. The residue was purified by flash column chromatography (AcOEt/hexanes 1:1) to give an anomeric mixture of **15** as a white solid (3.14 g, 92%). ^{1}H NMR ($CDCl_3$, 400 MHz): *δ* 7.37−7.22 (m, 5 H, aromatic H), 5.36 (t, $J = 3.2$ Hz, 1H), 5.25 (m, 1H), 5.17−5.04 (m, 2H), 4.76 (dd, $J = 12.4$ and 2.4 Hz, 1H), 4.24 (dd, $J = 10.4$ and 2.4 Hz, 1H),

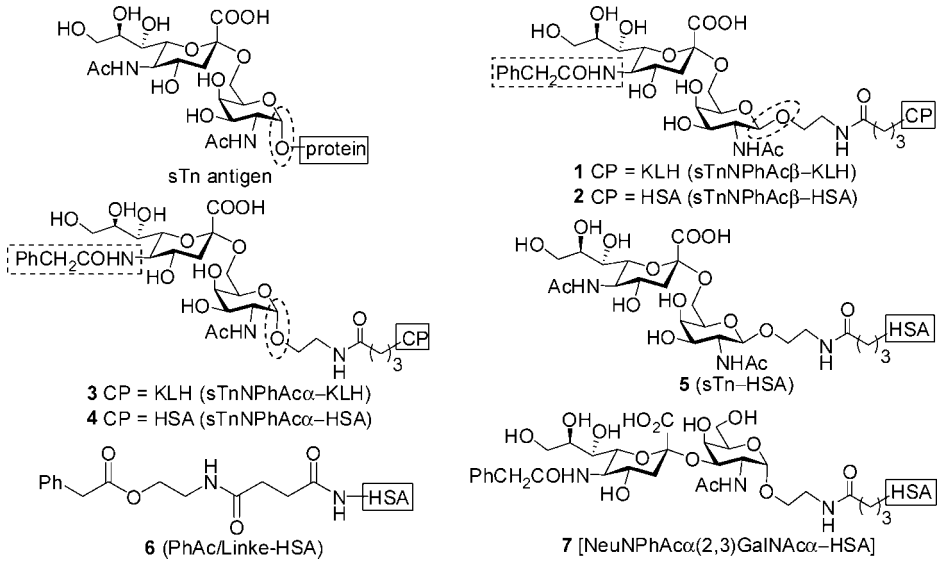

Figure 1. Structures of sTn antigen and the conjugates used in this research.

4.15 (dd, $J = 12.4$ and 8.0 Hz, 1H), 4.05 (d, $J = 10.4$ Hz, 1H), 3.78 (s, 3H, $COOCH_3$), 3.44 (d, $J = 2.4$ Hz, 1H), 2.58−2.44 (m, 2H), 2.14 (s, 3H), 2.07 (s, 3H), 2.03 (s, 3H), 1.81 (s, 3H), 1.16 (t, $J = 8.0$ Hz, 3H). ^{13}C NMR ($CDCl_3$, 100 MHz): δ 171.3, 170.9, 170.8, 170.7, 170.5, 168.6, 134.5, 129.7, 129.2, 127.6, 85.1, 72.7, 72.3, 69.0, 68.7, 62.6, 53.0, 49.7, 44.0, 37.5, 22.9, 21.2, 21.1, 21.0, 20.8, 14.3. HR ESI MS (*m*/*z*) calcd. for $C_{28}H_{37}NNaO_{12}S$ $(M + Na)^+$ 634.1934, found 634.1943.

2-Azidoethyl [Methyl 4,7,8,9-tetra-*O*-acetyl-3,5-dideoxy-5-phenylacetamido-D-glycero-α-D-galacto-2-nonulopyranosylonate]-(2→6)-*O*-2-acetamido-2-deoxy-α-D-galactopyranoside (16). A mixture of **15** (0.32 g, 0.52 mmol), **11** (0.16 g, 0.48 mmol), and activated MS 3Å (1.5 g) in anhydrous CH_3CN (5.0 mL) was stirred at rt for 2 h under an atmosphere of argon. After the mixture was cooled to −35 °C, NIS (0.44 g, 1.93 mmol) and TfOH (18 μL, 0.193 mmol) were added with stirring. The reaction was kept at −35 °C for 1 h and then quenched with the addition of Et_3N. The solid material was filtered off and washed with DCM. The combined filtrate and washings were washed with aqueous $Na_2S_2O_3$ and water, dried over anhydrous Na_2SO_4, and concentrated under vacuum. The residue was dissolved in 65% HOAc/H_2O (v/v, 5 mL) and heated at 65 °C for 1.5 h. The mixture was concentrated and the residue was purified by flash column chromatography (CH_2Cl_2/MeOH 30:1) to afford **16** as a white solid (212 mg, 52%), $R_f = 0.35$ (CH_2Cl_2/MeOH 15:1) and its β-anomer (64 mg, 15.7%), $R_f = 0.40$ (CH_2Cl_2/MeOH 15:1). **16**: ^{1}H NMR ($CDCl_3$, 400 MHz): δ 7.37−7.22 (m, 5 H, aromatic H), 5.98 (d, $J = 8.4$ Hz, 1H), 5.36−5.29 (m, 1H), 5.24 (dd, $J = 8.4$ and 2.0 Hz, 1H), 5.16 (d, $J = 9.2$ Hz, 1H), 4.89 (d, $J = 3.2$ Hz, 1H), 4.80−4.73 (m, 1H), 4.36−4.30 (m, 2 H), 4.09−3.99 (m, 3H), 3.98−3.92 (m, 2H), 3.89−3.82 (m, 2H), 3.78 (s, 3H, $COOCH_3$), 3.74 (dd, $J = 10.4$ and 3.2 Hz, 1H), 3.67−3.60 (m, 2H), 3.55−3.47 (m, 1H), 3.44 (d, $J = 3.2$ Hz, 2H), 3.37−3.30 (m, 1H), 2.61 (b, -OH), 2.54 (dd, $J = 12.8$ and 4.0 Hz, 1H, H-3′e), 2.15, 2.11, 2.05, 2.03 (4s, 4 × 3H, Ac), 1.90 (t, $J = 12.0$ Hz, 1H, H-3′a), 1.83 (s, 3H, Ac). ^{13}C NMR ($CDCl_3$, 100 MHz): δ 172.6, 171.5, 171.1, 170.8, 170.5, 170.4, 168.3, 134.5, 129.7, 129.1, 127.6, 99.0, 98.0, 72.9, 70.6, 69.2, 69.1, 68.7, 68.4, 67.7, 67.5, 63.7, 62.7, 53.2, 50.8, 50.5, 49.5, 44.0, 37.8, 23.4, 21.3, 21.1, 21.0, 20.8. HR ESI MS (*m*/*z*) calcd. for $C_{36}H_{49}N_5NaO_{18}$ $(M + Na)^+$ 862.2970, found 862.2983.

***N*-{2-*O*-{[(3,5-Dideoxy-5-phenylacetamido)-D-glycero-α-D-galacto-2-nonulosonic acid]-(2→6)-*O*-2-acetamido-2-deoxy-α-D-galactopyranosyl]-ethyl} 4-Pentenamide (18).** To a stirred solution of **16** (44.0 mg, 0.052 mmol) in MeOH (4 mL) was added a NaOMe solution in MeOH (0.1 N, 0.4 mL). After the mixture was stirred at rt overnight, it was neutralized with Amberlite 15 (H^+) resin. The resin was filtered off and washed with MeOH. The filtrate and washings were combined and concentrated to a small volume (ca. 3 mL), to which was added an aqueous NaOH solution (0.5 N, 0.5 mL). After the solution was stirred at rt overnight, it was neutralized with 2 N HCl to pH 7. Then, the reaction mixture was concentrated in vacuum to give **17**, which was used directly in the next step without further purification. HR ESI MS (*m*/*z*) calcd. for $C_{27}H_{38}N_5Na_2O_{14}$ $(M - H + 2Na)^+$ 702.2211, found 702.2222. A solution of **17** in H_2O (4 mL) was stirred with 10% Pd/C under a H_2 atmosphere at rt overnight. After argon was introduced to remove H_2, MeOH (4 mL) and 4-pentenoic anhydride (18 μL) were added sequentially. The mixture was stirred at rt overnight. After the catalyst was filtered off and washed with H_2O/MeOH, the filtrate and washings were combined and concentrated, and the residue was first extracted with DCM to remove any nonpolar materials and then purified on a Biogel P-2 column using distilled water as the eluent to give **18** after lyophilization as a white solid (28 mg, 75% from **16**). ^{1}H NMR (D_2O, 400 MHz): δ 7.41−7.30 (m, 5 H, Ar), 5.88−5.79 (m, 1H, CH═), 5.09 (s, 1H), 5.02 (t, $J = 10.8$ Hz, 1H, ═CH), 4.81 (d, $J = 3.2$ Hz, 1H, H-1), 4.13 (dd, $J = 11.2$ and 3.2 Hz, 1H, H-2), 3.97−3.44 (m, 18H), 3.32 (d, $J = 9.2$ Hz, 1H), 3.30−3.26 (m, 1H), 2.71 (dd, $J = 12.4$ and 4.0 Hz, 1H, H-3′e), 2.38−2.28 (m, 4H), 2.01 (s, 3H, Ac), 1.65 (t, $J = 12.4$ Hz, 1H, H-3′a). ^{13}C NMR (D_2O, 100 MHz): δ 176.5, 175.9, 174.7, 173.5, 137.2, 135.3, 129.4, 129.3, 127.6, 115.9, 100.5, 97.4, 72.8, 72.0, 69.8, 68.7, 68.6, 68.2, 68.0, 66.8, 63.9, 63.0, 52.2, 50.0, 42.9, 40.6, 39.2, 35.3, 29.6, 22.3. HR ESI MS (*m*/*z*) calcd. for $C_{32}H_{46}N_3Na_2O_{15}$ $(M - H + 2Na)^+$ 758.2724, found 758.2759.

***N*-{2-*O*-{[3,5-Dideoxy-5-phenylacetamido)-D-glycero-α-D-galacto-2-nonulosonic acid]-(2→6)-*O*-2-acetamido-2-deoxy-α-D-galactopyranosyl}-ethyl} 4-Oxo-butanamide (19).** To the stirred solution of **18** (25 mg, 0.035 mmol) in MeOH (5 mL) at −78 °C, ozone was bubbled until a blue color appeared and remained for 1 h. After introducing nitrogen to remove the remaining ozone, Me_2S (0.5 mL) was added at −78 °C. The resultant solution was allowed to warm to rt over a period of 1 h and stand for another 1 h before it was condensed in vacuum. The crude product was purified by a Biogel P-2 column using

distilled water as the eluent to give **19** after lyophilization as a white solid. ^{1}H NMR (D_2O, 400 MHz): δ 7.40−7.30 (m, 5 H, Ar), 5.42−5.35 (m, 1H, hydrated CHO), 4.82 (d, J = 3.2 Hz, 1H, H-1), 4.15−4.09 (m, 1H), 3.98−3.46 (m, 19H), 3.36−3.28 (m, 2H), 2.73−2.54 (m, 2H), 2.47−2.32 (m, 2H), 2.01 (s, 3H, Ac), 1.96−1.84 (m, 1H), 1.68−1.60 (m, 1H). ^{13}C NMR (D_2O, 100 MHz): δ 178.5, 175.9, 174.7, 173.7, 135.3, 129.3, 129.2, 127.6, 100.5, 97.4, 72.8, 72.1, 69.9, 69.8, 68.7, 68.6, 68.3, 67.9, 66.6, 64.0, 63.0, 52.2, 50.0, 42.9, 40.6, 39.2, 32.3, 29.0, 27.4, 22.2. HR ESI MS (*m*/*z*) calcd. for $C_{31}H_{44}N_3Na_2O_{16}$ $(M - H + 2Na)^+$ 760.2517, found 760.2552.

Procedure for the Coupling between 19 and KLH or HAS. A solution of **19** (10 mg), KLH or HSA (10 mg), and $NaBH_3CN$ (10 mg) in 0.1 M $NaHCO_3$ (0.3 mL, pH 7.5−8.0) was allowed to stand at rt in the dark for 4 days with occasional shaking. The reaction mixture was then purified by a Biogel A 0.5 column using 0.1 M phosphate buffered saline (PBS) (I = 0.1, pH =7.8) as the eluent. The fractions containing the glycoconjugates, positively characterized by both the bicinchoninic acid (BCA) assay for proteins and the Svennerholm method for sialic acid, were combined and dialyzed against distilled water for 2 d. It was then lyophilized to give the expected glycoconjugates **3** and **4** (ca. 10 mg) as white powders.

2-Pent-4-enamidoethyl 2-Phenylacetate (21). To a solution of *N*-(2-hydroxyethyl)-4-pentenamide (**20**, 0.3 g, 2.1 mmol) in pyridine (5 mL) were added phenylacetic anhydride (1.06 g, 4.2 mmol) and DMAP (25 mg, 0.21 mmol) at 0 °C. After stirring at rt overnight, the mixture was extracted with AcOEt, and the extract was washed with saturated $NaHCO_3$ aqueous solution and brine, dried over anhydrous Na_2SO_4, and concentrated under vacuum. The residue was purified by flash column chromatography (AcOEt/hexanes 1:2) to give **21** as oil (0.5 g, 92%). ^{1}H NMR ($CDCl_3$, 400 MHz): δ 7.35−7.26 (m, 5 H, Ar), 5.81−5.73 (m, 1H, CH═), 5.62 (brs, 1 H, NH), 5.06−4.97 (m, 2H, ═CH_2), 4.16 (t, J = 6.0 Hz, 2H), 3.63 (s, 2H, PhCH_2), 3.47 (dd, J = 10.4 and 5.6 Hz, 2H), 2.29 (dd, J = 14.8 and 5.6 Hz, 2H), 2.16 (t, J = 7.2 Hz, 2H). ^{13}C NMR ($CDCl_3$, 100 MHz): δ 172.5, 171.8, 137.1, 134.1, 129.4, 128.9, 127.5, 115.8, 63.8, 41.5, 38.8, 35.8, 29.6. HR GCEI MS (*m*/*z*) calcd. for $C_{15}H_{19}NO_3$ $(M)^+$ 261.1365, found 261.1372.

4-Oxo-4-[2-(2-phenylacetoxy)ethylamino]butanoic Acid (22). To the solution of **21** (0.1 g, 0.383 mmol) in DMF (2 mL) was added OsO_4 (1 mg, 3.83 μmol) at rt. After it was stirred for 5 min, oxone (0.94 g, 1.53 mmol) was added in one portion and the mixture was stirred at rt for 3 h. Na_2SO_3 was added to reduce the remaining Os(VIII). The reaction mixture was extracted with AcOEt, and the extract was washed with 1 N HCl and brine, dried over Na_2SO_4, and concentrated in vacuum. The residue was purified by flash column chromatography (AcOEt) to give **22** as a white solid (0.07 g, 65%). ^{1}H NMR ($CDCl_3$, 400 MHz): δ 7.35−7.26 (m, 5 H, Ar), 5.98 (brs, 1 H, NH), 4.16 (t, J = 5.6 Hz, 2H), 3.63 (s, 2H, PhCH_2), 3.48 (q, J = 5.6 Hz, 2H), 2.64 (t, J = 5.6 Hz, 2H), 2.38 (t, J = 6.4 Hz, 2H). ^{13}C NMR ($CDCl_3$, 100 MHz): δ 176.6, 172.8, 172.0, 134.0, 129.5, 128.9, 127.5, 63.5, 41.4, 39.0, 30.8, 29.7. HR GCEI MS (*m*/*z*) calcd. for $C_{14}H_{17}NO_5$ $(M)^+$ 279.1107, found 279.1106.

Synthesis of Conjugate 6. To the stirred solution of **22** (10 mg, 0.036 mmol), *N*-hydroxysuccinimide (9.0 mg, 0.078 mmol), and DMAP (catalytic amount) in anhydrous CH_2Cl_2 (2 mL) was added DIC (9.9 mg, 0.078 mmol) at 0 °C. After the mixture was stirred at 0 °C for 2 h, it was concentrated under vacuum, and the residue was dissolved in anhydrous DMF (0.5 mL) and cooled to 0 °C. Then, a 0.1 mL solution of HSA (10 mg) in 50 mM carbonate buffer (pH 9.1) was added dropwise. After the mixture was stirred at 0 °C overnight, it was diluted with water and washed with AcOEt. The aqueous layer was dialyzed against H_2O and then lyophilized to give **6** as a white powder (9 mg).

Analysis of the Carbohydrate Loading Levels of Glycoconjugates 3 and 4 (*8*). The solution of an exactly weighed glycoconjugate (0.5 mg) in distilled water (1.0 mL) was mixed with the resorcinol reagent (2.0 mL). The mixture was heated in a boiling water for 30 min. It was cooled to rt, and to this mixture was added an extraction solution (1-butanol acetate and 1-butanol, 85:15 v/v, 3.0 mL). The mixture was shaken vigorously before it was allowed to stand still for ca. 10 min to allow the organic layer to separate well from the inorganic layer. The organic layer was transferred to a 1.0 cm cuvette, and its absorbance at 580 nm was determined by a UV−vis spectrometer, using a blank organic solution as the control. The sialic acid content of the glycoconjugate was determined against a calibration curve created with the standard NeuNPhAc solution analyzed under the same conditions. The carbohydrate loading of each glycoconjugate was calculated according to the following equation.

$$\text{sTnNPhAc loading (w/w \%)} = \frac{\text{sTnNPhAc content (mg) in sample}}{\text{weight of sample (mg)}} \times 100\% \quad (1)$$

Immunization of Mouse. A total of 0.1 mL of an emulsion of sTnNPhAcα-KLH **3** containing 2 μg of sTnNPhAc and Titermax Gold adjuvant (Sigma) was intramuscularly injected to each of 5 female C57BL/6 mice at the age of 6−8 weeks (Jackson Laboratories, Bar Harbor, ME) on day 0, day 14, day 21, and day 28, respectively. The mice were bled on day −1 prior to the initial immunization and on day 27 and day 35 after immunization. Blood samples of 5 mice collected on each date were pooled and then clotted to obtain serum, which was stored at −80 °C before use.

ELISA. ELISA plates were incubated with a 100 μL solution of sTnNPhAcα-HSA (**4**, 2 μg/mL), or other HSA conjugates including **2**, **5**, **6**, and **7**, in the coating buffer (0.1 M bicarbonate, pH 9.6) at 4 °C overnight, which was followed by washing 3 times with PBS buffer containing 0.05% Tween-20. Pooled antisera diluted 1:300 to 1:72900 in serial half-log dilutions in PBS buffer containing 0.02% sodium azide (100 μL/well) were added in the coated ELISA plates, and the plates were incubated at 4 °C overnight. The plates were washed again with PBS buffer and then incubated with alkaline phosphatase linked goat antimouse kappa, IgM, or IgG2a antibody (1:1000 dilution) or with alkaline phosphatase linked antimouse IgG1 or IgG3 antibody (1:2000 dilution) for 1 h at rt. Finally, the plates were washed with PBS buffer and developed with 100 μL of PNPP solution (1.67 mg/mL in PNPP buffer) for 30 min at rt for colorimetric readout using a plate reader at 405 nm wavelength. For titer analysis, the OD values were plotted against dilution numbers, and a best-fit line was obtained. The equation of this line was used to calculate the dilution number at which an OD value of 0.5 was achieved, and this dilution number gives the antibody titer.

RESULTS AND DISCUSSION

The synthesis of sTnNPhAc, as well as its protein conjugates **3** and **4**, is shown in Scheme 2. First, a new and short route was developed to prepare glycosyl acceptor **11** from *N*-acetylgalactosamine **8**. Treating **8** with 2-chloroethanol in the presence of a catalytic amount of acetyl chloride produced 2-chloroethyl glycoside **9** (*28*), of which the anomeric α-configuration was affirmed by ^{1}H NMR ($J_{1,2}$ = 3.2 Hz). The chlorine atom in **9** was then substituted by an azido group after reacting with sodium azide at 80 °C in the presence of monobenzo-15-crown-5 to afford **10** in a quantitative yield. The reaction progress was monitored by ^{13}C NMR, since on TLC the R_f values of **9** and **10** were similar, but their ^{13}C NMR spectra were very different. The chemical shift of the carbon

Scheme 2

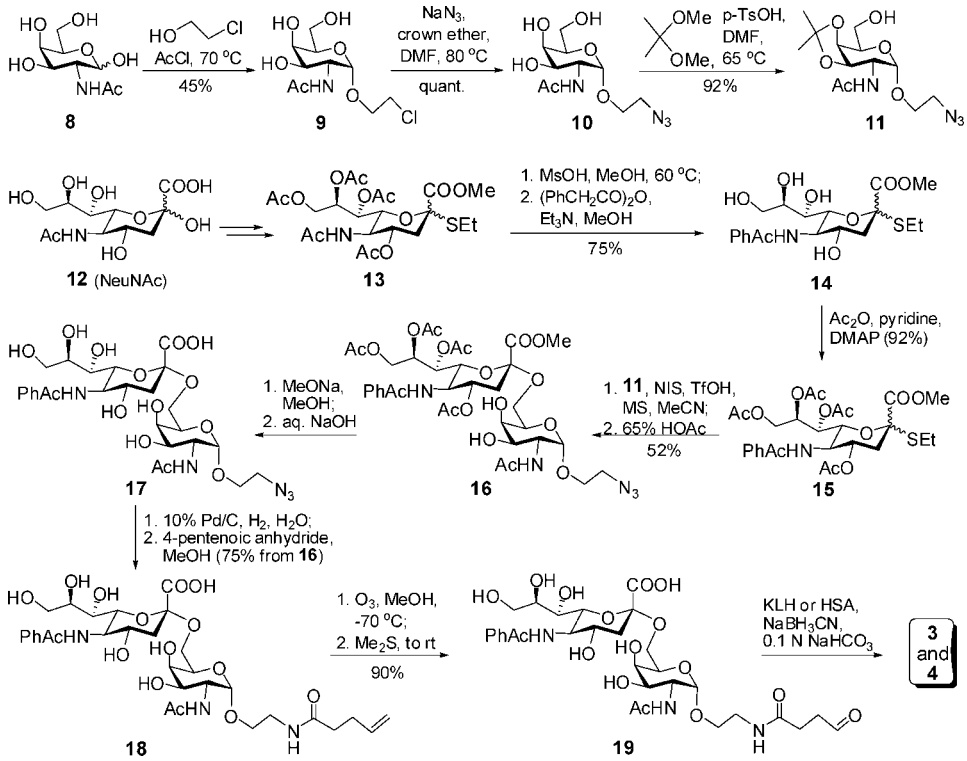

Scheme 3

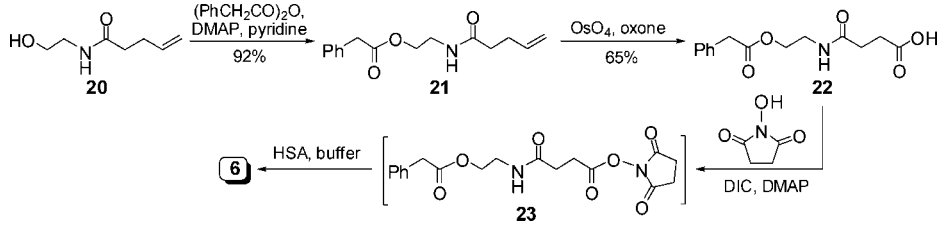

linked to the azido group in **10** was 50.6, while the same carbon in **9** appeared at δ 43.8. Finally, the 3,4-hydroxyl groups in **10** were selectively protected as acetonide under acidic conditions to give a high yield (92%) of **11**.

For the synthesis of sTn antigen and related derivatives, the most difficult step is probably the sialylation reaction. In our previous synthesis of sTn derivatives (*7*), Boons method (*29*) was used to obtain good yields and stereoselectivity for α-sialosides. In the present work, we planned to directly use *N*-phenylacetylthiosialoside **15** as a glycosyl donor with the hope of saving a few synthetic steps. Thus, after *N*-acetyl sialic acid (NeuNAc, **12**) was transformed into **13** by an established procedure (*7*), its *N*-acetyl group was replaced with a phenylacetyl group in two steps including deacetylation under acidic conditions to remove both *O*- and *N*-acetyl groups and then selective phenylacetylation of the free amino group. Thereafter, the hydroxyl groups were protected again by acetyl groups to give **15** as a mixture of α- and β-anomers. Since both α and β anomers could act as glycosyl donors, the mixture was directly applied to the subsequent sialylation reaction.

The sialylation of **11** by **15** was performed in CH_3CN using *N*-iodosuccinamide (NIS) and triflic acid (TfOH) as promoters to give a clean reaction (judged by TLC). ^{1}H NMR of the product showed that it was a mixture of α- and β-anomers (3.3:1.0). The anomers were nearly inseparable by column chromatography. Fortunately, after the isopropylidene group was removed, the resultant diol products were readily separated to afford the desired α-disaccharide **16** (52%), as well as the β anomer (16%). The α-configuration of sialic acid in **16** was assigned on the basis of the unique downfield shift of the NMR signal of H-3′e (δ 2.54) compared to that of β-linked sialic acids (δ 2.42), which have been observed in all sialosides. Moreover, the strong correlation between C-1′ and H-3′a, but not between C-1′ and H-3′e, in the HMBC spectrum of **16** suggests that the dihedral angle between C-1′ and H-3′a is close to 180°, which further proves the α-configuration of the sialyl residue in **16**. Therefore, the sialylation reaction using **15** as a sialyl donor gave an excellent yield and good stereoselectivity. Finally, all protecting groups in **16** were removed after treatments first with a methanolic solution of NaOMe and then with a methanolic/aqueous solution of NaOH to afford **17**, which was directly used in the next step for conjugation to proteins.

The protein conjugates of **17** were prepared by an established procedure (*6*). First, the azido group in **17** was reduced to form a primary amine, which was regioselectively acylated for the introduction of a pentenoyl group. The product **18** was purified with a Biogel P2 column using distilled water as the eluent, and its identity and purity were confirmed by NMR and HR MS. Next, the C═C double bond in **18** was selectively oxidized by ozone in methanol to afford aldehyde **19** which was purified with a Biogel P2 column. The ^{1}H NMR spectra of **19** showed the hydrated aldehyde proton signals (δ 5.3−5.5) with the disappearance of signals of protons linked to C═C double bond. Finally, **19** was coupled to carrier proteins, KLH and HSA, by

reductive amination carried out in a 0.1 N $NaHCO_3$ buffer solution in the presence of $NaBH_3CN$. Aldehyde **19** was used in excess, and unreacted **19** was readily separated from the conjugate products on a Biogel A 0.5 column. Column fractions containing the desired glycoconjugates, which gave positive results in both sialic acid assays and protein assays, were combined and dialyzed against water. Lyophilization of the resultant aqueous solution afforded **3** and **4** as white fluffy solids. Glycoconjugate **7** used as a coating antigen in this study was prepared from the 2,3-linked disaccharide by a similar procedure.

The antigen loading levels of glycoconjugates **3**, **4**, and **7** were analyzed by measurements of their sialic acid contents as reported in the literature (*8*). It was found that they contained 4.0−5.3% (w/w) of sugars, respectively. These loading levels were similar to those obtained previously (*7*). The KLH conjugate **3** was used as a vaccine for immunization of animals, and the HSA conjugates **4** and **7** were employed as the coating antigen in immunological assays.

HSA conjugate **6**, which contains the linker and the phenylacetyl group as an ester, was prepared according to Scheme 3. Acylation of **20** by phenylacetic anhydride followed by oxidative cleavage of the C═C double bond in the resultant **21** using OsO_4 and oxone (*30*) afforded carboxylic acid **22**, which was then converted into an active ester **23** for conjugation with HSA. An attempt to purify **23** by silica gel column chromatography resulted in decomposition on the column; therefore, it was directly applied to the conjugation step without purification. Because **6** did not contain sialic acid, its hapten loading level was determined by MALDI TOF MS. The molecular weight of **6** was found to be 80 186. On the basis of the molecular weights of HSA (66 592) and **22** (262), we estimated that on average each HSA molecule was modified by 51 copies of the phenylacetylated linker in **6**.

The immunological property of **3** as a vaccine was examined in C57BL/6 mouse, and the animal immunizations and the enzyme-linked immunosorbent assays (ELISA) to evaluate antibody responses were performed according to the protocols described for the β-linked conjugate **1** (*7*). Thus, 0.1 mL of an emulsion of **3** (containing 2 μg of carbohydrate antigen) and Titermax Gold adjuvant were injected to each of a group of 5 mice intramuscularly on days 0, 14, 21, and 28, respectively. These mice were bled three times on day −1, day 27, and day 35, respectively, prior to and after immunization. Blood samples of all 5 mice collected on each date were pooled for the preparation of antisera, and each serum would give a mean antibody concentration. The titers of total antibody and individual antibody isotypes including IgM, IgG1, IgG2a, and IgG3 of the antisera were assessed by ELISA. The antibody titer is the serum dilution number at which the optical density (OD) of an ELISA experiment reaches 0.5. Consequently, the ELISA OD values of each serum were plotted against serum dilution numbers, and the best-fit line was obtained for the calculation of antibody titer. sTnNPhAcα-HSA **4** was used as the capture antigen to coat plates in ELISA for the detection of sTnNPhAc-reactive antibodies, and the plate-bound antibodies were analyzed by various antiantibodies (*7*). The use of HSA conjugate as the capture antigen in ELISA allowed us to eliminate any interference potentially caused by KLH and detect antibodies specific for sTnNPhAc or the linker. Similarly, HSA conjugates of other antigens were employed to detect antibodies reactive to the specific antigen.

Figure 2 shows the observed total antibody and IgM, IgG1, IgG2a, and IgG3 antibody titers of the obtained sera. Day −1 serum did not show any binding to **4**, while day 27 and day 35 antisera both displayed high total antibody titers, with the latter higher than the former, suggesting a progressive immune response to **3** produced in animals. Detailed analysis of the

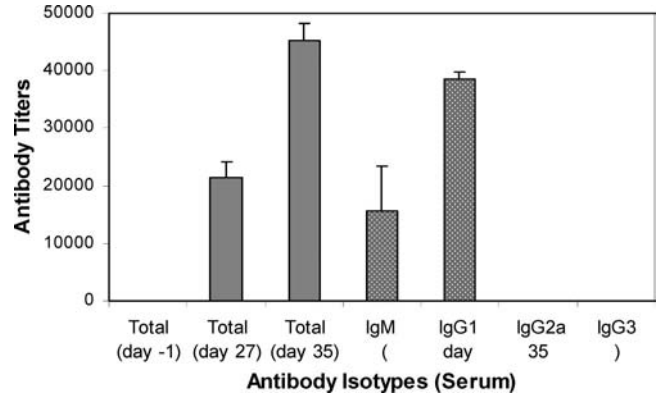

Figure 2. Total antibody titers of day −1, day 27, and day 35 sera and IgM, IgG1, IgG2a, and IgG3 antibody titers of day 35 serum determine by ELISA with **4** as the coating antigen. All antibody titers were obtained with pooled sera of five replicate animals.

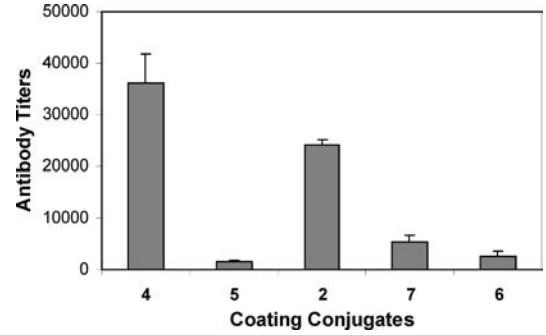

Figure 3. Titers of total antibody reactive to sTnNPhAcα, sTn, sTnNPhAcβ, NeuNPhAcα2,3GalNAc, and PhAc/linker, respectively, in the pooled day 35 serum derived from five replicate mice inoculated with sTnNPhAcα-KLH **3**. For ELISA, after the plates were coated with **4**, **5**, **2**, **7**, and **6**, respectively, they were treated with the antiserum, and the antibodies bound to the plates were then analyzed.

antibody isotypes revealed that **3** provoked mainly IgG1 antibody, which indicates a strong T cell dependent immune response. As usual, IgM antibody as the first line of antibody response to foreign antigens was also observed. These results were very similar to those derived from the β-linked conjugate vaccine **1** (*7*). It is apparent that the unnatural sTn derivative sTnNPhAc, whether it is α- or β-linked to a carrier protein, could form functional vaccines that elicited strong T cell dependent immunity useful for the treatment of cancer.

We also investigated the reactivity of the antiserum obtained with sTnNPhAcα-KLH **3** to natural sTn, sTnNPhAcβ, and NeuNPhAcα(2,3)GalNAcα, the linker between the antigen and protein, and isolated phenylacetyl functionality by means of ELISA, and the results are depicted in Figure 3. In these studies, ELISA plates were first coated with sTnNPhAcα-HSA **4**, sTn-HSA **5**, sTnNPhAcβ-HSA **2**, NeuNPhAcα(2,3)GalNAcα-HSA **7**, and PhAc/linker-HSA **6**, respectively, and then treated with the day 35 antiserum described above. It was demonstrated that the antiserum showed very strong binding to **2**, with a titer only slightly lower than that of **4**, indicating that the sTnNPhAcα-elicited antibodies could hardly differentiate the reducing end anomeric configurations of the capture antigens in ELISA. On the other hand, the antiserum produced a very low antibody titer with **7**-coated plate and did not exhibit major cross-reactivity with **5**- and **6**-coated plates. The significantly lower reactivity of the antiserum to **7** than to **4** suggest that the majority of antibodies raised by the glycoconjugate vaccine were specific to the whole antigen, sTnNPhAc, rather than to its partial structures such as NeuNPhAc and the phenylacetyl group or to the linker, as glycoconjugates **4** and **7** are only different in terms

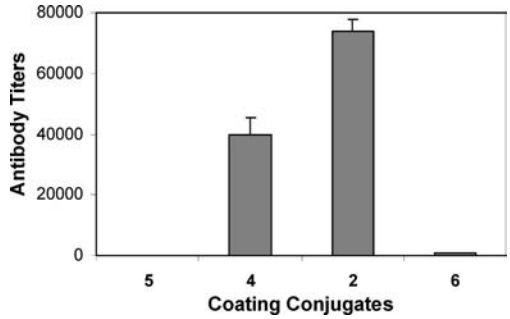

Figure 4. Titers of total antibody reactive to sTn, sTnNPhAcα, sTnNPhAcβ, and PhAc/linker, respectively, in the pooled serum derived from five replicate mice inoculated with sTnNPhAcβ -KLH **1**. For ELISA, after the plates were coated with **5**, **4**, **2**, and **6**, respectively, they were treated with the antiserum, and the antibodies bound to the plates were then analyzed.

of their inner glycosidic linkage, α(2,6)- vs α(2,3)-linkage, while they showed very different reactivity to the antiserum. The extremely low reactivity of the antiserum to sTn-HSA **5**, which differs from **4** only in the acyl group linked to the sialic acid 5-*N*-position, further proves that the **3**-induced immune response was specific to sTnNPhAc. Meanwhile, because **5** contains the same linker, its low reactivity to the antiserum further proves that no significant level of antibodies against the linker was induced. Moreover, the low reactivity of the antiserum to **6** also suggests that the antiserum did not contain a significant level of antibodies against the linker or the phenylacetyl group in a slightly different form, namely, as an ester.

We have also examined the reactivity of the antiserum obtained with sTnNPhAcβ-KLH **1** (*7*) to natural sTn, α-linked sTnNPhAc, the linker, and the isolated phenylacetyl functionality. For ELISA, again, the plates were first coated with sTn-HSA **5**, sTnNPhAcα-HSA **4**, sTnNPhAcβ-HSA **2**, and PhAc/linker-HSA **6**, respectively, and then treated with the anti-sTnNPhAcβ serum. As shown in Figure 4, the anti-sTnNPhAcβ serum had very strong binding to both **4**- and **2**-coated plates, but only a very low antibody titer was observed with **6**-coated plate and no cross-reactivity was detected with **5**-coated plate. These results further support the conclusions derived from the experiments described above.

In summary, a new and highly efficient method was developed for the synthesis of sTnNPhAc antigen and its α-linked protein conjugates. Immunological studies of sTnNPhAcα-KLH in mice have shown that it could provoke a strong and robust T cell dependent immune response, and the results were very similar to those previously obtained with sTnNPhAcβ-KLH (*7*). Moreover, the antisera derived from sTnNPhAcα- and sTnNPhAcβ-KLH-inoculated mice showed very little difference in reacting with sTnNPhAcα- and sTnNPhAcβ-coated plates in ELISA experiments, while the antisera did not show significant binding to natural sTn, NeuNPhAcα(2,3)GalNAc—an α(2,3)-linked analogue of sTnNPhAc, or to the free phenylacetyl functionality and the linker. These results, together with the results from our previous studies (*7*, *8*), led us to conclude that sTnNPhAc can indeed elicit a specific immune response and the elicited immune response recognize the whole antigen instead of merely the unnatural functionality or other partial structures of sTnNPhAc. More interestingly, it seems that the reducing end configuration of sTnNPhAc or its unnatural linkage to conjugate proteins had very little or no influence on its immunological identity or on the recognition of sTnNPhAc by the provoked antibodies. These results have proven the designing principles of glycoconjugate vaccines that have carbohydrate antigens coupled to carrier proteins via artificial linkages, which is very important for the understanding of the functions of carbohydrate-based vaccines and for future design of novel glycoconjugate vaccines. They can also help to explain why an unnatural GM3 analogue-provoked antibody was specifically cytotoxic to cancer cells that were metabolically engineered to express the same GM3 analogue (*26*), but not to normal cells, though normal cells could also use the engineering precursor to express unnatural sialic acids or even a low level of the unnatural GM3 analogue. The results have further demonstrated that the new linker does not have any obvious influence on the immunological properties of the resultant glycoconjugates and that the linker does not provoke any immune response. Therefore, this linker and the associated coupling strategy can be safely employed in the development of glycoconjugate cancer vaccines. The conclusions of this work should be of general significance in the field of conjugate vaccine research.

ACKNOWLEDGMENT

This work was financially supported by an NIH/NCI grant (R01 CA95142). Ms. Admira Bosnjakovic provided the disaccharide used in the synthesis of **7**. We thank Dr. B. Shay and Dr. L. Hryhorczuk for MS measurements, and Dr. B. Ksebati for some NMR measurements.

Supporting Information Available: ^{1}H and ^{13}C NMR and MS spectra of involved synthetic intermediates and products. This material is available free of charge via the Internet at http://pubs.acs.org.

LITERATURE CITED

(1) Hakomori, S. (2001) Tumor-associated carbohydrate antigens defining tumor malignancy: Basis for development of anti-cancer vaccines. *Adv. Exp. Med. Biol. 491*, 369–402.

(2) Danishefsky, S. J., and Allen, J. R. (2000) From the laboratory to the clinic: A retrospective on fully synthetic carbohydrate-based anticancer vaccines. *Angew. Chem., Int. Ed. 39*, 837–863.

(3) Ragupathi, G. (1998) Carbohydrate antigens as targets for active specific immunotherapy. *Cancer Immunol. Immunother. 46*, 82–87.

(4) Jennings, H. J., and Sood, R. K. (1994) Synthetic glycoconjugates as human vaccines, in *Neoglycoconjugates: Preparation and Applications* (Lee, Y. C., and Lee, R. T., Eds.) pp 325—371, Academic Press, San Diego.

(5) Lee, Y. C., and Lee, R. T. (1994) *Neoglycoconjugates: preparation and applications*, Academic Press, San Diego.

(6) Xue, J., Pan, Y., and Guo, Z. (2002) Neoglycoprotein cancer vaccines: Synthesis of an azido derivative of GM3 and its efficient coupling to proteins through a new linker. *Tetrahedron Lett. 43*, 1599–1602.

(7) Wu, J., and Guo, Z. (2006) Improving the antigenicity of sTn antigen by modification of its sialic acid residue for development of glycoconjugate cancer vaccines. *Bioconjugate Chem. 17*, 1537–1544.

(8) Pan, Y. B., Chefalo, P., Nagy, N., Harding, C. V., and Guo, Z. (2005) Synthesis and immunological properties of N-modified GM3 antigens as therapeutic cancer vaccines. *J. Med. Chem. 48*, 875–883.

(9) Buskas, T., Li, Y., and Boons, G. J. (2004) The immunogenicity of the tumor-associated antigen Lewis (y) may be suppressed by a bi-functional cross-linker required for coupling to a carrier protein. *Chem. Eur. J. 10*, 3517–3524.

(10) Ni, J., Song, H., Wang, Y., Stamatos, N. M., and Wang, L. X. (2006) Toward a carbohydrate-based HIV-1 vaccine: synthesis and immunological studies of oligomannose-containing glycoconjugates. *Bioconjugate Chem. 17*, 493–500.

(11) Mawas, F., Niggemann, J., Jones, C., Corbel, M. J., Kamerling, J. P., and Vliegenthart, J. F. G. (2002) Immunogenicity in a

mouse model of a conjugate vaccine made with a synthetic single repeating unit of type 14 pneumococcal polysaccharide coupled to CRM197. *Infect. Immun. 70*, 5107–5114.
(12) Yonezawa, S., Tachikawa, T., and Sato, E. (1992) Sialosyl-Tn antigens. Its distribution in normal human tissues and expression in adenocarcinoma. *Am. J. Clin. Pathol. 98*, 167–174.
(13) Itzkowitz, S. H., Bloom, E. J., and Kim, Y. S. (1990) Sialosyl-Tn. A novel mucin antigen associated with prognosis in colorectal cancer patients. *Cancer (Phila) 66*, 1960–1966.
(14) Kobayashi, H., Terao, T., and Kawashima, Y. (1992) Serum sialyl Tn as an independent predictor of poor prognosis in patients with epithelial ovraian cancer. *J. Clin. Oncol. 10*, 95–101.
(15) Leivonen, M., Nordling, S., Lundin, J., and Haglund, C. (2001) sTn and prognosis in breast cancer. *Oncology 61*, 299–305.
(16) Bresalier, R. S., Niv, Y., Byrd, J. C., Duh, Q. Y., Toribara, N. W., Rockwell, R. W., Dahiya, Y., and Kim, Y. S. (1991) Mucin production by human colonic carcinoma cells correlates with their metastatic potential in animal models of colon cancer metastasis. *J. Clin. Invest. 87*, 1037–1045.
(17) Adluri, S., Helling, F., Ogata, S., and Livingston, P. O. (1995) Immunogenicity of synthetic TF-KLH and sTn-KLH conjugates in colorectal carcinoma patients. *Cancer Immunol. Immunother. 41*, 185–192.
(18) Livingston, P. O., Zhang, S., and Lloyd, K. O. (1997) Carbohydrate vaccines that induce antibodies against cancer. 1. Rationale. *Cancer Immunol. Immunother. 45*, 1–9.
(19) Ragupathi, G., Koganty, R. R., Qiu, D., Lloyd, K. O., and Livingston, P. O. (1998) A novel and efficient method for synthetic carbohydrate conjugate vaccine preparation: synthesis of sialyl Tn-KLH conjugate using a 4-(4-N-maleimidomethyl) cyclohexane-1-carboxyl hydrazide (MMCCH) linker arm. *Glycoconjugate J. 15*, 217–221.
(20) Ragupathi, G., Howard, L., Cappello, S., Koganty, R., and Livingston, P. O. (1999) Vaccines prepared with sialyl-Tn and sialyl-Tn trimers using the 4-(4-maleimidomethyl)cyclohexane-1-carboxyl hydrazide linker group result in optimal antibody titers against ovine submaxillary mucin and sialyl-Tn-positive tumor cells. *Cancer Immunol. Immunother. 48*, 1–8.
(21) MacLean, G. D., Reddish, M., Koganty, R. R., Wong, T., and Longenecker, B. M. (1993) Immunization of breast cancer patients using a synthetic sialyl-Tn glycoconjugate plus Detox adjuvant. *Cancer Immunol. Immunother. 36*, 215–222.
(22) Miles, D. W., Towlson, K. E., Graham, R., Reddish, M., Longenecker, B. M., and Rubens, R. D. (1996) A randomized phase II study of sialyl-Tn and DETOX-B adjuvant with or without cyclophosphamide pretreatment for the active specific immunotherapy of breast cancer. *Br. J. Cancer 74*, 1292–1296.
(23) Kayser, H., Zeitler, R., Kannicht, C., Grunow, D., Nuck, R., and Reutter, W. (1992) Biosynthesis of a nonphysiological sialic acid in different rat organs, using N-propanoyl-D-hexosamines as precursors. *J. Biol. Chem. 267*, 16934–16938.
(24) Mahal, K. L., Yarema, K. J., and Bertozzi, C. R. (1997) Engineering chemical reactivity on cell surfaces through oligosaccharide biosynthesis. *Science 276*, 1125–1128.
(25) Liu, T., Guo, Z., Yang, Q., Sad, S., and Jennings, H. J. (2000) Biochemical engineering of surface α(2−8)polysialic acid for immunotargeting cancer cells. *J. Biol. Chem. 275*, 32832–32836.
(26) Wang, Q., Zhang, J., and Guo, Z. (2007) Efficient glycoengineering of GM3 on melanoma cell and monoclonal antibody-mediated selective killing of the glycoengineered cancer cell. *Bioorg. Med. Chem. 15*, 7561–7567.
(27) Chefalo, P., Pan, Y., Nagy, N., Harding, C., and Guo, Z. (2006) Effective metabolic engineering of GM3 on tumor cells by N-phenylacetyl-D-mannosamine. *Biochemistry 45*, 3733–3739.
(28) Sanki, A., and Mahal, L. K. (2006) A one-step synthesis of azide-tagged carbohydrates: Versatile intermediates for glycotechnology. *Synlett* 455–459.
(29) De Meo, C., Demchenko, A. V., and Boons, G.-J. (2001) A stereoselective approach for the synthesis of α-sialosides. *J. Org. Chem. 66*, 5490–5497.
(30) Travis, B. R., Narayan, R. S., and Borhan, B. (2002) Osmium tetroxide-promoted catalytic oxidative cleavage of olefins: an organometallic ozonolysis. *J. Am. Chem. Soc. 124*, 3824–3825.

BC800243F

Supporting Information for:

Synthetic and Immunological Studies of *5'-N*-phenylacetyl sTn to Develop Carbohydrate-Based Cancer Vaccines and to Explore the Impacts of Linkage between Carbohydrate Antigens and Carrier Proteins

Qianli Wang, Sandamali Amarasingha Ekanayaka, Jian Wu, Junping Zhang, and Zhongwu Guo*

Department of Chemistry, Wayne State University, 5101 Cass Avenue, Detroit, Michigan 48202, USA

(^{1}H- and ^{13}C-NMR Spectra and MS of synthetic intermediates and products)

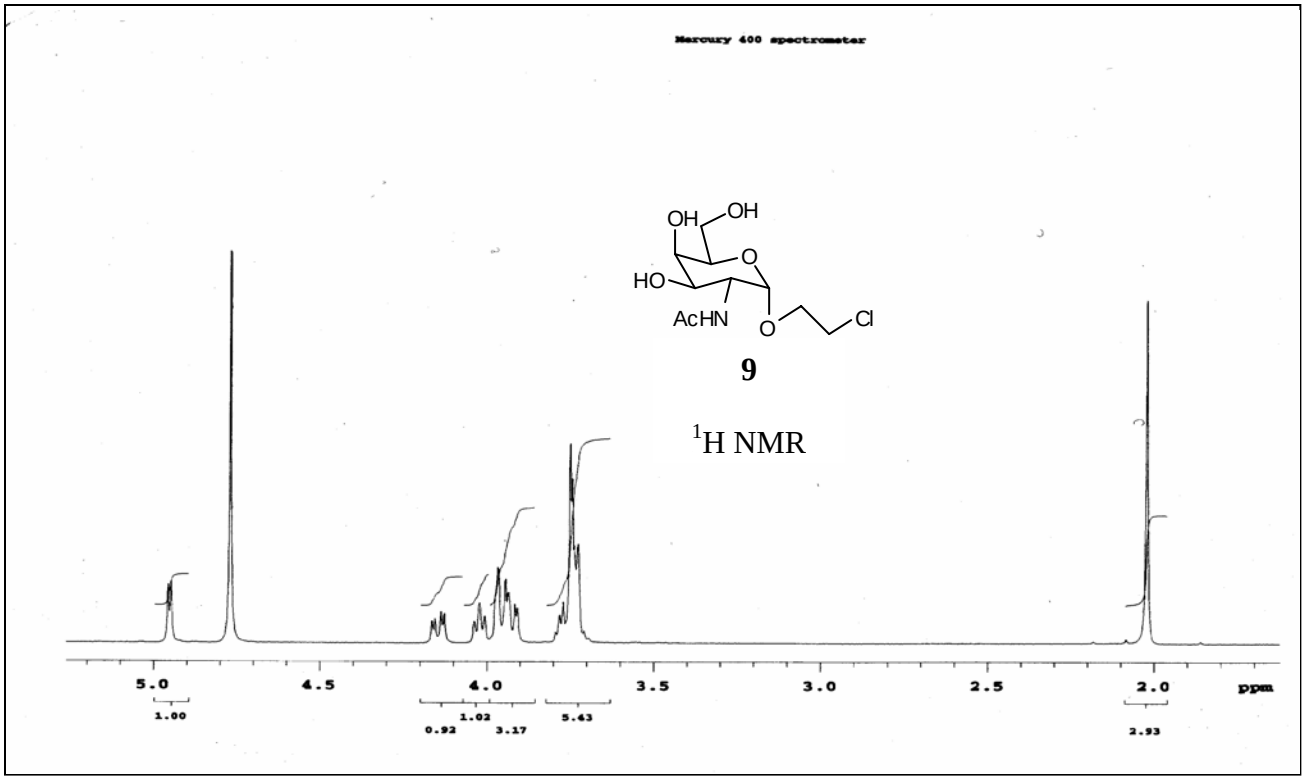

9

^{1}H NMR

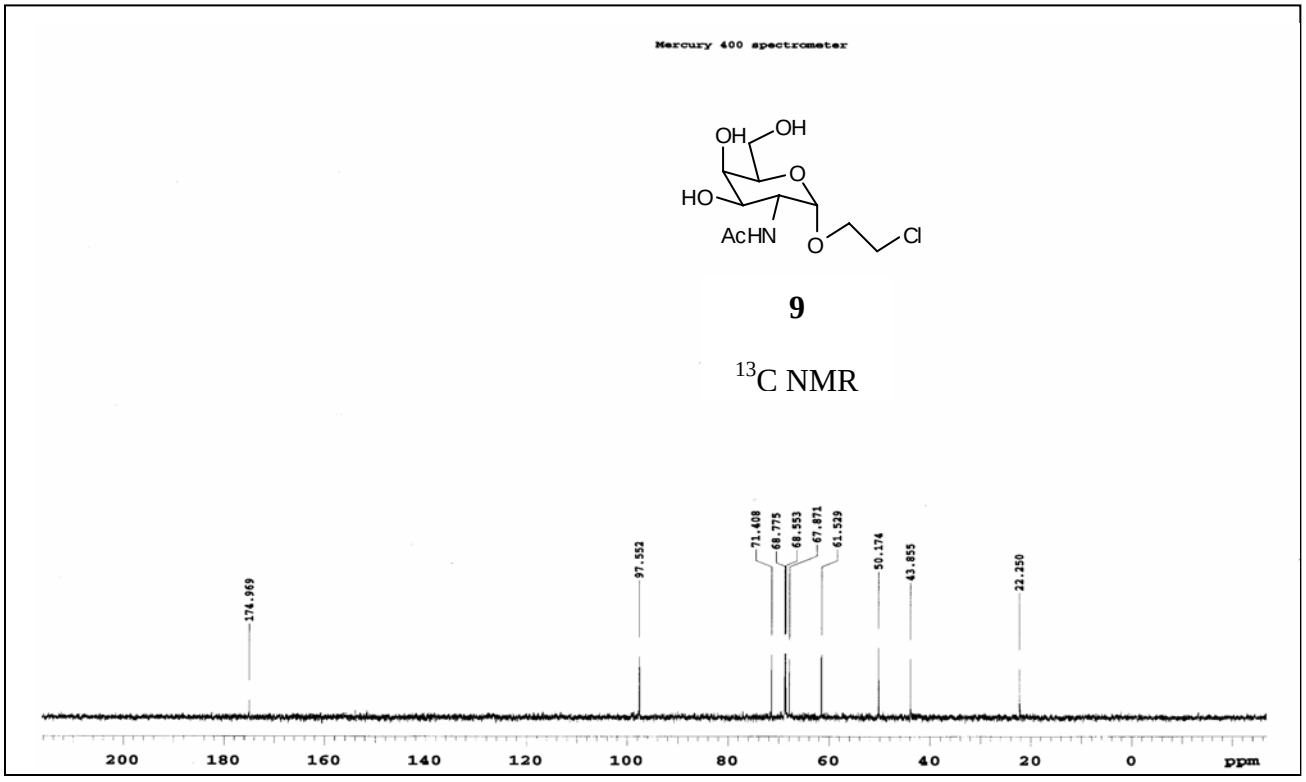

9

^{13}C NMR

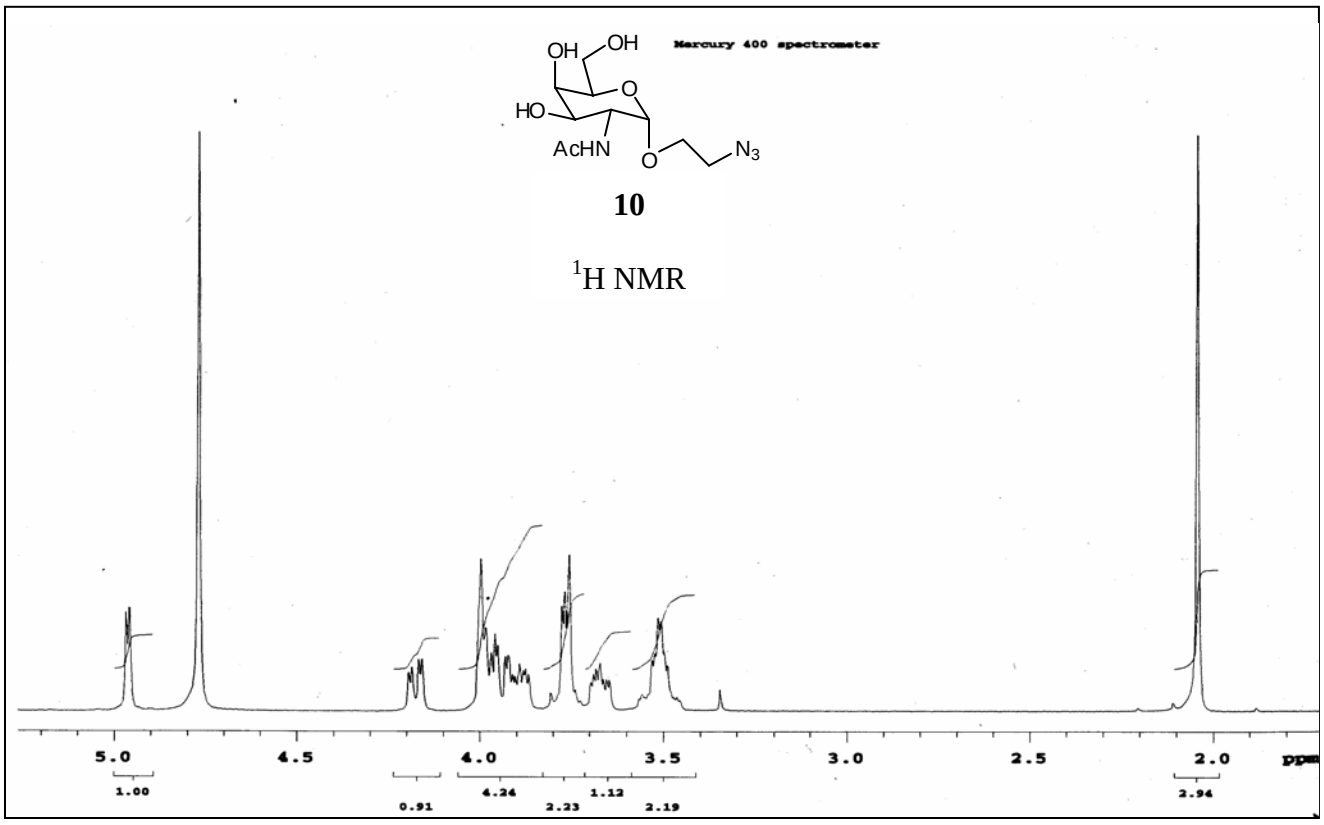

10

^{1}H NMR

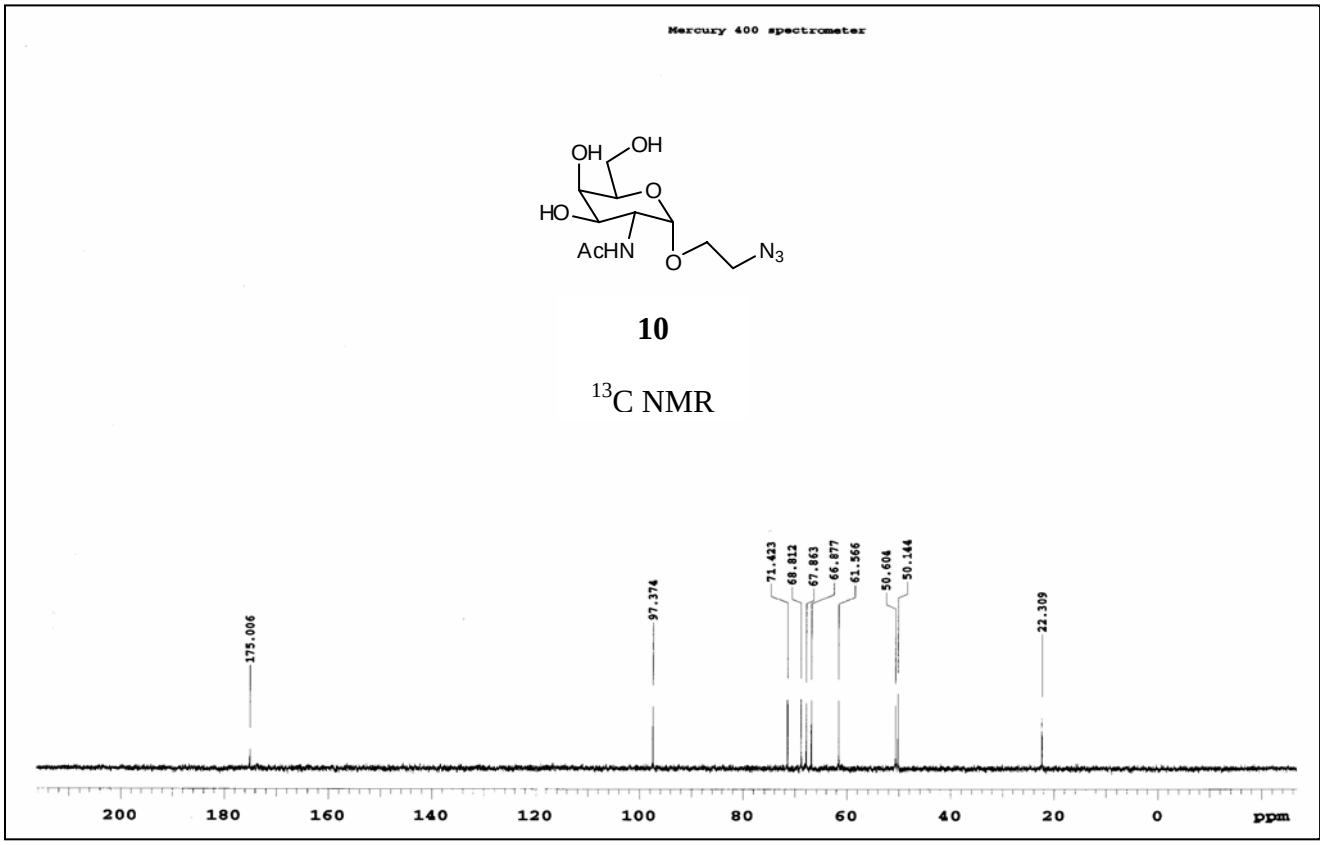

10

^{13}C NMR

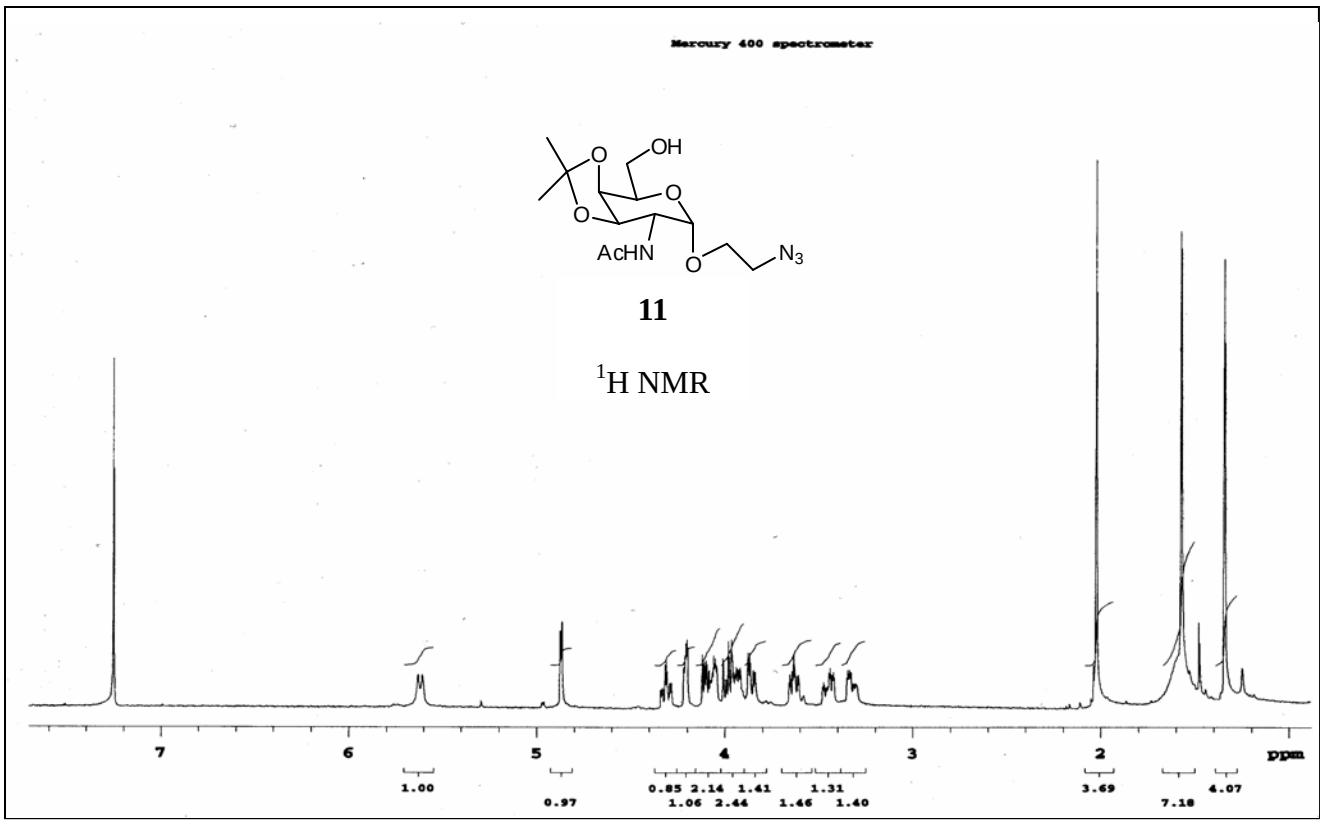

11

^{1}H NMR

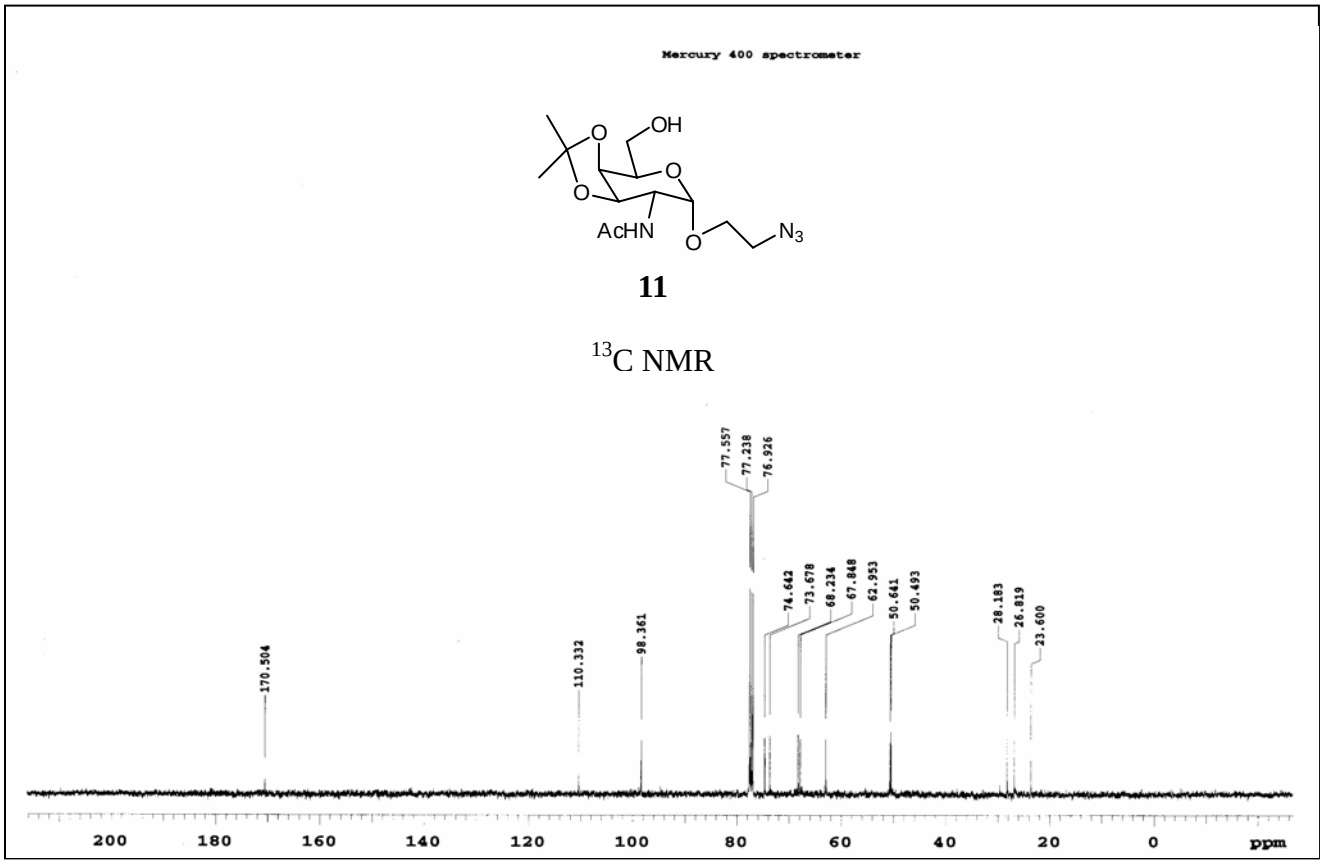

11

^{13}C NMR

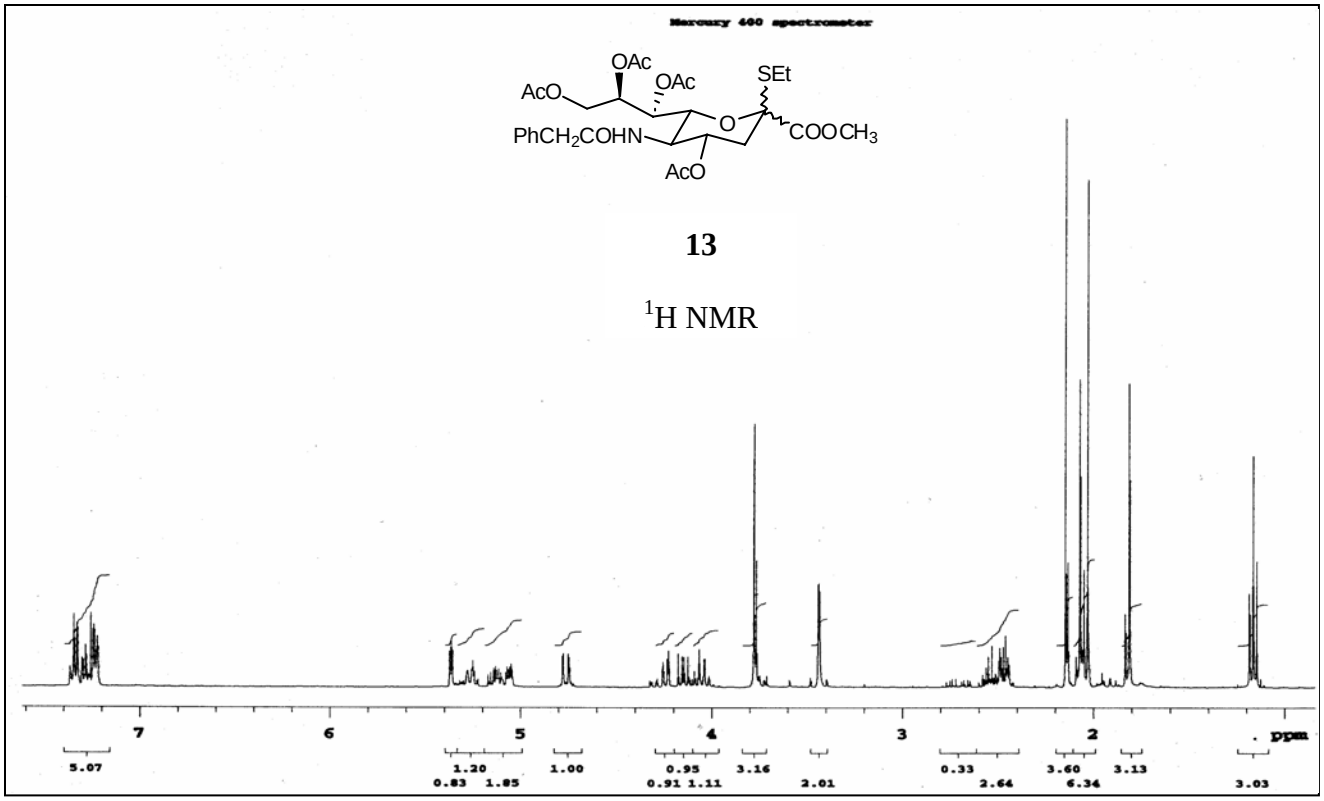

13

^{1}H NMR

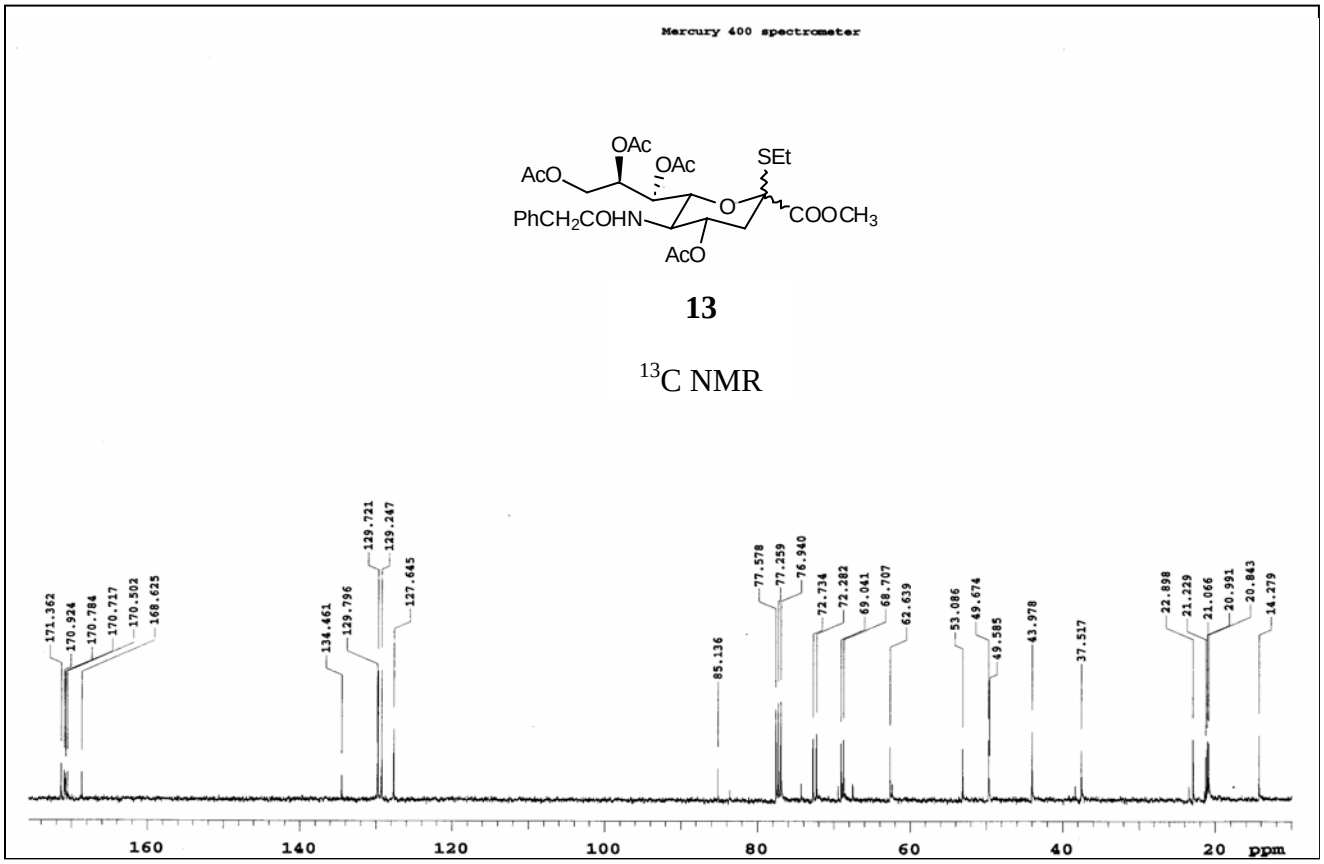

13

^{13}C NMR

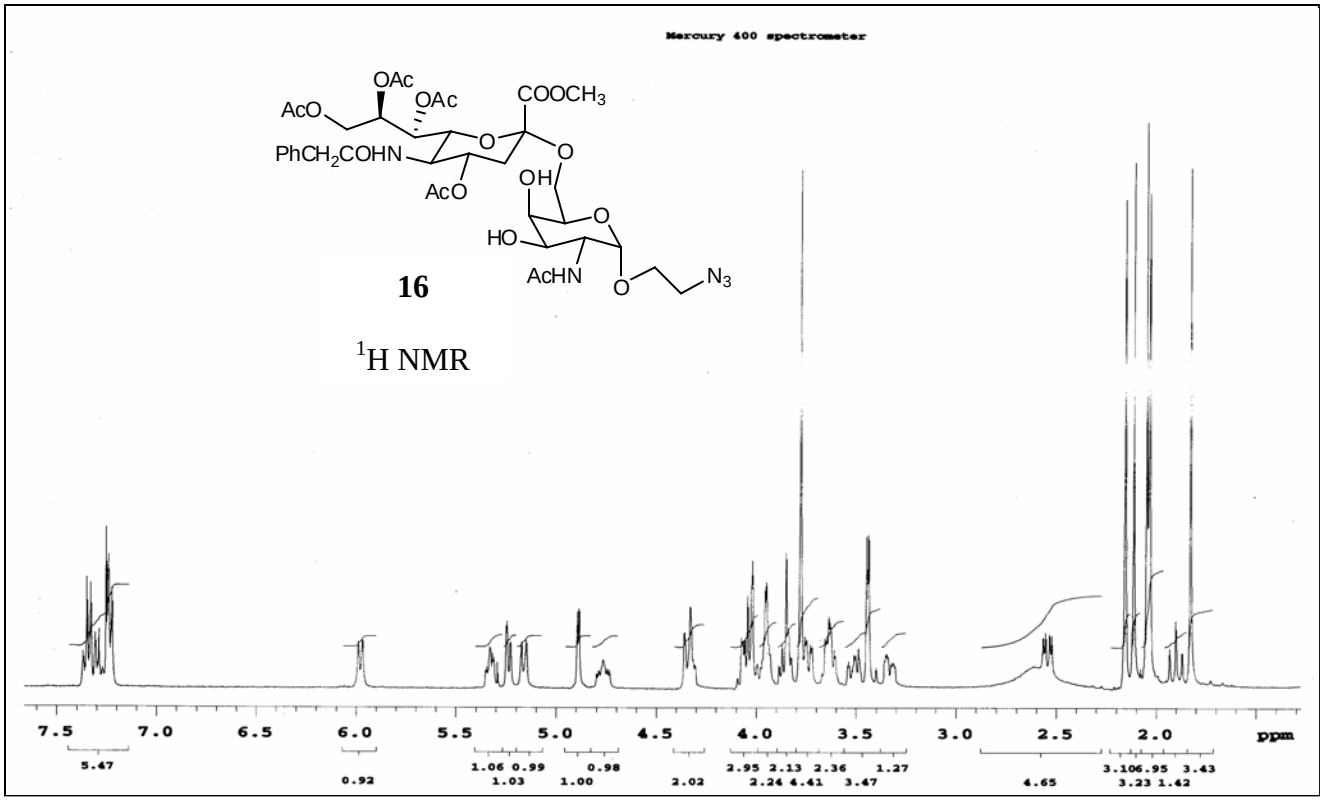
Mercury 400 spectrometer
OAc
OAc
AcO
COOCH3
PhCH2COHN
O
O
AcO
OH
O
HO
AcHN
O
N3
16
1H NMR
7.5
7.0
6.5
6.0
5.5
5.0
4.5
4.0
3.5
3.0
2.5
2.0
ppm
5.47
0.92
1.06 0.99
1.03
1.00
0.98
2.02
2.95 2.13 2.36 1.27
2.24 4.41 3.47
4.65
3.10 6.95 3.43
3.23 1.42

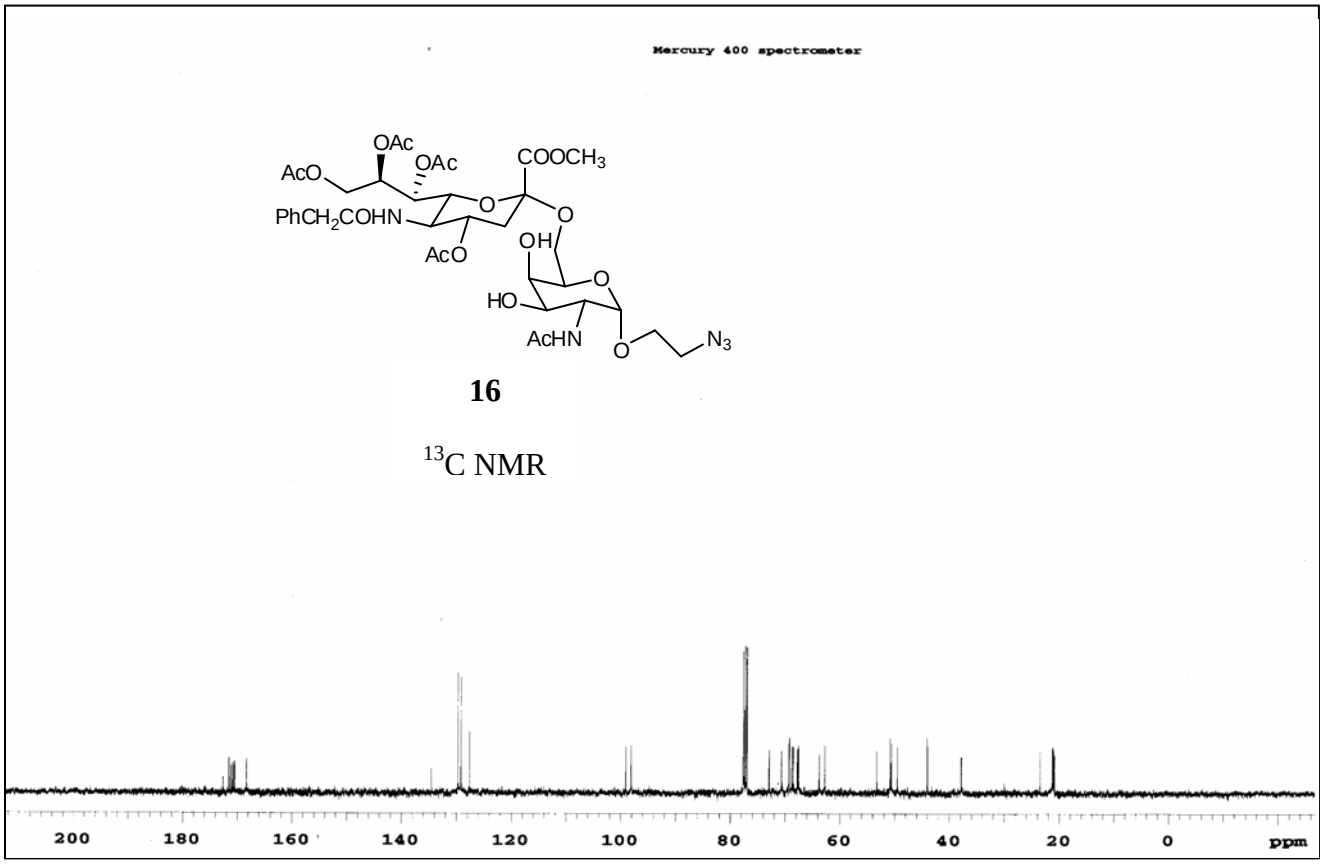
Mercury 400 spectrometer
OAc
OAc
AcO
COOCH3
PhCH2COHN
O
O
AcO
OH
O
HO
AcHN
O
N3
16
13C NMR
200
180
160
140
120
100
80
60
40
20
0
ppm

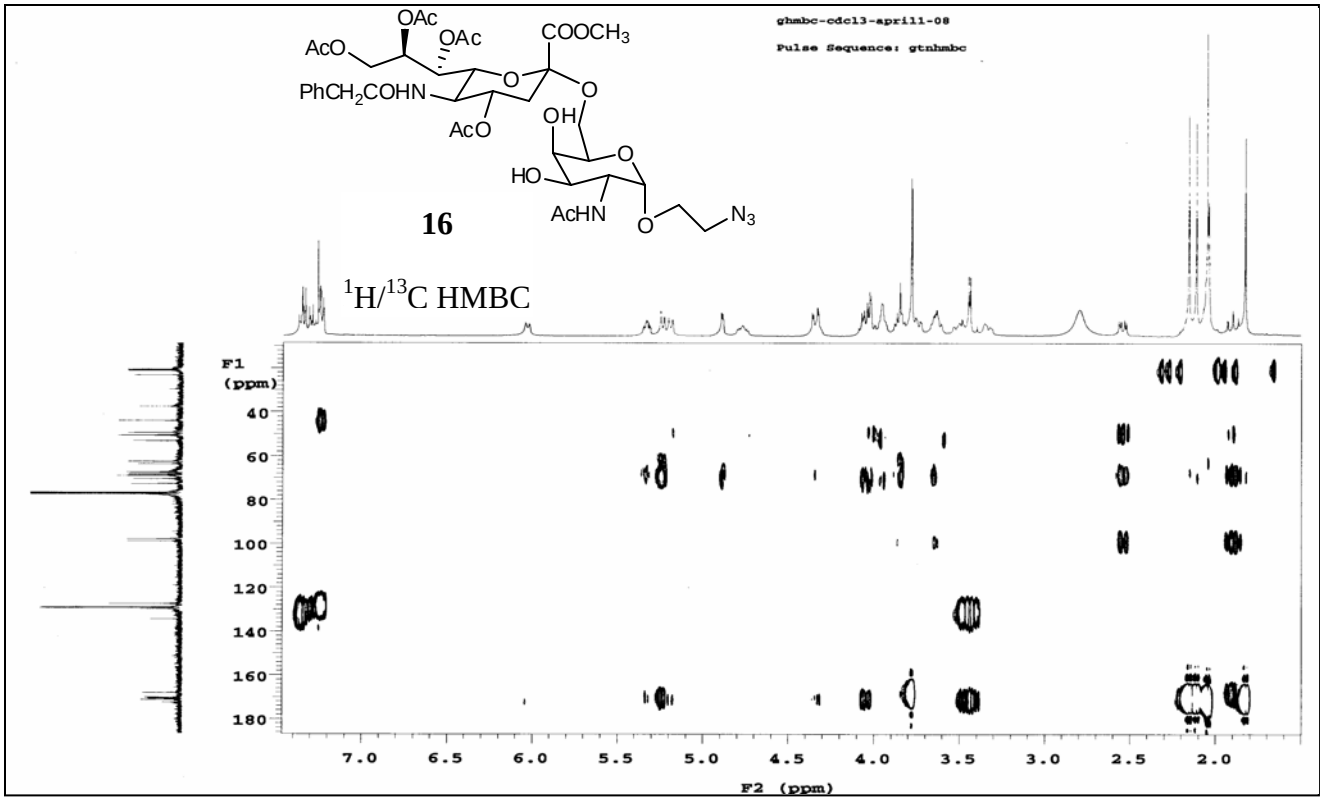
ghmbc-cdcl3-april1-08
Pulse Sequence: gtnhmbc
OAc
OAc
AcO
COOCH3
PhCH2COHN
AcO
OH
HO
AcHN
N3
16
1H/13C HMBC
F1 (ppm)
F2 (ppm)

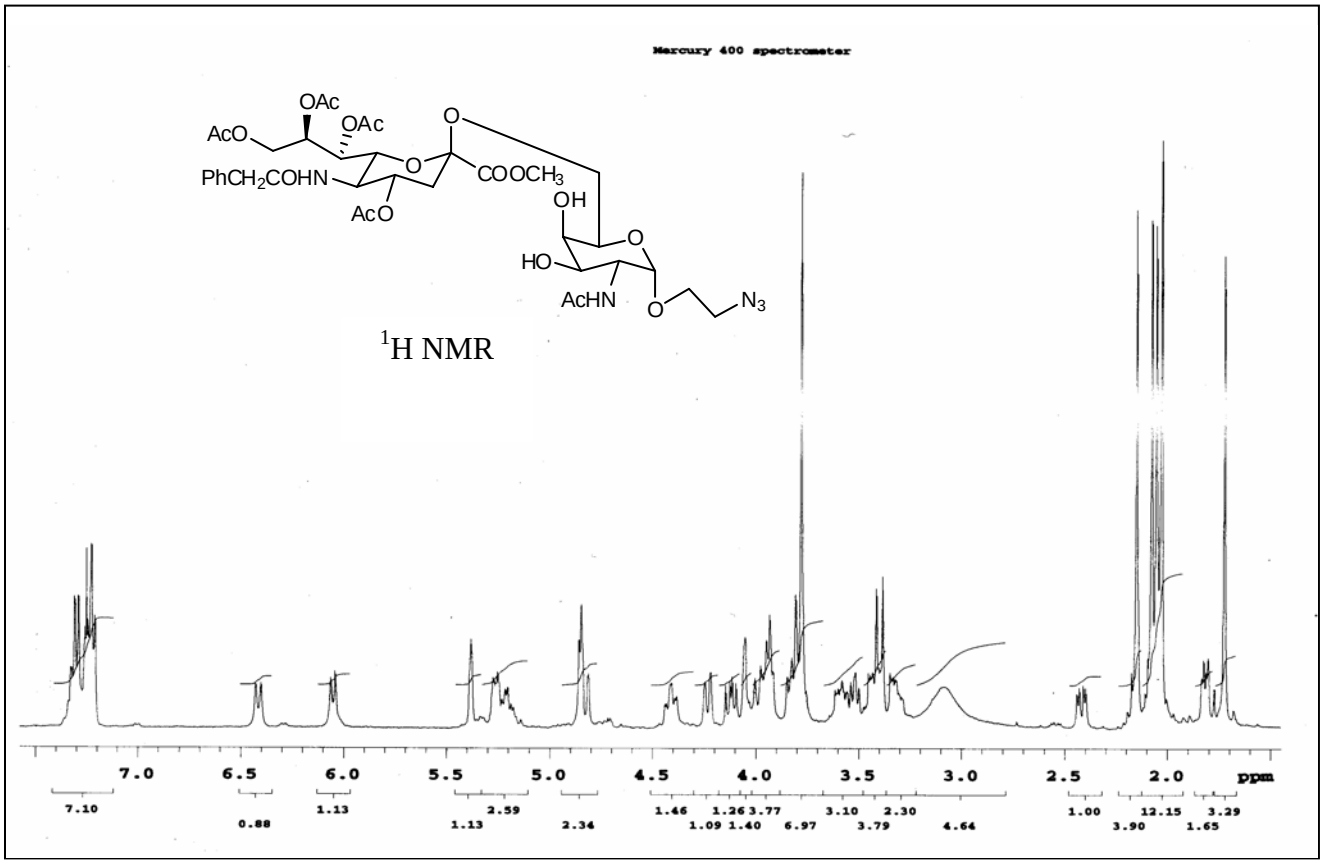
Mercury 400 spectrometer
OAc
OAc
AcO
PhCH2COHN
AcO
COOCH3
OH
HO
AcHN
N3
1H NMR
ppm

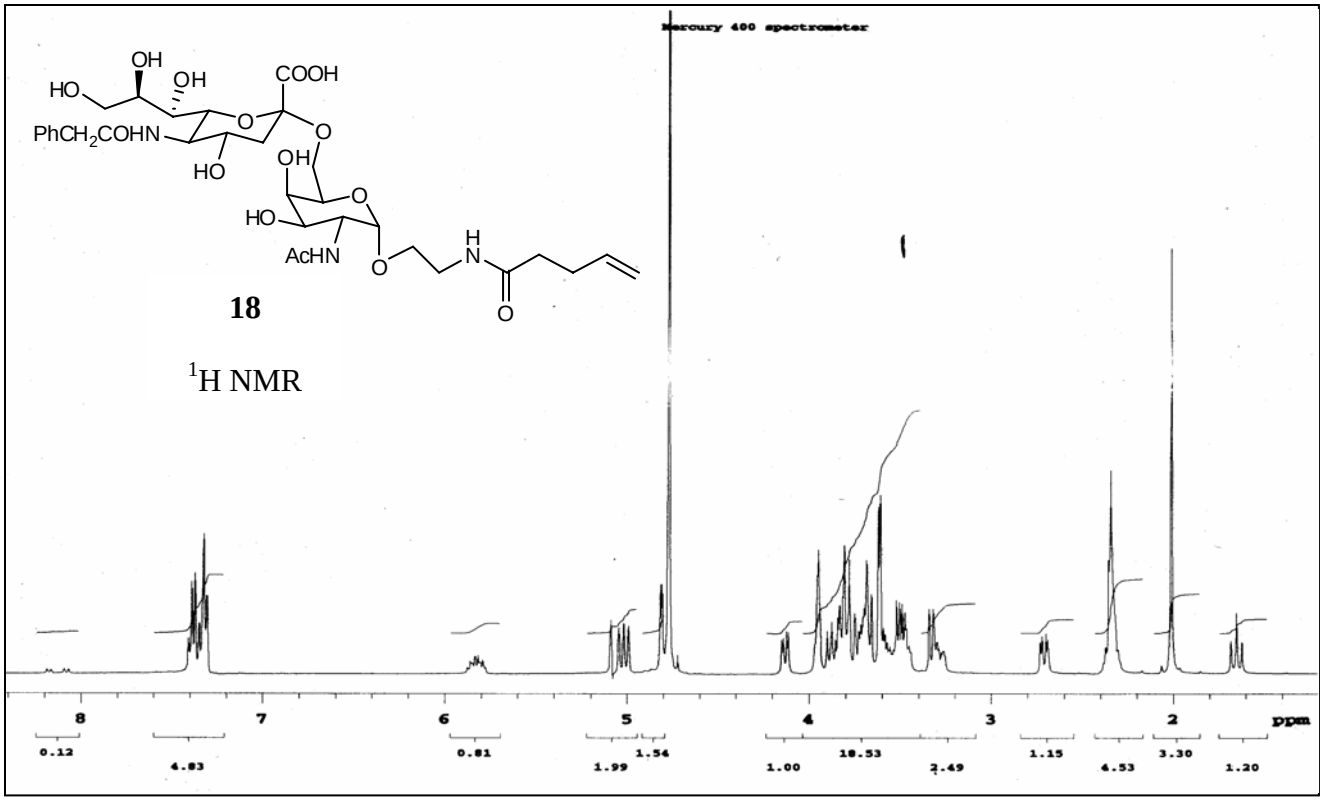
Mercury 400 spectrometer
OH
HO
OH
COOH
PhCH2COHN
O
HO
OH
O
HO
AcHN
O
H
N
O
18
1H NMR
8
7
6
5
4
3
2
ppm
0.12
4.83
0.81
1.99
1.54
1.00
10.53
2.49
1.15
4.53
3.30
1.20

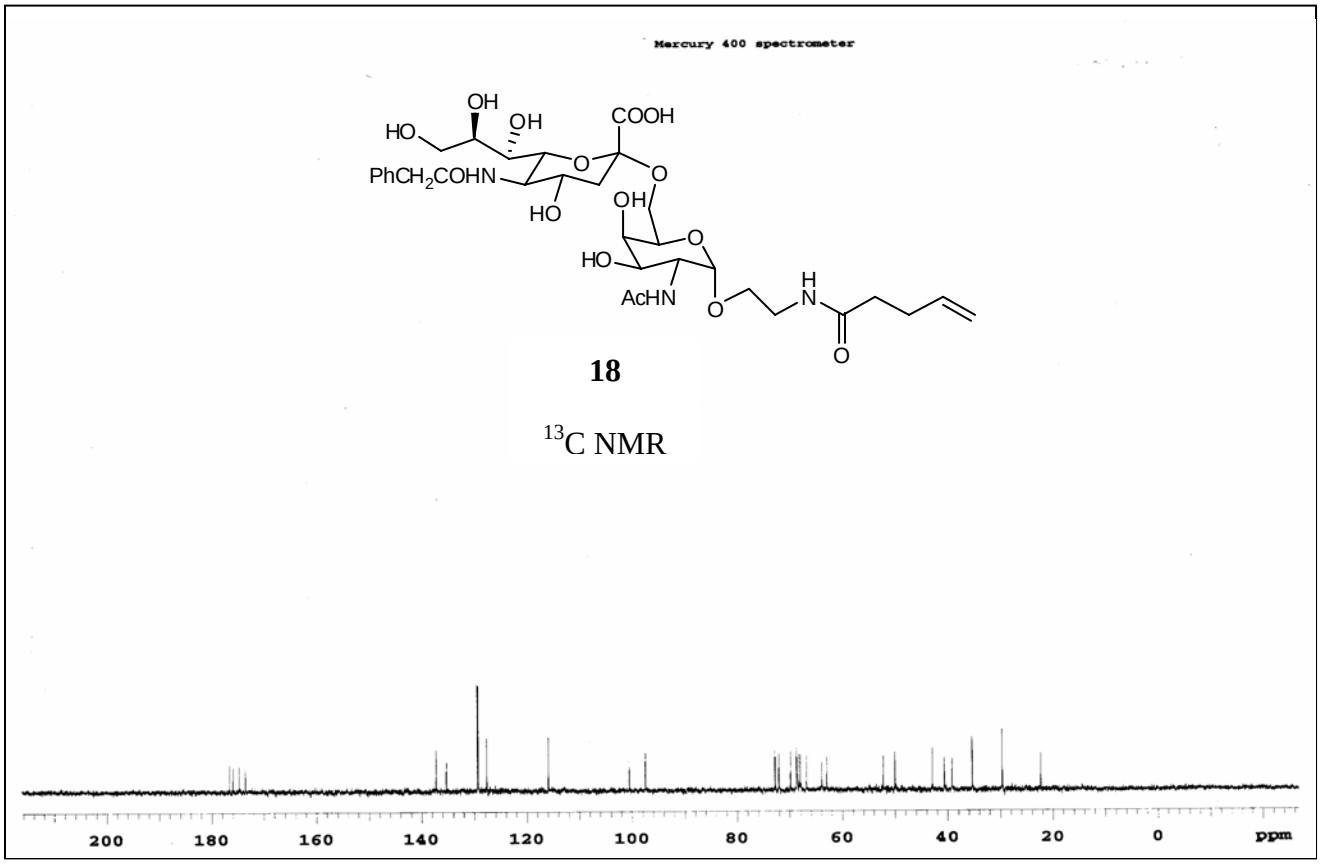
Mercury 400 spectrometer
OH
HO
OH
COOH
PhCH2COHN
O
HO
OH
O
HO
AcHN
O
H
N
O
18
13C NMR
200
180
160
140
120
100
80
60
40
20
0
ppm

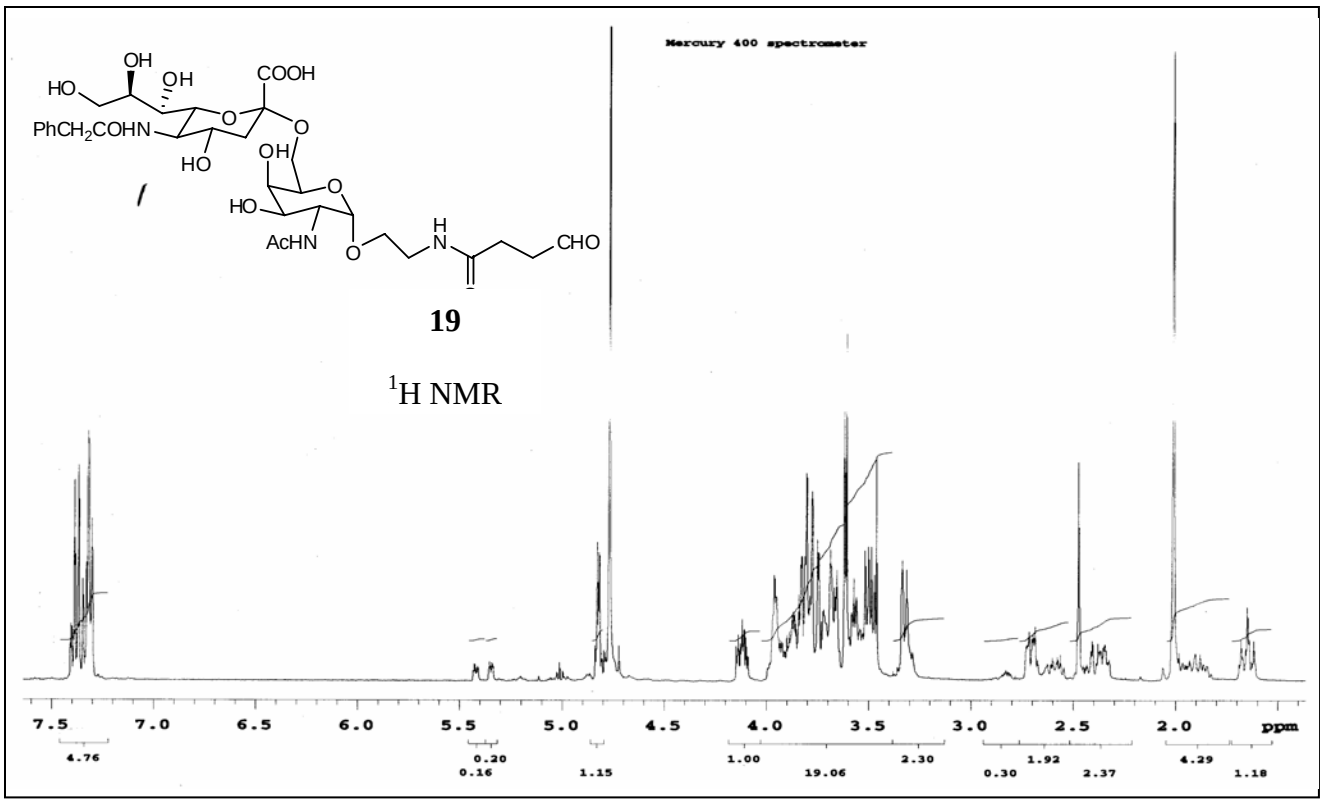

19

^{1}H NMR

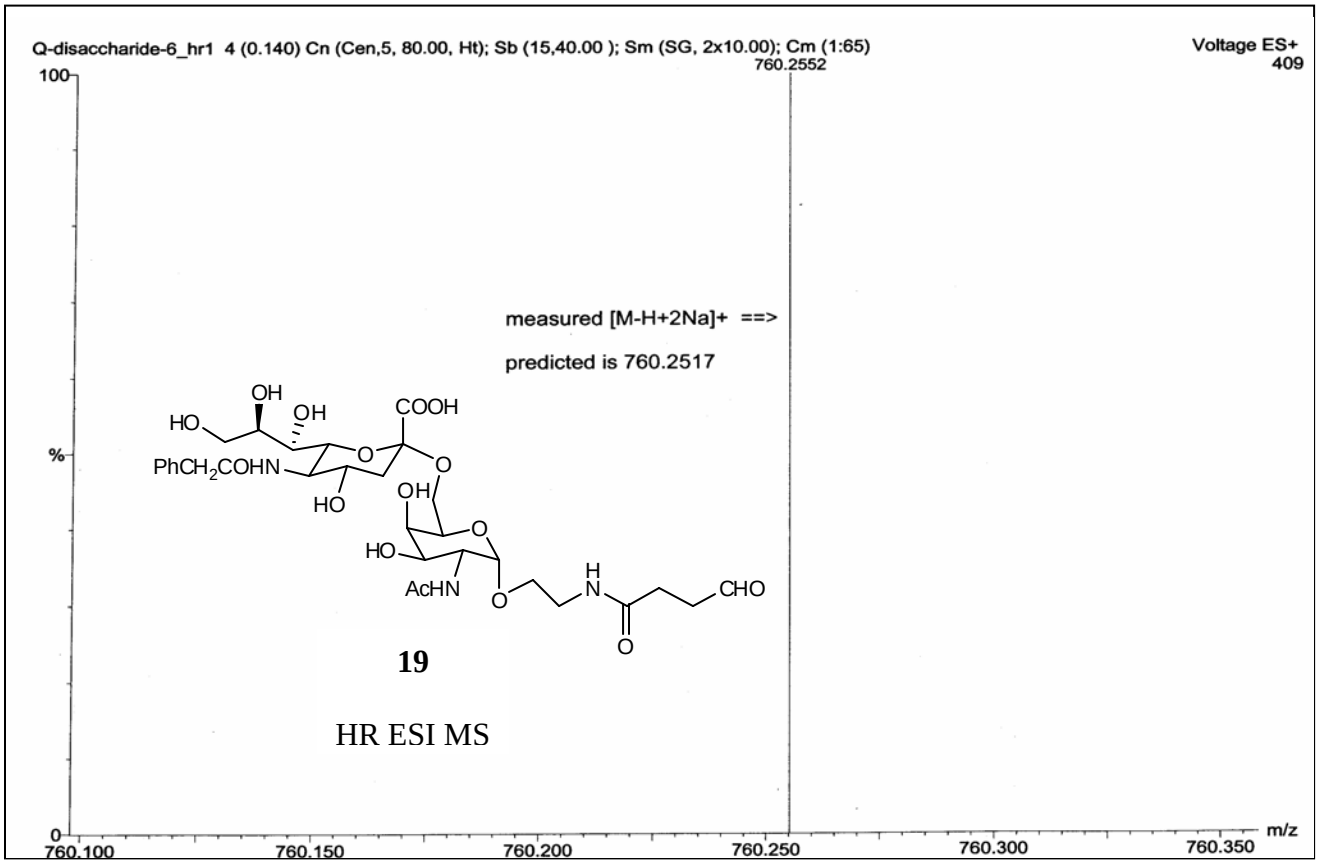

19

HR ESI MS

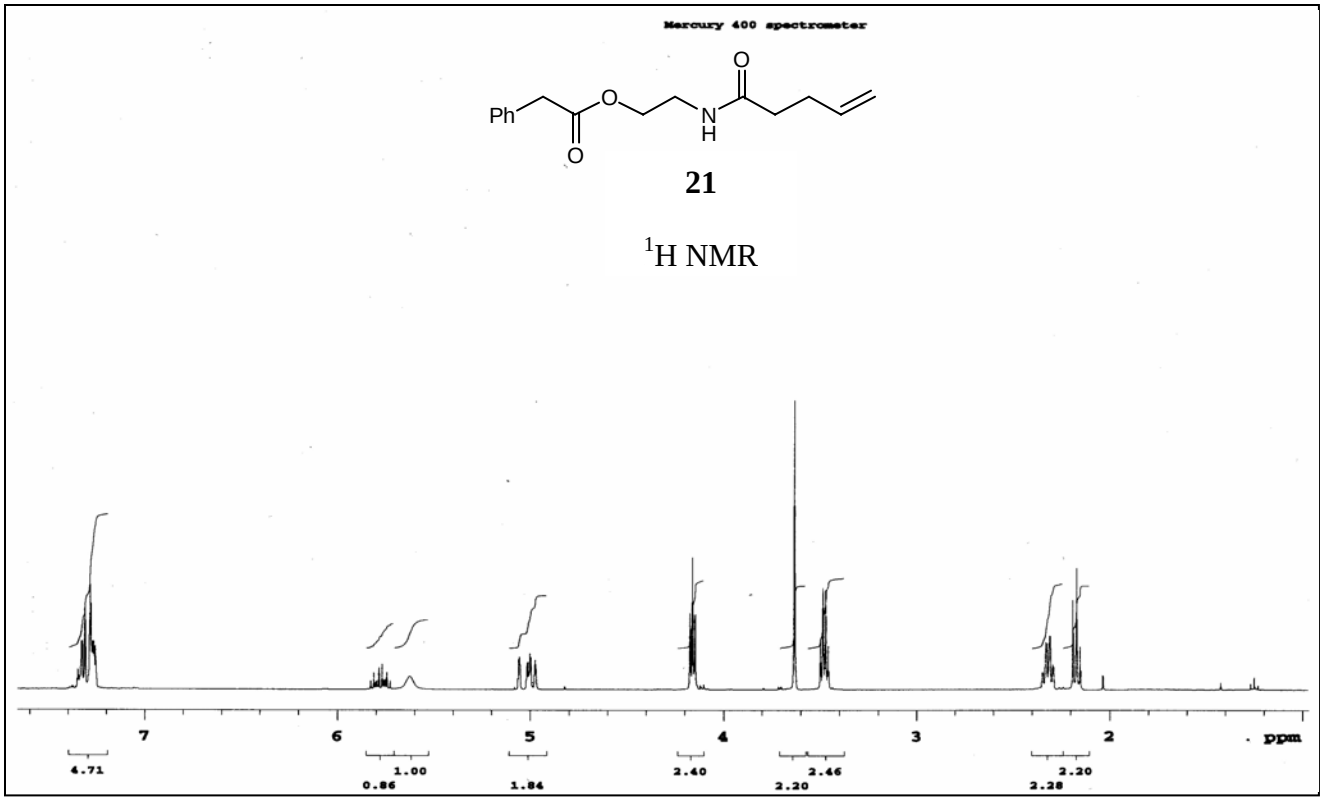

21

^{1}H NMR

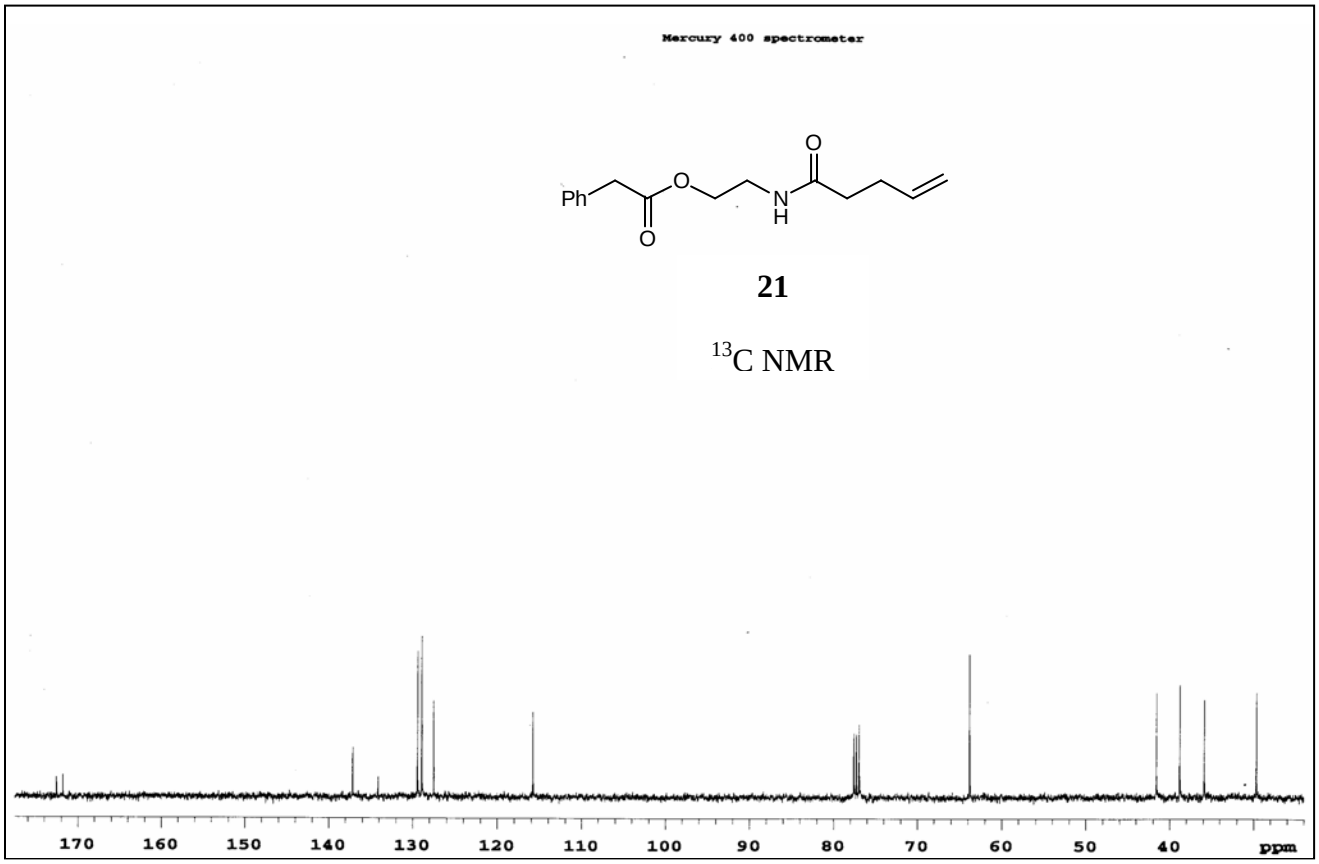

21

^{13}C NMR

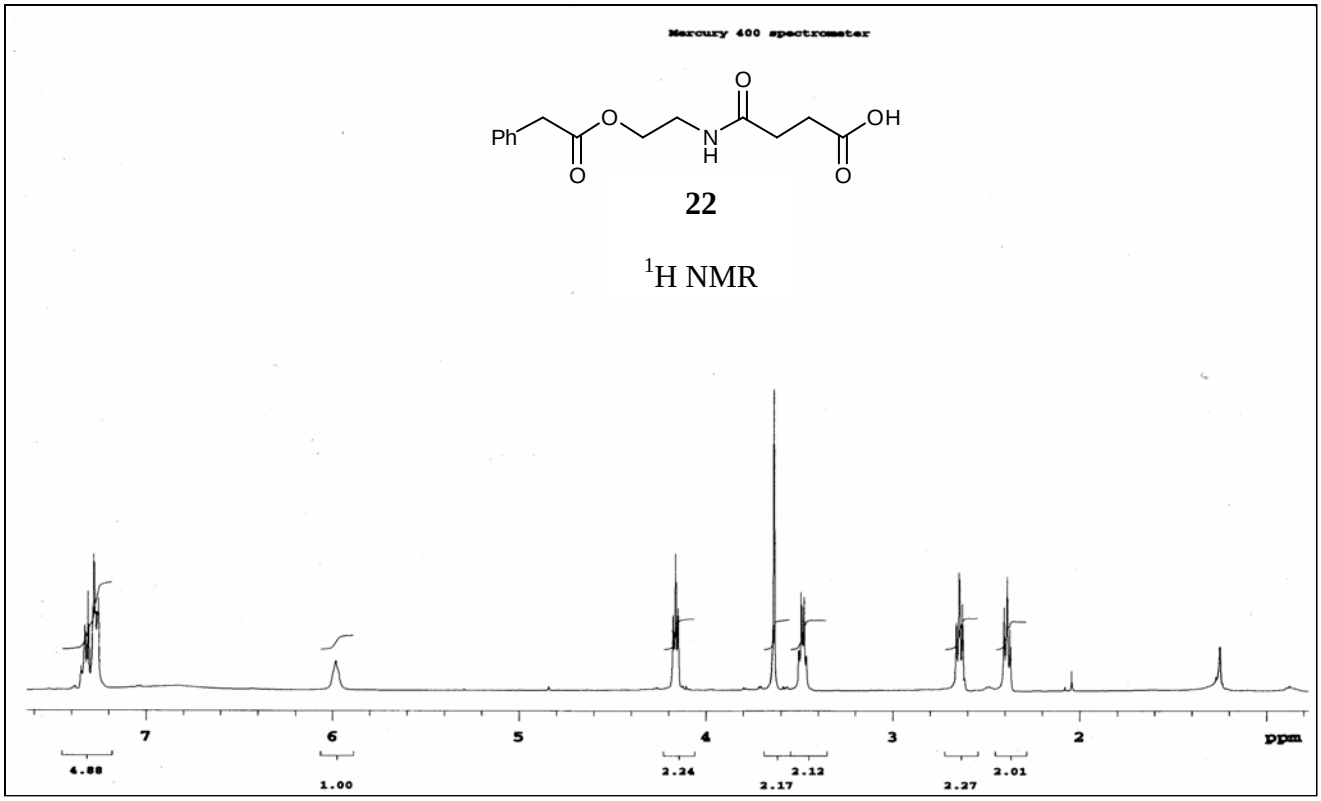

22

^{1}H NMR

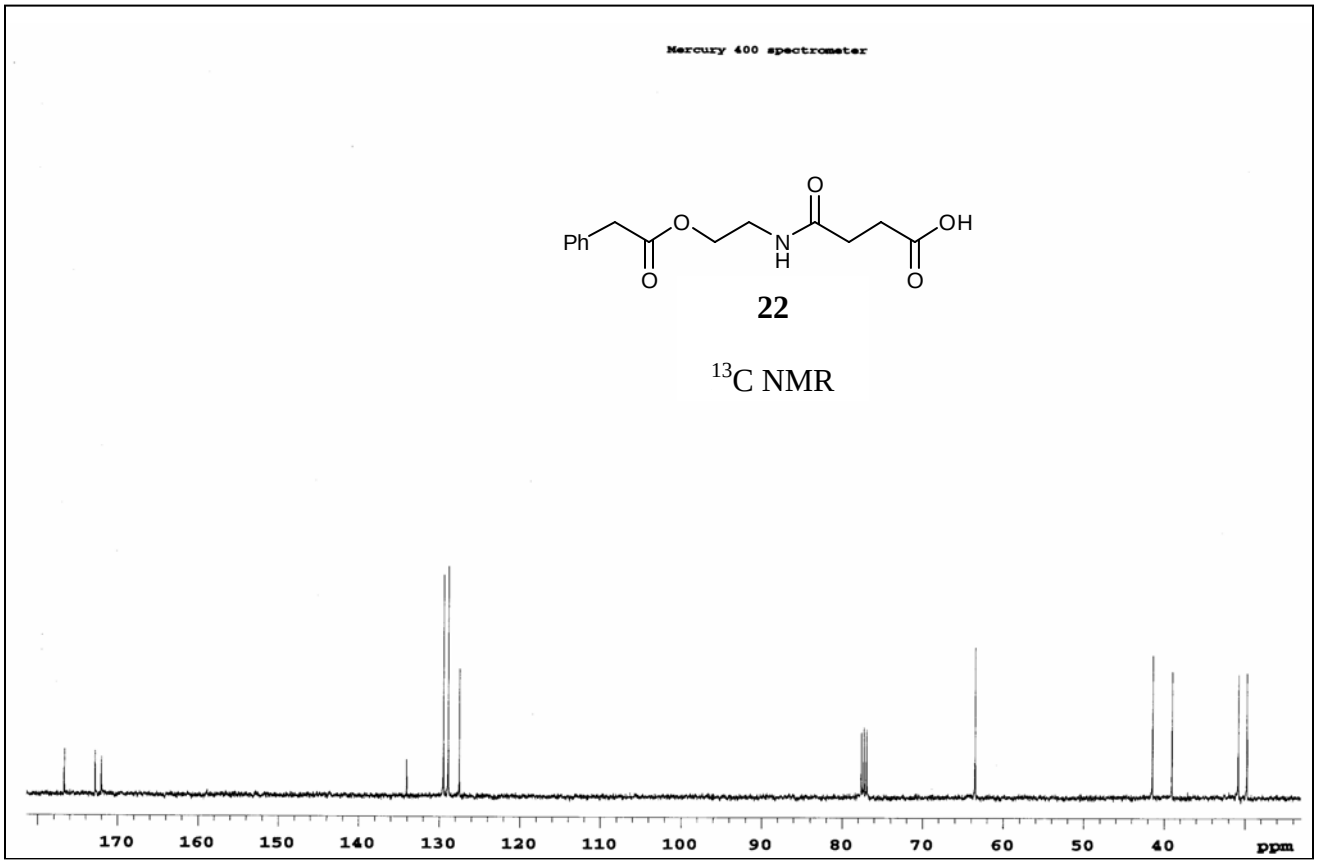

22

^{13}C NMR

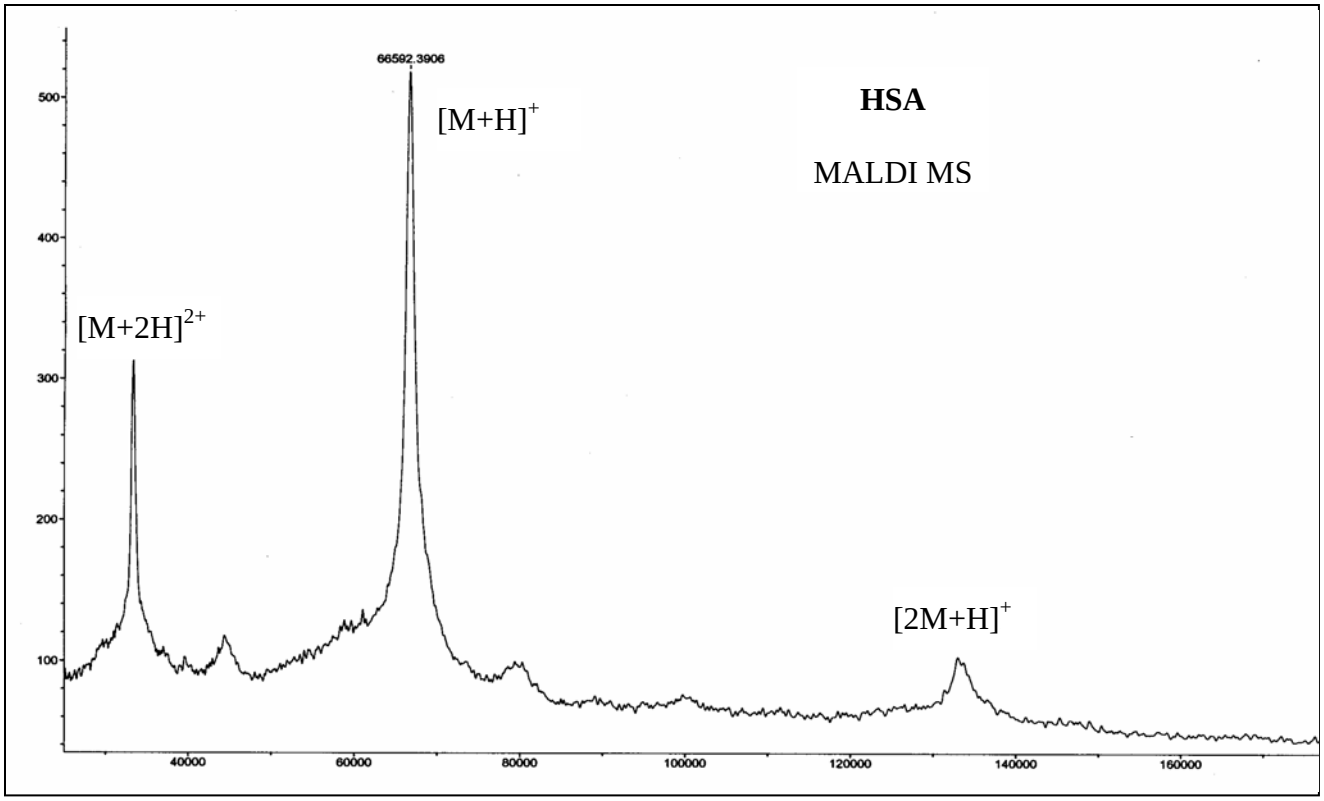
66592.3906
[M+H]+
HSA
MALDI MS
[M+2H]2+
[2M+H]+
500
400
300
200
100
40000
60000
80000
100000
120000
140000
160000

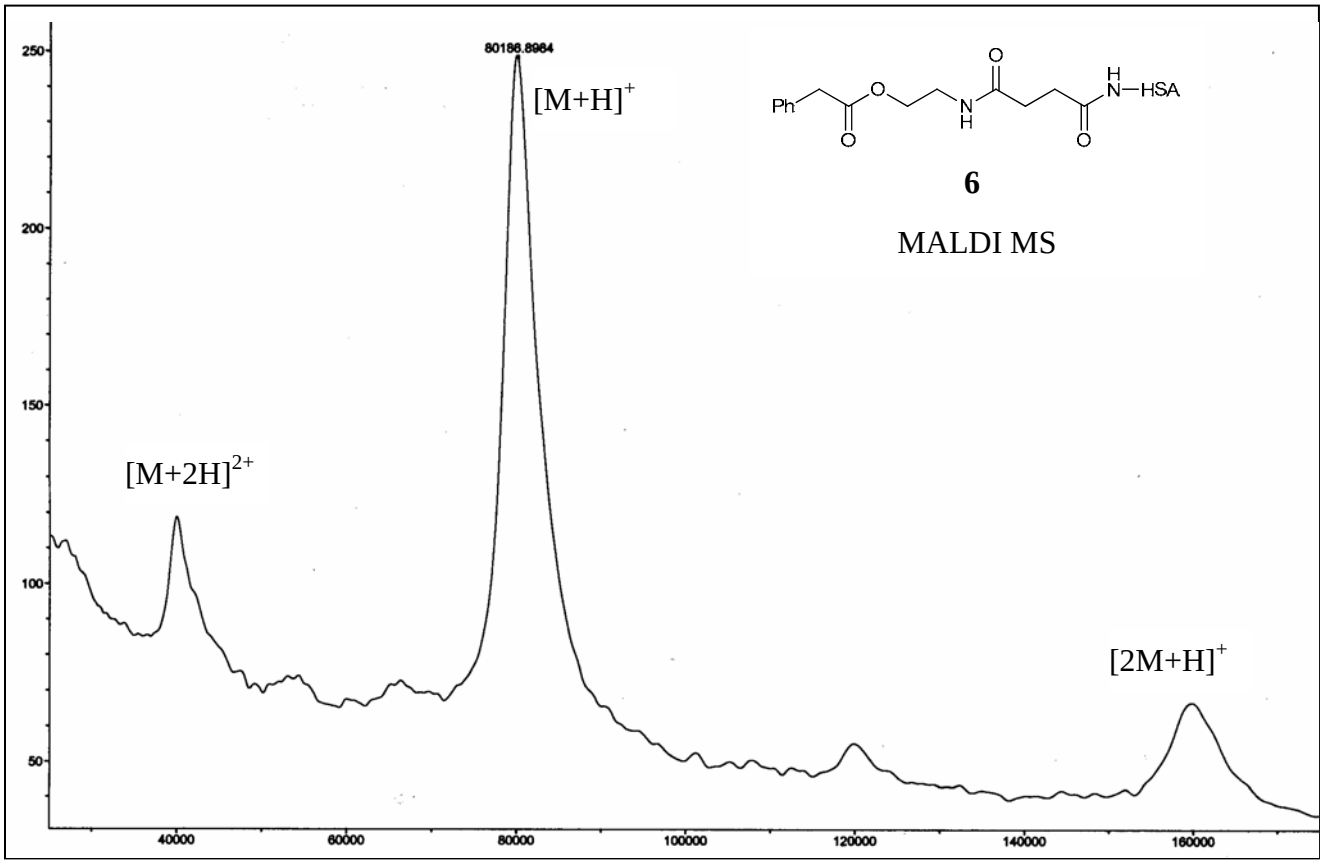
80186.8984
[M+H]+
Ph
O
N
H
HSA
6
MALDI MS
[M+2H]2+
[2M+H]+
250
200
150
100
50
40000
60000
80000
100000
120000
140000
160000

Optimization of Labile Esters for Esterase-Assisted Accumulation of Nitroxides into Cells: A Model for In Vivo EPR Imaging

Scott R. Burks,[†,‡,§] Jiahong Ni,[†] Sukumaran Muralidharan,[†] Andrew Coop,[#] Joseph P. Y. Kao,*[,†,‡,§] and Gerald M. Rosen*[,†,§,#]

Medical Biotechnology Center, University of Maryland Biotechnology Institute, Department of Physiology, University of Maryland School of Medicine, Center for EPR Imaging In Vivo Physiology, University of Maryland, and Department of Pharmaceutical Sciences, University of Maryland School of Pharmacy, Baltimore, Maryland 21201. Received April 15, 2008; Revised Manuscript Received August 11, 2008

Nitroxide-based electron paramagnetic resonance (EPR) imaging agents are useful quantitative probes of O_2 concentration in vivo in real time. Lipophilic, labile alkanoyloxymethyl esters of nitroxides can cross the blood−brain barrier, and after hydrolysis, the corresponding anionic nitroxide is intracellularly entrapped at levels sufficient to permit O_2 measurements. The utility of nitroxides as EPR imaging agents depends critically on their ability to accumulate in the brain to high levels. In this study, we systematically investigated the relationship between the structure of the alkanoyl moiety and the ability of the corresponding labile ester to deliver nitroxide intracellularly. We demonstrate, in a cultured cell model, that for nitroxide labile esters with unbranched alkanoyl chains, increasing the chain length improves intracellular loading. Moreover, by studying an isomeric series of labile esters, we conclude that branching of the alkanoyl chain drastically reduces intracellular loading. These structural insights improve our general ability to use labile esters to deliver carboxylates intracellularly, and suggest a strategy for enhancing delivery of nitroxide imaging agents across the blood−brain barrier in a living animal.

INTRODUCTION

Molecular oxygen is fundamental to many aspects of brain physiology. For example, in neurons, it is essential for the synthesis and catabolism of neurotransmitters such as dopamine, norepinephrine, and serotonin. Importantly, diverse pathophysiologies, including stroke, drug abuse, and neurodegenerative disorders such as Alzheimer's and Parkinson's diseases, are associated with acute or chronic alterations in brain O_2 concentration. In vivo measurement of O_2 in the brain in real time is not a trivial task. Blood oxygen level dependent (BOLD) MR imaging is only capable of qualitative O_2 measurements in vivo (*1*−*3*). Therefore, an alternative, minimally invasive imaging method for *quantitation* of O_2 in the living brain is highly desirable for pathophysiological studies.

Molecular oxygen, being paramagnetic, broadens the electron paramagnetic resonance (EPR) spectral lines of other paramagnetic species, such as nitroxides or trityl radicals. Changes in EPR spectral line width for these compounds have been used to measure O_2 concentrations in homogeneous solutions (*2*, *4*). The development of very-low-frequency EPR spectroscopy and imaging (*2*) along with suitable imaging probes makes it feasible to quantitate local O_2 concentrations in animals in real time. The concentration of O_2 in the vasculature of tumors has been successfully measured by EPR imaging using trityl radicals (*2*). Because of their large size and ionic charge, trityls cannot cross the blood−brain barrier or be intracellularly localized. Therefore, trityl radicals are unsuitable for O_2 measurements in the brain. Like trityls, suitably designed nitroxides are relatively resistant to bioreduction, but have the advantages of chemical flexibility and ease of chemical synthesis. Moreover, nitroxides are attractive probes for O_2 imaging in the brain because they can be prepared as small labile esters that can cross the blood−brain barrier to enter brain tissue.

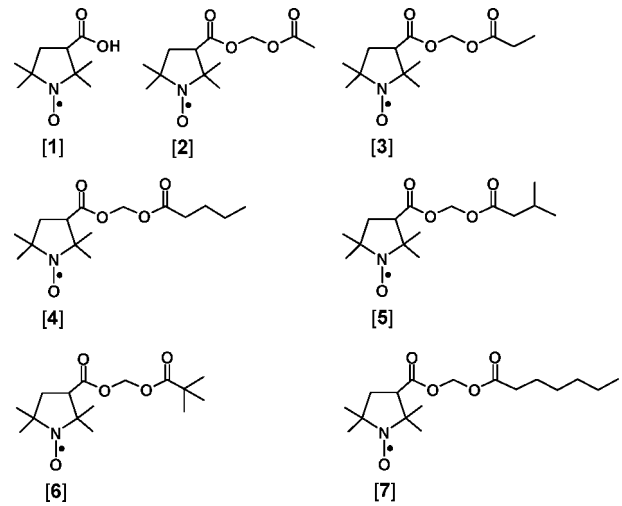

Figure 1. 3-Carboxy-2,2,5,5-tetramethyl-1-pyrrolidinyloxyl [**1**] and its labile ester derivatives characterized in this study.

Previously, we demonstrated that the lipophilic labile ester, 3-acetoxymethoxycarbonyl-2,2,5,5-tetramethyl-1-pyrrolidinyloxyl [**2**] (Figure 1), can cross the cell membrane and enter the cytosol, where it is hydrolyzed by intracellular esterases to yield membrane-impermeant 3-carboxy-2,2,5,5-tetramethyl-1-pyrrolidinyloxyl [**1**], which, being anionic at physiologic pH, becomes trapped intracellularly (*5*, *6*) (Scheme 1). In vivo, **2** is also able cross the blood−brain barrier to enter brain tissue, where it is hydrolyzed to **1**, making local O_2 measurements possible (*4*).

* Corresponding author. Address: 725 W. Lombard St., Baltimore, MD 21201. E-mail: kao@umbi.umd.edu; Tel: 410-706-4167. E-mail: grosen@umaryland.edu; Tel: 410-706-0514.
[†] University of Maryland Biotechnology Institute.
[‡] University of Maryland School of Medicine.
[§] Center for EPR Imaging.
[#] University of Maryland School of Pharmacy.

10.1021/bc8001562 CCC: $40.75 © 2008 American Chemical Society
Published on Web 09/11/2008

Scheme 1. Esterase-Assisted Intracellular Accumulation of Nitroxide 1

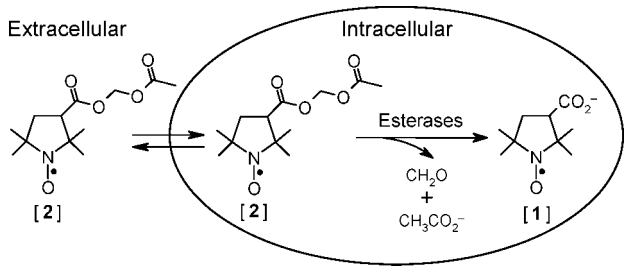

Although we have shown that nitroxide **2** is a usable pro-imaging agent (*4*−*6*), the potential utility of nitroxides as EPR imaging agents can be maximized by entrapping the highest concentrations of nitroxide **1** in the brain. We reasoned that increasing the lipophilicity of the labile ester pro-imaging agents would enhance their ability to cross biological membranes, and thus result in higher levels of trapped nitroxide **1**. In the present study, we synthesized a family of labile 3-alkanoyloxymethoxycarbonyl nitroxide esters that can be hydrolyzed to nitroxide **1** (Figure 1). Using our previous in vitro cell model (*5, 6*), we examined the ability of cells to accumulate nitroxide **1** when incubated with the different labile ester pro-imaging agents.

EXPERIMENTAL PROCEDURES

General Materials and Methods. Reagents and solvents from commercial vendors were used without further purification. Reagents were obtained from Aldrich Chemical Co. (Milwaukee, WI), and solvents were from VWR (West Chester, PA). Silica gel (230−400 mesh) and TLC plates (Silica Gel 60 F254) were from EMD Chemicals Inc. (Gibbstown, NJ). Cell culture media and biochemicals were from Invitrogen Corp. (Carlsbad, CA). 3-Carboxy-2,2,5,5-tetramethyl-1-pyrrolidinyloxyl [**1**] was prepared as described by Rozantsev (*7*). 3-Acetoxymethoxycarbonyl-2,2,5,5-tetramethyl-1-pyrrolidinyloxyl [**2**] was prepared as previously described (*6*). IR spectra were recorded on an FT-IR spectrometer (model 1600, Perkin-Elmer, Norwalk, CT) in $CHCl_3$. Mass spectrometric analysis was performed by the Mass Spectrometry Facility in the Department of Chemistry and Biochemistry at the University of Maryland, College Park. Elemental analyses were performed by Atlantic Microlab, Inc. (Norcross, GA). *Origin 8.0* software (OriginLab Corp., Northampton, MA) was used for data analysis. Unless otherwise indicated, standard deviations are reported for measurements.

Synthesis of 3-(2,2-Dimethylpropanoyl)oxycarbonyl-2,2,5,5-tetramethyl-1-pyrrolidinyloxyl [6]. To a solution of nitroxide [**1**] (0.25 g, 1.3 mmol) in DMSO (2 mL) was added K_2CO_3 (0.37 g, 2.7 mmol). After the reaction mixture was stirred at room temperature for 5 min, chloromethyl pivalate (0.2 g, 0.19 mL, 1.4 mmol) was added. Stirring was continued at room temperature for 3 h before the mixture was diluted with CH_2Cl_2 (50 mL) and brine (100 mL). The organic layer was dried over anhydrous $MgSO_4$ and evaporated under high vacuum to remove traces of DMSO. The resulting crude product was purified by chromatography on silica gel; elution with 1% (v/v) acetone in $CHCl_3$ afforded compound [**6**] (0.29 g, 75% yield). IR ($CHCl_3$): 1753 cm^{-1} (broad ester peak). Anal. Calcd for $C_{15}H_{26}NO_5$: C, 59.98; H, 8.73; N, 4.66 Found: C, 59.90; H, 8.84; N, 4.53.

Synthesis of 3-Chloromethoxycarbonyl-2,2,5,5-tetramethyl-1-pyrrolidinyloxyl [8]. This compound was prepared following the general procedure of Harada et al. (*8*). A mixture of CH_2Cl_2 (20 mL) and 20 mL of aqueous solution containing 3-carboxy-2,2,5,5-tetramethyl-1-pyrrolidinyloxyl [**1**] (0.5 g, 2.7 mmol), $NaHCO_3$ (0.9 g, 10.8 mmol), and tetrabutylammonium bisulfate (91 mg, 0.27 mmol) was stirred for 10 min at room temperature before addition of chloromethyl chlorosulfate (0.54 g, 0.33 mL, 3.3 mmol). The reaction mixture was vigorously stirred at room temperature for 2 h, during which the yellow color of the nitroxide moved from the aqueous phase into the organic phase. The CH_2Cl_2 phase was separated, washed with brine (100 mL), dried over anhydrous Na_2SO_4, filtered, and evaporated under reduced pressure to yield compound [**8**] (0.54 g, 85% yield). TLC (silica gel, 2:1 (v/v) hexane/EtOAc) showed only one spot. The product was used in subsequent reactions without further purification.

Synthesis of 3-Pentanoylmethoxycarbonyl-2,2,5,5-tetramethyl-1-pyrrolidinyloxyl [4]. A mixture of chloromethyl ester [**8**] (0.75 g, 3.2 mmol), K_2CO_3 (0.88 g, 6.4 mmol), and DMSO (2 mL) was stirred at room temperature for 5 min before addition of pentanoic acid (0.33 g, 0.34 mL, 3.2 mmol) and a few crystals of NaI. The reaction mixture was stirred at room temperature overnight and then diluted with CH_2Cl_2 (50 mL) and brine (100 mL). The organic phase was dried over anhydrous $MgSO_4$, filtered, and evaporated under high vacuum to remove traces of DMSO. The resulting crude product was purified on silica gel (7:3 (v/v) hexane/EtOAc) to give compound [**4**] (0.76 g, 80% yield). IR ($CHCl_3$): 1753 cm^{-1} (broad ester peak). Anal. Calcd for $C_{15}H_{26}NO_5$: C, 59.98; H, 8.73; N, 4.66. Found: C, 59.94; H, 8.83; N, 4.72.

Synthesis of 3-Propanoylmethyloxycarbonyl-2,2,5,5-tetramethyl-1-pyrrolidinyloxyl [3]. This nitroxide was synthesized using propionic acid in the procedure for nitroxide [**4**]; the yield was 85%. IR ($CHCl_3$): 1752 cm^{-1} (broad ester peak). HR FAB MS (*m/z*): calculated for $C_{13}H_{22}NO_5$ (M^+) 272.1498; found, 272.1498. Anal. Calcd for $C_{13}H_{22}NO_5$: C, 57.33; H, 8.14; N, 5.14. Found: C, 57.46; H, 8.00; N, 5.10.

Synthesis of 3-(3-Methylbutanoyl)methoxycarbonyl-2,2,5,5-tetramethyl-1-pyrrolidinyloxyl [5]. This nitroxide was synthesized using isovaleric acid in the procedure for nitroxide [**4**]; the yield was 74%. IR ($CHCl_3$): 1753 cm^{-1} (broad ester peak). Anal. Calcd for $C_{15}H_{26}NO_5$: C, 59.98; H, 8.73; N, 4.66. Found: C, 59.86; H, 8.81; N, 4.71.

Synthesis of 3-Heptanoylmethoxycarbonyl-2,2,5,5-tetramethyl-1-pyrrolidinyloxyl [7]. This nitroxide was synthesized using heptanoic acid in the procedure for nitroxide [**4**]; the yield was 84%. IR ($CHCl_3$): 1753 cm^{-1} (broad ester peak). Anal. Calcd for $C_{15}H_{26}NO_5$: C, 62.17; H, 9.21; N, 4.26. Found: C, 62.33; H, 9.40; N, 4.22.

Determination of log *P* Values of Labile Esters. For each of the labile esters, the $\log_{10}$ of the octanol−water partition coefficient (log *P*) was determined. The log *P* values of ester **2**−**7** were evaluated from their capacity factors (k') as determined by HPLC on a reverse-phase column (Kromasil 100 RP-C8; Higgins Analytical, Mountain View, CA), with a mobile phase consisting of methanol and 0.02 M sodium phosphate buffer (pH 6.0) in a volume ratio of 7:3 (*9, 10*). The measurements were performed using isocratic elution (1 mL/min) on a Waters HPLC equipped with a diode-array detector (model 600; Milford, MA); the absorbance at 222 nm was used to construct the chromatograms. The capacity factor is defined as $k' = (t_R - t_0)/t_0$, where t_R and t_0 are, respectively, the elution times of the compound of interest and the void marker (thiourea). To generate a log *P* vs log k' calibration line, we used nine compounds with known log *P* values (in parentheses): caffeine (−0.07), 2-butanone (0.29), cycloheximide (0.55), benzyl alcohol (1.10), hydrocortisone (1.53), acetophenone (1.58), nitrobenzene (1.85), anisole (2.11), and naphthalene (3.37) (*11, 12*). The calibration line (Supporting Information Figure S1) was used to convert the log k' values of esters **2**−**7** into the corresponding log *P* values. Two to four replicates of each measurement were made.

Kinetics of Nitroxide Reduction by Ascorbate. The background buffer used for all kinetic measurements was a 9:1 (v/v) mixture of Dulbecco's phosphate buffered saline (Ca^{2+}- and Mg^{2+}-free) and absolute ethanol (final pH 7.3). Diethylenetriamine-*N*,*N*,*N*′,*N*′,*N*″-pentaacetic acid (DTPA; 0.5 mM) was added to the background buffer to sequester trace heavy metal ions. Nitroxide esters **2**−**7** were each dissolved in absolute ethanol to make a 20 mM stock solution. A 200 mM stock solution of crystalline L-ascorbic acid (Sigma Ultra grade) was prepared in deionized water (18.3 MΩ·cm resistivity) that had been sparged with argon gas for 30 min; the solution was maintained at 0 °C under N_2 atmosphere. Each experimental sample contained 50 μM nitroxide in background buffer. At time zero, 2 mM ascorbate was added to the sample, which was immediately transferred into a quartz flat cell and placed in the EPR spectrometer for spectroscopic measurement (details below). The amplitude of the downfield peak in the nitroxide EPR spectrum was monitored over 20−25 min. In all cases, peak amplitude as a function of time was fitted well by a single-exponential decay characterized by an apparent first-order rate constant, k_{red} (see Figure S2 in Supporting Information for typical data set and nonlinear curve fit). All experiments were conducted at 23 °C. Duplicate measurements were performed for each nitroxide labile ester; the sequence of measurements was randomized.

Cellular Loading of Nitroxides. Jurkat lymphocytes were cultured and loaded with nitroxides as previously described (*5*, *6*). Briefly, a suspension of 1.8×10^7 cells, at a density of 2×10^7 mL^{-1}, was incubated for 70 min at room temperature in serum-free RPMI 1640 medium containing the indicated concentration of the appropriate nitroxide labile ester and 0.0015% (w/v) of the surfactant Pluronic F-127 (BASF Corp, Florham Park, NJ). After incubation, cells were washed 3 times in Hanks' Balanced Salt Solution (HBSS), and resuspended in 400 μL HBSS. To lyse cells, 120 μM digitonin was added to each cell suspension, which was then sonicated for 1 min in a bath sonicator (model G112SPIG, Laboratory Supplies Company, Inc., Hicksville, NY). The lysate was assayed for nitroxide content by EPR spectroscopy. Each loading experiment was repeated two to four times.

EPR Spectroscopy. EPR spectra were recorded on an X-band spectrometer (model E-109, Varian Inc., Palo Alto, CA) at the following settings: microwave power, 20 mW; microwave frequency, 9.55 GHz; field set, 3335 G; modulation frequency, 1 kHz; modulation amplitude, 0.5 G; field sweep, 80 at 26.7 G min^{-1}. Where the amplitude of only the center spectral line was required, the sweep width was 8 G. EWWIN software (Scientific Software Solutions, Northville, MI) was used for spectrometer control and data acquisition. The nitroxide signal was measured as the peak-to-trough amplitude of the center line of the three-line spectrum.

RESULTS AND DISCUSSION

To adjust the lipophilicity of EPR pro-imaging agents systematically, we synthesized a series of alkanoyloxymethyl esters of **1** in which the hydrophobicity and steric bulk of the alkanoyl moiety was varied (Figure 1). Compound **6** was synthesized through the procedure developed for **2** (*6*), with commercially available chloromethyl pivalate used instead of bromomethyl acetate as the alkylating agent to esterify nitroxide **1** (Scheme 2A). However, for compounds **3**, **4**, **5**, and **7**, it was simpler to prepare the chloromethyl ester **8**, which could undergo reaction with a series of inexpensive carboxylic acids to yield the corresponding labile esters (Scheme 2B).

Previously, we had shown that compound **2** is relatively resistant to bioreduction (*5*, *6*). The new compounds **3**−**7**, bearing different alkanoyloxymethyl ester functions but the identical nitroxide moiety as **2**, are expected to be similar to compound **2** in their resistance to reduction. We assessed the susceptibility of all seven compounds used in this study to reduction by 2 mM ascorbate. The apparent first-order rate constants for reduction (k_{red}) of compounds **2**−**7** are given in Table 1. The differences in the values are not statistically significant. When all measurements were pooled, the mean value for compounds **2**−**7** is $k_{red} = 7.7\ (\pm 0.7) \times 10^{-2}\ min^{-1}$ ($n = 12$).

Scheme 2. Synthesis of Nitroxide Labile Esters

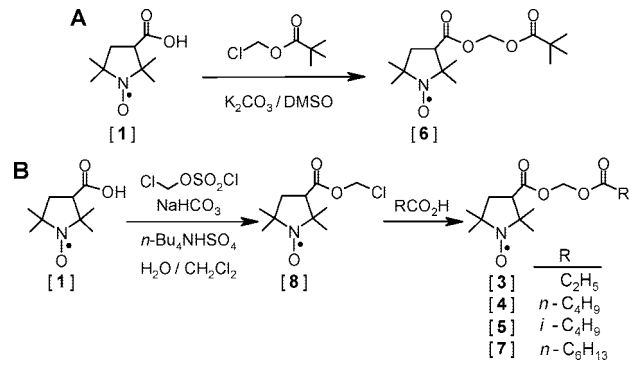

Table 1. Log *P* Values and Reduction Kinetics of Nitroxide Labile Esters 2−7

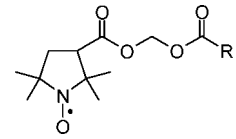

ester	R	log *P*	k_{red}[a] ($\times 10^{-2}$ min^{-1})
2	$-CH_3$	1.12	7.2
3	$-CH_2CH_3$	1.33	7.4
4	$-(CH_2)_3CH_3$	2.67	8.1
5	$-CH_2CH(CH_3)_2$	2.62	8.0
6	$-C(CH_3)_3$	2.60	8.0
7	$-(CH_2)_5CH_3$	3.54	7.6

[a] Apparent first-order rate constant for reduction by 2 mM ascorbate at pH 7.3, 23 °C. Each value is the average from two experiments.

To investigate the effectiveness of the various labile esters to deliver nitroxide **1** intracellularly, we incubated Jurkat lymphocytes with the esters over a range of concentrations and assayed the intracellular content of nitroxide **1**. We first compared the intracellular loading after incubation with esters **2**, **3**, **4**, and **7**—a family in which the length of the alkanoyl chain was systematically increased. The results are presented in Figure 2. It can be seen that, while increasing the alkanoyl chain length from 2 to 3 had a negligible effect on intracellular loading (compare results for esters **2** and **3**), increasing the chain length to 5 (ester **4**) resulted in a substantial enhancement of intracellular loading. A further increase of the chain length to 7 (ester **7**), however, brought no additional improvement in loading.

We next investigated the effect of branching in the alkanoyl chain in the labile ester on intracellular loading of nitroxide **1** by incubating the cells with the isomeric esters **4**, **5**, and **6**. The results in Figure 2 show that, while ester **4**, with an *n*-pentanoyl moiety, gave high intracellular levels of nitroxide **1**, esters **5** and **6**, with 3-methylbutanoyl (isovaleryl) and 2,2-dimethylpropanoyl (pivaloyl) moieties, respectively, gave very poor intracellular loading of nitroxide **1**. These findings indicate that increased branching in the alkanoyl chain drastically diminished the ability of the labile ester to deliver nitroxide **1** intracellularly.

Besides changing the steric bulk of the labile ester, increased branching in the alkanoyl chain is also expected to decrease the lipophilicity of the molecule. A commonly used measure

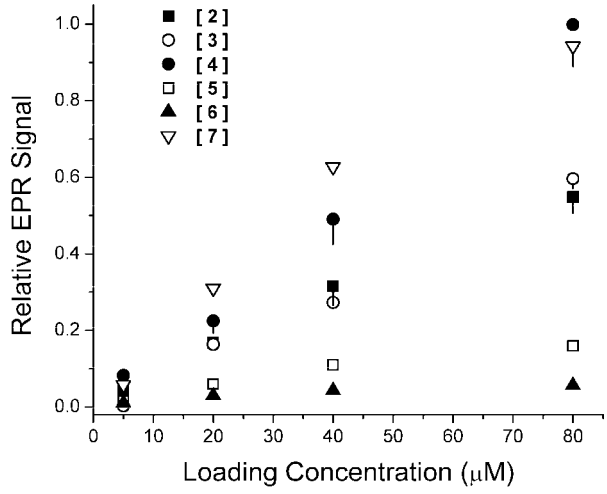

Figure 2. Intracellular loading of nitroxide **1** after Jurkat lymphocytes were incubated with various concentrations of the labile esters **2**−**7**. Error bars represent standard deviations; where not shown, the error bar is smaller than the symbol. For visual clarity, only down error bars are shown.

of lipophilicity is the $\log_{10}$ of the octanol−water partition coefficient, log *P*. The experimentally determined log *P* values for esters **2**−**7** (Table 1) show that lipophilicity does decrease with increased alkanoyl chain branching, but the effect is very slight. Thus, the isomeric esters **4**, **5**, and **6**, with primary, secondary, and tertiary alkanoyl chains, respectively, have log *P* values that decrease systematically but slightly, from 2.67 down to 2.60. Moreover, intracellular loading of the branched-chain esters **5** and **6** is much worse than that of straight-chain esters that are either less lipophilic (**2** and **3**) or more lipophilic (**7**). Therefore, the differences in lipophilicity cannot be invoked to explain differential intracellular loading. A reasonable inference is that intracellular esterases that hydrolyze alkanoyloxymethyl esters have a strong preference for straight over branched alkanoyl chains.

Having investigated the relationship between labile ester structure and the levels of intracellularly entrapped nitroxide **1**, we must investigate this relationship in vivo. Our cellular incubation model provided extremely promising data regarding the ability to load cells with nitroxides, but ultimate application of these compounds will depend on the ability of the lipophilic nitroxide esters to cross the blood−brain barrier. In anticipation of using the labile esters for EPR imaging of O_2 in living brain, studies are under way to determined the pharmacokinetics and pharmacodynamics of esters **3**, **4**, **5**, and **7**.

ACKNOWLEDGMENT

This work was supported in part by the National Institutes of Health through grants DA-023473 and EB-2034 (to G.M.R.), DA-19634 (to A.C.), and GM-56481 (to J.P.Y.K.).

Supporting Information Available: Additional figures. This material is available free of charge via the Internet at http://pubs.acs.org.

LITERATURE CITED

(1) Baudelet, C., and Gallez, B. (2002) How does blood oxygen level-dependent (BOLD) contrast correlate with oxygen partial pressure (pO_2) insider tumors. *Magn. Reson. Med. 48*, 980–986.

(2) Elas, M., Williams, B. B., Parasca, A., Mailer, C., Pelizzari, C. A., Lewis, M. A., River, J. N., Karczmar, C. S., Barth, E. D., and Halpern, H. J. (2003) Quantitative tumor oxymetric images from 4D electron paramagnetic resonance imaging (EPRI): Methodology and comparison with blood oxygen level-dependent (BOLD) MRI. *Magn. Reson. Med. 49*, 682–691.

(3) Matsumoto, K., Bernardo, M., Subramanian, S., Choyke, P., Mitchell, J. M., Krishna, M. C., and Lizak, M. J. (2006) MR assessment of changes of tumor in response to hyperbaric oxygen treatment. *Magn. Reson. Med. 56*, 240–246.

(4) Shen, J., Liu, S., Miyake, M., Liu, W., Pritchard, A., Kao, J. P. Y., Rosen, G. M., Tong, Y., and Liu, K. J. (2006) Use of 3-acetoxymethoxycarbonyl-2,2,5,5-tetramethyl-1-pyrrolidinyloxyl as an EPR oximetry probe: potential for *in vivo* measurement of tissue oxygenation in mouse brain. *Magn. Reson. Med. 55*, 1433–1440.

(5) Rosen, G. M., Burks, S. R., Kohr, M. J., and Kao, J. P. Y. (2005) Synthesis and biological testing of aminoxyls designed for long-term retention by living cells. *Org. Biomol. Chem. 3*, 645–648.

(6) Kao, J. P. Y., and Rosen, G. M. (2004) Esterase-assisted accumulation of 3-carboxy-2,2,5,5-tetramethyl-1-pyrrolidinloxyl into lymphocytes. *Org. Biomol. Chem. 2*, 99–102.

(7) Rozantsev, E. G. (1970) *Free Nitroxyl Radicals*, p 206, Plenum Press, New York.

(8) Harade, N., Hongu, M., Tanaka, T., Kawaguchi, T., Hashiyama, T., and Tsujihara, K. (1994) A simple preparation of chloromethyl esters of the blocked amino acids. *Synth. Commun. 24*, 767–772.

(9) Lambert, W. J. (1993) Modeling oil-water partitioning and membrane permeation using reverse-phase chromatography. *J. Chromatogr., Sect. A 656*, 469–484.

(10) Namjesnik-Dejanovic, K., and Cabaniss, S. E. (2004) Reverse-phase HPLC method for measuring polarity distributions of natural organic matter. *Environ. Sci. Technol. 38*, 1108–1114.

(11) Leo, A, Hansch, C., and Elkins, D. (1971) Partition coefficients and their uses. *Chem. Rev. 71*, 525–616.

(12) Singh, P., and Roberts, M. S. (1996) Local deep tissue penetration of compounds after transdermal application: Structure-tissue penetration relationships. *J. Pharmacol. Exp. Ther. 279*, 908–917.

BC8001562

Supporting Information for:

Optimization of labile esters for esterase–assisted accumulation of nitroxides into cells: A model for *in vivo* EPR imaging

Scott R. Burks,[†,‡,§] Jiahong Ni,[†] Sukumaran Muralidharan,[†] Andrew Coop,[#]

Joseph P.Y. Kao,[*,†,‡,§] and Gerald M. Rosen[*,†,§,#]

[†]Medical Biotechnology Center, University of Maryland Biotechnology Institute, Baltimore, MD, 21201

[‡]Department of Physiology, University of Maryland School of Medicine, Baltimore, MD, 21201

[§]Center for EPR Imaging In Vivo Physiology, University of Maryland, Baltimore, MD 21201

[#]Department of Pharmaceutical Sciences, University of Maryland School of Pharmacy, Baltimore, MD 21201

*Corresponding author. Address: 725 W. Lombard St. Baltimore, MD 21201. E-mail: kao@umbi.umd.edu; Tel: 410-706-4167. E-mail: grosen@umaryland.edu; Tel: 410-706-0514.

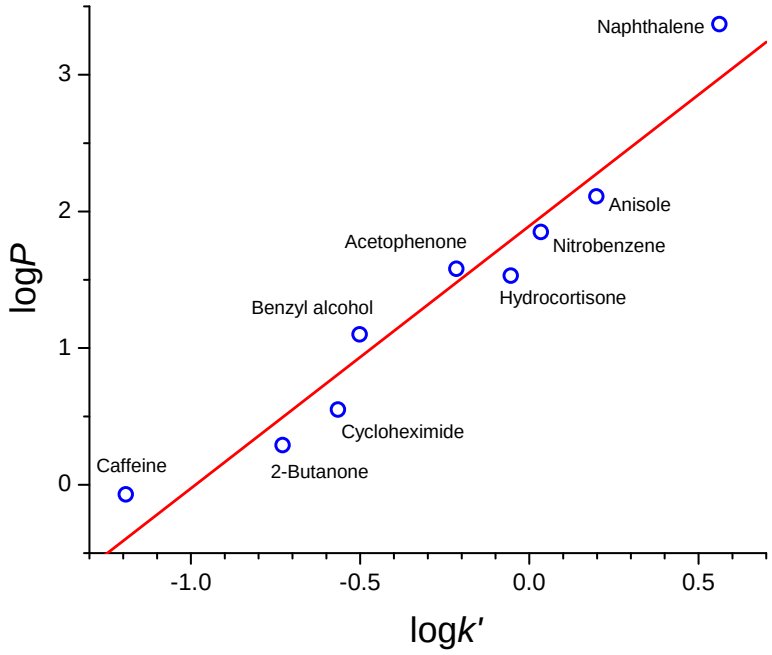

Figure S1. Standard calibration line of log*P* vs. log*k'*.

For each of nine standard compounds, the known log*P* value was plotted against the log*k'* value determined by the capacity factor method through HPLC on a C8 reverse-phase column (see Experimental Procedures for details). The red line is a linear least-squares fit to the data:

$$\log P = b + m \cdot \log k'$$

where $b = 1.89 \pm 0.10$ and $m = 1.92 \pm 0.18$.

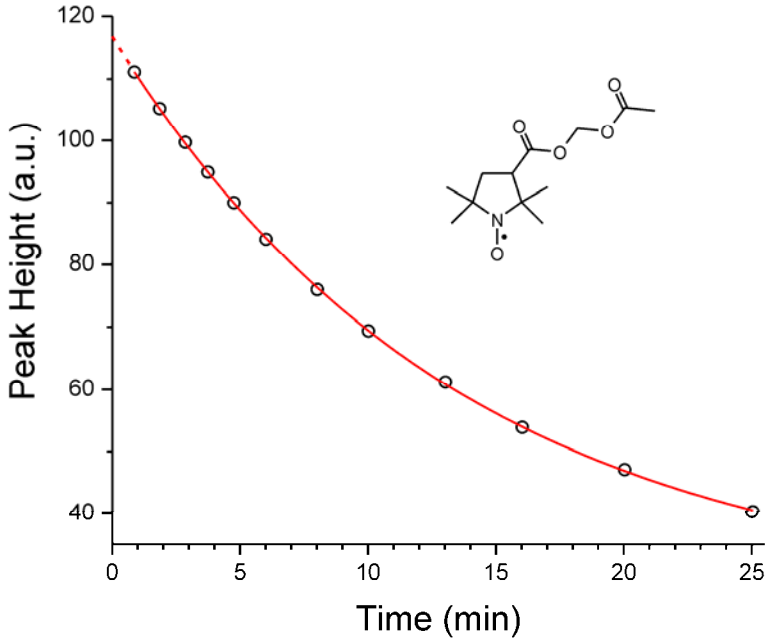

Figure S2. Kinetics of reduction of nitroxide labile ester [**2**] **by ascorbate.**

At time zero, 2 mM ascorbate was added to a solution of 50 μM nitroxide labile ester [**2**] and 0.5 mM DTPA in a 9:1 (v/v) mixture of Dulbecco's Phosphate Buffered Saline (Ca^{2+}- and Mg^{2+}-free) and absolute ethanol (final pH 7.3). The reaction mixture was transferred immediately to a flat quartz cell, and the amplitude of the downfield peak of the nitroxide spectrum was monitored over 25 min in an X-band EPR spectrometer (model E-109, Varian Associates, Palo Alto, CA). The amplitude of the downfield peak is plotted against time (circles). The data are well-fit by a single exponential decay (red curve) with an apparent first-order rate constant of $k_{red} = 7.4 \times 10^{-2}$ min^{-1}. Data from a replicate experiment performed ~1 hr later yielded an essentially identical result ($k_{app} = 7.1 \times 10^{-2}$ min^{-1}). All six compounds tested ([**2**] - [**7**]) showed similar kinetics of reduction by ascorbate—mean from all measurements: $k_{red} = 7.7 (\pm 0.7) \times 10^{-2}$ min^{-1} ($n = 12$).

Multifunctional Inorganic-Binding Beads Self-Assembled Inside Engineered Bacteria

Anika C. Jahns,[†] Richard G. Haverkamp,[‡] and Bernd H. A. Rehm*[,†]

Institute of Molecular Biosciences and Institute of Technology and Engineering, Massey University, Private Bag 11222, Palmerston North, New Zealand. Received May 16, 2008; Revised Manuscript Received July 23, 2008

Multifunctional shell−core nano/microbeads with a hydrophobic biopolymer core and a designed protein coat for selective binding of an inorganic substance and antibodies were self-assembled inside engineered bacteria. Hybrid genes were constructed to produce tailormade bead-coating proteins in the bacterium *Escherichia coli*. These fusion proteins contained a binding peptide for an inorganic material, the antibody binding ZZ domain, and a self-assembly promoting as well as biopolymer synthesizing enzyme. Production of these multidomain fusion proteins inside *E. coli* resulted in self-assembly of beads comprising a biopolyester core and displaying covalently bound binding sites for specific and selective binding of an inorganic substance and any antibody belonging to the immunoglobulin G class. Engineered beads were isolated and purified from the respective *E. coli* cells by standard cell disruption procedures. Bead morphology and the binding functionalities displayed at the bead surface were assessed by the enzyme-linked immunosorbent assay, transmission electron microscopy, elemental analysis, backscattering electron density, analytical density ultracentrifugation, and atomic force microscopy. These analyses showed that bacteria can be engineered to produce fusion proteins mediating self-assembly of spherical biopolymer beads with binding affinity to gold and/or silica and antibodies. Spherical structures of this type could conceivably serve as nano/microdevices for bioimaging in medical approaches where an antibody mediated targeted delivery of an inorganic contrast agent would be desired.

INTRODUCTION

Biological structures that specifically bind inorganics exert numerous potential biomedical applications. Therefore, the exploration of nature's structures for this purpose and the establishment of novel production methods is of great interest. In particular, beads (nano or microbeads) made of biological and inorganic materials are suitable for a variety of applications such as, e.g., diagnostics (*1, 2*), imaging (*3*), and drug delivery (*4*). In binding assays, it was demonstrated that nanobeads displaying an antibody at high density show a higher binding affinity than the antibody itself enhancing the sensitivity of a diagnostic assay (*5*). Molecular biomimetic approaches have been used to specifically coat biological nanostructures, such as, e.g., self-assembling virus beads, with various inorganics for applications in imaging, biosensing, laboratory methods, and electronics (*6, 7*). Genetically engineered proteins for inorganics (GEPI) have been obtained using combinatorial approaches including phage display or cell surface display in order to select peptides binding inorganics (*8*). Peptides were isolated specifically binding (noble) metals, semiconducting oxides, and other technological compounds (*7*−*11*). This ultimately enabled the use of biological structures with protein components as templates for the defined nanoscale deposition of inorganics as well as control of geometrical shapes and sizes of inorganic nanobeads. This was achieved by engineering of proteins contributing to these structures enabling display of GEPIs for binding of inorganics (*7*−*11*). This resembles the morphogenesis in hard tissues (such as bones, dental tissues, mollusk shells, spicules) which is controlled by inorganic-binding proteins.

In this study, microbial polymer inclusions (50−300 nm) were conceived as biological template structures (*12*−*14*). These spherical inclusions are self-assembled inside the bacterial cell mediated by a single protein, the polyester synthase (PhaC) (*15, 16*). The polymer inclusions serve as reserve materials and comprise a hydrophobic polyester core surrounded by at least the PhaC protein (*17*). This natural polyester is composed of (*R*)-3-hydroxy fatty acids. Interestingly, PhaC catalyzes the core polymer synthesis as well as is required for the self-assembly. Moreover, PhaC has been found to remain covalently attached to the polymer core (*18, 19*). Further structural proteins (e.g., PhaP) have been found to specifically hydrophobically interact with the polymer core, but are not required for self-assembly (*15, 20*−*22*). Protein engineering of the synthase or structural proteins demonstrated that various functional proteins can be displayed at the polymer inclusions surface and that these inclusions can be stably maintained outside the cell as beads (*18, 23*−*28*). Here, it was demonstrated that genetic fusions of GEPIs to PhaC or previously engineered PhaC enabled production of beads that bind inorganic and biological molecules simultaneously. In this study, the antibody binding domain of protein A from *Staphylococcus aureus* was used as an additional binding functionality, which ultimately enabled the production of spherical nano/microbeads that could specifically bind not only any specific antibody but also an inorganic as suitable contrast agent applicable for, e.g., bioimaging approaches (*29*) (Figure 1). Moreover, the use of engineered *E. coli* as a cell factory to produce functionalized beads in one step provides an efficient and economic production strategy.

EXPERIMENTAL PROCEDURES

Bacterial Strains, Plasmids, Oligonucleotides, and DNA Constructs. Bacterial strains, plasmids, and oligonucleotides used in this study are listed in Table 1. *E. coli* XL1-Blue was grown at 37 °C, BL21(DE3) at 25 °C. When required, ampicillin

* Corresponding author. E-mail: b.rehm@massey.ac.nz. Phone: +64 6 350 5515; ext. 7890. Fax: +64 6 350 5688.
[†] Institute of Molecular Biosciences.
[‡] Institute of Technology and Engineering.

10.1021/bc8001979 CCC: $40.75 © 2008 American Chemical Society
Published on Web 09/09/2008

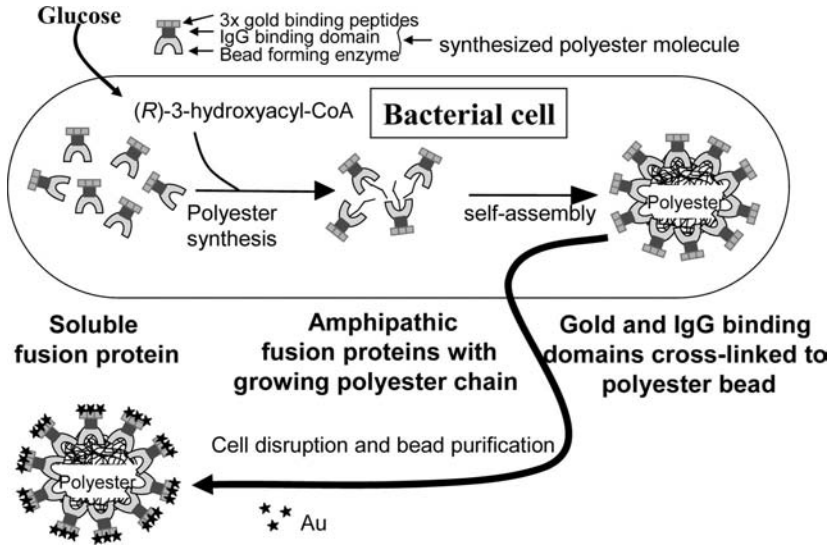

Figure 1. Schematic overview of polymer bead assembly.

75 μg/mL, tetracycline 12.5 μg/mL, or chloramphenicol 50 μg/mL were added. All chemicals were purchased from Sigma-Aldrich (St. Louis, MO).

General cloning procedures and isolation of DNA were performed as described elsewhere (*30*). DNA primers, deoxynucleoside triphosphate, T4 DNA ligase, and Taq polymerase were purchased from Invitrogen (CA, USA). DNA sequences of new plasmid constructs were confirmed by DNA sequencing according to the chain termination method using an automatic sequencer (Applied Biosystems, 3730 DNA Analyzer).

Gold-Binding Beads. To enable production of fusion proteins mediating production of polymer beads selectively binding gold, the GBP1 (*31*) encoding DNA sequence was inserted as a DNA fragment, composed of hybridized oligonucleotides GNI and GNII (Table 2), into the restriction enzyme sites *Xba*I/*Nde*I of plasmid pCWE. The resulting pCWE-GN-phaC contained the respective hybrid gene and was transformed into *E. coli* XL1-Blue harboring the plasmid pMCS69, which mediates synthesis of the polymer precursor required for bead production.A DNA sequence showing three repeats of the gold-binding peptide (*32*) was synthesized (DNA 2.0, Inc., CA, USA). The corresponding *Xba*I/*Sun*I fragment was inserted into plasmid pCWE, which was previously engineered to encode a pentaglycine linker and the ZZ domain of protein A both fused to the N terminus PhaC. The resulting plasmid pCWE-3xGN-G_5-ZZ-phaC was used to transform *E. coli* XL1Blue (pMCS69). To enable overproduction of the respective fusion protein, the corresponding hybrid gene was overexpressed under the control of the strong T7 promoter. Therefore, the hybrid genes were inserted into the *Xba*I/*Bam*HI site of vector pET-14b. The resulting plasmid pET-14b-3xGN-G_5-ZZ-phaC was used to transform *E. coli* BL21(DE3) harboring plasmid pMCS69.

Bead formation was assessed by analyzing the polyester constituting the bead core using gas chromatography−mass spectrometry as previously described (*16*). Moreover, beads formed inside the bacterial cell were stained with Nile red and observed using fluorescence microscopy as well as subjected to electron microscopy (*16*).

Silica-Binding Beads. To produce polymer beads with silica/antibody binding properties, the DNA sequence encoding the silica-binding peptide (*33*) encoding *Xba*I/*Nde*I DNA fragment, which was generated by hybridization of oligonucleotides SNI and SNII (Table 2), was ligated to the 5′ end of *phaC* in plasmid pCWE. Together with pMCS69, this construct led to bead formation in *E. coli* XL1Blue. To achieve overproduction of the respective fusion proteins at the bead surface and thereby enhance the binding density, hybrid genes encoding fusion proteins were expressed under control of the strong T7 promoter. Therefore, the 1838 bp *Xba*I/*Bam*HI fragment was inserted into the respective sites of plasmid pET-14b and then transformed into *E. coli* BL21(DE3) cells harboring the plasmid pMCS69. A hybrid gene similar to the hybrid gene encoding the extended gold-binding fusion protein was also constructed by using the oligonucleotides SN+I and SN+II (Table 2). This hybrid gene was inserted into plasmid pCWE which resulted in plasmid pCWE-SN-G_5-ZZ-phaC. The hybrid gene comprising the 2261 bp *Xba*I/*Bam*HI fragment was then subcloned into the respective sites of pET-14b to enable overexpression under T7 promoter control.

Multifunctional Beads. To synthesize polymer beads with gold, silica, and antibody binding capability, the SN-G_5-ZZ(−)phaC sequence was amplified by PCR using oligonucleotides 3′PhaC-*Blp*I and *Bam*HI-SN+ (Table 2). The PCR product was confirmed by DNA sequencing and ligated into *Bam*HI/*Blp*I site of plasmid pET-14b-3xGN-G_5-ZZ(−)phaC which resulted in plasmid pET-14b-3xGN-G_5-ZZ(−)phaC/SN-G_5-ZZ(−)phaC. This new plasmid was used to transform competent *E. coli* BL21(DE3) cells harboring pMCS69 and to mediate production of multifunctional beads.

Isolation of Polymer Beads. The polymer beads were isolated by harvesting respective cells using centrifugation for 20 min at 6000 × *g* and 4 °C. The sediment was washed and suspended in 3 volumes of 50 mM phosphate buffer (pH 7.5). Cells were passed through a French Press two times at 16 kpsi. The cell lysate (0.75 mL) was loaded onto a glycerol gradient (88% and 44% (v/v) glycerol in phosphate buffer). After ultracentrifugation for 2.5 h at 100 000 × *g* and 10 °C, beads could be isolated from a white layer above the 88% glycerol layer. The PHA beads were washed with 10 volumes phosphate buffer (50 mM, pH 7.5) and centrifuged at 100 000 × *g* for 60 min at 10 °C. The sediment containing the PHA beads was suspended in phosphate buffer and stored at 4 °C.

Gold-Binding Assay. The gold-binding was carried out at 20 °C in PKT buffer (10 mM KPO_4 (pH 7), 0.1 M KCl, 1% Triton X-100) with 250 μM $HAuCl_4$ and 200 μM sodium ascorbate according to Brown (*31*). For a 10 mL assay, a 1 mg/mL bead protein solution was used. The whole assay was incubated on a shaker until a pink color appeared, indicating the formation of colloidal gold. To let the gold bind to the peptides, the solution was further incubated. To wash the

Table 1. Bacterial Strains, Plasmids, and Oligonucleotides Used for the Generation of Hybrid Genes as Well as Engineered Bacteria in Order to Produce Designed Biopolymer Beads

E.coli strain, plasmid, or oligonucleotide	genotype	source or reference
	Strains	
XL1-Blue	recA1, endA1, gyrA96, thi-1, hsdR17 ($r-_k$, $m+_k$), supE44, relA1, -, lac[F′, proAB, lacI^q, lacZΔM15, Tn10(Tc^r)]	*47*
BL21(DE3)	F-, *ompT*, *hsdS*$_B$ (r_B- m_B-), *gal*, *dcm* (DE3)	Novagen
	Plasmids	
pBHR68	PHB biosynthesis operon from *Cupriavidus necator* in pBluescript SK−	*48*
pHAS	pET-14b containing *Nde*I/*Bam*HI-inserted phaC gene from *C. necator*	*49*
pET-14b	Ap^r, T7 promoter	Novagen
pET-14b-ZZ(−)phaC	pET-14b containing *Xba*I/*Bam*HI fragment comprising gene *ZZ-phaC*	*28*
pCWE	pBluescript SK- derivative containing the PHA synthase gene from *C. necator*	*16*
pCWE-ZZ(−)phaC	pCWE derivative containing the ZZ domain-encoding *Nde*I fragment lacking the signal sequence-encoding region	*28*
pMCS69	pBBR1MCS derivative containing genes *pha*A and *pha*B of *C. necator* colinear to *lac* promoter	*50*
pCWE-GNphaC	pCWE derivative containing a *Xba*I/*Nde*I fusion of GN to 5′ end of *phaC*	this study
pCWE-SNphaC	pCWE derivative containing a *Xba*I/*Nde*I fusion of SN to 5′ end of *phaC*	this study
pCWE- 3xGN-G_5-ZZ(−)phaC	pCWE derivative containing *Xba*I/*Sun*I fusion of 3GN to 5′ end of ZZ(−)*phaC*	this study
pCWE-SN-G_5-ZZ(−)phaC	pCWE derivative containing *Xba*I/*Sun*I fusion of SN+ to 5′ end of ZZ(−)*phaC*	this study
pET-14b-3xGN-G_5-ZZ(−)phaC	pET-14b derivative containing 2345 bp *Xba*I/*Bam*HI fragment of pCWE-3xGN-G_5-ZZ(−)phaC	this study
pET-14b-SN-G_5-ZZ(−)phaC	pET-14b derivative containing 2261 bp *Xba*I/*Bam*HI fragment of pCWE-SN-G_5-ZZ(−)phaC	this study
pET-14b-SNphaC	pET-14b derivative containing 1838 bp *Xba*I/*Bam*HI fragment of pCWE-SNphaC	this study
pET-14b-3xGN-G_5-ZZ(−)phaC /SN-G_5-ZZ(−)phaC	pET-14b-3xGN-G5-ZZ(−)phaC derivative containing bp *Bam*HI/*Blp*I SN-G_5-ZZ(−)phaC PCR product	this study
	Oligonucleotides	
GNI	5′-P-CTA GAA ATA AGG AGA TAT AGC AAT GCA TGG CAA AAC CCA GGC GAC CAG CGG CAC CAT TCA GAG CCA −3′	this study
GNII	5′-P-TAT GGC TCT GAA TGG TGC CGC TGG TCG CCT GGG TTT TGC CAT GCA TTG CTA TAT CTC CTT ATT T −3′	this study
SNI	5′-P-CTA GAA ATA AGG AGA TAT AGC AAT GAG CCC GCA TCC GCA TCC GCG CCA TCA TCA TAC CCA −3′	this study
SNII	5′′-P-TAT GGG TAT GAT GAT GGC GCG GAT GCG GAT GCG GGC TCA TTG CTA TAT CTC CTT ATT T −3′	this study
SN+I	5′-P-CTA GAA ATA AGG AGA TAC TAG TAT GAG CCC GCA TCC GCA TCC GCG CCA TCA TCA TAC CCT CGA GC −3′	this study
SN+II	5′-P-GTA CGC TCG AGG GTA TGA TGA TGG CGC GGA TGC GGA TGC GGG CTC ATA CTA GTA TCT CCT TAT TT −3′	this study
3′PhaC-*Blp*I	5′- GCT CAG CGG TCA TGC CTT GGC TTT GAC GTA TCG CCC −3′	this study
*Bam*HI-SN+	5′- GGA TCC AAT AAG GAG ATA CTA GTA TGA GCC CGC ATC CGC AT −3′	this study

Table 2. Identified Peptide Fragments of Proteins Analyzed by MALDI-TOF/MS

protein	identified peptide fragments
SN-G_5-ZZ-PhaC	F34-R56, E37-R56, V175-R190, I217-R228, F269-R279, F300-R323 L324-R334, I349-R361, N362−K388, Y404-R417, H418-R432, N433-R453 G541-K567, L551-K567, E633-K652
3xGN-G_5-ZZ-PhaC	T5-K32 or F120-R142 or F62-R84, E65-R84 or E123-R142 N85−K106 or N143−K164, V174-R181, V203-R218, Q219-K244, I245-R256 Y257−K272, D260-K272, D260-R282, R283-R290, F284-R290, T291-R307 F297-R307, A308-K321, I326-R351, F328-R351, L352-R362, N367-R374 G375-R389, I377-R389, N390−K416, Y432-R445, H446-R460, N461-R481 I488-L517, Q553-A568, L569-N595, Y625−N633, P638−H660, I661−F680 G683-R700

unbound gold out of the sample, the assay was centrifuged at 4000 × *g* for 15 min. The resulting sediment was suspended in 1 mL PKT buffer and loaded on a sucrose gradient (2.25 M − 0 M, 0.25 M increments, sucrose in PKT buffer). This gradient was undergoing ultracentrifugation for approximately 16 h at 100 000 × *g*. The resulting layer at 2 or 2.25 M sucrose, consisting of beads and gold, was washed with PKT buffer and centrifuged in an ultracentrifuge for 1 h at 100 000 × *g*. The sediment was used for TEM analysis and AFM measurements.

Silica-Binding Assays. The silica-binding assay was performed at room temperature according to Dickerson et al. (*34*). 1 mg/mL bead protein was dissolved in 50 mM potassium phosphate buffer, pH 7.5. The silica solution was freshly prepared by dissolving tetramethyl orthosilicate (TMOS, Sigma-Aldrich, St. Louis, MO) in 1 mM HCl to a final concentration of 1 M. The silica solution was then added to the protein solution so that the final concentration of TMOS in the silica-binding assay was 0.1 M. This mixture was then incubated on a shaker for 10 min and centrifuged for 5 min at 13 000 rpm. The sediment was washed three times with 50 mM potassium

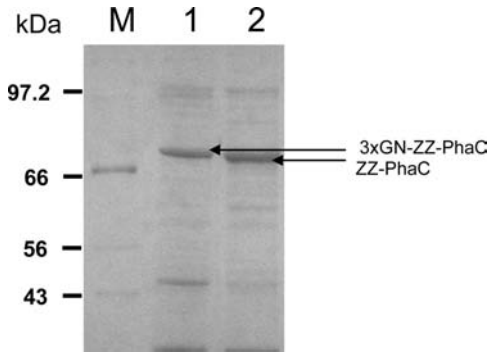

Figure 2. Protein profile of polymer beads displaying gold binding peptides. M, molecular mass standard (New England Biolabs, United Kingdom); Lane 1, polymer beads from *E. coli* BL21(DE3) (pET-14b-3xGN-G_5-ZZ(−)phaC); lane 2, polymer beads from *E. coli* BL21(DE3) (pET-14b-ZZ(−)phaC).

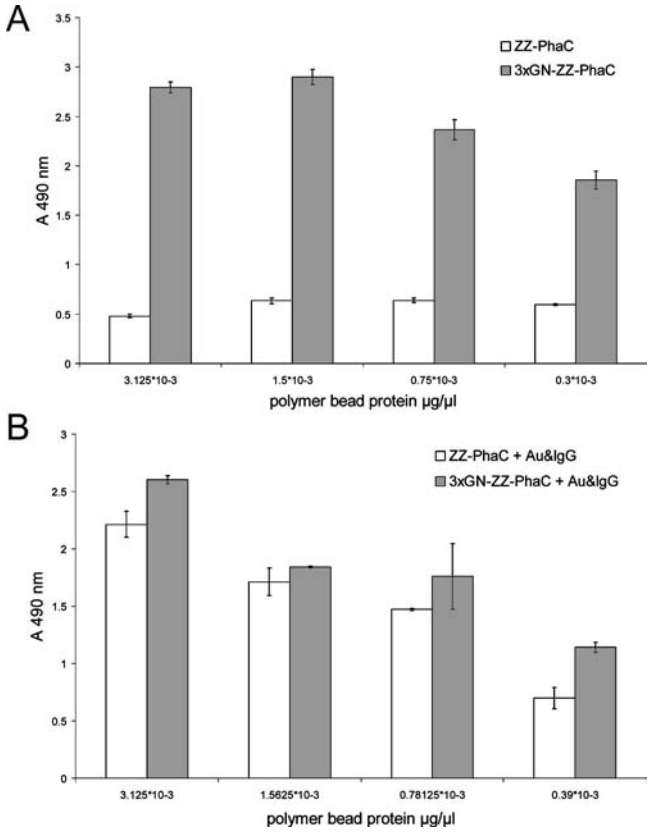

Figure 3. (A) Gold binding of various polymer beads assessed by ELISA. Polymer beads were isolated from *E. coli* BL21(DE3) harboring pET-14b-3xGN-G_5-ZZ(−)phaC (black columns) or pET-14b-ZZ(−)phaC (white columns). Streptavidin−HRP conjugate was used to detect bound 10 nm biotin−gold. Measurements were conducted in triplicates, the standard deviation is indicated. (B) Impact of gold binding on IgG binding of various polymer beads assessed by ELISA. Polymer beads were isolated from *E. coli* BL21(DE3) harboring pET-14b-3xGN-G_5-ZZ(−)phaC and incubated with gold followed by an incubation with human IgG (3xGN-ZZ-PhaC + Au&IgG, black columns). As controls, beads isolated from *E. coli* BL21(DE3) harboring pET-14b-ZZ(−)phaC were used and treated in the same way (gold incubation followed by human IgG incubation as ZZ-PhaC + Au&IgG, white columns). Goat polyclonal antihuman IgG-horseradish peroxidase conjugate was used for detection of bound human IgG. All measurements were conducted in triplicate; standard deviations are indicated.

phosphate buffer, pH 7.5, to remove unbound silica. To investigate the bead density changes due to silica binding, the washed sediments were suspended in 50 mM potassium phosphate buffer, pH 7.5, and separated using a sucrose gradient

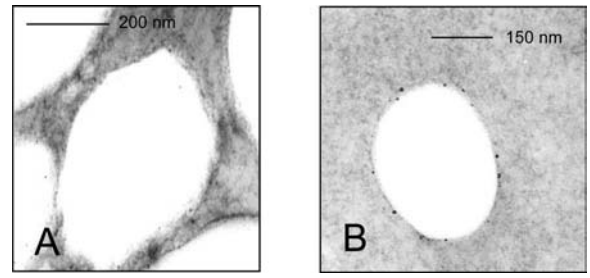

Figure 4. TEM images of polymer beads after incubation with colloidal gold. (A) Polymer beads displaying ZZ(−)phaC protein at the surface. (B) Polymer beads coated with the engineered protein 3xGN-G_5-ZZ(−)phaC mediating display of the gold-binding peptide.The pictures show slices through polymer beads embedded in BSA.

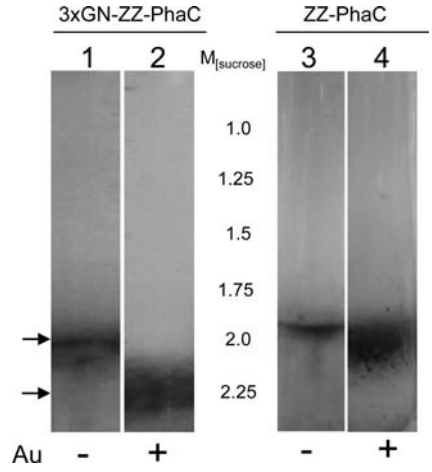

Figure 5. Gold binding to polymer beads demonstrated by density-dependent migration in a sucrose gradient using ultracentrifugation. Arrows indicate where the beads accumulated in the sucrose gradient after ultracentrifugation after incubation with 250 μM colloidal gold (+) and without (−). Lanes 1,2, polymer beads from *E. coli* BL21(DE3) (pET-14b-3xGN-G_5-ZZ(−)phaC); lanes 3,4, polymer beads from *E. coli* BL21(DE3) (pET-14b-ZZ(−)phaC.

(0−2.25 M sucrose in 0.25 M increments, sucrose in 50 mM potassium phosphate buffer, pH 7.5). These gradients underwent ultracentrifugation at 100 000 × *g* for 16 h at 10 °C. The resulting layers or sediments were washed in 50 mM potassium phosphate buffer, pH 7.5, and used for further investigations. In another silica binding assay, 0.5 mg/mL bead protein suspension was mixed with 0.003 g/mL SiO_2 (silica beads with a size range 1−5 μm) in potassium phosphate buffer and incubated on a shaker at room temperature for 4 h. The mixture was separated by sucrose gradient ultracentrifugation. The protein concentration of resulting layers and sediments was determined by Bradford (*35*). To qualitatively assess the binding of the engineered polymer beads to silica beads, fluorescence microscopy was used. For this purpose, the polymer beads were selectively stained with the hydrophobic fluorescent dye Nile red.

ELISA. For the enzyme-linked immunosorbent assay (ELISA), the wells of microtiter plates were coated with 100 μL of a polymer bead suspension (normalized to protein concentration, in a range from 0.05 μg/μL to 0.4 × 10^{-3} μg/μL) and incubated overnight at 4 °C. After being blocked with 3% (w/v) bovine serum albumin for 2 h, each well was incubated with 10 nm gold−biotin (Nanocs Inc., New York, USA) for 2 h followed by 1 h incubation with streptavidin−horseradish peroxidase conjugate (streptavidin-HRP; Sigma-Aldrich, St. Louis, MO). After each step, the wells were washed several times with phosphate-buffered saline containing 0.05% Tween 20. As substrate, 100 μL of an *o*-phenylenediamine solution (Abbott

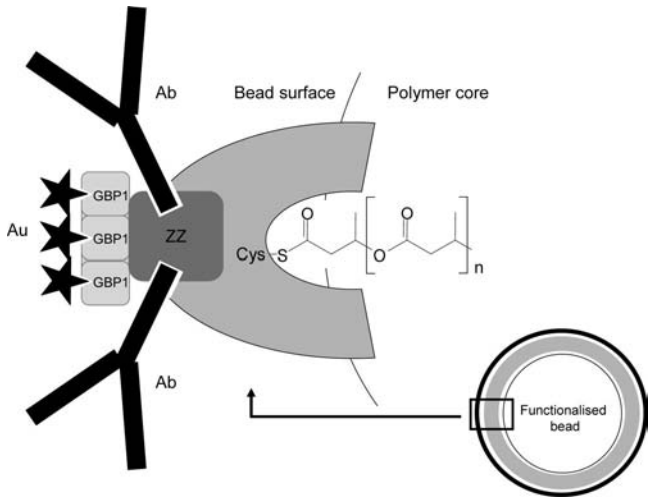

Figure 6. Scheme of the surface of a bifunctional gold/antibody binding polymer bead.

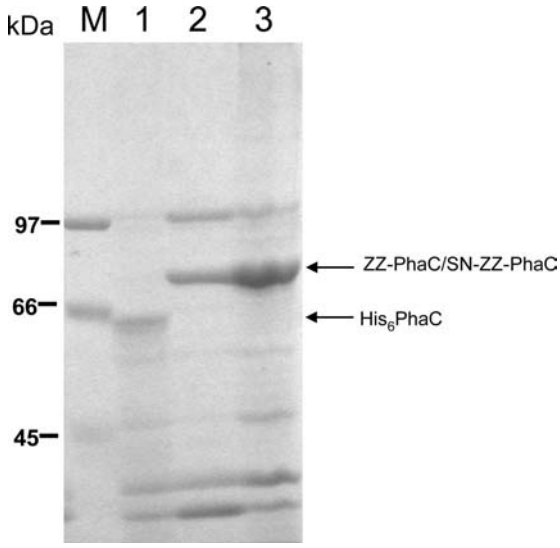

Figure 7. Protein profile of polymer beads displaying silica binding peptides. M, molecular mass standard (Amersham Biosciences, USA); lane 1, polymer beads from *E. coli* BL21(DE3) (pHAS); lane 2, polymer beads from *E. coli* BL21(DE3) (pET-14b-ZZ(−)phaC); lane 3, polymer beads from *E. coli* BL21(DE3) (pET-14b-SN-G_5-ZZ(−)phaC).

Diagnostics, IL, USA) was added to each well, and after 15 min, the reaction was stopped by adding 100 μL of 1 N H_2SO_4. The amount of substrate conversion was measured at a wavelength of 490 nm using a microtiter plate reader.

Protein Analysis. Bead protein profiles were routinely analyzed by sodium dodecyl sulfate (SDS)−polyacrylamide gel electrophoresis (PAGE) as described elsewhere (*36*). The gels were stained with Coomassie brilliant blue G250.

In order to identify proteins linked to the polymer beads, the bead proteins were separated by SDS-PAGE and protein bands of interest were cut off the gel. Proteins were subjected to MALDI-TOF mass spectrometry. Identification of tryptic peptides was performed by collision-induced dissociation tandem mass spectrometry and enabled identification of fusion proteins.

To identify N-terminally fused GEPIs, fusion proteins were subjected to N terminal sequencing using Edman degradation.

Microscopic Analysis. Atomic force microscopy imaging was performed on an Asylum Research MFP-3D instrument (Asylum Research, Santa Barbara, CA) in ac mode. All images were recorded in potassium phosphate buffer solution at a concentration of beads corresponding to 1−10 μg protein/mL.

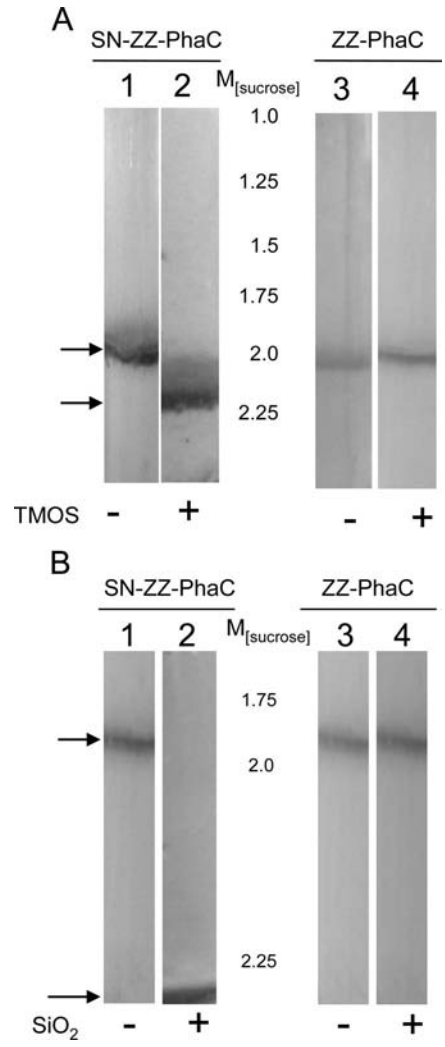

Figure 8. Silica binding to polymer beads demonstrated by density-dependent migration in a sucrose gradient using ultracentrifugation. (A) Images of tubes used for density assessment. Arrows indicate where the beads accumulated in the sucrose gradient after (+) and without (−) TMOS incubation. Lanes 1,2, polymer beads from *E. coli* BL21(DE3) (pET-14b-SN-G_5-ZZ(−)phaC); lanes 3,4, polymer beads from *E. coli* BL21(DE3) (pET-14b-ZZ(−)phaC). (B) Images of tubes used for density assessment. Arrows indicate the areas where the main part of the beads accumulated after SiO_2 binding (+) and without (−). Lanes 1,2, polymer beads from *E. coli* BL21(DE3) (pET-14b-SN-G_5-ZZ(−)phaC); lanes 3,4, polymer beads from *E. coli* BL21(DE3) (pET-14b-ZZ(−)phaC).

Higher bead concentrations were not used, as they resulted in scattering of the laser, which obscured the signal reflected from the cantilever and inhibited AFM operation. Approximately 100 μL of bead suspension was placed on a gold-coated mica substrate shortly before imaging. AFM cantilevers were either silicon Ultrasharp NSG11 (NT-MDT Co, Moscow, Russia) with force constants in the range 5−25 N/m and a tip radius around 10 nm, or silicon nitride TR400PSA (Olympus Corporation, Japan) with a force constant around 0.08 N/m and a tip radius <20 nm. Images of 512 × 512 points were collected at line scan frequencies of 1−8 Hz.

For transmission electron microscopy (TEM) analysis, cells or beads were prepared as described previously (*26*). Sections were stained and assessed using a Philips CM10 TEM. To visualize the gold binding, the beads were incubated with colloidal gold as described above in the gold-binding assay. Beads with bound colloidal gold or control beads not binding colloidal gold were then subjected to TEM sample preparation.

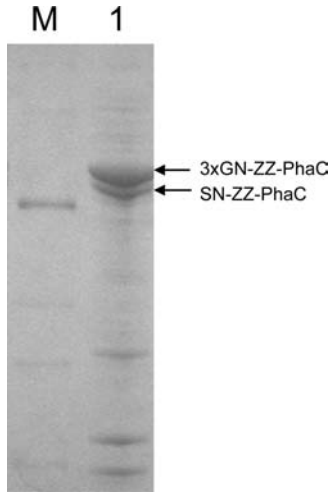

Figure 9. Protein profile of polymer beads displaying both binding activities (gold and silica). Lane M, molecular mass standard (New England Biolabs, U.K.); lane 1, polymer beads from *E. coli* BL21 (DE3) (pET-14b-3xGN-G_5-ZZ(−)phaC/SN-G_5-ZZ(−)phaC).

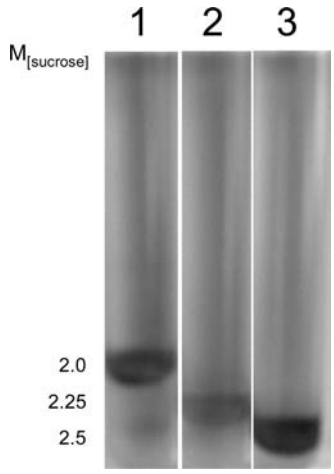

Figure 10. Different polymer beads were incubated with gold and silica and purified via ultracentrifugation of a sucrose gradient. Lane 1, pET-14b-ZZ(−)phaC; lane 2, pET-14b-3xGN-G_5-ZZ(−)phaC; lane 3, pET-14b-3xGN-G_5-ZZ(−)phaC/SN-G5-ZZ(−)phaC.

For elemental analysis, freeze-dried bead samples were mounted, using double-sided tape, on an aluminum specimen stub and then carbon-coated for EDS (energy dispersive spectrometry). Analysis was done using EDAX EDS system (EDAX, Mahwah, USA) in a FEI Quanta 200 SEM (scanning electron microscope; FEI, Eindhoven, The Netherlands). For imaging the gold in the samples, the BSED (back-scattered electron detection) mode was used.

RESULTS

Design and Production of Bifunctional Gold/Antibody Binding Beads. The capability of bacteria to produce intracellular granules with a hydrophobic biopolymer core and proteins attached to its surface from various cheap carbon and energy sources, such as, e.g., glucose, was utilized in this study to produced tailormade nano/microbeads suitable for molecular biomimetics.

The bead-forming and coating protein PhaC was engineered to enable simultaneous bead surface display of the gold-binding peptide GBP1 (*31*) and the antibody (IgG) binding ZZ domain (*37*). This strategy harnesses nature's capability to covalently cross-link the PhaC protein to polymer inclusions, which can be isolated and maintained as spherical beads with defined surface binding functionality (*26*). In order to produce the various multifunctional fusion proteins in the bacterium *E. coli* that mediate production of gold-binding polymer beads, the respective hybrid genes were constructed and inserted into an overexpression vector under control of the strong T7 promoter. In general, bead formation was monitored by polyester accumulation analysis, fluorescence microscopy of Nile red stained cells, and TEM. A fusion protein with only one gold-binding peptide did not mediate production of beads showing gold-binding affinity (data not shown). However, the use of three gold-binding peptide repeats, a pentaglycine spacer region followed by the IgG-binding domain fused to PhaC, mediated formation of beads with specific gold and antibody binding properties. This fusion protein 3xGN-G_5-ZZ-PhaC at the bead surface was demonstrated by SDS-PAGE and confirmed by MALDI-TOF/MS and N-terminal sequencing (Figure 2, Table 2). The SDS-PAGE analysis also showed an additional but less abundant 97 kDa protein, which was identified as copurified ATPase (Accession No. P0ABB9*)* derived from the production host *E. coli*.

To quantitatively assess the gold-binding activity of these novel polymer beads, an enzyme-linked immunosorbent assay was established employing the binding of biotinylated gold particles. Biotinylated gold particles bound to the beads were detected using streptavidin−HRP conjugate. The absorbance at 490 nm was increased at least 10-fold using the gold-binding peptide displaying beads when compared to the control beads not displaying the peptide (Figure 3A). Furthermore, elemental analysis and back-scattered electron density analysis was applied to confirm the presence of gold bound to the engineered beads (data not shown). The bead shape and size distribution was assessed by atomic force microscopy (data not shown).

The triple gold-binding peptide-ZZ-PhaC fusion protein additionally showed IgG binding activity due to a functional ZZ domain between the gold-binding peptides and PhaC. This activity was assessed by ELISA as previously described (*28*) (Figure 3B). The gold binding was visualized by transmission electron microscopy (TEM) (Figure 4). To further study gold binding and its impact on bead density, sucrose density gradients using ultracentrifugation were applied. The incubated samples as well as control samples were analyzed by sucrose gradient ultracentrifugation. Samples that were not incubated with colloidal gold formed a layer located at a density corresponding to <2 M sucrose ($d = 1.33$ g/mL). Control beads, PhaC(−)ZZ beads only displaying the IgG binding domain, when incubated with gold did not show a shift in density. In contrast, beads displaying the gold-binding peptides migrated further in the density gradient and formed a layer corresponding to a density of <2.25 M sucrose ($d = 1.4$ g/mL) when incubated with gold (Figure 5). Overall, these data suggested that the engineered beads displayed both binding functionalities (Figure 6).

Design and Production of Bifunctional Silica/Antibody Binding Beads. As described above for the design of the gold/antibody-binding peptide displaying beads, hybrid genes were constructed to enable production of multifunctional fusion proteins mediating formation of silica/antibody-binding polymer beads. Hybrid genes were overexpressed in *E. coli* and the resulting beads were isolated and characterized (Figure 7). The fusion protein SN-G_5-ZZ-PhaC was confirmed by MALDI-TOF/MS and N terminal sequencing (Table 2). The SDS-PAGE analysis also showed an additional but less abundant 97 kDa protein, which was identified as copurified ATPase (accession no. P0ABB9*)* derived from the production host *E. coli*.

The ability of the respective beads displaying silica-binding peptides to bind silica was shown using two different methods assessing either binding of silica to the bead surface or binding

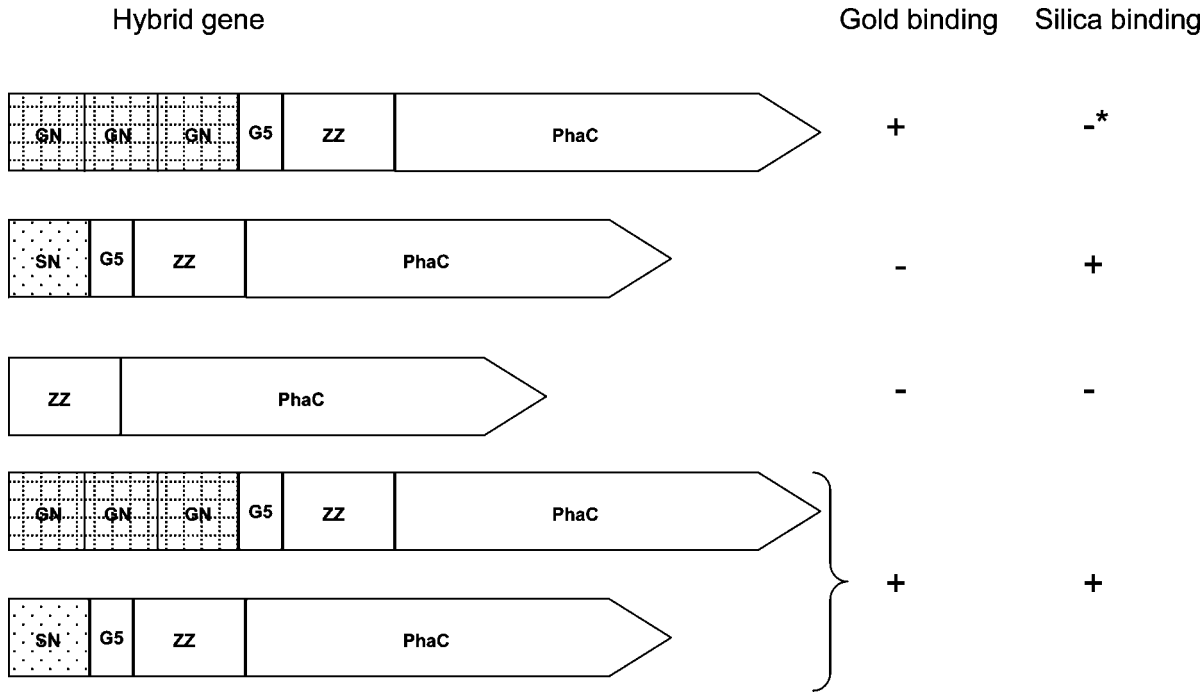

Figure 11. Schematic overview of hybrid genes used in this study. The bracket combining the last two constructs illustrates that both genes are located on the same plasmid. Gold binding ability was assessed as described above, and the silica binding ability was assessed using TMOS precipitation as described above. Binding is indicated by +, nonbinding by -; -* indicates a slightly increased unspecific silica binding compared to the control.

of the engineered polymer beads to commercially available silica beads. Beads displaying silica-binding peptides and control beads were incubated with TMOS dissolved in HCl and then separated by sucrose density ultracentrifugation as described in the Experimental Procedures. Different migration behavior of the engineered and control beads was observed representing a change in bead density (Figure 8A). PhaC(−)ZZ beads formed a layer at the 2 M sucrose (d = 1.33 g/mL) independent of treatment with TMOS. The respective beads self-assembled using fusion protein SN-G_5-ZZ-PhaC showed a density greater than the control beads and assembled at 2.25 M sucrose (d = 1.4 g/mL) after treatment with TMOS. These findings were additionally confirmed by elemental analysis showing silica only present in the engineered bead samples (data not shown). The direct fusion of the silica-binding peptide to the N terminus of PhaC resulting in SN-PhaC did not result in an increased density. These beads always behaved like the control beads without binding peptide.

Commercially available silica beads (silicon dioxide, 1−5 μm; Sigma-Aldrich, St. Louis, MO) were used as a second method to qualitatively assess silica binding by the engineered beads. Fusion and control beads were incubated with silica beads and separated using sucrose density ultracentrifugation as described in the Experimental Procedures. Protein determination by Bradford (*35*) was used to quantify binding. The respective control beads PhaC(−)ZZ showed about 85% of the protein content at a density corresponding to the polymer beads not bound to the commercial silica beads, and about 15% was found at much greater density in the sediment colocalizing with the commercial silica beads. In contrast, about 70% of beads displaying the silica-binding peptide employing fusion protein SN-G_5-ZZ-PhaC colocalized with the commercial silica beads when separated in sucrose density ultracentrifugation (Figure 8B).

Design and Production of Multifunctional Gold/Silica/Antibody Binding Beads. As described for the design of the bifunctional beads, hybrid genes mediating production of multifunctional gold/silica/antibody-binding polymer beads were constructed and overexpressed in *E. coli*. Two different hybrid genes each encoding a fusion protein comprising bead forming and inorganic binding domain were coexpressed to mediate production of multifunctional beads (Figure 9). The fusion proteins were confirmed by MALDI-TOF/MS (data not shown).

The gold and IgG binding ability of the respective beads was confirmed using ELISA as described above (data not shown). The silica-binding ability of the respective engineered beads was confirmed as described above (data not shown). To assess the multifunctionality, the respective engineered beads were incubated subsequently with colloidal gold and TMOS, and vice versa. After each incubation step, the samples were purified via sucrose density ultracentrifugation as described in the Experimental Procedures. As controls, the respective bifunctional polymer beads were incubated the same way as beads displaying the ZZ domain only. After incubation with colloidal gold followed by TMOS incubation, PhaC(−)ZZ beads accumulated in an area corresponding to 2 M sucrose (d = 1.33 g/mL), whereas bifunctional gold/antibody binding beads formed a layer located at a density of 2.25 M sucrose (d = 1.4 g/mL). Multifunctional gold/silica/antibody binding beads treated the same way migrated even further and formed a layer corresponding to a density of 2.5 M sucrose (d = 1.45 g/mL; Figure 10).

DISCUSSION

In this study, it was shown that microorganisms can be genetically modified to produce polymer inclusions that perform as beads displaying binding sites for antibodies and various inorganics at the same time. Thus, the bioengineering of polymer inclusions provides a valid molecular tool to generate novel hybrid materials that combine biological and inorganic agents suitable for numerous potential biomedical applications (*2*−*5*). Different hybrid genes were constructed (Figure 11) and successfully overexpressed, and the engineered protein functions could be displayed at the respective bead surfaces (Figures 2, 7, and 9). The gold/antibody binding polymer beads displaying the triple gold-binding peptide GBP1 (*38, 39*) showed strong gold binding in ELISA, which was established as a tool to quantitatively assess the gold binding. Control beads that did

not display this special binding peptide showed no significant gold binding (Figure 3A). These findings were confirmed by density-based migration behavior of the different beads in a sucrose gradient. Only beads displaying the gold-binding peptide showed an increased density after incubation with colloidal gold. TEM assessment of the polymer beads indicated specific gold binding to respectively engineered beads (Figure 4). However, the density of bound colloidal gold was rather low, which could be due to the isolation procedure applied to beads after binding the colloidal gold as well as the TEM sample preparation method. Additionally, no interference of both displayed binding domains—gold-binding and IgG-binding—was found. Moreover, it could be demonstrated that polymer beads engineered to bind gold and antibodies bind as much IgG as polymer beads displaying only the antibody binding domain (Figure 3B).

To test the possibility that the polymer beads in general can be designed to bind any inorganic, the protein bead surface was designed to bind silica. The binding of silica, obtained as precipitate from an aqueous TMOS solution, increased the density of the respective engineered beads, whereas the control beads without engineered binding sites showed no increased density (Figure 8A,B). Further confirmation of the successful functional displaying of the silica-binding peptide was obtained by assessing the binding of engineered SN-G_5-ZZ-PhaC and PhaC(−)ZZ control beads to commercial silica particles. Control beads showed only a minor background reaction compared to the binding ability of the engineered beads (Figure 8 C,D). A direct fusion of the silica-binding peptide to the N terminus of PhaC did not result in functional silica-binding polymer beads. Therefore, the exposure of the binding peptide—gained by employing the IgG binding ZZ domain as spacer—seems to be required for functionality. Elemental analysis using energy dispersive spectrometry proved the existence of silica in samples that were expected to precipitate silica out of TMOS, e.g., silica-binding peptide displaying beads. Silica could not be detected in control samples treated the same way. Due to the displayed ZZ domain, the engineered beads were additionally able to bind IgG as well as the control beads only displaying the ZZ domain. In contrast to the gold binding, it was not possible to obtain clear evidence that IgG binding and silica binding do not interfere with each other. This is due to the lack of an ELISA protocol for silica binding to the beads.

The multifunctional beads designed in this study were not only able to bind IgG antibodies plus gold and/or silica, but were also able to specifically bind all three compounds. However, it was shown that a deposition of silica at the bead surface impaired binding of gold, whereas beads with gold attached to their surface showed no weaker silica deposition as in the absence of gold. These data suggested that the silica deposition could block the binding sites for gold at the bead surface. Additionally, multifunctional beads incubated with gold and silica showed a higher density in sucrose gradients than observed for bifunctional beads. This indicates a possible binding of the silica to the already bound gold particles. Overall, this study clearly demonstrated that bacterial polymeric inclusions can be engineered as biomimetic tools to specifically and simultaneously bind biological and inorganic compounds, which could enable applications of these beads in diagnostic medicine as well as biotechnology. Numerous particles composed of various materials such as organic polymers, semiconductors, lipids, carbon or silica material have been produced and proposed for various biomedical applications (*40*−*46*). In contrast to the one-step manufacturing process described in this study for the production of new polymer beads, all other particles requiring functionalization were obtained by a process comprising at least two steps such as, e.g., bead production and chemical cross-linking of a functionality.

This biomimetic approach offers a tool to produce beads with covalently cross-linked functionalities in one step. These shell−core biobeads with specific binding properties could, for example, be applicable in medical bioimaging procedures in which antibody-based targeting of contrast agents is of special interest. In a previous study, it was demonstrated that a scFv immobilized at the surface of these beads showed a 75-fold increase in binding affinity when compared with the respective soluble scFv (*26*). Thus, the engineered beads could provide a very sensitive diagnostic tool. Moreover, the module like composition of these small biobeads offers versatile targeting of different tissues by simply incubating the beads with the relevant targeting antibody. Due to the displayed antibody binding functionality, an antibody of choice or even a combination of antibodies could be easily combined with bound gold to generate a contrast agent for bioimaging applications.

ACKNOWLEDGMENT

This work was supported by the New Zealand Foundation for Research Science and Technology and the Massey University Research fund. Ms. Anika Jahns received a Technology for Industry doctoral fellowship. This research has been facilitated by access to the Australian Proteome Analysis Facility established under the Australian Government's Major National Research Facilities program.

LITERATURE CITED

(1) Addinall, S. G., Bi, E., and Lutkenhaus, J. (1996) FtsZ ring formation in fts mutants. *J. Bacteriol. 178*, 3877–84.
(2) Karhanek, M., Kemp, J. T., Pourmand, N., Davis, R. W., and Webb, C. D. (2005) Single DNA molecule detection using nanopipettes and nanoparticles. *Nano Lett. 5*, 403–7.
(3) Jiang, W., Papa, E., Fischer, H., Mardyani, S., and Chan, W. C. (2004) Semiconductor quantum dots as contrast agents for whole animal imaging. *Trends Biotechnol. 22*, 607–9.
(4) Panyam, J., and Labhasetwar, V. (2003) Biodegradable nanoparticles for drug and gene delivery to cells and tissue. *Adv. Drug Delivery Rev. 55*, 329–47.
(5) Soukka, T., Harma, H., Paukkunen, J., and Lovgren, T. (2001) Utilization of kinetically enhanced monovalent binding affinity by immunoassays based on multivalent nanoparticle-antibody bioconjugates. *Anal. Chem. 73*, 2254–60.
(6) Mao, C., Solis, D. J., Reiss, B. D., Kottmann, S. T., Sweeney, R. Y., Hayhurst, A., Georgiou, G., Iverson, B., and Belcher, A. M. (2004) Virus-based toolkit for the directed synthesis of magnetic and semiconducting nanowires. *Science 303*, 213–7.
(7) Tamerler, C., and Sarikaya, M. (2007) Molecular biomimetics: utilizing nature's molecular ways in practical engineering. *Acta Biomater. 3*, 289–99.
(8) Sarikaya, M., Tamerler, C., Jen, A. K., Schulten, K., and Baneyx, F. (2003) Molecular biomimetics: nanotechnology through biology. *Nat. Mater. 2*, 577–85.
(9) Zin, M. T., Ma, H., Sarikaya, M., and Jen, A. K. (2005) Assembly of gold nanoparticles using genetically engineered polypeptides. *Small 1*, 698–702.
(10) Oren, E. E., Tamerler, C., and Sarikaya, M. (2005) Metal recognition of septapeptides via polypod molecular architecture. *Nano Lett. 5*, 415–9.
(11) Thai, C. K., Dai, H., Sastry, M. S., Sarikaya, M., Schwartz, D. T., and Baneyx, F. (2004) Identification and characterization of Cu(2)O- and ZnO-binding polypeptides by Escherichia coli cell surface display: toward an understanding of metal oxide binding. *Biotechnol. Bioeng. 87*, 129–37.
(12) Rehm, B. H. A. (2006) Biopolyester particles produced by microbes or using polyester synthases: Self-assembly and potential applications In *Microbial Bionanotechnology: Biological self-assembly systems and biopolymer-based nanostructures*, Rehm, Bernd H. A., Ed., pp 1−34.

(13) Rehm, B. H. A. (2006) Genetics and biochemistry of polyhydroxyalkanoate granule self-assembly: the key role of polyester synthases. *Biotechnol. Lett. 28*, 207–13.
(14) Rehm, B. H. A. (2007) Biogenesis of microbial polyhydroxyalkanoate granules: a platform technology for the production of tailor-made bioparticles. *Curr. Issues Mol. Biol. 9*, 41–62.
(15) Peters, V., Becher, D., and Rehm, B. H. A. (2007) The inherent property of polyhydroxyalkanoate synthase to form spherical PHA granules at the cell poles: the core region is required for polar localization. *J. Biotechnol. 132*, 238–45.
(16) Peters, V., and Rehm, B. H. A. (2005) In vivo monitoring of PHA granule formation using GFP-labeled PHA synthases. *FEMS Microbiol. Lett. 248*, 93–100.
(17) Rehm, B. H. A. (2003) Polyester synthases: natural catalysts for plastics. *Biochem. J. 376*, 15–33.
(18) Peters, V., and Rehm, B. H. A. (2006) In vivo enzyme immobilization by use of engineered polyhydroxyalkanoate synthase. *Appl. Environ. Microbiol. 72*, 1777–83.
(19) Hezayen, F. F., Steinbuchel, A., and Rehm, B. H. A. (2002) Biochemical and enzymological properties of the polyhydroxybutyrate synthase from the extremely halophilic archaeon strain 56. *Arch. Biochem. Biophys. 403*, 284–91.
(20) Potter, M., Muller, H., Reinecke, F., Wieczorek, R., Fricke, F., Bowien, B., Friedrich, B., and Steinbuchel, A. (2004) The complex structure of polyhydroxybutyrate (PHB) granules: four orthologous and paralogous phasins occur in *Ralstonia eutropha*. *Microbiology 150*, 2301–11.
(21) Jurasek, L., and Marchessault, R. H. (2004) Polyhydroxyalkanoate (PHA) granule formation in *Ralstonia eutropha* cells: a computer simulation. *Appl. Microbiol. Biotechnol. 64*, 611–7.
(22) York, G. M., Stubbe, J., and Sinskey, A. J. (2001) New insight into the role of the PhaP phasin of *Ralstonia eutropha* in promoting synthesis of polyhydroxybutyrate. *J. Bacteriol. 183*, 2394–7.
(23) Baeckstroem, T. B., Brockelbank, J. A., and Rehm, B. H. A. (2007) Recombinant *Escherichia coli* produces tailor-made biopolyester granules for applications in fluorescence activated cell sorting: Functional display of the mouse interleukin-2 and myelin oligodendrocyte glycoprotein. *BMC Biotechnol. 7*, 3.
(24) Banki, M. R., Gerngross, T. U., and Wood, D. W. (2005) Novel and economical purification of recombinant proteins: intein-mediated protein purification using in vivo polyhydroxybutyrate (PHB) matrix association. *Protein Sci. 14*, 1387–95.
(25) Barnard, G. C., McCool, J. D., Wood, D. W., and Gerngross, T. U. (2005) Integrated recombinant protein expression and purification platform based on *Ralstonia eutropha*. *Appl. Environ. Microbiol. 71*, 5735–42.
(26) Grage, K., and Rehm, B. H. A. (2008) In Vivo Production of scFv-displaying biopolymer beads using a self-assembly-promoting fusion partner. *Bioconjugate Chem. 19*, 254–62.
(27) Peters, V., and Rehm, B. H. A. (2008) Protein engineering of streptavidin for in vivo assembly of streptavidin beads. *J. Biotechnol. 134*, 266–74.
(28) Brockelbank, J. A., Peters, V., and Rehm, B. H. A. (2006) Recombinant *Escherichia coli* strain produces a ZZ domain displaying biopolyester granules suitable for immunoglobulin G purification. *Appl. Environ. Microbiol. 72*, 7394–7.
(29) Sharma, P., Brown, S., Walter, G., Santra, S., and Moudgil, B. (2006) Nanoparticles for bioimaging. *Adv. Colloid Interface Sci. 123*−*126*, 471–85.
(30) Sambrook, J., Fritsch, E. F., and Maniatis, T. (1989) *Molecular cloning: a laboratory manual*, Cold Spring Harbor Laboratory Press, Plainview, NY.
(31) Brown, S. (1997) Metal-recognition by repeating polypeptides. *Nat. Biotechnol. 15*, 269–272.
(32) Brown, S., Sarikaya, M., and Johnson, E. (2000) A genetic analysis of crystal growth. *J. Mol. Biol. 299*, 725–735.
(33) Naik, R. R., Brott, L. L., Clarson, S. J., and Stone, M. O. (2002) Silica-precipitating peptides isolated from a combinatorial phage display peptide library. *J. Nanosci. Nanotechnol. 2*, 95–100.
(34) Dickerson, M. B., Naik, R. R., Sarosi, P. M., Agarwal, G., Stone, M. O., and Sandhage, K. H. (2005) Ceramic nanoparticle assemblies with tailored shapes and tailored chemistries via biosculpting and shape-preserving inorganic conversion. *J. Nanosci. Nanotechnol. 5*, 63–67.
(35) Bradford, M. M. (1976) A rapid and sensitive method for the quantitation of microgram quantities of protein utilizing the principle of protein-dye binding. *Anal. Biochem. 72*, 248–54.
(36) Laemmli, U. K. (1970) Cleavage of structural proteins during assembly of head of bacteriophage-T4. *Nature 227*, 680–685.
(37) Lowenadler, B., Jansson, B., Paleus, S., Holmgren, E., Nilsson, B., Moks, T., Palm, G., Josephson, S., Philipson, L., and Uhlen, M. (1987) A gene fusion system for generating antibodies against short peptides. *Gene 58*, 87–97.
(38) Tamerler, C., Duman, M., Oren, E. E., Gungormus, M., Xiong, X., Kacar, T., Parviz, B. A., and Sarikaya, M. (2006) Materials specificity and directed assembly of a gold-binding peptide. *Small 2*, 1372–8.
(39) Tamerler, C., Oren, E. E., Duman, M., Venkatasubramanian, E., and Sarikaya, M. (2006) Adsorption kinetics of an engineered gold binding peptide by surface plasmon resonance spectroscopy and a quartz crystal microbalance. *Langmuir 22*, 7712–8.
(40) Chenevier, P., Veyret, B., Roux, D., and Henry-Toulme, N. (2000) Interaction of cationic colloids at the surface of J774 cells: a kinetic analysis. *Biophys. J. 79*, 1298–309.
(41) Nayak, S., and Lyon, L. A. (2005) Soft nanotechnology with soft nanoparticles. *Angew. Chem., Int. Ed. Engl. 44*, 7686–708.
(42) Schultz, D. A. (2003) Plasmon resonant particles for biological detection. *Curr. Opin. Biotechnol. 14*, 13–22.
(43) Alivisatos, A. P., Johnsson, K. P., Peng, X., Wilson, T. E., Loweth, C. J., Bruchez, M. P., Jr., and Schultz, P. G. (1996) Organization of 'nanocrystal molecules' using DNA. *Nature 382*, 609–11.
(44) Venkatesan, N., Yoshimitsu, J., Ito, Y., Shibata, N., and Takada, K. (2005) Liquid filled nanoparticles as a drug delivery tool for protein therapeutics. *Biomaterials 26*, 7154–63.
(45) Burns, A., Sengupta, P., Zedayko, T., Baird, B., and Wiesner, U. (2006) Core/shell fluorescent silica nanoparticles for chemical sensing: towards single-particle laboratories. *Small 2*, 723–6.
(46) Burns, A., Ow, H., and Wiesner, U. (2006) Fluorescent core-shell silica nanoparticles: towards "Lab on a Particle" architectures for nanobiotechnology. *Chem. Soc. Rev. 35*, 1028–42.
(47) Bullock, W. O., Fernandez, J. M., and Short, J. M. (1987) XL1-BLUE - a high-efficiency plasmid transforming RecA *Escherichia coli* strain with β-galactosidase selection. *Biotechniques 5*, 376.
(48) Spiekermann, P., Rehm, B. H. A., Kalscheuer, R., Baumeister, D., and Steinbuchel, A. (1999) A sensitive, viable-colony staining method using Nile red for direct screening of bacteria that accumulate polyhydroxyalkanoic acids and other lipid storage compounds. *Arch. Microbiol. 171*, 73–80.
(49) Yuan, W., Jia, Y., Tian, J. M., Snell, K. D., Muh, U., Sinskey, A. J., Lambalot, R. H., Walsh, C. T., and Stubbe, J. (2001) Class I and III polyhydroxyalkanoate synthases from *Ralstonia eutropha* and *Allochromatium vinosum*: Characterization and substrate specificity studies. *Arch. Biochem. Biophys. 394*, 87–98.
(50) Hoffmann, N., Amara, A. A., Beermann, B. B., Q, Q. S., Hinz, H. J., and Rehm, B. H. A. (2002) Biochemical characterization of the *Pseudomonas putida* 3-hydroxyacyl ACP: CoA transacylase, which diverts intermediates of fatty acid de novo biosynthesis. *J. Biol. Chem. 277*, 42926–42936.

BC8001979

HPMA as a Scaffold for the Modular Assembly of Functional Peptide Polymers by Native Chemical Ligation

Ivo R. Ruttekolk,[†] Falk Duchardt,[‡] Rainer Fischer,[⊥,‡] Karl-Heinz Wiesmüller,[||] Jörg Rademann,[§] and Roland Brock*,[†]

Department of Biochemistry, Nijmegen Centre for Molecular Life Sciences, Radboud University Nijmegen Medical Centre, PO Box 9101, 6500 HB Nijmegen, The Netherlands, Eberhard Karls University Tübingen, Department of Molecular Biology, Interfaculty Institute for Cell Biology, Auf der Morgenstelle 15, 72076 Tübingen, Germany, Leibniz Institute for Molecular Pharmacology (FMP), Robert-Rössle-Str. 10, 13125 Berlin, Germany, Free University Berlin, Institute for Chemistry and Biochemistry, Takustr. 3, 14195 Berlin, Germany, and EMC microcollections GmbH, Sindelfinger Straβe 3, 72072 Tübingen, Germany. Received May 29, 2008; Revised Manuscript Received July 25, 2008

Synthetic peptides are valuable tools in fundamental and applied biomedical research. On one hand, these molecules provide highly efficient access to competitive inhibitors of molecular interactions and enzyme substrates by rational design. On the other hand, peptides may serve as powerful vectors to mediate cellular uptake of molecules that otherwise enter cells only poorly. The coupling of both such functionalities provides access to molecules interfering with molecular processes inside the cell. However, the combination of several functionalities on one synthetic peptide may be compromised by problems associated with the synthesis of long peptides. Native chemical ligation enables the chemoselective coupling of fully deprotected functional building blocks. However, peptide thioesters are still not accessible by standard solid-phase peptide synthesis. Here, we demonstrate the cofunctionalization of a thioester-activated *N*-hydroxypropyl methacrylamide (HPMA) copolymer (28 500 Da) with the cell-penetrating peptide (CPP) nonaarginine and a bioactive peptide as independent building blocks by native chemical ligation. Nonaarginine was employed as a cell-penetrating peptide (CPP), a fluorescein-labeled analogue of a pro-apoptotic peptide as a biofunctional cargo. Incorporation of the fluorescein label enabled the highly sensitive quantification of the coupling stoichiometry by fluorescence correlation spectroscopy (FCS) using 0.4 pmol/12 ng of labeled construct. A construct only bearing the functional cargo peptide required cellular import by electroporation in order to show activity. In contrast, a construct combining all functionalities was active upon incubation of cells, validating the modular nature of the approach.

INTRODUCTION

Peptides provide a rich source of bioactive molecules, and numerous peptides and analogues are now used as drugs (*1*−*3*). In fundamental biological and biomedical research, peptides have become a highly valuable tool for defining the principles of molecular recognition (*4*).

However, given the poor capacity of peptides to enter cells, most applications of bioactive peptides have focused on extracellular targets, recombinant proteins, or cell lysates. In order to mediate cellular entry, over the past years, conjugation with cell-penetrating peptides has received increasing attention. Cell-penetrating peptides are a diverse class of peptides of 8 to 30 amino acids in length that promote the cellular uptake of the cargo molecules they are connected to (*5*). In our hands, nonaarginine has proven to be a CPP of choice (*6*). This CPP is very well tolerated by cells, has high import efficiency, and moreover, truncated sequences also show high activity as a CPP, rendering purification less problematic (*7*).

For the cellular import of peptides, in most cases, the conjugation with the CPP occurs by N-terminal elongation during solid-phase peptide synthesis. However, especially for longer peptides, purity and postsynthesis workup may become limiting factors. Moreover, in order to streamline the process from in vitro to intracellular testing, one may want to render a peptide that has shown activity in an in vitro assay competent for cell entry without the need for de novo synthesis of a cell-penetrating analogue.

Native chemical ligation (NCL) has proven to be a potent technique for the efficient and chemoselective coupling of fully deprotected peptides (*8*, *9*). In its original form, a peptide bearing an N-terminal cysteine residue forms an amide bond with another peptide, carrying a C-terminal thioester-activated amino acid. In spites of its success in the synthesis of longer polypeptides, the lack of protocols to generate the required C-terminal thioesters by standard solid-phase Fmoc peptide chemistry is still a limiting factor for its broader application.

As an alternative approach to overcome these limitations, we describe here the modular coupling of cysteine-bearing unprotected peptides to thioester-activated hydroxypropyl methacrylamide copolymer (HPMA). The HPMA serves as a linear scaffold to which the functional peptides are linked. HPMA has been demonstrated to be biocompatible and has therefore been used as a drug carrier in numerous applications (*10*−*12*). Furthermore, conjugation with the Tat-derived CPP (*13*) has

* To whom all correspondence should be addressed: Department of Biochemistry, Nijmegen Centre for Molecular Life Sciences, Radboud University, Nijmegen Medical Centre, PO Box 9101 (Route 286), 6500 HB Nijmegen, The Netherlands, Ph.: +31-24-3666213, Fax: +31-24-3616413, E-mail: r.brock@ncmls.ru.nl.

[†] Nijmegen Medical Centre.

[‡] Eberhard Karls University Tübingen.

[§] Leibniz Institute for Molecular Pharmacology and Free University Berlin.

[||] EMC microcollections GmbH.

[⊥] Present address: Wacker Chemie AG, Hanns-Seidel-Platz 4, 81737 München, Germany.

10.1021/bc800222e CCC: $40.75 © 2008 American Chemical Society
Published on Web 09/09/2008

been shown to facilitate the uptake of HPMA−doxorubicin conjugates (*14*).

The pro-apoptotic peptide AVPIAQK (*15, 16*) served as a bioactive cargo. This peptide corresponds to the seven N-terminal amino acids of the Smac (second mitochondria-derived activator of caspase) protein (*17*). Smac is a pro-apoptotic protein, that, following an apoptotic stimulus, is released from mitochondria and inhibits the antiapoptotic action of IAPs (inhibitor of apoptosis proteins) (*18*). Introduction of this peptide into cells specifically enhances the controlled cell death, i.e. apoptosis, in cells exposed to ligands of death receptors such as the tumor necrosis factor receptor or Fas (*16*). This peptide exerts this activity only when introduced into the cytoplasm. We had shown for this peptide previously that measurement of cell viability provides a reliable readout for comparing import efficiencies of different delivery strategies (*15*).

With respect to the quantification of coupled peptides per polymer, three options were considered. The first option had been the implementation into the synthesis protocol by photometric determination of a leaving group that is released upon coupling of a bioactive moiety (*19*). The second option is based on the degradation of an aliquot of the conjugate postsynthesis and quantification of a suitable degradation product of the bioactive moiety (*20*). Finally, the third option is based on the spectroscopic quantification of a functional group per unit weight of polymer. Using a fluorescently labeled conjugate of the bioactive moiety, we chose options 2 and 3. Confocal fluorescence-correlation spectroscopy (FCS) was employed as the analytical method to follow the release of a degradation product according to option 3 (*21*). This technique provides information on the average number and size of fluorescently labeled molecules diffusing through a confocal detection volume. FCS works at concentrations of probe molecules in the lower nanomolar to subnanomolar range and in microliter volumes, therefore reducing sample consumption to a minimum.

Our results show that the functionalization of HPMA via NCL occurs with uniform yields. By addressing the activity and cellular uptake of HMPA conjugated to the AVPIAQK peptide or R9 alone or to a combination of both peptides, it is established that all three molecular entities act as functionally independent building blocks.

EXPERIMENTAL PROCEDURES

Reagents. The preactivated hydroxypropyl methacrylamide copolymer *N*-methacrylateglycylglycine *p*-nitrophenyl ester (poly(HPMA-*co*-methacrylate-Gly-Gly-*p*-nitrophenyl ester)) was supplied by Polymer Laboratories (Shropshire, Great Britain). It has a linear structure, an average molecular weight (MW) of 28.5 kDa (M_w/M_n: 1.32) and a total nitrophenol content of 8.28 mol %. On the basis of the specifications provided by the manufacturer, we estimated 12.5 reactive groups per molecule. Rink amide resin was from Rapp Polymers (Tübingen, Germany). Fmoc amino acids were purchased from Novabiochem (Läufelingen, Switzerland) and Senn Chemicals (Dielsdorf, Switzerland). The other chemicals for synthesis were supplied by Fluka (Deisenhofen, Germany), PD-10 columns by GE Healthcare (Uppsala, Sweden), and Sephacryl S-200 HR gel from Pharmacia Biotech (Uppsala, Sweden). Cell culture media were purchased from PAN biotech (Aidenbach, Germany). The agonistic anti-Fas-antibody was supplied by Biomol (Hamburg, Germany), cycloheximide by SIGMA (Steinheim, Germany), and Alexa647-labeled Annexin V by Invitrogen (Karlsruhe, Germany).

Peptide Synthesis. Peptides were synthesized by automated solid-phase peptide synthesis using Fmoc/tBu chemistry. Fluorescein-labeled peptides were synthesized on Nα-carboxyfluorescein-labeled lysyl-Rink amide resin ((Fluo(Trt))-Lys-Rink), unlabeled peptides on Rink amide resin (*22*). Purity was determined by analytical RP-HPLC (Nucleosil 100, 250 × 2 mm, C18 column, 5 μm particle diameter; Grom, Herrenberg, Germany), identity was validated via MALDI-TOF-mass spectrometry. For the R9-amide analogue CYRRRRRRRRR, the tyrosine residue was included to enable detection at 280 nm. Concentrations were determined by UV/vis spectroscopy of peptides and conjugates diluted 1000-fold in Tris/HCl buffer pH 8.8 assuming an extinction coefficient for fluorescein E_{492} = 78 000 L/(mol × cm).

Synthesis of the Peptide with a Lysine-Coupled Cysteine Residue. Ala-Val-Pro-Ile-Ala-Gln(Trt)-Lys(Boc)-Lys(Dde)-Lys(Boc)-Leu-Lys(Boc)-εLys(Fluo) (15 μmol) was synthesized on (Fluo(Trt))-Lys-Rink amide resin. The peptide was N-terminally protected by reaction with boc-anhydride (32.7 mg, 150 μmol) in dimethylformamide (DMF) (1 mL) containing *N*,*N*-diisopropylethylamine (DIPEA) (29.8 μL, 180 μmol) for 24 h at 20 °C. After cleavage of the Dde-protecting group by hydrazine hydrate (2% v/v in DMF, 2 × 1 mL, 5 min, 20 °C), the ε-amino group was conjugated with Fmoc-Cys(Trt)-OH (87.9 mg, 150 μmol) using 1-hydroxybenzotriazole (20.3 mg, 150 μmol) and diisopropylcarbodiimide (23.5 μL, 150 μmol) in DMF (1 mL, 24 h, 20 °C). Following removal of the Fmoc-protecting group by piperidine (20% v/v in DMF), the peptide was cleaved off the resin and side chains deprotected using a mixture of 92.5% TFA, 2.5% triisopropylsilane, 2.5% 1,2-ethanedithiole, and 2.5% H_2O (v/v/v), precipitated in cold diethyl ether (4 °C) and spun down (4000 rpm, 5 min). The precipitate was washed with cold diethyl ether twice. Then, the precipitate was dissolved in a mixture of acetonitrile/water (4 mL, 1:1, v/v) and lyophilized.

Synthesis of HPMA−Peptide Conjugates. Poly(HPMA-*co*-methacrylate-Gly-Gly-*p*-nitrophenylester) (4 mg) was dissolved in anhydrous DMSO (200 μL), and benzylmercaptan (50 μL) was added. After 15 min, peptide was dissolved in this solution (4.4 to 11.2 mM corresponding to an 8- to 20-fold excess over polymer and 0.64 to 1.60 excess over reactive groups, respectively) and incubated for 30 min at 20 °C. After addition of thiophenol (50 μL) and incubation for 16 h at 20 °C, phosphate buffer (100 mM) and guanidinium chloride (6 M), pH 7.5 (200 μL), were added and the mixture incubated for 72 h at 20 °C. Finally, the reaction mixture was diluted with PBS (700 μL) and purified twice with a PD-10 column followed by lyophilization. The formation of a conjugate was validated using analytical gel filtration chromatography (ÄKTA-explorer fast protein liquid chromatography (FPLC) station; flow, 0.25 mL/min; 4 °C; Sephacryl S-200 HR-column, 150 × 10 mm). Absorption was detected at 215 nm (peptide bonds), 280 nm (aromatics), and 492 nm (fluorescein).

Microscopy. HeLa cells were incubated with HPMA-$(H_2N\text{-AVPIAQKK(C)KLK}\epsilon\text{K(Fluo)-NH}_2)_n(\text{CYR}_9\text{-NH}_2)_m$ denoted as AVPIAQK-HPMA-R9 and HPMA-$(H_2N\text{-AVPIAQKK(C)KLK}\epsilon\text{K(Fluo)-NH}_2)_n$ denoted as AVPIAQK-HPMA (each 20 μM with respect to the AVPIAQK peptide) in RPMI medium (45 min, 37 °C) and afterward analyzed by confocal laser scanning microscopy using an LSM 510 confocal microscope (Carl Zeiss, Göttingen) equipped with a Plan-Apochromat 63× N.A. 1.4 Oil DIC objective.

Determination of Stoichiometry by FCS. Autocorrelation measurements were performed in a 384-well plate (175 μm, low-base design, MMI, Eching, Germany) using a ConfoCor 2 fluorescence correlation spectroscope equipped with a C-Apochromat 40× N.A. 1.2 water immersion lens (Carl Zeiss, Jena, Germany) and a TCS SP5 fluorescence correlation spectroscope equipped with an HCX PL APO 63× N.A. 1.2 water immersion lens (Leica Microsystems, Mannheim, Germany). A solution of 25 nM peptide−HPMA was incubated in

Scheme 1. Coupling of the AVPIAQK Analogue to a Preactivated HPMA (Poly(hydroxypropyl Methacrylamide)-*co*-(Methacrylate-Gly-Gly-Nitrophenyl Ester))[a]

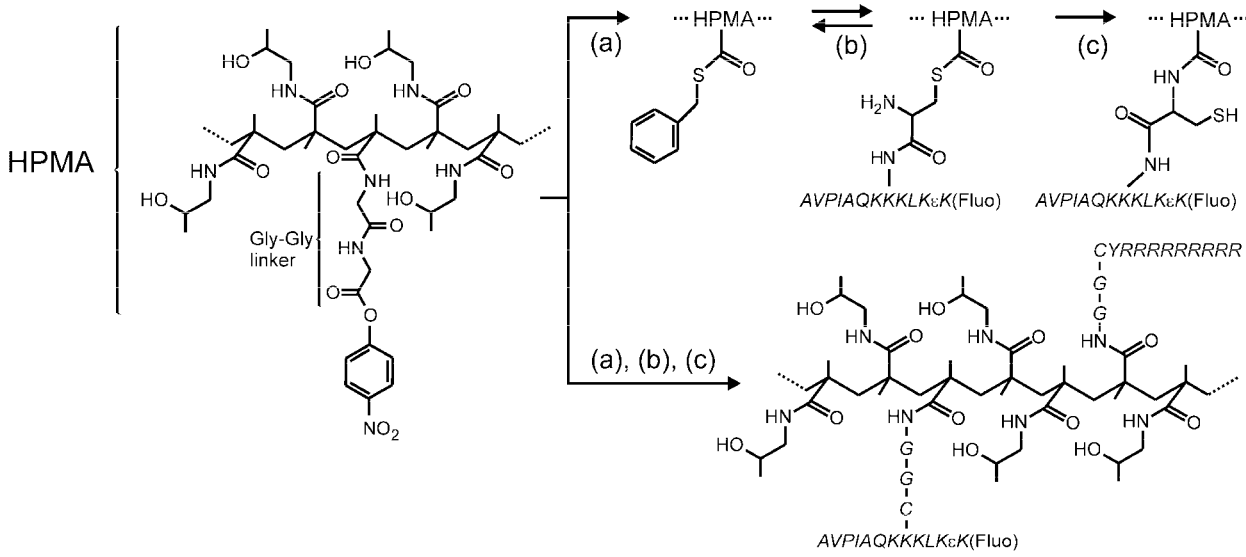

[a] (a) DMSO (anhydrous), benzylmercaptane; (b) DMSO (anhydrous), thiophenol; (c) DMSO, thiophenol, phosphate buffer (100 mM), guanidiniumchloride (6 M, pH 7.5). Amino acids represented in single letter code are printed in italics.

PBS-buffer containing 30 U/mL proteinase K for 1.5 h at RT. During this incubation, autocorrelation measurements were performed in regular intervals until the diffusional autocorrelation time and the amplitude of the autocorrelation function had reached a minimum. After digestion, the number of particles and the fpm of intact and completely digested samples were compared. The ratio of the number of particles after and before digestions represents the stoichiometry of peptides per polymer.

Bioactivity of Electroporated Conjugates. HeLa cells were detached by trypsination. Cells (4×10^5 cells in 200 μL serum-containing medium) were electroporated with the indicated peptides or conjugates in a 4 mm cuvette (peqlab Biotechnologie GmbH, Germany) using a 12.5 ms, 350 mV, 1700 μF pulse (Fischer, Germany). After incubation for 10 min on ice, the cells were washed by centrifugation, transferred to a 96-well microtiter plate (2×10^4 cells per well), and incubated in 200 μL serum-containing RPMI medium with anti-Fas antibody (100 ng/mL, human activating mouse IgM, clone CH11) and CHX (2 μg/mL) for 20 h at 37 °C and 5% CO_2. Dead cells were removed by washing twice with PBS, whereas the attached cells were stained with crystal violet (100 μL, 0.5% w/v crystal violet, 20% methanol v/v, 80% PBS) (15 min, 20 °C). After removal of excess dye by washing with cold water, the intracellular dye was resolved in 100 μL methanol and the absorption at 550 nm was determined.

Caspase-3 Activity Assay. HeLa cells were incubated with medium containing constructs for 30 min at 37 °C. After one washing step, cells were treated as indicated with agonistic Fas antibody (100 ng/mL) and CHX (2 μg/mL) for the induction of apoptosis followed by incubation for a further 3 h. Cells were harvested by scraping, washed with ice−cold PBS, and lysed in lysis buffer (1% Triton, 150 mM NaCl, pH 7.7, supplemented with protease inhibitor cocktail tablets (Roche Diagnostics, Mannheim, Germany) for 30 min on ice. The protein content in lysates was determined using a commercially available Bradford protein assay kit (Bio Rad Laboratories, München, Germany). Equivalents of 30 μg protein for each sample were diluted in caspase activity buffer (20 mM HEPES, 10 mM dithiothreitrol, 10% glycerol, 100 mM NaCl, pH 7.5). Fluorogenic caspase-3 substrate (Ac-DEVD-AMC, Calbiochem, Bad Soden, Germany) was added to the samples to a final concentration of 2 μM. The efficiency of the substrate cleavage by active caspase-3 was analyzed immediately after substrate addition and after 3 h incubation at 37 °C using a luminescence spectrometer LS50B (PerkinElmer, Norwalk, CT).

RESULTS AND DISCUSSION

Synthesis and Analytical Characterization of HPMA Conjugates. In order to ensure broad applicability of a polymer-based approach, robust synthesis procedures as well as reliable analytical methods to determine coupling efficiencies are required. To validate our protocol, a series of coupling reactions with structurally different peptides was performed and, for selected peptides, also repeated several times. As a bioactive peptide, the pro-apoptotic AVPIAQK peptide was selected. This peptide requires a free N-terminus for biological activity. Therefore, in this case, the cysteine residue required for NCL was introduced via coupling to a lysine side chain (Supporting Information Scheme 1). A protease-releasable fluorescent reporter group was introduced by C-terminal elongation with the tripeptide Lys-Leu-Lys, followed by a fluorescein-labeled lysine residue (*22*). The HPMA was obtained as a preactivated hydroxypropyl methacrylamide copolymer poly(HPMA-*co*-methacrylate-Gly-Gly-*p*-nitrophenyl ester) (linear structure, average MW 28.5 kDa, total nitrophenol content 8.28 mol %) with about 12.5 reactive groups per molecule. The active ester was first transesterified to a benzylmercaptyl-thiol ester in water-free DMSO, as we were concerned that due to its high reactivity the nitrophenyl ester moiety would engage in reactions with nucleophilic functional groups other than the sulfhydryl group of the N-terminal cysteine residue. Next, the polymer was incubated with peptide in water-free DMSO. After 16 h, aqueous buffer was added. The products were purified by gel filtration chromatography (Figure 1). The chemoselectivity of this modified one-pot ligation protocol was validated in an independent experiment using control peptides with and without an N-terminal cysteine residue (Supporting Information Figure 1).

For the determination of loading efficiency, two independent approaches were evaluated. First, the absorption per weight was measured for a defined amount of polymer. Second, the number of fluorescent particles before and after digestion of peptide-coupled HPMA with 30 U/mL proteinase K (Figure 2) was determined by fluorescence correlation spectroscopy. Due to the nanomolar sensitivity and microliter measurement volumes of

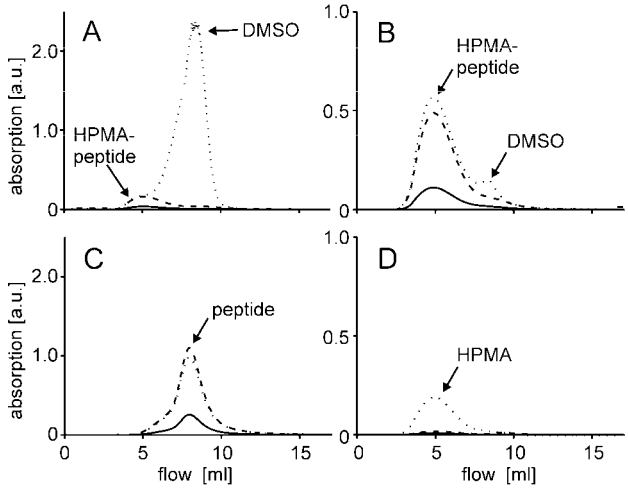

Figure 1. Analytical gel filtration chromatography of the HPMA(H_2N-AVPIAQKK(C)KLKεK(Fluo)-NH_2) conjugate: (A) crude reaction mixture, (B) after purification with a desalting column, (C) unbound peptide H_2N-AVPIAQKK(C)KLKεK(Fluo)-NH_2, and (D) free HPMA. Chromatograms were recorded at 215 nm (dotted lines), 280 nm (solid lines), and 492 nm (dashed lines).

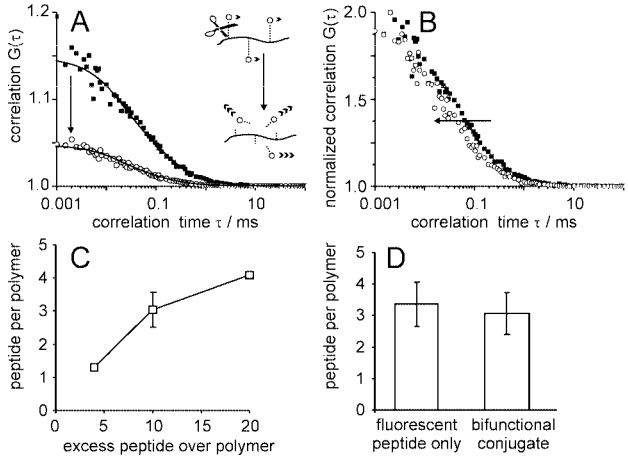

Figure 2. Quantification of peptide loading per polymer by fluorescence correlation spectroscopy (FCS). One aliquot of the HPMA−peptide conjugate AVPIAQK-HPMA-R9 was digested by addition of proteinase K (30 U/mL) to the polymer conjugate solution (10 μM). After incubation for 1.5 h at 37 °C, the solution was diluted in PBS (500-fold) and transferred to a 384-well plate. A reference aliquot was prepared in the same way in the absence of proteinase K. (A) Autocorrelation functions for the digested sample (open circles) and the undigested control (filled squares). (B) Superposition of the autocorrelation functions normalized to an amplitude of 1 to better visualize the shift toward shorter diffusional autocorrelation times. (C) Positive correlation of peptides coupled per polymer and the excess of peptide over polymer in the coupling reaction. Values were taken from Table 1. The excess relates to the excess of the fluorescently labeled analogue. (D) The coupling efficiency was independent from the presence of a second peptide. The conjugates for which the coupling efficiency was only determined by absorption-per-weight are not included in this graph.

FCS, only 0.4 pmol, corresponding to 12 ng of the labeled construct, was required for one measurement. Digestion led to a decrease of the amplitude of the autocorrelation function (Figure 2A), corresponding to an increase in the number of fluorescent particles. The completeness of the reaction was confirmed by following the reaction over time. The stoichiometry of peptide loading was derived by calculating the number of particles before and after digestion (Table 1). The release of the fluorescent reporter group from the scaffold was also reflected by the shift in the diffusional autocorrelation time from approximately 100 to 35 μs (Figure 2B).

The results obtained by FCS corresponded very well to those obtained by the absorption-per-weight-based methods. A slightly lower loading efficiency was obtained by the latter. This may be due to the presence of counterions in the polymer preparation, leading to an overestimate of the amount of material. Due to the fact that the FCS-based method is not affected by salt that compromises a correct determination of weight and requires much smaller amounts, we judge this method to be superior.

For the coupling efficiency, there was a positive correlation between the ratio of peptide in the coupling reaction over reactive groups (Figure 2C). Typically, with a molar excess of 10 with respect to the polymer, corresponding to 0.8 peptides per reactive group, about 3 peptides were coupled per polymer. Interestingly, in the tested concentration ranges, addition of a nonfluorescent peptide did not affect the coupling efficiency of the fluorescently labeled peptide (Figure 2D). This observation indicates that, at these concentrations, peptides did not compete for reactive groups. Also, for R9, the AVPIAQK peptide and a fluorescein-labeled cysteinyl-ε-lysyl moiety, similar coupling yields were obtained. This result indicates the suitability of the coupling protocol for the testing of larger collections of structurally diverse peptides, without the need for the optimization of coupling conditions for each individual case.

Moreover, by dividing the total fluorescence through the average number of molecules, information on the average fluorescence per molecule (fpm) was obtained. In principle, for polymers carrying several fluorescently labeled particles, the fpm should be a function of the stoichiometry of loading. However, due to self-quenching, the fpm can also be lower than expected (*23*). The fpm for the HPMA conjugates relative to the value of the free peptide was around 1, independent of the coupling efficiency. This result confirms the presence of fluorescence quenching. The molecular brightness of the polymers therefore does not provide information on the coupling efficiency.

We relate to quenching as a reduction of fluorescence per particle due to the spatial proximity of several fluorophores, not to the complete extinction of fluorescence for those polymers carrying more than one fluorophore. One could argue that, for particles carrying several fluorophores, fluorescence is quenched completely and these conjugates could not be detected. Then, for the undigested sample, only those conjugates carrying one fluorophore could be detected. Upon digestion, fluorescent groups would be cleaved off polymers carrying several fluorophores, resulting in their dequenching. As a consequence, the number of particles per polymer would be overestimated.

However, in our view, the very good agreement of the determination of coupling efficiency based on absorbance-per-weight and the FCS-based method argue against a total quenching of fluorescence for polymers carrying several fluorescein moieties. Assuming a Poissonian distribution of coupling efficiency, then at an average coupling ratio of 3 about 15% of the conjugates carry only 1 fluorophore. 80% of the peptides would be coupled to polymers carrying two or more fluorophores. If all these moieties would only become visible after release from the polymer, then a coupling efficiency of 6−7 would be derived.

Coupling to HPMA Preserves the Activity of the AVPIAQK Peptide. Next, we intended to establish that conjugation of the peptide to the polymer does not compromise its biological activity. Previously, for the AVPIAQK-peptide we had employed electroporation as a means for CPP-independent cytoplasmic delivery (*15*). The free and the HPMA-coupled peptide as well as their counterparts with the reverse sequence were loaded into HeLa cells by electroporation. The

Table 1. Summary of Coupling Reactions[a]

conjugate	fold excess	excess over reactive group	fluo-analogue per polymer	reactive groups coupled to fluo-analogue	rfpm[b]	used in figure
AVPIAQK(Fluo) -HPMA-YR9[d]	4:4:1	0.64	1.3	10%	1.1	
AVPIAQK(Fluo) -HPMA-R9[d]	10:10:1	1.6	3.4	27%	1.0	2, 4B, 5
AVPIAQK(Fluo) -HPMA[d]	20:1	1.6	4.6[c]	33%		4C
AVPIAQK(Fluo) -HPMA[d]	10:1	0.8	3.3	26%	1.0	3, 5
KQAIPVA(Fluo) -HPMA[e]	20:1	1.6	4.4[c]	33%		3
AVPIAQK(Fluo) -HPMA[d]	20:1	1.6	4.1(3.4[c])	33%	1.1	2
HPMA-R9(Fluo)[f]	10:1	0.8	2.7	22%	0.8	4A
AVPIAQK(Fluo) -HPMA-R9(Fluo)[d]	10:10:1	1.6	3.5	28%	0.9	
Cys(Fluo)-HPMA-R9	10:10:1	1.6	2.3	18%	1.1	

[a] For the bifunctional conjugates, information on coupling efficiency was obtained for the fluorescein-labeled analogue only. [b] The relative fluorescence per molecule (rfpm) was determined by dividing the fluorescence per molecule for the conjugate as determined by FCS through the one of the released peptide. [c] Loading efficiency determined by measuring the absorption per unit weight of peptide-coupled polymer. [d] AVPIAQK(Fluo) relates to Ala-Val-Pro-Ile-Ala-Gln-Lys-Lys(Cys)-Lys-Leu-Lys-εLys(Fluo) (see experimental procedures). [e] KQAIPVA(Fluo) relates to Lys-Gln-Ala-Ile-Pro-Val-Ala-Lys(Cys)-Lys-Leu-Lys-εLys(Fluo) (see experimental procedures). [f] R9(Fluo) relates to Cys-Arg_9-εLys(Fluo).

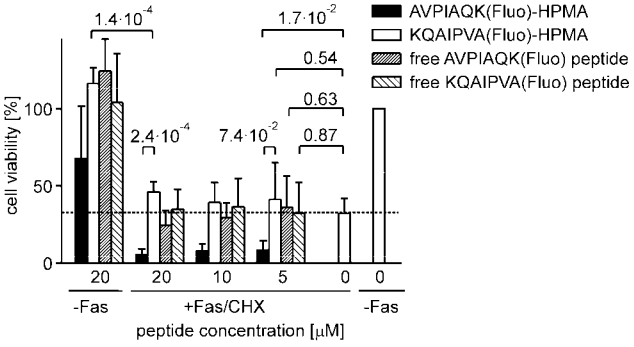

Figure 3. Enhancement of apoptosis induction by electroporated HPMA−conjugates. The concentration was adjusted with respect to the fluorescent moiety. In this case, peptide loading was determined by absorption per weight (Table 1). Cell viability was determined by crystal violet staining. AVPIAQK(Fluo) relates to Ala-Val-Pro-Ile-Ala-Gln-Lys-Lys(Cys)-Lys-Leu-Lys-εLys(Fluo) (see Experimental Procedures); KQAIPVA(Fluo) relates to Lys-Gln-Ala-Ile-Pro-Val-Ala-Lys(Cys)-Lys-Leu-Lys-εLys(Fluo) (see Experimental Procedures). The statistical significance was determined by a two-tailed unpaired Student's *t* test.

AVPIAQK-peptide does not induce apoptosis by itself. Instead, it increases cell death in the presence of an apoptosis-inducing stimulus, as for example an agonistic anti-Fas antibody. Stimulation with anti-Fas alone reduced cell viability by 64% (Figure 3). With the AVPIAQK peptide at a concentration of 20 μM, cell viability was reduced by a further 8%. In comparison, the HPMA-conjugated AVPIAQK peptide at a concentration of 20 μM (related to the fluorescein moiety, i.e., AVPIAQK peptide) reduced the viability by a further 29%. This difference in activity indicates that conjugation to the HPMA strongly promotes the activity of the peptide, possibly by protection from proteolytic degradation. The reverse sequences had no effect on cell viability. For the HPMA constructs, electroporated in the absence of an apoptotic stimulus viability was also fully maintained, demonstrating the biocompatibility of the HPMA scaffold.

Cellular Uptake and Bioactivity of Bifunctional Conjugates. Having established that the HPMA is inert with respect to cell entry and that the HPMA-conjugated AVPIAQK−peptide fully maintains activity, we next cofunctionalized the HPMA with the AVPIAQK−peptide and nonaarginine to obtain conjugates competent for cell entry. Both the HPMA conjugate functionalized with R9 only as well as the one cofunctionalized with R9 and the AVPIAQK peptide efficiently entered cells (Figure 4). In contrast to what we typically observe for free R9, a large part of the fluorescence was localized close to the plasma membrane. In addition, there was homogeneous intracellular fluorescence. Inside the nucleus, the nucleoli were

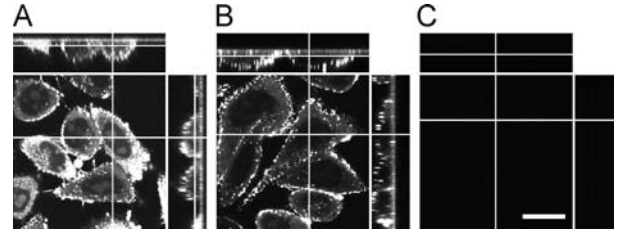

Figure 4. Cellular uptake and subcellular distribution of HPMA−peptide conjugates. Confocal microscopy of cells incubated (A) with HPMA-R9, (B) the bifunctional AVPIAQK-HPMA-R9 conjugate, and (C) a conjugate bearing the functional peptide only (AVPIAQK-HPMA) (20 μM). One confocal slice as well as orthogonal sections along the indicated lines are shown. Cells were incubated with the respective conjugate at a concentration of 20 μM with respect to the fluorescent moiety for 45 min at 37 °C. The bar denotes 20 μm.

visible, an observation that we and others have made for cell-penetrating conjugates before (*24*). For the bifunctional HPMA construct, only the AVPIAQK moiety was fluorescently labeled. The intracellular fluorescence therefore provided direct evidence for the cofunctionalization of the HPMA scaffold with the nonaarginine.

Finally, we assessed whether the bifunctional HPMA conjugate would also combine both biological functions, namely, cell entry and apoptosis enhancement. To fully establish that the conjugates acted by enhancement of apoptosis and to exclude the possibility that a reduction of cell viability was due to general cell toxic effects, we determined the activity of the executioner caspase 3 in cell lysates as an apoptosis-specific readout.

Neither of the constructs led to an increase of caspase 3 activity beyond the approximate 2-fold increase in activity observed for control cells incubated in the absence of stimulus and conjugate (Figure 5). The apoptotic stimulus increased the caspase 3 activity 3.5-fold. For the conjugate bearing the AVPIAQK moiety alone, no further increase was observed, consistent with the inability of this molecule to enter the cells. In contrast, the bifunctional conjugate increased the caspase 3 activity by up to 8-fold in a concentration-dependent manner. Some increase in activity to 5.3-fold was also observed for the conjugate bearing the nonaarginine moiety only. This activity may be due to a higher sensitivity of the apoptosis-induced cells to the import of a polycation (*25*). In the absence of the proapoptotic stimulus, there was no cytotoxic activity for either of the constructs. This result, in conjunction with the absence of activity for the electroporated reverse KQAIPVA(Fluo)-HPMA conjugate, validates the biocompatibility of the conjugates.

At present, the molecular basis for the different subcellular localization of the HPMA conjugates in comparison to free CPPs is not understood. To this point, we have not resolved whether this distribution is a consequence of a poor induction of

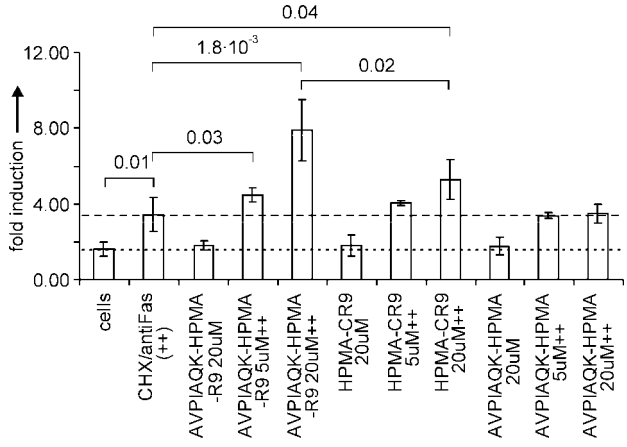

Figure 5. Bioactivity of HPMA conjugates. HeLa cells were incubated with different concentrations of the counjugates for 30 min at 37 °C. Afterward, the cells were washed and apoptosis was induced by stimulation with an agonistic anti-Fas antibody (100 ng/mL) and cycloheximide (CHX, 2 μg/mL).For measurements of the caspase-3 activity, cells were harvested 3 h after induction of apoptosis. The figure shows averages and standard deviations of two independent cell stimulations that were analyzed twice/three times by a colorimetric caspase assay. The biological activity is expressed as fold-induction of caspase 3 activity in relation to lysates of untreated cells obtained at $t = 0$. The results of the individual assays were normalized on the basis of the accumulated absorbance of all samples. The pointed line indicates the increase of caspase 3 activity during the 3 h incubation period of the assay in the absence of an apoptotic stimulus. The dashed line indicates the Fas stimulus-dependent increase in caspase activity, ++ the presence of the apoptotic stimulus. Concentrations were derived from the absorption of fluorescein. The statistical significance was determined by a two-tailed unpaired Student's *t* test.

endocytosis and therefore increased association with the plasma membrane or of differential vesicular trafficking of HPMA-loaded vesicles. For free cell-penetrating peptides, sequestration within the endolysosomal compartment is also a major limitation for bioactivity (*15*). Typically, these vesicles are distributed throughout the cell (*24*). More importantly with respect to their application, the localization close to the plasma membrane is not associated with the induction of membrane damage as validated by the biocompatibility of the conjugates in the absence of an apoptotic stimulus.

CONCLUSIONS

In summary, our results show that the HPMA-based strategy provides a convenient access to cell-penetrating bioactive peptides. Peptides mediating cell entry and bioactivity are coupled as fully unprotected building blocks to the preactivated HPMA polymers by native chemical ligation. Due to the modular nature of the approach, shorter peptides may be employed, which facilitates the synthesis of cell-penetrating conjugates especially for longer bioactive peptides. Therefore, the modular nature of the approach represents a considerable shortcut for testing the activity of peptides inside a cell. The assessment of bioactivity and uptake for the individual conjugates confirmed that the functionality of the three molecular elements, i.e., scaffold, bioactive peptide, and CPP, combine independently in a modular fashion.

The coupling reaction proceeded with little day-to-day variation. Our results indicate that the coupling efficiency correlates positively with the excess of peptide over functional groups. In further studies, it will therefore be highly interesting to systematically assess the effect of variations of either the number of bioactive peptides or the CPP with respect to bioactivity, uptake, and trafficking. Also, the incorporation of peptides known to promote endosomal release as a further element will be a promising option to explore for increasing bioactivity (*26*). These advancements will strongly promote the development and application of functional peptides in fundamental and applied biomedical research (*27*).

ACKNOWLEDGMENT

R.B. gratefully acknowledges financial support from the Volkswagen Foundation ("Nachwuchsgruppen an Universitäten" I/77 472) and the DFG (BR2443/5-1), F.D. is a scholar of the Graduiertenkolleg 794. J.R. acknowledges financial support from the DFG (RA895/4-1) and from the Fonds der Chemischen Industrie.

Supporting Information Available: Supplemental experimental data providing further information on the synthesis of the peptide with a cysteine residue coupled to a lysine side chain, demonstrating the chemoselectivity of the coupling reaction, and on self-quenching of polymer-coupled fluorophores. This material is available free of charge via the Internet at http://pubs.acs.org.

LITERATURE CITED

(1) Bray, B. L. (2003) Large-scale manufacture of peptide therapeutics by chemical synthesis. *Nat. Rev. Drug Discovery 2*, 587–593.

(2) Hruby, V. J., and Balse, P. M. (2000) Conformational and topographical considerations in designing agonist peptidomimetics from peptide leads. *Curr. Med. Chem. 7*, 945–970.

(3) Leader, B., Baca, Q. J., and Golan, D. E. (2008) Protein therapeutics: a summary and pharmacological classification. *Nat. Rev. Drug Discovery 7*, 21–39.

(4) Cooper, W. J., and Waters, M. L. (2005) Molecular recognition with designed peptides and proteins. *Curr. Opin. Chem Biol. 9*, 627–631.

(5) Fischer, R., Fotin-Mleczek, M., Hufnagel, H., and Brock, R. (2005) Break on through to the other side - Biophysics and cell biology shed light on cationic cell-penetrating peptides. *ChemBioChem 6*, 2126–2142.

(6) Wender, P. A., Mitchell, D. J., Pattabiraman, K., Pelkey, E. T., Steinman, L., and Rothbard, J. B. (2000) The design, synthesis, and evaluation of molecules that enable or enhance cellular uptake: peptoid molecular transporters. *Proc. Natl. Acad. Sci U.S.A 97*, 13003–13008.

(7) Mitchell, D. J., Kim, D. T., Steinman, L., Fathman, C. G., and Rothbard, J. B. (2000) Polyarginine enters cells more efficiently than other polycationic homopolymers. *J. Peptide Res. 56*, 318–325.

(8) Dawson, P. E., Muir, T. W., Clark-Lewis, I., and Kent, S. B. H. (1994) Synthesis of proteins by native chemical ligation. *Science 266*, 776–779.

(9) Tam, J. P., Xu, J., and Eom, K. D. (2001) Methods and strategies of peptide ligation. *Biopolymers 60*, 194–205.

(10) Duncan, R. (2003) The dawning era of polymer therapeutics. *Nat. Rev. Drug Discovery 2*, 347–360.

(11) Kopecek, J., and Bazilova, H. (1973) Poly[N-(2-hydroxypropyl)methacrylamide]. I. Radical polymerization and copolymerization. *Eur. Polym. J. 9*, 7–14.

(12) Kopecek, J., Kopeckova, P., Minko, T., and Lu, Z. (2000) HPMA copolymer-anticancer drug conjugates: design, activity, and mechanism of action. *Eur. J. Pharm. Biopharm. 50*, 61–81.

(13) Schwarze, S. R., Ho, A., Vocero-Akbani, A., and Dowdy, S. F. (2000) In vivo protein transduction: Delivery of a biologically active protein into the mouse. *Science 285*, 1569–1572.

(14) Nori, A., Jensen, K. D., Tijerina, M., Kopeckova, P., and Kopecek, J. (2003) Tat-conjugated synthetic macromolecules facilitate cytoplasmic drug delivery to human ovarian carcinoma cells. *Bioconjugate Chem. 14*, 44–50.

(15) Fotin-Mleczek, M., Welte, S., Mader, O., Duchardt, F., Fischer, R., Hufnagel, H., Scheurich, P., and Brock, R. (2005) Cationic cell-penetrating peptides interfere with TNF signaling by induction of TNF receptor internalization. *J. Cell Sci. 118*, 3339–3351.

(16) Fulda, S., Wick, W., Weller, M., and Debatin, K. M. (2002) Smac agonists sensitize for Apo2L/Trail- or anticancer drug-induced apoptosis and induce regression of malignant glioma in vivo. *Nat. Med. 8*, 808–815.

(17) Wu, G., Chai, J., Suber, T. L., Wu, J. W., Du, C., Wang, X., and Shi, Y. (2000) Structural basis of IAP recognition by Smac/DIABLO. *Nature 408*, 1008–12.

(18) Du, C., Fang, M., Li, Y., Li, L., and Wang, X. (2000) Smac, a mitochondrial protein that promotes cytochrome c-dependent caspase activation by eliminating IAP inhibition. *Cell 102*, 33–42.

(19) Searle, F., Gac-Breton, S., Keane, R., Dimitrijevic, S., Brocchini, S., Sausville, E. A., and Duncan, R. (2001) N-(2-hydroxypropyl)methacrylamide copolymer-6-(3-aminopropyl)-ellipticine conjugates. Synthesis, in vitro, and preliminary in vivo evaluation. *Bioconjugate Chem. 12*, 711–718.

(20) Ding, H., Prodinger, W. M., and Kopecek, J. (2006) Identification of CD21-binding peptides with phage display and investigation of binding properties of HPMA copolymer-peptide conjugates. *Bioconjugate Chem. 17*, 514–523.

(21) Rigler, R., Mets, Ü., Widengren, J., and Kask, P. (1993) Fluorescence correlation spectroscopy with high count rate and low background: Analysis of translational diffusion. *Eur. Biophys. J. 22*, 169–175.

(22) Fischer, R., Mader, O., Jung, G., and Brock, R. (2003) Extending the applicability of carboxyfluorescein in solid-phase synthesis. *Bioconjugate Chem. 14*, 653–660.

(23) Chen, R. F., and Knutson, J. R. (1988) Mechanism of fluorescence concentration quenching of carboxyfluorescein in liposomes: energy transfer to nonfluorescent dimers. *Anal. Biochem. 172*, 61–77.

(24) Duchardt, F., Fotin-Mleczek, M., Schwarz, H., Fischer, R., and Brock, R. (2007) A comprehensive model for the endocytic uptake of cationic cell-penetrating peptides. *Traffic 8*, 848–866.

(25) Law, B., Quinti, L., Choi, Y., Weissleder, R., and Tung, C. H. (2006) A mitochondrial targeted fusion peptide exhibits remarkable cytotoxicity. *Mol. Cancer Ther. 5*, 1944–1949.

(26) Wadia, J. S., Stan, R. V., and Dowdy, S. F. (2004) Transducible TAT-HA fusogenic peptide enhances escape of TAT-fusion proteins after lipid raft macropinocytosis. *Nat. Med. 10*, 310–315.

(27) Vicent, M. J., and Duncan, R. (2006) Polymer conjugates: nanosized medicines for treating cancer. *TRENDS Biotechnol. 24*, 39–47.

BC800222E

Supplemental material for:

HPMA as a scaffold for the modular assembly of functional peptide polymers by native chemical ligation

Ivo R. Ruttekolk,[†] Falk Duchardt,[‡] Rainer Fischer,[‡,⊥] Karl-Heinz Wiesmüller,[‖] Jörg Rademann,[§] Roland Brock[*,†]

[†] Department of Biochemistry, Nijmegen Centre for Molecular Life Sciences, Radboud University Nijmegen Medical Centre, PO Box 9101, 6500 HB Nijmegen, The Netherlands

[‡] Eberhard Karls University Tübingen, Department of Molecular Biology, Interfaculty Institute for Cell Biology, Auf der Morgenstelle 15, 72076 Tübingen, Germany

[§] Leibniz Institute for Molecular Pharmacology (FMP), Robert-Rössle-Str. 10, 13125 Berlin, Germany and: Free University Berlin, Institute for Chemistry and Biochemistry, Takustr. 3, 14195 Berlin, Germany

[‖] EMC microcollections GmbH, Sindelfinger Straße 3, 72072 Tübingen, Germany.

[⊥] Present address: Wacker Chemie AG, Hanns-Seidel-Platz 4, 81737 München, Germany

*to whom all correspondence should be addressed:

Department of Biochemistry, Nijmegen Centre for Molecular Life Sciences, Radboud University Nijmegen Medical Centre, PO Box 9101 (Route 286), 6500 HB Nijmegen, The Netherlands

Ph.: +31-24-3666213

Fax: +31-24-3616413

E-mail: r.brock@ncmls.ru.nl

Supplemental material – contents

1. Supplemental scheme 1 - Synthesis of the proapoptotic peptide with a cysteine residue coupled to a lysine side chain
2. Validation of the chemoselectivity of the modified native chemical ligation protocol
3. Further evidence for self-quenching of the polymer-coupled fluorophores using fluorescence spectroscopy

1) Supplemental Scheme 1 – Synthesis of the proapoptotic peptide with a cysteine residue coupled to a lysine side chain

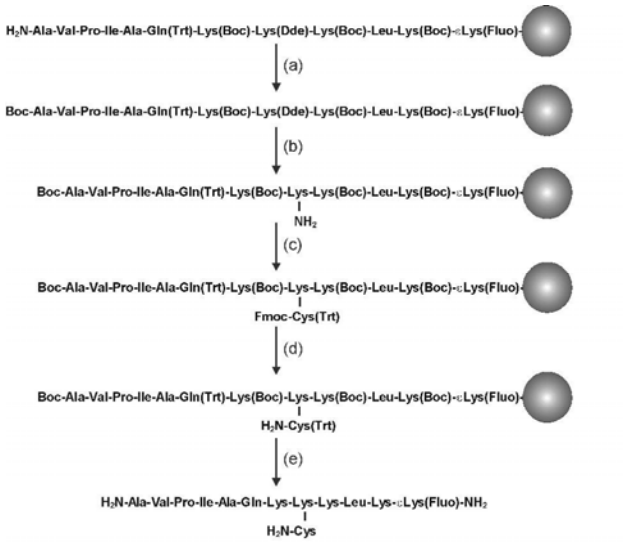

Synthesis of a proapoptotic peptide with a cysteine residue coupled to a lysine side chain for native chemical ligation to a thioester-preactivated HPMA polymer. (a) Boc-anhydride (78.6 mg, 360 μmol), DIPEA (29.8 μL, 180 μmol), DMF; (b) hydrazine hydrate (2 % v/v), DMF, 2 x 5 min; (c) Fmoc-Cys(Trt)-OH (87.9 mg, 150 μmol), 1-hydroxybenzotriazole (20.3 mg, 150 μmol), diisopropylcarbodiimide (23.5 μL, 150 μmol), DMF, 24 h; (d) piperidine (20 % v/v), DMF, 2 x 5 min; (e) triisopropylsilane (2.5 % v/v), 1,2-ethanedithiole (2.5 % v/v), H_2O (2.5 % v/v), trifluoracetic acid, 3 h; boc = tert-butyloxycarbonyl; Fmoc = 9-fluorenylmethoxycarbonyl.

2) Validation of the chemoselectivity of coupling using a modified native chemical ligation (NCL) protocol. Conversion of the highly reactive HPMA-nitrophenyl ester into a benzyl thioester and incubation with peptide in water-free DMSO are modifications of the standard NCL protocol. In order to validate the chemoselectivity of this modified NCL protocol, after incubation of the HPMA-co-methacrylate-Gly-Gly-p-nitrophenylester with a benzylmercaptan-thiol ester, the polymer was incubated either with a peptide containing an N-terminal cysteine residue (H_2N-CKLKεK(Fluo)-NH_2) or an analog in which this residue was replaced by an alanine residue (H_2N-AKLKεK(Fluo)-NH_2). Only the cysteine-containing peptide was ligated to the polymer (Suppl. Figure 1). For the control peptide, gel filtration retarded the DMSO as well as the free peptide.

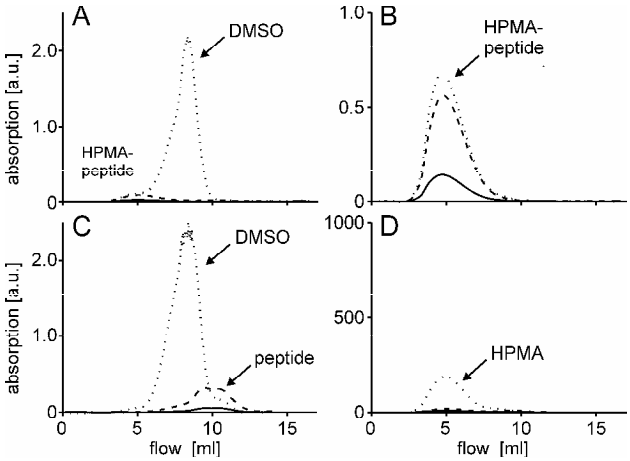

Suppl. Figure 1. Chemoselectivity of the modified NCL protocol. (A,B) Analytical gel filtration chromatography of the HPMA thioester after reaction with the peptide H_2N-CKLKεK(Fluo)-NH_2 before (A) and after (B) removal of DMSO with a desalting column. (C, D) Analytical gel filtration chromatography after incubation of the HPMA thioester with the peptide H_2N-AKLKεK(Fluo)-NH_2 before (C) and after (D) purification with a desalting column (dotted line: absorption at 215 nm, solid line: absorption at 280 nm, dashed line: absorption at 492 nm)

3) Characterization of polymer-coupled peptides by fluorescence spectroscopy. Further evidence for self quenching was obtained by comparison of adsorption and emission spectra of both the free peptide and the peptide-loaded polymer (Suppl. Figure 2). Recording of absorption and fluorescence emission spectra confirmed that conjugation of the peptide to the polymer affected the spectral characteristics of fluorescein. Spectroscopically determined absorbance and fluorescence spectra indicate bathochrome shifts of few nanometres. The shift in the absorption spectrum could even be observed with the naked eye as solutions of the polymer conjugates appeared more orange, whereas unconjugated peptides appeared more yellow.

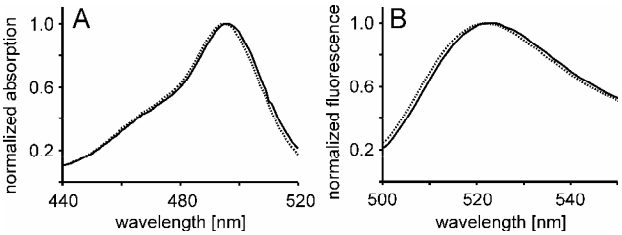

Suppl. Figure 2. Characterization of photophysical shifts occurring upon HPMA conjugation of peptides. (A) Normalized absorbance and (B) fluorescence emission spectra of the free, fluorescein-labeled AVPIAQK analog (dashed line) and the HPMA-AVPIAQK conjugate (solid line). The conjugate and the free peptide were dissolved in Tris/HCl pH 8.8 to a concentration of 2.0 μM with respect to the fluorescein moiety.

The Inhibitory Potencies of Monoclonal Antibodies to the Macrophage Adhesion Molecule Sialoadhesin Are Greatly Increased Following PEGylation

Julie Ducreux,[†] Rita Vanbever,[†] and Paul R. Crocker*[,‡]

Department of Pharmaceutical Technology, School of Pharmacy, Université Catholique de Louvain (UCL), 1200 Brussels, Belgium, and Wellcome Trust Biocentre, College of Life Sciences, University of Dundee, Dundee DD1 5EH, United Kingdom.
Received June 26, 2008; Revised Manuscript Received August 7, 2008

PEGylation of antibodies is known to increase their half-life in systemic circulation, but nothing is known regarding whether PEGylation can improve the inhibitory potency of antibodies against target receptors. In this paper, we have examined this question using antibodies directed to Sialoadhesin (Sn), a macrophage-restricted adhesion molecule that mediates sialic acid dependent binding to different cells. Anti-Sn monoclonal antibodies (mAbs), SER-4 and 3D6, were conjugated to PEG 5 kDa or and PEG 20 kDa, resulting in the incorporation of up to 3 molecules of PEG per mAb molecule. Following purification of PEGylated mAbs by anion exchange chromatography, it was shown that PEGylation had little or no effect on antigen binding activity but led to a dramatic increase in inhibitory potency that was proportional to both the size of the PEG and the degree of derivatization. Thus, PEGylation of antibodies directed to cell surface receptors could be a powerful approach to improve the therapeutic efficacy of antibodies, not only by increasing their half-life in vivo, but also by increasing their inhibitory potency for blocking receptor−ligand interactions.

INTRODUCTION

The modification of proteins with poly(ethylene glycol) (PEG) is now a well-established technique. At a therapeutic level, a number of benefits of PEGylation have been found, including the prolongation of protein half-life in the body, reduced degradation by metabolic enzymes, and elimination of its immunogenicity (for reviews, see *refs 1, 2*). PEG is a highly motile polymer which, when conjugated to a protein, can mask antigenic sites and sterically hinder access of proteolytic enzymes. Given the flexibility and large hydrated volume of PEG chains, another potential advantage of coupling PEG to proteins such as antibodies is an enhancement in their inhibitory potency via steric effects. This could be particularly useful for antibodies directed to cell surface proteins designed to disrupt receptor−ligand interactions. For example, blocking antibodies directed to endothelial cell adhesion molecules like VCAM and ICAM are potentially useful for treatment of inflammatory diseases due to their key roles in leukocyte recruitment and activation (*3, 4*).

Sialoadhesin (Sn, Siglec-1, CD169) is a macrophage-restricted adhesion molecule and a member of the Siglec family of sialic acid binding immunoglobulin (Ig)-like lectins (*5*). It contains 17 Ig-like domains and mediates sialic acid dependent adhesion to a range of cell types including lymphoid and myeloid cells (*6*). The sialic acid binding site of Sn is located on the surface of domain 1 and has been characterized at the atomic level by X-ray crystallography (*7*). Sn was originally characterized in the mouse as a non-phagocytic sialic acid dependent sheep erythrocyte receptor expressed on macrophage subsets (*8*), especially those in secondary lymphoid organs (*9*). Sn can be upregulated on monocytes and macrophages during inflammatory responses, including autoimmune diseases such as rheumatoid arthritis (*10*) and experimental autoimmune encephalomyelitis (*11*), and on macrophages that infiltrate human breast tumors (*12*). Studies on Sn-deficient mice have shown that Sn is able to exacerbate T cell dependent inflammatory responses in a model of autoimmune uveoretinitis (*13*) and in genetically determined demyelination neuropathies of the central and peripheral nervous systems (*14*). These results suggest an important role for Sn during inflammatory and immune responses (*15*).

SER-4 and 3D6 are monoclonal rat IgG2a anti-Sn antibodies directed to two distinct epitopes of mouse Sn, domains 2 and/or 3 for SER-4, and domain 1 for 3D6 (*6, 16, 17*). When used separately, each antibody can partially inhibit Sn-dependent adhesion, and when mixed together, a synergistic effect on inhibition was observed (*5, 18*). These antibodies therefore provide a useful model system to explore the potential of PEGylation in increasing inhibitory potency of antibodies directed close to the ligand binding site of Sn. The present study describes the preparation and characterization of PEG-mAbs directed to Sn and demonstrates that PEGylation can lead to a dramatic increase in the inhibitory potency of anti-Sn mAbs. This approach could lead to improved therapeutic efficacy for a range of immune and inflammatory disorders, not only for Sn, but also for other adhesion molecules important in cell-to-cell interactions in inflammatory and immune responses and potentially more broadly for other membrane receptors.

EXPERIMENTAL PROCEDURES

PEG. PEG reagents were purchased from Nektar Therapeutics (Huntsville, AL). Two succinimidyl α-methylbutanoate-PEG (abbreviated SMB-PEG) reagents were used: a 5 kDa linear PEG chain and a 20 kDa linear PEG chain. Modification of mAb with PEG molecules is abbreviated as, for example, SER-4−2PEG 5 kDa and denotes a modification of SER-4 mAb with 2 linear PEG chains of 5 kDa.

* Author to whom correspondence should be addressed. Phone: (44) 1382 345781. fax: (44) 1382 345783. E-mail: p.r.crocker@dundee.ac.uk.
[†] Université Catholique de Louvain.
[‡] Wellcome Trust Biocentre.

10.1021/bc800259z CCC: $40.75 © 2008 American Chemical Society
Published on Web 09/23/2008

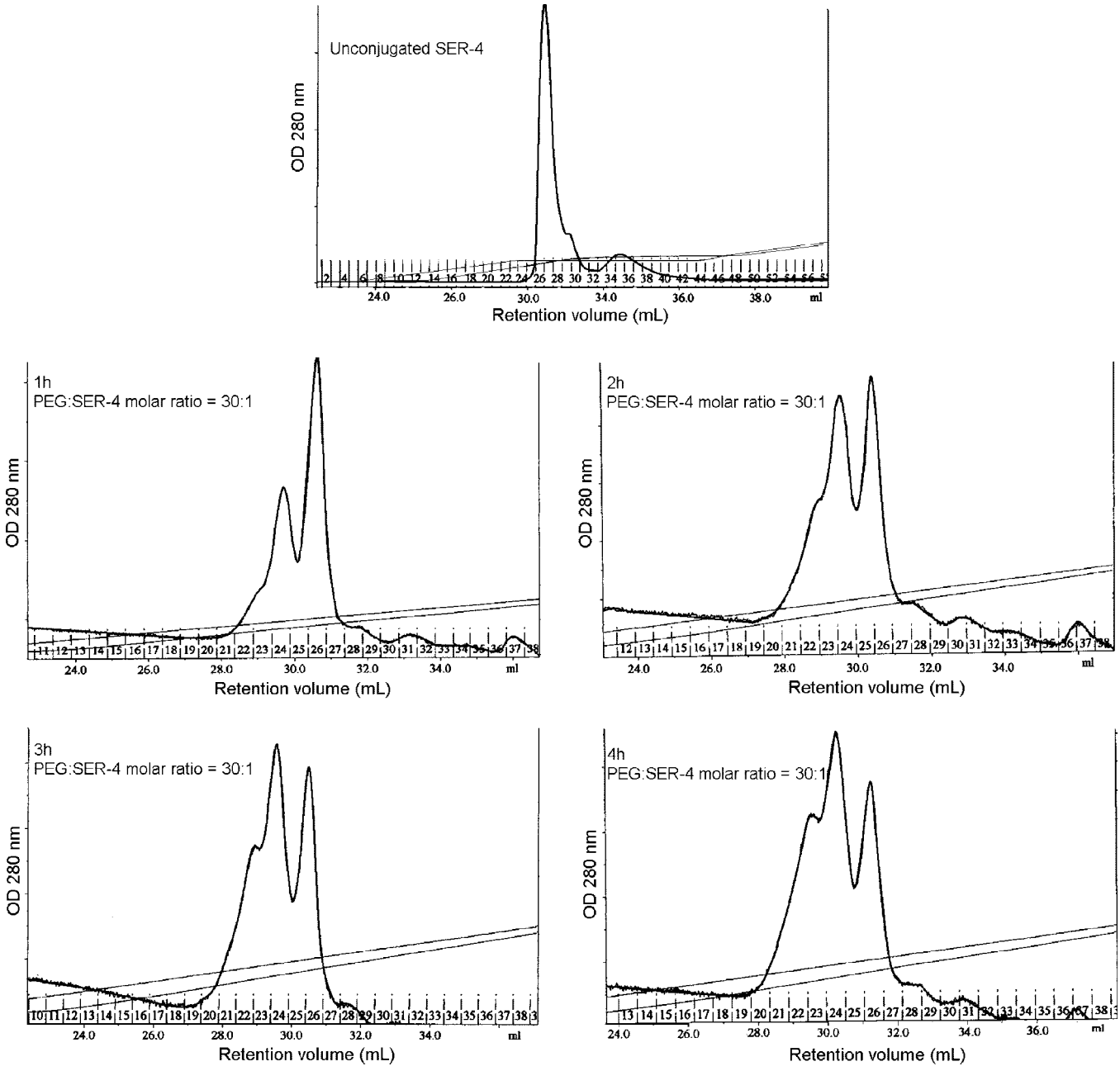

Figure 1. Anion exchange chromatograms of unconjugated SER-4 mAb (top) and modified SER-4 mAb following PEGylation in PBS pH 7.4 with initial PEG 5 kDa/SER-4 molar ratio of 30:1 and incubation for the different times indicated.

Purification of SER-4 and 3D6 Monoclonal Antibodies. Hybridomas producing SER-4 and 3D6 mAbs were expanded in IMDM + L-glutamine + 25 mM HEPES medium (Gibco, Invitrogen Corporation) supplemented with 10% hybridoma serum (FBS Gold from PAA Laboratories GmbH) and 1% penicillin/streptomycin. The conditioned supernatant was passed through a 0.2 μm filter to remove protein aggregates and cell debris and the SER-4 and 3D6 IgGs were purified from supernatants by affinity chromatography using a Protein-G Sepharose column. Bound IgGs were eluted with 0.1 M glycine (pH 3), and fractions containing protein were neutralized by the addition of 0.1 volume 1 M Tris (pH 8) and dialyzed into PBS. SER-4 and 3D6 mAbs were further purified by anion exchange Mono Q HR 5/5 high-performance liquid chromatography (HPLC) column (Amersham, Biosciences, UK). The flow rate was 0.5 mL/min, and the column was maintained at 4 °C. A salt gradient was used for elution: Buffer A was 25 mM Tris (pH 8); buffer B was 25 mM Tris, 1 M NaCl (pH 8).

Preparation of mAb-PEG Conjugates. SMB-PEG was allowed to react with free amino groups of SER-4 or 3D6 mAbs (2 mg/mL) at a SMB-PEG:antibody ratio 30:1 in PBS, pH 7.4, for 3 h at room temperature. The reaction was stopped by addition of 0.1 M glycine, and the mixture was then desalted with a PD-10 column (Amersham, Biosciences, UK) equilibrated with 25 mM Tris, pH 8. Anion exchange Mono Q HR 5/5 HPLC column chromatography was used to separate and purify PEG conjugates. Fractions were analyzed by SDS-PAGE using 7.5% and 12% acrylamide gels for nonreducing and reducing conditions, respectively (*19*), and stained in Brilliant Blue G-Colloidal suspension (Sigma). MALDI TOF-mass spectrometry analysis was also performed on fractions in order to confirm the size and the degree of

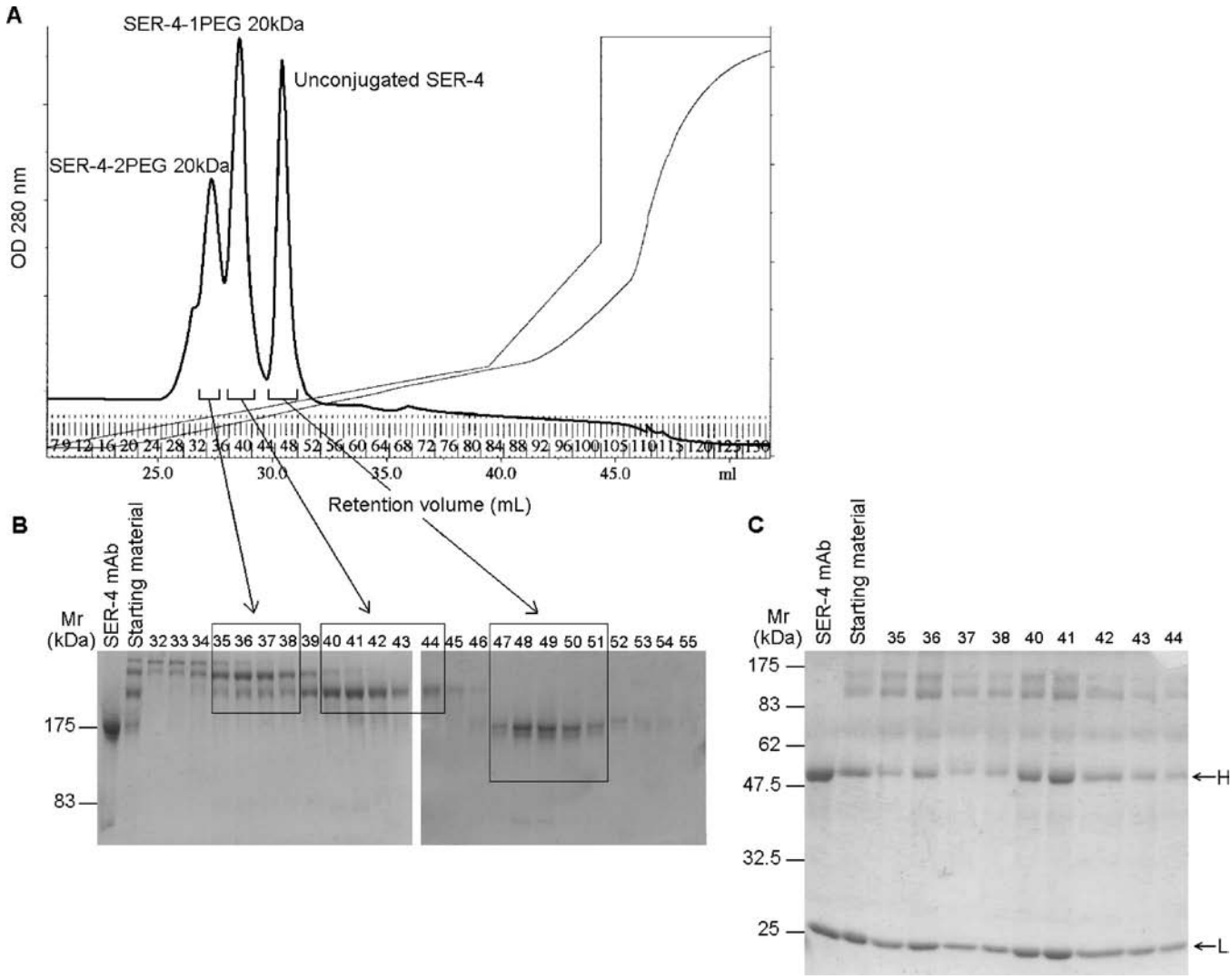

Figure 2. SER-4 mAb was conjugated to PEG 20 kDa (3 h in PBS pH 7.4 at room temperature) and PEG conjugates were purified by anion exchange chromatography (A). Fractions were analyzed by SDS-PAGE under nonreducing and reducing conditions to determine the degree of attachment and location of PEG on heavy and light chains. Sizes of molecular markers are shown. Under nonreducing conditions (B), SDS-PAGE stained with Coomassie blue shows 3 different degree of PEGylation. Under reducing conditions (C), arrows show heavy (H) chains of SER-4 at ~50 kDa and light (L) chains of SER-4 at 25 kDa. The band running between the 62 and 83 kDa markers in all tracks is a contaminant protein that was also present in the buffer-only lane (not shown).

modification of the different PEGylated products (Applied Biosystems 4700 Proteomics Analyzer).

Biotin Labeling of mAbs. Biotin labeling of SER-4 and 3D6 mAbs was performed using EZ-Link NHS-LC-Biotin reagent (Pierce, Rockford, IL) according to the manufacturer's procedure. Briefly, SER-4 or 3D6 mAbs (2 mg/mL) were mixed with 20-fold molar excess of *N*-hydroxysuccinimide (NHS)-activated biotin in PBS, pH 7.4, for 1 h at room temperature. Unreacted NHS-biotin was removed from the reaction mixture using PD-10 columns (Amersham, Biosciences, UK). Concentrations of biotin-labeled SER-4 or 3D6 were measured using a BCA protein assay kit (Pierce, Rockford, IL).

Antibody Binding Activity of PEG-mAb Conjugates. The antibody binding activities of each PEGylated product were determined by a competitive immunoassay using human Fc-chimera Sn (domains 1 to 3) immobilized on microtiter plate. 96 well Immulon-4 plates (Thermo, Milford, MA) were coated with 10 μg/mL antihuman IgG (Fc specific) mAb (Sigma) diluted in 0.1 M bicarbonate coating buffer (pH 9.6) and blocked with PBS + 5% skimmed milk. After washing, human Fc-chimera Sn was adsorbed to wells at a concentration of 2 μg/mL in PBS + 0.1% BSA. The wells were washed and incubated with biotin-labeled SER-4 or 3D6 anti-Sn mAb (0.1 μg/mL) mixed with serial dilutions of either unlabeled mAbs or mAb-PEG conjugates in PBS + 0.1% BSA. After washing, horseradish peroxidase conjugated streptavidin was added (Caltag). The wells were washed and the peroxidase activity was measured using 0.4 mg/mL *O*-phenylenediamine dihydrochloride (OPD) in 0.05 M phosphate-citrate buffer containing 0.014% H_2O_2 (Sigma) as substrate, and the absorbance at 450 nm was measured. The inhibition of biotin-labeled mAbs binding to Sn by PEG conjugates was compared to the inhibition seen with unlabeled mAbs. The percentage of biotin-labeled mAbs binding was determined by the following formula:

$$Abs_{\text{with competitor}} \times 100/Abs_{\text{without competitor}}$$

where $Abs_{\text{with competitor}}$ = absorbance when biotin-labeled mAbs are in competition with PEG conjugates or parent mAbs.

$Abs_{\text{without competitor}}$ = absorbance when biotin-labeled mAbs are used alone (100% of binding).

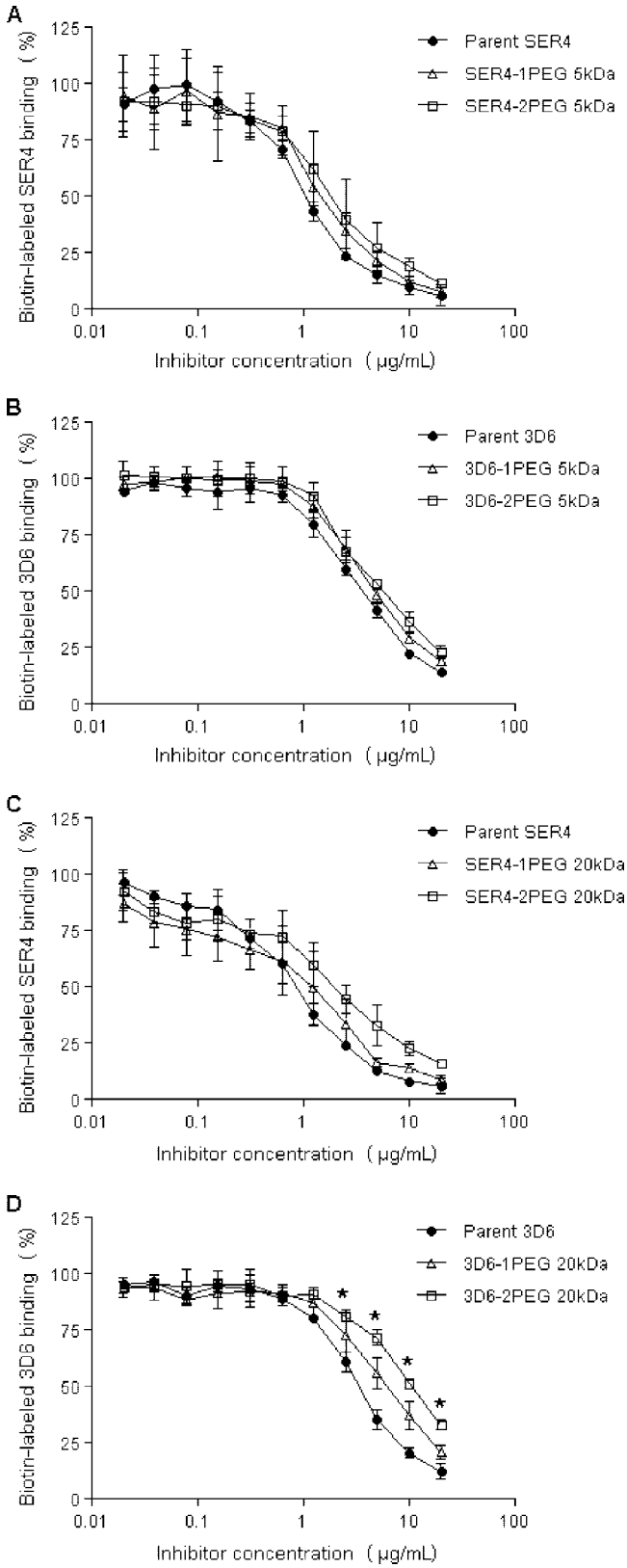

Figure 3. Binding activity of PEGylated mAbs. Conjugates of SER-4 (A,C) and of 3D6 (B,D) were tested at several concentrations for their ability to competitively inhibit the binding of biotin-labeled SER-4 and 3D6, respectively, to Sn-coated microtiter plates. Panels A and B: PEGylation of both mAbs with 1 (open triangles) or 2 (open squares) molecules of PEG 5 kDa does not affect the binding activity of mAbs. Panels C and D: Both SER-4 and 3D6 modified with 2 (open squares) molecules of PEG 20 kDa show a slight reduction of binding activity when compared to unconjugated mAbs (solid circles). * indicates a statistically significant difference in binding inhibition compared to unconjugated mAbs (Tukey test, $P < 0.001$). Each data point represents the mean ± SD ($n = 3$ in duplicate wells).

Solid-Phase Red Blood Cell (RBC) Binding Assay. To assess the inhibitory potency of PEGylated mAbs, RBC binding assays were carried out. Briefly, 96 well Immulon-4 plates were coated with antihuman IgG (Fc specific) mAb (Sigma) followed by incubation with human Fc-chimera Sn (domains 1 to 3). After washing, the wells were incubated for 1 h with 50 μL PBS + 0.1% BSA containing serially diluted unconjugated mAbs or PEG conjugates, used alone or in combination. One hundred microliters of freshly prepared human RBC at 0.5% volume/volume were then added directly to the wells, mixed, and incubated for 30 min at room temperature (*18*). The wells were gently washed with PBS + 0.1% BSA several times. To determine RBC binding quantitatively, the plate was dried, fixed with methanol for 5−10 min, and dried again, and the bound RBC were measured using 0.4 mg/mL *O*-phenylenediamine dihydrochloride (OPD) in 0.05 M phosphate−citrate buffer containing 0.014% H_2O_2 (Sigma). The absorbance at 450 nm was taken using a 96 well plate reader (Roses and Anthos 2001).

The percentage of inhibition of RBC binding was determined by the following formula:

$Abs_{with\ mAbs} \times 100/Abs_{without\ mAbs}$

where $Abs_{with\ mAbs}$ = absorbance when PEG conjugates or parent mAbs were previously incubated with Sn.

$Abs_{without\ mAbs}$ = absorbance when Sn is only incubated with RBC (100% of RBC binding).

Statistics. All results are expressed as mean ± standard deviation (SD). The one-way analysis of variance (ANOVA) test and Tukey test were performed to demonstrate statistical differences ($P < 0.05$), using the software *GraphPad Prism 5* for Windows.

RESULTS AND DISCUSSION

PEGylation of Anti-mouse Sn mAbs. Following purification by protein G-Sepharose and anion-exchange chromatography, both antibodies were PEGylated using either 5 kDa or 20 kDa SMB-PEG, a succinimidyl-α-methylbutanonate derivative of NHS-PEG with a significantly longer half-life in solution (*20, 21*). PEGylation was carried out at pH 7.4, a condition that favors selective coupling to the N-terminal residues over surface-exposed lysine residues. Since IgG molecules are composed of 2 identical light chains (25 kDa) and 2 identical heavy chains (50−70 kDa), between 1 and 4 PEG molecules can, in principle, be attached per IgG molecule. PEGylation was monitored by anion-exchange chromatography (Figure 1). Under the conditions used, the more strongly PEGylated antibodies eluted first in the increasing salt gradient (Figure 2A), presumably as a result of a charge-shielding effect of PEG that weakens their binding to the anion exchange resin (*2*). Initial experiments using 5 kDa SMB-PEG showed that a molar ratio of 30:1 PEG/mAb resulted in ∼33% of antibody molecules incorporating PEG after 1 h at room temperature (Figure 1). When the time of incubation was increased to 3 h, up to ∼70% of antibody molecules were labeled with PEG (Figure 1), but longer incubations did not lead to improved yields. Similar findings were made using SMB-PEG 20 kDa (not shown).

Anion exchange chromatography showed 3 peaks following PEGylation with SMB-PEG 5 kDa (Figure 1, 3 h time) and up to 4 peaks following PEGylation with SMB-PEG 20 kDa (Figure 2A). The 20 kDa-PEGylated mAbs were eluted with a lower salt concentration than 5 kDa-PEGylated mAbs. This may be due to a greater shielding effect of 20 kDa-PEG chains resulting from their increased length and mobility.

Characterization of SER-4-PEG and 3D6-PEG. *PEGylation Analysis.* SDS-PAGE was used under nonreducing and reducing conditions to investigate the attachment and location of PEG to mAbs. With 20 kDa-PEG, the starting material

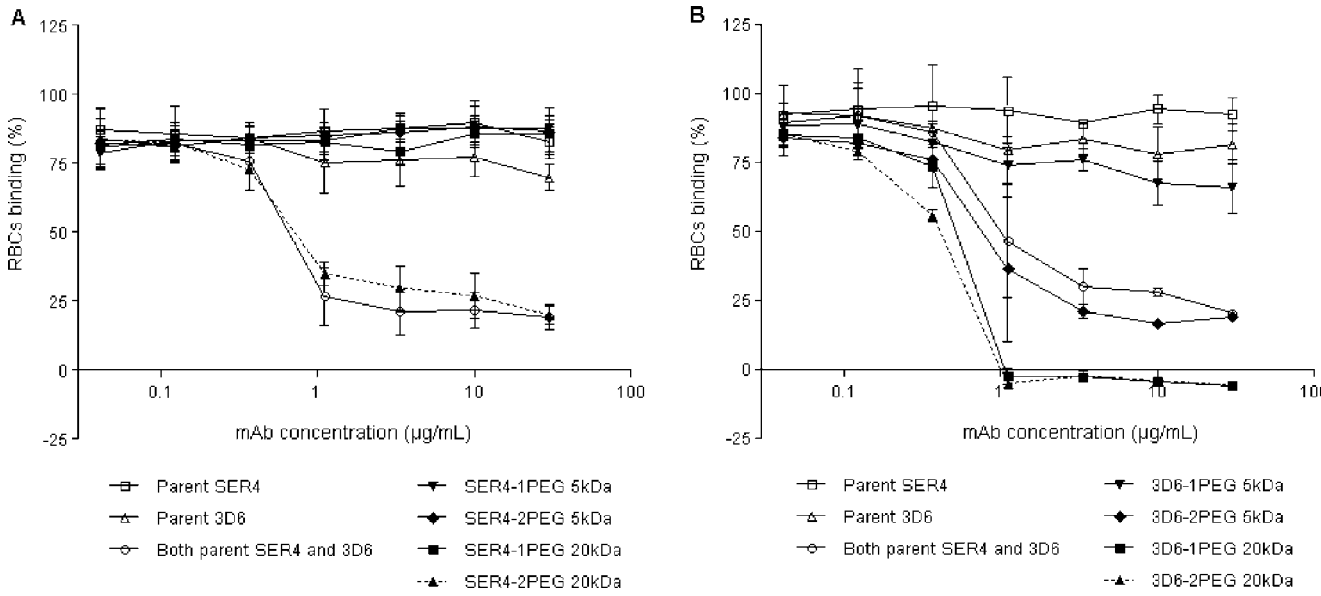

Figure 4. Inhibitory potency of PEGylated SER4 and 3D6 mAbs. A truncated form of Sn (domains 1 to 3) fused to the Fc region of human IgG1 was coated on wells at a concentration of 2 μg/mL. Wells were then preincubated with serially diluted unconjugated mAbs or PEG conjugates prior to the addition of human RBC. A preincubation of wells with SER-4 carrying 2 molecules of PEG 20 kDa reduced binding by about 75% (A). In the case of 3D6, a preincubation of wells with 3D6−2PEG 5 kDa resulted in ∼75% inhibition, and a complete inhibition of RBC binding was seen with 3D6 carrying either 1 or 2 molecules of PEG 20 kDa (B). Each data point represents the mean ± SD ($n = 3$ in duplicate wells).

showed the presence of four bands under nonreducing conditions, which corresponded to parent IgG (lower band) and 3 different degrees of PEGylation (Figure 2B). Similar findings were made with both SER-4 and 3D6, and only the data for SER-4 are shown. Following anion-exchange chromatography, the first peak (fractions 32−34) contained doubly and triply derivatized mAbs, the second peak (fractions 35−38) was strongly enriched in doubly derivatized mAb, and the third peak (fractions 40−44) was strongly enriched with singly derivatized mAb (Figure 2B). The fourth peak (fractions 47−51) contained underivatized mAb. These interpretations were supported by analysis of selected fractions by MALDI-TOF mass spectrometry (data not shown).

When these fractions were analyzed under reducing conditions, introduction of PEG was only observed with the heavy chains, suggesting that the N-terminal residues of the light chains were not readily conjugated under the conditions used (Figure 2C). Interestingly, heavy chains contained both one and two PEG molecules per heavy chain, suggesting that both the N-terminal residue and an internal lysine residue were modified on the same chain. These findings indicate that each mAb pool is heterogeneous with respect to the PEG modification, with each heavy chain containing 0, 1, or 2 PEG molecules, although the total number of PEG molecules per antibody molecule rarely exceeded 2.

Binding Activity of PEGylated mAbs. To investigate whether SMB-PEG modification affected the antigen-binding activity, derivatized SER-4 and 3D6 mAbs were tested in a competitive inhibition enzyme-linked assay (Figure 3). For this purpose, SER-4 and 3D6 mAbs were labeled with biotin and the abilities of parent mAbs and PEGylated mAbs (with 1 or 2 molecules of PEG 5 kDa and 20 kDa) to inhibit the binding of biotin-labeled mAb to antigen were compared. We showed that PEGylation of both mAbs with 1 or 2 molecules of PEG 5 kDa did not affect the inhibitory activity of mAbs (Figure 3A,B). However, both the SER-4 and 3D6 mAbs containing 2 molecules of PEG 20 kDa showed a slight reduction in inhibitory activity when compared with unlabeled mAbs (Figure 3C,D). This difference was statistically significant only in the case of 3D6 mAb ($P < 0.001$). These results showed that PEGylation of N-terminal residues of anti-Sn mAbs had little or no effect on their antigen binding strength.

Effect of PEGylation on Inhibitory Potency of SER-4 and 3D6. Human RBC bind strongly to Sn in a sialic acid dependent manner, and this provides a useful model system to study adhesion mediated by the receptor (*17*). To investigate whether PEGylation of anti-Sn mAbs could enhance their inhibitory potency, we used a well-defined solid-phase RBC binding assay in which recombinant Sn is coated on a plate and allowed to bind RBC in the presence and absence of anti-Sn mAbs (*5*). As shown previously (*5*), we found that neither SER-4 nor 3D6 mAb was able to inhibit binding when added alone, but in combination, they reduced binding by about 75% (Figure 4). When the inhibitory activities of PEGylated mAbs were analyzed, SER-4 carrying 2 molecules of PEG 20 kDa resulted in about 75% inhibition, but incorporation of 1 or 2 molecules of PEG 5 kDa or 1 molecule of PEG 20 kDa had no effect (Figure 4A). As SER-4 is directed to domains 2/3 of Sn, it is likely that the steric effects of 2 molecules of PEG 20 kDa are sufficient to mask the sialic acid binding pocket on domain 1 of Sn and inhibit the binding of RBC.

In the case of 3D6, no increased inhibition was seen with 1 molecule of PEG 5 kDa, but 2 molecules of PEG 5 kDa resulted in ∼75% inhibition. Strikingly, complete inhibition of RBC binding was seen with 3D6 carrying either 1 or 2 molecules of PEG 20 kDa with an IC_{50} values of 0.5 and 0.35 μg/mL, respectively (Figure 4B).

Finally, we compared inhibitory potency of antibodies when used in combination. A total of sixteen combinations of SER-4-PEG and 3D6-PEG were compared to the parent SER-4 and 3D6 combination in solid-phase RBC binding assays, and the IC_{50} values were calculated (Figure 5). All combinations of PEGylated antibodies were better inhibitors than the mixture of unlabeled SER-4 and 3D6. As expected,

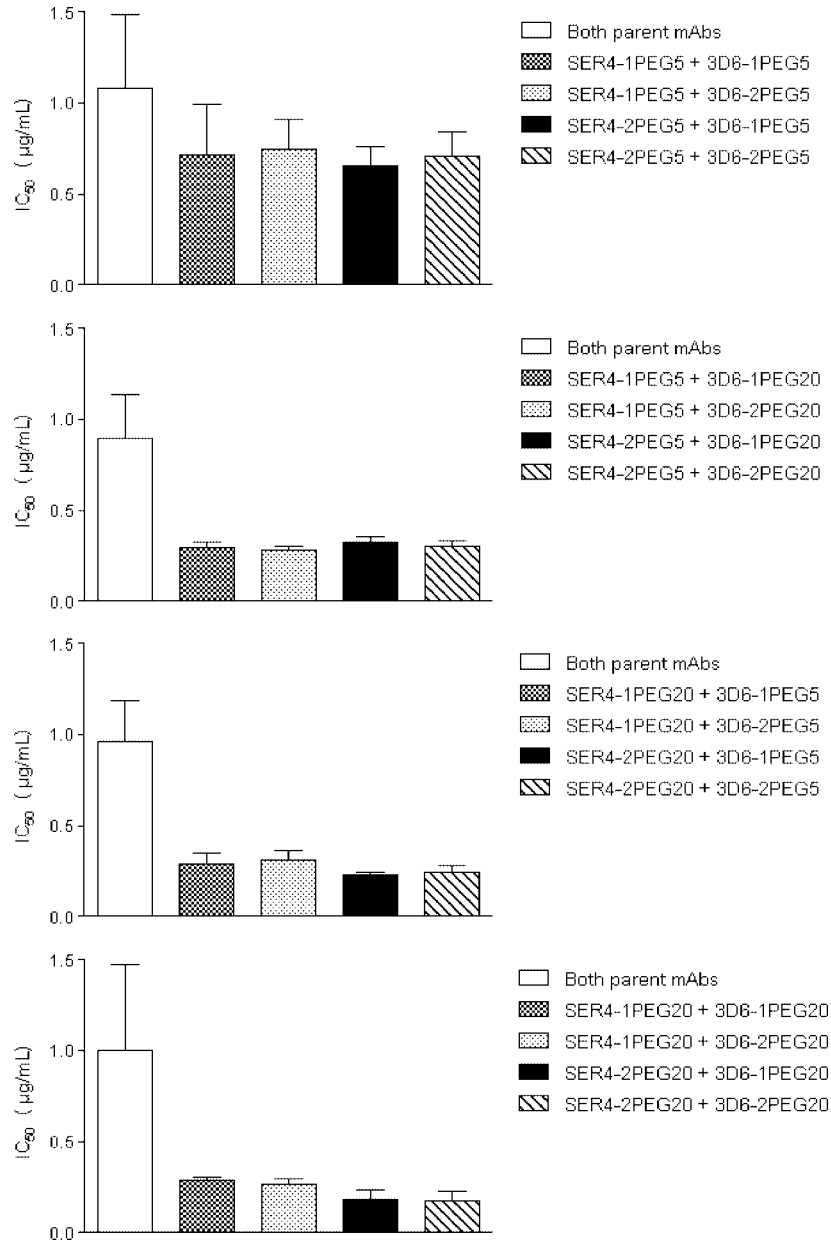

Figure 5. Inhibitory potency of PEGylated SER4 and 3D6 mAbs used in combination. A truncated form of Sn (domains 1 to 3) was coated on wells at a concentration of 2 μg/mL. Wells were then preincubated with serially diluted unconjugated mAbs or PEG conjugates in combination prior to the addition of human RBC. A total of sixteen combinations of SER-4-PEG and 3D6-PEG were compared to the parent SER-4 and 3D6 combination in RBC binding assays and concentrations inhibiting 50% of RBC binding (IC_{50}) were compared. All combinations of PEGylated antibodies were better inhibitors than the mixture of unlabeled SER-4 and 3D6. Bar represents the mean values of $IC_{50} \pm$ SD ($n = 3$ in duplicate wells).

the inhibitory potency further increased in line with the degree of PEGylation, with the most potent combination containing SER-4 and 3D6, each with 2 molecules of PEG 20 kDa, resulting in an IC_{50} of 0.3 μg/mL compared to an IC_{50} of $\sim$1.0 μg/mL using the mixture of non-PEGylated SER-4 and 3D6 mAbs (Figure 5).

In conclusion, this study shows that PEGylation of antibodies directed to the macrophage adhesion molecule, Sn, can have a dramatic effect on the inhibitory potency with minimal impact on binding strength. The pattern of results seen using the two antibodies directed to different epitopes, two sizes of PEG and different extents of derivatization fits very well with the concept of PEG-dependent steric hindrance. Thus, PEGylation of antibodies directed to cell surface receptors leads not only to increased circulating half-life, but also increased inhibitory potency that could be potentially exploited in a therapeutic setting such as in autoimmune or inflammatory diseases.

ACKNOWLEDGMENT

We would like to thank Sharon Shepherd for assistance with the FPLC analysis and purifications and the 'FingerPrints' proteomics facility (University of Dundee, Scotland) for providing the mass-spectrometry analysis of PEGylated conjugates. This research was funded by a "FIRST EUROPE" grant (Walloon Region, Belgium and European social fund) and a Wellcome Trust Senior Fellowship awarded to PRC. Rita Vanbever is a Chercheur Qualifié of the Fonds National de la Recherche Scientifique (FNRS, Belgium).

LITERATURE CITED

(1) Veronese, F. M., and Pasut, G. (2005) PEGylation, successful approach to drug delivery. *Drug Discovery Today 10*, 1451–1458.

(2) Fee, C. J., and Van Alstine, J. M. (2006) PEG-proteins: Reaction engineering and separation issues. *Chem. Eng. Sci. 61*, 924–939.

(3) Davis, L. S., Kavanaugh, A. F., Nichols, L. A., and Lipsky, P. E. (1995) Induction of persistent T cell hyporesponsiveness in vivo by monoclonal antibody to ICAM-1 in patients with rheumatoid arthritis. *J. Immunol. 154*, 3525–3537.

(4) Soriano, A., Salas, A., Salas, A., Sans, M., Gironella, M., Elena, M., Anderson, D. C., Pique, J. M., and Panes, J. (2000) VCAM-1, but not ICAM-1 or MAdCAM-1, immunoblockade ameliorates DSS-induced colitis in mice. *Lab. Invest. 80*, 1541–1551.

(5) Crocker, P. R., Mucklow, S., Bouckson, V., McWilliam, A., Willis, A. C., Gordon, S., Milon, G., Kelm, S., and Bradfield, P. (1994) Sialoadhesin, a macrophage sialic acid binding receptor for haemopoietic cells with 17 immunoglobulin-like domains. *EMBO J. 13*, 4490–4503.

(6) van den Berg, T. K., Breve, J. J., Damoiseaux, J. G., Dopp, E. A., Kelm, S., Crocker, P. R., Dijkstra, C. D., and Kraal, G. (1992) Sialoadhesin on macrophages: its identification as a lymphocyte adhesion molecule. *J. Exp. Med. 176*, 647–655.

(7) May, A. P., Robinson, R. C., Vinson, M., Crocker, P. R., and Jones, E. Y. (1998) Crystal structure of the N-terminal domain of sialoadhesin in complex with 3′ sialyllactose at 1.85 Å resolution. *Mol. Cell 1*, 719–728.

(8) Crocker, P. R., and Gordon, S. (1996) Properties and distribution of a lectin-like hemagglutinin differentially expressed by murine stromal tissue macrophages. *J. Exp. Med. 164*, 1862–1875.

(9) Schadee-Eestermans, I. L., Hoefsmit, E. C., van de Ende, M., Crocker, P. R., van den Berg, T. K., and Dijkstra, C. D. (2000) Ultrastructural localisation of sialoadhesin (siglec-1) on macrophages in rodent lymphoid tissues. *Immunobiology 202*, 309–325.

(10) Hartnell, A., Steel, J., Turley, H., Jones, M., Jackson, D. G., and Crocker, P. R. (2001) Characterization of human sialoadhesin, a sialic acid binding receptor expressed by resident and inflammatory macrophage populations. *Blood 97*, 288–296.

(11) van den Berg, T. K., van Die, I. V., de Lavalette, C. R., Dopp, E. A., Smit, L. D., van der Meide, P. H., Tilders, F. J., Crocker, P. R., and Dijkstra, C. D. (1996) Regulation of sialoadhesin expression on rat macrophages. Induction by glucocorticoids and enhancement by IFN-beta, IFN-gamma, IL-4, and lipopolysaccharide. *J. Immunol. 157*, 3130–3138.

(12) Nath, D., Hartnell, A., Happerfield, L., Miles, D. W., Burchell, J., Taylor-Papadimitriou, J., and Crocker, P. R. (1999) Macrophage-tumour cell interactions: identification of MUC1 on breast cancer cells as a potential counter-receptor for the macrophage-restricted receptor, sialoadhesin. *Immunology 98*, 213–219.

(13) Jiang, H. R., Hwenda, L., Makinen, K., Oetke, C., Crocker, P. R., and Forrester, J. V. (2006) Sialoadhesin promotes the inflammatory response in experimental autoimmune uveoretinitis. *J. Immunol. 177*, 2258–2264.

(14) Kobsar, I., Oetke, C., Kroner, A., Wessig, C., Crocker, P., and Martini, R. (2006) Attenuated demyelination in the absence of the macrophage-restricted adhesion molecule sialoadhesin (Siglec-1) in mice heterozygously deficient in P0. *Mol. Cell. Neurosci. 31*, 685–691.

(15) Crocker, P. R., Hartnell, A., Munday, J., and Nath, D. (1997) The potential role of sialoadhesin as a macrophage recognition molecule in health and disease. *Glycoconj. J. 14*, 601–609.

(16) Crocker, P. R., Werb, Z., Gordon, S., and Bainton, D. F. (1990) Ultrastructural localization of a macrophage-restricted sialic acid binding hemagglutinin, SER, in macrophage-hematopoietic cell clusters. *Blood 76*, 1131–1138.

(17) Crocker, P. R., Kelm, S., Dubois, C., Martin, B., McWilliam, A. S., Shotton, D. M., Paulson, J. C., and Gordon, S. (1991) Purification and properties of sialoadhesin, a sialic acid-binding receptor of murine tissue macrophages. *EMBO J. 10*, 1661–1669.

(18) Crocker, P. R., and Gordon, S. (1989) Mouse macrophage hemagglutinin (sheep erythrocyte receptor) with specificity for sialylated glycoconjugates characterized by a monoclonal antibody. *J. Exp. Med. 169*, 1333–1346.

(19) Laemmli, U. K. (1970) Cleavage of structural proteins during the assembly of the head of bacteriophage T4. *Nature 227*, 680–685.

(20) Roberts, M. J., Bentley, M. D., and Harris, J. M. (2002) Chemistry for peptide and protein PEGylation. *Adv. Drug Delivery Rev. 54*, 459–476.

(21) Chapman, A. P. (2002) PEGylated antibodies and antibody fragments for improved therapy: a review. *Adv. Drug Delivery Rev. 54*, 531–545.

BC800259Z

Bioconjugate Chemistry

NOVEMBER 2008
Volume 19, Number 11

© Copyright 2008 by the American Chemical Society

REVIEWS

A Semiempirical Model of Tumor Pretargeting

Guozheng Liu* and Donald J. Hnatowich

Division of Nuclear Medicine, Department of Radiology, University of Massachusetts Medical School, Worcester, Massachusetts 01655. Received July 3, 2008; Revised Manuscript Received September 4, 2008

This article provides an overview of a semiempirical pretargeting model now under development. After a brief review of the pretargeting concept, the strategies available, and the complexities of optimizing the dosage and timing, a semiempirical model is described that is not only capable of optimizing dosage and timing but also capable of predicting the results of pretargeting as a function of most pretargeting variables. The model requires knowledge of the pharmacokinetics of both the pretargeting agent (usually an antibody) and the effector, the accessibility of the pretargeting antibody for the effector, and their quantitative relationships in vivo. Several misconceptions that often surround pretargeting are also clarified.

INTRODUCTION

Conventional targeting of solid tumor with radiolabeled antibodies has vastly improved recently with the development of high-affinity antibodies and small antibody-like constructs. Similar improvements have also been made in parallel in the pretargeting of solid tumors for both imaging and therapy (*1*−*10*) such that encouraging results are now increasingly being reported in clinical trials of pretargeting (*11*). Pretargeting is popularly considered as a means of separating tumor targeting and radionuclide delivery and thus differs from conventional targeting in which the two are bound and administered together (*2, 3, 12*−*18*). The concept, strategies, applications, and prospects of pretargeting have been frequently reviewed (*1, 2, 9, 14, 16*−*29*), but the description of the pretargeting process therein remains largely qualitative, and pretargeting investigations are generally performed with dosages and timing selected largely by trial and error. Recently, we have made efforts to understand the pretargeting process quantitatively (*30*−*33*).

The justification for these efforts is the promise of greatly improved tumor-to-nontumor (T/NT) radioactivity ratios achieved shortly after administration of the radiolabeled effector compared to the conventional targeting with radiolabeled antibodies (*34*−*39*). By attaching the radionuclide to a small effector designed for rapid pharmacokinetics, the nuclide not only reaches the tumor rapidly but also clears rapidly from most normal tissues. The rapidly improving T/NT ratios of the radionuclide permit early imaging and reduce unwanted radiation exposure to normal tissues. The T/NT ratios in some tissues reached in hours by pretargeting are often equivalent to those achievable in days by conventional targeting, and more favorably, the T/NT ratios by pretargeting in some other tissues such as liver and spleen may actually exceed those by conventional targeting. This latter favorable outcome will result if the antibody becomes sequestered in these tissues (but not the tumor) and thereby becomes "invisible" to the radiolabeled effector. However, suggestions that pretargeting will provide a higher percent tumor accumulation of the radiolabeled effector may not be correct

* Guozheng Liu, Ph D; guozheng.liu@umassmed.edu; Phone: (508) 856-1958; Fax: (508) 856-6363. Donald J. Hnatowich, Ph D; donald.hnatowich@umassmed.edu; Phone: (508) 856-4256; Fax: (508) 856-6363.

10.1021/bc8002748 CCC: $40.75 © 2008 American Chemical Society
Published on Web 10/08/2008

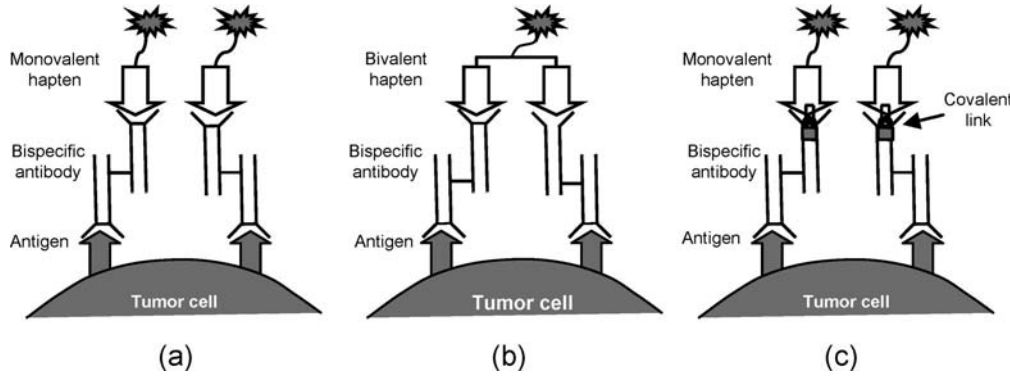

Figure 1. The principle of pretargeting strategies of bispecific antibody: (a) with monovalent hapten of moderate affinity; (b) with bivalent hapten of moderate affinity; and (c) with monovalent hapten of infinitive affinity.

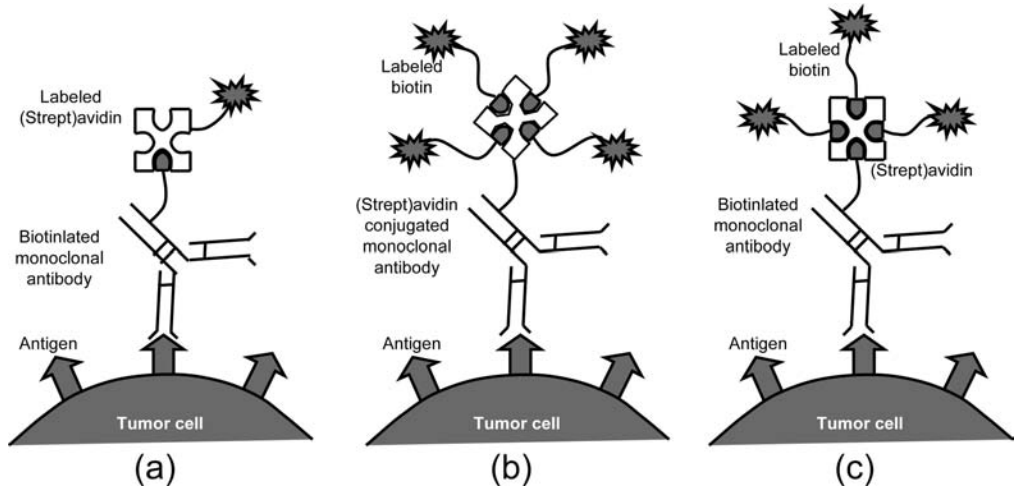

Figure 2. The three strategies of (strept)avidin/biotin pretargeting system: (a) two-step pretargeting with biotinylated antibody and radiolabeled (strept)avidin; (b) two-step pretargeting with (strept)avidin conjugated antibody and radiolabeled biotin; and (c) three-step pretargeting with biotinylated antibody, (strept)avidin, and radiolabeled biotin.

(*15*, *22*, *27*−*29*), since the rapid pharmacokinetics of the effector will limit the efficiency of its delivery into tumor and thus limit the percent accumulation (*40*).

Since the concept, approaches, applications, and prospects of pretargeting have been adequately reviewed (*1*, *2*, *9*, *14*, *16*−*29*), there is little need for another comprehensive coverage of past studies. Instead, this contribution focuses on the difficulty of optimization in pretargeting and describes a semiempirical model under development in this laboratory that not only is capable of optimizing dosage and timing but also is capable of predicting the results of pretargeting as a function of most pretargeting variables. We begin with an introduction briefly summarizing the different pretargeting systems and conclude with a discussion of the utility of the semiempirical model. Because pretargeting has been exclusively applied to tumor as the target, this report will refer throughout to pretargeting in this context, with the understanding that in the future normal tissues as targets may benefit from pretargeting as well.

PRETARGETING SYSTEMS

At least three systems have now been used for pretargeting: bispecific antibody/hapten (*41*, *42*), (strept)avidin/biotin (*43*), and oligomer/complementary oligomer (*44*−*46*), each with several distinct strategies. The simplest strategy includes two injections, and more complicated strategies may add one or more intermediate injections to clear the pretargeting antibody in the circulation, to amplify the number of the targeting sites on the cell surface, to block the binding sites of the pretargeting antibody still in blood and normal tissues, or, in the case of (strept)avidin/biotin pretargeting, to avoid the interference of endogenous biotin.

Concerning first the bispecific antibody/hapten system, the usual strategies involve two injections, although a blocking or clearing agent may be administered intermediately between the antibody and effector (*47*−*50*). Three types of hapten effectors have been reported: monovalent of moderate affinity, bivalent of moderate affinity, and monovalent of infinitive affinity. Figure 1 schematically illustrates the binding patterns of the three haptens. A monovalent hapten of moderate affinity (a) was reported to provide insufficient tumor retention (*51*−*54*). As a result, bivalent haptens (b) are usually used. The rationale for the use of bivalent hapten is that bivalency has been reported to provide enhanced binding affinity to the tethered antibody on tumor compared to the untethered antibody in circulation (*25*). The most recent effort to enhance binding affinity (*1*) involves a covalent bond formed automatically following the binding of the hapten to the antibody (c). Since this covalent bond will presumably form in circulation as well, whether this strategy provides lower T/NT ratios compared to the affinity enhancement remains to be seen.

Figure 2 illustrates three streptavidin/biotin strategies. In contrast to the bispecific antibody/hapten system, the streptavidin/biotin system is more flexible, since both (strept)avidin

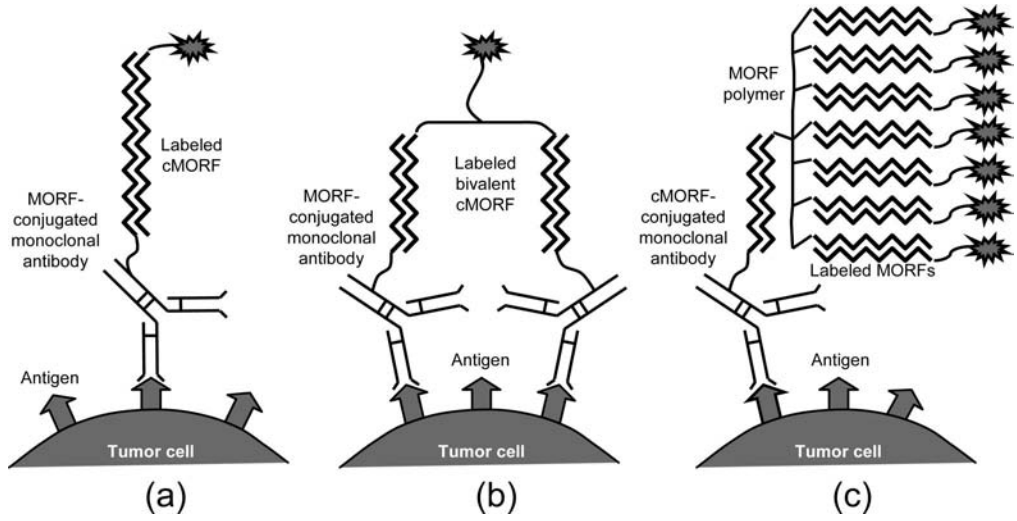

Figure 3. Three MORF/cMORF pretargeting strategies under development: (a) traditional two-step pretargeting, (b) affinity enhancement pretargeting, and (c) amplification pretargeting.

and biotin can be used as effectors. However, using radiolabeled (strept)avidin as effector and a biotinylated antibody (biotin is a small molecule also known as vitamin H) as pretargeting agent (a) is no longer being pursued (*43, 55−59*), because the slow pharmacokinetics of the radiolabeled (strept)avidin (*60, 61*) violates the principle of pretargeting whereby the radiolabel is to be attached to an effector with rapid pharmacokinetics. Therefore, the radiolabel is now attached to biotin and the (strept)avidin to the antibody (b). A potential complication of this strategy is the interference by endogenous biotin (*62, 63*) and the immunogenicity of streptavidin (*64*). Avidin may be a less immunogenic substitute for streptavidin (*65*) possibly only because its glycosylation encourages rapid accumulation into the liver (*66*). While a simple two-step strategy was used initially to show proof-of-concept (*67−70*), most studies now include a clearing step prior to effector administration. Increasing the pretargeting interval, i.e., the time between injections, would accomplish the same goal of clearing the pretargeting antibody but perhaps at the expense of reduced antibody expression in tumor due to internalization. Evidence has been presented that certain antibodies internalize more rapidly after conjugation with streptavidin (*71, 72*).

Another pretargeting strategy (c) of the same system involves three steps, the stepwise administration of biotin-antibody, avidin, and radiolabeled biotin (*43, 56, 73, 74*). The avidin serves multiple purposes: it clears the biotinylated antibody into the liver, helps clear endogenous biotin, and may modestly amplify the signal on the tumor sites by as much as a factor of 3 (*75*).

Within the oligomer/complementary oligomer system, the most extensively studied strategy thus far is to use phosphorodiamidate morpholino oligomers (MORFs). Other DNA analogues have been little used for a variety of reasons including instability of the native phosphodiester DNAs to nucleases (*44, 76*), the high binding affinity of phosphorothioate DNAs to serum and tissue proteins (*77*), and the aqueous insolubility of peptide nucleic acids (PNA) depending upon base sequence (*78*). MORFs exhibit high hybridization affinities to their complements (cMORFs), good hydrophilicity, and fast renal clearance (*79*). The different MORF/cMORF pretargeting strategies now under development are shown in Figure 3, including (a) the traditional two-step pretargeting, (b) affinity enhancement pretargeting, and (c) amplification pretargeting. While investigations of the latter two strategies continue (*80, 81, 78, 82, 83*), emphasis thus far has been on the first (*30−33, 46, 84−87*) because of its relative simplicity.

Although not described in this article, several miscellaneous studies could be considered pretargeting such as the use of enzyme/substrate interactions as a recognition system (*88*) and the use of MORF/cMORF binding to quantitate the internalization of antibodies (*89*).

FUNDAMENTAL DIFFICULTIES IN OPTIMIZING DOSAGE AND TIMING IN PRETARGETING

Although pretargeting has improved radionuclide delivery over conventional targeting, the improvement comes with a degree of complexity not shared by conventional targeting. Compared to the two variables of conventional targeting (dosage of radiolabeled antibody and detection time), there are four dosage-and-timing-associated variables in two-step pretargeting strategies (dosage of the pretargeting antitumor antibody, the pretargeting interval, the dosage of labeled effector, and the detection time) and considerably more in three-step strategies. The relationship between the two variables in conventional targeting is relatively simple. Provided that antigenic sites are not saturated, the percent of radioactivity accumulating in tumor does not vary greatly with the dosage of radiolabeled antibody but varies only with time. By contrast, in pretargeting, the accumulation in tumor of the radiolabel, now on the effector, will be influenced by changes in any of the pretargeting variables. Furthermore, there are at least three more system-associated variables (the pretargeting antibody, the radiolabeled effector, and the tumor model) compared to only two in conventional targeting (the radiolabeled antibody and the tumor model). Therefore, optimization of pretargeting is comparatively difficult especially in clinical trials (*40*).

In practice, optimization in pretargeting is almost always achieved experimentally. Theoretically, mathematical modeling could provide a method of simplifying the optimization. Several reports on purely mathematical modeling have appeared. For example, one report simulated an antibody/hapten pretargeting system (*90*), but the quantitatively predictive accuracy may have been compromised by the use of an oversimplified pharmacokinetic model and assumed parameters. A similar attempt at mathematical modeling compared a biotin/streptavidin two-step pretargeting strategy to a conventional targeting, but once again assumed parameters were used in the model (*91*). Similar observations may apply to additional reports (*92, 93*). In general, thus far pure mathematical modeling has not been able to predict optimal pretargeting conditions. In referring to those attempts, it has been stated that "some of the apparent anomalies between

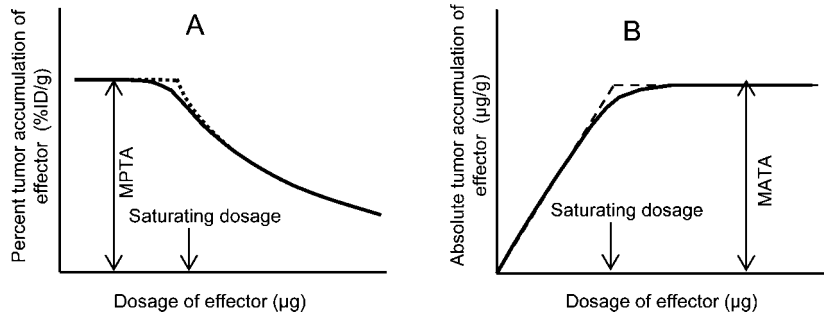

Figure 4. Schematic illustration of the relationship between the percent (A) and the absolute (B) tumor accumulation of effector and its dosage in pretargeting. The dotted lines represent theoretical curves (*30*).

the model and experience may be the result of using assumed parameters in the model which are not truly representative" (*29*).

While previous reports on experimental optimization do not describe a generalized approach, two reports, both concerning the bispecific antibody/hapten two-step strategy, deserve mention. One study optimized the pretargeting interval, antibody dosage, effector dosage, and detection time (*54*) by considering each variable separately while holding the others fixed at arbitrary values. In the second study (*94*), the influence of antibody dosage on the pharmacokinetics of a bispecific antibody was first determined, and an antibody dosage below antigen saturation was selected for the optimization of the pretargeting interval. Thereafter, optimization of the dosages of effector and antibody was achieved by increasing the effector dosage at fixed antibody dosage and vice versa. The pretargeting interval was arbitrarily set and, as the authors stated, "this interval might require further adjustment if either the bsMAb or peptide dosage changes".

More difficulties have been encountered in the optimization of the streptavidin/biotin pretargeting system, since most of these strategies involve three-steps. Among these three-step studies, those of Sharkey et al. (*63*) and Axworthy et al. (*95*) did not rely solely on trial and error. In the latter study, the dosage of antibody−streptavidin was first optimized by measuring antigen saturation. Then, the streptavidin accessibility was measured by histochemical examinations of tumor at two time points. Subsequently, at a fixed antibody dosage and a fixed pretargeting interval, a dosage of the clearing agent capable of removing more than 90% of the circulating antibody−streptavidin was selected along with an optimal dosage range of the radiolabeled biotin. However, optimization is always conditional on the selection of antibody dosage and pretargeting interval. Any change in these or other variables such as different antibodies will require a corresponding change in dosage of the clearing agent and dosage of the effector. Thus, these optimization studies provide limited general guidance (*36, 96*−*100*).

Similar optimization studies based purely on experimental observations of the MORF/cMORF pretargeting system have encountered similar difficulties even for the simplest two-step strategy. In one example (*85*), the influence of pretargeting interval on the pretargeting results was first examined, followed by the influence of the pretargeting antibody dosage. It subsequently became apparent that this optimization is incomplete, resulting in incorrect conclusions about the accessibility of antibody and antigen saturation (*30*).

In principle, any pretargeting strategy can be fully optimized experimentally provided that sufficient studies with variations in these variables have been performed, but besides being impractical in most cases, the optimization conditions of one system established in this manner will not apply to another. Furthermore, optimization in this manner would be extremely difficult in the clinic (*101*−*105*).

QUANTITATIVE UNDERSTANDING OF PRETARGETING − A SIMIEMPIRICAL MODEL

Recently, we have made efforts to understand pretargeting quantitatively beginning with the relatively simple two-step strategy of the MORF/cMORF pretargeting system (*30*−*33*). A semiempirical model capable of estimating the optimal tumor accumulation and optimal T/NT ratios for any combination of pretargeting variables was designed that will hopefully lead to an understanding of how each variable influences the pretargeting outcome. The influences of different pretargeting variables on both percent and absolute tumor accumulations (%ID/g and μg/g) of the effector and its radioactivity levels in normal organs were first examined so that several quantitative relationships could be established. These relationships are summarized below.

1. Maximum Percent and Maximum Absolute Tumor Accumulations (MPTA and MATA) of Effector. The tumor accumulation of radiolabeled effector has been expressed quantitatively by the following equation:

$$\text{Tumor accumulation of effector (\%ID/g)} = F \times f \times W^{-1} \times \int_{t=0}^{t=\infty} E \times C(\%\text{ID/g})_{\text{blood}} \times \mathrm{d}t \quad (1)$$

where F is the cardiac output; f is the fraction of the cardiac output reaching tumor; W is the tumor weight; E is the tumor trapping fraction of effector (defined as the retained fraction of effector molecules reaching the tumor); and C_{blood} is the blood level of free effector (i.e., effector in circulation not bound to circulating antibody) (*33*). This equation may be used to describe how the radiolabeled effector, tumor model, and pretargeting antibody influence the tumor accumulations of effector.

When the effector dosage is above that required to saturate the antibody in tumor, E will become zero, since additional effector arriving cannot be retained. However, at effector dosages below that required to saturate the antibody in tumor, E will be a constant of effector dosage, since during the entire delivery process (from $t = 0$ to infinity), the same fraction of effector reaching tumor will be trapped. Therefore, under these conditions E can be placed outside the integral sign in eq 1. Furthermore, under these conditions the tumor accumulation will be a maximum in percent, i.e., the maximum percent tumor accumulation (MPTA) as shown in eq 2:

$$\text{MPTA of effector (\%ID/g)} = F \times f \times W^{-1} \times E \times \int_{t=0}^{t=\infty} C(\%\text{ID/g})_{\text{blood}} \times \mathrm{d}t \quad (2)$$

By eq 2, the MPTA will vary with the tumor host (via F), tumor type and size (via f, W, and E), and the effector (via E and the integral of C) (*33*). The MPTA will not change with different antibodies provided that each antibody is not entirely inaccessible.

The influence of effector dosage on percent tumor accumulation is demonstrated schematically in Figure 4A. As shown, the percent tumor accumulation of the effector is a constant at its maximum value (MPTA) below the saturating dosage. Beyond this saturating dosage, the percent tumor accumulation gradually declines.

As shown in Figure 4B, the absolute tumor accumulation of radiolabeled effector (μg/g = %ID/g × dosage of effector (μg)/100%) increases linearly with the increasing dosage of effector until the saturating dosage is reached. Thereafter, the absolute tumor accumulation of the effector becomes constant at its maximum value (MATA), as further effector cannot bind to the saturated antibody localized in tumor.

2. Tumor Saturating Dosage of Effector and Accessibility of Antibody in Tumor. The number of moles of a monovalent effector accumulated in tumor at the point of saturation will equal the number of moles of antibody in tumor after corrected for groups per molecule and accessibility (*30, 31*). Thus, the tumor saturating dosage of effector ($SD_{effector}$) is related to the administered antibody dosage by eq 3:

$$\frac{SD_{effector}}{MW_{effector}} \times MPTA = \frac{D_{antibody}}{MW_{antibody}} \times \%ID/g_{antibody} \times gpm \times accessibility \quad (3)$$

where $MW_{effector}$ is the molecular weight of the effector; $D_{antibody}$ and $MW_{antibody}$ are, respectively, the dosage and the molecular weight of the antibody; the $\%ID/g_{antibody}$ is the tumor accumulation of antibody; gpm is the number of the effector-binding sites on each antibody; and the accessibility is the fraction of the effector-binding antibody in tumor still accessible to the effector at the time of effector administration. Since the MATA in μg is equal to the product of the number of micromoles of effector in tumor and its molecular weight, it is related to administered antibody dosage by eq 4:

$$\text{MATA of effector} = \frac{MW_{effector}}{MW_{antibody}} \times D_{antibody} \times \%ID/g_{antibody} \times gpm \times accessibility \quad (4)$$

Unless a pretargeting antibody is radiolabeled, its tumor accumulation ($\%ID/g_{antibody}$) is difficult to measure. It is commonly assumed that the pharmacokinetics of an antibody may be accurately traced by its radioactivity if radiolabeled with a limited gpm and with care leading to preserved integrity and immunoreactivity. Although this assumption is valid in at least one case of an antibody (*30*), we recently found that the biodistribution of antibodies can differ significantly when labeled with the same chelator but with different linker between the antibody and the chelator (*32*). We therefore believe that, for the purposes of prediction, measuring the biodistribution of radiolabeled antibody should be assumed to provide only an approximate measure of the pharmacokinetics of the unlabeled antibody. Fortunately, it is not the concentration of the antibody but the concentration of the accessible antibody, i.e., the product of $\%ID/g_{antibody}$ × accessibility, that is important. This concentration of accessible antibody can be measured by observing how the tumor accumulation of the radiolabeled effector changes with increasing effector dosage as in Figure 4. In a recent study, we measured the accessible level of a pretargeting antibody using this effector dosage escalation approach (see below).

3. Quantitative Presentation of Effector Levels in organs. Simple considerations will illustrate how the effector levels in tumor and normal tissues may be predicted (*31*). As mentioned above, before saturation of the antibody, the percent tumor accumulation of the effector is the MPTA. After saturation, the percent accumulation of effector in tumor will be the bound effector in tumor and the free effector present in blood within the tumor as in eq 5:

$$\text{Tumor accumulation of effector} = \%ID/g_{total\ effector\ in\ tumor} = \frac{D_{antibody} \times \%ID/g_{antibody} \times gpm \times accessibility}{MW_{antibody}} \times \frac{MW_{effector}}{D_{effector}} + \%ID/g_{free\ effector\ in\ tumor} \quad (5)$$

At the time of effector administration, the level of antibody in circulation is usually sufficiently low such that the antibody in blood becomes saturated with the effector. Thus, the total effector level in blood is the sum of both antibody-bound and free, as expressed in eq 6:

$$\%ID/g_{total\ effector\ in\ blood} = \frac{D_{antibody} \times \%ID/g_{antibody\ in\ blood} \times gpm}{MW_{antibody}} \times \frac{MW_{effector}}{D_{effector}} + \%ID/g_{free\ effector\ in\ blood} \quad (6)$$

In the same manner, the level of effector in an organ equals the level of effector bound to antibody plus the level of free effector in that organ. However, we have found experimentally that the effector-bound antibody in any organ other than kidney (see below) is in equilibrium with the effector-bound antibody in blood (*31*). Therefore, these organ levels can be obtained from the antibody-bound effector in blood, the organ to blood ratios of bound effector ($R_{O/B}$), and the free effector in that organ:

$$\%ID/g_{total\ effector\ in\ organ} = (\%ID/g_{total\ effector\ in\ blood} - \%ID/g_{free\ effector\ in\ blood}) \times R_{O/B} + \%ID/g_{free\ effector\ in\ organ} \quad (7)$$

Since the effector clears through kidney, the sole exception to eq 7 is this organ. The radioactivity level of effector in this organ is a function of the effector itself and is approximately independent of the accumulation of antibody.

If the pharmacokinetics of the pretargeting antibody and effector and the accessibility of the antibody are known, the biodistribution of the labeled effector under any conditions can be calculated using the above quantitative relationships (*31*). Since the application of these relationships requires experimental data, this model is semiempirical.

UTILITY OF THE SEMIEMPIRICAL MODEL

Besides helping to optimize dosage and timing, the semiempirical model may provide useful guidance in the selection of a pretargeting strategy including the selection of antibody and effector (pretargeting pair), their evaluation in preclinical studies, and, if encouraging, their use in clinical trials. Even though empirical measurement will continue to play an important role in each step, we believe that quantitative understanding may be helpful in reducing the number of empirical measurements needed.

Observations Useful in the Optimization of Timing and Dosages. The following observations resulting from studies on a two-step MORF/cMORF pretargeting strategy in a given mouse tumor model will be of general guidance for the optimization of T/NT ratios and tumor accumulations in the two-step strategies of other pretargeting systems (*33*).

a. Any dosage of pretargeting antibody is acceptable that is below that required to saturate the tumor antigenic sites. Higher antibody dosages may benefit diffusion into tumor against a binding site barrier or pressure gradient but will result in increased blood levels and therefore lower T/NT ratios.

b. Any pretargeting interval is acceptable that provide a set of acceptable T/NT ratios of antibody in all normal organs of interest. The T/NT ratios of the antibody usually improve steadily with increasing pretargeting interval over at least several days. If desired or necessary, acceptable T/NT ratios may be achieved at an earlier pretargeting interval through the use of an antibody clearance agent.

c. The optimal dosage of radiolabeled effector is the dosage just sufficient to saturate the accessible antibody in tumor.

d. Any detection time is acceptable that provides an acceptably low level of free radiolabeled effector in circulation and tissues (except kidney) compared to the level of effector bound to pretargeting antibody.

As an example of the application of these guidelines, in the case of the two-step MORF/cMORF strategy, optimization of the dosage and timing began by separately measuring the pharmacokinetics of both the labeled pretargeting antibody and the ^{99m}Tc-labeled cMORF effector and by measuring dosage saturation of tumor by antibody. The antibody results provided an estimate of the MORF-antibody concentration in tumor and provided a means of selecting the pretargeting interval. In this case, a time was chosen when the antibody reached 1−2%ID/g in blood. Knowledge of the pharmacokinetics of the labeled effector provided a means of selecting an acceptable detection time when the labeled effector was essentially cleared from circulation, in this case a blood level of 0.04%ID/g at about 3 h. The accessible level of the pretargeting antibody was then accurately measured by dosage escalation of the labeled effector so that the optimal dosage of the effector could be predicted.

Selection of Pretargeting Pairs. Any comparison of different pretargeting pairs should be under optimal conditions of dosage and timing for each. Fortunately, because of the quantitative relationships provided by the semiempirical model, the experiments required to obtain the optimal conditions may not all be necessary. Using the two-step pretargeting strategy again as the example, one prediction from eq 2 is that the nature of the pretargeting antibody normally does not influence the MPTA. It has been reported correctly that the pretargeting antibody affects percent tumor accumulation of effector (*36, 106*−*109*), but these percent tumor accumulations were not at the MPTA defined by eq 2. Thus, two pretargeting antibodies may differ in their level of tumor accumulation but still provide the same MPTA of the effector (*33*).

Selection of the antibody should therefore be dictated by the desired effector T/NT ratios rather than a desired effector MPTA. The effector T/NT ratios by pretargeting can be roughly estimated from the T/NT ratios of the radiolabeled antibody, but an accurate prediction of effector T/NT ratios requires the T/NT ratios of the accessible antibody. The tumor accessible level of antibody can be measured accurately by effector dosage escalation. Antibodies in blood may be assumed to be completely accessible to the effector. Since effector-bound antibody in any organ (other than kidney) is in equilibrium with the effector-bound antibody in blood, it becomes relatively easy to estimate the accessible levels of the antibody in these organs using the empirical organ/blood ratios of the accessible antibody. In this way, the effector T/NT ratios achievable with that antibody can be predicted with reasonable accuracy.

Another observation useful in the selection of the pretargeting antibody is its influence on the MATA. Higher absolute concentration of effector binding sites will lead to higher MATA, which can be achieved by increasing the dosage of the pretargeting antibody (*30*), increasing the gpm of pretargeting antibody (*110*), choosing a pretargeting antibody with better tumor accumulation (*33*), or, perhaps more effectively, using an amplification mechanism (*78, 82, 83*).

Concerning the selection of the effector, although any effector will be suitable, provided it is not trapped in any normal organs, the semiempirical model shows that the MPTA of different effectors can be different and usually the effectors providing higher MPTA will be preferred. The selection among effectors can be accomplished by measuring their MPTA values by effector dosage escalation. No further studies are required. As such, judgment can be reached on which effector is superior in tumor accumulation with no need of a pretargeting study under optimal pretargeting conditions.

The Semiempirical Model and the Clinic. The ultimate objective of pretargeting optimization studies is to improve tumor targeting in the clinic. In principle, the above observations obtained from the model MORF/cMORF pretargeting studies in animals should apply equally well in patients.

The main complication in clinical translation is tumor variation. Tumors originating from the same organ may differ in antigenic expression from patient to patient, and the antigenic expression of metastases may vary from its primary tumor. Experimentally, tumor type can greatly influence tumor accumulation of both antibody and effector. For example, tumor accumulation of a labeled cMORF in the LS174T tumor model (*31*) was 2−4 times higher than that in the CWR22 model (*32*). Similarly, the tumor accumulation of another labeled effector in one tumor model (*111*) was 10 times that in another (*112*). It can be easily understood from eq 2 that the MPTA of an effector may be different for different tumor models.

A better understanding of how tumor properties influence tumor accumulation of both antibody and effector would certainly be helpful both in selecting a pretargeting antibody dosage that does not saturate tumor antigenic sites and in selecting the saturating dosage of effector. Because experiences thus far on the use of different tumor models for pretargeting are limited, our understanding of the tumor influence on the pretargeting results is also limited. For example, whereas tumor size was found to correlate inversely with the effector accumulation in tumor in one tumor model (*31*), it was found to have no influence on the effector accumulation in another (*32*).

Planning a pretargeting study in a cancer patient might proceed by administering the radiolabeled pretargeting antibody at a tracer dosage that is expected to be below the antigen saturation dosage. By both noninvasive imaging and blood sampling, knowledge of the pharmacokinetics of the antibody can be obtained that will help to select an acceptable pretargeting interval. Thereafter, a dosage of labeled effector that is expected to just saturate the antibody in tumor may be selected on the basis of the assumption of an accessibility in tumor comparable to that in blood. In this way, an estimate of the MPTA and the T/NT ratios can be made. Presumably, a strategy of this complexity may have more relevance to tumor radiotherapy than imaging.

General Applicability to Other Pretargeting Systems and Strategies. Thus far, the development and applications of the semiempirical model have been limited to the two-step MORF/cMORF model pretargeting system. However, the semiempirical model should apply equally well to other two-step pretargeting systems and strategies, provided that the pharmacokinetic parameters are available, possibly after minor modifications. For example, a valency correction will be required in the application of eqs 1−6 to the streptavidin/biotin system if multiple biotin binding sites are present. Furthermore, for any system or strategy, it will be necessary to confirm in connection with eq 7 that the accessible levels of effector binding sites in blood and normal organs are in equilibrium. Otherwise, all quantitative relationships should remain valid.

CONCLUDING REMARKS

A semiempirical model of pretargeting is under continuous development and has been applied thus far to the two-step MORF/cMORF pretargeting strategy in mouse tumor models. The resulting observations may be used as a guide for the optimization of dosage and timing, leading to a set of optimal conditions with much less effort than required by trial and error. Even though the application of this model to the clinic has yet to be attempted, its utility is readily apparent, since the

pretargeting mechanism and the quantitative relationships should be identical for patients as subjects. Nevertheless, despite these pretargeting observations, the ability to select an optimal pretargeting procedure for a patient by semiempirical analysis must await further studies on how tumor variance influences tumor accumulations of both the pretargeting antibody and the effector.

ACKNOWLEDGMENT

Financial support is from NIH (CA 94994 and CA107360).

LITERATURE CITED

(1) Corneillie, T. M., Whetstone, P. A., and Meares, C. F. (2006) Irreversibly binding anti-metal chelate antibodies: Artificial receptors for pretargeting. *J. Inorg. Biochem. 100*, 882–890.
(2) Sharkey, R. M., and Goldenberg, D. M. (2006) Advances in radioimmunotherapy in the age of molecular engineering and pretargeting. *Cancer Invest. 24*, 82–97.
(3) Goldenberg, D. M., and Sharkey, R. M. (2006) Advances in cancer therapy with radiolabeled monoclonal antibodies. *Q. J. Nucl. Med. Mol. Imaging 50*, 248–264.
(4) Sharkey, R. M., Karacay, H., Cardillo, T. M., Chang, C. H., McBride, W. J., Rossi, E. A., Horak, I. D., and Goldenberg, D. M. (2005) Improving the delivery of radionuclides for imaging and therapy of cancer using pretargeting methods. *Clin. Cancer Res. 11*, 7109s–7121s.
(5) Sharkey, R. M., and Goldenberg, D. M. (2005) Perspectives on cancer therapy with radiolabeled monoclonal antibodies. *J. Nucl. Med. 46*, 115s–127s.
(6) Bethge, W. A., and Sandmaier, B. M. (2005) Targeted cancer therapy using radiolabeled monoclonal antibodies. *Technol. Cancer Res. Treat. 4*, 393–405.
(7) Govindan, S. V., Griffiths, G. L., Hansen, H. J., Horak, I. D., and Goldenberg, D. M. (2005) Cancer therapy with radiolabeled and drug/toxin-conjugated antibodies. *Technol. Cancer Res. Treat. 4*, 375–391.
(8) DeNardo, S. J. (2005) Radioimmunodetection and therapy of breast cancer. *Semin. Nucl. Med. 35*, 143–151.
(9) Gruaz-Guyon, A., Janevik-Ivanovska, E., Raguin, O., De Labriolle-Vaylet, C., and Barbet, J. (2001) Radiolabeled bivalent haptens for tumor immunodetection and radioimmunotherapy. *Q. J. Nucl. Med. 45*, 201–206.
(10) Mulford, D. A., Scheinberg, D. A., and Jurcic, J. G. (2005) The promise of targeted α-particle therapy. *J. Nucl. Med. 46*, 199s–204s.
(11) Reilly, R. M. (2006) Radioimmunotherapy of solid tumors: the promise of pretargeting strategies using bispecific antibodies and radiolabeled haptens. *J. Nucl. Med. 47*, 196–199.
(12) Meredith, R. F., and Buchsbaum, D. J. (2006) Pretargeted radioimmunotherapy. *Int. J. Radiat. Oncol. Biol. Phys. 66*, 57s–59s.
(13) DeNardo, G. L., Sysko, V. V., and DeNardo, S. J. (2006) Cure of incurable lymphoma. *Int. J. Radiat. Oncol. Biol. Phys. 66*, 46s–56s.
(14) Goldenberg, D. M., Sharkey, R. M., Paganelli, G., Barbet, J., and Chatal, J. F. (2006) Antibody pretargeting advances cancer radioimmunodetection and radioimmunotherapy. *J. Clin. Oncol. 24*, 823–834.
(15) Van de Wiele, C., Revets, H., and Mertens, N. (2004) Advances and prospects. *Q. J. Nucl. Med. Mol. Imaging 48*, 317–325.
(16) Goldenberg, D. M. (2003) Advancing role of radiolabeled antibodies in the therapy of cancer. *Cancer Immunol. Immunother. 52*, 281–96.
(17) Fritzberg, A. R. (1998) Antibody pretargeted radiotherapy: a new approach and a second chance. *J. Nucl. Med. 39* (2), 36N.
(18) Chang, C. H., Sharkey, R. M., Rossi, E. A., Karacay, H., McBride, W., Hansen, H. J., Chatal, J. F., Barbet, J., and Goldenberg, D. M. (2002) Molecular advances in pretargeting radioimunotherapy with bispecific antibodies. *Mol. Cancer Ther. 1*, 553–563.
(19) Goldenberg, D. M., Rossi, E. A., Sharkey, R. M., McBride, W. J., and Chang, C. H. (2008) Multifunctional antibodies by the Dock-and-Lock method for improved cancer imaging and therapy by pretargeting. *J. Nucl. Med. 49*, 158–163.
(20) Sharkey, R. M., Karacay, H., McBride, W. J., Rossi, E. A., Chang, C. H., and Goldenberg, D. M. (2007) Bispecific antibody pretargeting of radionuclides for immuno single-photon emission computed tomography and immuno positron emission tomography molecular imaging: an update. *Clin. Cancer Res. 13*, 5577s–5585s.
(21) Gruaz-Guyon, A., Raguin, O., and Barbet, J. (2005) Recent advances in pretargeted radioimmunotherapy. *Curr. Med. Chem. 12*, 319–338.
(22) Boerman, O. C., van Schaijk, F. G., Oyen, W. J., and Corstens, F. H. (2003) Pretargeted radioimmunotherapy of cancer: progress step by step. *J. Nucl. Med. 44*, 400–411.
(23) Goodwin, D. A., and Meares, C. F. (2001) Advances in pretargeting biotechnology. *Biotechnol. Adv. 19*, 435–450.
(24) McQuarrie, S. A., Xiao, Z., Miller, G. G., Mercer, J. R., and Suresh, M. R. (2001) Modern trends in radioimmunotherapy of cancer: pretargeting strategies for the treatment of ovarian cancer. *Q. J. Nucl. Med. 45*, 160–166.
(25) Barbet, J., Kraeber-Bodéré, F., Vuillez, J. P., Gautherot, E., Rouvier, E., and Chatal, J. F. (1999) Pretargeting with the affinity enhancement system for radioimmunotherapy. *Cancer Biother. Radiopharm. 14*, 153–166.
(26) Wilbur, D. S., Pathare, P. M., Hamlin, D. K., Stayton, P. S., To, R., Klumb, L. A., Buhler, K. R., and Vessella, R. L. (1999) Development of new biotin/streptavidin reagents for pretargeting. *Biomol. Eng. 16*, 113–118.
(27) Stoldt, H. S., Aftab, F., Chinol, M., Paganelli, G., Luca, F., Testori, A., and Geraghty, J. G. (1997) Pretargeting strategies for radio-immunoguided tumour localisation and therapy. *Eur. J. Cancer 33*, 186–192.
(28) Goodwin, D. A., and Meares, C. F. (1997) Pretargeting: general principles. *Cancer 80*, 2675s–2680s.
(29) Goodwin, D. A. (1995) Tumor pretargeting: almost the bottom line. *J. Nucl. Med. 36*, 876–879.
(30) Liu, G., He, J., Dou, S., Gupta, S., Rusckowski, M., and Hnatowich, D. J. (2005) Further investigations of morpholino pretargeting in mice - establishing quantitative relations in tumor. *Eur. J. Nucl. Med. Mol. Imaging 32*, 1115–1123.
(31) Liu, G., Dou, S., He, J., Liu, X., Rusckowski, M., and Hnatowich, D. J. (2007) Predicting the biodistribution of radiolabeled cMORF effector in MORF-pretargeted mice. *Eur. J. Nucl. Med. Mol. Imaging 34*, 237–246.
(32) Liu, G., Dou, S., Pretorius, P. H., Liu, X., Rusckowski, M., and Hnatowich, D. J. (2008) Pretargeting CWR22 prostate tumor in mice with MORF-B72.3 antibody and radiolabeled cMORF. *Eur. J. Nucl. Med. Mol. Imaging 35*, 272–280.
(33) Liu, G., Dou, S., Rusckowski, M., and Hnatowich, D. J. (2008) An experimental and theoretical evaluation of the influence of pretargeting antibody on the tumor accumulation of effector. *Mol. Cancer Ther. 7*, 1025–1032.
(34) Karacay, H., Brard, P. Y., Sharkey, R. M., Chang, C. H., Rossi, E. A., McBride, W. J., Ragland, D. R., Horak, I. D., and Goldenberg, D. M. (2005) Therapeutic advantage of pretargeted radioimmunotherapy using a recombinant bispecific antibody in a human colon cancer xenograft. *Clin. Cancer Res. 11*, 7879–7885.
(35) Sharkey, R. M., Cardillo, T. M., Rossi, E. A., Chang, C. H., Karacay, H., McBride, W. J., Hansen, H. J., Horak, I. D., and Goldenberg, D. M. (2005) Signal amplification in molecular imaging by pretargeting a multivalent, bispecific antibody. *Nat. Med. 11*, 1250–1255.
(36) Pagel, J. M., Hedin, N., Subbiah, K., Meyer, D., Mallet, R., Axworthy, D., Theodore, L. J., Wilbur, D. S., Matthews, D. C., and Press, O. W. (2003) Comparison of anti-CD20 and anti-CD45 antibodies for conventional and pretargeted radioimmu-

notherapy of B-cell lymphomas. *Blood 101*, 2340–2348.
(37) Subbiah, K., Hamlin, D. K., Pagel, J. M., Wilbur, D. S, Meyer, D. L., Axworthy, D. B, Mallett, R. W., Theodore, L. J., Stayton, P. S., and Press, O. W. (2003) Comparison of immunoscintigraphy, efficacy, and toxicity of conventional and pretargeted radioimmunotherapy in CD20-expressing human lymphoma xenografts. *J. Nucl. Med. 44*, 437–445.
(38) Magnani, P., Paganelli, G., Modorati, G., Zito, F., Songini, C., Sudati, F., Koch, P., Maecke, H. R., Brancato, R., Siccardi, A. G., and Fazio, F. (1996) Quantitative comparison of direct antibody labeling and tumor pretargeting in uveal melanoma. *J. Nucl. Med. 37*, 967–971.
(39) Sung, C., and van Osdol, W. W. (1995) Pharmacokinetic comparison of direct antibody targeting with pretargeting protocols based on streptavidin-biotin binding. *J. Nucl. Med. 36*, 867–876.
(40) Wu, A. M. (2001) Tools for pretargeted radioimmunotherapy. *Cancer Biother. Radiopharm. 16*, 103–108.
(41) Reardan, D. T., Meares, C. F., Goodwin, D. A., McTigue, M., David, G. S., Stone, M. R., Leung, J. P., Bartholomew, R. M., and Frincke, J. M. (1985) Antibodies against metal chelates. *Nature 316* (6025), 265–268.
(42) Goodwin, D. A., Meares, C. F., McTigue, M., et al. (1986) Rapid localization of haptens in sites containing previously administrated antibody for immunoscintigraphy with short half-life tracers [abstract]. *J. Nucl. Med. 27*, 959s.
(43) Hnatowich, D. J., Virzi, F., and Rusckowski, M. (1987) Investigations of avidin and biotin for imaging applications. *J. Nucl. Med. 28*, 1294–1302.
(44) Kuijpers, W. H., Bos, E. S., Kaspersen, F. M., Veeneman, G. H., and van Boeckel, C. A. (1993) Specific recognition of antibody-oligonucleotide conjugates by radiolabeled antisense nucleotides: a novel approach for two-step radioimmunotherapy of cancer. *Bioconjugate Chem. 4*, 94–102.
(45) Rusckowski, M., Qu, T., Chang, F., and Hnatowich, D. J. (1997) Pretargeting using peptide nucleic acid (PNA). *Cancer 80*, 2699–2705.
(46) Liu, G., Mang'era, K., Liu, N., Gupta, S., Rusckowski, M., and Hnatowich, D. J. (2002) Tumor pretargeting in mice using ^{99m}Tc-labeled morpholino, a DNA analog. *J. Nucl. Med. 43*, 384–391.
(47) Boerman, O. C., van Eerd, J., Oyen, W. J., and Corstens, F. H. (2001) A 3-step pretargeting strategy to image infection. *J. Nucl. Med. 42*, 1405–1411.
(48) Kranenborg, M. H., Oyen, W. J., Corstens, F. H., Oosterwijk, E., van der Meer, J. W., and Boerman, O. C. Rapid imaging of experimental infection with technetium-99m-DTPA after anti-DTPA monoclonal antibody priming. *J. Nucl. Med. 38*, 901–906.
(49) Goodwin, D. A., Meares, C. F., McCall, M. J., McTigue, M., and Chaovapong, W. (1988) Pre-targeted immunoscintigraphy of murine tumors with indium-111-labeled bifunctional haptens. *J. Nucl. Med. 29*, 226–234.
(50) Mirallie, E., Sai-Maurel, C., Faivre-Chauvet, A., Regenet, N., Chang, C. H., Goldenberg, D. M., Chatal, J. F., Barbet, J., and Thedrez, P. (2005) Improved pretargeted delivery of radiolabelled hapten to human tumour xenograft in mice by avidin chase of circulating bispecific antibody. *Eur. J. Nucl. Med. Mol. Imaging 32*, 901–909.
(51) Le Doussal, J. M., Gruaz-Guyon, A., Martin, M., Gautherot, E., Delaage, M., and Barbet, J. (1990) Targeting of indium 111-labeled bivalent hapten to human melanoma mediated by bispecific monoclonal antibody conjugates: imaging of tumors hosted in nude mice. *Cancer Res. 50*, 3445–3452.
(52) Goodwin, D. A., Meares, C. F., McTigue, M., Chaovapong, W., Diamanti, C. I., Ransone, C. H., and McCall, M. J. (1992) Pretargeted immunoscintigraphy: effect of hapten valency on murine tumor uptake. *J. Nucl. Med. 33*, 2006–2013.
(53) Goodwin, D. A., Meares, C. F., Watanabe, N., McTigue, M., Chaovapong, W., Ransone, C. M., Renn, O., Greiner, D. P., Kukis, D. L., and Kronenberger, S. I. (1994) Pharmacokinetics of pretargeted monoclonal antibody 2D12.5 and ^{88}Y-Janus-2-(p-nitrobenzyl)-1,4,7,10-tetraazacyclododecanetetraacetic acid (DOTA) in BALB/c mice with KHJJ mouse adenocarcinoma: a model for ^{90}Y radioimmunotherapy. *Cancer Res. 54*, 5937–5946.
(54) Kranenborg, M. H., Boerman, O. C., Oosterwijk-Wakka, J. C., de Weijert, M. C., Corstens, F. H., and Oosterwijk, E. (1998) Two-step radio-immunotargeting of renal-cell carcinoma xenografts in nude mice with anti-renal-cell-carcinoma X anti-DTPA bispecific monoclonal antibodies. *Int. J Cancer. 75*, 74–80.
(55) Paganelli, G., Riva, P., Deleide, G., Clivio, A., Chiolerio, F., Scassellati, G. A., Malcovati, M., and Siccardi, A. G. (1988) In vivo labelling of biotinylated monoclonal antibodies by radioactive avidin: a strategy to increase tumor radiolocalization. *Int. J. Cancer Suppl. 2*, 121–125.
(56) Paganelli, G., Pervez, S., Siccardi, A. G., Rowlinson, G., Deleide, G., Chiolerio, F., Malcovati, M., Scassellati, G. A., and Epenetos, A. A. (1990) Intraperitoneal radio-localization of tumors pre-targeted by biotinylated monoclonal antibodies. *Int. J. Cancer 45*, 1184–1189.
(57) Pimm, M. V., Fells, H. F., Perkins, A. C., and Baldwin, R. W. (1988) Iodine-131 and indium-111 labelled avidin and streptavidin for pre-targetted immunoscintigraphy with biotinylated anti-tumour monoclonal antibody. *Nucl. Med. Commun. 9*, 931–941.
(58) Khawli, L. A., Alauddin, M. M., Miller, G. K., and Epstein, A. L. (1993) Improved immunotargeting of tumor with biotinlated monoclonal antibodies and radiolabeled streptavidin. *Antibody Immunoconj. Radiopharm. 6*, 13–27.
(59) Saga, T., Weinstein, J. N., Jeong, J. M., Heya, T., Lee, J. T., Le, N., Paik, C. H., Sung, C., and Neumann, R. D. (1994) Two-step targeting of experimental lung metastases with biotinylated antibody and radiolabeled streptavidin. *Cancer Res. 54*, 2160–2165.
(60) Yao, Z., Zhang, M., Kobayashi, H., Sakahara, H., Nakada, H., Yamashina, I., and Konishi, J. (1995) Improved targeting of radiolabeled streptavidin in tumors pretargeted with biotinylated monoclonal antibodies through an avidin chase. *J. Nucl. Med. 36*, 837–841.
(61) Rusckowski, M., Fritz, B., and Hnatowich, D. J. (1992) Localization of infection using streptavidin and biotin: an alternative to nonspecific polyclonal immunoglobulin. *J. Nucl. Med. 33*, 1810–1815.
(62) Rusckowski, M., Fogarasi, M., Fritz, B., and Hnatowich, D. J. (1997) Effect of endogenous biotin on the applications of streptavidin and biotin in mice. *Nucl. Med. Biol. 24*, 263–268.
(63) Sharkey, R. M., Karacay, H., Griffiths, G. L., Behr, T. M., Blumenthal, R. D., Mattes, M. J., Hansen, H. J., and Goldenberg, D. M. (1997) Development of a streptavidin-anti-carcinoembryonic antigen antibody, radiolabeled biotin pretargeting method for radioimmunotherapy of colorectal cancer. Studies in a human colon cancer xenograft model. *Bioconjugate Chem. 8*, 595–604.
(64) Knox, S. J., Goris, M. L., Tempero, M., Weiden, P. L., Gentner, L., Breitz, H., Adams, G. P., Axworthy, D., Gaffigan, S., Bryan, K., Fisher, D. R., Colcher, D., Horak, I. D., and Weiner, L. M. (2000) Phase II trial of yttrium-90-DOTA-biotin pretargeted by NR-LU-10 antibody/streptavidin in patients with metastatic colon cancer. *Clin. Cancer Res. 6*, 406–414.
(65) Caliceti, P., Chinol, M., Roldo, M., Veronese, F. M., Semenzato, A., Salmaso, S., and Paganelli, G. (2002) Poly(ethylene glycol)-avidin bioconjugates: suitable candidates for tumor pretargeting. *J. Controlled Release 83*, 97–108.
(66) Sinitsyn, V. V., Mamontova, A. G., Checkneva, Y. Y., Shnyra, A. A., and Domogataky, S. P. (1989) Rapid blood clearance of biotinylatedIgG after infusionof avidin. *J. Nucl. Med. 30*, 66–69.
(67) Virzi, F., Fritz, B., Rusckowski, M., Gionet, M., Misra, H., and Hnatowich, D. J. (1991) New indium-111 labeled biotin derivatives for improved immunotargeting. *Int. J. Rad. Appl. Instrum. B 18*, 719–726.

(68) Hnatowich, D. J., Fritz, B., Virzi, F, Mardirossian, G., and Rusckowski, M. (1993) Improved tumor localization with (strept)avidin and labeled biotin as a substitute for antibody. *Nucl. Med. Biol. 20*, 189–195.
(69) Alvarez-Diez, T. M., Polihronis, J., and Reilly, R. M. (1996) Pretargeted tumour imaging with streptavidin immunoconjugates of monoclonal antibody CC49 and ^{111In}-DTPA-biocytin. *Nucl. Med. Biol. 23*, 459–466.
(70) Goodwin, D. A., Meares, C. F., and Osen, M. (1998) Biological properties of biotin-chelate conjugates for retargeted diagnosis and therapy with the avidin/biotin system. *J. Nucl. Med. 39*, 1813–1818.
(71) Casalini, P., Luison, E., Menard, S., Colnaghi, M. I., Paganelli, G., and Canevari, S. (1997) Tumor pretargeting: role of avidin/streptavidin on monoclonal antibody internalization. *J. Nucl. Med. 38*, 1378–1381.
(72) Muzykantov, V. R., Christofidou-Solomidou, M., Balyasnikova, I., Harshaw, D. W., Schultz, L., Fisher, A. B., and Albelda, S. M. (1999) Streptavidin facilitates internalization and pulmonary targeting of an anti-endothelial cell antibody (platelet-endothelial cell adhesion molecule 1): a strategy for vascular immunotargeting of drugs. *Proc. Natl. Acad. Sci. U.S.A. 96*, 2379–2384.
(73) Chinol, M., Paganelli, G., Sudati, F., Meares, C., and Fazio, F. (1997) Biodistribution in tumour-bearing mice of two 90Y-labelled biotins using three-step tumour targeting. *Nucl. Med. Commun. 18*, 176–182.
(74) Nakamoto, Y., Saga, T., Sakahara, H., Yao, Z., Zhang, M., Sato, N., Zhao, S., Nakada, H., Yamashina, I., and Konishi, J. (1998) Three-step tumor imaging with biotinylated monoclonal antibody, streptavidin and ^{111}In-DTPA-biotin. *Nucl. Med. Biol. 25*, 95–99.
(75) Kassis, A. I., Jones, P. L., Matalka, K. Z., and Adelstein, S. J. (1996) Antibody-dependent signal amplification in tumor xenografts after pretreatment with biotinylated monoclonal antibody and avidin or streptavidin. *J. Nucl. Med. 37*, 343–352.
(76) Bos, E. S., Kuijpers, W. H., Meesters-Winters, M., Pham, D. T., de Haan, A. S., van Doornmalen, A. M., Kaspersen, F. M., van Boeckel, C. A., and Gougeon-Bertrand, F. (1994) In vitro evaluation of DNA-DNA hybridization as a two-step approach in radioimmunotherapy of cancer. *Cancer Res. 54*, 3479–3486.
(77) Hnatowich, D. J. (1997) Pharmacokinetic considerations in the development of oligomers as radiopharmaceuticals. *Q. J. Nucl. Med. 41*, 91–100.
(78) Wang, Y., Chang, F., Zhang, Y., Liu, N., Liu, G., Gupta, S., Rusckowski, M., and Hnatowich, D. J. (2001) Pretargeting with amplification using polymeric peptide nucleic acid (PNA). *Bioconjugate Chem. 12*, 807–816.
(79) Summerton, J., and Weller, D. (1997) Morpholino antisense oligomers: design, preparation, and properties. *Antisense Nucleic Acid Drug Dev. 7*, 187–195.
(80) He, J., Liu, G., Vanderheyden, J. L., Dou, S., Rusckowski, M., and Hnatowich, D. J. (2005) Affinity enhancement bivalent morpholino for pretargeting: initial evidence by surface plasmon resonance. *Bioconjugate Chem. 16*, 338–345.
(81) He, J., Liu, X., Zhang, S., Liu, G., and Hnatowich, D. J. (2005) Affinity enhancement bivalent morpholinos for pretargeting: surface plasmon resonance studies of molecular dimensions. *Bioconjugate Chem. 16*, 1098–1104.
(82) He, J., Liu, G., Gupta, S., Zhang, Y., Vanderheyden, J. L., Rusckowski, M., and Hnatowich, D. J. (2004) Amplification targeting: amodified pretargeting approach with potential for signal amplification-proof of a concept. *J. Nucl. Med. 45*, 1087–1095.
(83) Chen, X., Dou, S., Liu, G., Liu, X., Wang, Y., Chen, L., Rusckowski, M., and Hnatowich, D. J. (2008) Synthesis and in vitro characterization of a dendrimer-MORF conjugate for amplification pretargeting. *Bioconjugate Chem. 19*, 1518–1525.
(84) Liu, G., Zhang, S., He, J., Liu, N., Gupta, S., Rusckowski, M., and Hnatowich, D. J. (2002) The influence of chain length and base sequence on the pharmacokinetic behavior of ^{99m}Tc-morpholinos in mice. *Q. J. Nucl. Med. 46*, 233–243.
(85) Liu, G., Liu, C., Zhang, S., He, J., Liu, N., Gupta, N., Rusckowski, M., and Hnatowich, D. J. (2003) Investigations of technetium-99m morpholino pretargeting in mice. *Nucl. Med. Commun. 24*, 697–705.
(86) Liu, G., He, J., Dou, S., Gupta, S., Vanderheyden, J. L., Rusckowski, M., and Hnatowich, D. J. (2004) Pretargeting in tumored mice with radiolabeled morpholino oligomer showing low kidney uptake. *Eur. J. Nucl. Med. Mol. Imaging 31*, 417–424.
(87) Liu, G., Dou, S., Mardirossian, G., He, J., Zhang, S., Liu, X., Rusckowski, M., and Hnatowich, D. J. (2006) Successful radiotherapy of tumor in pretargeted mice by ^{188}Re radiolabeled phosphorodiamidate morpholino oligomer, a synthetic DNA analog. *Clin. Cancer Res. 12*, 4958–1964.
(88) Bagshawe, K. D., Sharma, S. K., and Begent, R. H. (2004) Antibody-directed enzyme prodrug therapy (ADEPT) for cancer. *Expert Opin. Biol. Ther. 4*, 1777–1789.
(89) Liu, G., Dou, S., Yin, D., Squires, S., Liu, X., Wang, Y., Rusckowski, M., and Hnatowich, D. J. (2007) A novel pretargeting method for measuring antibody internalization in tumor cells. *Cancer Biother. Radiopharm. 22*, 33–39.
(90) Yuan, F., Baxter, L. T., and Jain, R. K. (1991) Pharmacokinetic analysis of two-step approaches using bifunctional and enzyme-conjugated antibodies. *Cancer Res. 51*, 3119–3130.
(91) Sung, C., and van Osdol, W. W. (1995) Pharmacokinetic comparison of direct antibody targeting with pretargeting protocols based on streptavidin-biotin binding. *J. Nucl. Med. 36*, 867–76.
(92) Sung, C., van Osdol, W. W., Saga, T., Neumann, R. D, Dedrick, R. L, and Weinstein, J. N. (1994) Streptavidin distribution in metastatic tumors pretargeted with a biotinylated monoclonal antibody: theoretical and experimental pharmacokinetics. *Cancer Res. 54*, 2166–2175.
(93) van Osdol, W. W., Sung, C., Dedrick, R. L., and Weinstein, J. N. (1993) A distributed pharmacokinetic model of two-step imaging and treatment protocols: application to streptavidin-conjugated monoclonal antibodies and radiolabeled biotin. *J. Nucl. Med. 34*, 1552–1564.
(94) Sharkey, R. M., Karacay, H., Richel, H., McBride, W. J., Rossi, E. A., Chang, K., Yeldell, D., Griffiths, G. L., Hansen, H. J., and Goldenberg, D. M. (2003) Optimizing bispecific antibody pretargeting for use in radioimmunotherapy. *Clin. Cancer Res. 9*, 3897s–913s.
(95) Axworthy, D. B., Reno, J. M., Hylarides, M. D., Mallett, R. W., Theodore, L. J., Gustavson, L. M., Su, F., Hobson, L. J., Beaumier, P. L., and Fritzberg, A. R. (2000) Cure of human carcinoma xenografts by a single dosage of pretargeted yttrium-90 with negligible toxicity. *Proc. Natl. Acad. Sci. U.S.A. 97*, 1802–1807.
(96) Schultz, J., Lin, Y., Sanderson, J., Zuo, Y., Stone, D., Mallett, R., Wilbert, S., and Axworthy, D. (2000) A tetravalent single-chain antibody-streptavidin fusion protein for pretargeted lymphoma therapy. *Cancer Res. 60*, 6663–6669.
(97) Goshorn, S., Sanderson, J., Axworthy, D., Lin, Y., Hylarides, M., and Schultz, J. (2001) Preclinical evaluation of a humanized NR-LU-10 antibody-streptavidin fusion protein for pretargeted cancer therapy. *Cancer Biother. Radiopharm. 16*, 109–123.
(98) Yao, Z., Zhang, M., Axworthy, D. B., Wong, K. J., Garmestani, K., Park, L., Park, C. W., Mallett, R. W., Theodore, L. J., Yau, E. K., Waldmann, T. A., Brechbiel, M. W., Paik, C. H., Pastan, I., and Carrasquillo, J. A. (2002) Radioimmunotherapy of A431 xenografted mice with pretargeted B3 antibody-streptavidin and ^{90}Y-labeled 1,4,7,10-tetraazacyclododecane-N,N′,N″,N″-tetraacetic acid (DOTA)-biotin. *Cancer Res. 62*, 5755–5760.
(99) Pagel, J. M., Lin, Y., Hedin, N., Pantelias, A., Axworthy, D., Stone, D., Hamlin, D. K., Wilbur, D. S., and Press, O. W. (2006) Comparison of a tetravalent single-chain antibody-streptavidin fusion protein and an antibody-streptavidin chemical conjugate for pretargeted anti-CD20 radioimmunotherapy of B-cell lym-

phomas. *Blood 108*, 328–336.
(100) Lin, Y., Pagel, J. M., Axworthy, D., Pantelias, A., Hedin, N., and Press, O. W. (2006) A genetically engineered anti-CD45 single-chain antibody-streptavidin fusion protein for pretargeted radioimmunotherapy of hematologic malignancies. *Cancer Res. 66*, 3884–3892.
(101) Breitz, H. B., Weiden, P. L., Beaumier, P. L., Axworthy, D. B., Seiler, C., Su, F.-M., Graves, S., Bryan, K., and Reno, J. M. (2000) Clinical optimization of pretargeted radioimmunotherapy (PRITTM) with antibody-streptavidin conjugate and ^{90}Y-DOTA-biotin. *J. Nucl. Med. 41*, 131–140.
(102) Forero, A., Weiden, P. L., Vose, J. M., Knox, S. J., LoBuglio, A. F., Hankins, J., Goris, M. L., Picozzi, V. J., Axworthy, D. B., Breitz, H. B., Sims, R. B., Ghalie, R. G., Shen, S., and Meredith, R. F. (2004) Phase 1 trial of a novel anti-CD20 fusion protein in pretargeted radioimmunotherapy for B-cell non-Hodgkin lymphoma. *Blood 104*, 227–236.
(103) Sharkey, R. M., Juweid, M., Shevitz, J., Behr, T., Dunn, R., Swayne, L. C., Wong, G. Y., Blumenthal, R. D., Griffiths, G. L., Siegel, J. A., et al. (1995) Evaluation of a complementarity-determining region-grafted (humanized) anti-carcinoembryonic antigen monoclonal antibody in preclinical and clinical studies. *Cancer Res. 55*, 5935s–5945s.
(104) Kraeber-Bodere, F., Faivre-Chauvet, A., Ferrer, L., Vuillez, J. P., Brard, P. Y., Rousseau, C., Resche, I., Devillers, A., Laffont, S., Bardiès, M., Chang, K., Sharkey, R. M., Goldenberg, D. M., Chatal, J. F., and Barbet, J. (2003) Pharmacokinetics and dosimetry studies for optimization of anti-carcinoembryonic antigen x anti-hapten bispecific antibody-mediated pretargeting of Iodine-131-labeled hapten in a phase I radioimmunotherapy trial. *Clin. Cancer Res. 9*, 3973s–3981s.
(105) Kraeber-Bodere, F., Rousseau, C., Bodet-Milin, C., Ferrer, L., Faivre-Chauvet, A., Campion, L., Vuillez, J. P., Devillers, A., Chang, C. H., Goldenberg, D. M., Chatal, J. F., and Barbet, J. (2006) Targeting, toxicity, and efficacy of 2-step, pretargeted radioimmunotherapy using a chimeric bispecific antibody and 131I-labeled bivalent hapten in a phase I optimization clinical trial. *J. Nucl. Med. 47*, 247–255.
(106) Karacay, H., Sharkey, R. M., McBride, W. J., Griffiths, G. L., Qu, Z., Chang, K., Hansen, H. J., and Goldenberg, D. M. (2002) Pretargeting for cancer radioimmunotherapy with bispecific antibodies: role of the bispecific antibody's valency for the tumor target antigen. *Bioconjugate Chem. 13*, 1054–1070.
(107) Cardillo, T. M., Karacay, H., Goldenberg, D. M., Yeldell, D., Chang, C. H., Modrak, D. E., Sharkey, R. M., and Gold, D. V. (2004) Improved targeting of pancreatic cancer: experimental studies of a new bispecific antibody, pretargeting enhancement system for immunoscintigraphy. *Clin. Cancer Res. 10*, 3552–3561.
(108) Rossi, E. A., Sharkey, R. M., McBride, W., Karacay, H., Zeng, L., Hansen, H. J., Goldenberg, D. M., and Chang, C. H. (2003) Development of new multivalent-bispecific agents for pretargeting tumor localization and therapy. *Clin. Cancer Res. 9*, 3886s–3896s.
(109) van Schaijk, F. G., Boerman, O. C., Soede, A. C., McBride, W. J., Goldenberg, D. M., Corstens, F. H., and Oosterwijk, E. (2005) Comparison of IgG and F(ab′)2 fragments of bispecific anti-RCCxanti-DTIn-1 antibody for pretargeting purposes. *Eur. J. Nucl. Med. Mol. Imaging 32*, 1089–1095.
(110) He, J., Liu, G., Dou, S., Gupta, S., Rusckowski, M., and Hnatowich, D. J. (2007) An improved method for covalently conjugating morpholino oligomers to antitumor antibodies. *Bioconjugate Chem. 18*, 983–988.
(111) van Schaijk, F. G., Oosterwijk, E., Molkenboer-Kuenen, J. D., Soede, A. C., McBride, B. J., Goldenberg, D. M., Oyen, W. J., Corstens, F. H., and Boerman, O. C. (2005) Pretargeting with bispecific anti-renal cell carcinoma x anti-DTPA(In) antibody in 3 RCC models. *J. Nucl. Med. 46*, 495–501.
(112) van Schaijk, F. G., Broekema, M., Oosterwijk, E., van Eerd, J. E., McBride, B. J., Goldenberg, D. M., Corstens, F. H., and Boerman, O. C. (2005) Residualizing iodine markedly improved tumor targeting using bispecific antibody-based pretargeting. *J. Nucl. Med. 46*, 1016–1022.

BC8002748

COMMUNICATIONS

Chemical Engineering of Mesenchymal Stem Cells to Induce a Cell Rolling Response

Debanjan Sarkar,[†] Praveen Kumar Vemula,[†] Grace S. L. Teo,[†] Dawn Spelke,[†] Rohit Karnik,[‡] Le Y. Wee,[†] and Jeffrey M. Karp*,[†]

Harvard-MIT Division of Heath Sciences and Technology, Department of Medicine, Brigham and Women's Hospital, Harvard Medical School, 65 Landsdowne Street, and Department of Mechanical Engineering, Massachusetts Institute of Technology, 77 Massachusetts Avenue, Cambridge, Massachusetts 02139. Received August 10, 2008; Revised Manuscript Received October 3, 2008

Covalently conjugated sialyl Lewis X (SLeX) on the mesenchymal stem cell (MSC) surface through a biotin−streptavidin bridge imparts leukocyte-like rolling characteristics without altering the cell phenotype and the multilineage differentiation potential. We demonstrate that the conjugation of SLeX on the MSC surface is stable, versatile, and induces a robust rolling response on P-selectin coated substrates. These results indicate the potential to increase the targeting efficiency of any cell type to specific tissue.

Cell therapy including platelet transfusions, bone marrow cell infusion, and islet cell transplantation have had a profound impact on improving patient quality of life and extending patient survival overall, and have demonstrated an impressive safety record (*1*). Culture expanded mesenchymal stem cells (MSCs), also referred to as connective tissue progenitor cells, have been approved for a limited number of applications (*2*) and have recently entered preclinical and clinical trials for treatment of numerous ailments including heart disease (*3*−*5*), brain and spinal cord injury (*6*), cartilage and bone injury (*7*, *8*), Crohn's disease (*9*), and graft versus host disease during bone marrow transplantation (*10*). The significant interest in MSC based therapies is due to their convenient isolation, lack of significant immunogenicity (*10*−*12*), lack of ethical controversy, and potential to differentiate into tissue specific cell types. However, a significant barrier to the effective implementation of all cell therapies is the inability to deliver these cells under minimally invasive conditions with high efficiency of engraftment within tissues of interest. Systemic infusion is thus a desired mode of cell delivery; however, systemically administered culture expanded MSCs home at low efficiencies (*13*−*16*).

The white blood cells (i.e., leukocytes) and hematapoetic stem cells have evolved mechanisms for effective and specific tissue targeting (i.e., "homing" or "trafficking") that have been dissected at the cellular, molecular, and biophysical level. This includes a multistep adhesion and activation cascade that allows leukocytes to adhere to the luminal surface of the vascular endothelium and subsequently migrate into the underling tissues. It is well-established that transient rolling-type interactions (mediated by selectins) and transition to firm adhesion (mediated by integrins) are absolutely essential and limiting components of leukocyte and hematopoetic cell trafficking (*17*−*20*). The blood vessels in each tissue are known to exhibit particular surface properties that can direct the trafficking of circulating cells. In addition, upon an active stimulus such as inflammation, specific homing receptors or ligands are expressed on the surface of the endothelium within the inflamed tissue.

Current MSC transfusion experiments have shown that only subsets of MSCs have the capacity to home to specific tissues (*21*) and that MSCs may lose their capacity to home after cell culture (*22*). This is complicated by the heterogeneity in receptor expression on MSCs and the changes in receptor expression observed during culture (*23*−*25*). The limited homing efficiency of MSCs is likely due to a lack of relevant cell surface adhesion molecules.

The central hypothesis for this work is that surfaces of cells that exhibit poor homing capabilities such as culture expanded MSCs (*26*−*29*) can be engineered to possess leukocyte-like adhesion properties, without otherwise altering function, in order to promote more effective rolling, adhesion, and ultimately *in vivo* homing. The proof of principle for this hypothesis is provided by recent work by Sackstein et al., which showed enhanced bone marrow engraftment of systemically administered MSCs (*30*). Strategies for modification of cell surfaces to promote adhesion are typically elaborate and include genetic modifications, insertion of glycosylphosphatidylinositol-modified proteins into the membrane, and metabolic delivery of specific moieties to the cell surface (*31*). While it has been shown that cells modified using *N*-hydroxy-succinimide ester coupling to cell surface amine groups retain viability and the ability to be cultured (*32*, *33*), this simple strategy has not been explored for promoting stem cell homing. Here, we demonstrate that it is possible to use this simple strategy to covalently couple the sialyl Lewis X (SLeX) moiety onto the surface of mesenchymal stem cells (MSCs) through biotin−streptavidin chemical modifications (Scheme 1) without compromising MSC viability, adhesion, proliferation, and multidifferentiation potential. We further show that this modification of SLeX homing receptors onto the surface of MSCs can promote a cell rolling response *in vitro* on substrates coated with P-selectin. A simple coupling scheme that is minimally invasive on the cell makes this

* Corresponding author. E-mail: jeffkarp@mit.edu. Tel: +1-617-8179174. Fax: +1-617-768-8338. Homepage: www.karplab.net.
[†] Harvard Medical School.
[‡] Massachusetts Institute of Technology.

10.1021/bc800345q CCC: $40.75 © 2008 American Chemical Society
Published on Web 10/31/2008

Scheme 1[a]

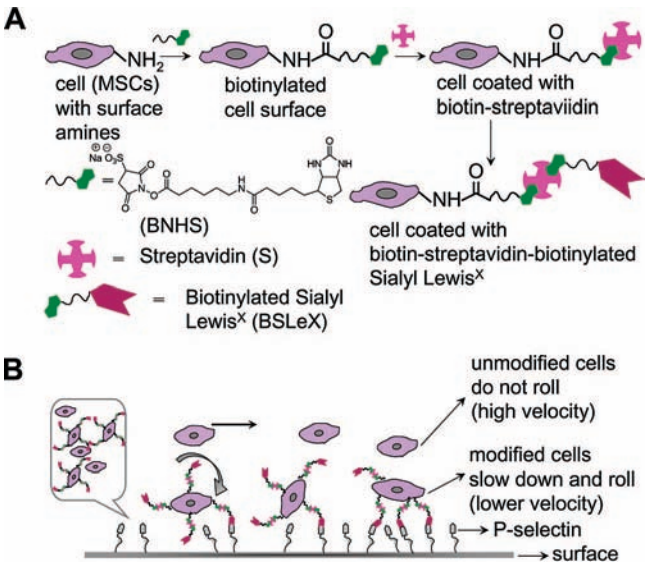

[a] (A) Modification of MSCs by SLeX using biotin−streptavidin. (B) Schematic presentation for rolling of SLeX modified MSCs on a P-selectin coated surface.

approach a simple method to potentially target any cell type to specific tissues via the circulation.

The free amine groups present on the surface of cells are available to react with the *N*-hydroxy-succinimide group of biotinyl-*N*-hydroxy-succinimide to biotinylate the cell surface. To improve the biotinylation efficiency, sulfonated biotinyl-*N*-hydroxy-succinimide (sulfo-NHS-Biotin, BNHS) was used. BNHS is water-soluble, which limits its transport through the cell membrane and thus facilitates maximal interaction of the NHS group with the cell membrane. After biotinylating the MSC surface, cells were incubated with streptavidin to form biotin−streptavidin complexes. The strong interaction between biotin and streptavidin stabilized the streptavidin on the cell surface. The streptavidin was then complexed with biotinylated-SLeX (sialyl-Lewis^X-PAA-Biotin, BSLeX; see Supporting Information) to introduce SLeX on the cell surface. It is believed that the absence of targeting agents such as SLeX on the surface of MSCs is responsible for their poor homing characteristics (*30*). Thus, we anticipated that synthetic immobilization of SLeX on the cell surface would induce a homing response through promoting cell rolling as shown in Scheme 1.

To assess the cell modification by BNHS and streptavidin, rhodamine-conjugated streptavidin (S) was added to biotinylated cells (BNHS+S), and incubated for 20 min. Subsequently, excess unbound S was removed by multiple washes with buffer, and the fluorescence intensity of the cells was measured. The controls used for this experiment were cells treated with only S (a control to assess the nonspecific adsorption of S), cells treated with both biotin (B) and S (B+S) to examine the need for covalent conjugation of biotin to the cell surface, and cells treated with only PBS to probe the impact of cell modifications on cell function and phenotype. The total fluorescence intensity was normalized to the group treated with PBS. All experiments were performed on ~80−90% confluent monolayers on tissue culture polystyrene, and fluorescence was only observed in regions with cells. Cells functionalized with BNHS (covalent attachment) had considerably higher fluorescence intensity compared to cells treated with B+S, indicating that cells that were covalently functionalized using the NHS moiety had greater amounts of streptavidin immobilized on their surfaces. After 7 days, the fluorescence intensity of BNHS+S treated cells was much higher compared to B+S and S controls (noncovalent

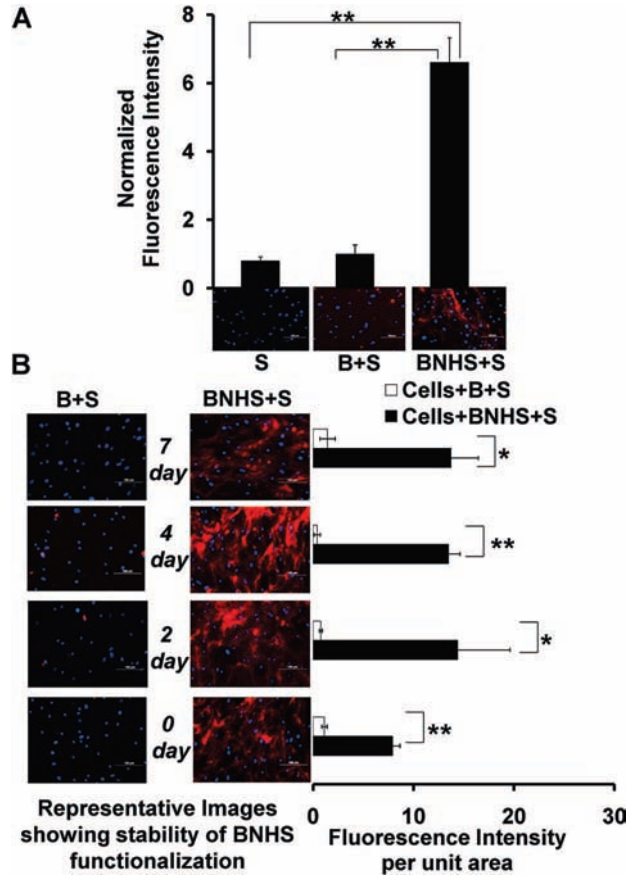

Figure 1. (A) Modification of the MSCs measured as a function of fluorescent signal 7 days after addition of S. (B) Accessibility (and stability) of covalently conjugated or adsorbed biotin on the MSC surface measured by addition of S at each time point.

and nonspecifically adsorbed, respectively), indicating that the conjugation of streptavidin to the biotinylated cells was efficient and stable (Figure 1A). By enumerating the number of DAPI stained nuclei with surrounding rhodamine fluorescence, after 7 days of the modification, the percentage of cells modified by BNHS+S was found to be 97 ± 1%, which was significantly higher than the controls B+S (10.5 ± 1.7%, $P = 0.004$) and S (2.3 ± 0.4%, $P = 0.008$). To assess the temporal accessibility of biotin on the cell surface, rhodamine−streptavidin was added at each time point to the biotinylated cells, and following multiple washes, the fluorescence intensity was measured (Figure 1B).

Specifically, MSCs were covalently functionalized with BNHS or functionalized via adsorption with native biotin (B) as a negative control. In both cases, experiments were conducted for 3 separate samples per group (triplicate) per time point. Each sample was processed and imaged. S was added on days 0, 2, 4, and 7, and after removing excess S by buffer washes, the fluorescence intensity was assessed (Figure 1B). An increase in the fluorescence intensity at day 2 compared with day 0 was observed, which may indicate the rearrangement and reorientation of the biotin moiety on the cell surface. The fluorescence intensity was stabilized and retained thereafter for up to 7 days and was significantly higher than the negative control at all time points ($P < 0.05$). This indicates the stability and accessibility of biotin on the cell surface via covalent immobilization chemistry. Presumably, streptavidin−biotin conjugated moieties, such as SLeX, would remain stably conjugated to the cell surface, accessible to interact with host biology. These results indicate the versatility and stability of the present approach.

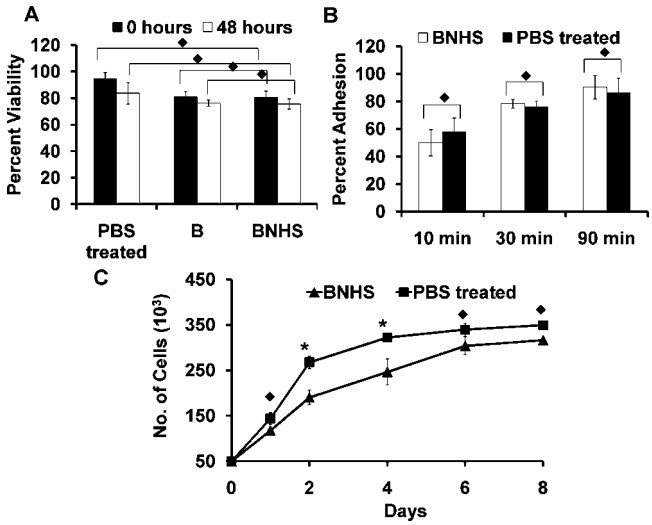

Figure 2. (A) Viability of the BNHS modified cells immediately after modification (0 h) and after 48 h. (B) Adherence of BNHS modified cells measured at 10, 30, and 90 min compared to the PBS treated cells. (C) Proliferation of the BNHS modified cells over an 8 day period compared to PBS treated cells. Error bars denote standard deviation from three separate experiments.

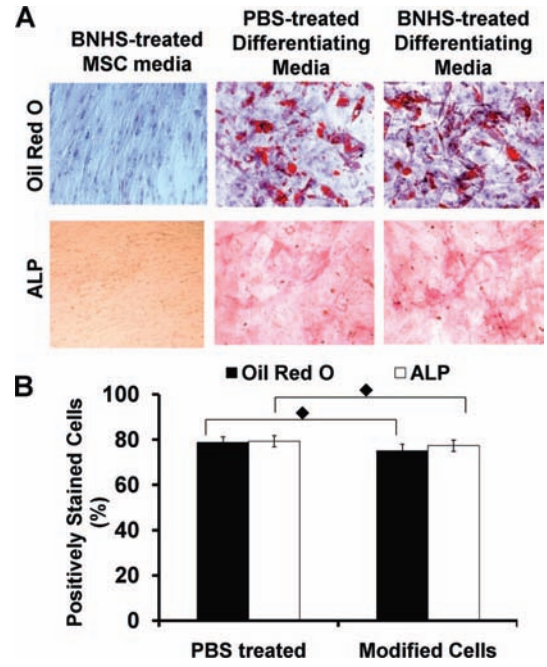

Figure 3. (A) Alkaline phosphatase (ALP) and oil red O (ORO) staining, 23 days after addition of osteogenic and adipogenic differentiation media, respectively. Negative controls (BNHS modified cells cultured in expansion media) showed no ORO or ALP staining. Positive controls (PBS treated cells in differentiating media) showed positive ORO and ALP staining. Experimental group (BNHS modified cells cultured in respective differentiating media) showed positive staining for both ORO and ALP. (B) Percentage of positively stained cells for ORO and ALP staining for PBS treated and BNHS modified cells. Error bars represent standard deviation from three separate treatments.

To gain insight into the effect of covalent modification on cell characteristics such as viability, proliferation, adhesion, and ability to differentiate into multiple lineages, a series of experiments were performed. The cell viability was not considerably affected up to 48 h after BNHS+S modification compared to the control groups (Figure 2A). Specifically, 95% and 85% of PBS treated cells were viable after 0 and 48 h, respectively, whereas cells treated with B (noncovalent) were 81% and 76% viable and cells treated with BNHS (covalent) were 79% and 75% viable. This indicates that the BNHS+S modification did not induce substantial cell toxicity. Cell adhesion characteristics were also not affected, as shown by the adhesion dynamics to tissue culture plastic of BNHS modified and PBS treated cells after 10, 30, and 90 min. This clearly indicates that the covalent modification of the cell surface did not compromise the ability of cells to interact with their extracellular environment (Figure 2B). On the contrary, BNHS modification inhibited the proliferation compared to the unmodified PBS treated cells on day 2 ($P = 0.01$, $n = 3$) and day 4 ($P = 0.02$, $n = 3$) (Figure 2C); however, both groups attained a confluent monolayer. This indicates that the covalent modification of the cell surface by biotin−streptavidin conjugation may have short-term negative impacts on proliferation but does not alter the normal substrate colonization characteristics of the MSCs.

Positive staining for oil red O (ORO) and alkaline phosphatase (ALP), indicators for adipogenic and osteogenic differentiation, respectively, was retained after BNHS modification (Figure 3; see Figure S1 in Supporting Information for higher magnification images). No differences in ORO or ALP staining were observed between BNHS modified cells and those treated with PBS after induction of osteogenic and adipogenic differentiation. Covalently modified MSCs cultured in nondifferentiating conditions (i.e., in MSC expansion medium) did not stain positively for osteogenic and adipogenic markers and the modification did not affect the number of positively stained cells compared to positive controls as shown in Figure 3B ($P > 0.05$, $n = 3$).

Taken together, the results suggest that BNHS modification of MSCs does not impair the potential for multilineage differentiation. However, it is important in future work to examine if other lineages are affected by the modification and if the trophic and immunomodulatory properties of MSCs are compromised. This work focused on examining the impact of cell surface modification with BNHS and S on cell function and phenotype. Although it is anticipated that the specific ligand attached through the streptavidin bridge would have a limited effect on these cell properties, each application would require extensive characterization for the candidate targeting ligand.

Since all experiments were performed with MSCs between passage 4 and 6, cell surface markers of passage 6 MSCs were examined by flow cytometry and immunofluorescence (data not shown). MSCs did not express hematopoetic markers CD34 or CD45 (0% of cells) but were shown to express high levels of MSC markers including CD90 and CD146 (100% of cells) as evidenced by flow cytometry. Immunofluorescence showed 0% expression of CXCR4 and 100% expression of MSC markers CD146, CD90, and CD271.

After examining the characteristic properties of MSCs with BNHS+S, BSLeX was introduced on cell surface as shown in Scheme 1, and its ability to impart a homing response was investigated via cell rolling within a standard parallel plate flow chamber system. Typically, culture expanded MSCs do not express ligands on their surface to enable cell rolling on selectin coated surfaces (*30*). MSCs modified with BNHS+S and biotinylated SLeX showed considerably lower velocities on immobilized P-selectin substrates compared to PBS treated cells ($P = 0.003$, $n = 3$) and cells treated with physically adsorbed BSLeX ($P = 0.04$, $n = 3$) (Figure 4A). Specifically, the interaction between SLeX and P-selectin reduced the velocity from ~65 μm/s to ~2 μm/s at a wall shear stress 0.366 dyne/cm^2. This clearly indicates that covalent modification of MSCs by biotin−streptavidin followed by SLeX−biotin induces a cell rolling response for culture expanded MSCs that is not typically observed.

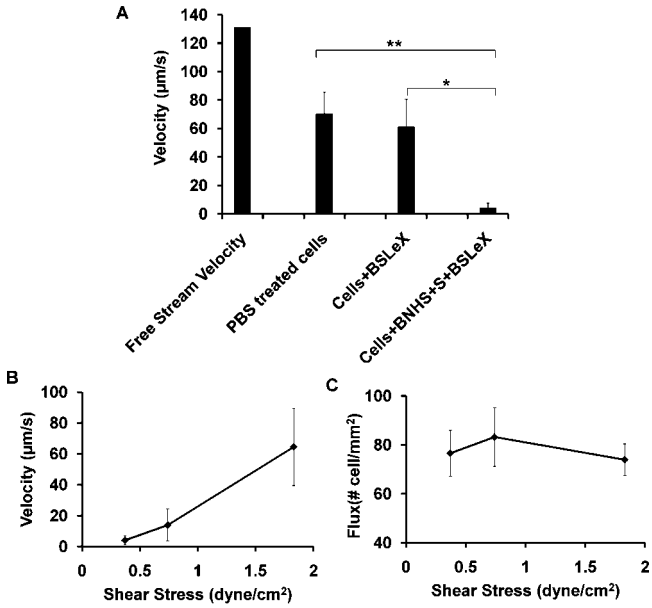

Figure 4. (A) Velocity of SLeX modified cells and controls on P-selectin treated surfaces at the shear stress of 0.366 dyne/cm^2. (B) Effect of shear stress on the rolling velocity. (C) Effect of shear stress on the number of interacting cells per unit area for the cells modified with SLeX.

The effect of flow rate and thus different shear stresses on the rolling characteristics is shown in Figure 4B,C. As shear stress is increased from 0.366 to 1.89 dyne/cm^2, the velocity of the modified cells increased whereas the number of cells interacting with P-selectin substrate remained relatively constant at ~75 cells/mm^2 (for 1 mM BNHS concentration) whereas the PBS treated cells displayed a near constant flux of ~20 cells/mm^2. This indicates that cells modified with SLeX interact with P-selectin substrates via recognized cell rolling based adhesion phenomena. The sharp increase in rolling velocity with increase in shear stress (Figure 4B), yet unchanged flux, may indicate that the SLeX is not uniformly distributed on the cell surface, or perhaps that the distribution of SLeX is unlike the clustering that typically appears on microvilli. Future work is thus required to characterize and optimize these parameters prior to *in vivo* homing studies. Together, this work demonstrates the potential to induce a leukocyte-like cell rolling response that may be useful to increase concentrations of MSCs and other cell types within specific tissues after systemic administration.

In conclusion, we have shown a novel, platform method for imparting a rolling response through functionalization of primary human MSCs with SLeX through combined covalent and biotin−streptavidin chemistries. Contrary to enzymatic modifications and retroviral transduction methods, the present approach is a simple, yet versatile method to engineer the cell membrane to induce a homing response. Importantly, covalently modified cells showed similar viability, proliferation, adhesion, and differentiation potential (as judged by ORO and ALP staining for adipogenic and osteogenic differentiation, respectively) compared to PBS treated cells. Apart from the specific interactions between SLeX and P-selectin to induce a rolling response, there are several other important cellular and molecular features that are crucial to induce and sustain cell trafficking behavior including cell deformability and cell−substrate contact area that is typically dictated by microvillus extensions (*33*), firm adhesion, and transmigration. Future work will involve characterizing the impact of the covalent immobilization methodology on these parameters and investigating coimmobilization of other adhesion molecules to further enhance the potential for an effective *in vivo* homing response. It would also be important to characterize the impact of engineered MSCs on the latter stages of cell homing that involve transendothelial migration and chemotaxis in response to soluble cues. We anticipate that the present approach to covalently modify the cell surface and immobilize required ligands is not limited to MSCs or the SLeX ligand. Hence, this technology should have broad implications on cellular therapies that utilize systemic administration and require targeting of cells to specific tissues.

ACKNOWLEDGMENT

We thank C. J. Mao and L. B. Huang for flow cytometry and immunoflourescence studies.

Supporting Information Available: Detailed materials and methods, fluorescent measurements and images of ORO and ALP staining. This material is available free of charge via the Internet at http://pubs.acs.org.

LITERATURE CITED

(1) Gastineau, D. A. (2004) Will regulation be the death of cell therapy in the United States? *Bone Marrow Transplant 33*, 777–80.

(2) Picinich, S. C., Mishra, P. J., Mishra, P. J., Glod, J., and Banerjee, D. (2007) The therapeutic potential of mesenchymal stem cells. Cell- & tissue-based therapy. *Expert Opin. Biol. Ther. 7*, 965–73.

(3) Burt, R. K., Loh, Y., Pearce, W., Beohar, N., Barr, W. G., Craig, R., Wen, Y., Rapp, J. A., and Kessler, J. (2008) Clinical applications of blood-derived and marrow-derived stem cells for nonmalignant diseases. *JAMA 299*, 925–36.

(4) Hashemi, S. M., Ghods, S., Kolodgie, F. D., Parcham-Azad, K., Keane, M., Hamamdzic, D., Young, R., Rippy, M. K., Virmani, R., Litt, H., and Wilensky, R. L. (2008) A placebo controlled, dose-ranging, safety study of allogenic mesenchymal stem cells injected by endomyocardial delivery after an acute myocardial infarction. *Eur. Heart J. 29*, 251–9.

(5) Abdel-Latif, A., Bolli, R., Tleyjeh, I. M., Montori, V. M., Perin, E. C., Hornung, C. A., Zuba-Surma, E. K., Al-Mallah, M., and Dawn, B. (2007) Adult bone marrow-derived cells for cardiac repair: a systematic review and meta-analysis. *Arch. Intern. Med. 167*, 989–97.

(6) Sykova, E., Jendelova, P., Urdzikova, L., Lesny, P., and Hejcl, A. (2006) Bone marrow stem cells and polymer hydrogels--two strategies for spinal cord injury repair. *Cell Mol. Neurobiol. 26*, 1113–29.

(7) Filho Cerruti, H., Kerkis, I., Kerkis, A., Tatsui, N. H., da Costa Neves, A., Bueno, D. F., and da Silva, M. C. (2007) Allogenous bone grafts improved by bone marrow stem cells and platelet growth factors: clinical case reports. *Artif. Organs 31*, 268–73.

(8) Gupta, M. C., Theerajunyaporn, T., Maitra, S., Schmidt, M. B., Holy, C. E., Kadiyala, S., and Bruder, S. P. (2007) Efficacy of mesenchymal stem cell enriched grafts in an ovine posterolateral lumbar spine model. *Spine 32*, 720–6, discussion 727.

(9) Garcia-Olmo, D., Garcia-Arranz, M., Herreros, D., Pascual, I., Peiro, C., and Rodriguez-Montes, J. A. (2005) A phase I clinical trial of the treatment of Crohn's fistula by adipose mesenchymal stem cell transplantation. *Dis. Colon Rectum 48*, 1416–23.

(10) Maitra, B., Szekely, E., Gjini, K., Laughlin, M. J., Dennis, J., Haynesworth, S. E., and Koc, O. N. (2004) Human mesenchymal stem cells support unrelated donor hematopoietic stem cells and suppress T-cell activation. *Bone Marrow Transplant 33*, 597–604.

(11) Aggarwal, S., and Pittenger, M. F. (2005) Human mesenchymal stem cells modulate allogeneic immune cell responses. *Blood 105*, 22–1815.

(12) Le Blanc, K., Tammik, L., Sundberg, B., Haynesworth, S. E., and Ringden, O. (2003) Mesenchymal stem cells inhibit and stimulate mixed lymphocyte cultures and mitogenic responses

independently of the major histocompatibility complex. *Scand. J. Immunol. 57*, 11–20.
(13) Zhang, M., Mal, N., Kiedrowski, M., Chacko, M., Askari, A. T., Popovic, Z. B., Koc, O. N., and Penn, M. S. (2007) SDF-1 expression by mesenchymal stem cells results in trophic support of cardiac myocytes after myocardial infarction. *Faseb J. 21*, 3197–207.
(14) Barbash, I. M., Chouraqui, P., Baron, J., Feinberg, M. S., Etzion, S., Tessone, A., Miller, L., Guetta, E., Zipori, D., Kedes, L. H., Kloner, R. A., and Leor, J. (2003) Systemic delivery of bone marrow-derived mesenchymal stem cells to the infarcted myocardium: feasibility, cell migration, and body distribution. *Circulation 108*, 863–8.
(15) Chen, J., Li, Y., Wang, L., Zhang, Z., Lu, D., Lu, M., and Chopp, M. (2001) Therapeutic benefit of intravenous administration of bone marrow stromal cells after cerebral ischemia in rats. *Stroke 32*, 1005–11.
(16) Kawada, H., Fujita, J., Kinjo, K., Matsuzaki, Y., Tsuma, M., Miyatake, H., Muguruma, Y., Tsuboi, K., Itabashi, Y., Ikeda, Y., Ogawa, S., Okano, H., Hotta, T., Ando, K., and Fukuda, K. (2004) Nonhematopoietic mesenchymal stem cells can be mobilized and differentiate into cardiomyocytes after myocardial infarction. *Blood 104*, 3581–7.
(17) Lawrence, M. B., and Springer, T. A. (1991) Leukocytes roll on a selectin at physiologic flow rates: distinction from and prerequisite for adhesion through integrins. *Cell 65*, 859–73.
(18) Salas, A., Shimaoka, M., Chen, S., Carman, C. V., and Springer, T. (2002) Transition from rolling to firm adhesion is regulated by the conformation of the I domain of the integrin lymphocyte function-associated antigen-1. *J. Biol. Chem. 277*, 50255–62.
(19) Ley, K., Laudanna, C., Cybulsky, M. I., and Nourshargh, S. (2007) Getting to the site of inflammation: the leukocyte adhesion cascade updated. *Nat. Rev. Immunol. 7*, 678–89.
(20) Greenberg, A. W., Kerr, W. G., and Hammer, D. A. (2000) Relationship between selectin-mediated rolling of hematopoietic stem and progenitor cells and progression in hematopoietic development. *Blood 95*, 478–86.
(21) Wynn, R. F., Hart, C. A., Corradi-Perini, C., O'Neill, L., Evans, C. A., Wraith, J. E., Fairbairn, L. J., and Bellantuono, I. (2004) A small proportion of mesenchymal stem cells strongly expresses functionally active CXCR4 receptor capable of promoting migration to bone marrow. *Blood 104*, 2643–2645.
(22) Rombouts, W. J., and Ploemacher, R. E. (2003) Primary murine MSC show highly efficient homing to the bone marrow but lose homing ability following culture. *Leukemia 17*, 160–70.
(23) Meirelles, L. d. S., Chagastelles, P. C., and Nardi, N. B. (2006) Mesenchymal stem cells reside in virtually all post-natal organs and tissues. *J. Cell. Sci. 119*, 2204–2213.
(24) Jones, E. A., Kinsey, S. E., English, A., Jones, R. A., Straszynski, L., Meredith, D. M., Markham, A. F., Jack, A., Emery, P., and McGonagle, D. (2002) Isolation and characterization of bone marrow multipotential mesenchymal progenitor cells. *Arthritis Rheum. 46*, 3349–60.
(25) Simmons, P. J., and Torok-Storb, B. (1991) Identification of stromal cell precursors in human bone marrow by a novel monoclonal antibody, STRO-1. *Blood 78*, 55–62.
(26) Barbash, I. M., Chouraqui, P., Baron, J., Feinberg, M. S., Etzion, S., Tessone, A., Miller, L., Guetta, E., Zipori, D., Kedes, L. H., Kloner, R. A., and Leor, J. (2003) Systemic delivery of bone marrow-derived mesenchymal stem cells to the infarcted myocardium: feasibility, cell migration, and body distribution. *Circulation 108*, 863–868.
(27) Chen, J., Li, Y., Wang, L., Zhang, Z., Lu, D., Lu, M., and Chopp, M. (2001) Therapeutic benefit of intravenous administration of bone marrow stromal cells after cerebral ischemia in rats. *Stroke 32*, 1005–1011.
(28) Kawada, H., Fujita, J., Kinjo, K., Matsuzaki, Y., Tsuma, M., Miyatake, H., Muguruma, Y., Tsuboi, K., Itabashi, Y., Ikeda, Y., Ogawa, S., Okano, H., Hotta, T., Ando, K., and Fukuda, K. (2004) Nonhematopoietic mesenchymal stem cells can be mobilized and differentiate into cardiomyocytes after myocardial infarction. *Blood 104*, 3581–3587.
(29) Jiang, W., Ma, A., Wang, T., Han, K., Liu, Y., Zhang, Y., Zhao, X., Dong, A., Du, Y., Huang, X., Wang, J., Lei, X., and Zheng, X. (2006) Intravenous transplantation of mesenchymal stem cells improves cardiac performance after acute myocardial ischemia in female rats. *Transplant Int. 19*, 570–580.
(30) Sackstein, R., Merzaban, J. S., Cain, D. W., Dagia, N. M., Spencer, J. A., Lin, C. P., and Wohlgemuth, R. (2008) Ex vivo glycan engineering of CD44 programs human multipotent mesenchymal stromal cell trafficking to bone. *Nat. Med. 14*, 181–187.
(31) Mahal, L. K., and Bertozzi, C. R. (1997) Engineered cell surfaces: Fertile ground for molecular landscaping. *Chem. Biol. 4*, 415–422.
(32) Hausmann, S., Claus, R., and Walzel, H. (1995) Short-term culture of surface-biotinylated cells: Application in non-radioactive analysis of surface protein shedding. *Immunol. Lett. 48*, 175–180.
(33) Yago, T., Leppanen, A., Qiu, H., Marcus, W. D., Nollert, M. U., Zhu, C., Cummings, R. D., and McEver, R. P. (2002) Distinct molecular and cellular contributions to stabilizing selectin-mediated rolling under flow. *J. Cell. Biol. 158*, 99–787.

BC800345Q

Supporting Information for:

Cell Surface Conjugation of Sialyl Lewis X Induces a Rolling Response for Human Mesenchymal Stem Cells

*Debanjan Sarkar[†], Praveen Kumar Vemula[†], Grace S. L. Teo[†], Dawn Spelke[†], Rohit Karnik[§], Le Y. Wee[†], Jeffrey M. Karp[†] **

[†]Harvard-MIT Division of Heath Sciences & Technology
Department of Medicine, Brigham and Women's Hospital, Harvard Medical School
65 Landsdowne Street, Cambridge, MA 02139, USA

[§]Department of Mechanical Engineering, Massachusetts Institute of Technology,
77 Massachusetts Avenue, Cambridge, MA 02139, USA

**Corresponding Author*
E-mail: jeffkarp@mit.edu
Tel: +1-617-8179174
Fax: +1-617-768-8338
Homepage: www.karplab.net

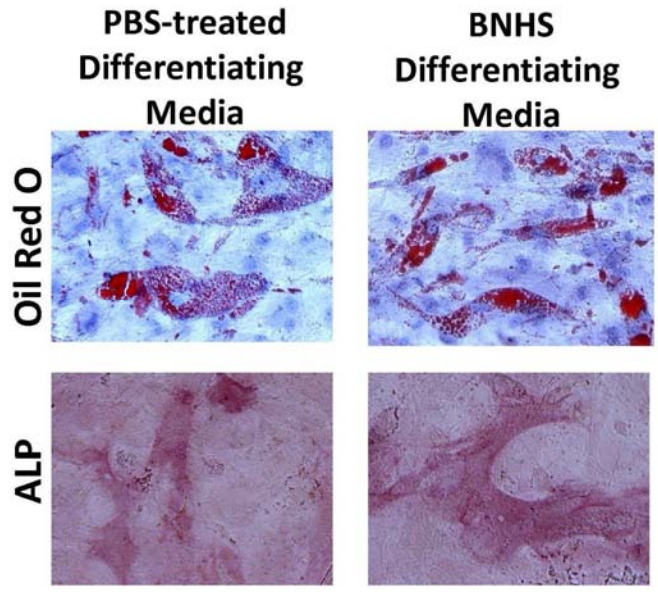

Figure S1. Alkaline phosphatase (ALP) and Oil Red O (ORO) staining, 23 days after addition of osteogenic and adipogenic differentiation media, respectively. Negative controls (BNHS modified cells cultured in expansion media) showed no ORO or ALP staining. Positive controls (PBS treated cells in differentiating media) showed positive ORO and ALP staining. Experimental group (BNHS modified cells cultured in respective differentiating media) showed similar positive staining for both ORO and ALP compared to the unmodified cells. 20X magnification.

Experimental Section:

Materials

P-selectin was purchased from R&D systems (Minneapolis, MN) and biotinylated sialyl Lewis(x)-poly(acrylamide) (sialyl-Lewis^X-PAA-Biotin) was purchased from Glycotech (Gaithersburg, MD). Primary human MSCs were obtained from the Center for Gene Therapy at Tulane University which has a grant from NCRR of the NIH, Grant # P40RR017447. α-MEM, Fetal Bovine Serum, L-Glutamine and Penn-Strep were purchased from Invitrogen. All other

chemicals and reagents were purchased from Sigma Aldrich (St. Louis, MO) and were used without further modification unless specified.

Mesenchymal Stem Cell Culture and Characterization

Primary human MSCs obtained from the Center for Gene Therapy at Tulane University were isolated from human marrow of healthy consenting donors and thoroughly characterized as previously described (Sekiya, I., Larson, B. L., Smith, J. R., Pochampally, R., Cui, J.-G., Prockop, D. J. (2002) Expansion of human adult stem cells from bone marrow stroma: Conditions that maximize the yields of early progenitors and evaluate their quality. *Stem Cells 20*, 530-41.). MSCs were maintained in expansion medium that consisted of 15% Fetal Bovine Serum (selected for its ability to expand MSCs), 1% (v/v) L-Glutamine, 1% (v/v) Penn-Strep, and α-MEM. All experiments were performed using MSCs at passage number 4-6. For MSC characterization, passage 6 cells were incubated for 10 minutes in non-enzymatic cell dissociation solution (Sigma). After washing with PBS containing 1% FBS and 0.05% NaN3 (FACS buffer), cells were filtered using a 40 μm cell strainer and incubated for 30 minutes using the following mouse IgG1, k antibodies: 1.) CD34 fluorescein isothiocyanate (FITC) conjugated antibody (diluted at 1:800 with FACS buffer), 2.) CD45 FITC-conjugated antibody (diluted at 1:800), 3.) CD90 FITC-conjugated antibody (diluted at 1:400), 4.) and CD146 R phycoerythrin (R-PE) conjugated antibody (diluted at 1:400). After staining, cells were washed again with FACS buffer and fluorescence levels were determined using a BD FACS Calibur flow cytometer and analyzed using the Cell Quest software.

Covalent Conjugation of Biotin (and Streptavidin) to the MSC surface

5000 cells in 200 µL MSC cell expansion media were added to the wells of a 96 well plate for a period of 24-48 hours to reach ~80-90 % confluency. To chemically modify the cells, media was aspirated from the wells and the cells were gently washed with 200 µL of phosphate buffer saline (PBS, pH 7.4 without Ca/Mg) at room temperature in each well. 100 µL of 1 mM BNHS solution in PBS, pH 7.4 without Ca/Mg was added to each well for 20-25 minutes at room temperature. After designated times, the cells in each well were washed twice with 200 µL of phosphate buffer saline (PBS, pH 7.4 without Ca/Mg). Then to each well, 50 µL of streptavidin solution (50 µg/mL in PBS, pH 7.4 without Ca/Mg) was added for 20 minutes at room temperature.

Stability of Covalently Conjugated Biotin (and Streptavidin) on the MSC surface

To characterize the stability of streptavidin bound to covalently conjugated biotin, 200 µL of S (rhodamine-conjugated streptavidin) solution made from 50 µg/mL in PBS, pH 7.4 without Ca/Mg was added for 20 minutes at room temperature on PBS, Biotin, and BNHS treated cells. After the addition of S, the cells were thoroughly washed with PBS and the fluorescence intensity of microscopic images was measured (day 0). Cells in separate wells were incubated for 7 days at 37 °C and 5% CO_2 with media changes every 2 days followed by examination of the fluorescence intensity.

Accessibility of Biotin on the MSC surface

To characterize the accessibility of the biotin on the cell surface after BNHS modification, 200 µL of S solution (50 µg/mL in PBS, pH 7.4 without Ca/Mg) was added for 20 minutes at room

temperature on either Biotin or BNHS treated cells after 0, 2, 4 and 7 days. After addition of S, the cells were fixed with 4% formaldehyde solution and stained with 100 µL of DAPI solution (1 µg/mL in PBS) after treatment with 100 µL of 0.1% TRITON X solution in PBS. The fluorescence intensity of microscopic images from BNHS and Biotin treated cells were analyzed using Nikon quantitative software (NIS-Elements version 3).

Viability, Adhesion and Proliferation Characteristics

The viability of the cells was examined using trypan blue exclusion. Briefly, cells were plated into 12 well plates, left to adhere over night and the cells were treated with BNHS solution as described above. The cells were incubated for 48 hours at 37 °C and 5% CO_2. The media was then aspirated (similar quantities of floating cells were observed between the groups – typically 1-5 per well) and the cells were detached with 200 µL of cell dissociation solution. 300 µL of media was added and the total 500 µL of the cell dispersion was collected in an eppendorf tubes. From this 10 µL of cell dispersion was diluted to 1:1 with 4% trypan blue solution and cells were counted in a hemocytometer to determine the number of viable (non-blue) and nonviable (blue) cells. The controls for this experiment included PBS treated cells and the cells treated with biotin and S without NHS (non covalent). Cell adhesion was quantified by measuring the number of adherent cells on tissue culture surfaces in 96 well plates after BNHS treatment. Briefly, 80-90% confluent cells in a T25 flask were biotinylated with BNHS as described above. 5000 cells were added to each well of a 96 well plate in 200 µL of MSC cell expansion media followed by incubation at 37°C. The non-adhered cells were removed by washing with PBS. Proliferation was quantified by manually tabulating the number of cells within a T25 flask at multiple time points with light microscopy at 10X.

Differentiation of cells

Multi-lineage differentiation potential of the BNHS modified and PBS treated cells was examined by treating cells with osteogenic and adipogenic induction media followed by respective colorimetric histological staining.

Osteogenic Differentiation

MSCs seeded in the wells of 24 well plates were cultured in MSC expansion media until reaching 90% confluence. For cell modification, cells were biotinylated with 1mM BNHS followed by conjugation with streptavidin (50 µg/mL) in PBS at room temperature. Osteogenic differentiation was induced by culturing the cells for 23 days in osteogenic induction media (from Lonza –MSCs Osteogenic Single Quote kit) containing dexamethasone, β-glycerophosphate, L-ascorbic acid-2-phosphate, and α-MEM. For a positive control, PBS-treated (un-modified) cells were maintained in osteogenic induction medium and for a negative control, BNHS modified cells were maintained in MSC expansion media. The media in both groups was changed every 3 days. Osteogenesis was evaluated by cell membrane associated alkaline phosphatase activity. Alkaline phosphatase activity was examined after 23 days by carefully aspirating the medium and washing the cells with distilled water. The cells were fixed with 3.7% formaldehyde solution for 15 min at room temperature followed by rinsing with distilled water. 0.06% Red Violet LB salt solution in Tris HCl was added with distilled water containing DMF and Naphthol AS MX-PO_4. The plates were incubated for 45 minutes and then the wells were rinsed 3 times with distilled water and visualized with light microscopy.

Adipogenic Differentiation

MSCs seeded in 4 wells of a 24 well plate were cultured in cell expansion media until reaching 100% confluence. Typically cells were biotinylated with 1mM BNHS followed by conjugation

with streptavidin (50 µg/mL) in PBS at room temperature. Adipogenic differentiation was induced by culturing the cells for 23 days in adipogenic induction media (from Lonza –MSCs Adipogenic Single Quote kit containing h-Insulin (recombinant), L-Glutamine, Dexamethasone, Indomethacin, IBMX (3-isobuty-l-methyl-xanthine), Pen/Strep) and adipogenic maintenance media (from Lonza –MSCs Adipogenic Single Quote kit containing h-Insulin (recombinant), L-Glutamine, Pen/Strep). As a positive control, PBS-treated (un-modified) cells were maintained in adipogenic induction medium, and as a negative control the BNHS modified cells were maintained in normal MSC expansion media. The media in both groups were changed every 3 days in a periodic exposure of induction and maintenance media as suggested by the supplier (Lonza). Adipogenesis was evaluated by Oil Red O staining. Following aspiration of the media, cells were washed once with PBS, and fixed in PBS with 3.7 % formaldehyde for 30 min at room temperature. Following fixation cells were rinsed with distilled water for a few minutes, and incubated with isopropanol containing an Oil Red O working solution (prepared by diluting 30 mL of 0.5% isopropanol / Oil Red O solution with 20 mL of distilled water). After 45 minutes culture well were rinsed twice with distilled water and 1 mL of hematoxylin was added to each well for 1 minute followed by aspiration and washing with distilled water. The wells were viewed using an inverted phase contrast microscope. Lipid droplets appeared red and nuclei appeared blue.

The percentage of cells that positively stained for alkaline phosphatase (an indicator of osteogenic differentiation) and for Oil Red O (an indicator of adipogenic differentiation) was calculated by enumerating the number of stained and unstained cells in 3 wells per group (3 fields per well)

Preparation of P-selectin Surfaces

Glass surfaces used for the preparation of P-selectin surface was cleaned by Piranha solution and subsequently washed with double distilled water three times. The cleaned surfaces were dried overnight under vacuum. P-selectin (700 μL of a 5 μg/mL solution) was placed on top of the glass surface and incubated on a plate shaker for 18 hours at room temperature. All the P-selectin surfaces were prepared fresh before the flow chamber assay.

Flow Chamber Assay

For flow chamber experimentation, the cells were biotinlyated with BNHS as described above in a T25 flask. 200 µL of S solution (50 µg/mL in PBS, pH 7.4 without Ca/Mg) was added for 20 minutes at room temperature to BNHS treated cells. Cells were washed twice with 1 mL of phosphate buffer saline (PBS, pH 7.4 without Ca/Mg) at room temperature in each well followed by addition of 1 mL of 4µg/mL biotinylated SLeX (Biotin-PAA-SLeX in PBS, pH 7.4 without Ca/Mg) at room temperature. The cells were detached from the flask by using 1 mL of cell dissociation solution and then resuspended in MSC expansion media (~10^5 cells/mL) for analysis of cell velocities within a parallel plate flow chamber.

The rolling characteristics of the cells were assessed using a rectangular parallel plate flow chamber (Glycotech, Gaithersburgh, MD) with 127 µm gasket thickness and a length of 6 cm. For the majority of experiments, a flow rate of 20 µL/min corresponding to a wall shear stress of 0.366 dyne/cm^2 was used. To monitor cell rolling, phase contrast microscopy (TE2000-U Inverted Nikon Microscope with a DS-Qi1 Monochrome Cooled Digital Camera) was utilized and images were recorded in a 10X field at 10 second intervals. The velocity of the cells was calculated by measuring the distance cells travelled within a 10 second interval. A cell was

classified as rolling if it rolled for 10 seconds while remaining in the field of view and if it translated at an average velocity less than 50% of the calculated free stream velocity of a non-interacting cell. The number of interacting cells was calculated manually based on number of cells remaining adhered in the field view for 10 seconds. To assess the effect of shear rate and the concentration of BNHS added to the cells, the rolling velocity and the flux of the cells were measured at flow rates of 20, 40 and 100 µL/min corresponding to 0.366, 0.73 and 1.89 dyne/cm^2, respectively.

Statistical Analysis:

For multiple pairwise comparisons, a two-tailed Student's t test was used with the Bonferroni correction. Error bars in bar graphs represent standard deviations, and statistical significance is denoted by ◆ $P > 0.05$, * $P < 0.05$, ** $P < 0.01$, *** $P < 0.001$.

Redmond Red as a Redox Probe for the DNA-Mediated Detection of Abasic Sites

Marisa C. Buzzeo and Jacqueline K. Barton*

Division of Chemistry and Chemical Engineering, California Institute of Technology, Pasadena, California 91125. Received August 6, 2008; Revised Manuscript Received September 9, 2008

Redmond Red, a fluoropore containing a redox-active phenoxazine core, has been explored as a new electrochemical probe for the detection of abasic sites in double-stranded DNA. The electrochemical behavior of Redmond Red-modified DNA at gold surfaces exhibits stable, quasi-reversible voltammetry with a midpoint potential centered around −50 mV versus NHE. Importantly, with Redmond Red positioned opposite an abasic site within the DNA duplex, the electrochemical response is significantly enhanced compared to Redmond Red positioned across from a base. Redmond Red, reporting only if well-stacked in the duplex, represents a sensitive probe to detect abasic sites electrochemically in a DNA-mediated reaction.

Since its discovery, the ability of DNA to conduct charge has been exploited in a variety of arenas, including time-resolved spectroscopy (*1*−*3*), conductivity measurements (*4*−*7*), and the development of biosensors (*8*). Our group, in particular, has explored the versatility of this intrinsic property of DNA by performing extensive electrochemical studies on surfaces modified with DNA duplexes (*9*−*15*). Typically in such systems, thiol-modified oligonucleotides are tethered to a gold electrode at the 5′ terminus by a Au−S bond and further modified at the opposite end with a redox probe, thus allowing the duplexes to act as an extension of the conducting medium. The reduction of the attached probe, as observed voltammetrically, serves as an indicator of the transport of charge via the DNA duplex. Importantly, it has been shown that DNA-mediated charge transport is remarkably sensitive to the integrity of the base stack; upon introduction of a single base mismatch located between the electrode and the redox probe, measured currents are dramatically diminished (*9, 10*). This behavior not only provides conclusive evidence that the observed electrochemical reactions are indeed DNA-mediated, but also allows naturally occurring perturbations, which may only subtly interrupt π-stack overlap, to be detected (*11*−*15*).

Among these possibly destabilizing defects are abasic sites, which appear naturally and frequently among DNA sequences as the result of hydrolytic cleavage of the glycosidic bond (*16*−*23*). Specific enzymes are responsible for correcting these damaged sites prior to transcription and replication. When this repair pathway is delinquent, however, the persistence of these defects can impart deleterious effects on genetic encoding, leading to the development of cancer, among other diseases (*24*−*26*). Because they represent a potential threat, the reliable and specific detection of abasic sites is critical, although still very much under exploration. Development of an electrochemical system to detect these unwanted sites specifically could contribute to the understanding of their occurrence and repair. Here, we employ Redmond Red (RR), obtained as a commercially available phosphoramidite and used commonly as a fluorophore, as a new redox probe for the detection of abasic sites. We find that the width of the covalently tethered phenoxazine derivative is particularly well accommodated when positioned opposite an abasic site within a DNA duplex, thus facilitating efficient DNA-mediated reduction as a "turn on" probe for their presence (Figure 1).

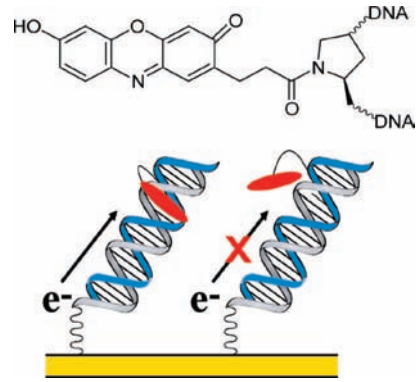

Figure 1. Structure of Redmond Red (RR), an electroactive phenoxazine derivative covalently tethered to DNA, along with a schematic representation of the basis of the abasic site probe. With Redmond Red placed opposite an abasic residue (left), DNA-mediated reduction can proceed, but if opposite a base (right), RR is excluded from the duplex and DNA-mediated reduction cannot proceed. Note that the three-ring phenoxazine core is comparable in size to a base pair.

Alkane thiol-modified DNA strands were synthesized as described previously (*14, 15*) with Redmond Red internal to the sequence and hybridized to a complement containing an abasic site in the opposite position. All syntheses were performed using standard phosphoramidite chemistry. Redmond Red-modified strands were cleaved from the solid support resin using 0.05 M K_2CO_3 in MeOH at ambient temperature for 12−17 h. Complementary strands were cleaved using concentrated NH_4OH at 60 °C for 8−12 h. Samples were purified twice by reversed-phase HPLC and characterized by MALDI-TOF mass spectrometry and UV−visible spectroscopy (see Supporting Information). For those oligonucleotides containing an abasic site, the commercially available tetrahydrofuranyl analogue was used (*27*); the naturally occurring, hemiacetal abasic residue is unstable and reactive on the time scale of DNA synthesis.

Freshly etched gold macroelectrodes were incubated with 50 μM modified duplex DNA overnight at 5 °C in the presence of 100 mM $MgCl_2$ to encourage formation of densely packed films. Electrochemical measurements were performed at ambient

* Author to whom correspondence should be addressed. E-mail: jkbarton@caltech.edu.

10.1021/bc800339y CCC: $40.75 © 2008 American Chemical Society
Published on Web 10/03/2008

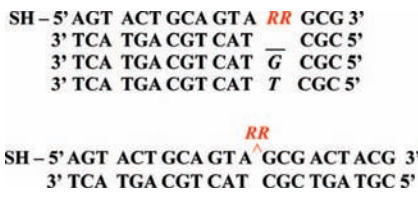

Figure 2. Sequences employed to determine the sensitivity of the DNA-mediated reduction of Redmond Red to the presence of the opposing base. Shown are the thiol-modified strands, along with the variable complementary strands, where "*RR*" indicates a Redmond Red moiety, and "__" an abasic site.

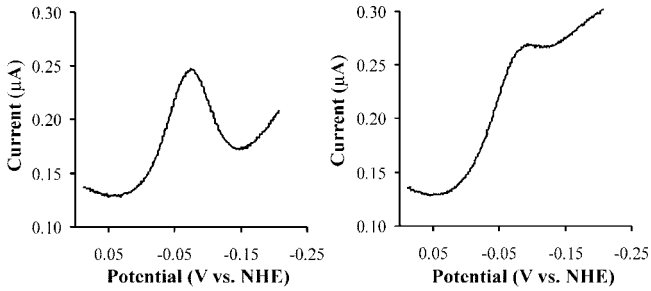

Figure 3. Electrochemical reduction at a ^{RR}DNA-modified electrode, observed by square wave voltammetry, when RR is positioned opposite an abasic site (left) or a guanine residue (right); the reductive signal is significantly attenuated in the latter case. Peak areas were determined by integrating above the baseline of the voltammograms, thus accounting for differences in the background responses.

temperature in phosphate buffer (5 mM sodium phosphate, 50 mM NaCl, pH 7) using a CH Instruments 760B potentiostat. A saturated calomel electrode served as a reference electrode, and a platinum wire as a counter. Square wave voltammograms were recorded at a frequency of 15 Hz and an amplitude of 0.025 V. Under such conditions, Redmond Red-modified DNA (^{RR}DNA) displays stable, quasi-reversible voltammetry with a midpoint potential centered around −50 mV versus NHE. The measured peak currents scale linearly with scan rate, indicating that RR behaves as a surface-bound species, as anticipated, and is not under diffusional control.

To test if the observed voltammetric response is in fact dependent on the presence of an abasic site, the same thiolated ^{RR}DNA was then hybridized to complementary sequences containing a guanine (G) or thymine (T) opposite the probe, and the resulting voltammetry recorded (see Figure 2 for sequences). The observed reductive signal is severely affected. Figure 3 shows a comparison of typical square wave voltammograms obtained for both assemblies, and Figure 4 presents a comparison of the average peak areas measured for the different sequences. More than a 2-fold increase is consistently observed when RR is situated opposite an abasic site versus an intact DNA strand. It therefore becomes apparent that inclusion of an opposing base precludes well-stacked insertion of RR into the duplex, thus preventing efficient reduction through the π-stack. Conversely, when an abasic residue is located on the complementary strand, the phenoxazine derivative, itself having a similar dimension to a base pair, is now able to insert into the duplex and become available for DNA-mediated reduction. The enhancement of signal seen for the well-stacked Redmond Red is consistent with earlier results that have shown the redox signal to reflect how well the probe is coupled into the base stack (*14*, *28*). This discrimination of abasic sites indicates that the DNA-mediated reduction of RR can provide a convenient means by which to detect the abasic defect.

We also investigated whether or not RR would respond voltammetrically to a base deletion. A complementary strand was synthesized in which the position opposite the RR was

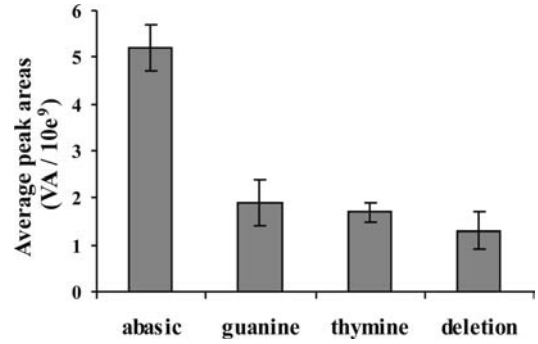

Figure 4. Bar chart representation of the differences observed in peak areas for the reduction of Redmond Red when positioned opposite an abasic residue, a base, or a deletion site within a DNA duplex. Peak areas, determined from square wave voltammetry, have all been normalized to the area of the gold surface as determined by sulfuric acid etches performed immediately prior to measurement. Error bars shown represent one standard deviation of the measurement.

occupied not by an abasic site, but instead by the base that corresponds to the next position on the RR strand; in short, no complementary base was assigned to RR (Figure 2). Under these conditions, we considered that the RR may be pinched out of the sequence, allowing the bases above the probe to fully hybridize and thus inhibiting reduction of the phenoxazine moiety. For these experiments, the length of the oligonucleotide was extended by six bases in order to prevent fraying above the probe site while keeping the position of Redmond Red relative to the electrode surface constant. As observed by both cyclic and square wave voltammetry, duplexes containing the deleted site do indeed consistently yield diminished currents, and the magnitude of the effect (300% increase for an abasic site) is in line with those results observed when a G or T is situated opposite RR (Figure 4). This indicates that the probe is, in fact, excluded from the base stack in order to allow for the remaining bases to hybridize and is therefore not available for reduction in a DNA-mediated fashion.

Early work first demonstrated the sensitivity of electrochemical techniques to the presence of abasic sites resulting from depurination in chromosomal DNA: differential poloragraphic responses were observed for nondenatured DNA versus the apurinic form (*29*−*31*). More recently, studies have reported the detection of these damaged sites specifically in synthetic oligonucleotides using chronopotentiometric and square wave voltammetric techniques (*32*−*35*). These systems, however, possess intrinsic limitations that prevent them from serving as practical diagnostics. In the first example, the target DNA must be consumed via acid-induced oligonucleotide digestion (*32*), while the other detection schemes are specific to thymine-related mutations (*33*−*35*). Here, the redox probe is covalently attached to the DNA, the target oligonucleotide remains intact, and the electrochemical measurement is fast, simple, and selective. Moreover, electrocatalytic coupling may provide enhanced signal discrimination, thus affording the increased sensitivity needed on the genomic scale (*11*, *12*).

The studies presented here once again highlight how sensitive DNA-mediated charge transport chemistry can be in reporting on DNA structure. Earlier we used DNA-mediated electrochemistry to characterize perturbations in the *intervening* DNA structures using a well-stacked probe, but here how well the probe is itself stacked serves as a specific reporter of local conformation. The selective enhancement found with RR opposing an abasic residue confirms that, to detect efficient reduction of the probe at a distance from the electrode, the reduction must be DNA-mediated. The dependence of probe detection on the spatial constraints of the duplex underscores

the general sensitivity of DNA-mediated charge transport chemistry to local DNA conformation.

ACKNOWLEDGMENT

We are grateful to the National Institutes of Health (GM 61077) for their financial support.

Supporting Information Available: Synthetic details, electrochemical experimental conditions, and characterization data (HPLC, MS, UV−vis, T_m) of modified DNA. This material is available free of charge via the Internet at http://pubs.acs.org.

LITERATURE CITED

(1) Wan, C., Fiebig, T., Kelley, S. O., Treadway, C. R., Barton, J. K., and Zewail, A. H. (1999) Femtosecond dynamics of DNA-mediated electron transfer. *Proc. Natl. Acad. Sci. U.S.A. 102*, 6014–6019.

(2) Takada, T., Kawai, K., Cai, X., Sigimoto, A., Fujitsuka, M., and Majima, T. (2004) Charge separation in DNA via consecutive adenine hopping. *J. Am. Chem. Soc. 126*, 1125–1129.

(3) Lewis, F. D., Zhu, H., Daublain, P., Cohen, B., and Wasielewski, M. R. (2006) Hole mobility in DNA A tracts. *Angew. Chem., Int. Ed. 45*, 7982–7985.

(4) Hihath, J., Xu, B., Zhang, P., and Tao, N. (2005) Study of single-nucleotide polymorphisms by means of electrical conductance measurements. *Proc. Natl. Acad. Sci. U.S.A. 102*, 16979–16983.

(5) van Zalinge, H., Schiffrin, D. J., Bates, A. D., Starikov, E. B., Wenzel, W., and Nichols, R. J. (2006) Variable-temperature measurements of the single-molecule conductance of double stranded DNA. *Angew. Chem., Int. Ed. 45*, 5499–5502.

(6) Wierzbinski, E., Amdt, J., Hammond, W., and Slowinksi, K. (2006) In situ electrochemical distance tunneling spectroscopy of ds-DNA molecules. *Langmuir 22*, 2426–2429.

(7) Guo, X., Gorodetsky, A. A., Hone, J., Barton, J. K., and Nuckolls, C. (2008) Conductivity of a single DNA duplex bridging a carbon nanotube gap. *Nat. Nanotechnol. 3*, 163–167.

(8) Drummond, T. G., Hill, M. G., and Barton, J. K. (2003) Electrochemical DNA sensors. *Nat. Biotechnol. 21*, 1192–1199, and references therein.

(9) Kelley, S. O., Jackson, N. M., Hill, M. G., and Barton, J. K. (1999) Long range electron transfer through DNA films. *Angew. Chem., Int. Ed. 38*, 941–945.

(10) Kelley, S. O., Boon, E. M., Jackson, N. M., Hill, M. G., and Barton, J. K. (1999) Single-base mismatch detection based on charge transduction through DNA. *Nucleic Acids Res. 27*, 4830–4837.

(11) Boon, E. M., Ceres, D. M., Drummond, T. G., Hill, M. G., and Barton, J. K. (2000) Mutation detection by electrocatalysis at DNA-modified electrodes. *Nat. Biotechnol. 18*, 1096–1100.

(12) Boal, A. K., and Barton, J. K. (2005) Electrochemical detection of lesions in DNA. *Bioconjugate Chem. 16*, 312–321.

(13) Gorodetsky, A. A., Dietrich, L. E. P., Lee, P. E., Demple, B., Newman, D. K., and Barton, J. K. (2008) DNA binding shifts the redox potential of the transcription factor SoxR. *Proc. Natl. Acad. Sci. U.S.A. 105*, 3684–3689.

(14) Gorodetsky, A. A., Green, O., Yavin, E., and Barton, J. K. (2007) Coupling into the base pair stack is necessary for DNA-mediated electrochemistry. *Bioconjugate Chem. 18*, 1434–1441.

(15) Gorodetsky, A. A., Ebrahim, A., and Barton, J. K. (2008) Electrical detection of TATA binding protein at DNA-modified microelectrodes. *J. Am. Chem. Soc. 130*, 2924–2925.

(16) Vesnaver, G., Chang, C.-N., Eisenberg, M., Grollman, A. P., and Breslauer, K. J. (1989) Influence of abasic and anucleosidic sites on the stability, conformation, and melting behavior of a DNA duplex: correlations of thermodynamic and structural data. *Proc. Natl. Acad. Sci. U.S.A. 86*, 3614–3618.

(17) Lindahl, T. (1993) Instability and decay of the primary structure of DNA. *Nature 362*, 709–715.

(18) Krokan, H. E., Standal, R., and Slupphaug, G. (1997) DNA glycosylases in the base excision repair of DNA. *Biochem. J. 325*, 1–16.

(19) Gelfand, C. A., Plum, G. E., Grollman, A. P., Johnson, F., and Breslauer, K. J. (1998) Thermodynamic consequences of an abasic lesion in duplex DNA are strongly dependent on base sequence. *Biochemistry 37*, 7321–7327.

(20) Lhomme, J., Constant, J.-F., and Demeunynck, M. (1999) Abasic DNA structure, reactivity, and recognition. *Biopolymers 52*, 65–83.

(21) Kuzminov, A. (2001) Single-strand interruptions in replicating chromosomes cause double-strand breaks. *Proc. Natl. Acad. Sci. U.S.A. 98*, 8241–8246.

(22) Schärer, O. D., and Jiricny, J. (2001) Recent progress in the biology, chemistry, and structural biology of DNA glycosylases. *BioEssays 23*, 270.

(23) Yu, S.-L., Lee, S.-K., Johnson, R. E., Prakash, L., and Prakash, S. (2003) The stalling of transcription at abasic sites is highly mutagenic. *Mol. Cell. Biol. 23*, 382–388.

(24) Loeb, L. A. (1985) Apurinic sites as mutagenic intermediates. *Cell 40*, 483–484.

(25) Guillet, M., and Boiteux, S. (2003) Origin of endogenous DNA abasic sites in *Saccharomyces cerevisiae*. *Mol. Cell. Biol. 23*, 8386–8394.

(26) Boiteux, S., and Guillet, M. (2004) Abasic sites in DNA: repair and biological consequences in *Saccharomyces cerevisiae*. *DNA Repair 3*, 1–12.

(27) Lin, Z., Hung, K. N., Grollman, A. P., and de los Santos, C. (1998) Solution structure of duplex DNA containing an extrahelical abasic site analog determined by NMR spectroscopy and molecular dynamics. *Nucleic Acids Res. 26*, 2385–2391.

(28) Boon, E. M., Jackson, N. M., Wightman, M. D., Kelley, S. O., Hill, M. G., and Barton, J. K. (2003) Intercalative stacking: a critical feature of DNA charge-transport electrochemistry. *J. Phys. Chem. B 107*, 11805–11812.

(29) Paleček, E. (1960) Oscillographic polarography of highly polymerized deoxyribonucleic acid. *Nature 188*, 656–657.

(30) Oliński, R., Walter, Z., Wiaderkiewicz, R., Lukášová, E., and Paleček, E. (1980) Changes in DNA properties due to treatment with the pesticides malathion and DDVP. *Radiat. Environ. Biophys. 18*, 65–72.

(31) Jelen, F., Fojta, M., and Paleček, E. (1997) Voltammetry of native double-stranded, denatured, and degraded DNAs. *J. Electroanal. Chem. 427*, 49–56.

(32) Dolinnaya, N. G., Jan, M. R., Kawde, A.-N., Oretskaya, T. S., Tashlitsky, V. N., and Wang, J. (2006) Electrochemical detection of abasic site-containing DNA. *Electroanalysis 18*, 399–404.

(33) Morita, K., Sankaran, N. B., Huang, W., Seino, T., and Sato, Y. (2006) Electrochemical SNPs detection using an abasic site-containing DNA on a gold electrode. *Chem. Commun.* 2376–2378.

(34) Morita, K., Nishizawa, S., and Teramae, N. (2006) Use of an abasic site-containing DNA for electrochemical SNP detection. *Nucleic Acids Symp. Ser. 50*, 91–92.

(35) Huang, W., Morita, K., Sankaran, N. B., Nishizawa, S., and Teramae, N. (2006) Electrochemical detection at low temperature for a specific nucleobase of target nucleic acids by an abasic site-containing DNA binding ligand. *Electrochem. Commun. 8*, 395–398.

BC800339Y

Supporting Information

Redmond Red as a Redox Probe for the DNA-mediated Detection of Abasic Sites

Marisa C. Buzzeo and Jacqueline K. Barton
Division of Chemistry and Chemical Engineering, California Institute of Technology
Pasadena, California 91125

1. Synthesis of modified DNA
2. Electrochemical experimental conditions
3. Characterization data
    S1. HPLC chromotagrams of Redmond Red modified DNA
    S2. HPLC chromotagrams of DNA containing abasic site
    S3. MALDI-TOF mass spectra
    S4. UV-vis spectra of Redmond Red modified DNA
    S5. Melting temperature analyses

1. Synthesis of modified DNA

All syntheses were performed using standard phosphoramidite chemistry. Thiol-modified DNA strands were synthesized as previously described using a C_6-disulfide phosphoramidite, available from Glen Research. Treatment with excess dithiothreitol in 10 mM Tris buffer (pH 8) for 30 min at ambient temperature resulted in cleavage of the disulfide bond and concomitant removal of the dimethoxytrityl (DMT) protecting group. Nap-5 Sephadex columns (GE Healthcare) were used to isolate the thiolated strands, and reversed-phase HPLC was used to purify the DNA before and after disulfide cleavage (see Figure S1). Redmond Red was incorporated into the DNA sequence at the desired position as a phosphoramidite (also available from Glen Research). Given the sensitivity of Redmond Red to typical cleavage and deprotection conditions (NH_4OH at 60 ºC), less harsh conditions were employed (K_2CO_3/MeOH at ambient temperature for 12 – 17 h) for strands containing this modification. Accordingly, phosphoramidites containing more labile protecting groups than standard reagents were required for synthesis (Glen Research). All synthesized DNA strands were purified by reversed-phase HPLC before and after removal of DMT protecting groups using a Varian DYNAMAX C18 semi-preparative column. Isolated products were characterized by MALDI-TOF mass spectrometry, UV-visible spectroscopy, and melting temperature analysis of hybridized duplexes. Representative purification and characterization data are shown below

2. Electrochemical experimental conditions

Prior to self-assembly, gold macroelectrodes (1.6 mm nominal diameter, BAS) were polished on a clean, damp microcloth (Buehler) with alumina slurries of decreasing particle size (1.0 μm, 0.05 μm, Buehler). Electrodes were then etched in H_2SO_4 to expose a fresh, clean surface as well as determine the working area, and rinsed copiously with deionized H_2O. Immediately following, a 20 μl droplet of 50 μM duplex DNA was immobilized on the gold surface and monolayers were allowed to self-assemble overnight at 5 ºC. Duplexes were incubated in the presence of 100 mM $MgCl_2$ in order to encourage the formation of densely packed films. Electrodes were rinsed thoroughly in phosphate buffer (5 mM sodium phosphate, 50 mM NaCl, pH 7) prior to electrochemical measurement.

3. Characterization data

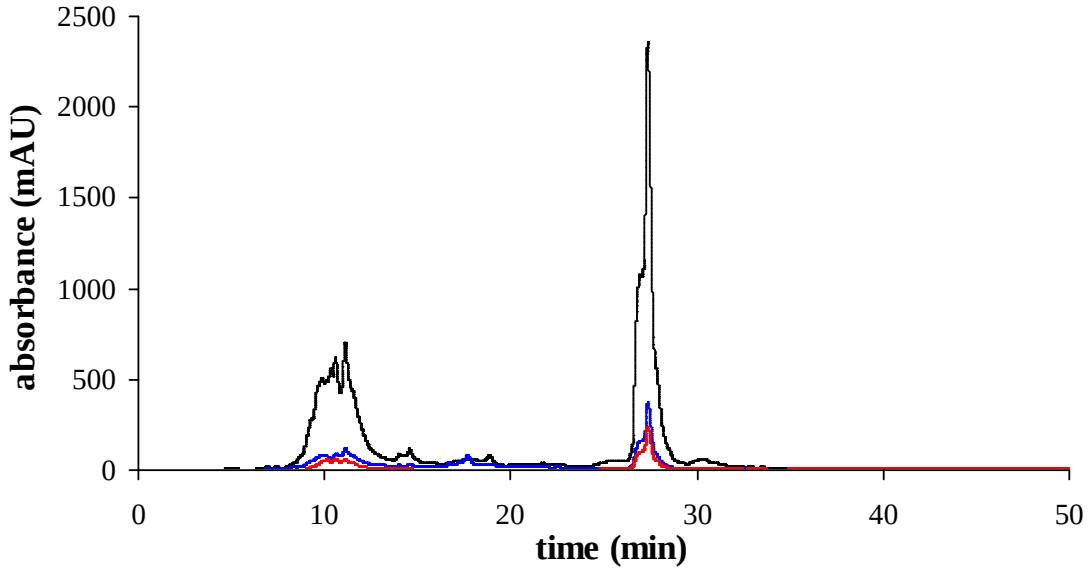

Figure S1a. HPLC chromatogram for Redmond Red-modified DNA (SH- 5' AGT ACT GCA GTA *RR* GCG 3'), prior to disulfide cleavage and DMT deprotection (black: 260nm, blue: 295 nm, red: 580 nm). Failed oligonucleotide syntheses appear around 10 min, while the product elutes around 28 min. Gradient: 100% 50mM NH_4OAc / 0% MeCN to 50% 50 mM NH_4OAc / 50% MeCN in 50 min (1% / min), at 3.5 ml / min.

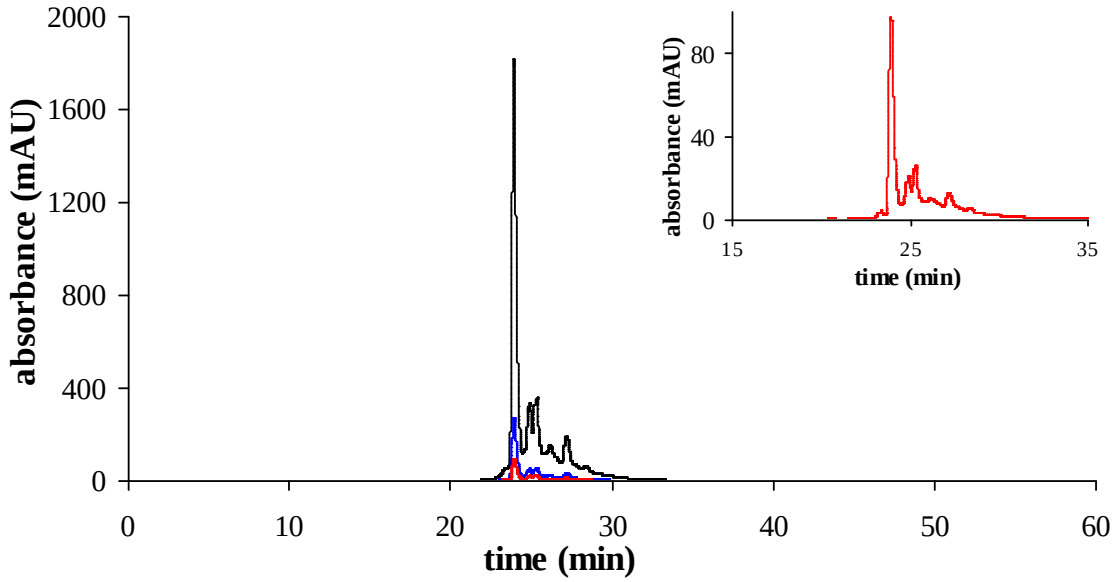

Figure S1b. HPLC chromatogram for Redmond Red-modified DNA, following disulfide cleavage achieved by treatment with DTT (black: 260nm, blue: 295 nm, red: 580 nm). The first main peak, centered around 24 min, corresponds to the product. Mass spectrometry confirmed that the side peaks that follow are not the desired product. Gradient: 100% 50mM NH_4OAc / 0% MeCN to 40% 50 mM NH_4OAc / 60% MeCN in 80 min (0.5% / min), at 3.5 ml / min. Inset: magnified view of the spectrum recorded at 580 nm.

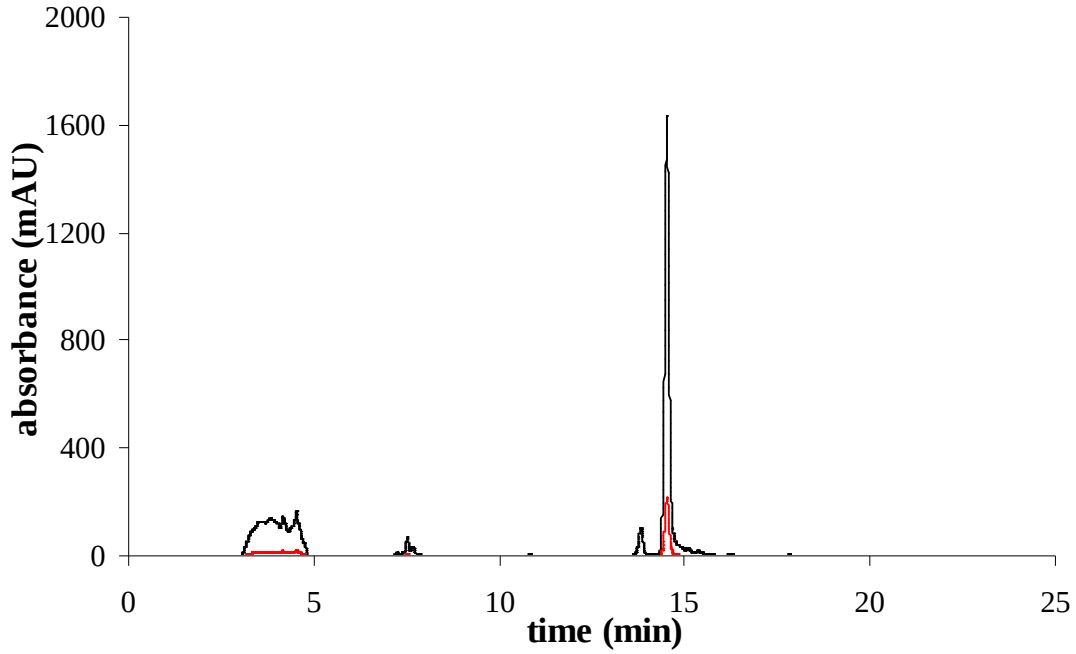

Figure S2a. HPLC chromatogram for DNA strand containing an abasic site (5' CGC __ TAC TGC AGT ACT 3' where "__" indicates the abasic site), prior to removal of DMT protecting group (black: 260nm, red: 294 nm). Product peak appears around 14 min. Gradient: 95% 50mM NH_4OAc / 5% MeCN to 35% 50 mM NH_4OAc / 65% MeCN in 40 min (2% / min), at 3.5 ml / min.

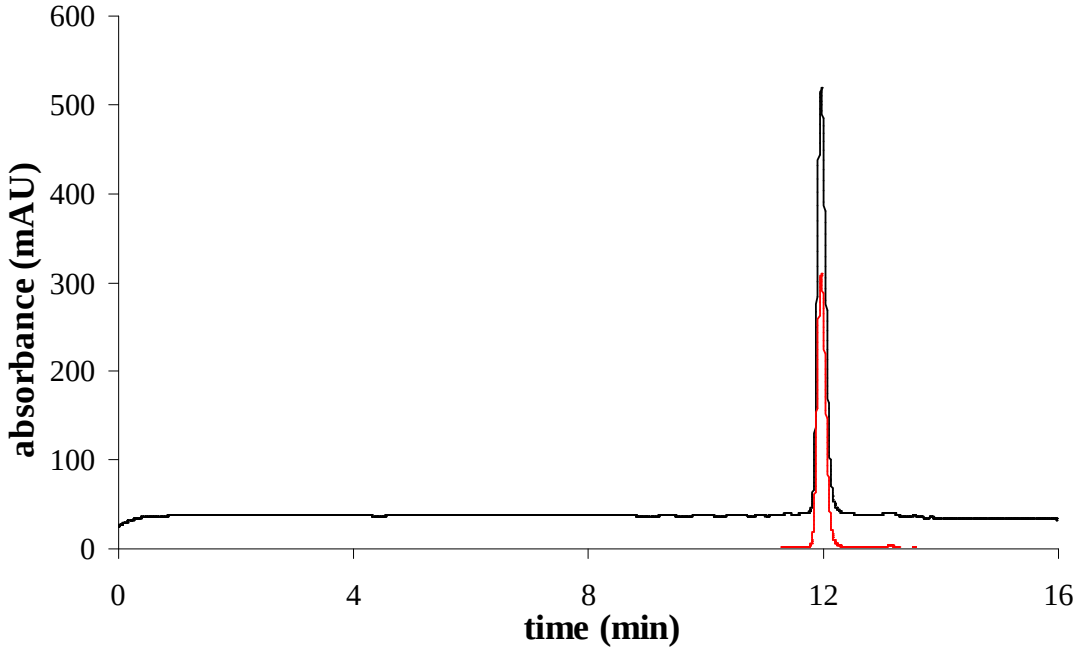

Figure S2b. HPLC chromatogram for DNA strand containing an abasic site, (5' CGC __ TAC TGC AGT ACT 3') following deprotection (black: 260nm, red: 294 nm). Deprotection is achieved by incubating DNA in 80% CH_3HOOH for 30 min and then precipitating with cold EtOH. Gradient: 95% 50mM NH_4OAc / 5% MeCN to 75% 50 mM NH_4OAc / 25% MeCN in 40 min (0.5% / min), at 3.5 ml / min. Product confirmed by mass spectrometry.

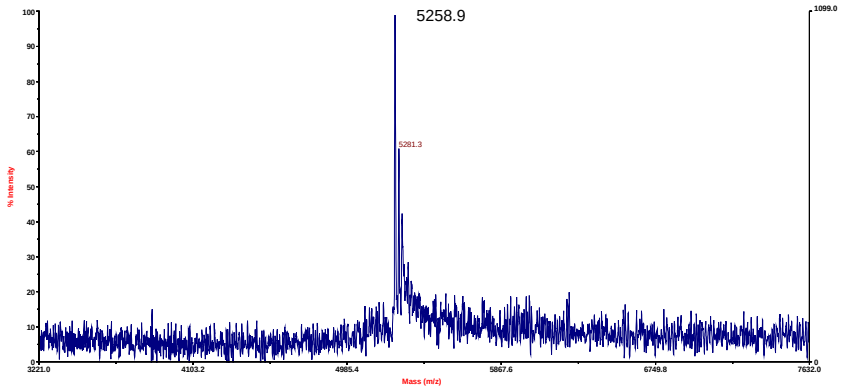

Figure S3a. Mass spectrum of thiolated, Redmond Red modified DNA (^{RR}DNA): SH- 5' AGT ACT GCA GTA *RR* GCG 3'; m/z = 5259 (expected 5254).

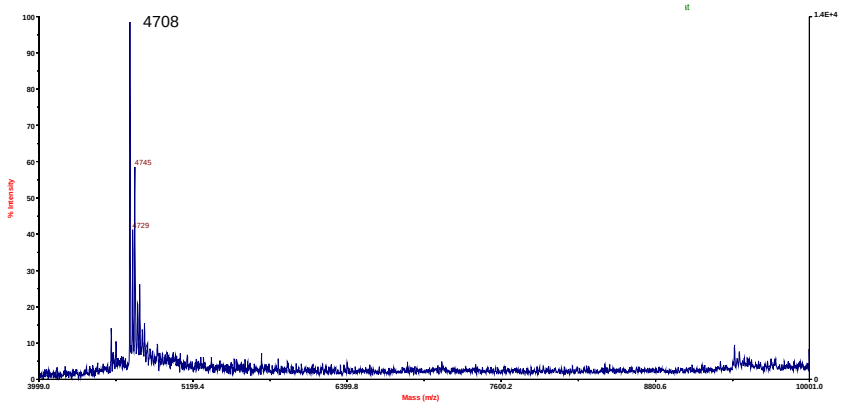

Figure S3b. Mass spectrum of complementary strand containing an abasic site opposite RR: 5' CGC __ TAC TGC AGT ACT 3', where "__" indicates an abasic site; m/z = 4708 (expected 4706).

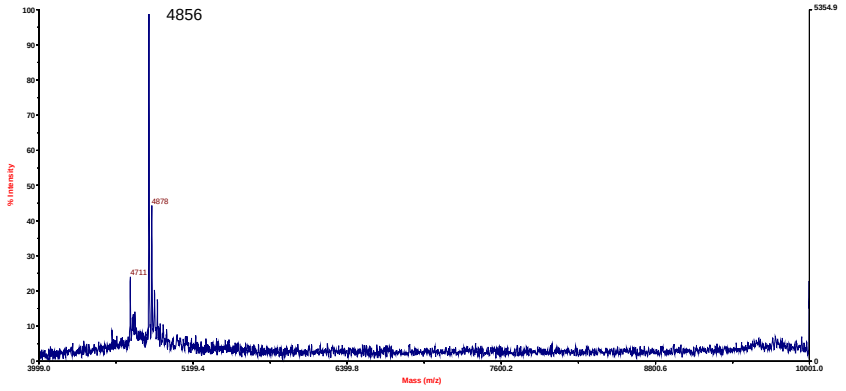

Figure S3c. Mass spectrum of complementary strand containing G opposite RR: 5' CGC *G* TAC TGC AGT ACT 3'; m/z = 4856 (expected 4854).

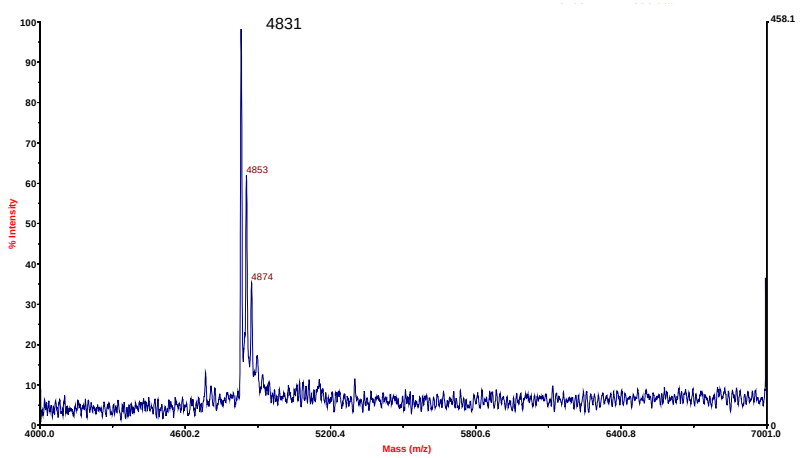

Figure S3d. Mass spectrum of complementary strand containing G opposite RR: 5' CGC *G* TAC TGC AGT ACT 3'; m/z = 4831 (expected 4830).

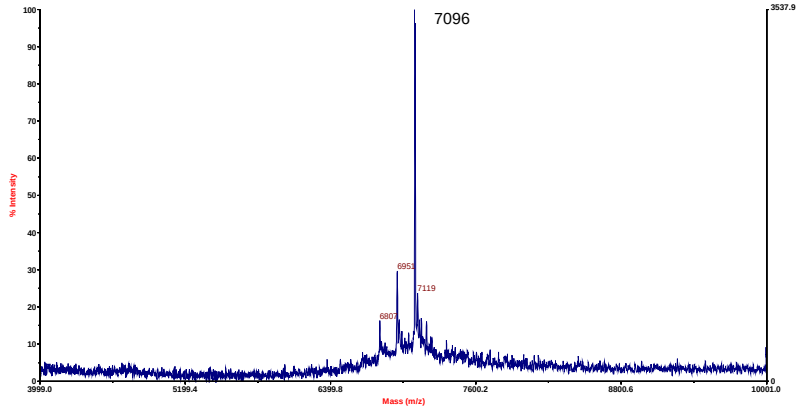

Figure S3e. Mass spectrum of thiolated, Redmond Red modified DNA (^{RR}DNA): SH- 5' AGT ACT GCA GTA *RR* GCG ACT ACG 3'; m/z = 7096 (expected 7091).

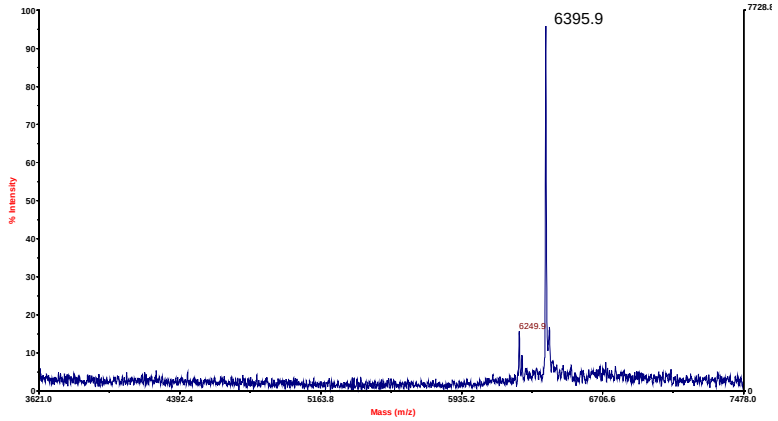

Figure S3f. Mass spectrum of complementary strand containing a 'deletion site' opposite RR: 5' CGT AGT CGC TAC TGC AGT ACT 3'; m/z = 6396 (expected 6393).

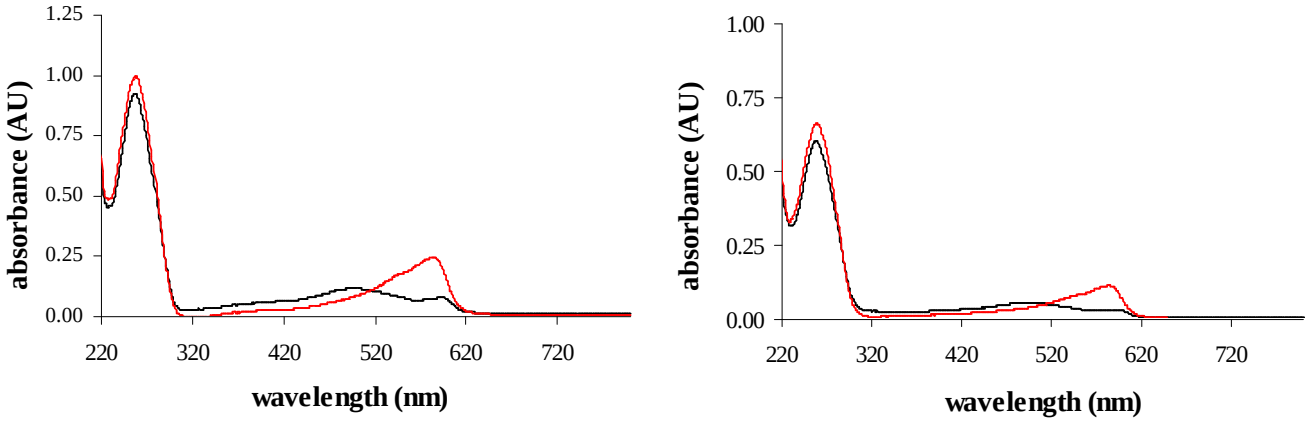

Figure S4. UV-vis spectra of Redmond Red-modified DNA at room temperature (black) and at 80 ºC (red), with characteristic maxima at 260 nm (DNA) and 580 nm (RR). At elevated temperatures, the interactions between Redmond Red and the DNA bases are discouraged, thus increasing the absorbance observed at 580 nm. Left: SH – 5' AGT ACT GCA GTA *RR* GCG 3' (15mer); right: SH – 5' AGT ACT GCA GTA *RR* GCG ACT ACG 3' (21mer).

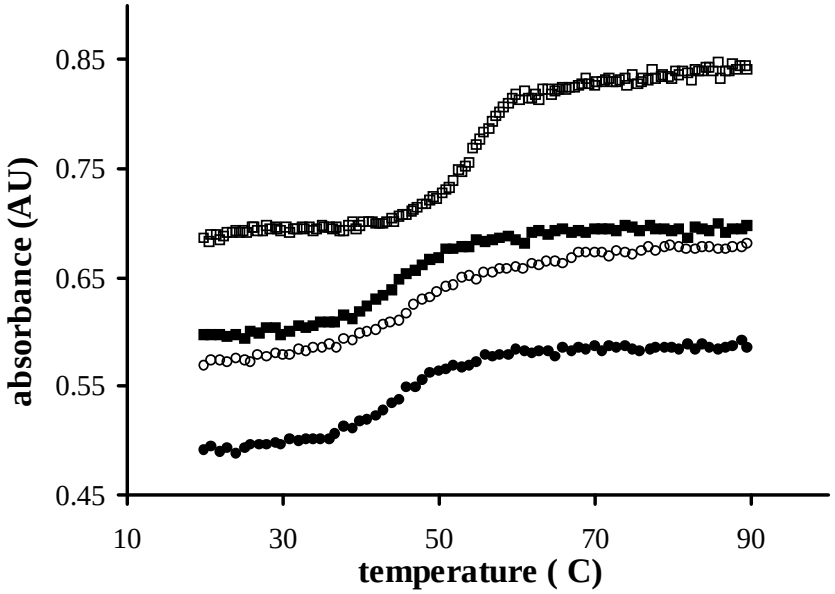

Figure S5. Melting temperature analysis for the four different duplexes employed: Redmond Red opposite a spacer site (closed circles, T_m = 45 ºC), guanine (open circles, T_m = 47 ºC), thymine (closed squares, T_m = 45 ºC) and a deleted site (open squares, T_m = 54 ºC). For these measurements, duplexes were heated to 90 ºC and then cooled back down to 15 ºC, at a typical rate of 0.5 ºC/min. Absorbance values at 260 nm were recorded at every degree interval.

ARTICLES

Dual Function Labeling of Biomolecules Based on DsRed-Monomer

A. M. Goulding,[#] Y. Rahimi,[#] S. Shrestha, and S. K. Deo*

Department of Chemistry and Chemical Biology, Indiana University Purdue University Indianapolis, Indianapolis, Indiana 46202. Received April 9, 2008; Revised Manuscript Received September 17, 2008

Unavailability of fusion tags that possess both affinity and visualization properties is a hurdle for biomolecular research. Typically, either a choice is made between an affinity tag and a reporter tag or both are employed in tandem if a fusion can be made at both termini of the target biomolecule. In this work, we have developed a site-specific genetic fusion approach employing DsRed-Monomer, a red fluorescent protein, that provides for both affinity and reporter functionality in a single tag. As a proof-of-concept, two fusion proteins, bradykinin-DsRed-Monomer and calmodulin-DsRed-Monomer, were prepared for the study. These fusion proteins were purified using a copper-immobilized column based on the inherent copper-binding property of DsRed-Monomer. Spectroscopic characterization of fusion proteins and comparison with native DsRed-Monomer showed no effect of fusion on the properties of DsRed-Monomer. Further, bradykinin-DsRed-Monomer was employed in the development of a competitive fluorescence immunoassay for the peptide bradykinin. Calmodulin-DsRed-Monomer was used to detect binding of the calmodulin ligand chlorpromazine, based on a change in the fluorescence of DsRed-Monomer upon binding of chlorpromazine to calmodulin. The studies performed demonstrate the application of DsRed-Monomer as a dual function tag indicating the potential usefulness of DsRed-monomer in proteomics and biomolecular research.

INTRODUCTION

Protein purification and its detection/localization are both essential components of proteomics and biomolecular research (*1*−*3*). Proteins are routinely purified utilizing affinity purification strategies with either chemical or biological tags (*4*−*8*). For efficient purification, either peptides or proteins are used as affinity tags (*9*−*11*). A single affinity tag is now seldom used because of its limitations on purification effectiveness, but is rather used in tandem to achieve better results (*12*−*14*). For protein detection or localization, fluorescent probes such as fluorescent proteins, quantum dots, or fluorophores have to be fused to the protein as reporter tags (*15*−*20*). This requires two separate tags to be fused to the protein to accomplish protein purification and detection, which limits the flexibility in terms of available termini for protein fusions. Hence, the availability of a single tag that will aid in both purification and detection/visualization of the protein will prove significant in today's biomolecular research. However, there are only a few reports published on methods that demonstrate dual functionality of tags used. In one of the reports, a six-histidine tag was engineered within the loop of green fluorescent protein (GFP), which was utilized for affinity purification and optical detection of a target protein (*21*). Although six-histidine tag insertion resulted in a 40% loss of the fluorescence activity of GFP, the remaining GFP fluorescence was sufficient for the detection of the fused target protein. In another report, a carrier protein fused to the target protein was labeled with a stilbene reporter using the phosphopantetheinyltransferase (PPTase) (*22*). When the stilbene reporter binds to the anti-stilbene antibody, the fluorescence of the stilbene reporter group is turned on. The stilbene-labeled fusion protein can then be purified using the antibody-bound column. Dye and antidye−antibody combinations have also been used as dual function tags (*23*). The major problem with the aforementioned antibody-based purification is the high cost and low stability of the immobilized antibody.

This manuscript describes site-specific tagging of peptides/proteins of interest with a red fluorescent protein, specifically DsRed-Monomer. Here, we demonstrate that DsRed-Monomer serves as a dual function tag based on its inherent fluorescence and copper-binding properties. Recently, we have established that DsRed-Monomer can bind copper ions and this property can be utilized in a single step affinity-based purification method (*24*). Using a copper-immobilized column, we were able to isolate more than 95% of the DsRed-Monomer from a crude *E. coli* extract with higher than 95% purity. In the work presented here, we demonstrate that the DsRed-Monomer can be used as an affinity tag for purification of fused peptides/proteins, and that the fluorescence of DsRed can be utilized as a reporter to perform bioassays. The advantages of a DsRed-Monomer-based tagging system include flexibility to attach target protein to either termini, the ability to perform site-specific genetic encoding, and achievement of efficient detection over low cellular autofluorescence due to its excitation−emission in the red region of the spectrum. In addition, protein-based affinity tags have been shown to aid in proper folding of the fused target protein, thereby enhancing the solubility of the fusion protein compared to peptide-based tags (*9*). Furthermore, the copper-immobilized columns needed for the purification are cheaper and more stable compared to the antibody-immobilized columns.

* Author to whom correspondence should be addressed. sdeo@iupui.edu, 317-278-7532.

[#] Equally contributed to work.

10.1021/bc800147k CCC: $40.75 © 2008 American Chemical Society
Published on Web 10/17/2008

DsRed-Monomer is a monomeric variant of native tetrameric DsRed (*25, 26*). It is a 28 kDa autofluorescent protein that shows broad excitation and emission bands with wavelength maxima at 584 and 591 nm, respectively. It matures faster than the native DsRed, and is pH- and temperature- (up to 37 °C) stable (*26*−*28*). The excellent physical properties and far-red fluorescence of DsRed allow for its use as a reporter in a variety of applications. To demonstrate the ability of DsRed-Monomer to function as a dual-function tag and to show its flexibility in genetic fusions of peptides/proteins, we constructed two fusion proteins. As a proof-of-concept, a fusion protein between a peptide, bradykinin, and DsRed-Monomer was constructed through the N-terminus of DsRed-Monomer. Bradykinin is a vasodilator peptide consisting of Arg-Pro-Pro-Gly-Phe-Ser-Pro-Phe-Arg residues (*29*). Another fusion protein between DsRed-Monomer and a model protein calmodulin (CaM) was constructed through the N-terminus of DsRed-Monomer. CaM is a Ca^{2+}-binding protein that is involved in the regulation of several cellular responses through its interaction with other proteins (*30, 31*). In the absence of Ca^{2+}, the CaM has a collapsed conformation (*32, 33*). In the presence of Ca^{2+}, CaM changes its conformation from a collapsed to a "dumbbell" configuration exposing its hydrophobic region that acts as a docking area for target peptides, proteins, and the tricyclic phenothiazene class of compounds (*32, 34*−*37*). The bradykinin-DsRed-Monomer fusion protein was expressed in *E. coli*, purified using a copper-immobilized column, and employed in the development of an immunoassay for bradykinin. The calmodulin-DsRed-Monomer (CaM-DsRed-Monomer) fusion protein was also expressed in *E. coli* and purified using a copper-immobilized column. This fusion protein was further employed to evaluate binding of a known CaM ligand, chlorpromazine to the fusion protein (*35, 37*).

EXPERIMENTAL SECTION

Reagents. The pDsRed-Monomer was purchased from Clonetech (Palo Alto, CA). Plasmid pVCU-1 containing the gene for calmodulin was kindly supplied by Prof. Sylvia Daunert from the University of Kentucky. Luria−Bertani (LB) broth and agar were purchased from DIFCO Laboratories (Detroit, MI). Bradykinin peptide, chlorpromazine hydrochloride, ampicillin, bovine serum albumin (BSA), and Coomassie brilliant blue R250 stain were obtained from Sigma Laboratories (St. Louis, MO). The chelex column and 96-well neutravidin-coated white microtiter plates were purchased from Pierce Technology (Rockford, IL). The Hi-Trap chelating column was from Amersham Bioscience. Rabbit antibradykinin antibody was purchased from Fitzgerald (Concord, MA). Goat antirabbit Fc specific biotinylated secondary antibody was obtained from ICN Biomedicals (Aurora, OH). ProTEV protease was obtained from Promega (Madison, WI).

Apparatus. Cell cultures were grown in a Fisher Scientific orbital shaker, and centrifuged using a Beckman J2-MI centrifuge (Palo Alto, CA). The fractions were lyophilized using a Fisher Bench Top freeze-dryer. Fluorescence measurements were performed on the Varian Cary Eclipse fluorescence spectrophotometer (Palo Alto, CA). All fluorescence intensities reported are the average of three replicates and have been corrected for the contribution of the background.

Plasmid Construction and Protein Expression. *Construction of Bradykinin-DsRed-Monomer Fusion.* The plasmid pDsRed-Monomer was used as a template for the PCR reaction. Primers were designed that encoded the DNA sequence for the bradykinin peptide, Arg-Pro-Pro-Gly-Phe-Ser-Pro-Phe-Arg. Using two consecutive PCRs, the DNA sequence for the peptide was inserted at the N-terminus of the DsRed-Monomer sequence present in the plasmid pDsRed-Monomer. Primer 1 coded for the three amino acid linker, Gly-Ser-Gly and the Arg-Pro-Pro part of bradykinin; Primer 2 encoded the remaining part of bradykinin, Gly-Phe-Ser-Pro-Phe-Arg and the linker Gly-Ser. Briefly, the steps involved include two PCRs using primer designed to encode for the bradykinin sequence and a three amino acid linker between the bradykinin and the DsRed-Monomer sequence (Forward Primer PCR1-GTCGACTCTAGAGGATGGTAGTGGTAGACCACCAGG CCCCCGGGTACCGGTC, Reverse Primer PCR1-GACCGGTACCCGGGGGCCTGG TGGTCTACCACTACCATCCTCTAGAGTCGAC, Forward Primer PCR2-GGTAGA CCACCAGGCTTCAGTCCATTTAGAGGTAGTCCCCGGGTACCGGT, Reverse Primer PCR2-GACCGGTACCCGGGGACTACCTCTAAATGGACTGAAGCCTGGT GGTCTAC). After each PCR step, digestion was performed with Dpn I to digest the original plasmid, leaving the plasmid with the inserted bradykinin DNA intact. This plasmid was then transformed into *E. coli* ER2566 strain. The colonies were picked, and miniprep was performed. DNA sequencing was performed to confirm the insertion of the bradykinin DNA sequence. The plasmid (pSKD103) with the entire bradykinin sequence and the linker sequence at the N-terminus of the DsRed-Monomer gene was obtained after the second step of PCR and employed for the expression of the fusion protein.

Construction of Calmodulin-DsRed-Monomer Fusion. The PCR primers were designed to introduce the sequences for the restriction enzymes, *Sph*I and *Xma*I on the CaM gene (Forward Primer-ATATATGCATGCGATGGCTGATCAGCTGACTGACGAGCAG, Reverse Primer- ATATATCCCGGGCCTTAGCCATCATAACCTGAACGAACTC). The plasmid PVUC-1 was used as a template (*36*). The CaM gene obtained after PCR and the pDsRed-Monomer were digested with *Sph*I and *Xma*I followed by ligation of the CaM gene into pDsRed-monomer plasmid to obtain pSKD104. The plasmid pSKD104 was transformed into *E. coli* ER2566 strain. The colonies were picked, and miniprep was performed. DNA sequencing was utilized to determine the sequence of the fusion protein.

Construction of CaM-DsRed-Monomer Fusion with TEV Protease Cleavage Site between CaM and DsRed-Monomer. To construct this fusion gene, the same primers, restriction enzymes, and molecular biology techniques were used as above for the CaM-DsRed-Monomer fusion. However, a new reverse primer was designed (new CaM Reverse Primer-CCCGGG*CCCCTGGAAGTACAGGTTTTCC*TTAGC-CATCATAACCTGAACG) which incorporated the TEV cleavage site, Glu-Asn-Leu-Tyr-Phe-Gln-Gly, before the *Xma*I restriction site. The DNA coding for TEV cleavage site is in italics and the DNA coding for *Xma*I is underlined. The PCR product was ligated into pDsRed-Monomer plasmid to obtain the plasmid pSKD105. This plasmid was transformed into *E. coli* JM107 strain.

Fusion Protein Expression. The cells containing the plasmid (pSKD103, pSKD104, and pSKD105) that encodes for fusion proteins were grown in Luria−Bertani (LB) broth containing ampicillin with shaking at 250 rpm at 37 °C to an optical density of 0.5 measured at 600 nm. Protein expression was induced using IPTG (1 mM) and the cells expressing bradykinin-DsRed-Monomer were allowed to grow further at 37 °C for an additional 3 h. The cells expressing calmodulin-DsRed-Monomer were allowed to grow at 37 °C overnight after induction with IPTG. The cells expressing CaM-TEV recognition site-DsRed-Monomer fusion protein were allowed to grow a further 16 h at 30 °C. The cells were harvested by centrifugation at 4 °C, 4000 × *g*, for 15 min and were sonicated using 20s on and 20 s off for 5 min. The crude fusion proteins were obtained by centrifugation at room temperature, 4000 × *g* for 30 min. Subsequently, the fusion proteins were purified as described below.

Fusion Protein Purification. The fusion proteins were purified on a Hi-Trap Chelating column (GE Healthcare). These columns are packed with Chelating Sepharose High Performance, a highly cross-linked agarose bead. These agarose beads have iminodiacetic acid coupled by stable ether groups, through a spacer arm of seven atoms. The column was prepared by washing with 5 mL of distilled water to remove ethanol used to store the column. Copper was immobilized on the column by passing through the column a volume of 0.5 mL of 0.1 M $CuSO_4$. The column was washed with an additional 5 mL of distilled water. Any non-immobilized copper was removed by passing 5 mL of acidic buffer (0.02 M sodium acetate containing 1.0 M NaCl, pH 4.0) through the column. The column was next equilibrated with 5 mL of binding buffer (50 mM sodium phosphate buffer containing 300 mM NaCl, pH 8.0). Crude fusion proteins in binding buffer were loaded onto the copper-immobilized column and incubated for 30 min at 37 °C. The column was then washed with 20 mL of binding buffer followed by 20 mL of wash buffer (50 mM sodium phosphate buffer containing 2 mM imidazole and 300 mM NaCl, pH 8.0). Purified fusion proteins were eluted with 5 mL of elution buffer (50 mM sodium phosphate containing 300 mM NaCl and 10 mM imidazole, pH 8.0). For the entire purification procedure, a flow rate of about 6 mL/min was used. Eluted fractions which displayed fluorescence emission characteristics of DsRed-Monomer were collected, and the purity was determined by SDS-PAGE using Coomassie staining solution. A dialysis step was performed using the buffer, 50 mM sodium phosphate containing 100 mM NaCl, pH 7.4, for bradykinin-DsRed-Monomer and buffer, 30 mM Tris containing 10 mM calcium, pH 7.2 for the CaM-DsRed-Monomer protein. Protein concentration was determined by using the Bradford assay.

Determination of Protein Recovery after Purification. To determine the recovery of protein, 180 mg of purified bradykinin-DsRed-Monomer/Calmodulin-DsRed-Monomer fusion protein was loaded onto the copper column. Purification steps outlined in the earlier section were followed, and the concentrations of eluted proteins were determined.

Protease Cleavage of CaM from CaM-DsRed-Monomer. Promega ProTEV protease was used according to the manufacturer's recommendations with the supplied buffer to cleave the CaM from the purified CaM-DsRed-Monomer fusion. The reaction was allowed to continue for 24 h at 37 °C. Complete cleavage of CaM was verified by running an SDS-PAGE gel with Coomassie staining.

Fluorescence Spectra. A volume of 200 μL of 1.0 μM DsRed-Monomer-bradykinin fusion protein and 1.0 μM of Calmodulin-DsRed-Monomer was placed into different wells of a microtiter plate, and excitation and emission scans of the protein were obtained at room temperature using a Cary Eclipse fluorescence spectrophotometer.

UV−visible Spectra. A volume of 1 mL of 1.0 μM DsRed-Monomer-bradykinin and 1.0 μM of Calmodulin-DsRed-Monomer fusion proteins were placed in a cuvette, and the absorption spectra of the proteins were recorded at room temperature using an Agilent 8453 UV/vis Spectrometer from Agilent Technologies (Santa Clara, CA).

Bradykinin Assay Development. *Dilution Study.* Standard solutions of bradykinin-DsRed-Monomer fusion protein were prepared by serially diluting the stock solution of the protein in assay buffer 1 (50 mM sodium phosphate containing 100 mM NaCl, pH 7.4). A volume of 100 μL of these solutions was mixed with 100 μL of assay buffer 1 and placed in a microtiter plate, and the fluorescence intensity was measured using an excitation maximum wavelength of 558 nm and an emission wavelength maximum of 591 nm. All fluorescence intensities were obtained in triplicate.

Binder Dilution Study Using Bradykinin-DsRed-Monomer. A volume of 100 μL of biotinylated goat antirabbit secondary antibody (10 μg/mL) in assay buffer 1 was added to the neutravidin-coated 96-well white microtiter plate and incubated for 2 h at room temperature with shaking at 250 rpm. The wells of the plate were washed 3 times with the wash buffer (50 mM sodium phosphate containing 150 mM NaCl, pH 7.4). Next, 100 μL of different concentrations of antibradykinin antibody in assay buffer 1 were added to the wells coated with secondary antibody. An incubation step was performed for 2 h at room temperature with shaking at 250 rpm followed by a wash step to remove unbound antibody. A volume of 50 μL of 0.1 μM concentration of the bradykinin-DsRed-Monomer fusion protein mixed with 50 μL of assay buffer 1 was added to the well plate, and incubation was performed for 2 h at room temperature. After a wash step, 200 μL of assay buffer 1 was added to the plate, and fluorescence emission readings were monitored at 591 nm.

Dose−Response Curve for Bradykinin. The primary (1:100 dilution) and secondary antibody (10 μg/μL) were immobilized on the wells of a microtiter plate as described earlier. A dose−response curve was generated for bradykinin by simultaneously incubating different concentrations of 50 μL of bradykinin peptide and 50 μL of 0.1 μM bradykinin-DsRed-Monomer fusion protein with immobilized antibradykinin antibody on a microtiter plate. The plate was incubated at room temperature for 2 h with shaking at 250 rpm. The plate was washed three times with the wash buffer to remove any unbound components. The fluorescence intensity was measured as described before.

Calmodulin Ligand-Binding Study. *Dilution Study.* Standard solutions of calmodulin-DsRed-Monomer fusion protein were prepared by serially diluting the stock solution of the protein in assay buffer 2 (30 mM Tris containing 10 mM calcium, pH 7.2). A volume of 100 μL of these solutions was mixed with 100 μL of assay buffer 2 and placed in a microtiter plate, and the fluorescence intensity was measured using an excitation maximum wavelength of 558 nm and the emission wavelength maximum of 591 nm. All fluorescence intensities were obtained in triplicate.

Dose−Response Curve for Chlorpromazine. Different concentrations of chlorpromazine were prepared by diluting in assay buffer 2. A volume of 100 μL of 1 μM calmodulin-DsRed-Monomer was mixed with different concentrations of 100 μL of chlorpromazine. The fluorescence intensity was monitored corresponding to DsRed-Monomer excitation/emission wavelength. A control study was performed using DsRed-Monomer and chlorpromazine. In another control study, solutions of varying concentrations of chlorpromazine (1×10^{-3} to 1×10^{-6} M) were excited at 556 nm and the fluorescence emission was monitored at 591 nm.

RESULTS AND DISCUSSION

The results described in this study demonstrate dual application of DsRed-Monomer. Reporter proteins, such as DsRed-Monomer, are commonly fused to the target protein for fluorescent-based bioassay development. However, if the same reporter protein can also function as an affinity purification tag, then this will reduce the assay development time and will simplify the assay development process. To demonstrate the versatility of DsRed-Monomer as a dual-function tag, we selected a peptide, bradykinin, and a protein, calmodulin, as fusion partners in this proof-of-concept study.

The DNA encoding for the bradykinin peptide and the gene for calmodulin were fused to the gene coding for the DsRed-Monomer using genetic engineering tools to construct two gene fusions. Plasmids pSKD103 and pSKD104 containing the fusion genes were transformed into *E. coli* cells and the fusion proteins

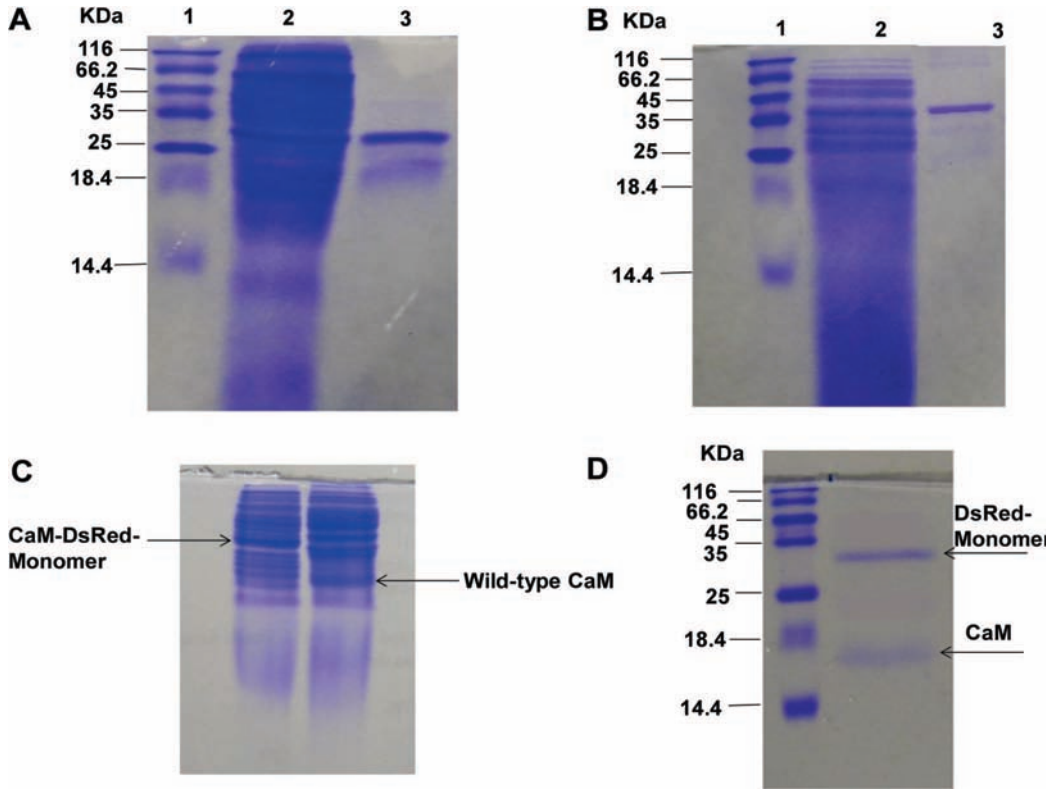

Figure 1. Pictures of SDS-PAGE (12.5% acrylamide) gels of purified fusion proteins. (A) Bradykinin-DsRed-Monomer. Lane 1: Molecular weight protein marker. Lane 2: Crude bradykinin-DsRed-Monomer. Lane 3: Purified bradykinin-DsRed-Monomer. (B) DsRed-Monomer-Calmodulin (CaM). Lane 1: Molecular weight protein marker. Lane 2: Crude CaM-DsRed-Monomer. Lane 3: Purified CaM-DsRed-Monomer. (C) Comparison of protein expression yield. Lane 1: expression of CaM-DsRed-monomer. Lane 2: Expression of wild-type CaM. (D) Protease cleavage of DsRed-Monomer from CaM-TEV recognition site-DsRed-Monomer. Lane 1: Molecular weight protein marker. Lane 2: Separated CaM and DsRed-Monomer proteins.

were expressed. The fusion proteins were purified using a copper-immobilized column utilizing DsRed-Monomer as an affinity tag. Briefly, copper was first immobilized on an iminodiacetic acid containing chelating column and crude fusion proteins were passed through the column. Purified fusion protein fractions were collected after a wash step by passing through an elution buffer containing imidazole. The elution of the purified fusion proteins were monitored by the pink coloration of the protein and by measuring its fluorescence. Purity of fusion proteins was verified by SDS-PAGE using Coomassie staining (Figure 1). Single bands corresponding to the molecular weight of the bradykinin-DsRed-Monomer fusion protein (27 kDa, Figure 1A) and calmodulin-DsRed-Monomer (41.5 kDa, Figure 1B) were observed (Figure 1). We have also performed an expression study to compare the effect of fusion of calmodulin to DsRed-monomer on the expression yield. For this study, we expressed wild-type calmodulin and calmodulin-DsRed-Monomer proteins under identical conditions. The conditions followed were the same as that used for the expression of the protein described in Experimental Section. An SDS-PAGE was performed (Figure 1C) that showed similar expression yield for calmodulin and calmodulin-DsRed-Monomer protein. Additionally, the total protein yields for the two proteins were similar. These observations indicate that fusion of the target protein to DsRed-Monomer does not affect the expression of the target protein. Concentrations of the purified fusion proteins were determined using the Bradford assay. Percent recovery of the purified protein was estimated by passing a known quantity of purified fusion proteins through the copper-immobilized column. The purification procedure was followed, and the concentration of eluted protein was determined. The amount of eluted protein was compared to the amount of protein initially loaded on the column, and recoveries were calculated to be 95% and 96% for bradykinin-DsRed-Monomer and calmodulin-DsRed-Monomer fusion proteins, respectively.

Table 1. Characteristics of DsRed Fusion Proteins

	DsRed-Monomer	Bradykinin-DsRed-Monomer	Calmodulin-DsRed-Monomer
$\lambda_{excitation}$, nm	556	556	556
$\lambda_{emission}$, nm	597	597	597
absorbance maxima, nm	480, 556	480, 556	480, 556
ε, M^{-1} cm^{-1}	34 715	40 427	59 000

To demonstrate that the target protein can be separated after purification from DsRed-Monomer if desired, we incorporated a TEV protease cleavage site between CaM- and DsRed-Monomer. The fusion protein was purified using a copper-bound column employing DsRed-Monomer as an affinity tag. The DsRed-Monomer was cleaved off easily and completely from the CaM-TEV recognition site-DsRed-Monomer fusion protein within 24 h time period. This was verified by running the reaction mixture on an SDS-PAGE gel. Figure 1 D shows two bands corresponding to CaM and DsRed-Monomer. Therefore, we can say that although DsRed-Monomer is a large affinity tag it can be efficiently separated from the target protein if desired.

Although variants of DsRed have been employed as fusion tags in other studies, there are no published reports on fusions of DsRed-Monomer. Therefore, spectral characteristics of the fusion proteins were first evaluated to determine any effect of peptide/protein fusion on the DsRed-Monomer protein structure and fluorescence emission (Table 1). Fluorescence excitation−emission scans were performed for both fusion proteins. An excitation wavelength maximum of 556 nm and an emission wavelength maximum of 591 nm were obtained for both fusion proteins, which is characteristic of the DsRed-Monomer (*24*).

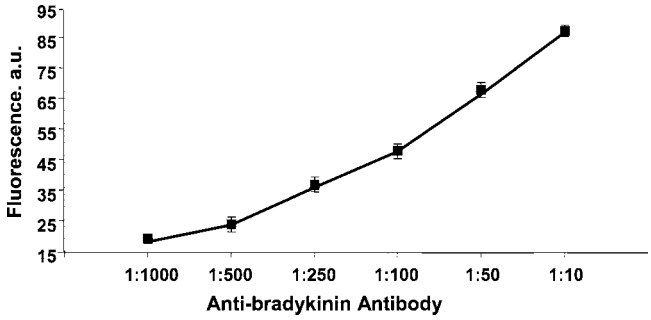

Figure 2. Binder dilution curve obtained by incubating a volume of 100 μL of varying dilutions of antibradykinin antibody immobilized on a microtiter well plate with 50 μL of 0.1 μM bradykinin-DsRed-Monomer fusion protein and 50 μL of assay buffer 1.

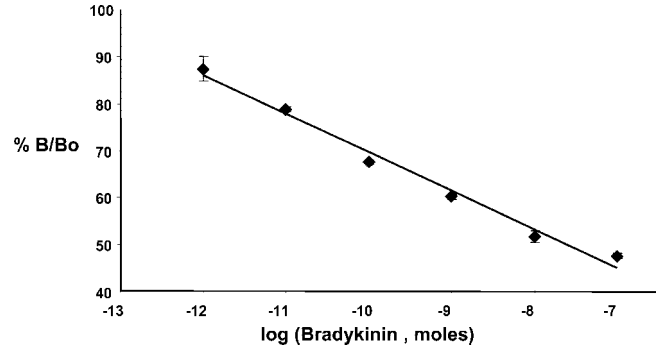

Figure 3. Dose−response curve for bradykinin peptide obtained by incubating 50 μL of 0.1 μM bradykinin-DsRed-Monomer protein and 50 μL of different concentrations of free bradykinin peptide with immobilized antibradykinin antibody. B corresponds to light intensity obtained from the sample containing free bradykinin and B_0 corresponds to light intensity obtained from the sample without the free bradykinin.

UV−visible absorbance spectra of both fusion proteins showed two peaks at 480 and 556 nm, which are similar to that observed in the case of DsRed-Monomer protein (*28*). A comparison of spectral properties of fusion proteins with the DsRed-Monomer protein showed no effect of peptide/protein fusion on the DsRed-Monomer fluorescence activity. These studies indicated that the fusion of a peptide/protein to DsRed-Monomer does not affect the fluorescence activity of the protein.

Next, to demonstrate the function of DsRed-Monomer as an optical tag, we performed studies that utilized DsRed-Monomer in assay development based on its inherent fluorescence. In that respect, a solid-phase competitive fluorescence immunoassay for the detection of bradykinin was developed using antibradykinin antibody and bradykinin-DsRed-Monomer fusion protein. A dilution study for the bradykinin-DsRed-Monomer fusion protein was performed to determine the concentration of the fusion protein that can be used in the development of the assay. On the basis of the dilution curve, a concentration of 0.1 μM was employed for the peptide immunoassay study. The next step in the assay was to study the binding between the bradykinin-DsRed-Monomer fusion protein and the antibradykinin antibody. For this study, biotinylated secondary antibody was immobilized on neutravidin-coated well plates. Varying dilutions of antibradykinin antibody were then immobilized on the plate through the secondary antibody. The fluorescence signal was measured after incubation of the bradykinin-DsRed-Monomer fusion protein on the plate. As expected, with increasing amounts of antibradykinin antibody a higher fluorescence signal was observed, because higher amounts of bradykinin-DsRed-Monomer fusion protein could bind to the antibody (Figure 2). From this curve, a 1:100 dilution of the antibradykinin antibody was selected for generating a dose−response curve for the bradykinin peptide.

A dose−response curve for bradykinin was generated by employing a competitive assay design (Figure 3). For this assay design, the antibradykinin antibody was immobilized on a neutravidin-coated plate through a biotinylated secondary antibody using biotin−neutravidin interaction. The free bradykinin peptide and the bradykinin-DsRed-Monomer fusion protein were added simultaneously to the antibradykinin antibody immobilized on a plate, and were allowed to compete to bind to the same antibody. The amount of antibradykinin antibody and the bradykinin-DsRed-Monomer fusion protein is kept fixed. With increasing amount of free bradykinin, less of the fusion protein could bind to the antibody, yielding a reduction in the fluorescence signal compared to the signal obtained in the absence of the free peptide. Therefore, the plot of the ratio of fluorescence intensity in the presence of free bradykinin upon the fluorescence signal in the absence of free bradykinin against the log units of the moles of free bradykinin showed a linear response with a negative slope (Figure 3). The dose−response curve was linear over 5 orders of magnitude, extending from 1×10^{-12} to 1×10^{-7} mol of bradykinin. A detection limit of 1 pmol for bradykinin peptide was calculated using a S/N ratio of 3. A detection limit of 1 pmol of bradykinin peptide was calculated using a signal-to-noise (S/N) ratio of 3. In normal plasma samples, approximately 2.1×10^{-11} mol of bradykinin are found; however, under diseased conditions the level of bradykinin increases (*38, 39*). Therefore, a higher bradykinin level will fall well within the working range of our assay. These results indicate that the assay developed in this study can be used in clinical diagnostics to test levels of bradykinin and is comparable to existing assays for bradykinin detection (*29, 40−42*). The effect of matrix on the fluorescence activity of DsRed-Monomer was evaluated by incubating bradykinin-DsRed-Monomer protein in plasma samples. Comparison of the fluorescence of DsRed-Monomer in clear plasma samples and in buffer samples showed an insignificant effect of matrix on the activity of the protein. This indicates that our assay could be employed in plasma screening of bradykinin if desired.

Spectroscopic and purification analysis of calmodulin-DsRed-Monomer fusion protein showed that proteins of interest could be fused to the DsRed-Monomer without affecting its copper-binding affinity and fluorescence. This should prove useful in visualization of fusion proteins followed by their isolation. Furthermore, we wanted to demonstrate that fusion with DsRed-Monomer can also be utilized in the optical detection of the interactions of fused target protein with its ligands. In that respect, calmodulin is a well-studied protein with known ligands that are commercially available; therefore, we decided to study binding of CaM ligands to calmodulin-DsRed-Monomer fusion protein. This can be performed in two ways. The calmodulin-DsRed-Monomer fusion protein can be genetically encoded to study calmodulin interacting proteins/ligands *in vivo*, or the isolated fusion protein can be used to study calmodulin interacting molecules *in vitro*. It has been reported by other groups that the fusion protein between green fluorescent protein (GFP) and calmodulin can be utilized in screening ligands that bind calmodulin (*35, 43, 44*) in solution-phase assay. On the basis of this, we performed a solution-based study by mixing calmodulin-DsRed-Monomer and a known representative CaM ligand, chlorpromazine. Addition of chlorpromazine resulted in a quenching of CaM-DsRed-Monomer fluorescence. This change in fluorescence can be attributed to the conformational change that occurs in CaM upon binding its ligand. It has been hypothesized previously that the conformational change in CaM may lead to a change in the microenvironment of fused fluorescent proteins affecting the fluorescence output of these proteins. A dose−response curve was generated by varying the

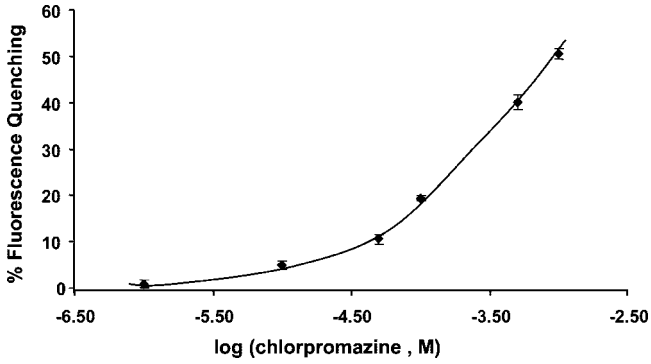

Figure 4. Dose−response curve for chlorpromazine generated by monitoring fluorescence change upon addition of different concentrations of chlorpromazine to calmodulin-DsRed-Monomer fusion protein. Fluorescence was measured using a 556 nm excitation wavelength maximum and a 591 nm emission wavelength maximum.

amount of chlorpromazine and relating it to the change in fluorescence intensity (Figure 4). A detection limit of 5×10^{-6} M was obtained for chlorpromazine, which is comparable to that achieved with other reported fluorescence-based assays for chlorpromazine (*34*, *35*). A control study was performed by adding chlorpromazine to DsRed-Monomer protein, which did not result in fluorescence quenching (data not shown). In another control study, we evaluated the effect of fluorescence excitation at 556 nm on chlorpromazine, which is inherently fluorescent. For this study, solutions of varying concentrations of chlorpromazine were excited at 556 nm, and the emission was monitored at 591 nm. The fluorescence intensity obtained from these samples was same as the buffer blank, demonstrating no effect of fluorescence excitation on chlorpromazine. Overall, the study performed shows that the binding between CaM and its ligand can be monitored using the fluorescence of DsRed-Monomer and the observed fluorescence quenching is due to the specific binding of chlorpromazine to CaM. We hypothesize that binding of other phenothiazene-based CaM ligands would yield similar results and could be evaluated if desired. It should be noted that the fluorescence change observed upon binding of ligands to CaM may not be universally applicable to other target protein−ligand pairs. Nevertheless, the fluorescence of DsRed-Monomer could still be used in the evaluation of target-protein ligand pair using a solid-phase assay technique.

In summary, through this study we have demonstrated a dual function of DsRed-Monomer as an affinity and a reporter tag. The combination of fluorescence and affinity properties of DsRed-Monomer makes it a unique reporter for *in vivo* and *in vitro* protein analysis. We believe that in the future new vectors based on DsRed-Monomer could be designed that allow the insertion of any protein. The recombinant proteins produced could then be expressed in different organisms, monitored optically, purified, and employed in assay development. Further, if desired, protease cleavage sites could be incorporated into fusion protein designs to isolate the target protein following purification. We do not anticipate any problems with the protease cleavage between DsRed-Monomer and the target protein, because this technique is well-developed and has been performed with DsRed previously (*45*−*49*). In one of these studies, the substrate of the hepatitis C virus protease fused to the DsRed-Express was cleaved about 54% by the membrane protease within 24 h. In another report, the 6-histidine tag fused to DsRed-Monomer incorporating the cleavage site for tobacco etch virus (TEV) protease was cleaved completely within 24 h (*46*). Additionally, the DsRed-tetramer/GFP pair has been employed to design fluorescence resonance energy transfer assays for the detection of protease activity by inserting substrate for the protease between the genes of the two fluorescent proteins (*47*−*49*). This is the first report on the fusion of a peptide/protein to DsRed-Monomer and its use as a label in a peptide detection assay as well as in the detection of protein−ligand binding. We envision that the DsRed-Monomer can be employed as a tag to visualize and isolate protein−protein interactions directly from cells expanding its utility in fundamental biomolecular research.

ACKNOWLEDGMENT

We would like to thank the National Institutes of Health and the National Science Foundation for their support. We would like to thank Prof. Sylvia Daunert from the University of Kentucky for providing the pVUC-1 plasmid. We appreciate funding from IUPUI Research Support Funds Grant. We would like to thank Christopher Konz for supplying plasma samples.

LITERATURE CITED

(1) O'Rourke, N. A., Meyer, T., and Chandy, G. (2005) Protein localization studies in the age of 'Omics'. *Curr. Opin. Chem. Biol. 9*, 82–7.

(2) Chen, I., Howarth, M., Lin, W., and Ting, A. Y. (2005) Site-specific labeling of cell surface proteins with biophysical probes using biotin ligase. *Nat. Methods 2*, 99–104.

(3) Hu, Y., Huang, X., Chen, G. Y., and Yao, S. Q. (2004) Recent advances in gel-based proteome profiling techniques. *Mol. Biotechnol. 28*, 63–76.

(4) Meredith, G. D., Wu, H. Y., and Allbritton, N. L. (2004) Targeted protein functionalization using His-tags. *Bioconjugate Chem. 15*, 969–82.

(5) Zhang, Z., Edwards, P. J., Roeske, R. W., and Guo, L. (2005) Synthesis and self-alkylation of isotope-coded affinity tag reagents. *Bioconjugate Chem. 16*, 458–64.

(6) Whetstone, P. A., Butlin, N. G., Corneillie, T. M., and Meares, C. F. (2004) Element-coded affinity tags for peptides and proteins. *Bioconjugate Chem. 15*, 3–6.

(7) Chen, B., Cao, H., Yan, P., Mayer, M. U., and Squier, T. C. (2007) Identification of an orthogonal peptide binding motif for biarsenical multiuse affinity probes. *Bioconjugate Chem. 18*, 1259–65.

(8) Tanaka, T., Kamiya, N., and Nagamune, T. (2004) Peptidyl linkers for protein heterodimerization catalyzed by microbial transglutaminase. *Bioconjugate Chem. 15*, 491–7.

(9) Waugh, D. S. (2005) Making the most of affinity tags. *Trends Biotechnol. 23*, 316–20.

(10) Cull, M. G., and Schatz, P. J. (2000) Biotinylation of proteins in vivo and in vitro using small peptide tags. *Methods Enzymol. 326*, 430–40.

(11) Larive, C. K., Lunte, S. M., Zhong, M., Perkins, M. D., Wilson, G. S., Gokulrangan, G., Williams, T., Afroz, F., Schoneich, C., Derrick, T. S., Middaugh, C. R., and Bogdanowich-Knipp, S. (1999) Separation and analysis of peptides and proteins. *Anal. Chem. 71*, 389R–423R.

(12) Braud, S., Moutiez, M., Belin, P., Abello, N., Drevet, P., Zinn-Justin, S., Courcon, M., Masson, C., Dassa, J., Charbonnier, J. B., Boulain, J. C., Menez, A., Genet, R., and Gondry, M. (2005) Dual expression system suitable for high-throughput fluorescence-based screening and production of soluble proteins. *J. Proteome Res. 4*, 2137–47.

(13) Burckstummer, T., Bennett, K. L., Preradovic, A., Schutze, G., Hantschel, O., Superti-Furga, G., and Bauch, A. (2006) An efficient tandem affinity purification procedure for interaction proteomics in mammalian cells. *Nat. Methods 3*, 1013–9.

(14) Tropea, J. E., Cherry, S., Nallamsetty, S., Bignon, C., and Waugh, D. S. (2007) A generic method for the production of recombinant proteins in Escherichia coli using a dual hexahistidine-maltose-binding protein affinity tag. *Methods Mol. Biol. 363*, 1–19.

(15) Miyawaki, A., Sawano, A., and Kogure, T. (2003) Lighting up cells: labelling proteins with fluorophores. *Nat. Cell Biol.*

Suppl. S1–7.
(16) Chapman, S., Oparka, K. J., and Roberts, A. G. (2005) New tools for in vivo fluorescence tagging. *Curr. Opin. Plant Biol. 8*, 565–73.
(17) Dubertret, B., Skourides, P., Norris, D. J., Noireaux, V., Brivanlou, A. H., and Libchaber, A. (2002) In vivo imaging of quantum dots encapsulated in phospholipid micelles. *Science 298*, 1759–62.
(18) Lidke, D. S., Nagy, P., Heintzmann, R., Arndt-Jovin, D. J., Post, J. N., Grecco, H. E., Jares-Erijman, E. A., and Jovin, T. M. (2004) Quantum dot ligands provide new insights into erbB/HER receptor-mediated signal transduction. *Nat. Biotechnol. 22*, 198–203.
(19) Patterson, G. H., and Lippincott-Schwartz, J. (2002) A photoactivatable GFP for selective photolabeling of proteins and cells. *Science 297*, 1873–7.
(20) Adams, S. R., Campbell, R. E., Gross, L. A., Martin, B. R., Walkup, G. K., Yao, Y., Llopis, J., and Tsien, R. Y. (2002) New biarsenical ligands and tetracysteine motifs for protein labeling in vitro and in vivo: synthesis and biological applications. *J. Am. Chem. Soc. 124*, 6063–76.
(21) Paramban, R. I., Bugos, R. C., and Su, W. W. (2004) Engineering green fluorescent protein as a dual functional tag. *Biotechnol. Bioeng. 86*, 687–97.
(22) Shute, T. S., Matsushita, M., Dickerson, T. J., La Clair, J. J., Janda, K. D., and Burkart, M. D. (2005) A site-specific bifunctional protein labeling system for affinity and fluorescent analysis. *Bioconjugate Chem. 16*, 1352–5.
(23) Watt, R. M., and Voss, E. W. (1977) Mechanism of quenching of fluorescein by anti-fluorescein IgG antibodies. *Immunochemistry 14*, 533–51.
(24) Rahimi, Y. (2007) Metal affinity-based purification of a red fluorescent protein. *Chromatographia 65*, 1612–1112.
(25) Rahimi, Y., Shrestha, S., and Deo, S. K. (2006) In *Proceedings of the 14th International Symposium on Bioluminescence and Chemiluminescence* (Kricka, L. J., and Stanley, P. E., Eds.) San Diego.
(26) Shrestha, S., and Deo, S. K. (2006) Anthozoa red fluorescent protein in biosensing. *Anal. Bioanal. Chem. 386*, 515–24.
(27) Verkhusha, V. V., Kuznetsova, I. M., Stepanenko, O. V., Zaraisky, A. G., Shavlovsky, M. M., Turoverov, K. K., and Uversky, V. N. (2003) High stability of Discosoma DsRed as compared to Aequorea EGFP. *Biochemistry 42*, 7879–84.
(28) Goulding, A. M., Hunt, E. A., Shrestha, S., Dria, K., and Deo, S. K. (2008) Biochemical and spectroscopic characterization of non-natural variants of DsRed-monomer. *Protein Eng. Des. Sel.*, in press.
(29) Ueno, A., Ohishi, S., Kitagawa, T., and Katori, M. (1979) Enzyme immunoassay of bradykinin. *Adv. Exp. Med. Biol. 120A*, 195–202.
(30) Trewhella, J. (1992) The solution structures of calmodulin and its complexes with synthetic peptides based on target enzyme binding domains. *Cell Calcium 13*, 377–90.
(31) Daunert, S., Bachas, L. G., Schauer-Vukasinovic, V., Gregory, K. J., Schrift, G., and Deo, S. K. (2007) Calmodulin-mediated reversible immobilization of enzymes. *Colloids Surf., B: Biointerfaces 58*, 20−27.
(32) Kuboniwa, H., Tjandra, N., Grzesiek, S., Ren, H., Klee, C. B., and Bax, A. (1995) Solution structure of calcium-free calmodulin. *Nat. Struct. Biol. 2*, 768–76.
(33) Babu, Y. S., Bugg, C. E., and Cook, W. J. (1988) Structure of calmodulin refined at 2.2 A resolution. *J. Mol. Biol. 204*, 191–204.
(34) Douglass, P. M., Salins, L. L., Dikici, E., and Daunert, S. (2002) Class-selective drug detection: fluorescently-labeled calmodulin as the biorecognition element for phenothiazines and tricyclic antidepressants. *Bioconjugate Chem. 13*, 1186–92.
(35) Dikici, E., Deo, S. K., and Daunert, S. (2003) Drug detection based on the conformational changes of calmodulin and the fluorescence of its enhanced green fluorescent protein fusion partner. *Anal. Chim. Acta 500*, 237–245.
(36) Schauer-Vukasinovic, V., Cullen, L., and Daunert, S. (1997) Rational design of a calcium sensing system based on induced conformational changes of calmodulin. *J. Am. Chem. Soc. 1119*, 11102–11103.
(37) Watt, S. J., Oakley, A., Sheil, M. M., and Beck, J. L. (2005) Comparison of negative and positive ion electrospray ionization mass spectra of calmodulin and its complex with trifluoperazine. *Rapid Commun. Mass Spectrom. 19*, 2123–30.
(38) Cugno, M., Agostoni, P., Brunner, H. R., Gardinali, M., Agostoni, A., and Nussberger, J. (2000) Plasma bradykinin levels in human chronic congestive heart failure. *Clin. Sci. 99*, 461–6.
(39) Cugno, M., Nussberger, J., Biglioli, P., Alamanni, F., Coppola, R., and Agostoni, A. (2001) Increase of bradykinin in plasma of patients undergoing cardiopulmonary bypass: the importance of lung exclusion. *Chest 120*, 1776–82.
(40) Decarie, A., Drapeau, G., Closset, J., Couture, R., and Adam, A. (1994) Development of digoxigenin-labeled peptide: application to chemiluminoenzyme immunoassay of bradykinin in inflamed tissues. *Peptides 15*, 511–8.
(41) Geiger, R., and Miska, W. (1986) Determination of bradykinin by enzyme immunoassay. *Adv. Exp. Med. Biol. 198*, 531–6.
(42) Ueno, A., Oh-ishi, S., Kitagawa, T., and Katori, M. (1981) Enzyme immunoassay of bradykinin using β-D-galactosidase as a labeling enzyme. *Biochem. Pharmacol. 30*, 1659–64.
(43) Baird, G. S., Zacharias, D. A., and Tsien, R. Y. (1999) Circular permutation and receptor insertion within green fluorescent proteins. *Proc. Natl. Acad. Sci. U.S.A. 96*, 11241–6.
(44) Miyawaki, A., Llopis, J., Heim, R., McCaffery, J. M., Adams, J. A., Ikura, M., and Tsien, R. Y. (1997) Fluorescent indicators for Ca2+ based on green fluorescent proteins and calmodulin. *Nature 388*, 882–7.
(45) Martin, M. M., and Jean, F. (2006) Single-cell resolution imaging of membrane-anchored hepatitis C virus NS3/4A protease activity. *Biol. Chem. 387*, 1075–80.
(46) Wu Y., Z. Y., Song, J., Hu, X., Ding, Y., and Zhang, Z. (2008) Using green and red fluorescent proteins to teach protein expression, purification, and crystallization. *Biochem. Mol. Biol. Educ. 36*, 43–54.
(47) Hsu, Y. Y., Liu, Y. N., Wang, W., Kao, F. J., and Kung, S. H. (2007) In vivo dynamics of enterovirus protease revealed by fluorescence resonance emission transfer (FRET) based on a novel FRET pair. *Biochem. Biophys. Res. Commun. 353*, 939–45.
(48) Kohl, T., Heinze, K. G., Kuhlemann, R., Koltermann, A., and Schwille, P. (2002) A protease assay for two-photon crosscorrelation and FRET analysis based solely on fluorescent proteins. *Proc. Natl. Acad. Sci. U.S.A. 99*, 12161–6.
(49) Mizuno, H., Sawano, A., Eli, P., Hama, H., and Miyawaki, A. (2001) Red fluorescent protein from Discosoma as a fusion tag and a partner for fluorescence resonance energy transfer. *Biochemistry 40*, 2502–10.

BC800147K

Chemical Activation of Lipoplexes Formed from DNA and a Redox-Active, Ferrocene-Containing Cationic Lipid

Christopher M. Jewell,[†] Melissa E. Hays,[†] Yukishige Kondo,[‡] Nicholas L. Abbott,*[,†] and David M. Lynn*[,†]

Department of Chemical and Biological Engineering, University of Wisconsin - Madison, 1415 Engineering Drive, Madison, Wisconsin 53706, and Department of Industrial Chemistry, Tokyo University of Science, Tokyo, Japan. Received May 22, 2008; Revised Manuscript Received August 2, 2008

We recently reported that the ferrocene-containing cationic lipid BFDMA [bis(11-ferrocenylundecyl)dimethylammonium bromide] can be used to mediate cell transfection, and that levels of transfection depend critically upon the oxidation state of the ferrocenyl groups of the lipid. Here, we report that the redox activity of BFDMA can be exploited to transform lipoplexes formed from oxidized BFDMA (which do not transfect cells) to lipoplexes that are "active" (and thus mediate high levels of transgene expression) by treatment with the chemical reducing agent glutathione (GSH). We demonstrate that GSH can be used to reduce the ferrocenium groups of oxidized BFDMA rapidly both (i) in solution and (ii) in lipoplexes formed by mixing oxidized BFDMA and DNA. Lipoplexes transformed in this manner mediate levels of cell transfection *in vitro* that are comparable to levels of transfection mediated by lipoplexes prepared by mixing DNA and reduced BFDMA. We demonstrate further that the chemical reduction of oxidized BFDMA leads to changes in the zeta potentials of these lipoplexes (e.g., from negative to positive). Characterization of lipoplex internalization using confocal microscopy demonstrated that these changes in zeta potential correlate to differences in the extents to which these lipoplexes are internalized by cells. These results provide a framework from which to interpret differences in cell transfection mediated by reduced and oxidized BFDMA. When combined, the results of this study suggest the basis of an approach that could be used to transform lipoplexes actively or "on-demand" and provide spatial and/or temporal control over the transfection of cells in a range of different fundamental and applied contexts.

INTRODUCTION

Cationic lipids are used widely as agents for the delivery of DNA to cells because they can interact with DNA to form nanoscale aggregates (or "lipoplexes") with sizes, charges, and other properties that can be used to address several critical barriers to cell transfection (*1*−*6*). Numerous past studies have identified a wide range of structural features and physical properties of cationic lipids that are important for the transfer of DNA into cells (*1*−*12*). This past work has contributed broadly to the development of cationic lipids and lipid-based formulations that can be used to promote high levels of cell transfection *in vitro* and *in vivo*.

Past studies on the development of cationic lipids for DNA delivery have focused, in large measure, on the design of lipids and lipoplex formulations that are (i) stable in extracellular environments (*13*−*15*) and/or (ii) unstable in (or designed to be responsive to) conditions found in intracellular environments (*16*−*27*). The former goal is often accomplished by the conjugation or incorporation of chemical functionality that resists protein adsorption or prevents the premature disruption of lipid/DNA interactions (*13*−*15*). The second goal has been addressed generally by the design of lipids containing functional groups that respond to changes in pH (*16*−*19, 26*), redox-potentials (*19*−*23*), or enzyme concentrations (*19, 24, 25*) present in intracellular environments. The broad motivations for the design of lipoplexes having this combination of properties are clear, as effective lipoplex-mediated transfer of DNA into cells will ultimately require lipoplexes that address effectively both extracellular barriers and intracellular barriers to the transport, internalization, and processing of DNA by cells.

In contrast to the work described above, less work has been focused on the development of lipoplexes or other nonviral DNA delivery systems that are designed to be transformed chemically or physically in extracellular environments (*27*). Lipoplexes that could be transformed in extracellular environments (for example, from states that may be "inactive", and, thus, unable to transfect cells, to states that are "active" and, thus, able to transfect cells efficiently) could be useful in a broad range of fundamental and applied contexts. For example, the ability to exert spatial and/or temporal control over the "activation" of inactive lipoplexes *in vitro* could lead to new methods for the patterning of cell transfection or the delivery of DNA to defined subpopulations of cells, and could thus contribute broadly to the development of new tools for both basic and applied biomedical research. The ability to exert such control could also prove useful for the localization of DNA delivery *in vivo*.

The work reported here builds upon the results of several past studies by our groups (*28*−*42*) and others (*43*−*50*) demonstrating that redox-active amphiphiles containing ferrocenyl groups can be used to exert spatial and/or temporal control over a broad range of properties of aqueous systems (*28*−*36, 43*−*50*) and interactions with macromolecular species (*37*), including DNA (*38*−*42*). Of particular relevance to the study described here, we reported recently that a two-tailed, ferrocene-containing cationic lipid [bis-(11-ferrocenylundecyl)dimethylammonium bromide (BFDMA; Figure 1)] (*44, 45, 47*) can be used to transfect cells (*38, 39*). One important outcome of these past studies was the observation that the oxidation state of the ferrocenyl groups of the BFDMA used to form lipoplexes with DNA plays a critical role in determining the ability of lipoplexes to promote transgene expression (*38, 39*). Lipoplexes formed

* E-mail: abbott@engr.wisc.edu, dlynn@engr.wisc.edu.
[†] University of Wisconsin - Madison.
[‡] Tokyo University of Science.

10.1021/bc8002138 CCC: $40.75 © 2008 American Chemical Society
Published on Web 10/03/2008

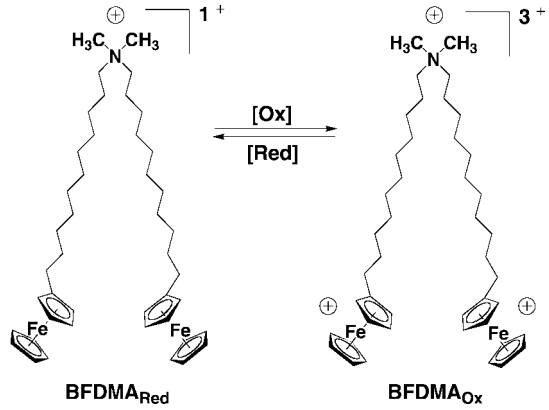

Figure 1. Structure of BFDMA, a redox-active cationic lipid. The charge of BFDMA can be cycled between +1 (reduced) and +3 (oxidized) by oxidation or reduction of the ferrocenyl groups at the end of each hydrophobic tail.

from DNA and reduced BFDMA (which has an overall net charge of +1) can be used to mediate high levels of cell transfection. However, lipoplexes formed using DNA and oxidized BFDMA (which has an overall net charge of +3) generally promote very low levels of cell transfection (*38, 39*). In subsequent studies aimed at characterizing the physical properties of lipoplexes formed from reduced and oxidized BFDMA, we identified differences in lipoplex sizes (*38, 39, 41*), internal dynamics (*41*), zeta potentials (*41*), and nanostructures (*42*) that correlated to these large differences in cell transfection. The results of these past studies, when combined, suggest that changes in the physical properties (and thus the transfection behaviors) of lipoplexes formed from reduced and oxidized BFDMA can be understood broadly in terms of changes in the amphiphilicity of BFDMA that occur upon the oxidation or reduction of ferrocene (*38, 39, 41, 42*). Because the redox state of ferrocenyl surfactants can, in general, be transformed rapidly and reversibly in aqueous environments (e.g., using either chemical or electrochemical methods) (*28*−*50*), these past results also suggest a basis for the development of methods that could permit active or reversible control over the ability (or the inability) of lipoplexes formed from BFDMA to transfect cells.

This current investigation sought to determine whether it was possible to exploit the redox activity of ferrocene to transform "inactive" lipoplexes formed from oxidized BFDMA to lipoplexes that are "active" and, thus, able to transfect cells. We report here that it is possible to transform or "activate" lipoplexes formed from DNA and oxidized BFDMA to lipoplexes that mediate high levels of transfection by treatment with a chemical reducing agent (glutathione, GSH). We demonstrate that GSH can be used to reduce the ferrocenium groups of oxidized BFDMA rapidly both (i) in solution and (ii) in lipoplexes formed by mixing oxidized BFDMA and DNA, and that lipoplexes transformed in this manner mediate levels of cell transfection *in vitro* that are comparable to levels of transfection mediated by lipoplexes prepared by the direct mixing of DNA and reduced BFDMA. We demonstrate further that the chemical reduction of the oxidized BFDMA in these lipoplexes leads to changes in zeta potentials (e.g., from negative values to positive values) and that these changes in zeta potential correlate to significant differences in the extents to which these lipoplexes are internalized by cells.

Our results demonstrate that it is possible to transform both the physicochemical properties and the biological behaviors of nanoscale aggregates of DNA and a redox-active cationic lipid. The results of this study, in combination with the results of our past studies (*38, 39, 41, 42*), suggest a basis for the development of methods for the transformation of cationic lipids and/or lipoplexes actively or "on-demand" in ways that could be used to provide spatial and/or temporal control over the transfection of cells *in vitro* or *in vivo*.

MATERIALS AND METHODS

Materials. Bis-(11-ferrocenylundecyl)dimethylammonium bromide (BFDMA) was synthesized as previously described (*45*). Glutathione (GSH) and lithium sulfate monohydrate were purchased from Sigma Aldrich (St. Louis, MO). Dodecyltrimethylammonium bromide (DTAB) was purchased from Acros Organics (Morris Plains, NJ). Plasmid DNA encoding enhanced green fluorescent protein [pEGFP-N1 (4.7 kb), >95% supercoiled] was purchased from the Waisman Clinical Biomanufacturing Facility at the University of Wisconsin - Madison. Plasmid DNA encoding firefly luciferase [pCMV-Luc, >95% supercoiled] was purchased from Elim Biopharmaceuticals, Inc. (San Francisco, CA). Deionized water (18 MΩ) was used to prepare all buffers and salt solutions. Dulbecco's modified Eagle's medium (DMEM), OptiMEM cell culture medium, phosphate-buffered saline (PBS), fetal bovine serum (FBS), Lipofectamine 2000, live/dead viability/cytotoxicity assay kits, calcein AM, and Lysotracker Red were purchased from Invitrogen (Carlsbad, CA). Bicinchoninic acid (BCA) protein assay kits were purchased from Pierce (Rockford, IL). Glo Lysis Buffer and Steady-Glo Luciferase Assay kits were purchased from Promega Corporation (Madison, WI). Cy5 Label-IT nucleic acid labeling kits were purchased from Mirus Bio (Madison, WI). Glass inset dishes used for laser scanning confocal microscopy (LSCM) were purchased from MatTek (Ashland, MA). All commercial materials were used as received without further purification unless otherwise noted.

General Considerations. Oxidation of BFDMA was conducted at 75 °C using a bipotentiostat (Pine Instruments, Grove City, PA) and a three-electrode cell to maintain a constant potential of 500 mV between the working electrode and a Ag/AgCl reference electrode. Platinum mesh (1.0 in^2) was used as the working and counter electrodes. The progress of oxidation was followed by monitoring current passed at the working electrode and by UV/visible spectrophotometry, as described previously (*38, 39*). All UV/visible absorbance values were recorded using a Beckman Coulter DU520 UV/vis spectrophotometer (Fullerton, CA). All zeta potential measurements were performed using a Zetasizer 2000HS instrument (Malvern Instruments, Worcestershire, UK). Fluorescence microscopy images used to evaluate the expression of enhanced green fluorescent protein (EGFP) in cell transfection experiments were recorded using an Olympus IX70 microscope and were analyzed using the *Metavue* version 7.1.2.0 software package (Molecular Devices; Toronto, Canada). Fluorescence, luminescence, and absorbance measurements used to characterize cytotoxicity, luciferase expression, and total cell protein were made using a PerkinElmer EnVision multilabel plate reader (Calcein AM: Ex, 492 nm; Em, 535 nm. Ethidium homodimer-1: Ex, 535 nm; Em, 620 nm. Luciferase: Em, 700 nm cutoff. BCA: Abs 560 nm). For DNA used in LSCM experiments, DNA was labeled using a Label-IT nucleic acid labeling kit according to the manufacturer's protocol (labeling density ~100 labels per plasmid). Labeled DNA was purified by ethanol precipitation, and labeling densities were determined using a UV/vis spectrophotometer, as described by the manufacturer of the labeling kit. LSCM was performed using a Bio-Rad Radiance 2100 MP Rainbow laser scanning confocal microscope equipped with a multiphoton laser. LSCM images were processed using the LaserSharp 2000 processing kit (Bio-Rad; Hercules, CA), *ImageJ* 1.38× (National Institutes of Health, Washington, DC; and Photoshop CS2 (Adobe Systems; San Jose, CA).

Preparation of Reduced and Oxidized BFDMA Solutions. Solutions of reduced BFDMA were prepared by dissolving a desired mass of reduced BFDMA in aqueous Li_2SO_4 (1.0 mM) followed by serial dilution with water over the desired concentration range (see text). Solutions of oxidized BFDMA were prepared by electrochemical oxidation of a 1.0 mM Li_2SO_4 solution containing reduced BFDMA, followed by serial dilution to desired concentrations, as described previously (*38*, *39*).

Preparation of Lipoplexes. Lipoplexes prepared from oxidized and reduced BFDMA were prepared in the following general manner. A solution of plasmid DNA (24 μg/mL in water) was added to a vortexing solution of aqueous Li_2SO_4 containing an amount of reduced or oxidized BFDMA sufficient to give the final lipid concentrations reported in the text. Total sample volumes for UV/vis absorbance experiments and zeta potential experiments were 1.0 mL. Sample volumes for LSCM and cell transfection experiments were 500 and 50 μL, respectively. Lipoplexes were allowed to stand at room temperature for at least 30 min before characterization or use in cell transfection experiments. Lipoplexes prepared to characterize the kinetics of reduction of BFDMA upon addition of GSH were used immediately after preparation.

Characterization of Transformation of Lipoplexes upon Addition of GSH. Experiments involving the addition of GSH to lipoplexes were performed by adding a negligible volume (0.5−5 μL) of a concentrated solution of GSH (0.5 M) to solutions of lipoplexes in an amount sufficient to yield the GSH/lipid molar ratios described in the text. Time-dependent changes in the oxidation state of BFDMA upon the addition of GSH to lipoplexes were characterized by measuring UV/vis absorbance spectra at wavelengths ranging from 400 to 800 nm. For these experiments, lipoplexes were prepared at higher lipid concentrations (but at equivalent lipid/DNA charge ratios) compared with lipoplexes prepared for use in transfection experiments to allow characterization of absorbance spectra. Following the acquisition of an initial wavelength scan, a kinetic scan was initiated by monitoring the absorbance of the solution at 5 s intervals at a wavelength of 630 nm (a wavelength characteristic of the absorbance of oxidized BFDMA). GSH was then added to the lipoplex solution, and the absorbance at 630 nm was monitored until a plateau in the measured value was observed. A second wavelength scan was performed over the range 400−800 nm at the conclusion of the kinetic experiment. For experiments involving measurements made on solutions of reduced BFDMA, DTAB was added immediately prior to measurement of absorbance to eliminate clouding observed in BFDMA solutions at concentrations greater than 100 μM. Note that DTAB does not absorb light in the visible region of interest of 400−800 nm. For experiments for which GSH was added to transform lipoplexes formed using oxidized BFDMA (described above), DTAB was added at the conclusion of each experiment before making a final absorbance measurement.

Characterization of Zeta Potential. Experiments designed to characterize the zeta potentials of lipoplexes after preparation or after exposure to GSH were conducted in the following general manner. For each sample prepared as described above, 1 mL of lipoplex solution was injected into the inlet of a Zetasizer 2000HS instrument, and measurements were made at ambient temperature using an electrical potential of 150 V. A minimum of four measurements were recorded for each sample, and the Henry equation was used to calculate zeta potentials from measurements of electrophoretic mobility (*51*). For this calculation, we assumed the viscosity of the solution to be the same as that of water.

General Protocols for Transfection and Characterization of Gene Expression. COS-7 cells used in transfection experiments were grown in clear or opaque polystyrene 96-well culture plates (for experiments using pEGFP-N1 and pCMV-Luc, respectively) at initial seeding densities of 15 000 cells/well in 200 μL of growth medium (90% Dulbecco's modified Eagle's medium, 10% fetal bovine serum, penicillin 100 units/mL, streptomycin 100 μg/mL). After plating, all cells were incubated at 37 °C for 24 h. At approximately 80% confluence, culture medium was aspirated and replaced with 200 μL of serum-free media (OptiMEM), followed by addition of 50 μL of lipoplex samples. Lipoplexes prepared as described above were added to assigned wells via pipet in replicates of three, and the cells were incubated for 4 h at 37 °C, at which point lipoplex-containing media was aspirated from all wells and replaced with 200 μL of serum-containing medium. Samples were incubated for an additional 48 h prior to characterization of transgene expression. For experiments conducted using lipoplexes formed using pEGFP-N1, cell morphology and relative levels of EGFP expression were characterized using phase contrast and fluorescence microscopy. For experiments conducted using lipoplexes formed using pCMV-Luc, quantitative cytotoxicity measurements were conducted using a commercially available fluorescence live/dead assay kit according to the manufacturer's instructions. Luciferase protein expression was determined using a commercially available luminescence-based luciferease assay kit using the manufacturer's specified protocol. Samples were compared with signals from control wells and/or normalized against total cell protein in each respective well using a commercially available BCA assay kit (Pierce). Lipoplexes formed using Lipofectamine 2000 were used as a positive control and prepared according to the manufacturer's instructions.

Characterization of Internalization of Lipoplexes Using LSCM. COS-7 cells were grown in glass inset confocal microscopy dishes at initial seeding densities of 2.4×10^5 cells in 2.0 mL of growth medium [90% (v/v) Dulbecco's modified Eagle's medium, 10% (v/v) fetal bovine serum, 100 units/mL penicillin, 100 μg/mL streptomycin]. Cells were allowed to grow overnight to approximately 90% confluence. Growth medium was then replaced with 2.0 mL of serum-free culture medium (OptiMEM), and 500 μL of lipoplex solutions (prepared using Cy5-labeled plasmid DNA) were added to sample dishes to achieve the final concentrations described in the text. Cells were incubated for 4 h at 37 °C, and media was aspirated and replaced with 2 mL of PBS buffer. Immediately prior to imaging, cells were incubated with solutions of calcein AM (live cell stain) and Lysotracker Red (endosome/lysosome stain) according to the manufacturer's protocols. Extents of internalization of fluorescently labeled DNA were then evaluated using LSCM. LSCM images were acquired using a 60×/1.40 NA oil immersion objective. Calcein AM, Lysotracker Red, and Cy5-labeled DNA were excited sequentially using laser lines at 488, 543, and 637 nm, respectively. Fluorescence emission signals were collected for three individual channels using direct scanning mode ($N = 1$, scan speed = 50 lps) and merged to create three-color images.

RESULTS AND DISCUSSION

The results of our past studies demonstrate that the oxidation state of the ferrocene groups in BFDMA influences significantly both the physical properties of BFDMA/DNA aggregates and the ability of these aggregates to transfect cells *in vitro* (*38*, *39*, *41*, *42*). Because the oxidation state of ferrocenyl surfactants can be transformed readily using a variety of chemical or electrochemical methods (for example, using electrochemical potentials applied to electrodes or a range of different chemical oxidizing or reducing agents) (*28*−*50*), BFDMA offers the potential to formulate lipoplexes with physical properties or behaviors that can be transformed

actively or reversibly. This investigation sought to determine (i) whether it was possible to use chemical reducing agents to reduce the ferrocenium groups in lipoplexes formed using DNA and oxidized BFDMA and (ii) whether the reduction of oxidized BFDMA could cause changes in the physical properties of lipoplexes sufficient to alter the ability of these aggregates to transfect cells. In the sections below, we describe the treatment and transformation of lipoplexes formed from oxidized BFDMA using GSH, a naturally occurring chemical reducing agent found in both extracellular and intracellular environments and involved in numerous biochemical processes and synthetic pathways (*52*).

Chemical Reduction of Oxidized BFDMA and Oxidized BFDMA/DNA Lipoplexes Using GSH. GSH has been demonstrated in previous studies to mediate the chemical reduction of ferrocenium species to ferrocenyl species (*53, 54*). It was not clear at the outset of this study, however, whether GSH could be used to promote the reduction of oxidized BFDMA or whether the reduction of oxidized BFDMA within lipoplexes could be made to occur at rates, or to extents, that would be useful in the context of cell transfection. We thus conducted a series of initial experiments to characterize the ability of GSH to mediate the reduction of oxidized BFDMA in solution (i.e., in the absence of DNA). Characterization of solutions of oxidized BFDMA in aqueous Li_2SO_4 using UV/vis spectrophotometry demonstrated that the addition of GSH (at molar excesses ranging from 10-fold to 50-fold) could be used to cause the quantitative reduction of oxidized BFDMA to reduced BFDMA (see Figure S1, Supporting Information). Additional experiments demonstrated that reduction occurred rapidly at high concentrations of GSH (e.g., within seconds to minutes in the presence of a 50-fold excess of GSH; reduction occurred more slowly (e.g., over ~90 min) in the presence of a 10-fold excess of GSH). The results of these initial experiments demonstrated the feasibility of reducing oxidized BFDMA using GSH and provided a baseline for characterization of the reduction of oxidized BFDMA in lipoplexes using UV/vis spectrophotometry.

We next conducted a series of experiments to determine whether it was possible to use GSH to reduce the oxidized BFDMA present in lipoplexes formed by mixing plasmid DNA and oxidized BFDMA. For these experiments, we used lipoplexes formed using oxidized BFDMA and plasmid DNA at a lipid/DNA charge ratio (CR) of 4.1:1. This charge ratio was chosen for these initial experiments on the basis of our past transfection results demonstrating that lipoplexes formed from oxidized BFDMA at a CR of 4.1:1 do not transfect cells, but that lipoplexes formed using reduced BFDMA at a CR of 1.4:1 mediate high levels of cell transfection (*39*). [We note here, in this context, that lipoplexes formed from DNA and oxidized BFDMA (which has a net charge of +3) at a CR of 4.1:1 contain the same molar ratio of BFDMA and DNA as lipoplexes formed from DNA and reduced BFDMA (which has a net charge of +1) at a CR of 1.4:1 (*39*).]

Figure 2 shows the UV/vis absorbance spectrum (over wavelengths ranging from 400 to 800 nm) of a solution of lipoplexes formed using oxidized BFDMA (dotted curve). Inspection of these data reveals an overall shape similar to that of solutions of oxidized BFDMA, and an absorbance peak at 630 nm that is diagnostic of oxidized BFDMA (as reported in past studies (*38, 39*); see also Figure S1, Supporting Information). Figure 2 also shows the UV/vis absorbance spectrum of a solution of lipoplexes of oxidized BFDMA after the addition of a 50-fold molar excess of GSH. Inspection of these data (solid gray curve) reveals large changes in the absorbance spectrum. In particular, we note the loss of the absorbance peak at 630 nm and the appearance of a new maximum in absorbance at

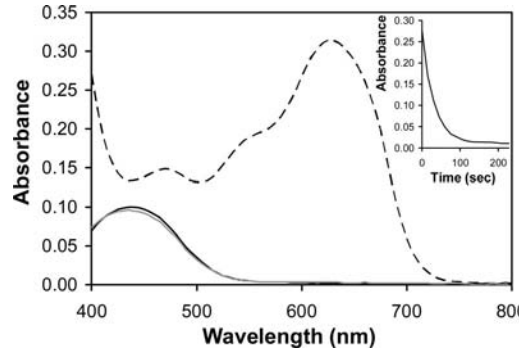

Figure 2. UV/visible absorbance spectra for solutions of lipoplexes formed from DNA and reduced (dark solid line) or oxidized (dark dashed line) BFDMA. The light solid line corresponds to lipoplexes formed from DNA and oxidized BFDMA and treated with a 50-fold excess of GSH. Inset: Decrease in absorbance vs time for lipoplexes formed from DNA and oxidized BFDMA upon treatment with a 50-fold excess of GSH. Absorbance was monitored at the absorbance maximum for oxidized BFDMA (630 nm).

445 nm. The maximum in absorbance at 445 nm indicates the presence of reduced BFDMA (*38, 39*), and the overall shape of this new absorbance spectrum is identical to that of the absorbance spectrum of lipoplexes formed using reduced BFDMA (at a CR of 1.4:1; see Figure 2, dark solid curve) (*38, 39*). These observations, when combined, demonstrate that (i) GSH is able to reduce the BFDMA in aggregates formed by the mixing of DNA and oxidized BFDMA and (ii) that the reduction of oxidized BFDMA occurs quantitatively under these conditions (e.g., as evidenced by the complete disappearance of the peak in absorbance at 630 nm). Subsequent investigation of the time dependence of the decrease in absorbance at 630 nm also demonstrated that the reduction of oxidized BFDMA occurred rapidly at higher concentrations of GSH (e.g., over a period of ~100 s in the presence of 50-fold excess GSH; see Figure 2, inset). Further characterization revealed this transformation to occur more slowly at lower concentrations of GSH (e.g., treatment of lipoplexes with a 10-fold molar excess of GSH resulted in the complete reduction of oxidized BFDMA, but this transformation occurred over a period of ~90 min; data not shown).

Characterization of Levels of Cell Transfection Mediated by Transformed Lipoplexes. The results above demonstrate that GSH can be used to chemically reduce BFDMA in lipoplexes formed from oxidized BFDMA and plasmid DNA. We next performed a series of experiments to determine whether transformation of the redox state of BFDMA in these lipoplexes could change the ability of these lipoplexes to mediate cell transfection *in vitro*. These experiments were conducted using the COS-7 cell line, a plasmid DNA construct encoding enhanced green fluorescent protein (EGFP), and transfection protocols similar to those used in our past studies (*38, 39*). To evaluate the general feasibility of this approach, we conducted a series of transfection experiments using lipoplexes at CRs identical to those used for the experiments described above (but at a lower overall concentration of BFDMA of 10 μM). As noted above, lipoplexes prepared using oxidized BFDMA at a CR of 4.1:1 were found to be "inactive" and did not mediate high levels of cell transfection in our past studies, but lipoplexes prepared using reduced BFDMA at a CR of 1.4:1 did mediate high levels of transgene expression (*38, 39*). This series of initial experiments was thus designed to determine whether the addition of GSH to solutions of lipoplexes formed from oxidized BFDMA could be used to produce solutions of lipoplexes that promote high levels of cell transfection.

Figure 3 shows representative fluorescence microscopy images of cells 48 h after treatment with lipoplexes prepared using

Figure 3. Representative fluorescence micrographs (100× magnification; 1186 μm × 899 μm) of EGFP expression in COS-7 cells treated with lipoplexes formed from (A) pEGFP-N1 and 10 μM reduced BFDMA, (B) pEGFP-N1 and oxidized BFDMA, and (C) pEGFP-N1 and oxidized BFDMA and treated with a 20-fold excess of GSH following lipoplex formation. Images were acquired at 48 h after exposure of cells to lipoplexes in serum-free medium (see text).

(A) reduced BFDMA, (B) oxidized BFDMA, or (C) lipoplexes prepared using oxidized BFDMA and treated with a 20-fold excess of GSH prior to addition to cells (see Materials and Methods section for additional details of transfection protocols). Inspection of the images in Figure 3A,B reveals that lipoplexes prepared using reduced BFDMA mediated high levels of EGFP expression and that lipoplexes prepared using oxidized BFDMA did not. These results are consistent with the results of our past studies (*38, 39*) and illustrate the significant influence of the oxidation state of BFDMA on levels of cell transfection. Inspection of the image in Figure 3C, however, reveals levels of EGFP expression that are (i) significantly higher than those shown in Figure 3B and (ii) qualitatively similar to the high levels of EGFP expression shown in Figure 3A. We conclude on the basis of these results that the addition of GSH to lipoplexes formed using oxidized BFDMA can be used to "activate" or transform solutions of these "inactive" lipoplexes to lipoplexes that mediate levels of transgene expression that are qualitatively similar to those formed using reduced BFDMA.

To characterize the ability of GSH-treated lipoplexes to mediate cell transfection more quantitatively, and across a greater range of lipid/DNA charge ratios, we conducted a second set of transfection experiments using lipoplexes formed from BFDMA and a plasmid DNA construct encoding firefly luciferase (pCMV-Luc). These transfection experiments were performed in a manner identical to our past experiments used to quantify the ability of reduced and oxidized BFDMA to mediate cell transfection (*38, 39*). These experiments were conducted using lipoplexes prepared at molar concentrations of BFDMA ranging from 2 to 60 μM. These molar concentrations correspond to lipid/DNA CRs ranging from 0.3:1 to 8.3:1 (for lipoplexes prepared using reduced BFDMA) and from 0.8:1 to 24.8:1 (for lipoplexes prepared using oxidized BFDMA). A table comparing lipid/DNA CRs to the molar concentrations of BFDMA used in the experiments described below can be found in a past publication (*39*).

Figure 4 shows quantitative luciferase expression results (expressed as relative light units normalized to total cell protein) for cells treated with lipoplexes prepared using concentrations of reduced BFDMA (white bars) or oxidized BFDMA (gray bars) ranging from 2 to 60 μM. Figure 4 also shows levels of luciferase expression for experiments using GSH-treated lipoplexes over this same range of BFDMA concentrations (black bars). The results of experiments using lipoplexes prepared using reduced and oxidized BFDMA (white bars and gray bars) are in general agreement with the results of our past studies (*38, 39*), and confirm that reduced BFDMA mediates high levels of cell transfection over a broad range of lipid concentrations, while oxidized BFDMA, in general, does not. Inspection of the data corresponding to levels of transfection mediated by GSH-treated lipoplexes reveals that these aggregates are also able to mediate

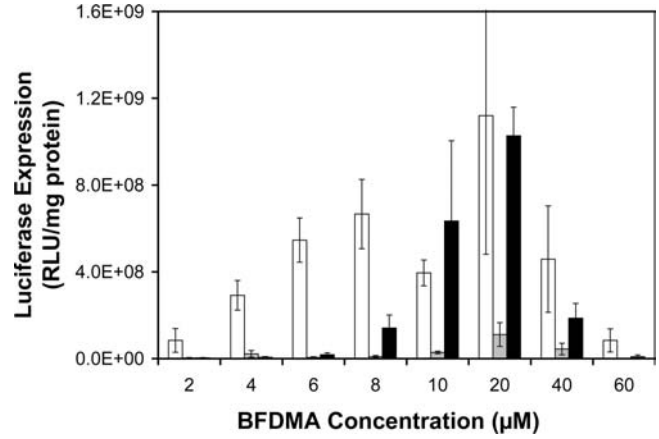

Figure 4. Normalized luciferase expression in COS-7 cells mediated by lipoplexes formed from reduced BFDMA (white bars), oxidized BFDMA (gray bars), and oxidized lipoplexes treated with a 20-fold excess of GSH prior to addition to cells (black bars). Experiments were performed in Opti-MEM with an exposure time of 4 h.

transgene expression at lipid concentrations ranging from 8 to 40 μM at levels that are, in several cases, comparable to the levels of expression mediated by lipoplexes formed from reduced BFDMA. The levels of transfection mediated in control experiments using lipoplexes formed from reduced BFDMA and treated with 20 μM GSH prior to addition to cells were identical (within error) to the levels of luciferase expression mediated by lipoplexes formed from reduced BFDMA alone (data not shown). These results, when combined, provide support for the view that the levels of gene expression mediated by the GSH-treated lipoplexes formed from oxidized BFDMA shown in Figure 4 result from the chemical reduction of oxidized BFDMA and not from any potential general influence of added GSH on cell transfection.

Inspection of the data in Figure 4 also demonstrates that levels of luciferase expression mediated by reduced BFDMA are a function of lipid concentration: levels of luciferase expression increase up to concentrations of 20 μM and decrease at concentrations higher than 40 μM (at which levels of lipid cytotoxicity become high) (*38, 39*). Further inspection of the results using GSH-treated lipoplexes of oxidized BFDMA reveals a similar concentration dependence (black bars), but over a more narrow range of concentrations (e.g., from 8 to 40 μM). We note that the decrease in luciferase expression at higher lipid concentrations (e.g., from 40 to 60 μM) again results, at least in part, from significant increases in the cytotoxicity of BFDMA at these concentrations (as described above; see also Figure S2 in the Supporting Information for results showing levels of cytotoxicity corresponding to transfection experiments in Figure

Table 1. Zeta Potentials of BFDMA Lipoplexes[a]

sample	500 μM BFDMA	10 μM BFDMA
Red BFDMA	26.5 ± 2.3 mV	27.6 ± 5.5 mV
Red BFDMA + GSH	26.9 ± 6.3 mV	26.3 ± 1.9 mV
Ox BFDMA	−16.0 ± 0.5 mV	−18.9 ± 3.1 mV
Ox BFDMA + GSH	30.3 ± 1.0 mV	17.6 ± 0.9 mV

[a] Concentrations given correspond to concentrations of BFDMA used in UV/vis spectrophotometry (500 μM; second column) and cell transfection and DNA internalization (10 μM; third column) experiments. Note that, in all cases, lipid/DNA charge ratios were fixed at 1.4:1 for reduced lipoplexes and 4.1:1 for oxidized lipoplexes (see text).

4). The specific reasons for the much lower levels of luciferase transfection at lower lipid concentrations (e.g., from 2 to 8 μM) are not yet completely understood. However, the results shown in Figures 3 and 4, when combined, do demonstrate that the treatment of lipoplexes formed from oxidized BFDMA (at concentrations ranging from 10 to 20 μM) with GSH can be transformed or activated in a manner that leads to lipoplexes that transfect cells at levels similar to those mediated by lipoplexes formed from reduced BFDMA. In the sections below, we demonstrate that these large changes in transfection behavior may result, at least in part, from large changes in the zeta potentials of lipoplexes upon treatment with GSH.

Characterization of the Zeta Potentials of Lipoplexes upon Treatment with GSH. We reported previously that the zeta potentials of lipoplexes formed from DNA and reduced BFDMA are negative at low lipid concentrations and positive at the lipid concentrations that promote the highest levels of transfection (e.g., 20 μM) (*41*). In contrast, lipoplexes formed using oxidized BFDMA were measured to remain negative or nearly neutral over the broad range of lipid concentrations used in the transfection experiments described above (as measured both in aqueous Li_2SO_4 and in serum-free cell culture media). Because particles with positive zeta potentials are generally internalized by cells more readily than particles with negative zeta potentials (e.g., by nonspecific endocytosis) (*55*, *56*), these results provided a framework from which to interpret and evaluate the large differences in cell transfection mediated by reduced and oxidized BFDMA (e.g., Figure 4) (*42*). The results shown in Figures 3 and 4 demonstrate clearly that the treatment of lipoplexes of oxidized BFDMA with GSH leads to large changes in EGFP and luciferase expression. We sought to understand whether these large increases in the transfection behavior of these lipoplexes could also be understood in terms of changes in zeta potentials that occur upon treatment with GSH.

Table 1 shows zeta potentials measured for lipoplexes formed from reduced or oxidized BFDMA either (i) before or (ii) after the addition of GSH. For these experiments, lipoplexes were formed at lipid/DNA CRs of 4.1:1 at total lipid concentrations of either 500 or 10 μM. These conditions were evaluated to permit comparison to the results of both UV/vis spectrophotometry experiments shown in Figure 2 ([BFDMA] = 500 μM) and the results of cell transfection experiments shown in Figures 3−5 ([BFDMA] = 10 μM).

The results shown in Table 1 demonstrate that the zeta potentials of lipoplexes formed from reduced BFDMA were positive (approximately +27 mV) and that the zeta potentials of lipoplexes formed from oxidized BFDMA were negative (from approximately −16 mV to −18 mV) at both lipid concentrations. These results are in general agreement with the results of our past study (*41*). The data in Table 1 also demonstrate that the addition of a 20-fold molar excess of GSH to lipoplexes of reduced BFDMA results in no significant changes in zeta potential. We note, however, that the addition of a 20-fold molar excess of GSH to lipoplexes of oxidized BFDMA results in large changes in zeta potential. In particular, the zeta potentials of these lipoplexes were found to change from negative to positive upon treatment with GSH (e.g., values of approximately +30 mV and +18 mV for lipoplexes prepared at 500 μM and 10 μM lipid, respectively). These results, when combined with those shown in Figure 2, provide additional support for the view that the treatment of lipoplexes of oxidized BFDMA with GSH results in chemical reduction of the ferrocenium groups of BFDMA. These results also suggest that these GSH-treated lipoplexes are able to reorganize physically over periods of ∼30 min in a manner that results in lipoplexes with positive zeta potentials. Additional experiments will be required to characterize changes in the nanostructures of these GSH-transformed lipoplexes and understand the dynamics of this physical transformation more completely. We demonstrate below, however, that these changes in zeta potential are consistent with large differences in the extents to which these lipoplexes are internalized by cells.

Characterization of the Internalization of Lipoplexes Using Confocal Microscopy. The data described above, and the results of our past studies (*41*), suggest that the redox state of the ferrocenyl groups of BFDMA could influence transfection, at least in part, by its influence on the zeta potentials of lipoplexes (which could, in turn, result in differences in the rates at which, or the extents to which, lipoplexes are internalized by cells). To characterize the internalization of lipoplexes by cells directly, we conducted a series of experiments using laser scanning confocal microscopy (LSCM) and lipoplexes formed using plasmid DNA labeled with a fluorescent probe (Cy5). Figure 5 shows representative LSCM images corresponding to cells incubated with (A,B) lipoplexes formed from reduced BFDMA, (C) lipoplexes formed from oxidized BFDMA, or (D) lipoplexes formed from oxidized BFDMA and then treated with a 20-fold excess of GSH prior to addition to cells. In these images, Cy5-labeled DNA is false-colored blue; the green and red fluorescence signals in these images correspond to calcein AM (a whole-cell stain) and Lysotracker Red (an endosome/lysosome stain), respectively. These experiments were conducted using lipoplexes prepared at charge ratios and lipid concentrations identical to those used in the transfection experiments shown in Figure 3. Lipoplexes were added to cells and incubated for 4 h before acquisition of the fluorescence microscopy images shown in Figure 5 (see Materials and Methods for additional details).

Figure 5A shows a representative image of cells treated with lipoplexes of reduced BFDMA at a magnification of 600×. The image in Figure 5B shows an enlarged view of a portion of the image shown in Figure 5A. Inspection of these two images reveals DNA to be present in three different locations: (i) in large aggregates that appear to be associated with (but not internalized by) cells, (ii) in endosomes and/or lysosomes (e.g., as identified by plain white arrows in Figure 5B), and (iii) in small, punctate blue fluorescent spots in the cytosol that are not colocalized with endosomes or lysosomes (e.g., as identified by starred white arrows in Figure 5B). (We note here for clarity that the endosome/lysosome stain used in this experiment is red, but that the vesicles in these images, in general, appear as yellow or orange/yellow in cases where calcein is also colocalized; stained vesicles that also contain Cy-5 labeled DNA appear as punctate magenta-colored spots in these images).

The images in Figure 5A,B demonstrate that lipoplexes formed from reduced BFDMA are internalized readily during the 4 h period over which they were exposed to cells. These results contrast to the results shown in the image in Figure 5C, which corresponds to cells treated with lipoplexes of oxidized BFDMA. Inspection of this image reveals that these cells do contain areas of faint punctate blue fluorescence (e.g., as

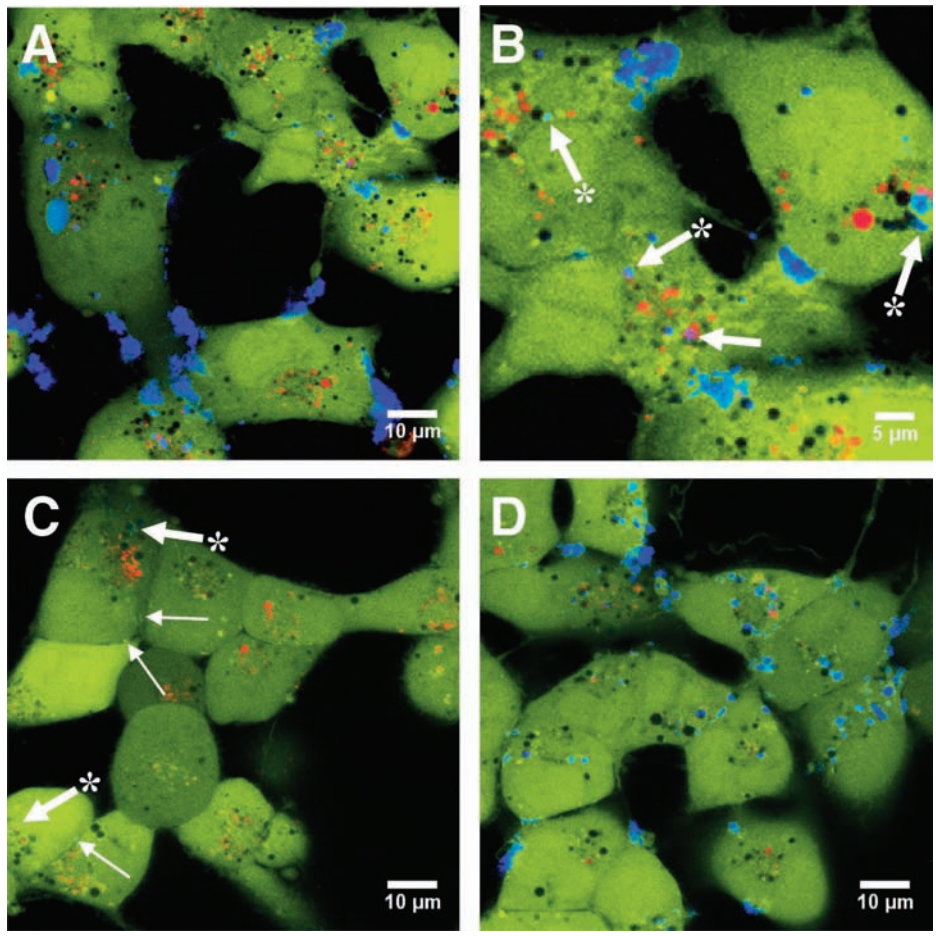

Figure 5. Representative confocal fluorescence micrographs showing DNA internalization in COS-7 cells treated with lipoplexes formed from (A,B) fluorescently labeled pEGFP-N1 and 10 μM reduced BFDMA, (C) fluorescently labeled pEGFP-N1 and 10 μM oxidized BFDMA, and (D) fluorescently labeled pEGFP-N1 and 10 μM oxidized BFDMA and treated with a 20-fold excess of GSH following lipoplex formation. Images were acquired 4 h after addition of lipoplexes (see Materials and Methods). Fluorescence signals correspond to Cy5 (fluorescently labeled DNA; blue signal), calcein AM (live cell stain; green signal), and Lysotracker Red (endosome/lysosome stain; red signal). See text for explanation of arrows. See Figure S3 of the Supporting Information for a high resolution reproduction of this image.

identified by starred white arrows), but that these punctate structures are both smaller in size and less numerous than those observed in Figure 5B. Inspection of this image also reveals small areas of faint blue fluorescence that are associated with, but apparently not internalized by, these cells (e.g., as identified by thin plain white arrows). The results shown in Figure 5C are representative of the sizes and numbers of punctate structures observed within cells treated with lipoplexes of oxidized BFDMA. We note, however, that considerable variability existed in the amounts of DNA that were associated with cell membranes. A comparison of the results in Figure 5C to those in Figure 5A,B suggests that the redox state of BFDMA influences significantly the internalization of lipoplexes by cells over the 4 h incubation period investigated in this study. We note that these apparent differences in extents of internalization correlate with the results of zeta potential measurements discussed above (Table 1) and provide a basis for interpreting the large differences in cell transfection mediated by reduced and oxidized BFDMA (e.g., Figures 3 and 4). Figure 5D shows images of cells that were incubated in the presence of GSH-treated lipoplexes for 4 h and reveals small, punctate blue fluorescent spots in nearly all cells. These results also correlate with our measurements of changes in zeta potential and cell transfection described above, and provide additional support for the view that chemical reduction of oxidized BFDMA by GSH can be used to activate lipoplexes of oxidized BFDMA that are otherwise inactive and do not transfect cells efficiently.

The observation of lipoplexes in Figure 5A,B,D that are colocalized with intracellular vesicles is consistent with the internalization of lipoplexes by endocytosis and, in general, with the results of past studies investigating the internalization of polyplexes formed using a range of other lipids (*1*−*6*). In this context, the observation of lipoplexes that are not colocalized with endosomes or lysosomes is an interesting result and suggests that lipoplexes formed from reduced BFDMA (or GSH-treated lipoplexes of oxidized BFDMA) may be able to mediate escape from these intracellular vesicles (or, alternatively, that they could potentially enter cells through a mechanism that does not involve endocytosis). Additional experiments will be required to characterize mechanisms of lipoplex internalization and trafficking quantitatively and determine the ultimate fates of lipoplexes of BFDMA more completely. In the context of this present study, however, we do observe that differences in transfection measured using reduced and oxidized BFDMA appear to correlate with a limited ability of oxidized BFDMA to mediate the transport of DNA into cells as compared to reduced BFDMA.

SUMMARY AND CONCLUSIONS

We have demonstrated that it is possible to exploit the redox properties of ferrocene to chemically activate or transform "inactive" lipoplexes formed from oxidized BFDMA and DNA to lipoplexes that mediate high levels of cell transfection by treatment with the chemical reducing agent glutathione (GSH).

Our results demonstrate that GSH can be used to reduce the ferrocenium groups of oxidized BFDMA rapidly and quantitatively both (i) in solution and (ii) when it is present as a component of a lipoplex. The results of our cell transfection experiments demonstrate that lipoplexes of oxidized BFDMA treated with GSH mediate levels of transgene expression that are, in several cases, comparable to those mediated by lipoplexes prepared by mixing DNA and reduced BFDMA.

We suggested in a previous report (*41*) that the dependence of cell transfection on the oxidation state of BFDMA could arise from differences in the zeta potentials of lipoplexes formed from either reduced or oxidized BFDMA. Characterization of the zeta potentials of lipoplexes in this present study revealed that the surface charges of lipoplexes of oxidized BFDMA undergo large changes in zeta potential (e.g., from negative to positive) upon treatment with GSH. In addition, the results of our confocal microscopy experiments using lipoplexes formulated using fluorescently labeled DNA suggested that differences exist in the levels at which lipoplexes of reduced BFDMA and lipoplexes of oxidized BFDMA were internalized by cells. These experimental results, when combined, provide experimental support for the proposition that the oxidation state of BFDMA influences cell transfection, at least in part, through its influence on the zeta potentials of lipoplexes formed from reduced and oxidized BFDMA.

In summary, we have demonstrated that it is possible to transform both the physicochemical properties and the biological behaviors of nanoscale aggregates of DNA and a redox-active cationic lipid by treatment with a chemical reducing agent. These results suggest the basis of a general approach that could, with further development, lead to methods for the transformation of cationic lipids and/or lipoplexes actively or "on-demand" in ways that could be used to provide spatial and/or temporal control over the transfection of cells *in vitro* or *in vivo*.

ACKNOWLEDGMENT

Financial support was provided by the National Institutes of Health (1 R21 EB006168) and the National Science Foundation (CTS-0754921). We are grateful to Lance Rodenkirch, Michael Hendrickson, and the W. M. Keck Center for Biological Imaging at the UW for access to and assistance with confocal microscopy facilities. We thank Selin Aytar and John Muller for many helpful discussions. D.M.L. is a Research Fellow of the Alfred P. Sloan Foundation.

Supporting Information Available: Results of additional experiments, including characterization of GSH-mediated reduction of oxidized BFDMA and characterization of cytotoxicity. This material is available free of charge via the Internet at http://pubs.acs.org.

LITERATURE CITED

(1) Kabanov, A. V., Felgner, P. L., and Seymour, L. W. (1998) *Self-Assembling Complexes for Gene Delivery: From Laboratory to Clinical Trial*, John Wiley and Sons, New York.

(2) Zabner, J. (1997) Cationic lipids used in gene transfer. *Adv. Drug Delivery Rev. 27*, 17–28.

(3) Nishikawa, M., and Huang, L. (2001) Nonviral vectors in the new millennium: delivery barriers in gene transfer. *Hum. Gene Ther. 12*, 861–70.

(4) de Lima, M. C. P., Simoes, S., Pires, P., Faneca, H., and Duzgunes, N. (2001) Cationic lipid-DNA complexes in gene delivery: from biophysics to biological applications. *Adv. Drug Delivery Rev. 47*, 277–294.

(5) Audouy, S. A. L., de Leij, L. F. M. H., Hoekstra, D., and Molema, G. (2002) In vivo characteristics of cationic liposomes as delivery vectors for gene therapy. *Pharm. Res. 19*, 1599–1605.

(6) Zhang, S. B., Xu, Y. M., Wang, B., Qiao, W. H., Liu, D. L., and Li, Z. S. (2004) Cationic compounds used in lipoplexes and polyplexes for gene delivery. *J. Controlled Release 100*, 165–180.

(7) Mahato, R. I., Rolland, A., and Tomlinson, E. (1997) Cationic lipid-based gene delivery systems: Pharmaceutical perspectives. *Pharm. Res. 14*, 853–859.

(8) Miller, A. D. (1998) Cationic Liposomes for Gene Therapy. *Angew. Chem., Int. Ed. 37*, 1768–1785.

(9) Bally, M. B., Harvie, P., Wong, F. M. P., Kong, S., Wasan, E. K., and Reimer, D. L. (1999) Biological barriers to cellular delivery of lipid-based DNA carriers. *Adv. Drug Delivery Rev. 38*, 291–315.

(10) Safinya, C. R. (2001) Structures of lipid-DNA complexes: supramolecular assembly and gene delivery. *Curr. Opin. Struct. Biol. 11*, 440–448.

(11) Martin, B., Sainlos, M., Aissaoui, A., Oudrhiri, N., Hauchecorne, M., Vigneron, J. P., Lehn, J. M., and Lehn, P. (2005) The design of cationic lipids for gene delivery. *Curr. Pharm. Des. 11*, 375–394.

(12) Khalil, I. A., Kogure, K., Akita, H., and Harashima, H. (2006) Uptake pathways and subsequent intracellular trafficking in nonviral gene delivery. *Pharmacol. Rev. 58*, 32–45.

(13) Lewis, J. G., Lin, K. Y., Kothavale, A., Flanagan, W. M., Matteucci, M. D., DePrince, R. B., Mook, R. A., Hendren, R. W., and Wagner, R. W. (1996) A serum-resistant cytofectin for cellular delivery of antisense oligodeoxynucleotides and plasmid DNA. *Proc. Natl. Acad. Sci. U.S.A. 93*, 3176–3181.

(14) Hong, K. L., Zheng, W. W., Baker, A., and Papahadjopoulos, D. (1997) Stabilization of cationic liposome-plasmid DNA complexes by polyamines and poly(ethylene glycol)-phospholipid conjugates for efficient in vivo gene delivery. *FEBS Lett. 400*, 233–237.

(15) Wheeler, J. J., Palmer, L., Ossanlou, M., MacLachlan, I., Graham, R. W., Zhang, Y. P., Hope, M. J., Scherrer, P., and Cullis, P. R. (1999) Stabilized plasmid-lipid particles: construction and characterization. *Gene Ther. 6*, 271–281.

(16) Budker, V., Gurevich, V., Hagstrom, J. E., Bortzov, F., and Wolff, J. A. (1996) pH-sensitive, cationic liposomes: A new synthetic virus-like vector. *Nat. Biotechnol. 14*, 760–764.

(17) Demeneix, B., Behr, J., Boussif, O., Zanta, M. A., Abdallah, B., and Remy, J. (1998) Gene transfer with lipospermines and polyethylenimines. *Adv. Drug Delivery Rev. 30*, 85–95.

(18) Gerasimov, O. V., Boomer, J. A., Qualls, M. M., and Thompson, D. H. (1999) Cytosolic drug delivery using pH- and light-sensitive liposomes. *Adv. Drug Delivery Rev. 38*, 317–338.

(19) Guo, X., and Szoka, F. C. (2003) Chemical approaches to triggerable lipid vesicles for drug and gene delivery. *Acc. Chem. Res. 36*, 335–341.

(20) Tang, F. X., and Hughes, J. A. (1998) Introduction of a disulfide bond into a cationic lipid enhances transgene expression of plasmid DNA. *Biochem. Biophys. Res. Commun. 242*, 141–145.

(21) Tang, F. X., and Hughes, J. A. (1999) Use of dithiodiglycolic acid as a tether for cationic lipids decreases the cytotoxicity and increases transgene expression of plasmid DNA in vitro. *Bioconjugate Chem. 10*, 791–796.

(22) Ajmani, P. S., Tang, F. X., Krishnaswami, S., Meyer, E. M., Sumners, C., and Hughes, J. A. (1999) Enhanced transgene expression in rat brain cell cultures with a disulfide-containing cationic lipid. *Neurosci. Lett. 277*, 141–144.

(23) Wetzer, B., Byk, G., Frederic, M., Airiau, M., Blanche, F., Pitard, B., and Scherman, D. (2001) Reducible cationic lipids for gene transfer. *Biochem. J. 356*, 747–756.

(24) Meers, P. (2001) Enzyme-activated targeting of liposomes. *Adv. Drug Delivery Rev. 53*, 265–72.

(25) Prata, C. A., Zhao, Y., Barthelemy, P., Li, Y., Luo, D., McIntosh, T. J., Lee, S. J., and Grinstaff, M. W. (2004) Charge-

reversal amphiphiles for gene delivery. *J. Am. Chem. Soc. 126*, 12196–7.
(26) Choi, J. S., MacKay, J. A., and Szoka, F. C. (2003) Low-pH-sensitive PEG-stabilized plasmid-lipid nanoparticles: Preparation and characterization. *Bioconjugate Chem. 14*, 420–429.
(27) Wolff, J. A., and Rozema, D. B. (2008) Breaking the bonds: Non-viral vectors become chemically dynamic. *Mol. Ther. 16*, 8–15.
(28) Gallardo, B. S., Hwa, M. J., and Abbott, N. L. (1995) In-situ and reversible control of the surface-activity of ferrocenyl surfactants in aqueous-solutions. *Langmuir 11*, 4209–4212.
(29) Bennett, D. E., Gallardo, B. S., and Abbott, N. L. (1996) Dispensing surfactants from electrodes: Marangoni phenomenon at the surface of aqueous solutions of (11-ferrocenylundecyl)trimethylammonium bromide. *J. Am. Chem. Soc. 118*, 6499–6505.
(30) Gallardo, B. S., Metcalfe, K. L., and Abbott, N. L. (1996) Ferrocenyl surfactants at the surface of water: Principles for active control of interfacial properties. *Langmuir 12*, 4116–4124.
(31) Gallardo, B. S., and Abbott, N. L. (1997) Active control of interfacial properties: A comparison of dimeric and monomeric ferrocenyl surfactants at the surface of aqueous solutions. *Langmuir 13*, 203–208.
(32) Gallardo, B. S., Gupta, V. K., Eagerton, F. D., Jong, L. I., Craig, V. S., Shah, R. R., and Abbott, N. L. (1999) Electrochemical principles for active control of liquids on submillimeter scales. *Science 283*, 57–60.
(33) Rosslee, C., and Abbott, N. L. (2000) Active control of interfacial properties. *Curr. Opin. Colloid Interface Sci. 5*, 81–87.
(34) Rosslee, C. A., and Abbott, N. L. (2001) Principles for microscale separations based on redox-active surfactants and electrochemical methods. *Anal. Chem. 73*, 4808–4814.
(35) Luk, Y. Y., and Abbott, N. L. (2003) Surface-driven switching of liquid crystals using redox-active groups on electrodes. *Science 301*, 623–626.
(36) Rosslee, C. A., Khripin, C., Foley, T. M. D., and Abbott, N. L. (2004) Using "prosurfactants" to enhance rates of delivery of surfactants. *AIChE J. 50*, 708–714.
(37) Hays, M. E., and Abbott, N. L. (2005) Electrochemical control of the interactions of polymers and redox-active surfactants. *Langmuir 21*, 12007–12015.
(38) Abbott, N. L., Jewell, C. M., Hays, M. E., Kondo, Y., and Lynn, D. M. (2005) Ferrocene-containing cationic lipids: influence of redox state on cell transfection. *J. Am. Chem. Soc. 127*, 11576–11577.
(39) Jewell, C. M., Hays, M. E., Kondo, Y., Abbott, N. L., and Lynn, D. M. (2006) Ferrocene-containing cationic lipids for the delivery of DNA: Oxidation state determines transfection activity. *J. Controlled Release 112*, 129–138.
(40) Hays, M. E., Jewell, C. M., Lynn, D. M., and Abbott, N. L. (2007) Reversible condensation of DNA using a redox-active surfactant. *Langmuir 23*, 5609–5614.
(41) Hays, M. E., Jewell, C. M., Kondo, Y., Lynn, D. M., and Abbott, N. L. (2007) Lipoplexes formed by DNA and ferrocenyl lipids: effect of lipid oxidation state on size, internal dynamics and zeta-potential. *Biophys. J. 93*, 4414–4424.
(42) Pizzey, C. L., Jewell, C. M., Hays, M. E., Lynn, D. M., Abbott, N. L., Kondo, Y., Golan, S., and Talmon, Y. (2008) Characterization of the nanostructure of complexes formed by a redox-active cationic lipid and DNA. *J. Phys. Chem. B 112*, 5849–5857.
(43) Saji, T., Hoshino, K., and Aoyagui, S. (1985) Reversible formation and disruption of micelles by control of the redox state of the head group. *J. Am. Chem. Soc. 107*, 6865–6868.
(44) Kakizawa, Y., Sakai, H., Nishiyama, K., Abe, M., Shoji, H., Kondo, Y., and Yoshino, N. (1996) Solution properties of double-tailed cationic surfactants having ferrocenyl groups in their hydrophobic moieties. *Langmuir 12*, 921–924.
(45) Yoshino, N., Shoji, H., Kondo, Y., Kakizawa, Y., Sakai, H., and Abe, M. (1996) Syntheses of cationic surfactants having two ferrocenylalkyl chains. *J. Jpn. Oil Chem. Soc. 45*, 769–775.
(46) Sakai, H., Imamura, H., Kakizawa, Y., Abe, M., Kondo, Y., Yoshino, N., and Harwell, J. H. (1997) Active control of vesicle formation using a redox-active surfactant. *Denki Kagaku 65*, 669–672.
(47) Kakizawa, Y., Sakai, H., Yamaguchi, A., Kondo, Y., Yoshino, N., and Abe, M. (2001) Electrochemical control of vesicle formation with a double-tailed cationic surfactant bearing ferrocenyl moieties. *Langmuir 17*, 8044–8048.
(48) Takei, T., Sakai, H., Kondo, Y., Yoshino, N., and Abe, M. (2001) Electrochemical control of solubilization using a ferrocene-modified nonionic surfactant. *Colloid Surf., A 183*, 757–765.
(49) Tsuchiya, K., Sakai, H., Saji, T., and Abe, M. (2003) Electrochemical reaction in an aqueous solution of a ferrocene-modified cationic surfactant mixed with an anionic surfactant. *Langmuir 19*, 9343–9350.
(50) Sakai, H., Imamura, H., Kondo, Y., Yoshino, N., and Abe, M. (2004) Reversible control of vesicle formation using electrochemical reaction. *Colloid Surf., A 232*, 221–228.
(51) Hunter, R. J. (1981) *Zeta Potential in Colloid Science*, Academic Press, New York.
(52) Meister, A., and Anderson, M. E. (1983) Glutathione. *Annu. Rev. Biochem. 52*, 711–760.
(53) Wring, S. A., Hart, J. P., and Birch, B. J. (1991) Voltammetric behavior of screen-printed carbon electrodes, chemically modified with selected mediators, and their application as sensors for the determination of reduced glutathione. *Analyst 116*, 123–129.
(54) Schreyer, S. K., and Mikkelsen, S. R. (1999) A synthetic cysteine oxidase eased on a ferrocene-cyclodextrin conjugate. *Bioconjugate Chem. 10*, 464–469.
(55) Tomlinson, E., and Rolland, A. P. (1996) Controllable gene therapy. Pharmaceutics of non-viral gene delivery systems. *J. Controlled Release 39*, 357–372.
(56) Vijayanathan, V., Thomas, T., and Thomas, T. J. (2002) DNA nanoparticles and development of DNA delivery vehicles for gene therapy. *Biochemistry 41*, 14085–14094.

BC8002138

Chemical Activation of Lipoplexes Formed from DNA and a Redox-Active, Ferrocene-Containing Cationic Lipid

Christopher M. Jewell,[1] Melissa E. Hays,[1] Yukishige Kondo,[2] Nicholas L. Abbott,[1,*] and David M. Lynn[1,*]

[1]Department of Chemical and Biological Engineering, University of Wisconsin – Madison, 1415 Engineering Drive, Madison, Wisconsin 53706, [2]Department of Industrial Chemistry, Tokyo University of Science, Tokyo, Japan

Supporting Information

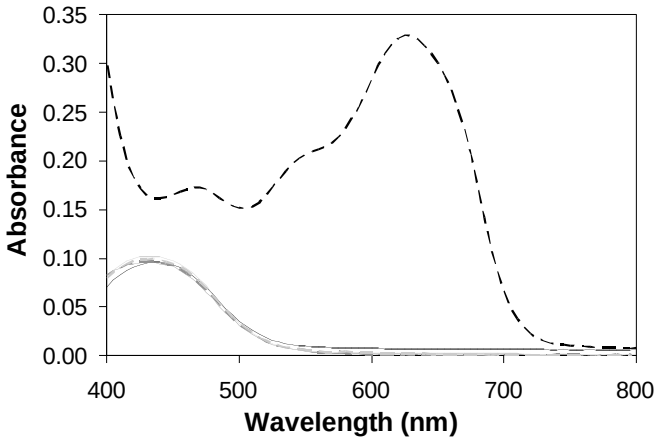

Figure S1: UV/visible absorbance spectra for solutions of reduced BFDMA (dark solid line) or oxidized BFDMA (dark dashed line). Also shown are spectra corresponding to solutions of oxidized BFDMA treated with GSH at a 50-fold excess (dark grey solid line), 30-fold excess (dark grey dashed line), 20-fold excess (light grey solid line), and 10-fold excess (light grey dashed line). See Experimental Section of main text for experimental details.

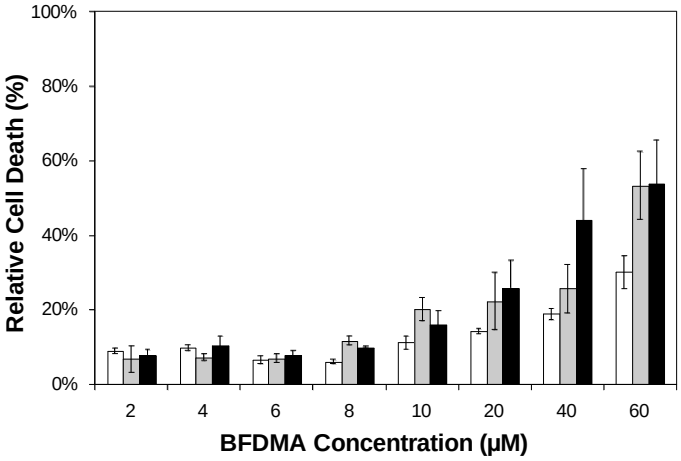

Figure S2: Relative cell death in COS-7 cells resulting from exposure to lipoplexes formed from reduced BFDMA (white bars), oxidized BFDMA (grey bars), and oxidized lipoplexes treated with a 20-fold excess of GSH prior to addition to cells (black bars). Experiments were performed in Opti-MEM with an exposure time of 4 h, and data correspond to luciferase expression data shown in Figure 4. See experimental section of main text for experimental details.

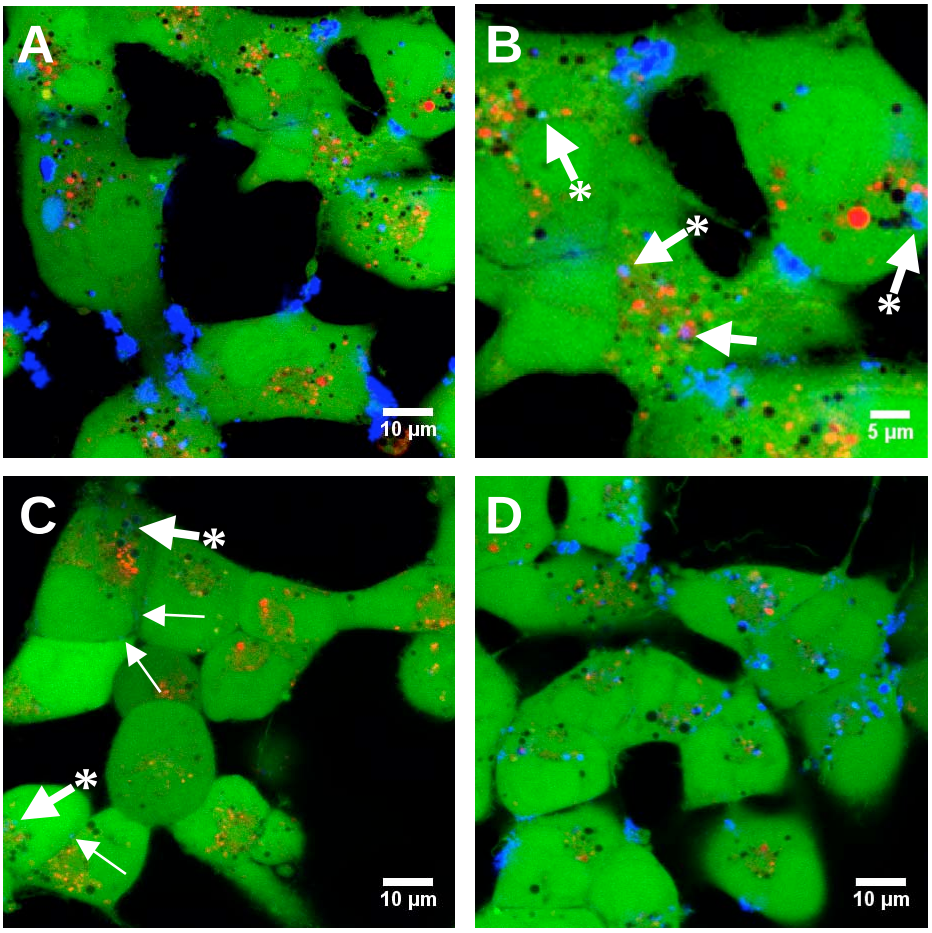

Figure S3: High-resolution reproduction of the images in Figure 5 of the main text showing representative confocal fluorescence micrographs of DNA internalization in COS-7 cells treated with lipoplexes formed from A-B) fluorescently-labeled pEGFP-N1 and 10 µM reduced BFDMA, C) fluorescently-labeled pEGFP-N1 and 10 µM oxidized BFDMA, and D) fluorescently-labeled pEGFP-N1 and 10 µM oxidized BFDMA and treated with a 20-fold excess of GSH following lipoplex formation. Images were acquired 4 h after addition of lipoplexes (see Materials and Methods). Fluorescence signals correspond to Cy5 (fluorescently-labeled DNA; blue signal), calcein AM (live cell stain; green signal), and Lysotracker Red (endosome/lysosome stain; red signal). See main text for explanation of arrows.

Peptide-Mediated Cellular Uptake of Cryptophane

Garry K. Seward, Qian Wei, and Ivan J. Dmochowski*

Department of Chemistry, University of Pennsylvania, 231 South 34th Street, Philadelphia, Pennsylvania 19104-6323. Received June 1, 2008; Revised Manuscript Received August 24, 2008

Cryptophane-A has generated considerable interest based on its high affinity for xenon and potential for creating biosensors for ^{129}Xe nuclear magnetic resonance (NMR) spectroscopy. Here, we report the cellular delivery of three peptide-functionalized cryptophane biosensors. Cryptophanes were delivered using two cationic cell penetrating peptides into several human cancer and normal cell lines. An RGD peptide targeting $\alpha_v\beta_3$ integrin receptor was shown to increase specificity of cryptophane cell uptake. Labeling the peptides with Cy3 made it possible to monitor cellular delivery using confocal laser scanning microscopy. The peptido-cryptophanes were determined to be relatively nontoxic by MTT assay at the micromolar cryptophane concentrations that are required for ^{129}Xe NMR biosensing experiments.

INTRODUCTION

Magnetic resonance imaging (MRI) identifies molecules at high spatial resolution within deep tissue and can facilitate the diagnosis of many diseases. However, MRI suffers from low sensitivity and high background signals due to intrinsic ^{1}H signals from water and fat. In MRI procedures involving human subjects, signals are typically enhanced using gadolinium- or iron-oxide-based agents at approximately 0.1 mmol/kg. However, it has been challenging using these contrast agents to identify biomolecular targets, such as proteins, which are typically present in cells at low concentrations (*1, 2*). Moreover, U.S. and European agencies recently issued advisories regarding the risks posed by gadolinium agents in patients with impaired renal function. These findings motivate studies of non-proton-based, hyperpolarized MRI agents such as ^{129}Xe, ^{13}C, and ^{3}He, which enable physiological assays, and provide potentially more sensitive methods for studying proteins and metabolites (*3*−*5*). ^{129}Xe is particularly attractive due to its large chemical shift window and laser polarization of nuclear spins, which enhances ^{129}Xe NMR signals by more than 10 000-fold. Importantly, the environmental sensitivity of the xenon chemical shift allows the simultaneous detection of multiple species in solution. ^{129}Xe NMR biosensing has been elegantly demonstrated using a cryptophane organic host molecule that binds xenon and can be targeted to specific analytes in solution (*6*).

Cryptophanes are versatile host molecules whose size can be tuned to bind xenon and a variety of organic solvents and cationic species (*7*). In cryptophane-A, two cyclotriveratrylenes are joined by three ethylene linkers to form a 1-nm-diameter pseudospherical cage with internal volume of ∼95 Å^3. Hill et al. showed that a tricarboxylate-modified cryptophane-A binds xenon with comparable affinity in buffer (K_A = 30 000 M^{-1}) and human plasma (K_A = 22 000 M^{-1}) at 310 K (*8*). This avidity for xenon has motivated the design of cryptophane-A biosensors for detecting protein binding (*9*) or enzyme-related activity (*10*) by laser-polarized ^{129}Xe nuclear magnetic resonance (NMR) spectroscopy. Biotin-functionalized cryptophanes produced a 1−4 ppm change in ^{129}Xe NMR chemical shift upon streptavidin binding (*11*−*14*). Similarly, peptide-decorated cryptophane-A reported cleavage by matrix metalloproteinase-7 (MMP-7), which is secreted from many human tumors (*10*). Importantly, the cryptophane did little to affect MMP-7 activity, with peptide cleavage producing a 0.5 ppm change in ^{129}Xe NMR chemical shift. These results motivate the development of cryptophane biosensors for in vivo ^{129}Xe NMR studies. However, very few water-soluble cryptophanes (*15*) have been synthesized, and little is known about their biological activity. We are not aware of any cell or animal studies involving cryptophanes that have been reported up to this time. In the current study, we investigated the uptake of peptide-modified cryptophane-A in human cancer, fibroblasts, and red blood cells.

Cryptophane-A has poor (low micromolar) water solubility and a molecular weight of 895 g/mol, which limits spontaneous intracellular diffusion, as can occur with smaller drug-like compounds. Thus, in order to test cryptophane cellular compatibility, one possible delivery method involves the use of polycationic peptides that help to solubilize the cryptophane and are rich in the basic amino acids arginine and lysine. These peptides, known generally as cell penetrating peptides (CPPs), can transport through cell membranes covalently attached cargo such as therapeutics, nucleic acids, and imaging agents (*16*−*19*). In one example, porphyrins useful for photodynamic therapy were delivered to cellular compartments by conjugating a segment of the human immunodeficiency transcriptional activator (HIV-1 TAT) or short peptides containing 6−9 consecutive arginines (*20*). Buckminsterfullerene, which is similar to cryptophane-A in molecular weight and chemical formula, was delivered to HEK-293 cells by attaching oligomers of lysine (*21*). These studies highlight the utility of CPPs for improving cellular uptake and bioavailability of large organic molecules.

Another cell delivery method involves the specific targeting of cell surface receptors, such as integrins (*22*−*24*), somatostatin (*25*−*27*), or folate (*28*). Integrin receptors are overexpressed in a variety of cancer cells and linked to tumor metastasis and invasion (*29, 30*). It is found that the $\alpha_v\beta_3$ integrin receptor in particular is substantially up-regulated in fast-growing tumor cells, compared to minimum expression in most normal tissues (*31, 32*). A cyclic tripeptide RGD sequence is known to target the $\alpha_v\beta_3$ integrin receptor (ABIR) (*33*−*36*). More recently, it was demonstrated that linear multimeric $(RGD)_n$ sequences also target the ABIR and promote the uptake of near-infrared-emitting cypate in A549 nonsmall cell carcinoma cells (*37*).

* To whom correspondence should be addressed. Department of Chemistry, University of Pennsylvania, 231 South 34th St., Philadelphia, PA 19104-6323. E-mail: ivandmo@sas.upenn.edu, Phone: 215-898-6459, Fax: 215-898-2037.

10.1021/bc8002265 CCC: $40.75 © 2008 American Chemical Society
Published on Web 10/17/2008

This strategy of selectively delivering biologically active molecules is particularly useful for imaging tumors, which overexpress a large number of cell surface receptors.

In the present study, we report the synthesis of cryptophane-A conjugated to HIV-1 TAT (residues 48−60), a nonamer of D-arginine, or the $(RGD)_4$ dodecamer. Cell penetrating peptides were chosen to examine initially whether cryptophanes could be delivered to cells and to measure the effects of nonspecific delivery on cell viability. The $(RGD)_4$ peptide was chosen for its ability to target cells overexpressing ABIR (*37*). Cysteine incorporation within these peptides provided a route for subsequent labeling with Cy3. Cell uptake and cytotoxicity were measured for AsPC-1 and CAPAN-2 pancreatic cancer cells, HFL-1 human lung fibroblasts, and human red blood cells.

EXPERIMENTAL PROCEDURES

Reagents. Organic reagents and solvents were used as purchased from the following commercial sources: Sigma-Aldrich: dimethyl sulfoxide (DMSO), dimethylformamide (DMF), methanol, triisopropylsilane (TIS), 2,6-lutidine, piperidine, 3-(4,5-dimethyl-2-thiazolyl)-2,5-diphenyl-2*H*-tetrazolium bromide (MTT); Fisher: sodium chloride, copper(II) sulfate, trifluoroacetic acid (TFA), diethyl ether (Et_2O), glutathione; Alfa Aesar: cesium carbonate, L-glutathione; Novabiochem: 2-(1*H*-benzotriazole-1-yl)-1,1,3,3-tetramethyluronium hexafluorophosphate (HBTU), *N*-methylmorpholine (0.4 M), O-(2-azidoethyl)-O′-(*N*-diglycolyl-2-aminoethyl)heptaethyleneglycol ($(PEG)_7$ linker), Rink amide resin, Fmoc-protected amino acids including Fmoc-L-Lys(Boc)-OH, Fmoc-Gly-OH, Fmoc-L-Arg(Pbf)-OH, Fmoc-Gln(Trt)-OH, Fmoc-Cys(tButhio)-OH, Fmoc-L-Pro-OH); GE Healthcare*:* Cy3 monoreactive dye pack, Sephadex G-25 size exclusion column; Calbiochem: tris(2-carboxyethyl)phosphine hydrochloride (TCEP-HCl), cyclo-Arg-Gly-Asp-D-Phe-Val (cyclo-RGDfV); Invitrogen: RPMI medium 1640, Dulbecco's phosphate buffered saline (DPBS), anti-CD51 mouse antibody; Pierce: Ellman's reagent. For biological assays, all solutions were prepared using deionized water purified by Mar Cor Premium grade Mixed Bed Service Deionization. The standard buffer is defined herein as 50 mM Tris, 5 mM $CaCl_2$, 300 mM NaCl, pH 7.2.

General Methods. All air- and moisture-sensitive reactions were performed under dinitrogen with glassware oven-dried and then flamed under partial vacuum. Peptides were generated using a Protein Technologies PS3 Peptide Synthesizer. HPLC analysis was performed on an Agilent 1100 system equipped with a quaternary pump and diode array detector using a Zorbax Rx-C8 semipreparative (9.4 × 250 mm, 5 μm) or analytical column (4.6 × 150 mm, 5 μm). The gradient eluent was composed of two solvents: 0.1% aqueous TFA (solvent A) and a 0.1% solution of TFA in CH_3CN (solvent B). Mass identification of all peptide-containing compounds was performed by the Wistar Institute Proteomics Facility using an Applied Biosystems Voyager 6030 MALDI-TOF mass spectrometer. UV−visible spectra for peptides and peptide-cryptophane-A conjugates were measured using an Agilent 89090A spectrophotometer. Fluorescence spectra were collected for Cy3-labeled peptides dissolved in standard buffer (λ_{ex} = 552 nm) using a Varian Cary Eclipse fluorescence spectrophotometer in small volume, 1-cm path length quartz cuvettes at rt (1 nm steps, 5 nm excitation and emission slits). The 96 well fluorescence measurements were made using a Labsystems Fluoroskan II microplate reader.

Peptide Synthesis and Purification. Peptides **1**−**3** (Scheme 1) were prepared by solid-phase synthesis using standard Fmoc amino acid protection chemistry on Rink Amide resin (0.1 mmol scale). Couplings of Fmoc-protected amino acids to the resin were carried out with HBTU and *N*-methylmorpholine to generate the activated ester. The resin was swelled in DMF (10 min) prior to synthesis. Amino acids were then added sequentially until 3-azidoproponic acid was attached at the N-terminus as the final step. All residues were coupled onto resin by the following procedure: removal of Fmoc group (20% piperidine solution in DMF, 2 × 5 min), wash (DMF, 6 × 30 s), activation (amino acid/HBTU/*N*-methylmorpholine, 1 × 30 s) coupling (amino acid/HBTU/*N*-methylmorpholine, 1 × 20 min), rinse (DMF, 3 × 30 s). Cleavage from the resin was accomplished with a mixture of TFA, TIS, and water (90/5/5) at rt for 3 h. The cleavage cocktail removed side chain protecting groups from all amino acids except for cysteine, which was protected by *t*-butylthiol. Semipreparative HPLC purification of all Cys-protected peptides was accomplished with a gradient: time 0, A/B = 100/0; 0−25 min, linear increase to A/B = 75/25; 25−27 min, linear change to A/B = 20/80; 27−37 min, A/B = 20/80. Selective cysteine deprotection was later performed by treating with TCEP (1 equiv) for 30 min, and running the reaction mixture through a NAP-10 gel filtration to remove TCEP.

Scheme 1. Synthesis of Peptides 1−3 and Peptide−Cryptophane Conjugates I−III[a]

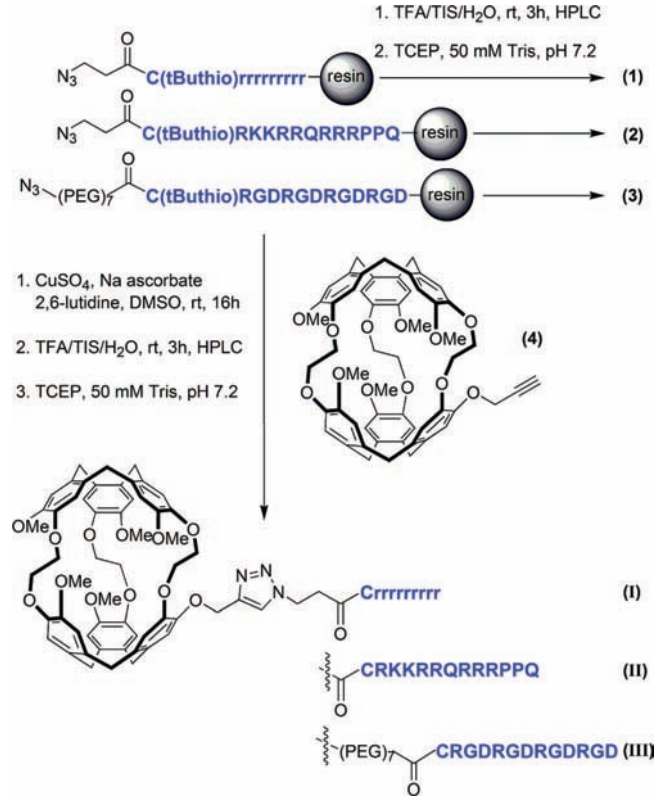

[a] Azidopeptide on solid support was reacted with monopropargyl-cryptophane-A via a Cu(I)-mediated [3 + 2] cycloaddition reaction. $(PEG)_7$ = -$(CH_2)_2$-O-$(CH_2CH_2O)_7$-$CH_2CH_2NHCOCH_2OCH_2$.

The peptide sequences prepared were as follows: N_3−CH_2CH_2−CONH−Crrrrrrrrr (D-Arg_9, **1**), N_3−CH_2CH_2−CONH−CGRKKRRQRRRPPQ (TAT, **2**), and N_3−$CH_2CH_2O(PEG)_7$−CONH−CRGDRGDRGDRGD (RGD_4, **3**). MALDI MS calculated for D-Arg_9 peptide, $C_{60}H_{119}N_{40}O_{12}S_1$ ($M + H^+$) 1623.97; found 1624.09. MALDI MS calculated for TAT peptide, $C_{76}H_{139}N_{39}O_{18}S_1$ ($M + H^+$) 1918.09; found 1919.15. MALDI MS calculated for RGD_4 peptide $C_{73}H_{128}N_{29}O_{33}S_1$ ($M + H^+$) 1970.90; found 1971.07. Pure peptides **1**−**3** were studied as-is, or subsequently conjugated with Cy3.

Synthesis of Peptide−Cryptophane Conjugates, I−III. [3 + 2] Cycloaddition reactions between azide-terminated peptides (still attached to solid support) and monopropargylated cryptophane-A **4** were performed to generate the peptide−cryptophane-A conjugates (Scheme 1) following established protocols

(*10*). Briefly, an aqueous solution of copper (II) sulfate (0.006 mmol, 0.5 equiv) was added to the resin containing azidopeptide (20 mg, maximum 0.0124 mmol azidopeptide, 1 equiv) followed by 2,6-lutidine (2.78 mL, 0.024 mmol, 2 equiv), sodium ascorbate (0.018 mmol, 1.5 equiv), and **4** (21 mg, 0.024, 2 equiv). Monopropargylated cryptophane-A was synthesized as previously described (*10*). The suspension was degassed with N_2 and stirred at rt for 16 h. The resin was then transferred to a fritted reaction vessel and washed sequentially with CH_2Cl_2, MeOH, water, and 1:1 MeOH/CH_2Cl_2 before drying under vacuum.

Cleavage from the resin was accomplished with a mixture of TFA, TIS, and water (90/5/5) at rt for 3 h. The Cys-protected peptide−cryptophane conjugates were precipitated and washed with anhydrous Et_2O before drying under vacuum. Analytical HPLC was performed using a gradient: time 0, A/B = 75/25; 0−25 min, linear increase to A/B = 50/50; time 25−27 min, linear change to A/B = 20/80; 27−37 min, A/B = 20/80. HPLC traces and retention times are provided in the Supporting Information. The cysteine was subsequently deprotected with TCEP in order to generate conjugates **I**−**III** (Scheme 1). MALDI MS calculated for $C_{116}H_{173}N_{40}O_{24}S_1$ (D-Arg_9-cryptophane, **I**) ($M + H^+$) 2542.33; found 2542.08. MALDI MS calculated for $C_{132}H_{193}N_{39}O_{30}S_1$ (TAT-cryptophane, **II**) ($M + H^+$) 2836.45; found 2836.96. MALDI MS calculated for $C_{129}H_{182}N_{29}O_{45}S_1$ ($(RGD)_4$-cryptophane, **III**) ($M + H^+$) 2889.26; found 2889.07. An extinction coefficient for **I**−**III**, 9300 M^{-1} cm^{-1} at 280 nm in water, was determined from solutions containing a weighed sample, as described previously (*10*).

Cysteine Labeling with Cy3. The pure Cys-protected peptides and Cys-protected peptide−cryptophane-A conjugates were dissolved in Tris buffer (50 mM, pH 7.2) at a concentration of 60 μM. Cysteine labeling with the Cy3-maleimide construct was performed according to the manufacturer's protocol. As described previously, cysteine was deprotected with TCEP, which was then removed by NAP-10 column. Cy3 dye was added dropwise and reacted for 3 h. The reaction was quenched by addition of glutathione (1 equiv). The reaction mixture was run through a NAP-10 gel filtration column before analytical HPLC purification.

For Cy3-labeled **I**−**III**, HPLC elution was achieved with the following gradient: time 0, A/B = 75/25; 0−25 min, linear increase to A/B = 50/50; 25−27 min, linear change to A/B = 20/80; 27−37 min, A/B = 20/80. MALDI MS calculated for $C_{153}H_{215}N_{44}O_{33}S_3$ (Cy3-**I**) ($M + H^+$) 3304.57; found 3304.82. MALDI MS calculated for $C_{170}H_{235}N_{43}O_{39}S_3$ (Cy3-**II**) ($M + H^+$) 3586.69; found 3587.84. MALDI MS calculated for $C_{167}H_{224}N_{33}O_{54}S_3$ (Cy3-**III**) ($M + H^+$) 3639.50; found 3640.07. Extinction coefficients used to determine solution concentrations of Cy3-labeled **I**−**III** were ε_{280} = 12 300 M^{-1} cm^{-1} and ε_{552} = 150 000 M^{-1} cm^{-1} in water.

For Cy3-labeled **1**−**3**, HPLC elution was achieved with the following gradient: time 0, A/B = 100/0; 0−25 min, linear increase to A/B = 75/25; 25−27 min, linear change to A/B = 20/80; 27−37 min, A/B = 20/80. HPLC traces and retention times are provided in the Supporting Information. MALDI MS calculated for $C_{97}H_{161}N_{44}O_{21}S_3$ (Cy3-**1**) ($M + H^+ - H_2O$) 2356.30; found 2357.68. MALDI MS calculated for $C_{113}H_{181}N_{43}O_{27}S_3$ (Cy3-**2**) ($M + H^+ - 2H_2O$) 2632.29; found 2632.12. MALDI MS calculated for $C_{110}H_{170}N_{33}O_{42}S_3$ (Cy3-**3**) ($M + H^+ - N_2$) 2697.12; found 2696.37. The concentration of Cy3-labeled peptides **1**−**3** in solution was determined using ε_{552} = 150 000 M^{-1} cm^{-1}, and accounting for the fraction labeled. Cy3 labeling efficiency was determined using Ellman's reagent according to manufacturer's protocol.

Cell Culture. HFL-1 human diploid lung fibroblasts and AsPC-1 and CAPAN-2 human pancreatic carcinoma cell lines were obtained from the Cell Culture Core of the Center for Molecular Studies in Liver and Digestive Diseases (University of Pennsylvania Medical School, Philadelphia, PA). NCI-H1975 cells were from Dr. Intae Lee and red blood cells were from Dr. Don Siegel (University of Pennsylvania Medical School, Philadelphia, PA). All cells were grown in 25 cm^2 tissue culture flasks in RPMI-1640 with 25 mM HEPES supplemented with 2 mM L-glutamine, 15% fetal calf serum, 100 units of penicillin, and 100 units of streptomycin. Cells were subcultured weekly, or more frequently, as needed.

Cytotoxicity Assays. In 96 well plates, 25 000 cells were plated per well and allowed to grow overnight. Nonfluorescently labeled peptide−cryptophane conjugates **I**−**III** were added from a stock solution in DPBS to wells in triplicate at final concentrations of 2, 10, 25, 50, 80, and 100 μM and incubated for 24 h in the dark. The medium was removed and the cells were washed thrice with DPBS before being treated with 20 μL of MTT for 3 h. The medium was removed once more and the resulting crystals were solubilized in DMSO. Absorbance at 540 nm was recorded in each well using the plate reader. Absorbance readings were subtracted from the value of wells containing untreated cells, and the reduction in cell growth was calculated as a percentage of control absorbance in the absence of any treatment. Data show the mean of at least three independent experiments ± SD.

Cell Uptake Studies. Cells were grown to confluence on LabTek 8-well microscope slides with glass coverslip bottoms. For uptake studies, cells were incubated with 2 μM solutions of Cy3-labeled **I**, **II**, or **III** for 15 min. For blocking studies, cells were pretreated for 45 min with an 100 μM solution of a cyclic RGDfV peptide containing D-phenylalanine that was previously identified to bind tightly to the integrin $\alpha_v\beta_3$ receptor (*37, 38*). In the antibody blocking studies, cells were pretreated for 30 min with 10 μM blocking anti-α antibody. For visualizing the results of both the uptake and blocking studies, the medium was removed and the cells were washed three times with DPBS. Cells were visualized using an Olympus FV1000 confocal laser scanning microscope with 543 nm (HeNe) laser excitation and Cy3 emission filter under 40× magnification (Olympus UApo/340 40×, 1.15 W).

Time-Dependent Cellular Uptake. Cells were plated at 10 000 cells per well in a CoStar 96-well plate and allowed to grow overnight. Cy3-labeled **I**, **II**, or **III** was added to the wells at a concentration of 10 μM and incubated for 0, 1, 2, 4, 8, and 24 h at 37 °C. At the end of the incubation time, the loading medium was removed, and the cells were washed thrice with DPBS. The cells were solubilized by the addition of 100 μL of 0.25% Triton X-100 in DPBS. To determine conjugate concentration, samples were excited at 544 nm and fluorescence at 590 nm was recorded using a plate reader. The cell numbers were then quantified using the CyQuant reagent (Molecular Probes) according to manufacturer protocol.

RESULTS AND DISCUSSION

Synthesis and Characterization of Peptide−Cryptophane Conjugates. Monopropargylated cryptophane-A **4** was synthesized in 12 nonlinear steps and 3% overall yield (*10*). The yields of purified peptides (**1**−**3**) were 80−85% for all peptide coupling and cleavage steps, based on the maximum possible yield from starting resin. Azidopeptides, while still attached to the solid support, were reacted with **4** by a copper (I)-catalyzed [3 + 2] cycloaddition in 80−89% yield (*39*−*41*). Peptide−cryptophane conjugates (with Cys still protected) were cleaved from the resin, and purified by reverse-phase HPLC (Supporting Information Figures S1−S3). The cysteine was deprotected before use with TCEP to yield **I**−**III**. The deprotected cysteines showed no evidence of disulfide formation leading to cryptophane dimer-

ization on the time scale of hours when purified by HPLC. The free thiols, however, may interact with endogenous sulfhydryls when introduced into cells.

The $(RGD)_4$ linear peptide was chosen to target ABIR, because it was readily synthesized and attached to cryptophane using established protocols (*10*). Furthermore, polypeptides of similar length were found to confer excellent cryptophane water solubility. In constrast, the cryptophane−$(RGD)_4$ conjugate presented solubility problems, most likely due to charge interactions between the repeating sequence of arginine and glutamic acid residues. A prior version of conjugate **III** was synthesized without the PEG_7 linker separating the cryptophane from the RGD tetramer. This prototype exhibited poor water solubility, which prevented its usefulness for *in vitro* cell studies. Addition of the PEG_7 linker increased water solubility, allowing concentrations up to 120 μM when DMSO (10% final concentration) was added to the buffer solutions.

The cysteine sulfhydryl group on the peptides and peptide−cryptophane conjugates was deprotected and reacted with maleimide-functionalized Cy3 to generate Cy3-labeled **1**−**3** and **I**−**III**. Mixtures of fluorescently labeled and unlabeled conjugates were obtained after reverse-phase HPLC purification (Supporting Information Figures S4−S6). For the cryptophane−peptide conjugates **I**−**III**, Cy3 labeling efficiencies of 50−69% were determined from the ratio of dye absorbance at 552 nm to the cryptophane absorbance at 280 nm. Cy3 labeling efficiencies were initially lower than expected. To improve yields, the reducing agent TCEP was removed from the solution by gel filtration chromatography before the addition of the Cy3 monoreactive dye pack. Removal of TCEP improved Cy3 conjugation yields by about 10%.

Ellman's reagent was used to determine the Cy3 labeling efficiencies for **1**−**3**, and confirmed the previous measurements determined for Cy3-labeled **I**−**III**. The 5,5′-dithiobis(2-nitrobenzoic acid) reacted with any free (previously unreacted) sulfhydryl groups to yield 2-nitro-5-thiobenzoic acid, which was quantified by measuring absorbance at 412 nm (ε_{412} = 14 150 M^{-1} cm^{-1}) (*42*). This assay found slightly higher Cy3 labeling efficiencies for **1**−**3** (60−72%) than for **I**−**III** (47−70%), which was in good agreement with the previously described ratiometric (A_{552}/A_{280}) UV−vis measurements for Cy3-labeled **I**−**III**.

Cell Toxcity Assays. The cytotoxicity of the cryptophane conjugates was evaluated in AsPC-1, CAPAN-2, and HFL-1 cell lines by exposing cells to increasing concentrations of **I**, **II**, or **III** as shown in Figure 1. The $(RGD)_4$−cryptophane conjugate **III** showed 25−30% proliferation inhibition of the various cell lines at the highest concentration studied (100 μM). Slightly higher amounts of cytotoxicity were also found for the D-Arg_9- and TAT-cryptophane conjugates, **I** and **II**, in both the AsPC-1 and CAPAN-2 cell lines. In general, the three conjugates appeared to be more toxic to HFL-1 fibroblast cells than either AsPC-1 or CAPAN-2 cancer cells. The toxicity profile is comparable to that of the similarly sized fullerene C_{60} molecule, which decreased viability of HEK cells by 10−50% over a similar range of concentrations (*43*). For compound **III**, 50% inhibition of proliferation was not reached in any of the cell lines at the concentrations tested. Compounds **I** and **II** showed 50% inhibition at 60 and 75 μM in HFL-1 fibroblasts. **I** also showed IC_{50} of 75 μM in AsPC-1 cells and more than 100 μM in CAPAN-2. **II** had IC_{50} values of 100 μM in AsPC-1 cells, while 50% inhibition was not reached in CAPAN-2 cells at 100 μM. Increased toxicity for compounds **I** and **II** as compared to **III** is thought to be a result of cryptophane delivery to the cell nucleus by TAT or D-Arg_9 nuclear localization peptides. For compound **III**, 10% DMSO was required to work at the higher concentrations. Cell viability assays for this compound were performed using 10% DMSO at all sample concentrations, and these viability data were normalized to cells treated with 10% DMSO without cryptophane. In absolute terms, 10% DMSO alone reduced cell counts by 2000−3500, corresponding to a 8−14% decrease compared to untreated cells.

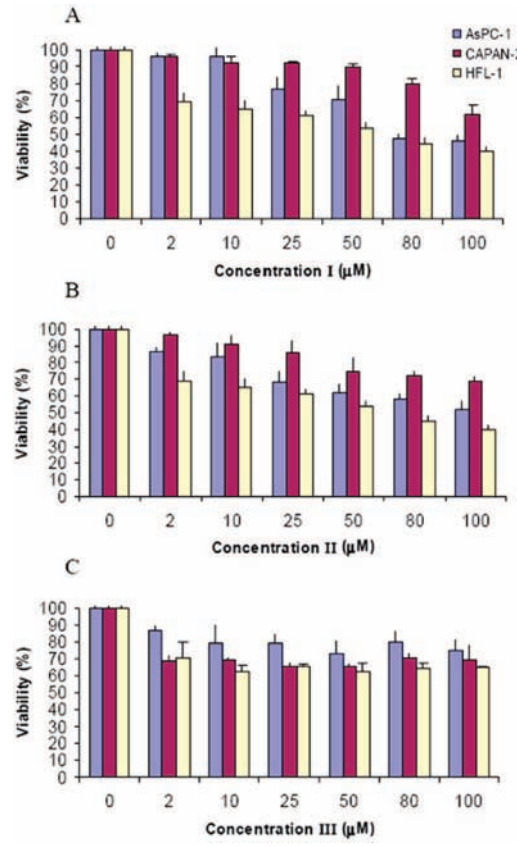

Figure 1. Cytotoxicity assay for conjugates **I** (A), **II** (B), and **III** (C) in AsPC-1 (blue), CAPAN-2 (maroon), and HFL-1 (off-white) cells. %Viability was determined via MTT assay after 24 h incubation with increasing concentrations of each conjugate, as compared to untreated cells.

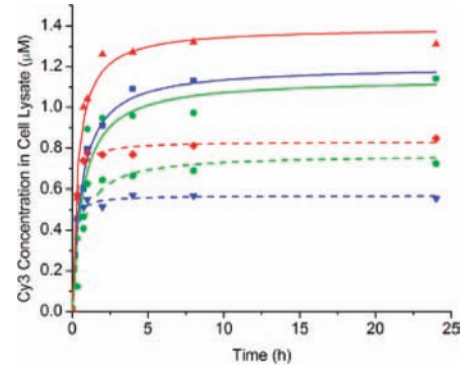

Figure 2. Uptake of peptides (solid lines) was measured for **1** (blue squares), **2** (red triangles), and **3** (green circles) and peptide−cryptophane conjugates (dashed lines) for **I** (blue inverted triangles), **II** (red diamonds), and **III** (green pentagons) by CAPAN-2 cells over 24 h.

Cell Uptake Studies. The time-dependent uptake of Cy3-labeled peptide−cryptophane conjugates **I**−**III** and peptides **1**−**3** at 10 μM was investigated in CAPAN-2 cells (Figure 2). All conjugates showed similar uptake kinetics with a rapid accumulation of compounds within the first hour. Maximum uptake was achieved by 4 h, and a plateau was observed for the remaining 20 h. In order to quantify cell uptake for each time point, 10 000 cells containing each fluorescent compound were placed in 100 μL lysis buffer. The concentrations of

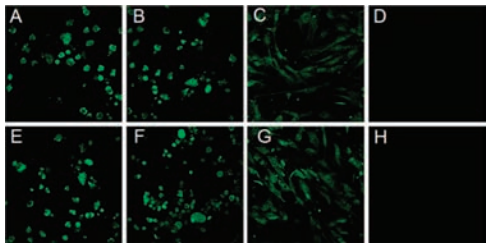

Figure 3. Cellular uptake of 2 μM Cy3-labeled **I** (top row) and **II** (bottom row) in AsPC-1 (A,E), CAPAN-2 (B,F), and HFL-1 cells (C,G) after 1 h incubation at 37 °C. Uptake of **I** and **II** was inhibited after 1 h incubation at 4 °C (D,H).

fluorescent peptides and conjugates were quantified by fluorometry after generating a fluorescence standard curve for Cy3 in the same lysis buffer, and correcting for the Cy3-labeling efficiency of each compound. Fluorescent peptides **1**−**3** were measured in the cell lysate solution at concentrations of 1.0−1.4 μM, whereas fluorescent cryptophane conjugates **I**−**III** were determined to be 500−800 nM. Within the error of the measurements, we cannot draw distinctions regarding the uptake efficiency of the three peptide motifs.

A procedure was developed to estimate the intracellular concentration of each compound from the lysate data. When detached from the surface, the CAPAN-2 cells were spherical and measured with a microscope to be ~35 μm in diameter. The average cell volume was calculated, and the fraction of the 100 μL cell lysate originally occupied by the cells was determined to be 0.0050. Thus, the measured cell lysate concentrations of 500−800 nM gave an approximate range of intracellular concentrations of 100−160 μM for **I**−**III** after the 24-h incubation period. This corresponds to 10−16-fold enrichment of **I**−**III** inside the cell (originally present in the media at 10 μM). Support for this finding comes from ratiometric measurements (Supporting Information Figures S7−S9) showing a range of fluorescence intensities that is 4−20 times greater inside the CAPAN-2 cells than the surrounding cell media. Importantly, these intracellular concentrations are within the limits of detection for laser-polarized ^{129}Xe NMR experiments (*43*).

Confocal laser scanning microscopy (CLSM) confirmed cellular delivery of cryptophane with the D-Arg$_9$− and TAT−cryptophane conjugates, **I** and **II** (Figure 3). After 1-h exposure to Cy3-labeled **I** and **II**, fluorescence was seen evenly distributed throughout most AsPC-1, CAPAN-2, and HFL-1 cells. Cy3-labeled **I** and **II** translocated into the cell nucleus, as was expected for conjugates of these peptides (*45*−*47*). After 1-h incubation at 4 °C with Cy3-labeled **I** and **II**, no fluorescence was observed (Figure 3D,H) by CLSM, which confirmed that uptake occurred via an energy-dependent endocytic pathway.

Cell uptake of Cy3-labeled **III** was also confirmed by CLSM. After 30-min incubation and rigorous cell washing, fluorescence was observed in NCI-H1975, CAPAN-2, and AsPC-1 cells (Figure 4A−C). Translocation of Cy3-labeled **III** was not observed in red blood cells, as expected, as these cells do not express $\alpha_v\beta_3$ integrin receptor (Figure 4D). In contrast to Cy3-labeled **I** and **II**, Cy3-labeled **III** was not observed to cross the nuclear membrane. In general, nuclear internalization of imaging agents is undesirable because of potential mutagenic effects on healthy cells. To determine whether uptake of **III** was mediated by ABIR, cells were preincubated with 100 μM cyclic RGDfV peptide, which is known to bind $\alpha_v\beta_3$ integrin receptor with high affinity (*48*). Figure 4D shows that the cyclic RGDfV peptide inhibited uptake of (RGD)$_4$−cryptophane as indicated by reduction in fluorescence. Internalization was also inhibited by coincubation with 10 μM anti-α_v mouse antibody (Figure 4F). Cyclic RGDfV and anti-α_v mouse antibody blocking groups also inhibited uptake in HFL-1 and CAPAN-2 cells (data not shown). These blocking data suggest that the (RGD)$_4$-labeled conjugate was specifically recognized by the $\alpha_v\beta_3$ integrin receptor and the α_v subunit is critical for cellular uptake of **III**.

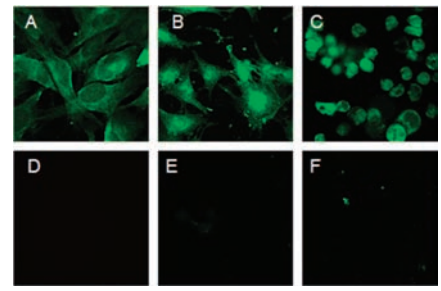

Figure 4. Uptake of 2 μM Cy3-labeled **III** targeting $\alpha_v\beta_3$ integrin in NCI-H1975 (A), HFL-1 (B), and CAPAN-2 (C) cells after 30 min incubation at 37 °C. Red blood cells (D) did not uptake this compound. Targeting in NCI-H1975 was successfully blocked with 100 μM cyclic RGDfV peptide (E) and 10 μM anti-α_v antibody (F).

Attempts at performing hyperpolarized ^{129}Xe NMR spectroscopy were made with compound **III** in isolated cells in culture. However, these experiments were unsuccessful due to the limited solubility of **III** and inability to achieve sufficient cell density within the detection volume. The requirement for incorporating DMSO in the buffers used to solubilize **III** further complicated the NMR data collection, as ^{129}Xe NMR chemical shift is very sensitive to solvent composition. The requirement for DMSO also made it difficult to achieve the high density of viable cells required for these NMR experiments.

Conjugates **I**−**III** have molecular weights of 2500–3500 Da and their transport and clearance properties in vivo are not yet known. Fullerenes, which are similar in size and chemical composition, have been found to localize to a variety of tissues in rats with large accumulations in the liver, spleen, and kidneys, suggesting that these compounds are cleared rapidly (*49*, *50*). PEG coatings may be used to improve bioavailability if the biodistribution of cryptophane is found to be similar to that of fullerene (*51*).

CONCLUSION

Cryptophane-A was conjugated to (D-Arg)$_9$, TAT, and (RGD)$_4$ peptides using a modified [3 + 2] cycloaddition reaction. This reaction provides a facile route for synthesizing chemically stable peptide−cryptophane conjugates (*40*, *52*). All compounds were examined for cell toxicity, and fluorescently labeled with Cy3 to facilitate cellular imaging studies by CLSM.

Conjugates **I** and **II** were delivered nonspecifically to all cell types tested and showed little cytotoxicity in concentration ranges that are relevant for solution-based hyperpolarized ^{129}Xe NMR experiments. Conjugate **III**, which contained an (RGD)$_4$ $\alpha_v\beta_3$ integrin receptor binding motif, was selectively delivered to cells expressing this receptor and excluded from human red blood cells. **III** was similarly nontoxic as **I** and **II**. Importantly for laser-polarized ^{129}Xe NMR studies, cryptophane concentrations in excess of 100 μM were achieved in CAPAN-2 cells using the three peptides.

An important goal of these studies is to identify cell delivery motifs that can be attached to cryptophane and effectively discriminate between cancer and normal cells. The results of this initial study are very promising, and motivate the search for peptides and small molecules that promote the cellular delivery of even higher concentrations of cryptophanes, with reduced toxicity, in order to facilitate in vivo NMR studies. As examples, the transportan and penetratin CPP sequences were shown previously to deliver higher concentrations of attached cargo than TAT and (D-Arg)$_9$ peptides (*53*, *54*). Additional cell

targeting motifs will be explored for use with other cancer biomarkers. Finally, protocols must be developed to perform ^{129}Xe MRI experiments using xenon biosensors in tissue samples, where higher cellular density (and associated cryptophane per unit volume) will improve ^{129}Xe MR signals. This work demonstrates that, due to their limited cytotoxicity and ready delivery to cells expressing specific cell surface receptors, cryptophanes offer considerable promise for in vivo xenon biosensing experiments.

ACKNOWLEDGMENT

We thank Intae Lee for providing cells and helpful discussions; Jeffery Saven, Ronen Marmorstein, and Scott Diamond for access to instrumentation; the Cell Culture Core of the University of Pennsylvania Center for Molecular Studies in Liver and Digestive Diseases for cells; Tobias Baumgart and Eric Meggers for access to cell culture facilities. This work was supported by the DOD (W81XWH-04-1-0657), NIH (1R21CA110104, 1R33CA110104, 1S10RR021113-01), and Camille and Henry Dreyfus Foundation.

Supporting Information Available: HPLC analysis of peptide−cryptophane conjugates **I**−**III** and Cy3-labeled peptides **1**−**3**, and CLSM images of Cy3-labeled peptide **3** in CAPAN-2 cells. This material is available free of charge via the Internet at http://pubs.acs.org.

LITERATURE CITED

(1) Degani, H., Gusis, V., Weinstein, D., Feilds, S., and Strano, S. (1997) Mapping pathophysiological features of breast tumors by MRI at high spatial resolution. *Nat. Med. 3*, 780–782.

(2) Foster-Gareau, P., Heyn, C., Alejski, A., and Rutt, B. K. (2003) Imaging single mammalian cells with a 1.5 T clinical MRI scanner. *Magn. Reson. Med. 49*, 968–971.

(3) Golman, K., Zandt, R. I., Lerche, M., Pehrson, R., and Ardenkjaer-Larsen, J. H. (2006) Metabolic imaging by hyperpolarized ^{13}C magnetic resonance imaging for in vivo tumor diagnosis. *Cancer Res. 66*, 10855–10860.

(4) Hopkins, S. R., Levin, D. L., Emami, K., Kadlecek, S., Yu, J., Ishii, M., and Rizi, R. R. (2007) Advances in magnetic resonance imaging of lung physiology. *J. Appl. Physiol. 102*, 1244–1254.

(5) Mugler, J. P., Driehuys, B., Brookeman, J. R., Cates, G. D., Berr, S. S., Bryant, R. G., Daniel, T. M., deLange, E. E., Downs, J. H., Erickson, C. J., Happer, W., Hinton, D. P., Kassel, N. F., Maier, T., Phillips, C. D., Saam, B. T., Sauer, K. L., and Wagshul, M. E. (1997) MR imaging and spectroscopy using hyperpolarized Xe-129 gas: Preliminary human results. *Magn. Reson. Med. 37*, 809–815.

(6) Spence, M. M., Rubin, S. M., Dimitrov, I. E., Ruiz, E. J., Wemmer, D. E., Pines, A., Yao, S. Q., Tian, F., and Schultz, P. G. (2001) Functionalized xenon as a biosensor. *Proc. Natl. Acad. Sci. U.S.A. 98*, 10654–10657.

(7) Collet, A. (1996) Cryptophanes. *Comp. Supramol. Chem. 2*, 325–365.

(8) Hill, P. A., Wei, Q., Eckenhoff, R. G., and Dmochowski, I. J. (2007) Thermodynamics of xenon binding to cryptophane in water and human plasma. *J. Am. Chem. Soc. 129*, 9262–9263.

(9) Spence, M. M., Ruiz, E. J., Rubin, S. M., Lowery, T. J., Winssinger, N., Schultz, P. G., Wemmer, D. E., and Pines, A. (2004) Development of a functionalized xenon biosensor. *J. Am. Chem. Soc. 126*, 15287–15294.

(10) Wei, Q., Seward, G. K., Hill, P. A., Patton, B., Dimitrov, I. E., Kuzma, N. N., and Dmochowski, I. J. (2006) Designing Xe-129 NMR biosensors for matrix metalloproteinase detection. *J. Am. Chem. Soc. 128*, 13274–13283.

(11) Spence, M. M., Rubin, S. M., Dimitrov, I. E., Ruiz, E. J., Wemmer, D. E., Pines, A., Yao, S. Q., Tian, F., and Schultz, P. G. (2001) Functionalized xenon as a biosensor. *Proc. Natl. Acad. Sci. U.S.A. 98*, 10654–10657.

(12) Lowery, T. J., Garcia, S., Chavez, L., Ruiz, E. J., Wu, T., Brotin, T., Dutasta, J. P., King, D. S., Schultz, P. G., Pines, A., and Wemmer, D. E. (2006) Optimization of xenon biosensors for detection of protein interactions. *ChemBioChem 7*, 65–73.

(13) Ruiz, E. J., Sears, D. N., Pines, A., and Jameson, C. J. (2006) Diastereomeric Xe chemical shifts in tethered cryptophane cages. *J. Am. Chem. Soc. 128*, 16980–16988.

(14) Hilty, C., Lowery, T. J., Wemmer, D. E., and Pines, A. (2006) Spectrally resolved magnetic resonance imaging of a xenon biosensor. *Angew. Chem., Int. Ed. 45*, 70–73.

(15) Huber, G., Brotin, T., Dubois, L., Desvaux, H., Dutasta, J. P., and Berthault, P. (2006) Water soluble cryptophanes showing unprecedented affinity for xenon: Candidates as NMR-based biosensors. *J. Am. Chem. Soc. 128*, 6239–6246.

(16) Gupta, B., Levchenko, T. S., and Torchilin, V. P. (2005) Intracellular delivery of large molecules and small particles by cell-penetrating proteins and peptides. *Adv. Drug Delivery Rev. 57*, 637–651.

(17) Wright, L. R., Rothbard, J. B., and Wender, P. A. (2003) Guanidinium rich peptide transporters and drug delivery. *Curr. Protein Pept. Sci. 4*, 105–124.

(18) Goun, E. A., Pillow, T. H., Jones, L. R., Rothbard, J. B., and Wender, P. A. (2006) Molecular transporters: Synthesis of oligoguanidinium transporters and their application to drug delivery and real-time imaging. *ChemBioChem 7*, 1497–1515.

(19) Goun, E. A., Shinde, R., Dehnert, K. W., Adams-Bond, A., Wender, P. A., Contag, C. H., and Franc, B. L. (2006) Intracellular cargo delivery by an octaarginine transporter adapted to target prostate cancer cells through cell surface protease activation. *Bioconjugate Chem. 17*, 787–796.

(20) Sibrian-Vazquez, M., Jensen, T. J., Hammer, R. P., and Vicente, M. G. H. (2006) Peptide-mediated cell transport of water soluble porphyrin conjugates. *J. Med. Chem. 49*, 1364–1372.

(21) Yang, J. H., Wang, K., Driver, J., Yang, J. H., and Barron, A. R. (2007) The use of fullerene substituted phenylalanine amino acid as a passport for peptides through cell membranes. *Org. Biomol. Chem. 5*, 260–266.

(22) Belvisi, L., Bernardi, A., Colombo, M., Manzoni, L., Potenza, D., Scolastico, C., Giannini, G., Marcellini, M., Riccioni, T., Castorina, M., LoGiudice, P., and Pisano, C. (2006) Targeting integrins: Insights into structure and activity of cyclic RGD pentapeptide mimics containing azabicycloalkane amino acids. *Bioorg. Med. Chem. 14*, 169–180.

(23) Harris, T. D., Kalogeropoulos, S., Nguyen, T., Liu, S., Bartis, J., Ellars, C., Edwards, S., Onthank, D., Silva, P., Yalamanchili, P., Robinson, S., Lazewatsky, J., Barrett, J., and Bozarth, J. (2003) Design, synthesis, and evaluation of radiolabeled integrin alpha(v)beta(3) receptor antagonists for tumor imaging and radiotherapy. *Cancer Biother. Radiopharm. 18*, 627–641.

(24) Temming, K., Schiffelers, R. M., Molema, G., and Kok, R. J. (2005) RGD-based strategies for selective delivery of therapeutics and imaging agents to the tumour vasculature. *Drug Resist. Updates 8*, 381–402.

(25) Cescato, R., Schulz, S., Waser, B., Eltschinger, V., Rivier, J. E., Wester, H. J., Culler, M., Ginj, M., Liu, Q. S., Schonbrunn, A., and Reubi, J. C. (2006) Internalization of sst(2), sst(3), and sst(5) receptors: Effects of somatostatin agonists and antagonists. *J. Nucl. Med. 47*, 502–511.

(26) Ginj, M., Zhang, H. W., Waser, B., Cescato, R., Wild, D., Wang, X. J., Erchegyi, J., Rivier, J., Macke, H. R., and Reubi, J. C. (2006) Radiolabeled somatostatin receptor antagonists are preferable to agonists for in vivo peptide receptor targeting of tumors. *Proc. Natl. Acad. Sci. U.S.A. 103*, 16436–16441.

(27) Reubi, J. C., Eisenwiener, K. P., Rink, H., Waser, B., and Macke, H. R. (2002) A new peptidic somatostatin agonist with high affinity to all five somatostatin receptors. *Eur. J. Pharmacol. 456*, 45–49.

(28) Hilgenbrink, A. R., and Low, P. S. (2005) Folate receptor-mediated drug targeting: From therapeutics to diagnostics. *J. Pharm. Sci. 94*, 2135–2146.

(29) Byzova, T. V., Goldman, C. K., Pampori, N., Thomas, K. A., Bett, A., Shattil, S. J., and Plow, E. F. (2000) A mechanism for modulation of cellular responses to VEGF: Activation of the integrins. *Mol. Cell 6*, 851–860.

(30) Byzova, T. V., Kim, W., Midura, R. J., and Plow, E. F. (2000) Activation of integrin alpha(v)beta(3) regulates cell adhesion and migration to bone sialoprotein. *Exp. Cell Res. 254*, 299–308.

(31) Cairns, R. A., Khokha, R., and Hill, R. P. (2003) Molecular mechanisms of tumor invasion and metastasis: An integrated view. *Curr. Mol. Med. 3*, 659–671.

(32) Felding-Habermann, B. (2003) Integrin adhesion receptors in tumor metastasis. *Clin. Exp. Metastas. 20*, 203–213.

(33) Pierschbacher, M. D., Hayman, E. G., and Ruoslahti, E. (1985) The cell attachment determinant in fibronectin. *J. Cell. Biochem. 28*, 115–126.

(34) Pierschbacher, M. D., and Ruoslahti, E. (1984) Cell attachment activity of fibronectin can be duplicated by small synthetic fragments of the molecule. *Nature 309*, 30–33.

(35) Ruoslahti, E. (2003) The RGD story: a personal account. *Matrix Biol. 22*, 459–465.

(36) Ruoslahti, E., and Pierschbacher, M. D. (1986) Arg-Gly-Asp - a versatile cell recognition signal. *Cell 44*, 517–518.

(37) Ye, Y. P., Bloch, S., Xu, B. G., and Achilefu, S. (2006) Design, synthesis, and evaluation of near infrared fluorescent multimeric RGD peptides for targeting tumors. *J. Med. Chem. 49*, 2268–2275.

(38) Gottschalk, K. E., and Kessler, H. (2002) The structures of Integrins and integrin-ligand complexes: Implications for drug design and signal transduction. *Angew. Chem., Int. Ed. 41*, 3767–3774.

(39) Tornøe, C. W., Christensen, C., and Meldal, M. (2002) Peptidotriazoles on solid-phase: [1,2,3]-Triazoles by regiospecific copper(I)-catalyzed 1,3-dipolar cycloadditions of terminal alkynes to azides. *J. Org. Chem. 67*, 3057–3064.

(40) Punna, S., Kuzelka, J., Wang, Q., and Finn, M. G. (2005) Head-to-tail peptide cyclodimerization by copper-catalyzed azide-alkyne cycloaddition. *Angew. Chem., Int. Ed. 44*, 2215–2220.

(41) Rostovtsev, V. V., Green, L. G., Fokin, V. V., and Sharpless, K. B. (2002) A stepwise Huisgen cycloaddition process: Copper(I)-catalyzed regioselective "ligation" of azides and terminal alkynes. *Angew. Chem., Int. Ed. 41*, 2596–2599.

(42) Riddles, P. W., Blakeley, R. L., and Zerner, B. (1983) Reassessment of Ellman's reagent. *Methods Enzymol. 91*, 49–60.

(43) Rouse, J. G., Yang, J. Z., Barron, A. R., and Monteiro-Riviere, N. A. (2006) Fullerene-based amino acid nanoparticle interactions with human epidermal keratinocytes. *Toxicol. In Vitro 20*, 1313–1320.

(44) Lowery, T. J., Rubin, S. M., Ruiz, E. J., Spence, M. M., Winssinger, N., Schultz, P. G., Pines, A., and Wemmer, D. E. (2003) Applications of laser-polarized Xe-129 to biomolecular assays. *Magn. Reson. Imaging 21*, 1235–1239.

(45) Lindgren, M., Gallet, X., Soomets, U., Hallbrink, M., Brakenhielm, E., Pooga, M., Brasseur, R., and Langel, U. (2000) Translocation properties of novel cell penetrating transportan and penetratin analogues. *Bioconjugate Chem. 11*, 619–626.

(46) Lindgren, M., Hallbrink, M., Prochiantz, A., and Langel, U. (2000) Cell-penetrating peptides. *Trends Pharmacol. Sci. 21*, 99–103.

(47) Zorko, M., and Langel, U. (2005) Cell-penetrating peptides: mechanism and kinetics of cargo delivery. *Adv. Drug Delivery Rev. 57*, 529–545.

(48) Haubner, R., Wester, H. J., Burkhart, F., Senekowitsch-Schmidtke, R., Weber, W., Goodman, S. L., Kessler, H., and Schwaiger, M. (2001) Glycosylated RGD-containing peptides, tracer for tumor targeting and angiogenesis imaging with improved biokinetics. *J. Nucl. Med. 42*, 326–336.

(49) Bolskar, R. D., Benedetto, A. F., Husebo, L. O., Price, R. E., Jackson, E. F., Wallace, S., Wilson, L. J., and Alford, J. M. (2003) First soluble M@C-60 derivatives provide enhanced access to metallofullerenes and permit in vivo evaluation of Gd@C-60[C(COOH)(2)](10) as a MRI contrast agent. *J. Am. Chem. Soc. 125*, 5471–5478.

(50) Xu, J. Y., Li, Q. N., Li, J. G., Ran, T. C., Wu, S. W., Song, W. M., Chen, S. L., and Li, W. X. (2007) Biodistribution of Tc-99m-C-60(OH)(x) in Sprague-Dawley rats after intratracheal instillation. *Carbon 45*, 1865–1870.

(51) Tabata, Y., and Ikada, Y. (1999) Biological functions of fullerene. *Pure Appl. Chem. 71*, 2047–2053.

(52) Rostovtsev, V. V., Green, L. G., Fokin, V. V., and Sharpless, K. B. (2002) A stepwise Huisgen cycloaddition process: Copper(I)-catalyzed regioselective "ligation" of azides and terminal alkynes. *Angew. Chem., Int. Ed. 41*, 2596–2599.

(53) Bendifallah, N., Rasmussen, F. W., Zachar, V., Ebbesen, P., Nielsen, P. E., and Koppelhus, U. (2006) Evaluation of cell-penetrating peptides (CPPs) as vehicles for intracellular delivery of antisense peptide nucleic acid (PNA). *Bioconjugate Chem. 17*, 750–758.

(54) Myrberg, H., Lindgren, M., and Langel, U. (2007) Protein delivery by the cell-penetrating peptide YTA2. *Bioconjugate Chem. 18*, 170–174.

BC8002265

Supporting Information

Peptide-Mediated Cellular Uptake of Cryptophane

*Garry K. Seward, Qian Wei, Ivan J. Dmochowski**

Department of Chemistry, University of Pennsylvania, 231 South 34th St., Philadelphia, PA 19104-6323

Figures S1-S3

HPLC conditions and traces are included for purification of Cys-protected cryptophane-peptide conjugates, precursors to **I-III**.

Similar retention times were obtained for Cy3-labeled **I-III**.

Figures S4-S6

HPLC conditions and traces are included for purification of Cy3-labeled peptides **1-3**.

Similar retention times were obtained for the unlabeled peptides **1-3**.

Figures S7-S9

Confocal micrographs of CAPAN-2 cells incubated with Cy3-labeled **3**.

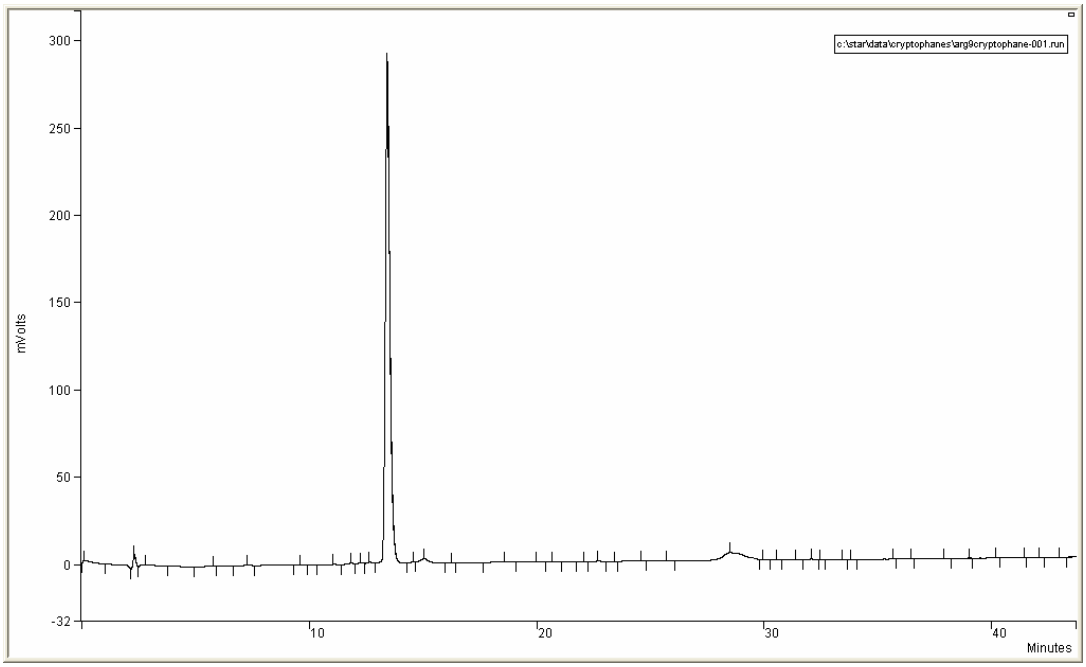

Figure S1. HPLC trace for Cys-protected cryptophane-peptide conjugate precursor to **I**. Column: Zorbax Rx-C8, 80 Å, 5 μm, 9.4 mm x 250 mm (Agilent); flow rate: 3 mL/min; injected volume: 1 mL; wavelength detection: 215 nm; gradient: 25 to 50% buffer B. Buffer A: H_2O, 0.1% TFA. Buffer B: acetonitrile, 0.1% TFA. Retention time: 13.41 min.

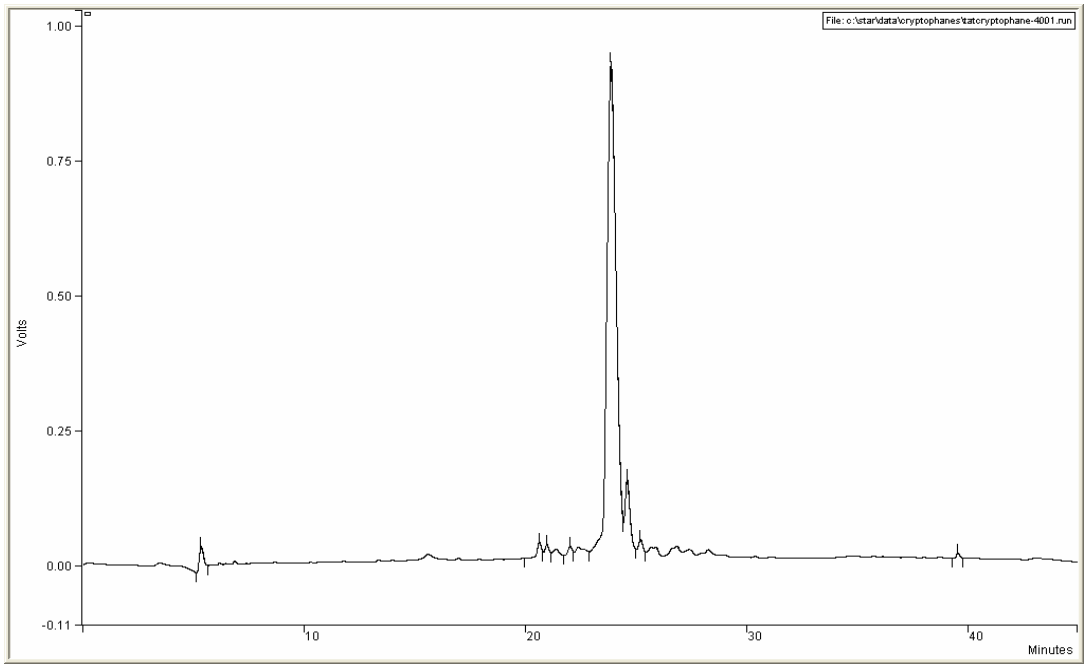

Figure S2. HPLC trace for Cys-protected cryptophane-peptide conjugate precursor to **II**. Column: Zorbax Rx-C8, 80 Å, 5 μm, 9.4 mm x 250 mm (Agilent); flow rate: 3 mL/min; injected volume: 1 mL; wavelength detection: 215 nm; gradient: 25 to 50% buffer B. Buffer A: H_2O, 0.1% TFA. Buffer B: acetonitrile, 0.1% TFA. Retention time: 23.86 min.

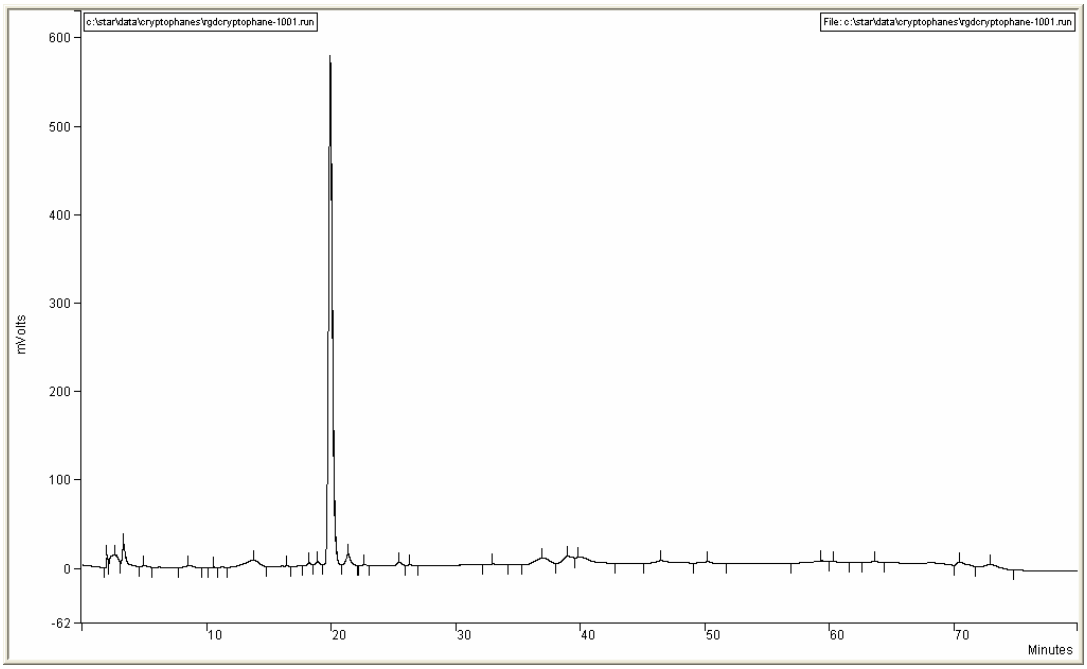

Figure S3. HPLC trace for Cys-protected cryptophane-peptide conjugate precursor to **III**. Column: Zorbax Rx-C8, 80 Å, 5 μm, 9.4 mm x 250 mm (Agilent); flow rate: 3 mL/min; injected volume: 1 mL; wavelength detection: 215 nm; gradient: 25 to 50% buffer B. Buffer A: H_2O, 0.1% TFA. Buffer B: acetonitrile, 0.1% TFA. Retention time: 19.01 min.

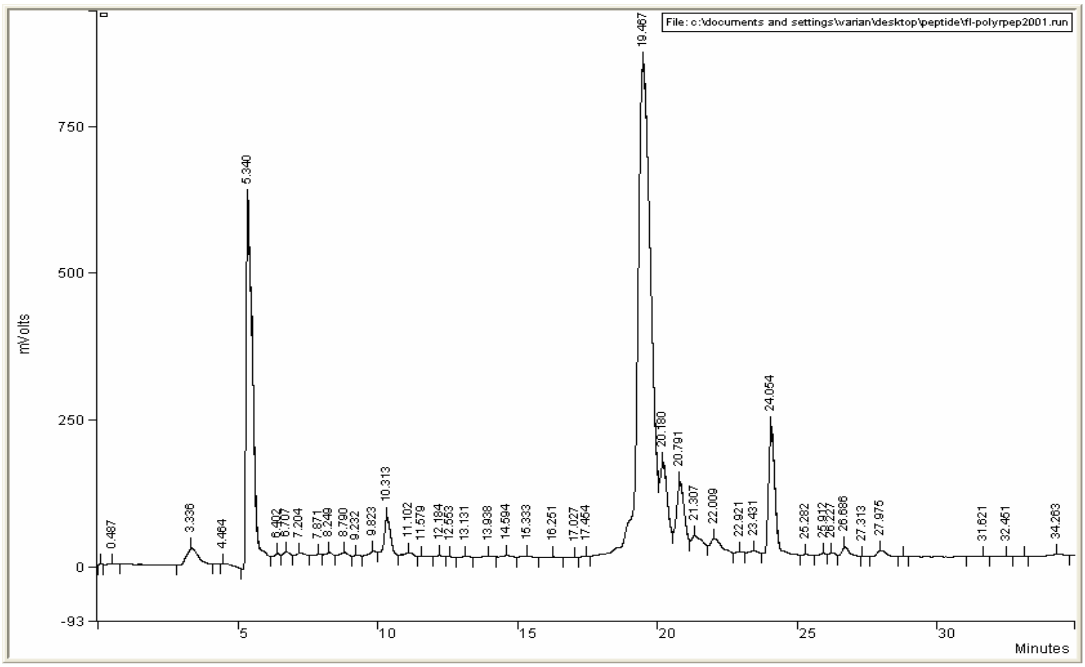

Figure S4. HPLC trace for Cy3-labeled peptide **1** (Cy3-**1**). Column: Zorbax Rx-C8, 80 Å, 5 μm, 9.4 mm x 250 mm (Agilent); flow rate: 3 mL/min; injected volume: 1 mL; wavelength detection: 215 nm; gradient: 0 to 25% buffer B. Buffer A: H_2O, 0.1% TFA. Buffer B: acetonitrile, 0.1% TFA. Retention time: 19.47 min.

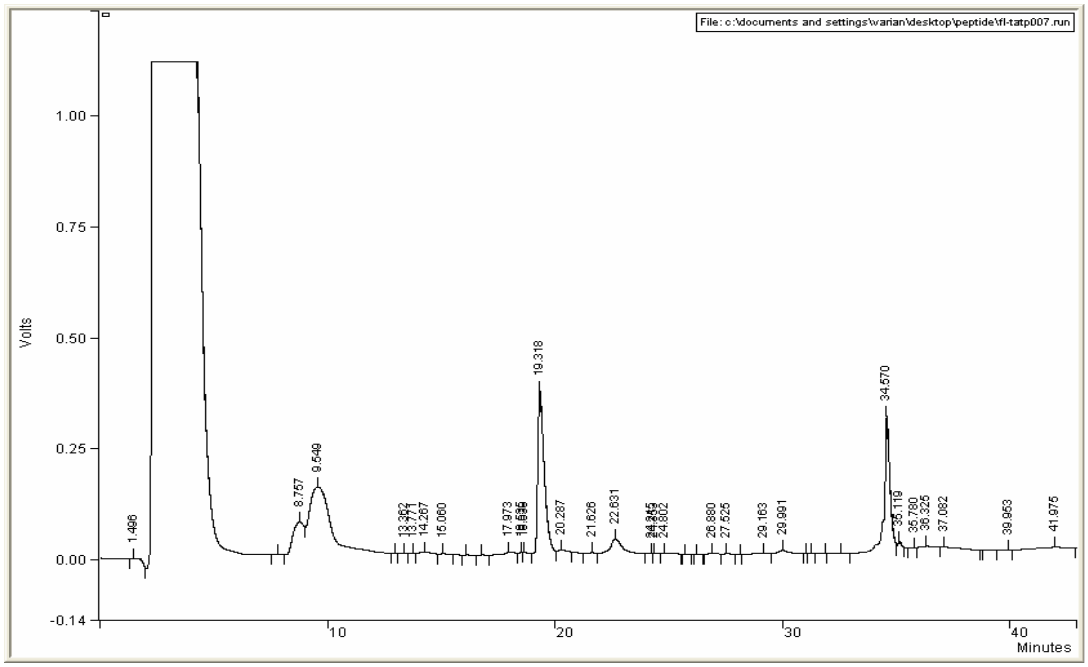

Figure S5. HPLC trace for Cy3-labeled peptide **2** (Cy3-**2**). Column: Zorbax Rx-C8, 80 Å, 5 μm, 9.4 mm x 250 mm (Agilent); flow rate: 3 mL/min; injected volume: 1 mL; wavelength detection: 215 nm; gradient: 0 to 25% buffer B. Buffer A: H_2O, 0.1% TFA. Buffer B: acetonitrile, 0.1% TFA. Retention time: 19.32 min.

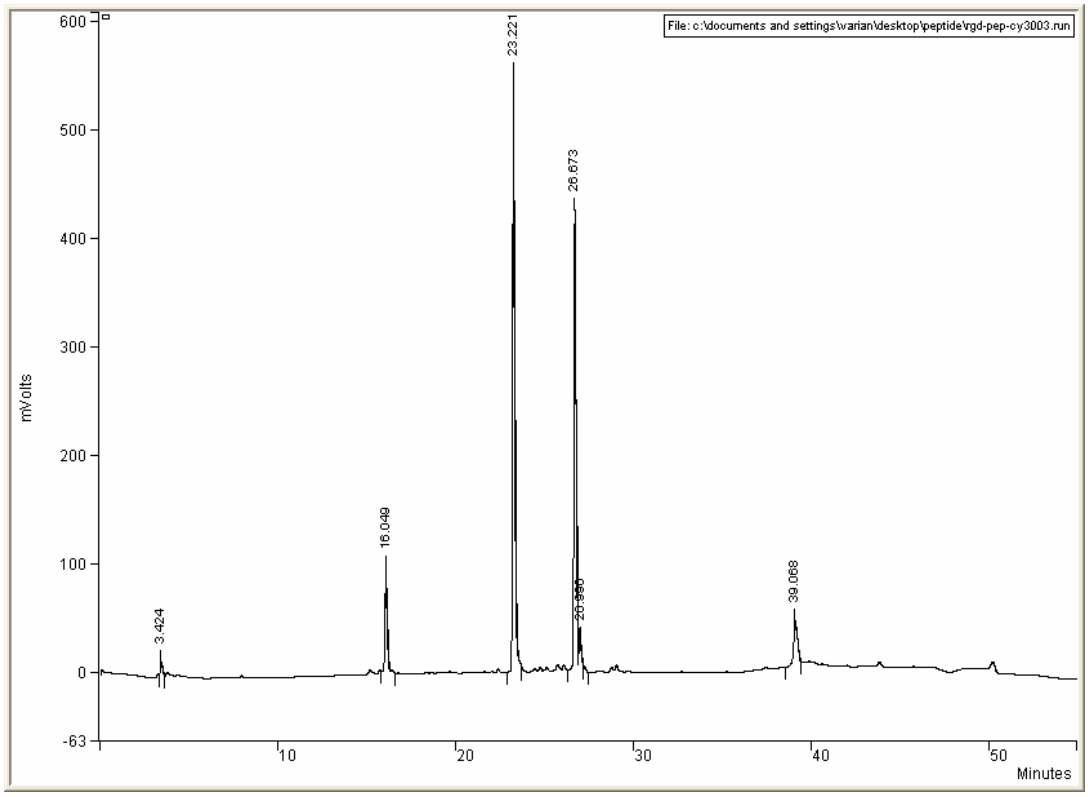

Figure S6. HPLC trace for Cy3-labeled peptide **3** (Cy3-**3**). Column: Zorbax Rx-C8, 80 Å, 5 μm, 9.4 mm x 250 mm (Agilent); flow rate: 3 mL/min; injected volume: 1 mL; wavelength detection: 215 nm; gradient: 0 to 25% buffer B. Buffer A: H_2O, 0.1% TFA. Buffer B: acetonitrile, 0.1% TFA. Retention time: 23.22 min.

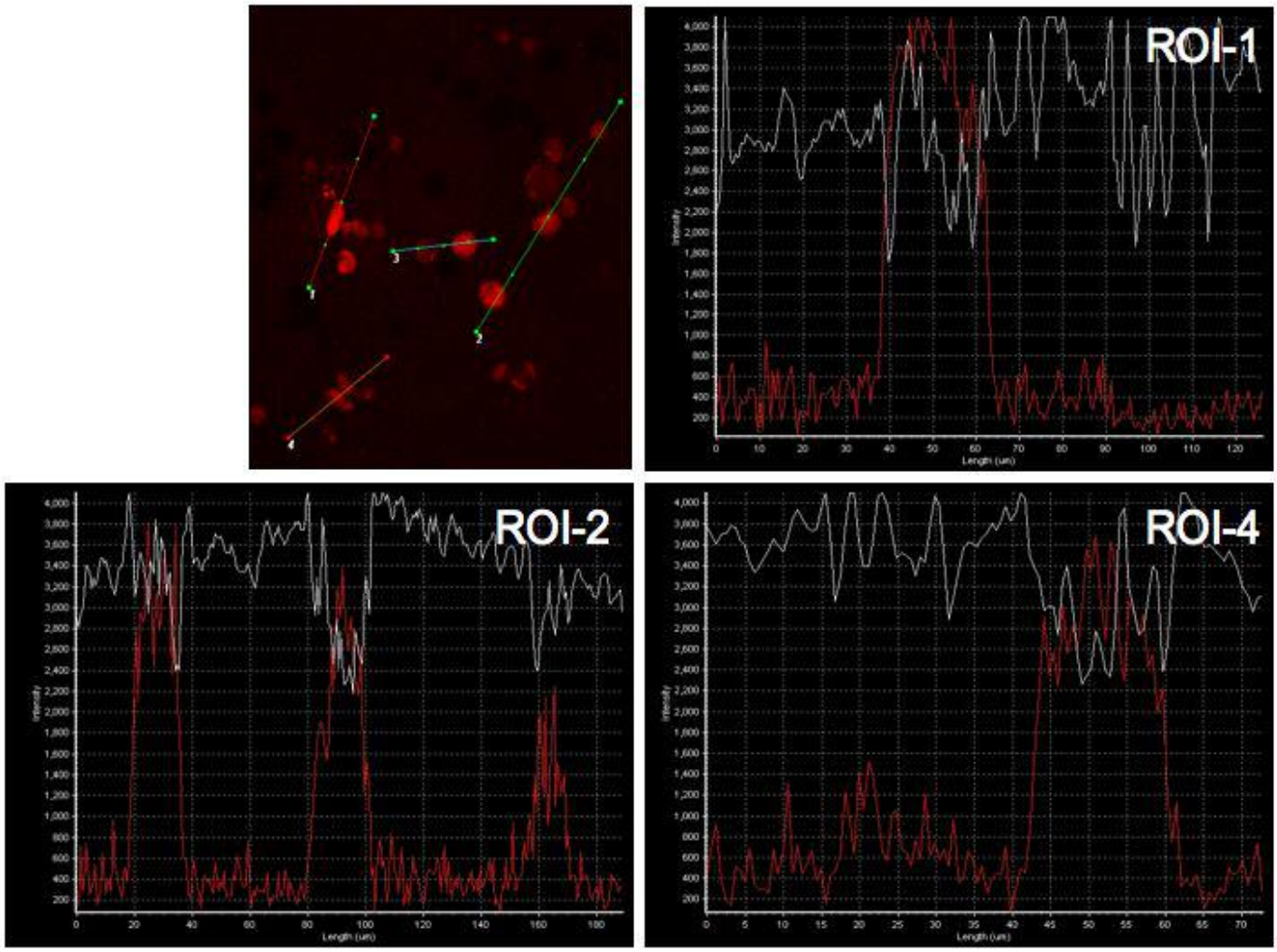

Figure S7. Sample Confocal Data Set 1. Confocal image of CAPAN-2 cells incubated with10 μM Cy3-**3** for 1 h. Cells were not washed and media was not changed before imaging. Images were taken using an Olympus FV1000 confocal laser scanning microscope with 543 nm (HeNe) laser excitation and Cy3 emission filter under 40x magnification (Olympus UApo/340 40x, 1.15 W). Region of Interest (ROI) intensity analysis (red lines) shows fluorescence intensity that is 7-20 times as intense inside cells than in the surrounding solution.

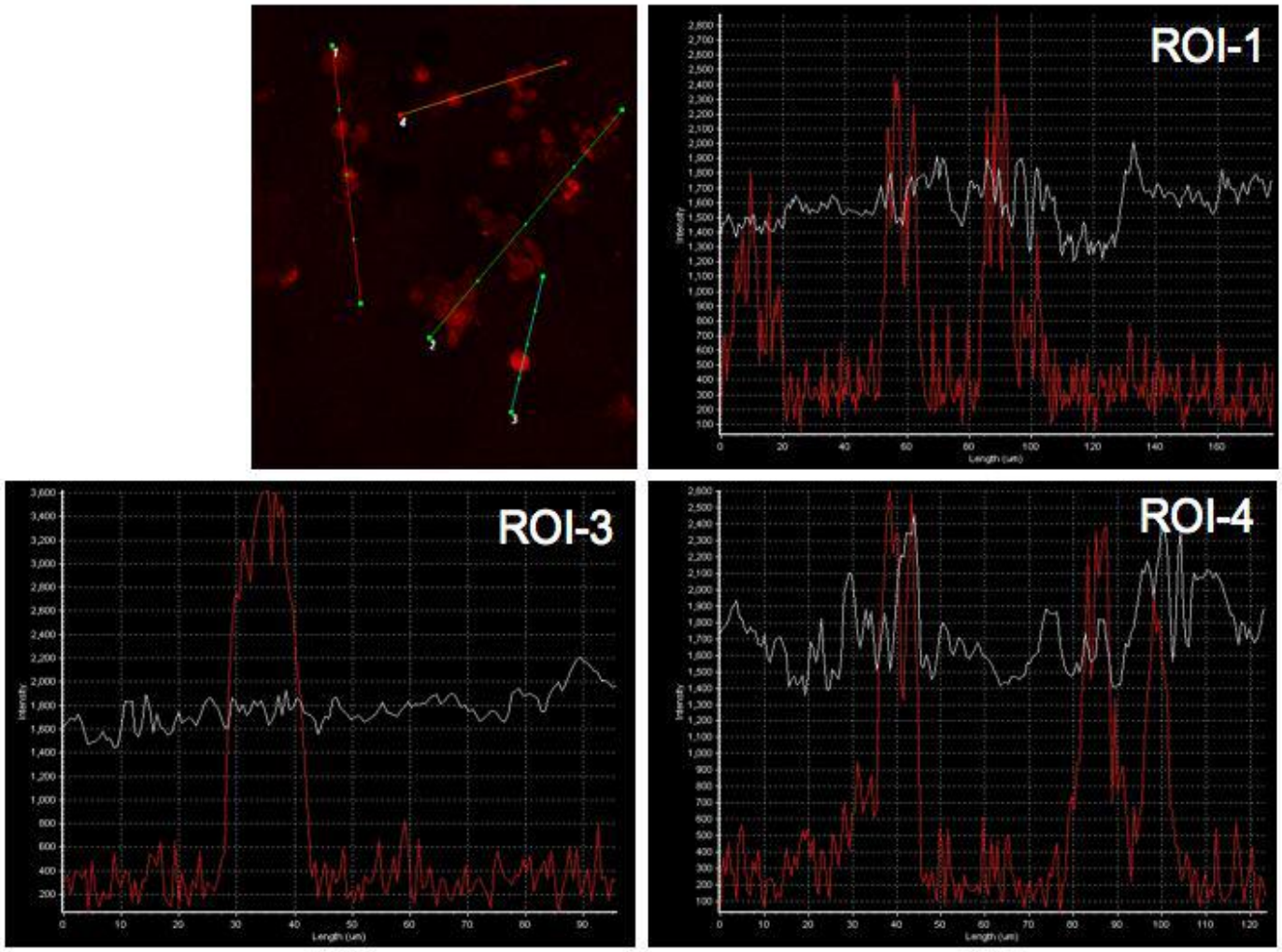

Figure S8. Sample Confocal Data Set 2. Confocal image of CAPAN-2 cells incubated with 10 μM Cy3-**3** for 1 h. Cells were not washed and media was not changed before imaging. Images were taken using an Olympus FV1000 confocal laser scanning microscope with 543 nm (HeNe) laser excitation and Cy3 emission filter under 40x magnification (Olympus UApo/340 40x, 1.15 W). Region of Interest (ROI) intensity analysis (red lines) shows fluorescence that is 10-15 times more intense inside cells than in the surrounding solution.

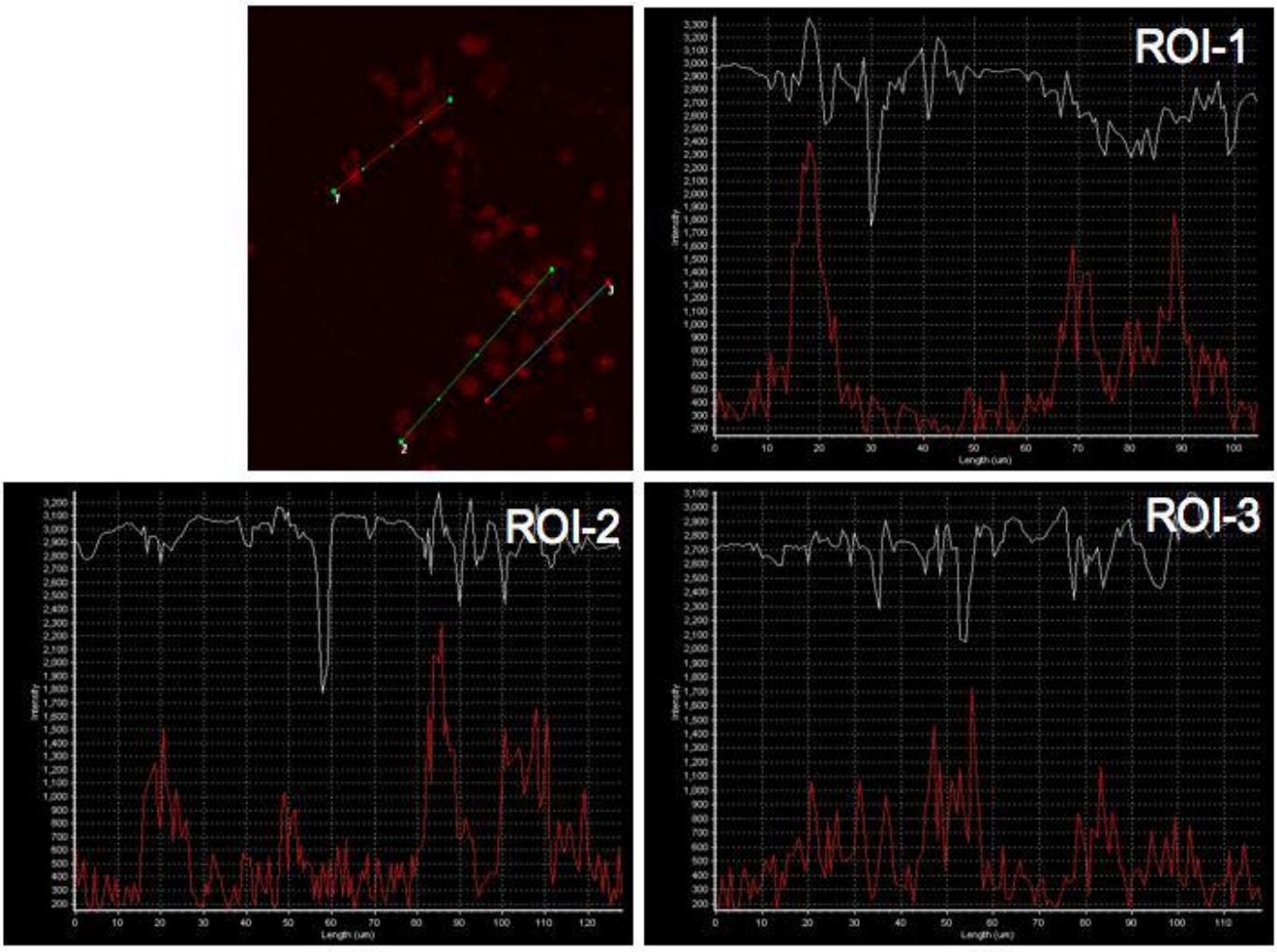

Figure S9. Sample Confocal Data Set 3. Confocal image of CAPAN-2 cells incubated with 10μM Cy3-**3** for 1 h. Cells were not washed and media was not changed before imaging. Images were taken using an Olympus FV1000 confocal laser scanning microscope with 543 nm (HeNe) laser excitation and Cy3 emission filter under 40x magnification (Olympus UApo/340 40x, 1.15 W). Region of Interest (ROI) intensity analysis (red lines) shows fluorescence intensity that is 4-8 times more intense inside cells than in the surrounding solution.

A Facile Method for the Construction of Oligonucleotide Microarrays

Dalip Sethi, A. Kumar, K. C. Gupta,* and P. Kumar*

Institute of Genomics and Integrative Biology (CSIR), Delhi University Campus, Mall Road, Delhi-110007, India. Received June 14, 2008; Revised Manuscript Received September 17, 2008

In recent years, the oligonucleotide-based microarray technique has emerged as a powerful and promising tool for various molecular biological studies. Here, a facile protocol for the construction of an oligonucleotide microarray is demonstrated that involves immobilization of oligonucleotide−trimethoxysilyl conjugates onto virgin glass microslides. The projected immobilization strategy reflects high immobilization efficiency (∼36−40%) and signal-to-noise ratio (∼98), and hybridization efficiency (∼32−35%). Using the proposed protocol, aminoalkyl, mercaptoalkyl, and phosphorylated oligonucleotides were immobilized onto virgin glass microslides. Briefly, modified oligonucleotides were reacted first with 3-glycidyloxypropyltriethoxysilane (GOPTS), and subsequently, the resultant conjugates were directly immobilized onto the virgin glass surface by making use of silanization chemistry. The constructed microarrays were then used for discrimination of base mismatches. On subjecting to different pH and thermal conditions, the microarray showed sufficient stability. Application of this chemistry to manufacture oligonucleotide probe-based microarrays for detection of bacterial meningitis is demonstrated. Single-step reaction for the formation of conjugates with the commercially available reagent (GOPTS), omission of capping step and surface modification, and efficient immobilization of oligonucleotides onto the virgin glass surface are the key features of the proposed strategy.

INTRODUCTION

Oligonucleotide arrays have emerged as a powerful and convenient tool for parallel and high-throughput experimentation in molecular biological research (*1*−*6*). Array technology has considerably simplified the process involved in disease diagnosis and gene mapping, as it offers advantages of using a very small amount of biological probes (nanomoles and picomoles), along with the capability of analyzing thousands of analytes in parallel (*7*).

Direct syntheses (in situ) of oligonucleotides on the chip surface following conventional or photolithographic methods and immobilization of presynthesized oligonucleotides on the selected substrates are the two predominant methods for construction of oligonucleotide microarrays. The in situ synthesis protocol allows the preparation of high-density oligonucleotide microarrays; however, it suffers from certain drawbacks (*8*−*12*). The deposition method, on the other hand, offers flexibility in the sense that a variety of biomolecules can be immobilized on the surface of choice but limited to generation of low to medium density arrays (*14*−*19*). Therefore, the deposition method has become a method of choice for routine applications in research and commercial laboratories. The choice of surface and the chemistry employed for attachment of oligonucleotides are the key factors that govern the quality of constructed microarray. Out of various surfaces used, glass is a substrate of choice owing to its widespread availability, low cost, well-characterized silane chemistry for functionalization, and favorable optical properties, which permits highly sensitive laser-induced fluorescence imaging.

For the attachment of oligonucleotides, various covalent and noncovalent oligonucleotide immobilization techniques have been documented. The simplest of them is the immobilization of probes via electrostatic adsorption onto a charged priming layer like aminopropyl or polylysine-coated glass slides; however, it results in poor hybridization efficiency (*13*). Covalent attachment of probes onto the solid support is a preferred approach, as it results in higher stability and hybridization efficiency as compared to noncovalent immobilization. Some commonly used attachment chemistries (surface-probe) are semicarbazide-aldehyde (*14*), epoxide-amine (*15*), aldehyde-amine (*16*), gold-thiol (*17*, *18*), and thiol-thiol (*19*) interactions. Various hetero- and homobifunctional reagents have also been reported for tethering oligonucleotides to polymeric surfaces (*20*−*24*). In addition to the covalent chemistries employed for the fabrication of arrays, some "organic−inorganic" interactions have also been utilized to realize immobilization of oligonucleotides. Attachment of thiol-modified probes to metallic gold via sulfur−gold linkage and phosphorylated oligonucleotides on zirconylated surface are the representative examples of this approach (*18*, *25*).

Here, we describe a simple two-step method that involves attachment of modified oligonucleotides (aminoalkyl, mercaptoalkyl, and phosphorylated oligomers) onto a virgin glass surface. The first step involves the reaction between a modified probe and a commercially available reagent, 3-glycidyloxypropyltriethoxysilane (GOPTS), to form a silylated conjugate, which, in turn, reacts with silanol functionalities of the glass slide to result in surface-bound oligonucleotides. The proposed strategy not only resulted in signal reproducibility but also showed superior spot morphology and homogeneity. The study undertaken herein includes investigation of optimal time required for the formation of oligomer−trimethoxysilyl conjugate followed by their immobilization on a virgin glass surface and determination of the threshold concentration of conjugate required for visualization. The thermal and pH stability of constructed microarrays was evaluated. The constructed microarrays were compared with the standard method to clearly

* Correspondence address. Dr. P. Kumar, Institute of Genomics and Integrative Biology, Delhi University Campus, Mall Road, Delhi-110007, India. Tel: +91-11-27666156, Fax: +91-11-27667471, E-mail: pkumar@igib.res.in. Dr. K.C. Gupta, Institute of Genomics and Integrative Biology, Delhi University Campus, Mall Road, Delhi-110007, India. Tel: +91-11-27662491, Fax: +91-11-27667471, E-mail: kcgupta@igib.res.in.

10.1021/bc800241k CCC: $40.75 © 2008 American Chemical Society
Published on Web 10/22/2008

highlight the advantages of the projected strategy in terms of immobilization and hybridization efficiency.

EXPERIMENTAL PROCEDURES

Chemicals and Reagents. Virgin glass microslides (75 × 22 mm^2), *N*-methylimidazole (NMI), and 3-glycidyloxypropyltrimethoxysilane (GOPTS) were obtained from Sigma-Aldrich Chemical Co., St. Louis, MO. Absolute ethanol was procured from Tedia Company Inc., Fairfield, U.S. 4,5,6,7-Tetrachlorofluorescein (TET) phosphoramidite was obtained from Applied Biosystems Inc., Foster City, CA. All other reagents used were of analytical grade and used as received from the commercial source, unless specified.

Instrumentation. Scan Array Lite Scanner (GSI Lumonics), Speed Vac concentrator (Hetovac VR-1), Lambda Bio 20 UV−vis spectrophotometer (Perkin-Elmer, USA), and *Quant Array* software for quantification of fluorescence intensity of the spots (Packard Biosciences, USA) were used.

Cleaning of Glass Slides. The glass slides were treated with 1 M NaOH for 1 h followed by washing with MilliQ water (3 × 150 mL). Then, the slides were treated with 1.5 M HCl for 1 h followed by extensive washings with MilliQ water (3 × 150 mL). Finally, the slides were immersed in absolute ethanol (2 × 150 mL, for 15 min each), dried, and stored under inert atmosphere.

Reagents and Buffers. (i) GOPTS solution (0.0136 M): Prepared by dissolving 30 μL GOPTS in 10 mL of dimethylformamide (DMF)/tetrahydofuran (THF)/acetonitrile (ACN). (ii) Reaction buffer (0.1 M NMI): Prepared by dissolving 80 μL in 10 mL of MilliQ water. (iii) Washing buffer: 125 mM SSC buffer containing 750 mM sodium chloride, pH 7.0. (iv) Hybridization buffer: 125 mM SSC buffer containing 1 M sodium chloride, pH 7.0.

Oligonucleotide Synthesis and Purification. Oligonucleotides, used in this study, were synthesized on 0.2 μmol scale on a Pharmacia LKB Gene Assembler Plus using the standard phosphoramidite approach following the manufacturer's protocol (*26*). Labeled oligonucleotides were prepared by performing the last coupling with TET-phosphoramidite in an analogous manner to that of normal nucleoside−phosphoramidites, except that an extended coupling time (5 min) was employed. A list of oligonucleotide sequences assembled along with their deprotection conditions and yields are given in Table 1. The ammoniacal solutions in all the cases were concentrated in a speed vac; the residue obtained was dissolved in water (200 μL) and applied onto a desalting column (reverse-phase ODS-silica gel column). The oligonucleotides were eluted with 30% acetonitrile in water, concentrated, purified, and stored at 4 °C.

Determination of Optimal Conditions Required for Immobilization of Modified Oligonucleotides on a Virgin Glass Microslide. *Preparation of Oligonucleotide−Trimethoxysilyl Conjugate.* Oligonucleotide sequence, TET-d(CTT CTT TTT CCT GTT ACC GT)-OPO_3^{2-} (0.6 nmol), dissolved in the reaction buffer (100 μL), was allowed to react with a GOPTS solution (100 μL) prepared in DMF for 8 h on an Eppendorf mixer. The reaction mixture was then concentrated, and the viscous material obtained was suspended in MilliQ water (40 μL) and centrifuged. The supernatant was collected and concentrated. The residue was finally dissolved in 10% DMSO in water to fix the concentration of the probe solution to 5 μM and then spotted (0.5 μL) manually using a 2 μL pipetteman onto a virgin glass microslide. After spotting, the microslide was kept at 45 °C for 35 min. The slide was washed with 1× SSC buffer (2 × 50 mL for 15 min each), followed by MilliQ water (2 × 50 mL), and dried under vacuum. Subsequently, the spots on the microslide were visualized under a laser scanner and quantified.

Likewise, the experiment was performed in other solvent systems, viz., THF/water (1:1, v/v) and ACN/water (1:1, v/v).

Time Kinetics for the Synthesis of Conjugate. To determine the optimum time required for the formation of conjugates, a kinetic study was performed. Twelve Eppendorfs were equally charged with GOPTS solution (100 μL) in DMF and TET-labeled oligonucleotide, TET-d(CTT CTT TTT CCT GTT ACC GT)-OPO_3^{2-} (0.6 nmol in 100 μL reaction buffer). The Eppendorfs were kept at 45 °C and withdrawn at different time intervals. Subsequently, the reaction mixture was worked up and microarray constructed, as described above. After usual washings and drying, the spots on the microslides were scanned under a laser scanner and quantified. The extent of reaction was evaluated by plotting fluorescence intensity of the spots against time. A similar study was carried out with aminoalkyl and mercaptoalkylated oligonucleotides.

Threshold Concentration of the Conjugate Required for Visualization. In order to determine the threshold concentration of conjugate required for visualization under a laser scanner, oligomer−trimethoxysilyl conjugate, TET-d(CTT CTT TTT CCT GTT ACC GT)-OPO_3^--$CH_2CH(OH)CH_2O(CH_2)_3$-Si-$(OMe)_3$, was dissolved in 10% DMSO in MilliQ water and spotted manually in duplicate in different concentrations (0.5, 1, 2.5, 5, 10, and 20 μM) on a glass microslide. The spotted slide was kept in a humidity chamber at 45 °C for 35 min, followed by washings with the washing buffer (2 × 50 mL for 15 min each) and MilliQ water (2 × 50 mL). The slide was dried under vacuum and scanned under a laser scanner.

Likewise, the conjugates of aminoalkyl and mercaptoalkylated probes were studied.

Evaluation of Glass Surface for Immobilization. In order to evaluate the homogeneity of glass surface, an experiment was performed. An oligomer−trimethoxysilyl conjugate, TET-d(CTT CTT TTT CCT GTT ACC GT)-OPO_3^--$CH_2CH(OH)CH_2O(CH_2)_3$-Si-$(OMe)_3$ (5 μM), was spotted manually on virgin glass microslides at different locations and kept at 45 °C for 35 min. After washing and drying, as described above, the slide was scanned.

Hybridization Studies. Oligonucleotide sequence, d-(ACG GTA ACA GGA AAA AGA AG)-OPO_3^- (0.6 nmol), dissolved in 100 μL of reaction buffer, was mixed with 100 μL solution of GOPTS in DMF. The reaction mixture was agitated for 270 min at 45 °C. Then, the solution was concentrated under vacuum to obtain a syrupy residue of oligonucleotide−trimethoxysilyl conjugate, which was resuspended in MilliQ water (40 μL). The mixture was centrifuged to get rid of excess GOPTS as undissolved material. The supernatant was concentrated under vacuum to obtain a residue, which was reconstituted in MilliQ water containing 10% DMSO (v/v) to make an oligonucleotide conjugate concentration to 5 μM. The conjugate was then spotted manually in duplicate on a glass slide. The spotted microslide was incubated at 45 °C in a humidity chamber for 35 min, followed by washings with washing buffer (3 × 50 mL for 15 min each) and then subjected to hybridization experiment. The microslide was kept in a hybridization chamber and treated with a solution of the complementary fluorescent oligonucleotide, TET-d(CTT CTT TTT CCT GTT ACC GT) (40 μL, 40 μM), prepared in hybridization buffer, under a coverslip at 45 °C for 1 h and then at 25 °C for 12 h. After removal of coverslip, the glass microslide was then washed with hybridization buffer (3 × 50 mL for 15 min each) to get rid of excess complementary oligomer. Subsequently, the microslide was dried, examined under a laser scanner, and quantified.

Similarly, the aminoalkyl and mercaptoalkylated oligonucleotide conjugates were immobilized on a microslide and hybridization assay was performed.

Table 1. Oligonucleotide Sequences Synthesized, Their Deprotection Conditions, and Yields

no	oligonucleotiode sequence	deprotection conditions	yield (A_{254} nm, OD)
1	TET-d (CTT CTT TTT CCT GTT ACC GT)OPO_3^{2-}	aq NH_4OH, 16 h, 60 °C followed by aq AcOH (80%), 4 h	24.3
2	d (AGC GTA ACA GGA AGA AGC TG)OPO_3^{2-}	same conditions	25.6
3	d (AGC GTA ACA GGA AGA TGC TG)OPO_3^{2-}	same conditions	23.4
4	d (AGC GTA CCA GGA AGA TGC TG)OPO_3^{2-}	same conditions	28.6
5	d (TTT TTT TTT TTT TTT TTT TT)OPO_3^{2-}	same conditions	24.2
6	d (AGC GTA ACA GGA AGA AGC TG)OPO_2-$(CH_2)_6NH_2$	aq NH_4OH, 16 h, 60 °C	20.2
7	d (AGC GTA ACA GGA AGA TGC TG)OPO_2- $(CH_2)_6NH_2$	same conditions	21.5
8	d (AGC GTA CCA GGA AGA TGC TG)- OPO_2- $(CH_2)_6NH_2$	same conditions	20.6
9	d(TTT TTT TTT TTT TTT TTT TT)- OPO_2- $(CH_2)_6NH_2$	same conditions	24.4
10	d (AGC GTA ACA GGA AGA AGC TG)OPO_2-$(CH_2)_6SH$	aq NH_4OH, 16 h, 60 °C containing 0.1 M DTT	21.1
11	d (AGC GTA ACA GGA AGA TGC TG)OPO_2- $(CH_2)_6SH$	same conditions	25.2
12	d (AGC GTA CCA GGA AGA TGC TG)- OPO_2- $(CH_2)_6SH$	same conditions	20.3
13	d(TTT TTT TTT TTT TTT TTT TT)- OPO_2- $(CH_2)_6SH$	same conditions	24.3
14	TET-d (CAG CTT CTT CCT GTT ACG CT)	aq NH_4OH, 16 h, 60 °C	24.1
15	TET-d(GCT GCG GTA GGT GGT TCA A) F. primer	same conditions	22.7
16	TET-d(TTG TCG CGG ATT TGC AAC TA) R. primer	same conditions	23.1
17	d(ACG TGT CAG CTG CAC ATT CGT)-OPO_3^{2-} (probe sequence)	aq NH_4OH, 16 h, 60 °C Followed by aq AcOH (80%), 4 h	23.5
18	d(CGT CGA GTC GGG CAT CTT TTT)-OPO_3^{2-} (control)	same conditions	24.5

Detection of Base Mismatches. The specificity of the system was demonstrated by immobilizing oligomer−trimethoxysilyl conjugates on virgin glass microslides. Four oligonucleotide conjugates, viz., d(ACG GTA ACA GGA AAA AGA AG)-OPO_3^--$CH_2CH(OH)CH_2O(CH_2)_3$-$Si(OMe)_3$, d(ACG GTA ACA GGA AAA AGC AG)-OPO_3^--$CH_2CH(OH)CH_2O(CH_2)_3$-$Si(OMe)_3$, d(ACG GTA ACA CGA AAA AGC AG)-OPO_3^--$CH_2CH(OH)CH_2O(CH_2)_3$-$Si(OMe)_3$, and d(TTT TTT TTT TTT TTT TTT TT)-OPO_3^--$CH_2CH(OH)CH_2O(CH_2)_3$-$Si(OMe)_3$ (5 μM), having zero, one, and two mismatches and noncomplementary probe, were spotted on a virgin glass slide and processed as described above. Subsequently, the spots on the microslide were hybridized with a complementary labeled TET-d(CTT CTT TTT CCT GTT ACC GT) and kept at 45 °C for 1 h and then at room temperature for 12 h. After washings with hybridization buffer (3 × 50 mL for 15 min each), the microslide was subjected to laser scanning followed by quantification. Under identical conditions, conjugates of aminoalkyl and mercaptoalkylated oligomers were immobilized, hybridized, and quantified.

In order to demonstrate that the epoxy group of GOPTS specifically reacts with terminal functional groups of end-modified oligonucleotides, a comparative study was performed. Conjugates of two oligonucleotide sequences, viz., TET-d(CTT CTT TTT CCT GTT ACC GT) and TET-d(CTT CTT TTT CCT GTT ACC GT)-OPO_3^{2-}, were prepared, as described above and after usual workup, the conjugates (5 μM) were spotted manually on virgin glass slide. After usual washings, the spots were visualized under a laser scanner and quantified.

Quantification of Immobilized Oligonucleotides. To quantify the density of immobilized oligonucleotides, an oligomer sequence, TET-d(CTT CTT TTT CCT GTT ACC GT)-OPO_3^{2-}, diluted to different concentrations (0.05, 0.10, 0.25, 0.50, 0.75, 1.0, 2.0 μM), was spotted on a glass microslide in duplicates. After drying the spots under vacuum, the microslide was visualized under a laser scanner and the fluorescence signal intensity corresponding to each spot was measured. Using these values, a standard curve was plotted between fluorescence intensity (A.U.) and concentration (μM) of the spot.

Thermal and pH Stability. To evaluate the thermal stability of probe immobilization, a microarray was constructed by spotting oligonucleotide−trimethoxysilyl conjugates at a concentration of 5 μM. The fabricated microarrays were treated under PCR-like conditions for 0, 5, and 10 cycles in 1× SSC buffer (pH 7). PCR parameters were as follows: 94 °C for 30 s (denaturing step), 54 °C for 30 s (annealing step), and 72 °C for 30 s (extension step). After thermocycling, the slide was washed, dried, and visualized under a laser scanner.

The pH stability was evaluated by preparing microarrays in a similar way and then subjecting them to washings with 1× SSC buffer of different pH (7, 8, and 9) (3 × 50 mL for 15 min each). The microslides, after usual washings and drying, were visualized under a laser scanner.

Detection of Bacterial Meningitis. *PCR-Amplification.* The PCR reaction was performed in 25 μL PCR Eppendorf containing 0.25 mM dNTPs (of each dATP, dCTP, dGTP, and dTTP), forward primer TET-d(GCT GCG GTA GGT GGT TCA A), and reverse primer TET-d(TTG TCG CGG ATT TGC AAC TA) (0.4 μM of each), genomic DNA (50 ng/reaction), Taq-polymerase (0.75 units), and MilliQ water. All PCR reactions were performed on an MJ Research thermocycler using the following profile: (1) 5 min at 95 °C (initial denaturation step); (2) 35 cycles of 50 s at 95 °C (denaturation step), 40 s at 58 °C (annealing step), 1 min at 72 °C (extension step); (3) 7 min at 72 °C (final extension step); hold temperature: 4 °C. The labeled PCR-amplifications, 111bp fragment of *ctrA* gene (*Neisseria meningitidis*; serogroup A), were analyzed by agarose gel electrophoresis, and detection was performed by ethidium bromide (10 μg/mL) in standard TAE buffer, pH 8.

PCR Amplicon Capture. Two oligonucleotide−trimethoxysilyl conjugates, d(ACG TGT CAG CTG CAC ATT CGT)-OPO_3^--$CH_2CH(OH)CH_2O(CH_2)_3$-$Si(OMe)_3$ (complementary) and d(CGT CGA GTC GGG CAT CTT TTT)-OPO_3^--$CH_2CH(OH)CH_2O(CH_2)_3$-$Si(OMe)_3$ (control, noncomplementary) were immobilized on the glass slide as described above. Amplicons were hot-denatured (5 min, 95 °C), cooled on ice (10 min), and used for the hybridization assay. After usual washings, the slide was visualized under a laser scanner.

Signal Evaluation and Quantification. Microarrays were scanned on a Scan Array Lite Scanner (GSI Lumonics) fitted with a Cy3 optical filter with 30 μm resolution; laser power and PMT were set to 85% and 80%, respectively. Spot intensities were quantified using *Quant Array* software (Packard Bioscience) and graphs were plotted in Microsoft *Excel*.

For each experimental condition tested on the microarrays, the experiments were repeated 2−3 times. The immobilization and hybridization data presented are the average of these repetitions, and the error bars represent the percentage error (∼3−5%) observed on this average.

RESULTS AND DISCUSSION

Homo- and heterobifunctional cross-linkers have been finding extensive use for various applications, such as preparation of affinity matrices, modification and stabilization of diverse structures, identification of ligand and receptor binding sites,

Scheme 1. Immobilization of Oligonucleotides on Virgin Glass via Oligonucleotide−Trimethoxysilyl Conjugates[a]

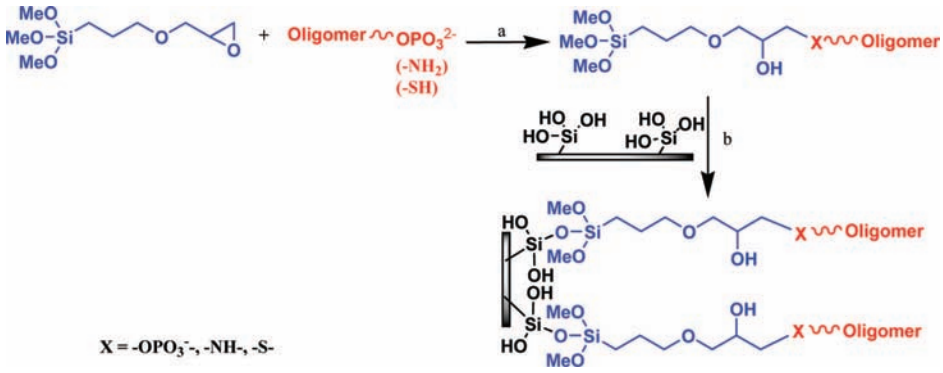

[a] Conditions: (a) 45 °C, 4.5 h (phosphoryl-oligomer); 45 °C, 3 h (aminoalkyl-oligomer); 45 °C, 2 h (mercaptoalkyl-oligomer); and (b) 45 °C, 35 min.

structural studies, and so forth. Of these, heterobifunctional reagents, which contain two different functional groups, have proven to be more advantageous, as cross-linking can be controlled both selectively and sequentially. By taking advantage of the differential reactivity of the two reactive groups, these reagents are finding extensive use in DNA microarray technology for tethering oligonucleotides to solid surfaces (*20*−*24*). Recently, immobilization of biomolecules on glass/silicon wafers has gained importance, as these are being used in constructing microarrays of biomolecules (e.g., oligonucleotide, peptide, protein, polysaccharides, and so forth). The primary aim of the present investigation was to design a facile and economical protocol for immobilization of aminoalkyl, mercaptoalkyl, and phosphorylated oligonucleotides, as they can easily be synthesized using commercially available reagents and chemicals, onto the virgin glass surface. While designing such a protocol, the following points were kept in mind: (i) the methodology should not require modified surfaces, (ii) the reagents should be commercially available and inexpensive, and (iii) the protocol should not involve complex chemistry and stringent reaction conditions. Guided by these considerations, we could find out three reagents, viz., 3-glycidyloxypropyltrimethoxy silane (GOPTS), 3-isocyanatopropyltriethoxysilane (IPTS), and 3-mercaptopropyltriethoxysilane (MPTS), for this purpose. Among these reagents, IPTS can be used for immobilization of amino- and mercaptoalkylated oligonucleotide, however, due to highly moisture-sensitive nature, the results are not reproducible. MPTS results in immobilization of mercaptoalkylated oligomers via disulfide linkage, which is quite a labile linkage. Only GOPTS, which fulfills all the requirements, was considered to be the reagent of choice for immobilization of modified oligonucleotides ($-NH_2$, -SH, and $-OPO_3^{2-}$). The epoxy function present at one of the ends can react efficiently with a vast variety of nucleophiles as well as electrophiles under mild conditions, and the trimethoxysilyl functions at the other end of the reagent can specifically react with silanol functionalities on the virgin glass surface following silanization chemistry (Scheme 1). By taking advantage of these points, a rapid and clean protocol has been developed for immobilization of oligonucleotides bearing different functional groups.

Optimization of Reaction Conditions. In order to find an appropriate solvent system for the preparation of oligonucleotide−trimethoxysilyl conjugates, we surveyed the literature and observed that trialkoxysilane groups get hydrolyzed in aqueous solution in the presence of either strong ionizable acids or bases (*27*−*29*). However, the rate of hydrolysis is very dependent on the presence of an organic solvent in the reaction mixture (*30*, *31*). Among the various solvent systems reported, viz., acetone−water, methanol−water, dioxane−water, ethanol−water, and DMF−water, the slowest rate of hydrolysis of

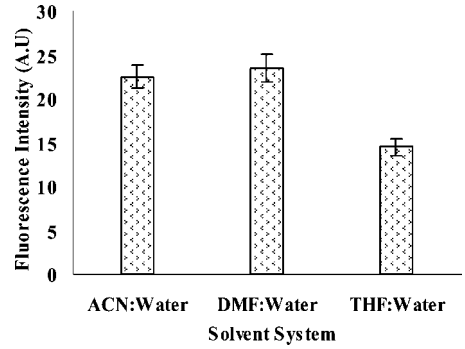

Figure 1. Effect of solvent systems on the reaction of end-modified oligonucleotides with GOPTS.

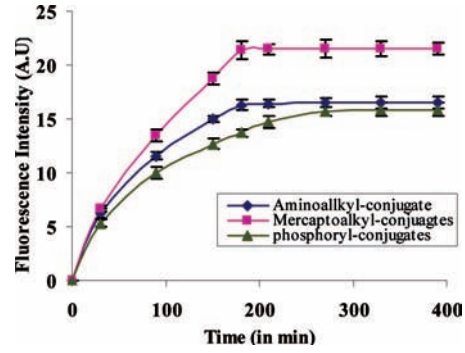

Figure 2. Kinetic study of the reaction between fluorescent-labeled end-modified oligonucleotides with GOPTS.

trialkoxysilanes was observed in DMF−water system, where DMF is believed to inhibit the hydrolysis of alkoxysilanes. Keeping these observations in mind, we carried out the conjugate formation (reaction between modified oligonucleotide and GOPTS) in DMF−water (1:1, v/v) using 0.1 M NMI, a nonionizable base, as reaction buffer. Even if, under such conditions, some of the trialkoxysilyl groups may get hydrolyzed, the use of a large excess of the conjugate for the immobilization reaction would hardly affect the efficacy of the system. Therefore, in order to evaluate the formation of oligonucleotide−trimethoxysilyl conjugates, three solvent systems, viz., ACN/water (1:1, v/v); DMF/water (1:1, v/v), and THF/water (1:1, v/v), were assessed. After carrying out the reaction for 8 h, the conjugate was spotted manually on a virgin glass microslide and incubated at 45 °C for 30 min. The results revealed that maximum fluorescence intensity (A.U.) of the spots was observed in case of DMF/water (1:1, v/v) containing 0.1 M NMI, indicating that the conjugation reaction proceeded efficiently in this solvent system (Figure 1). Therefore, in the

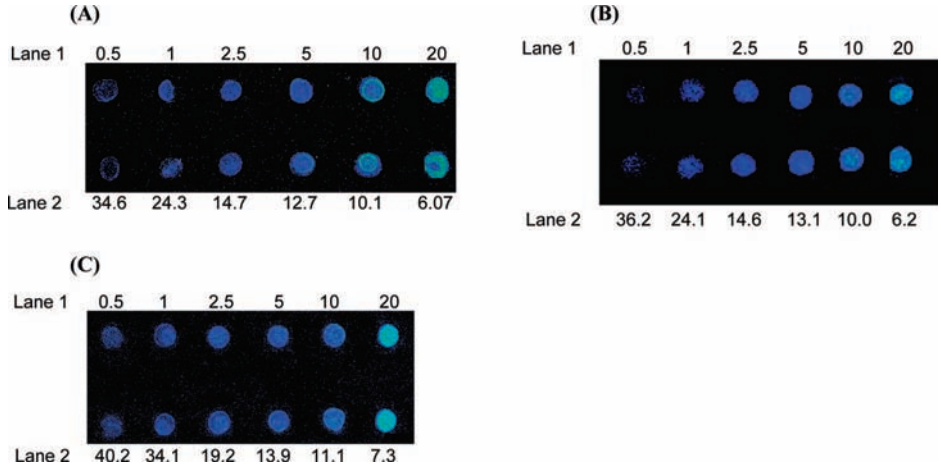

Figure 3. Pictorial representation of immobilization efficiency (%, lane 2) vs concentration (μM, lane 1) of (A) phosphoryl−trimethoxysilyl conjugate, (B) aminoalkyl−trimethoxysilyl conjugate, and (C) mercaptoalkyl−trimethoxysilyl conjugate.

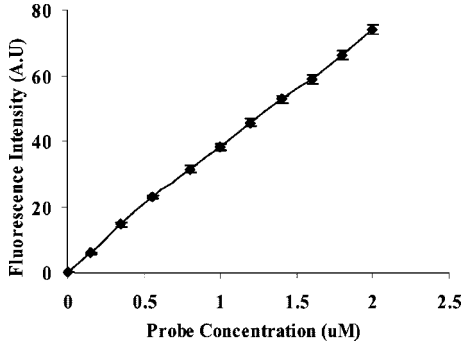

Figure 4. Correlation between concentrations of spotted labeled probe and fluorescence intensity. Fluorescent oligonucleotide was spotted in 0.05−2.0 μM concentrations.

rest of the experiments, oligonucleotide−trimethoxysilyl conjugates were prepared in DMF/water solvent system (1:1, v/v).

With the aim of determining the time required for the completion of reaction between aminoalkyl, mercaptoalkyl, and phosphorylated oligonucleotides and epoxy groups of GOPTS, kinetic studies were undertaken at 45 °C. Phosphorylated oligonucleotide, TET-d(CTT CTT TTT CCT GTT ACC GT)-OPO_3^{2-}, taken in twelve Eppendorf tubes, was allowed to react with GOPTS, and the tubes were withdrawn at different time intervals. After the usual workup, a microarray was constructed, as mentioned in the Experimental Section. The slide was visualized under a laser scanner, and fluorescence intensity (A.U.) of the spots was determined, which was subsequently plotted against time (min), as shown in Figure 2. The results indicate that the formation of the conjugate essentially completes in 180 min (3 h) in the case of aminoalkyl, 120 min (2 h) for mercaptoalkyl, and 270 min (4.5 h) for phosphorylated oligomers. In the subsequent experiments, a respective time period was employed for the preparation of conjugates between modified probes and GOPTS.

To determine the threshold concentration of the conjugate required for visualization under a laser scanner, an oligonucleotide−trimethoxysilyl conjugate, TET-d(CTT CTT TTT CCT GTT ACC GT)-OPO_3^--$CH_2CH(OH)CH_2O(CH_2)_3$-$Si(OMe)_3$, serially diluted from 20 μM to 0.5 μM, was spotted manually on a virgin glass slide and incubated at 45 °C. After the usual workup, the slide was scanned under a laser scanner and the spots were quantified. The pictorial view of the slide is depicted in Figure 3A. Similar experiments were carried out for aminoalkyl and mercaptoalkylated oligonucleotide conjugates (Figure 3B,C). The immobilization efficiency against each concentration was determined with the help of a standard curve (Figure 4). The results revealed that immobilization efficiency followed an inverse relation with concentration of spotted conjugates. The spots corresponding to 0.5−2.5 μM concentration were visible; however, to construct a good quality biochip, a concentration of 5 μM was selected and used for immobilization purposes.

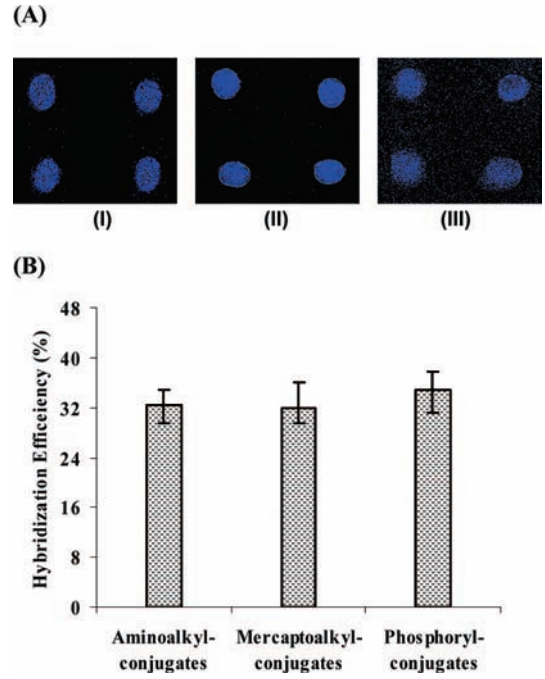

Figure 5. (A) Immobilization of (I) d(AGC GTA ACA GGA AGA AGC TG)OPO_3-$(CH_2)_6$NH- $CH_2CH(OH)CH_2O(CH_2)_3$-$Si(OMe)_3$, (II) d(AGC GTA ACA GGA AGA AGC TG)OPO_3-$(CH_2)_6$S-$CH_2CH(OH)CH_2O(CH_2)_3$-$Si(OMe)_3$, and (III) d(AGC GTA ACA GGA AGA AGC TG)OPO_3^--$CH_2CH(OH)CH_2O(CH_2)_3$-$Si(OMe)_3$ on a virgin glass surface followed by hybridization with labeled oligomer, TET-d(CAG CTT CTT CCT GTT ACG CT). (B) Quantitative hybridization efficiency.

Homogeneity of virgin glass microslides procured from Sigma Chemical Co., USA, was evaluated by manually spotting the TET-labeled conjugate at different positions on the glass microslides. The fluorescence intensity of spots was found to be in the range ~25.3−27.2 A.U., which showed that the density of silanol functionalities on the glass surface was present almost uniformly throughout the glass surface. The stability of the

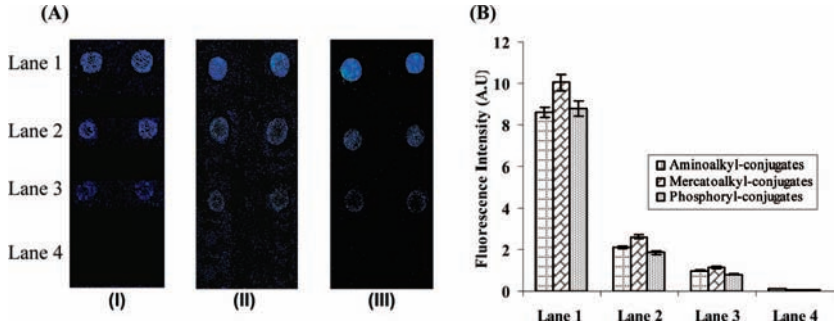

Figure 6. (A) Detection of base mismatches and specificity of immobilization after hybridization with TET-labeled complementary oligomer. Lane 1: zero mismatch. Lane 2: one mismatch. Lane 3: two mismatches. Lane 4: noncomplementary oligomer. Slide (I): Aminoalkyl−trimethoxysilyl conjugates. Slide (II): mercaptoalkyl−trimethoxysilyl conjugates. Slide (III): phosphoryl−trimethoxysilyl conjugates. (B) A histogram showing respective fluorescence intensity. Lane 1: Perfect match. Lane 2: One mismatch. Lane 3: Two mismatch. Lane 4: Non-complementary.

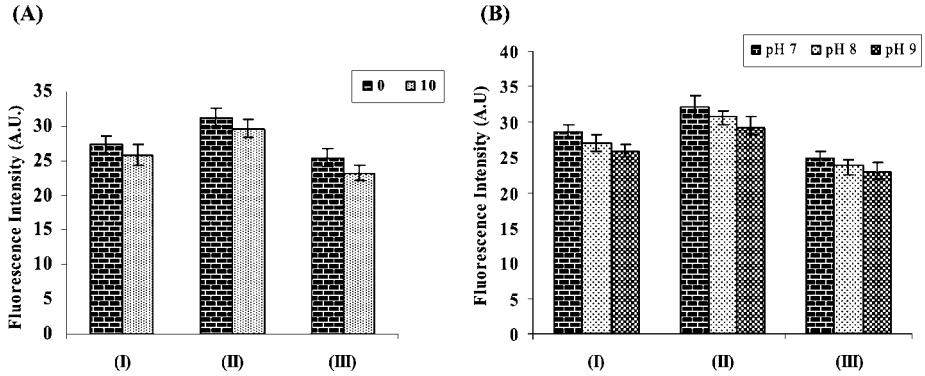

Figure 7. (A) Thermal stability of immobilized conjugates on glass slide and comparison of fluorescence signals obtained after 10 cycles of PCR-like conditions. (B) Stability of immobilized conjugates at pH 7−9.

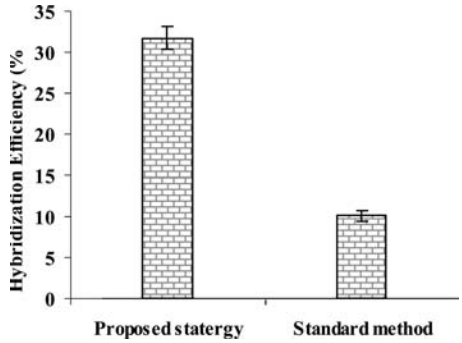

Figure 8. Comparison of hybridization efficiency of the proposed strategy with the standard one, viz., NTMTA.

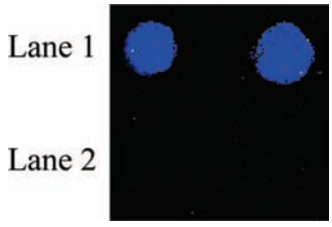

Figure 9. Detection of bacterial meningitis. Lane 1: Probe sequence. Lane 2: Control probe (non-complementary).

oligomer−trimethoxysilyl was also checked on storage at 4 °C for up to 30 days, and it was found to be stable.

Hybridization Assay. The applicability of the projected strategy was evaluated by performing hybridization assay of slides fabricated via immobilization of the trimethoxysilyl conjugates of aminoalkyl, mercaptoalkyl, and phosphorylated oligomers onto the glass slides at 5 μM concentration. The microarrays constructed were visualized by hybridizing them with the corresponding complementary TET-labeled oligonucleotides. After thorough washings and drying, the microslides were screened under a laser scanner and the fluorescent spots were visualized, as depicted in Figure 5A. The fluorescent spots on the microslides were quantified using *QuantArray* software. The quantification data is shown in Figure 5B. The proposed strategy resulted in high hybridization efficiency (∼32−35%). Furthermore, the spot morphology was also found to be almost identical.

Specificity of Chemistry and Base Mismatch Detection. To demonstrate the specificity of the proposed chemistry and the extent of involvement of internucleotidic phosphodiester groups in the formation of conjugates, a study was performed using TET-labeled phosphorylated oligomer and its nonphosphorylated labeled analogue, as described in the Materials and Methods section. Fluorescence intensity of spots of nonphosphorylated oligomer was only ∼10% as compared to that of phosphorylated oligonucleotides.

In order to demonstrate the specificity of the microarrays, four oligonucleotide−trimethoxysilyl conjugates having zero (d(AGC GTA ACA GGA AGA AGC TG)OPO_3^{2-}), one (d(AGC GTA ACA GGA AGA TGC TG)OPO_3^{2-}), and two (d(AGC GTA CCA GGA AGA TGC TG)OPO_3^{2-}) mismatches and a non-complementary sequence, d(TTT TTT TTT TTT TTT TT)OPO_3^{2-}, to the TET-d(CAG CTT CTT CCT GTT ACG CT) were immobilized onto a virgin glass slide. After the usual washings with SSC buffer and MilliQ water, the microarrays were subjected to a hybridization step with a labeled oligomer (complementary to zero mismatch sequence). Figure 6A(I) clearly shows the base mismatches. The results revealed that the fluorescence intensity of spots decreased for single-mismatch and was reduced to minimal for double-mismatch as compared to that of the perfect complementary oligomer.

Hybridization of the non-complementary oligonucleotide did not result in significant signal after hybridization, implying the specificity of the hybridization. Similarly, specificity of other microarrays constructed using amino- and mercaptoalkylated oligonucleotide−trimethoxysilyl conjugates was evaluated as depicted in Figure 6A(II and III). The quantification data are shown in Figure 6B.

Thermal and pH Stability. The thermal stability of constructed microarray was evaluated by subjecting it to 0, 5, and 10 cycles of PCR-like conditions. The percentage reduction in fluorescence intensity was observed to be ∼8.2% for phosphorylated oligomer conjugates, ∼5.8% for aminoalkylated oligomer, and ∼4.9% for mercaptoalkylated oligomer conjugates (Figure 7A), indicating that constructed microarrays are sufficiently stable to be used in biological research. The stability of constructed microarrays was also analyzed at different pHs (7, 8, and 9). The results indicated that the constructed microarrays are sufficiently stable in SSC buffers of different pH. The decrease in fluorescence intensity was ∼5% at pH 8 and ∼10% at pH 9 as compared to fluorescence intensity at pH 7 for the oligomer conjugates (Figure 7B).

Comparison of the Projected Strategy with Standard NTMTA Method. The efficacy of the proposed method was demonstrated by comparing with the NTMTA method (*20*). For comparison purposes, an equal concentration of an oligonucleotide (each at 5 μM) was used in all three methods. However, different reaction conditions as well as time were employed, as reported. After immobilization and hybridization with labeled complementary target, the slides were subjected to usual washings and drying. The slides were then subjected to scanning under a laser scanner for quantification, and the hybridization efficiency for each method was calculated. The hybridization efficiency of the proposed method (∼32−35%) was found to be significantly higher than the standard method, NTMTA (∼10.2%), as shown in Figure 8.

Detection of Bacterial Meningitis. In order to devise a biochip for the diagnosis of the bacterial infection, a microarray was constructed on a glass microslide using a unique probe sequence of the *CtrA* gene and a non-complementary probe sequence as control, as described in the Materials and Methods section. Subsequently, the spots on the glass surface were subjected to hybridization with the labeled PCR amplicons. After washings and drying, the slide was visualized under a laser scanner. Figure 9 shows the pictorial view of the slide. Spots of probe sequence specific to *ctrA* gene of bacteria (*N. Meningitidis*) showed fluorescence, while the spots pertaining to the control did not fluoresce at all, signifying the specificity of the system to prepare biochips for the detection of bacterial meningitis in humans.

CONCLUSIONS

An efficient and facile method for fabricating oligonucleotide microarrays has been developed employing conjugates of oligonucleotides. The method permits attachment of modified probes, which can be synthesized easily on the machine itself using commercially available reagents, onto virgin glass slides with high immobilization and hybridization efficiency and signal-to-noise ratio (∼98). The protocol offers an added advantage that it bypasses the capping step. The method involves commonly used reagents, chemicals, and simple chemistry; it is hoped that this will provide individuals, particularly the end users or nonchemists, an easy access to an oligonucleotide microarray for various applications including diagnosis of genetic as well as infectious diseases.

ACKNOWLEDGMENT

Financial support from the Department of Biotechnology, New Delhi, India, is gratefully acknowledged. One of the authors, D.S., acknowledges the University Grants Commission (UGC), New Delhi, India, for the award of Research Fellowship to carry out his work. Authors are thankful to Dr. Sunil Gupta and Dr. Shashi Khare, National Institute of Communicable Diseases (NICD), Delhi, India, for providing meningitis sample and facilities.

Supporting Information Available: Morphology, homogeneity and the reproducibility data in the projected method and comparison with the standard method, NTMTA. This material is available free of charge via the internet at http://pubs.acs.org.

LITERATURE CITED

(1) Mao, H., Lu, Z., Zhang, H., Liu, K., Zhao, J., Jin, G., Gu, S., and Yang, M. (2008) Colorimetric oligonucleotide array for genotyping of hepatitis C virus based on the 5′ non-coding region. *Clin. Chim. Acta 388*, 22–27.

(2) Sosnowski, R. G., Tu, E., Butler, W. F., O'Connell, J. P., and Heller, M. J. (1997) Rapid determination of single base mismatch mutations in DNA hybrids by direct electric field control. *Proc. Natl. Acad. Sci. U.S.A. 94*, 1119–1123.

(3) Zhu, T., Budworth, P., Han, B., Brown, D., Chang, H. S., Zou, G., and Wang, X. (2001) Toward elucidating the global gene expression patterns of developing Arabidopsis: Parallel analysis of 8300 genes by a high-density oligonucleotide probe array. *Plant Physiol. Biochem. 39*, 221–242.

(4) Drobyshev, A., Mologina, N., Shik, V., Pobedimskaya, D., Yershov, G., and Mirzabekov, A. (1997) Sequence analysis by hybridization with oligonucleotide microchip: identification of β-thalassemia mutations. *Gene 188*, 45–52.

(5) Boudreau, C. R., Yang, I., and Liau, L. M. (2005) Gliomas: advances in molecular analysis and characterization. *Surgical Neurology 64*, 286–294.

(6) Gallagher, J., Howlin, J., McCarthy, C., Murphy, E. P., Bresnihan, B., FitzGerald, O., Godson, C., Brady, H. R., and Martin, F. (2003) Identification of Naf1/ABIN-1 among TNF-α-induced expressed genes in human synoviocytes using oligonucleotide microarrays. *FEBS Lett. 551*, 8–12.

(7) Loy, A., and Bodrossy, L. (2006) Highly parallel microbial diagnostics using oligonucleotide microarrays. *Clin. Chim. Acta 363*, 106–119.

(8) Southern, E. M., Case-green, S. C., Elder, J. K., Johnson, M., Mu, K. U., Wang, J., and Williams, J. C. (1994) Arrays of complementary oligonucleotides for analysing the hybridization behaviour of nucleic acids. *Nucleic Acids Res. 22*, 1368–1373.

(9) Moorcroft, M. J., Meuleman, W. R. A., Latham, S. G., Nicholls, T. J., Egeland, R. D., and Southern, E. M. (2005) In situ oligonucleotide synthesis on poly(dimethylsiloxane): a flexible substrate for microarray fabrication. *Nucleic Acids Res. 33*, e75.

(10) Fodor, S. P., Read, J. L., Pirrung, M. C., Stryer, L., Lu, A. T., and Solas, D. (1991) Light directed spatially addressable parallel chemical synthesis. *Science 251*, 767–773.

(11) Singh-Gasson, S., Green, R. D., Yue, Y., Nelson, C., Blattner, F., Sussman, M. R., and Cerrina, F. (1999) Mask-less fabrication of light director oligonucleotide arrays using a digital micromirror array. *Nat. Biotechnol. 17*, 974–978.

(12) McGall, G. H., and Fidanza, J. A. (2001) Photolithographic synthesis of high density oligonucleotide arrays. *Methods Mol. Biol. 170*, 71–101.

(13) Burns, N. L., Van Alstine, J. M., and Harris, J. M. (1995) Poly(ethylene glycol) grafted to quartz: analysis in terms of a site-dissociation model of electro-osmotic fluid flow. *Langmuir 11*, 2768–2776.

(14) Podyminogin, M. A., Lukhtonaov, E. A., and Reed, M. W. (2001) Attachment of benzaldehyde-modified oligodeoxynucleotide probes to semicarbazide-coated glass. *Nucleic Acids Res. 29*, 5090–5098.

(15) Lamature, J. B., Beattie, K. L., Burke, B. E., Eggers, M. D., Ehrlich, D. J., Fowler, R., Hollis, M. A., Hollis, B. B., Kosicki,

B. B., Reich, R. K., and Smith, S. R. (1994) Direct detection of nucleic acid hybridization on the surface of a charge coupled device. *Nucleic Acids Res. 22*, 2121–2125.

(16) Defrancq, E., Hoang, A., Vinet, F., and Dumy, P. (2003) Oxime bond formation for the covalent attachment of oligonucleotides on glass support. *BioMed. Chem. Lett. 13*, 2683–2686.

(17) Brockman, J. M., Frutos, A. G., and Corn, R. M. (1999) A multistep chemical modification procedure to create DNA arrays on gold surfaces for the study of protein-DNA interactions with surface plasmon resonance imaging. *J. Am. Chem. Soc. 121*, 8044–8051.

(18) Herne, T. M., and Tarlov, M. J. (1997) Characterization of DNA probes immobilized on gold surfaces. *J. Am. Chem. Soc. 119*, 8916–8920.

(19) Rogers, Yu-H., Baucom, P. J., Huang, Z. J., Bogdanov, V., Anderson, S., and Boyce-Jacino, M. T. (1999) Immobilization of oligonucleotides onto a glass support via disulfide bonds: a method for preparation of DNA microarrays. *Anal. Biochem. 266*, 23–30.

(20) Kumar, P., Choithani, J., and Gupta, K. C. (2004) Construction of oligonucleotide arrays on a glass surface using a heterobifunctional reagent, N-(2-trifluoroethanesulfonatoethyl)-*N*-(methyl)-triethoxysilylpropyl-3-amine (NTMTA). *Nucleic Acids Res. 32*, e80.

(21) Kumar, P., Agarwal, S. K., and Gupta, K. C. (2004) N-(3-Tri-fluoroethanesulfonyloxypropyl)-anthraquinone-2-carboxamide: A new heterobifunctional reagent for immobilization of biomolecules on a variety of polymer surfaces. *Bioconjugate Chem. 15*, 7–11.

(22) Patnaik, S., Swami, A., Sethi, D., Pathak, A., Garg, B. S., Gupta, K. C., and Kumar, P. (2007) N-(Iodoacetyl)-N′-(anthraquinon-2-oyl)-ethylenediamine (IAED): A new heterobifunctional reagent for the preparation of biochips. *Bioconjugate Chem. 11*, 474–483.

(23) Hermanson, G. T. (1996) *Bioconjugate Techniques*, pp 239−242, Academic Press, San Diego.

(24) Chehade, K. A., and Spielmann, H. P. (2000) Facile and efficient synthesis of 4-azidotetrafluoroaniline: a new photoaffinity reagent. *J. Org. Chem. 65*, 4949–4953.

(25) Nonglaton, G., Benitz, I. O., Guisle, I., Piplier, M., Leger, J., Dubreuil, D., Tellier, C., Talham, D. R., and Bujoli, B. (2004) New approach to oligonucleotide microarrays using zirconium-phosphonate modified surfaces. *J. Am. Chem. Soc. 126*, 1497–1502.

(26) Pharmacia LKB. Gene assembler plus manual, Uppsala, Sweden, 1988.

(27) Torry, S. A., Campbell, A., Cunliffe, A. V., and Tod, D. A. (2006) Kinetic analysis of organosilane hydrolysis and condensation. *Int. J. Adhes. Adhes. 26*, 40–49.

(28) Shen, Y., Wu, T., Zhang, Y., and Li, J. (2005) Comparison of two typed (3-mercaptopropyl)trimethoxysilane-based networks on Au substrates. *Talanta 65*, 481–488.

(29) Li, H., Shih, W. Y., and Shih, W.-H. (2007) Stable aqueous ZnS quantum dots obtained using (3-mercaptopropyl)trimethoxysilane as a capping molecule. *IOP Nanotechnol. 18*, 495605.

(30) Jiang, H., Zheng, Z., and Wang, X. (2008) Kinetic study of methyltriethoxysilane (MTES) hydrolysis by FTIR spectroscopy under different temperatures and solvents. *Vib. Spectrosc. 46*, 1–7.

(31) Jiang, H., Zheng, Z., Li, Z., and Wang, X. (2006) Effects of temperature and solvents on the hydrolysis of alkoxysilane under alkaline conditions. *Ind. Eng. Chem. Res. 45*, 8617–8622.

BC800241K

Poly(2-methacryloyloxyethyl phosphorylcholine) for Protein Conjugation

Andrew Lewis,*,† Yiqing Tang,† Steve Brocchini,‡,§ Ji-won Choi,‡ and Antony Godwin*,‡

Biocompatibles UK Ltd, Weydon Lane, Farnham, Surrey GU9 8QL, PolyTherics Ltd, 2 Royal College Street, London NW1 0TU, and The School of Pharmacy, University of London, 29 Brunswick Square, London WC1N 1AX, United Kingdom. Received June 17, 2008; Revised Manuscript Received September 19, 2008

The water-soluble, biocompatible polymer poly(2-methacryloyloxyethyl phosphorylcholine) (PMPC) was evaluated for protein conjugation. PMPC is a zwitterionic polymer that is able to form a more compact conformation in aqueous solution than poly(ethylene glycol) (PEG). While a terminally functionalized N-hydroxysuccinimide derivative of PMPC was not efficient for conjugation to an amine moiety on interferon-α2a (IFN), we found that a bis-thiol specific derivative of PMPC could be conjugated after reduction of the disulfide bonds in IFN. Utilizing PMPC that displayed a similar hydrodynamic volume to 20 kDa PEG, we evaluated the *in vitro* antiviral and antiproliferative activity and pharmacokinetics of a PMPC-IFN conjugate. As a hygroscopic zwitterionic polymer, PMPC is able to form a compact conformation in aqueous solution, which was found to be more compact than PEG. This suggests that PMPC protein conjugates may display different plasma elimination characteristics than PEG protein conjugates. PMPC-IFN displayed marked resistance to antibody binding in Western blot analysis with a polyclonal anti-IFN antibody while displaying comparable *in vitro* antiviral and antiproliferative activity to PEG-IFN. During an *in vivo* pharmacokinetic study, the absorption $t_{1/2}$ for PMPC-IFN was considerably extended compared to the native IFN and 20 kDa PEG analogue. This is also consistent with the SDS-PAGE result where an apparent reduction in mobility through a hydrated medium was observed. The elimination $t_{1/2}$ was also vastly extended over the native IFN and twice the value of 20 kDa PEG-IFN. This suggests that tissue migration of PMPC-IFN occurs more slowly than the 20 kDa PEG-IFN despite their similarity in hydrodynamic volume, leading to an an improved depot effect, which could explain the longer elimination $t_{1/2}$. In this study, we demonstrate a potential use of PMPCylation as a novel tool for enhancing the pharmacokinetic profile of therapeutic proteins in ways that complement PEGylation.

INTRODUCTION

Medicines that are derived from proteins form a significant proportion of new medicines that are being approved for clinical use. As is well-known, protein-based medicines are burdened by several limitations that increasingly have to be overcome in order for the medicine to gain regulatory approval. Many limitations can be addressed by the covalent conjugation of poly(ethylene glycol) (PEG) to a protein. Protein PEGylation is clinically proven to favorably alter the protein's pharmacokinetics by prolonging its circulation time and to decrease the protein's toxicity profile, especially with respect to the reduction of immunogenicity (*1*−*4*). Prolonging the circulation time is critical for reducing the frequency of administration, thus further lowering the propensity for immunological side effects.

Additional advantages of PEGylation include the potential to increase water solubility and the storage stability of a protein. PEGylation can also decrease the propensity for protein aggregation. Such formulation advantages are critical in preventing the protein from losing activity or from becoming immunogenic. Although existing conjugation technologies often result in significantly less biological activity of the PEG−protein conjugate *in vitro*, the improved bioavailability and reduced immunogenicity *in vivo* leads to a safer and more efficacious medicine. While PEGylation is clinically proven, it is not without limitation, and there are a variety of obstacles and pitfalls to overcome in the continued development of a novel PEGylated biopharmaceutical (*5*). To further improve the properties of polymer−protein conjugates, there is considerable ongoing effort on many different strategies. One strategy is to conjugate other biocompatible, water-soluble macromolecules to proteins. The water-soluble polymers derived from 2-methacryloyloxyethyl phosphorylcholine (MPC) **1** are well-known to be biocompatible.

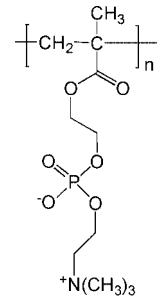

1

Since its earliest reported synthesis in the late 1970s (*6*), the methacrylate-functional monomer, 2-methacryloyloxyethyl phosphorylcholine (MPC), has been the mainstay component used in the synthesis of phosphorylcholine-bearing polymers. These materials have been periodically reviewed with respect to their highly biocompatible nature and consequent application in the medical device field (*7*−*14*). They have found widespread commercialization as bulk materials for contact lenses (*15*, *16*), as coatings on a number of devices including coronary stents (*17*), extracorporeal circuits (*18*, *19*), guidewires (*20*), ureteric

* Corresponding authors. Andrew.Lewis@biocompatibles.com (Tel: ++44 1252 732819). Antony.godwin@polytherics.co.uk (Tel: ++44 207 691 3580).
† Biocompatibles UK Ltd.
‡ PolyTherics Ltd.
§ University of London.

10.1021/bc800242t CCC: $40.75 © 2008 American Chemical Society
Published on Web 10/31/2008

stents and nephrostomy drains (*21*), and tympanostomy tubes (*22*), and as additives in contact lens solutions and cosmetic creams (*23*).

It was the use of MPC polymer (PMPC) coatings on coronary stents to deliver antirestenosis therapies in the bloodstream that demonstrated the potential of PMPC materials in the field of drug delivery (*24*−*36*). In recent years, there have been reports of the use of water-soluble copolymers of MPC for solubilization of drugs such as paclitaxel and amphotericin B (*37*−*39*). A variety of different nanocarrier systems based on PMPC have been described, including blended systems with other polymers such as PLA (*40*, *41*) and DNA complexing systems for gene delivery (*42*−*46*). Some systems have the ability to self-assemble into micelles (*47*, *48*) and polymersomes (*45*, *49*) with drug-carrying properties. Often, these polymers have been made by employing specialized methods of polymerization such as atom transfer radical polymerization (ATRP) (*50*−*53*) and reversible addition−fragmentation chain transfer (RAFT) (*54*) in order to afford more controlled polymer molecular weight distributions and architectures such as diblock copolymers, with low polydispersities.

Miyamoto *et al.* first reported the use of carboxyl-terminated PMPC and PEO polymers that were covalently conjugated to the enzyme papain and demonstrated that the polymers maintained the activity of the enzyme when stored for four weeks compared to native enzyme, the activity of which diminished within one week (*55*). In this case, the PMPC conjugate was more stable than the PEO analogue, with studies suggesting that PMPC induced a small change in the tertiary structure of the papain and inhibited self-digestion of the enzyme. Chiba *et al.* have made terpolymers containing PMPC, cationic DMAEA, and *p*-nitrophenylcarbonyloxyethyl methacrylate to conjugate to hepatitis B surface antigen for specific delivery of DNA to human hepatocytes (*56*). Similar terpolymers with BMA instead of DMAEA have been conjugated to interleukin-2 (IL-2) to target anticancer drugs to tumor cells expressing IL-2 receptors (*57*). Although there has been a very recent report on the use of end-functionalized PMPC for protein conjugation (*58*), there remains no reports on the conjugation of PMPC polymers to therapeutically relevant proteins in an effort to increase the plasma half-life *in vivo*. Since PMPC polymers have a long history of being biocompatible while also being structurally fundamentally different from PEG, it is appropriate to evaluate water-soluble PMPC polymers for therapeutic protein conjugation. Here, we describe the first such example, in which well-defined PMPC made *via* ATRP has been conjugated to interferon-α2a using a novel disulfide bridging linker, and its effects were evaluated in both *in vitro* bioassays and *in vivo* pharmacokinetic study.

MATERIALS AND METHODS

Materials. Reagents and solvents were purchased from either Sigma-Aldrich or Acros and used as received unless otherwise stated. Interferon-α2a (IFN) was purchased from Peprotech (cat. no. 300-02A). The HiLoad Superdex 200 prep grade (cat. no. 17-1069-01), PD-10 (Sephadex G-25 desalting, cat. no. 52-1308-00), HiTrap SP FF cation-exchange (cat no. 17-5054-01), and HiTrap Q FF anion-exchange (cat. no. 17-5053-01) columns were purchased from GE Healthcare. Phosphate buffered saline (PBS) for SEC analysis was prepared from tablets (Oxoid, cat. no. BR0014G). The water used for buffer preparation was deionized and of ultrapure grade I standard.

Instrumentation. Proton NMR experiments were performed on a 400 MHz Bruker NMR spectrometer at 298 K. Samples were prepared by dissolving approximately 10−20 mg of each sample in 0.75 mL of deuterated methanol, chloroform, or water.

The SEC system comprised a guard column and two Viscotek 7.8 mm × 30 cm $GMPW_{xl}$ columns connected to a Viscotek model 270 series dual detector (right-angle laser light scattering (RALLS) and viscometer) and a Viscotek VE 3580 RI detector. The three detectors together comprised the triple detection SEC system referred to herein. The equipment was calibrated using a PEG standard of Mw 21 450 (Polymer Laboratories). The SEC eluent that was used was either 0.2 M $NaNO_3$ with 10% acetonitrile or PBS at pH 7.3 using a flow rate of 0.7 mL/min. The triple detection SEC system was controlled using Viscotek *OmnicSEC 3.1* software. Samples were prepared at a concentration between 3 and 5 mg/mL in the eluent and filtered through 0.2 μm Anotop 10 filters (Whatman cat. no. 6809-1022). All samples were run in triplicate and the results averaged.

The d*n*/d*c* value used (0.142) for the MPC polymers was obtained from a sample of the polymer run at concentrations of 5, 4, 3, 2, and 1 mg/mL (from a stock solution of 80 mg PMPC in 4 mL buffer) on the triple detection SEC system. Conventional calibration was obtained using a set of PEG standards (Polymer Laboratories and Fluka) with Mp values of 167.7, 126.5, 82.3, 40.0, 19.2, and 12.3 kDa on the same SEC system.

The field flow fractionation system comprised a Wyatt Eclipse F separation system (350 μm thick channel; 10 000 MWCO regenerated cellulose membrane) and an Agilent 100 series autosampler running water (with 0.02% w/v azide) at 1 mL/min channel flow and 3 mL/min cross-flow. The analysis system comprised Wyatt DAWN EOS enhanced optical system and Wyatt Optilab DSP Interferometric refractometer. The system was controlled and data analyzed using Wyatt *ASTRA* software v 4.90.04. DAWN calibration was performed with toluene and normalization with BSA monomer.

General ATRP of PMPC Homopolymer Synthesis. The typical protocols of ATRP synthesis of PMPC homopolymers using ethyl 2-bromoisobutyrate, *N*-succinimidyl 2-bromo-2-methylpropionate **3**, Fmoc-protected 2-(2-aminoethoxy)ethyl 2-bromoisobutyrate, and bis-sulfide linker initiator **8** are given below.

Ethyl 2-bromoisobutyrate (0.25 g, 0.127 mmol, 1 equiv) was mixed with 10 mL methanol, and the mixture was subsequently purged with nitrogen over 30 min. Catalysts Cu(I)Br (18.2 mg, 0.127 mmol, 1 equiv) and 2,2′-bipyridine (39.7 mg, 0.254 mmol, 2 equiv) were added to the mixture under nitrogen, and the solution became dark brown immediately under stirring. Solid MPC (6.35 g, 2.16 mmol) was then added to the reaction mixture under nitrogen atmosphere, which followed a temperature increase of 2 to 3 °C due to exothermal polymerization. After 3 h, the reaction was stopped by exposure to air in order to oxidize Cu(I) to Cu(II), and with the addition of 50 mL methanol, the dark brown color of the solution became blue quickly. The blue solution was passed through a silica column to remove the copper catalyst, and the polymer was eluted by adding 150 mL of methanol. The collected solution was evaporated by rotary evaporation to remove methanol, and the colorless solid was further dried under vacuum for 20 h; mass = 6.00 g.

PMPC Bis-Sulfone 10 Synthesis. *(i) Synthesis of ATRP Initiator* **8.** A 50 mL round-bottom flask was charged with the succinimidyl ester bis-sulfide **6** prepared using the procedures already described (*59*) (1 g, 1.88 mmol, 1 equiv) . The flask was sealed with a septum and purged with argon for approximately 1 min. Anhydrous dichloromethane (100 mL) was then added and a solution allowed to form. To the stirred solution, neat 2-(2-aminoethoxy)ethanol (207 μL, 2.13 mmol, 1.13 equiv) was added dropwise and the resulting solution allowed to stir at RT overnight. Volatiles were then removed under vacuum to leave a sticky residue, which was immediately dissolved in ethyl acetate (50 mL). The resulting organic phase was washed with 3 × 30 mL of deionized water (the last 30

mL was acidified with several drops of 0.1 N HCl) and with a saturated brine solution (30 mL). The organic phase was then dried with magnesium sulfate, filtered under gravity, and the solvent removed under vacuum in a 100 mL round-bottom flask. The sticky residue afforded **7**, which was further dried in a vacuum oven at RT overnight and used without further purification. Accurate weighing of the material **7** in the drying flask was not possible, but it appeared to be of high yield and so was taken to be quantitative for the next step. The residue contained in the 100 mL round-bottom flask was sealed with a septum and placed in an argon atmosphere. Anhydrous dichloromethane (10 mL) was then added and a homogeneous solution allowed to form by stirring. Neat 2-bromoisobutyryl bromide (225 μL, 2.06 mmol, 1.1 equiv) was then added. Next, 4-dimethylaminopyridine (11 mg, 0.05 equiv) in dichloromethane (1 mL) was added and the resulting solution allowed to stir at RT overnight. The reaction solution was diluted with ethyl acetate (50 mL), transferred to a separating funnel, and washed in succession with deionized water (50 mL), 0.1 M sodium bicarbonate (15 mL), deionized water (15 mL), and finally with saturated brine (20 mL). The organic phase was dried with magnesium sulfate, filtered under gravity, and the volatiles removed under vacuum to leave a sticky product that was allowed to further dry in a vacuum oven at RT (0.7 g, 56% yield). Final purification was performed using dry flash chromatography. A no. 2 sintered glass funnel (4 cm diameter) was filled with approximately 3 cm depth of silica (BDH, code 153325P). A portion of the product (0.3 g) was dissolved in a small volume of dichloromethane and added to the silica. The column was then eluted with 25 mL portions of dichloromethane, ethyl acetate/hexane (1:2 v/v), ethyl acetate/hexane (1:1.5 v/v), and ethyl acetate/hexane (1:1 v/v). The elution of compounds was followed by TLC analysis (ethyl acetate/hexane 1:1 v/v, UV lamp detection) of the fractions obtained. The ethyl acetate/hexane (1:1.5 v/v) fractions were shown to contain the major product (Rf ~0.4), and these fractions were combined and the volatiles removed under vacuum to leave the desired product **8** (0.13 g). ^{1}H NMR: ($CDCl_3$) δ 1.89 (s, 6H, Ar-CH_3); 2.35 (s, 6H, $(CH3)_2CBr$); 3.19 (A2B2X, 4H, CH_2S); 3.69 (br m, 4H, OCH_2CH_2O); 3.76 (t, 2H, NCH_2CH_2O); 3.79 (m, 1H, COCH); 4.37 (t, 2H, CH_2N); (br s, 1H, NH); 7.06, 7.14 (AB q, 8H, SO_2Ar); 7.60, 7.74 (AB q, 4H, COAr). High resolution mass spectrometry analysis for $C_{33}H_{38}BrNO_5S_2$: theoretical masses should be to 2 sig figs at most (672.14).

(ii) Polymerization Using ATRP Initiator **8.** The bis-sulfide linker initiator **8** (120 mg, 0.18 mmol, 1 equiv) was dissolved in 7 mL methanol, and the mixture was purged with nitrogen over 30 min. After adding Cu(I)Br catalyst (25.8 mg, 0.18 mmol, 1 equiv) and bipyridine (56.2 mg, 0.36 mmol, 2 equiv), solid MPC monomer (3.68 g, 12.6 mmol) was added to the reaction mixture under nitrogen and the solution stirred for 16 h. The reaction was stopped by exposure to air and adding methanol (50 mL). The solution was then eluted through a silica plug (SiO_2 = 30 g) to remove catalyst, and 200 mL methanol was used to further elute the polymer. After solvent evaporation in a rotary evaporator in a 40 °C water bath, the polymer was further dried under vacuum overnight; mass = 3.50 g.

(iii) Fractionation of PMPC Bis-Sulfide **9** *and Oxidation to PMPC Bis-Sulfone* **10.** A solution of the crude PMPC bis-sulfide polymer in deionized water (150 mg/mL) was loaded (2.0 mL) onto a Superdex 200 column running with a pH 4.0, 20 mM sodium acetate mobile phase at 1 mL/min, and with UV detection at 280 nm. Fractions of elute were collected every 1 min during peak elution. Typically, three runs were performed and fractions 60−61, 61−62, and 62−63 min were combined since this was equivalent to the peak of 20 kDa PEG when run under the same conditions. The 9 mL obtained was then concentrated to approximately 2 mL using a 7 mL ICON centrifugal concentrator (MWCO 7000; Pierce). The sample was diluted to 6 mL using deionized water and then reconcentrated to about 1 mL. This step was then repeated.

The 1 mL of concentrated PMPC bis-sulfide in water was diluted with methanol (1 mL) and under stirring Oxone was added (7 mg). The 2 mL solution was then allowed to stir at RT overnight. The solution was then diluted to 2.5 mL with deionized water (0.5 mL) and loaded onto a PD-10 desalting column (pre-equilibrated with deionized water) to remove Oxone. After discarding the 2.5 mL of flowthrough, the column was eluted with a further 3.5 mL of deionized water and the eluent allowed to drip into 35 mL of ice-chilled acetone. The solid that precipitated was isolated by centrifugation (4000 rpm, 20 min) with the liquid phase decanted away and the solid dried under vacuum; mass = 27 mg.

Conjugation of PMPC-NHS 4 to IFN. Representative Procedure. To a 1 mL solution of IFN (1 mg/mL, PBS pH 7.7) was added PMPC-NHS ester **4** (192 mg) at RT. The mixture was vortexed for several seconds until homogeneous and then placed at 4 °C for 2 h. The reaction solution was then diluted with 3.2 mL of 25 mM sodium acetate buffer pH 4.0 (no NaCl) and loaded onto a pre-equilibrated 1 mL HiTrap SP FF column (collecting 1 mL load fractions L1 to L4; 0.2 mL for L5). Unreacted polymer was removed by washing the column with 10 mL of fresh buffer (collecting 1 mL wash fractions, W1 to W10). Protein species were then eluted with 10 mL of pH 4.0 acetate buffer containing 1 M NaCl (collecting 1 mL elution fractions E1 to E10). Two fractions containing the highest concentration of protein species (E1 and E2; A280 nm = 0.182 and 0.360, respectively) were combined and purified by SEC, collecting fractions every 1 min. Fractions were analyzed by SDS-PAGE for conjugation.

Conjugation of MPC Bis-Sulfone 10 to IFN; *in vivo* Sample Preparation Described. IFN (1 mg) was reconstituted with deionized water (1 mL) and reduced with the addition of dithiothreitol (DTT, 10 μL of a 0.4 M stock solution, 4 mM DTT final concentration) at RT for 30 min. The DTT was then removed and the buffer exchanged to PBS pH 8.2, 5 mM EDTA, using a PD-10 column pre-equilibrated with PBS pH 8.2, 5 mM EDTA. After loading the 1 mL of protein solution, the column was eluted with 5 mL of fresh buffer (collecting 1 mL elution fractions E1 to E5). Fractions E3 and E4 were identified as containing reduced protein by their A280 nm readings (typically 0.700 and 0.250, respectively) and were combined to give a 2 mL solution.

Five milligrams of the PMPC-bis-sulfone **10** was then added to the reduced IFN and the polymer allowed to dissolve with gentle shaking. The solution was then placed at 4 °C overnight. An oxidizing glutathione solution (50 μL; 1.5 mg reduced glutathione and 3.0 mg oxidized glutathione in 1 mL of PBS, pH 8.2) was then added and the solution incubated at 4 °C for further 48 h. The solution was then diluted to 2.5 mL with fresh buffer (0.5 mL) and buffer exchanged to 10 mM Tris, pH 8.0 (no NaCl), using a PD-10 column (3.5 mL solution resulting). A second batch of IFN was also PMPCylated as described (0.6 mg IFN, 2.5 mg PMPC-bis-sulfone). The two PMPCylated IFN solutions in 10 mM Tris were combined, and the polymer−protein conjugate was isolated by ion exchange chromatography followed by size-exclusion chromatography as described below.

For ion exchange, a 1 mL HiTrap Q FF anion-exchange column was equilibrated with 10 mM Tris buffer, pH 8.0 (no NaCl). The protein solution was loaded onto the column using a peristaltic pump and the filtrate collected as the load fraction. The column was then washed with 10 mL of fresh 10 mM Tris buffer to remove any unreacted PMPC polymer (collecting 1 mL wash fractions W1 to W10). The column was then eluted

with 5 mL of 10 mM Tris buffer containing 0.7 M NaCl to elute all protein species (collecting 1 mL elution fractions E1 to E5). The two fractions containing the highest concentration of protein species (E2 and E3; A280 nm = 0.799 and 0.166, respectively) were subsequently combined and purified by SEC in a single run (PBS pH 7.3). Fractions were collected every 1 min during the peak elution and stored immediately at 4 °C. Fractions 68−69, 69−70, 70−71, and 71−72 min were pooled to give the sample for *in vivo* evaluation.

SDS-PAGE. SDS-PAGE was carried out using either NuPAGE 4−12% or 12% Bis-Tris gels (1 mm, 10 or 12 wells, Invitrogen cat. nos. NP0321BOX and NP0342BOX, respectively). SeeBlue prestained molecular weight marker proteins (5 μL, Invitrogen cat. no. SEE50225) with an apparent mass range from 3 to 191 kDa were used for calibration. Aqueous solutions of polymers were prepared between 1 and 4 mg/mL. To a 20 μL sample of each polymer was added 5 μL of LDS running buffer (Invitrogen cat. no. 1191942). The resulting mixtures were vortexed, and between 10 and 25 μL of each was added to the appropriate well. The running conditions were 200 V for approximately 50 min in MOPS SDS running buffer (Invitrogen cat. no. 124555). After running, the gels were placed in a protein fixing solution of methanol/water/acetic acid 50: 40:10 v/v/v and stained using a colloidal blue stain (Invitrogen cat. no. 46-7015).

Quantification of Protein in PMPC Conjugates. The concentration of IFN in a pooled conjugate solution was determined by Micro BCA assay according to the manufacturer's instructions (Micro BCA assay kit, Pierce cat. no. 23235). Briefly, 150 μL of reagent was mixed with 150 μL of sample and incubated for 3 h at 37 °C. Absorbance was then measured at 570 nm. The concentration was determined after obtaining a standard curve from different concentrations of unconjugated IFN standard (see Supporting Information). The PMPC polymer on its own did not interfere with the Micro BCA assay.

Hemolysis. A 2-fold dilution series was made for each of the PMPC and PEG polymers (100 mg/mL stock in PBS) in RPMI 1640 media (with L-glutamine; Invitrogen cat. no. 21875-034) to give a range from 4 mg/mL to 31.25 μg/mL. To 96-well V-bottom tissue culture plates were added 100 μL of each dilution in duplicates. Triton-X (1%) was used as positive control. Red blood cells (RBCs) were prepared by layering 20 mL of single donor blood on 10 mL of Ficoll-Paque PLUS (GE Healthcare cat. no. 17-1440-02). After a 15 min centrifugation at 600 *g*, RBCs could be isolated as sediment. A 2% solution was prepared by diluting the RBC solution in RPMI 1640 media, then aliquoted into the sample plate (100 μL/well). After the desired incubation period at 37 °C (up to 3 h), the plates were centrifuged at 600 *g* for 10 min to sediment the RBCs. Following this, 100 μL of the supernatant fraction was carefully transferred to a new 96-well flat-bottom tissue culture plate, and the absorbance was measured at 490 nm using a spectrophotometer.

Western Blot Analysis. For the Western blot analysis, the SDS-PAGE gel following an electrophoresis step was assembled for a wet electroblotting and the resolved proteins transferred onto nitrocellulose membrane (Hybond ECL; GE Healthcare cat. no. RPN2020D). The condition used was 100 V for 1 h in transfer buffer (25 mM Tris, 192 mM glycine, 20% methanol). Cold packs and magnetic stirrer were used to dissipate heat generated during the transfer. After the transfer was complete, the membrane was blocked in 5% skimmed milk/TBST (10 mM Tris, 150 mM NaCl, 1% Tween 20) for 1 h at RT on a rocking platform, then briefly washed 5 times with TBST by agitation. Primary polyclonal anti-IFN-α rabbit antibody (R&D Systems cat. no. 31130-1) was then added at a dilution of 1:10 000 and was allowed to bind from overnight to 72 h at 4 °C on a rocking platform. Membrane was then washed for 15 min twice with TBST by agitation on a shaker. Secondary anti-rabbit HRP-conjugated antibody (GE Healthcare cat. no. NA934-1 ML) was added at a dilution of 1:10 000 and incubated for 1 h at RT on a rocking platform, and the membrane was subsequently washed by agitation with TBST twice at 15 min per wash. Bands containing IFN were identified and visualized by chemiluminescence using ECL reagent as per manufacturer's instruction (GE Healthcare cat. no. RPN2209) and by exposing the membrane onto an autoradiography film (Hyperfilm ECL; GE Healthcare cat. no. RPN1674K) in a dark room.

Antiviral Activity of PMPC-IFN. Antiviral activity of PMPC-IFN was analyzed using lung fibroblast cells, A549 (ECACC, cat. no. 86012804). A549 cells were cultured in DMEM media (high glucose with D-glucose; Invitrogen cat. no. 10938-025) supplemented with 10% fetal calf serum (FCS, EU approved, heat-inactivated; Invitrogen cat. no. 10108-165) and antibiotics (penicillin−streptomycin solution; Invitrogen cat. no. 15070-063). Before plating, cells were trypsinized and suspended at a concentration of 0.2×10^6 cells/mL. Cells were then plated at 50 μL/well on 96-well flat-bottom tissue culture plates and were allowed to adhere at 37 °C. On the following day, PMPC-IFN samples were diluted in DMEM/10% FCS at twice the desired concentration and added to wells (50 μL/well) in quadruplicate. After 24 h, media were removed and a working dilution of encephalomyocarditis virus (EMCV; LGC Promochem cat. no. VR-129B) was added to each well (50 μg/mL). The plates were then cultured until virus-induced cell death was observed. Media containing the virus was removed and the cells washed with PBS (300 μL/well) to remove cellular debris. Cells were then stained with 4% formaldehyde/0.1% methyl violet 2B (50 μL/well; Sigma-Aldrich cat. no. 19809-9) for 30 min. Stain was then removed by aspiration and the plates washed twice in PBS (300 μL/well). Solubilization of the stain was achieved by agitation with 10% SDS (50 μL/well) and the absorbance was measured at 570 nm using a spectrophotometer. If the absorbance exceeded the upper limit of detection, the stain was diluted by adding 150 μL of water into each well and subsequently removing 100 μL of solution. The optical densities were plotted against the IFN concentration and a curve fit was drawn using a nonlinear regression to determine the 50% effective dose (ED_{50}).

Antiproliferative Activity of PMPC-IFN. Antiproliferation activity of PMPC-IFN was measured in lymphoblast cells, Daudi (ECACC cat. no. 85011437). Daudi cells were cultured in RPMI 1640 supplemented with 10% FCS and antibiotics. For seeding, cells were suspended in 0.2×10^6 cells/mL and plated into 96-well U-bottom tissue culture plates at 20 000 cells/well (100 μL/well). PMPC-IFN samples were diluted in RPMI 1640/10% FCS at twice the desired concentration and 100 μL added to each well in quadruplicates. After 72 h, 20 μL of MTT (Sigma-Aldrich cat. no. M5655-1G; 5 mg/mL in RPMI 1640; filtered) was added to each well and incubated for 5 h at 37 °C. The plates were then centrifuged at 500 g for 10 min and the supernatant carefully removed. To each well was added 50 μL of DMSO (Sigma-Aldrich cat. no. 154938-2 L) and the solution agitated until the purple formazan crystals were completely dissolved. The solution was then transferred to a 96-well flat-bottom tissue culture plate for better optical uniformity, and the absorbance was measured at 570 nm using a spectrophotometer.

Pharmacokinetic Study of PMPC-IFN in Mice. The pharmacokinetic properties of PMPC-IFN were investigated in a mouse model using C57BL/6 mice. IFN (Roferon-A, Roche) and 40 kDa PEG-IFN (Pegasys, Roche) were also tested in parallel as references. The time courses were determined according to the published half-lives of IFN and PEGylated IFNs. Time points selected for IFN were 0.5, 1, 2, 4, 6, and

Table 1. Characterization and Comparison of PMPC to PEG by GPC Using PEG Calibration and Triple Detection

	triple detection GPC		conventional GPC[a]			RT (~25 °C)		37 °C	
polymer batch	M_n[b] (kDa)	M_w/M_n	M_n[b] (kDa)	M_w/M_n	ratio[c]	Rh[d] (nm)	IV[e] (dL/g)	Rh (nm)	IV (dL/g)
PMPC-1	15.5	1.08	9.0	1.26	0.58	2.37	0.052	2.40	0.054
PMPC-2	22.0	1.16	12.7	1.30	0.58	2.93	0.065	2.97	0.067
PMPC-3	58.1	1.19	26.6	1.33	0.46	5.00	0.120	5.18	0.124
PMPC-4	89.5	1.41	37.0	2.01	0.41	6.83	0.176	7.06	0.184
PMPC-5	100.7	1.58	–	–	–	7.61	0.202	–	–
PEG-12 k	8.7	1.16	9.2	1.26	1.05	3.25	0.231	–	–
PEG-20 k	16.5	1.06	15.6	1.16	0.95	–	–	–	–
PEG-21.5 k[f]	20.7	–	–	–	–	4.95	0.363	–	–
PEG-40 k	36.1	1.05	33.0	1.22	0.91	6.64	0.498	–	–

[a] PEG calibration. [b] kDa. [c] The ratio of M_n values determined by conventional GPC using PEG calibrants to M_n values determined by triple detection. [d] Hydrodynamic radius. [e] Intrinsic viscosity. [f] PEG calibrant standard with a M_w value of 21 450 Da.

12 h post-injection and for PMPC-IFN and PEG-IFN the time points were 1, 2, 6, 12, 24, 48, and 72 h post-injection. For each time point, 5 mice were injected subcutaneously. At selected time points, mice were sacrificed and the serum collected by incubating the blood for 30 min at RT followed by centrifugation at 600 g for 10 min at 15 °C to sediment the blood cells. Serum samples were then stored at −80 °C until use. A fixed amount of two sets of pooled serum from 5 mice was assayed using an antiviral assay.

Data Analysis and Statistics. Data analyses were performed using GraphPad *Prism 5.0* software. All statistical values shown are expressed as mean ± SEM.

RESULTS AND DISCUSSION

PMPC Synthesis. It was first necessary to evaluate the properties of PMPC in comparison to PEG. We prepared a series of PMPC polymers with different molecular weights by ATRP using ethyl 2-bromoisobutyrate as the initiator and methanol as the solvent at RT. The ATRP of PMPC in methanolic medium is well-controlled, affording narrow molecular weight distributions (*51, 52*). The polydispersity (M_w/M_n) from conventional SEC and triple detection SEC in Table 1 suggest a controlled polymerization especially at low target DP, and the molecular weight of PMPC measured by conventional GPC was close to target molecular weight. However, with high target molecular weights (entries 4 and 5), the polymerization lost some control, which led to higher polydispersities, attributable to the fast conversion at increased monomer concentration (*51, 52*). The molecular weight from conventional GPC using PEG calibrant was significantly lower than the target at higher molecular weight (sample PMPC-3 and PMPC-4), a trend observed in the literature (*52*). The yield of PMPC polymers made by ATRP was high, above 90% within the period of 10 to 24 h.

The molecular weight characteristics of five PMPC polymers (batches PMPC-1 to PMPC-5; Table 1) were obtained by conventional SEC (using PEG calibrants) and by triple detection SEC for absolute molecular weight determination. All these PMPC polymers were soluble to at least 10 mg/mL in aqueous buffers between pH values of 4.0 to 7.3. The triple detection system comprised refractive index, light scattering (90°), and viscometry detectors, and the molecular weight characteristics were obtained using a d*n*/d*c* value of 0.142 (the value is almost the same as that reported in the literature (*39*), 0.142 for $PMPC_{96}-BMA_{76}$ at 632.8 nm). The molecular weight characteristics of PMPC-2 and PMPC-3 were also determined by field flow fractionation where M_n (M_w/M_n) values of 27.1 kDa (1.16) and 63.3 kDa (1.17) were obtained, respectively. Four commercial PEG samples (from 12 to 40 kDa) were used for comparison (Table 1).

As expected, the zwitterionic character of the PMPC polymers afforded a more compact conformation in aqueous solution compared to the more open solution conformation of PEG (*60, 61*). This can be seen by comparing the hydrodynamic radii between PMPC and PEG polymers of different absolute molecular weights (Table 1). The molecular weights (M_n) that were obtained by light scattering and by conventional SEC using PEG calibrants also illustrate the difference in PMPC and PEG solution conformations. Little change in PMPC hydrodynamic radii occurred when measured at 37 °C, suggesting that the more dense structure of PMPC could be maintained *in vivo*. More compact PMPC−protein conjugates might be expected to display different tissue uptake characteristics than that observed for their analogous PEG−protein conjugates. Ultimately, the maintenance of a smaller solution conformation of the conjugated polymer could be important to minimize the potential for accumulation of the polymer within the body. For example, the more dense structure of PMPC may result in different extravasation properties into malignant tissue when compared to PEG. Since the denser conformation of PMPC results in a lower viscosity than PEG of comparable solution size, this lower relative viscosity may have advantages in terms of dosing and avoiding safety issues of blood viscosity changes.

Initial Evaluation of PMPC for Protein Conjugation. Before examining PMPC conjugation to IFN, hemolysis assays were conducted with PMPC alone. No hemolysis was observed with any of the PMPC or control PEG polymers at concentrations up to 4 mg/mL for up to 3 h using blood from human donors. This is not surprising, given that PMPC polymers have been primarily developed for use within the body, particularly in applications where blood contact is required such as guidewires (*20*), stents (*17*), extracorporeal circuits (*18*), and blood filtration applications (*62, 63*).

PMPC polymers were compared to PEG using SDS-PAGE in conditions suitable for the analysis of PEG and IFN. Notably, there was no evidence of PMPC staining with the standard protein stains of colloidal blue and silver after background destaining. An increase in molecular weight of the protein bands after conjugation in SDS-PAGE would therefore be indicative of PMPC conjugation. When PEG is used for protein conjugation, the PEG is stained strongly with barium iodide and is slightly stained by colloidal blue and silver.

It was also necessary to determine the properties of PMPC elution over an ion-exchange column suitable for protein purification. Often, non-conjugated polymeric species that are uncharged such as unreacted PEG can be removed by ion-exchange chromatography during the purification of the charged protein−polymer conjugate. Since PMPC is zwitterionic, we were concerned that any unconjugated PMPC might be difficult to remove by ion-exchange chromatography in the presence of protein species. The loading of a 2.5 mg/mL solution of PMPC-2 (1 mL) in 20 mM sodium acetate at pH 4.0 to a cation-exchange column (SP FF) was followed by a 5 mL wash with the same buffer, and then 3 mL of acetate buffer, pH 4.0, with 1 M NaCl added was used to elute any remaining species bound to the

Scheme 1. Synthesis of PMPC-NHS 4

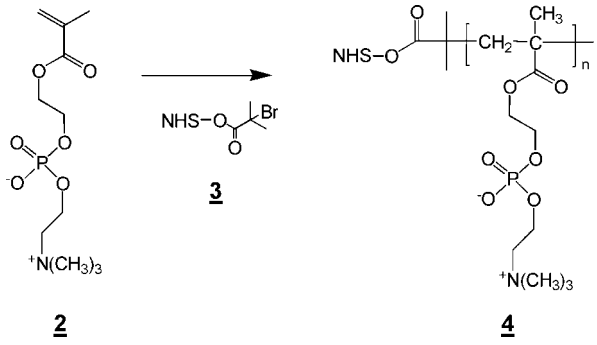

Table 2. Characteristics of PMPC-NHS

polymer	M_n PEG equivalent (Da)	NHS[a] (%)
PMPC-NHS-1	6800	46
PMPC-NHS-2	8700	51

[a] The H NMR integral at 2.9 ppm used for the four protons in NHS and the integral at 0.8 to 1.4 for the three protons of the main chain methyl on MPC.

column. These conditions are often used to remove unreacted PEG, while the protein species are retained on the column until the application of the high salt elution buffer. By spotting the fractions collected on a TLC plate and staining with phosphomolybdic acid for detection, PMPC polymer was found to pass straight through the column in the loading fraction and low salt wash in the same manner as PEG, confirming that PMPC−protein conjugates would be suitable for purification by ion-exchange chromatography.

Preparation of Functional PMPC Polymers for Protein Conjugation. Many PEGylation reactions have been conducted by acylation of protein amines with PEG reagents that are functionalized at one terminus with an *N*-hydroxysuccinimide (NHS) active ester. Using the initiator **3** (*64*), we prepared the NHS-functionalized PMPC polymer **4** (Scheme 1). A linear relationship of the evolution of M_n *vs* conversion demonstrated that the polymerization had a living characteristic (unpublished data), and the relatively low polydispersities (PD 1.2−1.3) showed a controlled polymerization. However, the NHS functional group on the PMPC polymer was sensitive to hydrolysis due to the hygroscopicity of MPC monomer and polymer. Monitoring proton NMR spectra of the polymer indicated that the ratio of NHS and methyl group on PMPC backbone gradually decreased with storage, meaning a loss of the NHS functional group over time. The data in Table 2 shows that only half of the PMPC sample remained functionalized with the NHS groups at the time of conjugation.

A series of experiments were performed under different conditions, varying pH (6.5 to 8.0), NHS ester to protein equivalence (20 to 840), and reaction time (2 to 18 h). Although many different conditions were tried for the MPCylation of IFN using an PMPC-NHS ester, no evidence of conjugation was found by SDS-PAGE analysis. One reaction sample (pH 7.7) was purified by ion-exchange and then size-exclusion chromatography, but only non-conjugated IFN was observed after analyzing the chromatographic fractions by SDS-PAGE, which confirmed that the PMPC-NHS ester had not undergone reaction with IFN. Since proton NMR analysis of PMPC-NHS indicated that a significant proportion of the polymer was functionalized (49%), some conjugation was expected to be observed, given the sufficient excess that was used. The PMPC-NHS **4** was however shown to be reactive toward the small molecule benzylamine in methanol by the disappearance in the NMR spectrum of the diagnostic NHS ester methylene signals at 2.9 ppm. This suggests that the accessibility of the linker group on the relatively large PMPC polymer may be low toward large protein molecules in an aqueous environment. We also wanted to prepare a functional PMPC polymer capable of thiol-selective conjugation. Amine conjugation is less efficient and selective than thiol-based conjugation in mild conditions (i.e., pH 6.5 to 7.5) that are appropriate for maintaining the activity of most therapeutic proteins. Many therapeutically relevant proteins do not have accessible cysteines that can be used for conjugation, so amine conjugations have predominated. Since cysteines are found paired as disulfides in many therapeutically relevant proteins, we have recently prepared PEG reagents that are capable of site-specific conjugation to both sulfur atoms that derived from a disulfide bond (*59*−*67*). Such reagents are capable of exploiting the increased efficiency and selectivity of native thiols in proteins.

Our PEGylation reagents **5** have a substituted propenyl conjugating moiety that comprises an electron-withdrawing group (e.g., carbonyl), an α,β-unsaturated double bond, and α β′-sulfonyl group that is prone to elimination as sulfinic acid (Scheme 2). The electron-withdrawing group promotes thiol addition, and the conjugated double bond in the PEG monosulfone **5** is required to initiate a sequence of interactive and sequential addition−elimination reactions (Scheme 2). The addition of the first thiolate anion allows the elimination of a sulfinic acid derivative. This generates another conjugated double bond at the α,β′-position for the addition of a second thiolate. If the two thiols are derived from a disulfide bond, a three-carbon bridge is formed between the two cysteine sulfur atoms. This juxtaposition of chemical functionality leads to a latently cross-conjugated moiety capable of thermodynamically driven bis-alkylation with the two sulfur atoms that are liberated by the mild reduction of an accessible disulfide within a protein. This results in PEG conjugation *via* a three-carbon bridge that links the two original sulfur atoms (Scheme 2).

To avoid conducting a post-polymerization reaction that involved an acylation or alkylation reaction at the PMPC terminus, we elected to prepare an ATRP initiator that would provide the terminal bis-sulfone moiety (Scheme 3). Since the bis-sulfone end group can undergo *in situ* elimination of one sulfinyl moieties to give alkenyl monosulfones such as **5** (Scheme 2), the bis-sulfide initiator **8** (Scheme 3) was chosen, as it was more likely to be stable during the polymerization. The functionalized ATRP initiator **8** was prepared in two steps from the NHS activated bis-sulfide **6** with an overall crude yield of 55%. After purification, the initiator **8** was used in the ATRP conditions to give the PMPC bis-sulfide **9**. The bis-sulfide initiator is soluble in methanol and stable under the condition of ATRP and purification. The polymerization of MPC initiated by **8** followed the general protocol; copper(I) catalyst was mixed with nitrogen-purged methanol solution of initiator **8** first, followed by the addition of MPC powder. It is observed that the bis-sulfide functional group on α-bromoester has no remarkable effect on the initiation of ATRP of MPC, which was fast and showed controlled polymerization (PD 1.2−1.4), compared to other initiators used in this study, such as ethyl 2-bromoisobutyrate, *N*-succinimidyl 2-bromo-2-methylpropionate **3** (*64*), and Fmoc-protected 2-(2-aminoethoxyl)ethyl 2-bromoisobutyrate (*68*). The PMPC bis-sulfide terminated polymers **9** were prepared with number average molecular weights ranging from approximately 20 to 50 kDa as determined by triple detection SEC (Table 3).

The bis-sulfide polymers **9** displayed narrow molecular weight distributions with polydispersities (M_w/M_n) that ranged from 1.2 to 1.4. These are the expected values for polymers that are prepared from a controlled radical polymerization reaction. PEG, however, has been prepared over many decades and is routinely

Scheme 2. Mechanism for Bridging PEGylation

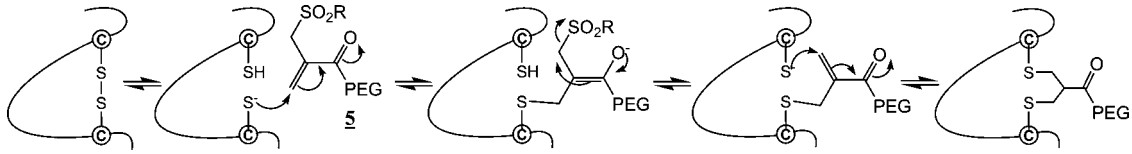

Scheme 3. Synthesis of the Bis-Sulfide Initiator 8 Followed by Its Polymerzation to Give the Precursor PMPC Bis-Sulfide 9 That Was Then Oxidized with OXONE to Give the Desired PMPC Bis-Sulfone 10

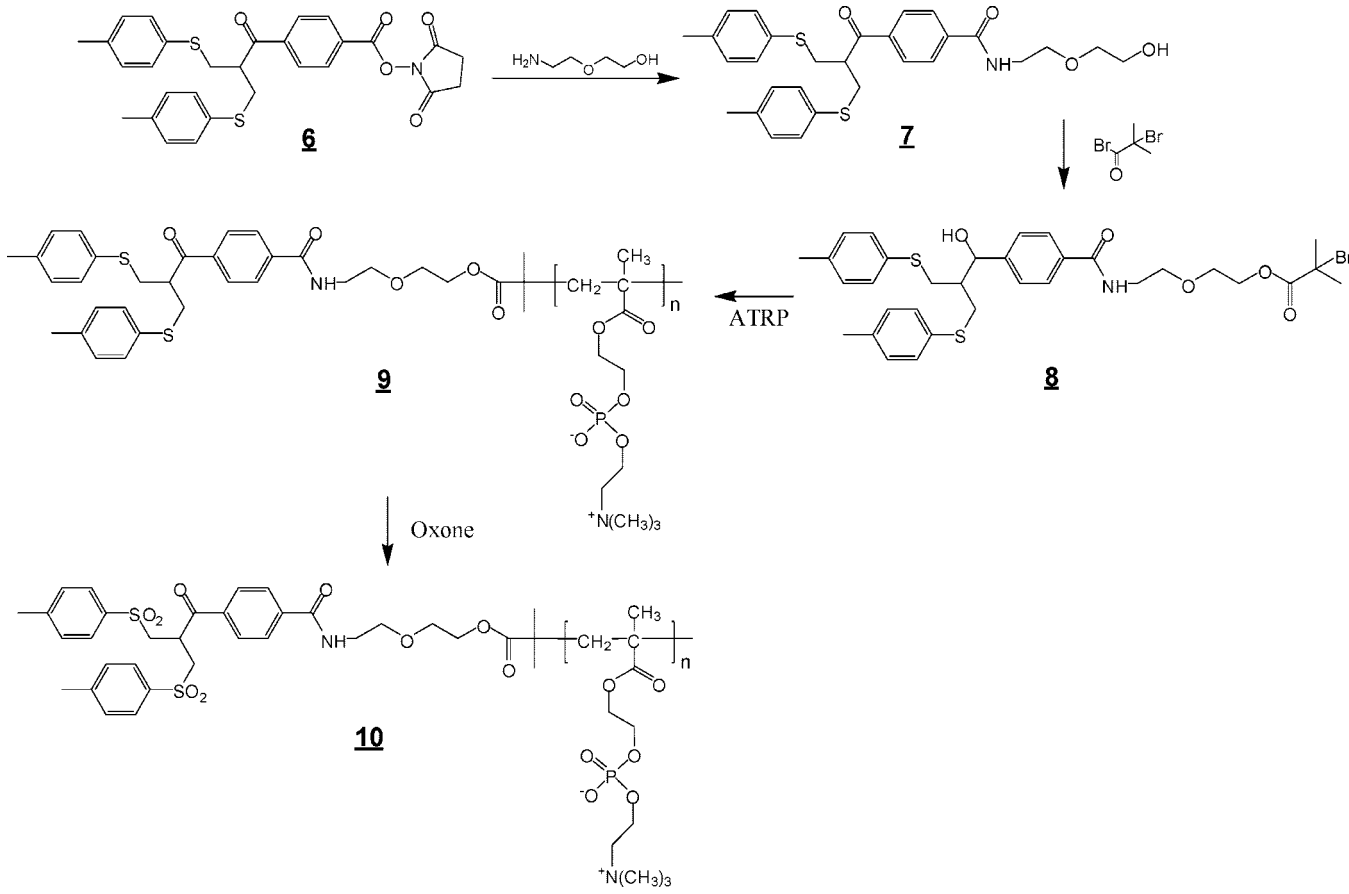

Table 3. Analysis of PMPC Bis-Sulfide Polymers 9 by Triple Detection SEC

PMPC bis-sulfide	*M*n (kDa)	M_w/M_n
PMPC bis-sulfide **9a**	21.2	1.20
PMPC bis-sulfide **9b**	25.5	1.24
PMPC bis-sulfide **9c**	37.8	1.19
PMPC bis-sulfide **9d**	47.2	1.28

available at polydispersities of less than 1.1 for molecular weights less than 40 kDa.

To improve homogeneity during conjugate preparation and characterization, it was decided to fractionate the PMPC bis-sulfide polymer **9** to reduce the polydispersity. Our initial experiments were conducted by running PMPC bis-sulfide batches **9c** and **9d** (2 mL of 85 to 150 mg/mL solutions loaded) separately over a Superdex 200 size-exclusion column with HPLC-grade water as the mobile phase (1 mL/min). The UV absorbance at 280 nm was used to detect the polymer, and 1 mL fractions were collected separately every minute during peak elution. Some of the fractions from both the **9c** and **9d** fractionations were then pooled into three batches (fractions 60−67 min, 68−75 min, and 82−85 min) and their molecular weight characteristics determined by triple detection SEC analysis (Table 4). The polydispersities of all three pooled samples were between 1.13 and 1.17, compared to 1.19 to 1.24

Table 4. Triple Detection SEC Analysis of Fractionated PMPC Bis-Sulfide Polymers 9c and 9d That Were Fractionated Separately in Water Using a Superdex 200 Column and Then Pooled

pooled PMPC fractions from SEC fractionation	M_n (kDa)	M_w (kDa)	M_w/M_n
60−67 min[a]	56.3	65.6	1.17
68−75 min[a]	46.5	52.4	1.13
80−86 min[a]	32.9	37.8	1.15
62−66 min[b]	44.2	51.3	1.16
72−75 min[b]	31.6	38.9	1.23
82−85 min[b]	29.1	34.5	1.19

[a] Fractions from **11c** and **11d** pooled. [b] Fractions from **11c** only pooled.

before fractionation. Combining a select fraction (**4** from **8**) from **11c** fractionation only did not lead to a reduction in polydispersity (Table 4). Later fractionations of PMPC were performed using a mobile phase of 20 mM sodium acetate at pH 4.0 to minimize any pH-related conformational changes in the polymer and to minimize the resulting polydispersities. We found that the retention times of the fractionated samples when rerun on the SEC column were reproducible under these conditions after oxidation of the end group to the bis-sulfone **12** form (Table

Table 5. Reproducible Retention Times of PMPC Bis-Sulfone 10 That Was Fractionated as PMPC Bis-Sulfone 10 Using a Superdex 200 Column at pH 4.0 with Sodium Acetate Buffer and Comparison with 20 kDa and 30 kDa PEG

PMPC SEC fractions pooled	peak[a] for pooled PMPC rerun on SEC	PEG comparison data: peak[a] and M_n
57−60 min	58.3 min	55.4 min; 30 kDa
60−63 min	60.2 min	61.3 min; 20 kDa

[a] Time of maximum peak height.

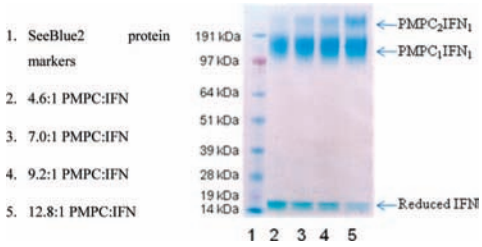

Figure 1. SDS-PAGE gel showing reaction solutions for PMPC disulfide bond conjugation to IFN. Ratios indicate the mass to mass ratio of PMPC that was added to reduced IFN.

5). In a further fractionation, the retention times of 20 and 30 kDa PEG polymers ($M_w/M_n = 1.12$) were used (Table 5) to decide which PMPC fractions to pool so that a comparison with PEG could be made after protein conjugation. To prepare PMPC for the conjugation to IFN for the *in vivo* study, the fractions from 60−61, 61−62, and 62−63 min were combined. This is equivalent to the peak elution when 20 kDa PEG is run under the same condition, which indicates an equivalence of hydrodynamic volume of PMPC to that of a 20 kDa PEG. It should be noted that we were further able to fractionate the resulting PMPC-IFN conjugates using the same method during conjugate purification (i.e., by SEC on the Superdex 200 column).

Treatment of the PMPC bis-sulfide **9** overnight with the mild oxidant Oxone gave the desired PMPC bis-sulfone **10** with no trace of the starting bis-sulfide of **9** when analyzed by proton NMR (see Supporting Information). The MPC pendant group signals in the NMR spectrum were consistent with the starting compound and were therefore thought to be unaffected by the oxidation.

PMPC Bis-Sulfone 10 Conjugation to IFN. To utilize the PMPC bis-sulfone **10** for protein conjugation first requires that an accessible disulfide bond in the protein is reduced to give the two free sulfhydrals. Initial conjugations to IFN were thus performed after reducing both of the disulfide bonds of IFN using 4 mM DTT. Following the removal of DTT using a pre-equilibrated PD-10 column, PMPC was added in increasing amounts (4.6 to 12.8:1 PMPC/IFN by mass) to the reduced IFN. Conjugation was performed at pH 8.2 for *in situ* generation of the protein thiol reactive monosulfone from the bis-sulfone **10** added to the conjugation. The reaction solutions were analyzed by SDS-PAGE (Figure 1), which showed two tight bands at high molecular weight. These were attributable to the mono- and di-PMPCylated IFN. Unreacted IFN was also observed in these gels. The relative intensities of the conjugated proteins indicated that the reaction was moderately efficient. Also, increasing the amount of PMPC afforded greater yields of mono- and di-PMPCylated protein.

Mono-PMPC-IFN could be isolated from the reaction mixture using anion-exchange chromatography followed by size-exclusion chromatography (Figures 2 and 3, respectively). The PMPC-IFN bound to the HiTrap Q FF anion-exchange column (elution with 0.05 M NaCl) but less well than the non-conjugated protein (elution with 0.15 to 0.7 M NaCl) due to changes in surface charge density post-polymer conjugation. Similarly to

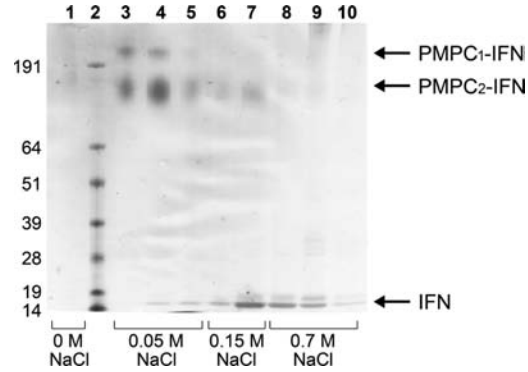

Figure 2. SDS-PAGE gel of anion-exchange chromatography fractions showing a typical purification of a PMPC-IFN reaction.

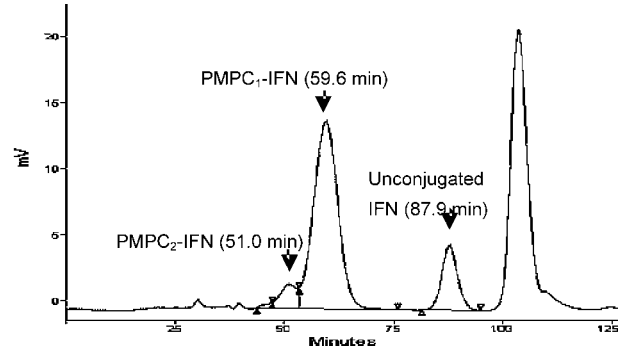

Figure 3. Representative size-exclusion chromatogram showing isolation the mono-PMPC-IFN. Column, HiLoad 16/60 Superdex 200 prep grade; mobile phase, PBS pH 7.3, 250 mM NaCl, 1.0 mL per min; A280 nm detection.

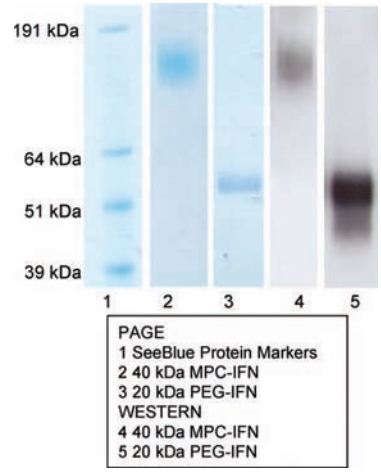

Figure 4. SDS-PAGE and Anti-IFN Western blot for *in vivo* PMPC-IFN candidate (lanes 2 and 3) and comparison with the 20 kDa disulfide bond PEG-IFN (lanes 4 and 5).

PEGylation, this difference was exploited for an effective separation of the two protein species as well as unreacted PMPC for the chromatography step. To ensure that all of the unreacted IFN was removed from the product, a second purification step was performed using size-exclusion chromatography. Fractions were collected every minute (Figure 3), and those fractions forming the peak for mono-PMPC-IFN were then pooled for further study.

SDS-PAGE and Western blot analysis using a polyclonal anti-IFN-α antibody was performed on the purified PMPC-IFN and compared to the 20 kDa PEG-IFN prepared by the same disulfide bond conjugation method (Figure 4). In both methods,

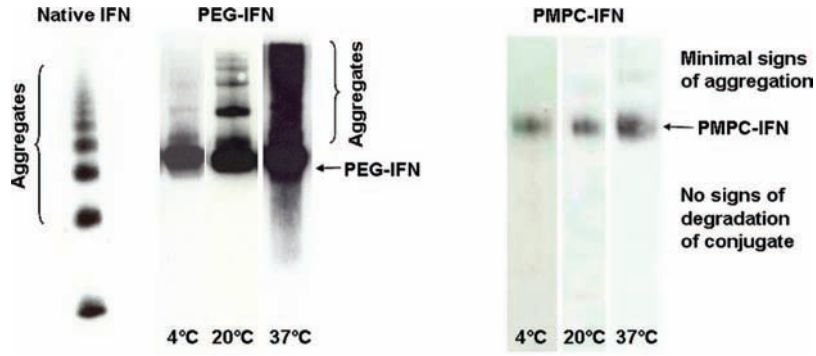

Figure 5. Stability of PEG-IFN (left) and PMPC-IFN (right) after 7 days at 4, 20, and 37 °C. PMPC-IFN shows high resistance toward self-aggregation. Of note, PMPC-IFN required longer incubation with anti-IFN antibody than PEG-IFN.

Table 6. Antiviral and Antiproliferative Activity of 20 kDa PEG-IFN, 20 kDa PEG equivalent PMPC-IFN, and 40 kDa PEG-IFN (Pegasys)

conjugates	ED_{50} (pg/mL)	IFN activity (%)
	Antiviral Activity	
IFN	12 ± 1	100
20 kDa PEG-IFN	75 ± 30	16.1
20 kDa PEG eq. PMPC-IFN	66 ± 10	18.1
	76 ± 4	15.8
	Antiproliferative Activity	
IFN	17 ± 2	100
20 kDa PEG-IFN	435 ± 116	3.9
20 kDa PEG eq. PMPC-IFN	524 ± 113	3.2

Table 7. Comparison of Absorption and Elimination Half-Lives of PMPC-IFN Conjugates

species	absorption $t_{1/2}$ (h)	elimination $t_{1/2}$ (h)	t_{max} (h)
IFN	<0.5[a]	0.8 ± 0.1	0.8 ± 0.2
PMPC-IFN	7.3 ± 0.3	24 ± 2	16 ± 4
PEG-IFN[b]	3.3	12.3	4
Pegasys[c]	7.4 ± 0.2	>50	16 ± 4

[a] No data point before 0.5 h. [b] Literature value (*2*). [c] In agreement with literature.

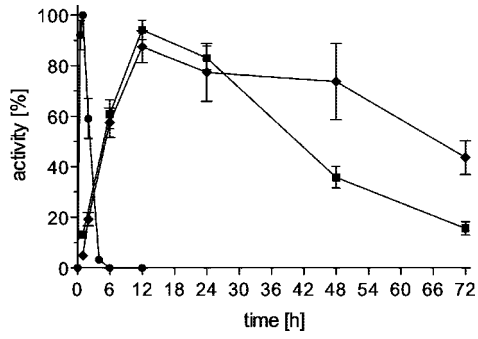

Figure 6. Pharmacokinetic profiles of IFN (●), 40 kDa PEG-IFN (◆), and 20 kDa PEG equivalent PMPC-IFN (■). Percentage activity of IFN, PEG-IFN, and PMPC-IFN was measured from their respective maximal activity.

purified PMPC-IFN was shown as a single high molecular weight band with no detectable free unconjugated IFN present. Of note, optimal detection of PMPC-IFN by Western blot required an incubation time with primary antibody of at least 72 h compared to that of PEG-IFN, which required 24 h. Furthermore, the migration distance of PMPC-IFN was less than that of the PEG-IFN conjugate of equivalent hydrodynamic volume. Given the property of the PMPC polymer to form a much more compact structure than the PEG of equivalent size in aqueous condition, the greater retention seen with the PMPC-IFN is likely due to the much greater size of the unravelled PMPC polymer in the presence of SDS.

Native IFN is known to aggregate over time if not stored correctly. Both the PEG and PMPC-IFN conjugates were stored at 4, 20, and 37 °C for one week and Western blot analysis performed (Figure 5). The PEG-IFN showed minimal aggregation at 4 °C, but severe aggregation at 20 and 37 °C. Notwithstanding the lower intensity of staining for the PMPC-IFN due to the increased resistance toward antibody binding, there was little suggestion of aggregation and no signs of degradation across all storage temperatures. This is indicative of an increased stability of the PMPC-IFN conjugate relative to the PEG-IFN and native protein.

Antiviral and Antiproliferative Activity of PMPC-IFN. We evaluated the *in vitro* antiviral and antiproliferative activities of the 20 kDa PEG equivalent PMPC-IFN and compared them against native IFN and 20 kDa PEG-IFN. EMCV and A549 cells for the antiviral assay and Daudi cells for proliferative assay were used (*69*). The ED_{50} values for the assays are shown in Table 6. The results for PMPC-IFN and PEG-IFN show a significant reduction in both activities compared to the native IFN. This is due to steric shielding by PEG or PMPC that is also seen with commercially available PEGylated IFNs and many other PEGylated proteins (*1*) as well as contribution by the linker that is inserted at the disulfide (*66*). Notably, the PMPC-IFN conjugate showed similar activities to the 20 kDa PEG-IFN, which shares the same hydrodynamic volume, in both assays (18.1% and 16.1% for antiviral, respectively; 3.2% and 3.9% for antiproliferative, respectively). Contrary to the Western blot results where IFN-specific antibody showed a markedly reduced detection of PMPC-IFN compared to PEG-IFN, the two *in vitro* assays both suggest that the degree of steric hindrance imposed by PMPC and PEG on protein−receptor interaction are similar at least in terms of their ability to trigger downstream immunological responses.

Pharmacokinetic Study of PMPC-IFN. The pharmacokinetic properties of a 20 kDa PEG equivalent PMPC-IFN were evaluated and compared to those of commercially available IFN-α2a (Roferon-A) and 40 kDa PEG-IFN-α2a (Pegasys) and the absorption and elimination half-life ($t_{1/2}$) determined in a mouse model. The representative absorption and elimination half-lives of IFN, 20 kDa PEG equivalent PMPC-IFN, and 40 kDa PEG-IFN are shown in Figure 6, and the average values presented in Table 7. A commercial formulation of IFN (Roferon-A) showed a mean elimination half-life of 0.8 h. An accurate absorption half-life could not be measured, as no ascending trend was seen within the time points tested indicating its entry into bloodstream within 30 min of subcutaneous injection. The commercial formulation of 40 kDa PEG-IFN (Pegasys) showed a mean absorption half-life of 7.4 h. Elimination half-life was measured as >50 h, as two out of three $t_{1/2}$ values exceeded the range of

time course tested in this study (>60 h). Similarly, the mean absorption and elimination half-lives of 20 kDa PEG equivalent PMPC-IFN showed a substantial extension of blood retention time over that of unconjugated IFN (7.3 and 24 h, respectively). This compares favorably to both IFN (<1 h) and the published value of 12 h for 20 kDa disulfide bond PEGylated IFN (*66*). Alternatively, similar $t_{1/2}$ values were also obtained when the data points from individual data sets were pooled to obtain a combined pharmacokinetic profile.

Taken together, these results clearly indicate that the conjugation of PMPC to IFN leads to a substantial extension in the elimination half-life of IFN. Surprisingly, despite their equivalent solution size, the extension of half-life observed for a 20 kDa PEG equivalent PMPC-IFN was greater than that reported for a 20 kDa disulfide PEGylated IFN. Together with the indication that the PMPCylated IFN is able to retain similar biological activity to its PEGylated equivalent while providing improved protein shielding from IFN-specific antibodies over PEG, these results demonstrate potentially novel properties of PMPC polymer in addition and complementary to the pharmacokinetic improvements to conjugated therapeutic agents.

CONCLUSIONS

IFN can be successfully conjugated with high efficiency to the biocompatible PMPC polymer. Compared to PEG of an equivalent mass, PMPC forms a more compact conformation in aqueous solution. At equivalent hydrodynamic size (20 kDa), this has enabled us to conjugate a dense polymer to IFN, which presented different properties to IFN conjugated with a more flexible PEG. The PMPC-IFN showed remarkable resilience to IFN-specific antibody in the Western blot analysis using a polyclonal anti-IFN antibody compared to PEG-IFN and IFN. While this is not a definitive endeavor to assess the effect of PMPC on immunogenicity, it is a crude indication of how effective PMPC may be on shielding immunogenic epitopes. Considering the dense nature of PMPC compared to PEG, it is also interesting that in the antiviral and antiproliferative assays PMPC-IFN demonstrated a similar potency to PEG-IFN of an equivalent hydrodynamic size. This strongly indicates that the physiological differences between the two biocompatible polymers do not affect their ability to trigger the two immune responses. In the *in vivo* pharmacokinetic study, the absorption half-life for PMPC-IFN was considerably extended compared to the native IFN and also to its disulfide-conjugated PEG analogue reported by Shaunak et al. (*66*), and similar to that of the reference 40 kDa PEG-IFN formulation. This is also consistent with the SDS-PAGE result where an apparent reduction in mobility through a hydrated medium (tissue or gel) was observed. There was also a marked increase in the elimination half-life for PMPC-IFN compared to the native IFN. The $t_{1/2}$ value placed the PMPC-IFN between 20 kDa PEG-IFN and the reference 40 kDa PEG-IFN in its ability to remain in the bloodstream. These results suggest that the tissue migration of the PMPC-IFN occurs more slowly than the 20 kDa PEG-IFN despite their similarity in hydrodynamic volume, leading to an improved depot effect in the tissue and a subsequent longer elimination half-life. Taken together, this work demonstrates a potential for PMPCylation of therapeutic proteins as a novel tool for modifying their *in vivo* characteristics in ways that are similar to PEGylation while offering improved pharmacokinetic enhancement and epitope masking.

ACKNOWLEDGMENT

The authors would like to thank Dr. Christine Wallrapp of CellMed AG for her help in the preclinical study.

Supporting Information Available: Proton NMR of PMPC bis-sulfone **10**. This material is available free of charge via the Internet at http://pubs.acs.org.

LITERATURE CITED

(1) Veronese, F. M., and Pasut, G. (2005) PEGylation, successful approach to drug delivery. *Drug Discovery Today 10*, 1451–8.
(2) Fishburn, C. S. (2008) The pharmacology of PEGylation: Balancing PD with PK to generate novel therapeutics. *J. Pharm. Sci.*
(3) Harris, J. M., and Chess, R. B. (2003) Effect of pegylation on pharmaceuticals. *Nat. Rev. Drug Discovery 2*, 214–21.
(4) Molineux, G. (2002) Pegylation: engineering improved pharmaceuticals for enhanced therapy. *Cancer Treat. Rev. 28*, 13–6, Suppl A.
(5) Gaberc-Porekar, V., Zore, I., Podobnik, B., and Menart, V. (2008) Obstacles and pitfalls in the PEGylation of therapeutic proteins. *Curr. Opin. Drug Discovery Dev. 11*, 242–50.
(6) Kadoma, Y., Nakabayash, N., Masahara, E., and Yamauchi, J. (1978) Synthesis and hemolysis test of the polymer containing phosphorylcholine groups. *Kobunshi Ronbunshu 35*, 423–427.
(7) Ishihara, K., and Iwasaki, Y. (1998) Reduced protein adsorption on novel phospholipid polymers. *J. Biomater. Appl. 13*, 111–27.
(8) Ishihara, K., Nomura, H., Mihara, T., Kurita, K., Iwasaki, Y., and Nakabayashi, N. (1998) Why do phospholipid polymers reduce protein adsorption? *J. Biomed. Mater. Res. 39*, 323–30.
(9) Ishihara, K. (2000) New polymeric biomaterials-phospholipid polymers with a biocompatible surface. *Front. Med. Biol. Eng. 10*, 83–95.
(10) Lewis, A. L. (2000) Phosphorylcholine-based polymers and their use in the prevention of biofouling. *Colloids Surf., B: Biointerfaces 18*, 261–275.
(11) Nakabayashi, N., and Williams, D. F. (2003) Preparation of non-thrombogenic materials using 2-methacryloyloxyethyl phosphorylcholine. *Biomaterials 24*, 2431–5.
(12) Lewis, A. L. (2004) Phosphorylcholine (PC) Technology. In *Encyclopedia of Biomaterials and Biomedical Engineering*, pp 1198−1211.
(13) Nakabayashi, N., and Iwasaki, Y. (2004) Copolymers of 2-methacryloyloxyethyl phosphorylcholine (MPC) as biomaterials. *Biomed. Mater. Eng. 14*, 345–54.
(14) Lewis, A. L. (2006) PC Technology as a platform for drug delivery: from combination to conjugation. *Expert Opin. Drug Delivery 3*, 289–98.
(15) Young, G., Bowers, R., Hall, B., and Port, M. (1997) Clinical comparison of Omafilcon A with four control materials. *CLAO J. 23*, 249–58.
(16) Young, G., Bowers, R., Hall, B., and Port, M. (1997) Six month clinical evaluation of a biomimetic hydrogel contact lens. *CLAO J. 23*, 226–36.
(17) Lewis, A. L., and Stratford, P. W. (2002) Phosphorylcholine-coated stents. *J. Long Term Eff. Med. Implants 12*, 231–50.
(18) De Somer, F., Francois, K., van Oeveren, W., Poelaert, J., De Wolf, D., Ebels, T., and Van Nooten, G. (2000) Phosphorylcholine coating of extracorporeal circuits provides natural protection against blood activation by the material surface. *Eur. J. Cardiothorac. Surg. 18*, 602–6.
(19) Pappalardo, F., Della Valle, P., Crescenzi, G., Corno, C., Franco, A., Torracca, L., Alfieri, O., Galli, L., Zangrillo, A., and D'Angelo, A. (2006) Phosphorylcholine coating may limit thrombin formation during high-risk cardiac surgery: a randomized controlled trial. *Ann. Thorac. Surg. 81*, 886–91.
(20) Gobeil, F., Juneau, C., and Plante, S. (2002) Thrombus formation on guide wires during routine PTCA procedures: a scanning electron microscopic evaluation. *Can. J. Cardiol. 18*, 263–9.
(21) Russell, J. (2000) Bacteria, biofilms and devices: The possible protective role of phosphorylcholine materials. *Journal of Endourology 14*, 39–42.

(22) Berry, J. A., Biedlingmaier, J. F., and Whelan, P. J. (2000) In vitro resistance to bacterial Biofilm formation on coated fluoroplastic tympanostomy tubes. *Otolaryngol Head Neck Surg. 123*, 246–51.
(23) Chrit, L., Bastien, P., Biatry, B., Simonnet, J. T., Potter, A., Minondo, A. M., Flament, F., Bazin, R., Sockalingum, G. D., Leroy, F., Manfait, M., and Hadjur, C. (2007) In vitro and in vivo confocal Raman study of human skin hydration: assessment of a new moisturizing agent, pMPC. *Biopolymers 85*, 359–69.
(24) Airoldi, F., Di Mario, C., Ribichini, F., Presbitero, P., Sganzerla, P., Ferrero, V., Vassanelli, C., Briguori, C., Carlino, M., Montorfano, M., Biondi-Zoccai, G. G., Chieffo, A., Ferrari, A., and Colombo, A. (2005) 17-beta-estradiol eluting stent versus phosphorylcholine-coated stent for the treatment of native coronary artery disease. *Am. J. Cardiol. 96*, 664–7.
(25) Armstrong, J., Gunn, J., Arnold, N., Malik, N., Chan, K. H., Vick, T., Stratford, P., Cumberland, D. C., and Holt, C. M. (2002) Angiopeptin-eluting stents: observations in human vessels and pig coronary arteries. *J. Invasive Cardiol. 14*, 230–8.
(26) Berrocal, D. H., Gonzalez, G. E., Morales, C., Gelpi, R. J., and Grinfeld, L. R. (2006) Irinotecan-eluting stents inhibited neointimal proliferation in hypercholesterolemic rabbit aortas. *Catheter Cardiovasc. Interv. 68*, 89–96.
(27) Burke, S. E., Kuntz, R. E., and Schwartz, L. B. (2006) Zotarolimus (ABT-578) eluting stents. *Adv. Drug Delivery Rev. 58*, 437–46.
(28) Han, Y., Liang, M., Kang, J., Qi, Y., Deng, J., Xu, K., and Yan, C. (2007) Estrogen-eluting stent implantation inhibits neointimal formation and extracellular signal-regulated kinase activation. *Catheter Cardiovasc. Interv. 70*, 647–53.
(29) Huang, Y., Liu, X., Wang, L., Verbeken, E., Li, S., and De Scheerder, I. (2003) Local methylprednisolone delivery using a BiodivYsio phosphorylcholine-coated drug-delivery stent reduces inflammation and neointimal hyperplasia in a porcine coronary stent model. *Int. J. Cardiovasc. Intervent. 5*, 166–71.
(30) Kipshidze, N. N., Iversen, P., Kim, H. S., Yiazdi, H., Dangas, G., Seaborn, R., New, G., Tio, F., Waksman, R., Mehran, R., Tsapenko, M., Stone, G. W., Roubin, G. S., Iyer, S., Leon, M. B., and Moses, J. W. (2004) Advanced c-myc antisense (AVI-4126)-eluting phosphorylcholine-coated stent implantation is associated with complete vascular healing and reduced neointimal formation in the porcine coronary restenosis model. *Catheter Cardiovasc. Interv. 61*, 518–27.
(31) Kwok, O. H., Chow, W. H., Law, T. C., Chiu, A., Ng, W., Lam, W. F., Hong, M. K., and Popma, J. J. (2005) First human experience with angiopeptin-eluting stent: a quantitative coronary angiography and three-dimensional intravascular ultrasound study. *Catheter Cardiovasc. Interv. 66*, 541–6.
(32) Lewis, A. L., and Vick, T. A. (2001) Site-specific drug delivery from coronary stents. *Drug Delivery Systems and Science 1*, 65–71.
(33) New, G., Moses, J. W., Roubin, G. S., Leon, M. B., Colombo, A., Iyer, S. S., Tio, F. O., Mehran, R., and Kipshidze, N. (2002) Estrogen-eluting, phosphorylcholine-coated stent implantation is associated with reduced neointimal formation but no delay in vascular repair in a porcine coronary model. *Catheter Cardiovasc. Interv. 57*, 266–71.
(34) Radke, P. W., Griesenbach, U., Kivela, A., Vick, T., Judd, D., Munkonge, F., Willis, S., Geddes, D. M., Yla-Herttuala, S., and Alton, E. W. (2005) Vascular oligonucleotide transfer facilitated by a polymer-coated stent. *Hum. Gene Ther. 16*, 734–40.
(35) Shin, E. K., Han, S. H., Ahn, T. H., Kang, W. C., Chung, W.-J., Shin, M.-S., Koh, K. K., and Choi, I. S. (2005) Favourable outcome of high dose dexamethasone eluting biodivysio drug delivery phosphoylcholine coated stent compared with unloaded stent. *Eur. Heart J. 26*, 706.
(36) Walter, D. H., Cejna, M., Diaz-Sandoval, L., Willis, S., Kirkwood, L., Stratford, P. W., Tietz, A. B., Kirchmair, R., Silver, M., Curry, C., Wecker, A., Yoon, Y. S., Heidenreich, R., Hanley, A., Kearney, M., Tio, F. O., Kuenzler, P., Isner, J. M., and Losordo, D. W. (2004) Local gene transfer of phVEGF-2 plasmid by gene-eluting stents: an alternative strategy for inhibition of restenosis. *Circulation 110*, 36–45.
(37) Konno, T., Watanabe, J., and Ishihara, K. (2003) Enhanced solubility of paclitaxel using water-soluble and biocompatible 2-methacryloyloxyethyl phosphorylcholine polymers. *J. Biomed. Mater. Res. A 65*, 209–14.
(38) Wada, M., Jinno, H., Ueda, M., Ikeda, T., Kitajima, M., Konno, T., Watanabe, J., and Ishihara, K. (2007) Efficacy of an MPC-BMA co-polymer as a nanotransporter for paclitaxel. *Anticancer Res. 27*, 1431–5.
(39) Yusa, S., Fukuda, K., Yamamoto, T., Ishihara, K., and Morishima, Y. (2005) Synthesis of well-defined amphiphilic block copolymers having phospholipid polymer sequences as a novel biocompatible polymer micelle reagent. *Biomacromolecules 6*, 663–70.
(40) Konno, T., Kurita, K., Iwasaki, Y., Nakabayashi, N., and Ishihara, K. (2001) Preparation of nanoparticles composed with bioinspired 2-methacryloyloxyethyl phosphorylcholine polymer. *Biomaterials 22*, 1883–9.
(41) Konno, T., Watanabe, J., and Ishihara, K. (2004) Conjugation of enzymes on polymer nanoparticles covered with phosphorylcholine groups. *Biomacromolecules 5*, 342–7.
(42) Lam, J. K., Ma, Y., Armes, S. P., Lewis, A. L., Baldwin, T., and Stolnik, S. (2004) Phosphorylcholine-polycation diblock copolymers as synthetic vectors for gene delivery. *J. Controlled Release 100*, 293–312.
(43) Mu, Q. S., Ma, Y. H., Lewis, A. L., Armes, S. P., and Lu, J. R. (2004) Complexation of DNA with biocompatible diblock copolymers. *Prog. Colloid Polym. Sci. 128*, 199–202.
(44) Chim, Y. T., Lam, J. K., Ma, Y., Armes, S. P., Lewis, A. L., Roberts, C. J., Stolnik, S., Tendler, S. J., and Davies, M. C. (2005) Structural study of DNA condensation induced by novel phosphorylcholine-based copolymers for gene delivery and relevance to DNA protection. *Langmuir 21*, 3591–8.
(45) Lomas, H., Canton, I., MacNeil, S., Armes, S. P., Ryan, A. J., Lewis, A. L., and Battaglia, G. (2007) Biomimetic pH sensitive polymersomes for efficient DNA encapsulation and delivery. *Adv. Mater. 19*, 4239–4243.
(46) Zhao, X., Pan, F., Zhang, Z., Grant, C., Ma, Y., Armes, S. P., Tang, Y., Lewis, A. L., Waigh, T., and Lu, J. R. (2007) Nanostructure of polyplexes formed between cationic diblock copolymer and antisense oligodeoxynucleotide and its influence on cell transfection efficiency. *Biomacromolecules 8*, 3493–3502.
(47) Armes, S. P., Du, J., Giammona, G., Lewis, A. L., Licciardi, M., and Tang, Y. (2006) New folate-functionalised biocompatible block copolymer micelles as potential anti-cancer drug delivery systems. *Polymer 47*, 2946–2955.
(48) Giacomelli, C., Le Men, L., Borsali, R., Lai-Kee-Him, J., Brisson, A., Armes, S. P., and Lewis, A. L. (2006) Phosphorylcholine-based pH-responsive diblock copolymer micelles as drug delivery vehicles: light scattering, electron microscopy, and fluorescence experiments. *Biomacromolecules 7*, 817–28.
(49) Du, J., Tang, Y., Lewis, A. L., and Armes, S. P. (2005) pH-sensitive vesicles based on a biocompatible zwitterionic diblock copolymer. *J. Am. Chem. Soc. 127*, 17982–3.
(50) Feng, W., Zhu, S., Ishihara, K., and Brash, J. L. (2005) Adsorption of fibrinogen and lysozyme on silicon grafted with poly(2-methacryloyloxyethyl phosphorylcholine) via surface-initiated atom transfer radical polymerization. *Langmuir 21*, 5980–7.
(51) Lobb, E. J., Ma, I., Billingham, N. C., Armes, S. P., and Lewis, A. L. (2001) Facile synthesis of well-defined, biocompatible phosphorylcholine-based methacrylate copolymers via atom transfer radical polymerization at 20 °C. *J. Am. Chem. Soc. 123*, 7913–4.
(52) Ma, I. Y., Lobb, E. J., Billingham, N. C., Armes, S. P., Lewis, A. L., Lloyd, A. W., and Salvage, J. P. (2002) Synthesis of biocompatible polymers 1. Homopolymerisation of 2-methacryloyloxyethyl phosphorylcholine via ATRP in protic solvents: an optimisation study. *Macromolecules 35*, 9306–9314.

(53) Ma, I. Y., Tang, Y., Billingham, N. C., Armes, S. P., Lewis, A. L., Lloyd, A. W., and Salvage, J. P. (2003) Well-defined biocompatibles block copolymers via atom transfer radical polymerization of 2-methacryloyloxyethyl phosphorylcholine in protic media. *Macromolecules 36*, 3475–3484.

(54) Stenzel, M. H., Barner-Kowollik, C., Davis, T. P., and Dalton, H. M. (2004) Amphiphilic block copolymers based on poly(2-acryloyloxyethyl phosphorylcholine) prepared via RAFT polymerisation as biocompatible nanocontainers. *Macromol. Biosci. 4*, 445–53.

(55) Miyamoto, D., Watanabe, J., and Ishihara, K. (2004) Effect of water-soluble phospholipid polymers conjugated with papain on the enzymatic stability. *Biomaterials 25*, 71–6.

(56) Chiba, N., Ueda, M., Shimada, T., Jinno, H., Watanabe, J., Ishihara, K., and Kitajima, M. (2007) Development of gene vectors for pinpoint targeting to human hepatocytes by cationically modified polymer complexes. *Eur. Surg. Res. 39*, 23–34.

(57) Chiba, N., Ueda, M., Shimada, T., Jinno, H., Watanabe, J., Ishihara, K., and Kitajima, M. (2007) Novel immunosuppressant agents targeting activated lymphocytes by biocompatible MPC polymer conjugated with interleukin-2. *Eur. Surg. Res. 39*, 103–10.

(58) Samanta, D., McRae, S., Cooper, B., Hu, Y., Emrich, T., Pratt, J., Charles, S. P. (2008)End-funtionalized phophorylcholine methacrylates and their use in protein conjugation*Biomacromolecules 9*, 2891–2897.

(59) Brocchini, S., Balan, S., Godwin, A., Choi, J. W., Zloh, M., and Shaunak, S. (2006) PEGylation of native disulfide bonds in proteins. *Nat. Protoc. 1*, 2241–52.

(60) Lowe, A. B., and McCormick, C. L. (2002) Synthesis and solution properties of zwitterionic polymers. *Chem. Rev. 102*, 4177–89.

(61) Mahon, J.,Zhu, S. (2008) Interactions of poly(2-methacryloyloxyethyl phosphorylcholine) with various salts studied by size exclusion chromatography*Colloid Polym Sci.*, *286*, 1443−1454.

(62) Iwasaki, Y., Yamasaki, A., and Ishihara, K. (2003) Platelet compatible blood filtration fabrics using a phosphorylcholine polymer having high surface mobility. *Biomaterials 24*, 3599–604.

(63) Lewis, A. L., Freeman, R. N., Redman, R. P., Tolhurst, L. A., Kirkwood, L. C., Grey, D. M., and Vick, T. A. (2003) Wettable phosphorylcholine-containing polymers useful in blood filtration. *J. Mater. Sci. Mater. Med. 14*, 39–45.

(64) Lecolley, F., Tao, L., Mantovani, G., Durkin, I., Lautru, S., and Haddleton, D. M. (2004) A new approach to bioconjugates for proteins and peptides (”pegylation”) utilising living radical polymerisation. *Chem. Commun. (Camb.)* 2026–7.

(65) Brocchini, S., Godwin, A., Balan, S., Choi, J. W., Zloh, M., and Shaunak, S. (2008) Disulfide bridge based PEGylation of proteins. *Adv. Drug Delivery Rev. 60*, 3–12.

(66) Shaunak, S., Godwin, A., Choi, J. W., Balan, S., Pedone, E., Vijayarangam, D., Heidelberger, S., Teo, I., Zloh, M., and Brocchini, S. (2006) Site-specific PEGylation of native disulfide bonds in therapeutic proteins. *Nat. Chem. Biol. 2*, 312–3.

(67) Balan, S., Choi, J. W., Godwin, A., Teo, I., Laborde, C. M., Heidelberger, S., Zloh, M., Shaunak, S., and Brocchini, S. (2007) Site-specific PEGylation of protein disulfide bonds using a three-carbon bridge. *Bioconjugate Chem. 18*, 61–76.

(68) Licciardi, M., Tang, Y., Billingham, N. C., Armes, S. P., and Lewis, A. L. (2005) Synthesis of novel folic acid-functionalized biocompatible block copolymers by atom transfer radical polymerization for gene delivery and encapsulation of hydrophobic drugs. *Biomacromolecules 6*, 1085–96.

(69) Meager, A., Gaines Das, R., Zoon, K., and Mire-Sluis, A. (2001) Establishment of new and replacement World Health Organization International Biological Standards for human interferon alpha and omega. *J. Immunol. Methods 257*, 17–33.

BC800242T

Supplementary information. Proton NMR of PMPC bis-sulfone **12**

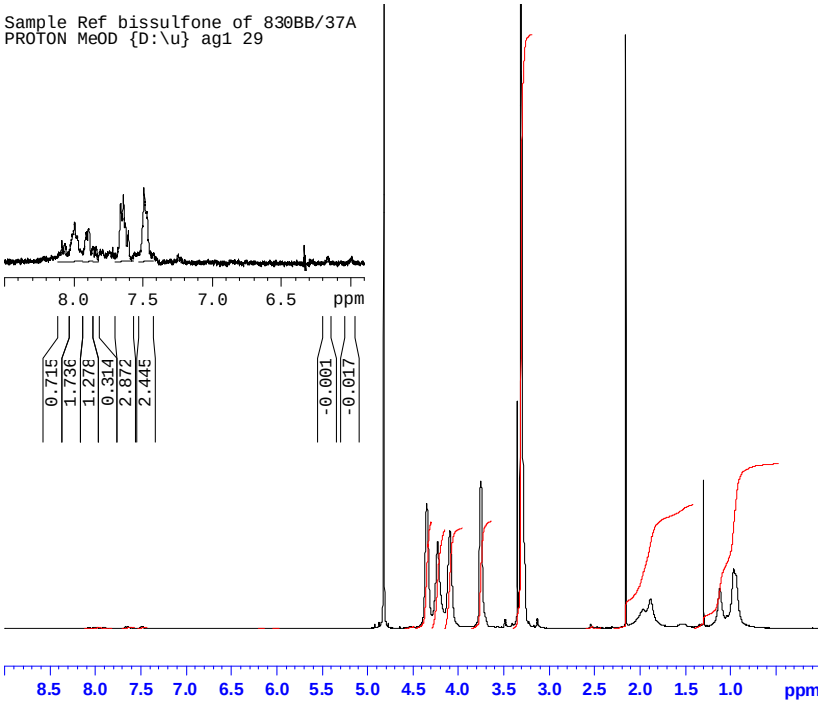

LHRH Receptor-Mediated Delivery of siRNA Using Polyelectrolyte Complex Micelles Self-Assembled from siRNA-PEG-LHRH Conjugate and PEI

Sun Hwa Kim,[†,‡] Ji Hoon Jeong,[§] Soo Hyeon Lee,[†] Sung Wan Kim,[‡] and Tae Gwan Park*[,†]

Department of Biological Sciences, Korea Advanced Institute of Science and Technology, Daejeon 305-701, South Korea, Center for Controlled Chemical Delivery, Department of Pharmaceutics and Pharmaceutical Chemistry, University of Utah, Salt Lake City, Utah 84112, and College of Pharmacy, Sungkyunkwan University, Suwon 440-746, South Korea. Received June 20, 2008; Revised Manuscript Received August 18, 2008

Polyelectrolyte complex (PEC) micelles modified with cancer cell targeting moieties were prepared for intracellular delivery of vascular endothelial growth factor (VEGF) small interfering RNA (siRNA). A luteinizing hormone-releasing hormone (LHRH) peptide analogue was coupled as a cancer targeting ligand to the distal end of the poly(ethylene glycol) (PEG)−siRNA conjugate. The siRNA-PEG-LHRH conjugate self-assembled to form nanosized PEC micelles upon mixing with poly(ethylenimine) (PEI) via ionic interactions. The PEC micelles showed spherical morphology with a hydrodynamic diameter of ca. 150 nm. For LHRH receptor overexpressing ovarian cancer cells (A2780), the PEC micelles with LHRH exhibited enhanced cellular uptake compared to those without LHRH, resulting in increased VEGF gene silencing efficiency via receptor-mediated endocytosis. This study showed that PEC micelles decorated with specific cell-recognizable targeting ligands could be used for targeted delivery of siRNA.

INTRODUCTION

RNA interference (RNAi) induced by small interfering RNA (siRNA) has recently been recognized as a potential therapeutic tool for silencing genes linked to human diseases (*1*, *2*). High sequence specificity and relatively small dose requirement of siRNA make it even more attractive to use RNAi technology for treatment of various diseases including cancer (*3*, *4*). Despite high therapeutic potentials of siRNAs, critical delivery problems remain to be solved for clinical applications (*5*). The most challenging hurdles in siRNA delivery are serum instability of siRNA during circulation in the bloodstream, poor cellular uptake, and limitation in targeted delivery to specific tissues or cells. To address such problems, various delivery systems, including cationic lipids (*6*, *7*), cationic polymers and peptides (*8*−*10*), viral vectors (*11*), and varied modified siRNA (*12*), have been introduced.

In our previous studies, we showed the possibility of using a polyelectrolyte complex (PEC) micelle-based siRNA delivery system in a systemic cancer therapy (*13*). The PEC micelles are composed of two essential components, PEG-conjugated siRNA (siRNA-PEG) and a polycation, polyethylenimine (PEI). The siRNA−PEG conjugate was covalently coupled via a disulfide linkage, which can be reduced to release intact siRNA in the reductive cytosolic condition. The PEC micelles can be self-assembled to form a core−shell structure via electrostatic interactions between the two oppositely charged polyelectrolytes of siRNA and PEI, resulting in the formation of an insoluble core. At the same time, the siRNA/PEI inner core can be stabilized by the PEG chains exposed on the surface. The distinctive core−shell structure confers stability on PEC micelles in the bloodstream, possibly leading to prolonged circulation. The PEG shell layer could sterically shield the polyelectrolyte complex core from accessibility of serum proteins, thereby protecting the PEC micelles from aggregation and enzymatic degradation of siRNA. In addition, owing to their small size (<150 nm), the PEC micelles can be passively localized to tumor sites through loosened tight junctions of endothelium in the vicinity of highly proliferative cancer cells (*13*). Extended retention of the micelles is also expected due to lack of lymphatic drainage in solid tumors (enhanced permeation and retention effect, EPR). The delivery systems based on VEGF siRNA-PEG/PEI PEC micelles showed dramatic target gene silencing and retardation of tumor growth in cancer xenografted animal models, when administered locally and systemically.

Cell-specific ligands, including antibodies, sugar molecules, vitamins, and hormones, have been popularly employed to confer tissue- or cell-specificity on gene carriers (*14*, *15*). Specific interaction between a targeting ligand and its cellular receptor generally enhances the cellular uptake of gene carriers by a mechanism called receptor-mediated endocytosis. Therefore, increasing specific cellular uptake by targeted gene delivery can significantly improve therapeutic efficacy with a much lower dose (*5*, *16*, *17*). In this study, cell-specific targeting property was added to the PEC micellar delivery system by employing luteinizing hormone releasing hormone (LHRH) as a cancer targeting moiety (Figure 1). The PEC micelle-based cancer targeting system for VEGF siRNA was demonstrated.

EXPERIMENTAL PROCEDURES

Materials. A peptide analogue of LHRH was synthesized and purified by Peptron Inc. (Daejeon, South Korea). The modified sequence of LHRH peptide was Gln-His-Trp-Ser-Tyr-DLys-Leu-Arg-Pro (MW 1196) with N-terminal pyroglutamation and C-terminal amidation, often referred to as Leuprolide Acetate in the literature (*18*−*20*). A heterofunctional poly(eth-

* Corresponding author. Tae Gwan Park, Ph.D., Department of Biological Sciences, Korea Advanced Institute of Science and Technology, Daejeon 305-701, South Korea. Tel: +82-42-869-2621; fax: +82-42-869-2610; E-mail: tgpark@kaist.ac.kr.

[†] Korea Advanced Institute of Science and Technology.

[‡] University of Utah.

[§] Sungkyunkwan University.

10.1021/bc800249n CCC: $40.75 © 2008 American Chemical Society
Published on Web 10/14/2008

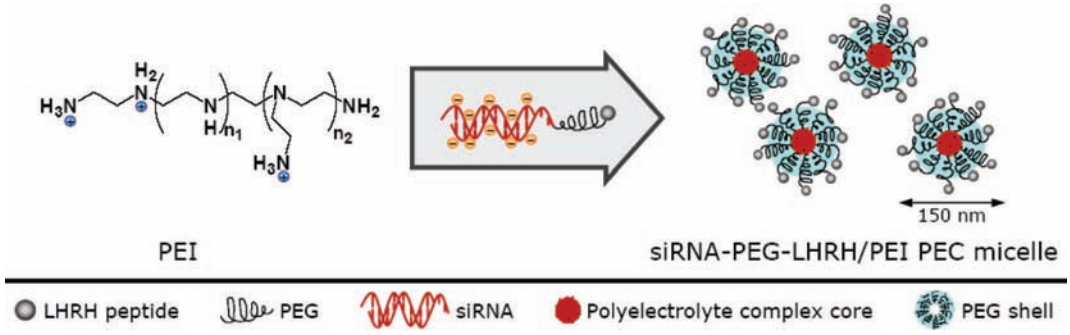

Figure 1. A schematic diagram of the preparation for siRNA-PEG-LHRH/PEI PEC micelles in an aqueous phase.

ylene glycol) (NH_2-PEG-COOH, MW 3400) derivative and methoxy-PEG with a sulfhydryl group (mPEG-SH, MW 3400) were obtained from Nektar (Huntsville, AL). *N*-Succinimidyl-3-(2-pyridyldithio)propionate (SPDP) was purchased from Pierce (Rockford, IL). Branched poly(ethylenimine) (PEI, MW 25 000), 1-ethyl-3-(3-dimethylaminopropyl) carbodiimide hydrochloride (EDC), and dithiothreitol (DTT) were obtained from Sigma-Aldrich (St. Louis, MO). A human VEGF siRNA was supplied from Qiagen Inc. (Valencia, CA). A synthetic VEGF siRNA has a sense strand (5′-GAGUACCCUGAUGAGAUCdTdT-3′) modified with or without 3′-hexylamine and an antisense strand (5′-GAUCUCAUCAGGGUACUCCdTdT-3′). For FACS analysis and confocal microscopy, the 5′-end of the sense strand of VEGF siRNA was further modified with indocarbocyanine dye (Cy3) (Dharmacon Research, Lafayette, CO). Fetal bovine serum (FBS) and Roswell Park Memorial Institute 1640 medium (RPMI 1640) were obtained from Gibco BRL (Grand Island, NY). All other chemicals and reagents were of analytical grade and used without further purification.

Preparation of siRNA-PEG-LHRH Conjugate. siRNA−PEG conjugate with a disulfide bond (siRNA-s-s-PEG) was prepared according to the previous methods (*9, 13*). siRNA-PEG-LHRH conjugate was synthesized with the modified procedure (Figure 2A). To synthesize sulfhydryl-PEG-LHRH, the α-amino group of NH_2-PEG-COOH (17 mg, 5 μmol) in PBS solution (1 mL, pH 7.5) was first activated with SPDP (15.6 mg, 50 μmol) dissolved in DMSO (50 μL) at room temperature. After 1 h reaction, unreacted SPDP was removed during dialysis against deionized water (MWCO 2000). The terminal carboxyl group of 2-pyridyl disulfide-PEG-COOH derivative was then conjugated to the ε-amino group of a lysine residue in LHRH peptide (12 mg, 10 μmol) with EDC (9.6 mg, 50 μmol) in a final volume of 5 mL PBS solution at room temperature overnight. The medium pH was maintained in the range of 5−6 by adding HCl. Four hundred micrograms of DTT (50 mM) was then added to the reaction solution and incubated for 3 h, followed by dialysis (MWCO 2000) against deionized water and then lyophilized. To conjugate the sulfhydryl-PEG-LHRH segment to siRNA via a disulfide bond, the siRNA−2-pyridyl disulfide conjugate was first prepared on the basis of the previous studies (*7, 12*). The 2-pyridyl disulfide activated siRNA (300 μg, 20 nmol) was reacted with sulfhydryl-PEG-LHRH conjugate (1 mg, 200 nmol) in PBS solution (pH 7.5) at room temperature for 24 h. Unreacted siRNA or PEG molecules were removed by extensive dialysis against deionized and distilled water (MWCO 10 000). The siRNA-PEG-LHRH conjugate was concentrated using a speed vacuum pump and adjusted to a concentration of 0.5 mg/mL in deionized water.

Characterization of siRNA-PEG-LHRH Conjugate and siRNA-PEG-LHRH/PEI PEC Micelles. Each reaction step was evaluated with various analytical methods including mass and size analysis. PEG-LHRH conjugate, PEG (NH_2-$PEG_{3,400}$-COOH), and sulfhydryl-$PEG_{3,400}$-LHRH were analyzed by MALDI-TOF (Kratos AXIMA-LNR) mass spectrometry. 3-Hydroxypicolinic acid (HPA) used as a matrix was dissolved in deionized water at a concentration of 0.05 M. Ammonium citrate (0.05 M) was added to the matrix solution (HPA/ammonium citrate = 8:1). The sample was dissolved in water at a concentration of 0.5 mM. The sample (50 μL) and the matrix solution (50 μL) were mixed and the resulting mixture (1 μL) was placed on the MALDI plate. The sample crystallization was carried out by a rapid solvent evaporation method. The siRNA-PEG-LHRH conjugate and other substrates (naked siRNA, sulfhydryl-PEG-LHRH, and LHRH) were analyzed by high-performance size-exclusion chromatography (HPLC-SEC, Waters 510 HPLC pump system) with UV detection at 280 nm. Samples were loaded into Shodex protein KW-800 column (Showa Denko, Japan). The mobile phase was composed of 50 mM NaCl and 50 mM Tris-HCl (pH 8.0) and the flow rate was fixed at 1.0 mL/min.

Gel mobility retardation assay was performed to analyze and isolate the synthesized siRNA-PEG-LHRH conjugate. To confirm the cleavage of the disulfide bond between siRNA and PEG segment in a simulated intracellular environment, 1 μg of siRNA-PEG-LHRH or siRNA-PEG was incubated in 50 μL RPMI 1640 media with or without 10 mM glutathione (GSH) for 2 h at 37 °C. The cleaved siRNA and siRNA conjugate (siRNA-PEG and siRNA-PEG-LHRH) were run on 2% agarose gel and visualized with ethidium bromide staining. The siRNA-PEG-LHRH/PEI PEC micelles were formed by mixing the siRNA-PEG-LHRH conjugate with PEI in PBS solution (pH 7.2) at an N/P ratio of 12 and stabilizing the mixing solution for 15 min at room temperature (Figure 1). The particle size and morphology of siRNA-PEG-LHRH/PEI PEC micelles were observed by atomic force microscope (PSIA XE-100 AFM system, separated $x-y$ and z scanner, scan size 50 × 50 μm^2). The sample solution was loaded on a freshly cleaved mica surface and dried in a vacuum oven at room temperature. AFM image was taken from a 2.5 × 2.5 μm^2 area. The particle size distribution of siRNA-PEG-LHRH/PEI PEC micelles was evaluated by using a dynamic light scattering (DLS) instrument (Zeta-Plus, Brookhaven, New York).

Cells and Cell Culture. Human ovarian carcinoma A2780 cells (LHRH receptor positive cancer cell line) were obtained from American type Culture Collection (ATCC). Human ovarian cancer SK-OV-3 cells (LHRH receptor negative cancer cell line) were purchased from the Korean Cell Line Bank (KCLB, Seoul, Korea). Cells were cultured in RPMI 1640 medium supplemented with 10% fetal bovine serum at 37 °C in a humidified atmosphere of 5% of CO_2. Cells were reseeded 24 h before cell transfection experiments.

Cellular Uptake of siRNA-PEG-LHRH/PEI PEC Micelles. To visualize the LHRH receptor-mediated cellular uptake of siRNA-PEG-LHRH/PEI PEC micelles by confocal microscopy and FACS analysis, red fluorophore Cy3-labeled siRNA and siRNA conjugates (siRNA-PEG and siRNA-PEG-LHRH)

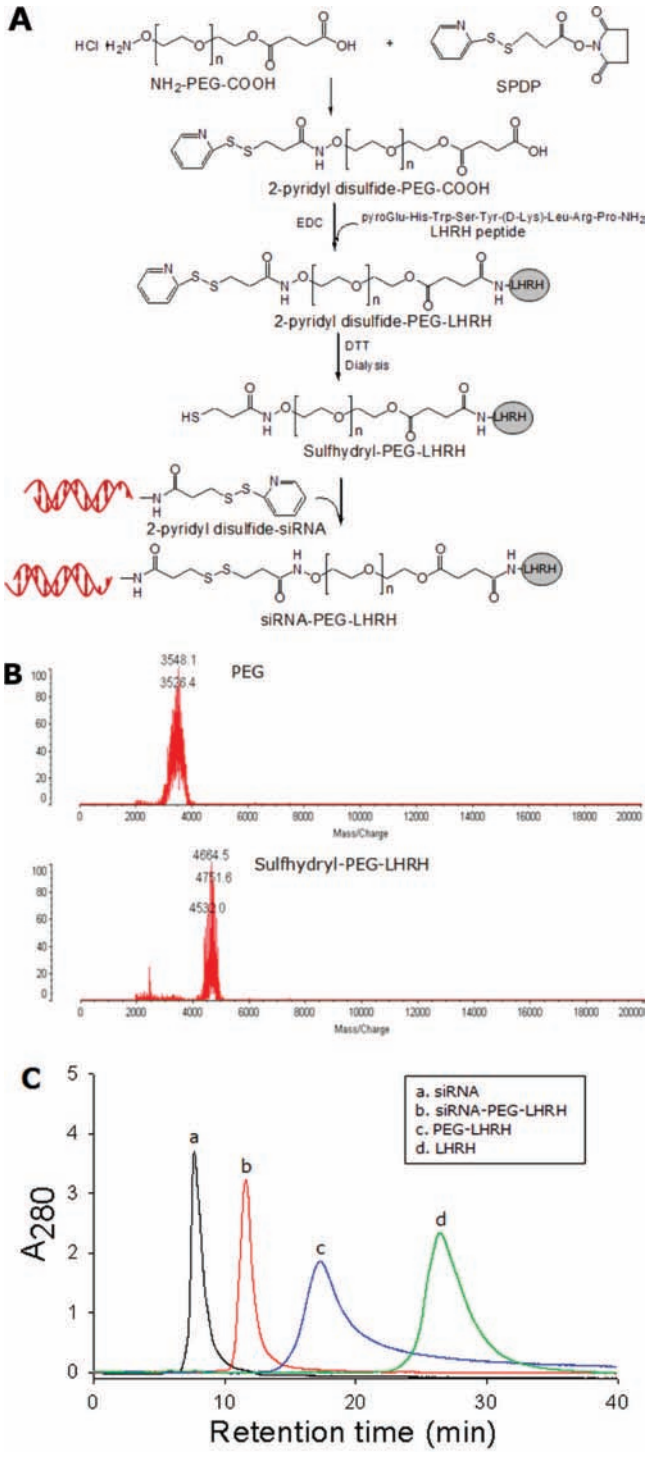

Figure 2. (A) Synthetic scheme of siRNA-PEG-LHRH conjugate containing a disulfide linkage between siRNA and PEG. (B) MALDI-TOF MS spectra for $PEG_{3,400}$ (upper panel) and sulfhydryl-$PEG_{3,400}$-LHRH (lower panel). (C) HPLC-SEC analysis of naked siRNA, siRNA-PEG-LHRH, sulfhydryl-PEG-LHRH, and LHRH peptide.

were utilized. For confocal microscopy, A2780 cells were incubated in a cell culture chamber slide at a density of 1×10^4 cells per well in 10% FBS containing RPMI 1640 medium for 24 h at 37 °C. After replacement of the culture medium, the cells were transfected with PEI complexes of siRNA, siRNA-PEG, and siRNA-PEG-LHRH at an N/P ratio of 16, which has been already optimized in our previous work (*6*, *7*). Thirty picomoles of various siRNA formulations was loaded into the medium per well. The cells were incubated for 1 h, washed three times with cold PBS solution, and fixed with 1% (w/v) *p*-formaldehyde solution. The slides were covered with a mounting solution (SuperMount, InnoGenex, San Ramon, CA). The cells were imaged by confocal laser scanning microscope (LSM 510, Carl-Zeiss Inc., USA) with a 543 nm helium−neon laser. To investigate LHRH receptor-targeted delivery of siRNA using FACS, the cells cultured in a 6-well plate (3.0×10^5 cells/well) were transfected with 30 nM siRNA and siRNA conjugates (siRNA-PEG and siRNA-PEG-LHRH), which were complexed with PEI (0.93 μg) at an N/P ratio of 16. For the LHRH ligand competition assay, free LHRH agonist (1 μM) was added to the transfection medium 30 min before the treatment of siRNA-PEG-LHRH/PEI PEC micelles. The harvested cells were fixed in 0.5% (w/v) *p*-formaldehyde solution. The extents of intracellular uptake of various siRNA formulations were monitored by flow cytometry (FACScan, Becton Dickinson) using *CELLQUEST* software (PharMingen).

RT-PCR Analysis. Reverse transcriptase-polymerase chain reaction (RT-PCR) analysis was performed to estimate the expression level of LHRH receptor in human ovarian cancer A2780 and SK-OV-3 cells. Total RNA was extracted from the cells (5×10^6) using RNeasy Mini Kit (Qiagen, Valencia, CA) according to the protocol supplied by the manufacturer, and the treatment with the RNase-Free DNase Set (Qiagen, Valencia, CA) was subsequently performed. One microgram of total RNA harvested from the cells was subjected to RT-PCR using SuperScript III One-Step RT-PCR System with Platinum Taq DNA Polymerase (Invitrogen, Carlsbad, CA). The primer sequences used were as follows: LHRH primer sequences (forward, 5′-GACCTTGTCTGGAAAGATCC-3′; reverse, 5′-CAGGCTGATCACCACCATCA-3′) and human $\beta\beta_2$-microglobulin (internal standard) primer sequences (forward, 5′-ACCCCCACTGAAAAAGATGA-3′; reverse, 5′-A TCTTC-AAACCTCCATGATG-3′). The PCR primers were supplied from Bioneer Co. (Daejeon, South Korea). Reverse transcription was performed at 45 °C for 60 min for the synthesis of cDNA followed by 5 min of incubation at 95 °C for the denaturation of DNA−RNA heteroduplexes. The following condition of thermal cycling was used for amplification: PCR amplification, 28 cycles at 94 °C for 1 min, at 55 °C for 50 s, and at 72 °C for 1 min; final extension, 1 cycle at 60 °C for 10 min. The PCR products were analyzed by 0.8% agarose gel electrophoresis and visualized by staining with ethidium bromide. The PCR products for LHRH receptor and human β_2-microglobulin were 319 bp and 114 bp in length, respectively.

LHRH Receptor-Mediated VEGF Gene Suppression by siRNA-PEG-LHRH/PEI PEC Micelles. Two types of human ovarian carcinoma cell lines were used to investigate LHRH receptor-mediated VEGF gene silencing. A2780 (LHRH receptor-overexpressing cell line) and SK-OV-3 (LHRH receptor-deficient cell line) were seeded in a 6-well plate at a density of 3.0×10^5 cells per well and incubated for 24 h prior to transfection experiment. The medium was replaced with a fresh one containing 50 nM siRNA formulations (siRNA-PEG/PEI and siRNA-PEG-LHRH/PEI) and incubated for 4 h at 37 °C. After exchanging the transfection medium with fresh medium containing 10% FBS, the cells were further incubated at 37 °C for 6 h. The medium was removed and supplemented with fresh medium containing 10% FBS and 20 μg/mL of heparin. The amount of VEGF released from the cells for 18 h was analyzed by using enzyme-linked immunosorbent assay (Quantikine human VEGF immuno-detection kit, R&D Systems, Minneapolis, MN) according to the manufacturer's instruction. The data were given as mean ± standard deviation (SD) of three independent measurements. Statistical analysis was performed

with a student's *t* test. Statistical significance was assigned for *P* value of <0.01.

RESULTS AND DISCUSSION

Systemic siRNA delivery based on nonviral vectors has been scarcely reported mainly due to lack of non-cytotoxic cationic lipid and polymer carriers that can effectively deliver nucleic acid drugs to a target tumor site. In addition to maintaining superior colloidal stability during systemic circulation, nanosized siRNA/carrier complexes should be efficiently transported from blood vessels to a cancerous tissue and finally taken up by the target cells. Our previous studies showed that the PEC micelle-based delivery system can be potentially exploited as an efficient and non-cytotoxic systemic siRNA delivery vehicle, which can partially overcome the challenging delivery barriers. The systemic administration of VEGF siRNA-PEG/PEI PEC micelles demonstrated significant accumulation of the PEC micelles in a tumor region presumably via an EPR effect, leading to dramatic retardation of tumor growth in an animal tumor model (*13*). These results suggest that the therapeutic effect of siRNA can be further enhanced by adding cancer cell specificity to the PEC micelles.

An LHRH analogue, (pyroE)-H-W-S-Y-(dK)-L-R-P(amide), was selected as a cancer targeting ligand, since the LHRH receptor is known to be overexpressed especially in prostate, breast, and ovarian cancer cells, but barely expressed in healthy human tissues (*18*, *19*). In addition, the LHRH analogue is resistant to *in vivo* degradation and has a high binding affinity toward LHRH receptor. Several LHRH agonists have been successfully used as a targeting moiety for cancer-targeted drug delivery (*20*). A conjugate of siRNA-PEG-LHRH containing a disulfide linkage between siRNA and PEG was synthesized as shown in Figure 2A. Prior to the conjugation of the LHRH peptide to PEG, the primary amine group of a heterofunctional PEG derivative (NH_2-PEG-COOH) was reacted with an active NHS group of a heterofunctional cross-linking reagent, *N*-succinimidyl-3-(2-pyridyldithio)propionate (SPDP). The terminal carboxylic group of the PEG derivative was then activated by EDC chemistry and used for the conjugation of an LHRH peptide. Since the N-terminal α-amino group of the peptide was blocked, the ε-amine group of a lysine residue in the LHRH peptide was the only one that participated in the coupling reaction. The 2-pyridyl disulfide-PEG-LHRH conjugate was then treated with 50 mM DTT to generate a free sulfhydryl group (-SH). The synthesis of SH-PEG-LHRH was confirmed by MALDI-TOF mass spectrometry (Figure 2B). An siRNA derivatized with primary amine at the 3′-end of a sense strand was separately activated using SPDP to produce 2-pydridyl disulfide-modified siRNA. The 2-pyridyl disulfide-activated siRNA was coupled to SH-PEG-LHRH via a sulfhydryl exchange reaction. The resulting siRNA-PEG-LHRH containing a disulfide linkage between siRNA and PEG (siRNA-ss-PEG-LHRH) was further purified by a gel elution method. The conjugation was monitored by size exclusion chromatography (SEC). Figure 2C exhibits chromatography profiles for naked siRNA (MW 15 000, line a), siRNA-PEG-LHRH (MW 19 596, line b), sulfhydryl-PEG-LHRH (MW 4596, line c), and LHRH peptide (MW 1196, line d). The four conjugates were well-separated depending on their molecular weights. However, it should be noticed that the siRNA-PEG-LHRH was eluted later than naked siRNA. The LHRH analogue has a slightly positive charge of +1 under basic pH regime between 7 and 12. Thus, the siRNA-PEG-LHRH conjugate might have a hairpin structure with the formation of a PEG loop due to the ionic interaction between the negatively charged siRNA and the slightly positively charged LHRH peptide. The self-folded structure of siRNA-PEG-LHRH may have a smaller hydrodynamic size than

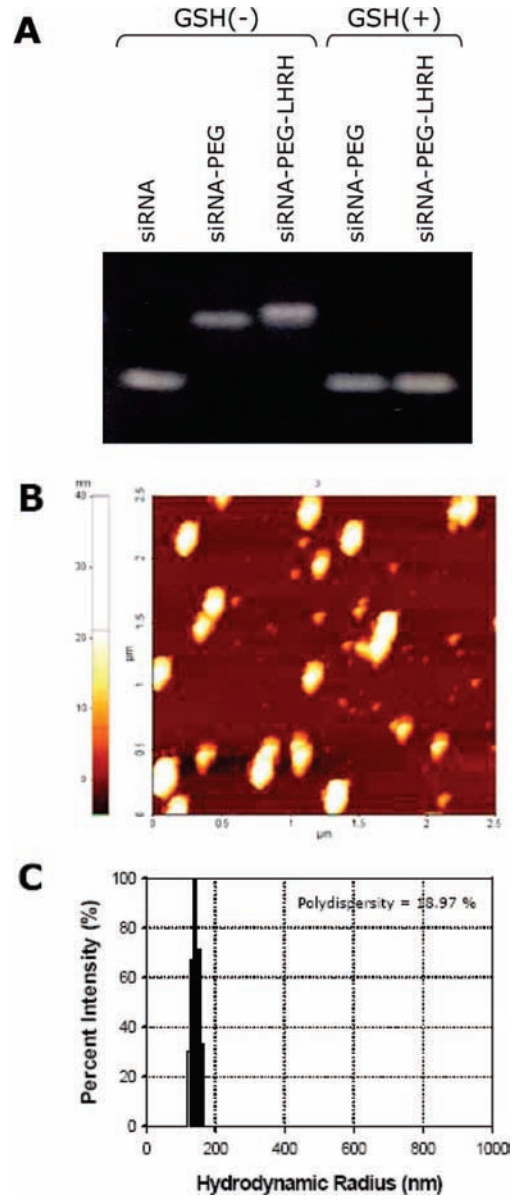

Figure 3. (A) Electrophoretic mobility shift assay for the analysis of siRNA-PEG-LHRH conjugation and disulfide bond cleavage under reducing conditions. GSH (+) and GSH (−) represent the treatment with and without 10 mM glutathione (GSH). (B) Representative AFM image of siRNA-PEG-LHRH/PEI PEC micelles at N/P ratio of 16. (C) Particle size distribution of siRNA-PEG-LHRH/PEI PEC micelles at N/P ratio of 16. Percent polydispersity = (polydispersity index)$^{1/2}$ × 100.

linear naked siRNA, resulting in the delayed elution. However, since electrostatic interactions between LHRH and siRNA were weak, the folded structure of siRNA-PEG-LHRH conjugate was likely to be readily dissociated upon interaction with highly charged PEI. The inner core part of the siRNA-PEG-LHRH/PEI PEC micelles could be formed by preferential electrostatic interactions between siRNA and PEI with releasing LHRH moieties on the shell surface.

The synthesis of the siRNA-PEG-LHRH conjugate was further verified by an electrophoretic mobility shift assay. The migration of the purified siRNA-PEG-LHRH in an electrophoretic field was significantly retarded, compared to that of unmodified siRNA (Figure 3A). This result directly shows the successful conjugation of SH-PEG-LHRH with siRNA. The incubation of siRNA-PEG-LHRH with GSH caused the complete reduction of the disulfide linkage between siRNA and PEG, leading to the generation of an intact form of siRNA (Figure

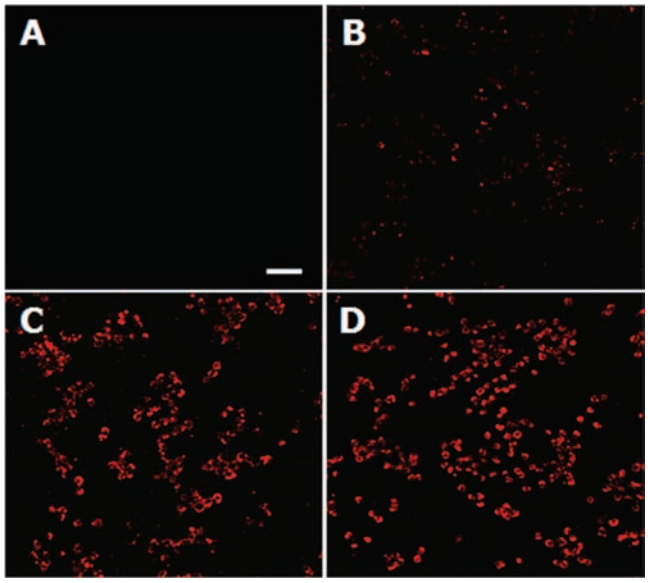

Figure 4. Confocal microscopy images of human ovarian cancer A2780 cells after no treatment (A) and treatment with (B) siRNA/PEI, (C) siRNA-PEG/PEI, and (D) siRNA-PEG-LHRH/PEI. Red signal represents Cy3 dye-labeled siRNA. Scale bar: 50 μm.

3A, lane 5). Considering that the concentration of GSH (10 mM) is similar to that of cytosolic GSH ranging between 0.5 and 10 mM (*21*), it can be deduced that free siRNA could be successfully rescued from the conjugates in a highly reductive environment of the cytoplasm. Since the presence of PEG in siRNA-PEG-LHRH may limit the access of the cytoplasmic RNA-induced silencing complex (RISC) due to the steric hindrance effect, we hypothesized that the reducible release of intact siRNA from the PEG chain in the cytoplasm may facilitate the incorporation of siRNA into RISC, which may lead to the enhanced silencing of a target gene.

The electrostatic interaction of siRNA-PEG-LHRH with PEI in an aqueous medium led to the spontaneous formation of PEC micelles. The resulting PEC micelles exhibit a spherical shape, as visualized by atomic force microscopy (Figure 3B). The spherical morphology could also be observed with ODN-PEG/PEI and siRNA-PEG/PEI PEC micellar formulations (*9*, *22*). The hydrodynamic diameter of the PEC micelles determined by a light scattering method was 142 nm with a narrow size distribution (polydispersity = 18.9%) (Figure 3C).

LHRH receptor-targeted delivery of siRNA-PEG-LHRH/PEI PEC micelles was studied in human ovarian carcinoma cells (A2780) using Cy3-conjugated siRNA. A2780 cells are known to overexpress LHRH receptor (*20*). Confocal microscopy observation demonstrated that the introduction of LHRH considerably increased the cellular uptake extent of siRNA-PEG-LHRH/PEI PEC micelles, as compared to the PEC micelles without LHRH ligand, siRNA-PEG/PEI (Figure 4). The enhanced cellular uptake of siRNA-PEG-LHRH/PEI PEC micelles can be attributed to a receptor-mediated endocytosis process. Enhanced intracellular delivery of LHRH−drug conjugate in ovarian cancer cells was also reported in previous studies (*18*, *19*). In the serum containing medium, the siRNA-PEG/PEI PEC micelles either with or without targeting ligands showed much higher intracellular siRNA delivery efficiencies than non-PEGylated siRNA/PEI polyelectrolyte complexes. The enhanced cellular uptake was primarily due to the improved stability of the PEC micelles in the presence of serum proteins. The surface-exposed PEG segments could stabilize the PEC micelles by forming a thermodynamically favorable core−shell structure and minimizing nonspecific binding of serum components to the PEC micelles, which can effectively prevent serum protein-mediated interparticulate aggregation (*22*, *23*). Receptor-mediated cellular uptake of siRNA-PEG-LHRH/PEI PEC micelles was further studied using flow cytometry. The extent of cellular uptake of LHRH-modified PEC micelles was increased by about 50% in an arbitrarily gated region (M1), compared to that of siRNA-PEG/PEI without LHRH (Figure 5). The presence of excess free LHRH peptide (1 μM) in the transfection medium significantly reduced the cellular uptake of siRNA-PEG-LHRH/PEI PEC micelles, suggesting that free LHRH peptides could

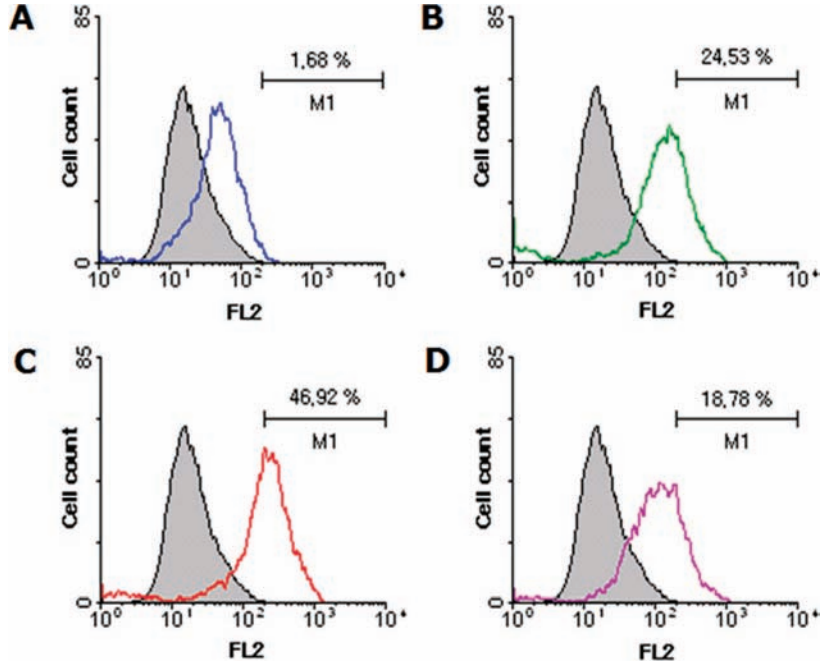

Figure 5. Flow cytometry histogram profiles from human ovarian cancer A2780 cells treated with (A) siRNA/PEI, (B) siRNA-PEG/PEI, and (C) siRNA-PEG-LHRH/PEI. (D) LHRH ligand competition assay was performed by adding free LHRH peptide (1 μM) 30 min prior to addition of siRNA-PEG-LHRH/PEI. Untreated control group is shown in filled graph. M1 presents an arbitrarily gated region (fluorescence intensity: 600−10 000).

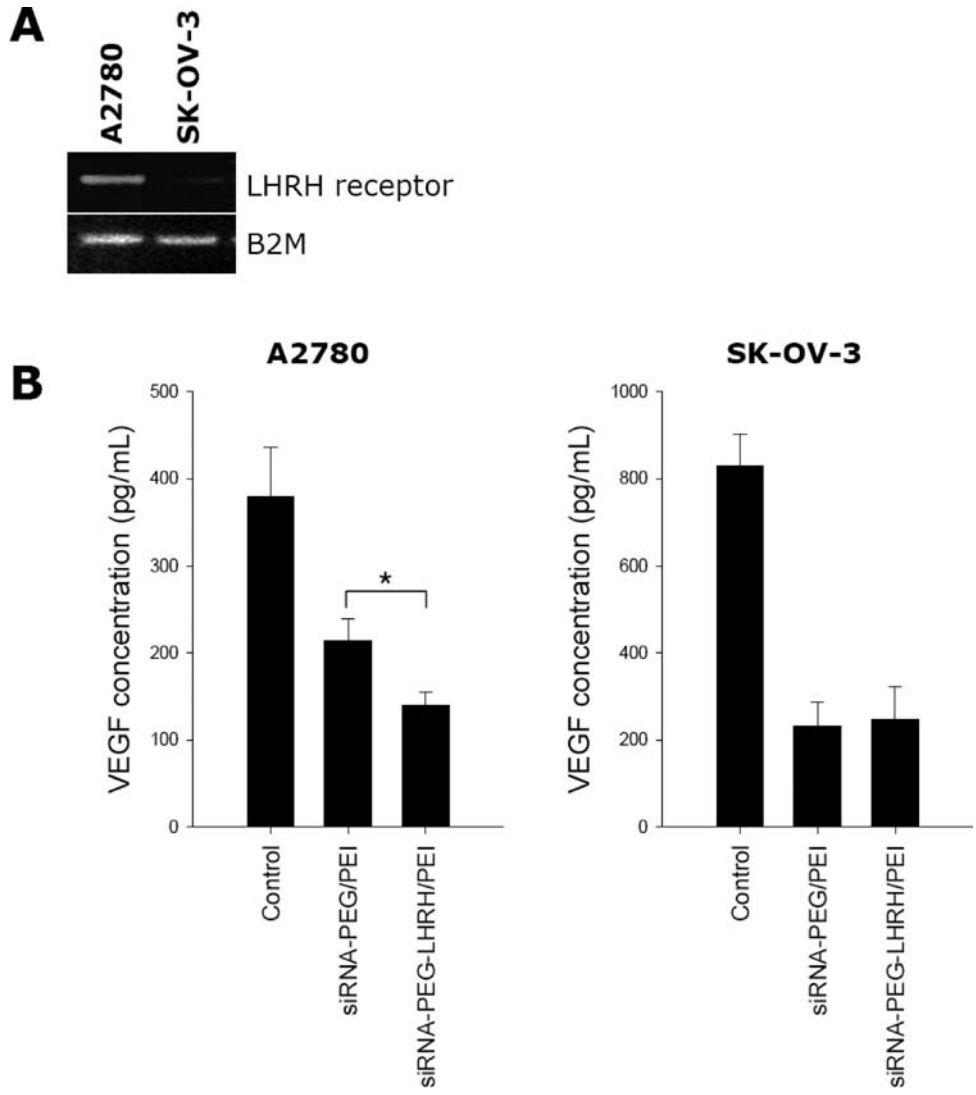

Figure 6. (A) RT-PCR analysis of mRNA expression of LHRH receptor in human ovarian carcinoma A2780 and SK-OV-3 cells. LHRH receptor (upper panel) and human β_2-microglobulin (B2M, lower panel) used as an internal standard have 319 and 114 bp, respectively. (B) LHRH receptor-mediated VEGF gene silencing in A2780 and SK-OV-3 cells. Cells were transfected with VEGF siRNA-PEG/PEI and VEGF siRNA-PEG-LHRH/PEI PEC micelles. Data were expressed as mean ± standard deviation ($n = 3$). * = $P < 0.01$.

compete with LHRH-modified PEC micelles for binding to LHRH receptors on the cell surface. In conjunction with the result from confocal microscopy, the flow cytometry result clearly demonstrates that the enhanced cellular uptake of siRNA-PEG-LHRH/PEI PEC micelles was mainly due to the specific interaction between LHRH moiety of PEC micelles and its cellular receptor, resulting from receptor-mediated endocytosis.

The potential therapeutic use of the siRNA-PEG-LHRH/PEI PEC micellar system was evaluated using VEGF-silencing siRNA. Two types of human ovarian cancer cells, A2780 and SK-OV-3, were used for comparatively analyzing gene silencing efficiency. Prior to the test of LHRH receptor-mediated gene silencing, the expression of LHRH receptor for the two cells was estimated by RT-PCR analysis as depicted in Figure 6A. Semiquantitative RT-PCR showed that a high level of LHRH receptor expression was detected in A2780 cells, while LHRH receptor expression in SK-OV-3 cells was negligible, in good agreement with previous reports (*22, 23*). For further *in vitro* transfection studies, the level of cellular toxicity of each formulation was evaluated using a cell viability assay (*24*). No detectable cytotoxicity was observed with all the formulations used in this experiment, suggesting that gene silencing was directly related to siRNA-induced RNAi (data not shown). For A2780 cells, the PEC micelles tethered with LHRH showed a higher inhibition extent of VEGF expression (139.4 ± 15.2 pg/mL) than those without LHRH (214.1 ± 25.4 pg/mL). In contrast, for SK-OV-3 cells, the LHRH targeting moiety did not affect the VEGF gene silencing efficiency, in which the PEC micelles with and without LHRH exhibited almost the same level of VEGF expression, 245.0 ± 77.8 pg/mL and 231.8 ± 56.3 pg/mL, respectively. Since various cancer cell lines exhibit a wide range of VEGF expression level depending on the cell type, SK-OV-3 cells secreted about a 2-fold higher amount of VEGF (832.2 ± 77.5 pg/mL) than A2780 cells (379.0 ± 56.9 pg/mL) prior to transfection. After transfecting siRNA-PEG-LHRH/PEI PEC micelles, SK-OV-3 cells apparently showed greater gene silencing percent (70.4 ± 9.4%) than A2780 cells (63.2 ± 4.0%). This was likely because the two cells have inherently different cellular uptake extents of PEC micelles and intracellular RNAi activities, resulting in different gene silencing efficiencies even when using the same transfection agent (*22, 23*). Although LHRH receptor-positive A2780 cells had lower VEGF silencing efficiency than LHRH receptor-deficient SK-OV-3 cells, they showed significantly improved gene silencing efficiency only when transfected with the LHRH-modified PEC micelles. The results suggest that the enhanced VEGF gene silencing by VEGF siRNA-PEG-LHRH/PEI PEC micelles was

mainly attributable to improved cellular uptake via an LHRH receptor-mediated endocytosis mechanism.

CONCLUSIONS

Here, we demonstrated that siRNA-PEG-LHRH/PEI PEC micelles could be used for cancer-targeted delivery of therapeutic siRNA. We have successfully synthesized and purified siRNA-PEG-LHRH conjugate, and prepared siRNA-PEG-LHRH/PEI PEC micelles in a nanometer size range. An LHRH receptor-targeted siRNA formulation (siRNA-PEG-LHRH/PEI PEC micelle) enhanced the intracellular delivery of siRNA for A2780 cells, due to LHRH-specific receptor−ligand interaction. VEGF siRNA-PEG-LHRH/PEI PEC micelles specifically inhibited VEGF expression in cancer cells in an LHRH receptor-specific manner. On the basis of the current formulation strategy, many different cancer targeting ligands such as folic acid, transferrin, peptides, antibodies, and growth factors could be similarly tethered to the distal end of the PEG chain in the siRNA-PEG/PEI micellar formulation for cancer-targeted delivery of siRNA therapeutics.

ACKNOWLEDGMENT

This work was supported by the grant from the Ministry of Science and Technology, Republic of Korea (F104AA010002-07A0101-00210).

LITERATURE CITED

(1) Hammond, S. M., Caudy, A. A., and Hannon, G. J. (2001) Post-transcriptional gene silencing by double-stranded RNA. *Nat. Rev. Genet. 2*, 110–9.

(2) Elbashir, S. M., Harborth, J., Lendeckel, W., Yalcin, A., Weber, K., and Tuschl, T. (2001) Duplexes of 21-nucleotide RNAs mediate RNA interference in cultured mammalian cells. *Nature 411*, 494–8.

(3) Kim, S. H., Mok, H., Jeong, J. H., Kim, S. W., and Park, T. G. (2006) Comparative evaluation of target-specific GFP gene silencing efficiencies for antisense ODN, synthetic siRNA, and siRNA plasmid complexed with PEI-PEG-FOL conjugate. *Bioconjugate Chem. 17*, 241–4.

(4) Hiroi, N., Funahashi, A., and Kitano, H. (2006) Comparative studies of suppression of malignant cancer cell phenotype by antisense oligo DNA and small interfering RNA. *Cancer Gene Ther. 13*, 7–12.

(5) McNamara, J. O., II, Andrechek, E. R., Wang, Y., Viles, K. D., Rempel, R. E., Gilboa, E., Sullenger, B. A., and Giangrande, P. H. (2006) Cell type-specific delivery of siRNAs with aptamer-siRNA chimeras. *Nat. Biotechnol. 24*, 1005–15.

(6) Jeong, J. H., Kim, S. H., Kim, S. W., and Park, T. G. (2006) Intracellular delivery of poly(ethylene glycol) conjugated antisense oligonucleotide using cationic lipids by formation of self-assembled polyelectrolyte complex micelles. *J. Nanosci. Nanotechnol. 6*, 2790–5.

(7) Yano, J., Hirabayashi, K., Nakagawa, S., Yamaguchi, T., Nogawa, M., Kashimori, I., Naito, H., Kitagawa, H., Ishiyama, K., Ohgi, T., and Irimura, T. (2004) Antitumor activity of small interfering RNA/cationic liposome complex in mouse models of cancer. *Clin. Cancer Res. 10*, 7721–6.

(8) Park, T. G., Jeong, J. H., and Kim, S. W. (2006) Current status of polymeric gene delivery systems. *Adv. Drug Delivery Rev. 58*, 467–86.

(9) Kim, S. H., Jeong, J. H., Lee, S. H., Kim, S. W., and Park, T. G. (2006) PEG conjugated VEGF siRNA for anti-angiogenic gene therapy. *J. Controlled Release 116*, 123–9.

(10) Jeong, J. H., Kim, S. W., and Park, T. G. (2003) Novel intracellular delivery system of antisense oligonucleotide by self-assembled hybrid micelles composed of DNA/PEG conjugate and cationic fusogenic peptide. *Bioconjugate Chem. 14*, 473–9.

(11) Fountaine, T. M., Wood, M. J., and Wade-Martins, R. (2005) Delivering RNA interference to the mammalian brain. *Curr. Gene Ther. 5*, 399–410.

(12) Hamada, M., Ohtsuka, T., Kawaida, R., Koizumi, M., Morita, K., Furukawa, H., Imanishi, T., Miyagishi, M., and Taira, K. (2002) Effects on RNA interference in gene expression (RNAi) in cultured mammalian cells of mismatches and the introduction of chemical modifications at the 3′-ends of siRNAs. *Antisense Nucleic Acid Drug Dev. 12*, 301–9.

(13) Kim, S. H., Jeong, J. H., Lee, S. H., Kim, S. W., and Park, T. G. (2008) Local and systemic delivery of VEGF siRNA using polyelectrolyte complex micelles for effective treatment of cancer. *J. Controlled Release 129*, 107–16.

(14) Wu, G., Yang, W., Barth, R. F., Kawabata, S., Swindall, M., Bandyopadhyaya, A. K., Tjarks, W., Khorsandi, B., Blue, T. E., Ferketich, A. K., Yang, M., Christoforidis, G. A., Sferra, T. J., Binns, P. J., Riley, K. J., Ciesielski, M. J., and Fenstermaker, R. A. (2007) Molecular targeting and treatment of an epidermal growth factor receptor-positive glioma using boronated cetuximab. *Clin. Cancer Res. 13*, 1260–8.

(15) Ikeda, Y., and Taira, K. (2006) Ligand-targeted delivery of therapeutic siRNA. *Pharm. Res. 23*, 1631–40.

(16) Schiffelers, R. M., Ansari, A., Xu, J., Zhou, Q., Tang, Q., Storm, G., Molema, G., Lu, P. Y., Scaria, P. V., and Woodle, M. C. (2004) Cancer siRNA therapy by tumor selective delivery with ligand-targeted sterically stabilized nanoparticle. *Nucleic Acids Res. 32*, e149.

(17) Bazan-Peregrino, M., Seymour, L. W., and Harris, A. L. (2007) Gene therapy targeting to tumor endothelium. *Cancer Gene Ther. 14*, 117–27.

(18) Dharap, S. S., Qiu, B., Williams, G. C., Sinko, P., Stein, S., and Minko, T. (2003) Molecular targeting of drug delivery systems to ovarian cancer by BH3 and LHRH peptides. *J. Controlled Release 91*, 61–73.

(19) Dharap, S. S., and Minko, T. (2003) Targeted proapoptotic LHRH-BH3 peptide. *Pharm. Res. 20*, 889–96.

(20) Dharap, S. S., Wang, Y., Chandna, P., Khandare, J. J., Qiu, B., Gunaseelan, S., Sinko, P. J., Stein, S., Farmanfarmaian, A., and Minko, T. (2005) Tumor-specific targeting of an anticancer drug delivery system by LHRH peptide. *Proc. Natl. Acad. Sci. U.S.A. 102*, 12962–7.

(21) Wang, W., and Ballatori, N. (1998) Endogenous glutathione conjugates: occurrence and biological functions. *Pharmacol. Rev. 50*, 335–56.

(22) Jeong, J. H., Kim, S. H., Kim, S. W., and Park, T. G. (2005) Polyelectrolyte complex micelles composed of c-raf antisense oligodeoxynucleotide-poly(ethylene glycol) conjugate and poly(ethylenimine): effect of systemic administration on tumor growth. *Bioconjugate Chem. 16*, 1034–7.

(23) Jeong, J. H., Kim, S. H., Kim, S. W., and Park, T. G. (2005) In vivo tumor targeting of ODN-PEG-folic acid/PEI polyelectrolyte complex micelles. *J. Biomater. Sci. Polym. Ed. 16*, 1409–1419.

(24) Mosmann, T. (1983) Rapid colorimetric assay for cellular growth and survival: application to proliferation and cytotoxicity assays. *J. Immunol. Methods 65*, 55–63.

BC800249N

Sites of Modification of Hemospan, a Poly(ethylene glycol)-Modified Human Hemoglobin for Use As an Oxygen Therapeutic

Kim D. Vandegriff,*[,†] Ashok Malavalli,[†] Gnel M. Mkrtchyan,[†] Stephanie N. Spann,[†] Dale A. Baker,[†,‡] and Robert M. Winslow[†,‡]

Sangart Inc., 6175 Lusk Boulevard, San Diego, California, 92121, and Department of Bioengineering, University of California, San Diego, La Jolla, California 92093. Received June 30, 2008; Revised Manuscript Received September 2, 2008

Hemospan is an acellular hemoglobin-based oxygen therapeutic in clinical trials in Europe and the United States. The product is prepared by site-specific conjugation of maleimide-activated poly(ethylene) glycol (PEG, MW ~5500) to human oxyhemoglobin through maleimidation reactions either (1) directly to reactive Cys thiols or (2) at surface Lys groups following thiolation using 2-iminothiolane. The thiolation/maleimidation reactions lead to the addition of ~8 PEGs per hemoglobin tetramer. Identification of PEG modified globins by SDS-PAGE and MALDI-TOF reveals a small percentage of protein migrating at the position for unmodified globin chains and the remaining as separate bands representing globin chains conjugated with 1 to 4 PEGs per chain. Identification of PEG modification sites on individual α and *β* globins was made using reverse-phase HPLC, showing a series of α globins conjugated with 0 to 3 PEGs and a series of *β* globins conjugated with 0 to 4 PEGs per globin. Mass analysis of tryptic peptides from hemoglobin thiolated and maleimidated with *N*-ethyl maleimide showed the same potential sites of modification regardless of thiolation reaction ratio, with seven sites identified on *β* globins at *β*8, *β*17, *β*59, *β*66, *β*93, *β*95, and *β*132 and three sites identified on α globins at α7, α16, and α40.

INTRODUCTION

Hemospan is a new class of hemoglobin-based oxygen therapeutic, designed using site-specific, maleimide poly(ethylene glycol) (PEG) conjugation chemistry with oxyhemoglobin (Hb) (*1, 2*). Hemospan, also referred to as MP4 or MalPEG-Hb in the literature, has been the subject of extensive biochemical (*2*−*6*) and physiologic studies (*7*−*10*). The product has completed phase I (*11*) and phase II clinical trials in Sweden (*12*) and the U.S., with phase III trials just finished in Europe.

Several general benefits have been attributed to PEG conjugation to proteins, including decreased immunogenicity, prolonged intravascular retention time, and increased colloidal osmotic pressure as a function of PEG mass and protein concentration (*3*). A recent study using small-angle X-ray scattering to obtain the three-dimensional structure of Hemospan in solution (P5K6 in that study) showed that PEGylation increases the macromolecular dimensions of hemoglobin from a maximum particle dimension of 70 Å for Hb to 130 Å for P5K6; in addition, PEGylation introduces an intermolecular repulsive effect that increases with PEG mass (*6*). Even though this PEGylated Hb molecule is not cross-linked intramolecularly and, therefore, remains capable of tetramer−dimer dissociation upon dilution (*13*), the PEG surface shielding and intermolecular repulsion prolong the circulatory half-life of Hemospan to approximately 20 h in surgical patients (*12*).

In the present study, we describe the number and distribution of PEG polymers on the individual α and *β* globin subunits in Hemospan. Because the maleimide−PEG raw material has a relatively wide mass distribution (~5500 ± 750 Da), sites of modification, under reaction conditions specified for Hemospan, were identified by mass analysis using a small molecular weight model, i.e., *N*-ethyl maleimide (NEM) in the place of maleimide−PEG. NEM as a model compound was validated recently in a study of modification sites in a similar product made using thiolation/maleimidation reactions with deoxyHb (*14*). Thiolation/maleimidation under Hemospan reaction conditions with oxyHb shows both similar and dissimilar sites compared to the same reaction conditions carried out on deoxyHb reported by Iafelice (*14*). A primary difference is that the *β*93Cys is modified in Hemospan, leading to higher O_2 affinity (*2, 4*).

EXPERIMENTAL SECTION

Hemospan Production. Hemospan was prepared using the process described earlier (*2*), with a small increase in processing temperature from 6° ± 2 to 10 °C, which does not affect the final reaction product. Briefly, stroma-free Hb was purified from human red blood cells and diluted to 1 mM (in tetramer) in phosphate-buffered saline (PBS), pH 7.4. Hb thiolation was carried out using a 10-fold molar excess (over Hb tetramer) of 2-iminothiolane (2-IT, Sigma Aldrich, St. Louis, MO) for 4 h at 10 °C. This was followed by PEG conjugation using a 20-fold molar excess (over Hb tetramer) of maleimide-activated PEG (MW ~5500 Da) (NOF Corp., Tokyo, Japan) for 2 h at 10 °C. The PEG-modified hemoglobin was diafiltered against lactated Ringer's solution using 70 kD tangential flow filtration to remove both unreacted Hb and maleimide-activated PEG. The final product was concentrated to a final Hb concentration of 4.2 g/dL.

NEM-Hb Production. NEM-Hb was prepared using the same reaction conditions described above for PEG conjugation. Hb was first reacted with a 10-fold molar excess of 2-IT for 4 h at 10 °C, followed by reaction with 20-fold molar excess of *N*-ethyl maleimide (NEM) (in the place of maleimide-activated PEG) for 2 h at 10 °C. NEM-modified Hb was dialyzed against lactated Ringer's solution to remove unreacted NEM.

Degree of Hemoglobin Modification. The degree of thiolation and maleimidation (or PEGylation) was evaluated from the number of reactive thiols on Hb after the thiolation and

* Corresponding author. kvandegriff@sangart.com; 858-450-2414, Telephone; 858-450-2499, Fax.
† Sangart Inc.
‡ University of California.

10.1021/bc8002666 CCC: $40.75 © 2008 American Chemical Society
Published on Web 10/07/2008

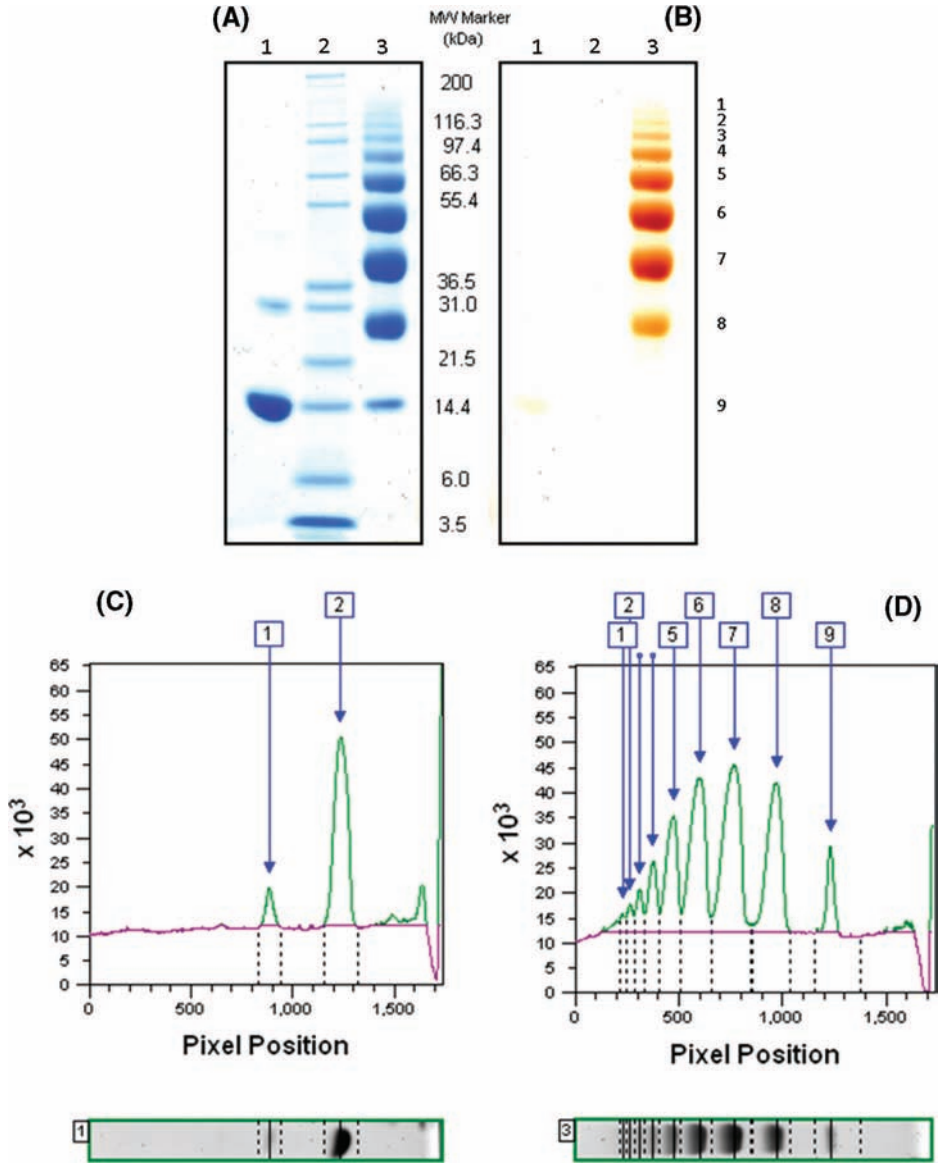

Figure 1. SDS-PAGE of Hb and Hemospan. (A) Coomassie blue staining, specific for protein; (B) iodine staining, specific for PEG. Lanes: (1) Hb; (2) MW markers; (3) Hemospan. Densitometry maps for Hb (C) and Hemospan (D) are shown for protein staining; the densitometry peaks for Hemospan are identified on the right side of (B).

maleimidation reactions. Free thiols were measured by disulfide exchange with the 4,4′-dipyridinedisulfide to produce the corresponding 4-thiopyridone (4-TP), measured at 324 nm ($\varepsilon = 1.98 \times 10^4$ M^{-1} cm^{-1}) (*15*). The difference between the number of free thiols immediately following thiolation versus post-maleimidation corresponds to the number of PEG or NEM molecules conjugated to the hemoglobin tetramer.

Two additional test methods were used to evaluate the degree of PEGylation: (1) ^{1}H NMR spectroscopy (Varian 400 MHz; Inova; performed at Spectral Data Services, Inc., Champaign, IL), using D_2O as the solvent, (trimethylsilyl)propionic acid-D4 as internal standard, and comparing spectra of Hemospan with samples of pure PEG (10 mg) dissolved in D_2O following the method of Jackson (*16*). The NMR signal at 3.5−3.9 ppm represents the chemical shift for the oxyethylene groups in PEG, and the integrated signal for pure PEG was used to calculate the amount of PEG in the hemoglobin conjugate. (2) A dry weight method was performed using Hb and Hemospan at equal concentrations in heme by subtracting the dry weight of Hb from the dry weight of PEG-conjugated Hb to calculate the number of ∼5 kD PEGs conjugated per Hb molecule. Dry weights were made following lyophilization (Virtis, Gardiner, NY) and oven-drying at 130 °C until weights no longer changed.

Table 1. Percent of Total for the Protein-Stained Gels for Hb and Hemospan (Figure 1A) According to the Densitometry Maps Shown in Figure 1C,D, Ranked from the Top to the Bottom of the Gels, and Percent of total for the Hemospan PEG-Stained Gel from Figure 1B, Ranked from the Top to the Bottom of the Gel

Hb (protein stain)		Hemospan (protein stain)		Hemospan (PEG stain)		
peak	density (%)	peak	density (%)	peak	density (%)	PEGs
1	9.36	1−2	2.30	1−2	2.83	>4
2	90.64	3−4	8.16	3−4	12.01	>4
		5	12.55	5	17.06	4
		6	22.49	6	26.65	3
		7	28.09	7	27.87	2
		8	20.94	8	13.57	1
		9	5.47	9	ND[a]	0

[a] ND = not detected.

Degree of PEGylation by SDS-PAGE and MALDI-TOF Mass Spectrometry (MS). Hemospan was analyzed by sodium dodecylsulfate/polyacrylamide gel electrophoresis (SDS-

PAGE) on Bis-Tris precast gels (Invitrogen), with a 4−12% gradient. Experiments were carried out under conditions to avoid removing conjugated PEG from the globins, and so heating and β-mercaptoethanol treatments were not employed in the SDS process. To confirm dissociation of globins, control experiments were performed on Hb both with and without heating and β-mercaptoethanol treatment in which no differences in band separation were observed. Gels were stained differentially using Coomassie blue for protein and iodine for PEG (*17*, *18*), and bands were analyzed by densitometry (Image Scanner, PowerLook 1120). Protein and PEG-conjugated globin bands were electroeluted for MALDI-TOF analysis by mixing samples with sinapinic acid in 50% acetonitrile/0.1% formic acid. An intact Hemospan solution sample was submitted independently for MALDI-TOF mass analysis. Samples were air-dried on the MALDI sample plate and analyzed on an Applied Biosystems Voyager DE mass spectrophotometer.

Degree of PEGylation by Reverse-Phase HPLC. Reverse-phase high-performance chromatography (RP HPLC) was used for analysis of modified globins. The modified hemoglobin solution was eluted on a C_3 column (4.6 × 50 mm) (Agilent 1100 series) at a flow rate of 2 mL/min at 50 °C in 35−40% acetonitrile with 0.1% trifluoroacetic acid (TFA) over 1 min, followed by 40−51% acetonitrile with 0.1% TFA over 11 min.

Mass Analysis by Electrospray Mass Spectrometry (ESI-TOF MS). Hb and NEM-Hb were desalted on a PD-10 column containing Sephadex G-25 medium (GE) and submitted for ESI-TOF analysis on an Agilent ESI-TOF mass spectrometer. Samples were electrosprayed into the TOF reflectron analyzer at an ESI voltage of 4000 V and a flow rate of 200 μL/min (50:50 acetonitrile/water/0.1% formic acid v/v) using flow injection with an Agilent microwell autosampler. The averaged mass spectrum was converted to a neutral charge state spectrum using a maximum entropy deconvolution algorithm (MaxEnt) as part of the *Analyst* data analysis software (Agilent).

Sites of Hemoglobin Maleimidation. Sites of thiolation/maleimidation in Hemospan were identified using NEM-Hb as a model compound. To evaluate potential preferences of Hb residues to react with 2-IT, Hb was subjected to thiolation under identical reaction conditions at four different ratios of Hb to 2-IT (1:3, 1:5, 1:7, and 1:10). NEM was added subsequently at a Hb/NEM molar ratio of 1:20 in each case. NEM-Hb samples prepared at the molar reaction ratio of 1:10:20 were run in triplicate. The same sites were found to be modified for all ratios tested, and samples prepared at the lower reaction ratios were run only once. NEM-Hb samples were subjected to SDS-PAGE on Bis-Tris precast gels, with a 4−12% gradient. Gels were stained with Coomassie blue. After staining, NEM-Hb bands were excised and pretreated prior to in-gel trypsin digestion. Reduction of disulfide linkages was performed using 10 mM dithiothreitol, followed by alkylation with 55 mM iodoacetamide (Sigma-Aldrich, St. Louis, MO). In-gel digestion with trypsin (Promega) was performed overnight at 37 °C at an estimated (1:30) enzyme to substrate ratio in 50 mM ammonium bicarbonate. Tryptic peptides were extracted from the gel using acetonitrile and formic acid and subjected to analysis by LC/MS/MS (Scripps Research Institute, MS Lab, San Diego, CA). Separation was performed on a laser-pulled, 100 μm ID C_{18} column with a tip of <5 μm that was also used as the nanoelectrospray emitter. Gradient elution was used with 0.1% formic acid/acetonitrile as the mobile phases, from 5% to 60% acetonitrile over 90 min, and then maintained for an additional 20 min with flow rates of ~200 nL/min. MS/MS analysis was performed on a LTQ-DECA (Thermoelectron Corp.) and Agilent LC/MSD Trap ion trap mass spectrometer. Data-dependent scanning was used to maximize the number of peptides sequenced in the highly complex mixture. This mode of operation uses preset criteria to select unique peptides on-the-fly for undergoing MS/MS. Sequences were searched by MASCOT (Matrix Science, Limited), with Sequest search engine software (University of Washington, WA) using either NCBInr (nonredundant) or SwissProt 55.1 databases. To improve searching efficiency, taxonomic categories were limited to mammalian proteins. Only peptides producing good quality fragmentation spectra and scoring higher than the threshold required for the 95% confidence level for MASCOT were used for protein identification.

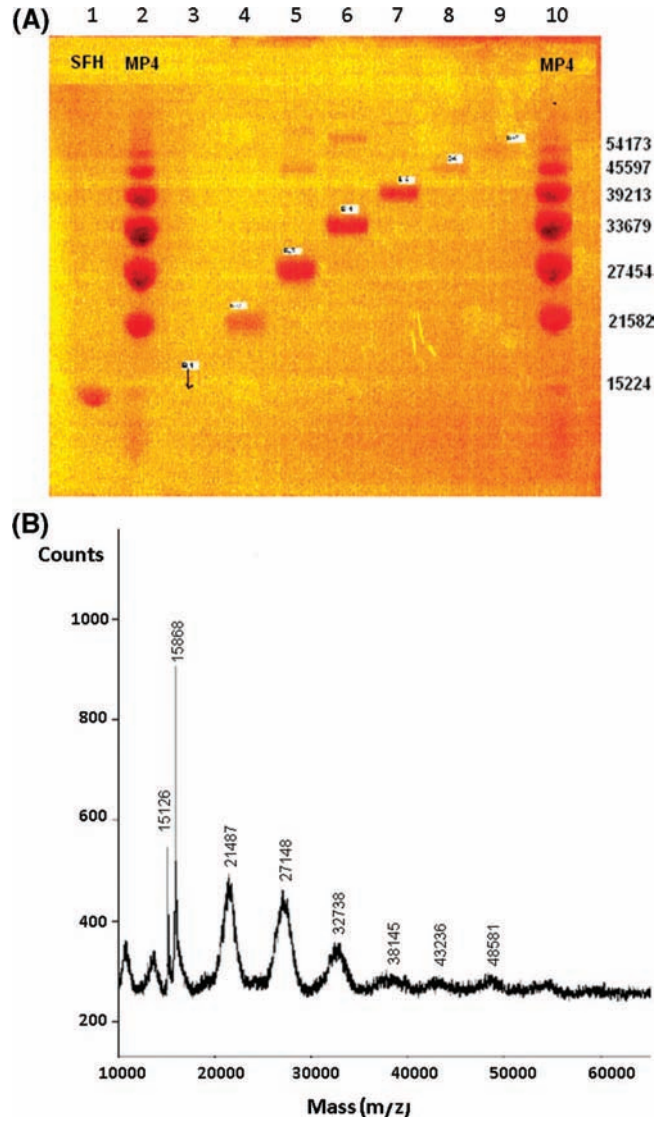

Figure 2. (A) SDS-PAGE of Hb (SFH) is shown in lane 1; Hemospan (MP4) is shown in lanes 2 and 10. Each Hemospan (MP4) band from lane 1 was extracted from the gel and rerun on SDS-PAGE (lanes 3−9). These bands were subjected to MALDI-TOF for mass determination, and the masses for each band are shown on the right-hand side of the gel. (B) Intact Hemospan was subjected to MALDI-TOF, showing peaks for unmodified globins (α = 15 126; β = 15 868) and additional peaks, increasing in mass by a factor of ~5.5 kDa, corresponding to the number of conjugated PEGs.

RESULTS

Degree of PEG Modification. The primary method used to measure the degree of PEGylation in Hemospan was the colorimetric technique (*15*). Unmodified Hb was used as a standard for this method, because human oxyHb contains two reactive thiols at the βCys93 residues. For 12 separate Hemospan lots prepared at Sangart's manufacturing facility, the oxyHb standard prepared prior to thiolation and PEGylation showed

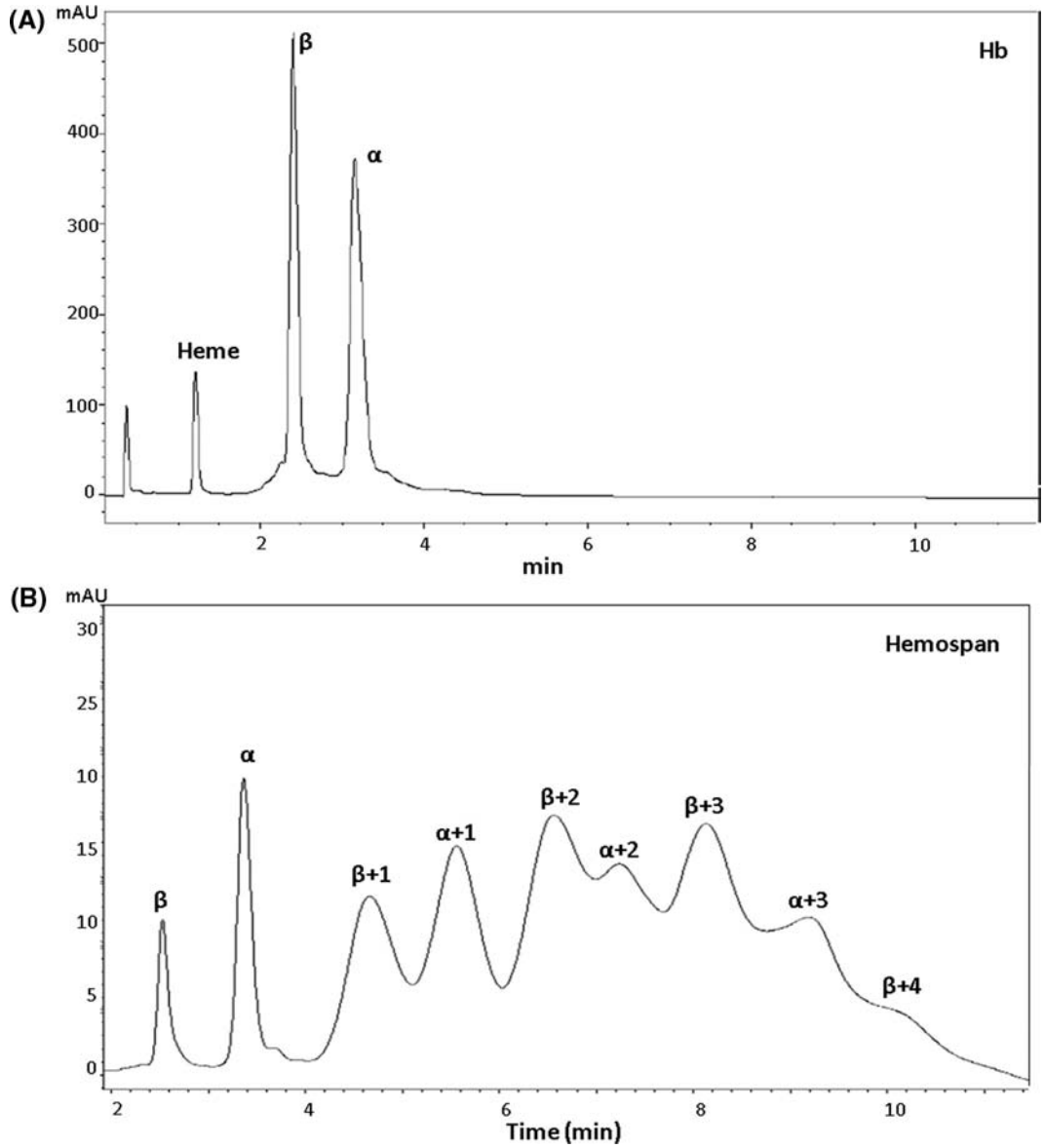

Figure 3. C_3 RP HPLC of Hb (A) and Hemospan (B); UV detection at 210 nm. Free heme and unmodified β and α globin peaks are assigned in (A). Unmodified β and α globin peaks and globin chains with increasing numbers of attached PEGs are assigned in (B). Note expanded scale in (B).

2.1 ± 0.03 (average ± standard deviation) free thiols. Following thiolation and PEGylation, the number of PEGs per Hb tetramer was 7.9 ± 0.2, with 0.4 ± 0.1 residual free thiols remaining. Degree of PEGylation measurements were also performed on single lots of Hemospan by ^{1}H NMR or dry weight analysis, giving values of 7.2 and 7.6, respectively. Therefore, on the basis of three independent measures, the average number of conjugated PEGs per Hb tetramer in Hemospan is 7−8. Thus, in addition to the two residing, reactive thiols on the β chains, the thiolation reaction with 2-IT at a 10-fold molar excess to Hb tetramer provides, on average, an additional 5−6 sites of PEG conjugation on the Hb tetramer, with <1 free thiol remaining.

Globin Analysis by SDS-PAGE. Representative SDS-PAGE of Hb and Hemospan are shown in Figure 1, with Coomassie blue staining for proteins (Figure 1A) and iodine staining for PEG (Figure 1B). In Figure 1A, Hb (lane 1) shows a major band migrating at ~15 kDa, corresponding to α and β globins migrating at the same position. A higher molecular weight protein band can also be seen in lane 1, migrating near the protein MW marker at ~31 kDa. To determine if the Hb solution contained any non-Hb, red cell protein, this band was treated with trypsin, and the tryptic peptides were extracted from the gel and subjected to LC/MS/MS analysis. The primary protein hit was identified as human hemoglobin β chain, with 95% sequence coverage and a mass of 16 102. A secondary protein was also present and was identified as carbonic anhydrase, with 57% sequence coverage and a mass of 28 909. Hemospan (lane 3) shows multiple bands by protein staining, with increasing molecular weights. Densitometry maps for Hb and Hemospan from the protein-stained gels are displayed in Figure 1C,D, with peaks ranked from the top to the bottom of the gel; percentages of total for the peaks are shown in Table 1.

Differential staining with iodine in Figure 1B, which is specific for PEG, shows no detectable band for either Hb or the protein MW markers (lanes 1 and 2, respectively). For Hemospan (lane 3), all bands stained for both protein and PEG, with the exception of one band seen by protein staining alone that migrated at ~15 kDa. To assess lot-to-lot consistency, densitometry of the ~15 kDa band from the 12 Hemospan lots tested showed $6.2 \pm 2.1\%$ (average ± standard deviation) of combined non-PEGylated globins. Each Hemospan band was

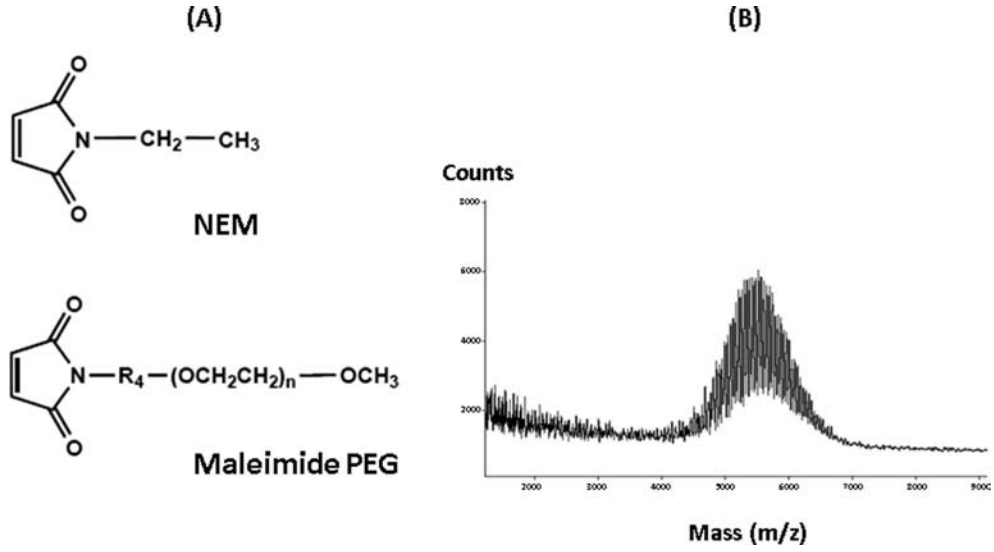

Figure 4. (A) Chemical structures of NEM and maleimide PEG, where R_4 is an alkyl linker between the maleimide functional group and the oxyethylene backbone in PEG. The number of repeating oxyethylene units in PEG (*n*) is approximately 114 for a ~5.5 kDa polymer. (B) MALDI-TOF analysis of the free maleimide−PEG.

extracted from the gel and rerun on SDS-PAGE (Figure 2A, lanes 3−9). The individual bands were also subjected to MALDI-TOF for mass determinations, with the measured masses reported on the right side of Figure 2A, aligned with their respective bands. The SDS-PAGE bands showed masses for globins with an increasing number of attached PEGs (~5.5 kDa for each PEG): lane 3, 0 PEGs (MW = 15 224); lane 4, 1 PEG (MW = 21 582); lane 5, 2 PEGs (MW = 27 454); lane 6, 3 PEGs (MW = 33 679); lane 7, 4 PEGs (MW = 39 213). Lighter bands were observed at positions with masses = 45 597 and 54 173, making up <10% of the total.

The MALDI-TOF spectrum for intact Hemospan is shown in Figure 2B as a series of mass peaks corresponding to unmodified α and β chains at 15 126 and 15 868, respectively, and additional peaks following, increasing in mass by a factor of ~5.5 kDa, again corresponding to the number of attached PEG units per globin in close agreement with the mass of the extracted SDS-PAGE bands in Figure 2A.

Globin Analysis by Reverse-Phase (RP) HPLC. RP HPLC (C_3) provides a protein separation method based on hydrophobicity and size. Using this method, the heme groups are stripped from the hemoglobin tetramers, and the subunit globins dissociate. Since human hemoglobin β chains are more hydrophilic compared to α chains, the individual chains can be resolved (*19*). Representative C_3 chromatograms of Hb and Hemospan are shown in Figure 3A and B, respectively. The heme peak and unmodified α and β globin peaks from Hb are identified in Figure 3A. The chromatographic profile for Hemospan is shown on an expanded scale in Figure 3B, with unmodified α and β globin peaks and seven additional, less well resolved modified globin peaks. Each peak was fractionated and run separately on the C_3 column, showing that they are made up of individual components (data not shown). Lot-to-lot consistency was assessed for the 12 Hemospan lots by integration of the well-resolved peaks for the unmodified β and α globins, showing 1.2 ± 0.2% and 4.8 ± 0.2% (average ± standard deviation), respectively, thus reflecting a high degree of consistency between manufacturing lots. This consistency was also observed in the PEGylated peaks that were not subject to integration. Tentative assignments for the peaks of the modified globins were defined based on globin chain hydrophobicity and degree of PEGylation and independently from PEG conjugation to individual α and β chains identified by MALDI-TOF (data not shown).

ESI-TOF Mass Spectrometry. To increase the resolution for determining the number of sites of maleimidation, ESI-TOF mass spectra were run on unmodified Hb and NEM-Hb. NEM has the same functionally reactive group as maleimide-activated PEG but with a lower, well-defined mass (126 Da) (Figure 4A, top), in marked contrast to the large mass and size distribution of free PEG (~5500 ± 750 Da) (Figure 4A, bottom), as demonstrated by its MALDI-TOF spectrum shown in Figure 4B. The NEM-Hb reaction was carried out using the same thiolation molar ratio of 2-IT to Hb used in the manufacturing process for the 12 lots of Hemospan, and the thiolated-Hb product was then reacted with NEM at the same molar ratio as used in the manufacturing process with PEG. The degree of maleimidation for NEM-Hb was 8.2. ESI-TOF spectra for Hb and NEM-Hb are shown in Figure 5A and B, respectively. For Hb, the $[M + H]^+$ ions at m/z = 15 127 and 15 867 correspond to unmodified α and β globins, respectively. For NEM-Hb, thiolated-NEM attachments by mass units are as follows: NEM alone = 126 mu; thiolated + NEM (Th + NEM) = 227 mu. The ESI-TOF results in Figure 5B show clearly defined peaks for α globin, with 0, 1, 2, or 3 Th + NEM modified sites, and β globin with 1 NEM-only modified site plus 1, 2, 3, or 4 Th + NEM modified sites. Free β globin could not be clearly resolved. These findings are in good agreement with the number of PEGylated sites found for Hemospan using either SDS-PAGE (Figure 2) or RP HPLC (Figure 3B).

Sites of Hemoglobin Modification. The simplified model system for maleimide PEGylation by using NEM as a substitute for PEG was used to evaluate the sites of Hb modification at ratios of Hb/2-IT/NEM of 1:3:20, 1:5:20, 1:7:20, and 1:10:20. At these ratios, the degree of maleimidation was determined to be 4.1, 5.3, 6.3, and 8.2 conjugated NEM sites per Hb tetramer, respectively. Each NEM-modified Hb sample was subjected to SDS-PAGE and trypsin digestion, followed by LC/MS/MS to identify modified-hemoglobin tryptic peptides by the increase in the atomic mass unit of modified peptides (amu), such that the addition of NEM alone is equal to +126 amu compared to addition of 2-IT + NEM = +227 amu. Regardless of the ratio of Hb/2-IT/NEM used, the same 10 modified residues were identified (Table 2). Tryptic peptides with 2-IT + NEM modified terminal Lys residues showed a mass increase of approximately 227 amu. The tryptic peptide in the β chain with NEM-modified

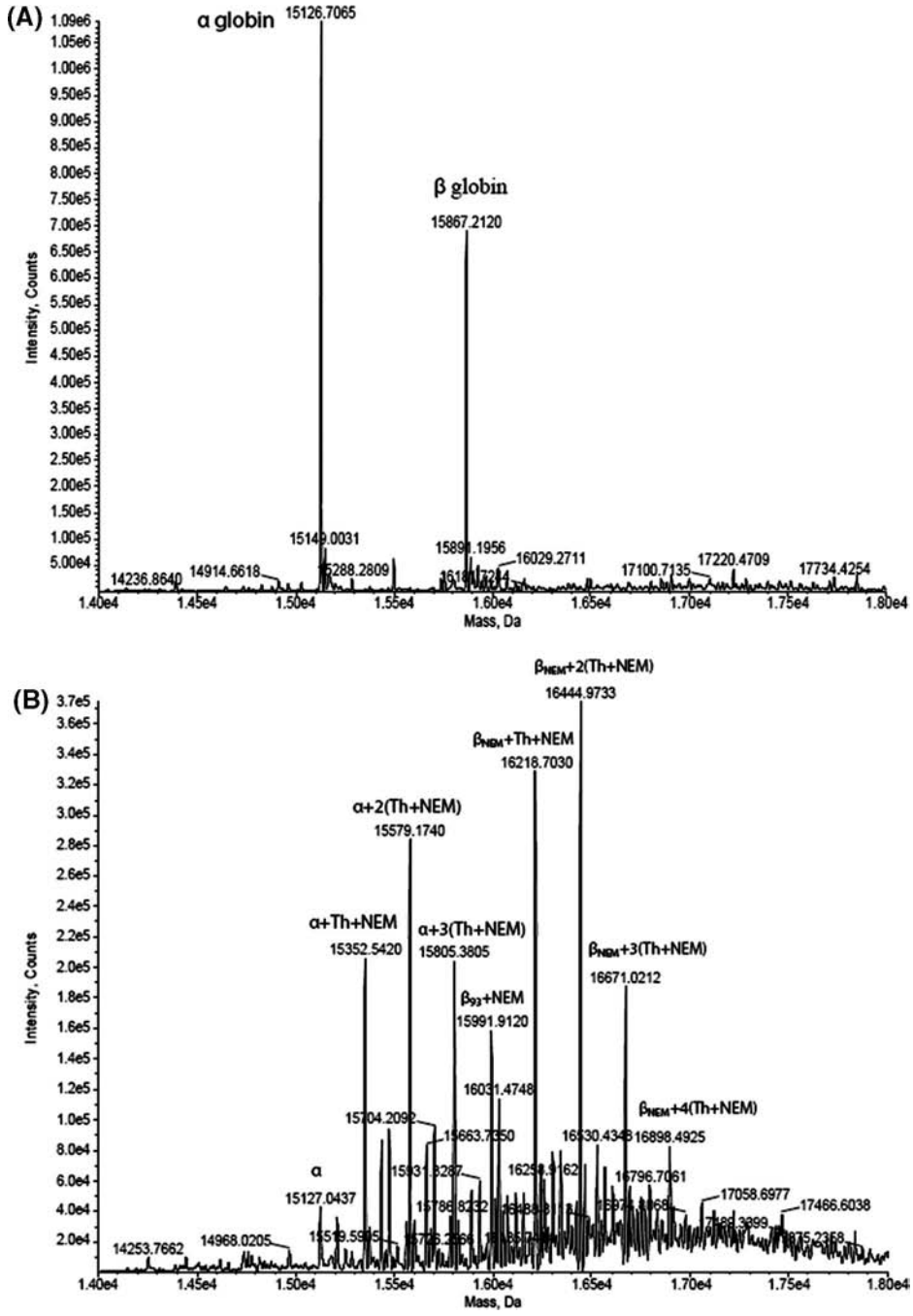

Figure 5. (A) ESI-TOF mass spectrum of Hb, showing α chain with a mass of 15 127 Da and β chain with a mass of 15 867 Da. (B) ESI-MS of NEM-Hb; peaks are identified as unmodified α globin, α globin plus the number of thiolated + NEM (Th + NEM) groups, β globin + NEM (i.e., β93Cys), and β globin plus the number of thiolated + NEM groups (Th + NEM). Little or no unmodified β globin could be resolved.

Cys at position 93 and with 2-IT + NEM modified terminal Lys at position 95 showed a mass increase of approximately 353 amu.

Considering a tetrameric hemoglobin molecule, a total of 20 potentially modifiable residues have been identified. Three thiolated-maleimidated sites were identified on the α globin: αLys7, αLys16, and αLys40. Six thiolated-maleimidated sites were identified on β globin: βLys8, βLys17, βLys59; βLys66, βLys95, βLys132, and one NEM-modified only site at βCys93. The globin distribution shows a preference for reactivity at β chains. These sites are depicted on a molecular diagram of human oxyhemoglobin in Figure 6 (PDB entry 2DN1) (*20*).

DISCUSSION

Hemospan has been the subject of many studies, including structural (*6*), functional (*7*−*10*), and clinical (*11, 12*), but the sites of chemical modification have not been defined until now. In this study, we present chemical analysis of the Hemospan product, including average degree of PEGylation, number of PEGs per globin, and sites of maleimidation.

Hemospan is human oxyHb modified using monofunctional maleimide PEG (∼5.5 kDa), with an average of 7−8 linear PEG polymers conjugated on the surface of the protein and <0.5 free thiol. An earlier publication on the reaction process used in the development of MP4 reported the degree of PEGylation to be 6.1 ± 0.2 (*2*). The higher number reported in the present study for Hemospan is most likely due to improvements in processing efficiency and controls at the manufacturing scale.

According to SDS-PAGE (Figures 1), the starting Hb product shows ∼90% α and β globins migrating at the same elution position at ∼16 kDa. However, a larger protein component making up ∼10% of the total by densitometry migrates at ∼31

Table 2. NEM-Hb Tryptic Peptides Obtained by Trypsin Digestion of NEM-Hb and Identified Using LC-ESI MS/MS[a]

α Chains	
VLSPADK[7]	**(A)**
TNVK[11]	(A)
AAWGK[16]	**(A)**
VGAHAGEYGAEALERMFLSFPTTK[40]	**(C)**
TYFPHFDLSHGSAQVK[56]	(E)
GHGK[60]K[61]	(E)
VADALTNAVAHVDDMPNALSALSDLHAHK[90]	(FG)
LRVDPVNFK[99]	(G)
LLSHCLLVTLAAHLPAEFTPAVHASLDK[127]	(H)
FLASVSTVLTSK[139]	(H)
YR	(HC)
β Chains	
VHLTPEEK[8]	**(A)**
SAVTALWGK[17]	**(A)**
VNVDEVGGEALG RLLVVYPWTQRF FESFGDLSTPDAVMGNPK[59]	**(E)**
VK[61]	(E)
AHGK[65]**K**[66]	**(E)**
VLGAFSDGLAHLDNLK[82]	(EF)
GTFATLSE LHC[93]**DK**[95]	**(F, FG)**
LHVDPENFRLLG NVLVCVLAHHFGK[120]	(GH)
EFTPPVQAAYQK[132]	**(H)**
VVAGVANALAHK[144]	(HC)
YH	(HC)

[a] The same modified peptides were identified at all ratios of Hb/2-IT/NEM studied (see text for details). Lys (K) residues hit by trypsin are identified by their chain sequence number. The β Cys (C) residue is also identified by its chain sequence number. Helical assignments for the terminal Lys residues in each peptide are shown to the right in parentheses. Identified modified peptides and helices are shown in bold. Modified residues are underlined.

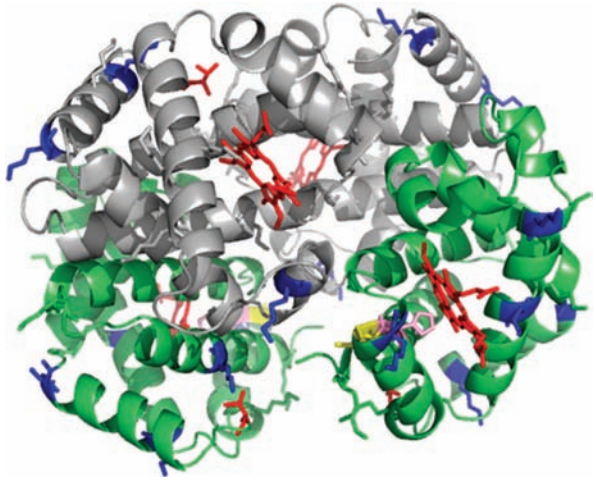

Figure 6. Three-dimensional structural model of tetrameric oxyHb (PDB entry 2DN1 (*20*)). α chains are shown in silver, β chains in green, and hemes in red. All Lys residue side chains are depicted. Modified Lys residues identified in this study are shown in blue, and the modified β93Cys is shown in yellow next to the proximal β92His residue (shown in pink) in contact with the β hemes.

kDa. This band was sequenced by tryptic digestion, matched against known protein sequences, and found to be primarily human β globin but with a lower score also identifying residual carbonic anhydrase. These data suggest that this band may be a mixture of nondissociated αβ dimer, a fraction of ββ dimer, which was identified by mass analysis by LC/MS/MS, that could arise through disulfide bridge formation between β globins since β-mercaptoethanol was not used, and possibly a small fraction of the red cell enzyme, carbonic anhydrase.

By SDS-PAGE, the Hemospan product comprises ∼5% unmodified α and β chains, ∼85% α and β chains conjugated to 1−4 PEGs, and ∼10% globin chains with >4 PEGs. Globins with >4 PEGs were also seen as minor peaks in the MALDI-TOF spectrum (Figure 2B), RP HPLC analysis of Hemospan (Figure 3B), and with NEM-globin modifications by ESI-TOF experiments (Figure 5B). Hemospan, which is not cross-linked intramolecularly, is dissociable at dilute concentrations, but even under fully dissociating conditions in high salt, <1% of the product exists as free, nonPEGylated αβ dimer (*13*), and haptoglobin has been reported to disappear transiently in human trials (*11*).

NEM was used as a simple model system in place of PEG (see Figure 4A) for the maleimidation reaction to evaluate the sites of hemoglobin modification by mass analysis. Reaction with NEM stabilizes the thiolated sites from forming disulfide bonds and provides a small molecular weight marker for mass analysis. Thus, any site found that reacted with NEM can react with PEG in the PEGylation reaction. Regardless of the Hb/2-IT reaction ratio used, the same Lys residues were identified, showing an equal propensity for thiolation, without kinetic preference. At the reaction ratio of 1:10:20 used to produce Hemospan, ∼8 maleimidated sites per Hb tetramer were measured for either NEM or PEG reactions, showing that PEGylation over a distribution of sites is not different from the reaction with the small maleimide model.

Out of 20 potential sites of modification identified by the NEM/tryptic peptide analysis on the Hb tetramer (see Table 2), less than half are modified on average under the conditions of the Hemospan reaction, and the product can best be described as Hb modified with PEG over a distribution of surface sites. Heterogeneity in sites of PEGylation does not necessarily extrapolate to functional heterogeneity. We have reported previously on the kinetics of CO binding (*13*) and heme loss (*5*), in which intramolecular (i.e., differences between subunits) showed a higher signal compared to intermolecular heterogeneities. The primary reason for this appears to be the modified β93Cys residues immediately adjacent to the β-subunit proximal histidines (β92His) directly bound to β hemes. There appears to be a preference for thiolation of Lys residues within β subunits, with six modified β Lys residues identified by tryptic digestion compared to only three sites on the α chains. Another preference may be reaction at the A helices on both α and β chains, with 8 out of 20 modified sites in this region of the molecule. On the three-dimensional structure showing these sites in Figure 6, there is a tendency to identify these sites at the outer corners of the A helical structures. No clear relation of modified sites to relative solvent accessibilities were found in the PDB entry 2DN1 (*21*), particularly considering that the β93Cys shows zero relative solvent accessibility in either oxy- or deoxyHb conformations by this method.

A similar method has been used to identify sites of thiolation and maleimidation to deoxygenated human Hb with 5−8 PEG chains conjugated per Hb tetramer (*14*). In that study, they showed (1) that NEM modification does not interfere with tryptic proteolysis at sites flanking the modified site, (2) that terminal Val residues were not modified, and, as we also have found here, (3) that the sites of modification do not depend on the kinetics of the reaction. A comparison between their study on human Hb bound to PEG under deoxygenated conditions and ours with Hemospan shows the same sites modified on α chains at Lys7 and Lys16 and on the β chains at Lys8, Lys17, Lsy59, and Lys66. Otherwise, they reported more modifications to α chains but not to βLys132, as we report here. A notable distinction is that the β93Cys was modified less so or not at all in the deoxyHb reaction but is clearly modified in Hemospan,

likely contributing to Hemospan's ligand binding effects reported for O_2 and CO (*4, 13*).

CONCLUSION

The two-step method of oxyHb thiolation and PEG maleimidation offers a simple, reliable method to produce a modified hemoglobin-based oxygen carrier that is being tested clinically to impart hemodynamic stability in surgery patients. In addition to the intrinsic β93Cys thiols that are PEGylated, the thiolation reaction is specific for 18 out of a total of 44 surface Lys residues. For the reaction under our process conditions, the β93Cys residue and 9 Lys residues are modified per $\alpha\beta$ dimer, distributed over the surface of hemoglobin, with a preponderance on the β subunits and a tendency for a higher proportion of modification on the A helical corners of either α or β chains. At this time, the reason for specificity of the thiolation reaction of the Lys residues identified here has not been determined.

ACKNOWLEDGMENT

This work was supported in part by the National Institutes of Health Bioengineering Partnership Grant HL064395. All authors are employees of Sangart, Inc. and hold stock options in the company.

LITERATURE CITED

(1) Acharya, A. S., Manjula, B. N., and Smith, P. (1996) Hemoglobin crosslinkers. U.S. Patent 5,585,484.

(2) Vandegriff, K. D., Malavalli, A., Wooldridge, J., Lohman, J., and Winslow, R. M. (2003) MP4, a new nonvasoactive PEG-Hb conjugate. *Transfusion 43*, 509–516.

(3) Manjula, B. N., Tsai, A., Upadhya, R., Perumalsamy, K., Smith, P. K., Malavalli, A., Vandegriff, K. D., Winslow, R. M., Intaglietta, M., Prabhakaran, M., Friedman, J. M., and Acharya, A. S. (2003) Site-specific PEGylation of hemoglobin at Cys-93(β): correlation between the colligative properties of the PEGylated protein and the length of the conjugated chain. *Bioconjugate Chem. 14*, 464–472.

(4) Vandegriff, K. D., Bellelli, A., Samaja, M., Malavalli, A., Brunori, M., and Winslow, R. M. (2004) Kinetics of NO and O_2 binding to a maleimide poly(ethylene glycol)-conjugated human haemoglobin. *Biochem. J. 382*, 183–189.

(5) Vandegriff, K. D., Malavalli, A., Minn, C., Jiang, E., Lohman, J., Young, M. A., Samaja, M., and Winslow, R. M. (2006) Oxidation and haeme loss kinetics of poly(ethylene glycol)-conjugated hemoglobin (MP4): dissociation between *in vitro* and *in vivo* oxidation rates. *Biochem. J. 399*, 463–471.

(6) Svergun, D. I., Ekström, F., Vandegriff, K. D., Malavalli, A., Baker, D. A., Nilsson, C., and Winslow, R. M. (2008) Solution structure of poly(ethylene) glycol-conjugated hemoglobin revealed by small-angle X-ray scattering: implications for a new oxygen therapeutic. *Biophys. J. 94*, 173–181.

(7) Winslow, R. M., Lohman, J., Malavalli, A., and Vandegriff, K. D. (2004) Comparison of PEG-modified albumin and hemoglobin in extreme hemodilution in the rat. *J. Appl. Physiol. 97*, 1527–1534.

(8) Tsai, A. G., Vandegriff, K. D., Intaglietta, M., and Winslow, R. M. (2003) Targeted O_2 delivery by low-P50 hemoglobin: a new basis for O_2 therapeutics. *Am. J. Physiol. 285*, H1411–H1419.

(9) Drobin, D., Kjellström, B. T., Malm, E., Malavalli, A., Lohman, J., Vandegriff, K. D., Young, M. A., and Winslow, R. M. (2004) Hemodynamic response and oxygen transport in pigs resuscitated with maleimide-polyethylene glycol-modified hemoglobin (MP4). *J. Appl. Physiol. 96*, 1843–1853.

(10) Young, M. A., Riddez, L., Kjellström, B. T., Bursell, J., Winslow, F., Lohman, J., and Winslow, R. M. (2005) MalPEG-hemoglobin (MP4) improves hemodynamics, acid-base status, and survival after uncontrolled hemorrhage in anesthetized swine. *Crit. Care Med. 33*, 1794–1804.

(11) Björkholm, M., Fagrell, B., Przybelski, R., Winslow, N., Young, M., and Winslow, R. M. (2005) A phase I single blind clinical trial of a new oxygen transport agent (MP4), human hemoglobin modified with maleimide-activated polyethylene glycol. *Haematologica 90*, 505–515.

(12) Olofsson, C., Ahl, T., Johansson, T., Larsson, S., Nellgård, P., Ponzer, S., Fagrell, B., Przybelski, R., Keipert, P., Winslow, N., and Winslow, R. M. (2006) A multi-center clinical study of the safety and activity of maleimide-polyethylene glycol hemoglobin (Hemospan®) in patients undergoing major orthopedic surgery. *Anesthesiology 105*, 1153–1163.

(13) Vandegriff, K. D., Young, M. A., Lohman, J., Bellelli, A., Samaja, M., Malavalli, A., and Winslow, R. M. (2008) CO-MP4, a poly(ethylene) glycol-conjugated hemoglobin derivative and carbon monoxide carrier that reduces myocardial infarct size in rats. *Br. J. Pharmacol. 154*, 1649–1661.

(14) Iafelice, R., Cristoni, S., Caccia, D., Russo, R., Rossi-Bernardi, L., Lowe, K. C., and Perrella, M. (2007) Identification of the sites of deoxy haemoglobin pegylation. *Biochem. J. 403*, 189–196.

(15) Ampulski, R., Ayers, V., and Morell, S. (1969) Determination of the reactive sulfhydryl groups in heme proteins with 4,4′-dipyridinedisulfide. *Anal. Biochem. 32*, 163–169.

(16) Jackson, C. C., Charlton, J., Kuzminski, K., Lang, G., and Sehon, A. (1987) Synthesis, isolation, and characterization of conjugates of ovalbumin with monomethoxypolyethylene glycol using cyanuric chloride as the coupling agent. *Anal. Biochem. 165*, 114–127.

(17) Kurfürst, M. M. (1992) Detection and molecular weight determination of polyethylene glycol-modified hirudin by staining after sodium dodecyl sulfate-polyacrylamide gel electrophoresis. *Anal. Biochem. 200*, 244–248.

(18) Skoog, B. (1979) Determination of polyethylene glycols 4000 and 6000 in plasma protein preparations. *Vox Sang. 37*, 345–349.

(19) Masala, B., and Manca, L. (1994) Detection of globin chains by reversed-phase high-performance liquid chromatography. *Methods Enzymol. 231*, 21–44.

(20) Park, S. Y., Yokoyama, T., Shibayama, N., Shiro, Y., and Tame, J. R. (2006) 1.25 Å resolution crystal structures of human haemoglobin in the oxy, deoxy and carbonmonoxy forms. *J. Mol. Biol. 360*, 690–701.

(21) Porollo, A. A., Adamczak, R., and Meller, J. (2004) POLYVIEW: a flexible visualization tool for structural and functional annotations of proteins. *Bioinformatics 20*, 2460–2462.

BC8002666

Synthesis and Spectroelectrochemistry of *N*-Cobaltacarborane Porphyrin Conjugates

Erhong Hao,[†] Min Zhang,[‡] Wenbo E,[‡] Karl M. Kadish,*[,‡] Frank R. Fronczek,[†] Brandy H. Courtney,[†] and M. Graça H. Vicente*[,†]

Department of Chemistry, Louisiana State University, Baton Rouge, Louisiana 70803, and Department of Chemistry, University of Houston, Houston, Texas 77204. Received June 30, 2008; Revised Manuscript Received August 13, 2008

N-Substituted porphyrins are well-known for the distortion they exhibit of the porphyrin plane through the sp^3 hybridization of one of the pyrrolenic units. They have served as model compounds in investigations of many biochemical processes. In this paper, we developed an efficient route to *N*-substituted porphyrins, and report the synthesis of a series of new *N*-substituted cobaltacarborane−porphyrins containing one or two cobaltabisdicarbollide anions linked by $(CH_2CH_2O)_2$ chains to either the core porphyrin nitrogens or to a *meso*-aminophenyl group. These conjugates show different degrees of distortion of the porphyrin macrocycle, which affect their spectroscopic and electrochemical properties. In particular, the core *N*-substituted conjugates show significant fluorescence quenching in comparison with the noncore substituted macrocycles. The X-ray structures of two targeted core *N*-cobaltacarborane porphyrin conjugates are presented. The electrochemical and spectroelectrochemical properties of these porphyrin conjugates were investigated; while the peripheral *N*-substituted cobaltacarboranylporphyrins undergo three reversible reductions and three reversible oxidations (two attributed to the porphyrin and one to the Co^{III} cluster), the core *N*-substituted porphyrins exhibit complicated electrochemical behavior with coupled chemical reactions.

INTRODUCTION

In the past few decades, porphyrin and related compounds have assumed broad importance in diverse areas of medicine, catalysis, and molecular electronics (*1*). Structural modification and conformational distortion of porphyrin macrocycles are widely studied because they may have the potential to control the properties and functions of tetrapyrroles in biological systems. In particular, porphyrins with substituents at a pyrrolenic nitrogen atom, i.e., *N*-substituted porphyrins, are of biochemical significance and have served as model compounds in investigations of biochemical processes (*2*−*8*). These compounds are well-known for the distortion of the porphyrin plane through the sp^3 hybridization of one of the pyrrolenic units. They are also powerful inhibitors of the enzyme ferrochelatase, which is essential for the formation of heme for hemoglobin, myoglobin, and cytochromes, and have been shown to be produced in a biochemical monooxygenation process catalyzed by cytochrome P-450 enzymes (*2*−*8*). The unique structures of synthetic *N*-substituted porphyrin derivatives has led to their investigation for potential applications in the fields of catalysts (*9*), molecular recognition (*10, 11*), medicine (*12*), and energy transfer (*13*). In addition, interesting new macrocycles have been reported from the ring expansion or reduction of *N*-substituted porphyrins and analogues (*14*−*17*). Despite the potential wide range of applications of these compounds and the important role they have played in understanding biological processes, the synthetic routes currently available to obtain *N*-substituted porphyrins are limited and most employ harsh conditions that result in low yields of the target molecules.

Recently, porphyrins bearing boron clusters have been identified as useful agents in boron neutron capture therapy (BNCT) of cancer because of their abilities to localize in tumors and their high boron content (*18, 19*). Among the boron clusters, the metallacarboranes and in particular the cobaltabisdicarbollide anion $[Co(C_2B_9H_{11})_2]^-$ and its adducts have attracted much attention because of their remarkable chemical, thermal, and photostabilities (*20*). As part of our studies of the development of new boron-containing porphyrins and derivatives, we recently reported the synthesis of porphyrin−cobaltacarborane conjugates, via an efficient nucleophilic ring-opening reaction of [3,3′-Co(8-$C_4H_8O_2$-1,2-$C_2B_9H_{10}$)(1′,2′-$C_2B_9H_{11}$)] by porphyrins containing phenol or pyridinum groups at the peripheral *meso*-positions (*21*). Herein, we report that the core porphyrin nitrogen atoms can also function as the nucleophilic species in the ring-opening reaction of [3,3′-Co(8-$C_4H_8O_2$-1,2-$C_2B_9H_{10}$)(1′,2′-$C_2B_9H_{11}$)], and this methodology allows the efficient synthesis of *N*-cobaltacarboranyl−porphyrins in high yields. Using as the starting porphyrins, free-base *meso*-tetraphenylporphyrin (H_2TPP) and octaethylporphyrin (H_2OEP), both mono- and di-*N*-substituted derivatives were obtained in high yields by slight modification of the reaction conditions. These compounds show unique and characteristic optical spectra and strong fluorescence quenching. We also report the synthesis of two new *N*-cobaltacarboranyl−porphyrins from the reaction of mono-(*p*-aminophenyl)triphenylporphyrin with [3,3′-Co(8-$C_4H_8O_2$-1,2-$C_2B_9H_{10}$)(1′,2′-$C_2B_9H_{11}$)]. The electrochemical and spectroelectrochemical properties for both types of compounds are reported, and comparisons are made to the individual monomeric units under the same experimental conditions.

EXPERIMENTAL PROCEDURES

Electrochemical and Spectroelectrochemical Measurements. Cyclic voltammetry (CV) measurements were performed at 298 K on an EG&G model 173 potentiostat coupled with an EG&G model 175 universal programmer in deaerated PhCN solution containing 0.1 M TBAP as a supporting electrolyte. A three-electrode system was utilized and consisted of a glassy carbon working electrode, a platinum wire counter electrode,

* E-mail: vicente@lsu.edu.
[†] Louisiana State University.
[‡] University of Houston.

10.1021/bc800265w CCC: $40.75 © 2008 American Chemical Society
Published on Web 10/24/2008

and a saturated calomel reference electrode (SCE). The reference electrode was separated from the bulk of the solution by a fritted-glass bridge filled with the solvent/supporting electrolyte mixture. UV−visible spectroelectrochemical experiments were performed with a home-built thin-layer cell (*22*) that had a light transparent platinum net working electrode. Potentials were applied and monitored with an EG&G PAR model 173 potentiostat. Time evolution of the UV−visible spectra was recorded with a Hewlett-Packard model 8453 diode array spectrophotometer.

Syntheses. All reactions were monitored by TLC using 0.25 mm silica gel plates with or without UV indicator (60F−254). Silica gel Sorbent Technologies 32−63 μm was used for flash column chromatography. ^{1}H and ^{13}C NMR were obtained on either a DPX-250 or a ARX-300 Bruker spectrometer. Chemical shifts (δ) are given in ppm relative to actone-d_6 (2.05 ppm, ^{1}H; 206.0 ppm, ^{13}C) unless otherwise indicated. Electronic absorption spectra were measured on a Perkin-Elmer Lambda 35 UV−vis spectrophotometer, and fluorescence spectra were measured on a Perkin-Elmer LS55 spectrometer. Mass spectra were obtained on an Applied Biosystems QSTAR XL. All solvents were obtained from Fisher Scientific (HPLC grade) without further purification. Cs[Co($C_2B_9H_{11}$)$_2$] was obtained from Katchem, Ltd, Czech Republic, *meso*-tetraphenylporphyrin (H_2TPP, **1**), and octaethylporphyrin (H_2OEP, **2**) were obtained from Frontier Scientific, Logan, Utah. 5-(4-Aminophenyl)-10,15,20-triphenylporphyrin and its zinc complex were synthesized according to a literature method (*23*). Intensity data were collected for the μ-EtO-cobaltacarborane, porphyrin **3** (as the monohydrate, bis pyridine solvate), and porphyrin **4** at $T = 110$ K using graphite monochromated Mo Kα radiation (λ = 0.710 73 Å) on a Nonius KappaCCD diffractometer fitted with an Oxford Cryostream cooler. Data reduction included absorption corrections by the multiscan method, using HKL SCALEPACK (*24*). Structures were solved by direct methods and refined by full-matrix least-squares, using SHELXL97 (*25*). Crystallographic data (excluding structure factors) for the structures in this paper have been deposited with the Cambridge Crystallographic Data Centre as supplementary publication no. CCDC 704151-704153. Copies of the data can be obtained, free of charge, on application to CCDC, 12 Union Road, Cambridge, CB2 1EZ, UK, (fax: +44- (0)1223-336033 or e-mail: deposit@ccdc.cam.ac.uk).

***N*-Cobaltacarborane Tetraphenylporphyrin (3).** H_2TPP (**1**) (61.4 mg, 0.10 mmol) and [3,3′-Co(8-$C_4H_8O_2$-1,2-$C_2B_9H_{10}$(1′,2′-$C_2B_9H_{10}$)] (65.4 mg, 0.16 mmol) were dissolved in ODCB (25 mL). The reaction solution was heated at 140 °C, and the color changed to green in about 15 min. Two hours later, TLC indicated no starting H_2TPP left, and the reaction was stopped by cooling. The reaction mixture was directly loaded on silica gel column using toluene to elute ODCB and trace H_2TPP. Then, the title porphyrin was eluted using dichloromethane and recrystallized from chloroform/hexane. After drying under vacuum, porphyrin **3** was obtained in 81% yield (82.8 mg), along with 4.7% (6.8 mg) of porphyrin **5**. For the title porphyrin, HRMS (MALDI-TOF) for $C_{52}H_{59}N_4O_2B_{18}Co$: *m*/*z* calcd, 1025.5788, found 1025.5717. ^{1}H NMR ($CDCl_3$): 9.32 (d, 2H, $J = 5.0$ Hz, β-H), 9.08 (d, 2H, $J = 5.0$ Hz, β-H), 8.85 (s, 2H, β-H), 8.54 (b, 4H, o-phenyl-H), 8.32 (d, 2H, $J = 7.75$, o-phenyl-H), 8.23 (d, 2H, $J = 7.75$, o-phenyl-H), 8.15 (s, 2H, β-H), 8.00 (m, 6H, m, p-phenyl-H), 7.87 (m, 6H, m, p-phenyl-H), 3.91 (s, 2H, car-H), 3.30 (s, 2H, car-H), 3.07 (t, 2H, OCH_2), 2.71 (t, 2H, OCH_2), 0.71 (t, 2H, OCH_2), 0.1−4.0 (br, 17H, BH), −4.83 (t, 2H, NCH_2). UV−vis (CH_2Cl_2) λ_{max} (nm) 450 (ε 320, 500), 613 (13 800), 669 (38 300).

Crystal data for **3**: $C_{52}H_{59}B_{18}CoN_4O_2 \cdot 2C_5H_5N \cdot H_2O$, dark blue, FW = 1201.76, triclinic, space group $P\bar{1}$, $a = 14.488(2)$, $b = 15.269(2)$, $c = 15.850(3)$ Å, $\alpha = 66.662(7)$, $\beta = 76.501(6)$, $\gamma = 83.995(7)°$, $V = 3130.2(8)$ Å^3, $Z = 2$, $D_{calc} = 1.275$ g cm^{-3}, $\mu = 0.326$ mm^{-1}, $T = 110$ K, $\theta_{max} = 32.6°$, 73 501 measured reflections, 22 598 independent ($R_{int} = 0.118$), 10 070 with $I > 2\sigma(I)$, $R_1 = 0.094$, w$R(F^2) = 0.163$, $S = 1.030$, 813 refined parameters, $\Delta\rho_{max} = 0.98$ eÅ^{-3}, $\Delta\rho_{min} = -1.06$ eÅ^{-3}.

***N*-Cobaltacarborane Octaethylporphyrin (4).** H_2OEP (**2**) (53.5 mg, 0.10 mmol) and [3,3′-Co(8-$C_4H_8O_2$-1,2-$C_2B_9H_{10}$(1′,2′-$C_2B_9H_{10}$)] (43.3 mg, 0.11 mmol) were dissolved in 10 mL of ODCB. The reaction solution was stirred at 140 °C for 2 h until TLC indicated no H_2OEP left. The reaction mixture was purified on a silica gel column using dichloromethane/hexane for elution. The first purple fraction was collected, recrystallized from chloroform/hexane, and dried under vacuum to yield the title porphyrin (86.1 mg, 89%). HRMALDI-TOF-MS for $C_{44}H_{75}N_4O_2B_{18}CoNa$: *m*/*z* calcd, 968.6934 [M + Na]$^+$, found 968.6957. ^{1}H NMR ($CDCl_3$): 10.67 (s, 2H, meso-H), 10.41 (d, 2H, meso-H), 4.28−4.42 (m, 8H, CH_2), 4.18−4.22 (m, 2H, car-H), 4.04−4.15 (m, 8H, CH_2), 3.59 (brs, 2H, car-H), 3.02−3.05 (m, 2H, OCH_2), 2.27−2.30 (m, 2H, OCH_2), 1.96−2.01 (t, 12H, CH_3), 1.47−1.53 (t, 12H, CH_3), 0.09−0.22 (m, 2H, OCH_2), 0.1−4.0 (br, 17H, BH), −5.60−5.57 (m, 2H, NCH_2). UV−vis (acetone) λ_{max} (nm) 400 (ε 145, 500), 539 (9, 200), 562 (12, 400), 581 (10, 200).

Crystal data for **4**: $C_{44}H_{75}B_{18}CoN_4O_2$, FW = 945.59, garnet red, triclinic, space group $P\bar{1}$, $a = 11.140(7)$, $b = 15.492(8)$, $c = 16.413(11)$ Å, $\alpha = 64.83(3)$, $\beta = 87.51(3)$, $\gamma = 84.12(4)°$, $V = 2550(3)$ Å^3, $Z = 2$, $D_{calc} = 1.231$ g cm^{-3}, $\mu = 0.378$ mm^{-1}, $T = 110$ K, $\theta_{max} = 22.9°$, 21 636 measured reflections, 6832 independent ($R_{int} = 0.074$), 4358 with $I > 2\sigma(I)$, $R_1 = 0.070$, w$R(F^2) = 0.126$, $S = 1.086$, 628 refined parameters, $\Delta\rho_{max} = 0.25$ eÅ^{-3}, $\Delta\rho_{min} = -0.35$ eÅ^{-3}.

***N,N*-Dicobaltacarborane Tetraphenylporphyrin (5).** Monosubstituted porphyrin **3** (26.0 mg, 0.025 mmol), [3,3′-Co(8-$C_4H_8O_2$-1,2-$C_2B_9H_{10}$(1′,2′-$C_2B_9H_{10}$)] (20.1 mg, 0.05 mmol), and K_2CO_3 (35 mg, 0.25 mmol) were stirred in ODCB (10 mL) and then the reaction mixture was heated to 140 °C until the disappearance of starting porphyrin **3** (monitored by TLC). The reaction mixture was purified on a silica gel column using dichloromethane/ethyl acetate for elution. The main green fraction was collected, recrystallized from chloroform/hexane, and dried under vacuum to yield the title porphyrin (26.6 mg, 73%). HRMALDI-TOF-MS for $C_{60}H_{87}N_4O_4B_{36}Co_2Na$: *m*/*z* calcd, 1458.8903, found 1458.8850; *m*/*z* calcd, 1481.8801 [M + Na]$^+$, found 1481.8874; *m*/*z* calcd, 1435.9006 [M − Na]$^-$, found 1435.9014. ^{1}H NMR (acetone-d_6): 8.97 (d, 2H, $J = 4.9$ Hz, β-H), 8.79 (m, 4H, β-H), 8.53 (b, 2H, o-phenyl-H), 8.33 (m, 4H, o-phenyl-H), 8.17 (t, 2H, o-phenyl-H), 8.01 (m, 9H, m, p-phenyl-H), 7.91 (m, 3H, m, p-phenyl-H), 7.77 (d, 2H, $J = 4.7$, β-H), 4.24 (brs, 4H, car-H), 3.48 (br s, 4H, car-H), 2.93 (brs, 4H, OCH_2), 2.49 (brs, 2H, OCH_2), 2.43 (brs, 2H, OCH_2), 0.69 (brs, 4H, OCH_2), 0.1−4.0 (br, 34H, BH), −2.64 (s, 1H, NH), −4.30 (m, 2H, NCH_2), −5.83 (m, 2H, NCH_2). UV−vis (CH_2Cl_2) λ_{max} (nm) 465 (ε 285, 950), 696 (58, 250).

***N,N*-Dicobaltacarborane Octaethylporphyrin (6).** Monosubstituted porphyrin **4** (48.5 mg, 0.05 mmol), [3,3′-Co(8-$C_4H_8O_2$-1,2-$C_2B_9H_{10}$(1′,2′-$C_2B_9H_{10}$)] (30.5 mg, 0.075 mmol), and $NaHCO_3$ (42.3 mg, 0.5 mmol) were stirred in 10 mL of ODCB. The reaction mixture was heated at 140 °C until complete disappearance of porphyrin **4** by TLC monitoring. The reaction mixture was purified on a silica gel column using dichloromethane/ethyl acetate for elution. The main fraction was collected, recrystallized from chloroform/hexane, and dried under vacuum to yield the title porphyrin (26.6 mg, 73%). HRMALDI-TOF-MS for $C_{52}H_{103}N_4O_2B_{36}Co_4Na_2$: *m*/*z* calcd, 1401.0078 [M + Na]$^+$, found 1401.0092. ^{1}H NMR (acetone-d_6): 11.38 (s, 1H, meso-H), 11.33 (s, 2H, meso-H), 11.09 (s,

Scheme 1[a]

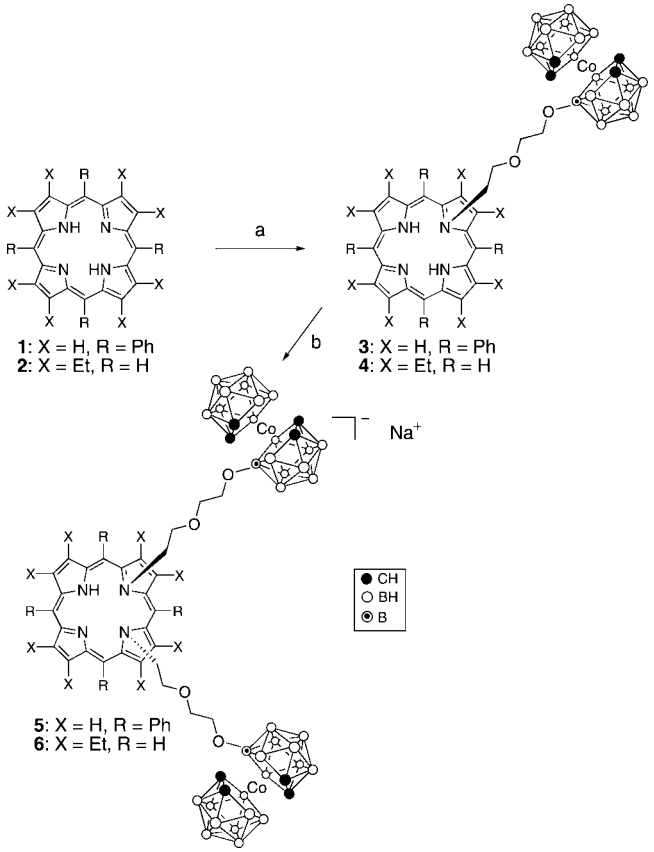

[a] Conditions: (a) [3,3′-Co(8-$C_4H_8O_2$-1,2-$C_2B_9H_{10}$)(1′,2′-$C_2B_9H_{11}$)], ODCB, 140 °C, 2 h (81−89%); (b) [3,3′-Co(8-$C_4H_8O_2$-1,2-$C_2B_9H_{10}$)(1′,2′-$C_2B_9H_{11}$)], $NaHCO_3$, ODCB, 140 °C, 2 h (73−83%).

1H, meso-H), 3.93−4.36 (m, 16H, CH_2), 3.81 (brs, 4H, car-H), 3.38 (brs, 4H, car-H), 2.85 (m, 4H, OCH_2), 2.36 (brs, 4H, OCH_2), 1.85−1.88 (m, 12H, CH_3), 1.44−1.56 (m, 6H, CH_3), 1.27−1.42 (m, 6H, CH_3), 0.12 (brs, 4H, OCH_2), 0.1−4.0 (br, 34H, BH), −5.41−5.35 (m, 2H, NCH_2), −6.44−6.38 (m, 2H, NCH_2). UV−vis (acetone) λ_{max} (nm) 427 (ε 141, 500), 573 (9, 800), 617 (5, 300).

Scheme 2[a]

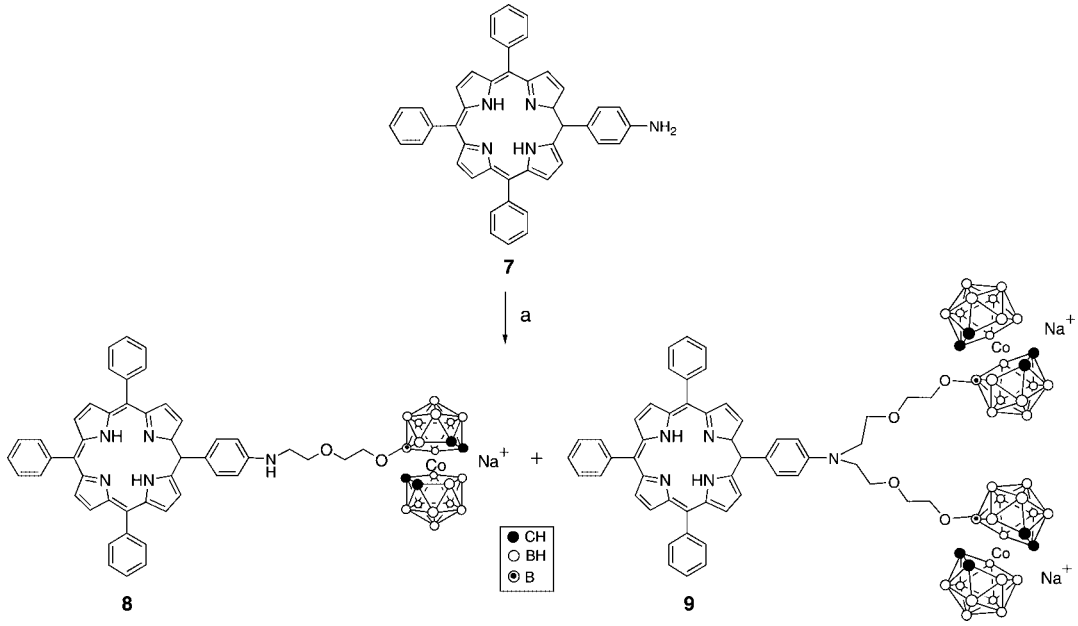

[a] Conditions: (a) [3,3′-Co(8-$C_4H_8O_2$-1,2-$C_2B_9H_{10}$)(1′,2′-$C_2B_9H_{11}$)], $CHCl_3/CH_3CN$ 1:1, reflux (46% of **8** and 26% of **9**).

5-(*N*-Cobaltacarboranephenyl)-10,15,20-triphenylporphyrin (8) and 5-(*N*,*N*-dicobaltacarboranephenyl)-10,15,20-triphenylporphyrin (9). Aminoporphyrin **7** (33.0 mg, 0.05 mmol) and [3,3′-Co(8-$C_4H_8O_2$-1,2-$C_2B_9H_{10}$(1′,2′-$C_2B_9H_{10}$)] (41.0 mg, 0.1 mmol) were dissolved in a mixture of 2.5 mL $CHCl_3$ and 5 mL CH_3CN. The reaction mixture was left refluxing overnight. The crude product was purified on a silica gel column using chloroform/ethyl acetate for elution, giving two major fractions **8** and **9** which were recrystallized from chloroform/hexane and dried under vacuum. Porphyrin **8** was obtained in 46% yield (25.7 mg). HR-MALDI-TOF-MS for $C_{52}H_{59}N_5O_2B_{18}Co_2Na$: *m*/*z* calcd, 1063.5794 $[M + H]^+$, found 1063.5802; *m*/*z* calcd 1039.5818 $[M - Na]^-$, found 1039.5863. ^1H NMR (acetone-d_6): 9.02 (d, 2H, β-H), 8.83 (m, 6H, β-H), 8.22 (m, 6H, o-phenyl-H), 7.95 (d, 2H, o-Ar-H), 7.81 (m, 9H, m,p-phenyl-H), 7.07 (d, 2H, p-Ar-H), 5.23 (b, 1H, NH), 4.38 (s, 2H, OCH_2), 4.31 (s, 2H, OCH_2), 3.83 (t, 2H, OCH_2), 3.66 (m, 4H, car-H), 3.50 (t, 2H, NCH_2), 1.6−3.0 (br, 17H, BH), −2.67 (s, 2H, NH). ^{13}C NMR (acetone-d_6) 149.6, 142.9, 142.8, 136.4, 135.1, 130.3, 128.6, 127.6, 122.7, 120.7, 120.2, 111.8, 72.6, 70.2, 69.2, 55.3, 47.2, 44.2. UV−vis (acetone) λ_{max} (nm) 415 (ε 242, 200), 515 (15, 900), 555 (11, 600), 589 (6, 600), 651 (5, 600). Porphyrin **9** was obtained in 26% (20.4 mg) yield. HR-MALDI-TOF-MS for $C_{60}H_{87}N_5O_4B_{36}Co_2Na_2$: *m*/*z* calcd, 1496.8910 $[M + H]^+$, found 1496.9001; *m*/*z* calcd, 1472.8933 $[M - Na]^-$, found 1472.8957. ^1H NMR (acetone-d_6): 9.08 (d, 2H, β-H), 8.84 (m, 6H, β-H), 8.23 (m, 6H, o-phenyl-H), 8.08 (d, 2H, o-Ar-H), 7.80 (m, 9H, m,p-phenyl-H), 7.26(d, 2H, p-Ar-H), 4.42 (br, 4H, OCH_2), 4.30 (br, 8H, OCH_2), 3.90 (br, 8H, OCH_2), 3.70 (br, 8H, car-H), 1.6−3.0 (br, 34H, BH), −2.60 (s, 2H, NH). ^{13}C NMR (acetone-d_6) 148.6, 142.7, 136.5, 135.0, 134.9, 129.5, 128.4, 127.4, 122.6, 120.5, 120.0, 111.1, 72.7, 69.0, 68.9, 55.3, 51.6, 47.0. UV−vis (acetone) λ_{max} (nm) 413 (ε 222, 600), 516 (15, 800), 559 (13, 000), 591 (7, 900), 651 (6, 300).

RESULTS

Synthesis. The synthesis of zwitterionic cobaltacarborane [3,3′-Co(8-$C_4H_8O_2$-1,2-$C_2B_9H_{10}$(1′,2′-$C_2B_9H_{10}$)] was first reported in 1997 (*26*) and then modified by Teixidor et al. (*27*). Upon refluxing the cobaltabisdicarbollide anion $[Co(C_2B_9H_{11})_2]^-$ in 1,4-dioxane in the presence of BF_3•Et_2O, [3,3′-Co(8-$C_4H_8O_2$-

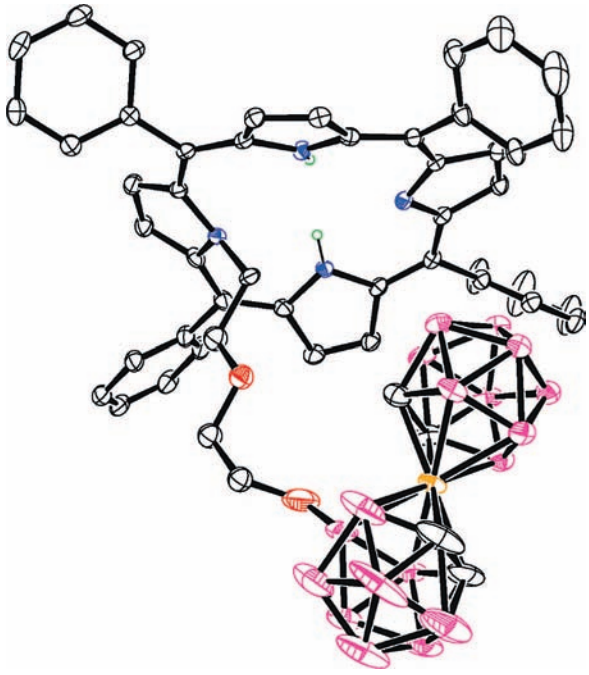

Figure 1. Molecular structure of *N*-cobaltacarborane porphyrin **3**. The C-H and B-H hydrogen atoms, and the hydrogen-bonded pyridine and water molecules are not shown for clarity.

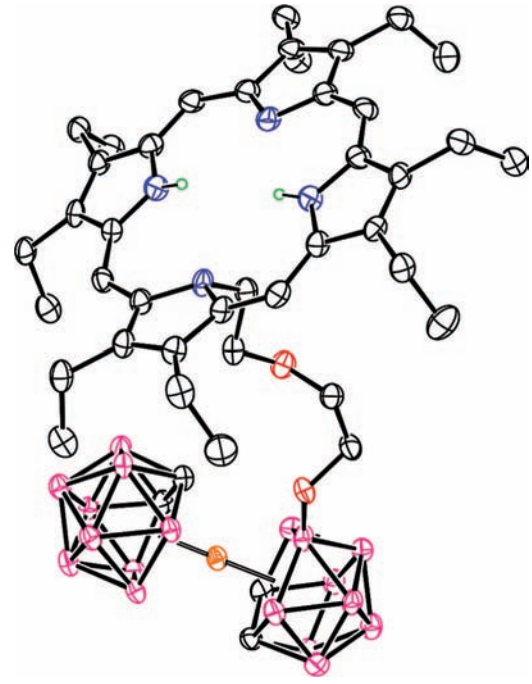

Figure 2. Molecular structure of *N*-cobaltacarborane porphyrin **4**. The C-H and B-H hydrogen atoms are not shown for clarity.

1,2-$C_2B_9H_{10}$(1′,2′-$C_2B_9H_{10}$)] was isolated in 80% yield, along with a slightly less polar minor fraction of [8,8′-μ-(C_2H_5O)-3,3′-Co(1,2-$C_2B_9H_{10}$)$_2$] in 4% yield. The structure of this minor fraction was confirmed by X-ray crystallography (see Supporting Information, Figure S1). The cobaltacarborane [8,8′-μ-(C_2H_5O)-3,3′-Co(1,2-$C_2B_9H_{10}$)$_2$] has been previously synthesized in low yield (5%) from [Co($C_2B_9H_{11}$)$_2$]$^-$, by refluxing in acetic anhydride in the presence of sulfuric acid (*28*). The structure of [8,8′-μ-(C_2H_5O)-3,3′-Co(1,2-$C_2B_9H_{10}$)$_2$] is similar to the known methyloxonium derivative [8,8′-μ-(CH_3O)-3,3′-Co(1,2-$C_2B_9H_{10}$)$_2$] (*29*) in that the C_2B_3 pentagonal planes bound to the cobalt atom are nonparallel due to the short oxygen bridge (mean B−O = 1.517(2) Å, B−O−B = 95.41(11)°), forming a dihedral angle of 26.48(10)°.

The reaction of metal-free H_2TPP (**1**) or H_2OEP (**2**) with [3,3′-Co(8-$C_4H_8O_2$-1,2-$C_2B_9H_{10}$(1′,2′-$C_2B_9H_{10}$)] in refluxing ODCB yielded the corresponding monosubstituted *N*-cobaltacarborane porphyrins **3** and **4**, in 81% and 89% yield, respectively (Scheme 1). Similar yields were obtained using chloroform as the solvent in the presence of $NaHCO_3$, but the reaction took 10 days for completion, instead of 2 h in ODCB. Small amounts of the disubstituted derivatives **5** or **6** (1−5%) were also isolated under the above reaction conditions. Higher yields (73−83%) of the *N*,*N*-dicobaltacarborane porphyrins were obtained upon reaction of the monosubstituted derivatives **3** or **4** with [3,3′-Co(8-$C_4H_8O_2$-1,2-$C_2B_9H_{10}$(1′,2′-$C_2B_9H_{10}$)] in refluxing ODCB and in the presence of a base ($NaHCO_3$). Porphyrins **3**−**6** are highly basic and were isolated in their core-protonated forms. On the other hand, monoaminoporphyrin **7** (*23*) reacted with [3,3′-Co(8-$C_4H_8O_2$-1,2-$C_2B_9H_{10}$(1′,2′-$C_2B_9H_{10}$)] in a mixture of chloform and acetonitrile (v/v = 1/2) to produce the *N*-substituted derivatives **8** and **9** in 46% and 26% yields, respectively (Scheme 2).

The structures of porphyrins **3**−**6**, **8**, and **9** were confirmed by HRMS, NMR, and, in the case of **3** and **4**, by single-crystal X-ray crystallography (Figures 1−6). The molecular structures of porphyrins **3** and **4**, shown in Figures 1 and 2, respectively, are rare examples of singly protonated *N*-substituted porphyrins. The crystal of porphyrin **3** was grown from pyridine/cyclohexane and the two inner porphyrin NHs form hydrogen bonds with one water molecule, which also forms two additional hydrogen bonds with two solvent pyridine molecules, as seen in Figure S2 of the Supporting Information. On the other hand, the crystal of porphyrin **4** was grown from dichloromethane/methanol, and this molecule is less distorted from planarity than **3**, as shown in Figure 2. The NMR spectra confirmed the proposed structures for porphyrins **3**−**6**, **8**, and **9**, and confirmed the remarkable regioselective in the formation of di-*N*,*N*-substituted porphyrins **5** and **6**. The UV−vis and fluorescence spectra are also consistent with the assigned structures.

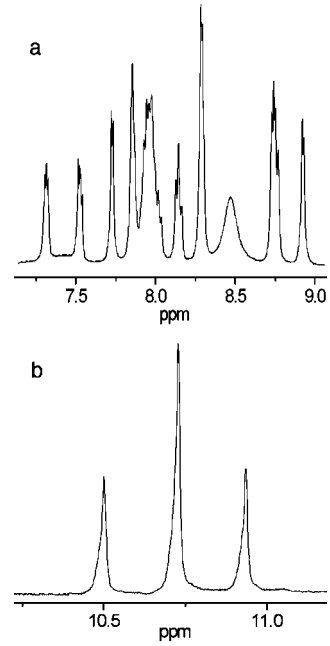

Figure 3. ^{1}H NMR (aromatic region only) in acetone-d_6 of (a) porphyrin **5** and (b) porphyrin **6**.

Electrochemistry and Spectroelectrochemistry. Two types of electrochemical behavior are obtained, one for conjugates

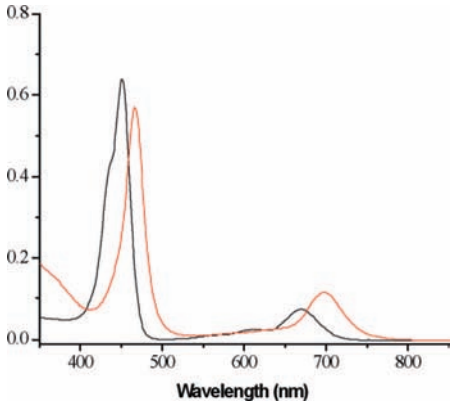

Figure 4. UV−visible spectra of porphyrins **3** (black) and **5** (red) in acetone at 2×10^{-6} M.

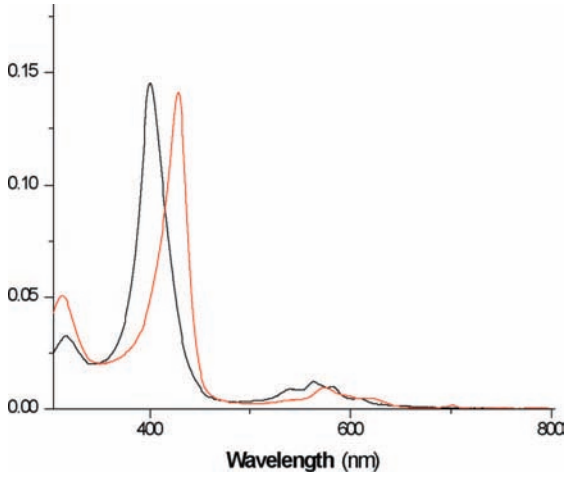

Figure 5. UV−visible spectra of porphyrins **4** (black) and **6** (red) in acetone at 1×10^{-6} M.

3−**6** where the porphyrin−cobaltabisdicarbollide linkage is at one or two of the four central porphyrin nitrogens (Scheme 1) and the other for conjugates **8** and **9**, which are linked at a single *meso* position of the macrocycle as seen in Scheme 2. Cyclic voltammograms for reduction and oxidation of the six conjugates are shown in Figures 7 and 8, but are well-defined only in the case of compounds **8** and **9** (Figure 7); compounds **3**−**6** exhibit irreversible processes due to coupled chemical reactions which occur during or after electron transfer, and this leads to the more complicated cyclic voltammograms (Figure 8). A summary of peak potentials for all of the investigated compounds in PhCN is given in Table 1.

In order to investigate the site of electron transfer, the reduced and oxidized forms of the conjugates were monitored by thin-layer spectroelectrochemistry. Examples of the spectral changes

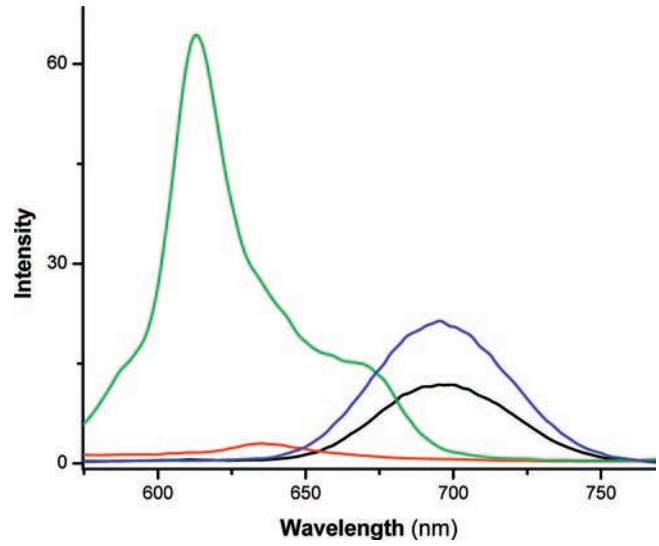

Figure 6. Fluorescence spectra of porphyrins **3** (blue), **5** (black), **4** (green), and **6** (red) in acetone at 1×10^{-6} M.

during the oxidation and reduction are shown in Figures 9−12 and a summary of the UV−visible data is given in Table 2 which includes H_2TPP for comparison.

DISCUSSION

In the absence of a nucleophilic group at the macrocycle periphery, metal-free porphyrins H_2TPP (**1**) and H_2OEP (**2**) reacted with zwitterionic [3,3′-Co(8-$C_4H_8O_2$-1,2-$C_2B_9H_{10}$)(1′,2′-$C_2B_9H_{10}$)] to give the corresponding mono-*N*- (**3** and **4**) and di-adjacent (**5** and **6**) *N*,*N*-cobaltacarboranyl porphyrins, in their core-protonated forms, in high yields. On the other hand, in agreement with our previous reports showing that free-base porphyrins containing one or multiple nucleophilic groups (hydroxyl, pyridyl, phenol) at the macrocycle periphery react with [3,3′-Co(8-$C_4H_8O_2$-1,2-$C_2B_9H_{10}$)(1′,2′-$C_2B_9H_{10}$)] preferentially at these sites (*21*), monoaminoporphyrin **7** produced the *N*-substituted derivatives **8** and **9** in low to moderate yields, probably due to steric hindrance and the low nucleophilicity of the amino group.

The spectroscopic properties of the new *N*-cobaltacarborane porphyrin conjugates were investigated, and two X-ray structures of the mono-*N*-cobaltacarborane porphyrins **3** and **4** were obtained, which show the different degrees of distortion from planarity in these molecules. In the molecular structure of porphyrin **3** (Figure 1), the two protonated pyrrolenic rings are located adjacent to the alkylated ring and are rotated in the opposite sense. Since there is a negative charge on the cobaltacarborane moiety, this molecule is zwitterionic. On the other hand, the structure of porphyrin **4** (Figure 2) is less distorted from planarity than the corresponding H_2TPP derivative

Table 1. Half-Wave Potentials ($E_{1/2}$, V vs SCE) and Site of Electron Transfer for Oxidation and Reduction of Porphyrin-Linked Cobaltabisdicarbollide Conjugates in PhCN, 0.1 M TBAP

			oxidation			reduction		
linkage	compound	# of cobalt centers	Co^{III}/Co^{IV}	P^b		P^b		Co^{III}/Co^{II}
-	**Cobaltabisdicarbollide**	1	1.65					−1.34
-	**H_2TPP**	−		1.33	1.05	−1.15	−1.54	
meso	**8**	1	1.64[a]	0.96	0.83	−1.20	−1.56	−1.35
	9	2	1.62[a]	0.93	0.78	−1.22	−1.58	−1.37
central N	**3**	1	1.60	1.46[a]	1.26[a]	−0.49[a]	−1.17[a]	−1.38
	4	1			1.39[a]	−0.76[a]	−1.39	−1.39
central N	**5**	2	1.57	1.12[a]	0.87	−1.04[a]	−1.18[a]	−1.40
	6	2	1.64[a]		1.64[a]	−0.74[a]	−1.39	−1.39

[a] Peak potential, E_p, at scan rate of 0.10 V/s. [b] P = porphyrin centered redox reactions.

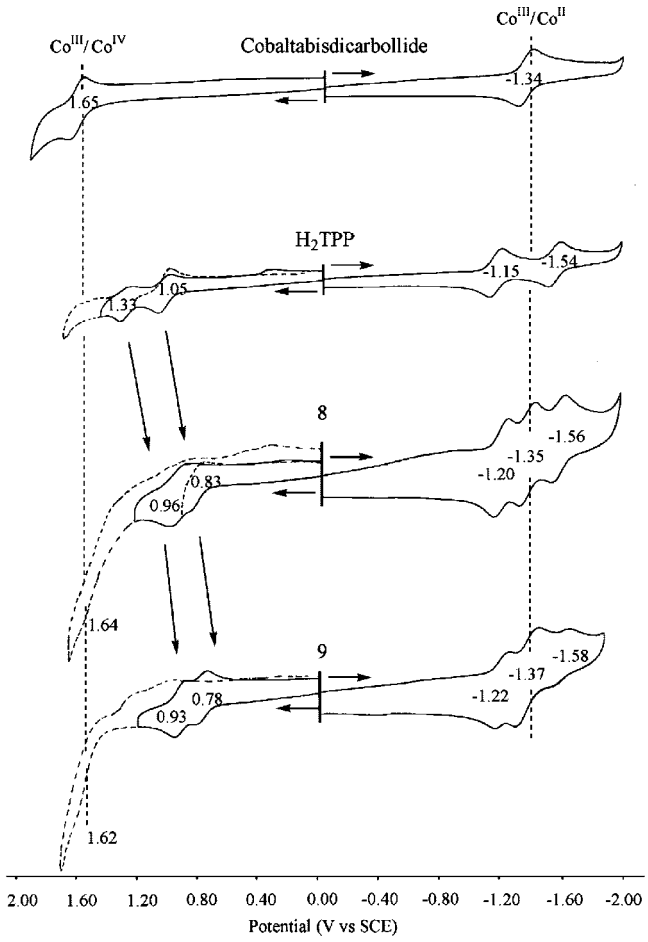

Figure 7. Cyclic voltammograms of cobaltabisdicarbollide, H_2TPP, and *meso*-substituted conjugates **8** and **9** in PhCN containing 0.1 M TBAP.

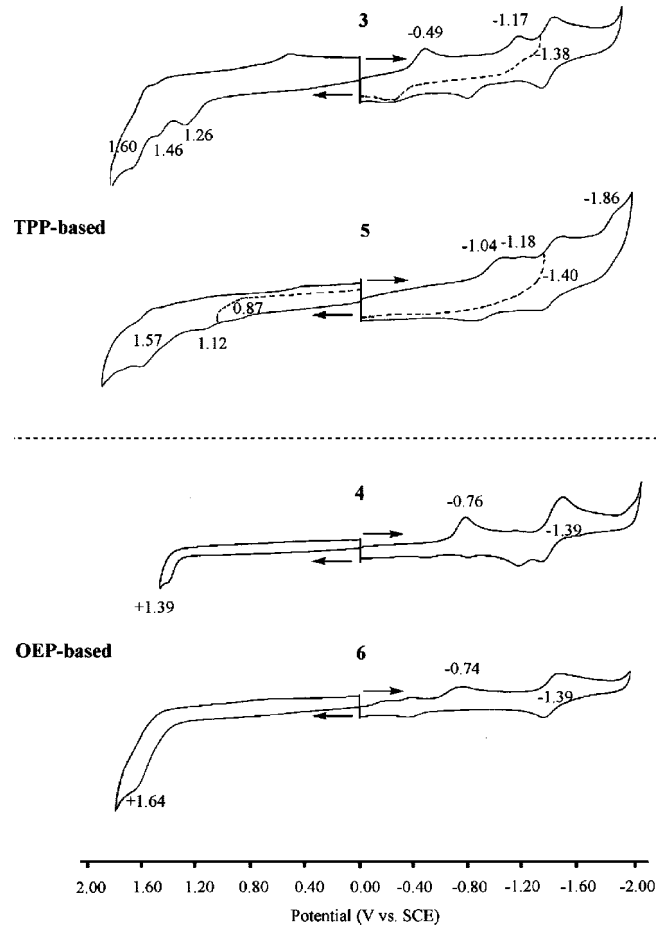

Figure 8. Cyclic voltammograms of *N*-substituted conjugates **3**−**6** in PhCN containing 0.1 M TBAP.

3, most likely because of the lack of hydrogen bonding to a water molecule, as exists in **3**, (see Supporting Information Figure S2) and perhaps lower steric hindrance of the pyrrolic ethyl groups of H_2OEP compared with the *meso*-phenyl groups of H_2TPP (*30*). In **4**, the porphyrin N atom carrying the cobaltacarborane substituent lies 0.371(4) Å out of the plane of the other three N atoms, and the cobaltacarborane-carrying pyrrole ring forms a dihedral angle of 17.2(5)° with the plane of the other 19 atoms in the porphyrin ring. This is quite similar to the conformation found in the analogous compound in which the substituted N atom carries an ethoxycarbonylmethyl group (*2*), where the dihedral angle is 19.1° and the substituted N atom lies 0.28 Å out of the N_3 plane. In that structure, there is also a lack of intermolecular hydrogen bonding involving the porphyrin N atoms.

The ^{1}H NMR of porphyrin **3** shows the NCH_2 signals at −4.83 ppm, in agreement with data reported for *N*-methyl-TPP (*12*), while the NCH_2 signals for porphyrin **4** appear at −5.57 ppm. The ^{1}H NMR spectrum of porphyrin **4** also shows two singlet resonances for the four *meso*-protons at 10.67 and 10.61 ppm, which are split into two signals of the same intensity (1:1). In contrast, the ^{1}H NMR spectrum of the disubstituted porphyrin **5** gave two different NCH_2 peaks at −5.80 ppm and −4.25 ppm, and one NH peak at −2.64 ppm. The ^{1}H−^{1}H COSY NMR spectrum for porphyrin **5** shows that the two hydrogen atoms of the NCH_2 are in different environments and therefore generate the two observed peaks at −5.80 ppm and −4.25 ppm. The symmetry observed in the ^{1}H and ^{13}C NMR spectra of porphyrin **5** indicates that the two alkylated nitrogen atoms are adjacent to each other (Figure 3a). The eight β-protons are split into 2:4:2, suggesting adjacent *N*-substitution. Similarly, the ^{1}H NMR spectrum of porphyrin **6** shows three resonances for the *meso*-protons, split into 1:2:1 (Figure 3b), which further indicates that the two substituents are on adjacent nitrogen atoms. Porphyrins **5** and **6** were isolated as the monocations due to the strong basicity of the corresponding free bases. Their remarkable regioselective formation has been previously observed in

Table 2. UV-visible Spectral Data (λ, nm ($\varepsilon \times 10^{-4}$ M^{-1} cm^{-1})) for Neutral and Reduced Porphyrin-Linked Cobaltabisdicarbollide Conjugates in PhCN, 0.1 M TBAP

	initial compound						after reduction				
cpd	Soret band		visible band				1st		2nd		3rd
H_2TPP		421 (22.0)	517 (2.2)	553 (2.2)	593 (0.7)	648 (0.5)	448 (7.3)	780 (1.5)	624 (2.4)		
8	314 (3.3)	424 (18.5)	520 (1.3)	561 (1.0)	594 (0.5)	654 (0.5)	488 (7.2)	780 (1.4)	348 (2.1)		606 (1.1)
9	315 (5.3)	421 (14.9)	521 (1.2)	564 (1.1)	598 (0.6)	657 (0.6)	455 (7.4)	780 (3.4)	348 (2.6)		607 (1.2)
3	318 (3.3)	441 (14.1)	542 (0.8)	576 (1.1)	616 (1.2)	667 (1.2)	436 (15.7)		510 (2.2)	850 (1.0)	358 (2.0)
4	316 (3.6)	404 (15.6)	540 (0.9)	566 (1.2)	581 (1.0)	610 (0.4)	413 (9.9)		437 (4.4)	793 (0.2)	
5	320 (2.3)	437 (7.8)	535 (1.0)	578 (1.1)	618 (0.9)	677 (0.8)	500 (2.1)		500 (1.9)	850 (2.7)	374 (1.9)
6	317 (4.3)	417 (8.6)	548 (0.6)	581 (0.7)	630 (0.4)	659 (0.1)	417 (3.7)		434 (6.3)	628 (4.0)	

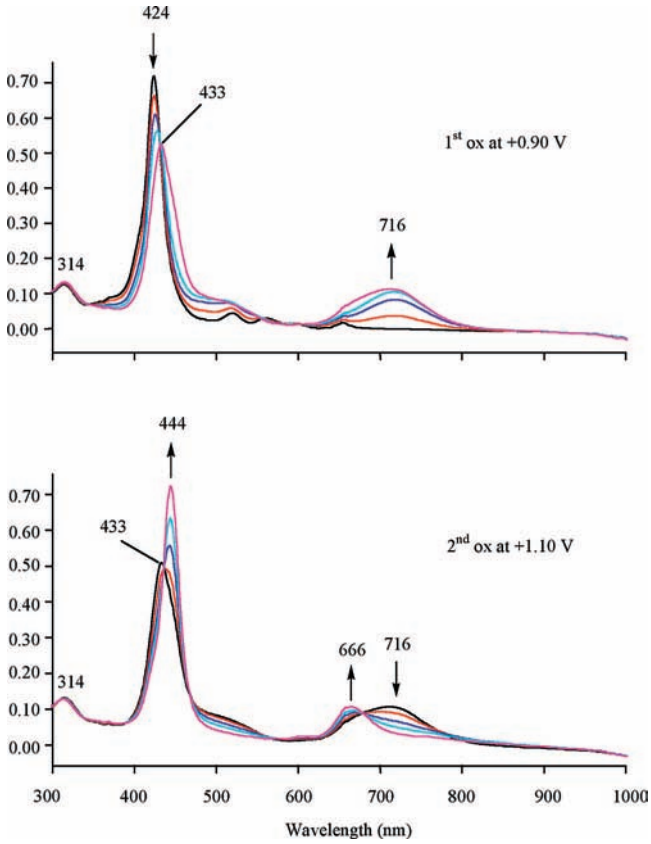

Figure 9. Thin-layer UV−visible spectral changes upon the (a) first and (b) second oxidations of porphyrin conjugate **8** in PhCN containing 0.1 M TBAP.

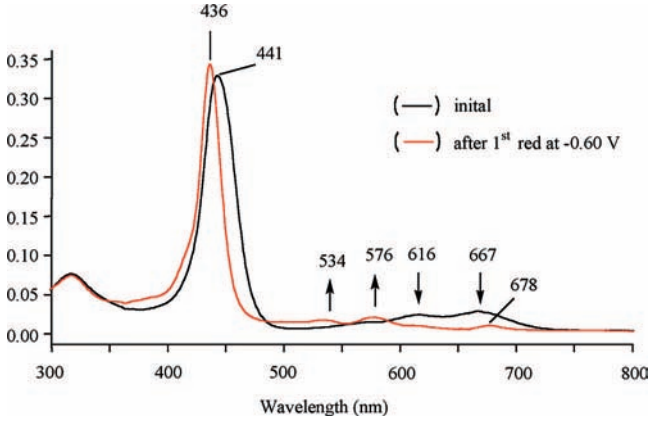

Figure 10. Thin-layer UV−visible spectral changes before (black line) and after (red line) the first reduction of porphyrin conjugate **3** in PhCN, 0.1 M TBAP.

N-alkylation reactions (*30*−*36*). The *N*-methylations of H_2TPP and H_2OEP using a variety of methylation reagents are reported to give adjacent *N*,*N*-dimethyl derivatives due to attack from the less sterically hindered side of the mono-*N*-methylated derivative. The regioselectivity of this reaction has been confirmed by X-ray structures in both cases (*30*, *34*).

N-Substitution is known to increase the degree of nonplanarity of the porphyrin macrocycle, and as a consequence, bathochromic shifts are usually observed in the optical spectra of *N*-substituted porphyrins, which correlate with the degree of conformation distortion (*5*). Significant red-shifts (15−32 nm) in the Soret bands of porphyrins **3**−**6** were observed (Figures 4 and 5), in comparison with the starting porphyrins H_2TPP (**1**) and H_2OEP (**2**) as well as with the *meso*-substituted porphyrins

Scheme 3[a]

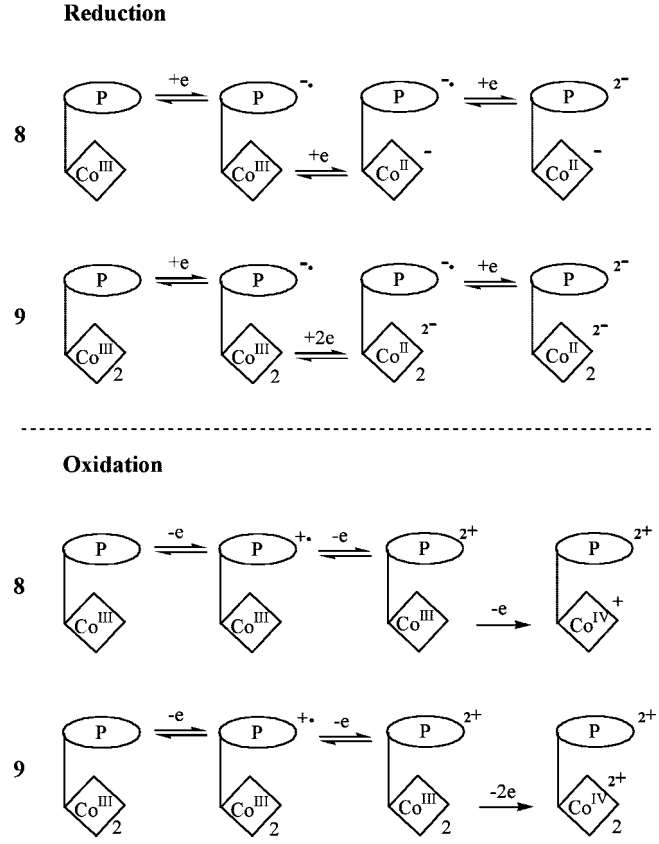

[a] Site of electron transfer at the porphyrin or cobaltabisdicarbollide part of conjugates **8** and **9**.

8 and **9** (see Supporting Information, Figures S3 and S4), which result from the distortion of the porphyrin macrocycle upon *N*-substitution. The fluorescence emission spectra of porphyrins **3**−**6** (Figure 6) show nearly complete fluorescence quenching for all *N*-substituted porphyrins (more than 90% as compared with starting porphyrins **1** and **2**), and this is due to strong distortions of the porphyrin planar conformation by the cobaltocarboranes attached to the central nitrogen atom(s). On the other hand, *N*-substituted porphyrins **8** and **9** showed similar spectroscopic data to the starting aminoporphyrin, since in these compounds, there is no significant distortion of the porphyrin macrocycle.

Electrochemistry. The unlinked cobaltbisdicarbollide undergoes two reversible metal-centered reactions (*37*) at $E_{1/2} = -1.34$ V ($Co^{III/II}$) and 1.65 V ($Co^{III/IV}$), while the unlinked free base porphyrin H_2TPP, **1**, displays four reversible reactions, two oxidations and two reductions (*38*). Conjugates **8** and **9** are characterized by six electron transfer processes, four of which are assigned to the porphyrin part of the molecule and two to the cobalt center of the cobaltabisdicarbollide. The cobalt-centered reactions of **8** and **9** occur at $E_{1/2} = -1.35$ to -1.37 V for reduction and $E_p = 1.62$ to 1.64 V for oxidation at a scan rate of 0.1 V/s, and are at virtually identical potentials as for reduction and oxidation of unlinked cabaltabisdicarbollide under the same solution conditions (see dashed lines in Figure 7).

As indicated above, H_2TPP undergoes two reversible one-electron oxidations (at $E_{1/2} = 1.05$ and 1.33 V), and two one-electron oxidations are also seen for conjugates **8** (0.83 and 0.96 V) and **9** (0.78 and 0.93 V). The easier oxidations of **8** and **9** as compared to H_2TPP result from the electron-donating substituent $PhNR_2$ at one *meso*-position of the porphyrin macrocycle. Easier oxidations have also been reported for porphyrins containing $PhNR_2$ substituents at all four *meso* positions of a porphyrin

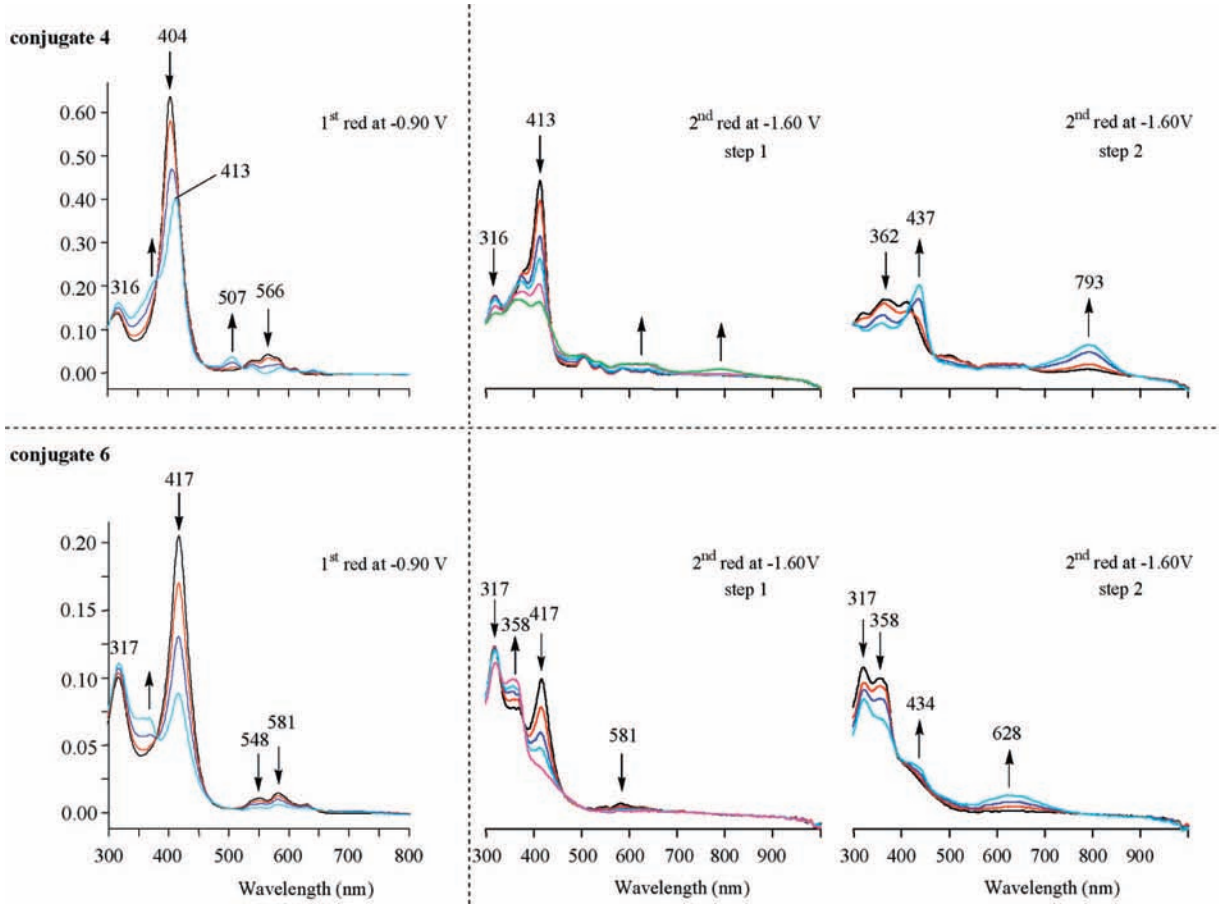

Figure 11. Spectral changes of the *N*-substituted conjugates **4** (top) and **6** (bottom) during reduction processes in PhCN containing 0.1 M TBAP.

macrocycle (*41*−*43*). The difference in potential between the first oxidation of H_2TPP and the first oxidation of conjugate **8** is 220 mV, while the difference in the $E_{1/2}$ value between the second oxidation of the two compounds is 370 mV. A further negative shift in $E_{1/2}$ of 30−50 mV is then seen upon going from conjugate **8** to conjugate **9** in PhCN, 0.1 M TBAP.

The two reversible reductions of H_2TPP at $E_{1/2} = -1.15$ and −1.54 V can be compared to similar electroreduction potentials for conjugate **8** at −1.20 and −1.56 V and conjugate **9** at −1.22 and −1.58 V (Figure 7). Here, the two conjugates are only 10−20 mV harder to reduce than H_2TPP. This lack of a substantial substituent effect on reductions is consistent with what has been observed in the literature for porphyrins with four $PhNR_2$ as *meso* substituents (*41*−*43*).

The reversible reduction potentials of porphyrin **8** at −1.35 V and porphyrin **9** at −1.37 V are unambiguously assigned to the Co^{III}/Co^{II} processes of the linked cobaltabisdicarbollide. The peak currents for reduction of the unlinked cobaltabisdicabollide and **8** are about equal in PhCN, consistent with one electron being transferred in each case. These contrast with what is seen for reduction of **9** where the peak current of the $Co^{III/II}$ process is approximately double that of **8**, consistent with the addition of two electrons, one to each electroactive cobaltabisdicarbollide group on the compound. Changing the number of cobaltabisdicarbollide groups from one to two does not affect the values of $E_{1/2}$, suggesting that no interaction occurs between these two redox centers in conjugate **9**.

A summary of peak potentials for all of the investigated compounds in PhCN is given in Table 1. The reduction of **8** and **9** first proceeds via a one-electron addition to the porphyrin macrocycle giving a π-anion radical, after which one electron is added to each cobaltabisdicarbollide unit at a more negative potential of −1.35 to −1.37 V. Further reduction at the porphyrin macrocycle then occurs at $E_{1/2} = -1.56$ to −1.58 V as shown in Figure 7. This reduction mechanism is shown graphically in Scheme 3 which also includes data for the oxidations. In this case, the first two one-electron abstractions from **8** or **9** ($E_{1/2} = 0.78$ to 0.96 V) involve the porphyrin part of the molecule, and the third electron abstraction involves the cobalt center of the cobaltabisdicarbollide. Additional proof for these assignments is given by spectroelectrochemical data described on the following pages.

Because irreversible chemical reactions are coupled to the electron transfers of **3**−**6**, attempts to assign a mechanism of electron transfer are tenuous at best, and this is made more difficult by the fact that compounds **3** to **6** not only have different core porphyrin structures (H_2TPP vs H_2OEP) but also differ in the number of linked cobaltabisdicarbollide groups (1 or 2) on the central nitrogen atoms. Nonetheless, several comparisons can be made from the current−voltage curves in Figure 8. The first is that **3** and **4**, which have a single linked *N*-substituted cobaltabisdicarbollide group, both show current−voltage curves characteristic of a chemical reaction following electron transfer (an electrochemical EC mechanism). The peak potential for the first reduction of **3** is located at $E_p = -0.49$ V for a scan rate of 0.1 V/s, while the E_p of **4** is located at −0.76 V under the same experimental conditions. This 270 mV difference in peak potential between E_p for reduction of **3** and **4** is similar in magnitude to potential separations for reductions of many metalloporphyrins with OEP and TPP core structures where the TPP derivatives are always easier to reduce (*38*−*40*). In fact, the 280 mV difference in $E_{1/2}$ between the first reduction of H_2TPP (−1.15 V vs SCE) and H_2OEP (−1.43 V) in PhCN,

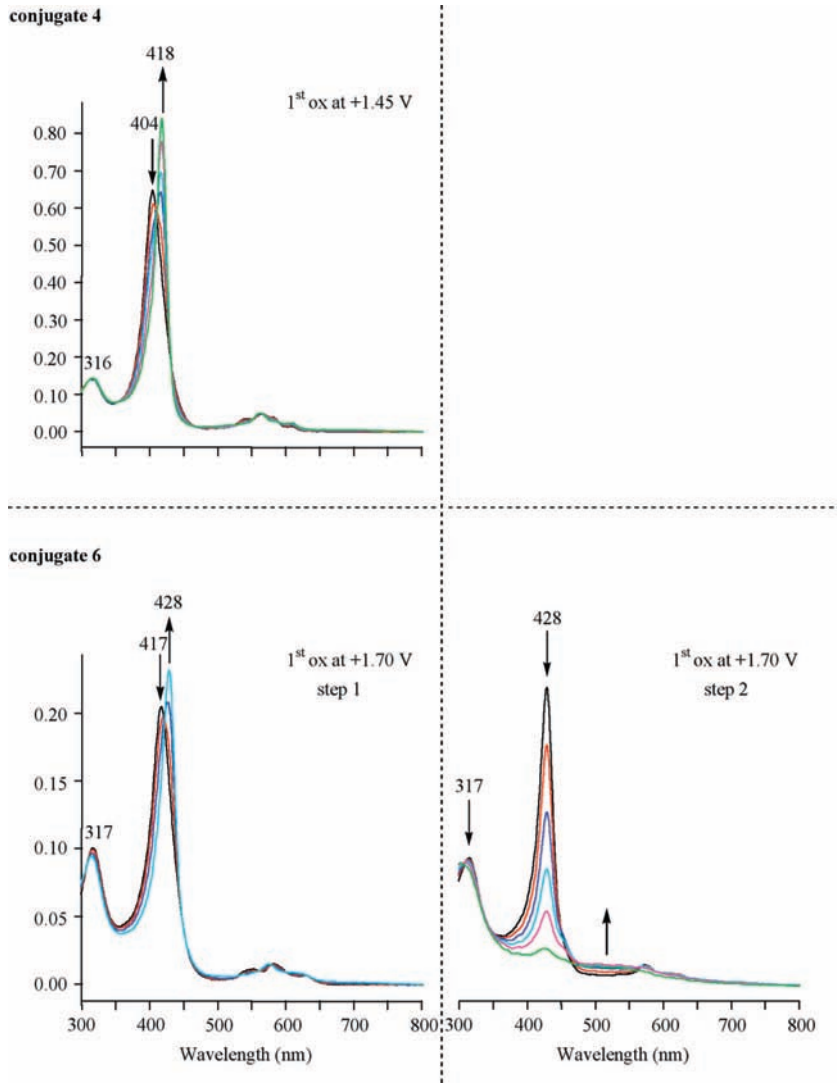

Figure 12. Spectral evolutions of the *N*-substituted conjugates **4** (top) and **6** (bottom) during oxidation processes in PhCN containing 0.1 M TBAP.

0.1 M TBAP, is experimentally the same as the ΔE_p value between the first reduction of **3** and **4** under the same solution conditions.

One can also compare the E_p values for reduction of **3** and **4** to $E_{1/2}$ values for reduction of H_2TPP or H_2OEP (see *refs 38–40* and voltammograms of free-base porphyrins in Supporting Information Figure S5). Conjugate **3** ($E_p = -0.49$ V) is 660 mV easier to reduce than H_2TPP ($E_{1/2} = -1.15$ V), while conjugate **4** (−0.76 V) is 670 mV easier to reduce than H_2OEP (−1.43 V).

Altogether, three reductions are seen for conjugate **3** in PhCN containing 0.1 M TBAP. As mentioned above, the first is irreversible and occurs at $E_p = -0.49$ V. The next two reductions are located at $E_p = -1.17$ V and $E_{1/2} = -1.38$ V and are similar to processes also seen for conjugate **5**. This might suggest that the cobaltabisdicarbollide group dissociates from the porphyrin after the first electron transfer in **5**. The measured redox potentials observed for reaction of the cobalt groups in the H_2TPP-based conjugates (−1.38 and 1.60 V for **3** and −1.40 and 1.57 V for **5**) are similar to $E_{1/2}$ values for the unlinked comparison compound (−1.34 and 1.65 V), and this suggests that in the ground state there are only weak electronic interactions between the porphyrin and cobaltabisdicarbollide groups within the conjugate.

Irreversible oxidation processes are observed at 1.39 and 1.64 V for conjugates **4** and **6**, respectively. Two reduction processes are observed at $E_p = -0.76$ and $E_{1/2} = -1.39$ V in conjugate **4**, while conjugate **6** undergoes several irreversible reduction processes and one reversible reduction at $E_{1/2} = -1.39$ V. Comparison of these values with redox potentials of H_2OEP leads to the conclusion that the reduction at $E_{1/2} = -1.39$ V occurs at the Co(III) center of the cobaltabisdicarbollide group and the oxidation at $E_p = 1.39$ V occurs at the porphyrin macrocycle.

The *N*-cobaltacarboranyl porphyrins **8** and **9** undergo three reversible reductions, two of which are assigned to porphyrin macrocycle reactions and one is characterized by Co^{III} to Co^{II}. They also have two reversible porphyrin ring-centered oxidations and one irreversible Co^{III}/Co^{IV} oxidation.

The core *N*-substituted porphyrins exhibit complicated electrochemical behavior with coupled chemical reactions. However, the cobalt-centered reaction site could be assigned by comparison with the $E_{1/2}$ of the unlinked cobaltabisdicarbollide.

Spectroelectrochemistry. When the intensity of a porphyrin Soret band significantly decreases after a reduction or oxidation, the electron transfer site is generally porphyrin ring-centered, leading to the formation of a π-anion or π-cation radical (*38, 40*). However, when the Soret band is only slightly shifted in wavelength and undergoes little or no change in molar absorptivity upon reduction or oxidation, the electron transfer site can often be assigned as the metal-centered. Thus, comparisons

between the observed spectral changes during oxidation or reduction of the conjugates with spectral changes obtained during oxidation or reduction of H_2TPP and H_2OEP may shed light on the probable site of electron transfer in the investigated compounds.

The changes in spectra during oxidations of conjugate **8** are shown in Figure 9. As the oxidation proceeds, the original Soret band at 424 nm decreases in intensity and shifts to 433 nm and a new band grows at 716 nm. These changes are consistent with formation of a porphyrin π-cation radical during the first electron abstraction. In the second oxidation process, a new intense Soret band grows in 444 nm and a well-defined visible band at 666 nm is also observed. Similar spectral changes are observed during the two oxidations of H_2TPP in PhCN, 0.2 M TBAP (Supporting Information, Figure S6).

The UV−visible spectral evolution upon the first one-electron reduction of **8** or **9** is also similar to spectral changes upon reduction of H_2TPP (Table 2) and is assigned to reactions occurring at the conjugated π-ring system of the porphyrin. During reductions of conjugates **8** and **9**, the Soret band decreases in intensity and a new Soret band is seen at 455−488 nm together with a broad band between 600 and 900 nm, which can be interpreted as formation of a porphyrin π-anion radical. The second reduction of **8** and **9** occurs at the linked cobaltabisdicarbollide. As Co^{II} is formed, there is a decreased intensity of the band at about 314 nm (characteristic of Co^{III}) and an increased intensity of the absorption at the 348 nm band which is assigned to Co^{II}.

In the case of the *N*-substituted conjugates, an assignment of the electron transfer site is less clear. As seen in Figure 10, the spectral evolution of **3** during the first reduction shows a blue shift of the Soret band from 441 nm (Soret band of H_2TPP) to 436 nm. The UV−visible spectrum of the singly reduced conjugate looks similar to that of neutral H_2TPP, thus suggesting loss of the cobaltabisdicarbollide group after the first reduction.

In the case of conjugates **4** and **6**, comparisons may be made with spectral changes during the reduction or oxidation of H_2OEP. When a potential of −0.90 V is applied to a solution of **4** or **6**, a similar evolution of the spectra is seen (Figure 11) and the final spectra can be interpreted in terms of porphyrin π anion radical formation. The second reduction involves two steps for these two conjugates, and here the electron transfer occurs at both the porphyrin π-ring system and the metal center of the cobaltabisdicarbollide group.

For conjugate **6** (Figure 12), a two-step electron transfer occurs during the first oxidation. The intensity of the Soret band at 417 nm decreases and a new band grows at 428 nm. No spectral changes are observed at 317 nm, suggesting that the electron transfer in this step occurs at the porphyrin π-ring system. The Soret band at 428 nm disappears during the second step electron transfer, as the intensity of the band at 317 nm decreases. This band is characteristic for Co(III), and the second electron transfer is therefore proposed to occur at the cobalt center. However, for conjugate **4**, only a one-step electron transfer is observed during the first oxidation, and the spectral changes are similar to the initial oxidation step of conjugate **6**. The results indicate that, for conjugate **4**, the electron transfer occurs at only the porphyrin π-ring system in the first oxidation, while for conjugate **6**, a two-step electron transfer occurs during the first oxidation process, one electron being abstracted from the porphyrin π-ring system and another from the cobaltabisdicarbollide group.

ACKNOWLEDGMENT

This work was partially supported by the National Institutes of Health, grant number CA098902 (M.G.H.V.). The support of the Robert A. Welch Foundation (Grants E-680 to K.M.K.) is gratefully acknowledged.

Supporting Information Available: The molecular structure of [8,8′-μ-(C_2H_5O)-3, 3′-Co(1,2-$C_2B_9H_{10}$)$_2$], and of conjugate **3** showing the intermolecular hydrogen bonding, UV−visible and fluorescence spectra for porphyrins **8** and **9**, cyclic voltammograms of H_2TPP and H_2OEP, and spectral changes of H_2TPP upon the first and second oxidations. This material is available free of charge via the Internet at http://pubs.acs.org.

LITERATURE CITED

(1) Kadish, K. M., Smith, K. M., Guilard, R. Eds. (2000) *The Porphyrin Handbook*, Academic Press, Boston.
(2) McLaughlin, G. M. (1974) Crystal and molecular structure of a non-metallo N-substituted porphyrin 21 ethoxycarbonylmethyl-2, 3,7,8,12,13,17,18-octaethylporphyrin. *J. Chem. Soc., Perkin Trans. 2*, 136–139.
(3) Lavallee, D. K., Kopelove, A. G., and Anderson, O. P. (1978) Structures and properties of N-methyltetraphenylporphyrin complexes. The crystal and molecular structure of chloro-N-methyl-.alpha.,.beta.,.gamma.,.delta.-tetraphenylporphinatozinc(II) and the chelate effect of zinc(II), cobalt(II), and cadmium(II) N-methylporphyrin complexes. *J. Am. Chem. Soc. 100*, 3025–3033.
(4) Lavallee, D. K. (1987) *The Chemistry and Biochemistry of N-Substituted Porphyrins*, VCH Publishers, Weinheim.
(5) Venkateshrao, S., Yin, J., Jarzecki, A. A., Schultz, P. G., and Spiro, T. G. (2004) Porphyrin distortion during affinity maturation of a ferrochelatase antibody, monitored by resonance raman spectroscopy. *J. Am. Chem. Soc. 126*, 16361–16367.
(6) Jarzecki, A. A., and Spiro, T. G. (2005) Porphyrin distortion from resonance raman intensities of out-of-plane modes: computation and modeling of N-methylmesoporphyrin, a ferrochelatase transition state analog. *J. Phys. Chem. A 109*, 421–430.
(7) Cochran, A. G., and Schultz, P. G. (1990) Antibody-catalyzed porphyrin metallation. *Science 249*, 781–783.
(8) Dailey, H. A. (1996) Mechanisms of Metallocenter Assembly (Eichorn, G. L., Marzilli, L. G., and Hausinger, R. P. Eds.) pp 77−89, VCH, New York.
(9) Ito, A., Konishi, K., and Aida, T. (1996) Free bases of chiral *N*-substituted porphyrins as catalysts for asymmetric reaction. *Tetrahedron Lett. 37*, 2585–2588.
(10) Konishi, K., Yahara, K., Toshishige, H., Aida, T., and Inoue, S. (1994) A novel anion-binding chiral receptor based on a metalloporphyrin with molecular asymmetry. Highly enantioselective recognition of amino acid derivatives. *J. Am. Chem. Soc. 116*, 1337–1344.
(11) Setsune, J.-I., and Takeda, H. (1995) Synthesis of N,N′-(trimethylene)-linked porphyrin-cyclen composite. *Tetrahedron Lett. 33*, 5903–5904.
(12) Lavallee, D. K., Xu, Z., and Pina, R. (1993) Synthesis and properties of new cationic-periphery porphyrins, tetrakis(p-(aminomethyl)phenyl)porphyrin and N-methyltetrakis(p-(aminomethyl)phenyl)porphyrin. *J. Org. Chem. 58*, 6000–6008.
(13) Tsukahara, K., Sawai, N., Hamada, S., Koji, K., Onoue, Y., Nakazawa, T., Nakagaki, R., Nozaki, K., and Ohno, T. (1999) Photophysical and photochemical properties of viologen-linked *N*-Alkylporphyrin diads and their metal complexes. *J. Phys. Chem. B 103*, 2867–2877.
(14) Vicente, M. G. H. (2000) Reactivity and functionalization of b-substituted porphyrins and chlorins. In *The Porphyrin Handbook*, (Kadish, K. M., Smith, K. M., Guilard, R. Eds.) pp 149−199, Chapter 4, *Volume 1: Synthesis and Organic Chemistry*, Academic Press, Boston.
(15) Ishimaru, Y., Sumida, S., and Iida, T. (2001) Regio- and stereoselective reduction of intramolecular *N*-strapped porphyrins to phlorins. *Tetrahedron Lett. 42*, 419–421.
(16) (a) Ruppert, R., Jeandon, C., Sgambati, A., and Callot, H. L. (1999) Reduction of N-arylporphyrins to N-arylphlorins: opposite stereochemical courses as a function of the reducing

agent. *Chem. Commun.* 2123–2124. (b) Krattinger, B., and Callot, H. J. (1999) Alkylation and reduction of porphyrins and N-substituted porphyrins: new routes to chlorins and phlorins. *Eur. J. Org. Chem.* 1857–1867. (c) Smith, K. M., Pandey, P. K., and Snow, K. M. (1986) Nickel(II)-promoted rearrangements of some *N*-substituted porphyrins. *J. Chem. Soc., Chem. Comm.* 1498–1499.

(17) Paolesse, R., Nardis, S., Stefanelli, M., Fronczek, F. R., and Vicente, M. G. H. (2005) Hemiporphycene from expansion of a corrole ring. *Angew. Chem., Int. Ed. 44*, 3047–3050.

(18) Barth, R. F., Coderre, J. A., Vicente, M. G. H., and Blue, T. E. (2005) Boron neutron capture therapy of cancer: current status and future prospects. *Clin. Cancer Res. 11*, 3987.

(19) Renner, M. W., Miura, M., Easson, M. W., and Vicente, M. G. H. (2006) Recent progress in the syntheses and biological evaluation of boronated porphyrins for boron neutron-capture therapy. *Curr. Med. Chem. Anti-Cancer Agents 6*, 145–158.

(20) Sivaev, I. B., and Bregadze, V. I. (1999) Chemistry of cobalt bis(discarbollides). A review. *Collect. Czech. Chem. Commun. 64*, 783–805.

(21) (a) Hao, E., and Vicente, M. G. H. (2005) Expeditious synthesis of porphyrin−cobaltacarborane conjugates. *Chem. Commun.* 1306–1308. (b) Hao, E., Jensen, T. J., Courtney, B. H., and Vicente, M. G. H. (2005) Synthesis and cellular studies of porphyrin-cobaltacarborane conjugates. *Bioconjugate Chem. 16*, 1495–1502. (c) Sibrian-Vazquez, M., Hao, E., Jensen, T. J., and Vicente, M. G. H. (2006) Enhanced cellular uptake with a cobaltacarborane-porphyrin-HIV-1 Tat 48−60 conjugate. *Bioconjugate Chem. 17*, 928–934. (d) Hao, E., Sibrian-Vazquez, M., Fronczek, F. R., Garno, J., and Vicente, M. G. H. (2007) Syntheses, aggregation and cellular studies of porphyrin-cobaltacarborane conjugates. *Chem. Eur. J. 32*, 9035–9042.

(22) Lin, X. Q., and Kadish, K. M. (1985) Vacuum-tight thin-layer spectroelectrochemical cell with a doublet platinum gauze working electrode. *Anal. Chem. 57*, 1498–1501.

(23) Luguya, R., Jaquinod, L., Fronczek, F. R., Vicente, M. G. H., and Smith, K. M. (2004) Synthesis and reactions of *meso*-(*p*-nitrophenyl)porphyrins. *Tetrahedron 60*, 2757–2763.

(24) Otwinowski, Z., Minor, W. (1997) Processing of X-ray diffraction data collected in oscillation mode (Carter, C. W., Jr., and Sweet, R. M. Eds.) *Macromolecular Crystallography, Part A*, Methods in Enzymology Volume *276*, pp 307−326, Academic Press, New York.

(25) Sheldrick, G. M. *SHELXL97*. University of Göttingen, Germany, 1997.

(26) Plešek, J., Heømánek, S., Franken, A., Cisarova, I., and Nachtigal, C. (1997) Dimethyl sulfate induced nucleophilic substitution of the [bis(1,2-dicarbollido)-3-cobalt(1-)]ate ion. Syntheses, properties and structures of its 8,8′-μ-sulfato, 8-phenyl and 8-dioxane derivatives. *Collect. Czech. Chem. Commun. 62*, 47–56.

(27) Teixidor, F., Pedrajas, J., Rojo, I., Vinas, C., Kivekas, R., Sillanpaa, R., Sivaev, I., Bregadze, V., and Sjoberg, S. (2003) Chameleonic capacity of [3,3′-Co(1,2-$C_2B_9H_{11}$) $_2$]$^-$ in coordination. generation of the highly uncommon S(thioether)-Na bond. *Organometallics 22*, 3414–3423.

(28) Plešek, J., Heømánek, S., Baše, K., Todd, L., and Wright, W. F. (1976) Zwitterionic compounds of the 8,8′-R-3-commo-3-cobaltabis(1,2-dicarba-closo-dodecaborane(11). *Collect. Czech. Chem. Commun. 41*, 3509–3515.

(29) Šubrtová, V., Petøièek, V., Linek, A., and Jecny, J. (1976) The crystal and molecular structure of 8,8′-OCH_3(B_9C_2H10) $_2$Co. *Z. Kristallogr. 144*, 139–141.

(30) Abeysekera, A. M., Grigg, R., Trocha-Grimshaw, J., and Henrick, K. (1980) N-methylation of etioporphyrin I and octaalkyl-5-azaporphyrins: x-ray structure of trans-N_a,N_b-dimethyletioporphyrin I triiodide. *Tetrahedron 36*, 1857–1868.

(31) Lavallee, D. K., and Anderson, O. P. (1982) Crystal and molecular structure of a free-base N-Methylporphyrin: N-Methyl-5,10,15,20-tetrakis(p-bromophenyl)porphyrin. *J. Am. Chem. Soc. 104*, 4707–4708.

(32) McLaughlin, G. M. (1974) Crystal and molecular structure of 1,3,6,8-tetra-azatricyclo[4.4.1.1^{3,8}]-dodecane, the 2:1 condensation product of formaldehyde and 1,2-diaminoethane, and the conformation of this system. *J. Chem. Soc., Perkin Trans. 2*, 136–140.

(33) Al-Hazimi, H. M. G., Jackson, A. H., Johnson, A. W., and Winter, M. (1977) N-methylated tetraphenylporphins. *J. Chem. Soc. Perkin I* 98–103.

(34) Senge, M. O., Kalisch, W. W., and Runge, S. (1997) N-Methyl derivatives of highly substituted porphyrins - the combined influence of both core and peripheral substitution on the porphyrin conformation. *Liebigs Ann. Recueil* 1345–1352.

(35) Stolzenberg, A. M., Simerly, S. W., Steffey, B. D., and Haymond, G. S. (1997) The synthesis, properties, and reactivities of free-base and Zn(II)-*N*-methyl hydroporphyrin compounds. The unexpected selectivity of the direct methylation of free-base hydroporphyrin compounds. *J. Am. Chem. Soc. 119*, 11843–11854.

(36) (a) Broadhurst, M. L., Grigg, R., and Shelton, G. (1970) N-Alkylation of porphins and related macrocycles. *J. Chem. Soc., Chem. Comm.* 231–233. (b) Grigg, R., Shelton, G., Sweeney, A., and Johnson, A. W. (1972) N-methylation and electrophilic substitution reactions of octa-alkyl-porphins, octaethylchlorin, and metalloporphins. *J. Chem. Soc. Perkin I* 1789–1799.

(37) Rudakov, D. A., Shirokii, V. L., Knizhnikov, V. A., Bazhanov, A. V., Vecher, E. I., Maier, N. A., Potkin, V. I., Ryabtsev, A. N., Petrovskii, P. V., Sivaev, I. B., Bregadze, V. I., and Eremenko, I. L. (2004) Electrochemical synthesis of halogen derivatives of bis(1,2-dicarbollyl)cobalt(III). *Russ. Chem. Bull. 53*, 2554–2557.

(38) Kadish, K. M., Caemelbecke, E. V., Royal, G. (1999) Electrochemistry of metalloporphyrins in nonaqueous media. *The Porphyrin Handbook, Volume 8: Electron Transfer* (Kadish, K. M., Smith, K. M., and Guilard, R. Eds.) pp 1−97, Chapter 55, Academic Press, Boston.

(39) Kadish, K. M., Royal, G., Caemelbecke, E. V., Gueletti, L. (1999) Metalloporphyrins in nonaqueous media: database of redox potentials. *The Porphyrin Handbook Volume 9: Database of Redox Potentials and Binding Constants* (Kadish, K. M., Smith, K. M., and Guilard, R. Eds.) pp 90−117, Chapter 59, Academic Press, Boston.

(40) Kadish, K. M. (1986) The electrochemistry of metalloporphyrins in nonaqueous media. In *Progress in Inorganic Chemistry*. Volume 34 (Lippard, S. J. Ed.) pp 435−605, John Wiley, New York.

(41) Malinski, T., Chang, D., Bottomley, L. A., and Kadish, K. M. (1982) Substituent effects on the redox reactions of para-substituted tetraphenylporphyrin complexes of ruthenium(II). *Inorg. Chem. 21*, 4248–4253.

(42) Bettelheim, A., White, B. A., Raybuck, S. A., and Murray, R. W. (1987) Electrochemical polymerization of amino-, pyrrole-, and hydroxy-substituted tetraphenylporphyrins. *Inorg. Chem. 26*, 1009–1017.

(43) Guilard, R., Barbe, J. M., and Fahim, M. (1992) Synthesis of carbenoid-bonded binuclear porphyrins which contain a single hydrophobic chain. Spectroscopic and electrochemical characterization of (P)SnFe(CO) $_4$. *New J. Chem. 16*, 815–820.

BC800265W

Supporting Information

Synthesis and Spectroelectrochemistry of *N*-Cobaltacarborane Porphyrin Conjugates

Erhong Hao,[a] *Min Zhang,*[b] *Wenbo E,*[b] *Karl M. Kadish,*[b,*] *Frank R. Fronczek,*[a]

Brandy H. Courtney[a] *and M. Graça H. Vicente*[a,1]

[a]Department of Chemistry, Louisiana State University, Baton Rouge, LA 70803, USA

[b]Department of Chemistry, University of Houston, Houston, TX 77204, USA

[1] Corresponding author. Phone: (225) 578 7405, Fax: (225) 578 3458, E-mail : vicente@lsu.edu

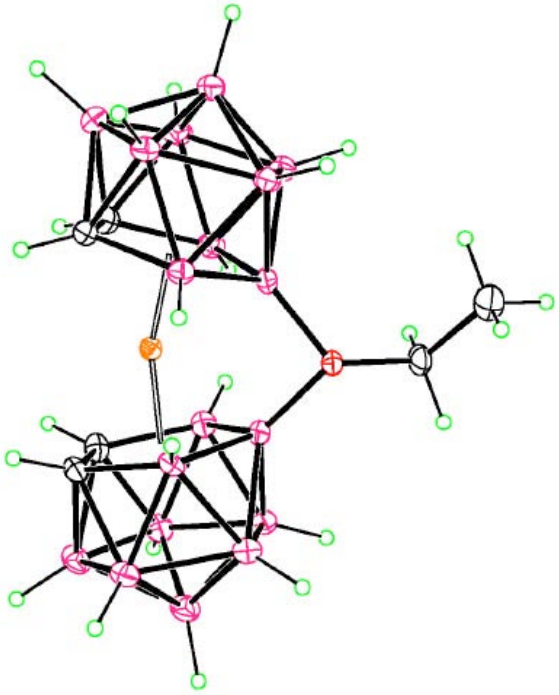

Figure S1. Molecular structure of [8,8'-μ-(C_2H_5O)-3, 3'-Co(1,2-$C_2B_9H_{10}$)$_2$].

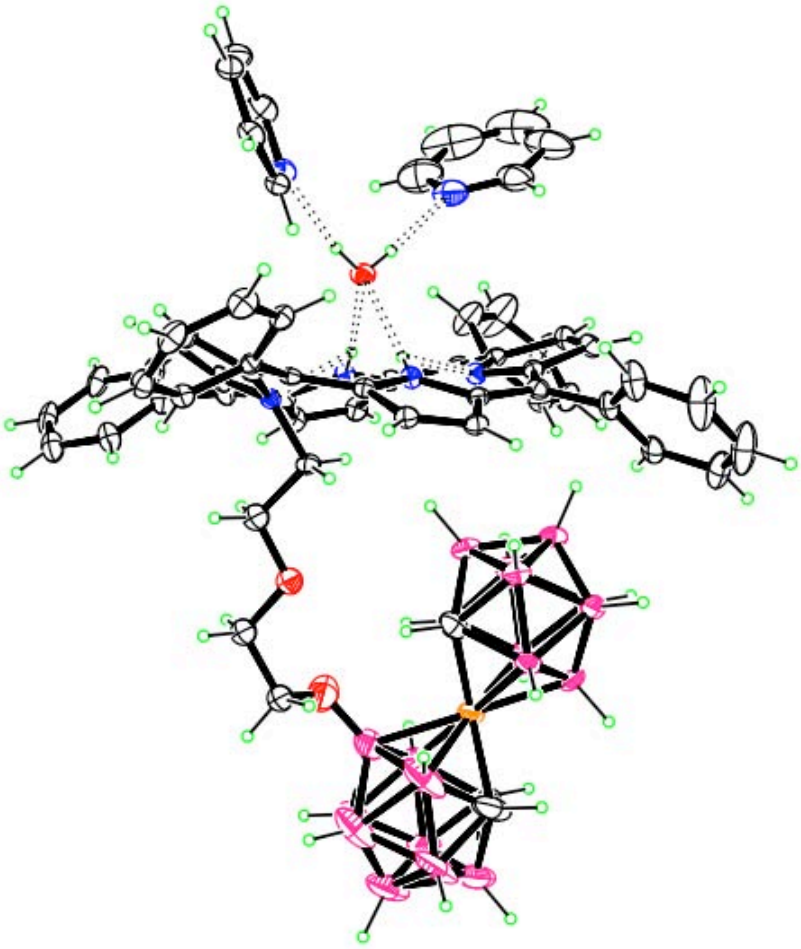

Figure S2. Molecular structure of *N*-cobaltacarborane porphyrin **3** showing the hydrogen-bonded water and pyridine molecules.

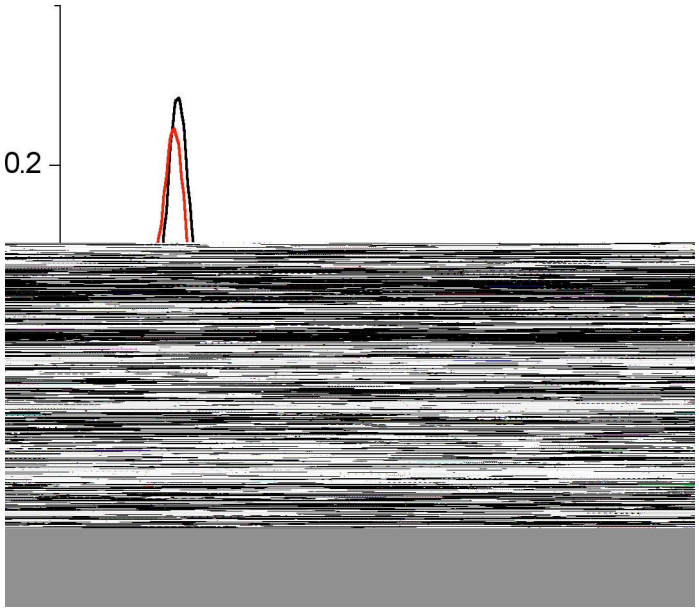

Figure S3. UV-visible spectra of porphyrins **8** (black) and **9** (red) in acetone at 1×10^{-6} M

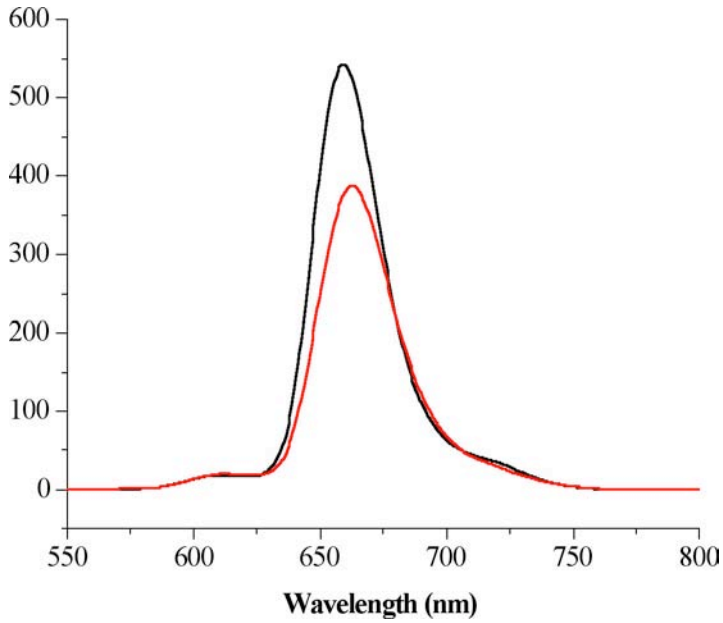

Figure S4. Fluorescence spectra of porphyrins **8** (black) and **9** (red) in acetone at 1×10^{-6} M.

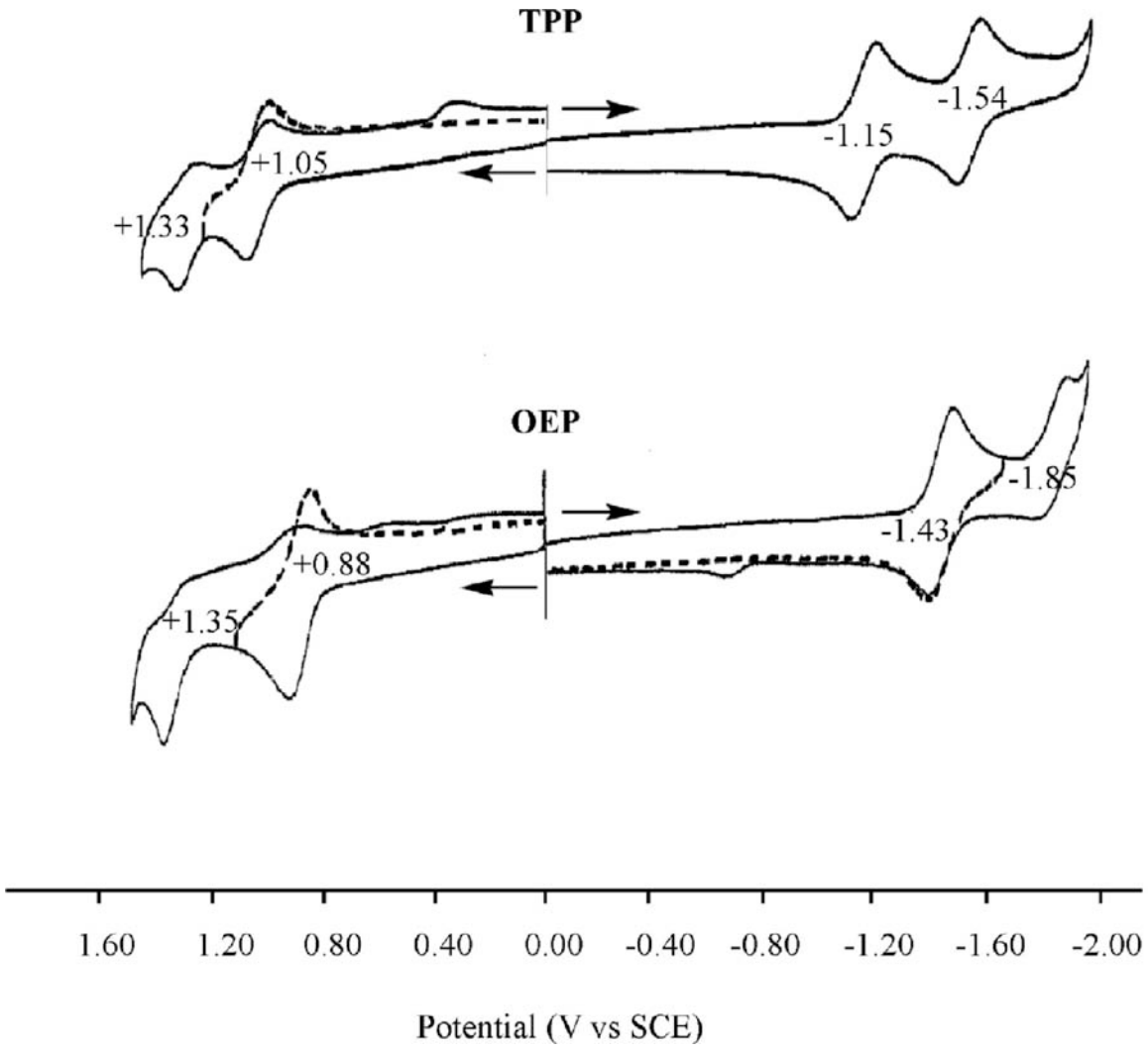

Figure S5. Cyclic voltammogramms of H_2TPP and H_2OEP in PhCN containing 0.1 M TBAP.

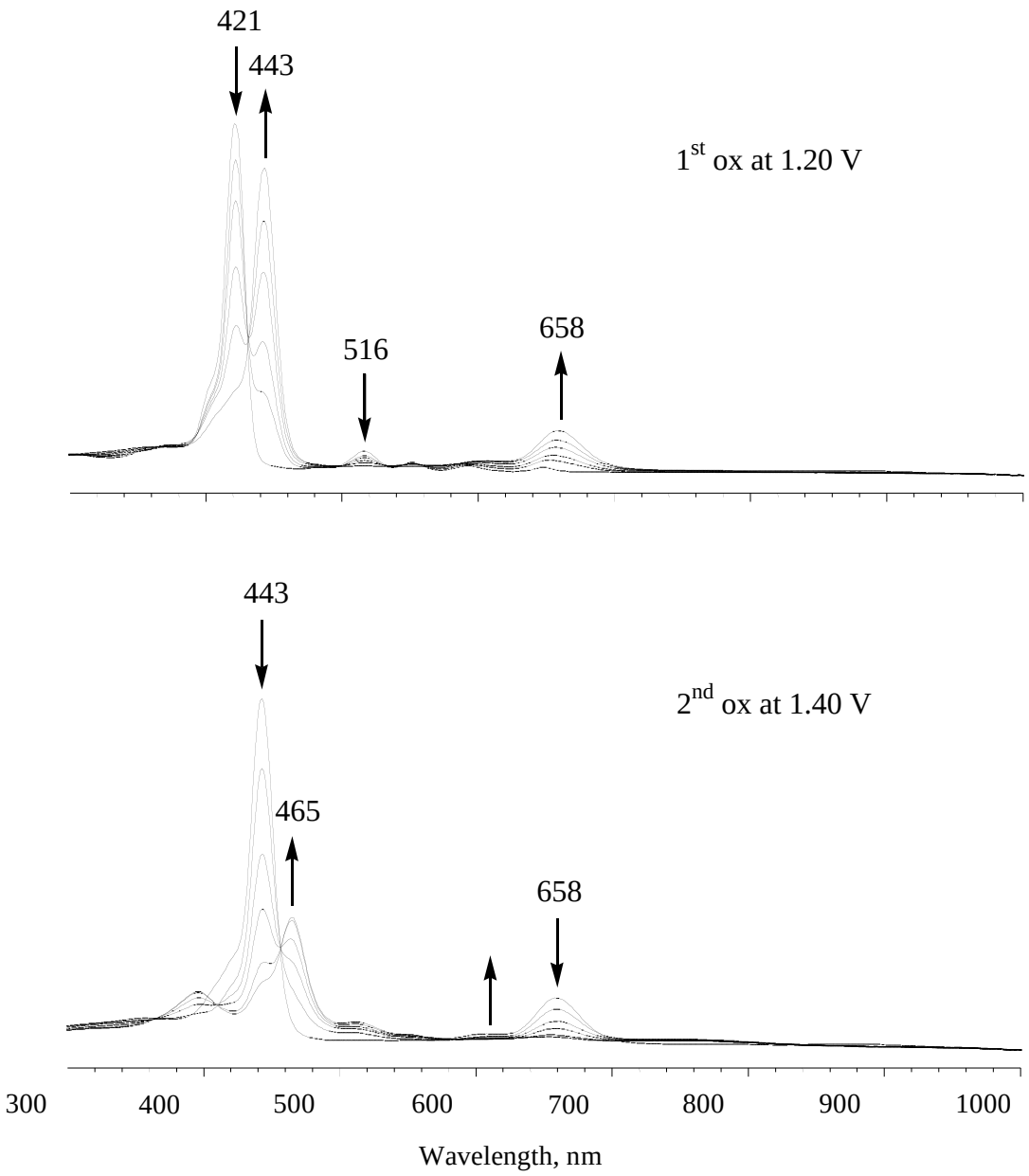

Figure S6. Spectral changes of H_2TPP upon the first and second oxidations in PhCN containing 0.2 M TBAP.

Cellular Delivery and Biological Activity of Antisense Oligonucleotides Conjugated to a Targeted Protein Carrier

Hyunmin Kang, Md. Rowshon Alam, Vidula Dixit, Michael Fisher, and Rudy L. Juliano*

Division of Molecular Pharmaceutics, School of Pharmacy, CB 7360, University of North Carolina, Chapel Hill, North Carolina 27599. Received July 1, 2008; Revised Manuscript Received September 5, 2008

Targeted delivery can potentially improve the pharmacological effects of antisense and siRNA oligonucleotides. Here, we describe a novel bioconjugation approach to the delivery of splice-shifting antisense oligonucleotides (SSOs). The SSOs are linked to albumin via reversible S−S bonds. The albumin is also conjugated with poly(ethylene glycol) (PEG) chains that terminate in an RGD ligand that selectively binds the $\alpha v\beta 3$ integrin. As a test system, we utilized human melanoma cells that express the $\alpha v\beta 3$ integrin and that also contain a luciferase reporter gene that can be induced by delivery of SSOs to the cell nucleus. The RGD-PEG-SSO-albumin conjugates were endocytosed by the cells in an RGD-dependent manner; using confocal fluorescence microscopy, evidence was obtained that the SSOs accumulate in the nucleus. The conjugates were able to robustly induce luciferase expression at concentrations in the 25−200 nM range. At these levels, little short-term or long-term toxicity was observed. Thus, the RGD-PEG-albumin conjugates may provide an effective tool for targeted delivery of oligonucleotides to certain cells and tissues.

INTRODUCTION

Antisense and siRNA oligonucleotides exhibit considerable promise as therapeutic agents (*1, 2*). While there are numerous examples of *in vivo* biological effects of oligonucleotides administered in free form, that is without use of a delivery system (*3, 4*), some investigators have suggested that oligonucleotide-based therapeutics could be enhanced via effective delivery strategies (*5, 6*). In this context, a variety of approaches have been pursued that generally fall into two broad categories. First, there are many reports dealing with the use of various types of nanoparticles for oligonucleotide delivery, including liposomes, lipoplexes, micelles, polymeric nanocarriers, and metallic particles, as discussed in several recent reviews and articles (*7*−*12*). A second strategy has been to synthesize conjugates of oligonucleotides with various peptides including so-called cell-penetrating peptides (*13, 14*), or peptides able to bind to specific cell surface receptors, and thus promote targeting of the conjugate (*15, 16*).

Both of these general approaches have advantages and liabilities. Even relatively small nanoparticles (∼100 nm diameter) are quite large in molecular terms, with masses in the millions of daltons. Nanoparticles cannot readily pass across the capillary endothelium in most normal tissues, and thus their biodistribution is limited to tissues that have extensive fenestrations in the endothelium such as liver, spleen, and some types of tumors (*17*−*19*). Nanoparticles are also scavenged by the phagocytes of the reticuloendothelial system (*20*), thus reducing their delivery to desired sites in the body, although this can be partially attenuated by surface modifications such as conjugation with poly(ethylene glycol) (PEG) (*21*). In contrast, oligonucleotides themselves, being relatively small with masses of several thousand daltons, are rapidly cleared from the bloodstream via renal excretion but nonetheless have broad distribution in many tissues (*22*−*24*). The pharmacokinetics and biodistribution of peptide−oligonucleotide conjugates has only been studied to a limited degree; however, a recent analysis of a peptide−morpholino oligonucleotide conjugate indicated broad distribution to various tissues (*25*).

With these considerations in mind, it seemed desirable to develop intermediate-sized delivery agents for oligonucleotides that might avoid renal clearance and thus have a longer circulation time than free oligonucleotides, but not have the same size constraints on biodistribution as typical nanoparticles. As an initial step in that direction, we report on the synthesis and characterization of macromolecular-scale oligonucleotide carriers based on human serum albumin (HSA). Some of the surface amino groups of albumin are conjugated with PEG chains that terminate in a targeting ligand, namely, a cyclic RGD (Arg-Gly-Asp) peptide. This ligand provides high-affinity binding to the $\alpha v\beta 3$ integrin, which is strongly expressed in angiogenic endothelia and in some tumor cells (*26*). Additional surface amino groups are used to link antisense oligonucleotides to the albumin via bioreversible S−S bridges. In this study, the antisense molecule used was a 2′-*O*-Me-phosphorothioate splice switching oligonucleotide (SSO) (*27*) that was designed to correct splicing of an aberrant luciferase reporter gene. Effective delivery of the SSO to the cell nucleus results in increased luciferase activity and thus provides an easily monitored positive readout.

Albumin has been extensively studied as a nontoxic carrier for conventional drugs (*28, 29*), and thus, we felt that it might have merit as a macromolecular carrier for oligonucleotides as well. The RGD-albumin-SSO conjugates we developed were tested in a cell culture model and were found to provide highly effective receptor-specific delivery. The endocytotic pathway of the conjugates involved trafficking via smooth vesicles rather than clathin-coated pits, and ultimately led to substantial nuclear accumulation of the splice switching oligonucleotide. This resulted in a marked increase in luciferase activity, an effect that was fully inhibited by excess RGD peptide, indicating receptor-dependent delivery. Thus, at the cell culture level, this approach has led to a highly

* Corresponding author. arjay@med.unc.edu, phone, 919 966 4383.

10.1021/bc800270w CCC: $40.75 © 2008 American Chemical Society
Published on Web 10/01/2008

specific and effective delivery system in the macromolecular or subnanoscale size range.

EXPERIMENTAL PROCEDURES

Materials. Human serum albumin (HSA) was purchased from Sigma-Aldrich (St. Louis, MO, USA). Alexa Fluor 488 C5 maleimide and a CBQCA amino assay kit were obtained from Invitrogen (Carlsbad, CA, USA). Dual-functionalized poly-(ethylene glycol), Malhex-NH-PEG-O-C_3H_6-CONHS (MW 5000), was from Rapp Polymere (Tubingen, Germany). Cyclo-[RGDfK(Ac-SCH_2CO)] peptide was purchased from Peptide International (Louisville, KY, USA). Sulfosuccinimidyl 6-(3′-[2-pyridyldithio]-propionamido) hexanoate (Sulfo-LC-SPDP) was from Thermo Fisher Scientific (Rockford, IL, USA). Glass-bottom tissue culture plates were obtained from MatTek (Ashland, MA, USA). Splice shifting oligonucleotide 623, or a mismatched version, was synthesized by an oligonucleotide core facility at University of North Carolina at Chapel Hill. These oligonucleotides were 2′-*O*-Me phosphorothioates functionalized with thiol groups at the 5′ position; in some cases, a Tamra fluorophore was included at the 3′ position (*15*).

Cells. A375SM melanoma cells that express the $\alpha v\beta 3$ integrin were stably transfected with a plasmid, pLuc/705, containing an aberrant intron inserted into the firefly luciferase coding sequence (*15*). The resulting A375SM-Luc705-B cells were grown in Dulbecco's Modified Eagle's Medium (DMEM) (Gibco/Invitrogen, Carlsbad, CA, USA) supplemented with 10% feta bovine serum (FBS).

Preparation of Albumin Conjugates with Cyclic RGD PEG or Cysteine PEG. Human serum albumin (denoted as A) (5 mg, 7.4×10^{-8} mol) was reacted with either L-cysteine (0.05 mg, 3.67×10^{-7} mol) or Alexa Fluor 488 C5 maleimide (0.27 mg, 3.67×10^{-7} mol) in phosphate buffered saline (PBS) supplemented with 1 mM EDTA (pH 7.4) for 4 h at room temperature to conjugate the single surface thiol group on albumin; this was followed by dialysis (MW cutoff 3500). The amino groups of the albumin were then reacted with Malhex-NH-PEG-O-C_3H_6-CONHS (11 mg, 2.21×10^{-6} mol) in PBS/1 mM EDTA (pH 7.4) for 4 h at room temperature. The product, a human albumin derivative with PEG-maleimide groups on the surface (termed PA), was purified from unincorporated PEG materials by dialysis (MW cutoff 100 000). The average number of PEG groups conjugated to albumin was determined by using the CBQCA assay, according to the manufacturer's instruction, to measure residual free amino groups. The thiol group on cyclic RGDfK needed for conjugation with the maleimide group on albumin was freshly generated by 1 h incubation of cyclo-[RGDfK(Ac-SCH_2CO)] (5 mg, 7.35×10^{-6} mol) in pH 7.0 deprotection buffer (HEPES (50 mM), NH_2OH (50 mM) and EDTA (30 mM)) at room temperature. The maleimide groups on the albumin derivative were then reacted with the thiol group of cyclic RGDfK (or cysteine as a control) in PBS with 1 mM EDTA (pH 7.4) overnight at room temperature and purified by dialysis (MW cutoff 100 000).

Conjugation of RGD-PEG-Albumin with Oligonucleotides. PEG−albumin conjugates, derivatized with either cyclo RGD (termed RPA, 9.2 mg, 7.35×10^{-8} mol) or cysteine (termed CPA, 8.7 mg, 7.35×10^{-8} mol), were reacted with dual functional sulfosuccinimidyl 6-(3′-[2-pyridyldithio]propionamido)hexanoate (1.2 mg, 2.21×10^{-6} mol) linker in PBS with 1 mM EDTA (pH 7.4) for 4 h at room temperature, and purified by dialysis (MW cutoff 100 000). Thiol-derivatized 623 oligonucleotide (or a mismatch version) (see Table 1) was then added to the intermediate in PBS with 1 mM EDTA (pH 7.4), and the reaction was maintained at room temperature for 24 h and purified by dialysis (MW cutoff 100 000). The average number of oligonucleotides linked to albumin was determined as 9.8 by observing the release of pyridine-2-thione (λ_{max} = 343 nm) from the reaction intermediate. This was also confirmed by monitoring the increase in OD260 subsequent to the oligonucleotide conjugation.

Table 1. Oligonucleotides Used in This Study[a]

623	5′-GTTATTCTTTAGAATGGTGC-3′
623-Tamra	5′-GTTATTCTTTAGAATGGTGC-Tamra-3′
623-SH	5′-HS-$(CH_2)_6$-GTTATTCTTTAGAATGGTGC-3′
Tamra-623-SH	5′-HS-$(CH_2)_6$-GTTATTCTTTAGAATGGTGC-Tamra-3′
MM	5′-GTAATTATTTATAATCGTCC-3′
MM-Tamra	5′-GTAATTATTTATAATCGTCC-Tamra-3′
MM-SH	5′-HS-$(CH_2)_6$-GTAATTATTTATAATCGTCC-3′
Tamra-MM-SH	5′-HS-$(CH_2)_6$-GTAATTATTTATAATCGTCC-Tamra-3′

[a] All oligonucleotides consist of 2′-OMe ribose residues with a phosphorothioate backbone.

Physical Characterization of the RGD-PEG-Albumin-Oligonucleotide Conjugates. The cyclic RGD derivatized albumin conjugate of oligonucleotide (termed RPAO) was analyzed by gel filtration fast protein chromatography (FPLC) (GE Healthcare) using a Superose 6 10/300 size exclusion column. The size and polydispersity of the conjugates were determined by a quasi-elastic dynamic light scattering (QELS) method as they eluted from the column (Wyatt, Santa Barbara, CA, USA).

Oligonucleotide Treatment of Cells and Luciferase Assay. A375SM-Luc705-B cells were seeded onto 12 well plates at 1×10^5 cells per well in medium containing 10% FBS. After 24 h, cells were rinsed, placed in OPTI-MEM (Gibco/Invitrogen, Carlsbad, CA, USA), and treated with free 623 oligonucleotide, various versions of the PEG-albumin-623 oligonucleotide conjugates, or 623 oligonucleotide complexed with Lipofectamine 2000 per manufacturer's instruction. After 4 h of treatment, FBS was added to each well to 1%. After 24 h, cells were washed with DMEM medium containing 10% FBS and incubated in DMEM supplemented with 1% FBS for 48 h prior to harvest. Activation of luciferase gene expression due to correction of splicing by oligonucleotide 623 was determined using a Luciferase assay kit (Promega, Madison, WI, USA) on a Monolight 2010 instrument (Analytical Luminescence Laboratory, San Diego, CA, USA).

Cellular Uptake and Confocal Microscopy. Cells were seeded onto either 12 well plates at 1×10^5 cells per well for cellular uptake measurements or in 12 well glass-bottom plates at 2×10^4 cells per well for live cell analysis by confocal microscopy. After treatment of cells with Tamra labeled oligonucleotide derivatives for 24 h, the cells were either lysed for measurement of Tamra fluorescence using a Nanodrop microfluorimeter (Nanodrop Technologies, Wilmington, DE, USA) or washed with DMEM containing 10% FBS and then placed in DMEM without phenol red, supplemented with 1% FBS, for confocal microscopy analysis. Colocalization of Tamra-labeled oligonucleotides with Alexa 488 labeled Transferrin or Dextran (Molecular Probes, Beaverton, OR, USA) in live cells was also examined by confocal microscopy. An Olympus confocal microscope with a 60× objective lens was used, and the data were processed using Fluoview software (Olympus, Center valley, PA, USA) as described previously (*15*).

Toxicity Studies. Cells were treated with various concentrations of oligonucleotides or conjugates as described above. After 48 h of treatment, cells were trypsinized and viable cells were counted using a Cellzone electric particle counter (Elmhurst, IL, USA) for short-term toxicity studies or replated at low density in 6 well plates containing a mixture of 1% low gelling temperature agarose (SeaKem, Rockland, ME, USA) supplemented with DMEM-H/10% FBS for 14 day studies of colony forming ability as described previously (*15*).

Scheme 1. Preparation of RGD Targeted HSA Oligonucleotide Conjugates[a]

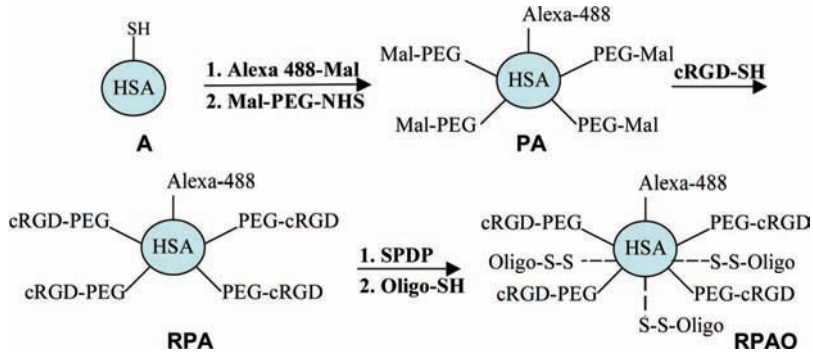

[a] Alexa 488-Mal = Alexa Fluor 488 C5 maleimde; Mal-PEG-NHS = Malhex-NH-PEG-O-C_3H_6-CONHS; cRGD-SH = cyclo[RGDfK-$COCH_2SH$]; SPDP = Sulfo-LC-SPDP; Oligo-SH = 623-SH, Tamra-623-SH, MM-SH, or Tamra-MM-SH (see Table 1).

Table 2. Measurement of Available Amino Groups on HSA by CBQCA

	CBQCA fluorescence (%)	number of estimated surface amino groups
HSA	100.00 ± 2.2	59
HSA-PEG	81.3 ± 3.3	48

Nuclease Stability. Micrococcal nuclease (400 gel units) was added to solutions of 623-Tamra or RPA-623-Tamra and the samples were incubated for various periods of time at 37 °C. The reactions were then stopped by the addition of EDTA (50 mM), and the fluorescent samples were analyzed on 10% polyacrylamide gels and examined under long-wavelength ultraviolet illumination to detect possible nucleolytic cleavage of the Tamra-labeled oligonucleotides.

RESULTS

Synthesis and Characterization of PEG-Albumin-Antisense Conjugates. The overall strategy for preparation of the various conjugates is outlined in Scheme 1. First, the single sulfhydryl group on human serum albumin was labeled with the green fluorophore Alexa 488 (in some cases, the sulfhydryl was simply blocked by forming an S−S bridge with cysteine). Subsequently, several surface amino groups were reacted with Mal-PEG-NHS to form a pegylated albumin (PA). The number of PEG chains conjugated to PA was determined by using a CBQCA assay to quantitate the number of exposed amino groups on albumin before and after the reaction with PEG; this indicated that approximately 10 PEG chains were conjugated per albumin molecule (Table 2). After purification of the PA conjugate, excess thiol-containing cyclic RGD peptide was reacted with the terminal maleimide groups on PA to form RGD-PEG-albumin (RPA). As a control, cysteine was used instead of RGD to react with the PA; this product was termed CPA. After purification, additional exposed amino groups were reacted with the bifunctional reagent Sulfo-LC-SPDP, and then, the 623 oligonucleotide (or mismatch version) was conjugated to form RPA-Oligonucleotide (RPAO) (also termed RPA-623). In some cases, the 623 oligonucleotide included a 3′ Tamra (red) fluorophore (with the resulting product termed RPA-623-Tamra). The number of oligonucleotides linked to the conjugate was determined in two ways (Figure 1). First, formation of the colored product pyridine-2-thione (λ_{max} = 343 nm) was monitored as the 5′-thiol oligonucleotide reacted with the SPDP-conjugated albumin. Second, the OD260 was determined before and after the conjugation reaction. Both of these methods led to close agreement with 8−11 oligonucleotides linked per albumin in various preparations.

The polyacrylamide gel migration behavior of the starting materials and the conjugates is illustrated in Figure 2A. The

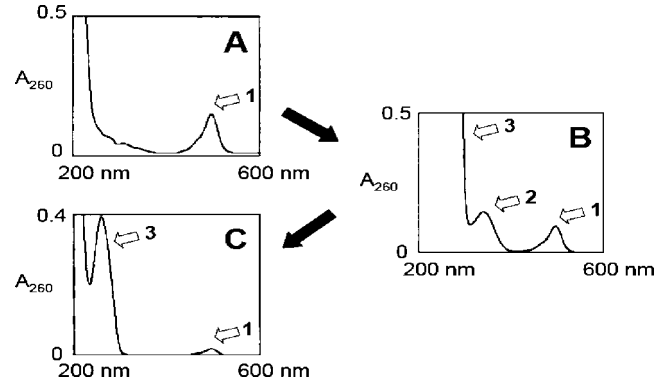

Figure 1. Cleavable disulfide formation between RPA and oligonucleotide. UV spectra of (A) RPA, (B) reaction mixture of RPA-SPDP and 623-SH, and (C) RPA-623. Peak 1: Alexa 488. Peak 2: Pyridine-2-thione. Peak 3: 623. Spectra of diluted samples are shown to include peak 2 and peak 3.

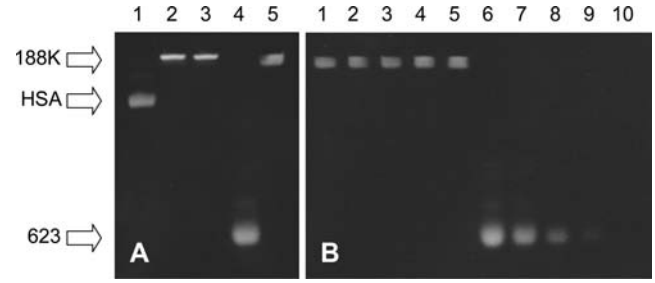

Figure 2. Polyacrylamide gel (10%) electrophoresis analysis of conjugates (A) and nuclease resistance (B). Panel (A): (1) HSA-Alexa 488, (2) PA-Alexa 488, (3) RPA-Alexa 488, (4) 623-Tamra, (5) RPA-623-Tamra. Panel B: RPA-623-Tamra (1−5) and 623-Tamra (6−10) were digested with Micrococcal nuclease (400 gel units) for 0 h (1,6), 1 h (2,7), 2 h (3,8), 4 h (4,9), and 12 h (5,10).

623-Tamra and RPA-623-Tamra are detected by their red fluoresence, while the RPA is detected by its green (Alexa 488) fluorescence. As seen, Alexa 488-modified human serum albumin migrated well into the gel, consistent with its molecular weight of 68 kDa, while the unconjugated 623-Tamra oligonucleotide migrated near the dye front. Both RPA and RPA-623-Tamra failed to significantly enter the gel, indicating molecular size greater than the largest molecular weight marker used (188 kDa). We also used gel analysis to evaluate the relative nuclease stability of 623-Tamra versus that of RPA-623-Tamra. As seen in Figure 2B, although 623-Tamra is a rather stable 2′-*O*-Me-phophorothioate oligonucleotide, incubation with micrococcal nuclease caused a gradual degradation of this material. In contrast, there was no loss of Tamra-labeled

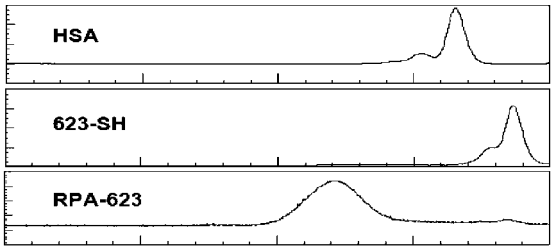

	Polydispersity Mw/Mn	Hydrodynamic radius Rh(z)
HSA	1.000 ± 0.003	2.2 nm
RPA-623	1.092 ± 0.013	6.0 nm

Figure 3. FPLC/QELS analysis. Starting materials (HSA and 623 oligonucleotide) and the final RPA-623 product were analyzed for relative molecular size using FPLC/QELS as described in experimental procedures. The faster migrating shoulder peaks seen in the HSA and 623-SH samples likely represent S−S bridged dimers.

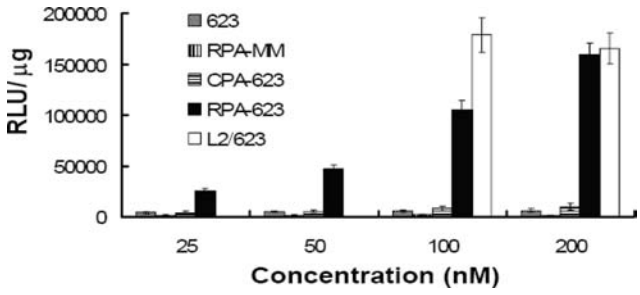

Figure 4. Dose response and specificity studies. Cells were treated with free 623, RPA-MM, CPA-623 (prepared by conjugating cysteine with the maleimide on PEG), RPA-623 at 25 to 200 nM, or 623 complexed with Lipofectamine 2000 (1.5 ug/mL) at 100 and 200 nM (L2/623) as described in experimental procedures. Luciferase activity was determined after 72 h from the cell lysates and expressed as relative luminescence units (RLUs) per ug of protein. Results are means and standard errors of three determinations.

oligonucleotide from the RPA-623-Tamra conjugate. This suggests that the oligonucleotides linked to PEG−albumin are partially protected against nuclease degradation.

The molecular size of the RPA-623 conjugate was estimated using size-exclusion chromatography and quasi-elastic laser light scattering. As indicated in Figure 3, the RPA-623 conjugate is heterodisperse, migrating as a broad peak while albumin has a sharper migration profile. The hydrodynamic radius of the RPA-623 conjugate was estimated at approximately 6 nm, while that of albumin was estimated at 2.2 nm. Thus, the average radius of the conjugate is about 2.7 times that of the ummodified albumin carrier. The albumin−oligonucleotide conjugates were stable during several weeks' storage in buffer at 4 °C, with no indication of aggregation.

Pharmacological Effect of the PEG-Albumin-Antisense Oligonucleotide Conjugates. In order to evaluate the pharmacological effectiveness of the conjugates, A375SM-Luc705-B cells were incubated with various concentrations of "free" 623 oligonucleotide, 623 complexed with Lipofectamine 2000, or several versions of the conjugates, and the increase in luciferase activity was quantitated. As indicated in Figure 4, treatment with the RPA-623 conjugate resulted in a concentration-dependent increase in luciferase activity over the range 25−200 nM, while use of a mismatched oligonucleotide version (RPA-MM), or a version where the PEG chains were terminated with cysteine (CPA-623), failed to achieve an effect. Free 623 also did not cause a significant increase in luciferase activity, while 623 complexed with Lipofectamine 2000 had a strong effect. It is interesting to note that the magnitude of the effect achieved

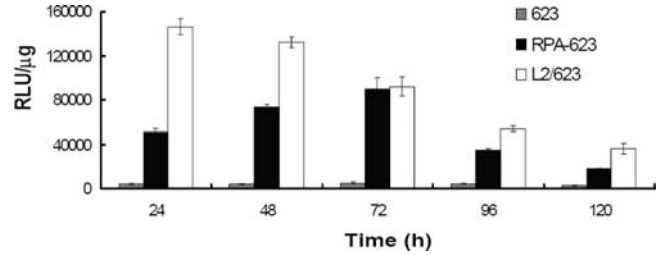

Figure 5. Time response studies. Cells were treated with 200 nM of free 623, RPA-623, or 623 complexed with Lipofectamine 2000 (1.5 ug/mL) (L2/623). After 24 h, cells were washed and placed in DMEM/1% FBS. Luciferase activity was determined from cell lysates collected at various times and expressed as relative luminescence units (RLUs) per microgram of cell protein as described in experimental procedures. Results are means and standard errors of three determinations.

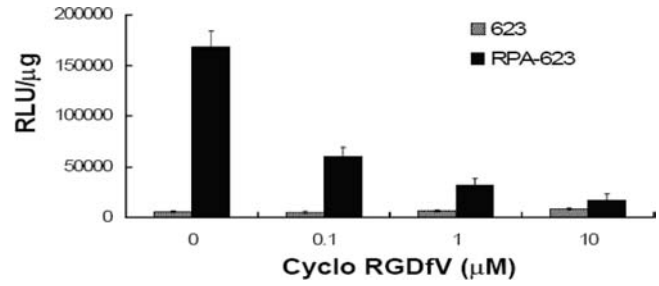

Figure 6. Inhibition of 623 antisense effect by excess cRGD peptide. Free cyclo RGDfV peptide at the indicated concentrations was added to the cells 30 min prior to treatment with either free 623 (100 nM) or RPA-623 (100 nM). Luciferase activity was determined after 48 h from cell lysates and expressed as relative luminescence units (RLUs) per microgram of cell protein. Results are means and standard errors of three determinations.

by the RPA-623 conjugate almost equaled that of the Lipofectamine complex; the latter is often considered the "gold standard" for delivery of oligonucleotides to cells in culture. The time course of luciferase activation differed markedly between RPA-623 and the 623-Lipofectamine complex. Thus, as seen in Figure 5, treatment with RPA-623 resulted in activity that rose gradually, attained a maximum at 72 h post-treatment, and then gradually declined. In contrast, use of the 623-Lipofectamine complex resulted in a rapid rise of activity within 24 h of treatment followed by a monotonic decline. This pattern suggests that the Lipofectamine complex rapidly delivers olgonucleotide to the cytosol and nucleus, while delivery of oligonucleotide from the RPA-623 conjugate involves a more complex and protracted trafficking within the cell. The intracellular delivery mediated by the RPA-623 conjugate clearly involves the $\alpha v\beta 3$ integrin since, as seen in Figure 6, incubation with excess cyclic RGD peptide completely blocks the ability of the conjugate to activate luciferase. At the concentrations used, the RGD peptide does not cause cell detachment or other obvious toxicity.

Uptake and Subcellular Distribution of the Conjugates. We examined the total cellular accumulation of the various materials using a Nanodrop fluorimeter assay, as seen in Figure 7. Total uptake was approximately linear with time in all cases. The highest uptake was observed with 623-Tamra complexed with Lipofectamine 2000, followed by RPAO (either 623 or mismatched), followed by CPA-623 and free 623-Tamra.

We also examined the subcellular distribution of the 623-Tamra labled oligonucelotide after delivery by the conjugates or via complexation with Lipofectamine. As seen in Figure 8, live cells treated with either RPA-623-Tamra or a Lipofectamine 2000/623-Tamra complex displayed substantial intracellular Tamra fluorescence at 24 h, including material present in

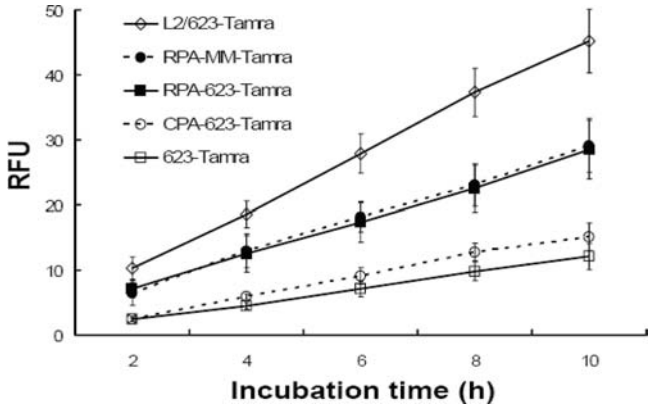

Figure 7. Cellular accumulation. Cells were treated with 100 nM of free 623-Tamra, 623-Tamra complexed with Lipofectamine 2000 (1.5 ug/ml) (L2/623), RPA-MM-Tamra, RPA-623-Tamra, or CPA-623-Tamra. After each incubation period, cells were washed and lysates were analyzed using a Nanodrop fluorimeter for uptake measurements. Results are means and standard errors of three determinations.

cytoplasmic vesicles as well as in the nucleus. By contrast, cells treated with free 623-Tamra or with CPA-623-Tamra exhibited less intracellular fluorescence with no evidence of nuclear accumulation. These observations suggest that the RGD-PEG-albumin conjugate can provide effective delivery of the pendant oligonucleotides to the cell nucleus.

To further understand the cellular uptake and trafficking of the conjugates, we coincubated them with well-known markers for different endocytotic pathways and then compared their subcellular distributions. In these studies, we used transferrin as a marker for clathrin-coated vesicle-mediated uptake and dextran as a marker for smooth vesicle endocytosis (*30*). These molecules were labeled with Alexa 488, a green fluorophore, while the RPA-623-Tamra conjugate displays a red fluorescence. As seen in Figure 9, at early time points (2 h) there was little overlap of the RPA-623-Tamra fluorescence with that of transferrin, but there was substantial overlap with the dextran fluorescence. At later time points, there was fluorescence overlap in both cases, although it was most pronounced for dextran. Nuclear accumulation of Tamra fluorescence was observed at the later time points, similar to that seen in Figure 8. These observations suggest that the RGD-PEG-albumin-oligonucleotide conjugate (RPAO) is initially taken up via smooth vesicle endocytosis, but later the material enters endomembrane compartments that are accessible via both the coated vesicle and smooth vesicle pathways. Inhibitor studies were consistent with this interpretation. Thus, as seen in Figure 10, cellular accumulation of the RPA-623-Tamra was inhibited by nontoxic concentrations of β-cyclodextrin and by cytochalasin D (as well as by excess RGD peptide). This indicates that the RPA-623-Tamra is taken up by an actin-dependent pathway that involves smooth vesicles rich in lipid-raft components (*30*).

Lack of Cytotoxicity of the Conjugates. We examined the cytotoxicity of the RPA-623 conjugate using both short-term and long-term assays. A375MLuc705 cells were treated with RPA-623, free 623, or 623 complexed with Lipofectamine. For the short-term assay, cell number was determined immediately after the incubation period. The long-term assay involved colony formation in soft agar over a 14 day period. As seen in Figure 11, there was little acute or long-term toxicity of RPA-623 even when used at concentrations needed to obtain a strong pharmacological effect.

DISCUSSION

Albumin has a long history as a biodegradable, nontoxic carrier for conventional low molecular weight drugs (*28, 29*). Here, we have employed human serum albumin as a targetable carrier for antisense oligonucleotides. The splice-switching oligonucleotide (SSO) termed 623 was conjugated to albumin via reversible S−S linkages. RGD-PEG chains were also conjugated in order to provide stabilization and the ability to target a specific cell surface receptor, the $\alpha v\beta 3$ integrin. This approach has provided a highly efficient carrier system that could be exploited in a variety of ways. The overall strategy is very flexible, and one could easily visualize using many other high-affinity ligands in addition to RGD peptides, thus offering the possibility of "targeting" to many types of cell surface receptors. The "payload" of the conjugates is quite high, with an average of 10 oligonucleotides of approximately 7000 MW conjugated per albumin; this means that the molecular mass of the payload is similar to the total mass of the albumin. PEGylation seems necessary, since in preliminary studies (not shown), we found that conjugation of the oligonucleotides to albumin in the absence of PEG led to nonspecific binding to cells. Interestingly, the PEG moieties also seemed to provide some protection against oligonucleotide degradation mediated by an endonuclease.

The RGD-PEG-albumin-oligonucleotide conjugate (RPA-623-Tamra) was taken up by cells in an RGD-dependent

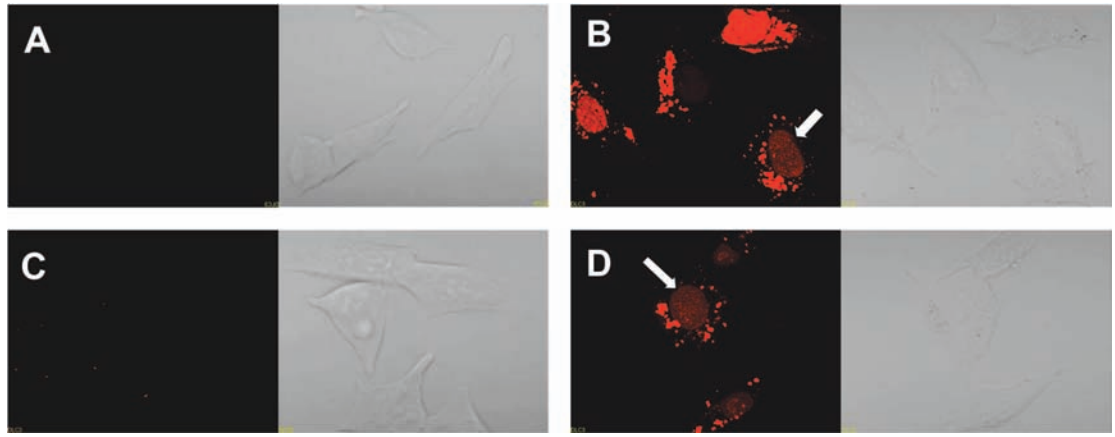

Figure 8. Confocal microscopy analysis of 623 uptake. Cells were treated with 100 nM of either (A) free 623-Tamra, (B) 623-Tamra complexed with Lipofectamine 2000 (1.5 ug/mL), (C) CPA-623-Tamra, or (D) RPA-623-Tamra as described in experimental procedures. After 24 h, cells were washed with DMEM containing 10% FBS and placed in DMEM supplemented with 1% FBS without phenol red for analysis on an Olympus confocal fluorescence microscope as described in experimental procedures. Arrows indicate Tamra fluorophore accumulated in nuclei.

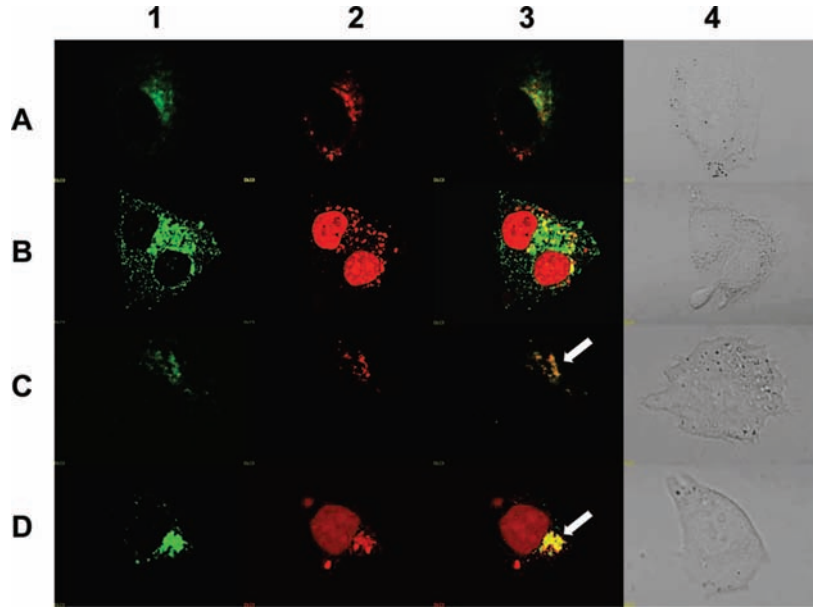

Figure 9. Colocalization of 623 with endosomal pathway markers. RPA-623-Tamra (100 nM) prepared by conjugating an HSA surface thiol group to a cysteine instead of Alexa 488 was coincubated with (A) Transferrin-Alexa 488 (200 nM) for 2 h, (B) Transferrin-Alexa 488 (100 nM) for 24 h, (C) Dextran-Alexa-488 (2 uM) for 2 h, and (D) Dextran-Alexa-488 (2 uM) for 24 h. Live cells were observed for (1) Alexa-488, (2) Tamra, (3) merged images of Alexa-488 and Tamra, and (4) differential interference contrast (DIC) image using an Olympus confocal fluorescence microscope as described in experimental procedures. Arrows represent colocalization of Alexa 488 and Tamra fluorophores.

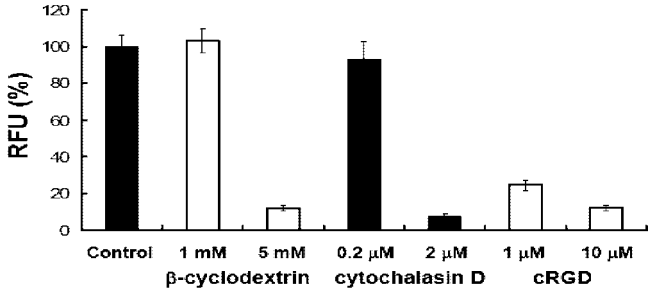

Figure 10. Cellular uptake inhibition. Cells were treated with β-cyclodextrin, cytochalasin D, or cyclo RGDfV (cRGD) for 30 min prior to treatment with either free 623-Tamra (100 nM) control or RPA-623-Tamra (100 nM). After 4 h, cells were washed and lysates were analyzed using a Nanodrop fluorimeter for uptake measurements. Results (RFU) are expressed as percentages relative to RFU of control (no inhibition) and are means and standard errors of three determinations.

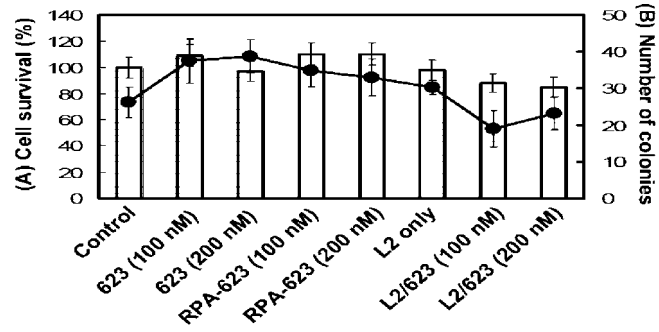

Figure 11. Toxicity studies. Cells were treated with free 623, 623 complexed with Lipofectamine 2000 (1.5 ug/ml) (L2/623), or RPA-623 under the same conditions as used for luciferase induction experiments. After 48 h, cells were trypsinized and viable cells were counted for short-term studies (A, shown as bars). Alternatively cells were replated in 6 well plates containing a mixture of 1% low gelling temperature agarose and complete DMEM medium with 10% FBS for long-term toxicity studies (B, shown as circles and a line). After 14 days, surviving colonies larger than 25 cells were counted. Survival is expressed as colonies per 100 cells plated.

fashion and was initially delivered to smooth-walled endosomes rich in lipid rafts and then trafficked to additional endomembrane compartments. Thus, the initial path of entry of the RGD conjugates seems similar to that of integrins themselves, which utilize smooth-walled vesicles, including caveolae, for internalization (*31*, *32*). Eventually, 623 oligonucleotide was delivered to the nucleus where it exerted a strong effect in terms of correcting splicing of the aberrant luciferase reporter gene. This effect was attained when the conjugate was used at oligonucleotide concentrations in the 25−200 nM range.

It is interesting to note that the degree of nuclear delivery and the subsequent effect on luciferase were very similar using the RPA conjugate and utilizing a Lipofectamine 2000 complex. However, given the long history of therapeutic use of albumin and of various PEGylated proteins (*33*), it seems likely that delivery using the albumin conjugates will be far less toxic *in vivo* than delivery obtained with cationic lipid complexes (*34*). It will also be of interest to see if the current albumin carrier technology can be adapted to the delivery of duplex siRNAs, as well as single-stranded antisense compounds.

The RPA-623 complex is polydisperse with an average hydrodynamic radius of about 6 nm. This is substantially smaller than the size of most nanoparticles currently being used to carry therapeutic agents (*35*); however, it is large by molecular standards. Thus, egress of the RPA-623 conjugates from the bloodstream in many normal tissues will be limited to some degree. It seems likely that RPA-623 will be able to exit capillaries via the so-called "large pore" system that allows egress of proteins as large as pentavalent IgM, but will have restricted access to the more abundant small pore system that largely excludes molecules >4.5 nm (*18*). In some tumors, as well as inflamed tissues, gaps in the endothelium allow egress of larger molecules, possible including the RPA conjugates (*36*). In contrast, an unconjugated oligonucleotide (5−15 000 da) is likely to have a much broader tissue distribution. In the current case, it may be possible to devise PEG-albumin-oligonucleotide conjugates that utilize smaller or fewer PEG molecules, thus reducing hydrodynamic radius and allowing more extensive

tissue distribution; this issue remains to be explored. In any case, further development of this intermediated-sized delivery system for oligonucleotides will entail substantial *in vivo* experimentation. Here, we have simply explored the basic aspects of the system at the cellular level.

ACKNOWLEDGMENT

This work was supported by NIH grant P01GM059299 to R.L.J. We thank Betsy Clarke for expert editorial assistance. Authors also thank Dr. Ashutosh Tripathy of the UNC Macromolecular Interactions Core Facility for his helpful advice on light scattering experiments.

LITERATURE CITED

(1) Chan, J. H., Lim, S., and Wong, W. S. (2006) Antisense oligonucleotides: from design to therapeutic application. *Clin. Exp. Pharmacol. Physiol. 33*, 533–40.

(2) de Fougerolles, A., Vornlocher, H. P., Maraganore, J., and Lieberman, J. (2007) Interfering with disease: a progress report on siRNA-based therapeutics. *Nat. Rev. Drug Discovery 6*, 443–53.

(3) Crooke, S. T. (2004) Progress in antisense technology. *Annu. Rev. Med. 55*, 61–95.

(4) Kim, D. H., and Rossi, J. J. (2007) Strategies for silencing human disease using RNA interference. *Nat. Rev. Genet. 8*, 173–84.

(5) Mescalchin, A., Detzer, A., Wecke, M., Overhoff, M., Wunsche, W., and Sczakiel, G. (2007) Cellular uptake and intracellular release are major obstacles to the therapeutic application of siRNA: novel options by phosphorothioate-stimulated delivery. *Exp. Opin. Biol. Ther. 7*, 1531–8.

(6) Russ, V., and Wagner, E. (2007) Cell and tissue targeting of nucleic acids for cancer gene therapy. *Pharm. Res. 24*, 1047–57.

(7) Derfus, A. M., Chen, A. A., Min, D. H., Ruoslahti, E., and Bhatia, S. N. (2007) Targeted quantum dot conjugates for siRNA delivery. *Bioconjugate Chem. 18*, 1391–6.

(8) Fattal, E., Couvreur, P., and Dubernet, C. (2004) "Smart" delivery of antisense oligonucleotides by anionic pH-sensitive liposomes. *Adv. Drug Delivery Rev. 56*, 931–46.

(9) Gilmore, I. R., Fox, S. P., Hollins, A. J., and Akhtar, S. (2006) Delivery strategies for siRNA-mediated gene silencing. *Curr. Drug Delivery 3*, 147–5.

(10) Li, W., and Szoka, F. C., Jr. (2007) Lipid-based nanoparticles for nucleic acid delivery. *Pharm. Res. 24*, 438–49.

(11) Sanguino, A., Lopez-Berestein, G., and Sood, A. K. (2008) Strategies for in vivo siRNA delivery in cancer. *Mini Rev. Med. Chem. 8*, 248–55.

(12) Vinogradov, S. V., Batrakova, E. V., and Kabanov, A. V. (2004) Nanogels for oligonucleotide delivery to the brain. *Bioconjugate Chem. 15*, 50–60.

(13) Abes, S., Moulton, H., Turner, J., Clair, P., Richard, J. P., Iversen, P., Gait, M. J., and Lebleu, B. (2007) Peptide-based delivery of nucleic acids: design, mechanism of uptake and applications to splice-correcting oligonucleotides. *Biochem. Soc. Trans. 35*, 53–5.

(14) Juliano, R. L. (2005) Peptide-oligonucleotide conjugates for the delivery of antisense and siRNA. *Curr. Opin. Mol. Ther. 7*, 132–6.

(15) Alam, M. R., Dixit, V., Kang, H., Li, Z. B., Chen, X., Trejo, J., Fisher, M., and Juliano, R. L. (2008) Intracellular delivery of an anionic antisense oligonucleotide via receptor-mediated endocytosis. *Nucleic Acids Res. 36*, 2764–76.

(16) Cesarone, G., Edupuganti, O. P., Chen, C. P., and Wickstrom, E. (2007) Insulin receptor substrate 1 knockdown in human MCF7 ER+ breast cancer cells by nuclease-resistant IRS1 siRNA conjugated to a disulfide-bridged D-peptide analogue of insulin-like growth factor 1. *Bioconjugate Chem. 18*, 1831–40.

(17) Jain, R. K. (1999) Transport of molecules, particles, and cells in solid tumors. *Annu. Rev. Biomed. Eng. 1*, 241–63.

(18) Rippe, B., Rosengren, B. I., Carlsson, O., and Venturoli, D. (2002) Transendothelial transport: the vesicle controversy. *J. Vasc. Res. 39*, 375–90.

(19) Scherphof, G. L. (1991) In vivo behavior of liposomes; interaction with the mononuclear phagocyte system and implications for drug targeting, In *Targeted Drug Delivery* (Juliano, R. L. Ed.), Springer Verlag, Berlin.

(20) Aderem, A., and Underhill, D. M. (1999) Mechanisms of phagocytosis in macrophages. *Annu. Rev. Immunol. 17*, 593–623.

(21) van Vlerken, L. E., Vyas, T. K., and Amiji, M. M. (2007) Poly(ethylene glycol)-modified nanocarriers for tumor-targeted and intracellular delivery. *Pharm. Res. 24*, 1405–14.

(22) Agrawal, S., and Zhang, R. (1997) Pharmacokinetics of oligonucleotides. *Ciba Found Symp. 209*, 60–75, discussion 75−8.

(23) Cossum, P. A., Sasmor, H., Dellinger, D., Truong, L., Cummins, L., Owens, S. R., Markham, P. M., Shea, J. P., and Crooke, S. (1993) Disposition of the 14C-labeled phosphorothioate oligonucleotide ISIS 2105 after intravenous administration to rats. *J. Pharmacol. Exp. Ther. 267*, 1181–90.

(24) DeLong, R. K., Nolting, A., Fisher, M., Chen, Q., Wickstrom, E., Kligshteyn, M., Demirdji, S., Caruthers, M., and Juliano, R. L. (1997) Comparative pharmacokinetics, tissue distribution, and tumor accumulation of phosphorothioate, phosphorodithioate, and methylphosphonate oligonucleotides in nude mice. *Antisense Nucleic Acid Drug Dev. 7*, 71–7.

(25) Amantana, A., Moulton, H. M., Cate, M. L., Reddy, M. T., Whitehead, T., Hassinger, J. N., Youngblood, D. S., and Iversen, P. L. (2007) Pharmacokinetics, biodistribution, stability and toxicity of a cell-penetrating peptide-morpholino oligomer conjugate. *Bioconjugate Chem. 18*, 1325–31.

(26) Stupack, D. G., and Cheresh, D. A. (2004) Integrins and angiogenesis. *Curr. Top. Dev. Biol. 64*, 207–38.

(27) Sazani, P., and Kole, R. (2003) Therapeutic potential of antisense oligonucleotides as modulators of alternative splicing. *J. Clin. Invest. 112*, 481–6.

(28) Di Stefano, G., Fiume, L., Baglioni, M., Busi, C., Bolondi, L., Farina, C., Mori, F., Chieco, P., Pariali, M., Kratz, F., Molin, L., Salmaso, S., and Caliceti, P. (2008) Doxorubicin coupled to lactosaminated albumin: effect of heterogeneity in drug load on conjugate disposition and hepatocellular carcinoma uptake in rats. *Eur. J. Pharm. Sci. 33*, 191–8.

(29) Temming, K., Meyer, D. L., Zabinski, R., Senter, P. D., Poelstra, K., Molema, G., and Kok, R. J. (2007) Improved efficacy of $\alpha v\beta 3$-targeted albumin conjugates by conjugation of a novel auristatin derivative. *Mol. Pharm. 4*, 686–94.

(30) Kirkham, M., and Parton, R. G. (2005) Clathrin-independent endocytosis: new insights into caveolae and non-caveolar lipid raft carriers. *Biochim. Biophys. Acta 1745*, 273–86.

(31) Caswell, P. T., and Norman, J. C. (2006) Integrin trafficking and the control of cell migration. *Traffic 7*, 14–21.

(32) White, D. P., Caswell, P. T., and Norman, J. C. (2007) $\alpha v\beta 3$ and $\alpha 5\beta 1$ integrin recycling pathways dictate downstream Rho kinase signaling to regulate persistent cell migration. *J. Cell Biol. 177*, 515–25.

(33) Ryan, S. M., Mantovani, G., Wang, X., Haddleton, D. M., and Brayden, D. J. (2008) Advances in PEGylation of important biotech molecules: delivery aspects. *Expert Opin. Drug Delivery 5*, 371–83.

(34) Lv, H., Zhang, S., Wang, B., Cui, S., and Yan, J. (2006) Toxicity of cationic lipids and cationic polymers in gene delivery. *J. Controlled Release 114*, 100–9.

(35) Juliano, R. L. (2007) Biological Barriers to Nanocarrier-Mediated Delivery of Therapeutic and Imaging Agents, In *Nanobiotechnology II* (Mirkin, C., and Niemeyer, C. Eds.) pp 263−278, Wiley-VCH, Weinheim, Germany.

(36) Greish, K. (2007) Enhanced permeability and retention of macromolecular drugs in solid tumors: a royal gate for targeted anticancer nanomedicines. *J. Drug Targeting 15*, 457–64.

BC800270W

Quantum Dots Bearing Lectin-Functionalized Nanoparticles as a Platform for *In Vivo* Brain Imaging

Xiaoling Gao,[†,‡] Jun Chen,[†] Jiyao Chen,[§] Bingxian Wu,[†] Hongzhuan Chen,*[,‡] and Xinguo Jiang*[,†]

Department of Pharmaceutics, School of Pharmacy, Fudan University, P.O. Box 130, 138 Yixueyuan Road, Shanghai 200032, P.R. China, Department of Pharmacology, Institute of Medical Sciences, Shanghai Jiaotong University School of Medicine, 280 South Chongqing Road, Shanghai 200025, P.R. China, and Surface Physics Laboratory (National Key Laboratory), Physics Department, Fudan University, Shanghai 200433, P.R. China. Received July 1, 2008; Revised Manuscript Received September 16, 2008

Delivery of imaging agents to the brain is highly important for the diagnosis and treatment of central nervous system (CNS) diseases, as well as the elucidation of their pathophysiology. Quantum dots (QDs) provide a novel probe with unique physical, chemical, and optical properties, and become a promising tool for *in vivo* molecular and cellular imaging. However, their poor stability and low blood−brain barrier permeability severely limit their ability to enter into and act on their target sites in the CNS following parenteral administration. Here, we developed a QDs-based imaging platform for brain imaging by incorporating QDs into the core of poly(ethylene glycol)−poly(lactic acid) nanoparticles, which was then functionalized with wheat germ agglutinin and delivered into the brain via nasal application. The resulting nanoparticles, with high payload capacity, are water-soluble, stable, and showed excellent and safe brain targeting and imaging properties. With PEG functional terminal groups available on the nanoparticles surface, this nanoprobe allows for conjugation of various biological ligands, holding considerable potential for the development of specific imaging agents for various CNS diseases.

INTRODUCTION

Delivery of imaging agents to the brain is highly important for the diagnosis and treatment of central nervous system (CNS) diseases (*1*−*3*), which also offers the opportunity to examine the structural, functional, and biochemical changes in the brain that will lead to new insights regarding the pathophysiology of these disorders. However, brain delivery of agents is often restricted by the blood−brain barrier (BBB), which is formed by tight junctions within the capillary endothelium, preserving brain homeostasis as well as preventing active agents against doing their jobs in the brain (*4*).

Quantum dots (QDs), semiconductor nanocrystals with unique physical, chemical, and optical properties, are now emerging as a revolutionary means for imaging and optical detection (*5*−*7*) and achieving more and more attention in neuroscience (*8*, *9*). Functionalized QDs obtained by attaching to ligands such as antibodies (*10*), peptides (*11*), and carbohydrates (*12*) have been used for *in vivo* molecular and cellular imaging. TAT-conjugated quantum dots have been described for brain imaging following intra-arterial administration (*13*). A recent report suggested that transferrin-conjugated quantum rods as probes were efficient for transmigration across an *in vitro* BBB (*14*). However, the major drawbacks of these previous QDs-based imaging techniques are their poor stability in aqueous media and in the biological systems (*15*−*17*). Encapsulations of QDs with amphiphilic copolymers (*10*) and phospholipids (*18*) have been previously presented to increase the solubility and stability of QDs but limited by their low payload capacity and lack of brain delivery ability. In general, the poor stability and lack of BBB permeability severely limit the ability of QDs to enter into and act on the target sites in the CNS following parenteral administration.

Previous studies in our laboratory and others have demonstrated that intranasal administration offers a practical, noninvasive, alternative route for drug delivery to the brain (*19*−*21*). Our recent work suggested that it is possible to deliver agents carried by certain lectin-functionalized nanoparticles into the brain via intranasal administration (*22*−*24*). Continuing these efforts, here we developed a quantum dots-based nanoplatform for brain imaging by encapsulating QDs into the core of poly(ethylene glycol)−poly(lactic acid) (PEG-PLA) nanoparticles and conjugating the nanoparticles with wheat germ agglutinin (WGA) to improve their brain delivery. This innovative approach raises new possibilities for the development of QDs-based specific imaging agents for various CNS diseases. To address the feasibility of this nanoplatform, we evaluate the particle size, zeta potential, internal structure, biobinding activity, and stability under *in vitro* settings, as well as biodistribution, brain delivery, and imaging property of the resulting nanoparticles in animals following intranasal administration.

EXPERIMENTAL PROCEDURES

Preparation of WGA-Functionalized Quantum Dots-Loaded Nanoparticles (WGA-QDs-NP). WGA-QDs-NP were prepared by incorporating tri-*n*-octylphosphine oxide-coated CdSe/ZnS QDs (TOPO-QDs) into PEG-PLA nanoparticles followed by conjugating the resulting nanoparticles with Traut's reagent-thiolated WGA via maleimide groups at the ends of the PEG spacers (Scheme 1). TOPO-QDs, high-quality, hydrophobic QDs (size: 7.2 nm, emission wavelength: 607 nm), were synthesized as described previously (*25*) and kindly provided by Dr. Yang Yue (National Laboratory for Infrared Physics, Shanghai Institute of Technical Physics, Chinese Academy of Sciences). Methoxy-PEG-PLA and maleimide-PEG-PLA were synthesized by ring-opening polymerization of D,L-lactide (99.5% pure, PURAC) initiated by methyl-PEG and maleimide-

* Corresponding authors. Prof. Xinguo Jiang, Tel.: 086-021-54237381, Fax: 086-021-54237381, E-mail: xgjiang@shmu.edu.cn, and Prof. Hongzhuan Chen, Tel.: 086-021-63846590-776451. Fax: 086-021-64674721. E-mail: yaoli@shsmu.edu.cn.

[†] School of Pharmacy, Fudan University.

[‡] Shanghai Jiaotong University School of Medicine.

[§] Physics Department, Fudan University.

10.1021/bc8002698 CCC: $40.75 © 2008 American Chemical Society
Published on Web 10/16/2008

Scheme 1. Preparation of Lectin-Functionalized Quantum Dots-Loaded Nanoparticles 80 × 99 mm² (600 × 600 DPI)

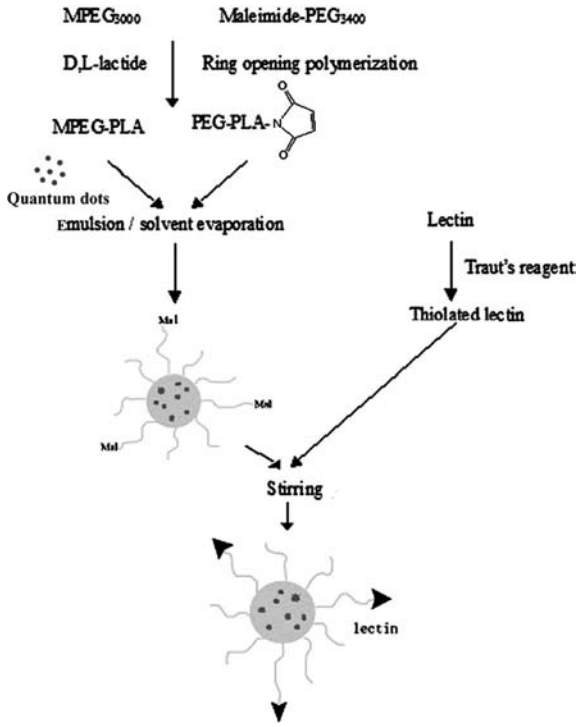

PEG, respectively, using stannous octoate as catalyst (*26*). QDs-loaded PEG-PLA nanoparticles were prepared with a blend of maleimide-PEG_{3400}-PLA_{54000} and methyl-PEG_{3000}-PLA_{49000} using an emulsion/solvent evaporation technique. Briefly, 1 mg maleimide-PEG-PLA and 9 mg methyl-PEG-PLA were dissolved in 0.5 mL of dichloromethane containing 3.2×10^{-5} mol/L QDs. The solution was then emulsified by sonication (220 w, 30 s) on ice in 2 mL of a 1% aqueous sodium cholate solution. The emulsion obtained was diluted into 8 mL of a 0.5% aqueous sodium cholate solution under moderate magnetic stirring. Five minutes later, dichloromethane was evaporated at low pressure at 30 °C using Büchi rotavapor R-200 (Büchi, Germany). Then, the nanoparticles were centrifuged at 21 000 *g* for 45 min using TJ-25 centrifuge (Beckman Counter, USA) equipped with an A-14 rotor. The supernatant was discarded, and the obtained nanoparticles were subjected to a 1.5 × 20 cm sepharose CL-4B column and eluted with 0.05 M HEPES buffer (pH 7.0) containing 0.15 M NaCl to remove the QDs un-entrapped or absorbed to the exterior of the nanoparticles. Then, the QDs-loaded nanoparticles were incubated with 2-iminothiolane-thiolated WGA at the ratio of thiolated lectin to maleimide 1:3 for 9 h for WGA conjugation. After that, the resulting WGA-QDs-NP were purified with a 1.5 × 20 cm Sepharose CL-4B column.

Morphology, Particle Size, and Zeta Potential of WGA-QDs-NP. Morphological examination of the nanoparticles was performed by transmission electron microscopy following negative staining with sodium phosphotungstate solution. The mean diameter and zeta potential of the nanoparticles were determined by dynamic light scattering analysis using Zeta Potential/Particle Sizer NICOMPTM 380 ZLS, respectively.

Internal Structure and Payload Capacity of WGA-QDs-NP. In order to determine the internal structure of WGA-QDs-NP, the nanoparticles were diluted to appropriate concentration and observed under a freeze−fracture electron microscope (JEOL 2010, JEOL, Japan) as described below. First, the samples were suspended in a microperforated grid under controlled temperature (25 °C) and humidity conditions (95−99%) and blotted gently to form a 100−250 nm thick liquid film with a filter paper. The liquid film was then immediately plunged into liquid ethane at its freezing point (−183 °C), producing a vitrified specimen, and kept under liquid nitrogen until loaded onto a cryogenic sample holder. Vitrified samples were observed under the freeze−fracture electron microscope at 200 kV using a magnification of 40 000. Images were recorded using a Gatan 832 multiscan CCD camera.

Haemagglutination Test. The retention of the bioactivity of WGA following covalent coupling to the surface of nanoparticles was confirmed by a haemagglutination test. Unmodified QDs-loaded NP and WGA-QDs-NP were incubated with 20% (v/v) suspension of fresh rat blood in 0.9% NaCl at 37 °C for 30 min, respectively. After that, the mixtures were observed under a fluorescence microscope (Olympus IX71), and the images were taken and colored with Image-Pro Plus.

Stability of WGA-QDs-NP in Aqueous Solution and in Serum. WGA-QDs-NP were prepared as 5 mg/mL solution in water and stored at 4 °C for one week and in serum for 24 h, respectively. After that, the solutions were diluted to appropriate concentration with the morphology and internal structure of the nanoparticles observed under freeze−fracture electron microscopy as described above.

Optical Properties of WGA-QDs-NP. The optical properties of WGA-QDs-NP were characterized by a luminescence spectrometer and compared with those of QDs at the excitation wavelength of 400 nm and emission wavelength between 550 and 650 nm. The excitation slit was 10.0 nm, E_m slit 2.5 nm, scan speed 30 nm/min, and the scan times 10 with a delay of 120 s.

Biodistribution of WGA-QDs-NP Following Intranasal Administration. Biodistribution of WGA-QDs-NP following intranasal administration in BALB/c nude mice was investigated by a NightOWL II LB983 NC320 *in vivo* optical imaging system (Berthold Technologies, Oak Ridge, TN) consisting of a highly sensitive Peltier cooled backlit CCD camera (2184 × 1472 pixels). The animal experiments were performed according to the protocols evaluated and approved by the ethical committee of Fudan University. First, nude mice (25−30 g) were anesthetized with sodium pentobarbital (50 mg/kg, i.p.) and imaged for the signal of autofluorescence. After that, the animals were given intranasally with WGA-QDs-NP at the dose of about 40 mg/kg (QDs 3.2×10^{-8} mol/kg) in 10 μL (5 μL each nostril) and imaged at 2 min and 1, 2, 3, 4, and 8 h postadministration, respectively ($n = 6$ for the time points of 2 min and 1, 2, and 3 h; $n = 3$ for the time points of 4 and 8 h). For imaging, mice were placed in the light-tight chamber, the filters for excitation and emission were set at 530 and 600 nm, respectively, and the photon emission was integrated over a period of 5 s. After that, a gray scale reference image was collected under white light. For localization of the photon emission, gray scale and pseudocolor images were merged using *WinLight* (*32*) software. From the luminescent images, regions of interest (ROIs) were drawn, and the peak and integrated bioluminescence flux (photons/s) were calculated utilizing the software.

To determine the biodistribution of WGA-QDs-NP in various organs, three hours following administration, three mice were euthanized and fixed by heart perfusion with their brains, hearts, livers, spleens, lungs, and kidneys collected for imaging under the NightOWL II LB 983 imaging system. After that, the brain tissues were immersed in 4% paraformaldehyde for 24 h, dehydrated in sucrose solution, embedded in Tissue-Tek O.C.T compound (Sakura Finetek, USA) and stored at −70 °C until frozen sectioning. Finally, the sections were transferred to microscope slides, counterstained with 4′,6-diamidino-2-phenylindole (DAPI), and observed under a fluorescence micro-

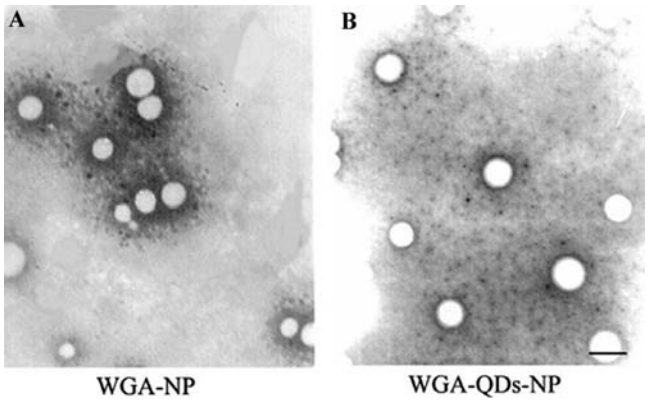

Figure 1. Transmission electron micrograph of (A) quantum dots-free WGA-conjugated nanoparticles (WGA-NP) and (B) WGA-conjugated quantum dots-loaded nanoparticles (WGA-QDs-NP) negatively stained with phosphotungstic acid solution, respectively. Bar, 100 nm. 80 × 48 mm (600 × 600 DPI).

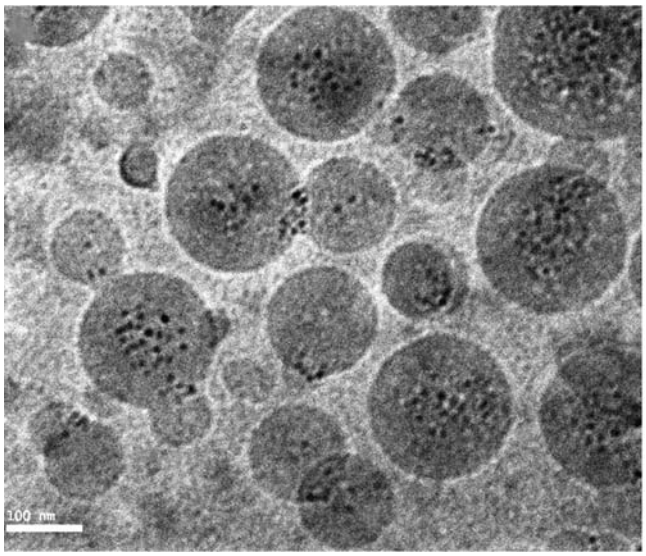

Figure 2. Internal structure of WGA-conjugated quantum dots-loaded nanoparticles (WGA-QDs-NP) exhibited by freeze−fracture electron microscopy. Bar, 100 nm. 80 × 68 mm (600 × 600 DPI).

scope (Olympus IX71) to determine the distribution of WGA-QDs-NP in the CNS.

RESULTS

Characterization of WGA-QDs-NP. The resulting nanoparticles exhibited a spherical shape under the examination of a transmission electron microscope (Figure 1B) with a number-based average diameter (95.3 ± 41.0 nm) comparable to that of the QDs-free WGA-functionalized nanoparticles (Figure 1A, 92.0 ± 33.7 nm). The zeta potential of WGA-QDs-NP was −22.67 ± 1.21 mV, which was also similar to that of QDs-free WGA-functionalized nanoparticles (−18.9 ± 2.4 mV). We examined the internal structure of WGA-QDs-NP with freeze−fracture electron microscopy, finding out that numerous QDs were encapsulated into each nanoparticle and most of them located at the center of the particles (Figure 2). We believe this phenomenon is mainly resulted from the strong hydrophobic interaction between TOPO and PLA fragment of the polymer, which composes the core of the resulting PEG-PLA nanoparticles (*27*).

The retention of WGA's bioactivity following covalent coupling to the surface of the QDs-loaded nanoparticles was confirmed by haemagglutination test. It was exhibited that the erythrocytes agglutinated following their incubation with WGA-QDs-NP and all the red fluorescence of QDs specifically stuck to the surface of the erythrocytes (Figure 3A). But in the case of the unmodified QDs-loaded nanoparticles, the fluorescent signals dispersed at random and did not show any specific affinity to erythrocytes (Figure 3B). This evidence clearly suggested that WGA, treated through the covalent coupling procedure, still retained the carbohydrate binding bioactivity and the incorporation of QDs into the nanoparticles did not alter the biobinding activity of the lectin-functionalized nanoparticles.

Stability of WGA-QDs-NP in aqueous solution and in serum was evaluated under freeze−fracture electron microscopy, respectively. The photos showed that WGA-QDs-NP dispersed well in water without significant changes in particle size even after one week storage (Figure 4A). Furthermore, they retained their structures and loadings after 24 h incubation in serum (Figure 4B). Such telling results strongly suggested the excellent solubility and stability of the present nanoplatform, indicating its potential to serve as a probe for imaging in the biological systems.

Optical properties of WGA-QDs-NP were characterized by a luminescence spectrometer and compared with those of QDs. The spectral curves of QDs reduced in intensity with increased light exposure, while those of WGA-QDs-NP showed a slightly blue shift but remained unchanged under the same scan condition (Figure 5), suggesting that the incorporation of QDs in the core of PEG-PLA nanoparticles also significantly improved their photostability.

Biodistribution of WGA-QDs-NP Following Intranasal Administration. Biodistribution of WGA-QDs-NP following intranasal administration was investigated in BALB/c nude mice by a dedicated imaging system. It was shown that, under the present imaging settings, autofluorescence of nude mice is negligible (Figure 6A, the first photo named "Blank") and fluorescent signals of WGA-QDs-NP in brain increased with exposure time, reaching peak at 3−4 h following administration, but almost disappeared at 8 h (Figure 6A,B). We also found that, 8 h following administration, certain amounts of fluorescent signals were detected near the urethra (photo taken when the animal was in supine position; Figure 6A, the last photo). Therefore, we deduced that at least part of WGA-QDs-NP were eliminated by filtration and excretion through the kidney.

To better understand the distribution of WGA-QDs-NP in different areas of the brain, 3 h following administration, three mice were euthanized with their brain collected, frozen-sectioned, and observed under a fluorescence microscope following nuclear staining with DAPI. It was shown that, 3 h after intranasal administration, fluorescence signals of WGA-QDs-NP were detected in the olfactory bulb, olfactory tract, cortex, caudate-putamen, hippocampus, third ventricle, dorsal third ventricle, and lateral ventricle (Figure 7), suggesting that the imaging agents distributed quickly and extensively into the CNS.

In addition, we found that the imaging agents described herein presented excellent brain targeting property following intranasal administration. Three hours following the administration, three mice were euthanized and fixed by heart perfusion with their brains, hearts, livers, spleens, lungs, and kidneys collected for imaging. The data showed that the relative average fluorescent intensities of WGA-QDs-NP in the tissues at this time point followed the order of brain ≥ lung > liver > kidney > heart > spleen (Figure 8A,B). These results clearly suggested the efficient brain targeting property of the present nanoplatform, which is very important for its safe and efficient *in vivo* imaging.

DISCUSSION

In the present study, we first developed a QDs-based imaging platform for brain imaging by incorporating QDs into the core

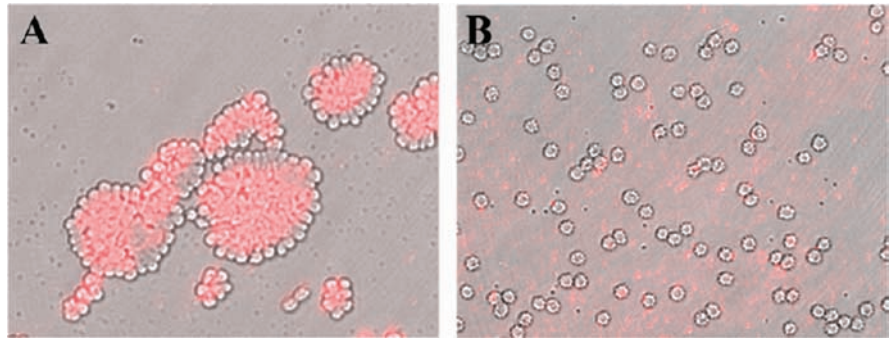

Figure 3. Interactions between erythrocytes and (A) WGA-conjugated quantum dots-loaded nanoparticles (WGA-QDs-NP) or (B) unmodified quantum dots-loaded nanoparticles (QDs-NP): erythrocytes suspension (4%, 200 mL) incubated with WGA-QDs-NP (10 mg/mL, 50 mL) and QDs-NP (10 mg/mL, 50 mL) at 37 °C for 30 min, respectively. 80 × 31 mm (300 × 300 DPI).

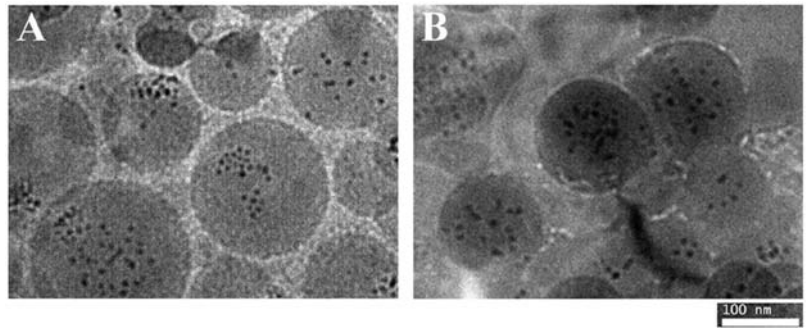

Figure 4. Freeze−fracture electron micrograph of WGA-conjugated quantum dots-loaded nanoparticles (WGA-QDs-NP) after (A) one week storage in aqueous solution and (B) 24 h incubation in serum. 80 × 33 mm (600 × 600 DPI).

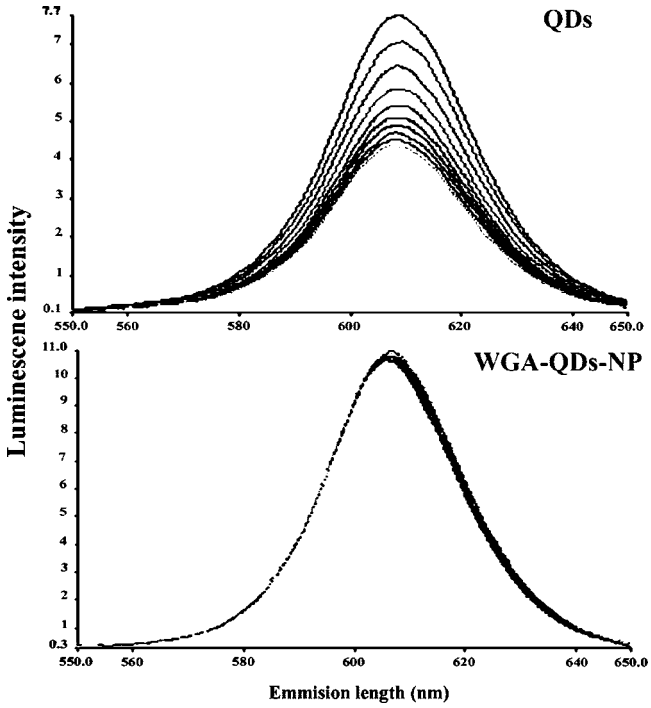

Figure 5. Luminescence emission spectra of quantum dots (QDs) (upper) and WGA-QDs-NP (lower) at the excited wavelength of 400 nm, respectively. The spectral curves of QDs reduced in intensity sequentially with the increase of light exposure, while those of WGA-QDs-NP showed a slightly blue shift but remained unchanged under the same scan condition (Ex: 400 nm, Em scan range: 550−650 nm; Ex slit: 10.0 nm; Em slit: 2.5 nm; Scan speed: 30 nm/min; Scan times: 10; Delayed: 120 s). 80 × 83 mm (600 × 600 DPI).

of PEG-PLA nanoparticles, which was then functionalized with WGA and delivered into the brain via nasal application. The resulting nanoparticles, with high payload capacity, are water-soluble, stable, and showed excellent and safe brain targeting and imaging properties. With the flexibility of having PEG functional terminal groups on the nanoparticles surface, this nanoprobe allows for conjugation of various biological ligands (e.g., sugars, peptides, proteins, and antibodies) as "smart nanoparticles" for targeting and imaging in various brain disorders.

Brain delivery properties of nanoparticles are essential for effective brain imaging *in vivo*. Our newly developed QDs-based nanoplatform showed the following advantages for *in vivo* brain imaging: First, WGA-QDs-NP stayed in the brain for more than 4 h (Figure 6), offering enough time for the recognition and binding of the imaging agents with the disorder regions in the CNS. Second, the imaging agents were almost cleared 8 h after administration (Figure 6), therefore supplying a safe technique for *in vivo* imaging. Third, the imaging agents distributed quickly and extensively into the CNS (Figure 7), which might provide a good opportunity for the recognition and binding of imaging agents with their targets. Furthermore, the excellent brain targeting property of WGA-QDs-NP following intranasal administration could thereby reduce potential toxicity to the peripheral organs (Figure 8).

The mechanism of brain delivery of WGA-QDs-NP is not clear yet. However, our previous work demonstrated that the enhancement of brain delivery of agents carried by WGA-functionalized nanoparticles was mediated by the substrates of WGA — *N*-acetyl-D-glucosamine and sialic acid, which were abundantly observed in the nasal cavity (*28*, *29*). It is well-documented that nasal mucosa was composed of the respiratory region, which had the highest degree of vascularization and was mainly responsible for drug absorption into the circulation, and olfactory mucosa, which played a vital role in the transport of drugs into the brain and cerebrospinal fluid (*30*). WGA, specifically binding to *N*-acetyl-D-glucosamine and sialic acid, presented a great affinity to the olfactory epithelium while a

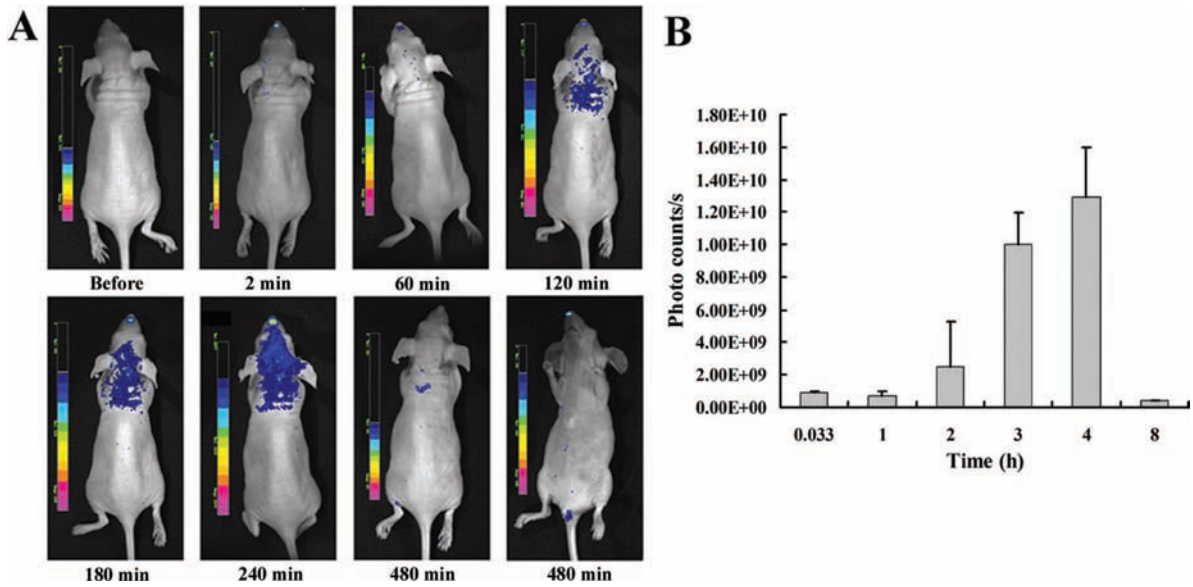

Figure 6. Distribution and retention of WGA-conjugated quantum dots-loaded nanoparticles (WGA-QDs-NP) in the brain following intranasal administration. (A) Representative optical images taken before, 2 min, and 1, 2, 3, 4, and 8 h after dose under a dedicated imaging system designed for small animals imaging. (B) Quantification of the luminescence signal from WGA-QDs-NP in the brain over time following intranasal administration ($n = 6$ for the time points of 2 min and 1, 2, 3 h; $n = 3$ for the time points of 4 and 8 h). 176 × 85 mm (300 × 300 DPI).

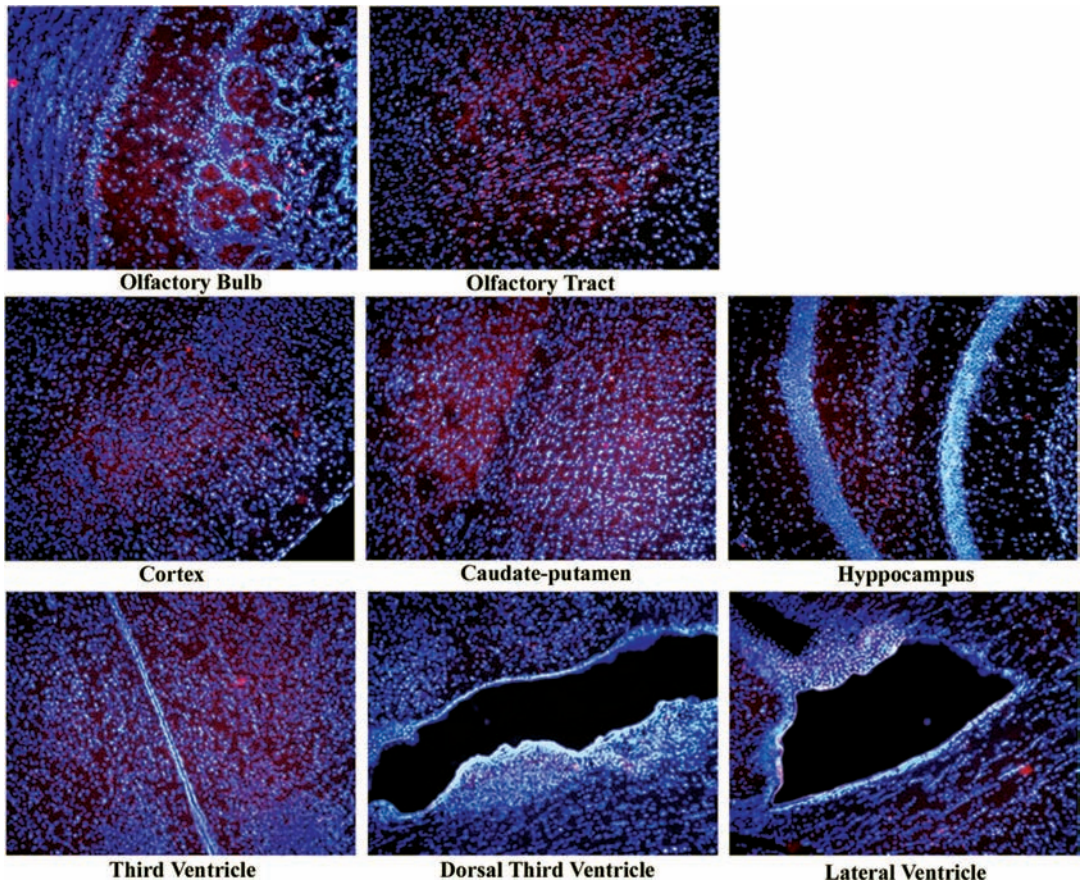

Figure 7. Distribution of WGA-conjugated quantum dots-loaded nanoparticles (WGA-QDs-NP, red) in the olfactory bulb, olfactory tract, cortex, caudate-putamen, hippocampus, third ventricle, dorsal third ventricle, and lateral ventricle of nude mice 3 h after intranasal application. 176 × 145 mm (300 × 300 DPI).

moderate degree to the respiratory epithelium (*29*, *31*). Accordingly, our previous data also showed that the affinity of WGA-NP to the olfactory mucosa was higher than that to the respiratory one (*24*). It has been well-presented that, following an intranasal administration to rats, wheat germ agglutinin−horseradish peroxidase (WGA-HRP) concentrated in the olfactory bulb, while a negligible amount of label was detected in the same location after intravenous administration of WGA-HRP or intranasal administration of unconjugated HRP (*32*). Therefore, we deduced that at least part of WGA-NP enter the brain via olfactory mucosa. If this is true, it would become much easier to understand why WGA-QDs-NP achieved such good

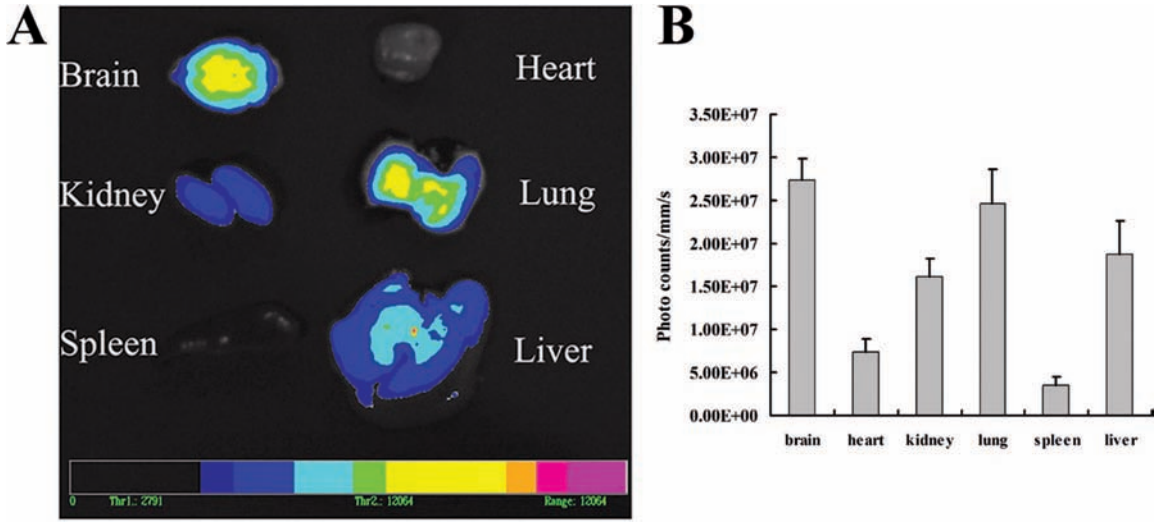

Figure 8. Distribution of WGA-conjugated quantum dots-loaded nanoparticles (WGA-QDs-NP) in various organs following intranasal administration in nude mice. (A) Representative optical image taken 3 h after dosing under a dedicated imaging system designed for small animal imaging. (B) Quantification of the luminescence signal from WGA-QDs-NP in various organs 3 h following intranasal application ($n = 3$). 176 × 81 mm (300 × 300 DPI).

brain targeting property. Previous research also strongly suggested that WGA-HRP can pass BBB following intravenous administration by absorptive-mediated mechanism (*33*). So, it is also possible WGA-NP achieve brain delivery via the systemic pathway.

The safety of QDs is now one of the major concerns for *in vivo* QDs-based imaging techniques. A recent paper suggested that cytotoxicity of QDs, which is mainly induced by the release of Cd^{2+} ions into the cellular environment, was greatly reduced by coating the bare QDs with polymers (*34*). In the present paper, QDs were entrapped into the core of nanoparticle and did not show any leakage after 24 h incubation in serum (Figure 4B). Therefore, the toxicity of QDs was considered to be low. The coating polymer PEG-PLA is a well-developed copolymer, and its safety has been well-acknowledged (*35*). In addition, the amount of WGA in the systemic circulation is far less than that required for the development of blood clots (*36*). Therefore, the application of WGA-QDs-NP is believed to be safe. Actually, no obvious side effects were observed in our experiments (data not shown). However, since the safety of the probe is now one of the major concerns for *in vivo* imaging, the long-term side effects of WGA-QDs-NP still need to be considered very carefully and deserve further research before their further application.

The emerging nanostructure QDs offer numerous potential applications in bioimaging *in vitro* and *in vivo*. However, conventional QDs-based imaging often encounters their poor stability in aqueous solution and in the biological systems, which was mainly caused by photocatalytic destruction of the mercaptoacetic acid coating and precipitation of the nanocrystals (*15*−*17*). Here, the use of TOPO-QDs encapsulation into PEG-PLA nanoparticles enables their potential application in imaging *in vivo*. Our data clearly suggested that QDs were encapsulated into the core of PEG-PLA nanoparticles with high loading efficiency (Figure 2) without changing the morphology, size, zeta potential, or biobinding activity of the lectin-functionalized nanoparticles (Figure 1, Figure 3). We believe that this phenomenon is mainly contributed by the strong hydrophobic interaction between TOPO and PLA fragment of the polymer, which composed the core of the resulting PEG-PLA nanoparticles (*27*). In the course of primary emulsification, TOPO-QDs coating with PLA remained inside the oil droplets while the hydrophilic group PEG migrated to the water surface. Upon solvent evaporation, the nanoparticles core solidified, forming solid nanoparticles with higher stability compared with both micelles and liposomes. The advantages of this preparation procedure were obvious. By using it, we obtained nanoparticles with high payload capacity and improved stability in both water and serum (Figure 4). In addition, the photostability of the encapsulated QDs was significantly improved compared with that of free QDs. In contrast, previous works in which QDs were encapsulated in the chloroform/ethanol solvent mixture to obtain QDs-loaded micelles had several drawbacks such as low payload (one QD per micelle) and easy aggregation (*10*).

Taking advantage of the thiolated-protein conjugating ability of maileimide group at the end of PEG, we successfully conjugated WGA to the surface of the QDs-loaded nanoparticles under mild condition without changing the biobinding ability of WGA. By incorporating PEG-PLA with other functional terminal groups such as biotin, amino (*11*), and carboxyl groups at the end of PEG, we can also further modify the nanoparticles with various biological ligands for specific molecular and cellular imaging (*17*). Therefore, WGA-QDs-NP described herein provided the following advantages to serve as a nanoplatform for bioimaging: (1) high payload capacity; (2) improved stability in aqueous solution and in biological system; (3) increased optical stability; (4) biobinding activity; and (5) flexibility of having PEG functional terminal groups available on the surface of nanoparticles, which allows conjugation of various biological ligands for specific molecular imaging. Further study is needed to fully optimize WGA-QDs-NP and to address the potential application of this nanoplatform in specific CNS disorders such as Alzheimer's disease and brain tumors.

ACKNOWLEDGMENT

The study was supported by National Key Basic Research Program (2007CB935800), National Natural Science Foundation of China (No. 30801442), and Grants from Shanghai Education Committee and Institute of Medical Sciences, Shanghai Jiaotong University School of Medicine. The authors also acknowledged Dr. Kunpeng Li and Prof. Ming Yao for their technical assistances in freeze−fracture electron microscopy and *in vivo* optical imaging, respectively.

Supporting Information Available: Distribution of WGA-QDs-NP in different areas of the brain and various organs 4 h

following intranasal administration in nude mice. This material is available free of charge via the Internet at http://pubs.acs.org.

LITERATURE CITED

(1) Kandimalla, K. K., Wengenack, T. M., Curran, G. L., Gilles, E. J., and Poduslo, J. F. (2007) Pharmacokinetics and amyloid plaque targeting ability of a novel peptide-based magnetic resonance contrast agent in wild-type and Alzheimer's disease transgenic mice. *J. Pharmacol. Exp. Ther. 322*, 541–549.

(2) Poduslo, J. F., Ramakrishnan, M., Holasek, S. S., Ramirez-Alvarado, M., Kandimalla, K. K., Gilles, E. J., Curran, G. L., and Wengenack, T. M. (2007) In vivo targeting of antibody fragments to the nervous system for Alzheimer's disease immunotherapy and molecular imaging of amyloid plaques. *J. Neurochem. 102*, 420–433.

(3) Sun, C., Veiseh, O., Gunn, J., Fang, C., Hansen, S., Lee, D., Sze, R., Ellenbogen, R. G., Olson, J., and Zhang, M. (2008) In vivo MRI detection of gliomas by chlorotoxin-conjugated superparamagnetic nanoprobes. *Small 4*, 372–379.

(4) Pardridge, W. M. (2005) The blood-brain barrier: bottleneck in brain drug development. *NeuroRx. 2*, 3–14.

(5) Bruchez, M., Jr., Moronne, M., Gin, P., Weiss, S., and Alivisatos, A. P. (1998) Semiconductor nanocrystals as fluorescent biological labels. *Science 281*, 2013–2016.

(6) Chan, W. C., Maxwell, D. J., Gao, X., Bailey, R. E., Han, M., and Nie, S. (2002) Luminescent quantum dots for multiplexed biological detection and imaging. *Curr. Opin. Biotechnol. 13*, 40–46.

(7) Michalet, X., Pinaud, F. F., Bentolila, L. A., Tsay, J. M., Doose, S., Li, J. J., Sundaresan, G., Wu, A. M., Gambhir, S. S., and Weiss, S. (2005) Quantum dots for live cells, in vivo imaging, and diagnostics. *Science 307*, 538–544.

(8) Pathak, S., Cao, E., Davidson, M. C., Jin, S., and Silva, G. A. (2006) Quantum dot applications to neuroscience: new tools for probing neurons and glia. *J. Neurosci. 26*, 1893–1895.

(9) Corbin, J. G., and Haydar, T. F. (2007) Quantum dots for neuroscience research: new tools for old problems? *Nanomed. 2*, 579–581.

(10) Gao, X., Cui, Y., Levenson, R. M., Chung, L. W., and Nie, S. (2004) In vivo cancer targeting and imaging with semiconductor quantum dots. *Nat. Biotechnol. 22*, 969–976.

(11) Cai, W., Shin, D. W., Chen, K., Gheysens, O., Cao, Q., Wang, S. X., Gambhir, S. S., and Chen, X. (2006) Peptide-labeled near-infrared quantum dots for imaging tumor vasculature in living subjects. *Nano Lett. 6*, 669–676.

(12) Babu, P., Sinha, S., and Surolia, A. (2007) Sugar-quantum dot conjugates for a selective and sensitive detection of lectins. *Bioconjugate Chem. 18*, 146–151.

(13) Santra, S., Yang, H., Stanley, J. T., Holloway, P. H., Moudgil, B. M., Walter, G., and Mericle, R. A. (2005) Rapid and effective labeling of brain tissue using TAT-conjugated CdS:Mn/ZnS quantum dots. *Chem. Commun. 25*, 3144–3146.

(14) Xu, G., Yong, K. T., Roy, I., Mahajan, S. D., Ding, H., Schwartz, S. A., and Prasad, P. N. (2008) Bioconjugated quantum rods as targeted probes for efficient transmigration across an in vitro blood-brain barrier. *Bioconjugate Chem. 19*, 1179–1185.

(15) Kloepfer, J. A., Bradforth, S. E., and Nadeau, J. L. (2005) Photophysical properties of biologically compatible CdSe quantum dot structures. *J. Phys. Chem. B. 109*, 9996–10003.

(16) Algar, W. R., and Krull, U. J. (2007) Luminescence and stability of aqueous thioalkyl acid capped CdSe/ZnS quantum dots correlated to ligand ionization. *ChemPhysChem 8*, 561–568.

(17) Susumu, K., Uyeda, H. T., Medintz, I. L., Pons, T., Delehanty, J. B., and Mattoussi, H. (2007) Enhancing the stability and biological functionalities of quantum dots via compact multifunctional ligands. *J. Am. Chem. Soc. 129*, 13987–13996.

(18) Dubertret, B., Skourides, P., Norris, D. J., Noireaux, V., Brivanlou, A. H., and Libchaber, A. (2002) In vivo imaging of quantum dots encapsulated in phospholipid micelles. *Science 298*, 1759–1762.

(19) Wang, F., Jiang, X., and Lu, W. (2003) Profiles of methotrexate in blood and CSF following intranasal and intravenous administration to rats. *Int. J. Pharm. 263*, 1–7.

(20) Zhang, Q. Z., Jiang, X. G., and Wu, C. H. (2004) Distribution of nimodipine in brain following intranasal administration in rats. *Acta Pharmacol. Sin. 25*, 522–527.

(21) Graff, C. L., and Pollack, G. M. (2005) Nasal drug administration: potential for targeted central nervous system delivery. *J. Pharm. Sci. 94*, 1187–1195.

(22) Gao, X., Tao, W., Lu, W., Zhang, Q., Zhang, Y., Jiang, X., and Fu, S. (2006) Lectin-conjugated PEG-PLA nanoparticles: preparation and brain delivery after intranasal administration. *Biomaterials 27*, 3482–3490.

(23) Gao, X., Chen, J., Tao, W., Zhu, J., Zhang, Q., Chen, H., and Jiang, X. (2007) UEA I-bearing nanoparticles for brain delivery following intranasal administration. *Int. J. Pharm. 340*, 207–215.

(24) Gao, X., Wu, B., Zhang, Q., Chen, J., Zhu, J., Zhang, W., Rong, Z., Chen, H., and Jiang, X. (2007) Brain delivery of vasoactive intestinal peptide enhanced with the nanoparticles conjugated with wheat germ agglutinin following intranasal administration. *J. Controlled Release 121*, 156–167.

(25) Yu, W. W., Qu, L., Guo, W., and Peng, X. (2003) Experimental determination of the extinction coefficient of CdTe, CdSe, and CdS nanocrystals. *Chem. Mater. 15*, 2854–2860.

(26) Zhang, Y., Zhang, Q. Z., Zha, L. S., Yang, W. L., Wang, C. C., Jiang, X. G., and Fu, S. K. (2004) Preparation, characterization and application of pyrene-loaded methoxy poly(ethylene glycol)-poly(lactic acid) copolymer nanoparticles. *Colloid Polym. Sci. 282*, 1323–1328.

(27) Gref, R., Minamitake, Y., Peracchia, M. T., Trubetskoy, V., Torchilin, V., and Langer, R. (1994) Biodegradable long-circulating polymeric nanospheres. *Science 263*, 1600–1603.

(28) Berger, G., Kogan, T., Skutelsky, E., and Ophir, D. (2005) Glycoconjugate expression in normal human inferior turbinate mucosa: a lectin histochemical study. *Am. J. Rhinol. 19*, 97–103.

(29) Takami, S., Getchell, M. L., and Getchell, T. V. (1994) Lectin histochemical localization of galactose, N-acetylgalactosamine, and N-acetylglucosamine in glycoconjugates of the rat vomeronasal organ, with comparison to the olfactory and septal mucosae. *Cell Tiss. Res. 277*, 211–230.

(30) Illum, L. (2000) Transport of drugs from the nasal cavity to the central nervous system. *Eur. J. Pharm. Sci. 11*, 1–18.

(31) Melgarejo Moreno, P., Hellín Meseguer, D., and Melgarejo Moreno, C. (1998) Olfactory epithelium of the rat. Lectin-mediated histochemical studies. *An. Otorrinolaringol. Ibero. Am. 25*, 471–480.

(32) Thorne, R. G., Emory, C. R., Ala, T. A., and Frey, W. H., II (1995) Quantitative analysis of the olfactory pathway for drug delivery to the brain. *Brain Res. 692*, 278–282.

(33) Banks, W. A., and Broadwell, R. D. (1994) Blood to brain and brain to blood passage of native horseradish peroxidase, wheat germ agglutinin, and albumin: pharmacokinetic and morphological assessments. *J. Neurochem. 62*, 2404–2419.

(34) Zhang, T., Stilwell, J. L., Gerion, D., Ding, L., Elboudwarej, O., Cooke, P. A., Gray, J. W., Alivisatos, A. P., and Chen, F. F. (2006) Cellular effect of high doses of silica-coated quantum dot profiled with high throughput gene expression analysis and high content cellomics measurements. *Nano Lett. 6*, 800–808.

(35) Plard, J., and Bazile, D. (1999) Comparison of the safety profiles of PLA50 and Me.PEG-PLA50 nanoparticles after single dose intravenous administration to rat. *Colloids Surf., B: Biointerfaces 16*, 173–183.

(36) Freyssinet, J. M., Thevenon, D., Souque, A., and Suscillon, M. (1982) Reversible inhibition of the in vitro coagulation of human plasma by lectins. *Thromb. Haemost. 48*, 120–124.

BC8002698

SUPPORTING INFORMATION

Quantum Dots-Bearing Lectin-Functionalized Nanoparticles as a Platform for *In Vivo* Brain Imaging

Xiaoling Gao, [†,‡] Jun Chen, [†] Jiyao Chen, [§] Bingxian Wu, [†] Hongzhuan Chen, *[,‡] Xinguo Jiang*[,†]

Department of Pharmaceutics, School of Pharmacy, Fudan University, P.O. Box 130, 138 Yixueyuan Road, Shanghai 200032, P.R. China, Department of Pharmacology, Institute of Medical Sciences, Shanghai Jiaotong University School of Medicine, 280 South Chongqing Road, Shanghai 200025, P.R. China, and Surface Physics Laboratory (National Key Laboratory), Physics Department, Fudan University, Shanghai 200433, P.R. China

List of contens:

Figure S1: Distribution of WGA-conjugated quantum dots-loaded nanoparticles in different areas of nude mice brain 4 h after intranasal application.

Figure S2: Distribution of WGA-conjugated quantum dots-loaded nanoparticles in various organs of nude mice 4 h following intranasal administration.

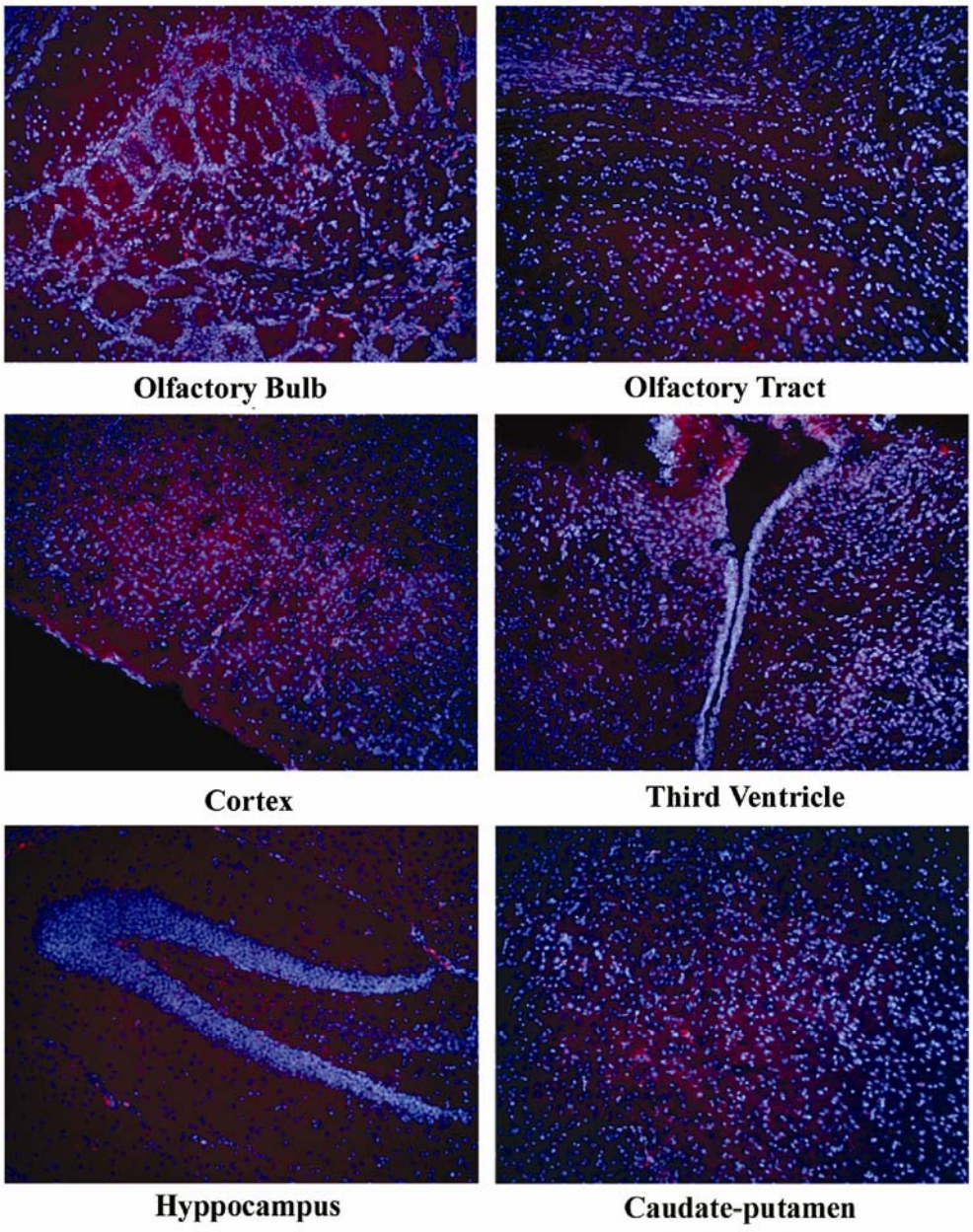

Figure S1: Distribution of WGA-conjugated quantum dots-loaded nanoparticles in olfactory bulb, olfactory tract, cortex, caudate-putamen, hippocampus and third ventricle of nude mice 4 h after intranasal application. The animals were anesthetized and given intranasally with WGA-QDs-NP at the dose of about 40 mg/kg (QDs 3.2×10^{-8} mol/kg). Four hours following administration, the mice were euthanized and fixed by heart perfusion with their brains collected for section, stain and observation under a fluorescence microscope.

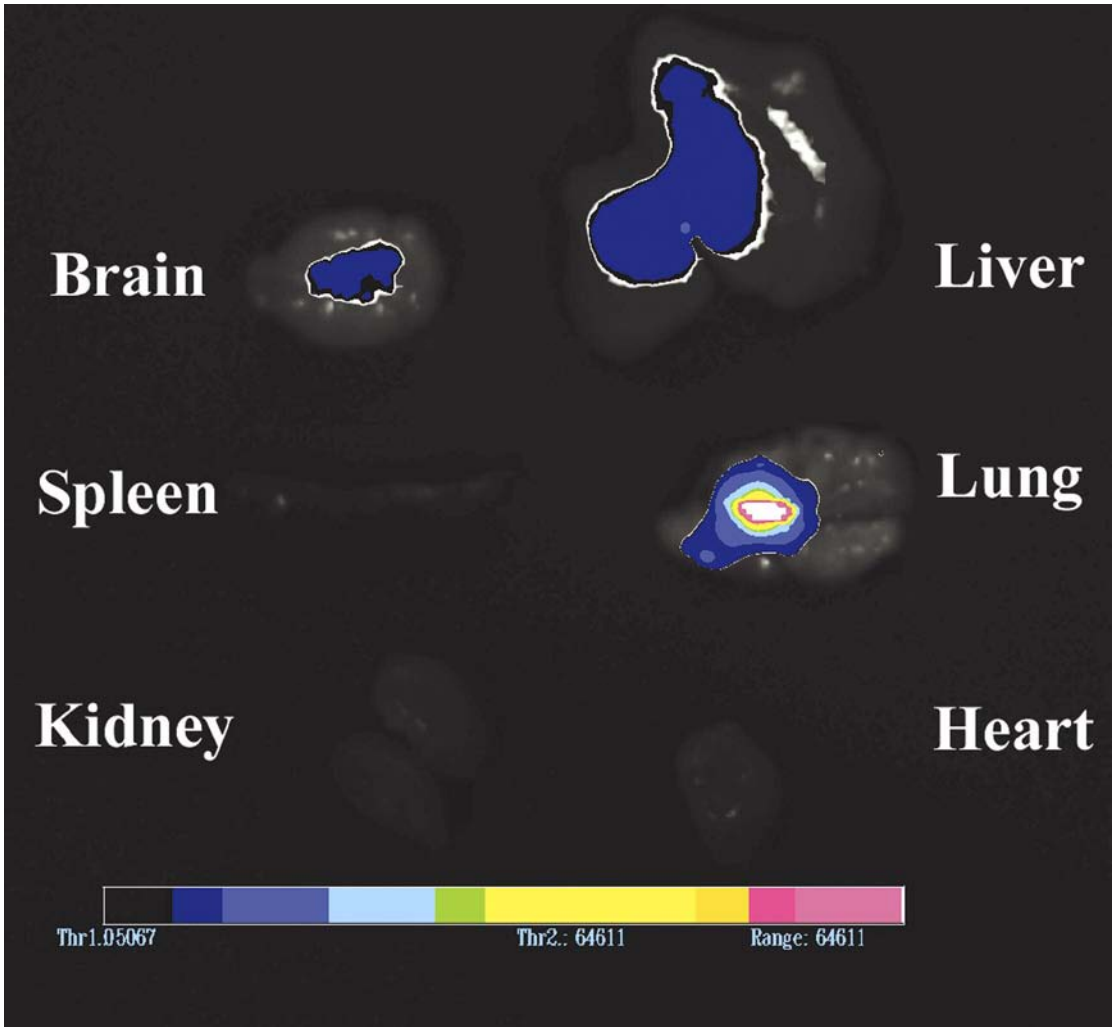

Figure S2: Distribution of WGA-conjugated quantum dots-loaded nanoparticles (WGA-QDs-NP) in various organs of nude mice 4h following intranasal administration. The animals were anesthetized and given intranasally with WGA-QDs-NP at the dose of about 40 mg/kg (QDs 3.2×10^{-8} mol/kg). Four hours following administration, the mice were euthanized and fixed by heart perfusion with their brains, hearts, livers, spleens, lungs and kidneys collected for imaging under the NightOWL II LB 983 imaging system.

Synthesis of Peptide Nucleic Acid FRET Probes via an Orthogonally Protected Building Block for Post-Synthetic Labeling of Peptide Nucleic Acids at the 5-Position of Uracil

Bereket Y. Oquare and John-Stephen Taylor*

Department of Chemistry, Washington University in St. Louis, One Brookings Drive, St. Louis, Missouri 63130. Received July 9, 2008; Revised Manuscript Received August 27, 2008

We report the design and synthesis of an orthogonally protected peptide nucleic acid (PNA) building block, Fmoc-PNA-U′-(Dde)-OH, and its use in the construction of PNA FRET probes. This building block allows for the post-synthetic attachment of reporter groups to the amino group attached to the 5-position of uracil (U) following selective deprotection of the Dde group. We illustrate the use of this building block for the synthesis of a series of FAM Cy5 donor acceptor pairs and their ability to detect a target DNA sequence.

The ability to directly detect and image gene expression inside living cells and organisms would greatly aid biological and biomedical research. One approach to image gene expression is to use antisense probes targeted to the mRNA of interest. Because endogenous mRNA transcripts are of very low copy number (1−10 000 copies/cell), it is critical that the signal from an antisense probe is greater than the background signal from the unbound agent in the cell. To accomplish this, various types of fluorogenic antisense probes have been developed that are designed to become fluorescent only upon binding to the target mRNA, most notably molecular beacons and binary FRET[1] probes.

Molecular beacons consist of a single antisense agent that bears a fluorescent donor on one end and a quencher on the other (*1, 2*). In the absence of the target, the molecular beacon folds in such a way to bring the donor in close proximity to the quencher, which quenches the fluorescence of the donor. In the presence of a target, the beacon unfolds to form a duplex, thereby distancing the quencher from the donor, which results in a strong fluorescence signal. In principle, molecular beacons should show high specificity and signal-to-noise, but in practice, nonspecific interactions with other biomolecules in a cell can open the beacon and activate fluorescence, as can cleavage of the backbone or linkers, which diminish the signal-to-noise.

Binary FRET probes consist of a pair of antisense agents, one bearing a donor fluorophore, and the other, an acceptor fluorophore. When present in low concentrations, energy transfer from the donor to the acceptor can only take place efficiently in the presence of a complementary template sequence which brings the two components together. As a result, binary FRET probes cannot be activated by nonspecific binding or degradation as can molecular beacons, and should possess much higher specificity and signal-to-noise. The first report of using binary FRET probes to detect a nucleic acid sequence in vitro came in 1988 (*3*), but it was not until 2000 that detection of an mRNA by a binary FRET probe in living cells was reported. Tsuji and co-workers showed that a pair of FRET probes could detect about 10 000 copies of c-fos mRNA produced from an over-expression vector by fluorescence microscopy (*4*). Later, they showed that they could detect about 900 copies by using time-resolved fluorescence imaging (*5*). They have also been able to detect about 10 000 copies of IL-2 mRNA by flow cytometry (*6*). To improve signal-to-noise, Bao and co-workers have developed dual FRET molecular beacons, in which the donor and acceptor probes are made into molecular beacons, which only become fluorescent when bound to the target mRNA. More recently, Kool and co-workers demonstrated the ability to detect mRNA in vivo by flow cytometry with a new class of quenched autoligating FRET probes (*7*).

Though the initial results in detecting mRNA in living cells by the binary FRET probes are promising, obtaining adequate signal-to-noise has been a problem. The FRET probes used in the previous cellular studies were all constructed from DNA, which can be degraded in vivo and thereby reduce the signal. Also, the RNA of DNA−RNA hybrids can be cleaved by RNaseH, which would further reduce the signal. Another disadvantage of DNA is that it is negatively charged, making it difficult to penetrate regions of folded RNA that would have high negative electrostatic potential. Peptide nucleic acids (PNAs) are a synthetic mimic of DNA with an electrically neutral amide backbone that recognize DNA or mRNA in a sequence-specific manner by Watson−Crick base pairing rules (*8*). PNA has become a particularly attractive nucleic acid analogue for the development of therapeutics and diagnostics because of its ability to form more stable duplexes with RNA than DNA, its stability to proteases and nucleases, and its ability to invade regions of secondary structure in RNA and not activate RNase H (*9, 10*).

PNA has recently been used for the construction of binary FRET probes in which the donor and acceptor fluorophores were attached to the ends of two PNAs (*11*). To maximize the FRET signal, however, the two PNAs had to bind to sites separated by about 7 bases. In designing FRET probes for folded mRNA in vivo, it would be easier if one only had to target a single

* To whom correspondence should be addressed: Department of Chemistry, Campus Box 1134, Washington University, One Brookings Drive, St. Louis, MO 63130. E-mail: taylor@wustl.edu.

[1]Abbreviations: Boc, *tert*-butyloxycarbonyl; Bhoc, benzhydryloxycarbonyl; Cy5, cyanine-5; Dde, 1-(4,4-dimethyl-2,6-dioxocyclohex-1-ylidene)ethyl; DCM, dichloromethane; DIEA, diisopropylethylamine; DMF, *N*,*N*-dimethylformamide; EDC, *N*,*N*-dimethylpropylethlydicarbodimide; ESI, electrospray ionization; EtOAc, ethyl acetate; FAB, fast atom bombardment; FAM, 5-(and-6)-carboxyfluorescein; FRET, fluorescence energy transfer; Fmoc, 9-fluorenylmethoxycarbonyl; HATU, *O*-(7-azabenzotriazole-1-yl)-*N*,*N*,*N*′,*N*′-tetramethyluronium hexafluorophosphate; MeOH, methanol; Mtt, methyltrityl; NHS, *N*-hydroxysuccinamide; NMP, *N*-methyl-2-pyrrolidinone; PNA, peptide nucleic acid; TFA, trifluoroacetic acid; THF, tetrahydrofuran; TMS, tetramethylsilane.

10.1021/bc800284x CCC: $40.75 © 2008 American Chemical Society
Published on Web 10/03/2008

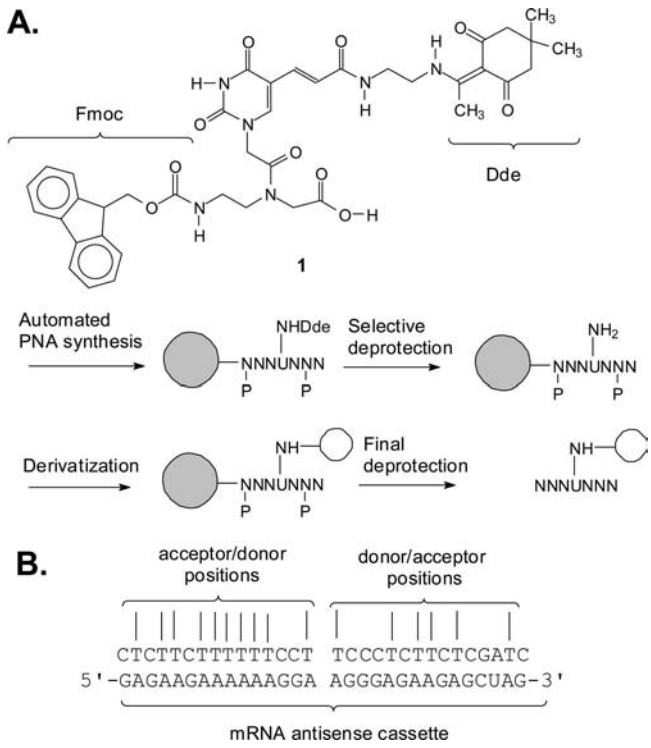

Figure 1. (A) Structure of the orthogonally protected Fmoc-PNA-U′-(Dde)-OH building block and its use for selectively derivatizing T's of PNAs. (B) Antisense cassette sequence and the possible complementary binary FRET PNA probes that could be prepared.

accessible site, rather than two accessible sites that are within 5−10 nt of each other, which would be much rarer. When targeting a single site, however, one of the fluorophores would have to be attached to an internal position of the PNA to maximize the FRET signal. More recently, PNAs internally labeled at C's with donor and acceptor fluorophores were used to create ligatible FRET probes (*12*).

Unlike endogenous genes, trans-genes can be genetically engineered to produce a high number of transcripts and to have any desired sequence. To take advantage of these features for the development of binary PNA FRET probes, we have undertaken the design and synthesis of mRNA cassettes that can be appended to a transgene to tag the mRNA with a repeating antisense site. Such a multimeric antisense tag would allow for the simultaneous binding of multiple binary FRET probes and could thereby greatly amplify the signal from such probes. To obtain an optimal signal output from a binary FRET probe requires that the distance between donor and acceptor can be varied, and the optimal placement of the donor and acceptor may ultimately depend on the number of cassettes and the conformation of the mRNA in vivo. Our initial design of an antisense cassette sequence is one that is devoid of secondary structure and is purine-rich. The sequence contains numerous A's and A-tracts, making it possible to easily vary the position of donor or acceptor fluorophores in a pair of adjacent PNAs through the use of a derivatizable T (Figure 1). Runs of purines in the mRNA sequence would also make it possible to further increase the affinity of a probe by triplex clamp formation. The purine-rich nature of the antisense cassette is also optimal for the complementary PNA sequence, as empirical rules dictate that optimal PNAs have <60% purine content and no more than four purines or three guanines in a row (http://www.appliedbiosystems.com/support/seqguide.cfm) (*13*).

PNAs have been derivatized with fluorophores directly through the amino group at the amino terminus, or at both amino or carboxy termini via addition of amino acids such as lysine or cysteine. Internally labeled PNAs have been prepared by Fmoc or Boc synthesis via derivatization of alkylamino derivative of the amino groups of A, C, and G (*14*) or at C or T by Boc synthesis through an aminoalkyl-modified backbone (*15*). For detecting our antisense cassette, however, we required an Fmoc PNA building block for derivatizing at T. We have previously developed a building block for introducing C5-thiomethyl uracil (U) into PNA by Fmoc synthesis, which can be post-synthetically derivatized via maleimide-linked reagents, though we found that a large excess of the maleimide is required to obtain a good yield of product (*16*). For our purposes, we decided to develop a new Fmoc building block for introducing a donor or acceptor fluorophore to a T through an amine linker. Furthermore, we wished that the linker have a well-defined orientation so that it might also be used to better report on the relative orientation between donor and acceptor groups. To this end, we designed two routes to a C5-derivative of U, compound **1**, containing a Dde-protected alkylamino group, which we show can be selectively deprotected and derivatized prior to complete deprotection of the PNA (Figure 1). We chose the Dde group because it has been previously shown to be compatible with Fmoc PNA synthesis and orthogonal to the other protecting groups (*17*). We also demonstrate the application of our building block to the synthesis of a binary FRET probe for the detection of the DNA sequence corresponding to our antisense mRNA cassette.

EXPERIMENTAL SECION

General Procedures. All reactions were performed under an argon or nitrogen atmosphere unless otherwise specified. All commercially available materials were used without further purification unless otherwise noted. Anhydrous solvents for reactions, such as DMF, DCM, and THF, were either used as obtained from Sigma-Aldrich or distilled from an appropriate drying agent, or dried with 4 Å molecular sieves. Analytical thin-layer chromatography (TLC) was performed using either Sigma-Aldrich's precoated silica gel plastic sheets 60 F_{254} (layer thickness of 250 μm) or general-purpose precoated silica gel glass sheets 60 F_{254} (250 μm) for compounds that are difficult to resolve on the plastic TLC plates. Molecules were visualized using UV light unless otherwise stated. Flash column chromatography was carried out on E. Merck (Bodman Industries, Aston, PA) silica gel 60 (40−63 μm) using the stated solvent system. ^{1}H NMR and ^{13}C NMR spectra were obtained on a Varian Mercury 300, Varian Oxford 300, and VarianUnityPlus 300 (all 300 MHz for ^{1}H NMR and 75 MHz for ^{13}C NMR spectrometers). The chemical shifts are expressed in parts per million (ppm) using deuterated NMR solvents in reference to TMS at 0 ppm.

Synthesis of *tert*-Butyl 2-(5-iodo-2,4-dioxo-3,4-dihydropyrimidin-1(2*H*)-yl) Acetate (3). To a suspension of iodouracil **2** (11.9 g, 50 mmol) and anhydrous K_2CO_3 (7.6 g, 55 mmol) in anhydrous DMF (175 mL) at 0 °C, *tert*-butylbromoacetate (9.75 g, 50 mmol) in anhydrous DMF (25 mL) was slowly added via syringe under a nitrogen atmosphere. After addition, the resulting reaction mixture was warmed to rt and vigorously stirred for 24 h. The byproduct precipitate of KBr salt was filtered under vacuum and washed with 10 mL of DMF. The solvent was evaporated in vacuo, and diluted with EtOAc (200 mL) and washed with water (3 × 100 mL). The aqueous phase was back-extracted with EtOAc (3 × 100 mL). The organic layers were combined, dried over Na_2SO_4, and evaporated to dryness in vacuo to yield the crude product. The product was then precipitated by adding cold water, collected in a sintered glass filter, and dried in vacuum overnight to give compound **3** as a white solid, 16.5 g, 94% yield. ^{1}H NMR (300 MHz, DMSO-d_6) δ (ppm): 11.8 (s, 1 H), 8.2 (s, 1 H), 4.4 (s, 2 H), 1.4 (s, 9

H). ^{13}C NMR (75 MHz, DMSO-d_6) δ (ppm): 177.5, 166.9, 161.0, 150.5, 150.1, 81.9, 67.9, 49.0, 27.6. ESI-MS (positive ion mode) calcd for $C_{10}H_{14}IN_2O_4$ $[M + H]^+$ 352.99; found 353.00.

Synthesis of (*E*)-3-(1-(2-*tert*-Butoxy-2-oxoethyl)-2,4-dioxo-1,2,3,4-tetrahydropyrimidin-5-yl)acrylic Acid (4). To a clean, dry 250 mL round-bottom flask was added *tert*-butyl-2-(5-iodo-2,4-dioxo-3,4-dihydropyrimidin-1(2*H*)-yl) acetate (**3**) (5.28 g, 15 mmol) and *N*-tetrabutylammonium bromide (5.80 g, 18 mmol), and dissolved in anhydrous DMF (70 mL). Then, acrylic acid (2.16 g, 30 mmol) in dry DMF (10 mL) was slowly added to the reaction mixture via a stainless steel syringe under nitrogen. A mixture of DMF/water/DIEA (10:10:10 mL) was added via syringe, and the reaction was evacuated (freed of any oxygen gas) and kept with stirring at rt under nitrogen. The catalyst, $Pd(OAc)_2$ (3% mol, 1.01 g, 4.5 mmol), was added under nitrogen. The flask was again evacuated and kept under nitrogen atmosphere. The reaction mixture was then heated to 80−90 °C in an oil bath for 16 h. The reaction mixture turned black for the first few hours, and then palladium particles precipitated while the solution turned yellow. The black particles were filtered under vacuum, and the DMF was evaporated in vacuo at an elevated temperature. The reaction mixture was then washed with water (25 mL) and diethyl ether (5 × 50 mL). The organics were combined, dried over Na_2SO_4, and evaporated to give the crude product as yellow oil. The product (**4**) was then precipitated by adding DCM/Et_2O mixture and a few drops of hexane in an ice bath. The product was collected by vacuum filtration in a sintered glass funnel and dried in vacuum overnight to give compound **4** as a yellow powder, 2.4 g, 54% yield. ^{1}H NMR (300 MHz, DMSO-d_6) δ (ppm): 12.3 (br, 1 H), 11.8 (s, 1 H), 8.3 (s, 1 H), 7.2 (d, J = 16 Hz, 1 H), 6.8 (d, J = 16 Hz, 1 H), 4.4 (s, 2 H), 1.4 (s, 9 H). ^{13}C NMR (75 MHz, DMSO-d_6) δ (ppm): 168.5, 167.4, 162.9, 150.4, 149.3, 137.3, 118.5, 108.4, 82.8, 50.4, 28.3. LR ESI-MS (positive mode) calcd for $C_{13}H_{17}IN_2O_6$ $[M + H]^+$ 297.11; found 297.11.

Synthesis of (*E*)-2,5-Dioxopyrrolidin-1-yl-3-(1-(2-*tert*-butoxy-2-oxoethyl)-2,4-dioxo-1,2,3,4-tetrahydropyrimidin-5-yl)acrylate (5). To (*E*)-3-(1-(2-*tert*-butoxy-2-oxoethyl)-2,4-dioxo-1,2,3,4-tetrahydropyrimidin-5-yl)acrylic acid (**4**) (0.59 g, 2.0 mmol) and NHS (0.46 g, 4 mmol) and DIEA (1.1 mL, 0.83 g, 6.4 mmol) in anhydrous DMF (20 mL) at 0 °C was added EDC·HCl (0.81 g, 4.2 mmol) in dry DMF (10 mL) dropwise via syringe under nitrogen. The reaction mixture was then warmed to rt and stirred for 12 h. The reaction was judged over by TLC, and the solvent was evaporated in vacuo. The crude product was purified by flash chromatography on a silica gel with 5% MeOH in DCM. The solvents were evaporated, and the product was dried in vacuum overnight to give 0.59 g **5** as a white solid in 75% yield. The product was immediately used for the next step owing to its instability. ^{1}H NMR (300 MHz, DMSO-d_6) δ (ppm): 8.1 (s, 1 H), 7.6 (d, J = 16 Hz, 1 H), 7.2 (d, J = 16 Hz, 1 H), 4.5 (s, 2 H), 2.8 (s, 4 H), 1.5 (s, 9 H); ^{13}C NMR (75 MHz, DMSO-d_6) δ (ppm): 177.5, 170.3, 166.4, 162.6, 161.9, 151.6, 149.4, 142.9, 109.2, 107.1, 82.2, 50.0, 27.5, 25.4.

Synthesis of the TFA Salt of 2-(1-(2-Aminoethylamino)-ethylidene)-5,5-dimethyl-1,3-cyclohexanedione (6). *tert*-Butyl 2-(1-(4,4-dimethyl-2,6-dioxocyclohexylidene)ethylamino) ethylcarbamate (*18*), (0.84 g, 2.6 mmol) was suspended in dry DCM (11.25 mL) and cooled to 0 °C. TFA (3.75 mL, 25%) was added dropwise via a syringe under atmospheric pressure. The reaction was allowed to occur at 0 °C for 30 min, and then warmed to rt and stirred for another 30 min. After 1 h, the reaction was judged complete by TLC analysis in 5% MeOH/DCM (R_f = 0). The solvent was evaporated in vacuo, and the residual TFA was removed by repeatedly evaporating from chloroform in small portions to give the product **6** as a yellow oil in quantitative yield (0.58 g). The product was immediately used for the next step without further purification, owing to its high instability. ^{1}H NMR (300 MHz, $CDCl_3$) δ (ppm): 3.9 (t, J = 16 Hz, 2 H), 3.3 (t, J = 16 Hz, 2 H), 2.7 (s, 3 H), 2.5 (s, 4 H), 1.1 (s, 6 H).

Synthesis of (*E*)-*tert*-Butyl 2-(5-(3-(2-(1-(4,4-dimethyl-2,6-dioxocyclohexylidene)ethylamino)ethylamino)-3-oxoprop-1-enyl)-2,4-dioxo-3,4-dihydropyrimidin-1(2*H*)-yl)acetate (7). The basic form of compound **6** (0.17 g, 0.77 mmol) was freshly prepared by addition of DIEA until about pH 7−7.5 as judged by pH paper, and dissolved in dry DMF (5 mL). The solution was then slowly added via syringe under nitrogen to a reaction flask containing the NHS ester **5** (0.250 g, 0.64 mmol) in dry DMF (5 mL) at 0 °C and then warmed to rt and stirred for 4−6 h under nitrogen. The solvent was evaporated in vacuo, and the crude reaction mixture was dissolved in 70 mL of DCM and was extracted with 1 M aq HCl (3 × 30 mL). The aqueous phase was back-extracted with DCM, and the organic layers were combined and concentrated in vacuo to give the crude product, which was chromatographed on silica gel with 5% MeOH in DCM to give 0.27 g compound **7** as a pure white solid in 85% yield. TLC in 5% MeOH/DCM, R_f = 0.25. ^{1}H NMR (300 MHz, CD_3OD) δ (ppm): 7.9 (s, 1 H), 7.2 (d, J = 16 Hz, 1 H), 7.1 (d, J = 16 Hz, 1 H), 4.5 (s, 2 H), 3.7 (t, J = 6 Hz, 2 H), 3.5 (t, J = 6 Hz, 2 H), 2.6 (s, 3 H), 2.4 (s, 4 H),1.5 (s, 9 H) 1.0 (s, 6 H). ^{13}C NMR (75 MHz, CD_3OD) δ (ppm): 200.0, 176.1, 169.7, 168.4, 164.0, 151.8, 149.3, 134.5, 122.0, 110.7, 109.0, 84.1, 53.5, 51.0, 49.9, 43.5, 39.9, 31.0, 28.4, 18.4. LR ESI-MS (positive ion mode) calcd for $C_{25}H_{35}N_4O_7$ $[M + H]^+$ 503.25; found 503.24.

Synthesis of (*E*)-2-(5-(3-(2-(1-(4,4-Dimethyl-2,6-dioxocyclohexylidene)ethylamino)ethylamino)-3-oxoprop-1-enyl)-2,4-dioxo-3,4-dihydropyrimidin-1(2*H*)-yl) Acetic Acid (8). Compound **7** (2.5 g, 5.0 mmol) was dissolved in CH_2Cl_2 (15 mL), and TFA (15 mL) was slowly added dropwise via syringe at 0 °C. The reaction mixture was then warmed to rt after addition of the reagents and stirred for 4 h. The reaction was monitored by TLC (5% MeOH in DCM) until the disappearance of the starting material and appearance of a new spot near the baseline. After the reaction was complete, the solvent was evaporated in vacuo, and the residual TFA was coevaporated several times with chloroform, and the resulting solid was triturated with methanol. The solid product was dried in vacuo and isolated by filtering through a sintered glass funnel under vacuum to afford 2.2 g of compound **8** as a white solid (quantitative yield). ^{1}H NMR (300 MHz, DMSO-d_6) δ (ppm): 13.2 (t, J = 6 Hz, 1 H), 11.7 (s, 1 H), 8.4 (t, J = 6 Hz, 1 H), 8.1 (s, 1 H), 7.1 (d, J = 16 Hz, 1 H), 7.0 (d, J = 16 Hz, 1 H), 4.5 (s, 2 H), 3.6 (m, 2 H), 3.4 (m, 2 H), 2.5 (s, 3 H), 2.3 (s, 4 H), 0.9 (s, 6 H). ^{13}C NMR (75 MHz, DMSO-d_6) δ (ppm): 196.4, 173.2, 169.3, 166.1, 162.3, 149.8, 148.4, 132.1, 120.9, 108.2, 52.4, 49.0, 42.0, 40.3, 38.7, 38.4, 29.8, 27.9, 17.3. LR ESI-MS (positive ion mode): calcd for $C_{21}H_{27}N_4O7$ $[M + H]^+$ 447.19; found 447.18.

Synthesis of (*E*)-*tert*-Butyl 2-(*N*-(2-(((9*H*-fluoren-9-yl)methoxy) carbonylamino)ethyl)-2-(5-(3-(2-(1-(4,4-dimethyl-2,6-dioxocyclohexylidene)ethylamino)ethylamino)-3-oxoprop-1-enyl)-2,4-dioxo-3,4-dihydropyrimidin-1(2*H*)-yl)acetamido) Acetate (10). To a solution of carboxylic acid **8** (2.2 g, 5.1 mmol) and amine **9** (19) (1 equiv, 2.2 g, 5.1 mmol) in dry DMF (30 mL) was added redistilled DIEA (2.1 mL, 1.5 g, 11.7 mmol) via syringe under nitrogen, and the temperature was lowered to 0 °C. In a separate round-bottom flask, HATU (1.2 equiv, 2.3 g, 6.1 mmol) was dissolved in anhydrous DMF (10 mL) and transferred to the reaction mixture via syringe under a nitrogen, at 0 °C. The reaction was kept at 0 °C for 1 h and then warmed to rt and

stirred for 8 h. The reaction was monitored by TLC (5% MeOH in DCM). The reaction mixture was worked up by pouring into 100 mL of DCM and washed with water (8 × 50 mL). The aqueous and DCM layers did not separate completely, and both the clear organic layer and emulsion layer were collected, dried over Na_2SO_4, and evaporated in vacuo. The crude product was purified by flash chromatography with 5% MeOH in DCM to give 3.9 g of compound **10** as a white solid in 93% yield. TLC: 5% MeOH/DCM ($R_f = 0.20$). ^{1}H NMR (300 MHz, acetone-d_6) δ (ppm): 13.5 (t, $J = 6$ Hz, 1 H), 10.4 (s, 1 H), 7.9 (d, $J = 16$ Hz, 2 H), 7.8 (s, 1 H), 7.7 (d, $J = 16$ Hz, 2 H), 7.4 (t, $J = 16$ Hz, 2 H), 7.3 (t, $J = 16$ Hz, 2 H), 7.2 (d, $J = 16$ Hz, 1 H), 7.1 (d, $J = 16$ Hz, 1 H), 4.8 (s, 2 H), 4.4−4.2 (m, 3 H), 4.0 (s, 2 H), 3.7−3.3 (m, 8 H), 2.6 (s, 3 H), 2.3 (s, 4 H), 1.5 (s, 9 H), 1.0 (s, 6 H). ^{13}C NMR (75 MHz, acetone-d_6) δ (ppm): 205.7, 162.8, 162.3, 161.1, 158.9, 148.6, 144.5, 141.5, 132.9, 127.9, 127.4, 125.5, 121.4, 120.2, 109.3, 109.2, 80.3, 66.5, 66.3, 49.2, 48.7, 47.4, 42.6, 39.2, 39.0, 27.8, 27.6, 17.2. LR MS-ESI (positive ion mode) calcd for $C_{44}H_{532}N_6O_{10}$ $[M + H]^+$ 825.38; found 825.36.

Synthesis of (*E*)-2-(*N*-(2-(((9*H*-Fluoren-9-yl)methoxy)carbonylamino)ethyl)-2-(5-(3-(2-(1-(4,4-dimethyl-2,6-dioxocyclohexylidene)ethylamino)ethylamino)-3-oxoprop-1-enyl)-2,4-dioxo-3,4-dihydropyrimidin-1(2*H*)-yl)acetamido)acetic Acid; Fmoc-U′ (Dde)-OH (1). TFA (7 mL) was slowly added via syringe at 0 °C to a solution of compound **10** (0.825 g, 1.0 mmol) in DCM (7 mL). The reaction mixture was then warmed to rt and stirred for 4−5 h. The reaction was monitored by TLC (DCM/MeOH, 5:1) and judged complete in 4−5 h after which the solvents were evaporated in vacuo and the residual TFA coevaporated with CCl_4 several times, and then evaporated from methanol to give 0.77 g of Fmoc-U′(Dde)-OH (**1**) as a white solid in quantitative yield. ^{1}H NMR (300 MHz, DMSO-d_6) δ (ppm): 13.3 (t, $J = 6$ Hz, 1 H), 11.7 (s, 1 H), 8.4 (t, $J = 6$ Hz, 1 H), 8.0 (s, 1 H), 7.9 (d, $J = 16$ Hz, 2 H), 7.7 (d, $J = 16$ Hz, 2 H), 7.4 (t, $J = 16$ Hz, 2 H), 7.3 (t, $J = 16$ Hz, 2 H), 7.1 (d, $J = 16$ Hz, 1 H), 7.0 (d, $J = 16$ Hz, 1 H), 4.8 (s, 2 H), 4.3−4.2 (m, 3 H), 4.0 (s, 2 H), 3.6−3.2 (m, 8 H), 2.5 (s, 3 H), 2.3 (s, 4 H), 0.9 (s, 6 H). ^{13}C NMR (75 MHz, DMSO-d_6) δ (ppm): 196.3, 173.0, 170.3, 166.1, 162.3, 149.7, 148.6, 143.8, 140.7, 132.1, 127.5, 127.0, 125.1, 120.6, 120.0, 108.0, 65.4, 52.3, 48.2, 47.7, 46.7, 41.9, 38.3, 29.7, 27.8, 17.2. LR ESI-MS (positive ion mode) calcd for for $C_{40}H_{45}N_6O_{10}$ $[M + H]^+$ 769.32; found 769.28.

Synthesis of (*E*)-*tert*-Butyl 2-(3-(2,4-dioxo-1,2,3,4-tetrahydropyrimidin-5-yl)acrylamido)ethylcarbamate (13). To the (*E*)-3-(2,4-dioxo-1,2,3,4-tetrahydropyrimidin-5-yl)acrylic acid (**11**) (*20*) (0.55 g, 3.0 mmol) and *N*-hydroxysuccinimide, NHS, (0.38 g, 3.3 mmol) was added anhydrous DMF (10 mL) under nitrogen. Then, mono-Boc ethylenediamine (**12**) (0.72 g, 4.5 mmol) (Alfa Aesar) and diisopropylamine (0.85 g, 1.2 mL, 6.6 mmol) in DMF (5 mL) were added dropwise via syringe to the reaction mixture. The reaction mixture was cooled to 0 °C with stirring under nitrogen. Then, EDC·HCl (0.632 g, 3.3 mmol) dissolved in anhydrous DMF (10 mL) was slowly added to the reaction mixture at 0 °C. After addition, the reaction mixture was allowed to warm to rt and stirred overnight. The DMF was evaporated at elevated temperature (100−110 °C) in vacuo. The crude product was purified by flash chromatography by using 5% MeOH in DCM to afford 0.83 g of compound **13** as an off-white solid in 85% yield. Analytically pure compound was obtained by recrystallization from ethanol/ether. ^{1}H NMR (300 MHz, DMSO-d_6) δ (ppm): 11.3 (s, 1 H), 8.1 (t, $J = 7$ Hz, 1 H),7.9 (s, 1 H), 7.1 (d, $J = 16$ Hz, 1 H), 7.0 (d, $J = 16$ Hz, 1 H), 6.8 (t, $J = 6$ Hz, 1 H), 3.2 (m, 2 H), 3.0 (m, 2 H), 1.4 (s, 9 H). ^{13}C NMR (75 MHz, DMSO-d_6) δ (ppm): 165.9, 162.8, 155.5, 150.2, 144.7, 132.4, 120.5, 107.8, 77.5, 40.2, 38.5, 28.1. ESI-MS (positive ion mode) calcd for $C_{14}H_{21}N_4O_5$ $[M + H]^+$ 325.1512; found 325.1512.

Synthesis of (*E*)-*N*-(2-Aminoethyl)-3-(2,4-dioxo-1,2,3,4-tetrahydropyrimidin-5-yl)acrylamide (14). Compound **13** (0.70 g, 2.2 mmol) was dissolved in DCM (12 mL), and TFA (4 mL) was slowly added via syringe at 0 °C. The reaction mixture was warmed to rt and stirred for 2 h. The reaction was monitored by TLC in 10% MeOH/DCM until the disappearance of the starting material and appearance of a new spot (product) near the baseline. When the reaction was complete, the solvent was evaporated in vacuo, and the remaining solvent was evaporated with small portions of carbon tetrachloride. The product was precipitated by adding a small amount of methanol to give a brownish white solid (0.49 g, 99%). ^{1}H NMR (300 MHz, DMSO-d_6) δ (ppm): 9.2 (br, 3 H), 8.3 (t, $J = 6$ Hz, 1 H),7.9 (s, 1 H), 7.2−7.1 (d, $J = 16$ Hz, 1 H), 7.0−6.9 (d, $J = 16$ Hz, 1 H), 3.4−3.3 (m, 2 H), 2.9 (t, $J = 6$ Hz, 1 H). ^{13}C NMR (75 MHz, DMSO-d_6) δ (ppm): 166.5, 162.8, 150.3, 145.0, 132.9, 120.0, 107.6, 38.7, 36.7. LR ESI-MS (positive ion mode) calcd for $C_9H_{13}N_4O_3$ $[M + H]^+$ 225.10; found 225.09.

Synthesis of (*E*)-*N*-(2-(1-(4,4-Dimethyl-2,6-dioxocyclohexylidene)ethylamino)ethyl)-3-(2,4-dioxo-1,2,3,4-tetrahydropyrimidin-5-yl)acrylamide (16). Compound **14** (0.45 g, 2.2 mmol) was freshly prepared as described above and dissolved in dry DMF, and DIEA was slowly added at 0 °C until the pH of the solution was slightly basic. Dde-OH (**15**) (available from Aldrich) (0.48 g, 2.6 mmol) in DMF was then slowly added via syringe. The reaction mixture was refluxed under nitrogen for 24 h. The solvent was evaporated at elevated temperature and then coevaporated with EtOH to almost complete dryness. The product was then precipitated out of ethanol in an ice bath to give 0.72 g of compound **16** as a pale brown solid in 84% yield. TLC: in 5% MeOH/DCM ($R_f = 0.25$). ^{1}H NMR (300 MHz, DMSO-d_6) δ (ppm): 13.2 (t, $J = 6$ Hz, 1 H), 11.3 (s, 2 H), 8.3 (t, $J = 6$ Hz, 1 H), 7.9 (s, 1 H), 7.1 (d, $J = 16$, 1 H), 7.0 (d, $J = 16$, 1 H), 3.6 (m, 2 H) 3.4 (m, 2 H), 2.5 (s, 3 H), 2.3 (s, 4 H), 0.9 (s, 6 H). ^{13}C NMR (75 MHz, DMSO-d_6) δ (ppm): 196.3, 173.0, 166.3, 162.8, 150.2, 145.0, 132.9, 119.9, 107.6, 107.0, 52.2, 41.9, 40.2, 38.6, 38.3, 29.6, 27.8, 17.2. ESI-MS (positive ion mode) calcd for $C_{19}H_{25}N_4O_3$ $[M + H]^+$ 389.1825; found 389.1822.

Synthesis of (*E*)-*tert*-Butyl 2-(5-(3-(2-(1-(4,4-dimethyl-2,6-dioxocyclohexylidene)ethylamino)ethylamino)-3-oxoprop-1-enyl)-2,4-dioxo-3,4-dihydropyrimidin-1(2*H*)-yl)acetate (7) from 16. A solution of compound **16** (0.6 g, 1.5 mmol) and anhydrous K_2CO_3 (0.24 g, 1.7 mmol) were dissolved in anhydrous DMF (8 mL). A solution of *t*-butylbromoacetate (0.30 g, 1.5 mmol) in anhydrous DMF (4 mL) was slowly added via syringe at 0 °C. The reaction mixture was warmed up to rt and stirred under nitrogen overnight. The precipitate of KBr was filtered and washed several times with methanol (3 × 10 mL). The filtrates were combined, evaporated in vacuo at an elevated temperature, and coevaporated with EtOH to almost complete dryness. The crude product was dissolved in 100 mL DCM and extracted with water (5 × 30 mL), 1 M HCl (2 × 20 mL), and finally with brine (1 × 20 mL). The aqueous phases were back-extracted with DCM (1 × 100 mL), and the organics were combined, dried over Na_2SO_4, and evaporated in vacuo. The product was purified by flash chromatography by using 5% MeOH in DCM to give 0.69 g of compound **7** as a crystalline white solid in 92% yield with identical spectra as described for **7** prepared from **5**.

General PNA Synthesis, Purification, and Characterization Procedures. Anhydrous diethyl ether, DIEA, TFA, *meta*-cresol, hydrazine, and hydroxylamine hydrochloride were purchased from Sigma (St. Louis, MO). High-purity anhydrous DMF and NMP solvents for the synthesis and dilution of the

PNA monomers were used as obtained from either Applied-Biosystems (Foster City, CA) or Sigma-Aldrich (St. Louis, MO), HATU was purchased either from Applied Biosystems or GenScript Corp. (Piscataway, NJ). The Fmoc PNA monomers A, C, G, T, and reagents for peptide nucleic acid (PNA) synthesis were from Applied Biosystems or ASM-Research Chemicals (Hannover, Germany). ε-Boc-α-Boc-Lys and ε-Mtt-α-Fmoc-Lys were from EMD Chemicals (Gibbstown, NJ). Cy5-NHS was from Amersham Biosciences Inc. (Piscataway, NJ). FAM-NHS was from Molecular Probes (Eugene, Oregon). Ultrafree-MC 0.2 μM filtered microcentrifuge tubes were used for cleavage of the PNA from the resin (Millipore Inc., Bedford, MA). Labeling of PNAs with fluorophore groups was carried out in anhydrous solvents unless otherwise specified. The synthesis of the PNAs was carried out by solid-phase Fmoc PNA synthesis on Fmoc-XAL-PEG-PS resin on an Expedite 8909 DNA/PNA synthesizer (Applied Biosystems) on a 2 μmol scale. DNA (ODNs) templates for fluorescence solution studies were purchased from Integrated DNA Technologies Inc. (Coralville, IA). Crude PNA FRET donor and acceptor probes were analyzed and purified by reversed-phase high-performance liquid chromatography (RP-HPLC) on a Beckman instrument equipped with a UV array detector. PNAs were eluted with a 65 min, 1 mL/min, 0−70% linear gradient of acetonitrile in 0.1% aqueous TFA on Varian Microsorb-MV column (C-18, 5 μm, 300 Å pore size, 4.6 × 250 mm). The PNAs were characterized by UV−vis on a Bausch and Lomb Spectronic1001 spectrophotometer or on a Varian Cary 100 Bio UV−visible spectrophotometer and by fluorescence spectroscopy on a Varian Cary Eclipse fluorescence spectrophotometer in phosphate buffered saline (PBS, pH 7.0, 100 mM). MALDI-TOF mass spectrometry was carried out on a PerSeptive Voyager MALDI-TOF instrument using a sinapinic acid matrix (10 mg in 1 mL of 0.1% TFA in 2:1 H_2O-CH_3CN, mixed 1:1 with PNA). For PNAs with fluorescent tags, we were unable to obtain good MALDI spectra and instead relied on UV to identify the fractions containing the desired PNA by the ratio of the PNA and fluorophore absorbance at 260 nm to the fluorophore absorbance maximum in PBS. Estimated molar extinction coefficients at 260 nm were obtained from available data for PNA (*21*) and the fluorophores (http://www.basic.northwestern.edu/biotools/OligoCalcModifications.html) and also used to determine PNA concentration.

Incorporation of Fmoc-U′(Dde)-OH into PNA and Selective Dde Deprotection. PNAs were synthesized using Fmoc-protected monomers and Fmoc-XAL-PEG-PS universal support on an 8909 Expedite PNA synthesizer using Bhoc-protected Fmoc PNA monomers and the PNA building block, Fmoc-U′-(Dde)-OH **1**. The resin was divided into three microcentrifuge reaction tubes. One tube was treated twice with 2% hydrazine in DMF for 30 min to remove the Dde group (*22*) (1 mL/2 μmol of the protected PNA resin). Another tube was treated with 1 mL of $NH_2OH·HCl$/imidazole deprotection cocktail mixture (1 volume of DMF plus 5 volumes of 1.25 g of $NH_2OH·HCl$ and 0.918 g of imidazole in 5 mL of NMP) (*17*) for 3 h to remove the Dde group. The third reaction tube was not treated. Following completion of the reactions, the Fmoc was removed with 1 mL 20% piperidine/DMF for 20 min, and repeated. Then the resin was washed 5 × 1 mL of 1:1 DCM/DMF. The resins were then treated with 200 μL of TFA/*m*-cresol (4:1) for 90 min at rt to remove the Bhoc protecting groups and cleave the PNA from the resin. The solution was removed and the remaining resin treated a second time. The solutions were combined, and the PNA was precipitated by treatment with cold anhydrous diethyl ether (1 mL). The PNAs were then recovered as white pellets by spinning them down in a centrifuge at 2000 rpm (3 × 5 min) and removing the ether. The crude PNAs were purified by reversed-phase HPLC as described in the experimental section by monitoring the UV absorbance at 260 nm. The desired fractions were collected and concentrated to dryness on a centrifugal evaporator overnight. The PNAs were redissolved in pure water and analyzed and characterized by UV, and further characterized by MALDI-TOF mass spectrometry using sinapinic acid matrix. PNA **18**: MALDI $(M + H)^+$ Calcd 4327.7, found 4326.9; PNA **20** $(M + H)^+$ Calcd 4163.6, via hydrazine deprotection: found 4161.7; via hydroxylamine/imidazole deprotection 4162.7.

Solid-Phase Synthesis of the PNA-FAM 22 Donor Probes. The donor probes were synthesized on the Expedite 8909 PNA synthesizer using Fmoc-protected monomers and the universal support Fmoc-XAL-PEG-PS in which one of the monomers was the PNA building block, Fmoc-U′-(Dde)-OH, and with ε-Boc-α-Boc-Lys at the N-terminus. The resin was treated with 1 mL of the deprotection mixture ($NH_2OH·HCl$/imidazole in NMP/DMF) for 3 h and washed thoroughly with DCM/DMF (1:1) mixture (5 × 1 mL). The resin was then swelled with DMF (250 μL) and DIEA (11 μL) for 5 min, and a 10-fold molar excess of FAM-NHS (10 equiv, 10 mg) was dissolved in a separate tube with 100 μL of anhydrous DMF, vortexed for a few seconds to completely dissolve the activated FAM-NHS, and immediately added to the resin all at once and stirred for 4−6 h at rt. The resin was washed with DCM/DMF (1:1) mixture (5 × 1 mL) to remove excess reagents and thoroughly dried by purging with nitrogen gas for several minutes. The PNAs were then cleaved from the resin and deprotected with 200 μL of TFA/*m*-cresol (4:1) cocktail mixture as described above. The crude PNA-FAM conjugates **22** were then recovered as yellow-colored pellets by precipitation from cold anhydrous diethyl ether (3 × 1 mL). The crude PNAs were dissolved in 500 μL of water containing 0.1% TFA filtered using an Xpertek syringe filters (13 mm, 0.45 μm) before HPLC injection. The crude PNA-FAM donors **22** were purified by reversed-phase HPLC with conditions described in the General Procedures section. The HPLC fractions containing the PNAs were collected, concentrated to dryness on a centrifugal evaporator overnight and redissolved in freshly distilled deionized water, and characterized by UV in pH 7 PBS buffer. The expected ratio of 500/267 nm absorbances for PNA **22** was 0.60 based on an estimated absorbance of 70 000 M^{-1} cm^{-1} for FAM at 500 nm and 116 200 M^{-1} cm^{-1} at 260 nm (119 000 M^{-1} cm^{-1} minus 20% hypochromicity for the PNA plus 20 000 M^{-1} cm^{-1} for FAM); found: 0.52 for PNA **22-0**, 0.51 for **22-7**, and 0.61 for **22-13.**

Solid-Phase Synthesis of the PNA-Cy5 FRET Acceptor Probe 24 via ε-Mtt-α-Fmoc-Lys. The PNA was synthesized on the Expedite 8909 PNA synthesizer as described above and ε-Mtt-α-Fmoc-Lys was added to the C-terminus. After the PNA synthesis was completed, the Mtt group was selectively deprotected by treating the resin with 1% TFA in DCM (5 × 1 mL) for 5 min (*23, 24*). After 3 cycles of the reaction, the yellow color of the deprotection mixture (an indication of trityl group deprotection) started to fade away and finally cleared, indicating the completion of the reaction. The resin was then thoroughly washed with DCM/DMF (1:1) mixture (5 × 1 mL) to remove the deprotected Mtt group and excess reagents. Then, it was swelled with DMF (250 μL) and DIEA (11 μL) for 5 min, and Cy5-NHS ester (1 mg) in 100 μL of anhydrous DMF was immediately added to the resin and stirred for 4 h. The excess reagents were washed away with 5 × 1 mL DCM/DMF (1:1). Fmoc was removed with two treatments of 1 mL of 20% piperidine/DMF for 20 min and then washed 5 × 1 mL of DCM/DMF (1:1). The PNA was cleaved from the resin with 200 μL of TFA/*m*-cresol (4:1) for 90 min, followed by filtration to remove the crude PNA. The cleavage step was repeated one

Scheme 1. Synthesis of Fmoc-U′-(Dde)-OH 1 from Iodouracil via Intermediate 7

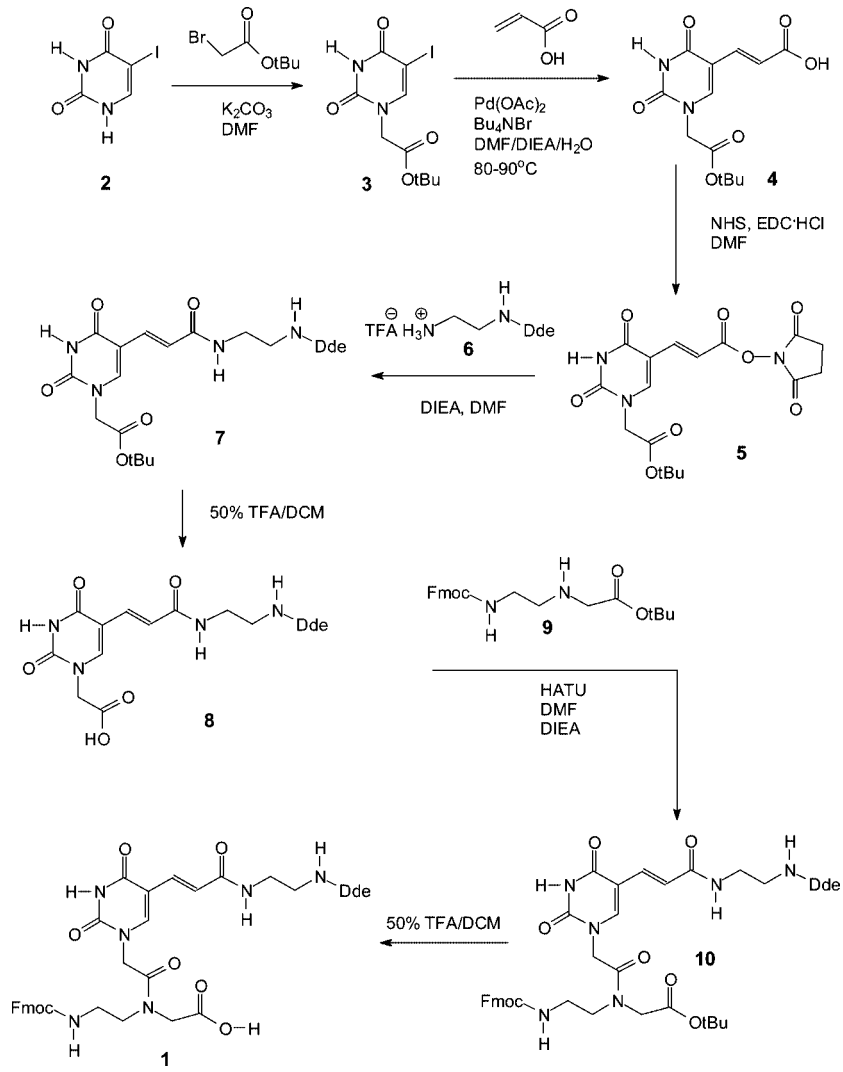

more time, and the filtrates were combined in one tube. The PNA-Cy5 FRET acceptor probe **24** was recovered by precipitation with cold anhydrous diethyl ether (1 mL). The crude PNA-Cy5 conjugate was purified by reversed-phase HPLC and characterized by UV in pH 7 PBS buffer. The expected ratio of the absorbances at 650 and 260 nm for PNA **24** was 2.3, based on an estimated absorbance of 250 000 M^{-1} cm^{-1} for Cy5 at 650 nm, and 108 600 M^{-1} cm^{-1} at 260 nm (123 200 M^{-1} cm^{-1} minus 20% hypochromicity for the PNA plus 10 000 M^{-1} cm^{-1} for Cy5): found 2.0.

Fluorescence Resonance Energy Transfer (FRET) Studies. The acceptor probe (PNA-Cy5 **24**) was added to the FRET donor probe (PNA-FAM **22**) with or without a DNA template and allowed to equilibrate at the concentration and time indicated in the Figure 2 legend. The emission spectrum was then recorded from 450 to 800 nm with excitation at 490 nm with 5 nm excitation and emission slit windows. The emission maximum for the PNA-Cy5 **24** probe was at 667 nm.

RESULTS AND DISCUSSION

Building Block Synthesis. Two synthetic routes were developed to the building block **1**. In route I (Scheme 1), commercially available iodouracil **2** was alkylated at N1 with *tert*-butyl bromoacetate in the presence of potassium carbonate in anhydrous DMF under nitrogen at room temperature for 24 h to give the *tert*-butyl ester **3** in 94% yield. The iodo group of **3** was replaced with an acryloyl group via Heck reaction with acrylic acid to give the carboxylic acid **4** in 54% yield. The carboxylic acid **4** was converted into an NHS ester **5** with *N*-hydroxysuccinamide and EDC in anhydrous DMF overnight in 75% yield. The NHS ester was coupled with the TFA salt of mono-Dde-protected ethylenediamine **6** (*18*) to give compound **7** in about 85% yield.

Compound **7** was converted to the Fmoc building block **1** in three additional steps. In the first step, compound **7** was treated with 50% TFA/DCM from 0 °C to rt for 4 h to give the carboxylic acid **8** in a quantitative yield without disturbing the Dde group. The carboxylic acid **8** was then coupled with *tert*-butyl-*N*-Fmoc-aminoethyl-glycinate **9** (*19*) by activation with HATU in the presence of DIEA in anhydrous DMF to give compound **10** in 93% yield. Finally, deprotection of the *tert*-butyl ester group of **10** with 50% TFA in dichloromethane afforded the desired PNA building block **1** in quantitative yield and in 30% overall yield from iodouracil.

We also investigated a second route to **7** that, though two steps longer, may be preferable for large-scale synthesis due to the ease of synthesis and purification of the intermediates and the better overall yield (Scheme 2). Acrylic acid **11** was first prepared in two steps in 85% yield from commercially available 5′-hydroxymethyluracil (*20*). We initially planned to couple **11** with mono-Dde protected ethylenediamine **6** as we had done in the first route, but due to the instability of **6**, we decided to

Scheme 2. Synthesis of Intermediate 7 from Uracil Acrylic Acid 11

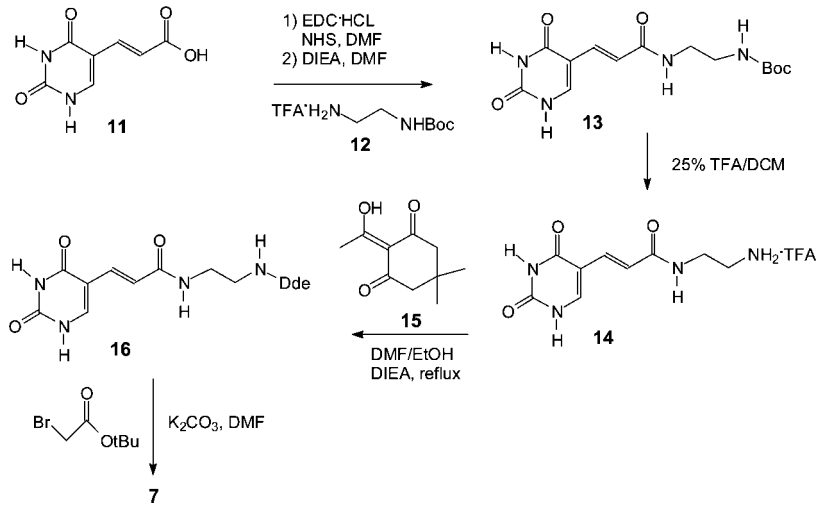

Scheme 3. Synthesis of the PNA-U′-(Dde) 18 and PNA-U′-(NH_2) 20

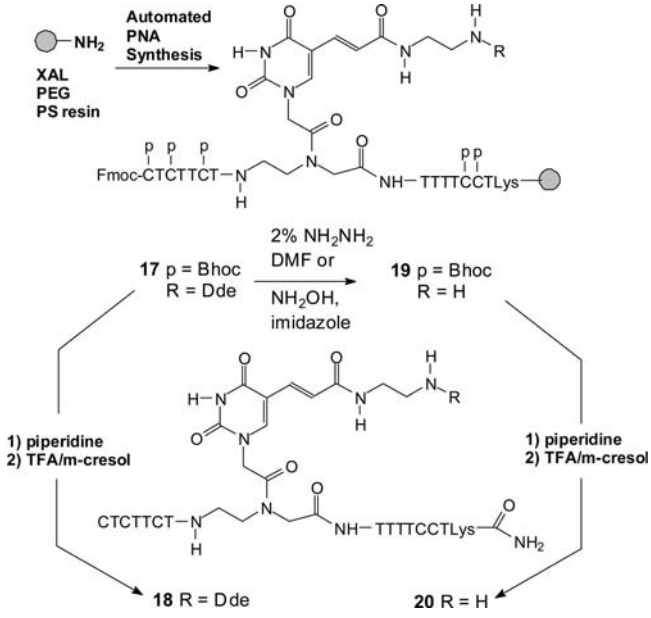

couple the more stable mono-Boc-protected ethylenediamine **12** and convert the Boc group to a Dde group. Thus, acrylic acid **11** was converted to the NHS ester in 87% yield by first forming the NHS ester with EDC and then adding commercially available mono-Boc ethylenediamine **12** in the presence of DIEA in dry DMF. The *tert*-butyl protecting group was then deprotected with 25% TFA/DCM for 3 h to give the TFA salt **14** in quantitative yield. The TFA salt was refluxed with Dde-OH **15** in the presence of DIEA in anhydrous DMF to give compound **16** in 84% yield. Compound **16** was alkylated with *tert*-butyl bromoacetate in the presence of potassium carbonate in anhydrous DMF under nitrogen at rt for 12 h to afford compound **7** in 90% yield. Compound **7** was converted to the PNA building block **1** as previously described in 43% overall yield for nine steps from hydroxymethyluracil.

Incorporation of Dde-U into PNA. To demonstrate that the Dde-U building block **1** was compatible with automated PNA synthesis and that the Dde group can be selectively removed, we synthesized CTCTTCTU(Dde)TTTTCCTK, **18**, and CTCTTCTU(NH_2)TTTTCCTK, **20**, according to Scheme 3. First, Dde-U was incorporated into PNA by solid-phase automated Fmoc PNA synthesis with standard Bhoc monomers on a XAL-PEG-PS resin to give the solid-phase intermediate **17**, followed by treatment with TFA/*m*-cresol to give the Dde-protected PNA **18** as confirmed by HPLC and MALDI analysis. The ability of the Dde group to survive strongly acidic deprotection conditions demonstrates its orthogonality to acid-labile amine protecting groups such as Mtt that would therefore allow selective derivatization of other sites on the PNA.

We then examined 2% hydrazine/DMF (*22*) and NH_2OH/imidazole (*17*) as methods for removing the Dde group from the solid-supported PNA **19** to give **20** (Scheme 3). Following either treatment, the PNA was first treated with piperidine to remove the Fmoc group and then cleaved from the support and completely deprotected with TFA/*m*-cresol. HPLC and MALDI analysis of the major product from both deprotection methods showed the same peak corresponding to the Dde deprotected PNA **20**. In practice, the hydroxylamine reagent is preferable, as it is compatible with the Fmoc group, which undergoes a significant amount of deprotection with hydrazine (*17*).

Synthesis of FAM/Cy5 FRET Probes. We selected a FAM/Cy5 FRET system to maximize detection sensitivity. Cy5 has a red-shifted absorption maxima which minimizes background signal due to direct excitation of Cy5 upon irradiation of fluorescein. Because the Cy5 emission is also red-shifted, there is less background signal due to fluorescein emission at the Cy5 emission maximum. In spite of its red-shifted absorption spectrum, Cy5 still has sufficient overlap between its absorption spectrum and that of fluorescein to give a good FRET signal (*7*, *25*). To determine the optimal positioning of the donor relative to the acceptor for maximum FRET, we synthesized PNAs with the fluorescein attached to three different sites (PNA-FAM **22-0**, **22-7**, and **22-13**), and Cy5 to a single site on the ε-amino end of a carboxy-terminal lysine group on the acceptor PNA-Cy5 **24** (Scheme 3).

The FRET donor PNA-FAMs were prepared by removing the Dde group from the corresponding PNAs **21-0**, **21-7**, **21-13** with NH_2OH/imidazole, followed by coupling with the NHS ester of 5/6-carboxyfluorescein (FAM) in the presence of DIEA for 2 h. To help drive the coupling to completion, the support was additionally treated with 100 μL of HATU (0.2 M) in DMF an additional 2 h at room temperature. The support was then washed several times with DCM/DMF, followed by cleavage and deprotection with TFA/*m*-cresol to afford the crude PNA as a colored pellet. The PNAs were then purified by reverse phase HPLC in 0.1% aqueous TFA. When dissolved at pH 7, the fluorescein adopts the open fluorescent form as shown in Scheme 4. The FRET acceptor PNA-Cy5 **24** was prepared by selectively deprotecting a carboxy-terminal ε-Mtt-α-Fmoc-Lys PNA **23** with 1% TFA/DCM and coupling with the NHS ester

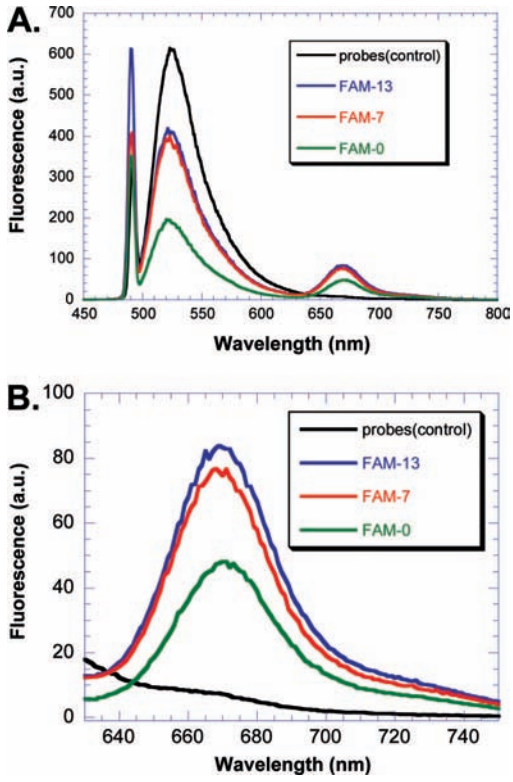

Figure 2. DNA-templated FRET system. PNA-FAM donor **22-0**, **7**, or **13** (2 μM), and PNA-Cy5 **24** (4 μM) were incubated with template DNA (2 μM) or without (control), in 100 mM PBS buffer pH 7.4 at 37 °C for 3 h. (A) The emission spectrum was then recorded from 450−800 nm with excitation at 491 nm, with 5 nm emission and excitation slit windows. (B) Expansion of the 630−750 nm region of the FRET signal.

of Cy5. The PNA was then treated with piperidine to remove the Fmoc group and then cleaved from the column and completely deprotected with TFA/*m*-cresol to give PNA-Cy5 **24**.

FRET Experiments. The donor and acceptor PNAs were then examined for their ability to detect a cDNA sequence by FRET. Fluorescence spectra were obtained with excitation at 491 nm in the presence of 2 μM PNA-FAM and 2 μM DNA and 4 μM PNA-Cy5. Fluorescence emission from fluorescein appears at 525 nm and that from Cy5 at 667 nm (Figure 2). The results clearly show a decrease in fluorescein emission and an increase in Cy5 emission for all the donor acceptor pairs. Maximal FRET was observed for fluorescein donors in positions 7 and 13. The similar FRET efficiencies for such two different spacings can be explained by similar donor acceptor distances resulting from the helical nature of the PNA·DNA duplex (*26*). Given the helical repeat of a PNA·DNA duplex as between 13 Å (*27*) and 15.6 Å (*28*), the fluorescein at position 7 will be out of phase with the Cy5, while the fluorescein at position 13 will be in-phase with the Cy5. The donor with fluorescein in position 0 showed more quenching but less Cy5 emission, indicating other quenching pathways were operating, presumably due to the formation of fluorescein-Cy5 complexes (*29*).

CONCLUSION

In conclusion, we have developed a new Fmoc-PNA building block **1** containing an orthogonally Dde protected alkyl amino group linked to C5 of uracil. We demonstrated that this building block could be incorporated into PNAs site-specifically and then selectively deprotected and derivatized with donor and acceptor fluorophores. Several fluorescein/Cy5 binary PNA probes were shown to detect the DNA sequence corresponding to the antisense mRNA cassette, but the optimal positioning for detecting a single or multimeric mRNA cassette remains to be determined. Further modification of the PNAs will also be required to render them membrane-permeable before they can be used to detect single and multiple mRNA cassettes in living cells.

Scheme 4. Synthesis of the PNA FRET Donor and Acceptor Probes 22 and 24

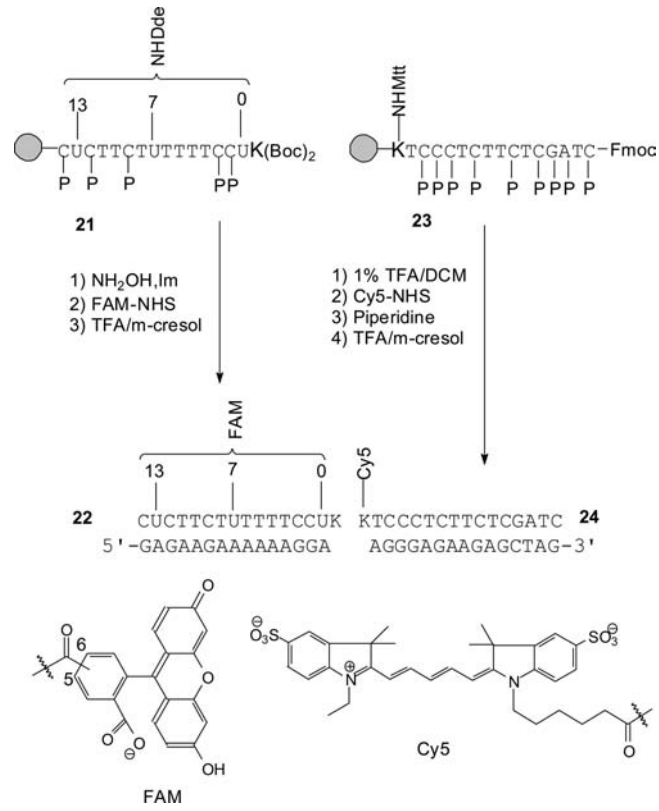

ACKNOWLEDGMENT

We thank Dan Gu and Dian Su for acquiring the MALDI data. This work was supported by the National Institutes of Health as a Program of Excellence in Nanotechnology (1U01 HL080729-01) grant and by the Washington University NIH Mass Spectrometry Resource (Grant No. P41 RR000954) and Washington University NMR facility (Grant No. RR1571501).

Supporting Information Available: Proton and ^{13}C NMR spectra of the intermediates and final product. This material is available free of charge via the Internet at http://pubs.acs.org.

LITERATURE CITED

(1) Santangelo, P., Nitin, N., and Bao, G. (2006) Nanostructured probes for RNA detection in living cells. *Ann. Biomed. Eng. 34*, 39–50.

(2) Fang, X., Mi, Y., Li, J. J., Beck, T., Schuster, S., and Tan, W. (2002) Molecular beacons: fluorogenic probes for living cell study. *Cell Biochem. Biophys. 37*, 71–81.

(3) Cardullo, R. A., Agrawal, S., Flores, C., Zamecnik, P. C., and Wolf, D. E. (1988) Detection of nucleic acid hybridization by nonradiative fluorescence resonance energy transfer. *Proc. Natl. Acad. Sci. U.S.A. 85*, 8790–4.

(4) Tsuji, A., Koshimoto, H., Sato, Y., Hirano, M., Sei-Iida, Y., Kondo, S., and Ishibashi, K. (2000) Direct observation of specific messenger RNA in a single living cell under a fluorescence microscope. *Biophys. J. 78*, 3260–74.

(5) Tsuji, A., Sato, Y., Hirano, M., Suga, T., Koshimoto, H., Taguchi, T., and Ohsuka, S. (2001) Development of a time-resolved fluorometric method for observing hybridization in living cells using fluorescence resonance energy transfer. *Biophys. J. 81*, 501–15.

(6) Ishibashi, K., and Tsuji, A. (2003) IL-2 or IL-4 mRNA as a potential flow cytometric marker molecule for selective collection of living T helper 1 or T helper 2 lymphocytes. *Anal. Chem. 75*, 2715–23.

(7) Abe, H., and Kool, E. T. (2006) Flow cytometric detection of specific RNAs in native human cells with quenched autoligating FRET probes. *Proc. Natl. Acad. Sci. U.S.A. 103*, 263–8.

(8) Nielsen, P. E., Egholm, M., Berg, R. H., and Buchardt, O. (1991) Sequence-selective recognition of DNA by strand displacement with a thymine-substituted polyamide. *Science 254*, 1497–1500.

(9) Nielsen, P. E. (2004) PNA technology. *Mol. Biotechnol. 26*, 233–48.

(10) Lundin, K. E., Good, L., Stromberg, R., Graslund, A., and Smith, C. I. (2006) Biological activity and biotechnological aspects of peptide nucleic acid. *Adv. Genet. 56*, 1–51.

(11) Robertson, K. L., Yu, L., Armitage, B. A., Lopez, A. J., and Peteanu, L. A. (2006) Fluorescent PNA probes as hybridization labels for biological RNA. *Biochemistry 45*, 6066–74.

(12) Dose, C., and Seitz, O. (2008) Single nucleotide specific detection of DNA by native chemical ligation of fluorescence labeled PNA-probes. *Bioorg. Med. Chem. 16*, 65–77.

(13) Xi, C., Balberg, M., Boppart, S. A., and Raskin, L. (2003) Use of DNA and peptide nucleic acid molecular beacons for detection and quantification of rRNA in solution and in whole cells. *Appl. Environ. Microbiol. 69*, 5673–8.

(14) Seitz, O., and Kohler, O. (2001) Convergent strategies for the attachment of fluorescing reporter groups to peptide nucleic acids in solution and on solid phase. *Chemistry 7*, 3911–25.

(15) Englund, E. A., and Appella, D. H. (2005) Synthesis of gamma-substituted peptide nucleic acids: a new place to attach fluorophores without affecting DNA binding. *Org. Lett. 7*, 3465–7.

(16) Cai, J., Li, X., and Taylor, J. S. (2005) Improved nucleic acid triggered probe activation through the use of a 5-thiomethyluracil peptide nucleic acid building block. *Org. Lett. 7*, 751–4.

(17) Diaz-Mochon, J. J., Bialy, L., and Bradley, M. (2004) Full orthogonality between Dde and Fmoc: the direct synthesis of PNA-peptide conjugates. *Org. Lett. 6*, 1127–9.

(18) Zhang, Z., and Fan, E. (2005) Solid-phase and solution-phase syntheses of oligomeric guanidines bearing peptide side chains. *J. Org. Chem. 70*, 8801–10.

(19) Thomson, S. A., Josey, J. A., Cadilla, R., Gaul, M. D., Hassman, C. F., Luzzio, M. J., Pipe, A. J., Reed, K. L., Ricca, D. J., Wiethe, R. W., and Noble, S. A. (1995) Fmoc mediated synthesis of peptide nucleic acids. *Tetrahedron 51*, 6179–94.

(20) Ressner, E. C., Fraher, P., Edelman, M. S., and Mertes, M. P. (1976) Synthesis of 5-substituted uracil derivatives. *J. Med. Chem. 19*, 194–6.

(21) Nielsen, P. E. (2004) *Peptide Nucleic Acids: Protocols and Applications*, Taylor & Francis, Cincinnati.

(22) Bycroft, B. W., Chan, W. C., Chharbra, S. R., and Hone, N. D. (1993) A novel lysine-protecting procedure for continuous flow solid phase synthesis of branched peptides. *J. Chem. Soc., Chem. Commun.* 778–9.

(23) Bourel, L., Carion, O., Gras-Masse, H., and Melnyk, O. (2000) The deprotection of Lys(Mtt) revisited. *J. Pept. Sci. 6*, 264–70.

(24) Thiam, K., Loing, E., Verwaerde, C., Auriault, C., and Gras-Masse, H. (1999) IFN-gamma-derived lipopeptides: influence of lipid modification on the conformation and the ability to induce MHC class II expression on murine and human cells. *J. Med. Chem. 42*, 3732–6.

(25) Marti, A. A., Li, X., Jockusch, S., Stevens, N., Li, Z., Raveendra, B., Kalachikov, S., Morozova, I., Russo, J. J., Akins, D. L., Ju, J., and Turro, N. J. (2007) Design and characterization of two-dye and three-dye binary fluorescent probes for mRNA detection. *Tetrahedron 63*, 3591–3600.

(26) Clegg, R. M., Murchie, A. I., Zechel, A., and Lilley, D. M. (1993) Observing the helical geometry of double-stranded DNA in solution by fluorescence resonance energy transfer. *Proc. Natl. Acad. Sci. U.S.A. 90*, 2994–8.

(27) Eriksson, M., and Nielsen, P. E. (1996) Solution structure of a peptide nucleic acid-DNA duplex. *Nat. Struct. Biol. 3*, 410–3.

(28) Lukeman, P. S., Mittal, A. C., and Seeman, N. C. (2004) Two dimensional PNA/DNA arrays: estimating the helicity of unusual nucleic acid polymers. *Chem. Commun. (Camb.)* 1694–5.

(29) Dietrich, A., Buschmann, V., Muller, C., and Sauer, M. (2002) Fluorescence resonance energy transfer (FRET) and competing processes in donor-acceptor substituted DNA strands: a comparative study of ensemble and single-molecule data. *J. Biotechnol. 82*, 211–31.

BC800284X

Synthesis of PNA FRET Probes via an Orthogonally Protected Building Block for Post-Synthetic Labeling of PNAs at the 5-Position of U.

Bereket Y. Oquare and John-Stephen Taylor*
Department of Chemistry, Washington University in St. Louis, One Brookings Drive,
St. Louis, Missouri 63130

*To whom correspondence should be addressed:

Department of Chemistry
Campus Box 1134
Washington University
One Brookings Drive
St. Louis, MO 63130
email: taylor@wustl.edu

		Page
Figure S1.	^{1}H NMR spectrum of **3**.	S2
Figure S2.	^{13}C NMR spectrum of **3**.	S3
Figure S3.	^{1}H NMR spectrum of **4**.	S4
Figure S4.	^{13}C NMR spectrum of **4**.	S5
Figure S5.	^{1}H NMR spectrum of **5**.	S6
Figure S6.	^{13}C NMR spectrum of **5**.	S7
Figure S7.	^{1}H NMR spectrum of **6**.	S8
Figure S8.	^{1}H NMR spectrum of **7**.	S9
Figure S9.	^{13}C NMR spectrum of **7**.	S10
Figure S10.	^{1}H NMR spectrum of **11**.	S11
Figure S11.	^{13}C NMR spectrum of **11**.	S12
Figure S12.	^{1}H NMR spectrum of **13**.	S13
Figure S13.	^{13}C NMR spectrum of **13**.	S14
Figure S14.	^{1}H NMR spectrum of **14**.	S15
Figure S15.	^{13}C NMR spectrum of **14**.	S16
Figure S16.	^{1}H NMR spectrum of **16**.	S17
Figure S17.	^{13}C NMR spectrum of **16**.	S18
Figure S18.	^{1}H NMR spectrum of **8**.	S19
Figure S19.	^{13}C NMR spectrum of **8**.	S20
Figure S20.	^{1}H NMR spectrum of **10**.	S21
Figure S21.	^{13}C NMR spectrum of **10**.	S22
Figure S22.	^{1}H NMR spectrum of **1**.	S23
Figure S23.	^{13}C NMR spectrum of **1**.	S24

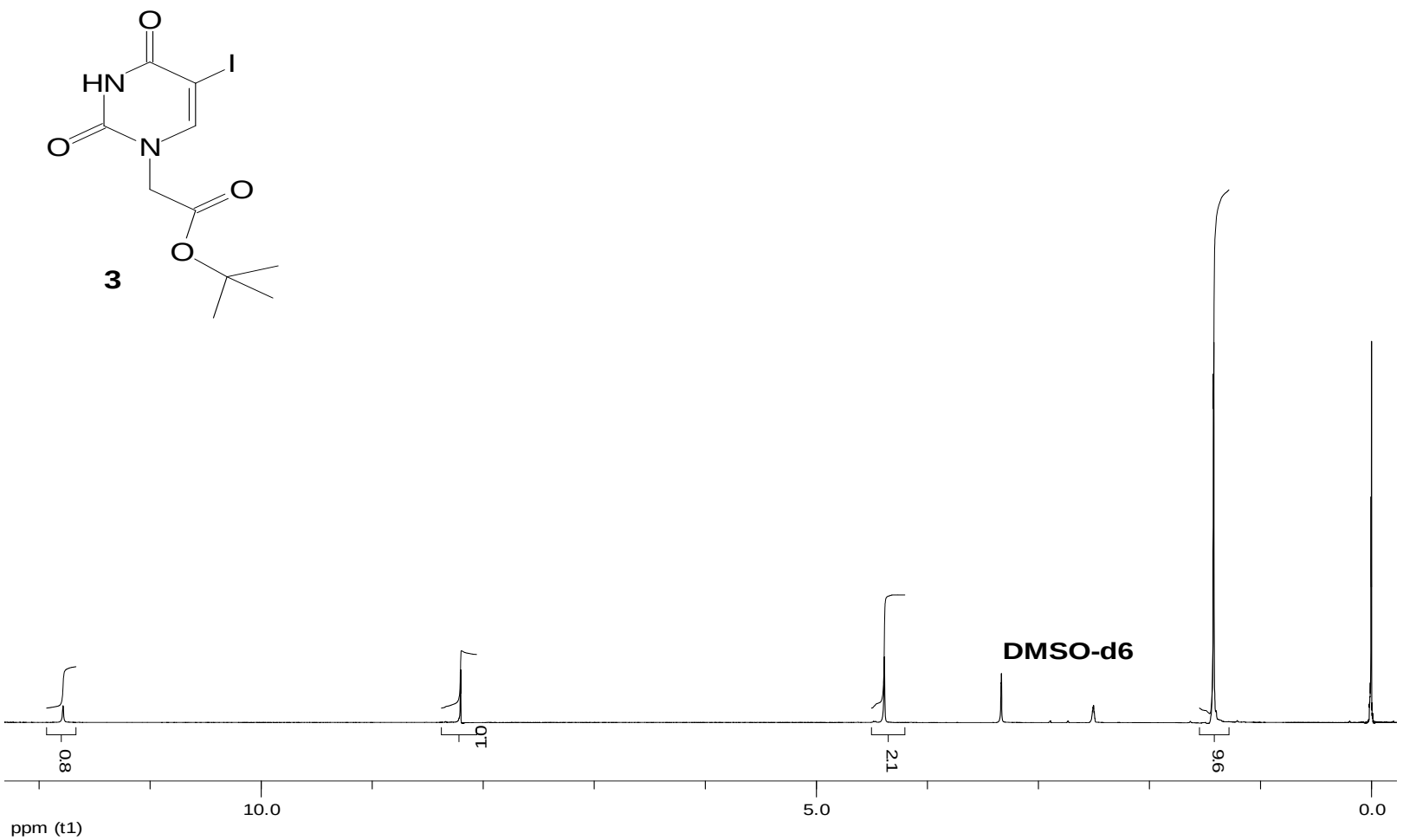

Figure S1. ^{1}H NMR (300MHz, DMSO-d_6) spectrum of tert-butyl 2-(5-iodo-2,4-dioxo-3,4-dihydropyrimidin-1(2H)-yl)acetate (3).

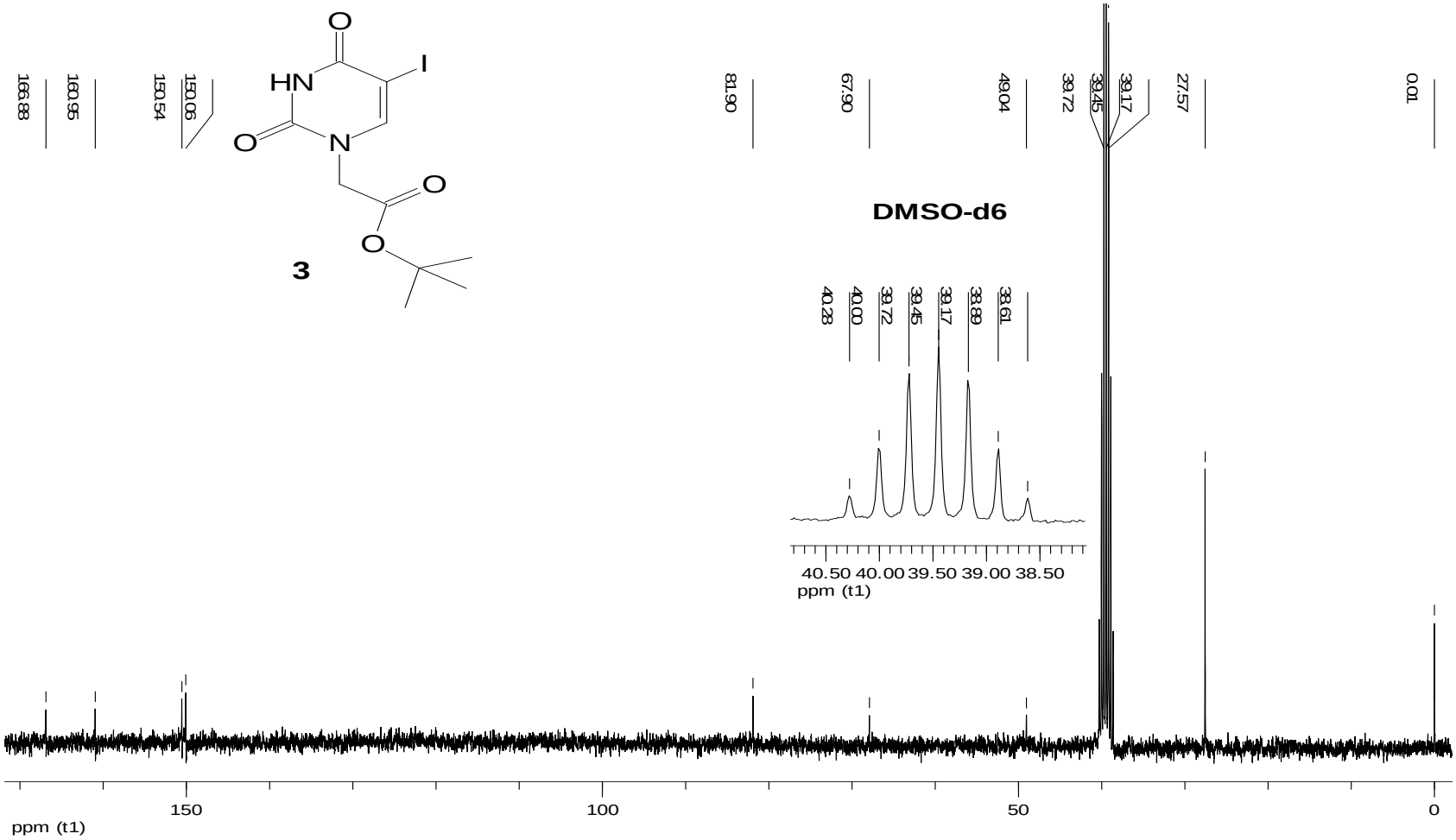

Figure S.2 ^{13}C NMR (75 MHz, DMSO-d_6) spectrum of tert-butyl 2-(5-iodo-2,4-dioxo-3,4-dihydropyrimidin-1(2H)-yl) acetate (3).

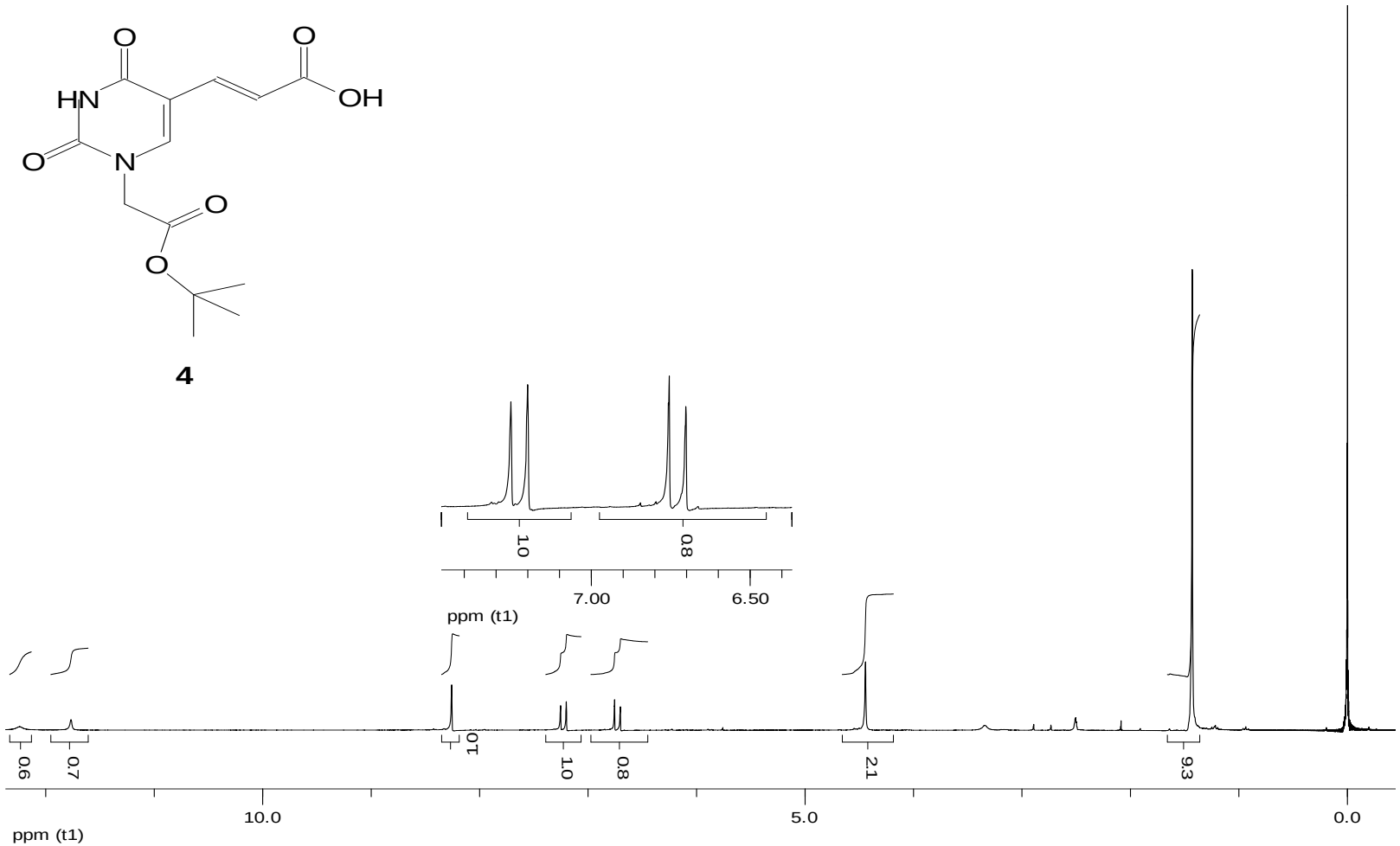

Figure 3.3 ^{1}H NMR (300 MHz, DMSO-d_6) spectrum of (E)-3-(1-(2-tert-butoxy-2-oxoethyl)-2,4-dioxo-1,2,3,4-tetrahydropyrimidin-5-yl)acrylic acid (4).

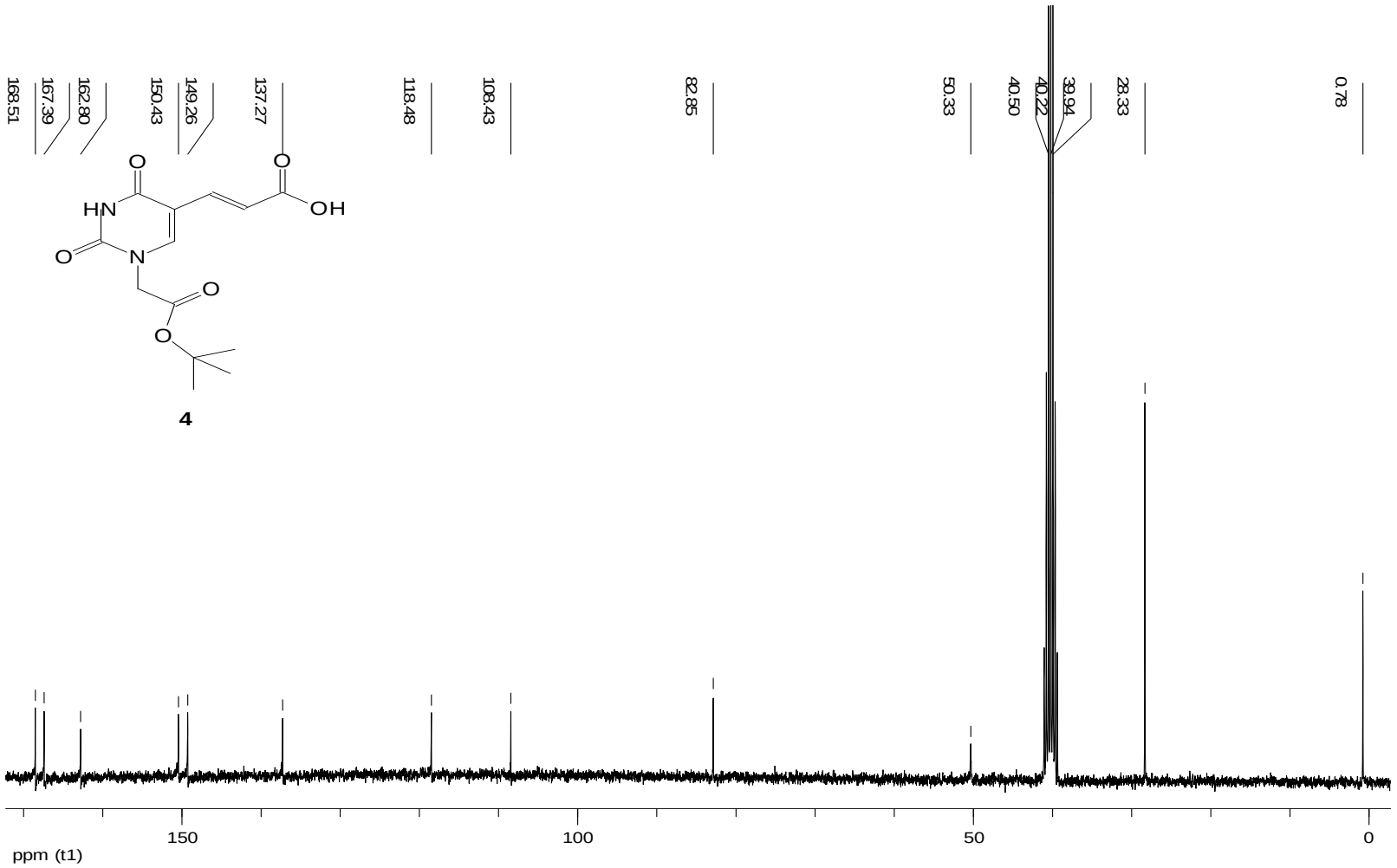

Figure S4. **^{13}C NMR (300 MHz, DMSO-d_6) spectrum of (E)-3-(1-(2-tert-butoxy-2-oxoethyl)-2,4-dioxo-1,2,3,4-tetrahydropyrimidin-5-yl)acrylic acid (4).**

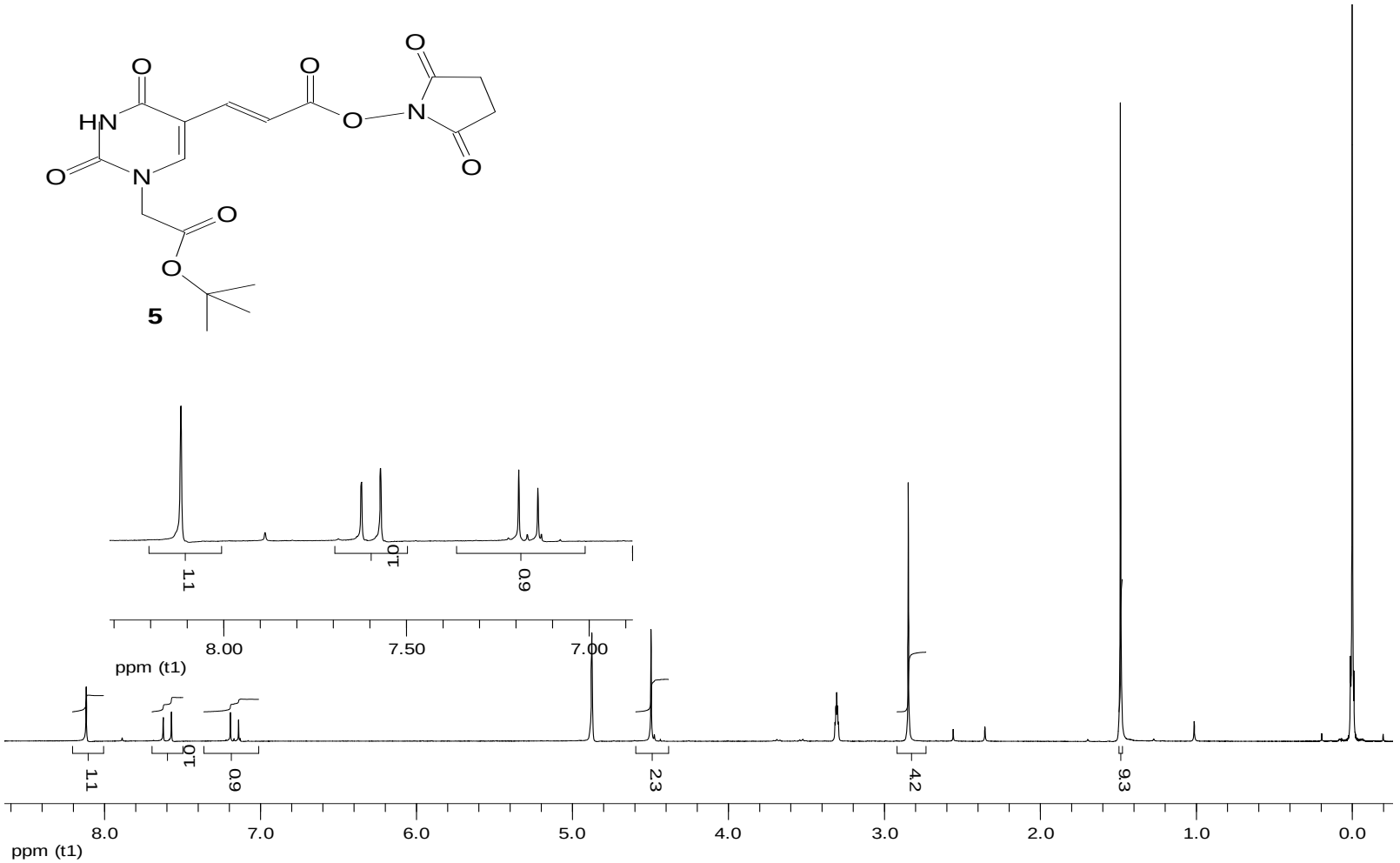

Figure S5. ^{1}**H NMR (300 MHz, DMSO-d$_6$) spectrum of (E)-2,5-dioxopyrrolidin-1-yl-3-(1-(2-tert-butoxy-2-oxoethyl) -2,4-dioxo- 1,2,3,4-tetrahydropyrimidin-5-yl)acrylate (5).**

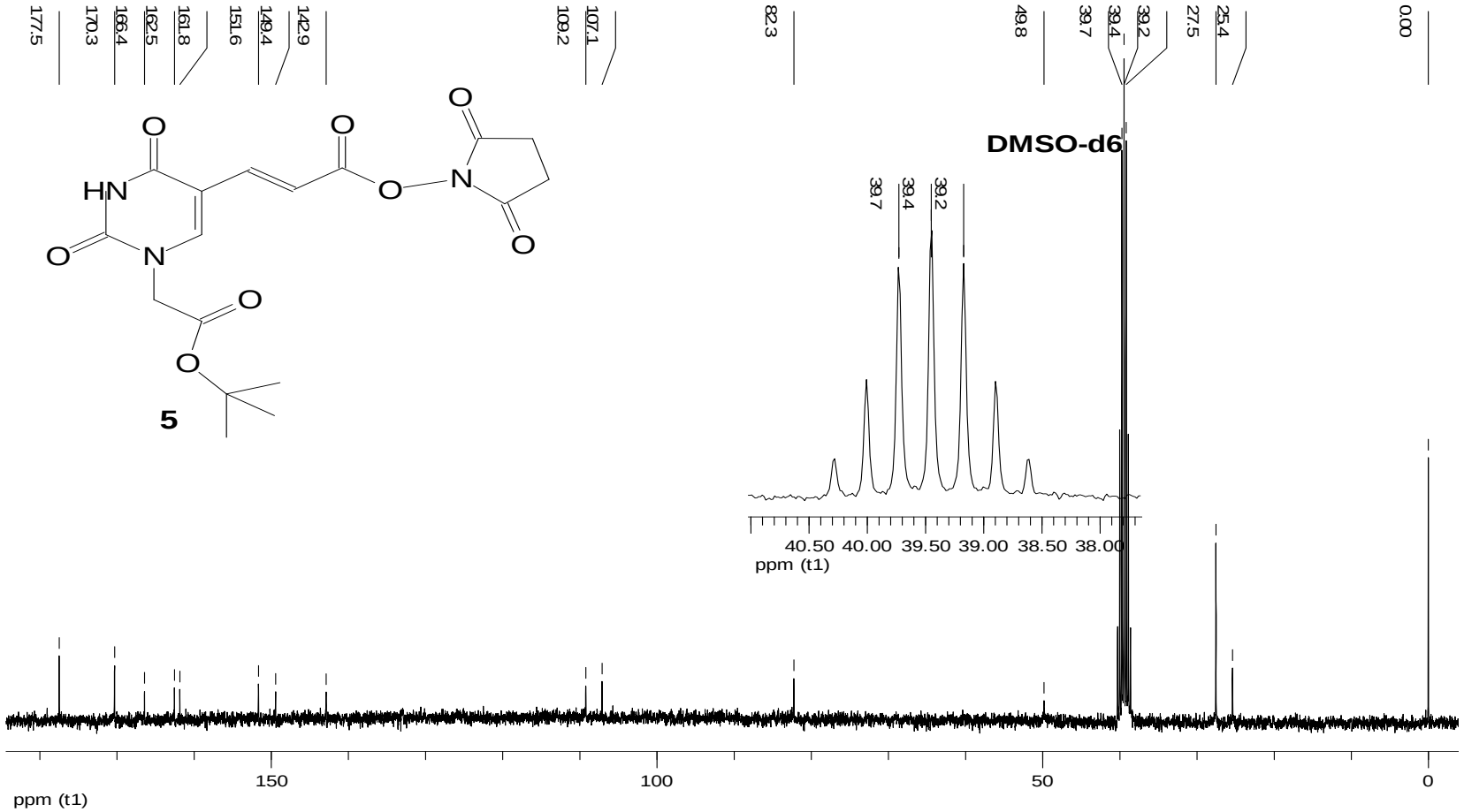

Figure S6. **^{13}C NMR (75 MHz, DMSO-d_6) spectrum of (E)-2,5-dioxopyrrolidin-1-yl-3-(1-(2-tert-butoxy-2-oxoethyl)-2,4-dioxo-1,2,3,4-tetrahydropyrimidin-5-yl)acrylate (5).**

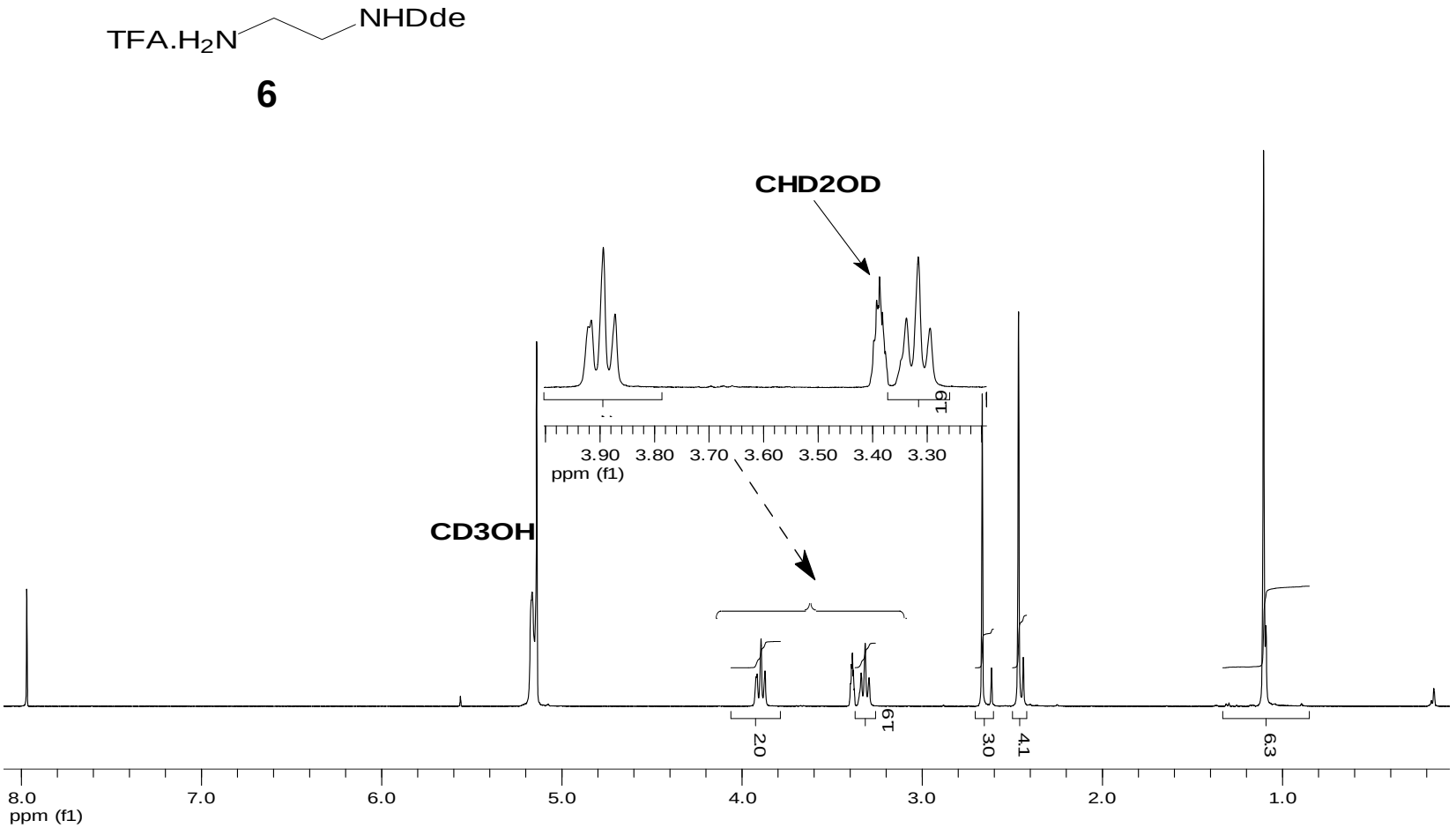

Figure S7. **^{1}H NMR (300 MHz, CD_3OD) spectrum of Synthesis of 2-(1-(2-aminoethylamino)ethylidene)-5,5-dimethyl-1,3-cyclohexanedione (6).**

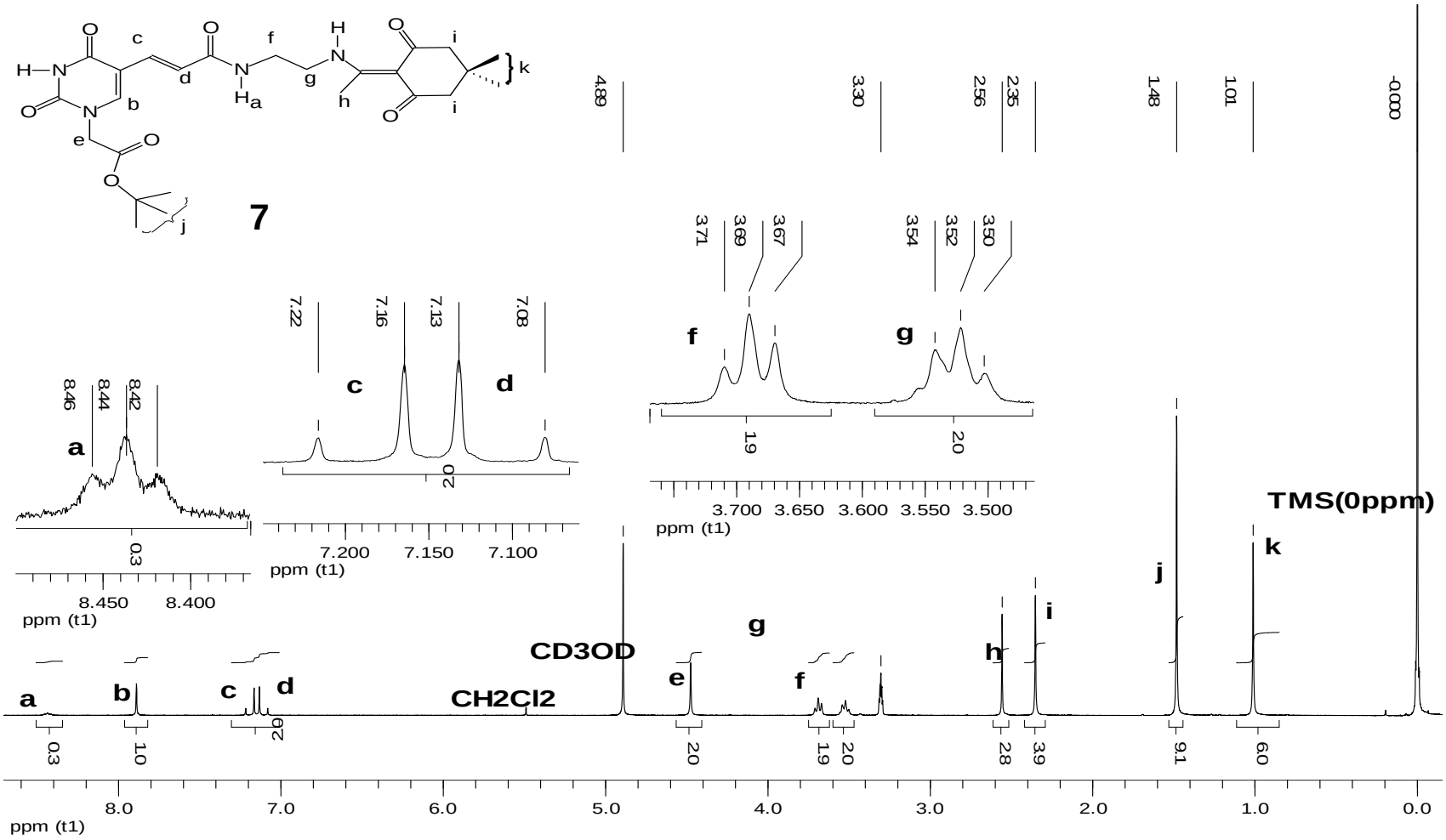

Figure S8. ^{1}H NMR (300 MHz, CD_3OD) spectrum of(E)-tert-butyl 2-(5-(3-(2-(1-(4,4-dimethyl-2,6-dioxocyclohexylid-ene)ethylamino)ethylamino)-3-oxoprop-1-enyl)-2,4-dioxo-3,4-dihydropyrimidin1(2H)-yl)acetate (7).

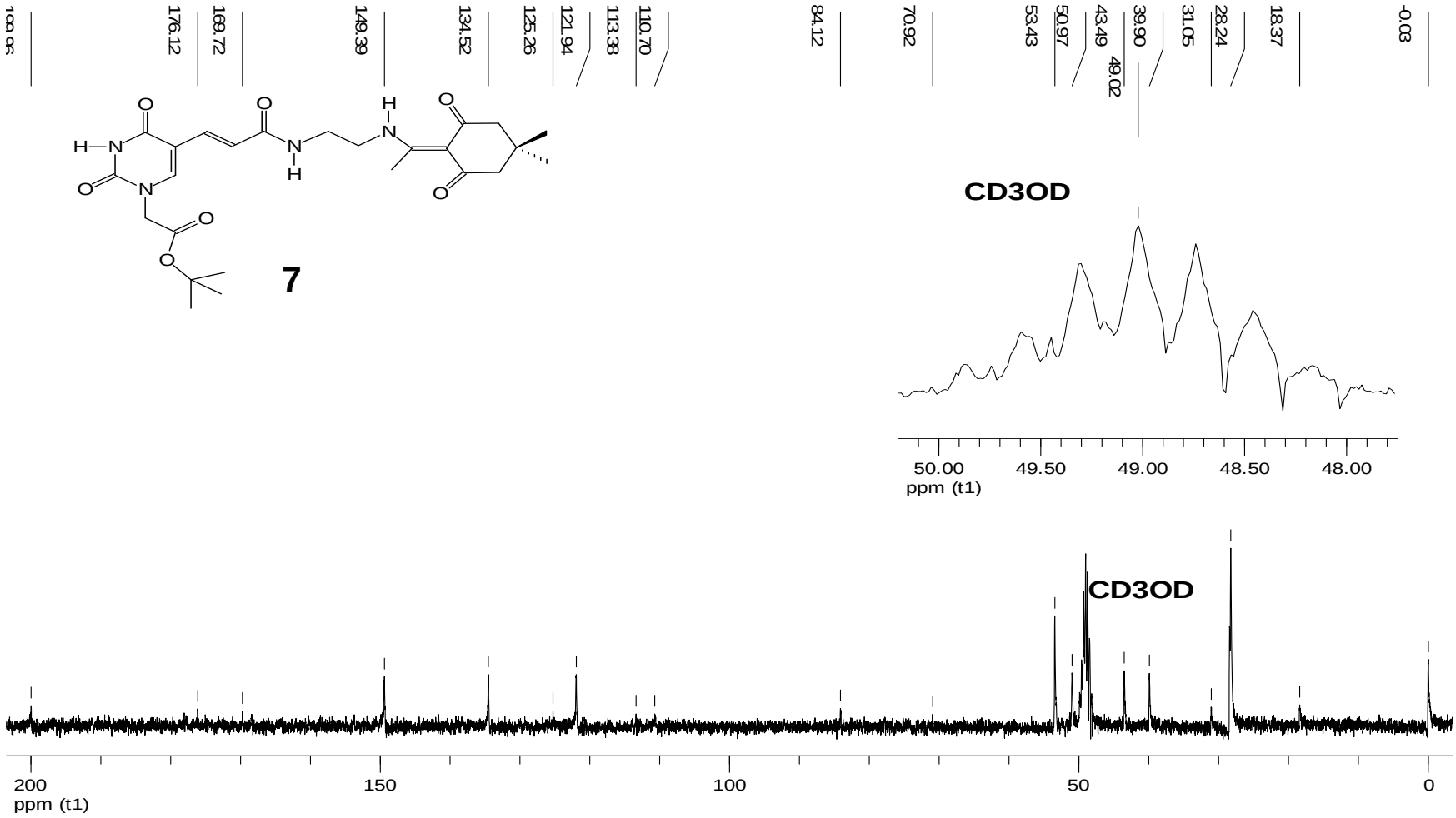

Figure S9. ^{13}C NMR (75 MHz, CD_3OD) spectrum of(E)-tert-butyl 2-(5-(3-(2-(1-(4,4-dimethyl-2,6-dioxocyclohexylid-ene)ethylamino)ethylamino)-3-oxoprop-1-enyl)-2,4-dioxo-3,4-dihydropyrimidin1(2H)-yl)acetate (7).

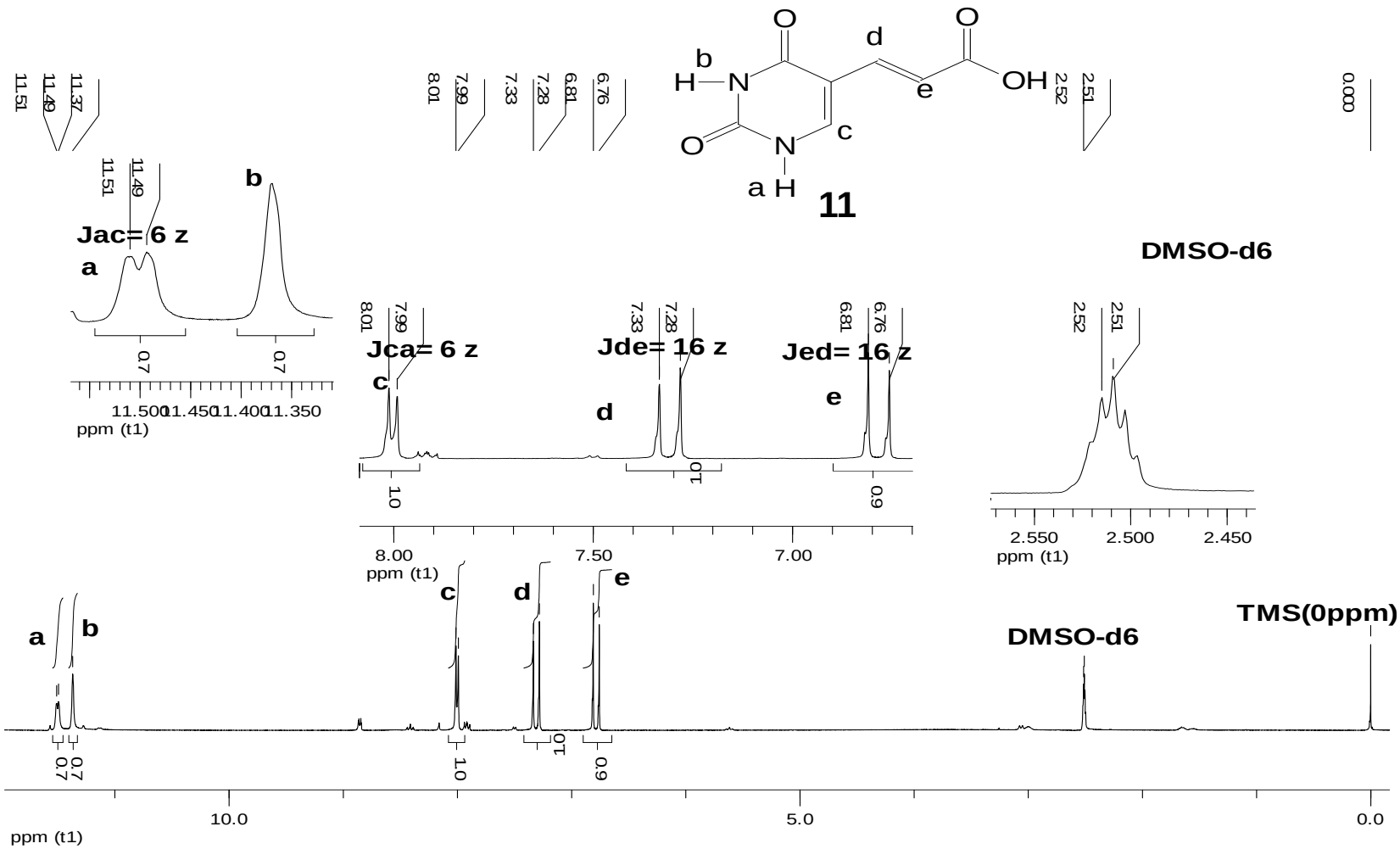

Figure S10. ^{1}H NMR(300 MHz, DMSO-d_6) spectrum of (E)-3-(2,4-dioxo-1,2,3,4-tetrahydropyrimidin-5-yl)acrylic acid (11).

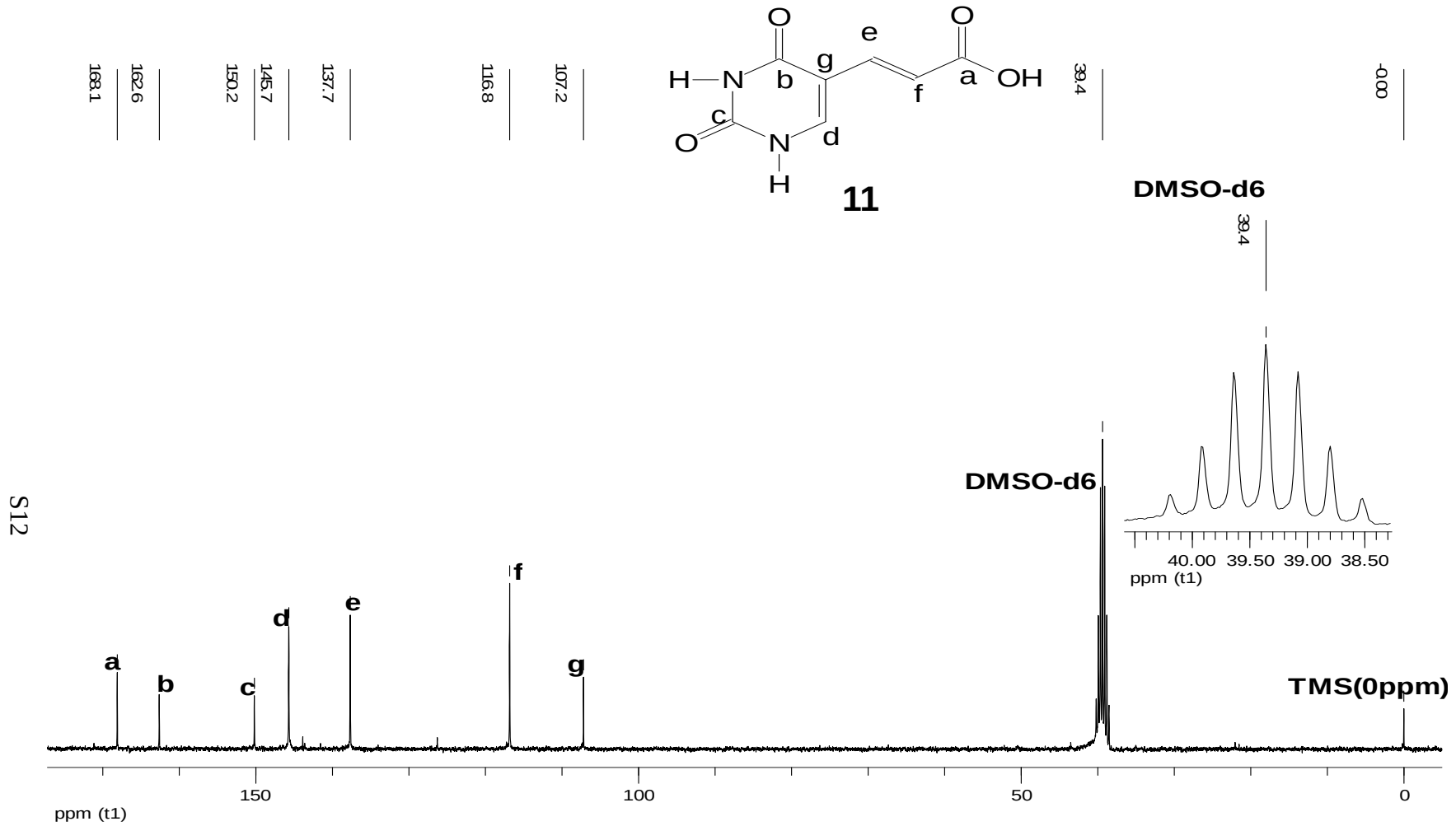

Figure S11. ^{13}C NMR(75 MHz, DMSO-d_6) spectrum of (E)-3-(2,4-dioxo-1,2,3,4-tetrahydropyrimidin-5-yl)acrylic acid (11).

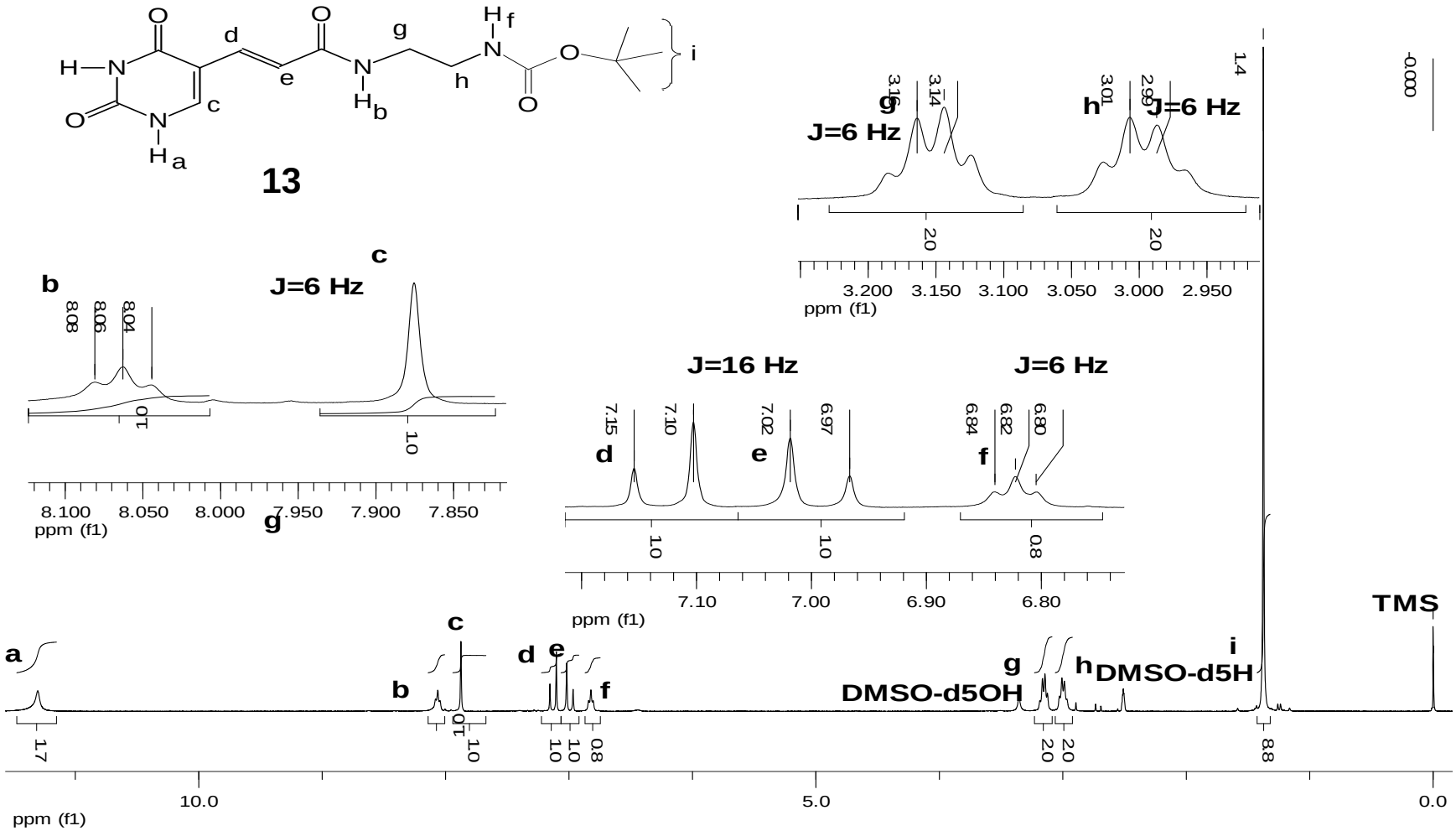

Figure S12. ^{1}**H NMR (300 MHz, DMSO-d$_6$) spectrum of (E)-tert-butyl-2-(3-(2,4-dioxo-1,2,3,4-tetrahydropyrimidin-5-yl) acrylamido)ethylcarbamate (13).**

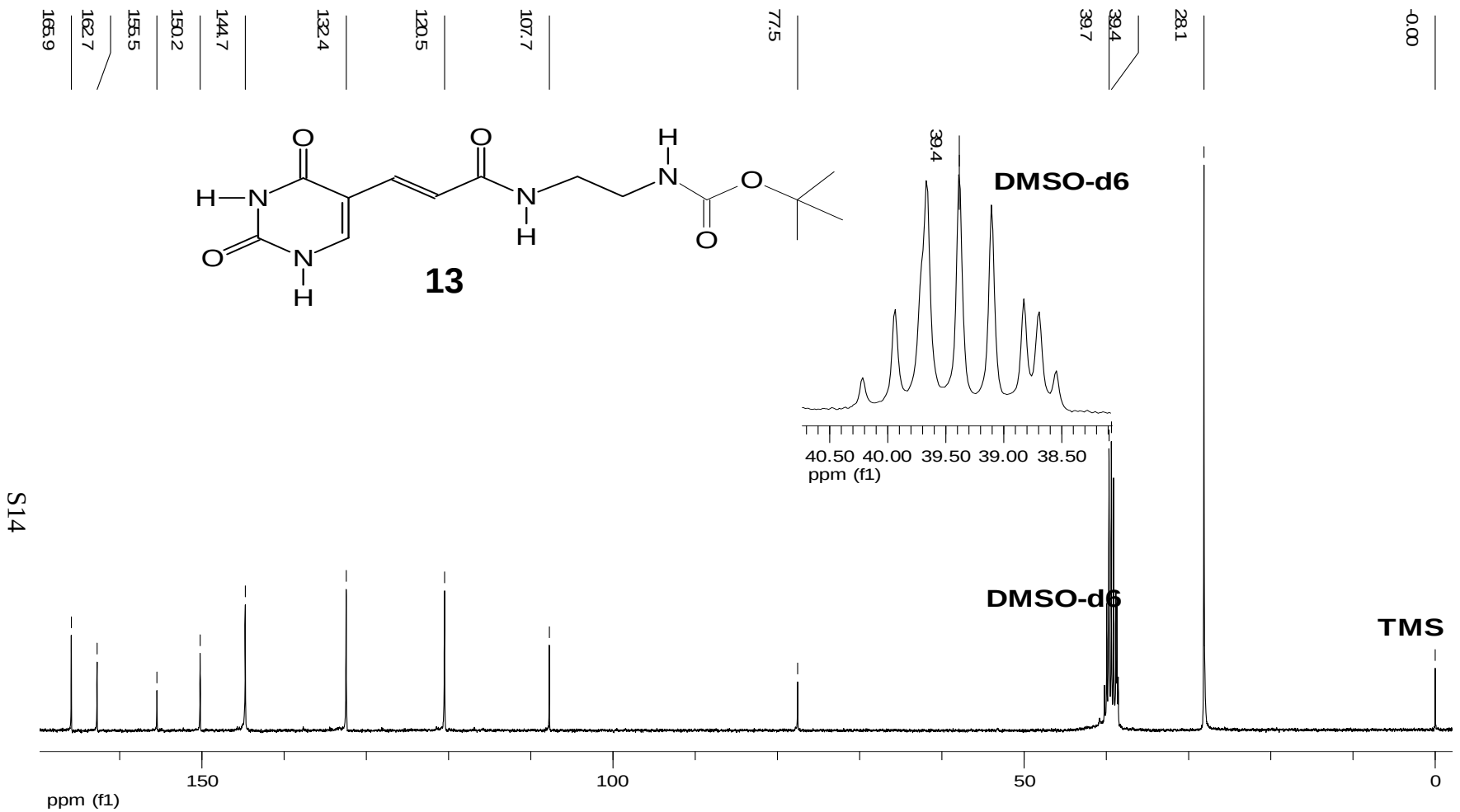

Figure S13. ^{13}C NMR (75 MHz, DMSO-d_6) spectrum of (E)-tert-butyl 2-(3-(2,4-dioxo-1,2,3,4-tetrahydropyrimidin-5-yl)acrylamido)ethylcarbamate (13).

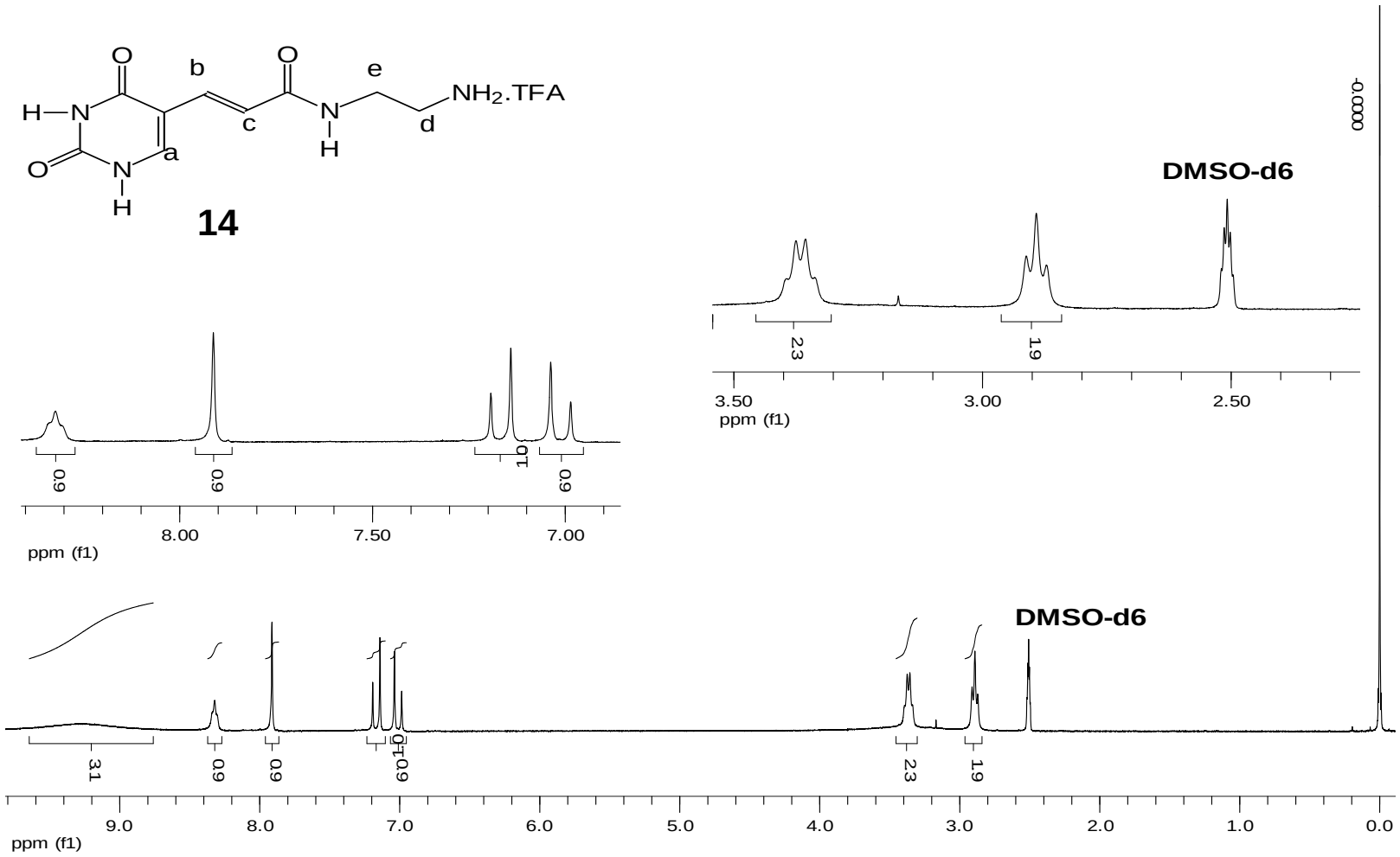

Figure S14. ^{1}H NMR (300 MHz, CD3OD) spectrum of (E)-N-(2-aminoethyl)-3-(2,4-dioxo-1,2,3,4-tetrahydropyrimidin-5-yl) acrylamide (14).

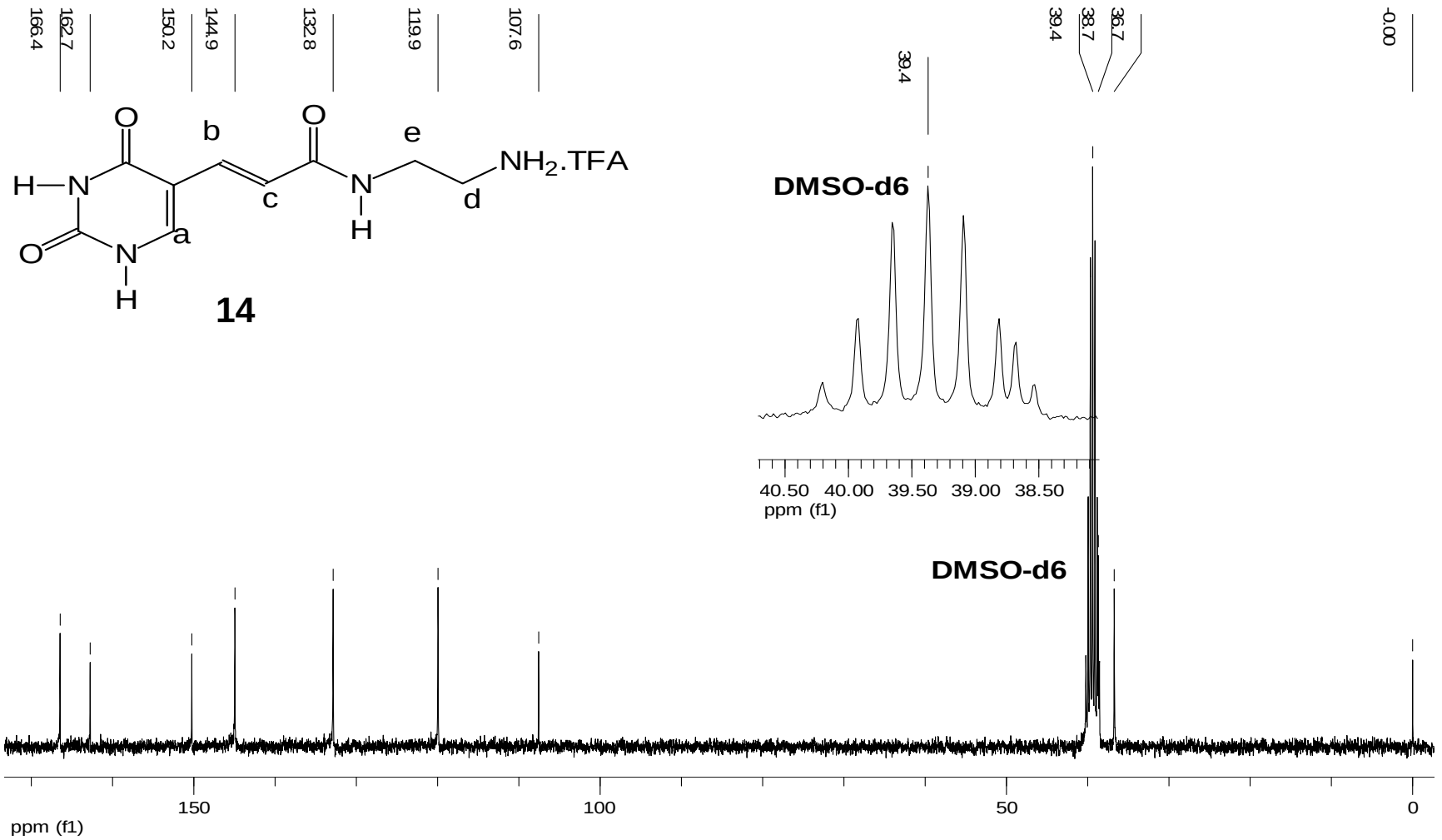

Figure S15. ^{13}C NMR (75 MHz, DMSO-d_6) spectrum of (E)-N-(2-aminoethyl)-3-(2,4-dioxo-1,2,3,4-tetrahydropyrimidin-5-yl) acrylamide (13).

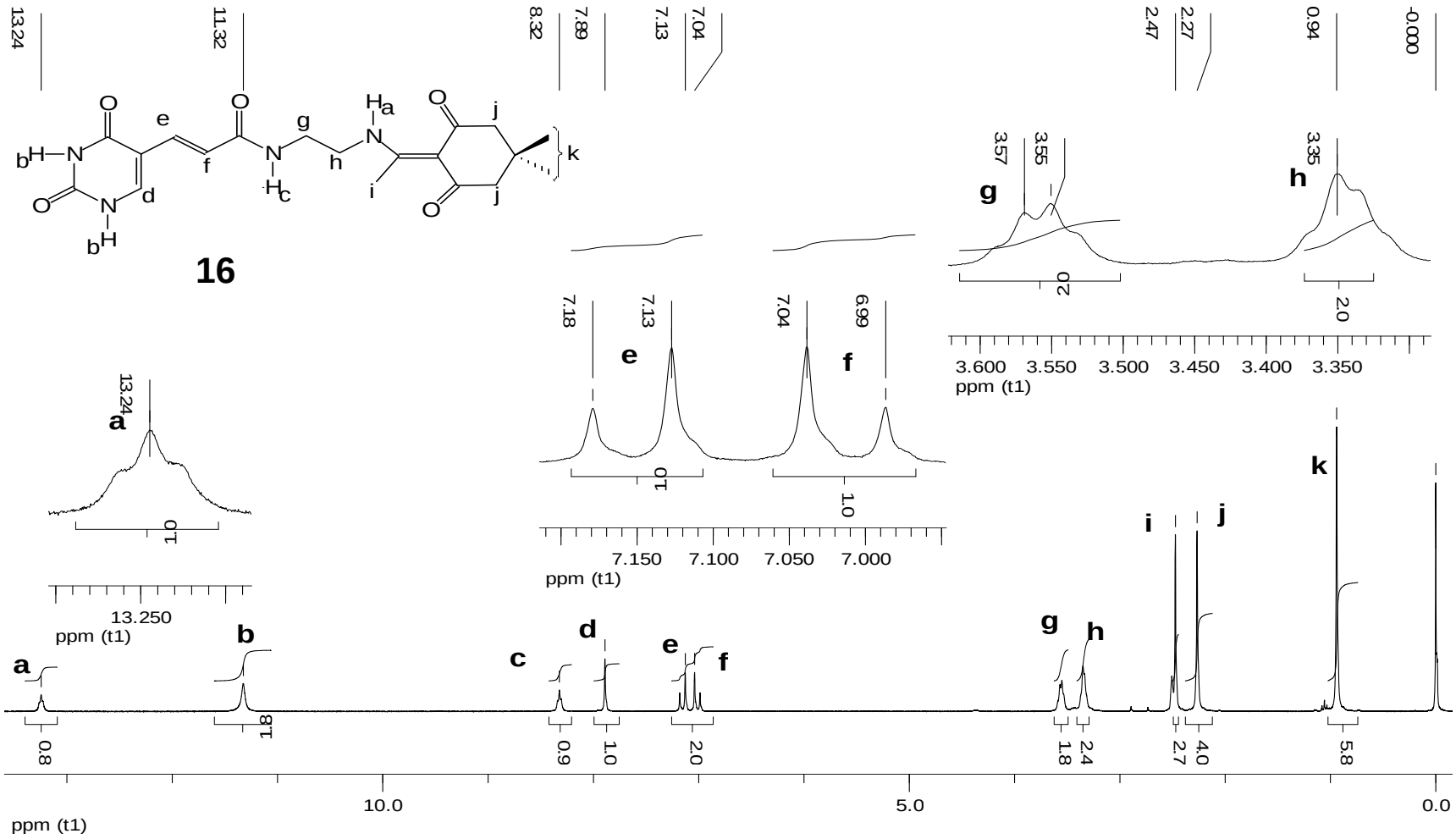

Figure S16. **^{1}H NMR (300 MHz, DMSO-d_6) spectrum of (E)-N-(2-(1-(4,4-dimethyl-2,6-dioxocyclohexylidene)ethylamino) -ethyl)-3-(2,4-dioxo-1,2,3,4-tetrahydropyrimidin-5-yl)acrylamide (16).**

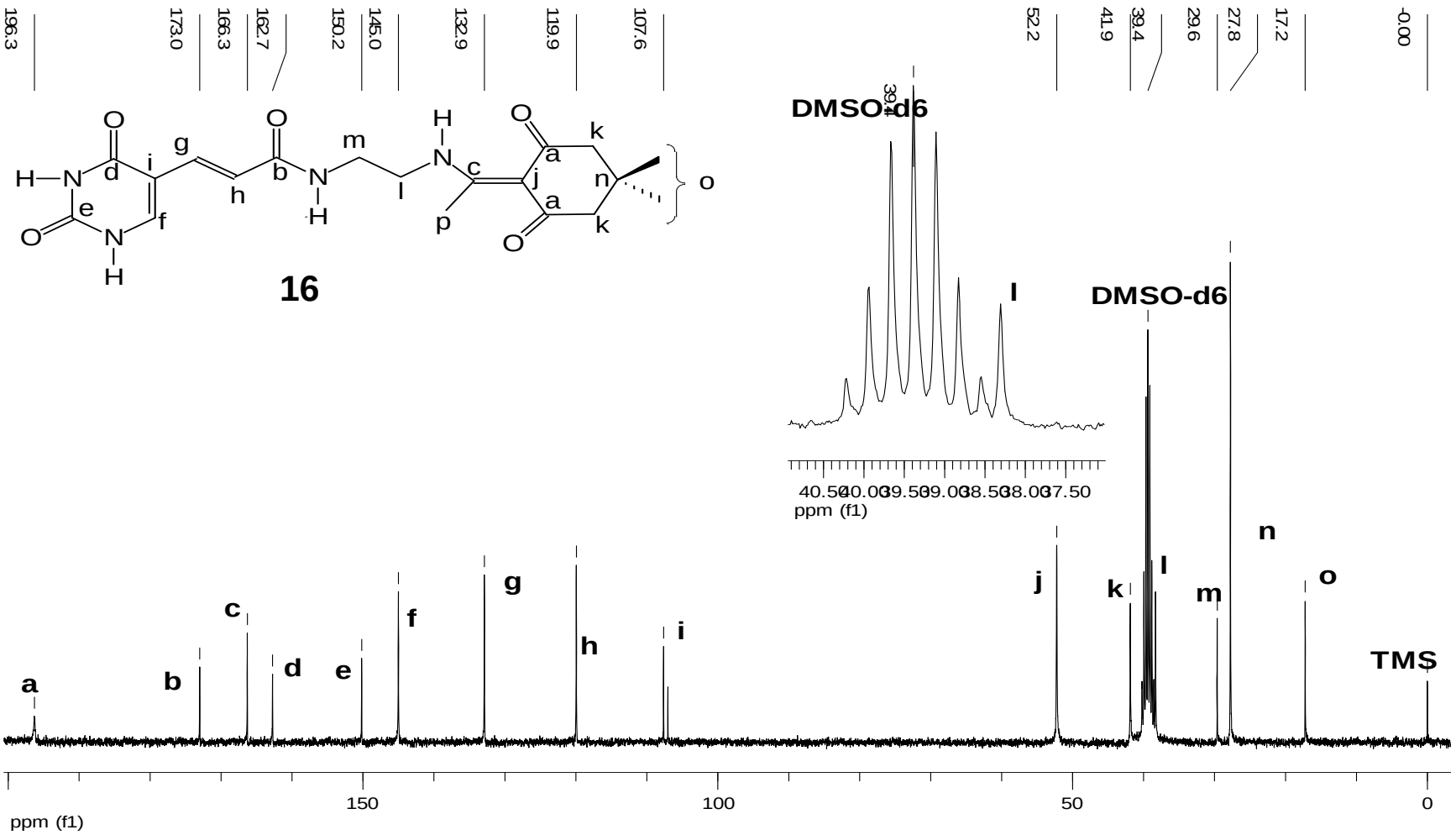

Figure S17. ^{13}**C NMR (75 MHz, DMSO-d$_6$) spectrum of (E)-N-(2-(1-(4,4-dimethyl-2,6-dioxocyclohexylidene)ethylamino) -ethyl)-3-(2,4-dioxo-1,2,3,4-tetrahydropyrimidin-5-yl)acrylamide (16).**

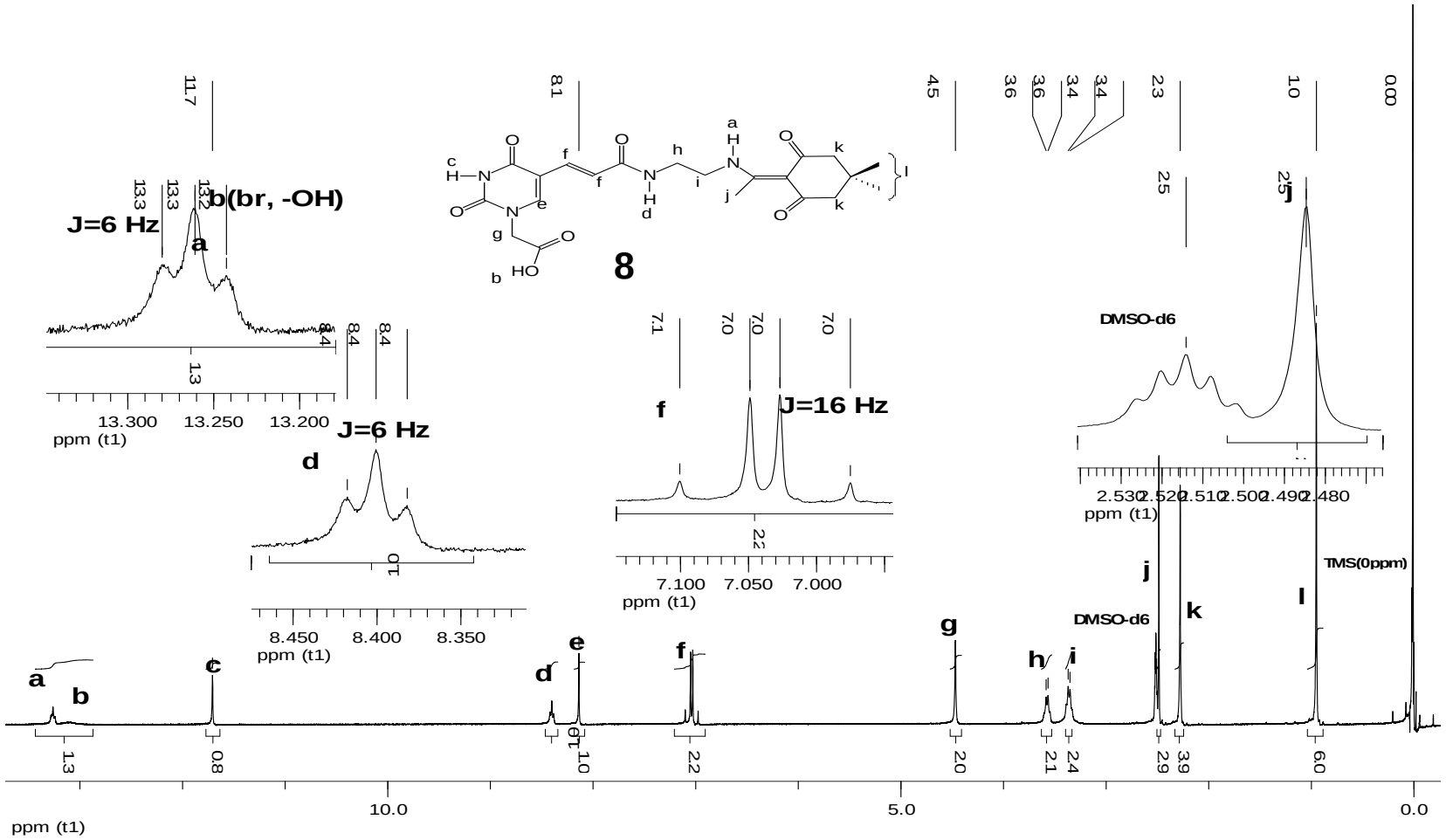

Figure S18. **^{1}H NMR (300 MHz, DMSO-d_6) spectrum of (E)-2-(5-(3-(2-(1-(4,4-dimethyl-2,6-dioxocyclohexylidene)ethyl-amino)ethylamino)-3-oxoprop-1-enyl)-2,4-dioxo-3,4-dihydropyrimidin-1(2H)-yl) acetic acid (8)**

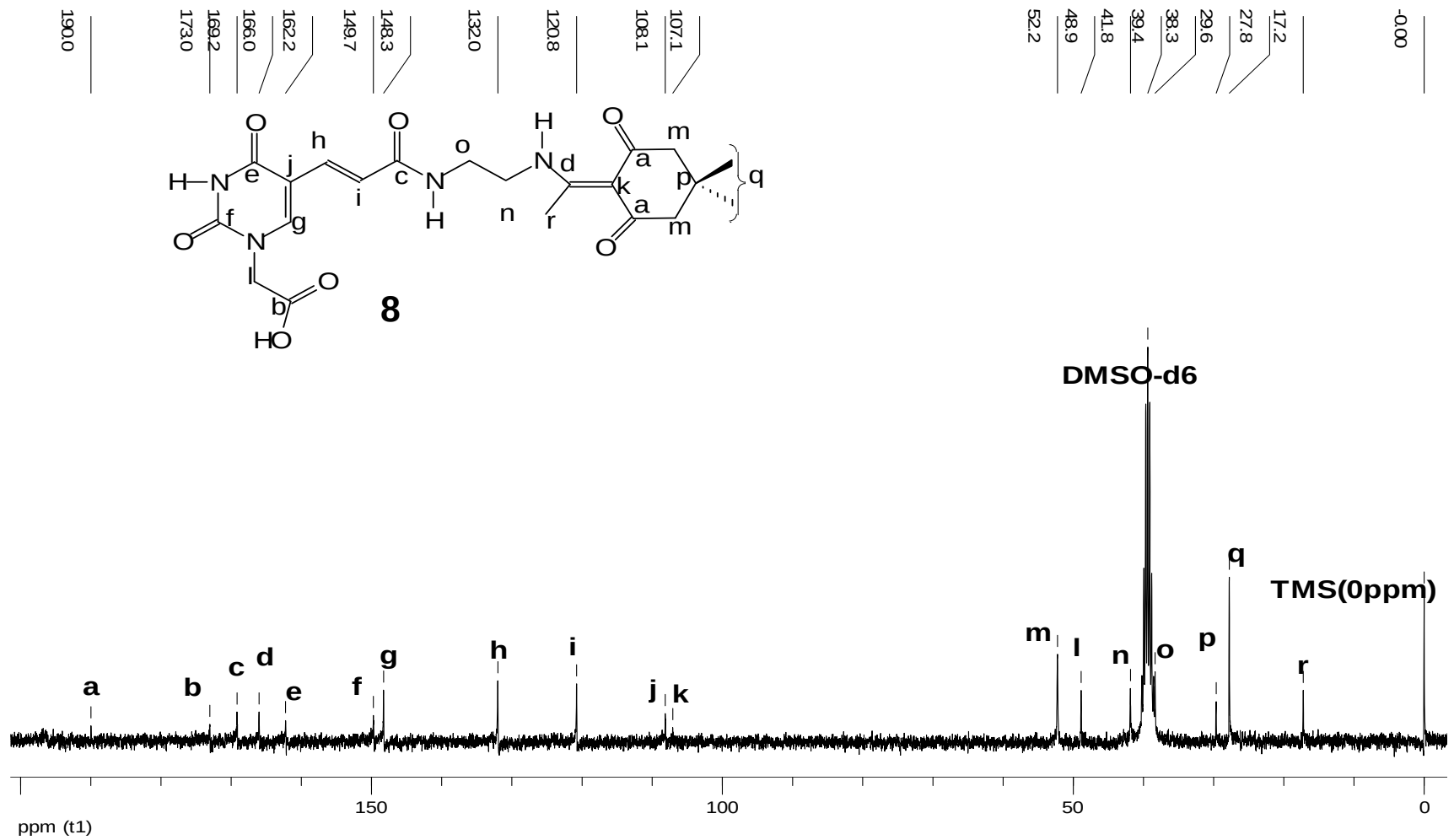

Figure S19. ^{13}**C NMR (75 MHz, DMSO-d$_6$) spectrum of (E)-2-(5-(3-(2-(1-(4,4-dimethyl-2,6-dioxocyclohexylidene)ethyl-amino)ethylamino)-3-oxoprop-1-enyl)-2,4-dioxo-3,4-dihydropyrimidin-1(2H)-yl) acetic acid (8).**

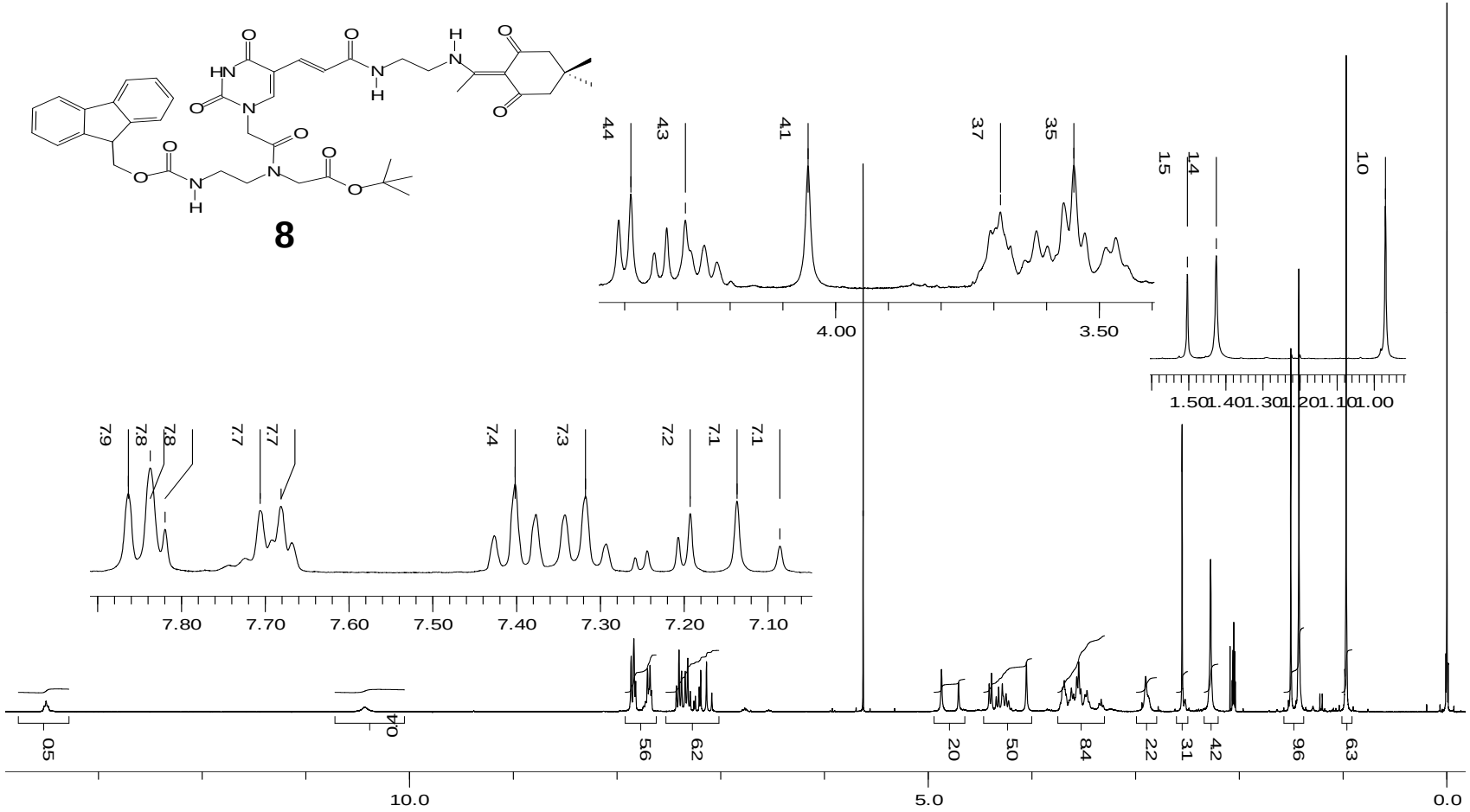

Figure S20. ^{1}H NMR (300 MHz, CD_3COCD_3) spectrum of (E)-tert-butyl 2-(N-(2-(((9H-fluoren-9-yl)methoxy)carbonylamino)ethyl)-2-(5-(3-(2-(1-(4,4-dimethyl-2,6-dioxocyclohexylidene)ethylamino)ethylamino)-3-oxoprop-1-enyl)-2,4-dioxo-3,4-dihydropyrimidin-1(2H)-yl)acetamido) acetate (10).

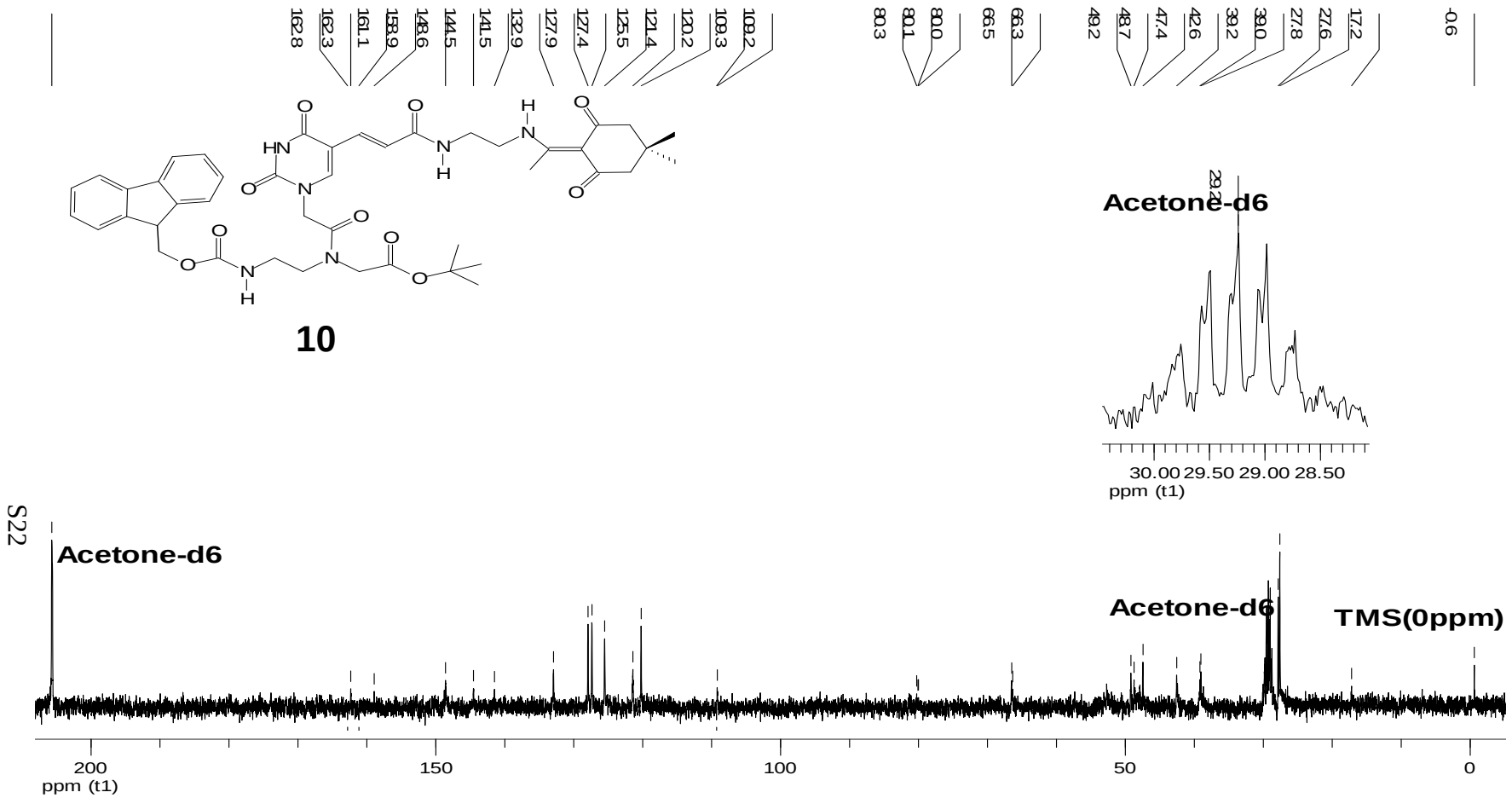

Figure S21. ^{13}C NMR (75 MHz, CD_3COCD_3) spectrum of (E)-tert-butyl 2-(N-(2-(((9H-fluoren-9-yl)methoxy)carbonylamino)ethyl)-2-(5-(3-(2-(1-(4,4-dimethyl-2,6-dioxocyclohexylidene)ethylamino)ethylamino)-3-oxoprop-1-enyl)-2,4-dioxo-3,4-dihydropyrimidin-1(2H)-yl)acetamido) acetate (10).

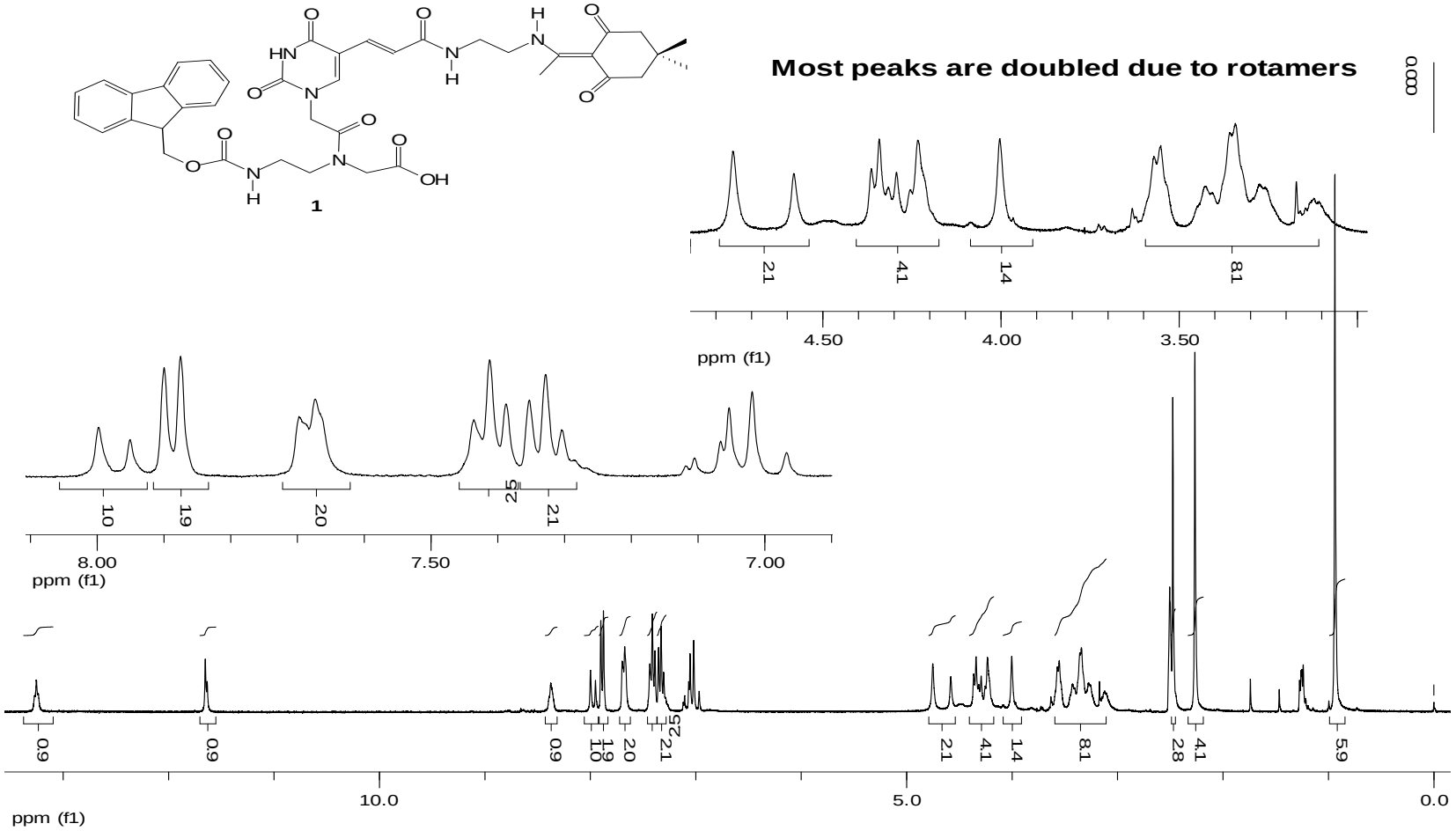

Figure S22. ^{1}H NMR (300 MHz, DMSO-d_6) spectrum of (E)-2-(N-(2-(((9H-fluoren-9-yl)methoxy)carbonylamino)ethyl)-2-(5-(3-(2-(1-(4,4-dimethyl-2,6-dioxocyclohexylidene)ethylamino)ethylamino)-3-oxoprop-1-enyl)-2,4-dioxo-3,4-dihydropyrimidin-1(2H)-yl)acetamido)acetic acid; Fmoc-U' (Dde)-OH (1).

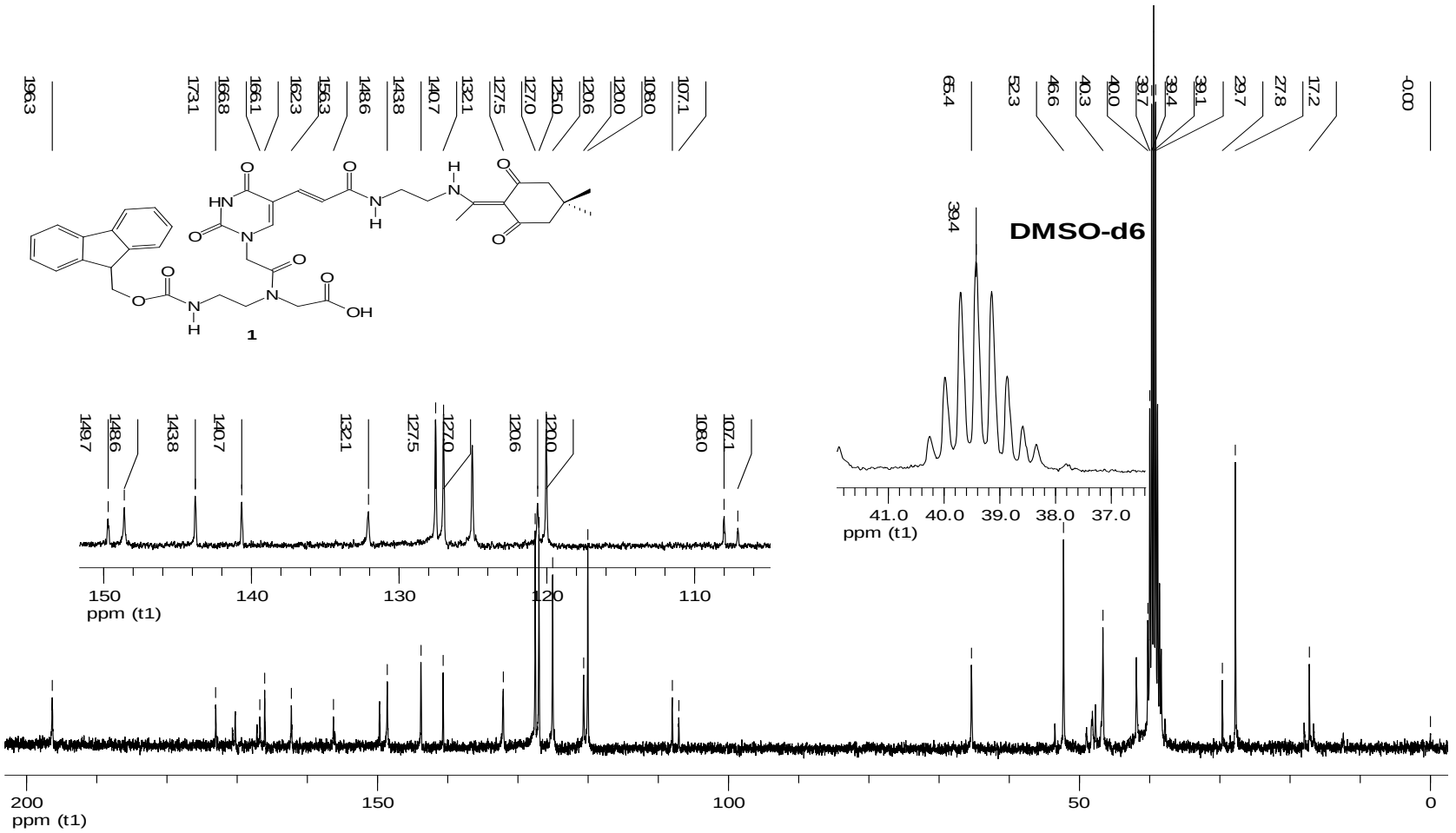

Figure S23. ^{13}C NMR (75 MHz, DMSO-d_6) spectrum of (E)-2-(N-(2-(((9H-fluoren-9-yl)methoxy)carbonylamino)ethyl)-2-(5-(3-(2-(1-(4,4-dimethyl-2,6-dioxocyclohexylidene)ethylamino)ethylamino)-3-oxoprop-1-enyl)-2,4-dioxo-3,4-dihydropyrimidin-1(2H)-yl)acetamido)acetic acid; Fmoc-U' (Dde)-OH (1).

NLS Peptide Conjugated Molecular Beacons for Visualizing Nuclear RNA in Living Cells

Nitin Nitin and Gang Bao*

Department of Biomedical Engineering, Georgia Institute of Technology and Emory University, Atlanta, Georgia 30332.
Received July 27, 2008; Revised Manuscript Received September 23, 2008

Imaging the expression and localization of RNAs in live-cell nucleus can provide important information on RNA synthesis, processing, and transport. Here, we report the development of a bifunctional molecular beacon (NLS-MB) composed of a single nuclear localization sequence (NLS) peptide conjugated to a molecular beacon for efficient delivery and imaging of endogenous RNAs in the nuclei of living cells. We characterized the NLS-MBs by comparing their signal-to-noise ratios with unmodified molecular beacons and determined their efficiency of nuclear import. We demonstrated the specificity and sensitivity of the method by observing in living cells the localization and colocalization of small nuclear RNAs (snRNA) U1 and U2 at discrete foci in the nucleoplasm, and the localization of small nucleolar RNA U3 in the nucleolus. These snRNAs were chosen because of their essential roles in RNA biogenesis. The results were validated using *in situ* hybridization as positive control and random beacons as negative control. This novel approach may be applied to imaging other nuclear RNAs and pre-mRNAs in living cells.

INTRODUCTION

Imaging RNA molecules in the nuclei of living cells can provide important spatial and temporal information on the dynamics of RNA synthesis, processing, and transport. Specifically, in eukaryotic cells, RNA molecules especially mRNAs (mRNA) are processed post-transcriptionally in the nucleus, including splicing, capping, polyadenylation, and methylation. These processing steps are carried out by multiple protein nanomachines and ribonucleoprotein (RNP) complexes (*1, 2*). The mature RNA molecules (including mRNA and rRNA) are then exported to the cytoplasm. Further, many viral genes are processed in the cell nucleus, including transcription and replication of viral RNAs. Therefore, the ability to detect and localize RNA molecules (including small nuclear RNAs) in live-cell nuclei may provide a powerful tool not only for studies of basic biology but also for disease detection and diagnosis. This ability will also complement the approaches of imaging RNA in the cytoplasm of living cells (*3, 4*) so that an integrated picture of RNA transport, distribution, and localization in the cell cytoplasm and nucleus can emerge.

Extensive efforts are being made to develop new approaches to image RNA in living cells. One novel approach uses a fusion protein, GFP-MS2, to track the localization and dynamics of RNA in living cells with single molecule sensitivity (*5*). Although a very powerful technique in tracking RNA dynamics, this method relies on transfecting cells to express GFP-MS2 as a reporter and add to the target RNA multiple (20−25) MS2 binding sequences. Therefore, this technique lacks the ability to image endogenous RNAs, which is important for diagnostic applications especially in vivo and may not be ideal for imaging small RNAs, since binding multiple MS2-GFPs may significantly perturb their structure and dynamics. Further, imaging assays have been performed by introducing fluorescently labeled linear oligonucleotide (ODN) probes into living cells for RNA expression, tracking, and localization studies (*6*−*8*). This approach, however, lacks the ability to distinguish background from true signal. In addition, although 2′-*O*-methyl backbone chemistry has been used to improve the affinity of linear ODN probes for binding to the target sequence (*7, 8*), in many cases the (*9*) increased affinity is associated with decreased specificity of the probe (*9*). To enhance detection specificity and increase signal-to-background ratio, two linear probes with a fluorescence resonance energy transfer (FRET) pair of (donor and acceptor) fluorophores have been used (*6*). This approach, however, may still have a high background signal due to direct excitation of the acceptor and emission detection of the donor fluorescence. Further, this dual-probe approach may be difficult to be used in targeting small nuclear RNAs.

Molecular beacon based approaches have been developed to image endogenous RNA in live cells. Molecular beacons are dual-labeled antisense oligonucleotide (ODN) probes with a fluorophore at one end and a quencher at the other end. In contrast to fluorescently labeled linear ODN probes, molecular beacons are designed to form a stem-loop (hairpin) structure in the absence of a complementary target so that fluorescence of the fluorophore is quenched (*10*). Hybridization with target RNA opens the hairpin and physically separates the reporter from the quencher, allowing a fluorescence signal to be emitted upon excitation. Molecular beacons have been used to image endogenous RNA localization in the cytoplasm of living cells as well as in live embryos during development (*3, 4, 7, 10*−*14*). However, most of the studies on live-cell RNA detection used microinjection to introduce linear or hairpin probes into cells. This delivery approach is labor-intensive when used for studying a large number of cells. Further, probes delivered using microinjection tend to nonspecifically accumulate in the nuclei of cells and thus have a high background signal. In some cases, no localized signal was observed (*12, 14*).

Here, we report the development of a bifunctional probe (NLS-MB) composed of a single nuclear localization sequence (NLS) peptide (*15*−*18*) conjugated to a molecular beacon (MB) for efficient delivery and imaging of endogenous snRNA and snoRNA in living cells. Using a combination of reversible membrane permeabilization and peptide-based delivery, we demonstrated the high specificity and sensitivity of the method

* To whom correspondence should be addressed. Tel: +1 404 385 0373; Fax: +1 404 894 4243; Email: gang.bao@bme.gatech.edu.

10.1021/bc800322a CCC: $40.75 © 2008 American Chemical Society
Published on Web 10/22/2008

Table 1. Design of NLS-Peptide Linked Molecular Beacons

NLS peptide (N terminus) C(Ahx)GGGPKKKRKVED (C terminus)
U1 snRNA Molecular Beacon 5′-Cy3-GCAGCCTGCCAGGTAAGTATGC(dT-C6-NH_2)GC-BHQ2−3′
U2 snRNA Molecular Beacon 5′-Cy3-CGAGCACAGATACTACACTTGGC(dT-C6-NH_2)CG-BHQ2−3′
U3 snoRNA Molecular Beacon 5′-Cy3-CGACCGGCTTCACGCTCAGGGG(dT-C6-NH_2)CG-BHQ2−3′
Negative Control Molecular Beacon 5′-Cy3-CGACGCGACAAGCGCACCGATACG(dT-C6-NH_2)CG-BHQ2−3′

by observing in living cells the localization and colocalization of snRNA U1 and U2 at discrete foci in the nucleoplasm and the localization of snoRNA U3 in the nucleolus. These small RNAs were chosen because U1 and U2 snRNAs are the key members of the spliceosome responsible for splicing of nuclear pre-mRNA (*15, 19*−*21*), and U3 snoRNA is one of the best characterized small nucleolar RNAs involved in the endonucleolytic cleavage of various pre-rRNAs (*22*). Our results clearly demonstrated the ability of the NLS-MBs in detecting snRNAs and snoRNAs in cell nucleus, which can be used to image other nuclear RNAs and pre-mRNAs in studying transcriptional and post-transcriptional processing of RNAs in living cells.

EXPERIMENTAL PROCEDURES

Molecular Beacon Design and Synthesis. Probes (as shown in Table 1) with modification in the stem region (dT-NH_2 on the quencher side) were synthesized by MWG Biotech, NC, and Biosearch Corp, CA. The molecular beacons were designed with regular DNA chemistry (deoxyribonucleotide backbone). The probes were purified using double HPLC. Probes for U1 and U2 snRNPs and U3 snoRNPs were designed with the Cy3 (fluorophore) and BHQ-II (quencher) pair. U2 snRNP probes were also designed to have Cy5 fluorophore and BHQ-III quencher. In all cases, the quencher was conjugated to the 3′-end, while the fluorophore was on the 5-end (Table 1).

Peptide Conjugation and Synthesis. In the conjugation scheme as shown in Figure 1, a nucleotide on the quencher-arm of a molecular beacon was modified with the dT-amine group and a 6-carbon spacer. To generate a stable linkage between a peptide and the modified molecular beacon, the NLS peptide was modified with a cysteine group at its N terminus. Amine-modified molecular beacons were reacted with a heterofunctional cross-linker sulfo-SMCC (Pierce Biotech) for 3 h at room temperature with intermediate shaking. The reaction was carried out with 1× (2 μm) molecular beacons and 20× (40 μm) sulfo-SMCC in PBS buffer. After 3 h, the excess of sulfo-SMCC was removed from the reaction mixture using centrifugal filter (YM-10) with a cutoff of 10 kDa. The resultant solution was brought to the same initial volume by adding PBS and reacted with 2× (4 μm) concentration of Cys-modified NLS peptide overnight at room temperature. Following this reaction, the peptide-linked molecular beacon complex was dialyzed overnight using Slide-A-Lyzer Dialysis Unit, 10K MWCO (Pierce Biotech Inc., Rockford, IL) to remove unconjugated peptide. The NLS peptide (99% purity) as shown in Table 1 was synthesized at SynPep Inc. The NLS peptide sequence was modified at its N terminus to introduce a cysteine residue. The aminohexanoic acid spacer (Ahx) equivalent to a length of ∼2 amino acids was introduced between the N terminus residue of NLS sequence and the cysteine residue to improve conjugation efficiency. Reaction between the thiol group (Cys) on an NLS peptide with the maleimide group introduced on a molecular beacon resulted in the formation of a thiol−maleimide bond, which is stable under physiological conditions, including the reducing intracellular environment.

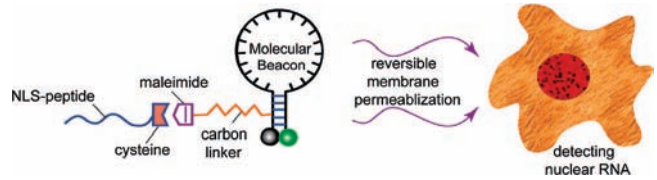

Figure 1. A schematic illustration of the design of a peptide-linked molecular beacon and its delivery into cell nucleus. The NLS peptide is covalently linked to the molecular beacon using a modified nucleotide (dT-C6-NH_2) in its quencher arm. The NLS-linked molecular beacons are delivered into the cytoplasm first using a reversible membrane permeabilization agent Streptolysin O (SLO), and the NLS peptide actively transports the probes into the nucleus of a living cell.

Cell Lines. All experiments in this study were carried out using HeLa cells. This cell line has been used in several nuclear transport studies and also in study of various snRNPs in fixed cells. HeLa cells were cultured using Dulbecco's modified Eagle's medium + fetal calf serum (10%) + horse serum (2.5%). HeLa cells were plated in T-25 (cell culture flask) using 1:10 dilution after each splitting cycle. A batch of HeLa was cultured only for about 10 splitting cycles. For imaging experiments, cells were plated on 4 well or 8 well Nalgene-Nunc chamber cover slides 24 h prior to the experiment.

Solution Assay for S/N of Modified and Unmodified Molecular Beacons. Measurements of signal-to-background ratio of peptide-linked molecular beacons and unmodified beacons were carried out using a SAFIRE microplate monochromator reader (TECAN, Austria). To determine the signal-to-background ratios, 200 nM conventional and peptide-linked molecular beacons were mixed with 200 nM of complementary target, respectively, in the microplate reader, and the fluorescence intensity at equilibrium (10 min incubation time) was recorded. The fluorescence signal of each molecular beacon type (conventional and peptide-linked) in the absence of target was recorded as background signal.

Cellular Delivery and Confocal Imaging. For cellular delivery of peptide-linked molecular beacons, experiments were carried out using HeLa cells (ATCC, VA). For imaging experiments, cells were cultured in a 4 well or 8 well Nalge Nunc culture plate with a glass coverslip bottom in their respective cell culture media (as described above) for 24 h before the experiment. For delivery, peptide-linked molecular beacons were mixed with activated streptolysin O (SLO) in serum-free media and incubated with the specific cells at 37 °C for 10 min. After incubation, the medium was changed to regular serum-rich media, and the cells were incubated for 1 h after changing the medium. We also conducted a control study in which NLS-conjugated, unquenched beacon probes were incubated with cells without streptolysin-O treatment. Our results indicate that there was essentially no uptake of unquenched beacons after 1 h of incubation without SLO (data not shown). Cells were then imaged alive using a confocal microscope (Axiovert LSM-100, Zeiss). For detection and imaging of localization of U1, U2 snRNPs, and U3 snoRNP, we used laser excitation at 543 nm with emission detection using a band-pass filter from 560−610 nm. For imaging colocalization of U1 and U2 snRNPs, we used both 543 and 640 nm laser excitation. The signal was detected using band-pass filter from 560−610 nm for Cy3 signal detection and long-pass filter from 660 nm for Cy5 signal detection.

RESULTS

Design of Peptide-Linked Molecular Beacons. In this study, we have designed and synthesized the peptide-linked molecular beacons targeting U1, U2 snRNAs, and U3 snoRNAs, as well as molecular beacons with a "random" probe sequence. The

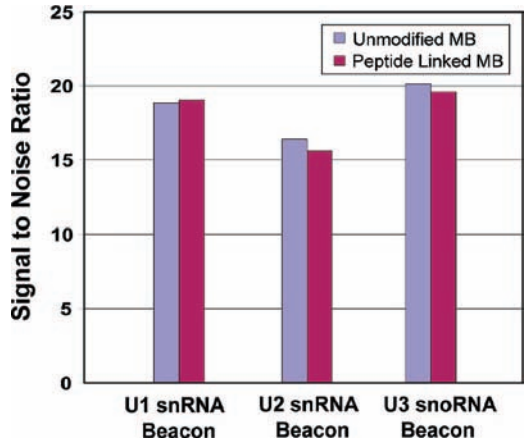

Figure 2. Signal-to-noise ratios of the NLS-linked and unmodified molecular beacons. For molecular beacons designed to target U1, U2 snRNAs, and U3 snoRNA, with and without the NLS peptide there is no significant difference in the signal-to-noise ratios.

specific oligonucleotide sequences of these MBs and the sequence of the NLS peptide are shown in Table 1, with the stem domain of a molecular beacon underlined. The design of these probes to target specific segments of small RNAs in the nuclei of living cells was based on previous fluorescence *in situ* hybridization (FISH) studies in fixed cells with linear oligonucleotide probes, which were shown to be able to access the target (*15, 16, 23*−*27*). The "random" beacon was designed as a negative control, with a 17-base probe sequence that does not have any exact match in the mammalian genome (*3, 4*). The probes used in this study are with deoxyribonucleotide backbone; the dye and quencher pairs (Cy3-BHQ-II and Cy5-BHQ-III) were selected to ensure effective quenching of the probes in their unhybridized state (stem-loop hairpin).

Signal-to-Noise Ratio of Peptide-Linked Molecular Beacons. To determine the possible effect of peptide conjugation on the molecular beacon function, in-solution hybridization assays were carried out to compare the signal-to-noise (S/N) ratios of the peptide-linked molecular beacons and unmodified beacons. When the positively charged NLS peptide is conjugated to a molecular beacon, the electrostatic interactions of the peptide with the negatively charged oligonucleotide hairpin may interfere with the probe-target (RNA) binding. As shown by the results in Figure 2, there were no significant changes in the S/N for each of the molecular beacons after modification with NLS peptide. This result is in agreement with our earlier results with Tat peptide-linked MBs for cytoplasmic delivery and mRNA detection (*4*).

Efficiency of Nuclear Delivery Using Peptide-Linked Molecular Beacons. To provide an estimate for the total concentration of NLS-MBs delivered into nucleus, we synthesized *unquenched*, U3-targeting hairpin probes with and without NLS peptide, respectively, and delivered them into the cytoplasm of living cells using SLO. Since U3 snoRNA does not have any target in the cytoplasm, there should be no specific signal in the cytoplasm; thus, this approach gives a good measure of probe distribution in the cytoplasm due to delivery but not probe−target hybridization. The total fluorescence signal was quantified in the cytoplasm and nucleus of approximately 40 cells. The average ratio of fluorescence intensity in the nucleus to total fluorescence in each cell was determined. A representative image of nuclear and cytoplasmic distribution of probes with and without NLS is shown in Figure 3A. There was a significant increase (∼3.3-fold increase) in the nuclear localization of NLS-conjugated probes compared to probes without the NLS peptides, as demonstrated in Figure 3B. Specifically, about 40% of the NLS-conjugated probes were

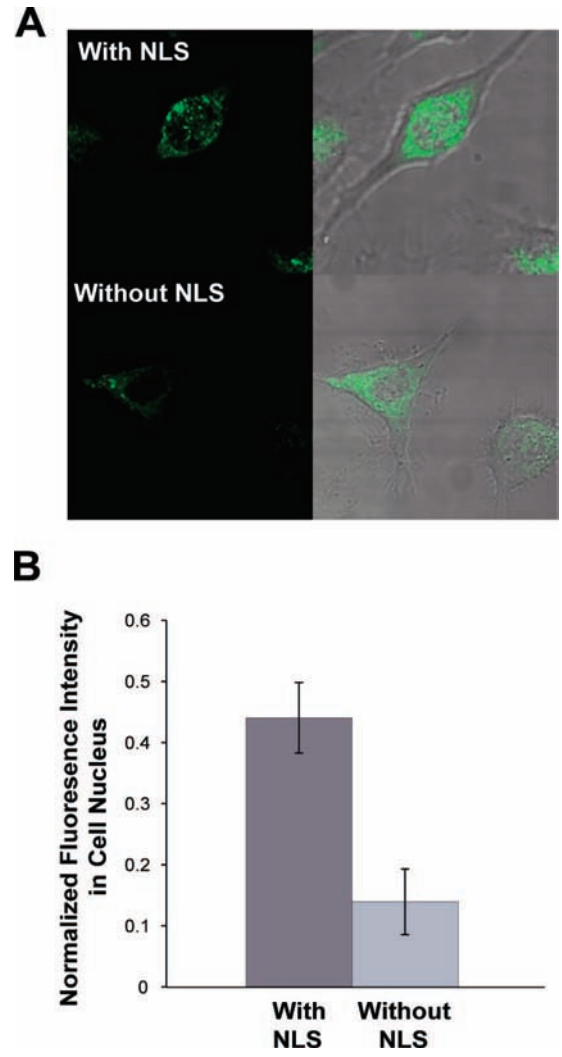

Figure 3. Efficiency of nuclear delivery of NLS-linked MB probes in living cells. (a) Fluorescence images of unquenched probes delivered to the cytoplasm of living cells using SLO. The NLS-conjugated probes show a much higher signal level in cell nucleus as compared with probes without the NLS peptide. (b) Quantification of nuclear delivery efficiency of probes with and without NLS peptide. The average fluorescence signal from NLS-conjugated probes in cell nucleus has a ∼3.3-fold increase compared with probes without NLS peptide.

delivered into the cell nucleus as compared to only about ∼10% of the probes without NLS peptide. This result is in agreement with a recent study using NLS-linked PNA probes (*28*).

Imaging of U3 snoRNP, U1, and U2 snRNPs in the Nuclei of Living Cells. To demonstrate the delivery of NLS-MBs into cell nuclei, and specific detection and imaging of an endogenous small RNA in the nuclei of living cells, we have performed detection assays to target U3 snoRNA and U1 and U2 snRNAs in the nucleus. The NLS-linked MBs targeting the respective small RNAs were introduced into the cell cytoplasm using a reversible cell membrane permeabilization method with Streptolysin O (SLO). The results for the detection of U3 snoRNP in the nucleus of a living cell are shown in Figure 4a. We observed very discrete localization of signal in the nucleolus and discrete peri-nucleolar foci in living cells with no detectable signal in the cytoplasm, consistent with the results obtained in previous studies (*24, 26, 27, 29*), indicating that U3 snoRNA is localized in the nucleolus and in certain cases associated with the cajal bodies. It is known that U3 snoRNA is processed in the cajal bodies prior to its transport and localization to the nucleolus. Furthermore, we observed heterogeneous localization (punctate pattern) of the U3 snoRNA in some nucleoli and a

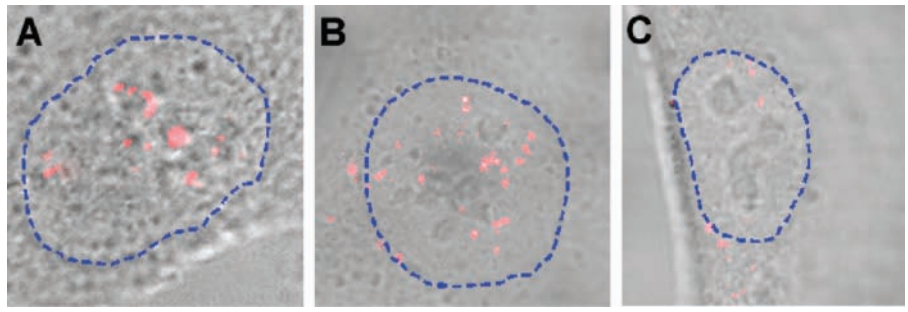

Figure 4. Imaging of U3 snoRNA, U1, and U2 snRNAs in the nucleus of living cells using NLS-linked molecular beacons. (a) Fluorescence signal of molecular beacons targeting U3 snoRNA in the nucleus of a living cell. Note that most of the localized signal was in the nucleolars, with no signal in the cytoplasm. (b) Imaging of U1 snRNA showing localized fluorescence signal in the nucleoplasm of a living cell excluding the nucleolus. Note that the discrete foci of U1 snRNPs are widely distributed in the nucleoplasm, with a few foci in the peri-nucleolar region. Note also the localized signal of U1 snRNPs in the peri-nuclear region of the cytoplasm, indicating the population of the U1 snRNAs exported to the cytoplasm for processing of its 5′ cap. (c) The fluorescence signal suggests that the localization of U2 snRNAs in the nucleus is similar to that of U1 snRNAs but with a much lower abundance.

uniform fluorescence pattern in others, also consistent with previous observations (*24*).

Shown in Figure 4b are the results of detection and imaging of U1 snRNPs using NLS peptide-linked MBs, clearly indicating the discrete localization of the U1 snRNPs in the nucleoplasm of HeLa cells but not in the nucleolus. The localized foci of U1 snRNPs are widely distributed in the nucleoplasm, with a few foci at discrete peri-nucleolar regions (marked with an arrow). This observation of widespread U1 snRNP localization in the nucleoplasm is in agreement with the results of the previous studies (*16, 23, 25, 30*). These studies have shown in fixed cells that U1 snRNPs are associated with both cajal bodies (processing of U1 snRNP after its import from cytoplasm) and speckles (site of assembly of splicing complex). In addition to widespread nucleoplasmic localization, we also observed some localized signal at discrete spots in the cytoplasmic, peri-nuclear region. This signal indicates a fraction of the U1 snRNPs exported to the cytoplasm. It has been suggested that U1 and some other snRNPs (excluding U6) are exported from the nucleus to the cytoplasm for assembly of the snRNP complexes and the processing of their cap (*31*−*33*). They are then imported back into the nucleus and further processed in the cajal bodies before transported to the speckle sites. This export process has been directly observed in *Xenopus* oocytes using labeled RNAs as well as EM-based high-resolution imaging (*17, 32*). These studies have also reported a rapid import of the snRNPs from the cytoplasm to nucleus after processing (*32*). The detection of both the cytoplasmic and nuclear portions of U1 snRNPs in live cells demonstrated clearly the high sensitivity of the molecular beacon based method.

Molecular beacon based imaging assays were performed to detect U2 snRNPs in live cells, and the results, displayed in Figure 4c, showed clear U2 localization at discrete foci in the nucleoplasm, excluding the nucleoli. In contrast to widespread localization of the U1 snRNPs in the nucleoplasm, the fluorescence signal of U2 snRNPs appeared at only a few discrete foci. This observation is in agreement with the results of the localization pattern obtained in previous studies (*16, 23*). We also observed the discrete signal of U2 snRNAs in the peri-nuclear region in the cytoplasm of living cells, confirming that U2 snRNPs, similar to U1 snRNPs, are exported to the cytoplasm for processing.

Taken together, the results in Figure 4 demonstrated that single NLS−peptide linked molecular beacons could be transported from the cytoplasm to the nucleus. To highlight the high specificity of the multifunctional probes in the nucleus, we have imaged RNA at discrete localizations (nucleoplasm vs nucleolus) with high signal to background ratio in the nuclei of living cells. However, it is unclear whether U1 and U2 snRNPs are restricted to the cajal bodies or the pattern observed in this study represents both the cajal bodies and the speckle sites. Answering this question through live-cell imaging studies would require the simultaneous labeling of some of the proteins in the speckle domains such as SF2/ASF (*34, 35*) as well as snRNAs. The combination of fusion proteins such as GFP with an exogenous probe for snRNA can provide valuable insight into the dynamics and function of RNAs in living cells. This will be pursued in a subsequent study.

Co-Localization of U1 and U2 snRNAs in Living Cells. U1, U2, and other members of the snRNP family, together with some non-snRNP proteins, form a splicing complex responsible for the trans-splicing of pre-mRNA transcripts. The assembly of this complex requires various snRNPs to come together to form a defined structure. Although in vitro characterization of the complex has been performed, there are still many unknowns concerning the assembly and inner workings of the spliceosome complex. For example, it is important to know the dynamics of U1 and U2 snRNPs, as they form a complex. As an initial effort, we have studied the colocalization of U1−U2 snRNAs in the cell nucleus to demonstrate the ability to simultaneously detect multiple RNAs in the nuclei of living cells. As shown in Figure 5a,c, some U1 and U2 snRNAs are colocalized at discrete foci in the nucleoplasm, with a more widespread distribution of U1 snRNPs, consistent with the results obtained using FISH with fixed cells (*15, 16*). This U1−U2 colocalization may be the first step toward the formation of the splicesosome. To our knowledge, this is the first direct observation of the colocalization of U1−U2 snRNAs in living cells.

In Situ Hybridization Studies with Fixed Cells. To confirm the observations in live cell studies, as a positive control we carried out fluorescence in situ hybridization (FISH) studies in fixed cells. The cells were fixed and permeablized according to the protocol described in the Experimental Section. The result of detecting U3 snoRNAs in fixed cells, shown in Figure 6a, clearly demonstrated the localization of U3 snoRNAs in the nucleoli, similar to what was observed in live cells. To validate our observations of the localization and colocalization of U1 and U2 snRNAs in living cells, we performed fluorescence in situ hybridization in fixed cells using probes targeted to U1 and U2 snRNAs. The results of the FISH studies are displayed in Figure 6b−d, which clearly show the discrete foci of colocalized U1 and U2 snRNAs. We also observed more widespread localization of the U1 snRNAs in the nucleoplasm of fixed cells. These observations are in good agreement with the results obtained from the live cell studies. In addition, we also observed few discrete foci of U1 and U2 snRNAs in the peri-nuclear region of cytoplasm in agreement with our live cell assay.

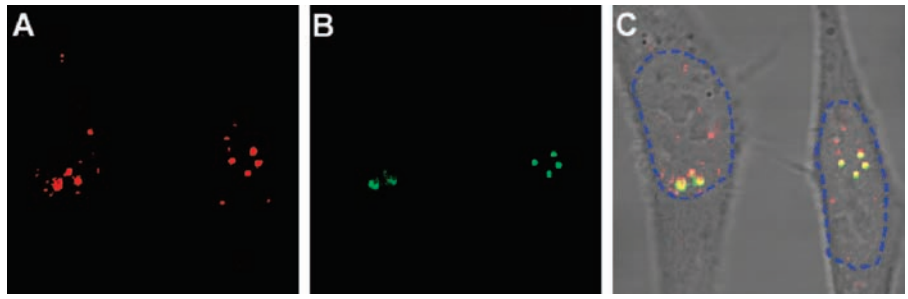

Figure 5. Co-localization of U1 and U2 snRNAs in the nucleoplasm of living cells imaged using peptide-linked molecular beacons. Shown in (a) and (b), respectively, are images of fluorescence signal from U1 and U2 snRNAs in the same living cell. (c) The overlay of the images in (a) and (b) indicating the co-localization of U1 and U2 snRNAs at discrete foci in nucleoplasm. In addition to the U1−U2 co-localized foci, U1 snRNAs can be observed at other foci in the nucleoplasm.

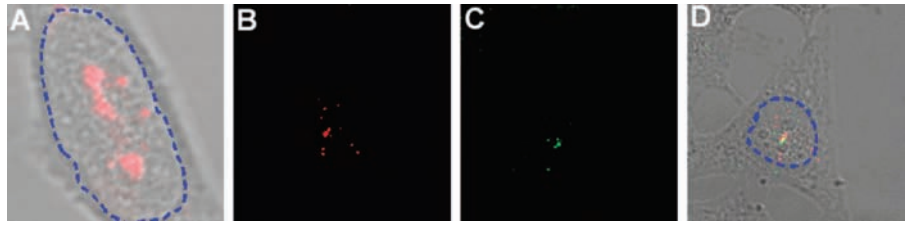

Figure 6. Fluorescence in situ hybridization (FISH) images of the U3 localization and U1−U2 co-localization in the nuclei of fixed cells. (a) FISH image of the U3 snoRNA in a fixed cell indicating that most of the signal was in the nucleolus, consistent with the live-cell results. Shown in (b) and (c), respectively, are FISH images of the U1 and U2 snRNAs localized at discrete foci in the nucleoplasm of the same fixed cell, in good agreement with that observed in live cells. (d) Overlay of the images in (b) and (c) shows the colocalization of U1 and U2 snRNAs in the nucleus of a fixed cell, confirming that observed in live cells.

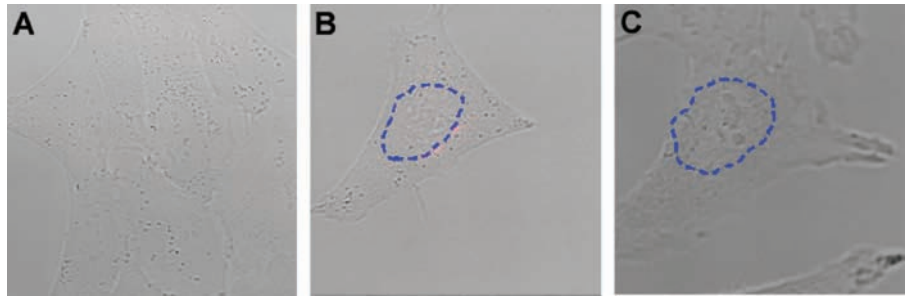

Figure 7. The results of negative control studies. (a) The low background signal from "random" beacons in the nuclei of living cells. These negative-control molecular beacons have no target in the mammalian genome thus indicating nonspecific opening of probes during delivery to and diffusion in the nucleus. (b) Fluorescence signal obtained by delivering U1-targeting molecular beacons without the NLS peptide. Only a few discrete foci in the peri-nuclear region in the cytoplasm could be observed but no significant signal in the nucleus of the living cell. (c) Fluorescence signal as a result of delivering unmodified molecular beacons targeting U3 snoRNA, indicating that without the NLS peptide attached to the U3-targeting beacons no significant signal could be detected in the nucleus or cytoplasm of a living cell.

Negative Control Studies. In order to determine the level of nonspecific interaction of NLS-MB in living cells, we carried out control studies with "random" molecular beacons, which have a specific sequence generated using "random walk", with no exact match in the mammalian genome. Figure 7a shows the signal from the NLS peptide-linked "random" beacons. Evidently, there was very low signal under the same imaging conditions as compared to the results shown in Figure 4. This clearly indicates that peptide-linked molecular beacons delivered to cells maintained their functionality during the course (∼1−1.5 h) of the study.

To further demonstrate that active transport of probes from the cytoplasm to nucleus is necessary for detecting nuclear RNAs (or RNAs in cell nuclei), we did a control study in which the molecular beacons designed to target U1 snRNAs and U3 snoRNA without any NLS peptide conjugated to them were delivered into the cytoplasm using SLO. Shown in Figure 7b and c are, respectively, the resulting images of U1- and U3-targeting molecular beacons. The image in Figure 7b shows discrete foci of U1 snRNA in the peri-nuclear region of the cytoplasm without any detectable signal in the nucleus, while no signal could be detected in the cytoplasm or in the nucleus from U3-targeting beacons (Figure 7c). This clearly indicates that, without conjugation of NLS peptides, molecular beacons cannot be actively transported to the nuclei of living cells. Since U1 snRNAs are exported from the nucleus for processing before being reimported back to the nucleus, their detection in the cytoplasm is in good agreement with our earlier results. Since U3 snoRNAs are being processed in the nucleus only, not exported to the cytoplasm, they should not be detected in the cytoplasm.

DISCUSSION

To detect specific RNAs in the nuclei of living cells, we have developed a peptide-linked molecular beacon, a bifunctional oligonucleotide probe that has both RNA targeting and nuclear delivery functions. Specifically, a single peptide with an NLS sequence was conjugated to a molecular beacon that targets an snRNA or snoRNA. To internalize the peptide-linked molecular beacons into the cytoplasm of living cells, we adopted a reversible permeabilization approach using streptolysin O (SLO). In some previous studies (*6*, *8*, *11*, *12*, *14*), probes (including

molecular beacons) were introduced into the cytoplasm of living cells by microinjection; however, upon microinjection most probes were nonspecifically sequestered in the nucleus, and molecular beacons had nonspecific opening in both the cytoplasm and the nucleus (*7*, *12*).

Unlike previous molecular beacon based studies in which high background signal was present in detecting RNAs in the nuclei of cells, the results presented in this study show highly specific targeting of nuclear RNAs with very low background levels (based on "random" beacon images and other negative controls). The significant difference between our results and that reported previously is believed to be a consequence of the delivery approach in introducing molecular beacons into living cells. The approach developed in this study allows for delivery of probes into the nucleus with high efficiency while maintaining the normal function of molecular beacons. Our results of detecting U1, U2 snRNAs, and U3 snoRNA, together with the control studies, provide strong evidence that the peptide-linked molecular beacons can be used not only to study fundamental RNA biology but also as a diagnostic imaging tool (*36*, *37*). In combination with our previous approaches (*4*), this method has the potential to image transcriptional and post-transcriptional processing of RNAs in living cells and provide an integrated picture of RNA distribution in the cell nucleus and cytoplasm. Although the delivery method presented in this study was used in cell culture assays, the NLS peptide can be combined with Tat and other cell penetrating peptides (CPPs) for in vivo delivery of probes. With molecular beacons designed to have near-infrared (NIR) reporter dyes, this approach can be further used to image RNAs in the cell nucleus of tissue samples.

In summary, in this study we have developed a novel method that allows for direct imaging of endogenous RNAs in the nuclei of living cells. This approach combines the high specificity and signal-to-noise ratio of molecular beacons with the ability of NLS peptide to effectively deliver oligonucleotide probes into the cell nucleus. This approach can be further combined with various protein tags to develop a comprehensive understanding of RNA biogenesis, transport, translation, and metabolism. This understanding will potentially lead to novel targets for therapeutic interventions in various diseases as well as significantly enhance our understanding of cell biology.

ACKNOWLEDGMENT

This work was supported by the NIH Roadmap Initiative in Nanomedicine through a Nanomedicine Development Center award PN2EY018244 (G.B.). We thank Phillip J. Santangelo for helpful discussions.

LITERATURE CITED

(1) Bentley, D. (2002) The mRNA assembly line: transcription and processing machines in the same factory. *Curr. Opin. Cell Biol. 14*, 336–42.

(2) Maniatis, T., and Reed, R. (2002) An extensive network of coupling among gene expression machines. *Nature 416*, 499–506.

(3) Santangelo, P. J., Nix, B., Tsourkas, A., and Bao, G. (2004) Dual FRET molecular beacons for mRNA detection in living cells. *Nucleic Acids Res. 32*, e57.

(4) Nitin, N., Santangelo, P. J., Kim, G., Nie, S., and Bao, G. (2004) Peptide-linked molecular beacons for efficient delivery and rapid mRNA detection in living cells. *Nucleic Acids Res. 32*, e58.

(5) Shav-Tal, Y., Darzacq, X., Shenoy, S. M., Fusco, D., Janicki, S. M., Spector, D. L., and Singer, R. H. (2004) Dynamics of single mRNPs in nuclei of living cells. *Science 304*, 1797–1800.

(6) Tsuji, A., Koshimoto, H., Sato, Y., Hirano, M., Sei-Iida, Y., Kondo, S., and Ishibashi, K. (2000) Direct observation of specific messenger RNA in a single living cell under a fluorescence microscope. *Biophys. J. 78*, 3260–74.

(7) Molenaar, C., Marras, S. A., Slats, J. C., Truffert, J. C., Lemaitre, M., Raap, A. K., Dirks, R. W., and Tanke, H. J. (2001) Linear 2′ O-Methyl RNA probes for the visualization of RNA in living cells. *Nucleic Acids Res. 29*, E89–9.

(8) Molenaar, C., Abdulle, A., Gena, A., Tanke, H. J., and Dirks, R. W. (2004) Poly(A)+ RNAs roam the cell nucleus and pass through speckle domains in transcriptionally active and inactive cells. *J. Cell Biol. 165*, 191–202.

(9) Demidov, V. V., and Frank-Kamenetskii, M. D. (2004) Two sides of the coin: affinity and specificity of nucleic acid interactions. *Trends Biochem. Sci. 29*, 62–71.

(10) Tyagi, S., and Kramer, F. R. (1996) Molecular beacons: probes that fluoresce upon hybridization. *Nat. Biotechnol. 14*, 303–8.

(11) Tyagi, S., and Alsmadi, O. (2004) Imaging native beta-Actin mRNA in motile fibroblasts. *Biophys. J. 87*, 4153–62.

(12) Perlette, J., and Tan, W. (2001) Real-time monitoring of intracellular mRNA hybridization inside single living cells. *Anal. Chem. 73*, 5544–50.

(13) Bratu, D. P., Cha, B. J., Mhlanga, M. M., Kramer, F. R., and Tyagi, S. (2003) Visualizing the distribution and transport of mRNAs in living cells. *Proc. Natl. Acad. Sci. U.S.A. 100*, 13308–13.

(14) Sokol, D. L., Zhang, X., Lu, P., and Gewirtz, A. M. (1998) Real time detection of DNA.RNA hybridization in living cells. *Proc. Natl. Acad. Sci. U.S.A. 95*, 11538–43.

(15) Carmo-Fonseca, M., Pepperkok, R., Carvalho, M. T., and Lamond, A. I. (1992) Transcription-dependent colocalization of the U1, U2, U4/U6, and U5 snRNPs in coiled bodies. *J. Cell Biol. 117*, 1–14.

(16) Matera, A. G., and Ward, D. C. (1993) Nucleoplasmic organization of small nuclear ribonucleoproteins in cultured human cells. *J. Cell Biol. 121*, 715–27.

(17) Feldherr, C. M., and Akin, D. (1990) EM visualization of nucleocytoplasmic transport processes. *Electron Microsc. Rev. 3*, 73–86.

(18) Feldherr, C. M., Lanford, R. E., and Akin, D. (1992) Signal-mediated nuclear transport in simian virus 40-transformed cells is regulated by large tumor antigen. *Proc. Natl. Acad. Sci. U.S.A. 89*, 11002–5.

(19) Collins, C. A., and Guthrie, C. (2000) The question remains: is the spliceosome a ribozyme? *Nat. Struct. Biol. 7*, 850–4.

(20) Maniatis, T., and Reed, R. (1987) The role of small nuclear ribonucleoprotein particles in pre-mRNA splicing. *Nature 325*, 673–8.

(21) Lerner, M. R., Boyle, J. A., Mount, S. M., Wolin, S. L., and Steitz, J. A. (1980) Are snRNPs involved in splicing? *Nature 283*, 220–4.

(22) Dragon, F., Gallagher, J. E., Compagnone-Post, P. A., Mitchell, B. M., Porwancher, K. A., Wehner, K. A., Wormsley, S., Settlage, R. E., Shabanowitz, J., Osheim, Y., Beyer, A. L., Hunt, D. F., and Baserga, S. J. (2002) A large nucleolar U3 ribonucleoprotein required for 18S ribosomal RNA biogenesis. *Nature 417*, 967–70.

(23) Carmo-Fonseca, M., Pepperkok, R., Sproat, B. S., Ansorge, W., Swanson, M. S., and Lamond, A. I. (1991) In vivo detection of snRNP-rich organelles in the nuclei of mammalian cells. *Embo J. 10*, 1863–73.

(24) Matera, A. G., Tycowski, K. T., Steitz, J. A., and Ward, D. C. (1994) Organization of small nucleolar ribonucleoproteins (snoRNPs) by fluorescence in situ hybridization and immunocytochemistry. *Mol. Biol. Cell 5*, 1289–99.

(25) Huang, S., and Spector, D. L. (1992) U1 and U2 small nuclear RNAs are present in nuclear speckles. *Proc. Natl. Acad. Sci. U.S.A. 89*, 305–8.

(26) Lange, T. S., Ezrokhi, M., Borovjagin, A. V., Rivera-Leon, R., North, M. T., and Gerbi, S. A. (1998) Nucleolar localization elements of Xenopus laevis U3 small nucleolar RNA. *Mol. Biol. Cell 9*, 2973–85.

(27) Narayanan, A., Lukowiak, A., Jady, B. E., Dragon, F., Kiss, T., Terns, R. M., and Terns, M. P. (1999) Nucleolar localization

signals of box H/ACA small nucleolar RNAs. *Embo J 18*, 5120–30.

(28) Cogoi, S., Codognotto, A., Rapozzi, V., Meeuwenoord, N., van der Marel, G., and Xodo, L. E. (2005) Transcription inhibition of oncogenic KRAS by a mutation-selective peptide nucleic acid conjugated to the PKKKRKV nuclear localization signal peptide. *Biochemistry 44*, 10510–10519.

(29) Narayanan, A., Eifert, J., Marfatia, K. A., Macara, I. G., Corbett, A. H., Terns, R. M., and Terns, M. P. (2003) Nuclear RanGTP is not required for targeting small nucleolar RNAs to the nucleolus. *J. Cell Sci. 116*, 177–86.

(30) Spector, D. L., Lark, G., and Huang, S. (1992) Differences in snRNP localization between transformed and nontransformed cells. *Mol. Biol. Cell 3*, 555–69.

(31) Izaurralde, E., Lewis, J., Gamberi, C., Jarmolowski, A., McGuigan, C., and Mattaj, I. W. (1995) A cap-binding protein complex mediating U snRNA export. *Nature 376*, 709–12.

(32) Pante, N., Jarmolowski, A., Izaurralde, E., Sauder, U., Baschong, W., and Mattaj, I. W. (1997) Visualizing nuclear export of different classes of RNA by electron microscopy. *RNA 3*, 498–513.

(33) Nakielny, S., and Dreyfuss, G. (1999) Transport of proteins and RNAs in and out of the nucleus. *Cell 99*, 677–90.

(34) Misteli, T. (2000) Cell biology of transcription and pre-mRNA splicing: nuclear architecture meets nuclear function. *J. Cell Sci. 113* (Pt 11), 1841–9.

(35) Misteli, T., Caceres, J. F., and Spector, D. L. (1997) The dynamics of a pre-mRNA splicing factor in living cells. *Nature 387*, 523–7.

(36) Lawrence, J. B., Marselle, L. M., Byron, K. S., Johnson, C. V., Sullivan, J. L., and Singer, R. H. (1990) Subcellular localization of low-abundance human immunodeficiency virus nucleic acid sequences visualized by fluorescence in situ hybridization. *Proc. Natl. Acad. Sci. U.S.A. 87*, 5420–4.

(37) Ambinder, R. F., and Mann, R. B. (1994) Epstein-Barr-encoded RNA in situ hybridization: diagnostic applications. *Hum. Pathol. 25*, 602–5.

BC800322A

Quantification of Isotope Encoded Proteins in 2-D Gels Using Surface Enhanced Resonance Raman

Giselle M. Knudsen,[†] Brandon M. Davis,[‡] Shirshendu K. Deb,[†] Yvette Loethen,[‡] Ravindra Gudihal,[†] Pradeep Perera,[‡] Dor Ben-Amotz,[‡] and V. Jo Davisson*[,†]

Department of Medicinal Chemistry and Molecular Pharmacology and the Bindley Bioscience Center at Discovery Park, and Department of Chemistry, Purdue University, West Lafayette, Indiana 47907. Received July 28, 2008; Revised Manuscript Received September 12, 2008

A strategy for quantification of multiple protein isoforms from a complex sample background is demonstrated, combining isotopomeric rhodamine 6G (R6G) labels and surface-enhanced Raman in polyacrylamide matrix. The procedure involves isotope-encoding by lysine-labeling with (R6G) active ester reagents, isoform separation by 2-DGE, fluorescence quantification using internal standardization to water, and silver nanoparticle deposition followed by surface-enhanced Raman detection. R6G sample encoding and standardization enabled the determination of total protein concentration and the distribution of specific isoforms using the combined detection approach of water-referenced fluorescence spectral imaging and ratiometric quantification. A detection limit of approximately 13.5 picomolar R6G-labeled protein was determined for the surface-enhanced Raman in a gel matrix (15-fold lower than fluorescence). High quantification accuracies for small differences in protein populations at low nanogram abundance were demonstrated for human GMP synthetase (hGMPS) either as purified protein samples in a single-point determination mode (3% relative standard deviation, RSD%) or as HCT116 human cancer cellular lysate in an imaging application (with 16% RSD%). These results represent a prototype for future applications of isotopic surface-enhanced resonance Raman scatter to quantification of protein distributions.

INTRODUCTION

Despite major advances in protein analysis, accurate and precise methodologies capable of assessing changes in protein distribution in biological systems represent a target for development. Specifically, post-translational modifications of proteins on the biological response time scale requires simultaneous monitoring of multiple protein isoforms to understand signaling. Examples include signal transduction pathways controlled by phosphorylation, such as activation of MAPK cascades, which are carefully tuned in terms of magnitude (*1, 2*), timing (*3*), duration (*4, 5*), and spatial regulation in response to specific stimuli (*6*). The relative changes in ERK1/2 isoforms can vary from 5% to 50% on the 10 min time scale in Ras activation (*3*) to 80−90% in response to amphetamine stimulation (*7*), and multiple isoforms are known for signaling proteins such as src kinase (*8*). Small changes in protein isoform content can translate into biologically meaningful distinctions due to downstream signal amplification. A different example is enzyme isoform diversity through post-translational modifications, such as those in GAPDH, which lead to variations of protein function aside from the catalytic activity (*9*−*11*).

Quantification of protein "isoforms" has been demonstrated using quantitative mass spectrometry (*12*) and differential gel electrophoresis (DIGE) (*13*). Bioconjugate chemistry combined with mass spectrometric methods have enabled a "bottom up" peptide analysis approach using stable isotope labeling of peptides, e.g., ICAT, iTRAQ, AQUA, or GIST (*12*). Label-free quantification methods are based on the abundance of specific ions sampled over a chromatographic peak (*12, 14*). This method requires careful selection of survey and fragment spectra (MS and MS/MS) sampling times relative to the chromatographic peak width. Recently, a targeted approach involving the use of multiple-reaction monitoring (MRM) to track a selected precursor ion, diagnostic of a specific molecular entity, has demonstrated an improved dynamic range 10^4-10^5 for phosphopeptide monitoring (*12, 15*). However, MRM has limitations in terms of reproducibility of proteome coverage, and the relative phosphorylation status for specific protein species is not readily accessible.

Comparative proteomic strategies using 2-DGE provide an avenue for potential quantification of changes in thousands of protein isoforms provided appropriate resolution of the targeted proteins in the sample (*16*). In practice, only the most abundant proteins in a proteome can be recovered in reasonable amounts for further analyses, and proteins with low levels of expression remain difficult to detect, quantify, and identify. This is a particularly important problem, because even in typical mammalian cells, the protein copy number can vary over a 10^6 range (*17*), and the expected number of unique protein entities can be as high as 10^5. This scenario is more challenging for serum proteomes (*18*), where the dynamic range has been estimated at up to 10^{12}.

Our efforts recently assessed the capacity of bioconjugation chemistry combined with silver-enhanced Raman detection based upon isotope ratio standardization in gel matrices to provide accurate quantification of proteins (*19*). Several limitations of fluorescence-based quantification may be addressed using surface-enhanced resonance Raman scattering (SERRS) spectroscopy. While internal standardization of single fluorophore content in gels has been demonstrated using Raman water signals (*20*), the capacity to multiplex with fluorescence requires the use of multiple dye classes. These distinct chemical modifications create higher-order separation problems for labeled

* Address all correspondence to V. Jo. Davisson: davisson@purdue.edu, 575 Stadium Mall Dr., West Lafayette, IN 47907 765-494-1414 (fax), 765-494-5238(office).

[†] Department of Medicinal Chemistry and Molecular Pharmacology and the Bindley Bioscience Center at Discovery Park.

[‡] Department of Chemistry.

10.1021/bc800325k CCC: $40.75 © 2008 American Chemical Society
Published on Web 10/17/2008

proteins in mixtures (*21*). Previous applications of surface-enhanced Raman-based detection for quantification have been limited due to variations in surface chemistry leading to large fluctuations in enhancement efficiency (*22, 23*). Isotopically encoded Raman active dyes such as Rhodamine 6-G (R6G) provided highly reproducible and quantitative SERRS-based concentration measurements (*24*). While Raman spectra of R6G isotopic variants are distinct, their physiochemical properties are virtually identical, thus making them ideal labels for internally standardized proteomic separations and quantification applications (*19, 24*).

Here, we present a new protein-encoding strategy that makes use of isotopic pairs of R6G-NHS ester labeling reagents for internally standardized ratiometric quantification analysis in silver-stained 2D gels (*19*). The ratiometric quantification accuracy, gel to gel reproducibility, and detection limit were assessed with a purified recombinant protein of interest, human GMP synthetase. The lower limit of detection for the SERRS measurement enabled a reduction in labeling and minimized separation artifacts. Three endogenous protein isoforms were quantified in cell lysates using internalized sample spiking with known quantities of recombinant hGMPS protein isoforms. The precision and accuracy in the resulting Raman-based quantifications justifies future development of the isotope edited internal standardized SERRS biomolecular quantification approach to protein isoform quantification methods.

MATERIALS AND METHODS

Materials. Isotope encoded d_0- or d_4-R6G NHS ester reagents were prepared by S. K. Deb as reported (*19*). All 2-DGE materials were from Biorad. Recombinant human GMP synthetase (hGMPS) was a gift from Justin C. Oliver, produced as described to >95% purity (*25*). All other reagents were purchased from Sigma.

Soluble Cell Lysate Preparation. HCT116 colon cancer cells (ATCC) were cultured using standard cell culture conditions in DMEM-F12 medium containing 10% FBS. Cells were harvested by trypsin release, then rinsed three times with PBS, and pelleted for storage at −80 °C. For lysis, thawed cell pellets were suspended in chilled lysis buffer containing 20 mM HEPES, pH 7.5, 0.25 M sucrose, 3 mM $MgCl_2$, 0.5% NP40, 2 mM DTT, and 1× Halt protease inhibitor cocktail (EDTA-free, Pierce). The cells (2×10^7 cells/mL) were homogenized with fifteen strokes of a 2 mL Dounce homogenizer and pestle B, and then cellular debris was pelleted at 12 000 *g* for 20 min at 4 °C. The supernatant was concentrated and buffer exchanged into 50 mM borate buffer pH 8.5 using 5 kDa MW cutoff ultrafree spin filters (Millipore), and the protein concentration was determined using the Biorad protein assay with BSA calibration. Prepared lysates were used immediately for labeling and 2-DGE analysis.

Protein Labeling. For lysate or recombinant protein sample labeling, 100−150 μg of protein was dissolved in 50 mM borate buffer pH 8.5 to a final volume of 200−1200 μL, to which was added 1 nmol (1 μL) of d_0- or d_4-R6G-NHS reagent stock dissolved in ethanol. After 1 h incubation in the dark at room temperature, the protein reaction was desalted on a PD-10 column (GE Healthsciences) into 50 mM Tris pH 7.5 buffer. The total protein eluate was concentrated then buffer exchanged with 8 M urea, 10 mM Tris pH 7.5, and 0.5% CHAPS on a 5k MW cutoff microspin filter, to remove any remaining unreacted dye. Protein concentration was determined using the Biorad protein assay, and dye content was assessed by UV−vis absorbance using $\varepsilon = 116\,000\ M^{-1}\ cm^{-1}$ at λ_{max} of 540 nm for R6G. These reaction conditions produce a low molar labeling efficiency (~0.1%), and were optimized using controlled mixtures of proteins with known pI and Mw and various dye/protein reaction stoichiometry, selecting for conditions that produced unaltered 2DGE images between labeled vs unlabeled samples (*20*). This method minimized the appearance of charge-shifts in the IEF dimension, due to potential side-reactions with Tyr, Thr, or Ser residues (*26*).

2D-PAGE. For isoelectric focusing, protein in a volume of less than 20 μL was diluted into sample rehydration buffer containing 8 M urea, 2% CHAPS, 50 mM DTT, 0.2% Bio-Lyte 3/10 ampholyte, and 0.001% bromophenol blue for rehydration of 11 cm, 3−10 nonlinear IPG strips. The IEF strips were focused under optimized conditions for mammalian cell lysates (*27*) over 16−20 h for a total of ~60 000 Vh using a shallow gradient over five voltage steps, reaching a maximum of 8000 V on a Biorad Protean IEF Cell apparatus. After focusing, the strips were reduced and alkylated in equilibration buffer containing 6 M urea, 0.375 M Tris pH 8.8, 4% SDS, 20% glycerol containing 2% DTT for 10 min, then 2.5% iodoacetamide for 10 min. For the second dimension, the strips were run on single well, precast, Criterion 12.5% acrylamide Tris-HCl gels. The gels were fixed in 50% methanol, 5% acetic acid for 1−2 h, followed by 50% methanol 1 h, then stored in water at 4 °C. Gels of non-R6G-labeled control protein samples were stained with SyproRuby according to the manufacturer protocol (Biorad).

Fluorescence Scanner Gel Documentation. Fluorescence images of 2D gels were recorded using a Typhoon fluorescence scanner (GE Life Sciences), with the following settings for R6G: 532 nm excitation, 580 (±30) nm bandpass emission filter, and 100 μm pixel size; and the photomultiplier voltage was adjusted for maximum dynamic range of signal, typically 650 V. For SyproRuby detection, 532 nm excitation and the 610 (±30) nm bandpass emission filters were used.

Silver Staining. Polyacrylamide gels were silver stained according to the Schevchenko method with modifications to minimize background staining (*28, 29*). Due to the importance of silver substrates for SERRS detection, details of the silver staining procedure are given here. The gels were reduced for 2 min in freshly prepared 2 mM sodium thiosulfate ($Na_2S_2O_3$). Then, the gels were rinsed twice in water over 5 min before incubation in chilled (4 °C) 0.1% silver nitrate solution for 20 min. The gels were then rinsed with two exchanges of water over 4 min, and then incubated in 10% sodium carbonate containing 0.04% formaldehyde until the protein spots had developed sufficient brown staining for visualization. Development was quenched before the appearance of excessive mirroring with a 2 min wash in 5% acetic acid. Where indicated, gels were preserved by soaking in 10% glycerol and drying between sheets of cellophane at room temperature.

***d_0/d_4*-R6G Ratiometric Accuracy.** The practical limits of the ratiometric quantification strategy were assessed using mixtures of separately labeled d_0- or d_4-R6G-recombinant hGMPS. Gel-to-gel reproducibility and precision were assessed for a 43% d_4-R6G composition sample, representing a 1.3-fold difference between d_0- and d_4-R6G concentrations. Three replicate gels containing 3 μg total of the mixed protein sample were separated by 2-DGE, silver stained, and then dried as described above. A practical detection limit was determined by sampling a series of 2-DGE samples containing 3 μg, 300 ng, 30 ng, or 3 ng total hGMPS protein. Here, the sample composition was selected to be 64.2% d_0-R6G, representing a 1.8-fold difference between d_0- and d_4-R6G samples, a value selected to be significant at picomolar R6G concentrations. For these samples, a single-point determination procedure was followed using a Senterra confocal Raman microscope (Bruker Optics) operated with *Opus* v 6 software.

The Senterra was equipped with a 532 nm laser and Olympus MPlan 20× (0.4 NA) or 50× (0.75 NA) objectives, with

collection spot size dimensions of 50 × 1000 μm, and 3−5 cm^{-1} resolution grating settings. The following settings were used to acquire spectra for 0.1−1 μg protein: 2 mW power, 2−5 scans, 30 s integration time; and for 1−10 ng protein: 5−10 mW, 5 scans, and 60 s integration. Data were fit using a manual curve fitting operation within *Opus* software around the signature 610 and 600 cm^{-1} peaks, using baseline subtraction between 619 and 587 cm^{-1}, and a Gaussian peak shape model. The ratio of areas of the 610 to 600 cm^{-1} peaks directly provided values of d_0/d_4 composition.

***d*$_0$/*d*$_4$-R6G-Labeled Spiked Lysate.** *Preparation.* To produce spiked lysate samples, HCT116 cell lysate was divided equally into three vials containing 750 μg lysate, to which was added 0, 1.5, or 3 μg of recombinant hGMPS. These samples were labeled in separate reactions to give two d_0-lysates containing w/w 0% or 0.2% spiked recombinant hGMPS and a single d_4-lysate containing 0.4% spiked recombinant hGMPS. Mixed composition d_0/d_4 samples were combined as follows: Sample A: 100 μg each of the d_0-labeled, 0% spiked, and d_4-labeled, 0.4% recombinant hGMPS-spiked lysates. Sample B: 100 μg each of the d_0-labeled, 0.2% spiked, and d_4-labeled, 0.4% spiked lysates. The d_0-R6G labeled, nonspiked lysate sample was also used as a control (Sample C).

Theoretical Percent d_4-R6G Composition in Spiked Lysates. The theoretical percent d_4-R6G composition in a given hGMPS protein spot was calculated as a function of the composition of endogenous hGMPS and the recombinant protein that was added to it. For each protein spot, endogenous (E) protein was defined as the mass (ng) of hGMPS present in 200 μg of cell-free lysate. The mass of recombinant (R) protein (ng) in a protein spot was calculated per 200 ng recombinant protein (or 0.1% w/w addition of recombinant protein to 200 μg of lysate). The theoretical composition of d_4-R6G (%) in samples A and B was then given by eqs 1 and 2.

$$\%d_4(\text{sample A}) = \frac{\left(\frac{E}{2} + 2R\right)}{(E + 2R)} \quad (1)$$

$$\%d_4(\text{sample B}) = \frac{\left(\frac{E}{2} + 2R\right)}{(E + 3R)} \quad (2)$$

Multispectral Fluorescence and Raman Imaging. Full spectral imaging was performed using a custom-built micro-Raman system (*30*), equipped with an air-cooled 514.5 nm Ar^+ laser (Melles-Griot) and an Olympus BX41 microscope. Raman scatter was collected using a 20× objective (Olympus ULWD MSPlan, 0.4 NA) and focused onto a circular-to-linear fiber bundle for detection using an imaging spectrograph (Acton Research, SpectraPro 300i) and a 1024 × 256 LN-cooled CCD (Princeton Instruments). Gel imaging was performed using a custom-written LabVIEW (National Instruments) program to raster scan the gel through the laser focus while collecting spectra from an array of points in the gel. The laser focal spot size was 10 μm in diameter and 100 μm in depth, effectively 10 pL focal volume, and the $x-y$ step size in fluorescence or Raman scatter images was 200 or 250 μm. Gels were placed on a low-fluorescence glass plate (Bio-Rad) under a small pool of Milli-Q water to prevent drying over the duration of the scan. Fluorescence imaging parameters were as follows: laser power, 1 mW at the sample; spectrograph grating, 300BLZ at 670 nm; exposure time, 5 ms; image size, ∼70 × 40 pixels = 17.5 × 10 mm; scan time = 10 min. SERRS imaging parameters were as follows: laser power, 14 mW at sample; spectrograph grating, 1200BLZ at 554 nm; exposure time, 1 s; image size, ∼48 × 48 pixels = 12 × 12 mm; scan time = 1 h.

Analysis of Multispectral Fluorescence and Raman Imaging. *Absolute Dye Quantification by Fluorescence.* For absolute R6G quantification in protein spots, the water-Raman subtraction method (WIS) of Loethen et al. (*20*) was applied to a small region of the gel containing the spiked sample. Calibration of dye concentration in solution was performed using d_0-R6G (calibration plot shown in Supporting Information Figure 1), and an additional region was imaged from the gel margin (protein-free) for calculating an average spectrum to be used as background. Savitzky-Golay second derivative solvent subtraction analysis of all spectra yielded the normalized value of R6G fluorescence to the water Raman band (*31*, *32*). Dye concentration was calculated over the volume of a protein spot using the protein-free R6G calibration and the normalized fluorescence spectral integration obtained from each image pixel. Using this method, a user-defined protein spot was selected as an internal standard for which the absolute molar amount of dye was quantified. Thus, the relative fluorescence in this spot could be used to normalize signal across replicate fluorescence gel images.

Automated SERRS Spectral Processing. To remove the fluorescence background from SERRS spectra, an automated method of polynomial fitting was used to model a composite fluorescence spectrum that could be subtracted (*33*). This procedure involved pixel by pixel comparison of the original spectra with a fourth-order polynomial fit and generating a composite spectrum by inputting the lesser of the original spectrum pixel value or the polynomial pixel value. Five or more iterations were performed to arrive at a composite spectrum that contained few or no Raman bands, smoothed using a second-order Savitsky-Golay width of 25 pixels (*32*), and subtracted from the original spectrum yielding a nearly null baseline SERRS spectrum.

Partial least-squares (PLS) modeling was used to quantify d_0- and d_4-R6G composition, using full-range, baseline-subtracted, second-derivative SERRS spectra. To generate the PLS model, a training set was collected with 200 spectra obtained for each of the following % d_4-R6G compositions: 100%, 75%, 50%, 25%, or 0% of a standard, d_0- or d_4-R6G-labeled purified protein (ferritin) (*19*). These spectra were weighted by standard deviation over the 200 spectra for each set, but otherwise were not manipulated for this analysis. The final calibration plots for PLS modeled training set data with observed versus expected % d_4-R6G composition had a linear R^2 correlation coefficient of 0.999 (Supporting Information Figure 2).

RESULTS

Quantitative Fluorescence and Raman Imaging. An analysis of cellular lysates as typical complex proteomic samples were used to establish the working protein and R6G concentrations for the overall quantitative fluorescence and Raman imaging strategy. Sample labeling used either 1A or 1B (Figure 1) (*19*) followed by 2-DGE separation, fluorescence spectral imaging, silver nanoparticle deposition, and Raman spectral imaging (Figure 2). In Figure 3 is shown the 2-DGE analysis of 30 μg soluble lysate sample prepared from HCT116 human colon cancer cells. This sample was labeled using R6G-NHS ester lysine labeling reagent 1A (Figure 1), at a ratio of 6.6 pmol dye per microgram protein to yield on average ∼0.1% labeling efficiency. Throughout this study, lower labeling levels were selected to minimize potential electrophoretic mobility shift effects (*34*). This reaction stoichiometry is reduced relative to typical sample labeling protocols (*35*), which yield approximately 1−2% protein labeling efficiency (*21*).

The absolute dye content in a single protein spot on the 2D gel was established using a water internal standardization method that compares the fluorescence of R6G to the water Raman signal (*20*). The corrected spectra for the R6G fluorescence intensity image is shown in Figure 3B, with sample

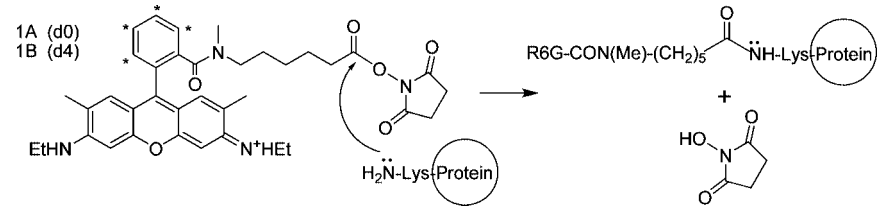

Figure 1. Structure of d_0- and d_4-R6G-NHS ester labeling reagents (1A and 1B); asterisks denote the sites of deuterium incorporation, and the site of nucleophilic attack by lysine residues for protein labeling is indicated.

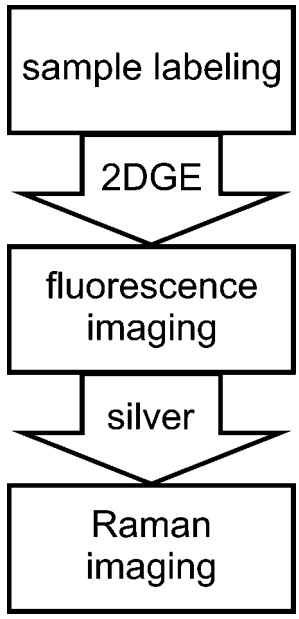

Figure 2. Sample handling workflow.

spectra from the designated protein spot shown in Figure 3C. The concentration of R6G in this protein spot was determined to be 3.1 nM, averaged over the gel volume with dimensions as drawn in Figure 3B. The detection limit was defined as 3× noise and routinely set at 0.2 nM. The Raman intensity image for this gel region (Figure 3D) accurately represented the fluorescence image (Figure 3B), and the Raman spectrum shown in Figure 3E was obtained from the selected protein spot containing 3.1 nM R6G.

Highlighted in these results is the use of a standard silver stain for acrylamide protein gels to generate a viable SERRS substrate formed *in situ*. Cryo EM imaging has shown that the sizes of brown, yellow, or blue−gray silver nanoparticles obtained in gels using silver deposition are typically 20−100 nm in size; these nanoparticles are within the range expected for surface-enhanced Raman substrates (*36, 37*). These sizes correlate well with data from size-controlled preparations of silver aggregates often used for surface-enhanced Raman (*38, 39*). Raman enhancement factors or efficacy were not analyzed, and no attempts to optimize the nanoparticle preparations (in terms of nanoparticle sizes, geometries, and roughness) were pursued.

GMP Synthetase Isoforms. For purposes of testing the feasibility of isotope edited internal standardization SERRS for protein isoform quantification, recombinant human GMP synthetase (hGMPS) posed a useful model protein. Human GMPS is encoded by a single gene (on the 3q chromosome), and only a single mRNA form has been reported; yet, it has been described in at least two distinct isoforms with different isoelectric points, as isolated from the T-lymphoma A3.01 cell line or produced in a recombinant baculovirus expression system (*40, 41*). A differential phosphopeptide analysis of the human tumor-derived cell line A431 indicated that Thr330 of hGMPS undergoes a phosphorylation event (*42*). Understanding which isoform is linked to a particular hGMPS function is an emerging question, with an example being the elevated expression in tamoxifen-resistant xenograft breast tumor 3366 cell line (*43*). The recombinant protein is purified as multiple species termed here as "isoforms", which resembled those found in endogenous HCT116 cell lysate as shown after 2-DGE separation (Figure 4). By fluorescence densitometry quantification using SyproRuby staining, the hGMPS protein species identified as E1−E4 in Figure 4B (MS/MS data in Supporting Information Table 1) comprised 0.1−0.2% of the total 200 μg protein lysate, or 200−400 ng, in the gel. Four species were also identified in recombinant hGMPS purified from an *E. coli* expression system (labeled R1−R4 in Figure 4C, MS/MS data in Supporting Information Table 2), suggesting that the modification of these putative hGMPS isoforms could originate from a similar chemical or biochemical process in both samples.

Gel-to-Gel Reproducibility of Ratiometric Quantification. An experiment was conducted to assess gel-to-gel reproducibility of the Raman spectral analyses using d_0- and d_4-R6G-labeled recombinant hGMPS at a fixed % d_4-R6G composition of 43%. Three replicate silver stained gels were prepared containing approximately 3 μg of total recombinant protein (or approximately 1 μg per protein species), and six Raman spectra were recorded for the most abundant hGMPS species (Figure 5). These spectra were submitted to Gaussian curve fitting analysis of the signature 611 and 600 cm^{-1} peaks to obtain d_0- and d_4-R6G composition directly; % d_4-R6G composition in each of the three gels (averaged over six spectra) was as follows: 43.3 ± 1.8%, 42.6 ± 0.6%, and 42.9 ± 1.3%. Percent relative standard deviation (RSD%) was used to summarize overall variance for the % d_4-R6G compositions, as described recently by Schröder et al. (*44*). Using single gel measurements (with $n = 6$ spectra), the RSD% for the three individual gels were 4.3%, 1.8%, and 3.1%. The value gained in recording data from three gels versus one gel was assessed by combining all eighteen spectra from the three gels, resulting in an RSD% of 3.0% overall. Therefore, there was no great advantage gained from recording SERRS spectra from multiple gels in this analysis, avoiding various sources of reproducibility error in 2-DGE (*44*). The result highlights the inherent accuracy in the ability of Raman to simultaneously detect isotopomeric dye populations in the same spectra.

Detection Limit of Ratiometric Quantification. To assess the practical detection limit of the ratiometric measurement, recombinant hGMPS samples were prepared in a 10-fold dilution series and developed on 2-DGE. In these samples, 64.2% d_4-R6G composition (or 1.8-fold difference between d_0- and d_4-R6G) was chosen to allow for absolute quantification errors over the range of nM to pM concentrations. The expected concentration of dye in the ~1 ng protein per spot sample was estimated as 75 pM based on 0.1% labeling efficiency, 76 kDa molecular weight, and approximate spot size of 0.5 × 0.5 mm^2. The most abundant protein species were quantified in each of these gels and found to contain % d_4-R6G of 63.9 ± 1.0%, 64.5 ± 1.2%, and 64.3 ± 2.5% for the 1 μg, 100 ng, and 10 ng per spot gels, respectively. Signal to noise ($S/N = 2$), acquisition

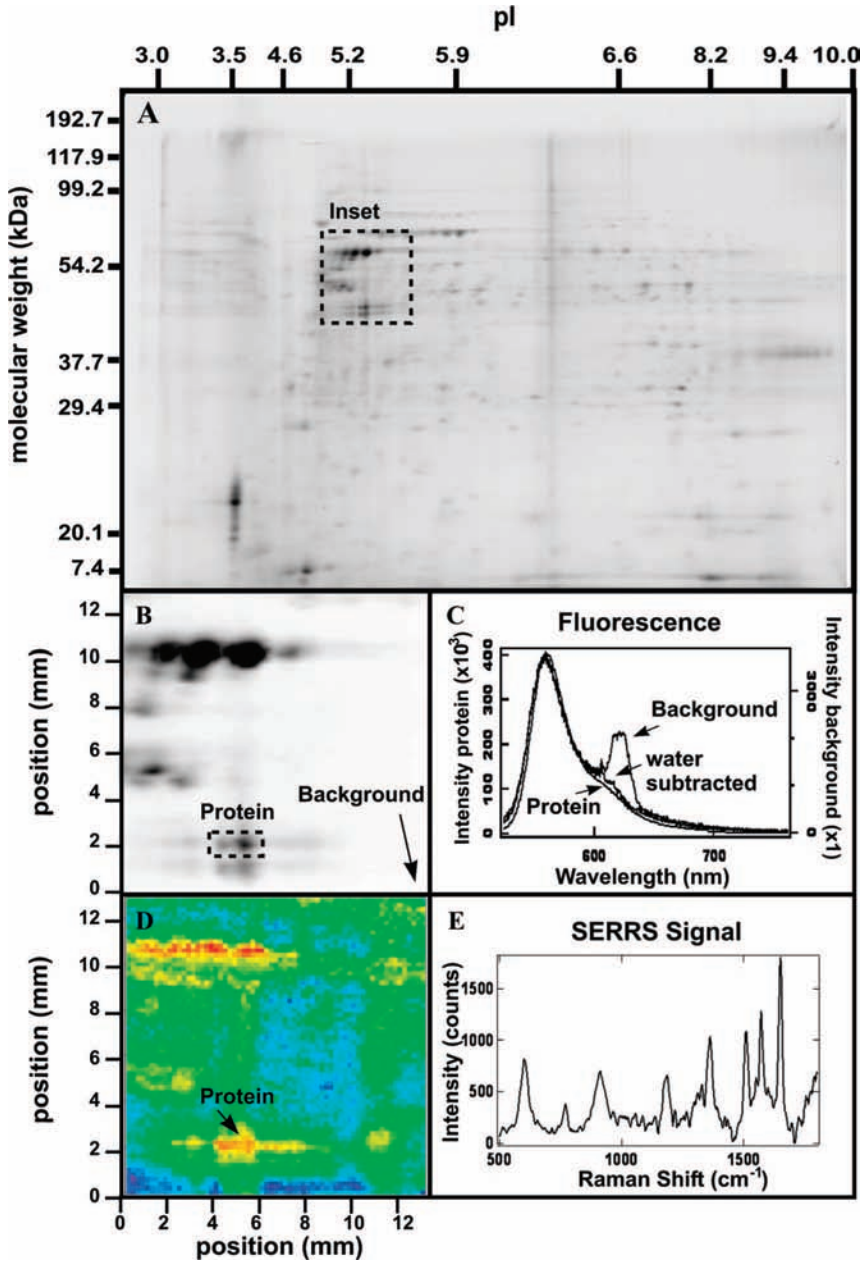

Figure 3. Shown here is a 2-DGE analysis of 30 μg of R6G-labeled lysate. (A) The full-sized fluorescence image was recorded with a Typhoon fluorescence scanner. (B) The 13 × 13 mm^2 inset region was further imaged using our confocal system by fluorescence (200 μm step size). (C) Representative fluorescence spectra are shown for protein (on the × 10^3 scale), background (on the 1× scale), and water-subtracted background (1× scale). (D) The gel was silver stained, then imaged by Raman in the same inset region, color coded for intensity at 1650 cm^{-1} from red (high) to blue (low). (E) A representative background-subtracted SERRS spectrum from the marked protein spot is shown.

time (~30 min), and background became limiting in the 1 ng gel for this simple Gaussian peak fitting method, and only three spectra could be manually fit for this sample. If, however, the peak-shaped model from the 1 μg−10 ng samples was applied to the 1 ng sample spectra, a % d_4-R6G of 64.9 ± 6.1% could be obtained (over $n = 3$ spectra). Thus, the practical protein detection limit was approximately 1 ng per spot for a simple single-point measurement method, comparable to silver stain (0.3−10 ng/spot), Sypro Ruby dye (1−2 ng), and Cyanine dye covalent labeling (0.25−0.95 ng) protein detection limits in gels (*45*, *46*). Using the metric of 3-fold variance in the 75 pM sample, the SERRS detection limit in terms of dye concentration was on the order of 13.5 pM.

Ratiometric Quantification of hGMPS Isoforms in Lysate. To evaluate the ratiometric quantification strategy in typical proteomic samples, an imaging-based internally standardized analysis was designed to quantify small-fold changes in hGMPS isoform distribution with a constant protein background in a complex cell lysate. In this experiment, two pairwise ratiometric analyses were performed with recombinant hGMPS spiked lysates. The tasks were to determine both the accuracy in % d_4-R6G composition for multiple hGMPS species and the composition of endogenous hGMPS in the lysate.

SERRS imaging was used for direct quantification of d_4-R6G composition in mixed lysate samples containing 0%, 0.2%, or 0.4% mass-spiked hGMPS, analyzed as samples A and B. The results reported in Table 1 were based upon single gel analyses for samples A and B (Figure 6), as justified by the gel-to-gel reproducibility experiment. Each pixel in Figure 6 represents a full R6G Raman (SERRS) spectrum. Representative SERRS spectra that compose the image maps of samples A and B are shown in Figure 6, and the complete data set is provided in Supporting Information Figure 3. These spectra (48 × 48 = 2304 per image) were fitted using a partial least-squares analysis

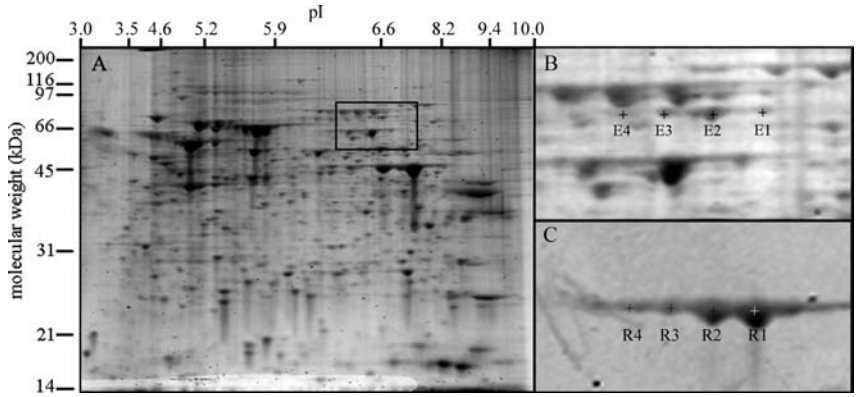

Figure 4. Shown here is a comparison between endogenous and recombinant hGMPS protein species in unlabeled, SyproRuby stained 2-D gels. (A) The full-scale fluorescence image of 200 μg of HCT116 lysate was recorded using a Typhoon scanner. (B) The inset region of panel A was enlarged and contrasted to show putative endogenous species of hGMPS, labeled E1-E4. (C) The 2-DGE image of 1 μg of recombinant hGMPS is shown on the same scale as panel B and contained four distinct species of hGMPS (R1−R4).

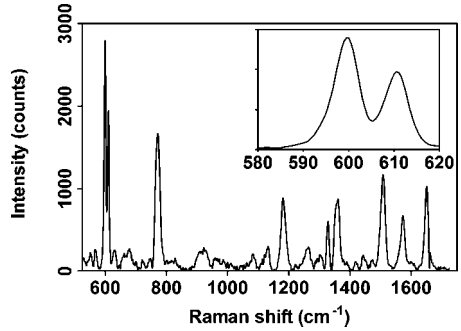

Figure 5. Baseline-corrected SERRS spectrum of d_0/d_4-R6G-labeled recombinant hGMPS in a 2-D gel. The inset spectrum shows an expanded view of the 600 cm^{-1} spectral region containing the well-resolved d_0 (right) and d_4 (left) peaks.

Table 1. Percent d_4-R6G Composition in hGMPS and Background Protein Species in Samples A and B, Determined by Full-Spectral Raman Analysis

protein species	% d_4 (sample A)	% d_4 (sample B)
1	86 ± 4	66 ± 5
2	76 ± 8	60 ± 5
3	70 ± 2	56 ± 9
4	50 ± 9	49 ± 9
b1	46 ± 8	45 ± 3
b2	43 ± 8	52 ± 8
b3	40 ± 13	46 ± 15
b4	46 ± 1	57 ± 5

that had been modeled using a training set of 1000 spectra recorded at controlled % d_4-R6G compositions (described in the Materials and Methods section). The % d_4-R6G compositions in each of the hGMPS and background species (Table 1) were calculated by PLS analysis and averaged over three spectra per protein spot.

As a measure of overall variance for this ratiometric quantification imaging method, the total RSD% were determined separately for samples A and B, using the average and standard deviations of replicate readings for the eight identified protein species reported in Table 1. For both samples A and B, the total RSD% are 16%. Using the high scan rate, low signal-to-noise Raman spectra, the quantification strategy had a total RSD% that was at least comparable with fluorescence-based methods evaluated at similar protein concentrations. For example, the total RSD% from native protein fluorescence detection was reported to be 12−16% (*44*), and data reported in a benchmarking study for the DIGE method had a total RSD% of ∼31% for four standard proteins analyzed with pooled sample internal standardization. By way of comparison, a recent

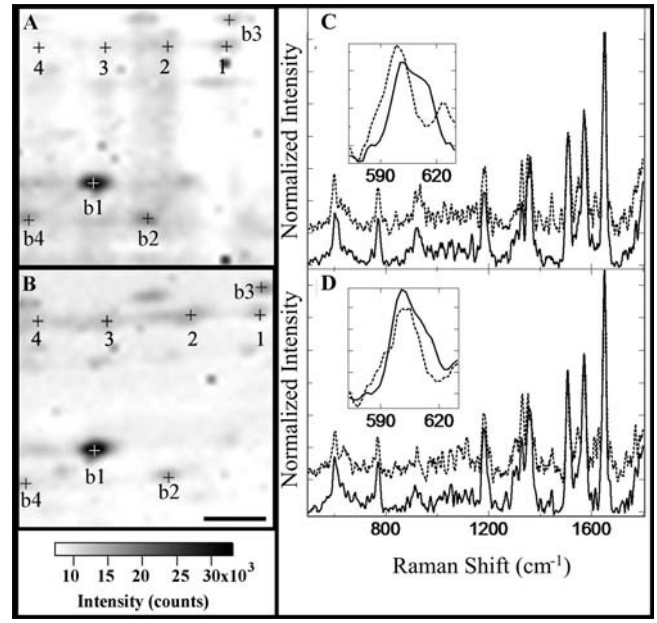

Figure 6. Raman mapping images are shown for samples A and B, in panels A and B respectively. Protein species labeled 1−4 in samples A and B were confirmed to be hGMPS by in gel trypsin digestion and MS/MS peptide sequencing (Supporting Information Table 3). Also shown are the background lysate proteins, labeled b1−b4, selected for % d_4-R6G composition calculations. Scale bar represents 2.5 mm. Representative baseline-corrected SERRS spectra from samples A and B are shown in panels C and D, respectively. Signal from the background protein species b1 (solid trace) is compared with signal from the hGMPS species 1 (dashed trace). The inset shows the signature d_0-R6G (611 cm^{-1}) and d_4-R6G (600 cm^{-1}) peaks, with d_4-R6G signal enrichment in the dashed hGMPS species traces as expected in these spiked samples. The full set of SERRS spectra from hGMPS and background species in samples A and B is provided in Supporting Information Figure 3.

report using the SILAC quantitative MS method, which also employs isotope encoding (*47*), had an overall RSD% of 11% within a narrow 3-fold difference range. The Raman spectra used here were acquired using settings optimized for speed in an imaging application, but which resulted in relatively high noise levels, and are the primary source of variance in these measurements.

hGMPS Isoform Quantification in HCT116 Lysate. The mass composition of endogenous hGMPS could be determined in the four putative isoforms of hGMPS (species 1−4) by defining the recombinant hGMPS sample as the internal standard. Recombinant hGMPS (*R*) was quantified indepen-

Table 2. Quantification of Endogenous Isoforms of hGMPS species (*E*) in Samples A and B, as Directly Determined from SERRS Spectra and Using Recombinant Protein (*R*) as an Internal Standard

hGMPS species	recombinant[a] (*R*) (ng/100 ng)	endogenous ($E_{(\text{Sample A})}$) (ng/100 μg lysate)	endogenous ($E_{(\text{Sample B})}$) (ng/100 μg lysate)
1	46.2	35.2 ± 2.5	34.6 ± 3.8
2	36.5	66.2 ± 9.6	65.5 ± 7.1
3	12.6	38.1 ± 1.5	37.2 ± 8.1
4	0.6	*nc*[b]	nc

[a] Recombinant protein distribution was normalized to 100 ng, equivalent to 0.1% w/w in 100 μg lysate. [b] The value of endogenous protein species **4** could not be calculated (nc).

dently by fluorescence densitometry analysis of the 2-DGE analysis shown in Figure 4C and with knowledge of the protein concentration. Given the Raman measured % d_4-R6G compositions reported in Table 1, it was possible to solve for the endogenous hGMPS (*E*) values reported in Table 2 using eqs 1 and 2. The % d_4-R6G compositions in samples A and B were determined from independent silver-enhanced Raman experiments; therefore, it is significant that the calculated endogenous protein values were consistent for these two experiments. For the least abundant hGMPS species (species 4), the endogenous amount could not be determined due to the low abundance in the recombinant internal standard. It was apparent that the mass distribution among endogenous isoforms of hGMPS, with the most abundant species E2 (Figure 4B) was pI-shifted to a more acidic form relative to the major recombinant species (R1 in Figure 4C). One interpretation would be that the most basic recombinant hGMPS species (R1) was an unmodified or native parent species, while the remaining putative hGMPS isoforms (2−4) were likely to be modified versions of this protein found in the endogenous sample.

DISCUSSION

The potential for application of isotope encoded internally standardized SERRS detection to quantification of multiple protein isoforms within a complex biological sample background is now apparent. R6G-protein encoding has enabled the absolute quantification of sample in hydrated gels using water-internal standardized fluorescence spectral imaging. The particular combination of chemical features in d_0- and d_4-R6G labeling reagents and in situ silver nanoparticle formation around protein in a gel matrix has enabled highly accurate relative quantification using SERRS detection with an established protein separation workflow. SERRS occurs when a molecular species occupies specific "hot spots" on metal surfaces such as silver, gold, or copper, with curvature features that are smaller than the wavelength of the incident light (*48*). Local electric field enhancement by metal surface plasmons lead to enhanced Raman scattering from adsorbed molecular species, by a factor of 10^6 or more. Furthermore, under electronic resonance (SERRS) conditions, enhancements on the order of 10^{14} can be obtained, thus allowing single molecule detection (*49, 50*). Isotope editing provides for the first time a solution to a recurring problem with variations in SERRS efficiencies (*51, 52*), enabling application of Raman features to quantitative biomolecular detection.

The inherent accuracy of isotope encoded internally standardized SERRS ratiometric quantification was demonstrated in analyses of gel-to-gel reproducibility and practical detection limits for the method. Sample to sample variations in gel efficiency (*44*) are eliminated through the use of internal standardization, as was demonstrated by comparison of error between single and multiple gel analyses. Furthermore, the ability to simultaneously monitor two isotopomeric species of R6G in a single SERRS spectral measurement allows for significant reduction of Poisson noise in the measurement due to variations in SERRS efficiency, therefore expanding the practical detection limit into the low picomolar dye concentration realm. For example, in the 10 ng per spot samples, the d_0 and d_4 peak area results obtained from five replicate measurements were 427 ± 260 and 746 ± 377 counts, respectively. If the variances in the peak areas were uncorrelated (Poisson noise), then it would not be possible to determine the value of the area ratio with an accuracy of better than about $\pm 50\%$. The fact that the experimentally measured standard deviation of the isotopic area ratios obtained from these same samples was $\pm 2.5\%$ indicates that most of the variance in the peak areas is highly correlated. In other words, because the d_0- and d_4-R6G chromophores are virtually chemically identical, the areas of the resulting SERRS peaks vary in unison, in spite of the large batch to batch variations in the SERRS activity of the sample.

On the basis of throughput and protein identification, mass spectrometry is often preferred over optical detection methods for quantitative proteomic analysis. However, it is arguable that the identity of a protein spot on a 2-D gel only needs to be determined once when studying the dynamics of the species in a known system. We have shown that it is possible to accurately determine relative compositions of isotopically labeled protein samples at low nanogram protein levels with the caveat that species identification and 2-D gel position must be proven at higher concentrations, since the SERRS detection limit is effectively 15-fold lower than fluorescence.

In this work, we have demonstrated accurate and precise quantification of three major species of human GMP synthetase through internal standardization. In a single-point determination mode, purified recombinant hGMPS species could be quantified in single gels with a 1−6% error over a 1 μg to 1 ng protein mass range. In an imaging application using automated spectral analysis, an RSD% of 16% could be obtained. Future applications will likely combine imaging and single-point determinations for high-accuracy quantification. This level of detection, accuracy, and precision in protein isoform quantification represents a new benchmark for isoform quantification (*13, 44, 47*) and sets the stage for future applications of isotopic surface-enhanced Raman to quantitative analysis of biomolecules.

CONCLUSION

In this study, we have demonstrated a new application of SERRS detection to the quantification of protein distributions, through the use of isotopically paired R6G lysine labeling reagents for sample encoding. By virtue of the inherent accuracy of Raman-based spectral quantification of isotopic dye populations, this strategy is uniquely positioned to overcome both the challenges of 2-DGE due to the reproducibility as well as variations in SERRS efficiency through ratiometric analyses. Furthermore, there is a strong implication in the matching of the detection capacity of SERRS limit of detection and dynamic range to the scale of protein abundances found in proteomic samples. In particular, an approach to accurately assess the graded variance in individual protein species has been established. This work has shown that the ratiometric comparisons that can be made by using isotopic variants of SERRS-active dyes as internal references results in highly accurate and precise quantification of protein distributions, and justifies the future development of SERRS-based biomolecular quantification using isotope encoded internal standardization.

ACKNOWLEDGMENT

We thank the Davisson and Ben-Amotz groups for critical reading of this manuscript. The authors were funded by NCI 1F32-CA123662 (G.M.K.), GM067195-04 and GM053155-10

(V.J.D.), NSF CHE 0455968 (D.B.A., P.P.), and GAANN Fellowship U.S. Dept. of Education (B.M.D.).

Supporting Information Available: The results are provided for MS/MS peptide sequence analysis confirming the identity of the isolated hGMPS protein species derived from HCT116 lysates, recombinant protein spots, and recombinant-spiked lysates. Also provided are the R6G in solution fluorescence calibration plot, PLS calibration plots for Raman training set data, and SERRS spectra from hGMPS and background species in Samples A and B. This material is available free of charge via the Internet at http://pubs.acs.org.

LITERATURE CITED

(1) MacKeigan, J. P., Murphy, L. O., Dimitri, C. A., and Blenis, J. (2005) Graded mitogen-activated protein kinase activity precedes switch-like c-Fos induction in mammalian cells. *Mol. Cell. Biol. 25*, 4676–4682.

(2) Whitehurst, A., Cobb, M. H., and White, M. A. (2004) Stimulus-coupled spatial restriction of extracellular signal-regulated kinase 1/2 activity contributes to the specificity of signal-response pathways. *Mol. Cell. Biol. 24*, 10145–10150.

(3) Fujioka, A., Terai, K., Itoh, R. E., Aoki, K., Nakamura, T., Kuroda, S., Nishida, E., and Matsuda, M. (2006) Dynamics of the Ras/ERK MAPK cascade as monitored by fluorescent probes. *J. Biol. Chem. 281*, 8917–8926.

(4) Oh, H., Ozkirimli, E., Shah, K., Harrison, M. L., and Geahlen, R. L. (2007) Generation of an analog-sensitive Syk tyrosine kinase for the study of signaling dynamics from the B cell antigen receptor. *J. Biol. Chem. 282*, 33760–33768.

(5) Irish, J. M., Czerwinski, D. K., Nolan, G. P., and Levy, R. (2006) Kinetics of B cell receptor signaling in human B cell subsets mapped by phosphospecific flow cytometry. *J. Immunol. 177*, 1581–1589.

(6) Ebisuya, M., Kondoh, K., and Nishida, E. (2005) The duration, magnitude and compartmentalization of ERK MAP kinase activity: Mechanisms for providing signaling specificity. *J. Cell Sci. 118*, 2997–3002.

(7) Shi, X., and McGinty, J. F. (2006) Extracellular signal-regulated mitogen-activated protein kinase inhibitors decrease amphetamine-induced behavior and neuropeptide gene expression in the striatum. *Neuroscience 138*, 1289–1298.

(8) Ingley, E. (2008) Src family kinases: Regulation of their activities, levels and identification of new pathways. *Biochim. Biophys. Acta 1784*, 56–65.

(9) Tisdale, E. J. (2002) Glyceraldehyde-3-phosphate dehydrogenase is phosphorylated by protein kinase Ci/l and plays a role in microtubule dynamics in the early secretory pathway. *J. Biol. Chem. 277*, 3334–3341.

(10) Seo, J., Jeong, J., Kim, Y., Hwang, N., Paek, E., and Lee, K.-J. (2008) Strategy for comprehensive identification of post-translational modifications in cellular proteins, including low abundant modifications: application to glyceraldehyde-3-phosphate dehydrogenase. *J. Proteome Res. 7*, 587–602.

(11) Sirover, M. A. (2005) New nuclear functions of the glycolytic protein, glyceraldehyde-3-phosphate dehydrogenase, in mammalian cells. *J. Cell. Biochem. 95*, 45–52.

(12) Bantscheff, M., Schirle, M., Sweetman, G., Rick, J., and Kuster, B. (2007) Quantitative mass spectrometry in proteomics: a critical review. *Anal. Bioanal. Chem. 389*, 1017–1031.

(13) Alban, A., David, S. O., Bjorkesten, L., ersson, C., Sloge, E., Lewis, S., and Currie, I. (2003) A novel experimental design for comparative two-dimensional gel analysis: Two-dimensional difference gel electrophoresis incorporating a pooled internal standard. *Proteomics 3*, 36–44.

(14) Zhang, R., Sioma, C. S., Wang, S., and Regnier, F. E. (2001) Fractionation of isotopically labeled peptides in quantitative proteomics. *Anal. Chem. 73*, 5142–5149.

(15) Wolf-Yadlin, A., Hautaniemi, S., Lauffenburger, D. A., and White, F. M. (2007) Multiple reaction monitoring for robust quantitative proteomic analysis of cellular signaling networks. *Proc. Natl. Acad. Sci. U.S.A. 104*, 5860–5865.

(16) Han, M. J., Herlyn, M., Fisher, A. B., and Speicher, D. W. (2008) Microscale solution IEF combined with 2-D DIGE substantially enhances analysis depth of complex proteomes such as mammalian cell and tissue extracts. *Electrophoresis 29*, 695–705.

(17) Gromov, P. S., Gromova, I., and Celis, J. E. (2006) Proteomic Analysis by Two-Dimensional Polyacrylamide Gel Electrophoresis, In *Proteomics for Biological Discovery* (Veenstra, T. D., and Yates, J. R., III, Eds.) pp 19−46, Chapter 2, John Wiley & Sons, Hoboken, NJ.

(18) Corthals, G. L., Wasinger, V. C., Hochstrasser, D. F., and Sanchez, J. C. (2000) The dynamic range of protein expression: a challenge for proteomic research. *Electrophoresis 21*, 1104–1115.

(19) Deb, S. K., Davis, B., Knudsen, G. M., Gudihal, R., Ben Amotz, D., and Davisson, V. J. (2008) Detection and relative quantification of proteins by SERRS using isotopic labels. *J. Am. Chem. Soc. 130*, 9624–9625.

(20) Loethen, Y. L., Knudsen, G. M., Davis, B., Gudihal, R., Davisson, V. J., and Ben-Amotz, D. (2008) Protein quantitation in 2-D gels using fluorescence with water raman as an internal standard. *J. Proteome Res. 7*, 1341–1345.

(21) Patton, W. F. (2002) Detection technologies in proteome analysis. *J. Chromatogr., B: Analyt. Technol. Biomed. Life Sci. 771*, 3–31.

(22) Campion, A., and Kambhampati, P. (1998) Surface-enhanced Raman scattering. *Chem. Soc. Rev. 27*, 241–250.

(23) Lacy, W. B., Olson, L. G., and Harris, J. M. (1999) Quantitative SERS measurements on dielectric-overcoated silver-island films by solution-deposition control of surface concentrations. *Anal. Chem. 71*, 2564–2570.

(24) Zhang, D. M., Xie, Y., Deb, S. K., Davisson, V. J., and Ben-Amotz, D. (2005) Isotope edited internal standard method for quantitative surface-enhanced Raman spectroscopy. *Anal. Chem. 77*, 3563–3569.

(25) Oliver, J. C. (2006) Chemical and Structural Dynamics of Guanosine Monophosphate Synthetase. Ph.D. Thesis, Purdue University, West Lafayette, IN, 173 p.

(26) Kalkhof, S., and Sinz, A. (2008) Chances and pitfalls of chemical cross-linking with amine-reactive N-hydroxysuccinimide esters. *Anal. Bioanal. Chem. 392*, 305–312.

(27) Leimgruber, R. M., Malone, J. P., Radabaugh, M. R., LaPorte, M. L., Violand, B. N., and Monahan, J. B. (2002) Development of improved cell lysis, solubilization and imaging approaches for proteomic analyses. *Proteomics 2*, 135–144.

(28) Mortz, E., Krogh, T. N., Vorum, H., and Gorg, A. (2001) Improved silver staining protocols for high sensitivity protein identification using matrix-assisted laser desorption/ionization-time of flight analysis. *Proteomics 1*, 1359–1363.

(29) Shevchenko, A., Wilm, M., Vorm, O., and Mann, M. (1996) Mass spectrometric sequencing of proteins from silver stained polyacrylamide gels. *Anal. Chem. 68*, 850–858.

(30) Xie, Y., Jiang, Y., and Ben-Amotz, D. (2005) Detection of amino acid and peptide phosphate protonation using Raman spectroscopy. *Anal. Biochem. 343*, 223–230.

(31) Loethen, Y. L., Zhang, D., Favors, R. N., Basiaga, S. B. G., and Ben-Amotz, D. (2004) Second-derivative variance minimization method for automated spectral subtraction. *Appl. Spectrosc. 58*, 272–278.

(32) Savitzky, A., and Golay, M. J. E. (1964) Smoothing and differentiation of data by simplified least squares procedures. *Anal. Chem. 36*, 1627–1639.

(33) Lieber, C. A., and Mahadevan-Jansen, A. (2003) Automated method for subtraction of fluorescence from biological Raman spectra. *Appl. Spectrosc. 57*, 1363–1367.

(34) Filatov Alexander, V., Krotov Grigory, I., Zgoda Victor, G., and Volkov, Y. (2007) Fluorescent immunoprecipitation analysis of cell surface proteins: a methodology compatible with mass-spectrometry. *J. Immunol. Methods 319*, 21–33.

(35) Unlu, M., Morgan, M. E., and Minden, J. S. (1997) Difference gel electrophoresis: a single gel method for detecting changes in protein extracts. *Electrophoresis 18*, 2071–2077.

(36) Emory, S. R., Haskins, W. E., and Nie, S. (1998) Direct observation of size-dependent optical enhancement in single metal nanoparticles. *J. Am. Chem. Soc. 120*, 8009–8010.

(37) Merril, C. R., Bisher, M. E., Harrington, M., and Steven, A. C. (1988) Coloration of silver-stained protein bands in polyacrylamide gels is caused by light scattering from silver grains of characteristic sizes. *Proc. Natl. Acad. Sci. U.S.A. 85*, 453–457.

(38) Evanoff, D. D., Jr., and Chumanov, G. (2005) Synthesis and optical properties of silver nanoparticles and arrays. *ChemPhysChem 6*, 1221–1231.

(39) Lee, P., and Meisel, D. (1982) Adsorption and surface-enhanced Raman of dyes on silver and gold sols. *J. Phys. Chem. 86*, 3391–3395.

(40) Hirst, M., Haliday, E., Nakamura, J., and Lou, L. (1994) Human GMP synthetase. Protein purification, cloning, and functional expression of cDNA. *J. Biol. Chem. 269*, 23830–23837.

(41) Lou, L., Nakamura, J., Tsing, S., Nguyen, B., Chow, J., Straub, K., Chan, H., and Barnett, J. (1995) High-level production from a baculovirus expression system and biochemical characterization of human GMP synthetase. *Protein Expression Purif. 6*, 487–495.

(42) Stover, D. R., Caldwell, J., Marto, J., Root, K., Mestan, J., Stumm, M., Ornatsky, O., Orsi, C., Radosevic, N., Liao, L., Fabbro, D., and Moran, M. F. (2004) Differential phosphoprofiles of EGF and EGFR kinase inhibitor-treated human tumor cells and mouse xenografts. *Clin. Proteomics 1*, 69–80.

(43) Besada, V., Diaz, M., Becker, M., Ramos, Y., Castellanos-Serra, L., and Fichtner, I. (2006) Proteomics of xenografted human breast cancer indicates novel targets related to tamoxifen resistance. *Proteomics 6*, 1038–1048.

(44) Schroeder, S., Zhang, H., Yeung, E. S., Jaensch, L., Zabel, C., and Waetzig, H. (2008) Quantitative gel electrophoresis: sources of variation. *J. Proteome Res. 7*, 1226–1234.

(45) Gade, D., Thiermann, J., Markowsky, D., and Rabus, R. (2003) Evaluation of two-dimensional difference gel electrophoresis for protein profiling. *J. Mol. Microbiol. Biotechnol. 5*, 240–251.

(46) Lopez, M. F., Berggren, K., Chernokalskaya, E., Lazarev, A., Robinson, M., and Patton, W. F. (2000) A comparison of silver stain and SYPRO ruby protein gel stain with respect to protein detection in two-dimensional gels and identification by peptide mass profiling. *Electrophoresis 21*, 3673–3683.

(47) Hanke, S., Besir, H., Oesterhelt, D., and Mann, M. (2008) Absolute SILAC for accurate quantitation of proteins in complex mixtures down to the attomole level. *J. Proteome Res. 7*, 1118–1130.

(48) Dieringer, J. A., McFarland, A. D., Shah, N. C., Stuart, D. A., Whitney, A. V., Yonzon, C. R., Young, M. A., Zhang, X. Y., and Van Duyne, R. P. (2006) Surface enhanced Raman spectroscopy: new materials, concepts, characterization tools, and applications. *Faraday Discuss. 132*, 9–26.

(49) Kneipp, K., Kneipp, H., Manoharan, R., Hanlon, E. B., Itzkan, I., Dasari, R. R., and Feld, M. S. (1998) Extremely large enhancement factors in surface-enhanced Raman scattering for molecules on colloidal gold clusters. *Appl. Spectrosc. 52*, 1493–1497.

(50) Nie, S., and Emory, S. R. (1997) Probing single molecules and single nanoparticles by surface-enhanced raman scattering. *Science 275*, 1102–1106.

(51) Deb, S. K., Davis, B., Ben Amotz, D., Davisson, V. J. Isotopic dye pairs for accurate optical concentration measurements using SERRS *Appl. Spectrosc.* in press.

(52) Graham, D., Mallinder, B. J., Whitcombe, D., Watson, N. D., and Smith, W. E. (2002) Simple multiplex genotyping by surface-enhanced resonance Raman scattering. *Anal. Chem. 74*, 1069–1074.

BC800325K

Quantification of Isotope Encoded Proteins in 2D Gels Using Surface Enhanced Resonance Raman

*Giselle M. Knudsen[1], Brandon M. Davis[2], Shirshendu K. Deb[1], Yvette Loethen[2], Ravindra Gudihal[1], Pradeep Perera[2], Dor Ben-Amotz[2], V. Jo Davisson[1]**

[1]Department of Medicinal Chemistry & Molecular Pharmacology and the Bindley Bioscience Center at Discovery Park and the [2]Department of Chemistry, Purdue University, West Lafayette, IN 47907.

Supporting Information Available.

Supplemental Table 1. MS/MS analysis of peptides matching hGMPS species in HCT116 lysate.

Supplemental Table 2. MS+MS/MS analysis of peptide coverage of hGMPS recombinant protein.

Supplemental Table 3. MS/MS identified peptides matching hGMPS species in recombinant-spiked sample.

Supplemental Figure 1. The fluorescence calibration plot of d_0-R6G in solution, used for water Raman internal standardization.

Supplemental Figure 2. The PLS model calibration plots for absolute versus expected d_0 and d_4 values, d_4 versus d_0-R6G composition, and %d_4-R6G composition.

Supplemental Figure 3. SERRS spectra from hGMPS and background species in Samples A and B, as shown in Figure 6.

Supplementary Table 1. MS/MS identification of hGMPS protein in 2DGE of HCT116 lysate. Putative hGMPS protein spots were selected for in-gel tryptic digestion using a protocol from the UCSF mass spectrometry facility (http://donatello.ucsf.edu/ingel.html), with zip tip treatment and using α-cyano-4-hydroxycinnamic acid matrix for MALDI preparation. MS/MS analysis was performed using a 4800 MALDI TOF/TOF analyzer from Applied Biosystems, and analyzed using ProteinPilot software v. 2.0, searching the Uniprot+Swissprot databases (2007.01.23) with the following settings: trypsin digestion, urea denaturation, iodoacetamide Cys alkylation, species *H. sapiens*, with special factors: phosphorylation emphasis, gel-based ID, and ID focus biological modifications. The search included 15652 proteins, and found only one protein with a score >1.30 (95%): SwissProt# P49915, human GMPS. The number of matched peptides and sequence coverage are listed below. These samples were analyzed through a service provided by the Purdue Proteomics Facility.

Sample	Unused[§]	Total	Peptides	%Coverage
E2□	24.48	24.48	13	28
E3	12.36	12.36	9	19
E4	2.07	2.07	2	3

□ Protein spot names are labeled in Figure 4B. Although E1 was also analyzed, no significant proteins could be identified from this species.

[§]Unused and Total refer to protein scoring used in ProteinPilot software to indicate a summed score for unique peptides that have been unused by other protein hits in the identification, out of the total available.

Supplementary Table 2. MS+MS/MS analysis of recombinant hGMPS species in 2DGE. Samples were selected and digested as described above for MALDI-MS/MS analysis, using an Applied Biosystems MALDI 4700 Protein Analyzer. The 4000 Series Explorer software was used for mass list export into GPS explorer software, searching the NCBInr database (2007.06.18) using the Mascot search engine software (v. 2.1) (www.matrixscience.com). Search settings were: combined MS+MS/MS scoring, species *H. sapiens*, 1 allowed missed cleavage, iodoacetamide modification of Cys, and variable modifications: phospho S,T, Y, Met-ox, Pyro-Glu. The number of matched peptides and sequence coverage are listed for the top hit in all cases: identification of gi|4504035, human GMPS.

Sample	Protein Score[§]	Peptides	%C.I.	Total Ion Score	Best Ion Score	%C.I. best ion
R1□	1,450	40	100	1,013	112	100
R2	1,510	37	100	1,134	141	100
R3	1,230	33	100	910	121	100

□ Protein spot names are labeled in Figure 4C.

[§]Individual peptide scores in Mascot are significant at >47, the protein score is derived from individual ion scores.

Supplementary Table 3. MS/MS analysis of Sample A and Sample B protein spots in 2DGE. Protein spots 1-4 were selected for in-gel tryptic digestion, followed by peptide extraction and LC-MS/MS analysis using an Agilent XCT plus coupled with an Agilent 1100 HPLC system. Masses were analyzed using Spectrum Mill software v. A.03.02.060, and searched against the IPI human database, v. 3.00, containing 47,094 sequences. MS/MS analysis settings were: tryptic digest, maximum 2 missed cleavages, fixed carbamidomethyl modification of Cys and variable modifications: phospho Thr/Ser/Tyr, oxidized Met, and pyro-Glu. Mass list parameters were precursor mass tolerance 2.5 Da, product mass tolerance 0.7 Da. Shown here are peptide information for identification of P49915, human GMPS.

Sample	#Spectra	Peptides	Score	%Coverage	Mean spectral intensity
1[1]	26	20	271.53	41	1.24E+08
2	18	14	192.37	22	9.26E+07
3	24	20	285.11	38	1.87E+08
4	21	20	263.56	36	1.33E+08

[1] Protein spot names are labeled in Figure 5.

Supplementary Figure 1. Rhodamine 6G Solution Fluorescence Calibration Plot. Error bars are 1 standard deviation of three replicate measurements for each concentration. The resultant calibration equation is:

Normalized Fluorescence Intensity = 0.0852*(Concentration in pM).

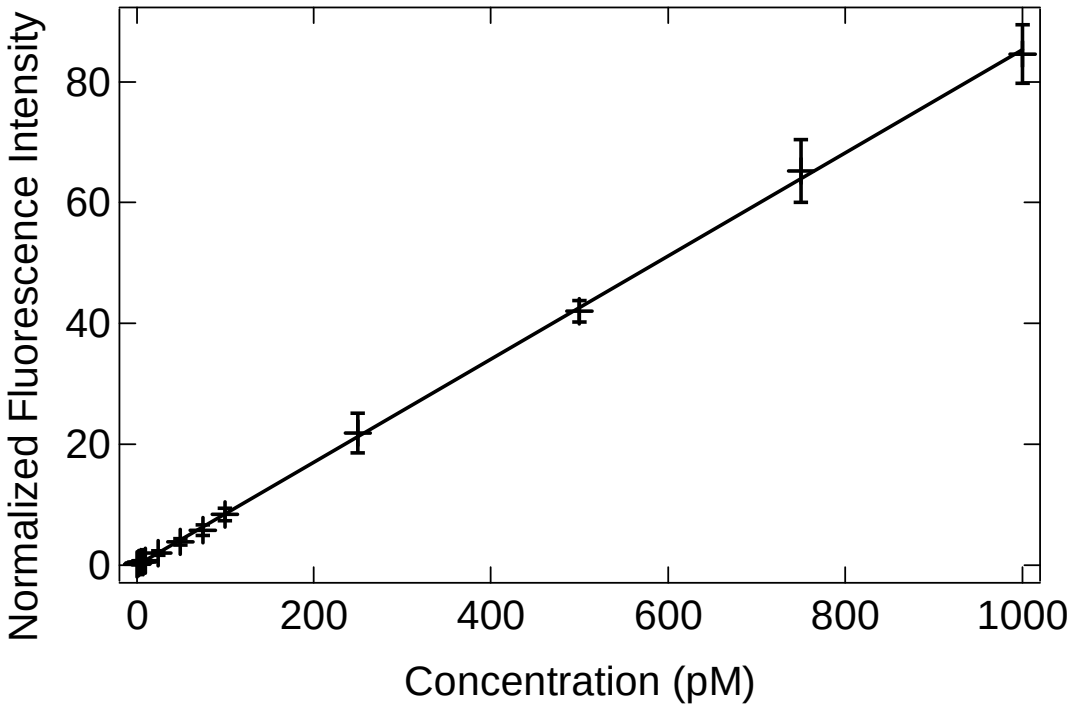

Supplementary Figure 2. PLS results obtained using a training set of 1000 Raman spectra with 100%, 75%, 50%, 25%, or 0% d_4-R6G labeled protein in SDS-PAGE gels stained with silver for surface enhancement of the Raman. The error bars are 95% CI. A linear correlation factor was used to absolutely quantify d_0-R6G (**A**) and d_4-R6G (**B**). Panel **C** shows the distribution of d_4:d_0 compositions, while panel **D** compares the measured and input (expected) $\%d_4$ composition, with an R^2 correlation coefficient of 0.999.

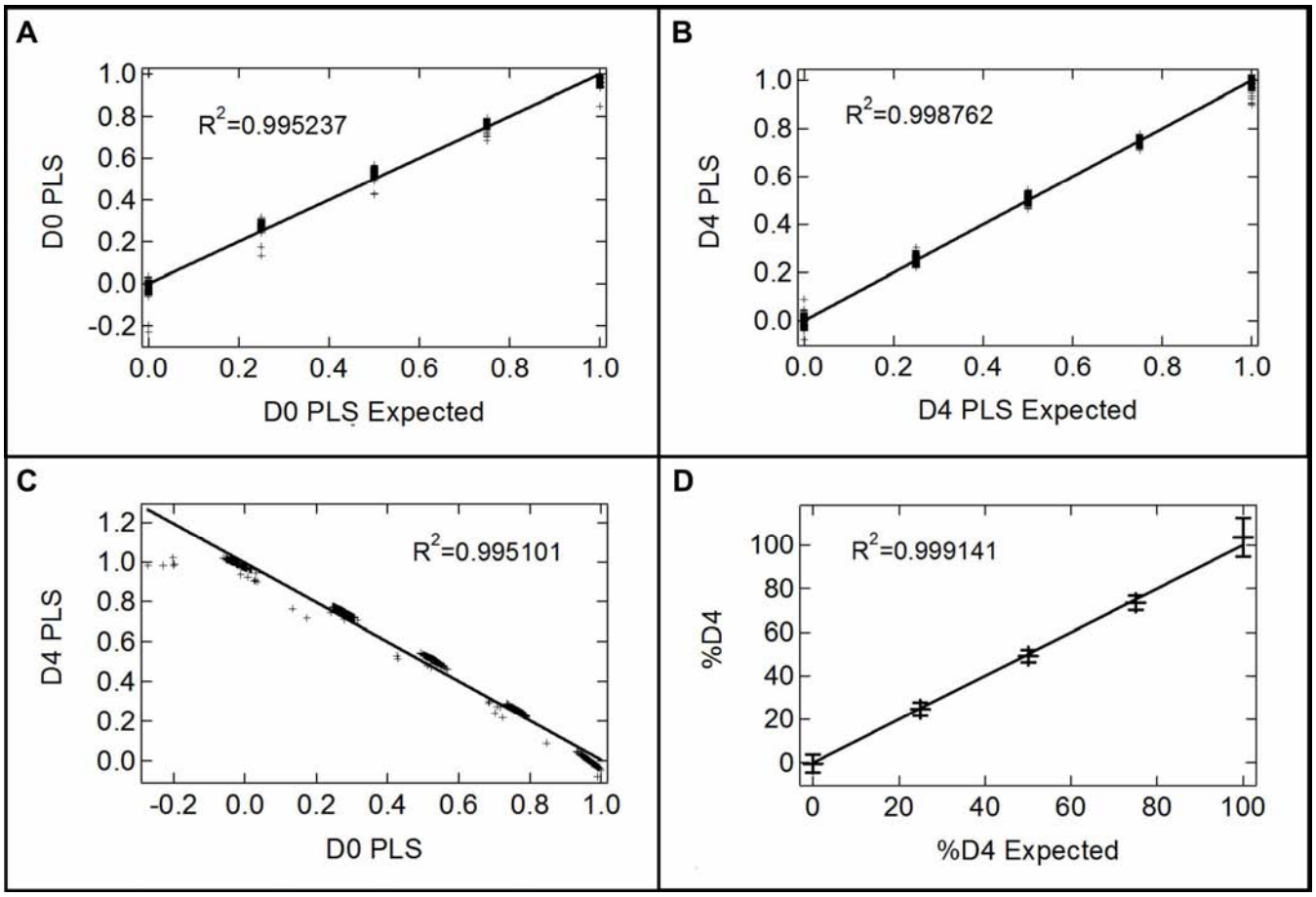

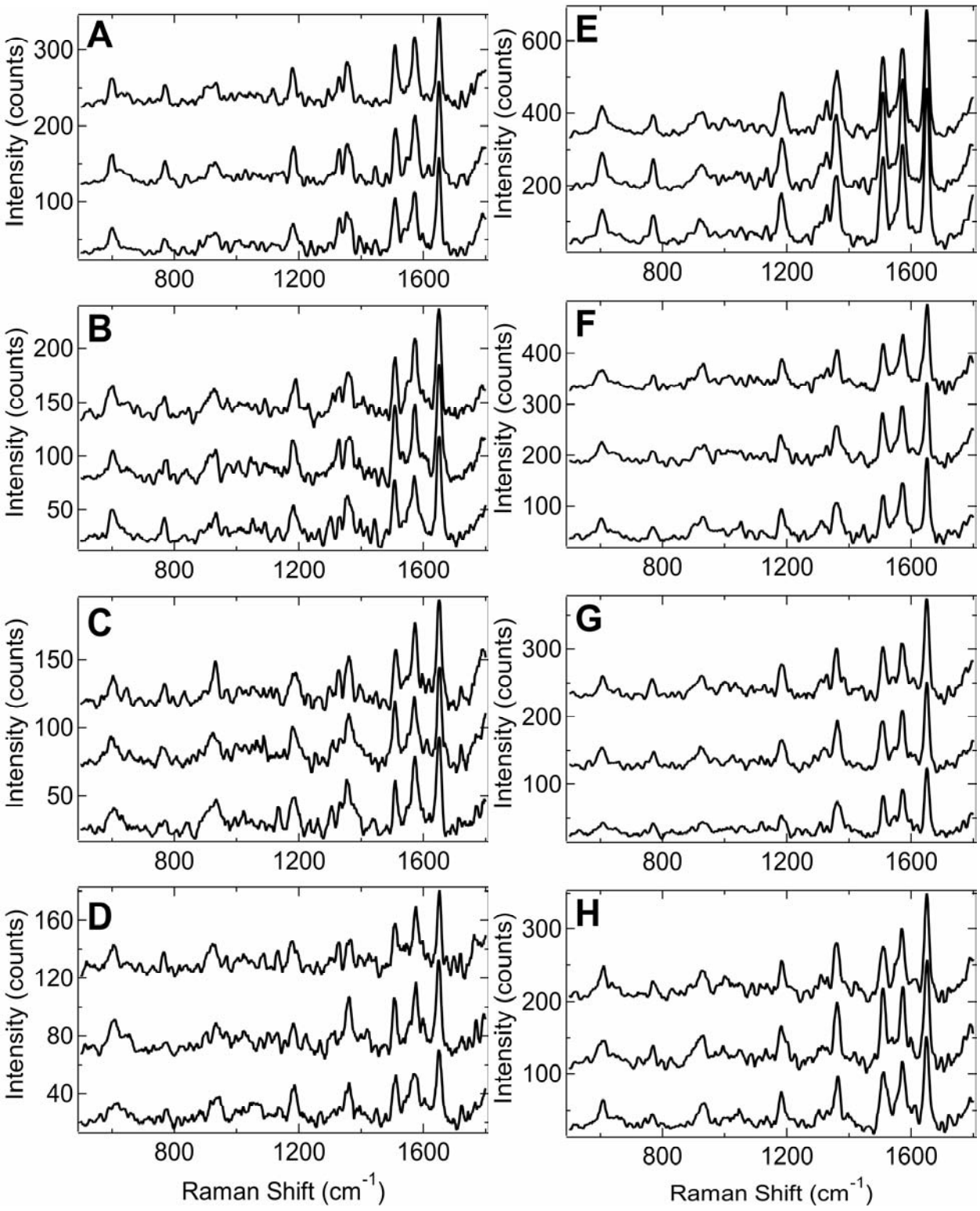
A
B
C
D
E
F
G
H
Intensity (counts)
Raman Shift (cm-1)
800
1200
1600

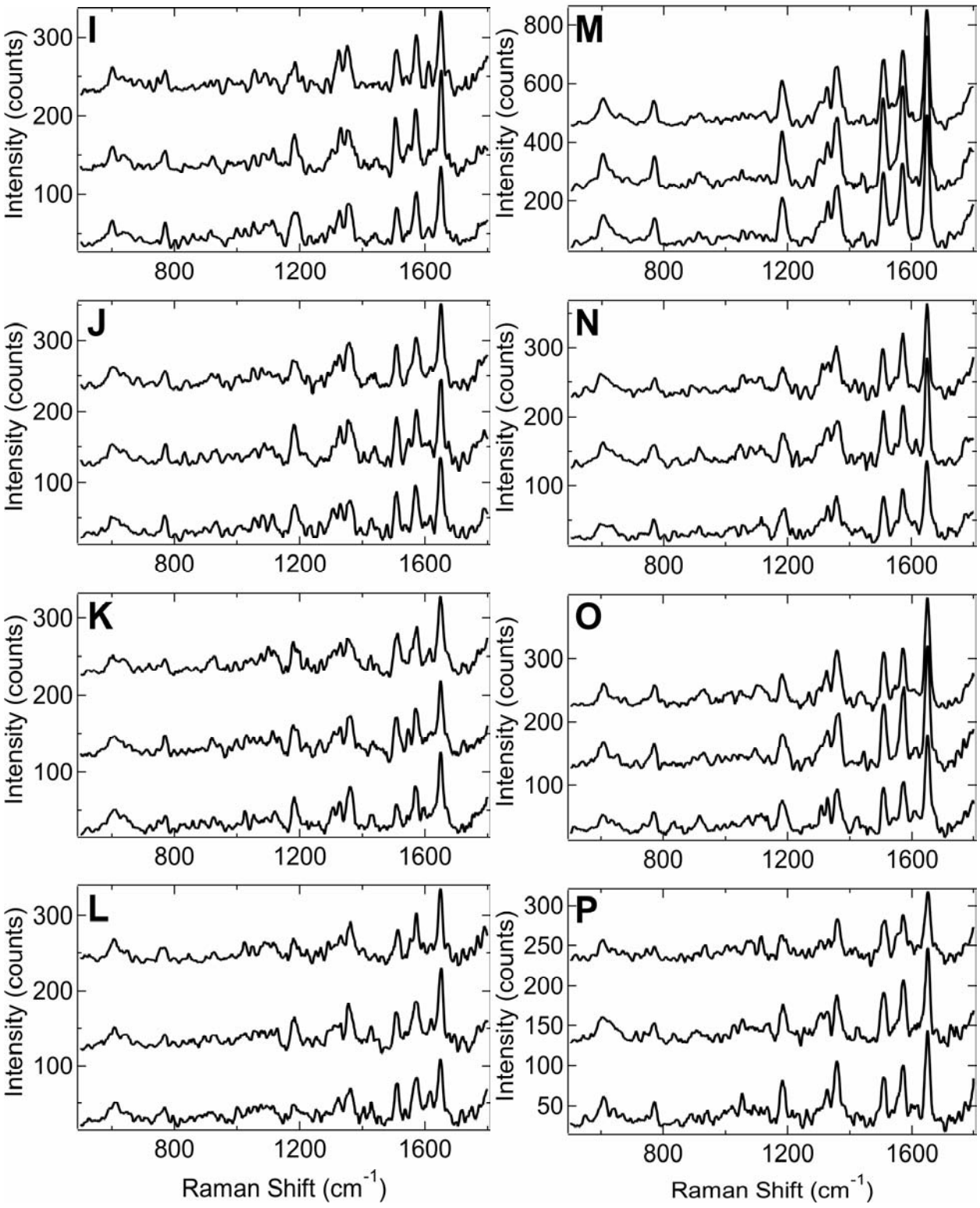

Supplementary Figure 3. SERRS spectra collected from protein species in Figure 6 for Samples A and B are shown after baseline correction and Savitsky-Golay smoothing as described in the experimental. The spectra are offset for clarity. Three replicate spectra are shown in each panel for a single protein species, and the panels are arranged in the order: hGMPS species 1, 2, 3, 4 background species b1, b2,

b3, b4 respectively in panels **A**, **B**, **C**, **D**, **E**, **F**, **G** and **H** for Sample A and in panels **I**, **J**, **K**, **L**, **M**, **N**, **O** and **P** for Sample B.

Site-Selective Glycosylation of Hemoglobin on Cys β93

Yalong Zhang,[†] Veer S. Bhatt,[‡] Guoyong Sun,[§] Peng G. Wang,[†,‡] and Andre F. Palmer*[,§]

Department of Chemistry, Biophysics Program and Department of Biochemistry, and Department of Chemical and Biomolecular Engineering, The Ohio State University, Columbus, Ohio 43210. Received July 29, 2008; Revised Manuscript Received September 17, 2008

In this work, we describe the synthesis and characterization of a novel glycosylated hemoglobin (Hb) with high oxygen affinity as a potential Hb-based oxygen carrier. Site-selective glycosylation of bovine Hb was achieved by conjugating a lactose derivative to Cys 93 on the β subunit of Hb. LC-MS analysis indicates that the reaction was quantitative, with no unmodified Hb present in the reaction product. The glycosylation site was identified by chymotrypsin digestion of the glycosylated bovine Hb followed with LC-MS/MS and from the X-ray crystal structure of the glycosylated Hb. The chemical conjugation of the lactose derivative at Cys β93 yields an oxygen carrier with a high oxygen affinity (P_{50} of 4.94 mmHg) and low cooperativity coefficient (n) of 1.20. Asymmetric flow field-flow fractionation (AFFFF) coupled with multiangle static light scattering (MASLS) was used to measure the absolute molecular weight of the glycosylated Hb. AFFFF-MASLS analysis indicates that glycosylation of Hb significantly altered the $\alpha_2\beta_2-\alpha\beta$ equilibrium compared to native Hb. Subsequent X-ray analysis of the glycosylated Hb crystal showed that the covalently linked lactose derivative is sandwiched between the β_1 and α_2 (and hence by symmetry the β_2 and α_1) subunits of the tetramer, and the interaction between the saccharide and amino acid residues located at the interface is apparently stabilized by hydrogen bonding interactions. The resultant structural analysis of the glycosylated Hb helps to explain the shift in the $\alpha_2\beta_2-\alpha\beta$ equilibrium in terms of the hydrogen bonding interactions at the $\beta_1\alpha_2/\beta_2\alpha_1$ interface. Taken together, all of these results indicate that it is feasible to site-specifically glycosylate Hb. This work has great potential in developing an oxygen carrier with defined chemistry that can target oxygen delivery to low pO_2 tissues and organs.

INTRODUCTION

Hemorrhagic shock is a well-documented clinical condition in which 50% of the blood volume is lost due to some trauma. The loss of oxygen carrying capacity results in the development of low pO_2 levels in key organs like the brain, liver, and heart. Therefore, it is imperative that resuscitation strategies first target oxygen delivery to these low pO_2 tissues and organs in order to preserve their function, before transporting oxygen to well-oxygenated sites in the body (*1*). Since hemoglobin (Hb) is responsible for oxygen transport and storage in red blood cells (RBC), it is not surprising that much effort has been spent to develop hemoglobin-based oxygen carriers (HBOCs) for treatment of hemorrhagic shock. The initial development of RBC substitutes was driven by the needs of the military (*2*). Early attempts toward developing a RBC substitute using acellular Hb in human recipients met with failure due to hypertension, short intravascular half-life, and nephrotoxicity (*3*). These problems have been attributed in large part to the affinity of Hb for nitric oxide (*4*) and dissociation of the $\alpha_2\beta_2$ tetramer into $\alpha\beta$ dimers that can further unfold to release cytotoxic heme that is eventually filtered through the renal glomeruli (*2, 5*−*7*).

In order to overcome the disadvantages associated with transfusing acellular Hb, several types of HBOCs have been developed over the past 20 years, such as cross-linked Hb (*8, 9*) polymerized Hb (*6, 10*−*15*), surface-conjugated Hb (*16*−*19*), liposome (*20*−*24*), and nanoparticle encapsulated Hb (*25*−*27*), and recombinant Hb (*7, 28, 29*).

In nature, glycoproteins possess a large hydration shield afforded by relatively small oligosaccharides (*30*), which will protect a protein from proteolysis and stabilize the protein by forming hydrogen bonds with amino acid residues on the protein surface. Glycosylation of Hb at Lys or N-terminal amines in the systemic circulation by glucose is a well-characterized non-enzymatic reaction (*31, 32*). Previously, oxidized dextran (*10, 33*) and oxidized raffinose (Hemolink, Hemosol Inc., Toronto, Canada) (*34*−*35*) were used to cross-link and polymerize Hb in order to increase its molecular radius and to prevent its extravasation through blood vessels. However, those early attempts at cross-linking and polymerizing Hb with oxidized saccharides yielded highly heterogeneous products with the resultant chemical modification of key amino acid residues that regulate oxygen affinity and the structural stability of the tetramer. In the case of Hemolink, Boykins et al. (*36*) confirmed that *O*-raffinose cross-linked and polymerized Hb was constrained in a locked T-state conformation that promotes heme instability. In addition, *in vivo* experiments also showed that Hemolink induced microvascular damage and increased the permeability of the microvasculature when compared to other HBOCs (*37*). In light of these results, recent advances in glycochemistry indicate that it is important and necessary to prepare homogeneous glycoproteins with specific glycosylation sites (*38*).

In the present study, the feasibility of site-selective glycosylation of bovine Hb (Figure 1) was investigated by conjugating a reactive lactose derivative to Cys β93. Bovine Hb was chosen as the source of Hb, since it has two cysteine residues per tetramer, each located at the Cys 93 position on the β subunit. Conversely, human Hb has 6 cysteine residues. Cys β93 is located in a conformationally plastic domain, which contains amino acid residues that regulate the allosteric properties of the Hb tetramer (*39*). Previous modification of Cys β93 with maleimide resulted in an increase in oxygen affinity and the

* To whom correspondence should be addressed. Department of Chemical and Biomolecular Engineering, The Ohio State University, 231A Koffolt Laboratories, 140 West 19th Avenue, Columbus, Ohio 43210. Tel: (614) 292-6033and E-mail: palmer.351@osu.edu.

[†] Department of Chemistry.

[‡] Biophysics Program and Department of Biochemistry.

[§] Department of Chemical and Biomolecular Engineering.

10.1021/bc8003205 CCC: $40.75 © 2008 American Chemical Society
Published on Web 10/17/2008

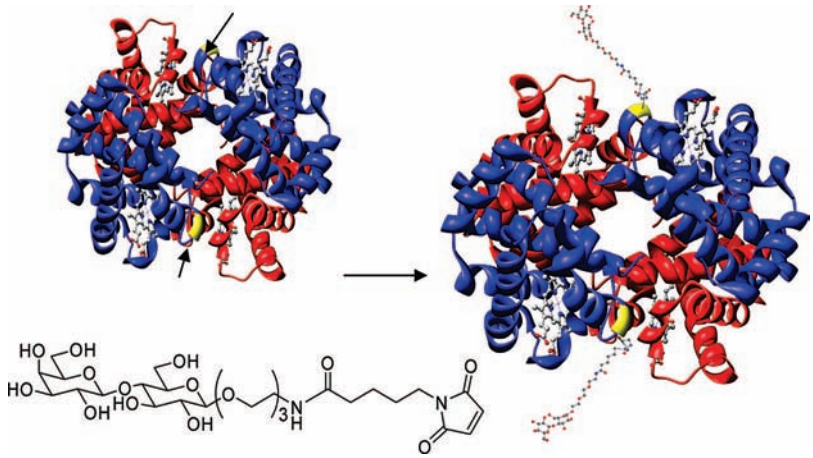

Figure 1. Site-selective glycosylation of bovine Hb at Cys β93 by the lactose derivative.

Scheme 1. Synthesis of Maleimide−Lactoside for Glycosylation of Bovine Hb.

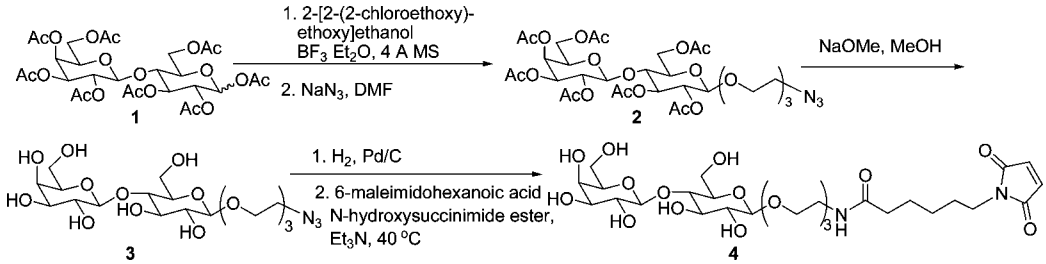

loss of some hydrogen bonds within the $\alpha_1\beta_2/\alpha_2\beta_1$ interface of Hb (*39*−*41*). In this study, the modified lactoside derivative could compensate for the lost hydrogen bonds by forming additional hydrogen bonds with amino acid residues within the $\alpha_1\beta_2/\alpha_2\beta_1$ interface in order to stabilize the tetrameric structure of Hb as well as to increase the molecular radius of Hb, therefore preventing its extravasation through the lumen of blood vessels and subsequent NO scavenging.

EXPERIMENTAL PROCEDURES

Materials. β-D-Lactose, 2-[2-(2-chloroethoxy)ethoxy]ethanol, and 6-maleimidohexanoic acid *N*-hydroxysuccinimide ester were purchased from Sigma-Aldrich (Milwaukee, WI) and used without further purification. HEMOX-solution, additive-A, and antifoaming agent were purchased from TCS Scientific Corp. (New Hope, PA). Bovine RBCs were purchased from QUAD 5 (Ryegate, MT). All other reagents, unless specified, were obtained from commercial sources and used without further purification. Solvents were distilled from the appropriate drying agents before use. Unless stated otherwise, all reactions were carried out at room temperature under a positive pressure of argon or nitrogen and were monitored by TLC on silica gel 60 F254 (0.25 mm, E. Merck, Gibbstown, NJ). Spots were detected under UV light or by anisole anhydride/H_2SO_4/MeOH (5/15/80). Column chromatography was performed on silica gel 60 (230−400 mesh) purchased from EMD Chemicals Inc. (Darmstadt, Germany). The ratio between silica gel and crude product ranged from 20 to 30:1 (w/w). For the characterization of reaction products, ^{1}H NMR spectra were recorded at 500 MHz, and chemical shifts referenced to $CDCl_3$ (7.26, $CDCl_3$). ^{13}C NMR spectra were recorded at 125 MHz, and ^{13}C chemical shifts referenced to $CDCl_3$ (77.00, $CDCl_3$).

Synthesis of *N*-3′,6′-Dioxa-9′-octyl-*O*-(β-D-glucopyranolsyl)-(1→4)-β-D-galactoside-6-maleimidohexanamide (maleimide−lactoside). The method of preparing maleimide−lactoside is shown in Scheme 1. First, the peracetyl-protected lactoside **1** was treated with 2-[2-(2-chloroethoxy)ethoxy]ethanol catalyzed by boron trifluoride and then reacted with sodium azide to yield 1-azido-4,6-dioxa-9-octyl-peracetyl-lactoside **2**. Second, the acetyl groups were removed by treating with sodium methoxide to yield compound **3**. Finally, the azido group of **3** was hydrogenated to an amine and reacted with 6-maleimidohexanoic acid *N*-hydroxysuccinimide ester to yield maleimide−lactoside **4**.

Hb Purification (*42, 43*). Hb was extracted from bovine RBCs suspended in 3.8% sodium citrate solution. RBCs were washed 3 times with 3 volumes of isotonic saline solution (0.9%) at 4 °C. Cells were then lysed with 2 volumes of hypotonic, 15 mOsM phosphate buffer (PB), pH 7.4, on ice for 1 h. Lysed cells were then filtered 3 times through glass wool and a filter paper to remove cell debris. The crude solution of Hb was dialyzed against 20 mM Tris-HCl buffer (pH = 8.2). This buffer was the starting buffer for the chromatographic purification of Hb. Hb purification was performed using an ÄKTA Explorer 100 system controlled by *Unicorn 5.1* software (GE Healthcare, Piscataway, NJ). Dialyzed Hb lysate was loaded onto a XK 26/40 (400 mm in length and 26 mm I.D., GE Healthcare, Piscataway, NJ) column packed with 120 mL Q-Sepharose XL resin (GE Healthcare, Piscataway, NJ) and eluted with a linear salt gradient (0 to 0.15 M NaCl in 5 column volumes). The eluted Hb was collected with a fraction collector (Frac 900, GE healthcare, Piscataway, NJ). The purity of Hb was assessed by SDS-PAGE. Pure Hb fractions were pooled for measurement of Hb concentration and methemoglobin (metHb) level. The concentrations of Hb and metHb in solution were determined using an adaptation of the cyanomethemoglobin (cyanometHb) method (*20, 44*). Hb solution was placed in a 1.5 mL cuvette and diluted with buffer (20 mM PB, pH 7.2) with a total volume of 1.0 mL (dilution factor: D_1) in order to yield an absorbance less than 1 at 630 nm (oxyHb + deoxyHb + metHb). Potassium cyanide (KCN) solution (50 μL, 10% KCN in 50 mM PB, pH 7.6) was added to the solution to convert metHb into cya-

nometHb, and the absorbance was measured at 630 nm to yield L_2 (since cyanometHb does not absorb at 630 nm), L_2 refers to the absorbance of oxyHb + deoxyHb. Thus, the concentration of metHb can be obtained from this equation: [metHb] = $D_1(L_1 - L_2)$/3.7 mM. To measure the concentration of Hb, potassium ferricyanide ($K_3Fe(CN)_6$) (50 μL, 20% $K_3Fe(CN)_6$ in 50 mM PB, pH 7.6) was mixed with diluted Hb solution (dilution factor: D_2), which converts oxyHb and deoxyHb into metHb. The solution was incubated for 5 min, and then KCN (50 μL, 10% KCN in 50 mM PB, pH 7.6) was added to the mixture to convert metHb to cyanometHb. The absorbance was measured at 540 nm (L_3). Thus, [Hb] = D_2L_3/11 mM.

Site-Selective Glycosylation of Hb. To a solution of Hb (60 mg, 9.34×10^{-4} mmol) in Tris-HCl buffer (20 mM, pH 8.2, 2.0 mL) was added maleimide−lactoside **4** (4.4 mg, 6.56×10^{-3} mmol) which was stirred at r.t. for 24 h. Sodium cyanoborohydride (12 mg, 9.34×10^{-2} mmol) was added to the reaction mixture, and the solution was stirred for another 24 h. The modified Hb was transferred to a Millipore centrifugal filter device (10 000 MW cutoff) and washed 4 times with Tris-HCl buffer (20 mM, pH 8.2, 2.0 mL) in a centrifuge at 5000 rpm to remove unreacted maleimide−lactoside **4** and sodium cyanoborohydride.

Analysis of Glycosylated Hb by LC-MS. LC-MS analysis of purified Hb and glycosylated Hb was performed on a Waters Alliance 2690 high-performance liquid chromatography (HPLC) system (Waters, Milford, MA) connected in series to a Waters LCT (Waters, Milford, MA) mass detector. Samples were analyzed using a Vydac C18 column (5 μm particle size, 1.0 × 250 mm) at a flow rate of 50 μL/min and injection volume of 10 μL. The mobile phase consisted of the following: phase A, 0.1% trifluoroacetic acid, and phase B, acetonitrile/0.1% trifluoroacetic acid. The percentage of phase B was increased according to a linear gradient from 0% to 65% in 45 min and then increased from 65% to 100% in 15 min. The amino acid sequence and molecular weight of bovine Hb was obtained from ProteinProspector at UCSF (http://prospector.ucsf.edu/).

Chymotrypsin Digestion of the β Chain of Glycosylated Hb. The β chain of glycosylated bovine Hb was purified via a Shimadzu HPLC LC-20AT (Columbia, MD) equipped with a Supelco bio wide pore C18 column (5 μm in particle size, 15 × 150 mm, and 300 Å in pore size, Sigma-Aldrich, Milwaukee, WI). The mobile phase and gradient were the same as those utilized in the LC-MS analysis. Twenty microliters of glycosylated bovine Hb (15 mg/mL) was injected into the RP-HPLC column, and the second peak was collected (22.67 min). The molecular weight of the collected fraction was confirmed by LC-MS 2010A (Shimadzu, Columbia, MD). The lyophilized protein was digested using a protocol similar to the reference (*45*) at the Campus Chemical Instrument Center (CCIC) at The Ohio State University by Dr. Liwen Zhang. Proteins were desalted using manual syringe protein traps from Michrom BioResources (Auburn, CA) and resuspended in 10 μL of water. Five microliteres of DTT (5 mg/mL) in 100 mM ammonium bicarbonate was incubated with the sample at 50 °C for 15 min to reduce all cysteine residues. Five microliters of iodoacetamide (15 mg/mL) in 100 mM ammonium bicarbonate was then added and incubated with the mixture in the dark for 15 min to alkylate the cysteine residues. Sequencing grade chymotrypsin from Roche was prepared as 25 ng/μL in 50 mM ammonium bicarbonate. The final buffer conditions for digestion were 25 mM ammonium bicarbonate and 5% acetonitrile. The digestion was carried out at 37 °C overnight and terminated by acidification. The digest was concentrated in a speed vac to ~30 μL for subsequent LC-MS/MS analysis.

LC-MS/MS Analysis of the β Chain of Glycosylated Hb. Capillary−liquid chromatography−nanospray tandem mass spectrometry (LC-MS/MS) was performed on a Thermo Finnigan LTQ mass spectrometer equipped with a nanospray source operated in positive ion mode at CCIC by Dr. Liwen Zhang. The LC system was an UltiMate Plus system from LC-Packings (Sunnyvale, CA) with a Famos autosampler and a Switchos column switcher. Five microliters of each sample was first injected into the trapping column (LC-Packings), and washed with 50 mM acetic acid. The injector port was switched to inject, and the peptides were eluted off the trap onto a 5 cm, 75 μm (inner diameter) ProteoPep II C18 reverse-phase column (New Objective, Inc. Woburn, MA) packed directly in the nanospray tip. Solvent A was composed of 50 mM acetic acid in water, and solvent B was composed of acetonitrile. Peptides were eluted directly off the column into the LTQ system at a flow rate of 300 nL/min. The gradient was initiated and maintained at 2% B for the first 3 min, then B was increased to 50% in 27 min, and further increased to 80% in 15 min. B was kept at 80% for another 5 min, then returned to 2% in 0.1 min. The total run time was ~65 min.

The MS/MS was acquired according to the standard conditions established at the CCIC. Briefly, a nanospray source operating at a spray voltage of 3 KV and a capillary temperature of 200 °C was used. The scan sequence of the mass spectrometer was based on the TopTen method; briefly, the analysis was programmed for a full scan to be recorded between 350 and 2000 Da, and a MS/MS scan was used to generate product ion spectra to determine the amino acid sequence in consecutive instrument scans of the ten most abundant peaks in the spectrum. The CID fragmentation energy was set to 35%. Dynamic exclusion was enabled with a repeat count of 30 s, exclusion duration of 350 s, and a low mass width of 0.5 and high mass width of 1.5 Da. Sequence information from the MS/MS data was processed using the *Mascot 2.0* active Perl script with standard data processing parameters. The data was later searched by *Mascot 2.0* (Matrix Science, Boston, MA) for protein identification and MassMatrix for the identification of cysteine glycosylation (*46*). Methionine oxidation and carbamidomethylation of cysteines were also considered as possible modifications.

Crystallization of Glycosylated Hb. Purified glycosylated Hb was used for all crystallization experiments. The protein was concentrated to 30 mg/mL in Tris-HCl Buffer (20 mM, pH 7.4), and a microbatch experiment was set up (*47*) under mineral oil (Sigma-Aldrich) at 25 °C. To find initial crystallization hits, sample drops were set up against commercial (Hampton Research, CA) as well as homemade screens in a ratio of 1:2. Crystalline forms could be observed in several different precipitants in the pH range 7.5−8.5. These conditions were optimized further by varying the concentration and pH of the corresponding crystallization reagent for each hit. Eventually, crystals grown in reagent droplets containing 25% w/v PEG MME 2000, 0.2 M trimethylamine *N*-oxide dehydrate, and 0.1 M Tris pH 8.25 were used to collect full data sets. These crystals grew as clustered thin plates with the longest dimension measuring 100 μm. They were flash-frozen after cryoprotection using 38% PEG MME 2000 and stored in liquid nitrogen until further use.

Data Collection and Processing. The X-ray intensity data to 3.5 Å resolution was collected at −160 °C using a R-AXIS IV++ imaging plate area detector and Cu K radiation generated from a rotating-anode X-ray generator (Rigaku-MSC, TX) operating at 46 kV and 90 mA. The temperature was maintained during data collection using an X-STREAM cryogenic device (Rigaku-MSC, TX). Although crystals diffracted to 3.3 Å, the completeness beyond 3.5 Å was lower than 20%. Therefore, the final data set was collected to 3.5 Å resolution. The data

were processed using the *CrystalClear* software, which is based on the d*TREK package (*48*). The crystals belong to the orthorhombic space group $P2_12_12_1$ with one molecule in the asymmetric unit. The unit-cell parameters are $a = 62.6$, $b = 74.0$, and $c = 129.8$ Å. Solvent analysis suggested only one molecule to be present in the asymmetric unit. Assuming that one protein molecule in the asymmetric unit has a molecular weight of 64 kDa, V_M was calculated to be 2.35 Å^3 Da^{-1}. The details of the crystallographic data are summarized in Table 1 in Supporting Information.

Structure Determination and Refinement. The structure of bovine Hb is already well-known (*46*). However, the protein can exist in different quaternary states depending on whether it is liganded (R-state) or not (T-state). Furthermore, several intermediate quaternary forms have been found to exist and are apparently governed by pH (*49*). Thus, structure determination could be pursued by molecular replacement (*49*, *50*) only when the correct quaternary model was provided. In doing so, three starting models of carbonmonoxy-bound Hb (*48*) with pdb 1g0a, 1g08, and 1g09 were evaluated. 1g0a clearly gave the best solution among all the models (*R*-factor, 37.0%; and correlation coefficient, 70.5%). Crystals of model (1g0a) were also grown at a pH (8.5) similar to that of our sample protein (8.25) further corroborating its validity as the correct model.

The model obtained from molecular replacement was refined using the program *REFMAC* (*51*). The initial steps of manual model building with the program coot (*52*) using $|2F_o - F_c|$ and $|F_o - F_c|$ Fourier maps yielded R and R_{free} factors of 0.322 and 0.357, respectively. Densities of the lactose and its succinimide linker were clearly evident (Figure 5) in the vicinity of Cys93 of the β subunit of the protein. Densities for all four bound heme groups and Fe^{3+} were clearly observed at this stage. The model thus obtained including the sugar and cofactors was subjected to several cycles of refinement alternating with several rounds of manual model building. Although the positions of water molecules were not sought at this resolution, there were good densities in $|2F_o - F_c|$ and $|F_o - F_c|$ for 8 water molecules, which seemed to hydrogen bond with various protein atoms. These were therefore included in the further refinement, to which they responded well. The R and R_{free} factors finally converged to 0.268 and 0.332, respectively. The refinement statistics are given in Table 2 (available in Supporting Information) (*53*, *54*). The program PROCHECK was used to validate the quality of the final structure (*54*). 91.1% of the residues were found in the most favored regions of the Ramachandran plot (*55*) and the remaining residues were in the additionally allowed regions.

Quality of the Model. The final coordinate set consists of 4582 non-hydrogen atoms from a total of 574 amino acid residues, one sugar-moiety covalently bound to Cys93 (on the β_1 subunit) via a succinimide linkage, four heme groups each with Fe^{3+} coordinated in the center, and two water molecules. The electron density map of the second sugar molecule was not as discernible, given the highly flexible nature of the linker. Thus, only one sugar molecule was incorporated into the final coordinate set. The protein structure exhibited a geometry close to ideal values, with root-mean-square (rms) deviations of 0.006 Å and 1.01 Å from standard values of bond lengths and bond angles, respectively. The overall mean B factor was found to be 91.2 Å^2. The high value of the B factors suggests that the quality of glycosylated Hb crystals is not good. Despite this, the electron density was very well defined for almost all of the main chain of the protein, all the heme groups, and even one of the covalently bound lactoses.

Oxygen Equilibria of Glycosylated Hb. Oxygen equilibrium curves of native Hb/glycosylated Hb were measured on a Hemox analyzer (TCS Scientific, New Hope, PA). This instrument simultaneously measures the Hb saturation via dual-wavelength spectrophotometry, while measuring the dissolved oxygen concentration with a Clark oxygen electrode. The temperature was maintained at 37 °C for all measurements. Samples were prepared by thoroughly mixing 500 μL of native Hb or glycoslylated Hb with 5 mL of the Hemox buffer (pH 7.4, TCS Instruments, Southampton, PA), 20 μL of Additive-A, 10 μL Additive-B, and 10 μL of antifoaming agent. The sample was saturated with compressed air at a pO_2 of 145 ± 2 mmHg. Then, the gas stream was switched to pure N_2 to deoxygenate the sample. The absorbance of oxy- and deoxy-Hb in solution was recorded as a function of pO_2 via dual-wavelength spectroscopy. Oxygen equilibrium curves were fit to a four-parameter (A_0, A_∞, P_{50}, n) Hill model (eq 1). In this model, the P_{50} represents the pO_2 at which Hb is half-saturated with O_2, and n is the Hill coefficient, while A_0 and A_∞ represent the absorbance at 0 mmHg and full saturation, respectively.

$$Y = \frac{\mathrm{Abs} - A_0}{A_\infty - A_0} = \frac{pO_2^n}{pO_2^n + P_{50}^n} \tag{1}$$

Molecular Weight Distribution Analysis of Glycosylated Hb. An asymmetric flow field-flow fractionator (AFFFF) (Wyatt Technology Corp., Santa Barbara, CA) coupled in series with a multiangle static light-scattering (MASLS) photometer (Wyatt Technology Corp.) and a differential interferometric refractometer (DIR) (Wyatt Technology Corp) was used to measure the absolute molecular weight distribution of native Hb and glycosylated Hb. During a typical experiment, the sample is injected into the AFFFF channel, where it is separated. The resultant eluent is then sent through the flow cell of the MASLS photometer, which continuously measures the macromolecule's Raleigh ratio (scattered light intensity) at 16 angles. The eluent is then sent through the flow cell of the DIR, which measures the macromolecule's concentration. Using a formulation of the angular distribution of scattered light derived by Zimm, it is possible to extract the molecular weight of each eluting monodisperse slice of the fraction (*56*). Hence, we can measure the absolute molecular weight of native and glycosylated Hb to evaluate whether glycosylation still favors the tetrameric structure of native Hb. All measurements were conducted at 25 °C. In preparation for AFFFF-MASLS-DIR experiments, all glassware was carefully cleaned, and all solutions were thoroughly filtered through 0.2 μm filters.

AFFFF-MASLS-DIR measures the weight average molecular weight (M_w) of native and glycosylated Hb in solution. M_w is defined as

$$M_w = \frac{\sum_i (c_i M_i)}{\sum_i c_i} \tag{2}$$

where c_i is the mass concentration of component i in solution and M_i is the molecular weight of component i in solution. In solution, the Hb tetramer will exist in equilibrium with $\alpha\beta$ dimers. Therefore, if C_T is the total mass concentration of Hb in the tetrameric and dimeric forms, then we can write expressions for the mass concentration of tetramer ($C_{\alpha_2\beta_2}$) and dimer ($C_{\alpha\beta}$) in solution if $x_{\alpha\beta}$ represents the mass fraction of $\alpha\beta$ dimers in solution.

$$C_{\alpha\beta} = C_T x_{\alpha\beta} \tag{3}$$

$$C_{\alpha_2\beta_2} = C_T(1 - x_{\alpha\beta}) \tag{4}$$

Substituting eqs 3 and 4 into eq 2 yields an expression for $x_{\alpha\beta}$ (eq 5).

$$x_{\alpha\beta} = \frac{M_w - M_{\alpha_2\beta_2}}{M_{\alpha\beta} - M_{\alpha_2\beta_2}} \tag{5}$$

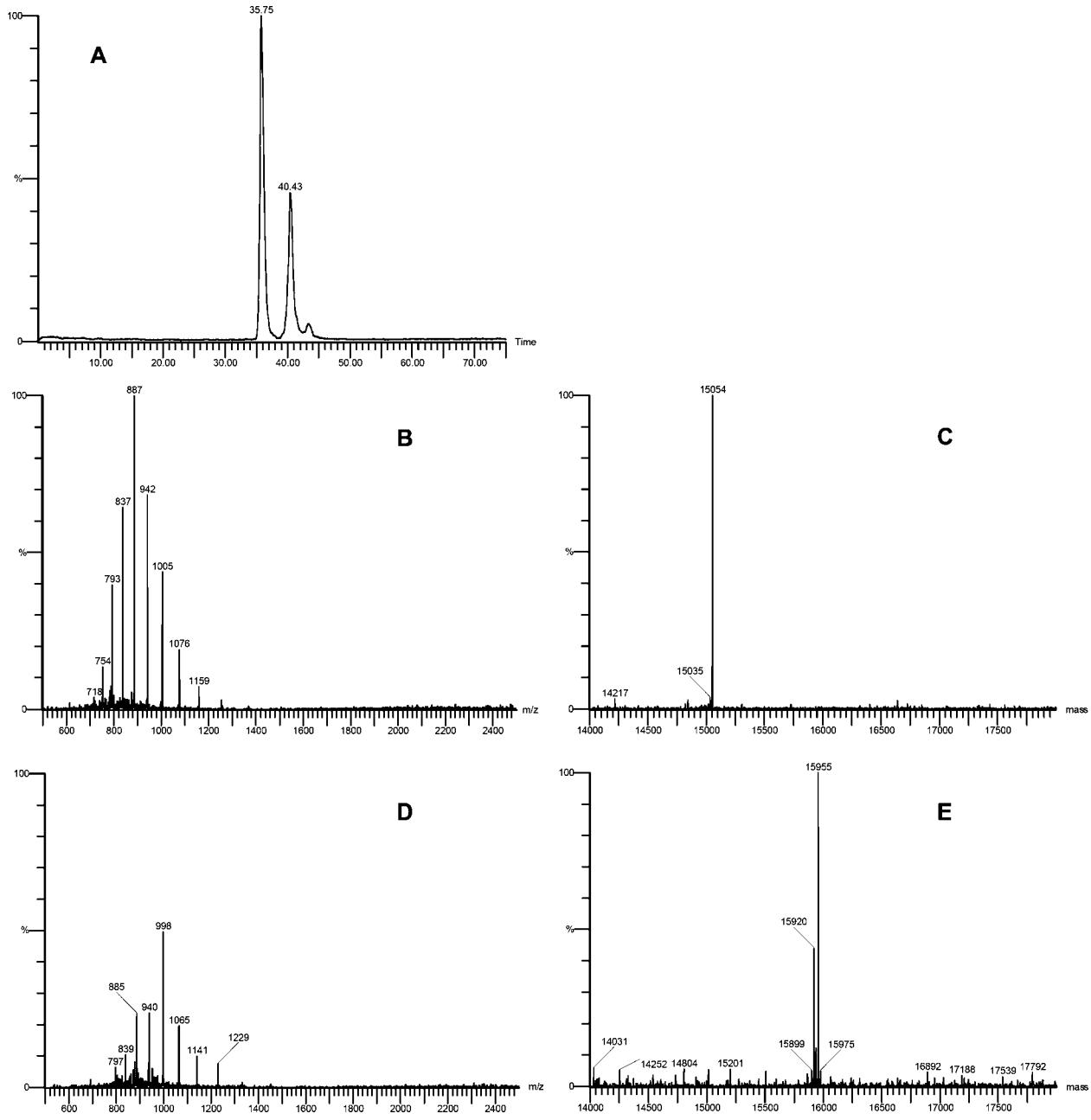

Figure 2. Analysis of bovine Hb by LC-MS. **A** represents the RP-HPLC chromatogram of bovine Hb. **B** represents the ESI-TOF mass spectra of the peak eluting at 35.75 min. **C** represents the deconvoluted molecular ion of the peak eluting at 35.75 min. **D** represents the ESI-TOF mass spectra of the peak eluting at 40.43 min. **E** represents the deconvoluted molecular ion of the peak eluting at 40.43 min.

Hence, substituting M_w (measured with AFFFF-MASLS-DIR), $M_{\alpha_2\beta_2}$(theoretical mass of tetrameric Hb), and $M_{\alpha\beta}$(theoretical mass of dimeric Hb) into eq 5 allows us to calculate $x_{\alpha\beta}$ and thus the mass fraction of tetrameric Hb ($x_{\alpha_2\beta_2} = 1 - x_{\alpha\beta}$).

RESULTS AND DISCUSSION

Preparation of Glycosylated Bovine Hb. Bovine Hb is a tetramer, which consists of two identical α chains and two identical β chains. The amino acid sequence of bovine Hb shows that only one cysteine, Cys-93, is located on the β chain. The molecular weight of the α chain and β chain are 15 053 and 15 955 Da, respectively. Since maleimide−lactoside **4** (M_w = 666 Da) can selectively react with thiol groups on cysteine residues, the reactive disaccharides can be selectively conjugated to Cys-93 on the β chain. As a result, the molecular weight of the β chain increases to 16 621 Da. In order to verify the glycosylation of bovine Hb by maleimide−lactoside **4**, the mass spectra of native bovine Hb and glycosylated Hb was measured by LC-MS (Figures 2 and 3, respectively).

In Figure 2, only two peaks were present in the RP-HPLC chromatogram (graph A). The ESI mass spectrum of the first peak (graph B) was deconvoluted to yield the mass of the molecular ion, 15 054 Da (graph C), which indicates that the first peak was due to the α chain of bovine Hb. The ESI mass spectrum of the second peak (graph D) was deconvoluted to yield the mass of the molecular ion, 15 955 Da (graph E), which indicates that the second peak was due to the β chain of bovine Hb. Comparing native bovine Hb (Figure 2) and glycosylated Hb (Figure 3), there was no significant difference in the retention time for both peaks in the LC chromatograms. Since it is the polarity of the molecule that determines the retention time in reverse-phase chromatography, this result indicates that the polarity of glycosylated Hb was not changed. The molecular

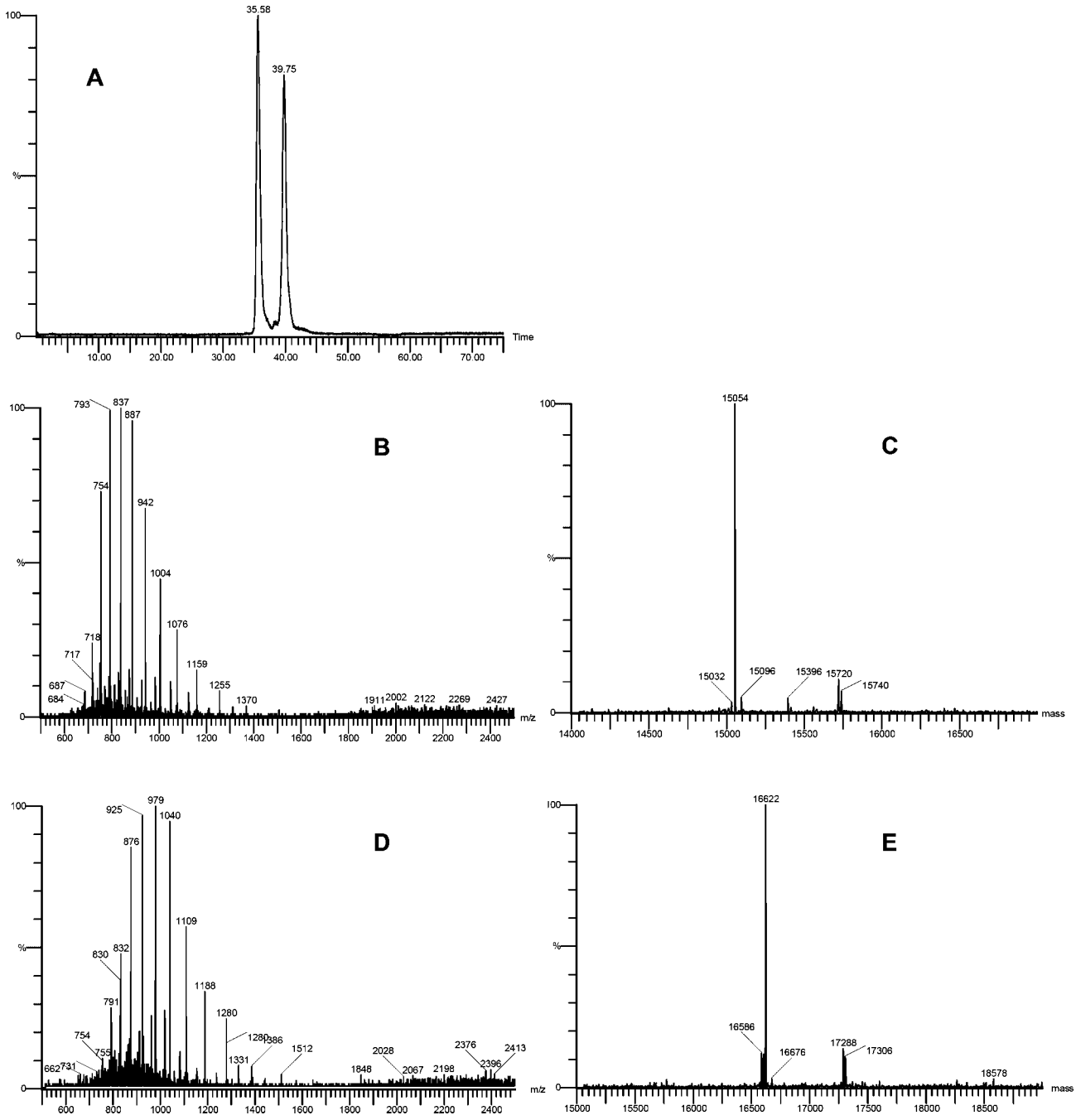

Figure 3. Analysis of glycosylated bovine Hb by LC-MS. **A** represents the RP-HPLC chromatogram of glycosylated bovine Hb. **B** represents the ESI-TOF mass spectrum of the peak eluting at 35.58 min. **C** represents the deconvoluted molecular ion of the peak eluting at 35.58 min. **D** represents the ESI-TOF mass spectrum of the peak eluting at 39.75 min. **E** represents the deconvoluted molecular ion of the peak eluting at 39.75 min.

weight of the α chain of the glycosylated Hb was 15 054 Da (Figure 3C), which was calculated by deconvolution of the ESI mass spectrum (Figure 3B). This result indicates that no lactoside derivative was conjugated to the α chain. However, the ESI mass spectrum of the second peak of Figure 3 (graph D) when deconvoluted (graph E) showed that the molecular weight of the β chain of glycosylated Hb increased to 16 622 Da. Therefore, the molecular weight difference between the β chain of natural Hb and glycosylated Hb is 667 Da, which is consistent with the molecular weight of maleimide−lactoside **4** (M_w = 666.3 Da). Therefore, LC-MS analysis of glycosylated Hb indicates that maleimide−lactoside is conjugated only to the β chain of Hb. Furthermore, the absence of a mass peak at 15 955 Da in graph E implies the absence of any unmodified β chains. This result shows that the conjugation reaction was quantitative and required no separation of unreacted protein products.

Determination of the Glycosylation Site on Bovine Hb. Tandem mass spectrometry was performed on the peptide fragments derived from the β chain of glycosylated bovine Hb digested by chymotrypsin, which will cleave the protein at Phe, Tyr, and Trp (*57*). The resulting data permit us to identify the conjugated latoside derivative, the chemotryptic peptides (AALSELHC*DKLHVDPENF) ($T_{\beta 85-102}$), and the glycosylation site in Figure 4 (The proteolytic MS-MS data are available in the Supporting Information). The calculated molecular weight for the glycosylated $T_{\beta 85-102}$ was 2704.3 Da. Peaks at 1271.56 (2+) and 848.08 (3+) were observed, which translate into

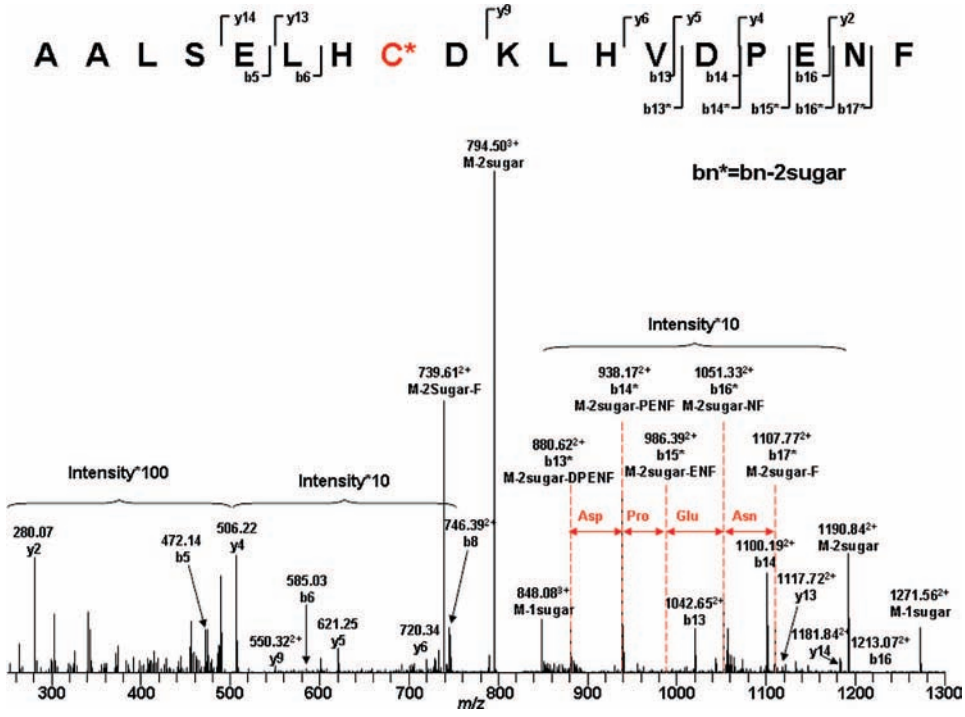

Figure 4. ESI-MS/MS spectra of the glycosylated β-globin chymotryptic peptides 85−102. *Represents the fragment containing the lactoside derivative.

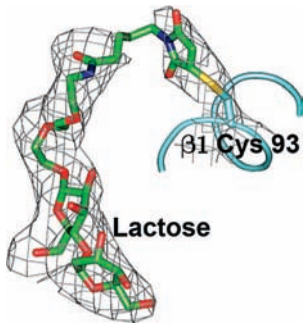

Figure 5. Succinimide linked lactose sandwiched between the β_1 and α_2 subunits of bovine Hb.

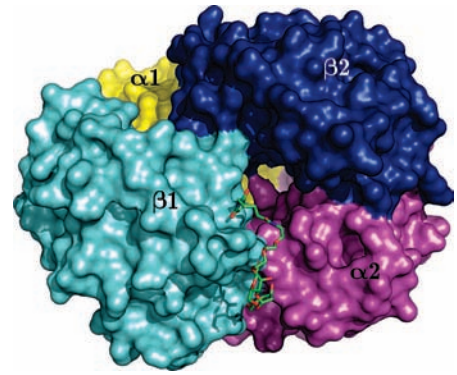

Figure 6. Final electron density map ($2F_o - F_c$) at 0.7σ showing β_1-Cys 93 covalently bound to the succinimide linked lactose.

molecular weights of 2542.12 and 2542.24 Da, respectively. The difference between the calculated molecular weight and the observed data was 162, which corresponds to the loss of one hexose. Peaks at 1190.84 (2+) and 794.50 (3+) were also observed, which correspond to a molecular weight 324 Da less than the calculated data (two hexoses lost). These observations confirm the conjugation of the lactoside derivative (a disaccharide) on this peptide fragment. Second, the peptide sequence were confirmed by observation of the ion series from b13 to b17, showing the loss of the DPENF sequence from the peptide fragment. Finally, the observation of y13 (1117.72^{2+}), y9 (550.32^{2+}), and b6 (585.03) indicate that the modified amino acid was located on the three peptide sequence HCD.

X-ray Structure of Glycosylated Hb. The complete amino acid sequence of bovine Hb shows that both α subunits consist of 141 and both β subunits consist of 145 amino acid residues. A sequence comparison with human Hb performed using CLUSTALW (*58*) shows 88% sequence identity in the α and 84% sequence identity in the β subunits. Thus, it is apparent that bovine Hb can serve as a good functional and structural mimic of human Hb.

It was found that the homogeneous lactoside glycosylated Hb can be crystallized and the crystal was analyzed to verify the site of modification and to access any structural changes associated with the glycosylation reaction. The crystal structure could provide definitive evidence that the Hb is glycosylated (Figures 5 and 6). The electron density of one succinimide-linked lactose could be found with slight discontinuity close to Cys β93 at 0.7σ cutoff in these maps. This result confirms the covalent glycosylation of the lactoside derivative at Cys β93. Since a significant deviation from native quaternary structure could strongly indicate a loss in function, this possibility had to be investigated. It was found that the structure of glycosylated bovine Hb was very similar to native bovine Hb (Figure 7). The overall rms deviation between the two structures was found to be as low as 0.40 Å. The overall quaternary fold is essentially identical to the native protein (pdb 1g0a) in most parts of the superimposition as seen in Figure 7. The only parts where there are discernible albeit minor differences in the fold are the two surface loops and the two glycosylation sites (red) compared with that of native Hb (blue). Since the Cys β93 residue forming the glycosylation site is part of a helix, this imposes severe geometrical constraints on it and, thus, probably prevents it from distorting the overall tertiary fold. The disturbance in the tertiary structure by chemical modification results in the breakage of the β94-β146 and β146-α40 hydrogen bonds (*39*−*41*). This loss

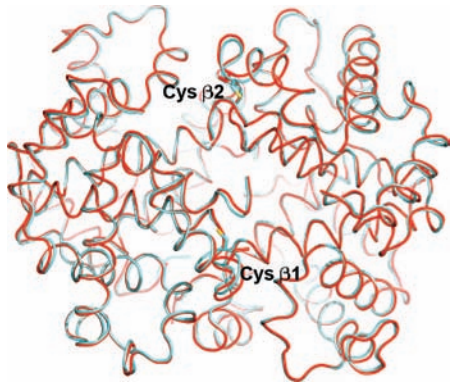

Figure 7. Superimposition of glycosylated bovine Hb (red) and native bovine Hb (blue).

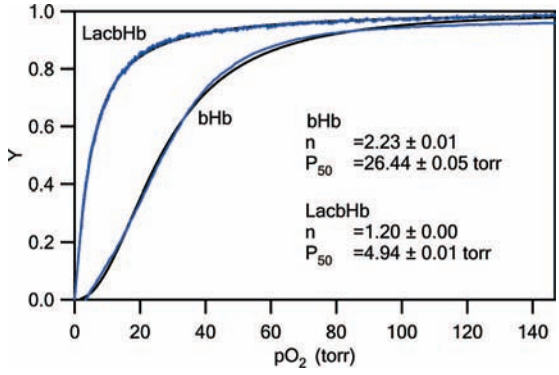

Figure 8. Oxygen dissociation curves of bovine Hb and glycosylated bovine Hb.

of hydrogen bonds will help to destabilize the T-state (*40*) and increase the oxygen binding affinity as well as decrease the cooperativity.

Oxygen Equilibria of Glycosylated Hb. The oxygen dissociation curves are shown in Figure 8 for native and glycosylated Hb. For native Hb, the P_{50} is 26.44 torr, while for glycosylated Hb, it is only 4.94 Torr. The P_{50} is an indicator of oxygen affinity and refers to the partial pressure of oxygen at which half of the HBOC is saturated with oxygen. The low P_{50} of the glycosylated Hb indicates that it has a higher affinity for oxygen versus native Hb. Furthermore, it was found that the cooperativity coefficient of glycosylated Hb is 1.2, which is almost half compared with that of native Hb (2.23). The cooperativity of hemoglobin is associated with the allosteric transition from T-state (tense) to R-State (relaxed) upon oxygenation (*39*). One reason for the decrease in cooperativity can be explained by the disturbance of the tertiary structure of Hb by maleimide modification of Cys β93. Another reason may be structural changes imposed by the glycosylation reaction. On the basis of the crystal structure (Figure 6), it was found that the lactose derivative is located within the $\alpha_1\beta_2/\alpha_2\beta_1$ interface. As a result, the additional hydrogen bonds between the disaccharide and various amino acid residues within the interface will hinder the transition from T-state to R-state and thus leads to a decrease in cooperativity. On the other hand, the additional hydrogen bonding interactions between the disaccharide and various amino acid residues at the interface could stabilize the overall tetrameric structure of Hb. This would be a novel feature of the glycosylated Hb and indicates that it should be more stable (not dissociate into $\alpha\beta$ dimers) in the bloodstream versus native Hb when transfused into patients. In addition, the high oxygen affinity of the glycosylated Hb indicates that it can be used to treat hemorrhagic shock by

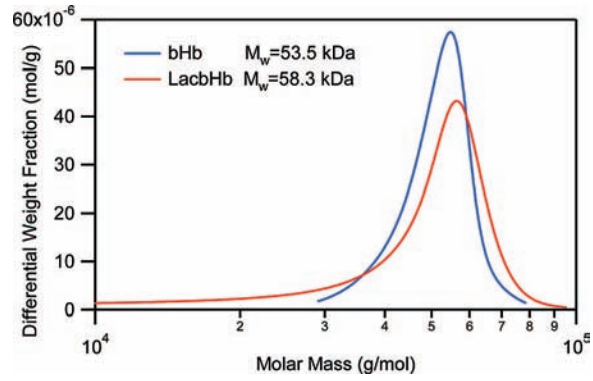

Figure 9. Differential molar mass distribution of bovine Hb (bHb, blue) and lactoside derivative conjugated to bovine Hb (LacbHb, red).

delivering oxygen to regions of the body with low oxygen levels instead of systemically.

AFFFF-MASLS-DIR of Glycosylated Hb. In order to prove our hypothesis that glycosylation of Hb will stabilize the tetrameric structure of Hb, an asymmetric flow field-flow fractionator (AFFFF) coupled in series with a multiangle static light-scattering (MASLS) photometer was used to measure the absolute molecular weight distribution of native Hb and glycosylated Hb. In aqueous solution, the Hb tetramer ($\alpha_2\beta_2$) exists in equilibrium with $\alpha\beta$ dimers. Because of this equilibrium, the measured molar mass of Hb in solution will be between that of the intact $\alpha_2\beta_2$ tetramer (64 kDa) and the $\alpha\beta$ dimer (32 kDa). In Figure 9, we observe this behavior. The average M_w for native Hb was calculated to be 53.5 kDa, and it was 58.3 kDa for glycosylated Hb. The molecular weights of the native Hb tetramer and dimer are 64 kDa and 32 kDa, respectively. If two lactose derivatives are conjugated to the native Hb tetramer, the resultant molecular weights of the glycosylated Hb tetramer and dimer are 65.334 kDa and 32.667 kDa, respectively. Therefore, substituting these values into eq 5 reveals that the mass fraction of $\alpha_2\beta_2$ is 0.67 for native Hb in solution and 0.78 for glycosylated Hb, respectively. Hence, the increase in the mass fraction of $\alpha_2\beta_2$ tetramer for glycosylated Hb indicates that the $\alpha_1\beta_2/\alpha_2\beta_1$ interface between adjacent $\alpha\beta$ dimers is more "sticky" for glycosylated Hb versus native Hb. The origin of this "stickyness" can be elucidated by recognizing that the sugar is sandwiched between the β_1 and α_2 subunits of the protein (Figure 6). Interestingly, hydrogen bonds are formed between the sugar molecule and amino acid residues within the $\alpha_2\beta_1$ interface, and it is this hydrogen bonding interaction that leads to the "stickyness" of the $\alpha\beta$ interface by stabilizing the overall tetrameric structure of Hb. This observation further explains why the equilibrium of glycosylated Hb favors the tetrameric structure when compared to native Hb. Therefore, an added benefit of the glycosylation reaction is that it can stabilize the tetrameric structure of Hb. As mentioned earlier, this feature will reduce the formation of $\alpha\beta$ dimers and therefore reduce the amount of Hb extravasation through the lumen of blood vessels and subsequent NO scavenging.

CONCLUSION

We describe in this work an approach for the site-selective chemical glycosylation of Hb as a potential HBOC. A lactoside derivative with a terminal maleimide moiety was synthesized and conjugated to Cys 93 on the β chain of bovine Hb. The glycosylation reaction was quantitative and required no special purification steps, which was confirmed by LC-MS. Chymotryptic digestion of the glycosylated β-globin chain followed by tandem mass spectroscopy and X-ray crystallography of the glycosylated Hb identified the glycosylation site at Cys β93.

The glycosylation of Cys β93 on Hb results in an oxygen carrier with a high oxygen affinity (P_{50} = 4.94 mmHg) and low cooperativity coefficient (1.20). The stability of the glycosylated Hb was evaluated by AFFFF-MASLS-DIR analysis. AFFFF-MASLS-DIR analysis showed that the tetrameric structure of glycosylated Hb was more stable compared to native Hb. Subsequent X-ray analysis of the glycosylated Hb crystal revealed that the lactose derivative is sandwiched between the β_1 and α_2 subunits of the protein. This indicates that the glycosylated Hb is stabilized by hydrogen bonding interactions between the disaccharide and amino acids within the interface. These hydrogen bonding interactions explain the stability of the glycosylated Hb versus native Hb. In conclusion, glycosylated Hb exhibits high oxygen affinity and improved tetrameric stability, which shows great potential as an artificial blood substitute.

ACKNOWLEDGMENT

A.F.P. acknowledges the support of National Institutes of Health grants R01HL078840 and R01DK070862. P.G.W. acknowledges the support of National Institutes of Health grants U54NSO5818301.

Supporting Information Available: NMR data for compounds **2**−**4,** the proteolytic MS-MS data, crystallographic data, and refinement statistics. This material is available free of charge via the Internet at http://pubs.acs.org.

LITERATURE CITED

(1) Mackenzie, C. F. (2001) Hemoglobin-based oxygen-carrying solutions and hemorrhagic shock. *Semin. Anesth. 20*, 71–77.
(2) Reid, T. J. (2003) Hb-based oxygen carriers: are we there yet? *Transfusion 43*, 280–287.
(3) Rabiner, S. F., O'Brien, K., Peskin, G. W., and Friedman, L. H. (1970) Further studies with stroma-free hemoglobin solution. *Ann. Surg. 171*, 615–622.
(4) Palmer, A. F. (2006) Molecular volume and HBOC-induced vasoconstriction. *Blood 108*, 3231–3232.
(5) Chang, T. M. S. (2006) Blood substitutes based on nanobiotechnology. *Trends Biotechnol. 24*, 372–377.
(6) Haney, C. R., Buehler, P. W., and Gulati, A. (2000) Purification and chemical modifications of hemoglobin in developing hemoglobin based oxygen carriers. *Adv. Drug Delivry Rev. 40*, 153–169.
(7) Chang, T. M. S. (2004) Hemoglobin-based red blood cell substitutes. *Artif. Organs 28*, 789–794.
(8) Hu, T., Manjula, B. N., Li, D., Brenowitz, M., and Acharya, S. A. (2007) Influence of intramolecular cross-links on the molecular, structural and functional properties of PEGylated haemoglobin. *Biochem. J. 402*, 143–151.
(9) Vuletich, D. A., Falzone, C. J., and Lecomte, J. T. J. (2006) Structural and dynamic repercussions of heme binding and heme-protein cross-linking in Synechococcus sp. PCC 7002 hemoglobin. *Biochemistry 45*, 14075–14084.
(10) Eike, J. H., and Palmer, A. F. (2004) Oxidized mono-, di-, tri-, and polysaccharides as potential hemoglobin cross-linking reagents for the synthesis of high oxygen affinity artificial blood substitutes. *Biotechnol. Prog. 20*, 953–962.
(11) Eike, J. H., and Palmer, A. F. (2004) Effect of Cl^- and H^+ on the oxygen binding properties of glutaraldehyde-polymerized bovine hemoglobin-based blood substitutes. *Biotechnol. Prog. 20*, 1543–1549.
(12) Eike, J. H., and Palmer, A. F. (2004) Effect of glutaraldehyde concentration on the physical properties of polymerized hemoglobin-based oxygen carriers. *Biotechnol. Prog. 20*, 1225–1232.
(13) Eike, J. H., and Palmer, A. F. (2004) Effect of $NaBH_4$ concentration and reaction time on physical properties of glutaraldehyde-polymerized hemoglobin. *Biotechnol. Prog. 20*, 946–952.
(14) Dimino, M. L., and Palmer, A. F. (2007) High O_2 affinity hemoglobin-based oxygen carriers synthesized via polymerization of hemoglobin with ring-opened 2-chloroethyl-β-D-fructopyranoside and 1-*O*-octyl-β-D-glucopyranoside. *Biotechnol. Bioeng. 97*, 462–472.
(15) Jia, Y., Ramasamy, S., Wood, F., Alayash, A. I., and Rifkind, J. M. (2005) Cross-linking with *O*-raffinose lowers oxygen affinity and stabilizes haemoglobin in a non-cooperative T-state conformation. *Biochem. J. 384*, 367–375.
(16) Nacharaju, P., Manjula, B. N., and Acharya, S. A. (2007) Thiolation mediated pegylation platform to generate functional universal red blood cells. *Artif. Cells, Blood Substitutes, Biotechnol. 35*, 107–118.
(17) Acharya, S. A., Acharya, V. N., Kanika, N. D., Tsai, A. G., Intaglietta, M., and Manjula, B. N. (2007) Non-hypertensive tetraPEGylated canine hemoglobin: correlation between PEGylation, O_2 affinity and tissue oxygenation. *Biochem. J. 405*, 503–511.
(18) Li, D., Manjula, B. N., and Acharya, A. S. (2006) Extension arm facilitated PEGylation of hemoglobin: correlation of the properties with the extent of PEGylation. *Protein J. 25*, 263–274.
(19) Hu, T., Prabhakaran, M., Acharya, S. A., and Manjula, B. N. (2005) Influence of the chemistry of conjugation of poly(ethylene glycol) to Hb on the oxygen-binding and solution properties of the PEG-Hb conjugate. *Biochem. J. 392*, 555–564.
(20) Arifin, D. R.; Palmer, A. F. (2003) Determination of size distribution and encapsulation efficiency of liposome-encapsulated hemoglobin blood substitutes using asymmetric flow field-flow fractionation coupled with multi-angle static light scattering. *Biotechnol. Prog., 19*, 1798–1811.
(21) Arifin, D. R., and Palmer, A. F. (2005) Polymersome encapsulated hemoglobin: a novel type of oxygen carrier. *Biomacromolecules 6*, 2172–2181.
(22) Arifin, D. R., and Palmer, A. F. (2005) Physical properties and stability mechanisms of poly(ethylene glycol) conjugated liposome encapsulated hemoglobin dispersions. *Artif. Cells, Blood Substitutes Biotechnol. 33*, 137–162.
(23) Arifin, D. R., and Palmer, A. F. (2005) Stability of liposome encapsulated hemoglobin dispersions. *Artif. Cells, Blood Substitutes Biotechnol. 33*, 113–136.
(24) Li, S., and Palmer, A. F. (2005) Structure and mechanical response of self-assembled poly(butadiene)-*b*-poly(ethylene oxide) colloids probed by atomic force microscopy. *Macromolecules 38*, 5686–5698.
(25) Zhao, J., Liu, C.-S., Yuan, Y., Tao, X.-Y., Shan, X.-Q., Sheng, Y., and Wu, F. (2007) Preparation of hemoglobin-loaded nanosized particles with porous structure as oxygen carriers. *Biomaterials 28*, 1414–1422.
(26) Salimi, A., Hallaj, R., and Soltanian, S. (2007) Immobilization of hemoglobin on electrodeposited cobalt-oxide nanoparticles: Direct voltammetry and electrocatalytic activity. *Biophys. Chem. 130*, 122–131.
(27) Patton, J. N., and Palmer, A. F. (2005) Photopolymerization of bovine hemoglobin entrapped nanoscale hydrogel particles within liposomal reactors for use as an artificial blood substitute. *Biomacromolecules 6*, 414–424.
(28) Miranda, J. J. L., Maillett, D. H., Soman, J., and Olson, J. S. (2005) Thermoglobin, oxygen-avid hemoglobin in a bacterial hyperthermophile. *J. Biol. Chem. 280*, 36754–36761.
(29) Hargrove, M. S., Whitaker, T., Olson, J. S., Vali, R. J., and Mathews, A. J. (1997) Quaternary structure regulates hemin dissociation from human hemoglobin. *J. Biol. Chem. 272*, 17385–17389.
(30) Dwek, R. A. (1996) Glycobiology: toward understanding the function of sugars. *Chem. Rev. 96*, 683–720.
(31) Higgins, P. J., and Bunn, H. F. (1981) Kinetic analysis of the nonenzymic glycosylation of hemoglobin. *J. Biol. Chem. 256*, 5204–5208.

(32) Haney, D. N., and Bunn, H. F. (1976) Glycosylation of hemoglobin *in vitro*: affinity labeling of hemoglobin by glucose-6-phosphate. *Proc. Natl. Acad. Sci. U.S.A. 73*, 3534–3538.
(33) Tam, S.-C., Blumenstein, J., and Wong, J. T.-F. (1976) Soluble dextran-hemoglobin complex as a potential blood substitute. *Proc. Natl. Acad. Sci. U.S.A. 73*, 2128–2131.
(34) Ali, A. C., and Campbell, J. A. (1997) Interference of *O*-raffinose cross-linked hemoglobin with routine Hitachi 717 assays. *Clin. Chem. 43*, 1794–1796.
(35) Adamson, J. G., and Moore, C. (1998) Hemolink, an O-raffinose crosslinked hemoglobin-based oxygen carrier. *Blood Substit. 2*, 62–81.
(36) Boykins, R. A., Buehler, P. W., Jia, Y., Venable, R., and Alayash, A. I. (2005) O-Raffinose crosslinked hemoglobin lacks site-specific chemistry in the central cavity: structural and functional consequences of β93Cys modification. *Proteins: Struct. Funct. Bioinf. 59*, 840–855.
(37) Baldwin, A. L., Wiley, E. B., and Alayash, A. I. (2004) Differential effects of sodium selenite in reducing tissue damage caused by three hemoglobin-based oxygen carriers. *J. Appl. Physiol. 96*, 893–903.
(38) Davis, B. G. (2002) Synthesis of glycoproteins. *Chem. Rev. 102*, 579–601.
(39) Vasquez, G. B., Karavitis, M., Ji, X., Pechik, I., Brinigar, W. S., Gilliland, G. L., and Fronticelli, C. (1999) Cysteines beta93 and beta112 as probes of conformational and functional events at the human hemoglobin subunit interfaces. *Biophys. J. 76*, 88–97.
(40) Cheng, Y., Shen, T.-J., Simplaceanu, V., and Ho, C. (2002) Ligand binding properties and structural studies of recombinant and chemically modified hemoglobins altered at β93 cysteine. *Biochemistry 41*, 11901–11913.
(41) Khan, I., Dantsker, D., Samuni, U., Friedman, A. J., Bonaventura, C., Manjula, B., Acharya, S. A., and Friedman, J. M. (2001) β93 Modified hemoglobin: kinetic and conformational consequences. *Biochemistry 40*, 7581–7592.
(42) Dimino, M. L., and Palmer, A. F. (2007) Purification of bovine hemoglobin via fast performance liquid chromatography. *J. Chromatogr., B: Anal. Technol. Biomed. Life Sci. 856*, 353–357.
(43) Sun, G., and Palmer, A. F. (2008) Preparation of ultrapure bovine and human hemoglobin by anion exchange chromatography. *J. Chromatogr., B: Anal. Technol. Biomed. Life Sci. 867*, 1–7.
(44) Eike, J. H., and Palmer, A. F. (2004) Effect of glutaraldehyde concentration on the physical properties of polymerized hemoglobin-based oxygen carriers. *Biotechnol. Prog. 20*, 1225–1232.
(45) Russell, W. K., Park, Z.-Y., and Russell, D. H. (2001) Proteolysis in mixed organic-aqueous solvent systems: applications for peptide mass mapping using mass spectrometry. *Anal. Chem. 73*, 2682–2685.
(46) Xu, H., Zhang, L., and Freitas, M. A. (2008) Identification and characterization of disulfide bonds in proteins and peptides from tandem MS data by use of the MassMatrix MS/MS search engine. *J. Proteome Res. 7*, 138–144.
(47) Chayen, N. E. (1997) The role of oil in macromolecular crystallization. *Structure 5*, 1269–1274.
(48) Pflugrath, J. W. (1999) The finer things in X-ray diffraction data collection. *Acta Crystallogr., Sect. D: Biol. Crystallogr. D55*, 1718–1725.
(49) Mueser, T. C., Rogers, P. H., and Arnone, A. (2000) Interface sliding as illustrated by the multiple quaternary structures of liganded hemoglobin. *Biochemistry 39*, 15353–15364.
(50) Navaza, J. (2002) On the computation of structure factors by FFT techniques. *Acta Crystallogr., Sect. A: Found. Crystallogr. A58*, 568–573.
(51) Murshudov, G. N., Vagin, A. A., and Dodson, E. J. (1997) Refinement of macromolecular structures by the maximum-likelihood method. *Acta Crystallogr., Sect. D: Biol. Crystallogr. D53*, 240–255.
(52) Emsley, P., and Cowtan, K. (2004) Coot: model-building tools for molecular graphics. *Acta Crystallogr., Sect. D: Biol. Crystallogr. D60*, 2126–2132.
(53) Engh, R. A., and Huber, R. (1991) Accurate bond and angle parameters for x-ray protein structure refinement. *Acta Crystallogr., Sect. A: Found. Crystallogr. A47*, 392–400.
(54) Laskowski, R. A., MacArthur, M. W., Moss, D. S., and Thornton, J. M. (1993) PROCHECK: a program to check the stereochemical quality of protein structures. *J. Appl. Crystallogr. 26*, 283–291.
(55) Ramachandran, G. N., and Sasisekharan, V. (1968) Conformation of polypeptides and proteins. *Adv. Protein Chem. 23*, 283–438.
(56) Zimm, B. H. (1948) The scattering of light and the radial distribution function of high-polymer solutions. *J. Chem. Phys. 16*, 1093–1099.
(57) Biringer, R. G., Amato, H., Harrington, M. G., Fonteh, A. N., Riggins, J. N., and Huhmer, A. F. R. (2006) Enhanced sequence coverage of proteins in human cerebrospinal fluid using multiple enzymatic digestion and linear ion trap LC-MS/MS. *Brief. Funct. Genomics Proteomics 5*, 144–153.
(58) Pearson, W. R., and Lipman, D. J. (1988) Improved tools for biological sequence comparison. *Proc. Natl. Acad. Sci. U.S.A. 85*, 2444–2448.

BC8003205

Supporting Information: Site-selective glycosylation of hemoglobin on Cys β93

Yalong Zhang[a], Veer S. Bhatt [b], Guoyong Sun[c], Peng G. Wang[a, b] and Andre F. Palmer[c*]

[a]*Department of Chemistry*

[b]*Biophysics Program and Department of Biochemistry*

[c]*Department of Chemical and Biomolecular Engineering*

The Ohio State University

Columbus, OH, 43210

U.S.A.

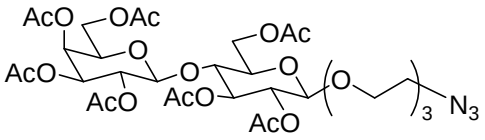

1-azido-3,6-dioxa-9-octyl-*O*-(2,3,6-tri-*O*-acetyl-β-D-glucopyranolsyl)-(1→4)-2,3,4,6-tetra-*O*-acetyl -β-D-galactoside (2). To a solution of peracetyl lactoside **1** (10.0 g, 14.7 mmol) in acetonitrile (150 mL) was added 2-[2-(2-chloroethoxy)ethoxy]ethanol (4.6 mL, 44.2 mmol) and 4 Å MS (Molecular Sieve) (2 g). The mixture was stirred at r.t. for 0.5 h and then cooled to 0 ºC. After that, boron trifluoride ether solution (3.9 mL, 29.4 mmol) was injected into the solution. The solution was slowly warmed to room temperature and stirred overnight. The solution was neutralized with saturated $NaHCO_3$ aqueous solution and extracted with ethyl acetate. The organic phase was dried with Na_2SO_4, filtered and concentrated. The crude product was purified by flash column chromatography with Hexanes/ EtOAc (1:1, v/v). The product (5.0 g, 6.35 mmol) in DMF (50 mL) was reacted with sodium azide (1.24 g, 19.1 mmol) and stirred at 80 ^{o}C overnight. The DMF was removed under reduced pressure and the crude product was purified by flash column chromatography with Hexanes/ EtOAc (1:1, v/v) to yield **2** (3.2 g) in an overall yield of 30% (two steps) as a colorless oil. ^{1}H NMR (500 MHz, $CDCl_3$) δ 1.97 (s, 3H), 2.05-2.06 (m, 9H), 2.07 (s, 3H), 2.13 (s, 3H), 2.16 (s, 3H), 3.41 (dd, *J* = 9.5, 4.3 Hz, 2H), 3.63-3.71 (m, 9H), 3.71-3.75 (m, 1H), 3.80 (t, *J* = 9.6 Hz, 1H), 3.86-3.93 (m, 2H), 4.07-4.16 (m, 3H), 4.48-4.51 (m, 2H), 4.58 (d, *J* = 8.0 Hz, 1H), 4.90 (dd, *J* = 9.5, 8.0 Hz, 1H), 4.96 (dd, *J* = 10.4, 3.5 Hz, 1H), 5.11 (dd, *J* = 10.5, 8.0 Hz, 1H), 5.20 (t, *J* = 9.4 Hz, 1H), 5.35-5.36

(m, 1H). ^{13}C NMR (125 MHz, $CDCl_3$) δ 20.49, 20.61, 20.69, 20.80, 20.85, 50.69, 60.81, 62.02, 66.63, 69.05, 69.14, 70.05, 70.40, 71.00, 71.69, 72.65, 72.84, 76.29, 100.64, 101.08, 169.07, 169.65, 169.76, 170.05, 170.14, 170.34, 170.36.

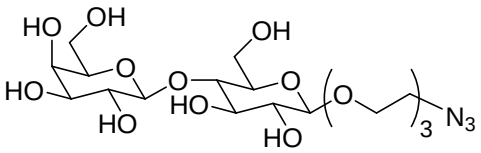

1-azido-3,6-dioxa-9-octyl-*O*-(β-D-glucopyranolsyl)-(1→4)-β-D-galactoside (3). To a solution of compound **2** (3.3 g, 4.16 mmol) in MeOH (20 ml) was added sodium methoxide (22.5 mg, 0.416 mmol). The mixture was stirred at r.t. for 5 h, and neutralized with Dowex 50WX2-100 (H^+) resin. The resultant solution was then concentrated under reduced pressure to yield **3** (1.7 g, 82%) as a white solid. ^{1}H NMR (500 MHz, D_2O) δ 3.23-3.26 (m, 1H), 3.41 (t, *J* = 5.2 Hz, 2H), 3.44-3.46 (m, 1H), 3.48-3.51 (m, 1H), 3.55-3.57 (m, 3H), 3.61-3.63 (m, 7H), 3.65-3.67 (m, 4H), 3.69-3.77 (m, 2H), 3.82 (d, *J* = 3.3 Hz, 1H), 3.87-3.89 (m, 1H), 3.94-3.99 (m, 1H), 4.34 (d, *J* = 7.9 Hz, 1H), 4.42 (d, *J* = 8.0 Hz, 1H). ^{13}C NMR (125 MHz, $CDCl_3$) δ 50.09, 60.03, 60.98, 68.71, 69.17, 69.45, 69.55, 69.65, 70.91, 72.48, 72.78, 74.26, 74.73, 75.31, 78.31, 102.04, 102.90.

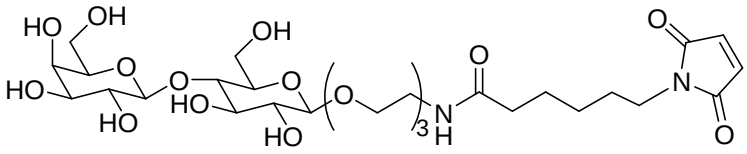

***N*-3',6'-dioxa-9'-octyl-*O*-(β-D-glucopyranolsyl)-(1→4)-β-D-galactoside-6-maleimido-hexanamide (maleimide-lactoside) (4).** To a solution of compound **3** (0.20 g, 0.40 mmol) in MeOH (10 mL) was added a catalytic amount of Pd/C. The mixture was stirred under hydrogen atmosphere at r.t. for 24 h. Consequently, the Pd/C was removed by filtration and the solution was concentrated under reduced pressure to yield the amine compound. The amine compound (50 mg, 0.106 mmol) in DMF (5.0 mL) was reacted with 6-maleimidohexanoic acid *N*-hydroxysuccinimide ester (34.0 mg, 0.111 mmol) and Et_3N (21 μL, 0.148 mmol). The solution was stirred at 40 ^{o}C overnight. The solvent was removed under reduced pressure and the residue was purified by flash chromatography with EtOAc:IPA:H_2O (6:3:1) to yield the

product as a colorless oil (26.1 mg) with an overall total yield of 37% (two steps). ^{1}H NMR (500 MHz, MeOD) δ 1.30-1.34 (m, 2H), 1.59-1.66 (m, 4H), 2.21 (t, *J* = 7.4 Hz, 2H), 3.29 (t, *J* = 8.3 Hz, 1H), 3.32-3.34 (m, 4H), 3.36-3.38 (m, 2H), 3.43-3.46 (m, 1H), 3.50-3.53 (m, 3H), 3.54-3.57 (m, 4H), 3.59-3.64 (m, 4H), 3.68-3.74 (m, 5H), 3.75-3.82 (m, 2H), 3.84-3.87 (m, 2H), 3.92 (dd, *J* = 12.2, 2.6 Hz, 1H), 4.01-4.05 (m, 1H), 4.38 (d, *J* = 7.6, 5.6 Hz, 2H), 6.83 (s, 2H). ^{13}C NMR (125 MHz, MeOD) δ 25.05, 25.92, 27.88, 35.41, 37.04, 38.92, 60.58, 61.09, 68.30, 68.90, 69.24, 69.80, 70.08, 70.14, 71.16, 73.34, 73.44, 74.90, 75.12, 75.69, 79.31, 102.90, 103.73, 133.98, 171.23, 174.73. HRMS: Calculated for $C_{28}H_{46}N_2O_{16}Na$ ($M+Na^+$) 689.2745; found 689.2744.

The proteolytic MS-MS data of the βChain of the glycosylated bovine hemoglobin

Trypsin

Measured m/z	Calculated M+H	Theoretical M+H	Protein Sequence	MASCOT Score	# Being detected
$821.36^{1+}/411.24^{2+}$	821.48	821.4073	^{1}MLTAEEK^{7}	490	19
$837.53^{1+}/419.31^{2+}$	837.62	837.4022	^{1}M$_{(Ox)}$LTAEEK^{7}	82	3
$950.38^{1+}/475.80^{2+}$	950.60	950.5094	^{8}AAVTAFWGK^{16}	1415	30
584.98^{3+}	1752.94	1752.8989	^{1}MLTAEEKAAVTAFWGK^{16}	481	12
$1328.82^{1+}/664.87^{2+}$	1328.74	1328.7169	^{17}VKVDEVGGEALGR^{29}	2542	47
551.30^{2+}	1101.60	1101.5535	^{19}VDEVGGEALGR^{29}	229	6
$425.56^{3+}/637.83^{2+}$	1274.66	1274.7256	^{30}LLVVYPWTQR^{39}	955	24
697.19^{3+}	2089.57	2089.9535	^{40}FFESFGDLSTADAVMNNPK^{58}	3403	45
$702.71^{3+}/1053.70^{2+}$	2106.13	2104.9484	^{40}FFESFGDLSTADAVM$_{(Ox)}$NNPK^{58}	881	14
613.32^{2+}	1225.64	1225.6245	^{65}KVLDSFSNGMK^{75}	272	9
549.17^{2+}	1097.34	1097.5296	^{66}VLDSFSNGMK^{75}	602	18
557.34^{2+}	1113.68	1113.5245	^{66}VLDSFSNGM$_{(Ox)}$K^{75}	35	1
$724.14^{3+}/1085.65^{2+}$	2170.30	2170.0597	^{76}HLDDLKGTFAALSELHC$_{(Cam)}$DK^{94}	287	4
843.66^{3+}	2528.98	2528.2238	^{82}GTFAALSELHC$_{(Cam)}$DKLHVDPENFK^{103}	75	2
782.76^{3+}	2346.28	2345.3704	^{95}LHVDPENFKLLGNVLVVVLAR^{115}	89	2
$422.55^{3+}/633.70^{2+}$	1265.40	1265.8304	^{104}LLGNVLVVVLAR^{115}	1039	22
$935.10^{3+}/623.63^{3+}$	1868.89	1868.9541	^{116}NFGKEFTPVLQADFQK^{131}	1416	36
$474.80^{3+}/711.88^{2+}$	1422.76	1422.7264	^{120}EFTPVLQADFQK^{131}	1029	21
589.36^{2+}	1177.72	1177.6800	^{132}VVAGVANALAHR^{143}	1396	18

Chymotrypsin

Measured m/z	Calculated M+H	Theoretical M+H	Protein Sequence	MASCOT Score	# Being detected
691.42^{2+}	1381.39	1381.7032	^{1}MLTAEEKAAVTAF^{13}	143	4
784.42^{2+}	1567.84	1567.7825	^{1}MLTAEEKAAVTAFW^{14}	110	3
570.02^{2+}	1139.08	1137.5786	^{3}TAEEKAAVTAF^{13}	27	1
663.13^{2+}	1325.26	1323.6579	^{3}TAEEKAAVTAFW^{14}	21	1
642.66^{3+}	1925.98	1926.0807	^{14}WGKVKVDEVGGEALGRLL^{31}	113	2
651.11^{2+}	1301.22	1300.7101	^{15}GKVKVDEVGGEAL^{27}	73	2
580.73^{3+}/870.77^{2+}	1740.54	1740.0014	^{15}GKVKVDEVGGEALGRLL^{31}	344	6
663.37^{1+}	663.37	663.3501	^{32}VVYPW^{36}	195	8
531.29^{2+}	1061.58	1061.5051	^{37}TQRFFESF^{44}	22	1
674.00^{2+}	1347.00	1346.6375	^{37}TQRFFESFGDL^{47}	40	1
782.32^{3+}/521.48^{3+}	1562.44	1562.7632	^{71}SNGMKHLDDLKGTF^{84}	243	9
527.05^{3+}	1579.15	1578.7581	^{71}SNGM$_{(ox)}$KHLDDLKGTF^{84}	25	1
603.28^{1+}	603.28	603.3348	^{85}AALSEL^{90}	42	2
418.98^{3+}/628.81^{2+}	1256.62	1256.6303	^{85}AALSELHC$_{(Cam)}$DKL^{95}	64	2
699.52^{3+}/1048.20^{2+}	2095.40	2094.9913	^{85}AALSELHC$_{(Cam)}$DKLHVDPENF^{102}	82	2
756.600^{2+}	1512.20	1510.6743	^{91}HC$_{(Cam)}$DKLHVDPENF^{102}	48	1
614.30^{3+}	1840.90	1839.9388	^{114}ARNFGKEFTPVLQADF^{129}	25	1
676.36^{2+}	1351.72	1351.6892	^{118}GKEFTPVLQADF^{129}	376	9
801.50^{3+}/1202.18^{2+}	2402.50	2402.3078	^{118}GKEFTPVLQADFQKVVAGVANAL^{140}	87	2
971.04^{2+}	1941.08	1941.0804	^{122}TPVLQADFQKVVAGVANAL^{140}	180	4
766.06^{2+}	1531.12	1530.8275	^{126}QADFQKVVAGVANAL^{140}	50	1
535.40^{2+}	1069.80	1069.6364	^{130}QKVVAGVANAL^{140}	95	3

Table 1. Data-collection statistics.

Values in parentheses are for the last shell.

Wavelength (Å)	1.54
Space group	$P2_12_12_1$
Unit-cell parameters (Å)	a = 62.6, b = 74.0, c = 129.8
V_M ($Å^3$ Da^{-1})	2.35
Solvent content (%)	47.7
Resolution range (Å)	24.5 - 3.5 (3.6 - 3.5)
No. of observed reflections	23286
No. of unique reflections	7999
Completeness (%)	96.4 (92.5)
R_{sym} (%)	13.1 (33.2)
I/I_σ	5.3 (2.4)

Table 2. Summary of crystallographic refinement.

PDB code	
Resolution limits (Å)	24.5 - 3.5
R_{cryst} (%)	26.8
R_{free} (%)	33.2
Total number of non-hydrogen atoms	4582
Total number of atoms in succinimide linked lactose	1(44)
Water molecules	8
R.m.s. deviations†(Å)	
Bond lengths	0.006
Bond angles	0.98
Dihedral angles	0.05
Overall G factor[§]	0.26
Average B factors $(Å)^2$	91.2
Residues in most favored regions (%)	91.1
Residues in additionally allowed regions (%)	8.9

†Target stereochemistry from literature[62] § As reported by PROCHECK[63]

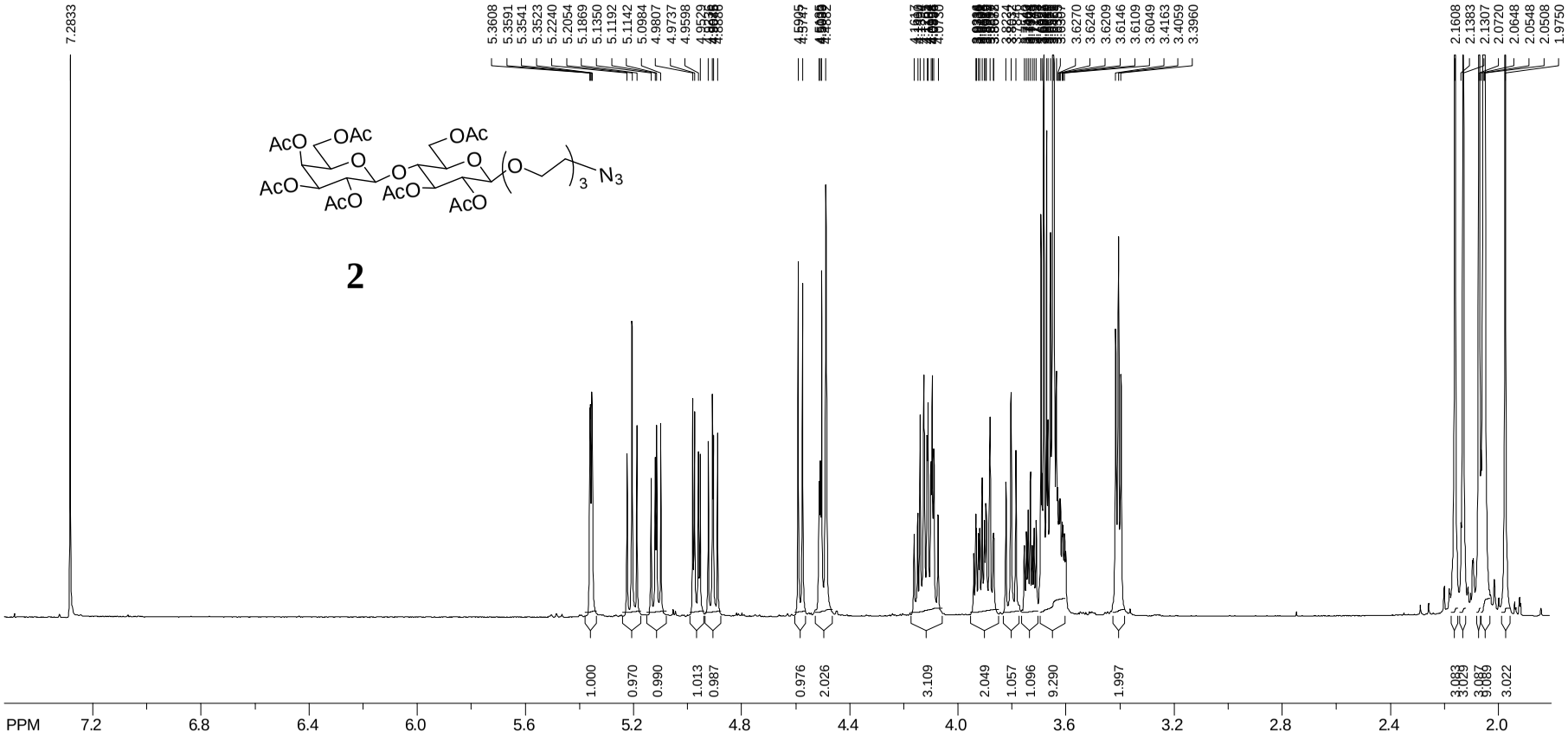

file: E:\Lab works\NMR\nmr-linker\peracetyl LacPEG(3)azide-8-11\1\1\fid expt <zg30>
transmitter freq.: 500.023088 MHz
time domain size: 65536 points
width: 10330.58 Hz = 20.660203 ppm = 0.157632 Hz/pt
number of scans: 16

freq. of 0 ppm: 500.020000 MHz
processed size: 32768 complex points
LB: 0.300 GB: 0.0000

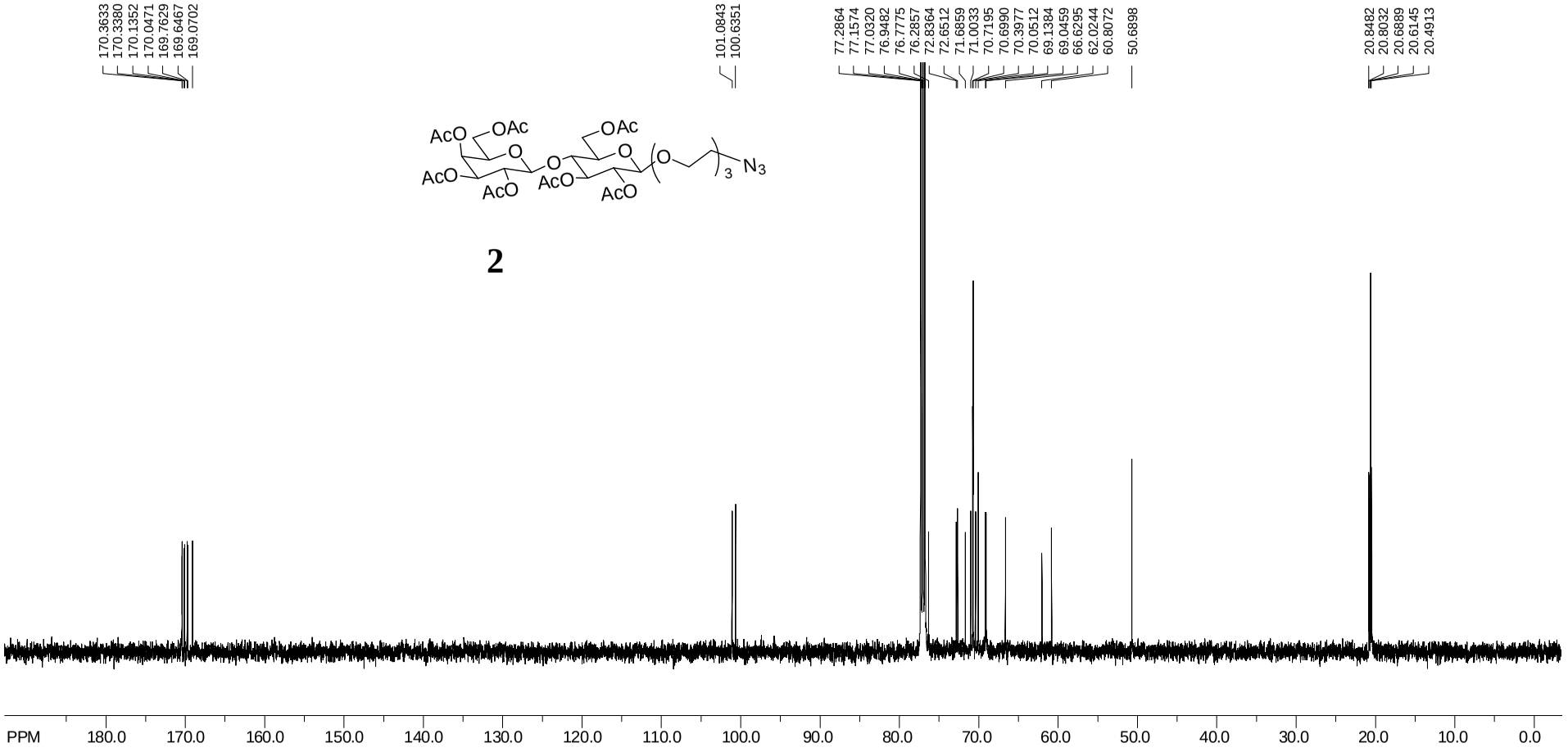

2

file: E:\Lab works\NMR\nmr-linker\peracetyl LacPEG(3)azide-8-11\2\fid expt: <zgpg30>
transmitter freq.: 125.742702 MHz
time domain size: 65536 points
width: 30030.03 Hz = 238.821256 ppm = 0.458222 Hz/pt
number of scans: 897

freq. of 0 ppm: 125.730129 MHz
processed size: 32768 complex points
LB: 1.000 GB: 0.0000

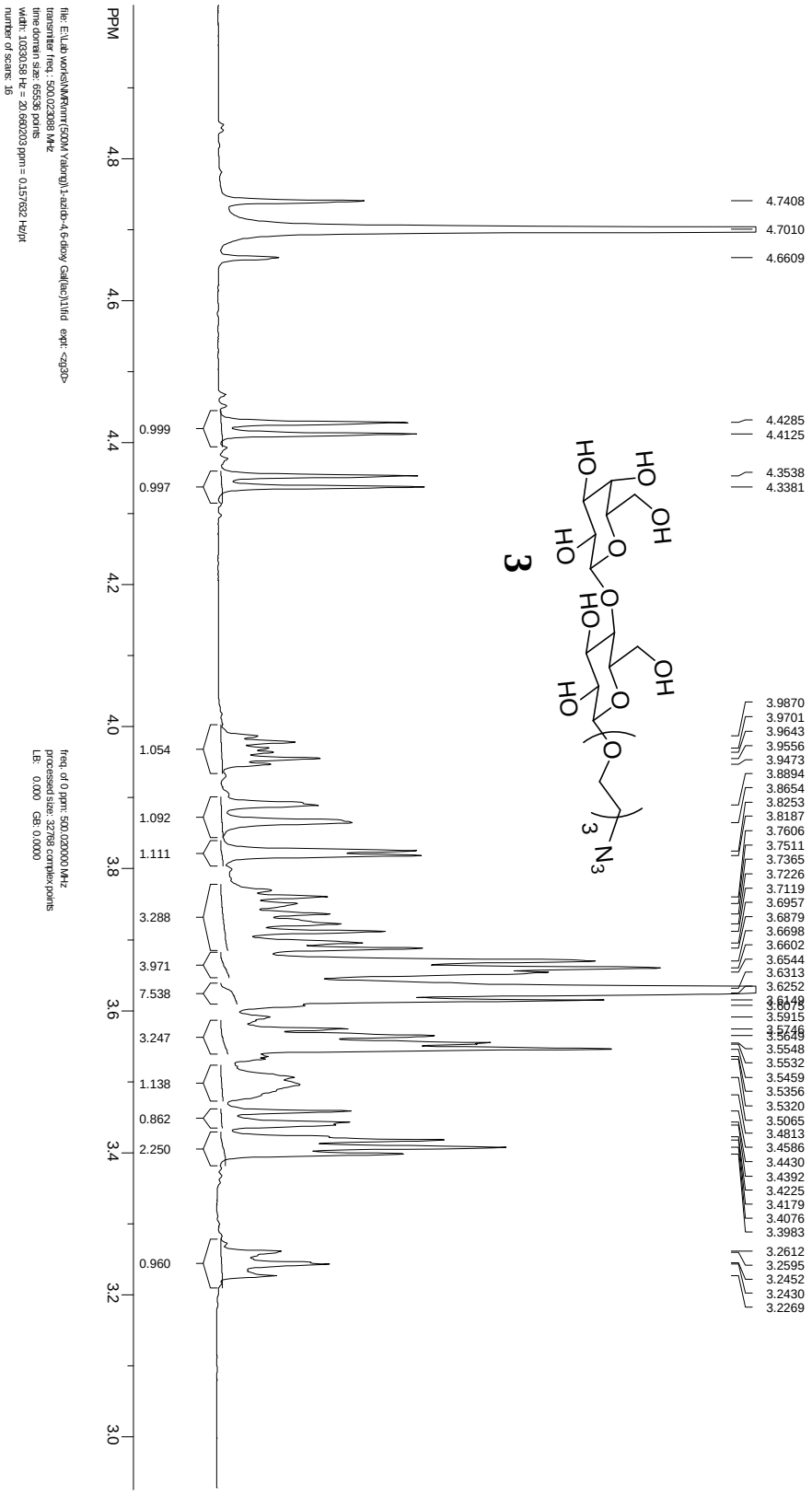
4.7408
4.7010
4.6609
4.4285
4.4125
4.3538
4.3381
3.9870
3.9701
3.9643
3.9556
3.9473
3.8894
3.8654
3.8253
3.8187
3.7606
3.7511
3.7365
3.7226
3.7119
3.6957
3.6879
3.6698
3.6602
3.6544
3.6313
3.6252
3.5915
3.5548
3.5532
3.5459
3.5356
3.5320
3.5065
3.4813
3.4586
3.4430
3.4392
3.4225
3.4179
3.4076
3.3983
3.2612
3.2595
3.2452
3.2430
3.2269
0.999
0.997
1.054
1.092
1.111
3.288
3.971
7.538
3.247
1.138
0.862
2.250
0.960
PPM
4.8
4.6
4.4
4.2
4.0
3.8
3.6
3.4
3.2
3.0
HO
OH
O
N3
3
file: E:\Lab work\NMR\nmr\[520M Yalong]\1-azido-4,6-dioxy Gal[(ac)1]\1\fid expt: <zg30>
transmitter freq.: 500.023088 MHz
time domain size: 65536 points
width: 10330.58 Hz = 20.660203 ppm = 0.157632 Hz/pt
number of scans: 16
freq. of 0 ppm: 500.020000 MHz
processed size: 32768 complex points
LB: 0.000 GB: 0.0000

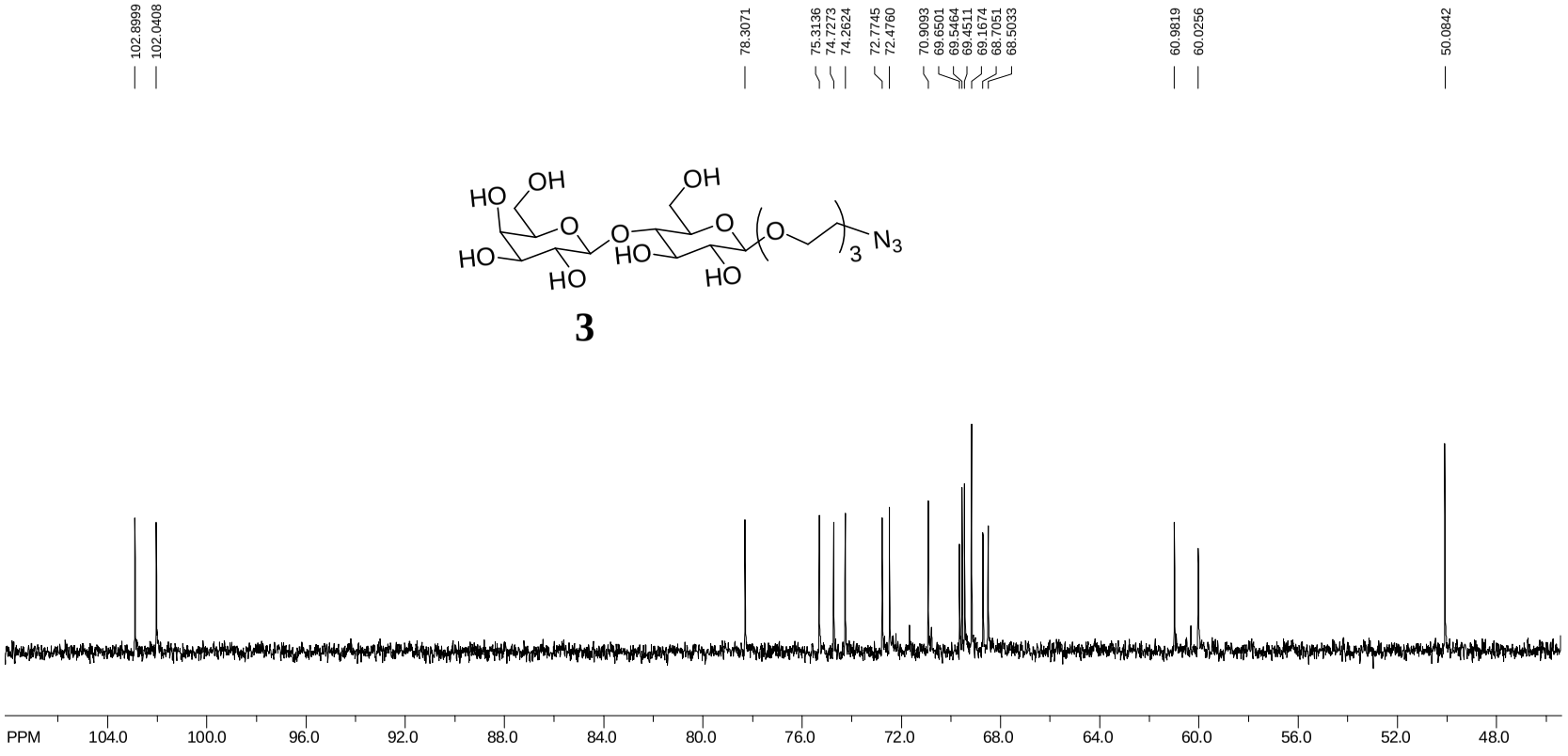

3

file: E:\Lab works\NMR\nmr(500M Yalong)\1-azido-4,6-dioxy Gal(lac)\2\fid expt: <zgpg30>
transmitter freq.: 125.742702 MHz
time domain size: 65536 points
width: 30030.03 Hz = 238.821256 ppm = 0.458222 Hz/pt
number of scans: 668

freq. of 0 ppm: 125.730129 MHz
processed size: 32768 complex points
LB: 0.000 GB: 0.0000

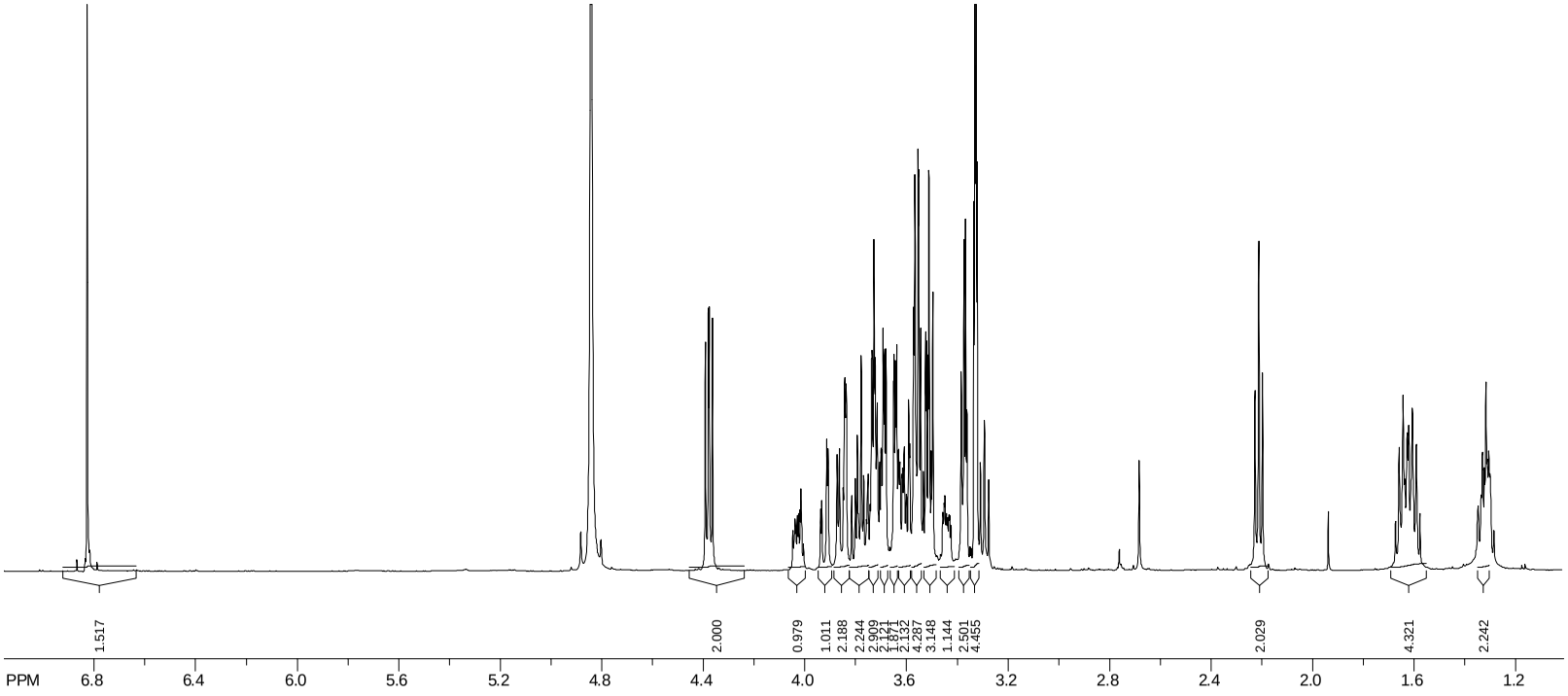

file: E:\Lab works\NMR\nmr(500M Yalong)\LacPEG(3)C(6)suc\1\fid expt: <zg30>
transmitter freq.: 500.023088 MHz
time domain size: 65536 points
width: 10330.58 Hz = 20.660203 ppm = 0.157632 Hz/pt
number of scans: 16

freq. of 0 ppm: 500.020000 MHz
processed size: 32768 complex points
LB: 0.000 GB: 0.0000

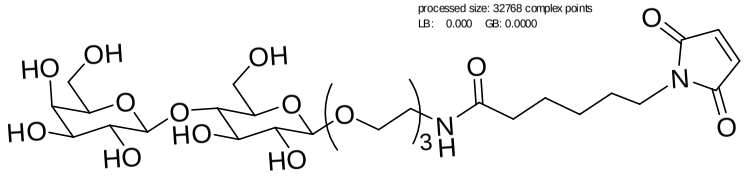

4

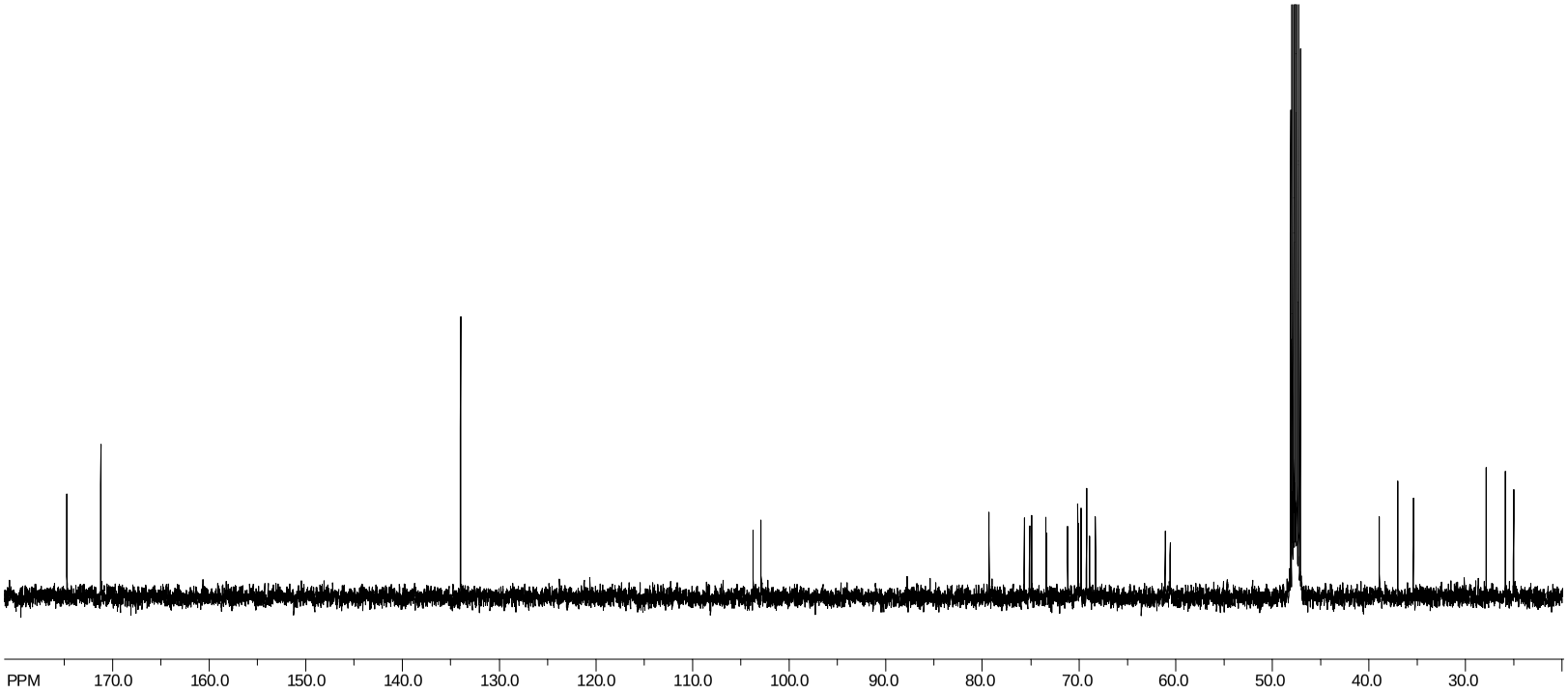

file: E:\Lab works\NMR\nmr(500M Yalong)\LacPEG(3)C(6)suc\2\fid expt: <zgpg30>
transmitter freq.: 125.742702 MHz
time domain size: 65536 points
width: 30030.03 Hz = 238.821256 ppm = 0.458222 Hz/pt
number of scans: 574

freq. of 0 ppm: 125.730129 MHz
processed size: 32768 complex points
LB: 0.000 GB: 0.0000

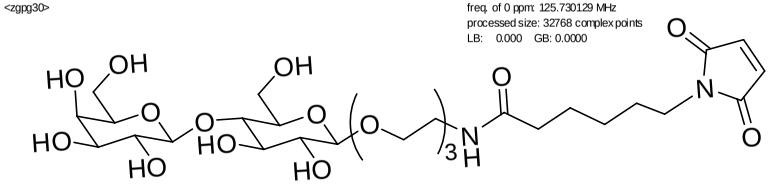

4

Unimolecular Micelles based on Hydrophobically Derivatized Hyperbranched Polyglycerols: Biodistribution Studies

Rajesh Kumar Kainthan[†] and Donald E. Brooks*[,†,‡]

Department of Pathology and Laboratory Medicine, Centre for Blood Research, and Department of Chemistry, University of British Columbia, Vancouver, British Columbia, Canada V6T 2B5. Received March 6, 2008; Revised Manuscript Received September 9, 2008

We recently reported the synthesis and testing of a new class of unimolecular micelles based on hyperbranched polyglycerols as second generation synthetic plasma expanders and as general drug delivery vehicles. A detailed biodistribution study of two derivatized hyperbranched polyglycerols of different molecular weights derivatized with hydrophobic groups and short poly(ethylene glycol) chains is reported in this article. In mice, these materials are nontoxic with circulation half-lives as high as 31 h, controllable by manipulating the molecular weight and the degree of PEG derivatization. Organ accumulation is low, presumably due to the "pegylation" effect. Thermal degradation and hydrolysis data suggest that these polymers are highly stable with a long shelf life, a major advantage for a pharmaceutical product. Degradation under acidic conditions has been observed for these polymers.

INTRODUCTION

There is a huge clinical demand for human serum albumin (HSA), with the world market being in the ~$1.5B/yr range (*1*). Because of supply and contamination problems with the human material, a number of alternatives have been developed as plasma expanders, but they all suffer from significant failings compared to the native protein (*2, 3*). While they can reproduce the osmotic function of HSA, none provide one of the most significant physiological functions of HSA, namely, the binding and transport in the circulation of a wide variety of small molecules including fatty acids, steroids, metal ions, and bilirubin, as well as hydrophobic drugs. Moreover, since most are linear polysaccharides, they increase plasma viscosity significantly, typically cause deleterious red cell aggregation, and exhibit a variety of complex physiological effects (*4*−*7*).

Our overall goal is to develop a second-generation synthetic substitute for HSA consisting of a dendritic biocompatible polymer that not only has superior volume replacement properties compared to other plasma expanders, due to its low intrinsic viscosity, but also will closely mimic the compatibility, binding, and transport properties of the natural material. Toward this end, we recently reported the synthesis and preliminary testing of several derivatized hyperbranched polyglycerols (dHPGs) functionalized with octadecyl chains and monomethyl poly(ethylene glycol) (MPEG-400) oligomers (*8*). A simple one-pot synthetic strategy has been developed with the aim of reducing the cost of synthesis in an industrial setting. These dHPGs were shown to be highly biocompatible using various *in vitro* hemocompatibility studies owing to the presence of PEG oligomers which protect the alkyl chains from interacting with cell membranes and plasma proteins. Being highly branched, these polymers have low intrinsic viscosity values and therefore are expected to increase blood viscosity only slightly. Moreover, they behave as unimolecular micelles and have been shown to bind fatty acids and model hydrophobic drugs, implying that these polymers can also be applied as general drug carriers (*8, 9*). Due to the presence of functionalizable hydroxyl groups, they can also be decorated with targeting groups for directed drug therapy or bioactive materials that could be active intracellularly.

An ideal synthetic plasma expander should have a reasonably long plasma circulation half-life compared to that of HSA (~15 days) and should be metabolized or excreted as soon as it leaves the blood compartment. The circulation half-life of a polymer generally increases with increase in molecular weight and size; however, organ accumulation and uptake by the reticuloendothelial system (RES) also increases. Therefore, a balance is often sought for optimum performance. Long-term tissue deposits are a potential problem and still remain one of the drawbacks of the currently used plasma expanders (*10*). A detailed study of the biodistribution of two dHPGs therefore was carried out in mice, the results of which are the subject of the current manuscript.

EXPERIMENTAL PROCEDURES

Materials. All chemicals were purchased from Sigma-Aldrich Canada Ltd. (Oakville, ON) and used without further purification except as noted. Glycidol (96%) was purified by vacuum distillation and stored over molecular sieves in a refrigerator (2−4 °C). 1,2-epoxyoctadecane was synthesized by the peroxidation of octadecene with *m*-chloroperbenzoic acid. α-epoxy,ω-methoxy poly(ethylene glycol) 350 (MPEG epoxide) was synthesized from a reaction of MPEG 350, sodium hydroxide, and epichlorohydrin. Two dHPGs of molecular weight 40 kDa (dHPG-40) and 83 kDa (dHPG-83) were prepared as previously reported (*8*).

Polymer Characterization. NMR spectra were recorded on a Bruker Avance 400 MHz NMR spectrometer using deuterated solvents (Cambridge Isotope Laboratories, 99.8% D) with the solvent peak as a reference. Molecular weights and polydispersities of the polymers were determined by gel permeation chromatography (GPC) connected to a multiangle laser light scattering (MALLS) detector (GPC-MALLS). The GPC system used consists of a Waters 2690 separation module fitted with a DAWN EOS MALLS detector from Wyatt Technology Corp.

* Corresponding author. Centre for Blood Research, Life Sciences Centre, 2350 Health Sciences Mall, University of British Columbia, Vancouver, BC V6T 1Z3, Canada. Fax: (604) 822-7742, E-mail address: don.brooks@ubc.ca (D. E. Brooks).

[†] Department of Pathology and Laboratory Medicine, Centre for Blood Research.

[‡] Department of Chemistry.

10.1021/bc800090v CCC: $40.75 © 2008 American Chemical Society
Published on Web 10/11/2008

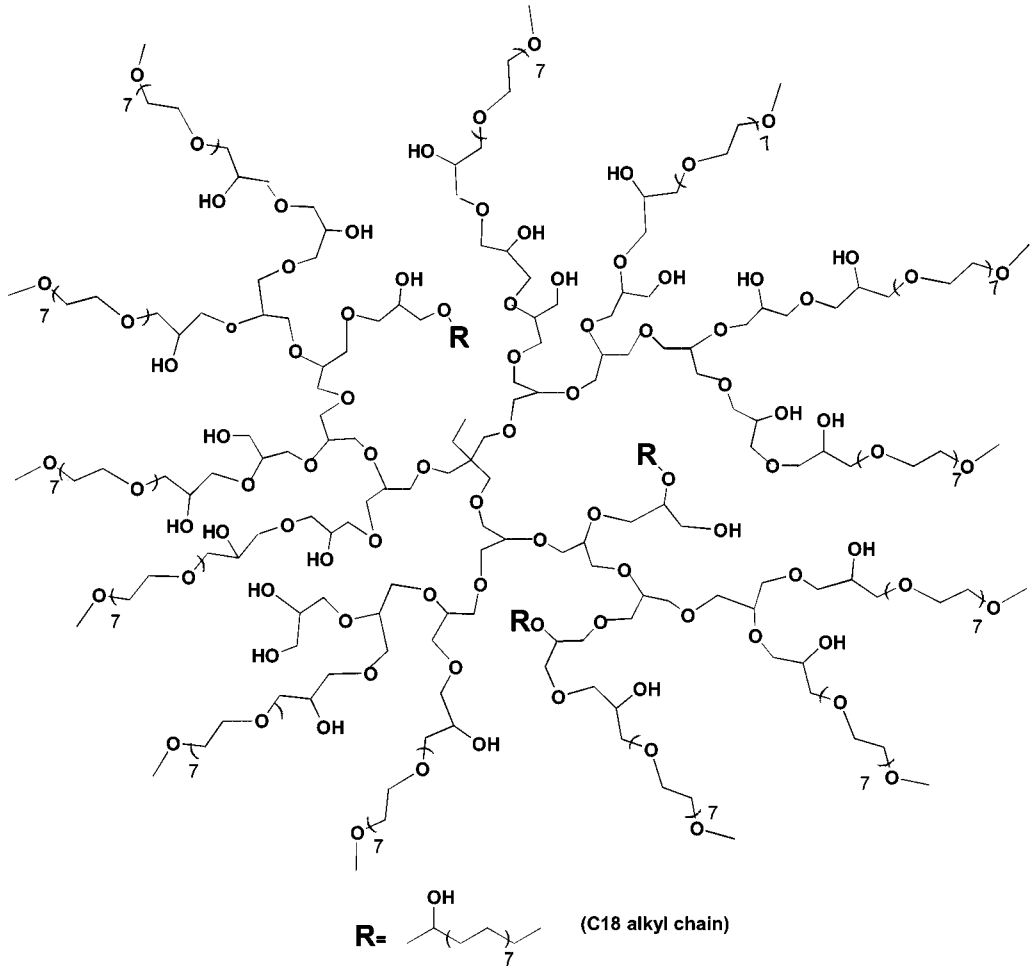

Figure 1. Structure of the derivatized hyperbranched polyglycerol (dHPG).

Table 1. Physical Characteristics of the dHPG Copolymers

polymer	C_{18} mol %	MPEG mol %	glycidol mol %	no. of C_{18}[a]	$M_n \times 10^{-4}$	M_w/M_n	$[\eta]$ (mL/g)	R_h nm (QELS)
dHPG- 40	1.6	20.4	78	4.4	4.0	1.5	7.2	6.5
dHPG-83	1.6	29.4	69	7.6	8.3	1.8	7.9	7.7

[a] Number of C18 chains per molecule; M_n number average molecular weight; M_w/M_n polydispersity; $[\eta]$ intrinsic viscosity; QELS quasi elastic light scattering; R_h average hydrodynamic radius.

with 18 detectors placed at different angles (laser wavelength = 690 nm) and a refractive index detector (Optilab DSP from Wyatt Technology Corp.). An Ultrahydrogel linear column with bead size 6−13 μm (elution range 10^3 to 5×10^6 Da) and an Ultrahydrogel 120 with bead size 6 μm (elution range 150 to 5×10^3 Da) from Waters were used. An aqueous 0.1 N $NaNO_3$ solution was used as the mobile phase at a flow rate of 0.8 mL/min. The dn/dc value for polyglycerol was determined to be 0.12 mL/g in aqueous 0.1 N $NaNO_3$ solutions and was used for molecular weight calculations. The data were processed using Astra software provided by Wyatt Technology Corp.

All thermogravimetric analyses, to study the thermal stability of the polymers, were performed on a TGA Q500 (TA Instruments, USA). A constant ramping temperature program (20.0 °C/min to 800 °C) was used in the experiments with a balance gas flow of 40 mL/min (Nitrogen) and a sample gas flow of 60 mL/min (Nitrogen). The real-time weight percentage and TGA chamber temperature were recorded. Analysis of the data was performed using TA Universal Analysis 2000 software (version 4.2E, TA Instruments, USA) to find the onset points.

***In Vitro* Aqueous Degradability.** The polymer dHPG-83 was dissolved in buffer solutions of pH 5 (30 mM acetate buffer with 70 mM $NaNO_3$) and 7.4 (30 mM phosphate buffer with 70 mM $NaNO_3$) at a concentration of 10 mg/mL and incubated at 37 °C. Samples were withdrawn at 1, 2, and 4 week intervals and analyzed by size exclusion chromatography for molecular weight characteristics.

Radiolabeling of dHPGs. Radiolabeling was done by partial conversion of hydroxyl groups to methoxides using tritiated methyl iodide. Briefly, 1 g of polymer was dissolved in 10 mL dimethylsulfoxide (DMSO) and approximately 5% of the hydroxyl groups were converted to potassium alkoxides by reaction with potassium hydride (35 mg). To this, 20 μL of tritiated methyl iodide (toluene solution) dissolved in 1 mL DMSO was added and the reaction mixture stirred at room temperature for 15 h; then, 5 mL water was added and the reaction mixture was acidified with dilute HCl. The polymer was purified by dialysis against water using a dialysis membrane of MWCO 1000 until the dialyzate contained low amounts of radioactivity; this normally took 24 h. The polymer solutions were then filtered through a syringe filter (0.2 μm) and the total polymer weight was determined from the total volume and the dry weight of a known volume (100 μL) of solution after freeze−drying (measured in duplicate). The polymer solution was then concentrated by evaporating off the water in a fume hood, and the final concentration of 100 mg/mL in 150 mM

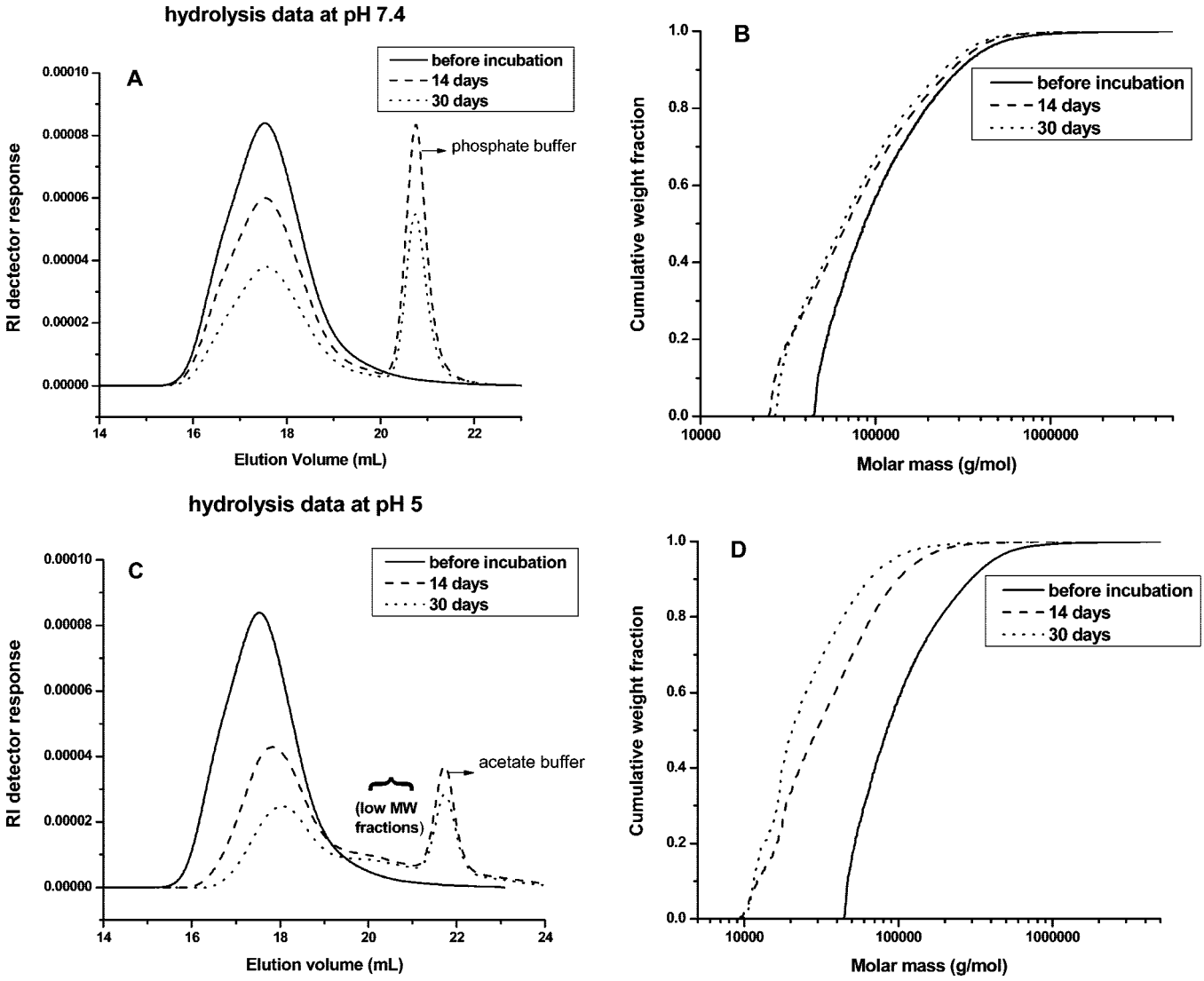

Figure 2. Time-dependent GPC chromatograms of dHPG-83 after incubation in buffer solutions of pH 7.4 and 5.0 at 37 °C.

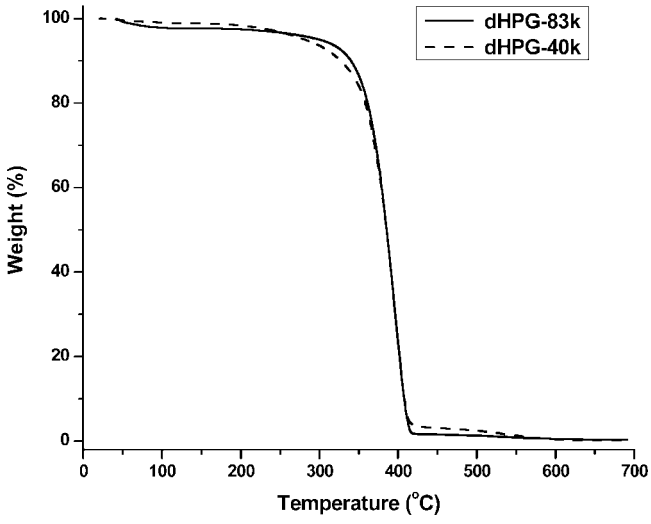

Figure 3. Thermal decomposition profiles of the dHPG polymers.

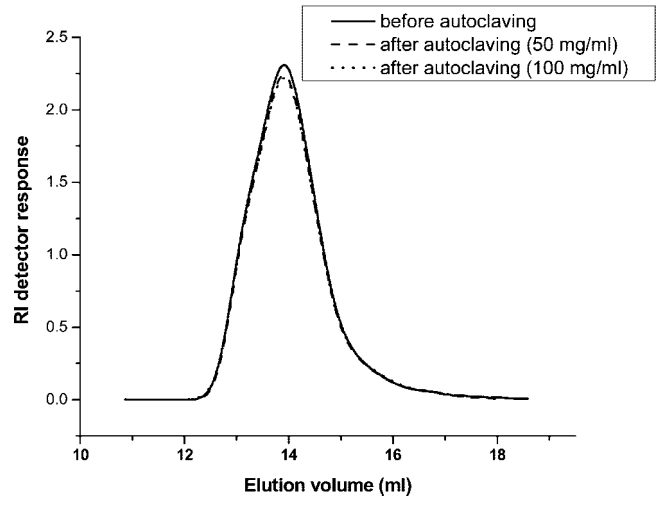

Figure 4. GPC chromatograms of dHPG-83 before and after autoclaving.

saline solution was made by appropriate dilution with an aqueous NaCl solution. This allowed the specific activity to be determined by counting an aliquot of solution.

Animal Studies. All animal experiment protocols were reviewed and approved by the Institutional Animal Care Committee (IACC) at UBC prior to conducting the studies. The care, housing, and use of animals were performed in accordance with the Canadian Council on Animal Care Guidelines. The studies were conducted at the British Columbia Cancer

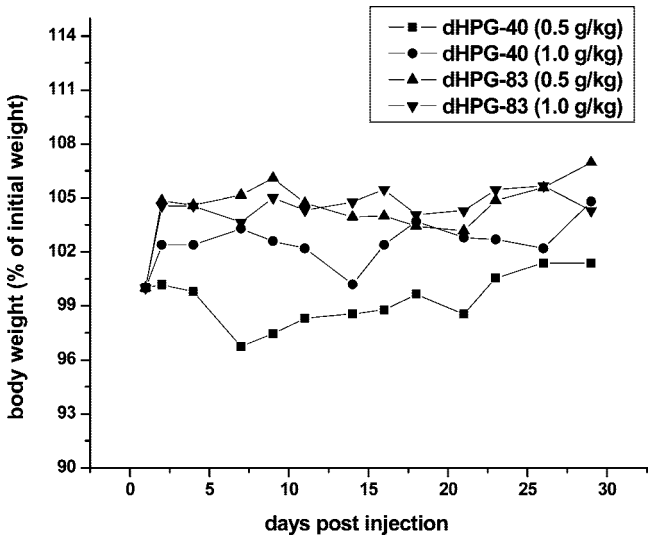

Figure 5. Change in body weight after administration of the dHPG polymers.

Research Centre under the supervision of Dr. Dawn Waterhouse and Prof. Marcel Bally.

Female Balb/C mice (7−11 weeks) were heated under a lamp for 1−2 min to increase blood circulation, and gently placed into a mouse restrainer for injection. The tail was wiped down with 70% isopropanol to clean the injection site and to aid in increasing circulation. Mice were injected intravenously (bolus) via lateral tail vein with a polymer solution of concentration 100 mg/mL (four mice per group) to a prescribed dose of 1 g/Kg. The injected volume was 200 μL/20 g mouse. Mice were then returned to their cages.

All animals were observed post-administration, at least once a day, and more if deemed necessary, during the pretreatment and treatment periods for mortality and morbidity. In particular, signs of clinical ill health were based on body weight loss, change in food consumption, and behavioral changes such as altered gait, lethargy, and gross manifestations of stress.

Blood was collected at various time intervals (30 min, 2, 4, 8, 24, and 48 h, and 7, 14, and 30 days) by cardiac puncture after termination by CO_2 inhalation. Plasma was separated by centrifuging samples at 2500 rpm for 15 min. Aliquots of plasma were placed in scintillation vials and analyzed with a Packard 1900 scintillation counter after adding 5 mL scintillation cocktail.

Mice in one group (time point 48 h) were housed in a metabolic cage. Urine and stools were collected as pooled samples at 1, 4, 8, 24, and 48 h post-injection. Aliquots of urine were analyzed by scintillation counting. Stool samples were pooled and made into a 30% homogenate in a known amount of water prior to obtaining aliquots for scintillation counting.

Upon termination, liver, spleen, kidney, lungs, and heart were removed from all the mice, weighed, and processed for scintillation counting. Livers (one lobe) were made into a 30% homogenate in a known amount of water using a polytron tissue homogenizer. Aliquots (in triplicate) of 200 μL homogenate were transferred to scintillation vials. All other organs were dissolved in 500 μL SOLVABLE. Vials were incubated at 50 °C overnight, then cooled prior to addition of 50 μL 200 mM EDTA, 25 μL 10 M HCl, and 200 μL 30% H_2O_2. This mixture was incubated at room temperature for 1 h prior to addition of 5 mL scintillation cocktail. Samples were analyzed by scintillation counting.

Evaluation of Antibody Mediated Clearance. Female Balb/c mice (total of 16) were individually weighed and divided into groups of 4. Mice in groups 3 and 4 received injections of dHPG- 83 every 2 weeks for 8 weeks. One week following the final injection, all mice received an i.v. injection of the radiolabeled dHPG-83, and blood was collected at different time points. Plasma was collected and assessed for polymer levels by scintillation counting.

RESULTS AND DISCUSSION

Synthesis and Characterization. The synthetic method we have employed for the dHPGs is a simple and efficient one-pot approach based on anionic ring-opening polymerization of epoxides. The structure of the polymer is given in Figure 1; the details of the synthesis have been described in an earlier manuscript (*8*). Briefly, an HPG of molecular weight 7000 g/mol was prepared by anionic ring-opening multibranching polymerization of glycidol from partially deprotonated trimethylolpropane using potassium methylate (*11*). HPG has numerous hydroxyl end groups, with the number per molecule being roughly equal to the degree of polymerization. Some of these were modified with C18 alkyl chains (2−5%) and MPEG-350 chains (mol wt 350) (20−40%) by sequential addition of 1,2-epoxyoctadecane and MPEG-epoxide. The unreacted alkyl epoxide was removed from the methanolic polymer solution by extraction with hexane. The final polymer product was purified by dialysis against water to remove any unreacted PEG chains and then freeze−dried. Two dHPGs of molecular weight 40 kDa and 83 kDa were prepared for biodistribution studies; their molecular characteristics are given in Table 1. The polymers were purified by dialysis. The molecular weight distributions of the polymer are narrow, in the range 1.5−1.8.

***In Vitro* Aqueous Degradability.** The dHPG polymer backbones contain −C−C− and −C−O−C− bonds only. Since these are not substrates for common enzymes in the circulation, no rapid enzymatic breakdown in blood is anticipated. We tested the stability of dHPG-83 in buffer solutions of pH 5 (lysosomal pH) and 7.4 (physiological pH) incubated at 37 °C by monitoring its molecular weight distribution profile over time by GPC. The chromatograms are shown in Figure 2. The RI traces indicated only a small decrease in peak molecular weight and the appearance of material in the 20 000−40 000 range after 14 and 30 days when the polymers were incubated at pH 7.4 (Figure 2A,B). However, the polymers degraded more noticeably at pH 5.0 and a much more prevalent lower molecular weight fraction, in the range 10 000−40 000, could be seen in the RI traces for the 15 and 30 day samples with an obvious reduction in the peak molecular weight (Figure 2C,D). The average molecular weight decreased from 83 to 20 K. Since the HPG core was reported earlier to be stable under similar conditions (*12*), the decrease observed might be due to degradation of the PEG chains, with the degradation of PEG under acidic conditions having been reported (*13*). However, the occurrence of relatively high molecular weight PEG chains would be expected to be relatively rare at the monomer concentrations used in the synthesis, so this is unlikely to be the whole explanation. A more detailed study of the degradation reaction is under way.

Thermal Degradation. A desirable property of dHPGs would be sufficient thermal stability to allow them to be autoclaved for sterilization. The core HPGs are thermally quite stable with onset of thermal decomposition in the range 360−390 °C (*14, 15*). The thermograms obtained for dHPG-40 and dHPG-83 are shown in Figure 3. It is evident from the figure that the derivatized HPGs are also highly stable up to a temperature of 300 °C with no indication of thermal decomposition. The onset of decomposition is around 350 °C. Aqueous solutions of dHPG at two different concentrations (50 mg/mL and 100 mg/mL) were autoclaved under standard conditions for sterilization, and the GPC chromatograms before and after the sterilization

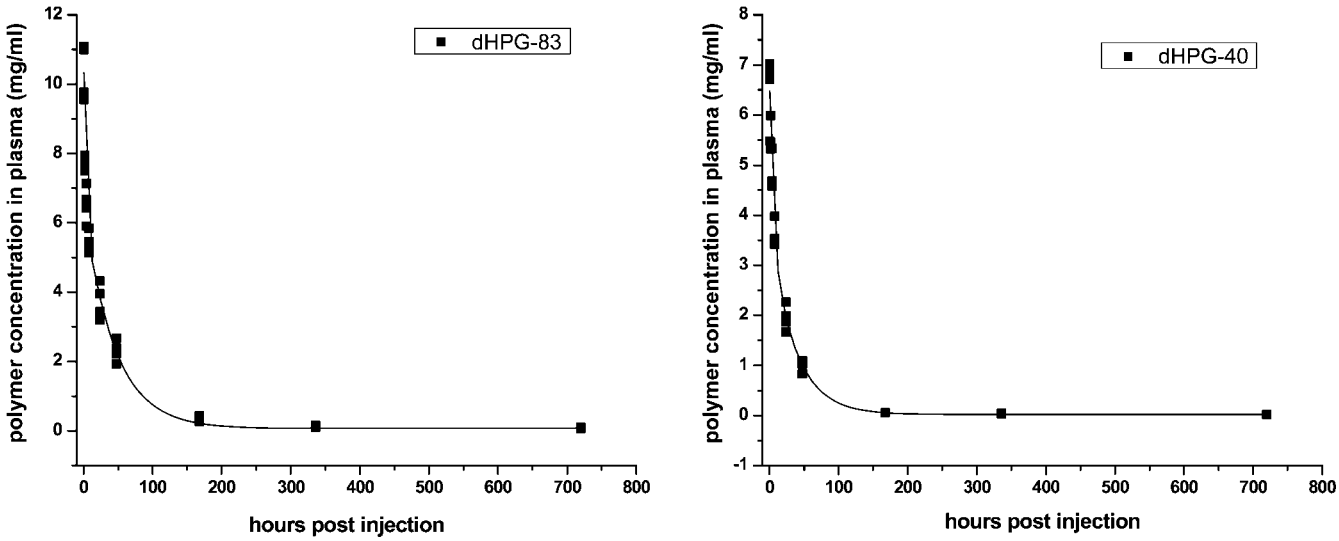

Figure 6. Plot of polymer concentration of dHPG polymers in plasma with respect to time.

Table 2. Rate Constants Determined from Pharmacokinetic Analysis of Polymer Concentrations in Plasma over Time[a]

polymer	P_0 (mg/mL plasma)	V_c (mL plasma)	α (h^{-1})	β (h^{-1})	$t_{1/2}$ (h)	k_{12} (h^{-1})	k_{21} (h^{-1})	k_2 (h^{-1})	$AUC_{0-\infty}$mg.mL^{-1}.h
dHPG-40	6.8 ± 1.4	2.94 ± 0.62	0.028 ± 0.007	0.20 ± 0.07	24.9 ± 6.2	0.060 ± 0.089	0.12 ± 0.05	0.046 ± 0.027	148.4 ± 44.9
dHPG-83	11.7 ± 0.4	1.7 ± 0.06	0.022 ± 0.002	0.61 ± 0.11	31.0 ± 2.9	0.249 ± 0.130	0.34 ± 0.06	0.040 ± 0.011	295.4 ± 29.9

[a] k_{12} and k_{21} represent the rate constants for transfer between the plasma and tissue compartments; k_2 is the rate constant for elimination.

procedure are shown in Figure 4. The chromatograms are indistinguishable with no change in molecular weight. These results demonstrate that aqueous solutions of dHPG polymers are sufficiently stable to allow them to be autoclaved.

Animal Studies. *Mouse Toxicity.* The derivatized HPGs dissolved in isotonic saline were injected i.v. into Balb/c mice at 0.5 g/Kg and 1 g/Kg, two mice per concentration per compound, and followed for 30 days for signs of toxicity and body weight loss. No untoward indicators were found, and all the animals grew normally with no signs of distress, as was found for underivatized HPGs (*16*). No signs of toxicity (e.g., lethargy, dry eyes, change in food consumption, altered gait, or scruffy coats) were observed. The animals were followed for 30 days for weight changes, and no weight loss was observed during this period (Figure 5). On autopsy, liver, gall bladder, spleen, lung, kidney, heart, intestine, lymph nodes, and bladder were examined macroscopically for gross pathology; all the organs appeared normal with no unusual finding observed.

Biodistribution. The circulating levels of both polymers are shown in Figure 6 as a function of time, expressed as milligrams polymer per milliliter of plasma. The data were analyzed by a standard two-compartment open pharmacokinetic model (*12, 17*). The rate constants (k_{12} - plasma to tissue, k_{21} - tissue back to plasma, and k_2 - elimination) calculated from the graphs are given in Table 2.

The plasma half-life for dHPG-40 was ~25 h, while that of dHPG-83 was ~31 h. The value for the area under the plasma concentration curve ($AUC_{0-\infty}$) was ~2 times that for the higher molecular weight polymer, implying that this polymer's tissue exposure was twice that of the lower molecular weight material. The results show that it is possible to adjust the retention time in blood and tissue exposure by manipulating the molecular weight through changes in the PEG content of the polymer, since both the dHPGs had similar HPG contents (16 000 and 24 000 for the low and high molecular weights, respectively, whereas the PEG contents were around 22 500 and 56 000). The core HPG molecular weight can also be varied with related effects as we have shown recently with higher molecular weight non-pegylated material (*12*). The plasma half-lives obtained for these polymers are consistent with the periods required for postoperative support in many cases (*18*). Lower molecular weight polymers, which would be excreted faster, can be made by reducing the molecular weight of HPG or degree of substitution with PEG; in some surgical settings, faster excretion is preferred. Even though the molecular weight of the dHPG-83 is double that of dHPG-40, the plasma half-life did not change dramatically. This might be due to the plasma half-life's dependence on many factors, one of which is the molecular size, which increases only weakly with molecular weight for hyperbranched polymers.

The plasma half-lives observed for these polymers are higher than those for linear polymers of similar molecular weights, presumably due to their globular shape and relative rigidity. For example, poly-*N*-(2-hydroxylpropyl)methacrylamide (HPMA), which has been extensively studied for anticancer drug delivery, has a circulation half-life of only 25 h for a molecular weight of 556 000 (*19*). The hydrodynamic radii of dHPG polymers are well above the glomerular filtration threshold, which is about 3.7−6.0 nm pore radius (*20*). Perhaps more relevant is the inability of dHPGs to pass through pores via reptation, an option available for linear polymers (*21, 22*). A related observation is that longer circulation times have been reported for pegylated polyester bow-tie dendrimers, which likewise cannot reptate (*13*).

The values for the distribution rate constants were calculated from the graphs and are summarized in Table 2. While the two polymers were eliminated from the system at essentially the same rate, the transfer of the higher molecular weight polymer dHPG-83 from blood to tissue (k_{12}) was about 4 times faster and the reverse process (k_{21}) almost 3 times faster than the rates for dHPG-40, consistent with the higher tissue accumulation observed for the higher molecular weight polymer as discussed below.

At termination, liver, spleen, lungs, and heart were collected and processed for scintillation counting. Levels of polymer in the organs were analyzed. The data was not corrected for the

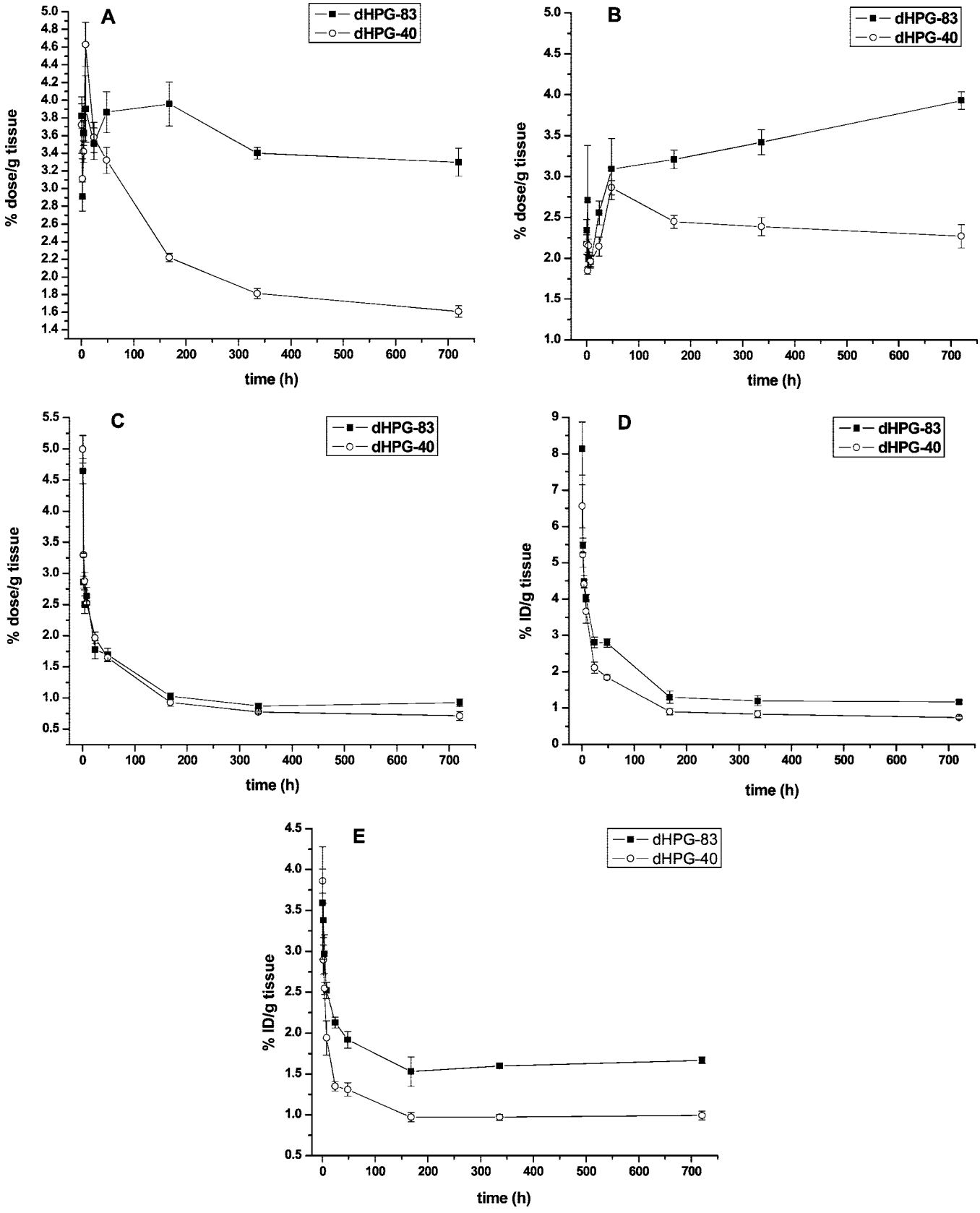

Figure 7. Levels of polymer accumulated over time in liver (A), spleen (B), kidney (C), lungs (D), and heart (E).

plasma present in these organs, so the high levels of radioactivity up to 48 h are largely due to the plasma present in them. Both polymers accumulate in liver and spleen to a small extent with values below 5% ID/g tissue (ID = initial dose) over the 30 day study period (Figure 7A,B). The low levels observed for these polymers compared to HPGs and other polymers reported in the literature evidently are due to the presence of PEG chains, supporting the concept that PEG grafting reduces uptake by the RES (*23, 24*). The levels in the organs were higher for the higher molecular weight polymer, which remained almost constant in liver and increased in spleen during the study period. A similar dependence of tissue accumulation on molecular weight has

Table 3. Polymer Levels in Urine and Feces at the Times Indicated[a]

	dHPG-83		dHPG-40	
time (h)	% dose in feces	% dose in urine	% dose in feces	% dose in urine
1	0.02	not collected	0.03	not collected
4	0.05	1.47	0.97	not collected
8	0.25	2.33	11.56	9.8
24	0.03	13.44	9.25	17.1
48	0.07	0.61	2.91	0.75

[a] Error bars are not shown as the data are obtained from pooled samples.

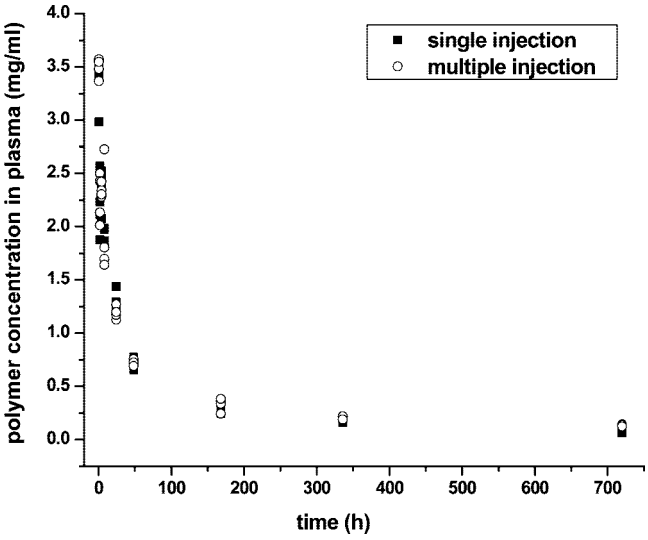

Figure 8. Plot of polymer concentration of dHPG-83 in plasma of animals preinjected with the polymer with respect to time.

been reported for other polymers, likely because the total tissue exposure was higher as indicated by the greater $AUC_{0-\infty}$value for dHPG-83 (Table 2) (*25*, *26*).

The levels of the lower molecular weight polymer in kidney, lungs, and heart were below 1% ID/g tissue (Figures 7C,D,E). The levels of the higher molecular weight polymer were around 1% in kidney and lungs and ~2% in heart. Similar organ accumulations have been reported for hetastarch, which is widely used clinically (*25*, *27*). These levels of apparent accumulation were accompanied by no gross effects on organ histology, however; the animals remained healthy throughout the observation period. The fate of the residual polymer in these organs after 30 days is unknown, and long-term toxicity studies are needed to assess the effect. However, the *in vitro* degradation data suggest that the polymer might degrade in the acidic compartments of the cells following uptake, resulting eventually in slow excretion from the body. Enzymatic degradation of polyethers has been reported earlier (*28*−*30*).

A metabolic study with a group of mice ($n = 4$) injected with the polymers was performed by collecting urine and feces as pooled samples at 1, 4, 8, 24, and 48 h. The values of polymer clearance into urine and feces are given in Table 3. Approximately 50% of dHPG-40 was excreted from the body within 24 h, with 27% through urine and 22% through feces. The dHPG-83 is mostly eliminated through urine with 17% eliminated within 24 h. Even though the amount of polymer present per unit mass of feces was similar for each, the total amount of dGHPG-83 excreted was only ~1% due to significantly lower amounts of feces excreted within 48 h for this group of animals. Most urinary excretion was over within 24 h for both polymers.

Evaluation of Antibody Mediated Clearance. We have not developed an enzyme-linked immunosorbent assay (ELISA) for the anti-dHPG polymer family due to the lack of a positive control. However, we have tested for evidence of antibody mediated clearance by attempting to sensitize mice with a sequence of prior injections before measuring the plasma depletion curve. If these dHPG polymers are immunogenic, the plasma half-lives of the polymer injected subsequently should be reduced due to the antibody mediated clearance mechanism (*31*−*33*). In order to study this, 16 mice were divided into groups of 4. Mice in groups 3 and 4 were injected with non-radiolabeled dHPG-83 every 2 weeks for 8 weeks at dose of 1 g/kg. One week following the final injection, all mice received an i.v. injection of the radiolabeled dHPG-83 at a dose of 1 g/kg, and blood was collected at different time points. Plasma was collected and assessed for polymer levels by scintillation counting. All the animals grew normally during the study period, and no signs of toxicity or weight loss were observed (data not shown). On autopsy, all organs appeared normal with no gross pathology.

The levels of dHPG-83 in the plasma for both the groups of animals, determined by scintillation counting, are shown as a function of time in Figure 8. It can be seen that the polymer levels are very similar with no significant change in plasma half-life, indicating that there is no significant antibody mediated clearance of the polymer.

The dHPG polymers, with potential applications as an albumin substitute or a general drug delivery vehicle, are highly biocompatible as evidenced by the *in vivo* results described above. The results also suggest that these polymers are non-immunogenic, as they can be administered in repeated doses without change in plasma half-lives. The polymers were well-tolerated by mice at doses as high as 1 g/kg. The plasma half-lives exceeded 24 h and can be controlled by varying the molecular weight through changing the polyglycerol core or the PEG content, as in the present case. The tested polymers are of sufficient size to not pass out immediately into the urine. The overall data considering the plasma half-life and the organ accumulation suggests that a derivatized HPG polymer with a number-average molecular weight of 40 000 is well-suited to an application as a plasma expander. The presence of radioactivity over relatively long periods of time suggests that these structures do not break down appreciably in the circulation over the time courses utilized. However, the *in vitro* degradation studies suggest that these PEG-containing polymers could degrade slowly, particularly under the acidic conditions of an intracellular environment.

ACKNOWLEDGMENT

This work was funded by grants from The Bayer Canadian Blood Services Hema-Quebec Partnership Fund (1614230, 1664725, 1721923) and a Canadian Institutes of Health Research Proof of Principle grant. We thank Canadian Institutes of Health Research, Natural Science and Engineering Research Council of Canada, the Canada Foundation for Innovation, Canadian Blood Services, Michael Smith Foundation for Health Research and BC Knowledge Development Fund for infrastructure support especially the LMB Macromolecular Hub at the UBC Centre for Blood Research. We thank Prof. Marcel Bally and Dr. Dawn Waterhouse for the animal experiments and Dr. Johan Janzen and Mrs. Irina Chafeeva for the help with the radiolabeling experiments.

LITERATURE CITED

(1) Roberts, I. (2002) Albumin and hypovolaemia: time to move on and generate new evidence. *Lancet 359*, 72–73.
(2) Mythen, M. G., and Salmon, J. B. (1993) The rational administration of colloids. *Blood Rev. 7*, 114–120.

(3) Barron, M. E., Wilkes, M. M., and Navickis, R. J. (2004) A systematic review of the comparative safety of colloids. *Arch. Surg. 139*, 552–563.
(4) Jonge, E., and Levi, M. (2001) Effects of different plasma substitutes on blood coagulation. *Crit. Care Med. 29*, 1261–1267.
(5) Treib, J., Baron, J. F., Grauer, M. T., and Strauss, R. G. (1999) An international view of hydroxyethyl starches. *Intensive Care 25*, 258–268.
(6) Brecher, M. E., Owen, H. G., and Bandarenko, N. (1997) Alternatives to albumin: starch replacement for plasma exchange. *J Clin. Apheresis 12*, 146–153.
(7) Chien, S. (1975) Biophysical behavior of red cells in suspensions. In *Red Blood Cell* (Surgenor, D. M., Ed.) pp 1032−1121, Academic Press, New York.
(8) Kainthan, R. K., Janzen, J., Kizhakkedathu, J. N., Devine, D. V., and Brooks, D. E. (2008) Hydrophobically derivatized hyperbranched polyglycerol as a human serum albumin substitute. *Biomaterials 29*, 1693–1704.
(9) Kainthan, R. K., Mugabe, C., Burt, H. M., and Brooks, D. E. (2008) Unimolecular micelles based on hydrophobically derivatized hyperbranched polyglycerols: ligand binding properties. *Biomacromolecules 9*, 886–895.
(10) Leuschner, J., Opitz, J., Winkler, A., Scharpf, R., and Bepperling, F. (2003) Tissue storage of 14 C-labelled hydroxyethyl starch (HES) 130/0.4 and HES 200/0.5 after repeated intravenous administration to rats. *Drugs R&D 4*, 331–338.
(11) Sunder, A., Hanselmann, H., Frey, H., and Mulhaupt, R. (1999) Controlled synthesis of hyperbranched polyglycerols by ring-opening multibranching polymerization. *Macromolecules 32*, 4240–4246.
(12) Kainthan, R. K., and Brooks, D. E. (2007) In vivo biological evaluation of high molecular weight hyperbranched polyglycerols. *Biomaterials 28*, 4779–4787.
(13) Gillies, E. R., Dy, E., Fréchet, J. M. J., and Szoka, F. C. (2005) Biological evaluation of polyester dendrimer: poly(ethylene oxide) "Bow-Tie" hybrids with tunable molecular weight and architecture. *Mol. Pharmaceutics 2*, 129–138.
(14) Siegers, C., Biesalski, M., and Haag, R. (2004) Self-assembled monolayers of dendritic polyglycerol derivatives on gold that resist the adsorption of proteins. *Chem.-Eur. J. 10*, 2831–2838.
(15) Kainthan, R. K., Hester, S., Levin, E, Devine, D. V., and Brooks, D. E. (2007) In vitro biological evaluation of high molecular weight hyperbranched polyglycerols. *Biomaterials 28*, 4581–4590.
(16) Kainthan, R. K., Janzen, J., Levin, E., Devine, D. V., and Brooks, D. E. (2006) Biocompatibility testing of branched and linear polyglycidol. *Biomacromolecules 7*, 703–709.
(17) Notari, R. E. (1980) *Biopharmaceutics and Clinical Pharmacokinetics, An Introduction*, Marcel Dekker, Inc., New York.
(18) Wilkes, N. J., Woolf, R. L., Powanda, M. C., Gan, T. J., Machin, S. J., Webb, A., Mutch, M., Bennett-Guerrero, E., and Mythen, M. (2002) Hydroxyethyl starch in balanced electrolyte solution (Hextend®)—pharmacokinetic and pharmacodynamic profiles in healthy volunteers. *Anesth. Analg. 94*, 538–544.
(19) Maeda, H., Seymour, L. W., and Miyamoto, Y. (1992) Conjugates of anticancer agents and polymers: advantages of macromolecular therapeutics in vivo. *Bioconjugate Chem. 3*, 351–362.
(20) Oliver, J. D., Anderson, S. T., Troy, J. L., Brenner, B. M., and Deen, W. M. (1992) Determination of glomerular size-selectivity in the normal rat with Ficoll. *J. Am. Soc. Nephrol. 3*, 214–28.
(21) Ogston, A. G., Preston, B. N., and Wells, J. D. (1973) On the transport of compact particles through solutions of chain-polymers. *Proc. R. Soc. London, Ser. B: Biol. Sci. A 333*, 297–309.
(22) Lee, C. C., Mackay, J. A., Frechet, J. M. J., and Szoka, F. C. (2005) Designing dendrimers for biological applications. *Nat. Biotechnol. 23*, 1517–1526.
(23) Okuda, T., Kawakami, S., Maeie, T., Niidome, T., Yamashita, F., and Hashida, M. (2006) Biodistribution characteristics of amino acid dendrimers and their PEGylated derivatives after intravenous administration. *J. Controlled Release 114*, 69–77.
(24) Woodle, M. C., and Lasic, D. D. (1992) Sterically stabilized liposomes. *Biochim. Biophys. Acta 1113*, 171–199.
(25) Mehvar, R. (2003) Recent trends in the use of polysaccharides for improved delivery of therapeutic agents: pharmacokinetic and pharmacodynamic perspectives. *Curr. Pharm. Biotechnol. 4*, 283–302.
(26) Hulme, B., Dykes, P. W., Appleyard, I., and Arkell, D. W. (1967) Retention and storage sites of radioactive polyvinylpyrrolidone. *J. Nucl. Med. 9*, 389–393.
(27) Klotz, U., and Kroemer, H. (1987) Clinical pharmacokinetic considerations in the use of plasma expanders. *Clin. Pharmacokinetics 12*, 123–135.
(28) Schramm, E., and Schink, B. (1991) Ether-cleaving enzyme and diol dehydratase involved in anaerobic polyethylene glycol degradation by a new Acetobacterium sp. *Biodegradation 2*, 71–79.
(29) Ohta, T., Tani, A., Kimbara, K., and Kawai, F. (2005) A novel nicotinoprotein aldehyde dehydrogenase involved in polyethyleneglycol degradation. *Appl. Microbiol. Biotechnol. 68*, 639–646.
(30) Kawai, F. (2002) Microbial degradation of polyethers. *Appl. Microbiol. Biotechnol. 58*, 30–38.
(31) Shek, P. N., and Heath, T. D. (1983) Immune response mediated by liposome-associated protein antigens. III. Immunogenicity of bovine serum albumin covalently coupled to vesicle surface. *Immunology 50*, 101–106.
(32) Harding, J. A., Engbers, C. M., Newman, M. S., Goldstein, N. I., and Zalipsky, S. (1997) Immunogenicity and pharmacokinetic attributes of poly(ethylene glycol)-grafted immunoliposomes. *Biochim. Biophys. Acta 1327*, 181–192.
(33) Li, W. M., Mayer, L. D., and Bally, B. M. (2002) Prevention of antibody-mediated elimination of ligand-targeted liposomes by using poly(ethylene glycol)-modified lipids. *J. Pharmacol. Exp. Ther. 300*, 976–983.

BC800090V

Folate and Folate−PEG−PAMAM Dendrimers: Synthesis, Characterization, and Targeted Anticancer Drug Delivery Potential in Tumor Bearing Mice

Prateek Singh, Umesh Gupta, Abhay Asthana, and Narendra K. Jain*

Pharmaceutics Research Laboratory, Department of Pharmaceutical Sciences, Dr. H. S. Gour University Sagar (M.P.) 470003 India. Received March 25, 2008; Revised Manuscript Received August 8, 2008

Ligand-mediated targeting of drugs especially in anticancer drug delivery is an effective approach. Dendrimers, due to unique surface topologies, can be a choice in this context. In the present study, PAMAM (polyamidoamine) dendrimers up to fourth generation were synthesized and characterized through infrared (IR), nuclear magnetic resonance (NMR), electrospray ionization (ESI) mass spectrometric, and transmission electron microscopic (TEM) techniques. Primary amines present on the dendritic surface were conjugated through folic acid and folic acid−PEG (poly(ethylene glycol))−NHS (*N*-hydroxysuccinimide) conjugates. Tumor in mice was induced through the use of KB cell culture. Prepared dendritic conjugates were evaluated for the anticancer drug delivery potential using 5-FU (5-fluorouracil) in tumor-bearing mice. Approximately 31% of 5-FU was loaded in folate−PEG−dendritic conjugates. Results indicated that folate−PEG−dendrimer conjugate was significantly safe and effective in tumor targeting compared to a non-PEGylated formulation. Tailoring of dendrimers via PEG−folic acid reduced hemolytic toxicity, which led to a sustained drug release pattern as well as highest accumulation in the tumor area.

INTRODUCTION

Nanoparticulate drug delivery systems containing anticancer agents have received much attention recently due to their unique accumulation behavior at the tumor site. Targeted anticancer drug delivery includes drug delivery by avoiding reticuloendothelial system (RES), utilizing the enhanced permeability and retention (EPR) effect and tumor specific targeting (*1*−*3*). Polymers have been used as drug carriers in the last 2−3 decades due to their ability to control drug release, to sustain circulation times, and to increase drug solubility. These drug carriers demonstrated higher affinity for preferential accumulation in tumor tissue as a result of EPR effect (*4*, *5*). Polymeric drug carriers encapsulate, complex, or conjugate drug molecules to deliver them to the desired site. In this context, applicability of dendrimers to deliver anticancer drugs and other bioactives is well-reported in the literature (*6*−*13*). These are a relatively new type of polymer known for their three-dimensional, monodispersed, highly branched, macromolecular nanoscopic (1−100 nm) architecture with a number of reactive end groups (*14*). Apart from drug delivery, dendrimers have recently been used successfully in the field of biomedicine and targeting (DNA and gene delivery, cancer diagonosis), catalysis, as light-harvesting devices, optical sensors, and so forth. Dendrimers have been reported to host both hydrophilic and hydrophobic drugs with high drug payload (*15*−*22*). Earlier dendrimers have successfully been delivered via transdermal, intravenous, and opthalamic routes, proving their transfection capabilities (*23*−*25*). The solubilization property of dendrimer makes them a promising carrier for insoluble drug delivery (*26*). However, toxicity problems with the surface cationic charge of dendrimers like polyamidoamine (PAMAM) and polypropyleneimine (PPI) pose a hurdle in their biomedical potential (*25*−*28*). Recently, surface-engineered/conjugated dendrimers, with drug molecules or targeting ligands or both, are receiving much attention as an alternative to the toxicity problems (*25*−*29*). In some reports, dendrimer−poly(ethylene glycol) (PEG) grafts were designed as a drug carrier that possesses an increased interior and biocompatible surface for the encapsulation of drugs like 5-fluorouracil, chloroquine phosphate, and so forth (*6*, *30*, *31*). In another study, PEGylated dendrimers encapsulating anticancer drugs adriamycin and methotrexate were prepared by extraction with chloroform from the mixtures of the PEGylated dendrimers and varying amounts of drug. Among the PEGylated dendrimers synthesized, the highest ability was achieved by the fourth-generation dendrimer having the PEG graft with average molecular weight of 2000 Da that could retain 6.5 adriamycin molecules or 26 methotrexate molecules per dendrimer molecule. The methotrexate-loaded PEG attached dendrimers slowly released the drug in an aqueous solution of low ionic strength (*32*).

The major drawback with the anticancer drug delivery is that these indiscriminately attack healthy cells as well as cancerous cells. The harmful side effects due to such therapy, however, can be reduced by developing a drug delivery system that is specific to tumor cells. To overcome this, a strategy called active targeting can be followed, wherein functionalities that respond to overexpressed receptors (e.g., folate conjugation on dendrimer surfaces) on tumor cells are attached to the drug carrier. Folate receptors (FR), which are 38 kDa glycosylphosphotidylinositol-anchored proteins, exist in three major forms, namely, FR-α, FR-β, and FR-γ. The FR-α form is overexpressed in many types of tumors including ovarian, endometrial, breast, renal cell carcinomas, and so forth. The fact that high-affinity FR binding is retained when folate is covalently linked via its γ-carboxyl group to a foreign molecule, combined with the prevalence of FR overexpression among tumors, makes it a good choice for targeted drug delivery to tumors (*33*, *34*). Tailored folic acid conjugated PAMAM dendrimers via EDC [1-ethyl-l-3-(3 methylaminopropyl carbodiimide)] linkage were more efficient in delivery of methotrexate (*9*, *35*). In another approach, PEGylation and folate conjugation were combined and a folate−PEG conjugate, capable of covalent coupling to primary amines present at the surface of polyplexes, was developed (*36*).

* Corresponding author. jnarendr@yahoo.co.in (Narendra K. Jain); umeshsemail@yahoo.co.in (Umesh Gupta), Tel./Fax.: +91-7582-264712.

10.1021/bc800125u CCC: $40.75 © 2008 American Chemical Society
Published on Web 10/25/2008

In the present study, a similar approach was designed in which PAMAM dendrimers up to fourth generation were synthesized, characterized, and conjugated to folic acid directly or indirectly through PEG4000 as spacer. 5-Fluorouracil, an anticancer drug, was encapsulated in both types of dendrimer−folic acid conjugates and assessed for their *in vitro* as well as *in vivo* anticancer potential in tumor-bearing mice.

EXPERIMENTAL PROCEDURES

Materials. Methyl acrylate, triethylamine, toluene, folic acid, PEG-4000, and ethylenediamine were purchased from Central Drug House, India. Thionyl chloride was obtained from Spectrochem, Mumbai (India). DMF (Dimethylformamide) was purchased from Merck, India. NHS (*N*-hydroxysuccinimide), and DSS (disuccinimidyl suberate) were purchased from Sigma Aldrich, Germany. DCC (*N*,*N*-dicyclohexyl carbodiimide) and culture medium RPMI 1640 were obtained from Hi Media, Mumbai (India). All the other common chemicals used were of analytical grade and were identified by respective chemical tests before their use in the study. The drug 5-fluorouracil was obtained as a generous gift from Cadila Pharmaceuticals Pvt. Ltd. India.

Synthesis and Characterization of 4.0 G PAMAM Dendrimers. Synthesis of PAMAM dendrimers was carried out following a two-step process, involving Michael addition of a suitable amine initiator core with methyl acrylate, and exhaustive amidation of the resulting esters with large excess of ethylenediamine, reported elsewhere (*14*).

Briefly, ethylenediamine (EDA) was used as an initiator core for the synthesis of dendrimers by attaching four acrylate moieties on each amino group of EDA (Scheme 1). Table 1 holds the molar equivalents of the reagents used in the synthesis of PAMAM dendrimers. The resulting compound was referred to as "generation −0.5G PAMAM tetra ester" (Scheme 1). This led to branching in the dendritic structure. The second step was used for amidation of the terminal carbomethoxy ($COCH_3$) groups of methylacrylate with EDA. This tetra ester with excess EDA gave "generation 0.0 PAMAM tetra amine". Similar steps were repeated for the synthesis of higher-generation PAMAM dendrimers, subsequently. The reaction sequence was followed by the removal of excess reagents by rotary vacuum evaporation (Superfit, India; 55−60 °C) at every step. Synthesis was carried out in the dark at room temperature (25 °C), using amber-colored round-bottom flask corked tightly. The reaction was carried out as per the quantities given in Table 1 and Scheme 1.

Dendrimers were subjected to physical and chemical characterization. Half- and full-generation dendrimers were distinguished by IR spectroscopy and chemical reaction of copper sulfate aqueous solution (1% w/v) with dendrimer (0.1% w/v in methanol). A synthesized 4.0 G dendritic system was characterized by IR, NMR, ESI mass spectroscopy, and transmission electron microscopy. In IR analysis, dendrimer samples were analyzed by the KBr pellet method in a Perkin-Elmer 783 IR spectrophotometer and displayed characteristic peaks at 3350.2 cm^{-1} (N−H stretch of primary amines); 3245 cm^{-1} (quarternary ammonium ion peak); 3190.0 cm^{-1} (antisymmetric N−H stretch of substituted primary amine); 1641.3 cm^{-1} (−C═O stretch); 2890 cm^{-1} (aliphatic C−H stretch); 1566.0, 1471.7, 1327.9 cm^{-1} (N−H bending of N substituted amide); 1118.4 cm^{-1} (CC bending). NMR spectroscopy (Bruker Advance DRX 300, Germany) was performed using D_2O as solvent and methanol as cosolvent at 300 MHz; δ 2.418, 2.436 ($-CH_2C$═O); δ 2.5−2.9 (amide-NH); δ 3.1−3.4 (-CH_2NH_2 terminal group); δ 4.762 (methanolic -OH) (Scheme 1).

ESI mass spectra were recorded on a Micromass Quattro II Triple Quadrupole mass spectrometer. The samples (dissolved in suitable solvents such as methanol/acetonitrile/water) were introduced into ESI source through a syringe pump at the rate of 5 μL/min. The ESI capillary was set at 3.5 KV and the cone voltage was 40 V. Spectra were collected in 6S scans, and the printouts were averaged spectra of 6−8 scans. Spectra recorded at high mass units were computerized decovoluted.

Transmission electron microscopy (TEM) of the prepared 4G PAMAM dendrimer was carried out after drying on 3 mm forman (0.5% plastic powder in amyl acetate) coated copper grid (300 mesh) at 60 KV (Philips Morgani, 268D trasmission electron microscope; Holland) after staining negatively, using uranyl acetate (4%). Photomicrographs (Figure 1A) were taken at suitable magnifications from the Electron Microscopy Section of Anatomy Division of All India Institute of Medical Sciences, New Delhi, India.

Synthesis and Characterization of PEG-4000 Bis Amine. PEG-4000 bis amine (H_2N-PEG4000-NH_2) was synthesized in three steps following a modified method reported by Zalipsky et al. (*37*). In the first step, PEG-4000 (19 g, 0.004 mol) was dissolved in toluene (100 mL) and dried by distillation. Dry pyridine (1.6 mL, 0.019 mol) was mixed to the above solution, and then thionyl chloride (4.36 mL, 0.059 mol) was added dropwise in a period of 30 min under reflux to the mixture. The mixture was heated for 4 h, cooled to room temperature (25 °C), filtered from pyridine hydrochloride, and toluene was evaporated in vacuum. The residue was dissolved in about 20 mL of dichloromethane (DCM), dried over anhydrous K_2CO_3, and filtered. The filtrate was treated with alumina (30 g, activated by heating at 120 °C for 2 h). Alumina was separated by filtration, and the filtrate was precipitated by cold ether. The polymer was recrystallized from dichloromethane (DCM) yielding 15 g (79%) of Cl-PEG-4000-Cl. In the second step, sodium azide (16 mmol, 1 g) was added to the solution of Cl-PEG-4000-Cl (3.6 g) in DMF (20 mL), and the mixture was placed in an oil bath maintained at 120 °C for 1 h; thereafter, DMF (20 mL) was added, and the mixture was stirred at 80 °C for 4 h, cooled, and filtered, and DMF was evaporated in vacuum. The residue was taken in DCM, filtered, and precipitated with cold ether. Yield was 3 g (83%) and N_3-PEG 4000-N_3 was formed. In the third and the final steps, N_3-PEG 4000-N_3 (1.6 g) was dissolved in absolute ethanol (40 mL), 10% Pd/C (0.1 g) was added, and the mixture was hydrogenated in a catalytic hydrogenation apparatus (Low-Pressure model PCHS 500, India) overnight. The catalyst was removed by filtration, and the polymer conjugate was precipitated using dry ether and was vaccuum-dried. A yield of 1.2 g (75%) NH_2-PEG 4000-NH_2 was obtained. PEG-4000 bis amine synthesis was characterized by IR spectroscopy, at every step.

Conjugation of Folic Acid to 4.0 G PAMAM Dendrimers. Folic acid was conjugated to 4.0 G PAMAM dendrimers surface through two approaches, i.e., direct conjugation and conjugation through PEG spacer (indirect).

Direct Conjugation. Preparation of NHS Ester of Folic Acid. The active ester of folic acid was prepared by a reported method (*38*). Briefly, folic acid (0.30 g, 0.68 mM) and triethylamine (0.15 mL, 1.0 mmol) were dissolved in DMSO (10 mL), and DCC (0.14 g, 0.68 mmol) was added to it. The solution was stirred for 1 h at room temperature in the dark, and NHS (0.12 g, 1.0 mmol) was added. The mixture was stirred overnight in the dark at room temperature, filtered via glass wool to remove the insoluble byproduct, dicyclohexylurea, and was precipitated using diethyl ether. The active ester of folic acid was collected by filtration, washed with dry tetrahydrofuran (THF) and dried under vacuum (Scheme 2). The NHS ester of folic acid was characterized through IR spectroscopy. Important peaks obtained for the folic acid were at 3545.0, 3415.3 cm^{-1} (N−H stretch of primary amine and amide); 3324.8 cm^{-1} (alkyl C−H and C═C stretch); 1694.8 cm^{-1} (aromatic C═C bending

Scheme 1. Synthesis of PAMAM Dendrimers up to Fourth Generation

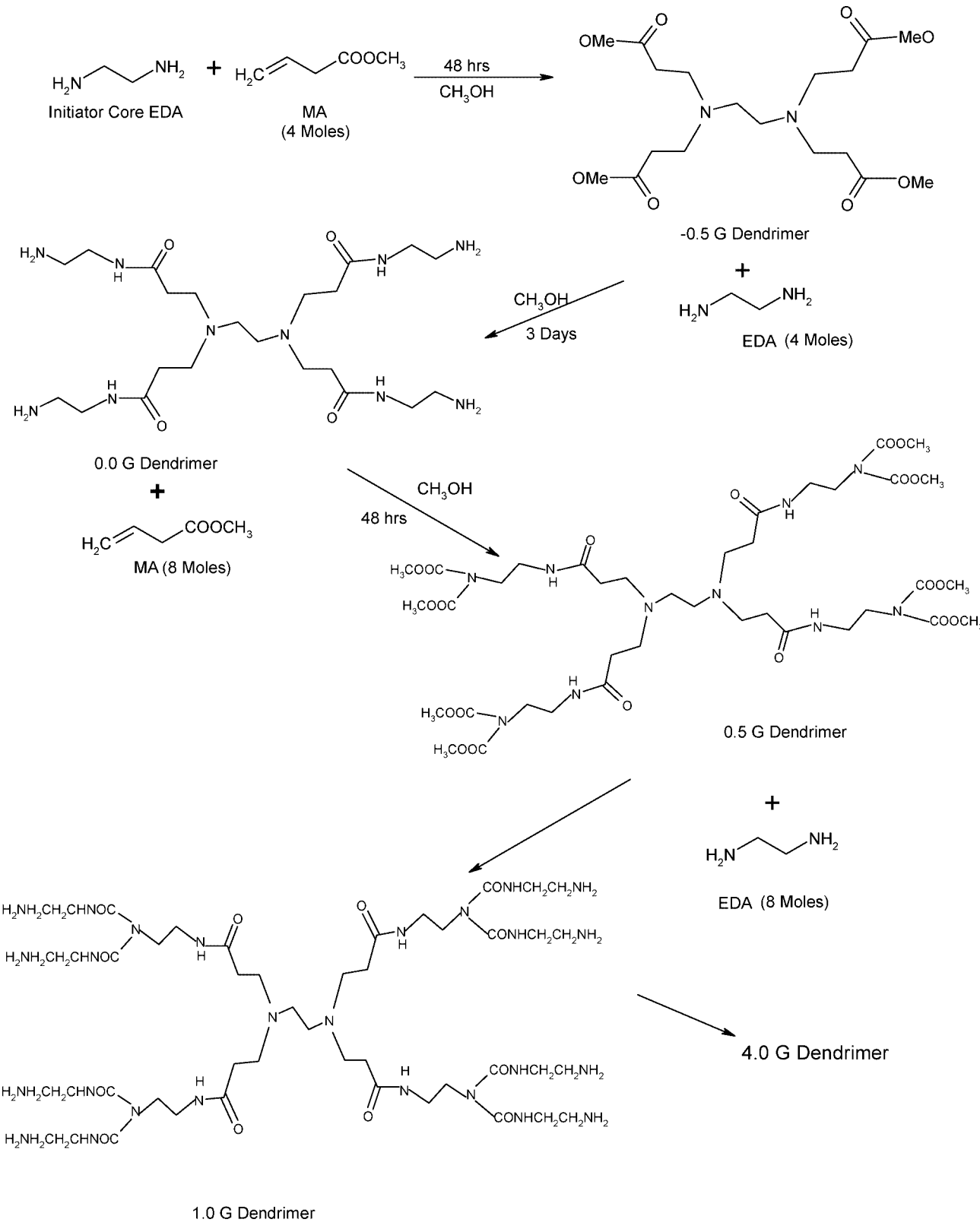

G- Generation, EDA- Ethylene Diamine, MA- Methylacrylate

and stretching); 1484.2 cm^{-1} (CH−NH−C=O amides bending); 837.8 cm^{-1} (aromatic C−H bending and benzene 1,4-disubstitution); and for the NHS conjugated folic acid 3691.6 cm^{-1} (amide N−H and C=O stretching); 3444.2 cm^{-1} (primary aliphatic amine N−H stretching); 2997.0 cm^{-1} (carboxylic acid C=O and O−H stretching unconjugated); 1712.7 cm^{-1} (ketones C=O unconjugated stretch), which confirmed the synthesis of NHS ester of folic acid.

Conjugation of Active Ester of Folic Acid to 4.0G PAMAM Dendrimers. The active ester of folic acid in DMSO (25 mg/mL) and that of amine-terminated 4.0 G PAMAM dendrimers in DMSO (10 mg/mL) were mixed and stirred for

Table 1. Details of the Reactants and Products in the Synthesis of PAMAM Dendrimers

generation	moles of reactant[a]	moles of reactant in excess	product mol. wt.	number of surface functional groups
−0.5G	4 moles (400 g) MA	5% excess of 4 moles	404	4
0.0G	4 moles (240 g) EDA	40 moles (10 equivalents)	516	4
0.5G	8 moles (800 g) MA	10% excess of 8 moles	1204	8
1.0G	8 moles (400 g) EDA	160 moles (20 equivalents)	1428	8
1.5G	16 moles (1600 g) MA	15% excess of 16 moles	2804	16
2.0G	16 moles (960 g) EDA	640 moles (40 equivalents)	3308	16
2.5G	32 moles (3200 g) MA	20% excess of 32 moles	6004	32
3.0G	32 moles (1920 g) EDA	1920 moles (60 equivalents)	6900	32
3.5G	64 moles (6400 g) MA	30% excess of 64 moles	12404	64
4.0G	64 moles (3840 g) EDA	5120 moles (80 equivalents)	14196	64

[a] MA = Methylacrylate, EDA = Ethylenediamine.

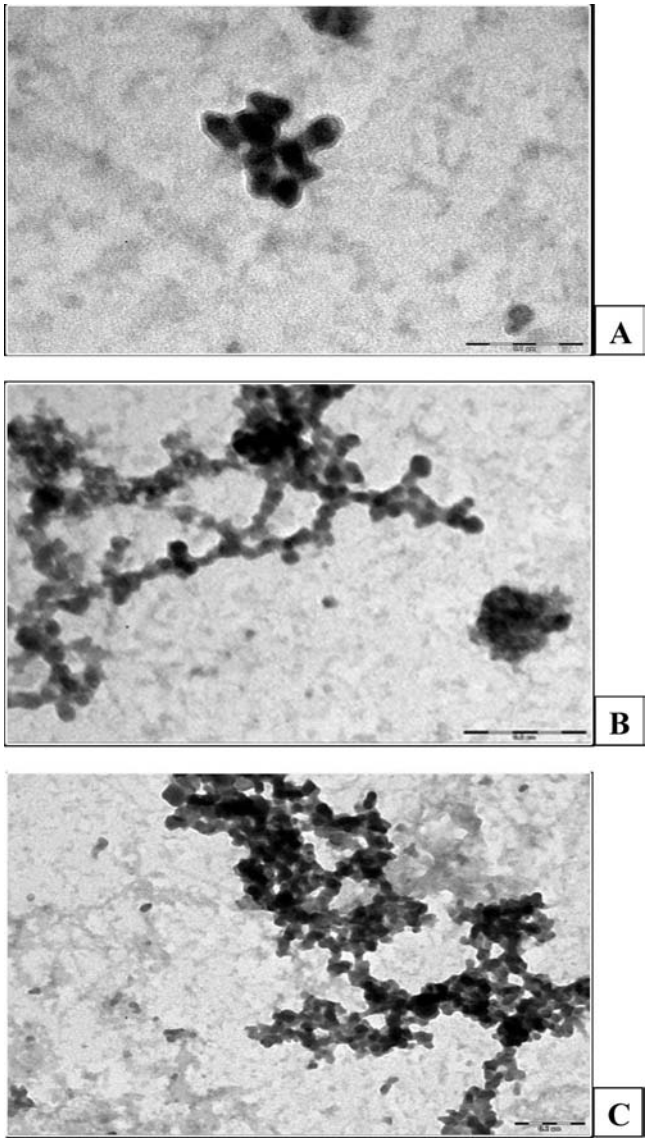

Figure 1. Electron microscopic photographs of (A) 4.0 G PAMAM dendrimers; (B) FA-PAMAM (folic acid−dendrimer conjugates); (C) FA-PEG-PAMAM (folic acid−PEG−dendrimer conjugates).

5 days at room temperature (25 °C) using a metabolic shaker. Acetone was added to the reaction mixture, and a yellow precipitate thus formed was collected by filtration and dried under vacuum. The crude product was dissolved in deionized water, and the pH was adjusted to 9.0 using 1 N NaOH solution. The solution was loaded to a Sephadex G-25 column using deionized water as effluent. Fractions containing the conjugate were collected, and the pH of the solution was adjusted to 3

Scheme 2. Preparation of NHS Ester of Folic Acid

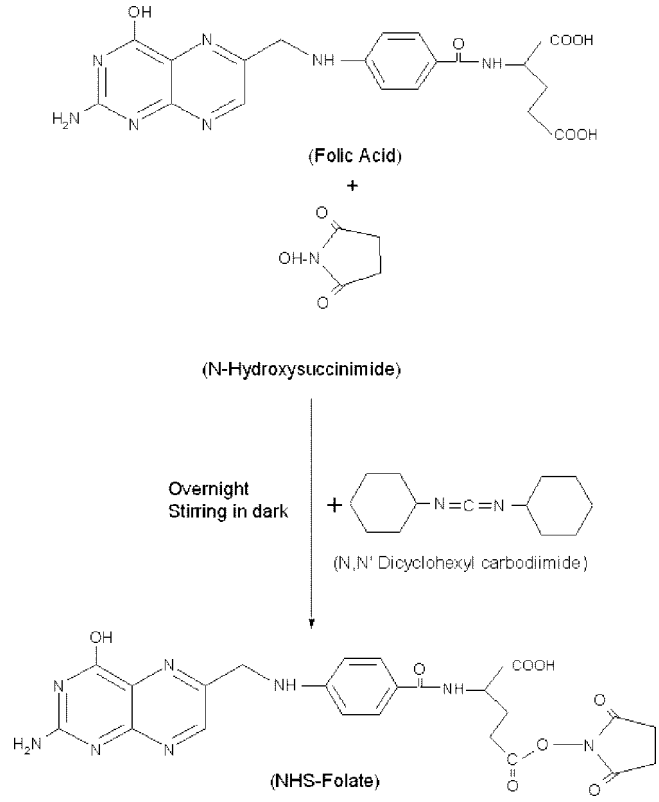

using 1 N HCl (*8*). The product was precipitated out, collected by filtration, and dried under vacuum.

Indirect Folic Acid Conjugation through PEG Spacer. Preparation of NHS-Activated Folate-Conjugated PEG. A similar method to that given in an earlier step was followed to obtain the NHS ester of folic acid. 65 mg (148 μmol) of FA-NHS (folic acid-*N*-hydroxy succinimide) ester was added to PEG-4000 bis-amine (900 mg, 225 μmol) in DMSO (5.0 mL) in the presence of triethylamine (4.0 μL). The mixture was stirred overnight, and the product was purified by filtration over a Sephadex G-25 column equilibrated with 0.1 M $NaHCO_3$ to remove unconjugated folic acid and unreacted PEG-bis amine fragments. Folate-containing product was detected by UV−visible spectrophotometer (Shimadzu 1601, Japan; absorbance at λ_{max} = 363 nm). The filtrate obtained was precipitated with acetone and dried under vacuum, yielding folate−PEG conjugate (NH_2-PEG-FA) as a pale yellow solid. Thereafter, 50 mg of the product was dissolved in DMSO (5.0 mL) containing triethylamine (4.0 μL) as a base, and a 10-fold excess of DSS (12.5 mg) was added. After stirring overnight, the PEG was precipitated by addition of acetone. The product was redissolved in DCM and filtered, and solvents were removed under reduced pressure. The product was then dissolved in DMSO and purified

Scheme 3. Synthesis of NHS-PEG4000-Folic Acid Conjugate from NHS-Folic Acid Conjugate

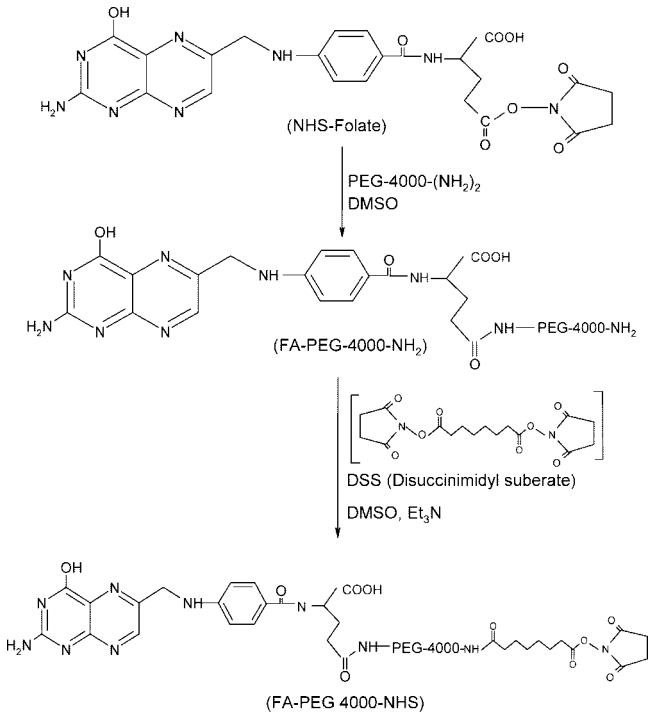

over a Sephadex G-25 column, using DMSO as an eluent (based on modified method) (*36*). The product was finally precipitated using acetone. NHS-PEG 4000-FA, so obtained (Scheme 3), was characterized at each step by IR spectroscopy. Important peaks in IR spectra were 3690.5 cm^{-1} (amide N−H and C═O stretching); 3400 cm^{-1} (primary aliphatic amine N−H stretching); 2911.5 cm^{-1} (alkyl C−H stretching); 112.5 cm^{-1} (strong peak of C−O of ether linkage); 1710.0 cm^{-1} (unconjugated C═O stretch); and 701.4 cm^{-1} (aromatic C−H bending), which confirmed the synthesis of NHS-PEG-FA.

Conjugation of NHS-PEG 4000-FA to 4.0 G PAMAM Dendrimers. The active ester NHS-PEG 4000-FA in DMSO (25 mg/mL) was conjugated to the amine-terminated 4.0 G PAMAM dendrimer in a similar manner to conjugation of FA-NHS in an earlier step (*8*).

Characterization of Folate Conjugated Systems. Synthesized folate conjugates were characterized by IR spectroscopy using the KBr pellet method. For NMR spectroscopy (Bruker Advance DRX 300, Country, Germany), folate conjugated 4.0 G PAMAM dendrimers were solubilized in D_2O using methanol as cosolvent and analyzed at 300.1299987 MHz. The electrospray mass spectra of folate conjugates were recorded on a Micromass Quattro II Triple Quadrupole mass spectrometer, similar to the PAMAM dendrimers. Similarly, TEM photomicrographs (Figure 1B,C) were taken at suitable magnifications using Philips Morgani, 268D; transmission electron microscope (Holland).

Drug Loading. 5-FU was loaded in PAMAM dendrimers and dendritic conjugates following the equilibrium dialysis method reported earlier (*39, 25*). Briefly, 1 mL of aqueous solution of 5-FU (1000 μg/mL) was mixed with 100 mg of 4.0 G PAMAM dendrimer, and the volume was increased to 10 mL with double-distilled water. The mixed solutions were incubated with slow magnetic stirring (50 rpm) using Teflon beads for 24 h. Percent drug encapsulation was confirmed indirectly through UV−visible spectrophotometry. The formulations having final drug concentrations were scanned against similar concentrations of dendritic solution without drug loading, as control (*40*). Similarly, drug was loaded in folic acid conjugated 4.0 G PAMAM (FA-PAMAM) and FA-PEG conjugated 4.0 G PAMAM (FA-PEG-PAMAM) dendrimers. The three different drug-loaded formulations so formed were drug-loaded 4.0 G PAMAM dendrimers (DF), drug-loaded folic acid conjugated 4.0 G PAMAM dendrimers (FA-DF), and drug-loaded FA-PEG conjugated 4.0 G PAMAM dendrimers (FA-PEG-DF).

***In Vitro* Studies.** *Entrapment Efficiency.* Ten milliliters each of three formulations (i.e., DF, FA-DF, and FA-PEG-DF) were taken separately in a cellophane bag (MWCO 12 000−14 000, Sigma, Germany). The contents were dialyzed under strict sink conditions against two portions of 50 mL water, and the unentrapped drug was allowed to pass out of the bag against perfect sink conditions for 10 min. The released drug was analyzed by UV−visible scanning after appropriate dilutions, indirectly. Similarly, dialyzed and diluted dendrimer solution without drug was taken as control. The percent entrapment of drug (% w/w in dendrimer solution) was determined indirectly.

In Vitro Release. For *in vitro* release studies, 5 mL of formulations (after complete removal of unentrapped drug) were taken in a dialysis bag and dialyzed against 100 mL of water as reservoir under sink conditions, separately. Aliquots of these formulations (i.e., DF, FA-DF, and FA-PEG-DF) were collected at hourly intervals for 24 h, and drug content was estimated by UV−visible spectrophotometer using water as control (*40*).

Hemolytic Toxicity. RBC suspension was obtained as per the well-known and reported procedure for hemolytic studies (*41*). Briefly, whole human blood was collected using heparin as anticoagulant in HiAnticlot blood collecting vials (Hi media, India) and centrifuged at 3000 rpm for 15 min. RBCs collected from the bottom were washed with normal saline (0.9% w/v) in double-distilled water until a clear, colorless supernatant was obtained above the cell mass. Cells were resuspended in normal saline. The RBC suspension so obtained was used further for hemolytic studies. To 1 mL of RBC suspension, 5 mL distilled water was added, which was considered to be 100% hemolytic. Similarly, 5 mL of normal saline was added to 1 mL of RBC suspension in another tube assumed to produce no hemolysis, hence acting as control. A half milliliter of formulation was added to 4.5 mL of normal saline and 1 mL of RBC suspension. Similarly, 0.5 mL of drug solution and 0.5 mL of dendrimer solution were taken in separate tubes and mixed with 4.5 mL of normal saline and 1 mL of RBC. Drug (i.e., 5-FU) and dendrimer in separate tubes were taken in such an amount that the resultant final concentrations of drug and dendrimer were equivalent in all the cases. The tubes were allowed to stand for half an hour with gentle intermittent shaking and were centrifuged for 15 min at 3000 rpm. The supernatants were taken and diluted with an equal volume of normal saline, and absorbance was taken at $\lambda_{max} = 540$ nm, against supernatant of normal saline diluted similarly, as control. The percent hemolysis was calculated for each sample by taking the absorbance of water as 100% hemolytic sample, using the following equation

$$\% \text{ hemolysis} = \left[\frac{AB_S}{AB_{100}}\right] \times 100$$

AB_S = Absorbance for the sample

AB_{100} = Absorbance for control

Similar procedure was followed for all the three formulations.

Stability Study. Formulations (i.e., DF, FA-DF, and FA-PEG-DF) were stored in tightly closed glass vials in dark (in amber colored vials) and light (in colorless vials) at 0 °C, room temperature (25−30 °C), and 50 °C (in controlled oven) for a period of seven weeks. Samples were analyzed weekly for up to seven weeks for any precipitation, turbidity, crystallization, change in color, consistency, and drug leakage. Data obtained

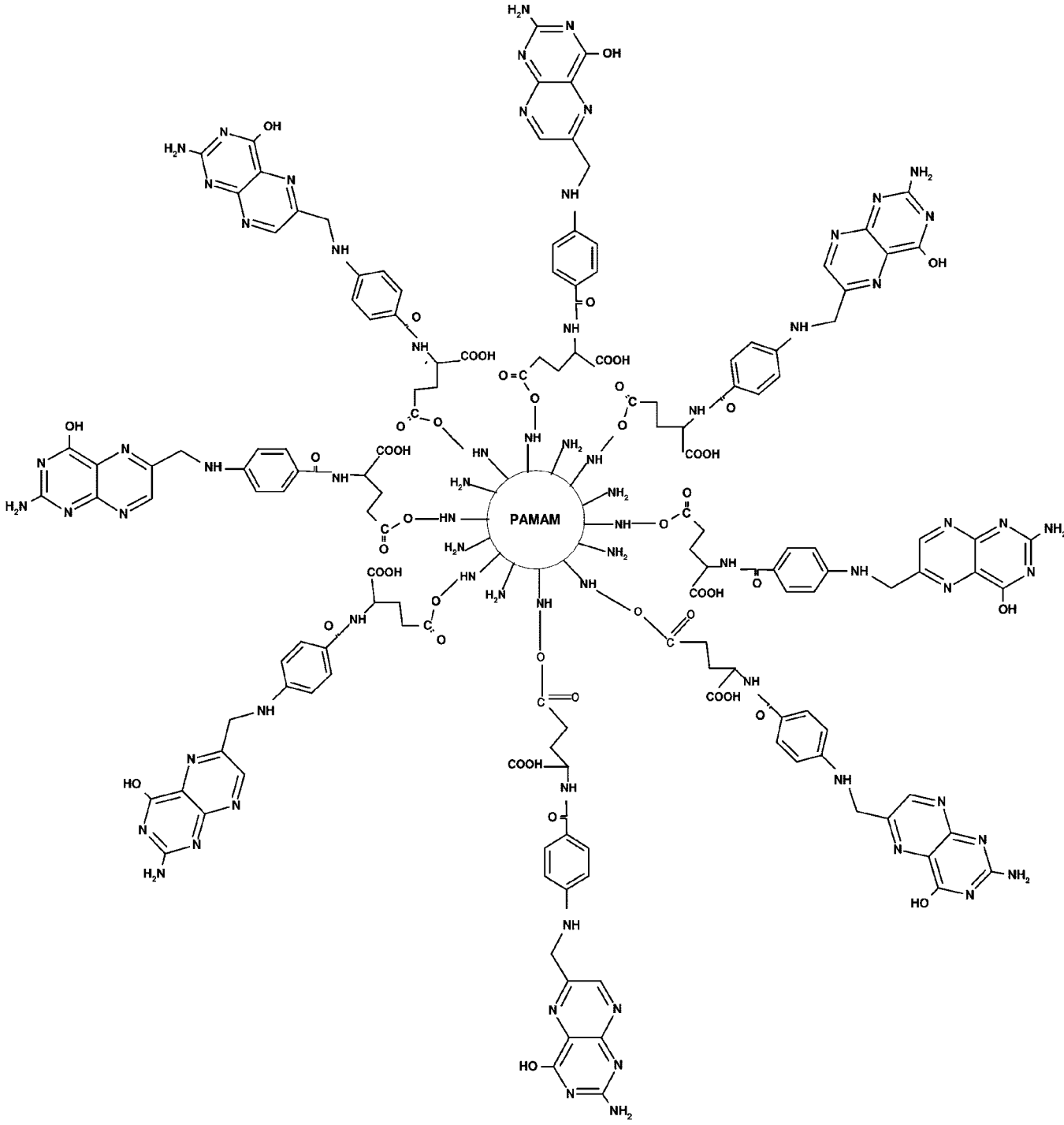

Figure 2. Chemical model structure of folic acid conjugated 4.0G PAMAM dendrimers.

were used for the analysis of any physical or chemical degradation, the required storage conditions, and the precautions required for storage. Leakage studies were performed for any increase in the release of drug from the formulations after storage at accelerated conditions. Formulations (2 mL) were kept in cellulose tubing (1200−1400 MWCO, Sigma, Germany) and dialyzed. The external medium (50 mL) was analyzed for content of the drug, spectrophotometrically. The procedure was repeated every week for up to seven weeks. The percentage increases in drug leakage from the formulations were used to analyze the effect of accelerated conditions of storage on the formulations (*6*).

***In Vivo* Studies.** *Tumor Induction in Mice.* Eight- to-nine-week-old female BALB/c mice (avg. body weight 25.0 ± 2.0 g) were used for the *in vivo* studies. The *in vivo* experimental protocol was duly approved by the Institutional Animal Ethical Committee of Dr. H.S. Gour University, Sagar, (M. P.) India. The KB cell line, which is human epidermoid carcinoma that overexpresses folate receptors, was purchased from the National Centre for Cell Science (NCCS, Pune; India), and grown continuously as a monolayer at 37 °C and 5% CO_2 in RPMI 1640 medium supplemented with penicillin (100 units/mL), streptomycin (100 μg/mL), and 10% heat inactivated fetal bovine serum (FBS). The culture was maintained *in vitro* for more than two months. KB cells were prepared for the injection in the female BALB/c mice. 1.5 mL 0.25% trypsin/1 mM EDTA solution was added and swirled to cover the plate and incubated at room temperature for 2 min, followed by addition of 5−7 mL serum-free media to harvest trypsinized cells from the plate and transfer to conical tube. These cells were centrifuged for 4

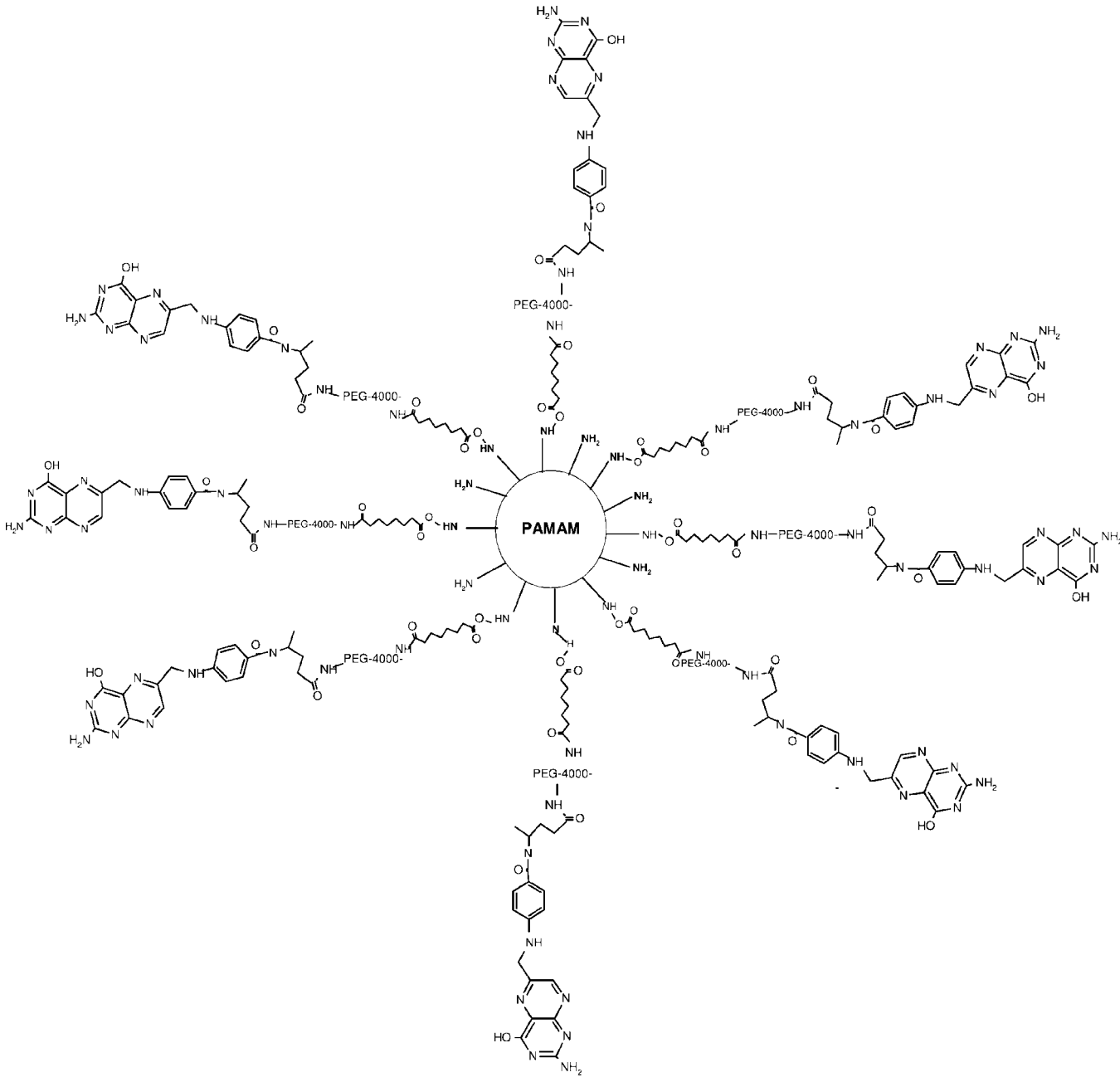

Figure 3. Chemical model structure of folic acid−PEG4000−4.0G PAMAM dendrimers.

min at 1200 rpm (25 °C); the supernatant was discarded and the pellet resuspended in serum-free medium. Cells were diluted with serum-free medium to the desired concentration (2×10^6 cells/0.2 mL) and placed on ice and injected cells immediately to maintain viability of cells. A tuberculin syringe (1 mL) was loaded with cells (KB tumor cells 2×10^6 cells/ 0.2 mL) using an 18-gauge hypodermic needle. Eight-week-old female BALB/c mice were maintained in hygienic and ventilated cages and fed a special low-folate diet (casein 100 g/kg, soya protein 100 g/kg, soyabean 70 g/kg, cellulose 47.5 g/kg, cornstarch 170 g/kg, sucrose 450 g/kg, mineral mix 45, folate-free vitamin mix 12.68 g/kg, choline 1.5 g/kg, BHT 0.014 g/kg, L-cystine 3.3 L-cystine) from one week prior to tumor inoculation until mice were sacrificed for *in vivo* performance (*42*). These KB tumor cells in serum-free medium suspension were inoculated in the subcutaneous space in the right flank of the mice. The mice were monitored daily for tumor onset by palpating the injection area with the index finger and thumb for the presence of the

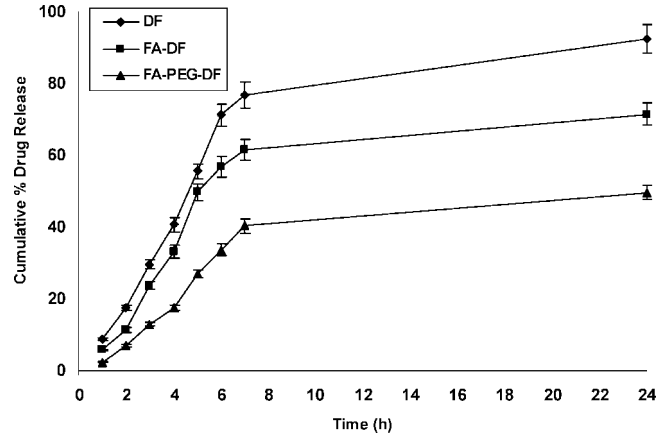

Figure 4. In vitro release studies ($n = 4$). Values represent mean ± SD.

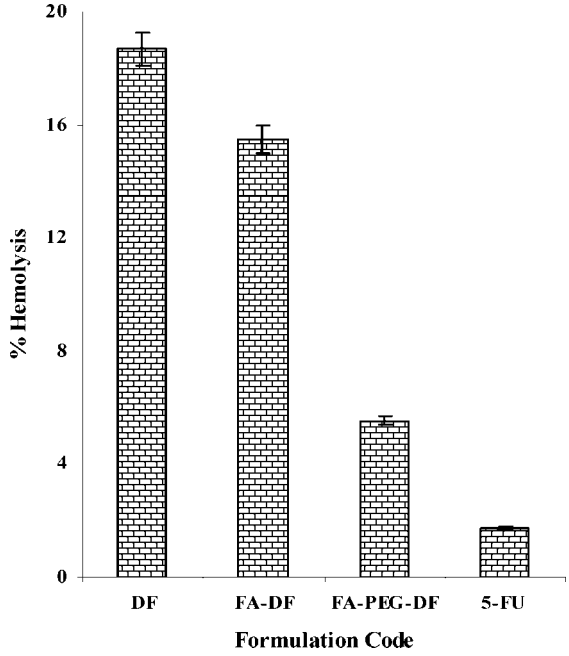

Figure 5. Percentage hemolytic toxicity of drug and different formulations ($n = 6$).Values represent means ± SD.

Table 2. Stability Studies for Different Formulations[a]

		dark			light		
parameters (after 7 weeks)	formulations	0 °C	RT	50 °C	0 °C	RT	50 °C
turbidity	DF	+	−	++	++	+	+++
	FA-DF	+	−	++	++	+	+++
	FA-PEG-DF	+	−	++	++	+	+++
precipitation	DF	+	−	++	+	+	+++
	FA-DF	+	−	++	+	+	+++
	FA-PEG-DF	+	−	++	+	+	+++
crystallization	DF	+	−	+	+	−	++
	FA-DF	+	−	+	+	−	+
	FA-PEG-DF	+	−	+	+	−	+
color change	DF	<	−	+	<	−	+++
	FA-DF	<	−	+	<	−	++
	FA-PEG-DF	<	−	+	<	−	+++
change in consistency	DF	+	−	<	++	−	≪
	FA-DF	+	−	<	++	−	≪
	FA-PEG-DF	++	−	<	++	−	≪

[a] − = no change; + = small change; ++ = considerable change; +++ = enough change; <, ≪ = extent of decrease as compared to initial.

tumor. Two to three weeks past inoculation, the mice injected with KB cells developed palpable solid tumors.

Pharmacodynamic Studies. Female BALB/c mice (avg. body weight 25.0 ± 2.0 g) were subcutaneously implanted with human epidermal carcinoma KB cells. Following the implantation, tumor cells were allowed to grow for another 21 days until well-established, at which time dosing with DF, FA-DF, FA-PEG-DF, and free drug solution (equivalent dose of 5-FU = 12 mg/kg) suspended in PBS was injected through tail vein of animals at day 0 and day 7. At a predetermined time, a major and minor axis of the tumor were measured using calipers. The formula used to compute tumor volume was as for the standard volume of an ellipsoid, where $V = 4/3\pi$ (1/2 length × 1/2 width × 1/2 depth) with an assumption that width equals depth and π equals 3; the formula (*43*) used was $V = 1/2 \times \text{length} \times \text{width}^2$.

Pharmacokinetic Studies. Calibration curves of 5-FU in serum and tissues of various organs were prepared using a reported HPLC method (*44*) with slight modifications. Briefly, a heparin-rinsed 1 mL tuberculin syringe was loaded with 0.1 mL heparin solution, and the anaesthetized female BALB/c mice, bearing appropriately sized primary tumors, was selected for the preparation of the standard curve. The chest cavity was opened with dissecting equipment to expose the heart. While the heart was pumping, the 27-gauge needle penetrated and blood was drawn into the 1 mL tuberculin syringe containing 0.1 mL heparin solution. Using scissors and forceps, organs and tumor were removed and weighed accurately. Later, they were placed in a separate well of a tissue culture plate containing HBSS in the freezer for further studies.

The blood sample was centrifuged at 3000 rpm for 10 min to separate RBCs and serum. The upper supernatant (serum) was collected separately with the help of a micropipette. The 100 μg/mL stock solution of 5-FU prepared in deionized distilled water was used, and aliquots of concentrations of 0.1, 0.3, 0.5, 1.0, 5.0, and 10.0 μg/mL in 10 mL volumetric flasks were prepared. From each of these concentrations, 100 μL (0.1 mL) volumes were withdrawn and transferred to labeled microcentifuged tubes. To each of these tubes, 100 μL of serum was added, and the tubes were vortexed at high speed for 10 min. After vortexing, the volume in each tube was increased to 1000 μL by adding 800 μL deionized water to get a concentration range 100−10 000 ng/mL. The prepared stocks were vortexed for another 10 min and then centrifuged at 3000 rpm at 15 °C (Beckman GS-15R microcentrifuge, USA). A control was also prepared in a similar fashion after adding 900 μL of deionized water to 100 μL of serum by vortexing and centrifuging at 3000 rpm at 15 °C. From each of these preparations, clear supernatant was removed and filtered through a 0.22 μm membrane filter (Gelman filter, Mumbai, India) using a syringe filtration assembly to a microcentrifuge tube. The drug sample in serum was in this way ready for preparation of the calibration curve. The retention time of drug was found to be 3.7 min.

Similarly, the drug samples in tissue of various organs like liver, spleen, kidney, and tumor were prepared. To each organ, the required amount of deionized water was added and homogenized for few minutes, followed by centrifugation at 4000 rpm, and the supernatant of each organ tissue was collected separately. The proper dilutions of tissue supernatant and drug concentration were made using deionized water to get a suitable concentration range. A set of concentrations were prepared for each organ.

The calibration curve data was obtained in the range 100−10 000 ng/mL. The HPLC column (Shimadzu, C_{18}, Japan) was cleaned thoroughly with deionized water and then with the mobile phase [water/methanol (85:15)]. The samples starting from blank to increasing concentration were injected and run through an HPLC column. The flow rate was kept at 1.0 mL/min at pressure of 102/101 bar, and the run time was adjusted to 10 min. The observations were taken at 260 nm wavelength in consideration of its retention time (RT) and area.

Biodistribution Studies. On the basis of the results observed in pharmacodynamic studies, FA-PEG-DF was found to be the most suitable in terms of efficacy and potential to carry 5-FU. This formulation (FA-PEG-DF) along with FA-DF was selected for further pharmacokinetic and tissue distribution studies in BALB/c mice (avg. wt. 25.0 ± 2.0 g) with KB cell induced tumor on their right flank as described earlier. Constant temperature conditions were maintained in the laboratory, avoiding any kind of stress on mice.

Mice were divided into three groups with each group comprising 12 tumor-induced mice and marked properly. Formulations (FA-PEG-DF and FA-DF) and plain drug (D) solubilized in saline at dosage of 12 mg/kg body weight were administered through the intravenous route in mice, separately. Following administration, blood samples were collected from

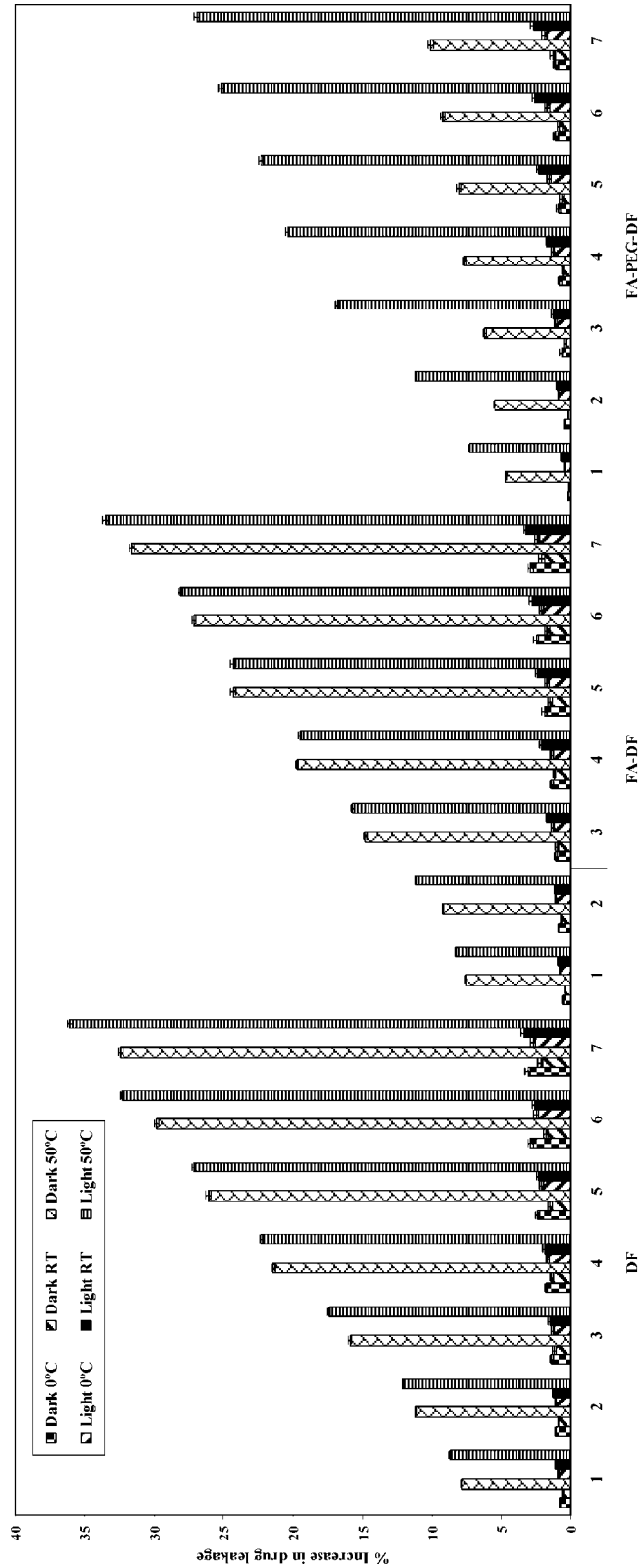

Figure 6. Percent increase in drug leakage from DF, FA-DF, and FA-PEG-DF formulations at accelerated conditions. Values represent means ± SD ($n = 4$).

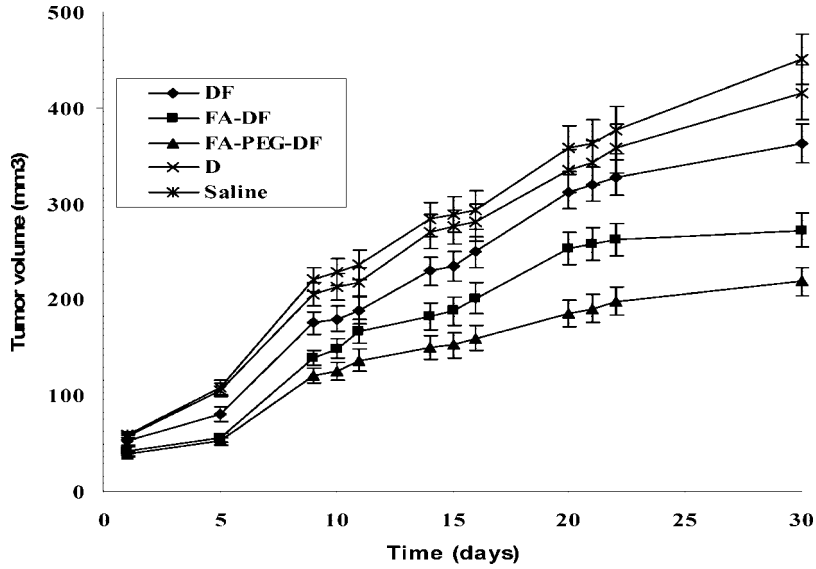

Figure 7. Screening data for tumor growth.

Table 3. Pharmacokinetic Parameters of DF, FA-DF, and 5-FU in Serum of BALB/c Mice[a]

formulation	AUC (0→t) (μg/mL/h)	MRT (h)	C_{max} (μg/mL)	t_{max} (h)
5-FU	19.96	0.09	31.8	0.1
FA-DF	19.78	0.58	4.2	1−2.5
FA-PEG-DF	14.16	1.21	1.28	2.5−5.0

[a] AUC = area under the curve, MRT =mean residence time, C_{max} = maximum drug concentration, t_{max} = time of peak concentration.

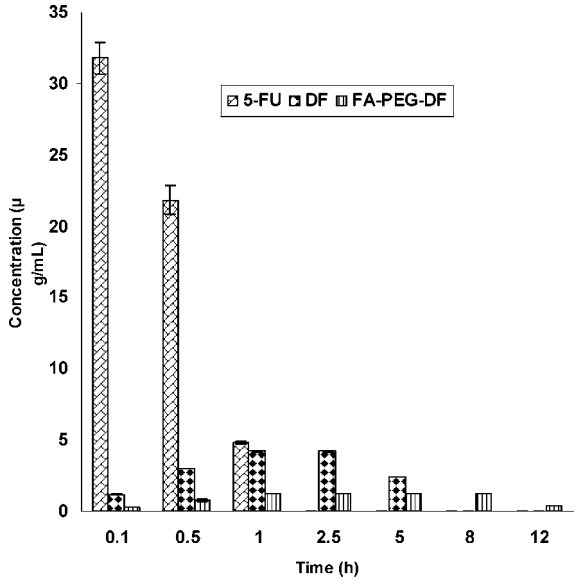

Figure 8. Plasma concentration vs time studies with the formulations DF and FA-PEG-DF.

tail vein at 0.1, 0.5, 1.0, 2.5, 5, 8, 12, and 24 h intervals. Not more then 0.3 mL withdrawals from each mouse were taken. In each case, blood was centrifuged at 3000 rpm for 10 min to separate RBCs and serum. The upper supernatant (serum) was collected separately with the help of a micropipette, mixed with 2 mL of ethyl acetate, and subsequently centrifuged to remove the organic layer, evaporated to dryness, and resuspended in the mobile phase for analysis of the presence of drug.

For biodistribution studies, mice were again divided into three groups with twelve mice in each. Each group received the same intravenous dose of different formulations and 5-FU similar to pharmacokinetic studies. Four mice from each group were sacrificed at 2, 8, and 24 h. Immediately after sacrificing the mice, organs, viz., spleen, kidney, liver, and tumor were carefully removed and weighed. Each of these specimens was stored under deep-freeze condition (−70 °C). Weighed tissue samples were suspended in 2 mL ethyl acetate and homogenized for 5 min. The homogenate was transferred to Eppendroff tube and centrifuged at 3000 rpm for 10 min at 4 °C. The organic layer was subsequently transferred into a second tube and evaporated to dryness under vacuum. The compound was resuspended in 1 mL of the mobile phase, vortexed, and then stored at deep-freeze condition (−70 °C) and analyzed for 5-FU by HPLC. In addition, one separate group of mice was injected with 181 mmol folic acid. This group was administered an equivalent dose of FA-PEG-DF, similar to the previous group through intravenous route, 15 min after administration of free folic acid. The pharmacokinetic and biodistribution parameters were calculated. The plasma concentration vs time were fitted to a biexponential equation

$$C_{(t)} = A_1 \times e^{-k_1 \times t} + A_2 \times e^{-k_2 \times t}$$

where $C_{(t)}$ is the drug concentration (*y*-axis) at time *t* (*x*-axis), A_1 and A_2 are the *y*-intercepts, and k_1 and k_2 are the slopes of apparent first-order elimination rate constants.

RESULTS AND DISCUSSION

Synthesis and Characterization of 4.0G PAMAM Dendrimers. Synthesis was carried out, taking increasing amounts of reactants in every progressive step (Table 1). Preliminary completion of synthesis was confirmed by copper sulfate color reaction, which results in a purple/blue color on reaction with primary amines. Full generations of the PAMAM dendrimers (e.g., 1.0G, 2.0G, 3.0G, etc.) gave purple color, whereas half-generations gave deep blue color, due to copper chelation at the terminal groups of dendrimers (*27*). Dendrimers were found to be oily liquids, and the intrinsic viscosity was higher in the case of full generation than half-generations, on complete removal of excess solvents and reagents. The color as seen was yellowish/ deep yellow to honey-like, and higher generations were found to be glassy masses.

IR, NMR, and ESI mass spectroscopy confirmed dendritic synthesis. In IR spectrum, the N−H stretch of surface primary amines was obtained at 3350.2 cm^{-1}, and the peak at 1641.3 cm^{-1} indicated the presence of −C═O groups in dendrimers. In NMR spectroscopic studies, chemical shifts of -CH_2NH_2

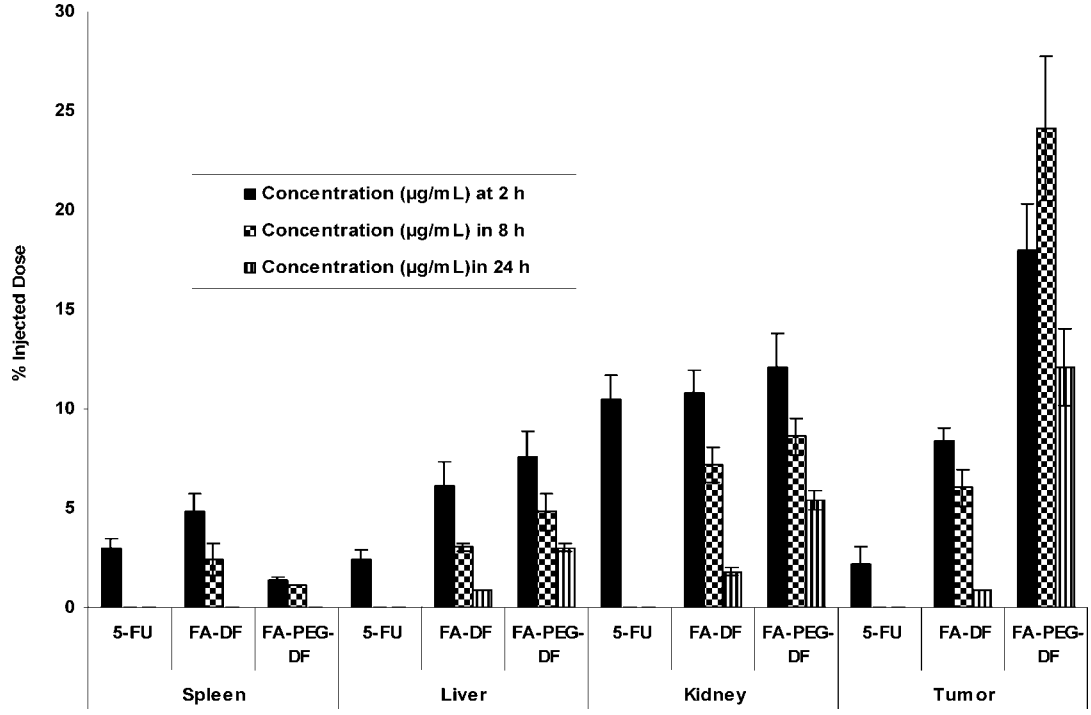

Figure 9. Tissue distribution data of plain drug (5-FU) and different formulations at different time intervals. Values represents means ± SD (n = 6).

terminal groups were obtained between δ 3.1 and 3.4 ppm, while peaks between δ 2.5 and 2.9 indicated the presence of amide NH in the structure. The NMR and IR spectra were found to be in accordance with the structure of PAMAM dendrimers (Scheme 1). The theoretical mass of the 4.0 G PAMAM dendrimers is about 14 196, and the report of the ESI mass study was 14 210; which is very close to the theoretically calculated mass (Table 1). TEM photographs of prepared 4.0 G PAMAM dendrimers revealed (Figure 1A) the size range of around 100 nm (*25, 27*).

Folic Acid Conjugation to 4.0 G PAMAM Dendrimers. The conjugation of folic acid on 4.0 G PAMAM dendrimer was accomplished using two methods by direct conjugation on the periphery and through the PEG spacer (Figures 2 and 3).

Direct Conjugation of Folic Acid. In the direct conjugation, NHS ester of folic acid (Scheme 2) was synthesized using DCC, NHS, and triethylamine (TEA) following a reported method (*38*). This NHS activated folic acid was conjugated to PAMAM dendrimers (*8*), and the synthesized folate conjugates were characterized using IR, NMR, and mass spectroscopy, which will be discussed in further sections.

Folic Acid Conjugation through PEG (Indirect Conjugation). In the second method, attachment of folic acid was accomplished through use of a PEG spacer, i.e., PEG bis amine (H_2N-PEG-4000-NH_2). PEG bis amine (NH_2-PEG 4000-NH_2) was synthesized in three successive steps (*37*), in which PEG-4000 was converted to Cl-PEG-4000-Cl using thionyl chloride and dry pyridine, then Cl-PEG-4000-Cl was converted to N_3-PEG-4000-N_3 using sodium azide, and thereafter N_3-PEG-4000-N_3 was used to get NH_2-PEG-4000-NH_2 (PEG bis amine) by a simple hydrogenation step (Catalytic Hydrogenator, Superfit, India) using Raney Nickel as catalyst. PEG bis amine synthesis was confirmed by IR spectroscopy at each step. The IR spectrum of PEG 4000 revealed peaks at 3430.7 cm^{-1} (O−H stretch); 1282.6 cm^{-1} (O−H deflection); 2886 cm^{-1} (C−H stretch); 1244 cm^{-1} (C−O deflection); 1112.5 cm^{-1} (strong peak of C−O stretch of ether), and so forth. Cl-PEG-4000-Cl displayed peaks at 670.2 cm^{-1} (strong, C−Cl stretch) and absence of O−H stretch peak at 3430.7 cm^{-1}, which was evident in PEG 4000. In the next step, conversion of Cl-PEG4000-Cl to N_3-PEG-4000-N_3 was confirmed through a peak at 2108 cm^{-1} (presence of N_3 groups). The last step in the synthesis of PEG bis amine was conversion of N_3-PEG-N_3 to H_2N-PEG-NH_2, which was again confirmed through the presence of N−H stretch of primary amines at 3350.2 cm^{-1}. Other important peaks obtained were at 3190.0 cm^{-1} (N−H stretch antisymmetric of substituted primary amine); 1566.0, 1471.7, 1327.9 cm^{-1} (N−H bending of N substituted amide); 3245.0 cm^{-1} (quaternary ammonium ion peak), and so forth.

NHS-activated folate-conjugated PEG was obtained through a series of aforementioned reaction sequences and was conjugated to amine-terminated 4.0 G PAMAM dendrimers similar to NHS-FA conjugation, as explained earlier (Scheme 3).

Characterization of Folic Acid-PAMAM and Folic Acid-PEG-PAMAM Conjugates. Conjugation of folic acid through both strategies (Figures 2 and 3) was again confirmed through IR, NMR, and ESI mass spectroscopic techniques. IR spectrum of FA-4.0 G PAMAM dendrimers revealed aromatic C−H bending at 826.6 cm^{-1}; ester unconjugated C═O stretching at 1262.5 cm^{-1}; and aromatic C═C bending and stretching at 1655.9 cm^{-1} due to attachment of folic acid, which contained aromatic rings. The IR spectrum of FA-PEG-4.0 G PAMAM dendrimers showed a strong and sharp peak of the C−O stretch ether linkage at 1117.8 cm^{-1}, which was due to the polyether b*a*ckbone of PEG, while other important peaks, which confirmed the conjugation, were at 2922.5 cm^{-1} (carboxylic acid C═O and O−H stretch unconjugated); 1626.4 cm^{-1} [aromatic C═C bending and stretching); 1461.4 cm^{-1}1 (CH−NH−C(═O) amides bending], and so forth. NMR spectral chemical shifts of folate-conjugated 4.0 G PAMAM dendrimers further confirmed conjugation. In FA-4.0 G PAMAM, a newer peak of R−(C═O)−NH−CH_2−CH_3 of folic acid linkage appeared at δ 1.0−2.0 ppm. Similarly, in FA-PEG 4.0 G PAMAM conjugate, a newer peak of the ether group of PEG appeared at δ 3.665 ppm, which was in contrast to its total absence in the 4.0 G NMR spectrum. The ESI mass of FA-4.0 G PAMAM

was 17 295, and for FA-PEG-4.0 G PAMAM, it was 49 730. The increase in mass after conjugation suggested that at least seven molecules of folic acid were attached by direct conjugation and eight molecules through PEG spacer. The electron microscopic analysis of dendrimers proves them to be nanometric, which was evident from TEM photographs (Figure 1B,C). The photographs revealed an increase in particle size on folate conjugation directly as well as through PEG spacer (*25*).

***In Vitro* Studies.** *Drug Loading, Formulation Development, and Entrapment Efficiency.* The drug, 5-FU, was encapsulated in all the conjugates, i.e., 4.0 G PAMAM dendrimer, folic acid−PAMAM dendrimer conjugates, and folic acid−PEG−PAMAM dendrimer conjugates. Drug loading was accomplished by the equilibrium dialysis method, i.e., excess drug interaction for prolonged duration with the dendrimeric systems. The loading of drug in PAMAM dendrimers as well as conjugates (FA-PAMAM, FA-PEG-PAMAM) was confirmed through UV−visible spectroscopy. Modified values of λ_{max} were observed and compared to the values of λ_{max} of 5-FU. Drug encapsulation was determined indirectly through dialysis using cellulose membrane (MWCO 12 000−14 000) and measuring the amount of unentrapped drug in the external sink. The data depict that there was less drug entrapment and retention inside the PAMAM (6.84% w/w) and FA-PAMAM (11.47% w/w) dendrimeric systems compared to the FA-PEG-PAMAM (31.45% w/w) dendrimeric system. Drug encapsulation was accomplished in both conjugates and PAMAM dendrimers through the equilibrium dialysis method. Encapsulation might be facilitated by hydrophilicity and aqueous partitioning of the drug molecules within the dendritic structures of folate conjugated and nonconjugated species. The formation of dendrimer−drug complex was confirmed indirectly, spectrophotometrically (*40*). Drug encapsulation was highest in the case of folic acid−PEG−PAMAM conjugates, which might be due to increased internal architecture of these conjugates leading to increased loading of the drug.

In Vitro Release and Hemolytic Toxicity. In vitro release studies were performed in the water under perfect sink conditions. The rate of drug release from FA-PEG-DF (49.6 ± 2.12% in 24 h) was observed to be lower compared to DF (92.3 ± 4.09% in 24 h) and FA-DF (71.4 ± 3.12% in 24 h) formulations (Figure 4). The rate of drug release of FA-PEG-DF was observed to be slowest, which could possibly be due to more dense and bulky (FA-PEG) surface-attached molecules providing a closed structure. The release pattern also indicated sustained release behavior of the drug for this formulation.

The hemolytic toxicity of the dendrimers imposes a constraint on its use as a drug delivery system. The toxicity is attributed to the polycationic nature of the PAMAM dendrimers. The percent hemolysis of RBC's with DF (18.67 ± 0.92%; $n = 6$) was comparatively higher, which may be a constraint on its use as a drug delivery system. However, FA-PEG-DF drastically reduced the hemolysis of RBC compared to FA-DF (Figure 5) from 15.47 ± 0.71% to 5.74 ± 0.28% ($n = 6$), which might be due to surface conjugation of the terminal -NH_2 groups by PEG resulting into increased biocompatible surface.

Stability Studies. The formulations were found to be most stable in the dark at room temperature. Formulation FA-PEG-DF displayed the best stability among all formulations (Table 2). Drug leakage was a minimum at room temperature compared to 0 and 50 °C for seven weeks, possibly due to the conformational change of the dendritic structure leading to a decrease in drug enclosing cavity (Figure 6). A drug leakage study again revealed that the FA-PEG-DF formulation was more stable than FA-DF and DF formulations. Finally, the FA-PEG-DF formulation was selected for further *in vivo* studies.

***In Vivo* Studies.** *Tumor Induction.* Female BALB/c mice were used for the tumor induction through KB cell lines. The mice were monitored daily for tumor onset by palpating up to three weeks.

Pharmacodynamic Studies. Pharmacodynamic studies were carried out to evaluate therapeutic efficacy of various dendritic formulations and plain drug solution (5-FU in PBS 7.4). The data obtained for each group were divided on the basis of different dendritic formulations, i.e., DF, FA-DF, FA-PEG-DF, plain 5-FU solution, and saline, as presented in Figure 7. As compared to drug (5-FU) entrapped in plain dendrimer (DF), folate conjugated PEG-4.0 G PAMAM (FA-DF) displayed a significant difference ($p < 0.05$) of the tumor growth with time. It was observed that after 20 days tumor volumes for mice treated with FA-PEG-DF and FA-DF were about 40% and 19% of those treated with DF. Also, from the tenth day onward (Figure 7) a significant difference in tumor growth was observed among the two formulations FA-DF and FA-PEG-DF. This may be attributed to the fact that the PEGylated system might be affecting 5-FU release, as observed previously in the *in vitro* data, justifying a relatively slow release compared to FA-DF and DF. Further, the FA-PEG-DF formulation, possibly due to prolonged systemic circulation, might have increased the chances of extracellular drug concentration at the tumorous site, which reflected better therapeutic potential at all time intervals in the pharmacodynamic study.

Pharamacokinetic Studies. Pharamacokinetic studies were carried out following intravenous administration to study the effect of PEGylation on the release profile and retention of dendritic formulations in systemic circulation. Serum concentrations of FA-PEG-DF were found to possess lower C_{max} compared to DF (Table 3 and Figure 8). However, the duration of C_{max} in the case of FA-PEG-DF was prolonged, i.e., from 2.5 to 8 h. This behavior was similar to the *in vitro* release profile, where drug release was lower in the case of FA-PEG-DF than that of DF (Figure 4). Also, FA-PEG-DF retarded the release of drug compared to the plain drug. Plasma drug concentration with DF was detected until the fifth hour, and thereafter no drug was detected. MRT of FA-PEG-DF was found to be near 12- and 3-fold that of free drug (5-FU) and DF, respectively. This indicated slow release of the drug from PEGylated dendritic systems compared to non-PEGylated and plain drug. Also, plasma concentration vs time studies revealed prolonged retention of PEGylated dendritic formulation (t_{max}, 2.5−5.0 h) in systemic circulation (Figure 8), although the blood level of the drug was observed to be lower at all time intervals as compared to DF and the plain drug solution (Table 3).

Biodistribution Studies. Biodistribution studies were conducted to evaluate drug delivery at various sites of interest, especially tumor. Plain drug, DF, and FA-PEG-DF formulations were found to have greater access to kidney (Figure 9). In the case of DF, drug concentration decreased rapidly, compared to FA-PEG-DF. The plain drug was not detected at the 8th and 24th hours of sampling. This observation suggests that kidney is the major clearance organ for dendritic systems and the bioactivity accounts for the higher concentration there. The kidney is known to express high levels of the folate receptors (*45*) and probably retained FA-PEG-DF for a longer duration compared to DF.

DF and FA-PEG-DF concentrations in liver were found to be considerably higher. However, DF concentration declined more rapidly compared to FA-PEG-DF. The liver, like the kidney, expresses high levels of folate receptors (*46*), thus supporting the larger uptake of FA-PEG-DF; whereas DF, although achieving higher concentration, was not retained for a long time. The drug levels observed in organs with both dendritic formulations, viz., DF and FA-PEG-DF, were higher as compared to plain drug. However, FA-PEG-DF was found to have scored much better against DF (Figure 9).

The drug levels observed in tumor tissues with both dendritic formulations, viz., DF and FA-PEG-DF, were higher compared to plain drug. However, FA-PEG-DF was found to have scored much better against DF (Figure 9). As folate receptors are expressed on solid tumors created by KB cells, the FA-conjugated dendritic formulation, FA-PEG-DF, displayed up to 15.5%, 20.1%, and 10% of ID (injected dose) at the 2nd, 8th, and 24th hour, respectively, at the tumor sites; whereas with DF, the scores were much lower, i.e., 7%, 5%, and 1.0% at 2nd, 8th, and 24th hour, respectively. In the case of plain drug, no active ingredient was detected at the 8th and 24th hour sampling. This indicated the localized action and higher retention potential of FA-PEG-DF at the tumorous site, thereby enhancing therapeutic efficacy. This above effect can be attributed to a synergistic effect of the modified vasculature at the tumor site as well as to the overexpression of folate receptors.

The specificity of targeted drug delivery was further addressed in a group of mice receiving 181 mmol folic acid 15 min before injection with FA-PEG-DF. At the eighth hour after injection, less than $0.5 \pm 0.01\%$ accumulation was observed in the tumor tissue. However, in the case of FA-PEG-DF administered to the group without prior dosing of free folic acid, up to $15.0 \pm 2.3\%$ drug uptake was noticed. This reduction in specificity may be attributed to blocking of the folate receptors with free folic acid at the tumorous tissue. This suggests that the difference in targeted and nontargeted dendritic conjugates is possibly due to specific uptake of these molecules through folate receptors overexpressed in the tumor.

The major drawback associated with anticancer drugs is their cytotoxicity and reduced availability of the appropriate dose at the tumor. The treatment of cancer requires the development of a "safe" and "effective" dosage form. The conventional mode of administration of such bioactives leads to their interaction with cancerous as well as normal cells. This not only precipitates toxicity but also adds to a considerable loss of dose before reaching the desired site. Any attempt to slightly modify the chemical structure of the drug to achieve results may reduce its efficacy. At the same time, the carrier systems need to be so designed that they bind to target cells as a result of their intrinsic affinity. An attractive approach may be the use of "ligands" that facilitate homing of therapeutic moieties at specific epitopes. The specific and selective binding of a ligand to its receptor site determines the biodistribution of anticancer drugs and hence exerts control over the pharmacokinetic properties of the drug (*47*, *48*). Dendrimers today are among the efficient carriers for drug delivery purposes. However, recently, emphasis of today's dendrimer research for drug delivery is mostly on surface-engineered dendrimers (*29*) pertaining to biocompatibility and toxicity (*28*) associated with the parent dendrimers like PAMAM (*49*) and PPI (polypropylene imine) dendrimers. To avoid the possible hazards in cancer chemotherapy, folate-based PAMAM dendritic systems having PEG residues were selected as drug carriers. The system was hypothesized to have the drug (i.e., 5-FU) within its internal cavities, which are shielded by exterior groups linked to folic acid and folate−PEG ligands. Earlier, this approach was proven to be efficient in anticancer drug targeting (*9*, *35*). The present study suggests that the PEGylation of dendrimers can extend the circulation time, and folate-conjugated systems may support the site-specific delivery of the bioactives. The developed formulation might be acting through the EPR effect as well as receptor-mediated endocytosis (RME), providing synergistic action thereby enhancing the therapeutic potential.

Conclusively, engineering of the dendritic surface with a targeting ligand such as folic acid can enhance the site-specific anticancer drug delivery. PEGylation of dendrimers can improve the circulation time of dendrimers in the body. In the present study, combination of both of these approaches displayed promising results in terms of efficacy and longer circulation time in the body. The present study was aimed at designing PAMAM dendrimers with more biocompatibility and less toxicity, but at the same time the ability to deliver drug at the desired site of action. The reduced toxicity and enhanced efficacy with FA-PEG-DF can be used most suitably as a controlled and targeted drug delivery system for the delivery of anticancer drugs like 5-FU. The formulation can be given through the intravenous route as a long-term circulatory nanoparticulate system.

ACKNOWLEDGMENT

The authors would like to acknowledge University Grants Commission (UGC) New Delhi, India, for the financial support to conduct this study.

Supporting Information Available: IR, NMR, and mass spectra of the 4.0G PAMAM dendrimer, FA-PAMAM (folic acid dendrimer conjugate), and FA-PEG-PAMAM (folic acid-PEG-dendrimer conjugates); and the IR spectra of intermediates of the PEG bis amine and NHS-PEG-folic acid. This material is available free of charge via the Internet at http://pubs.acs.org.

LITERATURE CITED

(1) Kwon, G. S., and Okano, T. (1996) Polymeric micelles as new drug carriers. *Adv. Drug Delivery Rev. 16*, 107–16.

(2) Brannon-Peppas, L., and Blanchette, J. O. (2004) Nanoparticle and targeted systems for cancer therapy. *Adv. Drug Delivery Rev. 56*, 1649–59.

(3) Brigger, I., Dubernet, C., and Couvreur, P. (2002) Nanoparticles in cancer therapy and diagnosis. *Adv. Drug Delivery Rev. 54*, 631–51.

(4) Duncan, R. (1999) Polymer conjugates for tumour targeting and intracytoplasmic delivery. The EPR effect as a common gateway? *Pharm. Sci. Technol. Today 2*, 441–49.

(5) Agarwal, A., Asthana, A., Gupta, U., and Jain, N. K. (2008) Tumor and dendrimers: A review on drug delivery aspects. *J. Pharm. Pharmacol. 60*, 1–19.

(6) Bhadra, D., Bhadra, S., Jain, S., and Jain, N. K. (2003) A PEGylated dendritic nanoparticulate carrier of fluorouracil. *Int. J. Pharm. 257*, 111–24.

(7) Tripathi, P. K., Khopade, A. J., Nagaich, S., Shrivastava, S., Jain, S., and Jain, N. K. (2002) Dendrimer grafts for delivery of 5-fluorouracil. *Pharmazie 57*, 261–64.

(8) Kono, K., Liu, M., and Frechet, J. M. J. (1999) Design of dendritic macromolecules containing folate or methotraxate residues. *Bioconjugate Chem. 10*, 1115–21.

(9) Quintana, A., Raczka, E., Piehler, L., Lee, I., Myc, A., Majoros, I., Patri, A. K., Thomas, T., and Mule, J., Jr. (2002) Design and function of a dendrimer- based therapeutic nanodevice targeted to tumor cells through the folate receptor. *Pharm. Res. 19* (9), 1310–16.

(10) Bhadra, D., Bhadra, S., and Jain, N. K. (2006) PEGylated dendritic nanoparticulate carriers of anticancer drugs. In *Nanotechnology for cancer therapy* (Amiji, M. M., Ed.) pp 523−549, Chapter 27, Academic Press, New York.

(11) Agarwal, A., Saraf, S., Asthana, A., Gupta, U., Tripathi, P. K., Gajbhiye, V., and Jain, N. K. (2008) Ligand based dendritic systems for tumor targeting. *Int. J. Pharm. 350*, 3–13.

(12) Kannan, S., Kolhe, P., Raykova, V., Glibatec, M., Kannan, R. M., Lieh-Lai, M., and Bassett, D. (2004) Dynamics of cellular entry and drug delivery by dendritic polymers into human lung epithelial carcinoma cells. *J. Biomater. Sci. Polym. Ed. 15*, 311–30.

(13) Gurdag, S., Khandare, J., Stapels, S., Matherly, L. H., and Kannan, R. M. (2006) Activity of dendrimer-methotrexate conjugates on methotrexate-sensitive and -resistant cell lines. *Bioconjugate Chem. 17*, 275–85.

(14) Tomalia, D. A., Baker, H., Dewald, J. R., Hall, M., Kallos, G., Martin, S., Roeck, J., Ryder, J., and Smith, P. (1985) A new class of polymers: starburst dendritic molecules. *Polym. J. 17*, 117–32.

(15) Tang, M. X., and Redemann, C. T., Jr. (1996) In vitro gene delivery by degraded polyamidoamine dendrimers. *Bioconjugate Chem. 7*, 703–14.

(16) Schatzlein, A. G., Zinselmeyer, B. H., Elouzi, A., Dufes, C., Chim, Y. T. A., Roberts, C. J., Davies, M. C., Munro, A., Gray, A. I., and Uchegbu, I. F. (2005) Preferential liver gene expression with polypropylene imine dendrimers. *J. Controlled Release 101*, 247–58.

(17) Bielinska, A., Kukowska-Latallo, J. F., Johnson, J., and Tomalia, D. A., Jr. (1996) Regulation of *in vitro* gene expression using antisense oligonucleotide or antisense expression plasmids transfected using starburst PAMAM dendrimers. *Nucleic Acid Res. 24*, 2176–82.

(18) Kukowska-Latallo, J. F., Bielinska, A. U., Johnson, J., Spindler, R., and Tomalia, D. A., Jr. (1996) Efficient transfer of genetic material into mammalian cells using Starburst polyamidoamine dendrimers. *Proc. Natl. Acad. Sci. U.S.A. 93*, 4897–02.

(19) Kihara, F., Arima, H., Tsutsumi, T., Hirayama, F., and Uekama, K. (2003) In vitro and in vivo gene transfer by optimised a-cyclodextrin conjugate with polyamido amine dendrimer. *Bioconjugate Chem. 14*, 342–50.

(20) Lim, Y. B., Kim, T., Lee, J. W., Kim, S. M., Kim, H. J., Kim, K., and Park, J. S. (2002) Self assembley ternary complex of cationic dendrimer, Cucurbituril and DNA non-covalent strategy in developing a gene delivery. *Bioconjugate Chem. 13*, 1181–85.

(21) Wiener, E. C., Brechbiel, M. W., Brothers, H., Magin, R. L., Gansow, O. A., Tomalia, D. A., and Lauterbur, P. C. (1994) Dendrimer-based metal chelates: a new class of magnetic resonance imaging contrast agents. *Magn. Reson. Med. 31*, 1–8.

(22) Newkome, G. R., Moorefield, C. N., Baker, G. R., Saunders, M. J., and Grossman, S. H. (1991) Unimolecular micelles. *Angew. Chem., Int. Ed. 30*, 1178–80.

(23) Vandamme, T. F., and Brobeck, L. (2005) Polyamindo amine dendrimers as ophthalmic vehicles for ocular delivery of pilocarpine nitrate and tropicamide. *J. Controlled Release 102*, 23–38.

(24) Chauhan, A. S., Sridevi, S., Chalasani, K. B., Jain, A. K., Jain, S. K., Jain, N. K., and Diwan, P. V. (2003) Dendrimer-mediated transdermal delivery: enhanced bioavailability of indomethacin. *J. Controlled Release 90*, 335–43.

(25) Agrawal, P., Gupta, U., and Jain, N. K. (2007) Glycoconjugated peptide dendrimers based nanoparticulate system for the delivery of chloroquine phosphate. *Biomaterials 28*, 3349–59.

(26) Gupta, U., Agashe, H. B., Asthana, A., and Jain, N. K. (2006) Dendrimers: novel polymeric nanoarchitectures for solubility enhancement. *Biomacromolecules 7*, 649–58.

(27) Bhadra, D., Yadav, A. K., Bhadra, S., and Jain, N. K. (2005) Glycodendrimeric nanoparticulate carriers of primaquine phosphate for liver targeting. *Int. J. Pharm. 295*, 221–33.

(28) Malik, N., Wiwattanapatapee, R., Klopsch, R., Lorenz, K., Frey, H., Weener, J. W., Meijer, E. W., Paulus, W., and Duncan, R. (2000) Dendrimers: relationship between structure and biocompatibility in vitro and preliminary studies on the biodistribution of ^{125}I labeled polyamodoamine dendrimers in vivo. *J. Controlled Release 65*, 133–48.

(29) Satija, J., Gupta, U., and Jain, N. K. (2007) Pharmaceutical and biomedical potential of surface engineered dendrimers. *Crit. Rev. Ther. Drug Carrier Syst. 24* (3), 261–315.

(30) Bhadra, D., Bhadra, S., and Jain, N. K. (2006) PEGylated peptide dendrimeric carriers for the delivery of antimalarial drug chloroquine phosphate. *Pharm. Res. 23* (3), 623–33.

(31) Gajbhiye, V., Kumar, P. V., Tekade, R. K., and Jain, N. K. (2007) Pharmaceutical and biomedical potential of PEGylated dendrimers. *Curr. Pharm. Des. 13*, 415–29.

(32) Kojima, C., Kono, K., Maruyama, K., and Takagishi, T. (2000) Synthesis of polyamidoamine dendrimers having poly(ethylene glycol) grafts and their ability to encapsulate anticancer drugs. *Bioconjugate Chem. 11*, 910–17.

(33) Garin-Chesa, P., Campbell, I., Saigo, P., Lewis, J., Old, L., and Rettig, W. (1993) Trophoblast and ovarian cancer antigen LK26, sensitivity and specificity in immunopathology and molecular identification as a folate-binding protein. *Am. J. Pathol. 142*, 557–67.

(34) Lu, Y., and Low, P. S. (2002) Folate-mediated delivery of macromolecular anticancer therapeutic agents. *Adv. Drug Delivery Rev. 54*, 675–93.

(35) Choi, Y., Thomas, T., Kotlyar, A., and Islam, M. T., Jr. (2005) Synthesis and functional evaluation of DNA-assembled polyamidoamine dendrimer clusters for cancer cell-specific targeting. *Chem. Biol. 12*, 35–43.

(36) Steenis-van, J. H., Maarseveen-van, E. M., Verbaan, F. J., Verrijik, R., Crommelin, D. J. A., Storm, G., and Hennink, W. E. (2003) Preparation and characterization of folate-targeted pEG-coated pDMAEMA-based polyplexes. *J. Controlled Release 87*, 167–76.

(37) Zalipsky, S., Gilon, C., and Zilkha, A. (1983) Attachment of drugs to polyethylene glycols. *Eur. Polym. J. 19* (12), 1177–83.

(38) Lee, R. J., and Low, P. S. (1994) Delivery of liposomes into cultured KB cells via folate receptor- mediated endocytosis. *J. Biol. Chem. 269*, 3198–204.

(39) Miklis, P., Cagin, T., and Goddard, W. A. (1997) Dynamics of Bengal Rose encapsulated in the Meijer dendrimer box. *J. Am. Chem. Soc. 119*, 7458–62.

(40) Jansen, J. F. G. A., Brabander-van den Berg, E. M. M., and Meijer, E. W. (1994) Encapsulation of guest molecules into a dendritic box. *Science 266*, 1226–29.

(41) Singhai, A. K., Jain, S., and Jain, N. K. (1997) Evaluation of an aqueous injection of Ketoprofen. *Pharmazie 52* (2), 149–51.

(42) Trasler, J., Deng, L., Melnyk, S., Pogribny, I., Tim, F. H., Sibani, S., Oakes, C., Li, E., James, S. J., and Rozen, R. (2003) Impact of Dnmt1 deficiency, with and without low folate diets, on tumor numbers and DNA methylation in Min mice. *Carcinogenesis 24* (1), 39–45.

(43) Yoo, H. S., and Park, T. G. (2004) Folate-receptor-targeted delivery of doxorubicin nano-aggregates stabilized by doxorubicin-PEG-folate conjugate. *J. Controlled Release 100*, 247–256.

(44) Wrightson, W. R., Myers, S. R., and Galandiuk, S. (1995) HPLC analysis of 5-Fu and FdUMP in tissue and serum. *Biochim. Biophys. Res. Commun. 216*, 808–13.

(45) Sikka, P. K., and McMartin, K. E. (1998) Determination of the folate transport pathways in culture rat proximal tubule cells. *Chem. Biol. Interact. 114*, 15–31.

(46) Zhao, X. B., and Lee, R. J. (2004) Tumor-selective targeted delivery of genes and antisense oligodeoxyribonucleotides via the folate receptor. *Adv. Drug Delivery Rev. 56*, 1193–204.

(47) De Wolf, F. A., and Brett, G. M. (2000) Ligand-binding proteins, their potential for application in systems for controlled delivery and uptake of ligands. *Pharmacol. Rev. 52* (2), 207–36.

(48) Molema, G. (2005) Design of vascular endothelium-specific drug-targeting strategies for the treatment of cancer. *Acta Biochim. Pol. 52*, 301–10.

(49) Roberts, J. C., Bhalgat, M. K., and Zera, R. T. (1996) Preliminary biological evaluation of polyamidoamine (PAMAM) starburst dendrimers. *J. Biomed. Mater. Res. 30*, 53–65.

BC800125U

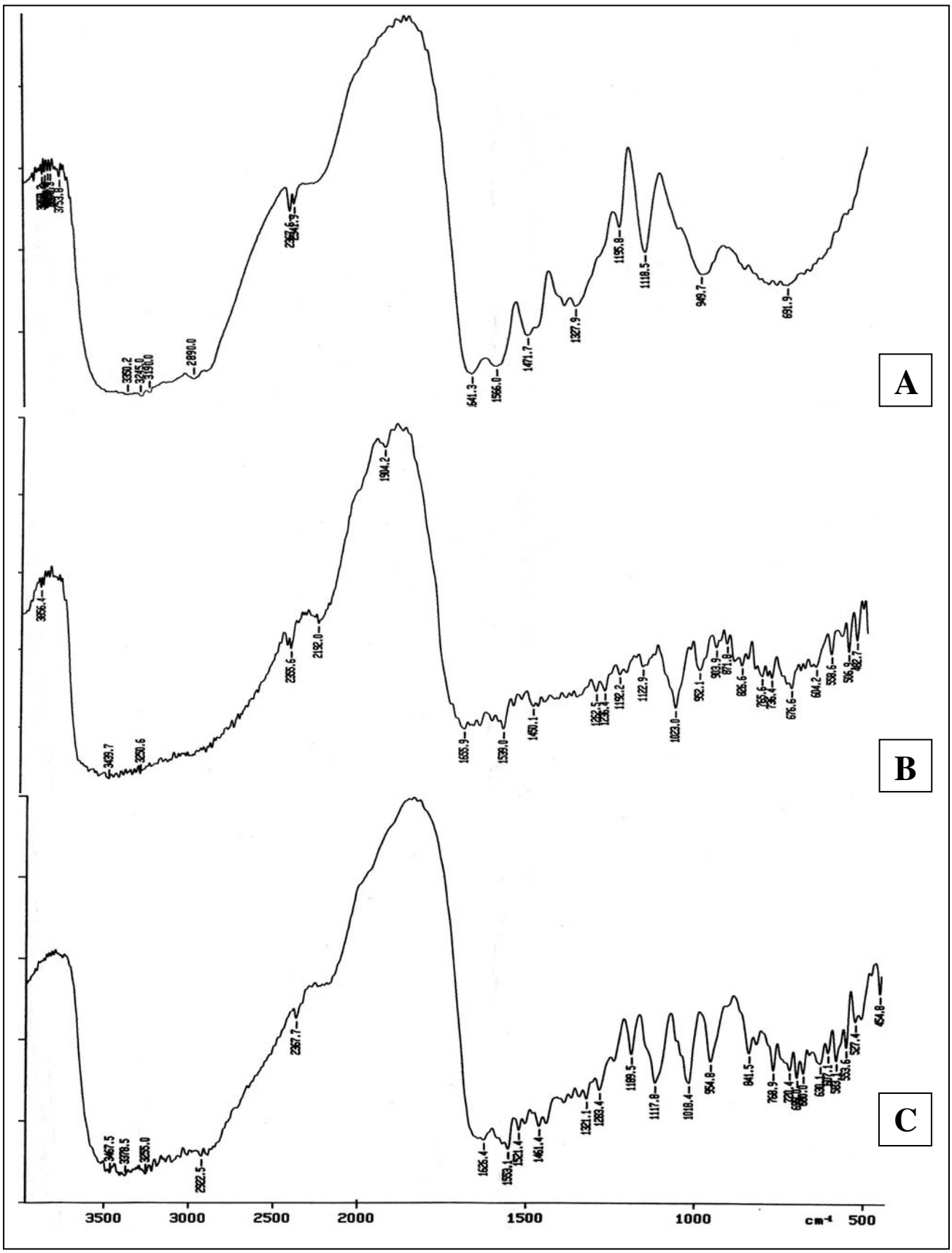

IR spectral analysis of A- 4.0 G PAMAM dendrimers; B- FA-PAMAM (Folic acid-dendrimer conjugates); C- FA-PEG-PAMAM (Folic acid-PEG-dendrimer conjugates).

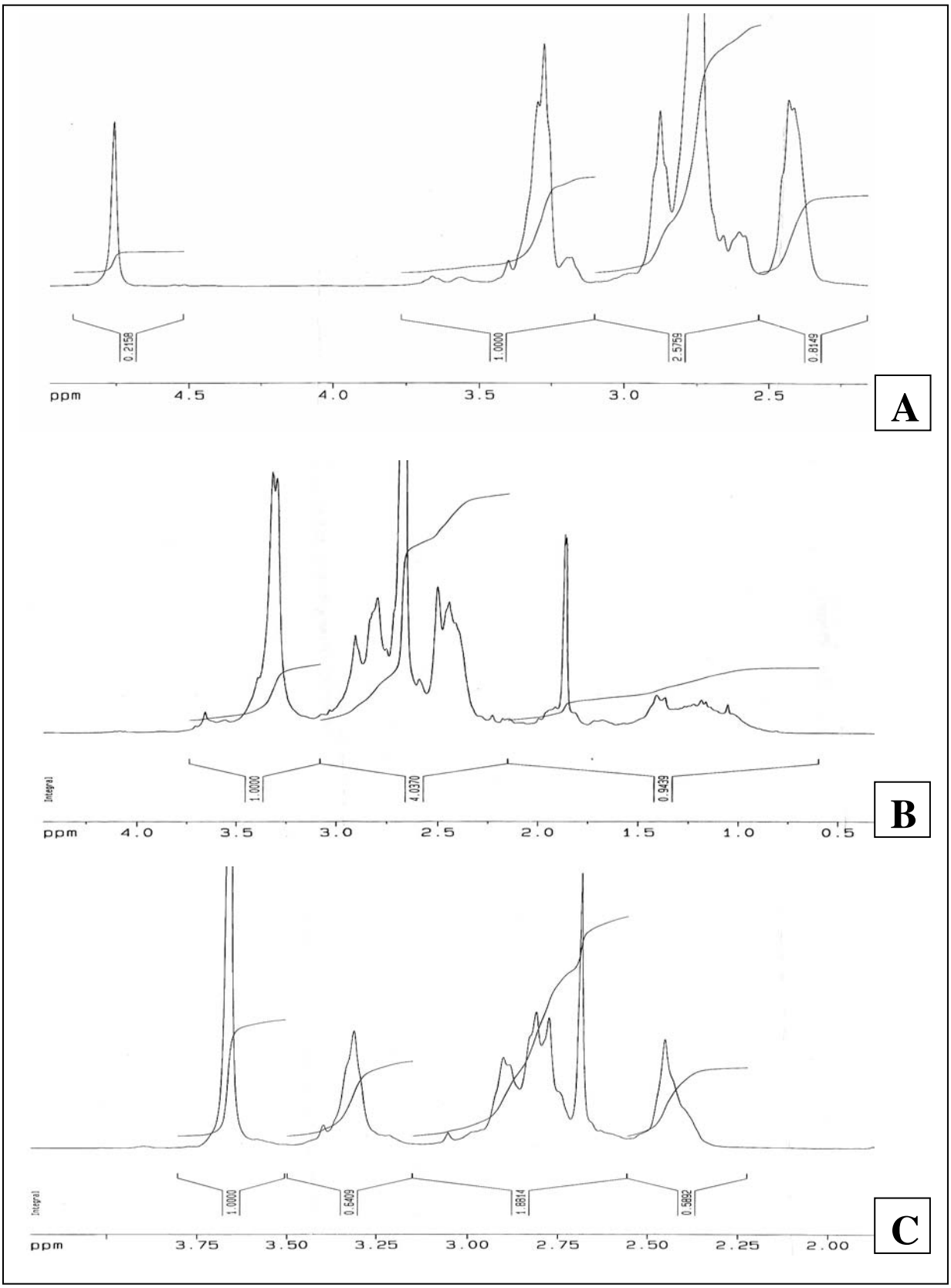

NMR spectral analysis of A- 4.0 G PAMAM dendrimers; B- FA-PAMAM (Folic acid-dendrimer conjugates); C- FA-PEG-PAMAM (Folic acid-PEG-dendrimer conjugates).

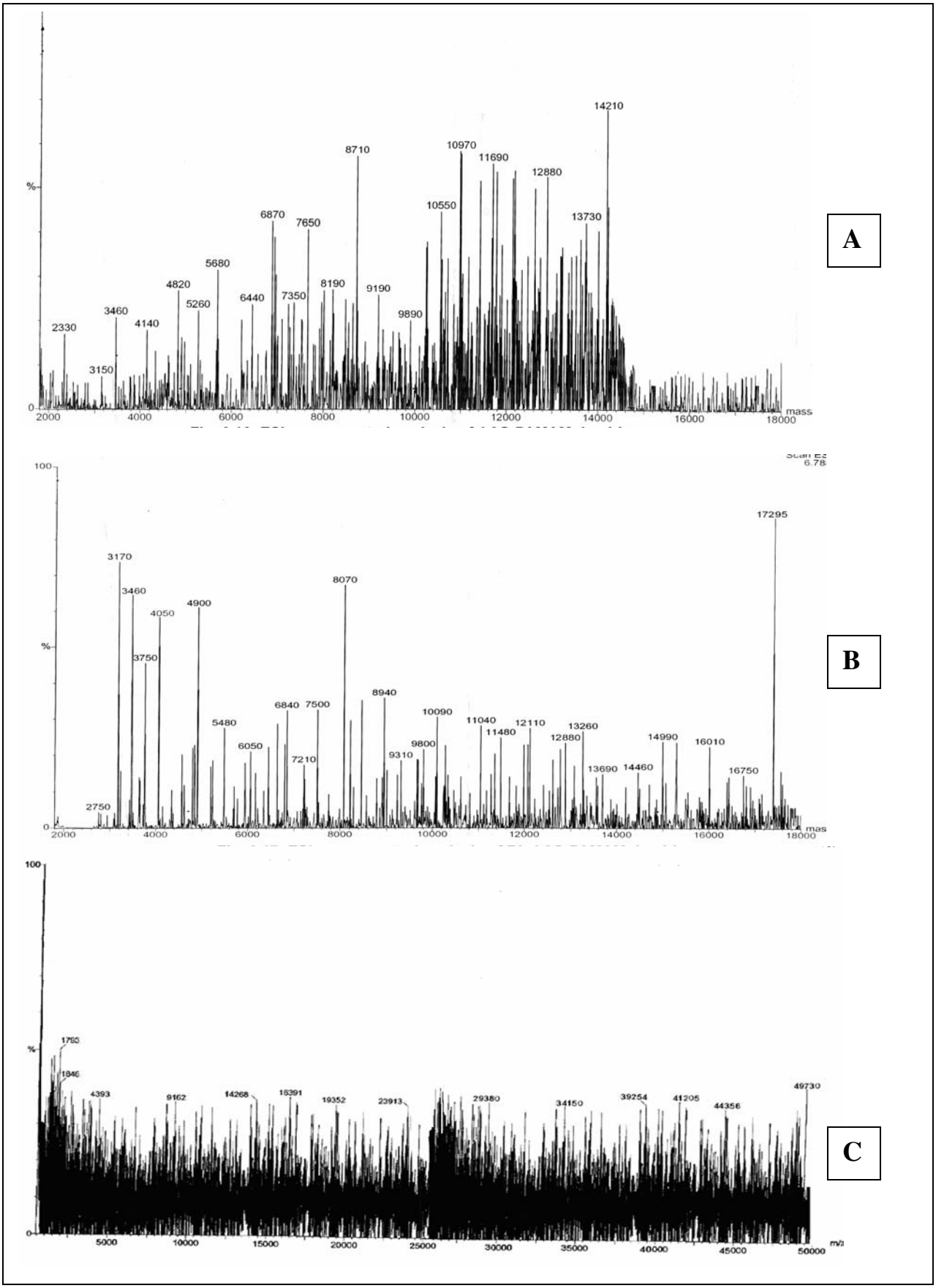

ESI mass spectral analysis of A- 4.0 G PAMAM dendrimers; B- FA-PAMAM (Folic acid-dendrimer conjugates); C- FA-PEG-PAMAM (Folic acid-PEG-dendrimer conjugates).

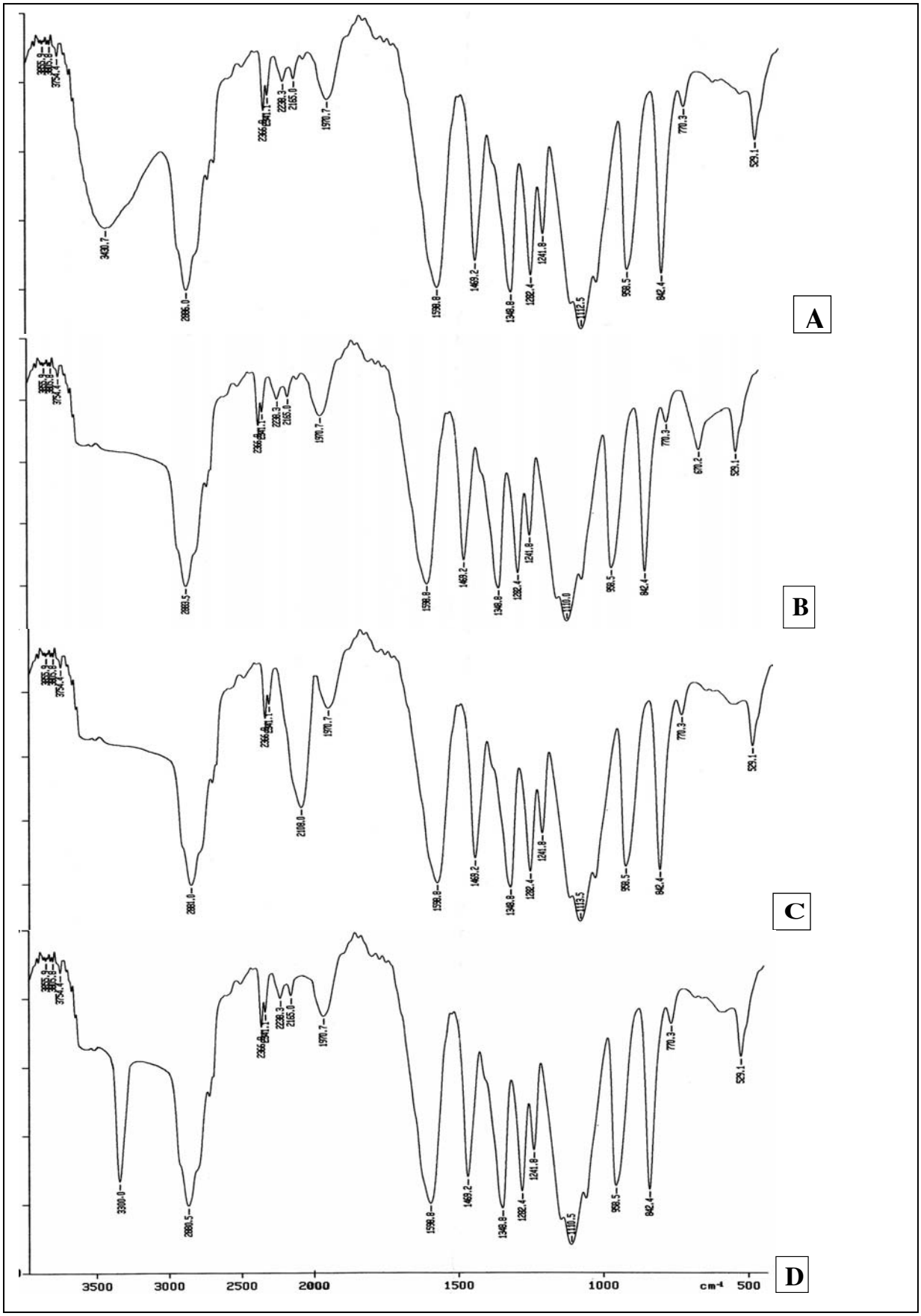

IR spectrum of the intermediates of NH_2 PEG 4000-NH_2 A-PEG4000; B-Cl-PEG4000-Cl; C-N_3-PEG4000-N_3, D- H_2N-PEG4000-NH_2.

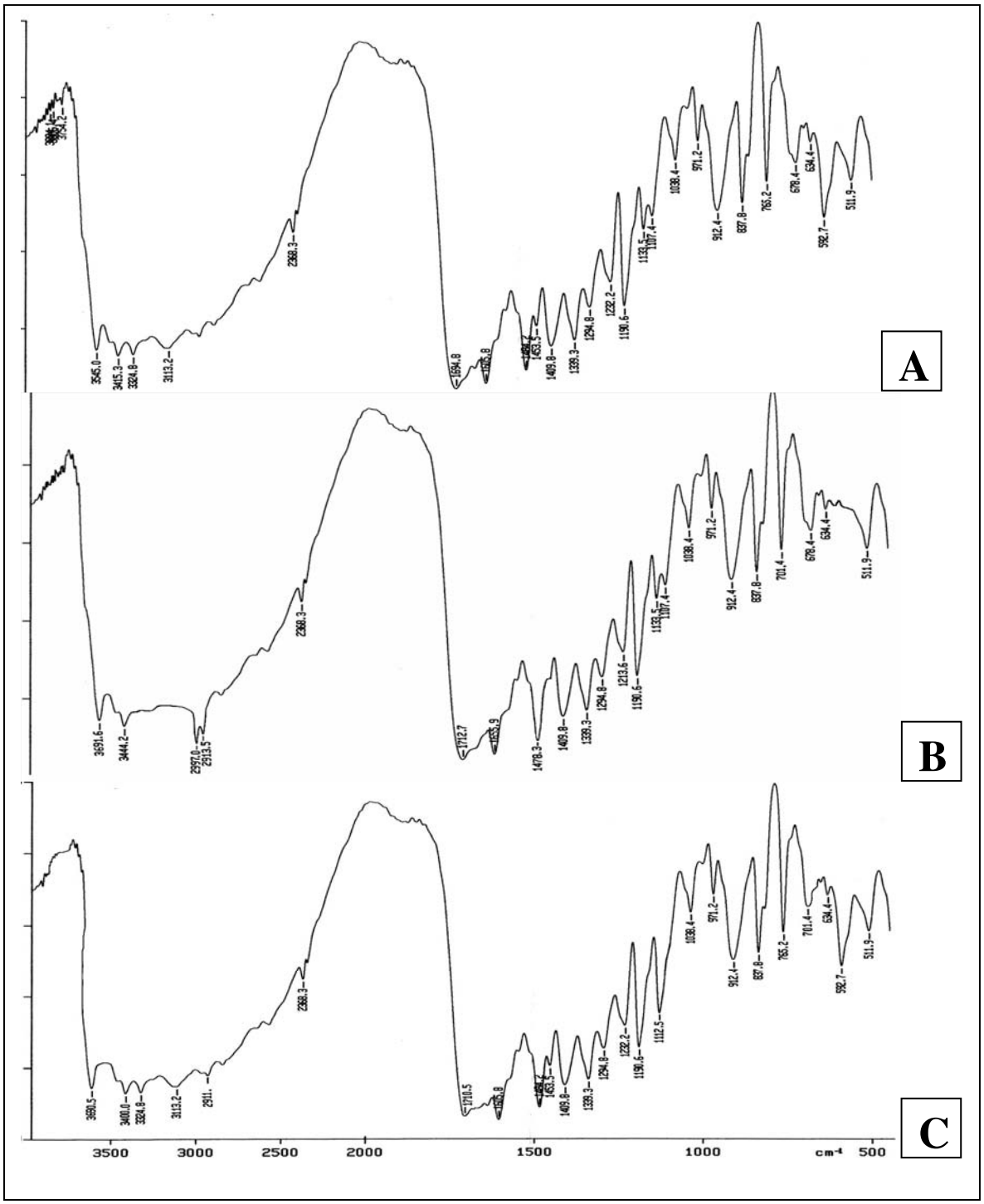

IR spectral analysis of A –Folic acid; B- Folic acid –NHS conjugates; C- NHS-PEG4000-Folic acid conjugates.

Development of Poly(ethylene glycol) Conjugated Lactoferrin for Oral Administration

Yasuhiro Nojima,[¶,†] Yosuke Suzuki,[†] Kazuma Iguchi,[†] Tuneo Shiga,[†] Aya Iwata,[†] Tomohito Fujimoto,[†] Kazuhiro Yoshida,[†] Hirohiko Shimizu,[‡] Takashi Takeuchi,[§] and Atsushi Sato*[,†]

School of Bioscience and Biotechnology, Tokyo University of Technology, 1404-1 Katakura, Hachioji, Tokyo 192-0982, Japan, NRL Pharma, Inc., East Building KSP, 3-2-1 Sakado, Takatsu-ku, Kawasaki, Kanagawa 213-0012, Japan, and Department of Veterinary Laboratory Medicine, Faculty of Agriculture, Tottori University, 4-101 Koyama-Minami, Tottori 680-8553, Japan.
Received June 26, 2008; Revised Manuscript Received August 22, 2008

Lactoferrin (LF) is an iron-binding glycoprotein that possesses multifunctional biological activities. Recent reports from clinical trials suggest that LF is potentially effective as a therapeutic protein against cancer and gangrene. However, pharmaceutical proteins such as LF are unstable in vivo. Therefore, to improve stability, we developed mono-PEGylated bovine LF (20k-PEG-bLf) with branched 20 kDa (2 × 10 kDa) poly(ethylene glycol) (PEG). We examined in vitro activities such as iron binding, IL-6 cell based assay, and resistance to a proteolytic enzyme in artificial gastric fluid. The 20k-PEG-bLf protein was fully active in iron binding and exhibited 69.6 ± 2.9% (mean ± S.E., $n = 6$) of the original anti-inflammatory activity. The proteolytic half-life increased 2-fold over that of unmodified LF. In vivo pharmacokinetic analyses were performed to examine absorption from the intestinal epithelium and serum clearance. Direct administration of 20k-PEG-bLf (30 mg/kg) into rat stomachs demonstrated that the amount of absorption from the intestinal tract increased approximately 10-fold relative to unmodified LF. Intravenous injection of the protein (1 mg/kg) revealed that 20k-PEG-bLf prolongs serum half-life by approximately 5.4-fold, and that the area under the curve (AUC) was increased approximately 9.2-fold compared to that of unmodified LF. PEGylation improved the physical and pharmacokinetic properties of bovine LF. This is the first report on the use of bioconjugation of LF for the development of a promising oral pharmaceutical agent.

INTRODUCTION

Lactoferrin (LF)[1] is an 80-kDa member of the transferrin family of iron-binding glycoproteins that is found in biological fluids such as milk, blood, cervical mucus, seminal fluids, saliva, and tears, and within the specific granules of polymorphonuclear leukocytes (*1*). It is a multifunctional protein that exhibits antimicrobial (*2*−*4*), antiviral (*5*), immunomodulation (*6*), antioxidation (*7*), anti-inflammation (*8*, *9*), antistress (*10*), and analgesic (*11*) effects, as well as enhancement of lipid metabolism (*12*). At present, LF is a commercially available fortified dairy product, but this multitude of biological activities has created great interest in the use of LF in drug discovery.

Agennix, Inc. (USA) has reported that orally administered Talactoferrin, an immunomodulatory recombinant human lactoferrin preparation, was effective in the treatment of patients with diabetic neuropathic foot ulcers (*13*) and in non-small-cell lung cancer (NSCLC) therapy in combination with cisplatin treatment in a phase I/II clinical trial (*14*). Talactoferrin has also been used in a recent renal cell carcinoma clinical trial (*15*). These findings suggest not only that LF is beneficial as a food supplement, but that it might also serve as a protein-based drug. In addition, LF reportedly inhibits hepatitis C viral entry into cells, suggestive of a use as a hepatitis C therapeutic agent (*16*−*18*).

Food proteins are generally absorbed from the intestine and transferred to the portal system, but the protein absorption dynamics of bovine LF (bLF) is extremely unique (*19*−*21*). Intact bLF goes directly to the intestine and is absorbed from intestinal epithelial cells by two possible pathways, specific receptor-mediated transcytosis and nonselective transcytosis. The incorporated bLF is then shifted to the lymphatic system, not the portal system, and transferred to the thoracic duct lymph. Thereafter, bLF enters systemic circulation. Accordingly, it is absolutely necessary that intact bLF reach and be absorbed from the intestine for it to exert its biological activities.

Native bLF has the drawback that it is susceptible to digestive juices. This phenomenon results in only a small amount of delivery to the intestinal tract. Therefore, enteric-coated (*22*) and liposomal formulations (*23*) have been developed to increase absorption efficiency of intact bLF.

Attempts have been made to alter biological therapeutic proteins, such as cytokines and antibodies, by covalent modification with a macromolecular substance, such as poly(ethylene glycol) (PEG). This technique, known as PEGylation, is used in drug delivery systems to improve the physical and pharmacokinetic properties of the native proteins (*24*). PEGylation imparts diminished immunogenicity and improved pharmacokinetic behavior (e.g., proteolytic resistance due to steric hindrance, inhibition of renal clearance due to the increased molecular mass after PEGylation), culminating in better pharmacological effects. Many proteins have been successfully PEGylated, including interferon-α (*25*, *26*), asparaginase (*27*), G-CSF (*28*), adenosine deaminase (*29*), and growth hormone receptor antagonist (*30*), and are now marketed drugs. To date,

* Corresponding author. Atsushi Sato, School of Bioscience and Biotechnology, Tokyo University of Technology, 1404-1 Katakura, Hachioji, Tokyo 192-0982, Japan. E-mail: atsato@bs.teu.ac.jp; Telephone: +81-42-637-2197; Fax: +81-42-637-2112.

¶ Present address: Department of Virology, Kitasato Research Center of Environmental Sciences, 1-15-1 Kitazato, Sagamihara, Kanagawa 228-0829, Japan.

† Tokyo University of Technology.

‡ NRL Pharma, Inc.

§ Tottori University.

[1]Abbreviations: LF, lactoferrin; PEG, poly(ethylene glycol); bLF, bovine lactoferrin; 20k-PEG-bLf, 20k PEG conjugated lactoferrin.

10.1021/bc800258v CCC: $40.75 © 2008 American Chemical Society
Published on Web 10/04/2008

most pharmaceutical proteins (including cytokines, antibody preparation, and PEGylated proteins) must be administered by subcutaneous, intramuscular, or intravenous injection in a hospital. Parenteral administration, however, places a burden on patients due to frequent hospital visits, increased costs, and difficulty and discomfort in self-injection. This has stimulated interest in the investigation of orally administered pharmaceutical proteins to improve the patients' quality of life; however, the progress to date in developing orally administered protein drugs has been inadequate (*31, 32*). The goal of this study was to develop a bLF amenable to oral administration by conjugating the protein to a branched PEG with a molecular mass of 20 kDa. We synthesized PEGylated bLF (20k-PEG-bLf) and characterized the in vitro biological activities and in vivo pharmacokinetics.

MATERIALS AND METHODS

Materials. Bovine lactoferrin (bLF) was acquired from MG Nutritionals (Melbourne, Australia). A 20-kDa (2 × 10 kDa) branched PEG of *N*-hydroxysuccinimidyl derivative (PEG-NHS, SUNBRIGHT GL2−200GS2) was purchased from the NOF Corp. (Tokyo, Japan). Heparin Sepharose 6 Fast Flow and PD-10 desalting columns were supplied by GE Healthcare (Uppsta, Sweden). Centriplus was supplied by Millipore (Billerica, MA). Titrisol, a concentrated iodine solution, was purchased from Merck KGaA (Darmstadt, Germany). Recombinant human IFN-γ was acquired from R&D systems (Minneapolis, MN). Calcitriol was purchased from Wako Pure Chemical Industries, Ltd. (Osaka, Japan). LPS from *E. coli* O127:B8 was purchased from Sigma (St. Louis. MO). The Cell Counting Kit-8 was purchased from Dojindo laboratories (Kumamoto, Japan). The Human IL-6 ELISA Kit was purchased from Kamakura Techno-Science (Kanagawa, Japan).

Experimental Animals. Wistar male rats (Institute for Animal Reproduction, Ibaragi, Japan) weighing 220−228 g were used in this study. The animals were maintained at a controlled temperature of 22 ± 2 °C with 12 h light/12 h dark cycles (light cycle 7:00−19:00), and were given standard chow (CE-2, Nihon Clea, Tokyo, Japan). All procedures were approved by the Animal Research Committee at Tottori University.

Preparation and Purification of 20 k-PEG-bLf. The PEGylated reaction mixture consisted of bLF and branched 20-kDa PEG-NHS reagent at a 1:10 molar ratio in phosphate buffered saline (PBS) pH 7.4. The final protein concentration was 0.5 mg/mL. The reaction was carried out for 1 h at 25 °C, and stopped by cooling (0−4 °C). The reaction mixture was applied to a column packed with Heparin Sepharose 6 Fast Flow resin, previously equilibrated with 10 mM sodium phosphate, pH 7.6. The column was washed with five column volumes of equilibration buffer to remove excess PEG reagent and byproduct. 20k-PEG-bLf was eluted with 300 mM sodium chloride, and unmodified bLF was eluted with 1 M sodium chloride at a flow rate of 2 mL/min. The 20k-PEG-bLf eluates were desalted using a PD-10 column and concentrated with Centriplus. Protein concentration was determined by the Bradford protein assay procedure with BSA as a standard.

SDS-PAGE Analysis. The reaction mixture and purified 20k-PEG-bLf were analyzed by sodium dodecyl sulfate (SDS)−polyacrylamide (7.5%) gel electrophoresis according to the methods of Laemmli (*33*) under nonreducing conditions and were stained with Coomassie Brilliant Blue (CBB). PEG-bLf and excess PEG reagents were specifically stained with Titrisol iodine solution according to the procedure of Kurfürst with some modifications (*34*). The SDS-PAGE gel was then rinsed with distilled water and placed in a 5% barium chloride solution for 10 min. The gel was washed with distilled water and transferred to 0.1 N Titrisol iodine reagent for 15 min. Excess Titrisol iodine was washed off with distilled water, and the PEG-conjugated proteins and excess PEG reagent were detected as brown bands.

N-Terminal Amino Acid Sequence. Unmodified bLF and purified 20k-PEG-bLf (600 μg/mL each) were digested with pepsin at a concentration of 60 ng/mL for 1 h at 37 °C. Digested proteins were subjected to SDS-PAGE and electroblotted to a PVDF membrane (Bio-Rad, Hercules, CA). Protein bands were visualized with CBB and excised from the membrane. Determination of the N-terminal amino acid sequence was carried out by automated Edman degradation on an Applied Biosystems model 470A sequencer.

Iron-Binding Assay. Starting with the native LF, apo- and iron-rebinding forms of bLF and 20k-PEG-bLf were prepared according to the method of Shimazaki et al. (*35*). The apo-LF was prepared in the presence of citrate. The reconstituted form of LF containing the ferric ions was prepared in the presence of bicarbonate. Iron concentration of each LF was determined using the method of Kirkpatrick et al. (*36*) with the Fe−C Test Kit (Wako Pure Chemicals, Osaka, Japan).

In Vitro Anti-Inflammation. A cell stimulation assay was carried out using the methods of Mattsby-Balzer et al. (*8*) and Håversen L et al. (*9*) with minor modifications. THP-1 (human monocyte leukemia cell line, JCRB0112) cells were obtained from the Health Science Research Resource Bank (Osaka, Japan) and grown in RPMI 1640 medium supplemented with 10% heat-inactivated fetal bovine serum (FBS) and 2 mM Glutamax (Invitrogen, Carlsbad, CA) in a CO_2 incubator at 37 °C. Logarithmic growth phase cells were treated with 20 ng/mL IFN-γ and 40 ng/mL calcitriol for 48 h to increase sensitivity against LPS. Following incubation, the cells were collected and suspended in cell assay medium (RPMI 1640 containing 10% FBS and 2 mM Glutamax) at a concentration of 1×10^6 cells/mL. The cells (400 μL) were then added to a 24-well plate. The cells were stimulated with LPS alone at a concentration of 100 ng/mL, with 100 ng/mL LPS plus 100 μg/mL test sample or with 100 μg/mL of the test sample alone at 37 °C for 24 h in a 5% CO_2 atmosphere. After incubation, culture supernatants were collected and IL-6 concentration was measured by ELISA.

Cytotoxicity of 20k-PEG-bLf. THP-1 cell suspension (100 μL of 1×10^6 cells/mL) was dispensed to each well of a 96-well plate in triplicate. Ten micrograms of unmodified bLF or 20k-PEG-bLf was added to each well and incubated at 37 °C for 24 h in an atmosphere of 5% CO_2. Cell Counting Kit-8 Solution (10 μL) was then added to each well, and the plate was incubated at 37 °C for 1 h in 5% CO_2. Cell viability was determined by measuring the absorbance at 450 nm (reference absorbance at 655 nm) using a microplate reader.

Proteolytic Digestion. Unmodified bLF or 20k-PEG-bLf was dissolved in 10 mM HCl at a concentration of 0.5 mg/mL and adjusted to pH 3.2. Pepsin was added to the protein solution at a final concentration of 20 ng/mL and incubated at 37 °C. Reaction mixture was collected at 0, 5, 10, 15, 20, 40, 60, and 100 min and terminated by the addition of SDS-PAGE loading buffer. Samples were heated at 95 °C for 5 min and analyzed by SDS-PAGE. The gel was stained with CBB, and the intensity of staining in each band was analyzed by *Image J* software.

Lymphatic bLF Transport from the Intestine. The experimental procedure was conducted according to the method of Takeuchi et al. (*19*) with some modifications. Eight-week-old Wistar rats ($n = 4-5$) were anesthetized with urethane (4 g/kg, s.c.) and sodium pentobarbital (0.1 mL, s.c.) before unmodified bLF (30 mg/kg or 300 mg/kg) or 20k-PEG-bLf (30 mg/kg) was injected intragastrically, over 1 min, using a 27-gauge needle. Thoracic lymph fluid was harvested and collected in heparinized tubes throughout the sampling period (at time zero and hourly after the injection for 4 h). The samples were centrifuged, and

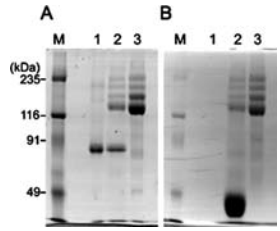

Figure 1. SDS-PAGE analysis of unmodified and PEGylated bLf. (A) Protein staining with Coomassie Brilliant Blue. Lanes: M, molecular weight marker; 1, unmodified bLF (2 μg); 2, PEGylation reaction mixture; 3, purified 20k-PEG-bLf (2 μg). (B) PEG-specific staining with iodine. Lanes: M and 1−3, same as in part A.

bLF concentration in the supernatant was determined by polyclonal antibody-based ELISA.

Pharmacokinetic Study. The experimental procedure was conducted according to the methods of Takeuchi et al. (*19*) with some modifications. Eight-week-old Wistar rats ($n = 6-10$) were anesthetized with sodium pentobarbital (60 mg/kg, i.p.), and a cannula for blood collection was inserted into the external jugular vein. Unmodified bLF (1 mg/kg or 10 mg/kg) or 20k-PEG-bLf (1 mg/kg) was injected into the femoral vein. The blood was collected from the external jugular vein through a cannula. Blood was collected at 0, 1, 5, 10, 15, 30, 60, 120, 180, and 240 min after sample administration. bLF blood concentration was determined quantitatively by polyclonal antibody-based ELISA.

Statistical Analysis. The Mann−Whitney test was used to determine statistical significance in the lymphatic transport study. The Student's unpaired *t* test was used to evaluate the area under the curve (AUC) in the pharmacokinetic study. *P* values of <0.05 were considered significantly different.

RESULTS

Preparation of 20 kDa-PEG Conjugate bLF. PEGylated bLF was generated as a result of the reaction between *N*-hydroxysuccinimide (NHS) ester derivatives of a 20 kDa branched PEG molecule and the free amino groups (ε- and α-amino groups) of bLF. Figure 1 shows the SDS-PAGE profile of unmodified bLF, the reaction mixture, and purified PEGylated bLF (PEG-bLf) detected by CBB (Figure 1A) and PEG-specific staining (Figure 1B). The reaction mixture contained various molecular weights of PEG-bLfs, unmodified bLF, and an excess of PEG reagent. CBB and PEG-specific staining showed that 20k-PEG-bLf was successfully purified by Heparin affinity chromatography from the PEGylation mixture. The proportions of mono, di, tri, and tetra PEGylated bLF were 81.7%, 12.2%, 3.2%, and 2.8%, respectively, as judged by the intensity of each stained band in the gel.

Iron-Binding Assay. LF has two domains, the N-lobe and the C-lobe. Each lobe contains an iron site where the ferric ion (Fe^{3+}) is tightly bound in the presence of HCO_3^{2-} (*37*). The iron-scavenging properties of LF are reportedly involved in antioxidative effects and antimicrobial activities. We measured the iron content of 20k-PEG-bLf and compared it to that of unmodified bLF. Representative data obtained from five independent experiments are shown in Table 1. 20k-PEG-bLf and unmodified bLF bound iron at the concentration of 1021 ng and 833.7 ng Fe^{3+} per mg of protein, respectively, revealing 122.5% relative binding activity of 20k-PEG-bLf to that of unmodified bLF. This result suggested that PEG modification did not affect the iron-binding ability of bLF.

In Vitro Anti-Inflammation. As an anti-inflammatory agent, bLF down-regulates LPS-induced IL-6 secretion in human monocytic cells (*8, 9*). The effect of 20k-PEG-bLf on this response was analyzed in the monocytic cell line THP-1.

Table 1. Iron-Binding Activities of 20k-PEG-bLf

protein	Fe concentration (ng/mg protein) apo-form	holo-form	relative binding ratio (% of unmodified bLF)
Unmodified bLF	79.7	913.4	100.0
20k-PEG-bLf	125.6	1146.6	122.5
BSA[a]	67.0	119.6	6.3

[a] BSA was used as a negative control.

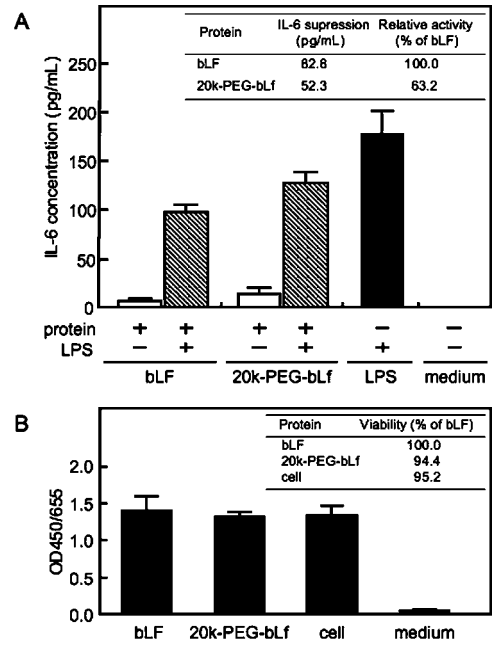

Figure 2. Inhibition of the LPS-induced IL-6 response in THP-1 cells by 20k-PEG-bLf. (A) ELISA comparison of IL-6 levels in supernatants from LPS stimulated THP-1 cells. Bovine LF (bLF) or 20k-PEG-bLf, at a dose of 100 μg/mL, was added after LPS (100 ng/mL) stimulation. All data represent means ± SD from triplicate wells. The inset shows the mean relative anti-inflammatory activity of 20k-PEG-bLf compared to that of bLF. The suppressed IL-6 concentrations were calculated by subtracting the values of "bLF + LPS" or "20k-PEG-bLf + LPS" from "cells treated with LPS only". (B) Viability of THP-1 cells treated with 20k-PEG-bLf. bLF or 20k-PEG-bLf (100 μg/mL) was added to THP-1 cells. All data represent means ± SD from triplicate wells. The inset shows the mean relative cell viability compared to that of bLF.

Representative data obtained from six independent experiments are shown in Figure 2A. No IL-6 was detected in the culture fluid of LPS-untreated cells, whereas IL-6 was slightly detected in the supernatants of cells treated with only 20k-PEG-bLf or unmodified bLF. Both 20k-PEG-bLf and unmodified bLF inhibited the LPS-induced IL-6 secretion, with mean reductions of 52.3 pg/mL and 82.8 pg/mL IL-6, respectively. Thus, the relative inhibitory activity of 20k-PEG-bLf was approximately 63.2% that of unmodified bLF. Six independent experiments revealed that the residual anti-inflammatory activity of 20k-PEG-bLf was 69.6 ± 2.9% (means ± S.E.) of the original. In order to rule out possible cell toxicity of the added samples, which could account for the observed inhibitory effect, we evaluated the effect of 20k-PEG-bLf on THP-1 cell viability. Neither 20k-PEG-bLf nor bLF affected cell viability, suggesting no cytotoxic effect from the added samples (Figure 2B).

Stability of 20k-PEG-bLf (Proteolytic Characterization). Artificial gastric fluid was used to compare the in vitro peptic susceptibility of unmodified bLF and 20k-PEG-bLf. Unmodified bLF (80 kDa) was degraded within 40 min, whereas 20k-PEG-bLf (predominantly mono PEG-bLf of 140 kDa) was still detectable at 100 min (Figure 3A). The PEGylation of bLF induced a 2-fold increase in the half-life of peptic digestion

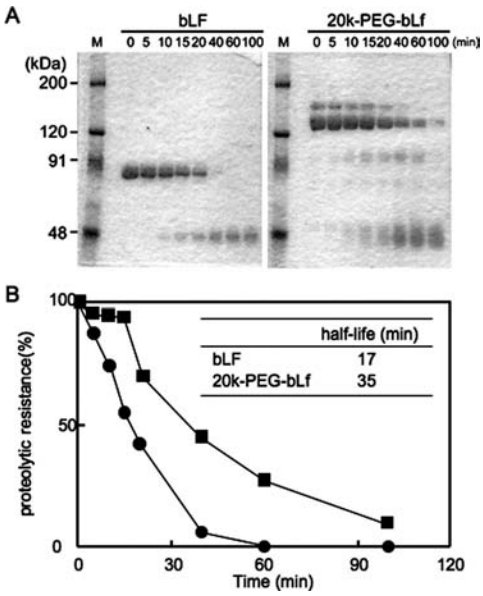

Figure 3. In vitro susceptibility of unmodified bLF and 20k-PEG-bLf to pepsin hydrolysis. (A) SDS-PAGE profile of pepsin-digested proteins. (B) Degradation rates of pepsin-digested unmodified bLF and 20k-PEG-bLf. Proteins were visualized with Coomassie Brilliant Blue, and residual protein bands were quantified using *Image J* software by reference to untreated bLF and 20k-PEG-bLf, which were arbitrarily set at 100%. Each data point was derived from one experiment, and all the time points were from the same incubation. The inset shows the half-life of resistance against pepsin digestion.

(Figure 3B), suggesting high stability of 20k-PEG-bLf in the gastrointestinal tract.

N-Terminal Amino Acid Sequence of Pepsin-Digested 20k-PEG-bLf. N-terminal amino acid sequences of pepsin-digested fragments from 20k-PEG-bLf were determined to estimate PEG conjugation sites on the 20k-PEG-bLf protein. Digestion of 20k-PEG-bLf with pepsin gave rise to four digestive fragments (Figure 4A, lane 2). Of these four, the three indicated by arrows specifically stained with iodine (data not shown), suggesting the presence of PEG-attached fragments. The following N-terminal amino acid sequences were obtained for the three PEG-attached fragments: Subfragment 1 (~105 kDa) - APRKNVRWXTIXQ (X stands for an uncertain residue); subfragment 2 (~80 kDa) - VVKLTVKFQL; and subfragment 3 (~60 kDa) - VKETYVFENL. These N-terminal amino acid sequences correspond to 1−13, 97−106, and 209−218, respectively, of mature bLF (689 amino acids length) (Figure 4B). These sequences are all in the N-terminal half of bLF. These results permit us to speculate that the N-terminal half of bLF is not a main target site of PEG modification.

Lymphatic Transport Study. Intact bLF is incorporated via the intestinal tract and transported into the thoracic duct lymph (*19*−*21*). To examine the absorption and transport of 20k-PEG-bLf in rats, 20k-PEG-bLf (30 mg/kg body weight) or unmodified bLF (30 or 300 mg/kg body weight) was administered intragastrically. bLF transport to the thoracic duct lymph was detected by ELISA (Figure 5). No bLF was detected before administration in either group. Unmodified bLF and 20k-PEG-bLf were detected 1 h after administration. The concentration of 20k-PEG-bLf continued to increase up to 4 h after administration, while the concentration of unmodified bLF (30 and 300 mg/kg body weight) remained constant. Consequently, the concentration of absorbed 20k-PEG-bLf (30 mg/kg body weight) at 4 h after administration was approximately 10-fold higher than that of absorbed unmodified bLF (30 mg/kg body weight), although no statistical difference was observed because of the large individual differences in absorbed 20k-PEG-bLf (Mann−Whitney test).

Pharmacokinetic Study. Pharmacokinetic parameters were determined by the intravascular administration of unmodified bLF and 20k-PEG-bLf in Wistar male rats. The mean serum concentrations of bLF versus time curves of 20k-PEG-bLf (1 mg/kg) and unmodified bLF (1 mg/kg, 10 mg/kg) are shown in Figure 6. No bLF was detected in the serum before injection. The concentration of bLF rapidly decreased and became undetectable by 60 and 120 min after administration of an unmodified bLF (1 mg/kg and 10 mg/kg), respectively. In contrast, 20k-PEG-bLf continued to be detected up to 240 min after intravenous administration. The area under the curve (AUC) of 20k-PEG-bLf was approximately 9.2-fold higher than that of unmodified bLF (1 mg/kg treatment group). 20k-PEG-bLf had a half-life of 42.4 min, whereas unmodified bLF (1 mg/kg) had a half-life of 7.8 min. Therefore, PEGylation of bLF led to a 5.4-fold prolongation of the half-life compared to unmodified bLF (1 mg/kg).

DISCUSSION

PEGylation is an established method for improving the pharmacokinetic properties and pharmacodynamic effects of therapeutic proteins (*24*). In most cases, PEGylated pharmaceutical proteins are administered parenterally. Few studies have reported on the oral administration of PEGylated proteins. Bioconjugation of PEG to granulocyte colony stimulating factor (G-CSF) enhanced oral delivery (*32*), suggesting that PEGylation could be a successful approach to not only parenteral formulation but oral formulation. Thus, this report encouraged us to attempt the PEGylation of oral bLF to achieve greater efficacy than that of unmodified bLF.

Lysine amino groups are most frequently used as PEGylation conjugation sites. This PEGylation, however, is nonspecific and may result in a high number of PEGylated mixtures. In cases where bLF was modified with the linear and small molecular mass of the PEG-NHS derivative (5 kDa), hyper-modified PEGylated bLF was formed, as judged by a smear pattern on SDS-PAGE gels (data not shown). This phenomenon may occur due to 54 internal lysine residues that act as potential conjugation sites in bLF. For example, analysis of several reactions with varying pH, temperature, and PEG-to-bLF ratios showed that the 20 kDa (this study) and 40 kDa PEG-NHS (data not shown) in the branched shape gave rise to a discrete band on SDS-PAGE.

The amino groups of proteins are considered to be suitable conjugation sites for PEGylation because they are the most represented groups and are highly reactive. This approach, however, frequently leads to reduction or loss of bioactivity, mainly because protein active sites are in or near conjugation sites, or are hindered by long polymer strands (so-called steric hindrance). In fact, PEGylated interferons (IFNs) (*25, 26*), which are now marketed for treatment of hepatitis B and C, show markedly reduced in vitro antiviral activity (e.g., PEG-IFN α2a (PEGASYS), 7%; PEG-IFN α2b (Intron), 28%). This reduced biological activity was largely compensated for by an extended in vivo half-life, eventually accounting for improved therapeutic efficacy. In contrast, our PEGylated bLF (20k-PEG-bLf) showed high residual in vitro activities. The iron binding activity was equivalent to that observed in native bLF, and the anti-inflammatory activity retained 69.6% of the action of native bLF. Thus, 20k-PEG-bLf would be a promising drug candidate for in vivo pharmacological study.

The proteolytic profiles showed that 20k-PEG-bLf displayed a significantly higher resistance to pepsin treatment compared to unmodified LF. Resistance to pepsin treatment of 20k-PEG-bLf revealed biphasic curves, high resistance (0−15 min) and

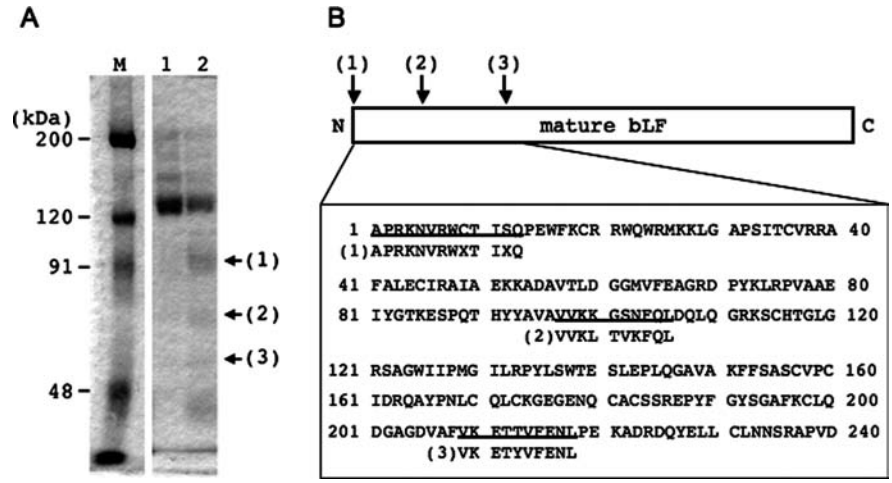

Figure 4. Deduced N-terminal amino acid sequences of pepsin-digested 20k-PEG-bLf fragments. (A) 20k-PEG-bLf was treated with pepsin at a concentration of 60 ng/mL for 60 min at 37 °C. Lanes: M, molecular weight markers; 1, undigested 20k-PEG-bLf; 2, 20k-PEG-bLf digested with pepsin. (B) Schematic diagram showing the location of the N-terminal amino acid sequences from pepsin-digested 20k-PEG-bLf.

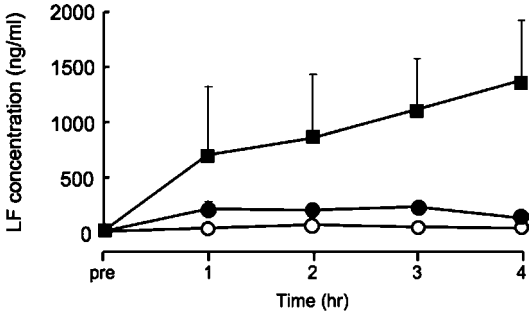

Figure 5. Changes in LF concentration in thoracic lymph over a 4 h time course. Open circles, closed circles, and closed squares show the data from bLF and 20k-PEG-bLf infusion into Wistar rats at a dosage of 30 mg/kg (bLF), 300 mg/kg (bLF), and 30 mg/kg (20k-PEG-bLf), respectively. Lymphatic fluid was collected every hour for 4 h, and LF concentration in thoracic lymph was measured by ELISA. Data represent means ± SE from 4−5 rats. The concentration of absorbed 20k-PEG-bLf (30 mg/kg body weight) at 4 h after administration was approximately 10-fold higher than that of absorbed unmodified bLF (30 mg/kg body weight).

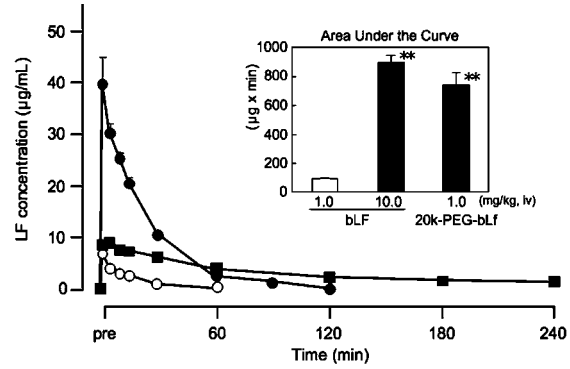

Figure 6. Pharmacokinetic profiles of unmodified bLF and 20k-PEG-bLf after intravenous injection. Open circles, closed circles, and closed squares show the data from rats injected at a dosage of 1 mg/kg (unmodified bLF), 10 mg/kg (unmodified bLF), and 1 mg/kg (20k-PEG-bLf), respectively. The inset shows the data from the area under the curve (AUC). Blood was collected at the indicated time points and assayed for bLF serum levels by ELISA. Data represent means ± SE from 5−7 rats. **Significant difference from unmodified bLF (1 mg/kg) administration ($P < 0.01$).

low resistance (15−100 min). The second curve slope apparently corresponds to fully released LF digestion.

The N-terminal region of LF contains unique clusters of basic amino acid residues that are involved in various biological functions such as antimicrobial and antiviral activities and affinity to heparin and LPS (*38*−*42*). The N-terminal amino acid sequences of pepsin-digested fragments from 20k-PEG-bLf indicate that the N-terminal portion of bLF was not modified with PEG. The high residual activities of 20k-PEG-bLf could be explained by this fact.

It has been reported that bLF taken up from the intestinal lumen is transported into the blood via the lymphatic, not portal, pathway in adult rats. The present study demonstrated enhanced uptake of PEGylated bLF from the rat intestine. PEGylated bLF might transfer across the small intestinal mucosal membranes by two possible pathways, specific receptor-mediated transcytosis and nonselective transcytosis. Considering that the ligand−receptor interaction could be reduced due to PEGylation, enhanced uptake of PEGylated bLF from the rat intestine could not be explained by specific receptor-mediated transcytosis. We, therefore, consider that this phenomenon may be mainly associated with nonselective transcytosis. The permeability of the epithelial membranes may be altered by PEGylation of bLF.

The area under the curve (AUC) of 20k-PEG-bLf was approximately 9.2-fold higher than that of unmodified bLF (1 mg/kg treatment group), and was similar to that of unmodified bLF (10 mg/kg treatment group). Approximately 4-fold higher serum concentration of unmodified bLF (10 mg/kg) than 20k-PEG-bLf (1 mg/kg) was detected 10 min postadministration, then decreased rapidly, and was undetectable 120 min postadministration. In contrast, the serum concentration of 20k-PEG-bLf (1 mg/kg) was detected 10 min postadministration, then decreased very slowly, and continued to be detected up to 240 min after intravenous administration, consequently giving rise to a similar AUC value to that of unmodified bLF (10 mg/kg).

Various attempts to deliver an intact molecule of bLF to the intestine have been made. Enteric-coated bLF resisted gastric digestion and was more efficiently absorbed than nonenteric-coated bLF (*20*, *22*). Liposomalization of bLF (bLF in enteric-formulated capsules protected in liposomes) reportedly enhances its anti-inflammatory activity, although liposomalization did not enhance the absorption of bLF from the intestine (*23*). These formulations, however, have the drawback that noncoated bLF is released from the capsules when they reach the intestine, resulting in degradation and inactivation of bLF in systemic circulation. In contrast, PEGylated bLF has the potential ability

not only of resistance to degradation in the stomach but also of stabilization in blood circulation.

In conclusion, PEGylated bLF with high biological activities and enhanced pharmacokinetic properties has been developed. PEGylation of bLF is a promising strategy for the improved oral delivery of bLF, and shows that the PEGylation technique may be a breakthrough in converting functional food proteins into pharmaceutical proteins.

ACKNOWLEDGMENT

We thank Professor H. Nyunoya and Associate Professor Y. Matsushita (Tokyo University of Agriculture and Technology, Tokyo, Japan) for determination of the N-terminal amino acid sequence. We also thank Kamakura Techno-Science Inc. (Kamakura, Japan) for large-scale preparation of purified 20k-PEG-bLf. This work was supported by grants from the New Energy and Industrial Technology Development Organization (NEDO).

LITERATURE CITED

(1) Levay, P. F., and Viljoen, M. (1995) Lactoferrin: a general review. *Haematologica 80*, 252–267.

(2) Farnaud, S., and Evans, R. W. (2003) Lactoferrin - a multifunctional protein with antimicrobial properties. *Mol. Immunol. 40*, 395–405.

(3) Arnold, R. R., Brewe, M., and Gauthier, J. J. (1980) Bactericidal activity of human lactoferrin: sensitivity of a variety of microorganisms. *Infect. Immun. 28*, 893–898.

(4) Lee, N. Y., Kawai, K., Nakamura, I., Tanaka, T., Kumura, H., and Shimazaki, K. (2004) Susceptibilities against bovine lactoferrin with microorganisms isolated from mastitic milk. *J. Vet. Med. Sci. 66*, 1267–1269.

(5) Ikeda, M., Sugiyama, K., Tanaka, T., Tanaka, K., Sekihara, H., Shimotohno, K., and Kato, N. (1998) Lactoferrin markedly inhibits hepatitis C virus infection in cultured human hepatocytes. *Biochem. Biophys. Res. Commun. 245*, 549–553.

(6) Yamauchi, K., Wakabayashi, H., Hashimoto, S., Teraguchi, S., Hayasawa, H., and Tomita, M. (1998) Effects of orally administered bovine lactoferrin on the immune system of healthy volunteers. *Adv. Exp. Med. Biol. 443*, 261–265.

(7) Ambruso, D. R., and Johnston, R. B., Jr. (1981) Lactoferrin enhances hydroxyl radical production by human neutrophils, neutrophil particulate fractions, and an enzymatic generating system. *J. Clin. Invest. 67*, 352–360.

(8) Mattsby-Baltzer, I., Roseanu, A., Motas, C., Elverfors, J., Engberg, I., and Hanson, LÅ. (1996) Lactoferrin or a fragment thereof inhibits the endotoxin-induced interleukin-6 response in human monocytic cells. *Pediatr. Res. 40*, 257–262.

(9) Håversen, L., Ohlsson, B. G., Hahn-Zoric, M., Hanson, L.Å., and Mattsby-Baltzer, I. (2002) Lactoferrin down-regulates the LPS-induced cytokine production in monocytic cells via NF-kappa B. *Cell. Immunol. 220*, 83–95.

(10) Kamemori, N., Takeuchi, T., Hayashida, K., and Harada, E. (2004) Suppressive effects of milk-derived lactoferrin on psychological stress in adult rats. *Brain. Res. 1029*, 34–40.

(11) Hayashida, K., Takeuchi, T., Shimizu, H., Ando, K., and Harada, E. (2003) Novel function of bovine milk-derived lactoferrin on antinociception mediated by mu-opioid receptor in the rat spinal cord. *Brain. Res. 965*, 239–245.

(12) Takeuchi, T., Shimizu, H., Ando, K., and Harada, E. (2004) Bovine lactoferrin reduces plasma triacylglycerol and NEFA accompanied by decreased hepatic cholesterol and triacylglycerol contents in rodents. *Br. J. Nutr. 91*, 533–538.

(13) Lyons, T. E., Miller, M. S., Serena, T., Sheehan, P., Lavery, L., Kirsner, R. S., Armstrong, D. G., Reese, A., Yankee, E. W., and Veves, A. (2007) Talactoferrin alfa, a recombinant human lactoferrin promotes healing of diabetic neuropathic ulcers: a phase 1/2 clinical study. *Am. J. Surg. 193*, 49–54.

(14) Wang, Y., Raghunadharao, D., Raman, G., Doval, D., Advani, S., Julka, P., Parikh, P., Patil, S., Nag, S., Madhavan, J., and Varadhachary, A. (2006) Adding oral talactoferrin to first-line NSCLC chemotherapy safely enhanced efficacy in a randomized trial. *J. Clin. Oncol. 2006 ASCO Annual Meeting Proceedings (Post-Meeting Edition) 24*, 7095.

(15) Jonasch, E., Stadler, W. M., Bukowski, R. M., Hayes, T. G., Varadhachary, A., Malik, R., Figlin, R. A., and Srinivas, S. (2008) Phase 2 trial of talactoferrin in previously treated patients with metastatic renal cell carcinoma. *Cancer. 113*, 72–77.

(16) Okada, S., Tanaka, K., Sato, T., Ueno, H., Saito, S., Okusaka, T., Sato, K., Yamamoto, S., and Kakizoe, T. (2002) Dose-response trial of lactoferrin in patients with chronic hepatitis C. *Jpn. J. Cancer. Res. 93*, 1063–1069.

(17) Kaito, M. (2005) Use of lactoferrin for chronic hepatitis C. *Hepatol. Res. 32*, 200–201.

(18) Ueno, H., Sato, T., Yamamoto, S., Tanaka, K., Ohkawa, S., Takagi, H., Yokosuka, O., Furuse, J., Saito, H., Sawaki, A., Kasugai, H., Osaki, Y., Fujiyama, S., Sato, K., Wakabayashi, K., and Okusaka, T. (2006) Randomized, double-blind, placebo-controlled trial of bovine lactoferrin in patients with chronic hepatitis C. *Cancer. Sci. 97*, 1105–1110.

(19) Takeuchi, T., Kitagawa, H., and Harada, E. (2004) Evidence of lactoferrin transportation into blood circulation from intestine via lymphatic pathway in adult rats. *Exp. Physiol. 89*, 263–270.

(20) Takeuchi, T., Jyonotsuka, T., Kamemori, N., Kawano, G., Shimizu, H., Ando, K., and Harada, E. (2006) Enteric-formulated lactoferrin was more effectively transported into blood circulation from gastrointestinal tract in adult rats. *Exp. Physiol. 91*, 1033–1040.

(21) Kitagawa, H., Yoshizawa, Y., Yokoyama, T., Takeuchi, T., Talukder, M. J., Shimizu, H., Ando, K., and Harada, E. (2003) Persorption of bovine lactoferrin from the intestinal lumen into the systemic circulation via the portal vein and the mesenteric lymphatics in growing pigs. *J. Vet. Med. Sci. 65*, 567–572.

(22) Shimizu, H. (2004) Development of an enteric-coated lactoferrin tablet and its application. *Biometals 17*, 343–347.

(23) Ishikado, A., Imanaka, H., Takeuchi, T., Harada, E., and Makino, T. (2005) Liposomalization of lactoferrin enhanced it's anti-inflammatory effects via oral administration. *Biol. Pharm. Bull. 28*, 1717–1721.

(24) Veronese, F. M., and Pasut, G. (2005) PEGylation, successful approach to drug delivery. *Drug Discovery Today 10*, 1451–1458.

(25) Wang, Y. S., Youngster, S., Grace, M., Bausch, J., Bordens, R., and Wyss, D. F. (2002) Structural and biological characterization of pegylated recombinant interferon alpha-2b and its therapeutic implications. *Adv. Drug Delivery Rev. 54*, 547–570.

(26) Bailon, P., Palleroni, A., Schaffer, C. A., Spence, C. L., Fung, W. J., Porter, J. E., Ehrlich, G. K., Pan, W., Xu, Z. X., Modi, M. W., Farid, A., Berthold, W., and Graves, M. (2001) Rational design of a potent, long-lasting form of interferon: a 40 kDa branched polyethylene glycol-conjugated interferon alpha-2a for the treatment of hepatitis C. *Bioconjugate Chem. 12*, 195–202.

(27) Kodera, Y., Tanaka, H., Matsushima, A., and Inada, Y. (1992) Chemical modification of L-asparaginase with a comb-shaped copolymer of polyethylene glycol derivative and maleic anhydride. *Biochem. Biophys. Res. Commun. 184*, 144–148.

(28) Cindric, M., Cepo, T., Galic, N., Bukvic-Krajacic, M., Tomczyk, N., Vissers, J. P., Bindila, L., and Peter-Katalinic, J. (2007) Structural characterization of PEGylated rHuG-CSF and location of PEG attachment sites. *J. Pharm. Biomed. Anal. 44*, 388–395.

(29) Levy, Y., Hershfield, M. S., Fernandez-Mejia, C., Polmar, S. H., Scudiery, D., Berger, M., and Sorensen, R. U. (1988) Adenosine deaminase deficiency with late onset of recurrent infections: response to treatment with polyethylene glycol-modified adenosine deaminase. *J. Pediatr. 113*, 312–317.

(30) Pradhananga, S., Wilkinson, I., and Ross, R. J. (2002) Pegvisomant: structure and function. *J. Mol. Endocrinol. 29*, 11–14.

(31) Calceti, P., Salmaso, S., Walker, G., and Bernkop-Schnürch, A. (2004) Development and in vivo evaluation of an oral insulin-PEG delivery system. *Eur. J. Pharm. Sci. 22*, 315–322.

(32) Jensen-Pippo, K. E., Whitcomb, K. L., DePrince, R. B., Ralph, L., and Habberfield, A. D. (1996) Enteral bioavailability of human granulocyte colony stimulating factor conjugated with poly(ethylene glycol). *Pharm. Res. 13*, 102–107.

(33) Laemmli, U. K. (1970) Cleavage of structural proteins during the assembly of the head of bacteriophage T4. *Nature 227*, 680–685.

(34) Kurfürst, M. M. (1992) Detection and molecular weight determination of polyethylene glycol-modified hirudin by staining after sodium dodecyl sulfate-polyacrylamide gel electrophoresis. *Anal. Biochem. 200*, 244–248.

(35) Shimazaki, K., and Hosokawa, T. (1991) A tentative method for rapid preparation of iron-saturated lactoferrin by affinity chromatography. *Anim. Sci. Technol. (Jpn.) 62*, 354–356.

(36) Kirkpatrick, C. H., Green, I., Rich, R. R., and Schade, A. L. (1971) Inhibition of growth of Candida albicans by iron-unsaturated lactoferrin: relation to host-defense mechanisms in chronic mucocutaneous candidiasis. *J. Infect. Dis. 124*, 539–544.

(37) Anderson, B. F., Baker, H. M., Norris, G. E., Rumball, S. V., and Baker, E. N. (1990) Apolactoferrin structure demonstrates ligand-induced conformational change in transferrins. *Nature 344*, 784–787.

(38) Shimazaki, K. (2000) Lactoferrin: a marvelous protein in milk. *Animal Sci. J. (Nihon. Chikusan. Gakkaiho.) 71*, 329–347.

(39) Tomita, M., Takase, M., Bellamy, W., and Shimamura, S. (1994) A review: the active peptide of lactoferrin. *Acta Paediatr. Jpn. 36*, 585–591.

(40) Elass-Rochard, E., Roseanu, A., Legrand, D., Trif, M., Salmon, V., Motas, C., Montreuil, J., and Spik, G. (1995) Lactoferrin-lipopolysaccharide interaction: involvement of the 28−34 loop region of human lactoferrin in the high-affinity binding to *Escherichia coli* 055B5 lipopolysaccharide. *Biochem. J. 312*, 839–845.

(41) Di, Biase, A. M., Pietrantoni, A., Tinari, A., Siciliano, R., Valenti, P., Antonini, G., Seganti, L., and Superti, F. (2003) Heparin-interacting sites of bovine lactoferrin are involved in anti-adenovirus activity. *J. Med. Virol. 69*, 495–502.

(42) van Berkel, P. H., Geerts, M. E., van Veen, H. A., Mericskay, M., de Boer, H. A., and Nuijens, J. H. (1997) N-terminal stretch Arg2, Arg3, Arg4 and Arg5 of human lactoferrin is essential for binding to heparin, bacterial lipopolysaccharide, human lysozyme and DNA. *Biochem. J. 328*, 145–151.

BC800258V

Design, Synthesis, and *In Vitro* Activity of Novel Drug Delivery Systems Containing Tuftsin Derivatives and Methotrexate

Katalin B. Bai,[†] Orsolya Láng,[§] Erika Orbán,[†] Rita Szabó,[†] László Köhidai,[§] Ferenc Hudecz,[†,‡] and Gábor Mezö*[,†]

Research Group of Peptide Chemistry, Hungarian Academy of Sciences, and Department of Organic Chemistry, Eötvös L. University, P.O. Box 32, 1518 Budapest 112, Hungary, and Department of Genetics, Cell and Immunobiology, Semmelweis University, Budapest, Nagyvárad tér 4. H-1089, Hungary. Received March 20, 2008; Revised Manuscript Received September 22, 2008

During the past decade, biodegradable polymers or oligopeptides recognized by cell-surface receptors have been shown to increase drug specificity, lowering systemic drug toxicity in contrast to small-size fast-acting drugs. The goal of the present study was to develop anticancer bioconjugates based on chemotactic drug targeting (CDT). These constructs are composed of methotrexate (Mtx) attached to a tuftsin-like peptide carrier through an enzyme-labile pentapeptide spacer (GFLGC) and several copies of a chemotactic targeting moiety (H-TKPR, For-TKPR, H-TKPKG, and Ac-TKPKG). Carriers with targeting moieties in the branches were prepared by solid-phase synthesis using mixed Boc and Fmoc strategies. The drug molecule connected to an enzyme-labile spacer was attached to the branched oligopeptide in solution. *In vitro* chemotaxis, cellular uptake, and cytotoxicity assays were carried out on the MonoMac6 cell line. The most effective conjugates with H-TKPR or Ac-TKPKG targeting moieties in the branches, which have the most advantageous chemotactic properties, can be internalized rapidly, and these conjugates trigger higher toxic effect than the free drug (Mtx). The results suggest that our tuftsin-based drug delivery systems might be potential candidates for targeting cancer chemotherapy.

INTRODUCTION

Numerous drug delivery systems (DDS) have been developed over the years to establish novel antitumor therapeutics. The main goal of these developments is the investigation of various approaches toward targeting toxic drugs to tumor cells using their conjugated forms with carriers and/or targeting moieties. In this way, a controlled location and higher concentration of toxic drugs can be reached at the site of action; furthermore, side effects and therapeutical doses can be reduced. The application of drug delivery systems for targeting chemotherapy might result in increased selectivity and efficiency in the cancer treatment (*1, 2*).

Peptide-based biodegradable conjugates represent one group of DDS. These conjugates consist of a drug molecule, an enzyme-labile or pH-sensitive spacer sequence, a biodegradable peptide carrier, and targeting moieties (e.g., peptide hormones, lectins, sugars, or antibodies) (*3*), which have been shown to bind to cell-surface receptors and can be internalized by receptor-mediated endocytosis. Chemotactic drug targeting (CDT), a special form of drug targeting, was investigated in our laboratory (*4*). Previously, we reported on the synthesis of chemotactic drug delivery systems for drug targeting. We used the well-known chemotactic peptides (For-Met-Leu-Phe and For-Nle-Leu-Phe) as targeting moieties, capable to bind to specific chemotactic receptors on phagocytic cells (*5*). In this study, we have further developed this system by modifying the chemotactic targeting moieties. Conjugates composed of chemotactically active ligands (chemotactic peptides), drug, and carrier induce chemotactic activity of target cells. In this way, responder cells accumulate in the high-concentration region of tissues, and internalization of the drug is also increased. To achieve conjugates suitable for CDT, chemotactic peptides as targeting moieties were built up as branches in the carrier.

In this study, a sequential oligopeptide, a tetratuftsin derivative, was applied as carrier. Human tuftsin, a naturally occurring tetrapeptide (H-TKPR-OH) was described by Najjar and Nishioka in 1970 (*6*). Tuftsin is the 289−292 sequence in the CH2 domain of the Fc fragment of the heavy chain of IgG (*7*). It is an immunopotentiating peptide, which stimulates phagocytosis and cell migration (*8*) and possesses antitumor activity (*9, 10*). In our present study, a tuftsin analogue (H-TKPK-OH) derived from canin and having human tuftsin-like activities, elongated with Gly at the *C*-terminal (H-TKPKG-OH), was used. The carrier in multifunctional conjugates was the H-$[TKPKG]_4$-NH_2 tetramer (OT20) (*11*). Inasmuch as the human tuftsin and its analogue have a chemotactic effect on monocytes (*12, 13*), these peptides and their formylated or acetylated derivatives at the *N*-terminal were attached to the carrier and applied as targeting moieties (H-TKPR, For-TKPR, H-TKPKG, Ac-TKPKG) in the branches.

Methotrexate, (*S*)-2-(4-(((2,4-diaminopteridin-6-yl)methyl)-methylamino)benzamido)pentanedioic acid (Mtx), an antimetabolite and antifolate molecule was incorporated as an anticancer drug. Mtx is used for chemotherapy in cancers and autoimmune diseases (*14*−*16*). It is mainly applied for the treatment of acute lymphoblastic leukemia (*17*), but it is also used against leishmania (*18, 19*) or in the treatment of rheumatoid arthritis (RA) (*20*). However, methotrexate could cause severe toxicity; the most frequent reactions include low white blood cell counts and toxicity of the liver and bone marrow resulting in immunosuppression.

To decrease the toxic side effects, the release of free drug molecules in target cells is important. The release of the Mtx from the conjugates can be influenced by the type of linkage applied between the drug and the carrier. The use of specific

* Correspondence to Dr. Gábor Mező, Research Group of Peptide Chemistry, Hungarian Academy of Sciences, Eötvös L. University, 1117 Budapest, Pázmány Péter sétány 1/A, Hungary; e-mail: gmezo@elte.hu; Tel: (+36)-1-209-0555/1426; Fax: (+36)-1-372-2620.

[†] Research Group of Peptide Chemistry, Hungarian Academy of Sciences, Eötvös L. University.

[‡] Department of Organic Chemistry, Eötvös L. University.

[§] Semmelweis University.

10.1021/bc800115w CCC: $40.75 © 2008 American Chemical Society
Published on Web 10/30/2008

oligopeptide sequences recognized by intracellular enzymes is a promising approach for increasing the site-specific release of the drug; therefore, Mtx was coupled to the carrier *via* a cathepsin B-cleavable tetrapeptide spacer sequence (GFLG). This linker is frequently used in drug conjugates and could be cleaved in the lysosomes (*21*, *22*). For the present study, the spacer sequence was elongated at the *C*-terminal with a cysteine to introduce a thiol group for conjugation through the thioether bond to the carrier.

In this paper, the synthesis and characterization as well as the chemotactic and cytotoxic properties of the new bioconjugates and their components (carrier, carrier with targeting moieties in the branches, Mtx, and Mtx-spacer) are reported. To ensure the release of the drug from the conjugates, enzymatic digestions were investigated using Cathepsin B. The chemotaxis, cellular uptake, and apoptosis assays were carried out on human MonoMac6 cell line, representing monocytic cells with a closely related pattern of surface receptors, and they display phenotypic and functional features of mature human monocytes and macrophages (*23*). Inasmuch as monocytes and macrophages express tuftsin receptors (*24*, *25*), MonoMac6 cells might express these receptors as well. In this way, we can ensure that our conjugates might be internalized by receptor-mediated endocytosis.

Chemotaxis assays were carried out with the Mtx-conjugates and with their components. Each of the conjugates could elicit significant chemotactic effect on MonoMac6 cells. Cellular uptake of the CF-labeled analogues of the conjugates was studied by flow cytometry. Rapid internalization of each CF-labeled conjugate was observed. We investigated the cytotoxicity of Mtx-conjugates and Mtx *via* apoptosis assay on the MonoMac6 cell line. Mtx-conjugates and the Mtx itself induced significant cell death at 1 μM concentration after 24 or 48 h. Our data show that MonoMac6 cells are highly susceptible to the toxic effects of the conjugates through enhanced cell death by necrosis.

Our results indicated that these kind of drug delivery systems are rather effective on the MonoMac6 cell line. Some of our conjugates were attractants for the cells, could be taken up considerably, and could elicit a toxic effect inside the cells.

EXPERIMENTAL PROCEDURES

Materials. Amino acid derivatives were purchased from Reanal (Budapest, Hungary) or NovaBiochem (Läufelfingen, Switzerland), MBHA and Rink-Amide MBHA resins were NovaBiochem products. Reagents for synthesis [*N*,*N*′-dicyclohexylcabodiimide (DCC), *N*,*N*′-diisopropylcarbodiimide (DIC), *N*-diisopropyl-ethylamine (DIEA), 1-hydroxybenzotriazole (HOBt), 1,8-diazabicyclo-[5.4.0]undec-7-ene (DBU), piperidine, trifluoroacetic acid (TFA), hydrogen fluoride (HF), *p*-cresol, *p*-thiocresol, thioanisole, phenol, 1,2-ethanedithiol (EDT), 1,4-DL-dithiothreitol (DTT), and 5(6)-carboxyfluorescein (CF) were purchased from Fluka (Buchs, Switzerland). Acetic anhydride (Ac_2O), dimethylsulfoxide (DMSO), and solvents for the synthesis were obtained from Reanal. HPLC-grade acetonitrile and 3-(4,5-dimethylthiazol-2-yl)-2,5-diphenyltetrazolium bromide (MTT) were ordered from Sigma-Aldrich Kft. (Budapest, Hungary). Methotrexate was purchased from Lederle Laboratories (Gosport, UK). Chloroacetic acid pentachlorophenyl ester (ClAc-OPcp) and formic acid trichlorophenyl ester (For-OTcp) were prepared in our laboratory from the appropriate acids and phenol derivatives (Fluka products) with DCC according to the method described by Martinezet al. (*26*).

Synthesis of the Components: H-TKPR-NH_2 (1), H-TKPKG-NH_2 (2), Ac-[TKPKG]$_4$-NH_2 (OT20) (3). The peptides were built up on MBHA resin (1.04 mmol/g capacity) by stepwise synthesis using standard Boc chemistry. The synthetic protocol was as follows: (i) washing of the resin with DCM (3 × 0.5 min), (ii) removal of Boc protecting groups with 33% TFA in DCM (2 + 20 min), (iii) DCM washing (5 × 0.5 min), (iv) neutralization with 10% DIEA in DCM (4 × 1 min), (v) DCM washing (4 × 0.5 min), (vi) coupling of 3 equiv Boc-amino acid derivative-DCC-HOBt (60 min), (vii) DMF washing (3 × 1 min), (viii) DCM washing (2 × 0.5 min), and (ix) ninhydrin or isatin assay (*27*, *28*). The following amino acid derivatives were applied: Boc-Thr(Bzl)-OH, Boc-Lys(ClZ)-OH, Boc-Pro-OH, Boc-Gly-OH, and Boc-Arg(Tos)-OH. After the synthesis, the components, which were used as control peptides in the bioassays, were cleaved from the resin simultaneously with the removal of the protecting groups in the presence of *p*-cresol, using HF (10 mL HF/1 g *p*-cresol). The cleavage was carried out at 0 °C for 90 min. The crude peptides were purified by reverse-phase high-performance liquid chomatography (RP-HPLC), and the purified components were characterized by analytical RP-HPLC and electrospray ionization mass spectrometry (ESI-MS) (Table 1).

Table 1. Characteristics of Compounds

code	R_t[a] (min)	[M][b] calculated	[M][b] found
1	7.8	499.3	499.5
2	7.6	528.4	529.7
3	12.5	2103.4	2103.2
4	11.4	4036.1	4035.7
5	14.6	4148.1	4147.8
6	10.8	4152.4	4152.0
7	13.9	4320.4	4320.1
8	11.5	4275.0	4274.9
9	14.6	4387.0	4386.8
10	10.8	4391.1	4391.1
11	14.1	4559.1	4559.4
12	24.5	930.7	930.3
13	22.3	6063.4	6063.4
14	23.0	6175.4	6175.5
15	23.2	6182.5	6182.3
16	23.4	6348.5	6348.8
17	31.3,32.1	851.9	852.3
18	26.0	5909.0	5909.2
19	26.6	6020.2	6020.9
20	26.7	6024.5	6024.2
21	26.9	6192.2	6192.3

[a] RP-HPLC column: Phenomenex Synergy C_{12} (4 μm, 80 Å, 250 × 4.6 mm); eluents: 0.1% TFA/water (A eluent), 0.1% TFA/acetonitrile-water 80:20 v/v (B eluent); flow rate 1 mL/min; gradient: 0 min 0% B, 5 min 0% B, 50 min 90% B. [b] ESI-MS was performed on a Bruker Esquire 3000+ ion trap mass spectrometer. Standard resolution mode resolving 2+ ions @ 13 000 u/s. Maximum resolution mode resolving 3+ and 4+ ions @ 1650 u/s. Extended mass range 200−6 000 *m*/*z* @ 27 000 u/s. Unsurpassed sensitivity in the low pg range.

Synthesis of the Branched Chain Oligopeptides: Ac-[TKPK(H-TKPR)G]$_4$-NH_2 (4), Ac-[TKPK(For-TKPR)G]$_4$-NH_2 (5), Ac-[TKPK(H-TKPKG)G]$_4$-NH_2 (6), Ac-[TKPK-(Ac-TKPKG)G]$_4$-NH_2 (7). The carrier backbone was built up on MBHA resin using the Boc strategy as described earlier (*29*). The following amino acid derivatives were applied: Boc-Thr(Bzl)-OH, Boc-Pro-OH, Boc-Gly-OH, Boc-Lys(ClZ)-OH in position 2, and Boc-Lys(Fmoc)-OH in position 4 in the repeat units. Prior to the synthesis of the branches, the *N*-terminus of the backbone was acetylated. Fmoc groups of the lysine side chains were removed selectively and the appropriate branches were built up in every second lysine residue using the mixed Fmoc/Bzl strategy. For this, the following amino acid derivatives were used: Fmoc-Arg(Pbf)-OH, Fmoc-Gly-OH, Fmoc-Lys(ClZ)-OH, Fmoc-Pro-OH, Fmoc-Thr(Bzl)-OH, and Z-Thr-OH.

In the case of peptides H-TKPR and H-TKPKG in the branches (peptides **4** and **6**), Z-Thr-OH was used for the incorporation of the *N*-terminal amino acid. In this way, a free amino terminus was formed in the branches after removal of the protecting groups with HF. In the case of For-TKPR and

Ac-TKPKG in the branches (branched peptides **5** and **7**), Fmoc-Thr(Bzl)-OH was applied. After the removal of the last Fmoc group from the *N*-terminus of the branches, a formyl (compound **5**) or acetyl group (compound **7**) was attached to the free α-amino groups using either For-OTcp (20 equiv in DMF for 3 h) or Ac_2O (Ac_2O/DIEA/DMF = 1:1:3 mL for 0.5 h).

The branched peptides were cleaved with HF, were purified and characterized in the same way as described above. Characteristics of the purified compounds are listed in Table 1.

Synthesis of the Branched Peptides with Chloroacetylated *N*-Terminal Lysine in the Backbone: ClAc-K(ClAc)-[TKPK(H-TKPR)G]$_4$-NH$_2$ (8), ClAc-K(ClAc)-[TKPK(For-TKPR)G]$_4$-NH$_2$ (9), ClAc-K(ClAc)-[TKPK(H-TKPKG)G]$_4$-NH$_2$(10),ClAc-K(ClAc)-[TKPK(Ac-TKPKG)-G]$_4$-NH$_2$ (11). The carrier backbone was built up on MBHA resin using the Boc strategy as described above, and a Boc-Lys(Boc)-OH was attached to the *N*-terminus using DIC/HOBt activation. Fmoc groups were removed and the branches were built up to form the chemotactic targeting sequences similarly to peptide **4**−**7**. Boc groups from *N*-terminal Lys were removed, and chloroacetylation was performed using 10 equiv of ClAc-OPcp in DMF. The chloroacetylated peptides were cleaved and worked up similarly to the previously described derivatives, but 10 mL HF/0.5 g *p*-cresol and 0.5 g *p*-thiocresol was used as the cleavage mixture that is suggested to haloacetylated peptides (*30*). The reaction time was 90 min at 0 °C. The crude peptides were purified by semipreparative RP-HPLC, and the purified components were characterized by analytical RP-HPLC and ESI-MS. Analytical data of chloroacetylated peptides are presented in Table 1.

Synthesis of Mtx$^{\gamma}$-GFLGC-NH$_2$ (12) and CF-GFLGC-NH$_2$ (17). The synthesis and isomer separation of Mtx-GFLGC-NH_2 peptide were published earlier (*4*). The Mtx-containing GFLGC peptide was built up on Rink-Amide MBHA resin using standard Fmoc chemistry. The synthetic protocol was as follows: (i) washing of the resin with DMF (3 × 1 min), (ii) removal of Fmoc protecting groups with 2% piperidine and 2% DBU in DMF (2 + 2 + 5 + 20 min), (iii) DMF washing (8 × 1 min), (iv) coupling of 3 equiv Fmoc-amino acid derivative-DIC-HOBt (60 min), (v) DMF washing (3 × 1 min), (vi) DCM washing (2 × 0.5 min), and (vii) ninhydrin or isatin assay (*27*, *28*). A trityl group was used for the side chain protection of Cys. The peptide was cleaved from the resin with 10 mL TFA using scavengers (phenol/thioanisole/EDT/water = 0.75 g/0.5 mL/0.25 mL/0.5 mL). The crude products were purified, and the isomers were separated by semipreparative RP-HPLC. CF-GFLGC-NH_2 was prepared in the same way, but the isomers of 5(6)-carboxyfluoresceine were not separated. The pure compounds were characterized by analytical HPLC and ESI-MS (Table 1).

Conjugation of the Chloroacetylated Peptides with Mtx$^{\gamma}$-GFLGC-NH$_2$ or CF-GFLGC-NH$_2$ (13−16 and 18−21). The chloroacetylated peptides were dissolved in 0.1 M Tris buffer (pH 8.2) at 10 mg/mL peptide concentration and Mtx$^{\gamma}$-GFLGC-NH_2 or CF-GFLGC-NH_2 was added to the solution in solid form at regular intervals. Under these conditions, thioether bonds can be formed between the chloroacetyl group of the branched peptides and the thiol group of the Cys in the spacer sequence resulting in compounds **13**−**16** and **18**−**21**. The conjugation reaction was monitored by analytical HPLC. At the end of the reaction, the mixtures were acidified and purified by RP-HPLC directly. The yields of the conjugations were 50−60% calculated for the carrier. The pure compounds were characterized by analytical RP-HPLC and ESI-MS (Table 1).

Reverse-Phase High-Performance Liquid Chomatography (RP-HPLC). Analytical RP-HPLC was performed on a Knauer (H. Knauer, Bad Homburg, Germany) HPLC system using a Phenomenex Synergy C_{12} column (4 μm, 80 Å, 250 × 4.6 mm I.D.) (Torrance, CA) as the stationary phase. Linear gradient elution (0 min 0% B, 5 min 0% B, 50 min 90% B) was used with the following eluents: 0.1% TFA/water (A eluent), 0.1% TFA/acetonitrile−water 80:20 v/v (B eluent). The flow rate was 1 mL/min at ambient temperature, and the peaks were detected at λ = 220 nm.

The crude peptides and conjugates were purified on a semipreparative Phenomenex Jupiter C_{18} column (10 μm, 300 Å, 250 × 10 mm I.D.) (Torrance, CA). The applied flow rate was 4 mL/min at ambient temperature, and the peaks were detected at λ = 220 nm. The same eluents as described above with an appropriate linear gradient were applied.

Electrosray Ionization Mass Spectromerty (ESI-MS). ESI-MS was performed on a Bruker Esquire 3000+ Ion trap mass spectrometer (Bremen, Germany), operating in continuous sample injection mode at 4 μL/min flow rate. Samples were dissolved in 50% acetonitrile/50% water containing 0.01% acetic acid. Mass spectra were recorded in positive ion mode in the *m*/*z* 200−1500 range.

Enzymatic Digestion by Cathepsin B. Conditions for digestion (enzyme concentration, pH, temperature) were chosen to approximate the lysosomal medium as a model for intracellular drug release. Compounds **12** and **15** were dissolved in a solution of 5 mM cysteine/2 mM EDTA (pH = 5). For the digestions, 200 μL aliquots of the solutions were used, and 0.1 unit of human liver cathepsin B (Merck Kft., Budapest, Hungary) was added to the solutions. The mixtures—giving the following initial concentrations: [cathepsin B]:[substrate] = 1:50—were incubated at 37 °C for 15 min and 1 h. Stabilities of the compounds were also measured without cathepsin B at pH 5 under the same conditions. After the incubation, the enzyme-containing solutions as well as the control samples were measured using tandem mass spectrometry, and the fragments were identified.

Cell Culture. Human monocytic MonoMac6 cells were grown in suspension in RPMI-1640 (Sigma Ltd. St. Louis, MO) supplemented with 10% heat-inactivated fetal calf serum (FCS; Gibco, Cergy-Pontoise, France) L-glutamine (2 mM) and gentamicin (35 μM). Cells were routinely maintained on plastic tissue culture dishes at 37 °C in an incubator with a humidified atmosphere containing 5% CO_2/95% air.

Chemotaxis Assay. The chemotactic ability of MonoMac6 cells was evaluated using a 96-well modified Boyden chamber (NeuroProbe, Gaithersburg, MD) (*31*). Polycarbonate filters with a pore size of 8 μm were used. Due to the requirements of cell-physiological experiments, the peptides were dissolved in an identical substance to culturing free of the ligand to be studied. For this purpose, RPMI-1640 supplemented with 10% heat-inactivated FCS, L-glutamine (2 mM/mL), and gentamicin (35 μM) was used. The concentration dependence of the chemotactic response was determined to be in the 0.0001−1 μM range. The 96-well plate was placed into the chamber, 395 μL of peptide solution was added to the bottom wells for each experiment, and the chamber was locked. The cells in medium (100 μL) at density of 10^5 cell/mL were applied to each of the top wells. The incubation time was 3 h at 37 °C in a humidified atmosphere containing 5% CO_2/95% air, allowing migration across the membrane. After the incubation, nonmigrated cells were removed from the upper surface of the membrane, and the number of cells, which were migrated into the 96-well plate through a filter, was determined by the 3-(4,5-dimethylthiazole-2-yl)-2,5-diphenyl-tetrazolium bromide (MTT) assay (*32*, *33*). For this, 20 μL of 12 μM MTT solution was added to wells. Cells were incubated with MTT at 37 °C for 24 h, then the plates were centrifuged at 2000 rpm for 5 min. Sample supernatants were removed, formazan crystals were solubilized in DMSO,

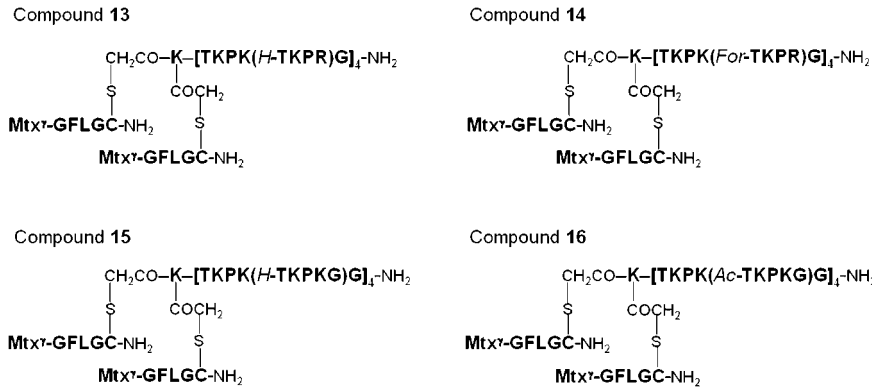

Figure 1. Schematic structure of the Mtx conjugates.

and the colorimetric measurement was carried out by an ELISA reader (Labsystems Multiscan MS-Reader, Helsinki, Finland) at $\lambda = 540$ and $\lambda = 620$ nm. Each data point represents the average of fifteen parallel measurements.

Cellular Uptake. MonoMac6 cells were cultured in RPMI-1640 supplemented with 10% FCS, L-glutamine (2 mM), and gentamicin (35 μM). Cell culture was maintained at 37 °C in a humidified atmosphere with 5% CO_2. To study the cellular uptake of fluorescent-labeled analogues of the conjugates, 10^5 cells per well were plated on 24-well plates. After 24 h incubation at 37 °C, cells were treated with the conjugates dissolved in serum-free RPMI-1640 for 1.5 h. The compounds were used in the 0.1−100 μM concentration range. Cells treated with serum-free medium for 1.5 h were used as control. After incubation, cells were washed with HPMI (glucose, $NaHCO_3$, NaCl, HEPES, KCl, $MgCl_2$, $CaCl_2$, $Na_2HPO_4 \times 2H_2O$) and were treated with trypsin for 10 min. The trypsinization was stopped by HPMI supplemented with 10% fetal calf serum, and cells were moved from the plate to FACS tubes. After washing, cells were resuspended in HPMI. The increase of the fluorescence of MonoMac6 cells after this preparation was monitored by flow cytometry (BD LSR II, BD Bioscience, San Jose, CA). Data were analyzed with *FACSDiVa* software. Fluorescence mean values of the untreated control were subtracted from the mean fluorescence of treated samples. Statistical analysis of data was performed using the Student's *t* test at the 95% confidence level.

Annexin V Apoptosis Assay. Mtx and Mtx-conjugates were dissolved in RPMI-1640 supplemented with 10% heat-inactivated FCS, L-glutamine (2 mM), and gentamicin (35 μM). Flow cytometry and cell staining was applied with fluorescein isothiocyanate- (FITC) labeled annexin-V (green fluorescence) (*34*−*37*), simultaneously with propidium iodide (PI) stain (red fluorescence) (*38*), to discriminate intact cells from apoptotic cells and necrotic cells after treatment with the conjugates and Mtx. The apoptotic/necrotic effect of Mtx and of conjugates was determined in the 0.01−1 μM range. Briefly, after cultured cells were pretreated with Mtx or conjugates for 3, 24, and 48 h at 37 °C in a humidified atmosphere containing 5% CO_2, cells were harvested and washed with phosphate-buffered saline (PBS). Cells were then resuspended in 100 μL of Annexin-V binding buffer (10 mM HEPES, 140 mM NaCl, and 2.5 mM $CaCl_2$, pH 7.4), incubated with 5 μL of Annexin-V-FITC at room temperature in the dark for 15 min followed by adding 400 μL of Annexin-V binding buffer to the cells. The cell suspensions were vortexed and analyzed immediately by flow cytometry using a Becton Dickinson FACS-Calibur flow cytometer with *Cell Quest* software (Becton Dickinson, Mountain View, CA). Finally, 5 μL PI was added to each tube, and the tubes were vortexed and analyzed again by flow cytometry. Untreated cells displayed 0% annexin+/PI− (early apoptosis) and 0% annexin−/PI+ (necrosis) after 3, 24, and 48 h incubation.

Statistical Evaluation of Data. Data shown in the figures demonstrate the averages ± SE values. The statistical analysis was done by the application of the *t* test of *Origin 7.0*.

RESULTS AND DISCUSSION

New anticancer drug delivery systems based on chemotactic drug targeting (CDT) were developed consisting of Mtx as the anticancer drug attached to an immunomodulatory carrier molecule through an enzyme-labile peptide spacer and targeting sequences with chemotactic activities. Four novel Mtx-conjugates (Figure 1), their Mtx-CF exchanged analogues, and their components were synthesized, purified, and characterized. These peptide conjugates were tested in various relevant biological assays: chemotaxis, cellular uptake, and cytotoxicity on the MonoMac6 cell line.

Synthesis. Linear peptides representing the components of the designed chemotactic branched oligopeptides and the carrier backbone (tetratuftsin derivative) were synthesized by standard Boc chemistry. The branches on carrier backbone were built up using Fmoc/Bzl strategy. In the case of the branched peptides without Mtx, the *N*-terminus of the backbone was acetylated (**4**−**7**), as outlined in Scheme 1. In the case of the drug or CF-labeled oligopeptide conjugates, an additional Lys residue was coupled to the *N*-terminus of the carrier backbone, and then both α- and ε-amino groups were chloroacetylated to form two conjugation sites (Scheme 2). Peptides were cleaved from the resin with liquid HF in the presence of appropriate scavengers. In addition, Mtx or CF containing spacer peptides (GFLG) elongated with a Cys residue at the *C*-terminus (Mtx$^{\gamma}$-GFLGC-NH_2 (**12**), CF-GFLGC-NH_2 (**17**)) were synthesized by Fmoc chemistry. The peptides were purified by RP-HPLC. The isomers (α, α-D, and γ) of Mtx containing peptide could be separated (*4*), but in case of the 5- and 6-carboxyfluoresceine derivatives, the separation was not successful. In order to form conjugates, the purified chloroacetylated branched oligopeptides were dissolved in 0.1 M Tris buffer (pH 8.2), and Mtx$^{\gamma}$-GFLGC-NH_2 or CF-GFLGC-NH_2 was added to the solution in solid form at regular intervals over 3 h at RT. Under these conditions, a thioether bond was formed between the chloroacetyl group of the branched oligopeptides and the thiol group of the cysteine in the spacer peptide resulting in compounds **13**−**16** (Scheme 2) and **18**−**21**. All compounds were purified by RP-HPLC and characterized by analytical HPLC and ESI-MS (Table 1). The chemoselective ligation followed by RP-HLPC purification resulted in conjugates (Figure 1) with 50−60% yields and 93−97% purity in all cases. While the two isomers of CF-

Scheme 1. Synthesis of Acetylated Branched Peptides

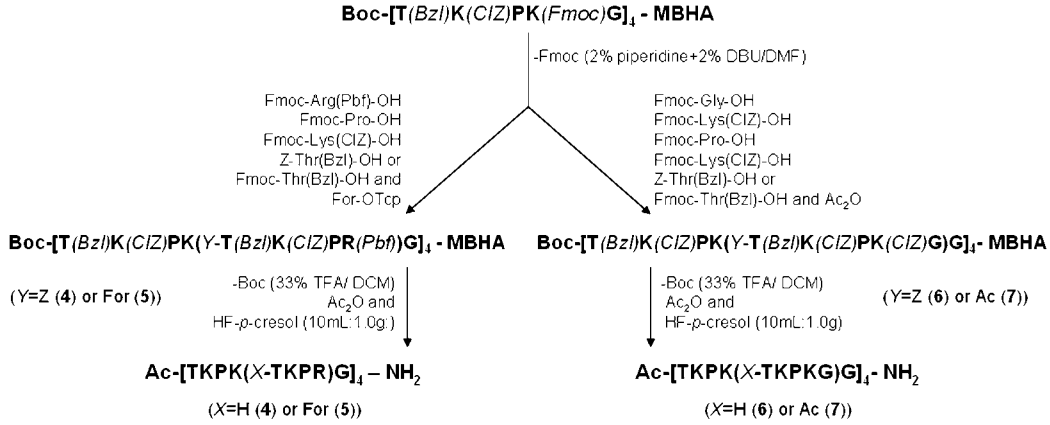

Scheme 2. Synthesis of Mtx-Conjugates

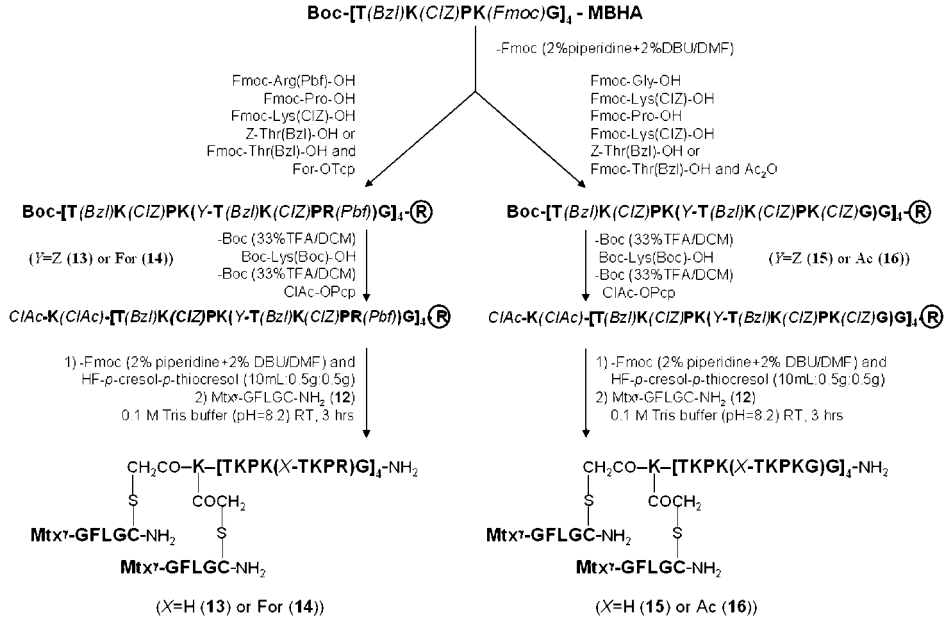

GFLGC-NH_2 were separated on the applied analytical HPLC column, the CF labeled conjugates (**18**−**21**) gave only single peaks.

Enzymatic Digestion by Cathepsin B. To determine the intracellular drug release enzymatic digestions with cathepsin B, a lysosomal enzyme, were carried out with the drug-spacer Mtx^{γ}-GFLGC-NH_2 (**12**) and conjugate **15** (Figure 1). In both cases, the main fragment split by cathepsin B was Mtx^{γ}-Gly-OH ($[M + H^+] = 512.3$), but Mtx^{γ}-Gly-Phe-OH ($[M + H^+] = 659.4$) and Mtx^{γ}-Gly-Phe-Leu-Gly-OH ($[M + H^+] = 829.5$) fragments were also identified by mass spectrometry. However, no significant enzymatic cleavage between Leu and Gly was observed (Figure 2). In the case of the conjugate (compound **15**), the multiple charged peaks of $[M + H^+] = 4560.0$ fragment (381.4 (12+); 415.4 (11+); 457.0 (10+); 506.3 (9+); 570.9 (8+); 652.5 (7+)) were also detected, which do not include the two Mtx^{γ}-GFLG sequences on the carrier backbone (Figure 3). No significant split in the oligotuftsin backbone could be detected, and the cleavage pattern did not change when the incubation time was increased from 15 min to 1 h. Our results suggested that the main cleavage site is between the Gly and Phe amino acid residues in the spacer sequence; thus, the drug can be released from the conjugates in the lysosomes. It is worth noting that the cleavage of the Ala-Cys bond in the lysosomal preparations was observed in the case of a conjugate of H-LLEDPVGTVAC-NH_2 (HSV epitope peptide) attached to the OT20 carrier through a thioether bond (*39*). On the basis of this similarity, we can hypothesize that peptides with Cys-amide at the *C*-terminus might provide a cleavage site for cathepsin B, which cannot be prevented by conjugation of Cys through thioether bond. This type of conjugation with an appropriate spacer sequence might provide some benefits to an effective drug release from drug delivery systems.

Chemotactic Activity of Compounds 1, 2, and 3. Chemotactic activity of H-TKPR-NH_2 (**1**), H-TKPKG-NH_2 (**2**), and Ac-[TKPKG]$_4$-NH_2 (OT20) (**3**) was examined. Compound **1** triggered a significant chemoattractant effect at 1 μM (337.9 ± 7.6%) and 10^{-3} μM (203.0 ± 5.0%), but at 10^{-1} μM, it was repellent (68.8 ± 18.2%), and at the other concentrations, it was neutral. In contrast, compound **2** was significantly repellent at 10^{-1} μM (55.6 ± 18.2%) and 10^{-4} μM (75.0 ± 7.8%), and neutral at the other concentrations. The tetratuftsin derivative carrier (**3**) also had chemorepellent behavior at 1 μM (56.5 ± 20.3%). However, no significant chemoattractant or chemorepellent effect was observed at the other concentrations on MonoMac6. These data indicated that the oligomerization of H-TKPKG-NH_2 (**2**) produced a carrier molecule (**3**) without a significant change of chemotactic activity (Supporting Information S2).

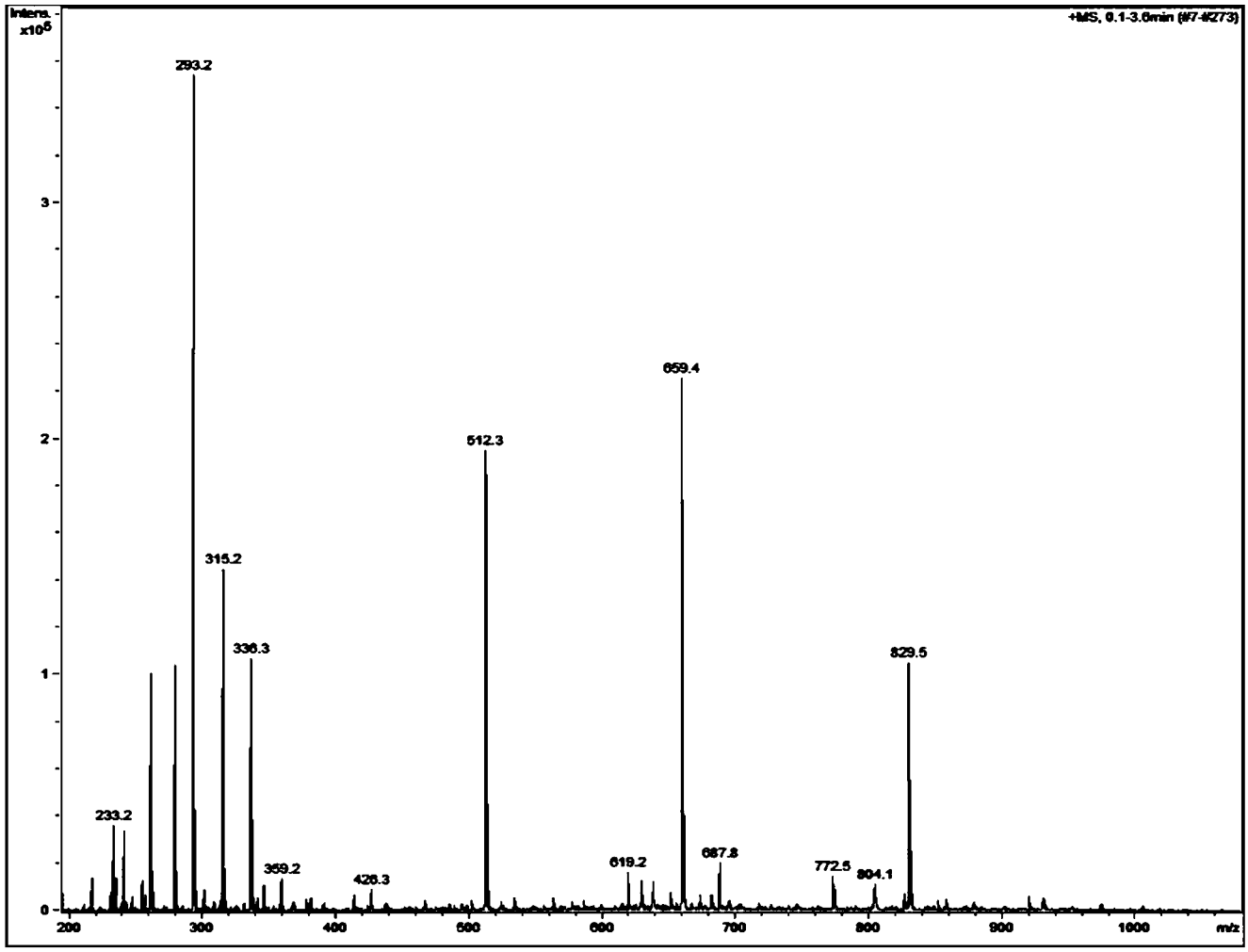

Figure 2. Mass spectrum of Mtx$^{\gamma}$-GFLGC-NH_2 (**12**) after digestion with cathepsin B.

Chemotactic Activity of Mtx and Mtx$^{\gamma}$-GFLGC-NH_2. Chemotactic activity of Mtx and Mtx$^{\gamma}$-GFLGC-NH_2 (**12**) molecules was also tested on MonoMac6. The Mtx itself was significantly repellent at the lower concentration range (10^{-2} μM, 47.3 ± 14.6%, 10^{-3} μM, 78.6 ± 19.6%; 10^{-4} μM, 66.9 ± 20.7%) and neutral at the higher concentrations. In contrast to Mtx, compound **12**, the drug containing enzyme sensible spacer sequence of the total CDT bioconjugate, was found to be significantly attractant at the lower concentration range (10^{-2} μM: 145.5 ± 4.8%, 10^{-3} μM: 153.5 ± 4.6%, 10^{-4} μM: 138.5 ± 6.5%), but it was repellent at the highest concentration (1 μM: 63.5 ± 16.1%). The effect of GFLGC on the repellent moiety of Mtx seems to be very advantageous with respect to the biological/clinical activity of the CDT bioconjugate (Supporting Information S3).

Chemotactic Activity of the Branched Peptides and the Mtx-Containing Bioconjugates. Four different targeting moieties in branches (H-TKPR, For-TKPR, H-TKPKG, Ac-TKPKG) were built up on the tetratuftsin carrier, resulting in the *N*-terminal acetylated branched peptides (**4**, **5**, **6**, **7**). In the case of the Mtx conjugates, chloroacetylation of both amino groups of Lys inserted in the *N*-terminus of the carrier was performed and these chloroacetylated branched peptides were conjugated with the Mtx$^{\gamma}$-GFLGC-NH_2 in solution (Scheme 2). This reaction resulted in four Mtx-containing conjugates (**13**, **14**, **15**, **16**). The four drug−oligopeptide conjugates as well as the corresponding branched oligopeptides were tested in chemotaxis assay on MonoMac6 cells. In the case of H-TKPR branches, the branched peptide (**4**) had a chemoattractant effect at 1 μM (115.1 ± 3.5%), and it was slightly repellent at the lower concentration range (10^{-2} μM, 82.6 ± 6.9%; 10^{-3} μM, 85.0 ± 6.1%) (Supporting Information S4). When Mtx$^{\gamma}$-GFLGC-NH_2 was coupled to the peptide resulting in compound **13**, significant chemoattractant behavior appeared over the whole concentration range (10^{-1} μM, 174.7 ± 4.3%; 10^{-2} μM, 306.9 ± 2.3%; 10^{-3} μM, 321.8 ± 2.3%; 10^{-4} μM, 289.6 ± 3.2%) (Figure 4A). In this case, the coupling of the Mtx$^{\gamma}$-GFLGC-NH_2 considerably amended the biological properties of the branched peptide.

In the case of the formylated branches, the branched peptide (**5**) had a chemoattractant effect at 1 μM (135.2 ± 7.4%), but it was repellent at the lower concentration range (10^{-2} μM, 57.5 ± 17.6%; 10^{-4} μM, 68.0 ± 16.7%) (Supporting Information S4). The conjugation with Mtx$^{\gamma}$-GFLGC-NH_2 does not modulate the chemotactic behavior of the molecule (**14**), the conjugate was still significantly attractant at 1 μM (157.6 ± 7.6%), and in the lower concentration range, it could elicit a chemorepellent effect (10^{-2} μM, 70.5 ± 14.1%; 10^{-4} μM, 73.9 ± 12.3%) (Figure 4B).

In case of H-TKPKG branches, the acetylated branched peptide (**6**) showed a biphasic effect; it could trigger a chemorepellent effect at the higher concentration range (1 μM, 53.3 ± 16.2%; 10^{-1} μM, 30.9 ± 20.3%), but it exhibited significant attractant chemotactic activity at the lower concentration range (10^{-2} μM, 388.9 ± 1.9%; 10^{-3} μM, 396.0 ± 2.1%; 10^{-4} μM, 251.4 ± 4.0%) (Supporting Information S4). The coupling of the Mtx$^{\gamma}$-GFLGC-NH_2 to the branched peptide resulted in adverse and less significant effects; the conjugate (**15**) was attractant at 10^{-1} μM (160.0 ± 1.9%), but it could

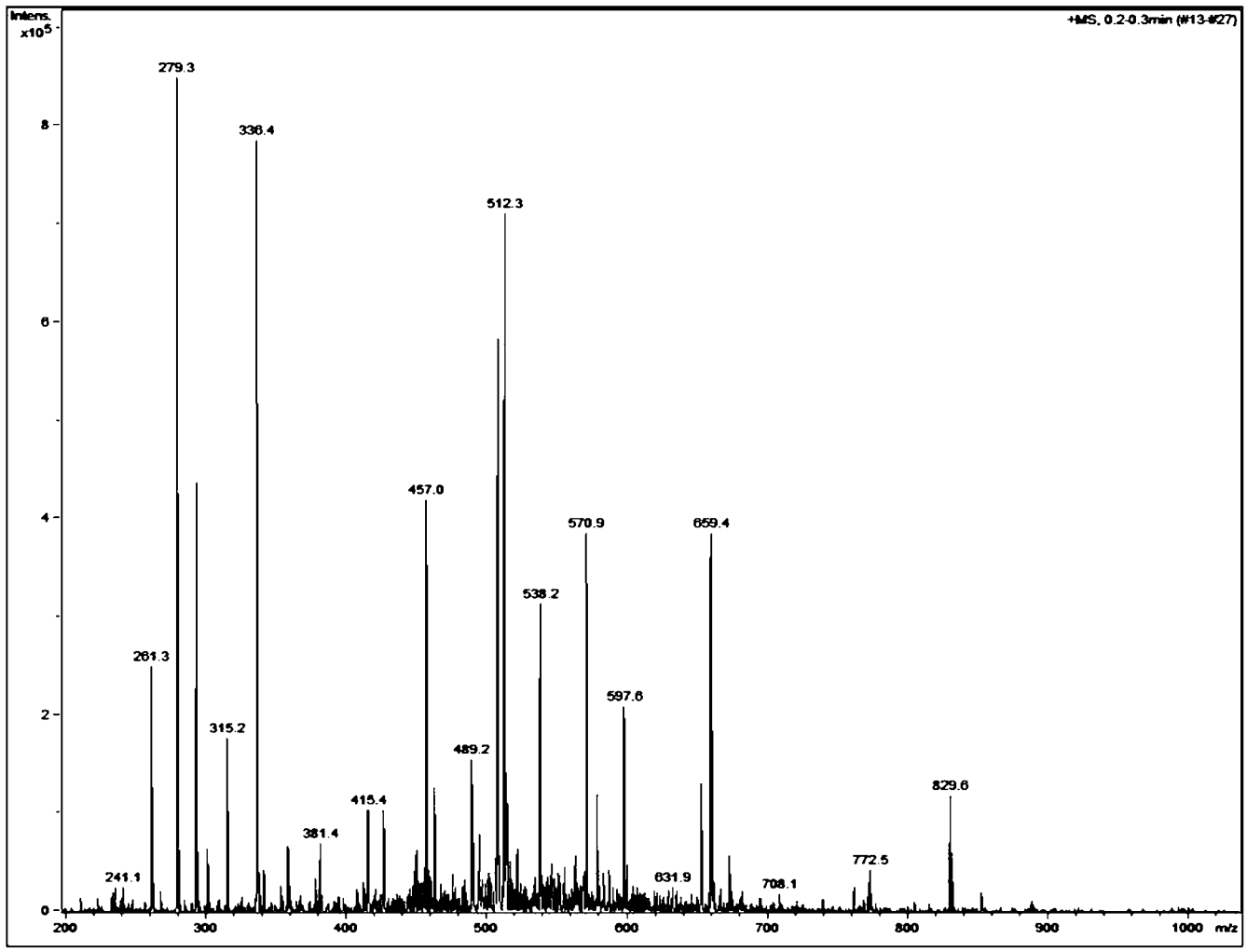

Figure 3. Mass spectrum of conjugate **15** after digestion with cathepsin B.

elicit a repellent effect in the lower concentration range (10^{-2} μM, 59.5 ± 19.3%; 10^{-3} μM, 71.9 ± 17.5%) (Figure 4C).

When the Ac-TKPKG branched peptide was studied, a significant attractant behavior was detected at 10^{-1} μM (139.6 ± 3.9%), which was retained, but shifted to the lower concentration range (10^{-2} μM: 146.1 ± 5.2%) after conjugation with Mtx$^{\gamma}$-GFLGC-NH_2 resulting in compound **16** (Supporting Information S4; Figure 4D).

Cellular Uptake of the CF-Labeled Conjugates. For the cellular uptake studies, the synthesis of CF-labeled conjugates was carried out. For this, CF-GFLGC-NH_2 was synthesized—similarly to Mtx$^{\gamma}$-GFLGC-NH_2—and coupled to the branched peptide *via* a thioether bond. Four CF-labeled conjugates (**18**, **19**, **20**, **21**) were studied. The mean fluorescence intensity of cells was quantitated by flow cytometry. After treatment for 90 min, cells were analyzed. We observed the concentration-dependent accumulation of fluorescence signal within the cells (Figure 5), indicating rapid internalization of each CF-labeled conjugate. A high level of internalization of the CF-labeled conjugates with For-TKPR branches was observed, while the internalization of the CF-labeled conjugates with H-TKPR branches was less pronounced (Figure 5A,B). Consequently, the formylation of the branches increased the cellular uptake of the conjugates. In the case of H-TKPKG branches, a relatively high internalization was observed, whereas the CF-labeled conjugates with Ac-TKPKG branches were internalized considerably within 90 min. In fact, the CF-labeled conjugates with Ac-TKPKG branches showed higher levels of internalization at all studied concentrations (Figure 5C,D). Consequently, the acetylation of the branches also increased the cellular uptake of the conjugates. The cellular uptake of the conjugates with H-TKPR branches was higher compared to the H-TKPKG branches. By the same token, the internalization of the conjugates with For-TKPR branches was compared to the conjugates with Ac-TKPKG branches: the rate of the cellular uptake was almost the same. A very high increase of fluorescence intensity in the cells was observed when the concentration of the conjugates was elevated from 4 μM to 20 μM. We believe that at lower concentration the conjugates are taken up in a receptor-mediated way, while at a higher concentration, they enter into the cells by fluidic endocytosis or the conjugates behave as cell penetrating peptides because of their strong positively charged character. The mechanism of the cellular uptake of these conjugates requires further study.

Apoptosis Assay. Phosphatidylserine (PS) is asymmetrically located in the lipid bilayer of the plasma membrane in mammalian cells. In cells undergoing apoptosis, PS is transferred from the cytoplasmic surface of the cell membrane to the outer surface of the plasma membrane and therefore serves as an early marker for apoptosis. By simultaneous staining with Annexin-V-FITC and PI, we could distinguish among intact cells, early apoptosis, late apoptosis, and cell death. Assessment of MonoMac6 cells exposed to 10^{-2}, 10^{-1}, and 1 μM Mtx and Mtx conjugates for different periods of time (3, 24, and 48 h) showed that 2−12% cells were undergoing necrosis (Figure 6; Supporting Information S5−6). MonoMac6 cells showed an an-

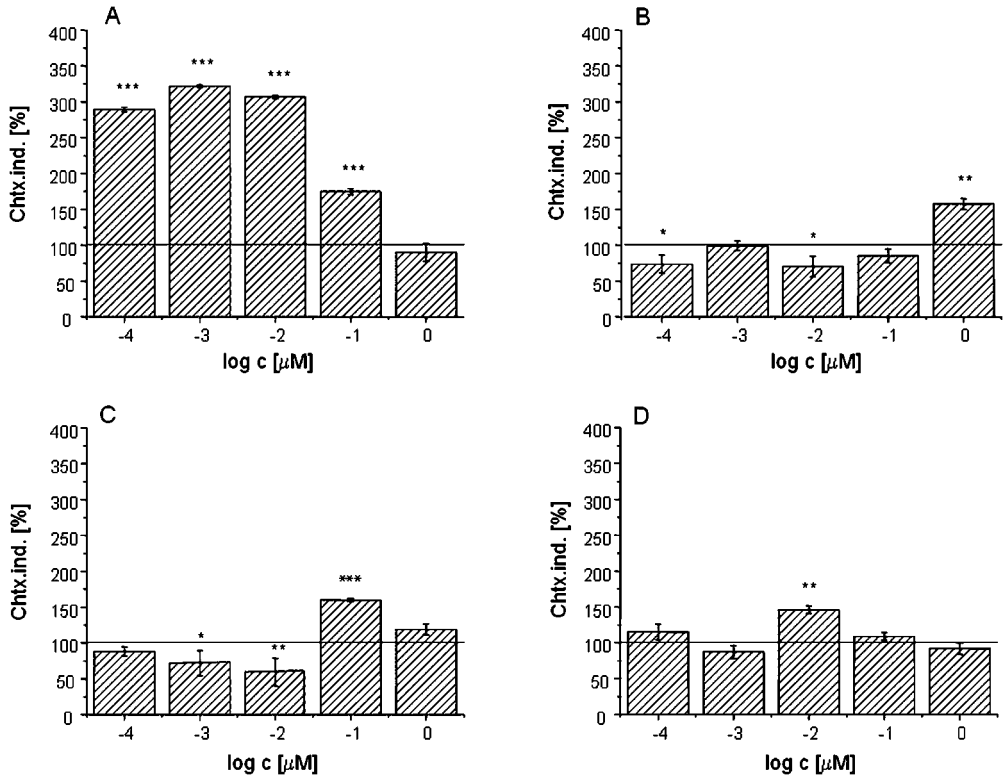

Figure 4. Chemotactic activity of Mtx conjugates with **A**, H-TKPR (**13**); **B**, For-TKPR (**14**); **C**, H-TKPKG (**15**); **D**: Ac-TKPKG (**16**) peptides in the branches. (* $p < 0.05$; ** $p < 0.01$; *** $p < 0.001$).

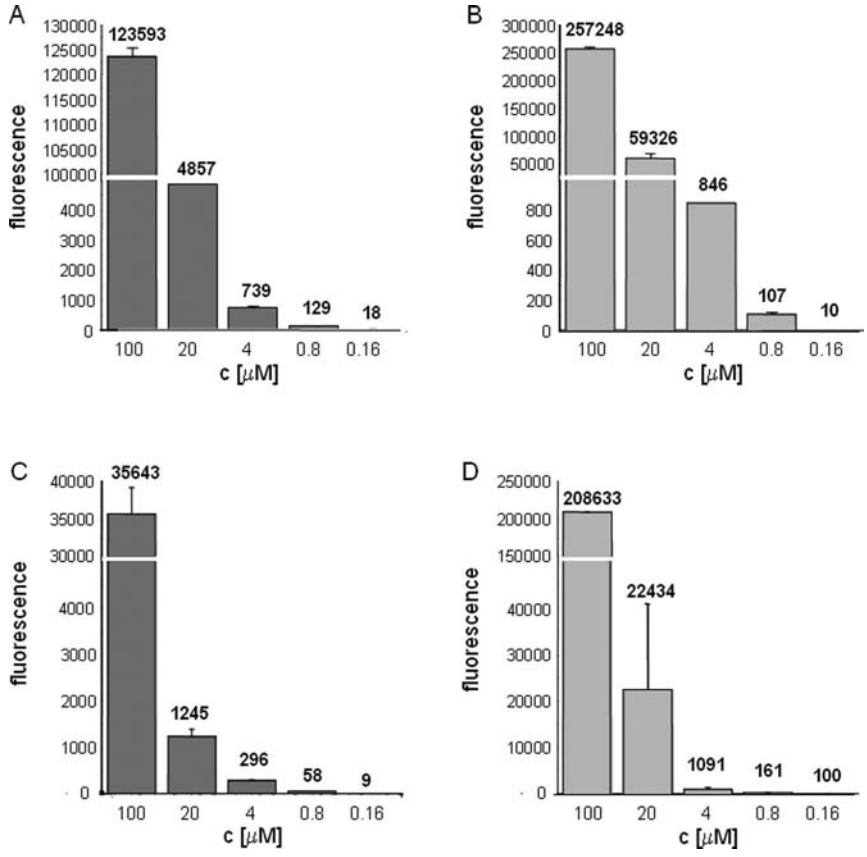

Figure 5. Cellular uptake of the CF-labeled conjugates with A, H-TKPR (**18**); B, For-TKPR (**19**); C, H-TKPKG (**20**); D, Ac-TKPKG (**21**) peptides in the branches.

nexin-/PI+ (indicating cell necrosis) pattern after 3, 24, and 48 h treatment with Mtx and Mtx conjugates in all concentrations. Only a few annexin+/PI− cells (indicating cell apoptosis) and annexin+/PI+ (indicating later stage of apoptotic cells) were observed. As it is shown in Figure 6 and Supporting Information S5−6, detection of MonoMac6 necrotic cells was dose- and

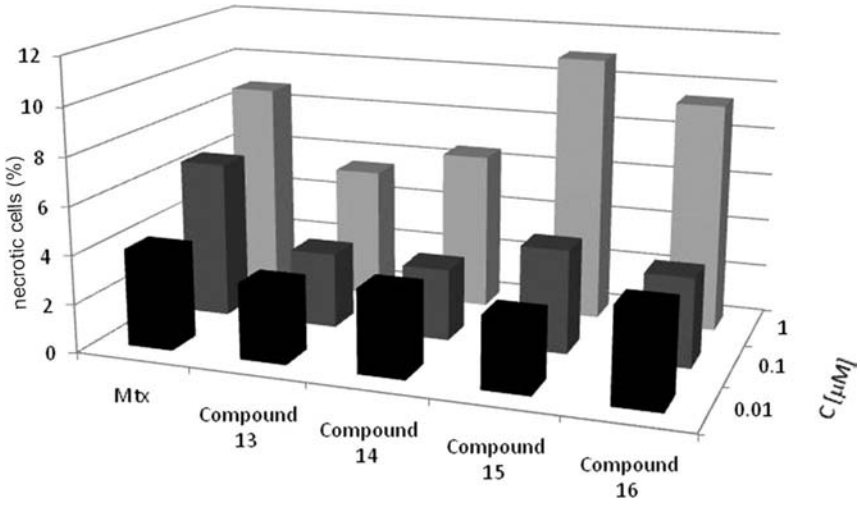

Figure 6. Effect of Mtx and Mtx-conjugates with H-TKPR (**13**), For-TKPR (**14**), H-TKPKG (**15**), and Ac-TKPKG (**16**) peptides in the branches in apoptotic assay on the MonoMac6 cell line after 24 h incubation.

time-dependent (maximum at 24 h, Figure 6). Mtx was more active than the conjugates at the concentrations of 0.01 and 0.1 μM, but at 1 μM dose, conjugates **15** and **16** showed higher toxity on MonoMac6 cells during the whole experiment.

CONCLUSION

In summary, new targeted peptide-based drug delivery systems were synthesized and biochemically characterized. These biodegradable conjugates consist of Mtx as the drug, an enzyme labile peptide spacer (GFLGC), a biodegradable peptide carrier (OT20), and four types of targeting peptide moieties (H-TKPR, For-TKPR, H-TKPKG, and Ac-TKPKG), which have been shown to bind to tuftsin receptors, and the conjugates can be internalized by receptor-mediated endocytosis. Inside the cells, in the lysosomes, the drug molecules could be released from the conjugates after enzymatic (cathepsin B) cleavage; therefore, our conjugates could elicit the proper anticancer effect. *In vitro* biological assays were performed with the prepared conjugates. Chemotaxis assays were carried out with the compounds and the branched peptides, as well as with the drug-conjugates. Each of the branched peptides and the drug conjugates could trigger a significant chemotactic effect on MonoMac6 cells, but the most effective conjugate was compound **13**, which was significantly attractant in a wide concentration range ($10^{-1}-10^{-4}$ μM). Rapid internalization of the CF-labeled conjugates was observed. Apoptosis assay was performed using simultaneous staining with Annexin-V-FITC and PI. MonoMac6 cells were undergoing necrosis after treatment with Mtx or with compunds **13**−**16**. Compounds **15** and **16** were the most effective ones; these conjugates triggered a higher toxic effect than the free drug (Mtx). Compound **13** induced necrosis in MonoMac6 cells. The effectiveness of compound **13** is comparable to that of the free drug at 3 or 48 h incubation (Supporting Information S5, S6). First and last, if we draw a parallel between Mtx and Mtx-conjugates (**13**, **14**, **15**, and **16**) we can conclude that the conjugates have many advantages in comparison with Mtx. The conjugates can attract the MonoMac6 cells in certain concentrations, especially compound **13**, which has the most advatageous chemotactic properties. Its significant chemoattractant behavior appears at a wide concentration range. Beside the chemotaxis, the conjugates can be internalized rapidly and at the same level as the Mtx, but the mechanism of internalization is different. Mtx can simply diffuse through the membrane without any specificity in contrast to the conjugates, which can be taken up by the cells through receptor-mediated endocytosis. By the same token, the conjugates are at least as cytotoxic as Mtx. To conclude the results of the biological assays, the most promising compounds are **13** and **16**. The results of the biological tests confirmed the feasibility of this new chemotactic drug targeting strategy for increasing the efficacy and specificity of chemotherapy especially in tumor treatments.

ACKNOWLEDGMENT

This work was supported by grants from the Hungarian National Science Fund (OTKA K 043576 and T 049814), ETT 202/2006, "Medichem 2" 1/A/005/2004, as well as GVOP-3.2.1.-2004-04-0005/3.0 and GVOP-3.2.1-2004-04-0352/3.0.

Supporting Information Available: (i) Chemotactic response of MonoMac6 cells induced by H-TKPR-NH_2, H-TKPKG-NH_2, the tetratuftsin derivative carrier (OT20), Mtx and Mtx$^{\gamma}$-GFLGC-NH_2; (ii) Chemotactic activity of the branched peptides withot drug molecule; (iii) Effect of Mtx and Mtx-conjugates with H-TKPR, For-TKPR, H-TKPKG, Ac-TKPKG peptides in the branches in apoptotic assay on MonoMac6 cell line after 3 and 48 h incubation. This material is available free of charge via the Internet at http://pubs.acs.org.

LITERATURE CITED

(1) Dubowchik, G. M., and Walker, M. A. (1999) Receptor-mediated and enzyme-dependent targeting of cytotoxic anticancer drugs. *Pharmacol. Ther. 83*, 67–123.
(2) Dass, C. R., and Choong, P. F. (2006) Carrier-mediated delivery of peptidic drugs for cancer therapy. *Peptides 27*, 3020–3028.
(3) Dharap, S. S., Wang, Y., Chandna, P., Khandare, J. J., Qiu, B., Gunaseelan, S., Sinko, P. J., Stein, S., Farmanfarmaian, A., and Minko, T. (2005) Tumor-specific targeting of an anticancer drug delivery system by LHRH peptide. *Proc. Natl. Acad. Sci. U.S.A. 102*, 12962–12967.
(4) Mezö, G., Láng, O., Jakab, A., Bai, K. B., Szabó, I., Schlosser, G., Láng, J., Köhidai, L., and Hudecz, F. (2006) Synthesis of oligotuftsin-based branched oligopeptide conjugates for chemotactic drug targeting. *J. Pept. Sci. 12*, 328–336.
(5) Niedel, J. E., and Cuatrecasas, P. (1980) Formyl peptide chemotactic receptors of leukocytes and macrophages. *Curr. Top. Cell. Regul. 17*, 137–169.
(6) Najjar, V. A., and Nishioka, K. (1970) "Tuftsin": a natural phagocytosis stimulating peptide. *Nature 228*, 672–673.
(7) Najjar, V. A. (1979) Biological and biochemical characteristics of the tetrapeptide tuftsin, Thr-Lys-Pro-Arg. *Adv. Exp. Med. Biol. 121*, 131–147.

(8) Nishioka, K., Constantopoulos, A., Satoh, P. S., and Najjar, V. A. (1972) The characteristics, isolation and synthesis of the phagocytosis stimulating peptide tuftsin. *Biochem. Biophys. Res. Commun. 47*, 172–179.

(9) Wleklik, M. S., Luczak, M., and Najjar, V. A. (1987) Tuftsin induced tumor necrosis activity. *Mol. Cell. Biochem. 75*, 169–174.

(10) Siemion, I. Z., and Kluczyk, A. (1999) Tuftsin: on the 30-year anniversary of Victor Najjar's discovery. *Peptides 20*, 645–674.

(11) Mezö, G., Kalászi, A., Reményi, J., Majer, Zs., Hilbert, A., Láng, O., Köhidai, L., Barna, K., Gaál, D., and Hudecz, F. (2004) Synthesis, conformation and immunoreactivity of new carrier molecules based on repeated tuftsin-like sequence. *Biopolymers 73*, 645–656.

(12) Zetter, B. R., Rasmussen, N., and Brown, L. (1985) An in vivo assay for chemoattractant activity. *Lab. Invest. 53*, 362–368.

(13) Lukács, K., Szabó, G., Sonkoly, I., Végh, E., Gács, J., Szekerke, M., and Szegedi, G. (1984) Stimulating effect of tuftsin and its analogs on the defective monocyte chemotaxis in systemic lupus erythematosus. *Immunopharmacology 7*, 171–178.

(14) Bleyer, W. A., Drake, J. C., and Chabner, B. A. (1973) Neurotoxicity and elevated cerebrospinal-fluid methotrexate concentration in meningeal leukemia. *N. Engl. J. Med. 289*, 770–773.

(15) Furst, D. E, and Kremer, J. M. (1988) Methotrexate in rheumatoid arthritis. *Arthritis Rheum. 31*, 305–314.

(16) Gardner-Medwin, J. M., and Powell, R. J. (1996) One patient, two unusual conditions and three basic lessons. *Ann. Rheum. Dis. 55*, 350–352.

(17) Farber, S., Diamond, L. K., Mercer, R. D., Sylvester, R. F., and Wolff, J. A. (1948) Temporary remissions in acute leukemia in children produced by folic acid antagonists, 4-aminopteroyl-glutamic acid, (aminopterin). *N. Engl. J. Med. 238*, 787–793.

(18) Mukhopadhyay, A., Chaudhuri, G., Arora, S. K., Sehgal, S., and Basu, S. K. (1989) Receptor-mediated drug delivery to macrophages in chemotherapy of leishmaniasis. *Science 244*, 705–707.

(19) Kóczán, G., Ghose, A. C., Mookerjee, A., and Hudecz, F. (2002) Methotrexate conjugate with branched polypeptide influences *Leishmania donovani* infection *in vitro* and in experimental animals. *Bioconjugate Chem. 13*, 518–524.

(20) Weinblatt, M. E. (1985) Toxicity of low dose methotrexate in rheumatoid arthitis. *J. Rheumatol. Suppl. 12*, 35–39.

(21) Etrych, T., Jelínková, M., Ríhová, B., and Ulbrich, K. (2001) New HPMA copolymers containing doxorubicin bound *via* pH-sensitive linkage: synthesis and preliminary *in vitro* and *in vivo* biological properties. *J. Controlled Release 73*, 89–102.

(22) Omelyanenko, V., Gentry, C., Kopeckova, P., and Kopecek, J. (1998) HPMA copolymer-anticancer drug-OV-TL16 antibody conjugates. II. Processing in epithelial ovarian carcinoma cells *in vitro*. *Int. J. Cancer 75*, 600–608.

(23) Ziegler-Heitbrock, H. W., Thiel, E., Futterer, A., Herzog, V., Wirtz, A., and Riethmuller, G. (1988) Establishment of a human cell line (MonoMac6) with characteristics of mature monocytes. *Int. J. Cancer 41*, 456–461.

(24) Chaudhuri, M. K., Konopińska, D., Bump, N. J., and Najjar, V. A. (1983) The similarity between tuftsin (Thr-Lys-Pro-Arg) receptors and tuftsin antibody: a case of induced molecular mimicry. *Ann. N.Y. Acad. Sci. 419*, 135–142.

(25) Chaudhuri, M. K., and Najjar, V. A. (1981) Tuftsin receptor and tuftsin antibody show identical binding properties. *Fed. Proc. 40*, 1737.

(26) Martinez, J., and Laur, J. (1982) Active esters of formic acid as useful formylating agents: improvements in the synthesis of formyl-amino acid esters, N-α-Formyl-Met-Leu-Phe-OH, and Formyl-Met-Lys-Pro-Arg, a phagocytosis stimulating peptide. *Synthesis* 979–981.

(27) Kaiser, E., Colescott, R. L., Bossinger, C. D., and Cook, P. I. (1970) Color test for detection of free terminal amino groups in the solid-phase synthesis of peptides. *Anal. Biochem. 34*, 595–598.

(28) Kaiser, E., Bossinger, C. D., Colescott, R. L., and Olser, D. B. (1980) Color test for terminal prolyl residues in the solid-phase synthesis of peptides. *Anal. Chim. Acta 118*, 149–151.

(29) Mezö, G., Manea, M., Jakab, A., Kapuvári, B., Bssze, Sz., Schlosser, G., Przybylski, M., and Hudecz, F. (2004) Synthesis and structural characterization of bioactive peptide conjugates using thioether linkage approaches. *J. Pept. Sci. 10*, 701–713.

(30) Ivanov, B. B., and Robey, F. A. (1996) Effective use of free thiols as scavengers for HF cocktails to deprotect bromo- and chloroacetylated synthetic peptides. *Pept. Res. 9*, 305–307.

(31) Boyden, S. (1962) The chemotactic effect of mixtures of antibody and antigen on polymorphonuclear leucocytes. *J. Exp. Med. 115*, 453–466.

(32) Mossmann, T. (1983) Rapid colorimetric assay for cellular growth and survival: application to proliferation and cytotoxicity assays. *J. Immunol. Methods 65*, 55–63.

(33) Alley, M. C., Scudiero, D. A., Monks, A., Hursey, M. L., Czerwinski, M. J, Fine, D. L., Abbott, B. J., Mayo, J. G., Shoemaker, R. H., and Boyd, M. R. (1988) Feasibility of drug screening with panels of human tumor cell lines using a microculture tetrazolium assay. *Cancer Res. 48*, 589–601.

(34) Tait, J. F., Gibson, D., and Fujikawa, K. (1989) Phospholipid binding properties of human placental anticoagulant protein-I, a member of the lipocortin family. *J. Biol. Chem. 264*, 7944–7949.

(35) Andree, H. A, Reutelingsperger, C. P., Hauptmann, R., Hemker, H. C., Hermens, W. T., and Willems, G. M. (1990) Binding of vascular anticoagulant alpha (VAC alpha) to planar phospholipid bilayers. *J. Biol. Chem. 265*, 4923–4928.

(36) Thiagarajan, P., and Tait, J. F. (1990) Binding of annexin V/placental anticoagulant protein I to platelets. Evidence for phosphatidylserine exposure in the procoagulant response of activated platelets. *J. Biol. Chem. 265*, 17420–17423.

(37) Koopman, G., Reutelingsperger, C. P., Kuijten, G. A., Keehnen, R. M., Pals, S. T., and van Oers, M. H. (1994) Annexin V for flow cytometric detection of phosphatidylserine expression on B cells undergoing apoptosis. *Blood 84*, 1415–1420.

(38) Darzynkiewicz, Z., Bruno, S., Del Bino, G., Gorczyca, W., Hotz, M. A., Lassota, P., and Traganos, F. (1992) Features of apoptotic cells measured by flow cytometry. *Cytometry 13*, 795–808.

(39) Tugyi, R., Mezö, G., Schlosser, G., Fellinger, E., Andreu, D., and Hudecz, F. (2008) Effect of conjugation with polypeptide carrier on the enzymatic degradation of herpes simplex virus glycoprotein D derived epitope peptide. *Bioconjugate Chem. 19*, 1652–1659.

BC800115W

Supporting Information

Design, Synthesis and *In Vitro* Activity of Novel Drug Delivery Systems, Containing Tuftsin Derivatives and Methotrexate

Katalin B. Bai[a], Orsolya Láng [b], Erika Orbán[a], Rita Szabó[a], László Kőhidai [b],

Ferenc Hudecz[a,c], Gábor Mező[a*]

[*]Correspondence to: Prof. Dr. Gábor Mező, Research Group of Peptide Chemistry, Hungarian Academy of Sciences, Eötvös L. University, 1117 Budapest, Pázmány P. stny. 1/A, Hungary; Tel.: (+36)-1-209-0555/1433; Fax: (+36)-1-372-2620; e-mail: gmezo@elte.hu

Table of Contents:

Chemotactic response of MonoMac6 cells induced by **A**: H-TKPR-NH_2 (**1**) , **B**: H-TKPKG-NH_2 (**2**), and **C**: the tetratuftsin derivative carrier (OT20) (**3**)……. S2

Chemotactic response of MonoMac6 cells induced by **A:** Mtx and **B**: Mtx^{γ}-GFLGC-NH_2 ... S3

Chemotactic activity of the branched peptides with **A**: H-TKPR (**4**); **B**: For-TKPR (**5**); **C**: H-TKPKG (**6**); **D**: Ac-TKPKG (**7**) peptides in the branches……... S4

Effect of Mtx and Mtx-conjugates with H-TKPR (**13**), For-TKPR (**14**), H-TKPKG (**15**), Ac-TKPKG (**16**) peptides in the branches in apoptotic assay on MonoMac6 cell line after 3 h incubation. S5

Effect of Mtx and Mtx-conjugates with H-TKPR (**13**), For-TKPR (**14**), H-TKPKG (**15**), Ac-TKPKG (**16**) peptides in the branches in apoptotic assay on MonoMac6 cell line after 48 h incubation..... S6

Figure1. Chemotactic response of MonoMac6 cells induced by **A**: H-TKPR-NH_2 (**1**) , **B**: H-TKPKG-NH_2 (**2**), and **C**: the tetratuftsin derivative carrier (OT20) (**3**) (* - $p<0.05$; ** - $p<0.01$; *** - $p<0.001$).

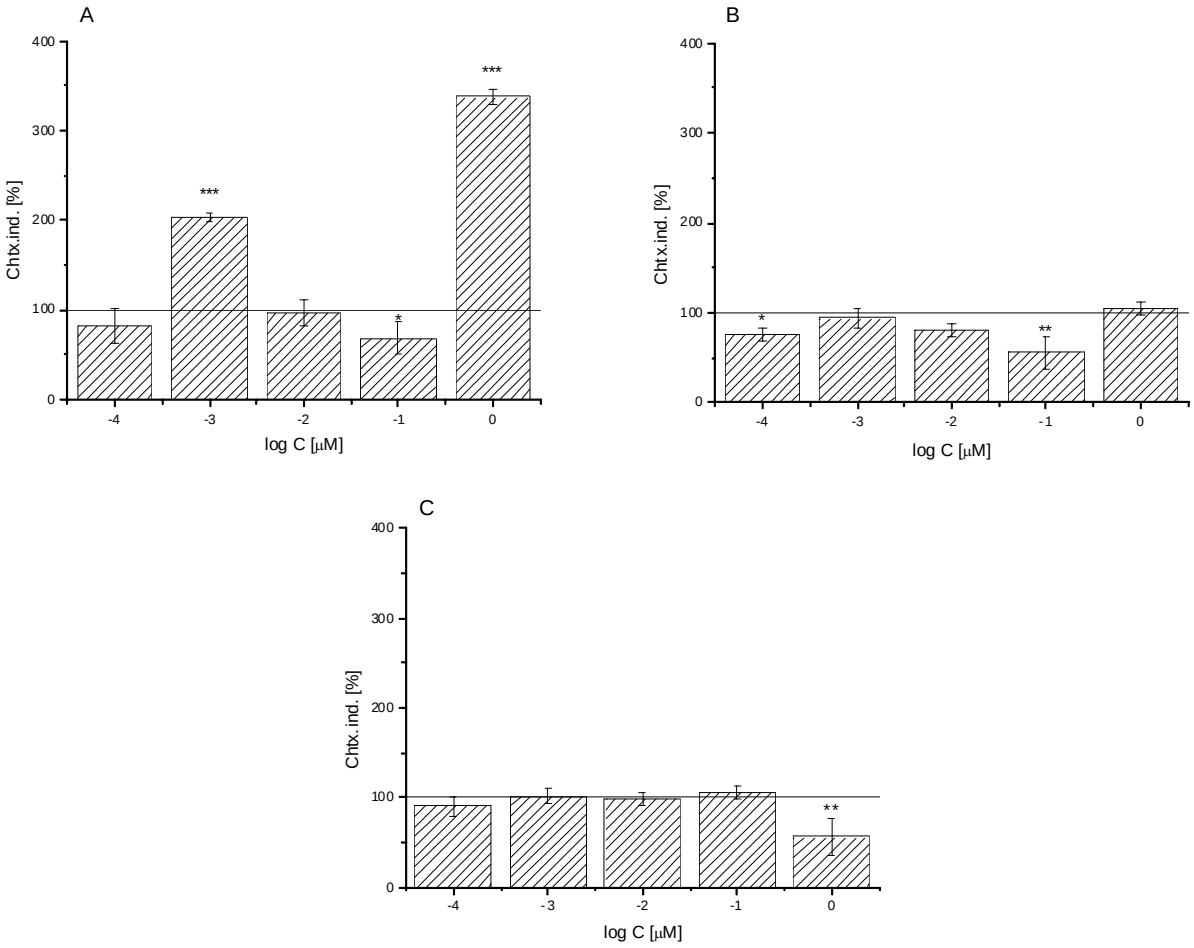

Figure 2. Chemotactic response of MonoMac6 cells induced by **A:** Mtx and **B**: Mtx^{γ}-GFLGC-NH_2 (**12**) (* - $p<0.05$; ** - $p<0.01$; *** - $p<0.001$).

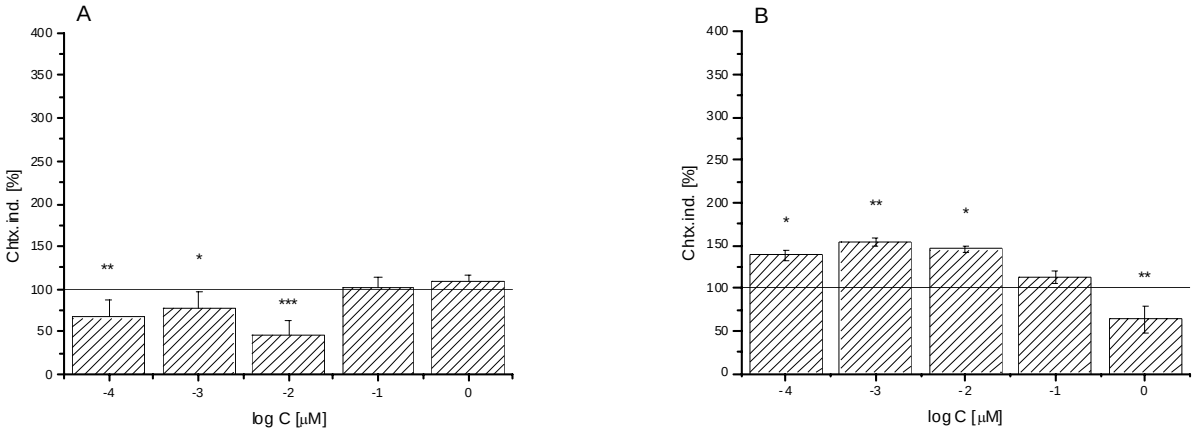

Figure3. Chemotactic activity of the branched peptides with **A**: H-TKPR (**4**); **B**: For-TKPR (**5**); **C**: H-TKPKG (**6**); **D**: Ac-TKPKG (**7**) peptides in the branches. (* - $p<0.05$; ** - $p<0.01$; *** - $p<0.001$).

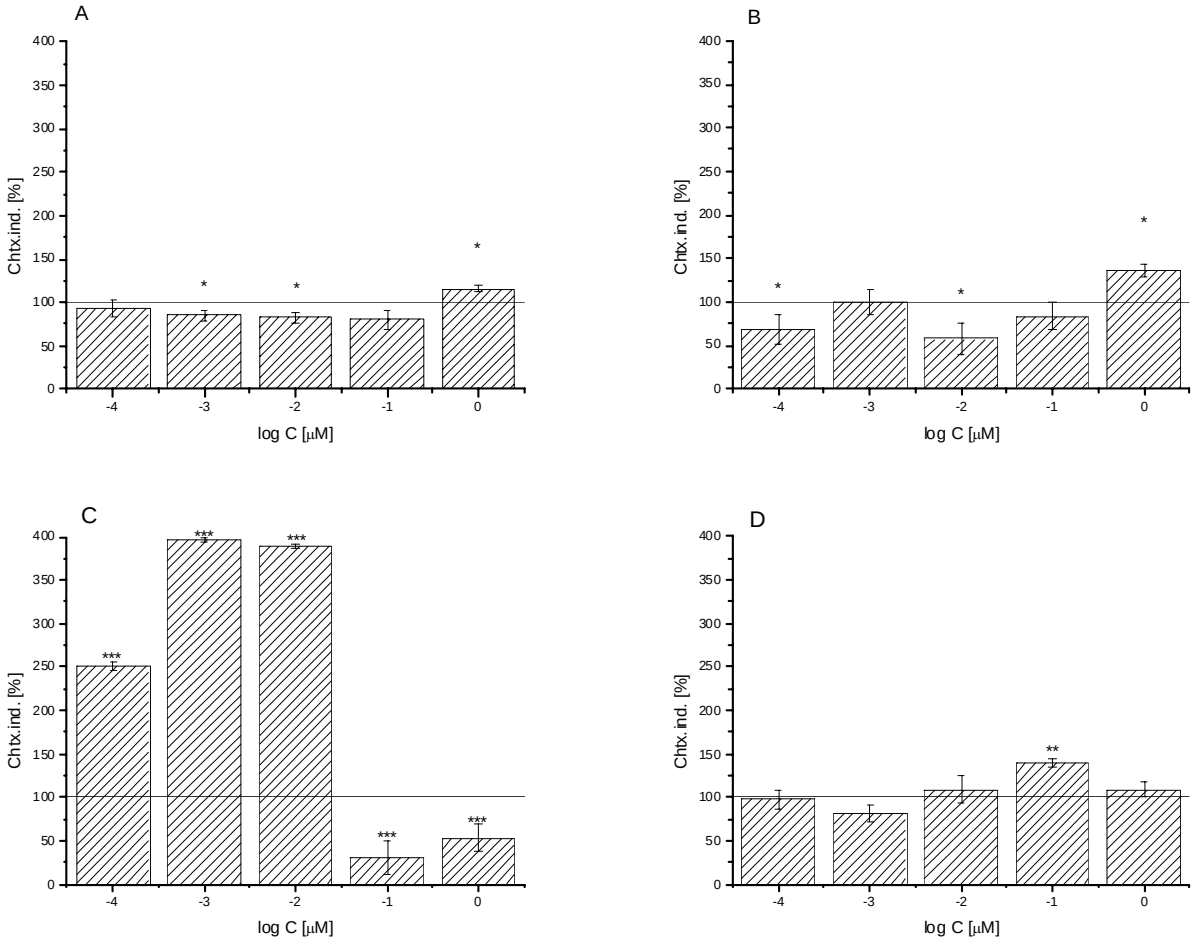

Figure 4. Effect of Mtx and Mtx-conjugates with H-TKPR (**13**), For-TKPR (**14**), H-TKPKG (**15**), Ac-TKPKG (**16**) peptides in the branches in apoptotic assay on MonoMac6 cell line after 3 h incubation.

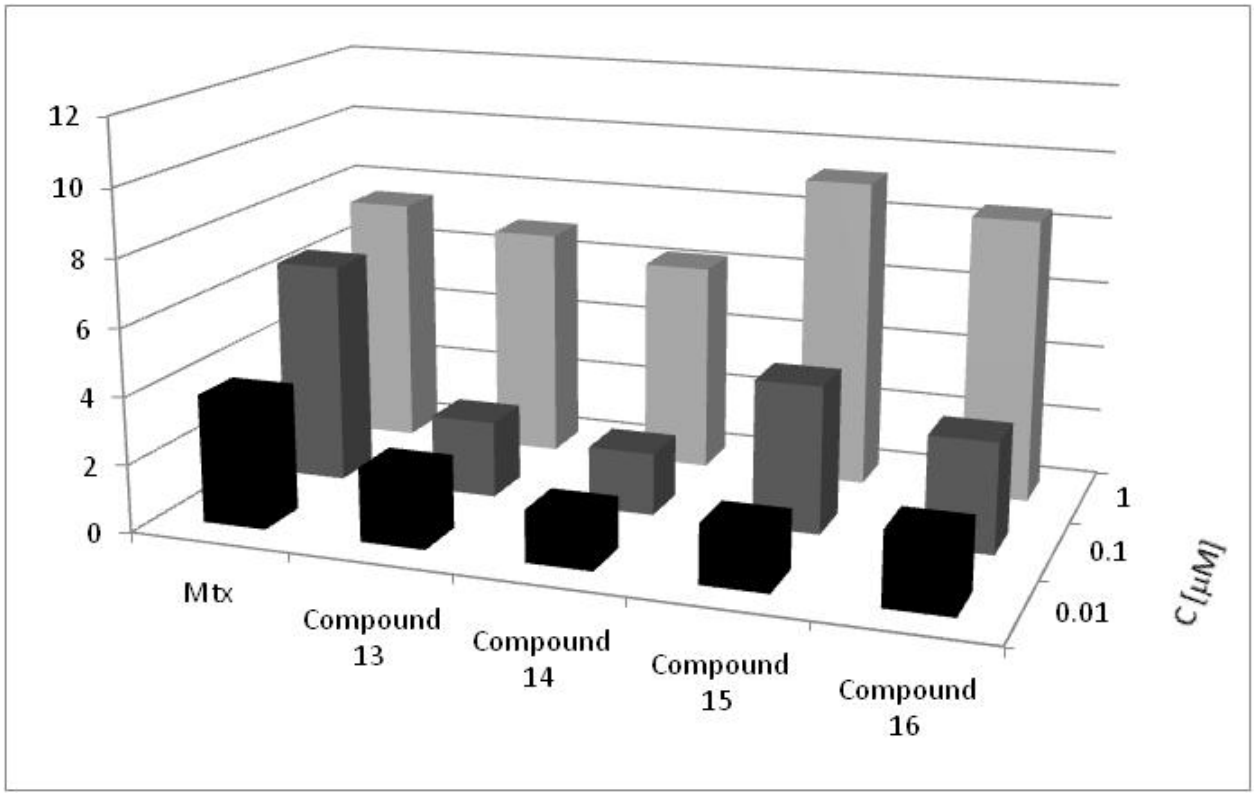

Figure 5: Effect of Mtx and Mtx-conjugates with H-TKPR (**13**), For-TKPR (**14**), H-TKPKG (**15**), Ac-TKPKG (**16**) peptides in the branches in apoptotic assay on MonoMac6 cell line after 48 h incubation.

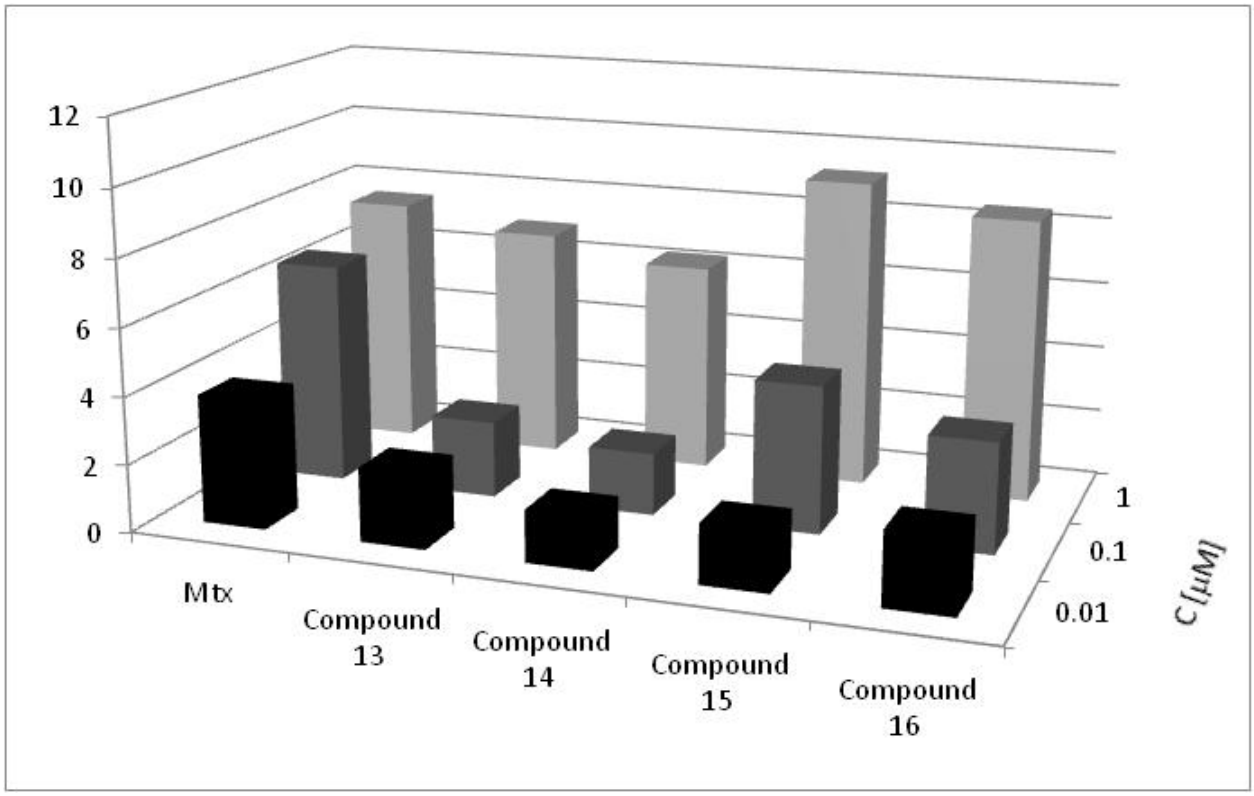

The Role of Polyamine Architecture on the Pharmacological Activity of Open Lactone Camptothecin−Polyamine Conjugates

Cristian Samor,*[,†] Andrea Guerrini,[†] Greta Varchi,[†] Giovanni Luca Beretta,[‡] Gabriele Fontana,[§] Ezio Bombardelli,[§] Nives Carenini,[‡] Franco Zunino,[‡] Carlo Bertucci,[||] Jessica Fiori,[||] and Arturo Battaglia[†]

Istituto CNR per la Sintesi Organica e Fotoreattività "I.S.O.F.", Area della Ricerca di Bologna, Via Gobetti 101, 40129 Bologna, Italy, Dipartimento di Oncologia Sperimentale e Laboratori, Fondazione IRCCS Istituto Nazionale Tumori, 20133 Milano, Italy, Indena SPA, viale Ortles 12, 20139 Milano, Italy, and Dipartimento di Scienze Farmaceutiche, Università di Bologna, Via Belmeloro 6, 40126 Bologna, Italy. Received January 25, 2008; Revised Manuscript Received August 19, 2008

A series of camptothecin open-ring lactone tripartate conjugates were synthesized, in which polyamine side chains with different architecture (ethane-1,2-diamine, spermidine, homospermidine, spermine, and 4,8,13,17-tetrazaicosane-1,20-diamine) are linked to the 21-carboxylic function through an amidic bond, while the 17-CH_2OH is acetylated. The rationale for the synthesis of these compounds was to explore the influence of the polyamine architecture on the activity of these CPT conjugates into cells, since the positively charged ammonium cations would favor interaction through electrostatic binding to the negatively charged DNA backbone. Topoisomerase I-mediated DNA cleavage assay was used to investigate the ability of these compounds to stimulate the DNA damage. The cleavage pattern was found to be similar to that of SN38 for all the new CPTs. The CPT tripartates were tested for growth inhibition ability against the human non-small-cell lung cancer carcinoma NCI-H460 cell line. Although these compounds were less potent than topotecan, SN38, and CPT after 1 h of treatment, the antiproliferative effects greatly increased after 72 h of exposure. The growth inhibition potency during long-term exposure is correlated with the number of charges of the 21-amide substituent. Both cleavage assay and *in vitro* effects support the interpretation that the compounds may have inhibitory activity also in the open-ring form. The architecture of the polyamine moiety is important for antiproliferative activity, and a balance between the hydrophilic and lipophilic properties of the polyamine is critical for CPT potency.

INTRODUCTION

Camptothecins (CPT, **1**, Figure 1) are an effective class of antitumor drugs, used in the treatment of a wide spectrum of human cancers. The molecular target of the CPTs family is the enzyme DNA topoisomerase I (topo I), a ubiquitous enzyme which is overexpressed in a variety of tumor cell lines and involved in the regulation of DNA topology during replication, recombination, and transcription (*1*−*4*). The drug stabilizes a reversible enzyme−DNA complex, which is termed the cleavable complex, thus preventing the ligation step of the enzyme action. These biochemical observations, integrated by crystallographic (*5*−*7*), UV−vis (*8, 9*), and NMR (*9*) spectroscopic information and quantum mechanic calculations (*9*−*14*), allowed the design of binding models for CPT with the covalent binary complex (*5, 11, 12, 15*).

Therapeutic applications of CPT have been limited by its low water solubility and by the high *in vivo* reactivity of the α-hydroxy-δ-lactone pharmacophore, which, under physiological conditions, reversibly hydrolyzes to the "ring-opened" carboxylate form (**1a**, Figure 1) (*16*). The latter is very toxic (*17*) and far less active with respect to inhibition of topo I (*18, 19*). In addition, the carboxylate form (**1a**) readily binds to human serum albumin, making it less accessible for cellular uptake (*20, 21*). This behavior gives rise to a drop in therapeutic efficacy, along with formulation difficulties (*21*). For these reasons, all the elements controlling the structure and lactone−carboxylate equilibrium are key factors in determine their potency. To avoid this inconvenience, a number of CPT analogues have been synthesized to improve lactone stability and aqueous solubility. These efforts have produced the two water-soluble semisynthetic analogues: topotecan (Hycamptin, **2**) (*22*) and irinotecan (Camptostar, **3**) (*23*), which received FDA approval for the clinical treatment of the ovarian, small-cell lung, and refractory colorectal cancers, while several other analogues are currently under development. Although **2** and **3** showed activity against a wide range of tumors, both of them have a relatively low therapeutic index and considerable toxic effects (*24*−*26*). In this regard, several prodrug strategies (*27*−*29*) have rapidly emerged to achieve site-specific delivery of

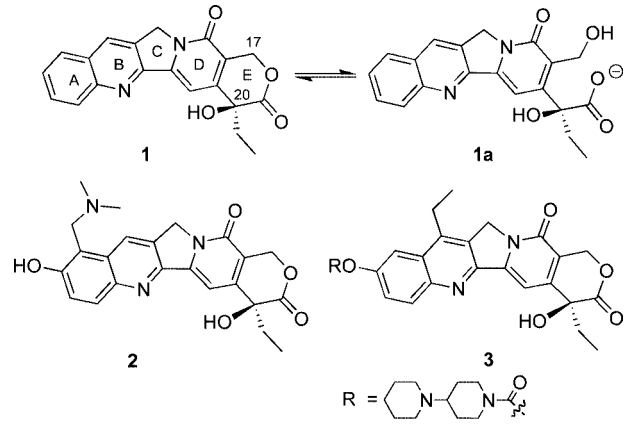

Figure 1. Camptothecin **1**, its carboxylate **1a**, and its FDA approved analogues Topotecan **2** and Irinotecan **3**.

* E-mail: csamori@isof.cnr.it. Phone: (039) 639-8286. Fax: (039) 6398349.
[†] I.S.O.F.
[‡] Fondazione IRCCS Istituto Nazionale Tumori.
[§] Indena SPA.
[||] Università di Bologna.

10.1021/bc800033r CCC: $40.75 © 2008 American Chemical Society
Published on Web 10/08/2008

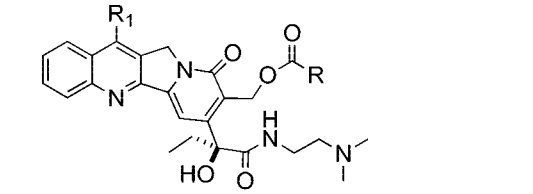

Compounds **I**: R_1= H, C_2H_5; R= Alk, Bz, NHR, OR

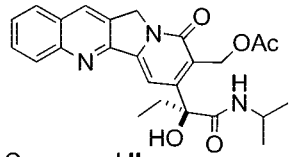

Compound **II**

Figure 2. 21-N^1,N^1-dimethylaminoethylamide (compound **I**) and 21-isopropyl amide (compound **II**) tripartates.

cytotoxic CPTs. Most of these strategies are based on the use of conjugates that maintain CPT in the closed-lactone form into the plasma compartment. To this end, it is known that the free 20-hydroxyl group favors the lactone ring-opening through intramolecular hydrogen bonding (*30*). Therefore, acylation of the 20-hydroxyl group would render the lactone moiety more stable toward ring opening (*31*). Accordingly, 20(*S*)-*O*-acyl esters (*32, 33*), 20(*S*)-*O*-carbonated linked tripeptide conjugates (*34*), and 20(*S*)-*O*-linked glycoconjugates (*35*) were synthesized and showed excellent *in vitro* cytotoxicity. Alternatively, reactive functional groups, such as amino, hydroxyl, and carboxylic acid substituents, were introduced in the quinoline (A/B) ring system as linkers for ligand conjugation (*36*−*41*).

A scarcely explored family of CPT conjugates is the tripartate prodrugs, which are characterized by an E-ring open form, where the C-21 position is linked to a *carrier* by an amidic bond, while the 17-hydroxy group is acetylated. The synthesis of these conjugates relies on the fact that the 17-OH-21-amide CPT derivatives (dipartates) are sufficiently stable to allow the 17-OH acylation, yielding more stable ester−amide tripartates (*42*). These 17-*O*-acylated 21-amides, which are stable under physiological conditions for several hours, are supposed to act through a two-step mechanism: the acyl moiety undergoes enzymatic hydrolysis, affording the corresponding dipartate 17-CH_2OH-21-amides (*43*−*45*), subsequently, the free 17-OH group anchimerically assists the spontaneous amide hydrolysis, which generates the lactone species through cyclization. Although only a few examples have been reported in the literature, their biological data showed that their action strongly depends on the structure of both the ester and the amide moieties. For example, the inhibitory activity of CPT tripartates bearing an acyl ester, a carbonate, or a carbamate moiety at the 17 position and a N^1,N^1-dimethylaminoethylamide group at the 21 position (compound **I**, Figure 2) showed higher *in vivo* activity than the 7-ethylcamptothecinic sodium salt (*43, 44*). Instead, the 17-*O*-acyl esters of CPT tripartates bearing an isopropylamide substituent at the 21 position (compound **II**, Figure 2) showed lower *in vitro* and *in vivo* activity than camptothecinic sodium salt (*42, 43*). This behavior is due to the different hydrolytic profile of the amide group of their corresponding 17-CH_2OH dipartates. Actually, the amidic bond of compound **I** hydrolyzes very rapidly at physiological pH, while the isopropyl amide group (compound **II**) hydrolyzed very slowly, being the rate-determining step in the generation of the lactone species.

Besides compounds of types **I** and **II**, two very efficient CPT PEGylate tripartates were reported (**4** and **5**, Figure 3), which show little *in vitro* efficacy in tissue cultures (*45*).

According to the authors, an initial rapid hydrolysis of the ester (or carbonate) affords the corresponding relatively stable and nonactive dipartates. Therefore, cyclization to the active lactone species, which occurs only within the tumor environment, is the rate-determining step (*46*).

The tripartate reactivity scenario is further complicated when considering the possibility that these compounds may exhibit intrinsic antitumor activity. Our recent results regarding the water-soluble CPT tripartate **6** (Figure 4) showed that this compound and its analogues maintain the same order of potency of their reference CPTs, despite the E ring opened form (*47*).

These results cannot be ascribed to the derivative lactonization, since no free CPT was recovered at the end of DNA cleavage assays, and the low amount of CPT detectable in plasma and tumor did not account for the observed efficacy. Thus, these 17-acetate-21 spermidine derivatives could represent the first example of an effective CPT drug with opened lactone ring.

To provide novel insights into this class of open-lactone conjugates, we have synthesized a family of 17-O-acyl protected tripartates of CPT bearing polyamines at the C21-carboxyl group. The ubiquitous polyamines, such as cadaverine, putrescine, spermidine, and spermine, are biosynthesized in humans and play an essential role as regulators of cell growth and differentiation (*48*−*50*). Many tumor types contain high levels of polyamines and an activated exogenous polyamines transporter (PAT) (*51*). Polyamines are organic cations, since the primary and secondary amino groups are protonated at physiological pH. The unique feature of polyamine structure is the presence of methylene groups, which favor hydrophobic interactions, and the presence of positive charges at defined distances, which can electrostatically interact with negatively charged DNA (*52*). In addition to this charge neutralization, polyamines interact with nucleic acid bases, dock into the major or minor grooves, and enter into multisite interactions depending on the ionic environment (*53, 54*). However, the mechanism of polyamine entry into mammalian cells remains poorly defined (*55*−*57*), and more data are needed on the transporters that are believed to facilitate specific delivery to tumor cells, in order to design proper prodrugs. Nevertheless, several attempts to design a polyamine vector have been reported, which are based on structure−activity studies aimed at explaining which polyamine sequence would be the most suitable to access the transporter (*58*−*62*). These studies suggest that small structural changes in the polyamine skeleton give rise to strong differences in their transport behavior and that linear polyamines are superior vectors to the branched ones (*54, 63*−*69*).

MATERIALS AND METHODS

General. All reactions were performed under an atmosphere of dry nitrogen using oven-dried glassware. Tetrahydrofuran, toluene, and ethyl ether were distilled from sodium benzophenone ketal. Dichloromethane and DMF were distilled from calcium hydride. All other solvents were HPLC grade. Reactions were magnetically stirred and monitored by thin-layer chromatography (TLC) with E. Merck silica gel 60-F254 plates. Flash column chromatography was performed with Merck silica gel (0.04−0.63 μm, 240−400 mesh) under high pressure. NMR spectra were recorded on a 400 MHz spectrometer. Unless otherwise stated, all NMR spectra were measured in $CDCl_3$ solutions and referenced to the $CHCl_3$ signal. All ^{1}H and ^{13}C shifts are given in ppm (s = singlet; d = doublet; t = triplet; dd = quadruplet; dt = doublet of triplets, m = multiplet; br s = broad signal). Coupling constants *J* are given in Hz. Assignments of proton resonances were confirmed, when possible, by selective homonuclear decoupling experiments or by correlated spectroscopy. IR spectra were recorded on a FT-IR ESP spectrometer as thin films on NaCl plates. Mass spectra were recorded on an ion trap spectrometer with an ionization

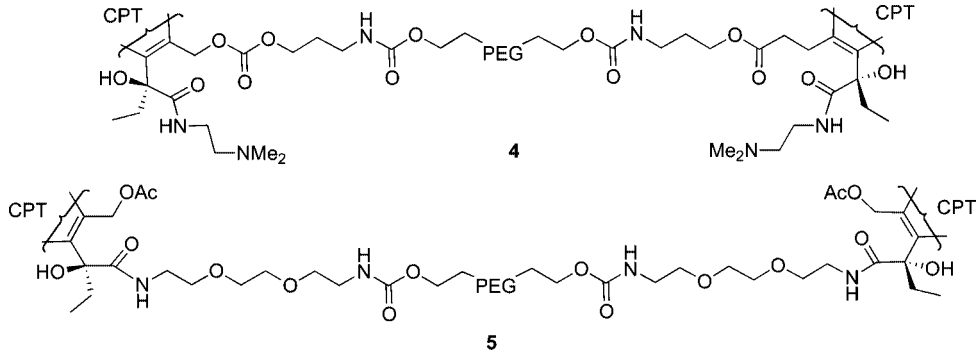

Figure 3. PEG-Tripartates **4** and **5**.

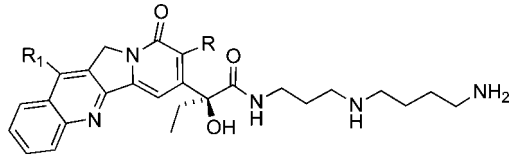

Figure 4. Compounds **6** and **7**.

potential of 70 eV. High-resolution mass spectra (HRMS) were performed with a resolution of 10 000 against a suitable mass standard. The commercially available reagents were used as received without further purification.

General Procedure. For the synthesis of tripartate conjugates **18**, **7**, and **19** from CPT **1** and *N*-^{t}BOC polyamines **13**, **14**, and **16**, respectively, CPT **1** (1.0 equiv), was suspended in 5.0 mL of dry pyridine, and the *N*-*t*BOC-polyamines **13**, **14**, and **16** (4.0 equiv) were added. The reaction was heated at 80 °C for 70 h, and than the solvent was removed under reduced pressure. Flash chromatography, CH_2Cl_2−MeOH (30:1), of the crude material afforded the derivatives 17-hydroxy-21-Boc-amides in 88%, 55%, and 10% yields, respectively, as yellow solids. These compounds (1.0 equiv) were dissolved in dry pyridine (5.0 mL), and acetic anhydride (20.0 equiv) was added. The reaction mixture was magnetically stirred for 2 h at 20 °C, and then the excess of solvent and reagent were removed under vacuum. The resulting solid residue was purified by silica gel flash chromatography, CH_2Cl_2−MeOH (30:1), affording the corresponding 17-*O*-acyl-21-*N*-^{t}Boc-amides in quantitative yield. To a cooled solution (0 °C) of these conjugates (1.0 equiv) in dry DCM (8.0 mL), TFA (15.7 equiv) was added dropwise with stirring over a period of 30 min. The reaction was stirred for 60 h at 0−4 °C, and then the solvent was removed under reduce pressure to obtain the tripartates **18**, **6**, and **19**, respectively, as pale yellow solids.

Compound 18. (88%); pale yellow solid. HRMS *m*/*z* calcd for $C_{26}H_{27}F_3N_4O_7$ $[M]^+$ 564,1832; *m*/*z* found 564,1841. ^{1}H NMR (400 MHz, DMSO-d_6/D_2O) δ 8.58 (s, 1 H, Ar), 8.08 (d, 1 H, J = 8.4 Hz, Ar), 8.01 (d, 1 H, J = 8.4 Hz, Ar), 7.81 (t, 1 H, J = 8.4 Hz, Ar), 7.64 (t, 1 H, J = 8.4 Hz, Ar), 7.53 (s, 1 H, Ar), 5.29 (d, 1 H, J = 11.2 Hz), 5.20 (d, 1 H, J = 11.2 Hz), 5.15 (s, 2 H, H-5), 3.38 (m, 1 H), 3.22 (m, 1 H), 2.86 (bt, 2 H), 2.22 (m, 1 H), 2.13 (m, 1 H), 1.95 (s, 3 H), 0.87 (t, 3 H, J = 7.8 Hz). ^{13}C NMR (100 MHz, DMSO-d_6) δ 174.1, 171.0, 161.3, 156.2, 153.4, 148.6, 144.9, 132.3, 131.1, 130.7, 129.7, 129.2, 128.7, 128.3, 123.9, 99.4, 79.3, 59.4, 51.0, 38.9, 37.3, 32.4, 21.4, 8.5.

Compound 6. (55%); pale yellow solid. HRMS *m*/*z* calcd for $C_{33}H_{39}F_6N_5O_9$ $[M]^+$ 763,2652; *m*/*z* found 763,2644. ^{1}H NMR (400 MHz, DMSO-d_6/D_2O) δ 8.63 (s, 1 H, Ar), 8.12 (d, 1 H, J = 8.4 Hz, Ar), 8.05 (d, 1 H, J = 8.4 Hz, Ar), 7.86−7.81 (m, 1 H, Ar), 7.70−7.65 (m, 1 H, Ar), 7.50 (s, 1 H, Ar), 5.29 (d, 1 H, J = 11.2 Hz, H-17), 5.24 (d, 1 H, J = 11.2 Hz, H-17), 5.21 (s, 2 H, H-5), 3.20−3.00 (m, 2 H), 2.88−2.80 (m, 4 H), 2.80−2.72 (m, 2 H), 2.18−2.28 (m, 1 H), 2.06−2.18 (m, 1 H), 1.95 (s, 3 H), 1.76−1.66 (m, 2 H), 1.60−1.48 (m, 4 H), 0.88 (t, 3 H, J = 7.8 Hz). ^{13}C NMR (100 MHz, DMSO-d_6) δ 173.9, 171.0, 161.3, 158.0 (q, CO_2H of TFA), 156.5, 153.4, 148.7, 144.9, 132.3, 131.1, 130.6, 129.7, 1292, 128.7, 128.3, 124.0, 99.5, 79.4, 59.5, 51.0, 46.8, 45.3, 38.9, 36.7, 32.3, 26.5, 24.8, 23.3, 21.4, 8.6.

Compound 19. (10%); pale yellow solid. HRMS *m*/*z* calcd for $C_{38}H_{47}F_9N_6O_{11}$ $[M]^+$ 934,3159; *m*/*z* found 934,3168. ^{1}H NMR (400 MHz, CD_3OD) δ 8.65 (s, 1 H, Ar), 8.18 (d, 1 H, J = 8.4 Hz, Ar), 8.07 (d, 1 H, J = 8.4 Hz, Ar), 7.88 (t, 1 H, J = 8.4 Hz, Ar), 7.83 (s, 1 H, H-14), 7.72 (t, 1 H, J = 8.4 Hz, Ar), 5.46 (d, 1 H, J = 11.2 Hz, H-17), 5.40 (d, 1 H, J = 11.2 Hz, H-17), 5.33 (s, 2 H, H-5), 3.18−3.00 (m, 12 H), 2.48−2.40 (m, 1 H, H-19), 2.34−2.26 (m, 1 H, H-19), 2.12−2.08 (m, 4 H), 2.06 (s, 3 H), 1.90−1.76 (m, 4 H), 1.06 (t, 3 H, J = 7.6 Hz). ^{13}C NMR (100 MHz, CD_3OD) δ 176.4, 173.2, 163.3, 158.5, 153.8, 149.7, 146.2, 133.4, 132.0, 131.0, 130.0, 129.8, 129.7, 129.1, 125.5, 102.2, 80.0, 60.5, 51.8, 46.7, 46.3, 45.9, 37.8, 37.1, 36.8, 33.2, 27.7, 27.5, 25.4, 24.3, 22.4, 8.3.

17-Acetylcamptothecin-21-benzylamide (*21*). CPT **1** (350 mg, 1.01 mmol), was suspended in dry benzyl amine (2.5 mL). The reaction mixture was heated at 45−50 °C for 2.5 h, and then the solvent was removed under reduced pressure. Water was then added, and the aqueous layer was extracted with CH_2Cl_2 (15 mL × 3). The combined organic extracts were dried over anhydrous Na_2SO_4, filtered, and concentrated under vacuum to afford 17-hydroxy-21-benzylamide as a yellow solid (440 mg, 96%). The crude material was used for the next step without further purification.

17-hydroxy-21-benzylamide (440 mg, 0.97 mmol) was dissolved in dry pyridine (10 mL), and acetic anhydride (1.8 mL, 19.4 mmol) was added. The reaction was stirred at room temperature until TLC analysis [CH_2Cl_2−MeOH (30:1)] showed complete consumption of the starting material (2.5 h). The solvent and the excess of reagent were then removed under vacuum, and water was added. The aqueous layer was extracted with CH_2Cl_2 (20 mL × 3). The organic layer was further washed with 5% HCl and dried over anhydrous Na_2SO_4, filtered, and concentrated in vacuo to afford **21** (480 mg, ∼100%) in quantitative yield as a pale yellow solid. HRMS *m*/*z* calcd for $C_{29}H_{27}N_3O_5$ $[M]^+$ 497,1951; *m*/*z* found 497,1964. ^{1}H NMR (400 MHz, $CDCl_3$) δ 8.19 (s, 1 H, Ar), 8.11 (d, 1 H, J = 8.4 Hz, Ar), 7.74 (t, 1 H, J = 8.4 Hz, Ar), 7.69 (d, 1 H, J = 8.4 Hz, Ar), 7.63 (s, 1 H, H-14), 7.51 (t, 1 H, J = 8.4 Hz, Ar), 7.35−7.20 (m, 5 H, Ar), 5.56 (d, 1 H, J = 12.0 Hz), 5.44 (d, 1 H, J = 12.0 Hz), 5.19 (d, 1 H, J = 16.4 Hz), 5.13 (d, 1 H, J = 16.4 Hz), 5.13 (s, 1 H, O*H*), 4.53 (dd, 1 H, J_1 = 4.8 Hz, J_1 = 6.4 Hz), 4.39 (dd, 1 H, J_1 = 14.8 Hz, J_1 = 6.4 Hz), 2.56−2.46 (m,

1 H, H-19), 2.38−2.28 (m, 1 H, H-19), 2.04 (s, 3 H), 1.08 (t, 3 H, $J = 7.6$ Hz). ^{13}C NMR (100 MHz, $CDCl_3$) δ 172.1, 171.1, 161.5, 157.0, 151.3, 148.0, 144.1, 137.7, 130.5, 130.1, 128.9, 128.6, 128.5, 128.0, 127.8, 127.7, 127.5, 127.2, 124.9, 100.7, 78.5, 58.7, 50.3, 43.5, 33.1, 20.9, 7.9.

17-Acetylcamptothecin-21-benzyl Ester (*23*). To a solution of **21** (480 mg, 0.97 mmol) in a 2:1 mixture of Ac_2O (12 mL) and AcOH (6 mL) was added granular $NaNO_2$ (1.34 g, 19.4mmol) in portions over 2 h at 0−4 °C. Evolution of brown gas occurred. The flask was kept in the ice bath for 2 h and allowed to warm to room temperature and further reacted for 24 h. The mixture was then poured into ice/water and extracted with CH_2Cl_2 (3×). The combined organic layers were washed with 5% Na_2CO_3 followed by H_2O and dried over Na_2SO_4. Evaporation of solvent afforded compound **22** as yellowish solid, which was immediately dissolved with anhydrous 1,4-dioxane (16 mL) and refluxed for 5 h. The reaction mixture was cooled to room temperature, and the solvent was removed under vacuum to give **23** (483 mg, ≈100%). The crude product was sufficiently pure for the following step. However, an analytical sample of **23** was purified by silica gel flash chromatography CH_2Cl_2−MeOH (30:1). **23**: HRMS *m*/*z* calcd for $C_{29}H_{26}N_2O_6$ $[M]^+$ 498,1791; *m*/*z* found 498,1798. ^{1}H NMR (400 MHz, $CDCl_3$) δ 8.33 (s, 1 H, Ar), 8.20 (d, 1 H, $J = 8.4$ Hz, Ar), 7.89 (d, 1 H, $J = 8.4$ Hz, Ar), 7.80 (t, 1 H, $J = 8.4$ Hz, Ar), 7.63 (t, 1 H, $J = 8.4$ Hz, Ar), 7.52 (s, 1 H, H-14), 7.33−7.24 (m, 5 H, Ar), 5.50 (d, 1 H, $J = 11.6$ Hz), 5.47 (d, 1 H, $J = 11.6$ Hz), 5.29 (d, 1 H, $J = 12.0$ Hz), 5.23 (s, 2 H), 5.16 (d, 1 H, $J = 12.0$ Hz), 4.32 (s, 1 H, O*H*), 2.41−2.24 (m, 2 H, H-19), 2.03 (s, 3 H), 0.95 (t, 3 H, $J = 7.6$ Hz). ^{13}C NMR (100 MHz, $CDCl_3$) δ 173.5, 171.0, 161.4, 153.4, 152.5, 148.7, 144.7, 134.7, 131.0, 130.5, 129.5, 128.8, 128.6, 128.6, 128.3, 128.1, 128.1, 127.8, 124.9, 99.8, 79.4, 68.2, 58.7, 50.2, 32.2, 20.9, 7.6.

17-Acetylcamptothecinic Acid (*20*). Crude **23** (226 mg, 0.45 mmol) was dissolved in THF−EtOH (1:1). Dry 10% Pd/C (48 mg) was carefully added to the reaction mixture, and the dissolved oxygen was removed under vacuum. Then, a balloon of hydrogen was mounted, and the mixture was stirred for 10 h at room temperature. The catalyst was removed by filtration through a celite pad, and the filtrate was concentrated under vacuum. The crude material was purified by silica gel flash chromatography CH_2Cl_2−MeOH (step gradient elution 20:1, 10:1) to afford **20**. HRMS *m*/*z* calcd for $C_{22}H_{20}N_2O_6$ $[M]^+$ 408,1321; *m*/*z* found 408,1330. ^{1}H NMR (400 MHz, DMSO-d_6) δ 8.64 (s, 1 H, Ar), 8.18 (d, 1 H, $J = 8.4$ Hz, Ar), 8.08 (d, 1 H, $J = 8.4$ Hz, Ar), 7.85−7.81 (m, 2 H, Ar), 7.68 (t, 1 H, $J = 8.4$ Hz, Ar), 5.90 (s, 1 H, O*H*), 5.61 (d, 1 H, $J = 10.4$ Hz), 5.39 (d, 1 H, $J = 10.4$ Hz), 5.20 (s, 2 H), 1.98−1.82 (m, 5 H, H-19 + Me), 0.82 (t, 3 H, $J = 7.6$ Hz). ^{13}C NMR (100 MHz, DMSO-d_6) δ 171.0, 161.8, 160.0, 153.9, 148.7, 143.5, 132.0, 130.9, 130.6, 129.7, 129.1, 128.5, 128.1, 123.6, 101.3, 80.6, 60.2, 50.6, 33.8, 21.5, 9.6.

General Procedure. For the preparation of tripartate conjugates **24**, **19**, and **25** from the addition reaction of **20** to N-^{t}BOC polyamines **15**, **16**, and **17**, respectively, to a solution of **20** (1 equiv) in dry DMF (2 mL) the polyamine (2 equiv) and Et_3N (3 equiv) were sequentially added. The reaction mixture was cooled at 0 °C and 1-[3-(dimethylamino)propyl]-3-ethylcarbodiimide hydrochloride (EDCI.HCl, 2.2 equiv) and *N*-hydroxybenzotriazole (HOBt, 2.1 equiv) were added. The mixture was stirred at 0 °C for 2 h, then warmed at 20 °C and reacted further for 40−50 h. The solvent was removed under reduced pressure, and the crude material was purified by silica gel flash chromatography in CH_2Cl_2−MeOH (step gradient elution 40:1, 30:1, and 15:1), to afford the corresponding 17-acetyl-21-*N*-^{t}BOC protected amides in 62%, 50%, and 27% yields, respectively. To a solution of these conjugates (1 equiv), in DCM (8 mL) TFA (15.7 equiv) was added dropwise at 0 °C. The solution was stirred for 60 h at 0−4 °C, and then solvents were removed under reduced pressure to afford the desire products **24**, **19**, and **25**, as pale yellow solids.

19: (50%); pale yellow solid.

Compound 24. (62%); pale yellow solid. HRMS *m*/*z* calcd for $C_{34}H_{43}F_6N_5O_9$ $[M]^+$ 779,2965; *m*/*z* found 779,2972. ^{1}H NMR (400 MHz, CD_3OD) δ 8.59 (s, 1 H, Ar), 8.13 (d, 1 H, $J = 8.4$ Hz, Ar), 8.02 (d, 1 H, $J = 8.4$ Hz, Ar), 7.83 (t, 1 H, $J = 8.4$ Hz, Ar), 7.78 (s, 1 H, H-14), 7.68 (t, 1 H, $J = 8.4$ Hz, Ar), 5.46 (d, 1 H, $J = 11.2$ Hz, H-17), 5.39 (d, 1 H, $J = 11.2$ Hz, H-17), 5.25 (s, 2 H, H-5), 3.10−2.90 (m, 8 H), 2.54−2.44 (m, 1 H, H-19), 2.33−2.24 (m, 1 H, H-19), 2.06 (s, 3 H), 1.82−1.66 (m, 8 H), 1.07 (t, 3 H, $J = 7.6$ Hz). ^{13}C NMR (100 MHz, CD_3OD) δ 174.5, 172.1, 162.2, 157.6, 152.5, 148.4, 144.8, 132.1, 130.7, 129.7, 128.7, 128.6, 128.5, 127.9, 124.5, 101.1, 78.7, 59.3, 50.5, 47.3, 46.9, 38.8, 38.4, 32.1, 26.3, 24.4, 23.5, 23.1, 21.4, 7.1.

Compound 25. (27%); pale yellow solid. HRMS *m*/*z* calcd for $C_{47}H_{63}F_{15}N_8O_{15}$ $[M]^+$ 1264,4173; *m*/*z* found 1264,4165. ^{1}H NMR (400 MHz, CD_3OD) δ 8.60 (s, 1 H, Ar), 8.14 (d, 1 H, $J = 8.4$ Hz, Ar), 8.03 (d, 1 H, $J = 8.4$ Hz, Ar), 7.85 (t, 1 H, $J = 8.4$ Hz, Ar), 7.80 (s, 1 H, H-14), 7.69 (t, 1 H, $J = 8.4$ Hz, Ar), 5.46 (d, 1 H, $J = 11.2$ Hz, H-17), 5.40 (d, 1 H, $J = 11.2$ Hz, H-17), 5.27 (s, 2 H, H-5), 3.18−3.00 (m, 20 H), 2.48−2.40 (m, 1 H, H-19), 2.34−2.26 (m, 1 H, H-19), 2.18−2.07 (m, 8 H), 2.06 (s, 3 H), 1.90−1.76 (m, 4 H), 1.06 (t, 3 H, $J = 7.6$ Hz). ^{13}C NMR (100 MHz, CD_3OD) δ 176.4, 173.2, 163.4, 158.4, 153.7, 149.6, 146.1, 133.3, 131.9, 131.0, 130.9, 129.9, 129.8, 129.7, 129.1, 125.5, 102.2, 80.0, 60.4, 51.7, 48.2, 46.8, 46.4, 45.9, 45.8, 45.8, 37.8, 37.1, 33.3, 30.9, 27.7, 27.5, 25.3, 24.1(2 C), 21.0, 8.3.

Growth Inhibition Assays. Human non-small-cell lung cancer NCI-H460 cells were cultured in RPMI 1640 containing 10% FCS. Cell sensitivity was assessed by growth inhibition assay after 1 or 72 h of drug exposure. Cells in the logarithmic phase of growth were seeded in duplicates into six-well plates. Twenty-four hours later, cells were exposed to the drug and counted with a Coulter counter 72 h after the beginning of drug exposure for 1 h of treatment and at the end of drug exposure in the case of 72 h of treatment. IC_{50} is defined as the inhibitory drug concentration causing a 50% decrease of cell growth over that of the untreated control.

Topoisomerase I-Dependent DNA Cleavage Assays. A gel-purified 751-bp *Bam*HI-*EcoRI* fragment of SV40 DNA was used for the cleavage assay (*1*). DNA fragments were uniquely 3′-end-labeled. Topoisomerase I-DNA cleavage reactions (20 000 cpm per sample) were done in 20 μL of 10 mM Tris-HCl (pH 7.6), 150 mM KCl, 5 mM $MgCl_2$, 15 μg/mL bovine serum albumin, 0.1 mM DTT, and the human recombinant enzyme (full-length topoisomerase I) for 30 min at 37 °C. Reactions were stopped using 0.5% SDS and 0.3 mg/mL of proteinase K for 45 min at 42 °C. Persistence of DNA cleavage at different time points was examined by adding 0.6 M NaCl after 30 min of incubation with 10 μM drug. After precipitation, DNA was resuspended in denaturing buffer (80% formamide, 10 mM NaOH, 0.01 mM EDTA, and 1 mg/mL dyes) before loading on a denaturing 8% polyacrylamide gel in Tris-borate EDTA buffer. Overall, DNA cleavage levels were measured with a PhosphoImager 425 mode (*2*).

Stability of Compound 18 in Cell Culture Medium and DNA Cleavage Buffer. The stability study was performed by using high-performance liquid chromatography (HPLC) coupled with mass spectrometry (LC-MS). In order to optimize the method, MS analyses in direct infusion mode were carried on a LCQ-Duo mass spectrometer (ThermoFinnigan, San Jose, CA), equipped with an electrospray ionization source (ESI),

operating in positive polarity under the following condition: spray voltage 4.5 kV, capillary temperature 200 °C. The mass spectra were recorded in total ion current (TIC) within 150 and 2000 *m/z* and in tandem mass modality (MS/MS). Quantitative LC-MS analyses of the cell culture media diluted 1:10 with 0.1% formic acid/acetonitrile 85:15 (v/v) were conducted on a Cap-LC liquid chromatograph interfaced with a Q-TOF hybrid mass analyzer (Micromass, Manchester, UK). Q-TOF micro was employed with a Z-spray ion source (source condition: capillary voltage 3.0 kV, source temperature 90 °C, desolvation temperature 250 °C). Chromatograms were acquired in the *m/z* range 100−600 (TIC modality). Reverse-phase chromatographic separations were obtained on a C18 Waters symmetry column (150 × 0.3 mm I.D., 3.5 μm), assembled with a security guard column (Waters Symmetry 300, C18 5 μm, NanoEase), using a gradient elution from A [water/acetonitrile/formic acid 95:5:0.1 (v/v/v)]/B [acetonitrile/water/formic acid 95:5:0.1 (v/v/v)] 80:20 (v/v), for 10 min, to A/B 10:90 (v/v), within 15 min, up to 25 min, to A/B 80:20 (v/v) within 25.10 min. Equilibration time at A/B 80:20 (v/v) was 15 min. The flow rate was 4.0 μL/min, and the injection volume was 0.3 μL.

Cell culture media (RPMI 1640 plus 10% FCS) containing 50 μM of compound **18**, after 1 and 72 h of incubation at 37 °C, and cleavage buffer (10 mM Tris-HCl (pH 7.6), 150 mM KCl, 5 mM $MgCl_2$, 15 μg/mL bovine serum albumin, 0.1 mM DTT) containing 50 μM of **18** after 1 h of incubation at 37 °C, were diluted 1: 10 with a mixture of 0.1% formic acid/acetonitrile 85:15 and analyzed by LC-Q-TOF system. To test whether the cell metabolism influences the E-ring closure of **18**, NCI-H460 cells (6×10^5) were seeded in cell culture flask (75 cm^2) and treated 24 h later with compound **18** for 1 h at the concentration corresponding to the IC_{80} value (about 60 μM). After 1 h exposure, cells and culture medium were immediately recovered and analyzed.

The analyses of standard compound **18** performed on the LCQ-Duo (see Supporting Information, Figure 8) showed the in-source fragmentation of its parent ion $[M + H]^+$ at 451.25 *m/z* to the main daughter ion at *m/z* 391.07. This fragmentation was confirmed by MS/MS analysis on the ion at *m/z* 451.25. The analyses on the LC-Q-TOF system (see Supporting Information, Figure 9) gave a more extensive in-source fragmentation, leading to the complete disappearance of compound **18** parent ion and the formation of the main fragment at 391.1938 *m/z* (exact mass) and other minor fragment at *m/z* 374.1770, 356.1726. CPT, a possible degradation product of **18**, was also analyzed by LC-MS ($[M + H]^+$ at 349.1090 *m/z*), and it was revealed in compound **18** standard solution as an impurity (3.66%). For calibration, five solutions of **18** (1.142 × 57.10 μM) were analyzed [equation curve: $y = 3.130 \pm 0.02112)x + 0.3937(\pm 0.5535)$; $r^2 = 0.9999$]; the limit of quantitation (LOQ) was measured at the concentration of 0.571 μM.

CHEMISTRY

To optimize the efficiency of this novel family of open-lactone ring CPTs, we explored the influence of the polyamine architecture on the activity of these CPT conjugates into cells. Since the molecular recognition events involved in polyamine transport are sensitive to the number of nitrogens present in the molecule and to the distance between them (*64*, *65*), the following polyamine scaffolds were selected for our investigation: ethane-1,2-diamine **8**, spermidine **9**, homospermidine **10**, spermine **11**, and 4,8,13,17-tetraza-icosane-1,20-diamine **12** (Figure 5).

Direct amidation of CPT **1** with N-protected polyamines **13**, **14** (*70*), **16** (*71*) was performed in pyridine at 80 °C according to a modified Adamovics's protocol (*42*) (Scheme 1). Sequential

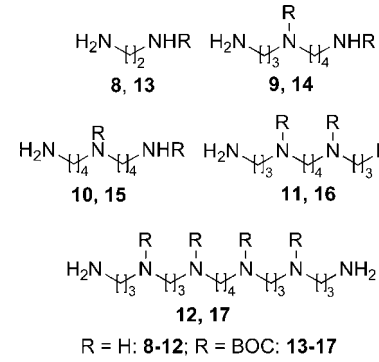

Figure 5. Structures of polyamines **8**−**12** and their correponding N-BOC derivatives **13**−**17**.

Scheme 1. Reactions of CPT with Polyamines

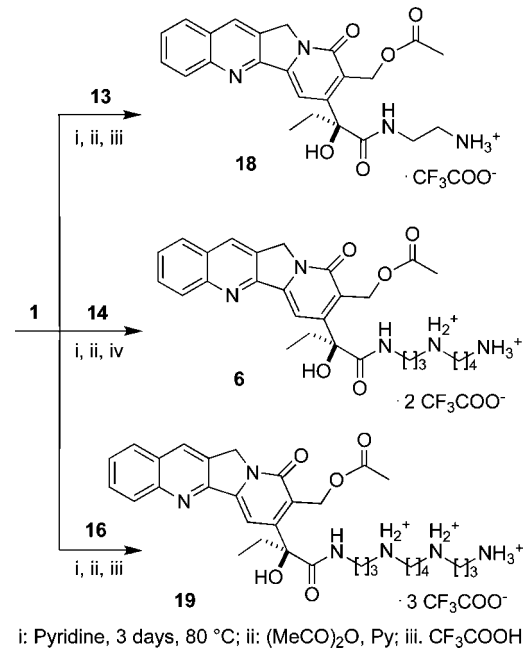

Scheme 2. Synthesis of 17-*O*-Acyl Protected Camptothecinic Acid 20

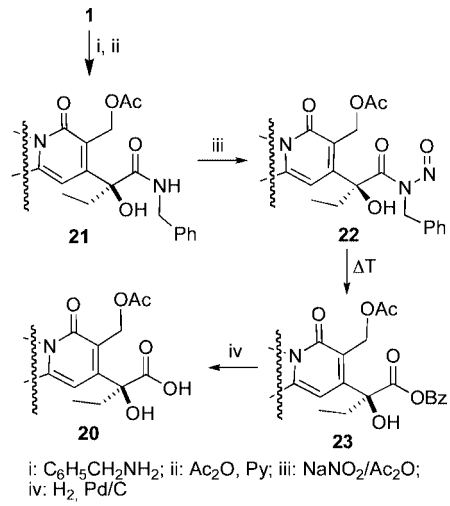

17-OH esterification of the resulting amides with Ac_2O followed by deprotection of the polyamine with trifluoroacetic acid afforded the tripartate conjugates **18**, **6**, and **19** as ammonium trifluoroacetates. Chemical yields of CPT amidation decreased with the enhancement of the polyamine length. For instance,

Scheme 3. Synthesis of Tripartates 19, 24, and 25

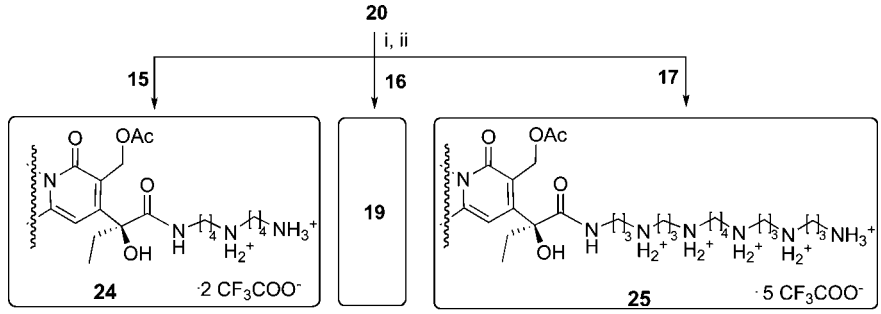

Table 1. Antiproliferative Activity of Camptothecin Derivatives on H460 Cells.[a]

	1 h exposure	72 h exposure	F.I.[b]
Topotecan	1.18 ± 0.24	0.015 ± 0.0027	79
SN38	0.22 ± 0.013	0.012 ± 0.001	18
CPT	0.18 ± 0.01	0.0059 ± 0.0024	30
18	6.04 ± 1.97	0.0023 ± 0.0004	2600
6	3.66 ± 0.34	0.048 ± 0.0075	76
19	2.1 ± 1.85	0.077 ± 0.019	28
24	7.7 ± 3.6	0.12 ± 0.03	64
25	1.44 ± 0.38	0.17 ± 0.027	8.5

[a] Sensitivity was assessed by growth inhibition assay after 1 or 72 h of drug exposure. Cells were counted 72 h after drug exposure for 1 h of treatment and at the end of drug exposure in the case of 72 h of treatment. The reported values are the mean ± SD of three independent experiments. [b] Fold increase: ratio between IC_{50} (μM) at 1 h and IC_{50} at 72 h.

chemical yields for the amidation of **1** were 88% and 55%, with the *N*-BOC derivatives **13** and **14**, respectively, but dropped to 10% when the spermine derivative **16** was used, while the coupling of CPT with polyamine **17** failed.

Such failure, along with the poor yields in the formation of compound **19**, prompted us to explore a more efficient protocol for the amidation reaction. We reasoned that 17-O-acyl camptothecinic acid **20** could be a suitable precursor for the synthesis of our tripartates. It has been reported that this naturally occurring compound can be either isolated from *Nothapodytes fetida* or obtained by acetylation of the corresponding sodium salt of **1** with Ac_2O in DMF (*72*). In our hands, this semisynthetic route was not reproducible, affording compound **20** in very low yield (<10%). Thus, we developed a new high-yielding and reproducible four-step synthesis, which afforded **20** in 80% starting from CPT. This methodology involves the one-pot sequential amidation of **1** with benzylamine, followed by acetylation of the free 17-OH group with acetic anhydride which provides the amide derivative **21** (Scheme 2).

Nitrosation of **21** with $NaNO_2$, in the presence of a mixture of Ac_2O and AcOH, afforded the corresponding *N*-nitroso amide **22**, which thermally rearranged to the benzylic ester **23**. Reductive debenzylation with H_2/Pd produced the target compound **20** in more than 80% overall yield. Amidation of **20** with **15**, **16**, and **17** (*73*) was performed according to a standard coupling procedure, using 1-ethyl-3-(3-dimethylaminopropyl) carbodiimide hydrochloride, in the presence of 1-hydroxybenzotriazole (Scheme 3). TFA removal of the *tert*-butoxy carbonyl protecting groups afforded the target conjugates **24**, **19**, and **25** as the trifluoroacetate salts.

BIOCHEMICAL ADN BIOLOGICAL EVALUATION

The CPT analogues were tested for growth inhibition ability against the human non-small-cell lung cancer carcinoma NCI-H460 cell line (Table 1) (*74*). The reduced potency of polyamine CPT derivatives with respect to topotecan, SN38, and CPT is likely related to the limited drug uptake, caused by their water-soluble salt formulation.

Although CPT derivatives were less potent than topotecan, SN38, and CPT after 1 h treatment, their antiproliferative effects increased after 72 h exposure. During long-term exposure, growth inhibition potency of **18** was higher than that of the reference drugs. Topoisomerase I-mediated DNA cleavage assay was carried out to investigate the ability of the compounds to stimulate DNA damage. Purified human topo I was used with SN38 as a reference compound (Figure 6A). Compound **18** exhibited DNA damage similar to that of SN38, and derivatives **6** and **19** revealed an intensity of DNA cleavage only slightly inferior to SN38, whereas **24** and **25** were substantially less efficient.

The cleavage pattern was found similar to that of SN38 for all the new CPTs. The stabilization of the ternary cleavable complex was also evaluated after the addition of a high salt concentration (0.6 M NaCl), which favors the drug−enzyme−DNA complex dissociation. As shown in Figure 6B, the compounds revealed DNA damage persistence similar to that of SN38. The best activity was achieved with compound **6**. The introduction of the homospermidine produced a reduction in the persistence of DNA damage with respect to spermidine (**24** vs **6**). A reduced persistence was also observed in the presence of a spermine instead of a spermidine (compound **19** vs **6**). Compound **18** was the least effective in stabilizing the DNA damage.

Compounds **18**, **6**, and **24**, which bear different polyamines in position C21, were tested for their capability to bind the DNA by evaluating the reduced migration in agarose gel of SV40 DNA plasmid (Figure 7). In comparison to compound **18**, compounds **6** and **24** revealed the most dose-dependent reduced migration of DNA plasmid. This feature was dependent on the number of positive charges carried by the polyamine residue (one for compound **18** and two for compounds **6** and **24**). Of note, the DNA binding affinity was also influenced by the architecture of the polyamine chain (compare **24** vs **6**), since homospermidine introduction at the C21 position, instead of spermidine, increased the capability to interact with DNA.

Stability studies of compound **18** in cell culture medium and cleavage buffer solutions were conducted on the ESI generated ion 391.1938, in single ion monitoring (SIM) modality (see Materials and Methods for details and Figure 10 in the Supporting Information section for representative sample TIC and SIM chromatograms).

As shown in Table 2, compound **18** was stable after 1 h of incubation at 37 °C both in cell culture medium and in cleavage buffer, because a marginal content of CPT (about 3%) was observed in both conditions. Appreciable degradation of **18** was observed when the compound was incubated in cell culture medium for 72 h, with the appearance of a significant amount of CPT. When the experiments were performed in the presence of cells, after 1 h of treatment at the IC_{80} value, no CPT was

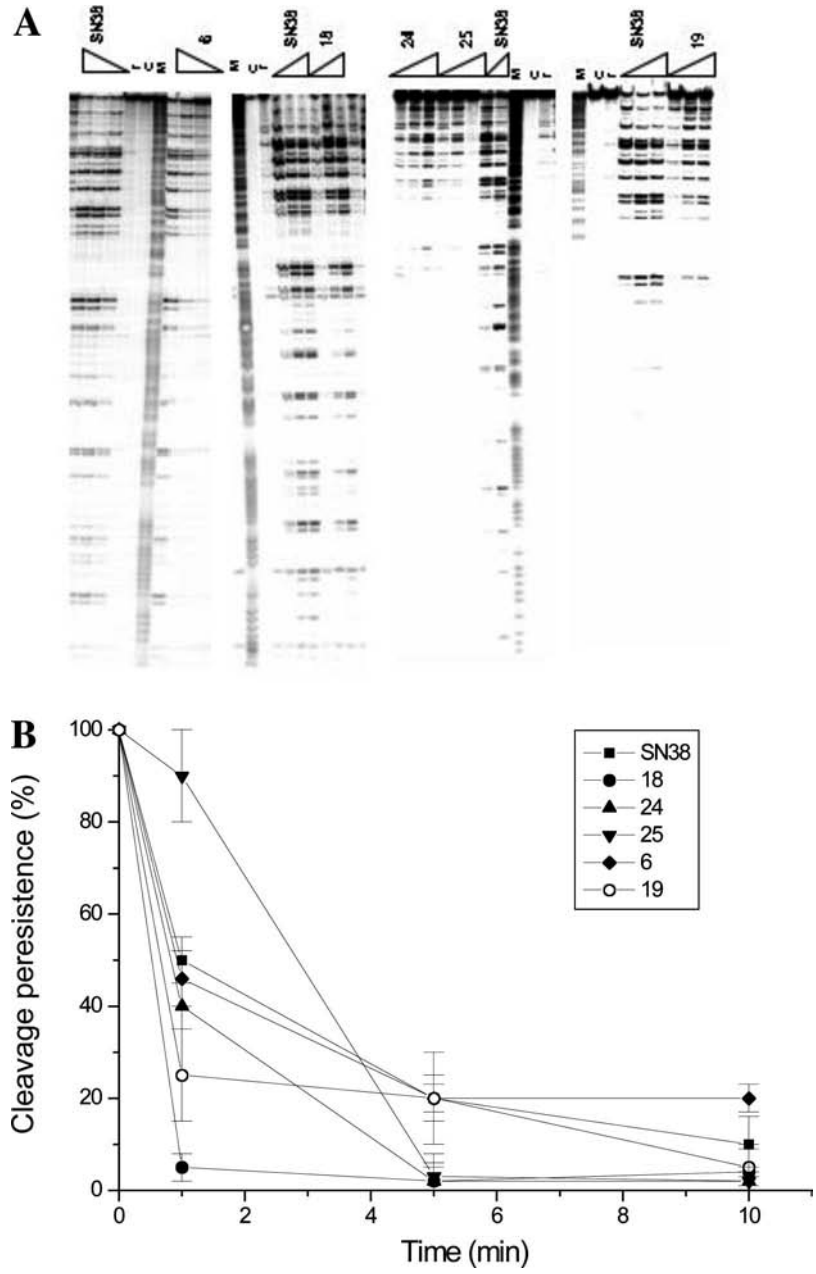

Figure 6. (A) Topoisomerase I-mediated DNA cleavage by SN38 and different camptothecin derivatives. Samples were reacted with 1, 10, and 50 μM drug at 37 °C for 30 min. Reaction was then stopped by adding 0.5% SDS and 0.3 mg/mL proteinase K and incubating for 45 min at 42 °C before loading on a denaturing 8% polyacrylamide gel. C, control DNA; T, reaction without drug; M, purine markers. (B) Persistence of topoisomerase I-mediated DNA cleavage in the presence of different compounds. The samples were reacted for 30 min with 10 μM drug in presence of top I. After this time, DNA damage was reversed by adding 0.6 M NaCl and incubating at 37 °C for 1, 5, and 10 min. The 100% value is referred to the extent of DNA cleavage at 30 min of incubation with top I. The experiment was repeated 3 times and the results of a representative value are reported.

found in the cell pellet; whereas a slight amount of CPT (3.7%) was recognized in cell culture medium (Table 2).

DISCUSSION AND CONCLUSION

The results reported in this study provide further evidence (*42*) that CPT polyamine conjugates with the open E-ring may be effective as cytotoxic agents and topo I inhibitors. Their activity was markedly dependent on the polyamine substituent. The introduction of suitable substituents in the open carboxylate form results in derivatives able to stabilize the cleavable complex. These CPT derivatives exhibited growth inhibition potency similar to or higher than that of topotecan, SN38, and CPT after long-term exposure. It is likely that the nature of the substituent is critical in promoting rapid intracellular drug accumulation and in achieving an optimal cytotoxic effect. Indeed, it is well-known that pharmacokinetic behavior at the cellular level is a critical determinant of the antitumor efficacy of CPTs, because as a consequence of the potential reversibility of the cleavable complex, adequate intracellular concentrations and exposure are required to produce a lethal extent of DNA damage. The growth inhibition potency during long-term exposure is correlated with the number of the charges of the substituent. Indeed, **18** was found the most active compound, while **25**, **24**, **19**, and **6**, which are the most charged derivatives, were the less active of the series. Interestingly, this pattern of activity was not observed after 1 h exposure for which, on the

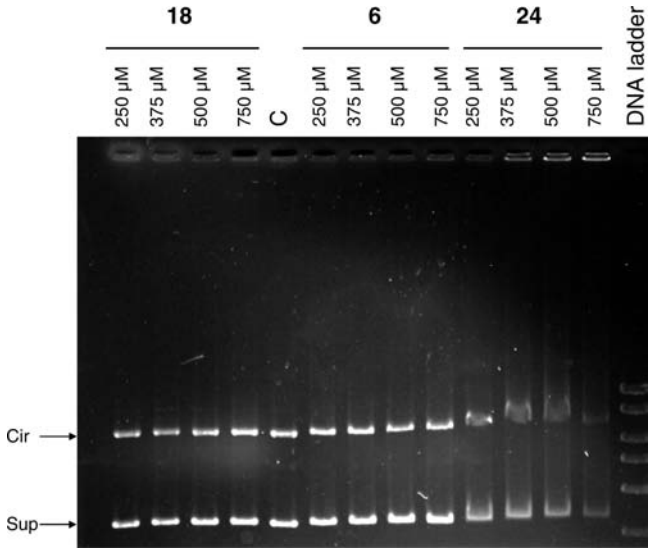

Figure 7. DNA binding of compounds **18**, **6**, and **24**. DNA and CPT analogues were incubated in 20 μL of phosphate buffered saline for 1 h at 37 °C in the presence of 100 ng of SV40 DNA plasmid at the indicated concentrations of compounds. Samples were analyzed on 0.7% agarose gel, followed by ethidium bromide staining. The arrows indicate the migration of the circular (Cir) and supercoiled (Sup) DNA plasmid.

Table 2. Stability of Compound 18[a]

experimental conditions		concentration (%)	
		18 (%)	CPT (%)
cell free conditions	medium (1 h)	96.4	3.6
	medium (72)	82.7	17.3
	cleavage buffer (1 h)	97.7	2.3
in presence of cells	medium (1 h)	96.3	3.7

[a] The amount of camptothecin produced by incubating compound **18** in different conditions was determined using LC/MS. The concentration of **18** added to cell culture medium or cleavage buffer was 50 μM. The experiments in presence of cells were performed by treating the cell culture at the IC_{80} value (about 60 μM) of **18** for 1 h and immediately harvesting both cell pellet and culture medium. The values are the means of three independent measures.

contrary, the most active derivative was **25**, which contains the longest polyamine side chain. The high antiproliferative activity observed for **18** after long-term exposure could suggest a major capability of this compound in promoting the E-ring closure, thus producing the structure of natural CPT. This feature is supported by an antiproliferative potency of **18** similar to that of CPT and by the formation of CPT (about 17%) after long-term incubation (72 h) in cell culture medium (Table 2). Thus, it is likely that, for this derivative, long-term exposure is required to produce E-ring closure. However, the cleavage assay and *in vitro* effects support the interpretation that the compounds may have inhibitory activity also in the open ring form. This feature is corroborated by the low amount of CPT (3.7%) observed incubating **18** for short-term exposure (1 h) in culture medium and by the absence of CPT recovered in the cells after this time exposure (Table 2). The architecture of the polyamine moiety is important for antiproliferative activity, and a balance between the hydrophilic and lipophilic properties of the polyamine is critical for CPT potency. The introduction of homospermidine instead of a spermidine in C21 reduced the antiproliferative effect after both short- and long-term exposure (compound **24** vs **6**). In addition, during short-term exposure, the potency seems to be correlated with the length of the polyamine, e.g., **25** versus topotecan; while during long-term exposure, a reduced potency was found for those compounds bearing long polyamine side chain. This observation supports a crucial role of the polyamine in the cellular pharmacokinetics.

The capability to stabilize the cleavable complex was found to be markedly dependent on the nature/length of the substituent linked to the 21-position of the CPT. Indeed, **24** and **25**, which carry a long polyamine moiety, displayed a low potency; on the contrary, **18** was very active in producing DNA damage. This feature appears independent from the capability of compound **18** to interact with the DNA in the absence of topo I (Figure 7) indicating that the ethyl-diamine moiety is more proficient than other substituents in fitting the CPT into the enzyme−DNA and thus producing more potent inhibition. Interestingly, reduced DNA damage was observed after exposure to a high concentration (50 μM) of **25** (Figure 6A). It is likely that this behavior is the result of the interaction between the long polyamine chain and the DNA substrate that, in so doing, inhibits the access of the enzyme into DNA sequences, thus reducing the cleavage efficacy of the compound. This hypothesis is also supported by the major capability of compounds **6** and **24** to interact with the DNA in the absence of topo I (Figure 7). Although of slight magnitude, compound **6** produced the more stable DNA damage, indicating that spermidine presents the best architecture for the interaction with the DNA in the presence of topo I. Our results support the efficacy per se of CPT with an open lactone ring in poisoning the topo I. Nevertheless, the antiproliferative activity and time-dependent effects probably reflect not only the inhibitory potency at target level but also the pharmacological behavior, which is determined by multiple and complex interactions, e.g., drug uptake, DNA interaction, and E-ring closure. The latter event could correlate with the properties of the polyamine moiety linked to the C21. Indeed, among the tested compounds, the most evident increase in cytotoxic potency found comparing short- and long-term exposure was observed for compound **18** (2600- vs 30-fold compared to CPT) that could indicate that the presence of an ethyl-diamine moiety may favor an efficient E-ring closure as a consequence of its easy release.

At concentrations of **18** required for cytotoxic effects during long-term exposure, the presence of free CPT was not measurable in cell culture medium. The expected amount on the basis of stability experiments (17%, Table 2) does not account for the activity reported in Table 1. Indeed, the potency of **18** is higher than that of CPT itself. In conclusion, although a contribution of CPT itself could not be ruled out, the available evidence supports that the CPT polyamine conjugates with the open E-ring may be active "per se".

Supporting Information Available: Figure 8, 9, 10, as described in the text, are provided. This material is available free of charge via the Internet at http://pubs.acs.org.

LITERATURE CITED

(1) Hsiang, Y.-H., Hertzberg, R., Hecht, S., and Liu, L. F. (1985) Camptothecin induces protein-linked DNA breaks via mammalian DNA topoisomerase I. *J. Biol. Chem. 260*, 14873–14878.

(2) Wang, J. C. (1996) DNA topoisomerases. *Annu. Rev. Biochem. 65*, 635–692.

(3) Champoux, J. J. (1998) Domains of human topoisomerase I and associated functions. *Prog. Nucleic Acid Res. Mol. Biol. 60*, 111–132.

(4) Wu, J. X., and Liu, L. F. (1997) Processing of topoisomerase I cleavable complexes into DNA damage by transcription. *Nucleic Acids Res. 25*, 4181–4186.

(5) Redinbo, M. R., Stewart, L., Kuhn, P., Champoux, J. J., and Hol, W. G. J. (1998) Crystal structures of human topoisomerase I in covalent and noncovalent complexes with DNA. *Science 279*, 1504–1513.

(6) Staker, B. L., Feese, M. D., Cushman, M., Pommier, Y., Zembower, D., Stewart, L., and Burgin, A. B. (2005) Structures of three classes of anticancer agents bound to the human topoisomerase I-DNA covalent complex. *J. Med. Chem. 48*, 2336–2345.

(7) Marchand, C., Antony, S., Kohn, K. W., Cushman, M., Ioanoviciu, A., Staker, B. L., Burgin, A. B., Lance Stewart, L., and Pommier, Y. (2006) A novel norindenoisoquinoline structure reveals a common interfacial inhibitor paradigm for ternary trapping of the topoisomerase I-DNA covalent complex. *Mol. Cancer Ther. 5*, 287–295.

(8) Sanna, N., Chillemi, G., Grandi, A., Castelli, S., Desideri, A., and Barone, V. (2005) New hints on the pH-driven tautomeric equilibria of the topotecan anticancer drug in aqueous solutions from an integrated spectroscopic and quantum-mechanical approach. *J. Am. Chem. Soc. 127*, 15429–15436.

(9) Bocian, W., Kawecki, R., Bednarek, E., Sitkowski, J., Pietrzyk, A., Williamson, M. P., Hansen, P. E., and Kozerski, L. (2004) Multiple binding modes of the camptothecin family to DNA oligomers. *Chem. Eur. J. 10*, 5776–5787.

(10) Fan, Y., Weinstein, J. N., Kohn, K. W., Shi, L. M., and Pommier, Y. (1998) Molecular modeling studies of the DNA-topoisomerase I ternary cleavable complex with camptothecin. *J. Med. Chem. 41*, 2216–2226.

(11) Kerrigan, J. E., and Pilch, D. S. (2001) A structural model for the ternary cleavable complex formed between human topoisomerase I, DNA, and camptothecin. *Biochemistry 40*, 9792–9798.

(12) Laco, G. S., Collins, J. R., Luke, B. T., Kroth, H., Sayer, J. M., Jerina, D. M., and Pommier, Y. (2002) Human topoisomerase I inhibition: Docking camptothecin and derivatives into a structure-based active site model. *Biochemistry 41*, 1428–1435.

(13) Lauria, A., Ippolito, M., and Almerico, A. M. (2007) Molecular docking approach on the Topoisomerase I inhibitors series included in the NCI anti-cancer agents mechanism database. *J. Mol. Modeling 13*, 393–400.

(14) Xiao, X., and Cushman, M. (2005) Effect of E-ring modifications in camptothecin on topoisomerase I inhibition: A quantum mechanics treatment. *J. Org. Chem. 70*, 9584–9587.

(15) Gupta, M., Fujimori, A., and Pommier, Y. (1995) Eukariotic DNA topoisomerases-I. *Biochim. Biophys. Acta 1262*, 1–14.

(16) Wall, M. E. (1969) *Biochemie und Physiologie der Alkaloide* (Mothes, K., and Schreiber, K., Eds.) pp 77−87, Akademie Verlag, Berlin.

(17) Slichenmeyer, W. J., Rowinsky, E. K., Donehower, R. C., and Kaufman, S. H. (1993) The current status of camptothecin analogs as antitumour agents. *J. Natl. Cancer Inst. 85*, 271–291.

(18) Wani, M. C., Nicholas, A. W., Manikumar, G., and Wall, M. E. (1987) Plant antitumor agents. Total synthesis oand antileukemic activity of ring A substituted camptothecin analogs. Structure activity correlations. *J. Med. Chem. 30*, 1774–1779.

(19) Giovanella, B. C., Hinz, H. R., Kozielski, A. J., Stehlin, J. S., Silber, R., and Potmesil, M. (1991) Complete growth-inhibition of human cancer xenografts in nude-mice by treatment with 20-(S)-camptothecin. *Cancer Res. 51*, 3052–3055.

(20) Fleury, F., Kudelina, I., and Nabiev, I. (1997) Interactions of lactone, carboxylate and self-aggregated forms of camptothecin with human and bovine serum albumins. *FEBS Lett. 406*, 151–156.

(21) Mi, Z., and Burke, T. G. (1994) Marked interspecies variations concerning the interactions of camptothecin with serum albumins - a frequency-domain fluorescence spectroscopic study. *Biochemistry 33*, 12540–12545.

(22) Kingsbury, W. D., Bohem, J C., Jakas, D. R., Holden, K. G., Hecht, S. M., Gallagher, G., Carafa, M. J., McCabe, F. L., Faucette, L. F., Johnson, R. K., and Hertzberg, R. P. (1991) Synthesis of water-soluble (aminoalkyl)camptothecin analogs - inhibition of topoisomerase-i and antitumor-activity. *J. Med. Chem. 34*, 98–107.

(23) Masuda, N., Fukuoka, Y., Kusunoki, K., Matsui, N., Takifuji, S., Kudoly, S., Negoro, M., Nishioka, K., Nakagawa, H., and Takada, J. (1992) A new derivative of camptothecin for the treatment of refractory or relapsed small-cell lung-cancer. *J. Clin. Oncol. 10*, 1225–1229.

(24) Macdonald, J. S., Benedetti, J. K., Modiano, M., and Alberts, D. S. (1997) Phase II evaluation of topotecan in patients with advanced colorectal cancer - A Southwest Oncology Group Trial (SWOG 9241). *Invest. New Drugs 15*, 357–359.

(25) Saltz, L. B., Schwartz, G. K., Ilson, D. H., Quan, V., and Kelsen, D. P. (1997) A phase II study of topotecan administered five times daily in patients with advanced gastric cancer. *Am. J. Clin. Oncol. 20*, 621–625.

(26) http://www.pharmcast.com/WarningLetters/Yr2003/Nov2003/Pfizer1103.htm.

(27) Dubowchik, G. M., and Walker, M. A. (1999) Receptor-mediated and enzyme-dependent targeting of cytotoxic anticancer drugs. *Pharmacol. Ther. 83*, 67–123.

(28) Huang, P. S., and Oliff, A. (2001) Drug-targeting strategies in cancer therapy. *Curr. Opin. Gen. Dev. 11*, 104–110.

(29) De Groot, F. M. H., Damen, E. W. P., and Scheeren, H. W. (2001) Anticancer prodrugs for application in monotherapy: Targeting hypoxia, tumor-associated enzymes, and receptors. *Curr. Med. Chem. 8*, 1093–1122.

(30) Fassberg, J., and Stella, V. J. (1992) A kinetic and mechanistic study of the hydrolysis of camptothecin and some analogs. *J. Pharm. Sci. 81*, 676–684.

(31) Zhao, H., Lee, C., Sai, P., Choe, Y. H., Boro, M., Pendri, A., Guan, S., and Greenwald, R. B. (2000) 20-O-acylcamptothecin derivatives: Evidence for lactone stabilization. *J. Org. Chem. 65*, 4601–4606.

(32) Yang, L.-X., Pan, X., and Wang, H.-J. (2002) Novel camptothecin derivatives. Part 1: Oxyalkanoic acid esters of camptothecin and their in vitro and in vivo antitumor activity. *Bioorg. Med. Chem. Lett. 12*, 1241–1244.

(33) Cao, Z., Harris, N., Kozielski, A., Vardeman, D., Stehlin, J. S., and Giovanella, B. (1998) Alkyl esters of camptothecin and 9-nitrocamptothecin: Synthesis, in vitro pharmacokinetics, toxicity, and antitumor activity. *J. Med. Chem. 41*, 31–37.

(34) De Groot, F. M. H., Busscher, G. F., Aben, R. W. M., and Scheeren, H. W. (2002) Novel 20-carbonate linked prodrugs of camptothecin and 9-aminocamptothecin designed for activation by tumour-associated plasmin. *Bioorg. Med. Chem. Lett. 12*, 2371–2376.

(35) Lerchen, H.-G., and Von dem Bruch, K. (2000) Synthesis of 20-O-linked 20(S)-camptothecin glycoconjugates: Impact of the side chain of the ester-linked amino acid on epimerization during the acylation reaction and on hydrolytic stability of the final glycoconjugates. *J. Prakt. Chem. 342*, 753–760.

(36) Prijovicha, Z. M., Leub, Y.-L., and Roffler, S. R. (2003) Stability of the new prodrug 9-aminocamptothecin glucuronide (9ACG) in the presence of human serum albumin. *Biochem. Pharmacol. 66*, 1181–1187.

(37) Matteucci, M., Lin, K.-Y., Huang, T., Wagner, R., Sternbach, D. D., Mehrotra, M., and Besterman, J. M. (1997) Sequence-specific targeting of duplex DNA using a camptothecin triple helix forming oligonucleotide conjugate and topoisomerase I. *J. Am. Chem. Soc. 119*, 6939–6940.

(38) Arimondo, P. B., Boutorine, A., Baldeyrou, B., Bailly, C., Kuwahara, M., Hecht, S. M., Sun, J.-S., Garestier, T., and Hélene, C. (2002) Design and optimization of camptothecin conjugates of triple helix-forming oligonucleotides for sequence-specific DNA cleavage by topoisomerase. *J. Biol. Chem. 277*, 3132–3140.

(39) Arimondo, P. B., Angenault, S., Halby, L., Boutorine, A., Schmidt, F., Monneret, C., Garestier, T., Sun, J.-S., Bailly, C., and Hélène, C. (2003) Spatial organization of topoisomerase I-mediated DNA cleavage induced by camptothecin-oligonucleotide conjugates. *Nucleic Acids Res. 31*, 4031–4040.

(40) Arimondo, P. B., Bailly, C., Boutorine, A., Ryabinin, V., Syniakov, A., Sun, J.-S., Garestier, T., and Hélène, C. (2001)

Directing topoisomerase I mediated DNA cleavage to specific sites by camptothecin tethered to minor- and major-groove ligands. *Angew. Chem., Int. Ed. 40*, 3045–3048.
(41) Wang, C. C., and Dervan, P. B. (2001) Sequence-specific trapping of Topoisomerase I by DNA binding polyamide-camptothecin conjugates. *J. Am. Chem. Soc. 123*, 8657–8661.
(42) Adamovics, J. A., and Hutchinson, C. R. (1979) Prodrug analogs of the anti-tumor alkaloid camptothecin. *J. Med. Chem. 3*, 310–314.
(43) Sawada, S., Yaegashi, T., Furuta, T., Yokokura, T., and Miyasaka, T. (1993) Chemical modification of an antitumor alkaloid, 20(S)-camptothecin: E-lactone ring-modified water-soluble derivatives of 7ethylcamptothecin. *Chem. Pharm. Bull. 41*, 310–313.
(44) Ogawa, T., Yaegashi,T., Sawada, S., Furuta, T. (2001) U.S. Patent 6,310,210 B1.
(45) Greenwald, R. B., Zhao, H., and Xia, J. (2003) Tripartate poly(ethylene glycol) prodrugs of the open lactone form of camptothecin. *Bioorg. Med. Chem. 11*, 2635–2639.
(46) This suggestion seems to be in contrast with literature results (*43*), claiming that the 17-OH-21-N^1,N^1-dimethylaminoethyl amide dipartates are not stable enough to survive cell tissue culture experiments, undergoing rapid cyclization to the lactone form at physiological pH. Hence, compound **4** should be *in vitro* active.
(47) Beretta, G. L., Petrangolini, G., De.Cesare, M., Pratesi, G., Perego, P., Tinelli, S., Tortoreto, M., Zucchetti, M., Frapolli, R., Bello, E., Manzotti, C., Fontana, G., Bombardelli, E., Battaglia, A., Samorì, C., and Zunino, F. (2006) Biological properties of IDN5174, a new synthetic camptothecin with the open lactone ring. *Cancer Res. 66*, 10976–10982.
(48) Cohen, S. S. (1998) *A Guide to the Polyamines*, Oxford University Press, Oxford.
(49) Igarashi, K., and Kashiwagi, K. (2000) Polyamines: Mysterious modulators of cellular functions. *Biochem. Biophys. Res. 271*, 559–564.
(50) Yoshida, M., Kashiwagi, K., Shigemasa, A., Taniguchi, S., Yamamoto, K., Makinoshima, H., Ishihama, A., and Igarashi, K. (2004) A unifying model for the role of polyamines in bacterial cell growth, the polyamine modulon. *J. Biol. Chem. 279*, 46008–46013.
(51) Cullis, P. M., Green, R. E., Merson.Davies, L., and Travis, N. (1999) Probing the mechanism of transport and compartmentalisation of polyamines in mammalian cells. *Chem. Biol. 6*, 717–729, and references therein.
(52) Bloomfield, V. A. (1997) DNA condensation by multivalent cations. *Biopolymers 44*, 269–282.
(53) Feuerstein, B. G., Williams, L. D., Basu, H. S., and Marton, L. J. (1991) Implications and concepts of polyamine-nucleic acid interactions. *J. Cell Biochem. 46*, 37–47.
(54) Kashiwagi, K., Yamaguchi, Y., Sakai, Y., Kobayashi, H., and Igarashi, K. (1990) Identification of the polyamine-induced protein as a periplasmic oligopeptide binding-protein. *J. Biol. Chem. 265*, 8387–8391.
(55) Fukuchi, J., Hiipakka, R. A., Kokontis, J. M., Nishimura, K., Igarashi, K., and Liao, S. (2004) TATA-binding protein-associated factor 7 regulates polyamine transport activity and polyamine analog-induced apoptosis. *J. Biol. Chem. 279*, 29921–29929.
(56) Uemura, T., Tachihara, K., Tomitori, H., Kashiwagi, K., and Igarashi, K. (2005) Characteristics of the polyamine transporter TPO1 and regulation of its activity and cellular localization by phosphorylation. *J. Biol. Chem. 280*, 9646–9652.
(57) Mani, K., Sandgren, S., Lilja, J., Cheng, F., Svensson, K., Persson, L., and Belting, M. (2007) HIV-Tat protein transduction domain specifically attenuates growth of polyamine deprived tumor cells. *Mol. Cancer Ther. 6*, 782–788.
(58) Vassylyev, D. G., Tomitori, H., Kashiwagi, K., Morikawa, K, and Igarashi, K. (1998) Crystal structure and mutational analysis of the *Escherichia coli* putrescine receptor. *J. Biol. Chem. 273*, 17604–17609.
(59) Phanstiel, O., IV, Price, H. L., Wang, L., Juusola, J., Kline, M., and Shah, S. M. (2000) The effect of polyamine homologation on the transport and cytotoxicity properties of polyamine-(DNA-intercalator) conjugates. *J. Org. Chem. 65*, 5590–5599.
(60) Wang, C., Delcros, J.-G., Cannon, L., Konate, F., Carias, H., Biggerstaff, J., Gardner, R. A., and Phanstiel, O. V. (2003) Defining the molecular requirements for the selective delivery of polyamine conjugates into cells containing active polyamine transporters. *J. Med. Chem. 46*, 5129–5138.
(61) Gardner, R. A., Delcros, J.-G., Konate, F., Breitbeil, I. I. I., Martin, B., Sigman, M., Huang, M., and Phanstiel, O. (2004) N-1-substituent effects in the selective delivery of polyamine conjugates into cells containing active polyamine transporters. *J. Med. Chem. 47*, 6055–6069.
(62) Phanstiel, O., IV, Kaur1, N., and Delcros, J.-G. (2007) Structure-activity investigations of polyamine-anthracene conjugates and their uptake via the polyamine transporter. *Amino Acids 33*, 305–313.
(63) Burns, M. R., Carlson, C. L., Vanderwerf, S. M., Ziemer, J. R., Weeks, R. S., Cai, F., Webb, H. K., and Graminski, G. F. (2001) Amino acid/spermine conjugates: Polyamine amides as potent spermidine uptake inhibitors. *J. Med. Chem. 44*, 3632–3644.
(64) Holley, J., Mather, A., Cullis, P., Symons, M. R., Wardman, P., Watt, R. A., and Cohen, G. M. (1992) Uptake and cytotoxicity of novel nitroimidazole-polyamine conjugates in ehrlich ascites tumor-cells. *Biochem. Pharmacol. 43*, 763–769.
(65) Siddiqui, A. Q., Merson-Davies, L., and Cullis, P. M. (1999) The synthesis of novel polyamine-nitroimidazole conjugates designed to probe the structural specificities of the polyamine uptake system in A549 lung carcinoma cells. *J. Chem. Soc., Perkin Trans. 1*, 3243–3252.
(66) Jakobs, A., Bernadou, J., and Meunier, B. (1997) Preparation of tetracationic metalloporphyrin - Spermine conjugates. *J. Org. Chem. 62*, 3505–3510.
(67) Rauter, H., Di.Domenico, R., Menta, E., Oliva, O., Qu, Y., and Farrell, N. (1997) Selective platination of biologically relevant polyamines. Linear coordinating spermidine and spermine as amplifying linkers in dinuclear platinum complexes. *Inorg. Chem. 36*, 3919–3927.
(68) Popaj, K., Guggisberg, A., and Hesse, M. (2000) Synthetic analogues to the spermidine-spermine alkaloid tenuilobine. *Helv. Chim. Acta 83*, 3021–3034.
(69) Dallavalle, S., Giannini, G, Alloatti, D., Casati, A., Marastoni, E., Musso, L., Merlini, L., Morini, G., Penco, S., Pisano, C., Tinelli, S., De.Cesare, M., Beretta, G. L., and Zunino, F. (2006) Synthesis and cytotoxic activity of polyamine analogues of camptothecin. *J. Med. Chem 49*, 5177–5186.
(70) Hu, V. W., and Hesse, M. (1996) The synthesis of p-Cumaroylspermidines. *Helv. Chim. Acta 79*, 548–559.
(71) Blagbrough, I. S., and Geall, A. J. (1998) Practical synthesis of unsymmetrical polyamine amides. *Tetrahedron Lett. 39*, 439–442.
(72) Bombardelli, E., and Verotta, L. (2000) U.S. Patent 6,121,277.
(73) Miller, K. A., Kumar, E. V. K. S., Wood, S. J., Cromer, J. R., Datta, A., and David, S. A. (2005) Lipopolysaccharide sequestrants: Structural correlates of activity and toxicity in novel acylhomospermines. *J. Med. Chem. 48*, 2589–2599.
(74) Marchesini, R., Colombo, A., and Caserini, C. (1996) Interaction of ionizing radiation with topotecan in two human tumor cell lines. *Int. J. Cancer 66*, 342–346.

BC800033R

The Role of Polyamine Architecture on the Pharmacological Activity of Open Lactone Camptothecin-Polyamine Conjugates

Cristian Samorì,[*,‡] *Andrea Guerrini,*[‡] *Greta Varchi,*[‡] *Giovanni Luca Beretta,*[§] *Gabriele Fontana,*[⊥] *Ezio Bombardelli,*[⊥] *Nives Carenini,*[§] *Franco Zunino,*[§] *Carlo Bertucci,*[†] *Jessica Fiori,*[†] *and Arturo Battaglia*[‡]

Istituto CNR per la Sintesi Organica e Fotoreattività "I.S.O.F.", Area della Ricerca di Bologna, Via Gobetti 101, 40129 Bologna, Italy, Dipartimento di Oncologia Sperimentale e Laboratori, Fondazione IRCCS Istituto Nazionale Tumori, 20133 Milano, Italy and [†]Dipartimento di Scienze Farmaceutiche, Università di Bologna, Via Belmeloro 6, 40126 Bologna, Italy

SUPPORTING INFORMATIONS

Contents:

Figure 8. LCQ Duo mass spectra (direct infusion) S2

Figure 9. LC/Q-TOF mass spectra S3

Figure 10. LC/Q-TOF SIM (**A**,**B**) and TIC (**C**) chromatograms S4

[*] E-mail. csamori@isof.cnr.it. Phone: (039) 639-8286. Fax: (039) 6398349.

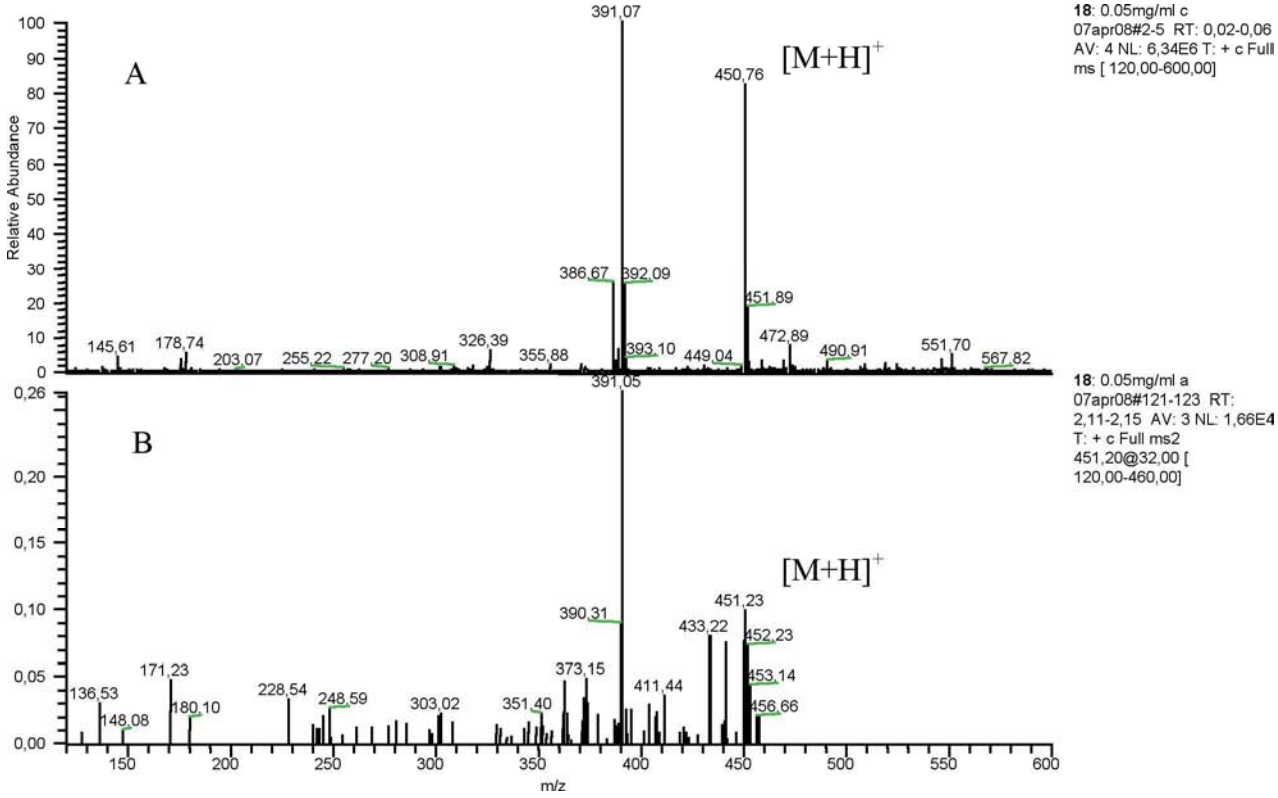

Figure 8. LCQ Duo mass spectra (direct infusion). **A**) Compound **18** mass spectrum (TIC), **B**) Compoud **18** MS/MS spectrum on the ESI generated ion 451.2

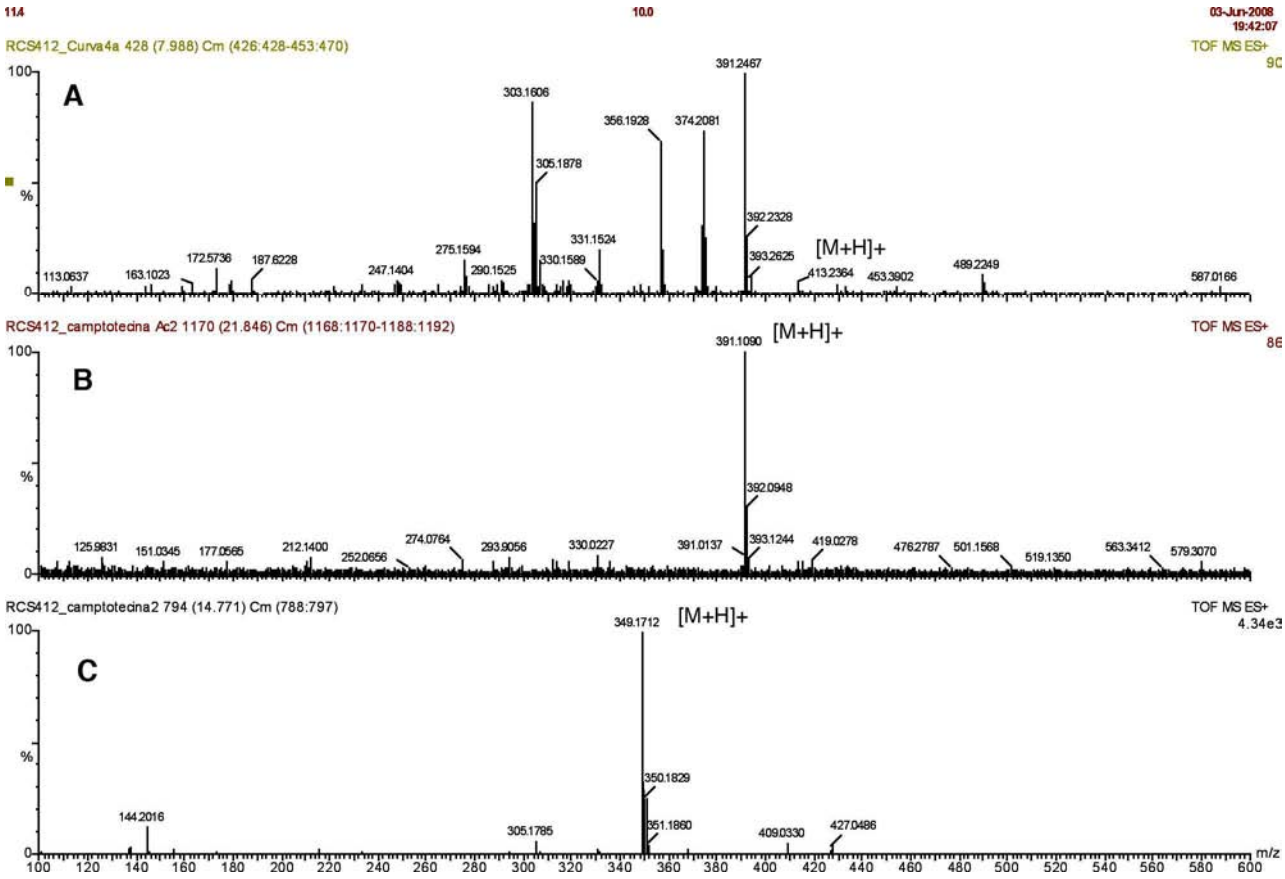

Figure 9. LC/Q-TOF mass spectra acquired on-line during the chromatographic analysis. **A**) Compound **18** mass spectrum, **B**) 20-acetyl-CPT mass spectrum, **C**) CPT mass spectrum.

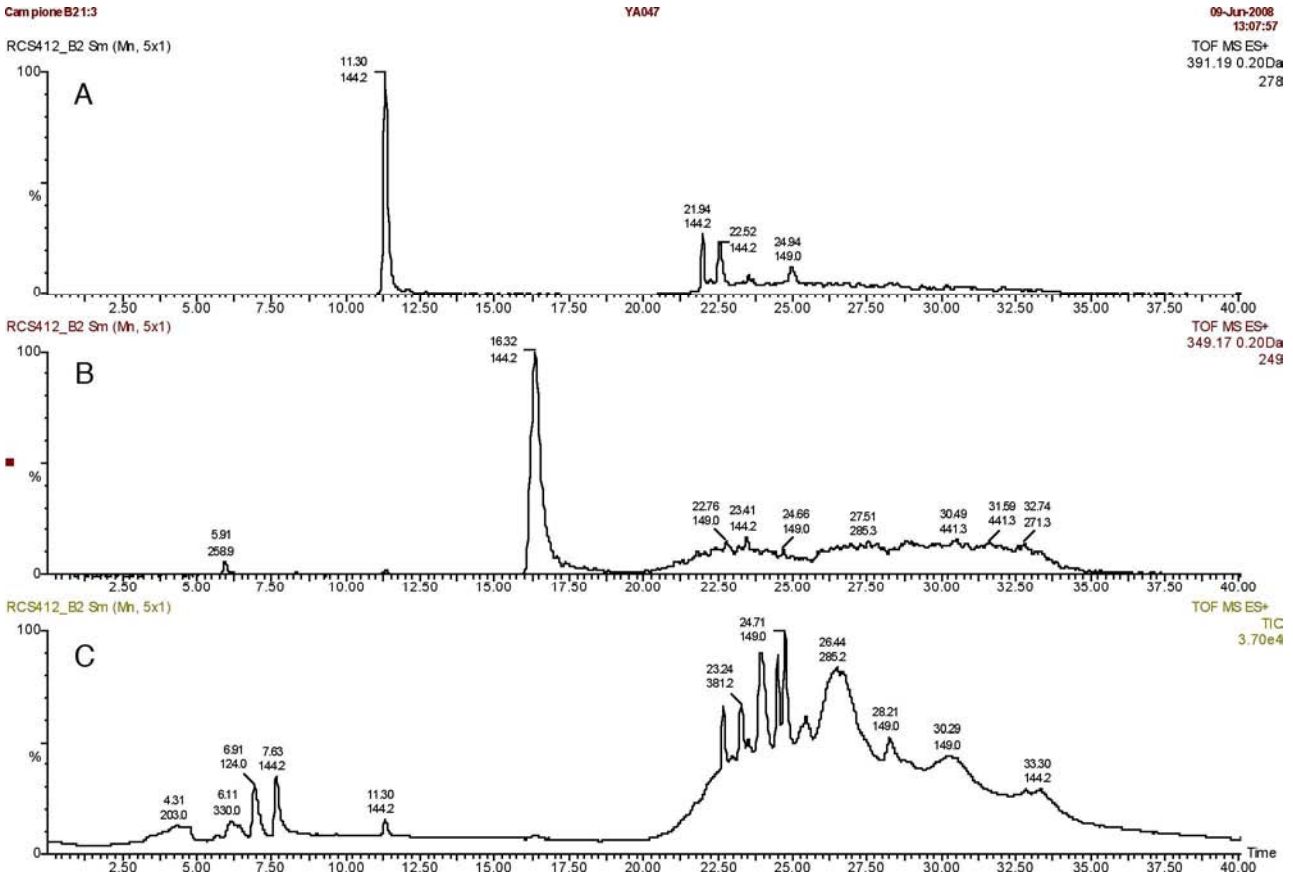

Figure 10. LC/Q-TOF SIM (**A**,**B**) and TIC (**C**) chromatograms of B2 sample solution. **A**) Compound **18** $[M+H]^+$ at 391.19 *m/z*, **B)** CPT $[M+H]^+$ at 349.17 *m/z*.

TECHNICAL NOTES

Aqueous Solubilization of Fullerenes Using Poly(amidoamine) Dendrimers Bearing Cyclodextrin and Poly(ethylene Glycol)

Chie Kojima, Yoko Toi, Atsushi Harada, and Kenji Kono*

Graduate School of Engineering, Osaka Prefecture University, Osaka, Japan. Received April 11, 2008; Revised Manuscript Received September 8, 2008

Fullerene has a unique structure and notable chemical and physical properties, which have been studied in diverse fields including biological applications. The extremely poor solubility of fullerenes in water limits their usage for biomedical applications. In this study, we synthesized polyamidoamine dendrimers having both β-cyclodextrin (CD) and poly(ethylene glycol) (PEG) and characterized the resulting dendrimers by ^{1}H NMR, IR, and gel permeation chromatography. We prepared 2.8 μM of aqueous fullerene solutions using these dendrimers. The clustering effect of CD and PEG at the surface of the dendrimer might be crucial for the solubilization of fullerene.

INTRODUCTION

Fullerene, C_{60}, has a unique structure and notable chemical and physical properties, which have been studied in diverse fields including biological applications. Fullerene has been reported to act as an antioxidant, a neuroprotective agent, and as anti-HIV and antimicrobial agents. In addition, fullerenes have photochemical properties, by which reactive oxygen species are generated in high quantum yields after irradiation to affect abnormal cells (*1*−*3*). However, extremely poor solubility in water limits their usage for biomedical applications. There are two strategies to improve the solubility. One is the chemical modification of C_{60}. Many researchers have designed a wide variety of fullerene derivatives as water-soluble fullerenes, such as fullerenes bearing carboxyl, hydroxyl, and amino groups, and water-soluble polymers, such as polyvinyl alcohol, poly(ethylene glycol) (PEG), and water-soluble dendrimers (*1*−*3*). However, modification is thought to lose and/or reduce the function of C_{60}. Alternatively, the addition of solubilizers has been shown to improve the solubility of C_{60} (*1*, *2*, *4*−*7*). Generally, this kind of molecular assembly may be unstable because of its dynamic properties. Further, without dispersing C_{60} at the molecular level, it may also cause loss and/or reduction of the function of C_{60} due to quenching.

Dendrimers are attractive polymers with unique structures, which have a monodispersed molecular weight, well-defined morphology, and an inner space capable of holding drug molecules, which is quite different from classical polymers (*8*). In addition, one of the major advantages of dendritic polymers is the modification and dense packing of functional moieties at the periphery (*8*−*11*). We previously modified dendrimers with PEG, as PEG is known to enhance water solubility and biocompatibility (*12*). We reported that these dendrimers could encapsulate anticancer drugs and photosensitizers (*12*, *13*). In the present study, we designed a solubilizer/carrier of C_{60} based on our PEG-modified dendrimers bearing cyclodextrin (CD) with dense packing. It has been reported that two CDs are complexed with one fullerene (*14*, *15*). The ability to complex with fullerene may be enhanced by accumulating CD at the periphery of the dendrimer. Therefore, we synthesized poly(amidoamine) (PAMAM) dendrimers modified with both CD and PEG, which may provide the benefit of clustering of CDs at the dendrimer periphery to improve the complex formation and also the exposure of the biocompatible and water-soluble surface for nanomedical applications. Previously, Arima et al. synthesized dendrimers modified with CDs for applications directed to gene delivery (*16*). They showed that the α-CD-modified PAMAM dendrimers exhibited the most effective transfection activity and were much improved over the dendrimers modified with mannose (*16*, *17*). In this study, we used β-CD for the binding CD because it does not tend to interact with PEG (*18*). We synthesized and characterized the PEG and CD-modified dendrimer and prepared a highly concentrated C_{60} aqueous solution using the dendrimer.

MATERIALS AND METHODS

Synthesis of PEG/CD-Modified Dendrimer. Monotosylated β-CD was synthesized according to the previous report (*19*). Briefly, to a 1% NaOH solution containing β-CD (20 g) was added CH_3CN solution containing *p*-toluenesulfonyl chloride (3.4 g) dropwise at room temperature. After 2 h, 1 M HCl was added to the reaction mixture to adjust the pH to 2.5. After the solution was stored at 4 °C overnight, the precipitation was harvested. The crude product was recrystallized from water. The yield was 2.3 g (7.8%). ^{1}H NMR (400 MHz, dimethylsulfoxide (DMSO)-d_6) δ 2.4 (s), 3.3−3.7 (m), 4.2−4.5 (m), 4.8 (m), 5.7 (m), 7.4 (d), 7.8 (d).

A generation 4 (G4) PAMAM dendrimer with ethylenediamine core was obtained from Sigma-Aldrich Corp. (St. Louis, MO). The G4 PAMAM dendrimer was reacted with monotosylated β-CD according to a previous report, with some modification (*16*). Briefly, the G4 PAMAM dendrimer (200 mg) and monotosylated β-CD (1.74 g) were dissolved in 4 mL of distilled DMSO. The mixture was stirred for 5 days at 60 °C under nitrogen gas. The product was purified using a Sephadex

* To whom correspondence should be addressed: Department of Applied Chemistry, Graduate School of Engineering, Osaka Prefecture University, 1-1 Gakuen-cho, Naka-ku, Sakai, Osaka 599-8531, Japan. Tel.: +81 72 254 9330; Fax: +81 72 254 9330; E-mail: kono@chem.osakafu-u.ac.jp.

10.1021/bc8001503 CCC: $40.75 © 2008 American Chemical Society
Published on Web 10/10/2008

Scheme 1. Preparation Method of the PEG/CD-Modified Dendrimer Including C_{60}

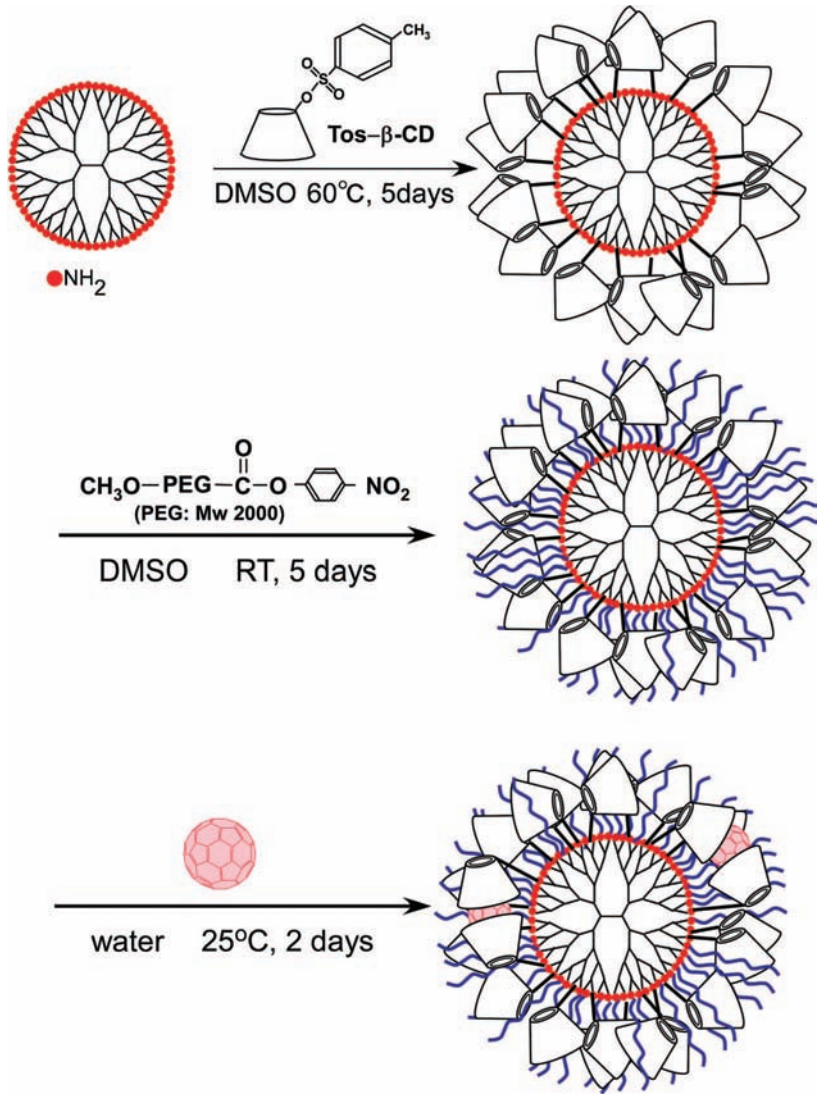

G-75 column with 0.1 M Na_2SO_4 aqueous solution as the eluent. The yield was 581 mg. Next, monomethoxy PEG (molecular weight: 2000) 4-nitrophenyl carbonate was bound to the CD-modified dendrimer according to our previous report (*12*). The CD-modified dendrimer (250 mg) and monomethoxy PEG 4-nitrophenyl carbonate (609 mg) were dissolved in 5 mL of distilled DMSO, and triethylamine (39 μL) was added. After stirring for 5 days at room temperature, the mixture was purified according to our previous report (*12*). The yield was 405 mg. PEG/CD-modified dendrimers at different ratios were also synthesized. The G4 PAMAM dendrimer (60 mg) and monotosylated β-CD (522 mg) dissolved in 1.6 mL of distilled DMSO were reacted and purified, as mentioned before. The yield was 145 mg. Next, pegylation was performed as mentioned before. The yield was 257 mg. Thin-layer chromatography of these compounds showed that free β-CD and PEG were free from contamination.

Characterization of the PEG/CD-Attached Dendrimer. The products were characterized by ^{1}H NMR, FTIR, fluorescamine assay, and gel permeation chromatography (GPC). ^{1}H NMR and FTIR were measured using a JNM-LA-400 instrument (JEOL, Japan) and FTIR-8400 (Shimadzu Corp., Japan), respectively. A fluorescamine assay was performed according to previous reports (*20, 21*). Fluorescamine reacted with primary amine was measured using an FP-6500 instrument (JASCO, Inc., Japan; $\lambda_{ex} = 390$ nm, $\lambda_{em} = 480$ nm). The GPC system (TSK-gel G3000PW and G4000PW; Toso Co., Ltd., Japan) had two detectors, a differential refractive index detector (RI-930; Jasco Inc., Japan) and a UV−vis detector ($\lambda = 220$ nm; UV-970; Jasco Inc., Japan). These dendrimers and the complexes with C_{60} were dissolved in water, and the sample solutions of 10−20 μL were injected. These dendrimers were eluted with 10 mM phosphate buffer containing 0.2 M sodium sulfate (pH 7.4) at 0.5 mL/min at 30 °C.

Preparation of C_{60} Aqueous Solutions with the PEG/CD-Modified Dendrimer. C_{60} aqueous solutions were prepared by mixing the solubilizers (free CD, 116 nmol, or dendrimers, 4 nmol) with C_{60} (0.25 mg) and stirring vigorously at 25 °C for 2 days. The suspension was centrifuged at 13 000 *g* for 20 min to remove the free C_{60} (*22*). The UV−vis spectra of the supernatant were measured using a V-560 instrument (JASCO, Inc., Japan). Those of the solubilizers themselves were also measured. Then, after water was removed, the residues were dissolved in toluene. The absorbance at 336 nm was measured ($\varepsilon = 5.7 \times 10^4$ M^{-1} cm^{-1}).

RESULTS AND DISCUSSION

Synthesis of the PEG/CD-Modified Dendrimer. Both PEG- and CD-modified dendrimers were synthesized according to Scheme 1. PAMAM dendrimer was reacted with monotosylated β-CD according to a previous report, with some modification,

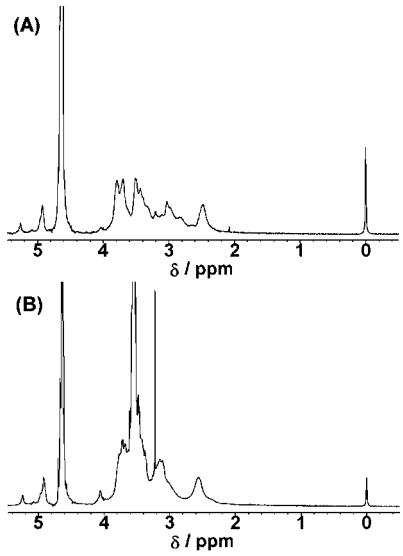

Figure 1. ^{1}H NMR spectra of the CD_{29}-modified dendrimer (A) and the PEG_{35}/CD_{29}-modified dendrimer (B) in D_2O.

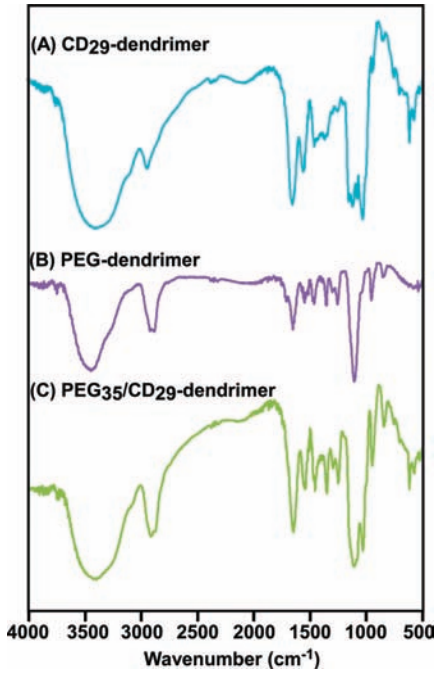

Figure 2. FTIR spectra of the CD_{29}-modified dendrimer (A), the PEG- modified dendrimer (B), and the PEG_{35}/CD_{29}-modified dendrimer (C).

to obtain the CD-modified dendrimer (*16*). Next, monomethoxy PEG 4-nitrophenyl carbonate was bound to the CD-modified dendrimer via urethane bonds, according to our previous report (*12*). These products were identified by ^{1}H NMR, as shown in Figure 1. The ^{1}H NMR spectrum of the CD-modified dendrimer had peaks which were derived from CD and the PAMAM dendrimer. From the ratio of the typical signal of CD (4.9−5.3 ppm) to the other signals except the solvent peak, the estimated number of CD molecules bound to the PAMAM dendrimer was 29. In the ^{1}H NMR spectrum of the PEG/CD-modified dendrimer, in contrast, the signals derived from CD, PEG, and the dendrimer were largely overlapped. It was difficult to estimate the number of PEG molecules bound to the CD-modified dendrimer from the ^{1}H NMR spectrum. Therefore, we analyzed the residual primary amino groups of the PEG/CD-modified dendrimer using fluorescamine assays. Fluorescamine fluoresces

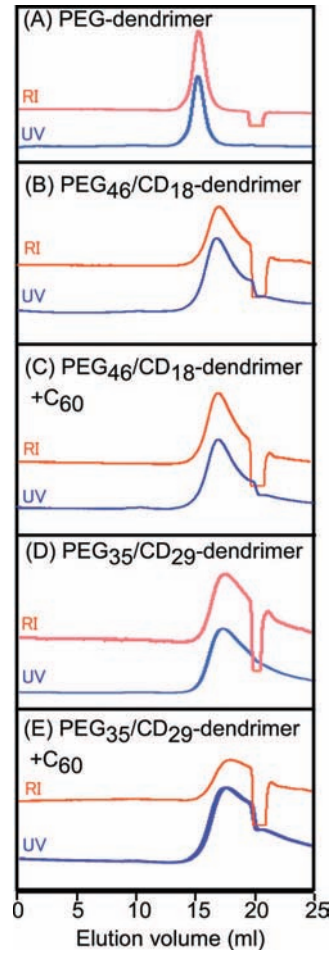

Figure 3. GPC profiles of the PEG-modified dendrimer (A), the PEG_{46}/CD_{18}-modified dendrimer (B,C), and the PEG_{35}/CD_{29}-modified dendrimer (D,E) before (B,D) and after (C,E) the addition of C_{60}. PEGs of 1, 2, 5, 10, 20, 50, and 140 kDa used as a standard were eluted at 20.6, 19.6, 18.6, 17.4, 16.4, 15.8, and 13.5 mL.

by reacting with a primary amino group (*20*, *21*). The fluorescamine assay of the PEG/CD-modified dendrimer indicates that the number of residual primary amino groups of the PEG/CD-modified dendrimers was 0.3 per dendrimer, suggesting that essentially every terminal amino group was attached to either a CD or PEG chain. Because the CD-modified dendrimer possessed 29 CD molecules in 64 terminal amino groups of the dendrimer, the PEG/CD-modified dendrimer may have 35 PEG chains and 29 CD molecules. We also synthesized the dendrimer with different contents of PEG and CD. This dendrimer was characterized as the PEG_{46}/CD_{18}-modified dendrimer by ^{1}H NMR and the fluorescamine assay.

Characterization of the PEG/CD-Modified Dendrimer. The CD-modified dendrimer and PEG/CD-modified dendrimer were characterized by FTIR spectrometry, as shown in Figure 2. The dendrimer modified with PEG chains at every terminal (PEG-dendrimer) was also analyzed as a control. The signals of both PEG and CD were observed in the PEG/CD-modified dendrimer, which is also consistent with the ^{1}H NMR results. It was reported that the FTIR spectra of the complex of PEG and CD have typical bands at 2800−3100 cm^{-1} and 3407 cm^{-1} (*23*). However, the PEG/CD-modified dendrimers did not exhibit these bands. This suggests that β-CD did not interact intra- or intermolecularly with PEG in these dendrimers. The PEG/CD-modified dendrimers were also characterized by GPC. The dendrimer modified with PEG chains at every terminal (PEG-dendrimer) was also analyzed as a control. The GPC profiles

Table 1. Summary of C_{60} Aqueous Solutions with Various Solubilizers

solubilizer	$[C_{60}]$	[solubilizer]	$[C_{60}]$/1 mM solubilizer	ref
PEG/CD-modified dendrimer	2.8 μM	2.0 μM	1.4 mM	this work
tetradecyl trimethylammonium hydroxide lauric acid	1.64 mM	100 mM	16.4 μM	*5*
humic acid (Mw = 10^3−10^5)	5.41 μM	1−100 mM (100 mg/mL)	54.1 nM−5.41 μM	*6*
fluoroalkyl end-capped acryloyl-morpholine oligomers (Mw = 4360)	29 μM	0.459 mM (2 g/L)	63 μM	*7*

are shown in Figure 3, in which the single peaks were observed. This suggests that the PEG/CD-modified dendrimer did not aggregate via the interaction between PEG and CD. As mentioned before, our IR analysis indicates that there were no interactions between CD and PEG in the PEG/CD-modified dendrimer. These data are also supported by a previous report demonstrating that the affinity of β-CD for PEG is much less than the affinity of α- and γ-CD for PEG (*18*). The peak tops of the dendrimers having both PEG and CD were shifted to a larger elution volume, as the ratios of CD in the dendrimer increased. The calculated molecular weights of the PEG-dendrimer, the PEG_{46}/CD_{18}-modified dendrimer, and the PEG_{35}/CD_{29}-modified dendrimer were 1.44×10^5 Da, 1.28×10^5 Da, and 1.18×10^5 Da, respectively, which is consistent with these chromatograms. In addition, the broader peaks of the PEG/CD-modified dendrimers were observed and compared with the PEG-dendrimer. This may be caused by the affinity of CD with the column gel. It is likely that the PEG/CD-modified dendrimers in our synthetic procedure are not obtained as a single molecule; different amounts of CD and PEG were attached to the dendrimer, although 29 or 18 molecules of CD and 35 or 46 molecules of PEG were attached on average. The broad peak may reflect the molecular distribution of the dendrimers. The large negative reflective indexes and the discontinuous UV peaks may come from the solvent of the sample, because the background RI and UV of the eluent (phosphate buffer containing Na_2SO_4) were affected by the injected sample solvent.

We then prepared C_{60} aqueous solutions with both PEG- and CD-modified dendrimers, according to the report of the preparation of the complexes between β-CD and C_{60} (*22*). Since free C_{60} could be removed by centrifugation due to aggregation, aqueous solutions of C_{60} were obtained as a supernatant. GPC analysis of the PEG/CD-modified dendrimer after the incubation with C_{60} was performed. Because the elution volume of the dendrimer in the absence and presence of C_{60} was almost the same, the complexes were formed in the dendrimer but did not form aggregates (Figure 3C,E).

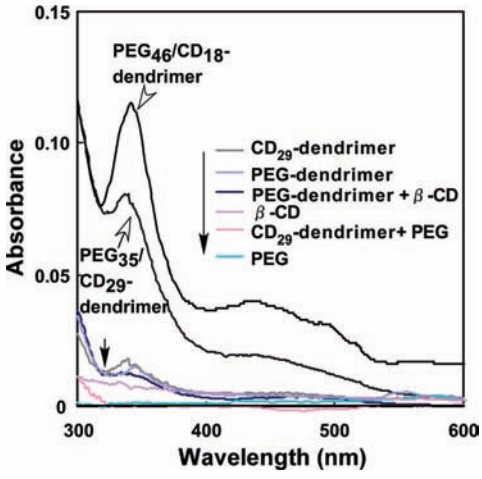

Figure 4. UV−vis spectra of C_{60} aqueous solutions containing the PEG_{46}/CD_{18}-modified dendrimer (2.0 μM), the PEG_{35}/CD_{29}-modified dendrimer (2.0 μM), the CD_{29}-modified dendrimer (2.0 μM), and the PEG_{64}-modfied dendrimer (2.0 μM), free CD (58 μM), free PEG (70 μM), or the mixtures. These spectra were obtained by subtracting the spectra of these compounds without C_{60} from those of the complex.

Solubilization of C_{60} by the PEG/CD-Modified Dendrimer. We prepared C_{60} aqueous solutions of the PEG/CD-modified dendrimers, the CD-modified dendrimer, the PEG-dendrimer, free CD, and free PEG. The corresponding UV−vis spectra are shown in Figure 4. We found that a more highly concentrated C_{60} aqueous solution was prepared using the CD-modified dendrimers than free CD, suggesting that the clustering of CD enhanced the ability to complex with C_{60}. Although it was previously reported that PEG interacts with C_{60} (*24*), under our conditions the PEG-modified dendrimer and free PEG did not dissolve C_{60} efficiently due to their low affinity. In the present study, the much stronger absorption derived from C_{60} was observed in the solution containing both PEG- and CD-modified dendrimers. This suggests that both PEG and CD of the dendrimer were crucial for the efficient complex formation with C_{60}. In other words, these data suggest that PEG was also involved in the interaction with C_{60} in the dendrimer. It is possible that C_{60} is complexed with CD and PEG, and that C_{60} is dispersed by surrounding it with PEG to enhance the interaction between C_{60} and the two CDs. Here, C_{60} was not rendered highly soluble by mixing the CD-modified dendrimer and free PEG or by mixing the PEG-modified dendrimer and free CD. Therefore, the effect of CD and PEG likely resulted from clustering at the surface of the dendrimer. Among the PEG/CD-modified dendrimers, the PEG_{46}/CD_{18}-modified dendrimer could solubilize slightly greater amounts of C_{60} than the PEG_{24}/CD_{29}-modified dendrimer. The attached CD molecules of the PEG_{24}/CD_{29}-modified dendrimer might be too crowded to interact with C_{60} at the surface of the dendrimer. It is also possible that the sufficient number of PEG chains at the surface of the dendrimer need to disperse the complex with C_{60}. Since the absorbance of C_{60} at 336 nm in toluene obeys the Beer−Lambert law, the amount of C_{60} was estimated from the absorbance of toluene solutions of the dendrimers. The numbers of complexed C_{60} molecules per PEG_{35}/CD_{29}-modified dendrimer and per PEG_{46}/CD_{18}-modified dendrimer were determined as 1.1 and 1.6, respectively. Figure 3 shows that the complex was not formed by the aggregation of C_{60} and the dendrimers, which is useful for the usage of C_{60} with their own function. The complex formed between C_{60} and both the PEG- and CD-modified dendrimers remains to be elucidated in detail. In addition, optimization of the bound ratios of CD and PEG to the dendrimer can improve the water solubility of C_{60}.

CONCLUSION

We synthesized and characterized PEG/CD-modified dendrimers. Highly concentrated C_{60} aqueous solutions with the dendrimer were prepared. We estimated the C_{60} concentration in the aqueous solution of the PEG_{46}/CD_{18}-modified dendrimer (2.0 μM) as 2.8 μM, although the solubility of C_{60} in pure water is reported as 2×10^{-24} M (*3*). Table 1 summarizes the previously reported C_{60} aqueous solutions by the simple mixing of C_{60} with various solubilizers in aqueous solution. Our C_{60}

aqueous solution has the highest observed concentration compared with the other methods involving the simple mixing of C_{60} with small amounts of the solubilizers in aqueous solution (*5*−*7*).

ACKNOWLEDGMENT

We are grateful to Akihiro Nomoto and Akiya Ogawa (Osaka Prefecture University) for their generous support in FTIR analysis. We also thank Sayako Tsumura for her kind support in fluorescamine assay. This work was supported by Grants from the Saneyoshi Scholarship Foundation, and in part by Grants-in-aid from the Ministry of Education, Culture, Sports, Science, and Technology of Japan (MEXT).

LITERATURE CITED

(1) Jensen, A. W., Wilson, S. R., and Schuster, D. I. (1996) Biological applications of fullerenes. *Bioorg. Med. Chem. 4*, 767–779.

(2) Bosi, S., Da Ros, T., Spalluto, G., and Prato, M. (2003) Fullerene derivatives: an attractive tool for biological applications. *Eur. J. Med. Chem. 38*, 913–923.

(3) Nakamura, E., and Isobe, H. (2003) Functionalized fullerenes in water. The first 10 years of their chemistry, biology, and nanoscience. *Acc. Chem. Res. 36*, 807–815.

(4) Jenekhe, S. A., and Chen, X. L. (1998) Self-assembled aggregates of rod-coil block copolymers and their solubilization and encapsulation of fullerenes. *Science 279*, 1903–1907.

(5) Li, H., Jia, X., Li, Y., Shi, X., and Hao, J. (2006) A salt-free zero-charged aqueous onion-phase enhances the solubility of fullerene C_{60} in water. *J. Phys. Chem. 110*, 68–74.

(6) Terashima, M., and Nagao, S. (2007) Solubilization of [60]fullerene in water by aquatic humic substances. *Chem. Lett. 36*, 302–303.

(7) Sawada, H., Iidzuka, J.-I., Maekawa, T., Takahashi, R., Kawase, T., Oharu, K., Nakagawa, H., and Ohira, K. (2003) Solubilization of fullerene into water with fluoroalkyl end-capped amphiphilic oligomersnovel fluorescence properties. *J. Colloid interface Sci. 263*, 1–3.

(8) Tomalia, D. A. (2005) Birth of a new macromolecular architecture: dendrimers as quantized building blocks for nanoscale synthetic polymer chemistry. *Prog. Polym. Sci. 30*, 294–324.

(9) Lee, C. C., MacKay, J. A., Frechet, J. M. J., and Szoka, F. C. (2005) Designing dendrimers for biological applications. *Nat. Biotechnol. 12*, 1517–1526.

(10) Gillies, E. R., and Frechet, J. M. J. (2005) Dendrimers and dendritic polymers in drug delivery. *Drug Discovery Today 10*, 35–43.

(11) Boas, U., and Heegaad, P. M. H. (2004) Dendrimers in drug research. *Chem. Soc. Rev. 33*, 43–63.

(12) Kojima, C., Kono, K., Maruyama, K., and Takagishi, T. (2000) Synthesis of polyamidoamine dendrimers having poly(ethylene glycol) grafts and their ability to encapsulate anticancer drugs. *Bioconjugate Chem. 11*, 910–917.

(13) Kojima, C., Toi, Y., Harada, A., and Kono, K. (2007) Preparation of polyethylene glycol-attached dendrimers encapsulating photosensitizers for application to photodynamic therapy. *Bioconjugate Chem. 18*, 663–670.

(14) Andersson, T., Nilsson, K., Sundahl, M., Westman, G., and Wennerstrom, O. (1992) C_{60} embedded in γ-cyclodextrin: a water-soluble fullerene. *J. Chem. Soc., Chem. Commun. 1992*, 604–606.

(15) Murthy, C. N., and Geckeler, K. E. (2001) The water-soluble β-cyclodextrin-[60]fullerene complex. *Chem. Commun. 2001*, 1194–1195.

(16) Arima, H., Kihara, F., Hirayama, F., and Uekama, K. (2001) Enhancement of gene expression by polyamidoamine dendrimer conjugates with α-, β-, and γ-cyclodextrins. *Bioconjugate Chem. 12*, 476–484.

(17) Wada, K., Arima, H., Tsutsumi, T., Chihara, Y., Hattori, K., Hirayama, F., and Uekama, K. (2005) Improvement of gene delivery mediated by mannosylated dendrimer/α-cyclodextrin conjugates. *J. Controlled Release 104*, 397–413.

(18) Harada, A., Okada, M., Li, J., and Kamachi, M. (1995) Preparation and characterization of inclusion complexes of poly(propy1ene) glycol with cyclodextrins. *Macromolecules 28*, 8406–8411.

(19) Vizitiu, D., Walkinshaw, C. S., Gorin, B. I., and Thatcher, G. R. J. (1997) Synthesis of monofacially functionalized cyclodextrins bearing amino pendent groups. *J. Org. Chem. 62*, 8760–8766.

(20) Udenfriend, S., Stein, S., Bohlen, P., Dairman, W., Leimgruber, W., and Weigele, M. (1972) Fluorescamine: a reagent for assay of amino acids, peptides, proteins, and primary amines in the picomole range. *Science 178*, 871–872.

(21) Yuba, E., Kojima, C., Sakaguchi, N., Harada, A., Koiwai, K., and Kono, K. (2008) Gene delivery to dendritic cells mediated by complexes of lipoplexes and pH-sensitive fusogenic polymer-modified liposomes. *J. Controlled Release 130*, 77–83.

(22) Liu, Y., Yang, Y.-W., Chen, Y., and Zou, H.-X. (2005) Polyrotaxane with cyclodextrins as stoppers and its assembly behavior. *Macromolecules 38*, 5838–5840.

(23) Rusa, C. C., and Tonelli, A. E. (2000) Separation of polymers by molecular weight thorough inclusion compound formation with urea and α-cyclodetrin hosts. *Macromolecules 33*, 1813–1818.

(24) Li, M., and Chen, Q. (2003) Interactions between fullerene (C_{60}) and poly(ethylene oxide) in their complexes as revealed by high-resolution solid-state ^{13}C NMR spectroscopy. *Polymer 44*, 2793–2798.

BC8001503

DECEMBER 2008
Volume 19, Number 12

© *Copyright 2008 by the American Chemical Society*

Bioconjugate Chemistry

REVIEWS

DNA-Mediated Electrochemistry

Alon A. Gorodetsky, Marisa C. Buzzeo, and Jacqueline K. Barton*

Division of Chemistry and Chemical Engineering, California Institute of Technology, Pasadena, California 91125. Received July 22, 2008; Revised Manuscript Received September 2, 2008

The base pair stack of DNA has been demonstrated as a medium for long-range charge transport chemistry both in solution and at DNA-modified surfaces. This chemistry is exquisitely sensitive to structural perturbations in the base pair stack as occur with lesions, single base mismatches, and protein binding. We have exploited this sensitivity for the development of reliable electrochemical assays based on DNA charge transport at self-assembled DNA monolayers. Here, we discuss the characteristic features, applications, and advantages of DNA-mediated electrochemistry.

1. INTRODUCTION

Since the elucidation of the double helical structure of DNA, scientists have been fascinated by the possibility that the stacked aromatic base pairs of the duplex may promote charge transport (CT) over significant distances (*1, 2*). Consequently, the nature of the conductive properties of duplex DNA has attracted substantial interest (*3*−*7*). Over the past two decades, a wide-ranging collection of experiments has both revealed the fundamental details of DNA-mediated CT and illustrated its potential for sensing applications.

Initial solution experiments featured photoinduced DNA-mediated CT between well-defined donor and acceptor sites (*8, 9*). While long-range CT has been shown to yield oxidative damage in DNA up to 200 Å away from the bound oxidant (*10, 11*), DNA CT has also been found to be exquisitely sensitive to the integrity of the base pair stack (*9, 12*) and to the coupling of the donors and acceptors with the DNA (*13*). Indeed, this sensitivity has prompted both the consideration of biological roles for DNA CT (*14*) and the construction of electrochemical DNA-based sensors for mutations, base lesions, and protein-binding (*15*).

Electrochemical techniques provide a particularly convenient means for the study of heterogeneous electron transfer at solid surfaces (*16*). Typically, redox-active molecules are modified with thiol-terminated alkyl chains and self-assembled as well-ordered monolayers on metal surfaces (*17*). Under an applied potential, electrons or holes are then transferred to pendant, redox-active head groups with the rates and yield of charge transfer (as measured electrochemically) providing information on the structure of the thiol terminated linker. In our laboratory, we have extended this methodology to the study and application of DNA-modified surfaces where charge transfer is *mediated* by the DNA monolayers, which are self-assembled onto conductive substrates.

Before embarking on a general discussion of the application of this methodology, it is important to have a clear understanding of the architecture of DNA-modified surfaces. Independent of the material employed, duplex DNA is modified at the 5′-end of a single strand with a linker, which allows it to interact with the electrode surface (Figure 1). In the case of gold, this tether is an alkane thiol; for graphitic surfaces, it is pyrene. Electrodes are then incubated with modified duplexes and an organized

* Author to whom correspondence should be addressed. E-mail: jkbarton@caltech.edu.

10.1021/bc8003149 CCC: $40.75 © 2008 American Chemical Society
Published on Web 11/04/2008

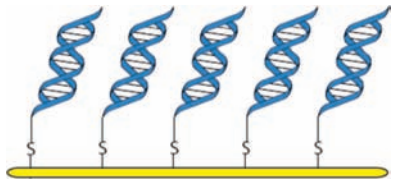

Figure 1. Schematic illustration of DNA duplexes in a close-packed monolayer immobilized on gold via an alkanethiol tether.

monolayer is allowed to self-assemble. A redox-active molecule is introduced either by exposure to a solution or through covalent attachment to the 5′-terminus of the single strand lacking the linker. Subsequent addition of an inert backfilling agent, such as mercaptohexanol, promotes the removal of nonspecifically adsorbed duplexes and single strands.

We have extensively characterized these DNA monolayers on both gold and graphite via electrochemical and physical techniques (*15*). Structural characterization has confirmed that the DNA duplexes within a DNA monolayer adopt an upright orientation, at an angle relative to the surface. The uniformity and reliability of this structure enables the duplexes to serve as an extension of the active electrode surface, thus allowing DNA-bound, redox-active molecules to be reduced via the π-stack. Importantly, fabrication of the surface with rigid, structurally defined DNA duplexes, rather than with single-stranded DNAs that can stick to the surface in ill-defined conformations, provides an enormous level of control and reliability in the construction of the monolayers. Moreover, since the electrochemistry of the DNA probe is remarkably sensitive to the integrity of the base pair stack, single base mismatches and lesions, located between the surface and the probe, dramatically attenuate the electrochemical yield of CT. These findings have been extended to general assays for the study of DNA/RNA hybrids and RNA transcripts. Furthermore, we have been able to detect a wide variety of DNA-binding proteins based on their association and electronic communication with the base pair stack. These data have underscored the strength and versatility of this methodology.

It is noteworthy that the CT properties of DNA monolayers are not simply of utility in the context of electrochemistry. The base pair stack of each individual duplex serves as a conduit for charge transfer, as recently confirmed by single molecule experiments within our laboratory (*18*). In fact, when considered in the context of an electrical circuit, the DNA duplexes and bound redox-active probes act as transducer elements with extraordinary gain; biochemical binding events such as hybridization are sensitively transduced into electrical signals. This emphasizes the role of DNA as a remarkably unique medium that provides unprecedented opportunities for studies and applications of long-range CT.

Finally, this review is by no means exhaustive but rather seeks to provide an overview of DNA-mediated electrochemical studies undertaken within our group. Here, we present our explorations of features characteristic of DNA-mediated CT that have been critical for applications of DNA monolayers as biosensors. In fact, several other reviews have detailed the use of electrochemical DNA sensors (*19*−*21*), and where appropriate, examples from other authors are presented.

2. SURFACE CHARACTERIZATION

For proper interpretation of experimental observations, extensive physical characterization of these self-assembled DNA monolayers is crucial. A gamut of experimental techniques can be utilized for investigating the structure and characteristics of DNA monolayers including (but not limited to) radioactive labeling (*22*−*25*), fluorescence self-interference (*26*−*28*), scanning tunneling microscopy (*29*−*31*), atomic force microscopy (*23*, *25*, *32*−*36*), scanning electrochemical microscopy (*37*−*39*), and surface plasmon resonance (*40*, *41*). When dense DNA monolayers are desired, the monolayers are assembled in the presence of Mg^{2+} to allow for close packing of the duplexes (schematically illustrated in Figure 1). Our group, in particular, has focused on surface characterization via radioactive labeling and scanning probe techniques. These investigations have indicated that DNA monolayers adopt an upright orientation and have predictable surface coverages, thereby allowing us to develop a detailed picture of DNA monolayer morphology.

Quantification of Surface Coverage via Radioactive Labeling. Radioactive labeling of the duplexes provides a reliable measure of surface coverage for DNA monolayers. In a typical radioactive labeling experiment, the 5′-end of the DNA complementary to the thiolated strand is labeled with polynucleotide kinase, and the amount of DNA is quantified directly via scintillation counting after self-assembly. On gold and graphite, these measurements indicated surface coverages of ∼40 pmol/cm^2 for well-packed DNA monolayers self-assembled in the presence of Mg^{2+} (*22*, *25*) and coverages of ∼12 pmol/cm^2 for loosely packed DNA monolayers in the absence of Mg^{2+} (*23*). Interestingly, the well-packed monolayer coverages obtained via radioactive labeling correspond to only ∼75−85% of the theoretical coverages of ∼60 pmol/cm^2 with DNA helices packed perpendicular to the surface. This fact strongly hinted that the DNA is oriented at an angle with respect to the surface.

The reliability and sensitivity of radioactive labeling relative to electrochemical assays cannot be understated. For example, monolayer formation can be *qualitatively* monitored via attenuation of an anionic probe such as ferri/ferrocyanide, $Fe(CN)_6^{3-/4-}$ (*22*). In addition, a cationic probe such as ruthenium hexammine can be utilized to quantify DNA coverages semiquantitatively (*42*, *43*), but this common electrochemical assay of surface coverage can lead to errors of up to 65% within each experiment (*44*). Accordingly, in our laboratory, radioactive labeling studies have proven to be particularly illuminating.

Scanning Tunneling Microscopy of DNA Monolayers. While radioactive labeling affords a quantitative measurement of the overall surface coverage, the electronic structure of local areas of a DNA monolayer can be probed via scanning tunneling microscopy (STM), providing atomic level information (*29*). Indeed, STM allows for the investigation of the electronic properties of DNA as a function of duplex orientation. Therefore, the images obtained yield information on not only the morphology but also the local density of states of the sample. At negative potentials, where the DNA adopts an upright orientation, agglomerates of duplexes are visible because the tip can electronically access the oriented DNA in an effective metal−molecule−metal junction. However, at positive potentials, the DNA is encouraged to lie down and the DNA film is effectively not visible to the STM tip. These data indicated that the DNA duplexes comprising a DNA monolayer aggregate in small hexagonal groups of ∼10 nm diameter. Furthermore, the inclusion of a mismatch within the monolayer dramatically attenuates communication between the tip and the surface, demonstrating that the STM is accessing the local density of states of the DNA π-stack.

Atomic Force Microscopy of DNA Monolayers. The morphology of self-assembled DNA monolayers can be further explored at the nanometer scale with atomic force microscopy (AFM). These investigations have indicated that 5′-tethered films are essentially smooth and featureless within the resolution of the AFM tip with the DNA dispersed in a uniform manner (*32*). AFM measurements also provide important information about the morphology and depth of the DNA monolayer at various substrate biases. By applying a large downward force to the

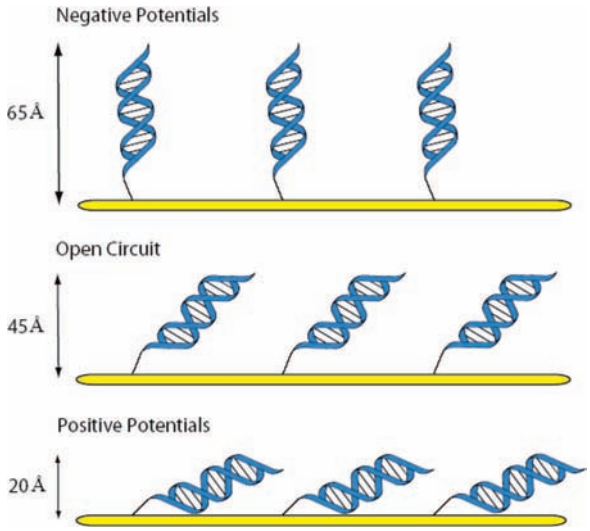

Figure 2. Schematic illustration of the modulation of the height of a DNA monolayer at different substrate potentials. At open circuit, imaging studies have shown that duplexes are oriented upright and at a ~45° angle relative to the surface. At positive potentials, the polyanionic DNA duplexes are attracted to the surface, while at negative potentials (used for most electrochemistry experiments described here), the duplexes are in an upright orientation with the helix axes perpendicular to the electrode surface.

monolayer with the AFM tip, a bare spot can be uncovered on the DNA-modified surface. Height contrast measurements between this bare spot and the surrounding DNA monolayer indicate a film depth which ranges from 4.2 to 4.6 nm for 15mer duplexes at open circuit on both gold and graphite. In fact, the height of these films can be reversibly modulated from 2 nm (the diameter of the duplex) at positive potentials to 5.5 nm (the full length of the duplex when normal to the surface) at negative potentials (Figure 2). These data, in conjunction with the above experiments, indicate that the duplexes adopt an upright orientation at negative potentials and are oriented at a ~45 ° angle with respect to the surface in the absence of an applied bias (*25, 32*).

In a complementary study, we also investigated alternative linkages of the thiol to the DNA. Interestingly, 3′- rather than 5′-grafted DNA monolayers did not adopt an upright orientation relative to the gold surface, as confirmed by their corresponding film depth of only ~2 nm. Since vertical orientation of the monolayer is absolutely essential for studies based on DNA-mediated CT, this work underscored the importance of considering linker placement when designing self-assembled DNA monolayers (*33*).

Several other AFM investigations of DNA monolayers are particularly noteworthy, especially when considering the electrochemical monitoring of DNA with larger macromolecules, such as proteins. Loosely packed DNA monolayers assembled in the absence of Mg^{2+} are necessary for improved accessibility of proteins, but such monolayers have a distinct "island" morphology since the DNA has room to lie flat on the gold surface in the absence of an applied potential (*23*). However, monolayers back-filled with a short-chain alkanethiol such as mercaptohexanol were demonstrated to adopt an upright orientation relative to the gold surface even at open circuit (*35, 36*). Furthermore, these studies showed that even loosely packed films formed from longer 24mer and 30mer duplexes adopt an upright orientation. This well-defined morphology of "deeper" monolayers is a crucial design point to consider in the sequence-specific detection of DNA binding proteins with extensive binding footprints.

3. DNA-MEDIATED ELECTROCHEMISTRY OF SMALL MOLECULES BOUND TO DNA

We have explored numerous redox-active probes in our investigations of DNA CT, and at first glance, many molecules appear adequate for these studies. The large collection of experiments conducted in our laboratory over the past decade, however, has taught us essential lessons regarding the selection of an appropriate redox probe. Three criteria are paramount: the species must (i) be electronically well-coupled to the base pair stack, (ii) be reliably linked to the duplex, and (iii) undergo stable reduction or oxidation within a potential window that does not compromise the integrity of the DNA monolayer. Furthermore, in addition to affording insight into the optimum probe design, our systematic studies clearly indicate that no one probe is ideally suited for every experiment. Instead, different markers offer distinct advantages and must be individually evaluated for specific applications.

The behavior of the redox probes employed in our studies do, however, display some common features when monitored electrochemically. When bound to DNA, small molecules appear to act as surface-bound species as indicated by a linear relationship between the peak current and scan rate. This relationship is not strictly linear for DNA-bound redox proteins, where the proteins are not situated in one fixed position or conformation and thus exhibit a slight diffusive component. Nonetheless, covalent probes bound to DNA typically do not display a square-root-dependence of the peak current on the scan rate that is indicative of free diffusion. In addition, DNA binding typically shifts the redox potential of the probe by 20−50 mV from direct reduction at the bare surface, and the voltammetry adopts a skewed shape relative to a classically adsorbed couple; the reductive and oxidative peaks are separated slightly due to the intervening DNA/alkanethiol spacer. Electrochemical reversibility and stability are also specific to each probe, but they can be investigated simply by repetitive cycling over the potential window of interest. Taken together, all of these features allow us to distinguish DNA-mediated processes from ones involving direct electrochemistry.

Early work in our laboratory employed probes that were not covalently attached to DNA but instead interacted with the base pair stack electrostatically or via intercalation (*22*). Although the majority of our studies have involved the intercalator methylene blue, we have also studied the interaction between DNA and anionic ferricyanide, cationic ruthenium hexammine, the tris-heteroleptic intercalator $Ir(bpy)(phen)(phi)^{3+}$, and the antitumor agent daunomycin (Figure 3). While these noncovalent markers have afforded a significant foundation for the study of DNA-mediated CT, they are intrinsically limited in the mechanistic detail and experimental control they can provide. As a result, more recent efforts have largely focused on developing covalently bound probes, specifically those that are electronically well-coupled to the base pair stack. This latter family began with investigations of cross-linked daunomycin and has been more recently expanded to include other covalently attached molecules such as anthraquinone and phenoxazine derivatives (Figure 3).

Electrochemistry of Small Molecules Non-Covalently Bound to DNA. In our earliest electrochemical experiments, methylene blue (MB), a well-studied aromatic intercalator that undergoes a $2e^-/1H^+$ reduction in aqueous systems, was employed as a reporter of DNA-mediated processes (*22*). Figure 4 shows a schematic illustration of the reduction of MB at a DNA monolayer; a reversible redox couple is seen with a midpoint potential centered at −10 to −50 mV vs NHE, shifted by ~30 mV from bare gold. The measured peak currents scale linearly with scan rate, indicating that the redox molecule is surface-bound, and a combination of electrochemical and

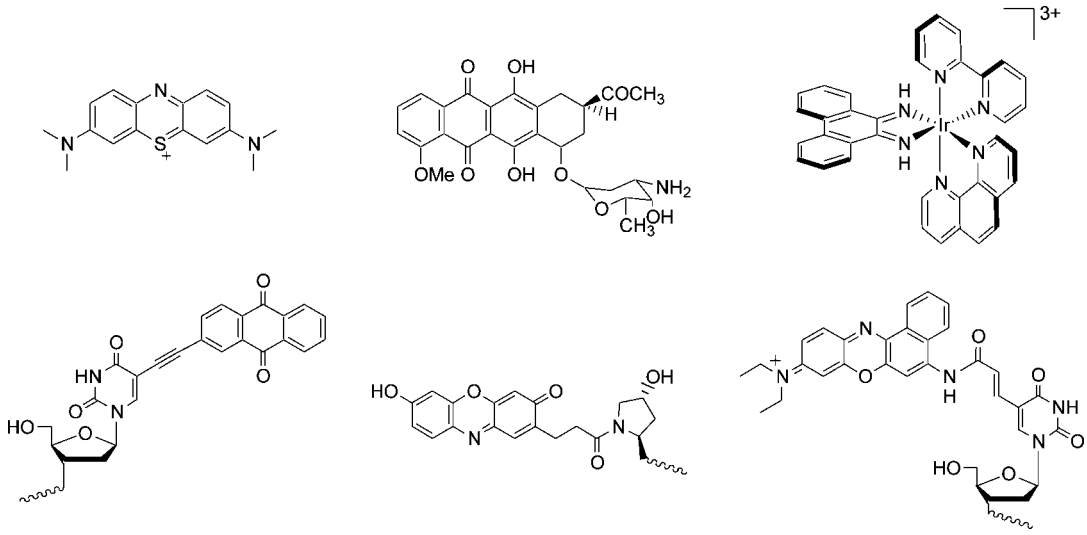

Figure 3. Chemical structures of redox-active probes which have been utilized to explore DNA-mediated CT. Noncovalent probes are on the top row (from left to right): methylene blue, daunomycin, and Ir(bpy)(phen)(phi)$^{3+}$. Covalent probes are on the bottom row (from left to right): anthraquinone, Redmond Red, and Nile Blue.

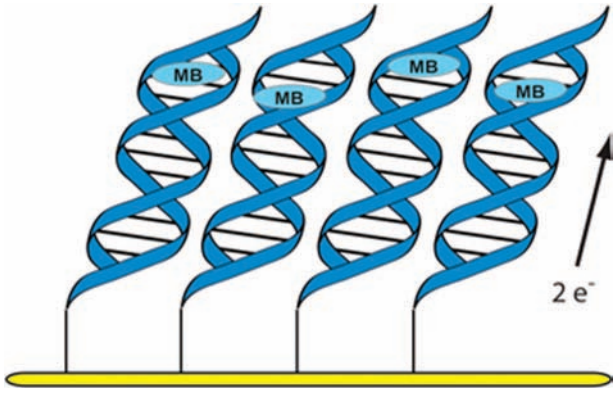

Figure 4. Schematic illustration of the reduction of methylene blue (blue) via DNA-mediated CT at a DNA monolayer. The probe is constrained to intercalate near the top of the monolayer.

spectroscopic measurements give a saturation value of 1.4 ± 0.2 molecules per duplex at high MB concentrations. This latter finding suggests that, for well-packed monolayers, MB is constrained to the top of the film. Any observed reduction, therefore, can be attributed to a DNA-mediated process, as the surface is inaccessible to the molecule.

To characterize this redox process in greater detail, a number of systematic studies were conducted (*44*−*49*). Initially, the behavior of the intercalator MB was compared to the groove-binder ruthenium hexammine (*47*). At high salt concentrations, where interaction with the charged duplex is inhibited, fewer molecules are reduced, thus illustrating the importance of efficient and tight binding to the monolayer for charge transfer. The reduction of these two probes was also monitored on surfaces that had been passivated with electropolymerized 2-naphthol. If the DNA were truly serving as a medium for charge transport, passivation would not affect the process being measured electrochemically. The reduction of ruthenium hexammine, which is thought to proceed via facilitated diffusion along the duplex, decreased by 70%, while reduction of MB was relatively unaffected. Although this study does not elucidate the mechanism of MB reduction, it supports the notion of a DNA-mediated process.

To further prove that the reduction of distally bound probes proceeds in a DNA-mediated fashion, we explored the electrochemistry of small molecules at DNA monolayers containing single base mismatches positioned between the electrode surface and the probe (*45*). It was theorized that, if the DNA base pairs combined to form a continuous, π-stacked conduit for charge transfer, the disruption of a single base pair, as in a mismatch, could interrupt the CT pathway. The presence of a single base mismatch causes no global change in the duplex structure, and yet, the inclusion of an intervening CA mismatch proved to have a dramatic effect on the efficiency of charge transfer to DM. These results are in excellent agreement with STM studies of matched and mismatched duplexes and with studies of photoinduced DNA CT in solution (*9*) (*vide supra*). Interestingly, not only could several mismatches be detected, but the DNA-mediated chemistry was also found to be independent of sequence context. Furthermore, this exquisite sensitivity to base pair stacking has since been observed for numerous intercalating probes including MB and Ir(bpy)(phen)(phi)$^{3+}$ but not for the groove-binding ruthenium hexammine. Thus, the observed electrochemistry is DNA-mediated and a general characteristic of the DNA, independent of the redox probe.

To increase the sensitivity of mismatch detection and further improve discrimination, MB was coupled to freely diffusing $Fe(CN)_6^{3-}$ in an electrocatalytic cycle (Figure 5). In this catalytic process, MB undergoes a $2e^-$ reduction via the base pair stack and, upon reduction to leucomethylene blue, loses some affinity for DNA, thus dissociating from the duplex (*45*, *46*). In turn, the cycle continues when leucomethylene blue is reoxidized by $Fe(CN)_6^{3-}$ in solution and binds again to DNA for another cycle of DNA-mediated reduction. It should be noted that $Fe(CN)_6^{3-}$ cannot be reduced directly at the negatively charged monolayer owing to repulsion from the polyanionic DNA monolayer. The entire process is effectively governed by the on/off kinetics of the methylene blue/leucomethylene blue redox couple, as confirmed by rotating disk electrode experiments (*48*). In fact, during the course of a single voltammogram, the DNA is repeatedly sampled, amplifying the absolute signal of MB and increasing the signal attenuation associated with a mismatch.

The detection of all naturally occurring mismatches and nearly all common lesions was achieved with the MB/$Fe(CN)_6^{3-}$ electrocatalytic couple via cyclic voltammetry and chronocoulometry (Figure 6). In addition, low detection limits were achieved in a chip-based format, with mismatch discrimination possible at electrodes as small as 30 μm in diameter (*46*). It should also be noted that the relatively stable GA mismatch could *not* be detected without the aid of the described catalytic

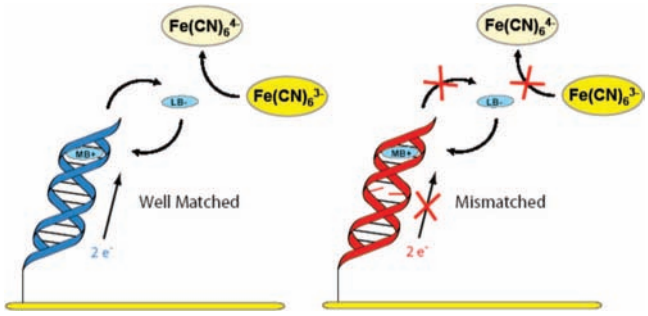

Figure 5. Schematic illustration of the methylene blue/ferricyanide electrocatalytic cycle on the DNA monolayer. DNA-bound methylene blue is reduced in a DNA-mediated reaction to leucomethylene blue (LB), which dissociates from the monolayer and is reoxidized by ferricyanide in solution; the reoxidized methylene blue returns to the DNA for another round of DNA-mediated electrochemistry. This electrochemical amplification leads to enhanced discrimination of all single base mismatches in DNA, since the intervening mismatch shuts down the DNA-mediated reaction and thus the electrocatalytic cycle.

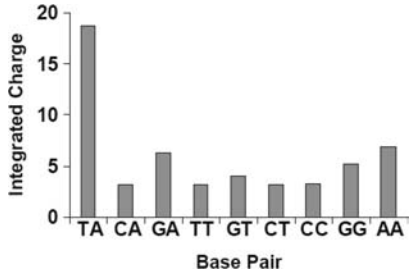

Figure 6. A comparison of the relative integrated charge obtained from chronocoulometry of 2 mM $Fe(CN)_6^{3-}$ and 0.5 μM MB at well-matched DNA monolayers (TA) and in the presence of various mismatches (adapted from ref *46*).

cycle, emphasizing the utility of electrocatalysis as an electrochemical tool. Furthermore, even base lesions that cause minor thermodynamic destabilization to the duplex could be detected with electrocatalysis: a systematic investigation revealed that the efficiency of CT was dramatically decreased even by subtle base modifications that altered base structure, steric bulk, or hydrogen bonding (*49*). Perhaps not surprisingly, modifications with methyl groups that do not participate in hydrogen bonding had little to no effect on the DNA-mediated electrochemistry. The sensitive detection of all single base mismatches independent of sequence context is remarkable and has proven to be valuable in the application of DNA electrochemistry for the diagnosis of single nucleotide polymorphisms.

MB electrochemistry was also extensively explored through self-assembled DNA monolayers on highly ordered pyrolytic graphite (HOPG), onto which the DNA is anchored to the surface via a pyrene moiety (*25*). As a surface, HOPG provides an attractive alternative since its accessible potential window is no longer limited by the oxidative reduction or desorption of thiols. The behavior of MB on graphite is quite similar to that on gold. Evidence that the charge transfer is DNA-mediated is provided by the facile detection of the CA and GT mismatches. The wider potential window afforded by HOPG allowed for the study of the voltammetry of $Ru(bpy)_2dppz^{2+}$ and $Os(phen)_2dppz^{2+}$. As expected, the electrochemistry of both intercalators was found to be DNA-mediated.

Electrochemistry of Small Molecules Covalently Bound to DNA. To facilitate the systematic investigation of charge transduction of DNA, it became necessary to employ redox-active probes that are covalently conjugated to the base pair stack. Our initial efforts focused on covalently attached daunomycin (DM), which can be site-specifically cross-linked to the exocyclic amine of guanine, forming a covalent bond, as shown in Figure 7 (*50*−*52*). Most importantly, this allows for controlled placement of the probe within the sequence. Since functionalization with DM occurs after the synthesis of the DNA, it does, however, necessitate that all guanines other than the one to be linked are replaced by inosine, a close base analogue. For the purpose of electrochemical measurements, this substitution has no influence on the results, but this requirement does have to be considered when developing sensing applications. Importantly, covalent attachment of this probe for DNA electrochemistry has made possible several seminal conclusions about DNA-mediated CT involving *ground-state* reactants.

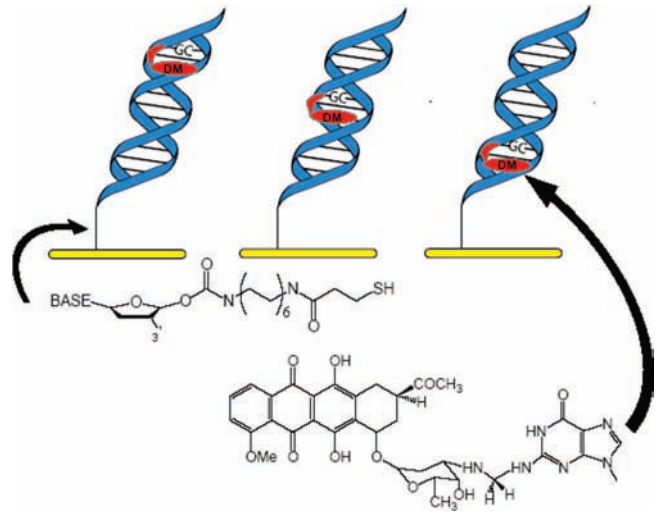

Figure 7. A schematic illustration of DNA duplexes with daunomycin covalently cross-linked at various separations from the electrode surface. Also depicted are the DM-guanine cross-link (right) and the thiol-terminated tether which connects the duplex to the electrode surface (left). This tether provides 16 σ bonds between the electrode and the base stack.

In initial experiments, the separation between the gold surface and the DM adduct was varied from 15 Å to 45 Å, and no effect on the yield or rate of electron transfer was observed (*50*). The inclusion of a mismatch in the intervening DNA, however, completely shuts off the electrochemistry of DM, conclusively demonstrating that CT is DNA-mediated. Subsequently, with DM held in a fixed position in the duplex, the length of the thiolated alkyl tether was varied to probe the effect of tether length on the rate of charge transfer (*51*). While the yield of CT remained the same regardless of chain length (the number of intervening methylene units was increased from 4 to 9), significantly, the rate of electron transfer decreased with increased tether length with a β_n of 1.0 per $-CH_2-$ unit, as expected for the variation in coupling with σ-bonded systems. Therefore, CT through the alkyl tether, not through 30 Å of π-stacked DNA, was the rate-limiting step of the DNA-mediated reduction. Taken together, these findings illustrate that the DNA−DM construct behaves as a single redox-active entity with dramatically different rates of CT through the stacked DNA and the σ-bonded alkyl chain.

In a later study, DM was employed to prove that DNA-mediated electrochemistry occurs via the base pair stack and not the sugar−phosphate backbone (*52*). With two DM moieties cross-linked to guanine residues, voltammograms of duplexes containing a nick in the backbone, a nick and a mismatch, a nick on both strands, and no modifications were compared. Nicks in the phosphate backbone do not attenuate CT, but, consistent with previous results, mismatches significantly attenuate the electrochemistry of DM. Interestingly, a later study

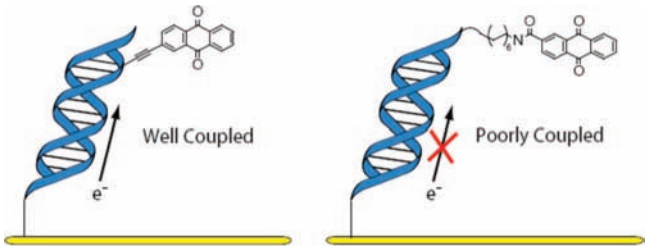

Figure 8. A schematic representation of the electrochemistry of anthraquinone derivatives that are well-coupled (left) and poorly coupled (right) to the base pair stack.

on HOPG showed that the electrochemistry of thiols incorporated within the sugar−phosphate backbone was DNA-mediated but proceeded at low yield (*53*). Therefore, while DNA electrochemistry proceeds through the base pair stack rather than through the sugar−phosphate backbone, it can promote reactions on the DNA backbone.

While DM afforded several key findings for our applications, it does possess some inherent limitations. As mentioned above, all guanine residues, other than the one to be linked, must be replaced by inosines, limiting its applicability in biosensors. Moreover, the stability of the linkage between DM and DNA is heat-sensitive. As a result, we have been focused on developing a new generation of probes that can be covalently attached to DNA with synthetic flexibility, are stable, and are electronically well-coupled to the base pair stack.

Through a variety of experiments conducted in both our laboratory and others, it has become apparent that efficient coupling of the probe to the base stack is critical for efficient DNA CT. Recently, the groups of Saito and Gooding introduced thymines modified with anthraquinone as effective, covalently attached probes of charge transfer at DNA-modified surfaces (*54*−*57*). Using this technology, Gooding and co-workers demonstrated the application of these modified probes to the detection of primer extension reactions (*54*, *55*), and Saito and co-workers demonstrated the photostimulated detection of mismatches with applications to genotyping of single nucleotide polymorphisms (*56*, *57*). However, the low current densities obtained in these studies led us to conduct a comparative study of anthraquinone linked to DNA through conjugated and saturated tethers (*58*). Importantly, we found efficient redox chemistry and mismatch sensitivity for anthraquinone only when linked through an alkyne and not when tethered by an alkyl chain (Figure 8). Thus, not only the choice of probe but also how the probe is coupled to the base pair stack are key to effective DNA-mediated CT.

More recently, we have investigated two phenoxazine-based probes, Redmond Red and Nile Blue, as covalent reporters of DNA CT (Figure 3). Redmond Red is commercially available, affording facile incorporation into DNA with no sequence restrictions (*59*), and Nile Blue can be attached in high yield to DNA by reacting its exocylic amine with a carboxy-NHS-ester-thymine (*60*). These probes can be incorporated via standard phosphoramidite chemistry, have virtually no sequence restrictions, are stable to light/heat, and support DNA-mediated electrochemistry. Accordingly, they are preferable to DM for routine use and high-throughput experiments; both of these probes have already been applied for electrochemical monitoring of protein/DNA interactions (*vide infra)*. Furthermore, Nile Blue has proven effective for detection of hybridization and has displayed electrocatalytic activity (unpublished results). Redmond Red, moreover, has proven to be a particularly sensitive reporter of abasic sites in DNA. The development of these probes holds great promise for future experiments.

4. ELECTROCHEMICAL DETECTION OF HYBRIDIZATION AND TRANSCRIPTION PRODUCTS

The studies described thus far report findings achieved with prehybridized duplexes on gold or graphite; the monolayers were formed exclusively via self-assembly of duplex DNA prior to electrochemical investigation. It is of tremendous importance, from both a fundamental and an applications perspective, to demonstrate similar behavior of DNA-mediated electrochemistry when duplexes are instead formed *in situ*. This approach allows for repeated, internally normalized investigations of a single surface, thereby laying the groundwork for the detection of lesions, mutations, and mismatches in chip-based genetic analysis.

Initial promising results have led current efforts to focus on the design and development of an electrochemical assay for the products of transcription. Consequently, we first explored DNA-mediated CT in DNA/RNA hybrids. Given the known correlation between several RNA sequences and the development of disease, the ability to simply and quantitatively detect the concentration of particular RNA sequences could ultimately be exploited for both disease diagnosis and chemotherapeutic design.

Electrochemical Detection of Mismatches *in Situ.* A comparative *in situ* experiment on modified gold surfaces allowed for a CA mismatch to be reversibly detected via DNA-mediated CT (*45*). DNA was immobilized on two separate electrodes, one bearing duplexes with well-matched complements, the second containing duplexes with a single base mismatch. Following exposure to a solution of DM, the electrodes exhibited the behavior expected for their respective complements, namely, the signals were much larger for the well-matched duplex. The duplexes were then dehybridized by heat denaturation and reincubated with the opposite complement; the resulting well-matched duplex exhibited an increased signal, while the response from the mismatched duplex displayed significant attenuation. Importantly, the signals observed for single-stranded DNA were qualitatively different from those observed for either mismatched or well-matched DNA, confirming duplex formation.

By utilizing the MB/$Fe(CN)_6^{3-}$ electrocatalytic couple, highly sensitive detection limits for hybridization have been achieved (*46*). Monolayers containing well-matched DNA were first self-assembled at gold microelectrodes manufactured in a chip-based format and investigated with chronocoulometry. The DNA was subsequently rehybridized with 100 pM mismatched complement before chronocoulometry was performed again (Figure 9). Dramatic signal attenuation was observed *in situ* in the presence of even a single mismatch. Controls performed with single-stranded DNA again yielded voltammetry which was broad, weak, irreproducible, and qualitatively different, again confirming duplex formation.

In addition to cyclic voltammetry and chronocoloumetry, an alternative electrochemical technique, electrochemical impedance spectroscopy, can also report on duplex formation *in situ*. Differences in the surface coverage are reflected in the electron-transfer resistance, (R_{ET}), as determined by this measurement. Using $Fe(CN)_6^{3-}$ as an electrochemical reporter, electrode surfaces were taken through several dehybridization/rehybridization cycles (using simple heat denaturation and room-temperature annealing), where the impedance at the surface was monitored at each step. The sensitivity of this technique allowed for excellent discrimination between dehybridized and rehybridized surfaces, allowing for label-free detection of duplex formation (*44*).

Electrochemistry through DNA/RNA Hybrids. As a complement to the hybridization studies described above, our laboratory has also investigated DNA-mediated charge transport through

Figure 9. A schematic representation of the protocol used for DNA electrochemistry before heat denaturation of DNA monolayers (left), after denaturation to yield single-stranded DNA (center), and after rehybridization with mismatched DNA (right). A dramatic attenuation in DNA-mediated CT is observed with hybridization of the mismatched strand compared to the well-matched DNA. Electrochemistry of the single-stranded monolayer gives a broad, weak, and irreproducible signal.

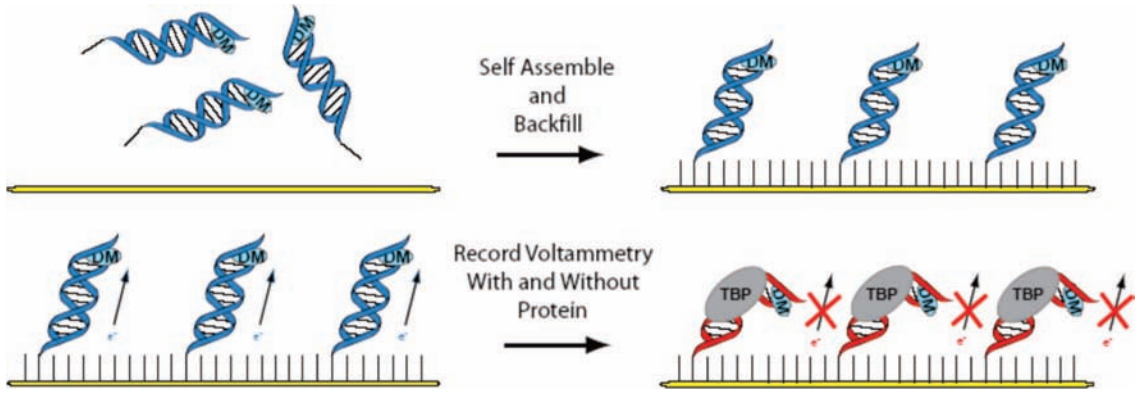

Figure 10. Illustration of the fabrication of DNA-modified gold electrodes for electrochemical analysis of protein binding and reaction. First, loosely packed DNA monolayers are formed and the surface is back-filled with mercaptohexanol for passivation. In the absence of protein, DNA-mediated redox chemistry to the DNA-bound probe is observed. Binding a protein that interrupts the base pair stack also interrupts the DNA-mediated redox chemistry, leading to an attenuation in the redox signal.

DNA/RNA hybrids directly. It is known that these naturally occurring intermediates adopt a conformation that more closely resembles A-form DNA, whereby the helix is significantly wider and more compact than canonical B-form. While these structural differences could potentially interfere with a charge transport pathway down the helix, electrochemical studies within our laboratory have demonstrated that DNA/RNA hybrids are indeed capable of conducting charge in a manner similar to DNA/DNA duplexes (*61*, *62*). Noncovalent MB reduced via a DNA/RNA hybrid exhibits nearly identical voltammetric behavior to that observed with DNA. Moreover, electrocatalytically coupling MB with $Fe(CN)_6^{3-}$ affords discrimination of all possible mismatches in DNA/RNA hybrids, as was monitored by chronocoulometry. These studies reveal that DNA-mediated CT can serve as an effective methodology for the detection of transcription products. Current efforts are now focused on the development of a sensitive and quantitative electrochemical hybridization assay for mRNA using covalently attached anthraquinone.

5. ELECTROCHEMICAL MONITORING OF PROTEIN/DNA INTERACTIONS

Self-assembled DNA monolayers also provide particularly convenient platforms for electrical monitoring of protein/DNA interactions. These interactions play crucial roles in many cellular processes such as transcription, repair, and replication. In particular, the association of transcription factors with DNA is an important area for exploration in proteomics and genomics; it is these interactions that control the developmental and regulatory responses of the cell, often in a complicated fashion. Therefore, the development of convenient and inexpensive methodologies for monitoring protein−DNA interactions remains of critical importance.

In a typical experiment, a loosely packed DNA monolayer is self-assembled with or without a covalently appended probe, and the surface is back-filled (Figure 10). Subsequently, voltammetry of the DNA-modified electrode is recorded before and after addition of protein. Detection of protein binding can be achieved in two ways: (1) proteins that perturb the base pair stack will attenuate the yield of DNA CT to a distally bound electroactive probe and (2) proteins featuring a redox-active cofactor such as an iron−sulfur cluster will cause the appearance of a new DNA-dependent electrochemical signal. These experiments have particularly benefited from the development of covalently attached probes which have allowed for conclusive quantification of the yield of DNA CT before and after protein binding. Furthermore, such electrochemical assays are general and based on exquisitely sensitive DNA-mediated electrochemistry, so a wide range of protein/DNA interactions and binding motifs can be sequence-specifically investigated in real time.

Detection of Transcription Factors. Our early studies at DNA−DM monolayers demonstrated that we could easily detect TATA-binding protein (TBP), a ubiquitous transcription factor that bends duplex DNA by ~90° (*23*). The addition of TBP to a DNA-modified surface results in distortion of the DNA and lowers the yield of DNA CT (Figure 10). Later, we extended this methodology to the detection of TBP at DNA-modified microelectrodes (*60*). At DNA monolayers modified with Nile Blue, TBP could be readily detected at either the macro- or microscale. However, microelectrodes allowed for the rapid detection of nanomolar concentrations of this transcription factor: 300 nM TBP could be reversibly detected with total signal loss in less than 30 s. Furthermore, 30 nM concentrations of TBP were detected even in the presence of micromolar amounts of bovine serum albumin, EndonucleaseIII, or *Bam*HI methyltransferase. These data hinted at the potential of assays based on DNA CT for the high-throughput, multiplexed electrical monitoring of numerous DNA binding proteins on a single chip.

Detection of Base-Flipping Enzymes. Methyltransferases are base-flipping enzymes that catalyze the transfer of a methyl group from *S*-adenosyl-methionine to adenine or cytosine within a DNA duplex. Establishing base flipping by a protein was historically quite difficult, usually requiring a crystal structure, but the electrical detection of base flipping using DNA electrochemistry has been found to be a sensitive, rapid, and attractive method for this characterization.

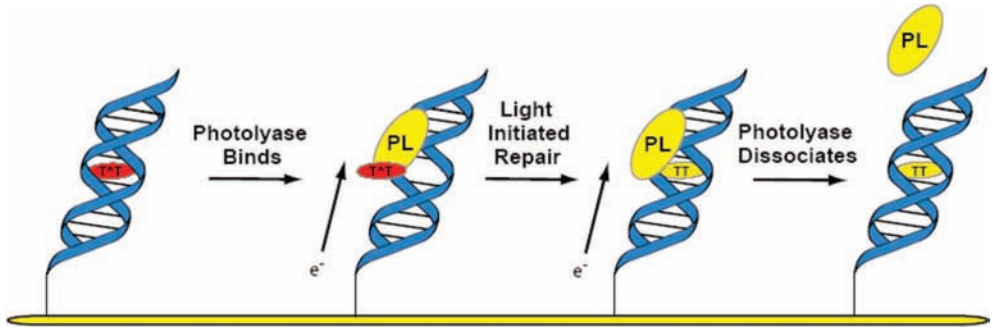

Figure 11. Schematic illustration using DNA electrochemistry to monitor the repair of thymine dimers in a DNA monolayer by photolyase. In the absence of photolyase, no signal is observed, but when the protein is added, a weak signal is observed due to binding of the T^T dimer. Control studies show that the signal corresponds to the flavin bound within the photolyase. Upon irradiation, the thymine dimer is repaired, the integrity of the base pair stack is restored, and the signal grows in intensity as more effective coupling of the protein-bound flavin to the DNA base pair stack is restored. Last, because the protein has a lower affinity for the undamaged DNA, it dissociates, leading to the slow loss of the protein redox signal.

While methyl substitution does not appreciably perturb the base pair stack, methyltransferases, in carrying out the base flip, significantly attenuate DNA-mediated CT. Upon the basis of this attenuation, we have detected base flipping in binding both uracil DNA glycosylase and *Hha*I methyltransferase to their cognate sequences (*23*). At a surface featuring a DNA−DM monolayer, for example, the addition of M.*Hha*I disrupts the integrity of the base pair stack with the concomitant decrease in the DM redox signal. Upon the basis of the crystal structure of the protein/DNA complex, it is apparent that, upon base flipping the internal cytosine of the recognition sequence 5′-GCGC-3′, M.*Hha*I also intercalates Gln 237, a nonaromatic residue into the base pair stack, filling the space occupied by the flipped-out cytosine, and interrupting the π-stacking within the duplex. Accordingly, electrochemistry experiments were conducted with a Q237W mutant enzyme. In this case, we expected that the mutant protein would insert the aromatic tryptophan residue into the π-stack upon base flipping, so little signal loss would be found; indeed, little attenuation in DM signal upon binding the mutant protein was observed. Moreover, to establish that the lack of attenuation was the result of restoration of the π-stack and not simply poor DNA binding by the mutant, we also examined binding of both wild-type and mutant M.*Hha*I to a DNA−DM monolayer containing an abasic site at the position of what would be the flipped-out cytosine. On this DNA−DM monolayer, the DM redox signal is only weakly detected both in the absence of protein and in the presence of wild-type M.*Hha*I, owing to the poor stacking of the duplex with an intervening abasic site. Nonetheless, in the presence of the Q237W mutant, the DM redox signal is restored. This enhanced signal for DM on binding the mutant reflects insertion of the tryptophan from the mutant protein within the base pair stack, so as to restore proper stacking in the DNA−DM duplex. Hence, DNA-binding proteins are seen to modulate DNA CT both positively and negatively, depending upon how they affect the conformation of the DNA.

Electrical Monitoring of Proteins in Real Time. Another advantage of monitoring protein binding to DNA electrically comes from the fact that this technique allows the sensitive detection of events in real time. This was illustrated first by showing double-stranded cleavage on a DNA−DM monolayer using the *Pvu*II restriction enzyme (*23*). In the presence of magnesium ion, *Pvu*II cleaves DNA sequence-specifically. Addition of *Pvu*II to a DNA monolayer containing the *Pvu*II recognition sequence with DM attached to the top of the film but without magnesium causes little perturbation in the DM redox signal. However, the addition of magnesium ion is seen to trigger loss of the DM signal; as the protein cleaves the DNA, the fragment containing the redox probe is released into solution. Interestingly, the kinetics of this signal loss parallels closely that seen for the protein restricting DNA in solution followed by DNA cleavage analysis using gel electrophoresis. The advantage of the electrochemistry technique, however, is clear: the restriction reaction can be monitored in real time.

Monitoring the repair of thymine dimers in DNA by photolyase provides another illustration of how protein/DNA reactions may be monitored sensitively and in real time using DNA electrochemistry (*63*). Photolyase is a repair enzyme from *E. coli* containing a flavin cofactor that binds pyrimidine dimers in duplex DNA and repairs them, upon photoactivation, in a reaction involving electron transfer from the reduced flavin cofactor to the dimer flipped out of the DNA duplex and bound in the pocket of the enzyme near the cofactor. Importantly, in monitoring photolyase reactions electrochemically on DNA monolayers, we did not utilize an externally bound DM redox probe; instead we depended upon the redox signal of the flavin, intimately bound in the protein pocket against the DNA. In binding the photolyase to a DNA monolayer containing the thymine dimer, we found first a weak redox signal arising at 40 mV versus NHE. Through control studies with apoprotein and a mutant, we assigned this redox signal to the flavin and attributed the weak signal to poor electrochemical coupling owing to the intervening destacked thymine dimer. We then carried out the repair reaction by illuminating the electrode surface. With irradiation, we observed an increase of almost an order of magnitude in the integrated flavin signal, and we confirmed repair of the thymine dimer using HPLC analysis. Thus, we could monitor *in real time*, as a function of irradiation, the repair of the thymine dimer by photolyase; as the photolyase repairs the thymine dimer, the base pair stack is restored, the photolyase becomes well-coupled into the base stack, and the flavin signal is enhanced (Figure 11) Subsequently, we found that, once the DNA is repaired, the protein dissociates from the monolayer and the signal intensity is lost.

The ability to monitor, in real time, the binding and chemical reaction of photolyase on DNA highlights the potential of DNA-mediated CT more generally in the analysis of DNA-binding proteins. DNA electrochemistry is unique in its sensitive reporting on DNA conformational changes that may be associated with protein reactions.

Electrochemistry of Base Excision Repair Enzymes Containing Iron Sulfur Clusters. Our DNA electrochemistry experiments with photolyase provide illustrations not only of how DNA electrochemistry can be used to assess DNA conformational changes associated with protein binding, but also how DNA electrochemistry may be utilized to measure the redox potentials of DNA-binding proteins in their active, DNA-bound form. For these experiments, no external redox probe, such as

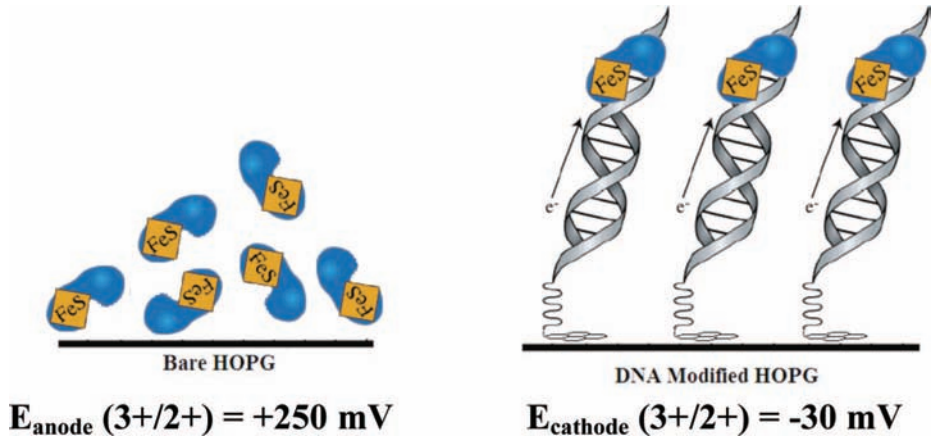

Figure 12. Schematic illustration of the electrochemistry of Endonuclease III in the presence and absence of DNA on graphite. DNA binding causes a potential shift negative of more than 200 mV.

MB or DM, was utilized. Importantly, we could determine the potential of the internally bound flavin cofactor and under conditions where the protein was bound to DNA to carry out its chemistry.

DNA electrochemistry has now been more generally applied in assessing the redox characteristics of DNA-binding proteins in their *active, DNA-bound* form. An illustrative example is found in the characterization of the redox chemistry associated with two base excision repair (BER) enzymes: MutY, a glycosylase that excises adenine from 8-oxoguanine:adenine mispairs, and Endonuclease III (EndoIII), a glycosylase that targets oxidized pyrimidines (*64*−*71*). Crystal structures of these enzymes indicated that they both contain an iron−sulfur cluster with the C-X_6-C-X_2-C-X_5-C motif in close proximity to the DNA backbone (*65*−*68*). This Fe_4S_4 motif, moreover, is conserved in base excision repair proteins from bacteria to man. Interestingly, in MutY, this cluster is not necessary for protein folding or stability but is crucial for DNA binding and *in vivo* activity (*69*). EPR experiments have demonstrated that the cluster is in its $[4Fe\text{-}4S]^{2+}$ form when isolated from the cell, but the protein cannot be reduced within a physiologically relevant window nor oxidized by ferricyanide without degradation (*70*, *71*). These studies, suggesting that redox activity was not associated with reaction by the repair proteins, were, however, conducted in the absence of DNA. Significantly, we found that EndoIII and MutY display stable, quasi-reversible signals with potentials of ∼90 mV versus NHE (*72*, *73*); at DNA-modified, surfaces, back-filled with mercaptohexanol for passivation; this potential is appropriate for a physiologically relevant redox switch. Importantly, these signals are not observed at surfaces back-filled with mercaptohexanol but lacking DNA. Furthermore, weak signals for the proteins on a surface containing a DNA duplex with an abasic site demonstrate that the observed redox processes for the proteins are DNA-mediated.

Experiments performed on DNA-modified, HOPG allowed for the direct comparison of the electrochemistry of EndoIII in the presence and absence of DNA (*74*). Qualitatively similar results were obtained in the presence of DNA on Au and HOPG. Due to its extended potential window, however, HOPG allows for the study of the electrochemistry of EndoIII also in the absence of DNA, a measurement made impossible by the potential window limit on gold. Oxidation of the $[4Fe\text{-}4S]^{2+/3+}$ form of the cluster without DNA led to an anodic signal at 250 mV versus NHE, which was followed by rapid decomposition, in confirmation of solution studies; reductive scans revealed a cathodic peak assigned to the $[4Fe\text{-}4S]^{2+/1+}$ couple of EndoIII. The ability to measure the redox potential of both free and bound EndoIII on the same surface thus allowed for the convincing demonstration that binding to DNA shifts the redox potential of the cluster by −200 mV and stabilizes its $[4Fe\text{-}4S]^{3+}$ state (Figure 12). The cluster therefore is redox-active at ambient temperature in its physiologically relevant, DNA-bound form.

These data underscore the importance of characterizing the redox chemistry of DNA-binding proteins in their biologically relevant, DNA-bound forms. Base excision repair enzymes represented an interesting target for us to study, given the ubiquity of the iron−sulfur clusters in these enzymes with no apparent function. In our laboratory, the finding that these repair proteins become activated to redox chemistry upon binding DNA presents an attractive context for possible DNA-mediated CT *in vivo*. Importantly, this is but one example, and other DNA-binding enzymes that contain a potential redox cofactor may also take advantage of this chemistry. DNA electrochemistry thus provides a first assay to characterize the redox chemistry of DNA-binding and, significantly, to begin to determine whether these proteins may utilize DNA-mediated redox chemistry within the cell.

Electrochemistry of a Transcription Factor Bound to DNA. SoxR is a 17 kDa transcription factor that binds DNA as a dimer with a [2Fe-2S] cluster in each monomer (*59*, *75*, *76*). The loss of the cluster does not affect protein folding, DNA binding, or promoter affinity, but oxidation of the cluster triggers the transcription of SoxS and the subsequent expression of over 100 other genes responsible for the oxidative stress response in bacteria. Interestingly, the redox potential of this cluster in the absence of DNA was determined as −290 mV vs NHE. Importantly, this measurement of the potential of SoxR led to a conundrum: given the reducing environment of the cell, the cluster would always be in its oxidized form, thereby making SoxR essentially constituitively activated *in vivo*. How does the cell keep this protein reduced and transcriptionally silent unless required? Since DNA-modified surfaces allow us to determine the redox potential of proteins in their DNA-bound forms, we explored the electrochemistry of the SoxR transcription factor on DNA-modified HOPG to ask what is the redox potential of SoxR in its physiologically relevant DNA-bound form.

To facilitate these experiments, self-assembled DNA monolayers were prepared on graphite with an appended redox-active probe, Redmond Red (*59*). Redmond Red provided a convenient internal reference for the voltammetry of the SoxR [2Fe-2S] cluster (Figure 13). With this extra probe for calibration, we could conclusively determine that binding to DNA shifts the redox potential of the [2Fe-2S] cluster of SoxR by 490 mV, to +200 mV in its DNA-bound form. Importantly, this potential shift provided a direct rationale for how SoxR stays transcriptionally silent *in vivo* until activated under oxidative conditions: the DNA-bound and physiologically relevant form is always

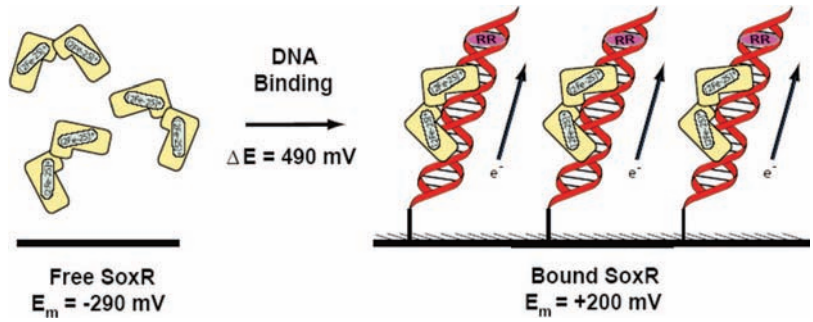

Figure 13. Schematic representation of the electrochemistry of SoxR on DNA-modified graphite with Redmond Red as an internal standard. Binding to DNA shifts the redox potential of SoxR by approximately 500 mV, and this shift likely reflects a substantial change in conformation on binding.

reduced and only conditions of extreme oxidative stress serve to oxidize and thereby activate this transcription factor. We are examining currently whether this activation occurs from a distance, by DNA-mediated CT.

It is interesting to note that the shift seen here on binding to DNA was opposite that seen for the base excision repair proteins and of a significantly larger magnitude. Thus, this large potential shift also provided insight into changes in the structure of SoxR on binding to DNA. Because the binding affinities for DNA of the oxidized and reduced protein are comparable, a significant structural difference between the free (low energy) and DNA-bound (high energy) forms of SoxR was postulated on the basis of electrochemical data. Later, crystal structures of SoxR with and without DNA (*77*) validated our proposal on the basis of these electrochemical data. These experiments once again underscore the importance of investigating the redox chemistry of DNA-binding proteins in their biologically relevant forms, bound to DNA.

6. CONCLUSION

The intrinsic ability of DNA to conduct charge along its base pair stack and the remarkable sensitivity of this chemistry to the integrity of the DNA duplex has intrigued us for over two decades. A combination of detailed structural characterization and careful experimental design has allowed the investigation of this chemistry on DNA-modified surfaces to explore the range and applications of DNA-mediated CT. Through a host of electrochemical studies, we have not only uncovered several fundamental properties of this chemistry but have also demonstrated its potential use in a variety of biosensing and biochemical applications.

DNA-modified surfaces offer an ideal platform on which to investigate CT. Structural studies have provided information on the morphology of these self-assembled monolayers, which are found to orient themselves upright and away from the surface, thereby creating an accessible conduit for the transport of charge. We have employed several different redox-active, DNA-bound molecules to serve as sensitive reporters of this process. While earlier work largely involved noncovalent intercalating moieties, subsequent studies have taken advantage of the precise control and improved electronic coupling afforded by covalent attachment.

In all cases, DNA-mediated CT displays an exquisite sensitivity to the stacking of the base pairs that intervene between the electrode surface and the pendant probe, allowing for the electrochemical discrimination of single base mismatches, lesions, and conformational perturbations. Our investigations are now being extended to DNA/RNA systems, with particular focus on the ability to detect products of transcription. Initial findings illustrated that DNA/RNA hybrids behave similarly to homologous DNA/DNA duplexes, allowing us the utilize DNA-mediated CT for development of a sensitive and quantitative hybridization assay. Finally, due to the possible DNA conformational changes associated with protein binding, we have also been able to demonstrate the sensitive detection of protein/DNA interactions and redox chemistry in real time and under their active, DNA-bound conditions.

This review is intended to survey the structural and electrochemical studies performed in our research group that have elucidated several key features of DNA-mediated charge transport. Much remains to be discovered with regard to the scope and fundamentals of this process. Can we harness this chemistry in the construction of highly sensitive nanoscale devices to detect proteins and RNA in real time in a multiplexed chip format? Are we, in fact, simply mimicking what Nature already exploits for long-range signaling among proteins in the cell that utilize DNA CT? Many more questions remain to be addressed, yet it is abundantly clear that DNA electrochemistry and, more generally, DNA CT, represent a remarkably rich field for study.

ACKNOWLEDGMENT

We gratefully acknowledge the NIH (GM61077) for their financial support. We are also very grateful to our many coworkers who have helped in elucidating this chemistry. We thank in particular Prof. M. G. Hill, without whom this chemistry could not have been discovered and described.

LITERATURE CITED

(1) Szent-Gyorgyi, A., Isenberg, I., and Baird, S. L. (1960) On the electron donating properties of carcinogens. *Proc. Natl. Acad. Sci. U.S.A. 46*, 1444–1449.

(2) Eley, D. D., and Spivey, D. I. (1962) Semiconductivity of organic substances. Part 9. Nucleic acid in the dry state. *Trans. Faraday Soc. 58*, 411–415.

(3) Boon, E. M., and Barton, J. K. (2002) Charge transport in DNA. *Curr. Opin. Struct. Biol. 12*, 320–329.

(4) Delaney, S., and Barton, J. K. (2003) Long-range DNA charge transport. *J. Org. Chem. 68*, 6475–6483.

(5) O'Neill, M. A., and Barton, J. K. (2005) *Sequence-Dependent DNA Dynamics: The Regulator of DNA-Mediated Charge Transport Charge Transfer in DNA, From Mechanism to Application* (Wagenknecht, H.-A., Ed.) pp 27−75, Wiley-VCH, Hoboken.

(6) Giese, B. (2000) Long-distance charge transport in DNA: The hopping mechanism. *Acc. Chem. Res. 33*, 631–636.

(7) Schuster, G. B. (2000) Long-range charge transfer in DNA: Transient structural distortions control the distance dependence. *Acc. Chem. Res. 33*, 253–260.

(8) Murphy, C. J., Arkin, M. R., Jenkins, Y., Ghatlia, N. D., Turro, N. J., and Barton, J. K. (1993) Long-range photoinduced electron transfer through a DNA helix. *Science 262*, 1025–1029.

(9) Kelley, S. O., Holmlin, R. E., Stemp, E. D. A., and Barton, J. K. (1997) Photoinduced electron transfer in ethidium-modified DNA duplexes: Dependence on distance and stacking. *J. Am. Chem. Soc. 119*, 9861–9870.
(10) Hall, D. B., Holmlin, R. E., and Barton, J. K. (1996) Oxidative DNA damage through long-range electron transfer. *Nature 382*, 731–735.
(11) Nunez, M. E., Hall, D. B., and Barton, J. K. (1999) Long-range oxidative damage to DNA: Effect of distance and sequence. *Chem. Biol. 6*, 85–97.
(12) Bhattacharya, P. K., and Barton, J. K. (2001) The influence of intervening mismatches on long-range guanine oxidation in DNA duplexes. *J. Am. Chem. Soc. 123*, 8649–8656.
(13) Williams, T. T., Dohno, C., Stemp, E. D. A., and Barton, J. K. (2004) Effects of the photooxidant on DNA-mediated charge transport. *J. Am. Chem. Soc. 126*, 8148–8158.
(14) Merino, E. J., Boal, A. K., and Barton, J. K. (2008) Biological contexts for DNA charge transport chemistry. *Curr. Opin. Chem. Biol. 12*, 229–237.
(15) Drummond, T. G., Hill, M. G., and Barton, J. K. (2003) Electrochemical DNA sensors. *Nat. Biotechnol. 21*, 1192–1199.
(16) Bard, A. J., Faulkner, L. R. (2001) *Electrochemical Methods*, 2nd ed., John Wiley & Sons, New York.
(17) Love, J. C., Estroff, L. A., Kriebel, J. K., Nuzzo, R. G., and Whitesides, G. M. (2005) Self-assembled monolayers of thiolates as a form of nanotechnology. *Chem. Rev. 105*, 1103–1169.
(18) Guo, X., Gorodetsky, A. A., Hone, J., Barton, J. K., and Nuckolls, C. (2008) Conductivity of a single DNA duplex bridging a carbon nanotube gap. *Nat. Nanotechnol. 3*, 163–167.
(19) Tarlov, M. J. and Steel, A. B. (2003) *Biomolecular Films: Design, Function and Applications* (Rusling, J. F., Ed.) Marcel Dekker, New York.
(20) Odenthal, K. J., and Gooding, J. J. (2007) An introduction to electrochemical DNA biosensors. *The Analyst 7*, 603–610.
(21) Boussicault, F., and Robert, M. (2008) Electron transfer in DNA and in DNA-Related Biological Processes Electrochemical Insights, *Chem. Rev. 108*, 2622–2645.
(22) Kelley, S. O., Barton, J. K., Jackson, N. M., and Hill, M. G. (1997) Electrochemistry of methylene blue bound to a DNA modified electrode. *Bioconjugate Chem. 8*, 31–37.
(23) Boon, E. M., Salas, J. E., and Barton, J. K. (2002) An electrical probe of protein-DNA interactions on DNA-modified surfaces. *Nat. Biotechnol. 20*, 282–286.
(24) Gore, M. R., Szalai, V. A., Ropp, P. A., Yang, I. V., Silverman, J. S., and Thorp, H. H. (2003) Detection of attomole quantitites of DNA targets on gold microelectrodes by electrocatalytic nucleobase oxidation. *Anal. Chem. 75*, 6586–6592.
(25) Gorodetsky, A. A., and Barton, J. K. (2006) Electrochemistry using self-assembled DNA monolayers on highly oriented pyrolytic graphite. *Langmuir 22*, 7917–7922.
(26) Rant, U., Arinaga, K., Fujita, S., Yokoyama, N., Abstreiter, G., and Tornow, M. (2004) Dynamical electrical switching of DNA layers on a metal surface. *Nano Lett. 4*, 2441–2445.
(27) Rant, U., Arinaga, K., Fujita, S., Yokoyama, N., Abstreiter, G., and Tornow, M. (2004) Structural properties of oligonucleotide monolayers on gold surfaces probed by fluorescence investigations. *Langmuir 20*, 100086–10092.
(28) Arinaga, K., Rant, U., Tornow, M., Fujita, S., Abstreiter, G., and Yokoyama, N. (2006) The role of surface charging during the coadsorption of mercaptohexanol to DNA layers on gold: direct observation of desorption and layer reorientation. *Langmuir 22*, 5560–5562.
(29) Ceres, D. M., and Barton, J. K. (2003) In situ scanning tunneling microscopy of DNA-modified gold surfaces: bias and mismatch dependence. *J. Am. Chem. Soc. 125*, 14964–14965.
(30) Hihath, J., Xu, B., Zhang, P., and Tao, N. (2005) Study of single nucleotide polymorphisms via electrical conductance measurements. *Proc. Natl. Acad. Sci. U.S.A. 102*, 16979–16983.
(31) Wierzbinski, E., Arndt, J., Hammond, W., and Slowinski, K. (2006) In Situ Electrochemical Distance Tunneling Spectroscopy of ds-DNA Molecules. *Langmuir 22*, 2426–2429.
(32) Kelley, S. O., Barton, J. K., Jackson, N. M., McPherson, L. D., Potter, A. B., Spain, E. M., Allen, M. J., and Hill, M. G. (1998) Orienting DNA helices on gold using applied electric fields. *Langmuir 14*, 6781–6784.
(33) Boon, E. M., Sam, M., Barton, J. K., Hill, M. G., and Spain, E. M. (2001) Morphology of 15-mer duplexes tethered to Au(111) probed using scanning probe microscopy. *Langmuir 17*, 5727–5730.
(34) Zhou, D., Sinniah, K., Abell, C., and Rayment, T. (2002) Use of atomic force microscopy for making addresses in DNA coatings. *Langmuir 18*, 8278–8281.
(35) Zhou, D., Sinniah, K., Abell, C., and Rayment, T. (2003) Label free detection of DNA hybridization at the nanoscale: a highly sensitive and selective approach using atomic-force microscopy. *Angew. Chem., Int. Ed. 42*, 4394–4397.
(36) Erts, D., Polyakov, B., Olin, H., and Tuite, E. (2003) Spatial and mechanical properties of dilute DNA monolayers on gold imaged by AFM. *J. Phys. Chem. B 107*, 3591–3597.
(37) Turcu, F., Schulte, A., Hartwich, G., and Schuhmann, W. (2004) Label free electrochemical recognition of DNA hybridization by means of modulation of the feedback current of SECM. *Angew. Chem., Int. Ed. 43*, 3482–3485.
(38) Liu, D., Li, C.-Z., Kraatz, H.-B., and Bard, A. J. (2005) Scanning electrochemical microscopy. 51. Studies of self-assembled monolayers of DNA in the absence and presence of metal ions. *J. Phys. Chem. B 109*, 5193–5198.
(39) Wain, A. J., and Zhou, F. (2008) Scanning electrochemical microscopy imaging of DNA microarrays using methylene blue as a redox-active intercalator. *Langmuir 24*, 5155–5160.
(40) Yang, X., Wang, Q., Wang, K., Tan, W., Yao, J., and Li, H. (2006) Electrical switching of DNA monolayers investigated by surface plasmon resonance. *Langmuir 22*, 5654–5659.
(41) Li, Y.-J., Xiang, J., and Zhou, F. (2007) Sensitive and label-free detection of DNA by surface plasmon resonance. *Plasmonics 2*, 79–87.
(42) Steel, A. B., Herne, T. M., and Tarlov, M. J. (1998) Electrochemical quantitation of DNA immobilized on gold. *Anal. Chem. 70*, 4670–4677.
(43) Yu, H.-Z., Luo, C.-Y., Sankar, D. G., and Sen, D. (2003) Voltammetric procedure for examining DNA-modified surfaces: quantitation, cationic binding activity, and electron-transfer kinetics. *Anal. Chem. 75*, 3902–3907.
(44) Ceres, D. M., Udit, A. K., Hill, H. D., Hill, M. G., and Barton, J. K. (2007) Differential ionic permeation of DNA-modified electrodes. *J. Phys. Chem. B 111*, 663–668.
(45) Kelley, S. O., Boon, E. M., Barton, J. K., Jackson, N. M., and Hill, M. G. (1999) Single-base mismatch detection based on charge transduction through DNA. *Nucleic Acids Res. 27*, 4830–4837.
(46) Boon, E. M., Ceres, D. M., Drummond, T. G., Hill, M. G., and Barton, J. K. (2000) Mutation detection by electrocatalysis at DNA-modified electrodes. *Nat. Biotechnol. 18*, 1096–1100.
(47) Boon, E. M., Jackson, N. M., Wightman, M. D., Kelley, S. O., Barton, J. K., and Hill, M. G. (2003) Intercalative stacking: a critical feature of DNA charge transport electrochemistry. *J. Phys. Chem. B 107*, 11805–11812.
(48) Boon, E. M., Barton, J. K., Bhagat, V., Nerissian, M., Wang, W., and Hill, M. G. (2003) Reduction of ferricyanide by methylene blue at a DNA-modified rotating-disk electrode. *Langmuir 19*, 9255–9259.
(49) Boal, A. K., and Barton, J. K. (2005) Electrochemical detection of lesions in DNA. *Bioconjugate Chem. 16*, 312–321.
(50) Kelley, S. O., Jackson, N. M., Hill, M. G., and Barton, J. K. (1999) Long range electron transfer through DNA films. *Angew. Chem., Int. Ed. 38*, 941–945.
(51) Drummond, T. G., Hill, M. G., and Barton, J. K. (2004) Electron transfer rates in DNA films as a function of tether length. *J. Am. Chem. Soc. 126*, 15010–15011.
(52) Liu, T., and Barton, J. K. (2005) DNA electrochemistry through the base pairs not the sugar-phosphate backbone. *J. Am. Chem. Soc. 127*, 10160–10161.

(53) Gorodetsky, A. A., and Barton, J. K. (2007) DNA-mediated electrochemistry of disulfides on graphite. *J. Am. Chem. Soc. 129*, 6074–6075.

(54) Di Giusto, D. A., Wlasoff, W. A., Giesebrecht, S., Gooding, J. J., and King, G. C. (2004) Multipotential electrochemical detection of primer extension reactions on DNA self-assembled monolayers. *J. Am. Chem. Soc. 126*, 4120–4121.

(55) Di Giusto, D. A., Wlasoff, W. A., Giesebrecht, S., Gooding, J. J., and King, G. C. (2004) Enzymatic synthesis of redox-labeled RNA and dual-potential detection at DNA-modified electrodes. *Angew. Chem., Int. Ed. 116*, 2809–2812.

(56) Okamoto, A., Kamei, T., Tanaka, K., and Saito, I. (2004) Photostimulated hole transport through a DNA duplex immobilized on a gold electrode. *J. Am. Chem. Soc. 126*, 14732–14733.

(57) Okamoto, A., Kamei, T., and Saito, I. (2006) DNA hole transport on an electrode: application to effective photoelectrochemical SNP typing. *J. Am. Chem. Soc. 128*, 658–662.

(58) Gorodetsky, A. A., Green, O., Yavin, E., and Barton, J. K. (2007) Coupling into the base pair stack is necessary for DNA-mediated electrochemistry. *Bioconjugate Chem. 18*, 1434–1441.

(59) Gorodetsky, A. A., Dietrich, L. E. P., Lee, P. E, Demple, B., Newman, D. K., and Barton, J. K. (2008) DNA binding shifts the redox potential of the transcription factor SoxR. *Proc. Natl. Acad. Sci. U.S.A. 105*, 3684–3689.

(60) Gorodetsky, A. A., Ebrahim, A., and Barton, J. K. (2008) Electrical detection of TATA binding protein at DNA-modified microelectrodes. *J. Am. Chem. Soc. 130*, 2924–2925.

(61) Boon, E. M., Barton, J. K., Pradeepkumar, P. I., Isaksson, J., Petit, C., and Chattopadhyaya, J. (2002) An electrochemical probe of DNA stacking in an antisense oligonucleotide containing a C3′-*endo*-locked sugar. *Angew. Chem., Int. Ed. 41*, 3402–3405.

(62) Boon, E. M., and Barton, J. K. (2003) DNA electrochemistry as a probe of base pair stacking in A-, B-, and Z-form DNA. *Bioconjugate Chem. 14*, 1140–1147.

(63) DeRosa, M. C., Sancar, A., and Barton, J. K. (2005) Electrochemically monitoring DNA repair by photolyase. *Proc. Natl. Acad. Sci. U.S.A. 102*, 10788–10792.

(64) David, S. S., and Williams, S. D. (1998) Chemistry of glycosylases and endonucleases involved in base-excision repair. *Chem. Rev. 98*, 1221–1262.

(65) Kuo, C. F., McRee, D. E., Fisher, C. L., O'Handley, S. F., Cunningham, R. P., and Tainer, J. A. (1992) Atomic structure of the DNA repair [4Fe-4S] enzyme endonuclease III. *Science 258*, 434–440.

(66) Thayer, M. M., Ahern, H., Xing, D., Cunningham, R. P., and Tainer, J. A. (1995) Novel DNA binding motifs in the DNA repair enzyme endonuclease III crystal structure. *EMBO J. 14*, 4108–4120.

(67) Fromme, J. C., and Verdine, G. L. (2003) Structure of a trapped endonuclease III-DNA covalent intermediate. *EMBO J. 22*, 3461–3471.

(68) Fromme, J. C., Banerjee, A., Huang, S. J., and Verdine, G. L. (2004) Structural basis for removal of adenine mispaired with 8-oxoguanine by MutY adenine DNA glycosylase. *Nature 427*, 652–656.

(69) Porello, S. L., Cannon, M. J., and David, S. S. (1998) A substrate recognition role for the $[4Fe\text{-}4S]^{2+}$ cluster of the DNA repair glycosylase MutY. *Biochemistry 37*, 6465–6475.

(70) Cunningham, R. P., Asahara, H., Bank, J. F., Scholes, C. P., Salerno, J. C., Surerus, K., Munck, E., McCracken, J., Peisach, J., and Emptage, M. H. (1989) Endonuclease III is an iron-sulfur protein. *Biochemistry 28*, 4450–4455.

(71) Fu, W., O'Handley, S., Cunningham, R. P., and Johnson, M. K. (1992) The role of the iron-sulfur cluster in *Escherichia coli* endonuclease III. A resonance raman study. *J. Biol. Chem. 267*, 16135–16137.

(72) Boon, E. M., Livingston, A. L., Chmiel, N. H., David, S. S., and Barton, J. K. (2003) DNA-mediated charge transport for DNA repair. *Proc. Natl. Acad. Sci. U.S.A. 100*, 12543–12547.

(73) Boal, A. K., Yavin, E., Lukianova, O. A., O'Shea, V. L., David, S. S., and Barton, J. K. (2005) DNA-bound redox activity of DNA repair glycosylases containing [4Fe-4S] clusters. *Biochemistry 44*, 8397–8407.

(74) Gorodetsky, A. A., Boal, A. K., and Barton, J. K. (2006) Direct electrochemistry of endonuclease III in the presence and absence of DNA. *J. Am. Chem. Soc. 128*, 12082–12083.

(75) Pomposiello, P. J., and Demple, B. (2001) Redox-operated genetic switches: the SoxR and OxyR transcription factors. *Trends Biotechnol. 19*, 109–114.

(76) Demple, B., Ding, H., and Jorgensen, M. (2002) *Escherichia coli* SoxR protein: sensor/transducer of oxidative stress and nitric oxide. *Methods Enzymol. 348*, 355–364.

(77) Watanabe, S., Kita, A., Kobayashi, K., and Miki, K. (2008) Crystal structure of the [2Fe-2S] oxidative-stress sensor SoxR bound to DNA. *Proc. Natl. Acad. Sci. U.S.A. 105*, 4121–4126.

BC8003149

COMMUNICATIONS

Tetrazine-Based Cycloadditions: Application to Pretargeted Live Cell Imaging

Neal K. Devaraj,[‡] Ralph Weissleder,[†,‡] and Scott A. Hilderbrand*[,†]

Center for Molecular Imaging Research, Massachusetts General Hospital/Harvard Medical School Charlestown, Massachusetts 02129, and Center for Systems Biology, Massachusetts General Hospital/Harvard Medical School Boston, Massachusetts 02114. Received October 15, 2008; Revised Manuscript Received October 21, 2008

Bioorthogonal tetrazine cycloadditions have been applied to live cell labeling. Tetrazines react irreversibly with the strained dienophile norbornene forming dihydropyrazine products and dinitrogen. The reaction is high yielding, selective, and fast in aqueous media. Her2/neu receptors on live human breast cancer cells were targeted with a monoclonal antibody modified with a norbornene. Tetrazines conjugated to a near-infrared fluorochrome selectively and rapidly label the pretargeted antibody in the presence of serum. These findings indicate that this chemistry is suitable for in vitro labeling experiments, and suggests that it may prove a useful strategy for in vivo pretargeted imaging under numerous modalities.

Bioorthogonal reactions for coupling materials in the presence of complex biological milieu are of great interest in biology and medicine. Such reactions have become key components in a variety of applications including protein engineering (*1*, *2*), immunoassay development (*3*), and cell surface modification (*4*, *5*). To date, only a few bioorthogonal reactions have been reported, the most popular being the Staudinger ligation and the [3 + 2] cycloaddition "click" reaction between azides and alkynes (*6*, *7*). Here, we report on the use of [4 + 2] Diels−Alder cycloadditions between a tetrazine and olefin as an alternative bioorthogonal reaction. The reaction is extremely selective, high yielding, and proceeds rapidly in aqueous media. The reaction partners show excellent stability in biological media and are simple to synthesize. The utility of this reaction is demonstrated by the specific labeling of Her2/neu receptors on breast cancer cells.

Recently, there has been tremendous interest in the use of the click reaction for biological labeling. The typical click reaction involves copper(I)-catalyzed coupling of an azide and terminal alkyne to generate a stable triazole (*7*). Until recently, the necessity of the copper catalyst precluded the use of this reaction in biological systems due to concerns regarding toxicity. Bertozzi and others have elegantly solved this problem by developing several new ring-strained cyclooctyne derivatives that do not require a catalyst (*4*, *8*, *9*). However, many of these derivatives have poor water solubility or require complex multistep synthesis and are not readily obtainable in large quantities. Despite these shortcomings, the cycloaddition reaction between azides and ring-strained cyclooctynes has been employed for imaging of cells (*4*) and zebra fish embryos (*10*).

Our search for alternative rapid, selective, and chemically accessible coupling reactions that do not require a catalyst led us to investigate the [4 + 2] Diels−Alder cycloaddition. Not only is the Diels−Alder reaction compatible with aqueous environments, but the second-order rate constants for this reaction are known to be enhanced up to several hundred-fold in aqueous media in comparison to organic solvents (*11*, *12*). Many Diels−Alder reactions are reversible (*13*) and therefore may not be suitable for biological labeling. The inverse electron demand Diels−Alder cycloaddition of olefins with tetrazines, however, results in irreversible coupling, giving dihydropyridazine products (Scheme 1). During this reaction, dinitrogen is released in a retro Diels−Alder step (*14*). A variety of tetrazines (*15*) and dienophiles including cyclic and linear alkenes or alkynes (*16*) have been studied in this reaction. Selection of the appropriate reaction partners allows for tuning of the coupling rate by several orders of magnitude (*15*, *16*).

Scheme 1

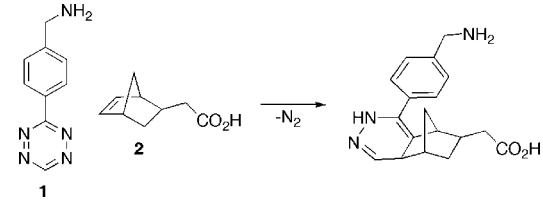

To probe the feasibility of the tetrazine−dienophile reaction as a tool for biological labeling, a modified norbornene (**2**) was selected as a model dienophile. Norbornenes offer an excellent balance between facile strain-promoted reactivity with tetrazines and overall chemical stability. Furthermore, a selection of norbornenes with additional conjugation handles are commercially available. In contrast, few tetrazines containing additional reactive groups have been reported. One potential starting point, dimethyl 1,2,4,5-tetrazine-3,6-dicarboxylate, has been investigated extensively, but is not stable in aqueous or protic media (*17*). Other amine-modified tetrazines such as 1,2,4,5-tetrazine-3,6-diamine (*18*) or 3,6-bis-(4-aminophenyl)-1,2,4,5-tetrazine (*19*) have been described, but have poor reactivity with dienophiles. In this communication, we detail

* Scott_Hilderbrand@hms.harvard.edu.
[†] Center for Molecular Imaging Research.
[‡] Center for Systems Biology.

10.1021/bc8004446 CCC: $40.75 © 2008 American Chemical Society
Published on Web 11/21/2008

the synthesis of a stable benzylamine-modified tetrazine with excellent dienophile reactivity and investigate its use in the bioorthogonal pretargeting of live cells.

The tetrazine, 3-(4-benzylamino)-1,2,4,5-tetrazine (**1**), is prepared by reaction of 4-(aminomethyl)benzonitrile with formamidine acetate and anhydrous hydrazine in the presence of elemental sulfur. The initial dihydrotetrazine product is oxidized to the tetrazine by treatment with sodium nitrite in acetic acid in 20% overall yield. The primary amine can be modified via standard amide-coupling procedures to prepare the near-infrared (NIR) fluorophore-modified conjugate, tetrazine-VT680 (**3**).

Tetrazine **1**, shows excellent stability in PBS buffer with little or no observed decomposition after prolonged standing at room temperature (data not shown). The stability of **1** in biological media is also very good, with only 15% decomposition observed after 15 h in fetal bovine serum (FBS) at 20.0 °C. Since both tetrazine **1** and norbornene **2** are asymmetric compounds, the Diels−Alder cycloaddition of these two components generates multiple isomeric dihydropyridazine products (Scheme S1 and Figure S5, Supporting Information) Analysis of the reaction products by LCMS indicates a clean reaction with >93% conversion to the dihydropyridazines. Tetrazine **1** reacts smoothly and rapidly with norbornene **2** in aqueous buffer and FBS with second-order rate constants of 1.9 and 1.6 M^{-1} s^{-1}, respectively. The use of more reactive tetrazines and highly strained dienophiles such as cyclooctynes will likely increase coupling rate constants by several orders of magnitude, and we are currently exploring these strategies (*20*).

Labeling of specific functional groups on live cells has emerged as a powerful application of bioorthogonal couplings. To demonstrate this, the tetrazine-based cycloaddition reaction was used to label antibodies bound to Her2/neu receptors on live SKBR3 cancer cells. Such strategies are of interest, because although antibodies show great specificity for antigens, their long blood half-lives result in high background signals when directly labeled with imaging agents or cytotoxins. Pretargeting offers the opportunity for un- or nonspecifically bound antibody to clear before chasing with a smaller, readily excreted molecule that selectively couples to the remaining antibody, drastically reducing background (*21*). Previous pretargeting strategies primarily have relied on the interaction between biotin and avidins to achieve specificity (*22*). Although these approaches have shown promise in the clinic, they suffer from problems such as immunogenicity and steric crowding resulting from the >50 kDa size of the avidins. A small molecule based pretargeting strategy may circumvent these problems.

To demonstrate the utility of the tetrazine−dienophile reaction for live-cell labeling, we used the FDA-approved monoclonal antibody trastuzumab (Herceptin) which binds to Her2/neu growth factor receptors (Figure 1) (*23*). Trastuzimab was simultaneously labeled with norbornene and tetramethyl rhodamine using standard coupling conditions. Human breast cancer SKBR3 cells, which overexpress Her2/neu, were incubated with 200 nM antibody, and then treated with 50 μM **3** in 10% FBS/HBSS solution for 30 min at 37 °C. After washing, the cells were imaged using both rhodamine and NIR fluorescence channels (Figure 2A,B). Significant labeling, which colocalizes, was observed (Figure 2C). Cells incubated with a control antibody, which contained rhodamine but not norbornene, showed no NIR labeling after exposure to **3** (Figure 2D and E). These experiments demonstrate the specificity of the tetrazine imaging agent for norbornene-modified antibody in the presence of live cells and serum. The reaction is rapid even with micromolar concentrations of the labeling agent and importantly in the presence of serum. These findings clearly indicate that this chemistry is suitable for in vitro experiments and suggests that it may prove a useful strategy for in vivo imaging under numerous modalities.

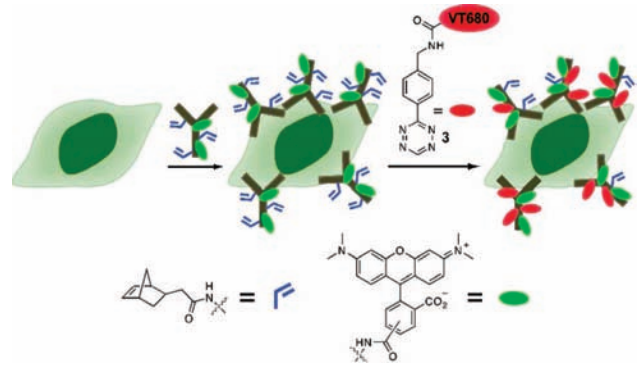

Figure 1. Pretargeting of SKBR3 cells with norbornene and tetramethylrhodamine co-labeled trastuzumab, followed by tagging the live cells with tetrazine-VT680 (**3**) via an inverse electron demand Diels−Alder coupling.

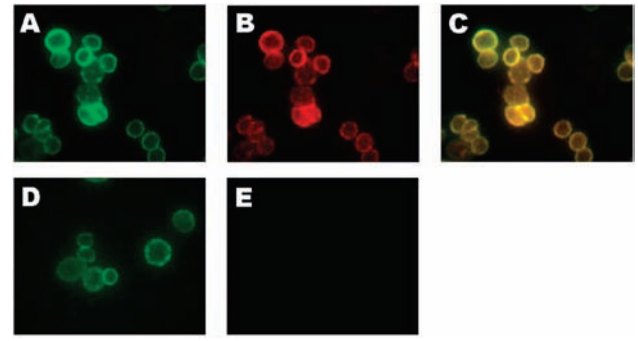

Figure 2. Fluorescent microscope images of SKBR3 human breast cancer cells after pretargeting trastuzumab antibodies modified with rhodamine and norbornene and subsequent labeling with **3**. (A) Rhodamine channel. (B) Near-IR channel (tetrazine-VT680). (C) Merged image of A and B. Images were also taken of cell surfaces targeted with a control antibody modified with only rhodamine and exposed subsequently to **3**. (D) Rhodamine channel. (E) Near-IR channel.

ACKNOWLEDGMENT

The authors would like to thank Drs. Fangwei Shao and Jered Haun for their assistance in the preparation of this manuscript. This research was supported in part by NIH grants U01-HL080731 and T32 − CA 79443.

Supporting Information Available: Detailed synthetic and cell labeling procedures, kinetic data, and full characterization for all compounds. This material is available free of charge via the Internet at http://pubs.acs.org.

LITERATURE CITED

(1) Link, J. A., Mock, M. L., and Tirrell, D. A. (2003) Non-canonical amino acids in protein engineering. *Curr. Opin. Biotechnol. 14*, 603–609.

(2) Wang, Q., Chan, T. R., Hilgraf, R., Fokin, V. V., Sharpless, K. B., and Finn, M. G. (2003) Bioconjugation by copper(I)-catalyzed azide-alkyne [3 + 2] cycloaddition. *J. Am. Chem. Soc. 125*, 3192–3193.

(3) Diamandis, E. P., and Christopoulos, T. K. (1991) The biotin-(strept)avidin system: principles and applications in biotechnology. *Clin. Chem. 37*, 625–636.

(4) Baskin, J. M., Prescher, J. A., Laughlin, S. T., Agard, N. J., Chang, P. V., Miller, I. A., Lo, A., Codelli, J. A., and Bertozzi, C. R. (2007) Copper-free click chemistry for dynamic *in vivo*

imaging. *Proc. Natl. Acad. Sci. U.S.A. 104*, 16793–16797.
(5) Link, J. A., and Tirrell, D. A. (2003) Cell surface labeling of *Escherichia coli* via copper(I)-catalyzed [3 + 2] cycloaddition. *J. Am. Chem. Soc. 125*, 11164–11165.
(6) Prescher, J. A., Dube, D. H., and Bertozzi, C. R. (2004) Chemical remodelling of cell surfaces in living animals. *Nature 430*, 873–877.
(7) Rostovtsev, V. V., Green, L. G., Fokin, V. V., and Sharpless, K. B. (2002) A stepwise huisgen cycloaddition process: copper (l)-catalyzed regioselective "ligation" of azides and terminal alkynes. *Angew. Chem., Int. Ed. 41*, 2596–2599.
(8) Codelli, J. A., Baskin, J. M., Agard, N. J., and Bertozzi, C. R. (2008) Second-generation difluorinated cyclooctynes for copper-free click chemistry. *J. Am. Chem. Soc. 130*, 11486–11493.
(9) Ning, X. H., Guo, J., Wolfert, M. A., and Boons, G. J. (2008) Visualizing metabolically labeled glycoconjugates of living cells by copper-free and fast huisgen cycloadditions. *Angew. Chem., Int. Ed. 47*, 2253–2255.
(10) Laughlin, S. T., Baskin, J. M., Amacher, S. L., and Bertozzi, C. R. (2008) In vivo imaging of membrane-associated glycans in developing zebrafish. *Science 320*, 664–667.
(11) Rideout, D. C., and Breslow, R. (1980) Hydrophobic acceleration of Diels-Alder reactions. *J. Am. Chem. Soc. 102*, 7816–7817.
(12) Graziano, G. (2004) Rate enhancement of Diels-Alder reactions in aqueous solutions. *J. Phys. Org. Chem. 17*, 100–101.
(13) Kwart, H., and King, K. (1968) The reverse Diels-Alder or retrodiene reaction. *Chem. Rev. 68*, 415–447.
(14) Sauer, J., Mielert, A., Lang, D., and Peter, D. (1965) Umsetzungen von 1.2.4.5-tetrazinen mit olefinen. zur struktur von dihydropyridazinen. *Chem. Ber. 98*, 1435–1445.
(15) Balcar, J., Chrisam, G., Huber, F. X., and Sauer, J. (1983) Reaktivität von stickstoff-heterocyclen gegenüber cyclooctin als dienophil. *Tetrahedron Lett. 24*, 1481–1484.
(16) Thalhammer, F., Wallfahrer, U., and Sauer, J. (1990) Reaktivität einfacher offenkettiger und cyclisher dienophile bei Diels-Alder-reaktionen mit inversem elektronenbedarf. *Tetrahedron Lett. 47*, 6851–6854.
(17) Kämpchen, T., Massa, W., Overheu, W., Schmidt, R., and Seitz, G. (1982) Zur kenntnis von reaktionen des 1,2,4,5-tetrazin-3,6-dicarbonsäure-dimethylesters mit nucleophilen. *Chem. Ber. 115*, 683–694.
(18) Lin, C.-H., Lieber, E., and Horwitz, J. P. (1954) The synthesis of *sym*-diaminotetrazine. *J. Am. Chem. Soc. 76*, 427–430.
(19) Soloducho, J., Doskocz, J., Cabaj, J., and Roszak, S. (2003) Practical synthesis of bis-substituted tetrazines with two pendant 2-pyrrolyl or 2-thienyl groups, precursors of new conjugated polymers. *Tetrahedron 59*, 4761–4766.
(20) During preparation of this manuscript the use of a cycloaddition reaction between a tetrazine and a strained trans-cyclooctene was reported for labeling a small protein: Blackman, M. L., Royzen, M., and Fox, J. M. (2008) Tetrazine ligation: fast bioconjugation based on inverse-electron-demand Diels–Alder reactivity. *J. Am. Chem. Soc. 130*, 13518–13519.
(21) Wu, A. M., and Senter, P. D. (2005) Arming antibodies: prospects and challenges for immunoconjugates. *Nat. Biotechnol. 23*, 1137–1146.
(22) Goldenberg, D. M., Sharkey, R. M., Paganelli, G., Barbet, J., and Chatal, J. F. (2006) Antibody pretargeting advances cancer radioimmunodetection and radioimmunotherapy. *J. Clin. Oncol. 24*, 823–834.
(23) Lewis, G. D., Figari, I., Fendly, B., Wong, W. L., Carter, P., Gorman, C., and Shepard, H. M. (1993) Differential responses of human tumor-cell lines to anti-P185(Her2) monoclonal-antibodies. *Cancer Immunol. Immun. 37*, 255–263.

BC8004446

Supporting Information:

General materials and methods. All chemicals were purchased from Sigma Aldrich unless noted and were used as received. The norbornene, (1S,2S,4S)-bicyclo[2.2.1]hept-5-en-2-yl acetic acid, was purchased from ChemBridge. All solvents were of reagent grade or higher and were used without further purification. Analytical HPLC and LC/MS were performed on a Waters 2695 HPLC equipped with a 2996 diode array detector, a Micromass ZQ4000 ESI-MS module, and a Grace-Vydac RPC18 column (model 218TP5210) at a flow rate of 0.3 mL/min. Preparative HPLC was performed on a Varian ProStar model 210 instrument equipped with a model 335 diode array detector, a model 701 fraction collector, and a Varian RPC18 column (model A6002250X212) at a flow rate of 21 mL/min. For all HPLC runs, solvent A consists of water with 0.1% TFA and solvent B is composed of acetonitrile with 10% water and 0.1% TFA. All UV/vis spectra and kinetics experiments were recorded on an Agilent 8453 diode array UV/vis spectrophotometer. Pseudo first order rate constants from all kinetics experiments were calculated using the Agilent UV/vis Chemstation software package Rev. A.10.01. Fluorescence measurements were obtained using a Varian Cary Eclipse fluorescence spectrophotometer. ^{1}H (400 MHz) and ^{13}C NMR (100 MHz) spectra were collected on a Bruker Advance-400 NMR spectrometer at ambient temperature in D_2O with 3-(trimethylsilyl)-propionic-2,2,3,3-D_4 acid sodium salt (TSP) as an internal standard. High-resolution electrospray ionization (ESI) mass spectra were obtained on a Bruker Daltonics APEXIV 4.7 Tesla Fourier transform mass spectrometer (FT-ICR-MS) in the Department of Chemistry Instrumentation Facility at the Massachusetts Institute of Technology.

Synthetic Procedures:

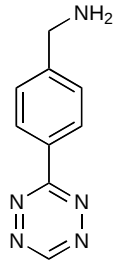

3-(*p*-Benzylamino)-1,2,4,5-tetrazine (**1**): To a thoroughly blended mixture of 4-(aminomethyl)benzonitrile hydrochloride (25 mmol, 4.21 g), formamidine acetate salt (100 mmol, 10.41 g) and sulfur (25 mmol, 801 mg) was added anhydrous hydrazine (7.84 mL, 250 mmol). After addition of the hydrazine, the reaction mixture becomes a thick clear slurry with gas evolution. After stirring vigorously for 20 h, the now yellow slurry is added to acetic acid (50 mL) and filtered through a glass frit. Sodium nitrite (125 mmol, 8.63 g) in 15 mL of water is then added to the acetic acid solution, cooled in an ice/water bath, over 15 min (**Caution**: the sodium nitrite addition generates a large amount of toxic nitrogen oxide gasses and should be performed in a well ventilated fume hood). During the sodium nitrite addition, the solution turns bright pink in color. The residue remaining after removal of the acetic acid by rotary evaporation at 60 °C and 5 torr is then washed with acetonitrile (3x20 mL) and filtered. After removal of the acetonitrile by rotary evaporation, the remaining viscous pink oil (~20 g) is dissolved in 250 mL of buffer A and partially purified in 5 portions by loading onto 70 g Varian Mega Bond Elute RPC18 flash chromatography cartridges eluting with buffer A containing 25% MeOH. The resulting pink fractions were combined, concentrated, and purified by preparative HPLC using a gradient from 0 to 25% buffer B over 30 min, giving **1** (0.92 g,

20%) as a pink crystalline solid after solvent removal. The purity of **1** was verified by analytical HPLC (Figure S1). ^{1}H NMR (400 MHz, D_2O): δ 10.41 (1H, s), 8.52 (2H, d, J = 8.4 Hz), 7.73 (2H, d, J = 8.4 Hz), 4.34 (2H, s). ^{13}C NMR (400 MHz, DMSO-d_6): δ 169.23, 160.49, 140.57, 135.05, 132.74, 131.91, 45.69. HRMS-ESI $[M+H]^+$ m/z calcd. for $[C_9H_{10}N_5]^+$ 188.0931, found 188.0935.

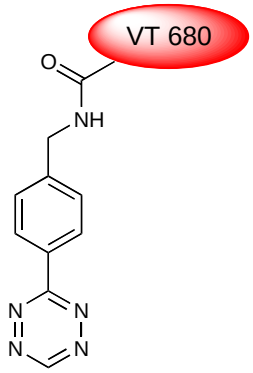

3-(*p*-Benzylamino)-tetrazine-VT680 conjugate (**3**): To a solution of **1** (15.0 mg, 0.08 mmol) in 2.5 mL of 0.1 M PBS, pH 8.3, was added VT680 NHS ester (12.4 mg, 0.01 mmol). The dark blue solution was allowed to stir overnight in the dark. Pure **3** (5.2 mg) was obtained following preparative HPLC of the reaction solution using a gradient from 0 to 25% buffer B over 30 min. Product purity was assessed by analytical LC/MS (Figure S9). The synthesis of **3** was confirmed by low resolution ESI mass spectrometry. The expected molecular weight of **3** was calculated to be approximately 1309 for $[M+H]^+$ from the molecular weight of **1** and the vendor supplied molecular weight of 1238 for the NHS ester of VT680. The experimentally observed molecular weight of **3** for $[M+H]^+$ is 1309.7.

Antibody labeling

Norbornene carboxylic acid ((1S,2S,4S)-bicyclo[2.2.1]hept-5-en-2-yl acetic acid) was stirred for three hours with 1.1 equivalents of disuccinimidyl carbonate in acetontrile using 1 equivalent of pyridine as base. After reaction, solvent and base were removed by rotary evaporation and the crude norbornene succinimidyl ester with N-hydroxysuccinimide side product was recovered. Commercially purchased humanized anti-HER2/neu antibody trastuzumab (Genentech, San Francisco, CA) in 0.1M sodium bicarbonate buffer (pH 8.2) was incubated for three hours at room temperature with a 5 molar excess of 5-(and-6)-carboxytetramethylrhodamine, succinimidyl ester (Invitrogen) and a 30 molar excess of crude norbornene succinimidyl ester. The antibody was then isolated and washed by centrifuge purification and stored in PBS buffer. Control antibody was modified in an identical manner but excluding the norbornene NHS.

Cell labeling and imaging

SKBR-3 human mammary carcinoma cell lines were maintained in complete McCoy's medium. Cells were incubated at 37 ^{o}C with 200 nM modified trastuzumab for 30 minutes and then washed twice with 10% fetal bovine serum (FBS) in Hanks balanced salt solution (HBSS). Tetrazine labeling was performed by incubating the cells for 30 minutes at 37 ^{o}C in 10% FBS/HBSS containing 50 μM of tetrazine-VT680. Cells were then washed twice with 10% FBS/HBSS and imaged with by fluorescence microscopy.

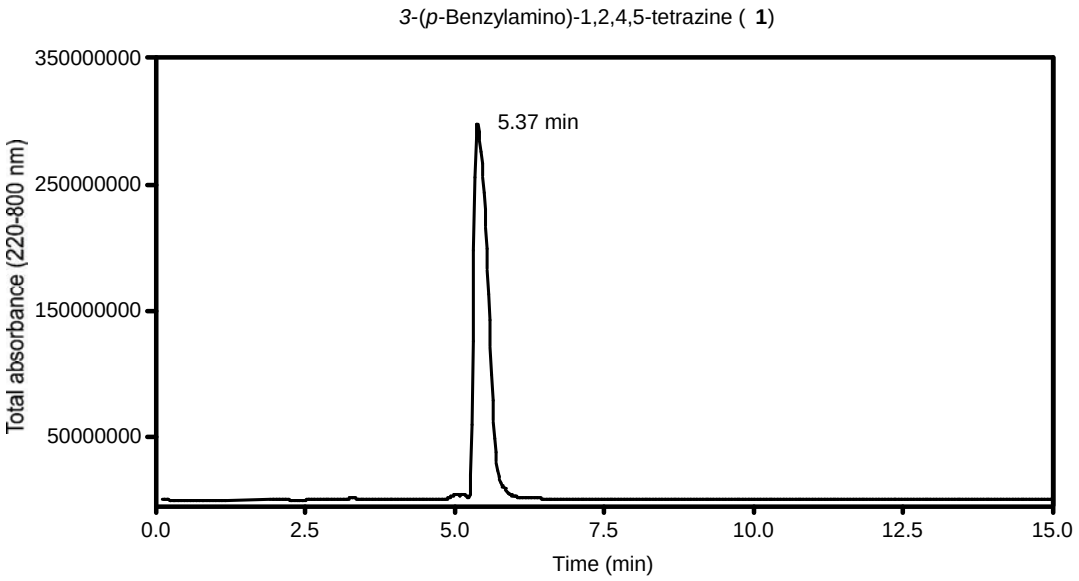

Figure S1. HPLC trace of purified 3-(*p*-Benzylamino)-1,2,4,5-tetrazine (**1**) using a gradient of 0 to 100 % buffer B over 15 min.

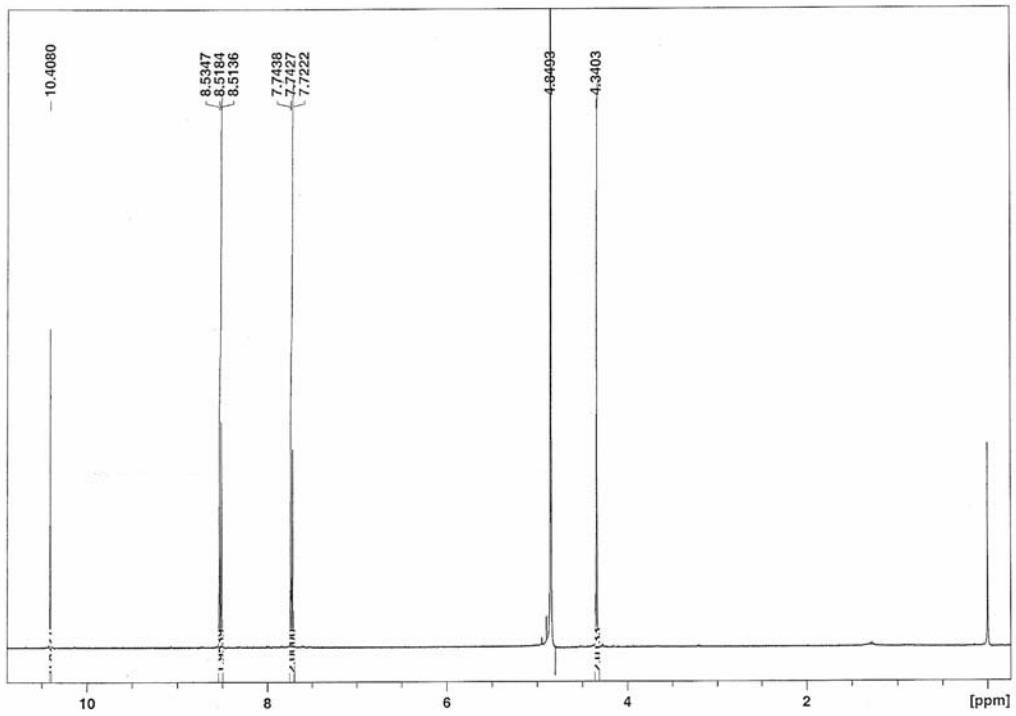

Figure S2. ^{1}H NMR of 3-(*p*-Benzylamino)-1,2,4,5-tetrazine (**1**) in D_2O with TSP as an internal standard.

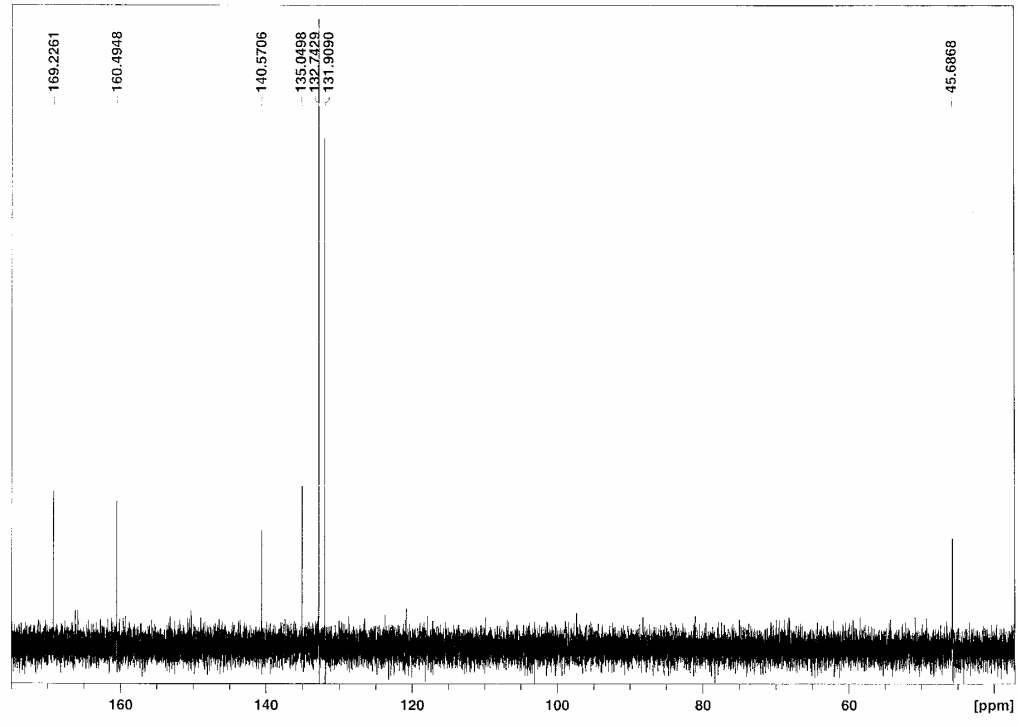

Figure S3. ^{13}C NMR spectrum of 3-(*p*-Benzylamino)-1,2,4,5-tetrazine (**1**) in D_2O with TSP as an internal standard.

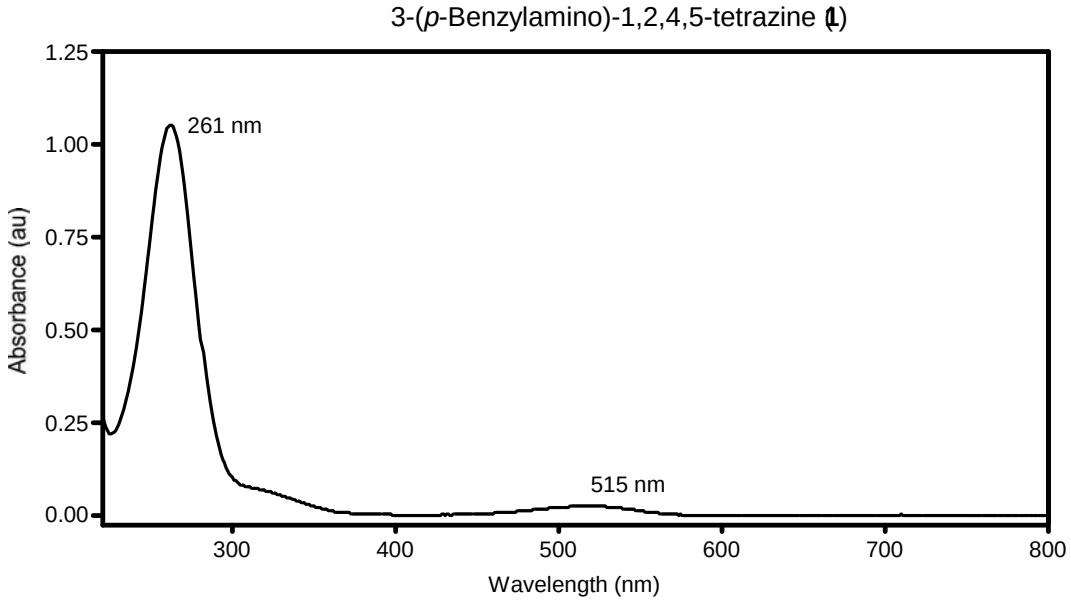

Figure S4. Absorption spectrum of 3-(*p*-Benzylamino)-1,2,4,5-tetrazine (**1**) in PBS, pH 7.4.

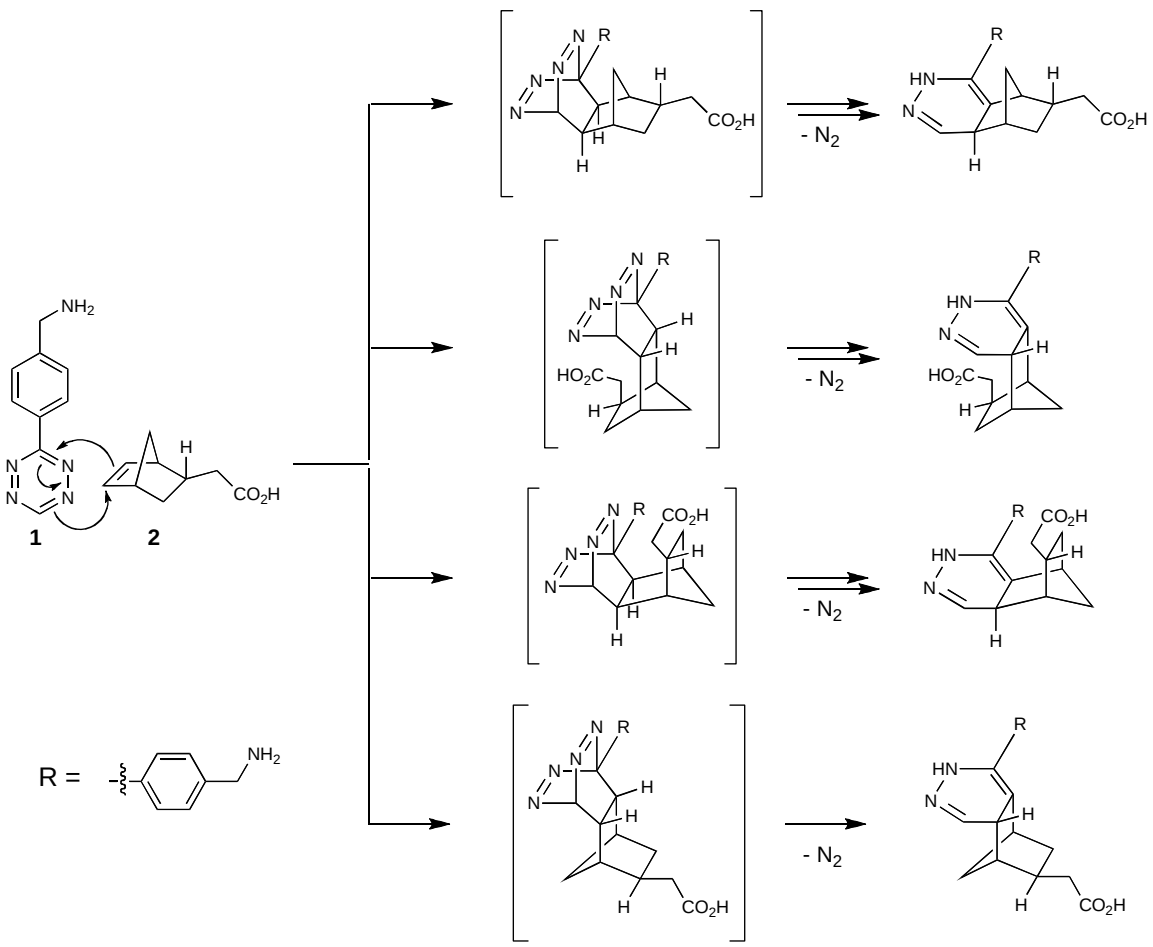

Scheme S1. The [4+2] cycloaddition reaction of 3-(*p*-Benzylamino)-1,2,4,5-tetrazine (**1**) with (1S,2S,4S)-bicyclo[2.2.1]hept-5-en-2-yl acetic acid (**2**) showing possible dihydropyridazine products.

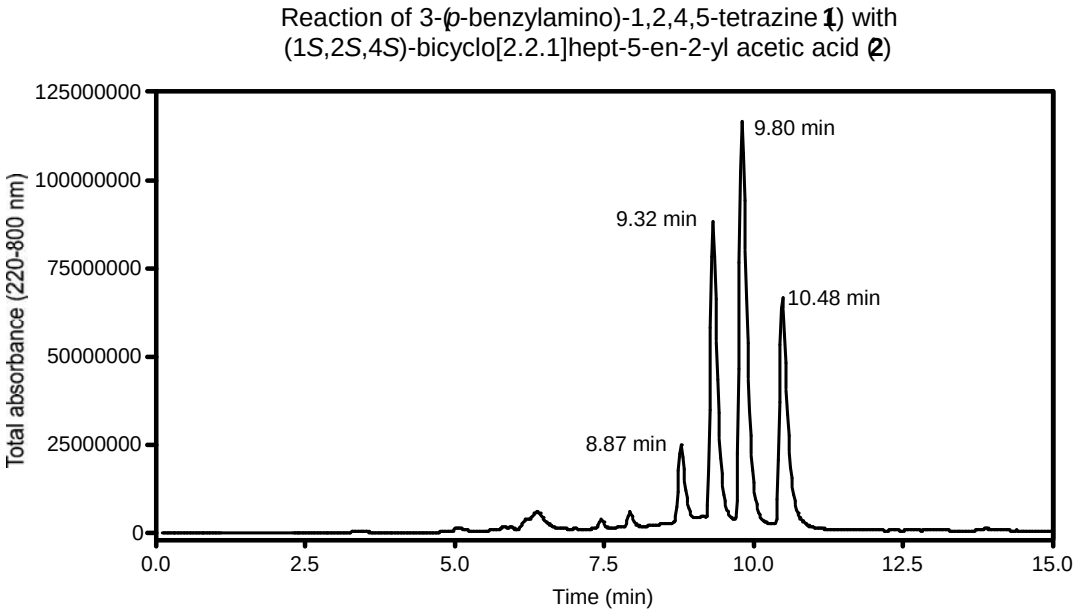

Figure S5. LC/MS chromatogram showing the four dihydropyridazine products formed from the reaction of a solution containing 5 mM 3-(*p*-Benzylamino)-1,2,4,5-tetrazine (**1**) and 6 mM (1S,2S,4S)-bicyclo[2.2.1]hept-5-en-2-yl acetic acid (**2**) in PBS, pH 7.4. The four products eluting at 8.87, 9.32, 9.80, and 10.48 min all have an observed mass of 312.3 amu. The mass for the dihydropyridazine products $[M+H]^+$ calculated for $C_{18}H_{22}N_3O_2^+$ is 312.2 amu. The HPLC trace was taken 15 min after preparing the reaction solution using a gradient of 0 to 100% buffer B over 15 min. The overall yield for conversion to the dihydropyridazine products is > 93%.

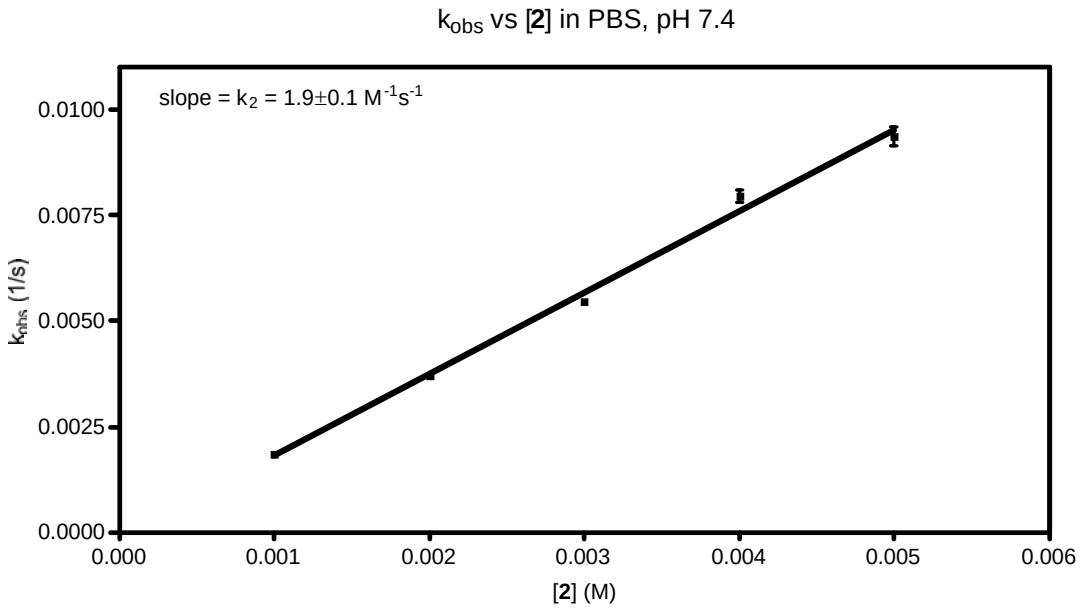

Figure S6. Plot of k_{obs} vs. the concentration of (1S,2S,4S)-bicyclo[2.2.1]hept-5-en-2-yl acetic acid (**2**) for the reaction of 1.0×10^{-4} M **1** with increasing concentrations of **2** in PBS, pH 7.4 at 20.0±0.1 °C. Each data point is the average of at least three independent trials. The second order rate constant (k_2) of 1.9 $M^{-1}s^{-1}$ is calculated from the slope of the graph using the relationship: $k_{obs}=[\mathbf{2}](k_2)$. Under these conditions all cycloaddition reactions were complete in less than 25 min.

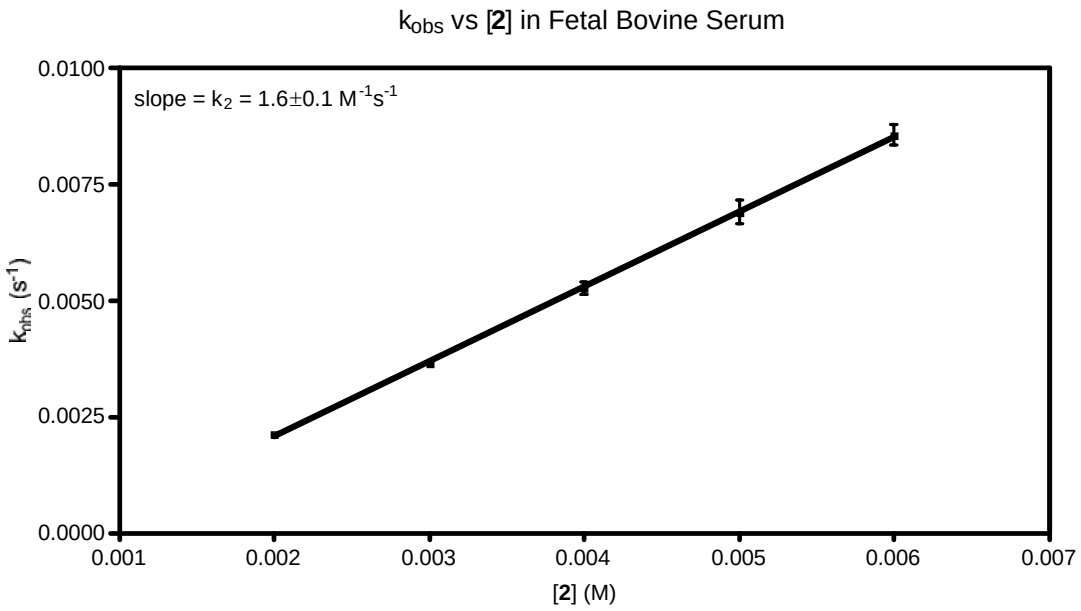

Figure S7. Plot of k_{obs} vs. the concentration of (1S,2S,4S)-bicyclo[2.2.1]hept-5-en-2-yl acetic acid (**2**) for the reaction of $2.0x10^{-4}$ M **1** with increasing concentrations of **2** in Fetal Bovine Serum (FBS) at 20.0±0.1 °C. Each data point is the average of at least three independent trials. The second order rate constant (k_2) of 1.6 $M^{-1}s^{-1}$ is calculated from the slope of the graph using the relationship: k_{obs}=[**2**](k_2). Under these conditions, all cycloadditon reactions were complete in less than 20 min.

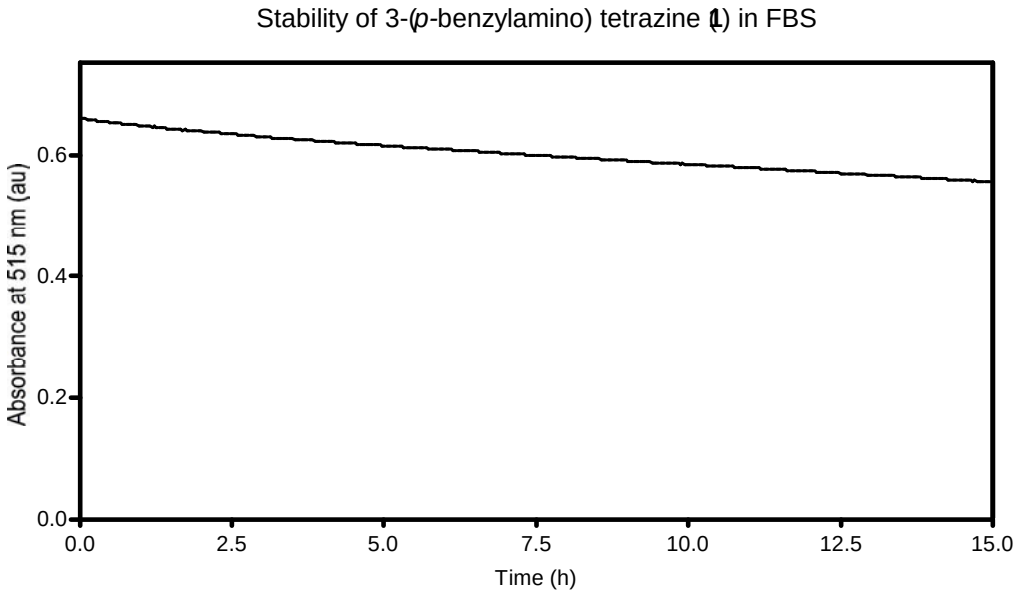

Figure S8. The solution stability of **1** in FBS at 20.0±0.1 °C monitored at 515 nm. After 15 h, a 15% decrease in absorption is observed.

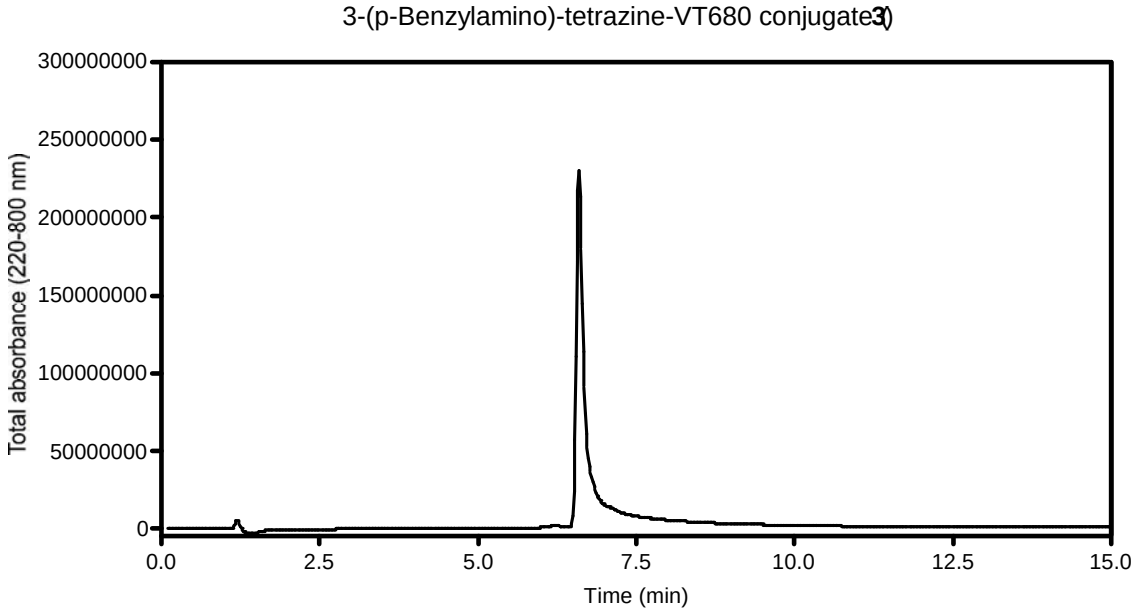

Figure S9. HPLC trace of the Tetrazine-VT680 (**3**) conjugate. The chromatogram was obtained using a gradient from 0 to 100% buffer B over 15 min.

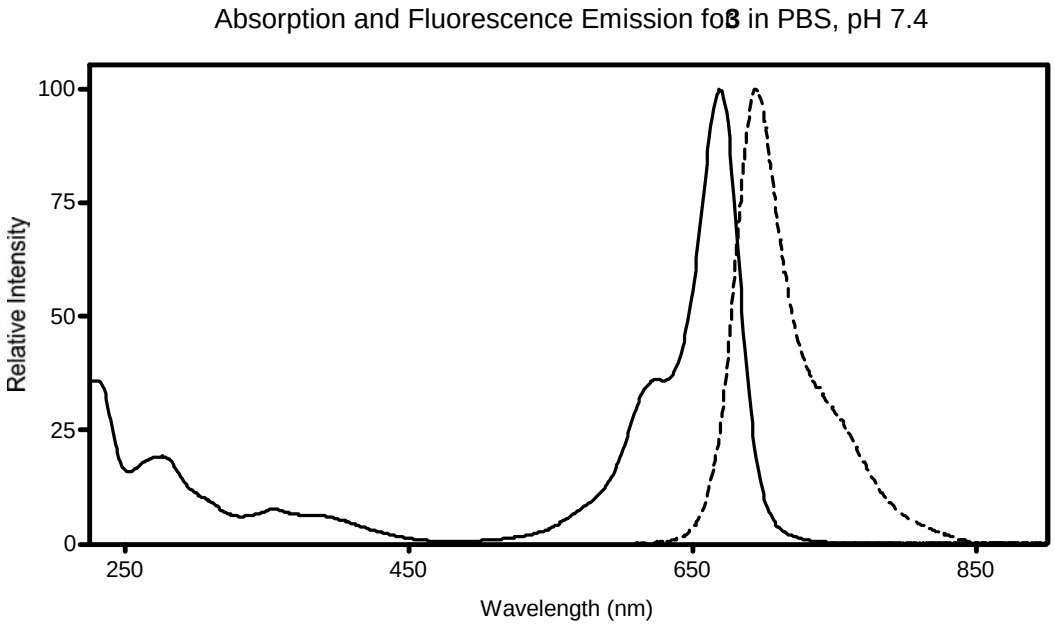

Figure S10. Absorption (solid) and fluorescence emission (dashed) traces of the tetrazine-VT 680 conjugate in PBS, pH 7.4. The fluorescence emission trace was acquired using an excitation wavelength of 600 nm. The absorption and emission maxima are at 669 and 694 nm, respectively.

A Peptide Targeted Contrast Agent Specific to Fibrin-Fibronectin Complexes for Cancer Molecular Imaging with MRI

Furong Ye,[†] Eun-Kee Jeong,[‡] Zhanjun Jia,[§] Tianxin Yang,[§] Denis Parker,[‡] and Zheng-Rong Lu[†,*]

Department of Pharmaceutics and Pharmaceutical Chemistry, Department of Radiology, and Department of Internal Medicine, University of Utah, Salt Lake City, and Veterans Affairs Medical Center, Salt Lake City, Utah. Received May 21, 2008; Revised Manuscript Received September 19, 2008

A peptide targeted contrast agent, CLT1-(Gd-DTPA), was synthesized for molecular imaging of fibronectin−fibrin complexes in tumor tissue with magnetic resonance imaging (MRI). The T_1 and T_2 relaxivities of CLT1-(Gd-DTPA) were 4.22 and 4.45 mM^{-1} s^{-1} at 3 T, respectively. The targeted contrast agent specifically bound to tumor tissue and resulted in significant tumor contrast enhancement at a dose of 0.1 mmol Gd/kg for at least 60 min in mice bearing HT-29 human colon carcinoma xenografts as shown in dynamic MR images. In contrast, a control nontargeted contrast agent, Gd(DTPA-BMA), was cleared rapidly with little tumor enhancement 60 min postinjection. Tumor enhancement with CLT1-(Gd-DTPA) was significantly reduced after coinjection with a 3-fold excess of free CLT1 peptide. The preliminary study has shown that CLT1-(Gd-DTPA) can specifically bind to the fibrin−fibronectin complexes in tumor tissues, resulting in significant tumor enhancement. The targeted contrast agent has a potential for cancer molecular imaging with MRI.

Magnetic resonance imaging (MRI) is a powerful imaging modality for morphological and functional imaging. MRI provides anatomical images of soft tissues with high spatial resolution and is effective for noninvasive imaging of physiological properties, e.g., diffusion, perfusion, and vascularity, of the tissues of interest (*1*). However, MRI has not been effectively used for molecular imaging because of its low sensitivity. The direct conjugation of targeting agents, e.g., peptides, antibodies, and proteins, to clinical MRI contrast agents, e.g., Gd(III) chelates, could not deliver a sufficient amount of contrast agents for MRI to effectively detect the molecular targets expressed on the surface of cells of interest (*2, 3*). Consequently, a large number of Gd(III) chelates have been incorporated into various targeted nanoparticles for MR molecular imaging to increase local concentration of contrast agents (*4*−*8*). Unfortunately, the size of these nanoparticles is much larger than the renal filtration threshold (ca. 4.5 nm), and they cannot be readily excreted from the body. Long-term tissue retention of high-dose Gd(III) based contrast agents may also cause toxic side effects such as systemic nephrogenic fibrosis (*9, 10*).

The limitations of MRI for molecular imaging can be overcome by proper selection of molecular biomarkers and using agents that can be readily excreted (*11*). Stable Gd(III) chelates have been proven safe in patients except those with intermediate and late-stage renal diseases. Since the amount of biomarkers expressed on the cell surface may not be sufficient for molecular imaging with MRI, other biomarkers with high local expression can be used for MR molecular imaging. It has been reported that tumor stroma have a unique meshwork of clotted plasma proteins that are not present in normal tissues (*12, 13*). The presence of the fibrin in tumor meshwork is known to associate with increased microvessel permeability in neoplastic tissues (*12*), and fibronectin in tumor stroma is also associated with tumor angiogenesis (*13*). The clotted plasma proteins might be attractive targets for molecular imaging with MRI. Recently, Ruoslahti and colleagues have identified peptides, including CLT1 and CLT2 peptides, which can specifically bind to the fibronectin−fibrin clots in various tumor tissues with little nonspecific binding to normal tissues (*14*). The incorporation of such peptides to Gd(III) chelates may result in targeted contrast agents for specific tumor imaging with MRI. As compared to nanoparticulate targeted contrast agents, the small molecular targeted contrast agents can rapidly diffuse into tumor tissue and bind to tumor meshwork. The unbound contrast agents can be rapidly excreted from the body via renal filtration. Consequently, significant signal enhancement of molecular targets can be visualized by MRI with minimal nonspecific background enhancement.

Here, we report a targeted contrast agent, a conjugate of a cyclic decapeptide CGLIIQKNEC (CLT1) and Gd-DTPA, for MR molecular imaging of fibrin−fibronectin complexes in tumor tissues. The peptide CLT1 was first synthesized using standard solid-phase peptide synthesis from Fmoc-protected amino acids (*15*) on a 2-chlorotrityl chloride resin. At the end of the peptide synthesis, an excess of DTPA dianhydride in DMSO was reacted with the peptide on the beads at room temperature for 4 h to conjugate DTPA at the N-terminal of the peptide. The resin was completely washed with water, DMF, dichloromethane, and methanol three times each. The CLT1−DTPA was then removed from the resin using TFA solution (TFA 94%, 1,2-ethanedithiol 2.5%, triisobutylsilane 2.5%, water 1%). The product was exposed to air for about 2 h to allow the formation of disulfide bonds for the cyclic peptide and then purified using preparative HPLC with a C18 column. CLT1−(Gd-DTPA) was finally prepared by complexation of CLT1−DTPA with $Gd(OAc)_3$ at pH 6. Excess $Gd(OAc)_3$ was removed by precipitation at pH 11. The final product was purified by preparative HPLC. The mass (m/z, $M + H^+$) of CLT1−(Gd-DTPA) was 1650.75 (calcd 1650.2) as determined by MALDI-

* Correspondence to Dr. Zheng-Rong Lu, 421 Wakara Way, Suite 318, Salt Lake City, UT 84108. Phone: 801 587-9450. Fax: 801 585-3614. E-mail: zhengrong.lu@utah.edu.

[†] Department of Pharmaceutics and Pharmaceutical Chemistry, University of Utah.

[‡] Department of Radiology, University of Utah.

[§] Department of Internal Medicine, University of Utah, and Veterans Affairs Medical Center, Salt Lake City.

10.1021/bc800211r CCC: $40.75 © 2008 American Chemical Society
Published on Web 12/03/2008

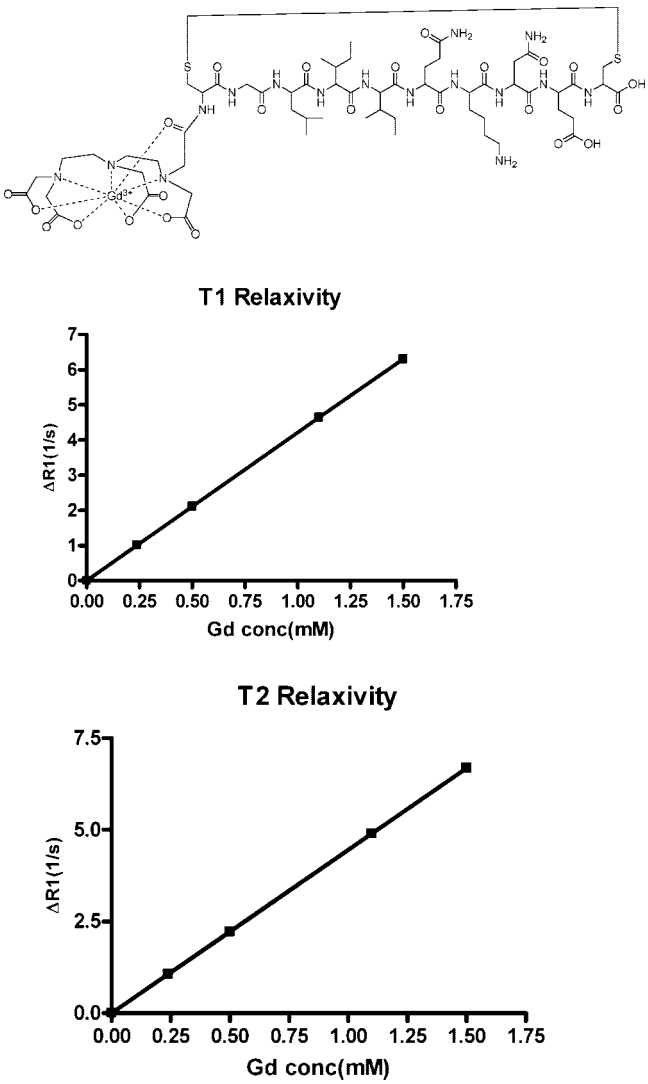

Figure 1. Chemical structure of CLT1−(Gd-DTPA) and plots of $1/T_1$ and $1/T_2$ versus the concentration of the contrast agent.

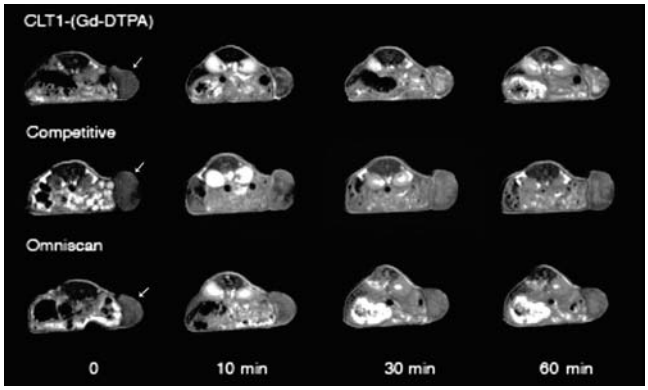

Figure 2. T_1-weighted 2D spin−echo images of mice bearing HT-29 xenografts before contrast and at 10, 30, and 60 min postinjection of CLT1−(Gd-DTPA), Omniscan and competitive mixture. Arrow points to the tumor tissue.

TOF mass spectrometry. The T_1 and T_2 relaxivities of CLT1−(Gd-DTPA) were determined on a Siemens Trio 3T scanner at room temperature using an inversion recovery (IR) prepared turbo spin−echo (TSE) imaging pulse sequence and a turbo spin−echo imaging sequence with turbo factor 3 (*16*), respectively. The T_1 and T_2 relaxivities of CLT1−(Gd-DTPA) were 4.22 and 4.45 mM^{-1} s^{-1} at 3 T. Figure 1 shows the

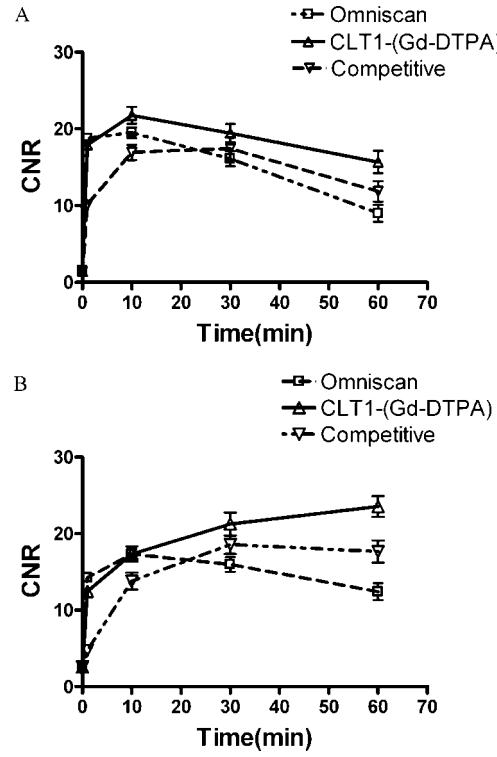

Figure 3. Plots of CNR versus time in tumor periphery (A) and inner area (B) before contrast and at 1, 10, 30, and 60 min postinjection of CLT1−(Gd-DTPA), Omniscan, and competitive mixture.

structure of CLT1−(Gd-DTPA) and the plots of the T_1 and T_2 water proton relaxation rates at various concentrations of the contrast agent at 3 T.

In vivo molecular imaging of fibrin−fibronectin complexes in tumor with the targeted contrast agent and MRI was evaluated in female athymic nu/nu mice bearing HT-29 human colon carcinoma xenografts with a T_1-weighted 2D spin−echo sequence. A clinical contrast agent, Gd(DTPA-BMA), was used as a control. Competitive targeting of free CLT1 peptide to CLT1−(Gd-DTPA) was also studied with coinjection of CLT1−(Gd-DTPA) and a 3-fold excess of free CLT1 peptide. A group of 3 mice was used for each contrast agent. The mice were anesthetized by intramuscular administration of a mixture of ketamine (45 mg/kg) and xylazine (6 mg/kg) for MRI. The CLT1−(Gd-DTPA) and Gd(DTPA-BMA) was intravenously injected at a dose of 0.1 mmol/kg. Contrast-enhanced MR images were acquired before and after injection at 1, 10, 30, and 60 min on a Siemens Trio 3T scanner using a human wrist coil. High-resolution 3D images were acquired with a 3D FLASH sequence with 25° flip angle, TR/TE = 7.8/2.7 ms, slice thickness 0.5 mm, field of view (FOV) 120 mm, voxel size 0.5 × 0.5 × 0.5 mm^3. T_1-weighted 2D axial tumor images were acquired with a 2D spin−echo sequence with TR 400 ms, TE 10 ms, 90° tip angle, and FOV 50 mm. Mice were sacrificed 24 h postinjection, and tumor tissues were removed and fixed with 3% paraformaldehyde and embedded in paraffin. Tissue sections (4 μm thickness) were incubated in 3% H_2O_2 for 10 min to block endogenous peroxidase activity and boiled in antigen retrieval solution for 15 min in microwave. The sections were then incubated with primary antibody overnight and secondary antibody the next day for visualization using the ABC kit (Santa Cruz Biotechnology).

Figure 2 shows the representative axial T_1-weighted 2D spin−echo images of the tumor tissues of the mice bearing HT-29 tumor xenografts before and after injection of the contrast agents. Significant enhancement was observed in tumor tissues for CLT1-(Gd-DTPA) 10 min postinjection, and strong en-

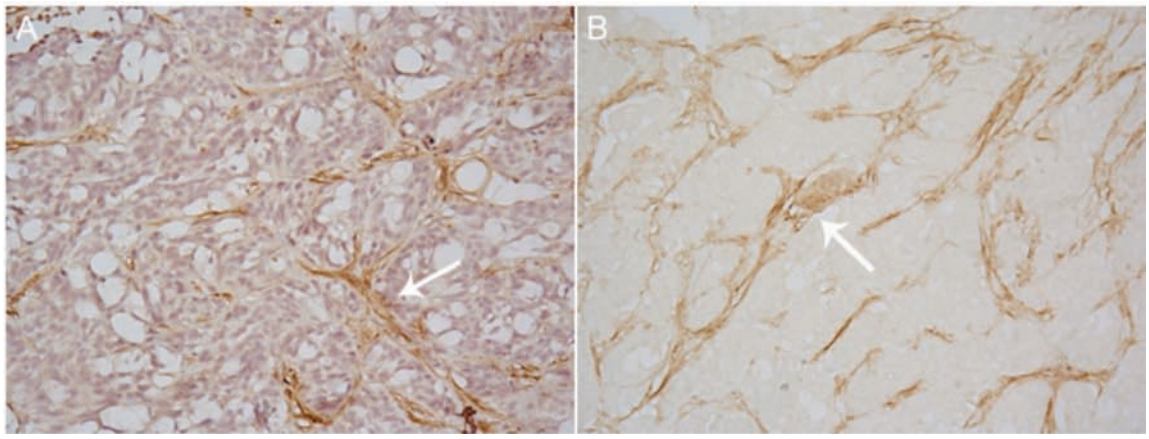

Figure 4. Staining of fibronectin in HT-29 tumor tissues with hemoxylin (A) or without hemoxylin (B) (40× magnification). Arrows point to the stained fibronectin (brown color) in the EES space, and blue in A indicates nuclus stained with hemoxylin.

hancement was visible in the tumor tissues at 60 min after injection. For the competitive study, the tumor enhancement with CLT1−(Gd-DTPA) was reduced after the coinjection of free peptide, which indicates that the free peptide recognizes the same binding site within tumor tissue as CLT1−(Gd-DTPA). The control agent Gd(DTPA-BMA) did not show a strong tumor enhancement as compared to CLT1−(Gd-DTPA).

MR signal intensity was also measured, and the contrast to noise ratio (CNR) in the tumor tissues was calculated as CNR $= (SI_{tissue} - SI_{muscle})/SD_{noise}$. Statistical analysis was perform using two-way ANOVA. Figure 3 shows the CNR of the tumor tissue in tumor periphery and inner areas before and at various time points after injecting the contrast agents. CLT1−(Gd-DTPA) showed higher CNR at 10 min after injection in the tumor periphery area and decreased gradually. At the same time, CNR in tumor inner area increased gradually during the period of 60 min postinjection. The CNR in both tumor periphery and inner tissue with Gd(DTPA-BMA) decreased rapidly after it reached the maximum values at 1 min postinjection. The CLT1−(Gd-DTPA) showed significantly higher CNR than the control Gd(DTPA-BMA) in tumor periphery since 10 min postinjection ($p < 0.05$) and in the tumor inner area since 30 min postinjection ($p < 0.05$). The results indicate binding and retention of the targeted contrast agent to tumor tissue. The presence of free peptide resulted in significant reduction of CNR in both tumor periphery and inner tumor tissue ($p < 0.05$) except at the point of 30 min postinjection. The result indicated that the presence of free peptide inhibited the binding of the targeted contrast agent to its target, resulting in decreased contrast enhancement in tumor tissue.

The plasma proteins fibrin(ogen) and fibronectin play a prominent role in hemostasis and wound healing. Fibrinogen is activated to form an insoluble fibrin clot following vascular injury. The clot also serves as a provisional matrix for adhesion and migration of cells or proteins including fibronectin, which is incorporated into the fibrin clot upon fibrin polymerization. The presence of the fibrin and fibronectin in tumor meshwork has also been reported in the literature due to the leakiness of tumor vasculature (*16*, *17*). CLT1 peptide was reported to specifically bind the fibrin−fibronectin complexes in tumor tissues (*14*). We further carried out immunohistochemical study to verify the presence of fibronectin in the HT-29 tumor tissues after MR imaging. Figure 4 shows the immunostaining of fibronectin in HT-29 tumor tissues with (Figure 4A) or without (Figure 4B) nucleus staining. The histochemical staining clearly indicated the existence of fibronectin in the extracellular spaces of tumor tissues.

It is a challenge for MRI to detect in vivo molecular targets with molecular imaging because of its low sensitivity. We have shown here that MRI can be effective for molecular imaging if suitable molecular targets are identified. The targeted contrast agent CLT1-(Gd-DTPA) had little nonspecific binding and accumulation in the normal tissue despite that the peptide was hydrophobic. It bound to its molecular target in tumor tissue, resulting in significant and prolonged tumor enhancement. The result was consistent to what was originally reported by Ruoslahti et al. in other tumor models, which further confirmed that CLT1 peptide had a high specificity to fibrin−fibronectin complexes in tumor stroma (*14*). Because of the high content of the fibrin−fibronectin complexes in the tumor stroma, the peptide was able to deliver a sufficient amount of Gd-DTPA chelates to the molecular targets to generate detectable signal enhancement for MRI. Since the contrast agent was a low molecular weight chelate with a small size, it was able to be cleared rapidly from the blood circulation and normal tissues, resulting in strong CNR in the tumor tissue.

MR molecular imaging of fibrin−fibronectin complexes in tumor tissue with CLT1−(Gd-DTPA) also has the potential to characterize tumor angiogenesis. It has been reported that the presence of fibrin in the tumor meshwork is associated with increased microvessel permeability in neoplastic tissues (*12*), and fibronectin in tumor stroma is also associated with tumor angiogenesis (*13*). The result suggested that CLT1−(Gd-DTPA) was able to detect the presence of fibrin−fibronectin complexes in the angiogenic tumor tissues. The correlation of fibrin−fibronectin complexes to tumor angiogenesis may provide an effective method for tumor angiogenesis imaging with MRI and CLT1−(Gd-DTPA). Accurate assessment of tumor angiogenesis is critical for tumor grading, assessment of tumor response to anticancer therapies, particularly antiangiogenesis therapies, and patient management.

Fibrin−fibronectin complexes are also present in the plasma clots of wounds and other pathologic tissues with leaky blood vessels such as atherosclerotic plaques. Ruoslahti and colleagues showed that fluorescein-labeled CLT peptides specifically bound to the injured blood vessel wall, not the intact arteries and tissues (*14*). It suggests that MRI with CLT1−(Gd-DTPA) may have broad applications, including molecular imaging of cancer, angiogenesis, vascular integrity, and assessment of wound healing, anthrosclerosis, and tumor response to antiangiogenesis therapies. As compared to other targeting moieties, including proteins, antibodies, and their fragments, the peptide targeted Gd(III) chelate is advantageous for MR molecular imaging due to its excellent tissue permeability and rapid clearance from nonspecific tissue or organs.

In summary, a targeted contrast agent CLT1−(Gd-DTPA) specific to fibrin−fibronectin complexes was prepared and preliminarily evaluated in an animal tumor model for effective

cancer MR molecular imaging. The targeted contrast agent had minimal nonspecific binding and accumulation in normal tissues. CLT1 peptide was able to deliver a sufficient amount of Gd-DTPA chelates to its molecular target for effective molecular imaging with MRI in tumor. CLT1−(Gd-DTPA) is a promising targeted contrast agent for MR molecular imaging of fibrin−fibronectin complexes. It has a great potential for cancer detection and diagnosis, characterization of tumor angiogenesis, and imaging wounds and atherosclerosis.

ACKNOWLEDGMENT

This research was supported in part by the NIH R01 CA097465. We greatly appreciate Dr. Yongen Sun and Ms. Melody Johnson for their technical assistance in animal handling and MRI data acquisition.

LITERATURE CITED

(1) Stephen, R. M., and Gillies, R. J. (2007) Promise and progress for functional and molecular imaging of response to targeted therapies. *Pharm. Res. 24*, 1172–85.

(2) Caravan, P., Ellison, J. J., McMurry, T. J., and Lauffer, R. B. (1999) Gadolinium(III) chelates as MRI contrast agents: structure, dynamics, and applications. *Chem. Rev. 99*, 2293–352.

(3) Gohr-Rosenthal, S., Schmitt-Willich, H., Ebert, W., and Conrad, J. (1993) The demonstration of human tumors on nude mice using gadolinium-labeled monoclonal antibodies for magnetic resonance imaging. *Invest. Radiol. 28*, 789–795.

(4) Sipkins, D. A., Cheresh, D. A., Kazemi, M. R., Nevin, L. M., Bednarski, M. D., and Li, K. C. (1998) Detection of tumor angiogenesis in vivo by $\alpha V\beta 3$-targeted magnetic resonance imaging. *Nat. Med. 4*, 623–6.

(5) Curtet, C., Maton, F., Havet, T., Slinkin, M., Mishra, A., Chatal, J. F., and Muller, R. N. (1998) Polylysine-(Gd-DTPA)$_n$ and polylysine-(Gd-DOTA)$_n$ coupled to anti-CEA F(ab′)$_2$ fragments as potential immunocontrast agents. Relaxometry, biodistribution, and magnetic resonance imaging in nude mice grafted with human colorectal carcinoma. *Invest. Radiol. 33*, 752–61.

(6) Ke, T., Jeong, E. K., Wang, X., Feng, Y., Parker, D. L., and Lu, Z.-R. (2007) RGD targeted poly(L-glutamic acid)-cystamine-(Gd-DO3A) conjugate for detecting angiogenesis biomarker $\alpha(v)\beta 3$ integrin with MR T_1 mapping. *Int. J. Nanomed. 2*, 191–9.

(7) Flacke, S., Fischer, S., Scott, M. J., Fuhrhop, R. J., Allen, J. S., McLean, M., Winter, P., Sicard, G. A., Gaffney, P. J., Wickline, S. A., and Lanza, G. M. (2001) Novel MRI contrast agent for molecular imaging of fibrin: implications for detecting vulnerable plaques. *Circulation 104*, 1280–5.

(8) Amirbekian, V., Lipinski, M. J., Briley-Saebo, K. C., Amirbekian, S., Aguinaldo, J. G., Weinreb, D. B., Vucic, E., Frias, J. C., Hyafil, F., Mani, V., Fisher, E. A., and Fayad, Z. A. (2007) Detecting and assessing macrophages in vivo to evaluate atherosclerosis noninvasively using molecular MRI. *Proc. Natl. Acad. Sci. U.S.A. 104*, 961–6.

(9) Ersoy, H., and Rybicki, F. J. (2007) Biochemical safety profiles of gadolinium-based extracellular contrast agents and nephrogenic systemic fibrosis. *J. Magn. Reson. Imaging 26*, 1190–7.

(10) Sieber, M. A., Pietsch, H., Walter, J., Haider, W., Frenzel, T., and Weinmann, H. J. (2008) A preclinical study to investigate the development of nephrogenic systemic fibrosis: a possible role for gadolinium-based contrast media. *Invest. Radiol. 43*, 65–75.

(11) Caravan, P., Das, B., Dumas, S., Epstein, F. H., Helm, P. A., Jacques, V., Koerner, S., Kolodziej, A., Shen, L., Sun, W. C., and Zhang, Z. (2007) Collagen-targeted MRI contrast agent for molecular imaging of fibrosis. *Angew. Chem., Int. Ed. Engl. 46*, 8171–3.

(12) Dvorak, H. F., Senger, D. R., Dvorak, A. M., Harvey, V. S., and McDonagh, J. (1985) Regulation of extravascular coagulation by microvascular permeability. *Science 227*, 1059–61.

(13) Neri, D., Carnemolla, B., Nissim, A., Leprini, A., Querzè, G., Balza, E., Pini, A., Tarli, L., Halin, C., Neri, P., Zardi, L., and Winter, G. (1997) Targeting by affinity-matured recombinant antibody fragments of an angiogenesis associated fibronectin isoform. *Nat. Biotechnol. 15*, 1271–5.

(14) Pilch, J., Brown, D. M., Komatsu, M., Järvinen, T. A., Yang, M., Peters, D., Hoffman, R. M., and Ruoslahti, E. (2006) Peptides selected for binding to clotted plasma accumulate in tumor stroma and wounds. *Proc. Natl. Acad. Sci. U.S.A. 103*, 2800–4.

(15) Wang, X. L., Ramusovic, S., Nguyen, T., and Lu, Z.-R. (2007) Novel polymerizable surfactants with pH-sensitive amphiphilicity and cell membrane disruption for efficient siRNA delivery. *Bioconjugate Chem. 18*, 2169–77.

(16) Hihamoto, R., Yagi, Y., and Pressman, D. (1959) Immunohistochemical studies of antibodies in anti-Murphy lym phosarcoma sera. *Cancer Res. 19*, 874–79.

(17) Stenman, S., and Vaheri, A. (1981) Fibronectin in human solid tumors. *Int. J. Cancer 27* (4), 427–435.

BC800211R

Design of DNA-Conjugated Polypeptide-Based Capture Probes for the Anchoring of Proteins to DNA Matrices

Ryan M. Schweller, Pamela E. Constantinou, Nicholas W. Frankel, Priyanka Narayan, and Michael R. Diehl*

Department of Chemistry, and Department of Bioengineering, Rice University, 6100 Main Street, MS 142 Houston, Texas 77005. Received August 22, 2008; Revised Manuscript Received November 11, 2008

A new method for protein surface functionalization was developed that utilizes DNA-conjugated artificial polypeptides to capture recombinant target proteins from the solution phase and direct their deposition onto DNA-functionalized matrices. Protein capture is accomplished through the coiled-coil association of an engineered pair of heterodimeric leucine zippers. Incorporating half of the zipper complex directly into the polypeptides and labeling these polymers with ssDNA enables the polypeptide conjugates to form intermediate linkages that connect the target proteins securely to DNA-functionalized supports. This synthetic route provides an important alternative to conventional DNA-conjugation techniques by allowing proteins to be outfitted site-specifically with ssDNA while minimizing the need for postexpression processing. We demonstrate these attributes by (i) using the capture probes to prepare protein microarrays, (ii) demonstrating control over enzyme activity via deposition of DNA, and, (iii) synthesizing finite-sized, multiprotein complexes that are templated on designed DNA scaffolds in near quantitative yield.

Protein coupling and immobilization strategies remain central to the investigation of protein interactions and constitute an important design element for a wide variety of protein detection technologies (*1*−*3*). To meet these needs, an array of polypeptide-based affinity tags has been implemented that can mediate the surface anchoring of proteins (*4, 5*). In addition to being expressed as small protein fusions, these functionalities offer significant advantages over physical adsorption as well as most direct covalent attachment schemes, since they provide control over the orientations of proteins on their supports and, in many circumstances, help preserve the native folded state of proteins (*6*).

Alternatively, DNA−protein conjugate molecules have been developed to facilitate protein immobilization onto DNA-coated matrices such as DNA microarrays (*7*−*9*) and organized molecular scaffolds formed from DNA (*10*). DNA-directed immobilization of proteins allows oligonucleotide sequences to encode the spatial positioning and composition of multiple proteins on solid supports via the controlled deposition of DNA (*7*). This approach can simplify the preparation of solid supports for protein immobilization and provide sensitive control over protein deposition, since DNA-surface chemistries are more established and robust than most protein immobilization techniques. DNA-directed protein deposition can also provide routes to tune the quantitative activities of enzymes in ways that can be difficult to achieve using protein affinity tags alone and offer new opportunities to build artificial systems of interacting proteins with complex kinetic properties. Such control has been demonstrated by recent work to "program" the stoichiometric ratios of multiple enzymes immobilized on the surfaces of DNA-coated 96-well plates (*11*). Similarly, multienzyme complexes have been created using DNA as a molecular scaffold and used to explore how proximity effects influence their coupled-enzyme reaction dynamics (*11, 12*).

Despite the advantages of using DNA hybridization to direct protein deposition, various technical obstacles still limit the utility of this approach for a variety of applications. Particularly, the production of large numbers of DNA−protein conjugates remains challenging. Although commercially available cross-linking agents can be used to couple amine- or thiol-functionalized DNA strands to surface cysteine and lysine residues of proteins (*13, 14*), the efficiency of these reactions tends to be low, and postlabeling purification is generally required to isolate the conjugates. Furthermore, site-specific DNA conjugation through this route requires that the majority of surface cysteines and lysines are mutated to nonreacting residues. Even if these or alternative modifications are possible, the direct labeling of proteins with DNA may interfere with protein function (*14*). These issues can be avoided by coupling DNA to proteins indirectly through protein affinity tags. Protocols that employ intein tags along with expressed protein ligation (*15, 16*), DNA−streptavidin conjugates and biotin labeling (*7*), reactions of chemically modified DNA molecules with SNAP-tag fusion (*17*), and protein farnesyltransferase labeling coupled with click chemistry (*18*) have all been adopted for this purpose. However, most of these methods still require purification steps to isolate the DNA−protein conjugates. Consequently, a host of technological applications stand to benefit from the development of new synthetic routes to prepare DNA−protein conjugates that emulate the simple and robust processing afforded by commonly used protein affinity tags alone.

In this report, we describe a new synthetic strategy to couple proteins to DNA matrices that involves the production of DNA-conjugated polypeptide polymers **1** that function as capture probes by associating with recombinant affinity-tagged proteins in solution and then directing their deposition onto DNA-coated supports. These polymers are based on artificial proteins that some of us have previously used to control the surface immobilization of proteins (*19*) and to build finite-sized multiprotein complexes (*20*). With this system, protein capture is achieved through the coiled-coil association of an engineered parallel pair of heterodimeric leucine zippers, designated Z_E and Z_R. The zipper sequences are derived from polypeptides

* Corresponding author. Michael R. Diehl, Departments of Chemistry and Bioengineering, Rice University 6100 Main Street, MS 142, Houston, Texas 77005. Phone: (713) 348-4568. Fax: (713) 348-5877. E-mail: diehl@rice.edu.

10.1021/bc8003606 CCC: $40.75 © 2008 American Chemical Society
Published on Web 11/20/2008

Scheme 1. Synthetic Route to Employ Artificial Protein−DNA Conjugates for Recombinant Protein Capture

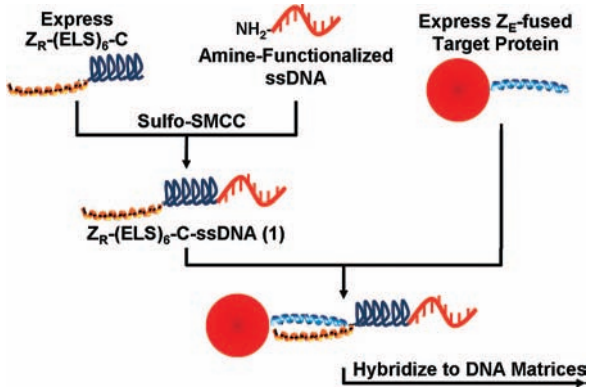

developed by Vinson et al. (*21*) and form exceptionally strong heterodimeric complexes ($K_D \sim 10^{-15}$ M) with much weaker homodimeric complexes ($K_D \sim 10^{-3}$ to 10^{-6} M). Half of the zipper complex is fused to a target protein as an affinity tag, while the other component is incorporated into the polymer as a genetic fusion. The polymers also contain a mechanically flexible and repetitive domain based on the elastomeric poly(VPGV$_\alpha$G) structural motif of the protein elastin (EL). Substitution of amino acids at the V$_\alpha$ position of this domain provides control over the hydrophilicity of the polymer and can be used to either direct or minimize physical adhesion of the polymers to functionalized surfaces (*19*). Here, we demonstrate that a DNA-conjugated version of these artificial proteins can be used to direct the self-assembly of target proteins onto DNA supports by forming a monovalent and stable intermediate linkage between immobilized ssDNA and the target proteins (Scheme 1).

The polypeptide polymers employed here contain the basic portion of the zipper complex (Z_R), a polymerized elastic "midblock domain" or ELS fragment (VPGVG VPG**S**G VPGVG VPG**S**G VPGVG), and a C-terminal cysteine, yielding Z_R-(ELS)$_6$-C. After the *in vivo* expression and purification of these polymers, sulfosuccinimidyl 4-[*N*-maleimidomethyl]cyclohexane-1-carboxylate (sulfo-SMCC) was used as a heterobifunctional cross-linker to couple an amine-functionalized oligonucleotide to the C-terminal cysteine of the polymers (*13*). The large shift in the isoelectric point of the polymers after DNA labeling allowed the conjugates to be purified to homogeneity using fast protein liquid chromatography (FPLC). Since the artificial proteins can sustain, without loss of function, lyophilization, resuspension in denaturing buffers, and extended dialysis, the labeling reactions can be scaled up, and this route allows concentrated stock solutions of Z_R-(ELS)$_6$-C-ssDNA to be prepared despite the intrinsic inefficiency of the sulfo-SMCC cross-linking reaction.

To test the ability of **1** to control the deposition of protein on DNA matrices, we labeled two samples of Z_R-(ELS)$_6$-C with different oligonucleotides containing non-complementary sequences. These polymers were then used as solution-phase capture probes that encode the spatial deposition of recombinant proteins onto DNA-printed microarrays (Figure 1). In this procedure, green fluorescent protein (GFP) and glutathione-*S*-transferase (GST) were chosen as target proteins and were expressed *in vivo* with C-terminal Z_E fusions. Protein capture was achieved by mixing samples of either Ni^{2+}-NTA purified target proteins (~1 mg/mL) or expressed proteins in unpurified cell lysates with a single conjugated version of **1** at a 3:1 molar ratio of target protein to polymer. After a brief incubation period (<30 min), these solutions were incubated for ~12 h over a custom-fabricated DNA microarray. Each array was washed and

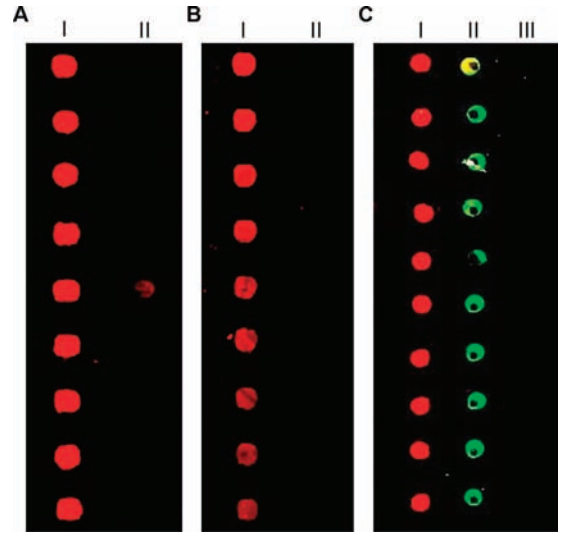

Figure 1. The use of artificial polypeptide conjugates to create protein microarrays encoded by DNA. Arrays probed with Alexa647-anti-GFP were prepared using purified GFP-Z_E (A) and cell lysates containing expressed GFP-Z_E (B). In both cases, column I denotes spots containing the complementary sequence for GFP-Z_E/polymer complex while a non-complementary control strand was spotted in column II. Images in A and B were cropped and placed together for clarity. The pitch between spots is 250 μm. (C) Two-component arrays were fabricated through a single incubation of precaptured GFP-Z_E and GST-Z_E proteins. Column I contains a complementary strand for GFP-Z_E/polymer complex, column II contains a complementary sequence for a second GST-Z_E /polymer complex, and column III contains spots of a non-complementary control strand. Multiprotein arrays were probed simultaneously with a mixture of Alexa647-anti-GFP and Cy3-anti-GST. The pitch between spots is 500 μm.

probed with fluorescently labeled antibodies (either Alexa647-anti-GFP or both Alexa647-anti-GFP and Cy3-anti-GST at 1 μg/mL) and scanned using a GenePix 4000B microarray scanner (Molecular Devices). DNA-directed self-assembly of both GFP-Z_E and GST-Z_E was found to be highly selective. As expected, arrays formed using either purified proteins or cell lysates demonstrated the oligonucleotide sequence-specific targeting of the proteins. Microarray spots containing the appropriate complementary ssDNA sequence possessed average signal-to-noise ratios (SNR) with a range of 20 to 60. Proteins appearing in the Cy3 channel tended toward the higher end of this range. On the other hand, average SNR values were significantly lower for spots containing non-complementary strands, an SNR range of 1.6 to 5. Furthermore, when precaptured protein solutions were combined for 1, 2, 4, or 8 h prior to their incubation on the microarray, we did not observe evidence of exchange between proteins displaying the zipper fusion.

We also examined the effect our DNA-directed immobilization strategy had on enzymatic activity. As a test case, we immobilized a β-lactamase enzyme (PSE-4) onto the surface of 96-well plates that were functionalized with streptavidin and then biotin-labeled oligonucleotides. DNA-directed deposition was performed using a similar procedure to that developed for the microarrays except that the PSE-4-Z_E fusion protein was prepared using standard periplasmic expression and lysis methods. Nitrocefin was used as a substrate for PSE-4, since the enzymatic opening of its β-lactam bond produced a detectable change in absorption at 485 nm using a Tecan Infinite 200 microplate reader. Measurements of nitrocefin hydrolysis rates again verified ability of **1** to selectively control enzyme deposition of target proteins (Figure 2B). Wells containing 5 μg of a complementary oligonucleotide to **1** showed a 4-fold increase in activity over wells that contained non-complementary sequences or where the ssDNA was omitted (Figure 2).

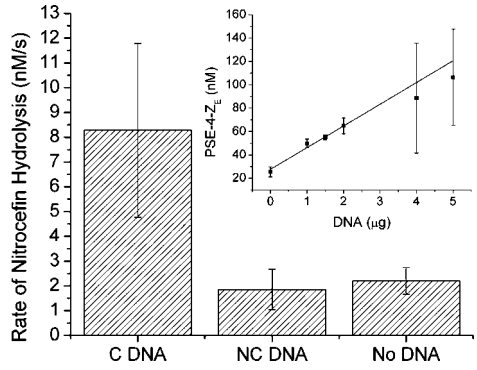

Figure 2. DNA-directed control over immobilized enzyme activity. A 4-fold increase in PSE-4-Z_E activity over background nitrocefin hydrolysis is seen in wells that were incubated with 5 μg of cDNA strands (C DNA) when compared to wells containing the same amount of a non-cDNA strand (NC DNA). Control wells where the DNA-functionalization step was omitted (No DNA) are also shown for comparison. The inset shows the linear dependence of PSE-4-Z_E activity on the amount of cDNA deposited in the wells.

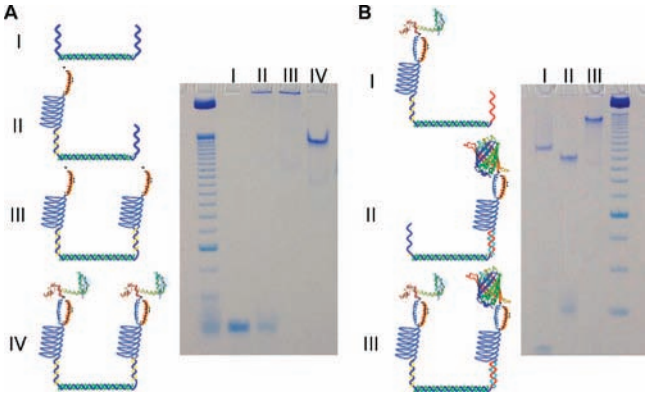

Figure 3. Non-denaturing PAGE-gels confirming the synthesis of multiprotein complexes. (A) Native PAGE-gel showing the successful formation of the complex containing two CaM-Z_E proteins assembled on a single DNA double helix. The dominant species observed in the individual lanes of the gel are indicated by Roman numerals. The labeling scheme is as follows: I. DNA scaffold alone; II. assemblies prepared at a 1 to 0.5 ratio of ssDNA scaffold to conjugates; III. a "half" complex composed of the DNA scaffolds and two artificial polypeptides; IV. complete assemblies formed at a 1:1:1 ratio of all assembly components. (B) Gel demonstrating the assembly of multiprotein complexes containing both a GFP-Z_E and a CaM-Z_E (III), templated on a DNA scaffold possessing two different "overhang" sequences. Partial complexes formed using only one type of protein and corresponding to either CaM-Z_E (I), or GFP-Z_E (II) are also shown.

Consistent with previous reports that utilize DNA-directed immobilization of enzymes (*11*), levels of PSE-4 activity were found to be linearly dependent on the amount of DNA that is immobilized in the wells (Figure 2 inset). Using soluble PSE-4-Z_E as a calibration standard, the hydrolysis rate was converted to PSE-4-Z_E concentration, yielding a slope of 18.6 nM PSE-4-Z_E per microgram of DNA.

Finally, the two different conjugated versions of **1** were synthesized and used to facilitate the self-assembly of multiprotein complexes onto molecular-scale scaffolds formed from DNA. Complexes containing either two GFP-Z_E proteins or a GFP-Z_E and a calmodulin protein (CaM-Z_E) were prepared (Figure 3). The DNA scaffold consisted of a 10-nm-long double helix (34 bases) flanked by unique single-strand "overhangs" comprising 20 bases on either end. The "overhangs" possessed either the same or orthogonal oligonucleotide sequences depending on whether single or multicomponent complexes were being synthesized. Multiprotein assemblies were synthesized by preincubating **1** with GFP-Z_E or CaM-Z_E, and then adding the DNA scaffold. In each case, the protein, polymer, and "overhang" concentrations were held at a 1:1:1 stoichiometry. Complex formation was examined using non-denaturing polyacrylamide gel electorphoresis (PAGE) and by staining for DNA and protein using Stains-All (Sigma). Clear separation between the scaffold and both partially and fully formed assemblies was observed. For each complex, gel intensity analysis indicated that the multiprotein complexes formed in high yield (>95%) using these conditions, proving that the association of the zipper complex and DNA-hybridization provided stable and selective linkages to drive the assembly process near quantitative yield, and that this process does not require the addition of large excesses of individual assembly components to form complete complexes.

In summary, we have demonstrated that DNA-conjugated artificial polypeptides can be used as protein capture probes that facilitate the oligonucleotide sequence-dependent deposition onto DNA-functionalized matrices. Furthermore, we have shown that these polymers allow the stoichiometries of enzymes to be deterministically controlled by forming a stable intermediate linkage between DNA-coated supports and target proteins. Importantly, our modular strategy separates the production of recombinant target proteins from DNA-conjugation procedures. Here, the synthesis of a single set of polymer allows diverse combinations of Z_E-tagged proteins to be immobilized for different applications. Furthermore, the selectivity and stability of the heterodimeric association of the leucine zipper system employed here permits target protein capture and pull down from unpurified cellular lysates and is compatible with a variety of protein expression systems and techniques. In this way, our strategy presents a flexible and versatile alternative to existing DNA-conjugation methods that is advantageous for applications where the ability to conjugate proteins with DNA is limiting, and in circumstances that require minimal postexpression processing of target proteins.

ACKNOWLEDGMENT

This research was generously supported by grants from the NSF (MCB-0645832) and the Welch Foundation (C-1625). P.E.C. was supported by a training fellowship awarded by the Program of the W.M. Keck Center for Interdisciplinary Bioscience (NIH grant No. T90 DK70121-03 and 5R90DK71504-3). We are also grateful for support from the NSF sponsored Center of Biological and Environmental Nanotechnology (CBEN) at Rice University.

Supporting Information Available: A detailed description of materials and methods, a listing of the amino acid and DNA sequences for all reagents, MALDI-TOF MS spectrum of the Z_R-$(ELS)_6$-C protein, FPLC chromatogram of the Z_R-$(ELS)_6$-C-ssDNA with the corresponding SDS-PAGE gel, Mircoarray from time-dependent incubations, and the full non-denaturing PAGE gel for the multiprotein complex. This material is available free of charge via the Internet at http://pubs.acs.org.

LITERATURE CITED

(1) Konig, T., and Skerra, A. (1998) Use of an albumin-binding domain for the selective immobilisation of recombinant capture antibody fragments on ELISA plates. *J. Immunol. Methods 218*, 73–83.

(2) MacBeath, G., and Schreiber, S. L. (2000) Printing proteins as microarrays for high-throughput function determination. *Science 289*, 1760–1763.

(3) Wu, G., Datar, R. H., Hansen, K. M., Thundat, T., Cote, R. J., and Majumdar, A. (2001) Bioassay of prostate-specific antigen (PSA) using microcantilevers. *Nat. Biotechnol. 19*, 856–860.

(4) Camarero, J. A. (2008) Recent developments in the site-specific immobilization of proteins onto solid supports. *Biopolymers 90*, 450–458.

(5) Rusmini, F., Zhong, Z., and Feijen, J. (2007) Protein immobilization strategies for protein biochips. *Biomacromolecules 8*, 1775–1789.

(6) Zhu, H., and Snyder, M. (2003) Protein chip technology. *Curr. Opin. Chem. Biol. 7*, 55–63.

(7) Niemeyer, C. M., Boldt, L., Ceyhan, B., and Blohm, D. (1999) DNA-Directed immobilization: efficient, reversible, and site-selective surface binding of proteins by means of covalent DNA-streptavidin conjugates. *Anal. Biochem. 268*, 54–63.

(8) Wacker, R., and Niemeyer, C. M. (2004) DDI-μFIA - A readily configurable microarray-fluorescence immunoassay based on DNA-directed immobilization of proteins. *ChemBioChem 5*, 453–459.

(9) Wacker, R., Schroder, H., and Niemeyer, C. M. (2004) Performance of antibody microarrays fabricated by either DNA-directed immobilization, direct spotting, or streptavidin-biotin attachment: a comparative study. *Anal. Biochem. 330*, 281–287.

(10) Erben, C. M., Goodman, R. P., and Turberfield, A. J. (2006) Single-molecule protein encapsulation in a rigid DNA cage. *Angew. Chem., Int. Ed. 45*, 7414–7417.

(11) Jung, G. Y., and Stephanopoulos, G. (2004) A functional protein chip for pathway optimization and in vitro metabolic engineering. *Science 304*, 428–431.

(12) Niemeyer, C. M., Koehler, J., and Wuerdemann, C. (2002) DNA-directed assembly of bienzymic complexes from in vivo biotinylated NAD(P)H:FMN oxidoreductase and luciferase. *ChemBioChem 3*, 242–245.

(13) Kukolka, F., and Niemeyer, C. M. (2004) Synthesis of fluorescent oligonucleotide-EYFP conjugate: towards supramolecular construction of semisynthetic biomolecular antennae. *Org. Biomol. Chem. 2*, 2203–2206.

(14) Niemeyer, C. M., Sano, T., Smith, C. L., and Cantor, C. R. (1994) Oligonucleotide-directed self-assembly of proteins: semi-synthetic DNA-streptavidin hybrid molecules as connectors for the generation of macroscopic arrays and the construction of supramolecular bioconjugates. *Nucleic Acids Res. 22*, 5530–5539.

(15) Kwon, Y., Coleman, M. A., and Camarero, J. A. (2006) Selective immobilization of proteins onto solid supports through split-intein-mediated protein trans-splicing. *Angew. Chem., Int. Ed. 45*, 1726–1729.

(16) Lovrinovic, M., Seidel, R., Wacker, R., Schroeder, H., Seitz, O., Engelhard, M., Goody, R. S., and Niemeyer, C. M. (2003) Synthesis of protein-nucleic acid conjugates by expressed protein ligation. *Chem. Commun. 7*, 822–823.

(17) Jongsma, M. A., and Litjens, R. H. (2006) Self-assembling protein arrays on DNA chips by auto-labeling fusion proteins with a single DNA address. *Proteomics 6*, 2650–2655.

(18) Duckworth, B. P., Chen, Y., Wollack, J. W., Sham, Y., Mueller, J. D., Taton, T. A., and Distefano, M. D. (2007) A universal method for the preparation of covalent protein-DNA conjugates for use in creating protein nanostructures. *Angew. Chem., Int. Ed. 46*, 8819–8822.

(19) Zhang, K., Diehl, M. R., and Tirrell, D. A. (2005) Artificial polypeptide scaffold for protein immobilization. *J. Am. Chem. Soc. 127*, 10136–10137.

(20) Diehl, M. R., Zhang, K., Lee, H. J., and Tirrell, D. A. (2006) Engineering cooperativity in biomotor-protein assemblies. *Science 311*, 1468–1471.

(21) Moll, J. R., Ruvinov, S. B., Pastan, I., and Vinson, C. (2001) Designed heterodimerizing leucine zippers with a range of pIs and stabilities up to 10^{-15} M. *Protein Sci. 10*, 649–655.

BC8003606

Supporting Information for

Design of DNA-Conjugated Polypeptide-based Capture Probes for the Anchoring of Proteins to DNA Matrices

Ryan M. Schweller, Pamela E. Constantinou, Nicholas W. Frankel, Priyanka Narayan and Michael R. Diehl*

Department of Chemistry, and Department of Bioengineering, Rice University, 6100 Main Street, MS 142 Houston, TX 77005.

Supporting Information

List of Contents

Detailed Materials and Methods
Table S1. List of Nucleotide Sequences Used for Conjugation and Self-Assembly
Table S2. List of Amino Acid Sequences for Artificial Proteins and Leucine Zipper Fusions
Figure S1. MALDI-TOF Spectrum of Artificial Proteins
Figure S2. Chromatograph and SDS-PAGE Gel of Artificial Protein-DNA Conjugates
Figure S3. Full Non-Denaturing PAGE Gel for Multi-Protein Assembly on a DNA Scaffold
Figure S4. 8 Hour Time Point Array and Corresponding Profile Plot

MATERIALS AND METHODS

General. All reagents were purchased from Sigma-Aldrich unless otherwise noted. All oligonucleotides were purchased from IDT DNA. The Alexa647-anti-green fluorescent protein (GFP) was purchased from Molecular Probes. Anti-GST antibodies were purchased from GE Healthcare and labeled in house using a Cy3 mono-reactive dye pack (GE Healthcare) and the resulting dye to antibody ratio (6 to 1) was determined according to the manufacturer's protocols.

All cloning procedures were carried out in the *E. coli* strain XL1-Blue (Stratagene). Expression was performed using BL21 (DE3) strains (Novagen). The sequences of the plasmids produced from each cloning step were verified using restriction mapping and DNA sequence analysis.

Primers sequences used to construct synthetic genes were designed using a web-based software tool (DNAWorks) (*1*). DNA sequences used for conjugation, surface-functionalization, and to form molecular scaffolds based on single DNA duplicies were designed using a program called SEQUIN (*2*). This software was used to minimize sequence repeats in the different strands used for conjugation and spotting, as well as those incorporated into the DNA scaffolds. All oligonucleotides were individually purified using denaturing PAGE protocols.

Plasmid Construction. Genes encoding for each domain of the artificial proteins including the basic portion of the zipper complex (Z_R) and the elastic 'mid-block domain' or ELS fragment (VPGVG VPG**S**G VPGVG VPG**S**G VPGVG) were constructed from synthetic oligonucleotides through PCR. During this process a C-terminal cysteine and a stop codon was introduced into the gene. The resulting fragments were directionally ligated into a pQE60 vector (Qiagen). This gene was then polymerized stepwise into larger Z_R-$(ELS)_2$-C, Z_R-$(ELS)_4$-C and Z_R-$(ELS)_6$-C constructs using the recursive directional ligation (RDL) procedure described in reference (*3*) with slight modifications. At each intermediate cloning step, two gene fragments were isolated from each vector by digestion with *Nco*I and *Bgl*I or *PflM*I and *Hind*III restriction endonucleases. These two fragments were then simultaneously inserted directionally into the *Nco*I and *Hind*III sites of a new pQE60 vector.

The recombinant target proteins containing Z_E fusions GST-Z_E, GFP-Z_E, calmodulin-Z_E (CAM-Z_E), and PSE-4-Z_E were all prepared using standard cloning procedures. Each of these genes contained a C-terminal Z_E and 6xHistidine (6xHis) for purification.

Protein Expression and Purification. To avoid proteolytic degradation of the Z_R fragment of the artificial proteins, and to facilitate Ni^{2+}-NTA purification, Z_R-$(ELS)_6$-C was co-expressed with a Z_E-6xHis gene that was created in pQE60 and then inserted into the *Nhe*I sites of a pREP4 vector (Qiagen). Both vectors contained the inducible, bacteriophage T5 promoter of the pQE plasmid. For expression, cells were grown in terrific broth (TB; 24 g of casein hydrolysate, 12 g of yeast extract, 4 mL glycerol, 17 mM KH_2PO_4, 72 mM K_2HPO_4), and antibiotics (50 mg/L ampicillin and 35 mg/L kanamycin). The cells were cultured at 37 ˚C until an OD_{600} of 1 was reached. Afterwards, expression was induced for 5 hours by adding 1 mM IPTG. Cells were then pelleted (5,000 RPM and 4 ˚C) an resuspended in lysis buffer (8 M urea, 10 mM Tris-HCl, 100 mM NaH_2PO_4, pH 8.0) and allowed to lyse overnight at 4 ˚C with vigorous stirring. The cell lysate was clarified by centrifugation and the supernatant was applied to a column containing Ni^{2+}-NTA resin. After washing with lysis buffer, the artificial protein was eluted using a buffer containing 6 M guanidine-HCl, 100 mM NaH_2PO_4, 10 mM Tris-HCl, pH 8.0. This buffer disassociates the Z_E/Z_R complex, allowing the Z_R-$(ELS)_6$-C to be eluted while the majority of the Z_E-6xHis proteins remain on the column. To remove excess Z_E-6xHis, the eluent was run through a second Ni^{2+}-NTA column. The flow through of this column was dialyzed with frequent water exchanges for 3 days and lyophilized. The protein purity was verified using SDS-PAGE and matrix-assisted laser desorption/ionization time-of-flight (MALDI-TOF) mass spectroscopy. The MALDI-TOF of the polymers gave peaks at 18652 m/z and 9323 m/z corresponding to the M^+ and M^{+2} polymer species, respectively. The Z_E-6xHis polypeptide was not present at detectable levels using either SDS-PAGE or MALDI-TOF analyses.

Cells expressing the target proteins were cultured similarly to those used for artificial protein production. However, expression was induced overnight at 23 ˚C. Purification of the

target proteins were carried out using standard native lysis and Ni^{2+}-NTA purification protocols with the exception of the PSE-4-Z_E. Cells containing these proteins lysed using an osmotic shock procedure that allows the outer membrane of cells to be broken using an osmotic shock buffer (30% sucrose, 1 mM EDTA, 30 mM Tris, pH 8.0). Protein expression and purification was verified using SDS-PAGE analysis while protein concentrations were determined using the Bradford method. For some experiments, clarified lysates were saved, aliquoted, and stored at -80 ˚C for experiments with unpurified proteins.

Artificial Protein-DNA conjugation. Artificial proteins were labeled with DNA as described in reference (*4*) with slight modifications. Briefly, concentrated stock solutions of Z_R-$(ELS)_6$-C (10 mg/mL) were prepared by dissolving the lyophilized polymers in 8 M Urea, 100 mM NaH_2PO_4, 10 mM Tris, pH 7.2. Disulfide bonds between polymers were then reduced by adding 400 mM tris(2-carboxyethyl)phosphine (TCEP) and incubated at 37 ˚C for 1.5 hours. Simultaneously, amine-labeled oligonucleotides, 20 bp in length, were reacted for one hour at 37 ˚C with the heterobifunctional crosslinker, sulfosuccinimidyl 4-[*N*-maleimidomethyl]cyclohexane-1-carboxylate (sulfo-SMCC). Afterwards, the reduced artificial protein and the DNA solutions were passed through two separate NAP-5 desalting columns, combined, and incubated for 2 hours at room temperatures and then overnight at 4 ˚C. The following day, the Z_R-$(ELS)_6$-C-ssDNA conjugates were isolated using a HiTrapQ ion-exchange column and fast protein liquid chromatography (FPLC). The peak fractions containing the conjugate were pooled and dialyzed with frequent water exchanges for 3 days and lyophilized. The polymers were then redissolved in Tris-EDTA (TE) buffer (pH 7.4) at a concentration of approximately 35 μM. The actual conjugate stock concentrations were determined from the OD_{260} using an extinction coefficient

from the appended ssDNA's extinction coefficient (ε_{260} = 185,000 M^{-1} cm^{-1}). Conjugate stock solutions were aliquoted and stored at -20 ˚C until needed.

DNA-Templated Protein Microarray Fabrication. DNA microarrays were fabricated by printing 5'-amine modified oligonucleotides on silyated (amine-aldehyde) functionalized slides (CEL Associates Inc). Oligonucleotide stocks were diluted appropriately with spotting buffer (40% glycerol in PBS, pH 6.6). For the single protein arrays, the arrays were printed in 90, 50, and 10 μM concentrations and a control strand was printed at 90 μM. The multi-protein arrays were all printed at 50 μM. A custom built microarrayer outfitted with SMP3 pins (Telechem Int.) was used for all printing. After printing, the slides were placed in a humid chamber for 45 minutes, and then allowed to dry outside the chamber for 10 minutes. The remaining free aldehyde groups were quenched in a solution of 25% ethanol and 0.25% $NaBH_4$ in PBS for 5 minutes. The slides were then thoroughly rinsed with milli-Q water (Millipore) and blocked using pre-hybridization buffer (20 mM Tris-HCl pH 7.4, 150 mM NaCl, 5 mM EDTA, 1% Tween 20, 0.1 mg/mL denatured herring sperm DNA, 0.1 mg/mL BSA, 3% dry milk) with gentle agitation for 2 hours. The arrays were then washed 3 times for 10 minutes each in wash buffer (20 mM Tris-HCl pH 7.4, 150 mM NaCl, 5 mM EDTA, 0.01% Tween 20), thoroughly rinsed with milli-Q water and dried under a nitrogen stream.

Artificial protein-DNA conjugates were used to direct the assembly of target proteins onto the DNA-spotted microarrays by first pre-incubating the target Z_E-fusion proteins individually with the artificial protein conjugates. A three-fold molar excess of target protein was typically maintained during these incubations. A reaction chamber was prepared by affixing a Gene Frame (AB Gene) to the microarrays. Mixtures of artificial proteins and target proteins

were brought to a final volume of 100 μL with hybridization buffer (20 mM Tris-HCl pH 7.4, 150 mM NaCl, 5 mM EDTA, 0.01% Tween 20, 0.1 mg/mL denatured herring sperm DNA, 0.5% dry milk) and perfused into the reaction chamber. For multi-protein array fabrication, two solutions of polymer-target protein complexes were prepared separately, combined into one solution, and introduced to the reaction chamber. The slides were left at room temperature to incubate overnight. Afterwards, the Gene Frames were removed and the slides were washed three times with wash buffer, rinsed with milli-Q water, and dried under nitrogen stream. New Gene Frames were applied to each array and a solution containing Alexa647-anti-GFP antibodies or both Alexa647-anti-GFP and Cy3-anti-GST antibodies were added at concentrations of 1 μg/mL for two hours. The slides were then washed 3 times for 10 minutes in wash buffer, rinsed briefly with milli-Q water and dried. The slides were immediately imaged on a GenePix 4000B microarray scanner (Molecular Devices) using a gain of 450.

The possibility of zipper exchange was also examined through a time-series study. Here, we prepared two leucine-zipper complexes: (1) a GFP-Z_E protein captured using a DNA-polypeptide conjugate and (2) an unconjugated Z_R-$(ELS)_6$-C polypeptide complexed to a GST-Z_E protein. The two captured proteins were mixed and incubated for periods of 1, 2, 4, or 8 hours before being applied to a printed microarray. Arrays were washed probed and scanned as in the two-channel experiments described above.

Surface-Immobilized β-Lactamase Assays. All reagents used to prepare substrates for these assays were dissolved in TE buffer (pH 7.4). 96-well plates were incubated with biotin-BSA (1 mg/mL) for 10 minutes. The plates were then blocked with casein (1 mg/mL) followed by BSA (1 mg/mL) for 1 minute each, and washed twice with TE buffer. Next, streptavidin (0.5 mg/mL)

was added to each well and incubated for 10 minutes. Afterwards, the streptavidin solutions were aspirated off and the plates were rinsed briefly with the casein solution and then twice with TE buffer. Biotin functionalized DNA was added to the appropriate wells to a final volume of 50 μL and incubated for 30 minutes. Certain wells were designated for controls that either omitted the DNA deposition or contained a non-complementary DNA strand. Excess DNA that did not bind the surface was removed by washing with casein and BSA as before. To immobilize enzymes, PSE-4-Z_E was pre-incubated in 3 fold excess of the Z_R-$(ELS)_6$-C-ssDNA conjugate for 30 minutes. The PSE-4-Z_E and conjugate solution were applied to the appropriate wells. The plate was left to incubate for 2 hours and then protein solutions were aspirated from the wells. After washing 4 times with TE buffer, each well was brought to a final volume of 100 μL by adding TE buffer. Subsequently, nitrocefin was added to each well, bringing the wells to a final volume of 200 μL and a final substrate concentration to 150 μM. The plates were scanned using a Tecan Infinite 200 microplate reader. Absorbance readings at 485 nm were monitored every 50 seconds for 3 hours at 25 ˚C. The steady-state reaction rates of the immobilized β-Lactamase enzymes were determined via linear regression analysis.

Synthesis and Characterization of Multi-Protein Assemblies. The DNA scaffold consisted of a single duplex of DNA (34 bases; 10 nm in length) flanked by unique single-strand 'overhangs' comprised of 20 bases on either end. To create scaffolds, strands were mixed stoichiometrically as estimated by A_{260}, and annealed from 95 ˚C to RT, over 1.5 hrs in TAE/Mg^{2+} buffer (40 mM Tris, 40 mM Acetic Acid, 2 mM EDTA, 12.5 mM Mg^{2+} Acetate, pH 8) for a final concentration of 1.8 μM. Target protein (either CaM-Z_E or GFP-Z_E) and its respective Z_R-$(ELS)_6$-C-ssDNA conjugate were mixed in a 1:1 ratio and incubated at 4 ˚C for at least 1 hr. DNA scaffold was

added in a 1:2 or 1:1 ratio with the protein mixture (depending on whether it was the single or two protein system) and incubated at RT for 1.5 hrs, then 4 ˚C for 30 min. A 7% non-denaturing PAGE gel was run at 200 V at 4 ˚C (SE 600 Ruby, GE Healthcare) in TAE/Mg^{2+} buffer. The DNA/protein complexes were visualized by staining with Stains-All (Sigma).

(1) Hoover, D. M., and Lubkowski, J. (2002) DNAWorks: an automated method for designing oligonucleotides for PCR-based gene synthesis. *Nucleic Acids Res. 30*, e43.

(2) Seeman, N. C. (1990) De novo design of sequences for nucleic acid structural engineering. *J. Biomol. Struct. Dyn. 8*, 573-581.

(3) Meyer, D. E., and Chilkoti, A. (2002) Genetically encoded synthesis of protein-based polymers with precisely specified molecular weight and sequence by recursive directional ligation: examples from the elastin-like polypeptide system. *Biomacromolecules 3*, 357-367.

(4) Kukolka, F., and Niemeyer, C. M. (2004) Synthesis of fluorescent oligonucleotide--EYFP conjugate: towards supramolecular construction of semisynthetic biomolecular antennae. *Org. Biomol. Chem. 2*, 2203-2206.

Table S1. List of nucleotide sequences used for conjugation and self-assembly. All sequences are listed in the 5' – 3' direction. AmMC6 indicates a 5' amino modifier on carbon 6 and 5Biosg represents a 5' biotin.

Sequence Name	**Nucleic Acid Sequence**
Conjugate1	/5AmMC6/CCAATGCGGTCTATCCAGCC
Conjugate2	/5AmMC6/CTACGGCAACTGTGGTCATC
scConjugate1	/5AmMC6/TTTTTTTTTTTTTTTTTTTTGGCTGGATAGACCGCATTCG
scConjugate2	/5AmMC6/TTTTTTTTTTTTTTTTTTTTGATGACCACAGTTGCCGTAG
sControl	/5AmMC6/TTTTTTTTTTTTTTTTTTTTCCGAGCAGGCGTGAGTCGTC
kcConjugate1	/5Biosg/TTTTTTTTTTTTTTTTTTTTGGCTGGATAGACCGCATTCG
kControl	/5Biosg/TTTTTTTTTTTTTTTTTTTTGATGACCACAGTTGCCGTAG
Scaffold Overhang1	CGTAGCAGGCACATCGTTGGCTGGATAGACCGCATTCG
Scaffold Overhang2	CGTAGCAGGCACATCGTTGATGACCACAGTTGCCGTAG
Scaffold1	GTCACGGACTGAGCGT
Scaffold2	CGATGTGCCT
Scaffold3	GCTACGACGCTC
Scaffold4	AGTCCGTGACTTGGCTGGATAGACCGCATTCG

Table S2. Amino acid sequences of the artificial polypeptide components.

Sequence Name	**Amino Acid Sequence**
Z_E	LEIEAAALEQENTALETEVAELEQEVQRLENIVSQYRTRYGPL
Z_R	LEIRAAALRRRNTALRTRVAELRQRVQRLRNEVSQYETRYGPL
ELS	VPGVGVPGSGVPGVGVPGSGVPGVGV
Z_R-$(ELS)_6$-C	MVGS-Z_R-GSNHGVG-$(ELS)_6$-VPGWLRSC

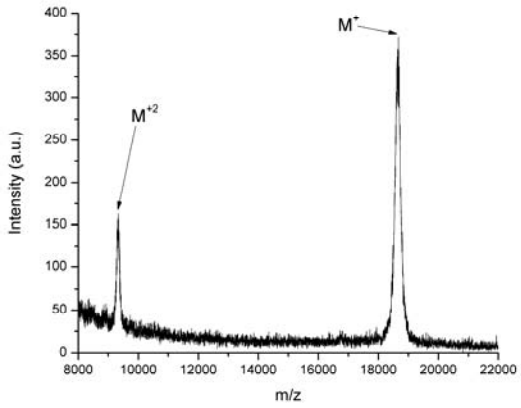

Figure S1. MALDI-TOF spectrum for the Z_R-$(ELS)_6$-C protein. The spectrum shows peaks at 9323 m/z and 18652 m/z, corresponding to the M^{+2} and M^{+} peaks, respectively. The calculated theoretical mass of the full-length polymers is 18793.5 Da, and 18662.3 Da if the N-terminal methionine is cleaved.

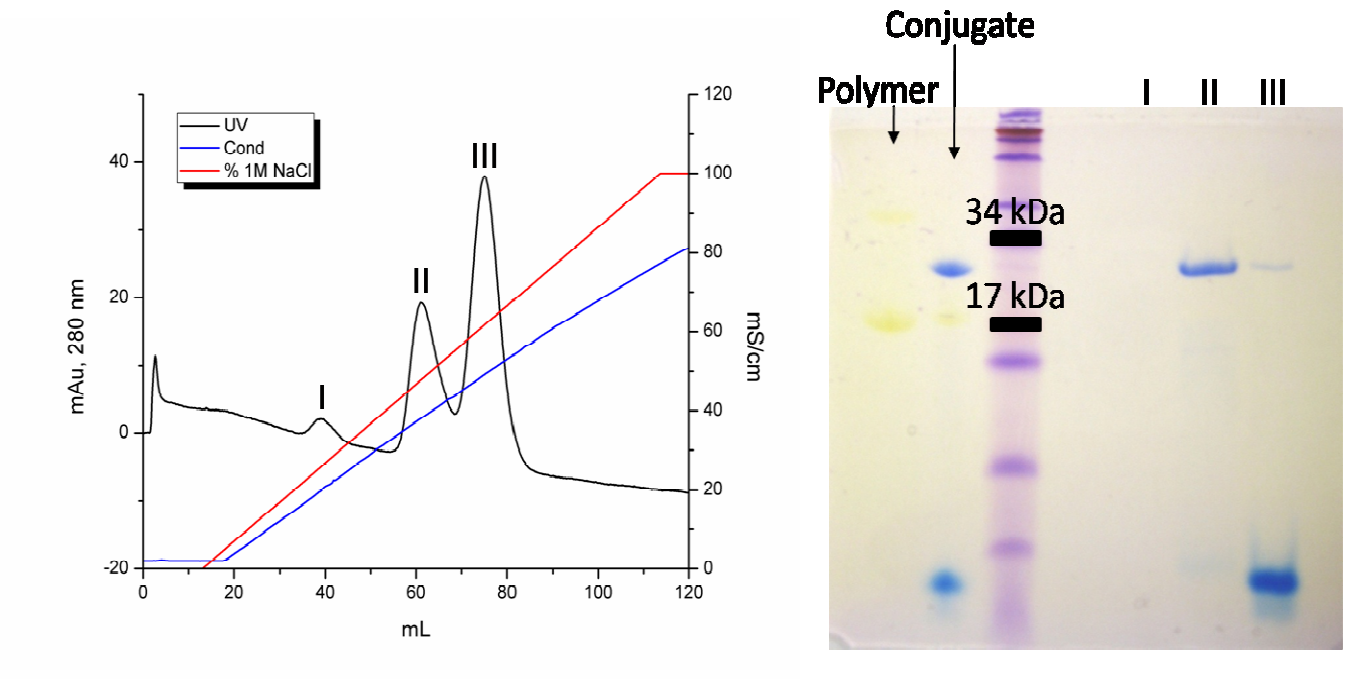

Figure S2. FPLC chromatogram and SDS-PAGE gel for conjugate synthesis and purification, indicating the absorption measured at 280 nm, gradient implemented, and measured conductivity. The chromatogram shows the characteristic 3 peaks from the crosslinking reaction: I. Unconjugated polymer; II. Conjugate; III. Unconjugated DNA. The corresponding gel shows purified polymer, the crosslinking reaction products (Conjugate), and a sample of each of the 3 peaks. The Stains-All stains DNA blue and protein yellow. The shift in the DNA band shows the presence of the conjugate in peak II.

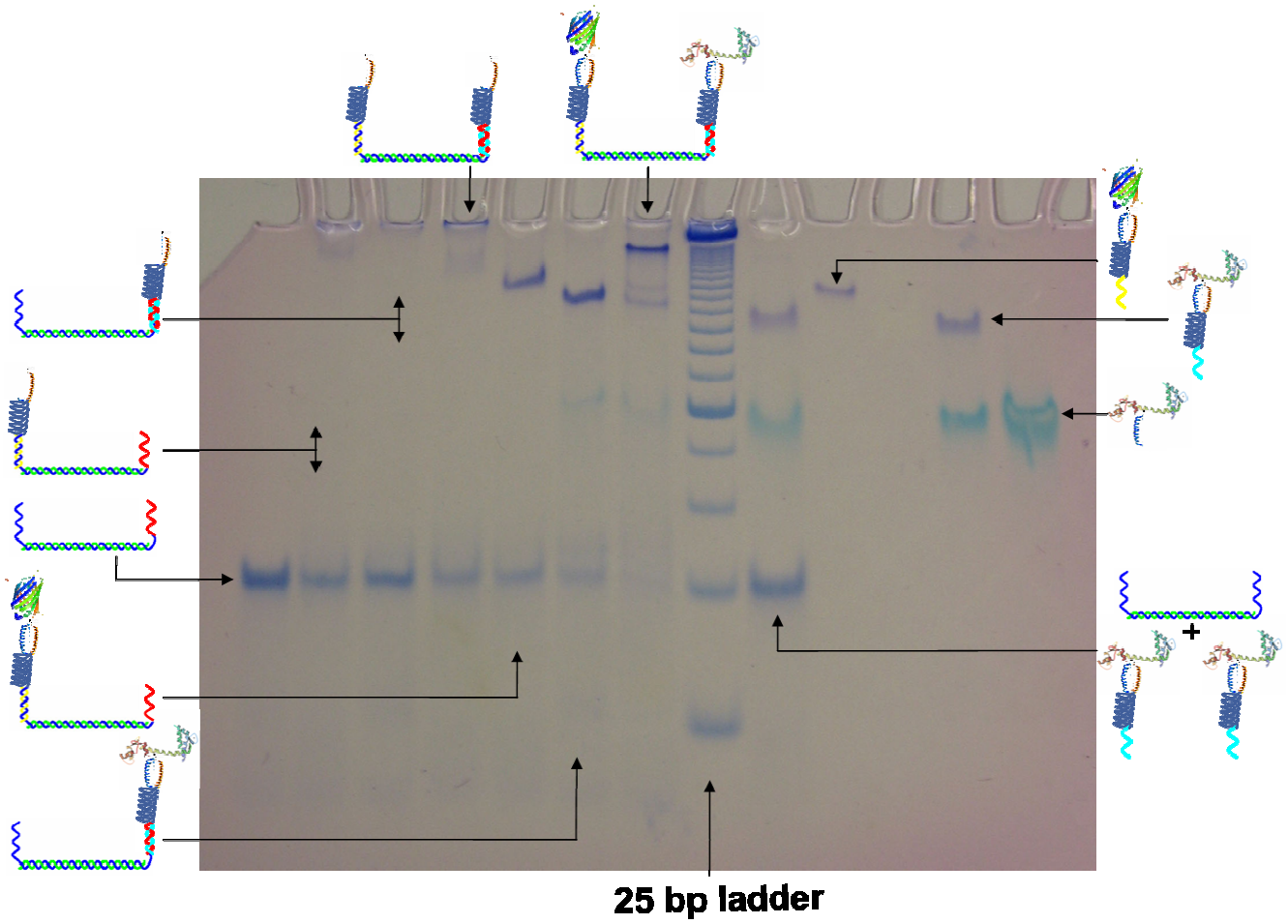

Figure S3. A non-denaturing PAGE gel displaying each of the components of the assembly individually as well as intermediate structures. The corresponding components of each lane are depicted at the periphery of the gel. From this analysis, we are able to adjust the volumes of individual protein stocks to compensate for errors in protein concentration measurements, in order to drive assembly formation more quantitatively.

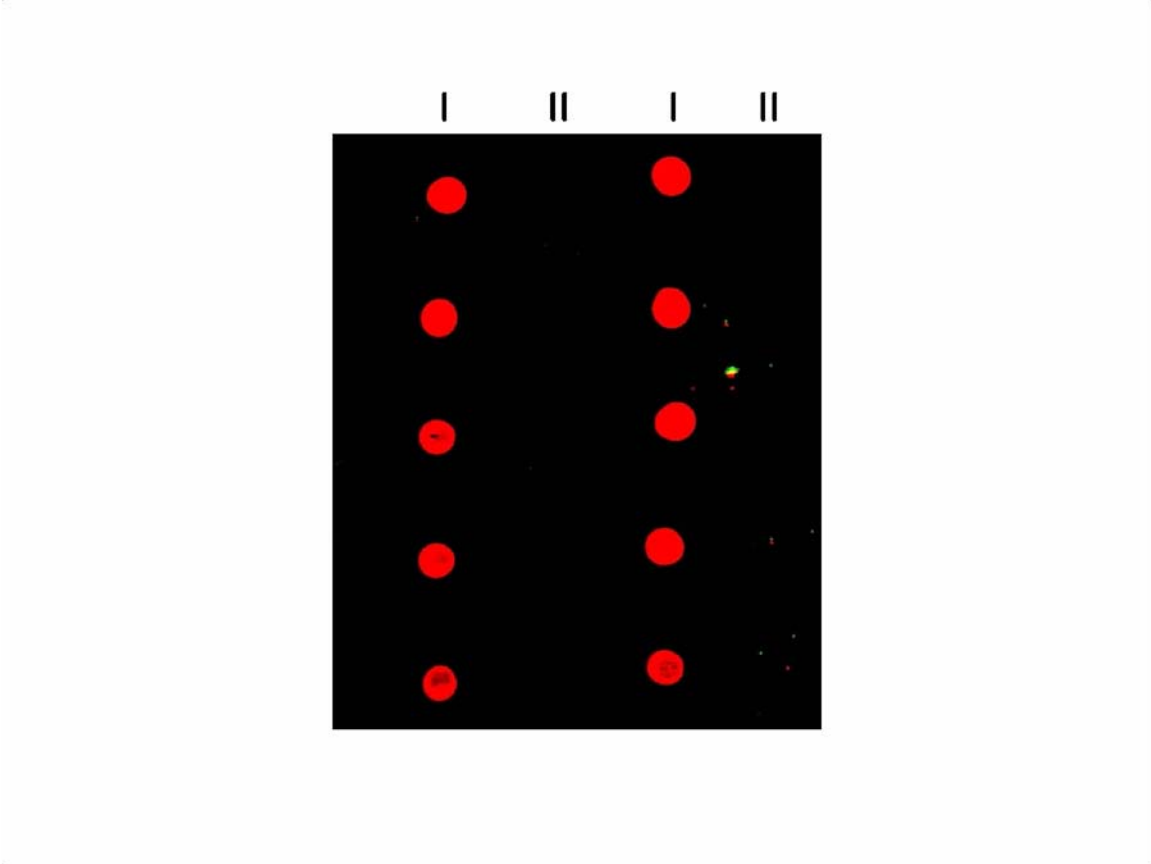

Figure S4. Microarray experiment showing the leucine zippers do not exchange between target proteins. Two protein complexes: (1) a GFP-Z_E protein captured using a DNA-polypeptide conjugate, and (2) a GST-Z_E complexed with an unconjugated Z_R-$(ELS)_6$-C polypeptide were mixed together for periods of 1-8 hours to test exchange. Afterwards, this solution was incubated for 16 hours over DNA-spotted array. Without exchange, the GST-Z_E protein should not immobilize on our arrays, and any exchange should result in the appearance of a GST-positive signal. All of the arrays show selective capture of the GFP-Z_E. We did not observe evidence of exchange in any experiments. The 8 hour time point is shown in the figure. The positive control strand was printed in lane I (the GFP positive lane), while a non-complementary strand is was printed in lane II : The GST signal (green) was lower than background in all spots in the array.

Fluorescently Labeled Risedronate and Related Analogues: "Magic Linker" Synthesis

Boris A. Kashemirov,[†] Joy Lynn F. Bala,[†] Xiaolan Chen,[†] F. H. Ebetino,[‡] Zhidao Xia,[§] R. Graham G. Russell,[§] Fraser P. Coxon,[||] Anke J. Roelofs,[||] Michael J. Rogers,[||] and Charles E. McKenna*[,†]

Department of Chemistry, University of Southern California, Los Angeles, California 90089-0744, Procter & Gamble Pharmaceuticals, Mason, Ohio 45040, University of Oxford, Nuffield Department of Orthopedic Surgery, Nuffield Orthopedic Center, Headington, Oxford, OX3 7LD United Kingdom, and Bone & Musculoskeletal Research Programme, Institute of Medical Sciences, University of Aberdeen, Aberdeen, AB25 2ZD United Kingdom. Received August 29, 2008; Revised Manuscript Received October 31, 2008

We report synthesis of the first fluorescently labeled conjugates of risedronate (**1**), using an epoxide linker strategy enabling conjugation of **1** via its pyridyl nitrogen with the label (carboxyfluorescein). Unlike prior approaches to create fluorescent bisphosphonate probes, the new linking chemistry did not abolish the ability to inhibit protein prenylation in vitro, while significantly retaining hydroxyapatite affinity. The utility of a fluorescent **1** conjugate in visualizing osteoclast resorption in vitro was demonstrated.

Nitrogen-containing bisphosphonates (N-BPs) are therapeutic agents for the treatment of diseases associated with increased bone resorption, such as osteoporosis and Paget's disease (*1, 2*). N-BPs inhibit farnesyl diphosphate synthase (FPPS), preventing the prenylation of small GTPase proteins that are crucial for the function and survival of bone-resorbing osteoclasts (*3*−*6*). Phosphonocarboxylate (PC) analogues of BPs are also able to inhibit bone resorption, but inhibit Rab geranylgeranyl transferase (RGGT), thereby selectively preventing the prenylation of Rab proteins (*7*).

Some N-BPs and PC analogues also demonstrate antitumor effects in vitro and in vivo (*1, 2*). However, it is unknown whether the antitumor effects of these drugs result from direct effects on tumor cells or derive chiefly from inhibition of bone resorption (*1, 2, 8*). Therefore, specific imaging probes to elucidate the skeletal distribution and cellular uptake of these drugs in bone and other tissues are highly desirable.

Fluorescent analogues of bisphosphonates are of increasing interest as biological probes exploiting the high bone affinity of these compounds. Recently, the primary aminoalkyl N-BP alendronate was coupled to Alexa Fluor 488 via the drug's γ-amino functionality; however, the conjugated labeled drug was obtained in only 7% purity (*9*). In a separate study, ε-amino N-BP pamidronate conjugated to IRDye78 or IRDye800CW was observed to bind to hydroxyapatite (HA) (*10, 11*). In all these cases, the imaging dyes were attached via an amide linkage at the terminal amino group of the drug (*9*−*12*), resulting in a large decrease in nitrogen basicity expected to lower greatly the inhibitory potency of the resulting conjugate. Also, this approach is not applicable to heterocyclic N-BPs such as risedronate (RIS, **1**), which lack a primary amine susceptible to facile acylation by activated esters of fluorescent labels. Thus, no successes in fluorescent labeling of any member of this class of drugs have yet been reported (*9*−*13*).

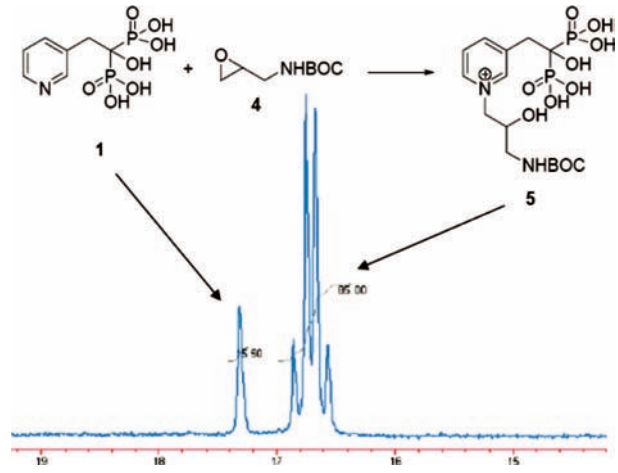

Figure 1. ^{31}P NMR spectrum of reaction mixture of **1** and **4** after 18 h at 40 °C.

We began our work with the concept of designing a universal linker, which, once attached to the drug, would permit conjugation with any fluorophore activated ester while, ideally, not adversely influencing bone affinity and retaining some ability to inhibit protein prenylation. On this basis, the phosphonate/carboxylate moieties (or the α-hydroxyl group) of the drug were considered to be unsuitable sites for attachment of a linker moiety. If a linker group could be connected via the pyridine nitrogen, a positively charged quaternary nitrogen atom would be generated, perhaps simulating a putative carbocation-like transition state analogue in the active site (*6*), thereby offering the possibility that the fluorescent conjugate could retain activity. Finally, this linking chemistry would need to be compatible with an incorporated primary amine group to allow subsequent conjugation of the drug−linker complex to an imaging molecule, and should address the low solubility of the drug in nonaqueous media.

In search of such a "magic" linker, we investigated the reaction of heterocyclic N-BPs with the epoxide **4** to generate N-alkylated analogues of the parent drugs **1**−**3** (Scheme 1). We find that epoxide **4** couples to the pyridine nitrogen of **1**−**3** under

* To whom correspondence should be addressed. Phone: +1 213 740 7007. Fax: + 1 213 740 0930. E-mail: mckenna@usc.edu.
[†] University of Southern California.
[‡] Procter & Gamble Pharmaceuticals.
[§] University of Oxford.
[||] University of Aberdeen.

10.1021/bc800369c CCC: $40.75 © 2008 American Chemical Society
Published on Web 11/25/2008

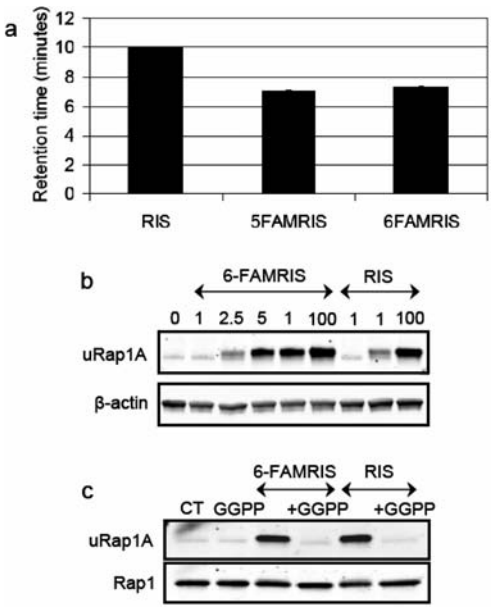

Figure 2. (a) Comparison of RIS (**1**) (**12**) and 6-FAMRIS (**13**) on hydroxyapatite column. (b, c) Western blot assays for unprenylated Rap1A (uRap1A). J774.2 macrophages were treated for 24 h with (b) 0−100 μM **13** or **1**; or (c) vehicle, 20 μM **13**, or 20 μM **1** in the presence or absence of 100 μM GGPP. Detection of β-actin (b) or total Rap1 (c) served as loading control.

Scheme 1[a]

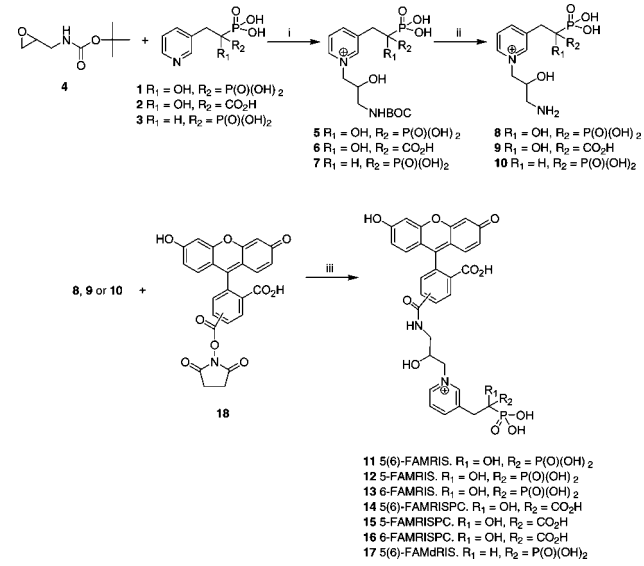

[a] Reagents: (i) ~5% MeOH/H_2O, 40−50 °C. (ii) 1:1 TFA/H_2O, room temperature; (iii) $NaHCO_3$/DMF, pH 8.3, room temperature, in darkness.

mild (pH nearly neutral, 40−50 °C) aqueous conditions, with high yields and regioselectivity (*14*). This linker affords the key functionalities referred to above: (1) a primary amine (after suitable deprotection) for facile conjugation to activated esters of fluorescent or other labels; (2) a permanent positive charge on the pyridinium nitrogen; and (3) a hydroxyl group (from the epoxide ring-opening) to balance the hydrophobic alkyl chain.

At 40 °C, nearly quantitative yields are achieved, affording intermediates **5**−**7** with less than 1% O-alkylation according to ^{31}P NMR (Figure 1). Aminohydroxypropane esters of 1-hydroxyethylidene-1,1-bisphosphonic acids were previously synthesized in aqueous conditions near neutral pH at 60−70 °C (*15*). Since we aimed to avoid forming ester linkages between the phosphonate group and the linker, the regioselectivity of our reaction was a welcome discovery. This linking strategy may be applicable to N-alkylation of other nitrogen-containing heterocycles (*16*).

Treatment of the N-*t*BOC-protected linker−drug intermediates **5**−**7** with TFA yielded the corresponding free amino forms **8**−**10**, which were then readily coupled to 5(6)-carboxyfluorescein via its succinimidyl ester (5(6)-FAM, SE, **18**). Individual isomers (5- and 6-FAM) of the labeled products may be isolated by semipreparative HPLC, although compounds **12**, **15**, and **16** were also synthesized directly from their respective isomerically pure FAM, SE starting materials. All labeled products were characterized by high-resolution mass, ^{1}H and ^{31}P NMR, UV absorption, and fluorescence emission spectra (see Supporting Information). FAM-labeled compound **11** showed no decomposition by analytical TLC after 1 week at room temperature in phosphate buffer (pH 7.2), demonstrating the stability of the labeled product.

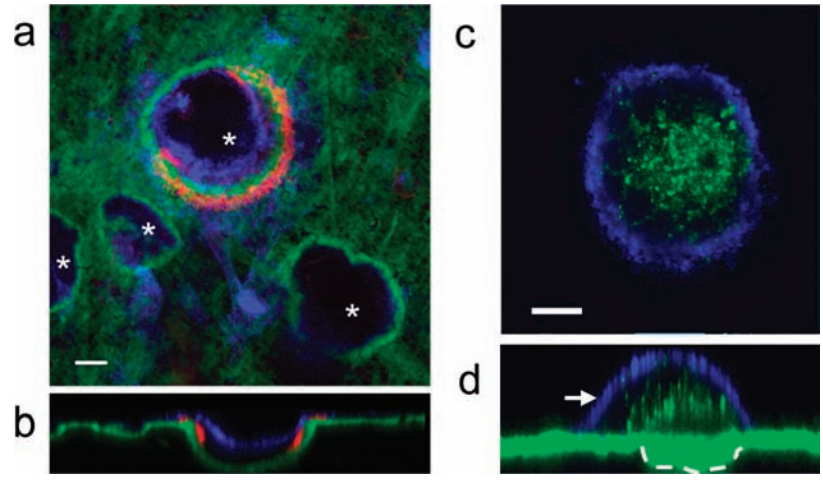

Figure 3. Binding and "recycling" of 5(6)-FAMRIS **11** to the surface of dentine (a, b) and uptake of **11** by rabbit osteoclast in vitro (c, d); bar = 10 μM. Rabbit osteoclasts were seeded onto dentine discs that had been precoated with **11** (green); osteoclasts were immunostained for VNR (blue), and actin rings of osteoclasts were visualized using TRITC-phalloidin (red; a, b only). (a) 1 μm *xy* image at the surface of the dentine; resorption pits identified by asterisks; (b) *zx* image of the same field-of-view. (c) 1 μm *xy* image 8 μm above the surface of the dentine and (d) *zx* image of the same osteoclast. *Z* position of (c) is denoted by arrow in (d). Dashed line in (d) shows the outline of the resorption pit. Note that detector gain in (c, d) was optimized to detect **11** intracellularly resulting in saturated signal from **11** at the dentine surface.

To investigate whether structural differences between **1** and labeled **12** and **13** could interfere with their role as imaging probes, a hydroxyapatite column was utilized as a model for their binding affinity to bone (*17*). The labeled compounds showed only a moderate decrease in retention time ($R_t = 7$ min) compared to **1** ($R_t = 10$ min) (Figure 2a). Probe **13** also inhibits the prenylation of the small GTPase Rap1A (at similar concentrations to RIS) (Figure 2b), an effect that could be reversed by the addition of exogenous GGPP (the isoprenoid required for prenylation of Rap1A; Figure 2c), indicating that the compound retains this activity of the parent N-BP. Fluorescent alendronate (F-ALN), where the primary amino nitrogen was converted to a neutral amide by the dye attachment chemistry, was inactive in this assay (*18*).

11, intensely labeled the surface of dentine, demonstrating its high affinity for a physiological mineralized substrate. Furthermore, following the culture of rabbit osteoclasts for 18 h on dentine discs precoated with **11** prior to seeding of the cells, **11** also labeled the newly exposed surface of resorption pits beneath actively resorbing osteoclasts (Figure 3a,b), indicating that **11** binds to newly exposed mineral surfaces after being released from the dentine surface during resorption (*18*). Other fluorescent bone-labeling agents with low bone affinity, such as calcein and xylenol orange, do not exhibit this recycling to resorption pits (*18*). In these cultures, **11** could also be detected within intracellular vesicles in resorbing osteoclasts (Figure 3c,d), in accordance with our previous studies demonstrating endocytic uptake of F-ALN by both macrophages and resorbing osteoclasts (*9, 18*).

In summary, we report the first synthesis of fluorescently labeled conjugates of drugs **1**−**3**, using a novel linking strategy. Advantages of the approach described include the exceptionally mild reaction conditions used to attach the linker to the drug (aqueous solution, pH near neutral, ∼room temperature), high yields, and regioselectivity. This approach has provided, for the first time, a fluorescent conjugate of an N-BP that inhibits protein prenylation.

ACKNOWLEDGMENT

Funding and compounds **1**−**3** were provided by Procter & Gamble Pharmaceuticals. Mass spectra were obtained by Dr. Ron New at the University of California Riverside. C.E. McKenna has been a consultant for P & G Pharmaceuticals.

Supporting Information Available: Detailed experimental procedures and data. This material is available free of charge via the Internet at http://pubs.acs.org.

LITERATURE CITED

(1) Russell, R. G. G. (2007) Bisphosphonates: mode of action and pharmacology. *Pediatrics 119 Suppl 2*, S150–62.

(2) Roelofs, A. J., Thompson, K., Gordon, S., and Rogers, M. J. (2006) Molecular mechanisms of action of bisphosphonates: current status. *Clin. Cancer Res. 12*, 6222s–6230s.

(3) Ebetino, F. H., Roze, C. N., McKenna, C. E., Barnett, B. L., Dunford, J. E., Russell, R. G. G., Mieling, G. E., and Rogers, M. J. (2005) Molecular interactions of nitrogen-containing bisphosphonates within farnesyl diphosphate synthase. *J. Organomet. Chem. 690*, 2679–2687.

(4) Kavanagh, K. L., Guo, K., Dunford, J. E., Wu, X., Knapp, S., Ebetino, F. H., Rogers, M. J., Russell, R. G. G., and Oppermann, U. (2006) The molecular mechanism of nitrogen-containing bisphosphonates as antiosteoporosis drugs. *Proc. Natl. Acad. Sci. U.S.A. 103*, 7829–7834.

(5) Kotsikorou, E., and Oldfield, E. (2003) A quantitative structure-activity relationship and pharmacophore modeling investigation of aryl-X and heterocyclic bisphosphonates as bone resorption agents. *J. Med. Chem. 46*, 2932–2944.

(6) Martin, M. B., Arnold, W., Heath, H. T., III, Urbina, J. A., and Oldfield, E. (1999) Nitrogen-containing bisphosphonates as carbocation transition state analogs for isoprenoid biosynthesis. *Biochem. Biophys. Res. Commun. 263*, 754–758.

(7) Coxon, F. P., Helfrich, M. H., Larijani, B., Muzylak, M., Dunford, J. E., Marshall, D., McKinnon, A. D., Nesbitt, S. A., Horton, M. A., Seabra, M. C., Ebetino, F. H., and Rogers, M. J. (2001) Identification of a novel phosphonocarboxylate inhibitor of Rab geranylgeranyl transferase that specifically prevents Rab prenylation in osteoclasts and macrophages. *J. Biol. Chem. 276*, 48213–48222.

(8) Lueftner, D., Henschke, P., and Possinger, K. (2007) Clinical value of bisphosphonates in cancer therapy. *Anticancer Res. 27*, 1759–1768.

(9) Thompson, K., Rogers, M. J., Coxon, F. P., and Crockett, J. C. (2006) Cytosolic entry of bisphosphonate drugs requires acidification of vesicles after fluid-phase endocytosis. *Mol. Pharmacol. 69*, 1624–1632.

(10) Zaheer, A., Lenkinski, R. E., Mahmood, A., Jones, A. G., Cantley, L. C., and Frangioni, J. V. (2001) In vivo near-infrared fluorescence imaging of osteoblastic activity. *Nat. Biotechnol. 19*, 1148–1154.

(11) Bhushan, K. R., Tanaka, E., and Frangioni, J. V. (2007) Synthesis of conjugatable bisphosphonates for molecular imaging of large animals. *Angew. Chem., Int. Ed. 46*, 7969–7971.

(12) Hirabayashi, H., Sawamoto, T., Fujisaki, J., Tokunaga, Y., Kimura, S., and Hata, T. (2001) Relationship between physicochemical and osteotropic properties of bisphosphonic derivatives: rational design for Osteotropic Drug Delivery System (ODDS). *Pharm. Res. 18*, 646–651.

(13) Maalouf, M. A., Wiemer, A. J., Kuder, C. H., Hohl, R. J., and Wiemer, D. F. (2007) Synthesis of fluorescently tagged isoprenoid bisphosphonates that inhibit protein geranylgeranylation. *Bioorg. Med. Chem. 15*, 1959–1966.

(14) Kashemirov, B. A., Bala, J. L. F., Chen, X., Ebetino, F. H., Xia, Z., Russell, R. G. G., Coxon, F. P., Rogers, M. J., and McKenna, C. E. (2007) P-146, 17th International Conference on Phosphorus Chemistry, Xiamen, China.

(15) Chuiko, A. L., Filonenko, L. P., Borisevich, A. N., and Lozinskii, M. O. (1993) Synthesis and properties of hydroxyaminoalkyl esters of (hydroxyethylidene)bis[phosphonic acid]. *Zh. Obshch. Khim. 63*, 1070–4.

(16) Chen, G., Heim, A., Riether, D., Yee, D., Milgrom, Y., Gawinowicz Mary, A., and Sames, D. (2003) Reactivity of functional groups on the protein surface: development of epoxide probes for protein labeling. *J. Am. Chem. Soc. 125*, 8130–3.

(17) Marma, M. S., Xia, Z., Stewart, C., Coxon, F., Dunford, J. E., Baron, R., Kashemirov, B. A., Ebetino, F. H., Triffitt, J. T., Russell, R. G. G., and McKenna, C. E. (2007) Synthesis and biological evaluation of α-halogenated bisphosphonate and phosphonocarboxylate analogues of risedronate. *J. Med. Chem. 50*, 5967–5975.

(18) Coxon, F. P., Thompson, K., Roelofs, A. J., Ebetino, F. H., and Rogers, M. J. (2008) Visualizing mineral binding and uptake of bisphosphonate by osteoclasts and non-resorbing cells. *Bone 42*, 848–60.

BC800369C

Fluorescently Labeled Risedronate and Related Analogs: "Magic Linker" Synthesis

*Boris A. Kashemirov[†], Joy Lynn F. Bala[†], Xiaolan Chen[†], F. H. Ebetino[‡], Zhidao Xia[§], R. Graham G. Russell[§], Fraser P. Coxon[‖], Anke J. Roelofs[‖], Michael J. Rogers[‖], and Charles E. McKenna[†,]**

†Department of Chemistry, University of Southern California, Los Angeles, CA, 90089 USA; [‡]Procter & Gamble Pharmaceuticals, Mason, OH, 45040, USA; [§]University of Oxford, Nuffield Department of Orthopedic Surgery, Nuffield Orthopedic Center, Headington, Oxford, OX3 7LD UK; [‖]Bone & Musculoskeletal Research Programme, Institute of Medical Sciences, University of Aberdeen, Aberdeen, AB25 2ZD UK.

*mckenna@usc.edu

SUPPLEMENTARY METHODS **2**

REAGENTS AND SPECTRAL MEASUREMENTS 2
CHEMICAL SYNTHESIS 3
Synthesis of tert-butyl (oxiran-2-ylmethyl)carbamate (4) from allylamine ***3***
General synthesis of N-alkylated drug intermediates 8, 9 and 10 ..... ***4***
Synthesis of 1-(3-amino-2-hydroxypropyl)-3-(2-hydroxy-2,2-diphosphonoethyl)pyridinium (**8**) 4
Synthesis of 1-(3-amino-2-hydroxypropyl)-3-(2-carboxy-2-hydroxy-2-phosphonoethyl)pyridinium (**9**) 5
Synthesis of 1-(3-amino-2-hydroxypropyl)-3-(2,2-diphosphonoethyl)pyridinium (**10**) 6
General synthesis of FAM-labeled compounds 11-17 ..... ***7***
Synthesis of 5(6)-FAMRIS (**11**) 9
Synthesis and HPLC Separation of 5- and 6-FAMRIS (**12** and **13**) 10
Synthesis of 5(6)-, 5-, and 6-FAMRISPC (**14** – **16**) 12
Synthesis of 5(6)-FAMdRIS (**17**) 14
UV ABSORPTION AND FLUORESCENCE EMISSION SPECTRA 15
HA BINDING AFFINITY 16
INHIBITION OF PROTEIN PRENYLATION 16
RABBIT OSTEOCLAST CULTURES ON DENTINE DISCS LABELED WITH 5(6)-FAMRIS 16

SUPPLEMENTARY FIGURES **18**

SUPPLEMENTARY FIGURE 1. 18
SUPPLEMENTARY FIGURE 2 19
SUPPLEMENTARY FIGURE 3 20
SUPPLEMENTARY FIGURE 4 21
SUPPLEMENTARY FIGURE 5 21
SUPPLEMENTARY FIGURE 6 22
SUPPLEMENTARY FIGURE 7 22
SUPPLEMENTARY FIGURE 8 23
SUPPLEMENTARY FIGURE 9 23
SUPPLEMENTARY FIGURE 10 24

SUPPLEMENTARY FIGURE 11 24
SUPPLEMENTARY FIGURE 12 25
SUPPLEMENTARY FIGURE 13 25
SUPPLEMENTARY FIGURE 14 26
SUPPLEMENTARY FIGURE 15 26
LITERATURE CITED 27

SUPPLEMENTARY METHODS

Reagents and Spectral Measurements. 5(6)-, 5-, and 6-carboxyfluorescein, succinimidyl ester (FAM, SE) were purchased from Sigma Aldrich. Compounds **1**, **2**, and **3** were kind gifts from Procter & Gamble Pharmaceuticals. All other compounds were purchased from Aldrich or Alfa Aesar. Triethylamine (TEA) was distilled from KOH; CH_2Cl_2 was distilled from P_2O_5; and allylamine was distilled under N_2. All other compounds were used as supplied by the manufacturer. Thin layer chromatography was performed on Merck Silica Gel 60 F_{254} plates, and the developed plates were visualized under a UV lamp at 354 nm. HPLC separations were performed on a Rainan Dynamax Model SD-200 system with a Rainan Dynamax absorbance detector Model UV-DII. NMR spectra were recorded on either 400 MHz Varian or 500 MHz Bruker spectrometers. UV spectra were recorded on a DU 800 spectrometer, and fluorescence emission spectra were taken on a Jobin Yvon Horiba FluoroMax-3 fluorimeter equipped with a DataMax Software version 2.20 (Jobin Yvon Inc). High resolution mass spectra were performed by Dr. Ron New at UC Riverside High Resolution Mass Spectrometry Facility on a PE Biosystems DE-STR MALDI TOF spectrometer with a WinNT (2000) Data System.

Chemical Synthesis.

Synthesis of tert-butyl (oxiran-2-ylmethyl)carbamate (**4**) from allylamine: Freshly distilled allylamine (2.3 mL, 30 mmol, 1.0 eq) in 10 mL dry CH_2Cl_2 was cooled in an ice bath (0 °C). To this cold solution, 6.54 g di-*tert*-butyl dicarbonate (30.0 mmol, 1.00 eq) in 20 mL dry CH_2Cl_2 was added. The solution was brought to rt and stirred for 4 h. The reaction mixture was then diluted with additional CH_2Cl_2 and washed with 5% citric acid solution, followed by brine. The organic layer was dried over Na_2SO_4 and concentrated in vacuo, yielding 3.3 g (68%) of the *tert*-butyl allylcarbamate. The ^{1}H NMR spectral data matched previously reported values for this compound (*1*).

^{1}H NMR ($CDCl_3$): δ 1.38 (s, 9H), 3.68 (br, 2H), 4.53 (brs, 1H), 5.02-5.16 (m, 2H), 5.72-5.84 (m, 1H).

The *tert*-butyl allylcarbamate (1.0 g, 6.4 mmol, 1.0 eq) was dissolved in 50 mL dry CH_2Cl_2. The solution was cooled to 0 °C and kept cold during addition of 2.8 g of 3-chlorobenzenecarboperoxoic acid ((MCPBA), (commercially available as 77% pure), 12 mmol, 1.9 eq). The solution was then brought to rt and stirred overnight. The reaction mixture was then diluted with additional CH_2Cl_2. The solution was washed with 10% Na_2SO_3, followed by washing with saturated $NaHCO_3$ 3x, and finally by washing with water. The organic layer was dried over Na_2SO_4 and concentrated in vacuo, yielding crude epoxide **4**. According to the ^{1}H NMR spectrum (*1*), the yield was 85%.

^{1}H NMR ($CDCl_3$): δ 1.44 (s, 9H), 2.59-2.78 (m, 2H), 3.04-3.54 (m, 3H), 4.75 (brs, 1H).

General synthesis of N-alkylated drug intermediates 8, 9 and 10. The parent drug is dissolved in water and the pH adjusted to 5.7-6.0 with 1 N NaOH. Epoxide **4** is dissolved in minimal methanol (MeOH) and added to the water solution, causing a slight precipitation to occur. The precipitate disappears on heating (40-50 °C) and as the reaction progresses. The reaction is monitored by ^{31}P NMR or by analytical reverse-phase HPLC. After 90-95% of the desired product is obtained (^{31}P NMR), the solvent is removed in vacuo, and the resulting white powder is washed with diethyl ether, filtered, and dried in a dessicator. Standard deprotection is performed with 1:1 trifluoroacetic acid (TFA): H_2O. After the reaction mixture is stirred for 3-4 h at rt, the solvent is removed in vacuo, and the resulting crystals are washed with diethyl ether and MeOH to yield the drug-linker conjugate for labeling reactions.

Synthesis of 1-(3-amino-2-hydroxypropyl)-3-(2-hydroxy-2,2-diphosphonoethyl)pyridinium (**8**):

The monosodium salt of (1-hydroxy-2-pyridin-3-ylethane-1,1-diyl)bis(phosphonic acid), **1** (287 mg, 0.94 mmol, 1.00 eq), was dissolved in 4 mL water, and the pH adjusted to 6.2 with 1 N NaOH. To this solution, 163 mg of **4** (0.94 mmol, 1.00 eq) in minimal MeOH was added. The reaction mixture was stirred at 40 °C for 18.5 h, yielding 90% of **5** by ^{31}P NMR. The solvent was removed in vacuo, and the residue was washed with diethyl ether, filtered, and dried in a dessicator. **5**, a white solid, was then used without further purification.

^{1}H NMR (D_2O): δ 1.27 (s, 9H), 3.07-3.30 (m, 4H), 3.95-4.03 (m, 1H), 4.18-4.27 (dd**,** *J* = 13.7 Hz, 3.7 Hz, 1H), 4.58-4.65 (part. obscured by HDO, about 1H), 7.75 (t, *J* = 6.8 Hz, 1H), 8.39 (d, *J* = 7.8 Hz, 1H), 8.43 (d, *J* = 6.5 Hz, 1H), 8.65 (s, 1H). ^{31}P{^{1}H} NMR (D_2O): δ 16.33 (d, *J* = 21.1 Hz, 1P), 16.55 (d, *J* = 21.1 Hz, 1P).

The entire sample of **5** was dissolved in 3 mL water. 3 mL TFA was slowly added, and the solution was stirred at rt for 3 h. According to ^{1}H NMR, a 100% yield of **8** was achieved. The solvent was then removed in vacuo, and the resulting solids were washed with ether, filtered, and dried, yielding **8** as white crystals, which were used without further purification.

^{1}H NMR (D_2O): 3.01 (t, *J* = 11 Hz, 1H), 3.31 (d, *J* = 12.6 Hz, 1H), 3.39 (t, *J* = 11.6 Hz, 2H), 4.25-4.33 (m, 1H), 4.36-4.44 (br, 1H), 7.88 (t, *J* = 6.6 Hz, 1H), 8.48 (d, *J* = 8.0 Hz, 1H), 8.58 (d, *J* = 5.5 Hz, 1H), 8.77 (s, 1H). ^{31}P{^{1}H} NMR (D_2O): δ 16.04 (d, *J* = 27.5 Hz, 1P), 16.40 (d, *J* = 27.5 Hz, 1P).

Synthesis of 1-(3-amino-2-hydroxypropyl)-3-(2-carboxy-2-hydroxy-2-phosphonoethyl)pyridinium (**9**):

Compound **2** (0.52 g, 2.10 mmol, 1.00 eq), 2-hydroxy-2-phosphono-3-pyridin-3-ylpropanoic acid, was dissolved in 10 mL water, and the pH adjusted to 5.9 with 1 N NaOH. To this solution, 0.45 g of **4** (2.57 mmol, 1.22 eq) in minimal MeOH was added. The reaction mixture was stirred at 50 °C for 6 h and then stirred at rt overnight, yielding 90% of **6** (^{31}P NMR). The solvent was removed in vacuo, and the residue was washed

with diethyl ether, filtered, and dried in a dessicator, leaving **6** (diastereoisomeric mixture), which was then used without further purification.

^{1}H NMR (D_2O): δ 1.27 (s, 9H), 3.00-3.23 (m, 3H), 3.45 (dd, *J* = 14.2 Hz, 3.6 Hz, 1H), 3.91-4.00 (m,1H), 4.19-4.27 (m, 1H), 4.58-4.64 (br, 1H), 7.78 (dd, *J* = 8.3 Hz, 6.2 Hz, 1H), 8.24-8.29 (m, 2H), 8.47 (d, *J* = 6.0 Hz, 1H), 8.49-8.53 (brd, 1H). ^{31}P{^{1}H} NMR (D_2O): δ 14.96 (s, 1P), 14.98 (s, 1P).

The entire sample of **6** was dissolved in 50:50 water:TFA (v/v). After stirring at rt for 4 h, a 100% yield of **9** was obtained (^{1}H NMR). The solvent was then removed in vacuo, and the residue was washed with diethyl ether, filtered, and dried, yielding **9** (a diastereoisomeric mixture) as white crystals, used without further purification.

^{1}H NMR (D_2O): δ 2.90 (m, 1H), 3.18-3.28 (m, 2H), 3.50 (m, 1H), 4.14-4.22 (m, 1H), 4.31-4.40 (m, 1H), 4.71-4.74 (m, 1H), 7.87 (dd, *J* = 8.3 Hz, 6.1 Hz, 1H), 8.34-8.39 (brd, 1H), 8.56-8.68 (m, 2H). ^{31}P{^{1}H} NMR (D_2O): δ 12.53 (s, 1P), 12.62 (s, 1P).

Synthesis of 1-(3-amino-2-hydroxypropyl)-3-(2,2-diphosphonoethyl)pyridinium (**10**):

Compound **3** (38.0 mg, 0.14 mmol, 1.00 eq), (2-pyridin-3-ylethane-1,1-diyl)bis(phosphonic acid), was dissolved in 1 mL water and the pH brought to 5.4 with 1 N NaOH. To this solution was added 25.5 mg of **4** (0.15 mmol, 1.07 eq) in minimal MeOH. The reaction mixture was stirred at 40 °C overnight, and the reaction was monitored by ^{31}P NMR. After 19 h, 20% of starting material **3** remained. Thus, an additional 5.30 mg (0.03 mmol, 0.21 eq) of **4** in MeOH was added to the reaction mixture. After 42 h, 90% of the desired product was obtained. The solvent was removed

in vacuo, and the resulting white powder was washed with diethyl ether, filtered, and dried, giving **7**, which was used without further purification.

^{1}H NMR (D_2O): δ 1.26 (s, 9H), 2.12 (tt, *J* = 21.2 Hz, 7.1 Hz, 1H), 3.09-3.24 (m, 4H), 3.94-4.00 (m, 1H), 4.22 (dd, *J* = 13.7 Hz, 9.6 Hz, 1H), 4.57-4.64 (m. 1H), 7.84 (dd, *J* = 8.6 Hz, 6.1 Hz, 1H), 8.40 (d, *J* = 8.1 Hz, 1H), 8.50 (d, *J* = 6.1 Hz, 1H), 8.69 (s, 1H). ^{31}P{^{1}H} NMR (D_2O): δ 17.20-17.28 (m, 2P).

The entire sample of **7** was dissolved in water. An equal volume of TFA was slowly added, and the solution was stirred at rt for 3 h, giving a 100% yield of **10** (^{1}H NMR). The solvent was removed in vacuo, and the residue was washed with diethyl ether and methanol, filtered, and dried, yielding **10** as white crystals, which was then used without further purification.

^{1}H NMR (D_2O): δ 2.18-2.36 (brt, 1H), 2.92 (brt, 1H), 3.14-3.28 (m, 3H), 4.16-4.24 (m, 1H), 4.60 (dd, *J* = 13.5 Hz, 9.5 Hz, 1H), 7.79 (dd, *J* = 8.7 Hz, 6.1 Hz, 1H), 8.37 (d, *J* = 8.2 Hz, 1H), 8.44 (d, *J* = 6.1 Hz, 1H), 8.64 (s, 1H). ^{31}P{^{1}H} NMR (D_2O): δ 17.2-18.0 (br, 2P).

General synthesis of FAM-labeled compounds 11-17. 8, 9, or **10** (3 eq) is dissolved in 0.1 N $NaHCO_3$. The pH is adjusted to 8.3 with solid Na_2CO_3. 5(6)-Carboxyfluorescein, *N*-hydroxysuccinimide ester (a mixture of 5-{[(2,5-dioxopyrrolidin-1-yl)oxy]carbonyl}-2-(6-hydroxy-3-oxo-3*H*-xanthen-9-yl)benzoic acid and 4-{[(2,5-dioxopyrrolidin-1-

yl)oxy]carbonyl}-2-(6-hydroxy-3-oxo-3*H*-xanthen-9-yl)benzoic acid*, 5(6)-FAM, SE, **18,** 1 eq), is dissolved in anhydrous DMF (~50 mg per 200 µL) and combined with the water solution, forming a dark red-orange solution with a small amount of precipitate. The pH is again adjusted to 8.9 with Na_2CO_3, dissolving all the precipitate, and the reaction mixture is stirred at rt overnight. The reaction mixture is purified by TLC with 100% MeOH as the eluant. The FAM label moves quickly with the solvent, giving a yellow upper band, while the phosphonate-containing compounds remain at the origin, and are extracted with water. The combined aqueous extracts are treated with Chelex (sodium form) to remove metals extracted from the silica, centrifuged, and concentrated in vacuo to yield a dark red-orange solid, which is dissolved in either water, 20% MeOH in 0.1 N triethylammonium acetate (TEAAc), or triethylammonium carbonate (TEAC) buffer (pH 7) and filtered through Nanosep 30K Omega filter. The product is purified by semi-preparative reverse-phase HPLC: Dynamax C18 (21.4 mm x 25 cm, 5 µm, 100 Å pore size) column, flow rate 8.0 mL/min, UV detection at 260 nm, gradient as follows: (Method A, used for **11**-**13**) 10% MeOH 0.1 N TEAAc or TEAC (pH 7) to 40% of 75% MeOH 0.1 N TEAAc or TEAC (pH 7) in 12 min, increasing to 70% of Buffer B in 100 min or (Method B, used for **14**-**17**) isocratic elution with 20% MeOH 0.1 N TEAC (pH 7) for 12 min, linearly increasing to 100% of 70% MeOH 0.1 N TEAC (pH 7) in 22 min (Supplementary Figures 2-3). The final amount of labeled product is calculated from the

* Systematic names obtained from IUPAC Nomenclature of Organic Chemistry generated by ACD/IUPAC Name Web Service™ (http://ilab.acdlabs.com/); note that numbering differs from trivial fluorescein numbering scheme.

UV absorption spectrum taking $\varepsilon = 73000\ M^{-1}cm^{-1}$ in 0.1 N phosphate buffer at pH 7.2(*2*, *3*), and the isolated eluate is lyophilized, yielding a red-orange solid.

Synthesis of 5(6)-FAMRIS (5-FAMRIS: 1-(3-{[3-carboxy-4-(6-hydroxy-3-oxo-3*H*-xanthen-9-yl)benzoyl]amino}-2-hydroxypropyl)-3-(2-hydroxy-2,2-diphosphonoethyl)pyridinium; 6-FAMRIS: 1-(3-{[4-carboxy-3-(6-hydroxy-3-oxo-3*H*-xanthen-9-yl)benzoyl]amino}-2-hydroxypropyl)-3-(2-hydroxy-2,2-diphosphonoethyl)pyridinium (**11**):

The following synthesis and purification steps were performed under minimal lighting. Intermediate **6** (177 mg, 0.36 mmol, 4.50 eq) was dissolved in 2 mL of 0.1 N $NaHCO_3$. The pH of the solution was adjusted to 8.3 with Na_2CO_3. To this solution was added 41.0 mg of **18** (0.08 mmol, 1.00 eq) in 200 μL anhydrous DMF, forming a dark red-orange solution with a small amount of precipitate. The pH was again adjusted to 8.1 with Na_2CO_3, causing the precipitate to dissolve. The reaction mixture was then stirred at rt for 3 h.

The reaction mixture was applied to TLC plates which were eluted with 100% MeOH. The dark orange band remaining at the origin was extracted with HPLC water, and the solution was treated with Chelex (sodium form) to remove metals extracted from the silica, then centrifuged and concentrated in vacuo to yield a dark red-orange solid, which was dissolved in HPLC water and filtered through Nanosep 30K Omega filters. The product was then purified by HPLC according to Method A with TEAAc buffers (Supplementary Figure 2). Peaks eluting from 25-75 min were collected. During evaporation of the buffer solution, product precipitated from the solution. Consequently,

a second HPLC purification was performed according to Method A but eluting with TEAC buffers (pH 7.5) (Supplementary Figure 2). This maintained basic conditions when the buffer was removed in vacuo. The final amount of labeled product was calculated from the UV absorption spectrum, and the solution was lyophilized to yield a bright reddish-orange solid (26 mg, 42%).

5(6)-FAMRIS, **11** (as a triethylammonium carbonate salt): ^{1}H NMR (D_2O): δ 3.33-3.39 (m, 2H), 3.43-3.66 (m, 2H), 4.08-4.42 (m, 3H), 4.72-4.80 (brd, 1H), 6.36-6.48 (m, 4H), 6.93 (d, 2H), 7.09 (s, 1H), 7.43 (s, 0.4 H), 7.68-7.87 (m, 2H), 8.06 (s, 0.6 H), 8.37-8.56 (m, 2H), 8.69-8.78 (2 s, 1H). ^{31}P{^{1}H} NMR (D_2O): δ 16.26 (d, J = 23 Hz, 1P), 16.50 (d, J = 23 Hz, 2P).

Synthesis and HPLC Separation of 5- and 6-FAMRIS (**12** and **13**): Intermediate **8** (149 mg, 0.30 mmol, 1.4 eq) was dissolved in 1 mL H_2O and 1.5 mL 0.1 N $NaHCO_3$. The pH was adjusted to 8.4 with additional Na_2CO_3. To this solution was added 100 mg of **18** (0.21 mmol, 1 eq) in ~700 μL anhydrous DMF in darkness. After the addition of the label, the pH was again adjusted to 8.4 to increase solubility of the label. The reaction mixture was stirred at rt in darkness for 3 h.

The solvent was then removed in vacuo, yielding a bright reddish-orange solid. The unpurified product was redissolved in water and purified by size exclusion chromatography (Sephadex G10 column eluted with 50 mM TEAAc). The bright orange compound can easily be seen traveling through the column. The first ~20 mL of compound eluted were analyzed by TLC (eluent, 100% MeOH) and showed no traces of

free 5(6)-FAM.

The solvent of this fraction was then removed in vacuo and redissolved in a 10% MeOH 0.1 N TEAAc buffer (pH 7). The product compounds were then purified by semi-preparative reverse-phase HPLC according to Method A (Supplementary Figure 2). 6-FAMRIS and 5-FAMRIS eluted at very different retention times, 27 and 44 min, respectively; each isomer was collected separately. Each fraction collected was analyzed by TLC (eluant, 100% MeOH) to ensure no traces of 5(6)-FAM was present. Each isomer was then concentrated in vacuo to remove buffer.

Compound **12** was also directly synthesized from 5-FAM, SE according to the method described above. The ^{1}H and ^{31}P NMR spectra and HPLC retention time corresponded to the peak eluting at 44 min, thus confirming our isomer assignments given to compounds **12** and **13** that were separated by HPLC (Supporting Figs. 3, 6-9). A slight difference can be seen, however, in the ^{1}H NMR spectra. Compound **12** synthesized from 5(6)-FAM, SE contains a minor singlet at δ 7.56, indicating a trace of the 6-isomer, which is absent from the product directly synthesized from the pure 5-isomer starting material. Detailed NMR descriptions given below correspond to the HPLC-separated products.

Compound **12** samples obtained from 5(6)-FAM, SE and from 5-FAM, SE were combined; the final amount was calculated from the UV absorption spectrum as described above, and the product obtained after lyophilization as a bright reddish-orange solid (11.9 mg, 8%).

The final amount of compound **13** was calculated from the UV absorption spectrum

as described above, and the product obtained after lyophilization as a bright reddish-orange solid (5.5 mg, 4%).

5-FAMRIS, **12** (retention time 44 min, as a triethylammonium acetate salt): ^{1}H NMR (D_2O): δ 3.37 (brt, 2H), 3.57 (dd, *J* = 14.1 Hz, 6.7 Hz, 1H), 3.61-3.69 (m, 1H), 4.22-4.31 (m, 1H), 4.36-4.45 (m, 1H), 4.79 (d, 1H), 6.61-6.71 (m, 4H), 7.11 (d, *J* = 9.2 Hz, 2H), 7.33 (d, *J* = 8.0 Hz, 1H), 7.56 (s, 0.14H), 7.83 (t, *J* = 7.2 Hz, 1H), 7.91 (d, *J* = 8.1 Hz, 1H), 8.15 (s, 1H), 8.44 (d, *J* = 8.3 Hz, 1H), 8.56 (d, *J* = 5.9 Hz, 1H), 8.74 (s, 1H). ^{31}P{^{1}H} NMR (D_2O): δ 16.47 (brs).

HRMS (positive ion MALDI, M^+): calcd 715.1089 m/z; found 715.1055 m/z; MS (negative ion MALDI, M^-): found 713.

6-FAMRIS, **13** (retention time of 27 min, as a triethylammonium acetate salt): ^{1}H NMR (D_2O): δ 3.27-3.37 (m, 2H), 3.44 (dd, *J* = 14 Hz, 6.9 Hz,1H), 3.58 (dd, *J* = 14 Hz, 4.9 Hz, 1H), 4.19 (brs, 1H), 4.35 (dd, *J* = 14 Hz, *J* = 9.3 Hz, 1H), 6.60-6.73 (m, 4H), 7.04 (d, *J* = 9.4 Hz, 2H), 7.53 (s, 1H), 7.81 (dd, *J* = 8.2 Hz, 6.4 Hz, 1H), 7.88 (d, *J* = 8.1 Hz, 1H), 7.95 (dd, *J* = 8.0 Hz, 1.6 Hz, 1H), 8.43 (d, *J* = 8.1 Hz, 1H), 8.53 (d, *J* = 6.5 Hz, 1H), 8.70 (s, 1H). ^{31}P{^{1}H} NMR (D_2O): δ 16.51 (brs).

HRMS (positive ion MALDI, M^+): calcd 715.1089 m/z; found 715.1082 m/z.

Synthesis of 5(6)-FAMRISPC (5-FAMRISPC: 1-(3-{[3-carboxy-4-(6-hydroxy-3-oxo-3*H*-xanthen-9-yl)benzoyl]amino}-2-hydroxypropyl)-3-(2-carboxy-2-hydroxy-2-phosphonoethyl)pyridinium; 6-FAMRISPC: 1-(3-{[4-carboxy-3-(6-hydroxy-3-oxo-3*H*-xanthen-9-yl)benzoyl]amino}-2-hydroxypropyl)-3-(2-carboxy-2-hydroxy-2-

phosphonoethyl)pyridinium (**14**): The following synthesis and purification steps were performed under minimal lighting. Intermediate **9** (158 mg, 0.36 mmol, 3.60 eq) was dissolved in 1 mL of water. The pH of the solution was adjusted to 8.3 with Na_2CO_3. To this solution was added 53 mg of **18** (0.1 mmol, 1.0 eq) in 200 μL anhydrous DMF, forming a dark red-orange solution with small amount of precipitate. The pH was again adjusted to 8.1 with Na_2CO_3, causing the precipitate to dissolve, and the reaction mixture was stirred at rt overnight.

The reaction mixture was directly placed on TLC plates with 100% MeOH as eluant. Free label moves quickly with the solvent, resulting in a yellow upper band, while phosphonate-containing compounds remain at the origin. The band with $R_f = 0$ was extracted from the silica with HPLC water. The solution was treated with Chelex (sodium form) to remove metals extracted from the silica, then centrifuged and concentrated in vacuo to yield a dark red-orange solid, which was dissolved in HPLC water and filtered through Nanosep 30K Omega filters. The solution was then purified by HPLC according to Method B. Peaks eluting at 25-40 min were collected together as **14**. The final amount was calculated from the UV absorption spectrum, and the product obtained after lyophilization as a bright reddish-orange solid (9.6 mg, 13%).

5(6)-FAMRISPC **14** (as a triethylammonium carbonate salt): ^{1}H NMR (D_2O): δ 3.27-3.62 (m, 3H), 4.03-4.40 (m, 2H), 6.42 (m, 4H), 6.92 (dd, *J* = 9.5 Hz, 3.5 Hz, 2H), 7.10 (d, *J* = 8.1 Hz, 1H), 7.42 (s, 0.4H), 7.70-7.86 (m, 2H), 8.06 (s, 0.6H), 8.27 (brs, 1H), 8.46-8.63 (m, 2H). $^{31}P\{^1H\}$ NMR (D_2O): δ 15.28 (brs, 1P).

HRMS (positive ion MALDI, M^+): calcd 679.1335 m/z; found 679.1321 m/z.

Single isomers of FAMRISPC were synthesized directly from isomerically pure starting materials (5-FAM, SE or 6-FAM, SE) according to the method above used for isomeric mixtures.

5-FAMRISPC, **15** (retention time 28 min, as a triethylammonium carbonate salt, 2 mg, 29%): ^{1}H NMR (D_2O): δ 3.39-3.52 (m, 2H), 3.55-3.63 (m, 1H), 4.14-4.23 (m, 1H), 4.30-4.40 (m, 1H), 6.43-6.60 (m, 4H), 7.04 (d, *J* = 9.0 Hz, 2H), 7.25 (d, *J* = 8.2 Hz, 1H), 7.77-7.86 (m, 2H), 8.08 (s, 1H), 8.23-8.33 (brs, 1H), 8.45-8.62 (m, 2H).

HRMS (positive ion MALDI, M^+): calcd 679.1324 m/z; found 679.1356 m/z.

6-FAMRISPC, **16** (retention time 25 min, as triethylammonium carbonate salt. 2.5 mg, 36%): ^{1}H NMR (D_2O): δ 3.31-3.45 (m, 2H), 3.47-3.55 (m, 1H), 4.05-4.15 (m, 1H), 4.24-4.34 (m, 1H), 6.45-6.59 (m, 4H), 7.00 (d, *J* = 9.0 Hz, 2H), 7.48 (s, 1H), 7.71-7.80 (m, 2H), 7.85 (dd, *J* = 8.1 Hz, *J* = 1.7 Hz, 1H), 8.21-8.27 (m, 1H), 8.47-8.55 (m, 2H).

HRMS (positive ion MALDI, M^+): calcd 679.1324 m/z; found 679.1321 m/z.

Synthesis of 5(6)-FAMdRIS (5-FAMdRIS: 1-(3-{[3-carboxy-4-(6-hydroxy-3-oxo-3*H*-xanthen-9-yl)benzoyl]amino}-2-hydroxypropyl)-3-(2,2-diphosphonoethyl)pyridinium; 6-FAMdRIS: 1-(3-{[4-carboxy-3-(6-hydroxy-3-oxo-3*H*-xanthen-9-yl)benzoyl]amino}-2-hydroxypropyl)-3-(2,2-diphosphonoethyl)pyridinium (**17**):

Intermediate **10** (53 mg, 0.1 mmol, 2.5 eq) was dissolved in 0.5 mL HPLC water and 0.5 mL of 0.1 N $NaHCO_3$. The pH was adjusted to 8.3 with Na_2CO_3. To this solution was added 18.0 mg of **18** (0.04 mmol, 1.00 eq) in 100 μL anhydrous DMF, forming a dark red-orange solution with a small amount of precipitate. The pH was again adjusted to 8.9

with Na_2CO_3, causing the precipitate to dissolve, and the reaction mixture was stirred at rt overnight.

The reaction mixture was purified by TLC with 100% MeOH as the eluant. The dark orange band at the origin was extracted from silica with water. The solution was treated with Chelex (sodium form) to remove metals extracted from the silica, then centrifuged and concentrated in vacuo to yield a dark red-orange solid, which were dissolved in 20% MeOH in 0.1 N TEAAc buffer (pH 7) and filtered through Nanosep 30K Omega filters. The solution was then purified by HPLC according to Method B. Peaks eluting from 27-45 min were collected as **17**. The final amount was calculated from the UV absorption spectrum, and the product obtained lyophilization as a bright reddish-orange solid (9.4 mg, 36%).

5(6)-FAMdRIS **17** (as triethylammonium acetate salt): ^{1}H NMR (D_2O): δ 2.07-2.27 (m, 1H), 3.10-3.27 (m, 2H), 3.35 (dd, *J* = 14.2 Hz, 6.8 Hz, 0.4H), 3.44-3.53 (m, 1H), 3.60 (dd, *J* = 14.2 Hz, 4.7 Hz, 0.6H), 4.08-4.16 (m, 0.4H), 4.18-4.25 (m, 0.6H), 4.25-4.40 (m, 1H), 4.71-4.77 (m, 1H), 6.40-6.52 (m, 4H), 6.96 (dd, *J* = 8.1 Hz, 4.1 Hz, 2H), 7.17 (d, *J* = 8.1 Hz, 0.6H), 7.44 (s, 0.4H), 7.72 (d, *J* = 8.1 Hz, 0.4H), 7.76-7.86 (m, 2H), 8.07 (d, *J* = 1.7 Hz, 0.6 H), 8.38 (t, *J* = 8.7 Hz, 1H), 8.47 (d, *J* = 5.9 Hz, 1H), 8.53 (d, *J* = 6.1 Hz, 1H), 8.67-8.71 (2 s, 1H). ^{31}P{^{1}H} NMR (D_2O): δ 16.51 (brs).

HRMS (positive ion MALDI, M^+): calcd 699.1139 m/z; found 699.1137 m/z.

UV absorption and fluorescence emission spectra. All samples were dissolved in water and diluted with 0.1 N phosphate buffer, pH 7.2. The final concentration is calculated

from the UV absorption spectrum at λ = 493 nm (ε = 73000 $M^{-1}cm^{-1}$ at pH 7.2) (*2*, *3*), assuming the labeled products have the same ε as 5(6)-FAM. Emission spectra were recorded using an excitation wavelength of 490 nm; the excitation and emission slits were set at a 1 nm spectral bandwidth. Integration time and increment were set to 0.5 s and 1 nm, respectively.

HA binding affinity. Column chromatography with hydroxyapatite ceramic spheres (20 μm, BioRad) was utilized to study the structural determinants of binding affinity (*4*). BPs were eluted by Fast Performance Liquid Chromatography (FPLC) in phosphate buffered (pH 7.0) solution with a gradient between 1 mM and 1 M over 50 min at a flow rate of 2 mLs/min and detected by UV absorbance.

Inhibition of protein prenylation. J774.2 macrophages were treated with 0-100 μM **13**, **1**, or vehicle and 20 μM **13** or 20 μM **1** in the presence or absence of 100 μM GGPP. Cells were lysed, and unprenylated Rap1A was detected by sodium dodecyl sulphate-polyacrylamide gel electrophoresis and immunoblotting using an antibody that preferentially binds to the unprenylated form of Rap1A *(5)*. Detection of β–actin or total Rap1 served as loading control.

Rabbit osteoclast cultures on dentine discs labeled with 5(6)-FAMRIS (11). Dentine discs in 96-well plates were pre-incubated with 100 μM **11** for 1 h, then washed 3 times in PBS prior to seeding with rabbit osteoclasts, isolated as described previously (*5*). After

24 h, cells were fixed using 4% paraformaldehyde and osteoclast membranes were stained using an antibody to the vitronectin receptor. F-actin was also visualized by counterstaining with 0.5 μg/ml of TRITC-phalloidin in PBS for 30 min (*5*). Samples were then analyzed by laser scanning confocal microscopy using a Zeiss LSM510 META system.

SUPPLEMENTARY FIGURES

a

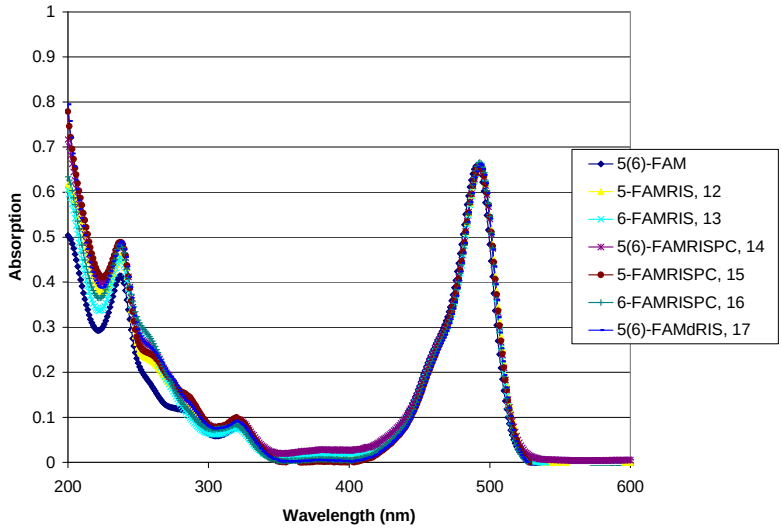

b

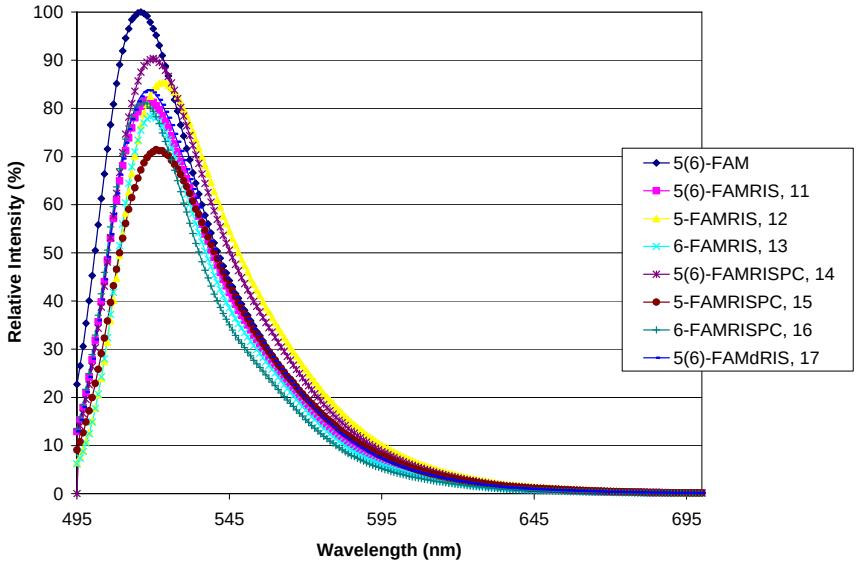

Supplementary Figure 1. UV absorption and fluorescence emission spectra of labeled compounds **11-17** normalized to 5(6)-FAM. All samples in 0.1 N phosphate buffer, pH 7.2, in 1 cm^3 cuvette. (A) Normalized at λ = 492 nm. (B) Normalized to 5(6)-FAM at 516 nm.

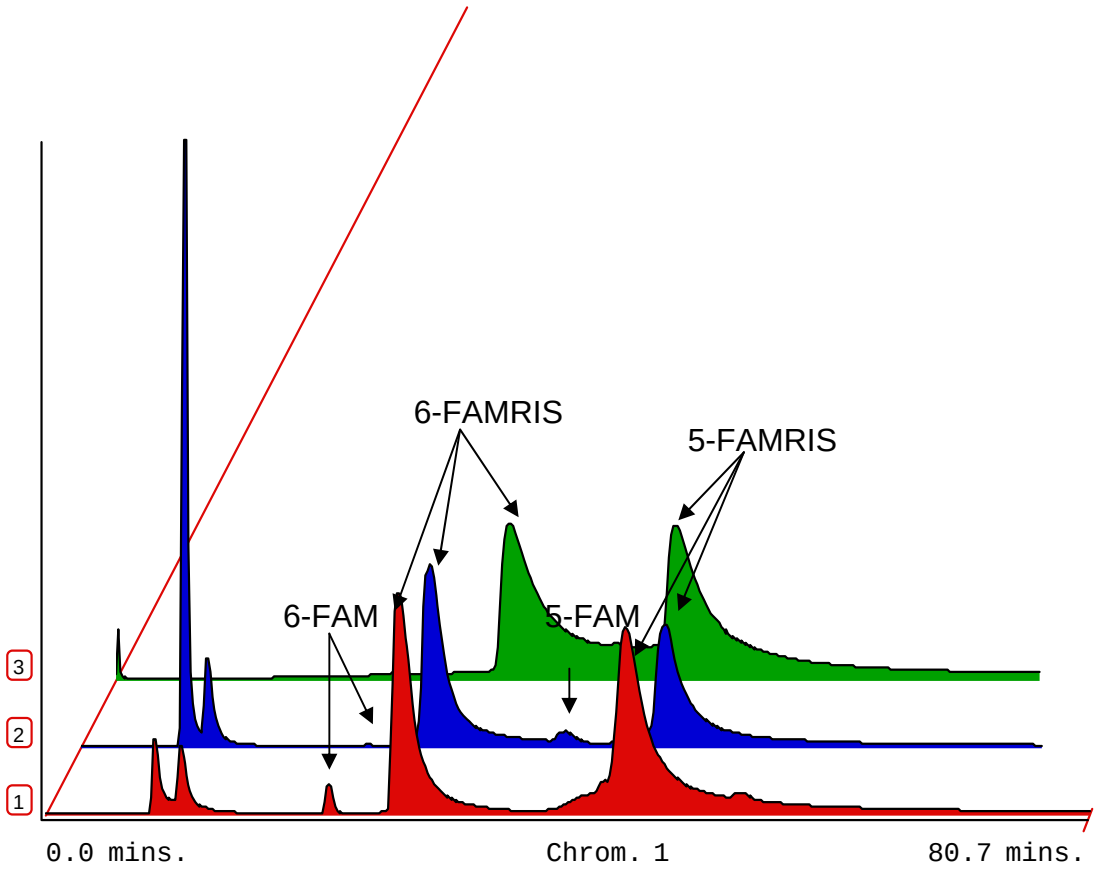

Supplementary Figure 2. Chromatograms for semi-preparative HPLC purification of 5(6)-FAMRIS, **11**. 1: Reaction mixture after size exclusion chromatography. 2: Reaction mixture after TLC purification (eluant, TEAAc buffer). 3: Reaction mixture after HPLC purification (eluant, TEAC buffer).

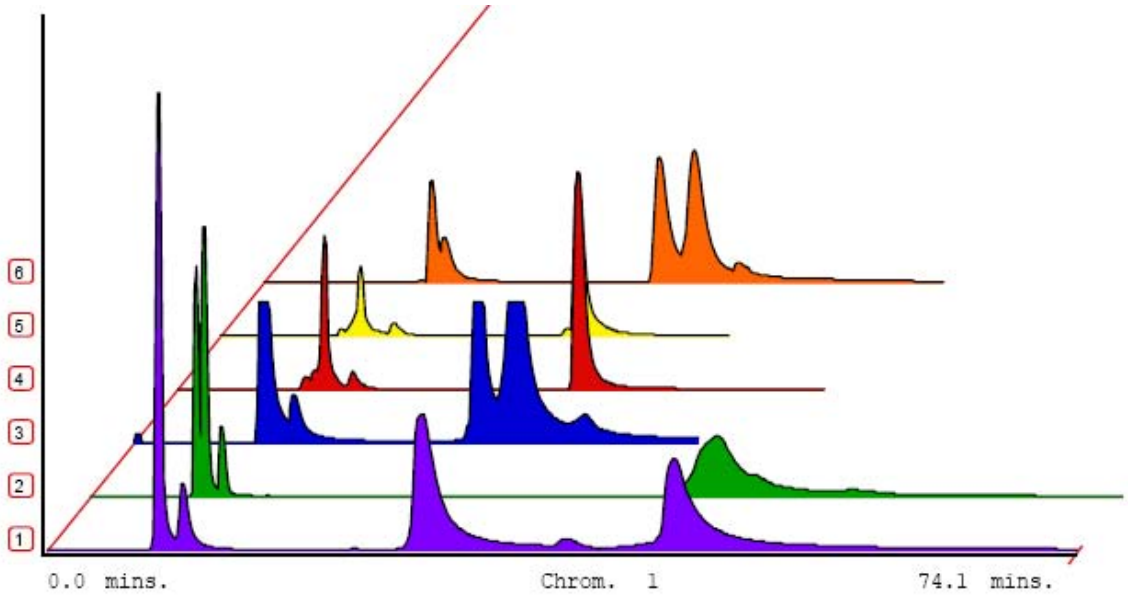

Supplementary Figure 3. Chromatograms for semi-preprative HPLC purifications of labeled compounds. 1: **11**, 5(6)-FAMRIS; 2: **12**, 5-FAMRIS; 3: **14**, 5(6)-FAMRISPC; 4: **15**, 5-FAMRISPC, 5: **16**, 6-FAMRISPC, 6: **17**, 5(6)-FAMdRIS. The unlabeled phosphonate-containing compounds elute at much shorter retention times.

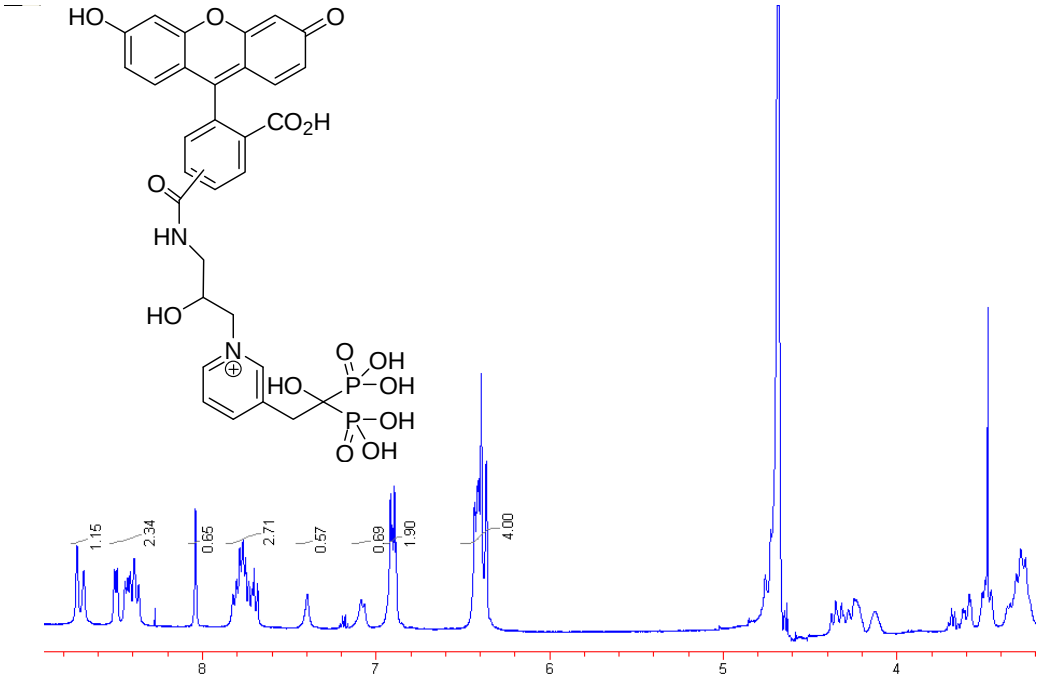

Supplementary Figure 4. ^{1}H NMR in D_2O of 5(6)-FAMRIS, **11**.

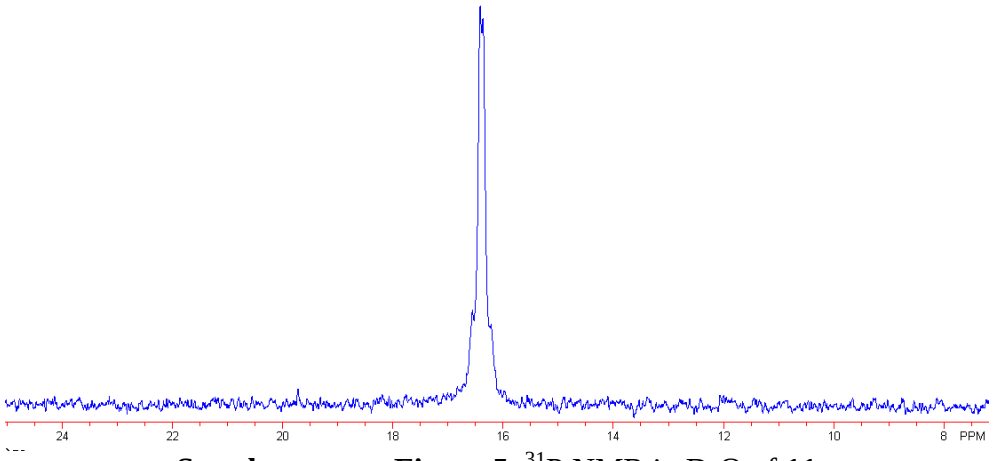

Supplementary Figure 5. ^{31}P NMR in D_2O of **11**

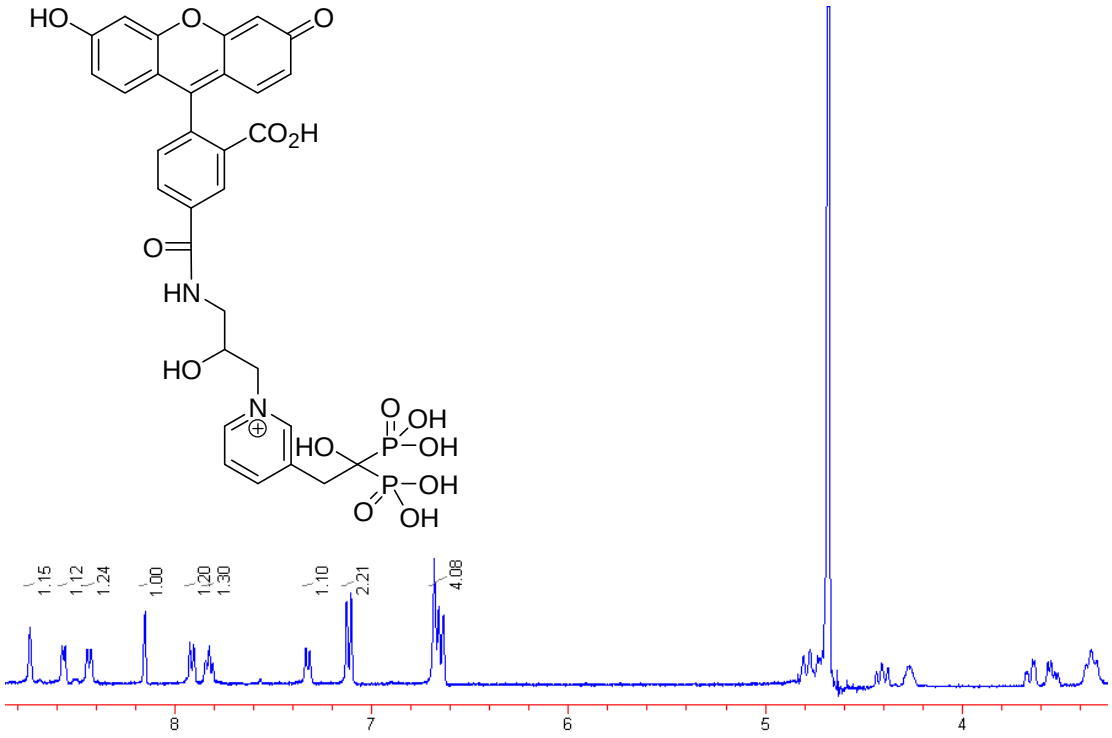

Supplementary Figure 6. ^{1}H NMR in D_2O of 5-FAMRIS, **12**.

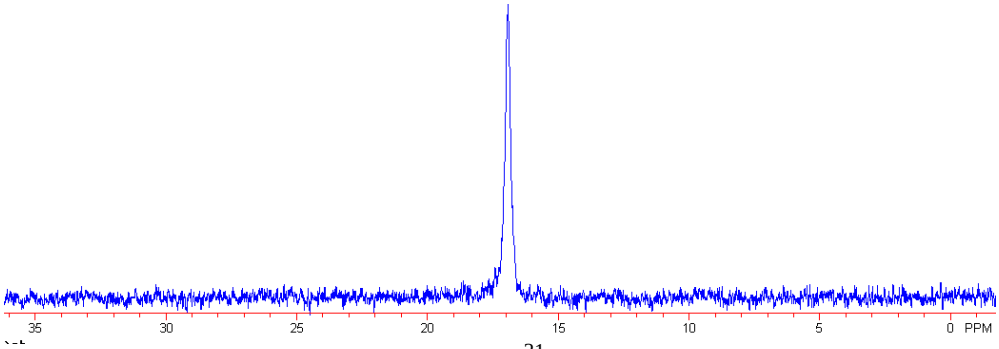

Supplementary Figure 7. ^{31}P NMR in D_2O of **12**.

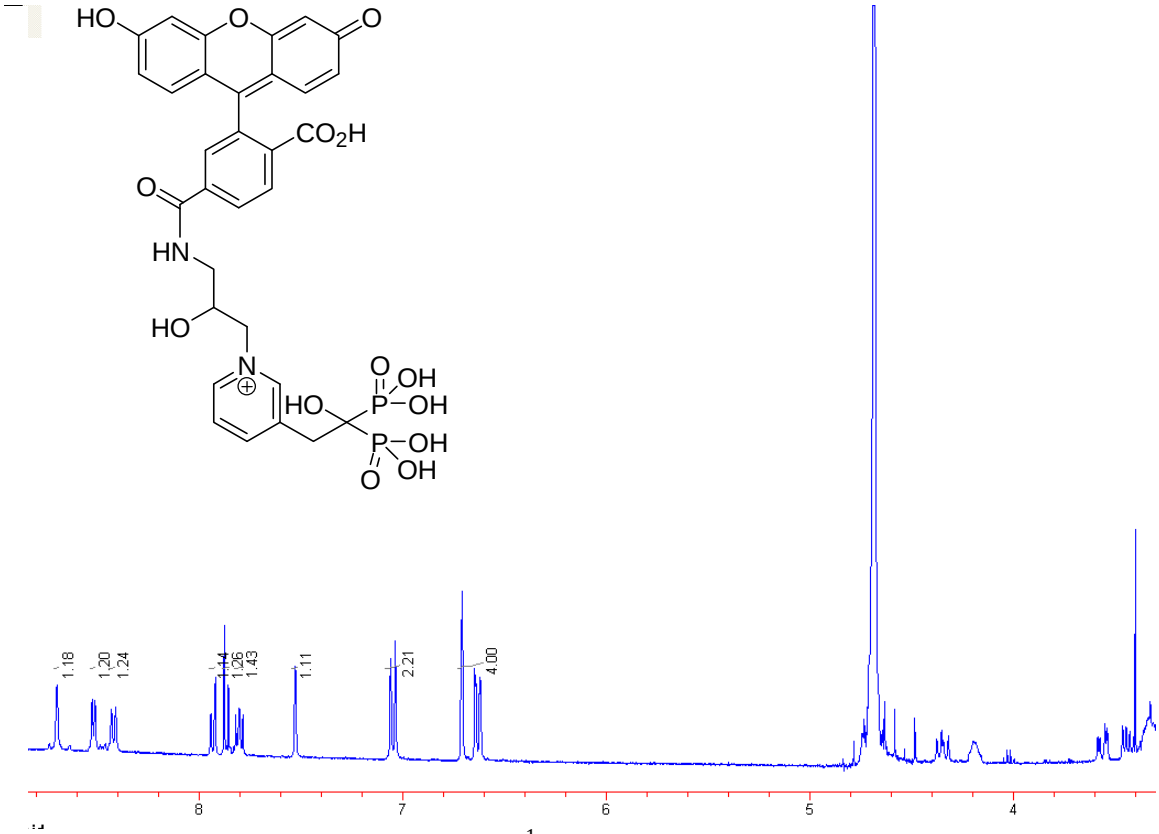

Supplementary Figure 8. ^{1}H NMR in D_2O of 6-FAMRIS, **13**.

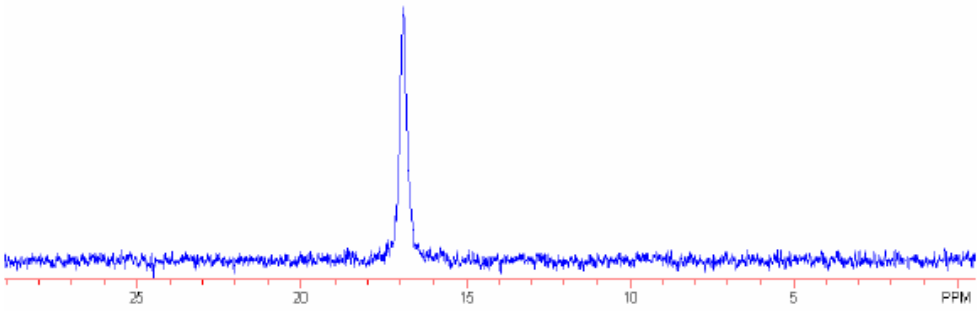

Supplementary Figure 9. ^{31}P NMR in D_2O of 13.

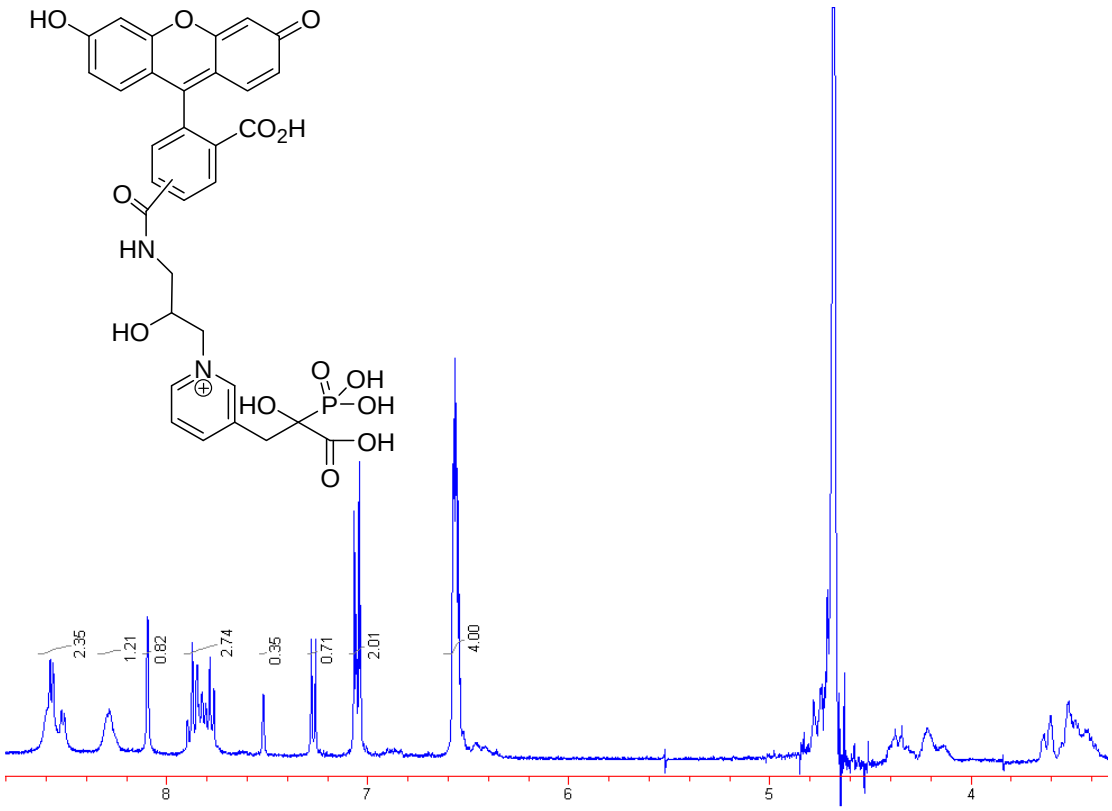

Supplementary Figure 10. ^{1}H NMR in D_2O of 5(6)-FAMRISPC, **14**.

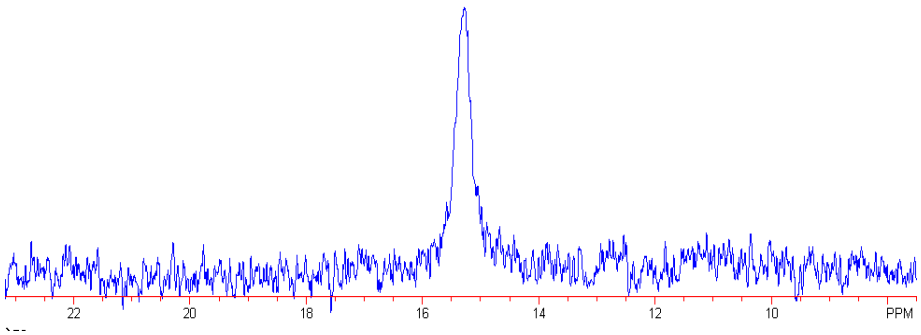

Supplementary Figure 11. ^{31}P NMR in D_2O of **14**.

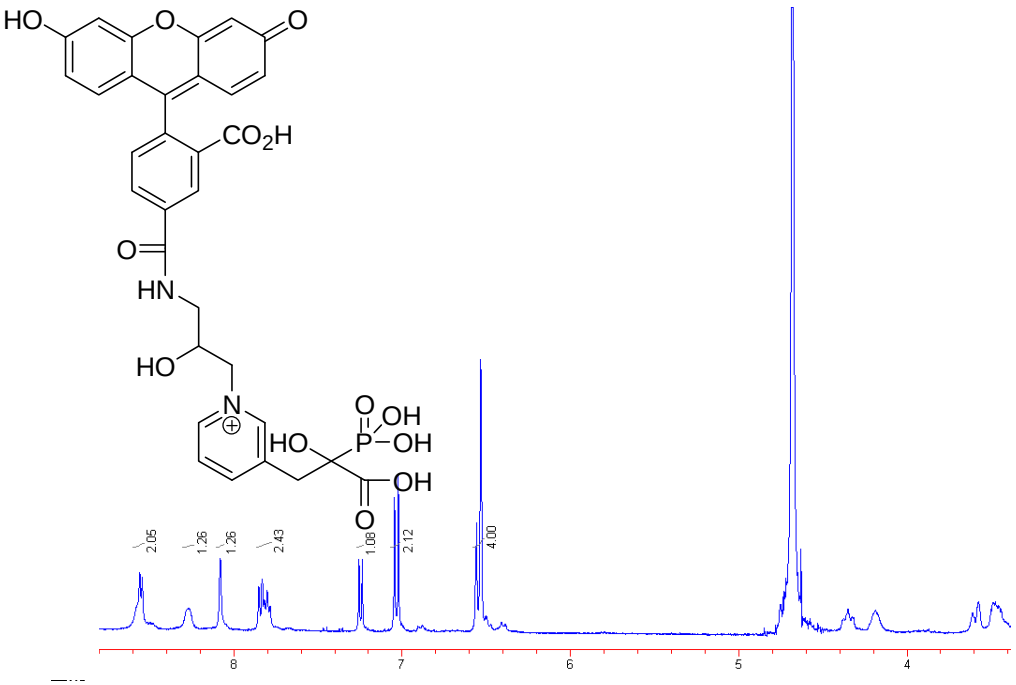

Supplementary Figure 12. ^{1}H NMR in D_2O of 5-FAMRISPC, **15**.

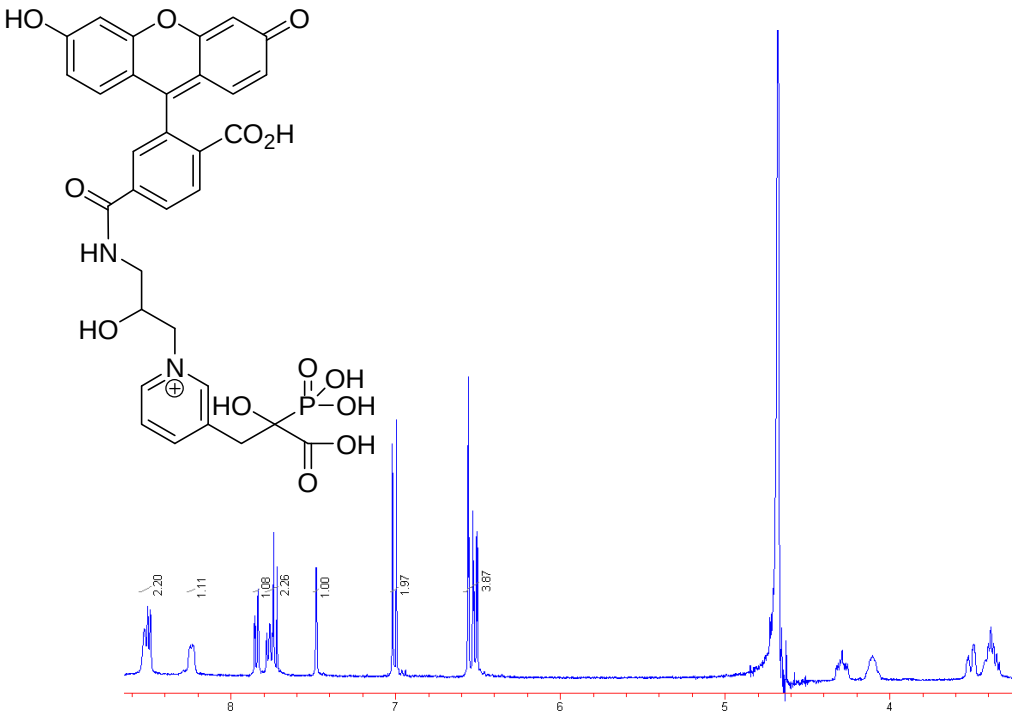

Supplementary Figure 13. ^{1}H NMR in D_2O of 6-FAMRISPC, **16**.

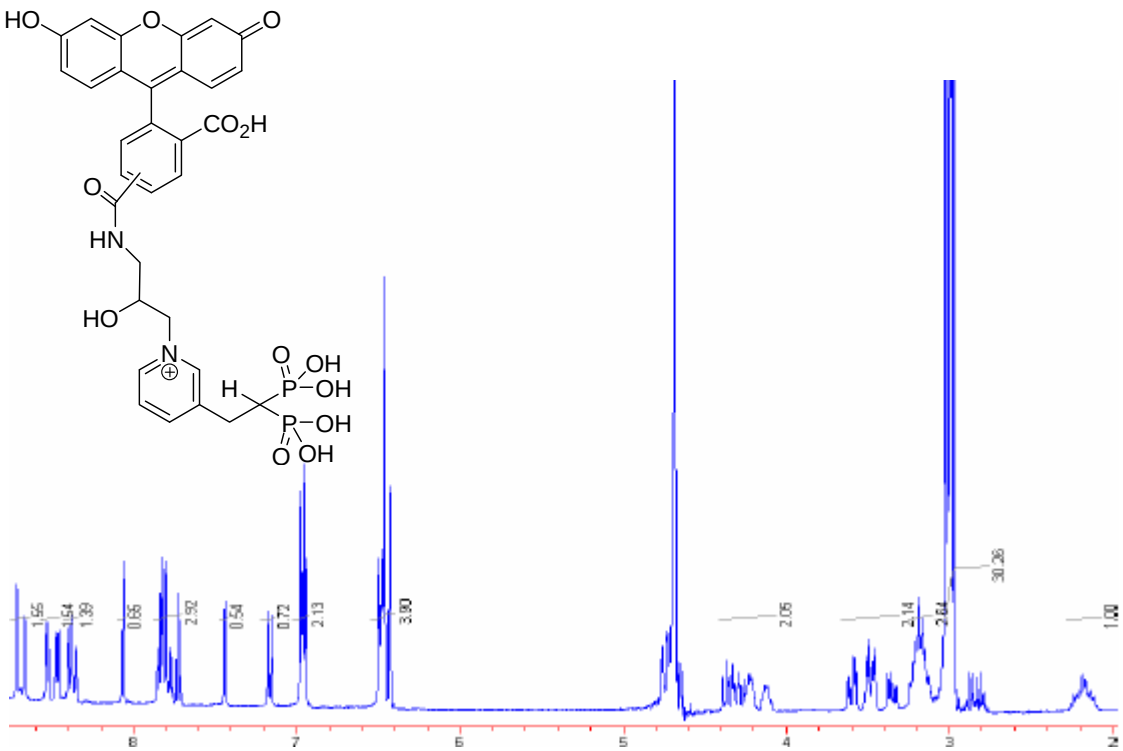

Supplementary Figure 14. ^{1}H NMR in D_2O of 5(6)-FAMdRIS, **17**.

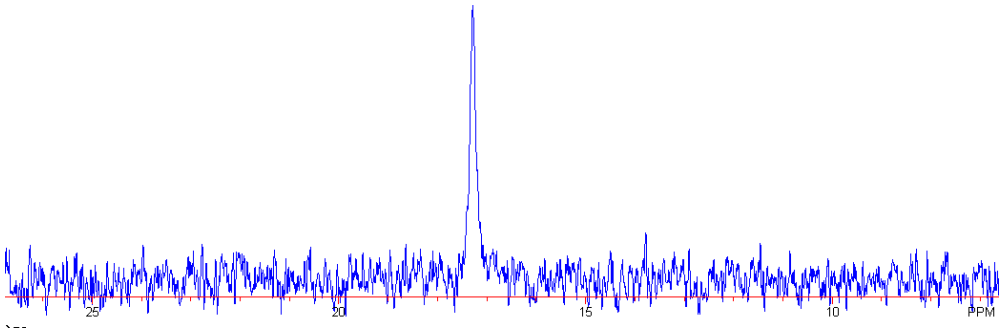

Supplementary Figure 15. ^{31}P NMR in D_2O of **17**.

Literature Cited

(1) Rocheblave, L., Bihel, F., De Michelis, C., Priem, G., Courcambeck, J., Bonnet, B., Chermann, J.-C., and Kraus, J.-L. (2002) Synthesis and antiviral activity of new anti-HIV amprenavir bioisosteres. *J. Med. Chem. 45*, 3321-3324.

(2) Kutyavin, I. V., Lokhov, S. G., Afonina, I. A., Dempcy, R., Gall, A. A., Gorn, V. V., Lukhtanov, E., Metcalf, M., Mills, A., Reed, M. W., Sanders, S., Shishkina, I., and Vermeulen, N. M. J. (2002) Reduced aggregation and improved specificity of G-rich oligodeoxyribonucleotides containing pyrazolo[3,4-d]pyrimidine guanine bases. *Nucleic Acids Res. 30*, 4952-4959.

(3) Mende, I., Hoffmann, P., Wolf, A., Lutterbuese, R., Kopp, E., Baeuerle, P. A., de Baey, A., and Kufer, P. (2005) Highly efficient antigen targeting to M-DC8+ dendritic cells via FcgRIII/CD16-specific antibody conjugates. *Int. Immunol. 17*, 539-547.

(4) Marma, M. S., Xia, Z., Stewart, C., Coxon, F., Dunford, J. E., Baron, R., Kashemirov, B. A., Ebetino, F. H., Triffitt, J. T., Russell, R. G. G., and McKenna, C. E. (2007) Synthesis and biological evaluation of a-halogenated bisphosphonate and Pphosphonocarboxylate analogues of risedronate. *J. Med. Chem. 50*, 5967-5975.

(5) Coxon, F. P., Thompson, K., Roelofs Anke, J., Ebetino, F. H., and Rogers Michael, J. (2008) Visualizing mineral binding and uptake of bisphosphonate by osteoclasts and non-resorbing cells. *Bone 42*, 848-60.

ARTICLES

Development and Characterization of New Cyclodextrin Polymer-Based DNA Delivery Systems

Virginie Burckbuchler,[†] Véronique Wintgens,[†] Christian Leborgne,[‡] Sophie Lecomte,[§] Nadine Leygue,[§] Daniel Scherman,[‡] Antoine Kichler,[‡] and Catherine Amiel*,[†]

Institut de Chimie des Matériaux Paris Est, Systèmes Polymères Complexes, Université Paris 12 Val de Marne, CNRS, 2-8 rue Henri Dunant, 94320 Thiais, France, FRE3087 CNRS-Généthon, 1 rue de l'Internationale, BP 60, 91002 Evry Cedex, France, and Laboratoire de Dynamique, Interactions et Réactivité, CNRS, 2-8 rue Henri Dunant, 94320 Thiais, France. Received February 22, 2008; Revised Manuscript Received September 18, 2008

In this study, we investigated whether a cyclodextrin polymer (polyβCD) complexed with cationic adamantyl derivatives (Ada) could be used as a vector for gene delivery. DNA compaction as a function of adamantyl/DNA phosphate ratio (A/P) by this new class of vector was demonstrated using surface enhanced Raman spectroscopy, ζ potential measurements, and DNA retardation assays. Transfection data highlight the relationship between *in vitro* gene delivery efficiency and the combination of several physical properties of the polyβCD/Ada/DNA polyplexes, including cationic polar headgroup valency and chemical structure of the spacer arm of Ada connectors, the adamantyl/DNA phosphate ratio (A/P) of the polyβCD/Ada/DNA polyplexes, and the ionic strength of the medium. Finally, when associating the best formulation with a fusogenic peptide, we reached transfection levels which were of the same order as those obtained with DOTAP.

1. INTRODUCTION

The delivery of DNA and other nucleic acid-based drugs such as siRNAs has a great potential in a wide variety of applications, including basic research and therapies for genetic and acquired diseases. However, the success of gene and siRNA therapies is largely dependent on the development of efficient delivery systems. One approach exploits the properties and tropisms of viruses. This is currently the most widely studied system, including in clinical trials (67% of the trials were done with viral vectors; for more details refer to the Web site http://www.wiley.co.uk/genetherapy/clinical/). All other approaches, collectively termed "nonviral gene delivery systems" try to mimick the efficiency of viral vectors by artificial means (*1*). The most studied nonviral approach consists of using structurally well-defined synthetic compounds, among which a majority is cationic, such as polymers (*2*−*4*), lipids (*5*−*7*), and peptides (*8*−*10*). These molecules share several functions that are essential for transfection: besides condensing the DNA, they usually form positively charged particles which efficiently enter the cell after binding to negatively charged proteoglycans on the outer face of the membrane (*11*). Depending on the carrier, these cationic vectors can also facilitate the escape into the cytosol of the DNA complexes from the lumen of intracellular endolysosomal compartments.

Despite the development of many compounds and a better understanding of the mechanism of transfection, the challenge of producing a nonviral vector with low toxicity and high transfection efficiency still remains. Indeed, polyethylenimines and cationic lipids, which are the most used cationic transfection agents, were shown to have measurable cytotoxicity *in vitro* and *in vivo* (*12*−*14*). Only a few attempts have been made to correlate the influence of the physicochemical properties of DNA complexes on transfection efficiency. The first studies were done with cationic lipid−DNA complexes (*15*−*18*). Structures of DNA complexes based on cationic polymers have also been studied (*19*−*21*), but without correlating the physicochemical characteristics of the DNA complexes with their capacity to deliver DNA (*22*, *23*). In this context, our work aims at both developing a versatile delivery system on the one hand and identifying the physicochemical properties required for an efficient gene transfer on the other hand.

We are developing an innovative system resulting from the association between a cyclodextrin polymer (polyβCD) which has found interest in the field of gene therapy (*24*−*26*) and amphiphilic cationic connectors (Figure 1A). This association is obtained through the formation of inclusion complexes. Cyclodextrins (CD) are cyclic water-soluble molecules of 6 (αCD), 7 (βCD), or 8 (γCD) α-D-glucose units with a cone-shaped architecture describing a cavity with an apolar interior which can induce an inclusion complex with a hydrophobic moiety (*27*, *28*). The hydrophobic group of the amphiphilic cationic connector forms an inclusion complex with the CD cavity of the polyβCD, and this results in a "polycation". The ternary complex, which is being called a "polyplex", is achieved via cooperative electrostatic interactions between the cationic charge of the connector and the negatively charged phosphate groups of DNA. This system should present several advantages: (i) the charge density of the vector is easily controlled by a simple addition of a connector to the vector (polyβCD/connector), (ii) it has been shown that CD can lower the cell

* Corresponding author. Telephone: + 33 1 49 78 12 19. Fax: + 33 1 49 78 12 08. E-mail address: amiel@glvt-cnrs.fr.
[†] Université Paris 12 Val de Marne.
[‡] FRE3087 CNRS-Généthon.
[§] Laboratoire de Dynamique, Interactions et Réactivité, CNRS.

10.1021/bc800070f CCC: $40.75 © 2008 American Chemical Society
Published on Web 11/24/2008

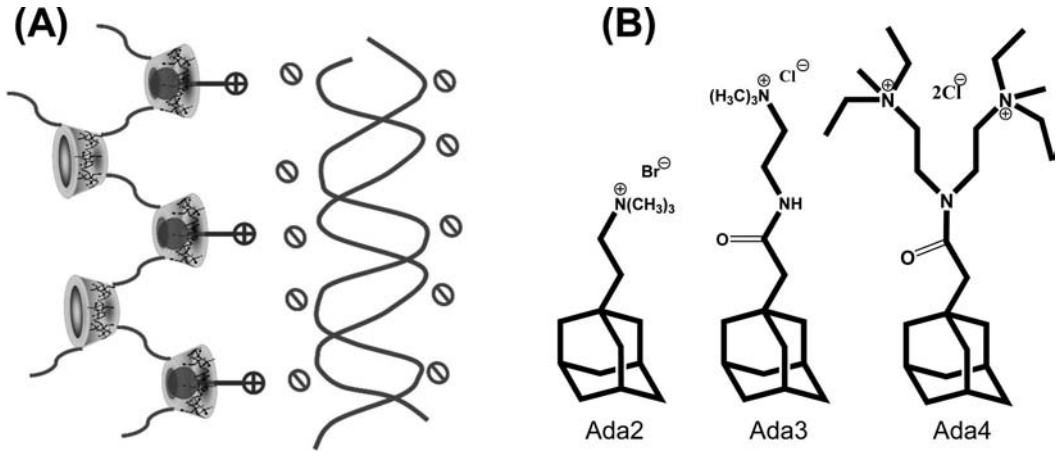

Figure 1. (A) Scheme of polyplex assembly between the cyclodextrin polymer (polyβCD), the connector (Ada), and DNA. (B) Chemical structure of the Ada connectors.

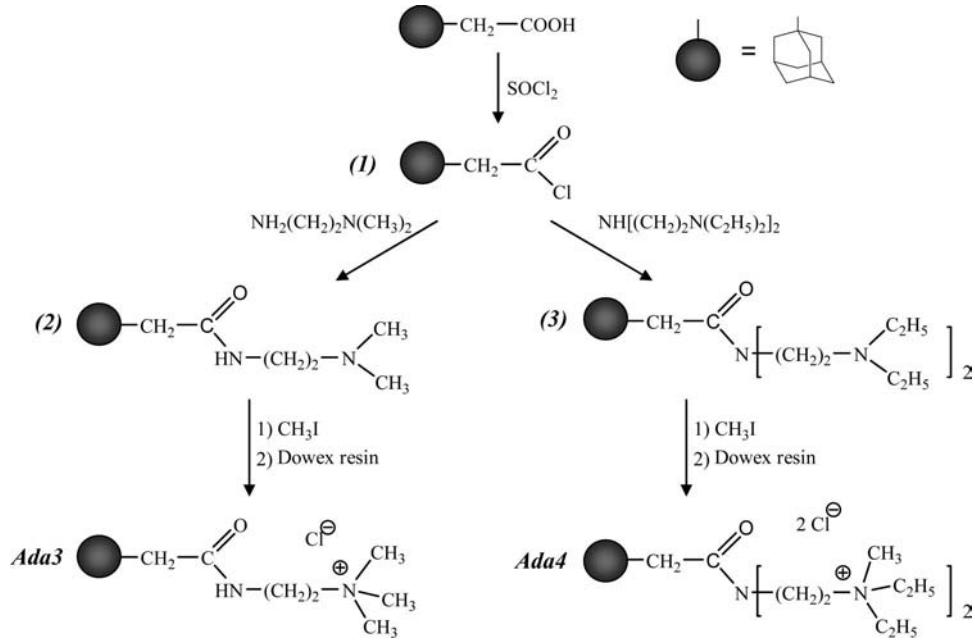

Figure 2. Synthesis scheme of the Ada3 and Ada4 connectors.

toxicity in transfection experiments (*29*) and increase transfection efficiency (*30, 31*), (iii) this vector can also be used for cell targeting using adamantane derivatives coupled to a specific compound recognized by cell receptors (*32*−*34*), and (iv) the polyplex characteristics and thus the transfection properties can be modified by changing the connectors.

In the present study, we have synthesized three different amphiphilic connectors (Figure 1B), which have in common the adamantyl hydrophobic group, which is well-known to make strong inclusion complexes, especially with βCD cavities. Several methods were then used to obtain information about DNA compaction and complexation. DNA mobility shift assays and ζ potential measurements allow the determination of the adamantyl/DNA phosphate ratio required for DNA complexation and the surface charge of the polyplexes. We have earlier elaborated a useful tool to study DNA compaction using surface enhanced Raman spectroscopy (SERS) (*35*). We can follow DNA compaction by monitoring the SERS signal of adenyl residues because the SERS signal of a nucleic acid mainly corresponds to the interaction of adenyl residues with silver colloid $(Ag)_n^+$. DNA compaction involves electrostatic interactions between the phosphate groups of DNA and the ammonium group of the vector. These intermolecular interactions will compete with silver adsorption of adenyl. In this study we also focused on the role of ionic strength in DNA complexation by using DNA retardation assays and small angle neutron scattering. Indeed, in cell culture media the ionic strength is about 170 mM (*36*), which probably influences DNA complexation. Finally, the *in vitro* transfection efficiency of these new DNA vectors was evaluated.

2. MATERIALS AND METHODS

2.1. Synthesis of the Cyclodextrin Polymer. The poly-β-cyclodextrin polymer (polyβCD) was synthesized by polycondensation of βCD (a gift from Roquette Company, France) and epichlorohydrin under strong alkaline conditions (*37*). A full description of the polyβCD synthesis and the polyβCD characterization has been published (*37, 38*). The polyβCD sample used in this study has an average molecular weight of M_w = 160 000 g mol^{-1} with a βCD content of 59% w/w, and its polydispersity index is M_w/M_n = 1.9.

2.2. Synthesis of Adamantanyl Connectors. Ada2 (2-(1-adamantyl)ethyltrimethylammonium bromide) was synthesized according to the previously published procedure (*35*).

The synthesis scheme of Ada3 and Ada4 connectors is described in Figure 2, and the experimental procedure was as follows:

Ada3 (2-(1-Carbamoylmethyladamantane)ethyltrimethylammonium Chloride). 1-Adamantane acetic acid (7 g, 36 mmol, Aldrich, Saint-Quentin-Fallavier, France) dissolved in 20 mL of thionyl chloride (Aldrich, Saint-Quentin-Fallavier, France) was placed in a distilled apparatus. After 1 h of reflux, thionyl chloride was removed by distillation and the apparatus was kept under vacuum. 5.8 g of 2-(1-adamantyl)ethanoyl chloride (**1**) as a pale pink liquid was obtained by distillation (75% yield). Compound **1** was characterized by ^{1}H NMR ($CDCl_3$, 300 MHz) δ (ppm): 1.8 − 1.7 (m, 12H; Ada), 2.1 (s, 3H; Ada), 2.7 (s, 2H; $-CH_2-CO$).

2-(1-Adamantyl)ethanoyl chloride (**1**) (2.12 g, 10 mM) was added dropwise to a solution of *N*,*N*′-dimethylethylenediamine (0.8 mL, 7 mmol, Aldrich, Saint-Quentin-Fallavier, France) in 15 mL of pyridine previously placed under argon at 0 °C. Then, the mixture was stirred overnight and protected from the light. The product was evaporated three times with acetone to remove pyridine. The obtained solid was dissolved in a solution of H_2SO_4 (10%, pH = 2.3) and then extracted with ether. Sodium hydroxide was added to the aqueous layer at 0 °C until pH = 10 and then extracted with ether. Before being dried over anhydrous $MgSO_4$, 2 g of product (**2**) was obtained as a beige solid (75% yield). Compound **2** was characterized by ^{1}H NMR ($CDCl_3$, 300 MHz): δ (ppm): 1.6 (m, 12H; Ada), 1.9 (m, 5H; Ada and Ada-CH_2-), 2.2 (s, 6H; -N(CH_3)$_2$), 2.4 (t, 2H; -N-CH_2), 3.3 (q, 2H; $-CH_2-NH$).

Compound **2** (2 g, 76 mmol) was dissolved in 5 mL of anhydrous dichloromethane, and then 1 mL of iodomethane (Aldrich, Saint-Quentin-Fallavier, France) was added drop by drop. The mixture was kept under reflux for 7 h and the solution was cooled to room temperature. Ether was added before filtration to obtain 2.6 g of Ada3 (80% yield) as a white solid. Iodide counterion was exchanged by chloride counterion with Dowex (2 × 8−100) anion exchange resin (Aldrich, Saint-Quentin-Fallavier, France).

Ada3 was characterized by ^{1}H NMR ($CDCl_3$, 300 MHz) δ (ppm): 1.6−1.7 (m, 12H; Ada), 1.9 (m, 3H; Ada), 2.0 (s, 2H; Ada-CH_2-), 2.4 (t, 2H; -N-CH_2), 3.5 (s, 9H; -CH_3), 3.8−3.9 (m, 2H; $-CH_2-CH_2-N$).

Ada4 (2-(1-Carbamoylmethyladamantane)di(ethyl(diethylmethylammonium)) dichloride). A solution of 2-(1-adamantyl)ethanoyl chloride (**1**) (1 g, 4.7 mmol, Aldrich, Saint-Quentin-Fallavier, France) in 10 mL of anhydrous ether was added drop by drop under argon to a solution of *N*,*N*,*N*′,*N*′-tetraethyldiethylenetriamine (1.33 mL, 5.1 mmol, Aldrich, Saint-Quentin-Fallavier, France) in a mixture of 30 mL of anhydrous ether and 0.65 mL of triethylamine. After 2 h of reflux, the white solid formed was filtered to eliminate triethylammonium chloride. The solution was evaporated to give 1.85 g (80% yield) of compound **3** as a yellow oil. Compound **3** was characterized by ^{1}H NMR ($CDCl_3$, 300 MHz) δ (ppm): 1.1 (m, 12H; -CH_3), 1.7 (m, 12H; Ada), 1.9 (m, 3H; Ada), 2.1 (s, 2H; Ada-CH_2-), 2.6 (m, 12H; $-N-C\underline{H}_2-CH_3$ and -CO-N-$CH_2-C\underline{H}_2$-), 3.4 (m, 4H, -CO−N−$C\underline{H}_2$-CH_2-).

To a solution of 1.5 g (3.8 mmol) of compound **3** in 50 mL of anhydrous dichloromethane was added drop by drop 1 mL of iodomethane. The mixture was kept under reflux for 2 h, and the solution was cooled to room temperature. The solution was filtered, and the solid product was washed with ether to give 1.8 g (70% yield) of Ada4 as a white solid. Iodide counterions were exchanged by chloride counterions with Dowex (2 × 8−100) anion exchange resin. Ada4 was characterized by ^{1}H NMR (DMSO, 300 MHz) δ (ppm): 1.2 (m, 12H; -CH_3), 1.6 (m, 12H; Ada), 1.9 (m, 3H; Ada), 2.1 (s, 2H; Ada-CH_2-), 3.0 (m, 6H; $^+N-CH_3$), 3.4 (m, 12H, $-CO-N-C\underline{H}_2-CH_2-$ and $-CH_2-CH_3$), 3.6 and 3.8 (m, 4H; $-CH_2-N^+$).

2.3. Polyplex Preparation. The vector composed of the polyβCD and the connector was generated by mixing a fixed amount of CD cavities of polyβCD [120 μmol·L^{-1} (10 equiv)] with various amounts of adamantyl connector ranging from 12 μmol·L^{-1} (1 equiv) to 120 μmol·L^{-1} (10 equiv). Polyplex formation was achieved by adding DNA plasmid solution in order to have a fixed 12 μmol·L^{-1} (1 equiv) of phosphate groups. All complexes were prepared in ultrapure water. PolyβCD/Ada/DNA polyplexes were prepared at various adamantyl/DNA phosphate ratios (A/P), which corresponds to the ratio between the number of adamantyl connectors and the DNA phosphate group number.

2.4. Physicochemical Characterization. *2.4.1. Fluorescence Measurements.* The association constants (determined with a standard deviation of 10%) between the cyclodextrin derivatives and the connectors were measured with a SLM Aminco 8100 fluorimeter (Bioritech, Chamarande, France). A complete description of the method was published previously (*39*). A fluorescent probe, 4-amino-*N*-*tert*-butylphthalimide, able to make inclusion complexes with CDs, was used as a competitor (*40*) for Ada2, Ada3, and Ada4. The cyclodextrin derivatives used in these experiments are βCD, (2-hydroxypropyl)-β-CD (HPβCD) (Aldrich, Saint-Quentin-Fallavier, France), and the synthesized polyβCD.

2.4.2. DNA Retardation Assays. The polymeric vector binding to the DNA at different adamantyl/DNA phosphate ratios (A/P) was determined by using a 1% agarose gel electrophoresis (w/v) containing ethidium bromide in a TBE buffer (89 mM Tris/89 mM boric acid/2 mM EDTA, pH = 8.3). Gels were run for 15 min at 100 V, and DNA was visualized using an UV illuminator.

2.4.3. ζ Potential. The ζ potential of the polyplexes were analyzed using a Zetasizer nano ZS (Malvern Instruments) at 25 °C. The measurements were performed in folded capillary cell (DTS 1060C, Malvern Instruments) with a 4 mW He−Ne laser at a wavelength of 633 nm. The ζ potential was automatically calculated from the electrophoretic mobility based on the Hemholtz−Smoluchowski relationship (*41*) for the polyplex polyβCD/Ada/DNA and based on the Hückel approximation for the vector polyβCD/Ada.

2.4.4. Surface Enhanced Raman Spectroscopy (SERS). The SERS experiments were carried out at 488 nm excitation of an argon ion laser on a Dilor XY Raman spectrophotometer (Horiba Jobin Yvon SAS, Longjumeau, France) equipped with a liquid-nitrogen-cooled CCD camera. Silver colloids for SERS measurements were prepared according to the Creighton method (*42*) and display an absorption band centered at 398 nm measured on a Cary 3 UV−visible spectrometer (Varian, Les Ulis, France). Polyplex samples were obtained by mixing 90 μL of colloid with 10 μL of polyplex aqueous solution and 10 μL of a 1 mM aqueous solution of $MgCl_2$. All SERS spectra were recorded after an incubation time of 20 min. The laser power was fixed at 40 mW at the sample, and the accumulation time was fixed at 180 s.

2.4.5. Small-Angle Neutron Scattering (SANS). The SANS experiments were carried out with the PACE spectrometer at the Laboratoire Léon Brillouin (LLB), Saclay, France. The experimental scattering vector **q** (**q** = $(4\pi/\lambda)\sin(\theta/2)$) range was $0.0032 < \mathbf{q}$ (Å^{-1}) < 0.12 and was covered by two sample-to-detector distances (3 m at the neutron wavelength of 6 Å^{-1} and 4.6 m at 13 Å^{-1}). The wavelength dispersion $\Delta\lambda/\lambda$ of the

velocity selector was 10%. The samples were kept in quartz cells (Hellma) with a path length of 2 mm for samples in D_2O. The collected data were normalized for the detector efficiency using the isotropic scattering of a 1 mm thick calibration sample of H_2O. The raw data were corrected for background from the solvent and sample cells. All the samples were prepared in D_2O to maximize the contrast between the β-cyclodextrin polymer (ρpolyβCD $= 2.29 \times 10^{10}$ cm^{-2}) and the solvent ($\rho D_2O = 6.41 \times 10^{10}$ cm^{-2}). The scattering length densities of Ada2, Ada3, and Ada4 are 0.22×10^{10} cm^{-2}, 0.46×10^{10} cm^{-2}, and 0.23×10^{10} cm^{-2}, respectively (without the counterions). In the SANS experiments, the DNA samples used are extracted from herring sperm (Sigma). Due to a lack of information regarding the relative composition in adenine, guanine, cytosine, and thymine, the scattering length density of the DNA sample could not been calculated (a theoretical value of 4.11×10^{10} cm^{-2} has been reported in the literature for the scattering length density of chicken erythrocyte nucleosomal DNA) (*43*).

The concentration of each compound in the polyplex formulation is as follows: $C_{poly\beta CD} = 10^{-2}$ M (corresponding to 10 equiv of βCD cavities), $C_{DNA} = 10^{-3}$ M (1 equiv of phosphate groups), $C_{Ada2} = 5 \times 10^{-3}$ M (5 equiv of adamantyl groups), and $C_{Ada3} = 5 \times 10^{-3}$ M (5 equiv of adamantyl groups). Because the scattered intensities of polyplex used under the concentration conditions of the other techniques are too weak to be detected, all sample concentrations are 10-fold higher in the SANS experiments.

2.5. Cell Culture and Transfection. In vitro cell transfection experiments have been performed using a plasmid DNA SMD2-LucΔITR (7.6 kb) encoding a luciferase gene on the human hepatocarcinoma cell line HepG2 (American type Culture Collection, Rockville, MD) and the human transformed embryonal kidney cells HEK293 (American type Culture Collection, Rockville, MD). Cells were plated 24 h before transfection in 24-well plates at 37 °C in a 5% CO_2/95% air incubator in a complete medium DMEM (Dulbecco's modified Eagle's medium) supplemented with 1% (v/v) of the penicillin−streptomycin antibacterial solution (Invitrogen) and 10% (v/v) fetal bovine serum (Invitrogen). For transfection, cells were used at 50−80% confluency and all the tests were performed in triplicate. Culture media was removed and replaced by a mixture of 400 μL of serum free DMEM and 100 μL of polyplex aqueous solution at the desired adamantyl/DNA phosphate ratio (A/P) containing 2 μg of plasmid DNA per well. After 3 h, the transfection medium was removed and replaced with 1 mL of complete medium. Luciferase activity was measured 24−48 h post-transfection. The luciferase assay was performed as described (*44*). Luciferase background was subtracted from each value, and the transfection efficiency was expressed as total light units/10 s/well and is the means of the triplicates. The protein content of the transfected cells was measured by using the BioRad protein assay.

Where indicated, the transfection experiments were done in the presence of the fusogenic peptide JTS-1 (Genepep), which has the following sequence: GLFEALLELLESLWELLLEA. The commercialized transfection agents PEI of 25 kDa (*2*) and the cationic lipid DOTAP (*7*) (*N*-(1-(2,3-dioleoyloxy)propyl)-*N*,*N*,*N*-trimethylammonium chloride) were used without peptide. DOTAP was used at a ± charge ratio of 4 whereas, for B-PEI, we used an amine to phosphate ratio of 13. Notably, in preliminary experiments, we found that these ratios were optimal for the transfection of HepG2 and HEK293 cells.

2.6. Cell Viability Assay. Cytotoxicity was evaluated by performing the 3-(4,5-dimethylthiazol-2-yl)-2,5-diphenyltetrazolium bromide (MTT; Sigma) assay (*45*). Briefly, one day after transfection, the cell culture medium was removed and replaced by serum-free DMEM containing 0.5 mg/mL MTT. After incubation at 37 °C for 3 h, the medium was removed and 200 μL of DMSO was added to each well to dissolve the formazan crystals produced from the reduction of MTT by viable cells. Absorbance was then measured at 570 nm. Untreated cells were used as control.

Table 1. Logarithm of the Binding Constants (Determined with a SD of 10%) for Different Cyclodextrin Derivatives (βCD, HPβCD, and polyβCD) to the Adamantyl Connectors (Ada2, Ada3, and Ada4) and Their Variation with the Addition of NaCl

	Ada2	Ada3	Ada4
$\log(K_{\beta CD})$	4.95	5.56	4.89
$\log(K_{HP\beta CD})$	3.95	3.98	3.18
+ NaCl 150 mM	*4.04*		*3.11*
$\log(K^{app}{}_{poly\beta CD})$	3.04	2.85	2.18
+ NaCl 150 mM	*3.72*		

3. RESULTS AND DISCUSSION

3.1. Chemical Structure of the Connectors. The adamantyl connectors described in Figure 1B have been synthesized in order to evaluate the influence of the chemical structure on the transfection efficiency, in terms of the spacer and the charge valency of the polar headgroup. The three connectors have in common a hydrophobic adamantyl group, which is well-known to form inclusion complexes with CDs. The Ada2 connector has a spacer formed by an alkyl chain, and the polar headgroup is monocationic. On the other hand, Ada3 and Ada4 have a spacer composed by an amide function which is able to form hydrogen bonds with DNA (*46*−*48*). Furthermore, Ada3 has a monocationic polar headgroup whereas Ada4 is bicationic.

3.2. Fluorescence Measurements. Table 1 shows the logarithm of the binding constants, obtained by fluorescence measurements, of the three adamantyl connectors (Ada2, Ada3, and Ada4) for the cyclodextrin derivatives βCD, HPβCD, and polyβCD. These three cyclodextrin derivatives have different cavity accessibilities with an encumbering which ranks as follows: βCD < HPβCD < polyβCD.

Adamantane derivatives show good affinities for βCD, as described in the literature (*49*). The logarithms of the binding constants are of the order of 5. HPβCDs have a higher steric hindrance than βCD due to their hydroxypropyl groups. This hindrance results in a decrease of the logarithm of the binding constants by one unit for Ada2 and by about 1.6−1.7 for Ada3 and Ada4 connectors. This corresponds to decreases from 20 to 30% of the binding energies. The measurements performed in a salt-rich medium in order to reduce the electrostatic repulsions of charges did not alter the binding efficiencies. Thus, the decrease of the binding constants is mainly due to a steric hindrance phenomenon. The lowest binding constants are obtained for polyβCD with Ada2, Ada3, and Ada4, as shown in Table 1. This is due to two complementary effects. On the one hand, the steric hindrance of the polyβCD, which is a branched cyclodextrin polymer, causes limited cavity accessibility. On the other hand, the polyelectrolyte behavior of the vector polyβCD/Ada generates unfavorable electrostatic repulsions between the connectors in solution and those which are already complexed in the CD cavity of the polyβCD. These electrostatic repulsions hinder complete complexation of free connectors. The Ada4 connector, with its two positive charges, is particularly sensitive to this effect, as shown by the low value of the logarithm of the binding constant ($\log(K^{app}{}_{poly\beta CD/Ada4}) = 2.18$). This value is lower by one unity than the one obtained for the complexation of polyβCD with Ada2 ($\log(K^{app}{}_{poly\beta CD/Ada2}) = 3.04$). The increase of this later value with NaCl salt addition ($\log(K^{app}{}_{poly\beta CD/Ada2}NaCl) = 3.72$) supports the explanation of unfavorable electrostatic repulsions (Table 1).

3.3. DNA Complexation and Compaction. *3.3.1. DNA Retardation Assay.* We determined, in a first set of experiments,

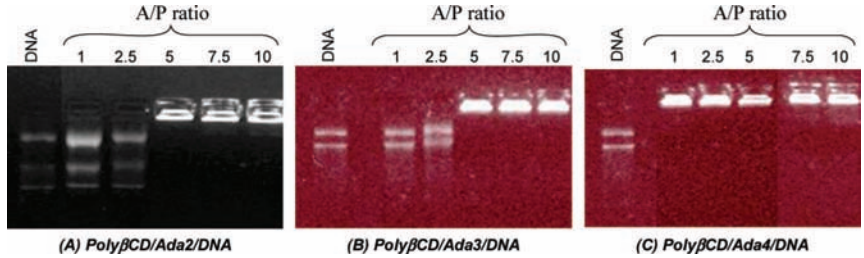

Figure 3. DNA retardation assay performed with the following DNA complexes: (A) Ada2 polyplexes, (B) Ada3 polyplexes, and (C) Ada4 polyplexes prepared at different adamantyl/DNA phosphate ratios (A/P).

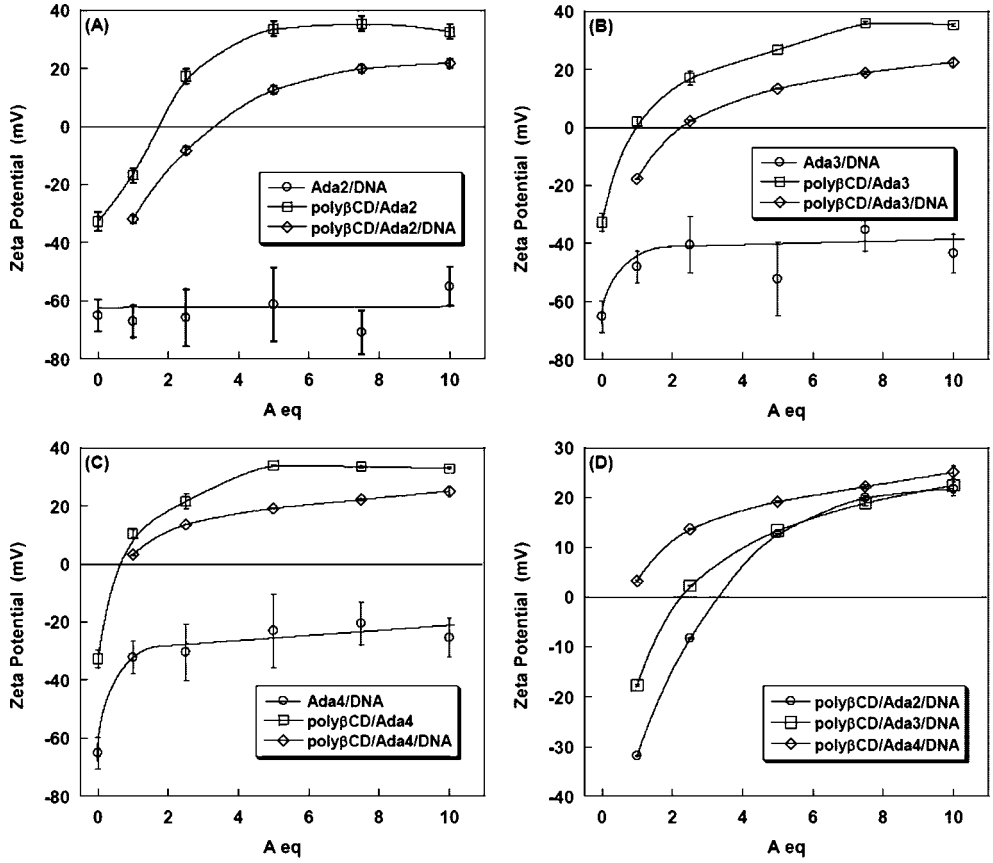

Figure 4. ζ potential of the three systems Ada/DNA vector, poly*β*CD/Ada vector, and poly*β*CD/Ada/DNA polyplex, at different adamantyl equivalents (A eq) (1 A eq = 12 μmol·L^{-1}), as a function of the connector: (A) Ada2, (B) Ada3, and (C) Ada4. (D) Comparison of the polyplex behavior according to the type of Ada connector.

the ability of the different vectors to interact with plasmid DNA by performing a gel shift mobility assay which allows us to identify the amount of cationic vector required to inhibit the migration of the plasmid DNA during gel electrophoresis. Figure 3 shows the results of the DNA retardation assay using Ada2, Ada3, and Ada4 polyplexes prepared at an adamantyl/DNA phosphate ratio (A/P) ranging from 1 to 10. The first lane of each gel corresponds to noncomplexed plasmid DNA. Notably, the different bands represent three forms of the plasmid DNA. It is also important to mention that the connectors Ada2, Ada3, and Ada4 alone, used in the absence of poly*β*CD, are not able to compact DNA (data not shown). The resulting gels show that the different vectors altered the DNA migration, which underscores that poly*β*CD is an essential component of the vector system. For Ada2 and Ada3 polyplexes, full retardation occurs at about the same charge ratio (i.e., A/P between 2.5 and 5). Ada4 polyplexes inhibit DNA retardation slightly more efficiently than the two other systems, since an A/P = 1 (equivalent to a ± ratio of 2) is sufficient due to its bicationic headgroup.

3.3.2. ζ Potential. In order to study more accurately the interactions of poly*β*CD/Ada with DNA, we performed ζ potential measurements of the polyplexes. Figure 4 reports the ζ potential as a function of the adamantyl equivalents (A eq) for the following different systems: connector/DNA, poly*β*CD/connector, and poly*β*CD/connector/DNA. We observed the same behaviors for the three connectors Ada2 (Figure 4A), Ada3 (Figure 4B), and Ada4 (Figure 4C). First, a connector/DNA mixture generates a negative ζ potential, proving the inability of the connector alone to mediate DNA complexation. The addition of poly*β*CD permits us to obtain a positive ζ potential value, indicating a DNA complexation which is consistent with the gel electrophoresis results. Notably, the DNA association with poly*β*CD/connector induces lower ζ potentials than the poly*β*CD/connector alone. This surface charge decrease, which is expected, is due to the neutralization of cationic charges by the anionic charges of the DNA. Figure 4D compares the ζ potential variation of the three polyplexes as a function of the adamantyl equivalents (A eq). At low A eq, Ada2 and Ada3 polyplexes have negative ζ potential values, indicating the

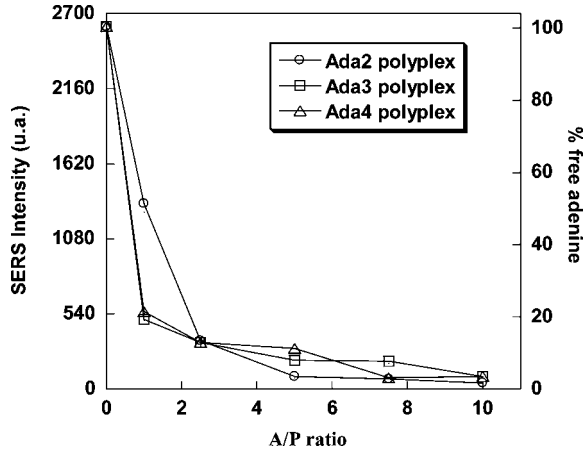

Figure 5. Influence of the nature of the connector on the SERS intensity of the polyplexes and on the percentage of free adenyl residues within the polyplexes.

presence of free DNA phosphate groups. Interestingly, a neutral surface charge of the polyplexes is obtained at an adamantyl equivalent of A/P ~ 3.3 for Ada2, A/P = 2.2 for Ada3, and of A/P = 1 for Ada4 polyplexes. These results underline that the ability of Ada4 to complex DNA depends on the chemical structure of the connectors. Of note, the Ada3 vector offers better DNA complexation properties than Ada2, probably due to the amide function of its spacer, which can create hydrogen bonds with the DNA bases. Finally, the even more efficient DNA complexation properties of Ada4 may be based on the combination of two effects: hydrogen bonding as with Ada3 and the multivalency of the polar headgroup.

3.3.3. Surface Enhanced Raman Spectroscopy (SERS). The Raman signal intensity of an adsorbed molecule on or near special metal surfaces such as silver colloids can be enhanced by factors of up to 10^8 relative to the signal obtained for the same compound at the same concentration by classical Raman spectroscopy. This enhancement of diffusion permits the detection of molecules at very low concentration (10^{-6} M to 10^{-10} M) and then is particularly attractive for DNA studies. The SERS advantage is its ability to analyze the adenyl bases availability in nucleic acids. In fact, it has been proven that adenine is a very good SERS active molecule because free adenine has a specific affinity for silver colloids. Thus, the SERS signal of nucleic acids is mainly due to the interaction of these residues with the silver colloid. The spectral intensity of the observed SERS signal is a function of the availability of these residues. We have shown that the SERS method can be used to study the DNA compaction (*35*). The DNA compaction was analyzed in terms of the SERS signal decrease of adenyl residues by monitoring the intensity of the band at 1046 cm^{-1}. This band is assigned to the vibrational motion of the $C(6)NH_2$ site (*35*) and acts as a probe of the amount of adenyl adsorbed onto the silver colloids.

Figure 5 shows the influence of the vector adamantyl/DNA phosphate ratio (A/P) on the adenyl residues accessibility of DNA at 1046 cm^{-1}. The first point at the origin corresponds to the reference SERS signal intensity of DNA alone at 1046 cm^{-1}. At low adamantyl/DNA phosphate ratio (A/P), the SERS intensity decreases strongly due to the formation of cooperative interactions between the cationic polar head of the connector and the anionic phosphate groups of DNA. Because of these interactions, which induce DNA reorganization, adenyl residues become more and more inaccessible to the silver colloids. The SERS intensity variation reveals an equivalent pattern for both polyβCD/Ada3 and polyβCD/Ada4 vectors whereas the polyβCD/Ada2 vector shows a milder variation. This indicates again that the polyβCD/Ada2 vector has less efficient DNA compaction properties. The formation of efficiently compacted polyplexes occurs at the adamantyl/DNA phosphate ratio 2.5 < A/P < 5 for the Ada2 polyplexes and at 1 < A/P < 2.5 for both Ada3 and Ada4 polyplexes. The free adenine percentage within the

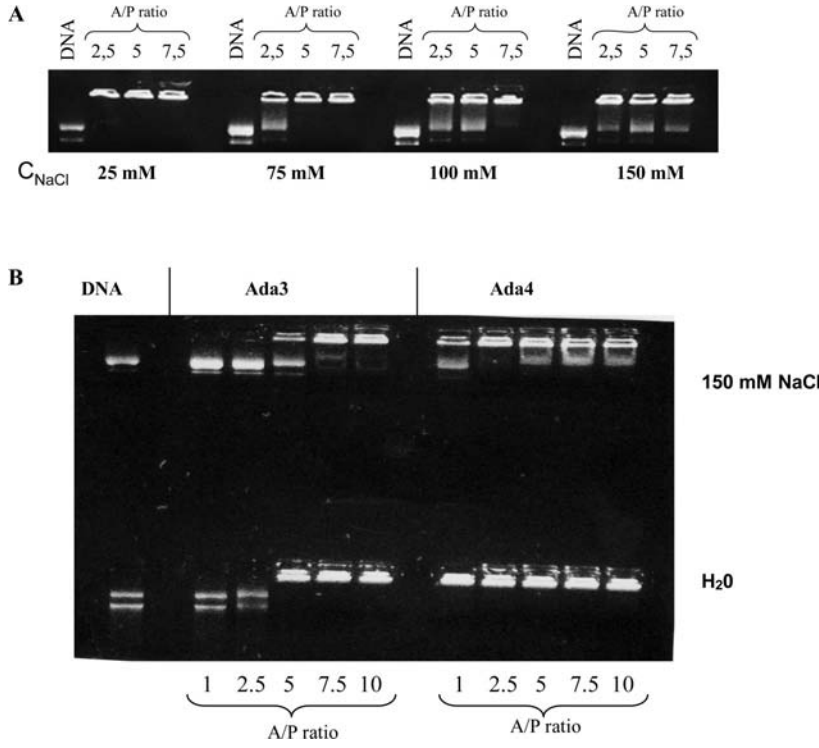

Figure 6. (A) Stability study of polyβCD/Ada2/DNA polyplexes at different adamantyl/DNA phosphate ratios (A/P = 2.5, 5, 7.5) in the presence of various NaCl concentrations (C_{NaCl} = 25, 75, 100, and 150 mM). (B) Stability of polyβCD/Ada3 and Ada4/DNA polyplexes at different adamantyl/DNA phosphate ratios (A/P = 1, 2.5, 5, 7.5, 10) in water or in the presence of 150 mM of NaCl.

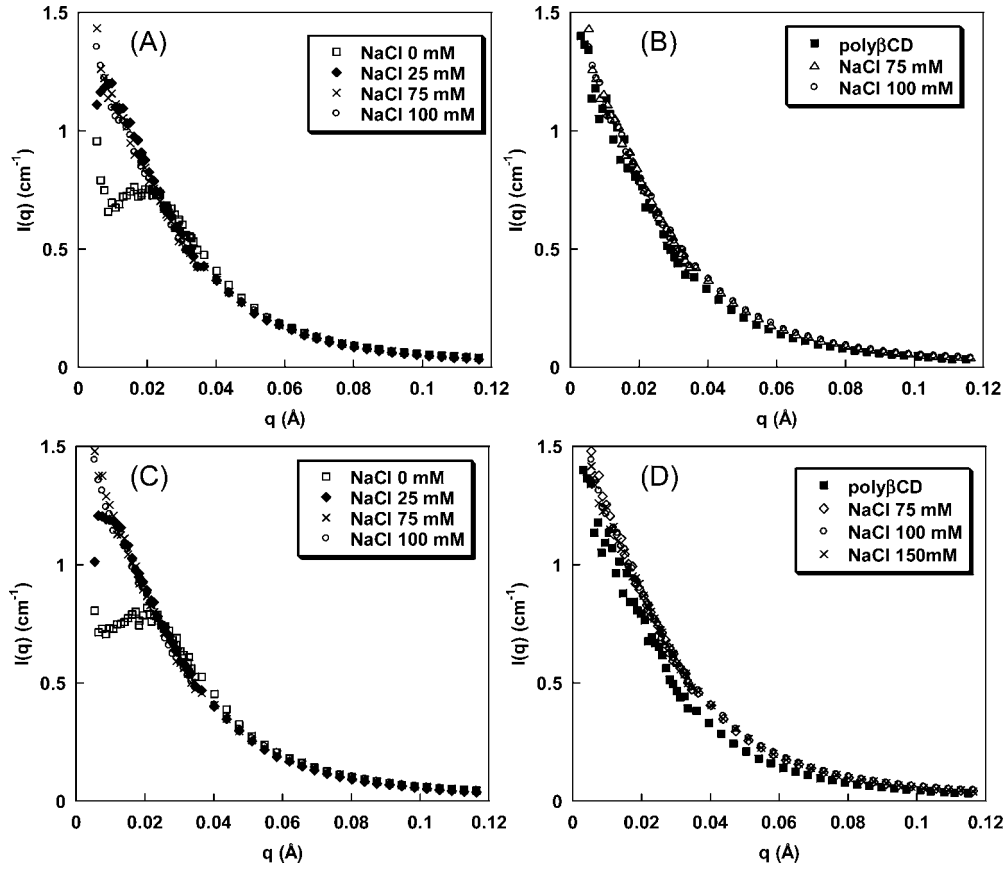

Figure 7. (A) Ionic strength influence on the scattered intensities of polyβCD/Ada2/DNA (10/5/1) polyplexes and (B) comparison of the scattering behavior of the polyβCD alone in solution with the scattering behavior of polyβCD/Ada2/DNA (10/5/1) polyplexes in 75 mM and 100 mM salt concentration. (C) Ionic strength influence on the scattered intensities of polyβCD/Ada3/DNA (10/5/1) polyplexes and (D) comparison of the scattering behavior of the polyβCD alone in solution with the scattering behavior of polyβCD/Ada3/DNA (10/5/1) polyplexes in 75, 100, and 150 mM salt concentration.

polyplex was estimated at different adamantyl/DNA phosphate ratios (A/P) by the probe band at 1046 cm^{-1} and corresponds to the intensity ratio $(I_{polyplex}/I_{DNA})_{1046cm}{}^{-1}$, where I_{DNA} is the reference SERS intensity of DNA and $I_{polyplex}$ is the SERS intensity of the polyplex at the adamantyl/DNA phosphate ratio (A/P). Under the preparation conditions of the neutral polyplex (from the ζ potential data), Ada2 polyplexes have nearly 10% (A/P = 3.3) of free adenyl residues, the Ada3 polyplex has 14% (A/P = 2.2), and the Ada4 polyplex has 21% (A/P = 1). The percentage of free adenyl residues decreases with an increase of the adamantyl/DNA phosphate ratio, which is an indication of the strength of DNA compaction. The Ada4 vector shows the highest free adenine percentage because the neutral polyplex was obtained at the lowest A/P ratio due to its bivalency. At highest adamantyl/DNA phosphate ratio, <5% of adenyl residues are free, suggesting a strong DNA compaction. These results clearly demonstrate that DNA compaction by the presented new vectors is efficient and depends on the nature of the connector.

3.4. Salt Effect on Polyplex Stability. Figure 6 shows the influence of ionic strength on the Ada2 polyplex stability. The Ada2 polyplexes have been prepared at three different adamantyl/DNA phosphate ratios, A/P = 2.5, 5, and 7.5, and at four different NaCl concentrations, C_{NaCl} = 25, 75, 100, and 150 mM (physiological salt conditions). At weak salt concentration (i.e., 25 mM), all DNA was retarded onto the gel, showing that Ada2 polyplex stability was unaffected. When the salt concentration was increased, the DNA retardation assays show a dissociation of the Ada2 polyplexes. This phenomenon depends on the adamantyl/DNA phosphate ratio and is demonstrated by the presence of the plasmid DNA which migrates toward the cathode in a similar manner as naked DNA. At C_{NaCl} = 75 mM, only the Ada2 polyplex with a A/P = 2.5 is partially dissociated. A concentration of C_{NaCl} = 100 mM induces dissociation of Ada2 polyplexes prepared at an adamantyl/DNA phosphate ratio of 2.5 and 5. Finally, under physiological salt conditions (C_{NaCl} = 150 mM), the Ada2 polyplexes are subject to a partial dissociation even at the highest adamantyl/DNA phosphate ratio tested. These results show that an increase of the ionic strength induces a partial dissociation of the Ada2 polyplexes which is probably due to a shielding of the electrostatic interactions. Notably, the polyβCD/Ada complex remains assembled because it has been demonstrated that an increase of the ionic strength reinforces hydrophobic interactions. A partial dissociation of the DNA complexes in the presence of 150 mM of NaCl was also observed with Ada3 and Ada4 (Figure 6B).

These results were complemented with small angle neutron scattering measurements. The ionic strength effect on Ada2 polyplex and Ada3 polyplex prepared at an adamantyl/DNA phosphate ratio A/P = 5, with different NaCl concentrations, C_{NaCl} = 0 (salt-free), 25, 75, 100, and 150 mM (physiological salt conditions), is shown in Figure 7A and 7C. These results express the influence of the salt addition on the conformation of the polyβCD chains and on their interactions with the polyplex and the surrounding medium. Under salt-free conditions, the scattering behaviors of both Ada2 polyplex (Figure 7A) and Ada3 polyplex (Figure 7C) show a clear diffusion peak which is characteristic of a polyelectrolyte (PEL) behavior. Indeed, these peaks indicate that, in the presence of connector Ada2 or Ada3, the polyplexes repulse each other by electrostatic interactions due to the global positive charge carried by the polyplexes. At weak ionic strength (C_{NaCl} = 25 mM), the

scattering behavior describes a poorly defined PEL peak, which indicates that the critical salt concentration which allows entire charge shielding is almost reached. The increase of the ionic strength at $C_{NaCl} = 75$ mM is sufficient to induce the disappearence of the PEL peaks obtained in salt-free conditions. The PEL peak is replaced by a monotonous intensity decrease as a function of **q**, which indicates a shielding of Coulombic repulsive interactions of polycationic chains. The same behavior is also observed at higher salt concentrations. Parts B and D of Figure 7 compare the diffusion behavior of Ada2 and Ada3 polyplexes, respectively, prepared at $C_{NaCl} = 75$ mM and above, with the scattering behavior of polyβCD alone in salt-free solution. In the case of Ada2 polyplexes (Figure 7B), their diffusion curves were superimposed with the one of polyβCD alone. This result shows that Ada2 polyplexes are dissociated for $C_{NaCl} \geq 75$ mM. From these data, it may be concluded that the weak charge density of the polyβCD/Ada2 vector does not permit the DNA complexation in the presence of salt.

In comparison, the diffusion curves of Ada3 polyplexes (Figure 7D), prepared at NaCl concentrations ranging from 75 to 150 mM, were not superimposed to the scattering behavior of polyβCD alone even under physiological salt conditions ($C_{NaCl} = 150$ mM). This result suggests that Ada3 polyplexes are less sensitive to the effect of salt than the Ada2 complexes, which is probably due to the hydrogen bond involved between the amide function of its spacer and the DNA bases.

3.5. In Vitro Transfection. After having studied the influence of the connector's chemical structure on polyβCD/Ada/DNA interaction properties, we evaluated the ability of the vectors to transfect DNA into cells. *In vitro* cell transfection experiments have been performed using a plasmid DNA encoding a *luciferase* gene on HepG2 and HEK293 cells. The addition of the JTS-1 peptide to polyplexes such as polylysine/DNA was previously shown to significantly increase the transfection efficiency, probably by improving the escape of the complexes from the endosomes (*50*). The adamantyl/DNA phosphate ratio (A/P) of the polyplexes used in the transfection studies was increased to increase the fraction of complexed connector, due to the poor apparent binding constant ($K^{app}_{poly\beta CD/Ada} < 10^3\ M^{-1}$) of Ada3 and Ada4 (Table 1). It should be specified that these constants are probably much lower than the ones in the ternary systems (not determined) where additional cooperative effects of coupled inclusion complex and electrostatic interactions might increase the affinity constants.

The transfection studies first revealed that the Ada2 polyplexes have only marginal DNA delivery efficiencies (data not shown). This was expected, since the ionic strength of the culture medium DMEM (i.e., 170 mM) probably induces polyplex dissociation before they can enter into the cells. Complexes generated with Ada3 were then evaluated on HepG2 cells by using increasing amounts of JTS-1 (Figure 8A). The results show that the addition of the fusogenic peptide is unable to increase the transfection activity above the control (i.e., without JTS-1). The same experiments were repeated using HEK293 cells, which are known to be more permissive to transfection than HepG2 cells. This time, the polyplexes generated with the highest dose of polyβCD/Ada3/JTS-1 allowed for a significantly higher transgene expression than polyplexes without JTS-1. However, the expression levels still remained several orders of magnitude lower than those obtained with B-PEI or DOTAP (Figure 8B).

Finally, we evaluated the transfection activity of the Ada4 vector on both cell lines. As shown in Figure 9, this formulation had a transfection efficiency which was of the same order as that of DOTAP on both cell lines. Notably, the efficiency of the Ada4 based complexes was dependent on the amount of added JTS-1 peptide (the difference between 10 and 40 μg of JTS-1 is significant on both cell lines). The best transfection results were obtained with the highest amount of peptide that was tested (i.e., 40 μg). Noteworthy also is the fact that the

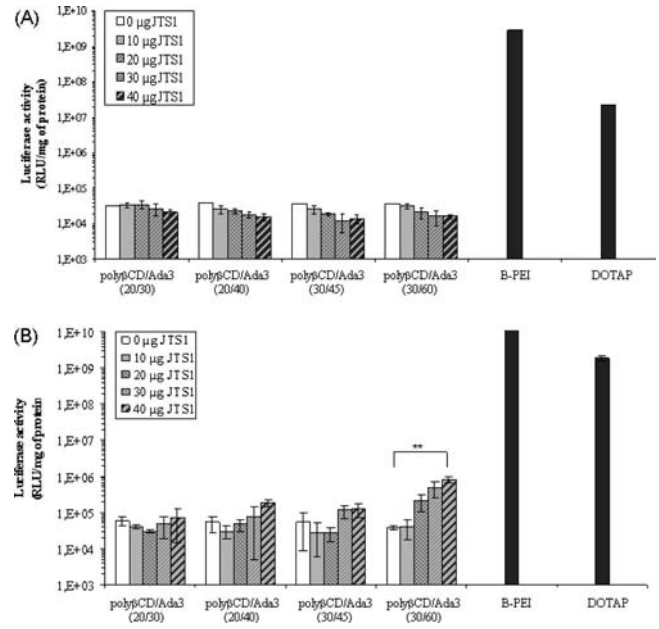

Figure 8. Transfection efficiency of Ada3-based polyplexes on (A) HepG2 cells and (B) HEK293 cells. Differences between formulations were determined using the Student's paired *t* test: $^{**}p < 0.01$.

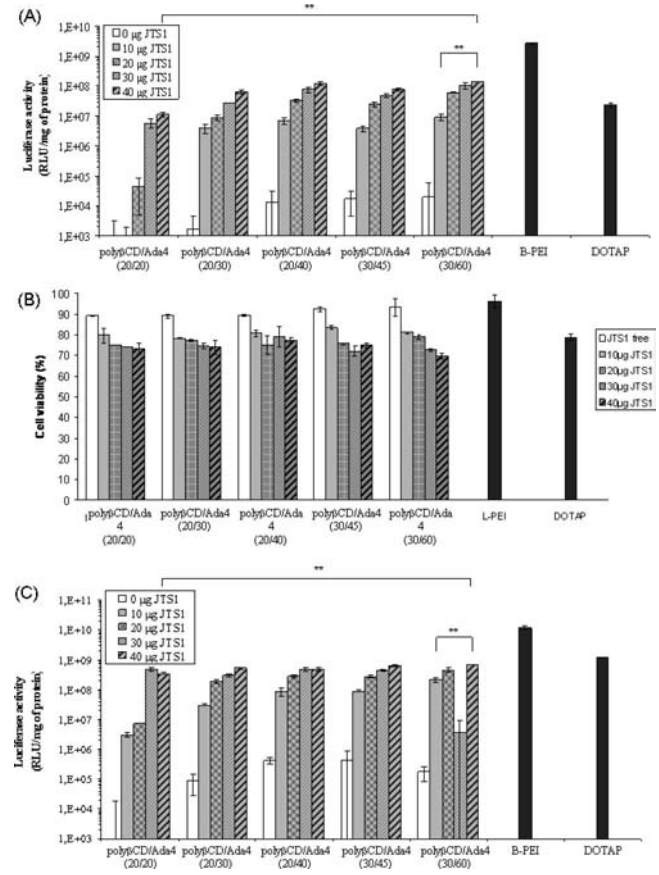

Figure 9. Transfection efficiency of Ada4 polyplexes on (A) HepG2 and (C) HEK293 cells. Differences between formulations were determined using the Student's paired *t* test: $^{**}p < 0.01$. (B) Evaluation of the cytotoxicity of the formulations. After 24 h of transfection of HepG2 cells, cell viability ($n = 2$) was measured. The results are given for the same formulations as those shown in part A.

transfection efficiency on HEK293 cells was not strongly modified when changing the polyβCD/Ada ratio (Figure 9C). However, the highest dose of polymer/Ada/JTS-1 led on both cell lines to the best transfection. From this study, it appears that the amide function of the Ada4 connector spacer associated with the double cationic charge of the polar head is the key parameter in the connector composition for DNA delivery. The toxicity of the polyβCD/Ada4/DNA $\pm$ JTS1 complexes on HepG2 cells following transfection was estimated by performing the MTT colorimetric assay (Figure 9B). The results indicate that the cytotoxicity of the complexes in the absence of the fusogenic peptide is very low. In fact, the cell viability decreases with the addition of JTS1. However, even with the highest amount of peptide, the cell viability remains of the same order as that observed with DOTAP.

4. CONCLUSION

We have presently demonstrated that cyclodextrin polymers (polyβCD) complexed with adamantyl cationic derivatives (Ada) constitute novel and efficient nonviral vectors for gene delivery. The design of the vector involves supramolecular inclusion complex interactions between polyβCD cavities and the hydrophobic part of the Ada connectors whereas, in the vector−DNA polyplex, additional supramolecular electrostatic interactions take part between the positive charges of Ada and the negative charges of DNA. The tailoring of the system was shown to be strongly dependent upon the chemical structure of the Ada connector: the nature of the spacer arm between the adamantyl moiety, and the charge valency of the connector. The physicochemical properties using three different Ada connectors have been extensively studied by different techniques testing the following properties: (i) the affinity between Ada connectors and polyβCD using fluorimetry, (ii) the DNA complexation and compaction using complementary experiments of gel electrophoresis, ζ potential, and SERS, and (iii) the structure of the polyplexes by SANS. The optimal properties were obtained with the Ada4 connector bearing a bivalent cationic charge and an amide function along its arm. This amide function proved to be important in the system, since the possible hydrogen bond interactions with DNA should have stabilized the polyplexes against dissociation under physiological conditions. *In vitro* transfection experiments performed on two cell lines (HepG2 and HEK293) correlated perfectly the results of the physicochemical study. The Ada4 vector, when associated with the fusogenic peptide JTS1, had a transfection efficiency similar to that of DOTAP.

Taken together, we would like to underscore that the improved reversibility of our system as compared to classical vectors makes the Ada4 formulation a very promising reagent for gene transfer. Further improvements of this vector should involve cell targeting. This can be easily realized by adding another adamantane derivative bearing a specific ligand recognized by cell receptors.

ACKNOWLEDGMENT

The authors thank the Laboratoire Léon Brillouin (LLB, Saclay, France) and Loïc Auvray for their assistance with the neutron scattering measurements.

LITERATURE CITED

(1) Wolff, J. A. (2002) The "grand" problem of synthetic delivery. *Nat. Biotechnol. 20*, 768–769.
(2) Boussif, O., Lezoualc'h, F., Zanta, M. A., Mergny, M. D., Scherman, D., Demeneix, B., and Behr, J. (1995) A versatile vector for gene and oligonucleotide transfer into cells in culture and in vivo: polyethylenimine. *Proc. Natl. Acad. Sci. 92*, 7297–7301.
(3) Wagner, E., Zenke, M., Cotten, M., Beug, H., and Birnstiel, M. (1990) Transferrin-polycation conjugates as carriers for DNA uptake into cells. *Proc. Natl. Acad. Sci. 87*, 3410–3414.
(4) Haensler, J., and Szoka, F. J. (1993) Polyamidoamine cascade polymers mediate efficient transfection of cells in culture. *Bioconjugate Chem. 4*, 372–379.
(5) Behr, J., Demeneix, B., Loeffler, J., and Perez-Mutul, J. (1989) Efficient gene transfer into mammalian primary endocrine cells with lipopolyamine-coated DNA. *Proc. Natl. Acad. Sci. 86*, 6982–6986.
(6) Felgner, P. L., Gadek, T. R., Holm, M., Roman, R., Chan, H. W., Wenz, M., Northrop, J. P., Ringold, G. M., and Danielsen, M. (1987) Lipofection: A Highly Efficient, Lipid-Mediated DNA-Transfection Procedure. *Proc. Natl. Acad. Sci. 84*, 7413–7417.
(7) Leventis, R., and Silvius, J. R. (1990) Interactions of mammalian cells with lipid dispersions containing novel metabolizable cationic amphiphiles. *Biochim. Biophys. Acta, Biomembr. 1023*, 124–132.
(8) Wyman, T. B., Nicol, F., Zelphati, O., Scaria, P. V., Plank, C., and Szoka, F. C. (1997) Design, Synthesis, and Characterization of a Cationic Peptide That Binds to Nucleic Acids and Permeabilizes Bilayers. *Biochemistry 36*, 3008–3017.
(9) Kichler, A., Pages, J. C., Leborgne, C., Druillennec, S., Lenoir, C., Coulaud, D., Delain, E., Le Cam, E., Roques, B. P., and Danos, O. (2000) Efficient DNA transfection mediated by the C-terminal domain of human immunodeficiency virus type 1 viral protein R. *J. Virol. 74*, 5424–5431.
(10) Kichler, A., Leborgne, C., and Bechinger, B. (2007) Characterization of the gene transfer process mediated by histidine-rich peptides. *J. Mol. Med. 85*, 191–201.
(11) Mislick, K. A., and Baldeschwieler, J. D. (1996) Evidence for the role of proteoglycans in cation-mediated gene transfer. *Proc. Natl. Acad. Sci. 93*, 12349–12354.
(12) Chollet, P., Favrot, M. C., Hurbin, A., and Coll, J.-L. (2002) Side-effects of a systemic injection of linear polyethylenimine-DNA complexes. *J. Gene Med. 4*, 84–91.
(13) Moghimi, S. M., Symonds, P., Murray, J. C., Hunter, A. C., Debska, G., and Szewczyk, A. (2005) A two-stage poly(ethylenimine)-mediated cytotoxicity: implications for gene transfer/therapy. *Mol. Ther. 11*, 990–995.
(14) Yew, N. S., and Scheule, R. K. (2005) Toxicity of cationic lipid-DNA complexes. *Adv. Genet. 53*, 189–214.
(15) Gershon, H., Ghirlando, R., Guttman, S. B., and Minsky, A. (1993) Mode of formation and Structural Features of DNA-Cationic Liposome Complexes Used for Transfection. *Biochemistry 32*, 7143–7151.
(16) Rädler, J. O., Koltover, I., Salditt, T., and Safinya, C. R. (1997) Structure of DNA-Cationic Liposome Complexes: DNA Intercalation in Multilamellar Membranes in Distinct Interhelical Packing Regimes. *Science 275*, 810–814.
(17) Reimer, D. L., Zhang, Y., Kong, S., Wheeler, J. J., Graham, R. W., and Bally, M. B. (1995) Formation of Novel Hydrophobic Complexes between Cationic lipids and Plasmid DNA. *Biochemistry 34*, 12877–12883.
(18) Sternberg, B., Sorgi, F. L., and Huang, L. (1994) New structures in complex formation between DNA and cationic liposomes vizualised by freeze-fracture electron microscopy. *FEBS Lett. 356*, 361–366.
(19) Nisha, C. K., Manorama, S. V., Ganguli, M., Maiti, S., and Kizhakkedathu, J. N. (2004) Complexes of poly(ethylene glycol)-based cationic random copolymer and calf thymus DNA: a complete biophysical characterization. *Langmuir 20*, 2386–2396.
(20) DeRouchey, J., Netz, R. R., and Rädler, J. O. (2005) Structural investigations of DNA-polycation complexes. *Eur. Phys. J. E 16*, 17–28.
(21) Evans, H. M., Ahmad, A., Ewert, K. K., Pfohl, T., Martin-Herranz, A., Bruinsma, R. F., and Safinya, C. R. (2003) Structural polymorphism of DNA-dendrime complexes. Phys. Rev. Lett. *91*, 075501(1−4).

(22) Volcke, C., Pirotton, S., Grandfils, C., Humbert, C., Thiry, P. A., Ydens, I., Dubois, P., and Raes, M. (2006) Influence of DNA condensation state on transfection efficiency in DNA/polymer complexes: An AFM and DLS comparative study. *J. Biotechnol. 125*, 11–21.

(23) Wolfert, M. A., Dash, P. R., Nazarova, O., Oupicky, D., Seymour, L. W., Smart, S., Strohalm, J., and Ulbrich, K. (1999) Polyelectrolyte Vectors for Gene Therapy: Influence of Cationic Polymer on Biophysical Properties of Complexes Formed with DNA. *Bioconjugate Chem. 10*, 993–1004.

(24) Pun, S. H., Bellocq, N. C., Liu, A., Jensen, G., Machemer, T., Quijano, E., Schuep, T., Wen, S., Engler, H., Heidel, J., and Davis, M. E. (2004) Cyclodextrin-Modified Polyethylenimine Polymers for Gene Delivery. *Bioconjugate Chem. 15*, 831–840.

(25) Arima, H., Kihara, F., Hirayama, F., and Uekama, K. (2001) Enhancement of Gene Expression by Polyamidoamine Dendrimer Conjugates with α-, *β*-, and *γ*-cyclodextrin. *Bioconjugate Chem. 12*, 476–484.

(26) Wolff, J. A.; Hagstrom, J. E.; Monahan, S. D.; Budker, V.; Rozema, D. B.; Slattum, P. M. Compositions and methods for drug delivery using amphiphile binding molecules. U.S. Patent 6,740,643, 2004.

(27) Li, S., and Purdy, W. C. (1992) Cyclodextrins and their applications in analytical chemistry. *Chem. Rev. 92*, 1457–1470.

(28) Manor, P. C., and Saenger, W. (1974) Topography of cyclodextrin inclusion complexes. III. Crystal and molecular structure of cyclohexaamylose hexahydrate, the water dimer inclusion complex. *J. Am. Chem. Soc. 96*, 3630–3639.

(29) Reineke, T. M., and Davis, M. E. (2003) Structural effects of carbohydrate-containing polycations on gene delivery. 1. Carbohydrate size and its distance from charge centers. *Bioconjugate Chem. 14*, 247–254.

(30) Cryan, S.-A., Donohue, R., Ravoo, B. J., Darcy, R., and O'Driscoll, C. M. (2004) Cationic cyclodextrin amphiphiles as gene delivery vectors. *J. Drug Delivery Sci. Technol.* 57–62.

(31) Cryan, S.-A., Holohan, A., Donohue, R., Darcy, R., and O'Driscoll, C. M. (2004) Cell transfection with polycationic cyclodextrin vectors. *Eur. J. Pharm. Sci. 21*, 625–633.

(32) Li, H., and Qian, Z. M. (2002) Transferrin/Transferrin Receptor-Mediated Drug Delivery. *Med. Res. Rev. 22*, 225–250.

(33) Forrest, M. L., Gabrielson, N., and Pack, D. W. (2005) Cyclodextrin-polyethylenimine conjugates for targeted *in vitro* gene delivery. *Biotechnol. Bioeng. 89*, 416–423.

(34) Davis, M. E., Pun, S. H., Bellocq, N. C., Reineke, T. M., Popielarski, S. R., Mishra, S., and Heidel, J. D. (2004) Self-Assembling Nucleic Acid Delivery Vehicles via Linear, Water-Soluble, Cyclodextrin-Containing Polymers. *Curr. Med. Chem. 11*, 179–197.

(35) Burckbuchler, V., Wintgens, V., Lecomte, S., Percot, A., Leborgne, C., Danos, O., Kichler, A., and Amiel, C. (2006) DNA compaction into new DNA vectors based on cyclodextrin polymer: Surface enhanced Raman spectroscopy characterization. *Biopolymers 81*, 360–370.

(36) Son, K. K., Tkach, D., and Hall, K. J. (2000) Efficient in vivo gene delivery by the negatively charged complexes of cationic liposomes and plasmid DNA. *Biochim. Biophys. Acta, Biomembr. 1468*, 6–10.

(37) Renard, E., Barnathan, G., Deratani, A., and Sébille, B. (1997) Polycondensation of cyclodextrins with epichlorohydrin. Influence of reaction conditions on the polymer structure. *Macromol. Symp. 122*, 229.

(38) Galant, C., Amiel, C., Wintgens, V., Sébille, B., and Auvray, L. (2002) Ternary Complexes with poly(*β*-cyclodextrin), Cationic Surfactant, and Polyanion in Dilute Aqueous Solution: A Viscometric and Small-Angle Neutron Scattering Study. *Langmuir 18*, 9687–9695.

(39) Burckbuchler, V., Boutant, V., Wintgens, V., and Amiel, C. (2006) Macromolecular Assemblies Based on Coupled Inclusion Complex and Electrostatic Interactions. *Biomacromolecules 7*, 2890–2900.

(40) Wintgens, V., and Amiel, C. (2004) New 4-amino-N-alkylphthalimides as fluorescence probes for *β*-cyclodextrin inclusion complexes and hydrophobic microdomains of amphiphilic systems. *J. Photochem. Photobiol. A 168*, 217–226.

(41) Budil, D. E., Lee, S., Saxena, S., and Freed, J. H. (1996) Nonlinear-Least-Squares Analysis of Slow-Motion EPR Spectra in One and Two Dimensions Using a Modified Levenberg-Marquardt Algorithm. *J. Magn. Reson., Ser. A 120*, 155–189.

(42) Creighton, J., Blatchford, C. G., and Albretch, M. J. (1979) Plasma resonance enhancement Raman scattering by pyridine adsorbed on silver or gold sol particles of size comparable to the excitation wavelength. *J. Chem. Soc., Faraday Trans. 2 75*, 790–798.

(43) Kassapidou, K., Jesse, W., Kuil, M. E., Lapp, A., Egelhaaf, S., and Van der Maarel, J. R. C. (1997) Structure and charge distribution in DNA and poly(styrenesulfonate) aqueous solutions. *Macromolecules 30*, 2671.

(44) Kichler, A., Leborgne, C., Coeytaux, E., and Danos, O. (2001) Polyethylenimine-mediated gene dlivery: a mechanistic study. *J. Gene Med. 3*, 135–144.

(45) Pagé, M., Bejaoui, N., Cinq-Mars, B., and Lemieux, P. (1988) Optimization of the tetrazolium-based colorimetric assay for the measurement of cell number and cytotoxicity. *Int. J. Immunopharmacol. 10*, 785–793.

(46) Soto, J., Bessodes, M., Pitard, B., Mailhe, P., Scherman, D., and Byk, G. (2000) Non-electrostatic complexes with DNA: towards novel synthetic gene delivery systems. *Bioorg. Med. Chem. Lett. 10*, 911–914.

(47) Narang, A. S., Thoma, L., Miller, D. D., and Mahato, R. I. (2005) Cationic Lipids with Increased DNA Binding Affinity for Nonviral Gene Transfer in Dividing and Nondividing Cells. *Bioconjugate Chem. 16*, 156–168.

(48) Cao, Z., Liu, W., Liang, D., Guo, G., and Zhang, J. (2007) Design of Poly(vinyldiaminotriazine)-Based Nonviral Vectors via Specific Hydrogen Bonding with Nucleic Acid Base Pairs. *Adv. Funct. Mater. 17*, 246–252.

(49) Cromwell, W. C., Bystrom, K., and Eftink, M. R. (1985) Cyclodextrin-adamantanecarboxylate inclusion complexes: studies of the variation in cavity size. *J. Phys. Chem. 89*, 326–332.

(50) Gottschalk, S., Sparrow, J. T., Hauer, J., Mims, M. P., Leland, F. E., Woo, S. L., and Smith, L. C. (1996) A novel DNA-peptide complex for efficient gene transfer and expression in mammalian cells. *Gene Ther. 3*, 48–57.

BC800070F

Specific Targeting of HER2 Overexpressing Breast Cancer Cells with Doxorubicin-Loaded Trastuzumab-Modified Human Serum Albumin Nanoparticles

Marion G. Anhorn,[†,§] Sylvia Wagner,[‡,§] Jörg Kreuter,[†] Klaus Langer,[†] and Hagen von Briesen*[,‡]

Fraunhofer Institute for Biomedical Engineering, Department of Cell Biology and Applied Virology, 66386 St. Ingbert, Germany, and Institute of Pharmaceutical Technology, Biocenter of Johann Wolfgang Goethe-University, 60438 Frankfurt/Main, Germany. Received February 25, 2008; Revised Manuscript Received September 23, 2008

Specific targeting of tumor cells to achieve higher drug levels in tumor tissue and to overcome cardiotoxic and other secondary effects is the major goal in cancer therapy. With trastuzumab as a humanized monoclonal antibody binding, the HER2 receptor specific targeting is possible. In the present study, target-oriented nanoparticles based on biodegradable human serum albumin (HSA) loaded with cytostatic drug doxorubicin were developed. The surface of the nanoparticles was modified by covalent attachment of trastuzumab. HER2 overexpressing breast cancer cells showed a good cellular binding and uptake of these nanoparticles. The specific transport of the cytostatic drug doxorubicin with this nanoparticulate formulation into the HER2 overexpressing breast cancer cells, their release, and biological activity was demonstrated. The results indicate that these cell-type specific drug-loaded nanoparticles could achieve an improvement in cancer therapy. To our knowledge, this is the first study demonstrating a specific trastuzumab-based targeting of HER2 overexpressing breast cancer cells with doxorubicin-loaded nanoparticles.

INTRODUCTION

Cytostatic drugs are very useful substances in the fight of tumor diseases. However, the main disadvantages of conventional chemotherapy are modest tumor response and dose limiting side effects because of nonspecific action of drugs to all fast proliferating tissues (*1*). One possibility to avoid these disadvantages is the development of colloidal drug carrier systems (*2*). In this regard, nanoparticles show a high drug loading efficiency with minor drug leakage as well as the ability to circumvent multidrug resistance paired with good storage stability. Using human serum albumin (HSA) as particle forming polymer has the following advantages (*3*): human serum albumin is a physiological starting material and particles made of HSA are biodegradable. Additionally, the production of these particles is easy and reproducible (*4*). Functional groups are located on the surface of the prepared particles. Consequently, covalent linkage, for example, with drug targeting ligands is possible.

Depending on the carrier system, a differentiation between passive and active drug targeting can be made (*5*). Malignant tumors induce an increased angiogenesis with the consequence of hypervascularization consisting of leaky vasculature in combination with poor lymphatic drainage (*6*). The pore size in the vasculature ranges from 200 to 600 nm in diameter. These characteristics lead to an enhanced extravasation and accumulation of carrier systems such as liposomes and nanoparticles. This phenomenon is called "enhanced permeability and retention (EPR) effect". Consequently, long-circulating nanoparticles with poly(ethylene glycol) modifications on their surface are able to conduct passive tumor targeting (*7*). A further approach is the covalent linkage of drug targeting ligands such as monoclonal antibodies on the surface of the drug carrier systems to specifically target malignant cells (*8*−*10*). Thus, an active targeting with the advantage of an efficient accumulation of drugs in tumor tissue with higher drug levels in target cells can be achieved.

Concerning drug targeting ligands, the focus of many groups is mainly on monoclonal antibodies (mAb) (*11*). Trastuzumab (Herceptin), a humanized monoclonal antibody targeting the HER2 receptor, was approved by the FDA in 1998. HER2 is a member of a family of four transmembrane epidermal growth factor receptor (EGFR) tyrosine kinases and is overexpressed in a variety of human cancer cells such as breast, lung, and ovarian carcinomas (*12*). HER2 overexpression is an adverse prognostic factor in women with breast cancer (*13*). Trastuzumab administered as single agent leads to response rates ranging from 15% to 30% (*13*). Increased response rates can be achieved by using the antibody in combination with conventional chemotherapy. In this context, some clinical trials showed that an anthracycline-containing regimen leads to a greater benefit in women whose tumors overexpress HER2 than regimes without anthracyclines (*14*). The main drawback of the combination of trastuzumab and anthracyclines is that both trastuzumab and anthracyclines show cardiotoxic effects. That is the reason why this antibody−drug combination is only used in clinical trials where physicians have the possibility to monitor the heart function of the patients. On the other hand, it could be expected that trastuzumab-modified nanoparticles as drug carrier system for anthracyclines could reduce these side effects due to the ability of the particles to transport the embedded drug specifically to the tumor cells (*15*). Furthermore, the antibody concentration of the drug carrier system is far below the concentrations used in a therapeutic trastuzumab regime and a therapeutic antibody effect is not intended. The antibody only has a ligand function within such a nanoparticulate system. Upon arrival at the tumor tissue, trastuzumab molecules which are covalently attached to the particle surface by poly(ethylene

* Corresponding author. Dr. Hagen von Briesen, Fraunhofer Institute for Biomedical Engineering, Ensheimer Strasse 48, D-66386 St. Ingbert, Germany. Phone: +49-(0)6894-980-286. Fax: +49-(0)6894-980-400. E-mail: hagen.briesen@ibmt.fraunhofer.de.

[†] Institute of Pharmaceutical Technology.

[‡] Fraunhofer Institute for Biomedical Engineering.

[§] Both authors contributed equally to this work.

10.1021/bc8002452 CCC: $40.75 © 2008 American Chemical Society
Published on Web 10/21/2008

glycol) cross-linker chains will lead to the entry of the drug-loaded particles into the tumor cells (*9, 16*). Due to the biodegradability of human serum albumin, the particles are degraded within the cells. Thereupon, the released cytostatic drug specifically kills the tumor cells without acting in nontarget cells such as heart tissue. Therefore, this approach could be an answer to the crucial combination of trastuzumab and doxorubicin with the possibility to offer this effective therapy to women with HER2 overexpressing cancer cells.

EXPERIMENTAL PROCEDURES

Human serum albumin (HSA, fraction V, purity 96−99%), glutaraldehyde 8% aqueous solution, and human IgG antibody were obtained from Sigma (Steinheim, Germany). Doxorubicin was obtained from Sicor (Milan, Italy). 2-Iminothiolane (Traut's reagent) and D-Salt Dextran desalting columns were purchased from Pierce (Rockford, USA). Trastuzumab (Herceptin) was obtained from Roche (Mannheim, Germany). The succinimidyl ester of methoxy poly(ethylene glycol) propionic acid with an average molecular weight of 5.0 kDa (mPEG5000-SPA) and the cross-linker poly(ethylene glycol)-α-maleimide-ω-NHS ester with an average molecular weight of 5.0 kDa (NHS-PEG5000-Mal) were purchased from Nektar (Huntsville, USA). All reagents were of analytical grade and used as received.

Preparation of Doxorubicin-Loaded Nanoparticles. An amount of 160 mg HSA was dissolved in 4 mL purified water and the solution was filtered through a 0.22 μm cellulose acetate membrane filter (Schleicher & Schuell, Dassel, Germany). An aliquot (500 μL) of this solution was added to 200 μL of a 0.5% (w/v) aqueous stock solution of doxorubicin. To this mixture, 300 μL of purified water was added. For lower drug loading of the particles, the 0.5% (w/v) doxorubicin stock solution was diluted to 0.05% (w/v) or 0.025% (w/v), respectively, before mixing with the aqueous HSA solution. In order to adsorb doxorubicin to human serum albumin in solution, the mixture was incubated under stirring (550 rpm) for 2 h at room temperature (*17*). For the preparation of nanoparticles by desolvation, 3 mL ethanol (96%, v/v) was added continuously (1 mL/min) with a tubing pump (Ismatec IPN, Glattbrugg, Switzerland). After protein desolvation, an aliquot of 4.7 or 11.75 μL 8% glutaraldehyde solution, respectively, was added to induce particle cross-linking (corresponding to 40% or 100% stoichiometric protein cross-linking, respectively). The cross-linking was performed for 24 h under constant stirring at ambient temperature. Aliquots (2.0 mL) of the resulting nanoparticles were purified by two cycles of differential centrifugation (16 100 *g*, 12 min) and redispersion. Within the first cycle, redispersion was performed with 2.0 mL purified water, whereas in the second cycle, nanoparticles were redispersed with phosphate buffer (pH 8.0) to a volume of 500 μL using a vortexer and ultrasonication. The polymer content of the doxorubicin-loaded nanoparticles was determined by gravimetry.

The collected supernatants were used to determine the non-entrapped doxorubicin by HPLC. The content of entrapped doxorubicin was calculated from the difference between total doxorubicin and unbound drug. For the quantification of doxorubicin, a Merck Hitachi D7000 HPLC system equipped with a LiChroCART 250−4 LiChrospher-100 RP-18 column (Merck, Darmstadt, Germany) was used. Separation was obtained using a mobile phase of water and acetonitrile (70:30) containing 0.1% trifluoroacetic acid at a flow rate of 0.8 mL/min. Doxorubicin was quantified by UV (250 nm) and fluorescence detection (excitation 560 nm, emission 650 nm).

Surface Modification of Drug-Loaded Nanoparticles. Drug-loaded HSA nanoparticles were prepared as described above and were modified as follows: One milliliter of HSA nanoparticle suspension dispersed in phosphate buffer (pH 8.0) was incubated with 250 μL of mPEG5000-SPA solution (60 mg/mL in phosphate buffer pH 8.0) or poly(ethylene glycol)-α-maleimide-ω-NHS ester, respectively, for 1 h at 20 °C under constant shaking (Eppendorf thermomixer, 600 rpm). The nanoparticles were purified by centrifugation and redispersion as described above. The content of the nanoparticles was determined by gravimetry.

For the thiolation step of the antibodies, trastuzumab and IgG were dissolved in phosphate buffer pH 8.0 at a concentration of 1.0 mg/mL. For the introduction of thiol groups, trastuzumab or IgG, respectively, were incubated with a 50-fold molar excess of 2-iminothiolane solution ($c = 1.14$ mg/mL; 40.2 μL) for 2 h as previously described by Steinhauser et al. (*16*). The antibodies were purified by size exclusion chromatography (SEC, D-Salt Dextran desalting column). The resulting solution contained thiolated antibody (trastuzumab or IgG, respectively) at a concentration of about 500 μg/mL. For the coupling reaction, 1.0 mL of the sulfhydryl-reactive nanoparticle suspension was incubated with 1.0 mL of the thiolated trastuzumab or IgG, respectively, to achieve a covalent linkage between antibody and the nanoparticle system. For the preparation of samples with adsorptively attached antibody, 1.0 mL of the mPEG5000-SPA modified nanoparticles were incubated with 1.0 mL of thiolated trastuzumab or IgG, respectively. The incubation of all samples was performed for 12 h at 20 °C under constant shaking (600 rpm). The samples were purified from unreacted antibody by centrifugation and redispersion as described earlier. To determine unbound antibody, the resulting supernatants were collected and analyzed by size exclusion chromatography (SEC) on a SW_{XL} column (7.8 mm × 30 cm) in combination with a TSKgel SW_{XL} guard column (6 mm × 4 cm) (Tosoh Bioscience, Stuttgart, Germany) using phosphate buffer (pH 6.6) as eluent at a flow rate of 1.0 mL/min. Aliquots of 20.0 μL were injected, and the eluent fraction was monitored by detection at 280 nm. In order to calibrate the SEC system for molecular weight, globular protein standards were used. The amount of antibody bound to the nanoparticle surface was calculated as difference between the amount of antibody obtained after thiolation and purification and the amount of antibody determined in the supernatant obtained after the conjugation step.

Nanoparticle Characterization. Nanoparticles were analyzed with regard to particle diameter and polydispersity by photon correlation spectroscopy (PCS) using a Malvern Zetasizer $3000HS_A$ (Malvern Instruments Ltd., Malvern, UK). The zeta potential was measured with the same instrument by Laser Doppler microelectrophoresis. Prior to both measurements, the samples were diluted with purified water. Particle content was determined by gravimetry. For this purpose, 50.0 μL of the nanoparticle suspension was pipetted into an aluminum weighing dish and dried for 2 h at 80 °C. After 30 min of storage in an exsiccator, the samples were weighed on a microbalance (Sartorius, Germany).

Cell Culture. For all experiments, HER2 overexpressing breast cancer cells SK-Br-3 (ATCC, LGC Promochem, Wesel) were used. The cells were cultured at 37 °C and 7.5% CO_2 in McCoy's 5A medium (PromoCell, Heidelberg) supplemented with 10% fetal calf serum (Invitrogen, Karlsruhe) and antibiotics (50 U/mL penicillin and 50 μg/mL streptomycin; Invitrogen, Karlsruhe).

As a control cell line, HER2 weakly expressing MCF7 cells were used. The cells were cultured at 37 °C and 7.5% CO_2 in RPMI 1640 medium (Invitrogen, Karlsruhe) supplemented with 10% fetal calf serum (Invitrogen, Karlsruhe) and antibiotics (50 U/mL penicillin and 50 μg/mL streptomycin; Invitrogen, Karlsruhe).

Cellular Binding of Nanoparticles. HER2 overexpressing SK-Br-3 cells were cultured in 24 well plates (Greiner,

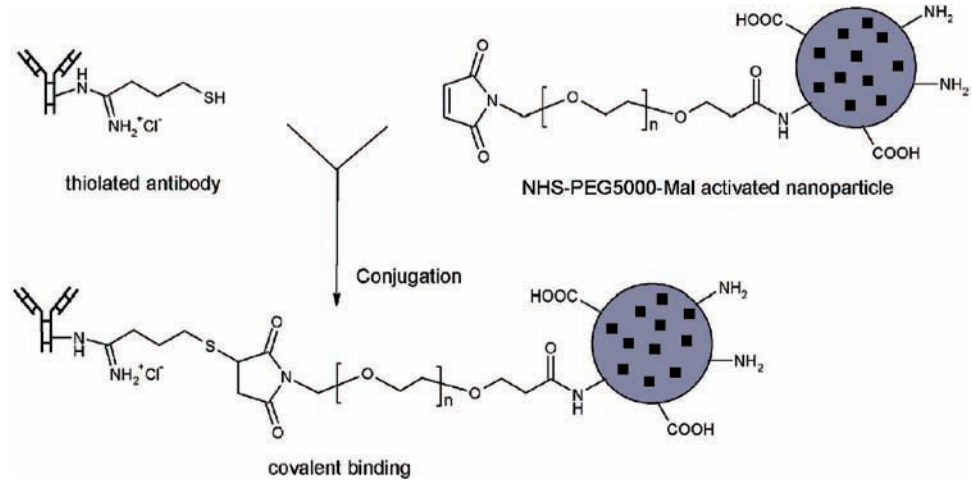

Figure 1. Covalent linkage of thiolated antibody to cross-linker-activated drug-loaded nanoparticle (black square = doxorubicin).

Frickenhausen) and treated with the different nanoparticle formulations for 4 h at 37 °C. After this incubation, the cells were washed twice with PBS (Invitrogen, Karlsruhe), then trypsinized and harvested. After washing with PBS and fixing with FACS-Fix (10 g/L PFA and 8.5 g/L NaCl in PBS, pH 7.4), flow cytometry (FACS) analysis was performed with 10 000 cells/sample, using *FACSCalibur* and *CellQuest Pro* software (Becton Dickinson, Heidelberg). Due to a green autofluorescence of these nanoparticles at 488/520 nm, this FACS analysis was possible.

For control experiment, HER2 weakly expressing MCF7 cells were cultured in 24 well plates (Greiner, Frickenhausen) and treated with the different nanoparticle formulations for 4 h at 37 °C. The sample preparation for flow cytometry analysis was performed as described before.

Cellular Uptake and Intracellular Distribution. Cellular uptake and intracellular distribution of the nanoparticles were studied by confocal laser scanning microscopy. SK-Br-3 cells were cultured on glass slides and treated with the different nanoparticle formulations for 4 h at 37 °C. After that incubation time, the cells were washed twice with PBS and the cell membranes were stained with 50 ng/μL Concanavalin A AlexaFluor 594 (Invitrogen, Karlsruhe) for 2 min. Cells were fixed with cold ethanol for 30 min. After fixation, the cells were washed and then embedded in Vectashield HardSet Mounting Medium (Axxora, Grünberg). The confocal microscopy study was performed with an Axiovert 200 M microscope with a 510 NLO Meta device (Zeiss, Jena), MaiTai femtosecond or an argon ion laser and the LSM Image Examiner software. The green autofluorescence of the nanoparticles was also used here.

Cellular Doxorubicin Recovery. Doxorubicin recovery was performed with flow cytometry (FACS) analysis. SK-Br-3 cells were cultured in 24 well plates (Greiner, Frickenhausen) and treated with the different nanoparticle formulations or free doxorubicin for 4 h at 37 °C. After this incubation, the cells were washed and incubated with fresh medium for different periods of time, and afterward trypsinized and harvested. Flow cytometry (FACS) analysis was performed after fixation with FACS-Fix (10 g/L PFA and 8.5 g/L NaCl in PBS, pH 7.4) with 10 000 cells/sample, using *FACSCalibur* and *CellQuest Pro* software (Becton Dickinson, Heidelberg). The red fluorescence of doxorubicin at 488/590 nm was used.

Biological Activity. Cell viability was determined in SK-Br-3 cells using WST-1 assay (Cell Proliferation Reagent; Roche Diagnostics) based upon the absorption measurement of formazan formation. Briefly, cells were cultured in 6 well plates and incubated with the different nanoparticulate formulations in PBS or PBS containing 100 μM chloroquine for 4 h at 37 °C. An amount of 10 000 cells/well were seeded in 96 well plates and further incubated for 7 d at 37 °C. The determination of cell viability was carried out after addition of WST-1 reagent and formazan measurement as described in the manufacturer's instruction manual.

For control experiment, HER2 weakly expressing MCF7 cells were used. The cell viability assay was performed as described before.

Statistical Analysis. Statistical analysis was made using the two-tailed Mann−Whitney U Test, which is equivalent to the Wilcoxon rank sum test (*18*−*20*). Statistical significance was defined at $P < 0.01$ values.

RESULTS AND DISCUSSION

Particle Preparation and Characterization. In the first step of the study, doxorubicin-loaded nanoparticles (Dox-NP) were prepared by using a well-established desolvation method (*17*). The nanoparticles were stabilized by two different amounts of glutaraldehyde. Therefore, nanoparticles were achieved with 40% (Dox-NP 40%) or 100% (Dox-NP 100%) stochiometric cross-linking of the particle matrix. Using 2-iminothiolane, thiol groups were introduced into the monoclonal antibody trastuzumab and the control antibody IgG. Finally, the drug-loaded particles were activated with a heterobifunctional poly(ethylene glycol)-α-maleimide-ω-NHS ester (NHS-PEG5000-Mal) or a monofunctional succinimidyl ester of methoxy poly(ethylene glycol) propionic acid (mPEG5000-SPA), respectively. In the first case, the heterobifunctional cross-linker leads to a covalent linkage between antibody and nanoparticle (Dox-NP-mAb) (Figure 1). In the second case, only an adsorptive binding between antibody and nanoparticle was expected because of the nonreactive methoxy group at the end of the poly(ethylene) glycol chain (Dox-NP + thiol mAb).

The results of the physicochemical characterization are presented in Tables 1 and 2 for 40% or 100% cross-linked nanoparticles, respectively. The resulting particles were characterized by particle diameters of 391.3 ± 14.0 nm and 385.2 ± 30.8 nm for 40% or 100% cross-linked nanoparticles, respectively. The polydispersity ranged between 0.053 ± 0.036 and 0.094 ± 0.057 indicating a monodisperse particle size distribution. Depending on the cross-linking degree, the doxorubicin loading was 51.39 ± 1.29 μg/mg for 40% cross-linked nanoparticles and 57.90 ± 0.44 μg/mg for 100% nanoparticles. Independent of whether the surface of the particles was modified or not, the particles showed a zeta potential between −40.1 ± 2.3 mV and −46.4 ± 3.4 mV.

Covalent linkage of trastuzumab to the particle surface was achieved with 14.92 ± 1.34 μg antibody/mg nanoparticle (40%

Table 1. Physicochemical Characteristics of Trastuzumab- and IgG-Modified Doxorubicin-Loaded HSA Nanoparticles with 40% Cross-Linked Particles ($n = 3$, mean ± SD)

HSA nanoparticles 40% cross-linking		unmodified	covalent binding of trastuzumab	covalent binding of IgG	adsorptive binding of trastuzumab	adsorptive binding of IgG
particle diameter	[nm]	391.3 ± 14.0	411.4 ± 2.3	408.6 ± 4.5	405.3 ± 1.6	402.5 ± 3.7
polydispersity		0.053 ± 0.036	0.045 ± 0.010	0.050 ± 0.062	0.026 ± 0.012	0.055 ± 0.027
zeta potential	[mV]	−41.4 ± 3.3	−44.0 ± 2.9	−46.3 ± 3.1	−40.1 ± 2.3	−41.5 ± 2.9
particle content	[mg/mL]	14.43 ± 0.11	14.09 ± 0.38	14.12 ± 0.36	14.05 ± 0.16	14.20 ± 0.25
antibody binding efficiency	[%]	-	90.3 ± 16.9	77.9 ± 19.6	20.7 ± 6.4	5.9 ± 7.6
	[μg/mg]	-	14.92 ± 1.34	13.80 ± 2.30	3.50 ± 1.13	0.93 ± 1.14
drug loading	[μg/mg]	51.39 ± 1.29	51.39 ± 1.29	51.39 ± 1.29	51.39 ± 1.29	51.39 ± 1.29

Table 2. Physicochemical Characteristics of Trastuzumab- and IgG-Modified Doxorubicin-Loaded HSA Nanoparticles with 100% Cross-Linked Particles ($n = 4$, mean ± SD)

HSA nanoparticles 100% cross-linking		unmodified	covalent binding of trastuzumab	covalent binding of IgG	adsorptive binding of trastuzumab	adsorptive binding of IgG
particle diameter	[nm]	385.2 ± 30.8	395.4 ± 1.7	402.2 ± 6.8	391.3 ± 6.8	397.7 ± 8.7
polydispersity		0.094 ± 0.057	0.080 ± 0.043	0.052 ± 0.034	0.055 ± 0.044	0.041 ± 0.048
zeta potential	[mV]	−42.6 ± 1.5	−46.4 ± 3.4	−43.7 ± 2.9	−41.2 ± 3.4	−43.8 ± 2.0
particle content	[mg/mL]	15.37 ± 0.34	14.24 ± 0.96	14.35 ± 1.13	14.30 ± 1.29	14.16 ± 1.57
antibody binding efficiency	[%]		90.6 ± 14.0	82.7 ± 15.5	39.2 ± 18.1	14.2 ± 5.0
	[μg/mg]		16.09 ± 3.71	15.39 ± 3.60	7.52 ± 5.29	2.73 ± 1.26
drug loading	[μg/mg]	57.90 ± 0.44	57.90 ± 0.44	57.90 ± 0.44	57.90 ± 0.44	57.90 ± 0.44

cross-linked nanoparticles) and 16.09 ± 3.71 μg trastuzumab/mg nanoparticle for the 100% cross-linked particles. With the control antibody IgG, similar results were obtained: Particles with a cross-linking degree of 40% showed a surface modification of 13.80 ± 2.30 μg antibody/mg nanoparticle, whereas more highly cross-linked particles resulted in a binding of 15.39 ± 3.60 μg IgG/mg nanoparticle on their surface.

In the case of preparations with antibodies bound by adsorption, a larger difference between the 40% and 100% cross-linked nanoparticles was observed: With a higher degree of cross-linking, the amount of adsorptively attached antibody increased from 3.50 ± 1.13 μg/mg (40%) to 7.52 ± 5.29 μg/mg (100%) for trastuzumab and from 0.93 ± 1.14 μg/mg (40%) to 2.73 ± 1.26 μg/mg (100%) for IgG. This may be due to a certain amount of covalent antibody binding by residues of monovalent bound glutaraldehyde. Under all preparation conditions, in the case of trastuzumab a more pronounced tendency to unspecific binding to particle surfaces was observed.

When comparing the results of nanoparticles with a covalent linkage to samples with only an adsorptive antibody attachment to the particle surface, it becomes obvious that the majority of the antibody molecules were covalently attached to the particle surface by the heterobifunctional PEG spacer. Only a minor part of the ligands were adsorbed to the nanoparticles or bound by monovalent glutaraldehyde.

Cellular Binding. HER2 overexpressing breast cancer cells SK-Br-3 were incubated with the same concentration (0.1 mg/mL referred to nanoparticles concentration) of nanoparticles with a covalent linkage of trastuzumab (Dox-NP-trastuzumab) as well as with samples with only an adsorptive attachment of trastuzumab on the particle surface (Dox-NP + thiol trastuzumab). Both nanoparticulate formulations showed good cellular binding. There was no difference in binding efficiency between the Dox-NP-trastuzumab and the Dox-NP + thiol trastuzumab (data not shown). Under the chemical point of view, covalent bonding is much stronger than adsorptive bonding. Particularly, this is true when the nanoparticles are administered into the bloodstream. The adsorptively bound antibodies are subjected to desorption processes. This phenomenon can be avoided by applying a covalent linkage between nanoparticle and antibody. Therefore, due to a supposed better stability of the covalent coupling, only the nanoparticle preparations with antibodies covalently linked by heterobifunctional PEG spacers were used for further cell culture experiments.

The SK-Br-3 cells were incubated with Dox-NP-trastuzumab nanoparticles (nanoparticle concentration corresponding to 2 μg/mL trastuzumab modification) with either 40% or 100% cross-linking. Just as the modality of mAb coupling, the degree of cross-linking had no influence on cellular binding efficiency (Figure 2a). Both nanoparticulate formulations, the 100% cross-linked as well as the 40% cross-linked Dox-NP-trastuzumab, displayed good cellular binding. Because there was no difference in cellular uptake between the 100% and 40% cross-linked nanoparticulate formulation (recognized on the same histogram shift, the same Y Mean fluorescence and the same percentage of positive cells, Figure 2a), further experiments were performed only with 100% cross-linked nanoparticles.

Specific targeting of tumor cells to achieve higher drug levels in tumor tissue and to overcome cardiotoxic and other secondary effects is the major goal in cancer therapy. With trastuzumab as a humanized monoclonal antibody, binding the HER2 receptor specific targeting is possible. HER2 overexpressing breast cancer cells SK-Br-3 were incubated with either nanoparticles modified with specific trastuzumab on surface (nanoparticle concentration corresponding to 2 μg/mL trastuzumab modification) or nanoparticles with unspecific control mAb IgG on the surface (concentration referred to specific nanoparticle concentration). As shown in Figure 2a, there was a specific targeting with Dox-NP-trastuzumab (73.80% positive cells for the 100% cross-linked nanoparticles and 73.07% positive cells for 40% cross-linked nanoparticles), whereas Dox-NP-IgG nanoparticles had a marginal cellular binding (5.57% positive cells). When the cells were incubated with increasing amounts of Dox-NP-trastuzumab, cellular binding increased in a concentration-dependent manner (see histograms and table in Figure 2b). Therefore, a highly specific targeting of HER2 overexpressing cancer cells could be shown with this trastuzumab-modified Dox-NP.

As a control experiment, we did flow cytometry binding studies with the trastuzumab-modified nanoparticles on the HER2 weakly expressing MCF7 breast cancer cell line. The MCF7 cells were incubated with either nanoparticles modified with specific trastuzumab on surface or control nanoparticles with IgG modification. As seen in Figure 3, trastuzumab-modified nanoparticles showed a marginal cellular binding, due to the low expression of HER2. Therefore, these MCF7 cells represented an optimal commonly used negative control. The comparison of the cellular binding of trastuzumab-modified

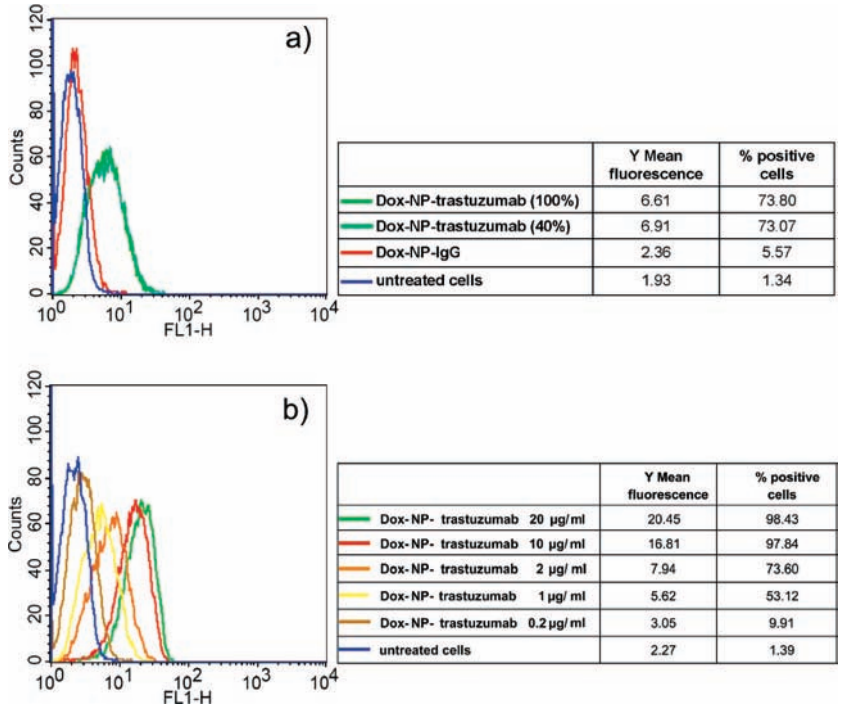

	Y Mean fluorescence	% positive cells
Dox-NP-trastuzumab (100%)	6.61	73.80
Dox-NP-trastuzumab (40%)	6.91	73.07
Dox-NP-IgG	2.36	5.57
untreated cells	1.93	1.34

	Y Mean fluorescence	% positive cells
Dox-NP- trastuzumab 20 µg/ml	20.45	98.43
Dox-NP- trastuzumab 10 µg/ml	16.81	97.84
Dox-NP- trastuzumab 2 µg/ ml	7.94	73.60
Dox-NP- trastuzumab 1 µg/ ml	5.62	53.12
Dox-NP- trastuzumab 0.2 µg/ ml	3.05	9.91
untreated cells	2.27	1.39

Figure 2. Specific cellular binding due to surface modification of nanoparticles with trastuzumab (40% or 100% cross-linked). (a) HER2 overexpressing SK-Br-3 cells were treated with Dox-NP-trastuzumab (40% or 100% cross-linked) or Dox-NP-IgG for 4 h at 37 °C. Flow cytometry (FACS) analysis was performed to quantify their cellular binding. The data are shown as histograms of the FL1-H-channel (autofluorescence of the nanoparticles) as well as a table with Y Mean fluorescence data and percentage of positive cells. Dark green: Dox-NP-trastuzumab (40% cross-linked). Light green: Dox-NP-trastuzumab (100% cross-linked). Red: Dox-NP-IgG. Blue: untreated control. (b) SK-Br-3 cells were incubated with different Dox-NP-trastuzumab concentrations for 4 h at 37 °C. Flow cytometry (FACS) analysis was performed to quantify their cellular binding. The data are shown as histograms of the FL1-H-channel (autofluorescence of the nanoparticles) as well as a table with Y Mean fluorescence data and percentage of positive cells. Green: 20 μg/mL referred to mAb concentration. Red: 10 μg/mL. Orange: 2 μg/mL. Yellow: 1 μg/mL. Brown: 0.2 μg/mL. Blue: untreated control.

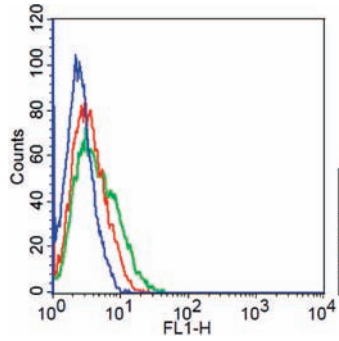

	Y Mean fluorescence	% positive cells
Dox-NP- trastuzumab	5.48	25.02
Dox-NP- IgG	3.95	10.54
untreated cells	2.65	1.35

Figure 3. Control of cellular binding on HER2 weakly expressing MCF7 cells. HER2 weakly expressing MCF7 cells were treated with Dox-NP-trastuzumab or Dox-NP-IgG for 4 h at 37 °C. Flow cytometry (FACS) analysis was performed to quantify their cellular binding. The data are shown as histograms of the FL1-H-channel (autofluorescence of the nanoparticles) as well as a table with Y Mean fluorescence data. Green: Dox-NP-trastuzumab. Red: Dox-NP-IgG. Blue: untreated control.

nanoparticles on HER2 overexpressing SK-Br-3 breast cancer cells, showing a really specific cellular binding (Figure 2a), and HER2 weakly expressing MCF7 breast cancer cells, showing a marginal cellular binding (Figure 3), demonstrated the specificity of our nanoparticulate drug targeting system.

Cellular Uptake and Intracellular Distribution. The cellular uptake and intracellular distribution of these nanoparticulate formulations were shown by confocal laser scanning microscopy (CLSM). HER2 overexpressing breast cancer cells were incubated with nanoparticles with covalent coupled trastuzumab on particle surface (Dox-NP-trastuzumab) as well as with control nanoparticles (Dox-NP-mPEG) (Figure 4). Green fluorescence of specifically uptaken Dox-NP-trastuzumab was visible within the inner part of the red-stained cell membrane (Figure 4f), whereas only some unspecific Dox-NP-mPEG stuck onto the outer part of the cell membrane (Figure 4c). Dox-NP-trastuzumab incubated cells were optically sliced in a stack of 0.75 μm thickness each by confocal laser scanning microscopy to prove the intracellular uptake. The picture series is displayed as a gallery (Supporting Information supplement 1). An animation of such a picture stack is shown in Supporting Information supplement 2 as well as the 3D projection of cells with internalized Dox-NP-trastuzumab in Supporting Information supplement 3. These movies demonstrate the intracellular uptake of the Dox-NP-trastuzumab.

In summary, this flow cytometry and CLSM data clarify the specific targeting and intracellular uptake of Dox-NP-trastuzumab.

Cellular Doxorubicin Recovery. In a next step, the specific transport of the cytostatic drug doxorubicin with this nanoparticulate formulation into the cancer cells, their release, and biological activity was proven. A first recovery experiment was

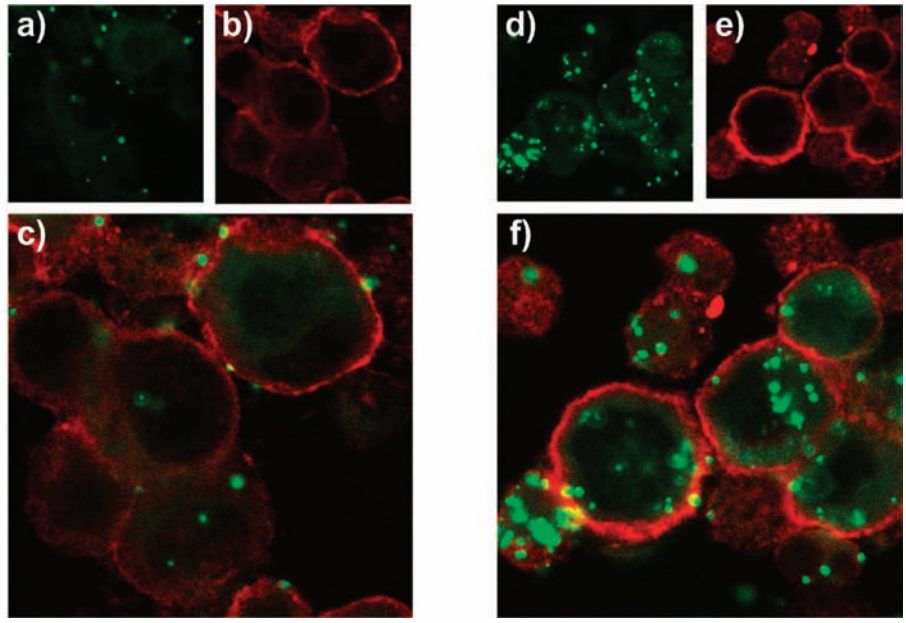

Figure 4. Cellular uptake and intracellular distribution of the nanoparticles studied by confocal laser scanning microscopy. SK-Br-3 cells were cultured on glass slides and treated with the different nanoparticle formulations for 4 h at 37 °C. The green autofluorescence of the nanoparticles was used, and the cell membranes were stained with Concanavalin A AlexaFluor 594 (red). Pictures were taken within inner sections of the cells. (a−c) Incubation of the cells with control nanoparticles without mAb modification. (d−f) Incubation of the cells with the specific Dox-NP-trastuzumab. (a) and (d) display the green nanoparticles channel; (b) and (e) display the red cell membrane; (c) and (f) overlay of the both fluorescence channels.

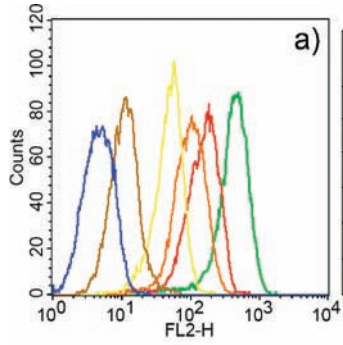

	Y Mean fluorescence	% positive cells
doxorubicin 50 µM	442.93	100.00
doxorubicin 15 µM	163.07	99.88
doxorubicin 10 µM	105.14	99.38
doxorubicin 5 µM	51.48	98.81
doxorubicin 1 µM	12.02	41.65
untreated cells	5.07	1.34

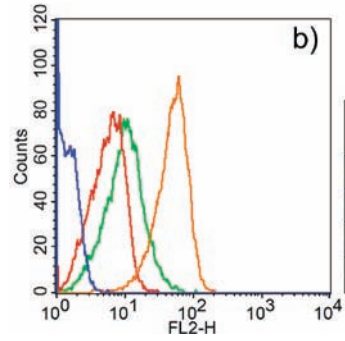

	Y Mean fluorescence	% positive cells
Dox-NP- trastuzumab	11.99	95.16
Dox-NP-IgG	6.47	83.74
doxorubicin	55.03	99.87
untreated cells	1.41	1.52

Figure 5. Doxorubicin recovery studied by flow cytometry: possibility of distinguishing different intracellular doxorubicin concentrations and the detection of nanoparticular transported doxorubicin. (a) HER2 overexpressing SK-Br-3 cells were treated with different concentrations of free doxorubicin for 4 h at 37 °C. Flow cytometry (FACS) analysis was performed to quantify their cellular binding. The data are shown as histograms of the FL2-H-channel (fluorescence of the doxorubicin) as well as a table with Y Mean fluorescence data and percentage of positive cells. Green: 50 μM doxorubicin concentration. Red: 15 μM. Orange: 10 μM. Yellow: 5 μM. Brown: 1 μM. Blue: untreated control. (One representative experiment out of two independent experiments is shown.) (b) HER2 overexpressing SK-Br-3 cells were treated with different nanoparticulate formulations or free doxorubicin for 4 h at 37 °C. Flow cytometry (FACS) analysis was performed to quantify their cellular binding. The data are shown as histograms of the FL2-H-channel (fluorescence of the doxorubicin) as well as a table with Y Mean fluorescence data and percentage of positive cells. Orange: free doxorubicin. Green: Dox-NP-trastuzumab. Red: Dox-NP-IgG. Blue: untreated control. (One representative experiment out of twelve independent experiments is shown.)

done as a flow cytometry analysis with the standard cell line SK-Br-3 and different concentrations of free doxorubicin to demonstrate the possibility of distinguishing different intracellular doxorubicin concentrations by flow cytometry. Use was made of the red fluorescence of doxorubicin in the FL2-H channel of the flow cytometer. Therefore, SK-Br-3 cells were

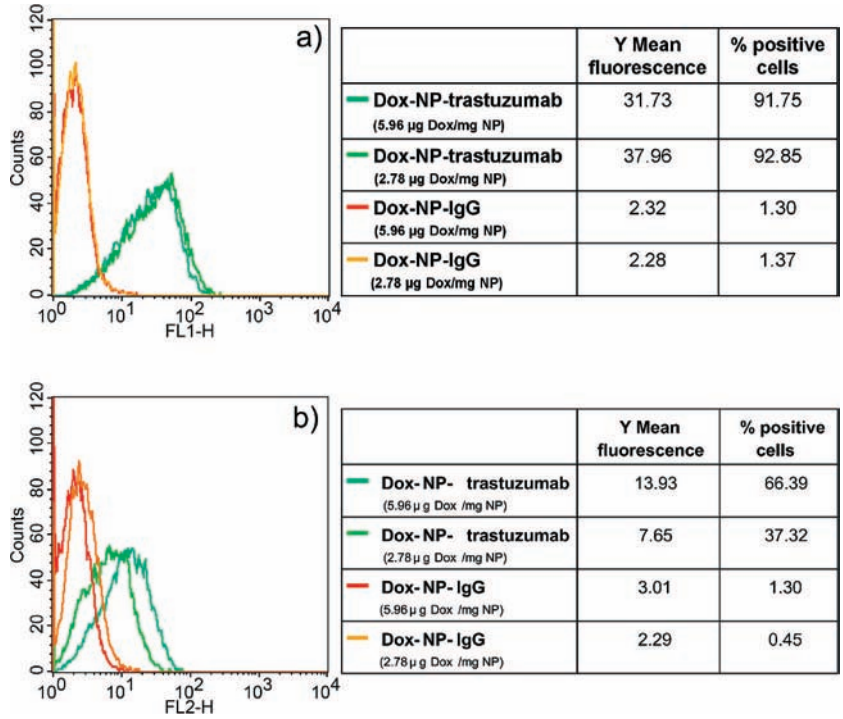

	Y Mean fluorescence	% positive cells
Dox-NP-trastuzumab (5.96 µg Dox/mg NP)	31.73	91.75
Dox-NP-trastuzumab (2.78 µg Dox/mg NP)	37.96	92.85
Dox-NP-IgG (5.96 µg Dox/mg NP)	2.32	1.30
Dox-NP-IgG (2.78 µg Dox/mg NP)	2.28	1.37

	Y Mean fluorescence	% positive cells
Dox- NP- trastuzumab (5.96 µ g Dox /mg NP)	13.93	66.39
Dox- NP- trastuzumab (2.78 µ g Dox /mg NP)	7.65	37.32
Dox- NP- IgG (5.96 µ g Dox /mg NP)	3.01	1.30
Dox- NP- IgG (2.78 µ g Dox /mg NP)	2.29	0.45

Figure 6. Doxorubicin recovery studied by flow cytometry. HER2 overexpressing SK-Br-3 cells were treated with different nanoparticulate formulations with different intraparticular doxorubicin concentrations for 4 h at 37 °C. Flow cytometry (FACS) analysis was performed to quantify their cellular binding. (a) The data are shown as histograms of the FL1-H-channel (autofluorescence of the nanoparticles) as well as a table with Y Mean fluorescence data and percentage of positive cells. (b) The data are shown as histograms of the FL2-H-channel (fluorescence of the doxorubicin) as well as a table with Y Mean fluorescence data and percentage of positive cells. Deep green: Dox-NP-trastuzumab nanoparticles with an intraparticular doxorubicin concentration of 5.96 μg doxorubicin/mg nanoparticle. Light green: Dox-NP-trastuzumab with an intraparticular doxorubicin concentration of 2.78 μg doxorubicin/mg nanoparticle. Red: control Dox-NP-IgG with an intraparticular doxorubicin concentration of 5.96 μg doxorubicin/mg nanoparticle. Orange: Dox-NP-IgG with an intraparticular doxorubicin concentration of 2.78 μg doxorubicin/mg nanoparticle.

incubated with different doxorubicin concentrations for 4 h at 37 °C. The results of flow cytometry analysis are shown in Figure 5a. A clear distinction between the different doxorubicin concentrations is possible with flow cytometry and *CellQuest Pro* software.

When the cells were incubated with doxorubicin-loaded nanoparticles with specific trastuzumab on particle surface (NP concentration corresponding to 15 μM doxorubicin concentration) or with doxorubicin-loaded nanoparticles with unspecific IgG (NP concentration corresponding to 15 μM doxorubicin) or with the same concentration of free doxorubicin (15 μM), different histograms were detected on the FL2-H channel (Figure 5b). Free doxorubicin showed the highest level of fluorescence intensity, followed by Dox-NP-trastuzumab and then Dox-NP-IgG (see table of Y Mean fluorescence Figure 5b). This effect demonstrated that different amounts of doxorubicin were transported to the cells by the different nanoparticulate formulations or free doxorubicin. Due to its specific cellular uptake, Dox-NP-trastuzumab transported more doxorubicin to the cells than the unspecific Dox-NP-IgG. The better uptake of free doxorubicin is a known phenomenon, but this is an unspecific transport to all kinds of cells responsible for all adverse secondary effects during a doxorubicin-based cancer therapy.

However, it was possible to influence the transported doxorubicin concentration by nanoparticles different in doxorubicin loading. HER2 overexpressing SK-Br-3 cells were treated with the specific Dox-NP-trastuzumab nanoparticles with an intraparticular doxorubicin concentration of 5.96 μg or 2.78 μg doxorubicin/mg nanoparticle or with the unspecific control Dox-NP-IgG nanoparticles with the same intraparticular doxorubicin concentration for 4 h at 37 °C. The flow cytometry data showed a better nanoparticulate cellular binding in the FL1-H-channel (Figure 6a) for the specific nanoparticulate formulations (over 90% positive cells) than the unspecific nanoparticulate formulations (approximately 1.3% positive cells), as already known. However, there was no difference in binding among the Dox-NP-trastuzumab nanoparticulate formulations with the different intraparticular doxorubicin concentrations, as well as among Dox-NP-IgG, meaning that the intraparticular doxorubicin concentration does not influence the cellular binding. However, there was a better transport of doxorubicin to the cells by higher loaded Dox-NP-trastuzumab than by lower loaded (see histogram and table in Figure 6b). This effect was also seen for unspecific nanoparticulate formulations. Thus, there was a possibility to influence the doxorubicin concentration transported to the cell. This could also be done by a higher amount of incubated nanoparticles, but a certain relation between the number of cells and the quantity of incubated nanoparticles should be maintained. Indeed, it is important for a nanoparticulate cancer therapy to administer highly loaded formulations in order to achieve a small drug infusion volume.

In a further recovery experiment, HER2 overexpressing SK-Br-3 cells were treated with Dox-NP-trastuzumab (NP concentration corresponding to 7 μM doxorubicin concentration), Dox-NP-IgG (0.1 mg/mL NP concentration corresponding to 7 μM doxorubicin concentration), or free doxorubicin (7 μM) for 4 h at 37 °C and were analyzed directly or further incubated with fresh medium for 20 or 44 h. Flow cytometry (FACS) analysis was performed to quantify their cellular binding and to investigate the doxorubicin processing. The data are shown as histograms of the FL2-H-channel for 4 h nanoparticle incubation only (Figure 7a), 4 h nanoparticle incubation and 20 h incubation time with medium (Figure 7b), and 4 h nanoparticle incubation and 44 h incubation time with medium (Figure 7c). For a better understanding of the results, we drew two lines in Figure 7a−c. The first goes through the histogram maximum of the histogram

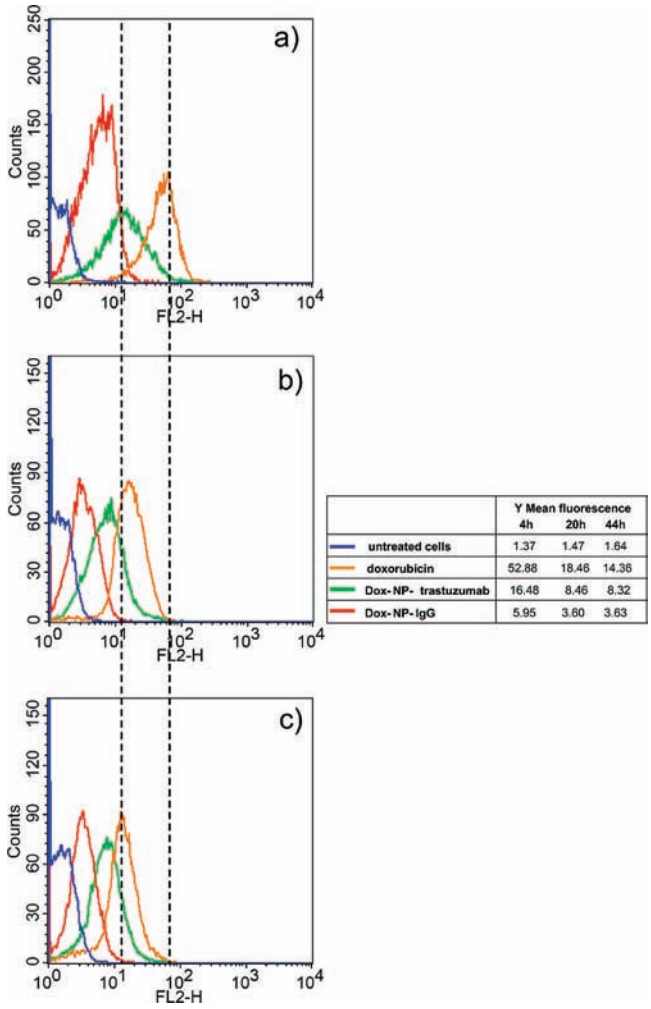

Figure 7. Doxorubicin recovery by flow cytometry: intracellular doxorubicin processing. HER2 overexpressing SK-Br-3 cells were treated with different nanoparticulate formulations or free doxorubicin for 4 h at 37 °C and incubated with fresh medium for different periods of time at 37 °C. Flow cytometry (FACS) analysis was performed to quantify their cellular binding. The data are shown as histograms of the FL2-H-channel (fluorescence of the doxorubicin) as well as a table with Y Mean fluorescence data. Orange: free doxorubicin. Green: Dox-NP-trastuzumab. Red: Dox-NP-IgG. Blue: untreated control. (a) 4 h nanoparticle incubation only. (b) 4 h nanoparticle incubation and 20 h incubation time with medium. (c) Four h nanoparticle incubation and 44 h incubation time with medium. (One representative experiment out of four independent experiments is shown.)

of free doxorubicin incubation analyzed after 4 h, and the second goes through the histogram maximum of the histogram of Dox-NP-trastuzumab after 4 h incubation. Both lines were elongated and cross the histograms after further 20 h and 44 h incubation. First of all, the already known histogram formation of doxorubicin transport to the cells was recognized: free doxorubicin was the best, followed by Dox-NP-trastuzumab and Dox-NP-IgG. However, if the cells were incubated with fresh medium and analyzed after 20 or 44 h a faster regression of the doxorubicin signal of free doxorubicin was recognized than of Dox-NP-trastuzumab. For the regression of the doxorubicin signal of free doxorubicin, we can read off values from approximately 65 (4 h incubation) to 13 (further 44 h incubation), which is a regression by a factor of 5. For the regression of the doxorubicin signal of Dox-NP-trastuzumab, we can read off values from approximately 13 (4 h incubation) to 8 (further 44 h incubation), which is a regression by a factor of 1.6. A reason for this observation could be the known drug efflux pumps of the cells. Free doxorubicin is transported out of the cells by these pumps, but nanoparticulate wrapped doxorubicin is saved. This sustained release effect could help to minimize the needed doxorubicin quantity for the cancer therapy in the future and to reduce secondary effects.

Biological Activity. In addition to the cellular uptake of the nanoparticulate doxorubicin, the therapeutic effect of these formulations was determined. HER2 overexpressing SK-Br-3 cells were incubated with the specific Dox-NP-trastuzumab or the unspecific Dox-NP-IgG in PBS for 4 h at 37 °C at a concentration of 15 μM referred to doxorubicin concentration, and a further incubation time of 7 d followed. Cell viability was determined using WST-1 assay based on the absorbance measurement of formazan formation. The formazan formation is only possible in the mitochondria of healthy cells; therefore, untreated cells set the 100% standard. After the incubation of Dox-NP-trastuzumab, the cells showed only a viability of 20.1% compared to cells incubated with Dox-NP-IgG reaching a viability of 56.5% (Figure 8a). Therefore, the Dox-NP-trastuzumab offered a better specific cellular uptake as well as a better cytotoxic activity.

To test whether the nanoparticles are entrapped within the endosomes or lysosomes and could not release their loaded cytostatic drug, chloroquine was used. Chloroquine is a weak basic reagent, which rapidly diffuses into the cells and accumulates in acidic compartments. This accumulation leads to an inhibition of lysosomal enzymes because of the pH increase. Lysosomal enzymes only work at acidic pH. Furthermore, chloroquine inhibits the fusion of endosome and lysosome, so entrapped agents are no longer degraded. The accumulation of chloroquine in endosomal vesicles induces an osmotic swelling of them, and therefore, the endosomes are destabilized and release the entrapped agents. However, there was no significant difference between the viability of the cells incubated with nanoparticulate formulations in either PBS (Figure 8a) or PBS containing chloroquine (Figure 8b). After incubation with Dox-NP-trastuzumab, there were 20.1% of healthy cells in the case of PBS incubations and 19.6% in the case of chloroquine use. The findings after incubation with Dox-NP-IgG were similar. There are 56.5% of healthy cells after incubation in PBS and 51.7% after incubation in PBS containing chloroquine. These results indicate that the nanoparticulate formulations are not entrapped in the endosomes or lysosomes, and the release of the cytostatic drug is not prohibited respectively.

In order to exclude whether or not these biological effects result from the trastuzumab surface modification of the nanoparticles and are mainly induced by the biological effect of trastuzumab itself, we compared doxorubicin-loaded trastuzumab-modified nanoparticles and unloaded trastuzumab-modified nanoparticles. As shown in Figure 9, the doxorubicin-loaded trastuzumab-modified nanoparticles had, as already known, a cytotoxic effect on cells, but the unloaded trastuzumab-modified nanoparticles did not alter the cell viability. Therefore, we can conclude that the trastuzumab modification of the particles had no influence on cell viability and the doxorubicin component of the particulate system must have caused the biological activity of our nanoparticulate system.

To demonstrate the specificity of our nanoparticulate system, we incubated the HER2 weakly expressing control cell line MCF7 with either the specific trastuzumab-modified nanoparticles or the unspecific IgG-modified nanoparticles (NP concentration corresponding to 1 μM doxorubicin). Both nanoparticulate formulations showed the same cytotoxicity due to an unspecific nanoparticle uptake of both nanoparticle formulations (Figure 10). These results verify the specificity and the biological activity of our newly designed ligand targeted nanoparticulate formulation based on human serum albumin with doxorubicin loading.

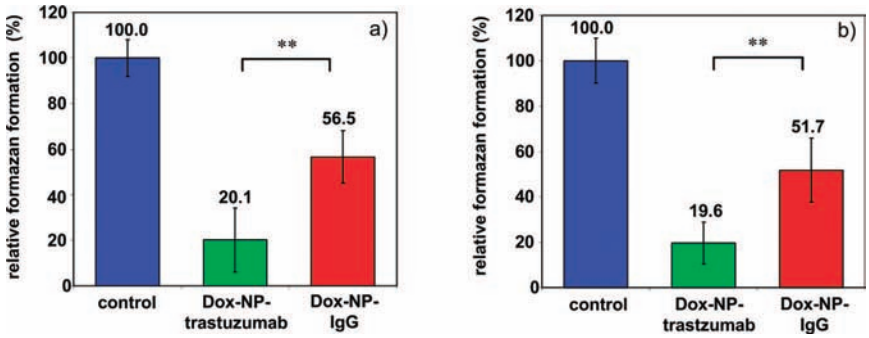

Figure 8. Cell viability assay: comparison between Dox-NP-trastuzumab and Dox-NP-IgG. HER2 overexpressing SK-Br-3 cells were incubated with the Dox-NP-trastuzumab or Dox-NP-IgG at the same concentration in (a) PBS or (b) PBS containing chloroquine for 4 h at 37 °C. After washing, the cells were further incubated for 7 d at 37 °C. The cell viability was determined after addition of WST-1 reagent and measurement of formazan formation, as described in the manufacturer's instructions manual. Untreated cells set the 100% standard. (internal control of each experiment $n = 9$, one representative experiment out of three independent experiments is shown for experiment (a))* *: The two samples are significantly different ($P < 0.01$, two-tailed Mann−Whitney U Test equivalent to the Wilcoxon rank sum test).

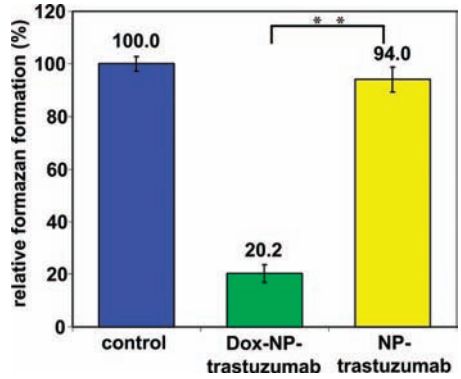

Figure 9. Cell viability assay: comparison between Dox-NP-trastuzumab and NP-trastuzumab. HER2 overexpressing SK-Br-3 cells were incubated with the Dox-NP-trastuzumab or NP-trastuzumab at the same concentration for 4 h at 37 °C. After washing, the cells were further incubated for 7 d at 37 °C. The cell viability was determined after addition of WST-1 reagent and measurement of formazan formation, as described in the manufacturer's instructions manual. Untreated cells set the 100% standard. (internal control of each experiment $n = 9$)* *: The two samples are significantly different ($P < 0.01$, two-tailed Mann−Whitney U Test equivalent to the Wilcoxon rank sum test).

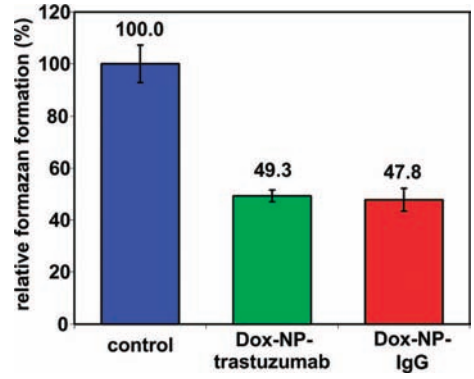

Figure 10. Cell viability assay: comparison between Dox-NP-trastuzumab and Dox-NP-IgG. HER2 weakly expressing MCF7 cells were incubated with the Dox-NP-trastuzumab or Dox-NP-IgG at the same concentration for 4 h at 37 °C. After washing, the cells were further incubated for 7 d at 37 °C. The cell viability was determined after addition of WST-1 reagent and measurement of formazan formation, as described in the manufacturer's instructions manual. Untreated cells set the 100% standard. (Internal control of each experiment $n = 9$)* *: The two samples are significantly different ($P < 0.01$, two-tailed Mann−Whitney U Test equivalent to the Wilcoxon rank sum test).

In the future, nanoparticle development for cancer chemotherapy will be a significant and expanding part of nanobiotechnology. The search for new tumor targets, novel ligands, new strategies for targeting, and particle stabilization will occupy science in the future to improve drug delivery at the tumor site while decreasing toxicity to normal tissues.

There already exist a lot of nanostructured formulations in order to reach this goal (for review, see Haley et al. (*21*)). For example, there are FDA-approved liposomal doxorubicin encapsulations (Doxil/Caelyx and Myocet) where the anthracycline pharmacokinetics are changed and cardiac risk is decreased but not eliminated (*22*−*25*). Anthracycline toxicity to normal tissue is reduced by liposomal encapsulation. After extravasation through tumor endothelium, liposomes disintegrate and deliver doxorubicin. Drug concentration has been measured 10 times higher in tumor tissue treated with Doxil compared to conventional free drug administration (*26*).

A further example is the first HSA-based nanoparticle formulation, Abraxane, approved by the FDA in 2005 and by the EMEA in 2008. The 130 nm large nanoparticles contain the cytostatic drug paclitaxel. Due to the bad solubility of paclitaxel in water, the conventional drug preparation (Taxol) contains polyethylated castor oil (Cremophor EL) and ethanol as vehicles. The drug incorporation in nanoparticles follows a new concept to improve drug solubility, with a variety of advantages compared to the standard paclitaxel therapy. Therefore, a nanoparticulate-bound paclitaxel infusion leads to a 33% increase in intratumoral concentrations and a 50% higher dose of delivered paclitaxel in comparison to a conventional paclitaxel infusion. Additionally, since nanoparticulate-bound paclitaxel is solvent-free, the infusion time is 30 min in contrast to the 3 h infusion for conventional taxol, and no premedication is required (*27, 28*).

In earlier studies, we have optimized and established a desolvation process to prepare human serum albumin nanoparticles (*4*). Previous studies have demonstrated that nanoparticles based on HSA were rapidly degraded after cellular uptake and led to a significant cellular accumulation of the entrapped drug (*29*). Therefore, we advanced this process to load human serum albumin based nanoparticles with the antineoplastic agent doxorubicin (*17*).

As already discussed, the specific targeting of cancer cells will be a breakthrough in cancer therapy. The treatment with monoclonal antibodies recognizing tumor-associated markers is a common strategy in cancer therapy. One of the most promising targets is the human epidermal growth factor receptor-2 (HER2), whose overexpression is strongly associated with poor prognosis. HER2 is a transmembrane tyrosine kinase

growth factor receptor, which is only marginally expressed in adult tissue (*30*), but is overexpressed in approximately 30% of human gastric, lung, and breast carcinoma. Trastuzumab (Herceptin), a humanized monoclonal antibody directed against the extracellular domain of HER2, is the only HER2-targeted therapy approved by the FDA for treatment of breast cancer (*31*). However, the best results in therapy were achieved when trastuzumab was given in combination with other cytotoxic agents. Because of its enhanced expression on tumor cells, its extracellular accessibility and its ability to internalize after antibody binding, HER2 represents a suitable target for tumor therapy with cell-specific nanoparticles. In a former study, we demonstrated an improvement of the specific uptake into HER2 overexpressing cells with trastuzumab surface-modified human serum albumin based nanoparticles (*9, 16*).

In the present study, we combined the specific trastuzumab-based nanoparticles with the cytostatic drug loading efficiency, to achieve a specific drug delivery system. Thus, we can conclude that we have developed a novel specific drug carrier system, which allowed us a specific transport of doxorubicin to HER2 overexpressing breast cancer cells. The duration of the uptaken doxorubicin within these cells was elongated and the drug was better saved against efflux, a known effect of nanoparticulate incorporated cytostatic drugs. Therefore, a minimization of needed doxorubicin volume in cancer therapy is presumed. Concerning the specificity and the minimized drug infusion volume, a reduction of the secondary side effects can be estimated. Due to the mAb directed specificity of the nanoparticles, our novel drug carrier system should be more efficient compared to the already known PEGylated liposomal doxorubicin carrier (Doxil or Caelyx). Additionally, nanoparticles show a higher loading capacity with a lower tendency of drug leakage than liposomes. Furthermore, a better stability of nanoparticles compared to liposomal formulations is known.

These trastuzumab-modified nanoparticles efficiently bind to and are specifically internalized in HER2 overexpressing breast cancer cells. They release the incorporated drug effectively. The combination of specific targeting with drug loading in these nanoparticulate formulations should lead to an improvement in cancer therapy.

ACKNOWLEDGMENT

The authors thank Daniel Sauer for his skilful technical assistance. This work was financially supported by the German Bundesministerium für Bildung und Forschung (BMBF) (Project 13N8671).

Supporting Information Available: Additional graphics and animated files as described in the text. Please refer to the pdf for descriptions. This material is available free of charge via the Internet at http://pubs.acs.org.

LITERATURE CITED

(1) Cirstoiu-Hapca, A., Bossy-Nobs, L., Buchegger, F., Gurny, R., and Delie, F. (2007) Differential tumor cell targeting of anti-HER2 (Herceptin) and anti-CD20 (Mabthera) coupled nanoparticles. *Int. J. Pharm. 331*, 190–196.

(2) Couvreur, P., and Vauthier, C. (2006) Nanotechnology: intelligent design to treat complex disease. *Pharm. Res. 23*, 1417–1450.

(3) Weber, C., Coester, C., Kreuter, J., and Langer, K. (2000) Desolvation process and surface characterisation of protein nanoparticles. *Int. J. Pharm. 194*, 91–102.

(4) Langer, K., Balthasar, S., Vogel, V., Dinauer, N., von Briesen, H., and Schubert, D. (2003) Optimization of the preparation process for human serum albumin (HSA) nanoparticles. *Int. J. Pharm. 257*, 169–180.

(5) Yokoyama, M., and Okano, T. (1996) Targetable drug carriers: present status and a future perspective. *Adv. Drug Delivery Rev. 21*, 77–80.

(6) Maeda, H., Wu, J., Sawa, T., Matsumura, Y., and Hori, K. (2000) Tumor vascular permeability and the EPR effect in macromolecular therapeutics: a review. *J. Controlled Release 65*, 271–284.

(7) Greenwald, R. B. (2001) PEG drugs: an overview. *J. Controlled Release 74*, 159–171.

(8) Nobs, L., Buchegger, F., Gurny, R., and Allemann, E. (2004) Current methods for attaching targeting ligands to liposomes and nanoparticles. *J. Pharm. Sci. 93*, 1980–1992.

(9) Wartlick, H., Michaelis, K., Balthasar, S., Strebhardt, K., Kreuter, J., and Langer, K. (2004) Highly specific HER2-mediated cellular uptake of antibody-modified nanoparticles in tumour cells. *J. Drug Targeting 12*, 461–471.

(10) Dinauer, N., Balthasar, S., Weber, C., Kreuter, J., Langer, K., and von Briesen, H. (2005) Selective targeting of antibody-conjugated nanoparticles to leukemic cells and primary T-lymphocytes. *Biomaterials 26*, 5898–5906.

(11) Adams, G. P., and Weiner, L. M. (2005) Monoclonal antibody therapy of cancer. *Nat. Biotechnol. 23*, 1147–1157.

(12) Harries, M., and Smith, I. (2002) The development and clinical use of trastuzumab (Herceptin). *Endocr. Relat. Cancer 9*, 75–85.

(13) Valabrega, G., Montemurro, F., and Aglietta, M. (2007) Trastuzumab: mechanism of action, resistance and future perspectives in HER2-overexpressing breast cancer. *Ann. Oncol. 18*, 977–984.

(14) Ferretti, G., Felici, A., Papaldo, P., Fabi, A., and Cognetti, F. (2007) HER2/neu role in breast cancer: from a prognostic foe to a predictive friend. *Curr. Opin. Obstet. Gynecol. 19*, 56–62.

(15) Pereverzeva, E., Treschalin, I., Bodyagin, D., Maksimenko, O., Langer, K., Dreis, S., Asmussen, B., Kreuter, J., and Gelperina, S. (2007) Influence of the formulation on the tolerance profile of nanoparticle-bound doxorubicin in healthy rats: focus on cardio- and testicular toxicity. *Int. J. Pharm. 337*, 346–356.

(16) Steinhauser, I., Spänkuch, B., Strebhardt, K., and Langer, K. (2006) Trastuzumab-modified nanoparticles: Optimisation of preparation and uptake in cancer cells. *Biomaterials 27*, 4975–4983.

(17) Dreis, S., Rothweiler, F., Michaelis, M., Cinatl, J., Jr., Kreuter, J., and Langer, K. (2007) Preparation, characterisation and maintenance of drug efficacy of doxorubicin-loaded human serum albumin (HSA) nanoparticles. *Int. J. Pharm. 341*, 207–214.

(18) Siegel, S., Castellan, N. J. (1988) Nonparametric statistics for the behavioral sciences (2nd edition), McGraw-Hill Education, New York.

(19) Sachs, L. (1992) Angewandte Statistik (7.Auflage), Springer-Verlag, Berlin.

(20) Heath, D. (1995) An Introduction to Experimental Design and Statistics for Biology, UCL Press, London.

(21) Haley, B., and Frenkel, E. (2008) Nanoparticles for drug delivery in cancer treatment. *Urol. Oncol. 26*, 57–64.

(22) Working, P. K., Newman, M. S., Sullivan, T., and Yarrington, J. (1999) Reduction of the cardiotoxicity of doxorubicin in rabbits and dogs by encapsulation in long-circulating, pegylated liposomes. *J. Pharmacol. Exp. Ther. 289*, 1128–1133.

(23) Waterhouse, D. N., Tardi, P. G., Mayer, L. D., and Bally, M. B. (2001) A comparison of liposomal formulations of doxorubicin with drug administered in free form: changing toxicity profiles. *Drug Saf. 24*, 903–920.

(24) Gabizon, A., Shmeeda, H., and Barenholz, Y. (2003) Pharmacokinetics of pegylated liposomal Doxorubicin: review of animal and human studies. *Clin. Pharmacokinet. 42*, 419–436.

(25) O'Brien, M. E., Wigler, N., Inbar, M., Rosso, R., Grischke, E., Santoro, A., Catane, R., Kieback, D. G., Tomczak, P., Ackland, S. P., Orlandi, F., Mellars, L., Alland, L., and

Tendler, C. (2004) Reduced cardiotoxicity and comparable efficacy in a phase III trial of pegylated liposomal doxorubicin HCl (CAELYX/Doxil) versus conventional doxorubicin for first-line treatment of metastatic breast cancer. *Ann. Oncol. 15*, 440–449.

(26) Lasic, D., Martin, F. (1995) Stealth Liposomes, in *Handbooks in Pharmacology and Toxicology* (Lasic, D., and Martin, F., Eds.) pp 22−41, CRC Press, Boca Raton, FL.

(27) Gradishar, W. J., Tjulandin, S., Davidson, N., Shaw, H., Desai, N., Bhar, P., Hawkins, M., and O'Shaughnessy, J. (2005) Phase III trial of nanoparticle albumin-bound paclitaxel compared with polyethylated castor oil-based paclitaxel in women with breast cancer. *J. Clin. Oncol. 23*, 7794–7803.

(28) Desai, N., Trieu, V., Yao, Z., Louie, L., Ci, S., Yang, A., Tao, C., De, T., Beals, B., Dykes, D., Noker, P., Yao, R., Labao, E., Hawkins, M., and Soon-Shiong, P. (2006) Increased antitumor activity, intratumor paclitaxel concentrations, and endothelial cell transport of cremophor-free, albumin-bound paclitaxel, ABI-007, compared with cremophor-based paclitaxel. *Clin. Cancer Res. 12*, 1317–1324.

(29) Wartlick, H., Spankuch-Schmitt, B., Strebhardt, K., Kreuter, J., and Langer, K. (2004) Tumour cell delivery of antisense oligonuclceotides by human serum albumin nanoparticles. *J. Controlled Release 96*, 483–495.

(30) Press, M. F., Cordon-Cardo, C., and Slamon, D. J. (1990) Expression of the HER-2/neu proto-oncogene in normal human adult and fetal tissues. *Oncogene 5*, 953–962.

(31) Tokunaga, E., Oki, E., Nishida, K., Koga, T., Egashira, A., Morita, M., Kakeji, Y., and Maehara, Y. (2006) Trastuzumab and breast cancer: developments and current status. *Int. J. Clin. Oncol. 11*, 199–208.

BC8002452

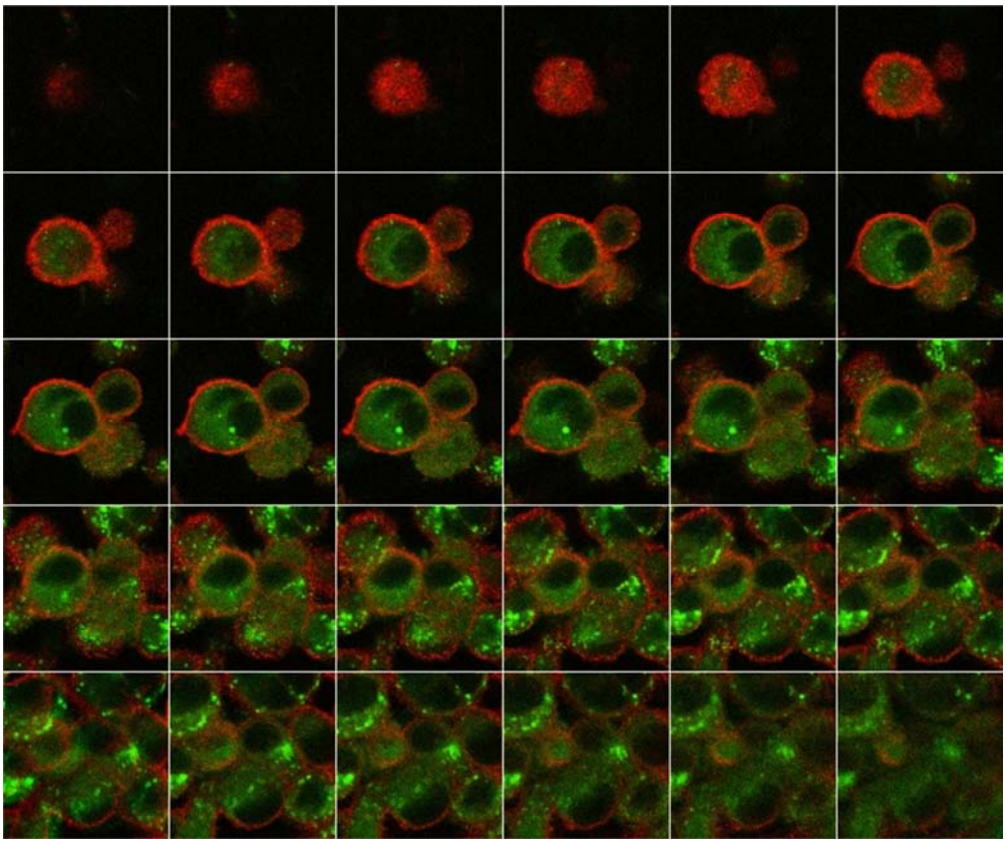

177x148mm (300 x 300 DPI)

Supporting Information

Specific targeting of HER2 overexpressing breast cancer cells with doxorubicin loaded trastuzumab modified human serum albumin nanoparticles

Marion G. Anhorn[†§], Sylvia Wagner[‡§], Jörg Kreuter[†], Klaus Langer[†], Hagen von Briesen[‡]*

Fraunhofer Institute of Biomedical Engineering, Department of Biohybrid Systems, 66386 St. Ingbert, Germany and Institute of Pharmaceutical Technology, Biocenter of Johann Wolfgang Goethe-University, 60438 Frankfurt / Main, Germany

[§]both authors contributed equally to this work

[†]Institute of Pharmaceutical Technology

[‡]Fraunhofer Institute of Biomedical Engineering

*Corresponding author:

Dr. Hagen von Briesen,

Fraunhofer Institute for Biomedical Engineering,

Ensheimer Strasse 48, D-66386 St.Ingbert, Germany

Phone: +49-(0)6894-980-286 Fax: +49-(0)6894-980-400

e-mail: hagen.briesen@ibmt.fraunhofer.de

List of content:

- Supplement 1: picture series of an optical stack
- Supplement 2: animation of an optical stack
- Supplement 3: 3D projection

Supplement 1

Cellular uptake and intracellular distribution of the nanoparticles studied by confocal laser scanning microscopy: optical stack.

SK-Br-3 cells were cultured on glass slides and treated with Dox-NP-trastuzumab for 24 h at 37°C. The green autofluorescence of the nanoparticles was used and the cell membranes were stained with Concanavalin A AlexaFluor 594 (red). Cells were optically sliced in a stack of 0.75 µm thickness each and the picture series is displayed as a gallery.

Supplement 2

Cellular uptake and intracellular distribution of the nanoparticles studied by confocal laser scanning microscopy: animation of an optical stack.

SK-Br-3 cells were cultured on glass slides and treated with Dox-NP-trastuzumab for 4 h. The green autofluorescence of the nanoparticles was used and the cell membranes were stained with Concanavalin A AlexaFluor 594 (red). Cells were optically sliced in a stack of 0.67 µm thickness each. The picture series was animated to demonstrate the intracellular uptake of the nanoparticles. The animation was done by the image processing program Image J.

Supplement 3

Cellular uptake and intracellular distribution of the nanoparticles studied by confocal laser scanning microscopy: 3D projection.

SK-Br-3 cells were cultured on glass slides and treated with Dox-NP-trastuzumab for 4 h. The green autofluorescence of the nanoparticles was used and the cell membranes were stained with Concanavalin A AlexaFluor 594 (red). Cells were optically sliced in a stack of 0.67 µm thickness each. A picture series of cells with internalized nanoparticles were semitransparently animated as a 3D projection to demonstrate the intracellular uptake of the nanoparticles. The animation was done by the image processing program Image J.

Design, Synthesis, and DNA Binding Properties of Photoisomerizable Azobenzene−Distamycin Conjugates: An Experimental and Computational Study

Sumana Ghosh,[‡] Dandamudi Usharani,[§] Ananya Paul,[‡] Susmita De,[§] Eluvathingal D. Jemmis,[†,§] and Santanu Bhattacharya*[,‡,||]

Department of Organic Chemistry and Department of Inorganic and Physical Chemistry, Indian Institute of Science, and Chemical Biology Unit, Jawaharlal Nehru Centre of Advanced Scientific Research, Bangalore 560 012, India. Received March 30, 2008; Revised Manuscript Received August 26, 2008

Here, we present the synthesis, photochemical, and DNA binding properties of three photoisomerizable azobenzene−distamycin conjugates in which two distamycin units were linked via electron-rich alkoxy or electron-withdrawing carboxamido moieties with the azobenzene core. Like parent distamycin A, these molecules also demonstrated AT-specific DNA binding. Duplex DNA binding abilities of these conjugates were found to depend upon the nature and length of the spacer, the location of protonatable residues, and the isomeric state of the conjugate. The changes in the duplex DNA binding efficiency of the individual conjugates in the dark and with their respective photoirradiated forms were examined by circular dichroism, thermal denaturation of DNA, and Hoechst displacement assay with poly[d(A-T).d(T-A)] DNA in 150 mM NaCl buffer. Computational structural analyses of the uncomplexed ligands using ab initio HF and MP2 theory and molecular docking studies involving the conjugates with duplex $d[(GC(AT)_{10}CG)]_2$ DNA were performed to rationalize the nature of binding of these conjugates.

INTRODUCTION

The distamycin and netropsin are well-known naturally occurring DNA minor groove binders (*1, 2*). These are known to selectively recognize A/T-rich base pairs via hydrogen bonding with base pairs together with van der Waals and electrostatic interactions with DNA (*3, 4*). Consequently, there is a continuing effort to modify natural distamycin A to enhance its sequence recognition and binding affinity with double-stranded (ds) DNA. In the past few years, various synthetic strategies have been developed to modify the distamycin scaffold to enhance the recognition efficiency together with mixed base-pair reading capacity. Thus, various new types of DNA binding molecules were designed to enhance and alter sequence specificity of distamycin to any desired target stretch of ds-DNA (*5, 6*). Another strategy to achieve improved DNA binding involved dimerization of DNA minor groove binders (MGB) (*7*−*9*). Although the gain in binding constant is often not as much as expected from dimerization, these modified ligands were found to recognize an extended stretch of 15−16 consecutive AT/GC base pairs with higher binding constant values (*10*−*12*).

We have been working on different DNA binding/cleaving molecules (*13*−*18*) and, in particular, with the distamycin analogues including its tail-to-tail dimers for improving their DNA recognition properties (*19*−*21*). We also reported the thermal stabilization of DNA upon conjugation of distamycin with oligodeoxynucleotides (*22*). In another effort, we have described the differences in their photochemical and DNA binding abilities of distamycin dimers connected through isomeric 2,2′ and 4,4′-dialkoxyazobenzene units (*23*). Herein we introduce the conjugates possessing an azobenzene moiety to which two distamycin arms has been connected via different types of linkages. The reason for choosing the azobenzene is due to its nearly reversible photoisomerization property (*24*). The light-induced isomerization of azobenzene is accompanied by significant changes in geometry and polarity of the chromophore (*25*). This unique property has already been widely exploited in various side chains and backbones of peptides, oligonucleotides, sugar scaffolds, and phospholipids to modify and regulate various biological processes (*26*−*30*). Indeed, an azobenzene group was also tethered into many transcription factors and at various positions of the T7-promoter site to modulate the transcription machinery in the presence of light (*31, 32*).

Here, we present the syntheses of three distamycin−azobenzene conjugates that vary in terms of the electronic nature of the linkage and in the length and the type of the spacer that connects them. The dimeric distamycin−azobenzene conjugates, **1**, **2**, and **3**, were synthesized using two different distamycin analogues, **Dist-1** and **Dist-2**. These distamycin analogues have an identical number of amide bonds for interaction with DNA bases, but they differ in terms of the number of N-methyl pyrrole rings and with respect to the position of partial charge developed along the distamycin backbone at physiological pH. So in the case of **1a**, **Dist-1** analogue is covalently connected to the 4,4′ (para) position of the electron-donating alkoxy substituted azobenzene moiety. On the other hand for ligands **2a** and **3a**, **Dist-1** and **Dist-2** units are covalently conjugated to the 4,4- position of the azobenzene core with *electron-withdrawing* carboxamido substituents, respectively, to furnish azobenzene−distamycin conjugates with a long or short spacer (Figure 1). We have examined the influence of the azobenzene moiety on the

* For correspondence. E-mail: sb@orgchem.iisc.ernet.in, Phone: +(91)-80-2293-2664, Fax: +(91)-80-2360-0529.

[‡] Department of Organic Chemistry, Indian Institute of Science.

[§] Department of Inorganic and Physical Chemistry, Indian Institute of Science.

[†] Present address: Indian Institute of Science Education and Research, Thiruvananthapuram, CET Campus, TVM 695016, Kerala, India.

[||] Jawaharlal Nehru Centre of Advanced Scientific Research.

10.1021/bc800130u CCC: $40.75 © 2008 American Chemical Society
Published on Web 11/08/2008

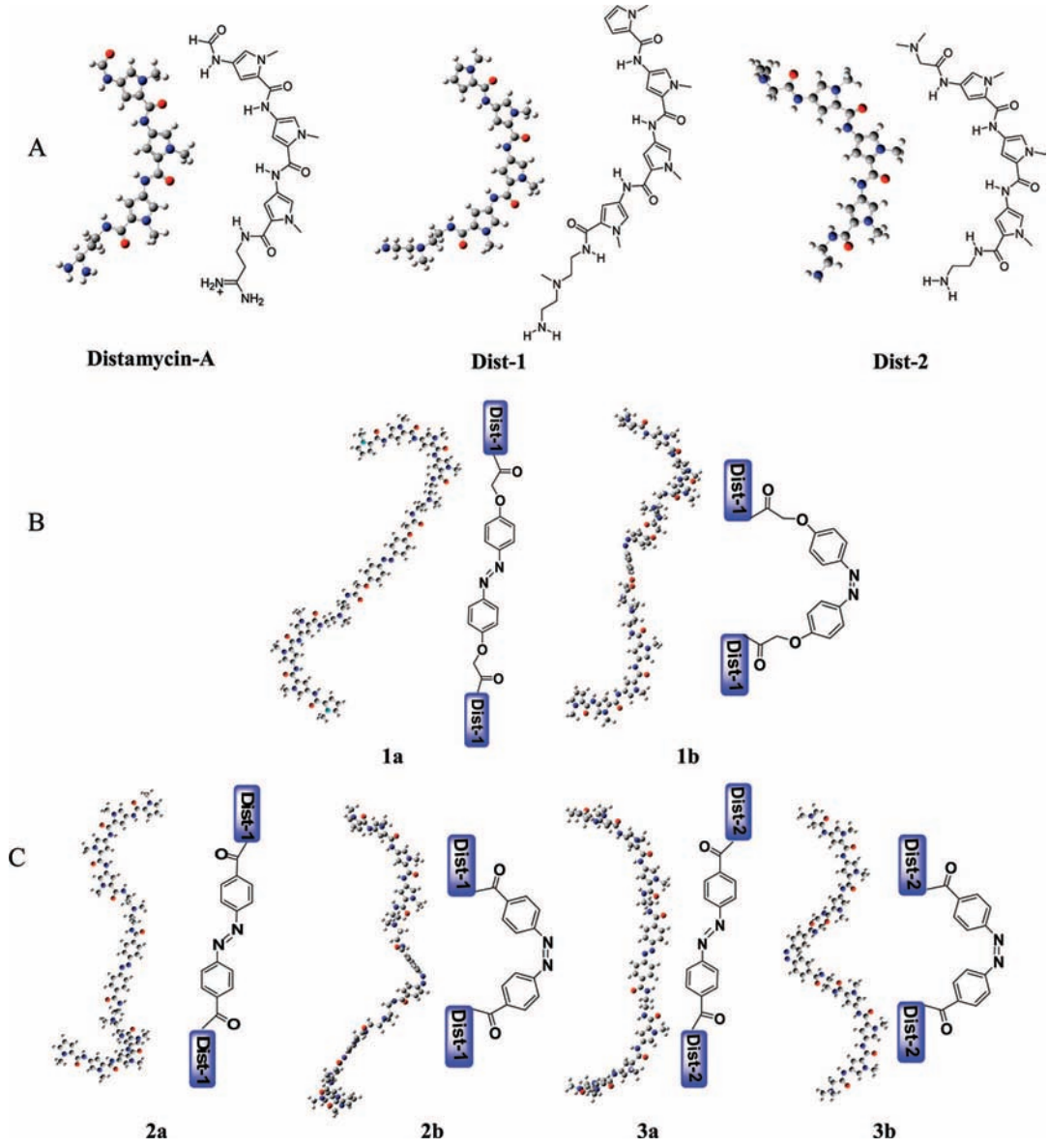

Figure 1. Chemical and optimized structures at the HF/3−21G level of theory of natural distamycin A, distamycin analogues, **Dist-1** and **Dist-2** (A), 4,4′-bis-alkoxyazobenzene containing **Dist-1** in **1a** (trans) and **1b** (cis) (B), 4,4′-bis-carboxamidoazobenzene containing **Dist-1** in **2a** (trans) and **2b** (cis); and (C) **Dist-2** in **3a** (trans) and **3b** (cis) linked via short spacer.

distamycin binding of the DNA minor groove and the changes in ds-DNA binding upon photoisomerization of the conjugate.

By examining the binding properties of these azobenzene−distamycin compounds (**1**, **2**, and **3**) with duplex DNA before and after photoillumination, we sought to address the following questions. Does the incorporation of azobenzene moiety in conjugates **1**, **2**, and **3** interfere with distamycin binding on DNA minor grooves in the ground state? How do the binding of distamycin arms vary upon changing the electronic nature of substituent (alkoxy vs carboxamido) on the azobenzene, e.g., between ligands **1** and **2**? How do ds-DNA binding characteristics vary with linker lengths between the long spacer based **2** and the short spacer based **3** for carboxamido-substituted azobenzene−distamycin conjugates? Finally, how much influence does the photoisomerization impart on the DNA binding properties of such azobenzene−distamycin conjugates?

We first illuminated ligand **1** at ∼360 nm and ligands **2** and **3** at ∼330 nm in solution to produce the corresponding photoisomeric forms. DNA binding properties and the changes in DNA binding efficiencies of individual conjugates in both their ground and photoisomerized states were studied by circular dichroism spectroscopy, thermal denaturation studies, and Hoechst displacement assay. We have also compared with **Dist-1** the DNA binding affinity of different photoirradiated forms of **1**, **2**, and **3** (in their photostationary state) designated as **1***, **2***, and **3***, respectively, to evaluate the effect of incorporation of azobenzene on DNA binding. The experimental results were then analyzed by ligand docking studies using duplex $d[(GC(AT)_{10}CG)]_2$ DNA scaffold. Both experimental and theoretical studies indicate that the duplex DNA binding is highly dependent on the linker length between the azobenzene and the distamycin. The linker length also influences the hydrogen bonding contacts between the pyrrole amide with DNA bases and helps to achieve proper shape complimentarity with the double helical DNA axis.

EXPERIMENTAL PROCEDURES

Synthesis. All reagents used in this study were of the highest purity available and were used without purification. Distamycin analogue, **Dist-1**, is a tetra *N*-methylpyrrole based oligopeptide, which has been synthesized and shown to interact with ds-DNA

along the minor groove surface as reported earlier (*33*). Compounds **4**, **8**, and **10** were prepared as described earlier (*33*−*36*).

4,4′-Dihydroxyazobenzene (*4*). A mixture of KOH (50 g, 760 mmol), *p*-nitrophenol (10 g, 72 mmol), and water (10 mL) was first heated to 120 °C and left to stand in a heating bath for 1 h. When the temperature slowly rose to 195−200 °C, the reaction vigorously started with the formation of large number of bubbles to give a brown viscous liquid. After the reaction was completed, the mixture was cooled and the products were dissolved in water. This afforded a dark red solution, which was acidified to pH 3 with concentrated HCl and extracted with ethyl acetate. Combined ethyl acetate extracts were dried over anhydrous Na_2SO_4 and removed to dryness under reduced pressure. Residue was recrystallized several times with distilled ethanol to give yellow crystals of **4** (*35*). The isolated yield was 4.0 g (43%). IR (cm^{-1}): 1600. ^1H NMR (300 MHz, DMSO-d_6) δ (ppm): 6.9 (d, $J = 9$ Hz, 4H), 8.2 (d, $J = 9$ Hz, 4H). ESI MS (positive ions): *m*/*z* calcd. 215.2 $[M + H]^+$, found 215.2 $[M + H]^+$.

4,4′-Bis(1-(carbomethoxy)methoxy)azobenzene (*5*). Methyl bromoacetate (1.2 mL, 13.0 mmol) was added to a mixture of 4,4′-dihydroxyazobenzene (0.8 g, 3.8 mmol), K_2CO_3 (5.4 g, 26.0 mmol), and 18-crown-6 (0.12 g, 0.46 mmol) in dry acetone (20 mL), and the mixture was refluxed for 15 h. The reaction mixture was then cooled to room temperature, filtered, and evaporated. The residue was dissolved in ethyl acetate, washed with water, and dried over anhydrous $MgSO_4$. The solvent was removed to dryness, and the crude product was purified by column chromatography over silica gel using EtOAc/hexane eluent (20:80) followed by EtOAc/hexane (30:70). This furnished 1.0 g of **5** as a yellow-colored solid (75%). IR (cm^{-1}): 1756.8, 1598.7. ^1H NMR (300 MHz, $CDCl_3$) δ (ppm): 3.83 (s, 6H), 4.7 (s, 4H), 7.01 (d, $J = 8.7$ Hz, 4H), 7.88 (d, $J = 9.0$ Hz, 4H). ESI MS (positive ions): *m*/*z* calcd. 359.4 $[M + H]^+$, found 359.4 $[M + H]^+$.

4,4′-Bis(1-(carboxylic acid)methoxy)azobenzene (*6*). Compound **5** (1.0 g, 2.8 mmol) was dissolved in 20 mL THF. A solution of 2.2 g (56 mmol) of NaOH in 50 mL water was added into the above solution and the mixture was heated under reflux for 2 h. Then, THF was removed under reduced pressure, and the remaining solution was cooled and acidified with 0.5 N HCl. The yellow solid that precipitated was filtered and dried over anhydrous P_2O_5. This furnished 0.74 g of acid, **6** (80% yield). IR (cm^{-1}): 3438.5, 1734.6, 1707.6, and 1600.6. ^1H NMR (300 MHz, DMSO-d_6) δ (ppm): 4.8 (s, 4H), 7.08 (d, $J = 9$ Hz, 4H), 7.82 (d, $J = 9.3$ Hz, 4H). ESI MS (positive ions): *m*/*z* calcd. 330.27 $[M]^+$, found 330.2 $[M]^+$.

4,4′-Bis(1-(chlorocarbonyl)methoxy)azobenzene (*7*). Compound **6** (150 mg, 0.5 mmol) was dissolved in 5.0 mL dry THF and into that 15 mL of distilled $SOCl_2$ was added under ice−cold condition. The reaction mixture was refluxed for 3 h. After that, both solvent and $SOCl_2$ were evaporated under vacuum. This resulted in the formation of a gummy acid chloride in ∼70% isolated yield. The acid chloride was directly used in the next step. IR (cm^{-1}): 1758.8, 1599.6.

4,4′-Bis[(1-carboxamide-*N*-2-2-[(2-aminoethyl)(methyl)amino[(1-methyl-4[(1-methyl-4[(1-methyl-4 [(1-methyl-1*H*-pyrrol-2-yl)carbonyl]amino-1*H*-pyrrol-2-yl)carbonyl]amino-1*H*-pyrrol-2-yl)carbon-yl]amino-1*H*-2-pyrrolecarboxamide]methoxy)azobenzene (*1*). The distamycin derivative, **Dist-1**, (0.6 g, 1.1 mmol) was dissolved in 15 mL of dry THF, and into it, 150 μL of *N*,*N*′-diisopropyl-*N*-ethylamine (DIEA) (0.9 mmol) was added. Acid chloride, **7**, (100 mg, 0.3 mmol) was dissolved in dry THF and added slowly into the above solution. The reaction mixture was stirred at room temperature for 4 h. The solvent was evaporated and the reaction mixture was adsorbed in neutral Al_2O_3 and eluted with $CHCl_3$ followed by MeOH/$CHCl_3$ (2:98) mixture. This furnished **1** as a yellow solid (0.2 g) in 53% isolated yield. ^1H NMR (300 MHz, DMSO-d_6) δ (ppm): 2.23 (s, 6H), 2.49 (s, 8H), 3.78, 3.83, 3.84, 3.87 (s, 12H), 4.56 (s, 4H), 6.04 (dd, $J_1 = 2.4$ Hz, $J_2 = 4.0$ Hz, 1H), 6.86 (m, 1H), 6.9−6.94 (m, 2H), 7.03 (bs, 2H), 7.07−7.1 (dd, 4H, $J_1 = 8.7$ Hz), 7.163 (bs, 1H), 7.22 (bs, 2H), 7.77−7.8 (dd, 4H, $J_1 = 8.7$ Hz), 9.8, 9.86, 9.9 (bs, 8H). ^{13}C NMR (125 MHz, DMSO-d_6) δ (ppm): 36.1, 42.0, 55.96, 72.52, 104.2, 104.73, 106.68, 108.16, 112.66, 115.3, 117.9, 118.45, 121.25, 122.2, 122.8, 124.1, 125.45, 126.32, 128.16, 145.56, 161.3, 163.2, 164.6, 167.22, 168.7, 169.88; ESI MS (positive ions): *m*/*z* calcd. 1475.58 $[M]^+$, 738.3 $[(M + H)/2]^+$, found 1475.6 $[M]^+$ (20%), 738.6 $[(M + H)/2]^+$, (100%). Anal. Calcd. for $C_{74}H_{86}N_{22}O_{12}.H_2O$: C, 59.5; H, 5.94; N, 20.63. Found: C, 59.1; H, 6.3; N, 20.3.

Azobenzene 4,4′-Dicarboxylic Acid (*8*). *p*-Nitrobenzoic acid (15 g, 67.5 mmol) and NaOH (50 g, 1.25 mmol) were mixed in water (225 mL), and the solution was heated on a water bath until the solid dissolved; hot aqueous glucose (100 g in 150 mL of water) was then added slowly into the above mixture at 50 °C whereupon a yellow precipitate was obtained, which immediately changed to a brown solution upon further addition of glucose. This reaction was highly exothermic. Then, a stream of air was passed into the mixture for 3 h and a light brown precipitate was obtained. This was filtered, dissolved in water, and acidified with acetic acid (25 mL) whereupon a light pink precipitate was obtained. This was filtered, washed with plenty of water (300 mL), and dried in a desiccator to obtain **8** (yield 9 g, 80%) as a brownish orange powder (*36*). ^1H NMR (300 MHz, DMSO-d_6) δ (ppm): 8.15 (d, 4H, $J = 8.7$ Hz), 7.99 (d, 4H, $J = 8.7$ Hz).

Azobenzene 4,4′-Dicarbonyl Chloride (*9*). To a suspension of **8** (1 g, 3.7 mmol) in 20 mL of 1,2-dichloromethane was added 2.0 g PCl_5 at 0 °C and then refluxed for 2 h. This afforded bright red crystals, which were filtered and recrystallized repeatedly from toluene to afford **9** (*36*) (0.84 g, 75%). IR (ν, cm^{-1}): 1776.12 (CO) and 1600 (N═N); ^1H NMR (300 MHz, $CDCl_3$) δ (ppm): 8.1 (d, $J = 8.7$ Hz, 4H), 8.32 (d, $J = 8.4$ Hz, 4H).

***N*-Methyldiethylenetriamine-Based Bis-Carboxamido Azobenzene−Distamycin Conjugate (*2*). Dist-1** (0.14 g, 0.30 mmol) was dissolved in 3.0 mL dry THF and into it DIEA (54 μL, 0.18 mmol) was added. Acid chloride, **9**, (18 mg, 0.06 mmol) dissolved in 4 mL dry THF was added slowly into the above solution. The reaction mixture was then stirred at room temperature for 12 h. The solvent was evaporated, and the reaction mixture was adsorbed in neutral alumina and first eluted with $CHCl_3$ followed by a mixture of MeOH/$CHCl_3$ (2:98) mixture. This furnished 0.04 g of **2** as an orange solid in overall 50% yield. ^1H NMR (300 MHz, $CDCl_3$) δ (ppm): 2.4 (bs, 6H), 2.7 (bs, 8H), 3.4−3.45, 3.55 (m, 8H), 3.71, 3.73, 3.86, 3.97 (s, 12H), 6.1 (dd, $J_1 = 2.4$ Hz, $J_2 = 3.6$ Hz, 1H), 6.64 (bs, 2H), 6.71, (bs, 1H), 6.76 (bs, 1H), 6.92 (bs, 2H), 7.1 (bs, 1H), 7.26 (bs, 1H), 7.58 (d, $J = 7.8$ Hz, 4H), 7.7 (d, $J = 8.4$ Hz, 4H). ^{13}C NMR (125 MHz, DMSO-d_6) δ (ppm): 36.5, 56.7, 105.2, 113.1, 118.3, 118.9, 122.6, 123.0, 123.3, 125.9, 126.8, 128.6, 128.9, 152.0, 153.5, 159.2, 162.0, 166.0, 167.22, 168.7, 169.88. ESI MS (positive ions): *m*/*z* calcd. 1415.53 $[M]^+$, found 1415.8 $[M]^+$. Anal. Calcd. for $C_{72}H_{82}N_{22}O_{10}.H_2O$: C, 60.32; H, 5.91; N, 21.49. Found: C, 59.9; H, 6.27; N, 21.1.

Azasuccinimidyl-1-methyl-4-[(1-methyl-4-nitro-1*H*-2-pyrrolyl)carbonyl]amino-1*H*-2-pyrrolecarboxylate (*11*). 1-Methyl-4-[(1-methyl-4-nitro-1*H*-2-pyrrolyl)carbonyl]amino-1*H*-2-pyrrole carboxylic acid **10** (0.15 g, 0.36 mmol) was dissolved in DMF (1 mL) and cooled in an ice bath. *N*-Hydroxysuccinimide (54 mg, 0.47 mmol) was added into the solution followed by dicyclohexyl carbodiimide (100 mg, 0.47 mmol). The

resulting solution was stirred for 1 h, first at 0 °C and then at room temperature for another 6 h. The precipitated dicyclohexyl urea was filtered off, and the filtrate was diluted with EtOAc. The EtOAc and DMF were evaporated under vacuum to obtain the succinimide ester of pyrrole carboxylic acid derivative **11** as a pure solid. The isolated yield was 0.15 g (80%). However, the product was found to be hydrolytically very unstable, and due to this, the product **11** was directly used for the next step without further purification.

2-*tert*-Butoxycarbonylamino-1-aminoethane (*12*). Ethylene diamine (3.35 mL, 50 mmol) was dissolved in dry THF and cooled in an ice bath. Triethyl amine (1.74 mL, 12.5 mmol) was added into it followed by dropwise addition of di *t*-butyl dicarbonate (2.7 g, 12.5 mmol). The reaction mixture was stirred for 12 h at room temperature. After that, the solvent was removed by rotary evaporation and the resultant mass was dissolved in ethyl acetate. The EtOAc layer was washed successively with 5 mL water and 5 mL brine and dried over anhydrous Na_2SO_4. The resultant solution was evaporated and adsorbed in neutral alumina column. It was first eluted with $CHCl_3$, followed by (1:99) MeOH/$CHCl_3$ mixture to obtain **12** as a pure solid. The isolated yield was 1.5 g (75%). ^{1}H NMR (300 MHz, $CDCl_3$) δ (ppm): 1.45 (s, 9H), 1.98 (bs, 2H), 3.16−3.21 (q, $J_1 = 5.4$ Hz, $J_2 = 5.1$ Hz, 2H), 5.03 (bs, 2H).

***N*-2[*tert*-Butoxycarbonylamino-1-aminoethane[1-methyl-4-[(1-methyl-4-nitro-1*H*-pyrrol-2-yl) carbonyl]amino-1*H*-2-pyrrole carboxamide (*13*).** A solution of **11** (0.2 g, 0.4 mmol) in dry THF was added dropwise into a solution of 12 (0.072 g, 0.45 mmol) in THF at room temperature. A catalytic amount of triethylamine was added and the resulting mixture was stirred at room temperature for 4 h. At the end of 4 h, the solvent was evaporated and directly adsorbed on silica. The resulting mixture was purified by eluting column with $CHCl_3$ followed by MeOH/$CHCl_3$ (3:97) mixture. This yielded 0.13 g of **13** (60%). ^{1}H NMR (300 MHz, $CDCl_3$) δ (ppm): 1.44 (s, 9H), 3.35−3.5 (m, 4H), 3.71, 3.82, 3.91 (s, 9H), 6.54 (s, 1H), 6.7 (s, 1H), 7.22 (bs, 2H), 7.6 (s, 2H), 7.74, 7.77, 8.12, 8.2 (bs, 4H). ESI MS (positive ions): *m*/*z* calcd. 556.7 $[M]^+$, found 557 $[M]^+$.

***N*-2[*tert*-Butoxycarbonylamino-1-aminoethane[1-methyl-4-[(1-methyl-4-[bromoethanamido]-1*H*-pyrrol-2-yl)carbonyl]amino-1*H*-2-pyrrolecaroboxamide (*14*).** 200 mg (0.36 mmol) of **13** was dissolved in 1.5 mL of dry DMF and hydrogenated over 90 mg of Pd/C (5%) for 20 h at room temperature. The catalyst, Pd/C, was filtered off and the residue was washed twice with 1 mL each of dry DMF. The combined filtrate and washings were collected together and mixed with 0.3 mL (1.7 mmol) of DIEA and was cooled to 0 °C. To this solution, 0.1 mL (1.0 mmol) of bromoacetyl bromide was added, and the resultant solution was stirred for 2 h at 0 °C and then at room temperature for 8 h. At the end of this period, the reaction mixture was washed with water and extracted with ethyl acetate. The crude reaction mixture obtained upon evaporation of ethyl acetate was adsorbed on silica gel and purified by column chromatography upon elution with $CHCl_3$ followed by MeOH/$CHCl_3$ (4:96) mixture. The product was isolated as a yellow solid. The isolated yield was 93 mg (40%). ^{1}H NMR (300 MHz, $CDCl_3$) δ (ppm): 1.4 (s, 9H), 3.3−3.45 (m, 4H), 3.83, 3.85, 3.87 (s, 9H), 3.96 (s, 2H), 6.54 (bs, 2H), 6.7 (s, 1H), 7.1 (s, 1H), 7.21 (bs, 2H), 8.2, 8.5, 8.63 (bs, 4H). ESI MS (positive ions): *m*/*z* calcd. 669.0 $[M + Na]^+$, 671.0 $[M + Na]^+$; found 669.2 $[M + Na]^+$, 671.2 $[M + Na]^+$.

***N*-2[*tert*-Butoxycarbonylamino-1-aminoethane[1-methyl-4-[(1-methyl-4-[dimethylaminoethanamido]-1*H*-2-pyrrolyl) carbonyl]amino-1*H*-2-pyrrolecarboxamide (*15*).** Compound **14** (0.05 g, 0.08 mmol) was dissolved in dry MeOH, the solution was cooled in an ice−water bath, and excess dimethylamine gas was passed into it in a screw-top pressure tube. The resultant mixture was then heated at 70 °C for 12 h. Excess dimethylamine was evaporated, and the residual mass was dissolved in ethyl acetate, washed with saturated $NaHCO_3$ solution, water and brine, and finally dried over anhydrous Na_2SO_4. The gummy mass obtained upon evaporation of solvents was purified by column chromatography on alumina using $CHCl_3$ followed by MeOH/$CHCl_3$ (2:98) mixture as eluent. This afforded **15** as a gum (35 mg, 75%). ^{1}H NMR (300 MHz, $CDCl_3$) δ (ppm): 1.4 (s, 9H), 2.3 (s, 6H), 3.05 (s, 2H), 3.3 (m, 2H), 3.45 (m, 2H), 3.84, 3.87, 3.9 (three s, 9H), 6.56 (s, 1H), 6.6 (s, 1H), 6.9 (s, 1H), 7.0 (s, 1H), 7.16 (s, 1H), 7.22 (s, 1H), 5.3, 6.8, 8.03, 8.16, 8.94 (bs, 5H). ESI MS (positive ions): *m*/*z* calcd. 611.8 $[M]^+$, found 612 $[M]^+$.

***N*-2[Diaminoethane[1-methyl-4-[(1-methyl-4-[bromoethanamido]-1*H*-2-pyrrol-yl)carbonyl]amino-1*H*-2-pyrrolecarboxamide (*16*).** To a solution of **15** (60 mg, 0.1 mmol) in dichloromethane (2 mL), an equal volume of trifluoroacetic acid (TFA) (2 mL, 26 mmol) was added into it under cold condition (0−5 °C), and the reaction was continued for 2 h at room temperature. After completion of the reaction, the excess TFA and solvent were removed by rotary evaporation. The residue was washed twice with $CHCl_3$ and finally dried to obtain **16** (40 mg, 80%). It was directly used without further purification due to its instability and high reactivity.

Ethylenediamine-Based Bis-Carboxamido Substituted Azobenzene Distamycin Conjugate (*3*). Compound **16** (0.2 g, 0.4 mmol) was dissolved in dry THF and into it 175 μL (1 mmol) diisopropyl ethylamine (DIEA) was added. The resultant mixture was stirred for 15 min at room temperature. Then, again 1.0 mmol of approximately 200 μL DIEA was added. A solution of 4,4′-bis(chlrocarbonyl) azobenzene, **9**, (6 mg, 0.02 mmol) was added dropwise, and the reaction mixture was allowed to stir at room temperature for 12 h. The solvent was evaporated, and the residue was purified by column chromatography on alumina eluted first with $CHCl_3$ followed by MeOH/$CHCl_3$ mixtures (2:98) and (4:96) as eluent. The product was obtained as an orange solid (40 mg, 40%). ^{1}H NMR (300 MHz, $CDCl_3$) δ (ppm): 2.35 (s, 6H), 3.06 (s, 2H), 3.6 (m, 4H), 3.84, 3.87, 3.9 (s, 9 H), 6.88 (s, 1H), 6.93 (s, 1H), 6.98 (s, 1H), 7.14 (s, 1H), 7.23 (s, 2H), 7.96 (d, $J = 8.1$ Hz, 4H), 8.1 (d, $J = 8.4$ Hz, 4H), 8.4, 9.03, 9.26 (bs, 4H). ^{13}C NMR (125 MHz, DMSO-d_6) δ (ppm): 36.5, 56.7, 105.2, 113.1, 118.3, 118.9, 122.6, 122.8, 124.1, 123.0, 123.3, 125.9, 126.8, 128.6, 128.9, 152.0, 153.5, 159.2, 162.0, 166.0, 167.22, 168.7, 169.88. ESI MS (positive ions): *m*/*z* calcd. 1257.34 $[M]^+$, 629.2 $[(M + H)/2]^+$, found 1257.7 $[M]^+$, 629.5 $[(M + H)/2]^+$. Anal. Calcd. for $C_{62}H_{72}N_{20}O_{10}\cdot 0.5H_2O$: C, 58.8; H, 5.81; N, 22.12. Found: C, 58.41; H, 6.23; N, 21.9.

Photoisomerization and UV−vis Analysis. Photoillumination of ligand **1** was carried out using a xenon lamp 450 with light intensity of ca. 40 W, which transmitted light around 360 nm. On the other hand for carboxamido substituted ligands **2** and **3**, photoillumination was done using a water-cooled high-pressure 250 W Hg lamp that transmitted light between 320 and 380 nm after passing through a set of bandpass chemical filters (*37*). The rate of isomerization was measured spectrophotometrically for each ligand (**1**, **2**, and **3**) in DMSO at a given concentration on a UV−vis spectrophotometer at 25 °C. Such spectral analysis as a function of time gave the approximate time required for reaching the photostationary state from each of the azobenzene−distamycin conjugates.

^{1}H NMR Spectroscopy. ^{1}H NMR experiments with each ligand for configurational analysis were carried out at 25 °C using a 300 MHz spectrometer. Individual samples of around 1 mM concentration were taken in d_6-DMSO, and the corresponding changes in the molecular configuration after photoillumination were determined by recording ^{1}H NMR spectros-

Scheme 1[a]

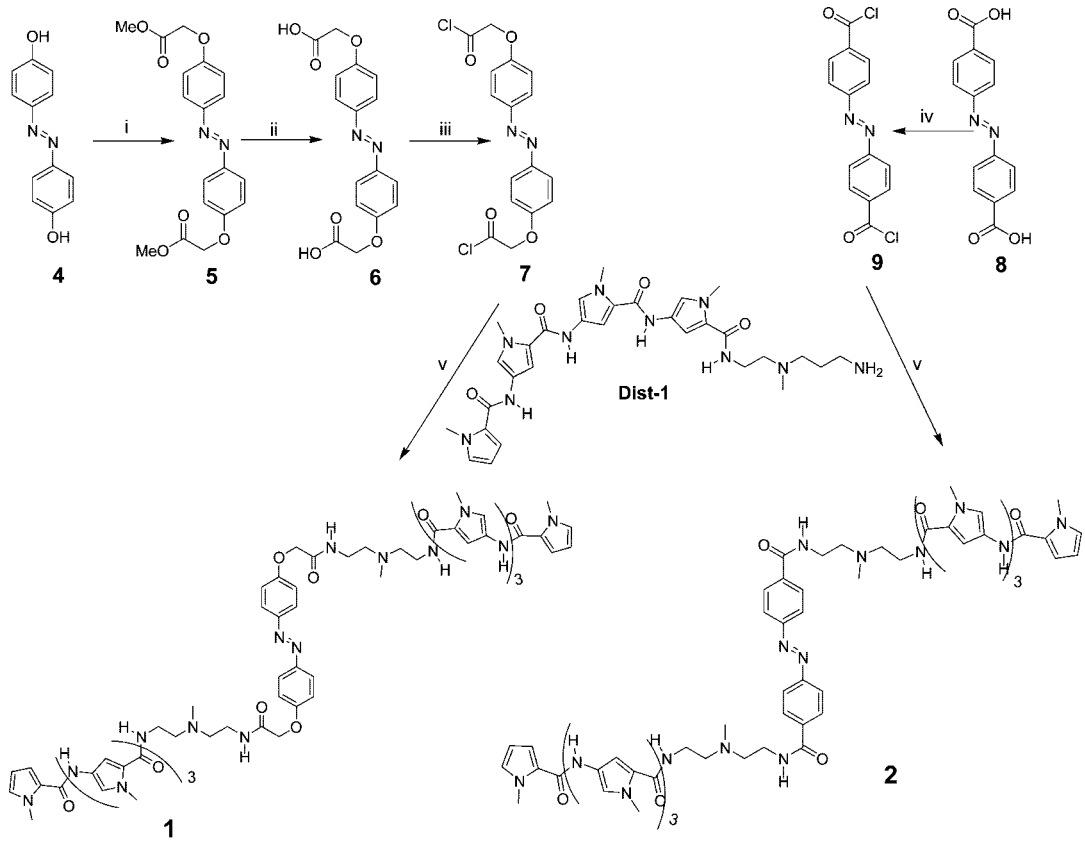

[a] Reagents, conditions, and yields. (i) Methyl bromoacetate, K_2CO_3, 18-crown-6, acetone, reflux, 14 h, 75%; (ii) 0.5 N NaOH, THF, reflux, 2 h, followed by acidification with 0.5 N HCl, 90%; (iii) $SOCl_2$, THF, reflux, 3 h, 90%; (iv) PCl_5, $ClCH_2CH_2Cl$, reflux 2 h, 75%; (v) DIEA, THF, RT, 4 h, 50%.

copy. Integration of the respective azobenzene protons allowed quantitative determination of the percentage of trans and cis forms of each sample in their photostationary states.

Circular Dichroism Spectroscopy. CD spectra were recorded on a spectropolarimeter equipped with a temperature controller. The experiments were performed in NaCl buffer (150 mM NaCl, 0.01 M Tris-HCl, 0.1 mM EDTA buffer at pH 7.4) using 20 μM duplex poly[d(A-T).d(T-A)] with or without the azobenzene−distamycin conjugates at 25 °C. All CD titrations were averaged over two acquisitions and the scan rate was maintained at 50 nm/min with optical cells of path length of 1 cm. Titration was performed under dark and utmost care was taken to minimize the isomerization of azobenzene−distamycin hybrids. The CD values were expressed in millidegree. The changes in ICD intensity at 336 nm were plotted against [ligand]/[DNA] ratio to obtain the concentration of conjugate required to saturate the ds-DNA binding.

Melting Temperature Measurements. The thermal stability of each ligand/ds-DNA complex was assessed from thermal denaturation studies. Using a UV−vis spectrophotometer equipped with a temperature-programmable cell block, the changes in absorbance at 260 nm were followed as a function of temperature. The samples were heated at 0.5 °C/min, and the absorbance values were recorded for every 0.5 °C rise in temperature. All T_m experiments were carried out in NaCl buffer at saturated [ligand]/[DNA] ratios.

Minor Groove-Bound Hoechst Displacement Assay. First, 0.25 μM Hoechst was taken in NaCl buffer and various aliquots of concentrated poly[d(A-T).d(T-A)] solutions were added progressively to saturate Hoechst binding on duplex DNA surface. The fluorescence intensity of Hoechst 33258 increased on binding with duplex poly[d(A-T).d(T-A)]. Each azobenzene−distamycin conjugate was then added individually into saturated solution of the Hoechst−DNA complex, and the displacement of Hoechst from ds-DNA was measured from a decrease in the fluorescence emission intensity at 464 nm (λ_{ex} = 355 nm) at 25 °C. Titration was performed under dark and care was taken to minimize the isomerization of azobenzene−distamycin conjugates. The apparent binding constant (K_{app}) has been calculated as $K_a = K_{app}[L_{50}]$, where K_a indicates the binding constant of Hoechst, which was found to be 1.5×10^7 M^{-1} by Scatchard analysis (*38*) with poly[d(A-T).d(T-A)] in NaCl buffer, and $[L_{50}]$ is the concentration of individual ligand achieving 50% quenching of DNA-bound Hoechst fluorescence.

Computational Details. All the bis-alkoxy and bis-carboxamido substituted azobenzene−distamycin conjugates (**1**−**3**) and **Dist-1** and **Dist-2** analogues were optimized at the HF/3−21G level of theory using *Gaussian 03* (*39*). Single point energies are obtained for the model azobenzenes **17** and **18** at the MP2/6−31+G* level of theory. The Mülliken atomic charges of the optimized ligands (**1**−**3**) obtained from the calculation at the HF/3−21G level of theory are used for docking studies. A nucleotide sequence of $d[GC(AT)_{10}CG]_2$ was generated from the nucgen program of *AMBER 8* (*40*) instead of poly[d(A-T).d(T-A)] DNA. The B-form of DNA built by this procedure is assigned with AMBERff03 force field (*41*) and minimized for 250 steps by steepest decent algorithm and a further 250 steps by the conjugate gradient method to remove the bad strains in the DNA. The modeled ds-DNA was then docked with the optimized ligand structures using AUTODOCK 3.05 version (*42*, *43*). The center of the macromolecule is the grid center with grid size of 80 × 80 × 126 and grid spacing of 0.4186 Å. Docking runs were performed using the Lamarckian genetic algorithm (LGA) with some modifications of the docking

Scheme 2[a]

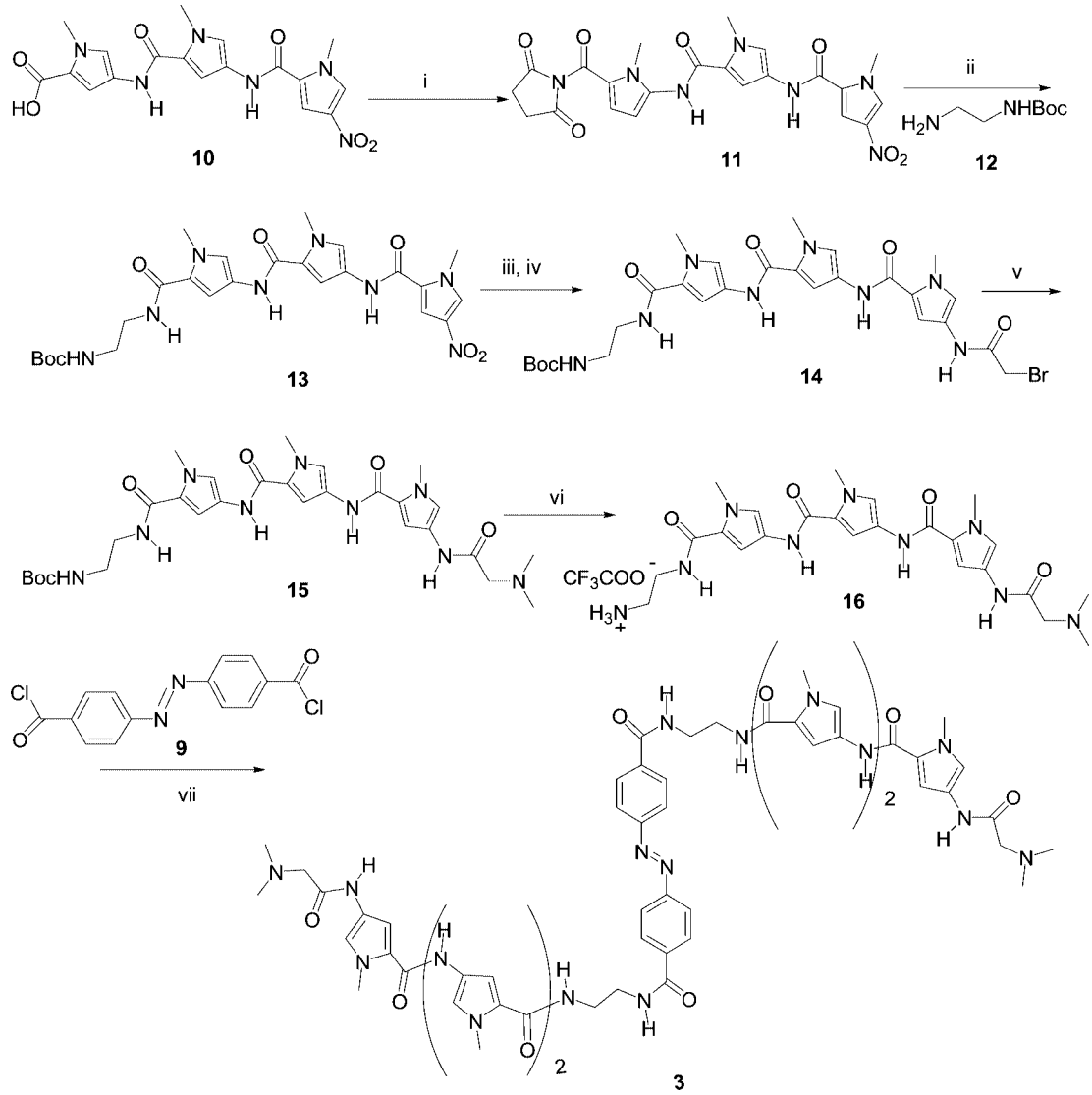

[a] Reagents, conditions, and yields: (i) DCC, NHS, DMF, 0 °C, 1 h, then RT, 6 h, 80%; (ii) THF, RT, 4 h, 60%; (iii) 5% Pd/C, DMF, 20 h, RT; (iv) DIEA, bromoacetyl bromide, 0 °C, 2 h, RT, 40%; (v) $NH(CH_3)_2$, MeOH, 70 °C, 12 h, 75%; (vi) CH_2Cl_2, TFA (1:1), RT, 2 h, 80%; (vii) DIEA, RT, 12 h, 40%.

Table 1. Stabilization Energies (kcal/mol) of Trans Isomers Relative to the Cis Isomers at HF/3–21G Level for Ligands 1−3 and at MP2/6–31+G* Level for the Model Azobenzenes 17 and 18 Using *Gaussian 03*

substitution	*trans*	energy
bis-alkoxide	**1a**	−13.1
	17a	−11.0
bis-carboximido	**2a**	−18.6
	3a	−15.4
	18a	−12.3

parameters. LGA was used because of the existence of 32−48 rotable bonds in these conjugates and to evaluate the right conjugate−DNA conformation, as it is known to reproduce various experimental ligand−DNA complex structures (*44*−*46*). Docking began with rigid docking of the initial Gaussian optimized structures. Docking of each ligand was derived from 20 different runs that were set to be obtained after a maximum of 500 000 energy evaluations or 25 000 000 generations, to give 20 conformations. The probability that docking solution in the population would undergo a local search was set to 0.06 and the constraint was set to a maximum of 300 iterations per search. The size of local search space (rho) was set to 1.0−0.01. A pseudo-Solis and Wets local search was then used to minimize

Scheme 3. Structures of the Trans and Cis Isomers of Model Azobenzenes 17 (Alkoxy Substituent) and 18 (Carboxamido Substituent)

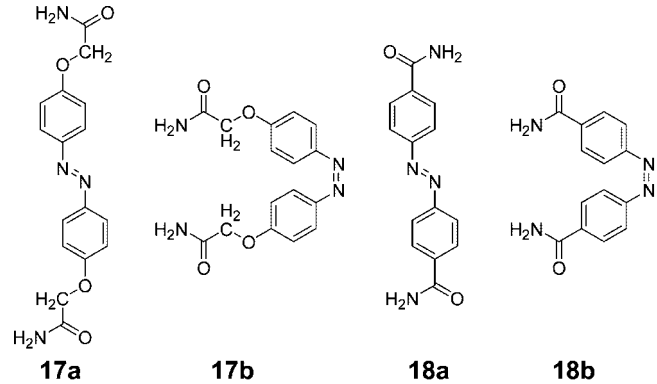

energy of the population where the population size was set to 50. The elitism number and the rates of gene mutation and gene crossover were 1, 0.02, and 0.08, respectively. The flexible docking procedure was repeated until substantial interactions of the extended binding mode of ligand with DNA were

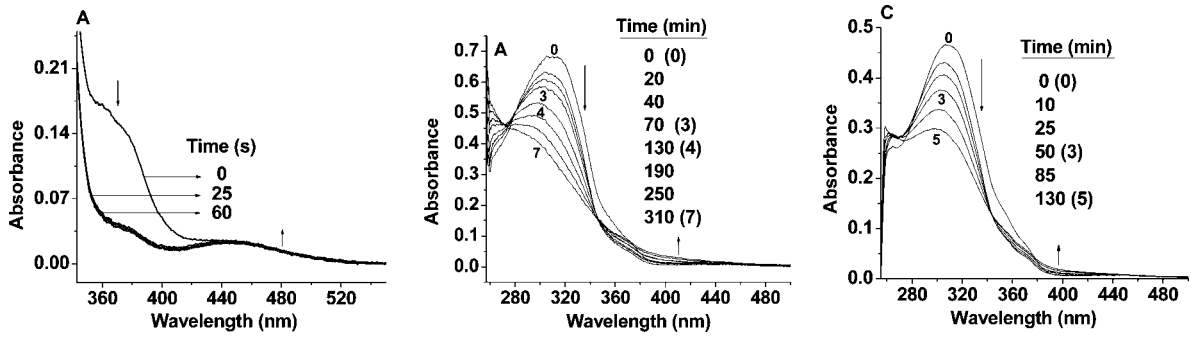

Figure 2. Changes in the absorption spectra of a solution of **1** in DMSO (12 μM, A), **2** (10 μM, B), and **3** (10 μM, C) upon photoillumination at appropriate λ values. Arrows indicate the nature of changes in the observed absorption region of $\pi-\pi^*$ and $n-\pi^*$ transitions of the azobenzene units, respectively.

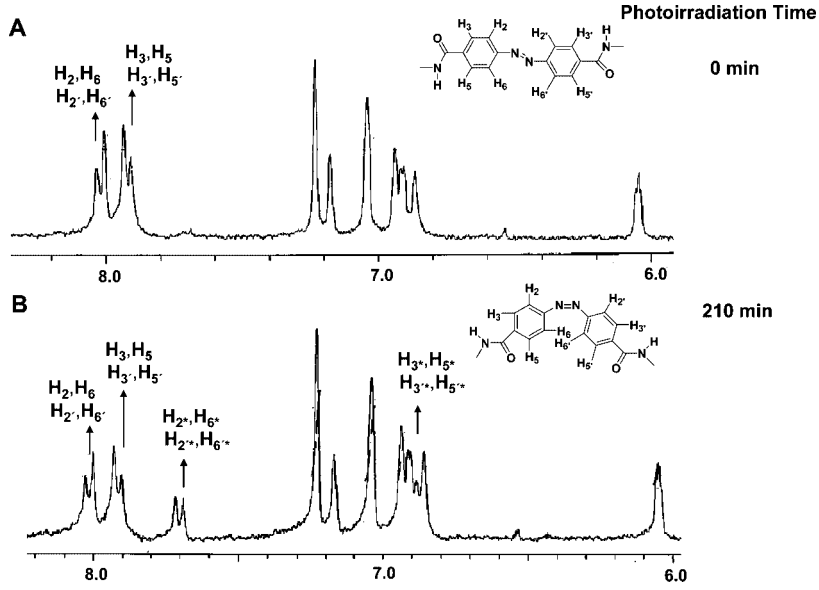

Figure 3. ^{1}H NMR spectra of a d_6-DMSO solution of **2** (1 mM) before (A) and after (B) 210 min of photoillumination at ~330 nm. Chemical shifts of the respective azobenzene protons before and after irradiation are indicated with respect to TMS as standard. The symbol * refers to the sample after irradiation.

obtained. Further, the lowest dock conformation obtained from the flexible docking was again submitted for rigid docking to remove the internal energy of ligand (steric clashes) and retain the hydrogen bonding interaction with ds-DNA bases.

RESULTS AND DISCUSSION

Synthesis. The key starting material **Dist-1** for the synthesis of **1** has been obtained following a procedure described earlier (*19*, *33*). The synthesis of **1** began with the alkylation of 4,4′-dihydroxy azobenzene, **4**, with 3.5 equiv of methyl bromoacetate in acetone under reflux conditions as summarized in Scheme 1. The dimethyl ester, **5**, was saponified and then converted to the corresponding acid chloride, **7**. This was then directly used for coupling with 4 equiv of **Dist-1** in dry THF in the presence of Hünig's base at room temperature to furnish **1** as a yellow solid in 50% isolated yield (Scheme 1).

The other starting material azobenzene 4,4′-dicarboxylic acid, **8**, and the corresponding azobenzene 4,4′-dicarbonyl chloride, **9**, were prepared according to the reported procedures (*35*). The synthesis of **2** was accomplished by amide bond formation between the amine tethered distamycin derivative, **Dist-1** (~4 equiv) and **9** in THF at room temperature (Scheme 1). The reaction mixture was chromatographically purified to furnish **2** as an orange solid in 50% isolated yield.

The synthesis of **3** began with tri-*N*-methylpyrrole based nitro acid, **10**, which was synthesized according to a reported procedure (*34*) The acid functionality was activated as NHS ester, **11**, and then directly coupled with **12** in dry THF at room temperature to furnish **13** in ~60% isolated yield. The nitro group present at the N-terminus of the oligopeptide derivative was hydrogenated over Pd/C (5%) in dry DMF followed by capping of the amine functionality by bromoacetyl bromide. The reactive bromide at the N-terminus of the oligopeptide derivative was coupled with dimethyl amine under reflux condition for 12 h to obtain **15**. The *tert*-butoxycarbonyl group present at the C-terminus of oligopeptide was deprotected using TFA to furnish primary amine, **16** (**Dist-2**). Then, ~4 equiv of **16** was directly used for coupling with **9** in dry THF at room temperature to afford **3** in 40% isolated yield (Scheme 2).

Optimized Ligand Structures. The conjugates (*1*−*3*) can give rise to many conformations, which arise due to the change in the dihedral angle around the central C−N═N−C bond of azobenzene. Among various possible conformational isomers, we have calculated the two most significant conformations, cis and trans, at the HF/3−21G level of theory using the *Gaussian 03* program package (*39*). The optimized structures of these ligands are shown in Figure 1. The letters "a" and "b" after structure number indicate trans and cis isomer, respectively. The trans isomers are found to be more stable compared to their respective cis isomers for all the ligands (Table 1). The order of relative stability of the trans isomers with respect to the corresponding cis isomers is **1** (−13.1 kcal/mol) < **3** (−15.4

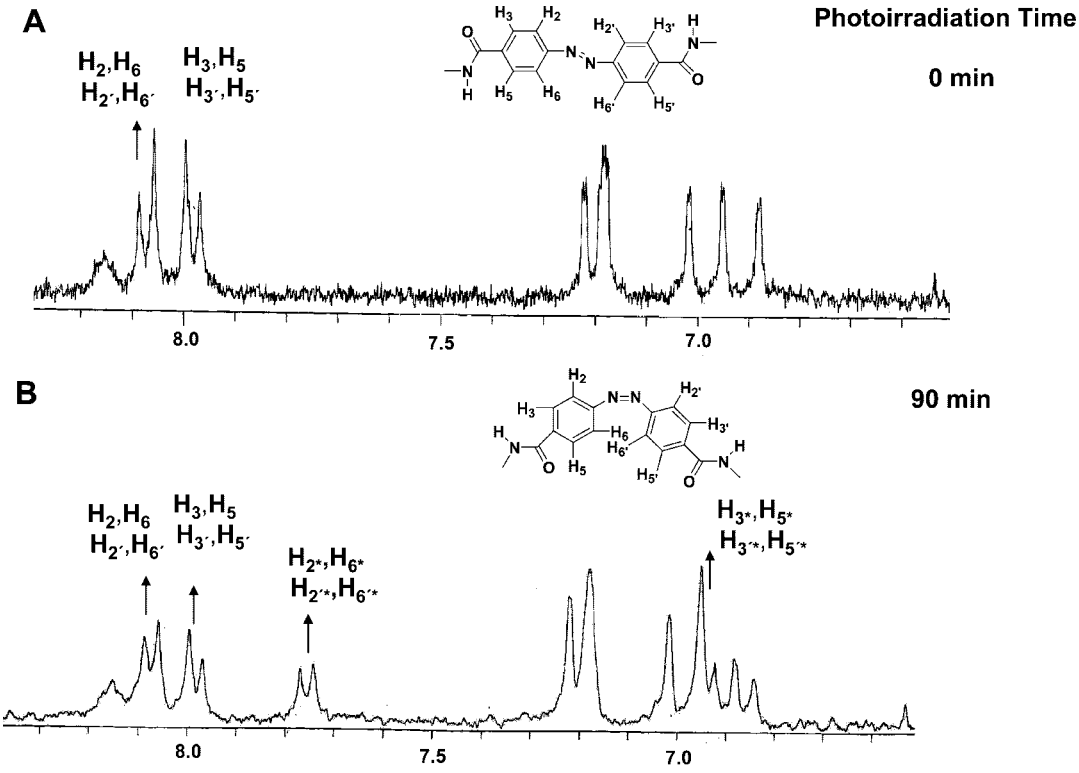

Figure 4. ^{1}H NMR spectra of a d_6-DMSO solution of **3** (1 mM) before (A) and after (B) 90 min of photoillumination at ∼330 nm. Chemical shifts of the respective azobenzene protons before and after irradiation are indicated with respect to TMS as standard. The symbol * refers to the sample after irradiation.

kcal/mol) < **2** (−18.6 kcal/mol). The ligands **1** and **2** feature long linker based **Dist-1**, and ligand **3** has short linker based **Dist-2** (Table 1). It shows that, for a constant linker length, trans isomers are relatively more stable for the electron-withdrawing bis-carboxamido-substituted azobenzenes **2** and **3** as compared to the electron-donating bis-alkoxy-substituted azobenzenes, **1** (Table 1).

In order to understand the electronic effect of the bis-carboxamido versus bis-alkoxy substituents, model azobenzenes **17** and **18** are studied. Structure **17** has OCH_2CONH_2 and structure **18** has $CONH_2$ substituents at the para position to mimic ligands **1** and **2** (or **3**), respectively, (Scheme 3). The trans isomers **17a** and **18a** are more stable in comparison to their respective cis isomers **17b** and **18b** by 11.0 and 12.3 kcal/mol, respectively, at the MP2/6−31+G* level of theory (Table 1). Thus, the trend in the relative energies for ligand **1** is also retained in the model azobenzenes **17** and **18**. This indicates that the bis-carboxamido substituents can stabilize the trans isomer more than the bis-alkoxy substituents.

The azobenzene moiety in the trans isomer is planar, but deviation from planarity is ∼50° in the cis isomer. As a result, the stabilization of the azobenzene π-orbital due to the delocalization in the substituents can only be observed in the trans isomer. The carboxamido group stabilizes the π-molecular orbital of the azobenzene in the trans isomer **18a** by 0.87 eV as compared to the trans isomer **17a** having an alkoxy group. This supports the greater stability of the trans isomers (**2a**, **3a**) of the carboxamido-substituted ligands over the trans isomer (**1a**) of alkoxy-substituted ligands.

Photoisomerization of the Ligands in Solution. As anticipated, the distamycin−azobenzene conjugates photoisomerize upon light illumination. Detailed investigation of the isomerization of azobenzene is important in order to know the composition of the trans and cis isomeric forms at the photostationary state. Accordingly, we followed this for each conjugate by UV−visible and ^{1}H NMR spectroscopy.

UV−vis Analysis. The isomerization process was assessed by irradiation of the distamycin−azobenzene conjugate **1** (12 μM) in DMSO solution at 360 nm (Figure 2A). Upon photoillumination, the absorption band intensity at ∼365 nm due to $\pi-\pi^*$ transition decreased with a considerable blue shift, while the band due to n−π^* transition at ∼450 nm increased. According to previous studies (*35*), the absorption band around 360 nm is due to the trans form of the azobenzene moiety, while that around 450 nm is ascribed to the *c*is form. Therefore, the irradiation indicates transformation of the trans azobenzene to the cis azobenzene moiety. This process continued over a period up to 60 s until the photostationary state was reached. Similarly, photoisomerization studies were individually conducted on 10 μM solution of compounds **2** and **3** in DMSO by UV−vis spectroscopy upon photoillumination at ∼330 nm. In both cases, the distamycin band appeared at ∼306 nm overlapped with the 330 nm $\pi-\pi^*$ absorption band of the −N═N− group, and a less intense n−π^* band appeared at around 370 nm (Figure 2B,C). During photoisomerization, the $\pi-\pi^*$ absorption bands for both ligands at 330 nm decreased along with the distamycin absorption band at ∼306 nm. For compound **2**, all curves passed through common points at 280 and 346 nm during 1 h irradiation (Figure 2B). Irradiation for a period longer than 1 h shifted the common point at 280 to 274 nm. Importantly, throughout the isomerization process, each sample maintained an apparent isosbestic point at ∼346 nm, and monotonous absorption enhancement was observed for the n−π^* transition at ∼380 nm. Photoillumination beyond 5 h, however, resulted in a loss of isosbestic point at 346 nm. So, photoisomerization might have led to different isomerized products that remain in an apparent equilibrium. Similarly, photoillumination of a 10 μM DMSO solution of conjugate **3** up to ∼130 min resulted in both a decrease and blue shift of the $\pi-\pi^*$ absorption intensity at ∼308 nm and enhancement of the n−π^* absorption band intensity at ∼370 nm via an apparent isosbestic point at ∼343 nm as shown

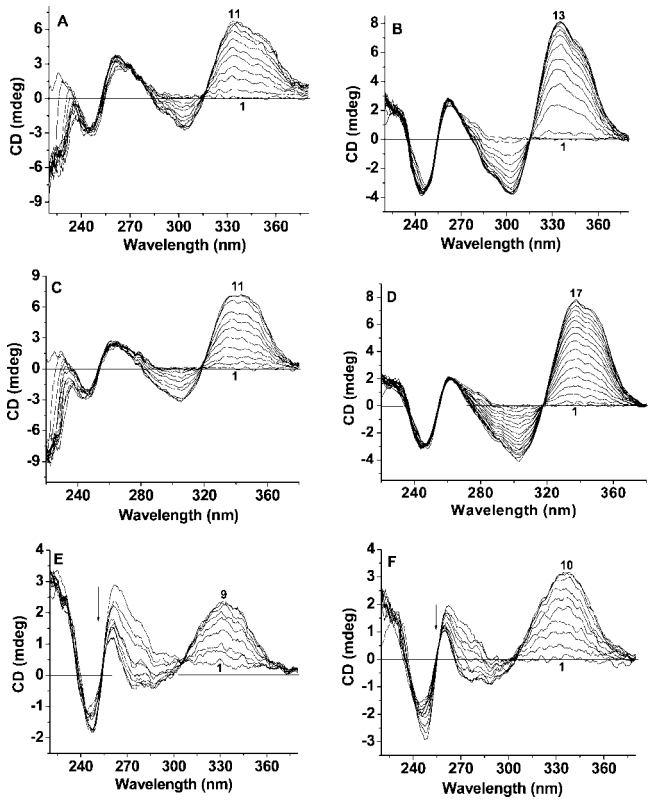

Figure 5. CD titration curves due to **1** in trans form (A), **1*** in cis form (B), **2** in trans form (C), **2*** in ~8/2 (trans/cis) isomeric form (D), **3** in trans form (E), **3*** in ~8/2 (trans/cis) isomeric form (F) carried out with 20 μM poly[d(A-T).d(T-A)] in 10 mM Tris-HCl, 150 mM NaCl, 0.1 mM EDTA at pH 7.4 at 25 °C. For all the panels, trace 1 corresponds to the CD spectrum of poly[d(A-T).d(T-A)] DNA alone. Addition of DNA enhances the ICD band at ~334 nm. Traces 9−11, 13, and 17 signify the corresponding saturation at a given [ligand]/poly[d(A-T).d(T-A)] ratios. No significant change in DNA band was observed for panels A to D upon ligand addition into a given DNA solution. In panels E and F, the down arrow indicates the decrease in DNA band with increasing ligand concentration.

in Figure 2C. Overall, the ligand **3** required ~2 h to reach the photostationary state.

Photoisomerization followed by ^{1}H NMR Spectroscopy. ^{1}H NMR spectroscopy is a very useful technique to determine the cis and trans composition of the ligands in the photostationary state. The changes in ^{1}H NMR spectra of 1 mM solution of **1**, **2**, and **3** in d_6-DMSO upon photoillumination at the respective wavelengths, after periodic time intervals of irradiation, are shown in Supporting Information Figure S4 and Figures 3 and 4. Irradiation of **1** for ~10 min completely shifts 3,3′,5,5′-*H*s (meta protons of azobenzene at ~7.1 ppm) and 2,2′,6,6′-*H*s (ortho protons of azobenzene at ~7.8 ppm) upfield at ~6.8 and ~6.86 ppm, respectively (Supporting Information Figure S4) as verified from reported observations (*35*). Compound **1** required ~10 min to reach the photostationary state with ~100% cis isomeric form. Similarly, upon photoillumination for ~1 h for symmetrical carboxamido-substituted azobenzene derivative, **2** the downfield protons of the azobenzene unit at ~7.9 ppm and ~8.0 ppm shifted upfield as doublets at ~7.7 ppm and ~6.9 ppm, respectively (Figure 3). Analysis of the integration after 3.5−4 h of irradiation revealed that only ~20% of the trans form has been converted into the cis form in the photostationary state. Similar characteristic features were also seen with the carboxamido ligand, **3** (Figure 4). However, unlike in **2** here the photostationary state was reached after 1.5 h, with a composition of ~8:2 (trans/cis) form.

The electronic character of the azobenzene in **1** is different from that in **2** and **3**. In **1**, the substituent is electron-donating, whereas in **2** and **3**, the substituent is electron-withdrawing. It is known both experimentally (*47, 48*) and theoretically (*49, 50*) that the electron-donating substituents render azobenzene susceptible to ready photoisomerization. The nature of spacer that connects distamycin with the azobenzene nucleus is also important. Thus, in **2**, the spacer is protonated, while in **3**, the sites of protonation are at the termini of the oligopeptide chains and not at the spacer unit. This explains why the isomerization is slower in **2** compared to **3**.

DNA Binding Properties. In order to assess the duplex DNA binding properties of each of these conjugates, circular dichroism spectroscopy, thermal melting, and Hoechst displacement assay were employed. For CD experiments, we carried out titration by adding different photoisomeric forms of each conjugates into the fixed (20 μM) poly[d(A-T).d(T-A)] solution in NaCl buffer, and the respective results are shown in Figure 5. The DNA binding properties of these conjugates were investigated starting with 4,4′-substituted bis-alkoxy derivative, **1** and **1***, to the bis-carboxamido-substituted long spacer based **2** and **2*** and short spacer based **3** and **3*** azobenzene−distamycin conjugates (where * indicates the photoirradiated form of the ligands at their respective photostationary states). To understand the mode of binding of azobenzene−distamycin conjugates with duplex DNA, the strength of ligand−DNA interactions were also assessed using molecular docking studies.

A. Circular Dichroism Spectral Titrations. We used circular dichroism spectroscopy to characterize the binding of azobenzene−distamycin conjugates both in their ground state and photoirradiated form to the duplex poly[d(A-T).d(T-A)]. Figure 5A−F shows the circular dichroism spectra from 220 to 380 nm obtained by incremental addition of individual conjugates into the fixed poly[d(A-T).d(T-A)] solution. CD measurements of each ligand with poly[d(A-T).d(T-A)] yielded a set of curves showing two pairs of bands. The intense negative and positive bands observed at 245 and 260 nm arise from the DNA molecule (intrinsic CD). The negative and positive CD bands centered at 303 and 336 nm arise solely from the induction of optical activity of the DNA-bound nonchiral azobenzene−distamycin hybrid molecule (extrinsic or induced CD) (*50*). The induced CD (ICD) values at 336 nm were plotted with the increase [ligand]/[DNA] ([D]/[P]) ratio to evaluate the extent of ligand−DNA interaction and saturation [D]/[P] ratio.

The parent distamycin derivative, **Dist-1**, required a [D]/[P] ratio of 0.2 to "saturate" DNA binding on its minor grooves. This corresponds to 2:1 binding mode, where two **Dist-1** ligands occupy five base pairs along the DNA minor groove (*21*).

During CD titration, there exists an equilibrium between the free ligand in solution and ligand bound to duplex DNA. With increasing DNA affinity of the ligand, the concentration of "free ligand" in solution will be lower. On comparing the binding affinity between trans and cis forms of ligand **1** (Figure 5A vs B), we see from the CD titration that the cis form of the ligand requires a lower concentration (saturation point or maximum ICD intensity at [D]/[P] ratio of 0.2) to cover most of the AT-base pairs along the duplex DNA minor groove than the corresponding trans form (saturation point or maximum ICD intensity at [D]/[P] ratio of 0.3) (Figure 6A). This indicates that at a comparable ligand concentration more trans form of ligand **1** remains free in solution as compared to the cis form in the presence of a fixed DNA concentration. This shows that binding of the cis form of ligand **1** is higher than that of the trans form.

An ICD enhancement at 336 nm was also observed with the ~8/2 (trans/cis) isomeric form of **2*** compared to the 100% trans form of **2** (Figure 5C vs D). The CD titration of **2** required ~0.47 [D]/[P] ratio, while ~8/2 (trans/cis) isomeric mixture of

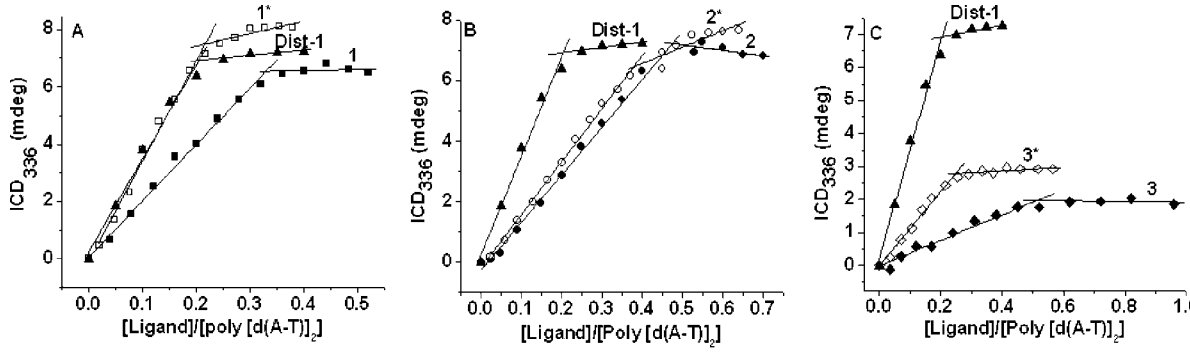

Figure 6. Changes in ICD intensities at 336 nm due to photoisomeric forms of ligands **1** (A), **2** (B), and **3** (C) during titration with 20 μM poly[d(A-T).d(T-A)] in 10 mM Tris-HCl, 150 mM NaCl, 0.1 mM EDTA buffer at pH 7.4 at 25 °C in dark condition. Different isomeric compositions of the ligands are as follows: **1** (∼100% trans), **1*** (∼100% cis), **2** (∼100% trans), **2*** (∼8/2 (trans/cis)), **3** (∼100% trans), and **3*** (∼8/2 (trans/cis)). Distamycin analogue, **Dist-1**, has also been included for comparison.

Table 2. Melting Temperatures (T_m), Apparent Binding Constants (K_{app}), and Saturation [D]/[P] Ratios Obtained from Binding of Dist-1 and Different Forms of 1, 2, and 3 with Poly[d(A-T).d(T-A)]

DNA + ligands	T_m (°C)[a]	ΔT_m (°C)[b]	$K_{app} \times 10^{-5}$ (M^{-1})[c]	[D]/[P]
Poly[d(A-T).d(T-A)] alone	64.7	−		
+ **Dist-1**	67.4	2.7	6.5	0.2
+ **1**	74.0	9.3	7.2	0.3
+ **1***	75.0	10.3	7.4	0.2
+ **2**	81.0	16.3	6.4	0.47
+ **2***	81.9	17.2	7.0	0.37
+ **3**	85.7	21.0	6.8	0.5
+ **3***	86.7	22.0	10.4	0.25

[a] T_m indicates the average melting temperature value of two independent melting experiments that has been done with the complexes of poly[d(A-T).d(T-A)] in the presence of different ligands in 150 mM NaCl, 10 mM Na_2HPO_4, 0.1 mM EDTA, pH = 7.4, at the saturated [D]/[P] ratio. The error is within ±0.2 °C. [b] ΔT_m corresponds to the difference in T_m between DNA alone and DNA−ligand complexes. [c] K_{app} = apparent binding constant obtained from Hoechst displacement assay.

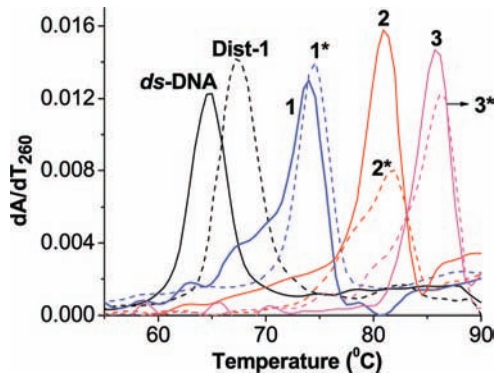

Figure 7. Thermal melting of 20 μM poly[d(A-T).d(T-A)] complexed with various azobenzene−distamycin ligands in NaCl buffer at saturating [D]/[P] ratios. The label of each curve corresponds to DNA: 20 μM poly[d(A-T).d(T-A)]. **Dist-1**: Distamycin analogue, at [D]/[P] = 0.2; **1** and **1*** at [D]/[P] = 0.3 and 0.2; **2** and **2*** at [D]/[P] = 0.47 and 0.37; **3** and **3*** at [D]/[P] = 0.5 and 0.25, respectively.

2* required 0.37 [D]/[P] ratio to saturate ligand binding on DNA minor grooves (Figure 6B). This improvement in ICD intensity and [D]/[P] ratio suggests higher binding of **2*** compared to **2**. A more significant improvement in ICD intensity at 336 nm was observed with the ∼8/2 (trans/cis) isomeric form of **3*** compared to **3** (Figure 5E vs F). The CD titration of 100% trans form of **3** required ∼0.50 [D]/[P] ratio, while ∼8/2 (trans/cis) isomeric mixture of **3*** required only 0.25 [D]/[P] ratio to saturate ligand binding on the DNA minor groove (Figure 6C).

B. Competition for DNA Minor Groove. The apparent binding constants of each ligand toward ds-DNA were evaluated by estimating their efficiency in replacing fully bound Hoechst 33258 from minor grooves of ds-DNA in NaCl buffer. In contrast to CD results, a subtle difference in apparent binding constant values between **1** and **1*** was not apparent from Hoechst displacement assay (Table 2). This is, however, not too surprising, as the binding constant of Hoechst 33258 to the minor groove of ds-DNA is considerably greater than that of distamycin. Interestingly, however, both isomeric forms of **1** rapidly quenched Hoechst fluorescence preferably when 50% of Hoechst was displaced from the duplex DNA minor groove (Supporting Information Figure S5). On the other hand, **2** and **2*** possessed comparable binding constants and manifested a similar type of Hoechst displacement curves (Supporting Information Figure S5). However, a significant difference in ICD intensity observed with **3** and **3*** correlates well with the lower concentration required by **3*** to remove Hoechst from the DNA minor grooves than that of **3**. This fact explains the significant difference in their apparent binding constant values ($K_{app} = 6.8 \times 10^{-5}$ M^{-1} and 10.4×10^{-5} M^{-1}) between the ground and photoisomerized forms of **3** (Supporting Information Figure S5 and Table 2).

C. Influence on DNA Melting. The thermal DNA melting experiment is an important method for the determination of the stability of ligand−ds-DNA complexes. It is known that minor groove binders like distamycin enhance the helix-to-coil transition temperature via recognition of AT-specific bases of ds-DNA (*19*). Here, the thermal denaturation experiments with all ligand−DNA complexes were performed at saturating [D]/[P] ratio in NaCl buffer by following the absorbance change at 260 nm with increase in temperature (Figure 7, Table 2). Importantly, the DNA melting experiment at the saturated [D]/[P] value for each ligand allows us to compare the duplex stability imposed by various alkoxy- and carboxamido-substituted azobenzene distamycin analogues.

The ligand-saturated DNA complexes of both irradiated and non-irradiated solutions of ligand **1** were found to stabilize ds-DNA almost to the same extent. The photoirradiated forms of **1** stabilize ds-DNA by ∼1 °C from that of its ground state. However, they were found to stabilize duplex DNA by ∼7.1 °C more compared to the distamycin analogue, **Dist-1** (Figure 7, Table 2). Such higher T_m for conjugate **1** indicates that a greater number of hydrogen bonding interactions together with other noncovalent interactions (hydrophobic, electrostatic, van der Waals) are responsible for the stabilization of such ligand−DNA complexes. Similarly, the ligand **2** and photoisomerized **2*** stabilized the duplex poly[d(A-T)]$_2$ to 81 and 81.9 °C, respectively, (i.e., by ∼14.5 °C more compared to distamycin analogue, **Dist-1**). The photoisomeric forms of **3** stabi-

Table 3. Free Binding Energies (Δ*G*), Docked Energies, and the Close Contact Distances of Amide Bond of Ligand with DNA Bases Obtained From *Autodock* Calculations of Dist-1, Dist-2, Hoechst, 1, 2, and 3 Ligands with Modeled Duplex [d(GC(AT)$_{10}$CG)]$_2$ DNA[a]

ligands	Δ*G* (kcal/mol)[b]	docked energies (kcal/mol)	closest distances between ligand and DNA bases (Å)	D1 (Å)	D2 (Å)
Dist-1	−7.0	−11.3	2.50, 2.74, 2.32, 2.54	-	-
Dist-2	−7.1	−11.5	2.21, 2.39, 2.53, 2.52, 2.11	-	-
Hoechst	−12.1	−13.0	2.26, 2.18	-	-
1a	−8.2	−21.9	3.35, 5.29, 6.54, 2.74, 4.61, 5.63	11.62	21.53
1b	−7.9	−21.6	3.49, 5.25, 5.78, 2.58, 2.92, 3.69, 4.85, 4.30, 2.56	8.02	14.06
2a	−10.3	−22.7	5.04, 6.61, 5.16, 3.56, 3.19, 5.62, 4.15, 4.24, 3.46	11.91	19.40
2b	−9.8	−22.3	4.14, 2.71,4.27, 3.86, 3.16, 3.49, 3.95, 2.56, 4.56, 3.98	8.17	11.91
3a	−12.9	−24.1	2.94, 4.87, 6.59, 2.61, 3.06, 2.56, 2.51	11.91	17.05
3b	−14.1	−25.3	2.39, 3.06, 2.73, 2.38, 4.65, 5.51, 4.90, 3.51, 2.17, 3.25	7.53	8.30

[a] The D1 and D2 are the distances in Å between azobenzene and linker containing azobenzene moiety of the ligands as shown in Scheme 4. [b] The values obtained by rigid docking of the lowest docked conformation of the ligands initially obtained from the flexible docking studies.

Scheme 4. Schematic Representation of D1 and D2 Distances in the trans and cis Azobenzene−Distamycin Conjugates[a]

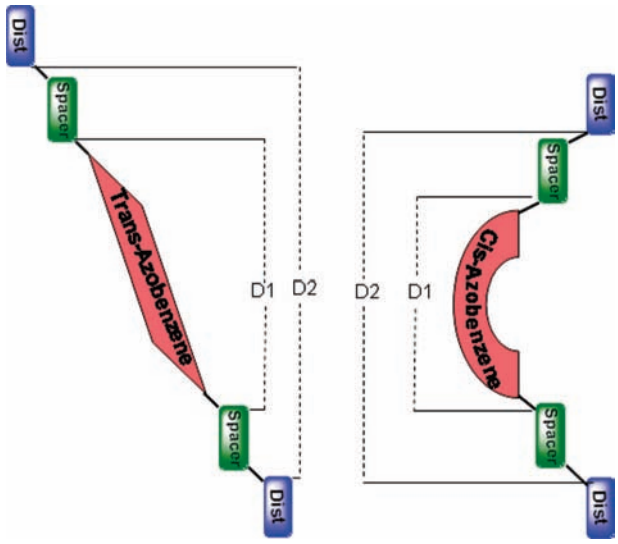

[a] Here, D1 represents the length of azobenzene, and D2 represents the length of azobenzene along with the spacer.

lized duplex poly[d(A-T).d(T-A)] to 85.7 and 86.7 °C, respectively, and ∼18−19 °C more compared to distamycin analogue, **Dist-1** (Figure 7, Table 2). It may be noted that in all cases the ΔT_m and the apparent binding constants (K_{app}) were higher for the photoirradiated forms of the conjugates even if they were small. Importantly, however, the ΔT_m was always achieved with photoirradiated forms of the conjugates at lower [D]/[P] ratio than the respective trans form.

We have also carried out the melting experiment with duplex poly[d(A-T).d(T-A)] in the presence of each ligand including their photoilluminated forms at a fixed [D]/[P] ratio of 0.5, which bring out the differences between trans and cis isomeric forms more clearly. Thus, at this [D]/[P] ratio of 0.5, while **1** stabilized poly[d(A-T).d(T-A)] by 11.5 °C, **1*** afforded a stabilization of 13.3 °C (Supporting Information Table SI-2). Similarly, under the same conditions, photoisomerized **2***and **3***, respectively, brought about 2.4 °C and >1 °C higher stabilization of poly[d(A-T).d(T-A)] than **2** and **3**. These results demonstrate greater stabilization of DNA by the photoisomerized forms of the distamycin−azobenzene conjugates. Hence, the cis form of the conjugates possess higher affinity toward duplex DNA.

D. Molecular Docking on DNA Duplex. To rationalize the experimental trends quantitatively using molecular modeling, initially a rigid docking of the optimized ligand structures with modeled duplex d[GC(AT)$_{10}$CG]$_2$ DNA were performed by *AUTODOCK* v 3.05 (*42*) However, favorable hydrogen bonding interactions between ligand and DNA bases obtained at this level did not adequately explain the experimental results. So, either one side or both sides of the linker atoms were chosen as rotable units for flexible docking of ligands. Finally, a rigid docking was performed with the lowest docked conformation obtained from the flexible docking studies. Such lowest docked conformations of different ligand−DNA complexes were considered for discussion below. The corresponding docking energies and free binding energies (Δ*G*) of all types of rigid and flexible dock conformations of ligand−DNA complexes are shown in Table 3 and Supporting Information Table SI-1. The docked energies and binding energies obtained from the molecular docking studies correlated well with the thermal melting values, as the stabilization of the overall ligand−DNA complexes is influenced by hydrogen bonding and other noncovalent interactions. The binding energies obtained from PreDICCTA (*52*) by supplying the experimental ΔT_m values were similar to these results.

A rigid docking of the **Dist-1** gave a binding free energy of −7.0 kcal/mol (Table 3). There are four hydrogen bonding contacts between the pyrrole amide bond of **Dist-1** and A/T base pairs of DNA in addition to the other noncovalent interactions with the oxo group of the ribose sugar moiety (Figure 8). The DNA base-pair recognition efficiency of **Dist-1** as obtained from the saturation [D]/[P] ratio is supported by the number of hydrogen bonding contacts.

The docking of **1**, **2**, and **3** showed that the azobenzene moiety allows both the distamycin arms to satisfy the extended mode of binding (*11*) unlike the hairpin conformation as observed with γ-amino butyric acid linker based distamycin derivatives (*53*). The isomer **1b** has more pyrrole amide bonds available for hydrogen bonding with the AT base pairs than **1a**. This was supported by higher ICD intensity and low [D]/[P] ratio of **1*** than **1** (Figure 6A, Table 2). One or both benzene moieties of the planar azobenzene group in the trans form (**1a**) approach the ds-DNA to be involved in hydrophobic interactions with the DNA bases. In addition, with long spacer (∼11 Å), the number of pyrrole amides that are able to form hydrogen bonds with the DNA bases decreases, while the nonplanar azobenzene moiety in the cis form prefers to remain out of the DNA helical surface and thus allow more pyrrole amide bonds to satisfy hydrogen bonding interactions with DNA bases (not shown).

The better hydrogen bonding contacts of the para-substituted **1b** over **1a** can also be explained by the difference in D1 and D2 distances. D1 corresponds to the length of azobenzene and D2 represents D1 and spacer length (Scheme 4). The D2 distance varies in the ligands due to variation of electron-donating vs electron-withdrawing substituent of the azobenzene moiety (**1, 2**) and also due to the existing spacer in **Dist-1** and **Dist-2** (Figure 1). In the case of trans to cis photoisomerization of **1**, the lowest-energy docked conformation has D1 = ∼3.5 Å and an overall decrease of D2 from 21.53 Å to 14.06 Å leading to an increase in hydrogen bonds (Table 3). The docked (−21.9 and −21.6 kcal/mol) and free binding energies (−8.2 and −7.9 kcal/mol) are in tune with the melting temperature values (Table 3). The subtle differences in docked and free

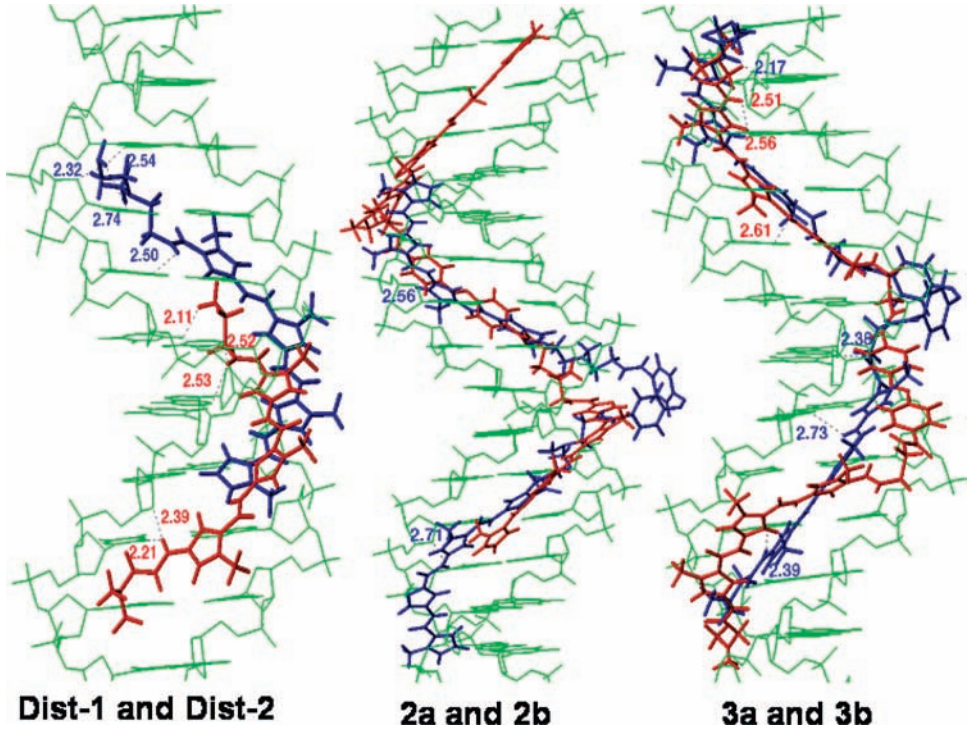

Figure 8. The docked conformations of **Dist-1**, **Dist-2**, and both isomeric forms of the ligands **2** and **3** with duplex d[GC(AT)$_{10}$CG]$_2$ DNA scaffold are shown. Ligand, **Dist-1**, and cis form of ligands **2b** and **3b** are shown in blue-colored capped sticks, whereas **Dist-2** and trans forms of ligand **2a** and **3a** are shown in red-colored capped sticks. The image is from *Sybyl 7.0* (*54*).

binding energies between **1a** and **1b** support the low variation in melting temperature at saturating [D[/[P] ratio and apparent binding constant (K_{app}) values. This explains the DNA binding features of the dialkoxy azobenzene−distamycin dimers **1a** and **1b**.

In the case of dicarboxy azobenzene−distamycin conjugatees also, the docked conformations of **2b** with ds-DNA show greater availability of the hydrogen bond contacts between pyrrole amide bonds and AT base pairs over **2a** (Figure 8, Table 3) as observed from the CD spectral titrations. As seen in **1a** and **1b**, a similar large variation of D1 = ∼3.7 Å around the azobenzene moiety and contraction of D2 from 19.4 Å to 11.91 Å, where D2 = [-(CH$_2$)$_2$NMe(CH$_2$)$_2$NHOCPhN═NPhCONH(CH$_2$)$_2$NMe-(CH$_2$)$_2$-], are observed during trans to cis photoisomerization (Table 3). This might cause a subtle improvement in [D]/[P] ratio of **2*** than that of **2**. The comparative binding constant values are proportional to that of **Dist-1**, as possible hydrogen bonding contacts seem to be similar for both cases (Table 3). The improved T_m values compared to **1** and **1**** can again be correlated with the higher docking (−22.7 and −22.3 kcal/mol) and free binding energies (−10.3 and −9.8 kcal/mol), as hydrogen bonding interactions together with other noncovalent interactions contribute to stabilizing the ligand−DNA complexes. Smaller differences in docking and free binding energies between both photoisomeric forms of **2** again quantify their small variation in both melting temperature and K_{app} values.

The docked conformation of **3b** has shown a larger number of hydrogen bonding contacts with DNA bases compared to **3a** (Figure 8). The trans to cis isomerization of **3** has shown a decrease in the length of D1= ∼4.4 Å around the azobenzene moiety and simultaneous contraction of D2 from 17.05 Å to 8.3 Å along the linker length containing the azobenzene moiety (Scheme 4, Table 3). This helps both distamycin arms in **3b** to align along the isohelical pitch of the DNA helical axis, which achieves a maximum number of hydrogen bonding contacts and favorable electrostatic interactions with DNA in comparison to **3a** (Table 3). These observations support higher ICD intensity, lower [D]/[P] ratio, and higher K_{app} value for **3*** than **3**. A higher apparent binding constant value of the photoirradiated form of **3** may be a consequence of its higher free binding energy of −14.1 kcal/mol compared to free binding energy of Hoechst 33258 (−12.1 kcal/mol). This implies that a greater difference in DNA binding affinity and apparent DNA binding constant between the ∼8/2 (trans/cis) isomeric form and the trans form can be achieved with short linker based conjugate, **3**, compared to the flexible, long linker based ligand **2**. Photoisomerization of azobenzene induced a greater change of D2 in **3** compared to the docked conformations of **1** and **2** (Table 3). This eventually caused a greater difference in DNA binding affinity between **3** and **3**** compared to both isomeric forms of **1** and **2**. Further, the shape of **3b** was found to be more appropriately matched with the DNA helical axis (Figure 8). Even the positive charge at the N-terminal position is relatively more freely available for electrostatic interaction with the phosphates of DNA. This in fact contributed to enhancing the ligand−DNA interaction of **3** compared to other ligands (**1**, **2**).

CONCLUSIONS

The combined experimental data established how distamycin binding on DNA minor grooves was influenced by the presence of an azobenzene core. From ^{1}H NMR and UV−vis spectroscopy, it has been found that the nature of the substituent with respect to the core azobenzene unit (**1** vs **2**) and the linker lengths between distamycin and azobenzene unit (**2** vs **3**) influence the rate and the extent of azobenzene isomerization. Thus, the DNA binding properties of such conjugates were found to directly depend on the orientation of the distamycin with respect to the azobenzene core linker length between azobenzene and distamycin moiety and on the position of positive charge along the oligopeptide backbone. The azobenzene core influenced the conformational freedom of the oligopeptide largely, thereby preventing favorable isohelical orientation of the distamycin units along the ds-DNA minor grooves. Thus, at room temperature, geometrical features of the

azobenzene core prevent simultaneous participation of both distamycin arms in an optimal DNA recognition process. This was manifested by a less intense ICD band and the requirement of high [ligand]/[DNA] ratio to saturate minor groove binding by azobenzene−distamycin hybrids compared to the distamycin alone. According to the results obtained from CD spectroscopy, the photoirradiated forms **1***, **2***, and **3*** favored DNA binding affinity compared to the corresponding trans form as evidenced from high ICD_{336} intensity and low [D]/[P] values for the cis form of the ligands.

Molecular docking studies indicate that during photoisomerization the difference in planarity of the azobenzene moiety together with the change in the length either around the azobenzene moiety (D1) or along the linker containing the azobenzene moiety (D2) determines the orientation of both distamycin arms along the DNA minor groove surface. This eventually causes a greater number of hydrogen bonding contacts between the pyrrole amide and the DNA bases in their cis geometry compared to that in the trans configuration. For example, a greater difference in D2 during photoisomerization for the short spacer based azobenzene−distamycin conjugates explains the relatively larger difference in the ICD intensity and the DNA binding constant values between **3** and **3***. CD spectra allowed measurements of the differences in the DNA binding affinity between trans and photoirradiated form of all the ligands. This was not, however, possible with the Hoechst displacement assay. Except for ligand **3**, there was very little difference in the apparent binding constant values between the isomeric forms of other ligands. This could be due to lower binding free energies of these ligands (**1a**, **1b**, **2a**, and **2b**) compared to Hoechst 33258 as a MGB. As expected, all the dimeric distamycin−azobenzene conjugates were able to stabilize polymeric alternating A/T-rich duplex DNA more effectively compared to the monomeric distamycin analogue, **Dist-1**. There is a gradual increase in the overall stability of DNA−ligand complexes as we move from **1a** to **3a**. Although no major differences in T_m values were observed between the conjugates before and after photoillumination at "saturating" [D]/[P] ratio based on ICD titration data, there was a perceptible increase in T_m values when DNA melting was performed at a constant [D]/[P] ratio of 0.5 with each ligand. This indicates that the cis isomeric forms of such conjugates stabilize ds-DNA more than their trans counterparts at a fixed ligand/DNA ratio.

Experimental and theoretical studies of DNA binding with ligands (**1**, **2**, and **3**) demonstrate the role of linker length between azobenzene and distamycin conjugates for achieving favorable DNA binding affinity and a perceptible difference in duplex DNA binding affinity during photoisomerization. Thus, it was possible to regulate distamycin binding on ds-DNA to some extent by properly anchoring a photoactive disubstituted azobenzene unit to the oligopeptide backbone using a short and rigid spacer.

In summary, the present study describes how specific alterations in a set of azobenzene−distamycin conjugates alter their molecular structure and geometry, which in turn influences their DNA binding affinity on the floor of the minor groove. This also gives significant leads for the design of MGBs, with structural prerequisites to selectively control DNA recognition in the presence of external stimulus. Such an approach reveals a way to control certain biological events where one can regulate the binding specificity and efficiency of small molecules on duplex DNA with light.

ACKNOWLEDGMENT

We thank the Department of Biotechnology, Government of India for funding this work. We also thank Centre for Modeling, Simulation and Design (CMSD), and High Performance Computing Facility (HPCF), University of Hyderabad, Maui High Performance Computing Center (MHPCC) at Hawaii and the Supercomputer Education and Research Centre (SERC) of Indian Institute of Science for computational facilities. D.U.R. and S.D. acknowledge CSIR for senior research fellowships.

Supporting Information Available: Spectral characterization data of the final compounds **1**−**3** and the optimized coordinates of all the ligands and the docked energies for rigid docking details. This material is available free of charge via the Internet at http://pubs.acs.org.

LITERATURE CITED

(1) Bailly, C., and Chaires, J. B. (1998) Sequence-specific DNA minor groove binders. Design and synthesis of netropsin and distamycin analogues. *Bioconjugate Chem. 9*, 513–38.

(2) Dervan, P. B. (2001) Molecular recognition of DNA by small molecules. *Biorg. Med. Chem. 9*, 2215–35.

(3) Wemmer, D. E., and Dervan, P. B. (1997) Targeting the minor groove of DNA. *Curr. Opin. Struct. Biol. 7*, 355–61.

(4) Bruice, T. C., Mei, H., He, G., and Lopez, V. (1992) Rational design of substituted tripyrrole peptides that complex with DNA by both selective minor-groove binding and electrostatic interaction with the phosphate backbone. *Proc. Natl. Acad. Sci. U.S.A. 89*, 1700–04.

(5) Buchmueller, K. L., Staples, A. M., Howard, C. M., Horick, S. M., Uthe, P. B., Le, N. M., Cox, K. K., Nguyen, B., Pacheco, K. A. O., Wilson, W. D., and Lee, M. (2005) Extending the language of DNA molecular recognition by polyamides: unexpected influence of imidazole and pyrrole arrangement on binding affinity and specificity. *J. Am. Chem. Soc. 127*, 742–50.

(6) Trauger, J. W., Baird, E. E., Mrksich, M., and Dervan, P. B. (1996) Extension of sequence-specific recognition in the Minor Groove of DNA by pyrrole-imidazole polyamides to 9−13 base pairs. *J. Am. Chem. Soc. 118*, 6160–66.

(7) Streltsov, S. A., Gromyko, A. V., Oleinikov, V. A., and Zhuze, A. L. (2006) The Hoechst 33258 covalent dimer covers a total turn of the double-stranded DNA. *J. Biomol. Struct. Dyn. 24*, 285–302.

(8) Correa, B. J., Canzio, D., Kahane, A. L., Reddy, P. M., and Bruice, C. T. (2006) DNA sequence recognition by Hoechst 33258 conjugates of hairpin pyrrole/imidazole polyamides. *Bioorg. Med. Chem. Lett. 16*, 3745–50.

(9) Joubert, A., Sun, X., Johansson, E., Bailly, C., Mann, J., and Neidle, S. (2003) Sequence-selective targeting of long stretches of the DNA minor groove by a novel dimeric bis-benzimidazole. *Biochemistry 42*, 5984–92.

(10) Buchmueller, K. L., Staples, A. M., Howard, C. M., Horick, S. M., Uthe, P. B., Le, N. M., Cox, K. K., Nguyen, B., Pacheco, K. A. O., Wilson, W. D., and Lee, M. (2004) Extending the language of DNA molecular recognition by polyamides: Unexpected influence of imidazole and pyrrole arrangement on binding affinity and specificity. *J. Am. Chem. Soc. 127*, 742–50.

(11) Trauger, J. W., Baird, E. E., and Dervan, P. B. (1998) Recognition of 16 base pairs in the minor groove of DNA by a pyrrole-imidazole polyamide dimer. *J. Am. Chem. Soc. 120*, 3534–35.

(12) Woods, C. R., Ishii, T., Wu, B., Bair, K. W., and Boger, D. L. (2002) Hairpin versus extended DNA binding of a substituted beta-alanine linked polyamide. *J. Am. Chem. Soc. 124*, 2148–52.

(13) Chaudhuri, P., Ganguly, B., and Bhattacharya, S. (2007) An experimental and computational analysis on the differential role of the positional isomers of symmetric bis-2-(pyridyl)-1*H*-benzimidazoles as DNA binding agents. *J. Org. Chem. 72*, 1912–23.

(14) Chaudhuri, P., Majumder, H. K., and Bhattacharya, S. (2007) Synthesis, DNA binding, and *Leishmania* topoisomerase inhibition activities of a novel series of anthra[1,2-d]imidazole-6,11-dione derivatives. *J. Med. Chem. 50*, 2536–40.

(15) Bhattacharya, S., and Mandal, S. S. (1995) Ambient oxygen activating water soluble cobalt-salen complex for DNA cleavage. *J. Chem. Soc. Chem. Commun.* 2489–90.
(16) Bhattacharya, S., and Mandal, S. S. (1996) DNA cleavage by intercalatable cobalt-bispicolylamine complexes activated by visible light. *Chem. Commun.* 1515–16.
(17) Mandal, S. S., Varshney, U., and Bhattacharya, S. (1997) Role of central metal ion and ligand charge in the DNA binding and modification by metallosalen complexes. *Bioconjugate Chem. 8*, 798–812.
(18) Mandal, S. S., Kumar, N. V., Varshney, U., and Bhattacharya, S. (1996) Metal-ion dependent DNA cleavage by transition metal complexes of a new water-soluble salen dereivative. *J. Inorg. Biochem. 63*, 265–272.
(19) Thomas, M., Varshney, U., and Bhattacharya, S. (2002) Distamycin analogues without leading amide at their *N*-termini - comparative binding properties to AT- and GC-rich DNA sequences. *Eur. J. Org. Chem.* 3604–15.
(20) Bhattacharya, S., and Thomas, M. (2001) DNA recognition by the first *tail-to-tail* linked distamycin-like oligopeptide dimers. *Chem. Commun.* 1464–65.
(21) Bhattacharya, S., and Thomas, M. (2000) DNA binding properties of novel distamycin analogs that lack the leading amide unit at the N-terminus. *Biochem. Biophys. Res. Commun. 267*, 139–44.
(22) Ghosh, S., Defrancq, E., Lhomme, J. H., Dumy, P., and Bhattacharya, S. (2004) Efficient conjugation and characterization of distamycin-based peptides with selected oligonucleotide stretches. *Bioconjugate Chem. 15*, 520–29.
(23) Ghosh, S., Usharani, D., De, S., Jemmis, E. D., and Bhattacharya, S. (2008) Photophysical and duplex-DNA-binding properties of distamycins based on 4,4'- and 2,2'-dialkoxyazobenzenes as the core. *Chem. Asian J. 3*, 1949–1961.
(24) Rau, H. *Photochemistry and Photophysics* (Rabek, J. F., Ed.) pp 119−41, Vol. II, CRC, Boca Raton, FL.
(25) Rau, H. (1990) Azo compounds, In *Studies in Organic Chemistry: Photochromism, Molecules and Systems* (Dürr, H., and Bonas-Laurent, H., Eds) pp 165−92, Vol *40*, Elsevier, Amsterdam.
(26) Flint, D. G., Kumita, J. R., Smart, O. S., and Woolley, G. A. (2002) Using an azobenzene cross-linker to either increase or decrease peptide helix content upon trans-to-cis photoisomerization. *Chem. Biol. 9*, 391–97.
(27) Asanuma, H., Liang, X., Yoshida, T., and Komiyama, M. (2001) Photocontrol of DNA duplex formation by using azobenzene-bearing oligonucleotides. *ChemBioChem 2*, 39–44.
(28) Liang, X., Asanuma, H., and Komiyama, M. (2002) Photoregulation of DNA triplex formation by azobenzene. *J. Am. Chem. Soc. 124*, 1877–83.
(29) Dohno, C., Uno, S., and Nakatani, S. (2007) Photoswitchable molecular glue for DNA. *J. Am. Chem. Soc. 129*, 11898–99.
(30) Srivastava, A., Ghorai, S., Bhattacharjya, A., and Bhattacharya, S. (2005) A tetrameric sugar-based azobenzene that gels water at various pH values and in the presence of salts. *J. Org. Chem. 70*, 6574–82.
(31) Guerrero, L., Smart, O. S., Weston, C. J., Burns, D. C., Woolley, G. A., and Allemann, R. K. (2005) Photochemical regulation of DNA-binding specificity of MyoD. *Angew. Chem., Int. Ed. 44*, 7778–82.
(32) Liu, M., Asanuma, H., and Komiyama, M. (2006) Azobenzene-tethered T7 promoter for efficient photoregulation of transcription. *J. Am. Chem. Soc. 128*, 1009–15.
(33) Bhattacharya, S., and Thomas, M. (2000) Facile synthesis of oligopeptide distamycin analogs devoid of hydrogen bond donors or acceptors at the N-terminus: sequence-specific duplex DNA binding as a function of peptide chain length. *Tetrahedron Lett. 41*, 5571–75.
(34) Bhattacharya, S., and Thomas, M. (2001) Facile synthesis of novel fluorescent distamycin analogues. *Tetrahedron Lett. 42*, 5525–28.
(35) Wei, W., Tomohiro, T., Kodaka, M., and Okuno, H. (2000) Selective synthesis and kinetic measurement of 1:1 and 2:2 cyclic compounds containing 1,4,7,10-tetraazacyclododecane and azobenzene units. *J. Org. Chem. 65*, 8979–87.
(36) Ameerunisha, S., and Zacharias, P. S. (1995) Characterization of simple photoresponsive systems and their applications to metal ion transport. *J. Chem. Soc., Perkin Trans. 2*, 1679–82.
(37) Kasha, M. (1948) Transmission filters for the ultraviolet. *J. Opt. Soc. Am. 38*, 929–34.
(38) McGhee, J. D., and Von Hippel, P. H. (1974) Theoretical aspects of DNA-protein interactions: co-operative and non-co-operative binding of large ligands to a one-dimensional homogeneous lattice. *J. Mol. Biol. 86*, 469–489.
(39) Frisch, M. J.; Trucks, G. W. et al. (2003) *Gaussian 03*, Gaussian, Inc., Wallingford, CT.
(40) Nicole, A. T. F. et. al. *AMBER 8*, University of California, San Francisco.
(41) Duan, Y., Wu, C., Chowdhury, S., Le, M. C., Xiong, G., Zhang, W., Yang, R., Cieplak, P., Luo, R., and Lee, T. (2003) A point-charge force field for molecular mechanics simulations of proteins based on condensed-phase quantum mechanical calculations. *J. Comput. Chem. 24*, 1999–2012.
(42) AutoDock 3.05, 10550 North Torrey Pines Road, La Jolla, CA 92037−1000.
(43) Morris, G. M., Goodsell, D. S., Halliday, R. S., Huey, R., Hart, W. E., Belew, R. K., and Olson, A. J. (1998) Automated docking using a Lamarckian genetic algorithm and an empirical binding free energy function. *J. Comput. Chem. 19*, 1639–62.
(44) Evans, D. A., and Neidle, S. (2006) Virtual screening of DNA minor groove binders. *J. Med. Chem. 49*, 4232–38.
(45) Detering, C., and Varani, G. (2004) Validation of automated docking programs for docking and database screening against RNA drug targets. *J. Med. Chem. 47*, 4188–4201.
(46) Chen, K, Adelstein, S. J., and Kassis, A. I. (2004) Molecular modeling of the interaction of iodinated Hoechst analogs with DNA: Implications for new radiopharmaceutical design. *J. Mol. Struct. (Theochem) 711*, 49–56.
(47) Singh, A. K., and Madhusoodnan, K. S. (1998) Effect of substituents and media on photochromic properties of azobenzene systems. *National Academy Science Letters (India) 21*, 243–46.
(48) Angiolini, L., Caretti, D., Giorgini, L., Salatelli, E., Altomare, A., Carlini, C., and Solaro, R. (2000) Optically active polymethacrylates with side-chain L-lactic acid residues connected to push−pull azobenzene chromophores. *Polymer 41*, 4767–80.
(49) Crecca, C. R., and Roitberg, A. E. (2006) Theoretical study of the isomerization mechanism of azobenzene and disubstituted azobenzene derivatives. *J. Phys. Chem. A 110*, 8188–8203.
(50) Diau, E. W. G. (2004) A new trans-to-cis photoisomerization mechanism of azobenzene on the S1 (n,π) surface. *J. Phys. Chem. A 108*, 950–56.
(51) Luck, G., Zimmer, C., Reinert, K. E., and Arcamone, F. (1977) Specific interactions of distamycin A and its analogs with (A-T) rich and (G-C) rich duplex regions of DNA and deoxypolynucleotides. *Nucleic Acids Res. 4*, 2655.
(52) Shaikh, S. A., and Jayaram, B. (2007) A swift all-atom energy-based computational protocol to predict DNA-ligand binding affinity and ΔT_m. *J. Med. Chem. 50*, 2240–44.
(53) Heckel, A., and Dervan, P. B. (2003) U-Pin polyamide motif for recognition of the DNA minor groove. *Chem. Eur. J. 9*, 3353–66.
(54) SYBYL 7.0, Tripos Inc., 1699 South Hanley Rd., St. Louis, MO, 63144.

BC800130U

Supporting Information

Design, Synthesis and DNA Binding Properties of Photoisomerizable Azobenzene-Distamycin Conjugates: An Experimental and Computational Study

Sumana Ghosh,[a] *Dandamudi Usharani,*[b] *Ananya Paul,*[a] *Susmita De,*[b] *Eluvathingal D. Jemmis,*[†,b] *and Santanu Bhattacharya**[,a,c]

[a]Department of Organic Chemistry, Indian Institute of Science, Bangalore 560 012, India.

[b]Department of Inorganic and Physical Chemistry, Indian Institute of Science, Bangalore, 560 012 India.

[c]Chemical Biology Unit, Jawaharlal Nehru Centre of Advanced Scientific Research, Bangalore 560 012, India.

[†]Present Address: Indian Institute of Science Education and Research, Thiruvananthapuram, CET Campus, TVM 695016, Kerala, India.

Running Title: Azobenzene-distamycin conjugates

*For correspondence, Phone: +(91)-80-2293-2664,

Fax: +(91)-80-23600529,

E-mail: sb@orgchem.iisc.ernet.in

Contents:

Spectral Characterization data of Final Compounds: **1, 2, and 3 (^{1}H-NMR, and ^{13}C-NMR Spectra) (Fig. SI-1, SI-2, SI-3)**	SI-3-5
^{1}H-NMR spectra of 2 before and after photoirradiation at ~360 nm (Fig. SI-4)	SI-6
Competition for DNA minor groove, Hoechst displacement Assay (Fig. SI-5)	SI-7
Docking and free binding energies of all the ligands (Dist-1 Dist-2 and 1, 2, 3) (Table SI-1)	SI-8
Melting temperatures (T_m) at fixed [D]/[P] ratio of 0.5 obtained from binding of different forms of 1, 2 and 3, with poly [d(A-T).d(T-A)]. (Table SI-2)	SI-9
The single point and relative energies of the lowest docked structure of *trans* and *cis* forms for the ligands 1-3 (Table SI-3)	SI-10
The total energies (hartree) and the cartesian coordinates of optimized structures of ligands (Dist-1 Dist-2, Hoechst, and 1, 2, 3)	SI-11
The total energies in hartree and the cartesian coordinates of the structures 17a, 17b, 18a and 18b at MP2/6-31+G* level of theory	SI-19

Materials and Methods. All reagents used in this study were of highest purity available and were used without purification. Thin-layer chromatography (TLC) was performed using silica gel-G and preparative column chromatography was done on silica gel (60–120 mesh size). Solvents such as CH_2Cl_2, $CHCl_3$ were dried over P_2O_5, Et_3N was dried over KOH, THF using sodium and benzophenone ketyl and DMF was vacuum distilled over anhydrous $MgSO_4$. ^{1}H-NMR spectra were recorded on a 300 or a 400 Hz spectrometer and ^{13}C-NMR spectra were recorded on a 500 Hz spectrometer. Chemical shifts (δ) are reported in ppm downfield from the internal standard (TMS). Electrospray ionization (ESI) mass spectra were used to characterize synthesized compounds. Abbreviations for the structures of azobenzene-distamycin conjugates **1-3** are given in the main manuscript.

A

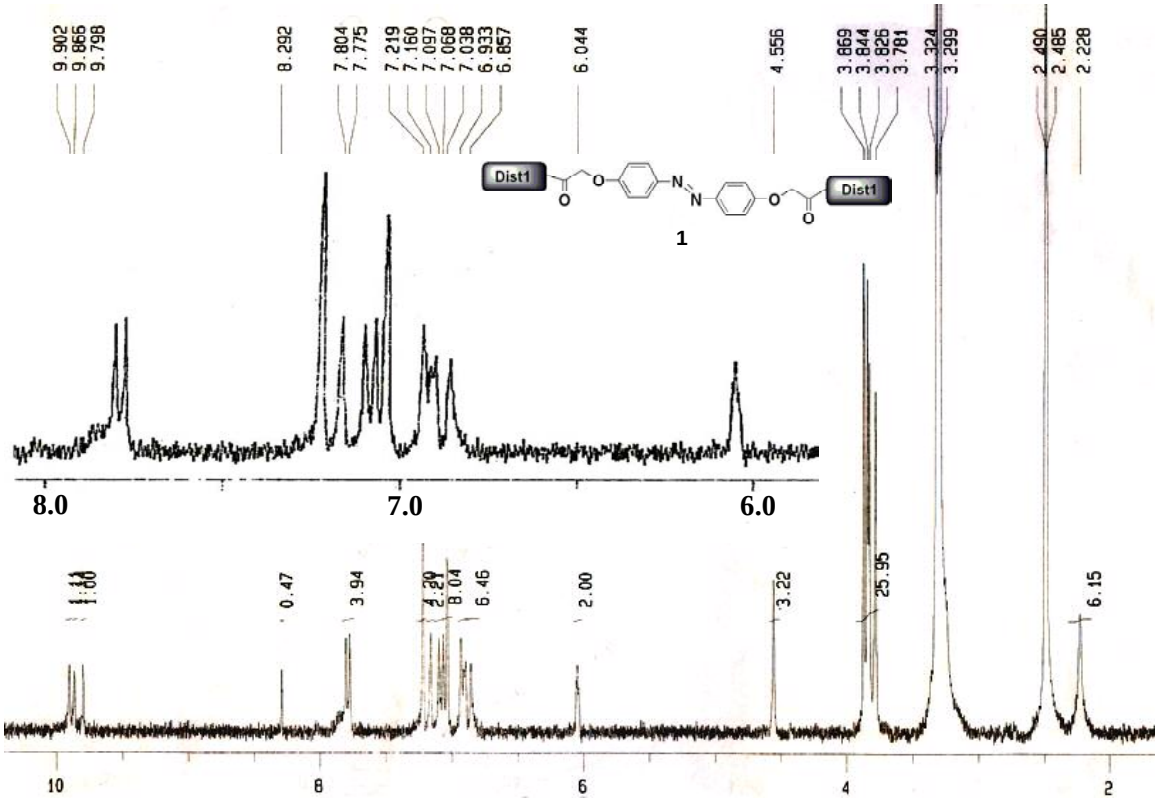

B

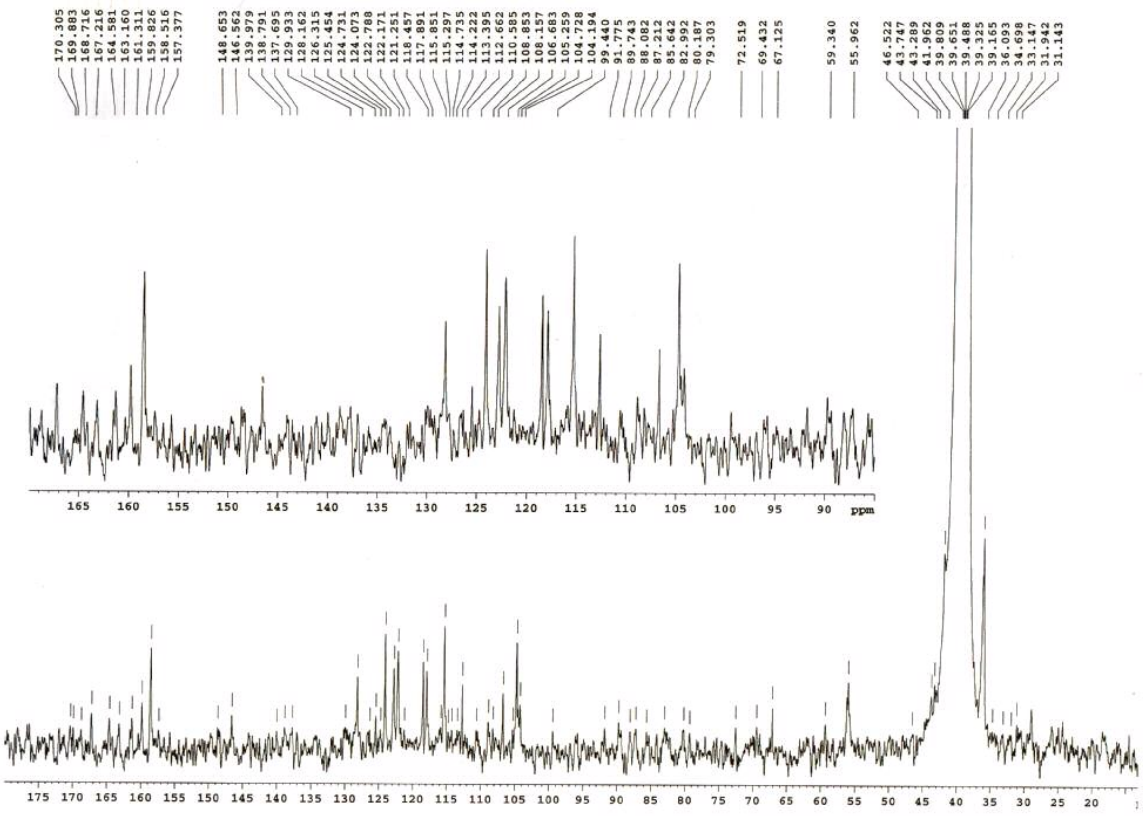

Figure S1. (A) ^{1}H-NMR (300 MHz, DMSO-d_6); (B) ^{13}C-NMR (125 MHz, DMSO-d_6) of **1**.

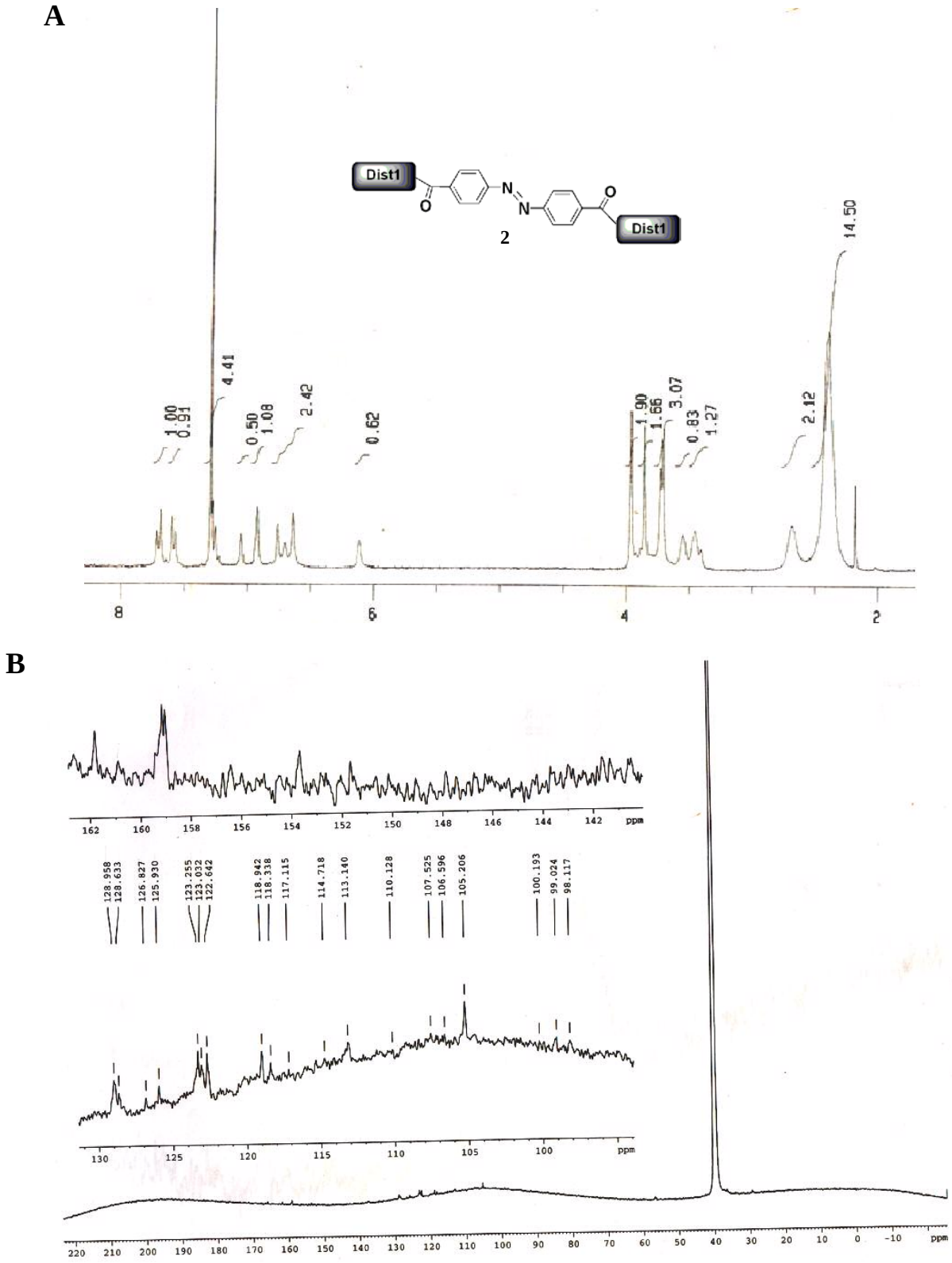

Figure S2. (A) ^{1}H-NMR (300 MHz, DMSO-d_6); (B) ^{13}C-NMR (125 MHz, DMSO-d_6) of **2**.

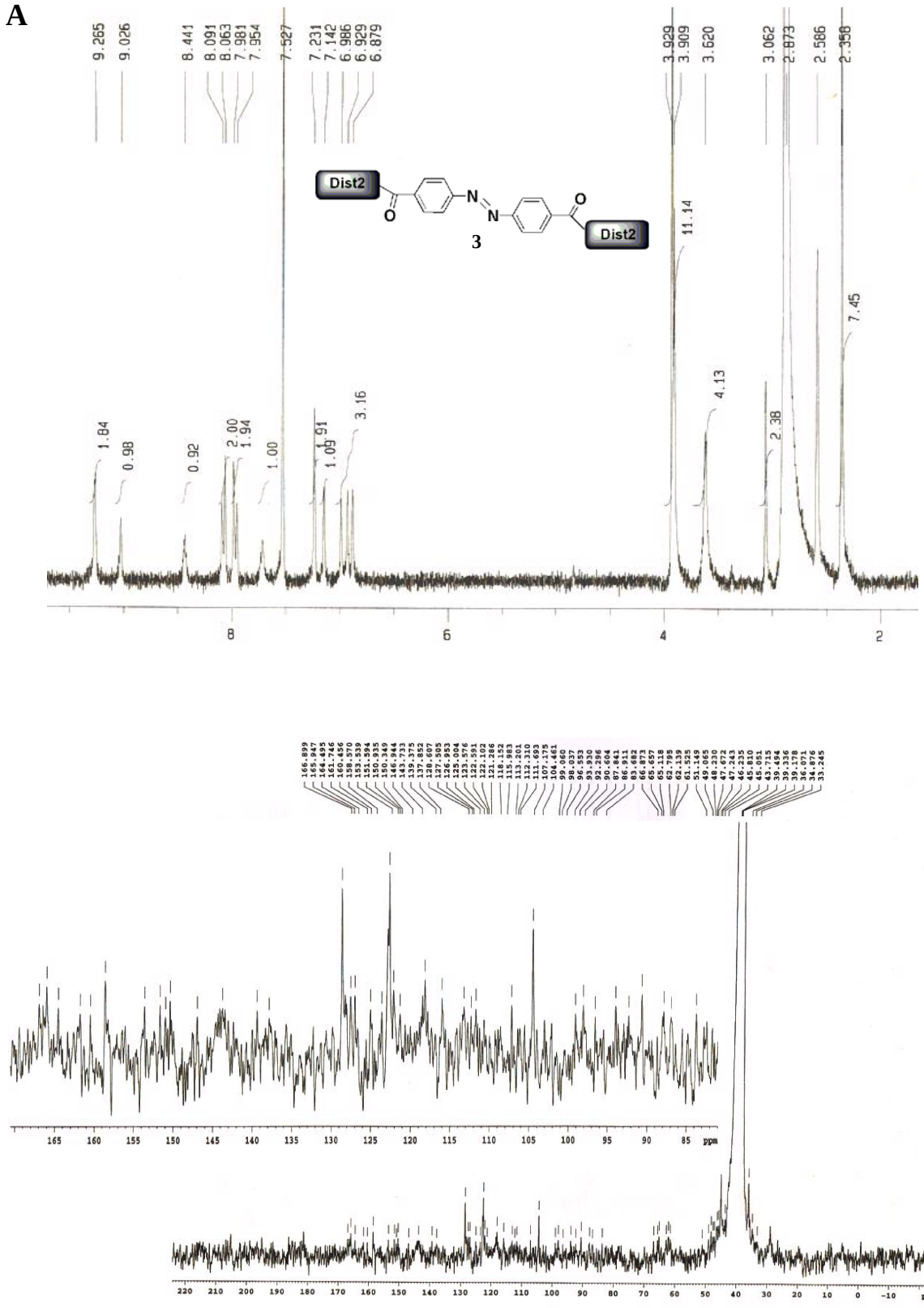

Figure S3. (A) ^{1}H-NMR (300 MHz, DMSO-d_6); (B) ^{13}C-NMR (125 MHz, DMSO-d_6) of **3**.

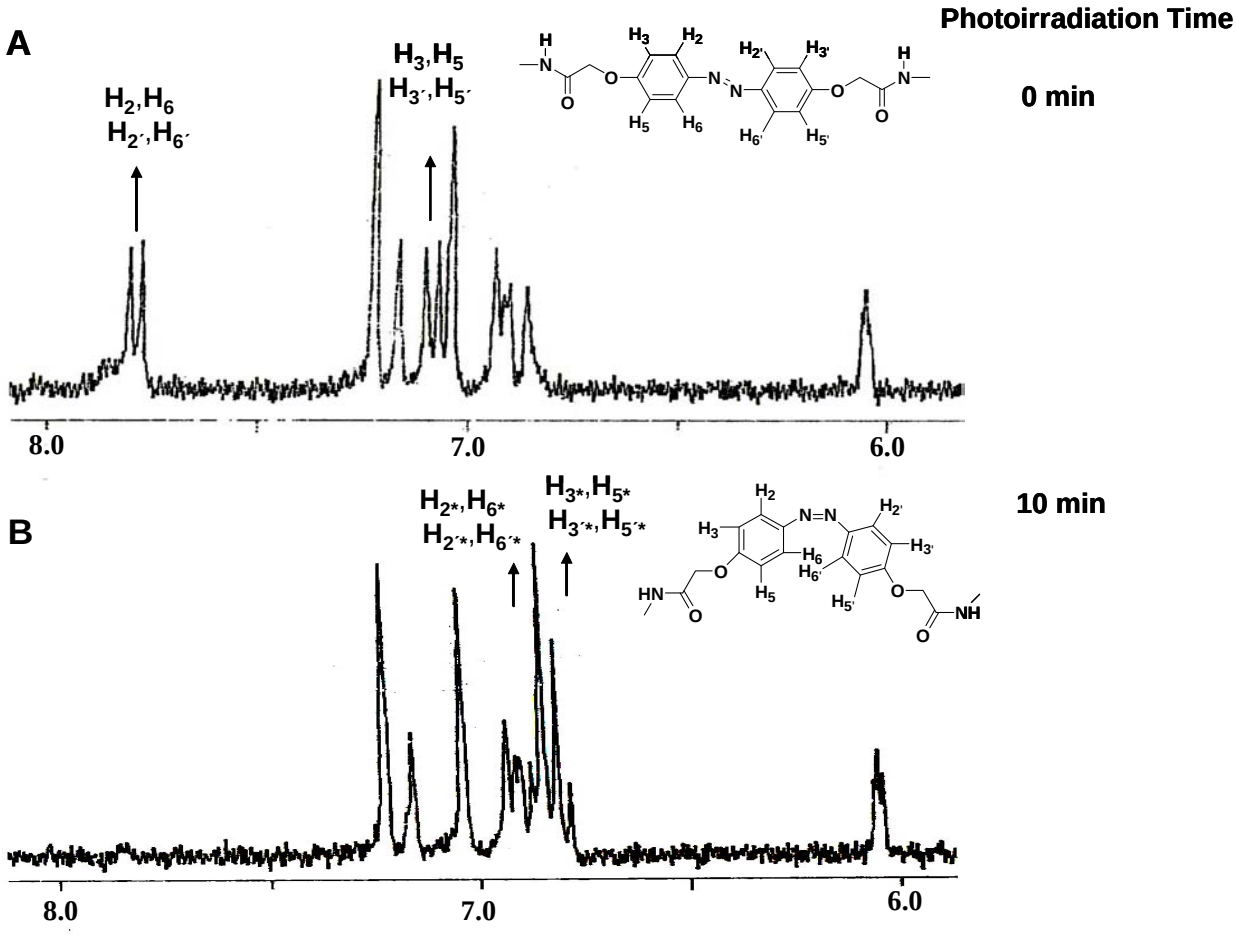

Figure S4. ^{1}H-NMR spectra of a d_6-DMSO solution of **1** (1 mM) before (A) and after (B) 10 min of photoirradiation at ~360 nm. Chemical shifts of the respective azobenzene protons before and after irradiation are indicated with respect to TMS as standard. The symbol '*' refers to the sample after irradiation.

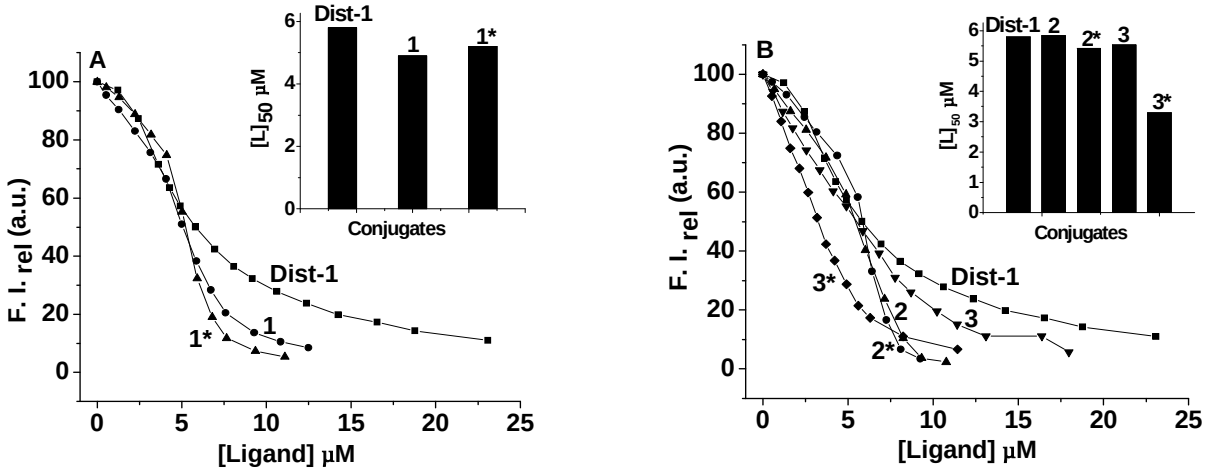

Figure S5. Changes in the fluorescence intensity of Hoechst 33258 upon addition of different azobenzene-distamycin conjugate into the saturated Hoechst-poly [d(A-T).d(T-A)] complex in NaCl buffer at 25 ^{o}C. Inset: Y-axis of the bar correspond to various ligand concentrations ($[L]_{50}$) to displace 50% Hoechst from DNA minor groove surface. Apparent binding constants (K_{app}) were calculated from the respective $[L]_{50}$ values and considering *Ka* (Hoechst) = 1.5×10^{7} M^{-1}, and [Hoechst 33258] = 250 nM. Here different isomeric compositions of the ligands are same as mentioned above.

Table SI-1. The docked and free binding energies (ΔG), number of rotable bonds, cluster (number of similar conformations) and number of amide bond contacts with DNA bases obtained form Autodock calculations of **Dist-1**, **Dist-2, Hoechst** and different photoisomeric forms of **1**, **2**,and **3** with modeled duplex $[d(GC(AT)_{10}CG)]_2$ DNA are tabulated.

Ligands	ΔG (kcal/mol)	Docked energy (kcal/mol)	Rotable bonds	Cluster	The bond distance between ligand and DNA bases (Å)
Dist-1	-7.0	-11.3	0	1	2.50, 2.74, 2.32, 2.54
Dist-2	-7.1	-11.5	0	1	2.21, 2.39, 2.53, 2.52, 2.11
Hoechst	-12.1	-13.0	0	1	2.26, 2.18
1a	-7.5	-7.5	0	1	
	-7.7	-19.9	10	1	
	-8.2a	**-21.9**	**0**	**1**	**3.35, 5.29, 6.54, 2.74, 4.61, 5.63**
1b	-11.0	-11.0	0	5	
	-7.0	-21.2	10	1	
	-7.9	**-21.6**	**0**	**9**	**3.49, 5.25, 5.78, 2.58, 2.92, 3.69, 4.85, 4.30, 2.56**
2a	10.3	-10.3	0	2	
	-7. 8	-18.2	8	1	
	-10.3	**-22.7**	**0**	**7**	**5.04, 6.61, 5.16, 3.56, 3.19, 5.62, 4.15,4.24, 3.46**
2b	-7.2	-7.2	0	1	
	-6.7	-18.6	8	1	
	-9.8	**-22.3**	**0**	**3**	**4.14, 2.71,4.27, 3.86, 3.16, 3.49, 3.95, 2.56, 4.56, 3.98**
3a	-14.3	-14.3	0	1	
	-6.7	-18.9	5	1	
	-12.9	**-24.1**	**0**	**5**	**2.94, 4.87, 6.59, 2.61, 3.06, 2.56, 2.51,**
3b	-7.1	-7.1	0	1	
	-13.6	-24.3	5	2	
	-14.1	**-25.3**	**0**	**14**	**2.39, 3.06, 2.73, 2.38, 4.65, 5.51, 4.90, 3.51, 2.17, 3.25**
	-13.7	-25.7	6	1	
	-14.1	**-25.9**	**0**	**20**	

[a]The values in bold obtained by rigid docking of the lowest docked conformation of the ligands initially obtained from the flexible docking studies.

Table SI-2. Melting temperatures (T_m) at fixed [D]/[P] ratio of 0.5 obtained from binding of different forms of **1**, **2** and **3**, with poly [d(A-T).d(T-A)].

DNA + Ligands	T_m(°C)[a]	ΔT_m(°C)[b]
Poly [d(A-T). d(T-A)] alone	64.7	-
+ 1	76.2	11.5
+ 1*	78.0	13.3
+ 2	81.3	16.6
+ 2*	83.7	19.0
+ 3	89.0	24.3
+ 3*	>90	>25.3

[a]T_m indicates the average melting temperature value of two independent melting experiments that has been done with the complexes of poly [d(A-T).d(T-A)] in the presence of different ligands in 150 mM NaCl, 10 mM Na_2HPO_4, 0.1 mM EDTA, pH = 7.4 at the saturated [D]/[P] ratio, The error is within ± 0.2 °C. [b]ΔT_m corresponds to the difference in T_m between DNA alone and DNA-ligand complexes.

Table SI-3: The single point and relative energies of the lowest docked structure of *trans* and *cis* forms for all the ligands **1-3** at HF/3-21g level of theory using Gaussian 03 program are given. The D1 and D2 are the distance around the azobenzene and azobenzene and spacer moiety as shown in scheme 4.

Ligand	Total energy in hartree	Relative energy in (kcal/mol)	D1 (Å)	D2 (Å)
1a (*trans*)	−4920.77349	0.0	11.62	21.53
1b (*cis*)	−4920.74933	15.2	8.02	14.06
2a	−4694.29540	0.0	11.91	19.40
2b	−4694.28781	4.8	8.17	11.91
3a	−4203.73143	0.0	11.91	17.05
3b	−4203.63689	59.3	7.53	8.30

The coordinates of docked conformation of these isomers can be obtained from the authors.

The total energies in hartree and the cartesian coordinates of optimized structures at HF/3-21g level of theory using Gaussian 03 program package are given.

Dist -1 Total energy = 1953.30907

7	10.618715000	6.144309000	2.160660000
1	9.816206000	6.376142000	2.718249000
6	10.294588000	5.372646000	0.949509000
6	9.890308000	3.952477000	1.362162000
7	9.492572000	3.150113000	0.197879000
6	10.632086000	2.664011000	-0.591220000
6	8.479060000	2.111289000	0.434557000
6	7.513092000	2.058555000	-0.757818000
7	6.479960000	1.035191000	-0.576569000
1	5.606123000	1.303139000	-0.186103000
6	6.738145000	-0.262559000	-0.856500000
8	7.849473000	-0.626987000	-1.230288000
6	5.619160000	-1.194798000	-0.688288000
7	5.776368000	-2.549715000	-0.787627000
6	4.293908000	-0.940137000	-0.442396000
6	7.023956000	-3.279632000	-1.055622000
6	4.567560000	-3.157130000	-0.600707000
6	3.625442000	-2.185238000	-0.386314000
7	2.250394000	-2.336025000	-0.156180000
6	1.603014000	-3.528232000	-0.124345000
1	1.739853000	-1.503588000	0.034821000
8	2.198088000	-4.593610000	-0.250855000
6	0.153949000	-3.450208000	0.073908000
7	-0.608766000	-4.559925000	0.312650000
6	-0.682405000	-2.362509000	0.037141000
6	-0.142718000	-5.949927000	0.425650000
6	-1.916559000	-4.187756000	0.435553000
6	-1.996773000	-2.829798000	0.266794000
7	-3.134018000	-2.010945000	0.298353000
6	-4.398968000	-2.461652000	0.498454000
1	-2.978637000	-1.032848000	0.202337000
8	-4.637673000	-3.644881000	0.717719000
6	-5.446467000	-1.440692000	0.437062000
7	-6.741992000	-1.705347000	0.786672000
6	-5.377916000	-0.131691000	0.029521000
6	-7.287274000	-2.980518000	1.275125000
6	-7.493059000	-0.578968000	0.611266000
6	-6.676293000	0.416123000	0.140021000
7	-7.008291000	1.737010000	-0.190424000
1	-6.266319000	2.308571000	-0.525971000
6	-8.254215000	2.264809000	-0.083906000
6	-8.382029000	3.665658000	-0.489473000
8	-9.202861000	1.602891000	0.326835000
6	-7.444233000	4.541074000	-0.975179000
7	-9.585904000	4.333052000	-0.423966000
6	-8.088993000	5.775103000	-1.212838000
6	-9.400848000	5.607633000	-0.862694000
6	-10.875037000	3.794066000	0.035510000
1	9.492482000	5.795963000	0.349551000
1	11.183973000	5.338539000	0.335490000
1	9.040994000	4.027031000	2.030950000
1	10.710626000	3.506241000	1.921076000
1	10.277387000	2.137850000	-1.466917000
1	11.237871000	3.494952000	-0.926438000
1	11.264527000	1.983475000	-0.019248000
1	8.920580000	1.128667000	0.575680000
1	7.915589000	2.359823000	1.324799000
1	8.056107000	1.833725000	-1.661949000
1	7.035591000	3.021393000	-0.867772000
1	3.838028000	0.018433000	-0.336096000
1	6.798834000	-4.334661000	-1.019096000
1	7.411793000	-3.014338000	-2.024445000
1	7.766784000	-3.035634000	-0.314375000
1	4.448571000	-4.209311000	-0.629129000
1	-0.406793000	-1.350540000	-0.158381000
1	-0.996592000	-6.560592000	0.676361000
1	0.288455000	-6.276661000	-0.505422000
1	0.606298000	-6.031839000	1.195935000
1	-2.690761000	-4.883996000	0.630020000
1	-4.515505000	0.381208000	-0.333053000
1	-8.328931000	-2.821364000	1.508536000
1	-7.186910000	-3.743412000	0.521766000
1	-6.757850000	-3.300360000	2.157424000
1	-8.530227000	-0.547532000	0.823720000
1	-11.606672000	4.584541000	-0.041408000
1	-11.169452000	2.957155000	-0.574871000
1	-10.798277000	3.459842000	1.056381000
1	-10.211337000	6.298090000	-0.893667000
1	-7.643379000	6.665249000	-1.591813000
1	-6.411639000	4.339619000	-1.149089000
1	11.190247000	6.951698000	1.995121000

Dist -2 Total energy = -1707.99271

7	-9.547391000	5.456294000	-0.964544000
1	-9.031343000	6.297310000	-1.142838000
6	-8.765499000	4.219322000	-1.041259000
6	-7.645420000	4.137242000	0.015098000
7	-6.884898000	2.889951000	-0.083241000
6	-7.377779000	1.741629000	0.437763000
1	-6.056491000	2.874539000	-0.632926000
8	-8.491577000	1.711032000	0.955804000
6	-6.487229000	0.576461000	0.341393000
6	-5.135976000	0.565740000	0.104722000
7	-6.890594000	-0.717818000	0.529946000
6	-4.707383000	-0.782037000	0.141391000
7	-3.380623000	-1.193959000	-0.045909000
6	-5.813354000	-1.547667000	0.399471000
6	-2.956783000	-2.482185000	0.022278000
1	-2.728193000	-0.489611000	-0.309036000
6	-1.503302000	-2.650994000	-0.108091000
8	-3.742720000	-3.410758000	0.184103000
7	-0.894670000	-3.838679000	-0.409496000
6	-0.521590000	-1.713765000	0.094993000
6	0.459959000	-3.661309000	-0.411132000
6	-1.539212000	-5.115366000	-0.754674000
6	0.724982000	-2.354630000	-0.097387000
7	1.967581000	-1.719674000	0.034213000
6	3.165619000	-2.319095000	-0.190850000
1	1.957454000	-0.789574000	0.389040000
8	3.244799000	-3.511161000	-0.471527000
6	4.324617000	-1.424647000	-0.074748000
7	5.614592000	-1.858048000	0.066256000
6	4.345328000	-0.053373000	-0.140819000
6	6.084962000	-3.242720000	0.229346000
6	6.449096000	-0.777166000	0.104967000
6	5.693362000	0.357457000	-0.026391000
7	6.129475000	1.689687000	-0.059158000
1	5.425878000	2.387429000	-0.174069000
6	7.426939000	2.082203000	0.047080000
8	8.345685000	1.291056000	0.188349000
6	7.617863000	3.597917000	-0.026812000
7	8.987625000	4.045629000	0.085605000
6	9.601678000	3.842209000	1.403870000
6	9.851907000	3.692411000	-1.047828000
6	-8.256819000	-1.205867000	0.774261000
1	7.208267000	3.941551000	-0.971997000
1	7.030332000	4.049050000	0.767254000
1	-8.334386000	4.136831000	-2.031440000
1	-9.429093000	3.380547000	-0.891833000
1	-6.955879000	4.963796000	-0.106788000
1	-8.085160000	4.192818000	1.000633000
1	-4.510463000	1.418446000	-0.033779000
1	-5.892766000	-2.599964000	0.495379000
1	-0.664628000	-0.700521000	0.396464000
1	1.134985000	-4.449115000	-0.626417000
1	-2.548521000	-5.096815000	-0.390518000
1	-1.533656000	-5.254919000	-1.828219000
1	-0.988099000	-5.918995000	-0.287436000
1	3.507543000	0.586797000	-0.302926000
1	5.323254000	-3.906359000	-0.132390000
1	6.993464000	-3.369200000	-0.342013000
1	6.288169000	-3.443994000	1.273428000

1	7.498588000	-0.872061000	0.218129000
1	8.951160000	4.254469000	2.167257000
1	10.539539000	4.382601000	1.438639000
1	9.785333000	2.796272000	1.621748000
1	9.373225000	4.001237000	-1.970498000
1	10.783968000	4.236515000	-0.958190000
1	10.063048000	2.630245000	-1.096407000
1	-8.861814000	-0.374969000	1.082796000
1	-8.659205000	-1.645711000	-0.129423000
1	-8.225421000	-1.955266000	1.552619000
1	-10.132069000	5.530964000	-0.153644000

Hoechst Total energy = -1354.64924

6	-2.562228000	0.365639000	0.005828000
6	-2.578823000	1.756892000	-0.099272000
6	-3.786672000	2.432960000	-0.172514000
6	-4.948039000	1.696374000	-0.136742000
6	-4.925173000	0.296059000	-0.029225000
6	-3.727205000	-0.381968000	0.043002000
6	-0.492926000	1.197109000	-0.020021000
1	-3.799181000	3.500061000	-0.254285000
1	-5.894490000	2.195472000	-0.191574000
1	-3.730764000	-1.448539000	0.124031000
7	-1.267506000	2.233719000	-0.110572000
7	-1.223238000	0.023725000	0.055581000
6	0.970131000	1.249530000	0.005542000
6	1.742182000	0.102014000	-0.039604000
6	1.571831000	2.517572000	0.071044000
6	3.114677000	0.256132000	-0.009644000
1	1.303550000	-0.872571000	-0.108894000
6	2.936935000	2.658158000	0.099952000
1	0.927539000	3.370411000	0.096049000
6	3.718997000	1.513229000	0.060655000
1	3.398949000	3.621759000	0.150773000
6	5.336184000	0.080874000	0.014529000
7	5.102285000	1.357879000	0.074235000
7	4.163689000	-0.647400000	-0.039251000
6	6.669505000	-0.516118000	0.005115000
6	6.885658000	-1.887883000	-0.053962000
6	7.767896000	0.330896000	0.058122000
6	8.163576000	-2.400360000	-0.060255000
1	6.062219000	-2.572583000	-0.095340000
6	9.048344000	-0.178914000	0.051985000
1	7.595753000	1.385820000	0.103664000
6	9.252449000	-1.546638000	-0.007281000
1	8.342543000	-3.453435000	-0.105434000
1	9.885842000	0.489796000	0.093326000
8	10.497389000	-2.119617000	-0.016761000
1	11.214342000	-1.475763000	0.021399000
6	-6.974805000	-0.272688000	1.203845000
6	-6.933076000	-0.458201000	-1.231111000
6	-8.027184000	-1.379546000	1.262702000
1	-7.481802000	0.689712000	1.180253000
1	-6.341791000	-0.316023000	2.079801000
6	-7.985688000	-1.563953000	-1.157465000
1	-7.438129000	0.495325000	-1.370829000
1	-6.270693000	-0.632016000	-2.068320000
1	-8.686675000	-1.208317000	2.104817000
1	-7.524080000	-2.337491000	1.400082000
1	-8.615649000	-1.523977000	-2.037783000
1	-7.480669000	-2.530338000	-1.130927000
7	-6.136862000	-0.476070000	0.008793000
7	-8.825519000	-1.363066000	0.030291000
6	-9.982671000	-2.258531000	0.078685000
1	-10.601863000	-1.999449000	0.928743000
1	-10.571863000	-2.132801000	-0.821409000
1	-9.702634000	-3.310879000	0.163671000
1	-0.863666000	-0.894913000	0.168006000
1	4.080897000	-1.635661000	-0.092728000
1	-7.480669000	-2.530338000	-1.130927000
7	-6.136862000	-0.476070000	0.008793000
7	-8.825519000	-1.363066000	0.030291000
6	-9.982671000	-2.258531000	0.078685000
1	-10.601863000	-1.999449000	0.928743000
1	-10.571863000	-2.132801000	-0.821409000
1	-9.702634000	-3.310879000	0.163671000
1	-0.863666000	-0.894913000	0.168006000
1	4.080897000	-1.635661000	-0.092728000

1a Total energy = -4920.96862

7	-0.709693000	-2.623333000	0.742888000
7	-1.105578000	-3.754554000	1.064257000
6	-2.401348000	-4.125033000	0.610055000
6	-3.221915000	-3.312778000	-0.149736000
6	-2.844236000	-5.390612000	0.968480000
6	-4.468958000	-3.753499000	-0.548767000
1	-2.875034000	-2.339290000	-0.422333000
6	-4.082740000	-5.837260000	0.575700000
1	-2.199038000	-6.009473000	1.556641000
6	-4.902967000	-5.017813000	-0.187160000
1	-5.086899000	-3.107215000	-1.135493000
1	-4.443729000	-6.808196000	0.839345000
6	0.585973000	-2.255577000	1.198200000
6	1.408190000	-3.077486000	1.965677000
6	1.031218000	-1.001283000	0.843085000
6	2.645198000	-2.640952000	2.361689000
1	1.056025000	-4.048981000	2.237461000
6	2.280479000	-0.551936000	1.238798000
1	0.390772000	-0.378921000	0.253076000
6	3.089811000	-1.372029000	1.999478000
1	3.296265000	-3.250347000	2.951480000
1	2.601034000	0.425787000	0.948114000
8	-6.119310000	-5.543762000	-0.532084000
8	4.338802000	-1.031671000	2.443555000
6	-7.046084000	-4.819922000	-1.328456000
1	-6.622200000	-4.561151000	-2.292659000
1	-7.365783000	-3.909662000	-0.833368000
6	4.908603000	0.238864000	2.161661000
1	5.030971000	0.388194000	1.094610000
1	4.297631000	1.042553000	2.557847000
6	-8.254061000	-5.722067000	-1.550400000
8	-8.330806000	-6.871520000	-1.177285000
7	-9.244141000	-5.096744000	-2.237146000
1	-9.152445000	-4.140087000	-2.499756000
6	6.275343000	0.282446000	2.834328000
8	6.724124000	-0.598380000	3.534819000
7	6.940759000	1.435386000	2.574262000
1	6.550279000	2.121389000	1.966234000
6	8.266068000	1.683982000	3.151664000
1	8.267334000	1.315922000	4.166114000
1	8.448562000	2.748359000	3.166345000
6	9.376087000	0.994250000	2.346571000
1	9.385212000	1.401124000	1.344053000
1	9.158526000	-0.068092000	2.281075000
6	-10.481211000	-5.804339000	-2.584412000
1	-10.934094000	-5.323191000	-3.438943000
1	-10.223866000	-6.817445000	-2.850670000
6	-11.481288000	-5.804474000	-1.419290000
1	-11.010050000	-6.252001000	-0.547780000
1	-11.730076000	-4.778533000	-1.179278000
7	-12.701418000	-6.516901000	-1.819936000
7	10.670843000	1.251798000	2.988905000
6	-13.982783000	-5.962531000	-1.359923000
1	-14.358581000	-6.475890000	-0.479396000
1	-13.853320000	-4.916709000	-1.113161000
6	11.785282000	1.664589000	2.132410000
1	12.462782000	0.840560000	1.911552000
1	11.400103000	2.047252000	1.199673000
6	12.560676000	2.808436000	2.803313000
1	11.882188000	3.635675000	2.946094000
1	12.943292000	2.500105000	3.765564000
6	-15.021537000	-6.073599000	-2.484851000
1	-14.673696000	-5.516403000	-3.342431000
1	-15.148664000	-7.106713000	-2.767884000
7	-16.322071000	-5.537127000	-2.072478000
1	-16.608663000	-4.652346000	-2.422424000
7	13.699923000	3.239614000	1.986780000
1	14.620814000	3.058768000	2.313731000
6	-12.605759000	-7.973703000	-1.644137000
1	-11.722348000	-8.351606000	-2.140619000

1	-12.553306000	-8.253279000	-0.591965000
1	-13.468886000	-8.456792000	-2.081281000
6	11.029962000	0.267583000	4.013842000
1	10.192729000	0.103594000	4.679099000
1	11.312601000	-0.692859000	3.580608000
1	11.859008000	0.631567000	4.607857000
6	13.507429000	3.975788000	0.869247000
6	14.725565000	4.312782000	0.117507000
8	12.376805000	4.318081000	0.526316000
6	15.966844000	3.736930000	0.219491000
7	14.783267000	5.259992000	-0.869118000
6	16.807301000	4.361765000	-0.731646000
1	16.242953000	2.933037000	0.863833000
6	16.049334000	5.299042000	-1.381568000
7	18.154271000	4.031765000	-0.933300000
1	16.328936000	5.968370000	-2.153972000
6	18.956977000	4.612712000	-1.861560000
1	18.540891000	3.352287000	-0.317677000
6	20.315494000	4.072380000	-1.941826000
8	18.563633000	5.528234000	-2.576927000
6	20.849377000	2.944196000	-1.370560000
7	21.293423000	4.669306000	-2.688606000
6	22.199095000	2.858183000	-1.781928000
1	20.340550000	2.238099000	-0.753464000
6	22.441953000	3.937890000	-2.590972000
7	23.077594000	1.832662000	-1.406378000
1	23.337395000	4.215474000	-3.084007000
6	24.367980000	1.738362000	-1.818469000
1	22.724072000	1.158544000	-0.765573000
6	25.091657000	0.554962000	-1.350838000
8	24.883661000	2.593157000	-2.531560000
6	24.625687000	-0.567410000	-0.712425000
7	26.438420000	0.404906000	-1.536533000
6	25.729281000	-1.424921000	-0.501044000
1	23.614583000	-0.778071000	-0.444891000
6	26.831633000	-0.795433000	-1.018840000
7	25.650029000	-2.676981000	0.123480000
1	27.837940000	-1.124772000	-1.045670000
6	26.709954000	-3.498873000	0.332346000
1	24.745339000	-2.967595000	0.418260000
6	26.404639000	-4.762050000	1.006152000
8	27.844078000	-3.192870000	-0.023882000
6	25.215445000	-5.251803000	1.483375000
7	27.380340000	-5.699566000	1.267200000
6	25.468382000	-6.520516000	2.050215000
1	24.264230000	-4.771583000	1.442590000
6	26.806759000	-6.759836000	1.898120000
1	24.757321000	-7.168000000	2.508140000
1	27.389291000	-7.602195000	2.190811000
6	-17.166544000	-6.282191000	-1.322179000
6	-18.423607000	-5.621314000	-0.940284000
8	-16.870956000	-7.429099000	-0.994671000
6	-18.726403000	-4.283937000	-0.994699000
7	-19.504478000	-6.273662000	-0.411106000
6	-20.037638000	-4.121585000	-0.489278000
1	-18.080731000	-3.498682000	-1.317392000
6	-20.490648000	-5.366887000	-0.143620000
7	-20.694748000	-2.888554000	-0.377461000
1	-21.426673000	-5.649926000	0.264459000
6	-21.944818000	-2.727145000	0.126904000
1	-20.212722000	-2.095484000	-0.736345000
6	-22.415378000	-1.342525000	0.205350000
8	-22.627350000	-3.680662000	0.486599000
6	-21.725528000	-0.167401000	0.040185000
7	-23.711704000	-1.030667000	0.509304000
6	-22.637755000	0.892756000	0.246396000
1	-20.685619000	-0.061379000	-0.173444000
6	-23.853558000	0.326941000	0.530657000
7	-22.303390000	2.251805000	0.168693000
1	-24.778416000	0.799533000	0.738629000
6	-23.174806000	3.270142000	0.385885000
1	-21.369685000	2.463959000	-0.101917000
6	-22.600534000	4.614684000	0.310162000
8	-24.360738000	3.067570000	0.625613000
6	-21.287475000	5.008981000	0.241724000
7	-23.377591000	5.740014000	0.327839000
6	-21.269368000	6.422134000	0.213129000
1	-20.428762000	4.375817000	0.239544000
6	-22.573535000	6.841453000	0.265506000
7	-20.103466000	7.197183000	0.148277000
1	-22.958837000	7.828049000	0.261651000
6	-20.084643000	8.553973000	0.115852000
1	-19.242158000	6.699520000	0.132563000
6	-18.755619000	9.164454000	0.050312000
8	-21.118755000	9.214814000	0.139860000
6	-17.511744000	8.587444000	0.010633000
7	-18.586008000	10.531584000	0.016991000
6	-16.556564000	9.626282000	-0.048294000
1	-17.290712000	7.544320000	0.021612000
6	-17.254120000	10.803157000	-0.042401000
1	-15.497707000	9.518005000	-0.089004000
1	-16.902145000	11.807939000	-0.075648000
6	-19.640273000	11.557073000	0.041064000
1	-19.158641000	12.522868000	0.004910000
1	-20.296187000	11.439186000	-0.804846000
1	-20.226308000	11.469918000	0.940338000
6	-24.844585000	5.805057000	0.403972000
1	-25.128533000	6.844237000	0.338256000
1	-25.286261000	5.251612000	-0.408248000
1	-25.190078000	5.382629000	1.332300000
6	-24.810673000	-1.969576000	0.779550000
1	-25.708603000	-1.387993000	0.922088000
1	-24.938363000	-2.644781000	-0.050450000
1	-24.598514000	-2.549617000	1.661641000
6	-19.666191000	-7.720003000	-0.193863000
1	-18.700629000	-8.182049000	-0.266936000
1	-20.085491000	-7.880961000	0.789490000
1	-20.334751000	-8.131538000	-0.939252000
6	13.711496000	6.165625000	-1.310363000
1	13.893749000	7.164027000	-0.933479000
1	13.696981000	6.189558000	-2.391091000
1	12.778671000	5.792144000	-0.933995000
6	21.175212000	5.898919000	-3.486137000
1	20.845922000	6.716564000	-2.866332000
1	22.149792000	6.116972000	-3.895381000
1	20.460018000	5.762747000	-4.279581000
6	27.356584000	1.352608000	-2.185205000
1	27.314160000	2.310596000	-1.693767000
1	28.352839000	0.944359000	-2.110003000
1	27.086508000	1.487209000	-3.218929000
6	28.810321000	-5.607527000	0.935353000
1	29.253035000	-4.754637000	1.421396000
1	29.284698000	-6.515926000	1.275680000
1	28.941252000	-5.498668000	-0.128048000

1b Total energy = **-**4920.94771

7	0.555129000	-4.529145000	5.155804000
7	-0.661720000	-4.417838000	5.342912000
6	1.231429000	-4.227921000	3.913901000
6	0.797712000	-4.666729000	2.673298000
6	2.447398000	-3.576615000	4.023589000
6	1.571730000	-4.433051000	1.554788000
1	-0.129231000	-5.191254000	2.580460000
6	3.209433000	-3.315335000	2.902070000
1	2.787099000	-3.280761000	4.994799000
6	2.767372000	-3.749072000	1.667315000
1	1.250835000	-4.762671000	0.588837000
1	4.137238000	-2.790087000	2.956774000
6	-1.591947000	-3.835499000	4.401564000
6	-1.382307000	-2.623861000	3.763172000
6	-2.805272000	-4.484969000	4.257804000
6	-2.377348000	-2.084081000	2.973670000
1	-0.456372000	-2.103417000	3.885273000
6	-3.791214000	-3.961785000	3.444598000
1	-2.966070000	-5.400004000	4.789809000
6	-3.572816000	-2.756749000	2.805782000
1	-2.231241000	-1.150973000	2.471003000
1	-4.724396000	-4.458210000	3.294681000
8	-4.529538000	-2.185473000	1.969576000
8	3.491622000	-3.507607000	0.502559000
6	-5.716639000	-1.629150000	2.542836000

1	-5.536603000	-1.261639000	3.547707000
1	-6.001796000	-0.800848000	1.910604000
6	4.713138000	-4.219014000	0.277654000
1	4.696218000	-5.194443000	0.752362000
1	4.798047000	-4.348905000	-0.791400000
6	5.922277000	-3.449564000	0.793365000
8	5.855997000	-2.517965000	1.577778000
7	7.096026000	-3.927972000	0.329839000
1	7.112973000	-4.662507000	-0.343482000
6	-6.851977000	-2.643210000	2.594091000
8	-6.699463000	-3.846959000	2.478419000
7	-8.058034000	-2.081507000	2.827697000
1	-8.152815000	-1.090730000	2.875879000
6	8.372258000	-3.346381000	0.763668000
1	9.158398000	-4.068484000	0.600813000
1	8.305830000	-3.133991000	1.819548000
6	-9.262656000	-2.908896000	2.967244000
1	-10.004483000	-2.356783000	3.525092000
1	-8.997555000	-3.795633000	3.520988000
6	-9.845132000	-3.296570000	1.600503000
1	-10.113286000	-2.391446000	1.070747000
1	-9.082312000	-3.813740000	1.024365000
6	8.701876000	-2.059443000	-0.005427000
1	8.800665000	-2.295104000	-1.056725000
1	7.881190000	-1.357763000	0.111242000
7	9.968706000	-1.511834000	0.493960000
7	-11.046916000	-4.117467000	1.797129000
6	10.972485000	-1.103519000	-0.491644000
1	10.757145000	-1.567259000	-1.441866000
1	10.992296000	-0.023312000	-0.633749000
6	12.360517000	-1.598283000	-0.055525000
1	12.330227000	-2.675335000	-0.000217000
1	12.620807000	-1.206749000	0.917600000
6	-12.178243000	-3.876145000	0.890030000
1	-12.206144000	-4.587038000	0.069348000
1	-12.095228000	-2.879978000	0.474326000
6	-13.495635000	-3.970479000	1.674011000
1	-13.597103000	-4.953275000	2.105957000
1	-13.487568000	-3.238605000	2.468811000
6	-10.748325000	-5.545265000	1.982584000
1	-10.354397000	-5.999457000	1.073485000
1	-10.018445000	-5.673363000	2.770467000
1	-11.645376000	-6.077740000	2.267318000
6	9.814673000	-0.586989000	1.620069000
1	10.773564000	-0.407690000	2.090262000
1	9.398507000	0.372695000	1.310667000
1	9.156193000	-1.015827000	2.363837000
7	-14.657756000	-3.724360000	0.816321000
1	-15.018880000	-2.800320000	0.751735000
7	13.406726000	-1.192983000	-0.998755000
1	13.958500000	-0.392794000	-0.789534000
6	13.547130000	-1.821782000	-2.188094000
6	14.696427000	-1.388167000	-2.995427000
8	12.755847000	-2.695432000	-2.539003000
6	15.803727000	-0.693313000	-2.579352000
7	14.853770000	-1.670381000	-4.325702000
6	16.656739000	-0.540454000	-3.697597000
1	16.010797000	-0.368046000	-1.584943000
6	16.039670000	-1.148235000	-4.758585000
7	17.897388000	0.110631000	-3.660913000
1	16.365962000	-1.237049000	-5.762818000
6	18.736180000	0.230787000	-4.722208000
1	18.137347000	0.565042000	-2.808297000
6	20.023192000	0.866025000	-4.410174000
8	18.422105000	-0.170111000	-5.838874000
6	20.627035000	0.995845000	-3.184590000
7	20.865379000	1.392239000	-5.351441000
6	21.875112000	1.629544000	-3.389862000
1	20.253142000	0.637527000	-2.251950000
6	21.989310000	1.864088000	-4.734553000
7	22.787366000	1.925842000	-2.368085000
1	22.780266000	2.322717000	-5.269984000
6	23.967076000	2.573528000	-2.553763000
1	22.576800000	1.565753000	-1.464129000
6	24.710569000	2.849180000	-1.317914000
8	24.353673000	2.894987000	-3.673363000
6	24.232508000	2.879822000	-0.031652000
7	26.036967000	3.183610000	-1.280999000
6	25.308241000	3.237251000	0.814408000
1	23.224000000	2.716230000	0.275086000
6	26.405968000	3.413312000	0.014105000
7	25.205283000	3.379107000	2.204457000
1	27.394987000	3.681699000	0.283199000
6	26.242351000	3.686252000	3.026221000
1	24.292147000	3.304395000	2.593815000
6	25.905283000	3.692538000	4.454874000
8	27.361684000	3.928243000	2.583465000
6	24.829678000	3.118856000	5.083865000
7	26.704465000	4.260430000	5.423510000
6	24.967829000	3.349127000	6.471590000
1	24.049978000	2.558720000	4.619999000
6	26.126465000	4.055067000	6.639392000
1	24.305750000	3.025750000	7.240826000
1	26.581883000	4.424401000	7.529028000
6	-15.159230000	-4.708146000	0.033287000
6	-16.378851000	-4.359310000	-0.709603000
8	-14.613715000	-5.807519000	-0.025042000
6	-17.238370000	-3.315475000	-0.477611000
7	-16.875637000	-5.086612000	-1.757427000
6	-18.288621000	-3.409694000	-1.420875000
1	-17.158701000	-2.589762000	0.299940000
6	-18.033278000	-4.509365000	-2.196418000
7	-19.368061000	-2.518040000	-1.492512000
1	-18.591593000	-4.902576000	-3.006631000
6	-20.358130000	-2.580220000	-2.419982000
1	-19.438972000	-1.844887000	-0.762482000
6	-21.330315000	-1.481661000	-2.345608000
8	-20.411013000	-3.487697000	-3.244607000
6	-21.175292000	-0.253534000	-1.752540000
7	-22.564693000	-1.510787000	-2.934788000
6	-22.361252000	0.482821000	-1.981818000
1	-20.301892000	0.105625000	-1.256363000
6	-23.198939000	-0.322102000	-2.707450000
7	-22.575876000	1.793821000	-1.536353000
1	-24.176765000	-0.122959000	-3.063592000
6	-23.704775000	2.510360000	-1.774170000
1	-21.856139000	2.196199000	-0.979494000
6	-23.695886000	3.883056000	-1.265461000
8	-24.662008000	2.030383000	-2.372404000
6	-22.662898000	4.623858000	-0.747262000
7	-24.815182000	4.669035000	-1.272714000
6	-23.175778000	5.901224000	-0.425874000
1	-21.648821000	4.313588000	-0.630366000
6	-24.505383000	5.895622000	-0.759945000
7	-22.416988000	6.942697000	0.125237000
1	-25.221685000	6.669912000	-0.663831000
6	-22.906867000	8.171461000	0.429497000
1	-21.458198000	6.745258000	0.302833000
6	-21.935549000	9.117990000	0.980694000
8	-24.086920000	8.458462000	0.251344000
6	-20.587746000	8.984832000	1.198392000
7	-22.302334000	10.385481000	1.377877000
6	-20.117297000	10.199977000	1.743559000
1	-19.988933000	8.127160000	0.991232000
6	-21.198112000	11.033313000	1.838626000
1	-19.115645000	10.427414000	2.025559000
1	-21.261721000	12.033938000	2.198188000
6	13.909738000	-2.365323000	-5.214074000
1	13.405791000	-1.649322000	-5.850914000
1	14.459094000	-3.064517000	-5.828747000
1	13.196147000	-2.886862000	-4.605551000
6	20.626609000	1.522498000	-6.797211000
1	20.318723000	2.533409000	-7.032369000
1	21.544547000	1.297969000	-7.321481000
1	19.858655000	0.828134000	-7.079608000
6	26.982691000	3.233599000	-2.406837000
1	27.628051000	4.091011000	-2.279239000
1	27.583738000	2.333392000	-2.425784000
1	26.423374000	3.322218000	-3.318323000
6	27.939588000	5.034881000	5.222098000
1	27.716072000	6.094211000	5.205618000
1	28.616797000	4.825090000	6.037812000

1	28.377873000	4.742591000	4.287380000
6	-16.279429000	-6.273679000	-2.389799000
1	-15.830161000	-6.001334000	-3.336385000
1	-15.534962000	-6.670989000	-1.726887000
1	-17.056515000	-7.005300000	-2.561177000
6	-23.194190000	-2.634293000	-3.646001000
1	-23.719476000	-2.247893000	-4.507792000
1	-22.424995000	-3.315767000	-3.955032000
1	-23.897335000	-3.137728000	-2.994719000
6	-26.156803000	4.299569000	-1.747811000
1	-26.812019000	5.135462000	-1.555946000
1	-26.133001000	4.079432000	-2.801655000
1	-26.511795000	3.426974000	-1.224739000
6	-23.648599000	10.975897000	1.327294000
1	-23.582751000	11.976546000	1.727793000
1	-24.005791000	11.006233000	0.311908000
1	-24.336586000	10.389047000	1.912302000

2a Total energy = -4694.48582

6	21.322527000	8.614129000	-1.951844000
6	19.953248000	8.682041000	-1.905575000
6	19.542481000	9.714261000	-2.779475000
6	20.678893000	10.241225000	-3.326982000
7	21.762018000	9.585744000	-2.825092000
1	19.310819000	8.096368000	-1.288185000
1	18.542881000	10.030930000	-2.966968000
1	20.798020000	11.031039000	-4.032169000
6	22.223033000	7.739203000	-1.191534000
8	23.422950000	7.951995000	-1.041084000
7	21.621878000	6.650307000	-0.645666000
1	20.674659000	6.456996000	-0.882994000
6	22.261104000	5.724713000	0.189272000
6	21.619970000	4.612192000	0.782844000
6	23.566837000	5.702548000	0.602726000
6	22.555898000	3.950113000	1.537468000
1	20.584067000	4.370813000	0.701277000
7	23.739073000	4.628946000	1.430030000
1	24.356389000	6.367674000	0.364302000
6	22.363488000	2.761944000	2.378400000
8	23.119523000	2.434645000	3.288090000
7	21.258886000	2.031799000	2.074528000
1	20.747035000	2.259428000	1.251597000
6	20.823477000	0.912169000	2.795736000
6	19.654146000	0.175383000	2.493566000
6	21.391920000	0.328665000	3.896851000
6	19.549544000	-0.831345000	3.420379000
1	18.954729000	0.400853000	1.720278000
7	20.608765000	-0.723487000	4.279611000
1	22.278731000	0.593228000	4.412882000
6	18.481765000	-1.831228000	3.552817000
8	18.250299000	-2.455016000	4.584100000
7	17.746613000	-2.019106000	2.426539000
1	18.051910000	-1.592735000	1.580309000
6	16.623218000	-2.852797000	2.339770000
6	15.840304000	-3.015527000	1.172648000
6	16.061636000	-3.637150000	3.311700000
6	14.828078000	-3.892035000	1.471723000
1	15.989331000	-2.509745000	0.245510000
7	14.966028000	-4.259309000	2.783308000
1	16.367966000	-3.783248000	4.315524000
6	13.736998000	-4.346996000	0.596568000
8	12.712587000	-4.888721000	1.008608000
7	13.920723000	-4.123679000	-0.724033000
6	12.888825000	-4.498648000	-1.696420000
1	14.793471000	-3.784400000	-1.056963000
6	11.695985000	-3.531453000	-1.656692000
1	13.345835000	-4.504128000	-2.675446000
1	12.524686000	-5.490437000	-1.475498000
7	10.703039000	-3.927635000	-2.657773000
1	12.045599000	-2.510167000	-1.804194000
1	11.262193000	-3.603135000	-0.671036000
6	9.288331000	-3.899712000	-2.265146000
6	10.955250000	-3.398730000	-4.000925000
6	8.615758000	-5.205314000	-2.710804000
1	8.761098000	-3.060166000	-2.708475000
1	9.214029000	-3.817833000	-1.189108000
1	10.859533000	-2.312631000	-4.039983000
1	11.952746000	-3.665434000	-4.327561000
1	10.251177000	-3.824136000	-4.703592000
7	7.185706000	-5.215099000	-2.381774000
1	8.725194000	-5.327115000	-3.777469000
1	9.092224000	-6.036373000	-2.212155000
6	6.297998000	-4.573948000	-3.170815000
1	6.881170000	-5.767557000	-1.614275000
6	4.855635000	-4.614516000	-2.764234000
8	6.643222000	-3.992792000	-4.191376000
6	4.411484000	-4.988889000	-1.502728000
6	3.936796000	-4.220801000	-3.721607000
6	3.064637000	-4.990735000	-1.210689000
1	5.105162000	-5.255478000	-0.731558000
6	2.587778000	-4.228196000	-3.434031000
1	4.300103000	-3.912619000	-4.678829000
6	2.148656000	-4.615598000	-2.181598000
1	2.709081000	-5.271856000	-0.243307000
1	1.863261000	-3.934315000	-4.164364000
7	0.737626000	-4.590409000	-1.974418000
7	0.343140000	-4.938453000	-0.852026000
6	-1.067841000	-4.912866000	-0.644639000
6	-1.982650000	-4.519699000	-1.609501000
6	-1.507035000	-5.301971000	0.607233000
6	-3.330119000	-4.531065000	-1.320590000
1	-1.625001000	-4.206896000	-2.566329000
6	-2.855831000	-5.306085000	0.895935000
1	-0.782302000	-5.592733000	1.338601000
6	-3.776257000	-4.935249000	-0.069018000
1	-4.019318000	-4.198118000	-2.069658000
1	-3.217551000	-5.590610000	1.861046000
6	-5.218444000	-4.973055000	0.338741000
7	-6.144603000	-4.900357000	-0.640295000
8	-5.531607000	-5.083299000	1.516963000
6	-7.575186000	-4.917734000	-0.313646000
1	-5.878411000	-4.914009000	-1.597343000
6	-8.067301000	-3.536769000	0.140689000
1	-7.741391000	-5.640921000	0.469921000
1	-8.127791000	-5.218391000	-1.191455000
7	-9.490376000	-3.623569000	0.491799000
1	-7.462369000	-3.202906000	0.978549000
1	-7.938650000	-2.835113000	-0.672464000
6	-10.385884000	-2.589082000	-0.030888000
6	-9.734569000	-3.983000000	1.891232000
6	-11.684278000	-3.233518000	-0.540898000
1	-10.618588000	-1.830661000	0.716326000
1	-9.922899000	-2.102826000	-0.875740000
1	-9.510217000	-3.160755000	2.572323000
1	-10.770231000	-4.267807000	2.029517000
1	-9.118218000	-4.827708000	2.168806000
7	-12.626222000	-2.232565000	-1.050381000
1	-12.177983000	-3.782156000	0.248502000
1	-11.428905000	-3.919235000	-1.333916000
6	-12.427553000	-1.647205000	-2.252628000
1	-13.387942000	-1.955880000	-0.475191000
6	-13.463511000	-0.709432000	-2.695148000
8	-11.430562000	-1.894583000	-2.927046000
6	-14.690781000	-0.434588000	-2.147188000
7	-13.323221000	0.057184000	-3.819297000
6	-15.314796000	0.534334000	-2.966628000
1	-15.114175000	-0.880303000	-1.275382000
6	-14.445606000	0.816374000	-3.988106000
7	-16.589115000	1.069426000	-2.730174000
1	-14.560468000	1.490921000	-4.796694000
6	-17.179213000	2.017060000	-3.502020000
1	-17.095790000	0.683921000	-1.965507000
6	-18.494475000	2.470400000	-3.044733000
8	-16.641313000	2.456889000	-4.513200000
6	-19.150294000	2.223319000	-1.864442000
7	-19.284665000	3.291221000	-3.801340000
6	-20.382454000	2.914623000	-1.910502000
1	-18.793870000	1.641410000	-1.044318000
6	-20.435490000	3.560724000	-3.118359000
7	-21.332590000	2.909210000	-0.879999000
1	-21.202098000	4.174953000	-3.514560000

6	-22.505210000	3.592882000	-0.913832000
1	-21.133090000	2.329646000	-0.096205000
6	-23.326504000	3.491513000	0.293767000
8	-22.845627000	4.245885000	-1.895049000
6	-23.022911000	2.963459000	1.523961000
7	-24.602654000	3.980533000	0.349046000
6	-24.156058000	3.135083000	2.351290000
1	-22.096236000	2.526596000	1.821783000
6	-25.112717000	3.763187000	1.596461000
7	-24.228512000	2.723731000	3.689046000
1	-26.093171000	4.056343000	1.869616000
6	-25.313999000	2.892766000	4.486294000
1	-23.420968000	2.274799000	4.058038000
6	-25.170080000	2.403334000	5.858441000
8	-26.342309000	3.420915000	4.073554000
6	-24.094081000	1.836684000	6.493138000
7	-26.205764000	2.469791000	6.765015000
6	-24.480125000	1.547715000	7.820741000
1	-23.131651000	1.648604000	6.074281000
6	-25.781433000	1.950021000	7.948695000
1	-23.877072000	1.103997000	8.578362000
1	-26.432507000	1.904789000	8.790503000
6	-27.555606000	3.005426000	6.531671000
1	-28.039072000	2.466751000	5.734147000
1	-28.116066000	2.891679000	7.447637000
1	-27.503048000	4.045165000	6.256514000
6	-25.347529000	4.643220000	-0.731711000
1	-25.402056000	4.002299000	-1.596157000
1	-26.340830000	4.849870000	-0.363607000
1	-24.858049000	5.559166000	-1.016464000
6	-18.987213000	3.824782000	-5.138904000
1	-18.793280000	3.019627000	-5.828157000
1	-19.848575000	4.388109000	-5.463819000
1	-18.118523000	4.460169000	-5.103496000
6	-12.172453000	0.088385000	-4.733253000
1	-12.030388000	-0.876756000	-5.189045000
1	-12.376009000	0.832083000	-5.488598000
1	-11.274758000	0.345700000	-4.195887000
6	14.141487000	-5.212556000	3.542027000
1	13.922105000	-4.789690000	4.512473000
1	13.233404000	-5.381440000	2.995993000
1	14.678731000	-6.143528000	3.671122000
6	20.945171000	-1.609182000	5.405003000
1	21.297556000	-1.004416000	6.228385000
1	20.061465000	-2.146606000	5.691288000
1	21.723420000	-2.302243000	5.111638000
6	25.036619000	4.270996000	2.023447000
1	25.519088000	5.173275000	2.371297000
1	24.862855000	3.602983000	2.845168000
1	25.664286000	3.792981000	1.282054000
6	23.148700000	9.856866000	-3.236385000
1	23.266891000	10.922087000	-3.375634000
1	23.808406000	9.504906000	-2.466861000
1	23.367371000	9.347748000	-4.166694000

2b Total energy = -4694.45620

7	0.575533000	9.870401000	-0.225712000
7	-0.575663000	9.870505000	0.221470000
6	1.365071000	8.682491000	-0.455903000
6	1.545309000	7.697643000	0.499998000
6	2.057642000	8.623976000	-1.653222000
6	2.408494000	6.648919000	0.247675000
1	1.019769000	7.746601000	1.429918000
6	2.892571000	7.558602000	-1.911973000
1	1.934761000	9.415416000	-2.363248000
6	3.086416000	6.572022000	-0.958079000
1	2.517273000	5.883763000	0.989009000
1	3.414012000	7.476598000	-2.842155000
6	-1.365171000	8.682699000	0.452294000
6	-1.545422000	7.697369000	-0.503106000
6	-2.057710000	8.624776000	1.649661000
6	-2.408591000	6.648762000	-0.250237000
1	-1.019904000	7.745864000	-1.433064000
6	-2.892621000	7.559524000	1.908966000
1	-1.934817000	9.416570000	2.359291000
6	-3.086484000	6.572465000	0.955569000
1	-2.517379000	5.883233000	-0.991185000
1	-3.414038000	7.477980000	2.839203000
6	-4.018987000	5.460497000	1.324475000
8	-4.346987000	5.280726000	2.489971000
7	-4.485545000	4.685522000	0.321969000
1	-4.336343000	4.939682000	-0.627676000
6	-5.366613000	3.547189000	0.605501000
1	-5.004677000	3.054327000	1.494118000
1	-5.319510000	2.855191000	-0.222571000
6	-6.823254000	3.986550000	0.812996000
1	-6.859175000	4.725065000	1.608130000
1	-7.183611000	4.448009000	-0.096975000
7	-7.643302000	2.807795000	1.119183000
6	-8.910824000	2.653371000	0.401395000
6	-7.715452000	2.490377000	2.547836000
1	-9.765422000	2.955037000	1.006574000
1	-8.896691000	3.258348000	-0.492085000
6	-9.080056000	1.193867000	-0.048492000
1	-8.339317000	3.198087000	3.095726000
1	-8.121037000	1.496412000	2.690329000
1	-6.724395000	2.509300000	2.981434000
1	-9.055675000	0.524033000	0.799241000
1	-8.261866000	0.949804000	-0.708289000
7	-10.348975000	0.983970000	-0.751594000
1	-11.103839000	0.562746000	-0.261354000
6	4.018932000	5.459873000	-1.326407000
8	4.346972000	5.279529000	-2.491804000
7	4.485464000	4.685395000	-0.323508000
1	4.336165000	4.939972000	0.626008000
6	5.366506000	3.546896000	-0.606460000
1	5.004457000	3.053460000	-1.494716000
1	5.319525000	2.855420000	0.222054000
6	6.823118000	3.986127000	-0.814423000
1	6.858937000	4.724129000	-1.610033000
1	7.183588000	4.448160000	0.095210000
7	7.643117000	2.807163000	-1.119969000
6	8.910740000	2.653208000	-0.402251000
6	7.715109000	2.488887000	-2.548443000
1	9.765250000	2.954569000	-1.007707000
1	8.896687000	3.258696000	0.490885000
6	9.080094000	1.193970000	0.048449000
1	8.338879000	3.196294000	-3.096832000
1	8.120716000	1.494853000	-2.690387000
1	6.723999000	2.507510000	-2.981933000
1	9.055634000	0.523648000	-0.798896000
1	8.262002000	0.950250000	0.708494000
7	10.349109000	0.984534000	0.751513000
1	11.103951000	0.563122000	0.261399000
6	10.511677000	1.413123000	2.023359000
6	11.795524000	1.095129000	2.654847000
8	9.625945000	2.034163000	2.606327000
6	12.819679000	0.298546000	2.209137000
7	12.146976000	1.584831000	3.882795000
6	13.827847000	0.307993000	3.200611000
1	12.850269000	-0.248378000	1.293761000
6	13.382441000	1.110286000	4.218693000
7	15.037867000	-0.394280000	3.106549000
1	13.859583000	1.359838000	5.130887000
6	16.016502000	-0.366841000	4.046476000
1	15.147798000	-0.981781000	2.311011000
6	17.220672000	-1.134497000	3.721759000
8	15.892003000	0.258908000	5.094352000
6	17.597416000	-1.724250000	2.541066000
7	18.215417000	-1.349013000	4.635686000
6	18.861690000	-2.321461000	2.749365000
1	17.057733000	-1.715168000	1.620808000
6	19.212887000	-2.074697000	4.051243000
7	19.579070000	-3.018252000	1.767075000
1	20.086229000	-2.366080000	4.575043000
6	20.810078000	-3.561501000	1.952912000
1	19.114479000	-3.173164000	0.900356000
6	21.400488000	-4.154508000	0.746402000
8	21.362369000	-3.541461000	3.048915000
6	21.074599000	-3.906693000	-0.563722000
7	22.446326000	-5.036449000	0.759679000

6	21.947351000	-4.672373000	-1.371912000
1	20.337122000	-3.220712000	-0.915304000
6	22.776030000	-5.361018000	-0.526042000
7	21.927663000	-4.674061000	-2.772660000
1	23.555917000	-6.039521000	-0.758279000
6	22.762218000	-5.409123000	-3.551382000
1	21.251589000	-4.086676000	-3.205935000
6	22.576181000	-5.254359000	-4.995128000
8	23.611173000	-6.151049000	-3.066443000
6	21.699574000	-4.469985000	-5.700888000
7	23.342864000	-5.950605000	-5.904254000
6	21.934476000	-4.691190000	-7.075966000
1	20.969156000	-3.805955000	-5.297604000
6	22.949058000	-5.605101000	-7.159945000
1	21.423326000	-4.235706000	-7.891936000
1	23.416887000	-6.032033000	-8.016361000
6	-10.511416000	1.411851000	-2.023692000
6	-11.795147000	1.093390000	-2.655186000
8	-9.625662000	2.032652000	-2.606881000
6	-12.819298000	0.296967000	-2.209183000
7	-12.146469000	1.582385000	-3.883453000
6	-13.827330000	0.305787000	-3.200802000
1	-12.849971000	-0.249458000	-1.293511000
6	-13.381848000	1.107554000	-4.219263000
7	-15.037309000	-0.396527000	-3.106525000
1	-13.858882000	1.356560000	-5.131663000
6	-16.015817000	-0.369669000	-4.046602000
1	-15.147289000	-0.983647000	-2.310712000
6	-17.219992000	-1.137193000	-3.721596000
8	-15.891213000	0.255484000	-5.094819000
6	-17.596967000	-1.726068000	-2.540540000
7	-18.214503000	-1.352481000	-4.635592000
6	-18.861160000	-2.323511000	-2.748672000
1	-17.057504000	-1.716217000	-1.620160000
6	-19.212070000	-2.077770000	-4.050821000
7	-19.578728000	-3.019585000	-1.766013000
1	-20.085273000	-2.369607000	-4.574601000
6	-20.809675000	-3.563022000	-1.951707000
1	-19.114325000	-3.173819000	-0.899073000
6	-21.400336000	-4.155117000	-0.744871000
8	-21.361723000	-3.543840000	-3.047848000
6	-21.074756000	-3.906267000	0.565133000
7	-22.446143000	-5.037101000	-0.757698000
6	-21.947652000	-4.671363000	1.373722000
1	-20.337390000	-3.219978000	0.916348000
6	-22.776119000	-5.360690000	0.528201000
7	-21.928273000	-4.671969000	2.774475000
1	-23.556031000	-6.039045000	0.760789000
6	-22.763033000	-5.406390000	3.553583000
1	-21.252181000	-4.084380000	3.207445000
6	-22.577432000	-5.250370000	4.997248000
8	-23.611815000	-6.148768000	3.069032000
6	-21.701454000	-4.464919000	5.702592000
7	-23.343986000	-5.946272000	5.906745000
6	-21.936608000	-4.685109000	7.077791000
1	-20.971344000	-3.800766000	5.298952000
6	-22.950708000	-5.599511000	7.162255000
1	-21.425940000	-4.228654000	7.893519000
1	-23.418531000	-6.025991000	8.018899000
6	-11.353419000	2.472338000	-4.743580000
1	-11.116004000	3.384003000	-4.220795000
1	-10.431549000	1.994048000	-5.027859000
1	-11.945486000	2.692618000	-5.618782000
6	-18.249895000	-0.896898000	-6.033327000
1	-18.252673000	0.179081000	-6.075941000
1	-17.385540000	-1.257437000	-6.566141000
1	-19.149274000	-1.290521000	-6.481671000
6	-23.103171000	-5.633598000	-1.930823000
1	-24.167603000	-5.674069000	-1.748438000
1	-22.896616000	-5.019329000	-2.786201000
1	-22.730197000	-6.636673000	-2.094644000
6	-24.416210000	-6.908627000	5.610601000
1	-24.802818000	-7.268381000	6.552493000
1	-25.200508000	-6.432878000	5.046508000
1	-24.031460000	-7.730790000	5.031104000
6	11.353967000	2.475184000	4.742546000
1	11.116538000	3.386614000	4.219353000
1	10.432105000	1.997032000	5.027075000
1	11.946069000	2.695858000	5.617624000
6	18.251110000	-0.892373000	6.033070000
1	18.253649000	0.183636000	6.074877000
1	17.386995000	-1.252716000	6.566407000
1	19.150713000	-1.285451000	6.481442000
6	23.103644000	-5.632002000	1.933123000
1	24.168047000	-5.672488000	1.750570000
1	22.897179000	-5.017117000	2.788079000
1	22.730813000	-6.634997000	2.097757000
6	24.415686000	-6.912137000	-5.607603000
1	24.802339000	-7.272344000	-6.549303000
1	25.199814000	-6.435535000	-5.043993000
1	24.031505000	-7.734098000	-5.027443000

3a Total energy = -4203.84108

7	-10.225101000	-3.055392000	1.458915000
6	-8.806857000	-3.193393000	1.128316000
6	-7.964093000	-3.424900000	2.392545000
1	-8.477648000	-2.284952000	0.649316000
1	-8.676244000	-4.029533000	0.457114000
7	-6.543182000	-3.552932000	2.057622000
1	-8.100496000	-2.593563000	3.069432000
1	-8.289664000	-4.338803000	2.862369000
6	-5.820293000	-2.465426000	1.716442000
1	-6.111445000	-4.439959000	2.175164000
6	-4.370957000	-2.667297000	1.395357000
8	-6.320009000	-1.347521000	1.680579000
6	-3.793568000	-3.904654000	1.141081000
6	-3.592337000	-1.524719000	1.329664000
6	-2.450727000	-3.998803000	0.846003000
1	-4.382525000	-4.799106000	1.144304000
6	-2.246718000	-1.617088000	1.041110000
1	-4.059863000	-0.579407000	1.505779000
6	-1.672755000	-2.851923000	0.802179000
1	-1.994264000	-4.943204000	0.643592000
1	-1.628508000	-0.745212000	0.993434000
7	-0.276381000	-2.850366000	0.510508000
7	0.238409000	-3.957532000	0.296917000
6	1.634425000	-3.957652000	0.004511000
6	2.409144000	-2.809563000	-0.060007000
6	2.207108000	-5.193692000	-0.232369000
6	3.754084000	-2.906920000	-0.344391000
1	1.945739000	-1.861347000	0.105709000
6	3.552041000	-5.287783000	-0.524482000
1	1.586866000	-6.064327000	-0.188460000
6	4.336361000	-4.148276000	-0.564462000
1	4.333625000	-2.009787000	-0.424187000
1	4.012375000	-6.231529000	-0.727101000
6	5.786503000	-4.344238000	-0.890368000
7	6.619865000	-3.321300000	-0.573846000
8	6.177982000	-5.385214000	-1.391570000
6	8.048673000	-3.362950000	-0.886493000
1	6.290906000	-2.578479000	0.001039000
6	8.428452000	-2.199214000	-1.817273000
1	8.246920000	-4.294838000	-1.388627000
1	8.634897000	-3.312929000	0.023751000
7	9.870311000	-2.155893000	-2.054596000
1	7.917443000	-2.326787000	-2.759397000
1	8.132373000	-1.253305000	-1.381178000
1	-10.623799000	-2.144975000	1.468223000
1	10.426602000	-1.530146000	-1.519295000
6	-10.963162000	-4.138617000	1.792590000
6	-12.389015000	-3.903937000	2.028897000
8	-10.449958000	-5.251258000	1.889948000
6	-13.136178000	-2.771092000	1.828190000
7	-13.222962000	-4.880440000	2.501353000
6	-14.467883000	-3.069845000	2.196724000
1	-12.789509000	-1.838035000	1.444653000
6	-14.487082000	-4.377041000	2.609254000
7	-15.531530000	-2.159006000	2.126244000
1	-15.301824000	-4.955474000	2.961024000
6	-16.819277000	-2.452953000	2.440675000
1	-15.299259000	-1.219653000	1.892089000

6	-17.769516000	-1.361578000	2.189592000
8	-17.137350000	-3.549201000	2.892156000
6	-17.615139000	-0.281787000	1.356691000
7	-19.023759000	-1.297836000	2.732444000
6	-18.813857000	0.467922000	1.405236000
1	-16.770408000	-0.072126000	0.739878000
6	-19.658206000	-0.181010000	2.266708000
7	-19.041376000	1.640424000	0.672573000
1	-20.641269000	0.078975000	2.564553000
6	-20.202406000	2.345908000	0.689071000
1	-18.269927000	2.001823000	0.157549000
6	-20.236162000	3.480993000	-0.241661000
8	-21.131816000	2.035775000	1.428054000
6	-19.453672000	3.688626000	-1.350635000
7	-21.133649000	4.510255000	-0.161840000
6	-19.886770000	4.889952000	-1.957860000
1	-18.694637000	3.037545000	-1.722175000
6	-20.918830000	5.373996000	-1.198469000
7	-19.339417000	5.435846000	-3.127183000
1	-21.494409000	6.253494000	-1.334375000
6	-19.751091000	6.600735000	-3.703772000
1	-18.607659000	4.916063000	-3.561930000
8	-20.639360000	7.284806000	-3.231609000
6	10.444468000	-3.004593000	-2.943389000
6	11.884398000	-2.843907000	-3.153112000
8	9.778785000	-3.851634000	-3.528568000
6	12.735941000	-1.868255000	-2.699383000
7	12.612132000	-3.718873000	-3.911771000
6	14.024659000	-2.163650000	-3.199839000
1	12.478747000	-1.026075000	-2.097148000
6	13.913677000	-3.310460000	-3.943151000
7	15.167514000	-1.389945000	-2.950844000
1	14.662919000	-3.838276000	-4.474276000
6	16.412785000	-1.688399000	-3.402815000
1	15.027563000	-0.529046000	-2.470888000
6	17.463914000	-0.776275000	-2.933247000
8	16.617306000	-2.649305000	-4.138481000
6	17.436080000	0.055490000	-1.841722000
7	18.697810000	-0.667052000	-3.513545000
6	18.693906000	0.698467000	-1.764448000
1	16.635932000	0.159064000	-1.143798000
6	19.445438000	0.236433000	-2.812278000
7	19.052075000	1.617102000	-0.768876000
1	20.436237000	0.490196000	-3.088985000
6	20.265117000	2.221988000	-0.682967000
1	18.345112000	1.855962000	-0.110742000
6	20.447181000	3.101803000	0.472890000
8	21.140248000	2.039405000	-1.522664000
6	19.660511000	3.268000000	1.586026000
7	21.538165000	3.915881000	0.603040000
6	20.296084000	4.218342000	2.416373000
1	18.750404000	2.757202000	1.807665000
6	21.449529000	4.599438000	1.781189000
7	19.804346000	4.655230000	3.654909000
1	22.185464000	5.294725000	2.093545000
6	20.414661000	5.582589000	4.445981000
1	18.953790000	4.239860000	3.968850000
8	21.454779000	6.128397000	4.129122000
6	19.635731000	5.855771000	5.728838000
1	19.519484000	4.905052000	6.237451000
1	18.635839000	6.200927000	5.447517000
7	20.322677000	6.772917000	6.617769000
6	19.869259000	6.687351000	8.007661000
1	19.947240000	5.664665000	8.355874000
1	20.510636000	7.303621000	8.623837000
1	18.838633000	7.023254000	8.142789000
6	20.401238000	8.151056000	6.117761000
1	19.417429000	8.622323000	6.048526000
1	21.012457000	8.734580000	6.794040000
1	20.871873000	8.146920000	5.149483000
6	-18.961287000	6.935841000	-4.965050000
1	-19.068748000	6.093263000	-5.639267000
1	-17.903694000	7.003042000	-4.691200000
7	-19.450403000	8.126298000	-5.633588000
6	-19.212857000	9.372444000	-4.894651000
1	-18.148242000	9.603417000	-4.805126000
1	-19.696137000	10.187374000	-5.417911000
1	-19.650800000	9.288433000	-3.914721000
6	-19.058588000	8.206188000	-7.042447000
1	-19.366956000	7.305915000	-7.559759000
1	-19.562983000	9.047581000	-7.499068000
1	-17.982736000	8.335521000	-7.180482000
6	-12.862834000	-6.263096000	2.846977000
1	-12.094034000	-6.271985000	3.601815000
1	-13.751776000	-6.748144000	3.220455000
1	-12.492581000	-6.781300000	1.978758000
6	-19.621870000	-2.210125000	3.719445000
1	-19.565963000	-1.774247000	4.708857000
1	-20.658081000	-2.371486000	3.458509000
1	-19.084202000	-3.138561000	3.694666000
6	-22.142017000	4.743673000	0.883669000
1	-21.781518000	5.482677000	1.587908000
1	-23.046577000	5.106837000	0.417133000
1	-22.331346000	3.815540000	1.388021000
6	12.114435000	-4.916583000	-4.606086000
1	11.388857000	-4.641438000	-5.352603000
1	12.961224000	-5.400651000	-5.068144000
1	11.643715000	-5.586177000	-3.905651000
6	19.176278000	-1.329737000	-4.736782000
1	19.120127000	-0.646557000	-5.574718000
1	20.203968000	-1.629340000	-4.588741000
1	18.561890000	-2.190152000	-4.920852000
6	22.654763000	4.063152000	-0.342703000
1	23.310702000	4.827869000	0.044163000
1	23.186149000	3.131808000	-0.441548000
1	22.286929000	4.351283000	-1.313654000

3b Total enegy = -4203.81647

7	7.342272000	1.106449000	2.231771000
6	6.451875000	2.257195000	2.081872000
6	5.015044000	1.809870000	1.764925000
7	4.120813000	2.960931000	1.615715000
6	4.161590000	3.723899000	0.502268000
8	4.986496000	3.531223000	-0.382454000
6	3.167016000	4.836425000	0.392671000
6	2.018730000	4.928605000	1.162406000
6	1.137998000	5.977543000	0.982424000
6	1.411066000	6.946888000	0.032651000
6	2.568588000	6.873196000	-0.723223000
6	3.427256000	5.807673000	-0.561263000
7	0.606664000	8.135104000	-0.135188000
7	-0.622292000	8.137673000	-0.255987000
6	-1.434982000	6.950827000	-0.390254000
6	-1.168611000	5.952865000	-1.311873000
6	-2.056696000	4.905449000	-1.462159000
6	-3.205732000	4.843369000	-0.690528000
6	-3.459277000	5.843281000	0.235175000
6	-2.593136000	6.906905000	0.366971000
6	-4.208136000	3.735210000	-0.768652000
8	-5.034648000	3.573869000	0.120848000
7	-4.172459000	2.940306000	-1.859682000
6	-5.074810000	1.791812000	-1.976217000
6	-6.508302000	2.240035000	-2.306707000
7	-7.406922000	1.091841000	-2.423367000
1	-6.866031000	2.877499000	-1.513978000
1	-6.505322000	2.783327000	-3.240428000
1	-5.076609000	1.250774000	-1.041304000
1	-4.718696000	1.153336000	-2.768492000
1	-3.605582000	3.172581000	-2.642804000
1	-1.822541000	4.130789000	-2.163502000
1	-4.344585000	5.773146000	0.831086000
1	-0.280542000	5.991114000	-1.906162000
1	-2.800550000	7.708202000	1.045542000
1	0.250420000	6.039014000	1.575503000
1	2.781392000	7.653287000	-1.424457000
1	1.779391000	4.175924000	1.885594000
1	4.311805000	5.714285000	-1.155112000
1	3.556112000	3.219743000	2.392060000
1	5.012470000	1.242151000	0.845971000
1	4.654830000	1.197023000	2.575377000
1	6.813830000	2.868705000	1.270829000

1	6.453201000	2.827452000	2.999378000
1	7.923454000	0.850648000	1.466665000
1	-7.990243000	0.862781000	-1.651459000
6	-7.377410000	0.301236000	-3.521573000
6	-8.403356000	-0.747934000	-3.570573000
8	-6.536902000	0.481524000	-4.401617000
6	-9.551040000	-0.839355000	-2.824117000
7	-8.382190000	-1.807129000	-4.438282000
6	-10.243831000	-1.997626000	-3.246278000
1	-9.887243000	-0.142481000	-2.090085000
6	-9.494337000	-2.573841000	-4.237792000
7	-11.471860000	-2.419129000	-2.718871000
1	-9.683742000	-3.455505000	-4.794263000
6	-12.161241000	-3.508320000	-3.147226000
1	-11.817603000	-1.912828000	-1.934526000
6	-13.471763000	-3.686786000	-2.509175000
8	-11.705035000	-4.262697000	-4.001135000
6	-14.230531000	-2.745956000	-1.858653000
7	-14.177618000	-4.858681000	-2.524071000
6	-15.434190000	-3.372116000	-1.458421000
1	-13.986297000	-1.716169000	-1.724711000
6	-15.367930000	-4.674038000	-1.879217000
7	-16.470455000	-2.725516000	-0.771845000
1	-16.076817000	-5.452655000	-1.761583000
6	-17.615338000	-3.331273000	-0.363433000
1	-16.358753000	-1.748535000	-0.620334000
6	-18.550028000	-2.478990000	0.373417000
8	-17.841799000	-4.513039000	-0.601836000
6	-18.390558000	-1.201052000	0.850173000
7	-19.801102000	-2.905748000	0.724635000
6	-19.587400000	-0.841404000	1.509083000
1	-17.520011000	-0.590128000	0.765318000
6	-20.436786000	-1.913067000	1.412521000
7	-19.817422000	0.392717000	2.133991000
1	-21.424010000	-2.018045000	1.782570000
6	-20.968924000	0.729310000	2.781296000
1	-19.077949000	1.060333000	2.088957000
8	-21.911955000	-0.033617000	2.875636000
6	7.307498000	0.348449000	3.352564000
6	8.325869000	-0.706231000	3.431968000
8	6.468691000	0.560384000	4.227171000
6	9.472868000	-0.827369000	2.688700000
7	8.297111000	-1.739743000	4.329905000
6	10.157357000	-1.977886000	3.144313000
1	9.813996000	-0.154438000	1.934867000
6	9.403742000	-2.519867000	4.151874000
7	11.382400000	-2.423203000	2.629701000
1	9.586796000	-3.386475000	4.733556000
6	12.063708000	-3.504740000	3.089261000
1	11.732039000	-1.942173000	1.831279000
6	13.373068000	-3.710527000	2.457140000
8	11.601859000	-4.231277000	3.964014000
6	14.140020000	-2.792763000	1.783670000
7	14.069839000	-4.886965000	2.503916000
6	15.338622000	-3.438934000	1.400414000
1	13.905190000	-1.764292000	1.625083000
6	15.261163000	-4.729257000	1.853698000
7	16.381787000	-2.818126000	0.700886000
1	15.962766000	-5.517032000	1.754606000
6	17.541853000	-3.430858000	0.349440000
1	16.229292000	-1.875018000	0.422894000
6	18.521665000	-2.579500000	-0.327357000
8	17.743666000	-4.617561000	0.585071000
6	18.531469000	-1.218100000	-0.506532000
7	19.660470000	-3.086240000	-0.890032000
6	19.715304000	-0.890677000	-1.204834000
1	17.799624000	-0.522371000	-0.162037000
6	20.388021000	-2.064140000	-1.427632000
7	20.093110000	0.408127000	-1.574756000
1	21.312297000	-2.220572000	-1.921424000
6	21.230591000	0.717446000	-2.259349000
1	19.480384000	1.145926000	-1.301243000
8	22.024542000	-0.129598000	-2.623254000
6	-20.913729000	2.133822000	3.373960000
1	-20.690202000	2.813435000	2.558984000
1	-20.071056000	2.170812000	4.071454000
7	-22.168569000	2.537140000	3.979278000
6	-22.308473000	3.988349000	4.118288000
1	-22.161741000	4.464125000	3.156335000
1	-23.311577000	4.212647000	4.456402000
1	-21.602111000	4.419770000	4.831129000
6	-22.509492000	1.802779000	5.204145000
1	-21.808127000	2.007129000	6.017168000
1	-23.499961000	2.098277000	5.525276000
1	-22.520529000	0.747891000	4.989412000
6	21.362111000	2.214259000	-2.522474000
1	21.322827000	2.710072000	-1.558799000
1	20.483089000	2.533757000	-3.091012000
7	22.612680000	2.562478000	-3.169221000
6	22.980965000	3.970499000	-3.005913000
1	22.994638000	4.225601000	-1.953320000
1	23.976460000	4.120378000	-3.402619000
1	22.300713000	4.652949000	-3.520452000
6	22.725332000	2.091363000	-4.555180000
1	23.721487000	2.308043000	-4.918766000
1	22.578422000	1.025042000	-4.576520000
1	22.003569000	2.577199000	-5.216808000
6	7.246451000	-2.048885000	5.311938000
1	6.627365000	-1.180253000	5.428429000
1	6.653642000	-2.886638000	4.967165000
1	7.712586000	-2.305181000	6.252944000
6	13.631395000	-6.167698000	3.079682000
1	12.838597000	-5.974320000	3.776643000
1	13.283919000	-6.827439000	2.294781000
1	14.469794000	-6.625211000	3.585295000
6	20.080331000	-4.495048000	-0.931568000
1	20.236794000	-4.868087000	0.066398000
1	19.323326000	-5.097086000	-1.406453000
1	20.998444000	-4.544786000	-1.496656000
6	-7.334081000	-2.151957000	-5.411127000
1	-6.708573000	-1.291637000	-5.552351000
1	-6.747452000	-2.983927000	-5.042603000
1	-7.802322000	-2.431498000	-6.344437000
6	-13.749710000	-6.157714000	-3.065780000
1	-12.956505000	-5.989225000	-3.768693000
1	-13.406008000	-6.798613000	-2.263803000
1	-14.592313000	-6.622404000	-3.557689000
6	-20.409944000	-4.212253000	0.432359000
1	-20.418628000	-4.391401000	-0.629992000
1	-19.850165000	-5.000404000	0.906825000
1	-21.420390000	-4.192409000	0.810955000

The total energies in hartree and the cartesian coordinates of the structures **17a**, **17b**, **18a** and **18b** at MP2/6-31+G* level of theory using Gaussian 03 program package are given.

17a Total energy =-1135.7685572

7	-0.331948000	-0.263647000	0.002009000
7	0.366534000	0.761918000	0.003368000
6	1.775518000	0.568800000	0.009905000
6	2.391920000	-0.668289000	0.015543000
6	2.557234000	1.715634000	0.010490000
6	3.770067000	-0.764448000	0.021819000
1	1.784303000	-1.547560000	0.015164000
6	3.928436000	1.629406000	0.016282000
1	2.067433000	2.667094000	0.005820000
6	4.542595000	0.384818000	0.021937000
1	4.224867000	-1.732391000	0.026991000
1	4.549926000	2.499054000	0.015877000
6	-1.740092000	-0.067710000	-0.004589000
6	-2.356277000	1.181650000	-0.008133000
6	-2.520465000	-1.202880000	-0.007627000
6	-3.723141000	1.277670000	-0.014440000
1	-1.744517000	2.057682000	-0.005541000
6	-3.903003000	-1.115140000	-0.014312000
1	-2.035735000	-2.157158000	-0.005100000
6	-4.506679000	0.126540000	-0.017616000
1	-4.222176000	2.223219000	-0.016559000
1	-4.484171000	-2.012597000	-0.017501000
8	5.911886000	0.393803000	0.028714000
8	-5.860052000	0.329893000	-0.025008000
6	6.665689000	-0.809781000	0.013534000
1	6.440898000	-1.406716000	-0.863657000
1	6.474867000	-1.406478000	0.898651000
6	-6.776158000	-0.755906000	-0.011357000
1	-6.664987000	-1.376772000	-0.893422000
1	-6.642226000	-1.374783000	0.869109000
6	8.138790000	-0.421181000	-0.022509000
8	8.547482000	0.715007000	-0.114128000
7	8.957852000	-1.501861000	0.042105000
1	8.580587000	-2.417956000	0.147011000
6	-8.180416000	-0.164410000	0.012070000
8	-8.425311000	1.020126000	0.081696000
7	-9.142324000	-1.119288000	-0.039154000
1	-8.899038000	-2.081338000	-0.128836000
1	9.948360000	-1.377333000	-0.016096000
1	-10.105350000	-0.855095000	0.013617000

17b Total energy =-1135.7509744

7	-0.619056000	2.839130000	-0.010497000
7	0.617111000	2.840510000	-0.007611000
6	-1.444157000	1.653808000	-0.078777000
6	-1.241247000	0.623804000	-0.983032000
6	-2.567752000	1.645041000	0.728855000
6	-2.150097000	-0.412209000	-1.056794000
1	-0.388574000	0.632313000	-1.627894000
6	-3.462815000	0.594784000	0.677930000
1	-2.730972000	2.468985000	1.392670000
6	-3.250365000	-0.432585000	-0.220705000
1	-2.007593000	-1.216828000	-1.747421000
1	-4.321973000	0.550893000	1.310085000
6	1.443891000	1.656942000	0.070999000
6	1.248972000	0.643016000	0.994861000
6	2.559950000	1.633858000	-0.746628000
6	2.158525000	-0.391596000	1.078961000
1	0.401308000	0.662923000	1.646163000
6	3.455533000	0.584456000	-0.685027000
1	2.717051000	2.445375000	-1.427020000
6	3.251343000	-0.426488000	0.233773000
1	2.021874000	-1.184267000	1.784448000
1	4.308297000	0.529231000	-1.324938000
8	4.118958000	-1.511737000	0.335727000
8	-4.116430000	-1.519498000	-0.310427000
6	5.422852000	-1.314804000	0.891072000
1	5.428231000	-0.503313000	1.611279000
1	5.682290000	-2.234622000	1.394800000
6	-5.415829000	-1.333907000	-0.881304000
1	-5.414319000	-0.537604000	-1.618186000
1	-5.670745000	-2.263938000	-1.368148000
6	-6.461565000	-1.012113000	0.178372000
8	-6.196765000	-0.638632000	1.308844000
7	-7.729025000	-1.137902000	-0.267878000
1	-7.911233000	-1.486792000	-1.183446000
6	6.459074000	-1.014990000	-0.184239000
8	6.185300000	-0.661406000	-1.318116000
7	7.731332000	-1.135668000	0.253313000
1	7.919355000	-1.466819000	1.174145000
1	8.489628000	-0.891026000	-0.350951000
1	-8.491538000	-0.878915000	0.324996000

18a Total energy =-907.4258678

7	0.359779000	0.502690000	-0.006122000
7	-0.361942000	-0.528346000	0.004212000
6	1.756818000	0.258130000	-0.015612000
6	2.566120000	1.402882000	-0.020634000
6	2.350698000	-1.018298000	-0.027705000
6	3.954710000	1.281687000	-0.023383000
1	2.088129000	2.378086000	-0.029886000
6	3.734090000	-1.132047000	-0.039163000
1	1.717576000	-1.898544000	-0.030734000
6	4.551855000	0.012606000	-0.024729000
1	4.564230000	2.180210000	-0.061485000
1	4.211615000	-2.106570000	-0.061930000
6	-1.759239000	-0.286423000	0.014269000
6	-2.352206000	0.989129000	0.027514000
6	-2.569592000	-1.431738000	0.018475000
6	-3.737355000	1.102513000	0.032320000
1	-1.719354000	1.869482000	0.043251000
6	-3.956457000	-1.311216000	0.031035000
1	-2.091064000	-2.406707000	0.014007000
6	-4.554738000	-0.043951000	0.026350000
1	-4.183046000	2.092735000	0.077545000
1	-4.594404000	-2.188906000	0.046730000
6	6.040625000	-0.194410000	-0.039146000
8	6.544693000	-1.236443000	-0.446839000
7	6.811840000	0.855158000	0.400022000
1	7.803049000	0.669195000	0.488787000
1	6.428493000	1.567623000	1.005112000
6	-6.056596000	0.019582000	0.039448000
8	-6.740686000	-0.919414000	0.434953000
7	-6.626136000	1.195365000	-0.387704000
1	-7.634389000	1.190787000	-0.479227000
1	-6.120087000	1.834727000	-0.984178000

18b Total energy =-907.4062382

7	-0.621849000	2.829577000	-0.053297000
7	0.621860000	2.829572000	0.053316000
6	-1.431133000	1.646591000	-0.016029000
6	-1.334765000	0.689389000	1.007071000
6	-2.477002000	1.570742000	-0.945931000
6	-2.258593000	-0.348872000	1.069579000
1	-0.550367000	0.765225000	1.753206000
6	-3.380449000	0.511943000	-0.892892000
1	-2.562399000	2.338503000	-1.709816000
6	-3.288240000	-0.453971000	0.122034000
1	-2.194452000	-1.100200000	1.850237000
1	-4.147720000	0.440017000	-1.658828000
6	1.431137000	1.646581000	0.016046000
6	1.334775000	0.689389000	-1.007066000
6	2.476995000	1.570715000	0.945957000
6	2.258599000	-0.348874000	-1.069576000
1	0.550387000	0.765239000	-1.753210000
6	3.380433000	0.511910000	0.892920000
1	2.562388000	2.338469000	1.709851000
6	3.288234000	-0.453993000	-0.122021000

1	2.194467000	-1.100190000	-1.850247000
1	4.147688000	0.439972000	1.658869000
6	4.238352000	-1.610716000	-0.252119000
8	3.948316000	-2.615778000	-0.893895000
7	5.438629000	-1.502497000	0.409727000
1	6.110344000	-2.237225000	0.225560000
1	5.815741000	-0.600257000	0.663399000
6	-4.238360000	-1.610690000	0.252114000
8	-3.948525000	-2.615562000	0.894277000
7	-5.438444000	-1.502639000	-0.410109000
1	-6.110212000	-2.237322000	-0.225954000
1	-5.815482000	-0.600460000	-0.664114000

Quantum Dot−Carrier Peptide Conjugates Suitable for Imaging and Delivery Applications

Cornelia Walther, Karolin Meyer, Robert Rennert, and Ines Neundorf*

Institute of Biochemistry, Faculty of Biosciences, Pharmacy and Psychology, University of Leipzig, Brüderstr. 34, 04103 Leipzig.
Received April 25, 2008; Revised Manuscript Received September 5, 2008

We developed multifunctional fluorescent nanoparticles suitable for the nonviral delivery of negatively charged molecules like RNA. Therefore, we incorporated the recently developed branched hCT-derived carrier peptide hCT(18−32)-k7 on the surface of luminescent quantum dots (QDs). Besides detailed characterization of our QD−peptide conjugates concerning stability, toxicity, and uptake mechanism. we used them for efficient RNA delivery into different cell lines. The results of our studies indicate the involvement of more than one endocytotic uptake pathway in the internalization process. Furthermore, we could show that the QD−peptide bioconjugates exhibit no effect on cell viability and possess high stability inside living cells. The efficacy of our newly designed constructs for oligonucleotide drug delivery is highlighted by the successful intracellular transport of Cy-3 labeled RNA. Moreover, by using the chemotherapeutic chloroquine the efficient release of the assemblies out of endosomes was demonstrated. These results prove that our multifunctional platforms are versatile tools for diagnostic and therapeutic imaging purposes applicable for biologically active siRNA or aptamer sequences.

INTRODUCTION

During the past decades, a large amount of potential drug candidates and future drug targets have been developed. Our main focus should now rest on the understanding and investigation of the biological action and processes these compounds exert and cause. For this reason, it is not only important to figure out how a probe enters a cell but also to follow its fate within the cell interior. Recently, a series of multifunctional nanoparticles has been developed that can be used in biomedical and pharmaceutical applications for diagnosis and therapy. Thereby, these probes can not only serve as vehicles for the delivery of therapeutic agents to their targets, but they can also act as tools for imaging. The latter can be realized by the use of luminescent semiconductor nanocrystals, also known as quantum dots (QDs). Due to unique spectroscopic properties, this new class of materials has attracted much attention (*1, 2*). Quantum dots have narrow, size-tunable emission spectra and possess a high quantum yield. They are excitable within a broad wavelength range and are exceptionally resistant to photobleaching and chemical degradation. All these advantages make them superior to conventionally used fluorophor systems like small organic dyes or fluorescent proteins. For this reason, they are widely applied as an alternative in many fluorescent-based (cell-) assays preferably when performing long-term and multicolor labeling experiments (*3*). However, certain requirements should be fulfilled by these particles: they should not exhibit any cytotoxicity, and they should be attached to a targeting moiety allowing them not only to penetrate the cell membrane but also to reach their target site within the cell interior.

Coating QDs with peptides is one approach that has become more and more accepted. For instance, attachment of cell-penetrating peptides (CPP) (*4, 5*), such as polyarginine and TAT-derived peptides, to the QD surface has allowed translocating QDs into cells (*6, 7*). Recently, CPP have become widely used vectors for the cellular delivery of molecules in basic and applied biomedical research. With their help, it is possible to introduce membrane-impermeable substances like peptide nucleic acids (PNA) (*8*), proteins (*9*), oligonucleotides (*10*), or nanoparticels (*11, 12*) into mammalian cells. There is a growing attraction in using CPP for drug delivery because many pharmacologically interesting molecules have often only poor bioavailability. Additionally, the attachment of the bioactive compound is easily achieved by covalent coupling or via complexation strategies. Cell-penetrating properties of the human hormone calcitonin (hCT) have been described recently. Human calcitonin, a 32 amino acid long peptide amide, is physiologically secreted by the thyroid gland and involved in the regulation of the calcium metabolism. Owing to a high permeability through the nasal epithelium, it is applied as an intranasal therapeutic (*13*). Structure−activity studies revealed that the truncated sequence hCT(9−32) can translocate through cell membranes, although the calcitonin receptor activating N-terminus (aa 1−8) of hCT is lacking (*14, 15*). By using hCT(9−32), efficient transport of different cargoes into cells like the antiproliferative drug daunorubicin, fluorophors, or even large proteins has been achieved (*16, 17*). Until now, several different hCT-derived carrier peptides have been developed and successfully used in internalization studies (*18, 19*). Moreover, we previously reported on branched hCT-derived analogues that very effectively transfected several cell lines, as well as primary cells, with plasmid DNA encoding the protein EGFP (*20, 21*). This branched design successfully combined the cell-penetrating properties of the hCT moiety with a positively charged side chain suitable for complexation of negatively charged molecules like oligonucleotides. However, so far little is known about the uptake mechanism of hCT-derived CPP. From several studies, it is known that the uptake is mediated by endocytosis. Recently, Foerg et al. postulated a lipid raft dependent pathway for hCT(9−32) and its branched derivative hCT(9−32)-br into cells (*22*). For future applications, a further careful analysis of the uptake mechanism is crucial. In particular, the correlation between attached cargoes and the entry pathway should be

* Corresponding author. Dr. Ines Neundorf, Faculty of Biosciences, Pharmacy and Psychology, Institute of Biochemistry, Brüderstr. 34, D-04103 Leipzig, Phone: +49 (0) 341 97 36 832, Fax: +49 (0) 341 97 36 909, E-mail: neundorf@uni-leipzig.de.

10.1021/bc800172q CCC: $40.75 © 2008 American Chemical Society
Published on Web 11/08/2008

investigated carefully. Results from these studies should help to design best-fitted hCT-derivatives.

The focus of this work was the design and characterization of a QD−peptide-based delivery system suitable for imaging and delivery purposes. Therefore, we covalently coupled a branched hCT-derived peptide to QD nanoparticles of different colors. For the first time, we present the successful delivery of nanoparticles with our hCT-derived CPP. Furthermore, the newly generated constructs were investigated concerning cellular toxicity, stability, and uptake mechanism. Additionally, we focused on the cellular transport of potent oligonucleotide drugs and chose Cy-3-labeled RNA for tracking the fate of the cargo in the cytoplasm. By using fluorescence microscopy, we could demonstrate an effective uptake of these QD−peptide−RNA conjugates and that the complex between the RNA and the QD−peptide conjugate is quite stable. Moreover, by the addition of chloroquine, a substance that assists the release out of endosomes, the assemblies of RNA and QD−peptide conjugates diffused in the cytoplasm.

EXPERIMENTAL PROCEDURES

Materials. Piperidine, thioanisole, ethanedithiole, trifluoroacetic acid (TFA) (HPLC grade), tris(2-carboxyethyl)phosphine (TCEP), Trypan blue, Hoechst 33342, and 5(6)-carboxyfluorescein (CF) were purchased from Fluka (Buchs, Switzerland). *N*,*N*-Diisopropylethylamine (DIEA), *O*-(7-azabenzotriazol-1-yl)-1,1,3,3-tetramethyluronium hexafluorophosphate (HATU), thiocresol, ethylenediaminetetraacetic acid (EDTA), methyl-β-cyclodextrin, wortmannin, chlorpromazine, 5-(*N*-ethyl-*N*-isopropyl)amiloride (EIPA), nystatin, and sulfosuccinimidyl 4-(*N*-maleimidomethyl)cyclohexane-1-carboxylate (sulfo-SMCC) were obtained from Sigma-Aldrich (Steinheim, Germany). Quantum Dots (T2-MP-EviTags) from Evident Technologies (New York, USA), diethyl ether from Merck (Darmstadt, Germany), and acetonitrile (ACN) were purchased from VWR Prolabo (Darmstadt, Germany). 4-(2′,4′-Dimethoxyphenyl-Fmoc-aminoethyl)-phenoxy resin (Rink amide) and N^{α}-Fmoc-protected amino acids were purchased from NovaBiochem (Läufelingen, Switzerland) and Iris Biotech (Marktredwitz, Germany). *N*,*N*′-Diisopropylcarbodiimide (DIC), *N*-hydroxybenzotzriazole (HOBt), and trifluoroacetic acid (TFA) (peptide grade) were obtained from Iris Biotech (Marktredwitz, Germany). *N*,*N*′-Dimethylformamide (DMF) and dichloromethane (DCM) were purchased from Biosolve (Valkenswaard, The Netherlands).

The following side chain protecting groups were chosen: trityl (Trt) for Cys and His; 2,2,4,6,7-pentamethyldihydrobenzofurane-5-sulfonyl (Pbf) for Arg; *tert*-butyl (tBu) for Thr and Glu; *tert*-butyloxylcarbonyl (Boc) or 1-(4,4-dimethyl-2,6-dioxocyclohex-1-ylidene)ethyl (Dde) according to the synthesis strategy.

For cell culture and colocalization studies, the following media, supplements, and substances were used: RPMI 1640 (with L-glutamine), Dulbecco's modified Eagle's medium (DMEM), trypsin/EDTA (1 × concentrate, 1:250 in PBS, trypsin 0.5 mg/mL, EDTA 0.22 mg/mL, pH 7−7.5), Dulbecco's phosphate buffered saline (PBS, pH 7.4), and fetal calf serum (FCS) were purchased from PAA Laboratories (Pasching, Austria), OptiMEM and Hank's balanced salt solution (HBSS) from Gibco/Invitrogen (Auckland, NZ). Transferrin from human serum as Texas Red or Alexa Fluor 488 conjugate and cholera toxin subunit B (recombinant) Alexa Fluor 488 or 647 conjugate were from Molecular Probes (Eugene, Oregon, USA). Cell culture flasks (75 cm^2) and 24-well plates were obtained from TPP (Trasadingen, Switzerland). 8-well chamber slides for microscopy were from ibidi (Munich, Germany). Human embryonic kidney (HEK 293) and human cervix carcinoma (HeLa) cell lines were obtained from the American type Culture Collection (ATCC).

Peptide Synthesis and Purification. Synthesis of the hCT derivatives was performed by automated multiple solid-phase peptide synthesis (SPPS) (Syro, MultiSynTech, Bochum, Germany) using orthogonal Fmoc/^{t}Bu strategy as described previously (*23*). All peptides were synthesized as C-terminal amides by using the Rink amide resin (30 mg, resin loading 0.45 mmol g^{-1}).

At first the sequence, hCT(19−32) was synthesized automatically. Then, (Dde)-Lys(Fmoc)-OH was introduced manually and elongated via the side chain of Lys (*18*) to obtain the branched peptides. Therefore, double-coupling reactions were carried out (1 h each) using 3-fold excess of amino acid, HATU, and DIEA. Afterward, the fragment was elongated automatically and (Dde)-hCT(18−32)-k7 was obtained, whereas the N-terminus of the side chain k7 was protected with Boc. After cleavage of the Dde protecting group with 2% hydrazine in DMF (v/v; 10 × 10 min at room temperature), the peptide was either modified with (5,6)-carboxyfluorescein (CF) or cysteine in order to obtain CF-hCT(18−32)-k7 or [C^{17}]-hCT(18−32)-k7, respectively. CF-coupling was performed for 2 h using a 1.5-fold excess of CF, HATU, and DIEA in DMF. Introduction of cysteine was performed as described above for (Dde)-Lys(Fmoc)-OH. For synthesis of a double-labeled conjugate, CF-labeling of the side chain occurred as described above. Subsequently, the hydroxyl groups of CF were protected with trityl by using 4 equiv of trityl chloride and DIEA in DCM for 16 h. Then, cysteine at position 17 was introduced after cleavage of the Dde protecting group.

Finally, the peptides were cleaved from the resins within 3 h at room temperature. Peptides without Cys were treated with TFA/thioanisol/thiocresol (90:5:5 v/v) and peptides containing Cys were treated with TFA/thianisol/ethanedithiol (90:7:3 v/v). Then, the peptides were precipitated from ice−cold diethyl ether, collected by centrifugation, lyophilized from water/*tert*-butyl alcohol (3:1 v/v), and analyzed by analytical RP-HPLC on a Vydac RP18-column (4.6 × 250 mm; 5 μm/300 Å) using linear gradients of 10−60% B in A (A = 0.1% TFA in water; B = 0.08% TFA in ACN) over 30 min and a flow rate of 0.6 mL min^{-1}. Purification of the peptides was achieved by preparative HPLC on a RP18 column (Waters, 5 μm, 25 × 300 mm) by using a linear gradient of 10−40% B in A over 50 min and a flow rate of 15 mL min^{-1}. Identification was performed by MALDI-TOF mass spectrometry (Voyager RP, Perseptive Biosystems), and purity was confirmed again by analytical RP-HPLC as described before.

The following peptides were synthesized: CF-hCT(18−32)-k7, [C^{17}]-hCT(18−32)-k7, and [C^{17}]-hCT(18−32)-k7(CF). Sequences and analytical data are shown in Table 1.

Preparation of QD−Peptide Conjugates. To obtain QD-[C^{17}]-hCT(18−32)-k7 conjugates, amine-functionalized quantum dots (QD; purchased from EvidentTech) were at first activated by adding approximately 1 mg of sulfo-SMCC to 200 μL of amine quantum dots (QD_{514}: $n = 2.3$ nmol) in 200 μL of 50 mM sodium phosphate pH 7.4. After shaking at room temperature for 60 min, the excess of the cross-linker was removed using a PD-10 desalting column equilibrated with conjugation buffer (1 mM EDTA, 0.1 M phosphate, 0.15 M NaCl, pH 7.2). Fractions containing the QD were collected, identified by tracking the fluorescence (Horiba Jobin Yvon Fluorolog-3), and combined. Coupling of the peptide was performed by first incubating the peptide with TCEP to obtain free sulfhydryl groups. Then, [C^{17}]-hCT(18−32)-k7 was mixed with the maleimide-activated QD in conjugation buffer (1 mM EDTA, 0.1 M phosphate, 0.15 M NaCl, pH 7.2) and incubated at 4 °C overnight. Afterward, the solution was concentrated using an Amicon filter device (MWCO 10 000). The conjugate was then purified by size exclusion chromatography with a

Table 1. Amino Acid Sequences, Molecular Masses and Retention Times of the Synthesized hCT-Derivatives

Peptide	Sequence	MW [Da] calc.	MW [Da] exp.	t_{ret} [min]
CF-hCT(18-32)-k7[a]	**CF**-KFHTFPQTAIGVGAP-NH_2 KKRKAPKKKRKFA┘	3523.2	3524.4	15.3
[C^{17}]-hCT(18-32)-k7	C^{17}KFHTFPQTAIGVGAP-NH_2 KKRKAPKKKRKFA┘	3268.0	3268.7	14.3
[C^{17}]-hCT(18-32)-k7(**CF**)	C^{17}KFHTFPQTAIGVGAP-NH_2 **CF**-KKRKAPKKKRKFA┘	3626.6	3627.8	14.7

[a]CF: 5(6)-carboxyfluorescein.

Superdex200 resin. At least 25−30 fractions were collected. The fluorescence of the fractions was recorded at the QD emission peak wavelength of 514 nm, and the peptide amount in each fraction was measured by Bradford assay. The Bradford readings and the fluorescence values at the QD emission peak wavelength were plotted vs the fraction number to generate elution profiles and to identify the fractions containing QD−peptide conjugate.

The same procedure was used to conjugate [C^{17}]-hCT(18−32)-k7 and [C^{17}]-hCT(18−32)-k7(CF) to QD_{617} (n = 2.4 nmol). QD−peptide conjugates with a QD to peptide ratio of 1:100 up to 1:300 were prepared.

Cell Culture. Cells were grown in 75 cm^2 culture flasks to confluence at 37 °C and 5% CO_2 in a humidified atmosphere (95%). HeLa cells were grown in supplemented RPMI 1640 (with L-glutamine) with 10% heat-inactivated fetal calf serum. HEK 293 cells were cultured in Dulbecco's modified Eagle's medium/Ham's F12 (without L-glutamine) containing 15% heat-inactivated fetal calf serum.

Resazurin-Based Cell Viability Assay. HEK 293 or HeLa cells were seeded in 96-well plates (15 000 and 50 000 cells/well, respectively). To investigate the influence of the inhibitors, peptides, and QD−peptide bioconjugates on the cell viability, we used the fluorimetric resazurin-based cell viability assay as described recently in ref *21*. The peptide or rather the QD−peptide bioconjugate was diluted to appropriate concentrations (0.01−2 μM for the QD−peptide bioconjugate, 100 μM of [C^{17}]-hCT(18−32)-k7 and CF-hCT(18−32)-k7) in standard cell culture medium. For testing the inhibitors, dilutions of wortmannin (200 nM), EIPA (100 μM), chloropromazine (20 μM), nystatin (27 μM), or methyl-β-cyclodextrin (10 mM) in serum free medium were prepared. For each data point, a triplicate of wells was prepared. Cells were incubated for 24 h with the peptide and QD−peptide solutions and for 60 min with the inhibitor solutions, and afterward, the resazurin-based *in vitro* toxicity assay was performed.

Untreated cells were investigated as the negative control, whereas cells incubated with a solution of 70% alcohol for 10 min were used as the positive control. Afterward, a freshly prepared resazurin solution (1:5 v/v in serum-free cell culture medium) was added (1:1 v/v), and the cells were incubated for 2 h under standard growth conditions. The cell viability was finally analyzed fluorimetrically by using a multiwell plate reader (Spectrafluor plus, Tecan, Crailsheim, Germany). The metabolic conversion of resazurin to the reduced resofurin by the living cells was measured at 595 nm (after excitation at 550 nm).

Fluorescence Microscopic Imaging. To characterize the peptide uptake by fluorescence microscopic imaging, living, unfixed cells were investigated. HeLa and HEK 293 cells seeded in 8-well chamber slides (40 000 and 100 000 cells/well, respectively) were incubated with 25 μM CF-hCT(18−32)-k7 for 30 and 60 min. 10 min prior to the end of the peptide incubation, Hoechst 33342 was added to a final concentration of 5 μg/mL for nuclear staining. To monitor the intracellular fate, cells were coincubated with either Alexa Fluor 647 labeled cholera toxine (final concentration of 10 μg/mL) or Texas Red labeled transferrin (final concentration of 50 μg/mL). To distinguish between internalized and cell surface-bound peptides, the remaining extracellular fluorescence was quenched with an acidic Trypan blue buffer (300 μM in glycine buffer, pH 4.5) for 1 min. Subsequently, cells were washed 3 times with PBS, suspended in HBSS (pH 7), and inspected by fluorescence imaging. The peptide uptake was analyzed using a Zeiss Axiovert 200 inverse phase-contrast fluorescence microscope provided with an ApoTome and a 63×/1.4 oil immersion objective.

Additionally, HeLa and HEK 293 cells, seeded in 8 well chamber slides (40 000 and 100 000 cells/well, respectively) were incubated with QD_{617}-[C^{17}]-hCT(18−32)-k7 (0.02 μM QD) for 45 up to 90 min as described above and simultaneously incubated with either cholera toxin Alexa Fluor 488 (10 μg/mL) or transferrin Alexa Fluor 488 (50 μg/mL). Finally, the cells were washed with PBS for several times, diluted in HBSS (pH 7), and imaged.

Flow Cytometry. HeLa and HEK 293 cells were seeded in 24-well plates (100 000 and 250 000 cells/well, respectively) and grown under standard growth conditions. Subconfluent cells were incubated with CF-hCT(18−32)-k7 (20 μM in serum free medium) for 60 min or with QD_{617}-[C^{17}]hCT(18−32)-k7 (0.01 μM QD in serum free medium) for 90 min. Then, cells were incubated with Trypan blue (300 μM in glycine buffer, pH 4.5) for 1 min in order to quench potentially remaining extracellular fluorescence caused by CF. Additionally, cells were washed with PBS (3 × 300 μL). Afterward, the cells were detached by incubation with trypsin/EDTA for 1 min. The catalytic activity of trypsin was stopped by addition of cell culture medium supplemented with 10% FCS (HeLa)/15% FCS (HEK 293). Then, trypsin/EDTA was removed, and the cells were resuspended in PBS and analyzed by a flow cytometer (Partec GmbH, Münster, Germany). At least 10 000 cells per sample were analyzed in order to get reproducible results. The mean fluorescence intensity of peptide-labeled cells was compared with untreated cells as control.

For inhibition of endocytosis pathways, cells were pretreated for 30 min with wortmannin (200 nM), EIPA (100 μM), chloropromazine (20 μM), nystatin (27 μM) or methyl-β-cyclodextrin (10 mM) (all inhibitor dilutions were prepared in serum free medium) prior to incubation with CF- or QD_{617}-

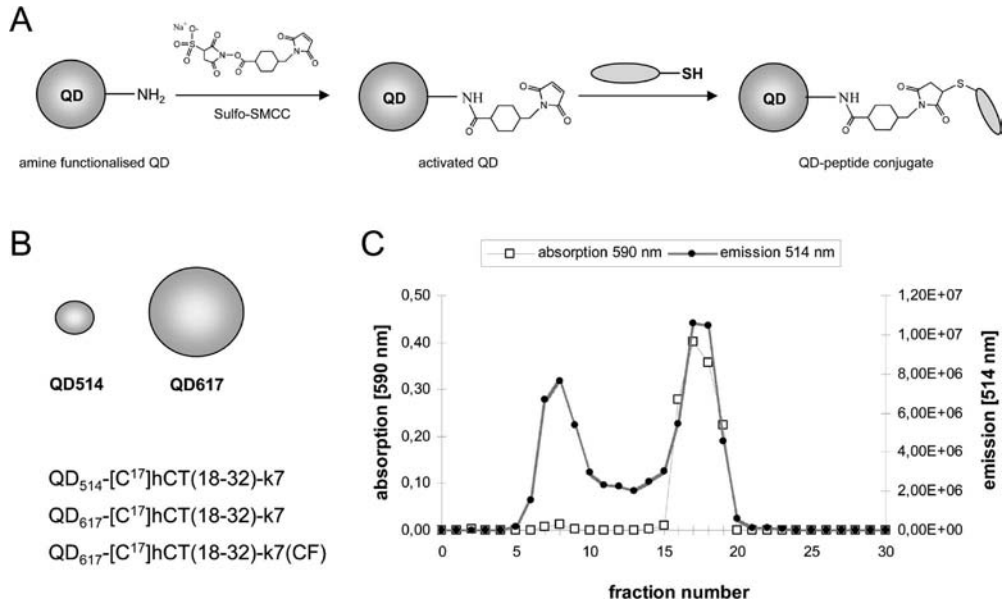

Figure 1. Synthesis of QD−peptide assemblies. (A) Amine-functionalized QDs were activated with sulfo-SMCC, subsequently followed by reaction with the thiol group of the peptide. (B) Two different QDs were used for bioconjugate generation. The double-labeled conjugate was created by coupling the CF-labeled peptide to QD_{617}. (C) Fractions collected by a Superdex200 column were measured by Bradford assay (absorption) and fluorescence spectroscopy (emission). QD−peptide fractions are represented by peaks with overlapping fluorescence and absorption spectra.

labeled hCT derivatives. All experiments were performed twice or triply in duplicate or triplicate.

The flow cytometric data were evaluated by using the software *FlowMax 3.0* (Partec).

Stability of QD-hCT-Peptide Conjugates. To determine the stability of the newly synthesized QD-hCT-peptide conjugates, HeLa and HEK 293 cells, respectively, were seeded in 8 well chamber slides (40 000 and 100 000 cells/well, respectively) and grown under standard growth conditions. Subconfluent cells were incubated with the double-labeled QD_{617}-[C^{17}]-hCT(18−32)-k7(CF) (0.02 μM QD) for 1.5 and 4 h. After 4 h incubation, the QD-hCT-peptide conjugate solution was removed and cell media were added. Fluorescence imaging was performed after 1.5, 4, and 24 h shortly after washing the cells 3−5 times with 200 μL HBSS (pH 7). At least 100 μL HBSS was added for fluorescence imaging that was performed using a Zeiss Axiovert 200 inverse phase-contrast fluorescence microscope provided with an ApoTome and a 63×/1.4 oil immersion objective.

Peptide-Mediated RNA Delivery. We complexed Cy-3-labeled RNAs of different lengths with QD_{514}-hCT-peptide conjugates: 83 base long RNA (5′-GGGAGAATTCCGACCA-GAAGAUUGAGAAGGGCGAUCUUCCGGCCGGACCUCA-ACCGGCGUAUGUGGCUCUACAUGGAUCCUCA-3′) and 101 base long RNA (sequence: 5′-GGAGCUCAGCCUUCA-CUGCCGGAGUGCAUUGUUGGCUGGGUGAUCGUGGU-GGAGACCUUACCCCUCUACGGGGGGGUGGAGGGCA-CCACGGUCGGAUCCAC-3′). Final concentrations at the cells were 0.4 μM RNA and QD_{514}-[C^{17}]-hCT(18−32)-k7 (0.04 μM QD) in 200 μL OptiMEM.

Prior to the peptide−RNA complexation, the RNA was de- and renatured. Therefore, the required volume of RNA stock solution was diluted with RNase- and DNase-free distilled water to a final volume of 10 μL, heated up to 70 °C for 5 min and slowly cooled down to room temperature. Then, the required volume of QD_{514}-[C^{17}]-hCT(18−32)-k7 solution was added and the noncovalent peptide−RNA complexation was carried out for 1 h at 37 °C. Afterward, preheated serum-free OptiMEM was added to reach a final volume of 200 μL. The QD-peptide-RNA solution was added to the cells and incubated for 1.5 and 6 h, respectively, at 37 °C. For nuclear staining, Hoechst 33342 was added to a final concentration of 5 μg/mL 10 min prior to the end of complex incubation. Finally, after 1.5 or 6 h the QD−peptide−RNA solution was removed and the cells were washed four times with 200 μL OptiMEM. 100 μL HBSS was added to the cells, and fluorescence microscopic imaging was performed as described above.

The influence of chloroquine was investigated as follows: prior to the addition of the QD−peptide−RNA solution, the cells were preincubated with 100 μL chloroquine (100 μM). After 1.5 h incubation, the QD−peptide−RNA solution was removed, and the cells were treated as described above.

RESULTS

Synthesis of QD-hCT-Peptide Conjugates. Peptides were coupled covalently to green (514 nm emission maximum, QD_{514}) and red (617 nm emission maximum, QD_{617}) emitting QDs. For efficient cell delivery, we incorporated the branched hCT-derivative hCT(18−32)-k7 on the surface of the QDs. We recently were able to show that this branched peptide was internalized very effectively in several cell lines (*21*). Furthermore, owing to the cationic sequence of the side chain an efficient complexation of negatively charged structures like oligonucleotides is possible. Synthesis of the QD−peptide conjugates was performed according to the manufacturer's protocol. Briefly, we first coupled the bifunctional cross-linker sulfo-SMCC to PEG-NH_2 functionalized QDs. Then, the peptide was introduced as [C^{17}]-hCT(18−32)-k7 that reacted selectively with the maleimide of the cross-linker (see Figure 1A for reaction scheme). We prepared QD−peptide conjugates with a QD to peptide ratio of 1:100 up to 1:300. Additionally, we synthesized a double-labeled conjugate where the peptide was labeled with 5(6)-carboxyfluorescein (CF) at the N-terminus of the side sequence k7 (see Figure 1B for details).

The coupling efficiency was determined by performing either a Bradford assay or, in the case of the double-labeled conjugate, by measuring the fluorescence of CF. For the red-emitting QDs, the assays revealed about 100 peptide molecules per quantum dot, whereas for the smaller green-emitting QDs, ratios of about 1:50 QD to peptide were determined.

Cellular Uptake in HeLa and HEK 293 Cells. Cellular uptake was studied in two different cell lines, HeLa and HEK

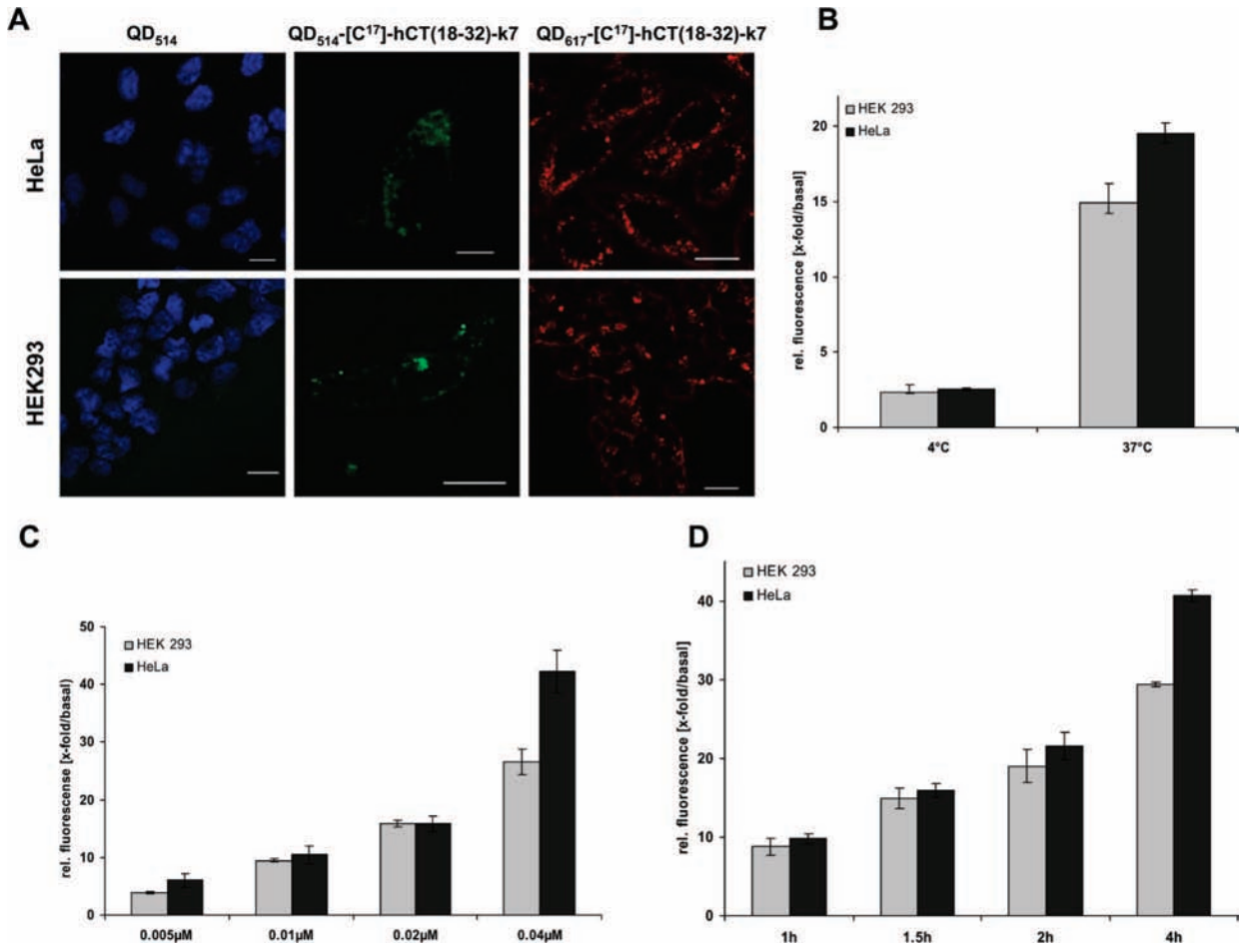

Figure 2. Internalization of QD−hCT carrier peptide conjugates in HeLa and HEK 293 cells. (A) Representative fluorescence microscopy images of QD_{514}-solution only (0.25 μM), QD_{514}-[C^{17}]-hCT(18−32)-k7 (0.04 μM QD concentration) and QD_{617}-[C^{17}]-hCT(18−32)-k7 (0.02 μM QD concentration). The scale bar is 20 μm. (B,C,D) Uptake of QD_{617}-[C^{17}]-hCT(18−32)-k7 (0.02 μM QD concentration) in HEK 293 and HeLa cells as determined by flow cytometry at either 37 or 4 °C for 90 min (B), at different concentrations for 90 min at 37 °C (C) and after incubation the cells up to 4 h at 37 °C.

293 cells, because these cell lines have often been used in recent reports (*6*, *22*, *23*). After incubation with nonconjugated QDs, we observed no detectable intracellular fluorescence, indicating that the nanoparticles were not able to enter the cells by themselves (shown for QD_{514} in Figure 2A). Cell internalization of the $QD_{617/514}$-[C^{17}]-hCT(18−32)-k7 conjugates was slow and occurred efficiently after 90 min of incubation. A punctuate and vesicular uptake pattern was observed in both cell lines pointing to an endocytotic entry pathway (Figure 2A). Subsequently, we studied in more detail the uptake of QD_{617}-[C^{17}]-hCT(18−32)-k7 conjugates in both cell lines by using flow cytometry. Uptake was significantly reduced at 4 °C (Figure 2B), supporting an energy-dependent internalization mechanism. This is in agreement with previously published results on QD−peptide delivery in both HEK 293 (*6*) and HeLa (*23*) cells. In addition, internalization of the QD−peptide bioconjugates is both concentration- (Figure 2C) and time-dependent (Figure 2D) in HEK 293 as well as in HeLa cells.

To get more insight into the entry mechanism, we investigated the uptake by the simultaneous delivery of AlexaFluor 488-conjugated cholera toxin subunit B (AF488-CtxB) or AlexaFluor 488-conjugated transferrin (AF488-Tf) into the cells. Like other microbial toxins, the active part of cholera toxin subunit B is internalized by an endocytosis pathway that is independent of clathrin and involves lipid rafts (*24*, *25*). However, labeled transferrin is commonly used to monitor clathrin-dependent uptake in cells (*26*). Therefore, cells were preincubated with the appropriate marker, and subsequently, the QD−bioconjugates were added. We inspected the cells after 45 min, the time point at which we assumed that cell entry of the QD−peptide assemblies occurred. Figure 3A,B shows the uptake of QD_{617}-[C^{17}]-hCT(18−32)-k7 conjugates in HeLa cells. No colocalization was found for QD−peptide conjugates and AF488-Tf, whereas after incubation with AF488-CtxB, colocalization of internalized QD−peptide conjugate and CtxB was evident as seen by the merged fluorescence on the plasma membrane. Quite different results were obtained after incubating HEK 293 cells with the QD−peptide conjugate and the two endocytosis markers (Figure 3C,D). Here, no colocalization within the cell was observed. Moreover, it seems that the entry of the markers into this cell line occurs very fast, while the QD−peptide conjugate is mostly present on the plasma membrane and only to a minor fraction in the cell interior. Even after inspecting the cells at different time points (15, 30, 60, 90, 120 min), we did not detect any degree of overlap in the fluorescence pattern (data not shown).

Inhibition of Endocytotic Pathways. To further characterize the uptake mechanism of the QD−peptide bioconjugates, we preincubated HeLa as well as HEK 293 cells with different inhibitors interfering with individual endocytotic pathways (*25*−*30*). After 30 min preincubation with these different inhibitors, we analyzed the cellular uptake of the QD−peptide conjugates (cells were incubated with bioconjugates for 90 min) by flow cytometry. Additionally, we tested the influence of the same inhibitors on the uptake of 5(6)-carboxyfluorescein (CF)-labeled hCT(18−32)-k7 in both cell lines to get some insights into the

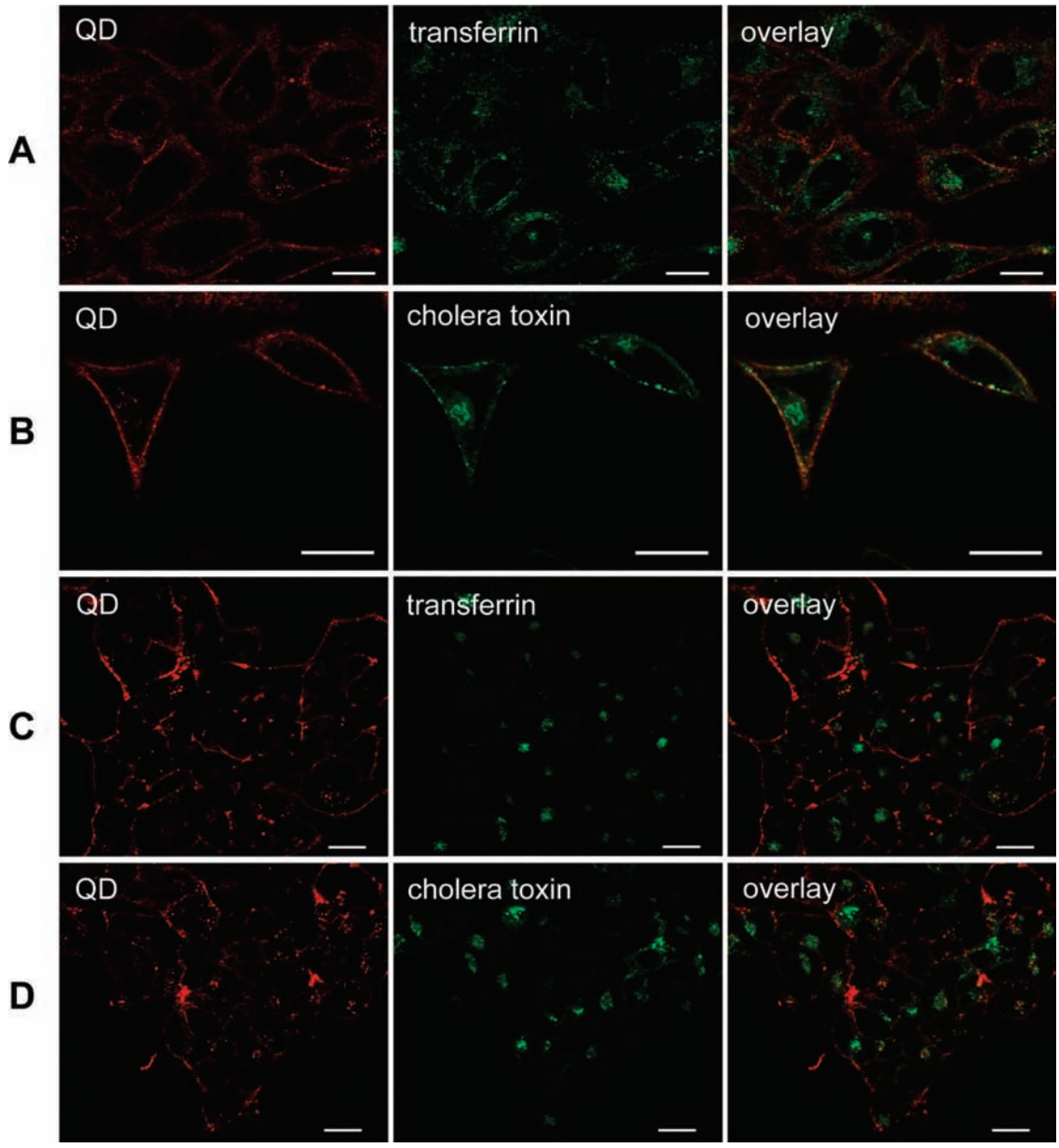

Figure 3. Colocalization study of QD_{617}-[C^{17}]-hCT(18−32)-k7 in HeLa (A,B) and HEK 293 (C,D) with transferrin or cholera toxin, respectively. Colocalized vesicels are visible in yellow, QD_{617}-[C^{17}]-hCT(18−32)-k7 conjugate in red, and endocytosis markers (transferrin and cholera toxin) in green. For colocalization studies with transferrin, cells were incubated with QD_{617}-[C^{17}]-hCT(18−32)-k7 and simultaneously stained with 50 μg/mL Alexa Fluor 488-conjugated transferrin for 45 min at 37 °C (A,C). For colocalization studies with Alexa Fluor 488-conjugated cholera toxin, cells were preincubated with 10 μg/mL cholera toxin at 4 °C, and the marker was then replaced by QD_{617}-[C^{17}]hCT(18−32)-k7 for 1 h at 37 °C (B,D). The scale bar is 20 μm.

influence of the cargo size on the internalization process. Unspecific bound peptides were detached from the outer leaflet of the cell membrane by trypsin digestion. Figure 4A,B demonstrates the uptake of QD_{617}-[C^{17}]-hCT(18−32)-k7 and CF-hCT(18−32)-k7 in HeLa and HEK 293 cells, respectively. We found out that the uptake of the QD−peptide conjugate in HeLa cells seems to follow two different pathways (see Figure 4A). The decreased uptake after depletion of cholesterol through MβCD proves the results from the colocalization studies and points to a lipid raft-dependent entry pathway. The second way is obviously mediated by macropinocytosis, a fact that is indicated by the influence of 5-(*N*-ethyl-*N*-isopropyl)amiloride (EIPA). Interestingly, the uptake of CF-hCT(18−32)-k7 is realized by a third pathway in HeLa cells that is clathrin-dependent. Upon preincubation with chlorpromazine, a marker that inhibits this endocytosis pathway, the uptake was decreased (see Figure 4A). The same pathways seem to be involved in the internalization process of CF-hCT(18−32)-k7 in HEK 293 cells (see Figure 4B). Surprisingly, the uptake of QD_{617}-[C^{17}]-hCT(18−32)-k7 was not negatively influenced after preincubating HEK 293 cells with any of the tested inhibitors. In contrast, here we observed an increase in uptake (see Figure 4B).

To eliminate influence of the tested inhibitors on cell viability and thus impair the results of the inhibition studies, we performed resazurin-based cell viability assays. As demonstrated in Figure 4C, the impact of the inhibitors on cell viability was negligible for HeLa as well as for HEK 293 cells in the tested concentration range.

Stability. By using the double-labeled compound, we investigated the stability of the QD−peptide bioconjugates after cell entry. Hence, we incubated HeLa and HEK 293 cells for 24 h with the conjugate QD_{617}-[C^{17}]-hCT(18−32)-k7(CF) and visualized the cells by fluorescence microscopy after 1.5, 4, and 24 h.

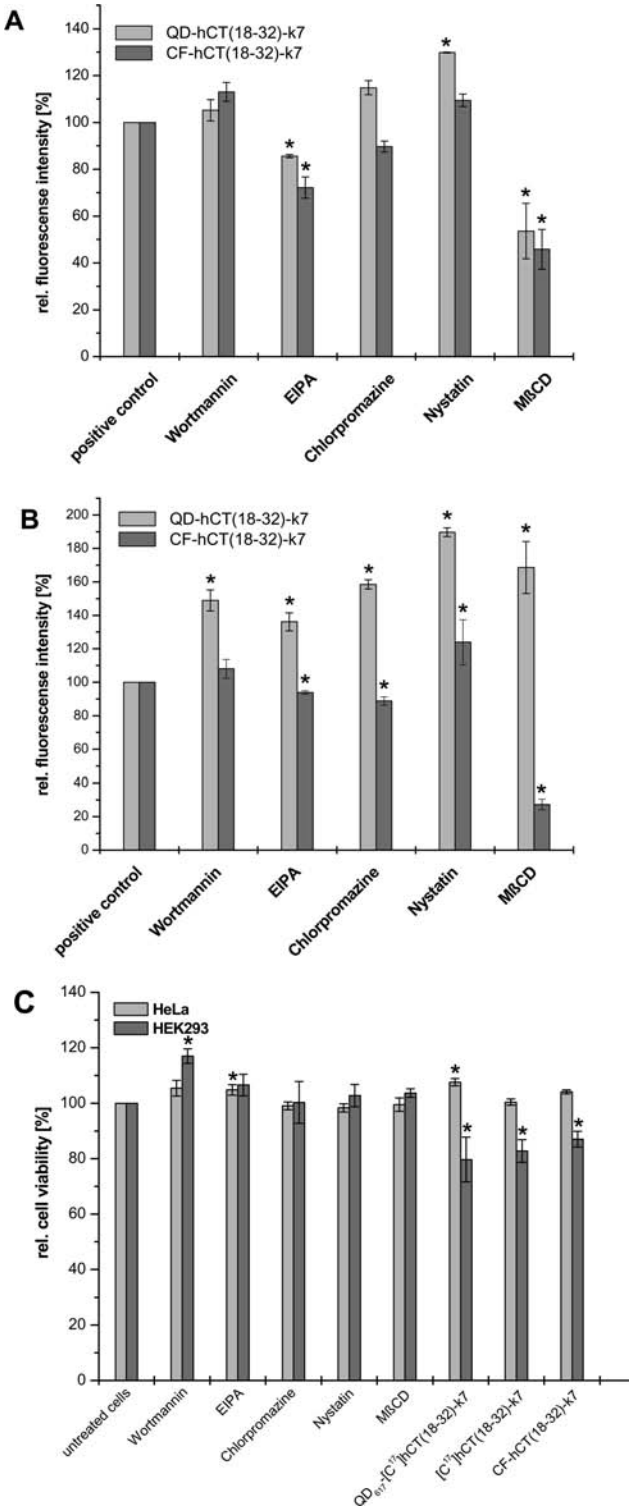

Figure 4. Endocytosis inhibition and toxicity studies. Panels A and B show uptake and endocytosis inhibition of CF-hCT(18−32)-k7 and QD_{617}-[C^{17}]-hCT(18−32)-k7 in HeLa (A) and HEK 293 (B) cells as determined by flow cytometry. The inhibition of endocytosis was performed by pretreating cells with 200 nM wortmannin, 100 μM EIPA, 20 μM chlorpromazine, 27 μM nystatin, and 10 mM methyl-β-cyclodextrin (MβCD) before incubation with QD_{617}-[C^{17}]-hCT(18−32)-k7 (0.02 μM QD) for 90 min or 20 μM CF-hCT(18−32)-k7 for 60 min. Cells incubated only with peptide or QD−peptide conjugate were used as control cells and set as 100%. Panel C shows relative cell viability of HeLa and HEK 293 cells after treatment with inhibitor for 60 min and peptide or QD−peptide solutions for 24 h (for details, see Experimental Section). Data are normalized to untreated cells (100% viability). Means were compared using Student's *t* test. A *P* value of <0.05 was considered significant and is indicated by an asterisk symbol (*).

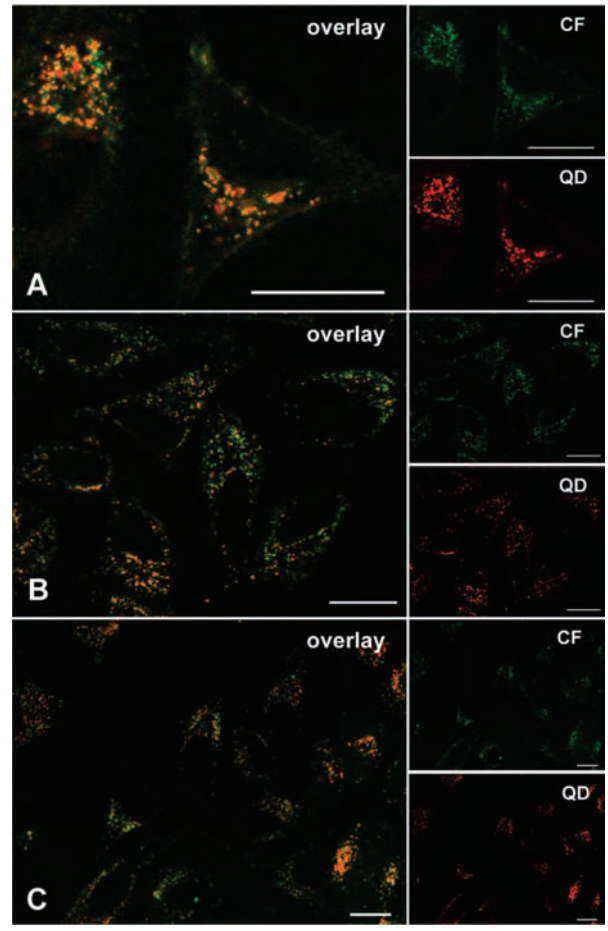

Figure 5. Stability of the new QD−hCT−peptide bioconjugates in HeLa cells. Colocalized vesicles are visible in yellow, carboxyfluorescein in green, and QDs in red. Cells were incubated with the double-labeled conjugate QD_{617}-[C^{17}]-hCT(18−32)-k7(CF) (0.02 μM QD concentration) for 1.5 h (Panel A) or 4 h (Panel B), and fluorescence imaging was performed at 1.5 h (Panel A), 4 h (Panel B), and 24 h (Panel C). The scale bar is 20 μm.

The merged fluorescence of the two fluorophors even after 24 h demonstrates that the conjugate seemed to be mostly intact (see Figure 5 for HeLa cells). In addition, it can be seen that the peptide-labeled nanoparticles were still entrapped in vesicles. The same results were obtained for HEK 293 cells (see Supporting Information Figure 2).

Furthermore, potential cytotoxic effects of the QD-CPP assemblies were assessed using a cell proliferation assay. The results confirmed no influence on cell viability for the QD−peptide conjugates in HeLa cells relative to untreated control cells (see Figure 4C). In contrast, cell viability was slightly reduced to 80% after incubating HEK 293 cells with the conjugate for 24 h.

Cargo Delivery. The main focus of this study was to create multifunctional particles for both imaging and transport of bioactive molecules. A major difference between this work and earlier studies is that the conjugated carrier peptides simultaneously function for the delivery of both the QD and an attached cargo. Furthermore, by complexing the cargo directly to the carrier peptide our approach circumvents the tradeoffs in the number of attached species on the QD surface. Since negatively charged oligonucleotides are not able to translocate the cell membrane by themselves, there is a great demand on effective delivery systems for siRNA or aptamers in gene regulation strategies. Therefore, as proof of our concept, we chose to transport Cy-3 labeled RNA into HeLa and HEK 293 cells. The Cy-3 label served for visualizing the fate of the cargo after cell

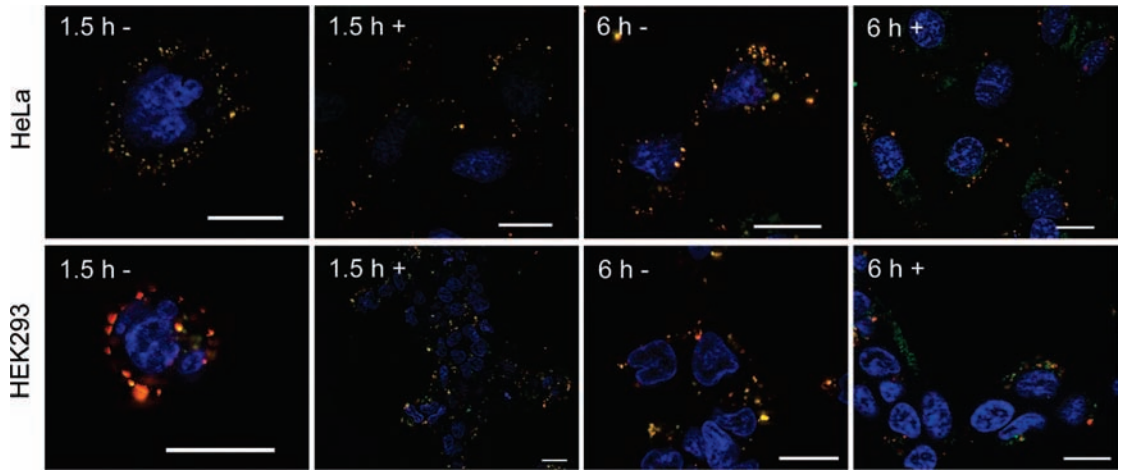

Figure 6. RNA delivery mediated by the QD_{514}-[C^{17}]-hCT(18−32)-k7 bioconjugate. Delivery of the 83 base long RNA in HeLa and HEK 293 cells. Colocalization is visible in yellow, Cy-3 labeled RNA in red, QD_{514}-[C^{17}]-hCT(18−32)-k7 in green, and the nucleus was stained with Hoechst 33342 in blue. The cells were incubated with QD-peptide-RNA either for 1.5 h (1.5 h -) or 6 h (6 h -). The influence of the pretreatment with 100 μM chloroquine for 1 h is shown in panels marked with +. The scale bar is 20 μm.

entry. Thus, we complexed QD_{514}-[C^{17}]-hCT(18−32)-k7 with RNAs of different lengths (either 83 or 101 bases long).

One major problem when using CPP for cargo delivery is their enclosure in endosomes after cell entry. The results from our internalization studies clearly showed entrapment of the QD−peptide conjugates in vesicles that may be endosomes or lysosomes. To overcome this difficulty, we also treated the cells with the antimalaria drug chloroquine. This cell-permeable base is described to neutralize the acidic environment in the endosomes leading to reduction of endolysosomal hydrolytic degradation and destabilization of the complex between carrier and cargo (*31*). Figure 6 shows HeLa (upper row) and HEK 293 (lower row) cells after incubation of complexes formed from QD_{514}-[C^{17}]-hCT(18−32)-k7 and the 83 base long RNA. Cells were inspected after 1.5 and 6 h. As described above, cellular distribution was monitored in preparations with or without the addition of chloroquine. It is evident that the complex is still intact after 6 h in both cell lines, whereas upon the addition of chloroquine, most of the substances have distributed into the cytoplasma. Only the green fluorescence coming from the QD−peptide conjugates was visible. The red fluorescence from the RNA was only merely seen. Therefore, we conclude that the RNA must have been detached from the complex with the peptides coupled to the QD surface. The same results were obtained after incubation of complexes formed from QD_{514}-[C^{17}]-hCT(18−32)-k7 and the 101 base long RNA in both tested cell lines (data not shown).

DISCUSSION

Over the past two decades there has emerged an immense interest in quantum dots as fluorescent probes for biomolecular and cell imaging owing to their unique spectroscopic properties. Several examples are now available demonstrating successful *in vitro* and *in vivo* applications of QDs in tissue staining and cell labeling. Here, different strategies for cell internalization have been followed, like nonspecific or specific binding to the cell surface or the use of antibody-coated QDs (*32*, *33*). Another promising approach for realizing effective cell uptake is the attachment of cell-penetrating peptides to the QD surface. This class of peptides is able to penetrate the cell membrane in a receptor-independent way and shuttle various cargoes into the cell at the same time. Recent advances have shown the applicability of CPP in an impressive mode, and until now, a series of different biomolecules has been successfully transported into diverse cell lines. Nevertheless, only a few studies exist that have investigated peptide-coated quantum dots especially for their stability, toxicity, and internalization mechanism. Recently, Ruan et al. published data concerning cellular uptake and intracellular fate of Tat-functionalized QDs (*23*). They observed an engulfment of Tat-QDs in vesicles where they were bound to the inner membrane, and the subsequent transport of these vesicles to the perinuclear region. Furthermore, they found vesicles loaded with Tat-QDs on the outer membrane resulting from vesicle shedding. Moreover, it was assumed that the Tat peptide-conjugated QDs are internalized by macropinocytosis. Another paper from the same group dealt with PEG/PEI-coated QDs. Herein, the authors could show an improvement concerning the escape from intracellular acidic organelles (*34*). A general major drawback in such applications is, however, the toxicity of PEI that was minimized in this study by grafted PEG segments.

Our work focused on the development of transport systems that contain photostable markers like QDs and are useful as fluorescent probes for imaging, tracking, and delivery purposes. Furthermore, we were interested in the stability and toxicity of the new constructs and their internalization mechanism. Therefore, we generated different QD−peptide bioconjugates by attaching cysteine-modified [C^{17}]-hCT(18−32)-k7 to the surface of PEG-coated QD. We also synthesized a double-labeled compound by coupling [C^{17}]-hCT(18−32)-k7(CF) to red emitting QD_{617}. By measuring the fluorescence of the second fluorophor CF and comparing it with a calibration curve, it was possible to determine the amount of peptides per QD_{617} to a ratio of about 100:1. In our experiments, this value barely differed from the one we obtained by Bradford assay. Generally, this ratio is in good agreement with values obtained in previous studies where peptides were attached on a QD surface (*11*). Moreover, by introducing a second fluorophor the determination of the amount of peptides on the QD surface is achieved in an easy way. Thus, long-time stability can simply be monitored. We determined that the double-labeled QD−peptide conjugate was stable at least over a period of one year (data not shown). A similar approach to quantify the number of peptides attached per QD was adopted by Derfus et al. (*35*). The disulfide bond of a cleavable cross-linker between FITC-labeled peptides and nanoparticles was reduced by 2-mercaptoethanol and the amount of FITC-labeled peptide was then quantified by fluorescence. However, our approach differs from other strategies where the therapeutic and delivery entities are simultaneously attached to

the QD surface. Thus, our newly formed constructs can directly serve as delivery and imaging tools.

Next, we analyzed the uptake and distribution of our QD−peptide conjugates in two cell lines, HEK 293 and HeLa. The first internalization experiments using fluorescence microscopy showed that the generated bioconjugates were able to cross the lipid barrier of the cells. Both HeLa and HEK 293 cells efficiently took up the peptide-coated QDs. Also, we detected no uptake of the QDs alone. This is in agreement with the study of Delehanty et al. on self-assembled quantum dot−peptide bioconjugates (*6*). Furthermore, the vesicular distribution pattern suggests an endocytotic mechanism. This was confirmed by investigating the uptake of QD_{617}-[C^{17}]-hCT(18−32)-k7 using flow cytometry. We found that uptake is reduced at 4 °C pointing to an energy-dependent internalization. Additionally, internalization of the studied QD−peptide conjugates is concentration- and time-dependent. Interestingly, these results were similar to previous studies using carboxyfluorescein (CF)-labeled hCT-derived peptides (*22*). In addition, recent studies on HEK 293 cells revealed that the uptake of CF-hCT(18−32)-k7 is temperature-, concentration-, and time-dependent. Here, it was also found that the uptake could not be displaced by the addition of unlabeled hCT(18−32)-k7 peptide, pointing to a receptor-independent uptake mechanism (*36*).

Accordingly, we studied the uptake in more detail because CPP are known to use several endocytotic pathways for cell internalization. For instance, most of the cationic peptides investigated so far enter the cells via clathrin-independent pathways including macropinocytosis (*37*−*39*). Therefore, we started with colocalization experiments by using fluorescent-labeled transferrin and cholera toxin subunit B to distinguish at first between clathrin-dependent (transferrin) and lipid raft-dependent (CTxB) endocytosis. Since we were interested in the processes of cell entry, we inspected the cells to an early stage, after 45 min, when most of the QD−peptide bioconjugates were passing the cell membrane, and only few constructs stayed inside the cell. From fluorescence imaging studies of HeLa cells incubated with QD_{617}-[C^{17}]-hCT(18−32)-k7 and AlexaFluor 488 labeled CTxB, we assume a lipid raft dependent uptake mechanism due to clear colocalization of both substances. It is known that HeLa cells have decreased caveolin-1 expression. Therefore, internalization of cholera toxin subunit B can occur via the clathrin-mediated pathway, too, but it was found out that the significant fraction is internalized via clathrin-independent pathways (*40*−*42*). For HEK 293 cells, the results were not as clear, since we could not detect any colocalization of our QD−peptide conjugates with neither transferrin nor CTxB. In both cases, the marker was very rapidly taken up by HEK 293 cells. However, we were additionally interested in the influence of the cargo size on the internalization process and compared the results of the QD−peptide bioconjugates to the uptake of CF-labeled hCT(18−32)-k7. In contrast to the QD−peptide conjugate, we detected colocalization with both markers transferrin and CTxB in HeLa cells (see Supporting Information Figure 1) indicating that CF-hCT(18−32)-k7 is internalized by both clathrin-dependent and -independent pathways. Again, we observed no colocalization after incubating HEK 293 cells with the peptides and either transferrin or CTxB.

Therefore, we decided to extend our studies by using several endocytotic inhibitors. We preincubated the cells with inhibitors for clathrin-dependent and -independent pathways, as well as for caveolin-dependent endocytosis and macropinocytosis. Our results show that the import of the conjugates was never fully blocked after preincubation with the inhibitors. Besides, we did not find any influence of wortmannin. Since wortmannin is reported to also affect the sorting pathways like recycling and degradation, it may have happened that internalization per se was not reduced but the fate of the peptides inside the cells was influenced. This has to be investigated further.

For HeLa cells, we conclude that the QD−peptide−bioconjugates appear to enter by macropinocytosis and lipid raft-dependent pathways. We could assess a strong influence of methyl-β-cyclodextrin (MβCD) to the amount of intracellular fluorescence. MβCD perturbs the function and organization of lipid rafts and is therefore a marker for raft processes. The results from the colocalization studies were consistent with this observation because they demonstrated simultaneous entrapment of hCT-QDs and cholera toxin subunit B also pointing to a lipid raft-dependent pathway. By using the inhibitor 5-(*N*-ethyl-*N*-isopropyl)amiloride (EIPA), the uptake of the bioconjugate was to some extent reduced as well, indicating that the internalization of the conjugate may occur by a second pathway that is macropincocytosis. Interestingly, when treating with the inhibitors we did not detect any decrease in uptake for the peptide-coated QDs in HEK 293 cells. Moreover, the inhibition of the pathways led to a dramatic increase in uptake in all cases. Recently, this effect was also reported by Duchardt et al. They detected a high increase in cellular fluorescence (4- to 7-fold) by flow cytometry after treatment with MβCD. They explained this observation on the one hand with the strong enrichment of the tested peptides at the plasma membrane. This fraction was also resistant to trypsin digestion (*38*). On the other hand, it may be that the inhibitors promote the uptake leading then to a more rapid internalization pathway. This could also be the case for the internalization of the QD−peptide conjugates in HEK 293 cells. Another explanation could be the retention of the QD−peptide conjugate inside the endosomal compartment and thus an inhibition of the rapid exit of its fragments out of the cytosol. Since we determined no relevant cytotoxicity for all tested inhibitors in the evaluated concentration range, we exclude the possibility that the increased uptake observed is due to any negative influence on cell viability.

In contrast, the CF-labeled peptide seemed to follow three different entry pathways in HeLa and HEK 293 cells. Additionally, the evaluation of the inhibition studies demonstrated strong evidence that EIPA, chlorpromazine, and MβCD influence the uptake. In HeLa cells, this is consistent with the observations we made by fluorescence microscopy where colocalization was found with fluorescent-labeled transferrin as well as with cholera toxin subunit B, pointing to both clathrin-dependent and -independent endocytosis. In addition, we detected reduced peptide uptake in the dependence of the particular inhibitors tested. Therefore, we assume that the most dominant entry pathway is lipid raft-dependent and that only a minor fraction of CF-hCT(18−32)-k7 peptides are internalized by clathrin-mediated endocytosis or macropinocytosis. The strong influence of MβCD to the uptake of CF-hCT(18−32)-k7 in HEK 293 cells is in our opinion not remarkable, since it is known that depletion of cholesterol can generally affect most of the endocytotic uptake pathways (*43*).

Interestingly, it seems that both tested substances labeled with cargoes of different sizes use more than one entry pathway. However, regarding the relatively high concentrations that are normally used to study CPP it is likely that the peptides enter through multiple pathways, i.e., fluid phase or nonspecific adsorptive endocytosis. In fact, Duchardt et al. concluded that peptide concentration is a key experimental condition when analyzing peptide uptake (*38*). In another study, it was hypothesized that, in HeLa cells, macropinocytosis operates at a low basal rate. Thus, an inhibition of clathrin- and caveolae-mediated pathways could result in the stimulation of macropinocytosis (*44*). However, the differences in the uptake of the QD−peptide conjugates concerning HEK 293 and HeLa cells could be explained on one hand by the involvement of a yet unknown

uptake pathway in HEK 293 cells. On the other hand, there is general disagreement regarding to what extent the exact uptake pathway can be elucidated by inhibition studies. This is because the sensitivity of a certain cell line to various inhibitors of endocytic uptake pathways is different. In fact, the results of these studies can only give some indication of how the uptake of a certain molecule or complex could happen. Nevertheless, in conclusion, our findings contribute to the understanding of how CPP and especially hCT-derived carrier peptides are able to enter the cell interior and how the attached cargo can influence the adopted pathway. Anyway, the dissection of such mechanistic aspects is crucial in the further development and application of such drug delivery vectors for pharmaceutical purposes.

Furthermore, we demonstrated that our newly developed QD-CPP assemblies exert no cytotoxic effects on HeLa cells and have only a minor influence on cell viability after incubation of HEK 293 cells for 24 h with the constructs. This could be due to aggregation of the QD−peptide conjugates after 24 h in the cell interior. The toxic influence of the CF-hCT(18−32)-k7 peptides may be due to their rapid internalization in this cell line (as observed by fluorescence microscopy), an effect that was also described by Delehanty et al. (*6*). Furthermore, we assessed the stability of the QD−peptide nanoparticles after exposure of the double-labeled QD−peptide conjugate for 24 h to both cell-lines. Still after 24 h, the constructs of QD and peptide seemed to be mostly intact, as indicated by the merged fluorescence. From this, we conclude that the QD surface can effectively help to protect the peptides from degradation. Considering future *in vivo* applications, this could be important because one major drawback in using peptides is often the lack of metabolic stability that restricts many *in vivo* experiments.

The past years have sparked great interest in the therapeutic potential of gene regulation and gene silencing. As a result, there have been great efforts in the development of different strategies to deliver siRNA or aptamers into mammalian cells. The aim of this work was therefore to provide tools that are not only helpful in imaging but also in drug delivery applications. According to this, our results from the delivery studies with Cy-3 labeled RNA demonstrate the versatility of our peptide−QD conjugates. RNA of different length was efficiently transported into HeLa and HEK 293 cells. Furthermore, with the help of chloroquine it was possible to deliver the conjugates into the cytosol. Recently, we were able to demonstrate that the addition of chloroquine is useful in improving transfection rates in several cell lines and does not influence cell viability in the tested concentrations (*21*). Other approaches like the addition of cationic lipids are common for achieving endosomal escape (*35*). However, depending on whether chloroquine was added or not the complex of QD−peptide conjugates and RNA persisted in vesicles or was discharged in the cytoplasma. Interestingly, upon release out of the vesicles it seems that the RNA has dissociated from the QD−peptide assembly. After 6 h, only the green fluorescence was visible in the cytosol originating from the QD-bioconjugate. The red fluorescence from the RNA was only merely seen. Therefore, it must be assumed that the RNA dissociated from the positively charged peptides coupled to the QDs. Since we could show that the QD−peptide conjugate was stable for at least 24 h, the green fluorescence is in fact assumed to derive from the intact QD−peptide bioconjugate. The problem in the use of QDs is that they are sequestered in vesicles after cell entry. Thus, they are not available for molecular recognition or targeting. By using our approach, this obstacle can be overcome, and the delivery of therapeutic RNA to its target can be realized. Therefore, our delivery systems could be very useful tools for the transport and monitoring of other structures like siRNA or aptamers.

CONCLUSION

The aim of this study was to develop fluorescent nanoparticles suitable for the nonviral delivery and monitoring of therapeutic oligonucleotides. Therefore, we incorporated in a first step hCT-derived carrier peptides on the surface of luminescent quantum dots. Second, we carefully characterized these new systems and could demonstrate that they are nontoxic and possess high stability inside cells. Furthermore, we found some key factors concerning their uptake mechanism. The last step demonstrated that our QD−peptide conjugates successfully deliver complexed RNA into cells. This explored approach could be easily adapted to the transport and tracking of other biologically active molecules important in gene therapy.

ACKNOWLEDGMENT

The authors thank R. Reppich-Sacher for recording the MALDI mass spectra and K. Löbner for help in cell culture experiments. Cy-3 labeled RNA was a gift from Prof. Dr. U. Hahn and is kindly acknowledged. I. Neundorf thanks Prof. Dr. A. G. Beck-Sickinger for generous access to all resources of the institute.

Supporting Information Available: Supplementary experimental figures and description of the figures. This material is available free of charge via the Internet at http://pubs.acs.org.

LITERATURE CITED

(1) Jaiswal, J. K., Mattoussi, H., Mauro, J. M., and Simon, S. M. (2003) Long-term multiple color imaging of live cells using quantum dot bioconjugates. *Nat. Biotechnol. 21*, 47–51.

(2) Smith, A. M., and Nie, S. (2004) Chemical analysis and cellular imaging with quantum dots. *Analyst 129*, 672–677.

(3) Watson, A., Wu, X., and Bruchez, M. (2003) Lighting up cells with quantum dots. *Biotechniques 34*, 296300, 302−303.

(4) Mae, M., and Langel, U. (2006) Cell-penetrating peptides as vectors for peptide, protein and oligonucleotide delivery. *Curr. Opin. Pharmacol. 6*, 509–514.

(5) Snyder, E. L., and Dowdy, S. F. (2005) Recent advances in the use of protein transduction domains for the delivery of peptides, proteins and nucleic acids in vivo. *Expert Opin. Drug Delivery 2*, 43–51.

(6) Delehanty, J. B., Medintz, I. L., Pons, T., Brunel, F. M., Dawson, P. E., and Mattoussi, H. (2006) Self-assembled quantum dot-peptide bioconjugates for selective intracellular delivery. *Bioconjugate Chem. 17*, 920–927.

(7) Lagerholm, B. C., Wang, M., Ernst, L. A., Ly, D. H., Liu, H., Bruchez, M. P., and Waggoner, A. S. (2004) Multicolor coding of cells with cationic peptide coated quantum dots. *Nano Lett. 4*, 2019–2022.

(8) Bendifallah, N., Rasmussen, F. W., Zachar, V., Ebbesen, P., Nielsen, P. E., and Koppelhus, U. (2006) Evaluation of cell-penetrating peptides (CPPs) as vehicles for intracellular delivery of antisense peptide nucleic acid (PNA). *Bioconjugate Chem. 17*, 750–758.

(9) Pooga, M., Kut, C., Kihlmark, M., Hallbrink, M., Fernaeus, S., Raid, R., Land, T., Hallberg, E., Bartfai, T., and Langel, U. (2001) Cellular translocation of proteins by transportan. *Faseb J. 15*, 1451–1453.

(10) Turner, J. J., Arzumanov, A. A., and Gait, M. J. (2005) Synthesis, cellular uptake and HIV-1 Tat-dependent trans-activation inhibition activity of oligonucleotide analogues disulphide-conjugated to cell-penetrating peptides. *Nucleic Acids Res. 33*, 27–42.

(11) Akerman, M. E., Chan, W. C., Laakkonen, P., Bhatia, S. N., and Ruoslahti, E. (2002) Nanocrystal targeting in vivo. *Proc. Natl. Acad. Sci. U.S.A. 99*, 12617–12621.
(12) Lewin, M., Carlesso, N., Tung, C. H., Tang, X. W., Cory, D., Scadden, D. T., and Weissleder, R. (2000) Tat peptide-derivatized magnetic nanoparticles allow in vivo tracking and recovery of progenitor cells. *Nat. Biotechnol. 18*, 410–414.
(13) Pontiroli, A. E., Alberetto, M., and Pozza, G. (1985) Intranasal calcitonin and plasma calcium concentrations in normal subjects. *Br. Med. J. (Clin. Res. Ed.) 290*, 1390–1391.
(14) Stroop, S. D., Nakamuta, H., Kuestner, R. E., Moore, E. E., and Epand, R. M. (1996) Determinants for calcitonin analog interaction with the calcitonin receptor N-terminus and transmembrane-loop regions. *Endocrinology 137*, 4752–4756.
(15) Neundorf, I., and Beck-Sickinger, A. G. (2005) Calcitonin-derived carrier peptides. *Curr. Pharm. Des. 11*, 3661–3669, Calcitonin-derived carrier peptides.
(16) Krauss, U., Kratz, F., and Beck-Sickinger, A. G. (2003) Novel daunorubicin-carrier peptide conjugates derived from human calcitonin segments. *J. Mol. Recognit. 16*, 280–287.
(17) Machova, Z., Muhle, C., Krauss, U., Trehin, R., Koch, A., Merkle, H. P., and Beck-Sickinger, A. G. (2002) Cellular internalization of enhanced green fluorescent protein ligated to a human calcitonin-based carrier peptide. *ChemBioChem 3*, 672–677.
(18) Rennert, R., Wespe, C., Beck-Sickinger, A. G., and Neundorf, I. (2006) Cell-penetrating peptides as vectors for peptide, protein and oligonucleotide delivery. *Biochim. Biophys. Acta 1758*, 347–354.
(19) Rennert, R., Neundorf, I., and Beck-Sickinger, A. G. (2008) Calcitonin-derived peptide carriers: mechanisms and application. *Adv. Drug Delivery Rev. 60*, 485–498.
(20) Krauss, U., Muller, M., Stahl, M., and Beck-Sickinger, A. G. (2004) In vitro gene delivery by a novel human calcitonin (hCT)-derived carrier peptide. *Bioorg. Med. Chem. Lett. 14*, 51–54.
(21) Rennert, R., Neundorf, I., Jahnke, H. G., Suchowerskyj, P., Dournaud, P., Robitzki, A., and Beck-Sickinger, A. G. (2008) Generation of carrier peptides for the delivery of nucleic acid drugs in primary cells. *ChemMedChem 3*, 241–253.
(22) Foerg, C., Ziegler, U., Fernandez-Carneado, J., Giralt, E., Rennert, R., Beck-Sickinger, A. G., and Merkle, H. P. (2005) Decoding the entry of two novel cell-penetrating peptides in HeLa cells: lipid raft-mediated endocytosis and endosomal escape. *Biochemistry 44*, 72–81.
(23) Ruan, G., Agrawal, A., Marcus, A. I., and Nie, S. (2007) Imaging and tracking of Tat peptide-conjugated quantum dots in living cells: new insights into nanoparticle uptake, intracellular transport, and vesicle shedding. *J. Am. Chem. Soc. 129*, 14759–14766.
(24) Nichols, B. J., Kenworthy, A. K., Polishchuk, R. S., Lodge, R., Roberts, T. H., Hirschberg, K., Phair, R. D., and Lippincott-Schwartz, J. (2001) Rapid cycling of lipid raft markers between the cell surface and Golgi complex. *J. Cell Biol. 153*, 529–541.
(25) Puri, V., Watanabe, R., Singh, R. D., Dominguez, M., Brown, J. C., Wheatley, C. L., Marks, D. L., and Pagano, R. E. (2001) Clathrin-dependent and -independent internalization of plasma membrane sphingolipids initiates two Golgi targeting pathways. *J. Cell Biol. 154*, 535–547.
(26) Thorstensen, K., and Romslo, I. (1988) Uptake of iron from transferrin by isolated rat hepatocytes. A redox-mediated plasma membrane process? *J. Biol. Chem. 263*, 8844–8850.
(27) Shpetner, H., Joly, M., Hartley, D., and Corvera, S. (1996) Potential sites of PI-3 kinase function in the endocytic pathway revealed by the PI-3 kinase inhibitor, wortmannin. *J. Cell Biol. 132*, 595–605.
(28) Swanson, J. A., and Watts, C. (1995) Macropinocytosis. *Trends Cell Biol. 5*, 424–428.
(29) Le, P. U., and Nabi, I. R. (2003) Distinct caveolae-mediated endocytic pathways target the Golgi apparatus and the endoplasmic reticulum. *J. Cell Sci. 116*, 1059–1071.
(30) Ikonen, E. (2001) Roles of lipid rafts in membrane transport. *Curr. Opin. Cell Biol. 13*, 470–477.
(31) Cheng, J., Zeidan, R., Mishra, S., Liu, A., Pun, S. H., Kulkarni, R. P., Jensen, G. S., Bellocq, N. C., and Davis, M. E. (2006) Structure-function correlation of chloroquine and analogues as transgene expression enhancers in nonviral gene delivery. *J. Med. Chem. 49*, 6522–6531.
(32) Zhou, M., Nakatani, E., Gronenberg, L. S., Tokimoto, T., Wirth, M. J., Hruby, V. J., Roberts, A., Lynch, R. M., and Ghosh, I. (2007) Peptide-labeled quantum dots for imaging GPCRs in whole cells and as single molecules. *Bioconjugate Chem. 18*, 323–332.
(33) Wu, X., Liu, H., Liu, J., Haley, K. N., Treadway, J. A., Larson, J. P., Ge, N., Peale, F., and Bruchez, M. P. (2003) Immunofluorescent labeling of cancer marker Her2 and other cellular targets with semiconductor quantum dots. *Nat. Biotechnol. 21*, 41–46.
(34) Duan, H., and Nie, S. (2007) Cell-penetrating quantum dots based on multivalent and endosome-disrupting surface coatings. *J. Am. Chem. Soc. 129*, 3333–3338.
(35) Derfus, A. M., Chen, A. A., Min, D. H., Ruoslahti, E., and Bhatia, S. N. (2007) Targeted quantum dot conjugates for siRNA delivery. *Bioconjugate Chem. 18*, 1391–1396.
(36) Rennert, R., Neundorf, I., Beck-Sickinger, A. G. (2007) Synthesis and application of peptides as drug carriers. *Nucleic Acid and Peptide Aptamers edition of the Methods in Molecular Biology series*, Humana Press Inc., Totowa, USA, accepted.
(37) Kaplan, I. M., Wadia, J. S., and Dowdy, S. F. (2005) Cationic TAT peptide transduction domain enters cells by macropinocytosis. *J. Controlled Release 102*, 247–253.
(38) Duchardt, F., Fotin-Mleczek, M., Schwarz, H., Fischer, R., and Brock, R. (2007) A comprehensive model for the cellular uptake of cationic cell-penetrating peptides. *Traffic 8*, 848–866.
(39) Futaki, S., Nakase, I., Tadokoro, A., Takeuchi, T., and Jones, A. T. (2007) Arginine-rich peptides and their internalization mechanisms. *Biochem. Soc. Trans. 35*, 784–787.
(40) Singh, R. D., Puri, V., Valiyaveettil, J. T., Marks, D. L., Bittman, R., and Pagano, R. E. (2003) Selective caveolin-1-dependent endocytosis of glycosphingolipids. *Mol. Biol. Cell 14*, 3254–3265.
(41) Torgersen, M. L., Skretting, G., van Deurs, B., and Sandvig, K. (2001) Internalization of cholera toxin by different endocytic mechanisms. *J. Cell Sci. 114*, 3737–3747.
(42) Kirkham, M., Fujita, A., Chadda, R., Nixon, S. J., Kurzchalia, T. V., Sharma, D. K., Pagano, R. E., Hancock, J. F., Mayor, S., and Parton, R. G. (2005) Ultrastructural identification of uncoated caveolin-independent early endocytic vehicles. *J. Cell Biol. 168*, 465–476.
(43) Kirkham, M., and Parton, R. G. (2005) Clathrin-independent endocytosis: new insights into caveolae and non-caveolar lipid raft carriers. *Biochim. Biophys. Acta 1745*, 273–286.
(44) Harush-Frenkel, O., Debotton, N., Benita, S., and Altschuler, Y. (2007) Targeting of nanoparticles to the clathrin-mediated endocytic pathway. *Biochem. Biophys. Res. Commun. 353*, 26–32.

BC800172Q

SUPPORTING INFORMATION

Quantum dot–carrier peptide conjugates suitable for imaging and delivery applications

Cornelia Walther, Karolin Meyer, Robert Rennert, Ines Neundorf

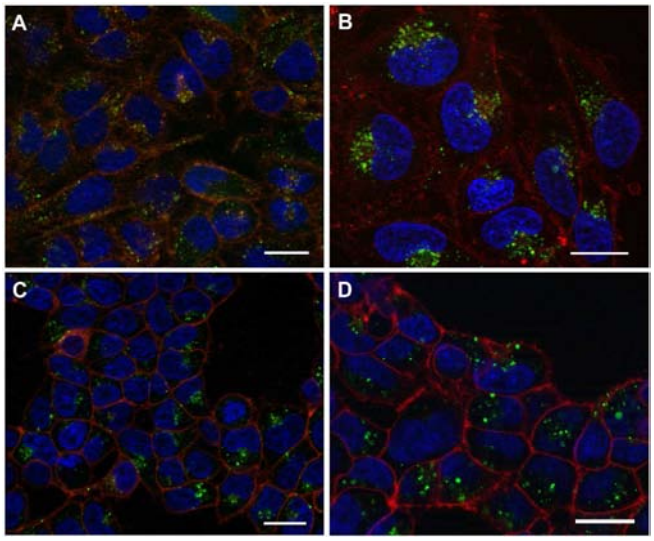

Figure 1. Cellular uptake of CF-hCT(18-32)-k7. Co-localisation study of CF-hCT(18-32)-k7 with either transferrin or cholera toxin in HeLa and HEK 293 cells. Co-localised vesicles are yellow, CF-labelled peptide is visible in green and endocytosis markers (transferrin or cholera toxin) are red. Panel A and B shows Hela and Panel C and D HEK 293 cells. For co-localisation studies with transferrin (A, C) cells were simultaneously incubated with 25 µM CF-hCT(18-32)-k7 for 30 min at 37°C and transferrin (50 µg/ml). For co-localisation studies with cholera toxin (B, D) cells were pre-incubated with 10 µg/ml cholera toxin (B: 30min at 4°C, D: 15 min at 37°C) and then incubated with 25 µM CF-hCT(18-32)-k7 (B: 1 h at 37°C, D: 15 min at 37°C). The scale bar is 20 µm.

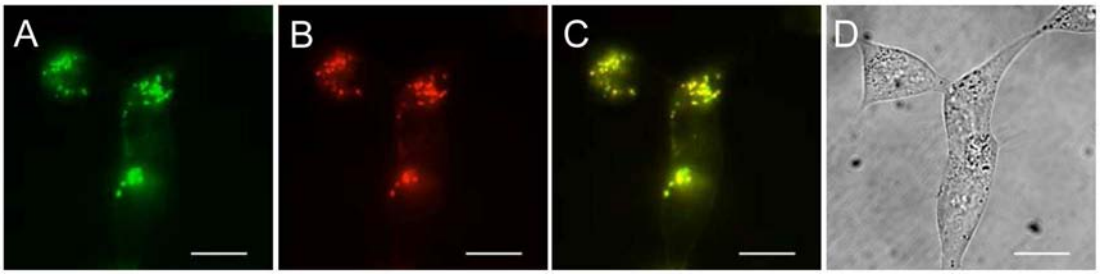

Figure 2. Stability of the QD-peptide bioconjugates in HEK 293 cells. Cells were incubated with the double-labelled conjugate QD_{617}-[C^{17}]-hCT(18-32)-k7(CF) for 4 h. QD-peptide solution was replaced by cell culture medium and fluorescence imgaging was performed after 24 h. (A) CF fluorescence, (B) QD fluorescence, (C) merge, (D) bright field. The scale bar is 20 µm.

Synthesis and Complexation Ability of a Novel Bis-(guanidinium)-tetrakis-(β-cyclodextrin) Dendrimeric Tetrapod as a Potential Gene Delivery (DNA and siRNA) System. Study of Cellular siRNA Transfection

S. Menuel,[†] S. Fontanay,[†] I. Clarot,[†] R. E. Duval,[†] L. Diez,[‡] and A. Marsura*[,†]

UMR 7565 SRSMC and UMR 7564 LCPME, CNRS, Nancy-Université, Faculté de Pharmacie 5 rue A. Lebrun, BP 80403, 54001 Nancy Cedex, France. Received May 14, 2008; Revised Manuscript Received October 6, 2008

The facile synthesis of a novel bis-(guanidinium)-tetrakis-(β-cyclodextrin) tetrapod, the first example of a new host family, was described, and the ability of the cyclodextrin CyD tetrapod to form molecular association with siRNA and DNA guest molecules was demonstrated. Affinity capillary electrophoresis was used to determine the binding constant with the evaluation of the shift in the electrophoretic mobility μ of injected siRNA when various CyD tetrapod concentrations were added to the run buffer. A significant association constant (K_a =16 000 M^{-1}) was obtained with borate buffer when double-stranded siRNA was primarily opened with the help of temperature. An efficient cellular transfection of siRNA into human embryonic lung fibroblasts was observed by fluorescence microscopy.

INTRODUCTION

Developing new, highly efficient, and nontoxic gene delivery carriers in cells remain an important challenge both in basic sciences and in clinical research fields. At the present time, viral vectors (clinical tests using adenoviruses, adeno-associate viruses, retroviruses, etc.) have been successfully applied, but their side effects such as severe pathogenicity limited further application (*1*). Besides, nonviral (cationic polymers, lipids, dendritic polymers, polyplexes, etc.) vectors have been studied as an alternative strategy for gene delivery because of their lower toxicity, non-immunogenicity, and convenient handling (*2*). However, the remaining difficulties with nonviral vectors remain with their relatively lower transfection efficiency than viral vectors. The poor performance was also due to polyplex aggregation as a consequence of decreasing water solubility induced by charge neutralization arising when electrostatic interaction between polyanionic DNA and polycationic vectors occurs (*3*).

Significant efforts for DNA delivery and more recently siRNA in cells have been conducted the past ten years through different nonviral approaches using macromolecular systems as carriers (*4*−*6*). Prosaically, two families of molecules are represented, on one hand nanoparticulate systems (*7*−*10*) and on the other hand polymeric systems (*11*−*15*).

Early in 1995, cyclodextrins (CyDs) and derivatives were introduced as potent carriers for phosphorothioate−ODN delivery. It was demonstated that cellular uptake was concentration and time dependent (*16*). Further, numerous contributions appear from that time in which either native and modified cyclodextrins were evaluated as ligands for nucleotides, oligonucleotides, and DNA (*17*−*19*).

Our first report on the subject suggested early in 1997 monothiogalactosyl and heptakis-thiogalactosyl-β-cyclodextrins as novel nonpolymeric efficient vectors for small antisense-ODN (*20*). Some other examples have been reported in the literature on complexes of CyD-DNA as, e.g., CyD−PAMAM dendrimeric conjugates (*21*) or bis-amidinium-CyDs polymers (*22, 23*) and their corresponding PEG derivatives, including monosaccharidyl inclusion polyplexes (*24*). The latter has been demonstrated further as totally biocompatible and efficient to transfect DNA in cells. In the same way, some liganded-CyDs cluster-organized, and dendrimers have been found able to form molecular associations with ODNs (*25, 26*). Furthermore recently, a family of sophisticated systems based on polymer−Cyd associations such as nanostructured multilayers using polylysine−CyD multilayers (*27*), polyelectrolyte multilayers (*28*), low weight or linear polyethyleneimine−CyD polymers (*29, 30*), or amphiphilic cationic CyDs (*31*) were successfully tested as *in vitro* nonviral gene delivery vectors. In parallel, the "molecular umbrella" tetrameric design and synthesis of nonviral noncyclodextrinyl vectors, notably based on the bottom-up construction of supramolecular systems, has been developed and has been shown to be able to cross the membrane of living cells and concentrate at the nucleus and therefore could be considered interesting molecular systems for nuclear drug targeting (*32*−*34*).

Here, we report in this way the synthesis of a novel bis-(guanidinium)-tetrakis-(β-cyclodextrin) dendrimeric tetrapod as a discrete molecular system, characterization of its self-assembly with a short interfering RNA (siRNA) oligonucleotide and single-stranded DNA, ability of the tetrapod to form molecular association with siRNA and DNA by affinity capillary electrophoresis, and siRNA *in vitro* transfection results.

EXPERIMENTAL SECTION

Materials. Chemicals for the synthesis, benzyl alcohol, and all other chemicals and solvents for electrophoresis experiments were of analytical grade and were purchased from Sigma-Aldrich. Ultrapure-grade water was obtained in a Milli-Q system from Millipore (Bedford, MA). MRC-5 cells (human pulmonary embryonic fibroblasts, ATCC CCL-171) were obtained from BioMerieux (France). The short interfering RNA (siRNA) oligonucleotide used is a 21 bp random duplex siRNA, purified and desalted, with no known homology to any mammalian

* Corresponding author. Fax: +33 3 83 68 23 45, Tel: +33 3 83 68 23 24, E-mail: Alain.Marsura@pharma.uhp-nancy.fr.
[†] UMR 7565 SRSMC.
[‡] UMR 7564 LCPME.

10.1021/bc800193p CCC: $40.75 © 2008 American Chemical Society
Published on Web 11/18/2008

Scheme 1. Synthetic Scheme of CyD Tetrapod 5

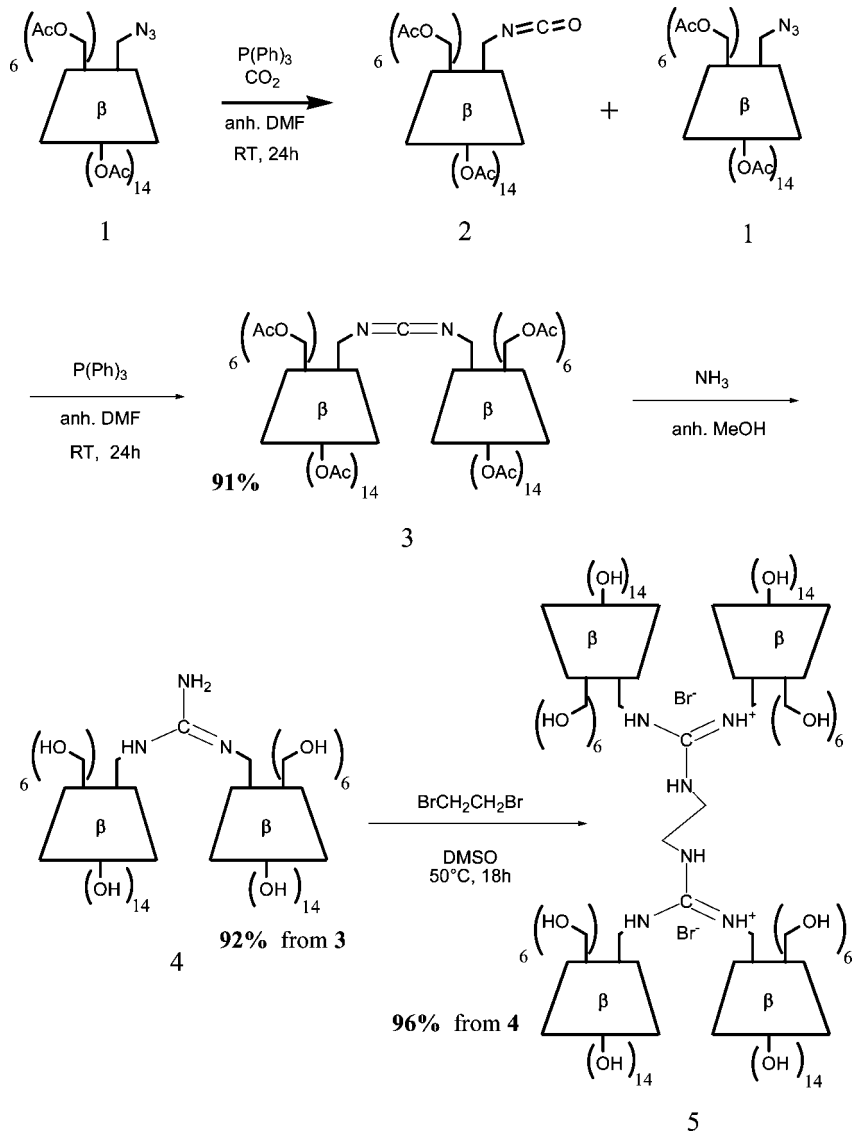

sequence, labeled by Cy3 fluorochrome. siRNA stock solution was provided by Eurogentec (siRNA 633790−637791 SCB-1, Eurogentec, France) at a concentration of 100 μM. Modified essential medium (MEM, 41090, Invitrogen) supplemented with 10% decomplemented fetal bovine serum (FBS, 10270, Invitrogen, lot 40Q5150K).

Synthesis. The pure tetrapod **5** was obtained in fairly good yield (96%) and in two steps from a carbodiimide-β-cyclodextrin dimer **3**, which is afforded by the "phosphine imide" strategy from the monoazido-CyD (Scheme 1). Compounds **1**, **2**, and **3** have been synthesized by known procedures in the literature (*35*, *36*).

Synthesis of 6-Monoguanidino-(bis-β-cyclodextrin) Dimer 4. Carbodiimide **3** (1.40 g; 0.615 mmol) (*35*) was dissolved in dichloromethane/methanol (5:1 by volume, 60 mL) and the solution was stirred at 25 °C under NH_3 for 18 h. After evaporation of the solvent, the residue was dissolved in methanol (5 mL) and precipitated with diethyl ether, filtered, and evaporated to dryness to give pure **4** (92%). FTIR (KBr): ν = 3374.5 cm^{-1} (OH);1736−1663 cm^{-1} (N═C−(NH_2)−NH). ESMS: 2292 [M + H^+]. ^{1}H NMR (400 MHz, D_2O, 25 °C, TMS): δ = 5.07 (m, 14H; H1), 3.95 (m, 14H; H3), 3.90−3.80 (m, 26H; H6a; H5), 3.71−3.62 (m, 16H; H6b; H2), 3.51 (m, 14H; H4). ^{13}C NMR (100 MHz, D_2O, 25 °C, TMS): δ = 175.1 (N═C−(NH_2)−NH), 102.2 (C1), 81.5 (C4), 73.4 (C2), 72.3 (C3), 72.2 (C6), 60.6 (C5).

Synthesis of the Bis-guanidinium-tetrakis-β-cyclodextrin Tetrapod 5. 6-Monoguanidino-(bis-β-cyclodextrin) dimer **4** (0.622 g; 0.271 mmol) and 1,2-dibromoethane (0.025 g; 0.135 mmol; 0.5 equiv) was dissolved in DMSO (25 mL), and the solution was stirred at 50 °C for 18 h under argon. The reaction was stopped by precipitation with diethyl ether (100 mL) at 25 °C and filtered. The residue was dissolved in methanol/water (1:2 by volume, 53 mL). This solution was concentrated to dryness, and the residue was dissolved in water (100 mL). After lyophilization, this solution gave pure **5** (96%). Found: C, 33.02; H, 6.53; N, 1.58; S, 5.31. $C_{127}H_{286}Br_2N_6O_{136}$, 10DMSO, 19$H_2O$ requires C, 32.96; H, 7.23; N, 1.57; S, 5.99. FTIR (KBr): ν = 3359.7 cm^{-1} (OH);1737 cm^{-1}; ($^+$NH═*C*−(NH_2)−NH, Br^-) 1639 cm^{-1}. ESMS: 3662 [M − (β-CyD−NH)$^+$]. MALDI-TOF: 4591 [M − 18]$^+$, 2292 [dipode **4** + H]$^+$. ^{1}H NMR (400 MHz, D_2O, 25 °C, TMS): δ = 5.10 (m, 28H; H1), 3.99 (m, 28H; H3), 3.95−3.81 (m, 52H; H6a; H5), 3.74−3.65 (m, 32H; H6b; H2), 3.50 (m, 28H; H4), 3.17 (m, 4H; CH_2). ^{13}C NMR (100 MHz, D_2O, 25 °C, TMS): δ = 174.0 (NHBr═*C*−(NH_2)−NH), 102.3 (C1), 81.6 (C4), 73.6 (C2), 72.4 (C3), 72.3 (C6), 60.7 (C5), 22.3 (CH_2).

Capillary Electrophoresis. All experiments were performed on a Beckman P/ACE 5500 model (Beckman, Fullerton, USA) equipped with a diode array detector (190−600 nm). Capillary temperature was controlled by coolant at 25.0 °C. An untreated

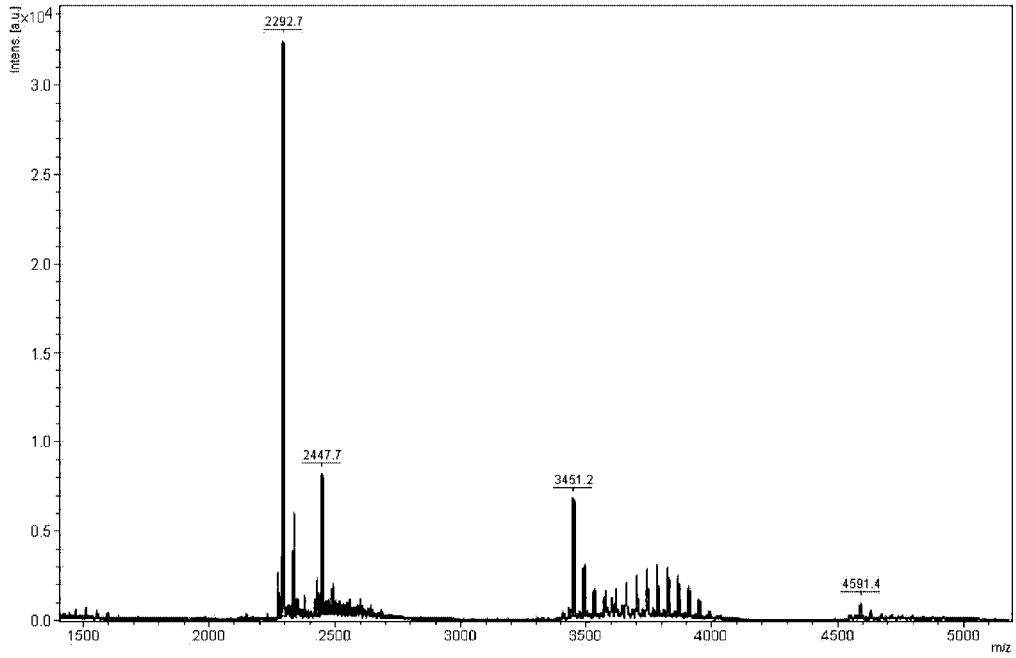

Figure 1. MALDI-TOF MS of Tetrapod **5**.

fused-silica capillary 75 μm i.d. with a total length of 47 cm (effective length 40 cm) was employed. All samples were injected in the hydrodynamic mode (10 s under pressure) at 20 kV. The experimental setup, data acquisition, and processing were governed using Beckman P/ACE Station software. The background electrolyte (BGE) was prepared by dissolving 2 μmol to 50 μmol of CyD tetrapod **5** in the appropriate borate buffer (25 mM, pH 9.3). Everyday, at the beginning of a run batch, the capillary was rinsed with 0.1 M sodium hydroxide (20 min) and ultrapure water (20 min). Before each injection, the capillary was successively rinsed with 0.1 M sodium hydroxide (2 min), ultrapure water (2 min), and BGE (2 min). All solutions introduced in the capillary were first percolated through an Alltech (Tampleuve, France) regenerated cellulose filter (0.45 μm pore size).

Electrophoresis Sample Preparation. Sample solutions were obtained by dissolving biological material in ultrapure water at the final concentration of 2 μM. Double-stranded siRNA was opened with temperature (94 °C) in the presence of CyD tetrapod **5** and diluted in run buffer at 0.2 μM before injection.

Cell Line, Cell Culture. The MRC5 cell line was cultured in Modified Essential Medium without antibiotics at 37 °C, 5% CO_2, under a humid atmosphere. Cell viability was determined by the trypan blue dye exclusion method. MRC-5 cells were plated at 5×10^5 cells/slide flask (170920, Nunc). For all experiments, cells were allowed to adhere and grow for 24 h in culture medium prior to siRNA transfection.

Transfection Complex (CyD Tetrapod/siRNA). First, we prepared an aqueous solution of tetrapod **5** at a final concentration of 2.5 mg/mL. The solution was sterilized through a 0.22 μm filter (SLGP033RS, Millipore). Second, we added 57.2 μL of this aqueous solution of CyD **5** to 12 μL of siRNA stock solution. After that, the solution was heated at 94 °C during 3 min, and then we controlled the cooling (less 0.8 °C per 5 s) until a final temperature of 2 °C was reached. This step is supposed to permit siRNA and CyD tetrapod **5** to complex together. Finally, we added this solution to 12 mL of MEM supplemented with 2% decomplemented fetal bovine serum in order to obtain our transfection solution.

***In Vitro* Transfection.** To start the transfection reaction, culture medium was replaced by 2 mL of this preparation (assay). Negative controls were transfected with either (i) CyD tetrapod **5** in the absence of any siRNA or (ii) siRNA in the absence of any CyD tetrapod **5**. Then, slides were incubated 37 °C, 5% CO_2, under a humid atmosphere, until appropriate times.

Table 1. Linear Regression Obtained with Equation 1 and Corresponding Binding Constants *K* for Single Stranded (ss) DNA in Phosphate Conditions (phos.) and for Single-Stranded DNA and Double- (ds) and Single-Stranded siRNA in Borate Conditions (bor.)

analyte	slope	intercept	corr. coef.	$K \pm$ s.d. M^{-1}
ss DNA phos.	1.818	7730.294	0.9996	4250 ± 750
ss DNA bor.	1.513	9189.418	0.9927	6050 ± 1550
ds siRNA bor.	~0	–	–	–
ss siRNA bor.	0.630	10187.151	0.9992	16150 ± 3700

^{1}H NMR and ^{13}C NMR Spectroscopy. ^{1}H NMR and ^{13}C NMR spectra were obtained using a Bruker DRX-400 (400 MHz and 100 MHz, respectively).

Fluorescence Microscopy. In order to perform fluorescent microscopy analysis, cells were fixed with a 4% formaldehyde solution (in PBS) for 1 min and subsequently washed 3 times with PBS. Then, cells were counterstained with Hoechst 33342 for 1 min and washed 3 times in PBS. Cells were mounted in PBS and examined by fluorescence microscopy with appropriate filters (microscope Axioskop SIP 48843, Zeiss, and camera AxioCam MRC, Zeiss). Observations were made after 6, 12, and 24 h of exposure with a 400× magnification.

RESULTS AND DISCUSSION

Synthesis and Characterization of CyD Tetrapod 5. Tetrapod **5** was synthesized according to our previous report (*37*) using the "phosphine imide" efficient strategy (also named Staudinger-Aza-Wittig tandem reaction) developed by our team in four steps from the monoazido-β-CyD (*35*). Scheme 1 shows the entire synthetic procedure of the tetrapod **5** available in a large-scale batch. The structure of **5** was confirmed by FTIR, ^{1}H and ^{13}C NMR, MALDI-TOF, and elemental analysis. Figure 1 shows the MALDI-TOF MS of **5**.

Self-Assemblies of CyD Tetrapod 5 and siRNA or DNA. Numerous analytical methods have been developed and applied in the study of the interactions between small ligands and biomacromolecules. Among them, some chromatographic

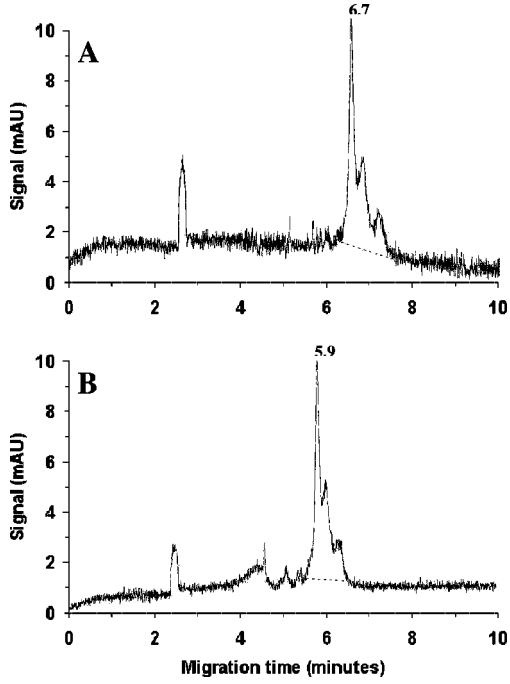

Figure 2. Electrophoregrams of single-stranded siRNA with background electrolyte containing 0 (A) and 25 μM of CyD (B). (Electrophoretic conditions were described in the Experimental Section).

methodologies, such as affinity chromatography or size exclusion, have also been employed to determine binding parameters (*38, 39*). Capillary electrophoresis (CE) is an attractive method for such determination. Low sample consumption, rapid analysis speed, and high efficiency are advantages that make this technology a major tool of association constant measurement. Several CE modes are available for such measurement, such as affinity capillary electrophoresis (ACE), Hummel-Dreyer method (HD), vacancy affinity capillary electrophoresis (VACE), vacancy peak method (VP), frontal analysis (FA), or frontal analysis continuous capillary eletrophoresis (FACCE) (*40*−*43*). Measurement in the ACE mode is based on the change in electrophoretic mobility of the biomolecule due to complexation to the ligand added at various concentrations in the background electrolyte. Both DNA and siRNA were used in this work to demonstrate the ability of **5** to form stable complexes with oligonucleotides.

The binding constants were estimated by the changes in the migration time of the analytes based on the different additions of **5** (2 to 50 μmol) in running buffers. For 1:1 association, the change in solute mobility with changing ligand concentration is related to the following equation (double reciprocal plot) (*44*).

$$\frac{1}{(\mu_i - \mu_f)} = \frac{1}{(\mu_c - \mu_f)K}\frac{1}{[\mathrm{CyD}]} + \frac{1}{(\mu_c - \mu_f)} \qquad (1)$$

where μ_i is the experimentally measured electrophoretic mobility of the solute, μ_f is the mobility of the free (uncomplexed) solute, μ_c is the electrophoretic mobility of the solute−ligand complex, K is the binding constant, and [CyD] is the equilibrium ligand concentration. Binding constants can be estimated by varying the ligand concentration at constant solute concentrations and fitting the data by linear regression to eq 1. To develop and optimize the electrophoresis methodology, a single-stranded DNA primer was primarily used. It is well-known that capillary electrophoresis of biological material such as DNA with BGE containing borates could lead to inappropriate complexation study. In a first approach, the single-stranded DNA under evaluation was used with two electrolyte conditions: borate 25 mM pH 9.3 and phosphate 50 mM pH 9.0. As illustrated in Table 1 lines 1 and 2, both conditions lead to equivalent binding constants (similar order) indicating that borates have no influence on the association process with the CyD tetrapod **5**.

SiRNA was first used without temperature treatment (double strand not open), and no binding constant could be determined as no modification of the analyte migration time was observed (Table 1, line 3). When siRNA was opened (single-stranded configuration), the addition of CyD to the background electrolyte led to a significant decrease of the electrophoretic mobility, as

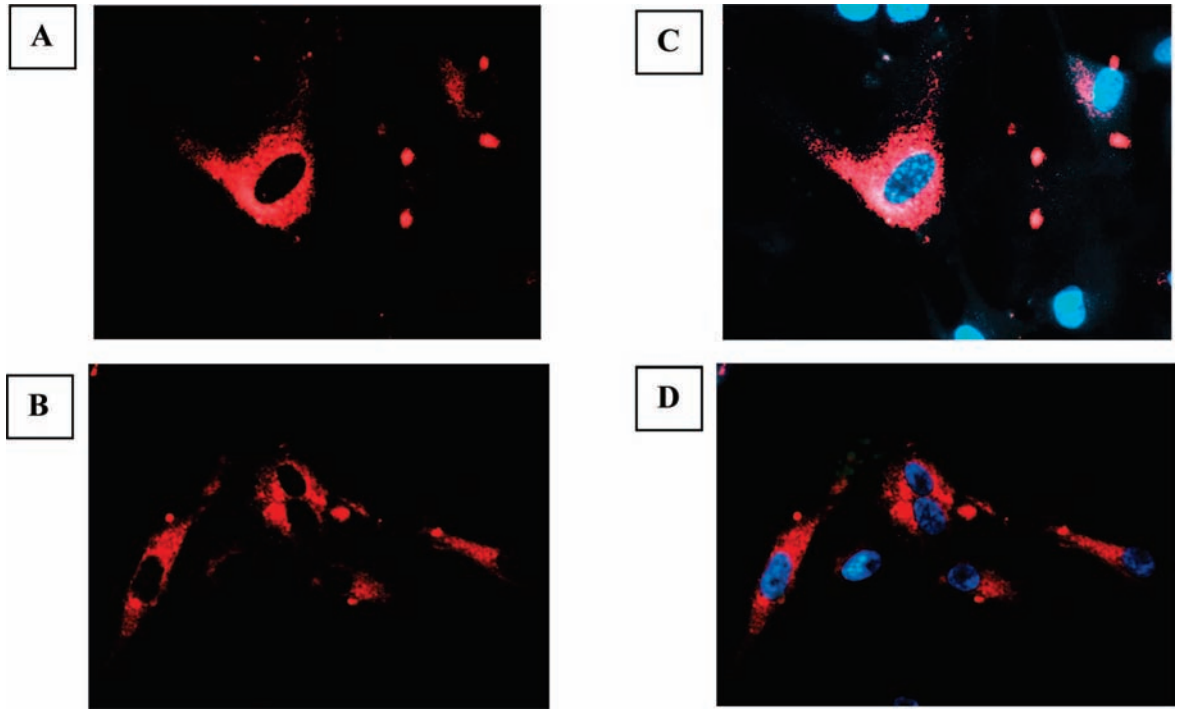

Figure 3. (A) Cy3-labeled siRNA at 6 h after injection; (B) after 12 h; (C) Cy3-labeled siRNA at 6 h after injection with Hoechst counterstained nuclei; (D) Cy3-labeled siRNA at 12 h after injection with Hoechst counterstained nuclei.

illustrated in Figure 2 for 0 and 25 μM of CyD added. The association constant obtained (16 150 M^{-1}, Table 1, line 4) indicates the ability of ligand **5** to form a strong association with such a biological molecule.

Toxicity Experiments. Toxicity experiments on tetrapod were performed *in vitro*, by measuring cellular viability (e.g., MTT assay) in the presence of increasing amounts of tetrapod. We have demonstrated that the tetrapod was poorly cytotoxic on MRC-5 cells, with a greater toxic effect for prolonged exposure times (e.g., 168 h), and concluded that it weakly affects MRC-5 cell viability (*37*).

Transfection Experiments. For transfection experiments, we used an siRNA labeled with Cy3 (see Experimental Section) to investigate the intracellular delivery and traffic of siRNA by the CyD tetrapod **5** in MRC-5 cells. Negative controls (see Experimental Section for details) showed no Cy3 labeling (data not shown), while numerous Cy3-stained cells, showing an intense red fluorescence, were detected in tetrapod-siRNA transfected MRC-5 cells, and thus until 6 h post-transfection (Figure 3A,C).

Hence, we demonstrated that a final concentration of 100 μM of scrambled siRNA is sufficient for an efficient cell transfection until 6 h of incubation with our tetrapod (Figure 3A). Nevertheless, the transfection reaction is clearly time-dependent, with a more intense fluorescence for 12 h transfected cells (Figure 3C). We observed the same staining at 24 h post-transfection. Figure 3B,D, showing parallel Hoechst 33342 (e.g., blue fluorescence) and Cy3 (e.g., red fluorescence) staining on the same field, at both 6 and 12 h, respectively. Hoechst labeling was used to counterstain nuclei of MRC-5 cells. Hence, we demonstrated a, siRNA transfection and/or localization in the cytoplasm (e.g., at the periphery of nucleus) of transfected MRC-5 cells.

We have also demonstrated that the efficiency of CyD tetrapod **5** is comparable to these of commercial compounds, i.e., PEI as previously described by Ikeda (*45*) and Ou (*46*); but it is noteworthy that CyD tetrapod **5** is also clearly less toxic than such compounds.

In summary, this novel tetrapod has high gene transfection efficiency, low cytotoxicity, and great potential for gene delivery *in vitro*. From the above data, bis(guanidinium)-tetrakis-(β-CD) **5** has a significantly high gene transfection in primary human lung fibroblast cell line (MRC-5), and it could be a promising gene carrier in many other primary cancer or stem cells. We actually attempted to validate the efficiency of delivery by silencing cellular "housekeeping" gene.

CONCLUSION

We synthesized a novel bis-(guanidinium)-tetrakis-(β-cyclodextrin) dendrimeric tetrapod for gene delivery systems. The compound presented here is the first example of a new molecular family including future CyD linear oligomeric analogues (penta-, hexapod, etc.) presently in progress. Tetrapod **5** could form 1:1 supramolecular water-soluble complexes with single-stranded DNA and siRNA as shown by capillary electrophoresis, and a better association with siRNA instead DNA was demonstrated. Elsewere, efficiency of siRNA and DNA transfection in cells is comparable to existing polyplex or polycationic systems. Toxicity experiments reveal that CyD tetrapod **5** is less cytotoxic than existing PEI cationic polymers. Finally, we can conclude that CyD tetrapod **5** is efficient not only for complexation of nucleic acids, but also for transfection of siRNA.

ACKNOWLEDGMENT

We thank the CNRS, MESR, and District of Nancy for financial supports. Pr. J.J. Gaumet for MALDI-TOF spectrum registration, Pr. A. Nicolas for providing electrophoresis facilities and discussion, Pr. C. Finance for Biological facilities, and Mr. E. Dubs for technical assistance in the synthesis of a cyclodextrin starting product. The service commun of NMR (UHP) is also acknowledged.

LITERATURE CITED

(1) Kay, M. A., Liu, D., and Hoogerbrugge, P. M. (1997) Gene therapy. *Proc. Natl. Acad. Sci. U.S.A. 94*, 12744–12746.
(2) Luo, D., and Saltzman, W. M. (2000) Synthetic DNA delivery systems. *Nat. Biotechnol. 18*, 33–37.
(3) Tang, M. X., and Szoka, F. C., Jr. (1997) The influence of polymer structure on the interactions of cationic polymers with DNA and morphology of the resulting complexes. *Gene Ther. 4*, 823–832.
(4) Boussif, O., Lezoualc'h, F., Zanta, M. A., Mergny, M. D., Scherman, D., Demeneix, B., and Behr, J. P. (1995) A versatile vector for gene and oligonucleotide transfer into cells in culture and in vivo: polyethyleneimine. *Proc. Natl. Acad. Sci. U.S.A. 92*, 7297–7301.
(5) Lungwitz, U., Breunig, M., Blunk, T., and Gopferich, A. (2005) Polyethyleneimine-based non-viral gene delivery systems. *Eur. J. Pharm. Biopharm. 60*, 247–260.
(6) Bolcato-Bellemin, A.-L., Bonnet, M. E., Creusat, G., Erbacher, P., and Behr, J. P. (2007) Sticky overhangs enhance siRNA-mediated gene silencing. *Proc. Natl. Acad. Sci. U.S.A. 104*, 16050–16055.
(7) Lambert, G., Fattal, E., and Couvreur, P. (2001) Nanoparticulate systems for the delivery of antisense oligonucleotides. *Adv. Drug Delivery Rev. 47*, 99–112, and refs cited therein.
(8) Felgner, P. L., Gadek, T. R., Holm, M., Roamn, R., Chan, H. W., Wenz, M., Northrop, J. P., Ringold, G. M., and Danielsen, M. (1987) Lipofection: a highly efficient lipid-mediated DNA-transfection procedure. *Proc. Natl. Acad. Sci. U.S.A. 84*, 7413–7417.
(9) Felgner, P. L., Barenholz, Y., Behr, J. P., Cheng, S. H., Cullis, P., Huang, L., Jessee, J. A., Seymour, L., Szoka, F., Thierry, A. R., Wagner, E., and Wu, G. (1997) Nomenclature for synthetic gene delivery systems. *Hum. Gene Ther. 8*, 511–512.
(10) Veena, V., Thomas, T., and Thomas, T. J. (2002) DNA nanoparticles and development of DNA delivery vehicles for gene therapy. *Biochemistry 41*, 14085–14094.
(11) Kichler, A., Leborgne, C., Coeytaux, E., and Danos, O. (2001) Polyethyleneimine-mediated gene delivery: a mechanistic study. *J. Gene Med. 3*, 134–144, and refs cited therein.
(12) Fischer, D., von Harpe, A., Kunath, K., Petersen, H., Li, Y., and Kissel, T. (2002) Copolymers of ethylene imine and N-(2-hydroxyethyl)-ethylene imine as tools to study effects of polymer structure on physicochemical and biological properties of DNA complexes. *Bioconjugate Chem. 13*, 1124–1133.
(13) Gebhart, C. L., Sriadibhatla, S., Vinogradov, S., Lemieux, P., Alakhov, V., and Kabanov, A. V. (2002) Designed and formulation of polyplexes based on pluronic-polyethyleneimine conjugates for gene transfer. *Bioconjugate Chem. 13*, 937–944.
(14) Kim, T.-i., Seo, H. J., Choi, J. S., Jang, H. S., Baek, J. U., Kim, K., and Park, J. S. (2004) PAMAM-PEG-PAMAM: Novel triblock copolymer as a biocompatible and efficient gene delivery carrier. *Biomacromlecules 5*, 2487–2492.
(15) Kim, T.-i., Baek, J. U., Yoon, J. K., Choi, J. S., Kim, K., and Park, J. S. (2007) Synthesis and characterization of a novel arginine-grafted dendritic block copolymer for gene delivery and study of its cellular uptake pathway leading to transfection. *Bioconjugate Chem. 18*, 309–317.
(16) Zhao, Q., Temsamani, J., and Agrawal, S. (1995) Use of cyclodextrins and its derivatives as carriers for oligonucleotide delivery. *Antisense Res. Dev. 5*, 185–192.
(17) Hirayama, F., and Uekama, K. (1999) Cyclodextrin-based controlled drug release system. *Adv. Drug Delivery Rev. 36*, 125–141.
(18) Redenti, E., Pietra, C., Gerloczy, A., and Szente, L. (2001) Cyclodextrins in oligonucleotide delivery. *Adv. Drug Delivery Rev. 53*, 235–244.

(19) Cserhati, T., and Forgas, E. (2001) Quantitaive relationship between the chemical structure of antisense nucleosides and their capacity to interact with cyclomalto-octaose. *Eur. J. Pharm. Biopharm. 51*, 39–44.
(20) Abdou, S., Collomb, J., Sallas, F., Marsura, A., and Finance, C. (1997) β-Cyclodextrin derivatives as carriers to enhance the antiviral activity of an antisense oligonucleotide directed toward a coronavirus intergenic consensus sequence. *Arch. Virol. 142*, 1585–1602.
(21) Arima, H., Kihara, F., Hirayama, F., and Uekama, K. (2001) Enhancement of gene expression by polyamidoamine dendrimer conjugates with α-, β-, and γ-cyclodextrins. *Bioconjugate Chem. 12*, 476–484.
(22) Gonzales, H., Hwang, S. J., and Davies, M. E. (1999) New class of polymers for the delivery of macromolecular therapeutics. *Bioconjugate Chem. 10*, 1068–1074.
(23) Hwang, S. J., Bellocq, N. C., and Davies, M. E. (2001) Effects of structure of β-cyclodextrin-containing polymers on gene delivery. *Bioconjugate Chem. 12*, 280–290.
(24) Shuai, X., Merdan, T., Unger, F., and Kissel, T. (2005) Supramolecular gene delivery vectors showing enhanced transgene expression and good biocompatibility. *Bioconjugate Chem. 16*, 322–329.
(25) Vargas-Berrenguel, A., Ortega-caballero, F., Santoyo-Gonzales, F., Garcia-Lopez, J. J., Gimenez-Martinez, J. J., Garcia-Fuentes, L., and Ortiz-Salmeron, E. (2002) Dendritic galactosides based on a b-cyclodextrin core for the construction of site-specific molecular delivery systems: synthesis and molecular recognition studies. *Chem. Eur. J. 8*, 812–827.
(26) Ortiz-Mellet, C., Defaye, J., and Garcia Fernandez, J. M. (2002) Multivalent cyclooligosaccharides: versatile carbohydrate clusters with dual role as molecular receptors and lectin ligands. *Chem. Eur. J. 8*, 1983–1992.
(27) Zhang, X., Sharma, K. K., Boeglin, M., Ogier, J., Mainard, D., Voegel, J.-C., Mély, Y., and Benkiral-Jessel, N. (2008) Transfection abilityand intracellular DNA pathway of nanostructured gene-delivery systems. *Nano Lett. 8*, 2432–2436.
(28) Jessel, N., Oulad-Abdelghani, M., Meyer, F., Lavalle, P., Haikel, Y., Schaaf, P., and Voegel, J.-C. (2006) Multiple and time-sheduled in situ DNA delivery mediated by β-cyclodextrin embedded in a polyelectrolyte multilayer. *Proc. Natl. Acad. Sci. U.S.A. 103*, 8618–8621.
(29) Huang, H., Tang, G., Wang, Q., Li, D., Shen, F., Zhou, J., and Yu, H. (2006) Two novel nonviral gene delivery vectors: low molecular weight polyethyleneimine cross-linked by (2-hydroxypropyl)-β-cyclodextrin or (2-hydroxypropyl)-γ-cyclodextrin. *Chem. Commun.* 2382–2384.
(30) Yamashita, A., Choi, H. S., Ooya, T., Yui, N., Akita, H., Kogure, K., and Harashima, H. (2006) Improved cell viability of linear polyethyleneimine through γ-cyclodextrin inclusion for effective gene delivery. *ChemBioChem 7*, 297–302.
(31) Cryan, S. A., Donohue, R., Ravoo, B. J., Darcy, R., and O'Droiscoll, C. M. (2004) Cationic cyclodextrin amphiphiles as gene delivery vectors. *J. Drug Delivery Sci. Technol. 14*, 57–62.
(32) Janout, V., Lanier, M., and Regen, S. L. (1997) Design and synthesis of molecular umbrellas. *J. Am. Chem. Soc. 119*, 640–647.
(33) Jing, B., Janout, V., and Regen, S. L. (2003) Fully detachable molecular umbrellas as peptide delivery agents. *Bioconjugate Chem. 14*, 1191–1196.
(34) Mehiri, M., Jing, B., Ringhoff, D., Janout, V., Cassimeris, L., and Regen, L. S. (2008) Cellular entry and nuclear targeting by a highly anionic molecular umbrella. *Bioconjugate Chem. 19*, 1510–1513.
(35) Charbonnier, F., Marsura, A., Roussel, K., Kovàcs, J., and Pintér, I. (2001) Studies on the synthesis and structure of new urea-linked sugar podando-coronand derivatives. *Helv. Chim. Acta 84*, 535–551.
(36) Charbonnier, F., Marsura, A., and Pintér, I. (1999) One-pot synthesis of a thioureido-β-cyclodextrin dimer. *Tetrahedron Lett. 40*, 6581–6583.
(37) Menuel, S., Duval, R. E., Cuc, D., Mutzenhardt, P., and Marsura, A. (2007) Molecular recognition of nucleotides by a new bis-(guanidinium)tetrakis-(β-cyclodextrin)-tetrapod. *New J. Chem. 31*, 995–1000.
(38) Wainer, I. W., Kaliszan, R., and Noctor, T. A. G. (1993) Biochromatography using immobilized biopolymers: A new approach to the determination of pharmacological properties. *J. Pharm. Pharmacol. 45*, 367–373.
(39) Pinkerton, T. C., and Koeplinger, K. A. (1990) Determination of warfarin-human serum albumin protein binding parameters by an improved Hummel-Dreyer high-performance liquid chromatographic method using internal surface reversed-phase columns. *Anal. Chem. 62*, 2114–2122.
(40) Tanaka, Y., and Terabe, S. (2002) Estimation of binding constants by capillary electrophoresis. *J. Chromatogr., B 768*, 81–92.
(41) Ostergaard, J., Schou, C., Larsen, C., and Heegaard, N. H. H. (2002) Evaluation of capillary electrophoresis-frontal analysis for the study of low molecular weight drug-human serum albumin interactions. *Electrophoresis 23*, 2842–2853.
(42) Busch, M. H. A., Carels, L. B., Boelens, H. F. M., Kraak, J. C., and Poppe, H. (1997) Comparison of five methods for the study of drug-protein binding in affinity capillary electrophoresis. *J. Chromatogr., A 777*, 311–328.
(43) Busch, M. H. A., Kraak, J. C., and Poppe, H. (1997) Principles and limitations of methods available for the determination of binding constants with affinity capillary electrophoresis. *J. Chromatogr., A 777*, 329–353.
(44) Connors, K. A. (1987) *Binding constants - The measurement of molecular complex stability*, John Wiley & Sons, New York.
(45) Ikeda, M., Minari, J., Shimada, N., Numata, M., Sakurai, K., and Shinkai, S. (2007) Complex formation between cationic beta-1,3-glucan and hetero-sequence oligodeoxynucleotide and its delivery into macrophage-like cells to induce cytokine secretion. *Org. Biomol. Chem. 21*, 2219–2224.
(46) Ou, M., Wang, X. L., Xu, R., Chang, C. W., Bull, D. A., and Kim, S. W. (2008) Novel biodegradable poly(disulfide amine)s for gene delivery with high efficiency and low cytotoxicity. *Bioconjugate Chem. 19*, 626–633.

BC800193P

Comparison of Cellular Uptake Using 22 CPPs in 4 Different Cell Lines

Judith Mueller, Ines Kretzschmar, Rudolf Volkmer, and Prisca Boisguerin*

Institut für Medizinische Immunologie, Charité - Universitätsmedizin Berlin, Hessische Str. 3−4, 10115 Berlin, Germany.
Received May 15, 2008; Revised Manuscript Received October 21, 2008

Cell-penetrating peptides (CPPs) are short peptides able to penetrate cell membranes and translocate different cargoes into cells. Although recently the topic of many research articles, to our best knowledge no single systematic study of CPPs has been carried out as yet, meaning information can only by gathered piece by piece from different sources. We therefore decided to start analytical screening of CPP specificity in cell lines. We used 22 different CPPs, which have all been published before, and present the first analytical screen in 4 selected cell lines (MDCK, HEK293, HeLa, and Cos-7). Furthermore, we examined the influence of different conditions, such as protease inhibitors, incubation conditions, endocytosis inhibitors, temperature, and cytotoxicity. We clearly demonstrate that the 22 CPPs can be classified into 3 groups based on their internalization properties, even after trypsinization. Moreover, we show that additional agents, which should increase cellular uptake or dissolve endosomal/lysosomal entrapped CPPs, only have low effects. Our intensive screening under standardized conditions provides the opportunity to compare cellular uptake of CPPs, an important step for the use of CPPs as peptidic vectors in the medical field.

INTRODUCTION

Over the past decade, intracellular drug delivery has become an emerging area of research in medical and pharmaceutical fields. However, cell membranes are impermeable to most molecules not actively imported by living cells, including practically all macromolecules and even many small molecules whose physicochemical properties prevent passive membrane diffusion. An increasingly popular class of membrane translocating agents is the cell penetrating peptides (CPPs) (reviewed in *refs 1, 2*).

Many CPPs (also known as "protein transduction domains") have now been characterized, revealing remarkable properties of cell penetration either on their own or as conjugates with a range of other types of biomolecules, such as peptides, proteins, liposomes, and nanoparticles (reviewed in ref *3*). The mechanism by which CPPs enter cells is not clear, although many recent papers have indicated different forms of endocytosis, implicating the involvement of well-characterized clathrin-mediated endocytosis (*4*), caveolae-mediated endocytosis (*5, 6*), or macropinocytosis (*7, 8*). Most likely, CPPs utilize multiple internalization mechanisms in combination (*9*).

Work in the CPP area stemmed from the discovery that the third helix of the Antennapedia homeodomain, pAntp (43−58) (*10*) and the trans-activating transcriptional activator, Tat, a protein encoded by HIV-1 (*11, 12*), can cross biological membranes. Within the last two decades, the number of peptides assigned to the family of CPPs has increased to about 100 (*13*). Nowadays, they can be divided into three classes: protein-derived peptides, model peptides, and designed peptides (*13, 14*). Protein-derived CPPs usually comprise the minimal effective sequence segment of the parent translocation protein and are also known as protein transduction domains or membrane translocation sequences. Examples are the Tat peptide (48−60) derived from the 86-mer Tat protein (*15*) or penetratin (43−58) derived from the homeodomain of *Drosophila* Antennapedia. Model CPPs comprise sequences designed with the aim of producing well-defined amphipathic α-helical structures or mimicking the structures of known CPPs. Examples are the model amphipathic peptide (MAP) (*16*) or polyarginine sequences (*17*). Designed CPPs are usually chimeric peptides comprising a hydrophilic and a hydrophobic domain of different origins, such as transportan, a fusion peptide of galanin and mastoparan (*18*). Here, we used 22 representative CPPs of these classes, as shown in Table 1.

No unambiguous definition of CPPs has been proposed, but generally, they comprise less than 30 amino acids. All known CPPs have a net positive charge at physiological pH and contain between approximately 17% (e.g., hCT(9−32)) and 100% (polyarginines) positively charged amino acids. With the exception of polyarginines, all other CPPs are amphipathic. Some of them acquire amphipathic characteristics when adopting an α-helical structure, as, for instance, the model peptide MAP, while others have distinct hydrophobic and hydrophilic parts, such as transportan.

However, the endocytic mechanism used (clathrin-mediated endocytosis, caveolar uptake, or macropinocytosis) defines the migration of these peptides into cells and depends on parameters such as the nature of the cationic agent itself and complex formation with cargo, as well as the nature and distribution of proteoglycans expressed on the cell surface (*9, 19*).

To the best of our knowledge, only a few studies comparing CPP cellular uptake have been performed up to now (*20*−*22*). Nevertheless, differences in numerous variables relating to the experimental procedures used by various groups make it hard to compare studies and form any conclusions, especially about the mechanism of internalization. These variables include the following: different sources and purity of CPP, label or cargo used, concentration of CPP, cell-type, density and stage of cell cycle, incubation time, and final end point or readout.

Since there has been no large-scale systematic attempt to determine which CPP sequence shows optimal cellular uptake, we decided to compare the uptake of 22 different CPPs in 4 cell lines, Cos-7, HEK293, HeLa, and MDCK (reasons for cell line selection are given in Experimental Procedures). In a first step, we defined standard conditions allowing direct comparison

* Phone: (+)49 (30) 450 524254, Fax: (+)49 (30) 450 524942, E-mail: prisca.boisguerin@charite.de, Homepage: http://immunologie.charite.de/arbeitsgruppen/ag-volkmer/.

10.1021/bc800194e CCC: $40.75 © 2008 American Chemical Society
Published on Web 11/19/2008

Table 1. Sequences of the CPPs Used in This Study[a]

	name	sequences	no. AA	pI	MW [Da]	ref
protein-derived peptides	SynB1	FITC-RGGRLSYSRRRFSTSTGR	18	12.30	2460	(*57*)
	Polyomavirus Vp1	FITC-APKRKSGVSK	10	11.26	1417	(*58*)
	Penetratin	FITC-RQILIWFQNRRMKWKK	16	12.31	2591	(*10*)
	HIV-1 Tat-(48−60)	FITC-GRKKRRQRRRPPQ	12	12.70	2078	(*15*)
	Bac1−15	FITC-RRIRPRPPLPRPRP	14	12.70	2123	(*59*)
	NF-kB	FITC-VQRKRQKLMP	10	12.02	1643	(*60*)
	SV40 T antigen	FITC-PKKKRKV	7	11.33	1242	(*61*)
	HATF3	FITC-ERKKRRRE	8	11.55	1517	(*62*)
	hCT(9−32)	FITC-LGTYTQDFNKFHTFPQTAIGVGAP	24	6.74	2970	(*63*)
	HIV-1 Rev-(34−50)	FITC-TRQARRNRRRRWRERQR	17	12.60	2797	(*17*)
	pVEC	FITC-LLIILRRRIRKQAHAHSK	18	12.48	3206	(*64*)
	Integrin	FITC-VTVLALGALAGVGVG	15	5.49	2456	(*37*)
designed peptides	DPV6	FITC-GRPRESGKKRKRKRLKP	17	12.19	1656	(*65*)
	$S4_{13}PV$	FITC-ALWKTLLKKVLKAPKKKRKV	20	11.51	2437	(*43*)
	Transportan	FITC-GWTLNSAGYLLGKINLKALAALAKKL	27	10.18	2736	(*18*)
	Pep-1	FITC-KETWWETWWTEWSQPKKKRKV	21	9.82	3201	(*66*)
	MPG	FITC-GALFLGWLGAAGSTMGAWSQPKKKRKV	27	11.33	2237	(*67*)
model peptides	MAP	FITC-KLALKLALKALKAALKLA	18	10.60	3208	(*16*)
	poly-P	FITC-VRLPPPVLRPPPVLRPPP	18	12.30	2357	(*68*)
	R7	FITC-RRRRRRR	7	12.78	1471	(*69*)
	R9	FITC-RRRRRRRRR	9	12.90	1783	(*69*)
others	pVEC-scrambled	FITC-IAARIKLRSRQHIKLRHL	18	12.48	2569	(*28*)

[a] CPPs were N-terminally labeled with FITC. Number of amino acids (no. AA), theoretical isoelectric points (pI), and molecular weights (MW) were calculated using the Protparam tool (http://www.expasy.ch/cgi-bin/protparam).

of the measured cellular uptake. Thereafter, we systematically analyzed the properties of the CPPs by changing one of the conditions, such as trypsinization, endocytosis modulators, or temperature. The resulting information, which includes determining the CPPs showing the highest cellular uptake, represents an important step for using CPPs in the clinical applications.

EXPERIMENTAL PROCEDURES

Peptides. The peptides used for the binding studies were automatically synthesized (Syro II, MultiSynTech) according to the Fmoc standard protocol. Peptides with a C-terminal carboxyl group were generated using TentaGel S PHB-aa-Fmoc (Rapp Polymere). For standard synthesis, Fmoc-aa-OH was used with the following side-chain protections: E-, D-(OtBu); S-, T-, Y-(tBu); K-, W-(Boc); N-, Q-, H-(Trt); R-(Pbf) (Novabiochem; Bachem). 5(6)-Carboxyfluorescin (FITC, Fluka) coupling was achieved using 1 equiv *N*-hydroxybenzotriazole (HOBt) and 1 equiv di-isopropylcarbodiimide (DIC) as activators, as reported in ref *23*.

The crude peptides were purified to >95% by preparative HPLC (Waters), and their identity was determined by analytical RP-HPLC (Waters) and MALDI TOF mass spectrometry (LaserTec BenchTopII, PerSeptive Biosystems).

Cell Culture. African green monkey kidney (Cos-7), human embryonal kidney (HEK293), human cervix carcinoma (HeLa), and Madin-Darby canine kidney (MDCK) cells were cultured in phenol red-free Dulbecco's modified Eagle medium (DMEM, Invitrogen) supplemented with 10% fetal bovine serum (FBS, Invitrogen) and 1% penicillin/streptomycin (pen/strep, Biochrom AG). The cells were seeded 1×10^5 cells/mL in 1.5 mL media in 6-well culture plates (Falcon, BD Biosciences) and allowed to grow until ~80% confluence. Unless otherwise indicated, 37 °C solutions were used and all incubations were performed at 37 °C, 5% CO_2.

Cell line selection was the result of intense screening of more than 90 papers published between 2000 and 2008, which determined CPP uptake in over 54 different cell lines. The cell lines mostly used were HeLa (46%), CHO (9%), MDCK (9%), Cos (7%), HEK293 (7%), MCF-7 (5%), Jurkat (5%), and NIH-3T3 (5%). All other cell lines are under the threshold of 5%. By screening the cellular uptake of CPPs in HeLa, Cos-7, HEK293, and MDCK cells, we intend to cover the commonly used cell lines.

Cellular Uptake. The cell layers were rinsed twice with PBS to completely remove the medium. One milliliter of a 100 μM peptide solution in PBS-G (PBS + 1% glucose) was applied for 30 min at 37 °C, 5% CO_2 (final CPP concentration 10 μM). Excess CPPs were removed by two rinses with PBS buffer (37 °C). Unless otherwise indicated, the cells were trypsinated for 10 min at 37 °C with 200 μL trypsin (0.05% trypsin /0.02% EDTA (w/v) solution (Biochrom AG)) before lysis. Then, cells were washed with 10 mL followed by 5 mL of PBS buffer, and centrifuged at 4000 rpm at 4 °C for 10 min (Eppendorf centrifuge 5810 R). The cell pellets were resuspended in 500 μL RIPA (50 mM Tris, 1 mM EDTA, 150 mM NaCl, 1% (v/v) NP40, 0.5% (v/v) deoxycholat, 0.1% (w/v) SDS, pH 7.5; Complete Mini, EDTA-free (Roche Diagnostica GmbH) freshly added) for lysis. The lysates were transferred into 1.5 mL Eppendorf tubes and incubated for 1 h at 4 °C. Finally, the samples were centrifuged at 8200 rpm at 4 °C for 10 min (Eppendorf centrifuge 5415 R).

The CPP concentrations were determined using 100 μL of lysat to measure FITC emission (Nunc 96 well plates U96 PP) on a microplate reader (FLUOstar Optima (excitation: 485 nm and emission: 520 nm)). The total protein contents were determined by a BCA assay. Five microliters of the sample and 200 μL of the BCA-reagent (reagent A: 1% (w/v) BCA-Na_2, 2% (w/v) Na_2CO_3, 0.16% (w/v) Na_2−Tatrat, 0.4% NaOH, 0.95% (w/v) $NaHCO_3$, pH 11.25. reagent B: 4% (w/v) $CuSO_4 \cdot 5H_2O$; A/B = 50:1) were mixed in a 96-well plate (Nunc Maxi Sorb) and incubated for 30 min at 37 °C. The solution was measured using a microplate reader (FLUOstar Optima (absorbance at 620 nm)), and thereafter, the concentration was calculated using a bovine serum albumin (BSA, Sigma-Aldrich) calibration curve.

Protease Inhibitor Test. The protease inhibitors (Sigma-Aldrich) were diluted in 900 μL DMEM (+1% pen/strep, without FBS) and mixed with 100 μL CPPs in PBS-G (final concentration 10 μM). The solutions were applied to the HeLa cells and incubated for 30 min at 37 °C, 5% CO_2. Peptides and inhibitors were omitted in the control sample. After 30 min incubation, CPPs and inhibitors were removed by two rinses with PBS (37 °C) buffer, and cells were lysed with RIPA as described above.

We used the following protease inhibitor concentrations: 50 μM leupeptin, 1 mM aprotinin, 1 mM glycerolphosphate,

10 μM phenanthroline, 1 mM ethylene diamine tetraacetic acid (EDTA), and 10 μM E-64 dissolved in H_2O; 20 μM MG-132 and 10 μM bestatin dissolved in dimethyl sulfoxide (DMSO) and 1 mM phenylmethylsulfonylfluoride (PMSF) dissolved in isopropanol. All inhibitors were purchase from Sigma-Aldrich or Calbiochem.

To determine the degradation product, cell lysates were analyzed by HPLC (Waters) equipped with a 5 μm (150 $\times$ 4.6 mm) C18 column, a precolumn containing the same adsorbent, and a fluorescence detector. HPLC conditions are described in ref *29*.

Endocytosis Inhibitor Test. The protease inhibitors (20 μM MG-132 and 1 mM EDTA) were diluted in 900 μL DMEM (+1% pen/strep, without FBS) and added to the cells at 37 °C. After 1 h, the endocytosis inhibitors were added and incubated for 30 min. Thereafter, 100 μL CPPs (100 μM in PBS-G) were applied to the different inhibitors (final CPP concentration 10 μM) and incubated for 30 min. Excess CPPs and inhibitors were removed by two rinses with PBS (37 °C), and then the cells were trypsinated and lysed with RIPA as described above.

All inhibitors were purchased from Sigma-Aldrich, and we used the following inhibitor concentrations: 30 μM chlorpromazine hydrochloride, 100 μM chloroquine diphosphate salt, 10 μM heparin sodium salt all dissolved in H_2O, as well as 100 μM nystatin dehydrate and 100 nM wortmannin dissolved in DMSO.

Besides the 37 °C incubation, we also performed incubations at 4 °C with the protease inhibitors (20 μM MG-132 and 1 mM EDTA) and the CPPs. To minimize possible side effects, we ensured that all solutions were pre-chilled to 4 °C.

Confocal Laser Scanning Microscopy. Confocal images were acquired with an inverted IX81 fluorescence microscope equipped with a Fluoview 1000 scanhead (Olympus, Tokyo, Japan) and a 60$\times$ (N.A. 1.35) oil-immersion objective at 25 °C. The green FITC fluorescence was excited with the 488 nm laser line of an Ar-ion laser, while the red trypan blue fluorescence was excited with a 543 nm He−Ne laser. The system was run in sequential scanning mode, where only one laser was active at a time, to avoid spectral overlap. The emission of FITC was recorded between 500 and 530 nm. For trypan blue, the emission was recorded from 570 to 670 nm. All measurements of peptide uptake were performed with living, nonfixed cells grown in a glass-bottom dish (World Precision Instruments). Cells were seeded at a density of 1×10^5/well 1 day before the experiment and cultured in DMEM (+1% pen/strep, without FBS).

Viability Assay. 100 μL containing 5×10^5 cells were seeded in 96-well microtiter plates (Falcon) and cultivated overnight. The next day, cells were rinsed twice with PBS, and subsequently, 100 μL DMEM (+1% pen/strep, without FBS) was added. Then, 10 μL of different peptide solution concentrations were applied, and cells were incubated for 2 h at 37 °C. Finally, cell viability was measured using colorimetric MTT dye.

After washing the cells with PBS, they were incubated with 10 μL of CCK-8 solution (Fluka) and 100 μL of DMEM (1% pen/strep) for 4 h, and cell viability was determined by measuring the absorbance of each sample due to the formazan product at 570 nm using a microplate reader (FLUOstar Optima).

RESULTS

Determining the Main Conditions. For our analytical evaluation of CPP uptake, we selected 22 different peptides (Table 1) corresponding to the three representative CPP families. Screening the literature revealed CPP concentrations varying from 1 μM to 50 μM (*24, 25*); a range over which the CPPs are normally not toxic (*9, 26*). Moreover, Duchardt et al. (*9*) demonstrated that CPP internalization could be enhanced by using concentrations of $\geq$10 μM. Time-dependent assays performed to determine the optimal incubation duration showed that 30 min is largely sufficient to measure cellular uptake. Longer incubation times (45 or 60 min) only increase the signal intensities by a factor of 1.4 (data not shown). For that reason, and also due to toxicity, we chose a CPP concentration of 10 μM and an incubation time of 30 min for all assays, unless stated otherwise.

To avoid artifacts during fluorescence measurements, some precautions had to be considered. For FACS (fluorescence activated cell sorting) or microplate reader measurements, the electrostatic interaction between the positively charged CPPs and the negatively charged plasma membrane have to be removed by trypsin treatment (*12, 27*). However, visualizing CPP cell translocation by microscopy using live cells is now standard procedure.

Influence of Protease Inhibitors on Cellular Uptake. A few studies have investigated the metabolic stability or the pattern of degradation of the CPPs (*28*−*31*). Proteolytic processing of the peptides could result in membrane-impermeable products, showing the importance of protease inhibiting agents. In uptake experiments with incubation time points up to 1 h or longer, the peptides need to be stable outside the membrane and should not be degraded within this time. Hence, evaluating peptide stability is an important parameter (*29*).

An attempt was made to inhibit degradation using several protease inhibitors covering the most common proteases, namely, phenanthroline, which inhibits matrix metalloproteases (MMPs); ethylenediaminetetraacetic acid (EDTA) as an inhibitor for metalloproteases; MG-132 as a proteasome inhibitor; bestatin, which inhibits aminopeptidase B and leucine aminopeptidase; E-64 as a broadband irreversible covalent cysteine protease inhibitor; phenylmethylsulfonyl fluoride (PMSF), which inhibits serine proteases; and finally, aprotinin, an inhibitor of serine proteases, particularly trypsin (see Table 1 in Supporting Information). All these protease inhibitors are often represented in commercially available protease inhibitor cocktails. In addition, we analyzed the influence of bovine serum albumin (BSA), which should saturate the proteases in order to increase amounts of intact peptides. Cells were incubated with inhibitors or BSA 2 h before CPP incubation and together with the CPPs for 30 min at 37 °C. Figure 1A shows the results using $S4_{13}PV$ as an example CPP in HeLa cells. In most of the cases, the protease inhibitors have a low or even negative influence on cellular uptake. Phenanthroline and bestatin have no influence, whereas E-64, PMSF, and aprotinin seem to reduce cellular uptake, probably due to toxic effects on the cells. Using BSA, we observed the greatest decrease in internalization. Only EDTA, MG-132, and the combination of both increased cellular uptake by preventing extracellular and intracellular peptide degradation. Neither protease inhibitor is toxic for the cells, either alone or in combination (Figure 1, B). To confirm the inhibitory effect of EDTA/MG-132, we analyzed the cell lysate of HeLa cells incubated with $S4_{13}PV$ (Figure 1C). Measurements of the peak areas revealed a reduction of the peaks at 14.03 and 26.76 min by more than 60% in the presence of EDTA/MG-132. On the other hand, the double peak (19.84 and 20.12 min) increased, which corresponds to cis−trans isomers of $S4_{13}PV$.

Despite the fact that the proteolytic activity strongly depends on the cell line, Trehin et al. (*30*) found that degradation patterns between different cell lines were comparable. Since our own observations agree with this result (data not shown), we choose EDTA and MG-132 as standard conditions for further analyses in different cell lines.

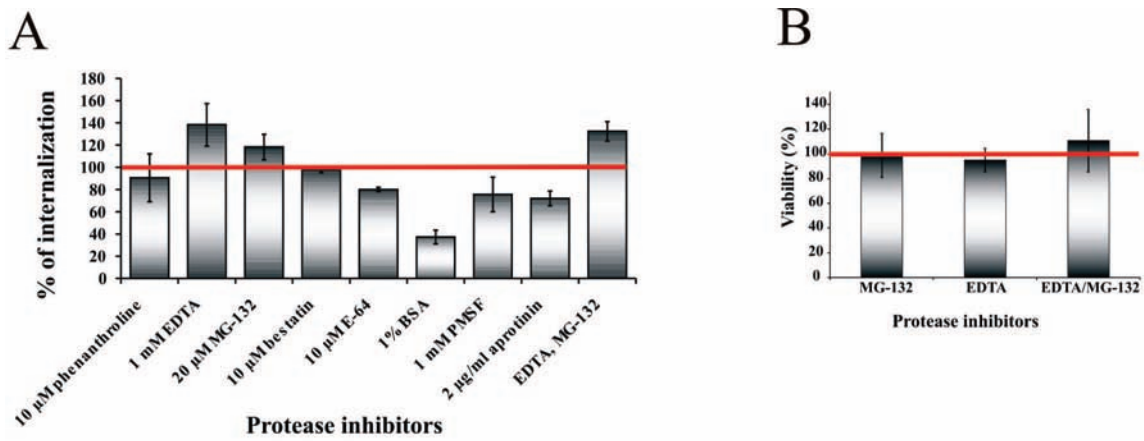

C

RT (min)	30 min		60 min	
	without EDTA/MG-132	with EDTA/MG-132	without EDTA/MG-132	with EDTA/MG-132
	Area (μV*sec)	Area (μV*sec)	Area (μV*sec)	Area (μV*sec)
8.60#	5,640,559 ± 425,440	5,576,152 ± 566,955	5,308,6309 ± 236,769	5,630,029 ± 269,295
14.25	1,700,976 ± 417,860	535,605 ± 57,605	20,133,217 ± 1,715,280	6,588,279 ± 802,522
17.33	-	-	8,138,655 ± 751,100	798.871 ± 73.294
19.84*	**31,973,845 ± 7,303,916**	**42,663,353 ± 4,894,256**	**51,362,552 ± 3,400,158**	**89.826.822 ± 12.537.915**
20.12*	**90,484,736 ± 20,066,428**	**123,380,469 ± 11,736,897**	**159,943,829 ± 17,597,539**	**196.522.584 ± 17,523,200**

Figure 1. Effects of protease inhibitors on CPP cellular uptake. (A) HeLa cells were preincubated for 2 h with the respective protease inhibitor followed by incubation with CPP $SV_{13}PV$ for 30 min at 37 °C. The data represent the mean of three independent experiments ± SEM. The best result is obtained using 1 mM EDTA and 20 μM MG-132 (last bar). The red line represents 100% internalization corresponding to the control without inhibitor. The data represent the mean of 2−3 independent experiments ± SEM. (B) Measurement of viability using the CCK-8 solution (Fluka): HeLa cells were preincubated for 2 h with either 20 μM MG-132 or 1 mM EDTA, or both together. The red line shows 100% viability, which corresponds to no toxic effect of the protease inhibitors. The data represent the mean of 2−3 independent experiments ± SEM. (C) Cell lysates of HeLa cells incubated with $S4_{13}PV$ in the presence or absence of the protease inhibitor (EDTA/MG-132) analyzed by HPLC. #: Peak at 8.60 min is due to medium impurity. *: The double peak at 19.84 and 20.12 min represents CPP-$S4_{13}PV$ and is due to proline cis−trans isomerization. Products at 14.03 and 26.78 min are potential degradation products, which are reduced by the protease inhibitors. The data represent the mean of 3 independent experiments ± SEM.

Quantitative Analyses of 22 Different CPPs and the Influence of Trypsinization. The CPPs listed in Table 1 were tested in Cos-7, HEK293, HeLa, and MDCK cells, and cellular uptake was quantified by fluorescence measurements using a microplate reader (Figure 2). Although all 22 CPPs are known from the literature and are supposed to have cell penetrating properties, they do not show the same degree of cellular uptake. In the first data set (Figure 2A - without trypsin), we could discriminate three groups of CPPs. The first group (<1000 SI/mg) comprises the nearly unmeasurable uptake of polyomavirus Vp1, poly-P, NF-kB, SV40 T antigen, HATF3, and hCT(9−32). The second group (between 1000 SI/mg and 10 000 SI/mg) includes SynB1, DPV6, HIV-1 Tat-(48−60), Pep-1, Bac1−15, MPG, integrin, and pVEC-scrambled. The third group comprises CPPs with high cellular uptake (>10 000 SI/mg), such as penetratin, $S4_{13}PV$, transportan, MAP, R7, R9, HIV-1 Rev-(34−50), and pVEC. Comparing one individual CPP among the four cell lines, we could determine approximately the same amount of uptake. Interestingly, three CPPs seem to be specific for one cell line: integrin for HEK293 cells (4-fold higher), $S4_{13}PV$ (3-fold higher), and MAP (2-fold higher) for HeLa cells (Figure 2A).

Flow cytometry and a microplate reader are both conventional tools to quantify cellular association of fluorochrome-tagged CPPs. However, neither method could discriminate between membrane-bound and internalized fluorochrome. To differentiate between CPPs that are within the cells and those stuck on the cell surface, we included a trypsinization step before cell lysis. Using this protocol, we could clearly demonstrate a more than 10-fold to over 100-fold decrease in signal intensities in most cases. Figure 2B shows that the CPPs with the highest internalization after trypsinization are the commonly used CPPs such as penetratin, $S4_{13}PV$, transportan, MAP, and R9, whereby MAP seems to be slightly more specific for HeLa. However, in most cases only up to 20% of the CPPs are within the cells after trypsinization (Figure 2C). Curiously, we could not measure high cellular uptake of HIV-1 Tat-(48−60), which is often reported to be within the same range as penetratin or R9. However, we could clearly confirm the efficiency of R9 compared to R7, which is in accordance with Tunnemann et al. (*26*).

Interestingly, integrin is still specific for HEK293 cells even after trypsinization (3-fold higher SI/mg protein compared to the other cells; details in Table 2). Likewise, we could observe penetratin specificity for HeLa cells (3-fold higher, details in Table 3 in the Supporting Information).

Altogether, in the majority of cases, the CPPs are located on the cell surface, and less than 10% are actually found within the cells. One exception is transportan, which shows high cellular uptake even after trypsinization. In HEK293 cells, we observed only a 6-fold decrease in signal intensity and only 2- to 3-fold reductions in Cos-7, HeLa, or MDCK cells. Some CPPs, such as NF-kB, SV40 T antigen, HATF3, and hCT(9−32), which previously showed very low internalization (without trypsin) also display low internalization after trypsin treatment.

Comparing both panels of Figure 2 clearly demonstrates that measurements in the absence of trypsin treatment always overestimated cellular uptake. The extent of the overestimation varied according to the cell lines and peptides. Moreover, the efficiency of the trypsin treatment is shown with integrin, which

A - without trypsin

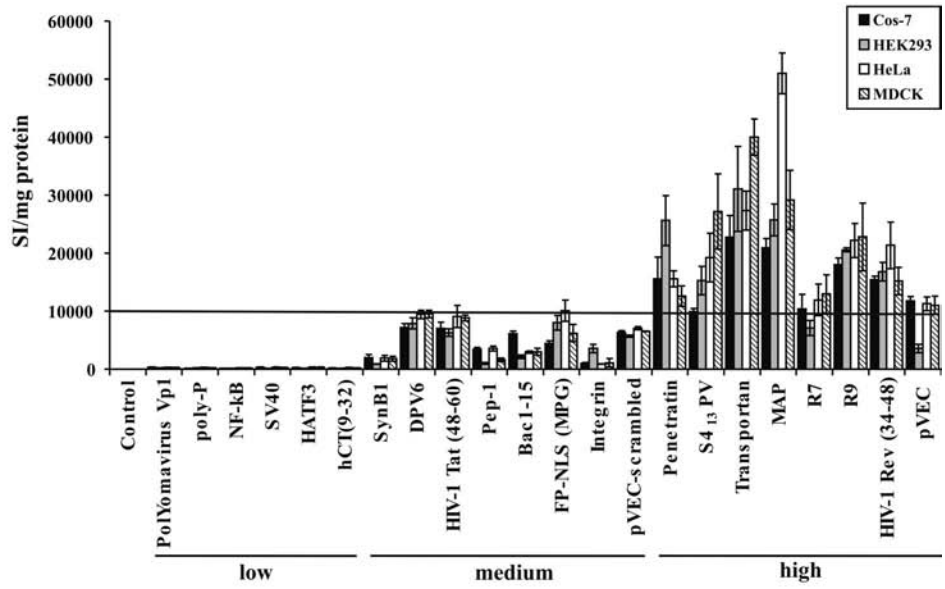

B - with trysin

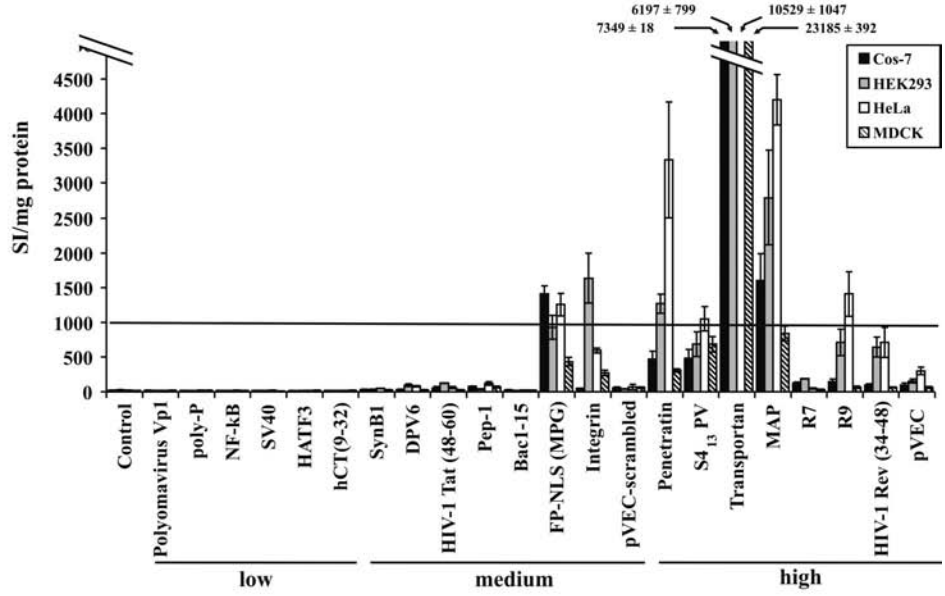

C - % of cellular up-take [B/A*100]

	Polyomavirus Vp1	poly-P	NF-kB	SV40	HATF3	hCT(9-32)	SynB1	DPV6	HIV-1 Tat (48-60)	Pep-1	Bac1-15	FP-NLS (MPG)	Integrin	pVEC-scrambled	Penetratin	$S4_{13}$PV	Transportan	MAP	R7	R9	HIV-1 Rev (34-48)	pVEC
Cos-7	6	19	14	7	6	11	2	0	1	2	0	32	5	1	3	5	32	8	1	1	1	1
HEK293	9	8	11	13	10	12	3	1	2	4	1	12	46	1	5	5	20	11	3	3	4	2
HeLa	7	7	11	7	6	7	3	1	1	3	1	12	67	1	21	5	39	8	0	6	3	3
MDCK	9	10	9	6	6	10	1	0	0	4	1	7	14	1	2	3	58	3	0	0	0	1

Figure 2. Comparison of CPP cellular uptake with or without a trypsinization step in Cos-7, HEK293, HeLa, and MDCK cells. (A) Cellular uptake without trypsin: Cells were preincubated for 2 h with the protease inhibitor (EDTA/MG-132) followed by incubation with CPPs for 30 min at 37 °C. After washing steps, the cells were lysed and analyzed by a microplate reader. The data represent the mean of 3−5 independent experiments ± SEM. Measured values and standard deviations are given in Supporting Information. (B) Cellular uptake with trypsin: Cells were preincubated for 2 h with the protease inhibitor (EDTA/MG-132) followed by incubation with CPPs for 30 min at 37 °C. The cells were treated with trypsin (10 min at 37 °C) before cell lysis. The data represent the mean of 3−5 independent experiments ± SEM. Measured values and standard deviations are given in Supporting Information. (C) For a better overview, the real CPP translocations within the cells were calculated as the relative percentage of internalization: (A[SI/mg protein]/B[SI/mg protein] · 100%). Gray boxes represent cellular uptake between 10% and 20%; black boxes over 20%.

Table 2. Details of Cellular Uptake[a]

effect of the	name	sequences	pI	Cos-7	HEK293	HeLa	MDCK
pI	Integrin	FITC-VTVLALGALAGVGVG	5.49	51 ± 1	1638 ± 360	595 ± 35	274 ± 39
	Pep-1	FITC-KETWWETWWTEWSQPKKKRKV	9.82	79 ± 4	39 ± 6	119 ± 26	72 ± 14
	Penetratin	FITC-RQILIWFQNRRMKWKK	12.31	472 ± 114	1269 ± 137	2748 ± 831	311 ± 22
sequence	pVEC	FITC-LLIILRRRIRKQAHAHSK	12.48	96 ± 28	154 ± 29	301 ± 53	65 ± 13
	pVEC-scrambled	FITC-IAARIKLRSRQHIKLRHL	12.48	60 ± 10	42 ± 1	77 ± 50	61 ± 9

[a] CPPs were N-terminally labeled with FITC. Theoretical isoelectric points (pI) were calculated using the Protparam tool (http://www.expasy.ch/cgi-bin/protparam). Cells were cultured as described in Experimental Procedures. The given values represent the signal intensity per mg cell protein (SI/mg cell protein). The data represent the mean of 3−5 independent experiments ± S.E.M.

is not a trypsin substrate. Trypsin is supposed to remove surface-bound peptide by the digestion of peptide and/or membrane proteins. This phenomenon could be clearly demonstrated by showing a decrease of 19-fold for Cos-7 cells, 3-fold for MDCK cells, and 2-fold for HEK293 cells. For HeLa cells, we only observed a 1.5-fold decrease, revealing the specificity for this cell line (see Supporting Information Table 3).We therefore used a standard protocol including a trypsin treatment before analysis of cell lysates by a microplate reader in all subsequent experiments.

Comparing CPP Distribution. Conflicting evidence has been presented concerning the role of individual endocytic pathways (*32*, *33*). We supposed that the apparent discrepancies were a consequence of the different experimental conditions with respect to cell lines, incubation times, and peptide concentrations. To investigate this, we performed experiments using a subset of the previously analyzed CPPs.

We used polyomavirus Vp1 as an example of a CPP with low cellular uptake (Figure 2B). Penetratin, HIV-1 Tat-(48−60), and R9 were used, since they are well-known in the literature. Furthermore, we used transportan, MPG, and integrin due to their high measured cellular uptake even after trypsinization (compare Figure 2A,B).

Figure 3 summarizes the distribution of the CPPs within the four cell lines. We only compared data from experiments using the same cell numbers and same incubation time. In the control picture (without CPPs), no self-fluorescence of the cells could be measured (Figure 3A, first panel). Additionally, to avoid misinterpretation due to extracellular fluorescence bound to cell membranes or working materials, we added trypan blue solution during each CLSM measurement. Trypan blue is unable to translocate intact cell membranes, which makes it a selective quencher for extracellular bound fluorophores (*34*−*36*). The trypan blue staining is only shown in the control of Figure 3A or in special cases revealing diverging phenomenon (Figure 3B).

First of all, by subjectively comparing the fluorescence pictures we could clearly reproduce the results obtained by the microplate reader (Figure 2). The three postulated groups of CPPs can be deduced with polyomavirus Vp1 showing the lowest cellular uptake (group 1), HIV-1 Tat-(48−60), MPG, and integrin with medium internalization (group 2) and penetratin, R9, transportan, and MAP with the highest adsorption (group 3).

Looking in detail at the CPP distribution, we observed that the CPPs were within the cells in all cases, even if a low cellular uptake was measured by the microplate reader. We detected low cytoplasmic dissemination only in the case of polyomavirus Vp1 (Figure 3A, second panel) and medium internalization in the case of integrin (Figure 3A, eighth panel) for all analyzed cell lines, which correspond to the low and medium results of Figure 2. CPPs such as penetratin, R9, MAP, and FP-NLS (MPG), which show good cellular uptake measured by the microplate reader—even after trypsinization—also revealed high cellular internalization (Figure 3A,B).

HIV-1-Tat-(48−60) mainly shows a vesicular distribution in all cells, and furthermore, a cytoplasmic and additionally nucleic localization (10−20%) in the case of HeLa and MDCK cells (Figure 3A, third panel). In general, the HIV-1 Tat-(48−60) distribution in cells seems to be more diffuse, showing a combination of punctuated fluorescence and more diffuse fluorescence in the cytoplasm and nucleus. Due to the additional cytoplasmic and nucleic distribution in HeLa and MDCK cells, the quantity of internalized CPP seems to be higher than in the other two cell lines, which does not correspond to the approximately equal distribution measured by the microplate reader (Figure 2). At this juncture, we could only postulate that the nuclear-located CPP could not be extracted and measured after cell lysis.

Penetratin (Figure 3A, fourth panel) displays a punctuated dispersion within the cells, as is also observed for the smac-penetratin construct used in HeLa cells (*21*). We observed an equal distribution of R9 with an additional cytoplasmic distribution found most strongly in MDCK cells (Figure 3A, fifth panel).

CLSM pictures of MAP (Figure 3A, sixth panel) demonstrated in most cases that the fluorescence appeared evenly distributed throughout the cytosol and nucleus, accompanied by a punctuated pattern, suggesting that non-endocytotic as well as endocytotic modes of uptake are involved. FP-NLS (MPG) (Figure 3A, seventh panel) show a comparable uptake to MAP but 2-fold lower as shown in Figure 2B. Integrin seems to be mostly located close to the cell membrane, especially in Cos-7 and HeLa cells, which is in agreement with Zhang et al. (*37*) (Figure 3A, eighth panel). The low internalization does not correspond to the middle signals in Figure 2B. The observed discrepancy between both methods could be explained by the pH-induced quenching effect of the FITC moiety within vesicles (*38*).

Transportan plays a special role in cellular uptake. Using the microplate reader, we recorded extremely high incorporation even after trypsinization. Images of confocal microscopy showed not only cytoplasmic vesicles but also intense cell damage (Figure 3B). 20−30% of the cells revealed a huge accumulation of transportan, correlating with the vital dye trypan blue staining, independent of the cell types. This lytic characteristic is also clearly demonstrated in the viability test showing a high cytotoxic effect with a transportan concentration up to 25 μM (Supporting Information Table 2). The same phenomenon could be observed in 5% of the HeLa cells incubated with MAP (data not shown).

Viability Test of the 22 Different CPPs. We also examined the cellular toxicity of the 22 different CPPs, since this is crucial to their use as effective delivery vehicles. To provide information about acute toxicity, we incubated cells for 2 h with all 22 FITC-labeled CPPs, at concentrations of 1 μM to 50 μM (Table 2 in Supporting Information). Most of the CPPs showed no cytotoxicity even at high concentrations (100% ± 20% viability). Using the three peptides $S4_{13}PV$, transportan, and MAP, we did observe a decrease in cell viability at a concentration of 25 μM. $S4_{13}PV$ seems the more critical candidate with a viability of 63−50% for Cos-7 and HEK293, complete cytotoxicity at 25 μM for HeLa and even at 10 μM for MDCK cells. Transportan caused decreased viability at 25 μM for Cos-7, HeLa, and MDCK cells (20−0%) but had a lower effect on HEK293 cells (~50%). MAP was only toxic at 25 μM for Hela

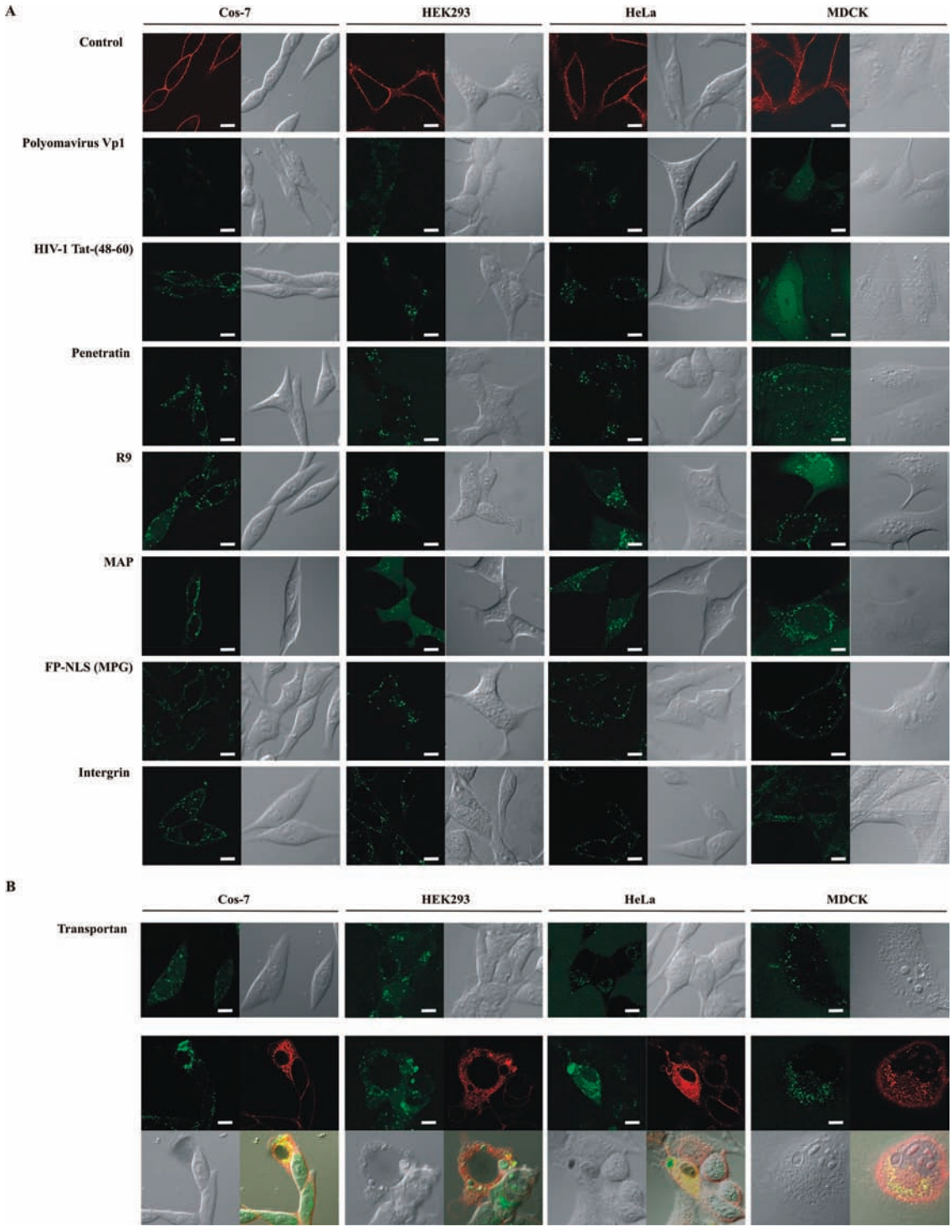

Figure 3. Example of CPP cellular uptake in Cos-7, HEK293, HeLa, and MDCK cells. As control, the four cell lines without peptides are shown as an overlay of the FITC staining (488 nm) and the trypan blue staining (543 nm) with the corresponding phase contrast images. Thereafter, the four different cell types are treated with 10 μM of the FITC-labeled CPPs for 30 min. For each condition, we show the fluorescence (488 nm) and phase contrast images. (A) Trypan blue staining is only shown to demonstrate the artifact as exemplified by transportan. Here, we additionally show the vital trypan blue staining and the corresponding merged images (B). The white bars represent 10 μm.

cells, whereas it had low or even no effect on Cos-7, MDCK, and HEK293 cells. The effect of decreasing cell viability by these three CPPs is not surprising because they are postulated to penetrate the cell by pore formation (*39*).

Because $S4_{13}PV$ shows some toxic effects, we further analyzed its cytotoxicity more precisely at a concentration of 10 μM. We used HeLa cells because their reduced viability (64 $\pm$ 24%) lies between the values of Cos-7 (89 $\pm$ 17%), HEK293 (95 $\pm$ 6%), and MDCK (33% $\pm$ 16%) cells. HeLa cells were incubated for 30 and 60 min with $S4_{13}PV$. Neither incubation time showed any cytotoxic effects on the cells (30 min, 100 $\pm$ 11%; 60 min, 102 $\pm$ 3%).

Altogether, these results substantiated our standard conditions (10 μM CPP for 30 min) as not affecting cell viability.

Influence of Endocytosis Inhibitors on the Cellular Uptake. To gain more insight into the mechanism(s) by which CPPs are taken up by cells, we selected the 8 CPPs from Figure 3 as well as 4 others from the 22 CPPs and tested them with

Table 3. Effects of Various Reagents on Cellular Uptake[a]

Cell line	Condition	Control	Penetratin	DPV6	HIV-1 Tat (48-60)	S4(13)PV	Transportan	MAP	R7	R9	HIV-1 Rev (34-48)	FP-NLS (MPG)	Integrin	pVEC-scrambled	Positive effect	Negative effect
Cos-7	37°C	1.00	1.00	1.00	1.00	1.00	1.00	1.00	1.00	1.00	1.00	1.00	1.00	1.00	/	/
	4°C	0.88	1.13	3.67	3.10	0.45	3.38	2.58	1.04	2.57	3.18	0.44	1.13	2.06	58	17
	Chlorpromazine	0.75	2.07	1.53	0.73	0.71	1.30	0.55	0.38	0.99	2.94	0.52	1.00	1.30	25	8
	Chloroquine	0.87	1.52	1.99	2.99	0.67	1.38	2.69	1.27	5.50	5.57	1.02	0.92	3.79	58	0
	Nystatin	0.77	0.76	0.58	0.36	1.00	1.01	1.04	0.18	0.88	0.52	0.36	0.75	2.00	8	33
	Heparin	0.96	0.88	6.72	4.01	0.43	2.70	1.05	2.67	2.23	5.02	0.27	0.57	2.41	58	17
	Wortmannin	0.82	0.82	0.91	0.45	0.33	3.78	0.35	0.23	0.68	1.01	0.17	1.69	0.69	8	42
HEK293	37°C	1.00	1.00	1.00	1.00	1.00	1.00	1.00	1.00	1.00	1.00	1.00	1.00	1.00	/	/
	4°C	0.80	0.62	0.38	0.27	0.20	3.04	6.71	0.36	0.30	0.33	1.34	0.12	2.34	25	58
	Chlorpromazine	0.76	1.09	0.65	0.24	0.75	1.36	0.51	0.19	0.67	0.59	0.63	0.05	4.92	8	25
	Chloroquine	0.89	0.85	0.68	0.48	1.15	2.75	0.79	0.76	0.65	0.68	0.84	1.16	3.27	17	8
	Nystatin	0.82	0.82	0.80	0.38	1.43	0.42	0.70	0.21	0.23	0.17	0.62	0.04	1.46	0	50
	Heparin	0.86	0.26	1.35	1.19	0.53	1.91	1.67	3.11	0.89	1.18	2.57	0.48	6.02	25	17
	Wortmannin	0.49	0.39	0.62	0.19	0.50	4.19	0.20	0.21	0.16	0.18	0.56	0.57	0.95	8	58
HeLa	37°C	1.00	1.00	1.00	1.00	1.00	1.00	1.00	1.00	1.00	1.00	1.00	1.00	1.00	/	/
	4°C	0.98	1.23	1.31	1.52	0.77	1.90	1.14	2.15	0.60	0.37	0.85	0.29	0.91	8	17
	Chlorpromazine	1.02	1.05	0.39	1.70	0.97	0.73	0.74	1.91	1.26	0.16	1.21	0.66	0.95	0	17
	Chloroquine	0.96	3.05	0.68	1.98	1.37	2.07	0.33	4.47	1.43	0.97	0.96	1.80	2.24	25	8
	Nystatin	1.02	1.16	0.53	1.72	0.40	2.05	1.32	2.19	0.41	0.70	1.11	1.44	1.85	25	8
	Heparin	0.88	1.55	3.21	5.27	1.08	1.39	0.14	8.40	0.24	0.76	0.15	0.10	4.77	33	33
	Wortmannin	0.80	0.53	0.52	0.45	0.74	2.76	0.26	0.93	0.16	0.19	0.60	2.04	0.67	17	42
MDCK	37°C	1.00	1.00	1.00	1.00	1.00	1.00	1.00	1.00	1.00	1.00	1.00	1.00	1.00	/	/
	4°C	0.90	2.30	0.71	0.89	1.55	2.81	0.29	1.39	1.03	0.89	1.32	0.35	0.90	17	8
	Chlorpromazine	1.11	1.79	1.67	1.43	0.95	4.25	1.76	1.53	3.34	2.60	1.62	0.57	1.37	25	0
	Chloroquine	1.15	1.15	0.97	1.06	0.27	6.10	1.71	0.80	1.23	1.76	0.66	0.08	0.85	8	17
	Nystatin	1.04	3.01	1.09	0.92	1.47	1.30	7.89	0.80	0.96	0.90	0.46	0.17	0.75	17	25
	Heparin	1.15	1.77	0.96	1.02	0.07	4.85	3.21	1.66	2.20	0.69	0.48	0.31	1.01	25	25
	Wortmannin	1.28	1.24	1.22	1.09	0.65	5.17	1.32	1.04	1.05	0.76	1.23	2.66	0.55	17	0

[a] The cells were treated with the reagents at the given concentrations, and later, CPPs (10 μM) were added to the medium. The cells were incubated for another 30 min and subjected to quantification (for more details see Experimental Procedures). The data represent the mean of 3−5 independent experiments. The results at the standard condition (37°C) are set at 1.00 with the other results relative to this value. As a control, we used cells with reagents but without CPPs. To quantify the significance of reagent effects, we determined a significant increase at >2.00 (black boxes) or a significant decrease at <0.50 (white boxes). On the right, we calculated the overall average effect (%) of the different reagents (positive effect = % of black boxes; negative effect = % of white boxes). The numbers marked in red represent the conditions used for confocal microscopy (see Figure 4 and Supporting Information Figure 1). Measured values and standard deviations are given in Supporting Information.

chemical inhibitors to block specific endocytotic pathways. We treated cells with the inhibitors (see Supporting Information Table 1) before adding the CPPs and then analyzed them using a microplate reader. Besides the standard conditions at 37 °C, we tested energy-dependent pathways by measuring at 4 °C. As direct endocytosis inhibitors, we used chlorpromazine as a clathrin-dependent endocytosis inhibitor and nystatin, which disrupts caveolar structures and functions. As endocytosis modulators, we utilized chloroquine inhibiting the acidification of endosomes and the fungal metabolite wortmannin inhibiting fluid-phase uptake and the homotypic fusion of early endosomes (*32*). Furthermore, heparin was used as a competitor of cell membrane-associated heparin sulfate proteoglycans (HSPGs).

The effects of the endocytosis inhibitors used are summarized in Table 3. Each box corresponds to a decimal number based on the standard condition (37 °C, no inhibitor) set to 1.00, with the threshold set at <0.50 for negative (white boxes) and >2.00 for positive effects (black boxes). All gray squares represent no difference, likened to the standard condition (raw data are given in the Supporting Information).

The overall effect of each inhibitor or condition for all the CPPs tested was calculated such that the percent of black boxes gives the average positive effect and the percent of white boxes the average negative effect (Table 3, right column).

By comparison of the four cell lines, the chosen conditions seem to have more positive effects on Cos-7 cells: 26 black boxes compared to 14 white boxes. The most positive effects were seen with heparin (58%), chloroquine (58%), and, curiously, at 4 °C (48%), suggesting an energy-independent pathway for uptake. Opposite effects were observed with HEK293 cells: 10 black boxes to 26 white boxes. The most frequent negative effects here were observed with 4 °C (58%), Nystatin (50%), and Wortmannin (58%).

For HeLa and MDCK cells, we found a more equal distribution of positive and negative effects (12 black boxes to 15 white boxes for HeLa and 13 black boxes to 8 white boxes for MDCK). HeLa and MDCK cells only showed an increase in cellular uptake using specific CPP/inhibitor combinations (no average positive effect ≥50%).

Altogether, most of the inhibitors used seem to have weak consequences for the cells: 44% of the conditions used have no effects on Cos-7, 50% on HEK293, 63% on HeLa, and 70% on MDCK cells (numbers of gray boxes).

To confirm the different activity of certain inhibitors, we used CLSM imaging to reevaluate the potential redistribution of some CPPs (Table 3, numbers marked in red; Figure 4 and Supporting Information Figure 1). Fluorescence images show the differences between the cellular uptake of selected CPPs without and with inhibitor. We again proved a reduced cellular uptake in the same cases as observed in Table 3, such as R9 with heparin in HeLa cells. On the other hand, we could only show an increase in cellular uptake when we previously found an increase over 2.00, such as integrin with wortmannin in MDCK cells or HIV-1 Tat-(48−60) with heparin in Cos-7 cells. Altogether, we could

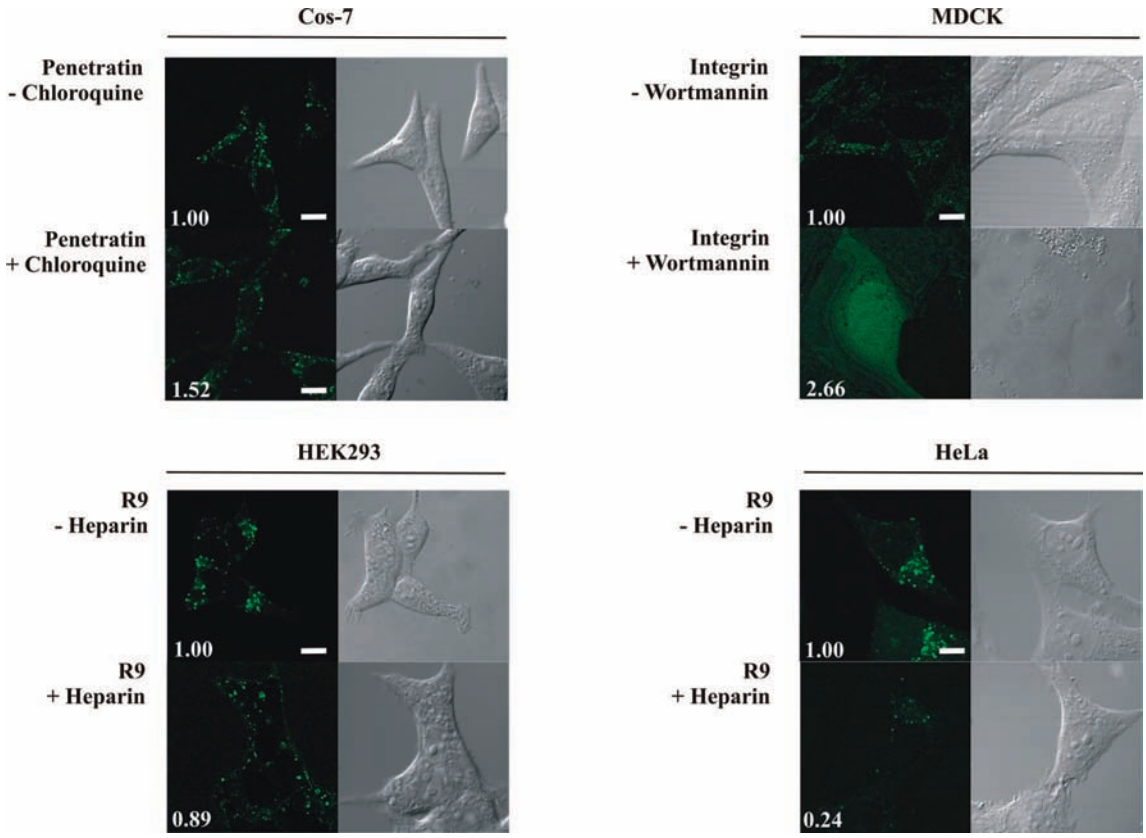

Figure 4. Example of cellular uptake and endocytosis inhibitors in Cos-7, HEK293, HeLa, and MDCK cells. Confocal microscopy sections of the four different cell types were treated with the endocytosis inhibitors for 30 min and afterward with 10 μM of FITC-labeled CPPs together with the inhibitors for an additional 30 min. For each condition, we show the fluorescence and phase contrast images. The percentage of cellular uptake measured by the microplate reader is given in the left lower corner of the fluorescence images. The white bars represent 10 μm.

visualize the same effects of the inhibitors by microscopy as observed in the microplate reader experiments.

DISCUSSION

In the past few years, defined experimental conditions have been established for the measurements of cellular uptake, a necessary step for reproducibility and avoiding artifacts. Approximately 100 000 cells (depending on the cell line) should be seeded in 6-well plates two days before the experiment in order to reach about 80% confluence on the day of measurement. Within one experiment, the same number of cells should always be seeded, since the uptake of CPPs depends on the peptide to cell ratio (*40*). To acquire images for confocal microscopy, the cells should not be confluent (40−60% is preferable). For example, endocytotic internalization was remarkably reduced especially in confluent Madin-Darby canine kidney (MDCK) epithelial cells. This effect was shown to be compound-unspecific, since also other compounds (FITC-dextran, TRITC-transferin, etc.), known to be internalized by endocytosis, lost their internalization efficiency (*41*).

To prevent extra- or intracellular degradation, we determined a combination of EDTA/MG-132 as the most efficient protease inhibitors (Figure 1). Although EDTA is known to interfere with many processes inside the cell, it has no toxic effect on the cells used in this study (see Figure 1B). The same was found for MG-132. Furthermore, the combination of both inhibitors has no influence on cell viability and morphology (see control experiment in Figure 3A, first panel). Curiously, BSA dramatically reduced CPP internalization. This is in contradiction to Palm et al. (*29*) who postulated the saturation of the proteases by BSA. Our results are in agreement with the function of BSA acting as a universal protein/peptide transporter in the serum. Therefore, it is most likely that BSA masks the CPPs and prevents their interaction with the cell membrane as reported by Kosuge et al. (*42*).

Toxic effects should be kept at a minimum if CPPs are used as drug delivery vehicles. For that reason and as deduced form literature, we used a final CPP concentration of 10 μM and an incubation time of 30 min by default. Applying these conditions, we observed no cytotoxicity, clearly demonstrated by the viability tests (Supporting Information Table 2). In general, at high concentrations toxic effects were observed on cell membranes and organelles as shown for MAP and especially for transportan. 20−30% of the cells revealed a huge accumulation of transportan (Figure 2B), which correlated with the vital dye trypan blue staining independently of the cell type. This is not surprising, since transportan penetrates the cell membrane by creating short-lived pores (*39*). The same phenomenon could be observed in 5% of the HeLa cells incubated with MAP (data not shown). Furthermore, the lytic property is clearly demonstrated in the viability test showing a high cytotoxic effect with transportan at a concentration up to 25 μM and also with MAP, but with lesser effects (Supporting Information Table 2).

Our analytical evaluation of the CPP internalization results in a classification into three groups: (1) CPPs with low cellular uptake [such as polyomavirus Vp1, poly-P, NF-kB, SV40 T antigen, HATF3, and hCT(9−32)]; (2) CPPs with medium internalization [e.g., SynB1, DPV6, HIV-1 Tat-(48−60), Pep-1, Bac1−15, MPG, and pVec-scrambled]; (3) CPPs with high cellular uptake [such as penetratin, $S4_{13}PV$, transportan, MAP, R7, R9, HIV-1 Rev-(34−50), and pVec]. This relationship found between the investigated CPPs is significantly influenced by additional trypsinization of the cells (Figure 2).

Nevertheless, comparing all results confirms that it is still a great challenge to predict a CPP's properties based only on primary sequences. CPPs with similar isoelectric points (pI) show different uptake activities. For example, penetratin (pI = 12.31) shows high cellular internalization in comparison to the low activity of poly-P with the same pI value (pI = 12.30). These results demonstrate that the positive charges of CPPs (pI = 10−12), which are postulated to be important for the interaction with HSPGs on the cell surface, are not always the portal guiding endocytosis (*19*). On the other hand, we also found CPPs with a low pI such as integrin (pI = 5.49), which revealed good internalization, especially with HEK293 cells.

The only point that can be ruled out is the correlation of the amino acid order within the primary sequence. pVEC could be detected, e.g., in HeLa cells (SI/mg = 239 ± 140), whereas the scrambled version showed practically no uptake (SI/mg = 77 ± 50). A similar effect could be observed with $S4_{13}PV$ (ALWKTLLKKVLKA-PKKKRKV; SI/mg = 10.000−39.000) and SV40 T antigen (PKKKRKV; SI/mg = 160−310): only the addition of the N-terminal sequence induces the cell penetrating properties of the sequence (*43*). These results imply that the sequence length and conformation of the CPP plays a more important role in cellular uptake than the accumulation of positive charge. However, it is also difficult to argue with the three-dimensional structure, since α-helices (e.g., transportan (*44*)) as well as β-structures (e.g., penetratin (*45*)) are reported to be important for cellular internalization via membrane perturbation.

Comparing our results, we could find some agreements with published reports, but also some basic differences. For example, the commonly used CPPs such as penetratin, MAP, and R9 also show the highest signal intensities in our analytical measurements, which is in agreement with the literature. Curiously, we could not measure high cellular uptake of HIV-1 Tat-(48−60), which often ranks in the same range as penetratin or R9 according to earlier published observations (*31*). Similarly, poly-P is less internalized compared to HIV-1 Tat-(48−60), penetratin, or polyarginines (*25*).

CPP-mediated delivery into the cytoplasm can be achieved by at least two independent mechanisms: (i) adsorptive endocytosis and subsequent release of the enclosed compounds from endosomes or lysosomes (*4, 8, 46*); and (ii) rapid crossing of the membrane by a seemingly energy-independent, not well understood mechanism referred to as transduction (*9, 47, 48*). For the 22 presented CPPs (Table 1), there is a consensus that different endocytosis pathways strongly contribute to cellular uptake, since only small effects could be detected after treatment with endocytosis inhibitors. 43−57% of the tested conditions showed no effects on the CPP internalization (gray boxes in Table 3) These results are in accordance with Duchardt et al. (*9*) showing that chlorpromazine seems to have no special effect using 10 μM CPPs or with Oehlke et al. (*49*) who demonstrated that chloroquine had no effect upon the internalization of MAP peptides.

However, chloroquine seems to have a special role as an endocytic modulator. Chloroquine is a lysosomotropic amine acting as a buffering agent and preventing endosome acidification. Chloroquine also slows down endocytosis, thus leaving more time for endosomal escape. Finally, by preventing the acidification of endocytic compartments, it inhibits associated degradative activities. This endocytic modulator has no clear increasing effect on the cellular uptake, but could significantly increase conjugate activity implying endocytic uptake of at least a portion, if not all, of the internalized conjugate (*50, 51*).

Furthermore, nystatin has no influence on the CPP internalization in HEK293, HeLa, and MDCK cells, as was also observed in human hepatoma cells (HepG2) and in buffalo green monkey (BGM) cells (*52*).

Treatment with heparin has been shown to inhibit CPP cellular uptake by capping the interaction between the negatively charged proteoglycan and the positively charged peptide (*19*). Nevertheless, the influence of heparin seems not as significant as predicted previously (*6, 46, 53*). The small differences observed between the cells could be due to differential expression of cell surface-expressed HPSGs. In fact, although all tissues express proteoglycans, the level of expression is determined by the state of differentiation and growth of the cell, and specific HPSG isoforms are known to be differentially expressed in different cell types (*54*).

Finally, wortmannin, which inhibits endosome fusion, seems to have a negative effect in combination with penetratin and R9, whereas it has no effect with HIV-1 Tat-(48−60) as described by Fischer et al. (*31*). All wortmannin treated cells show the typical phenomenon of enlarged endosomes, even without FITC-labeled CPPs, caused by inhibiting fusion with lysosomes (Supporting Information Figure 1).

Altogether, the endocytosis inhibitors had little effect on the cellular uptake of the 12 tested CPPs in Cos-7, HEK293, HeLa, and MDCK cell lines. Probably, the avoidance of endocytic routes could be achieved using higher CPP peptide concentrations between 25 and 40 μM as recommended by Tunnemann et al. (*26*) or Duchardt et al. (*9*). The equilibrium between the different states of internalization could be shifted to the cytoplasmic one by increasing the HIV-1 Tat-(48−60) concentration, as reported previously (*9, 55*). The uptake of R9 (endocytosis versus transduction) was shown to be dependent on the CPP concentration, as demonstrated with HeLa cells (*9*) and mouse C2C12 myoblasts (*26*).

CONCLUSION

Despite the high number of biological applications using CPPs, the precise mechanism of entry still appears controversial and certainly requires further investigation. Contradictory results are often reported and could stem from experimental variations: e.g., diversity of the CPP sequences, the wide variety of cell lines studied, the differing protocols applied to investigate the entry mechanism, etc.

Therefore, we performed a comparative screen using 22 CPPs in four cell lines under standardized conditions. Our results clearly revealed that the CPPs could be categorized by their behavior into three main groups showing high, medium, and low cellular uptake. This phenomenon still applies even after trypsinization. The use of endocytosis modulators to manipulate cellular uptake seemed to have fewer effects than often reported. Therefore, we propose a more sophisticated approach to modulate the cellular localization by varying the concentration, sequence length, and/or 3D structure of the analyzed CPP. Furthermore, even if the CPPs are trapped in endosomal/lysosomal vesicles, we believe that the quantity of available cytosolic CPPs is enough to initiate a biological reaction such as reported in Abes et al. (*56*). Chloroquine treatment, which does not lead to a significant redistribution of CPPs, as shown by fluorescence microscopy in our experiments (see also ref *50*), led to a concomitant improvement in oligonucleotide activity of the internalized CPP−conjugate, as shown in splicing correction experiments (*50, 51*). Another way to promote endosomal escape could be the conjugation of a viral fusion peptide such as the N-terminus of hemagglutinin (HA2), which has a better *in vivo* potential (*51*).

Having now in our hand a subset of CPPs with high cell penetrating properties, our future directions will include screening various CPPs together with or fused to elements (e.g., CPP

and peptidic inhibitors) to determine structure−activity relationships (SAR).

ACKNOWLEDGMENT

P.B. is supported in part by the Deutsche Forschungsgemeinschaft (DFG, VO 885/1). The authors thank Prof. Dr. Herrmann and Dr. Korte for advice and assistance with confocal microscopy.

Supporting Information Available: Additonal information as described in the text. This material is available free of charge via the Internet at http://pubs.acs.org.

LITERATURE CITED

(1) Jarver, P., and Langel, U. (2006) Cell-penetrating peptides--a brief introduction. *Biochim. Biophys. Acta 1758*, 260–3.

(2) Deshayes, S., Morris, M. C., Divita, G., and Heitz, F. (2005) Cell-penetrating peptides: tools for intracellular delivery of therapeutics. *Cell. Mol. Life Sci. 62*, 1839–49.

(3) Lindsay, M. A. (2002) Peptide-mediated cell delivery: application in protein target validation. *Curr. Opin. Pharmacol. 2*, 587–94.

(4) Richard, J. P., Melikov, K., Brooks, H., Prevot, P., Lebleu, B., and Chernomordik, L. V. (2005) Cellular uptake of unconjugated TAT peptide involves clathrin-dependent endocytosis and heparan sulfate receptors. *J. Biol. Chem. 280*, 15300–6.

(5) Ferrari, M. E., Nguyen, C. M., Zelphati, O., Tsai, Y., and Felgner, P. L. (1998) Analytical methods for the characterization of cationic lipid-nucleic acid complexes. *Hum. Gene Ther. 9*, 341–51.

(6) Fittipaldi, A., Ferrari, A., Zoppe, M., Arcangeli, C., Pellegrini, V., Beltram, F., and Giacca, M. (2003) Cell membrane lipid rafts mediate caveolar endocytosis of HIV-1 Tat fusion proteins. *J. Biol. Chem. 278*, 34141–9.

(7) Kaplan, I. M., Wadia, J. S., and Dowdy, S. F. (2005) Cationic TAT peptide transduction domain enters cells by macropinocytosis. *J. Controlled Release 102*, 247–53.

(8) Wadia, J. S., Stan, R. V., and Dowdy, S. F. (2004) Transducible TAT-HA fusogenic peptide enhances escape of TAT-fusion proteins after lipid raft macropinocytosis. *Nat. Med. 10*, 310–5.

(9) Duchardt, F., Fotin-Mleczek, M., Schwarz, H., Fischer, R., and Brock, R. (2007) A comprehensive model for the cellular uptake of cationic cell-penetrating peptides. *Traffic 8*, 848–66.

(10) Derossi, D., Joliot, A. H., Chassaing, G., and Prochiantz, A. (1994) The third helix of the Antennapedia homeodomain translocates through biological membranes. *J. Biol. Chem. 269*, 10444–50.

(11) Frankel, A. D., and Pabo, C. O. (1988) Cellular uptake of the tat protein from human immunodeficiency virus. *Cell 55*, 1189–93.

(12) Green, M., and Loewenstein, P. M. (1988) Autonomous functional domains of chemically synthesized human immunodeficiency virus tat trans-activator protein. *Cell 55*, 1179–88.

(13) Lindgren, M., Hallbrink, M., Prochiantz, A., and Langel, U. (2000) Cell-penetrating peptides. *Trends Pharmacol. Sci. 21*, 99–103.

(14) Zorko, M., and Langel, U. (2005) Cell-penetrating peptides: mechanism and kinetics of cargo delivery. *Adv. Drug Delivery Rev. 57*, 529–45.

(15) Vives, E., Brodin, P., and Lebleu, B. (1997) A truncated HIV-1 Tat protein basic domain rapidly translocates through the plasma membrane and accumulates in the cell nucleus. *J. Biol. Chem. 272*, 16010–7.

(16) Oehlke, J., Scheller, A., Wiesner, B., Krause, E., Beyermann, M., Klauschenz, E., Melzig, M., and Bienert, M. (1998) Cellular uptake of an α-helical amphipathic model peptide with the potential to deliver polar compounds into the cell interior nonendocytically. *Biochim. Biophys. Acta 1414*, 127–39.

(17) Futaki, S., Suzuki, T., Ohashi, W., Yagami, T., Tanaka, S., Ueda, K., and Sugiura, Y. (2001) Arginine-rich peptides. An abundant source of membrane-permeable peptides having potential as carriers for intracellular protein delivery. *J. Biol. Chem. 276*, 5836–40.

(18) Pooga, M., Hallbrink, M., Zorko, M., and Langel, U. (1998) Cell penetration by transportan. *Faseb J. 12*, 67–77.

(19) Poon, G. M., and Gariepy, J. (2007) Cell-surface proteoglycans as molecular portals for cationic peptide and polymer entry into cells. *Biochem. Soc. Trans. 35*, 788–93.

(20) El-Andaloussi, S., Jarver, P., Johansson, H. J., and Langel, U. (2007) Cargo-dependent cytotoxicity and delivery efficacy of cell-penetrating peptides: a comparative study. *Biochem. J. 407*, 285–92.

(21) Fotin-Mleczek, M., Welte, S., Mader, O., Duchardt, F., Fischer, R., Hufnagel, H., Scheurich, P., and Brock, R. (2005) Cationic cell-penetrating peptides interfere with TNF signalling by induction of TNF receptor internalization. *J. Cell Sci. 118*, 3339–51.

(22) Maiolo, J. R., Ferrer, M., and Ottinger, E. A. (2005) Effects of cargo molecules on the cellular uptake of arginine-rich cell-penetrating peptides. *Biochim. Biophys. Acta 1712*, 161–72.

(23) Fischer, R., Mader, O., Jung, G., and Brock, R. (2003) Extending the applicability of carboxyfluorescein in solid-phase synthesis. *Bioconjugate Chem. 14*, 653–60.

(24) Lebleu, B., Moulton, H. M., Abes, R., Ivanova, G. D., Abes, S., Stein, D. A., Iversen, P. L., Arzumanov, A. A., and Gait, M. J. (2008) Cell penetrating peptide conjugates of steric block oligonucleotides. *Adv. Drug Delivery Rev. 60*, 517–29.

(25) Pujals, S., and Giralt, E. (2008) Proline-rich, amphipathic cell-penetrating peptides. *Adv. Drug Delivery Rev. 60*, 473–84.

(26) Tunnemann, G., Ter-Avetisyan, G., Martin, R. M., Stockl, M., Herrmann, A., and Cardoso, M. C. (2008) Live-cell analysis of cell penetration ability and toxicity of oligo-arginines. *J. Pept. Sci. 14*, 469–76.

(27) Richard, J. P., Melikov, K., Vives, E., Ramos, C., Verbeure, B., Gait, M. J., Chernomordik, L. V., and Lebleu, B. (2003) Cell-penetrating peptides. A reevaluation of the mechanism of cellular uptake. *J. Biol. Chem. 278*, 585–90.

(28) Elmquist, A., and Langel, U. (2003) In vitro uptake and stability study of pVEC and its all-D analog. *Biol. Chem. 384*, 387–93.

(29) Palm, C., Jayamanne, M., Kjellander, M., and Hallbrink, M. (2007) Peptide degradation is a critical determinant for cell-penetrating peptide uptake. *Biochim. Biophys. Acta 1768*, 1769–76.

(30) Trehin, R., Nielsen, H. M., Jahnke, H. G., Krauss, U., Beck-Sickinger, A. G., and Merkle, H. P. (2004) Metabolic cleavage of cell-penetrating peptides in contact with epithelial models: human calcitonin (hCT)-derived peptides, Tat(47−57) and penetratin(43−58). *Biochem. J. 382*, 945–56.

(31) Fischer, R., Kohler, K., Fotin-Mleczek, M., and Brock, R. (2004) A stepwise dissection of the intracellular fate of cationic cell-penetrating peptides. *J. Biol. Chem. 279*, 12625–35.

(32) Jones, A. T. (2007) Macropinocytosis: searching for an endocytic identity and role in the uptake of cell penetrating peptides. *J. Cell Mol. Med. 11*, 670–84.

(33) Patel, L. N., Zaro, J. L., and Shen, W. C. (2007) Cell penetrating peptides: intracellular pathways and pharmaceutical perspectives. *Pharm. Res. 24*, 1977–92.

(34) Sahlin, S., Hed, J., and Rundquist, I. (1983) Differentiation between attached and ingested immune complexes by a fluorescence quenching cytofluorometric assay. *J. Immunol. Methods 60*, 115–24.

(35) Ma, Z., and Lim, L. Y. (2003) Uptake of chitosan and associated insulin in Caco-2 cell monolayers: a comparison between chitosan molecules and chitosan nanoparticles. *Pharm. Res. 20*, 1812–9.

(36) Wan, C. P., Park, C. S., and Lau, B. H. (1993) A rapid and simple microfluorometric phagocytosis assay. *J. Immunol. Methods 162*, 1–7.

(37) Zhang, L., Torgerson, T. R., Liu, X. Y., Timmons, S., Colosia, A. D., Hawiger, J., and Tam, J. P. (1998) Preparation of functionally active cell-permeable peptides by single-step ligation of two peptide modules. *Proc. Natl. Acad. Sci. U.S.A. 95*, 9184–9.

(38) Lanz, E., Slavik, J., and Kotyk, A. (1999) 2′,7′-Bis-(2-carboxyethyl)-5(6)-carboxyfluorescein as a dual-emission fluorescent indicator of intracellular pH suitable for argon laser confocal microscopy. *Folia Microbiol. (Praha) 44*, 429–34.

(39) Matsuzaki, K., Yoneyama, S., Murase, O., and Miyajima, K. (1996) Transbilayer transport of ions and lipids coupled with mastoparan X translocation. *Biochemistry 35*, 8450–6.

(40) Hallbrink, M., Oehlke, J., Papsdorf, G., and Bienert, M. (2004) Uptake of cell-penetrating peptides is dependent on peptide-to-cell ratio rather than on peptide concentration. *Biochim. Biophys. Acta 1667*, 222–8.

(41) Foerg, C., Ziegler, U., Fernandez-Carneado, J., Giralt, E., and Merkle, H. P. (2007) Differentiation restricted endocytosis of cell penetrating peptides in MDCK cells corresponds with activities of Rho-GTPases. *Pharm. Res. 24*, 628–42.

(42) Kosuge, M., Takeuchi, T., Nakase, I., Jones, A. T., and Futaki, S. (2008) Cellular internalization and distribution of arginine-rich peptides as a function of extracellular peptide concentration, serum, and plasma membrane associated proteoglycans. *Bioconjugate Chem. 19*, 656–64.

(43) Mano, M., Teodosio, C., Paiva, A., Simoes, S., and Pedroso de Lima, M. C. (2005) On the mechanisms of the internalization of S4(13)-PV cell-penetrating peptide. *Biochem. J. 390*, 603–12.

(44) Lindberg, M., Jarvet, J., Langel, U., and Graslund, A. (2001) Secondary structure and position of the cell-penetrating peptide transportan in SDS micelles as determined by NMR. *Biochemistry 40*, 3141–9.

(45) Magzoub, M., Eriksson, L. E., and Graslund, A. (2003) Comparison of the interaction, positioning, structure induction and membrane perturbation of cell-penetrating peptides and non-translocating variants with phospholipid vesicles. *Biophys. Chem. 103*, 271–88.

(46) Ferrari, A., Pellegrini, V., Arcangeli, C., Fittipaldi, A., Giacca, M., and Beltram, F. (2003) Caveolae-mediated internalization of extracellular HIV-1 tat fusion proteins visualized in real time. *Mol. Ther. 8*, 284–94.

(47) Fretz, M. M., Penning, N. A., Al-Taei, S., Futaki, S., Takeuchi, T., Nakase, I., Storm, G., and Jones, A. T. (2007) Temperature-, concentration- and cholesterol-dependent translocation of L- and D-octa-arginine across the plasma and nuclear membrane of CD34+ leukaemia cells. *Biochem. J. 403*, 335–42.

(48) Ziegler, A., Nervi, P., Durrenberger, M., and Seelig, J. (2005) The cationic cell-penetrating peptide CPP(TAT) derived from the HIV-1 protein TAT is rapidly transported into living fibroblasts: optical, biophysical, and metabolic evidence. *Biochemistry 44*, 138–48.

(49) Oehlke, J., Lorenz, D., Wiesner, B., and Bienert, M. (2005) Studies on the cellular uptake of substance P and lysine-rich, KLA-derived model peptides. *J. Mol. Recognit. 18*, 50–9.

(50) Abes, S., Williams, D., Prevot, P., Thierry, A., Gait, M. J., and Lebleu, B. (2006) Endosome trapping limits the efficiency of splicing correction by PNA-oligolysine conjugates. *J. Controlled Release 110*, 595–604.

(51) El-Andaloussi, S., Johansson, H. J., Lundberg, P., and Langel, U. (2006) Induction of splice correction by cell-penetrating peptide nucleic acids. *J. Gene Med. 8*, 1262–73.

(52) Ignatovich, I. A., Dizhe, E. B., Pavlotskaya, A. V., Akifiev, B. N., Burov, S. V., Orlov, S. V., and Perevozchikov, A. P. (2003) Complexes of plasmid DNA with basic domain 47−57 of the HIV-1 Tat protein are transferred to mammalian cells by endocytosis-mediated pathways. *J. Biol. Chem. 278*, 42625–36.

(53) Console, S., Marty, C., Garcia-Echeverria, C., Schwendener, R., and Ballmer-Hofer, K. (2003) Antennapedia and HIV transactivator of transcription (TAT) "protein transduction domains" promote endocytosis of high molecular weight cargo upon binding to cell surface glycosaminoglycans. *J. Biol. Chem. 278*, 35109–14.

(54) Jones, S. W., Christison, R., Bundell, K., Voyce, C. J., Brockbank, S. M., Newham, P., and Lindsay, M. A. (2005) Characterisation of cell-penetrating peptide-mediated peptide delivery. *Br. J. Pharmacol. 145*, 1093–102.

(55) Potocky, T. B., Menon, A. K., and Gellman, S. H. (2003) Cytoplasmic and nuclear delivery of a TAT-derived peptide and a beta-peptide after endocytic uptake into HeLa cells. *J. Biol. Chem. 278*, 50188–94.

(56) Abes, S., Moulton, H. M., Clair, P., Prevot, P., Youngblood, D. S., Wu, R. P., Iversen, P. L., and Lebleu, B. (2006) Vectorization of morpholino oligomers by the (R-Ahx-R)4 peptide allows efficient splicing correction in the absence of endosomolytic agents. *J. Controlled Release 116*, 304–13.

(57) Rousselle, C., Clair, P., Lefauconnier, J. M., Kaczorek, M., Scherrmann, J. M., and Temsamani, J. (2000) New advances in the transport of doxorubicin through the blood-brain barrier by a peptide vector-mediated strategy. *Mol. Pharmacol. 57*, 679–86.

(58) Saphire, A. C., Guan, T., Schirmer, E. C., Nemerow, G. R., and Gerace, L. (2000) Nuclear import of adenovirus DNA in vitro involves the nuclear protein import pathway and hsc70. *J. Biol. Chem. 275*, 4298–304.

(59) Sadler, K., Eom, K. D., Yang, J. L., Dimitrova, Y., and Tam, J. P. (2002) Translocating proline-rich peptides from the antimicrobial peptide bactenecin 7. *Biochemistry 41*, 14150–7.

(60) Lin, Y. Z., Yao, S. Y., Veach, R. A., Torgerson, T. R., and Hawiger, J. (1995) Inhibition of nuclear translocation of transcription factor NF-kappa B by a synthetic peptide containing a cell membrane-permeable motif and nuclear localization sequence. *J. Biol. Chem. 270*, 14255–8.

(61) Lanford, R. E., Kanda, P., and Kennedy, R. C. (1986) Induction of nuclear transport with a synthetic peptide homologous to the SV40 T antigen transport signal. *Cell 46*, 575–82.

(62) Ragin, A. D., Morgan, R. A., and Chmielewski, J. (2002) Cellular import mediated by nuclear localization signal peptide sequences. *Chem. Biol. 9*, 943–8.

(63) Trehin, R., Krauss, U., Muff, R., Meinecke, M., Beck-Sickinger, A. G., and Merkle, H. P. (2004) Cellular internalization of human calcitonin derived peptides in MDCK monolayers: a comparative study with Tat(47−57) and penetratin(43−58). *Pharm. Res. 21*, 33–42.

(64) Elmquist, A., Lindgren, M., Bartfai, T., and Langel, U. (2001) VE-cadherin-derived cell-penetrating peptide, pVEC, with carrier functions. *Exp. Cell Res. 269*, 237–44.

(65) De Coupade, C., Fittipaldi, A., Chagnas, V., Michel, M., Carlier, S., Tasciotti, E., Darmon, A., Ravel, D., Kearsey, J., Giacca, M., and Cailler, F. (2005) Novel human-derived cell-penetrating peptides for specific subcellular delivery of therapeutic biomolecules. *Biochem. J. 390*, 407–18.

(66) Morris, M. C., Depollier, J., Mery, J., Heitz, F., and Divita, G. (2001) A peptide carrier for the delivery of biologically active proteins into mammalian cells. *Nat. Biotechnol. 19*, 1173–6.

(67) Morris, M. C., Vidal, P., Chaloin, L., Heitz, F., and Divita, G. (1997) A new peptide vector for efficient delivery of oligonucleotides into mammalian cells. *Nucleic Acids Res. 25*, 2730–6.

(68) Fernandez-Carneado, J., Kogan, M. J., Castel, S., and Giralt, E. (2004) Potential peptide carriers: amphipathic proline-rich peptides derived from the N-terminal domain of gamma-zein. *Angew. Chem., Int. Ed. Engl. 43*, 1811–4.

(69) Wender, P. A., Mitchell, D. J., Pattabiraman, K., Pelkey, E. T., Steinman, L., and Rothbard, J. B. (2000) The design, synthesis, and evaluation of molecules that enable or enhance cellular uptake: peptoid molecular transporters. *Proc. Natl. Acad. Sci. U.S.A. 97*, 13003–8.

BC800194E

Supporting Information

Tabel 1: Consequences of protease inhibitors and endocytosis modulators

Effect of the	Treatment	Conc.	Consequences
Protease	Phenanthroline	10 µM	Inhibition of metallo proteases
	EDTA	1 mM	Inhibition of metallo proteases
	MG-132	20 µM	Inhibition of proteasom activity
	Bestatin	10 µM	Inhibition of aminopeptidase B and leucine aminopeptidase
	E-64	10 µM	Inhibition of cysteine proteases
	BSA	1%	For protease saturation
	PMSF	1 mM	Inhibition of serine proteases by sulfonylation
	Aprotinin	2 µg/ml	Inhibition of serine proteases especially trypsin
Endocytosis	37°C	-	Standard condition
	4°C	-	Inhibition of energy-dependent process
	Chlorpromazine	30 µM	Inhibition of clathrin-dependent endocytosis
	Chloroquine	100 µM	Inhibits acidification of endosomes
	Nystatin	100 µM	Disrupt caveolar structure and function
	Heparin	10 µM	Competitor of cell membrane-associated HSPGs
	Wortmannin	100 nM	Inhibits endosome fusion

Footnote: The concentrations given in the table are the concentrations used in this study. Additionally, a brief description of the proposed exerted effect on protease/endocytosis is given for each substance. EDTA: ethylenedinitrilotetraacetic acid, PMSF: phenylmethanesulphonylfluoride, BSA: bovine serum albumin, Glycerol-P: β-glycerol phosphate, HSPGs: heparin sulfate proteoglycans

Table 2: Viability Test

	Cos-7				HEK293				HeLa				MDCK			
CPPs	**1 µM**	**10 µM**	**25 µM**	**50 µM**	**1 µM**	**10 µM**	**25 µM**	**50 µM**	**1 µM**	**10 µM**	**25 µM**	**50 µM**	**1 µM**	**10 µM**	**25 µM**	**50 µM**
SynB1	108 ± 11	86 ± 11	96 ± 21	104 ± 4	109 ± 22	81 ± 17	90 ± 15	80 ± 3	105 ± 16	105 ± 21	87 ± 25	96 ± 25	100 ± 8	102 ± 11	99 ± 8	103 ± 19
Polyomavirus Vp1	106 ± 15	81 ± 9	106 ± 24	89 ± 1	108 ± 26	90 ± 15	97 ± 17	88 ± 16	102 ± 22	88 ± 3	90 ± 4	91 ± 20	95 ± 11	106 ±13	122 ±24	98 ± 11
Penetratin	114 ± 10	99 ± 7	110 ± 23	114 ± 11	113 ± 17	141 ± 11	105 ± 25	101 ± 17	94 ± 16	95 ± 22	76 ± 3	72 ± 26	98 ± 5	89 ± 10	112 ± 9	120 ± 19
DPV6	97 ± 07	83 ± 9	88 ± 10	93 ± 14	104 ± 20	115 ± 6	134 ± 7	114 ± 1	94 ± 8	92 ± 20	106 ± 16	102 ± 9	112 ± 13	84 ± 10	106 ± 18	117 ± 12
HIV-1 Tat-(48-60)	105 ± 12	99 ± 6	115 ± 10	93 ± 2	82 ± 15	83 ± 15	90 ± 13	94 ± 8	100 ± 20	80 ± 16	63 ± 22	50 ± 10	100 ± 0	100 ± 5	106 ± 6	100 ± 14
$S4_{13}PV$	97 ± 23	89 ± 17	63 ± 21	**12 ± 27**	94 ± 9	95 ± 6	50 ± 26	**11 ± 17**	105 ± 12	64 ± 24	**0**	**0**	106 ± 4	**33 ± 16**	**11 ± 1**	**5 ± 2**
Transportan	104 ± 12	86 ± 15	**20 ± 25**	**0**	90 ± 5	97 ± 7	50 ± 29	**14 ± 11**	108 ± 21	88 ± 19	**0**	**0**	102 ± 60	116 ± 13	**14 ± 1**	**7 ± 2**
MAP	99 ± 25	106 ± 11	55 ± 23	**6 ± 7**	107 ± 17	110 ± 7	113 ± 3	83 ± 16	92 ± 26	99 ± 19	**34 ± 10**	**6 ± 10**	102 ± 1	97 ± 14	66 ± 10	**46 ± 14**
Pep-1	98 ± 01	97 ± 15	93 ± 19	78 ± 11	87 ± 12	99 ± 1	81 ± 9	91 ± 18	96 ± 15	98 ± 17	104 ± 18	109 ± 27	106 ± 20	104 ± 19	105 ± 10	100 ± 14
Bac1-15	116 ± 17	91 ± 14	105 ± 2	100 ± 12	88 ± 21	104 ± 9	90 ± 13	73 ± 21	95 ± 15	99 ± 11	81 ± 27	88 ± 23	86 ± 9	89 ± 13	89 ± 11	93 ± 16
poly-P	104 ± 03	106 ± 15	94 ± 21	**47 ± 10**	87 ± 19	96 ± 23	82 ± 10	80 ± 9	92 ± 18	94 ± 21	92 ± 10	107 ± 20	98 ± 7	97 ± 10	99 ± 8	106 ± 7
R7	91 ± 12	97 ± 4	93 ± 8	94 ± 7	89 ± 14	84 ± 0	80 ± 9	69 ± 11	97 ± 14	87 ± 17	93 ± 26	97 ± 24	105 ± 7	101 ± 22	103 ± 12	110 ± 16
R9	91 ± 19	102 ± 8	108 ± 13	88 ± 17	99 ± 18	89 ± 10	72 ± 22	78 ± 9	92 ± 14	111 ± 1	98 ± 19	73 ± 23	104 ± 15	91 ± 6	81 ± 12	61 ± 25
NF-kB	102 ± 05	98 ± 10	67 ± 27	54 ± 25	93 ± 8	111 ± 0	89 ± 3	70 ± 9	103 ± 9	90 ± 12	90 ± 18	95 ± 15	104 ± 12	98 ± 20	102 ± 22	101 ± 11
SV40	105 ± 17	101 ± 29	103 ± 23	87 ± 14	106 ± 14	88 ± 9	104 ± 20	109 ± 9	87 ± 12	86 ± 6	89 ± 1	86 ± 18	101 ± 2	86 ± 8	102 ± 21	100 ± 6
HATF3	71 ± 01	83 ± 22	**49 ± 16**	**39 ± 20**	80 ± 16	76 ± 5	88 ± 17	81 ± 9	87 ± 15	100 ± 28	101 ± 10	105 ± 27	104 ± 20	102 ± 7	114 ± 15	120 ± 25
hCT(9-32)	118 ± 21	110 ± 4	111 ± 4	92 ± 10	89 ± 24	89 ± 2	78 ± 12	83 ± 25	95 ± 17	108 ± 10	100 ± 10	96 ± 10	96 ± 1	93 ± 8	102 ± 1	108 ± 13
HIV-1 Rev-(34-50)	114 ± 10	101 ± 11	98 ± 3	98 ± 20	94 ± 25	93 ± 26	78 ± 28	**26 ± 13**	85 ± 7	94 ± 16	74 ± 15	**34 ± 0**	94 ± 1	100 ± 10	76 ± 12	51 ± 11
FP-NLS (MPG)	108 ± 15	101 ± 2	116 ± 5	132 ± 5	97 ± 14	100 ± 17	95 ± 26	118 ± 16	99 ± 17	96 ± 13	111 ± 26	103 ± 15	103 ± 5	102 ± 6	83 ± 9	90 ± 12
pVEC	98 ± 26	91 ± 5	78 ± 9	52 ± 12	79 ± 14	71 ± 18	68 ± 12	52 ± 15	114 ± 26	112 ± 17	116 ± 30	94 ± 24	101 ± 9	102 ± 4	102 ± 4	97 ± 2
Integrin	97 ± 4	119 ± 16	117 ± 12	106 ± 3	76 ± 7	75 ± 1	95 ± 11	105 ± 15	96 ± 1	113 ± 22	98 ± 9	118 ± 25	105 ± 5	110 ± 4	101 ± 0	99 ± 4
pVEC-scrambled	79 ± 24	80 ± 8	90 ± 9	**37 ± 8**	72 ± 11	78 ± 26	74 ± 19	82 ± 29	103 ± 18	99 ± 15	102 ± 22	76 ± 15	103 ± 7	95 ± 22	94 ± 10	93 ± 10

Footnote: Measurement of the viability using the CCK-8 solution (Fluka). 100% shows no influence of the CPPs. Four different CPP concentrations were used (1 µM, 10 µM, 25 µM, and 50 µM) for each cell lines. The data represent the mean of 3-5 independent experiments ± S.E.M.; bold data indicated a viability ≤50%.

Table 3: Influence of trypsin treatment on the cellular uptake.

Without trypsin treatment												
CPP \ cell line	**Cos-7**			**HEK293**			**HeLa**			**MDCK**		
	M	**SD**	**CV**	**M**	**SD**	**CV**	**M**	**SD**	**CV**	**M**	**SD**	**CV**
control	19	4	21	26	8	31	28	6	21	24	7	29
Polyomavirus Vp1	339	64	19	206	11	5	285	10	4	229	42	18
poly-P	105	16	15	185	55	30	301	29	10	213	42	20
NF-kB	127	39	31	129	34	26	204	49	24	180	39	22
SV40	270	80	30	132	26	20	309	41	13	262	67	26
HATF3	265	54	20	153	5	3	322	24	7	328	62	19
hCT(9-32)	579	163	28	123	18	15	266	22	8	189	58	31
SynB1	1,970	547	28	869	60	7	1,898	503	27	1,802	431	24
DPV6	7,187	710	10	7,899	973	12	9,436	743	8	9,530	659	7
HIV-1 Tat-(48-60)	6,995	1,059	15	6,283	667	11	9,080	1,925	21	8,830	481	5
Pep-1	3,460	260	8	1,018	152	15	3,555	397	11	1,615	325	20
Bac1-15	6,092	461	8	2,148	312	15	2,954	176	6	2,957	608	21
FP-NLS (MPG)	4,433	453	10	7,982	1,266	16	10,062	1,852	18	6,213	1,468	24
Integrin	981	158	16	3,576	730	20	889	58	7	1,964	486	25
pVEC-scrambled	6,302	302	5	5,671	193	3	7,055	261	4	6,522	5	0
Penetratin	15,852	3,734	24	25,619	4,314	17	15,560	1,360	9	12,598	1,770	14
$S4_{13}PV$	9,931	539	5	15,286	2,455	16	19,226	4,212	22	27,207	6,490	24
Transportan	22,767	3,697	16	31,080	7,308	24	27,328	3,386	12	39,970	3,125	8
MAP	20,937	1,617	8	25,735	2,757	11	51,008	3,505	7	29,142	5,129	18
R7	10,410	2,461	24	7,108	1,295	18	11,935	2,717	23	12,940	3,301	26
R9	17,998	1,173	7	20,571	331	2	22,197	2,938	13	22,789	5,805	25
HIV-1 Rev-(34-50)	11,779	736	6	16,794	1,586	9	21,336	4,021	19	15,191	2,340	15
pVEC	6,302	302	5	6,805	719	11	11,262	1,167	10	11,027	1,594	14
With trypsin treatment												
CPP \ cell line	**Cos-7**			**HEK293**			**HeLa**			**MDCK**		
	M	**SD**	**CV**	**M**	**SD**	**CV**	**M**	**SD**	**CV**	**M**	**SD**	**CV**
control	20	5	25	23	6	26	22	4	18	17	5	29
Polyomavirus Vp1	20	4	20	18	2	11	22	1	5	19	4	21
poly-P	20	1	5	15	2	13	22	6	27	21	6	29
NF-kB	18	3	17	15	3	20	22	6	27	16	0	0
SV40	20	2	10	18	3	17	22	4	18	15	1	7
HATF3	16	4	25	16	1	6	18	4	22	20	2	10
hCT(9-32)	17	2	12	15	3	20	18	3	17	19	5	26
SynB1	33	4	12	29	8	28	48	2	4	24	7	29
DPV6	34	6	18	95	21	22	81	9	11	28	4	14
HIV-1 Tat-(48-60)	64	11	17	125	4	3	60	14	23	28	5	18
Pep-1	79	4	5	39	6	15	119	26	22	72	14	19
Bac1-15	26	7	27	19	2	11	22	2	9	22	5	23
FP-NLS (MPG)	1,411	116	8	928	171	18	1,257	160	13	435	59	14
Integrin	51	1	2	1,638	360	22	595	35	6	274	39	14
pVEC-scrambled	60	10	17	42	1	2	53	9	17	61	9	15
Penetratin	472	114	24	1,269	137	11	2,748	831	30	311	22	7
$S4_{13}PV$	481	132	27	689	179	26	1,052	172	16	686	110	16
Transportan	7,349	18	0	6,197	799	13	10,529	1,047	10	23,185	392	2
MAP	1,600	393	25	2,795	677	24	4,199	361	9	839	108	13
R7	129	10	8	189	3	2	48	7	15	32	8	25
R9	145	42	29	713	190	27	1,409	322	23	66	15	23
HIV-1 Rev-(34-50)	95	20	21	645	145	22	715	271	38	65	6	9
pVEC	96	28	29	154	29	19	301	53	18	65	13	20

Cells were pre-incubated for 2 h with the protease inhibitors (EDTA/MG-132) followed by incubation with CPPs for 30 min at 37°C. After washing steps the cells were lysed and analyzed by a microplate reader. For assays with trypsin, the cells were treated with trypsin (10 min at 37°C) before cell lysis. The data represent the mean (M) of 3-5 independent experiments with the corresponding standard deviation (SD) and correlation value (CV). The CV values for all cell assays are below the threshold of 30%.

Table 4: Effects of endocytosis modulators on cellular uptake - Raw data

Cell lines	Conditions	Control			Penetratin			DPV6			HIV-1 Tat-(48-60)			$S4_{13}PV$			Transportan		
		M	SD	CV	M	SD	CV	M	SD	CV	M	SD	CV	M	SD	CV	M	SD	CV
Cos-7	**37°C**	20	5	25	472	114	24	34	6	18	64	11	17	481	132	27	7,349	18	0
	4°C	18	5	28	534	138	26	123	18	15	197	23	12	217	23	11	24,813	115	0
	Chlorpromazine	16	3	19	975	138	14	52	20	38	46	11	24	344	99	29	9,533	592	6
	Chloroquine	20	3	15	718	200	28	67	10	15	190	12	6	320	32	10	10,109	2,236	22
	Nystatin	16	3	19	357	27	8	20	2	10	23	2	9	479	27	6	7,388	1,061	14
	Heparin	20	4	20	414	43	10	226	19	8	255	18	7	208	58	28	19,844	5,408	27
	Wortmannin	17	3	18	386	114	30	31	9	29	29	8	28	157	18	11	27,805	4,067	15
HEK293	**37°C**	23	6	26	1,269	137	11	95	21	22	125	4	3	689	179	26	6,197	799	13
	4°C	19	5	26	798	121	15	36	7	19	34	1	3	135	24	18	18,862	2,919	15
	Chlorpromazine	18	3	17	1,380	331	24	62	12	19	30	9	30	519	44	8	8,412	201	2
	Chloroquine	21	4	19	1,084	274	25	64	15	23	60	16	27	792	121	15	17,034	1,732	10
	Nystatin	19	4	21	1,042	69	7	76	15	20	47	8	17	984	68	7	2,589	542	21
	Heparin	20	5	25	324	56	17	128	5	4	150	25	17	362	27	7	11,838	3,794	32
	Wortmannin	11	3	27	492	45	9	59	8	14	24	5	21	348	4	1	25,970	3,059	12
HeLa	**37°C**	21	4	19	3,335	831	25	81	9	11	59	11	19	1,052	172	16	10,529	1,047	10
	4°C	21	5	24	1,374	326	24	107	24	22	90	3	3	808	198	25	19,985	4,514	23
	Chlorpromazine	22	4	18	1,178	175	15	32	5	16	100	15	15	1,017	207	20	7,709	1,731	22
	Chloroquine	20	6	30	3,415	51	1	55	9	16	117	26	22	1,447	305	21	21,840	4,276	20
	Nystatin	21	6	29	1,294	141	11	43	5	12	102	17	17	411	98	24	21,635	2,816	13
	Heparin	19	6	32	1,734	424	24	262	74	28	312	95	30	1,134	123	11	14,634	3,406	23
	Wortmannin	17	3	18	597	179	30	42	12	29	27	3	11	780	99	13	29,113	1,025	4
MDCK	**37°C**	17	5	29	311	22	7	28	4	14	28	5	18	686	110	16	4,637	78	2
	4°C	15	3	20	715	72	10	20	3	15	25	7	28	1,064	153	14	13,036	2,744	21
	Chlorpromazine	19	6	32	556	98	18	47	8	17	40	8	20	650	187	29	19,713	1,654	8
	Chloroquine	20	4	20	359	78	22	27	3	11	30	4	13	188	53	28	28,270	3,237	11
	Nystatin	18	2	11	936	135	14	31	6	19	26	1	4	1,008	179	18	6,046	688	11
	Heparin	20	4	20	549	96	17	27	3	11	29	3	10	46	12	26	22,499	1,930	9
	Wortmannin	22	3	14	386	72	19	34	1	3	31	7	23	448	65	15	23,952	4,476	19

The cells were treated with the reagents at the given concentrations and later CPPs (10 µM) were added to the medium. The cells were incubated for another 30 min and subjected to quantification (for more details see Experimental Procedures). The data represent the mean (M) of 3-5 independent experiments with the corresponding standard deviation (SD) and correlation value (CV). The CV values for all cell assays are below the threshold of 30%.

Table 4: Effects of endocytosis modulators on cellular uptake - Raw data (continuous)

Cell lines	Conditions	MAP			R7			R9			HIV-1 Rev (34-48)			FP-NLS (MPG)			Integrin			pVEC-scrambled		
		M	SD	CV	M	SD	CV	M	SD	CV	M	SD	CV	M	SD	CV	M	SD	CV	M	SD	CV
Cos-7	**37°C**	1,600	393	25	129	10	8	145	42	29	95	20	21	1,411	116	8	51	1	2	60	10	17
	4°C	4,127	479	12	134	118	88	374	66	18	301	47	16	614	113	18	58	12	21	123	22	18
	Chlorpromazine	875	98	11	49	4	8	144	20	14	279	47	17	738	118	16	51	23	45	77	4	5
	Chloroquine	4,309	920	21	164	24	15	800	212	27	529	122	23	1,435	232	16	47	13	28	226	43	19
	Nystatin	1,668	61	4	23	5	22	128	38	30	49	4	8	507	138	27	38	8	21	119	16	13
	Heparin	1,677	119	7	344	31	9	325	28	9	477	17	4	377	43	11	29	2	7	144	23	16
	Wortmannin	569	57	10	30	8	27	99	21	21	96	18	19	236	14	6	86	8	9	41	12	29
HEK293	**37°C**	2,795	677	24	189	3	2	713	190	27	645	145	22	928	171	18	1,638	360	22	42	1	2
	4°C	18,761	3,000	16	68	7	10	214	44	21	211	24	11	1,240	195	16	205	45	22	97	26	27
	Chlorpromazine	1,422	259	18	36	3	8	477	109	23	378	99	26	588	27	5	79	14	18	204	39	19
	Chloroquine	2,210	598	27	145	21	14	461	7	2	438	75	17	783	25	3	1,908	153	8	136	9	7
	Nystatin	1,949	356	18	39	5	13	165	8	5	108	17	16	571	129	23	70	16	23	61	6	10
	Heparin	4,661	968	21	589	154	26	637	76	12	761	83	11	2,386	479	20	779	29	4	250	16	6
	Wortmannin	552	22	4	39	8	21	112	22	20	117	23	20	519	102	20	930	183	20	40	11	28
HeLa	**37°C**	4,199	361	9	48	7	15	1,409	322	23	715	217	30	1,257	160	13	595	35	6	53	9	17
	4°C	4,798	304	6	104	13	13	839	159	19	267	56	21	1,068	209	20	173	40	23	63	10	16
	Chlorpromazine	3,121	216	7	92	2	2	1,774	296	17	113	12	11	1,517	361	24	51	23	45	66	15	23
	Chloroquine	1,388	379	27	215	63	29	2,011	339	17	697	104	15	1,209	270	22	1,071	313	29	154	18	12
	Nystatin	5,534	570	10	106	26	25	578	123	21	502	137	27	1,396	237	17	859	94	11	127	36	28
	Heparin	569	106	19	405	56	14	345	56	16	545	115	21	194	18	9	61	13	21	328	85	26
	Wortmannin	1,084	180	17	45	4	9	224	44	20	135	15	11	749	75	10	1,211	221	18	46	2	4
MDCK	**37°C**	839	108	13	32	8	25	66	15	23	65	6	9	435	59	14	274	39	14	61	9	15
	4°C	245	26	11	45	3	7	68	7	10	57	12	21	574	78	14	96	27	28	55	16	29
	Chlorpromazine	1,472	436	30	49	6	12	220	62	28	168	45	27	706	57	8	156	20	13	83	7	8
	Chloroquine	1,430	190	13	26	7	27	81	16	20	114	7	6	285	50	18	23	7	30	51	9	18
	Nystatin	6,618	1,768	27	26	4	15	63	11	17	58	8	14	199	20	10	46	6	13	46	13	28
	Heparin	2,691	798	30	53	1	2	144	38	26	45	13	29	209	61	29	84	25	30	62	17	27
	Wortmannin	1,106	284	26	33	8	24	69	9	13	49	10	20	534	107	20	726	194	27	33	1	3

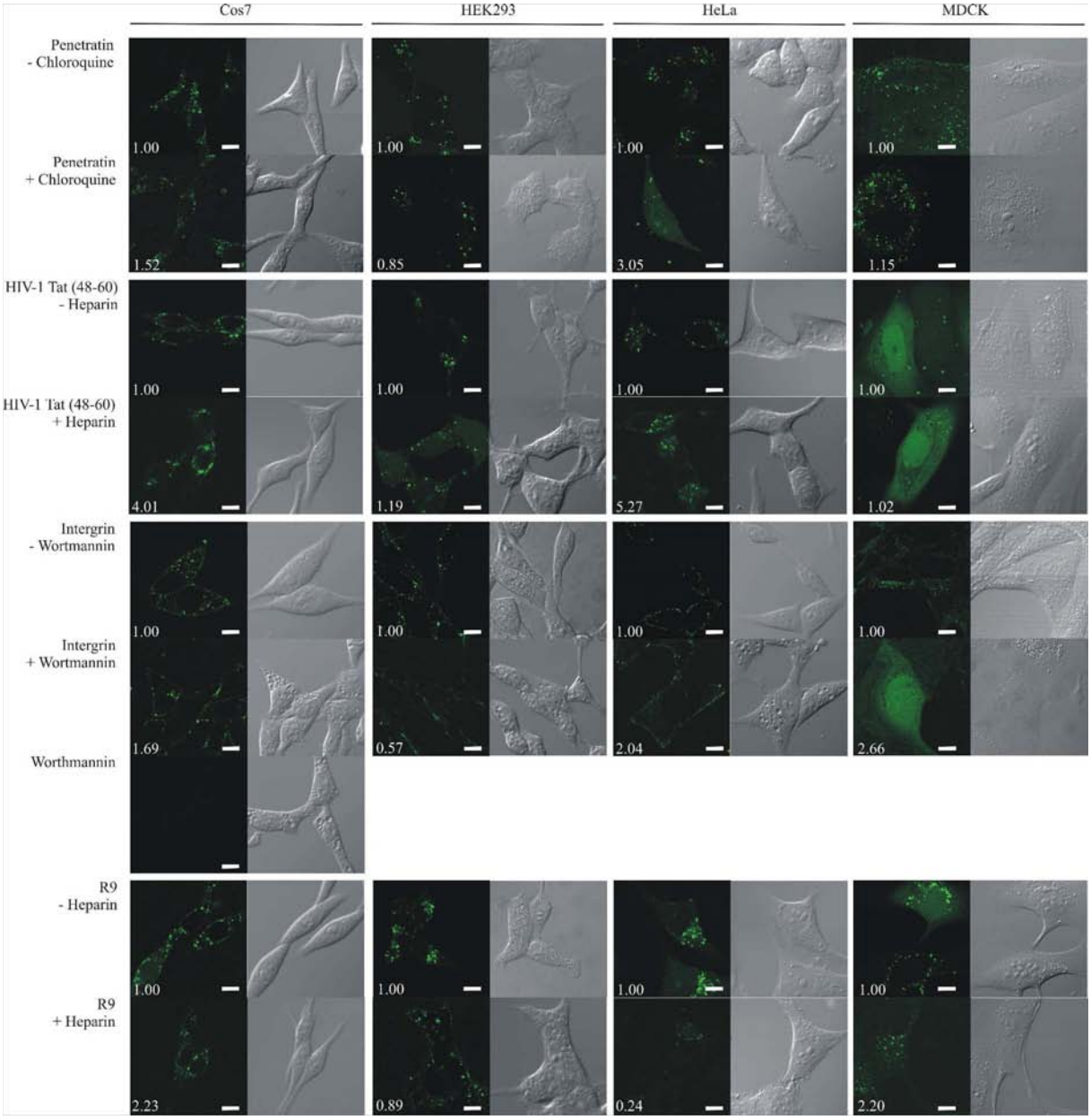

Figure 1: Example of cellular uptake and endocytosis modulators in Cos-7, HEK293, HeLa, and MDCK cells. Confocal microscopy sections of the four different cell types treated with the endocytosis modulators (concentrations see Experimental Section) for 30 min and afterwards with 10 µM of the FITC-labelled CPPs together with the inhibitors for additional 30 min. For each condition we show fluorescence and the phase contrast images. In the left upper corner of the fluorescence images the percentage of the cellular uptake measured by microplate reader is given (Table 3). The white bars represent 10 µm.

Enhanced Cell Uptake of Superparamagnetic Iron Oxide Nanoparticles Functionalized with Dendritic Guanidines

Amanda L. Martin,[†] Lisa M. Bernas,[II,§] Brian K. Rutt,[II,§] Paula J. Foster,[II,§] and Elizabeth R. Gillies*[,†,‡]

Department of Chemistry, Department of Chemical and Biochemical Engineering, Department of Medical Biophysics, and Imaging Research Laboratories—Robarts Research Institute, The University of Western Ontario, 1151 Richmond Street, London, Ontario N6A 5B7, Canada. Received May 20, 2008; Revised Manuscript Received October 14, 2008

Magnetic resonance imaging (MRI) is a powerful tool for the diagnosis of disease and the study of biological processes such as cancer metastasis and inflammation. Superparamagnetic iron oxide (SPIO) nanoparticles have been shown to be effective contrast agents for labeling cells to provide high sensitivity in MRI, but this sensitivity depends on the ability to label cells with sufficient quantities of SPIO, which can be challenging for nonphagocytic cells such as cancer cells. To address this issue, a novel cell-penetrating polyester dendron with peripheral guanidines was developed and conjugated to the surface of SPIO. The functionalized nanoparticles were characterized by transmission electron microscopy, infrared spectroscopy, and dynamic light scattering, and it was found that the surface functionalization reaction proceeded to completion and did not have any adverse effects on the SPIO. In GL261 mouse glioma cells, the dendritic guanidine exhibited remarkably similar cell-penetrating capabilities to the HIV-Tat_{47-57} peptide for the transport of fluorescein, and when conjugated to SPIO, it provided significantly enhanced uptake in comparison with nanoparticles having no dendron or dendrons with hydroxyl or amine peripheries. This uptake led to substantial decreases in the transverse relaxation time (T_2) of labeled cells relative to control cells. While the nanoparticles functionalized with dendritic guanidines exhibited somewhat greater toxicity than those functionalized with dendrons having hydroxyl or amine peripheries, they were still relatively nontoxic at the low concentrations required for labeling.

INTRODUCTION

Magnetic resonance imaging (MRI) is an important noninvasive technique for the diagnosis of disease and the study of biological processes. Since the inception of MRI, several million contrast agent injections have been performed. These agents increase the signal contrast between normal and diseased tissues by altering the nuclear relaxation times of water molecules in their vicinity. In addition to low molecular weight complexes based on gadolinium (Gd^{3+}) (*1*), a class of contrast agents of growing importance is superparamagnetic iron oxide (SPIO) nanoparticles (*2*). These nanoparticles induce local inhomogeneities in the magnetic field, resulting in regions of hypointensity in T2-weighted MR images. Several SPIO agents are clinically approved by the United States Food and Drug Administration for use in liver and spleen imaging, as well as gastrointestinal imaging (*3*). In vivo administration of SPIO has been investigated primarily by two routes. In some applications, SPIO is injected intravenously and reaches the target site either passively or by the conjugation of an active targeting group to the SPIO surface (*4, 5*). Alternatively, for the study of biological processes such as metastasis and stem cell transplantation, cells can be labeled with SPIO in vitro then tracked by MRI following in vivo injection (*6*−*8*). Recent work by Heyn and co-workers has demonstrated that even single SPIO labeled cells can be detected in vivo by MRI, thus illustrating the immense promise of this technique (*9*).

The ability to detect labeled cells by MRI depends on the quantity of SPIO in the cells. Thus, the efficiency with which cells can be loaded with SPIO is a major determinant for MR sensitivity at the single cell level. For biological applications, SPIO is typically coated with a water soluble polymer such as dextran (*10*) or poly(ethylene oxide) (*11, 12*) in order to provide water solubility and biocompatibility, but these polymers are not designed to significantly enhance the uptake of SPIO into cells. While cells such as macrophages can be readily labeled with adequate quantities of SPIO due to their inherent capability to phagocytose material in the extracellular medium, many other cell lines, including cancer cells do not readily phagocytose SPIO. This challenge can be overcome in some cases by the use of complexes formed between SPIO and transfection agents such as Superfect, Lipofectamine, and poly(L-lysine) (*13*); however, this is a multistep process that must be optimized on a case by case basis and care must be taken to control the size and polydispersity of the resulting complexes. An alternative approach that has been investigated involves the direct conjugation of cell-penetrating peptides such as HIV-Tat (*14, 15*) or protamine (*7*) to the SPIO surface. This method provides a well-defined agent that can be used to label cells in a single step, but a limitation is the availability of peptides on a large scale due to the expense of peptide or protein synthesis and concerns regarding immunogenicity when they are isolated from natural sources. In addition, due to the many reactive functional groups present in peptides, their conjugation to the nanoparticle surface is nontrivial, involving first activation and then conjugation via a multistep process. Thus, the goal of this work was the development of a simple and versatile process for modulating the cell uptake of SPIO via functionalization of the nanoparticle surface.

Well-defined branched molecules called dendrimers were anticipated to be an ideal backbone for the covalent functionalization of the SPIO surface in order to modulate biological properties and cell uptake (*16, 17*). Dendrimers are prepared

* Author to whom correspondence should be addressed. E-mail: egillie@uwo.ca. Phone: 519-661-2111 ext 80223. Fax: 519-661-3022.
[†] Department of Chemistry.
[‡] Department of Chemical and Biochemical Engineering.
[§] Department of Medical Biophysics.
[II] Imaging Research Laboratories—Robarts Research Institute.

10.1021/bc800209u CCC: $40.75 © 2008 American Chemical Society
Published on Web 11/18/2008

by a stepwise synthetic sequence providing molecules with well-defined molecular weight and composition. They can frequently be prepared on a multigram scale by exploiting very high yielding reactions and using a minimal number or even no chromatographic purification steps. Thus far, there have been a couple of reports of dendrimer coated SPIO for cell labeling, but in these cases, carboxyl terminated dendrimers were used as a stabilization agent during the nanoparticle synthesis and the mode of attachment of the dendrimer to the nanoparticle surface is still not well understood (*6, 18, 19*). For this work, it was proposed that by using wedges of dendrimers, commonly referred to as dendrons, the multiple functional groups at the dendron's periphery could allow for the introduction of multiple biological ligands in a well-defined display to modulate properties such as cell uptake and targeting, while the dendron's focal point would provide a site for attachment to the nanoparticle surface. Recent work by the groups of Goodman (*20*), Wender (*21*), and Harth (*22*) has demonstrated that dendrons functionalized at their peripheries with guanidines can significantly enhance the uptake of chromophores into cells in a manner similar to cell-penetrating peptides such as HIV-Tat (*23*) and protamine (*24*), which contain high levels of the amino acid arginine. However, the ability of these dendritic molecules to deliver large and challenging cargo such as nanoparticles into cells has not yet been demonstrated. With the aim of modulating the uptake of SPIO by cells for in vitro cell labeling, we describe here the preparation of a polyester dendron having multiple peripheral guanidine groups and its conjugation to SPIO. This new dendritic guanidine was found to have a cell penetrating capability very similar to that of the HIV-Tat_{47-47} peptide, and upon conjugation to SPIO, it was found to significantly enhance the cell uptake of the nanoparticles, leading to substantial changes in T2 in MR images. Its effect on the toxicity of the nanoparticles was also investigated.

EXPERIMENTAL PROCEDURES

General Procedures and Materials. All chemicals were purchased from commercial sources and used without further purification unless otherwise noted. Anhydrous acetonitrile, dichloromethane, and *N*,*N*-dimethylformamide (DMF) were obtained from a solvent purification system. Triethylamine was distilled from CaH_2. Column chromatography was performed using silica gel (0.063−0.200 mm particle size, 70−230 mesh). Dialysis was performed using a Spectra/Por regenerated cellulose membrane. Ultrafiltration was carried out using a 300 KDa molecular weight cutoff (MWCO) membrane of regenerated cellulose purchased from Amicon. Infrared spectra were obtained as thin films on NaCl plates or as KBr pellets. ^{1}H NMR spectra were obtained at 400 or 600 MHz, and ^{13}C NMR spectra were obtained at 100 or 150 MHz. Chemical shifts are reported in ppm and are calibrated against residual solvent signals of $CDCl_3$ (δ 7.26, 77.2) or CD_3OD (δ 3.31, 49.15). All coupling constants (*J*) are reported in Hertz. Transmission electron microscopy (TEM) was carried out using a carbon Formvar grid and a Phillips CM10 microscope operating at 80 kV with a 40 μm aperture. Dynamic light scattering (DLS) was performed at a concentration of 1 mg of iron/mL in water using a Malvern Zetasizer Nano-S instrument.

Quantification of Accessible Amine Groups on the Nanoparticle Surface. Amine functionalized, cross-linked dextran coated Fe_3O_4 nanoparticles (**1**) were prepared as previously reported (*7, 25*). The nanoparticles (0.81 mg of Fe, as determined spectrophotometrically following treatment with HCl and H_2O_2 (*7*)) were then diluted into 0.5 mL of 25 mM pH 7.4 citrate buffer, and the rhodamine derivative **2** (*26*) (18 mg, 0.025 mmol) was added, followed by diisopropylethylamine (DIPEA) (20 μL). The reaction mixture was stirred overnight in the dark at room temperature and then dialyzed against water for 24 h with several water changes. The UV−visible absorbance of the resulting solution was measured, and the concentration of conjugated dye **2** was calculated based on the extinction coefficient of the dye in water ($\varepsilon = 96100$ M cm^{-1}, $\lambda = 567$nm).

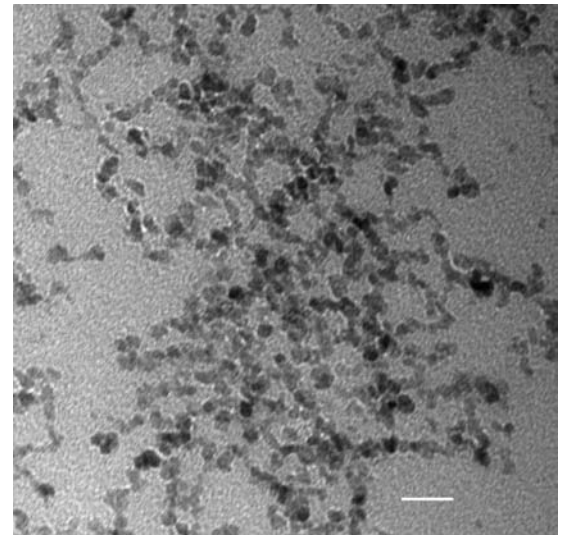

Figure 1. TEM image of nanoparticle **1** (scale bar = 20 nm).

Synthesis of Water Soluble Linker 4. Under a nitrogen atmosphere 2-(2-(2-(2-azidoethoxy)ethoxy)ethoxy)acetic acid **3** (*27*) (0.50 g, 2.2 mmol, 1.0 equiv), *N*-hydroxysuccinimide (0.25 g, 2.2 mmol, 1.0 equiv), and DCC (0.47 g, 2.3 mmol, 1.1 equiv) were dissolved in 20 mL of anhydrous acetonitrile. This solution was stirred at 65 °C for 6 h and then was cooled to room temperature, and the dicyclohexylurea byproduct was removed by filtration. The solvent was removed under reduced pressure to provide 0.69 g (96%) of the product **4** as a colorless oil. ^{1}H NMR (400 MHz, $CDCl_3$) δ: 4.53 (s, 2H), 3.81−3.79 (m, 2H), 3.73−3.65 (m, 8H), 3.39 (t, 2H, $J = 5.1$), 2.85 (br s, 4H). ^{13}C NMR (400 MHz, $CDCl_3$) δ: 169.2, 166.3, 71.5, 70.8, 70.2, 66.7, 50.9, 25.8. IR (cm^{-1}, thin film from CH_2Cl_2): 3330, 2930, 2870, 2110, 1820, 1790, 1740. MS calcd for $[M + H]^+$ ($C_{12}H_{19}O_7N_4$): 331.1. Found: (ES+) 331.1.

Conjugation of Linker 4 and Dye 2 to Nanoparticles (Synthesis of Nanoparticles 5). To a solution of nanoparticle **1** (10 mg of Fe) in 1.1 mL of 25 mM pH 7.4 citrate buffer was added linker **4** (8.2 mg, 25 μmol) in 0.25 mL of 1:1 DMSO/H_2O followed by the rhodamine derivative **2** (1.7 mg, 2.5 μmol) and DIPEA (50 μL). The solution was stirred overnight in the dark and then dialyzed against pure water for 24 h to provide nanoparticle **5**. The presence of the azide group on the nanoparticle surface was verified by IR spectroscopy (KBr pellet) (Figure 3a), while the amount of conjugated dye was quantified by UV−visible spectroscopy to be 0.21 μmol/mg of Fe.

Synthesis of *N*,*N*′-Bis(*tert*-butoxycarbonyl)-6-guanidinylcaproic Acid (8). 6-Aminocaproic acid (**6**) (0.51 g, 3.9 mmol, 1.0 equiv) was dissolved in 10:1 CH_3CN/H_2O (60 mL), and NEt_3 (4.0 mL) was added. At 0 °C, *N*,*N*′-bis(*tert*-butoxycarbonyl)-1H-pyrazole-1-carboxamidine (**7**) (1.0 g, 3.2 mmol, 0.83 equiv) was added and the mixture was stirred overnight. The reaction was then diluted with EtOAc (100 mL) and washed with saturated $NaHCO_3$ (2 × 50 mL), 1 M $KHSO_4$ (2 × 50 mL), and finally brine (50 mL). The organic phase was dried with $MgSO_4$ and filtered, and the solvent was removed under reduced pressure to yield 1.1 g (90%) of **8** as a white solid. ^{1}H NMR (400 MHz, $CDCl_3$) δ: 8.32 (t, 1H, $J = 4.6$), 3.41−3.36 (m, 2H), 2.34 (t, 2H, $J = 7.4$), 1.67−1.62 (m, 4H), 1.49 (s, 18H), 1.43−1.38 (m, 2H). ^{13}C NMR (100 MHz, $CDCl_3$) δ:

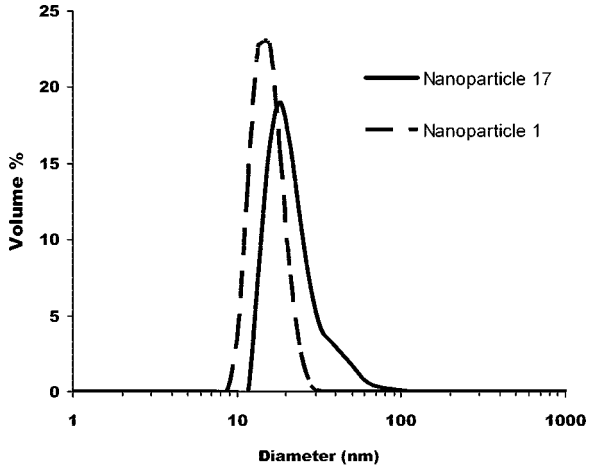

Figure 2. Hydrodynamic diameters of the nanoparticles prior to and after surface functionalization via the "click" reaction, as determined by dynamic light scattering.

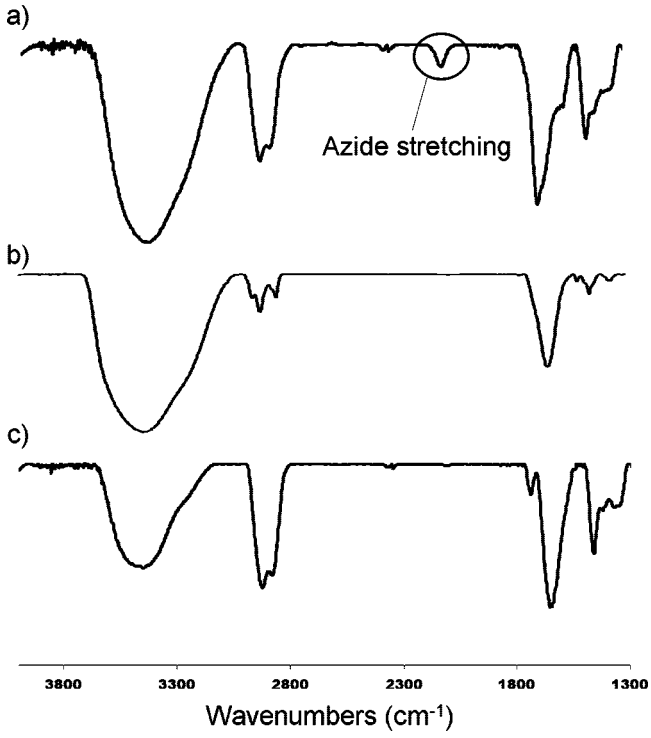

Figure 3. Infrared spectra of (a) nanoparticle **5**, (b) dendron **13**, and (c) functionalized nanoparticle **19**.

163.71, 156.34, 153.49, 83.27, 79.48, 40.92, 28.92, 28.47, 28.26, 28.17, 26.55, 24.67. IR (cm^{-1}, thin film from CH_2Cl_2): 3330, 3140, 2980, 2935, 1720, 1640, 1620. MS calcd for $[M + H]^+$ ($C_{17}H_{31}O_6N_3$): 373.5. Found: (ES+) 373.2.

Synthesis of Dendron 12. Dendron **11** (*28*) (50 mg, 21 μmol, 1.0 equiv) and the acid **8** (0.14 g, 0.38 mmol, 18 equiv) were dissolved in anhydrous *N*,*N*-dimethylformamide (DMF) (4.0 mL), and *O*-benzotriazole-*N*,*N*,*N*′,*N*′-tetramethyluronium hexafluorophosphate (HBTU) (0.14 g, 0.38 mmol, 18 equiv) was added, followed by 1-hydroxybenzotriazole (HOBt) (51 mg, 0.38 mmol, 18 equiv) and DIPEA (74 μL, 0.43 mmol, 20 equiv). The reaction mixture was stirred under nitrogen for 48 h. The product was purified by dialysis against DMF followed by silica gel chromatography using EtOAc and then 1:1 CH_2Cl_2/MeOH to provide 60 mg (65%) of **12** as a colorless oil. ^{1}H NMR (400 MHz, $CDCl_3$) δ: 11.48 (s, 8H), 8.30 (t, 8H, $J = 4.8$), 6.57−6.54 (m, 6H), 4.73 (d, 2H, $J = 2.2$), 4.31−4.16 (m, 28H), 3.51−3.47 (m, 16H), 3.39−3.35 (m, 16H), 2.60−2.64 (m, 1H), 2.55 (t, 16H, $J = 6.1$), 2.18 (t, 16H, $J = 7.4$), 1.66−1.54 (m, 24H), 1.49 (s, 144H), 1.37−1.33 (m, 16H), 1.27 (s, 3H), 1.25 (s, 6H), 1.23 (s, 12H). ^{13}C NMR (150 MHz, $CDCl_3$): δ 173.1, 171.9, 171.8, 171.7, 156.1, 153.2, 82.9, 80.0, 77.3, 75.8, 65.2, 65.0, 64.8, 53.0, 46.7, 46.5, 46.4, 40.7, 36.2, 34.9, 34.1, 28.6, 28.3, 28.0, 26.5, 26.0, 25.2, 17.8, 17.5, 17. 4. IR (cm^{-1}, thin film from CH_2Cl_2): 3330, 2980, 2930, 2120, 1740, 1735, 1725, 1640, 1615. MS: calcd for $[M + H]^+$ ($C_{198}H_{341}N_{32}O_{70}$): 4287.3. Found: (ES+) 4282.2.

Synthesis of Dendron 13. Dendron **12** (77 mg, 18 μmol) was dissolved in 2 mL of 1:1 trifluoroacetic acid/CH_2Cl_2, and the solution was stirred at room temperature for 2 h. The solvent was removed under reduced pressure to yield 63 mg (98%) of **13** as a colorless oil in the form of its TFA salt. ^{1}H NMR (600 MHz, CD_3OD): δ 4.77 (d, 2H, $J = 2.2$), 4.22 (m, 28H), 3.43 (t, 16H, $J = 6.7$), 3.16 (t, 16H, $J = 7.1$), 2.93 (t, 1H, $J = 2.3$), 2.56 (t, 16H, $J = 6.7$), 2.20 (t, 16H, $J = 7.4$), 1.64−1.55 (m, 24H), 1.41−1.37 (m, 16H), 1.35 (s, 3H), 1.29 (s, 6H), 1.26 (s, 12H). ^{13}C NMR (600 MHz, CD_3OD): δ 174.6, 174.1, 173.1, 173.0, 172.3, 77.0, 75.5, 65.0, 52.5, 46.2, 46.1, 46.0, 39.9, 35.8, 35.2, 34.9, 33.2, 28.5, 25.8, 24.9, 16.8. IR (cm^{-1}, thin film from THF/MeOH): 3400, 2930, 2120, 1650, 1460. MS: calcd for $[M + H]^+$ ($C_{118}H_{205}N_{32}O_{38}$): 2677.5. Found: (MALDI-TOF) 2678.4.

Synthesis of Dendron 14. Dendron **12** (25 mg, 5.8 μmol, 1.0 equiv) was dissolved in 0.5 mL of 1:1 THF/H_2O. To this was added 3-amino-1-azidopropane (*29*) (5.9 mg, 58 μmol, 10 equiv), $CuSO_4$ (15 μL of a 0.5 M solution in H_2O, 7.5 μmol, 1.3 equiv), sodium ascorbate (200 μL of a 0.5 M solution in H_2O, 100 μmol, 17 equiv), and finally bathophenanthrolinedisulfonic acid disodium salt (5.0 mg, 8.5 μmol, 1.5 equiv). The reaction mixture was stirred for 24 h at room temperature. The product was purified by dialysis against DMF to provide 15 mg (60%) of **14** as a viscous colorless oil. ^{1}H NMR (400 MHz, $CDCl_3$) δ: 11.49 (s, 8H), 8.32 (s, 8H), 6.61 (br s, 8H), 5.26 (br s, 2H), 4.25−4.16 (m, 28H), 3.65 (s, 2H), 3.50−3.46 (m, 16H), 3.40−3.36 (m, 16H), 2.57−2.54 (m, 16H), 2.43−2.40 (m, 1H), 2.21−2.17 (m, 16H), 1.66−1.54 (m, 24H), 1.49 (s, 144H), 1.37−1.33 (m, 16H), 1.25−1.21 (m, 24H). ^{13}C NMR (600 MHz, $CDCl_3$): δ 180.0, 173.2, 171.9, 171.8, 171.6, 156.1, 138.1, 83.0, 79.2, 70.5, 64.9, 64.8, 58.0, 46.4, 46.2, 40.7, 36.4, 36.2, 34.9, 34.1, 31.4, 28.8, 28.2, 28.0, 26.5, 25.3, 17.9, 17.8, 17.7. IR (cm^{-1}, thin film from CH_2Cl_2): 3330, 2980, 2935, 2240, 2100, 1740, 1735, 1645, 1615, 1575, 1455. MS: calcd for $[M + H^+]^+$ ($C_{201}H_{341}N_{36}O_{70}$): 4379.8. Found: (ES+) 4379.2.

Synthesis of Fluorescein Functionalized Dendron 16. Dendron **14** (10 mg, 2.3 μmol, 1.0 equiv) and fluorescein isothiocyanate isomer 1 (FITC) (3.5 mg, 9.2 μmol, 4.0 equiv) were dissolved in 2 mL of dry DMF. The resulting solution was cooled to 0 °C, and then 1 mL of dry triethylamine was added and the reaction mixture was stirred in the dark for 24 h. The product was purified by dialysis against DMF to provide 10 mg (95%) of the protected product as a viscous yellow oil. The protected derivative (10 mg, 2.2 μmol) was then dissolved in 2 mL of 1:1 trifluoroacetic acid/CH_2Cl_2, and the solution was stirred at room temperature for 2 h. The solvent was removed under reduced pressure to yield 8 mg (90%) of **16** as a viscous yellow oil. ^{1}H NMR (600 MHz, $CD_3OD/CDCl_3$ 1:1): δ 8.26 (d, 2H, $J = 9.4$), 8.09 (d, 2H, $J = 9.4$), 7.46 (d, 1H, $J = 8.8$), 7.39 (d, 1H, $J = 8.8$), 7.20−7.14 (m, 1H), 6.85 (d, 2H, $J = 9.4$), 5.24 (br s, 2H), 4.22−4.17 (m, 28H), 3.80 (br s, 2H), 3.43−3.40 (m, 16H), 3.23 (br s, 2H), 3.13−3.10 (m, 16H), 3.03 (br s, 2H), 2.70 (br s, 1H), 2.55−2.53 (m, 16H), 2.19−2.16 (m, 16H), 1.59−1.55 (m, 24H), 1.37−1.33 (m, 16H), 1.24−1.21 (m, 24H). ^{13}C NMR (600 MHz, $CDCl_3$): δ 174.5, 171.5, 170.9, 165.8, 162.0, 157.1, 156.0, 145.6, 129.7, 125.9, 125.1, 121.9, 121.8, 115.3, 70.1, 64.9, 64.8, 64.6, 48.9, 46.5, 40.9, 35.5, 34.9, 33.6,

28.1, 25.8, 24.9, 17.3, 17.1. IR (cm^{-1}, thin film from CH_2Cl_2/MeOH): 3369, 2980, 2930, 2102, 1739, 1681, 1674, 1652, 1594, 1526, 1456, 1436. MS: calcd for $[M + Na]^+$ ($C_{142}H_{234}NaN_{37}O_{41}S$): 3168.7. Found: (ES+) 3167.7.

Conjugation of Dendrons 9, 11, and 13 to Nanoparticle 5 (Synthesis of Nanoparticles 17, 18, and 19). The desired dendron (**9**, **11**, or **13**) (10 μmol, 2 equiv per azide) was dissolved in a minimum volume of water and was added to a solution of nanoparticle **5** (2 mg of Fe in 1 mL of water). To this was added sodium ascorbate (4 mg, 20 μmol) followed by $CuSO_4$ (1.2 mg, 5 μmol), and the reaction mixture was stirred overnight under a nitrogen atmosphere. The resulting solution was dialyzed against 10 mM ethylenediaminetetraacetic acid (EDTA), followed by pure water. IR spectroscopy (KBr pellet) on a lyophilized sample showed disappearance of the peak corresponding to the azides on the nanoparticles, confirming completion of the reaction (Figure 3c and the Supporting Information).

Cell Culture. GL261 mouse glioma cells obtained from the NCI-Frederick Cancer Research National Tumor Repository were maintained at 37 °C and 5% CO_2 in RPMI-1640 medium (Gibco) supplemented with 10% fetal bovine serum (FBS, Gibco).

Evaluation of the Cell Uptake of Dendron 16. Cells were plated at 8×10^5 cells/well in 6-well plates and allowed to adhere for 24 h. At this point, the medium was aspirated to remove dead cells and replaced with 1 mL of fresh medium to which dendron **16** or FITC-Tat_{47-57} (Ana Spec) was added at concentrations of 0.1, 1.0, or 10 μM. The cells were incubated at 37 °C for either 10 min or 1 h. At this point, the cells were washed twice in the plates with Hank's Buffered Salt Solution (HBSS, Gibco), detached using trypsin-EDTA for 3 min, quenched with RPMI/10% FBS, and then resuspended in 0.5 mL of HBSS and kept on ice until analysis. The cells were analyzed for fluorescein fluorescence by flow cytometry on a BD FACSCalibur flow cytometer (BD Biosciences, USA). Basal fluorescence was given by GL261 cells that were not incubated with the agents.

Evaluation of Cell Uptake of Nanoparticles 5, 17, 18, and 19. In order to assess cellular uptake of the nanoparticle agents, the experiment was carried out as described above, except that the agents were added at a concentration of 25 μg Fe/mL, and the cells were incubated for 30 min or 2 h and then analyzed by flow cytometry for rhodamine fluorescence.

Confocal Microscopy. Cells were plated on collagen-coated coverslips (BD Biosciences) in 6-well plates at a density of 5×10^5 cells/well and allowed to adhere overnight. Agents were then added at 25 μg of Fe/mL in 1 mL of fresh media, and the cells were incubated at 37 °C for 2 h. The cells were then washed with HBSS, fixed with 10% formalin for 10 min, washed again, and turned onto glass slides for confocal microscopy. Images were obtained using a confocal laser scanning microscope (LSM 510, Carl Zeiss Inc.) using a 63× (N.A. = 1.4) objective and an excitation wavelength of 543 nm (He−Ne laser).

Evaluation of Agent Toxicity. The cytotoxicity of the agents was evaluated using a colorimetric MTT assay (Sigma). Cells were plated at 5×10^4 cells/well in 50 μL in a 96-well plate and allowed to adhere overnight. Iron oxide agents were then added at varying concentrations up to ~200 μg Fe/mL, giving a total volume of 100 μL/well. After 24 h, the MTT reagent (10 μL) was added to the cells and the cells were returned to 37 °C for 3 h, during which time the MTT reagent was metabolized by viable cells, resulting in the formation of insoluble purple formazan crystals. The crystals were then solubilized by the addition of a detergent, and the plate was incubated for 4 h in the dark at room temperature. The absorbance read on a plate reader at 590 nm and normalized to the background at 650 nm is proportional to the number of viable cells.

Magnetic Resonance Imaging of Labeled Cells. GL261 cells were plated in T75 flasks and allowed to reach 80% confluency. Nanoparticle **19** was incubated with the cells at a concentration of 12 μg of iron per mL for 2 h. Control cells were incubated in the absence of nanoparticles. The cells were then washed in the flasks four times with HBSS, detached, and washed once more by resuspension in 5 mL of HBSS and centrifugation. The cells were transferred to mini NMR tubes (New Era Enterprises, Inc.) and centrifuged at 10000*g* for 5 min to form dense pellets. T2 measurements of unlabeled and labeled cell pellets were made using a spin echo sequence (TE = 12−300 ms, TR = 2500 ms, 2 mm slice thickness) on a 3T MRI scanner (GE).

RESULTS AND DISCUSSION

Preparation of Nanoparticles for Functionalization. A number of synthetic protocols ranging from aqueous to high temperature thermal decomposition methods have been reported for the synthesis of SPIO (*30*). For this work, the procedure involving the decomposition of $FeCl_2$ and $FeCl_3$ in the presence of ammonium hydroxide and dextran was used, as it readily provided water soluble nanoparticles for further functionalization (*25*). Treatment with epichlorohydrin followed by ammonium hydroxide, as described by Weissleder and co-workers, provided nanoparticle **1**, with a cross-linked dextran shell and surface amine groups (*7*).

These nanoparticles were characterized by transmission electron microscopy (TEM) (Figure 1), and the size of the iron oxide core was found to be approximately 5 nm, as previously reported (*31*). Dynamic light scattering was used to determine that the total hydrodynamic diameter of the nanoparticles, including the dextran coating, was 16 nm (Figure 2). The polydispersity index for the nanoparticles was relatively low at 0.26. The concentrations of iron in nanoparticle solutions were determined spectrophotometrically following nanoparticle degradation with hydrochloric acid and hydrogen peroxide (*7*). In addition, the dextran was quantified using the phenol sulfuric acid assay (*32*), and it was found that the mass ratio of dextran/iron in the nanoparticles was approximately 1.9:1, similar to what was expected based on previous reports (*31*). As the surface amine groups are critical for further functionalization of **1**, it was important to quantify the number of amine groups that were available for potential derivatization. By treatment of the nanoparticles with a large excess of the *N*-hydroxysuccinimidyl carbonate activated rhodamine derivative **2** (*26*), followed by removal of excess dye by dialysis, it was found that there were 23 μmol of amine available for functionalization per milligram of iron based on quantification of the dye by UV−visible spectroscopy. Although the concentration of reactive amines on the nanoparticle surface has not been explicitly quantified in this way before, conjugations to SPIO have generally been carried out at ratios on the order of micromoles of agent per milligrams of iron, thus indicating that nanoparticle **1** has more than enough amines available (*7, 33, 34*).

Amines provide good functional handles for bioconjugation reactions with a number of functional groups including carboxylic acids, *N*-hydroxysuccinimidyl esters, and isothiocyanates in water. However, when the biological ligands of interest have internal amines or other nucleophilic functional groups, the preparation and conjugation of the above derivatives can be problematic. Therefore, in order to develop a highly general technique to introduce dendrons with a wide variety of functional groups on their peripheries, surface amines on **1** were converted to azides using a water soluble linker (Scheme 1). Azides allow

Scheme 1

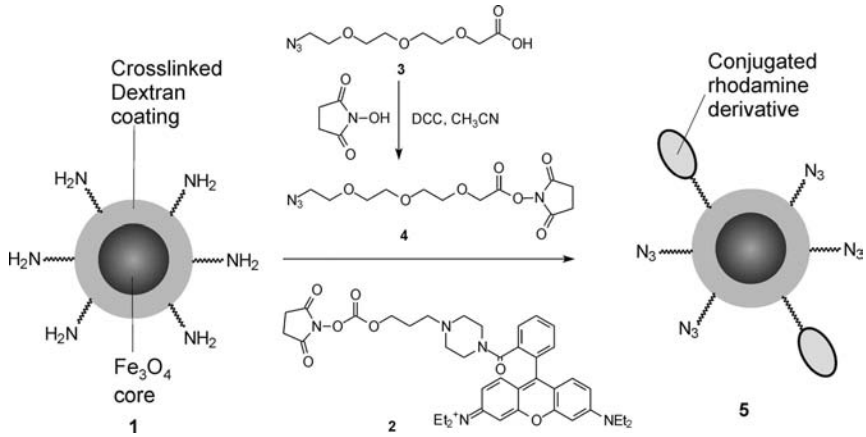

Scheme 2

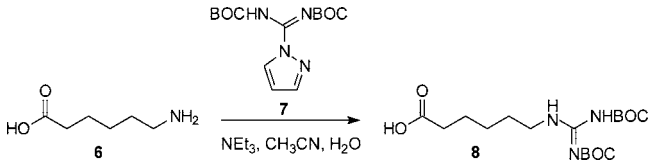

for highly chemoselective and functional group tolerant Cu(I) catalyzed "click" cycloaddition reactions with alkynes to be carried out on the nanoparticle surface under aqueous conditions (*35*). These cycloaddition reactions have been found to be very high yielding, even in the presence of significant steric hindrance (*36*), and are therefore ideal for the conjugation of macromolecules such as dendrons. This reaction has previously been demonstrated to be effective for conjugating molecules to the surface of SPIO (*37, 38*). As shown in Scheme 1, the linker **4** was prepared by the reaction of 2-(2-(2-(2-azidoethoxy)ethoxy)-ethoxy)acetic acid (*27*) (**3**) with *N*-hydroxysuccinimide using *N*,*N*′-dicyclohexylcarbodiimide in acetonitrile. This linker was then reacted with nanoparticle **1** in pH 7.4 citrate buffer at a ratio of 2.5 μmol of linker per milligram of iron to provide **5**. Due to the large excess of amines on the nanoparticle surface, the number of surface azides was limited by the quantity of linker added. The presence of the azide groups on the nanoparticle surface was verified using infrared (IR) spectroscopy by the presence of the distinctive azide stretch at 2100 cm^{-1} (Figure 3a).

In addition to the azide functional handles for conjugation of the dendrons, a fluorescent probe was required in order to characterize the biological properties of the nanoparticles, such as their cellular uptake and intracellular trafficking. This was accomplished in the same step using the rhodamine derivative **2** at a ratio of 0.25 μmol/mg of iron. After the reaction, all residual small molecules and salts were removed by dialysis. The quantity of conjugated dye on **5** was determined by UV−visible spectroscopy to be 0.21 μmol/mg of iron, thus verifying the high yield of the nanoparticle amine derivatization using *N*-hydroxysuccinimidyl derivatives. In addition, by comparison of the fluorescence with a sample having a normalized absorbance at 567 nm, it was determined that fluorescence quenching of the rhodamine by the nanoparticles was negligible.

Synthesis of a Dendritic Guanidine. For preparation of the dendritic guanidine transporter, a guanidine derivative with a carboxylic acid functional handle was prepared. 6-Aminocaproic acid (**6**) was reacted with *N*,*N*′-bis(BOC)-1-amidinopyrazole (**7**) to provide *N*,*N*′-bis(BOC)-6-guanidinylcaproic acid (**8**) as shown in Scheme 2. Selection of this linker length was based on previous reports demonstrating that guanidine functionalized dendrons with more flexible spacers exhibited increased cell-penetrating capabilities relative to those that were less flexible (*21*).

A polyester dendron based on 2,2-bis(hydroxymethyl)propionic acid was selected as the dendritic scaffold due to its ease of synthesis, biodegradability, and biocompatibility (*39*, *40*). The alkyne functionalized dendron **9** was prepared as previously reported (*41*), and then the peripheral hydroxyl groups were converted to amines by reaction with anhydride **10** followed by deprotection to provide **11**, with more nucleophilic functional handles for further derivatization (Scheme 3) (*28*). The guanidine derivative **8** was then coupled to the peripheral amines using *O*-benzotriazole-*N*,*N*,*N*′,*N*′-tetramethyluronium hexafluorophosphate (HBTU) and hydroxybenzotriazole (HOBt). Excess **8** and other byproducts were removed by dialysis and standard column chromatography to provide dendron **12**. Removal of the BOC protecting groups using 1:1 trifluoroacetic acid/dichloromethane provided dendron **13** with eight peripheral guanidine groups in the form of their trifluoroacetate salts. Overall, this synthetic route is simple and amenable to scale up, as no HPLC and only one standard column chromatography purification step is required throughout the entire synthesis.

In order to investigate the efficacy of the dendritic guanidine relative to the well established molecular transporter HIV-tat_{47-57}, a fluorescein labeled dendron was prepared. As shown in Scheme 4, an amine was introduced to the focal point of dendron **12** by reaction of the focal point alkyne with 3-amino-1-azidopropane (*29*) to provide **14**. This amine was then reacted with fluorescein isothiocyanate (FITC) (**15**). Excess FITC was removed by dialysis, and then dendron **16** was obtained upon removal of the BOC protecting groups.

Conjugation of Dendrons to Nanoparticles. With dendrons having peripheral hydroxyls (**9**), amines (**11**), or guanidine groups (**13**) in hand, each was conjugated to the surface of nanoparticle **5** to provide functionalized nanoparticles **17**, **18**, and **19**, respectively. As shown in Scheme 5, each coupling was carried out using click reaction conditions consisting of **5**, 5 mM $CuSO_4$, 20 mM sodium ascorbate, and 2 equiv of the dendron per azide group on the nanoparticle. After 24 h, excess reagents were removed by dialysis against 10 mM EDTA followed by water. The EDTA dialysis was critical in removing residual copper salts. In the absence of this step, high levels of toxicity were observed in preliminary work. Characterization of the resulting nanoparticles by TEM verified that the iron oxide core was not degraded during the conjugation and that the size remained approximately 5 nm. DLS showed that only a small increase in the hydrodynamic diameter of the nanoparticles was observed following conjugation, accompanied by a small increase in the polydisperity index to 0.28, which is consistent

Scheme 3

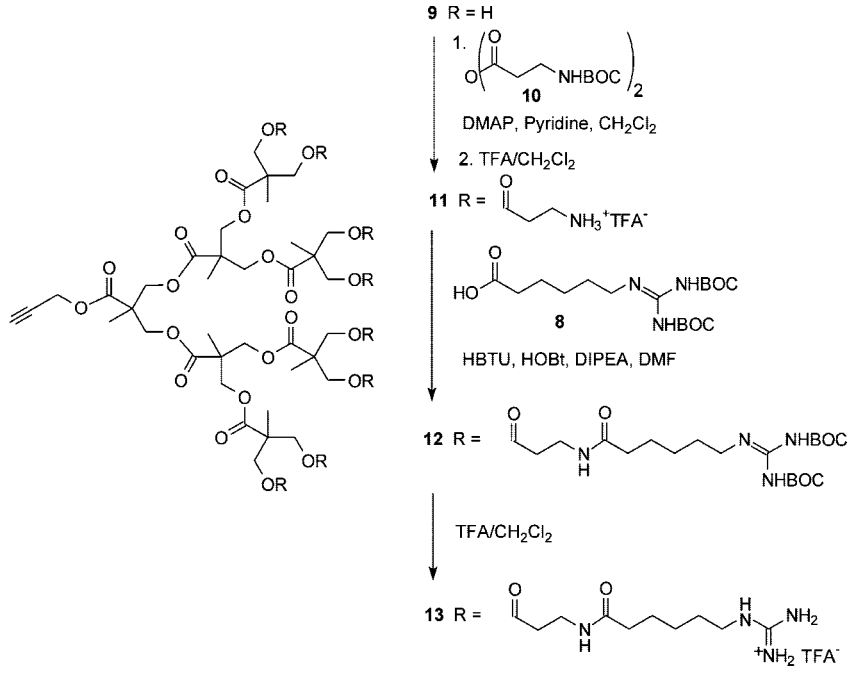

Scheme 4

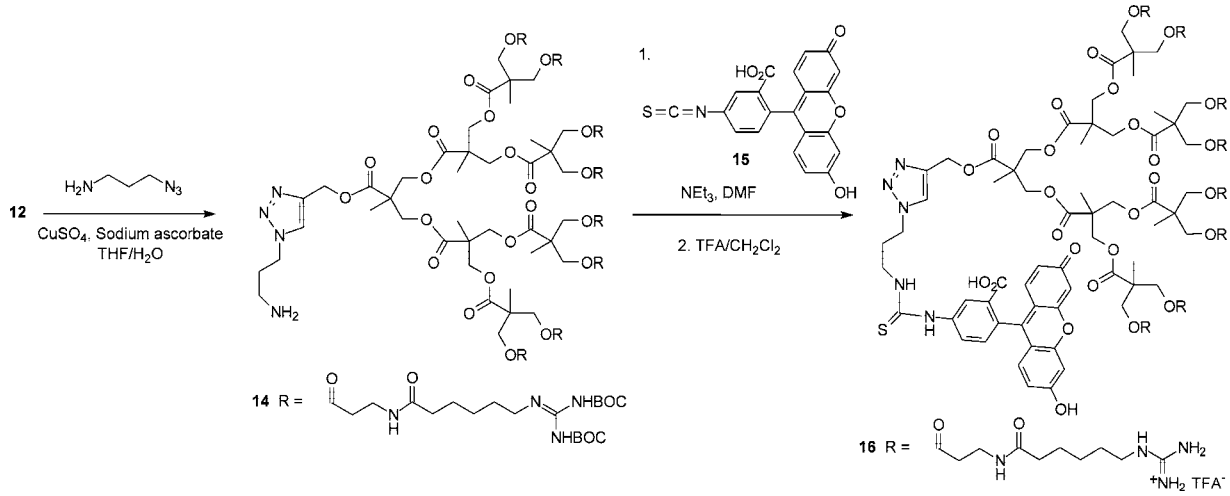

with the small size of the dendron relative to the initial nanoparticles and very minimal aggregation (Figure 2). IR spectroscopy on dried samples of the nanoparticles showed that, in the case of all three dendrons, the click reaction proceeded to completion with complete disappearance of the peak at 2100 cm^{-1} corresponding to the azide group. In addition, changes in the region of the spectrum corresponding to C═O stretching and N—H bending (~1500−1700 cm^{-1}) were observed, which is consistent with the introduction of the dendrons bearing multiple ester and amide groups (Figure 3b and c). In contrast, subjecting nanoparticle **5** to the click conditions in the absence of dendron did not lead to any change in the IR spectrum. Thus, the click reaction proved to be highly effective for the conjugation of dendrons having a variety of functional groups on their peripheries.

Biological Evaluation. GL261 mouse glioma cells were selected for biological studies because they are nonphagocytic cells, which are generally challenging to load with SPIO in the absence of a transfection agent. It is of significant interest to be able to track cancer cells using MRI in order to reach a better understanding of the cell invasion process, so the development of nanoparticles that are capable of more effectively labeling such cells would contribute significantly to the imaging studies. First, the efficacy of the fluorescein labeled dendritic guanidine transporter **16** was compared to that of a fluorescein labeled HIV-Tat_{47-57} oligopeptide (FITC-LC-YGRKKRRQRRR-NH_2) using flow cytometry. The effects of both incubation time and concentration were investigated. As shown in Figure 4, it was found that, at a concentration of 1.0 μM, dendron **16** and Tat_{47-57} exhibited very similar levels of uptake at both 10 min and 1 h time points. At a concentration of 10 μM, very similar uptake was observed after 10 min, while the uptake of Tat_{47-57} was approximately 2-fold higher after 1 h. Overall, both cell-penetrating agents exhibited time- and concentration-dependent uptake, and the similarity in the uptake of the new dendritic guanidine compared to Tat_{47-57} is remarkable, given that it does not contain a specific amino acid sequence and is an unoptimized structure.

Next, the cellular uptake of the functionalized SPIO nanoparticles **5**, **17**, **18**, and **19** was investigated. The cells were incubated for 30 min or 2 h with the nanoparticles at a concentration of 25 μg of iron per mL, and then cell uptake

Scheme 5

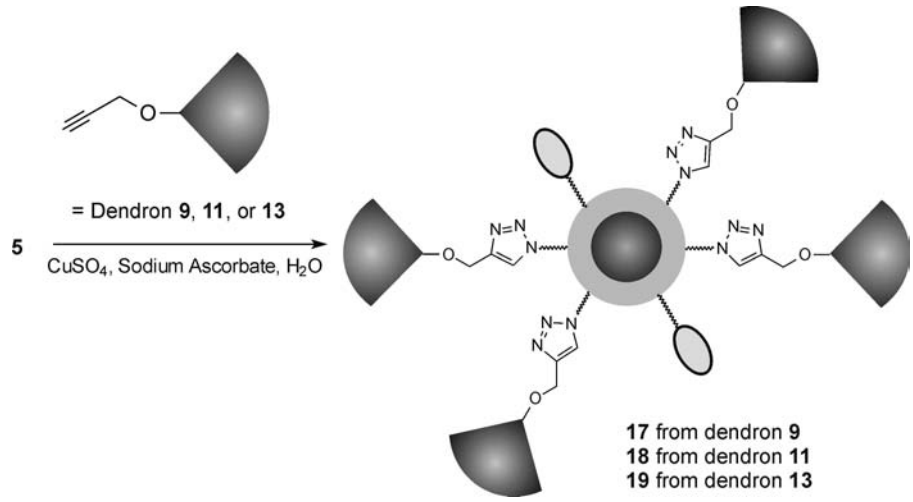

was assessed by flow cytometry based on the fluorescence of the rhodamine dye that was conjugated at the same density on each set of nanoparticles. After 30 min, only nanoparticle **19** gave rise to a new population of cells with increased fluorescence (Figure 5a) while the fluorescence of all other cells remained identical to that of control cells that were not exposed to any nanoparticles. After 2 h, cells incubated with nanoparticle **19** exhibited significantly increased fluorescence, as shown in Figure 5b, while cells incubated with all other nanoparticles remained at background levels. This result indicates that the dendritic guanidines specifically enhance the uptake of SPIO into GL261 cells and that the effect is not simply due to a cationic charge on the nanoparticles.

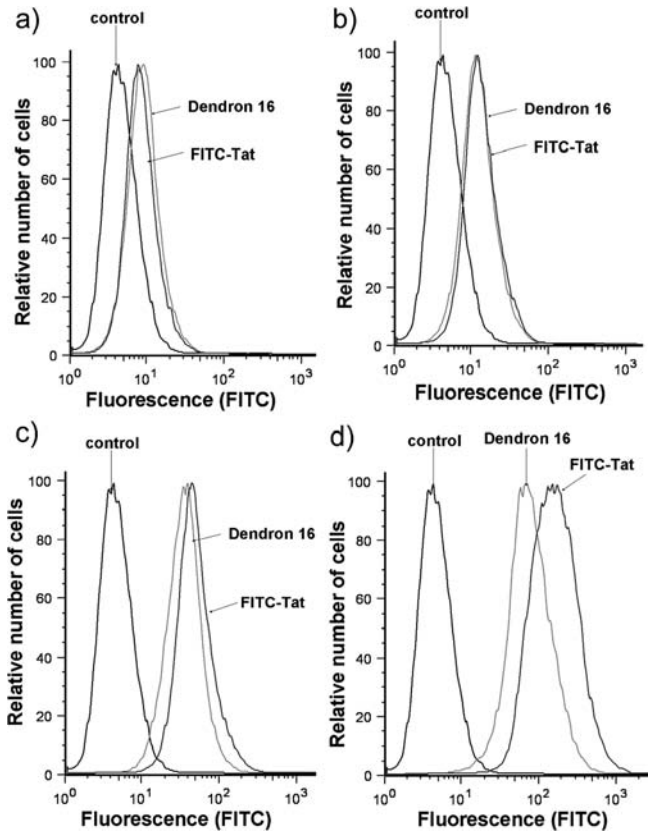

Figure 4. Flow cytometry analyses of GL261 cells following incubation with dendron **16** or HIV-Tat$_{47-57}$: (a) 1.0 μM for 10 min; (b) 1.0 μM for 1 h; (c) 10 μM for 10 min; (d) 10 μM for 1 h.

To verify the flow cytometry results, confocal microscopy was performed on cells following 2 h incubations with nanoparticles **5**, **17**, **18**, and **19** at a concentration of 25 μg of iron per mL. As shown in Figure 6, cells incubated with nanoparticle **19** were strongly fluorescent, while control cells and cells incubated with nanoparticles **5**, **17**, and **18** did not show any fluorescence using the same microscope settings. Based on the confocal images, it is difficult to determine the exact intracellular location of the nanoparticles or whether it is even a single compartment. Thus, further detailed microscopy studies will need to be carried out to determine this, as well as the effects of cell type, incubation time, and fixation (*42*). Dendritic guanidines have been demonstrated to provide delivery to different intracellular compartments depending on subtle differences in the dendritic structure (*22*), but it is not yet clear how a nanoparticle-based cargo may affect the intracellular trafficking. For this work, the location of the SPIO within cells is not a critical aspect of its ability to provide contrast, unless it causes undesirable alterations in the behavior of the labeled cells. No signs of nanoparticle toxicity were observed in the cells during this study.

To show that the enhanced uptake observed using flow cytometry and confocal microscopy results in an enhanced MRI response, GL261 cells were incubated with nanoparticle **19** at a concentration of 12 μg of iron per mL for 2 h, washed, and pelleted. T2 measurements of unlabeled and labeled cell pellets were made using a spin echo sequence on a 3T MRI scanner. T2 values were 65 and 6.1 ms for unlabeled and labeled cell

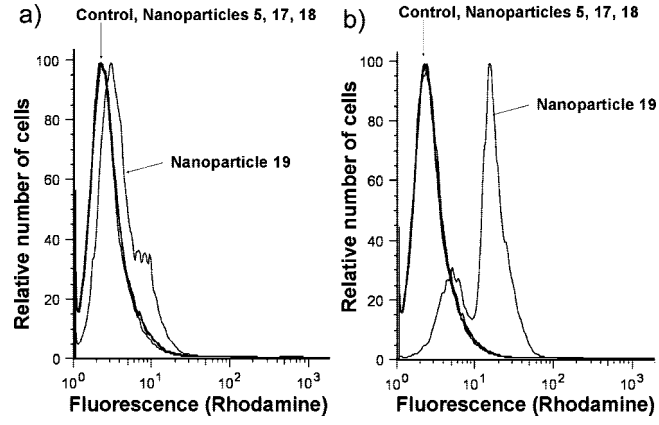

Figure 5. Flow cytometry analyses of GL261 cells following incubation with nanoparticles **5**, **17**, **18**, or **19** at a concentration of 25 μg Fe/mL for (a) 30 min or (b) 2 h.

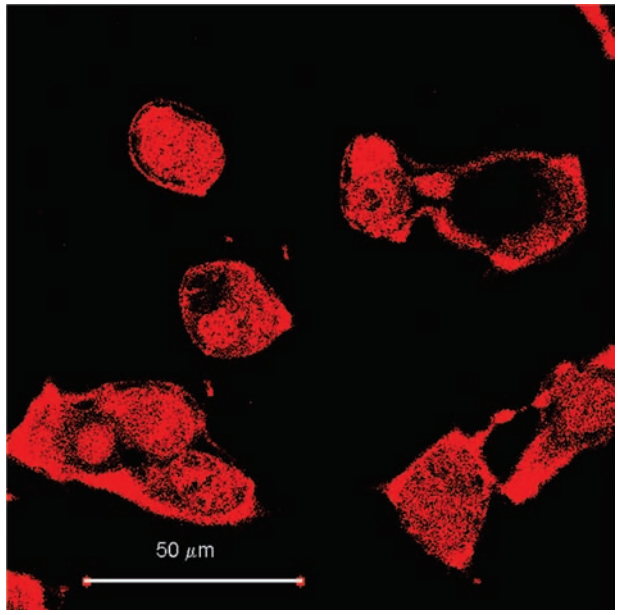

Figure 6. Confocal laser scanning microscopy image of GL261 cells following a 2 h incubation with nanoparticle **19** at a concentration of 25 μg of Fe/mL.

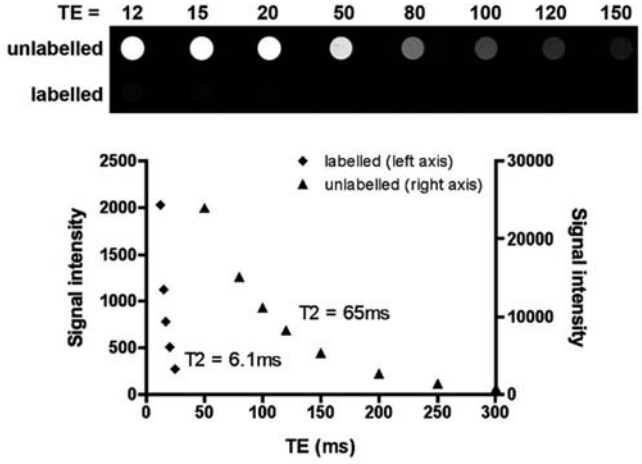

Figure 7. MRI signal intensity of unlabeled cells and cells labeled with nanoparticle **19**, measured at 3T using a spin echo sequence with varying echo times (TE).

pellets, respectively (Figure 7). This significant difference in T2 values illustrates the utility of these nanoparticles for labeling cells for detection by MRI.

Finally, to investigate the toxicities of the nanoparticles as a function of their surface coating, the GL261 cells were incubated with varying concentrations of nanoparticles **5**, **17**, **18**, and **19** for a 24 h period, and then an MTT assay was performed to quantitatively assess cell viability. The results of this assay are shown in Figure 8. Consistent with previous experiments demonstrating the high biocompatibilities of dendrimers based on 2,2-bis(hydroxymethyl)propionic acid (*39*, *43*), nanoparticle **17** exhibited a relatively similar toxicity profile to the underivatized nanoparticle **5** which is similar to those that have been widely used in a number of cell labeling applications (*44*−*46*). Nanoparticle **18**, prepared from the dendron **11** with peripheral amines, also had a similar toxicity profile. Guanidine functionalized nanoparticle **19** did exhibit somewhat increased toxicity, but it remained relatively nontoxic at the low concentrations used for cell labeling. It is possible that its toxicity at higher concentrations arises from their ability to penetrate and create defects in cell membranes, as has been observed for various

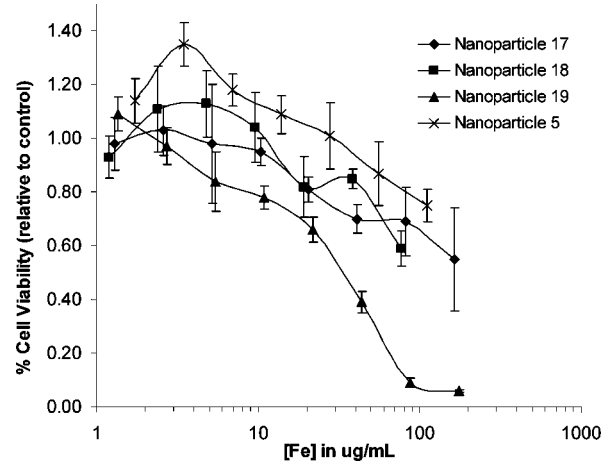

Figure 8. Viability of GL261 cells after a 24 h incubation with nanoparticles **5**, **17**, **18**, and **19**, as measured by the MTT assay. Error bars represent standard deviations on three measurements.

polycationic nanoparticles and transporters (*47*). It is likely that the toxicity of the nanoparticles can be modulated in the future by tuning the ratio of dendron to nanoparticles as well as the length and hydrophobicity of the linker used to conjugate the guanidine groups to the dendron periphery.

CONCLUSIONS

In conclusion, SPIO with surface azide groups was prepared and used to conjugate dendrons having various peripheral functional groups and focal point alkynes. In particular, a new dendritic guanidine was prepared and was found to have a cell penetrating capability remarkably similar to that of the HIV-Tat_{47-57} oligopeptide. Upon conjugation to the nanoparticle surface, this dendron provided significantly enhanced uptake of SPIO into GL261 mouse glioma cells in comparison to dendrons with hydroxyl or amine peripheries. This level of uptake was demonstrated to provide a decrease in the T2 of labeled cells relative to control cells by an order of magnitude. At the concentrations used for cell labeling, the functionalized nanoparticles were found to be relatively nontoxic. It is also noteworthy that the nanoparticles at all stages of synthesis were found to be stable over periods of months when stored at 4 °C in neutral solutions. This represents the first successful example of the transport of a biologically relevant nanoparticle cargo by a dendritic guanidine transporter and promises to provide improved labeling of cells with SPIO for enhanced sensitivity in cellular MRI. In the future, this dendron will also be investigated for its ability to transport other challenging cargo such as quantum dots and polymer assemblies. In addition, as this work demonstrates that dendrons are an effective means of presenting biologically relevant functionality on the nanoparticle surface, it is anticipated that this surface functionalization approach can be expanded to include other biological targeting ligands such as carbohydrates that can also benefit from a multivalent dendritic display.

ACKNOWLEDGMENT

We thank NSERC, the Canada Research Chairs Program, and the Ontario Institute for Cancer Research One Millimetre Cancer Challenge Program for funding this work. A.L.M. is supported by an Ontario Graduate Scholarship in Science and Technology. B.K.R. receives salary support from the Barnett-Ivey Heart and Stroke Foundation of Ontario Endowed Chair award. L.M.B. is supported by CIHR Grant MGC-14973. Jessica Watson is acknowledged for assistance in the preparation of compound **4** and Michael Maris for compound **8**.

Supporting Information Available: NMR spectra of all new molecules; IR characterization of dendrons **9** and **11** and nanoparticles **17** and **18**. This information is available free of charge via the Internet at http://pubs.acs.org.

LITERATURE CITED

(1) Caravan, P., Ellison, J. J., McMurry, T. J., and Lauffer, R. B. (1999) Gadolinium (III) chelates as MRI contrast agents: Structure, dynamics, and applications. *Chem. Rev. 99*, 2293–2352.

(2) Corot, C., Robert, P., Idée, J.-M., and Port, M. (2006) Recent advances in iron oxide nanocrystal technology for medical imaging. *Adv. Drug Delivery Rev. 58*, 1471–1504.

(3) Semelka, R. C., and Helmberger, T. K. (2001) Contrast agents for MR imaging of the liver. *Radiology 218*, 27–38.

(4) Tsourkas, A., Shinde-Patil, V. R., Kelly, K. A., Patel, P., Wolley, A., Allport, J. R., and Weissleder, R. (2005) In vivo imaging of activated endothelium using an anti-VCAM-1 magnetooptical probe. *Bioconjugate Chem. 16*, 576–581.

(5) Andee, J. H., Huh, Y. M., Jun, Y. W., Seo, J. W., Jang, J. T., Song, H. T., Kim, S., Cho, E. J., Yoon, H. G., Suh, J. S., and Cheon, J. (2007) Artificially engineered magnetic nanoparticles for ultra-sensitive molecular imaging. *Nat. Med. 13*, 95–99.

(6) Bulte, J. W. M., Douglas, T., Witwer, B., Zhang, S. C., Strable, E., Lewis, B. K., Zywicke, H., Miller, B., van Gelderen, P., Moskowitz, B. M., Duncan, I. D., and Frank, J. A. (2001) Magnetodendrimers allow endosomal magnetic labelling and in vivo tracking of stem cells. *Nat. Biotechnol. 19*, 1141–1147.

(7) Pittet, M. J., Swirski, P. K., Reynolds, F., Josephson, L., and Weissleder, R. (2006) Labelling of immune cells for in vivo imaging using magnetofluorescent nanoparticles. *Nat. Protoc. 1*, 73–78.

(8) Foster, P. J., Dunn, E. A., Karl, K. E., Snir, J. A., Nycz, C. M., Harvey, A. J., and Pettis, R. J. (2008) Cellular magnetic resonance imaging: In vivo imaging of melanoma cells in lymph nodes of mice. *Neoplasia 10*, 207–216.

(9) Heyn, C., Ronald, J. A., Mackenzie, L. T., MacDonald, I. C., Chambers, A. F., Rutt, K., and Foster, P. J. (2006) In vivo magnetic resonance imaging of single cells in mouse brain with optical validation. *Magn. Reson. Med. 55*, 23–29.

(10) Weissleder, R., Bogdanoc, A., Neuwelt, E. A., and Papisov, M. (1995) Long-circulating iron oxides for MR imaging. *Adv. Drug Delivery Rev. 16*, 321–334.

(11) Kohler, N., Fryxell, G. E., and Zhang, M. (2004) A bifunctional poly(ethylene glycol)silane immobilized on metallic oxide-based nanoparticles for conjugation with cell targeting agents. *J. Am. Chem. Soc. 126*, 7206–7211.

(12) Li, Z., Wei, L., Gao, M., and Lei, H. (2005) One-pot reaction to synthesize biocompatible magnetite nanoparticles. *Adv. Mater. 17*, 1001–1005.

(13) Frank, J. A., Miller, B. R., Arbab, A. S., Zywicke, H. A., Jordan, E. K., Lewis, B. K., Jr., and Bulte, J. W. M. (2003) Clinically applicable labelling of mammalian and stem cells by combining superparamagnetic iron oxides and transfection agents. *Radiology 228*, 480–487.

(14) Josephson, L., Tung, C., Moore, A., and Weissleder, R. (1999) High-efficiency intracellular magnetic labelling with novel superparamagnetic-tat peptide conjugates. *Bioconjugate Chem. 10*, 186–191.

(15) Lewin, M., Carlesso, N., Tung, C. H., Tang, X. W., Cory, D., Scadden, D. T., and Weissleder, R. (2000) Tat peptide-derivatized magnetic nanoparticles allow in vivo tracking and recovery of progenitor cells. *Nat. Biotechnol. 18*, 410–414.

(16) Fréchet, J. M. J., and Tomalia, D. , Eds. (2001) *Dendrimers and other dendritic polymers*, Wiley and Sons, Chichester and New York.

(17) Newkome, G. R., Moorefield, C. N., and Vögtle, F. (2001) *Dendrimers and dendrons: Concepts, syntheses, applications*, Wiley-VCH, Weinheim, Germany.

(18) Shi, X., Thomas, T. P., Myc, L. A., and Kotlyar, A., Jr. (2007) Synthesis, characterization, and intracellular uptake of carboxyl-terminated poly(amidoamine) dendrimer-stabilized iron oxide nanoparticles. *Phys. Chem. Chem. Phys. 9*, 5712–5720.

(19) Strable, E., Bulte, J. W. M., Moskowitz, B., Vivekanandan, K., Allen, M., and Douglas, T. (2001) Synthesis and characterization of soluble iron oxide-dendrimer composites. *Chem. Mater. 13*, 2201–2209.

(20) Chung, H. H., Harms, G., Seong, C. M., Choi, B. H., Min, C., Taulane, J. P., and Goodman, M. (2004) Dendritic oligoguanidines are intracellular translocators. *Biopolymers 76*, 83–96.

(21) Wender, P. A., Kreider, E., Pelkey, E. T., Rothbard, J., and VanDeusen, C. L. (2005) Dendrimeric molecular transporters: Synthesis and evaluation of tunable polyguanidino dendrimers that facilitate cellular uptake. *Org. Lett. 7*, 4815–4818.

(22) Huang, K., Voss, B., Kumar, D., Hamm, H. E., and Harth, E. (2007) Dendritic molecular transporters provide control of delivery to intracellular compartments. *Bioconjugate Chem. 18*, 403–409.

(23) Schwarze, S. R., and Dowdy, S. F. (2000) In vivo protein transduction: Intracellular delivery of biologically active proteins, compounds and DNA. *Trends Pharmacol. Sci. 21*, 45–48.

(24) Reynolds, F., Weissleder, R., and Josephson, L. (2005) Protamine as an efficient membrane-translocating peptide. *Bioconjugate Chem. 16*, 1240–1245.

(25) Molday, R. S., and MacKenzie, D. (1982) Immunospecific ferromagnetic iron-dextran reagents for the labelling and magnetic separation of cells. *J. Immunol. Methods 52*, 353–367.

(26) Nguyen, T., and Francis, M. B. (2003) Practical synthetic route to functionalized rhodamine dyes. *Org. Lett. 5*, 3245–3248.

(27) Gong, Y., Luo, Y., and Bong, D. (2006) Membrane activation: Selective vesicle fusion via small molecule recognition. *J. Am. Chem. Soc. 128*, 14430–14431.

(28) Li, B., Martin, A., and Gillies, E. R. (2007) Multivalent polymer vesicles via surface functionalization. *Chem. Commun.* 5217–5219.

(29) Hatzakis, N. S., Engelkamp, H., Velonia, K., Hofkens, J., Christianen, P. C. M., Svendsen, A., Patkar, S. A., Vind, J., Maan, J. C., Rowan, A. E., and Nolte, R. J. M. (2006) Synthesis and single enzyme activity of a clicked lipase-BSA hetero-dimer. *Chem. Commun.* 2012–2012.

(30) Jeong, U., Teng, X., Wang, Y., Yang, H., and Xia, Y. (2007) Superparamagnetic colloids: Controlled synthesis and niche applications. *Adv. Mater. 19*, 33–60.

(31) Shen, T., Weissleder, R., Papisov, M., Bogdanov, A., and Brady, T. J. (1993) Monocrystalline iron oxide nanocompounds (MION): Physicochemical properties. *Magn. Reson. Med. 29*, 599–604.

(32) Dubois, M., Gilles, K. A., Hamilton, J. K., Rebers, P. A., and Smith, F. (1956) Colorimetric method for determination of sugars and related substances. *Anal. Chem. 28*, 350–356.

(33) Zhao, M., Kircher, M. F., Josephson, L., and Weissleder, R. (2002) Differential conjugation of TAT peptide to superparamagnetic nanoparticles and its effect on cellular uptake. *Bioconjugate Chem. 13*, 840–844.

(34) Montet, X., Funovics, M., Montet-Abou, K., Weissleder, R., and Josephson, L. (2006) Multivalent effects of RGD peptides obtained by nanoparticle display. *J. Med. Chem. 49*, 6087–6093.

(35) Kolb, H. C., and Sharpless, K. B. (2003) The growing impact of click chemistry on drug discovery. *Drug Discovery Today 8*, 1128–1137.

(36) Helms, B., Mynar, J. L., Hawker, C. J., and Fréchet, J. M. J. (2004) Dendronized linear polymers via "click chemistry". *J. Am. Chem. Soc. 126*, 15020–15021.

(37) White, M. A., Johnson, J. A., Koberstein, J. T., and Turro, N. J. (2006) Toward the syntheses of universal ligands for metal oxide surfaces: Controlling surface functionality through click chemistry. *J. Am. Chem. Soc. 128*, 11356–11357.

(38) Sun, E. Y., Josephson, L., and Weissleder, R. (2006) "Clickable" nanoparticles for targeted imaging. *Mol. Imaging 5*, 122–128.

(39) Gillies, E. R., Dy, E., Fréchet, J. M. J., and Szoka, F. C. (2005) Biological evaluation of polyester dendrimer-poly(ethylene oxide) "bow-tie" hybrids with tunable molecular weight and architecture. *Mol. Pharmaceutics 2*, 129–138.

(40) Ihre, H., Padilla De Jesús, O. L., Szoka, F. C. J., and Fréchet, J. M. J. (2002) Polyester dendritic systems for drug delivery applications: Design, synthesis, and characterization. *Bioconjugate Chem. 13*, 433–452.

(41) Wu, P., Malkoch, M., Hunt, J. N., Vestberg, R., Kaltgrad, E., Finn, M. G., Fokin, V. V., Sharpless, K. B., and Hawker, C. J. (2005) Multivalent, bifunctional dendrimers prepared by click chemistry. *Chem. Commun.* 5775–5777.

(42) Potocky, T. B., Menon, A. K., and Gellman, S. H. (2005) Effects of conformational stability and geometry of guanidinium display on cell entry by beta-peptides. *J. Am. Chem. Soc. 127*, 3686–3687.

(43) Padilla De Jesús, O. L., Ihre, H. R., Gagne, L., Fréchet, J. M. J., and Szoka, F. C. J. (2002) Polyester dendritic systems for drug delivery applications: In vitro and in vivo evaluation. *Bioconjugate Chem. 13*, 453–461.

(44) Choi, S. H., Han, M. H., Moon, W. K., Son, K. R., Won, J. K., Kwon, B. J., Na, D. G., Weinmann, H. J., and Chang, K. H. (2006) Cervical lymph node metastases: MR imaging of gadofluorine M and monocrystalline iron oxide nanoparticle-47 in a rabbit model of head and neck cancer. *Radiology 241*, 753–762.

(45) Dodd, C. H., Hsu, H. C., Chu, W. J., Yang, P., Zhang, H. G., Jr., Zinn, K., Forder, J., Josephson, L., Weissleder, R., Mountz, J. M., and Mountz, J. D. (2001) Normal T-cell response and in vivo magnetic resonance imaging of T cells loaded with HIV transactivator-peptide-derived superparamagnetic nanoparticles. *J. Immunol. Methods 256*, 89–105.

(46) Schellenberger, E. A., Bogdanov, A. J., Hogemann, D., Tait, J., Weissleder, R., and Josephson, L. (2002) Annexin V-CLIO: A nanoparticle for detecting apoptosis by MRI. *Mol. Imaging 1*, 102–107.

(47) Leroueil, P. R., Berry, S. A., Duthie, K., Han, G., Rotello, V. M., McNerny, D. Q., Jr., and Orr, B. G. (2008) Wide varieties of cationic nanoparticles induce defects in supported lipid bilayers. *Nano Lett. 8*, 420–424.

BC800209U

Supporting Information:

Enhanced Cell Uptake of Superparamagnetic Iron Oxide Nanoparticles Functionalized with Dendritic Guanidines

Amanda L. Martin[†], Lisa M. Bernas[¶§], Brian K. Rutt[¶§], Paula J. Foster[¶§], and Elizabeth R. Gillies[†‡]*

[†]Department of Chemistry, [‡]Department of Chemical and Biochemical Engineering, [¶]Department of Medical Biophysics, [§]Imaging Research Labs – Robarts Research Institute, The University of Western Ontario, 1151 Richmond St., London, ON N6A 5B7, Canada.

Table of Contents:

1. NMR spectra of compounds **4**, **8**, **12**, **13**, **14**, and **16** ..…….……pg. 2-4
2. IR spectra of dendrons **9** and **11** and nanoparticles **17** and **18…**...…….....pg. 5-6

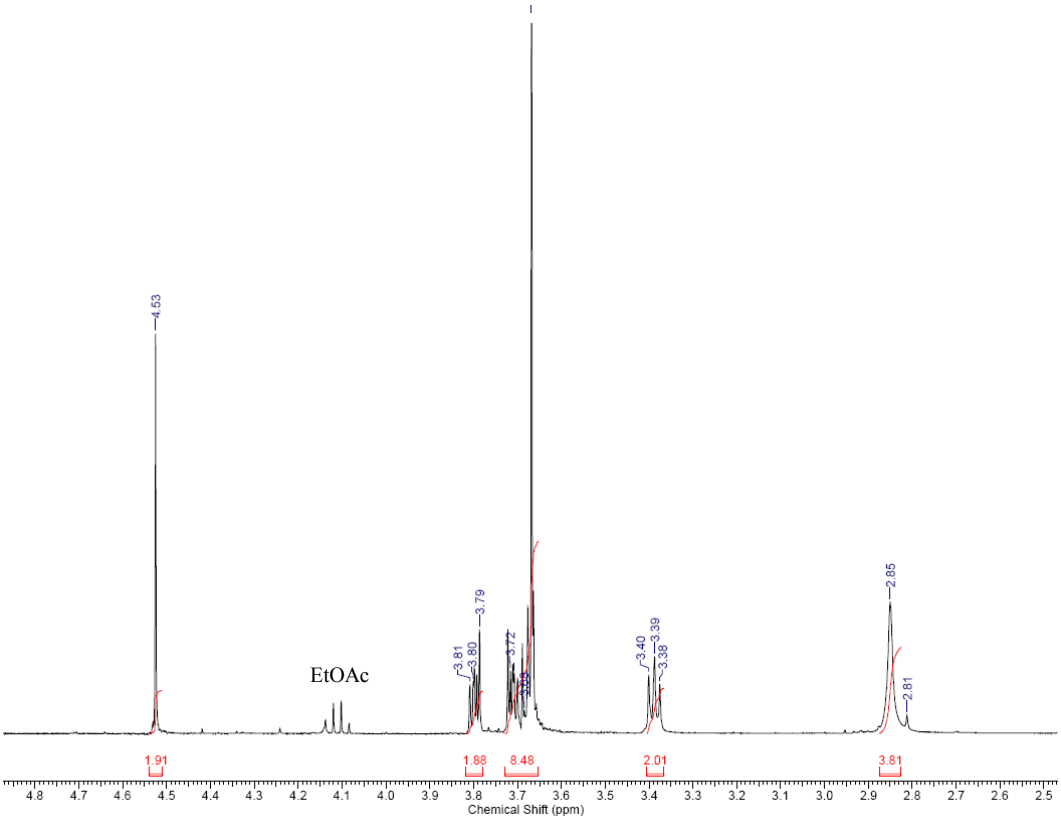

Figure 1. NMR spectrum of compound **4**.

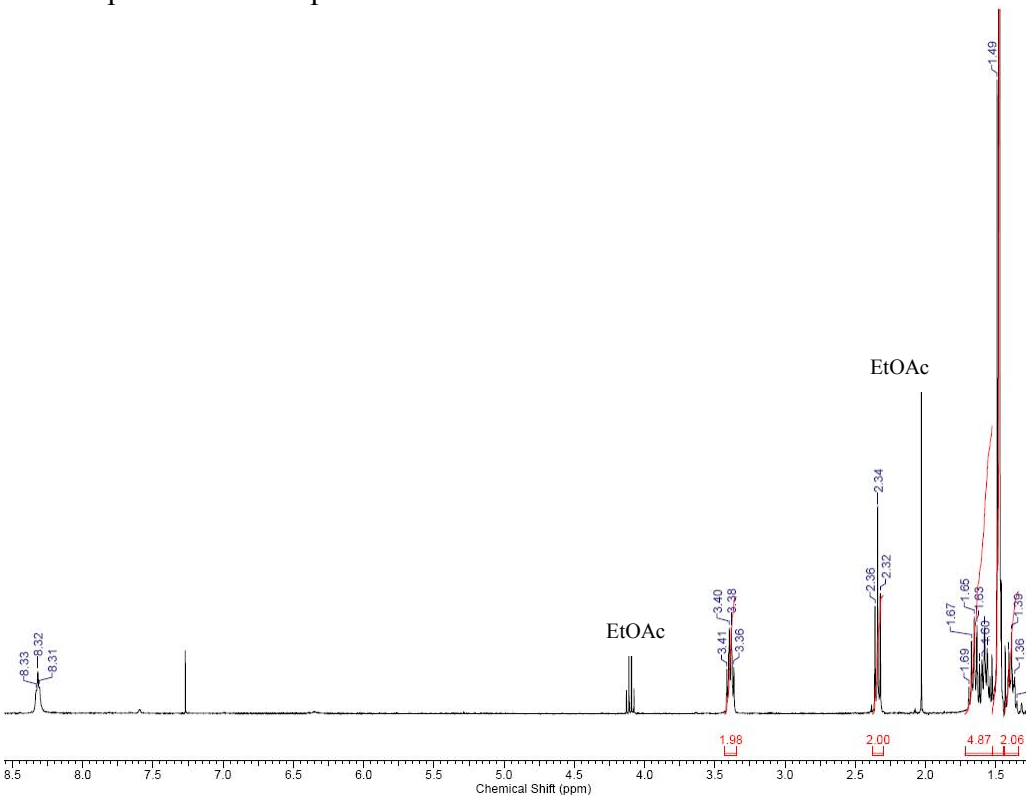

Figure 2. NMR spectrum of compound **8**.

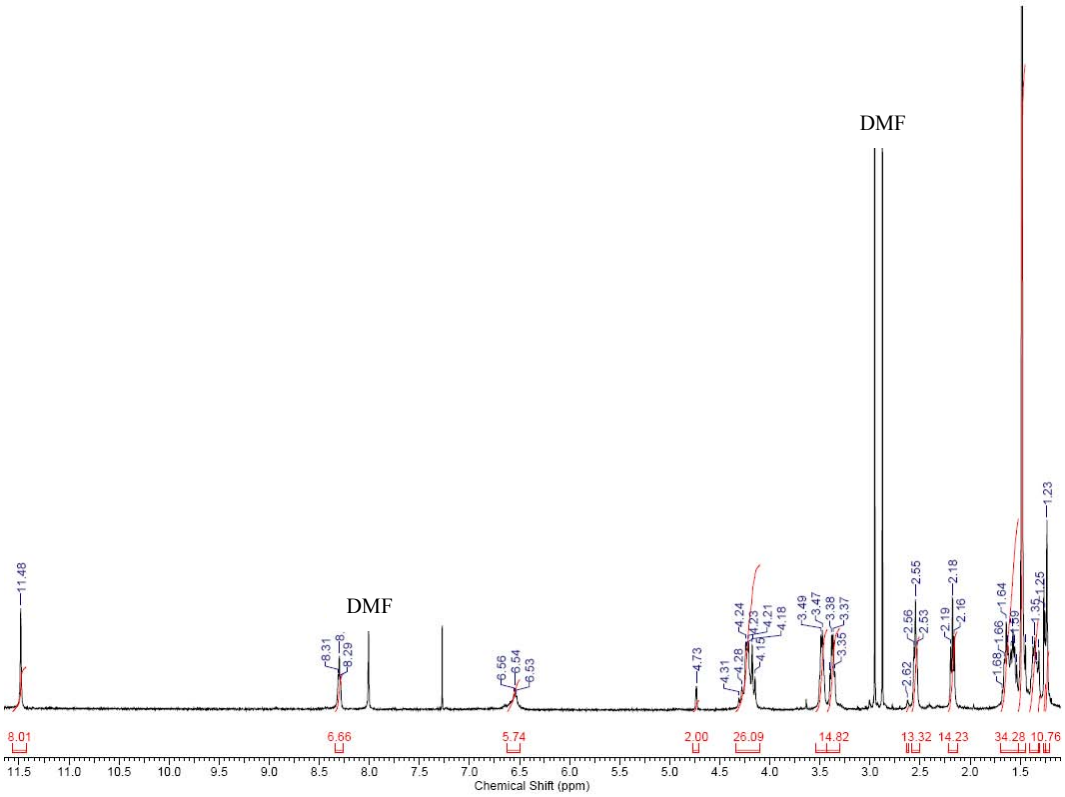

Figure 3. NMR spectrum of dendron **12**.

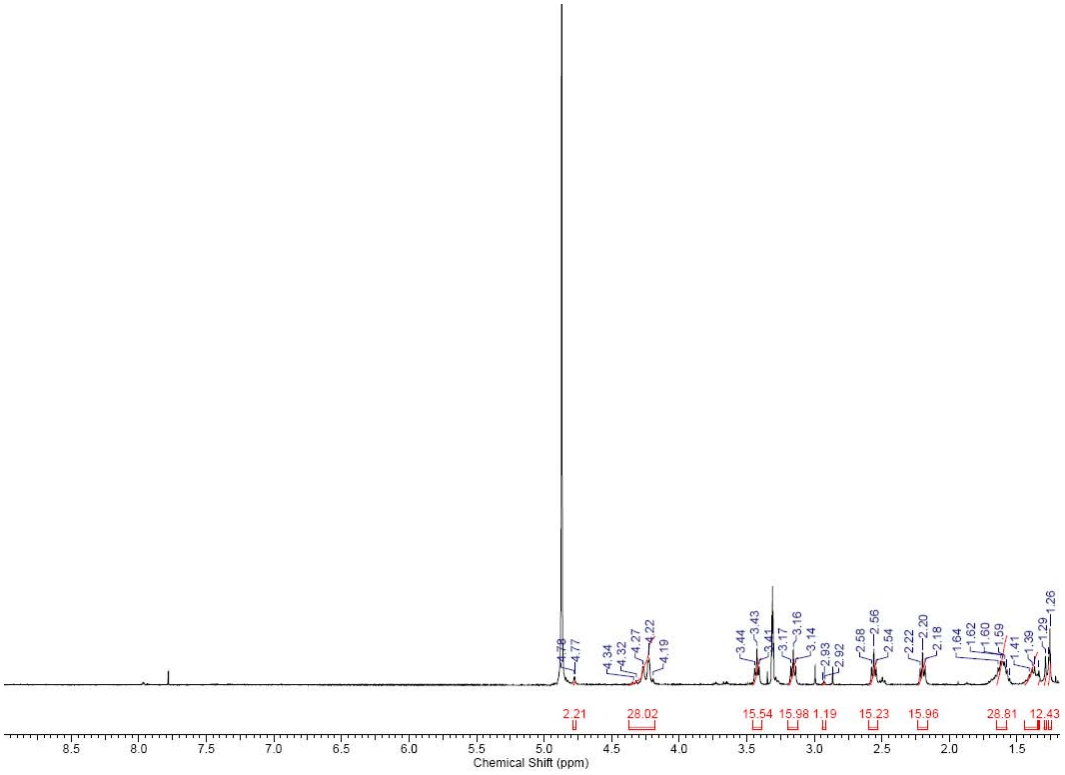

Figure 4. NMR spectrum of dendron **13**.

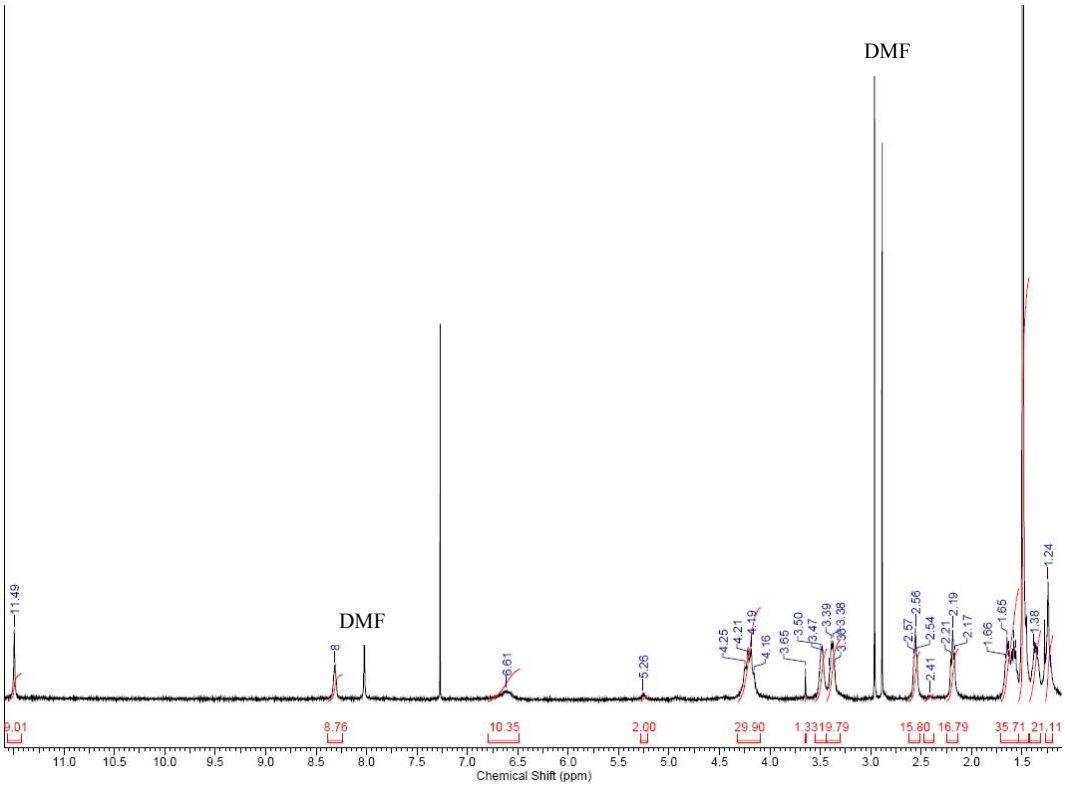

Figure 5. NMR spectrum of dendron **14**.

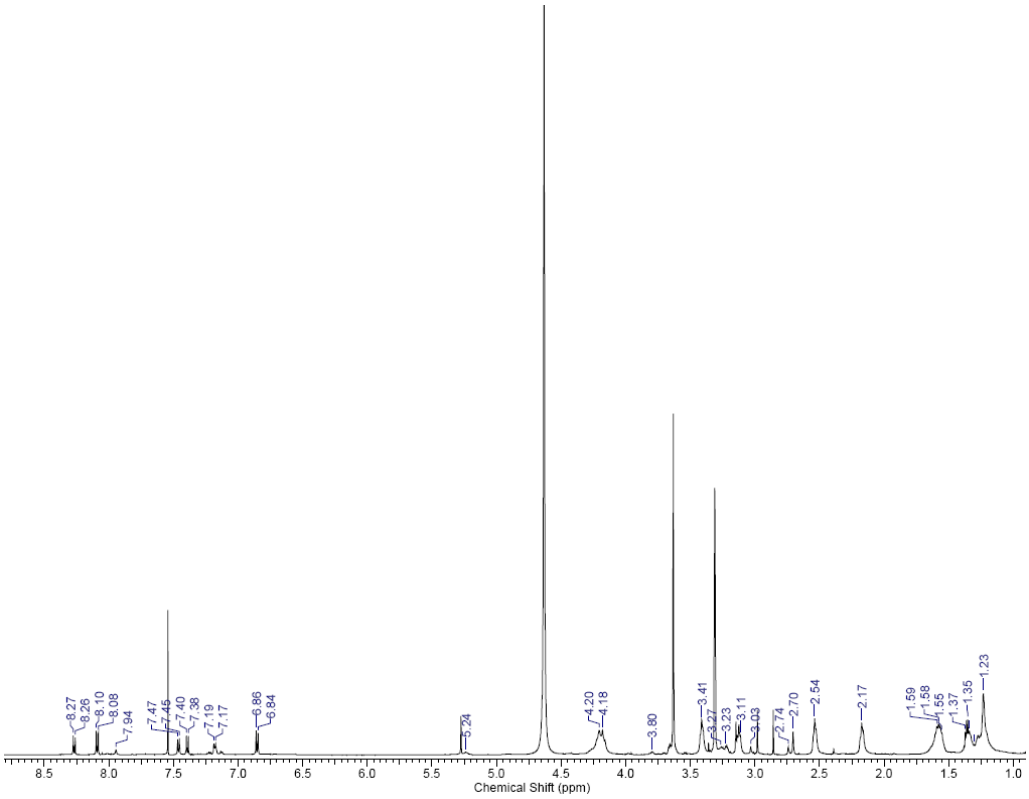

Figure 6. NMR spectrum of dendron **16**.

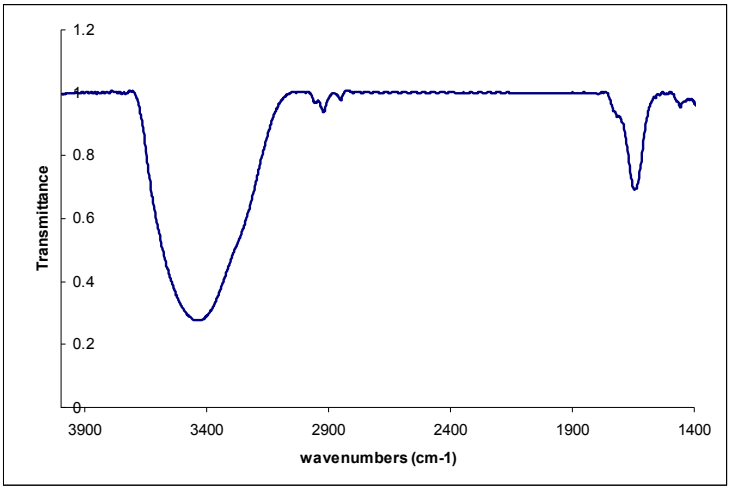

Figure 7. IR spectrum of dendron **9**.

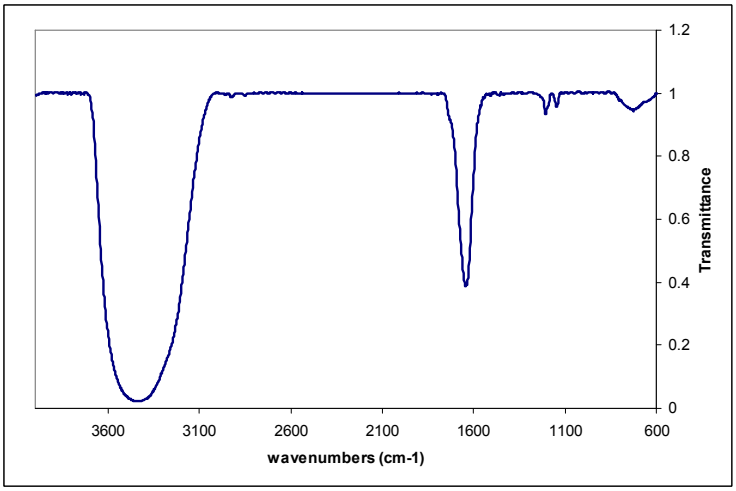

Figure 8. IR spectrum of dendron **11**.

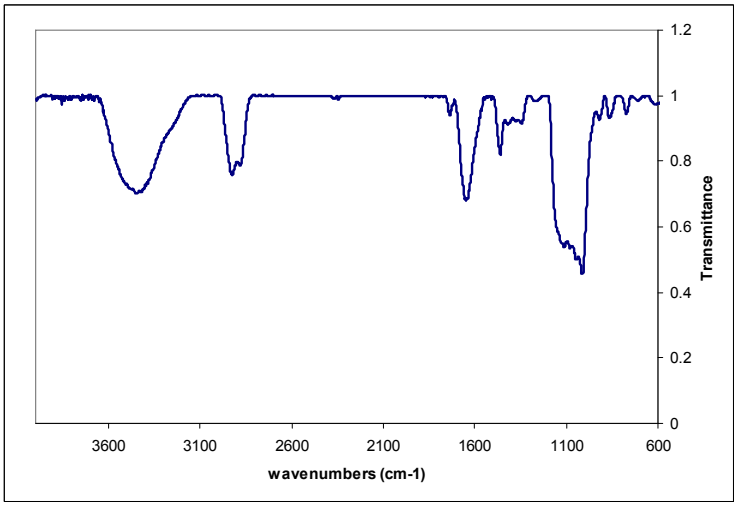

Figure 9. IR spectrum of nanoparticle **17.**

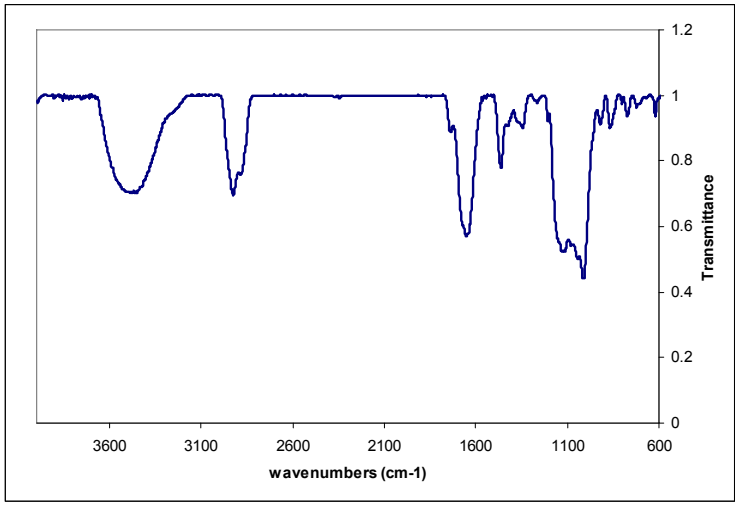

Figure 10. IR spectrum of nanoparticle **18**.

Influence of Ligand Valency on the Targeting of Immature Human Dendritic Cells by Mannosylated Liposomes

Socorro Espuelas,[†,‡] Christine Thumann,[§] Béatrice Heurtault,[†] Francis Schuber,[†] and Benoît Frisch*[,†]

Institut Gilbert Laustriat, UMR 7175-LC01 CNRS/Université Louis Pasteur, Département de Chimie Bioorganique, Laboratoire de Chimie Enzymatique et Vectorisation, Faculté de Pharmacie, 74 route du Rhin, 67400 Illkirch, France, Centro Galénico, Facultad de Farmacia, Universidad de Navarra, Pamplona, Spain, and Unité INSERM U748, Institut de Virologie, Université Louis Pasteur, 3 Rue Koeberlé, 67000 Strasbourg, France. Received June 24, 2008; Revised Manuscript Received September 9, 2008

An important challenge for the development of new generations of vaccines is the efficient delivery of antigens to antigen presenting cells such as dendritic cells. In the present study we compare the interaction of plain and targeted liposomes, containing mono-, di-, and tetraantennary mannosyl lipid derivatives, with human monocyte-derived immature dendritic cells (iDCs). Whereas efficient mannose receptor-mediated endocytosis by iDCs was observed for the mannosylated liposomes, in contrast, only nonspecific interaction with little uptake was observed with plain liposomes. In accordance with the clustering effect, liposomes prepared with multibranched mannosylated lipids displayed higher binding affinity for the mannose receptor than vesicles containing the monomannosylated analogs. Importantly, we have found that dimannosylated ligands present at the surface of the liposomes were as efficient as tetramannosylated ones to engage in multidentate interactions with the mannose receptor of iDCs, resulting in both cases in an effective uptake/endocytosis. This result will greatly facilitate, from a practical standpoint, the design of mannose-targeted vaccination constructs. Moreover, we showed that mannose-mediated uptake of liposomes did not result in an activation of iDCs. Altogether, our results suggest that antigen-associated targeted liposomes containing diantennary mannosylated lipids could be effective vectors for vaccines when combined with additional DC activation signals.

INTRODUCTION

Dendritic cells (DCs) are the most effective antigen presenting cells that play a key role in adaptive immunity against pathogens or tumor cells (*1, 2*). Immature dendritic cells (iDCs) present in peripheral tissues very actively endocytose exogenous antigens (*3*), after which these cells begin a maturation process that involves a down-regulation of their phagocytic ability and an up-regulation of antigen processing (reviewed by Guermonprez et al.) (*3*). This process is followed by the migration of iDCs to secondary lymphoid organs, where they turn into efficient antigen-presenting cells to naïve T-cells, via the MHC-I and MHC-II molecules, resulting in the activation of T-cells and in the initiation of antigen-specific immune responses or immunological tolerance (*4, 5*). In view of the antigen uptake and presentation competence of DCs, targeting of these cells might be a rational strategy for improving vaccine efficacy. Furthermore, enhancement of the interaction between the vaccine formulation bearing specific antigens and DCs could also be a potential method for increasing vaccine effectiveness.

Recognition and uptake of antigens by iDCs involves receptor-mediated endocytosis/phagocytosis via nonspecific pattern recognition receptors such as Toll-like receptors (TLR) and C-type lectins (*3*). C-type lectins are able to recognize specific pathogen-associated carbohydrate structures. Within the lectins superfamily, the mannose receptor family, composed of four members that include the mannose receptor (MR/CD206), DEC-205(CD205), Endo180, and the M-type phospholipase A2 receptor (*6*−*9*), is of particular importance (*10*). MR has been implicated in the recognition of mannose residues exposed on the surface of specific pathogens and in the internalization of mannosylated antigens, resulting in their enhanced presentation to T-cells (*11*). Furthermore, a recent study has demonstrated that the immunostimulatory properties of KLH (keyhole limpet hemocyanin), a xenoantigen widely used as a vaccine component, are partially triggered by its interaction with MR (*12*). Thus, mannosylation of peptide or protein antigens was shown to result in a 200−10,000-fold enhanced potency for the stimulation of specific T-cell clones, when compared with their nonmannosylated counterparts (*13*). As reviewed by Keler et al., MR-targeted vaccines present a promising approach (*14*). Consequently, the recent generations of antigen delivery systems to DCs involve the formulation of glycosylated antigen carriers such as liposomes, nanoparticles, or niosomes (*15*−*19*). Among the different vaccination vectors, liposomes are particularly attractive structures that are characterized by a marked absence of toxicity and a low intrinsic immunogenicity. These vesicles also offer a wide range of options for the design of vaccination constructs that include the size and (phospho)lipid composition of the vesicles, the mode of association of antigens, adjuvants, e.g. lipopeptide TLR ligands, and cytokines (IL-2...) (*20*−*22*).

Our group has previously synthesized a mannosylated amphiphilic derivative which was optimized to present a high affinity for MR and which could be easily incorporated into the bilayers of liposomes (*23*). This compound was composed of a tetramannosyl headgroup connected, via a polyethylene glycol spacer, to a lipid moiety. The tetramannosylated derivatives, when exposed on the surface of liposomes, showed a much higher affinity for concanavalin A than their monomannosylated analogs (*23*). In the present study, we have now synthesized and investigated a simplified ligand that contains only two mannose residues (Scheme 1). Our aim was to define the optimal

* To whom correspondence should be addressed. Phone: + 33 390 24 41 68. Fax: +33 390 24 43 06. E-mail: frisch@bioorga.u-strasbg.fr.

† Institut Gilbert Laustriat, UMR 7175-LC01 CNRS/Université Louis Pasteur.

‡ Universidad de Navarra.

§ Unité INSERM U748, Institut de Virologie, Université Louis Pasteur.

10.1021/bc8002524 CCC: $40.75 © 2008 American Chemical Society
Published on Web 11/24/2008

Scheme 1. Synthesis of the Dimannosylated Conjugate Man_2DOG

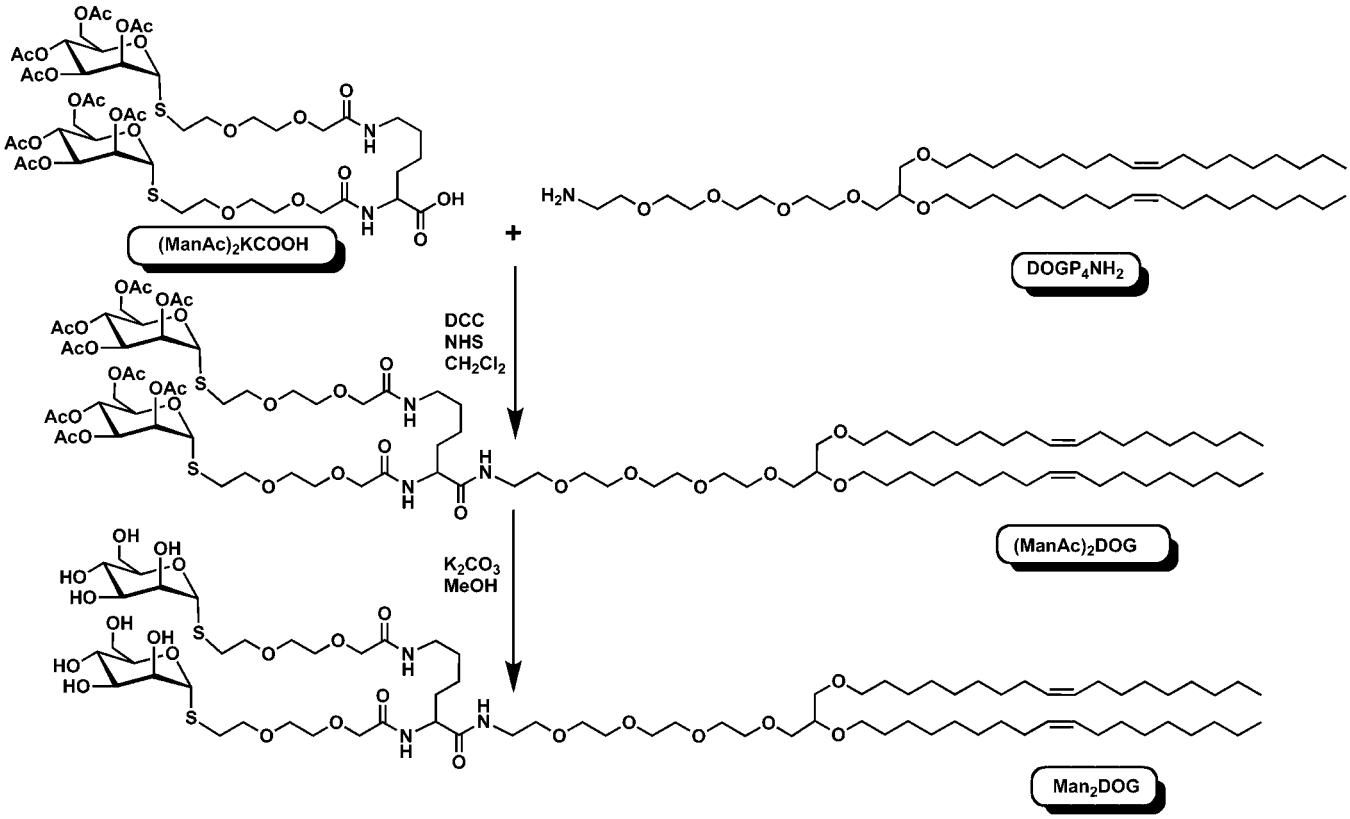

degree of ligand mannosylation (i.e., valency equal to 1, 2, or 4), yielding an efficient interaction and uptake of fluorescently labeled small unilamellar liposomes by human iDCs. The interaction of the mannosylated liposomes with the target cells was assessed by flow cytometry (*18*, *24*). In a second approach, clodronate, a nonpermeant cytotoxic molecule, was encapsulated in the mannosylated liposomes to explore their ability to interact with iDCs and to deliver intracellularly an active molecule. Collectively, our results indicate the following: (i) that targeting via mannosylated molecules is needed to observe an efficient internalization of liposomes by human iDCs, (ii) that targeted liposomes are able to release an active drug into iDCs without their activation, (iii) that, to target iDCs, multibranched mannosylated ligands are more efficient than monomannosylated ones, and, importantly, (iv) that targeting with dimannosylated ligands is as effective as targeting with tetramannosylated ones, thus greatly simplifying the design of DC targeted liposomes.

EXPERIMENTAL PROCEDURES

General. Reagent grade solvents were used without further purification. Egg yolk L-α-phosphatidylcholine (PC), L-α-phosphatidyl-DL-glycerol (PG) transesterified from egg yolk PC, cholesterol (recrystallized in methanol), dichloromethylenebisphosphonate (clodronate), yellow-colored 3-(4,5-dimethylthiazol-2-yl)-2,5-diphenyltetrazolium bromide (MTT), and mannan were purchased from Sigma-Aldrich (Saint-Quentin-Fallavier, France). 5(6)-Carboxyfluorescein (CF) was purchased from Eastman Kodak company (Rochester, NY) and purified according to Silvander et al. (*25*). The Hepes buffer used in this study corresponds to 10 mM Hepes containing 150 mM NaCl at pH 7.4. The mono- and tetramannosylated lipids, described in Scheme 2 (Man_1DOG and Man_4DOG), were synthesized according to (*23*). ^1H NMR and ^{13}C NMR spectra were recorded on a Bruker DPX 200 (200 MHz) and DPX 300 (300 MHz). Mass spectrometry was performed using a ESI/TOF Mariner spectrometer.

Synthesis. *$(ManAc)_2DOG$.* $(ManAc)_2KCOOH$ (50 mg, 44 μmol) (*23*), $DOGP_4NH_2$ (34 mg, 44 μmol) (*23*), DCC (10 mg, 48.4 μmol), and NHS (1 mg) were dissolved in 2 mL of anhydrous methylene chloride. After 1 h, the formed precipitate was removed by filtration and the organic phase was then washed with 3 × 6 mL of 5% (w/v) citric acid in water followed by 3 × 6 mL of water. After drying over $MgSO_4$, the solvent was evaporated to dryness. The reaction product $(ManAc)_2DOG$ (35 mg; yield 42%) was obtained after purification by chromatography on silica gel eluted with CH_2Cl_2/MeOH (30/1). ^1H NMR (δ ppm, $CDCl_3$/MeOD 1:1): 0.91 (t; 6H, $J = 6.6$ Hz, 2 × CH_3), 1.32 (m, 44H, 2 × 11 CH_2 allyl), 1.56 (m, 4H, 2 × OCH_2CH_2), 1.69−2.15 (m, 14H, $CH(CH_2)_3CH_2$ lys, 2 × $CH_2CH{=}CHCH_2$), 1.94, 1.97, 2.06, 2.15 (s, 24H, $OC(O)CH_3$), 2.80−3.03 (m, 4H, 2 × SCH_2), 3.30−3.82 (m, 39H, $CH(CH_2)_3CH_2$ lys, $NHCH_2(CH_2OCH_2)_4CH(CH_2O)O$, 2 × $SCH_2CH_2O(CH_2)_2$, 2 × $OCH_2(CH_2)_7$), 3.98−4.45 (m, 11H, CH_α-lys, 2 × $H_{4,6}$Man, 2 × $OCH_2C(O)NH$), 5.17−5.49 (m, 10H, 2 × $CH{=}CH$, 2 × $H_{2,3,5}$Man), 5.47 (d, 1H, $J = 1.76$ Hz, H_1Man), 7.8 and 8.1 (*NH*). ^{13}C NMR (δ ppm, $CDCl_3$/MeOD 1:1): 14.56 (CH_3), 20.59 − 20.69 − 20.75 and 20.78 ($OC(O)CH_3$), 23.74 (CH_2CH_3), 24.09 ($CH(CH_2)_3CH_2$lys), 27.24, 27.32 ($OCH_2CH_2CH_2$), 28.17 ($CH_2CH{=}CHCH_2$), 30.17, 30.32, 30.36, 30.47, 30.58, 30.63, 30.66, 30.80, 30.85, 31.17, 31.37, 31.52 (SCH_2, $OCH_2CH_2CH_2(CH_2)_4CH_2$, $CH{=}CHCH_2(CH_2)_4$-$CH_2CH_2CH_3$), 33.07, 33.63 ($OCH_2CH_2(CH_2)_6CH{=}CH(CH_2)_5$-$CH_2$), 33.38 ($C(O)NHCH_2CH_2$lys), 39.68, 40.41 ($C(O)NH$-$CH_2CH_2O$, $C(O)NHCH_2CH_2$lys), 53.86 ($C_\alpha$lys), 63.58 (C_6Man), 67.41, 70.38, 70.92, 72.14 (C_{2-5}Man), 70.48 ($CHCH_2O(CH_2)_8$), 71.08 − 71.11 − 71.17 − 71.28 − 71.42 − 71.47 − 71.54 − 71.58 − 71.90 − 71.98 − 72.08 − 72.53, 73.24 (SCH_2-$(CH_2OCH_2)_2C(O)$, $NHCH_2(CH_2OCH_2)_4$), 79.26 (OCH_2CHO), 83.76 (C_1Man), 130.82, 130.87 ($HC{=}CH$), 171.37, 171.44, 172.19, 172.29, 172.47, 172.54, 173.67 ($C(O)$). ESI-TOF MS (*m*/*z*), calculated for $C_{93}H_{161}N_3O_{31}S_2$ 1881.4, found ($M + Na^+$) 1904.0.

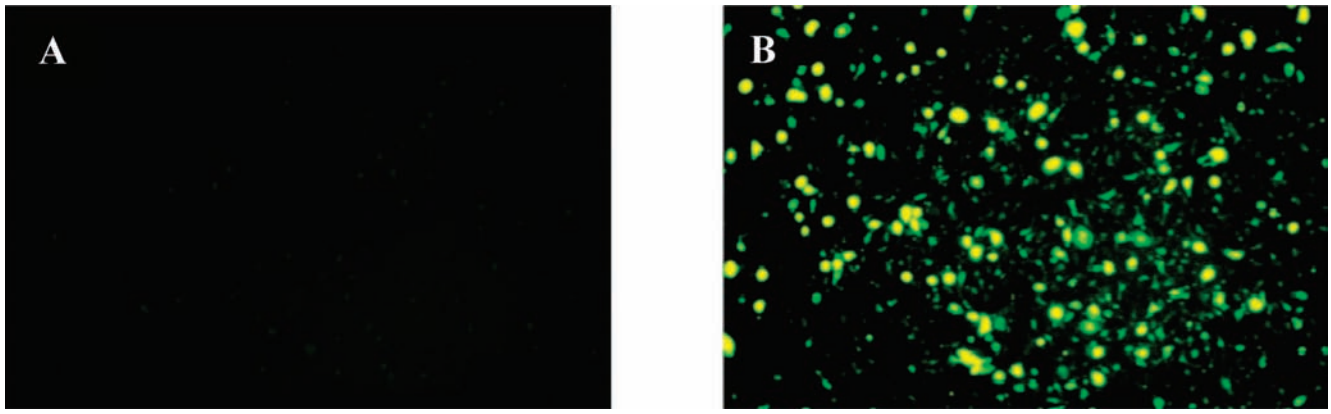

Figure 1. Epifluorescence images of human iDCs incubated at 37 °C for 2 h with 5(6)-carboxyfluorescein-encapsulated in plain (A) or Man_4-liposomes (6 mol % mannose) (B). Cells were observed with a Nikon Diaphot TMD inverted microscope with an epifluorescence attachment.

Man_2DOG. $(ManAc)_2$DOG (35 mg, 19 μmol) and potassium carbonate (7 mg, 50 μmol) were dissolved in 10 mL of anhydrous methylene chloride. After 3 h at room temperature and stirring, the organic phase was evaporated to dryness. The reaction product Man_2DOG (28 mg; yield 97%) was obtained after purification by chromatography on silica gel eluted with CH_2Cl_2/MeOH (7/3). ^{1}H NMR (δ ppm, $CDCl_3$/MeOD 1:1): 0.91 (t, 6H, $J = 6.6$ Hz, 2 × CH_3), 1.29 (m, 44H, 2 × 11 CH_2allyl), 1.58 (m, 4H, 2 × OCH_2CH_2), 1.73−2.15 (m, 14H, $CH(CH_2)_3CH_2$lys, 2 × $CH_2CH{=}CHCH_2$), 2.68−2.95 (m, 4H, 2 × SCH_2), 3.26−4.05 (m, 55H, $CH(CH_2)_3CH_2$lys, $NHCH_2(CH_2OCH_2)_4CH(CH_2O)O$, 2 × $SCH_2CH_2O(CH_2)_2O$, 2 × $OCH_2(CH_2)_7$, 2 × H_{2-6}Man, 2 × $OCH_2C(O)NH$), 4.41 (m, 1H, CH_αlys), 5.33−5.36 (m, 6H, 2 × C$H{=}$CH, 2 × H_1Man). ^{13}C NMR (δ ppm, $CDCl_3$/MeOD 1:1): 14.54 (CH_3), 23.75 (CH_2CH_3), 24.16 ($CH(CH_2)_3CH_2$lys), 27.25, 27.31 (OCH_2CH_2-CH_2), 28.16 ($CH_2CH{=}CHCH_2$), 30.18, 30.36, 30.48, 30.62, 30.80, 30.86, 31.16, 31.33 (SCH_2, $OCH_2CH_2CH_2(CH_2)_4CH_2$-$CH{=}CHCH_2(CH_2)_4CH_2CH_2CH_3$), 33.07, 33.63 ($OCH_2CH_2$-$(CH_2)_6CH{=}CH(CH_2)_5CH_2CH_2CH_3$), 33.30 ($C(O)NHCH_2$-$CH_2$lys), 39.72, 40.42 ($C(O)NHCH_2CH_2O$, $C(O)NHCH_2$lys), 53.11 ($C_\alpha$lys), 62.82 (C_6Man), 70.47, 71.12, 71.19, 71.43, 71.56, 71.70, 71.81, 71.95, 72.07, 72.17, 72.53 ($SCH_2(CH_2O$-$CH_2)_2C(O)$, $NHCH_2(CH_2OCH_2)_4$), 68.88, 73.08, 73.55, 75.03 (C_{2-5}Man), 79.28 (OCH_2CHO), 86.33 (C_1Man), 130.85 ($HC{=}CH$), 172.49, 172.62, 173.85 (C(O)). ESI-TOF MS (*m*/*z*) calculated for $C_{77}H_{145}N_3O_{23}S_2$ 1543.9, found ($M + Na^+$) 1567.9.

Liposome Preparation. Liposomes were prepared by mixing, in a round-bottom flask, phospholipids (PC, PG) and cholesterol (75/20/50 molar ratio), in chloroform with the appropriate mannosylated lipid at 0−16 mol % mannose content. After solvent evaporation under high vacuum, the dried lipid film was hydrated by vortex mixing after addition of 1 mL of Hepes buffer (for 10 μmol of lipids) containing 150 mM clodronate or 40 mM CF. The resulting suspension was sonicated at 25 °C for 1 h (5 s cycles interrupted for 1.25 s) under a continuous flow of nitrogen, using a 3 mm diameter probe sonicator (Vibra Cell, Sonics and Material Inc., Danbury, CT) at 300 W. The SUV (Small Unilamellar Vesicles) preparations were finally centrifuged for 10 min at 10,000*g* to remove the titanium dust originating from the probe. The liposomes were separated from unencapsulated CF or clodronate by passage through a 1 × 10 cm Sephadex G-75 column equilibrated with Hepes buffer. The size of the vesicles was determined by a photon correlation spectroscopy technique, using a Coulter (model N4SD) submicron particle analyzer (Coulter Electronics, FL). The liposomes were analyzed for phosphorus (*26*) and sugar content (*23*). All the liposome formulations were freshly prepared and sterilized (Millex filters 0.22 μm) before use with the cells. This formulation led to a clodronate concentration of 4.8 mM in the final liposome suspension. Encapsulated CF was quantified according to Barbet et al. (*27*). Mannosyl residues associated with the liposomes are expressed in mol % relative to the phospholipids: for example, four times more Man_1DOG molecules were used compared to the case of Man_4DOG to achieve the same mannose content.

Generation of Human Immature Dendritic Cells. iDCs were obtained by differentiation of monocytes isolated by countercurrent elutriation of peripheral blood mononuclear cell (PBMC) separated from the blood of healthy donors. Accordingly, the monocytes were then cultured in RPMI 1640 medium (GIBCO BRL, France) containing 10% fetal bovine serum (FBS) (GIBCO BRL, France), 1000 IU/mL GM-CSF, and 500 IU /mL IL-4 (PeproTech, USA) for 6 days. Cells were again fed with fresh medium containing cytokines on day 1 and with fresh cytokines on day 4. At day 6, the resulting cells, which were semi- to nonadherent, displayed DC morphology and their phenotype was analyzed as described below.

Uptake of 5(6)-Carboxyfluorescein-Encapsulated Liposomes by iDCs. Immature human dendritic cells were plated at 4 × 10^5 cells/mL in 6-well plates and incubated with (manno)liposomes containing CF for 30 min (2 h for microscopy and fluorometric experiments) at 37 °C with 5% CO_2. The medium used was RPMI 1640 supplemented with 5% heat inactivated FBS. After the incubation period, the cells were washed twice with cold PBS and finally fixed with 1.5% paraformaldehyde before flow cytometry analysis (FACS). Mannan was used in a competitive inhibition assay to confirm the specificity of the uptake of the ligands. Accordingly, the cells were preincubated for 10 min with 10 μg/mL of mannan followed by the liposomal formulation for an additional 30 min. The cells were then treated as above for FACS analysis (Figure 2). For spectrofluorometric analysis (Figure 3), after cold PBS treatment, the cells were lyzed with 1% Triton in PBS. The fluorescence was measured at $\lambda_{em} = 530$ nm (λ_{ex} 485 nm) with a fluorometer (Shimadzu, RF-5301, Kyoto, Japan). The relation between liposomal phospholipids and total CF fluorescence (Figure 3) was determined similarly after detergent lysis of the CF-loaded vesicles.

Microscopy. Epifluorescence microscopy of human iDCs was performed at 37 °C after 2 h of incubation with 5(6)-carboxyfluorescein encapsulated in plain or Man_4 liposomes (6 mol % mannose). Cells were observed with a Nikon Diaphot TMD inverted microscope with an epifluorescence attachment (FITC filter set: DM 510 B-2A) and equipped with a 10× magnification.

Effect of Mannosylated Liposomes on the Phenotype of iDCs. To evaluate the induction of maturation of iDCs by mannosylated liposomes, adherent and nonadherent cells were

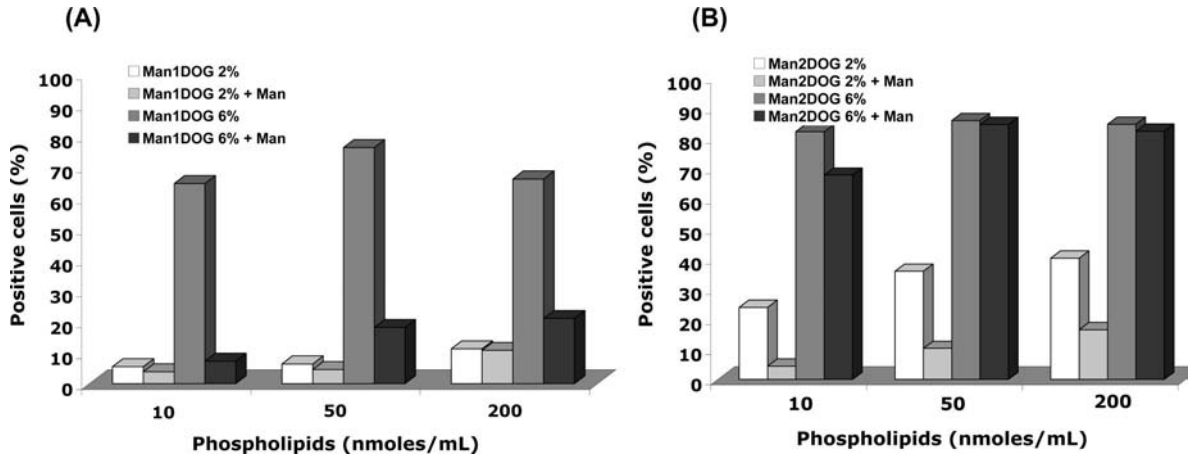

Figure 2. Quantification of fluorescently labeled iDCs observed after incubation with 5(6)-carboxyfluorescein-encapsulated liposomes targeted with Man_1DOG (A) or Man_2DOG (B). The cells were incubated at 37 °C for 30 min with varying concentrations (expressed in nmol/mL of phospholipids) of CF-liposomes containing the indicated amounts (expressed in mol % mannose) of Man_1DOG or Man_2DOG. (+) Man: mannan inhibition experiments. The cells were preincubated for 10 min with 10 μg of mannan/mL followed by an incubation with Man_1- or Man_2-liposome formulations for 30 min. The percentage of positive cells in the presence of plain liposomes was <10%. The data are from a representative experiment carried out twice with similar results.

harvested from T-75 flasks with cold PBS-EDTA. These cells were then recultured at 4×10^5 cells/mL in 6-well plates in media prepared with one volume of fresh RPMI containing 5% FBS and one volume of monocyte-conditioned medium (MCM) corresponding to cytokine-enriched medium from a 6-day culture of monocytes. After addition of LPS (1 μg/mL) or the different mannosylated formulations (0.1−50 nmol of phospholipids/mL), the cells were further incubated for 24−48 h before phenotypic analysis by flow cytometry.

Intracellular Activity of Clodronate Encapsulated in Liposomes on iDCs. Immature human dendritic cells generated as above were plated at 4×10^5 cells/mL in 48-well plates and incubated with (manno)liposomes containing clodronate for 48 h at 37 °C with 5% CO_2. The medium used was RPMI 1640 supplemented with 5% heat inactivated FCS. After the incubation, the cells were washed twice with cold PBS and their viability was evaluated as indicated below.

Cytotoxicity Assay. Cell viability was measured with the colorimetric MTT assay (*28*). Briefly, 5×10^5 DCs/mL, maintained in one volume of MCM and one volume of RPMI 1640 containing 5% FCS, was incubated in the presence of different concentrations of liposomes for 24, 48, or 72 h at 37 °C. Half of the medium was removed before addition of 60 μL of MTT (7.5 mg/mL in PBS lacking Ca^{2+} and Mg^{2+}) for 2 h at 37 °C. Solubilization of the formazan crystals was achieved by aspiration of 300 μL of supernatant followed by addition of 200 μL of 10% (v/v) Triton-X100 in acidified (0.4% concentrated HCl) isopropanol. The absorbance of quadruplicates at 540 nm was measured using a plate reader. The clodronate concentration versus cells was estimated considering a clodronate concentration of 4.8 mM in the final liposome suspension.

Phenotype Analysis by Flow Cytometry. Phenotypic characterization of dendritic cells was carried out by flow cytometry using a FACScan (Becton Dickinson). Cells resuspended in PBS (Becton Dickinson) were incubated for 15 min at 4 °C with saturating concentrations of the following panel of PE-labeled monoclonal antibodies: anti-CD83, anti-CD86, and anti-HLA DR. Specific anti-immunoglobulin isotypes mAbs (anti-IgG1 and anti-IgG2) were used as control. The percentage of positive cells was determined regarding the isotypic control (Figure 5) The mean fluorescence intensity (MFI) was determined for the cells stained with the specific marker antibody (Figure 5).

Statistical Analysis. The data of Figure 5 were analyzed using the Mann−Whitney test (SigmaStat, version 2.0, Jandel GmbH, Erkrath, Germany). Results were considered significantly different when $p < 0.05$.

RESULTS AND DISCUSSION

Synthesis of the Amphiphilic Dimannosyl Conjugate Man_2DOG. Our group has previously synthesized mono- and tetra-mannosylated derivatives which, when incorporated in liposomes, were promising molecules to target cells expressing mannose receptors (*23*). In the present work we first performed the synthesis of a dimannosylated derivative to investigate the influence of the mannose valency on the *in vitro* iDCs' targeting. The synthesis of Man_2DOG (Scheme 1) first required the production of lipid $DOGP_4NH_2$. This compound was synthesized in 6 steps starting from glycerol, tetraethylene glycol, and oleyl alcohol according to the procedure described previously by Espuelas et al. (*23*). Compound $(ManAc)_2KCOOH$ was obtained by introduction of two mannose groups on a L-lysine backbone as described (*23*). The carboxylic acid function of $(ManAc)_2$-KCOOH was activated with dicyclohexylcarbodiimide and *N*-hydroxysuccinimide at room temperature in the presence of diisopropylethylamine. $DOGP_4NH_2$ in CH_2Cl_2 was then added and the reaction was carried out for 12 h to give $(ManAc)_2DOG$. The final product, Man_2DOG, was obtained after removal of the acetyl protecting groups of the mannose residues with potassium carbonate in methanol.

Characterization of the Mannosylated Liposomes. Liposomes have been described as tools for the efficient presentation of ligands to cell surface receptors, which require multivalent interactions (*23*). Moreover, antigens associated with such vesicles were also shown to be more efficiently captured/endocytosed and presented by antigen presenting cells than free antigens in solution (*29*). We consequently formulated small unilamellar liposomes incorporating various amphiphilic mannosylated derivatives in their phospholipidic bilayers. The main characteristics of plain and mono- and tetramannosylated liposomes (see Scheme 2 for structures) have been previously reported (*23*). The sugar residues associated with these vesicles, determined by the resorcinol−sulfuric acid method, increased proportionally with the amount of mannosyl lipids added during liposome preparation (*23*). Mono- and tetramannosylated lipids were consequently found to be stably inserted into the bilayer of liposomes, leading to Man_1- and Man_4-liposomes, respectively (*23*). In the present work, Man_2-liposomes have been prepared by incorporation of the presently described Man_2DOG.

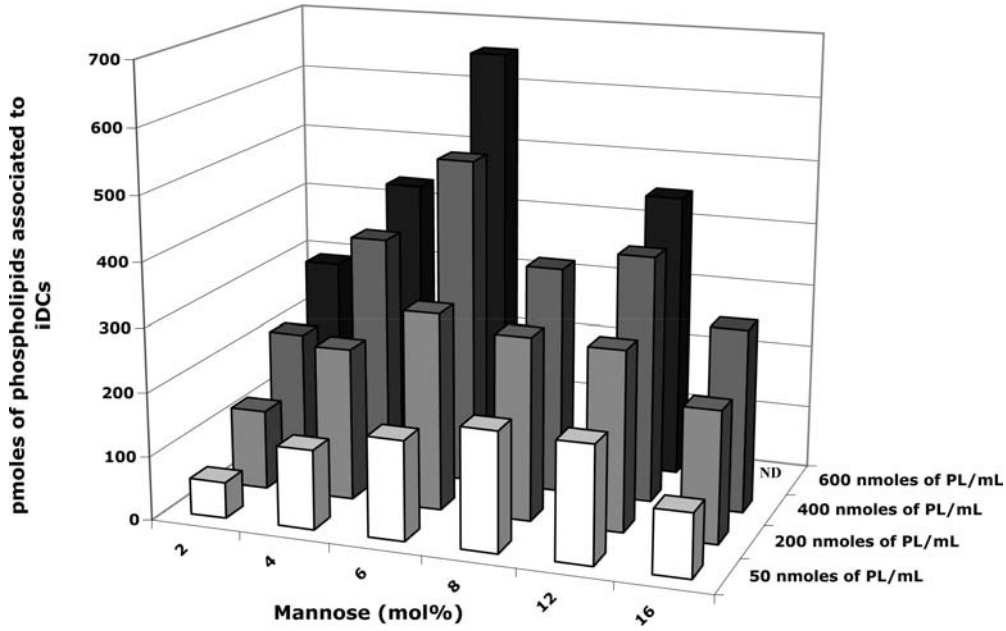

Figure 3. Quantification of cell-associated vesicles after incubation of iDCs with 5(6)-carboxyfluorescein-encapsulated liposomes containing varying amounts (2−16 mol % mannose) of Man_4DOG. The cells were incubated at 37 °C for 2 h with the given concentrations (in nmol/mL of phospholipids) of targeted CF-liposomes. The cell-associated vesicles (expressed as picomoles of phospholipids) were quantified by determination of the fluorescence of CF at $\lambda_{em} = 530$ nm (λ_{ex} 485 nm) after lysis of the cells with 1% Triton X-100. The results are expressed as picomoles phospholipids associated to iDCs as a function of nanomoles of liposomal phospholipids/mL of cell medium. Data are means of three experiments (SD < 10%). ND, not determined.

Scheme 2. Structures of the Mono- and Tetramannosylated Lipid Derivatives

Abbreviation	Structures
Man_4DOG	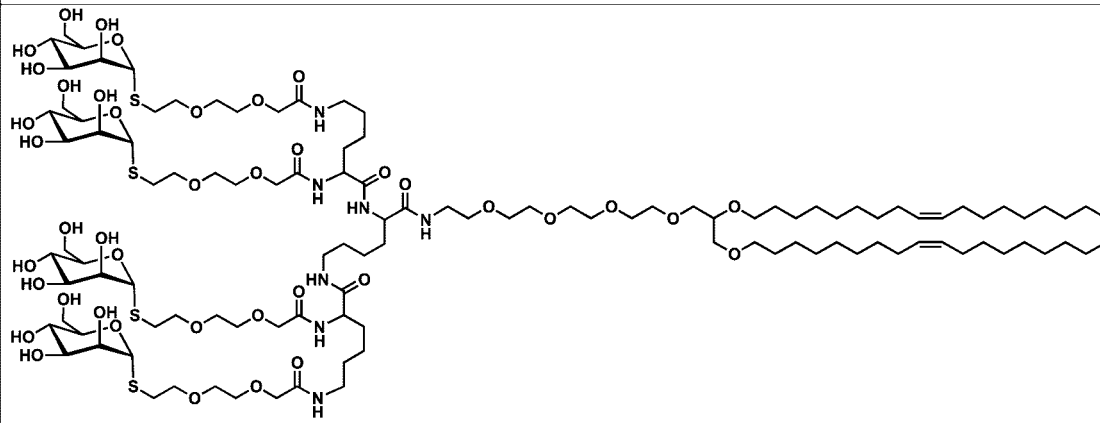
Man_1DOG	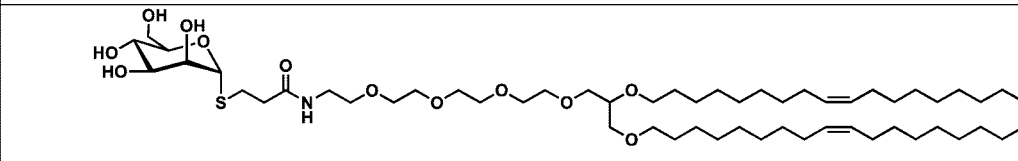

The size of the liposomes ranged between 70 nm for the plain vesicles and 110 nm for the liposomes containing the highest proportion of the tetramannosylated lipid (i.e., equivalent to 16 mol % mannose). Compared to plain vesicles, the presence of the mannosylated lipids had no apparent influence on their stability. Thus, about 60% retention of the encapsulated marker CF was observed after incubation of the different liposome populations for 24 h in a cell culture medium (RMPI in the presence of 5% heat-inactivated serum) at 37 °C.

Interaction of Targeted Liposomes Containing 5(6)-Carboxyfluorescein with Immature Human Dendritic Cells. The ability of the liposomes to interact with iDCs has been assessed with vesicles having encapsulated CF. Upon release of the CF in the cytoplasm, the fluorescence is dequenched and visible inside the cell. Figure 1 illustrates the dramatic difference between the fluorescence emitted by the cells after incubation with plain (Figure 1A) and targeted Man_4-liposomes (Figure 1B). In Figure 2, the cell-associated fluorescence has been expressed as percentage of CF positive cells (Figure 2A and 2B) after incubation with plain and Man_1- and Man_2-liposomes. The percentage of CF positive cells was <10% after incubation with plain liposomes. At this point it should be mentioned that although iDCs are known to display high endocytic/phagocytic activities (*3*) and to capture plain liposomes (*15, 18, 24, 30*), this uptake remains quite low for short incubation times such as the 2 h used in our study (*15, 30, 31*).

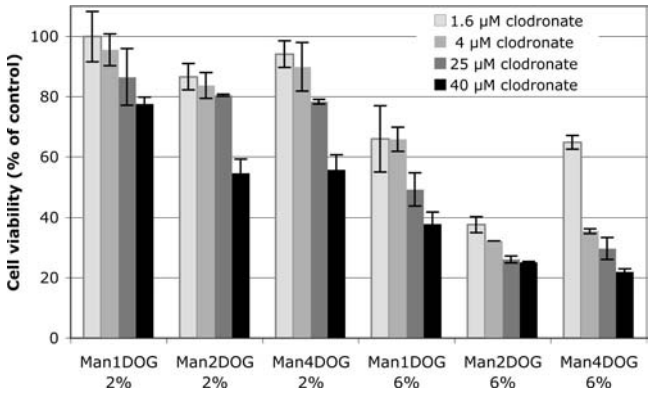

Figure 4. Cytotoxicity assay. Cytotoxicity of clodronate encapsulated in mannose-targeted liposomes. Human iDCs, plated at 4×10^5 cells/mL RPMI supplemented with 5% heat-inactivated FBS in 48-well plates, were incubated with the indicated liposomal formulations for 48 h. The cytotoxicity was measured with a MTT test. Data represent means of triplicates ± SEM.

As shown in Figure 2A, no significant fluorescence was found associated with iDCs after incubation with Man_1-liposomes at 2 mol % mannose, whereas for higher mannose densities (e.g., 6 mol %), about 60−70% of the cells were fluorescent, irrespective of the liposome concentration (10−200 nmol/mL). For the same mannose content, the behavior of the Man_2-liposomes was very different (Figure 2). Thus, about 20−40% of the cells were already fluorescent at a low dimannose density (2 mol %); moreover, the number of positive cells increased as a function of the concentration of liposomes. In the presence of Man_2-liposomes containing a mannose density of 6 mol %, the percentage of positive cells was about 80% regardless of the concentration of liposomes. Related to these points, which indicate that in agreement with literature (*32*−*34*) the mannose density and valency have a major impact on DC targeting, we have shown previously with galactosylated liposomes that lectin−sugar interactions were highly dependent on the surface density of monovalent ligands, with the occurrence of a threshold value of about 5 mol % (*35*). Accordingly, monomannosylated lipids inserted into the outer layer of the targeted liposomes could generate above a critical concentration—via lateral diffusion—a multivalent platform which adopts a favorable arrangement for high-affinity interaction with the MR receptor (*36*).

Incubation of iDCs with plain and Man_4-liposomes (6 mol % mannose) was performed at 4 °C (to determine binding) and 37 °C (to evaluate binding and endocytosis). For plain liposomes, after 2 h of incubation, only low levels of cell-associated fluorescence were observed (<10% of positive cells, Figure 1A) and no significant difference was found between 4 and 37 °C (data not shown). For the targeted liposomes, with concentrations varying from 0 to 330 nmol of phospholipids/mL, a low saturable binding was observed at 4 °C, reaching 600 MFI for the highest vesicle concentration; in contrast, at 37 °C, no saturation was found and a value of 1270 MFI was reached at the highest concentration used (data not shown). These results suggest that under our conditions the cell-associated fluorescence measured at 37 °C is predominantly due to vesicle uptake via endocytosis.

To demonstrate the specificity of the interaction of the targeted liposomes with mannose receptors (most likely the MR) present at the surface of DCs, we have performed competition experiments in the presence of free mannan. At a concentration of 10 μg/mL, mannan substantially inhibited the uptake of Man_1-liposomes (Figure 2A), indicating that these vesicles were predominantly endocytosed by DCs via a mannose-specific receptor. Inhibition of the uptake of constructs containing multivalent mannosyl ligands required, however, much higher mannan concentrations (up to 1 mg/mL) (data not shown). This observation confirms the occurrence of increased binding affinities resulting from multivalent interactions that are triggered by clustering effects (*32*−*34*).

In Figure 3, the cell-associated fluorescence was measured and reported in picomoles of phospholipids (PL) associated to iDCs as a function of nanomoles of PL/mL for the Man_4-liposomes. Increasing the concentration of targeted liposomes from 50 to 600 nmol of PL/mL resulted in an increase of fluorescence associated to iDCs regardless of the ligand density used (2−16 mol % mannose). Consequently, in this vesicle concentration range no uptake saturation could be observed during the 30 min of incubation. Furthermore, Figure 3 indicates that the optimal tetramannose density for liposome association with iDCs is reached around 6−8 mol %.

Cytotoxicity of Clodronate-Loaded Mannosylated Liposomes. Clodronate, a small hydrosoluble and cytotoxic molecule, does not readily enter cells. However, when encapsulated into liposomes, this drug was shown previously to be delivered intracellularly and this formulation was used extensively to selectively deplete mononuclear phagocytic cells such as macrophages (*37*). Under our experimental conditions, free clodronate was indeed found to become cytotoxic for iDCs at only very high concentrations, with an $IC_{50} \approx 2$ mM (data not shown). However, and in sharp contrast with macrophages, when human monocyte-derived iDCs were incubated for 48 h with clodronate encapsulated in plain liposomes, no toxicity could be detected in the concentration range tested (0−40 μM of clodronate) (data not shown). As already noted above (Figure 1A), this observation might be related to a lower ability of dendritic cells, compared to macrophages, to spontaneously capture particles either by phagocytosis or endocytosis (*38*) and consequently to a decreased intracellular delivery of the cytotoxic drug. Related to that latter point, macrophage depletion experiments have generally been performed with larger liposomes, i.e. 200−300 nm vs 70 nm in this study, and thus with a higher clodronate load; moreover, macrophages are also known for a great intrinsic sensitivity to the effect of this drug (*39*).

In sharp contrast, however, iDC viability was highly affected by clodronate entrapped in targeted liposomes (Figure 4). Thus, incorporation of our synthetic mono-, di-, and tetramannosylated lipids into clodronate-loaded liposomes was able to dramatically enhance the uptake of the vesicles by iDCs and, consequently, the cytotoxicity of the drug. Moreover, and in line with observations made above, the clodronate study confirmed that Man_1-liposomes were efficient only at the highest mannose density (6 mol %). Interestingly, at constant drug concentration, the cytotoxicity of liposomal clodronate increased with the density of the mannose residues present at the surface of the targeted vesicles and also with the valency of the branched mannosylated lipids, for Man_1 and Man_2 but not for Man_4 (Figure 4). It is possible that the dimannosyl lipid could cluster on the surface of the liposome in a topology as favorable for a multivalent interaction with the receptor as the tetramannosyl ligand.

As shown in Figure 4, a clodronate dose-dependent increase of toxicity was only observed with Man_1-liposomes (at 2 and 6 mol % mannose) and with multibranched lipids at low mannose densities (e.g., 2 mol %). With the di- or tetramannosylated lipids at the highest mannose density used (i.e., 6 mol %), very high toxicities were observed at already very low clodronate concentrations. The higher affinities of the multivalent constructs were confirmed by the competition studies with mannan. Thus, about 100-fold higher concentrations of the polysaccharide were needed to inhibit the interaction uptake of the multivalent-targeted liposomes with the DCs compared to Man_1-liposomes.

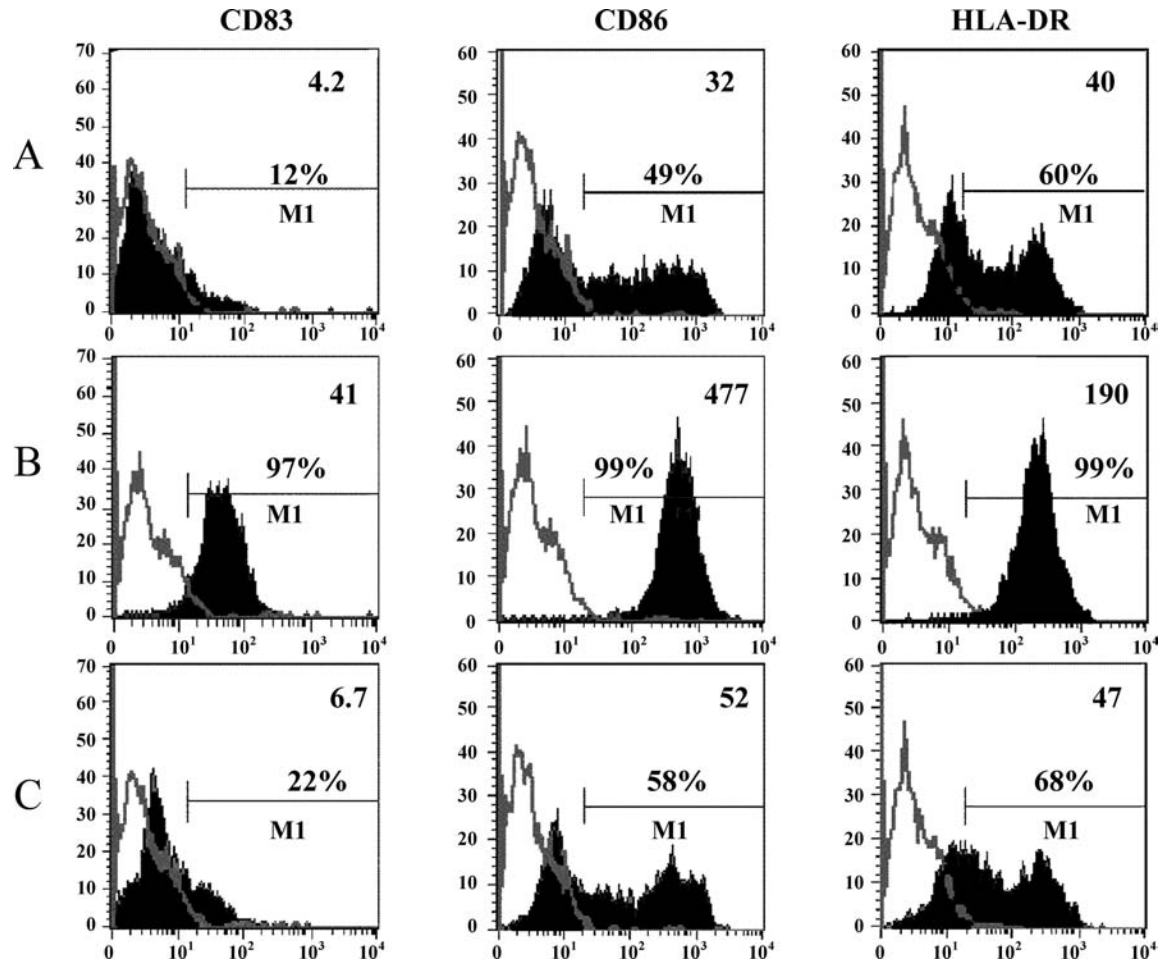

Figure 5. Absence of phenotypic maturation of human iDCs incubated in the presence of Man_4-liposomes. Monocytes maintained in culture for 6 days to differentiate into dendritic cells were cultured for an additional 24 h in the absence of stimuli (A) or in the presence of 1 μg/mL LPS (B) and Man_4-liposomes (200 nmol of phospholipids/mL. (C) Cells were stained with PE-conjugated Abs specific for the marker indicated (filled histogram) or an isotype-matched color Ab (thick gray line). Values indicated on histograms (M1) are the percentage of positive cells of the cells stained with the marker-specific Ab. In the right upper corners, the mean fluorescence intensities (MFI) are indicated. The results represent a single experiment with the same donor and are representative of five experiments that gave similar results: (A) untreated cells; (B) cells incubated with 1 μg/mL LPS; (C) cells incubated in the presence of Man_4-liposomes (6 mol % mannose). Compared to control cells (A), the presence of LPS as maturation agent, lead to a significant increase of surface markers ($p < 0.01$ at least for the three markers) while no significant modification of marker levels was observed ($p > 0.05$ for the three markers) for the cells incubated in the presence of Man_4-liposomes (C).

These results are in agreement with the ability of multivalent branched constructs to bind with increased affinity with the CRD (carbohydrate recognition domains) of the MR (*33*).

Several C-type lectins that recognize mannosyl moieties have been identified on the surface of human monocyte-derived DCs, such as MR and DC-SIGN (*14*). Whereas DC-SIGN binds internal mannose residues of linear N-linked oligosaccharides, MR shows a greater affinity for the terminal sugars in branched structures (*40*). We can thus hypothesize that the uptake of clodronate-loaded mannosylated liposomes via endocytosis is probably mediated by MR, although additional experiments would be necessary to prove this point.

The conclusions reached with the present studies corroborate the results obtained above with flow cytometric analysis of the fluorescence associated with iDCs after incubation with 5(6)-carboxyfluorescein loaded liposomes. A dramatic increase of fluorescence was thus observed for the targeted Man_1- and Man_2-constructs when the mannose surface density was increased from 2 to 6 mol % (Figure 2).

Taken together, our results indicate that the nontargeted liposomes used in our study are poor vectors to deliver nonpermeant molecules, such as clodronate, into iDCs. This diverges with the known uptake of plain liposomes by phagocytic cells used for the treatment of intramacrophage pathogens (*41, 42*). In contrast, however, targeted liposomes designed to interact with the mannose receptors present at the surface of DCs proved to be excellent carriers. In this respect, we have shown that the relatively simple diantennary mannosylated, when incorporated into liposomes, was as efficient as the more complex tetraantennary lipid. This might be explained by the ability of the diantennary ligand to engage into multivalent/multidentate interactions, favored by lateral diffusion at the surface of the vesicle. Importantly, this observation will simplify the chemical approach for the design of such targeted liposomes.

Activation/Maturation of Immature Dendritic Cells. DCs are capable of evolving from antigen-capturing cells (immature) to antigen-presenting cells (mature). This maturation, which represents a major step in the initiation of an immune response (*3*), would be of great interest if it could also be triggered by vaccination constructs. Related to this point, some studies have hinted that mannosylation of antigens might represent an effective means of triggering the maturation and enhancing the functional capacity of DCs *in vitro* (*43*). We were consequently interested in the evaluation of the impact of our mannosylated molecules, incorporated into liposomes, on the maturation of human iDCs.

Most typical features of immature dendritic cells were obtained after culturing monocytes for 6 days (Figure 5A, upper

row). DC maturation is accompanied by the expression of CD83 and the up-regulation of CD80 and CD86. After treatment of iDCs for 24 or 48 h with mannosylated liposomes, the levels of surface markers were determined and compared with those induced by LPS (1 mg/mL), used as a maturation control (Figure 5B, middle row). As shown in Figure 5C (lower row), the incubation of iDCs with Man_4-liposomes (6 mol %) did not induce any significant change ($p > 0.05$) in the phenotypic expression of surface markers typical of immature cells. Levels of MHC-II and costimulatory molecule CD86 did not change (Figure 5). Similar results were obtained for plain liposomes (data not shown).

We can conclude that, whereas the role of MR in antigen uptake is well documented (*44*, *45*), the suggestion that this receptor might also be endowed with signaling functions (*46*), resulting in DC maturation and activation, still needs solid experimental proof (*40*). A similar lack of dendritic cells' activation has been observed previously with other mannosylated liposomes prepared with branched trimannoside structures (*18*, *24*). However, as suggested before, immune responses generated by antigen delivery through mannosylated constructs might also need additional signals provided, for example, by TLR agonists (*47*−*49*).

CONCLUSION

Mannosylated liposomes are highly valuable vehicles to specifically deliver drugs or antigens to cells such as DCs, and this strategy shows great promise in the design of vaccines (*24*, *50*). Although monovalent mannosyl ligands, when inserted above a certain threshold in the bilayer of liposomes, can yield good interactions with mannose receptors, multivalent ligands that have higher affinities in accordance with the cluster effect, are more efficient for targeting. In this respect, the observation made in the present study that di- and tetraantennary ligands, when exposed at the surface of clodronate-loaded liposomes, exhibited similar cell delivery efficiencies with iDCs, is of practical value from a chemical standpoint. Indeed, the synthesis of a diantennary mannosyl ligand such as the one illustrated in Scheme 1 is much more straightforward than the tetraantennary equivalent. Based on the present work, we have recently applied with success the *in vivo* targeting to DCs of antitumor vaccination constructs (*51*) that codeliver MHC-I/II peptide epitopes and immune response activators such as TLR ligands (J.-S. Thomann et al., to be published).

LITERATURE CITED

(1) Banchereau, J., and Steinman, R. M. (1998) Dendritic cells and the control of immunity. *Nature 392*, 245–52.
(2) Steinman, R. M., and Banchereau, J. (2007) Taking dendritic cells into medicine. *Nature 449*, 419–26.
(3) Guermonprez, P., Valladeau, J., Zitvogel, L., Thery, C., and Amigorena, S. (2002) Antigen presentation and T-cell stimulation by dendritic cells. *Annu. Rev. Immunol. 20*, 621–67.
(4) Banchereau, J., Briere, F., Caux, C., Davoust, J., Lebecque, S., Liu, Y. J., Pulendran, B., and Palucka, K. (2000) Immunobiology of dendritic cells. *Annu. Rev. Immunol. 18*, 767–811.
(5) Steinman, R. M. (1991) The dendritic cell system and its role in immunogenicity. *Annu. Rev. Immunol. 9*, 271–96.
(6) East, L., and Isacke, C. M. (2002) The mannose receptor family. *Biochim. Biophys. Acta 1572*, 364–86.
(7) Higashi, N., Fujioka, K., Denda-Nagai, K., Hashimoto, S., Nagai, S., Sato, T., Fujita, Y., Morikawa, A., Tsuiji, M., Miyata-Takeuchi, M., Sano, Y., Suzuki, N., Yamamoto, K., Matsushima, K., and Irimura, T. (2002) The macrophage C-type lectin specific for galactose/N-acetylgalactosamine is an endocytic receptor expressed on monocyte-derived immature dendritic cells. *J. Biol. Chem. 277*, 20686–20693.
(8) Stahl, P. D., and Ezekowitz, R. A. (1998) The mannose receptor is a pattern recognition receptor involved in host defense. *Curr. Opin. Immunol. 10*, 50–5.
(9) Tacken, P. J., Torensma, R., and Figdor, C. G. (2006) Targeting antigens to dendritic cells in vivo. *Immunobiology 211*, 599–608.
(10) McGreal, E. P., Martinez-Pomares, L., and Gordon, S. (2004) Divergent roles for C-type lectins expressed by cells of the innate immune system. *Mol. Immunol. 41*, 1109–21.
(11) Taylor, P. R., Gordon, S., and Martinez-Pomares, L. (2005) The mannose receptor: linking homeostasis and immunity through sugar recognition. *Trends Immunol. 26*, 104–10.
(12) Presicce, P., Taddeo, A., Conti, A., Villa, M. L., and Della Bella, S. (2008) Keyhole limpet hemocyanin induces the activation and maturation of human dendritic cells through the involvement of mannose receptor. *Mol. Immunol. 45*, 1136–45.
(13) Tan, M. C., Mommaas, A. M., Drijfhout, J. W., Jordens, R., Onderwater, J. J., Verwoerd, D., Mulder, A. A., van der Heiden, A. N., Scheidegger, D., Oomen, L. C., Ottenhoff, T. H., Tulp, A., Neefjes, J. J., and Koning, F. (1997) Mannose receptor-mediated uptake of antigens strongly enhances HLA class II-restricted antigen presentation by cultured dendritic cells. *Eur. J. Immunol. 27*, 2426–35.
(14) Keler, T., Ramakrishna, V., and Fanger, M. W. (2004) Mannose receptor-targeted vaccines. *Expert Opin. Biol. Ther. 4*, 1953–62.
(15) Foged, C., Arigita, C., Sundblad, A., Jiskoot, W., Storm, G., and Frokjaer, S. (2004) Interaction of dendritic cells with antigen-containing liposomes: effect of bilayer composition. *Vaccine 22*, 1903–13.
(16) Jain, S., and Vyas, S. P. (2006) Mannosylated niosomes as adjuvant-carrier system for oral mucosal immunization. *J. Liposome Res. 16*, 331–45.
(17) Joralemon, M. J., Murthy, K. S., Remsen, E. E., Becker, M. L., and Wooley, K. L. (2004) Synthesis, characterization, and bioavailability of mannosylated shell cross-linked nanoparticles. *Biomacromolecules 5*, 903–13.
(18) White, K. L., Rades, T., Furneaux, R. H., Tyler, P. C., and Hook, S. (2006) Mannosylated liposomes as antigen delivery vehicles for targeting to dendritic cells. *J. Pharm. Pharmacol. 58*, 729–37.
(19) Takagi, H., Furuya, N., and Kojima, N. (2007) Preferential production of IL-12 by peritoneal macrophages activated by liposomes prepared from neoglycolipids containing oligomannose residues. *Cytokine 40*, 241–50.
(20) Altin, J. G., and Parish, C. R. (2006) Liposomal vaccines—targeting the delivery of antigen. *Methods 40*, 39–52.
(21) Espuelas, S., Roth, A., Thumann, C., Frisch, B., and Schuber, F. (2005) Effect of synthetic lipopeptides formulated in liposomes on the maturation of human dendritic cells. *Mol. Immunol. 42*, 721–9.
(22) Reddy, S. T., Swartz, M. A., and Hubbell, J. A. (2006) Targeting dendritic cells with biomaterials: developing the next generation of vaccines. *Trends Immunol. 27*, 573–9.
(23) Espuelas, S., Haller, P., Schuber, F., and Frisch, B. (2003) Synthesis of an amphiphilic tetraantennary mannosyl conjugate and incorporation into liposome carriers. *Bioorg. Med. Chem. Lett. 13*, 2557–60.
(24) Copland, M. J., Baird, M. A., Rades, T., McKenzie, J. L., Becker, B., Reck, F., Tyler, P. C., and Davies, N. M. (2003) Liposomal delivery of antigen to human dendritic cells. *Vaccine 21*, 883–890.
(25) Silvander, M., Bergstrand, N., and Edwards, K. (2003) Linkage identity is a major factor in determining the effect of PEG-ylated surfactants on permeability of phosphatidylcholine liposomes. *Chem. Phys. Lipids 126*, 77–83.
(26) Rouser, G., Fleischer, S., and Yamamoto, A. (1970) Two dimensional then layer chromatographic separation of polar lipids and determination of phospholipids by phosphorus analysis of spots. *Lipids 5*, 494–6.

(27) Barbet, J., Machy, P., Truneh, A., and Leserman, L. D. (1984) Weak acid-induced release of liposome-encapsulated carboxyfluorescein. *Biochim. Biophys. Acta 772*, 347–56.

(28) Pauwels, R., Balzarini, J., Baba, M., Snoeck, R., Schols, D., Herdewijn, P., Desmyter, J., and De Clercq, E. (1988) Rapid and automated tetrazolium-based colorimetric assay for the detection of anti-HIV compounds. *J. Virol. Methods 20*, 309–21.

(29) Fukasawa, M., Shimizu, Y., Shikata, K., Nakata, M., Sakakibara, R., Yamamoto, N., Hatanaka, M., and Mizuochi, T. (1998) Liposome oligomannose-coated with neoglycolipid, a new candidate for a safe adjuvant for induction of CD8+ cytotoxic T lymphocytes. *FEBS Lett. 441*, 353–6.

(30) Opanasopit, P., Higuchi, Y., Kawakami, S., Yamashita, F., Nishikawa, M., and Hashida, M. (2001) Involvement of serum mannan binding proteins and mannose receptors in uptake of mannosylated liposomes by macrophages. *Biochim. Biophys. Acta 1511*, 134–145.

(31) Arigita, C., Bevaart, L., Everse, L. A., Koning, G. A., Hennink, W. E., Crommelin, D. J., van de Winkel, J. G., van Vugt, M. J., Kersten, G. F., and Jiskoot, W. (2003) Liposomal meningococcal B vaccination: role of dendritic cell targeting in the development of a protective immune response. *Infect. Immun. 71*, 5210–8.

(32) Bedouet, L., Bousser, M. T., Frison, N., Boccaccio, C., Abastado, J. P., Marceau, P., Mayer, R., Monsigny, N., and Roche, A. C. (2001) Uptake of dimannoside clusters and oligomannosides by human dendritic cells. *Biosci. Rep. 21*, 839–855.

(33) Biessen, E. A., Noorman, F., van Teijlingen, M. E., Kuiper, J., Barrett-Bergshoeff, M., Bijsterbosch, M. K., Rijken, D. C., and van Berkel, T. J. (1996) Lysine-based cluster mannosides that inhibit ligand binding to the human mannose receptor at nanomolar concentration. *J. Biol. Chem. 271*, 28024–28030.

(34) Grandjean, C., Angyalosi, G., Loing, E., Adriaenssens, E., Melnyk, O., Pancre, V., Auriault, C., and Gras-Masse, H. (2001) Novel hyperbranched glycomimetics recognized by the human mannose receptor: quinic or shikimic acid derivatives as mannose bioisosteres. *ChemBioChem 2*, 747–757.

(35) Haensler, J., and Schuber, F. (1988) Preparation of neogalactosylated liposomes and their interaction with mouse peritoneal macrophages. *Biochim. Biophys. Acta 946*, 95–105.

(36) Engel, A., Chatterjee, S. K., Al-arifi, A., Riemann, D., Langner, J., and Nuhn, P. (2003) Influence of spacer length on interaction of mannosylated liposomes with human phagocytic cells. *Pharm. Res. 20*, 51–57.

(37) van Rooijen, N., and van Kesteren-Hendrikx, E. (2002) Clodronate liposomes: perspectives in research and therapeutics. *J. Liposome Res. 12*, 81–94.

(38) Reece, J. C., Vardaxis, N. J., Marshall, J. A., Crowe, S. M., and Cameron, P. U. (2001) Uptake of HIV and latex particles by fresh and cultured dendritic cells and monocytes. *Immunol. Cell Biol. 79*, 255–263.

(39) Monkkonen, J., Taskinen, M., Auriola, S. O., and Urtti, A. (1994) Growth inhibition of macrophage-like and other cell types by liposome- encapsulated, calcium-bound, and free bisphosphonates in vitro. *J. Drug Targeting 2*, 299–308.

(40) Frison, N., Taylor, M. E., Soilleux, E., Bousser, M. T., Mayer, R., Monsigny, M., Drickamer, K., and Roche, A. C. (2003) Oligolysine-based Oligosaccharide Clusters: selective recognition and endocytosis by the mannose receptor and dendritic cell-specific intercellular adhesion molecule 3 (ICAM-3)-grabbing nonintegrin. *J. Biol. Chem. 278*, 23922–23929.

(41) Gupta, C. M., and Haq, W. (2005) Tuftsin-bearing liposomes as antibiotic carriers in treatment of macrophage infections. *Methods Enzymol. 391*, 291–304.

(42) Khuller, G. K., Kapur, M., and Sharma, S. (2004) Liposome technology for drug delivery against mycobacterial infections. *Curr. Pharm. Des. 10*, 3263–74.

(43) Zhong, G., Wang, J., Xu, M., Xie, Z., Yu, M., Wang, J., Zhou, T., Gong, W., Sun, Y., Hu, M., Zhang, X., Shen, B., and Guo, N. (2005) Enhanced maturation and functional capacity of dendritic cells induced by mannosylated L2 domain of ErbB2 receptor. *Scand. J. Immunol. 62*, 108–16.

(44) Apostolopoulos, V., and McKenzie, I. F. (2001) Role of the mannose receptor in the immune response. *Curr. Mol. Med. 1*, 469–474.

(45) Sallusto, F., Cella, M., Danieli, C., and Lanzavecchia, A. (1995) Dendritic cells use macropinocytosis and the mannose receptor to concentrate macromolecules in the major histocompatibility complex class II compartment: downregulation by cytokines and bacterial products. *J. Exp. Med. 182*, 389–400.

(46) Cambi, A., and Figdor, C. G. (2003) Dual function of C-type lectin-like receptors in the immune system. *Curr. Opin. Cell Biol. 15*, 539–46.

(47) He, L. Z., Crocker, A., Lee, J., Mendoza-Ramirez, J., Wang, X. T., Vitale, L. A., O'Neill, T., Petromilli, C., Zhang, H. F., Lopez, J., Rohrer, D., Keler, T., and Clynes, R. (2007) Antigenic targeting of the human mannose receptor induces tumor immunity. *J. Immunol. 178*, 6259–67.

(48) Ramakrishna, V., Vasilakos, J. P., Tario, J. D., Jr., Berger, M. A., Wallace, P. K., and Keler, T. (2007) Toll-like receptor activation enhances cell-mediated immunity induced by an antibody vaccine targeting human dendritic cells. *J. Transl. Med. 5*, 5.

(49) Dan, J. M., Wang, J. P., Lee, C. K., and Levitz, S. M. (2008) Cooperative stimulation of dendritic cells by Cryptococcus neoformans mannoproteins and CpG oligodeoxynucleotides. *PLoS One 3*, e2046.

(50) Kojima, N., Biao, L., Nakayam, T., Ishii, M., Ikehara, Y., and Tsujimura, K. (2008) Oligomannose-coated liposomes as a therpeutic antigen-delivery and an adjuvant vehicle for induction of in vivo tumor immunity. *J. Control. Release 129*, 26–32.

(51) Roth, A., Rohrbach, F., Weth, R., Frisch, B., Schuber, F., and Wels, W. S. (2005) Induction of effective and antigen-specific antitumour immunity by a liposomal ErbB2/HER2 peptide-based vaccination construct. *Br. J. Cancer 92*, 1421–9.

BC8002524

Investigation of Insulin Loaded Self-Assembled Microtubules for Drug Release

Marsiyana M. Henricus, Karen T. Johnson, and Ipsita A. Banerjee*

Department of Chemistry, Fordham University, 441 East Fordham Road, Bronx, New York 10458. Received June 25, 2008; Revised Manuscript Received September 22, 2008

Self-assembled microtubules were used to entrap insulin for the preparation of new drug delivery devices. The interactions of insulin with the microtubules were probed by circular dichroism, zeta potential analysis, as well as FTIR spectroscopy. The morphologies of the insulin-loaded tubules were examined by AFM and TEM. We found that insulin loading was both pH- as well as concentration-dependent. The circular dichroism analysis indicated that, at pH range 6−7, the conformation change in the presence of the microtubules was minimal and hence would be the most appropriate conditions for insulin loading. The entrapment efficiency and release of insulin was found to be pH-dependent. Further, the controlled drug release studies indicated that, under acidic conditions, insulin release was extremely slow, and it is likely that the insulin is protected inside the microtubules. Thus, the microtubules may potentially protect the insulin from aggregation and release at lower pH (gastric pH) *in vivo*. However, at pH 6.5 (closer to intestinal pH) a sustained release was observed. Such new materials may inhibit the aggregation of peptides under suitable conditions and potentially be used for drug delivery, in particular, for other peptide-based drugs.

INTRODUCTION

Over the past several years, attention has been focused on research related to the development of nanomaterials for numerous applications such as biosensors, optoelectronics, catalysts, and drug delivery systems (*1*−*4*). In addition to their small size, nanomaterials can be altered to facilitate attachments to specific components, in order to improve biocompatibility and allow for more accurate intracellular and intercellular targeting (*5*−*7*). Nanoparticles consisting of polymers, ceramics, metals, as well as biological materials have been constructed to form various types of structures that offer unique characteristics to aid drug delivery (*8*−*11*). Many of the polymeric nanoparticles that have been developed are biodegradable, preventing the accumulation of the nanoparticles in the body in addition to ensuring the constant drug release over a period of time. Soft delivery systems such as surfactant micelles, liposomes engineered from phospholipids, and vegetable oil based materials have also been used to carry various types of biological materials and lipophilic drugs. In lieu of this, several lipid formulations have been developed to transport protein drugs and allow for their sustained release (*12*−*22*).

A rapidly growing drug delivery approach is the use of microtubules and nanotubes because of their large relative internal volumes, which can be functionalized on the internal and the external surface. Self-assembled lipid microtubes and carbon nanotubes (CNTs) have been utilized as drug delivery agents (*23*−*27*). Nanotubes and microtubules self-assembled from peptide bolaamphiphiles exhibit several properties that make them promising biomaterials, including facile self-assembly in aqueous solutions, biocompatibility, and ability to be functionalized (*28, 29*). For example, self-assembled peptide nanotubes have been used to immobilize enzymes such as lipase, which upon immobilization showed improved stability (*30*).

In this work, the peptide drug, insulin, was entrapped within self-assembled peptide microtubules. Insulin is an important hormone for the regulation of blood glucose levels and is implicated in diseases such as Diabetes type I and type II (*31*). Aggregation of insulin and consequent precipitation has been a major barrier to the development of long-term delivery methods for insulin (*32, 33*). Many methods have been used to protect insulin and other peptide drugs from physical inactivation, such as the addition of stability-enhancing additives, surfactants, and phenols (*34, 35*). Nanomaterials such as poly(alkyl cyanoacrylate), PLGA, poly(vinyl alcohol) gel spheres, hydroxypropyl methylcellulose phthalate microspheres, Eudragit L100 microspheres, and poly(γ-glutamic acid) nanoparticles shelled with chitosan have been functionalized with insulin for purposes of drug delivery (*36*−*40*). It is well-known that dicarboxylic amino acids have been successfully used to prevent agitation-induced aggregation in insulin (*41*). However, the rich potential of self-assembled tubular assemblies formed from synthetic amino acid bolaamphiphiles (two amino acid head groups connected by a hydrophobic tail group) for diminution of aggregation, entrapment of insulin, and preparation of a potential drug delivery device is yet to be explored. Here, we have examined highly biocompatible microtubules self-assembled from bis(*N*-α-amidotyrosyl-tyrosyl-tyrosine)-1,5-pentane dicarboxylate for controlled drug release of insulin. The main objective of the present study was to examine the interactions of insulin with the microtubule, determine entrapment efficiency, and study their release behavior. Such materials may potentially be useful for the encapsulation of other peptides and drugs and promote longer circulation times *in vivo*.

EXPERIMENTAL SECTION

Materials. 1-Hydroxy-benzotraizole hydrate, Tyr-Tyr-Tyr-methyl ester, DMF, EDAC (dimethylaminopropyl-*N*-ethylcarbodiimide hydrochloride), chloroform, methanol, TEA (triethyl amine), $NaHCO_3$, NaOH, HCl, and insulin from Porcine pancreas (≥27 USP units/mg) were purchased from Sigma Aldrich. Phosphate buffer solutions of various pH values were

* Author to whom all correspondence should be addressed. I. A. Banerjee. Phone: 718-817-4445. Fax: 718-817-4432. E-mail: banerjee@fordham.edu.

10.1021/bc800254n CCC: $40.75 © 2008 American Chemical Society
Published on Web 11/06/2008

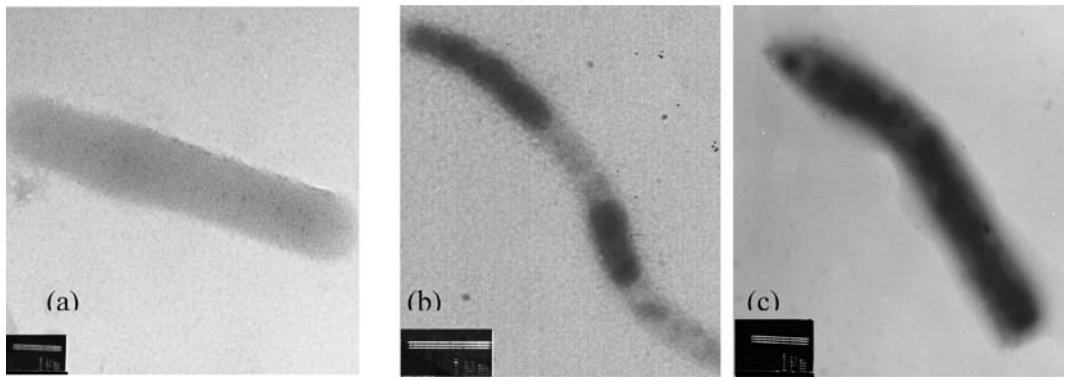

Figure 1. (a) TEM image of a self-assembled microtubule. (b) TEM image of partially loaded insulin microtubule at 0.2 mg/mL concentration of insulin. (c) Uniformly loaded insulin microtubule at 0.5 mg/mL concentration of insulin.

prepared, and the pH was adjusted by adding either HCl or NaOH as required; Brillant Blue G-250, 95% ethanol, and phosphoric acid were purchased from Fisher Scientific. All chemicals were used as received.

Methods. *Growth and Self Assembly of Microtubules.* The bolaamphiphile was synthesized and self-assembled according to previously established methods (*28, 29, 42*). Briefly, the bis(*N*-α-amido-tyr-tyr-tyrosine)-1,5-pentane dicarboxylate (8 mM) was self-assembled into microtubules at pH 5 over a period of two weeks. The assembled tubules were then sonicated, washed, and centrifuged twice at 4000 rpm for 3 h before incorporation of insulin.

Preparation of Insulin-Loaded Microtubules. Various concentrations of insulin in the range of 0.1 mg/mL to 2 mg/mL were incubated with the microtubules for a period of 72 h at 4 °C while mildly agitating the samples. The samples were then centrifuged and washed twice with nanopure water to remove any un-entrapped insulin. In order to determine the optimum pH for entrapment of insulin, the experiments were carried out in the pH range 4−10.

Measurement of Entrapment Efficiency. The amount of insulin loaded into the peptide microtubules was determined by measuring the difference between the total amount of insulin added into the peptide microtubules and the amount of unloaded insulin present in the supernatant after the loading process. In general, a concentration of 0.5 mg/mL of insulin was used in order to carry out the entrapment efficiency studies. The studies were carried out in varying pH, to determine the effect of pH on the loading capacity. The loaded microtubules (500 μL) were centrifuged at 4500 rpm at 4 °C for 5 h, and then the amount of free insulin in the clear supernatant was measured by the Bradford method (*43*). The entrapment efficiency was calculated using the following equation: $(X_1 - X_2/X_1) \times 100\%$, where X_1 is the concentration of the amount of insulin and X_2 is the concentration of the unloaded insulin. Therefore, entrapment efficiency of insulin in microtubules

$$= \frac{\text{total amount of insulin used} - \text{free insulin in supernatant}}{\text{total amount of insulin used}} \times 100 \quad (1)$$

Drug Release Studies of Insulin. The insulin-loaded microtubules (formed at pH 6) were washed and centrifuged thoroughly before conducting the release studies. In order to determine the pH effect on the release studies of insulin from the microtubules, we investigated the release of insulin at varying pH. Insulin-loaded microtubules (500 μL) were added to 1.5 mL of respective buffer solutions (pH 4−10) and the amount of insulin released was measured via the Bradford method. Measurements were carried out for a period of 5 h at 37 °C. All measurements were carried out in triplicate.

Characterization. *Circular Dichorism (CD) Spectroscopy.* CD measurements were carried out using a JASCO J-720 spectropolarimeter. Samples were scanned at least five times at the rate of 200 nm/min with a 0.5 nm step, 1 nm bandwidth, and then averaged. The path length of the quartz cell was 2 mm. In the experiments, a blank run made with buffer alone was subtracted from the experimental spectra for correction. The 190−250 nm spectra were used for analysis. All the spectra were smoothed and converted to the mean residue ellipticity $[\theta]$ in deg*cm^2/dmol.

FTIR Spectroscopy. In order to confirm the incorporation of insulin onto the microtubules, FTIR analyses were performed using Matteson Infinity IR equipped with DIGILAB, ExcaliBuv HE Series FTS 3100 software. The samples were dried at room temperature and mixed with KBr to make pellets and then analyzed. All spectra were taken at 4 cm^{-1} resolution with 50 scans taken for averaging. Sample measurements were carried between 400 and 4000 cm^{-1}.

Absorbance Spectroscopy. To determine the protein concentration using the Bradford method, absorbance measurements were carried out at λ_{max} of 595 nm using a Varian Cary 3 UV−visible spectrophotometer. Samples were diluted with appropriate amounts of buffer or nanopure water.

Zeta Potential Analysis. A NICOMP 380 ZLS zeta potential/particle sizer system (Santa Barbara, CA) was used to determine the zeta potential of the samples. Measurements of ζ-potential of the samples were carried out at 25 °C and at varying pH. The concentrations of the suspensions were adjusted within the operational limits of the instrument, and the suspension pH was adjusted by the addition of standard buffer solutions. The reported ζ-potential values are the average of at least five measurements (spread of values ± 5% of the reported mean values).

Atomic Force Microscopy. Atomic force microscopy was carried out using a Quesant Universal SPM Instrument by the tapping mode in air using a silicon nitride cantilever.

Transmission Electron Microscopy (TEM). The morphologies of the samples were analyzed by TEM (JEOL 120 EX) operated at 100 kV. Samples were washed twice and air-dried on carbon-coated copper grids before analysis.

RESULTS AND DISCUSSION

The microtubules were self-assembled in aqueous solution at pH 5. Both hydrogen bonding interactions between the amide and carboxyl groups as well as the hydrophobic interactions allowed for the facile self-assembly of the bolaamphiphile. The microtubules formed via self-assembly at room temperature within a period of two weeks. Details of the self-assembly of the microtubules are described elsewhere (*29*). A TEM image of a self-assembled microtubule before entrapment of insulin

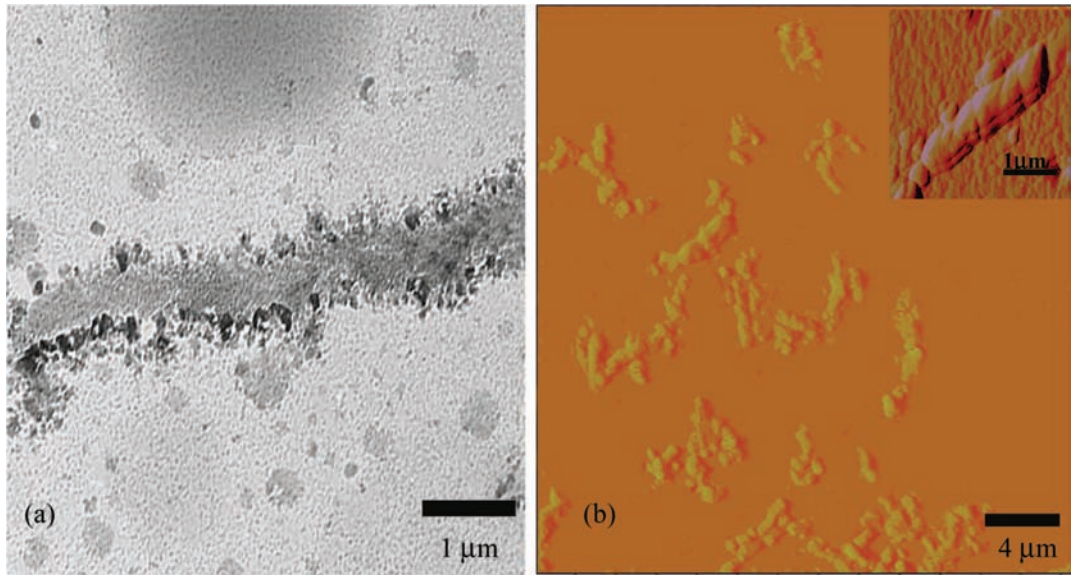

Figure 2. (a) TEM image of insulin-coated microtubules on the outside wall, at 1 mg/mL concentration of insulin. (b) AFM amplitude image of insulin-coated microtubules. Inset shows a single coated microtubule in the presence of a high concentration of insulin (1 mg/mL).

is shown in Figure 1a. The morphologies of the tubules after incorporation of insulin were examined by transmission electron microscopy and atomic force microscopy. On an average, we used tubules with an inner diameter of 500 nm to entrap the insulin. In order to determine optimum conditions for incorporation of insulin, it was incubated with the microtubules at varying pH for different periods of time. The concentration of insulin was also varied. By and large, we observed that, after 72 h, insulin was entrapped within the microtubules. The results obtained indicate that the incorporation of insulin was found to be not only pH-dependent but also concentration-dependent. At concentrations between 0.5 mg/mL and 0.6 mg/mL, at a pH range between 4 and 7, after incubation for 72 h, insulin was entrapped inside the microtubules. Figure 1a shows the TEM image of a microtubule before incubation with insulin. Figure 1b shows the TEM image of a microtubule after incubation for 72 h at pH 6 when the sample was incubated with 0.2 mg/mL insulin, while Figure 1c shows the TEM image of a microtubule where in the insulin is uniformly encapsulated after 72 h at pH 6 in the presence of 0.5 mg/mL insulin. As shown in figures 1b and 1c, the insulin appeared as darker areas in the microtubules (*44*). We also observed that, at higher pH, insulin tended to form aggregates and was not incorporated uniformly within the microtubules even at low concentrations (data not shown). At higher concentrations (between 0.8 mg/mL and 2 mg/mL), the insulin bound to the outside surface of the microtubules as well (Figure 2). The TEM image of insulin−microtubule (Figure 2a) shows the incorporation of insulin within the microtubules as well as formation of aggregates on the outside walls of the tubules. Those studies were also carried out after 72 h. The concentration of insulin used therein was 1 mg/mL. Figure 2b shows the AFM image of insulin-coated microtubules at pH 6, when the samples were incubated with 1 mg/mL of insulin. The inset shows a single microtubule, whose outside walls are coated with insulin. Thus, at lower concentrations, it appears that the inside loading mechanism of insulin may be similar to incorporation of nanoparticles via capillary effect as observed in previous work where the trends were similar (*45*, *46*), while at higher concentrations, they tend to adsorb onto the outside walls of the microtubules as well. Although the exact mechanism of entrapment of insulin is not clear yet, it is likely that, as the microtubules are exposed to the insulin solution, it diffuses inside due to a concentration gradient as well as due to capillary action. Hydrophobic interactions between the tyrosines of the

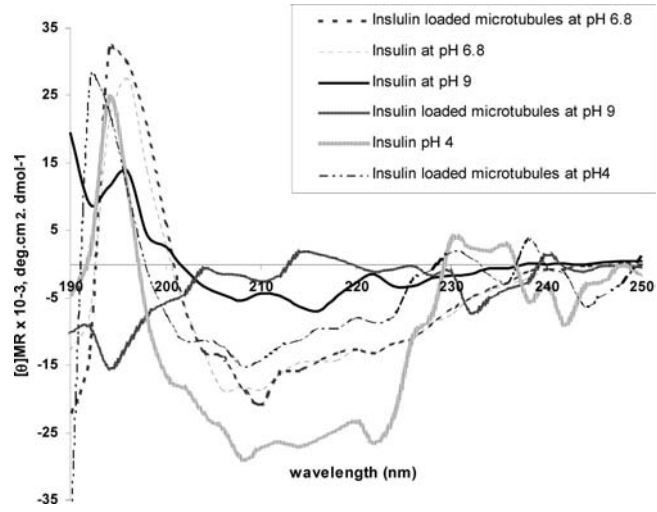

Figure 3. Comparison of CD spectra of insulin and insulin-loaded microtubules at varying pH.

bolaamphiphiles and the hydrophobic residues of insulin may also be involved. In addition, electrostatic interactions and hydrogen bonding also play a critical role.

Circular Dichroism. The conformational changes of insulin upon association with microtubules was evaluated using CD spectroscopy. Figure 3 indicates the CD spectra obtained in the presence and absence of microtubules under different pH conditions. At pH 4, the CD spectrum of insulin shows negative ellipticity at 208 and 222 nm as well as a positive band with a maximum at 192 nm. These peaks are indicative of typical α-helical structure (*47*). After incubation with the microtubules, however, there is a decrease in the negative ellipticity at 222 nm as well as 208 nm. This decrease in intensity upon binding is indicative that there is a reduction in the α-helical content; further, this indicates that interaction of insulin with microtubules at pH 4 may result in partial unfolding of the protein structure. Increasing the pH to 6.8 showed a reduction in the α-helical content of insulin by itself compared to that observed at pH 4; however, when bound to the microtubules, we did not observe significant changes in the secondary structure, except that there is a shift in the negative ellipticity band from 208 to 206 nm and a reduction in the intensity of the positive maxium

Table 1. Zeta Potential Analysis Comparison of Insulin Loaded Microtubules

pH	Zeta Potential of Microtubules (mV)	Zeta Potential of Insulin-Loaded Microtubules (mV)
pH 4	5.96	6.22
pH 5	5.51	6.72
pH 6	1.24	2.19
pH 7	0.18	2.17
pH 9	−1.81	−1.69

observed at 194 nm. At pH 9, however, upon incorporation of the microtubules, the protein seems to undergo unfolding, forming a random coil like structure, with a negative ellipticity band at 194 nm, and its structure is significantly different from that observed for insulin by itself in solution at pH 9. Also, at pH 9, the α helix content of insulin appears to be significantly less than that observed at lower pH and the CD spectrum becomes one that is more typical of that observed for β-sheet structures, characterized by a minimum in the ellipticity at 216 nm and a maxima at 196 nm. This trend is similar to previous observations of insulin CD studies (*48*). These studies indicate that the optimum pH for entrapping insulin within the microtubules would be around pH 6−7, as the conformation change was relatively minimal under those conditions.

Zeta Potential Analysis. The pH dependence on the ζ-potential of the tubules before and after entrapment of insulin is shown in Table 1. We observed that the ζ-potential of insulin-entrapped tubules was slightly higher compared to those of the tubules by themselves. Although changes in the ζ-potential are evident, no drastic changes were observed, which indicate that insulin was encapsulated within the tubules and not adsorbed on the outside as well. This effect is similar to those observed in the case of polymeric nanocapsules, wherein ζ-potential changes were negligible upon encapsulation (*49*). We observed that under basic conditions the ζ-potential of the insulin−tubules remained negative. Since the isoelectric point of insulin is 5.5, above its pI, insulin becomes negatively charged, resulting in favorable electrostatic interactions between microtubule and insulin and increased loading up to pH 7. At basic pH, the negatively charged insulin would have less attraction toward the negatively charged microtubules, resulting in significantly less incorporation of insulin due to the presence of deprotonated residues of insulin as well as the COO^- groups of the microtubules.

Infrared Spectroscopy. In order to confirm the incorporation of insulin, the samples were also analyzed by FTIR spectroscopy. Figure 4 shows the comparison of IR spectra of insulin and insulin-loaded tubules obtained at pH 6, when 0.5 mg/mL concentration of insulin was used. In the insulin-loaded tubules, peaks at 1293 cm^{-1} and 1269 cm^{-1} due to the C−O stretching vibrations are slightly blue-shifted compared to those observed for insulin at 1286 cm^{-1} and 1261 cm^{-1} due to C−O−H hydrogen bonding interactions (*50, 51*) between the microtubules and insulin. Peaks at 1487 cm^{-1} due to C═C aromatic stretching vibration seen in insulin are shifted to 1485 cm^{-1} in the insulin-loaded tubules. This peak is further shifted from the weak C═C aromatic stretching peak observed for the microtubules by themselves at 1492 cm^{-1} due to the presence of the tyrosine moieties in the microtubules. Peaks at 1592 cm^{-1} and 1569 cm^{-1} due to the amide N−H (1°-amide) II band and N−H (2°-amide) II band observed in the case of insulin-loaded microtubules are also blue-shifted to a small extent compared to those of insulin at 1590 cm^{-1} and 1567 cm^{-1}, respectively. Characteristic asymmetric stretching due to COO^- occurring in the region 1410−1460 cm^{-1} and a small peak at 1562 cm^{-1} are seen due to the amide II N−H bend of the microtubules. In the case of insulin alone (Figure 4a), an intense peak is observed at 1659 cm^{-1}, which is attributed to the amide I stretching

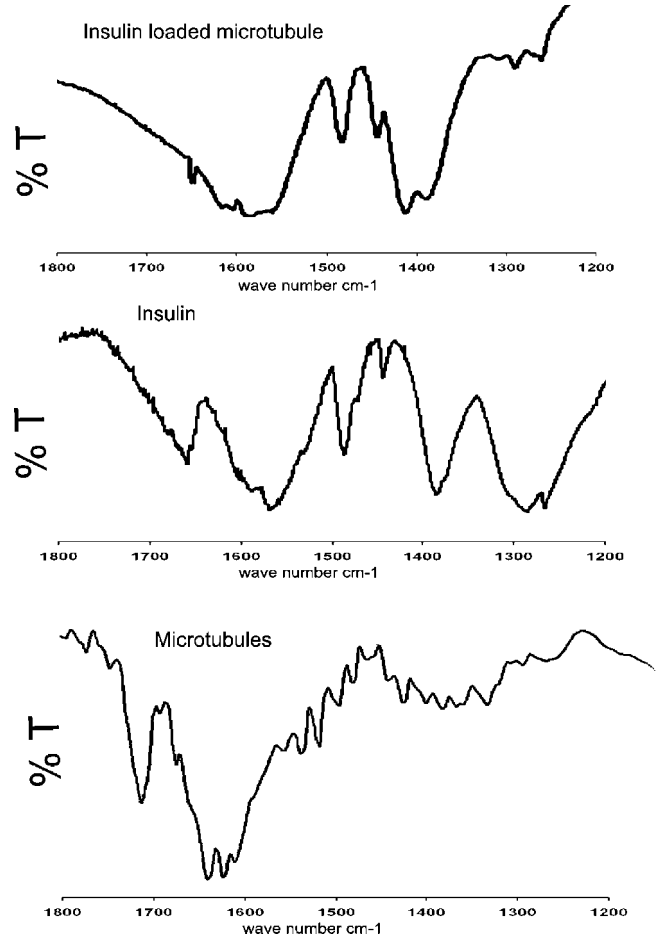

Figure 4. Comparison of FTIR spectra of insulin-loaded microtubules, insulin, and microtubules.

vibration and typical for α-helix conformation (*52*). This peak is also seen in the case of insulin-loaded tubules at 1652 cm^{-1}, though less intense due to interactions with the tubules indicating that the conformation of insulin is relatively similar in the microtubules. Overall, the broad peak centered around 1620 cm^{-1} for the insulin-loaded microtubules is mostly due to the combined contributions of both insulin and the microtubules, particularly the amide I C═O stretches (free and H-bound) at 1654 $cm^{-1}$and 1639 cm^{-1}, as well as the carboxylate peak at 1721 cm^{-1} of the microtubules. No distinct peak at 1721 cm^{-1} is observed for the insulin-loaded microtubules, indicating the involvement of COOH−HOOC interactions with insulin. It is to be noted that similar shifts were observed in the case of pH 4 samples as well (data not shown). These results further confirm that the insulin was loaded in the microtubules.

Entrapment Efficiency and *in Vitro* Release Behavior of Insulin Microtubules. The drug carrying capacity or entrapment efficiency of delivery systems is vital when determining the efficacy of a particular system. The entrapment efficiency of insulin within the microtubules was examined at various pH. The concentration of insulin was kept constant at 0.5 mg/mL, and the amounts of insulin encapsulated at various pH were calculated. As expected, the entrapment efficiency was found to be pH-dependent. This effect is shown in Figure 5. It was observed that the entrapment efficiency was highest in the pH 6−7 range At pH 6.8, the entrapment efficiency was found to be 80.5%, which was calculated to be 0.382 mg/mL. Subsequently, the entrapment efficiency became less at basic pH. It is most likely that there is charge repulsion between the deprotonated carboxylate groups of the microtubules and deprotonated amino acids of insulin at basic pH, leading to lesser

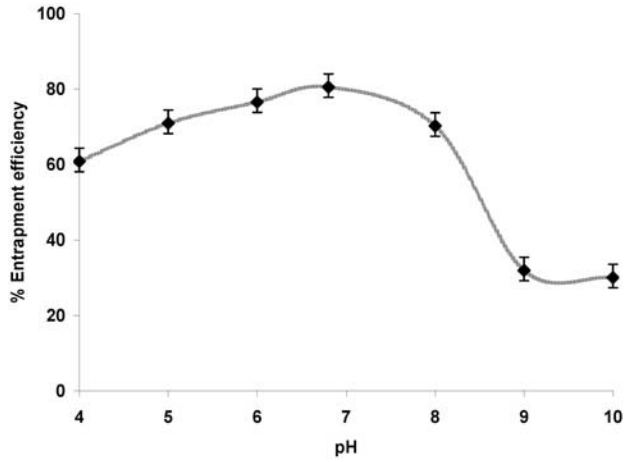

Figure 5. Effect of pH on the entrapment efficiency of insulin in the microtubules.

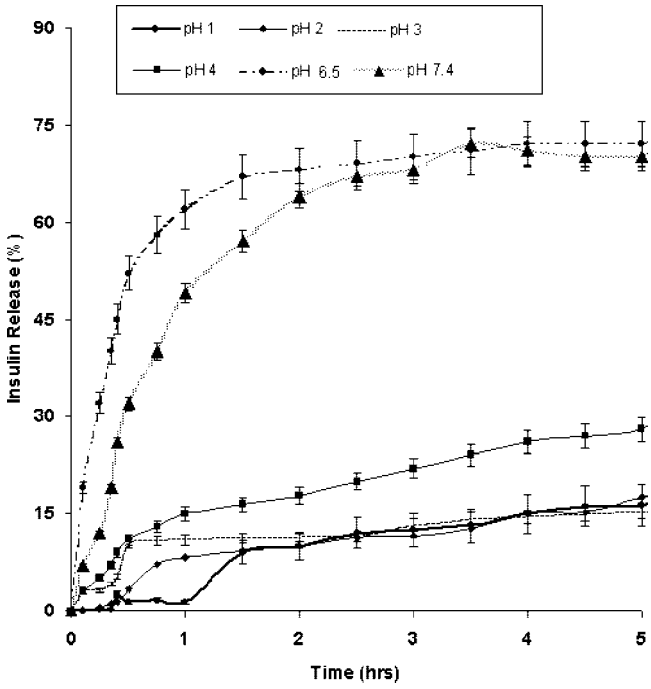

Figure 6. Effect of pH on the *in vitro* release of insulin from microtubules.

entrapment efficiency. Further, at higher pH, insulin tends to aggregate, making it more difficult for incorporation into the microtubules. A key benefit of this process is that insulin loading can be accomplished without the use of organic solvents or the addition of external additives.

The release of insulin was studied over a period of 5 h at 37 °C at varying pH. The *in vitro* release profiles of insulin from the microtubules at different pH are shown in Figure 6. In general, some of the drawbacks of peptide drugs include degradation in the stomach and inactivation by proteolytic enzymes in the luminal cavity. In order to mimic the conditions in the stomach, we studied the insulin release patterns at low pH (pH 1−3). We observed that, at low pH, the release was significantly slower, whereas a sustained release pattern was obtained at a pH of 6.5 (closer to the conditions in the duodenum). At pH 7.4 (closer to conditions at ileum), we observed a similar trend as that observed at pH 6.5, although the initial release was relatively faster. Overall, the release pattern of insulin was found to be pH-dependent and was characterized by an initial rapid release during the first hour (for pH 6.5 and 7.4) followed by a relatively sustained release. It appears that insulin release takes place via disassociation of insulin from the microtubules. At low pH, the dissociation of insulin is relatively less as the microtubules are highly protonated, and the strong hydrogen bonding interactions may allow for less insulin to be released. As the pH is increased, the release of insulin increases. Although *in vivo* conditions may vary, the microtubules appear to have higher insulin retention capacity at low pH, and thus, it is likely that under acidic conditions (for example, in gastric environment) the insulin may be protected inside the microtubules and may be more likely to release at intestinal pH (pH 6−7) where the absorption and action of the drug are necessary. Such materials may be applicable for insulin drug delivery systems. In order to further improve the conformational stability of the insulin within the microtubules while optimizing their delivery, future work will involve spray freeze−drying the insulin-loaded microtubules. The rapid freezing of the insulin-loaded microtubules may prevent phase separation of the drug, thwart crystalline growth in frozen water, and result in a more stable insulin delivery system. Further *in vivo* studies are ongoing and will be published separately.

CONCLUSIONS

In this work, we have utilized self-assembled microtubules formed from the peptide bolaamphiphile bis(*N*-α-amidotryosyl-tyrsol-tyrosine)-1,5-pentane dicarboxylate for entrapment of insulin. The interactions of insulin with the self-assembled microtubules were probed by circular dichroism, zeta potential analysis, as well as FTIR spectroscopy. The morphologies of the insulin-loaded tubules were examined by AFM and TEM. We found that insulin loading was both pH as well as concentration-dependent. The circular dichroism analysis indicated that, at pH 6−7, the conformation change upon interaction with microtubules was relatively minimal and hence would be the most appropriate conditions for insulin loading. The entrapment efficiency and release of insulin was found to be pH-dependent. Further, we also carried out controlled drug release studies, which indicated that, under acidic conditions, the insulin release was extremely slow, and it is likely that the insulin is protected inside the microtubules. However, at pH 6.5−7.4, a sustained release pattern was observed.

ACKNOWLEDGMENT

The authors thank Dr. Areti Tsiola at the Queens College Core Facilities Center for Biomolecular imaging for the use of the transmission electron microscope and Ed Nieves at the Albert Einstein School of Medicine for the use of the Circular Dichroism spectropolarimeter. I.B. thanks the Office of Research at Fordham University for the Faculty Research Grant support.

LITERATURE CITED

(1) Lim, S., Wei, J., Li, Q., and You, J. (2005) A glucose biosensor based on electrodeposition of palladium nanoparticles and glucose oxidase onto Nafion-solubilized carbon nanotube electrode. *Biosens. Bioelectron. 20*, 2341–2346.

(2) Balandin, A., Pokatilov, P., and Nika, D. (2007) Phonon engineering in hetero- and nanostructures. *J. Nanoelectron. Optoelectron. 2*, 140–170.

(3) Wang, M., Guo, D., and Li, H. (2005) High activity of novel Pd/TiO_2 nanotube catalysts for methanol electro-oxidation. *J. Solid State Chem. 178*, 1996–2000.

(4) Couvreur, P., Dubernetc, C., and Puisieux, F. (1995) Controlled drug delivery with nanoparticles: current possibilities and future trends. *Eur. J. Pharm. Biopharm. 41*, 2–13.
(5) Emerich, D., and Thanos, C. (2006) The pinpoint promise of nanoparticles-based drug delivery and molecular diagnosis. *Biomol. Eng. 23*, 171–184.
(6) Staples, M., Daniel, K., Cima, M., and Langer, R. (2006) Application of micro- and nano-electromechanical devices to drug delivery. *Pharm. Res. 23*, 847–863.
(7) LaVan, D., McGuire, T., and Langer, R. (2003) Small-scale systems for in vivo drug delivery. *Nat. Biotechnol. 21*, 1184–1191.
(8) Oh, K., Lee, K., Han, S., Cho, S., Kim, D., and Yu, S. (2005) Formation of core/shell nanoparticles with a lipid core and their application as a drug delivery system. *Biomacromolecules 6*, 1062–1067.
(9) Yih, T. C., and Al-Fandi, M. (2006) Engineered nanoparticles as precise drug delivery systems. *J. Cell. Biochem. 97*, 1184–1190.
(10) Raghuvanshi, R., Mistra, A., Talwar, G., Levy, R., and Labhasetwar, V. (2001) Enhanced immune response with combination of alum and biodegradable nanoparticles containing tetanus toxoid. *J. Microencapsulation 18*, 723–732.
(11) Kreuter, J., Ramage, P., Petrov, V., Hamm, S., Alyautdin, R., Briesen, H., and Begley, D. (2003) Direct evidence that poly-sorbate-80-coated poly (butylcyanoacrylate) nanoparticles deliver drugs to CNS via specific mechanisms requiring prior binding of drug to the nanoparticles. *Pharm. Res. 20*, 409–416.
(12) Malmsten, M. (2006) Soft drug delivery systems. *Soft Matter 2*, 760–769.
(13) Jr. Cudic, M., Chua, B., Deliyannis, G., and Jackson, D. (2004) An insect antibacterial peptide based drug delivery system. *Mol. Pharm. 1*, 220–232.
(14) Teng, X., Shchukin, D., and Mohwald, H. (2008) A novel drug carrier: lipophilic drug loaded polyglutamate/polyelectrolyte nanocontainers. *Langmuir 24*, 383–389.
(15) Malzert-Freon, A., Vrignaud, S., Saulnier, P., Lisowski, V., Benoit, J., and Rault, S. (2006) Formulation of sustained release nanoparticles loaded with a tripentone, a new anticancer agent. *Int. J. Pharm. 320*, 157–164.
(16) Yamaguchi, T. (1996) Lipid microspheres as drug carriers: a pharmaceutical point of view. *Adv. Drug Delivery Rev. 20*, 117–130.
(17) Igarashi, R., Takenaga, M., and Matsuda, T. (1996) Distribution of lipid microsphere preparations. *Adv. Drug Delivery Rev. 20*, 147–154.
(18) Mizushima, Y. (1996) Lipid microspheres (lipid emulsions) as a drug carrier-an overview. *Adv. Drug Delivery Rev. 20*, 113–115.
(19) Mayer, L., Hope, M., and Cullis, P. (1986) Vesicles of variable sizes produced by a rapid extrusion procedure. *Biochim. Biophys. Acta 858*, 161–168.
(20) Fang, J., Leu, Y., Chang, C., Lin, C., and Tsai, Y. (2004) Lipid nano/submicron emulsions as vehicles for topical flurbiprofen delivery. *Drug Delivery 11*, 97–105.
(21) Katre, N., Asherman, J., Schaefer, H., and Hora, M. (1998) Multivesicular liposome (DepoFoam) technology for the sustained delivery of insulin-like growth factor-I (IGF-I). *J. Pharm. Sci. 87*, 1341–1346.
(22) Oh, K., Han, S., Lee, H., Koo, H., Kim, R., Lee, K., Han, S., Cho, S., and Yuk, S. (2006) Core/shell nanoparticles with Lecithin lipid cores for protein delivery. *Biomacromolecules 7*, 2362–2367.
(23) Goldstein, A., Amory, J., Martin, S., Vernon, C., Matsumoto, A., and Yager, P. (2001) Testosterone delivery using glutamide-based complex high axial ratio microstructures. *Bioorg. Med. Chem. 9*, 2819–2825.
(24) Venkatesan, N., Yoshimitsu, J., Ito, Y., Shibata, N., and Takada, K. (2005) Liquid filled nanoparticles as a drug delivery tool for protein therapeutics. *Biomaterials 26*, 7154–7163.
(25) Baughman, R., Zakhido, A., and deHeer, W. (2002) Carbon nanotubes - the route toward applications. *Science 297*, 787–792.
(26) Iijima, S., and Ichihashi, T. (1993) Single-shell carbon nanotubes of 1 nm diameter. *Nature 363*, 603–605.
(27) Kam, N., Jessop, T., Wender, P., and Dai, H. (2004) Nanotube molecular transporters: internalization of carbon nanotubes-protein conjugates to mammalian cells. *J. Am. Chem. Soc. 126*, 6850–6851.
(28) Menzenski, M. Z., and Banerjee, I. A. (2007) Self-assembly of supramolecular nanostructures from phenyalanine derived bolaamphiphiles. *New J. Chem. 31*, 1674–1680.
(29) Spear, R. L., Tamayev, R., Fath, K. R., and Banerjee, I. A. (2007) Templated growth of calcium phosphate on tyrosine derived microtubules and their biocompatibility. *Colloids Surf., B 60*, 158–166.
(30) Yu, L., Banerjee, I. A., Gao, X., Nuraje, N., and Matsui, H. (2005) Fabrication and application of enzyme-incorporated peptide nanotubes. *Bioconjugate Chem. 16*, 1484–1487.
(31) Reaven, G. (1997) Role of insulin resistance in human disease. *Nutrition 13* (1), 64.
(32) Brange, J., and Havelund, S. (1983) Insulin pumps and insulin quality: Requirements and problems. *Acta Med. Scand. Suppl. 671*, 135–138.
(33) Brange, J., and Langkjær, L. (1993) Insulin structure and stability, In *Stability and Characterization of Protein and Peptide Drugs: Case Histories* (Wang, Y. J., and Pearlman, R., Eds.) pp 315−350, Plenum Press, New York.
(34) Wu, C.-S., and Yang, J. T. (1981) Conformation of insulin and its fragments in surfactant solutions. *Biochim. Biophys. Acta 667*, 285–293.
(35) Wang, Y., and Hanson, M. (1988) Parenteral formulations of proteins and peptides: stability and stabilizers. *J. Parenteral Sci. Technol. 42*, S3–S25.
(36) Jain, D., and Majumdar, D. K. (2006) Insulin loaded eudragit L100 microspheres for oral delivery: preliminary in vitro studies. *J. Biomater. Appl. 21*, 195–211.
(37) Nolan, C., Gelbaum, L., and Lyon, L. (2006) H NMR investigation of thermally triggered insulin release from poly(N-isopropylacrylamide) microgels. *Biomacromolecules 7*, 2918–2922.
(38) Ito, Y., Chung, D., and Imanishi, Y. (1994) Design and synthesis of a protein device that releases insulin in response to glucose concentration. *Bioconjugate Chem. 5*, 84–87.
(39) Sarmento, B., Ribeiro, A., Veiga, F., Ferreira, D., and Neufeld, R. (2007) Oral bioavailabilty of insulin contained in polysaccharide nanoparticles. *Biomacromolecules 8*, 3054–3060.
(40) Simon, M., Wittmar, M., Bakowsky, U., and Kissel, T. (2004) Self-assembling nanocomplexes from insulin and water-soluable branched polyesters, poly[(vinyl-3-(diethylamino)-propylcarbamate-*co*-(vinyl acetate)-*co*-vinyl alcohol)]-*graft*-poly(L-lactic acid): a novel carrier for transmucosal delivery of peptides. *Bioconjuate Chem. 15*, 841–849.
(41) Bringer, J., Heldt, A., and Grodsky, G. M. (1981) Prevention of insulin aggregation by dicarboxylic amino acids during prolonged infusion. *Diabetes 30*, 83–85.
(42) Kogiso, M., Ohnishi, S., Yase, K., Masuda, M., and Shimizu, T. (1998) Dicarboxylic oligopeptide bolaamphiphiles: proton-triggered self-assembly of microtubes with loose solid surfaces. *Langmuir 14*, 4978–4986.
(43) Ninfa, J., and Ballou, D. (2008) Quantification of Protein Concentration, *Fundamental Laboratory Approaches for Biochemistry and Biotechnology*, pp 83−88, Chapter 3, Wiley, New York.
(44) Caruso, F., Trau, D., Mohwald, H., and Renneberg, R. (2000) Enzyme encapsulation in layer-by-layer engineered polymer multilayer capsules. *Langmuir 16*, 1485–1488.
(45) Djalali, R., Chen, Y., and Matsui, H. (2003) Au nano-crystal growth on nanotubes controlled by conformations and charges of sequenced peptide templates. *J. Am. Chem. Soc. 125*, 5873–5879.

(46) Yu, L., Banerjee, I. A., Shima, M., Rajan, K., and Matsui, H. (2004) Size-controlled Ni nanocrystal growth on peptide nanotubes and their magnetic properties. *Adv. Mater. 16*, 709–712.

(47) Pittman, I., and Tager, H. S. (1995) A spectroscopic investigation of the conformational dynamics of insulin in solution. *Biochemistry. 34*, 10578–10590.

(48) Tiyaboonchai, W., Woiszwillo, J., Sims, R. C., and Middaugh, R. C. (2003) Insulin containing polyethylenimine-dextran sulfate nanoparticles. *Int. J. Pharm. 255*, 139–151.

(49) Aboubakar, M., Puisieux, F., Couvreur, P., and Vauthier, C. (1999) Physico-chemical characterization of insulin-loaded poly-(isobutylcyanoacrylate) nanocapsules obtained by interfacial polymerization. *Int. J. Pharm. 183*, 63–66.

(50) Xu, X., Li, H., Wang, C., Wu, T., and Han, S. (2004) Is the blue shift of C-H vibration in DMF-water mixture mainly caused by C-H--O interaction. *Chem. Phys. Lett. 394*, 405–409.

(51) Dzwolak, W., Loksztejn, A., and Smirnovas, V. (2006) New insights into the self-assembly of insulin amyloid fibrils: An H-D exchange FT-IR study. *Biochemistry 45*, 8143–8151.

(52) Dorkoosh, F., Verhoef, J., Amgats, M., Rafiee-Tehrani, M., Borchard, G., and Junginger, H. E. (2002) Peroral delivery systems based on superporous hydrogel polymers: release characteristics for the peptide drugs buserelin, octreotide and insulin. *Eur. J. Pharm. Sci. 15*, 433–439.

BC800254N

Signal Transduction of Hyaluronic Acid−Peptide Conjugate for Formyl Peptide Receptor Like 1 Receptor

Eun Ju Oh,[†] Jung-Wook Kim,[‡] Ji-Hyun Kong,[†] Sung Ho Ryu,[‡] and Sei Kwang Hahn*[,†]

Department of Materials Science and Engineering and Department of Life Science, Pohang University of Science and Technology (POSTECH), Pohang, Kyungbuk 790-784, Korea. Received June 25, 2008; Revised Manuscript Received October 13, 2008

Agonistic and antagonistic peptides for formyl peptide receptor like 1 (FPRL1) receptor have been investigated as novel drug candidates for inflammatory diseases such as sepsis, asthma, and rheumatoid arthritis. In this work, a novel protocol for the synthesis of hyaluronic acid (HA)−peptide (CWRYMVm) conjugate for FPRL1 receptor was successfully developed for further clinical applications of peptide drugs. Aminoethyl methacrylated HA (HA-AEMA) was synthesized by the coupling reaction of tetrabutyl ammonium salt of HA (HA-TBA) and AEMA using benzotriazol-1-yloxy-tris(dimethylamino) phosphonium hexafluorophosphate (BOP) in dimethyl sulfoxide (DMSO). Then, HA-AEMA was conjugated with CWRYMVm in water via Michael addition reaction between methacrylate group of HA-AEMA and thiol group in cysteine. The formation of HA−peptide conjugate was confirmed by ^{1}H NMR and gel permeation chromatography (GPC). The average number of conjugated peptide molecules could be controlled from 5 to 23 per single HA chain. The HA−peptide conjugate showed serum stability longer than four days. *In vitro* signal transduction activity of the HA−peptide conjugate for FPRL1 receptor was confirmed from the elevated levels of phospho-extracellular signal-regulated kinase (pERK) and calcium ion in FPRL1 overexpressing RBL-2H3 cells. The partially decreased biological activity of HA−peptide conjugates by the steric hindrance of HA was recovered after its degradation by hyaluronidase treatment.

INTRODUCTION

The formyl peptide receptor like 1 (FPRL1) receptor is one of the chemoattractant receptors encompassing G protein-coupled seven transmembrane domains. It is mostly expressed in phagocytic leukocytes and stimulates innate immunity, such as chemotactic migration, pro-inflammatory cytokine secretion, and degranulation (*1*). When inflammation and infection occur, chemotactic factors bind to specific heterotrimeric G protein-coupled receptors (GPCRs) such as FPRL1 receptor on the leukocyte surface (*2*). Activation of these receptors leads to directed migration, granule mobilization, and activation of the nicotinamide adenine dinucleotide phosphate (NADPH) oxidase (*3*). The reactive oxygen species generated by the oxidase are important for microbial killing and for intercellular signaling in astrocytoma cell lines, neutrophils, monocytes, T cells, and HUVECs (*1*, *3*). Several agonistic and antagonistic peptide sequences for the FPRL1 receptor have been investigated as drug candidates for inflammatory diseases such as sepsis, asthma, and rheumatoid arthritis (*4*−*6*). Trp-Lys-Tyr-Met-Val-DMet (WKYMVm) is one of the widely studied agonist peptides that selectively binds to and activates the FPRL1 receptor in FPRL1 overexpressing RBL-2H3 cells (*4*, *5*). Trp-Arg-Trp-Trp-Trp-Trp (WRWWWW) is an FPRL1 antagonist peptide that down-regulates the activation of FPRL1 by agonistic peptides, resulting in the complete inhibition of the intracellular calcium increase, extracellular signal-regulated kinase activation, superoxide generation, and chemotactic migration of cells toward agonistic peptides (*6*).

Recently, the bioconjugation technology using synthetic and natural polymers like poly(ethylene glycol) [PEG] and hyaluronic acid (HA) has been widely used for the development of various biopharmaceuticals with feasible pharmacokinetic characteristics (*7*). The chemical attachment of PEG to the biopharmaceuticals, such as protein and peptide drugs, has been reported to increase the drug efficacy by reducing renal clearance, decreasing the immunoresponse and alleviating the enzymatic degradation in the body. There are several commercialized PEGylation products, such as Neulasta (pegfilgrastim) by Amgen, Somavert (pegvisomant) by Pfizer, PEGASYS (peginterferon alfa-2a) by Roche, and so on. However, the negative effect of PEGylation has been also reported (*8*, *9*). A repeated injection of PEGylated liposomes has been reported to result in their diminished long-circulating characteristics by a so-called "accelerated blood clearance" (ABC) phenomenon (*8*). In addition, PEGylation of glucagon like peptide - 1 (GLP-1) has been reported to bring about a significant decrease in its cAMP activity (*9*). The branch-type PEGylation with a molecular weight of 43 000 Da caused even greater biological activity loss (*9*). As an alternative to replace the roles of PEG, HA has been investigated as a novel drug carrier for various protein and peptide drugs (*10*−*13*). HA is a natural linear polysaccharide composed of alternating disaccharide units of D-glucuronic acid and *N*-acetyl-D-glucosamine with $\beta(1\rightarrow4)$ interglycosidic linkage (*10*). HA is the only nonsulfated glycosaminoglycan (GAG) which is abundant in synovial fluid and extracellular matrix (ECM) (*10*). The fact that HA molecules from different sources have the same primary structure explains the molecular basis for its natural biocompatibility (*14*). HA plays important roles in the regulation of cell behavior including cell migration and proliferation (*15*−*18*). CD44 (*19*), RHAMM (*15*, *20*), and LYVE-1 (*21*) have been identified as HA receptors. Because of the various biological functions and unique physicochemical properties, HA and modified HA have been widely used for drug delivery (*11*, *12*), arthritis treatment (*22*), ophthalmic surgery (*23*), and tissue engineering (*24*). Especially for drug delivery applications, HA with a high molecular weight over 2 million was used for the

* Corresponding author. S. K. Hahn, Ph.D. Tel.: +82-54-279-2159; Fax: +82-54-279-2399; E-mail address: skhanb@postech.ac.kr.

[†] Department of Materials Science and Engineering.

[‡] Department of Life Science.

10.1021/bc800255y CCC: $40.75 © 2008 American Chemical Society
Published on Web 11/14/2008

sustained-release formulation of human growth hormone (*11*), and selectively cross-linked HA hydrogels were used for the encapsulation of erythropoietin (*12*). HA was also used for the conjugation with active cytotoxic agents, such as paclitaxel (*25*) and doxorubicin (*26*).

In this work, a novel bioconjugation protocol for FPRL1 peptide therapeutics was developed to make them suitable for *in vivo* applications. Bioconjugation of the peptide drug to HA increases its half-life in circulation contributing for a high efficacy. In contrast to PEGylation, HA can be conjugated with various numbers of peptide drug molecules per single HA chain, which enables multiple action of peptide drugs. The peptide drug used in this study was one of the agonistic peptides for FPRL1 receptor with a sequence of WRYMVm. In order to introduce a thiol group to the peptide molecule, cysteine was added to the end of the peptide sequence. Aminoethyl methacrylated HA (HA-AEMA) was newly synthesized in DMSO using the tetra-*n*-butylammonium salt of HA (HA-TBA) and benzotriazol-1-yloxy-tris(dimethylamino)phosphonium hexafluorophosphate (BOP), and *N*,*N*-diisopropylethylamine (DIPEA). CWRYMVm was conjugated to HA-AEMA via the Michael addition reaction between the methacryloyl group of HA-AEMA and the thiol group in cysteine. Michael addition, between electron-poor olefins and nucleophiles such as thiols, has been used for the bioconjugation of various biomolecules (*27*, *28*). The stability of peptide in fetal bovine serum (FBS) was investigated before and after its conjugation to HA. Since the binding of agonistic peptide to FPRL1 receptor induces the elevation of phospho-extracellular signal-regulated kinase (pERK) and calcium ion levels (*1*), the biological activity of HA−peptide conjugates was assessed from the intracellular level of pERK and calcium ion in FPRL1 overexpressing RBL-2H3 cells. RBL-2H3 cells have no FPRL1 showing similar characteristics to the other immune cells with FPRL1. Therefore, FPRL1 overexpressing RBL-2H3 (RBL-2H3/FPRL1) cells are a very good model system to check the FPRL1 downstream signaling such as pERK level.

MATERIALS AND METHODS

Materials. Sodium hyaluronate, the sodium salt of hyaluronic acid (HA), with a molecular weight of 200 000 was obtained from Denkikagaku Kogyo Co. (Tokyo, Japan). Peptide with a sequence of Cys-Trp-Arg-Tyr-Met-Val-DMet (CWRYMVm) was purchased from Peptron (Daejeon, Korea). Dowex 50WX8−40 ion-exchange resin, benzotriazol-1-yloxy-tris(dimethyl-amino)phosphonium hexafluorophosphate (BOP), 2-aminoethyl methacrylate hydrochloride (AEMA), *N*,*N*-diisopropylethylamine (DIPEA), tris(2-carboxyethyl) phosphine hydrochloride (TCEP), trifluoroacetic acid (TFA), and hyaluronidase from *Streptomyces hyalurolyticus* were purchased from Sigma-Aldrich (St. Louis, MO). Tetra-*n*-butylammonium hydroxide (TBA-OH) was obtained from Alfa Aesar (Ward Hill, MA). Dimethyl sulfoxide (DMSO) was obtained from Junsei Chemical Co. (Tokyo, Japan) and acetonitrile from J. T. Baker (Phillipsburg, NJ). Anti-rabbit polyclonal antibody to phospho-ERK was purchased from Cell Signaling Technology (Danvers, MA) and anti-mouse monoclonal antibody to GAPDH from Biogenesis (Poole, UK). Goat anti-rabbit IgG or goat anti-mouse IgG antibody conjugated to horseradish peroxidase was obtained from KPL (Gaithersburg, MD). Double-distilled water was used for the following experiments. All chemicals were used without further purification.

Synthesis of HA-AEMA. Ion exchange resin of Dowex 50WX-8−400 (25 g) was washed with 500 mL of water and filtered to remove the supernatant three times. Then, 1.5 molar excess of TBA-OH (48.9 mL) was added to the Dowex resin and mixed for 30 min. The filtered Dowex-TBA resin was washed with 500 mL of water and filtered again three times. Sodium salt of HA (MW = 200 K, 5 mmol) was dissolved in 200 mL of water, which was poured into the prepared Dowex-TBA (25 mmol) resin. After mixing for 3 h, the supernatant was filtered through 0.45 μm filter and lyophilized for 3 days. The resulting HA-TBA was dissolved in DMSO. Then, BOP, 2-AEMA and *N*,*N*-DIPEA were added to the solution and mixed for a day. Finally, the reaction product was dialyzed against a large excess amount of water and lyophilized for three days. The obtained HA-AEMA was characterized with ^{1}H NMR (NMR, DPX300, Bruker, Germany).

Synthesis of HA−Peptide Conjugates. Agonistic peptide for FPRL1 receptor (CWRYMVm) was dissolved in water. For the reduction of the disulfide bond between peptide molecules, 10-fold molar excess of TCEP as a reducing reagent was added to the peptide solution and mixed for 10 min. HA-AEMA was also dissolved in water. After complete dissolution, the HA-AEMA solution was mixed with the peptide solution. The number of peptide molecules per single HA chain in the feed was 5, 9, 19, 28, and 56, respectively. After the pH of the reaction mixture was adjusted to 8.74 by the addition of 1 N NaOH, the mixed solution was incubated at 37 °C for 16 h. Then, the reaction was stopped by dropping the pH to 7.0 with 1 N HCl. The solution was finally lyophilized for three days. HA−peptide conjugate was purified by fractionation using gel permeation chromatography (GPC). GPC analysis was performed using the following systems: Waters 1525 binary HPLC pump, Waters 2487 dual λ absorbance detector, Waters 717 plus autosampler, Superdex Peptide 10/300 GL column. The eluent was 30 vol % acetonitrile (ACN)/0.1 vol % trifluoroacetic acid (TFA), and the flow rate was 1 mL/min. The detection wavelengths were 210 nm for HA and 280 nm for the peptide, respectively. Three replicates were carried out to assess the average peptide content in HA−peptide conjugate and the bioconjugation efficiency (%).

Quantification of Peptide Content in HA−Peptide Conjugates. A peptide stock solution at a concentration of 1 mg/mL was used to prepare peptide standard solutions with concentrations of 10, 20, 40, 80, 160, and 320 μg/mL, respectively. HA−peptide conjugate solutions were also prepared by dissolving 1 mg of each HA−peptide conjugate sample in 1 mL of water. GPC analysis was carried out as described above. From the peak areas detected at 280 nm, a linear standard curve for peptide was obtained and used for the determination of the amount of peptide in HA−peptide conjugates.

***In Vitro* Serum Stability Test of HA−Peptide Conjugates.** In order to investigate the effect of HA conjugation on the serum stability of peptide, raw peptide and three HA−peptide conjugates were dissolved in 0.5 mL of water and mixed with 0.5 mL of fetal bovine serum (FBS), respectively. In HA−peptide conjugates, the number of peptide molecules per single HA chain was 5, 19, and 33, respectively. Because the peptide was not dissolved in serum completely, 50 vol % serum solution was used for the serum stability test. Then, the solutions were incubated at 37 °C for 96 h. The remaining amount of peptide was measured by GPC analysis after incubation for 12, 24, 48, 72, and 96 h. Three replicates were carried out.

Hyaluronidase Treatment of HA−Peptide Conjugates. In order to investigate the effect of HA conjugation on the signal transduction activity of peptide, three kinds of peptide samples were prepared, the raw peptide, HA−peptide conjugates, and HA−peptide conjugates after hyaluronidase treatment. In the HA−peptide conjugates, the number of peptide molecules per single HA chain was 5, 8, and 23, respectively. Each HA−peptide conjugate sample (0.4 mL, 1 mg/mL) was divided into two aliquots. One aliquot was mixed with 0.2 mL of hyaluronidase solution (400 units/mL), and the other was mixed with 0.2 mL

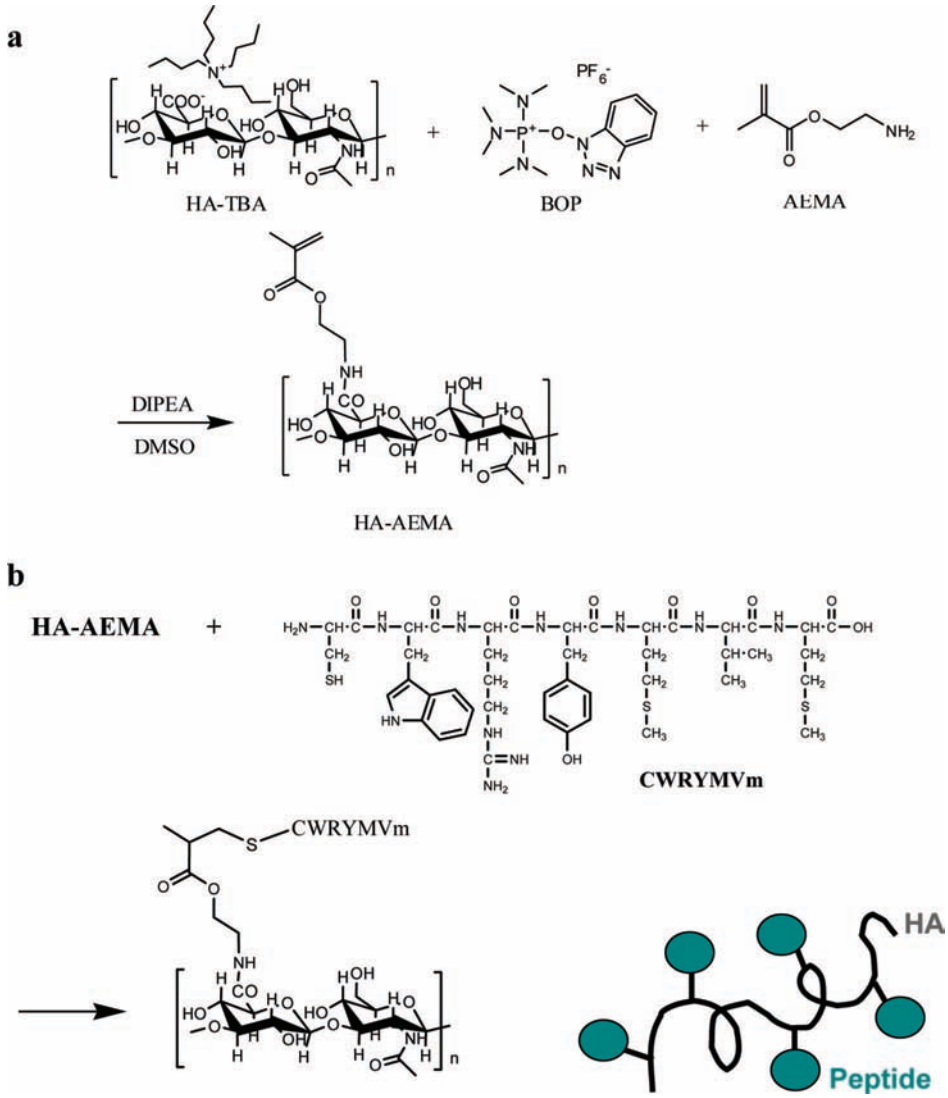

Figure 1. Schematic representations (a) for the synthesis of aminoethyl methacrylated hyaluronic acid (HA-AEMA) using *N*,*N*-diisopropylethylamine (DIPEA) and benzotriazol-1-yloxy-tris(dimethyl-amino)phosphonium hexafluorophosphate (BOP) and (b) for the conjugation of HA-AEMA with the peptide (CWRYMVm) for formyl peptide receptor like 1 (FPRL1) receptor.

of water. Then, the solutions were incubated at 37 °C overnight for the complete enzymatic degradation of HA. Three replicates were carried out for the following bioactivity tests measuring the intracellular level of pERK and calcium ion.

RBL-2H3 and RBL-2H3/FPRL1 Cell Cultures for Western Blot. RBL-2H3 cells and FPRL1 overexpressing RBL-2H3 (RBL-2H3/FPRL1) cells were cultured at 37 °C in a humidified incubator containing 5% CO_2, as described elsewhere (*29*). Dulbecco's modified Eagle's medium (DMEM) was supplemented with 20 vol % heat-inactivated FBS and 200 μg/mL of G418. The cells were subcultured every 3 days.

Stimulation of RBL-2H3/FPRL1 Cells with Peptide Samples. The prepared cells were aliquoted into 1×10^6 cells and stimulated with a control (no treatment), peptide (CWRYMVm), HA-AEMA, the mixture of peptide and HA-AEMA, and three HA−peptide conjugate samples with and without hyaluronidase treatment. For comparison, the peptide content in HA−peptide conjugate samples was adjusted to have the same amount as the peptide sample. The stimulation time varied from 0 to 30 min. After stimulation, the cells were washed with serum-free DMEM and lysed in lysis buffer at pH = 7.4 containing 0.5 M NaCl, 20 mM Tris-Cl, 0.25% Triton X-100, 1 mM EDTA, 1 mM EGTA, 10 mM β-glycerphosphate, 10 mM NaF, 1 mM benzamidine, 10 μg/mL aprotinin, 10 μg/mL leupeptin, 10 μg/mL pepatatin, 1.5 mM Na_3VO_4, 1 mM phenylmethylsulfonyl fluoride (PMSF), and 1 mM DTT. The detergent-insoluble material was pelleted by centrifugation at 12 000 *g* and 4 °C for 15 min, and the soluble supernatant fraction was used immediately or stored at −80 °C before use. Protein concentrations in the lysates were determined by Bradford protein assay. Three replicates were carried out.

Electrophoresis and Immunoblot Analysis for Western Blot. Protein samples were subjected to electrophoresis using 12 wt % SDS−polyacrylamide gel and the buffer system described by King and Laemmli (*30*). After the electrophoresis, the proteins were blotted onto nitrocellulose membrane and blocked by incubating with Tris-buffered saline, 0.05% Tween 20 containing 5% nonfat dried milk. Then, the membranes were incubated for 12 h with anti-rabbit polyclonal antibody to pERK (1/1000 dilution) or anti-mouse monoclonal antibody to GAPDH (1/2000 dilution) and washed with Tris-buffered saline. After incubating the membrane with a 1/5000 diluted goat anti-rabbit IgG or goat anti-mouse IgG antibody conjugated to horseradish peroxidase for 1 h, the antigen−antibody complexes were visualized by using the enhanced chemiluminescence (ECL) detection system. The phosphorylation of pERK was analyzed using the *Image J* 1.38 X program.

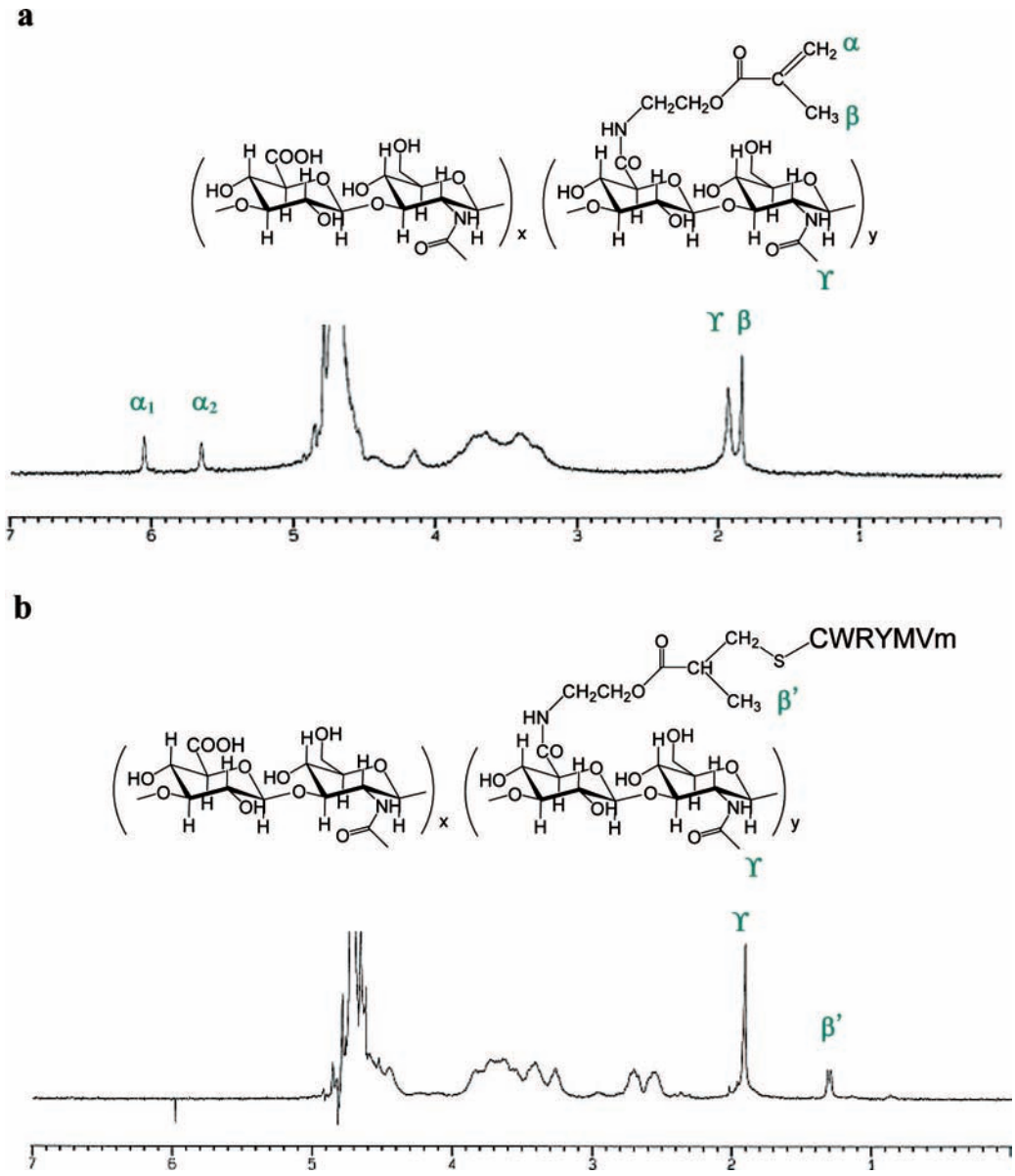

Figure 2. ^{1}H NMR spectra of (a) aminoethyl methacrylated hyaluronic acid (HA-AEMA) and (b) HA−peptide conjugate of HA-$(CWRYMVm)_{23}$ for formyl peptide receptor like 1 (FPRL1) receptor.

Calcium Imaging of the Cells. The intracellular calcium level was determined using fura-2-acetoxymethyl ester (Fura-2/AM) as described by Bae et al. (*31*). Briefly, the prepared cells were incubated in serum-free RPMI 1640 medium with 3 μM of Fura-2/AM at 37 °C for 50 min under continuous stirring. For each measurement, 2×10^6 cells were aliquoted in Ca^{2+}-free Locke's solution (154 mM NaCl, 5.6 mM KCl, 1.2 mM $MgCl_2$, 5 mM HEPES, pH 7.3, 10 mM glucose, and 0.2 mM EGTA). Changes in the fluorescence ratio were measured at the dual excitation wavelengths of 340 and 380 nm and emission wavelength of 500 nm, and the fluorescence images were also obtained.

Statistical Analysis. The data are expressed as means ± SD from several separate experiments. Statistical analyses and comparisons were carried out via *t*-test, and a value for $p < 0.05$ was considered statistically significant.

RESULTS AND DISCUSSION

Synthesis of HA−Peptide Conjugates for FPRL1 Receptor. The chemical modification of HA with AEMA was successfully carried out using the novel protocol as schematically shown in Figure 1a. HA-AEMA was synthesized by the coupling reaction of TBA salt of HA (HA-TBA) with AEMA using BOP in DMSO. DIPEA was used to release the free primary amine of AEMA. The chemical structure of HA-AEMA was analyzed by ^{1}H NMR. The methyl resonance of acetamido moiety of HA at $\delta = 1.85-1.95$ ppm was used as an internal standard (γ in Figure 2). The degree of AEMA modification was ca. 57 mol %, which was determined from the peak areas of methacrylate unit of AEMA at $\delta = 6.1$ and 5.6 ppm (α_1 and α_2 in Figure 2a). By changing the amount of AEMA added for the reaction, we could control the degree of AEMA modification in HA-AEMA up to 85 mol %. The peptide for FPRL1 receptor having a sequence of WRYMVm was modified with cysteine to prepare CWRYMVm with thiol groups. HA-AEMA was conjugated with CWRYMVm via the Michael addition reaction between methacryloyl groups in HA-AEMA and thiol groups in CWRYMVm (Figure 1b). ^{1}H NMR analysis of HA−peptide conjugate, HA-$(CWRYMVm)_{23}$, confirmed the formation of HA−peptide conjugate (Figure 2b). Before conjugation, there were double peaks at $\delta = 6.1$ and 5.6 ppm corresponding to two hydrogens on methacryloyl groups of HA-AEMA (α_1 and

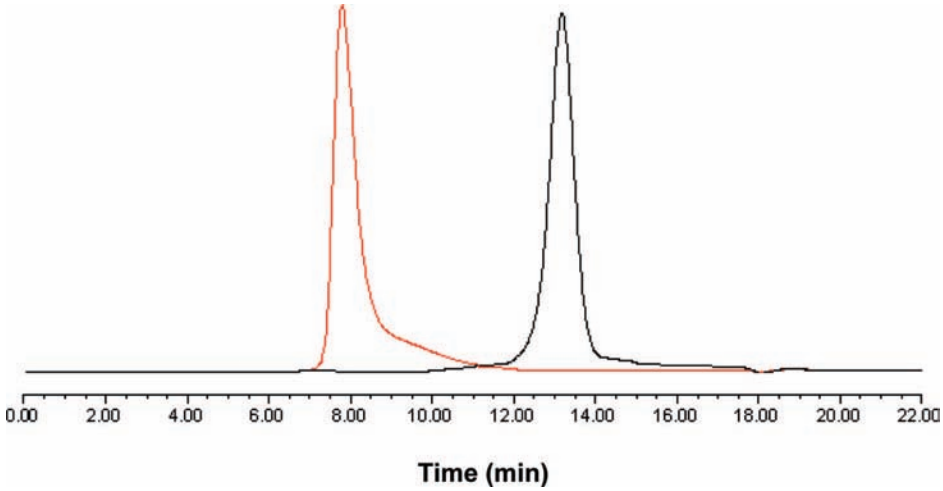

Figure 3. Gel permeation chromatograms (GPC) of the peptide (CWRYMVm) for formyl peptide receptor like 1 (FPRL1) receptor at a right peak and hyaluronic acid (HA)−peptide conjugate at a left peak detected at 280 nm.

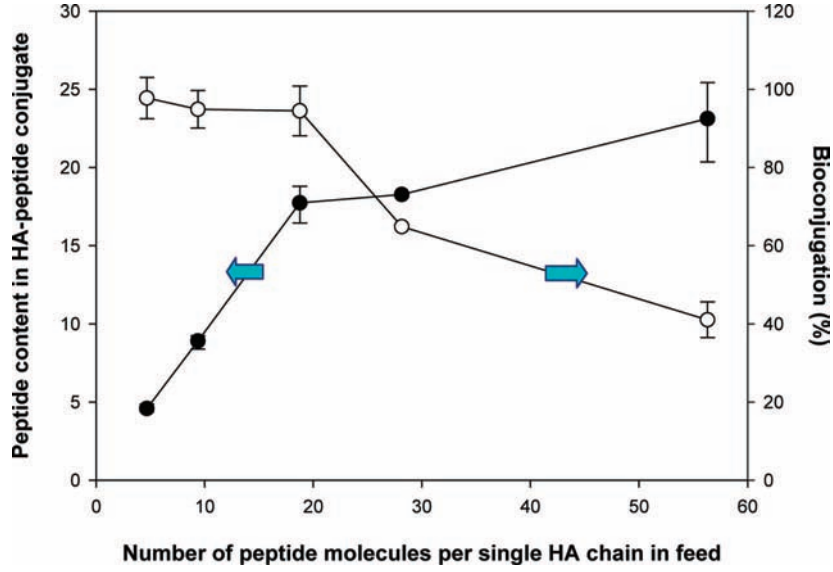

Figure 4. The content of peptide (CWRYMVm) for formyl peptide receptor like 1 (FPRL1) receptor in hyaluronic acid (HA)−peptide conjugates (the number of peptide molecules per single HA chain) (•, ⟸) and the resulting bioconjugation efficiency (%) (○, ⟹). The results are presented as means ± SD of three independent experiments.

α_2). After Michael addition reaction, the peaks at $\delta = 6.1$ and 5.6 ppm disappeared and the peak corresponding to -CH_3 of the methacryloyl group at $\delta = 1.8$ ppm (β) was shifted to the peak at $\delta = 1.3$ ppm (β'). The results from ^{1}H NMR analysis corroborated the successful formation of HA-AEMA and the subsequent HA−peptide conjugate.

Characterization of HA−Peptide Conjugates for FPRL1 Receptor. The formation of HA−peptide conjugate for FPRL1 receptor was also confirmed by GPC analysis as shown in Figure 3. The peak of HA−peptide conjugate appeared at a retention time of 8 min, while that of intact peptide appeared at a retention time of 13 min. The peak shift to the early retention time revealed that the peptide was conjugated to HA with a high molecular weight of 200 000 Da. The number of peptide molecules added per single HA chain in the reaction solution for the synthesis of HA−peptide conjugate was 5, 9, 19, 28, and 56, respectively. The resulting peptide contents in HA−peptide conjugate were quantified by measuring the peak area on GPC detected at 280 nm. Because HA is not detected at a wavelength of 280 nm, the peaks of HA−peptide conjugates at 280 nm resulted solely from the peptide molecules. The peptide content in HA−peptide conjugates at a retention time of 8 min increased with the feeding ratio of peptide molecules

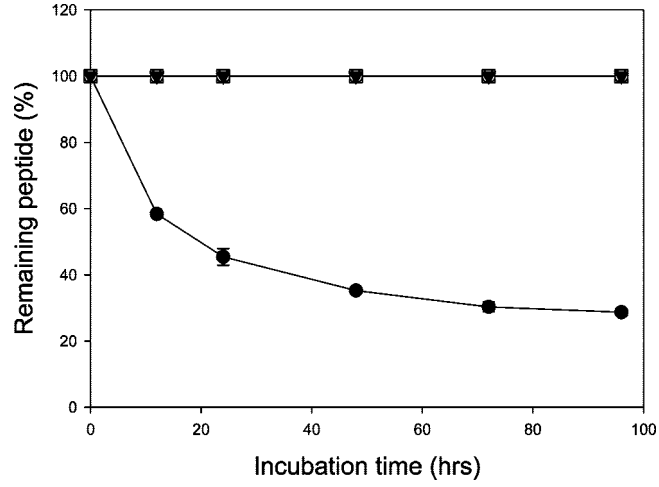

Figure 5. *In vitro* serum stability of peptide (CWRYMVm, ●) and hyaluronic acid (HA)−peptide conjugates in fetal bovine serum (FBS, 50 vol %) solution. The number of peptide molecules per single HA chain was 5 (○), 19 (▼), and 33 (□), respectively. The results are presented as means ± SD of three independent experiments.

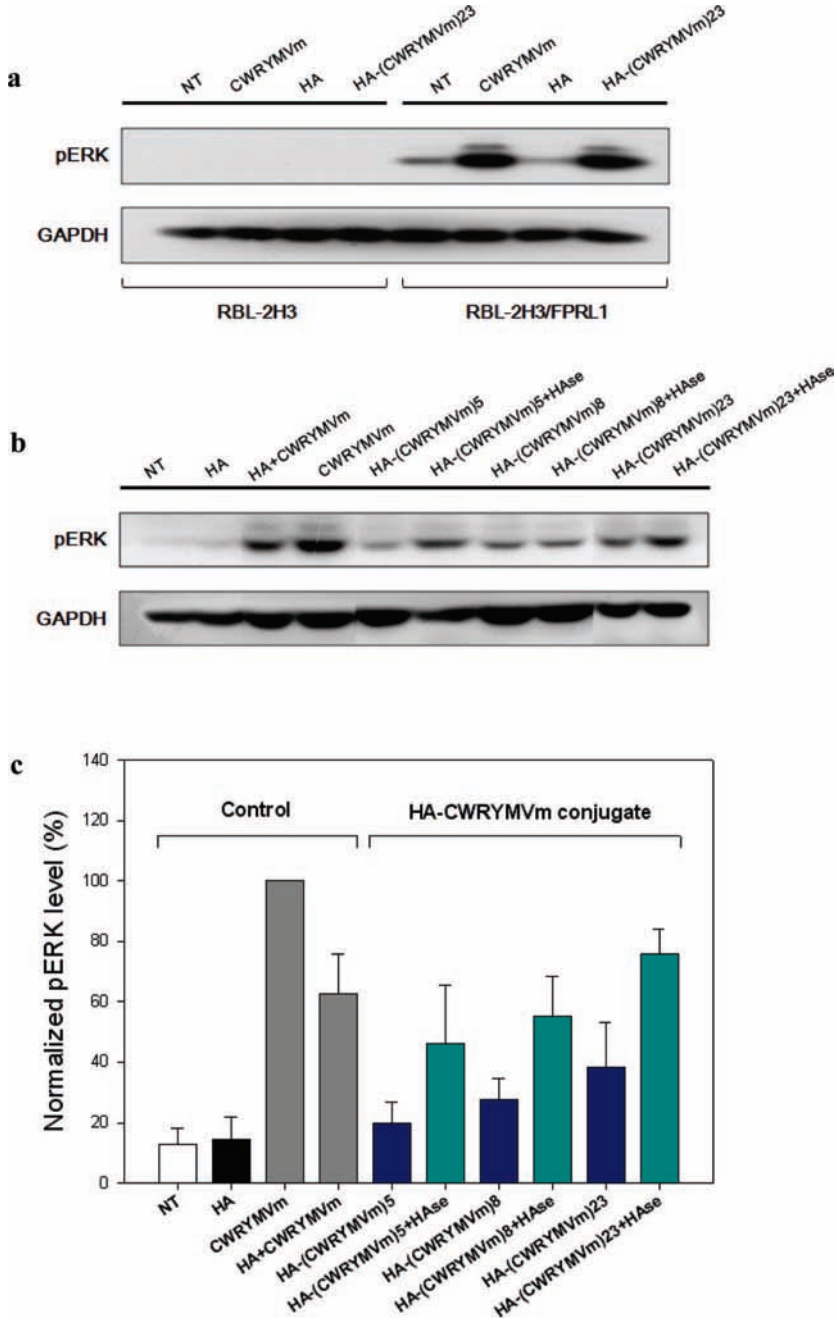

Figure 6. (a) Western blots for phospho-extracellular signal-regulated kinase (pERK) levels in the RBL-2H3 cells and formyl peptide receptor like 1 (FPRL1) overexpressing RBL-2H3 cells after stimulation for 5 min with a control (no treatment), peptide (CWRYMVm), aminoethyl methacrylated hyaluronic acid (HA-AEMA), and HA−peptide conjugate of HA-$(CWRYMVm)_{23}$ having 23 peptide molecules per single HA chain. (b) Western blots for pERK levels in the FPRL1 overexpressing RBL-2H3 cells after stimulation for 5 min with a control (no treatment), HA-AEMA, peptide (CWRYMVm), a mixture of HA-AEMA and peptide (HA + CWRYMVm), and three HA−peptide conjugate samples (HA-CWRYMVm) with and without hyaluronidase (HAse) treatment. The numbers 5, 8, and 23 represent the number of peptide molecules per single HA chain in HA−peptide conjugates. (c) Densitometry of Western blot bands for the samples in (b). The results were presented as means ± SE of three independent experiments.

to single HA chain (Figure 4). However, the degree of bioconjugation (%) decreased with increasing peptide content in the reactants. The bioconjugation (%) represents the molar ratio of peptide molecules in the HA−peptide conjugate to the total peptide molecules added initially for the conjugation reaction. When the number of peptide molecules per single HA chain in the feed was less than 19, the bioconjugation efficiency (%) was higher than 90%. The average number of conjugated peptide molecules could be controlled from 5 to 23 per single HA chain, as schematically shown in Figure 1b.

***In Vitro* Serum Stability of HA−Peptide Conjugates for FPRL1 Receptor.** Although several agonistic and antagonistic peptides for FPRL1 receptor have been identified in our group as promising new drug candidates for the inflammatory diseases such as sepsis, asthma, and rheumatoid arthritis (*4*−*6*), their short half-lives in the body should be elongated for further clinical applications. As expected, the peptide with a sequence of CWRYMVm was quite unstable in serum. After incubation in 50 vol % FBS solution for 3 days, only less than 30 wt % of the peptide remained with a big initial degradation of over 50 wt % in a day (Figure 5). However, HA−peptide conjugate showed notably increased serum stability in 50 vol % FBS solution. The peptide conjugated to HA did not degrade at all even after incubation for 4 days. The increased stability of peptide in serum by HA conjugation was the same for all three HA−peptide conjugates with different peptide contents. As the serum stability of the peptide drug is essential for the

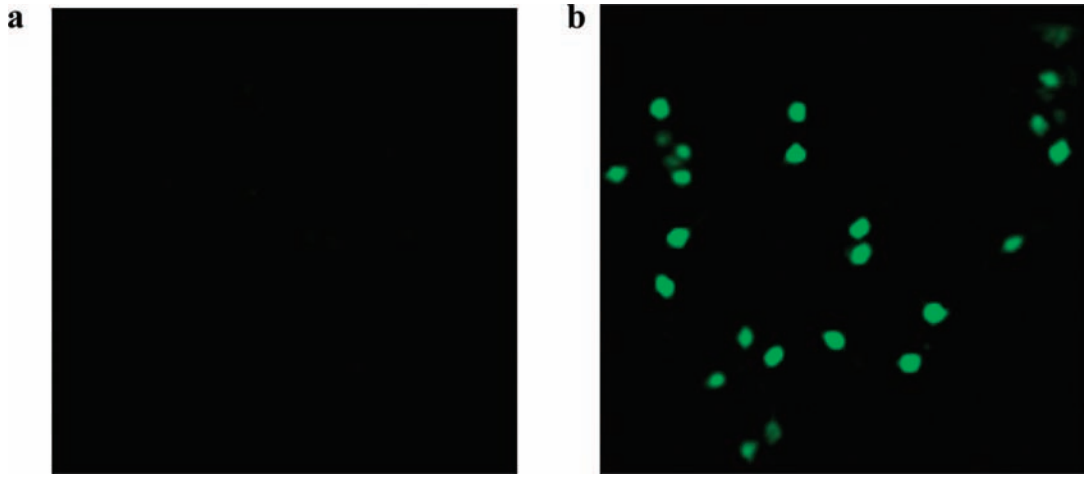

Figure 7. Calcium fluorescence imaging of the formyl peptide receptor like 1 (FPRL1) overexpressing RBL-2H3 cells after stimulation with (a) a control (no treatment) and (b) HA−peptide conjugate sample of HA-$(CWRYMVm)_{23}$ for FPRL1 receptor. The number of peptide molecules per single HA chain was 23.

application *in vivo*, the protocol for the conjugation of peptide to HA via Michael addition would be usefully exploited for the development of peptide therapeutics with good solubility and a feasible long half-life.

***In Vitro* Signal Transduction of HA−Peptide Conjugates for FPRL1 Receptor.** The signal transduction activity of HA−peptide conjugate for the FPRL1 receptor was assessed by measuring the elevation level of phospho-extracellular signal-regulated kinase (pERK) (Figure 6) and calcium ion (Figure 7) in RBL-2H3/FPRL1 cells. The band intensity was normalized to GAPDH to get the pERK level. When the cells were stimulated with the peptide or HA−peptide conjugate for FPRL1 receptor up to 30 min, the elevation of intracellular pERK level on Western blot was the highest at a stimulation time of 5 min in both cases. Therefore, the stimulation time was fixed at 5 min for the following cell activity tests. Figure 6a compares the pERK levels on Western blots in RBL-2H3/FPRL1 cells with those in RBL-2H3 cells after stimulation with a control (no treatment), peptide (CWRYMVm), HA-AEMA (HA), and HA−peptide conjugate having 23 peptide molecules per single HA chain. As there is no receptor for CWRYMVm in RBL-2H3 cells, the pERK levels were not elevated at all even after stimulation with peptide alone. However, in RBL-2H3/FPRL1 cells, the pERK levels elevated significantly after stimulation with both peptide alone and HA-$(CWRYMVm)_{23}$ samples. Figure 6b shows the pERK levels on Western blots after stimulation with a control (no treatment), HA-AEMA (HA), peptide (CWRYMVm), a mixture of HA-AEMA and peptide (HA + CWRYMVm), HA−peptide conjugates (HA-CWRYMVm), and hyaluronidase-treated HA−peptide conjugates (+HAse). The numbers 5, 8, and 23 represent the number of peptide molecules per single HA chain in HA−peptide conjugates. As a control, the pERK level by peptide alone was set to be 100% and the other data were normalized for comparison (Figure 6c). In the mixture of HA-AEMA and peptide, the pERK level decreased to ca. 63% compared with that of peptide alone. Moreover, the bioactivity of HA−peptide conjugates decreased to ca. 20%, 28%, and 38% depending on the amount of peptide per single HA chain. However, the bioactivity could be recovered up to ca. 76% after degradation of HA molecules by hyaluronidase treatment (+HAse). The decrease in the signal transduction activity of peptide molecules after being conjugated to HA might have resulted from the "steric hindrance" of HA chain reducing the access of peptide molecules to FPRL1 receptor. For the same reason, HA−peptide conjugate with a low peptide content of 5 per single HA chain [HA-$(CWRYMVm)_5$] showed a lower pERK level than HA-$(CWRYMVm)_{23}$, despite using the same peptide content for the Western blot analysis. After the hyaluronidase treatment (+HAse), however, the steric hindrance was thought to be alleviated, contributing to the increase of intracellular pERK level. There was a positive correlation between the pERK level and the content of peptide in HA−peptide conjugates with and without hyaluronidase treatment. According to the *t*-test, the *p*-value between HA-AEMA (HA) and [HA-$(CWRYMVm)_5$ + HAse] was 0.194, which means no significant elevation of pERK level after treatment with [HA-$(CWRYMVm)_5$ + HAse]. However, as the content of peptide in HA−peptide conjugates increased to 9 and 23, the *p*-value decreased to 0.056 and 0.004, respectively. The decreased *p*-value indicates that the biological activity of HA-CWRYMVm after hyaluronidase treatment significantly increased with the peptide content in HA-CWRYMVm conjugates. Bioconjugation of multiple peptides to a single HA chain might contribute to the development of long-acting formulation of peptide therapeutics. Previously, we have reported the effect of chemical modification of HA on its degradation (*32*, *33*). The chemical modification of carboxyl groups on HA was thought to make it more stable to enzymatic degradation by hyaluronidase contributing to the elongation of its half-life. The half-life of HA−peptide conjugate will be assessed by *in vivo* tests for further applications. Calcium imaging showed the same tendency as the Western blot analysis. Unlike the control, the RBL-2H3/FPRL1 cells treated by HA−peptide conjugate showed a bright fluorescence under UV light demonstrating its biological activity (Figure 7). Altogether with the stimulation test results of RBL-2H3/FPRL1 cells with agonistic peptides and HA−peptide conjugates, we could confirm the signal transduction activity of HA−peptide conjugates for the FPRL1 receptor. The novel protocol for the conjugation of HA-AEMA with the peptide of CWRYMVm would be usefully applied for various protein and peptide drugs with thiol groups. The HA−peptide conjugate for the FPRL1 receptor will be investigated further in murine models of inflammatory diseases such as sepsis, asthma, and rheumatoid arthritis for clinical applications to immunotherapeutics.

CONCLUSIONS

HA-AEMA was successfully synthesized and conjugated with CWRYMVm, one of the agonistic peptide drugs for the FPRL1 receptor, via Michael addition between the methacryloyl group of AEMA and the thiol group of cysteine. The formation of the HA−peptide conjugate was confirmed by ^{1}H NMR and GPC. HA−peptide conjugate could be prepared to have 5−23 peptide molecules per single HA chain by changing the initial feed ratio of peptide to HA repeat unit. The conjugation of peptide to HA molecules resulted in significantly enhanced serum stability. The signal transduction activity of HA−peptide

conjugate was confirmed by measuring the elevation level of pERK and calcium ion in FPRL1 overexpressing RBL-2H3 cells. The bioconjugation protocol using HA derivatives might be successfully applied for the development of peptide therapeutics with an elongated half-life and a feasible biological activity. *In vivo* tests of HA−peptide conjugate for FPRL1 receptor will be carried out in murine models of inflammatory diseases such as sepsis, asthma, and rheumatoid arthritis for further clinical applications to immunotherapeutics.

ACKNOWLEDGMENT

This study was supported by a grant of the Korea Healthcare Technology R&D Project, Ministry of Health & Welfare, Republic of Korea (A080711).

LITERATURE CITED

(1) Lee, M. S., Yoo, S. A., Cho, C. S., Suh, P. G., Kim, W. U., and Ryu, S. H. (2006) Serum amyloid A binding to formyl peptide receptor-like 1 induces synovial hyperplasia and angiogenesis. *J. Immunol. 177*, 5585–5594.

(2) Emilie, H., Fancois, B., Sophie, B., and Marie-Josephe, R. (2007) The role of β-arrestins in the formyl peptide receptor-like 1 internalization and signaling. *Cell. Signal. 19*, 1939–1948.

(3) Johan, B., Sara, P., Huamei, F., Ulf-Henrik, M., Kristoffer, H., Anna, K., and Claes, D. (2004) Cytochalasin B triggers a novel pertussis toxin sensitive pathway in TNF-alpha primed neutrophils. *BMC Cell Biol. 5*, 21–35.

(4) Seo, J. K., Choi, S. Y., Kim, Y., Baek, S. H., Kim, K. T., Chae, C. B., Lambeth, J. D., Suh, P. G., and Ryu, S. H. (1997) A peptide with unique receptor specificity: stimulation of phosphoinositide hydrolysis and induction of superoxide generation in human neutrophils. *J. Immunol. 158*, 1895–1901.

(5) Bae, Y. S., Song, J. Y., Kim, Y., He, R., Ye, R. D., Kwak, J. Y., Suh, P. G., and Ryu, S. H. (2003) Differential activation of formyl peptide receptor signaling by peptide ligands. *Mol. Pharmacol. 64*, 841–847.

(6) Bae, Y. S., Lee, H. Y., Jo, E. J., Kim, J. I., Kang, H. K., Ye, R. D., Kwak, J. Y., and Ryu, S. H. (2004) Identification of peptides that antagonize formyl peptide receptor-like 1-mediated signaling. *J. Immunol. 173*, 607–614.

(7) Healy, J. M., Lewis, S. D., Kurz, M., Boomer, R. M., Thompson, K. M., Wilson, C., and McCauley, T. G. (2004) Parmacokinetics and biodistribution of novel aptamer compositions. *Pharm. Res. 21*, 2234–2246.

(8) Ishida, T., Maeda, R., Ichihara, M., Irimura, K., and Kiwada, H. (2003) Accelerated clearance of PEGylated liposomes in rats after repeated injections. *J. Controlled Release 88*, 35–42.

(9) Pan, C. Q., Buxton, J. M., Yung, S. L., Tom, I., Yang, L., Chen, H., MacDougall, M., Bell, A., Claus, T. H., Clairmont, K. B., and Whelan, J. P. (2006) Design of a long acting peptide functioning as both a glucagon-like peptide-1 receptor agonist and a glucagon receptor antagonist. *J. Biol. Chem. 281*, 12506–12515.

(10) Laurent, T. C. (1998) *The chemistry, biology and medical applications of hyaluronan and its derivatives*, Portland Press, Wenner-Gren intern., London.

(11) Kim, S. J., Hahn, S. K., Kim, M. J., Kim, D. H., and Lee, Y. P. (2005) Development of a novel sustained release formulation of recombinant human growth hormone using sodium hyaluronate microparticles. *J. Controlled Release 104*, 323–335.

(12) Motokawa, K., Hahn, S. K., Nakamura, T., Miyamoto, H., and Shimoboji, T. (2006) Selectively crosslinked hyaluronic acid hydrogels for sustained release formulation of erythropoietin. *J. Biomed. Mater. Res. 78A*, 459–465.

(13) Nakamura, T., Kato, T., Togawa, H., Yasugi, K., Konishi, H., and Sekimori, Y. (2006) Conjugate of water-soluble modified hyaluronic acid and GLP-1 analogue. WO2006/095775.

(14) Kuo, J. W. (2006) *Practical aspects of hyaluronan based medical products*. CRC Press, Taylor & Francis Group, New York.

(15) Toole, B. (1998) Hyaluronan-cell interactions in morphogenesis. *The chemistry, biology, and medical applications of hyaluronan and its derivatives* (Laurent, T. C., Eds.) Portland Press, London.

(16) Brecht, M., Mayer, U., Schlosser, E., and Prehm, P. (1986) Increased hyaluronate synthesis is required for fibroblast detachment and mitosis. *Biochem. J. 239*, 445–450.

(17) Toole, B. (1991) *Cell Biology of Extracellular Matrix* (Hay, E. D., Eds.) Plenum, New York.

(18) Goldberg, R. L., and Toole, B. P. (1987) Hyaluronate inhibition of cell proliferation. *Arthritis Rheum. 30*, 769–778.

(19) Aruffo, A., Stamenkovic, I., Melnick, M., Underhill, C., and Seed, B. (1990) CD44 is the principal cell surface receptor for hyaluronate. *Cell 61*, 1303–1313.

(20) Entwistle, J., Hall, C. L., and Turley, E. A. (1996) HA receptors: regulators of signaling to the cytoskelecton. *J. Cell. Biochem. 61*, 569–577.

(21) Schledzewski, K., Falkowski, M., Moldenhauer, G., Metharom, P., Kzhyshkowska, J., Ganss, R., Demory, A., Falkowska-Hansen, B., Kurzen, H., Ugurel, S., Geginat, G., Arnold, B., and Goerdt, S. (2006) Lymphatic endothelium-specific hyaluronan receptor LYVE-1 is expressed by stabilin-I+, F4/80+, CD11b+ macrophages in malignant tumors and wound healing tissue in vivo and in bone marrow cultures in vitro: implications for the assessment of lymphangiogenesis. *J. Pathol. 209*, 67–77.

(22) Balazs, E. A., and Denlinger, J. L. (1993) Viscosupplementation: a new concept in the treatment of osteoarthritis. *J. Rheumatol. 20*, 3–9.

(23) Balazs, E. A. (1983) Sodium hyaluronate and viscosurgery. *Healon (sodium hyaluronate). A guide to its use in ophthalmic surgery* (Miller, D., and Stegmann, R., Eds.) Wiley, New York.

(24) Ohri, R., Hahn, S. K., Stayton, P. S., Hoffman, A. S., and Giachelli, M. (2004) Hyaluronic acid grafting mitigates calcification of glutaraldhyde-fixed bovine pericardium. *J. Biomed. Mater. Res. 70A*, 159–165.

(25) Luo, Y., Ziebell, M. R., and Prestwich, G. D. (2000) A hyaluronic acid-taxol antitumor bioconjugate targeted to cancer cells. *Biomacromolecules 1*, 208–218.

(26) Luo, Y., Bernshaw, N. J., Lu, Z. R., Kopecek, J., and Prestwich, G. D. (2002) Targeted delivery of doxorubicin by HPMA copolymer-hyaluronan bioconjugates. *Pharm. Res. 19*, 396–402.

(27) Oishi, M., Sasaki, S., Nagasaki, Y., and Kataoka, K. (2003) pH-responsive oligodeoxynucleotide (ODN)-poly(ethylene glycol) conjugate through acid-labile beta-thiopropionate linkage: preparation and polyion complex micelle formation. *Biomacromolecules 4*, 1426–1432.

(28) Metters, A., and Hubbell, J. (2005) Network formation and degradation behavior of hydrogels formed by Michael-type addition reactions. *Biomacromolecules 6*, 290–301.

(29) He, R., Sang, H., and Ye, R. D. (2003) Serum amyloid A induces IL-8 secretion through a G protein-coupled receptor, FPRL1/LXA4R. *Blood 101*, 1572–1581.

(30) King, J., and Laemmli, U. K. (1971) Polypeptides of the tail fibres of bacteriophage T4. *J. Mol. Biol. 62*, 465–477.

(31) Bae, Y. S., Bae, H., Kim, Y., Lee, T. G., Suh, P. G., and Ryu, S. H. (2001) Identification of novel chemoattractant peptides for human leukocytes. *Blood 97*, 2854–2862.

(32) Hahn, S. K., Park, J. K., Takashi, T., and Shimoboji, T. (2007) Synthesis and degradation test of hyaluronic acid hydrogels. *Intern. J. Biol. Macromol. 40*, 374–380.

(33) Oh, E. J., Kang, S. W., Kim, B. S., Jiang, G., Cho, I. H., and Hahn, S. K. (2008) Control of the molecular degradation of hyaluronic acid hydrogels for tissue augmentation. *J. Biomed. Mater. Res. 86A*, 685–693.

BC800255Y

Bioconjugate Chemistry 20th Anniversary

Subscriber access provided by SHEMYAKIN-OVCHINNIKOV INST

Article

Influence of the Molecular Charge on the Biodistribution of Bombesin Analogues Labeled with the [Tc(CO)]-Core

Elisa Garci#a Garayoa, Christian Schweinsberg, Veronique Maes, Luc Brans, Peter Bla#uenstein, Dirk A. Tourwe#, R. Schibli, and P. August Schubiger

Bioconjugate Chem., **2008**, 19 (12), 2409-2416• DOI: 10.1021/bc800262m • Publication Date (Web): 11 November 2008

Downloaded from http://pubs.acs.org on May 2, 2009

More About This Article

Additional resources and features associated with this article are available within the HTML version:

- Supporting Information
- Links to the 1 articles that cite this article, as of the time of this article download
- Access to high resolution figures
- Links to articles and content related to this article
- Copyright permission to reproduce figures and/or text from this article

View the Full Text HTML

ACS Publications
High quality. High impact.

Bioconjugate Chemistry is published by the American Chemical Society. 1155 Sixteenth Street N.W., Washington, DC 20036

Influence of the Molecular Charge on the Biodistribution of Bombesin Analogues Labeled with the [^{99m}Tc(CO)$_3$]-Core

Elisa García Garayoa,*[,†] Christian Schweinsberg,[†] Veronique Maes,[‡] Luc Brans,[‡] Peter Bläuenstein,[†] Dirk A. Tourwé,[‡] R. Schibli,[†] and P. August Schubiger[†]

Paul Scherrer Institute, Centre for Radiopharmaceutical Science, CH-5232 Villigen PSI, Switzerland, and Department of Organic Chemistry, Vrije Universiteit Brussel, 1050 Brussels, Belgium. Received June 27, 2008; Revised Manuscript Received September 26, 2008

The overexpression of Bombesin (BBS) receptors on a variety of human cancers make them interesting targets for tumor imaging and therapy. Analogues of the neuropeptide BBS have been functionalized with the (N$^{\alpha}$His)-chelator for labeling with the ^{99m}Tc-tricarbonyl core. The introduction of a βAla-βAla linker between the stabilized BBS binding sequence and the chelator led to increased tumor uptake but still rather unfavorable *in vivo* properties. Novel polar linkers, with different charge, have been introduced in the molecule and tested for their influence on the biodistribution. The new analogues showed a shift in hydrophilicity from a Log D = 0.9 to Log D values between 0.4 and −2.2. All compounds kept the increased stability in both human plasma ($t_{1/2}$ > 16 h) and in tumor cells ($t_{1/2}$ = 30−40 min). The compounds with Log D values between +1 and −1 showed the highest binding affinities with K_d values of <0.5 nM, as well as the highest cellular uptake. However, higher hydrophilicity (Log D < −1.8) led to lower affinity and a substantial decrease of internalization. The introduction of a positive charge (β^3hLys) resulted in unfavorable biodistribution, with increased kidney uptake. The introduction of an uncharged hydroxyl group (β^3hSer) improved the biodistribution, resulting in significantly better tumor-to-tissue ratios. The compound with one single negative charge (β^3hGlu) showed a significant increase in the tumor uptake (2.1 ± 0.6% vs 0.80 ± 0.35% ID/g in comparison to the βAla-βAla analogue) and also significantly higher tumor-to-tissue ratios. The specificity of the *in vivo* uptake was confirmed by coinjection with natural BBS. Moreover, the analogue provided a much clearer image of the tumor xenografts in the SPECT/CT studies. The introduction of a single negative charge may be useful in the development of new BBS analogues to obtain an improved biodistribution profile, with increased tumor uptake and better imaging.

INTRODUCTION

A variety of human carcinomas show an overexpression of peptide receptors for which natural neuropeptides feature high affinities. Thus, peptide-based radiopharmaceuticals exhibit a great potential for imaging and therapy of cancer (*1*−*5*). Their small size allows good penetration into tumor tissue and promotes more rapid blood clearance compared to other macromolecular carriers such as antibodies (*4*). This can result in high specific uptake and optimal tumor-to-background ratios for the visualization of tumors and small metastases as well as for therapeutic applications, depending on the radionuclide used (*4*). Peptides are readily synthesized and can withstand harsh conditions for labeling. Their chemical characteristics offer a broad range for functionalization and modification like the introduction of chelating systems and pharmacokinetic modifiers (*4*−*6*). There is evidence that for some cancer types not only one but several peptide receptors may be overexpressed in varying levels and regions in the tumor tissue (*7*). Therefore, it is of great interest to develop more than one peptide radiopharmaceutical to cover a broader range of possible targets as well as to obtain a more homogeneous distribution of the activity within the tumor mass.

Bombesin (BBS) is a tetradecapeptide with high affinity for the mammalian gastrin-releasing peptide receptor (GRP-R), a subtype of the BBS receptor superfamily, which is overexpressed in most human prostate and breast tumors as well as small-cell lung cancer and several other cancer types (*8*−*10*). A variety of BBS analogues has been designed, based either on the complete original peptide sequence or on the fragment (7−14). Several BBS analogues containing the appropriate chelating systems for radiolabeling with different radionuclides (e.g., ^{99m}Tc or ^{186}Re/^{188}Re, ^{64}Cu, ^{111}In, ^{177}Lu, and ^{18}F) show promising pharmacological properties (*4*−*6*, *11*−*14*). Of the different radionuclides useful in nuclear medicine, ^{99m}Tc is still the one with the broadest clinical application due to its favorable dosimetry, high specific activity, low cost, and ready availability from a ^{99}Mo/^{99m} Tc-generator. Its physical properties ($t_{1/2}$ = 6 h, energy γ = 140 keV, 98% abundance) are optimal for imaging using single photon emission computed tomography (SPECT) (*15*−*17*). In addition, a metal chelator applicable for ^{99m}Tc is usually also suitable for the therapeutic radionuclides ^{186}Re and ^{188}Re due to their similar chemical properties. Thus, a successful candidate for targeting GRP-R with ^{99m}Tc could be interesting for radiotherapeutic applications with Re isotopes (*16*). Our group successfully established a chelating system for both ^{99m}Tc(I) and ^{186}Re/^{188}Re(I) in the form of a tridentate chelator, the retro(N$^{\alpha}$His)Ac-chelator, for labeling of biomolecules with the tricarbonyl technique (*18*, *19*).

Some modifications of the BBS amino acid sequence, such as the exchange of Met^{14} with norleucine (Nle) and Leu^{13} with cyclohexylalanine (Cha), resulted in an improved stability in human plasma and in prostate and breast cancer cells. These modifications did not affect the binding affinity and cell internalization, but led to increased tumor-to-background ratios, although tumor uptake did not significantly change (*20*, *21*).

* Correspondence and requests should be addressed to Dr. E. García Garayoa. Center for Radiopharmaceutical Science. Paul Scherrer Institute, CH-5232 Villigen PSI, Switzerland. Phone: + 41-56-310 28 17. Fax: + 41-56-310 28 49. E-mail: elisa.garcia@psi.ch.

† Centre for Radiopharmaceutical Science.

‡ Vrije Universiteit Brussel.

10.1021/bc800262m CCC: $40.75 © 2008 American Chemical Society
Published on Web 11/11/2008

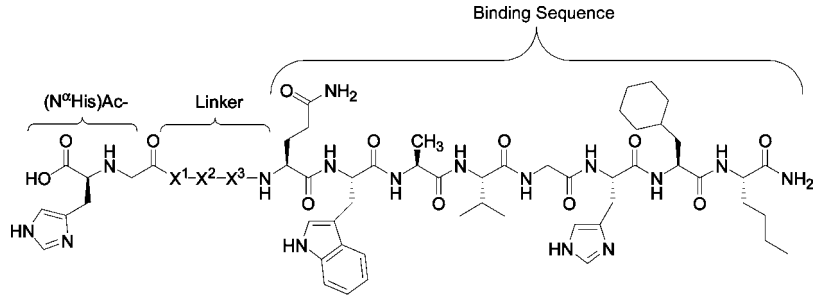

Compound	X^1	X^2	X^3
1		βAla	βAla
2	β³hSer	βAla	βAla
3	β³hGlu	βAla	βAla
4	β³hLys	βAla	βAla
5	β³hGlu	β³hGlu	βAla
6	β³hGlu	β³hGlu	β³hGlu

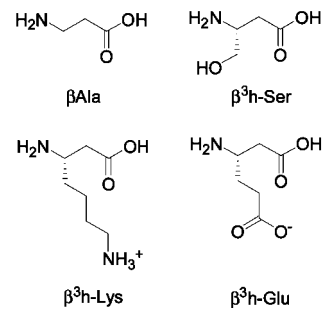

Figure 1. Chemical structure of the new BBS analogues.

Smith et al. reported on the positive influence of aliphatic spacers on the uptake of ^{99m}Tc-labeled BSS analogues into GRP-R-expressing tissues (*14*). With the introduction of a βAla-βAla[1]linker, we showed an additional improvement of the *in vivo* tumor uptake of stabilized BBS analogues labeled with the ^{99m}Tc-tricarbonyl core (*20*). Likewise, other recent papers report on the positive effects of polar linker moieties on ^{64}Cu-labeled DOTA-, NOTA-, and ^{99m}Tc(III)-labeled BBS conjugates (*22*−*24*). The BBS analogues with the ^{99m}Tc(CO)$_3$-His complex are more lipophilic than the above-mentioned peptides, since the His-imidazole residue (pK = 6) is not protonated at physiological pH values. An increase of the hydrophilicity of the molecule as well as the presence of charges may lead to new analogues with improved biodistribution profiles. New BBS derivatives were synthesized with different polar linkers inserted between the stabilized binding sequence and the retro(N$^\alpha$His)Ac-chelator. The spacers contain different β-amino acids (*25, 26*) either neutral or with a positive or negative charge in the side chain. In this study, we investigated the influence of these polar linkers and charges on the *in vitro* and *in vivo* behavior of new ^{99m}Tc(I)-labeled BBS analogues.

EXPERIMENTAL PROCEDURES

Chemicals and Equipment. Cell culture media DMEM GLUTAMAX-I, trypsin/EDTA, bovine serum albumin, and soybean trypsin inhibitor were obtained from Invitrogen (Basel, Switzerland), fetal calf serum (FCS), and antibiotic/antimycotic solution were obtained from Bioconcept (Allschwil, Switzerland). Bacitracin, HEPES, and Chymostatin were purchased from SIGMA (Buchs, Switzerland). All other chemicals were obtained from Fluka (Buchs, Switzerland) or Merck (Dietikon, Switzerland). For the determination of protein concentrations, a Pierce BCA Protein Assay kit from Socochim (Lausanne, Switzerland) was used. Na[^{99m}TcO$_4$] was eluted from a Mallinckrodt ^{99}Mo/^{99m}Tc generator (Tyco Healthcare, Petten, The Netherlands) using 0.9% saline. Sodium boranocarbonate was a gift from the provider of the generator. The radioactivity of *in vitro* and *in vivo* experiments was measured with a NaI-γ-counter (Packard Canberra Cobra II, Meriden, USA) or a NaI ionization chamber. The Fmoc-β^{3}homoamino acids were purchased from Fluka.

Peptide Synthesis and Radiolabeling with ^{99m}Tc. Peptide solid-phase synthesis was carried out on a Rink Amide Resin using the Fmoc-strategy as previously described (*20*). Purification of the peptides was done on a semipreparative HPLC system (Gilson) on a reversed-phase C_{18} column (DiscoveryBIO SULPELCO Wide Pore, 25 cm × 2.21 cm, 5 μm) with a linear gradient of 3% B to 100% B (solvent A = H_2O + 0.1% TFA and solvent B = CH_3CN + 0.1% TFA) in 30 min, a flow rate of 1 mL/min, and UV detection at 215 nm.

Each of the new spacers introduced between the binding sequence and the chelator contained three β-amino acids in form of a β-alanine (βAla), β^3-homoserine (β^{3}hSer), β^3-homolysine (β^{3}hLys), or β^3-homoglutamic acid (β^{3}hGlu). The (N$^\alpha$His)Ac moiety (retro[N^α-carboxymethyl-histidine]) was coupled to the N-terminus for labeling to [^{99m}Tc(CO)$_3$] (Figure 1) (*25, 26*).

Radiolabeling of the analogues was performed as previously described (*20*). For analyses and purification of the labeled peptides from the unlabeled compounds, a Macherey-Nagel CC Nucleosil 100−5 C_{18} RP column (5 μm, 250 × 4.6 mm) was used. Preparative HPLC for purification of the labeled peptides was performed using a Merck-Hitachi L-7100-system with an equipped two-channel scintillation detector interface (John Caunt Scientific Ltd., Eynsham, England) and a Rainin Dynamax absorbance detector model UV-1. HPLC solvents consisted of H_2O + 0.1% TFA (solvent A) and CH_3OH + 0.1% TFA (solvent B). The separation was performed with a linear gradient 50% A/50% B to 20% A/80% B in 25 min (1.0 mL/min). For the analytical HPLC of the labeled peptides, a Varian ProStar system was used with a Varian ProStar 230 Solvent Delivery Pump, a Varian Photodiode Array Detector model 330, a Varian ProStar Autosampler model 410, and a radiomatic Flo-one Beta Detector (Packard Canberra). HPLC solvents consisted of CH_3CN + 0.1% TFA (solvent A) and H_2O + 0.1% TFA (solvent B). The labeling control was performed with a linear gradient of 30% A/70% B to 80% A/20% B in 25 min (1.0 mL/min).

Octanol/Water Partition Coefficient Study. To compare the polarity of the different new analogues, the octanol/water partition coefficients were determined at pH = 7.4 by measuring the distribution of the radiolabeled peptides in 1-octanol and

[1]βAla is the exception to the general nomenclature of the β amino acids according to Abele and Seebach (*25, 26*)

PBS. Five microliters containing 500 kBq of radiolabeled compound in PBS were added to a vial containing 1.2 mL 1-octanol and PBS (1:1). After vortexing for 1 min, the vial was centrifuged for 5 min at 10 000 rpm to ensure complete separation of layers. Then, 40 μL of each layer were taken in a preweighed vial and measured in the γ-counter. Counts per unit weight of sample were calculated, and log D values were obtained using the formula

$$\log_{10}\mathrm{D} = \log_{10}\left(\frac{\text{counts in 1 g of octanol}}{\text{counts in 1 g of water}}\right)$$

Cell Culture. PC-3 human prostate cancer cell line was obtained from the European Collection of Cell Cultures (Salisbury, United Kingdom). Cells were maintained in Dulbecco's MEM with GLUTAMAX-I supplemented with 10% FCS, 100 IU/mL penicillin G sodium, 100 μg/mL streptomycin sulfate, and 0.25 μg/mL amphotericin B. Cells were incubated at 37 °C in an atmosphere containing 5% CO_2 and subcultured twice a week after detaching with trypsin-EDTA.

Metabolic Stability in Human Plasma and in PC-3 cells. The degradation of the radiolabeled analogues was investigated *in vitro* in human plasma from healthy donors. The analogues (3 MBq/mL, 1.5−2 pmol/mL) were incubated for different time periods (from 0 to 24 h) at 37 °C. After incubation, proteins were precipitated as follows: 250 μL of sample + 750 μL of acetonitrile/ethanol (1:1) and TFA (0.01%). The mixture was vortexed and centrifuged (10 min, 20 000 *g*) at 4 °C. The supernatant was filtered and analyzed by RP-HPLC equipped with a radioactivity detector. The stability in cell culture was evaluated with 2×10^6 cells in PBS. The analogues (3 MBq/mL, 1.5−2 pmol/mL) were incubated from 0 to 5 h at 37 °C. Afterward, proteins were precipitated, and the supernatant filtered and analyzed as above. All experiments were carried out 2−3 times. Different peaks corresponding to the intact peptide and the different degradation products were obtained in the radioactivity chromatograms. The percentage of intact peptide was determined for each incubation time.

Receptor Inhibition Studies. One day prior to the assay, PC-3 cells at confluence were placed in 48-well plates. Cells were incubated in a special binding buffer (50 mM HEPES, 125 mM NaCl, 7.5 mM KCl, 5.5 mM $MgCl\cdot 6H_2O$, 1 mM EGTA, 5 g/L BSA, 2 mg/L Chymostatin, 100 mg/L Soybean Trypsin inhibitor, 50 mg/L Bacitracin, pH 7.4) with increasing concentrations of the BBS analogues (0−30 000 nM) in the presence of 4 kBq of ^{99m}Tc-BBS(7−14), which is known to express a high binding affinity to the GRP receptor. After 1 h incubation at 37 °C, the cells were washed twice with cold PBS. Bound radioactivity was recovered by solubilizing the cells in 1 N NaOH (2×400 μL). The radioactivity was measured in the γ-counter. All experiments were carried out 2−3 times in triplicate.

Receptor Saturation Studies. One day prior to the assay, PC-3 cells at confluence were placed in 48-well plates and incubated for 1 h at 37 °C in the binding buffer described above with increasing concentrations of the labeled BBS analogues (0.01−2 nM). The concentration of total technetium-labeled peptide was calculated according to Bauer et al. (*15*). Nonspecific binding was determined by coincubation with 1 μM natural BBS. After incubation, the cells were washed twice with cold PBS, solubilized in 1 N NaOH (2×400 μL), and the radioactivity was measured in the γ-counter. Experiments were performed 2−3 times in triplicate.

Internalization. One day prior to the assay, PC-3 cells at confluence were placed in 6 well plates. Cells were incubated with the labeled analogues (4 kBq/well) in binding buffer for 5, 15, 30, 60, and 120 min at 37 °C to allow binding and internalization. Nonspecific binding was determined in the presence of 1 μM natural BBS. After incubation, cells were washed twice with cold PBS. Surface-bound activity was removed by acid wash (50 mM glycine/HCL, 100 mM NaCl, pH 2.8, 2×600 μL for 5 min at room temperature). Afterward, the plates were neutralized with 600 μL PBS and cells were lysed with 1 N NaOH (2×600 μL). Surface-bound and internalized activities were measured in the γ-counter. The protein concentration was determined and results were calculated as percentage of total added radioactivity per milligram of protein. All experiments were carried out 2−3 times in triplicate.

Externalization. One day prior to the assay PC-3 cells at confluence were placed in 6 well plates. Cells were incubated with the labeled analogues (20 kBq/well) in culture medium for 1 h at 37 °C to allow binding and maximal internalization. After incubation, the supernatant was discarded and each well washed twice with cold PBS. Afterward, the cells were incubated again at 37 °C in 2 mL culture medium for 30, 60, 150, or 300 min. At each time point, the supernatant was collected, the cells were washed twice with cold PBS, and the radioactivity remaining in the cells was recovered by lysing the cells with 1 N NaOH (2×600 μL). Radioactivity in the supernatant (released activity) and in the lysate (internalized activity) was determined in the γ-counter. Results are expressed as the percentage of the total activity associated with the cells. The protein concentration was determined, and results were calculated as the percentage of total added radioactivity per milligram protein. All experiments were carried out 2−3 times in triplicate.

Biodistribution Studies. All animal experiments were conducted in compliance with the Swiss animal protection laws and with the ethical principles and guidelines for scientific animal trials established by the Swiss Academy of Medical Sciences and the Swiss Academy of Natural Sciences. Female CD-1 nu/nu mice 6−8-week-old (Charles River Laboratories, Sulzfeld, Germany) were subcutaneously injected with 8×10^6 cells in 150 μL culture medium without supplements. About 3 weeks after tumor implantation, the mice (3−6 per group) were injected i.v. with 3.7 MBq of the radiolabeled peptides (peptide amount of 0.2 pmol/mouse). At 0.5 h, 1.5 or 5 h postinjection (p.i.), the animals were sacrificed by cervical dislocation. The different organs (heart, lung, spleen, kidneys, pancreas, stomach, small intestine, large intestine, liver, muscle, bone) and blood were collected from the animals, weighed, and the radioactivity measured in a γ-counter. To determine specificity of the *in vivo* uptake, one group of mice received a coinjection of 100 μg of unlabeled natural BBS and the radiolabeled analogue and sacrificed 1.5 h p.i. Results are presented as a percentage of injected dose per gram of tissue (%ID/g).

SPECT/CT Studies. Single photon emission computed tomography/X-ray computed tomography (SPECT/CT) images were performed postmortem 1.5 h after i.v. injection of the ^{99m}Tc-BBS analogues (20 MBq). Images were obtained on an X-SPECT-system (Gamma Medica Inc.) equipped with a single head SPECT device and a CT-device. SPECT data were acquired and reconstructed with *LumaGEM* (version 5.407). CT data were acquired by an X-Ray CT-system (Gamma Medica) and reconstructed with the software *Cobra* (version 4.5.1). Fusion of SPECT and CT data was performed with IDL *Virtual Machine* (version 6.0). Images were generated with *Amira* (version 3.1.1).

Statistical Analysis. All data are presented as the mean ± SD. Differences in the *in vivo* uptake in the biodostribution studies were analyzed by one-way ANOVA followed by Dunnett's comparison test. Differences between blocked and

control groups were analyzed by unpaired *t* test. $P \leq 0.05$ was considered statistically significant.

RESULTS

Peptide Synthesis and Radiolabeling. In the peptide syntheses, yields of 50−58% were obtained for the cold purified peptides (Table 1, Supporting Information). The labeling yields with the ^{99m}Tc-tricarbonyl core were higher than 90%. Pertechnetate and tricarbonyl represented a maximum of 3% and 5%, respectively. For both *in vitro* and *in vivo* studies, labeled and unlabeled peptide were separated by preparative RP-HPLC. After the separation, the labeled analogue was analyzed with analytical RP-HPLC and corresponded to more than 98% of the radioactivity.

Octanol/Water Coefficient. The reference compound (**1**) with the linker βAla-βAla showed a rather lipophilic character with a Log D of +0.9. The introduction of a hydroxyl group (**2**) changed the polarity to +0.4. The insertion of additional positive or negative charges resulted in a clear increase of hydrophilicity up to −2.2 for compound **6** (bearing three negative charges) (Table 1).

Metabolic Stability. All new analogues, based on the fragment BBS(7−14) with the same changes at positions 13 and 14 (Cha and Nle for Leu and Met, respectively) showed increased stability compared to the unmodified sequence with a $t_{1/2}$ of approximately 16 h in human plasma. Stability in PC-3 tumor cells was also higher for the new analogues ($t_{1/2} = 30-40$ min) especially for compound **4**, which showed a clear increase in cell stability with a $t_{1/2}$ of 80 min.

Binding Assays. The binding affinity was tested for both the labeled and the unlabeled analogues. In inhibition experiments, compounds **1** and **2** showed the highest affinity, with IC_{50} values of 5.1 and 6.8 nM, respectively. Compounds **3** to **5** had slightly lower affinities, whereas compound **6** showed a high decrease of affinity ($IC_{50} = 634$ nM) (Table 1). The ^{99m}Tc-labeled compounds **1** to **5** exhibited a saturable and highly specific binding. These analogues had high affinity for GRP receptors, with K_d values in the subnanomolar range under 0.5 nM (Table 1). Under the set conditions, the binding of the labeled compound **6** was very low in the range of unspecific binding and the K_d value was not determined.

Internalization/Efflux. For compounds **1** to **5**, more than 80% of the activity bound to PC-3 cells was internalized after 30 min. Internalization of compounds bearing a neutral spacer (**2**) or a single negative charge in the spacer (**3**) was comparable to the reference peptide **1** after 1 h (30% of total dose/mg protein). Compound **4** (with a single positive charge) showed the highest internalization value (40% of total dose/mg protein after 1 h), whereas compound **5** and especially compound **6** showed a lower internalization (15% and 1% of total dose/mg protein after 1 h, respectively). Results are depicted in Figure 2A. Due to its low affinity and internalization, compound **6** was not tested for externalization.

In the externalization experiments with analogues **3**, **4**, and **5**, the radioactivity was rapidly externalized with a release of approximately 70% in the first 2.5 h after maximal internalization. Release of compounds **1** and **2** was slower (45% of the internalized activity was released in the first 2.5 h). Percentages of 20−30% of analogues **3**, **4**, and **5** remained in the cells after 5 h, whereas the retention for analogues **1** and **2** was slightly higher with 40% of activity still associated with the cells at this time (Figure 2B).

Biodistribution and SPECT/CT Studies. The neutral or negatively charged compounds (analogues **1**, **2**, **3**, and **5**) were further tested in mice with PC-3 tumor xenografts (Table 2). Compound **4** with a positive charge was excluded from these studies due to the unfavorably high retention in kidneys and liver found in previous biodistribution studies in normal mice (Supporting Information Table 2).

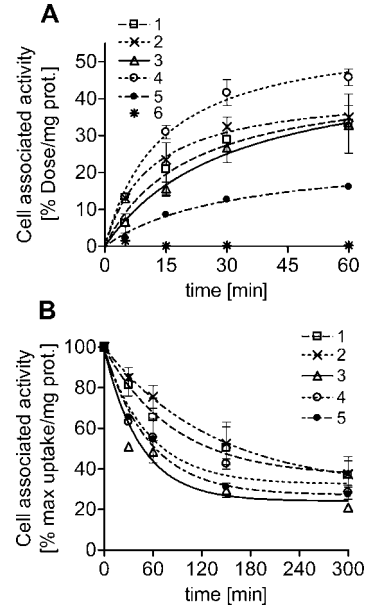

Figure 2. Time-course internalization (**A**) and externalization after maximal internalization (**B**) of the ^{99m}Tc-labeled BBS analogues in PC-3 cells after incubation at 37 °C. Data represent the percentage of internalized activity per milligram protein related to the total activity added to the cells ($n = 2-3$).

Compared to compound **1**, analogues **2** (neutral) and **3** (one negative charge) showed higher uptake in the receptor-expressing tissues (pancreas, colon, and tumor) at 0.5 h p.i. time (Table 2). Interestingly, the tumor uptake was significantly higher for analogue **3** compared to the reference **1** ($P \leq 0.05$), and the activity was retained longer (1% ID/g at 5 h p.i.) than for the other analogues (∼0.5% ID/g at 5 h p.i.).

Analogues **2**, **3**, and **5** showed a highly significant decrease in liver accumulation compared to the reference peptide **1** ($P \leq 0.01$) (Table 2). In spite of the higher kidney uptake of all new peptides at 0.5 h p.i., the activity washout from this organ was very fast, with the exception of compound **5**. Thus, the activity in the kidneys at later p.i. times was lower than 1% ID/g and similar for compounds **1**, **2**, and **3** (Table 2).

The higher tumor uptake in combination with a lower liver uptake and a faster clearance from blood and normal tissues led to high tumor-to-nontumor ratios for the new analogues especially for compound **3** after 1.5 h (tumor/kidney = 2.3 ± 0.8, tumor/liver = 6.3 ± 0.6) and 5 h (tumor/kidney = 3.5 ± 0.5, tumor/liver = 11.1 ± 1.3) (Figure 3).

In the blocking experiments, an excess of natural BBS was coinjected with the labeled analogues at 1.5 h p.i., and the uptake in the receptor-positive tissues pancreas, colon, and tumor was significantly reduced, thus indicating clearly a specific accumulation of radioactive tracer in these tissues (Table 2).

SPECT/CT images were acquired with compounds **1**, **3**, and **5** at 1.5 h p.i. The visualization of the tumor xenograft was clearer with **3** than with **1** and **5**, which corroborated the results obtained in the biodistribution studies (Figure 4). Compound **1** exhibited high uptake in the abdominal cavity due to the high hepatic, pancreatic, and intestinal uptakes (Figure 4A). The radioactivity in the abdominal area for compound **5** would be determined by the uptake in the kidneys, pancreas, and bowel (Figure 4C). Compound **3** showed lower renal and hepatic uptakes, and the abdominal activity would correspond to the uptake in pancreas and intestinal tract (Figure 4B).

The *in vivo* studies were performed with the HPLC purified analogues. We found that injection of nonpurified analogues

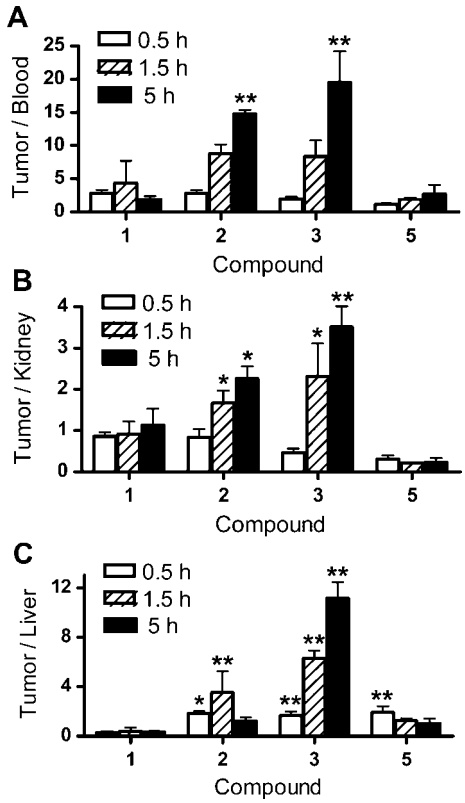

Figure 3. Tumor to nontumor ratios of the ^{99m}Tc-labeled BBS analogues in mice bearing PC-3 tumor xenografts (3.7 MBq/mouse i.v.) (n = 3−13). (**A**) Tumor-to-blood. (**B**) Tumor-to-kidney. (**C**) Tumor-to-liver. * ($P \leq 0.05$), ** ($P \leq 0.01$) vs reference compound **1** (one-way ANOVA and Dunnett's post hoc test).

Table 1. Characteristics of the new BBS analogues: retention time and polarity (LogD) of the ^{99m}Tc-labeled analogues, and binding affinity for GRP-receptors in PC-3 cells of the labeled (K_d values) and unlabeled (IC_{50} values) compounds (n = 2–3)[a]

Analogue	HPLC γ - trace t_R [min]	LogD	K_d [nM]	IC_{50} [nM]
1	16.8	0.9 ± 0.2	0.19 ± 0.12	5.1 ± 1.7
2	16.6	0.4 ± 0.1	0.05 ± 0.03	6.8 ± 3.2
3	16.6	−0.5 ± 0.1	0.08 ± 0.01	13.3 ± 3.0
4	14.9	−0.5 ± 0.1	0.14 ± 0.06	23.6 ± 12.0
5	16.7	−2.0 ± 0.2	0.36 ± 0.07	16.3 ± 8.3
6	15.7	−2.2 ± 0.4	n.d.	634.0 ± 221.7

[a] n.d. = non-determined.

led to higher uptake in blood and normal tissues (namely, kidney, lung, spleen, and liver) compared to the corresponding HPLC-purified analogues (unpublished data). No statistically significant differences were found in the uptake in receptor-positive tissues, which indicates that the presence of an excess of unlabeled peptide was not sufficient to block the receptors *in vivo*. Moreover, the injection of the HPLC-purified analogues with an amount of the corresponding unlabeled peptide similar to the nonpurified samples (100 pmol) resulted in biodistributions comparable to those of the HPLC-purified analogues. This demonstrated that the increased nonspecific uptake in healthy tissues was not due to the presence of unlabeled analogue but to other radioactive species that are not detected in the HPLC chromatogram and are eliminated after HPLC purification.

DISCUSSION

A variety of BBS analogues have been labeled with different radionuclides to investigate their potential for the detection and therapy of GRP-R-expressing neoplasms (*4*−*6*, *11*, *13*, *14*, *22*−*24*, *27*).

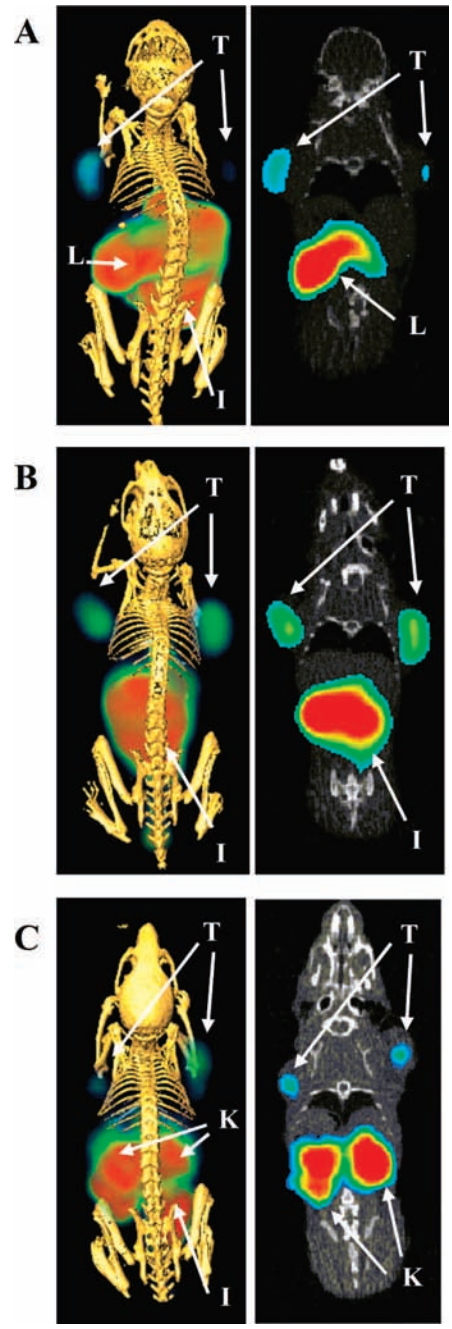

Figure 4. SPECT/CT image of nude mice bearing PC-3 tumor xenografts at 1.5 h p.i. of 20 MBq of the ^{99m}Tc-labeled BBS analogue. (**A**) Three-dimensional image (left) and coronal slice (right) of compound **1** (neutral). (**B**) Three-dimensional image (left) and coronal slice (right) of compound **3** (one negative charge). (**C**) Three-dimensional image (left) and coronal slice (right) of compound **5** (two negative charges). T = tumor; K = kidney; L = liver; I = intestinal activity.

Our work is focused on the development and characterization of new BBS derivatives radiolabeled with ^{99m}Tc using the tricarbonyl labeling technique (*18*, *19*). The amino acid sequence of our peptides is based on the fragment 7−14 of BBS (Figure 1), which has been modified as previously published to increase the stability (replacement of Leu^{13} with Cha, and Met^{14} with Nle). The additional introduction of a βAla-βAla linker (**1**) led to improved *in vivo* tumor uptake (*14*, *20*). However, the accumulation of activity in the liver increased, and the tumor-to-nontumor ratios were still rather low. High uptake in the liver and in the kidneys has also been reported for other ^{99m}Tc-labeled BBS analogues (*11*, *23*) and may obscure the detection of lesions in the abdomen. Moreover, high renal uptake could also induce

Table 2. Biodistribution of the ^{99m}Tc-labeled BBS analogues (3.7 MBq/mouse i.v.) in mice bearing PC-3 xenografts. The animals of the blocked group received a co-injection of 0.1 mg natural BBS. Data (mean ± SD) are expressed as percentage of injected dose per gram of tissue (n = 3-4)[a]

BBS	Organs	0.5 h	1.5a h	5 h	1.5 h blocked
1	Blood	0.58 ± 0.21	0.36 ± 0.66	0.23 ± 0.11	0.47 ± 0.07
	Kidney	1.82 ± 0.51	0.79 ± 0.35	0.39 ± 0.20	0.76 ± 0.19
	Liver	5.26 ± 1.26	2.36 ± 0.87	1.83 ± 0.75	2.13 ± 0.36
	Stomach	1.37 ± 0.62	0.73 ± 0.47	0.60 ± 0.33	1.23 ± 0.08
	Small intestine	5.00 ± 0.69	1.83 ± 0.57	0.32 ± 0.19	6.48 ± 2.88
	Colon	2.65 ± 0.30	4.36 ± 3.60	2.55 ± 1.77	1.11 ± 0.17
	Pancreas	19.00 ± 7.60	6.16 ± 1.80	0.69 ± 0.53	1.19 ± 0.07
	Tumor	1.53 ± 0.26	0.80 ± 0.35	0.41 ± 0.27	0.37 ± 0.09
2	Blood	1.05 ± 0.27	0.11 ± 0.01	0.04 ± 0.00	0.14 ± 0.03
	Kidney	3.51 ± 0.87	0.59 ± 0.10	0.24 ± 0.05	0.66 ± 0.30
	Liver	1.56 ± 0.19**	0.35 ± 0.23	0.46 ± 0.16**	1.02 ± 0.36
	Stomach	2.29 ± 1.18	0.62 ± 0.04	0.16 ± 0.06	0.39 ± 0.26
	Small intestine	5.54 ± 0.72	2.90 ± 1.27	0.50 ± 0.09	3.19 ± 0.29
	Colon	4.94 ± 0.24*	1.74 ± 0.39	1.79 ± 0.74	0.25 ± 0.20§§
	Pancreas	28.37 ± 2.82	10.07 ± 1.82	2.54 ± 0.93	1.12 ± 0.73§§
	Tumor	2.85 ± 0.15	0.97 ± 0.04	0.53 ± 0.09	0.45 ± 0.06§§
3	Blood	1.64 ± 0.23	0.25 ± 0.07	0.05 ± 0.00	0.41 ± 0.18
	Kidney	7.05 ± 1.69**	0.90 ± 0.10	0.28 ± 0.03	1.57 ± 1.31
	Liver	1.90 ± 0.24**	0.33 ± 0.12	0.09 ± 0.02**	2.40 ± 0.67
	Stomach	2.12 ± 0.14	1.17 ± 0.19	0.30 ± 0.05	0.38 ± .031
	Small intestine	7.25 ± 0.67	3.49 ± 1.25	0.52 ± 0.08	1.30 ± 0.21
	Colon	6.71 ± 1.49**	3.07 ± 0.51	2.96 ± 1.78	0.18 ± 0.03§§
	Pancreas	22.98 ± 6.95	11.01 ± 3.72	3.46 ± 2.20	0.42 ± 0.10§§
	Tumor	3.19 ± 0.68**	2.11 ± 0.60**	0.98 ± 0.23*	0.49 ± 0.29§§
5	Blood	2.00 ± 0.39	0.41 ± 0.01	0.19 ± 0.04	0.60 ± 0.23
	Kidney	7.37 ± 0.75**	3.53 ± 0.38**	2.17 ± 0.27**	3.99 ± 0.96
	Liver	1.16 ± 0.11**	0.61 ± 0.06	0.47 ± 0.02**	0.54 ± 0.22
	Stomach	1.23 ± 1.06	0.69 ± 0.09	0.67 ± 0.28	0.81 ± 0.11
	Small intestine	2.28 ± 0.48	0.83 ± 0.15	0.35 ± 0.08	1.03 ± 0.34
	Colon	2.38 ± 0.38	1.30 ± 0.15	0.68 ± 0.13*	0.30 ± 0.12§§
	Pancreas	9.05 ± 1.89	2.09 ± 1.08	2.33 ± 0.22	0.33 ± 0.10§
	Tumor	2.29 ± 0.80	0.76 ± 0.33	0.48 ± 0.22	0.55 ± 0.27

[a] n = 13 for compound 1 (21); * ($P \leq 0.05$), ** ($P \leq 0.01$) vs. reference compound 1 (one-way ANOVA and Dunnett's post hoc test); § ($P \leq 0.05$), §§ ($P \leq 0.01$) vs. unblocked group (unpaired t-test).

radiation nephrotoxicity. The modification of the polarity can change the pharmacokinetics of biomolecules and have a significant impact on the biodistribution as reported for several radiolabeled peptides (*21, 22, 28*−*30*). Therefore, new hydrophilic amino acid linkers were introduced into our BBS analogues to improve the *in vivo* distribution and to increase the tumor-to-background ratios. To avoid the introduction of new enzymatic cleavage sites, β^3homoamino acids were chosen for the syntheses of these linkers (Figure 1) (*26*). All new peptides showed a higher hydrophilicity compared to our reference peptide **1** (Table 1). A single hydroxyl group (β^3hSer, **2**) resulted only in a slight increase of polarity. The insertion of β^3hGlu (**3**) and β^3hLys (**4**) provided the molecule with a single negative and a single positive charge, respectively, and resulted in higher hydrophilicity. As expected, the increase in polarity was even more evident for analogues **5** and **6**, with two and three negative charges.

The linkers did not influence the metabolic stability of the peptides, which showed high plasma stability *in vitro* ($t_{1/2}$ = 16 h) as well as in PC-3 cells ($t_{1/2}$ = 30−40 min), similar to that of stabilized BBS analogues recently published (*21*). Besides a high stability, compounds **2** to **5** exhibited high binding affinities for GRP-R, in the range of ^{125}I-BBS and our previous BBS analogues (Table 1) (*21*), while the affinity of the unlabeled compound **6** was more than 100-fold lower than that of the reference **1**.

In vitro internalization studies in human prostate carcinoma PC-3 cells reflected an agonistic behavior for the new conjugates, which is consistent with data previously reported for BBS constructs with a similar amino acid sequence (Figure 2A) (*11,21,23,29*). The internalization of the analogues **1**, **2** (neutral), and **3** (one negative charge) was comparable, with a maximum of 30% of the total dose/mg protein. Since these three BBS analogues showed big differences in the molecular polarity and no differences in both affinity and internalization, polarity does not seem to be crucial for the internalization. However, analogue **4** (one positive charge) showed a slightly higher internalization than **1** to **3**, whereas the internalization of analogue **5** (two negative charges) was significantly decreased and that of compound **6** (three negative charges) was negligible. These results would indicate that a positive charge may favor internalization of the tricarbonyl-labeled analogues, while more than one negative charge would have an adverse influence, which is consistent with the results Parry et al. reported for the insertion of one and two glutamic acids into the linker of a ^{64}Cu-labeled DOTA-BBS(7−14). The Cu-labeled DOTA-complex already bears a single negative charge, and the introduction of the additional charges also led to a loss of binding affinity and internalization (*22*). This would underscore that not only the linker but also the chelating system may affect the properties of biomolecules, which has already been discussed by Decristoforo et al. for ^{99m}Tc-labeled peptides (*31*). Furthermore, the influence of different polar groups might be specific for each particular labeling approach. The results of the *in vitro* studies indicate that the number and position of negative charges may have a strong influence on the binding affinity and internalization of radiolabeled BBS analogues.

Biodistribution studies were performed in mice bearing PC-3 tumor xenografts to investigate the influence of the charge on the *in vivo* uptake into human tumor cells. The highest tumor

uptake at 0.5 h p.i. was obtained with analogue **3**, being similar to that of a previously reported analogue (*21*). Although compound **2** only showed a slightly lower tumor uptake, it was more rapidly cleared than analogue **3** (Table 2). The fast washout of analogue **3** from normal tissues together with a longer residence time in the tumor tissue resulted in more favorable tumor-to-tissue ratios (Figure 3). The uptake in pancreas and colon was higher than that in tumor for all analogues (Table 2), which is consistent with the presence of high amounts of GRP receptors in these tissues. Specific uptake in normal receptor-positive organs may preclude the use of peptide-based radiopharmaceuticals in clinics. In this respect, no colon uptake is to be expected in men, since human colon does not express GRP receptors. Human pancreas expresses bombesin receptors and might be a dose-limiting organ in radionuclide therapy. However, the levels of GRP receptors are lower than in murine pancreas. Furthermore, human pancreas is not a highly radiosensitive organ, and interestingly, analogue **3** showed a faster washout from pancreas than from tumor. The pancreas uptake observed with the radiolabeled analogues showed a good correlation with their binding affinity. However, no correlation was found between affinity and tumor uptake. This discrepancy may be due to a combination of a polarity-dependent tumor penetration and the affinity for the receptors. Thus, although a higher polarity seems to favor tumor penetration, the different affinity would determine the final binding to the receptors. The hydrophilic character of the analogues **2**, **3**, and **5** translated into a highly significant reduction of activity in the liver, which was comparable to or even clearly lower than that of other recently published ^{99m}Tc-labeled BBS analogues (*11, 21, 23, 32*). The increased polarity also resulted in higher kidney uptake, especially for analogue **5**. The biodistribution of **5** was less favorable, since it showed not only high uptake and retention in the kidneys but also lower uptake in receptor-positive tissues, which confirmed the *in vitro* results. In contrast, compounds **2** and **3** exhibited a much faster clearance from kidney, which led to the highest tumor-to-kidney ratios reported for ^{99m}Tc-labeled BBS agonists (*11, 29*). Analogue **3** also showed higher tumor-to-liver ratios (Figure 3), thus indicating that a single negative charge would be more favorable. Compound **4** was not included in these experiments because of its unsatisfying *in vivo* behavior in preliminary biodistribution studies in normal mice (Supporting Information Table 2). This analogue showed high kidney uptake and slow washout. The influence of the charge on renal uptake has been reported for radiolabeled peptides (*30, 33, 34*). It is known that interaction between positively charged peptides and the negatively charged surface of the proximal tubular cells may increase renal accumulation (*33, 34*). The positive charge on the Lys side chain of analogue **4** may contribute to the higher and persistent accumulation of radioactivity in the kidneys. High renal uptake may cause radiation nephrotoxicity, the most important dose-limiting factor that reduces the therapeutic index of radiopeptides.

Analogue **3** provided a better imaging of the tumor xenografts with a SPECT/CT system than analogues **1** and **5** (Figure 4), with an enhanced delineation of the xenografts and decreased radioactivity in the abdominal area. High abdominal accumulation of radioactivity may obscure the detection of tumors and metastases localized in this region, and it is a general observation reported not only for ^{99m}Tc-labeled BBS analogues (*11, 14, 29, 35*) but also for ^{64}Cu-labeled DOTA-BBS(7−14) (*22*), ^{64}Cu-NOTA-8-Aoc-BBN(7−14)NH_2 (*24*), or ^{68}Ga-labeled DOTA-BBS(6−14) (*36*). Therefore, in order to increase the potential of new radiolabeled BBS analogues in tumor targeting, it is very important to reduce the abdominal uptake.

In conclusion, we evaluated five new BBS analogues for their usefulness in imaging GRP-R-expressing neoplasms and could confirm the great impact of the polarity and charge on their *in vivo* behavior. Different linkers, consisting of polar β^3homoamino acids, were introduced between the binding sequence and the retro(N$^{\alpha}$His)Ac-chelator. A positive charge in the linker resulted in higher uptake and retention in kidney and liver. A hydroxyl group and especially a single negative charge in form of a β^3homoglutamic acid considerably ameliorated the biodistribution profile, with higher tumor uptake and retention, and significantly improved tumor-to-background ratios. However, additional negative charges led to a loss of binding affinity and internalization, and unfavorable biodistribution. The introduction of polar groups seems to be of great interest to improve the *in vivo* properties of ^{99m}Tc- or $^{186/188}$Re-labeled BBS analogues and increase their potential for imaging of GRP-R-expressing tumors. Further preclinical studies with therapeutic radionuclides will help to determine their potential use as radiotherapeutics.

ACKNOWLEDGMENT

The authors thank Ms. Olga Gasser, Dr. Alexander Hohn, and Mr. Alain Blanc for their technical assistance. This work was funded by an Oncosuisse grant (Nr. OCS 01311-02-2003) and by the Fund for Scientific Research-Flanders, Belgium, (grant nr. G.0036.04). V. Maes is a Postdoctoral Researcher of the Fund for Scientific Research-Flanders; Luc Brans thanks the "Institute for the Promotion of Innovation through Science and Technology in Flandres (IWT-Vlaanderen)" for a grant.

Supporting Information Available: Analytical data of the different analogues after synthesis and biodistribution data of compound **4** in normal mice at 0.5, 1.5 h (unblocked and blocked), and 5 h p.i. This material is available free of charge via the Internet at http://pubs.acs.org.

LITERATURE CITED

(1) Reubi, J. C. (2003) Peptide receptors as molecular targets for cancer diagnosis and therapy. *Endocr. Rev. 24*, 389–427.
(2) Heppeler, A., Froidevaux, S., Eberle, A. N., and Maecke, H. R. (2000) Receptor targeting for tumor localisation and therapy with radiopeptides. *Curr. Med. Chem. 7*, 971–994.
(3) Krenning, E. P., Kwekkeboom, D. J., Valkema, R., Pauwels, S., Kvols, L. K., and De Jong, M. (2004) Peptide receptor radionuclide therapy. *Ann. N.Y. Acad. Sci. 1014*, 234–245.
(4) Dijkgraaf, I., Boerman, O. C., Oyen, W. J. G., Corstens, F. H. M., and Gotthardt, M. (2007) Development and application of peptide-based radiopharmaceuticals. *Anticancer Agents Med. Chem. 7*, 543–551.
(5) Okarvi, S. M. (2004) Peptide-based radiopharmaceuticals: Future tools for diagnostic imaging of cancers and other diseases. *Med. Res. Rev. 24*, 357–397.
(6) Smith, C. J., Volkert, W. A., and Hoffman, T. J. (2005) Radiolabeled peptide conjugates for targeting of the bombesin receptor superfamily subtypes. *Nucl. Med. Biol. 32*, 733–740.
(7) Reubi, J., Gugger, M., and Waser, B. (2002) Co-expressed peptide receptors in breast cancer as a molecular basis for in vivo multireceptor tumour targeting. *Eur. J. Nucl. Med. Mol. Imaging 29*, 855–862.
(8) Markwalder, R., and Reubi, J. C. (1999) Gastrin-releasing peptide receptors in the human prostate: relation to neoplastic transformation. *Cancer Res. 59*, 1152–1159.
(9) Parry, J., Andrews, R., and Rogers, B. (2007) MicroPET imaging of breast cancer using radiolabeled bombesin analogs targeting the gastrin-releasing peptide receptor. *Breast Cancer Res. Treat. 101*, 175–183.
(10) Zhou, J., Chen, J., Mokotoff, M., Zhong, R., Shultz, L. D., and Ball, E. D. (2003) Bombesin/gastrin-releasing peptide receptor: a potential target for antibody-mediated therapy of small cell lung cancer. *Clin. Cancer Res. 9*, 4953–4960.

(11) Nock, B. A., Nikolopoulou, A., Galanis, A., Cordopatis, P., Waser, B., Reubi, J. C., and Maina, T. (2005) Potent bombesin-like peptides for GRP-receptor targeting of tumors with ^{99m}Tc: a preclinical study. *J. Med. Chem. 48*, 100–110.

(12) Zhang, H., Chen, J., Waldherr, C., Hinni, K., Waser, B., Reubi, J. C., and Maecke, H. R. (2004) Synthesis and evaluation of bombesin derivatives on the basis of pan-bombesin peptides labeled with indium-111, lutetium-177, and yttrium-90 for targeting bombesin receptor-expressing tumors. *Cancer Res. 64*, 6707–6715.

(13) Smith, C. J., Gali, H., Sieckman, G. L., Hayes, D. L., Owen, N. K., Mazuru, D. G., Volkert, W. A., and Hoffman, T. J. (2003) Radiochemical investigations of ^{177}Lu-DOTA-8-Aoc-BBN(7-14)NH_2: an in vitro/in vivo assessment of the targeting ability of this new radiopharmaceutical for PC-3 human prostate cancer cells. *Nucl. Med. Biol. 30*, 101–109.

(14) Smith, C. J., Gali, H., Sieckman, G. L., Higginbotham, C., Volkert, W. A., and Hoffman, T. J. (2003) Radiochemical investigations of ^{99m}Tc-N_3S-X-BBN(7-14)NH_2: An *in vitro/in vivo* structure-activity relationship study where X = 0-, 3-, 5-, 8-, and 11-carbon tethering moieties. *Bioconjugate Chem. 14*, 93–102.

(15) Bauer, R., and Pabst, H. W. (1982) Tc-genrators - yield of ^{99m}Tc and ratio to 'inactive' ^{99}Tc. *Eur. J. Nucl. Med. 7*, 35–36.

(16) Garcia-Garayoa, E., Schibli, R., and Schubiger, P. A. (2007) Peptides radiolabeled with Re-186/188 and Tc-99m as potential diagnostic and therapeutic agents. *Nucl. Sci. Technol. 18*, 88–100.

(17) Liu, S., and Edwards, D. S. (1999) ^{99m}Tc-labeled small peptides as diagnostic radiopharmaceuticals. *Chem. Rev. 99*, 2235–2268.

(18) Schibli, R., La Bella, R., Alberto, R., Garcia-Garayoa, E., Ortner, K., Abram, U., and Schubiger, P. A. (2000) Influence of the denticity of ligand systems on the in vitro and in vivo behavior of ^{99m}Tc(I)-tricarbonyl complexes: a hint for the future functionalization of biomolecules. *Bioconjugate Chem. 11*, 345–351.

(19) La Bella, R. L., Garcia-Garayoa, E., Bahler, M. B., Blauenstein, P., Schibli, R., Conrath, P., Tourwe, D., and Schubiger, P. A. (2002) A ^{99m}Tc(I)-postlabeled high affinity bombesin analogue as a potential tumor imaging agent. *Bioconjugate Chem. 13*, 599–604.

(20) Garcia Garayoa, E., Ruegg, D., Blauenstein, P., Zwimpfer, M., Khan, I. U., Maes, V., Blanc, A., Beck-Sickinger, A. G., Tourwe, D. A., and Schubiger, P. A. (2007) Chemical and biological characterization of new Re(CO) $_3$/[^{99m}Tc](CO) $_3$ bombesin analogues. *Nucl. Med. Biol. 34*, 17–28.

(21) Garcia Garayoa, E., Schweinsberg, C., Maes, V., Ruegg, D., Blanc, A., Blauenstein, P., Tourwe, D. A., Beck-Sickinger, A. G., and Schubiger, P. A. (2007) New [Tc-99m]bombesin analogues with improved biodistribution for targeting gastrin releasing-peptide receptor-positive tumors. *Q. J. Nucl. Med. Mol. Imaging 51*, 42–50.

(22) Parry, J. J., Kelly, T. S., Andrews, R., and Rogers, B. E. (2007) In vitro and in vivo evaluation of ^{64}Cu-Labeled DOTA-linker-bombesin(7−14) analogues containing different amino acid linker moieties. *Bioconjugate Chem. 18*, 1110–1117.

(23) Kunstler, J. U., Veerendra, B., Figueroa, S. D., Sieckman, G. L., Rold, T. L., Hoffman, T. J., Smith, C. J., and Pietzsch, H. J. (2007) Organometallic ^{99m}Tc(III) ′4 + 1′ bombesin(7−14) conjugates: synthesis, radiolabeling, and in vitro/in vivo studies. *Bioconjugate Chem. 18*, 1651–1661.

(24) Prasanphanich, A. F., Nanda, P. K., Rold, T. L., Ma, L., Lewis, M. R., Garrison, J. C., Hoffman, T. J., Sieckman, G. L., Figueroa, S. D., and Smith, C. J. (2007) [^{64}Cu-NOTA-8-Aoc-BBN(7−14)NH_2] targeting vector for positron-emission tomography imaging of gastrin-releasing peptide receptor-expressing tissues. *Proc. Natl. Acad. Sci. U.S.A. 104*, 12462–12467.

(25) Abele, S., and Seebach, D. (2000) Preparation of achiral and of enantiopure geminally disubstituted beta-amino acids for beta-peptide synthesis. *Eur. J. Org. Chem.* 1–15.

(26) Seebach, D., Beck, A. K., and Bierbaum, D. J. (2004) The world of beta- and gamma-peptides comprised of homologated proteinogenic amino acids and other components. *Chem. Biodivers. 1*, 1111–1239.

(27) Smith, C. J., Volkert, W. A., and Hoffman, T. J. (2003) Gastrin releasing peptide (GRP) receptor targeted radiopharmaceuticals: A concise update. *Nucl. Med. Biol. 30*, 861–868.

(28) Schottelius, M., Wester, H. J., Reubi, J. C., Senekowitsch-Schmidtke, R., and Schwaiger, M. (2002) Improvement of pharmacokinetics of radioiodinated Tyr3-octreotide by conjugation with carbohydrates. *Bioconjugate Chem. 13*, 1021–1030.

(29) Alves, S., Correia, J. D. G., Santos, I., Veerendra, B., Sieckman, G. L., Hoffman, T. J., Rold, T. L., Figueroa, S. D., Retzloff, L., McCrate, J., Prasanphanich, A., and Smith, C. J. (2006) Pyrazolyl conjugates of bombesin: a new tridentate ligand framework for the stabilization of fac-[M(CO)(3)](+) moiety. *Nucl. Med. Biol. 33*, 625–634.

(30) Christensen, E. I., Rennke, H. G., and Carone, F. A. (1983) Renal tubular uptake of protein: effect of molecular charge. *Am. J. Physiol. Renal Physiol. 244*, F436–F441.

(31) Decristoforo, C., and Mather, S. J. (2002) The influence of chelator on the pharmacokinetics of Tc-99m-labelled peptides. *Q. J. Nucl. Med. Mol. Imaging 46*, 195–205.

(32) Rogers, B. E., Bigott, H. M., McCarthy, D. W., Manna, D. D., Kim, J., Sharp, T. L., and Welch, M. J. (2003) MicroPET imaging of a gastrin-releasing peptide receptor-positive tumor in a mouse model of human prostate cancer using a ^{64}Cu-labeled bombesin analogue. *Bioconjugate Chem. 14*, 756–763.

(33) Antunes, P., Ginj, M., Walter, M. A., Chen, J., Reubi, J. C., and Maecke, H. R. (2007) Influence of different spacers on the biological profile of a DOTA-somatostatin analogue. *Bioconjugate Chem. 18*, 84–92.

(34) Akizawa, H., Arano, Y., Mifune, M., Iwado, A., Saito, Y., Mukai, T., Uehara, T., Ono, M., Fujioka, Y., Ogawa, K., Kiso, Y., and Saji, H. (2001) Effect of molecular charges on renal uptake of ^{111}In-DTPA-conjugated peptides. *Nucl. Med. Biol. 28*, 761–768.

(35) Reubi, J. C., Wenger, S., Schmuckli-Maurer, J., Schaer, J.-C., and Gugger, M. (2002) Bombesin receptor subtypes in human cancers: detection with the universal radioligand ^{125}I-[D-TYR^6, β-ALA^{11}, PHE^{13}, NLE^{14}] bombesin(6−14). *Clin. Cancer Res. 8*, 1139–1146.

(36) Schuhmacher, J., Zhang, H., Doll, J., Macke, H. R., Matys, R., Hauser, H., Henze, M., Haberkorn, U., and Eisenhut, M. (2005) GRP receptor-targeted PET of a rat pancreas carcinoma xenograft in nude mice with a ^{68}Ga-labeled bombesin(6−14) analog. *J. Nucl. Med. 46*, 691–699.

BC800262M

Supporting Information. Analytical data of the different analogues after synthesis and biodistribution data of compound **4** in normal mice at 0.5, 1.5 h (unblocked and blocked), and 5 h p.i. This information is available free of charge via the Internet at http://pubs.acs.org.

Table 1. Analytical data of the unlabeled BBS analogues.

Compound	Molecular formula	Yield of peptide synthesis	ES-MS			HPLC UV trace t_R [min]
			calcd M	[M+ H^+]	[M+2H^+]/2	
1	$C_{61}H_{90}N_{18}O_{14}$	55 %	1298.7	1299.5	650.5	12.0[1]
2	$C_{65}H_{97}N_{19}O_{16}$	50 %	1399.7	1401.0	701.0	14.4
3	$C_{67}H_{99}N_{19}O_{17}$	53 %	1441.7	1443.0	722.0	14.5
4	$C_{68}H_{104}N_{20}O_{15}$	58 %	1440.8	1442.0	722.0	14.2
5	$C_{70}H_{103}N_{19}O_{19}$	55 %	1513.8	1514.2	758.1	10.8
6	$C_{73}H_{107}N_{19}O_{21}$	56 %	1585.8	1586.9	793.9	10.8

[1] Gradient: 3% CH_3CN to 100% CH_3CN in 20 min (flow 1 mL/min)

Table 2. Biodistribution of ^{99m}Tc-labeled compound **4** (3 MBq/mouse i.v.) in BALB/c mice. The animals of the blocked group received a co-injection of 0.1 mg natural BBS. Data (mean ± SD) are expressed as percentage of injected dose per gram of tissue (n = 3).

BBS	Organs	0.5 h	1.5 h	5 h	0.5 h blocked
4	Blood	3.64 ± 1.23	0.22 ± 0.02	0.10 ± 0.02	3.70 ± 0.62
	Muscle	0.86 ± 0.18	0.15 ± 0.10	0.06 ± 0.03	0.78 ± 0.07
	Kidney	12.88 ± 2.84	7.08 ± 0.51	5.53 ± 1.60	11.93 ± 1.82
	Liver	10.66 ± 0.43	8.41 ± 0.29	4.82 ± 1.01	13.05 ± 1.63
	Stomach	3.21 ± 0.48	1.22 ± 0.11	0.69 ± 0.11	1.88 ± 0.26
	Small intestine	6.54 ± 0.27	5.41 ± 1.46	1.29 ± 0.08	5.65 ± 1.28
	Colon	4.82 ± 0.55	4.01 ± 0.96	4.67 ± 1.07	1.92 ± 0.28 *
	Pancreas	24.21 ± 4.45	10.45 ± 8.63	5.44 ± 0.99	1.42 ± 0.12 **

* ($P \leq 0.01$), ** ($P \leq 0.001$) vs. unblocked group (unpaired t-test).

For Review. Confidential - ACS

Bioconjugate Chemistry 20th Anniversary

Subscriber access provided by SHEMYAKIN-OVCHINNIKOV INST

Article

Identification of Small Molecule Binding Molecules by Affinity Purification Using a Specific Ligand Immobilized on PEGA Resin

Kouji Kuramochi, Yuka Miyano, Yoshihiro Enomoto, Ryo Takeuchi, Kazutomo Ishi, Yoichi Takakusagi, Takeki Saitoh, Keishi Fukudome, Daisuke Manita, Yoshifumi Takeda, Susumu Kobayashi, Kengo Sakaguchi, and Fumio Sugawara

Bioconjugate Chem., **2008**, 19 (12), 2417-2426• DOI: 10.1021/bc8002716 • Publication Date (Web): 26 November 2008

Downloaded from http://pubs.acs.org on May 2, 2009

More About This Article

Additional resources and features associated with this article are available within the HTML version:

- Supporting Information
- Access to high resolution figures
- Links to articles and content related to this article
- Copyright permission to reproduce figures and/or text from this article

View the Full Text HTML

ACS Publications
High quality. High impact.

Bioconjugate Chemistry is published by the American Chemical Society. 1155 Sixteenth Street N.W., Washington, DC 20036

Identification of Small Molecule Binding Molecules by Affinity Purification Using a Specific Ligand Immobilized on PEGA Resin

Kouji Kuramochi,[†,||] Yuka Miyano,[†,||] Yoshihiro Enomoto,[†,||] Ryo Takeuchi,[†] Kazutomo Ishi,[‡] Yoichi Takakusagi,[†] Takeki Saitoh,[†] Keishi Fukudome,[†] Daisuke Manita,[†] Yoshifumi Takeda,[‡] Susumu Kobayashi,[‡,§] Kengo Sakaguchi,[†,‡] and Fumio Sugawara*[,†,‡]

Department of Applied Biological Science, Genome and Drug Research Center, and Faculty of Pharmaceutical Sciences, Tokyo University of Science, 2641 Yamazaki, Noda, Chiba 278-8510, Japan. Received July 2, 2008; Revised Manuscript Received October 26, 2008

We investigated the application of resins used in solid-phase synthesis for affinity purification. A synthetic ligand for FK506-binding protein 12 (SLF) was immobilized on various resins, and the binding assays between the SLF-immobilized resins and FK506-binding protein 12 (FKBP12) were performed. Of the resins tested in this study, PEGA resin was the most effective for isolating FKBP12. This matrix enabled the isolation of FKBP12 from a cell lysate, and the identification of SLF-binding peptides from a phage cDNA library. We confirmed the interaction between SLF and these peptides using a cuvette type quartz crystal microbalance (QCM) apparatus. Our study suggests that PEGA resin has great potential as a tool not only for the purification and identification of small-molecule binding proteins but also for the selection of peptides that recognize target molecules.

INTRODUCTION

To elucidate the mechanism of action of biologically active small molecules, it is important to identify their target proteins (*1*). Affinity purification with ligand-immobilized beads has greatly contributed to screening for small molecule target proteins (*2*). Generally, agarose is used as a matrix for affinity purification. Unfortunately, however, agarose has a tendency to cause nonspecific binding of proteins, which can lead to problems during the screening procedure. Moreover, the yield as well as the variety of small ligands immobilized on an agarose matrix are limited because agarose is unstable in organic solvents. Several kinds of matrices, including a glycidyl methacrylate (GMA)-covered GMA-styrene copolymer (*3*−*7*), poly(methacrylate) polymers (*8*−*11*), and poly(acrylamide) polymers (*12*−*16*), have been developed to circumvent these problems (*2*). We are interested in applying resins used in solid-phase synthesis to the affinity purification of proteins (*17*). The resins have several attractive features as potential affinity matrices, including significant stability in both organic and aqueous media, chemical and physical stability, and high capacity loading of ligand. We have previously reported the affinity purification of a mammalian DNA polymerase β using its inhibitor-immobilized TentaGel resin.

In earlier studies, the fluorescent, radioisotope, or biotin-labeled derivatives immobilized on affinity beads were used as tools for identification of the target proteins derived from cell lysates (*18*−*21*). Indeed, several target proteins of small molecules, such as methotrexate (*7*, *22*, *23*), FK506 (*1*, *5*, *8*−*11*, *24*), and cyclosporin A (*25*−*27*), were isolated by these methods. Recently a phage-based method was reported (*28*). Phage particles can display a huge combinatorial library encoding peptides or proteins, which are derived from foreign DNA inserts as fusions of the phage capsid. Phage clones that specifically bind to the target molecules are first selected from the library. The corresponding amino acid sequences expressed on the phage surface can then be identified by sequencing the insert DNA of the phage clones. This method allows the rapid selection and identification of the ligand-binding peptides or proteins and has been successfully applied to the determination of binding proteins for FK506 (*29*), doxorubicin (*30*), HBC (*31*), and paclitaxel (*32*−*34*). Moreover, phage display technology can be used to efficiently identify the specific drug-binding site of the identified protein (*33*, *35*−*37*).

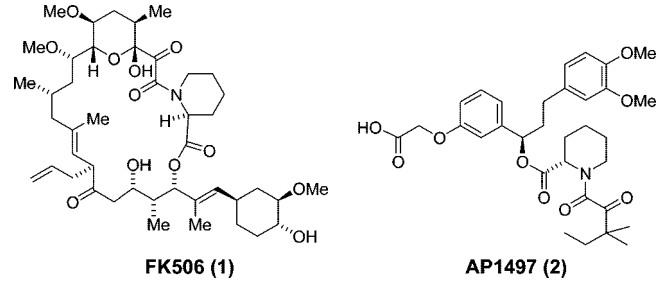

Figure 1. Structure of FK506 (**1**) and AP1497 (**2**). AP1497 is one of the synthetic ligands for FKBP12 (SLFs).

To evaluate the suitability of resins used in organic synthesis as affinity matrices, we focused on synthetic ligands for FK506-binding protein 12 (SLFs) as a model system (Figure 1). AP1497 (**2**) is one such SLF, which tightly binds to FK506 binding protein 12 (FKBP12) with a dissociation constant (K_D) of 20 nM (Figure 1) (*38*, *39*). Previous studies demonstrated that FK506-immobilized matrices captured FKBP12 from cell lysates (*1*, *5*, *8*−*11*, *24*) and that a biotinylated SLF derivative enabled the isolation of clones encoding FKBP12 from a T7 cDNA phage-display library (*40*, *41*). Thus, SLF is considered an ideal model ligand to evaluate matrices for affinity purification of target proteins from both cell lysates and phage cDNA libraries.

In this article, we have evaluated several resins used for organic syntheses as candidate affinity matrices for the identi-

* Corresponding author. Tel:+81-4-7124-1501(ext. 3400). Fax: +81-4-7123-9757. E-mail: sugawara@rs.noda.tus.ac.jp.
† Department of Applied Biological Science.
‡ Genome and Drug Research Center.
§ Faculty of Pharmaceutical Sciences.
|| These authors equally contributed to this work.

10.1021/bc8002716 CCC: $40.75 © 2008 American Chemical Society
Published on Web 11/26/2008

fication of small molecule-binding proteins. We isolated FKBP12 protein from Jurkat cell lysates using SLF-immobilized PEGA resin. We also isolated two SLF-binding phage clones, which displayed full-length FKBP12 and a SLF-binding peptide, from a phage cDNA library using SLF-immobilized PEGA resin.

EXPERIMENTAL PROCEDURES

General Chemistry. Dichloromethane was distilled from P_2O_5 prior to use. *N*,*N*-Dimethylformamide was distilled from calcium hydride prior to use. All other reagents were commercially available and used without further purification. All reactions were monitored by TLC, which was carried out on Silica Gel 60 F_{254} plates (Merck, Darmstadt, Germany). Flash chromatography separations were performed on PSQ 100B (Fuji Silysia Co., Ltd., Japan). ^{1}H and ^{13}C NMR spectra were recorded on Avance DRX-600 or DRX-400 (Bruker BioSpin, Rheinstetten, Germany), using $CDCl_3$ (with TMS for ^{1}H NMR and chloroform-*d* for ^{13}C NMR as the internal reference) solution, unless otherwise noted. Chemical shifts were expressed in δ (ppm) relative to Me_4Si or residual solvent resonance, and coupling constants (*J*) were expressed in Hz. Optical rotations were recorded on a P-1030 digital polarimeter (JASCO, Tokyo, Japan) at room temperature. Infrared spectra (IR) were recorded on a FT/IR-410 spectrometer (JASCO) using NaCl (neat) or KBr pellets (solid) and were reported on wavenumbers (cm^{-1}). Mass spectra (MS) were obtained on an ABIQSTAR pulsar i mass spectrometer (Applied Biosystems, Foster City, CA) under high resolution conditions, using poly (ethylene glycol) as internal standard. Amino HypoGel200 (loading, 0.92 μmol/mg; size, 90 μm) and amino HypoGel400 (loading, 0.70 μmol/mg; size, 90 μm) were purchased from RAPP plolymere (Tübingen, Germany). Amino NovaSyn resins (loading, 0.29 μmol/mg; size, 90 μm), amino NovaGel (loading, 0.83 μmol/mg; size, 75−150 μm), amino PEGA (loading, 0.40 μmol/mg; size, 150−300 μm), amino polystyrene (loading, 0.90 μmol/mg; size, 75−150 μm), and hydroxyamino Wang resins (loading, 2.0 μmol/mg; size, 100−200 μm) were purchased from novabiochem (San Diego, CA). AffiGel 102 Gels (loading, 15 μmol/mL; size, 70−300 μm) were purchased from Bio-Rad Laboratories (Hercules, CA). EAH Sepharose 4B (loading, 7−12 μmol/mL; size, 45−165 μm) was purchased from GE Healthcare Bio-Science Corp (Piscataway, NJ). The peptide (LSCLWAELSGKLWPLPAAQ) was purchased from GENIX TALK (Osaka, Japan).

General Biology. Fetal bovine serum (FBS) was purchased from Biowest (Loire Valley, French). Kanamycin sulfate, dimethyl sulfoxide (DMSO), and biotin were purchased from Wako Pure Chemical Industries (Tokyo, Japan). RPMI 1640 and 2-Mercaptoethanol were purchased from Nacalai Tesque (Kyoto, Japan). Protease inhibitor cocktail was obtained from Sigma-Aldrich (ST. Louis, MO). Streptavidin agarose gel was purchased from GE Healthcare (Buckinghamshire, U.K.).

(1*R*)-1-[3-[2-(4-Nitrophenoxy)-2-oxoethyl]phenyl]-3-(3,4-dimethoxyphenyl)-1-propanyl (2*S*)-1-(3,3-dimethyl-1,2-dioxopentyl)-2-piperidinecarboxylate (3). Compound **3** was prepared in ca. 4:1 tautomeric mixture according to our previous report (*41*). Major tautomer: $[\alpha]_D^{24} = -7.2$ (*c* 1.8, $CHCl_3$); ^{1}H NMR (600 MHz, $CDCl_3$) δ 8.27 (2H, m), 7.33 (2H, m), 7.31 (1H, m), 7.03 (1H, d, J = 7.7 Hz), 7.00 (1H, *br*s), 6.93 (1H, dd, J = 8.2 Hz, 2.5 Hz), 6.77 (1H, m), 6.68 (2H, m), 5.80 (1H, dd, J = 7.9 Hz, 5.7 Hz), 5.32 (1H, *br*d, J = 5.3 Hz), 4.96 (2H, s), 3.85 (6H, s), 3.35 (1H, brd, J = 12.7 Hz), 3.16 (1H, td, J = 13.1 Hz, 2.9 Hz), 2.57 (2H, m), 2.36 (1H, m), 2.24 (1H, m), 2.07 (1H, m), 1.72 (5H, m), 1.45 (1H, m), 1.35 (2H, m), 1.22 (3H, s), 1.21 (3H, s), 0.88 (3H, t, J = 7.4 Hz); ^{13}C NMR (100 MHz, $CDCl_3$) δ 207.8, 169.7, 167.3, 166.6, 157.7, 154.6, 148.9, 147.4, 145.6, 141.8, 133.3, 129.9, 125.3 (× 2), 122.2 (× 2), 120.4, 120.1, 114.6, 113.1, 111.7, 111.3, 76.4, 65.3, 55.9, 55.8, 51.2, 46.7, 44.1, 38.0, 32.4, 31.2, 26.3, 24.9, 23.4, 23.1, 21.1, 8.7; IR (neat) 3021, 2937, 2861, 1786, 1738, 1701, 1640, 1592, 1521, 1444, 1348, 1210, 1143, 1082, 1029, 992, 921, 864, 756 cm^{-1}; HRMS (ESI) calcd for $C_{38}H_{44}N_2O_{11}$ ($[M + Na]^+$) *m*/*z* 727.2837, found 727.2800.

General Method for the Preparation of SLF-Immobilized Resins (5). Dry resins (1 equiv) were swollen in pyridine. To the suspension of the resins was added a solution of **3** (0.3−1.9 equiv) and DMAP (1.2 equiv) in CH_2Cl_2. After the mixture was stirred at r.t. for 19 h, the mixture was filtrated and washed with CH_2Cl_2 five times. The filtrate was concentrated, and the residue was purified by silica gel chromatography (hexane/EtOAc = 4:1 to 1:1) to give the recovered AP1497 *p*-nitrophenyl ester. The amount of SLF immobilized on the dry resins was estimated by the amount of the recovered **3**.

The SLF-immobilized resins were suspended in Ac_2O-pyridine (1:1), and the suspension was stirred at r.t. for 3 h. Then the suspension was filtered and washed with CH_2Cl_2 three times, MeOH three times, and CH_2Cl_2 twice. The resulting resins were dried in vacuo.

The amount of SLF immobilized on 1 mg of dry PEGA resin (**5e**) was 0.19 μmol. Because the swelling volume of PEGA in water is reported to be 16 mL/g in the manufacturer's instruction, 1 g of PEGA resin swells up to 16 mL. Thus, the amount of SLF immobilized on 1 mL of wet PEGA resin (**5e**) was estimated to be 11−12 μmol.

General Method for the Preparation of Acetylated Resins (Control Resins) (6). Dry resins were swollen in pyridine (5.0 mL). To the suspension of the resins was added Ac_2O (5.0 mL), and the suspension was stirred at r.t. for 3 h. Then the suspension was filtered and washed with CH_2Cl_2 three times, MeOH three times, and CH_2Cl_2 twice. The resulting resins were dried in vacuo.

Synthesis of SLF-Immobilized AffiGel. Affigel 102 Gel was washed with DMF five times and swollen in DMF (*5*). To the suspension of the gel was added a solution of **3** (1.2 equiv) and DMAP (1.2 equiv) in DMF. After the mixture was stirred at r.t. for 16 h, the mixture was filtrated and washed with DMF five times. The filtrate was concentrated, and the residue was purified by silica gel chromatography (hexane/EtOAc = 4:1 to 1:1) to give the recovered **3**. The amount of SLF immobilized on the gel was estimated to be 15 μmol/mL by the amount of recovered **3**. The SLF-immobilized AffiGel were suspended in 20% DMF solution of Ac_2O, and the suspension was stirred at r.t. for 3 h. Then the suspension was filtered and washed with DMF three times and 20% aqueous solution of EtOH three times.

Synthesis of Acetylated AffiGel. Affigel 102 Gel was washed with DMF five times. The gel was suspended in 20% DMF solution of Ac_2O, and the suspension was stirred at r.t. for 3 h. Then the suspension was filtered and washed with DMF three times and 20% aqueous solution of EtOH three times.

Synthesis of SLF-Immobilized Sepharose 4B. EAH Sepharose 4B was washed with 1 mM aqueous solution of HCl three times and in 0.5 M aqueous NaCl, and swollen in dioxane/H_2O (1:1). To the suspension of the resins was added a solution of **3** (1.2 equiv) and DMAP (1.2 equiv) in dioxane/H_2O (1:1). After the mixture was stirred at r.t. for 16 h, the mixture was filtrated and washed with dioxane/H_2O (1:1) five times. The filtrate was concentrated, and the residue was purified by silica gel chromatography (hexane/EtOAc = 4:1 to 1:1) to give recovered **3**. The amount of SLF immobilized on the beads was estimated to be 7 μmol/mL by the amount of recovered **3.** The SLF-immobilized Sepharose 4B were suspended in 5% Ac_2O in dioxane, and the suspension was stirred at r.t. for 3 h. Then the suspension was filtered and washed with dioxane/H_2O five times and H_2O three times.

Synthesis of Acetylated Sepharose 4B. EAH Sepharose 4B was washed with 1 mM aqueous solution of HCl three times and in 0.5 M aqueous NaCl, and swollen in dioxane/H_2O (1:1). The gels were treated with 5% Ac_2O in dioxane, and the suspension was stirred at r.t. for 3 h. Then the suspension was filtered and washed with dioxane/H_2O five times and H_2O three times.

Bis(SLF-PEG-undecyl)disulfide (7). Compound **7** was prepared in ca. 4:1 tautomeric mixture from compound **3** according to our previous report (*41*). Major tautomer: $[\alpha]_D^{24} = -3.6$ (*c* 0.67, $CHCl_3$); ^{1}H NMR (600 MHz, $CDCl_3$) δ 7.31 (1H × 2, t, $J = 7.9$ Hz), 7.05 (1H × 2, *br*t, $J = 5.6$ Hz), 7.00 (1H × 2, *br*d, $J = 7.7$ Hz), 6.93 (1H × 2, *br*s), 6.86 (1H × 2, dd, $J = 7.9$ Hz, 2.0 Hz), 6.78 (1H × 2, m), 6.68 (1H × 2, *br*s), 6.67 (2H × 2, m), 6.09 (1H × 2, *br*m), 5.77 (1H, dd, $J = 7.9$ Hz, 5.6 Hz), 5.31 (1H × 2, d, $J = 5.4$ Hz), 4.50 (2H × 2, s), 3.86 (3H × 2, s), 3.85 (3H × 2, s), 3.63 (8H × 2, *br*s), 3.60 (2H × 2, m), 3.57 (2H × 2, m), 3.52 (2H × 2, m), 3.44 (2H × 2, m), 3.37 (1H × 2, *br*d, $J = 12.3$ Hz), 3.18 (1H × 2, td, $J = 13.1$ Hz, 2.9 Hz), 2.67 (2H × 2, t, $J = 7.4$ Hz), 2.61 (1H × 2, m), 2.53 (1H × 2, m), 2.38 (1H × 2, *br*d, $J = 13.7$ Hz), 2.25 (1H × 2, m), 2.15 (2H × 2, t, $J = 7.4$ Hz), 2.05 (1H × 2, m), 1.80−1.60 (12H × 2, m), 1.50 (1H × 2, m), 1.35 (4H × 2, m), 1.27 (10H × 2, brs), 1.23 (3H × 2, s), 1.21 (3H, s), 0.89 (3H × 2, *t*, $J = 7.4$ Hz); ^{13}C NMR (100 MHz, $CDCl_3$) δ 207.8 (× 2), 173.2 (× 2), 169.7 (× 2), 168.1 (× 2), 167.3 (× 2), 157.4 (× 2), 148.9 (× 2), 147.4 (× 2), 141.9 (× 2), 133.3 (× 2), 130.0 (× 2), 120.1 (× 2), 120.1 (× 2), 114.2 (× 2), 113.3 (× 2), 111.3 (× 2), 76.5 (× 2), 70.5 (× 4), 70.3 (× 2), 70.2 (× 2), 70.0 (× 2), 69.7 (× 2), 67.4 (× 2), 55.9 (× 2), 55.8 (× 2), 55.8 (× 2), 51.3 (× 2), 46.7 (× 2), 44.1 (× 2), 39.12 (× 2), 39.10 (× 2), 38.8 (× 2), 36.7 (× 2), 32.5 (× 2), 31.2 (× 2), 29.7 (× 2), 29.5 (× 2), 29.42 (× 2), 29.36 (× 2), 29.3 (× 2), 29.21 (× 2), 29.20 (× 2), 28.5 (× 2), 26.4 (× 2), 25.7 (× 2), 24.5 (× 2), 23.5 (× 2), 23.2 (× 2), 21.2 (× 2), 8.7 (× 2); IR (neat) 3342, 2928, 2857, 1738, 1645, 1517, 1444, 1351, 1261, 1141, 1030, 992 cm^{-1}; HRMS (ESI) calcd for $C_{102}H_{56}N_6O_{24}Na_2S_2$ 979.5198 ($[M + 2Na]^{2+}$), found 979.5220. Calcd for $C_{102}H_{56}N_6O_{24}NaS_2$ *m*/*z* 1936.0504 ($[M + Na]^+$), found 1936.0549.

Bis(Acetyl-PEG-undecyl)disulfide (Bis 11-(*N*-acetyl-3,6,9-trioxaundecyl-*N*-carbamoylundecyl)disulfide) (8). A solution of bis(amino-PEG-undecyl)disulfide (13.4 mg, 13.3 μmol) in Ac_2O (1 mL) and pyridine (1 mL) was stirred at r.t. for 20 h. Then the mixture was concentrated, and the residue was purified by silica gel chromatography ($CHCl_3$/MeOH = 20:1) to give **7** (10.4 mg, 90%) as a white solid. Mp = 88−89 °C; ^{1}H NMR (600 MHz, $CDCl_3$) δ 6.22 (1H ×2, *br*s), 6.11 (1H × 2, *br*s), 3.65 (8H × 2, *br*s), 3.57 (4H × 2, t, $J = 5.1$ Hz), 3.45 (4H × 2, m), 2.68 (2H × 2, t, $J = 7.3$ Hz), 2.17 (2H, x 2, t, $J = 7.9$ Hz), 1.99 (3H × 2, s), 1.69−1.60 (4H × 2, m), 1.37 (2H × 2, m), 1.27 (10H × 2, *br*s); ^{13}C NMR (100 MHz, $CDCl_3$) δ 173.2 (× 2), 170.0 (× 2), 70.39 (× 2), 70.38 (× 2), 70.1 (× 4), 69.9 (× 2), 69.8 (× 2), 39.2 (× 2), 39.1 (× 2), 39.0 (× 2), 36.6 (× 2), 29.36 (× 2), 29.33 (× 2), 29.27 (× 2), 29.2 (× 2), 29.1 (× 4), 28.4 (× 2), 25.6 (× 2), 23.1 (× 2); IR (neat) 3298, 3082, 2921, 2849, 1643, 1557, 1463, 1414, 1377, 1286, 1232, 1143, 997, 952 cm^{-1}; HRMS (ESI) calcd for $C_{42}H_{82}N_4O_{10}NaS_2$ 889.5364 ($[M + Na]^+$), found 889.5364.

Expression of Six Histidine-Tagged FK506-Binding Protein 12 (FKBP12). The cDNA encoding human FKBP12 was cloned into the expression vector pET28a(+) (Novagen) and was transformed into *Esherichia coli* BL21(DE3). A single colony was inoculated into 15 mL of LB medium containing 1% glucose and 50 μg/mL kanamycin, and cultured at 30 °C. The cells were grown overnight and then were transferred into 1 L of the same medium at 37 °C. After incubation for 3 h, the expression of FKBP12 was induced by adding IPTG to 1 mM. The culture was then continued for further 3 h at 37 °C. The cultured cells were harvested by centrifugation at 1500*g* for 10 min at 4 °C. The cells were resuspended in PBS and centrifuged at 1100*g* for 10 min at 4 °C. After removal of the supernatant, the cells were frozen using liquid N_2 and then stored at −80 °C.

Purification of His-Tagged FKBP12. The FKBP12-producing cells were sonicated in buffer A (50 mM phosphate (pH. 8.0), 300 mM NaCl, 10 mM imidazole, 1 mM phenylmethylsulfonyl fluoride (PMSF), 1 μg/mL leupeptin, and 1 μg/mL pepstatin A) and then centrifuged at 20400*g* for 30 min at 4 °C. The supernatant was filtered through a PVDF membrane (Millex, pore size 0.45 μm, Millipore, Billerica, MA) and then loaded onto a Ni-NTA resin (GE Healthcare) pre-equilibrated with buffer A. The column was washed with buffer B (50 mM phosphate (pH. 8.0), 300 mM NaCl, 20 mM imidazole), and buffer C (50 mM phosphate (pH. 8.0), 300 mM NaCl, and 30 mM imidazole). Bound proteins were then eluted with buffer D (50 mM phosphate (pH. 8.0), 300 mM NaCl, and 250 mM imidazole). The fractions containing the His-tagged FKBP12 were collected and dialyzed into TEMG buffer (50 mM Tris-HCl (pH 7.5), 1 mM EDTA, 50 mM NaCl, 10% glycerol, and 5 mM 2-mercaptoethanol) for purification by FPLC. The protein was loaded onto HiTrap DEAE column pre-equilibrated with TEMG buffer, and the flow-through fraction was then subjected to HiTrap SP column. The flow-through fraction was collected and dialyzed into FKBP buffer (25 mM Tris-HCl (pH 7.5), 50 mM NaCl, 1 mM $MgCl_2$, 1 mM $CaCl_2$, 10% glycerol, 5 mM 2-mercaptoethanol, and 0.05% Nonidet P-40) and then stored at −80 °C until use.

Binding Analysis between FKBP12 and the Resins. Each resin (4 mg) was pre-equilibrated with the FKBP12 buffer (400 μL) overnight. Then 600 μL of recombinant FKBP12 (1.61 mg/mL, 0.97 mg) was added to the resins. The resins were incubated at 4 °C for 4 h. The amount of FKBP12 in the supernatant was determined by the Bradford assay, with absorbance measured at 595 nm. The amount of FKBP12 bound to the resins was calculated by subtracting the amount of FKBP12 in the supernatant from the amount of total FKBP12. After the resins were washed with the FKBP12 buffer (850 μL) 5 times, the resulting resins were boiled at 90 °C in 250 μL of SDS−PAGE loading buffer (0.25 mM dithiothreitol, 0.5% SDS, 20 mM Tris-HCl (pH6.8), 2.5% glycerol, and 0.01% Bromo phenol blue). The supernatant of each sample was separated on a 15% acrylamide gel, visualized by CBB staining, and quantified using the ImageJ program.

Affinity Purification of FKBP12 from Jurkat Cell Lysates by the SLF-Immobilized PEGA Resin. All procedures were performed at 4 °C. Frozen Jurkat cells (1×10^7 cells) were suspended in 1 mL FKBP buffer containing protease inhibitors (1 mM phenylmethyl sulfonyl fluoride, 1 μg/mL leupeptin, and 1 μg/mL pepstatin A), sonicated twice for 5 s, and incubated on ice for 25 min. The cells were centrifuged at 15000 rpm for 20 min at 4 °C, and the supernatant was kept as cell lysate. After SLF-immobilized PEGA resin (4 mg) and control PEGA resin (4 mg), pre-equilibrated with FKBP buffer containing protease inhibitors, the resulting beads were added to 450 μL of Jurkat cell lysate. The mixtures (1 mL) were rotated gently for 4 h. The resins were washed 3 times with 850 μL of FKBP buffer containing protease inhibitors and were boiled at 90 °C in 50 μL of SDS−PAGE loading buffer (1.25 mM dithiothreitol, 2.5% SDS, 100 mM Tris-HCl (pH6.8) 12.5% glycerol, and 0.01% bromo phenol blue). Each sample was separated on a 15% acrylamide gel and visualized by silver staining. FKBP12 bound to the resins was detected by Western blotting with anti-FKBP12 goat polyclonal antibody (Santa Cruz Biotechnology, Inc., Santa Cruz, CA) and alkali phosphatase-conjugated antigoat IgG.

Construction of FKBP12 Phage Clone. Full length gene encoding human FKBP12 protein was obtained from a phage cDNA library by PCR with the two primers, FKBP-up (5′-GAATTCGATGGGAGTGCAGGTGGAAAC-3′) and FKBP-down (5′-AAGCTTTCATTCCAGTTTTAGAAGCTCC-3′). The amplified DNA was double digested with *Eco*R I and *Hin*d III endonucleases and concentrated by ethanol precipitation. The purified DNA was then ligated into T7-Select10-3b vector (Novagen) and subsequently packaged into phagemid (Novagen). The FKBP12 phage clone was amplified by infection into *E. coli* strain BLT5615.

Binding Analysis of FKBP12 Phage Clone to the SLF-Immobilized Resin or Control Resin. Each resin (100 μg) was pre-equilibrated with TBS (25 mM Tris-HCl, pH 7.5, 50 mM NaCl, 1 mM $MgCl_2$, 1 mM $CaCl_2$, 10% Glycerol, and 0.05% Nonidet P40) for 12 h at 4 °C. The FKBP12 phage clone was amplified by infection into *E. coli* strain BLT5615 as host cells, and the amplified phage clone (1×10^{10} plaque forming units (pfu)/mL) was added to the resin. After incubation at room temperature for 1 h, the resin was precipitated and the phage solution removed. The resin was then washed 10 times with Wash buffer (25 mM Tris-HCl, pH 7.5, 50 mM NaCl, 1 mM $MgCl_2$, 1 mM $CaCl_2$, 10% Glycerol, 0.05% Nonidet P40, and 5 mM 2-mercaptoethanol). Bound phage particles were subsequently removed from the resin by 15 min incubation in 1% SDS in TBS buffer. The eluted phage particles were amplified by infection into *Escherichia coli* strain BLT5615, and the titers of the phage particles from each resin were calculated. The phage clone with no inserted cDNA fragment (No Ins phage) was used in the same binding assay as the negative control.

Construction of T7 cDNA Phage Library. The T7 phage library was constructed using cloning kits for T7 phage display (T7 Select 10-3 OrientExpress cDNA Cloning System, Random Primer, Novagen) and cDNA derived from Colo205 cells according to the method given by the manufacturer. The primary titer of this T7 phage library was 3.3×10^5 pfu. The library was amplified with a titer of 1×10^{10} pfu/mL for screening.

Affinity Selection of SLF-Binding Phage Clones from T7 cDNA Phage Library Using the SLF-Immobilized PEGA Resin. A modified version of the biopanning technique given in the manufacturer's instructions (Novagen) was used in this study. The resin (100 μg) pre-equilibrated with TBS (25 mM Tris-HCl, pH 7.5, 50 mM NaCl, 1 mM $MgCl_2$, 1 mM $CaCl_2$, 10% glycerol, and 0.05% Nonidet P40) for 12 h at 4 °C. The T7 cDNA display library (1 mL, approximately 1×10^{10} pfu/mL) was added to the resin. After incubation at room temperature for 1 h, the resin was precipitated and the phage solution removed. The resin was then washed 10 times with Wash buffer (25 mM Tris-HCl, pH 7.5, 50 mM NaCl, 1 mM $MgCl_2$, 1 mM $CaCl_2$, 10% glycerol, 0.05% Nonidet P40, and 5 mM 2-mercaptoethanol). Adsorbed phage particles were subsequently removed from the resin by 15 min of incubation in 1% SDS solution. The eluted phage particles were amplified by infection into *E. coli* strain BLT5615 as host cells. The amplified phage was applied to subsequent rounds of biopanning. The titer was monitored at each panning step. The eluted phage solution at each step was used for the immediate infection of host cells. Incubation with shaking at 37 °C was continued until lysis was observed. Amplified phage titers of each round were estimated to be approximately $1-6 \times 10^{10}$ pfu/mL. After each round, the eluted phage titers were compared to those of the previous round.

Characterization of Binding Phage. After the seventh round, the eluted phage particles were applied to Luria−Bertani (LB) plates containing 50 μg/mL carbenicillin. Sixteen clones were randomly selected from the plate, and each clone was dissolved in phage extraction solution (20 mM Tris-HCl pH 8.0, 100 mM NaCl, and 6 mM $MgSO_4$). Phage DNA carrying insert cDNAs was amplified by PCR using a forward primer (5′-TGCTAACT-TCCAAGCGGACC-3′) and a reverse primer (5′-TTGCCCA-GAACTCCCCAA-3′). The PCR products were purified with ExoSAP-It (GE Healthcare) and used for cycle sequence PCR with a BigDye Terminator 3.1 Cycle Sequence Kit (Applied BioSystems). The resulting fragments were precipitated with ethanol. The purified PCR products were sequenced on an ABI PRISM 3100 Genetic Analyzer (Applied BioSystems). From the results, the deduced amino acid sequence present on the T7 phage capsid was determined.

Scheme 1. Synthesis of SLF-Immobilized Supports (5a−j) and Control Supports (6a−j)[a,b]

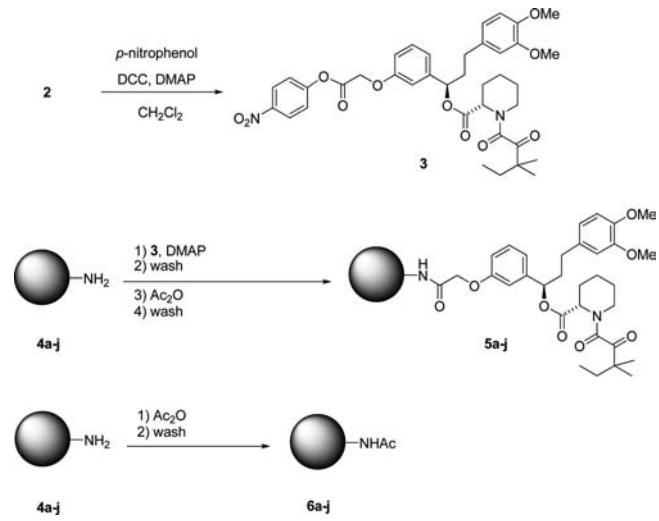

[a] (**a**) HypoGel 200, (**b**) HypoGel 400, (**c**) TentaGel, (**d**) NovaSynTG, (**e**) PEGA, (**f**) NovaGel, (**g**) polystyrene resins, (**h**) Wang resins (**i**) AffiGel, (**j**) Sepharose 4B. [b] The loading of SLF on **5** was estimated from the amount of the recovered **2**, resulting in **5a** (0.48 μmol/mg), **5b** (0.49 μmol/mg), **5c** (0.23 μmol/mg), **5d** (0.19 μmol/mg), **5e** (0.19 μmol/mg), **5f** (0.48 μmol/mg), **5g** (0.48 μmol/mg), **5h** (0.48 μmol/mg), **5i** (15 μmol/mL), and **5j** (7 μmol/mL).

Kinetic Analysis of the Binding between SLF and FKBP12 or SLF-Binding Peptide by QCM Apparatus. Kinetic analyses were performed by a 27 MHz QCM system (Affinix Q, Initium Inc., Tokyo, Japan). Disulfide linked SLF dimer or acetylated diulfide was immobilized on the gold electrode of the sensor chip (*41*). The sensor chip was set on the QCM apparatus and soaked in buffer (8 mL, 10 mM Tris-HCl, pH 8.0, and 200 mM NaCl). The frequency of the QCM was defined as zero position after equilibrium (3 min). Then an 8 μL aliquot of His-tagged FKBP12 or 20 amino acid peptide sequence (SLSCLWAELSGKLWPLPAAQ) was sequentially injected into the cuvette. The changes of the frequency were monitored over time. The kinetic analysis was performed by AQUA ver. 1.5 software (Initium Inc.).

RESULTS

Syntheses of SLF-Immobilized Supports and Control Supports. AP1497 (**2**) was immobilized on resins (**4a**−**h**), which are normally used for solid-phase syntheses, and commercially available agarose matrices (**4i** and **4j**) by two steps via its nitrophenyl ester **3** (Scheme 1) (*38*, *41*). After immobilization of **2** onto the resins, the residual amino groups were blocked with acetic anhydride, yielding SLF-immobilized supports (**5a**−**j**). The loading of the SLF molecule was estimated from the amount of recovered **3**. Typically, the SLF-immobilized supports were prepared with a loading of 0.007−0.49 μmol/mg. In addition, control matrices (**6a**−**j**) were prepared by acetylation of **4** with Ac_2O to check the binding specificity.

HypoGel200 (**4a**), Hypogel400 (**4b**), TentaGel (**4c**), and NovaSyn TG (**4e**) are polystyrene−polyethylene glycol graft polymers (*42*). The molecular masses of polyethylene glycol (PEG) in HypoGel200 and Hypogel400 are 200 and 400 Da, respectively. TentaGel and NovaSynTG resins have PEG chains with a molecular mass of about 2000−3000 Da. The major difference between TentaGel and NovaSyn TG is the structure of the linkers. The PEG chains in TentaGel are linked to the polystyrene core via benzyl ether or in the case of NovaSyn TG via ethyl ether. NovaGel (**4f**), (4′-*O*-methylpolyethyleneglycoxycarbonylaminomethyl)polystyrene, was prepared from a modified aminomethylated polystyrene by partial derivatization with PEG chains. NovaGel has PEG chains with a molecular mass of about 2000 Da. PEGA (**4e**) is a copolymer of dimethylacrylamide and PEG (*43*). The molecular mass of the PEG chains in PEGA resin is about 800 Da. Wang resin (**4h**) was linked to the polystyrene core via the hydroxymethylphenoxy group. AffiGel (**4i**) and Sepharose 4B (**4j**) are commercially available agarose supports and are usually used for target identification of biologically active compounds. All of the supports used in this paper had a similar particle size (45−300 μM).

Binding Analyses between FKBP12 and the SLF-Immobilized Supports. Binding analyses between recombinant FKBP12 and the resins for organic synthesis were performed by the Bradford method for protein quantification (Figure 2A) (*17*, *44*). An excess amount of FKBP12 (0.97 mg) was applied to each SLF-immobilized resin (**5a**−**h**) or control resin (**6a**−**h**). After incubation at 4 °C for 4 h, the amount of FKBP12 in the supernatant was determined using the Bradford assay. The amount of FKBP12 bound to the resins was calculated by subtraction of the amount of free FKBP from that of total FKBP12. As shown in Figure 2A, only SLF-immobilized PEGA resin (**5e**) bound a significant amount of FKBP12 (0.53 mg), i.e., >25-fold greater than that bound by the control PEGA resin (**6e**) (0.02 mg). After washing away the unbound FKBP12 with buffer 5 times, the resins were boiled with SDS sample buffer. Any eluted FKBP12 was detected by SDS−PAGE and visualized using CBB staining. Figure 2B shows that FKBP12 was eluted only from **5e**. In contrast, no bound FKBP was detectable using the other resins, even after loading in the presence of abundant quantities of FKBP. The binding specificity was also confirmed by a competition assay with free SLF (Supporting Information). Similarly, we compared the amount of FKBP12 binding to SLF immobilized on PEGA resin (**5e**) with that to AffiGel (**5i**), which is one of the matrixes widely utilized for affinity purification of proteins (Figure 2C). SDS−PAGE analyses indicated that very similar amounts of FKBP12 were captured by the SLF on both resins in significantly low background. We confirmed that both **5e** and **5i** absorbed almost the same amount of FKBP12 (approximately 180 μg/4 mg resin). Because the amount of SLF immobilized on **5e** and **5i** was 11−12 and 15 μmol/mL, respectively (see Experimental Procedures and ref *45* for details), these data indicate that FKBP12 specifically bound to SLF immobilized on PEGA resin with efficiency similar to that of the AffiGel matrix. In addition, we confirmed that the PEGA resin with other ligands, such as lithocolic acid (LCA, a DNA polymerase β inhibitor) and glutathione (GSH), was applicable for affinity purification (Supporting Information).

We next sought to isolate FKBP12 from Jurkat cell lysates with the SLF-immobilized PEGA resin (**5e**) in a small scale. After incubation with the cell lysates, the resins were washed and then bound proteins were analyzed by SDS−PAGE. A 12-kDa protein was detected in the eluted proteins from **5e** in the silver-stained gel but not in those from **6e** (Figure 3A). In addition, a polyclonal antibody against FKBP12 cross-reacted

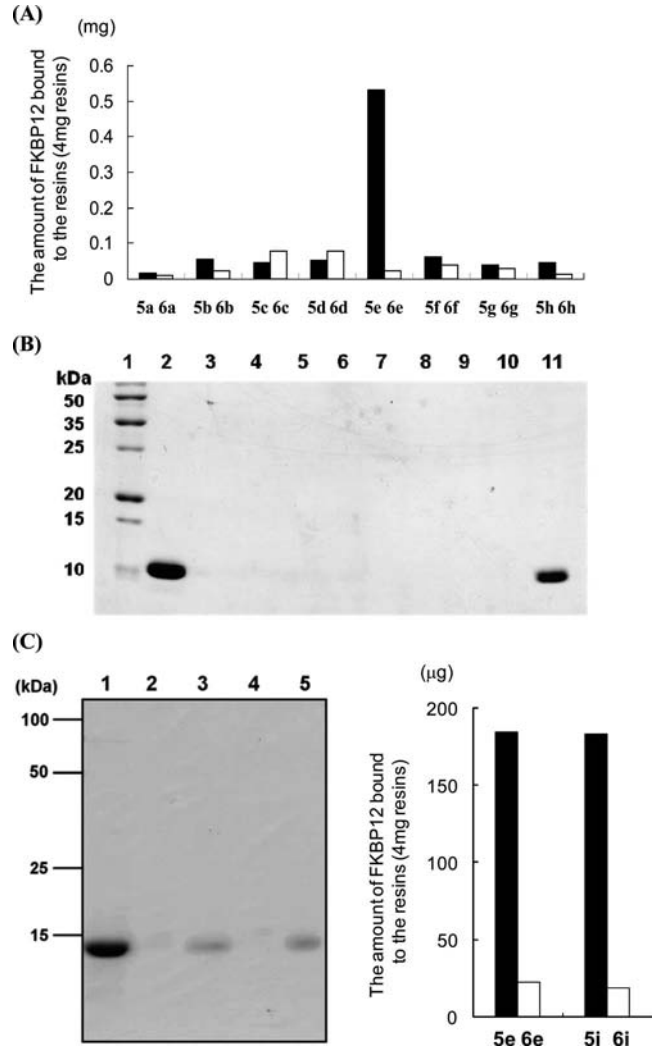

Figure 2. Binding analysis between recombinant FKBP12 and SLF-immobilized resins. (A) The amount of FKBP12 binding to resins **5a**−**h** and **6a**−**h**. A total of 0.97 mg of FKBP12 was applied onto **5a**−**h** and **6a**−**h**. After equilibrium, the amount of FKBP12 in the supernatant was determined by the Bradford assay. The amount of FKBP12 binding to resins **5a**−**h** and **6a**−**h** was calculated by subtraction of the amount of FKBP12 in the supernatant from the input FKBP12. (B) SDS−PAGE of FKBP eluted from **5a**−**h** and **6e**. After washing the resins to remove unbound FKBP12, the resins were boiled with SDS sample buffer. The eluted FKBP12 was analyzed by SDS−PAGE and visualized by CBB staining. Lane 1, molecular weight marker; lane 2, input FKBP12 (20%); lane 3, **5a**; lane 4, **5b**; lane 5, **5c**; lane 6, **5d**; lane 7, **5f**; lane 8, **5g**; lane 9, **5h**; lane 10, **6e**; lane 11, **5e**. (C) Comparison of FKBP12 binding between SLF-immobilized PEGA resin (**5e**) and AffiGel (**5i**). The bound FKBP12 protein on each resin was separated on a SDS−polyacrylamide gel (right) and quantified using ImageJ software (left). Lane 1, input FKBP12 (100%); lanes 2−5, elution from **6e** and **5e**, and **6i** and **5i**, respectively.

with this protein band (Figure 3B), indicating that the SLF-immobilized PEGA resin efficiently captured FKBP12 from the cell lysate.

Binding Analysis between FKBP12 Phage Clone and SLF-Immobilized PEGA Resin. To explore the suitability of PEGA resin as an affinity matrix for phage display, we conducted a T7 phage display screen using the SLF-immobilized PEGA resin. The binding of the T7 phage expressing FKBP12 clone (FKBP12 phage) to the SLF-immobilized PEGA resin was examined (Figure 4A). The phage particles were incubated with the SLF-immobilized PEGA (**5e**) or the control PEGA resins (**6e**). After removal of unbound phage, the bound phage particles were eluted and counted by infection into *E. coli*. The

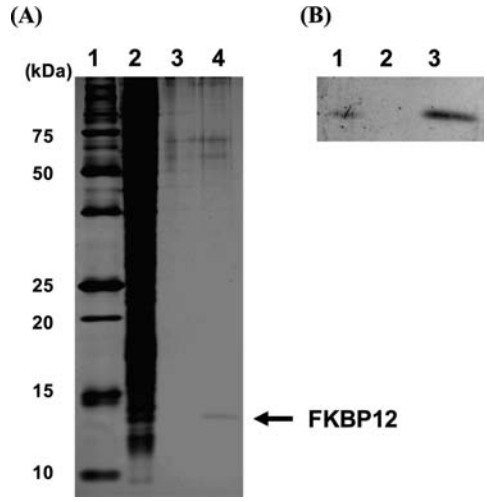

Figure 3. Affinity purification and detection of FKBP12 from Jurkat cell lysates using the SLF-immobilized PEGA resin. (A) SDS−PAGE analysis of the eluted samples from SLF-immobilized PEGA resin (**5e**) and control PEGA resin (**6e**). The protein bands on the gel were visualized after silver staining. Lane 1, molecular weight marker; lane 2, cell lysate; lane 3, elution from **6e**; lane 4, elution from **5e**. (B) Immunoblotting analysis for FKBP12. The eluted fractions were subjected to immunoblotting analysis using antihuman FKBP12 antibody. Lane 1, cell lysate; lane 2, elution from **6e**; lane 3, elution from **5e**.

recovery rate of the eluted phage particles from **5e** or **6e** is shown in Figure 4. **5e** trapped 600-fold more FKBP12 phages than **6e**. In contrast, there was little difference between the recovery rates of the phage with no insert cDNA (No Ins phage) from the two resins (i.e., **5e** and **6e**). These results indicate that the FKBP12 phage clone specifically binds SLF immobilized on the PEGA resin. We conducted the same binding analyses using AffiGel and Sepharose 4B (Figure 4 B and 4C). The SLF-immobilized AffiGel (**5i**) trapped 144-fold more FKBP12 phages than the acetylated AffiGel (**6i**), although the recovery rate was quite lower than that in the case of **5e** (Figure 4B). By contrast, the SLF-immobilized Sepharose 4B (**5j**) absorbed the FKBP12 phage clone with significantly high background. Our results indicate that PEGA resin may be a useful matrix for phage display screening.

Affinity Selection of SLF-Binding Phage Clones from the T7 Phage cDNA Library Using the SLF-Immobilized PEGA Resin. Isolation of FKBP12 phage from a phage cDNA library using the SLF immobilized PEGA resin was examined (Figure 5A). The T7 phage cDNA library was prepared with total RNA from Colo205 cells. The primary T7 phage library contained approximately 3.3×10^5 individual phage clones. The phage cDNA library was incubated with the SLF-immobilized PEGA (**5e**) or control PEGA resin (**6e**). After removal of unbound phage particles, the bound phage particles were eluted and amplified in *E. coli*. The resulting phages were then used in the next round of selection. Using **5e**, the recovery rate of eluted phage particles against input phage particles increased with each round of biopanning (Figure 5). By contrast, this ratio displayed little variation during each round of biopanning using **6e** (Figure 5). After the seventh round, we randomly selected 13 clones out of the eluted phage clones from **5e**. We then analyzed the deduced amino acid sequences displayed on the phage surface (Table 1A). Three clones (clone 1) encoded full-length FKBP12 including the 5′-terminal untranslated region. The other 9 clones displayed 20 amino acids (SLSCLWAELSGKLWPLPAAQ) on the phage surface, which are derived from a frameshift of the inserted cDNA. We also randomly selected 15 clones from the phages binding to **6e** and analyzed the corresponding sequences. Fourteen out of 15 clones binding to

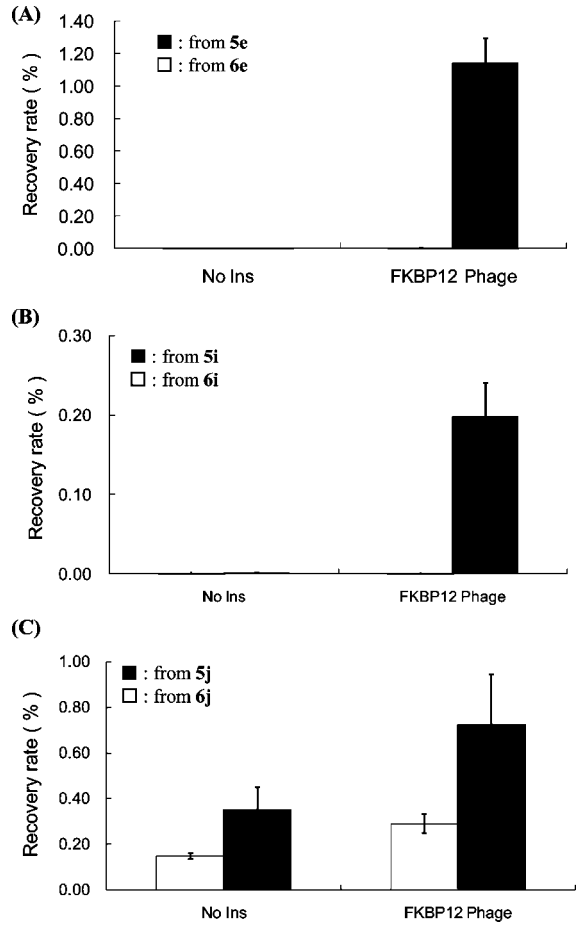

Figure 4. Binding analysis between FKBP12 phage clone and SLF-immobilized PEGA resin (A), AffiGel (B), or Sepharose 4B (C). Recovery rate of FKBP12 phage particles to the input phage particles from SLF-immobilized beads (filled column) or control beads (open column) is indicated. The phage clone with no insert cDNA (No Ins phage) was used in the same binding assay as the negative control. Values are the mean ± SD ($n = 6$).

6e encoded an individual short peptide, but no consensus sequences were identified.

Specific binding of clone 2 onto **5e** was confirmed using the same procedures as for FKBP12 phage (Figure 6). The recovery rate of clone 2 from **5e** was 9.5-fold higher than that from **6e**. However, there are no differences between the recovery of No Ins phage clone by **5e** and **6e**. These results indicate that clone 2 specifically recognizes SLF immobilized on the PEGA resin. Taken together, these results indicate that affinity selection of SLF-binding phage clones from the cDNA library was successfully achieved by the use of the SLF-immobilized PEGA resin. We searched for human genes homologous to the clone 2 peptide using PSI-BLAST (position-specific iterative BLAST). The clone 2 peptide displayed homology to various human gene products, but showed a relatively higher level of similarity to the 13 amino-acid sequence of group E Sox proteins (SoxE) (Supporting Information). This result suggests that SLF may bind to many kinds of proteins in human cells and that SoxE members are passive targets of SLF in vivo.

Kinetic Analysis of the Binding between SLF and the SLF-Binding Peptide Using a QCM Apparatus. We performed a kinetic analysis of the interaction between SLF and the clone 2 peptide (SLSCLWAELSGKLWPLPAAQ) using a cuvette type quartz crystal microbalance (QCM) apparatus (Affinix Q, Initium). Disulfide linked with SLF (Bis(SLF-PEG-undecyl)disulfide; **7**) or acetylated disulfide (bis(Acetyl-PEG-undecyl)disulfide; **8**) was immobilized onto the gold surface of

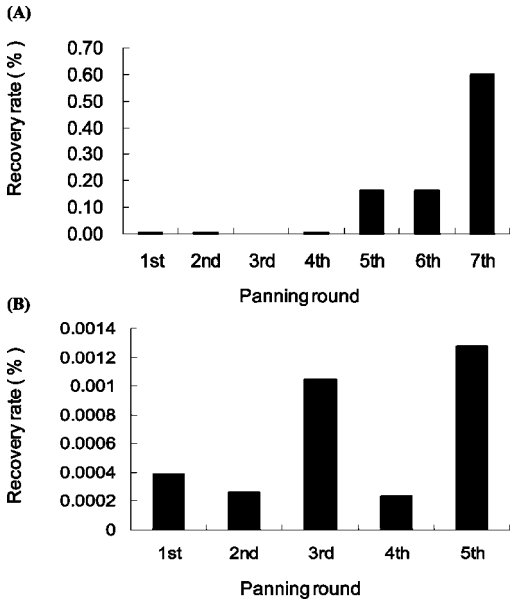

Figure 5. Recovery rate of SLF-binding phage particles after each round of biopanning. (A) The recovery rate obtained from the SLF-immobilized PEGA resin (**5e**). (B) The recovery rate obtained from the control PEGA resin (**6e**). The phage cDNA library derived from Colo205 cells was applied to **5e** or **6e**. After removal of unbound phage particles, bound phage particles were eluted and amplified by infection of *E. coli*. The resulting phage particles were used in the next round of selection. At each round, the recovery rates of the eluted phage particles to the input phage particles from the resins were calculated.

Table 1. Amino Acid Sequence of Peptide Displayed on the Phage Particle after the Biopanning Using (A) SLF-Immobilized PEGA Resin (5e) or (B) Control PEGA Resin (6e)

(A)

phage clone	sequence[a]	frequency[b]
1[c]	GRCWSTPPVAPPARSASAAA MGVQVETISPGDGRTFPKRG QTCVVHYTGMLEDGKKFDS SRDRNKPFKFMLGKQEVIRG WEEGVAQMSVGQRAKLTISP DYAYGATGHPGIIPPHATLV FDVELLKLE	3/13
2	SLSCLWAELSGKLWPLPAAQ	9/13

(B)

phage clone	sequence[a]	frequency[b]
1′	PAGISRELVDKLAAALE	2/15
2′	SHVRESGARTKAAVAQ	1/15
3′	RNLLWLE	1/15
4′	SGASPAV	1/15
5′	SPTLTHF	1/15
6′	TEKRQEDPYYCPRDR	1/15
7′	SAVCTKGRDLINASL	1/15
8′	SGTTVQSGGLGQGPGGLAKAS PVAGGPLGREVR	1/15
9′	SHSSGLNDHSHHGPGARHLPP PQGHAAWPP	1/15
10′	SSKHDF	1/15
11′	SPSRSRTLGSPAGGSGPGQAG REGEGGPGAAGQTGHR	1/15
12′	SVRGRKNIPQPSTLKQWGEGS QRVQMAPVPFAAEN	1/15
13′	SQEVSEKLPQG	1/15
14′	SKTIASSSPPS	1/15

[a] Amino acid sequences were determined from DNA sequences of the insert DNA. [b] Frequency is the number of sequences among the total phage clones selected. [c] The underlined sequence corresponds to the full-length sequence of the human FKBP12 protein.

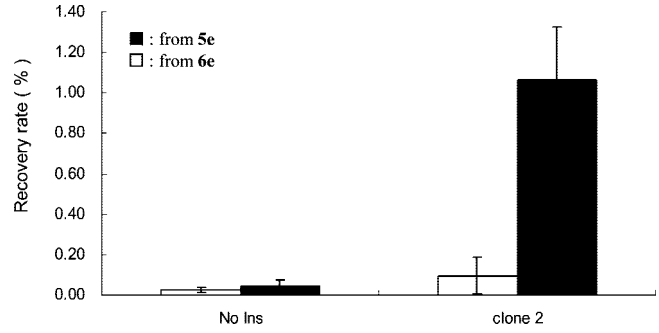

Figure 6. Binding analysis between the clone 2 and SLF-immobilized PEGA resin. Recovery rate of clone 2 to the input phage particles obtained from SLF-immobilized PEGA resin (filled column) or control PEGA resin (open column) is indicated. The phage clone with no insert cDNA (No Ins phage) was used in the same binding assay as the negative control. Values are the mean ± S.D. ($n = 6$).

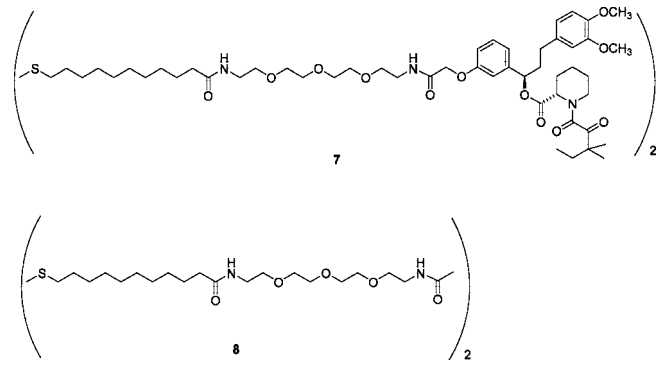

Figure 7. Structure of the disulfide linked with SLF (**7**) and acetylated disulfide (**8**).

the sensor chip (Figure 7). After washing the gold surface, the resulting sensor chip was mounted onto the QCM apparatus. As a positive control, recombinant FKBP12 was injected into the cuvette, and the QCM frequency shifts caused by the binding between the protein and small molecules conjugated to the sensor chip were monitored (red line in Figure 8A). The injection of protein significantly varied the frequency on the SLF-immobilized sensor chip. However, these frequency changes were only slight on the compound **8**-immobilized sensor chip, which was used as a negative control (Figure 8A, black line). Similarly, the addition of clone 2 peptide caused substantial frequency changes on the SLF-immobilized sensor chip but almost no change on the compound **8**-immbilized sensor chip (Figure 8B). The binding of FKBP12 or the clone 2 peptide against compound **7** was analyzed using the Langmuir adsorption model (Figure 9). The K_D values of the recombinant FKBP12 and clone 2 peptide with compound **7** were 0.027 μM and 5.8 μM, respectively. These results indicate that the clone 2 peptide (SLSCLWAELSGKLWPLPAAQ) specifically binds to SLF in vitro.

DISCUSSION

In this study, we investigated whether the resins used for solid-phase syntheses were suitable for affinity purification. To evaluate the capacity of the resins to act as an affinity matrix, synthetic ligand for FKBP12 (SLF), which specifically and tightly binds to FKBP12, was used as a model system. The efficacy of the SLF-immobilized resins was evaluated by affinity purification of FKBP12 from both a cell lysate and a phage cDNA library. Among the resins tested in this study, SLF-immbolized PEGA resin was the most effective at capturing FKBP protein. This result suggested that the favorable swelling

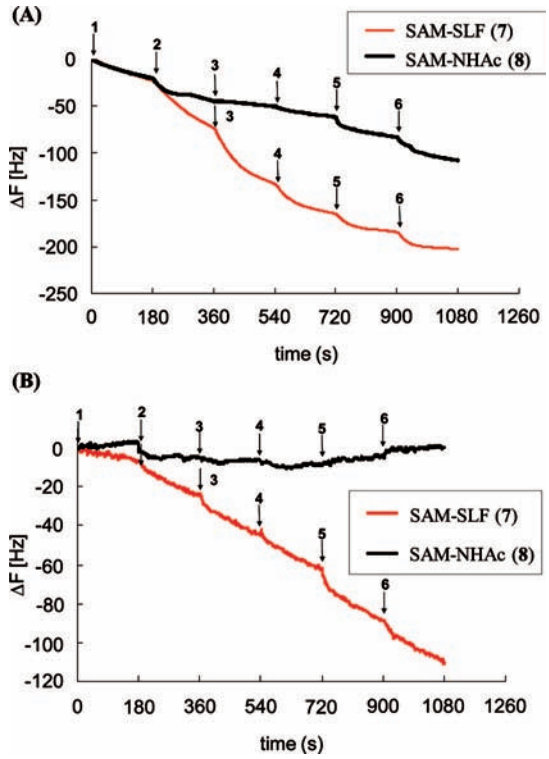

Figure 8. Kinetic analyses of the binding between SLF and SLF-binding peptides by using the QCM apparatus. (A) Time course of the frequency change of the SLF-immobilized (red) or control (black) sensor chip, responding to the addition of FKBP12. Various concentrations of FKBP12 were added to the cuvette. The resulting overall concentrations of FKBP12 in the cuvette were as follows: 1, 7.2 nM; 2, 21.6 nM; 3, 50.3 nM; 4, 79.0 nM; 5, 107.7 nM; 6, 136.4 nM. (B) Time course of the frequency change of the SLF-immobilized (red) or control (black) sensor chip, responding to the addition of clone 2 peptide. Various concentrations of the peptide were added to the cuvette. The resulting overall concentrations of the peptide in the quvette were as follows: 1, 0.3 μM; 2, 0.8 μM; 3, 1.3 μM; 4, 1.8 μM; 5, 4.8 μM; 6, 6.8 μM.

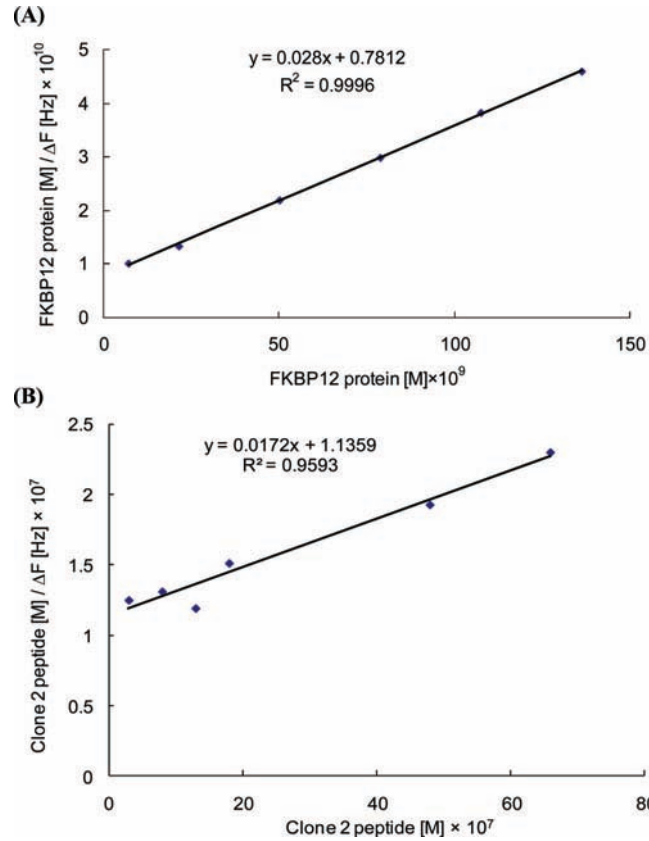

Figure 9. Langmuir isotherm plots for (A) FKBP12 and (B) clone 2 peptide binding with SLF-SAM (**7**) by QCM analyses.

properties of PEGA resin (16 mL/g) in aqueous media enabled affinity purification with high binding capacity and specificity. The swelling properties of the other resins are less favorable (e.g., 4 mL/g for TentaGel and NovaSyn TG resin in water). Furthermore, the hydrophilic nature of the PEGA matrix afforded easy access of the protein to the immobilized ligand on the resin.

Our previous report showed that TentaGel, which is PEG-coated polystyrene beads, was an effective resin for purifying DNA polymerase β. DNA polymerase β was purified from a Molt4 nuclear extract by LCA-immobilized TentaGel. In the present study, TentaGel was found to be unsuitable for purifying FKBP12. Tamura and co-workers also failed to isolate FKBP12 from a cell lysate with FK506-immobilized TentaGel, although the background itself was very low (*8*). These results suggest that hydrophobic ligands are poorly displayed on the surface of TentaGel resin, probably because the ligands have a tendency to form hydrophobic interactions with the polystyrene core by distorting the long flexible PEG chains (Mw 2000−3000 Da) (*8*). The very long PEG chains of TentaGel are not suitable for a spacer as affinity matrix when the hydrophobic ligands are immobilized on TentaGel. By contrast, DNA polymerase β binds to LCA-conjugated TentaGel because the hydrophilic carboxylic acid groups of LCA might prevent direct interaction with the polystyrene core.

Here, we demonstrate that SLF-immobilized PEGA resin can be used to purify FKBP12 from using Jurkat cell lysates with a low background. To our knowledge, this is the first case to exemplify that the target protein could be isolated from a cell lysate with a small ligand-immobilized PEGA resin. The hydrophilic PEG chains (Mw 800 Da) on the surface chains may act as a suitable linker not only to display the hydrophobic ligand on the surface but also to reduce nonspecific binding of proteins on the core. Auzanneau et al. reported that an antibody against *Streptococcus* Group A trisaccharide recognized the small molecule on PEGA resin (*14*). Sucholeiki et al. revealed that methotrexate-immobilized PEGA magnetic matrix specifically captured the folate binding protein from several kinds of proteins (bovine albumin, chicken albumin, folate binding protein, lysozyme, lactferrin, and lactoperoxidase precursor) (*16*). Taken together with our results, these observations indicated that PEGA resin could be applicable for affinity purification using small molecules with a variety of chemical properties as ligands.

We also investigated the application of the resins for phage display screening. Recently, several groups have succeeded in determining the ligand-binding site of the target protein by this screening method (*29*−*37*), where an avidin-coated matrix with a biotinylated compound was generally utilized. We found that the T7 phage displaying FKBP12 specifically bound the SLF immobilized on PEGA resin and that the PEGA matrix as well as AffiGel showed better signal-to-noise ratio than Sepharose 4B. These observations indicate that the PEGA resin is a useful matrix not only for affinity purification of proteins but also for phase display screening.

Using the SLF-immobilized PEGA resin, we successfully isolated 2 different clones out of the phage cDNA library derived from Colo205 cells. One clone (clone 1) encoded full length FKBP12 with the untranslated region, and the other phage clone (clone 2) displayed the 20 amino acid peptide (SLSCLWAELS-GKLWPLPAAQ, clone 2 peptide). We verified that the dissociation constant of the clone 2 peptide was 5.8 μM using the QCM apparatus, whereas interaction of the peptide with the

acetylated disulfide was barely detectable (K_D = 10.1 mM). Although the interaction between the peptide and SLF was weaker than that between FKBP12 and SLF (0.027 μM), these results suggest that the peptide specifically binds to SLF.

We also found that human SoxE proteins contain a region homologous to the clone 2 peptide. The SoxE proteins include Sox8, 9, and 10, which regulate transcription in various developmental processes, such as chondrogenesis, male sex determination, neural crest development, and gliogenesis (*46*−*48*). The 13 amino acids of SoxE proteins showing similarity to the clone 2 peptide are located in helix 2 of the HMG domain. This helix contacts the base pairs of the target DNA site and is followed by the C-terminal region of the HMG domain, including helix 3 and the C-terminal tail, which are required for interaction with numerous transcription factors (*49*−*51*). From these observations, we propose that SLF interferes with the binding between SoxE proteins and DNA and/or that the protein−protein interactions with transcription factors are inhibited by the conformational change of the C-terminal region of SoxE proteins due to the binding of SLF to the helix 2 domain. Therefore, although SLF does not exhibit a significant cellular response, it is possible that SLF might block certain cell differentiation pathways in which the SoxE proteins are involved.

In summary, we investigated the application of the resins used in solid-phase synthesis for affinity purification. Since resins used in solid-phase synthesis are chemically and physically stable, various approaches for synthesis and immobilization of small ligands are available by using the resins. Of the resins tested in this study, PEGA resin was the most effective for isolating FKBP12. This matrix enabled the isolation of FKBP12 from a cell lysate, and the identification of SLF-binding peptides from a phage cDNA library. Moreover, PEGA resin displayed as appropriate properties for affinity protein purification and phage display as AffiGel in our experimental conditions. Our study suggests that PEGA resin has great potential as a tool not only for the purification and identification of small-molecule binding proteins but also for the evolution and selection of peptides or antibodies that recognize target molecules. Further proteomics applications of PEGA resin are currently underway.

Supporting Information Available: Binding competition assays of FKBP12 absorption on the SLF-immobilized PEGA resin (Figure S1), preparation of lithocolic acid-immobilized resins (Scheme S1), binding analysis between a mammalian DNA polymerase β and the lithocolic acid-immobilized resins by the Bradford method (Figure S2), preparation of glutathione (GSH)-immobilized resins (Scheme S2), binding analysis between glutathione *S*-transferase (GST) and the glutathione (GSH)-immobilized resins by the Bradford method (Figure S3), and alignment between the clone 2 peptide and human Sox 8−10 proteins (Figure S4). This material is available free of charge via the Internet at http://pubs.acs.org.

LITERATURE CITED

(1) Lin, J., Jr., Lane, W. S., Friedman, J., Weissman, I., and Schreiber, S. L. (1991) Calcineurin is a common target of cyclophilin-cyclosporin A and FKBP-FK506 complexes. *Cell 66*, 807–815.

(2) Hermanson, G. T., Mallia, A. K., and Smith, P. K. (1992) The Matrix, *Immobilized Affinity Ligand Technique*, Chapter 1, pp 1−50, Academic Press, San Diego, CA.

(3) Kawaguchi, H., Asai, A., Ohtsuka, Y., Watanabe, H., Wada, T., and Handa, H. (1989) Purification of DNA-binding transcription factors by their selective absorption on the affinity latex particles. *Nucleic Acids Res. 17*, 6229–6240.

(4) Wada, T., Watanabe, H., Kawaguchi, H., and Handa, H. (1995) DNA affinity chromatography. *Methods Enzymol. 254*, 595–604.

(5) Shimizu, N., Sugimoto, K., Tang, J., Nishi, T., Sato, I., Hiramoto, M., Aizawa, S., Hatakeyama, M., Ohba, R., Hatori, H., Yoshikawa, T., Suzuki, F., Oomori, A., Tanaka, H., Kawaguchi, H., Watanabe, H., and Handa, H. (2000) High-performance affinity beads for identifying drug receptors. *Nat. Biotechnol. 18*, 877–881.

(6) Hiramoto, M., Shimizu, N., Nishi, T., Shima, D., Aizawa, S., Tanaka, H., Hatakeyama, M., Kawaguchi, H., and Handa, H. (2002) High-performance affinity beads for identifying anti-NF-kappa B drug receptors. *Methods Enzymol. 353*, 81–88.

(7) Uga, H., Kuramori, C., Ohta, A., Tsuboi, Y., Tanaka, H., Hatakeyama, M., Yamaguchi, Y., Takahashi, T., Kizaki, M., and Handa, H. (2006) A new mechanism of methotrexate action revealed by target screening with affinity beads. *Mol. Pharmacol. 70*, 1832–1839.

(8) Tamura, T., Terada, T., and Tanaka, A. (2003) A quantitative analysis and chemical approach for the reduction of nonspecific binding proteins on affinity resins. *Bioconjugate Chem. 14*, 1222–1230.

(9) Shiyama, T., Furuya, M., Yamazaki, A., Terada, T., and Tanaka, A. (2004) Design and synthesis of nobel hydrophilic spacers for the reduction of nonspecific binding proteins on affinity resins. *Bioorg. Med. Chem. 12*, 2831–2841.

(10) Yamamoto, K., Yamazaki, A., Takeuchi, M., and Tanaka, A. (2006) A versatile method of identifying specific binding proteins on affinity resins. *Anal. Biochem. 352*, 15–23.

(11) Mori, T., Takahashi, T., Shiyama, T., Tanaka, A., Hira, N., Tanaka, N., and Hosoya, K. (2006) An easy preparation of 'monolithic type' hydrophilic solid phase: Capability for affinity resins to isolate target proteins. *Bioorg. Med. Chem. 14*, 5549–5554.

(12) Cuatrecacas, P. (1970) Protein purification by affinity chromatography: Derivatizations of agarose and polyacrylamide beads. *J. Biol. Chem. 245*, 3059–3065.

(13) Baues, R. J., and Gray, G. R. (1977) Lectin purification on affinity columns containing reductively aminated disaccharides. *J. Biol. Chem. 252*, 57–60.

(14) Auzanneau, F.-I., Meldal, M., and Bock, K. (1995) Synthesis, characterization and biocompatibility of PEGA resins. *J. Pept. Sci. 1*, 31–44.

(15) Villain, M., Vizzavona, J., and Rose, K. (2001) Covalent capture: a new tool for the purification of synthetic and recombinant polypeptides. *Chem. Biol. 8*, 673–679.

(16) Sucholeiki, I., Toledo-Sherman, L. M., Hosfield, C. M., Boutilier, K., DeSouza, L. V., and Stover, D. R. (2004) Novel magnetic supports for small molecule affinity capture of proteins for use in proteomics. *Mol. Divers. 8*, 9–19.

(17) Kuramochi, K., Haruyama, T., Takeuchi, R., Sunoki, T., Watanabe, M., Oshige, M., Kobayashi, S., Sakaguchi, K., and Sugawara, F. (2005) Affinity capture of a mammalian DNA polymerase β by inhibitors immobilized to resins used in solid-phase organic synthesis. *Bioconjugate Chem. 16*, 97–104.

(18) Stockwell, B. R. (2004) Exploring biology with small organic molecules. *Nature 432*, 846–854.

(19) Piggott, A. M., and Karuso, P. (2004) Quality, not quantity: The role of natural products and chemical proteomics in modern drug discovery. *Comb. Chem. High Throughput Screen. 7*, 607–630.

(20) Jung, H. J., and Kwon, H. J. (2006) Chemical genomics with natural products. *J. Microbiol. Biotechnol. 16*, 651–660.

(21) Kim, Y. K., and Chang, Y.-T. (2007) Tagged library approach facilitates forward chemical genetics. *Mol. BioSyst. 3*, 392–307.

(22) Webber, S., Deits, T. L., Snyder, W. R., and Whiteley, J. M. (1978) The purification of rat and sheep liver dihydropteridine reductases by affinity chromatography on methotrexate-sepharose. *Anal. Biochem. 84*, 491–503.

(23) Gupta, S. V., Greenfield, N. J., Poe, M., Makulu, D. R., Williams, M. N., Moroson, B. A., and Bertino, J. R. (1977) Dihydrofolate reductase from a resistant subline of the L1210 lymphoma. Purification by affinity chromatography and ultraviolet difference spectrophotometric and circular dichroic studies. *Biochemistry 16*, 3073–3079.

(24) Fretz, H., Albers, M. W., Galat, A., Standaert, R. F., Lane, W. S., Burakoff, S. J., Bierer, B. E., and Schreiber, S. L. (1991) Rapamycin and FK506 binding proteins (Immunophilins). *J. Am. Chem. Soc. 113*, 1409–1411.

(25) Kieffer, L. J., Thalhammer, T., and Handschumacher, R. E. (1992) Isolation and characterization of a 40-kDa cyclophilin-related protein. *J. Biol. Chem. 267*, 5503–5507.

(26) Thalhammer, T., Kieffer, L. J., Jiang, T.-R., and Handschumacher, R. E. (1992) Isolation and partial characterization of membrane-associated cyclophilin and a related 22-kDa glycoprotein. *Eur. J. Biochem. 206*, 31–37.

(27) Moss, M. L., Palmer, R. E., Kuzmic, P., Dunlap, B. E., Henzel, W., Kofron, J. L., Mellon, W. S., Royer, C. A., and Rich, D. H. (1992) Identification of Actin and HSP 70 as cyclosporin A binding proteins by photoaffinity labeling and fluorescence displacement assays. *J. Biol. Chem. 267*, 22054–22059.

(28) Smith, G. P., and Petrenko, V. A. (1997) Phage display. *Chem. Rev. 97*, 391–410.

(29) Sche, P. P., McKenzie, K. M., White, J. D., and Austin, D. J. (1999) Display cloning: functional identification of natural product receptors using cDNA-phage display. *Chem. Biol. 6*, 707–716.

(30) Jin, Y., Yu, J., and Yu, Y. G. (2002) Identification of hNopp140 as a binding partner for doxorubicin with a phage display cloning method. *Chem. Biol. 9*, 157–162.

(31) Shim, J. S., Lee, J., Park, H. J., Park, S. J., and Kwon, H. J. (2004) A new curcumin derivative, HBC, interferes with the cell cycle progression of colon cancer cells via antagonization of the Ca^{2+}/calmodulin function. *Chem. Biol. 11*, 1455–1463.

(32) Rodi, D. J., Janes, R. W., Sanganee, H. J., Holton, R. A., Wallace, B. A., and Makowski, L. (1999) Screening of a library of phage-displayed peptides identifies human bcl-2 as a taxol-binding protein. *J. Mol. Biol. 285*, 197–203.

(33) Rodi, D. J., Agoston, G. E., Manon, R., Lapcevich, R., Green, S. J., and Makowski, L. (2001) Identification of small molecule binding sites within proteins using phage display technology. *Comb. Chem. High Throughput Screening 4*, 553–572.

(34) Boehmerle, W., Splittgerber, U., Lazarus, M. B., Mackenzie, K. M., Johnston, D. G., Austin, D. J., and Ehrlich, B. E. (2006) Paclitaxel induces calcium oscillations via an inositol 1,4,5-trisphosphate receptor and neuronal calcium sensor 1-dependent mechanism. *Proc. Natl. Acad. Sci. U.S.A. 103*, 18356–18361.

(35) Rodi, D. J., Soares, A. S., and Makowski, L. (2004) Quantitative assessment of peptide sequence diversity in M13 combinatorial peptide phage display libraries. *J. Mol. Biol. 322*, 1039–1052.

(36) Mandava, S., Makowski, L., Devarapalli, S., Uzubell, J., and Rodi, D. J. (2004) RELIC-A bioinformatics server for combinatorial peptide analysis and identification of protein-ligand interaction sites. *Proteomics 4*, 1439–1460.

(37) Makowski, L., and Rodi, D. J. (2003) Genome-wide characterization of the binding repertoire of small molecule drugs. *Hum. Genomics 1*, 41–51.

(38) Holt, D. A., Luengo, J. I., Yamashita, D. S., Oh, H.-J., Konialian, A. L., Yen, H.-K., Rozamus, L. W., Brandt, M., Bossard, M. J., Levy, M. A., Eggleston, D. S., Liang, J., Schultz, L. W., Stout, T. J., and Clardy, J. (1993) Design, synthesis, and kinetic evaluation of high-affinity FKBP ligands and the X-ray crystal structures of their complexes with FKBP. *J. Am. Chem. Soc. 115*, 9925–9938.

(39) Keenan, T., Yaeger, D. R., Courage, N. L., Rollins, C. T., Pavone, M. E., Rivera, V. M., Yang, W., Guo, T., Amara, J. F., Clackson, T., Gilman, M., and Holt, D. A. (1998) Synthesis and activity of bivalent FKBP12 ligands for the regulated dimerization of proteins. *Bioorg. Med. Chem. 6*, 1309–1335.

(40) McKenzie, K. M., Videlock, E. J., Splittgerber, U., and Austin, D. J. (2004) Simultaneous identification of multiple protein targets by using complementary-DNA phage display and a natural-product-mimetic probe. *Angew. Chem., Int. Ed. 6*, 4052–4055.

(41) Takakusagi, Y., Kuramochi, K., Takagi, M., Kusayanagi, T., Manita, D., Ozawa, H., Iwakiri, K., Takakusagi, K., Miyano, Y., Nakazaki, A., Kobayashi, S., Sugawara, F., and Sakaguchi, K. (2008) Efficient one-cycle affinity selection of binding proteins or peptide specific for a small-molecule using a T7 phage display pool. *Bioorg. Med. Chem. 16*, 9837−9846.

(42) Toy, P. H. *Tentagel. Electronic Encyclopedia of Reagents in Organic Synthesis* (Paquette, L. A., Fuchs, P. L., Wipf, P., Crich, D. C., Eds.) John Wiley & Sons, U.K., on-line publication http://www.mrw.interscience.wiley.com/eros/articles/rn00470/frame-.html.

(43) Meldal, M. (1992) PEGA: A flow stable polyethylene glycol dimethyl acrylamide copolymer for solid phage synthesis. *Tetrahedron Lett. 33*, 3077–3080.

(44) Bradford, M. M. (1976) A rapid and sensitive method for the quantitation of microgram quantities of protein utilizing the principle of protein dye binding. *Anal. Biochem. 72*, 248–254.

(45) The amount of SLF on PEGA resin (**5e**) is indicated as μmol per 1 mg of dry PEGA resin (μmol/mg), whereas the amount of SLF on AffiGel (**5i**) is indicated as μmol per 1 mL of wet AffiGel (μmol/mL). To compare the amount of SLF on **5e** with that on **5i**, the unit of the amount of SLF on **5e** is converted from μmol/mg into μmol/mL according to the calculation described in Experimental Procedures.

(46) Wegner, M. (1999) From head to toes: the multiple facets of Sox proteins. *Nucleic Acids Res. 27*, 1409–1420.

(47) Schepers, G. E., Bullejos, M., Hosking, B. M., and Koopman, P. (2000) Cloning and characterization of the Sry-related transcription factor gene Sox8. *Nucleic Acids Res. 28*, 1473–1480.

(48) Sock, E., Schmidt, K., Hermanns-Borgmeyer, I., Bösl, M. R., and Wegner, M. (2001) Idiopathic weight reduction in mice deficient in the high-mobility-group factor Sox8. *Mol. Cell. Biol. 21*, 6951–6959.

(49) Reményi, A., Lins, K., Nissen, L. J., Reinbold, R., Schöler, H. R., and Wilmanns, M. (2003) Crystal structure of a POU/HMG/DNA ternary complex suggests differential assembly of Oct4 and Sox2 on two enhancers. *Genes Dev. 17*, 2048–2059.

(50) Werner, M. H., Huth, J. R., Gronenborn, A. M., and Clore, G. M. (1995) Molecular basis of human 46X,Y sex reversal revealed from the three-dimensional solution structure of the human SRY-DNA complex. *Cell 81*, 705–714.

(51) Wiβmüller, S., Kosian, T., Wolf, M., Finzsch, M., and Wegner, M. (2006) The high-mobility-group domain of Sox proteins interacts with DNA-binding domains of many transcription factors. *Nucleic Acids Res. 34*, 1735–1744.

BC8002716

Supporting Information

Identification of small molecule binding molecules by affinity purification using a specific ligand immobilized on PEGA resin

Kouji Kuramochi,[†,#] Yuka Miyano,[†,#] Yoshihiro Enomoto,[†,#] Ryo Takeuchi,[†] Kazutomo Ishi,[‡] Yoichi Takakusagi,[†] Takeki Saitoh,[†] Keishi Fukudome,[†] Daisuke Manita,[†] Yoshifumi Takeda,[‡] Susumu Kobayashi,[‡,§] Kengo Sakaguchi,[†,‡] Fumio Sugawara[†,‡,]*

Department of Applied Biological Science, Genome and Drug Research Center, and Faculty of Pharmaceutical Sciences, Tokyo University of Science, 2641 Yamazaki, Noda, Chiba 278-8510, Japan.

† Department of Applied Biological Science.

‡ Genome and Drug Research Center.

§ Faculty of Pharmaceutical Sciences.

 # These authors equally contribute to this work.

Index

1. Binding competition assays of FKBP12 absorption on the SLF-immobilized PEGA resin

2. Preparation of lithocolic acid-immobilized resins

3. Binding analysis between a mammalian DNA polymerase β and the lithocolic acid-immobilized resins by Bradford method

4. Preparation of glutathione (GSH)-immobilized resins

5. Binding analysis between glutathione *S*-transferase (GST) and the glutathione (GSH)-immobilized resins by Bradford method

6. Alignment between the clone 2 peptide and human Sox 8~10 proteins

1. Binding competition assays of FKBP12 absorption on SLF-immobilized PEGA resin

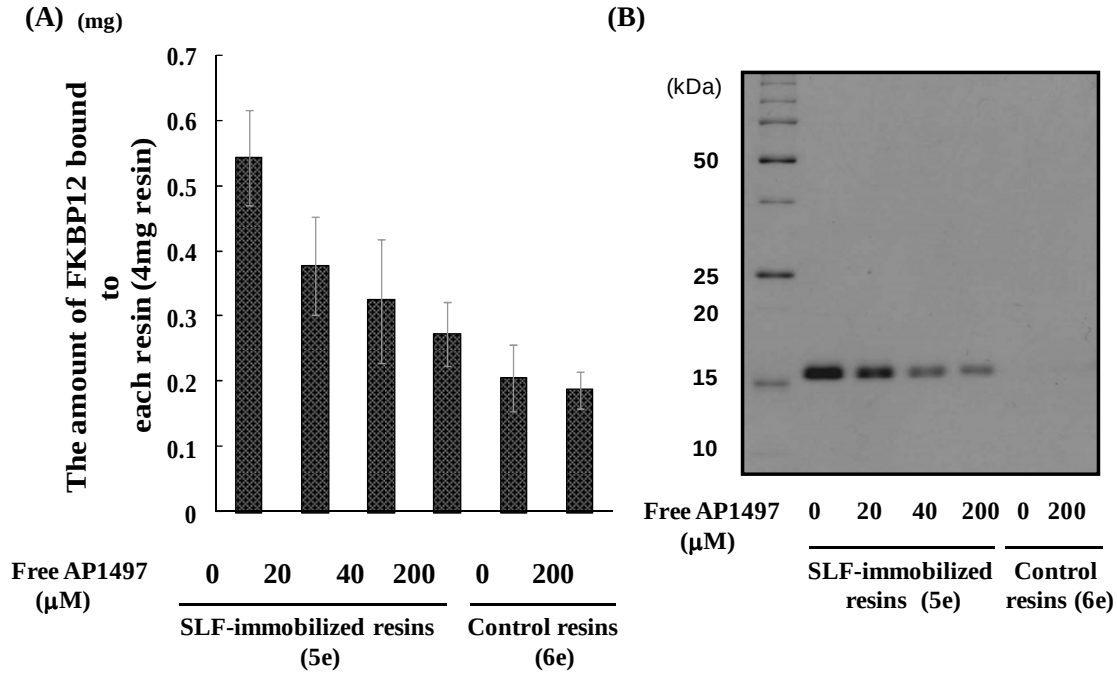

Figure S1. Binding competition assays of FKBP12 absorption on SLF-immobilized PEGA resin. The amount of FKBP12 bound to SLF-immobilized PEGA (**5e**) in the absence or presence of increasing concentration of free AP1497. As a control, the amount of FKBP12 bound to control PEGA (**6e**) is indicated. These experiments were performed according to the procedure described in text. (A) Total 0.97 mg of FKBP12 was applied to **5e** and **6e** in the absence or presence of increasing concentration of free AP1497. After equilibrium, the amount of FKBP12 in the supernatant was determined by Bradford assay. The amount of FKBP12 binding to resins **5e** and **6e** was calculated by subtraction of the amount of FKBP12 in the supernatant from that of input FKBP12. (B) SDS-PAGE of FKBP eluted from **5e** and **6e**. After washing the resins to remove unbound FKBP12, the resins were boiled with SDS sample buffer. The eluted FKBP12 was analyzed by SDS-PAGE and visualized by CBB staining. Values are mean±S.D. of a representative result conducted in triplicates.

2. Preparation of lithocolic acid (LCA)-immobilized resins

Scheme S1. Synthesis of LCA-immobilized resins (S4a-h).[a,b]

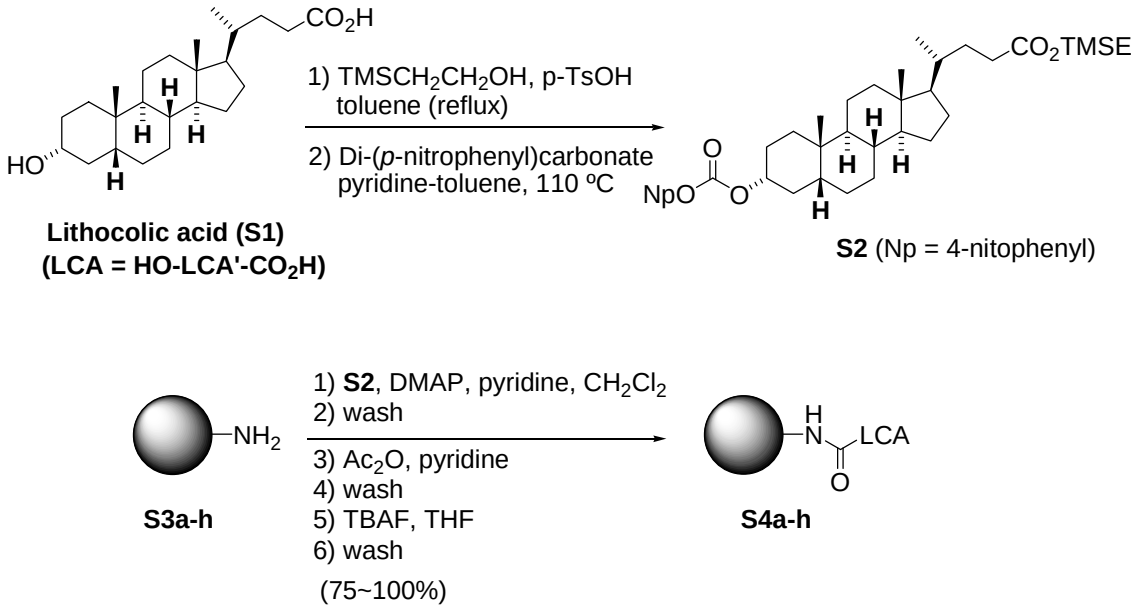

[a](**a**) HypoGel 200, (**b**) HypoGel 400, (**c**) TentaGel, (**d**) NovaSynTG, (**e**) PEGA, (**f**) NovaGel, (**g**) polystyrene resins, (**h**) Wang resins. [b]The loading of LCA on **S4** was estimated from the amount of the recovered **S2**, resulting as follows: **S4a** (0.80 μmol/mg), **S4b** (0.64 μmol/mg), **S4c** (0.22 μmol/mg), **S4d** (0.30 μmol/mg), **S4e** (0.76 μmol/mg), **S4f** (0.48 μmol/mg), **S4g** (0.48 μmol/mg), **S4h** (0.48 μmol/mg).

3. Binding analysis between a mammalian DNA polymerase β and the lithocolic acid (LCA)-immobilized resins by Bradford method

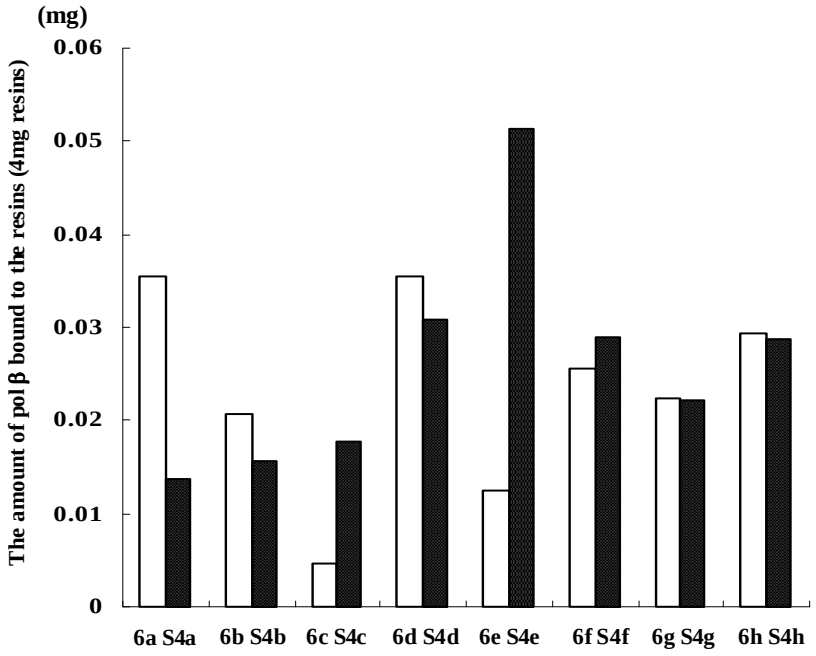

Figure S2. Binding analysis between recombinant DNA polymerase β (pol β) and lithocoloc acid (LCA)-immobilized resins (**S4a-h**). The amounts of pol β binding to LCA-immobilized resins (**S4a–h**) and control resins (**6a–h**) are indicated. Total 0.60 mg of pol β was applied to S**4a–h** (4 mg) and **6a–h** (4 mg). After equilibrium, the amount of pol β in the supernatant was determined by Bradford assay. The amount of pol β binding to resins **S4a–h** and **6a–h** was calculated by subtraction of the amount of pol β in the supernatant from that of input pol β. These experiments were performed according to the binding analyses described in text.

4. Preparation of glutathione (GSH)-immobilized resins

Scheme S2. Synthesis of (A) glutathione (GSH)-immobilized resins (S7a-h) and (B) control resins (S8a-h).[a]

(A)

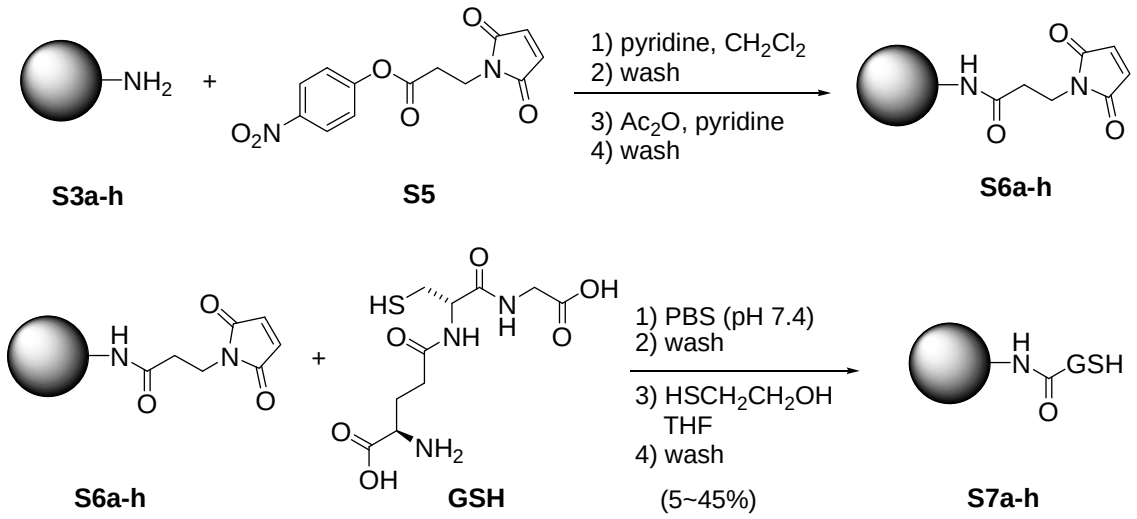

(B)

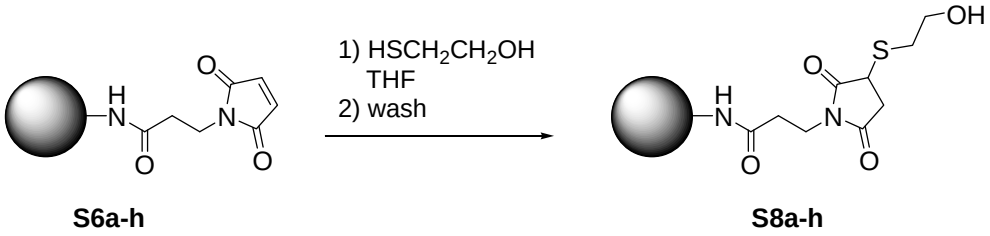

[a](**a**) HypoGel 200, (**b**) HypoGel 400, (**c**) TentaGel, (**d**) NovaSynTG, (**e**) PEGA, (**f**) NovaGel, (**g**) polystyrene resins, (**h**) Wang resins. [b]The loading of LCA on **S6a–h** was estimated from the amount of the recovered **GSH**, resulting as follows: **S7a** (0.083 μmol/mg), **S7b** (0.098 μmol/mg), **S7c** (0.133 μmol/mg), , **S7d** (0.123 μmol/mg), **S7e** (0.182 μmol/mg) , **S7f** (0.168 μmol/mg), **S7g** (~0.01 μmol/mg), **S7h** (~0.01 μmol/mg).

5. Binding analysis between glutathione *S*-transferase (GST) and glutathione (GSH)-immobilized resins by Bradford method

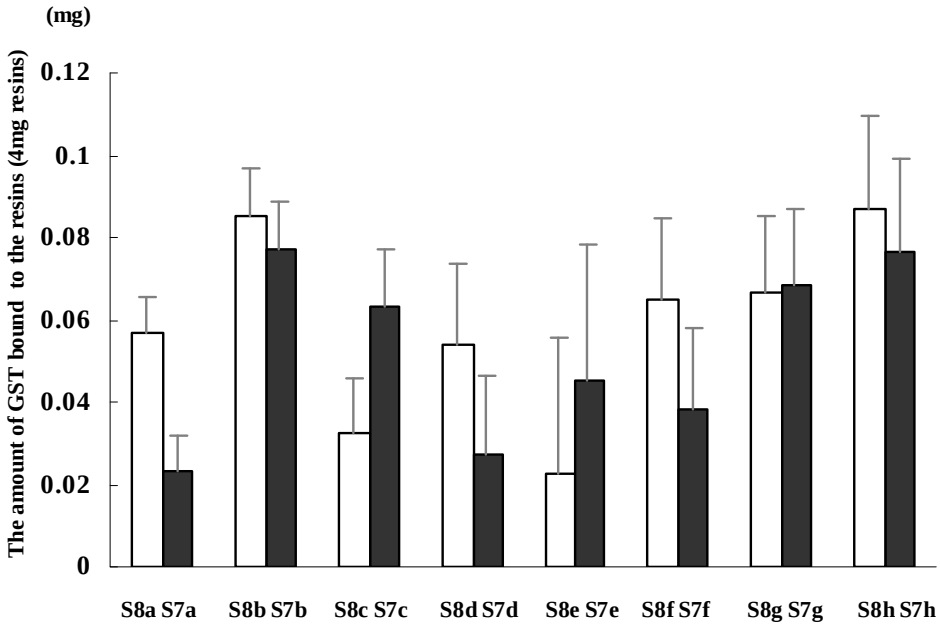

Figure S3. Binding analysis between glutathione *S*-transferase (GST) and glutathione (GSH)-immobilized resins (**S7a-h**). The amounts of GST binding to GSH-immobilized resins (**S7a–h**) and control resins (**S8a–h)** are indicated. Total 0.34 mg of GST was applied to **S7a–h** (4 mg) and **S8a–h** (4 mg). After equilibrium, the amount of GST in the supernatant was determined by Bradford assay. The amount of GST binding to resins **S7a–h** and **S8a–h** was calculated by subtraction of the amount of GST in the supernatant from that of input GST. These experiments were performed according to the binding analyses described in text. Values are mean±S.D. of a representative result conducted in triplicates.

6. Alignment between the clone 2 peptide and human Sox 8~10 proteins

```
clone 2:   7  AELS---GKLWPL  16
SOX8    : 130  AELSKTLGKLWRL  142
SOX9    : 133  AELSKTLGKLWRL  145
SOX10   : 132  AELSKTLGKLWRL  144
               ****   ******
```

Figure S4. Alignment between the clone 2 peptide and human Sox 8~10 proteins. The asterisk indicates identical amino acids.

Bioconjugate Chemistry 20th Anniversary

Subscriber access provided by SHEMYAKIN-OVCHINNIKOV INST

Article

A New PEG##-Alanine Active Derivative for Releasable Protein Conjugation

Gianfranco Pasut, Anna Mero, Francesca Caboi, Silvia Scaramuzza, Luigi Sollai, and Francesco M. Veronese

Bioconjugate Chem., **2008**, 19 (12), 2427-2431• DOI: 10.1021/bc800281s • Publication Date (Web): 24 November 2008

Downloaded from http://pubs.acs.org on May 2, 2009

More About This Article

Additional resources and features associated with this article are available within the HTML version:

- Supporting Information
- Access to high resolution figures
- Links to articles and content related to this article
- Copyright permission to reproduce figures and/or text from this article

View the Full Text HTML

ACS Publications
High quality. High impact.

Bioconjugate Chemistry is published by the American Chemical Society. 1155 Sixteenth Street N.W., Washington, DC 20036

A New PEG−β-Alanine Active Derivative for Releasable Protein Conjugation

Gianfranco Pasut,*[,†] Anna Mero,[†] Francesca Caboi,[‡] Silvia Scaramuzza,[‡] Luigi Sollai,[‡] and Francesco M. Veronese[†]

Department of Pharmaceutical Sciences, University of Padua, via F. Marzolo 5, 35131 Padua, Italy, and Bio-Ker S.r.l., Piscinamanna 09010 Pula (CA), Italy. Received July 7, 2008; Revised Manuscript Received November 3, 2008

A new PEGylating agent, PEG-βAla-NHCO-OSu, has been studied for protein amino conjugation using human growth hormone (hGH) and granulocyte colony stimulating factor (G-CSF) as model therapeutic proteins. This new activated PEG possesses a convenient property for protein modification when compared to other activated carboxylate PEGs, namely, lower reactivity. When this polymer reacts with a protein, its features lead to fewer PEG−protein conjugate isomers because it preferentially binds the most nucleophilic and exposed amines. Furthermore, the conjugates obtained with PEG-βAla-NHCO-OSu showed an interesting slow release of polymer chains upon incubation under physiological conditions. Further investigations determined that the PEG chains released are those coupled to histidine residues, and this finally yields less PEGylated species as well as free protein. This release allows a partial recovery of protein activity that is often remarkably and permanently reduced after stable PEGylation, and it occurs in water or blood without the involvement of enzymes. On the other hand, the rate of PEG release, tuned by the chemical structure of this new PEGylating agent, is not too high, and therefore, the achievement of a desired prolongation of protein half-life in vivo is still feasible. The pharmacokinetics of hGH-PEG6k-βAla conjugate was compared to that of native hGH in rats and monkeys, and the blood residence times were increased by 10- and 7-fold, respectively. The conjugate potency was evaluated in hypophysectomized rats demonstrating a superior pharmacodynamic profile with respect to native hGH.

INTRODUCTION

Biotechnology products are becoming more successful as therapeutic agents because of the important role of monoclonal antibodies (*1*). Besides important and promising results, several proteins still present relevant limitations for a safe therapeutic use, such as (i) the tendency to promote an immunological response, particularly in the case of heterologous proteins but also for human proteins administered at high doses (*2*), (ii) the physicochemical instability, both during shelf storage and in vivo after administration, and (iii) the short body residence time, especially for proteins with molecular weights below the kidney clearance threshold. Most of these problems can be overcome by PEGylation (the chemical link of polyethylene glycol), because it increases molecular weight of native drugs, shields critical protein sites (epitopes or amino acid sequences degraded by enzymes), reduces aggregation, and enhances water solubility (*3*−*6*). Altogether, these advantages lead to improved therapeutics that can be less frequently administered with respect to parent drugs, thus increasing patient compliance. PEGylation has already reached important results as demonstrated by the eight marketed PEG−protein conjugates (*5*). Despite its potentials, PEGylation is not devoid of open problems, such as the marked activity reduction of conjugated proteins that can in some cases prevent the exploitation of a conjugate, although this is often counterbalanced by the greater prolongation of conjugate in vivo half-life. A typical example is PEGylated interferon α-2a (PEGASYS), which retains only 7% of the native protein activity, but because of the half-life increase from 2.1 to 15 h, it has become a product with enhanced therapeutic value (*7*). Several research groups are now addressing this problem with interesting "releasable PEGs", although none of the conjugates reported so far entered the market. These PEGs take advantage of cleavable spacers that allow and control the release of conjugated protein in its fully active native form. Often, these systems are based on ester bonds which trigger the release, and the rate can be tuned by changing the neighboring chemical groups (*8*−*11*).

We recently developed a new PEGylating derivative, PEG-βAla-NHCO-OSu, which exhibited lower reactivity toward amines and higher stability in alkaline solutions, as compared to other *N*-hydroxysuccinimide activated PEGs (*12*). For protein PEGylation, this derivative was found useful because it preferentially reacts with the most nucleophilic and solvent-exposed protein amino groups, yielding a less heterogeneous mixture of conjugate isomers. This behavior was investigated with two therapeutic proteins, namely, human growth hormone (hGH) and granulocyte colony stimulating factor (G-CSF). Interestingly, the conjugates obtained with this PEGylating agent possess the property to slowly release some polymer chains, forming either fewer PEGylated protein isomers or native proteins also. To better understand the release mechanism, PEG-βAla-NHCO-OSu was conjugated to simple models revealing that the polymer is released when coupled to histidines. The PEG release rate was slow enough to ensure the conjugate half-life prolongation obtained by PEGylation.

The hGH conjugate was also investigated for the pharmacokinetic profile, in rats and monkeys, and the potency in hypophysectomized rats. It is worth noting that a single weekly

* Corresponding author. Gianfranco Pasut, Department of Pharmaceutical Sciences, University of Padua, via Marzolo 5, 35100 Padova, Italy. Phone: +39(0)49-8275693. Fax: +39(0)49-8275366. e-mail: gianfranco.pasut@unipd.it.

† University of Padua.

‡ Bio-Ker S.r.l.

10.1021/bc800281s CCC: $40.75 © 2008 American Chemical Society
Published on Web 11/24/2008

subcutaneous injection of hGH-PEG-βAla was equally potent to a daily subcutaneous injection of native hGH.

MATERIALS AND METHODS

Lyophilized rh-GH and rh-G-CSF were supplied by Bio-Ker (Pula, Cagliari, Italy). PEG-NH_2 of different molecular weights was purchased from Nektar (Huntsville, AL). *N*,*N*-Dicychlohexylcarbodiimide (DCC), *N*-hydroxysuccinimide (NHS), 2,4,6-trinitrobenzensulfonic acid (TNBS), *p*-nitrophenyl chloroformate, and organic solvents were purchased from Aldrich Chemie (Steinheim-West-Germany). Salts of analytical grade were from Merck. β-Alanine (βAla) was a Fluka product. Boc-NH-βAla-NHS was purchased from Novabiochem (Germany).

Gel filtration chromatography was performed with a Shimadzu (Kyoto, Japan) analytical HPLC system, using a Zorbax GF250 column (250 × 4.6 mm). Elution was carried out at a flow rate of 0.3 mL/min with 0.1 M PBS, 0.3 M NaCl containing 20% of acetonitrile. The effluent was monitored by recording the absorbance at 226 nm or at 280 nm.

Conjugate purification was carried out using an ion exchange SP-Sepharose fast flow (GE Healthcare, Uppsala, Sweden) loaded column (300 × 25 mm), with a Shimadzu HPLC (Kyoto, Japan). Elution was carried out at flow rate of 0.5 mL/min with a linear gradient of 0.1 M NaCl in water from 0% to 100% in 60 min. The effluent was monitored by recording the absorbance at 226 nm.

Protein concentrations were determined spectrophotometrically on a Perkin-Elmer Lambda-25 spectrophotometer. The concentrations of stock solutions of proteins and PEG−protein conjugates were evaluated from their absorbance at 280 nm. Extinction coefficients at 280 nm for PEG−proteins were considered unchanged from the native proteins.

PEG-βAla-NHCO-OSu Synthesis. PEG-βAla-NHCO-OSu was synthesized as previously reported (*12*). Briefly, PEG-NH_2 6 kDa (0.05 mmol), dissolved in CH_2Cl_2, reacted with Boc-NH-βAla-NHS (0.15 mmol) in the presence of Et_3N (0.1 mmol) to yield PEG-βAla-NH-Boc, which was purified by precipitation in Et_2O. The Boc protection group was removed by TFA hydrolysis, forming PEG-βAla-NH_2 that was recovered by evaporation of the solvent in a Rotavap, followed by precipitation in Et_2O. The dried PEG-βAla-NH_2 (0.042 mmol) dissolved in DMSO and reacted with di(*N*-succinimidyl) carbonate (0.21 mmol), for 12 h at 50 °C, gave the desired PEG-βAla-NHCO-OSu that was recovered by precipitation from Et_2O (yield 72%).

The degree of PEG activation was evaluated as reported elsewhere (*13*); briefly, an equimolar solution of PEG-βAla-NHCO-OSu and Gly-Gly was reacted and the unreacted amino groups determined by Snyder assay (*14*). The percentage of PEG-βAla-NHCO-OSu activation was 81%. Percentages of PEG dimer (below 5%), formed during the last step of the synthesis, and unreactive PEG (without the amino group, about 7%), present in the commercial batch of PEG-NH_2, were also determined. This may account for the reported percentage of PEG-βAla-NHCO-OSu activation.

^{1}H NMR ($CDCl_3$, 300 MHz) analysis of PEG-βAla-NHCO-OSu (PEG-βAla-NHCO-OSu) was performed by irradiating the sample with a pulse of 1444 Hz to suppress the signal of PEG$(OCH_2CH_2)_n$ hydrogens: σ 2.466 (t, 2H, NH-CO-CH_2-CH_2), σ 2.797 (s, 4H, -CH_2-, NHS), σ 3.364 (s, 3H, CH_3O), σ 3.538 (q, 2H, NH-CO-CH_2-CH_2).

Protein Conjugation with PEG-βAla-NHCO-OSu. PEG-βAla-NHCO-OSu was conjugated to either hGH or G-CSF as follows: a solution of 5 mg/mL of protein in 10 mM phosphate buffer pH 7 was left to react for 3 h at 4 °C with 3 molar excess of PEG-βAla-NHCO-OSu per each protein's amino group. The reaction was monitored by gel permeation chromatography (GPC), and after 3 h, the total amount of protein had reacted with PEG, as determined by GPC and MALDI-TOF analysis (see Supporting Information). The PEG−protein conjugate mixtures were fractionated by ion exchange chromatography, and the conjugate fractions were pooled and concentrated by ultrafiltration. The conjugate purity was checked by GPC, and the samples were eventually further purified by a second chromatographic step. The final solution was dialyzed against water, and a solution of trehalose was added to reach a ratio of 0.2 mg of trehalose for 0.8 mg of protein and lyophilized. Characterization was carried out by gel filtration chromatography.

PEG Release from Conjugates. The purified conjugate mixtures were dissolved in physiological buffer (10 mM Na_2HPO_4, 0.15 M NaCl; pH 7.4), at a concentration of 1 mg/mL (expressed as protein content) and incubated for 96 h at room temperature. At predetermined times, samples were withdrawn and analyzed by GPC using a Zorbax GF250 column (250 × 4.6 mm). Elution was carried out at a flow rate of 0.3 mL/min with 0.1 M PBS, 0.3 M NaCl, containing 20% of acetonitrile. The effluent was monitored by recording the absorbance at 226 nm or at 280 nm. The degree of PEG release was evaluated by both the variation in the peak area of the conjugates and the appearance of free protein peak. Solutions of hGH and G-CSF were studied under the same conditions.

Peptide Model Conjugation with PEG-βAla-NHCO-OSu. Triptorelin (pGlu-His-Trp-Ser-Tyr-DTrp-Leu-Arg-Pro-Gly-NH_2), Boc-Tyr, and Gly-Phe-Leu-Gly were used as models to evaluate the reactivity of the secondary amine of histidine, the tyrosine hydroxyl group, and the N-terminal amino group, respectively. Each peptide or protected amino acid (1 equiv) was dissolved in DMSO, and PEG-βAla-NHCO-OSu (0.33 equiv) was added under stirring. After dissolution, 1.5 equiv of Et_3N was added, the reaction was allowed to proceed for 12 h, diluted 1:1 with CH_2Cl_2, and finally washed with acidic water. The organic phase, dried over anhydrous sodium sulfate, was precipitated in diethyl ether. The product was recovered by filtration, dried under vacuum, and incubated in a solution of 10 mM Na_2HPO_4, 0.15 M NaCl, pH 7.4, at room temperature. The conjugate stability was evaluated by GPC or by RP-HPLC.

Animal Studies. All animal experiments were performed in accordance with the procedure described in the Guide for the Care and Use of Laboratory Animals.

Pharmacokinetic Study in Rats. Pharmacokinetic study in rats has been performed on male Sprague−Dawley rats, weighing about 300−350 g (Harlan Nossan). hGH content in serum samples was quantified by ELISA, using the Active Human Growth Hormone Elisa Kit supplied by Diagnostic System Laboratories Inc. (DSL), 445 Medical Centre Boulevard, Webster, TX. Four rats (group 1) have been administered once with 2.5 mg/kg b.w. of hGH-PEG-βAla subcutaneously on the back. Blood has been withdrawn at predose and 1, 2, 4, 8, 24, 32, 48, and 72 h after PEGylated h-GH administration. Four rats (group 2) have been administered once with 0.5 mg/kg b.w. of reference product (native hGH). Blood has been withdrawn at predose and 5, 15, 30, 60, and 90 min and 2, 3, 4, and 6 h after hGH administration. hGH content in serum samples was quantified by ELISA.

Pharmacokinetic Study in Monkeys. Pharmacokinetic study in monkeys has been done on young adult male rhesus monkeys (*Macaca mulatta*) 4 years old (4−7 kg). hGH content in the serum was quantified by ELISA as reported above. Three monkeys (group 1) have been administered once with 1.5 mg/kg b.w. of hGH-PEG-βAla, by subcutaneous injection. Blood (at least 1.0 mL) has been withdrawn at predose and 0.5, 1, 2, 4, 8, 12, 18, 24, 32, and 48 h after administration and every 24 h for 1 week. Three monkeys (group 2) have been administered once with 0.5 mg/kg b.w. of the reference product (native hGH), by subcutaneous injection. Blood (at least 1.0

Scheme 1. Synthesis of PEG-βAla-NHCO-OSu and Its Coupling with a Protein

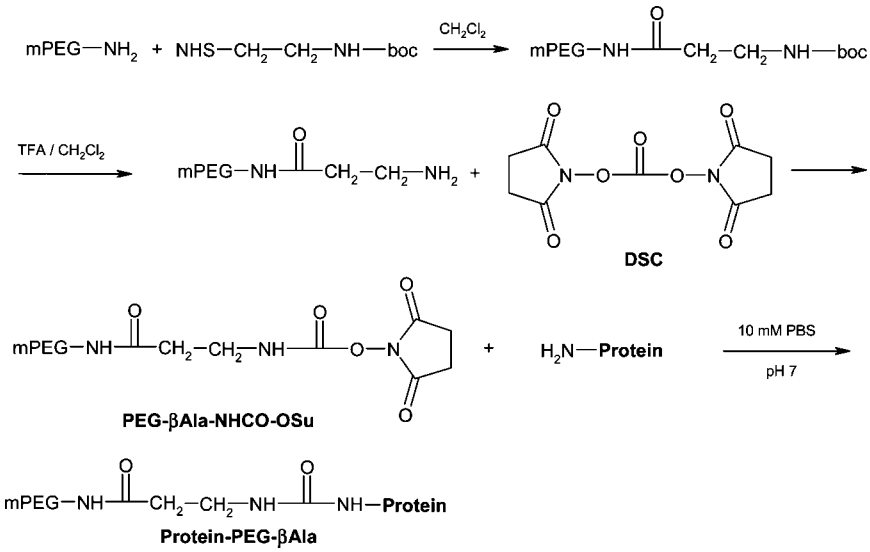

mL) has been withdrawn at predose, 5, 15, and 30 min, and 1, 1.5, 2, 3, 4, 6, 8, 10, 12, and 24 h after administration. hGH content in serum samples was quantified by ELISA.

Pharmacodynamic Study in Hypophysectomized Rats (Weight Gain Test). Pharmacodynamic study in rats was performed by treating hypophysectomized Sprague−Dawley rats, weighing 80−100 g. Animals were divided in three groups, eight rats in each: the first group was administered once with 240 μg/rat (protein equiv) of hGH-PEG-βAla by subcutaneous route on the back. The second group received daily 60 μg/rat/day of native hGH for 6 days by subcutaneous route on the back. The third was treated with vehicle by subcutaneous route on the back. Animal weight was monitored every two days until the end of the study.

RESULTS AND DISCUSSION

Preparation and Characterization of hGH and G-CSF Conjugates with PEG-βAla-NHCO-OSu. In Scheme 1, the synthesis of PEG-βAla-NHCO-OSu and the subsequent conjugation to protein amino groups are shown. Coupling reactions between PEG-βAla-NHCO-OSu and hGH or G-CSF were monitored by gel permeation chromatography (GPC) as reported in Figure 1 (panels A and B). After 3 h of incubation, nearly all protein amounts disappeared from the reaction mixture, yielding two new peaks that, on the basis of GPC and MALDI-TOF analysis, corresponded to mono- and di-PEGylated conjugates with traces of tri-PEGylated species (for MALDI-TOF analysis, see Supporting Information). In order to purify the conjugates from the excess of unreacted polymer and the free protein, a cationic exchange chromatography was carried out and purified reaction mixtures were checked by GPC.

The lower reactivity of PEG-βAla-NHCO-OSu with respect to the PEG-O-CH_2COOSu (PEG-SCM), a well-known PEGylating agent, was confirmed by studying both their chemical stability in alkaline solution and the conjugate isomers obtained after a coupling reaction with hGH (see Supporting Information). In particular, the half-life of NHS hydrolysis was 6.35 and 1.05 min for PEG-βAla-NHCO-OSu and PEG-O-CH_2COOSu, respectively. When PEG-SCM was conjugated to hGH under the same conditions of PEG-βAla-NHCO-OSu, diPEGylated and triPEGylated isomers were formed to a considerable degree while PEG-βAla-NHCO-OSu formed mainly monoPEGylated conjugates (see Supporting Information).

PEG Release from the Conjugates. The stability of hGH and G-CSF conjugates was assessed by GPC following incubation in PBS buffer at pH 7.4; Figure 2 shows the free protein release. After 96 h, the amount of released free hGH or G-CSF was found to be 21% and 29% of the starting conjugated proteins, respectively. In both cases, the GPC analysis revealed a decrease of diPEGylated species peak area during the time of

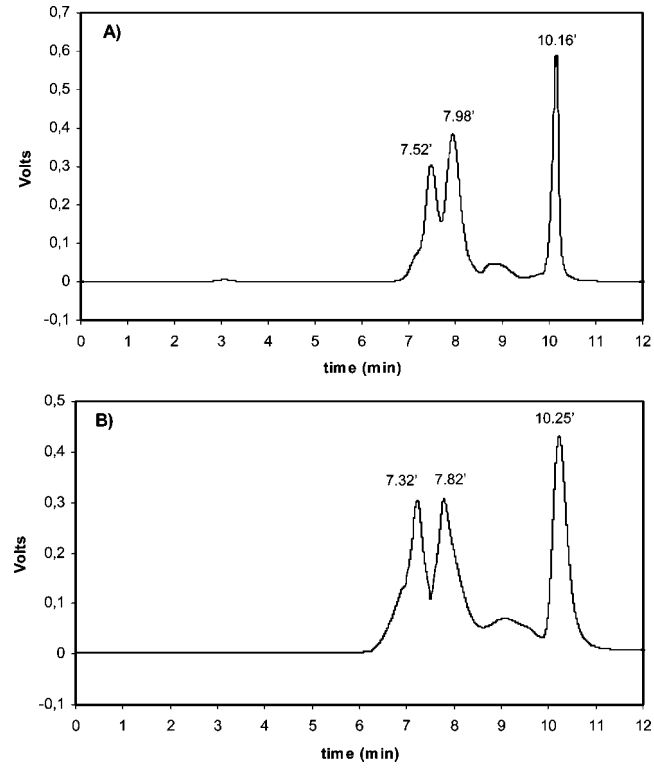

Figure 1. Gel filtration profile of reaction mixture of hGH (panel A) and G-CSF (panel B) with PEG-βAla-NHCO-OSu, after 3 h of reaction. (A) PEG/hGH reaction: peak at T_R = 7.52 min is di-PEGylated hGH conjugates, and peak at T_R = 7.98 min is mono-PEGylated hGH conjugates (as determined by MALDI-TOF analysis). (B) PEG/G-CSF reaction: peak at T_R = 7.32 min is di-PEGylated G-CSF conjugates, and peak at T_R = 7.82 min is mono-PEGylated G-CSF conjugates. The peaks at 10.16 min and 10.25 min are *N*-hydroxysuccinimide. The shoulders eluting with the first peaks of each chromatogram correspond to the tri-PEGylated conjugates. In both chromatograms, the peaks at about 9 min correspond to the unreacted protein.

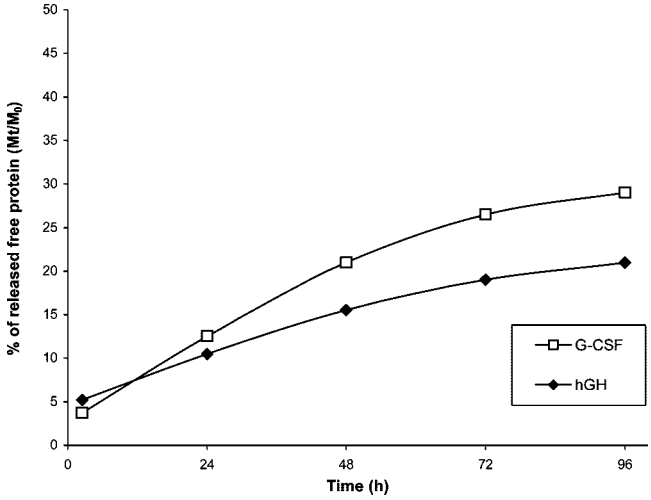

Figure 2. Protein release from hGH-PEG-βAla (♦) and G-CSF-PEG-βAla (□) conjugates during incubation in a solution of 10 mM Na_2HPO_4, 0.15 M NaCl, pH 7.4 at room temperature. The released hGH or G-CSF were evaluated by GPC analysis.

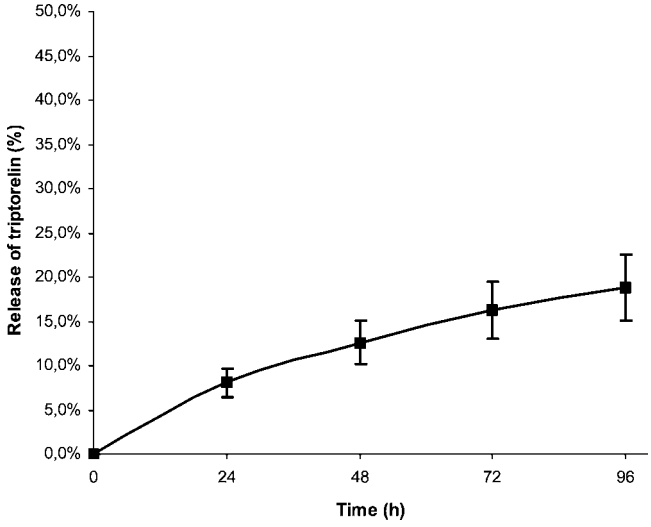

Figure 3. Triptorelin release after incubation of triptorelin-PEG-βAla conjugate in a solution of 10 mM Na_2HPO_4, 0.15 M NaCl, pH 7.4 at room temperature. The release was determined by GPC on the basis of formation of free peptide and decrease of conjugate amount.

the experiment with a concomitant small increase of mono-PEGylated conjugates and the formation of a peak of free protein.

PEG Release from Peptide Models. To gain insight into the release mechanism of PEG-βAla-NHCO-OSu, this polymer was studied with suitable models, namely, Triptorelin (pGlu-His-Trp-Ser-Tyr-DTrp-Leu-Arg-Pro-Gly-NH_2), Gly-Phe-Leu-Gly, and Boc-Tyr used to mimic the conjugation at His side chain; N-terminal amino group, and hydroxyl group of Tyr, respectively. The conjugate stability was studied following incubation in PBS. The Gly-Phe-Leu-Gly and Boc-Tyr conjugates showed negligible PEG release after 5 days of incubation, demonstrating the stability of the amide or carbamate bond between PEG-βAla-NHCO-OSu and the amine group of Gly or the hydroxyl group of Tyr, respectively. On the other hand, a release was observed in the case of triptorelin, where PEG is linked to the histidine secondary amine (see Figure 3). We expect that the coupling of PEG-βAla-NHCO-OSu to the Tyr hydroxyl group of a protein will probably occur to a very limited extent during common reaction conditions in water solutions,

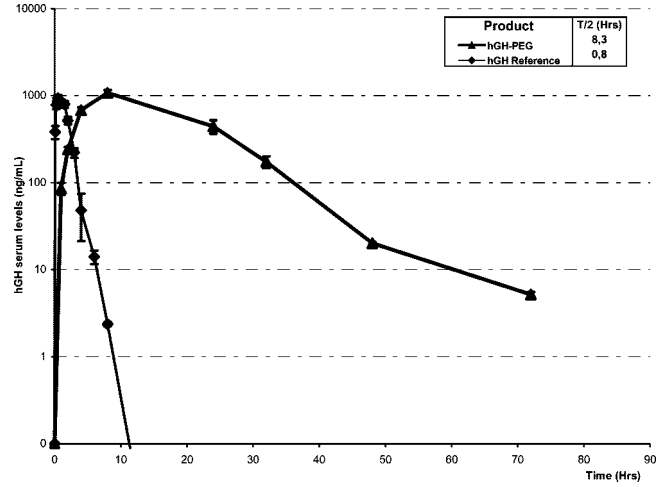

Figure 4. Pharmacokinetic profile of native hGH and hGH-PEG-βAla in rats (dose 2.5 mg/kg). PEGylation raised the hGH half-life from 0.8 to 8.3 h.

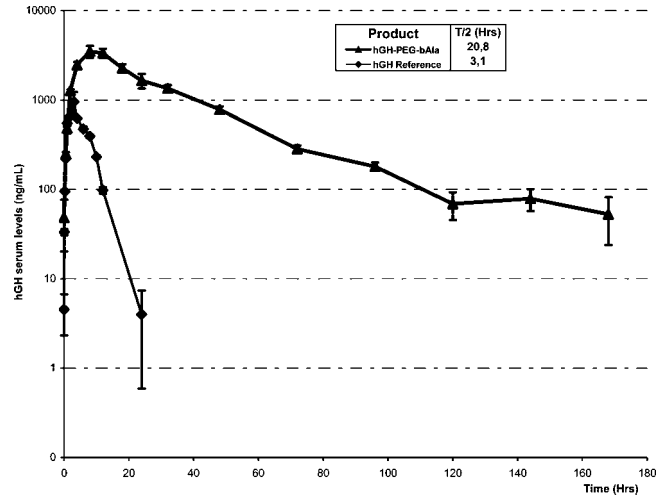

Figure 5. Pharmacokinetic profile of native hGH and hGH-PEG-βAla in monkeys (dose 1.5 mg/kg). As shown, after PEGylation the hGH half-life increased from 3.1 to 20.8 h.

where stronger nucleophiles are present, e.g., amino groups of lysines and N-terminal amino acid.

Pharmacokinetic Studies of hGH-PEG-βAla Conjugate in Rats and Monkeys. Pharmacokinetics studies were carried out in rats and monkeys for the hGH-PEG-βAla diconjugate fraction separated by cation exchange chromatography. The conjugation led to a great increase in blood residence time in both animal models; in fact, hGH half-life increased from 0.8 to 8.3 h in rats and from 3.1 to 20.8 h in monkeys, as shown in Figures 4 and 5, respectively. These data are comparable to those reported by other authors on hGH-PEG obtained by stable PEGylation (*15*), although a thorough comparison is difficult because several parameters are different in these two studies, as, for instance, the mass of PEG.

In Vivo Activity of hGH-PEG-βAla in Animal Model. The biological activity of hGH-PEG-βAla conjugate mixtures and their pharmacodynamic profiles were tested in hypophysectomized rats by evaluating the weight gain during one week observation of animals. A single subcutaneous injection of hGH-PEG-βAla (1 × 240 μg/rat, protein equiv) was found to be similar or slightly more potent than the same total amount of free hGH but given daily over a period of six days (6 × 40 μg/rat) (see Figure 6). Clark and co-workers reported similar results for hGH conjugated to 5 PEG 5 kDa chains (*15*). The

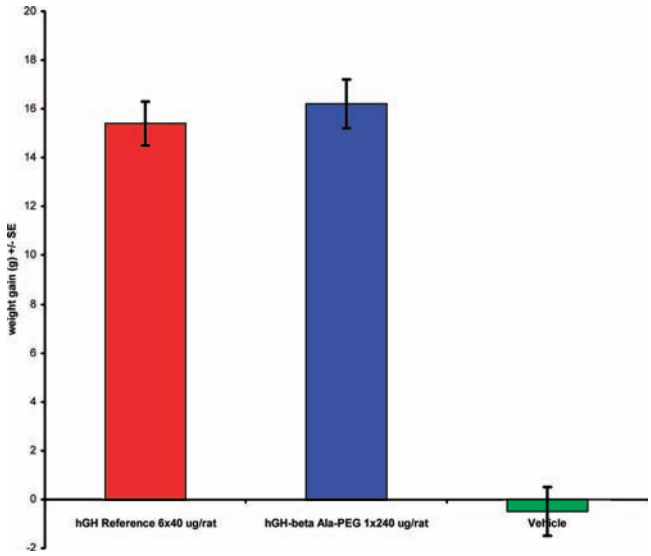

Figure 6. Weight gain in hypophysectomized rats given daily subcutaneous injections of hGH (6 × 40 μg/rat) or one weekly dose of hGH-PEG-βAla (1 × 240 μg/rat, protein equiv).

hGH−$(PEG)_5$ conjugate prepared by these authors had a half-life longer (15 h) than the hGH-PEG-βAla reported here (8.3 h), thus extending theoretically the protein activity over a longer period. The activity of these two different hGH−PEG conjugates are comparable, and this seems more in favor of the new hGH−PEG, which is still able to lead to a great pharmacodynamic response although showing a shorter half-life. Probably, this relevant response is partially due to the ability of this new PEG−βAla conjugate to slowly release in part the PEG chains, yielding either fewer PEGylated species or native hGH that are in any case more biologically active than the starting conjugate. Furthermore, the rate of PEG release does not compromise the beneficial half-life increase of the protein obtained after PEGylation.

CONCLUSION

Our study demonstrates that the new PEGylating agent, PEG-βAla-NHCO-OSu, can enhance the potential of PEG−protein conjugation. In fact, this polymer showed a higher stability in water at alkaline pH values, six times higher than that of PEG-SCM, and a lower reactivity toward amines that direct the coupling only toward the strongest and most solvent-exposed nucleophiles of a protein (*12*). Therefore, it forms fewer PEG−protein isomers than other commonly used PEG reagents. Furthermore, this PEG derivative showed the propensity to be slowly released from the protein conjugate when the polymer is attached to the side chain of histidine. As it is a phenomenon extremely relevant to recovering the protein activity that is often markedly reduced in the conjugated protein, this is one of the major limitations of PEGylation. The possibility to address this problem by using a simple approach, such as the coupling with PEG-βAla-NHCO-OSu, is particularly needed, and it could lead to the preparation of improved protein bioconjugates. In fact, beside the advantage of a prolonged in vivo half-life, these conjugates will possess the ability to recover the protein activity by slowly releasing the PEG chains attached.

The pharmacokinetic and pharmacodynamic data presented here support the effectiveness of PEG-βAla-NHCO-OSu as a new PEGylating agent for protein modification.

ACKNOWLEDGMENT

The research was supported by Bio-Ker.

Supporting Information Available: Experimental conditions of hGH conjugation with PEG-SCM, MALDI-TOF mass spectra of PEG-βAla-NHCO-OSu, PEG-βAla-NHCO-OSu/hGH reaction mixture and PEG-SCM/hGH reaction mixture. Half-life hydrolysis of PEG-βAla-NHCO-OSu and PEG-SCM in water. This material is available free of charge via the Internet at http://pubs.acs.org.

LITERATURE CITED

(1) Lawrence, S. (2004) The biotech drug market. *Nat. Biotechnol. 22*, 1496.
(2) Schellekens, H. (2005) Factors influencing the immunogenicity of therapeutic proteins. *Nephrol. Dial. Transplant. 20*, 3–9.
(3) Veronese, F. M., and Pasut, G. (2005) PEGylation, successful approach to drug delivery. *Drug Discovery Today 10*, 1451–1457.
(4) Veronese, F. M., and Harris, J. M. edrs. (2002) Theme issue on "Peptide and Protein Pegylation I". *Adv. Drug Delivery Rev. 54*, 453–606.
(5) Pasut, G., and Veronese, F. M. (2007) Polymer-drug conjugation, recent achievements and general strategies. *Prog. Polym. Sci. 32*, 933–961.
(6) Harris, J. M., and Chess, R. B. (2003) Effect of PEGylation on pharmaceuticals. *Nature Rev. Drug. Discovery 2*, 214–221.
(7) Reddy, K. R., Modi, M. W., and Pedder, S. (2002) Use of peginterferon α2a (40KD) (Pegasys®) for the treatment of hepatitis C. *Adv. Drug Delivery Rev. 54*, 571–586.
(8) Greenwald, R. B., Yang, K., Zhao, H., Conover, C. D., Lee, S., and Filpula, D. (2003) Controlled release of proteins from their poly(ethylene glycol) conjugates: drug delivery system employing 1,6-elimination. *Bioconjugate Chem. 14*, 395–403.
(9) Greenwald, R. B., Choe, Y. H., Conover, C. D., Shum, K., Wu, D., and Royzen, M. (2000) Drug delivery systems based on trimethyl lock lactonization: poly(ethylene glycol) prodrugs of amino-containing compounds. *J. Med. Chem. 43*, 475–487.
(10) Zhao, H., Yang, K., Martinez, A., Basu, A., Chintala, R., Liu, H. C., Janjua, A., Wang, M., and Filpula, D. (2006) Linear and branched bicin linkers for releasable PEGylation of macromolecules: controlled release in vivo and in vitro from mono- and multi-PEGylated proteins. *Bioconjugate Chem. 17*, 341–351.
(11) Peleg-Shulman, T., Tsubery, H., Mironchik, M., Fridkin, M., Schreiber, G., and Shechter, Y. (2004) Reversible PEGylation: a novel technology to release native interferon alpha2 over a prolonged time period. *J. Med. Chem. 7*, 4897–4904.
(12) Pasut, G., Caboi, F., Schrepfer, R., Tonon, G., Schiavon, O., and Veronese, F. M. (2007) New active poly(ethylene glycol) derivative for amino coupling. *React. Funct. Polym. 67*, 529–539.
(13) Pasut, G., Scaramuzza, S., Schiavon, O., Mendichi, R., and Veronese, F. M. (2005) PEG-epirubicin conjugates with high drug loading. *J. Bioact. Compat. Polym. 20*, 213–230.
(14) Snyder, S. L., and Sobocinski, P. Z. (1975) An improved 2,4,6-trinitrobenzenesulfonic acid method for the determination of amines. *Anal. Biochem. 64*, 284–288.
(15) Clark, R., Olson, K., Fuh, G., Mariani, M., Mortensen, D., and Teshima, G. (1996) Long-acting growth hormones produced by conjugation with polyethylene glycol. *J. Biol. Chem. 271*, 21969−21977.

BC800281S

A NEW PEG-βALANINE ACTIVE DERIVATIVE FOR RELEASABLE PROTEIN CONJUGATION

Gianfranco Pasut,[1] Anna Mero,[1] Francesca Caboi,[2] Silvia Scaramuzza,[2] Luigi Sollai[2] and Francesco M. Veronese[1]*

1. Department of Pharmaceutical Sciences, University of Padua, via F. Marzolo 5, 35131 Padua, Italy

2. Bio-Ker S.r.l., Piscinamanna 09010 Pula (CA), Italy.

*Corresponding Author.

e-mail: gianfranco.pasut@unipd.it

SUPPLEMENTARY INFORMATION

Experimental conditions of hGH conjugation with PEG-SCM 3

MALDI-TOF mass spectrometry analysis 3

Stability of PEG derivatives in alkaline solution 4

Figure A 5

Figure B 6

Figure C 7

Experimental conditions of hGH conjugation with PEG-SCM. A hGH solution of 5 mg/ml in 10 mM phosphate buffer pH 7 was left to react for 3 hours at 4°C with 3 molar excess of PEG-SCM per each protein's amino group. The reaction was monitored by gel permeation chromatography (GPC) and after three hours the total amount of protein reacted with PEG, as determined by GPC and MALDI-TOF analysis.

MALDI-TOF Mass Spectrometry analysis. Measurements were performed on a REFLEX time-of-flight instrument (Bruker-Franzen Analytik, Bremen, Germany) equipped with a SCOUT ion source operating in positive linear mode. Ions, formed by a pulsed UV laser beam (nitrogen laser, λ = 337 nm), were accelerated to 25 kV. Sinapinic acid (saturated solution in acetonitrile:water (50:50 v:v)) was used as a matrix. Samples were dissolved in 0.1% trifluoroacetic acid aqueous solution. 5 µl of the diluted sample solution was mixed with the same volume of matrix solution, and 1 µl of the resulting mixture was deposited on a stainless steel sample holder and allowed to dry before introduction into the mass spectrometer.

In figure A is shown the MALDI-TOF spectrum of PEG-βAla-NHCO-OSu as a single peak centered in 6101 Da. The mass spectrometry analysis of PEG-βAla-NHCO-OSu / hGH reaction mixture confirmed the results obtained from GPC. In fact, PEG-βAla-NHCO-OSu reacting with hGH formed mainly monoPEG-hGH (peak at 28151 Da) and diPEG-hGH (peak at 34261 Da) as shown in figure B. A small amount of free protein is still present (peak at 22144). The lower reactivity of PEG-βAla-NHCO-OSu as amino PEGylating agent with respect the most known and used PEG-SCM is also demonstrated by the MALDI-TOF analysis of PEG-SCM / hGH reaction mixture. PEG-SCM, reacting in the same conditions as PEG-βAla-NHCO-OSu, formed hGH-PEG conjugates with higher degree of PEGylation (figure C).

Stability of PEG derivatives in alkaline solutions. A concentrated solutions of PEG-βAla-NHCO-OSu and PEG-SCM were prepared in 1,4-dioxane at 20 mg/ml. 100 µl of these solutions were taken and diluted with 900 µl of 0.1M borate buffer pH 8, respectively. The increment of UV absorption at 260 nm of these solutions, due to NHS release from the polymer, was followed until reaching the steady state. The half-life of NHS hydrolysis was calculated using first order reactions mathematical model. The hydrolysis t½ was 6.35 min for PEG-βAla-NHCO-OSu, a value significantly higher than that of the commonly used PEG-SCM (t½ = 1.05 min).

Figure A: MALDI-TOF spectrum of new active PEG-βAla-NHCO-OSu derivative (from ref. 12).

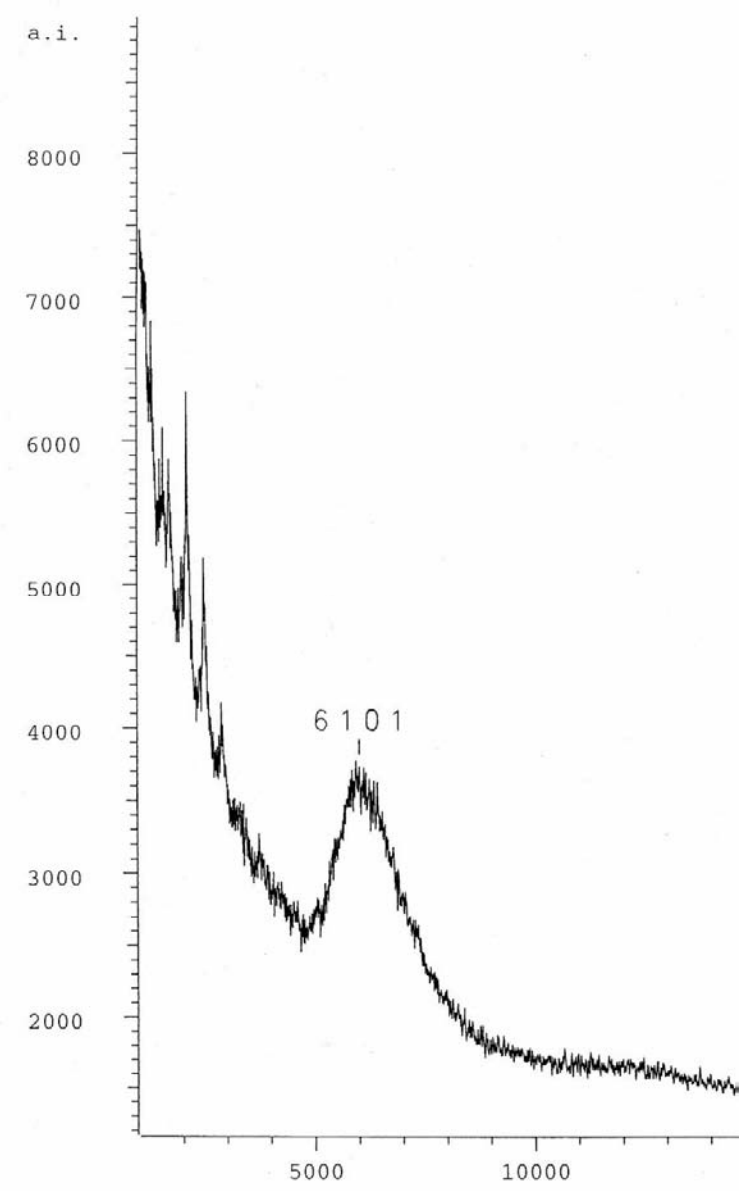

Figure B: MALDI-TOF spectrum of PEG-βAla-NHCO-OSu / hGH reaction mixture. The peak at 22144 m/z is the protein hGH, peak at 28151 m/z is the monoPEG hGH, peak at 34261 m/z is the diPEG-hGH (from ref. 12).

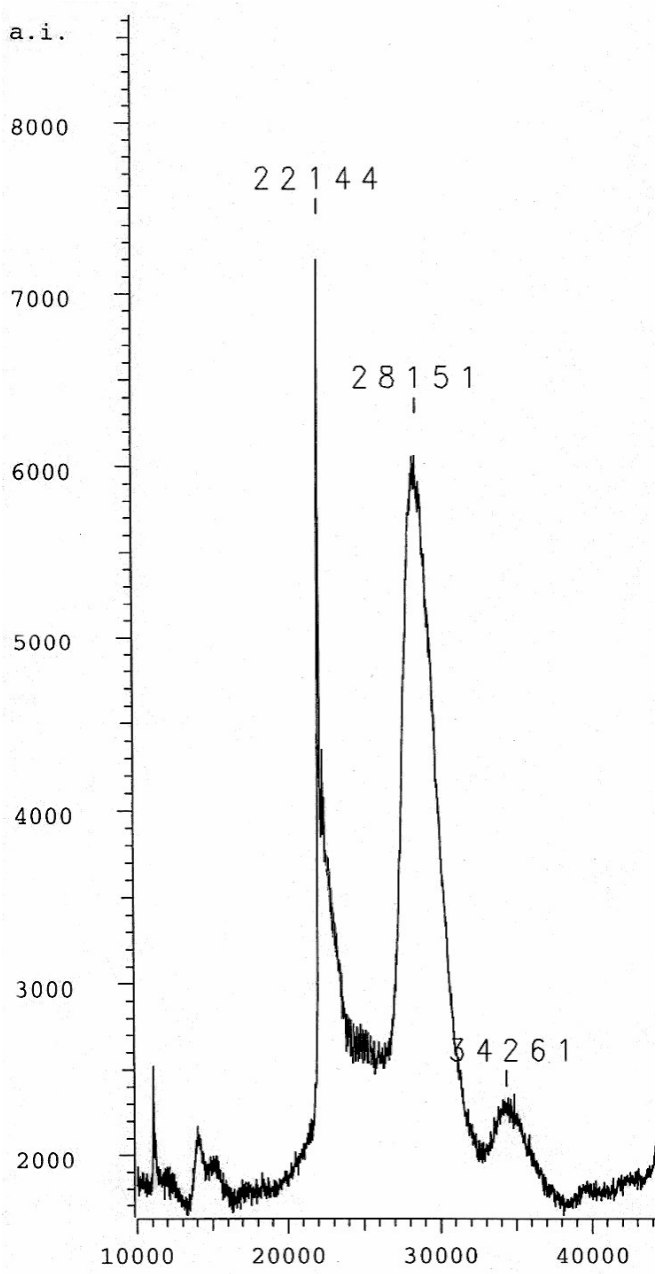

Figure C: MALDI-TOF spectrum of reaction mixture of PEG-SCM / hGH. The peak at 29033 m/z is the monoPEG-hGH, peak at 34814 m/z is the diPEG-hGH and peak at 40428 m/z is the triPEG-hGH (from ref. 12).

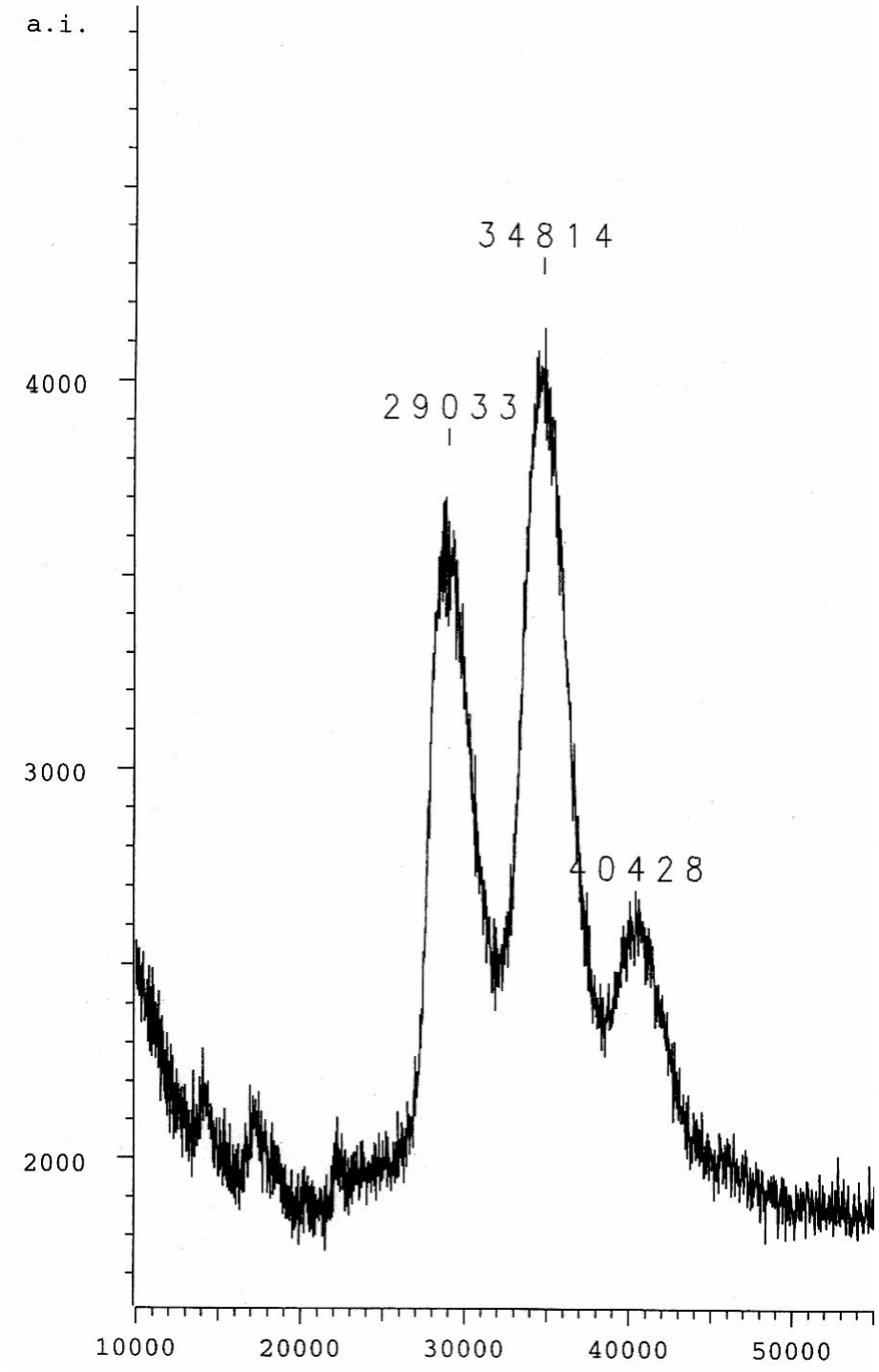

Subscriber access provided by SHEMYAKIN-OVCHINNIKOV INST

Article

Novel Glycated [Tc(CO)]-Labeled Bombesin Analogues for Improved Targeting of Gastrin-Releasing Peptide Receptor-Positive Tumors

Christian Schweinsberg, Veronique Maes, Luc Brans, Peter Bla#uenstein, Dirk A. Tourwe#, P. August Schubiger, Roger Schibli, and Elisa Garci#a Garayoa

Bioconjugate Chem., **2008**, 19 (12), 2432-2439• DOI: 10.1021/bc800319g • Publication Date (Web): 19 November 2008

Downloaded from http://pubs.acs.org on May 2, 2009

More About This Article

Additional resources and features associated with this article are available within the HTML version:

- Supporting Information
- Access to high resolution figures
- Links to articles and content related to this article
- Copyright permission to reproduce figures and/or text from this article

View the Full Text HTML

ACS Publications
High quality. High impact.

Bioconjugate Chemistry is published by the American Chemical Society. 1155 Sixteenth Street N.W., Washington, DC 20036

Novel Glycated [^{99m}Tc(CO)$_3$]-Labeled Bombesin Analogues for Improved Targeting of Gastrin-Releasing Peptide Receptor-Positive Tumors

Christian Schweinsberg,[†] Veronique Maes,[‡] Luc Brans,[‡] Peter Bläuenstein,[†] Dirk A. Tourwé,[‡] P. August Schubiger,[†,§] Roger Schibli,[†,§] and Elisa García Garayoa*[,†]

Paul Scherrer Institute, Centre for Radiopharmaceutical Science, CH-5232 Villigen PSI, Switzerland, Department of Organic Chemistry, Vrije Universiteit Brussel, 1050 Brussels, Belgium, and Department of Chemistry and Applied Biosciences, ETH Zurich, 8093 Zurich, Switzerland. Received July 25, 2008; Revised Manuscript Received October 14, 2008

Radiolabeled bombesin (BBS) analogues are promising pharmaceuticals for imaging of cancer cells expressing gastrin-releasing peptide receptors (GRPR). However, most of the radiolabeled BBS derivatives show a high accumulation of activity in the liver and a strong hepatobiliary excretion, both unfavorable for imaging and therapy of abdominal lesions. For this reason, we introduced hydrophilic carbohydrated linker moieties into our BBS analogues to reduce the abdominal accumulation and to improve the tumor-to-background ratios. A stabilized BBS(7−14) sequence bearing the (N$^{\alpha}$His)Ac-chelator was modified with amino acid linkers containing a lysine or propargylglycine residue. The ε-amino group of a lysine was either coupled to shikimic acid or reacted with glucose to form the Amadori conjugate. Alternatively, a glucose was attached to the peptide via "click" chemistry with the propargylglycine side chain. The peptides were synthesized on Rink amide resin using solid-phase peptide synthesis and labeled with ^{99m}Tc using the tricarbonyl technique. Binding and degradation were tested *in vitro* in GRPR-expressing PC-3 cells. Biodistribution and SPECT/CT imaging studies were performed in nude mice bearing PC-3 tumor xenografts. The new peptides showed a log *D* between −0.2 and −0.5 and kept the high affinity for GRPR with K_d values of <0.5 nM. *In vitro*, they were rapidly internalized into the tumor cells and showed an increased cellular retention and stability ($t_{1/2}$ > 35 min). *In vivo*, all new compounds exhibited higher tumor-to-background ratios compared to the nonglycated reference. Thus, the best results were obtained with the triazole coupled glucose with a 4-fold increased uptake and retention in tumor tissue (3.6 and 2.5%ID/g at 1.5 h and 5 h p.i, respectively) and a significantly reduced accumulation in the liver (0.6 vs 2.4%ID/g, 1.5 h p.i., respectively). Apart from higher tumor-to-liver ratios (17-fold, 1.5 h p.i.), both tumor-to-kidney and tumor-to-blood ratios could be significantly improved by a factor of 1.5 and 2.7, respectively (1.5 h p.i., $P < 0.05$). The imaging studies proved the reduction of abdominal background, and tumor xenografts could clearly be visualized. In conclusion, the introduction of a carbohydrated linker substantially improved the biodistribution properties of BBS analogues labeled with the ^{99m}Tc-tricarbonyl core.

INTRODUCTION

Modified neuropeptides have gained increasing attention for radiopharmaceutical applications like peptide receptor imaging (PRI) and peptide receptor radiotherapy (PRRT) (*1*−*5*). They bind with high affinity and selectivity to their corresponding receptors, which are overexpressed on a considerable number of cancers (*1*, *5*, *6*). Apart from somatostatin (sst) analogues like ^{111}In-DTPA-Octreotide (OctreoScan) or ^{90}Y- and ^{177}Lu-DOTA-TOC, which already are successful in the clinical treatment of neuroendocrine tumors and gastrinomas (*7*−*10*), additional receptor ligands are under investigation for targeting a broader range of tumor types. The tetradecapeptide bombesin (BBS) has recently been studied intensively due to its high affinity for the mammalian gastrin-releasing peptide receptor (GRPR) (*11*). GRPR shows high expression in most human prostate and breast tumors as well as small-cell lung, ovarian, endometrial, and other cancers (*12*−*14*). BBS derivatives have been labeled with various radionuclides like ^{99m}Tc, ^{64}Cu, ^{68}Ga, ^{111}In, ^{177}Lu, or ^{18}F and proved to be successful candidates for both PRI and PRRT (*15*−*21*). However, the modification of their pharmacokinetic profile is of high interest to reduce their frequent high hepatic accumulation and hepatobiliary excretion, which is problematic for imaging and therapy of abdominal lesions (*15*, *16*, *18*, *20*−*23*). Different modifiers offer the possibility to influence these unfavorable *in vivo* properties. Smith et al. investigated the positive effects of aliphatic and amino acid linkers for BBS analogues (*18*, *24*, *25*). Moreover, glycation by the Amadori reaction has been reported to provide radiohalogenated sst analogues with excellent physicochemical characteristics (*26*−*28*). These compounds were more hydrophilic but still exhibited a high receptor binding affinity, improved tumor uptake and tumor-to-nontumor ratios, and reduced hepatobiliary transfer and liver accumulation (*26*, *28*−*31*). Recent studies with ^{111}In- and ^{177}Lu-labeled DOTA-sst analogues confirmed the positive effects of glycation via Amadori rearrangement for radiolabeled metallopeptides (*32*), and interestingly, in addition the modification of neurotensin (NT) with the glycomimetic 3,4,5,-trihydroxyl-1-cyclohexene-1-carboxylic acid (shikimic acid) induced a reduction of both hepatic uptake and renal retention (*33*). Our group could already show an improvement of ^{99m}Tc-labeled BBS analogues by the introduction of a double β-alanine sequence and recently published the first promising results of a linker coupled to shikimic acid (*34*).

* Correspondence and requests should be addressed to Dr. E. García Garayoa. Center for Radiopharmaceutical Science. Paul Scherrer Institute, CH-5232 Villigen PSI, Switzerland. Phone: + 41-56-310 28 17. Fax: + 41-56-310 28 49. E-mail: elisa.garcia@psi.ch.

[†] Centre for Radiopharmaceutical Science.

[‡] Vrije Universiteit Brussel.

[§] ETH Zurich.

10.1021/bc800319g CCC: $40.75 © 2008 American Chemical Society
Published on Web 11/19/2008

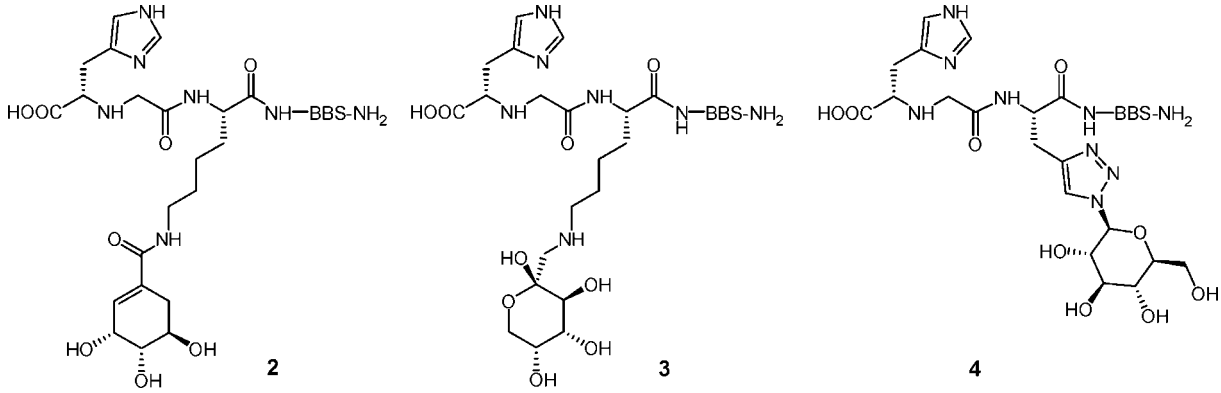

Figure 1. Chemical structure of the carbohydrated groups introduced into the linker sequence of the BBS analogues. **2** = Lysine-coupled shikimic acid; **3** = Amadori-product; **4** = triazole-coupled glucose.

Surprisingly, so far no further data of glycated BBS analogues have been published.

In this study, we investigated for the first time the influence of glycation on the biodistribution profile of radiolabeled BBS derivatives. We inserted carbohydrated linker moieties between the stabilized binding sequence BBS(7−14) and the N^{α}histidine-chelator by the application of established methods like the Amadori reaction, by the formation of a stable triazole bond via "click" chemistry, and by coupling of shikimic acid to a lysine residue (*33*, *35*, *36*). The peptides were labeled with ^{99m}Tc ($t_{1/2}$ = 6 h, 140 keV γ photon energy, 89% abundance) featuring a favorable dosimetry, high specific activity, low cost, and ready availability from a ^{99}Mo/^{99m}Tc-generator, and radiochemical properties optimal for single photon emission tomography (SPECT) (*37*). Moreover, the chemical similarities of the "matched pair" ^{99m}Tc/^{188}Re offer the opportunity to use successful ^{99m}Tc-labeled candidates for tumor targeting also for therapeutic applications labeled with ^{188}Re ($t_{1/2}$ = 17 h; 2.12 MeV $\beta^{-}{}_{max}$-radiation) (*37*). The new compounds were tested *in vitro* for binding affinity, internalization, efflux, and metabolic stability in the GRPR-expressing human prostate carcinoma cell line PC-3. *In vivo* biodistribution and SPECT/CT studies were performed in nude mice bearing PC-3 tumor xenografts.

MATERIALS AND METHODS

Chemicals and Equipment. All chemicals were obtained from Fluka (Buchs, Switzerland) or Merck (Dietikon, Switzerland). Cell culture media DMEM GLUTAMAX-I, trypsin/EDTA, bovine serum albumin, and soybean trypsin inhibitor were obtained from Invitrogen (Basel, Switzerland); fetal calf serum (FCS) and antibiotic/antimycotic solution were obtained from Bioconcept (Allschwil, Switzerland). Bacitracin, HEPES, and Chymostatin were purchased from SIGMA (Buchs, Switzerland). For the determination of protein concentrations, a Pierce BCA Protein Assay kit from Socochim (Lausanne, Switzerland) was used. Na[^{99m}TcO$_4$] was eluted from a Mallinckrodt ^{99}Mo/^{99m}Tc generator (Tyco Healthcare, Petten, The Netherlands) using 0.9% saline. Sodium boranocarbonate was a gift from the provider of the generator. The radioactivity of *in vitro* and *in vivo* experiments was measured with a NaI-γ-counter (Packard Canberra Cobra II, Meriden, USA) or a NaI ionization chamber.

Peptide Synthesis and Radiolabeling with ^{99m}Tc. The peptide solid-phase synthesis was carried out on a Rink Amide Resin with the Fmoc-strategy as previously described (*23*). The introduction of different carbohydrates (Figure 1) in the form of glucose or shikimic acid was performed as recently published (*33*, *35*, *36*, *38*). The purification of the peptides was done on a semipreparative HPLC system (Gilson) on a reverse-phase C_{18} column (Discovery BIO SULPELCO Wide Pore, 25 cm × 2.21 cm, 5 μm) with a linear gradient of 3% B to 100% B (solvent A = H_2O + 0.1% TFA and solvent B = CH_3CN + 0.1% TFA) in 30 min, a flow rate of 1 mL/min, and UV detection at 215 nm. Radiolabeling of the peptides with [^{99m}Tc(OH$_2$)$_3$(CO)$_3$]$^+$ was performed as previously described (*23*). For analyses and purification of the labeled peptides from the unlabeled compounds, a Macherey-Nagel CC Nucleosil 100−5 C_{18} RP column (5 μm, 250 = 4.6 mm) was used. Preparative HPLC for peptide purification was performed using a Merck-Hitachi L-7100-system with an equipped two-channel scintillation detector interface (John Caunt scientific Ltd., Eynsham, England) and a Rainin Dynamax absorbance detector model UV-1. HPLC solvents consisted of H_2O + 0.1% TFA (solvent A) and CH_3OH + 0.1% TFA (solvent B). The separation was performed with a linear gradient 50% A/50% B to 20% A/80% B for 25 min (1.0 mL/min). For the analytical HPLC of the labeled peptides, a Varian ProStar system was used with a Varian ProStar 230 Solvent Delivery Pump, a Varian Photodiode Array Detector model 330, a Varian ProStar Autosampler model 410, and a radiomatic Flo-one Beta Detector (Packard Canberra). HPLC solvents consisted of CH_3CN + 0.1% TFA (solvent A) and H_2O + 0.1% TFA (solvent B). The labeling control was performed with a linear gradient of 30% A/70% B to 80% A/20% B for 25 min (1.0 mL/min).

Octanol/Water Partition Coefficient Study. The octanol/water partition coefficients were determined at pH = 7.4. 5 μL containing 500 kBq of the radiolabeled compound in PBS was added to a vial containing 1.2 mL 1-octanol and PBS (1:1). After vortexing for 1 min, the vial was centrifuged for 5 min at 10 000 rpm to ensure complete separation of layers. Then, 40 μL of each layer was taken in a preweighed vial and measured in the γ-counter. Counts per unit weight of sample were calculated, and log D values were calculated as described by Pillarsetty et al. (*39*) using the formula

$$\log_{10} D = \log_{10}\left(\frac{\text{counts in 1 g of octanol}}{\text{counts in 1 g of water}}\right)$$

Cell Culture. PC-3 human prostate cancer cell line was obtained from European Collection of Cell Cultures (Salisbury, United Kingdom). Cells were maintained in Dulbecco's MEM with GLUTAMAX-I supplemented with 10% FCS, 100 IU/mL penicillin G sodium, 100 μg/mL streptomycin sulfate, and 0.25 μg/mL amphotericin B. Cells were incubated at 37 °C in an atmosphere containing 5% CO_2 and subcultured twice a week after detaching with trypsin-EDTA.

Metabolic Stability in PC-3 Cells. The stability in cell culture was evaluated with 2 × 10^6 cells in PBS. The analogues (3 MBq/mL, 1.5−2 pmol/mL) were incubated for 0.5, 1, 2.5, and 5 h at 37 °C. Afterward, proteins were precipitated as follows: 250 μL of sample + 750 μL of CH_3CN /ethanol (1:1)

Table 1. Sequence of BBS Analogues with New Carbohydrated Groups in the Linker[a]

		chelator	linker	binding sequence
reference	**1**	(N^{α}His)Ac	βAla-βAla	Gln-Trp-Ala-Val-Gly-His-Cha-Nle-NH_2
new peptides	**2**	(N^{α}His)Ac	**Lys(sha)**-βAla-βAla	Gln-Trp-Ala-Val-Gly-His-Cha-Nle-NH_2
	3	(N^{α}His)Ac	**Lys(Amd)**-βAla-βAla	Gln-Trp-Ala-Val-Gly-His-Cha-Nle-NH_2
	4	(N^{α}His)Ac	**Ala(^{N}TG)**-βAla-βAla	Gln-Trp-Ala-Val-Gly-His-Cha-Nle-NH_2

[a] **Lys(sha)** = Lysine-coupled shikimic acid; **Lys(Amd)** = Amadori-Product; **Ala(^{N}TG)** = triazole-coupled glucose.

and TFA (0.01%). The mixture was vortexed and centrifuged (10 min, 20 000 g) at 4 °C. The supernatant was filtered and analyzed by RP-HPLC equipped with a radioactivity detector. All experiments were carried out 2−3 times.

Receptor Inhibition Studies. One day prior to the assay, PC-3 cells at confluence were placed in 48 well plates. Cells were incubated in a special binding buffer (50 mM HEPES, 125 mM NaCl, 7.5 mM KCl, 5.5 mM $MgCl\cdot 6H_2O$, 1 mM EGTA, 5 g/L BSA, 2 mg/L Chymostatin, 100 mg/L Soybean Trypsin inhibitor, 50 mg/L Bacitracin, pH 7.4) with increasing concentrations of the BBS analogues (0−30 000 nM) in the presence of 4 kBq of ^{99m}Tc-BBS(7−14). After 1 h incubation at 37 °C, the cells were washed twice with cold PBS. Bound radioactivity was recovered by solubilizing the cells in 1 N NaOH (2 × 400 μL). The radioactivity was measured in the γ-counter. All experiments were carried out 2−3 times in triplicate.

Receptor Saturation Studies. One day prior to the assay, PC-3 cells at confluence were placed in 48 well plates and incubated for 1 h at 37 °C in the binding buffer described above with increasing concentrations of the labeled BBS analogues **2**−**4** (0.01−2 nM). The concentration of total technetium-labeled peptide was calculated according to Bauer et al. (*40*). Nonspecific binding was determined by coincubation with 1 μM BBS(1−14). After incubation, the cells were washed twice with cold PBS, solubilized in 1 N NaOH (2 × 400 μL), and the radioactivity measured in the γ-counter. Experiments were performed 2−3 times in triplicate.

Internalization and Externalization. One day prior to the assay, PC-3 cells at confluence were placed in 6 well plates. For internalization studies, cells were incubated with the labeled analogues (4 kBq/well) in binding buffer for 5, 15, 30, 60, and 120 min at 37 °C to allow binding and internalization. Nonspecific binding was determined in the presence of 1 μM BBS(1−14). After incubation, cells were washed twice with cold PBS. Surface-bound activity was removed by acid wash (50 mM glycine/HCL, 100 mM NaCl, pH 2.8, 2 = 600 μL for 5 min at room temperature). Afterward, the plates were neutralized with 600 μL PBS, and cells were lysed with 1 N NaOH (2 × 600 μL). Surface-bound and internalized activities were measured in the γ-counter. The protein concentration was determined and results were calculated as a percentage of total added radioactivity per milligram protein.

For externalization studies, PC-3 cells were incubated with the labeled analogues (20 kBq/well) in culture medium for 1 h at 37 °C to allow binding and maximal internalization. After incubation, the supernatant was discarded and each well washed twice with cold PBS. Afterward, the cells were incubated again at 37 °C in 2 mL culture medium for 30, 60, 150, or 300 min. At each time point, the supernatant was collected, the cells were washed twice with cold PBS and the radioactivity remaining in the cells was recovered by lysing the cells with 1 N NaOH (2 × 600 μL). Radioactivity in the supernatant (released activity) and in the lysate (internalized activity) was determined in the γ-counter. Results are expressed as a percentage of the total activity associated with the cells. The protein concentration was determined, and results were calculated as a percentage of total added radioactivity per milligram protein. All experiments were carried out 2−3 times in triplicate.

Biodistribution Studies. All animal experiments were conducted in compliance with the Swiss animal protection laws and with the ethical principles and guidelines for scientific animal trials established by the Swiss Academy of Medical Sciences and the Swiss Academy of Natural Sciences. Female CD-1 nu/nu mice 6−8 week-old (Charles River Laboratories, Sulzfeld, Germany) were subcutaneously injected with 8×10^6 PC-3 cells in 150 μL culture medium without supplements. About 3 weeks after tumor implantation, the mice (3−6 per group) were injected i.v. with 3.7 MBq radiolabeled peptides. At 0.5 h, 1.5, or 5 h postinjection (p.i.), the animals were killed by cervical dislocation. The different organs (heart, lung, spleen, kidneys, pancreas, stomach, small intestine, large intestine, liver, muscle, bone) and blood were collected, weighed, and the radioactivity measured in a γ-counter. Results are presented as the percentage of injected dose per gram of tissue (%ID/g). To determine the specificity of the *in vivo* uptake, one group of mice received a coinjection of 100 μg of unlabeled BBS(1−14) and the radiolabeled analogue and sacrificed at 1.5 h p.i.

SPECT/CT Studies. Single photon emission computed tomography/X-ray computed tomography (SPECT/CT) images were performed postmortem 1.5 h after i.v. injection of the ^{99m}Tc-BBS analogues (20 MBq). Images were obtained on an X-SPECT-system (Gamma Medica Inc.) equipped with a single head SPECT device and a CT device. SPECT data were acquired and reconstructed with LumaGEM (version 5.407). CT data were reconstructed with the software *Cobra* (version 4.5.1). Fusion of SPECT and CT data was performed with *IDL Virtual Machine* (version 6.0). Images were generated with *Amira* (version 3.1.1).

Statistical Analysis. All data are presented as the mean ± SD. Differences in the *in vivo* uptake in the biodostribution studies were analyzed by one-way ANOVA followed by Dunnett's comparison test. Differences between blocked and control groups were analyzed by unpaired *t* test. $P \leq 0.05$ was considered statistically significant.

RESULTS AND DISCUSSION

The modification of the biodistribution profiles of BBS analogues toward a reduction of abdominal accumulation is of high interest for both diagnostic and therapeutical applications. In this study, we investigated the influence of different glycated linkers on the *in vivo* behavior of ^{99m}Tc(CO)$_3$-labeled BBS derivatives. The amino acid sequence of the new peptides was based on the fragment 7−14 of BBS (Table 1), which had been successfully modified as previously published to increase the metabolic stability in human plasma and PC-3 tumor cells (replacement of Leu^{13} with Cha, and Met^{14} with Nle) (*23, 34*). The additional introduction of a βAla-βAla linker (compound **1**) led to improved *in vivo* tumor uptake (*18, 23*). However, the accumulation of activity in the liver was increased and the tumor-to-tissue ratios were still rather poor (tumor-to-blood = 4.3 ± 3.4; tumor-to-kidney = 0.9 ± 0.3; tumor-to-liver = 0.4 ± 0.3; at 1.5 h p.i.). A significant impact of polar linker moieties on the biodistribution was reported for several radiolabeled peptides, and in particular, carbohydrated compounds exhibited clearly improved pharmacokinetics (*21, 26, 34, 41, 42*). Therefore, we set out to synthesize three glycated BBS analogues (**2**, **3**, and **4**) for comparison with the unglycated

Table 2. Characteristics of the New BBS Analogues: Retention Time and Polarity (log *D*) of the ^{99m}Tc-Labeled Peptides, And Binding Affinity for GRP Receptors in PC-3 Cells of the Labeled (K_d Values) and Unlabeled (IC_{50} Values) Compounds ($n = 2-4$)

compound	HPLC γ − trace t_R [min]	log *D*	K_d [nM]	IC_{50} [nM]	$t_{1/2}$ in PC-3cell [min]
1	16.8	0.9 ± 0.2	0.18 ± 0.12	5.1 ± 1.7	30 ± 6
2	16.4	−0.2 ± 0.1	0.02 ± 0.01	6.5 ± 1.7	35 ± 11
3	16.7	−0.5 ± 0.1	0.18 ± 0.03	3.7 ± 1.7	37 ± 8
4	16.8	−0.5 ± 0.1	0.29 ± 0.16	3.2 ± 1.2	38 ± 5

^{99m}Tc(CO)$_3$-labeled compound **1**, which has recently been characterized by our group (*23*) (Table 1).

Compound **2** was modified with a linker bearing a lysine coupled to the glycomimetic shikimic acid at the ε-amino group, as recently published (*33*). Compound **3** was glycated by the "Amadori rearrangement", the Schiff base reaction of an aldose with a free amino group, known to form extremely stable carbohydrated peptide derivatives (*36, 43*). Finally, we investigated a clicked, carbohydrated BBS(7−14) analogue by the formation of a stable triazole bond between an alkyne in the linker and an azido glucose derivative (*35*) (Figure 1).

Radiolabeling of these novel carbohydrated peptides with $[^{99m}Tc(OH_2)_3(CO)_3]^+$ was performed at ligand concentrations of 10^{-5} M for 1 h at 75 °C. The HPLC traces of the ^{99m}Tc(CO)$_3$ complexes showed a general shift to longer retention times (16.4−16.9 min) compared to the unlabeled peptides (∼14.5 min) and the precursor $[^{99m}Tc(OH_2)_3(CO)_3]^+$ (∼9 min). Radiolabeling yields were higher than 95% for all derivatives, and the active complexes **2**−**4** were successfully separated from the unlabeled peptides to avoid a saturation of the GRPR in subsequent *in vitro*/*in vivo* experiments.

To compare the polarity of the $[^{99m}Tc(CO)_3]$-labeled new analogues **2**−**4**, the octanol/water partition coefficients were determined. The reference compound **1** bearing only the βAla-βAla-linker showed a rather lipophilic character with a log *D* of +0.9. The introduction of the shikimic acid changed the polarity of peptide **2** to −0.2, while the coupling to glucose resulted in log *D* values of −0.5 for both analogues **3** and **4** (Table 2).

***In Vitro* Studies.** The *in vitro* experiments were performed with PC-3 cells, which express a high level of GRPR. In order to investigate the potential of our three novel carbohydrated peptides **2**−**4** for specific targeting of GRPR, studies on receptor binding (Table 2) and cell internalization/cellular efflux (Figure 2) were performed. Additionally, the metabolic stability in tumor cells was investigated (Table 2). We already published an increased stability in PC-3 cells for compound **1** compared to the unmodified sequence (30 ± 6 min vs 5 ± 2 min, respectively) (*34*). The $t_{1/2}$ values of the novel peptides **2** (35 ± 11 min), **3** (37 ± 8 min), and **4** (38 ± 5 min) were slightly higher than for reference **1**, but the differences were not statistically significant (Table 2).

The affinity of the unlabeled analogues for GRPR was tested in inhibition experiments in competition with 4 kBq of ^{99m}Tc-BBS(7−14), which is known to express a high affinity for this receptor (*44*). All peptides exhibited a similar high affinity with IC_{50} values between 3 and 7 nM (Table 2). Furthermore, the receptor binding of the new analogues proved to be saturable and highly specific after radiolabeling with the ^{99m}Tc(CO)$_3$-core, with K_d values lower than 0.5 nM (Table 2). Interestingly, peptide **2** showed the highest affinity ($K_d = 0.02 \pm 0.01$ nM), about ten times higher than reference **1** ($K_d = 0.18 \pm 0.12$ nM) and the new peptides **3** ($K_d = 0.18 \pm 0.03$ nM) and **4** ($K_d = 0.29 \pm 0.16$ nM).

The internalization experiments showed a similar, rapid uptake into PC-3 cells reaching a plateau between 60 and 120 min (Figure 2). We found 29−37% of the total radioactivity per milligram of protein in the cell lysate after stripping the surface-bound activity off the cells with acidic buffer (pH 2.8). These results would reflect an agonistic behavior for the new compounds and are consistent with recently published BBS analogues with similar amino acid sequences (*15, 20, 34, 41*). The nearly complete blockade (<1% of the added radioactivity per milligram protein) by coincubation with an excess of BBS(1−14) demonstrated the high specificity for all new glycated BBS radiotracers. Variations in the bound radioactivity among the new peptides were statistically not significant. Additionally, efflux studies revealed a similar intracellular retention of the internalized activity of ∼35% up to 5 h for all new peptides **2**−**4** and the reference compound **1** (Figure 2). These results are in agreement with the similar metabolic stability of the new peptides we found in the degradation experiments with PC-3 cells (Table 2).

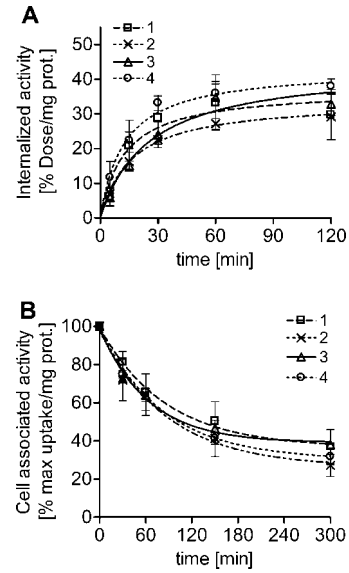

Figure 2. Time-course internalization (**A**) and externalization after maximal internalization (**B**) of the ^{99m}Tc-labeled BBS analogues in PC-3 cells after incubation at 37 °C. Data represent the percentage of internalized activity per milligram of protein related to the total activity added to the cells ($n = 2-3$).

Biodistribution Studies. Time-dependent biodistribution studies with the new radiotracers **2**−**4** have been performed in athymic mice, bearing PC-3 tumor xenografts. The new peptides **2** and **4** exhibited higher blood levels at 0.5 h p.i. (2.1 ± 0.7%ID/g and 1.8 ± 0.2%ID/g, respectively) than reference **1** (0.6 ± 0.2%ID/g). However, the clearance from the blood pool was fast and efficient for all new derivatives, providing low levels at 1.5 h p.i. for all new compounds (≤0.4% ID/g), similar to those published for the nonglycated ligand **1**.

All three new ligands **2**−**4** showed a relatively low liver uptake between 2.3 ± 0.3%ID/g (peptide **2**) and 1.3 ± 0.3%ID/g (peptide **3**) after 0.5 h. Peptides **2** and **4** showed a rapid elimination of activity from this organ (0.6 ± 0.1%ID/g and 0.6 ± 0.3%ID/g at 1.5 h p.i., respectively). Peptide **3** showed a slightly slower washout with 1.0 ± 0.1%ID/g (1.5 h p.i.) and 0.6 ± 0.2%ID/g (5 h p.i.). However, the uptake and retention of the carbohydrated peptides was significantly lower than the data reported for the nonglycated analogue **1** (5.3 ± 1.3 ID/g at 0.5 h p.i. and 2.1 ± 0.4%ID/g at 5 h p.i.).

Maximal tumor uptake was found at 0.5 h for all complexes. Compound **4** featured the highest accumulation at all p.i. times (5.6 ± 2.1, 3.6 ± 1.1, and 2.5 ± 1.3%ID/g at 0.5 h, 1.5, and 5 h p.i., respectively), which was significantly higher than that reported for peptide **1** ($P < 0.01$) (Table 3). Interestingly, the retention of **4** in the tumor was significantly higher than that of

Table 3. Biodistribution of the ^{99m}Tc-Labeled BBS Analogues (3.7 MBq/mouse i.v.) in Mice Bearing PC-3 Xenografts[a]

BBS	organs	0.5 h	1.5 h	5 h	1.5 h blocked
1	blood	0.58 ± 0.21	0.36 ± 0.66[b]	0.23 ± 0.11	0.47 ± 0.07
	stomach	1.37 ± 0.62	0.73 ± 0.47[b]	0.60 ± 0.33	1.23 ± 0.08
	kidney	1.82 ± 0.51	0.79 ± 0.35[b]	0.39 ± 0.20	0.76 ± 0.19
	liver	5.26 ± 1.26	2.36 ± 0.87[b]	1.83 ± 0.75	2.13 ± 0.36
	small intestines	5.00 ± 0.69	1.83 ± 0.57[b]	0.32 ± 0.19	6.48 ± 2.88
	pancreas	19.00 ± 7.60	6.16 ± 1.80[b]	0.69 ± 0.53	1.19 ± 0.07
	colon	2.65 ± 0.30	4.36 ± 3.60[b]	2.55 ± 1.77	1.11 ± 0.17
	tumor	1.53 ± 0.26	0.80 ± 0.35[b]	0.41 ± 0.27	0.37 ± 0.09
2	blood	2.12 ± 0.72	0.34 ± 0.10	0.11 ± 0.05	0.36 ± 0.08
	stomach	3.01 ± 0.23	1.50 ± 0.33	0.30 ± 0.10	0.90 ± 0.26
	kidney	7.20 ± 1.96	2.21 ± 0.38	0.99 ± 0.29	1.96 ± 0.62
	liver	2.28 ± 0.33**	0.57 ± 0.14*	0.22 ± 0.04**	0.87 ± 0.37
	small intestines	5.95 ± 1.68	5.52 ± 1.00	0.47 ± 0.07	2.84 ± 1.13
	pancreas	22.38 ± 8.10	16.05 ± 7.41	1.96 ± 1.64	2.16 ± 0.58[§§]
	colon	5.67 ± 2.59	4.57 ± 1.84	3.15 ± 1.31	0.48 ± 0.06[§§]
	tumor	3.79 ± 1.09*	2.83 ± 1.26**	0.62 ± 0.23	1.27 ± 0.62
3	blood	0.66 ± 0.21	0.16 ± 0.07	0.04 ± 0.01	0.15 ± 0.06
	stomach	1.53 ± 0.45	1.07 ± 0.10	0.58 ± 0.22	0.28 ± 0.09
	kidney	2.98 ± 0.84	1.89 ± 0.55	0.96 ± 0.15	1.52 ± 0.38
	liver	1.34 ± 0.33**	0.95 ± 0.10	0.61 ± 0.18**	2.07 ± 0.69
	small intestines	3.42 ± 0.15	2.88 ± 0.27	0.89 ± 0.08	1.88 ± 0.78
	pancreas	20.12 ± 6.60	18.56 ± 1.42	4.32 ± 1.58	1.52 ± 1.64[§§]
	colon	5.05 ± 1.10	4.53 ± 1.12	3.36 ± 0.46	0.52 ± 0.23[§§]
	tumor	2.37 ± 0.64	1.82 ± 0.43	0.71 ± 0.53	0.67 ± 0.20[§§]
4	blood	1.77 ± 0.16	0.34 ± 0.11[c]	0.07 ± 0.01	0.49 ± 0.15
	stomach	4.18 ± 0.20	1.82 ± 0.33[c]	0.54 ± 0.12	0.47 ± 0.11
	kidney	7.48 ± 0.53	2.65 ± 0.80[c]	0.95 ± 0.05	2.06 ± 0.71
	liver	1.74 ± 0.07**	0.64 ± 0.33**[c]	0.22 ± 0.01**	0.98 ± 0.80
	small intestines	8.51 ± 1.49	4.55 ± 1.24[c]	1.77 ± 0.46	3.64 ± 1.15
	pancreas	63.17 ± 8.23	26.96 ± 2.53[c]	3.70 ± 1.15	3.33 ± 0.28[§§]
	colon	12.93 ± 1.88	7.31 ± 1.22[c]	6.43 ± 0.79	0.74 ± 0.07[§§]
	tumor	5.64 ± 2.06**	3.62 ± 1.09**[c]	2.49 ± 1.32**	1.01 ± 0.09[§§]

[a] The animals of the blocked group received a coinjection of 0.1 mg BBS(1−14). Data (mean ± SD) are expressed as percentage of injected dose per gram of tissue ($n = 3-4$). [b] $n = 13$. [c] $n = 6$. * ($P \leq 0.05$). ** ($P \leq 0.01$) vs reference compound **1** (one-way ANOVA and Dunnett's posthoc test). [§] ($P \leq 0.05$). [§§] ($P \leq 0.01$) vs unblocked group (unpaired *t* test).

the other new peptides **2** and **3** and the reference **1**. Thus, in the case of complex **4**, 45% of the tumor-localized activity after 0.5 h still remained inside the tumor at 5 h p.i., compared to 16−29% for the other analogues.

Besides the increased tumor uptake, we observed high uptake of the radiopeptides in pancreas and colon, which are known to express GRPR in mice. The highest values in both organs were obtained for peptide **4** at 0.5 h p.i. (pancreas = 63%ID/g and colon 13.0% ID/g). Moreover, the specificity of tracer accumulation in GRPR-positive tissues was determined by coinjection with 0.1 mg BBS(1−14) per mouse. These experiments showed a clear reduction of radioactivity in the tumor xenografts and in pancreas and colon (Table 3), which would confirm that the *in vivo* uptake was due to receptor-specific interaction.

Despite the higher kidney uptake found for the new carbohydrated BBS analogues at early p.i. times (due to their increased hydrophilicity), it rapidly decreased, and the activity in the kidneys at later p.i. times was relatively low for all peptides (<1% ID/g, at 1.5 and 5 h p.i.) (Table 3). This would indicate that the tracers were not trapped in the renal tissue and renal excretion of the radiopeptides was very fast.

The increased hydrophilicity of the new peptides resulted in a decrease in hepatic activity. However, a relatively high and unspecific accumulation of activity was observed in the small intestine, which would indicate that hepatobiliary excretion partially contributes to the overall tracer elimination (Table 3). Biodistribution experiments in normal mice have been reported for ^{99m}Tc(III)-labeled BBS analogues, all modified with different lipophilic linkers, and, in the case of two compounds, an additional carboxylic group. All these complexes featured high uptake in hepatic tissue (7.2−9.4%ID/g) and relatively high renal accumulation between 1.8 and 6.0%ID/g at 1 h p.i (*20*).

Calculation of tumor-to-blood, tumor-to-liver, and tumor-to-kidney ratios (Figure 3) allowed comparisons with other radiolabeled BBS analogues, recently described in the literature. The highest tumor-to-blood ratios corresponded to compound **4** and were significantly higher than those of the reference peptide **1** at 1.5 h p.i. (11.5 ± 4.8 vs 4.3 ± 3.4, respectively; $P < 0.05$) and at 5 h p.i. (33.4 ± 4.2 vs 1.9 ± 0.5, $P < 0.01$). Compounds **2** and **3** showed similar tumor-to-blood ratios compared to peptide **1** at 0.5 and slightly higher at 1.5 and 5 h p.i. time, but the differences were not statistically significant, with the exception of compound **3** at 1.5 h (13.0 ± 7.1 vs 4.3 ± 3.4, respectively; $P < 0.01$).

Interestingly, compound **4** featured significantly increased tumor-to-kidney ratios already at 1.5 h p.i. (1.4 ± 0.4 for **4** vs 0.9 ± 0.3 for **1**; $P < 0.05$) but more remarkably at 5 h p.i. (2.6 ± 0.4 for **4** vs 1.1 ± 0.3 for **1**; $P < 0.01$). Tumor-to-kidney ratios for peptides **2** and **3** were not significantly different compared to the reference **1** at any p.i. time (Figure 3).

The most notable finding was the improvement of tumor-to-liver ratios for all new glycated radiotracers at all p.i. times compared to the nonglycated peptide **1** (Figure 3). This indicates a significant impact of carbohydration on tracer accumulation in the liver, which is particularly important since high accumulation of radioactivity in the liver has been reported not only for ^{99m}Tc-labeled BBS analogues but also for ^{64}Cu-DOTA-BBS(7−14), ^{64}Cu-NOTA-8-Aoc-BBN(7−14)NH_2, and ^{68}Ga-DOTA-BBS(6−14) (*19*, *21*, *22*). The positive effect of carbohydration on liver accumulation has already been published for other peptides, e.g., radiolabeled sst analogues. Carbohydrated conjugates of Tyr^3-octreotide (TOC) showed a significant decrease of tracer accumulation in the liver and the intestines, without any effect on the binding affinity and similar or even increased uptake in sst receptor expressing tissues and tumor xenografts (*26*).

A direct comparison of the *in vivo* results with other ^{99m}Tc-labeled BBS analogues published in the literature is somehow difficult, since no glycated BBS analogues have yet been described and most of the reported analogues are based on the unmodified BBS(7−14) sequence. Smith et al. reported on the biodistribution in SCID mice with PC-3 tumor xenografts of BBS analogues radiolabeled with the bidentate ^{99m}Tc(X)(CO_3)-DPR-complex (X = H_2O or $P(CH_2OH)_3$ and DPR = 2,3-diaminopropionic acid) (*24*). Maximal tumor uptake at 1 and 4 h p.i. (3.7 and 2.7%ID/g, respectively) was comparable to our glycated BBS analogue **4** (3.6 and 2.5%ID/g at 1.5 and 5 h p.i., respectively). However, the accumulation in the liver and kidneys was higher, and thus, tumor-to-liver and tumor-to-kidney ratios were lower compared to our glycated compound **4**. Alves et al. published *in vivo* data in PC-3 tumor xenografted SCID mice for a series of pyrazolyl BBS conjugates labeled with the ^{99m}Tc(I)-tricarbonyl-core (*41*). In this case, maximal tumor uptake (1.8%ID/g at 1 h p.i.), as well as tumor-to-tissue ratios, was lower than those of analogue **4**. Interestingly, they tested the effect of several linkers between the chelator and the binding sequence. They found that the polar seryserylserine featured a longer retention in the tumors at 4 h p.i. compared to two rather lipophilic linkers consisting of β-Ala or glycylglycylglycine. This supports the results obtained with our polar glycated compounds and indicates a general positive influence of polar linkers on the biodistribution of ^{99m}Tc(I)-triycarbonyl-

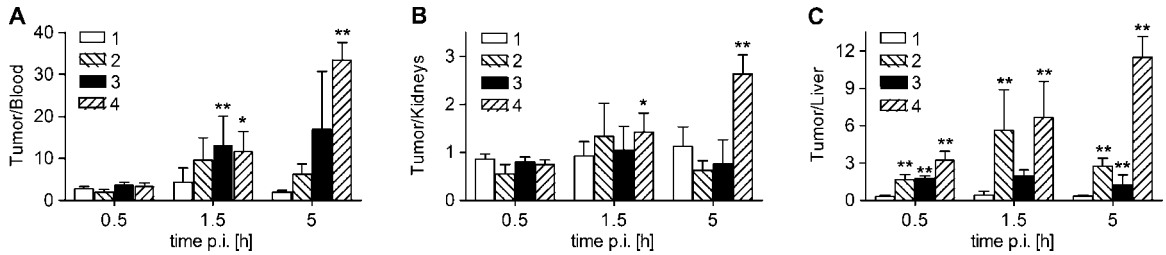

Figure 3. Tumor-to-tissue ratios of the ^{99m}Tc-labeled BBS analogues in mice bearing PC-3 tumor xenografts (3.7 MBq/mouse i.v.) ($n = 3-13$). (A) Tumor-to-blood. (B) Tumor-to-kidney. (C) Tumor-to-liver. * ($P \leq 0.05$), ** ($P \leq 0.01$) vs reference compound **1** (one-way ANOVA and Dunnett's posthoc test).

labeled BBS analogues. The same group reported recently a study with similar analogues incorporating 2-(*N,N′*-Bis(*tert*-butoxycarbonyl)diethylenetriamine) acetic acid (DTMA) as chelator for ^{99m}Tc (*45*). The *in vivo* behavior of the DTMA-BBS analogues was comparable to that of the pyrazolyl conjugates. Our results are also in agreement with a recent study with HYNIC and diphosphine BBS analogues (*46*). The authors found higher tumor uptake and better tumor-to-tissue ratios for the HYNIC analogue compared to the more lipophilic diphosphine tracer. Our analogue **4** showed slightly higher tumor uptake than the HYNIC conjugate (3.6%ID/g vs 3.0%ID/g at 1.5 h p.i., respectively). However, kidney and liver uptakes were lower, and consequently, tumor-to-kidney and tumor-to-liver ratios higher. Nock et al. reported on *in vivo* data for several ^{99m}Tc(V)-labeled BBS(1−14) analogues either with a hydrophilic or with a lipophilic character. Their results also indicated a strong impact of the polarity on the accumulation of the tracers in liver, kidneys, and tumors (*15*), the hydrophilic peptides showing the best tumor-to-nontumor ratios. Tumor-to-liver and tumor-to-blood ratios were comparable to those of our best compound (**4**). However, the glycated ^{99m}Tc(I)-labeled peptide **4** showed higher tumor-to-kidney values than the ^{99m}Tc(V)-labeled compound, which could be of interest for therapeutical applications with $^{186/188}$Re-labeled BBS.

SPECT/CT Imaging Studies. High accumulation of activity in the liver and gastrointestinal tract may hide the localization of cancerous lesions in the abdomen. Therefore, the reduced abdominal uptake by introduction of carbohydrates in addition to the increased tumor uptake is able to increase the potential of radiolabeled BBS, in general, and of ^{99m}Tc(CO)$_3$-labeled peptides, in particular. The new glycated analogues were further evaluated *in vivo* in SPECT/CT imaging experiments. Representative SPECT/CT images of the novel glycated radiotracer **4** and the nonglycated ligand **1** are depicted in Figure 4. The new conjugate **4** clearly provided a better imaging of the tumor xenografts than the reference compound **1**. The higher tumor uptake of conjugate **4** led to a clearer visualization of the xenografts compared to the nonglycated **1**. Furthermore, the lower liver and kidney uptakes resulted in decreased radioactive background in the abdominal area. Accumulation in small intestines due to hepatobiliary excretion as well as uptake in the GRPR-positive pancreatic and colon tissue were still high, in accordance with our *ex vivo* biodistribution data.

CONCLUSION

We evaluated three novel carbohydrated BBS derivatives for their usefulness in imaging GRPR-expressing neoplasms, and we could confirm the positive impact of glycation on the *in vivo* behavior of BBS analogues. In summary, the introduction of the polar carbohydrates had no effect on internalization, efflux, or metabolic stability *in vitro* but led to a significant reduction of abdominal accumulation, higher tumor uptake, and improved tumor-to-background ratios *in vivo*. The best results were obtained with a triazole coupled glucose, which ameliorated the biodistribution profile significantly. In this respect, the easy glycation via click reaction, using commercially available reagents, clearly offers an opportunity to improve the pharmacokinetic profiles of ^{99m}Tc- or ^{188}Re-labeled BBS analogues and increase their potential for imaging and therapy of GRPR-expressing tumors.

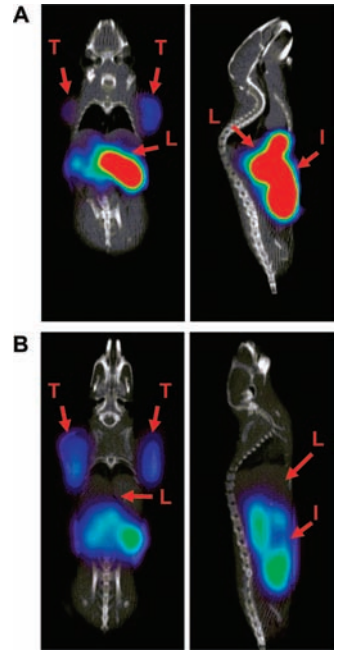

Figure 4. SPECT/CT image of nude mice bearing PC-3 tumor xenografts at 1.5 h p.i. of the ^{99m}Tc-labeled BBS analogues (20 MBq, i.v.). (A) Coronal (left) and sagittal (right) slices of compound **1** (nonglycated). (B) Coronal (left) and sagittal (right) slices of compound **4** (glycated via click reaction). T = tumor; L = liver; I = intestines.

ACKNOWLEDGMENT

The authors thank Mr. Alain Blanc, Ms. Olga Gasser, and Dr. Alexander Hohn for their technical assistance. This work was funded by an Oncosuisse grant (Nr. OCS 01311-02-2003) and by the Fund for Scientific Research-Flanders, Belgium, (grant Nr. G.0036.04). V. Maes is a Postdoctoral Researcher of the Fund for Scientific Research-Flanders; L. Brans thanks the Institute for the Promotion of Innovation through Science and Technology in Flanders (IWT-Vlaanderen) for a grant.

LITERATURE CITED

(1) Reubi, J. C. (2003) Peptide receptors as molecular targets for cancer diagnosis and therapy. *Endocr. Rev. 24*, 389–427.
(2) Heppeler, A., Froidevaux, S., Eberle, A. N., and Maecke, H. R. (2000) Receptor targeting for tumor localisation and therapy with radiopeptides. *Curr. Med. Chem. 7*, 971–994.

(3) Krenning, E. P., Kwekkeboom, D. J., Valkema, R., Pauwels, S., Kvols, L. K., and De Jong, M. (2004) Peptide receptor radionuclide therapy. *Ann. N.Y. Acad. Sci. 1014*, 234–245.
(4) Dijkgraaf, I., Boerman, O. C., Oyen, W. J. G., Corstens, F. H. M., and Gotthardt, M. (2007) Development and application of peptide-based radiopharmaceuticals. *Anticancer Agents Med. Chem. 7*, 543–551.
(5) Okarvi, S. M. (2008) Peptide-based radiopharmaceuticals and cytotoxic conjugates: Potential tools against cancer. *Cancer Treat. Rev. 34*, 13–26.
(6) Reubi, J., Gugger, M., and Waser, B. (2002) Co-expressed peptide receptors in breast cancer as a molecular basis for in vivo multireceptor tumour targeting. *Eur. J. Nucl. Med. Mol. Imaging 29*, 855–862.
(7) Krenning, E. P., Kwekkeboom, D. J., Bakker, W. H., Breeman, W. A. P., Kooij, P. P. M., Oei, H. Y., Vanhagen, M., Postema, P. T. E., Dejong, M., Reubi, J. C., Visser, T. J., Reijs, A. E. M., Hofland, L. J., Koper, J. W., and Lamberts, S. W. J. (1993) Somatostatin receptor scintigraphy with [^{111}In-DTPA-D-Phe^{1}]- and [^{123}I-Tyr^{3}]-octreotide - the rotterdam experience with more than 1000 patients. *Eur. J. Nucl. Med. Mol. Imaging 20*, 716–731.
(8) Gibril, F., Reynolds, J. C., Doppman, J. L., Chen, C. C., Venzon, D. J., Termanini, B., Weber, C., Stewart, C. A., and Jensen, R. T. (1996) Somatostatin receptor scintigraphy: Its sensitivity compared with that of other imaging methods in detecting primary and metastatic gastrinomas - A prospective study. *Ann. Intern. Med. 125*, 26-&.
(9) Otte, A., Mueller-Brand, J., Dellas, S., Nitzsche, E. U., Herrmann, R., and Maecke, H. R. (1998) Yttrium-90-labelled somatostatin-analogue for cancer treatment. *Lancet 351*, 417–418.
(10) de Jong, M., Breeman, W. A. P., Valkema, R., Bernard, B. F., and Krenning, E. P. (2005) Combination radionuclide therapy using Lu-177- and Y-90-labeled somatostatin analogs. *J. Nucl. Med. 46*, 13S–17S.
(11) Reubi, J. C., Wenger, S., Schmuckli-Maurer, J., Schaer, J.-C., and Gugger, M. (2002) Bombesin receptor subtypes in human cancers: detection with the universal radioligand 125I-[D-TYR^{6}, β-ALA^{11}, PHE^{13}, NLE^{14}] bombesin(6−14). *Clin. Cancer Res. 8*, 1139–1146.
(12) Smith, C. J., Volkert, W. A., and Hoffman, T. J. (2005) Radiolabeled peptide conjugates for targeting of the bombesin receptor superfamily subtypes. *Nucl. Med. Biol. 32*, 733–740.
(13) Markwalder, R., and Reubi, J. C. (1999) Gastrin-releasing peptide receptors in the human prostate: relation to neoplastic transformation. *Cancer Res. 59*, 1152–1159.
(14) Zhou, J., Chen, J., Mokotoff, M., Zhong, R., Shultz, L. D., and Ball, E. D. (2003) Bombesin/gastrin-releasing peptide receptor: a potential target for antibody-mediated therapy of small cell lung cancer. *Clin. Cancer Res. 9*, 4953–4960.
(15) Nock, B. A., Nikolopoulou, A., Galanis, A., Cordopatis, P., Waser, B., Reubi, J. C., and Maina, T. (2005) Potent bombesin-like peptides for GRP-receptor targeting of tumors with ^{99m}Tc: a preclinical study. *J. Med. Chem. 48*, 100–110.
(16) Zhang, H., Chen, J., Waldherr, C., Hinni, K., Waser, B., Reubi, J. C., and Maecke, H. R. (2004) Synthesis and evaluation of bombesin derivatives on the basis of pan-bombesin peptides labeled with indium-111, lutetium-177, and yttrium-90 for targeting bombesin receptor-expressing tumors. *Cancer Res. 64*, 6707–6715.
(17) Zhang, X., Cai, W., Cao, F., Schreibmann, E., Wu, Y., Wu, J. C., Xing, L., and Chen, X. (2006) ^{18}F-labeled bombesin analogs for targeting GRP receptor-expressing prostate cancer. *J. Nucl. Med. 47*, 492–501.
(18) Smith, C. J., Gali, H., Sieckman, G. L., Higginbotham, C., Volkert, W. A., and Hoffman, T. J. (2003) Radiochemical investigations of ^{99m}Tc-N_3S-X-BBN[7−14]NH_2: an *in vitro/in vivo* structure-activity relationship study where = = 0-, 3-, 5-, 8-, and 11-carbon tethering moieties. *Bioconjugate Chem. 14*, 93–102.
(19) Schuhmacher, J., Zhang, H., Doll, J., Macke, H. R., Matys, R., Hauser, H., Henze, M., Haberkorn, U., and Eisenhut, M. (2005) GRP receptor-targeted PET of a rat pancreas carcinoma xenograft in nude mice with a ^{68}Ga-labeled bombesin(6−14) analog. *J. Nucl. Med. 46*, 691–699.
(20) Kunstler, J. U., Veerendra, B., Figueroa, S. D., Sieckman, G. L., Rold, T. L., Hoffman, T. J., Smith, C. J., and Pietzsch, H. J. (2007) Organometallic ^{99m}Tc(III) '4 + 1' bombesin(7−14) conjugates: synthesis, radiolabeling, and in vitro/in vivo studies. *Bioconjugate Chem. 18*, 1651–1661.
(21) Parry, J. J., Kelly, T. S., Andrews, R., and Rogers, B. E. (2007) In vitro and in vivo evaluation of ^{64}Cu-labeled DOTA-linker-bombesin(7−14) analogues containing different amino acid linker moieties. *Bioconjugate Chem. 18*, 1110–1117.
(22) Prasanphanich, A. F., Nanda, P. K., Rold, T. L., Ma, L., Lewis, M. R., Garrison, J. C., Hoffman, T. J., Sieckman, G. L., Figueroa, S. D., and Smith, C. J. (2007) [^{64}Cu-NOTA-8-Aoc-BBN(7−14)NH_2] targeting vector for positron-emission tomography imaging of gastrin-releasing peptide receptor-expressing tissues. *Proc. Natl. Acad. Sci. U.S.A. 104*, 12462–12467.
(23) Garayoa, E. G., Ruegg, D., Blauenstein, P., Zwimpfer, M., Khan, I. U., Maes, V., Blanc, A., Beck-Sickinger, A. G., Tourwe, D. A., and Schubiger, P. A. (2007) Chemical and biological characterization of new Re$(CO)_3$/[^{99m}Tc]$(CO)_3$ bombesin analogues. *Nucl. Med. Biol. 34*, 17–28.
(24) Smith, C. J., Sieckman, G. L., Owen, N. K., Hayes, D. L., Mazuru, D. G., Kannan, R., Volkert, W. A., and Hoffman, T. J. (2003) Radiochemical investigations of gastrin-releasing peptide receptor-specific [^{99m}Tc(X)$(CO)_3$-Dpr-Ser-Ser-Ser-Gln-Trp-Ala-Val-Gly-His-Leu-Met-(NH_2)] in PC-3, tumor-bearing, rodent models: syntheses, radiolabeling, and in vitro/in vivo studies where Dpr = 2,3-diaminopropionic acid and = = H_2O or $P(CH_2OH)_3$. *Cancer Res. 63*, 4082–4088.
(25) Smith, C. J., Gali, H., Sieckman, G. L., Hayes, D. L., Owen, N. K., Mazuru, D. G., Volkert, W. A., and Hoffman, T. J. (2003) Radiochemical investigations of ^{177}Lu-DOTA-8-Aoc-BBN[7−14]NH_2: an in vitro/in vivo assessment of the targeting ability of this new radiopharmaceutical for PC-3 human prostate cancer cells. *Nucl. Med. Biol. 30*, 101–109.
(26) Schottelius, M., Wester, H. J., Reubi, J. C., Senekowitsch-Schmidtke, R., and Schwaiger, M. (2002) Improvement of pharmacokinetics of radioiodinated Tyr3-octreotide by conjugation with carbohydrates. *Bioconjugate Chem. 13*, 1021–1030.
(27) Wester, H. J., Schottelius, M., Scheidhauer, K., Meisetschlager, G., Herz, M., Rau, F. C., Reubi, J. C., and Schwaiger, M. (2003) PET imaging of somatostatin receptors: design, synthesis and preclinical evaluation of a novel ^{18}F-labelled, carbohydrated analogue of octreotide. *Eur. J. Nucl. Med. Mol. Imaging 30*, 117–122.
(28) Wester, H. J., Schottelius, M. K., Scheidhauer, J. C., Reubi, I., and Wolf, and Schwaiger, M. (2002) Comparison of radioiodinated TOC, TOCA and Mtr-TOCA: the effect of carbohydration on the pharmacokinetics. *Eur. J. Nucl. Med. Mol. Imaging 29*, 28–38.
(29) Haubner, R., Wester, H. J., Weber, W. A., Mang, C., Ziegler, S. I., Goodman, S. L., Senekowitsch-Schmidtke, R., Kessler, H., and Schwaiger, M. (2001) Noninvasive imaging of alpha(v)beta(3) integrin expression using F-18-labeled RGD-containing glycopeptide and positron emission tomography. *Cancer Res. 61*, 1781–1785.
(30) Schottelius, M., Rau, F., Reubi, J. C., Schwaiger, M., and Wester, H. A. (2005) Modulation of pharmacokinetics of radioiodinated sugar-conjugated somatostatin analogues by variation of peptide net charge and carbohydration chemistry. *Bioconjugate Chem. 16*, 429–437.
(31) Wester, H. J., Schottelius, M., Poethko, T., Bruus-Jensen, K., and Schwaiger, M. (2004) Radiolabeled carbohydrated somatostatin analogs: A review of the current status. *Cancer Biother. Radiopharm. 19*, 231–244.
(32) Antunes, P., Ginj, M., Walter, M. A., Chen, J., Reubi, J. C., and Maecke, H. R. (2007) Influence of different spacers on the

biological profile of a DOTA-somatostatin analogue. *Bioconjugate Chem. 18*, 84–92.

(33) Maes, V., Garcia-Garayoa, E., Blauenstein, P., and Tourwe, D. (2006) Novel ^{99m}Tc-labeled neurotensin analogues with optimized biodistribution properties. *J. Med. Chem. 49*, 1833–1836.

(34) Garcia-Garayoa, E., Schweinsberg, C., Maes, V., Ruegg, D., Blanc, A., Blauenstein, P., Tourwe, D. A., Beck-Sickinger, A. G., and Schubiger, P. A. (2007) New [^{99m}Tc]bombesin analogues with improved biodistribution for targeting gastrin releasing-peptide receptor-positive tumors. *Q. J. Nucl. Med. Mol. Imaging 51*, 42–50.

(35) Maes, V., Brans, L., Schweinsberg, C., Garcia-Garayoa, E., Blauenstein, P., Schubiger, P. A., and Tourwe, D. (2007) Click-carbohydrated [^{99m}Tc(CO) $_3$](N^{α}His)Ac-Bombesin(7−14) analogs. *Biopolymers 88*, 547–547.

(36) Maes, V., and Tourwe, D. (2006) Maillard glycation of peptides containing the (N^{α}His)Ac chelator for ^{99m}Tc(CO)$_3$ labeling. *Int. J. Pept. Res. Ther. 12*, 197–202.

(37) Garcia-Garayoa, E., Schibli, R., and Schubiger, P. A. (2007) Peptides radiolabeled with Re-186/188 and Tc-99m as potential diagnostic and therapeutic agents. *Nucl. Sci. Technol. 18*, 88–100.

(38) Kuijpers, B. H. M., Groothuys, S., Soede, A. C., Laverman, P., Boerman, O. C., van Delft, F. L., and Rutjes, F. P. J. T. (2007) Preparation and evaluation of glycosylated arginine-glycine-aspartate (RGD) derivatives for integrin targeting. *Bioconjugate Chem. 18*, 1847–1854.

(39) Pillarsetty, N., Cai, S., Ageyeva, L., Finn, R. D., and Blasberg, R. G. (2006) Synthesis and evaluation of [^{18}F] labeled pyrimidine nucleosides for positron emission tomography imaging of herpes simplex virus 1 thymidine kinase gene expression. *J. Med. Chem. 49*, 5377–5381.

(40) Bauer, R., and Pabst, H. W. (1982) Tc-generators - yield of ^{99m}Tc and ratio to 'inactive' ^{99}Tc. *Eur. J. Nucl. Med. 7*, 35–36.

(41) Alves, S., Correia, J. D. G., Santos, I., Veerendra, B., Sieckman, G. L., Hoffman, T. J., Rold, T. L., Figueroa, S. D., Retzloff, L., McCrate, J., Prasanphanich, A., and Smith, C. J. (2006) Pyrazolyl conjugates of bombesin: a new tridentate ligand framework for the stabilization of fac-[M(CO)$_3$]$^+$ moiety. *Nucl. Med. Biol. 33*, 625–634.

(42) Christensen, E. I., Rennke, H. G., and Carone, F. A. (1983) Renal tubular uptake of protein: effect of molecular charge. *Am. J. Physiol. Renal Physiol. 244*, F436–441.

(43) Albert, R., Marbach, P., Bauer, W., Briner, U., Fricker, G., Bruns, C., and Pless, J. (1993) Sdz-Co-611 - a highly potent glycated analog of somatostatin with improved oral activity. *Life Sci. 53*, 517–525.

(44) La Bella, R. L., Garcia-Garayoa, E., Bahler, M. B., Blauenstein, P., Schibli, R., Conrath, P., Tourwe, D., and Schubiger, P. A. (2002) A ^{99m}Tc(I)-postlabeled high affinity bombesin analogue as a potential tumor imaging agent. *Bioconjugate Chem. 13*, 599–604.

(45) Lane, S. R., Veerendre, B., Rold, T. L., Sieckman, G. L., Hoffman, T. L., Jurisson, S. S., and Smith, C. J. (2008) ^{99m}Tc(CO)$_3$-DTMA bombesin conjugates having high affinity for the GRP receptor. *Nucl. Med. Biol. 35*, 263–272.

(46) Faintuch, B. L., Teodoro, R., Duatti, A., Muramoto, E., Faintuch, S., and Smith, C. J. (2008) Radiolabeled bombesin analogs for prostate cancer diagnosis: preclinical studies. *Nucl. Med. Biol. 35*, 401–411.

BC800319G

Bioconjugate Chemistry 20th Anniversary

Subscriber access provided by SHEMYAKIN-OVCHINNIKOV INST

Article

Protease-Specific Nanosensors for Magnetic Resonance Imaging

Eyk Schellenberger, Franziska Rudloff, Carsten Warmuth, Matthias Taupitz, Bernd Hamm, and Jo#rg Schnorr

Bioconjugate Chem., **2008**, 19 (12), 2440-2445• DOI: 10.1021/bc800330k • Publication Date (Web): 14 November 2008

Downloaded from http://pubs.acs.org on May 2, 2009

More About This Article

Additional resources and features associated with this article are available within the HTML version:

- Supporting Information
- Access to high resolution figures
- Links to articles and content related to this article
- Copyright permission to reproduce figures and/or text from this article

View the Full Text HTML

ACS Publications
High quality. High impact.

Bioconjugate Chemistry is published by the American Chemical Society. 1155 Sixteenth Street N.W., Washington, DC 20036

Protease-Specific Nanosensors for Magnetic Resonance Imaging

Eyk Schellenberger,* Franziska Rudloff, Carsten Warmuth, Matthias Taupitz, Bernd Hamm, and Jörg Schnorr

Department of Radiology, Charité - Universitätsmedizin Berlin; Charitéplatz 1; 10117 Berlin, Germany. Received August 1, 2008; Revised Manuscript Received October 27, 2008

Imaging of enzyme activity is a central goal of molecular imaging. With the introduction of fluorescent smart probes, optical imaging has become the modality of choice for experimental *in vivo* detection of enzyme activity. Here, we present a novel high-relaxivity nanosensor that is suitable for *in vivo* imaging of protease activity by magnetic resonance imaging. Upon specific protease cleavage, the nanoparticles rapidly switch from a stable low-relaxivity stealth state to become adhesive, aggregating high-relaxivity particles. To demonstrate the principle, we chose a cleavage motif of matrix metalloproteinase 9 (MMP-9), an enzyme important in inflammation, atherosclerosis, tumor progression, and many other diseases with alterations of the extracellular matrix. On the basis of clinically tested very small iron oxide particles (VSOP), the MMP-9-activatable protease-specific iron oxide particles (PSOP) have a hydrodynamic diameter of only 25 nm. PSOP are rapidly activated, resulting in aggregation and increased T2*-relaxivity.

INTRODUCTION

The advent of fluorescent smart sensor probes activatable by proteases ignited the development of reporter probes (*1*) and instrumentation (*2*) establishing optical imaging as the modality of choice for *in vivo* detection of enzyme activity (*3*).

To take advantage of the high resolution and deep-tissue imaging capabilities of magnetic resonance imaging (MRI), suitable for whole-body imaging of humans, as well as the absence of radiation exposure, several new probe designs were introduced. Meade and co-workers developed a reporter probe activatable by β-galactosidase on the basis of a paramagnetic contrast agent and demonstrated its successful use for the visualization of gene transfer by MRI (*4*).

A paramagnetic polymerization probe was presented by Bogdanov et al., which allowed imaging of tissue peroxidase activity by MRI (*5*). Josephson and co-workers introduced magnetic relaxation switches sensing enzymatic activity based on superparamagnetic high-relaxivity probes for *in vitro* MRI (*6*). Upon protease activation, these sterically stabilized cross-linked iron oxide particles (CLIO) switch from large clustered high-relaxivity aggregates to smaller low-relaxivity single particles. This technique is not suitable for *in vivo* application, since the nonactivated clustered particles are too large to have a favorable bioavailability and, more importantly, activation by elevated enzyme activity in the target tissue *reduces* the relaxivity and consequently the contrast effect.

Here, we describe a new design of protease-sensitive nanosensors, which are based on electrostatically stabilized, citrate-coated very small iron oxide particles (VSOP) with a hydrodynamic diameter of 7.7 ± 2.1 nm (Figure 2a) instead of larger sterically stabilized nanoparticles (over 20 nm). We have previously developed a pharmacologically formulated variant of these superparamagnetic particles (VSOP-C184) for magnetic resonance angiography, which was successfully tested in a clinical phase 1 trial and currently undergoing clinical phase 2 testing (*7*).

As cleavage motif, we chose a recognition site for MMP-9 and MMP-2, which was previously used to prepare a MMP-9-activatable fluorescent probe (*8*, *9*). MMPs have been identified as important regulators of pathological remodeling of extracellular matrix in cancer and inflammation (*10*). Using fluorescent smart probes, Bremer et al. developed a new concept to monitor the success of MMP inhibition in cancer by *in vivo* imaging, which may ultimately enable monitoring of therapeutic responses in the large spectrum of diseases with alterations of the extracellular matrix (*11*).

EXPERIMENTAL PROCEDURES

Synthesis. (1) The synthesized fluorescein-labeled MMP-9 peptide NH_2-GG*PRQITA*G-K(FITC)-GGGG-RRRRR-G-RRRRR-amide (the italicized amino acids correspond to the MMP-9 substrate (*9*)) was confirmed by MALDI-TOF (MALDI 2, Shimadzu). The molecular weight was within 1 Da of the expected value. 1 mg of the MMP-9 peptide (in 100 μL DMSO) was reacted with 31 mg NHS-mPEG (*O*-[(*N*-succinimidyl)succinyl-aminoethyl]-*O*′-methyl-poly(ethylene glycol) 5000, Fluka) in 300 μL 0.1 M HEPES, pH 7.5, overnight at 4 °C. The resulting MMP-9-peptide-mPEG copolymer was purified by gel filtration with BioGel P6 (BioRad, in 10 mM HEPES, 140 mM NaCl, pH 7.5). The absence of unreacted MMP-9 peptide was confirmed by HPLC using a reverse-phase C18 column with acetonitrile/water gradient. The concentration of the peptide-mPEG copolymers was determined spectrophotometrically by measuring peptide-bound fluorescein absorption (absorption at 494 nm, extinction coefficient of 72 000 M^{-1} cm^{-1}).

(2) VSOP (VSOP-C200) was provided by Ferropharm GmbH. To prepare 6×-MMP-9-PSOP (with six peptide-mPEG copolymers per VSOP), 1.25 nmol VSOP (3.25 μmol Fe assuming 2600 iron atoms per particle, data from Ferropharm GmbH) in 250 μL HEPES buffer (10 mM HEPES, 140 mM NaCl, pH 7.5) were mixed with 7.5 nmol peptide-mPEG in 250 μL HEPES buffer and stirred immediately. Other ratios (3 to 16) were prepared accordingly. Hydrodynamic diameters of MMP-9-PSOPs were determined by dynamic light scattering (Zetasizer Nano ZS, Malvern Instruments) in the same buffer. Relaxivities were measured with an MR spectrometer at 0.94 T (Bruker, Minispec MQ 40) according to the manufacturer's instructions.

For quenching experiments (Figure 3), 50 pmol VSOP was mixed with different amounts of the peptide-mPEG copolymers (150 pmol to 800 pmol) in 200 μL and subjected to fluorescence

* E-mail: eyk.schellenberger@charite.de.

10.1021/bc800330k CCC: $40.75 © 2008 American Chemical Society
Published on Web 11/14/2008

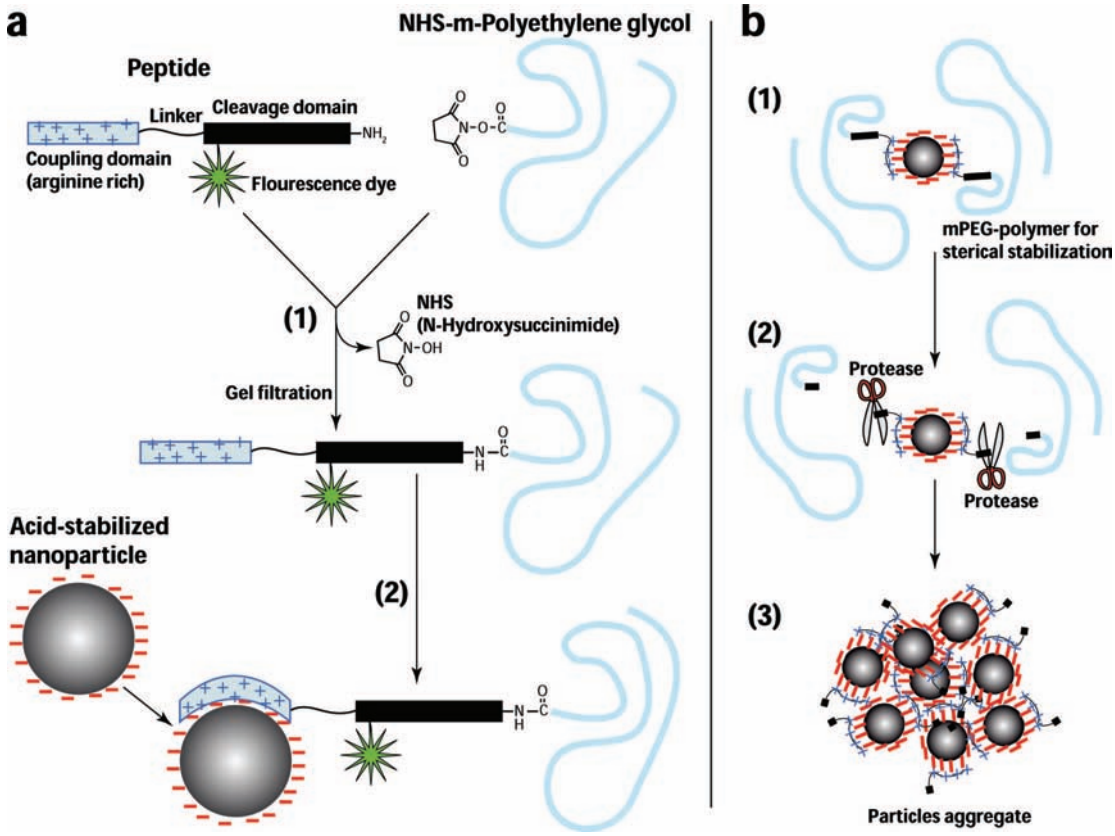

Figure 1. Synthesis and function of MMP-9-PSOP. (a) Synthesis. In step (1), the 25 amino acid peptides consisting of an arginine-rich coupling domain and a cleavage domain with the recognition site for MMP-9 linked by a glycine bridge are reacted with NHS-methyl-poly(ethylene glycol) (NHS-mPEG). The resulting peptide-mPEG copolymers are purified by gel filtration to remove unreacted mPEG and NHS. In step (2), peptide-mPEG are mixed with VSOPs, yielding MMP-9-PSOP. (b) Function. When sterically stabilized PSOP with an intact mPEG shell (1) are exposed to a protease specific to the cleavage motif, the peptide-mPEG are cut at the cleavage domain, resulting in a loss of sterical stabilization (2). The remaining particles aggregate due to the magnetic attraction of the iron oxide cores and the electrostatic attraction of the positive (arginine-rich coupling domain) and negative charged surface areas (acid shell).

measurements (excitation/emission 494/521 nm, Hitachi fluorescence spectrophotometer F-7000). Ratios of these quenched fluorescences and corresponding unquenched fluorescences of equal copolymer concentrations without VSOP addition were calculated and compared with the fluorescence of free fluorescein dye mixed with VSOP accordingly.

Enzyme Activation. To demonstrate the ability of MMP-9 to activate MMP-9-PSOP (0.125 nmol particles in 50 μL), hydrodynamic size measurements were carried out before and after adding MMP-9 (7.4 U MMP-9, human, Calbiochem) at 37 °C. For experiments with enzyme inhibition, MMP-2/MMP-9 Inhibitor II (30 μM final concentration, Calbiochem) was added before the addition of MMP-9 enzyme. The hydrodynamic diameters (Zetasizer) were monitored for 2 h. The incubation buffer for enzyme experiments was 10 mM HEPES, 140 mM NaCl, 1.3 mM $CaCl_2$, and 50 μM $ZnCl_2$, pH 7.5.

MR Imaging. For the MR experiments (Figure 4b), four different particle concentrations of 6×-MMP-9-PSOP (300 nM, 150 nM, 75 nM, and 38 nM particle concentration) were incubated with 1.3 U MMP-9 in 200 μL incubation buffer (see above) at 37 °C. All inhibitor experiments (Figure 4c,d) were done under identical conditions using a particle concentration of 300 nM. All enzyme reactions were imaged with a clinical 1.5-T MR scanner (Siemens Sonata). The gradient echo sequence with 12 echo times (TR = 100 ms, TE = 3.1−44.8 ms) was repeated 200 times over 50 min. The images were analyzed with OsiriX DICOM viewer, ImageJ (National Institutes of Health, USA), and Prism 5 (GraphPad Software). Curve fits for T2 calculation and enzyme inhibition (logarithmic inhibitor response curve, standard slope) were done with Prism 5.

Molecular Modeling. The 5 nm octahedral magnetite core of VSOP-C200 with approximately 2600 iron atoms and 75 citrate shell molecules per core (data provided by Ferropharm GmbH) was generated with CrystalMaker (CrystalMaker Software). Molecular modeling of MMP-9-PSOP was done based on the size measurements and the sequence of the MMP-9 peptide and NHS-mPEG (MW 5000) using the PyMOL Molecular Graphics System (*12*).

RESULTS

To add enzyme-sensing capability, we designed a construct shown in Figure 1a consisting of a peptide and a methyl-poly(ethylene glycol) polymer (mPEG, molecular weight 5000). The peptide consists of a cleavage domain with the enzyme recognition motif and a highly positively charged, arginine-rich coupling domain, which are connected by a linker sequence. For analysis by fluorescence methods, a fluorescine is coupled to the peptide. In a first step, this peptide was reacted with NHS-mPEG at the end of the cleavage domain. In a second step, after purification by gel filtration and HPLC control for purity, these peptide-mPEG copolymers were mixed in different ratios with the VSOP. A ratio of 6 peptide-mPEG per VSOP yielded MMP-9-PSOP with a hydrodynamic diameter of 24.9 ± 7.0 nm (Figure 2b). Mixtures with ratios between 6 and 16 peptide-mPEG consistently yielded particles with sizes around 24 nm,

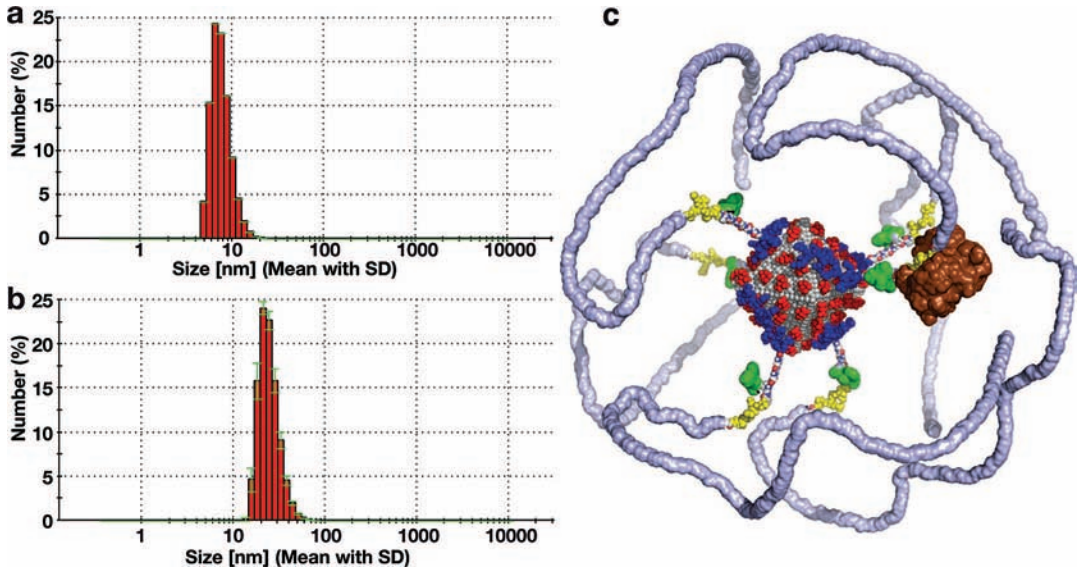

Figure 2. Size and model of MMP-9-PSOP. The hydrodynamic size distribution of the parent VSOP with 7.7 ± 2.1 nm is shown in (a). With the copolymers attached to the surface, the PSOP are still small at 25 nm with a narrow size distribution (b). For illustration, a model of MMP-9-PSOP based on the peptide sequence, the structure of mPEG, and the size measurements is shown in (c). The parent VSOP consists of a 5 nm magnetite core (gray) covered by a negatively charged citrate shell (red). The peptide-mPEG copolymers are electrostatically bound by the positively charged coupling domains (blue). The mPEG polymers (light blue) are linked to the coupling domain via the cleavage domain (yellow) and a linker peptide. A model of MMP-9 (*22*) (brown) is shown for size comparison at the cleavage domain. Fluorescein dyes (green).

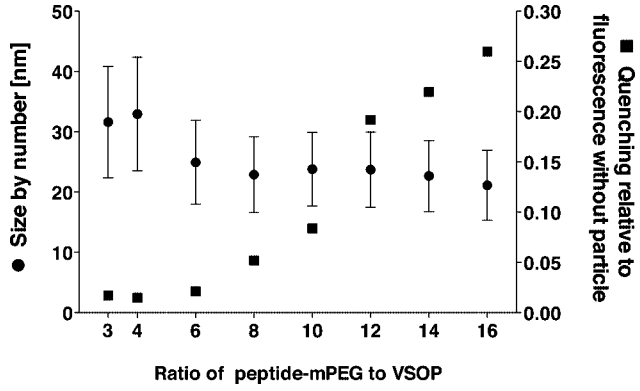

Figure 3. Dependence of size and fluorescence quenching on the ratio of peptide-mPEG copolymers to VSOP. Left axis: With an increasing number of peptide-mPEG copolymers per VSOP, the hydrodynamic size (mean of distribution by number, SD) of MMP-9-PSOP decreases slightly up to a ratio of 6 peptide-mPEG per VSOP and stays constant around 24 nm up to a ratio of 16. An average ratio of 6 peptide-mPEG per VSOP seems to be necessary for good steric stabilization. Below that ratio, the particles most likely form more dimers or multimers. Right axis: Due to the proximity of the copolymer-coupled fluorescein dyes to each other and to the nanoparticle cores, strong quenching of fluorescence can be observed for PSOP with ratios up to 8, proving nearly complete binding of the copolymers to the VSOP. With higher ratios, the quenching effect decreases, indicating incomplete coupling of copolymers due to saturation of the VSOP surface with peptide-mPEG copolymers.

whereas ratios below 6 resulted in particles over 30 nm in size, probably due to insufficient steric stabilization (Figure 3 and Table 1).

To evaluate the level of copolymer coupling to the VSOP surface, we measured the fluorescence quenching effect of the peptide-bound fluorescein, which is caused by nonradiative energy transfer due to the proximity of the dyes to each other and to the iron oxide cores (*13*). Compared with the fluorescence of the peptide-mPEG complexes without the particles, the fluorescence was strongly quenched up to ratios of 8 complexes per VSOP (Figure 3). PSOP with 6 complexes per VSOP had a quenched relative fluorescence of 0.02, indicating nearly complete coupling of the complexes to the VSOP surface. Higher ratios of complexes to particle cores showed a decreasing quenching effect, revealing incomplete coupling, most likely due to saturation of the VSOP surface. When free fluorescein was mixed with the particles (6 fluorescein dyes per VSOP) as control, the fluorescence was only reduced to 0.78, confirming that the reduction of copolymer fluorescence was not only caused by light absorption by the particles. Therefore, 6 peptide-mPEG copolymers per particle was considered a good ratio for further experiments.

For illustration, a model of MMP-9-PSOP (6 peptide-mPEG per particle), based on the sequence of the peptide-mPEG complexes and particle size measurements, is shown together with a crystal structure of MMP-9 in Figure 2c.

The function of the particles is explained in Figure 1b. When the sterically stabilized MMP-9-PSOP (1) are exposed to MMP-9, the protease cleaves the peptide at the recognition site (2), resulting in loss of the sterically stabilizing mPEG shell. Due to the superparamagnetic properties of the iron oxide cores and the ambivalent surface of the remaining particles with positively (coupling domains) and negatively (citrate coat of VSOP) charged areas, the particles aggregate driven by magnetic and electrostatic attraction (3).

This process has two important consequences: First, clustering of the superparamagnetic nanoparticles causes a substantial increase in R2-relaxivity, called magnetic switch (*6*). Second, the particles are converted from mPEG-covered stealth particles into highly aggregative particles with strongly charged surfaces (*14*). Conveniently, mPEG-5000 has been shown to be optimal for achieving stealth properties for nanoparticles (*15*). Consequently, once injected, the intact PSOP should remain for a long time in the blood circulation until they reach an MMP-9 expressing target tissue, where they are converted into aggregative particles and accumulate.

In contrast to mPEG-5000, peptide-mPEG copolymers made of mPEG-2000 (molecular weight 2000) or of branched mPEG-2000 did not yield stable particles but precipitating aggregates, presumably due to insufficient steric stabilization (data not

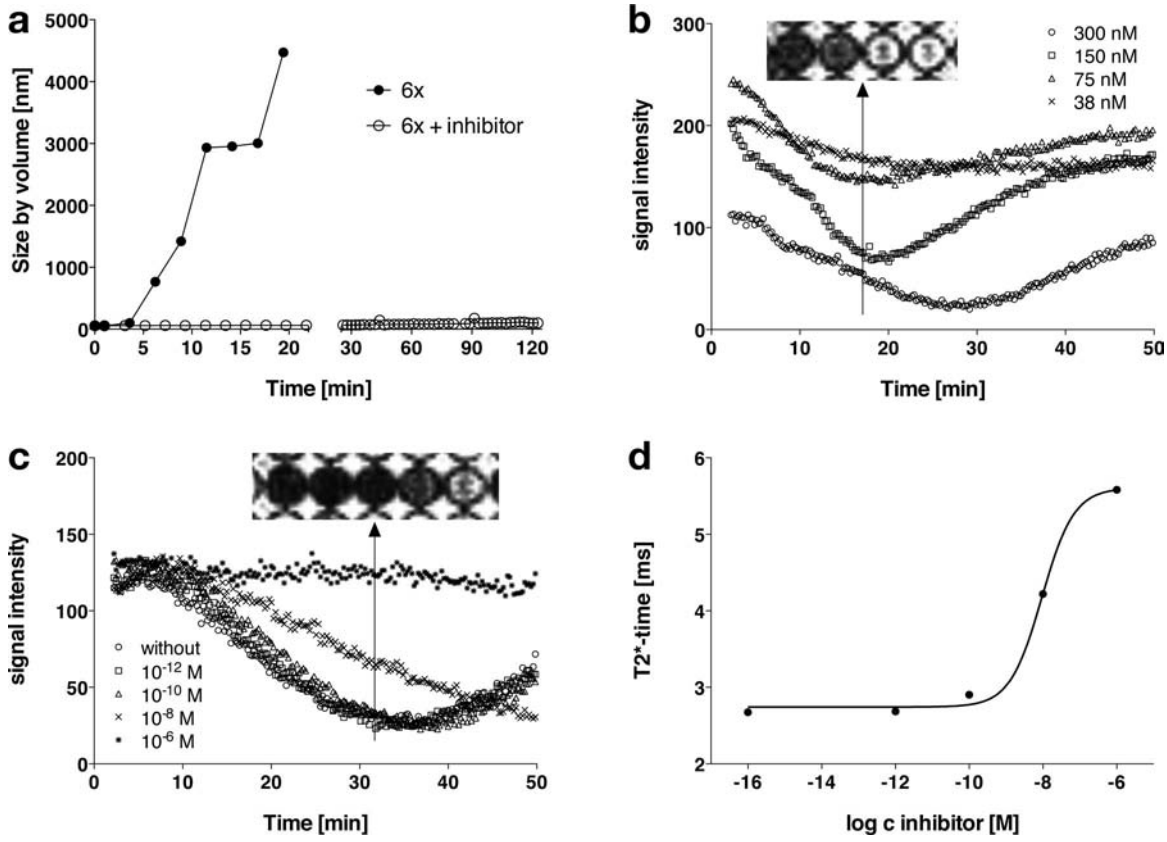

Figure 4. Function of PSOP. (a) Hydrodynamic size measurements. Time course of aggregation-induced size increase of the MMP-9-PSOP probe (0.125 nmol particles) induced by enzyme activation with 7.4 U of MMP-9. There was no probe activation when the experiments were done in the presence of 30 μM MMP-9-inhibitor. (b−c) MRI experiments. (b) Time course of activation of MMP-9-PSOP at four different particle concentrations. As aggregates form, the T2*-relaxivity of these particles increases, causing a drop in signal intensities on the gradient echo sequences to a minimum until no further decrease occurs because continuing aggregation and precipitation reduce the amount of water protons affected. MR image obtained at the time point indicated by the arrow. (c) Time course of signal intensities of MMP-9-PSOP (300 nM particle concentration) incubated with different concentrations of a MMP-9-inhibitor. (d) Inhibition of the T2*-time-shortening at the time point indicated by the arrow in (c). The 50% inhibitory concentration in this assay is approximately 10 nM. MR experiments were done with 1.3 U MMP-9 in 200 μL buffer.

Table 1. Properties of MMP-9-PSOP

size [nm]	24.9 ± 7.0
Peptide-mPEG copolymers per particle	6
R1 relaxivity [mM $Fe^{1-}s^{-1}$]	8.9
R2 relaxivity [mM $Fe^{1-}s^{-1}$]	41
Fe atoms per particle*	2600

* Data provided by Ferropharm GmbH. Relaxivities at 0.94 T.

shown). Another control experiment with uncoupled peptide and mPEG-5000 did not result in stable particles either (data not shown).

To demonstrate the function of MMP-9-PSOP, we measured the changes in size and T2* contrast in MRI following activation by MMP-9. Results are shown in Figure 4. First, we tested the activation of MMP-9-PSOP by monitoring hydrodynamic diameters (Figure 4a). Incubation of MMP-9-PSOP (6 peptide-mPEG per particle) with MMP-9 caused dramatic aggregation already after a few minutes leading to particle sizes exceeding the micrometer range. When the experiment was repeated in the presence of a MMP-9 inhibitor, the size remained almost unchanged over a period of 2 h.

To monitor the activation using MRI, we prepared 200 μL reactions with different concentrations of MMP-9-PSOP (300 nm, 150 nM, 75 nM, and 38 nM) and 1.3 U MMP-9 each. Approximately every 15 s, T2*-weighted images (gradient echo sequences with 12 echo times (TE) between 3.1 and 44.8 ms and a repetition time (TR) of 100 ms) were acquired over a period of 50 min. Figure 4b shows the time course of the signal intensities (for a TE of 10.6 ms). Depending on the concentration, the signal intensities decrease and reach a minimum at about 15 min for a concentration of 75 nM concentration and at about 27 min for 300 nM. The signal decrease was about 79% for 300 nM and 24% for 38 nM. The differences in the time it took to reach the signal minimum can be explained by the different amounts of peptide substrates to be cleaved by the MMP-9. The MR image in Figure 4b represents a snapshot taken at 17.6 min. Figure 4c shows the time course of signal intensities measured under the same conditions for 300 μM-MMP-9-PSOP incubated with different concentrations of a MMP-9-inhibitor. The signal drop is delayed at a concentration of 10 nM and nearly completely suppressed for the observation period of 50 min at a MMP-9-inhibitor concentration of 1 μM. T2* relaxation times for the different inhibitor concentrations were calculated from the MR images obtained at 32 min and analyzed using an inhibition function of Prism 5 software (log(inhibitor) vs response curve with standard slope, $R^2 = 0.996$). The 50% inhibitory concentration in this assay was 9.3 nm (95% confidence interval 4.2 nM to 21 nM).

DISCUSSION

After mixing with the VSOP, the peptide-mPEG copolymers adsorb at the strongly negatively charged VSOP citrate surface with their positively charged coupling domains. The resulting protease-specific iron oxide particles (PSOP) with the copolymers at the surface are no longer electrostatically but sterically stabilized, i.e., the natural tendency of superparamagnetic magnetite nanocores to aggregate is countered by the thick mPEG coat and not by the negatively charged surface of the

VSOP as before. Instead of PEG, other macromolecules such as dextran could provide sterical stabilization as well.

The results of the size measurements and *in vitro* MRI experiments presented here confirm the specific protease-sensing function of these newly developed PSOP. Upon incubation with MMP-9, the nanosensors start clustering after a few minutes, as can be shown by dynamic laser light scattering and MRI. This activation by protease activity was largely suppressed by preincubation with an MMP-2/MMP-9 inhibitor. Inhibition occurred in a typical, concentration-dependent manner (Figure 4d), proving that activation was due to the protease activity of MMP-9.

The PSOP comprise several key characteristics making them a good candidate for an enzyme reporter probe for *in vivo* MRI: Synthesis of the particles is fairly straightforward. They can be adapted to any proteases or possibly other cleaving enzymes. Poly(ethylene glycol)s have been proven to be biocompatible (listed in the pharmacopeia) and provide stealth properties, which is a prerequisite for a sufficiently long circulation time *in vivo* (*15*). Together with the nanosensors' small diameter of about 25 nm, these properties ensure good bioavailability in the desired target tissues. Unlike the caspase-3-sensitive nanosensors presented by Josephson and co-workers (*6*), which are clusters of approximately 45 nm sized CLIO monomers before activation and are cleaved into monomers by caspase-3, leading to a *decrease* in relaxivity and contrast effect, PSOP become larger upon activation and relaxivity increases. This property allows the *in vivo* application of the nanoparticles. The parent VSOP has been shown to be safe in preclinical (*16*) and clinical trials (*7*). In contrast to near-infrared fluorescence imaging, MRI with PSOP is a potential candidate for whole-body imaging of protease activity in humans. Moreover, the particles could be used to deliver therapeutics, or the accumulating magnetic cores themselves could serve as "theranostics" in clinical magnetic thermotherapy of cancer, which currently requires direct injection of magnetic nanoparticles into the tumor (*17*).

The *in vitro* experiments performed in this study have some limitations: First, the size measurements yielded meaningful results only until the aggregates started to precipitate, thereby dropping out of the measurement field of the zetasizer. In the MR experiments, the T2* contrast effect also started to decrease at a certain point in time, which is partially attributable to precipitation as well. Additionally, the fraction of water protons influenced by the magnetic field of the particles also decreases from a certain time onward as the aggregates continue to increase in size while their number decreases (*18*). Although precipitation due to aggregation is problematic for these *in vitro* settings, it is an intended and important mode of function for *in vivo* application. The accumulation of the particles in protease-expressing target tissues following the switch from a PEGylated stealth state to a highly surface-charged, aggregative state cannot be demonstrated with the types of experiments used here and remains to be shown *in vivo*. Although the aggregation effect and consequently the magnetic switch would be desirable for an enhanced contrast effect in the *in vivo* situation, it is not a necessity, since a particle binding to the target tissue due to the exposed charged surface is sufficient to produce a strong contrast effect (*19*−*21*).

We are convinced that the nanosensors presented here have great potential as reporter probes for assessing enzyme activity of proteases by *in vivo* MRI and can thus help diagnose diseases with pathologically altered protease activity or monitor protease inhibitor therapies.

ACKNOWLEDGMENT

VSOP was provided by Ferropharm GmbH. We thank Bettina Herwig for language editing.

LITERATURE CITED

(1) Weissleder, R., Tung, C. H., Mahmood, U., and Bogdanov, A. J. (1999) In vivo imaging of tumors with protease-activated near-infrared fluorescent probes. *Nat. Biotechnol. 17*, 375–378.

(2) Ntziachristos, V., Ripoll, J., Wang, L. V., and Weissleder, R. (2005) Looking and listening to light: the evolution of whole-body photonic imaging. *Nat. Biotechnol. 23*, 313–320.

(3) Weissleder, R., and Pittet, M. J. (2008) Imaging in the era of molecular oncology. *Nature 452*, 580–589.

(4) Louie, A. Y., Hüber, M. M., Ahrens, E. T., Rothbächer, U., Moats, R., Jacobs, R. E., Fraser, S. E., and Meade, T. J. (2000) In vivo visualization of gene expression using magnetic resonance imaging. *Nat. Biotechnol. 18*, 321–325.

(5) Bogdanov, A., Matuszewski, L., Bremer, C., Petrovsky, A., and Weissleder, R. (2002) Oligomerization of paramagnetic substrates result in signal amplification and can be used for MR imaging of molecular targets. *Mol. Imaging 1*, 16–23.

(6) Perez, J. M., Josephson, L., O'Loughlin, T., Hogemann, D., and Weissleder, R. (2002) Magnetic relaxation switches capable of sensing molecular interactions. *Nat. Biotechnol. 20*, 816–820.

(7) Taupitz, M., Wagner, S., Schnorr, J., Kravec, I., Pilgrimm, H., Bergmann-Fritsch, H., and Hamm, B. (2004) Phase I clinical evaluation of citrate-coated monocrystalline very small superparamagnetic iron oxide particles as a new contrast medium for magnetic resonance imaging. *Invest. Radiol. 39*, 394–405.

(8) Chen, J., Tung, C. H., Allport, J. R., Chen, S., Weissleder, R., and Huang, P. L. (2005) Near-infrared fluorescent imaging of matrix metalloproteinase activity after myocardial infarction. *Circulation 111*, 1800–1805.

(9) Kridel, S. J., Chen, E., Kotra, L. P., Howard, E. W., Mobashery, S., and Smith, J. W. (2001) Substrate hydrolysis by matrix metalloproteinase-9. *J. Biol. Chem. 276*, 20572–20578.

(10) Hu, J., Van den Steen, P. E., Sang, Q. X., and Opdenakker, G. (2007) Matrix metalloproteinase inhibitors as therapy for inflammatory and vascular diseases. *Nat. Rev. Drug Discovery 6*, 480–498.

(11) Bremer, C., Tung, C. H., and Weissleder, R. (2001) In vivo molecular target assessment of matrix metalloproteinase inhibition. *Nat. Med. 7*, 743–748.

(12) DeLano, W. L. (2002) *The PyMOL Molecular Graphics System*, DeLano Scientific, USA.

(13) Josephson, L., Kircher, M. F., Mahmood, U., Tang, Y., and Weissleder, R. (2002) Near-infrared fluorescent nanoparticles as combined MR/optical imaging probes. *Bioconjugate Chem. 13*, 554–60.

(14) Moghimi, S. M., and Szebeni, J. (2003) Stealth liposomes and long circulating nanoparticles: critical issues in pharmacokinetics, opsonization and protein-binding properties. *Prog. Lipid Res. 42*, 463–478.

(15) Shi, B., Fang, C., and Pei, Y. (2006) Stealth PEG-PHDCA niosomes: effects of chain length of PEG and particle size on niosomes surface properties, in vitro drug release, phagocytic uptake, in vivo pharmacokinetics and antitumor activity. *J. Pharm. Sci. 95*, 1873–1887.

(16) Wagner, S., Schnorr, J., Pilgrimm, H., Hamm, B., and Taupitz, M. (2002) Monomer-coated very small superparamagnetic iron oxide particles as contrast medium for magnetic resonance imaging: preclinical in vivo characterization. *Invest. Radiol. 37*, 167–177.

(17) Thiesen, B., and Jordan, A. (2008) Clinical applications of magnetic nanoparticles for hyperthermia. *Int. J. Hyperthermia* 1–8.

(18) Koh, I., Hong, R., Weissleder, R., and Josephson, L. (2008) Sensitive NMR sensors detect antibodies to influenza. *Angew. Chem., Int. Ed. Engl. 47*, 4119–4121.

(19) Kaufels, N., Korn, R., Wagner, S., Schink, T., Hamm, B., Taupitz, M., and Schnorr, J. (2008) Magnetic resonance imaging

of liver metastases: experimental comparison of anionic and conventional superparamagnetic iron oxide particles with a hepatobiliary contrast medium during dynamic and uptake phases. *Invest. Radiol. 43*, 496–503.

(20) Schnorr, J., Wagner, S., Abramjuk, C., Drees, R., Schink, T., Schellenberger, E. A., Pilgrimm, H., Hamm, B., and Taupitz, M. (2006) Focal liver lesions: SPIO-, gadolinium-, and ferucarbotran-enhanced dynamic T1-weighted and delayed T2-weighted MR imaging in rabbits. *Radiology.*

(21) Schellenberger, E., Schnorr, J., Reutelingsperger, C., Ungethum, L., Meyer, W., Taupitz, M., and Hamm, B. (2008) Linking proteins with anionic nanoparticles via protamine: ultrasmall protein-coupled probes for magnetic resonance imaging of apoptosis. *Small 4*, 225–230.

(22) Browner, M. F., Smith, W. W., and Castelhano, A. L. (1995) Matrilysin-inhibitor complexes: common themes among metalloproteases. *Biochemistry 34*, 6602–6610.

BC800330K

Bioconjugate Chemistry 20th Anniversary

Subscriber access provided by SHEMYAKIN-OVCHINNIKOV INST

Article

Dendrimer#Drug Conjugates for Tailored Intracellular Drug Release Based on Glutathione Levels

Raghavendra S. Navath, Yunus E. Kurtoglu, Bing Wang, Sujatha Kannan, Robert Romero, and Rangaramanujam M. Kannan

Bioconjugate Chem., **2008**, 19 (12), 2446-2455• DOI: 10.1021/bc800342d • Publication Date (Web): 24 November 2008

Downloaded from http://pubs.acs.org on May 2, 2009

More About This Article

Additional resources and features associated with this article are available within the HTML version:

- Supporting Information
- Access to high resolution figures
- Links to articles and content related to this article
- Copyright permission to reproduce figures and/or text from this article

View the Full Text HTML

ACS Publications
High quality. High impact.

Bioconjugate Chemistry is published by the American Chemical Society. 1155 Sixteenth Street N.W., Washington, DC 20036

Dendrimer−Drug Conjugates for Tailored Intracellular Drug Release Based on Glutathione Levels

Raghavendra S. Navath,[†,‡] Yunus E. Kurtoglu,[†] Bing Wang,[‡,§] Sujatha Kannan,[§] Robert Romero,[‡] and Rangaramanujam M. Kannan*[,†,‡]

Department of Chemical Engineering and Material Science, and Biomedical Engineering, Wayne State University, Detroit, Michigan 48202, Perinatology Research Branch, Eunice Kennedy Shriver National Institute of Child Health and Human Development, National Institutes of Health, DHHS, and Department of Pediatrics (Critical Care Medicine), Children's Hospital of Michigan, Wayne State University, Detroit, Michigan 48201. Received August 9, 2008; Revised Manuscript Received October 24, 2008

N-Acetyl-L-cysteine (NAC) is an antioxidant and anti-inflammatory agent with significant potential in clinical applications including stroke and neuroinflammation. The drug shows high plasma binding upon IV administration, requiring high doses and associated side effects. Through the use of an appropriate delivery vehicle, the stability and efficacy of NAC can be significantly improved. Dendrimers are an emerging class of nanoscale drug delivery vehicles, which enable high drug payloads and intracellular delivery. Poly(amidoamine) (PAMAM) dendrimer−NAC conjugates having cleavable disulfide linkages are designed for intracellular delivery based on glutathione levels. We have successfully synthesized two conjugates with a cationic G4-NH_2 and an anionic G3.5-COOH PAMAM dendrimer with NAC payloads of 16 and 18 per dendrimer, respectively, as confirmed by ^{1}H NMR and MALDI-TOF analysis. NAC release from the conjugates at intracellular and extracellular glutathione (GSH) concentrations were evaluated by reverse phase HPLC (RP-HPLC) analysis, and ∼70% of NAC payload was released within one hour at intracellular GSH concentrations (∼10 mM), whereas negligible NAC release was observed at extracellular GSH levels (2 μM). FITC-labeled conjugates showed that they enter cells rapidly and localize in the cytoplasm of lipopolysaccharide (LPS)-activated microglial cells (the target cells *in vivo*). The significantly improved efficacies of dendrimer−NAC conjugates in activated microglial cells was confirmed by measuring the nitrite inhibition in the cell culture medium, which is an indication of the antioxidative property of the drug. Both G4-NH_2 and G3.5-COOH conjugates showed significantly better nitrite inhibition both at 24 and 72 h compared to free NAC, by as much as a factor of 16. The results indicate that PAMAM dendrimer conjugates produce higher local NAC concentration inside the cells, with GSH-sensitive disulfide linker enabling efficient and rapid cellular release of the drug.

INTRODUCTION

N-Acetyl cysteine (NAC) is a clinically important antioxidant, antiapoptotic, and anti-inflammatory drug used in the treatment of neuroinflammation, AIDS, colon cancer, and detoxification of heavy metals (e.g., lead, mercury, arsenic) (*1*−*6*). NAC has been extensively studied as both a therapeutic agent and direct cysteine precursor (*7*). In the treatment of neuroinflammation, it acts at multiple neuroprotective sites and has recently been demonstrated to attenuate amniotic and placental cytokine responses after maternal infection induced by lipopolysaccharide (LPS) (*8*) and to restore the maternal fetal oxidative balance and reduce fetal death and preterm birth (*9*, *10*). Further, a higher dose of NAC remains a primary treatment for acetaminophen overdose and exposure to toxic chemicals and is routinely used in hospitals (*11*−*14*). However, the use of NAC requires higher and repeated dosing. This is due to the poor bioavailability and blood stability, caused by the presence of free sulfhydryl groups in NAC, which are capable of spontaneous oxidation and forming disulfide bonds with plasma proteins (*15*). Early pharmacokinetic studies have demonstrated low oral bioavailability of NAC (between 6% and 10%), which were attributed to low blood concentrations of NAC (*16*, *17*). The need for high doses can lead to cytotoxicity and side effects, including increased blood pressure (*18*). NAC is one of the very few drugs being explored for treating neuroinflammation in perinatal applications, where side effects can be very critical.

The design of appropriate dendrimer−NAC conjugates can improve the stability and bioavailability, and at the same time enable intracellular release. These are especially important in our eventual interest in perinatal and neonatal applications of dendrimers and NAC. The unique design of conjugates involves linking of the NAC via disulfide bonds to spacer molecules attached to dendrimers. The resulting structure of the conjugates described here achieves two major objectives to ensure efficacy: (a) it may restrict the protein binding of NAC, as the free sulfydryl groups are involved in disulfide linkages; (b) it may enable higher intracellular levels of NAC and better release of NAC from the conjugate, resulting from disulfide linkages that are cleaved in the presence of intracellular glutathione (GSH). The results on *in vitro* release and the cellular efficacy toward reducing neuroinflammation in activated microglial cells shows the improved efficacy of the conjugates.

Over the past few decades, polymeric carriers have been extensively explored for controlled delivery of drugs intracellularly and to targeted tissues (*19*). Dendrimers are emerging as a viable class of polymeric vehicles (∼5−15 nm) because of the large density of reactive functional groups and well-defined structure and monodispersity (*20*, *21*). This enables a

* Corresponding author. Department of Chemical Engineering and Material Science, Wayne State University, Detroit, Michigan 48202; E-mail: rkannan@eng.wayne.edu.

† Department of Chemical Engineering and Material Science, and Biomedical Engineering, Wayne State University.

‡ National Institutes of Health.

§ Children's Hospital of Michigan, Wayne State University.

10.1021/bc800342d CCC: $40.75 © 2008 American Chemical Society
Published on Web 11/24/2008

high drug payload, but the steric hindrance at the dendrimer surface can make drug release a challenge when ester or amide linkers are used, especially at higher generations (*22*). Active molecules could be encapsulated (*23*), complexed (*24*), or covalently linked (*25*) to the polymeric carrier. The polymer can improve the solubility, stability, and blood circulation times. Despite several significant achievements of the polymeric conjugates, clinical applications still remain elusive, partly due to the issues of drug release over an appropriate time interval. Common approaches in conjugate design involve the use of ester or amide linkers, which are cleaved hydrolytically or enzymatically (*26*). For practical applications in drug delivery, increasing the drug payload and engineering the drug release at the appropriate tissue are two key aspects in the design of polymer conjugates. For intravenous applications, it is highly desirable to design a linker that is stable during circulation but enables drug release when it reaches the target site. There is a need to design efficient polymer conjugates having cleavable bonds or linkers, with high drug payloads and appropriate release profiles.

Recently, specific chemical reactions, such as the disulfide reduction, have emerged as alternative mechanisms for drug release (*27, 28*). Polymeric delivery systems offer an avenue for GSH responsive targeted delivery of drugs to tumor tissue (*29, 30*). Various carriers such as gold nanoparticles (*31*), gold nanorods (*32*), mesoporous silica nanorods (*27*), nanoparticle inhibited β- galactosidase (*33*), poly (2-dimethylaminoethyl methacrylate) (PDMAEMA) (*34*), carbon nanotubes for siRNA delivery (*28*), poly (β-amino ester) (*35*), gelatin nanoparticles (*36*), methyl acryloylglycylglycine 4-nitrophenyl ester for DNA delivery (*37*) have been used in this regard with reductively cleavable disulfide spacers. Furthermore disulfide bonds have been incorporated in the synthesis of cleavable delivery systems for plasmid DNA (*38*), antisense oligonucleotides (*39*), peptide nucleic acids (*40*), toxins (*41*), and anticancer drugs (*42*) Therefore, in the present investigation we have combined a dendrimer-based delivery system with disulfide chemistry, to develop a GSH-responsive release system with a high drug payload. The disulfide bonds are easily cleavable, and hence the drug release is not compromised. The glutathione (GSH)-mediated release of biomolecules from monolayer-protected gold nanoparticle surfaces and manipulation of their bioactivity *in vitro* has been demonstrated (*31*). GSH is the most abundant thiol species in the cytoplasm and the major reducing agent in biochemical processes, providing a potential *in situ* releasing source in living cells. The intracellular GSH concentration (1−10 mM) is substantially higher than extracellular levels (0.002 mM in plasma) (*31*). More importantly, the GSH levels in cancer tissues can be many-fold higher than those in normal tissues (*30, 31*). Therefore, a GSH responsive linker will limit plasma release and can promote targeted release.

EXPERIMENTAL PROCEDURE

The experimental protocols, characterization methods, and NMR and MALDI spectra for the various compounds discussed in the paper are provided as part of the Supporting Information (R-I to R-XI).

Stability of Conjugates. Stabilities of NAC alone, GSH alone, GSH and NAC when they are present together, were evaluated as controls. The NAC and GSH concentrations used for stability studies were 0.2 mg/mL and 3 mg/mL (10 mM), respectively. The concentrations of GSH and NAC in these studies were chosen in relevance to the conjugate stability studies. Stability of conjugates was analyzed in physiological pH (PBS buffer) and in the presence of two different GSH concentrations (10 mM and 2 mM). The stability studies were carried out for a period of 17 h at 37 °C. The conjugates were dissolved at 1 mg/mL concentrations in 1 mL of PBS solution and required amount of GSH was added to trigger disulfide exchange reactions, resulting in the release of NAC from the conjugate. At specific time intervals, 30 μL samples were withdrawn and analyzed with HPLC. All experiments were run in triplicate for statistical analysis.

Flow Cytometry Analysis. Immortalized mouse microglial cells (BV-2 cells obtained by courtesy of Dr. Kuhn, Wayne State University) (passage 16) were grown overnight in 6-well plates using DMEM cell culture medium supplemented with 10% FBS and 1% penicillin−streptomycin. When the cells were 70% confluent, they were treated with FITC-labeled-PMAM-NH-CO-propionyl S-S-*N*-acetyl-cysteine conjugated (FITC PAMAM-NH-CO-Pr-S-S-NAC compound **2**) (equivalent to 10 μg/mL of FITC-PAMAM-NH-CO-Pr-S-S-NAC) for 15, 60, and 120 min. The cells were washed with phosphate buffered saline (PBS, pH = 7.4), trypsinized, and centrifuged at 1500 rpm for 5 min to obtain a cell pellet. The cells were then rinsed with PBS buffer, spun down three times, and resuspended in 1% formaldehyde, and analyzed using a flow cytometer (FACS caliber, Becton Dickinson) by counting 10 000 events. The mean fluorescence intensity of cells was calculated using the histogram plot.

Confocal Laser Scanning Microscopy. The procedure for cell culture and drug treatment was the same as described in the previous section. After treating BV-2 cells for 2 h with FITC PAMAM-NH-CO-Pr-S-S-NAC conjugate (equivalent to 10 μg/mL of FITC PAMAM-NH-CO-Pr-S-S-NAC), the cells were washed with PBS three times and fixed with 4% *para*-formaldehyde for 20 min. Images were captured under the confocal microscope (Zeiss LSM 310) using a magnification of 630×. The emission and excitation wavelengths were 488 and 518 nm for FITC.

Detection of Nitrite Production. The presence of L-PS induces nitrite production, and the subsequent suppression of this by the dendrimer conjugates is used to assess the efficacy. BV-2 cells (passage 16) were seeded in 24-well plates at 10^5/ml/well and incubated for 24 h. The medium was removed and 500 μL of fresh serum-free medium was added. The cells were exposed to 100 ng/mL of lipopolysaccharide (LPS) and various concentrations of dendrimer conjugates for 3 h. The medium was removed again, and 500 μL of fresh, serum-free medium containing 100 ng/mL of LPS was added. The cells were incubated for 24 and 72 h, and the culture medium was removed for analysis. Control treatments with various concentrations of free NAC, positive controls with LPS induction and no treatment, and negative controls without any LPS induction were also studied.

Accumulation of nitrite in the culture medium was used as a measure of NO formation. The nitrite concentration was determined by using the Griess reagent system (Cayman) that uses sulfanilamide and *N*-(1-naphthyl)ethylene diamine. In brief, 100 μL of supernatant from BV-2 cells exposed to different treatments was incubated with 50 μL of Griess reagent 1 (sulfanilamide) and 50 μL of Griess reagent 2 (*N*-(1-naphthyl)-ethylenediamine) for 10 min at room temperature. The absorbance at 540 nm was then measured, and nitrite concentration was determined using a curve calibrated with nitrite standards.

Intracellular GSH Measurement. Levels of intracellular reduced glutathione (GSH) was assessed spectrofluorimetrically by monochlobimane staining (*13*). Briefly, the procedure for culture and drug treatment was the same as described in the previous section. Cells seeded in collagen I coated 96-well plates were washed once with PBS and incubated with 50uM monochlobimane diluted in phenol red free medium. The fluorescence intensity was measured after 15 min at 37 °C. Excitation and emission wavelengths were 380 and 485 nm, respectively. Intracellular GSH reduced rate was calculated

Scheme 1

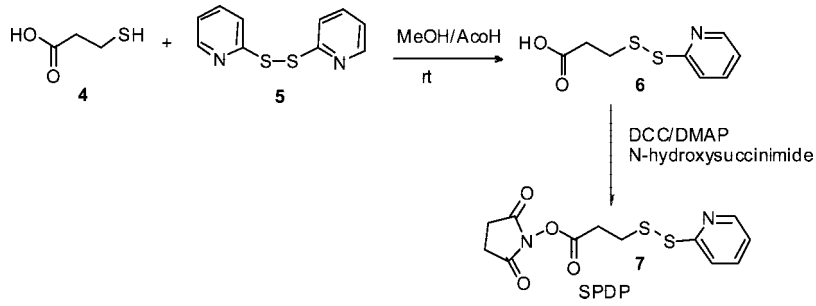

Scheme 2

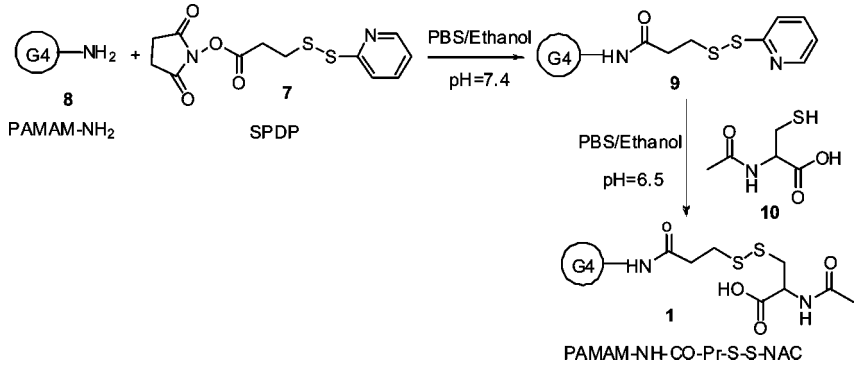

according to the following formula: [reduced rate (%) = (fluorescence intensity of EMEM control − fluorescence intensity of treatment group)/fluorescence intensity of EMEM control × 100%].

RESULTS AND DISCUSSION

This therapeutic efficacy of polymer conjugates can be enhanced, and side effects reduced, if intracellular drug release can be enhanced. This is especially true in neonatal applications of NAC, where high doses of NAC are used. To attain this objective, we have developed GSH-responsive dendrimer NAC conjugates incorporating a connecting disulfide spacer. Use of the disulfide spacer can provide extracellular stability with rapid degradation once internalized in cells, releasing the free NAC. In the present investigation, we have successfully synthesized and evaluated two dendrimer conjugates, a cationic PAMAM-NH-CO-Pr-S-S-NAC and an anionic G3.5-CO-Glutathione-S-S-NAC (G3.5-CO-GS-S-NAC) conjugate, for the first time in dendrimers with a disulfide bond between the drug and the dendrimer through a different spacer. The drug will be released at a rate dependent on GSH concentration.

PAMAM-NH-CO-Pr-S-S-NAC Conjugate Synthesis (1). To conjugate the NAC to dendrimers, the linker SPDP was appended to the dendrimer with the thiopyridine termination. The NAC was covalently attached to the PDP linked dendrimer by the formation of disulfide bonds. Synthesis of *N*-succinimidyl 3-(2-pyridyldithio)propionate (SPDP) was performed by a two-step procedure (Scheme 1). First, 3-mercaptopropionic acid was reacted by thiol−disulfide exchange with 2,2′-dipyridyl disulfide to give 2-carboxyethyl 2-pyridyl disulfide (Scheme 1, Supporting Information R-V). To facilitate linking of amine-terminated dendrimers to SPDP, the succinimide group was appended on SPDP to obtain *N*-succinimidyl 3-(2-pyridyldithio)propionate (Scheme 2, Supporting Information R-VI), by esterification with *N*-hydroxysuccinimide by using *N*,*N*′-dicyclohexylcarbodiimide. To introduce sulfhydryl-reactive groups, PAMAM-NH_2 dendrimers were reacted with the heterobifunctional cross-linker SPDP (Scheme 2, Supporting Information R-VI). The *N*-succinimidyl activated ester of SPDP couples to the terminal primary amines to yield amide-linked 2-pyridyldithiopropanoyl (PDP) groups (Scheme 2). After reaction with SPDP, PAMAM-NH-PDP was analyzed using RP-HPLC (data not shown) to determine the extent to which SPDP had reacted with dendrimers.

The samples were compared to unmodified PAMAM-NH_2 dendrimers. Samples were initially run on a linear gradient from 100:0 H_2O (0.1 wt % TFA)/acetonitrile to 10:90 H_2O (0.1 wt % TFA)/acetonitrile over 32 min. During this gradient, PAMAM-NH_2 was eluted after (13.1) compared to the modified PAMAM-NH-PDP dendrimer (data not shown). The increased retention time is in line with the addition of hydrophobic PDP groups. The slight broadening of the peaks and appearance of shoulder peaks for both PAMAM dendrimers and PAMAM-NH-PDP might reflect structural defects that occurred during synthesis of the dendrimer, for example, by incomplete alkylation of the primary amines or intramolecular cyclization. The absence of amine-terminated dendrimer in the pyridyl disulfide-modified dendrimers indicates the completion of the reaction as reflected from the HPLC analysis. The PAMAM-NH-PDP so obtained was reacted with water soluble NAC to get the desired conjugate. The linking of NAC to dendrimer via the formation of a disulfide bond was confirmed by HPLC, NMR, and MALDI-TOF (Table 1, Supporting Information R-VII). The NMR and the MALDI data for the drug payload agree very well with each other, as summarized in Table 1. The HPLC chromatogram reflected decreased retention time (Figure 2B) (15.0 min) with the addition of hydrophilic groups. The shift in retention times for the dendrimer conjugates confirms the conjugation with NAC; further, the shift to higher retention times indicates the hydrophobic nature imparted due to the spacer molecules and the NAC. The absence of the peaks corresponding to NAC and NAC-NAC and SPDP in the chromatogram for the conjugates confirms the purity of the compound synthesized. The chromatogram of the PAMAM-NH-CO-Pr-S-S-NAC conjugate showed the presence of a very small fraction of NAC-NAC as indicated by the slight hump at 8.2 min. Further, the appearance of methyl groups in NMR at 1.94 ppm confirms

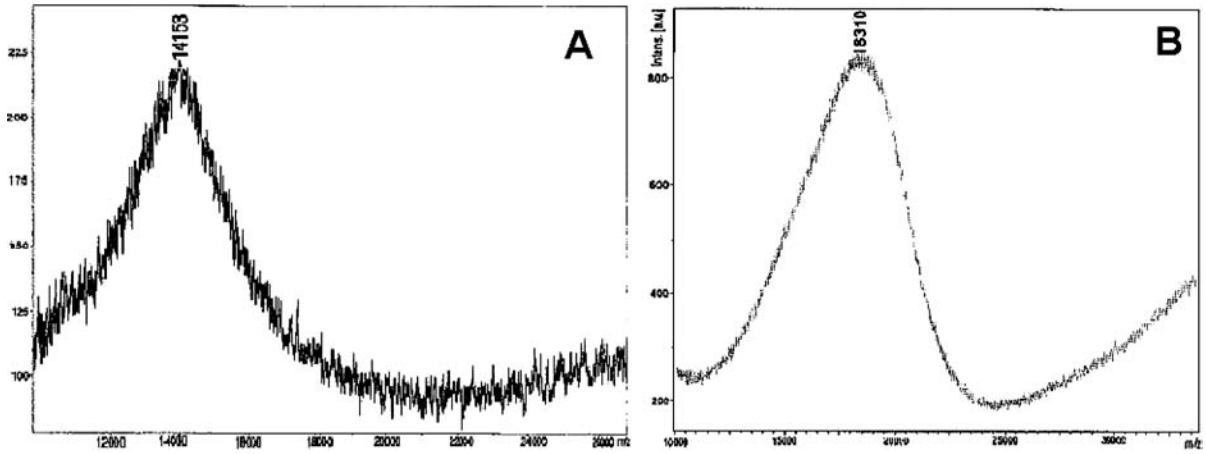

Figure 1. MALDI-TOF analysis of modified PAMAM dendrimers to determine the average number of coupled Pr-S-S-NAC groups. PAMAM-NH_2 before (A) and after (B) reaction with SPDP and followed by NAC reaction

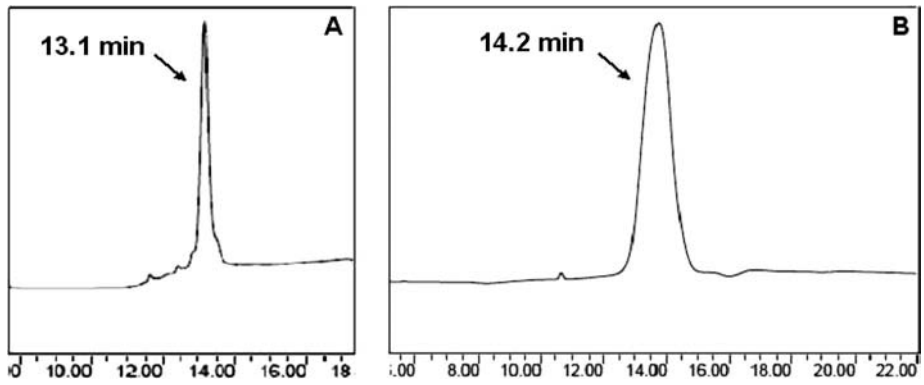

Figure 2. RP-HPLC analysis of the derivatization of PAMAM -NH_2 dendrimer with the heterobifuctional cross-linker SPDP and followed by NAC reaction. PAMAM-NH_2 (A); PAMAM-NH-CO-Pr-S-S-NAC (B).

Table 1. Molecular Weight Estimation (by ^{1}H-NMR, MALDI-TOF, and ESI-MS) of NAC and PAMAM-NAC Conjugates

	generation number	molecular weight by (NMR/ MALDI-TOF/ ESI-MS)	pay load	purity of conjugate	HPLC elution time	solubilityin PBS/H_2O
G4-NH_2	4	14.1kDa	-	100%	14.2	highly soluble
Pr-NAC	-	250 Da	-	-	-	-
G4-NH-CO-Pr-S-S-NAC	4	18.3kDa	16	99.2%	15.0	highly soluble
FITC	-	389 Da	--	99.5%	-	not soluble
FITC-G4-NH-CO-Pr-S-S-NAC-	4	19.0kDa	18	99.5%	16.0	highly soluble
G3.5-COOH	3.5	11.1kDa	-	100%	8.25	highly soluble
GS-S-NAC	-	468 kDa	-	99.1%		soluble
G3.5-CO-GS-S-NAC	3.5	19.7kDa	18	99.5%	12.5	highly soluble

the formation of disulfide bonds between the PAMAM-NH-PDP and NAC. The attachment of multiple copies of NAC to PAMAM-NH-PDP dendrimers was determined by MALDI-TOF. Analysis of the unmodified G4 dendrimer gave a broad M+ peak at 14.1 kDa (Figure 1A), which closely corresponds to the theoretical molecular mass of the dendrimer 14.2 kDa. Coupling of the G4 terminal amine groups with NAC resulted in a shift in the major peak to 18.3 kDa (Figure 1B, Table 1, Supporting Information R-VII). Each thiopropanoyl NAC group has a molecular mass of 250 Da. Therefore, these data indicate an average of 16 NAC molecules per dendrimer molecule (16 thiopropanoyl NAC groups per dendrimer molecule containing 64 amine terminal groups, $n = 3$; number of independent experiments, Table 1, Supporting Information R-VII). The PAMAM-NH-CO-Pr-S-S-NAC conjugate was tagged with fluorescent dye FITC (Scheme 3) for a cell uptake study (data not shown). The drug payloads in the conjugates have been kept moderate, in order to enable high solubilities of the conjugate for *in vivo* experiments.

PAMAM-CO-GS-S-NAC Conjugate Synthesis. *S*-(2-Thiopyridyl)glutathione, was prepared from the reaction of 2,2′-dithiodipyridine in excess and the corresponding peptide in a mixture of methanol and water at room temperature (Scheme 4). Upon completion of the reaction, methanol was removed *in vacuo* and the residue was washed with dichloromethane. The aqueous solution was subjected to reverse phase (RP) HPLC purification, and lyophilization of the eluent gave the pure product as a white solid (Supporting Information R-IX). This compound was reacted with NAC in PBS in pH = 7.4 to get the desired glutathione-*N*-acetyl cysteine (GS-S-NAC) (Scheme 4) intermediate and purified. The formation of a disulfide bond was confirmed by NMR and ESI-MS (Table 1, Supporting Information R-X). The appearance of methyl groups in NMR at 1.90 ppm indicates the formation of disulfide bond between

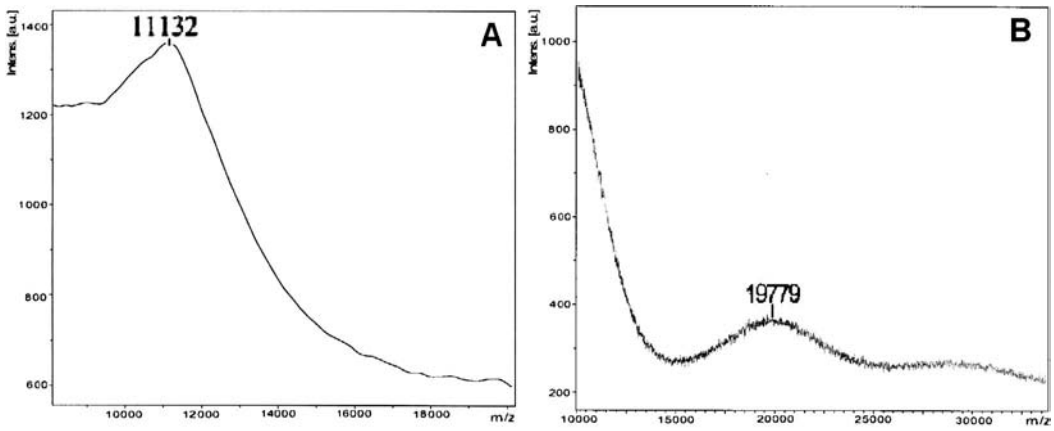

Figure 3. MALDI-TOF analysis of modified PAMAM-COOH dendrimers to determine the average number of coupled GS-S-NAC groups. PAMAM-COOH (A) and PAMAM-CO-GS-S-NAC (B).

Scheme 3

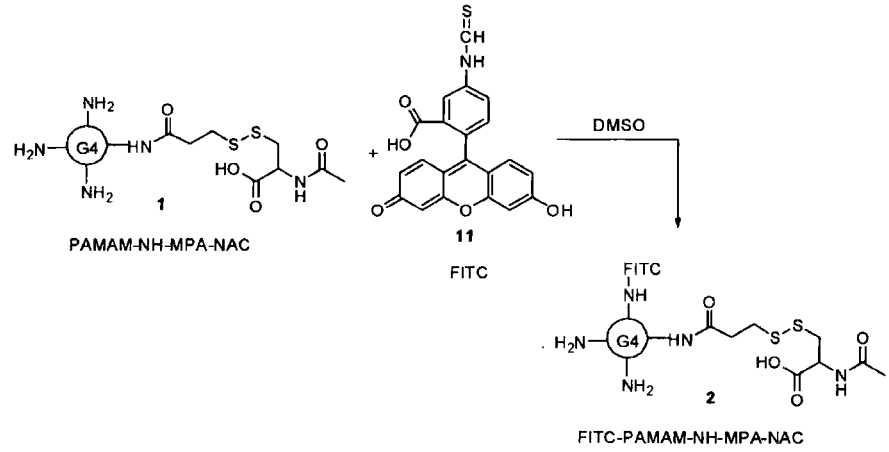

Scheme 4

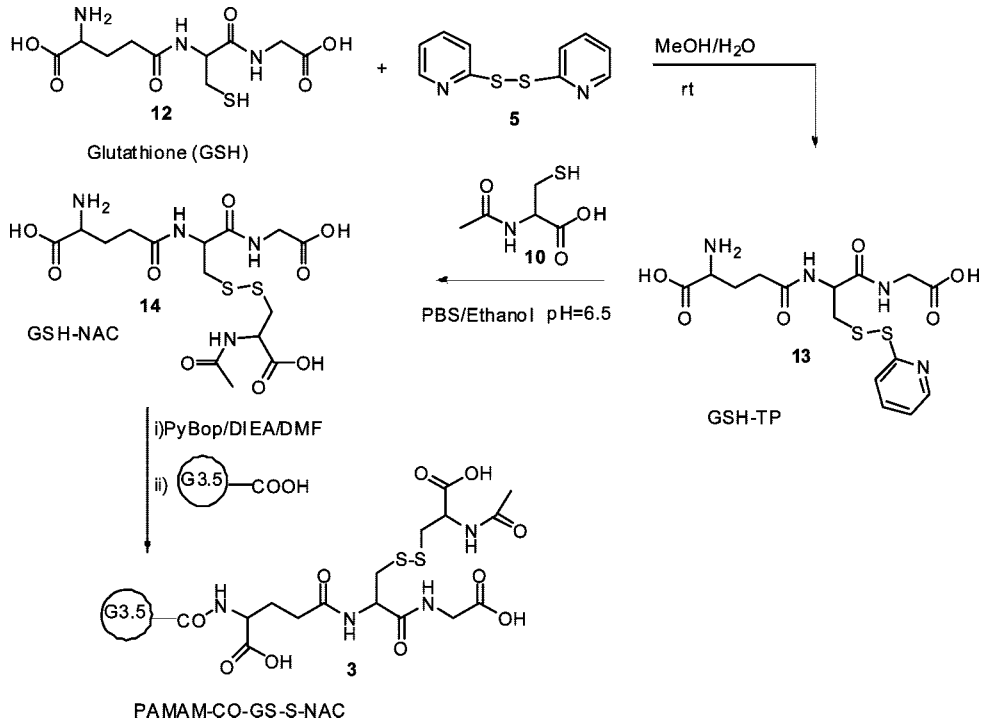

the GSH and NAC. To introduce the GS-S-NAC, PAMAM-COOH was reacted with GS-S-NAC in the presence of PyBop/DIEA to give the desired PAMAM-CO-GS-S-NAC conjugate (Scheme 4, Supporting Information R-XI). Introduction of GS-

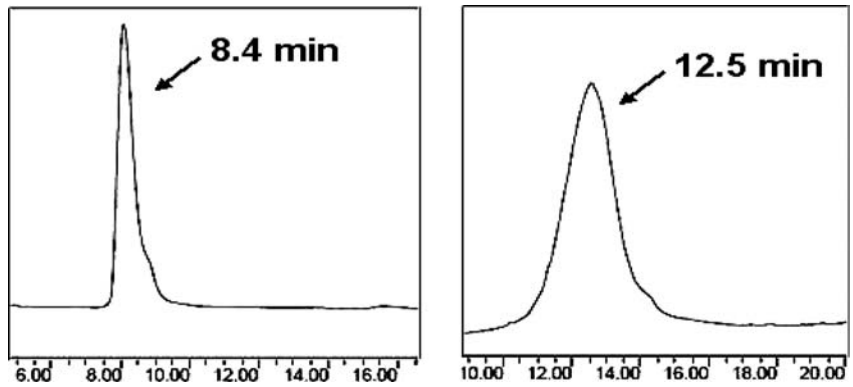

Figure 4. RP-HPLC analysis of the derivatization of PAMAM dendrimer with the GS-S-NAC. PAMAM-COOH (A), PAMAM-CO-GS-S-NAC (B).

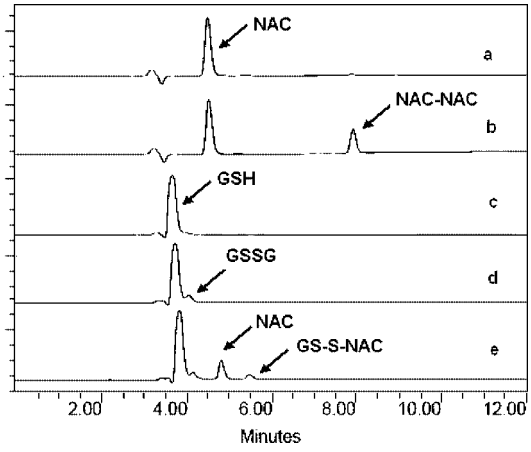

Figure 5. RP-HPLC UV absorbance chromatograms at 210 nm (arbitrary AU units) (a) NAC; (b) NAC and NAC-NAC; (c) GSH; (d) GSH and GSSG; (e) GSH, GSSG, NAC, and GS-S-NAC.

S-NAC was confirmed HPLC, NMR, and MALDI. The same type of MALDI analysis yielded approximately 19.7 kDa (Figure 3B, Supporting Information R-X) (18 GS-S-NAC groups for the PAMAM-COOH dendrimers). The number of GS-S-NAC groups was also determined via NMR analysis and the appearance of methyl protons at 1.70 and 1.92 ppm (Supporting Information R-XI) indicates the formation of GS-NAC conjugate with dendrimer. The NMR and MALDI data for the drug payload agree very well with each other, as summarized in Table 1.The yields of PAMAM-conjugates are high and reproducible.

Release Studies. The release of NAC from the conjugates was investigated in the presence of GSH at intracellular and extracellular concentrations (*31*). It was assumed that the release of NAC would occur by the disulfide exchange reaction. GSH and its oxidized form (GSSG) are responsible for forming the intracellular redox buffer. Intracellularly, GSH takes the role of attacking thiolate moiety and gets oxidized in the process while cleaving the existing disulfide bonds. Disulfide exchange reactions do not change the total number of disulfide bonds but rather shuffle the species forming them. In the present study, the release of NAC from the conjugates by disulfide exchange reaction was confirmed by the HPLC analysis and is discussed in detail in the following sections.

Free NAC had an elution time of 4.7 min (Figure 5a), whereas GSH eluted at 3.8 min (Figure 5c). Oxidized forms of NAC and GSH were also analyzed by HPLC and the oxidized form of NAC eluted (NAC-NAC) at 8.2 min (Figure 5b), while oxidized GSH (GSSG) eluted at 3.9 min (Figure 5d). The GSSG peak was very close to the GSH peak, and when both were injected together, GSSG appeared as a shoulder on the GSH peak (Figure 5d). On the other hand, NAC-NAC is more hydrophobic than NAC, as indicated by the higher elution times for the former than NAC in the chromatogram (Figure 5b). Hydrophilicity of NAC can be associated with its thiol group, and when this group is occupied, the molecule is rendered more hydrophobic, as suggested by the significant increase in its retention time when NAC-NAC (Figure 5b) was formed. A similar shift to higher retention was observed for GSSG, as indicated by the appearance of a shoulder on the peak seen for retention of GSH (Figure 5d). However, this shift in retention time of GSSG is not as significant (Figure 5d) as that seen for NAC-NAC (Figure 5b). The retention time of GS-S-NAC (Figure 5e) was 5.3 min, which was longer than both GSH (3.8 min) and NAC (4.7 min). This suggests that occupation of thiol groups reduces the hydrophilicity of both NAC and GSH.

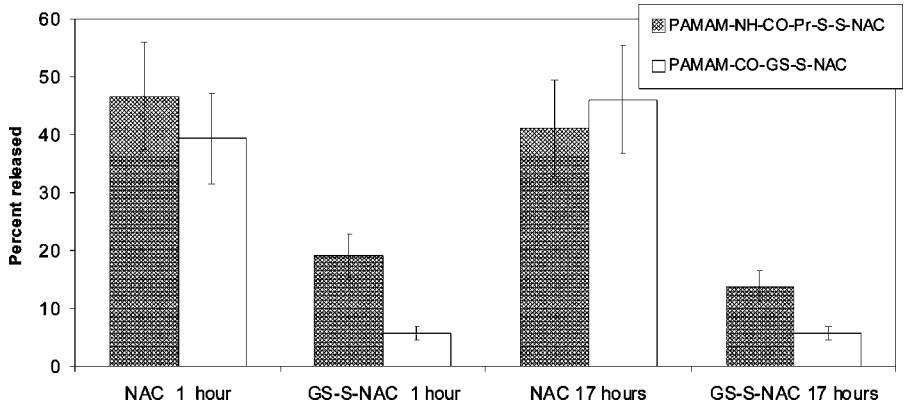

Figure 6. Release of NAC and GS-S-NAC from conjugates (in PBS with 10 mM GSH).

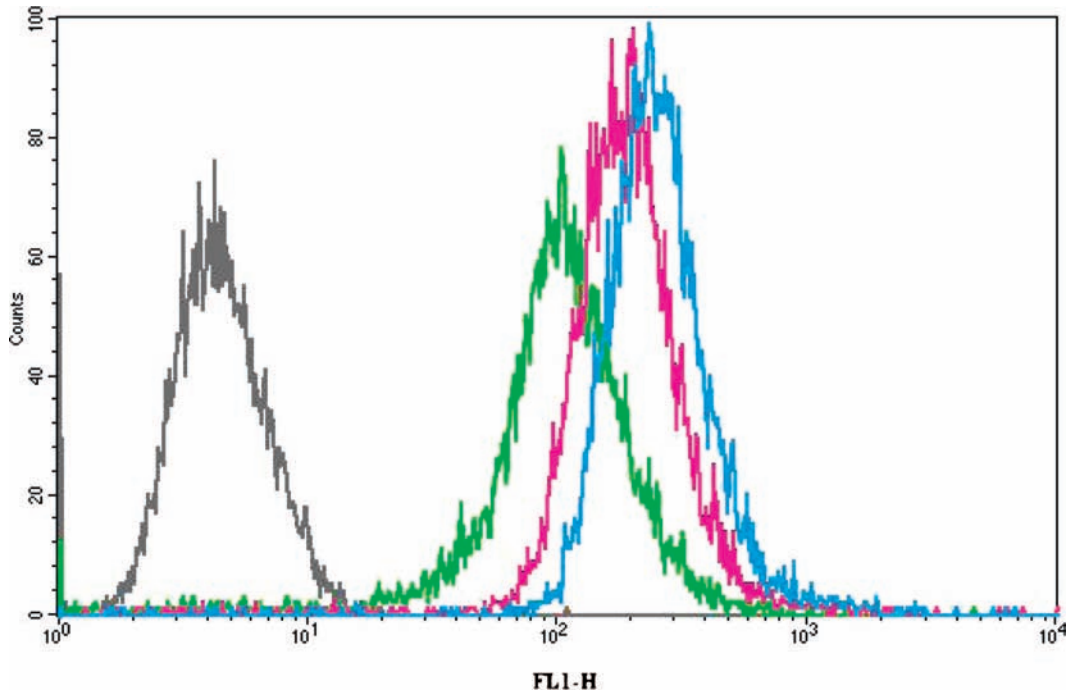

Figure 7. Flow cytometry of the cell entry dynamics of FITC-PAMAM-NH-CO-Pr-S-S-NAC- conjugate in the BV-2 microglial cell line. The log of FITC absorption intensity (FL1-H on *x*-axis) is plotted against the number of cells (counts on *y*-axis). The rapid increase in the cellular uptake of FITC-PAMAM-NH-CO-Pr-S-S-NAC within 15 min is evident.

Stability analysis of free NAC and free GSH suggests that both GSH and NAC go through slow oxidation and form their dimers (NAC-NAC and GSSG) by disulfide bond formation when dissolved in PBS. The rate of disulfide bond formation was relatively slow at 25% of NAC and GSH being converted to their oxidized form over 17 h. It was determined that, in addition to their dimers, when NAC and GSH were present together, they formed GS-S-NAC as well. The formation rates of GS-S-NAC were in agreement with the oxidation rates determined for both NAC and GSH separately. When NAC and GSH were present together where GSH was in excess, no detectable NAC-NAC was formed. The conjugates were also analyzed in the absence of GSH to verify the stability of the disulfide linkage at physiological pH. When the conjugates were placed in PBS buffer and analyzed for 17 h, both conjugates were stable and did not release any of the NAC they carried. The stability of the disulfide linkage shows that they are capable of carrying their payload without any release due to instability in aqueous media at physiological pH. The extent of the release of drug from both dendrimer−NAC conjugates was also analyzed at plasma and intracellular GSH concentrations. The conjugates and the GSH in required amounts were added to PBS solution, and the solution was analyzed at various time intervals by HPLC for up to 17 h. UV absorbance peak areas were used to determine the concentrations of each of the species in the solution, based on appropriate calibration curves. At plasma GSH concentration (2 μM), both G3.5-CO-GS-S-NAC and G4-NH-CO-Pr-S-S-NAC conjugates were very stable and they did not release any detectable levels of free NAC within a 17 h period. For both conjugates, 1% of the NAC payload was found in the release medium in reduced GS-S-NAC or NAC-NAC forms (data not shown). The limited release of NAC in reduced GS-S-NAC or NAC-NAC forms was very rapid and competed within 1 h. The remaining NAC stayed intact throughout the release study due to depletion of the reduced GSH in the media. This suggests that NAC releases from the conjugate rapidly but the amount of NAC released will be governed by the amount of reduced GSH available.

The expected release mechanisms of both PAMAM-NH-CO-Pr-S-S-NAC and PAMAM-CO-GS-S-NAC conjugates should be similar, with the only difference being the linker used. In the presence of excess GSH, the conjugates containing disulfide bonds can get shuffled by GSH in two possible ways. The conjugates may release NAC in the free form, while a GSH will attach onto the dendrimers forming the disulfide bond. The other possible way includes releasing of GS-S-NAC while the dendrimers have a free thiol group. The GS-S-NAC formed can be further shuffled by excess GSH present and can yield GSSG and NAC. The shuffling reactions will reach equilibrium where the concentration of each species is stabilized. These fast shuffling reactions will not change the total number of disulfide linkages, while slow oxidation reactions can also take place forming new disulfide bonds.

Both conjugates were analyzed for their release characteristics at intracellular GSH concentration (10 mM). The results suggest that both conjugates were able to release significant amounts of free NAC within an hour (Figure 6). PAMAM-NH-CO-Pr-S-S-NAC conjugate released 47% of the NAC payload in free form within 1 h. Additionally, 19% of NAC payload was found in GS-S-NAC oxidized form. The total NAC that was detached from the dendrimers within 1 h was 66%. The extent of NAC released did not change significantly after the initial release within 1 h; 41% of NAC payload was found in the free form and 14% was found as GS-S-NAC. The slight decrease in NAC content was most likely due to the error in concentration determination, and it was within standard error limits. Similarly, PAMAM-CO-GS-S-NAC conjugate released 39% of NAC in free form and another 6% in GS-S-NAC form within 1 h, yielding a 45% total NAC release. At 17 h, the free NAC content was determined as 46%, and 6% of NAC payload was in the GS-S-NAC form. At intracellular GSH concentration, no NAC-NAC was formed throughout the release studies. Absence of NAC-NAC can be explained by the excess amount of GSH present in the media, which can transfer the disulfide linkage onto either GSSG or GS-S-NAC by disulfide exchange reactions. After the initial rapid release of NAC, the concentrations

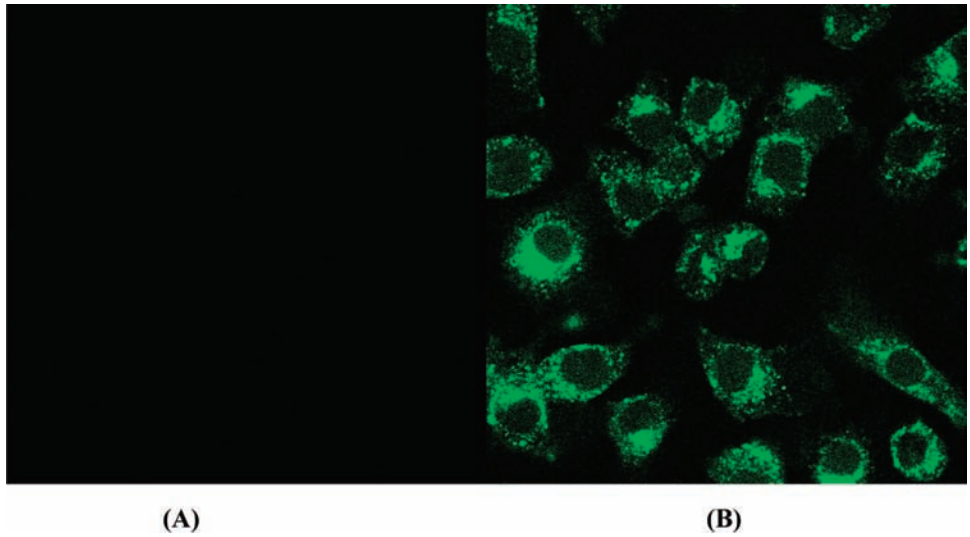

Figure 8. Confocal microscopy images (630×) after 2 h of treatment with (A) control and (B) FITC-PAMAM-NH-CO-Pr-S-S-NAC. The FITC-PAMAM-NH-CO-Pr-S-S-NAC conjugates appear to be mainly localized in the cytoplasm, while the nucleus appears to be relatively free of the presence of any fluorescence at this time scale.

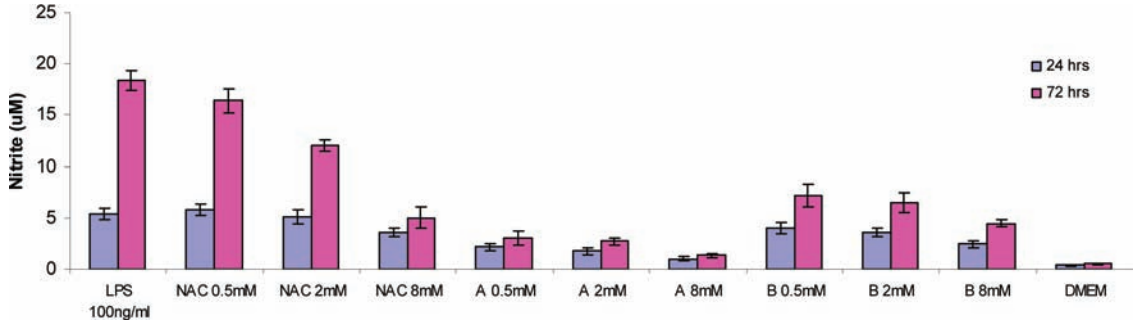

Figure 9. Efficacy assay of dendrimer−NAC conjugates. BV-2 cells were treated with 100 ng/mL of LPS and the indicated concentration of NAC, PAMAM-NH-CO-Pr-S-S-NAC (A) conjugate and PAMAM-CO-GS-S-NAC (B) conjugate for 3 h, and then incubated with 100 ng/mL of LPS for 24 and 72 h. Nitrite in culture medium was measured using Griess reagent system. Data are mean ± SD of three samples per group, and assessed by *t* test.

of analytes did not change significantly, which suggests that the cleavage is by fast exchange reactions which reach equilibrium within 1 h. The difference in drug release of the two conjugates may be explained by the different types of linkers used for attachment of NAC.

Our study shows fast release of NAC from the conjugates in intracellular GSH levels and the stability at plasma GSH levels; these results suggest the similar release mechanism for NAC from the conjugates. This study demonstrates that PAMAM dendrimer-based NAC delivery systems can be developed for various applications. The above results have significant implications in designing dendrimer-based drug delivery systems. Enzymatic release of drugs from dendritic delivery systems is challenging. Smaller generations were shown to be capable of enzymatic cleavage, but lower generations lack the enhancements higher generations have to offer, whereas higher generations face steric hindrance issues (*43, 44*). Commonly used pH-responsive release systems usually provide slower drug release over longer time periods unless the release takes place at a very low pH (*24, 44*). The two GSH-responsive delivery systems described here have very fast release kinetics at intracellular conditions and demonstrate that GSH can be used as a reliable releasing agent in dendrimer-based delivery systems. Interestingly, the thiol-containing drugs are capable of forming disulfide bonds, and this is one major contributing factor for their enhanced protein binding and reduced bioavailability. Further, this study shows that the covalent linking of the thiol-containing drugs by disulfide bonds would provide a means of releasing these drugs from the carrier systems at the targeted sites.

Cell Entry of Conjugates in BV-2 Microglial Cell. Cellular entry of FITC-PAMAM-NH-CO-Pr-S-S-NAC conjugate was evaluated using flow cytometry and confocal microscopy. The flow cytometry shows a significant fluorescence intensity increase within 15 min, as evidenced by a two order of magnitude increase in the fluorescence intensity (Figure 7). Subsequently, there was a moderate increase in fluorescence noted until 120 min. This shows that the FITC-PAMAM-NH-CO-Pr-S-S-NAC conjugates entered the cells rapidly.

The cellular entry was also visualized using confocal microscopy (Figure 8). It is evident that the FITC-PAMAM-NH-CO-Pr-S-S-NAC conjugate enters the cells and localizes mostly in the cytoplasm, while the nucleus appears to have relatively less fluorescence at this time scale. The cells without any treatment show no fluorescence. From the above results, it appears that FITC-PAMAM-NH-CO-Pr-S-S-NAC conjugates are transported inside the cells efficiently, perhaps by endocytosis (*45*).

Efficacy Assay of Conjugates. NAC exerts its therapeutic effects by decreasing the production of pro-inflammatory cytokines and reactive oxygen and nitrogen species. In our *in vivo* studies, we seek to use NAC to treat neuroinflammation induced by activated microglial cells in perinatal brain injury. Therefore, we evaluated the cellular efficacy of these conjugates in the BV-2 mouse microglial cell line that is activated by LPS.

Microglial cells activated by LPS release the free radical NO that can result in damage to membranes and DNA of the surrounding cells leading to cell death. The antioxidative properties of the conjugates were tested by measuring the nitrite levels as a marker of free radical NO production in the cell supernatant. Free NAC inhibited nitrite production in a dose-dependent manner after 72 h of incubation. At 24 h, a time point at which a relatively lower amount of NO is produced, only the highest concentration of free NAC (8 mM) inhibited nitrite release. Both PAMAM-NH-CO-Pr-S-S-NAC and PAMAM-CO-GS-S-NAC conjugates showed significant inhibition of nitrite production even at the lowest equivalent dose of NAC (0.5 mM). In fact, in both conjugates, with anionic and cationic terminal groups, 0.5 mM NAC in the conjugated form showed equivalent efficacy to 8 mM of free NAC. The conjugates did not show a significant dose dependence, at the three concentrations equivalent to free NAC, perhaps because significant suppression (>60%−80%) was seen even at the lowest concentrations (Figure 9) for both conjugates. Perhaps, the use of even lower concentration of conjugates may enable us to find dose dependence, but detailed dose dependence is beyond the scope of this study. At equivalent concentrations, the cationic PAMAM-NH_2-NAC conjugate showed slightly better efficacy than the anionic PAMAM-COOH-NAC conjugate. From these results, it appears that improved intracellular uptake and high drug payload in the dendrimer conjugate may be producing a high local drug concentration inside the cell to elicit a significant therapeutic response. It also suggests that an appreciable amount of the drug is released intracellularly even at these relatively short time intervals (especially for polymer conjugates).

The above results have significant implications in both understanding and manipulating drug release mechanisms and achieving controlled intracellular drug release in dendrimer-based delivery systems. The results suggest that GSH can be used as a reliable *in vivo* releasing agent in dendrimer-based delivery systems. As the most abundant thiol species in living cells, GSH is the most likely candidate for the disulfide reduction in previously reported drug delivery systems. The relatively rapid drug release at intracellular GSH levels is key in dendrimer-based conjugates where drug release is typically much slower. The manipulation of GSH concentration in living cells as demonstrated here conclusively proves that GSH-mediated release is a viable mechanism for releasing payloads from dendrimer conjugates.

CONCLUSIONS

We have developed dendrimer−NAC conjugates as drug delivery systems for the treatment of neuroinflammation associated with cerebral palsy in perinatal applications. The PAMAM dendrimer-based intracellular drug delivery system uses a linker that uses GSH as the releasing agent. Two conjugates were prepared, one based on an anionic PAMAM G3.5-COOH dendrimer and one based on a cationic PAMAM-G4-NH_2 dendrimer. NMR, MALDI, and HPLC showed that the conjugate synthesis was effective and successful. *In vitro* release studies at different GSH levels have shown that GSH is responsible for releasing payloads from a dendrimer carrier in buffer. Flow cytometry and confocal microscopy revealed that the conjugates enter the cells rapidly and localize in the cytoplasm. The efficacy was assessed in activated microglial cells using nitrite inhibition. Both conjugates showed significant efficacy even at drug levels 16 times lower than that of the free drug. These studies address a key challenge that relates to drug release from polymer in general, and dendrimers in particular. We have recently reported the intrinsic ability of PAMAM dendrimers to target activated microglial cells in animal models of neuroinflammation (*44*). Combined with the findings of these studies, which allow us to tailor the intracellular release based on glutathione levels, we will be able to design dendrimer−drug conjugates with increased *in vivo* efficacy.

ACKNOWLEDGMENT

This study was supported by the Intramural Research Program of the National Institute of Child Health and Human Development, NIH, DHHS.

Supporting Information Available: Experimental procedures, ^{1}H NMR, ^{13}C NMR, MALDI-TOF, ESI analysis of all intermediates and final products. This material is available free of charge via the Internet at http://pubs.acs.org.

LITERATURE CITED

(1) Louwerse, E. S., Weverling, G. J., and Bossuyt, P. M. (1995) Randomized, double-blind, controlled trial of acetylcysteine in amyotrophic lateral sclerosis. *Arch. Neurol. 52*, 559–564.

(2) Ferrari, G., Yan, C. Y., and Greene, L. A. (1995) N-Acetylcysteine (D- and L-stereoisomers) prevents apoptotic death of neuronal cells. *J. Neurosci. 15*, 2857–2866.

(3) Beloosesky, R, Gayle, A. D, and Ross, G. M. (2006) Maternal N-acetyl cysteine suppress fetal inflammatory cytokine responses to maternal lipoplysaccharide. *Am. J. Obstet. Gynecol. 195*, 1053–1057.

(4) Beichert, M., Nebe, C. T, Hack, V., Edler, L., Droge, W., Pittack, N, Daniel, V., Breitkreutz, R., Schuster, D., and Brust, J. (2000) Improvement of immune functions in HIV infection by sulfur supplementation: two randomized trials. *J. Mol. Med. 78*, 55–62.

(5) Estensen, R. D, Levy, M., and Klopp, S, J. (1999) N-Acetyl cysteine suppression of the proliferative index in the colon of patients with previous adenomatous colonic polyps. *Cancer Lett. 147*, 109–114.

(6) Ballatori, N. (1998) N-Acetyl cysteine as an antidote in methyl mercury poisoning. *Environ. Health Perspect. 106* (5), 267–271.

(7) Dilger, R. N, and Baker, D. H. (2007) Oral N-acetyl L-cysteine is a safe and effective precursor of cysteine. *J. Anim. Sci. 19*, 1–26.

(8) Beloosesky, R., Gayle, D. A., and Amidi, F. (2006) N-acetylcysteine suppresses amniotic fluid and placenta inflammatory cytokine responses to lipopolysaccharide in rats. *Am. J. Obstet. Gynecol. 194*, 268–273.

(9) Xu, D. X., Chen, Y. H., and Wang, H. (2005) Effect of N-acetylcysteine on lipopolysaccharide-induced intra-uterine fetal death and intra-uterine growth retardation in mice. *Toxicol. Sci. 88*, 525–533.

(10) Buhimschi, I. A., Buhimschi, C. S., and Weiner, C. P. (2003) Protective effect of N-acetylcysteine against fetal death and preterm labor induced by maternal inflammation. *Am. J. Obstet. Gynecol. 188*, 203–208.

(11) Van Schayck, C. P., Dekhuijzen, P. N., and Gorgels, W. J. (1998) Are anti-oxidant and anti-inflammatory treatments effective in different subgroups of COPD. A hypothesis. *Respir. Med. 92*, 1259–1264.

(12) Ben-Ari, Z., Vaknin, H., and Tur-Kaspa, R. (2000) N-Acetylcysteine in acute hepatic failure (non-paracetamol-induced). *Hepatogastroenterology 47* (33), 786–789.

(13) Vale, J. A., and Proudfoot, A. T. (1995) Paracetamol (acetaminophen) poisoning. *Lancet 346*, 547–552.

(14) Tepel, M., Van der Giet, M., and Schwarzfeld, C. (2000) Prevention of radiographic-contrast-agent-induced reductions in renal function by acetylcysteine. *N. Engl. J. Med. 343*, 180–184.

(15) Harada, D., Naito, S., and Otagiri, M. (2002) Kinetic analysis of covalent binding between N-acetyl-L-cysteine and albumin through the formation of mixed disulfides in human and rat serum in vitro. *Pharm. Res. 19*, 1648–1654.

(16) Borgström, L, Kågedal, B., and Paulsen, O. (1986) Pharmacokinetics of N-acetylcysteine in man. *Eur. J. Clin. Pharmacol. 31*, 217–222.
(17) Dilger, R. N., Toue, S., Kimura, T., Sakai, R., and Baker, D. H. (2007) Excess dietary L- cysteine, but not L-cystine, is lethal for chicks but not for rats or pigs. *J. Nutr. 322*, 331−338.
(18) Palmer, L. A., Doctor, A., Chhabra, P., Sheram, M. L., Laubach, V. E., Karlinsey, M. Z., Forbes, M. S., Macdonald, T, and Gaston, B. (2007) S-Nitrosothiols signal hypoxia-mimetic vascular pathology. *J. Clin. Invest. 117*, 2592–601.
(19) Rui, Y, Wang, S., Low, P. S., and Thompson, D. H.,. (1998) Diplasmenylcholine-folate liposomes: an efficient vehicle for intracellular drug delivery. *J. Am. Chem. Soc. 120*, 11213–11218.
(20) Lee, C. C., Mackay, J. A., Frechet, J. M. J., and Szoka, F. C. (2005) Designing dendrimers for biological applications. *Nat. Biotechnol. Rev. 23*, 1517–1526.
(21) Gillies, E. R, and Frechet, J. M. J. (2005) Dendrimers and dendritic polymers in drug delivery. *Drug Discovery Today 10*, 35–43.
(22) Najlah, M., Freeman, S., Attwood, D. D., and Emanuele, A. (2006) Synthesis, characterization and stability of dendrimer prodrugs. *Int. J. Pharm. 308*, 175–182.
(23) Alving, R. C., Steckt, A. E., Chapman, L. W., Waits, B. V., Jr., Hendrickst, D. L., Swartz, M. G, Jr., and Hansont, L. I. (1978) Therapy of leishmaniasis: Superior efficacies of liposome-encapsulated drugs. *Proc. Natl. Acad. Sci. U.S.A. 75*, 2959–2963.
(24) Patri, K. A., Kukowska-Latallo, F. J., and Baker, R. J., Jr. (2005) Targeted drug delivery with dendrimers: Comparison of the release kinetics of covalently conjugated drug and non-covalent drug inclusion complex. *Adv. Drug Delivery Rev. 57*, 2203–2214.
(25) Ulbrich, K., Etrych, T., Chytil, P., Jelinkova, M., and Rihova, B. (2003) HPMA copolymers with pH-controlled release of doxorubicin: In vitro cytotoxicity and in vivo antitumor activity. *J. Controlled Release 87*, 33–47.
(26) Duncan, R. (2003) The dawning era of polymer therapeutics. *Nat. Rev. Drug Discovery 2*, 347–360.
(27) Giri, S., Trewyn, B. G. P., Stellmaker, M. P., and Lin, V. S.-Y. (2005) Stimuli-responsive controlled-release delivery system based on mesoporous silica nanorods capped with magnetic nanoparticles. *Angew. Chem., Int Ed. 44*, 5038–5044.
(28) Kam, N. W. S., Liu, Z., and Dai, H. (2005) Functionalization of carbon nanotubes via cleavable disulfide bonds for efficient intracellular delivery of siRNA and potent gene silencing. *J. Am. Chem. Soc. 127*, 12492–12493.
(29) Perry, R. R., Mazetta, J., Levin, M., and Barranco, S. C. (1993) Glutathione levels and variability in breast tumors and normal tissue. *Cancer 72*, 783–787.
(30) Yeh, C. C., Hou, M. F., Wu, S. H., Tsai, S. M., Lin, S. K., Hou, L. A., Ma, H., and Tsai., L. Y. (2006) A study of glutathione status in the blood and tissues of patients with breast cancer. *Cell. Biochem. Funct. 24*, 555–559.
(31) Hong, R., Han, G., Fernandez, M. J., Kim, J. B., Forbes, S. N., and Rotello, M. V. (2006) Glutathione-mediated delivery and release using monolayer protected nanoparticle carriers. *J. Am. Chem. Soc. 128*, 1078–1079.
(32) Kou, X., Zhang, S., Yang, Z., Tsung, K. C., Stucky, D. G., Sun, L., Wang, J., and Yan, C. (2007) Glutathione- and cysteine-induced transverse overgrowth on gold nanorods. *J. Am. Chem. Soc. 129*, 6402–6404.
(33) Verma, A., Simard, M. J., Worrall, W. E. J., and Rotello, M. V. (2004) Tunable reactivation of nanoparticle-inhibited β-galactosidase by glutathione at intracellular concentrations. *J. Am. Chem. Soc. 126*, 13987–13991.
(34) You, Zi-Ye., Manickam, S. D., Zhou, H. Q., and Oupicky, D. (2007) Reducible poly(2-dimethylaminoethyl methacrylate): Synthesis, cytotoxicity, and gene delivery activity. *J. Controlled Release 122*, 217–225.
(35) Zugates, T. G., Anderson, G. D., Little, R. S., Lawhorn, E. B. I., and Langer, R. (2006) Synthesis of poly(β-amino esters) with thiol-reactive side chains for DNA delivery. *J. Am. Chem. Soc. 128*, 12726–12734.
(36) Kommareddy, S., and Amiji, M. (2005) Preparation and evaluation of thiol-modified gelatin nanoparticles for intracellular DNA delivery in response to glutathione. *Bioconjugate Chem. 16*, 1423–1432.
(37) Oupicky, D., Parker, L. A., and Seymour, W. L. (2002) Laterally stabilized complexes of DNA with linear reducible polycations: strategy for triggered intracellular activation of DNA delivery vectors. *J. Am. Chem. Soc. 124*, 8–9.
(38) Wagner, E., Cotten, M., Mechtler, K., Kirlappos, H., and Birnstiel, L. M. (1991) DNA-binding transferrin conjugates as functional gene-delivery agents: synthesis by linkage of polylysine or ethidium homodimer to the transferrin carbohydrate moiety. *Bioconjugate Chem. 2*, 226–231.
(39) Rajur, B. S., Roth, M. C., Morgan, R. J., and Yarmush, L. M. (1997) Covalent protein-oligonucleotide conjugates for efficient delivery of antisense molecules. *Bioconjugate Chem. 8*, 935–940.
(40) Filipovska, A., Eccles, M. R., Smith, R. A., and Murphy, M. P. (2004) Delivery of antisense peptide nucleic acids (PNAs) to the cytosol by disulphide conjugation to a lipophilic cation. *FEBS Lett. 556*, 180–186.
(41) Reiter, Y., Kreitman, J. R., Brinkmann, U., and Pastan, I. (1994) Cytotoxic and antitumor activity of a recombinant immunotoxin composed of disulfide-stabilized anti-TAC Fv fragment and truncated pseudomonas exotoxin. *Int. J. Cancer 58*, 142–149.
(42) Hinman, M. L., Hamann, R. P., Wallace, R., Menendez, T. A., and Durr, F. E. (1993) Upeslacis, Preparation and characterization of monoclonal antibody conjugates of the calicheamicins: A novel and potent family of antitumor antibiotics. *J. Cancer Res. 53*, 3336–3342.
(43) Najlah, M., Freeman, S., Attwood, D. D., and Emanuele, A. (2007) In vitro evaluation of dendrimer prodrugs for oral drug delivery. *Int. J. Pharm. 336*, 183–190.
(44) De Jesus, O. L. P., Ihre, H. R., Gagne, L., Frechet, J. M. J., and Szoka, F. C., Jr. (2002) Polyester dendritic systems for drug delivery applications: In vitro and in vivo evaluation. *Bioconjugate Chem. 13*, 453–461.
(45) Pillai, O., Inapagolla, R., Kannan, S., and Kannan, R. M. (2008) The effect of surface functionality on cellular trafficking of dendrimers. *Biomaterials 29*, 3469–3476.
(46) Kannan R. M., Iezzi, R., Kannan, S., and Rajaguru, B. (2007) Dendrimer-containing particles for sustained release of compounds, Provisional US patent, filed November.

BC800342D

Supporting Information

Dendrimer-drug conjugates for tailored intracellular drug release based on glutathione levels

Raghavendra S. Navath[1,2], Yunus E. Kurtoglu[1], Bing Wang[2,3], Sujatha Kannan[3], Robert Romero[2], and Rangaramanujam M. Kannan[1,2]*

Department of Chemical Engineering and Material Science, and Biomedical Engineering, Wayne State University, Detroit, Michigan 48202, [2]Perinatology Research Branch, National Instituted of Child Health and Human Development, National Institutes of Health, (NICHD/NIH), DHHS, [3]Department of Pediatrics (Critical Care Medicine), Children's Hospital of Michigan, Wayne State University, Detroit, MI, 48201, USA

***CORRESPONDING AUTHOR:** [1]Department of Chemical Engineering and Material Science, and Biomedical Engineering, Wayne State University, Detroit, Michigan 48202, [2]Perinatology Research Branch, National Instituted of Child Health and Human Development, National Institutes of Health, (NICHD/NIH), DHHS.

E-Mail: aa2293@wayne.edu

Materials(R-I):

Ethylenediamine-core poly(amidoamine) [PAMAM] dendrimers (Diagnostic grade generation 3.5 with -COOH end groups, and generation-4 with -NH_2 groups) were purchased from Dendritech. Other reagents were obtained from assorted vendors in the highest quality available. These include benzotriazol-1-yl-oxytripyrrolidinophosphonium hexafluorophosphate (PyBop, Aldrich), Diisopropyl ethylamine (Aldrich) dimethyl sulfoxide, (DMSO, Aldrich), dicyclohexylcarbodiimide (DCC, Aldrich), *N*-hydroxysuccinimde (Aldrich), 2, 2^1 –Dipyridyldisulfide (Aldrithiol, Aldrich) dimethylformamide (DMF, Aldrich) Ethanol (Aldrich) (N-Acetyl Cysteine (NAC, Aldrich), Glutathione (GSH, Aldrich), Acetonitrile (Aldrich) phosphate buffer saline (PBS, pH, 7.4, Aldrich) and Spectra/Por dialysis membrane (MWCO 1000).

Methods (R-II):

All ^{1}H and ^{13}C NMR spectra were recorded on Varian Mercury spectrometer 400MHz in DMSO. MALDI-TOF spectra were recoded on a Bruker Ultraflex system equipped with a pulsed nitrogen laser (337 nm), operating in positive ion reflector mode, using 19 kV acceleration voltage and a matrix of 2, 5 dihydroxybenzoic acid

Reverse Phase-HPLC Characterization (R-III)

HPLC characterization of conjugates was carried out with Waters HPLC instrument equipped with two pumps, an autosampler and dual UV detector interfaced to Breeze software. The mobile phase used was Acetonitrile / Water (both 0.14% TFA by w.) and water phase had a pH of 2.25. Mobile phases were freshly prepared, filtered and degassed prior to the use. Supelco Discovery BIO Wide Pore C5 HPLC Column (5 μm particle size, 25 cm × 4.6 mm length × I.D.) equipped with two C5 Supelguard Cartridges (5 μm particle size, 2 cm × 4.0 mm length × I.D.) was used for characterization of the conjugates as well as stability studies. Gradient method used for analysis was (100:0) Water: Acetonitrile to (60:40) Water-Acetonitrile in 25 minutes followed by returning to initial conditions in 5 minutes. The flow rate was 1 mL/min. The dual U.V. absorbance detector was used at 210 nm and 280 nm simultaneously. Calibration curves were prepared for NAC, GSH and their oxidized forms, based on UV absorbance peak area at 210nm. These calibrations were used in characterization and stability analysis.

Cell Culture (R-IV)

Mouse microglial cell line (BV-2) was obtained from Children's Hospital of Michigan Cell Culture Facility. Cells were grown in 75 mm^2 culture flasks using Dulbecco's Modified Eagle Medium (DMEM, Invitrogen) supplemented with 10% fetal bovine serum (FBS, Invitrogen) and 1% penicillin-streptomycin at 37^oC with 5% CO_2 in an incubator. The cells were subcultured every 48 hours and harvested from subconfluent cultures (60-70%) using 0.05% trypsin-EDTA (Invitrogen).

Preparation of 3-(2-Pyridyldithio)-propanoic acid (PDP) (6) (R-V)

3-(2-Pyridyldithio)-propanoic acid (**6**) was synthesized as a precursor for the generation of *N*- succinimidyl 3-(2-pyridyldithio)-propanoate (**7**) (SPDP). 2, 2^1 –Dipyridyldisulfide (**5**) (2.745 g, 0.0124 mol) was dissolved in 20 mL anhydrous ethanol. Acetic acid (0.75 mL) and 3-mercapto-propanoic acid (0.66 g, 0.0062 mol) were added and the solution was stirred at room temperature for 2 hours and subsequently the solvent was removed under reduced pressure to yield a viscous yellow oil, which was placed under high vacuum to remove all traces of acetic acid. The crude product was purified by a basic Al_2O_3 column using a 3:2 mixture of dichloromethane and ethanol as eluent. Once the yellow band corresponding to the thione by-product had eluted from the column, 4 mL of acetic acid per 100 mL solvent was added to elute the desired product. Fractions containing this compound were pooled and the solvent removed under reduced pressure. The resulting viscous oil was placed on a high vacuum line to remove all traces of acetic acid and yield the title compound (**6**) (1.04 g, 0.0048 mol, 78% yield). Calculated mass: 215.01; ESI: *m/z* 214.04 (M-1), 238.03 (M + Na). ^{1}H NMR (300 MHz; d_6-DMSO) δ, 2.59 (2H, t, J = 7.0), 2.98 (2H, t, J = 7.0), 7.23 (1H, ddd, J = 7.1, 4.8, 1.2), 7.75 (1H, d, J = 8.0), 7.8 (1H, td, J = 7.9, 1.4), 8.4 (1H, d, J = 4.9). ^{13}C NMR (75MHz, d_6-DMSO) δ 33.6, 33.7, 119.2, 121.1, 137.7, 149.5, 159.0, 172.7.

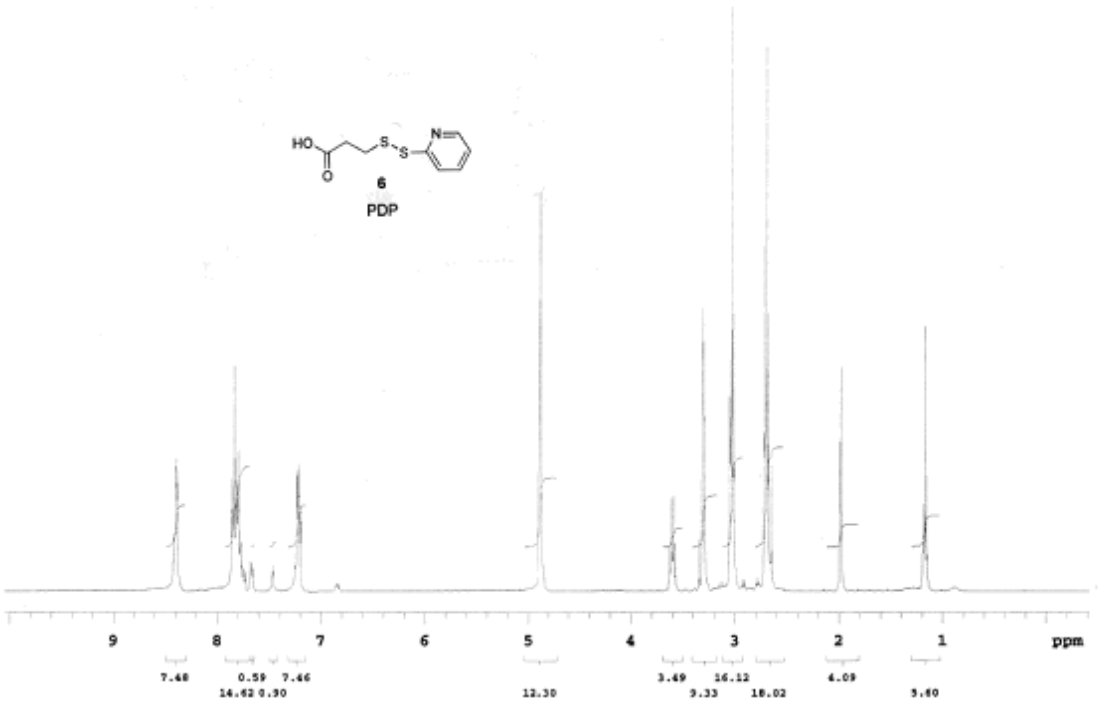
HO
O
S
S
N
6
PDP
9
8
7
6
5
4
3
2
1
ppm
7.48
0.59
7.46
14.62
0.30
12.30
3.49
16.12
9.33
18.02
4.09
5.60

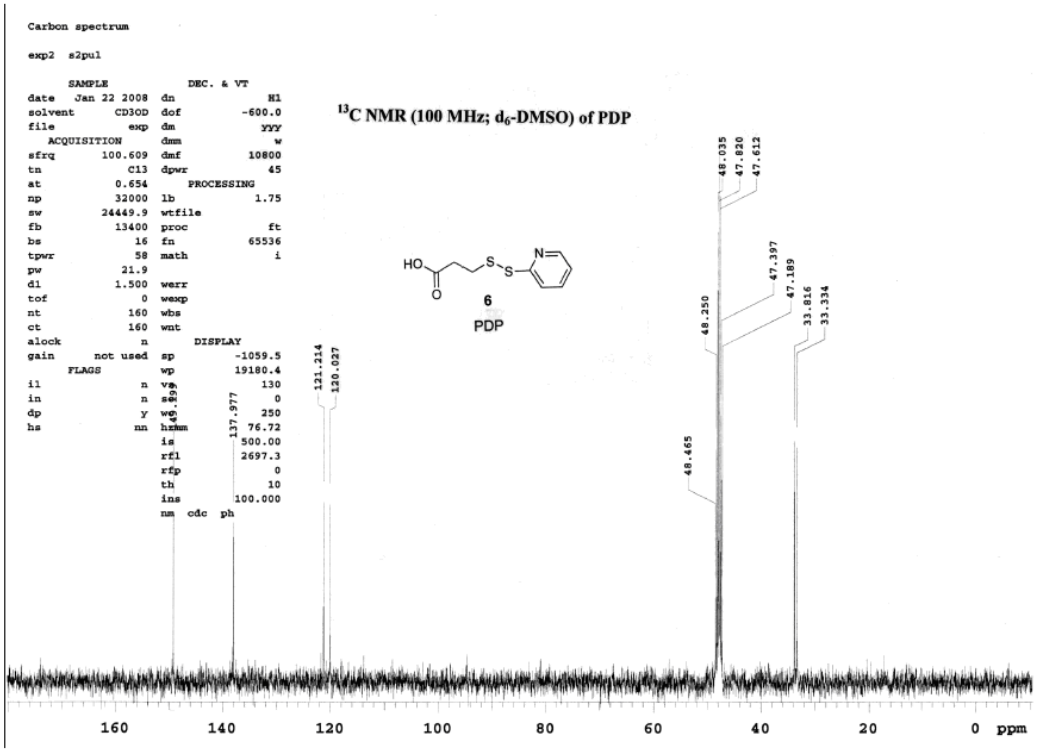
Carbon spectrum
exp2 s2pul
SAMPLE
date Jan 22 2008
solvent CD3OD
file exp
ACQUISITION
sfrq 100.609
tn C13
at 0.654
np 32000
sw 24449.9
fb 13400
bs 16
tpwr 58
pw 21.9
d1 1.500
tof 0
nt 160
ct 160
alock n
gain not used
FLAGS
il n
in n
dp y
hs nn
DEC. & VT
dn H1
dof -600.0
dm yyy
dmm w
dmf 10800
dpwr 45
PROCESSING
lb 1.75
wtfile
proc ft
fn 65536
math i
werr
wexp
wbs
wnt
DISPLAY
sp -1059.5
wp 19180.4
vs 130
sc 0
wc 250
hzmm 76.72
is 500.00
rfl 2697.3
rfp 0
th 10
ins 100.000
nm cdc ph
13C NMR (100 MHz; d6-DMSO) of PDP
HO
O
S
S
N
6
PDP
131.214
120.027
48.035
47.830
47.612
47.397
47.189
48.250
33.816
33.334
48.465
160
140
120
100
80
60
40
20
0
ppm

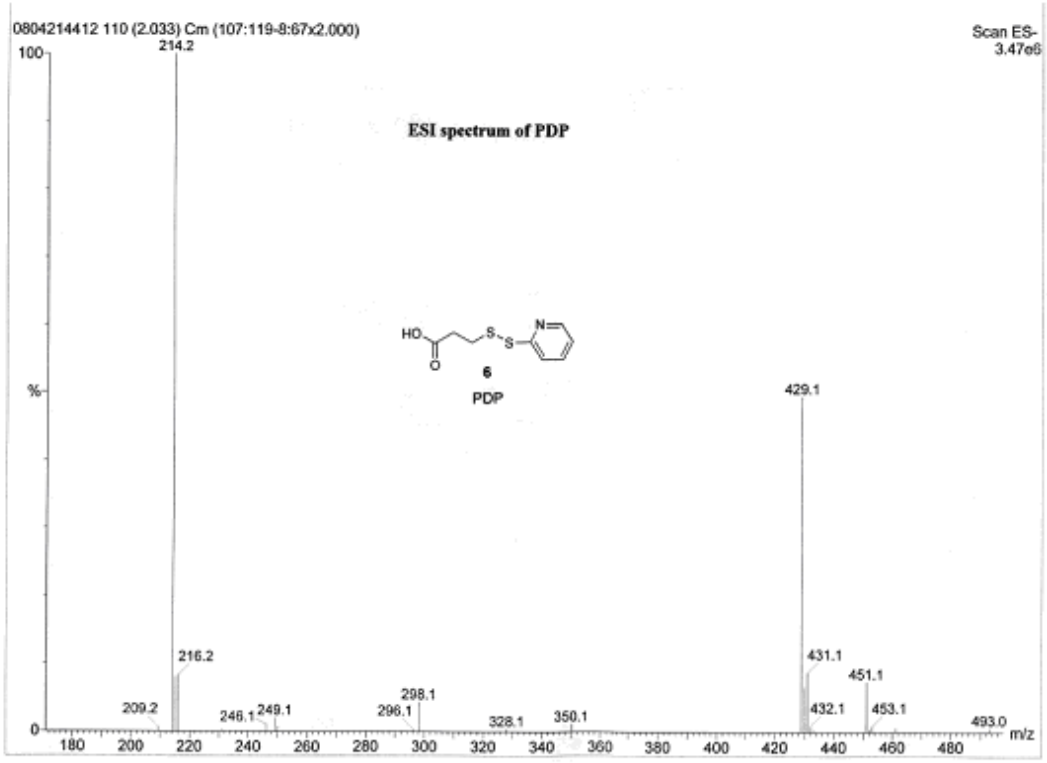

Preparation of *N*-Succinimidyl 3-(2-pyridyldithio)-propanoate (SPDP) (7) (R-VI)

3-(2-Pyridyldithio)-propanoic acid (**6**) (0.862 g, 0.004 mol) in anhydrous DCM (5 mL) was cooled to 0°C in an ice bath. *N*-hydroxysuccinimde (0.507 g, 0.0044 mol) was added followed by dicyclohexylcarbodiimide (0.91 g, 0.0044 mol), both in anhydrous DCM (2 mL). The solution was brought back up to room temperature and left stirring for 3 hours. The formation of a product was followed by silica gel TLC. After the reaction had reached completion the solution was filtered under vacuum from the urea precipitate and the solvent removed from the filtrate under reduced pressure to yield yellow oil. This crude material was purified via silica gel column chromatography using a 50:2 mixture of dichloromethane and methanol as the eluent. The fractions containing the product were combined and the solvent removed to yield colorless oil that crystallized overnight at -20°C (1.025 g, 0.0032 mol, 82% yield). Calculated mass: 312. ESI *m/z* 313.35 (M+H), 335.2 (M + Na). ^{1}H-NMR (300 MHz, d_6-DMSO) δ/ppm 2.81-2.83 (2H, m), 2.80 (H_2O, brs) 2.99-3.03(1H, m), 3.12-3.16 (5H, m), 7.25 (1H, ddd, J = 6.4, 4.8, 1.6), 7.76 (1H, d, J

= 7.1), 7.82 (1H, td, J = 7.5, 1.6), 8.48 (1H, d, J = 4.9). ^{13}C NMR (75, MHz; d_6-DMSO) δ/ppm 25.90, 30.97, 33.54, 120.22, 121.12, 138.60, 150.42, 159.5, 167.4, 170.76.

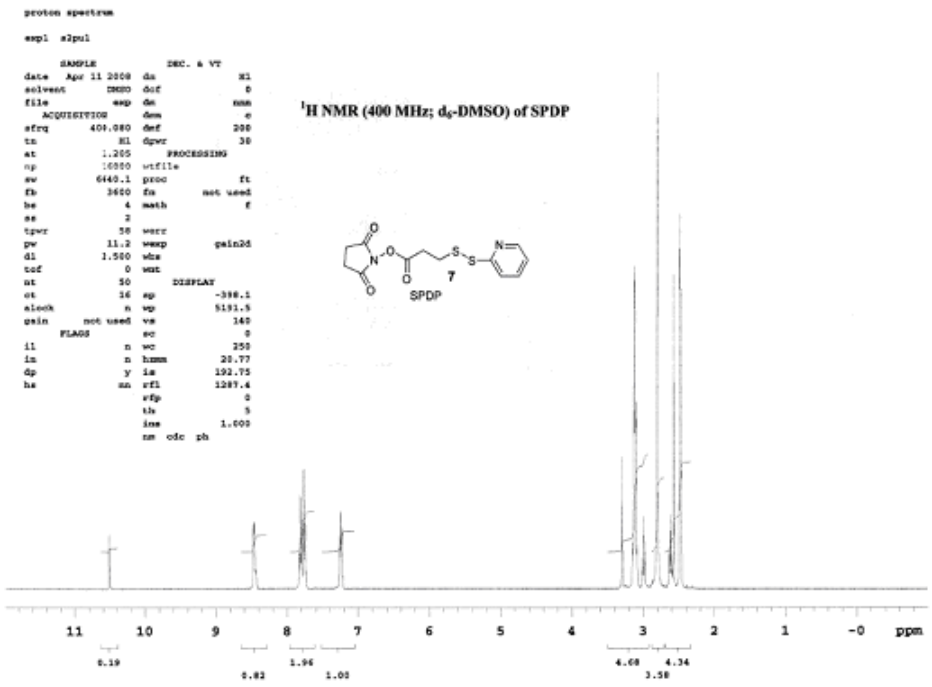

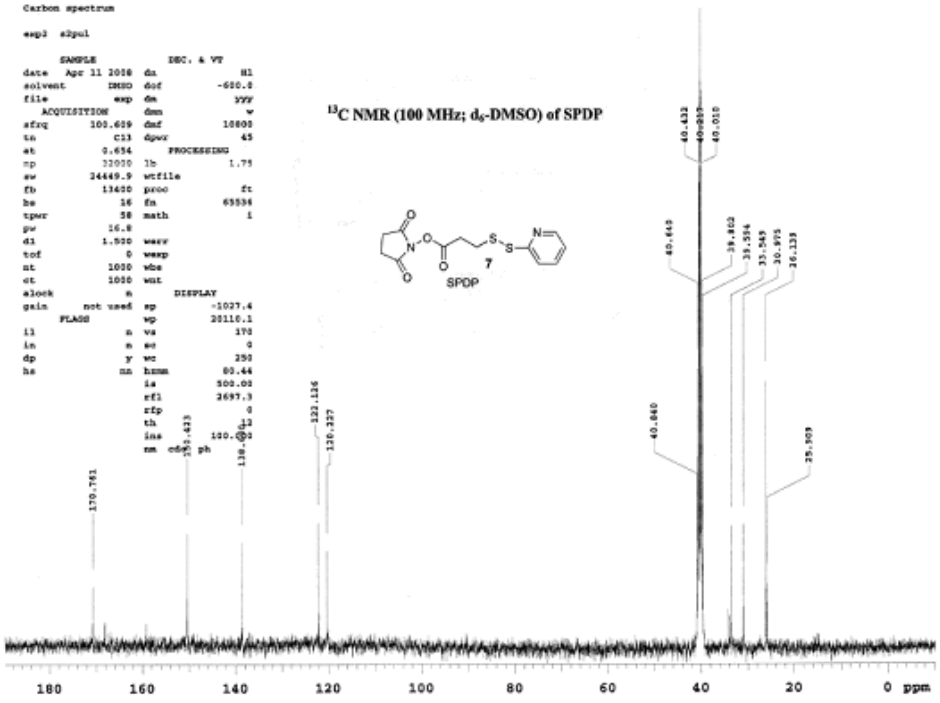

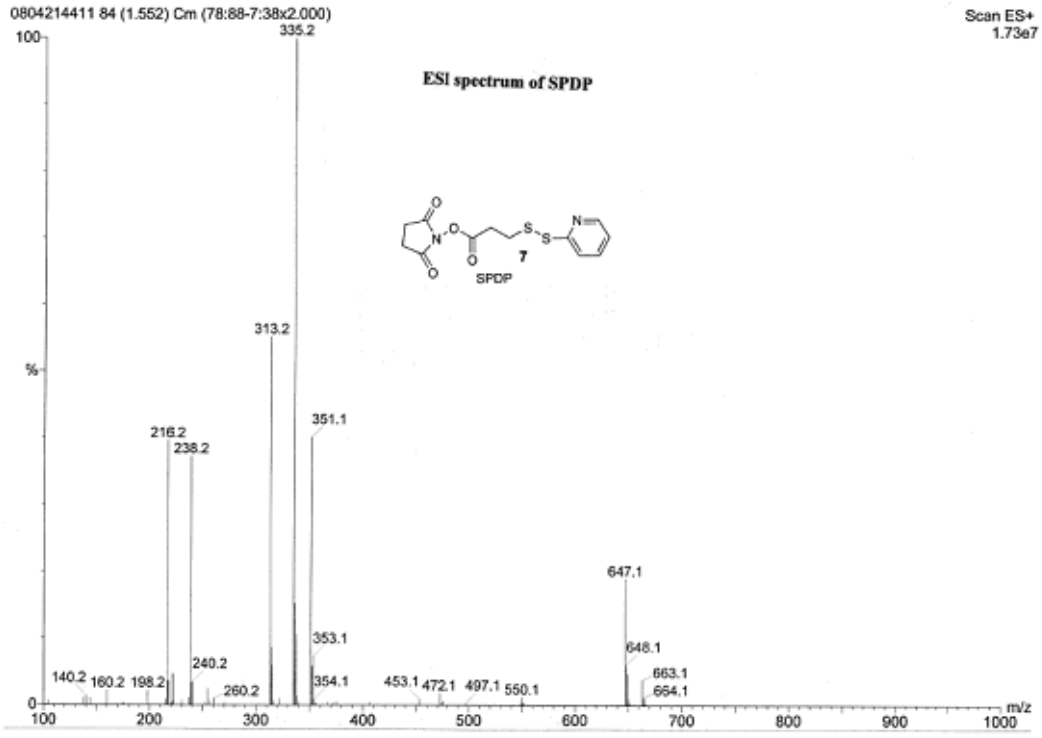

Preparation of PAMAM -NH-CO-Pr-S-S-NAC conjugate (1) (R-VII)

For the preparation of PAMAM-PDP (**9**) generation 4, SPDP (**7**) (351 mg, 1.126 mol) in ethanol (10 mL) was added to a solution of PBS buffer pH 7.4 (20 mL) and PAMAM-NH_2 dendrimer (**8**) (500 mg, 2.25 mol) to provide sufficient modification whilst preventing loss of product due to the precipitation of highly modified dendrimer. Reaction was stirred at room temperature for 2h. To this reaction N-Acetyl cysteine was added (**10**) (273 mg, 1.67 mol) at once, and stirred the reaction at room for 4 h. The reaction was monitored with HPLC. After completion of reaction, the reaction mixture was diluted with water and lyophilized to get *crude* product. The solid *crude* product was diluted with water and dialyzed against DMSO followed by PBS (pH = 7.4) to remove by-products and the excess of reactants and then replaced with deionized water (1 times 4l) for 12h days to remove salts. The water was lyophilized to get pure product in good yield(71%).

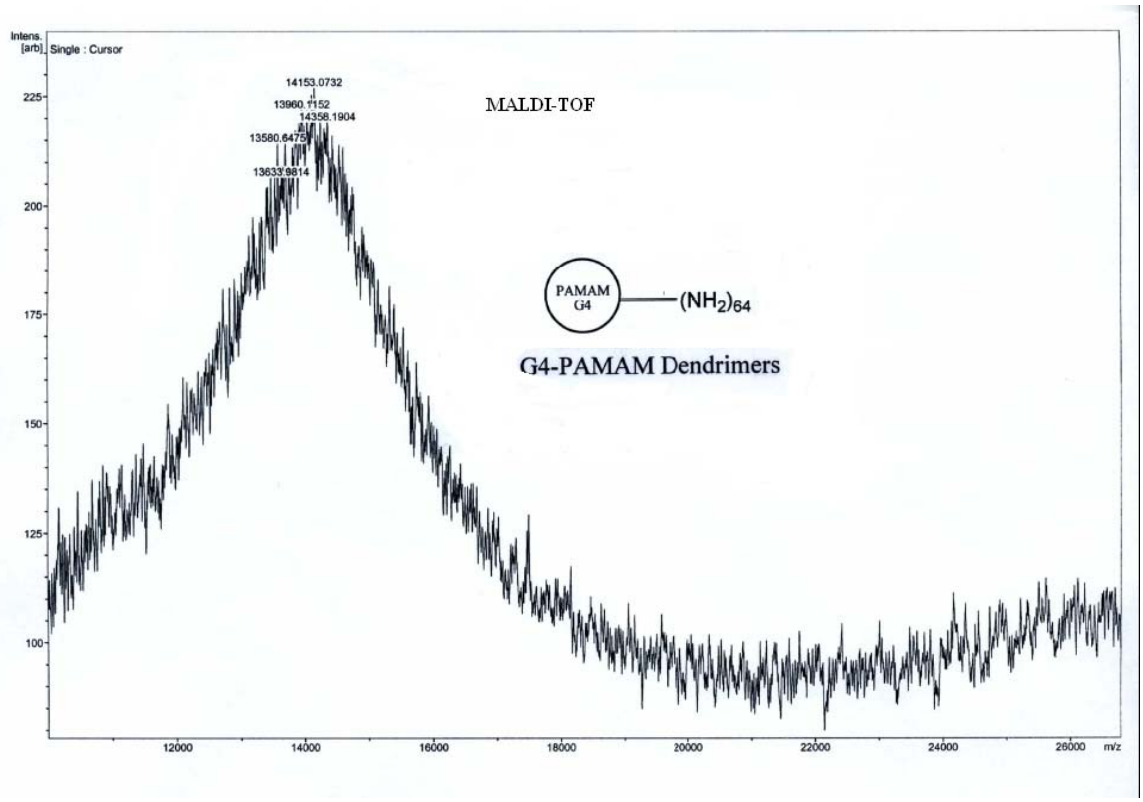

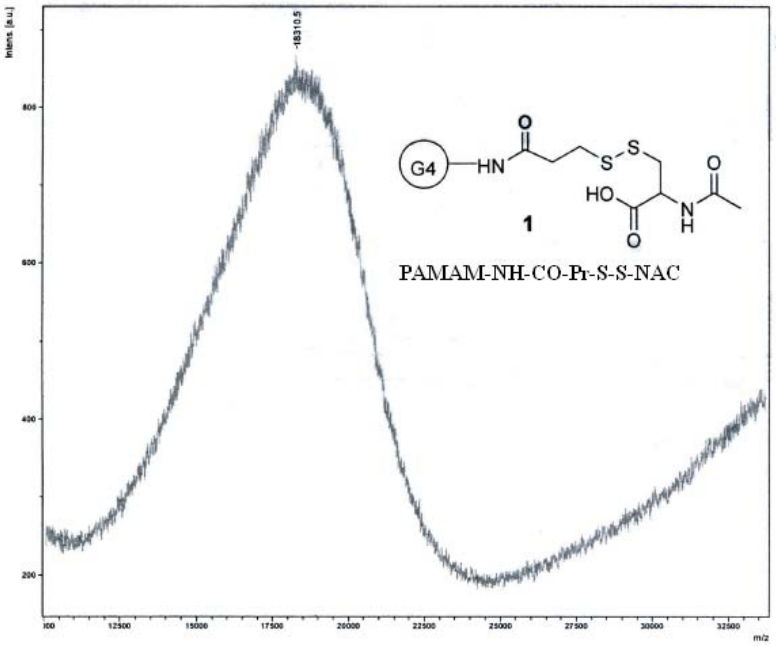

m/z	SN	Intens.	Area	Res.
18310.5	82.3	790.80	2920708	2

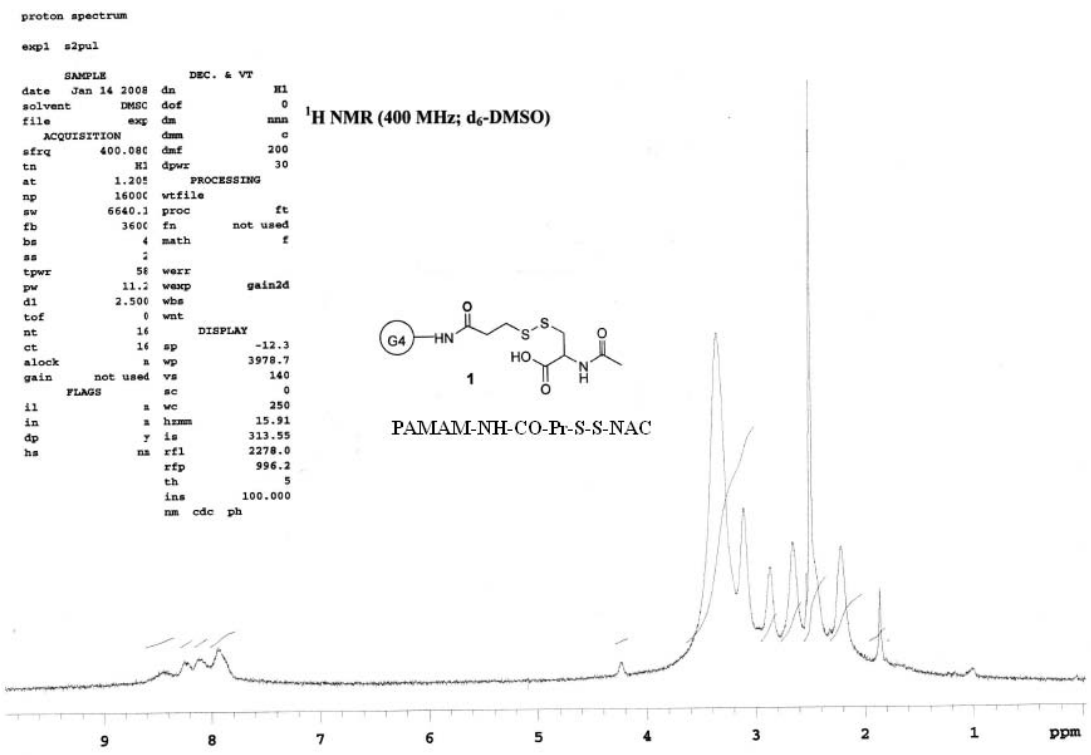

Synthesis of FITC-PAMAM –NH-CO-Pr-S-S-NAC conjugate for imaging (2) (R-VIII)

To a stirred solution of **PAMAM –CO-PR-S-S-NAC** (**1**) (50 mg, 2.73 mmole) in DMSO (2 mL) FITC was added (2.12 mg, 5.44 mmole) and the reaction was continued for 12h at room temperature in dark. Reaction was analyzed using RP-HPLC to determine the extent to which FITC had reacted with PAMAM-MPA-NAC conjugate (**1**). The samples were compared to unmodified dendrimer-conjugate. Samples were initially run on a linear gradient from 100: 0 H_2O/acetonitrile(0.1 wt % TFA) to 10:90 H_2O/acetonitrile (0.14 wt % TFA) over 32 min. During this gradient, dendrimer conjugate was eluted after 15 min compared to the modified FITC-dendrimer- conjugate (**2**) was eluted after 16.0 min. After completion of reaction the compound was dialyzed against DMSO followed by PBS to remove excess of reactants and then replaced with deionized water. The water was lyophilized get pure product in 88% yield.

_S_-(2-thiopyridyl) glutathione (13) (R-IX)

_S_-(2-thiopyridyl) glutathione (**13**) is prepared from the reaction of 2, 2[1]-dithiodipyridine (2.8 g, 0.0127 mol) and GSH (2 g, 0.0065 mol) in a mixture of methanol and water (1:1) stirred for 15h at room temperature. Upon completion of the reaction (monitored by TLC), most of methanol was removed in vacuo and the residue was dissolved in water washed with dichloromethane. The aqueous solution was subjected to reverse phase (RP) HPLC purification, and lyophlization of the eluent gave the pure product as a white solid in 80% yield. Calculated mass: 416. ESI _m/z_ 417 (M+H). ^{1}H-NMR (300 MHz, d_6-DMSO) δ/ppm 1.98-2.11(2H, m), 2.22-3.02 (2H, m), 2.98-3.08(1H, m), 3.18-3.22(1H, m), 3.65-3.71(2H, m), 3.95-402(1H, m), 4.57-4.62(1H, m), 7.0-7.07(1H, m), 7.72-7.87(2H, m), 8.24(2H, br.s., NH), 8.42-8.48(3H, m, NH_2, aromatic)

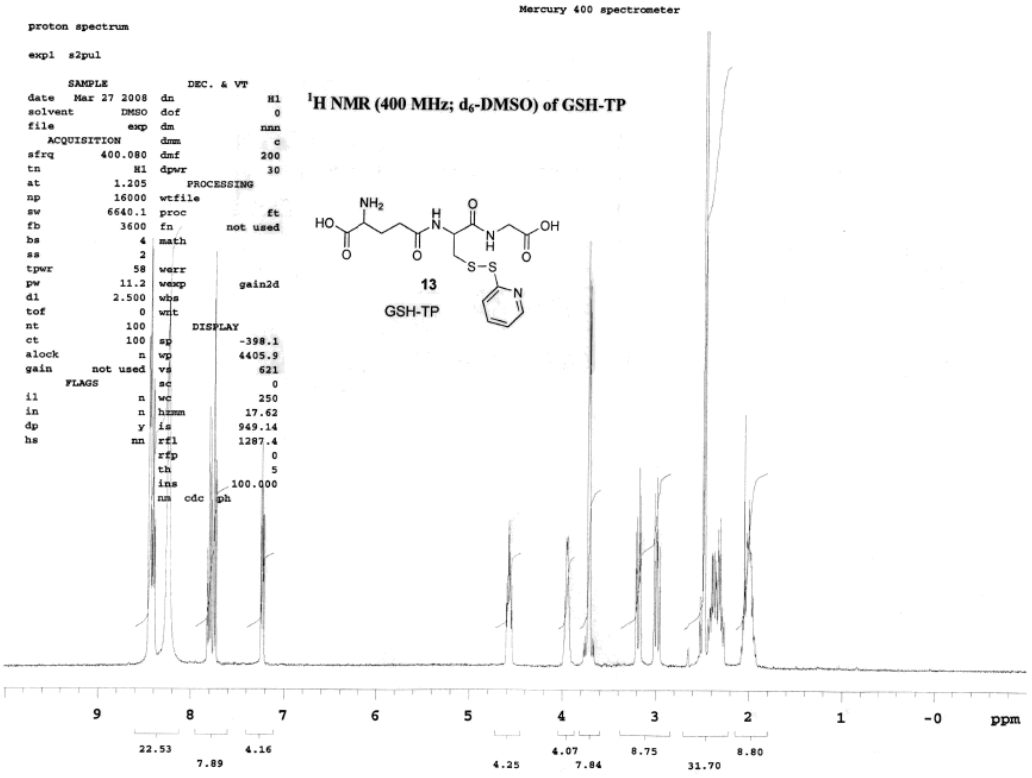

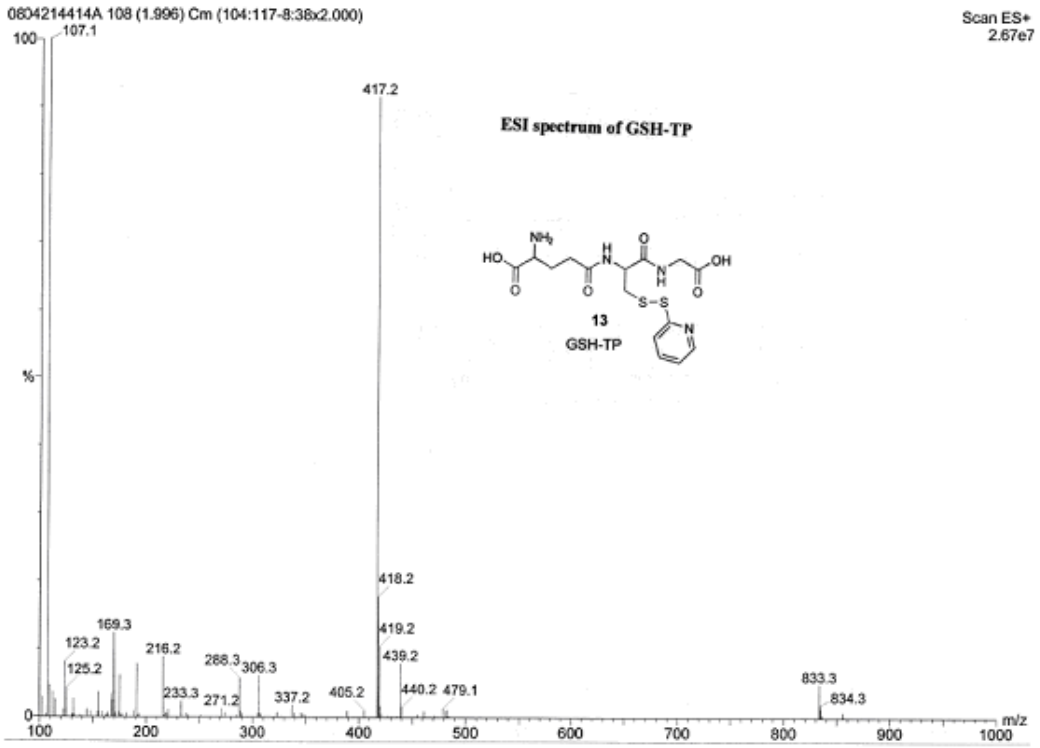

N-Acetyl –glutathione (14) (R-X)

S-(2-thiopyridyl) glutathione (**13**) (0.8 g, 0.0019 mol) was dissolved in PBS buffer pH= 7.4 (5 mL) and added NAC (**10**) (0.313 g, 0.0019 mol) at once, and the reaction mixture was stirred at room temperature for 2 h. After completion of reaction dichloromethane was added and the organic layer was separated to remove the corresponding thione by-product, this process was repeated five times. The aqueous solution was subjected to reverse phase (RP) HPLC purification, and lyophilization of the eluent gave the pure product as a white solid in 79% yield. Calculated mass: 468. ESI *m/z* 467 (M-H). ^{1}H NMR (300 MHz, d_6-DMSO) δ/ppm, 1.81 (3H, s), 1.90-2.0(2H, m), 2.28-2.37(2H, m), 2.79-2.86(3H, m), 3.07-3.17(2H, m), 3.69-3.78(2H, m), 4.40-4.46(1H, m), 4.52-4.58(1H, m). ^{13}C-NMR (75, MHz d6-DMSO) δ/ppm, 22.35, 26.09, 30.86, 51.26, 51.32, 51.64, 52.02, 169.36, 169.44, 170.89, 171.27, 172.02, 172.07.

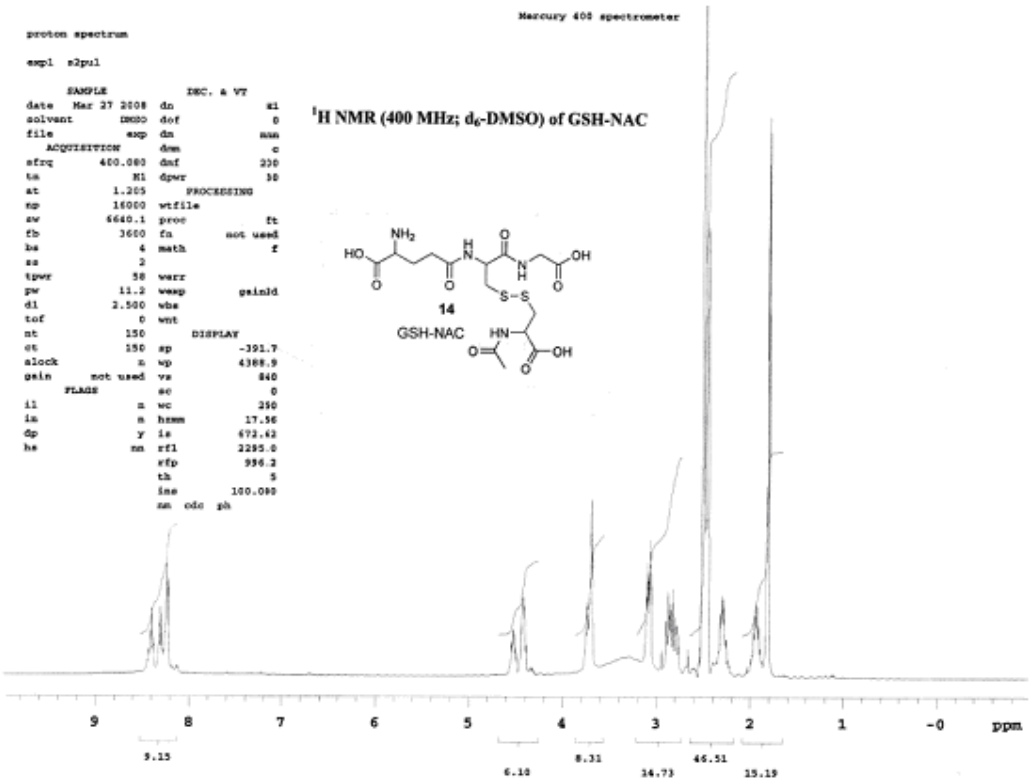
Mercury 400 spectrometer
proton spectrum
exp1 s2pul
SAMPLE
date Mar 27 2008
solvent DMSO
file exp
ACQUISITION
sfrq 400.080
tn H1
at 1.205
np 16000
sw 6640.1
fb 3600
bs 4
ss 2
tpwr 58
pw 11.2
d1 2.500
tof 0
nt 150
ct 150
alock n
gain not used
FLAGS
il n
in n
dp y
hs nn
DEC. & VT
dn H1
dof 0
dn nnn
dnm c
dnf 200
dpwr 30
PROCESSING
wtfile
proc ft
fn not used
math f
werr
wexp gainld
wbs
wnt
DISPLAY
sp -391.7
wp 4388.9
vs 840
sc 0
wc 250
hzmm 17.56
is 672.62
rfl 2295.0
rfp 956.2
th 5
ins 100.000
ln odc ph
^{1}H NMR (400 MHz; d_6-DMSO) of GSH-NAC
14
GSH-NAC
9.15
6.10
8.31
34.73
46.51
15.19
ppm

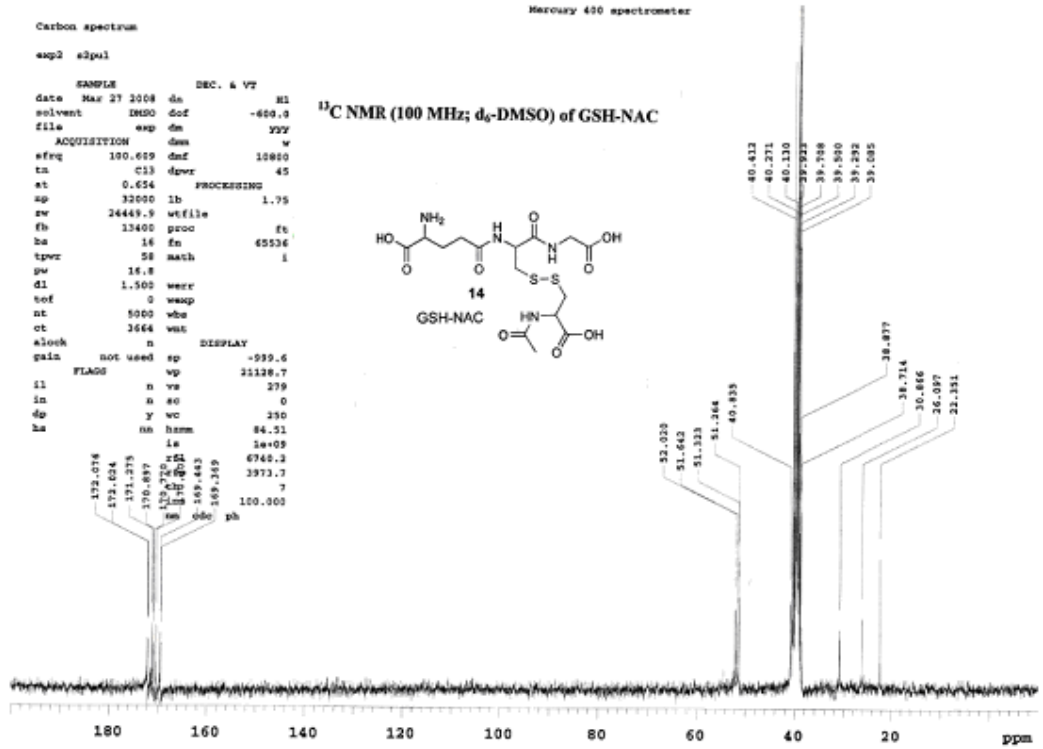
Mercury 400 spectrometer
Carbon spectrum
exp2 s2pul
SAMPLE
date Mar 27 2008
solvent DMSO
file exp
ACQUISITION
sfrq 100.669
tn C13
at 0.654
np 32000
sw 24449.9
fb 13400
bs 16
tpwr 58
pw 16.8
d1 1.500
tof 0
nt 5000
ct 3664
alock n
gain not used
FLAGS
il n
in n
dp y
hs nn
DEC. & VT
dn H1
dof -600.0
dn YYY
dnm w
dnf 10800
dpwr 45
PROCESSING
lb 1.75
wtfile
proc ft
fn 65536
math i
werr
wexp
wbs
wnt
DISPLAY
sp -999.6
wp 31128.7
vs 279
sc 0
wc 250
hzmm 84.51
is 1e+05
rfl 6748.3
rfp 3973.7
th 7
ins 100.000
ln odc ph
^{13}C NMR (100 MHz; d_6-DMSO) of GSH-NAC
14
GSH-NAC
ppm

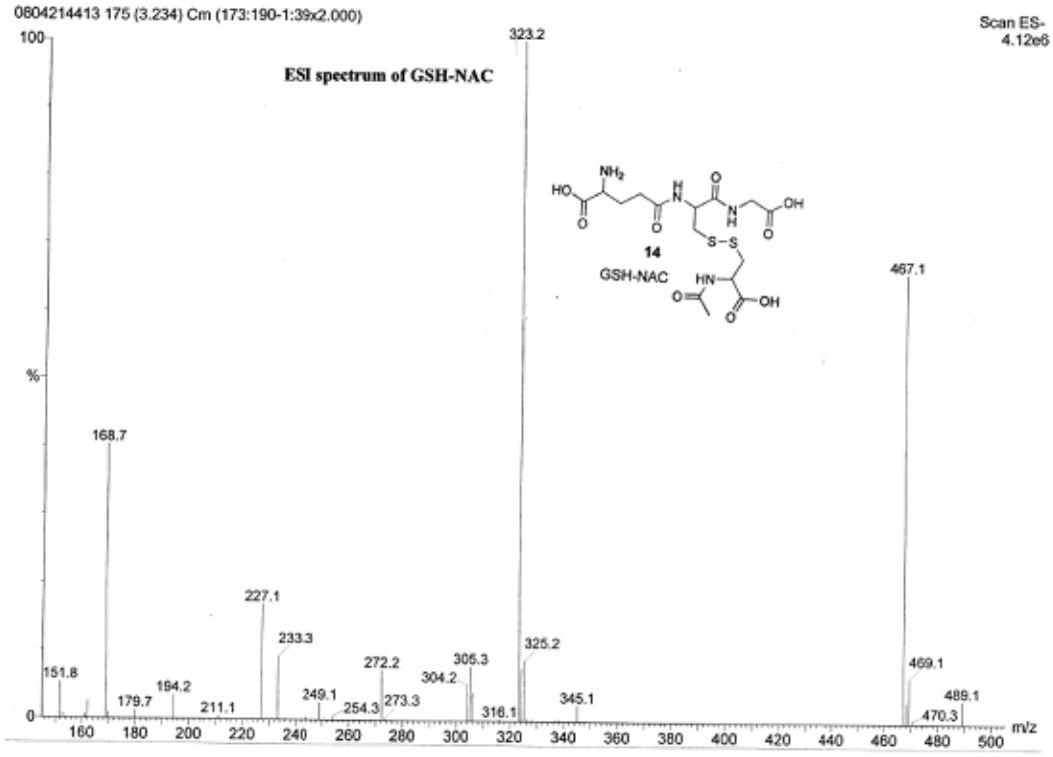

Preparation of PAMAM –CO-GS-S-NAC conjugate (3) (R-XI)

The anionic PAMAM-COOH generation-3.5 dendrimer (0.5 g, 0.043 mmol) was dissolved in DMSO/DMF (3:2, 20 mL) and DIEA (557 µL, 0.0059 mol) and PyBop (1.44 g, 0.0027 mol) were added and the reaction stirred for 1h. To this a solution of N-Acetyl-glutathione (**14**) (1.391 g, 0.0027 mol) was added in DMSO (10 mL) was stirred for 12 h at room temperature. The reaction was monitored with HPLC. After completion of reaction, it was diluted with water and lyophilized to get crude product. The solid crude product was diluted with water and dialyzed against DMSO followed by PBS (pH =7.4) to remove by-products and the excess of reactants and then replaced with deionized water for 12h to remove salts. The water was lyophilized get pure product in 78% yield .

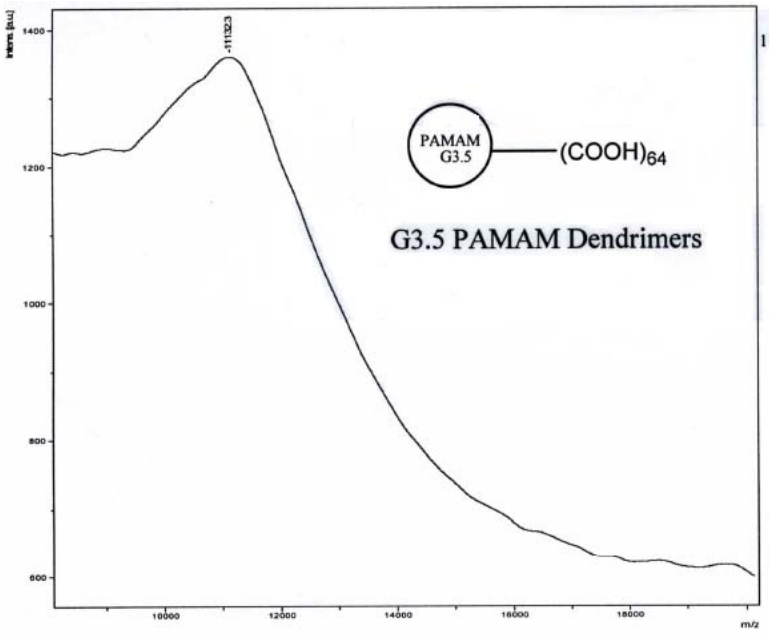

m/z	SN	Intens.	Area	Res.
11132.3	3083387.6	1359.82	7962503	4

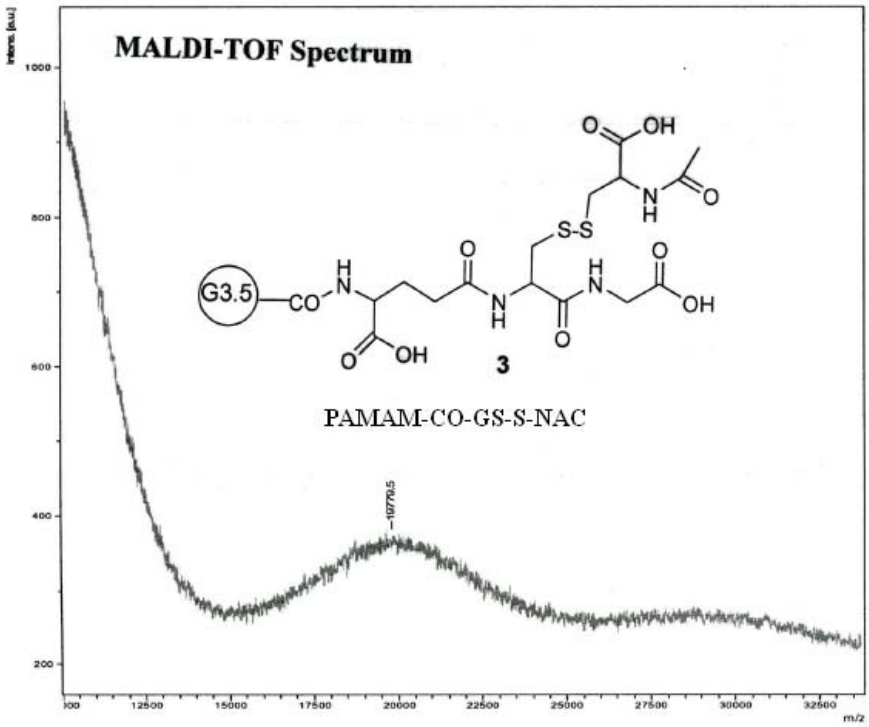

m/z	SN	Intens.	Area	Res.
19779.5	29.6	350.56	2159743	1

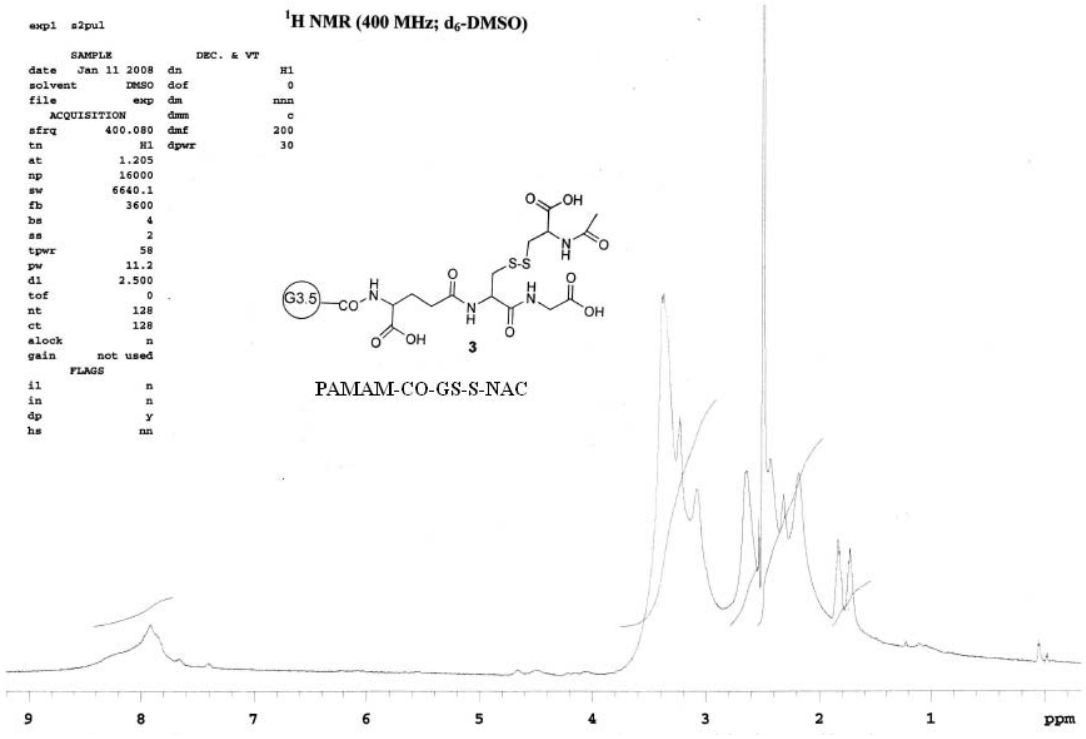

^{1}H NMR (400 MHz; d_6-DMSO)

Bioconjugate Chemistry 20th Anniversary

Subscriber access provided by SHEMYAKIN-OVCHINNIKOV INST

Article

Enhancement of Electrochemical Signal on Gold Electrodes by Polyvalent Esterase#Dendrimer Clusters

Martin Humenik, Christopher Po#hlmann, Yiran Wang, and Mathias Sprinzl

Bioconjugate Chem., **2008**, 19 (12), 2456-2461• DOI: 10.1021/bc800353z • Publication Date (Web): 19 November 2008

Downloaded from http://pubs.acs.org on May 2, 2009

More About This Article

Additional resources and features associated with this article are available within the HTML version:

- Supporting Information
- Access to high resolution figures
- Links to articles and content related to this article
- Copyright permission to reproduce figures and/or text from this article

View the Full Text HTML

ACS Publications
High quality. High impact.

Bioconjugate Chemistry is published by the American Chemical Society. 1155 Sixteenth Street N.W., Washington, DC 20036

Enhancement of Electrochemical Signal on Gold Electrodes by Polyvalent Esterase−Dendrimer Clusters

Martin Humenik, Christopher Pöhlmann, Yiran Wang, and Mathias Sprinzl*

Laboratorium für Biochemie, Universität Bayreuth, Universitätstrasse 30, 95440 Bayreuth, Germany. Received August 18, 2008; Revised Manuscript Received October 14, 2008

5′-Maleimide-oligodeoxynucleotide was conjugated with single sulfhydryl group of cystamine core poly(amidoamine) dendrimers of different generations. Amino groups on the dendrimer moiety were modified with maleimide and coupled to the cysteine 118 of esterase 2 from *Alicyclobacillus acidocaldarius* in a site-specific manner. Polyvalent esterase-dendrimer-oligodeoxynucleotide clusters were hybridized to capture oligodeoxynucleotides immobilized on a gold electrode. The amperometric signal of *p*-aminophenol was detected following the esterase-catalyzed hydrolysis of *p*-aminophenylbutyrate. The multiple anchoring of the esterase reporter via generation 3- and generation 5-derived clusters exhibited 10- and 100-fold signal enhancement, respectively, as compared to monovalent esterase−oligonucleotide conjugate. The polyvalent and monovalent reporters were comparable in their abilities regarding mismatch discrimination.

INTRODUCTION

Electrochemical sensors for the detection of DNA hybridization combine nucleic acid layers with electrochemical reporters to generate electrical signals. This type of sensors simplifies the data collection and makes it suitable for construction of portable DNA biosensors (*1, 2*). The improvement of biosensor sensitivity remains, however, a challenging task. Enhancement of the signal has been achieved by optimization of sensor design and performance of enzyme reporters. The physical optimization via minimization of the sensor surface (*3, 4*) and redox-recycling of electro-active substrate (*5, 6*) has improved detection limits dramatically. Nowadays, most frequently used reporter enzymes are alkaline phosphatase and horseradish peroxidase (*7*). The important task is to increase stability and specific activity of enzymes (*8, 9*), and to improve the quality of enzyme conjugation to the DNA hybridization event. Conjugation can be achieved either via interaction of streptavidin−enzyme and biotinylated ODN[1] (*6, 10*) or directly via covalently conjugated enzyme−ODN (*8, 11*).

We recently developed a sensitive enzyme−ODN reporter for electrochemical detection of DNA hybridization (*8*), which uses thermostable esterase 2 from *Alicyclobacillus acidocaldarius* (*12*) as a reporter enzyme. Single-chain esterase 2 provides the possibility for site-specific conjugation of the protein and ODN. EST−ODN conjugate with a 1:1 ratio of protein to oligonucleotide allowed the detection of attomoles of DNA (*8*). It is expected that the sensitivity of detection will be substantially improved if several reporter enzyme molecules are attached to one ODN. In the present study, we describe a site-specific chemistry for the preparation of ODN reporters equipped with multiply coupled esterase via dendrimer branching. We employed commercially available PAMAM dendrimers of generation 3 and generation 5 (Figure 1A), which differ in diameter, multivalency, and surface group density (*13, 14*). These polyvalent EST-dendrimer-ODN clusters were used in a DNA-directed immobilization assay on a gold electrode (Figure 1B). The capacity of signal enhancement and the ability of mismatch discrimination were determined and compared to monovalent EST−ODN conjugate (*8*).

MATERIALS AND METHODS

General. The organic bifunctional reagents sulfosuccinimidyl-4-(*N*-maleimidomethyl)cyclohexane-1-carboxylate and succinimidyl-[(*N*-maleimidopropionamido)-diethylene glycol] ester were purchased from Pierce (Rockford, IL, USA); G3 and G5 cystamine core PAMAM dendrimers and tris(2-carboxyethyl)phosphine were from Aldrich (Taufkirchen, Germany). 5′-Amino and 5′-sulfhydryl modified ODNs, equipped with C6 linker, were obtained from Biomers (Ulm, Germany). Biogel-P6 was from Biorad (München, Germany). SepPak C18 columns (Waters Corp., Eschborn, Germany) were used for desalting of oligonucleotides. Microcon YM10 centrifuge tubes (Millipore, Schwalbach, Germany) were used for desalting and concentration of dendrimer−ODN probes. Gel permeation chromatography was performed by using Pharmacia FPLC system on Sephacryl S-200 HR column (Pharmacia, Freiburg, Germany).

Preparation of Esterase 2 (C97S, E118C). Plasmid pET30a-EstC97S_E118C was derived from pT7-SCII-Est2 plasmid DNA (*12*) to replace Cys97 to Ser and Glu118 to Cys in esterase 2. The gene was expressed in *E. coli* BL21 (DE3). Esterase was purified according to published procedure (*12*) and stored at −20 °C in 100 mM Tris/HCl, pH 7.5, 20 mM $MgCl_2$, 200 mM KCl, 1 mM β-mercaptoethanol, and 50% glycerol. The esterase was dialyzed against 0.1 M Na-Pi, pH 7.2, before conjugation with oligonucleotides.

5′-Maleimide-ODN. 5′-Amino-modified ODN (50 nmol) in 0.1 M Na-Pi, pH 8.0, (100 μL) was treated with sulfo-SMCC (2.5 μmol, 50 μL in DMF). The reaction mixture was left at RT for 1 h and the 5′-maleimide-ODN was precipitated with ethanol and isolated by centrifugation. The pellet was dissolved in 0.1 M Na-Pi buffer, pH 7.4, (500 μL) and desalted on a Biogel P6 column. The procedure yielded typically 90% of 5′-

* Author to whom correspondence should be addressed. Fax: +49-921-55-2066; e-mail: mathias.sprinzl@uni-bayreuth.de.

[1]Abbreviations: EST, esterase 2 (C97S, E118C); G3/G5, generation 3/generation 5; FPLC, fast protein liquid chromatography; ODN, oligodeoxynucleotide; PAGE, polyacrylamide gel electrophoresis; PAMAM, poly(amidoamine) dendrimer; sulfo-SMCC, sulfosuccinimidyl-4-(*N*-maleimidomethyl)cyclohexane-1-carboxylate; SMEG, succinimidyl-[(*N*-maleimidopropionamido) diethylene glycol]; TCEP, tris(2-carboxyethyl)phosphine.

10.1021/bc800353z CCC: $40.75 © 2008 American Chemical Society
Published on Web 11/19/2008

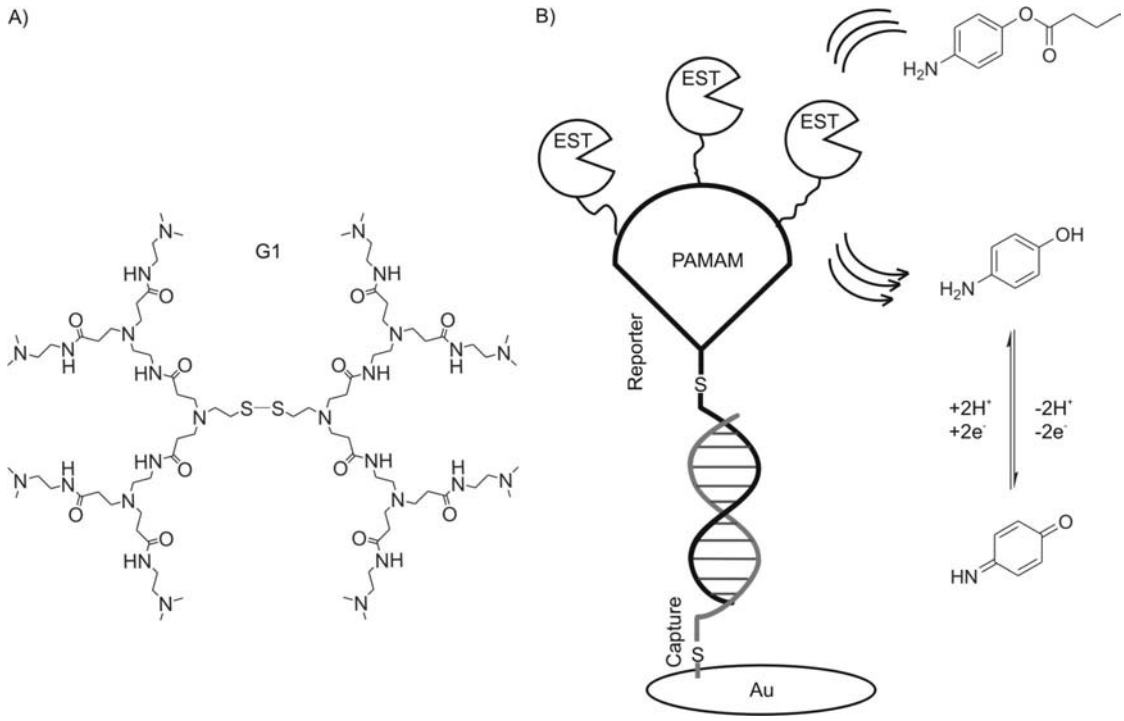

Figure 1. (A) Structure of the PAMAM containing a cystamine core (for simplicity, only the branching of G1 dendrimer is depicted). (B) Principle of the signal enhancement on a gold electrode; multivalent attachment of esterase 2 to ODN via PAMAM increases the amount of reporter enzyme per hybridization event in the vicinity of particular electrode.

maleimide-ODN as determined by A_{260} absorption. The purity and identity of the product were analyzed by HPLC and MALDI-TOF (Supporting Information).

Dendrimers−ODN Conjugates. Dendrimer G3 (100 nmol, 7.7 μL, in methanol) was added into triethylamine solution in DMF (25 μL, 123 mM) followed by solution of acetic anhydride in DMF (25 μL, 93 mM). The reaction mixture was left at RT for 2 h and used without purification for next steps. The acetylation of G5 PAMAM was performed under similar conditions, where 100 nmol of dendrimers (33.6 μL in methanol) was diluted with DMF to the end volume of 100 μL and treated with 0.9 μL of acetic anhydride (9.5 μmol) and 1.5 μL of triethylamine (11.5 μmol). The reaction mixture of acetylated dendrimer was then diluted with 3 volumes of buffer (50 mM Na-Pi, 150 mM NaCl, 5 mM EDTA, pH 6.3) treated by 1 μmol of TCEP (100 mM solution in the same buffer), followed by incubation at 37 °C for 1 h. The freshly prepared reaction mixture of sulfhydryl-activated dendrimer was combined with 100 nmol of 5′-maleimide-ODN (40 μM in 50 mM Na-Pi, 150 mM NaCl, 5 mM EDTA, pH 6.3). The reaction mixture was left at RT for 1 h and subsequently filtered through YM10 centrifuge tubes. The retained product was washed twice with 0.1 M Na-Pi buffer, pH 8.0, and collected in the same. Typically, 70% yield was obtained for dendrimer−ODN conjugates of generations 3 and 5. The reaction course was followed by urea-PAGE and HPLC. Product was characterized by MALDI-TOF (Supporting Information).

Maleimide Activation of Dendrimer−ODN Conjugates. Dendrimer−ODN conjugates in 0.1 M Na-Pi, pH 8.0, (15 nmol, 150 μL) were treated with bifunctional reagent SMEG (4.5 μmol, 90 μL in DMF) at RT for 1 h. Excess of the reagent was removed by a Biogel-P6 column affording 50% of maleimide-dendrimer-ODN of generation 3. G5-derived conjugate was isolated by 4× repeated filtration in YM10 centrifuge tubes against 50 mM Na-Pi, 150 mM NaCl, 5 mM EDTA, pH 6.3, yielding typically 70% maleimide-dendrimer-ODN conjugate.

Preparation of EST-Dendrimer-ODN Cluster. Esterase 2 (C97S, E118C) in 0.1 M Na-Pi buffer, pH 7.2, (70 μM) was treated with 1.4 mM TCEP at 37 °C for 30 min and isolated by filtration in YM10 centrifuge tubes removing TCEP. The esterase was collected in 50 mM Na-Pi, 150 mM NaCl, 5 mM EDTA, pH 6.3, and 360 μL of the protein solution (0.2 mM) was treated with G3 maleimide-dendrimer-ODN conjugate (0.1 mM, 90 μL in the same buffer) at 37 °C for 16 h. Product was purified by gel permeation chromatography on Sephacryl S-200 HR column (2 × 70 cm), eluted with 10 mM Tris/HCl, 10 mM KCl, pH 7.5, at a flow rate of 1 mL/min. The main peak of the product was collected (10−12 mL), concentrated under vacuum to one-fifth of the volume, and reloaded on the same column for the second round of chromatography.

Electrochemical Detection on Gold Electrodes. Chip modules and potentiostat were obtained from Siemens Corporate Technology (Erlangen, Germany). Each chip (11 mm × 13 mm) consisted of 8 individual 0.85-mm-diameter (0.6 mm^2) gold electrodes with spaces of 2.0 mm between the positions. Four electrodes were treated with a silver/silver chloride solution and served as reference electrodes. For measurements, a U-shaped 10 μL flow chamber was placed over the electrodes, and the printed circuit board of the chip was connected to the multi-potentiostat device. The potentiostat was connected to a PC through a serial interface SCB-68. *Labview 6.0* software was used to control the potentiostat, collect the data, and plot figures.

Immobilization of DNA on Gold Electrodes. The gold electrodes were rinsed with water and ethanol, and dried under air stream. The thiol group of the capture ODN (0.2 μM) was first reduced by treatment with 2 mM TCEP in 10 mM Na-Pi, 300 mM NaCl, pH 7.0, at 37 °C for 5 min. Activated capture ODN (1 μL) was spotted onto electrodes and incubated at ambient temperature in a humidity chamber for 16 h. Individual electrodes were washed three times with the same buffer. The sequences of the used capture ODNs are listed in Table 1S (Supporting Information).

EST Activity Measurements on the Gold Electrodes. Detection limits were estimated by serial dilution of EST−ODN conjugate or EST-dendrimer-ODN clusters in 20 mM Na-Pi, 300 mM NaCl, 2 mM EDTA, 0.05% Tween 20, 1 mg/mL BSA,

Table 1. Apparent Michaelis−Menten Constants Obtained from the Kinetic Measurement of Esterase Reporter Immobilized via Hybridization of Corresponding ODN Conjugate or Dendrimer−ODN Cluster on the Gold Electrode

	EST−ODN	EST-dendrimer-ODN	
		G3	G5
K_M^{app} [mM]	0.7 ± 0.1	0.9 ± 0.1	1.1 ± 0.4
I_{max} [nA s^{-1}]	6.6 ± 1.8	31.7 ± 3.6	57.8 ± 12.6
k_{cat} [nA s^{-1} nM^{-1}]	1.3 ± 0.3	6.3 ± 0.7	11.5 ± 2.5

pH 7.4. Different concentration of EST conjugates (1 μL) was applied onto each electrode equipped with immobilized perfect match capture ODN and incubated at 25 °C for 20 min. The electrodes were washed three times with 100 μL of 5 mM Na-Pi, 75 mM NaCl, 0.5 mM EDTA, 0.05% Tween 20, pH 7.4. The same experimental procedure was used for mismatch determination. Different capture ODNs comprising 1 to 3 mismatches were used. After hybridization at 50 °C and washing steps, the chip was placed into a potentiostat and 1 mM substrate, *p*-aminophenylbutyrate, in 0.1 M Na-Pi, pH 7.0, was pumped through a flow chamber at flow rate of 50 μL/min for 1 min. The flow was stopped and the current slope was measured to assay the EST activity (*8*).

Measurement of enzyme kinetics was conducted by using EST−ODN conjugate and EST-dendrimer-ODN clusters (5 nM) to hybridize with perfect match capture ODN on gold electrodes. Different concentrations of *p*-aminophenylbutyrate in 0.1 M Na-Pi, pH 7.0, were delivered over gold electrodes, and signal was recorded as described above.

RESULTS AND DISCUSSION

Preparation and Characterization of EST-Dendrimer-ODN Clusters. Primary amino groups on the surface of G3 and G5 PAMAM cystamine core dendrimers (*14*) had to be partially acetylated (*15*) to prevent the unspecific binding of the positively charged dendrimers to oligonucleotide polyanion. Approximately 60% acetylation ratio, estimated by MALDI-TOF (Supporting Information, Figures 3S and 4S), was found as an optimal shield of positive charge on the dendrimer surface and at the same time provides sufficient amount of free amino groups for further multiple EST coupling. The partially acetylated dendrimers were reduced and conjugated to 5′-maleimide-ODN (*16*). Bifunctional linker sulfo-SMCC was used to activate 5′-amino-ODN for monovalent conjugation as previously described (*8*). The free amino groups on the surface of dendrimer−ODN conjugate allow further modification with a maleimide linker. Multiple binding of nonpolar linkers such like SMCC decreases the solubility in aqueous environment. Therefore, ethylene glycol linker SMEG, which provides both better solubility and spacing between dendrimer and protein surface, was used. The formation of dendrimer products with different extent of maleimide activation was evident from smear on urea-PAGE and from peak broadening on HPLC (Supporting Information, Figures 1S and 2S). MALDI-TOF spectra also revealed broad molecular peaks, typical for dendrimers (*17, 18*) and dendrimer−ODN conjugates (*16*) and did not allow precise molecular mass determination of the product (Supporting Information, Figures 3S and 4S).

The wild-type esterase 2 contains only one cysteine at position 97, which is buried inside the structure and is not accessible for modification (*19*). Thus, replacements of cysteine 97 by serine and glutamine 118 by cysteine were performed to expose a reactive sulfhydryl group on the protein surface. EST-dendrimer-ODN clusters (Figure 2) were prepared by reaction of 8- and 16-fold excess of EST with maleimide-activated dendrimer−ODN of generations 3 and 5, respectively. Statistical mixtures of clusters (Figure 3A,B, lane 1), as reported also for other protein−dendrimer conjugates (*20, 21*), were obtained. The higher molecular mass clusters were separated from unreacted esterase and dendrimer−ODN conjugate by gel permeation chromatography on Sephacryl S 200 HR (Figure 3A,B). Monovalent EST−ODN conjugate was also prepared and purified as described (*8*).

The relative protein content of the purified clusters was determined from absorbance ratio at 260 and 280 nm, defined as

$$\frac{A_{260}}{A_{280}} = \frac{\varepsilon_p^{260} c_p + \varepsilon_o^{260} c_o}{\varepsilon_p^{280} c_p + \varepsilon_o^{280} c_o} \quad (1)$$

where A is absorbance at 260 or 280 nm and ε represents extinction coefficient, while c_p and c_o represent the concentration of protein and ODN, respectively. Experimental A_{260} and A_{280} values from different mixtures of esterase 2 and 5′-amino-modified ODN (from 0:1 to 18:1) were fitted to a hyperbolic curve (Figure 4). The resulting calibration curve allowed us to deduce the composition of the G3 cluster (7:1) and the G5 cluster (10:1). G3 and G5 PAMAMs significantly differ in the number of surface amino groups (4-fold) (*14*), whereas the observed loading difference between G3 and G5 dendrimer−ODN with the esterase was less than 2-fold. The different reactivities of smaller G3 and larger G5 maleimide-dendrimer-ODN conjugate toward bulky protein are probably reasons for observed deviations.

The amount of the esterase anchored on the gold electrode via hybridization between capture ODN and either monovalent EST−ODN conjugate or polyvalent G3/G5 clusters (Figure 1B) was tested. The intensities of the electrical signal in the presence of varied concentrations of *p*-aminophenylbutyrate were measured. Apparent kinetic parameters (Table 1) were calculated from the electrochemical version of the Lineweaver−Burk equation (eq 2) (*22*).

$$\frac{1}{I_{slope}} = \frac{K_M^{app}}{I_{max}} \times \frac{1}{[S]} + \frac{1}{I_{max}} \quad (2)$$

The apparent Michaelis−Menten constant (K_M^{app}) is a reflection of both the enzymatic affinity and the ratio of microscopic constants including diffusion of the product to the electrode surface. I_{slope} represents the increase of the current after the addition of substrate (this value was determined the first 5 s in stopped flow mode (*8*)), [S] is the bulk concentration of substrate, and I_{max} is the maximum current measured under substrate saturation. Different values of current slope against substrate concentration, with obvious similarity to Michaelis−Menten kinetics (Supporting Information, Figure 5S), were observed using 5 nM EST−ODN, G3 and G5 EST-dendrimer-ODN clusters. With the G3 and G5 clusters, the increase in maximal current I_{max} (Table 1) demonstrates that more esterase is brought to the electrode surface by a hybridization event if compared with monovalent EST−ODN. Additionally, catalytic efficiency k_{cat} corresponds with EST/ODN ratio obtained from the A_{260}/A_{280} dependence depicted in Figure 4.

Signal Enhancement on Gold Electrodes Using Multivalent EST-Dendrimer-ODN Clusters. The influence of polyvalent G3 and G5 EST-dendrimer-ODN clusters on signal enhancement was compared with monovalent EST−ODN conjugate (*8*). Different concentrations of EST bound ODN probes were assayed on the gold electrodes uniformly modified with perfectly matched capture ODN and resulted in linear dependences in all experiments (Figure 5). The lowest detectable ODN concentration using the EST−ODN conjugate was 3 pM, which is in agreement with results reported previously (*8*). The G3 and G5 EST-dendrimer-ODN clusters revealed upon the same experimental arrangement the lowest detectable target

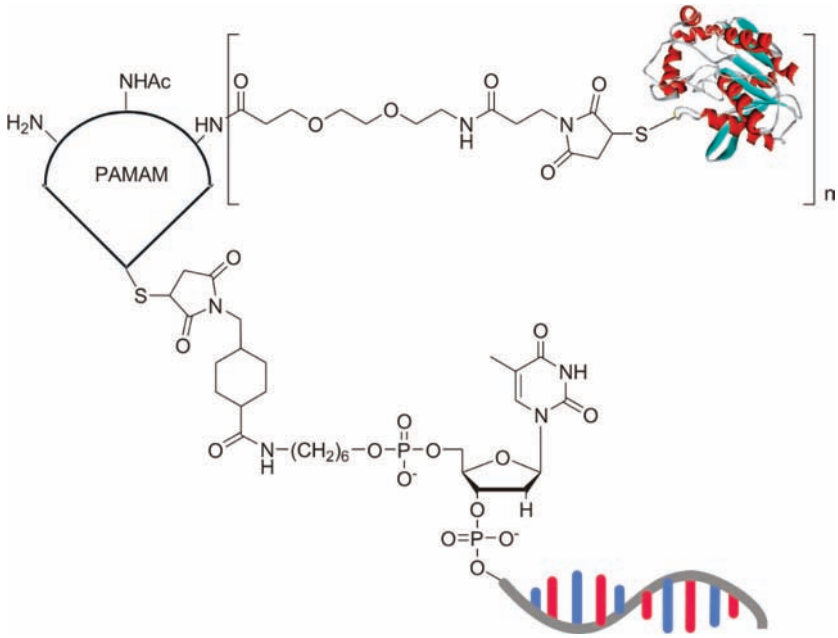

Figure 2. Schematic representation of esterase-dendrimer-ODN cluster. SMCC linker connects ODN and sulfhydryl group of PAMAM. Esterase is attached to the dendrimer surface via ethylene glycol linker in a site-specific manner (Cys118).

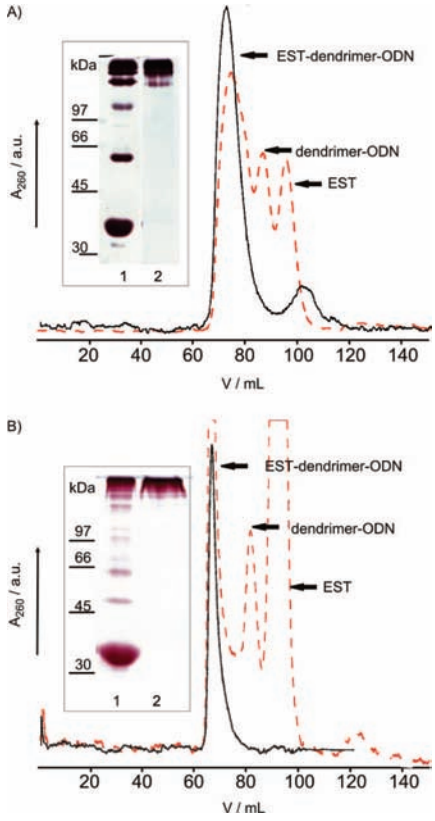

Figure 3. Purification of the EST-dendrimer-ODN cluster by gel permeation chromatography on Sephacryl 200 HR; clusters derived from G3 (A) and G5 PAMAM (B) were eluted in the void volume of the column. First (- -) and second (—) round of purification are presented. Inserts show 10% SDS-PAGE of crude reaction products (lane 1) and purified clusters (lane 2) after second round of gel permeation chromatography.

concentrations of 0.3 pM (Figure 5A) and 0.02 pM (Figure 5B), respectively. Strong enhancement of the signal were achieved at low concentrations of clusters (<10 pM), whereas at concentrations of >10 nM, no signal enhancement was observed. It is conceivable that at higher concentrations the

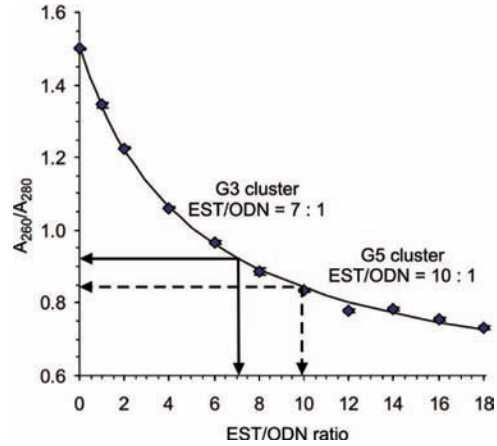

Figure 4. Estimation of the molecular EST/ODN ratio for EST-dendrimer-ODN cluster derived from G3 and G5 PAMAM; UV absorption was recorded at 260 and 280 nm for different mixtures of esterase 2 and 5′-amino-ODN (◆). The data were fitted to the hyperbolic plot (—). UV absorption of G3 (full line with arrows) and G5 cluster (dashed line with arrows) correspond to EST/ODN ratio 7:1 and 10:1, respectively.

advantage of the multiple esterase attachment was compromised by a large hydrodynamic volume of polyvalent EST−dendrimer moiety. On the other hand, at lower concentration levels, where most of the capture ODNs became unoccupied, the multiple enzyme binding significantly enhanced the signal. G3 and G5 clusters have comparable protein content (Figure 4), whereas diameters and corresponding areas of dendrimers differ significantly (4× and 8×, respectively) (*14*). Apparently, the dense protein loading of the G3 dendrimer surface may alter proper protein folding and substrate accessibility/diffusion summed in observed enzyme activity. Thus, G3 and G5 EST-dendrimer-ODN clusters differ by 10× in their signal enhancement abilities. The controlled spotting of G3 and G5 clusters either onto a bare gold electrode or onto an electrode layered with non-matched capture ODN excluded any possible unspecific binding of higher PAMAMs onto the gold surface (*23*) or to capture oligonucleotides (*24*).

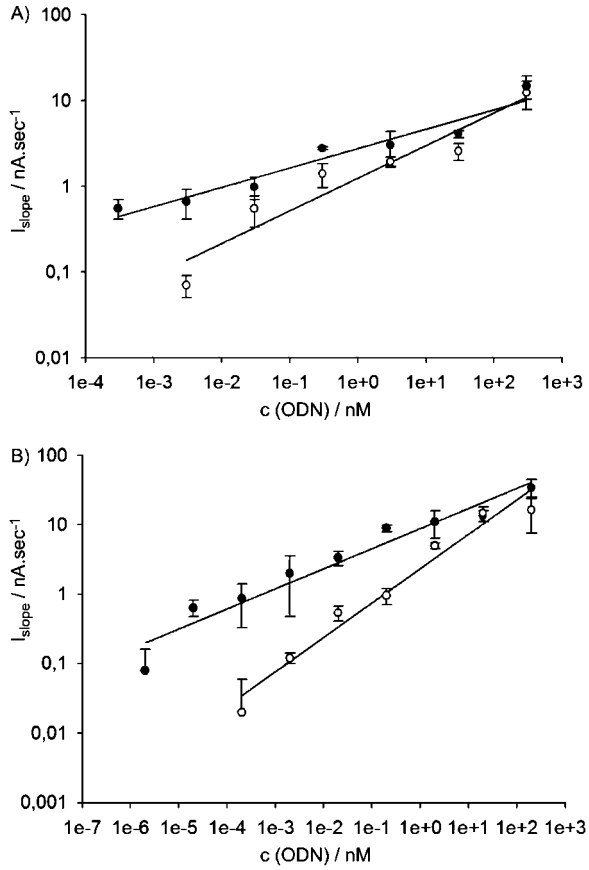

Figure 5. Detection of DNA hybridization on the gold electrodes equipped with uniform capture ODN. (A) Correlation of the signal with ODN concentration of G3 EST-dendrimer-ODN clusterd (•) and monovalent EST−ODN conjugate (○). (B) Analogous comparison for the G5 cluster.

Specificity of DNA hybridization and mismatch detection are important parameters of DNA analysis on biosensors. In order to test these parameters, gold electrodes were prepared with immobilized capture ODNs resulting in a perfect match and one, two, and three mismatched base pairs. The EST−ODN conjugate and EST-dendrimer-ODN clusters were then hybridized to these immobilized capture ODNs. Monovalent EST−ODN and polyvalent G3 and G5 clusters distinguished the perfect from the mismatched probes (Figure 6). The discrimination efficiency increased with the number of the nonmatched base pairs when EST−ODN and G3 clusters were assayed. However, the G5 cluster was not able to discriminate among the numbers of mismatches as efficiently as the G3 cluster.

CONCLUSION

In summary, we prepared EST-dendrimer-ODN clusters derived from G3 and G5 cystamine core PAMAM dendrimers. Efficient sulfhydryl−maleimide chemistry to connect ODN and dendrimer, which was polyvalently functionalized with esterase 2, was exploited. Although mutivalency of dendrimers was already applied in the construction of protein (*20*, *21*, *25*−*27*) and ODN (*16*, *28*, *29*) nanoscale devices, according to our knowledge the synthesis of polyvalent enzyme-dendrimer-ODN clusters had not yet been reported. DNA-directed hybridization of the presented polyvalent clusters on gold electrodes revealed 10- and 100-fold shifts of the detection limit to lower concentrations if compared among G3 and G5 clusters and monovalent EST−ODN conjugate (*8*). Hence, the multivalent binding of esterase to capture ODN resulted in detection limits of 3×10^{-13} M and 2×10^{-14} M for G3 and G5 dendrimer clusters, respectively. These detection limits are comparable with alternative methods of electrochemical DNA detection, which use horseradish peroxidase bound liposomes (*30*), ferrocene multiple labeling of gold nanoparticles (*31*), and cyclic DNA probes (*32*). The simple and efficient preparation and fairly improved detection limits emphasize the potential of the presented esterase 2-dendrimer-ODN construct in electrochemical detection of DNA.

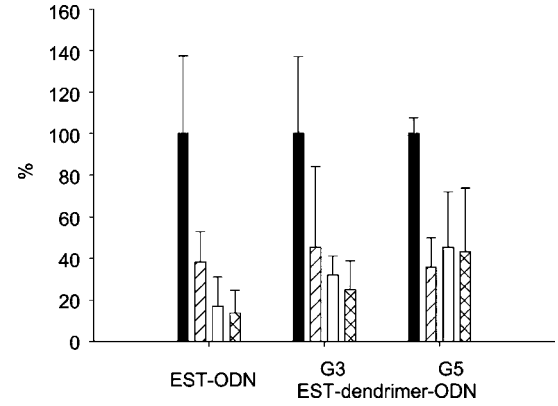

Figure 6. Mismatch discrimination ability of the EST−ODN conjugate and G3 and G5 clusters compared in the amperometric detection of immobilized capture probes. Perfectly matched capture and one, two, and three mismatches are presented as black, dashed, open, and crossed bars, respectively; the signal values for perfectly matched capture was set as 100%.

ACKNOWLEDGMENT

This work was supported by the Forschungskreis der Ernährungsindustrie, AiF 230 ZN.

Supporting Information Available: Figures 1S-5S and Table 1S as described in the text. This material is available free of charge via the Internet at http://pubs.acs.org.

LITERATURE CITED

(1) Drummond, T. G., Hill, M. G., and Barton, J. K. (2003) Electrochemical DNA sensors. *Nat. Biotechnol. 21*, 1192–1199.
(2) Sassolas, A., Leca-Bouvier, B. D., and Blum, L. J. (2008) DNA biosensors and microarrays. *Chem. Rev. 108*, 109–139.
(3) Paeschke, M., Wollenberger, U., Kohler, C., Lisec, T., Schnakenberg, U., and Hintsche, R. (1995) Properties of interdigital electrode arrays with different geometries. *Anal. Chim. Acta 305*, 126–136.
(4) Zhang, Y., Kim, H. H., and Heller, A. (2003) Enzyme-amplified amperometric detection of 3000 copies of DNA in a 10-microL droplet at 0.5 fM concentration. *Anal. Chem. 75*, 3267–3269.
(5) Niwa, O., Morita, M., and Tabei, H. (1990) Electrochemical-behavior of reversible redox species at interdigitated array electrodes with different geometries - consideration of redox cycling and collection efficiency. *Anal. Chem. 62*, 447–452.
(6) Nebling, E., Grunwald, T., Albers, J., Schafer, P., and Hintsche, R. (2004) Electrical detection of viral DNA using ultramicroelectrode arrays. *Anal. Chem. 76*, 689–696.
(7) Bakker, E. (2004) Electrochemical sensors. *Anal. Chem. 76*, 3285–3298.
(8) Wang, Y., Stanzel, M., Gumbrecht, W., Humenik, M., and Sprinzl, M. (2007) Esterase 2-oligodeoxynucleotide conjugates as sensitive reporter for electrochemical detection of nucleic acid hybridization. *Biosens. Bioelectron. 22*, 1798–1806.
(9) Zhang, Y., Pothukuchy, A., Shin, W., Kim, Y., and Heller, A. (2004) Detection of approximately 10(3) copies of DNA by an electrochemical enzyme-amplified sandwich assay with ambient O(2) as the substrate. *Anal. Chem. 76*, 4093–4097.

(10) Hwang, S., Kim, E., and Kwak, J. (2005) Electrochemical detection of DNA hybridization using biometallization. *Anal. Chem. 77*, 579–584.
(11) Caruana, D. J., and Heller, A. (1999) Enzyme-amplified amperometric detection of hybridization and of a single base pair mutation in an 18-base oligonucleotide on a 7-μm-diameter microelectrode. *J. Am. Chem. Soc. 121*, 769–774.
(12) Manco, G., Adinolfi, E., Pisani, F. M., Ottolina, G., Carrea, G., and Rossi, M. (1998) Overexpression and properties of a new thermophilic and thermostable esterase from *Bacillus acidocaldarius* with sequence similarity to hormone-sensitive lipase subfamily. *Biochem. J. 332*, 203–212.
(13) Svenson, S., and Tomalia, D. A. (2005) Dendrimers in biomedical applications-reflections on the field. *Adv. Drug Delivery Rev. 57*, 2106–2129.
(14) Tomalia, D. A., Huang, B., Swanson, D. R., Brothers, H. M., and Klimash, J. W. (2003) Structure control within poly(amidoamine) dendrimers: size, shape and regio-chemical mimicry of globular proteins. *Tetrahedron 59*, 3799–3813.
(15) Majoros, I. J., Keszler, B., Woehler, S., Bull, T., and Baker, J. R. (2003) Acetylation of poly(amidoamine) dendrimers. *Macromolecules 36*, 5526–5529.
(16) DeMattei, C. R., Huang, B. H., and Tomalia, D. A. (2004) Designed dendrimer syntheses by self-assembly of single-site, ssDNA functionalized dendrons. *Nano Lett. 4*, 771–777.
(17) Shi, X. Y., Lesniak, W., Islam, M. T., Muniz, M. C., Balogh, L. P., and Baker, J. R. (2006) Comprehensive characterization of surface-functionalized poly (amidoamine) dendrimers with acetamide, hydroxyl, and carboxyl groups. *Colloids Surf., A 272*, 139–150.
(18) Lesniak, W. G., Kariapper, M. S. T., Nair, B. M., Tan, W., Hutson, A., Balogh, L. P., and Khan, M. K. (2007) Synthesis and characterization of PAMAM dendrimer-based multifunctional nanodevices for targeting alpha(v)beta(3) integrins. *Bioconjugate Chem. 18*, 1148–1154.
(19) De Simone, G., Galdiero, S., Manco, G., Lang, D., Rossi, M., and Pedone, C. (2000) A snapshot of a transition state analogue of a novel thermophilic esterase belonging to the subfamily of mammalian hormone-sensitive lipase. *J. Mol. Biol. 303*, 761–771.
(20) Kluger, R., and Zhang, J. (2003) Hemoglobin dendrimers: Functional protein clusters. *J. Am. Chem. Soc. 125*, 6070–6071.
(21) van, B. I., Malda, H., Synowsky, S. A., van Dongen, J. L., Hackeng, T. M., Merkx, M., and Meijer, E. W. (2005) Multivalent peptide and protein dendrimers using native chemical ligation. *Angew. Chem., Int. Ed. 44*, 5052–5057.
(22) Kamin, R. A., and Wilson, G. S. (1980) Rotating-ring-disk enzyme electrode for biocatalysis kinetic-studies and characterization of the immobilized enzyme layer. *Anal. Chem. 52*, 1198–1205.
(23) Rahman, K. M. A., Durning, C. J., Turro, N. J., and Tomalia, D. A. (2000) Adsorption of poly(amidoamine) dendrimers on gold. *Langmuir 16*, 10154–10160.
(24) Bielinska, A. U., Kukowska-Latallo, J. F., and Baker, J. R. (1997) The interaction of plasmid DNA with polyamidoamine dendrimers: mechanism of complex formation and analysis of alterations induced in nuclease sensitivity and transcriptional activity of the complexed DNA. *Biochim. Biophys. Acta, Gene Struct. Exp. 1353*, 180–190.
(25) Fischer-Durand, N., Salmain, M., Rudolf, B., Juge, L., Guerineau, V., Laprevote, O., Vessieres, A., and Jaouen, G. (2007) Design of a new multifunctionalized PAMAM dendrimer with hydrazide-terminated spacer arm suitable for metal-carbonyl multilabeling of aldehyde-containing molecules. *Macromolecules 40*, 8568–8575.
(26) Patri, A. K., Myc, A., Beals, J., Thomas, T. P., Bander, N. H., and Baker, J. R. (2004) Synthesis and in vitro testing of J591 antibody-dendrimer conjugates for targeted prostate cancer therapy. *Bioconjugate Chem. 15*, 1174–1181.
(27) Wu, G., Barth, R. F., Yang, W. L., Chatterjee, M., Tjarks, W., Ciesielski, M. J., and Fenstermaker, R. A. (2004) Site-specific conjugation of boron-containing dendrimers to anti-EGF receptor monoclonal antibody cetuximab (IMC-C225) and its evaluation as a potential delivery agent for neutron capture therapy. *Bioconjugate Chem. 15*, 185–194.
(28) Choi, Y. S., Mecke, A., Orr, B. G., Holl, M. M. B., and Baker, J. R. (2004) DNA-directed synthesis of generation 7 and 5 PAMAM dendrimer nanoclusters. *Nano Lett. 4*, 391–397.
(29) Choi, Y., Thomas, T., Kotlyar, A., Islam, M. T., and Baker, J. R. (2005) Synthesis and functional evaluation of DNA-assembled polyamidoamine dendrimer clusters for cancer cell-specific targeting. *Chem. Biol. 12*, 35–43.
(30) Alfonta, L., Singh, A. K., and Willner, I. (2001) Liposomes labeled with biotin and horseradish peroxidase: a probe for the enhanced amplification of antigen-antibody or oligonucleotide--DNA sensing processes by the precipitation of an insoluble product on electrodes. *Anal. Chem. 73*, 91–102.
(31) Wang, J., Li, J., Baca, A. J., Hu, J., Zhou, F., Yan, W., and Pang, D. W. (2003) Amplified voltammetric detection of DNA hybridization via oxidation of ferrocene caps on gold nanoparticle/streptavidin conjugates. *Anal. Chem. 75*, 3941–3945.
(32) Patolsky, F., Weizmann, Y., and Willner, I. (2002) Redox-active nucleic-acid replica for the amplified bioelectrocatalytic detection of viral DNA. *J. Am. Chem. Soc. 124*, 770–772.

BC800353Z

SUPPORTING INFORMATION

Enhancement of Electrochemical Signal on Gold Electrodes by Polyvalent Esterase-Dendrimer Clusters

Martin Humenik, Christopher Pöhlmann, Yiran Wang, Mathias Sprinzl*

Laboratorium für Biochemie, Universität Bayreuth, Universitätstrasse 30, 95440 Bayreuth, Germany

*Author to whom correspondence should be addressed. Fax: +49-921-55-2432; e-mail: mathias.sprinzl@uni-bayreuth.de

PAGE analysis of G3 and G5 dendrimers and related ODN conjugates

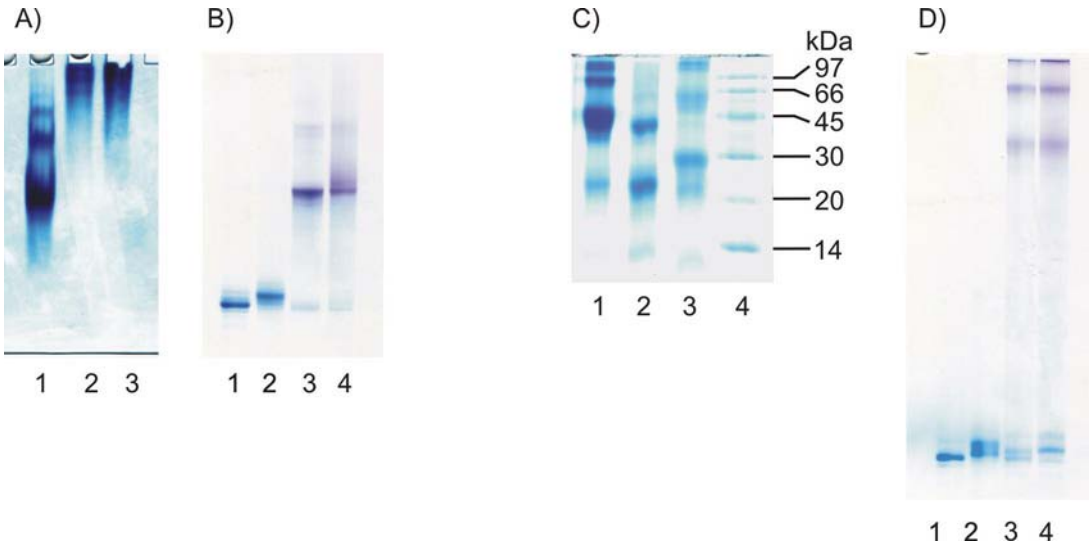

Figure 1S.: PAGE analysis of G3/G5 dendrimer-ODN preparations; A) Native PAGE (15%) of the G3 dendrimer acetylation; lane 1: G3 PAMAM dendrimer; lane 2: preparation of acetylated analog; lane 3: reduction of cystamine core of dendrimer by TCEP; B) Urea-PAGE (15%) of G3-ODN conjugation; lane 1: 5´-amino-ODN; lane 2: 5´-maleimide-ODN; lane 3: G3-ODN; lane 4: maleimide-G3-ODN; C) SDS-PAGE (20%) of G5 acetylated dendrimers and dendrimer-ODN conjugate; lane 1: acetylated dendrimer; lane 2: reduction of cystamine core of dendrimer by TCEP; lane 3: G5-ODN conjugate; lane 4: protein mass standard: D) Urea-PAGE analysis of G5 dendrimer ODN conjugation; lane 1 and lane 2 identical with B; lane 3 and lane 4 analogous to B in terms of G5 conjugation. Generally main band of the G3/G5 dendrimer (A and C, lane 1) is accompanied by trailing generation (half of molecular mass) and by oligomers originated from PAMAM synthesis (*S1*).

HPLC analysis of 5´-modiefied ODNs and dendrimer-ODN conjugates

High-pressure liquid chromatography was carried out on Beckman Gold HPLC system (Beckman Coulter GmbH, Krefeld, Germany) with variable-wavelength detector. Oligonucleotide conjugates were analyzed by reverse phase chromatography on Jupiter C-18 column (250×4.6 mm, 5 µm, Phenomenex, Aschaffenburg, Germany). Buffer A contained 0.01 M triethylammoniumacetate (TEAA) in water, pH = 6.8, buffer B contained 0.01 M TEAA in water, pH = 6.8 and 90% of CH_3CN. Elution was performed by gradient of B 5-50% over 30 min. Flow rate was 1 ml/min, detection by absorbance at 260 nm. Alternatively, ODN-dendrimer conjugates were analyzed by Gemini C6-Phenyl column (250×4.6 mm, 5 µm, Phenomenex, Aschaffenburg, Germany). Buffer A contained 0.1% TFA in water, buffer B contained 0.1% TFA in water and 90% of CH_3CN. Elution was performed by a gradient of B 0-50% over 30 min.

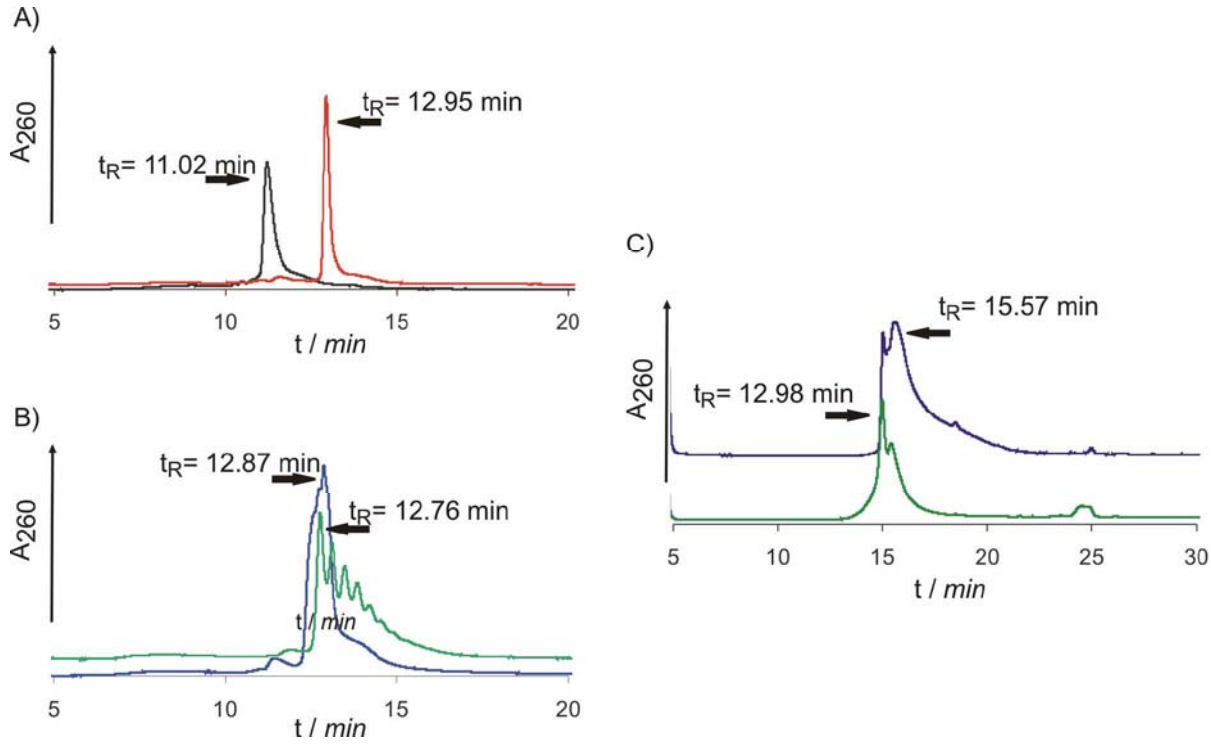

Figure 2S.: HPLC analysis of G3/G5 dendrimer ODN conjugation: A) 5´-amino-ODN, t_R = 11.02 min and 5´-maleimide-ODN, t_R = 12,95 min; B) G3-ODN, t_R = 12.87 min and maleimide-G3-ODN, $t_R \geq$ 12.76 min; A and B analyzed by C18 column and TEAA/CH_3CN elution buffer; C) G5-ODN, t_R = 12.98 min and maleimide-G5-ODN, $t_R \geq$ 15.57 min; analyzed by C6-Phenyl column and 0.1%TFA/H_2O/CH_3CN elution buffer.

Although, PAMAM dendrimers are protein like polyamides, it should be mentioned that G3 dendrimer-ODN conjugate was likely detectable under ODN like conditions (Urea-PAGE and HPLC on C18 reverse phase column and triethylammonium acetate / acetonitril system). However, G5 dendrimer-ODN conjugate, where dendrimer became a prevalent structural moiety, was better

analyzable under protein like conditions (SDS-PAGE and HPLC on C6 reverse phase colmn and 0.1 % TFA / H_2O / acetonitryl system).

MALDI-TOF analysis of ODNs, dendrimers and their conjugation products

MALDI-TOF mass spectrometry was performed on a Bruker Reflex III equipped with a 337 nm N_2 laser in the linear mode and 20 kV acceleration voltage.

Purchased G3 and G5 PAMAM dendrimers were diluted with MeOH to end concentration of 1 mM and reaction mixtures of acetylated dendrimers respectively were mixed with Sinapinic acid matrix (20 mg/ml, 50 % CH_3CN, 0.1% TFA in H_2O) to final concentration 0.1 mM. 0.5 µL was spotted onto target plate.

ODNs and G3/G5 dendrimer-ODN conjugates were desalted on SepPak C18 column eluted with 50 % CH_3CN in ddH_2O, dried and redissolved in matrix solution composed from 9 parts of 3-hydroxypicolinic acid (50 mg/ml in 50% CH_3CN / H_2O) and 1 part of diammonium citrate (50 mg/ml in H_2O) to final concentration 50-100 µM.

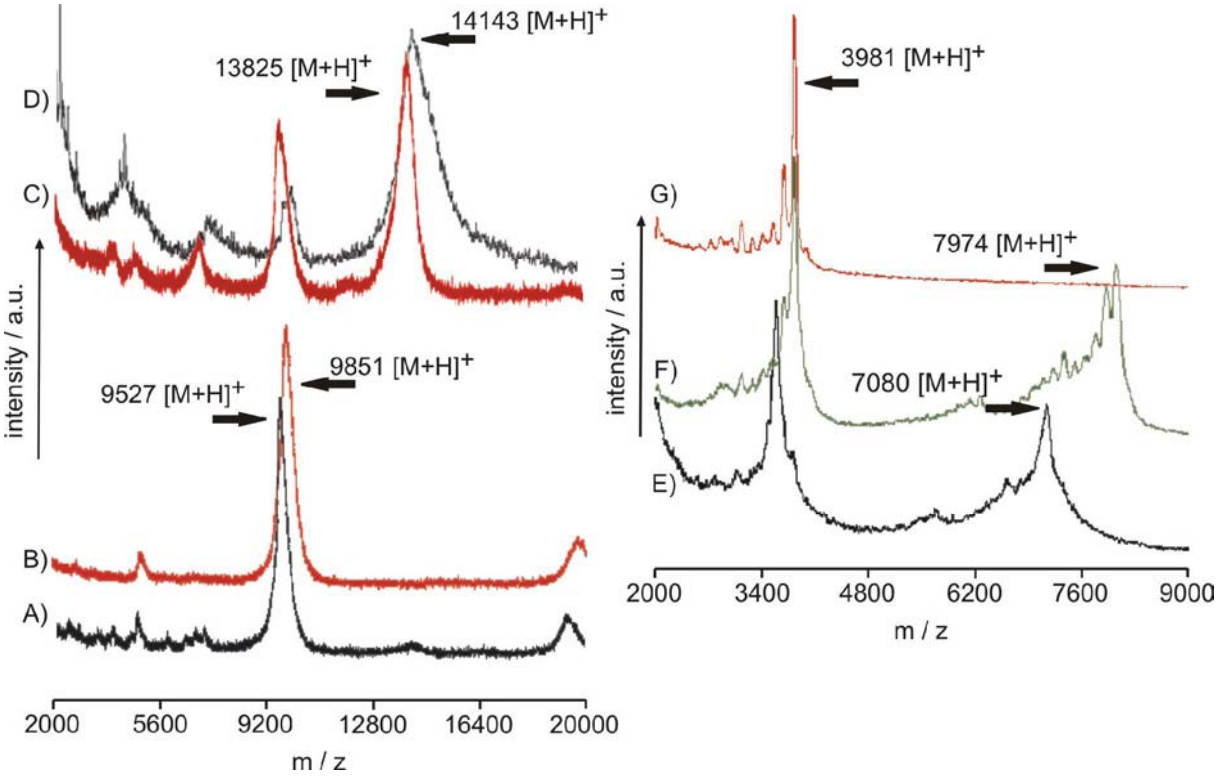

Figure 3S.: MALDI-TOF analysis of conjugates related to G3 dendrimer; A) 5´-amino-ODN; B) 5´-maleimide-ODN; C) G3-ODN; D) maleimide-G3-ODN; E) G3 PAMAM; F) G3 acetylated PAMAM; G) G3 sulfhydryl activated PAMAM.

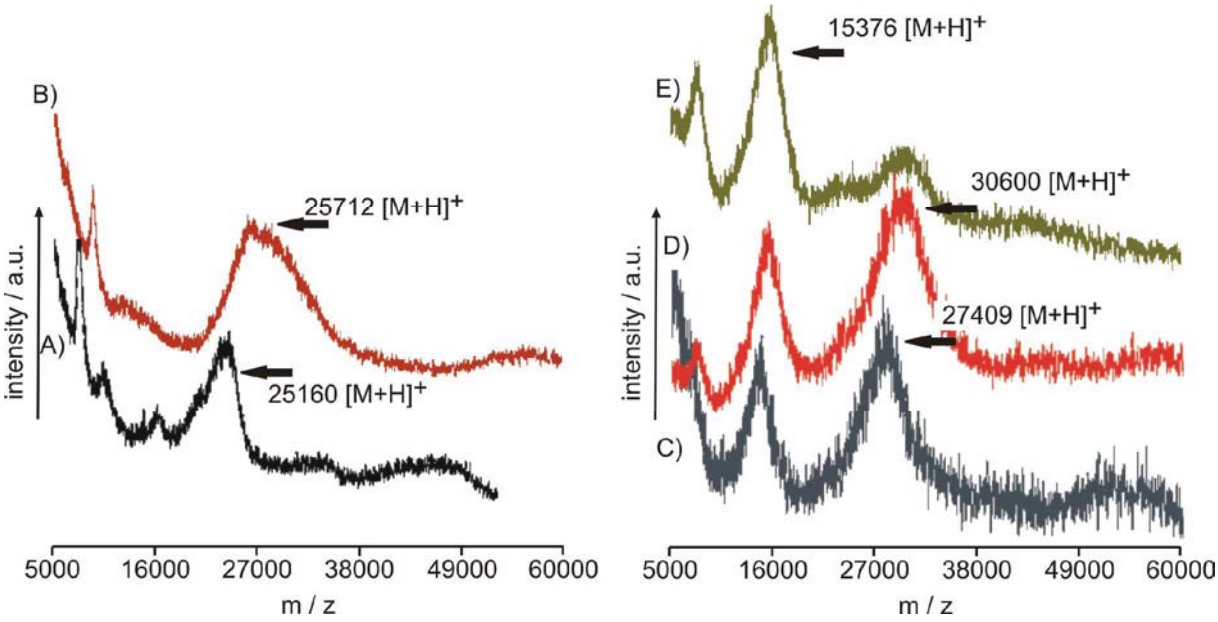

Figure 4S.: MALDI-TOF analysis of conjugates related to G5 dendrimer; A) G5-ODN; B) maleimide-G5-ODN; C) G5 PAMAM; D) G5 acetylated PAMAM **5**; E) G5 sulfhydryl activated PAMAM.

Table 1S.: Nucleotide sequences of capture and reporter ODNs

Capture ODN	**Sequence (5' – 3')**	**Modification**
Perfect match	TTT TTT GAC AGG CGA GGA ATA CAG GTA TTG	5'-SH
1 mismatch[a]	TTT TTT GAC AGG CGA GG**T** ATA CAG GTA TTG	5'-SH
2 mismatches	TTT TTT GAC AGG CGA G**CT** ATA CAG GTA TTG	5'-SH
3 mismatches	TTT TTT GAC AGG CGA G**CT T**TA CAG GTA TTG	5'-SH
Reporter ODN		
	TTT TTT TCA ATA CCT GTA TTC CTC GCC TGT C	5'-NH_2

[a] The base mismatches are shown underlined

Kinetic measurment on the gold electrode chip

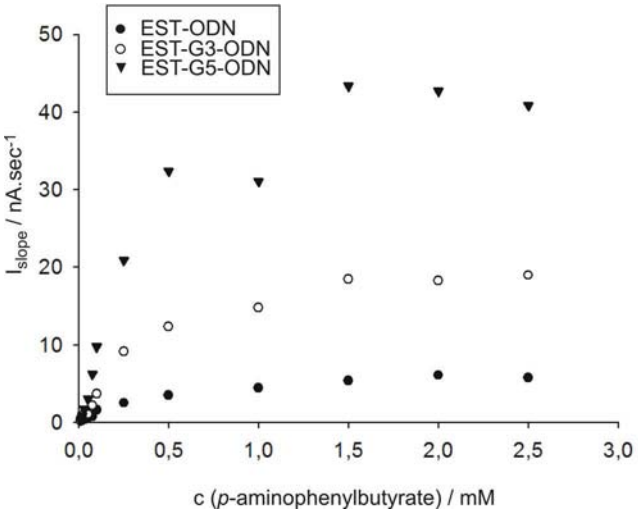

Figure 5S.: Dependence of the current slope on the substrate concentration obtained with different EST reporters on the gold electrode. Monovalent EST-ODN conjugate (●) and polyvalent EST clusters derived from G3 (○) and G5 (▼) dendrimer were assayed.

Literature cited

(S1) Sharma A, Mohanty DK, Desai A, Ali R. (2003) A simple polyacrylamide gel electrophoresis procedure for separation of polyamidoamine dendrimers. *Electrophoresis 16*, 2733-2739.

Subscriber access provided by SHEMYAKIN-OVCHINNIKOV INST

Article

Fluorine-18 Click Radiosynthesis and Preclinical Evaluation of a New F-Labeled Folic Acid Derivative

Tobias L. Ross, Michael Honer, Phoebe Y. H. Lam, Thomas L. Mindt, Viola Groehn, Roger Schibli, P. August Schubiger, and Simon M. Ametamey

Bioconjugate Chem., **2008**, 19 (12), 2462-2470• DOI: 10.1021/bc800356r • Publication Date (Web): 24 November 2008

Downloaded from http://pubs.acs.org on May 2, 2009

More About This Article

Additional resources and features associated with this article are available within the HTML version:

- Supporting Information
- Access to high resolution figures
- Links to articles and content related to this article
- Copyright permission to reproduce figures and/or text from this article

View the Full Text HTML

ACS Publications
High quality. High impact.

Bioconjugate Chemistry is published by the American Chemical Society. 1155 Sixteenth Street N.W., Washington, DC 20036

Fluorine-18 Click Radiosynthesis and Preclinical Evaluation of a New ^{18}F-Labeled Folic Acid Derivative

Tobias L. Ross,* Michael Honer, Phoebe Y. H. Lam, Thomas L. Mindt,† Viola Groehn,‡ Roger Schibli,† P. August Schubiger, and Simon M. Ametamey

Animal Imaging Center - PET, Center for Pharmaceutical Science of ETH, PSI and USZ, and Department of Chemistry and Applied Biosciences, ETH Zürich, 8093 Zürich, Switzerland, and Merck Eprova AG, 8200 Schaffhausen. Received August 20, 2008; Revised Manuscript Received October 24, 2008

The folate receptor (FR) is highly expressed on most epithelial cancer cells, while normal cells show only restricted expression of FR. As a result, the FR is an ideal target for receptor-based molecular imaging and therapy of cancer and has become a promising target in oncology. To date, several folate-based chemotherapeutics and imaging probes such as radiopharmaceuticals for single photon emission computed tomography (SPECT) have been developed. However, an ^{18}F-labeled folic acid derivative suitable for positron emission tomography (PET) imaging that can be routinely applied is still lacking. In this study, a new fluorinated and radiofluorinated folic acid derivative, $^{18/19}$F-click folate, was synthesized using click chemistry. In a convenient and very efficient two-step radiosynthesis, the isolated ^{18}F-click folate was obtained in good radiochemical yields of 25−35% with a specific activity of 160 ± 70 GBq/μmol after ≤90 min synthesis time. The new compound was pharmacologically evaluated *in vitro* and *in vivo*. The affinity of the non-radioactive ^{19}F-click folate to the FR was determined in displacement studies with FR expressing KB tumor cells using ^{3}H-folic acid. In these *in vitro* binding studies, a nanomolar affinity with a K_i of 9.76 ± 3.13 nM was found for ^{19}F-click folate. The ^{18}F-labeled click folate derivative was then applied for *in vivo* PET studies and *ex vivo* biodistribution experiments using nude mice bearing KB tumor xenografts. The *post mortem* dissection experiments showed a high specific uptake of ^{18}F-click folate derivative in FR-expressing tissues. Uptake in KB tumor xenografts and kidneys (FR-positive tissue) amounted to 3.13%ID/g (94% specific blockade) and 16.53%ID/g (75% specific blockade), respectively. PET imaging using ^{18}F-click folate permitted a visualization of KB tumors, and blockade studies confirmed the specific accumulation of the radiotracer *in vivo*. However, strong hepatobiliary excretion of the new tracer led to elevated accumulation of radioactivity in the abdominal region. In conclusion, the click chemistry approach is convenient to accomplish and provided high radiochemical yields of ^{18}F-click folate. The new tracer showed good *in vitro* but limited *in vivo* properties. Ultimately, the ^{18}F-click folate emphasizes the potential of ^{18}F-labeled folates for receptor-based tumor PET imaging.

INTRODUCTION

Folic acid **1** (see Scheme 1) is an essential dietary vitamin, namely, vitamin B_9. In eukaryotic cells, folic acid is needed in the one-carbon metabolism and *de novo* nucleotide production for DNA synthesis (*1*). In normal cells, folates are directly internalized by the ubiquitously expressed reduced-folate carrier (RFC), a membrane-spanning protein. The RFC has only a low, micromolar affinity to the oxidized forms of folic acid, but it has a high affinity to reduced forms of folic acid (*2*). Another possibility of folic acid uptake into cells is the endocytosis by a glycoprotein receptor, the folate receptor (FR) (*3*). The FR shows a high affinity (K_D ~1 nM) to oxidized forms of **1** (*4*−*7*). In highly proliferating cells, which have an increased demand of folate due to their amplified growth rate, the FR is considered to play a role in mediating elevated folate uptake (*1, 2, 6, 8, 9*). Furthermore, many malignant human endothelial cancer cells highly express the FR, while in normal tissue, only a restricted expression is found (*10, 11*). The degree of overexpression of the FR on human epithelial cancer cells ranges from 30-fold (ovarian carcinoma) up to 1400-fold (endometrial cancer) (*10*). Under physiological conditions, the FR is notably expressed only in choroid plexus, thyroid, and kidney. Hence, the FR is a very attractive molecular target for receptor-based tumor imaging and therapy (*12, 13*).

Over the past decade, several folate-based radiopharmaceuticals have been developed and have proven their potential as diagnostic tools for imaging FR-positive tumors and tissues (*14*). Most of them have been labeled with ^{111}In or with ^{99m}Tc, and some are currently in (pre)clinical studies for potential application as radiopharmaceuticals in diagnostic nuclear medicine (*15, 16*).

The folic acid structure offers two positions for derivatization, the α- and γ-carboxylic acid. Whether or not the binding affinity and *in vivo* pharmacological behavior is dependent on the site of derivatization and conjugation is still debated in the literature (*12, 14, 17*). The first findings in biological studies using folate-based drugs and (radio-)imaging agents indicated the necessity of a free α-carboxyl function to retain binding affinity to the receptor (*18*−*20*). Consequently, the γ-carboxyl group became the preferred site for derivatization for folate conjugates (*12, 14, 21*). In contrast, other studies reported that both the α- and γ-regisomer of a folate derivative showed almost no significant difference in binding affinity to the FR (*12, 14, 16, 17*). Furthermore, there is also evidence of unaltered FR binding affinity and successful endocytosis of drugs after omission of the whole glutamic acid residue (*16, 17, 22*).

Regarding PET imaging, fluorine-18 is the most commonly used radionuclide due to its excellent physical characteristics

* tobias.ross@pharma.ethz.ch.
† Department of Chemistry and Applied Biosciences, ETH Zürich.
‡ Merck Eprova AG.

10.1021/bc800356r CCC: $40.75 © 2008 American Chemical Society
Published on Web 11/24/2008

Scheme 1. Structures of Folic Acid (1) and [18]F-Labeled Folic Acid Derivatives, [18]F-Click Folate ([[18]F]3), α- and γ-[[18]F]FBA-Folate (α- and γ-[[18]F]2)

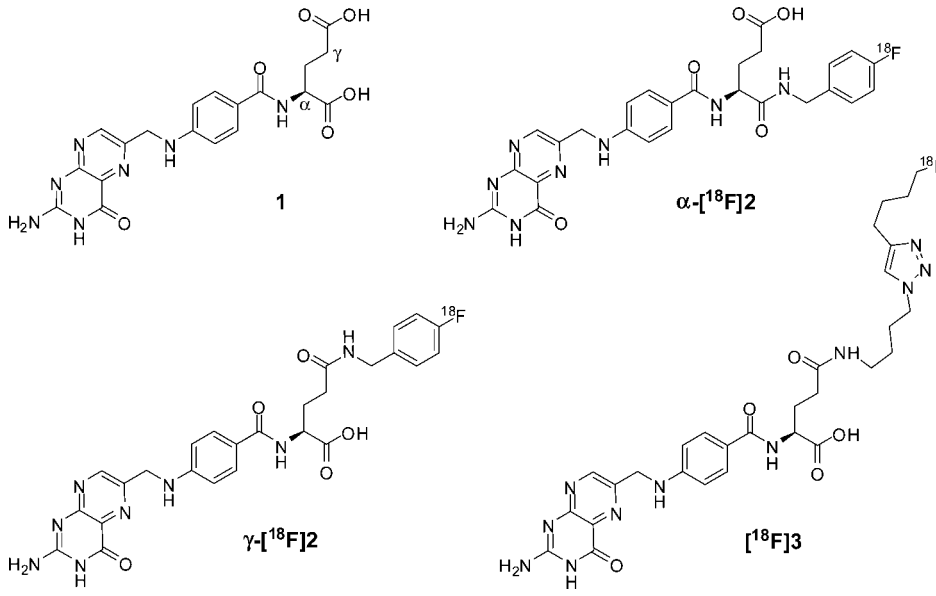

for imaging. The half-life of F−18 of 110 min allows complex radiosyntheses, extended pharmacological *in vivo* studies, and further offers the possibility of distribution and delivery of ^{18}F-radiopharmaceuticals to PET centers without radiochemistry laboratories. Moreover, the β^+-energy of only 635 keV reduces the range of the emitted positron before annihilation and thus provides high spatial resolution for PET imaging. Hence, an ^{18}F-labeled folate-based radiopharmaceutical would be of great interest.

We recently developed the first ^{18}F-labeled folate, the α/γ-[^{18}F]FBA-folate (**α/γ-[^{18}F]2**; see Scheme 1), using the prosthetic group 4-[^{18}F]fluorobenzylamine (4-[^{18}F]FBA), (*23*) which was coupled to native folic acid (*24*). Although the **α/γ-[^{18}F]2** showed promising results in *in vivo* PET studies, it was not suited for routine PET imaging due to unfavorable radiochemistry (*24*). The multistep radiosynthesis of **α/γ-[^{18}F]2** included the three-step preparation of 4-[^{18}F]fluorobenzylamine and the coupling with the activated esters of native folic acid. Subsequently, the **α/γ-[^{18}F]2** was isolated in radiochemical yields of only ∼5% by means of semipreparative HPLC. Moreover, the use of native folic acid caused the formation of both regioisomers of the activated ester and thus resulted in the formation of both the **α-** and **γ-[^{18}F]2**, which could not be separated by semipreparative HPLC. However, *in vitro* cell assays revealed similar binding affinities of the separately synthesized reference compounds, **α-2** and **γ-2** (IC_{50} (**α-2**), 71 ± 8 nM; IC_{50} (**γ-2**), 62 ± 6 nM).

Another approach by Al Jammaz et al. was also based on prosthetic group labeling, but no pharmacological data have been provided so far (*25*).

In 2002, a Cu(I)-catalyzed version of the Huisgen 1,3-dipolar cycloaddition of terminal alkynes and azides has been discovered, which dramatically enhances yields and reduces reaction times from days to hours (*26, 27*). In addition, the new catalyzed variant leads only to one regioisomer, the 1,4-triazoles, while the classic alkyne−azide cycloaddition gave a mixture of 1,4- and 1,5-triazoles. Due to an extraordinary efficiency and selectivity, the new variant of this cycloaddition had such a huge impact on various fields of chemistry that it has become the most famous representative of the so-called click reactions (*28, 29*). The first use of this click cycloaddition in PET chemistry was reported by Marik and Sutcliffe in 2006, who used ^{18}F-labeled alkynes for a click reaction with azide-functionalized peptides (*30*). Since then, several studies have proven its accessibility toward ^{18}F-labeling with high efficiency and outstanding robustness (*31*).

The aim of this study was to develop a new ^{18}F-labeled folic acid derivative as a potential radiopharmaceutical for routine PET imaging of FR-positive tumors. In order to develop a robust and high-yielding ^{18}F-labeling, which is suitable for large-scale routine productions, the click chemistry approach was chosen. On the basis of the report of Marik and Sutcliffe (*30*), the click approach was expanded to ^{18}F-labeling of folates. Furthermore, click chemistry provides a regiospecific coupling with the ^{18}F-labeled moiety and exclusively leads to one regioisomer, in this study, to the γ-isomer. As mentioned before, literature data are controversial and do not exclusively indicate one of the regioisomers. We chose the γ-isomer, as in our previous studies, we found slightly better FR affinity for this regioisomer (*24*). The new "^{18}F-click folate" (**[^{18}F]3**; see Scheme 1) was evaluated *in vitro* and *in vivo* using nude mice bearing FR-positive KB tumor xenografts.

EXPERIMENTAL PROCEDURES

General. Reagents and solvents were purchased from Sigma-Aldrich Co. or Merck AG. All chemicals were used as supplied unless stated otherwise. The *N2-N,N*-dimethylaminomethylene-10-formylpteoric acid was generously provided by Merck Eprova AG, Schaffhausen, Switzerland. ^{3}H-Folic acid (**[^{3}H]1**) was purchased from Moravek Biochemicals Inc. (USA). Nuclear magnetic resonance spectra were recorded with a Bruker 400 or 500 MHz spectrometer with the corresponding solvent signals as an internal standard. Chemical shifts are reported in parts per million (ppm) relative to tetramethylsilane (0.00 ppm). Values of the coupling constant, *J*, are given in hertz (Hz); the following abbreviations are used in the experimental section for the description of P^{1P}H-NMR spectra: singlet (s), doublet (d), triplet (t), multiplet (m), doublet of doublets (dd). The chemical shifts of complex multiplets are given as the range of their occurrence. Low-resolution mass spectra (LR-MS) were recorded with a Micromass Quattro micro API LC-ESI. Water-sensitive reactions were run under argon in flame-dried glassware. Reactions were monitored by thin layer chromatography (TLC, performed on EM Science 0.25-mm-thick, precoated silica gel 60 F-254 glass-supported plates) or HPLC. HPLC was

performed on a Merck-Hitachi L-7000 system equipped with a L-7400 tunable absorption detector. Analytical HPLC was performed with a reversed-phase column (XBridge C18, 5 μm, 4.6 × 150 mm, Waters AG) using the following solvent system: 0.1% TFA_{aq} (solvent A), acetonitrile (solvent B); flow, 1 mL/min; 0-1 min, 95% A; 1-15 min, 95% → 5% A; 15-20 min, 5% A; 20-22 min, 5% → 95% A; 22-25 min, 95% A. Semipreparative HPLC was performed with a reversed-phase semipreparative column (XBridge C18, 5 μm, 10 × 150 mm, Waters AG), flow, 3 mL/min; isocratic NH_4HCO_3 solution (10 mM, 88%)/CH_3CN (12%).

Analytical radio-HPLC was performed on an Agilent 1100 series HPLC system equipped with a GabiStar (Raytest) radiodetector using a reversed-phase column (Gemini 5 μ C18, 250 × 4.6 mm, Phenomenex) with a solvent system and gradient as follows: 10 mM NH_4HCO_3 solution (solvent A), methanol (solvent B); flow, 1 mL/min; 0−30 min, A 90% → 40%; 30−40 min, A 40%; 40−45 min, A 40% → 90%. Semipreparative radio-HPLC was carried out on an HPLC system equipped with a Merck-Hitachi L-6200A intelligent pump, a Knauer Variable Wavelength Monitor UV-detector, and an Eberline RM-14 radiodetector using a reversed-phase column (Gemini 5 μ C18, 250 × 10 mm, Phenomenex) with a solvent system and gradient as follows: 10 mM NH_4HCO_3 solution (solvent A), ethanol (solvent B); flow, 2 mL/min; 0−30 min, A 90% → 40%; 30−40 min, A 40%; 40−45 min, A 40% → 90%. Determination of relative lipophilicity was perfomed on the Agilent 1100 system using the reversed-phase Gemini 5 μ C18 (250 × 4.6 mm, Phenomenex) column and an isocratic solvent system as follows: 80% water (pH 2 with H_3PO_4) and 20% acetonitrile.

PET imaging was performed with the 16-module variant of the quad-HIDAC tomography (Oxford Positron Systems). This small animal PET camera system provides an ultrahigh resolution of less than 0.9 mm^3 (*32*, *33*).

Synthesis of 6-[^{19}F]fluoro-1-hexyne (5). 5-Hexyne-1-yl *p*-tosylate (**4**) (330 mg, 1.3 mmol) (prepared by tosylation of 5-hexyne-1-ol according to the procedure described by van Hest et al. (*34*)), Kryptofix 2.2.2 (620 mg, 1.6 mmol), and KF (97 mg, 1.6 mmol) in dry THF (12 mL) were stirred at reflux for 20 h. Fractionated distillation of the volatile components at ambient pressure gave **5** as a 42% solution in THF (200 mg, 62%): Bp. 65−70 °C/1 atm.

^{1}H NMR ($CDCl_3$) δ 4.51 (t, 1H, J = 6.0 Hz), 4.40 (t, 1H, J = 6.0 Hz), 2.23 (dt, 2H, J = 7.6 and 2.8 Hz), 1.95 (t, 1H, J = 2.8 Hz), 1.80−1.73 (m, 2H), 1.65−1.61 (m, 2H) ppm.

Synthesis of γ-(4-Azido-butyl)-folic Acid Amide (6). 6 was prepared according to the procedure described by Mindt et al. (*35*).

N-BOC-amino-butane-azide was prepared from mono-BOC-diaminobutane according to the procedure described by Link et al. (*36*). After deprotection in CH_2Cl_2/TFA (20%) at room temperature overnight, the TFA salt of 4-azido-butane-amine was obtained as a colorless oil (0.44 g, 94%). The activated ester of α-protected glutamic acid, BocGluOMe, was formed by the use of 2-(1*H*-benzotriazol-1-yl)-1,1,3,3-tetramethyluroniumhexafluorophosphate (HBTU). The activated ester was coupled to the TFA salt of 4-azido-butane-amine to furnish BOC-Glu(4-azido-butyl)-OMe as colorless oil (330 mg, 92%). After deprotection in CH_2Cl_2/TFA (20%) at room temperature overnight, the TFA salt of Glu(4-azido-butylamide)OMe was obtained as a pale yellow oil (740 mg, quantitative). The activated ester (HBTU) of *N2*-*N*,*N*-dimethylaminomethylene-10-formyl-pteroic acid was coupled to the TFA salt of Glu(4-azido-butylamide)OMe to furnish the *N2*-*N*,*N*-dimethylaminomethylene-10-formyl-α-*O*-methyl-γ-(4-azido-butyl) folic acid amide as a yellow solid (290 mg, 92%). After deprotection in 1 M NaOH at room temperature overnight, the pH was adjusted to ∼2 to precipitate the penta-hydrochloride salt of **6** as a yellow powder (75 mg, quantitative).

Synthesis of γ-(4-(4-[^{19}F]fluorobutyl)triazo-1-yl)butyl-folic Acid Amide (^{19}F-click folate, 3). 6 (penta-hydrochloride salt, 14 mg, 0.02 mmol) was suspended in ^{t}BuOH/H_2O (1:1, 2 mL), and **5** (48 mg, 0.2 mmol), $Cu(OAc)_2$ (0.8 mg, 20 mol %) and sodium ascorbate (1.5 mg, 40 mol %) were added. The mixture was stirred at 75 °C until HPLC indicated complete conversion of the azide starting material (∼30 min). The mixture was cooled to room temperature, and the resulting suspension was dissolved by addition of a few drops 1 M NaOH. Adjustment of pH to 2 by addition of 1 M HCl resulted in precipitation of the product. The mixture was centrifuged (10 min at 3500 rpm) and the pale yellow supernatant decanted. Drying of the solid provided a brown powder (20 mg). The crude product was dissolved in 0.1 M NaOH (0.4 mL) and purified by semiprep HPLC. The collected fractions containing the product were concentrated under reduced pressure and the residue dissolved in 1 M NaOH (1 mL). Adjustment to pH 2 by addition of 1 M HCl resulted in precipitation of **3**. Centrifugation (10 min at 3500 rpm), decantation of the pale yellow supernatant, and drying of the solid provided the penta-hydrochloride salt of **3** as a yellow powder (9 mg, 53%).

^{1}H NMR (DMSO-d_6) δ 12.02−11.85 (bs, 1H), 8.66 (s, 1H), 8.19 (d, 1H, J = 7.8 Hz), 7.86−7.80 (m, 2H), 7.65 (d, 2H, J = 8.7 Hz), 7.35−6.95 (broad m, 2H), 6.65 (d, 2H, J = 8.7 Hz), 4.53−4.47 (m, 3H), 4.40 (t, 1H, J = 5.8 Hz), 4.32−4.23 (m, 3H), 3.54−3.32 (bs, 1H), 3.08−2.97 (m, 2H), 2.62 (t, 2H, J = 6.6 Hz), 2.22−2.13 (m, 2H), 2.09−2.00 (m, 1H), 1.98−1.88 (m, 1H), 1.79−1.60 (m, 6H), 1.36−1.26 (m, 2H) ppm. ^{13}C NMR (DMSO-d_6) δ 173.8, 171.5, 166.3, 160.7, 155.0, 153.5, 150.7, 149.1, 148.5, 146.5, 129.0, 128.0, 121.7, 121.4, 111.2, 84.2, 83.0, 52.2, 48.8, 45.9, 37.7, 32.0, 29.3, 27.2, 26.5, 26.1, 24.8, 24.5 ppm. LR-MS: $[M + H]^+$ = 638.24 (calc. for $C_{29}H_{36}FN_{11}O_5$: 637.67). Elemental analysis (calculated % values for $C_{29}H_{36}N_{11}O_5(HCl)_5$ in parenthesis) C 42.72 (42.48), H 5.18 (5.04), N 18.17 (18.79).

Production of n.c.a. [^{18}F]fluoride. N.c.a. [^{18}F]fluoride was produced via the ^{18}O(p,n)^{18}F nuclear reaction at a Cyclone 18/9 cyclotron (IBA, Belgium). Isotopically 97% enriched [^{18}O]water was irradiated by a 18 MeV proton beam using a 2.1 mL liquid target. The [^{18}F]fluoride/[^{18}O]water solution was transferred from the target to a manipulator-equipped syntheses hot cell using a helium stream.

Synthesis of γ-(4-(4-[^{18}F]Fluorobutyl)triazo-1-yl)butyl-folic Acid Amide (^{18}F-click folate, [^{18}F]3). N.c.a. [^{18}F]fluoride (∼20−30 GBq) was trapped on an anion exchange cartridge (Sep-Pak Light Accell Plus QMA, Waters AG), preconditioned with 5 mL 0.5 M potassium carbonate solution and 5 mL water, while the [^{18}O]water was recovered for recycling. The n.c.a. [^{18}F]fluoride was directly eluted into a 10 mL sealed reaction vessel using a solution of potassium carbonate (2 mg) and Kryptofix 2.2.2 (10 mg) in 1.5 mL acetonitrile/water (4:1). At 85−90 °C, the solvents were removed by reduced pressure and a stream of nitrogen. Subsequently, 0.8−1.0 mL of dry acetonitrile was added three times and evaporated to dryness. To the obtained dry [^{18}F]fluoride−cryptate complex, **4** (25 μL) in 1.0 mL acetonitrile was added. The reaction vessel was connected via a PTFE tubing with a second 10 mL reaction vessel containing copper(I)iodide (2.5 mg), and the second reaction vessel was placed in a dry ice/isopropanol cooling bath. The reaction mixture in reaction vessel one was heated to 95−100 °C, while the ^{18}F-labeled product **[^{18}F]5** was co-distilled with acetonitrile to the second reaction vessel (bp (**5**) = 106 °C (*30*)). **[^{18}F]5** was given in a radiochemical yield of 70−85% and a radiochemical purity of 95−99%. After 12 min, the second reaction vessel containing **[^{18}F]5** in 0.6−0.8 mL acetonitrile was

disconnected and allowed to warm to ambient temperature. To this mixture 0.8 mL water, 10 μL DIPEA, 20 μL 2,6-lutidine, and **6** as its penta-hydrochloride salt (1.5 mg, 2 μmol) in 0.2 mL DMF were added successively. The mixture was heated to 80 °C and was allowed to cool down to 60 °C within 20 min. The **[^{18}F]3** content of the crude mixture was 65−80% according to analytical radio-HPLC. The product was isolated by semi-preparative HPLC in radiochemical yields of 25−35%. The HPLC solvents were removed under reduced pressure and a stream of nitrogen at 100 °C. The dry product was then formulated in physiological phosphate buffer solution (PBS, 0.15 M).

***In Vitro* Cell Binding Assays.** Cell binding assays were performed with KB cells, a human nasopharyngeal epidermal carcinoma cell line overexpressing the FR (*3*). Cells were continuously cultured as monolayers in 75 cm^2 flasks at 37 °C in humidified atmosphere (7.5% CO_2). The cells were folate-starved in folate-deficient RPMI 1640 medium supplemented with fetal calf serum (10%, heat-inactivated), L-glutamine, and antibiotics (penicillin, 100 IU/mL; streptomycin, 100 μg/mL). Such compositions, with fetal calf serum as the only folate source in the medium, are known to provide a final folate concentration of ∼3 nmol/mL, which is at the low end of the physiological serum concentration in humans (*37*).

After a growing period of 2−3 days, a cell suspension in pure, ice−cold folate-deficient RPMI 1640 medium (without further additives) was prepared. The cell suspension was distributed to 1.5 mL vials, ∼7000 cells per tube (∼240 μL). A dilution series of eight different concentrations in a range from 5.0×10^{-6} to 5.0×10^{-11} M for native folic acid and in the range from 5.0×10^{-6} to 5.8×10^{-12} M for **3** were prepared. The cells were incubated as triplicates of each concentration together with **[^{3}H]1** (10 μL, ∼25 kBq/μL, specific activity 1.203 GBq/μmol) at 2−4 °C for 30 min. Nonspecific binding was determined in the presence of native folic acid at a concentration of 10^{-3} M. After centrifugation, 10 min at 800 × *g*, and 4 °C, the supernatant was discarded. The cell pellets were resuspended and lysed at the same time using a 1 M NaOH solution (0.5 mL). Preliminary comparative experiments showed that an additional washing step before the lysis is not necessary. The lysed cells were vortexed and transferred into scintillation tubes containing 4 mL of a scintillation cocktail (Ultima Gold, PerkinElmer). Radioactivity in the tubes was recorded by β-counting (LS6500, Beckman USA). The IC_{50} values were determined from the displacement curves using the *Origin 8.0* software (OriginLab Corp., USA). K_i values were calculated according to the Cheng-Prusoff equation (*38*) using a K_D of **[^{3}H]1** of 1 nM.

***In Vitro* Metabolite Studies in Plasma and Liver Microsomes.** The **[^{18}F]3** solution (∼20 MBq, 35 μL) was incubated with human or murine plasma (0.5 mL) in a shaking water bath at 37 °C. Aliquots of 70 μL were taken at different time points over a period of 0−120 min. Plasma proteins were precipitated by addition of 140 μL acetonitrile and removed by centrifugation for 10 min at 10 000 × *g* (room temperature). Aliquots of the supernatant were analyzed by radio-HPLC (analytical HPLC system).

The **[^{18}F]5** solution (∼20 MBq, 35 μL) was incubated with human or murine liver microsomes (BD Gentest, BD Biosciences, USA) in a shaking water bath at 37 °C (0.5 mg protein per mL). Control samples were incubated with heat-inactivated microsomes. Each sample contained 10% 10 mM NADPH solution or PBS for control samples. Proteins were precipitated by addition of 250 μL acetonitrile at different time points over a period of 0−30 min and removed by centrifugation for 5 min at 10 000 × *g* (4 °C). Aliquots of the supernatant were analyzed by radio-HPLC (analytical HPLC system).

***In Vivo* Studies.** *Animals.* Animal studies complied with Swiss and local laws on animal protection and husbandry. Male NMRI nude mice were purchased from Charles River (Germany) and maintained on a folate-deficient rodent diet to reduce their serum folate concentration to a level comparable to human serum levels (*39*). After a 3−4 day acclimatization period, 0.1 mL of a KB tumor cell suspension (50×10^6 cells/mL) was inoculated subcutaneously into the right axilla of each mouse. The cell suspension for inoculation was achieved by cell harvest of subconfluent cells using 1 mM EDTA solution in PBS. Cells were washed once with PBS and after centrifugation (1000 × *g*, 5 min, 20 °C) resuspended in PBS for inoculation. The animal experiments were performed 10−14 days after inoculation, when the tumors had reached weights of 80−300 mg.

Ex Vivo Biodistribution Studies. Animals were injected with ∼2 MBq, 12.5 pmol, (max. volume 100 μL per injection) of **[^{18}F]3** via a lateral tail vein. In the blockade group ($n = 4$), each animal received 200 μg of native folic acid (2 mg/mL folic acid in PBS) via intravenous injection 10 min prior to the radiotracer injection. The control group ($n = 4$) received an injection of PBS. Animals were sacrificed by decapitation 45 min after radiotracer injection. Tumours, organs, and tissues were dissected and measured in the γ-counter (Wizard, PerkinElmer). The incorporated radioactivity was expressed as percentage injected dose per gram of tissue (%ID/g; ((cpm tissue/g tissue/cpm injected) × 100).

PET Imaging Studies. PET experiments were performed with the 16-module variant of the quad-HIDAC tomograph (Oxford Positron Systems) (*33*). Animals were lightly restrained and injected with 6−12 MBq, 37.5−75.0 pmol of the radiotracer (90−110 μL per injection) via a lateral tail vein. In the blockade group ($n = 3$), each animal received 200 μg of native folic acid (2 mg/mL folic acid in PBS) via intravenous injection 10 min prior to the radiotracer injection, whereas the control group ($n = 3$) received a corresponding volume of PBS. Animals were anesthetized with isoflurane (Abbott) in an air/oxygen mixture and scanned as described previously (*40*). The PET scans were acquired from 15 to 45 min post-injection. For a comparison of [^{18}F]**3** tumor uptake with 2-[^{18}F]fluoro-2-deoxy-D-glucose ([^{18}F]FDG), two animals were rescanned with [^{18}F]FDG four days after the [^{18}F]**3** study. Each animal received ∼9 MBq of [^{18}F]FDG and was scanned 30−60 min after injection.

RESULTS AND DISCUSSION

Radiochemistry. The ^{18}F-labeling is based on a prosthetic group approach using the Cu(I)-catalyzed 1,3-dipolar cycloaddition of alkynes and azides (Scheme 2), also referred to as click chemistry (*26*, *27*). The prosthetic group, 6-[^{18}F]fluoro-1-hexyne **[^{18}F]5**, could be successfully produced from the corresponding *p*-tosylate precursor **4** according to a procedure reported by Marik et al. (*30*). The **[^{18}F]5** was purified by co-distillation with acetonitrile at the same time the ^{18}F-labeling step was carried out. Within 12 min, the ^{18}F-labeled alkyne **[^{18}F]5** was obtained and isolated in excellent radiochemical yields of 70−85% with radiochemical purities of ≥95%. The **[^{18}F]5** was collected by condensation in a second reaction vial, which was placed in a dry ice/*i*-propanol cooling bath. The second reaction vessel already contained CuI as catalyst for the following 1,4-triazole formation by cycloaddition with the γ-azide-functionalized folic acid derivative, γ-(4-azido-butyl)-folic acid amide **6**. This click reaction worked best in a 1:1-mixture of acetonitrile and 0.15 M PBS. Although additional bases are generally not necessary when this click reaction is performed in aqueous systems (*28*), a 1:2 mixture of DIPEA and 2,6-lutidine was found optimal for enhancing coupling efficiency and reducing side-product formation. However, the initial step in the click mechanism is the coordination of the

Scheme 2. Radiosynthesis of ^{18}F-Click Folate ([^{18}F]3) via the 1,3-Dipolar Cu(I)-Catalyzed Cycloaddition of n.c.a. 6-[^{18}F]Fluoro-1-Hexyne ([^{18}F]5) and γ-(4-Azido-Butyl)-Folic Acid Amide (6)[a]

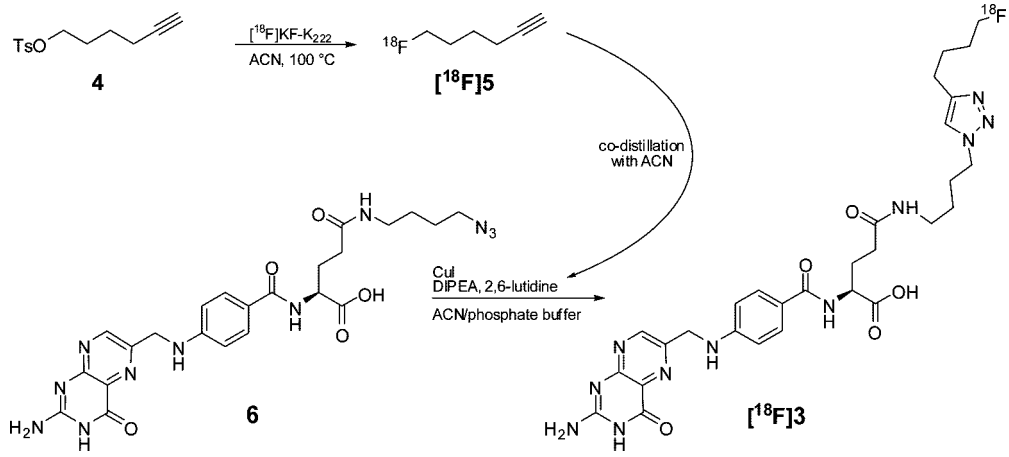

[a] **4**: 5-hexynyl-*p*-tosylate (precursor for **[^{18}F]5**).

Cu(I)-catalyst to the alkyne, forming an acetylide, which is exothermic and favored in aqueous systems, but slightly endothermic in pure organic systems (e.g., in acetonitrile approximately −0.6 kcal/mol), where generally base addition is needed to facilitate this acetylide formation (*41*). Furthermore, previous studies demonstrated that nitrogen bases such as pyridine or 2,6-lutidine suppress side-product formation and often improve yields (*27, 29, 30*). After subsequent addition of PBS, DIPEA, 2,6-lutidine, and finally the γ-azide-functionalized folate **6** in DMF to the reaction mixture, the orange solution was stirred for 20 min at elevated temperatures of 80 → 60 °C. A good conversion of 65−80% to the ^{18}F-click folate **[^{18}F]3** in the reaction mixture was observed by analytical HPLC within 15−20 min. Higher temperatures up to 110 °C increased the coupling yield to some extent, but led to a deteriorated product/side-product ratio. Likewise, elongated reaction times of 45−60 min did not significantly enhance the radiochemical yield. The click chemistry step succeeds without the need for protection groups and directly provides the final product **[^{18}F]3**.

[^{18}F]3 was purified by reversed-phase semipreparative HPLC. The product peak (retention time 17.5 min, full width at half-maximum = 1.0 min) was collected in a reaction vessel, and HPLC solvents (∼3−4 mL) were evaporated under reduced pressure and a stream of nitrogen at 100 °C within 10−15 min. The dry product was redissolved in physiological PBS and formulated for biological applications. After an overall synthesis time of approximately 90 min, the isolated product was obtained in radiochemical yields of 25−35%, with a radiochemical purity of ≥99% and a specific activity of 160 ± 70 GBq/μmol. The **[^{18}F]3** was identified by analytical HPLC by coinjection with its nonradioactive reference compound **3**.

The extraordinary efficiency of the 1,3-dipolar click cycloaddition of alkynes and azides (*28*) could be successfully transferred to ^{18}F-labeling of a new folic acid derivative and has been proven to be very reliable and high-yielding. In comparison to other multistep procedures for preparing ^{18}F-labeled folic acid derivatives (*24, 25*), this two-step click chemistry approach is much more suitable for routine productions. Its robustness and the high radiochemical yields provide sufficient amounts of the ^{18}F-labeled radiotracer within adequate synthesis times. Furthermore, the regiospecific coupling results only in the γ-isomer and precludes complicated separation methods or the use of regioisomeric mixtures. Consequently, this radiosynthetic strategy is particularly suitable for large-scale production of ^{18}F-labeled folates for routine applications in PET imaging.

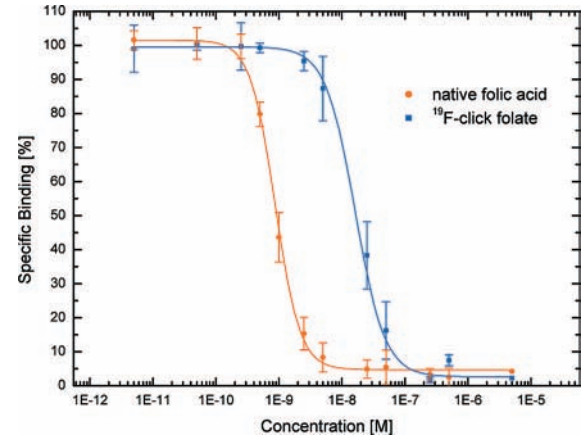

Figure 1. Displacement curves of native folic acid and ^{19}F-click folate (**3**) using ^{3}H-folic acid (1 nM) and human KB cells in cell suspension showing the mean ± SD percentage of specific binding. Nonspecific binding was determined in the presence of native folic acid at a concentration of 10^{-3} M.

***In Vitro* Cell Binding Assays.** Human KB cells (human nasopharyngeal epidermal carcinoma cell line overexpressing the FR) were kept under folate-deficient conditions to reproduce a folate concentration similar to that of human serum. The IC_{50} values of native folic acid and **3** were obtained by displacement studies (Figure 1) using ^{3}H-folic acid (Moravek Biochemicals, USA). The mean IC_{50} of three independent experiments with **3** was determined as 18.0 ± 7.1 nM, which is higher compared to the value for native folic acid (IC_{50} = 1.12 ± 0.44 nM, n = 3). Applying the IC_{50} values to the Cheng-Prusoff equation (*38*) with the assumption that the K_D of ^{3}H-folic acid is 1 nM (*4−7*) gave a K_i value of 9.76 ± 3.13 nM for **3**. Thus, the binding affinity of this new folic acid derivative is in the low nanomolar range but more than 1 order of magnitude lower compared to that of native folic acid (K_i = 0.61 ± 0.19 nM).

***In Vitro* Metabolite Studies in Plasma and Liver Microsomes.** To test the plasma stability of the new tracer, **[^{18}F]3** was incubated in human or murine plasma at 37 °C. Aliquots were taken and analyzed by radio-HPLC over a period of 0−120 min. As PET imaging studies with [^{18}F]-labeled radiotracers are typically performed at early time points after injection, a maximum incubation time of 120 min for the plasma stability study was considered to be sufficient. For all time points examined, no metabolic degradation or defluorination of the radioactive compound was detectable.

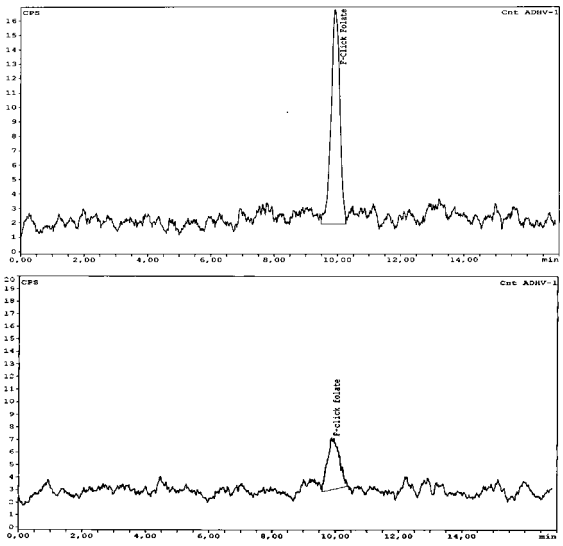

Figure 2. Radio-HPLC chromatograms of the metabolite study using **[^{18}F]3** in human liver microsomes. The first chromatogram shows **[^{18}F]3** at 0 min incubation. In the second chromatogram, only unmetabolized parent compound is detected after 30 min incubation.

Table 1. *Ex Vivo* Biodistribution Studies Using [^{18}F]3 in NMRI Nude Mice Bearing KB Tumor Xenografts[a]

organ/tissue	control[b]		blockade[b]	
lung	0.85	±0.04	0.18	±0.04
liver	1.71	±0.14	0.81	±0.23
kidney	**16.53**	**±2.22**	**3.89**	**±3.52**
brain	0.26	±0.10	0.16	±0.26
heart	0.90	±0.22	0.12	±0.04
spleen	0.33	±0.12	0.08	±0.02
stomach	2.50	±0.60	6.14	±5.14
intestine	19.59	±5.26	42.73	±16.78
bone	1.89	±0.50	1.15	±0.93
blood	0.13	±0.01	0.19	±0.14
urine	49.92	±15.58	39.68	±14.21
feces	56.00	±27.64	134.87	±46.71
bile	667.36	±530.09	618.60	±300.88
KB tumor	**3.13**	**±0.83**	**0.19**	**±0.08**

[a] Animals were sacrificed 45 min post-injection. Data are expressed as percent injected dose per gram tissue (%ID/g). [b] In the blockade group ($n = 4$), 200 μg native folic acid was injected into each animal 10 min prior to the radiotracer, whereas the control group ($n = 4$) received a corresponding volume of PBS.

Further investigation of the metabolic stability of **[^{18}F]3** *in vitro* was carried out in human and murine liver microsomes. To analyze whether ^{18}F-click folate is degraded by enzymes present in these microsomal preparations, the radiotracer was incubated at 37 °C for 30 min. Radio-HPLC analysis of the samples revealed that **[^{18}F]3** is stable in human and murine liver microsomes, since no radioactive metabolites or defluorination were detected (Figure 2).

Biodistribution Studies. The *in vivo* binding specificity of **[^{18}F]3** to the FR on KB tumor cells was first analyzed by *post mortem* biodistribution studies under control and blockade conditions. The blockade group received 200 μg native folic acid 10 min prior to radiotracer administration, whereas the control animals were injected with a corresponding volume of PBS. Radioactivity accumulation in KB tumors at 45 min post-injection amounted to 3.13 ± 0.79%ID/g, while tracer uptake in blocked animals was reduced by more than 90% to 0.19%ID/g (Table 1). Highly specific uptake of the radiotracer was also identified in the kidneys, which are known to express the FR under physiological conditions (*42*−*44*). Control animals showed a kidney accumulation of 16.53 ± 2.22%ID/g, which was reduced to 3.89 ± 3.52%ID/g in the blockade group (77% specific uptake). Highest nonspecific accumulation of radioactivity was found in the bile, pointing to hepatobiliary elimination of **[^{18}F]3** as the major elimination pathway. Moderate activity accumulation was evident in urine, feces, and intestine.

***In Vivo* PET Imaging.** Mice bearing a FR-expressing KB tumor in the area of their right shoulder were injected with **[^{18}F]3** and scanned 15−45 min post-injection to assess whether tumors can be visualized by PET imaging. As expected from the *ex vivo* biodistribution data, tracer uptake in excretory organs was predominant, but tumors were nevertheless clearly visualized (Figure 3, top row). Tracer uptake in KB tumors was found to be heterogeneous with higher activity accumulation in the rim of the tumors, suggesting better delivery of the radiotracer to the outer portions of the tumor mass. A similar heterogeneous distribution of the radiotracer in KB tumor xenografts was also found in a previous study using **α/γ-[^{18}F]2** (*24*). Due to the fast growth of certain tumor types, the centers of larger xenografts (≥300 mg) are often insufficiently perfused, which may lead to a necrotic tumor center (*45*, *46*). However, there are also indications that KB xenografts, showing a heterogeneous radiotracer uptake, exhibit a homogeneous expression of the FR and good vascularization, and only high intratumoral pressure causes an insufficient radiotracer uptake in the tumor center (*47*).

In agreement with previous studies (*24*, *40*), ^{18}F-FDG uptake in the KB tumor xenografts was negligible (Figure 3, bottom row). The KB tumor model is one example where ^{18}F-FDG PET imaging fails. In such cases, a receptor-based imaging approach using specific ligands such as folic acid derivatives for targeting the FR could overcome these difficulties.

The binding specificity of **[^{18}F]3** to the FR on KB tumor cells was also demonstrated by *in vivo* PET studies under control and blockade conditions. The blockade group received 200 μg native folic acid 10 min prior to radiotracer administration, whereas the control animals were injected with a corresponding volume of PBS. All animals were scanned from 15 to 45 min after radiotracer application. Figure 4 shows a corresponding series of horizontal whole body sections under both experimental conditions. Tumors and kidneys were only visualized in the absence of competing folic acid, supporting the specificity of [^{18}F]3 binding to the FR *in vivo*. The cortex of kidneys (proximal tubules) is known to express the FR under physiological conditions where renal reabsorption of folates takes place (*42*−*44*).

In correspondence to *post mortem* dissection studies (Table 1), PET experiments revealed the highest accumulation of radioactivity in excretory organs of the abdominal region (gall bladder, intestine, urinary bladder, kidneys). The extremely high tracer concentration in bile and, consequently, in the intestines results from the strong hepatobiliary elimination of the radiotracer. A high abdominal accumulation of the radiotracer is undesirable and hampers tumor visualization in this region. Previous studies using the first ^{18}F-labeled folate, **α/γ-[^{18}F]2** (*24*), also showed a prominent hepatobiliary elimination of the radiotracer.

Strong hepatobiliary elimination often correlates with the degree of lipophilicity of a drug. As a consequence, higher lipophilicity generally results in increased hepatobiliary excretion. For comparison of the relative lipophilicity, the retention factors (k'-values) of native folic acid, **α**- and **γ-2** and **3** were determined using a reversed-phase HPLC system (*48*). The k'-value of native folic acid as a reference with the lowest lipophilicity was found to be 0.30. Both regioisomers, **α**- and **γ-2**, gave identical k'-values of 0.67, which indicate an increased lipophilicity in comparison to native folic acid. The k'-value of 2.28 for **3** points to a much higher lipophilicity. Consequently,

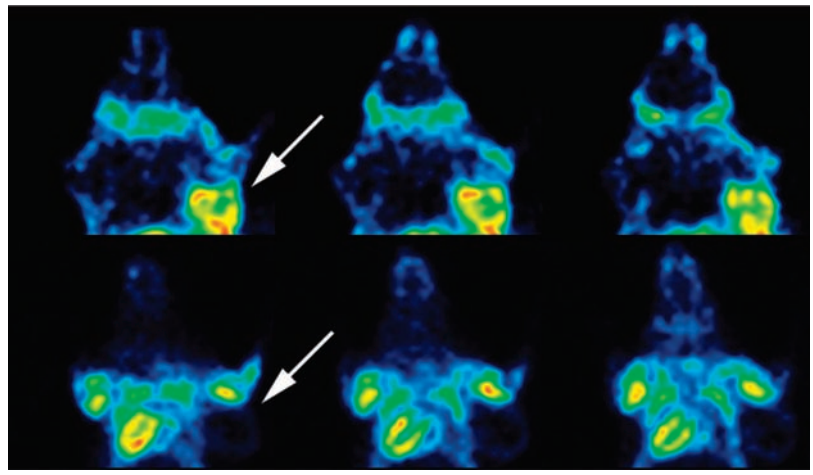

Figure 3. Representative series of horizontal PET images through the head and thorax region of an NMRI nude mouse bearing a KB tumor xenograft next to the right forelimb (arrows). The mouse was injected with **[^{18}F]3** and imaged from 15 to 45 min post-injection (top row). The same mouse was injected with ^{18}F-FDG four days later and scanned from 30 to 60 min post-injection (bottom row). Visualization of the FR-positive tumor was only possible with **[^{18}F]3**.

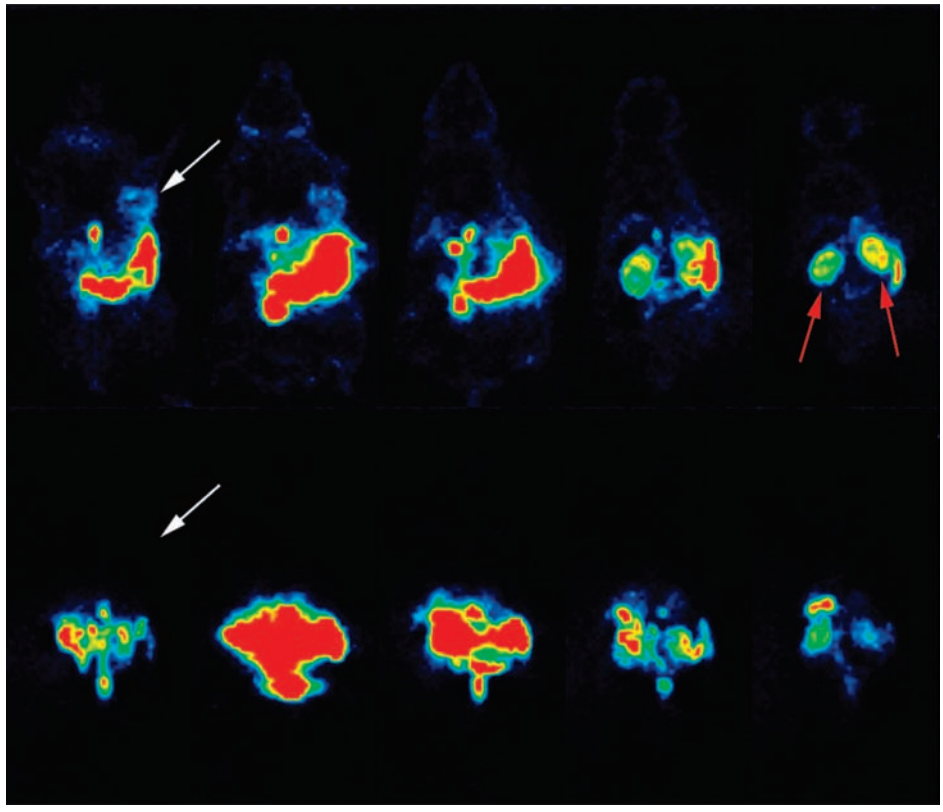

Figure 4. Series of horizontal whole body PET images (ventral to dorsal) of two NMRI nude mice bearing a KB tumor xenograft next to the right forelimb (white arrows). Mice were injected with **[^{18}F]3** under control conditions (top row) or blockade conditions (bottom row) and imaged from 15 to 45 min post-injection. Uptake in FR-positive tumor and kidneys (red arrows) is only present in the control animal demonstrating the specificity of tracer uptake.

the lipophilicity of the fluorinated folates may well correlate with the degree of hepatobiliary elimination.

CONCLUSIONS

On the basis of click chemistry, a new fluorinated folic acid derivative, ^{19}F-click folate, was synthesized and evaluated *in vitro*. ^{19}F-click folate showed nanomolar affinity for the FR on KB tumor cells, which was in a comparable range to that of native folic acid.

The click chemistry approach was successfully applied to the radiolabeling of the corresponding ^{18}F-labeled folic acid derivative. In a two-step radiosynthesis, the ^{18}F-click folate was labeled with fluorine-18 in very good radiochemical yields and high radiochemical purities. The time-saving and robust radiosynthesis and especially the high radiochemical yields are particularly suitable for large-scale productions as needed for routine PET imaging.

In biodistribution studies, a high specificity of ^{18}F-click folate to the FR was observed. High radioactivity accumulation in gall bladder and intestines indicated a pronounced hepatobiliary elimination of ^{18}F-click folate. This finding was confirmed by PET imaging where a high nonspecific accumulation of

radioactivity in the abdominal region was detected. The high specificity of ^{18}F-click folate proves the potential of this class of compounds; however, further investigations toward novel ^{18}F-labeled folates with reduced lipophilicity are warranted.

ACKNOWLEDGMENT

We thank Sabine Baumann, Claudia Keller, and Marianne Kehl for their support with the *in vivo* experiments; Andrea Weber for her help with the *in vitro* tests; and Dr. Cristina Müller for advice and discussion on folates and their pharmacology.

Supporting Information Available: ^{1}H and ^{13}C NMR spectra of compound **3** and **5**. Radio-HPLC chromatograms of quality control, plasma stability studies, and liver microsomes metabolite studies. This material is available free of charge via the Internet at http://pubs.acs.org.

LITERATURE CITED

(1) Leamon, C. P., and Low, P. S. (2001) Folate-mediated targeting: from diagnostic to drug and gene delivery. *Drug Discovery Today 6*, 44–51.

(2) Antony, A. C. (1992) The biological chemistry of folate receptors. *Blood 79*, 2807–2820.

(3) Antony, A. C. (1996) Folate receptors. *Annu. Rev. Nutr. 16*, 501–521.

(4) McHugh, M., and Cheng, Y. C. (1979) Demonstration of a high affinity folate binder in human cell membranes and its characterization in cultured human KB cells. *J. Biol. Chem. 254*, 11312–11318.

(5) Antony, A. C., Utley, C. S., Marcell, P. D., and Kolhouse, J. F. (1982) Isolation, characterization and comparison of the solubilized particulate and soluble folate binding proteins from human milk. *J. Biol. Chem. 257*, 10081–10089.

(6) Kamen, B. A., and Capdevila, A. (1986) Receptor-mediated folate accumulation is regulated by the cellular folate content. *Proc. Natl. Acad. Sci. U.S.A. 83*, 5983–5987.

(7) Kane, M. A., and Waxman, S. (1989) Biology of disease−role of folate binding proteins in folate metabolism. *Lab. Invest. 60*, 737–746.

(8) Ross, J. F., Chaudhuri, P. K., and Ratnam, M. (1994) Differential regulation of folate receptor isoforms in normal and malignant tissues in vivo and in established cell lines. *Cancer 73*, 2432–2443.

(9) Toffoli, G., Cernigoi, C., Russo, A., Gallo, A., Bagnoli, M., and Biocchi, M. (1997) Overexpression of folate binding protein in ovarian cancers. *Int. J. Cancer 74*, 193–198.

(10) Garin-Chesa, P., Campbell, I., Saigo, P. E., Lewis, J. L., Jr., Old, L. J., and Rettig, W. J. (1993) Trophoblast and ovarian cancer antigen LK26. Selectivity and specificity in immunopathology and molecular identification as a folate-binding protein. *Am. J. Pathol. 142*, 557–567.

(11) Weitmann, S. D., Lark, R. H., Coney, L. R., Fort, D. W., Frasca, V., Zurawski, V. R., Jr., and Kamen, B. A. (1992) Distribution of the folate receptor GP38 in normal and malignant cell lines and tissues. *Cancer Res. 52*, 3396–3401.

(12) Ke, C. Y., Mathias, C. J., and Green, M. A. (2003) The folate receptor as a molecular target for tumor-selective radionuclide delivery. *Nucl. Med. Biol. 30*, 811–817.

(13) Leamon, C. P., and Jackman, A. L. (2008) Exploitation of the folate receptor in the management of cancer and inflammatory disease. *Vitamines & Hormones. Volume 79: Folic Acid and Folates* (Litwack, G., Ed.) pp 203−233, Chapter 7, Academic Press/Elsevier.

(14) Ke, C. Y., Mathias, C. J., and Green, M. A. (2004) Folate-receptor-targeted radionuclide imaging agents. *Adv. Drug Delivery Rev. 56*, 1143–1160.

(15) Siegel, B. A., Dehdashti, F., Mutch, D. G., Podoloff, D. A., Wendt, R., Sutton, G. P., Burt, R. W., Ellis, P. R., Mathias, C. J., Green, M. A., and Gershenson, D. M. (2003) Evaluation of ^{111}In-DTPA-folate as a receptor-targeted diagnostic agent for ovarian cancer: initial clinical results. *J. Nucl. Med. 44*, 700–707.

(16) Müller, C., Dumas, C., Hoffmann, U., Schubiger, P. A., and Schibli, R. (2004) Organometallic ^{99m}Tc-technetium(I)- and Re-rhenium(I)-folate derivatives for potential use in nuclear medicine. *J. Organomet. Chem. 689*, 4712–4721.

(17) Leamon, C. P., DePrince, R. B., and Hendren, R. W. (1999) Folate-mediated drug delivery: Effect of alternative conjugation chemistry. *J. Drug Targeting 7*, 157–169.

(18) McAlinden, T. P., Hynes, J. B., Patil, S. A., Westerhof, G. R., Jansen, G., Schornagel, J. H., Kerwar, S. S., and Freisheim, J. H. (1991) Synthesis and biological evaluation of a fluorescent analogue of folic acid. *Biochemistry 30*, 5674–5681.

(19) Wang, S., Luo, J., Lantrip, D. A., Waters, D. J., Mathias, C. J., Green, M. A., Fuchs, P. L., and Low, P. S. (1997) Design and synthesis of [^{111}In]DTPA-folate for use as a tumor-targeted radiopharmaceutical. *Bioconjugate Chem. 8*, 673–679.

(20) Guo, W., Hinkle, G. H., and Lee, R. J. (1999) ^{99m}TC-HYNIC-folate: A novel receptor-based targeted radiopharmaceutical for tumor imaging. *J. Nucl. Med. 40*, 1563–1569.

(21) Sudimack, J., and Lee, R. J. (2000) Targeted drug delivery via the folate receptor. *Adv. Drug Delivery Rev. 41*, 147–162.

(22) Ke, C.-Y., Mathias, C. J., and Green, M. A. (2001) Targeting the tumor-associated folate receptor with ^{111}In-DTPA conjugate of pteroic acid. *J. Nucl. Med. 42*, 114P–115P.

(23) Dollé, F., Hinnen, F., Vauffrey, F., Tavitian, B., and Crouzel, C. (1998) A general method for labelling oligodeoxynucleotides with ^{18}F for in vivo PET imaging. *J. Label. Compd. Radiopharm. 39*, 319–330.

(24) Bettio, A., Honer, M., Müller, C., Brühlmeier, M., Müller, U., Schibli, R., Groehn, V., Schubiger, P. A., and Ametamey, S. M. (2006) Synthesis and preclinical evaluation of a folic acid derivative labeled with ^{18}F for PET imaging of folate receptor-positive tumors. *J. Nucl. Med. 47*, 1153–1160.

(25) Al Jammaz, I., Al-Otaibi, B., Okarvi, S., and Amartey, J. (2006) Novel synthesis of [^{18}F]-fluorobenzene and pyridinecarbohydrazide-folates as potential PET radiopharmaceuticals. *J. Label. Compd. Radiopharm. 49*, 125–137.

(26) Tornøe, C. W., Christensen, C., and Meldal, M. (2002) Peptidotriazoles on solid phase: [1,2,3]-triazoles by regiospecific copper(I)-catalyzed 1,3-dipolar cycloadditions of terminal alkynes to azides. *J. Org. Chem. 67*, 3057–3064.

(27) Rostovtsev, V. V., Green, L. G., Fokin, V. V., and Sharpless, K. B. (2002) A stepwise Huisgen cycloaddition process: copper(I)-catalyzed regioselective "ligation" of azides and terminal alkynes. *Angew. Chem., Int. Ed. 41*, 2596–2599.

(28) Kolb, H. C., Finn, M. G., and Sharpless, K. B. (2001) Click Chemistry: diverse chemical function from a few good reactions. *Angew. Chem., Int. Ed. 40*, 2004–2021.

(29) Bock, V. D., Hiemstra, H., and van Maarseveen, J. H. (2006) Cu^{I}-catalyzed alkyne-azide "click" cycloadditions from a mechanistic and synthetic perspective. *Eur. J. Org. Chem.*, 51–68.

(30) Marik, J., and Sutcliffe, J. L. (2006) Click for PET: rapid preparation of [^{18}F]fluoropeptides using CuI catalyzed 1,3-dipolar cycloaddition. *Tetrahedron Lett. 47*, 6681–6684.

(31) Ross, T. L. (2008) Recent advances in fluorine-18 radiopharmaceuticals: the click chemistry approach applied to fluorine-18. *Curr. Radiopharm.*, in press.

(32) Jeavons, A. P., Chandler, R. A., and Dettmar, C. A. R. (1999) A 3D HIDAC-PET camera with submillimetre resolution for imaging small animals. *IEEE Trans. Nucl. Sci. 46*, 468–473.

(33) Missimer, J., Madi, Z., Honer, M., Keller, C., Schubiger, P. A., and Ametamey, S. M. (2004) Performance evaluation of the 16-module quad-HIDAC small animal PET camera. *Phys. Med. Biol. 49*, 2069–2081.

(34) Van Hest, J. C. M., Kiick, K. L., and Tirrell, D. A. (2000) Efficient incorporation of unsaturated methionine analogues into proteins *in vivo*. *J. Am. Chem. Soc. 122*, 1282–1288.

(35) Mindt, T. L., Müller, C., Melis, M., de Jong, M., and Schibli, R. (2008) "Click-to-Chelate": *in vitro* and *in vivo* comparison of a $^{99m}Tc(CO)_3$-labeled N(t)-histidine folate derivative with its isostructural, clicked 1,2,3-triazole analogue. *Bioconjugate Chem. 19*, 1689–1695.

(36) Link, A. J., Vink, M. K. S., and Tirrell, D. A. (2004) Presentation and detection of azide functionality in bacterial cell surface proteins. *J. Am. Chem. Soc. 126*, 10598–10602.

(37) Antony, A. C., Kane, M. A., Portillo, R. M., Elwood, P. C., and Kolhouse, J. F. (1985) Studies of the role of a particulate folate-binding protein in the uptake of 5-methyltetrahydrofolate by cultured human KB cells. *J. Biol. Chem. 260*, 14911–14917.

(38) Cheng, Y. C., and Prusoff, W. H. (1973) Relationship between the inhibition constant (K_i) and the concentration of inhibitor which caused 50% inhibition (I_{50}) of an enzymatic reaction. *Biochem. Pharmacol. 22*, 3099–3108.

(39) Mathias, C. J., Wang, S., Lee, R. J., Waters, D. J., Low, P. S., and Green, M. A. (1996) Tumor-selective radiopharmaceutical targeting via receptor-mediated endocytosis of gallium-67-deferoxamine-folate. *J. Nucl. Med. 37*, 1003–1008.

(40) Honer, M., Brühlmeier, M., Missimer, J., Schubiger, A. P., and Ametamey, S. M. (2004) Dynamic imaging of striatal D_2 receptors in mice using quad-HIDAC PET. *J. Nucl. Med. 45*, 464–470.

(41) Himo, T., Lovell, T., Hilgraf, R., Rostovtsev, V. V., Noodleman, L., Sharpless, K. B., and Fokin, V. V. (2005) Copper(I)-catalyzed synthesis of azoles. DFT study predicts unprecedented reactivity and intermediates. *J. Am. Chem. Soc. 127*, 210–216.

(42) Goresky, C. A., Watanabe, H., and Johns, D. G. (1963) The renal excretion of folic acid. *J. Clin. Invest. 42*, 1841–1849.

(43) Morshed, K. M., Ross, D. M., and McMartin, K. E. (1997) Folate transport proteins mediate the bidirectional transport of 5-methyltetrahydrofolate in cultured human proximal tubule cells. *J. Nutr. 127*, 1137–1147.

(44) Birn, H. (2006) The kidney in vitamin B_{12} and folate homeostasis: characterization of receptors for tubular uptake of vitamins and carrier proteins. *Am. J. Physiol. Renal Physiol. 291*, 22–36.

(45) Mathias, C. J., Lewis, M. R., Reichert, D. E., Laforest, R., Sharp, T. L., Lewis, J. S., Yang, Z. F., Waters, D. J., Snyder, P. W., Low, P. S., Welch, M. J., and Green, M. A. (2003) Preparation of ^{66}Ga- and ^{68}Ga-labeled Ga(III)-deferoxamine-folate as potential folate-receptor-targeted PET radiopharmaceuticals. *Nucl. Med. Biol. 30*, 725–731.

(46) Zanzonico, P., O'Donoghue, J., Chapman, J. D., Schneider, R., Cai, S., Larson, S., Wen, B., Chen, Y., Finn, R, Ruan, S., Gerweck, L., Humm, J., and Ling, C. (2004) Iodine-124-labeled iodo-azomycin-galactoside imaging of tumor hypoxia in mice with serial microPET scanning. *Eur. J. Nucl. Med. Mol. Imaging 31*, 117–128.

(47) Müller, C., Forrer, F., Schibli, R., Krenning, E. P., and de Jong, M. (2008) SPECT study of folate receptor-positive malignant and normal tissues in mice using a novel ^{99m}Tc-radiofolate. *J. Nucl. Med. 49*, 310–317.

(48) Nowotnik, D. P., Feld, T., and Nunn, A. D. (1993) Examination of some reversed-phase high-performance liquid chromatography systems for determination of lipophilicity. *J. Chromatogr. 630*, 105–115.

BC800356R

Supporting Information for:

Click Chemistry Radiosynthesis and Preclinical Evaluation of a New ^{18}F-Labelled Folic Acid Derivative

Tobias L. Ross, Michael Honer, Phoebe Y. H. Lam, Thomas L. Mindt*, Viola Groehn[#], Roger Schibli*, P. August Schubiger, Simon M. Ametamey

*Animal Imaging Center - PET, Center for Pharmaceutical Science of ETH, PSI and USZ, ETH Zürich, 8093 Zürich; *Department of Chemistry and Applied Biosciences, ETH Zürich, 8093 Zürich; [#]Merck Eprova AG, 8200 Schaffhausen*

^{1}H- and ^{13}C-NMR spectra of γ-(4-(4-[^{19}F]fluorobutyl)triazo-1-yl)butyl-folic acid amide (^{19}F-click folate):

DRX-500: 1H of MT382/A in DMSO at 298K

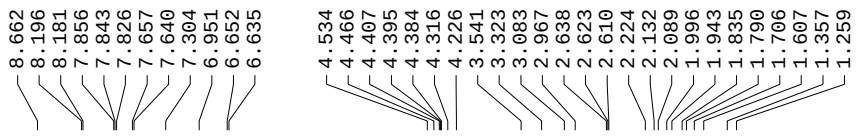

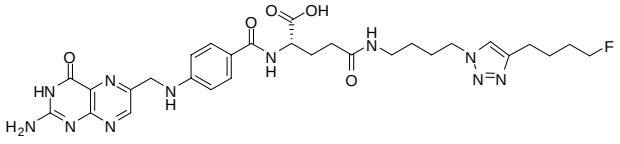

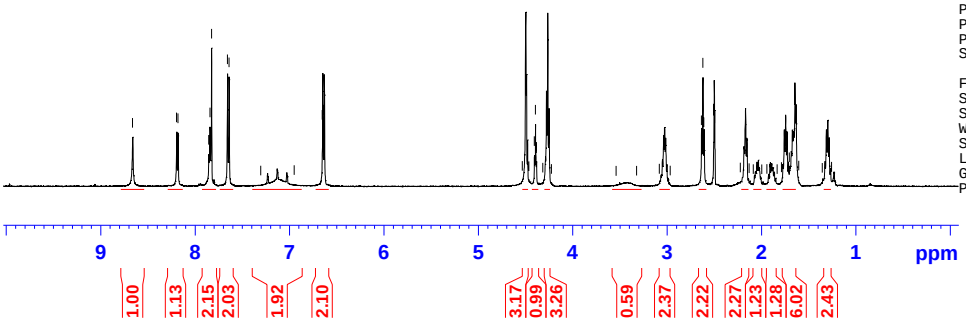


```
Current Data Parameters
NAME          R47MT382-A
EXPNO                  1
PROCNO                 1

F2 - Acquisition Parameters
Date_           20061124
Time               15.39
INSTRUM          drx500
PROBHD   5 mm BBO BB-1H
PULPROG          zgpr.ok
TD                32768
SOLVENT           CDCl3
NS                    4
DS                    0
SWH           10000.000 Hz
FIDRES         0.305176 Hz
AQ             1.6385000 sec
RG                  256
DW               50.000 usec
DE                6.00 usec
TE                298.0 K
D1            0.10000000 sec
d12           0.00002000 sec
d13           0.00000300 sec

======== CHANNEL f1 ========
NUC1                 1H
P1                 9.30 usec
PL1               -4.00 dB
PL9               55.00 dB
SFO1        500.1316955 MHz

F2 - Processing parameters
SI                16384
SF          500.1300052 MHz
WDW                  EM
SSB                   0
LB                 0.10 Hz
GB                    0
PC                 1.00
```

DRX-500: 13C{1H} of in CDCl3 at 298K

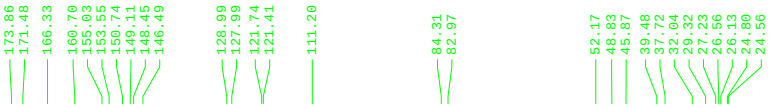

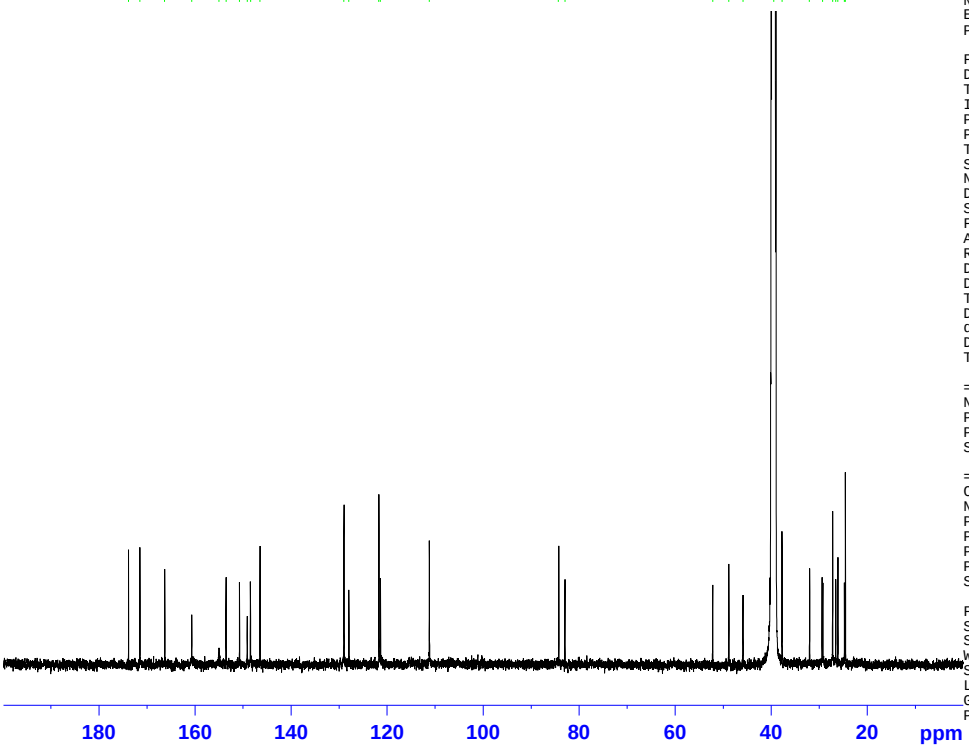


```
Current Data Parameters
NAME          R47MT382-A
EXPNO                  2
PROCNO                 1

F2 - Acquisition Parameters
Date_           20061126
Time               14.36
INSTRUM          drx500
PROBHD   5 mm BBO BB-1H
PULPROG          zgpg30
TD                65536
SOLVENT           CDCl3
NS                32768
DS                    4
SWH           30030.029 Hz
FIDRES         0.458222 Hz
AQ             1.0912410 sec
RG                32768
DW               16.650 usec
DE                6.00 usec
TE                298.0 K
D1            4.00000000 sec
d11           0.03000000 sec
DELTA         3.90000010 sec
TD0                   1

======== CHANNEL f1 ========
NUC1                13C
P1                6.00 usec
PL1              -3.00 dB
SFO1        125.7703643 MHz

======== CHANNEL f2 ========
CPDPRG2          waltz16
NUC2                 1H
PCPD2             64.00 usec
PL2               -4.00 dB
PL12              12.75 dB
PL13              21.00 dB
SFO2        500.1320005 MHz

F2 - Processing parameters
SI                32768
SF          125.7578484 MHz
WDW                  EM
SSB                   0
LB                 2.00 Hz
GB                    0
PC                 1.40
```

^{1}H-NMR spectrum of 6-[^{19}F]fluoro-1-hexyne:

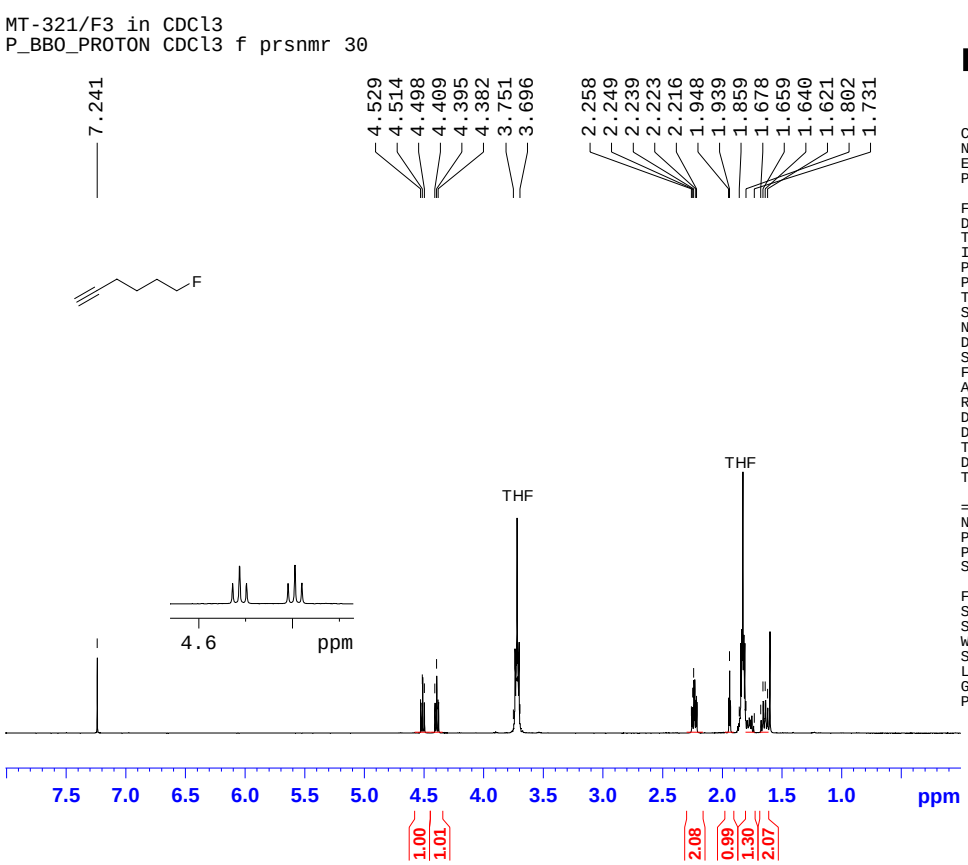


```
Current Data Parameters
NAME          R47MT380F3
EXPNO                  1
PROCNO                 1

F2 - Acquisition Parameters
Date_           20061120
Time               13.33
INSTRUM            av400
PROBHD   5 mm PABBO BB-
PULPROG             zg30
TD                 65536
SOLVENT            CDCl3
NS                    16
DS                     2
SWH             8278.146 Hz
FIDRES          0.126314 Hz
AQ              3.9584243 sec
RG                   256
DW                60.400 usec
DE                 6.00 usec
TE                297.7 K
D1           1.00000000 sec
TD0                    1

======== CHANNEL f1 ========
NUC1                  1H
P1                 14.00 usec
PL1                -1.00 dB
SFO1         400.1324710 MHz

F2 - Processing parameters
SI                 32768
SF           400.1300172 MHz
WDW                   EM
SSB                    0
LB                  0.30 Hz
GB                     0
PC                  1.00
```

Radio-/UV-HPLC chromatogram of quality control test of "^{18}F-click folate":

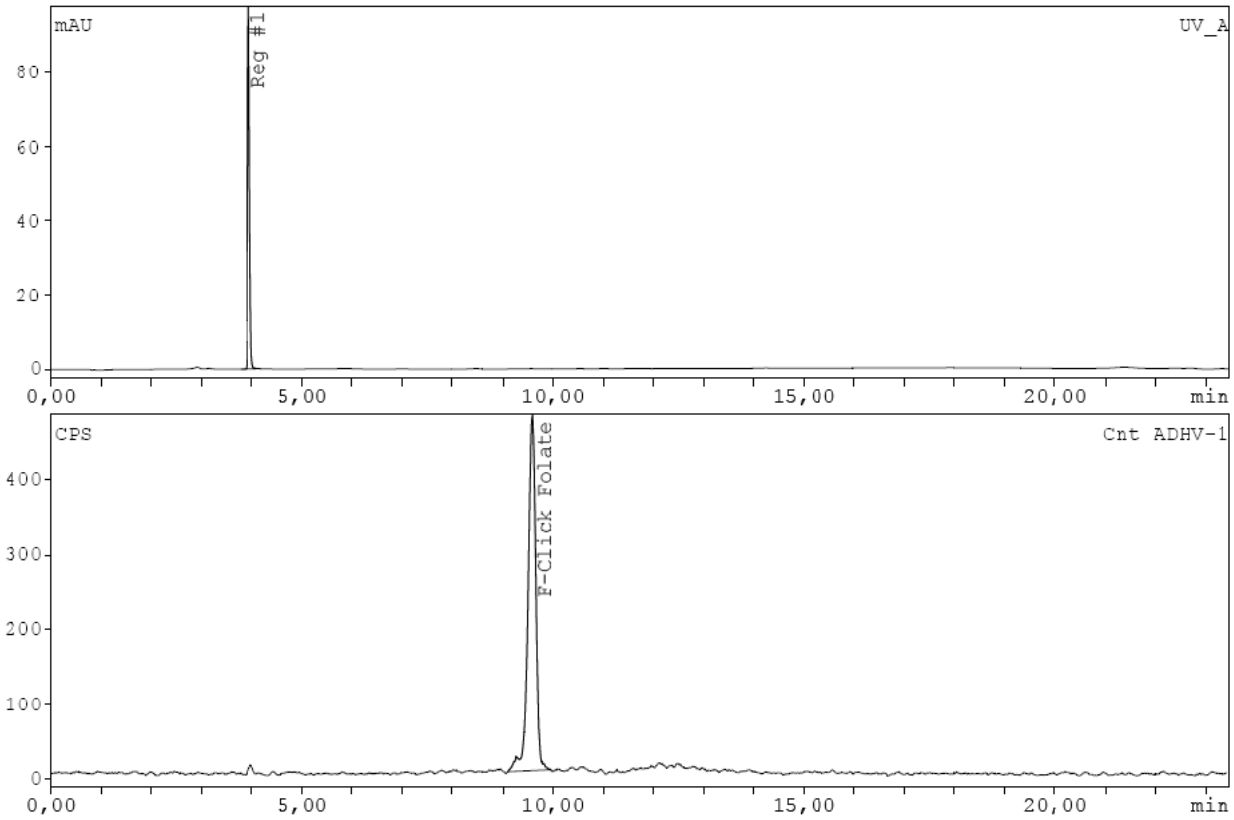

Radio-HPLC chromatogram of human plasma stability tests (0 min incubation):

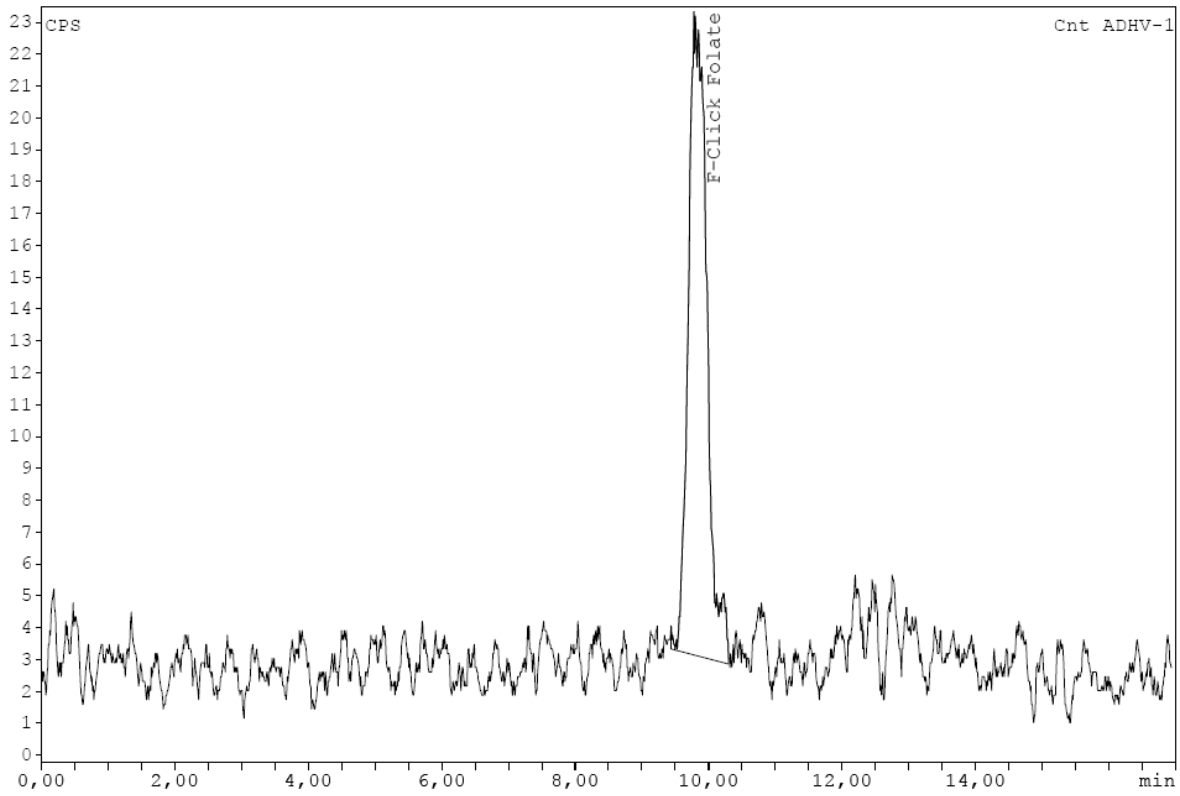

Radio-HPLC chromatogram of human plasma stability tests (5 min incubation):

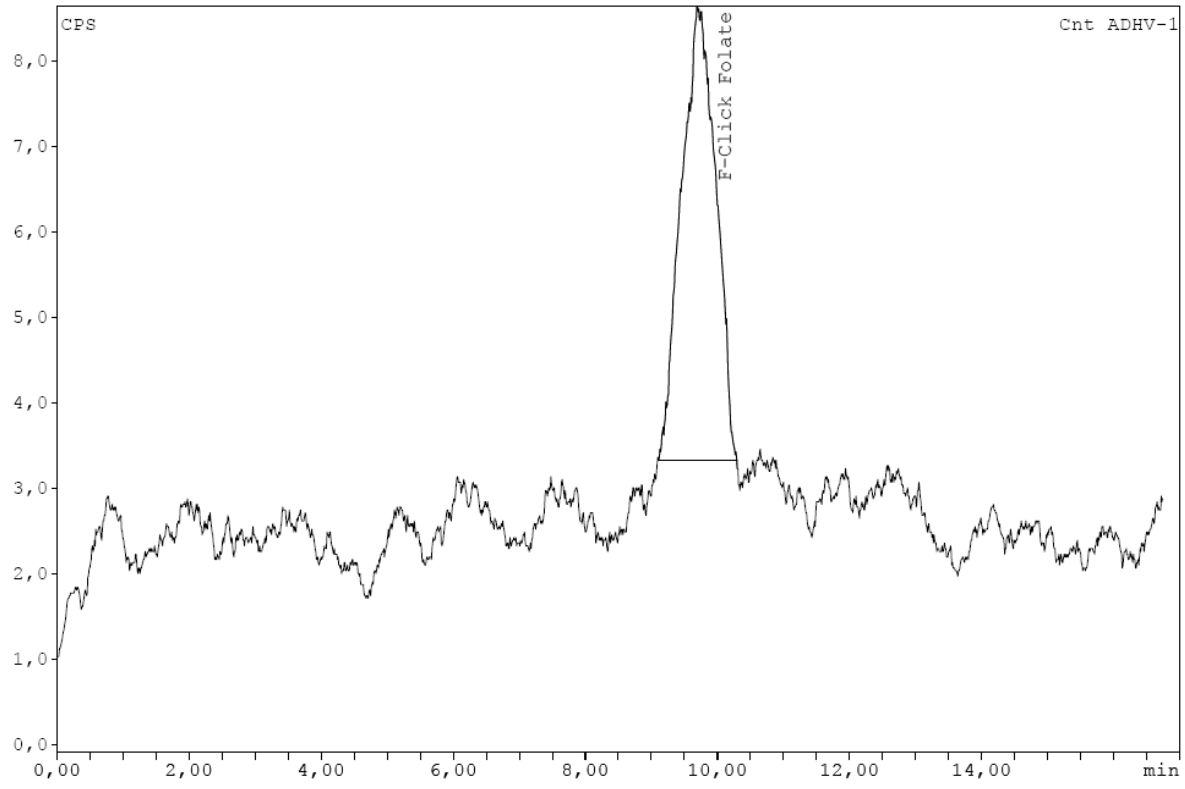

Radio-HPLC chromatogram of human plasma stability tests (30 min incubation):

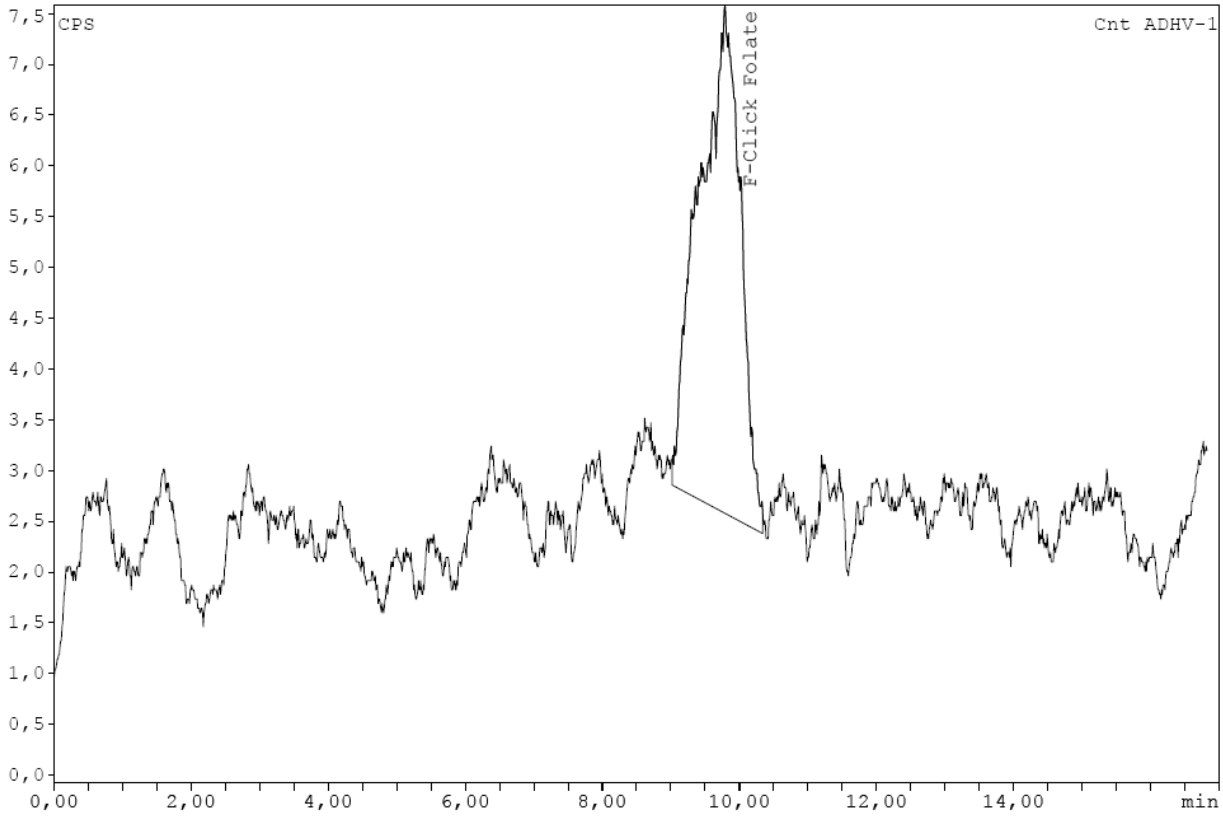

Radio-HPLC chromatogram of human plasma stability tests (120 min incubation):

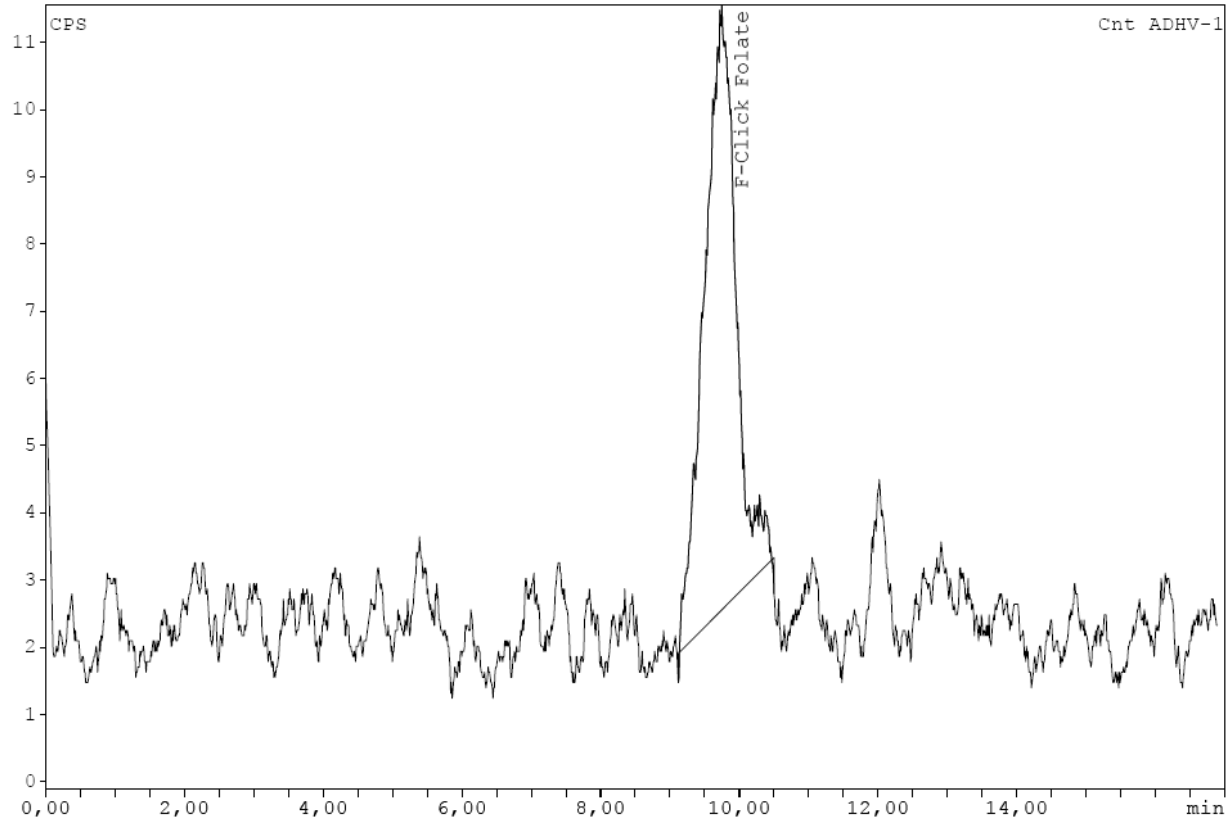

Radio-HPLC chromatogram of murine liver microsome studies (0 min):

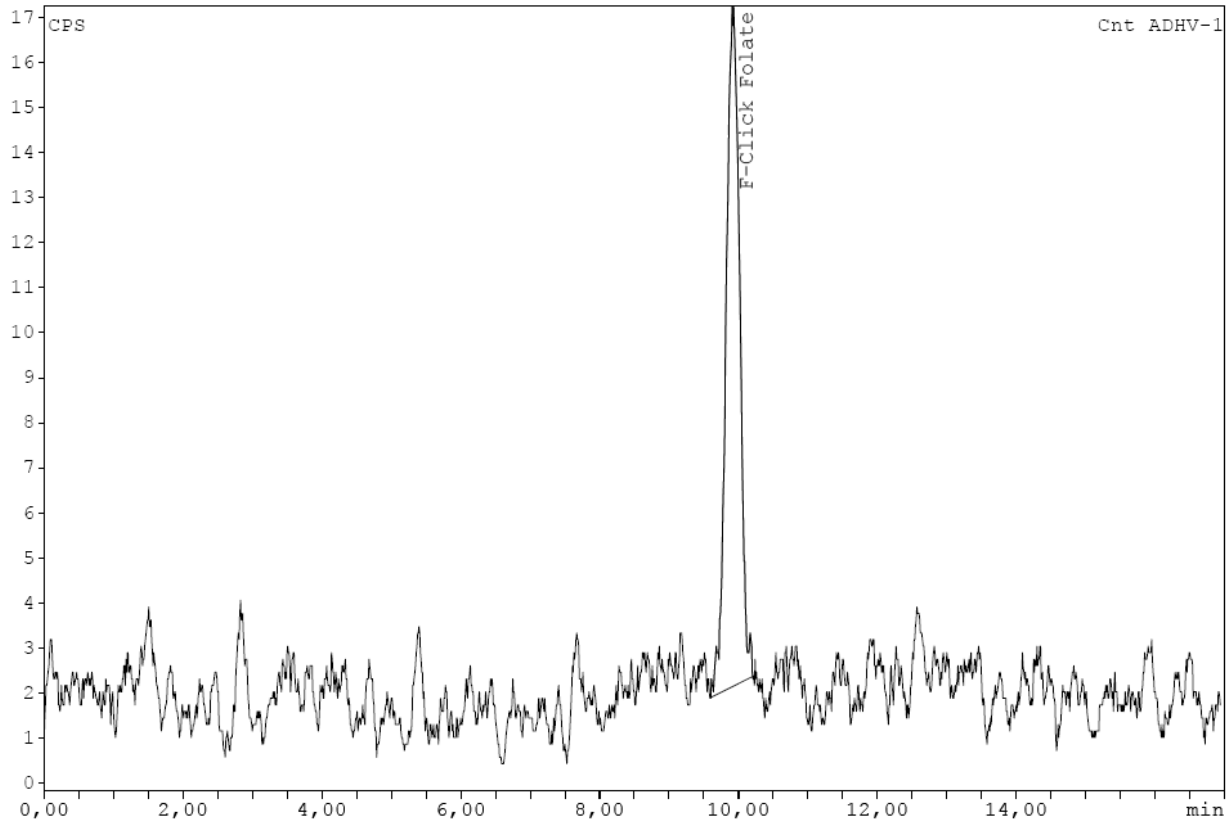

Radio-HPLC chromatogram of murine liver microsome studies (5 min):

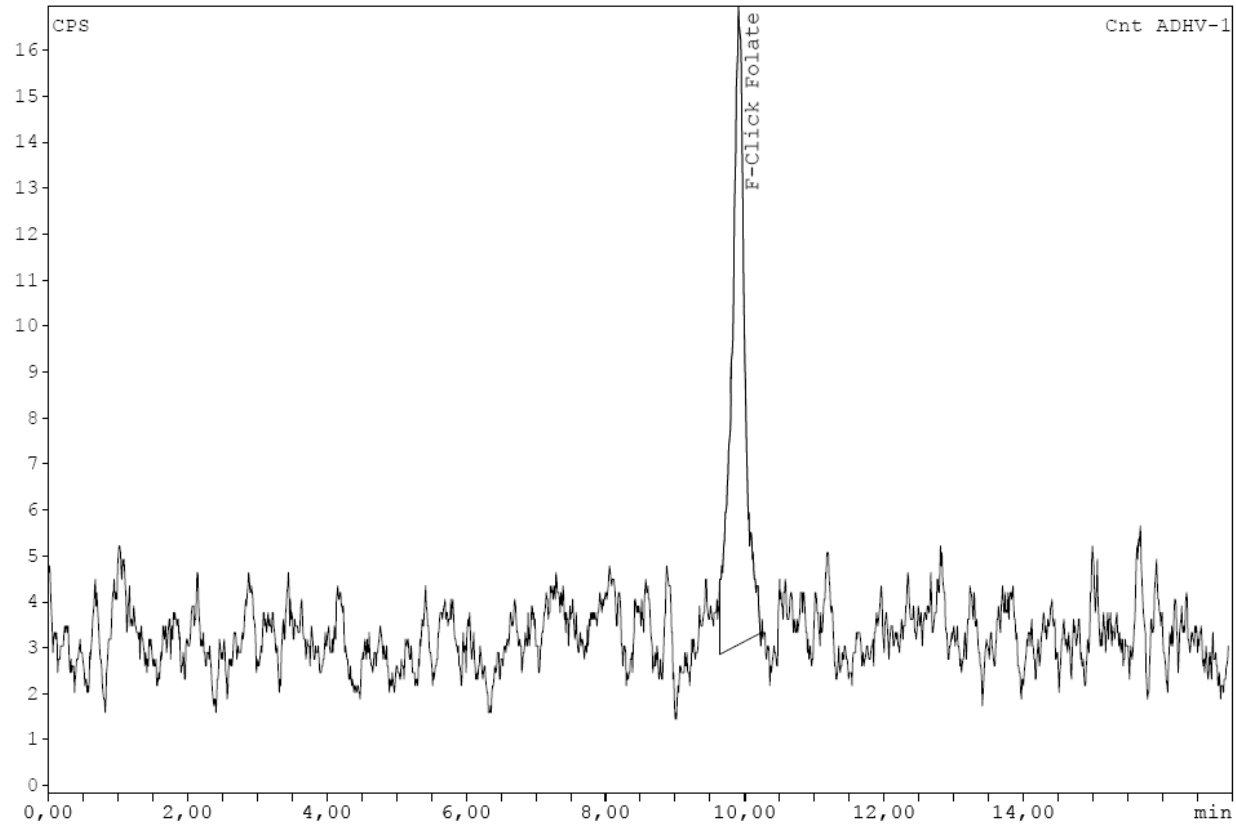

Radio-HPLC chromatogram of murine liver microsome studies (30 min):

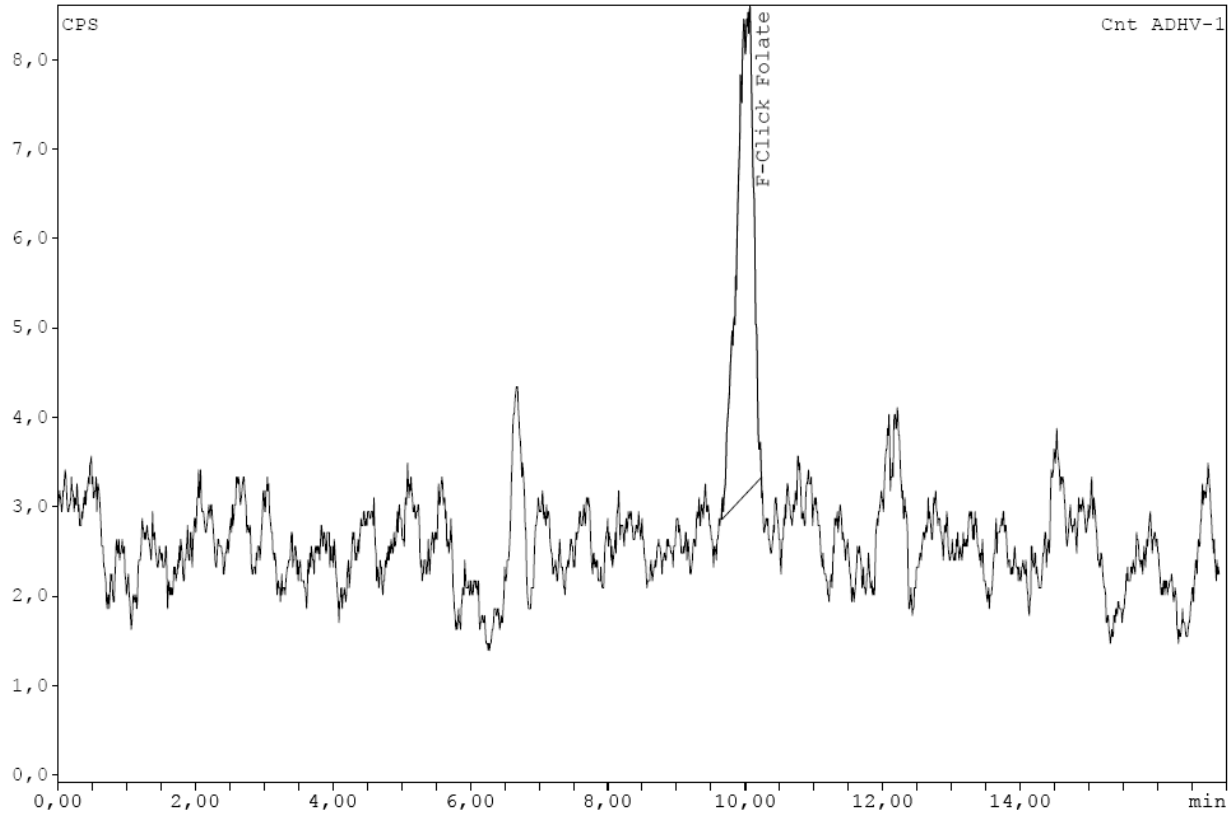

Radio-HPLC chromatogram of human liver microsome studies (0 min):

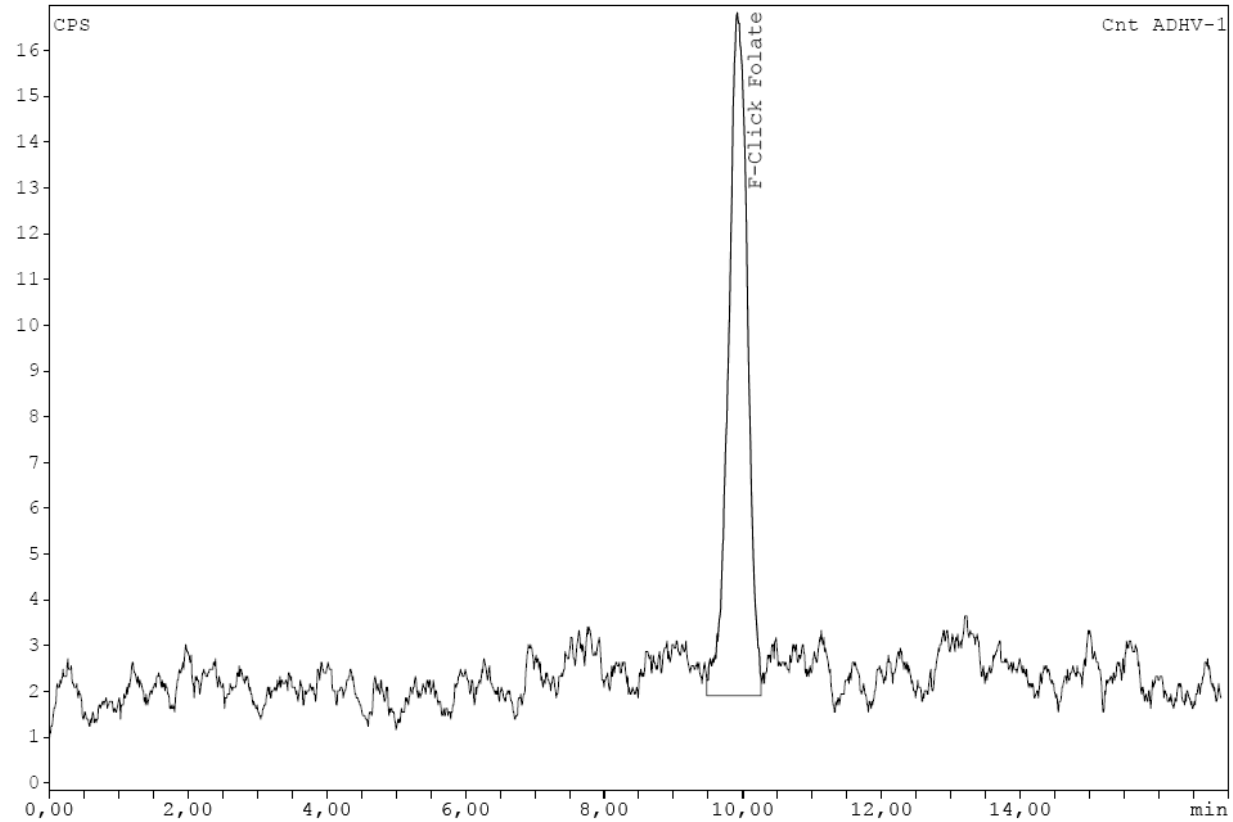

Radio-HPLC chromatogram of human liver microsome studies (5 min):

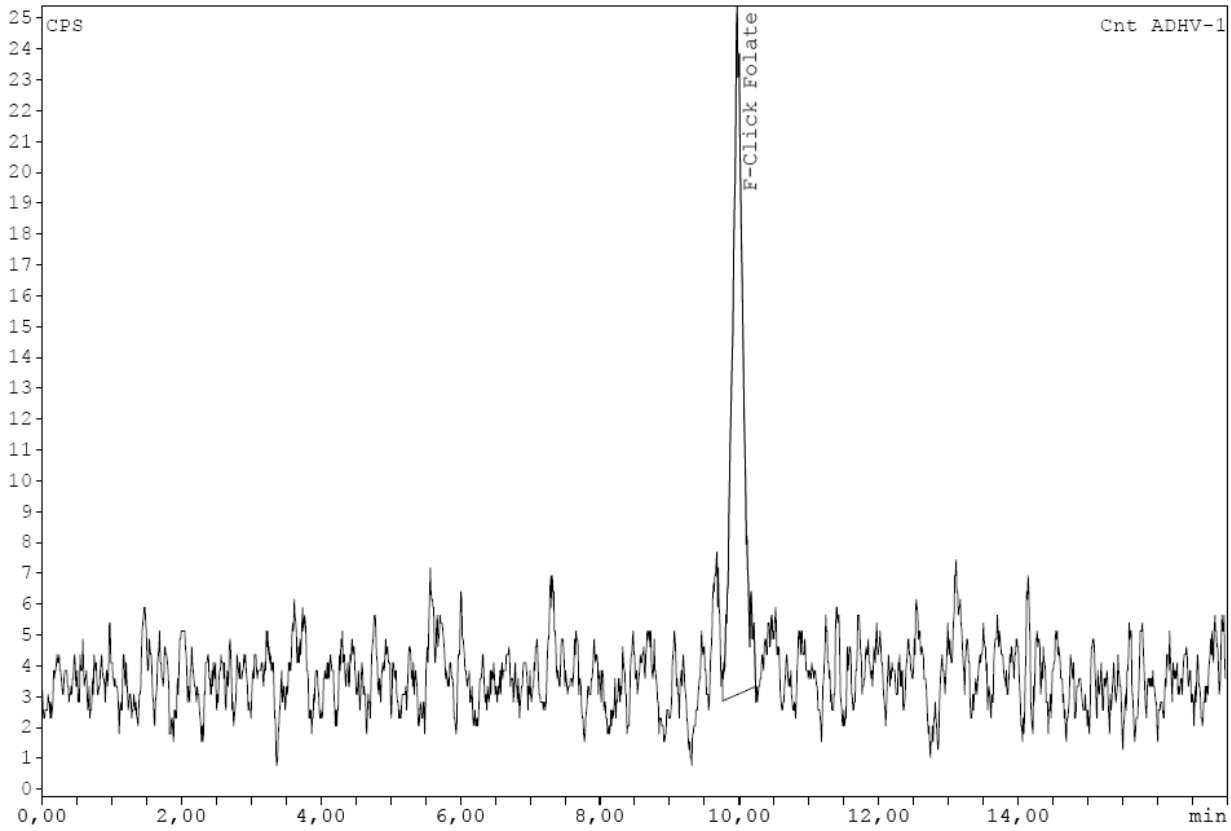

Radio-HPLC chromatogram of human liver microsome studies (30 min):

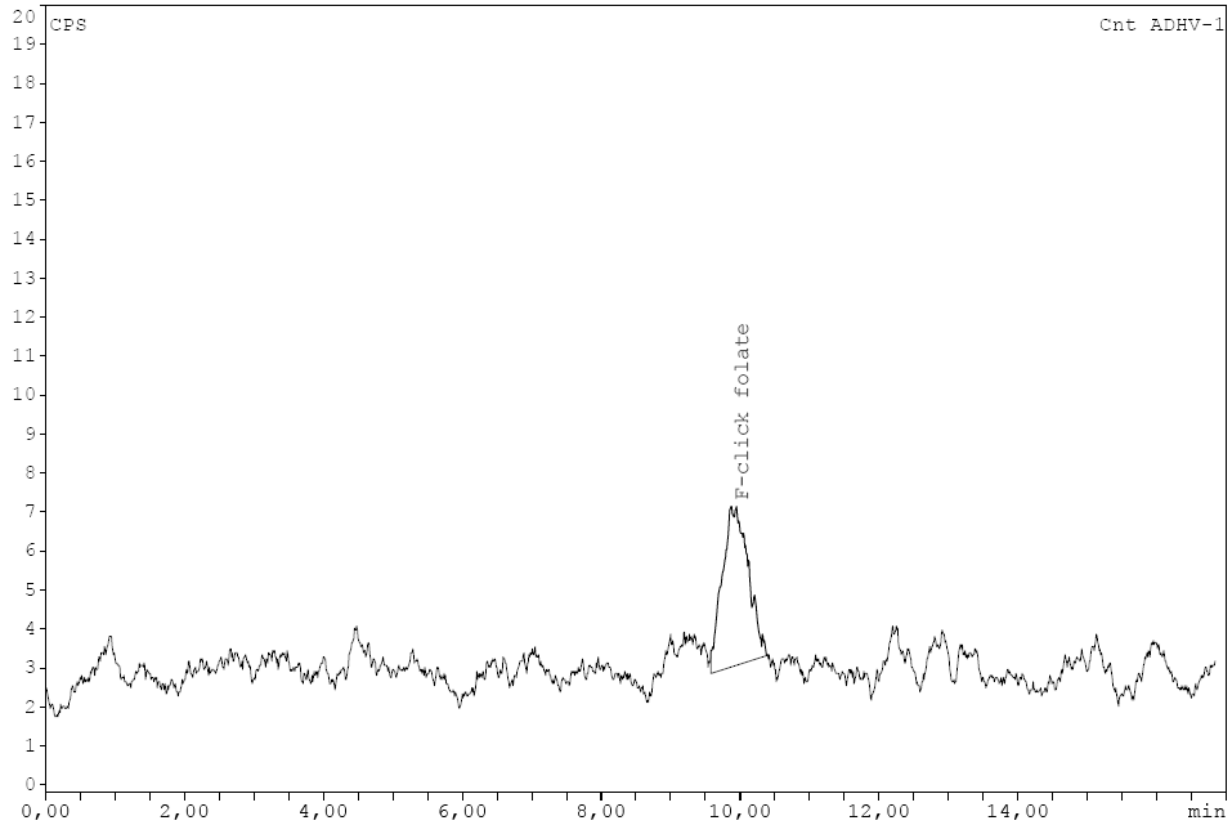

Bioconjugate Chemistry 20th Anniversary

Subscriber access provided by SHEMYAKIN-OVCHINNIKOV INST

Article

Paramagnetic Lipid-Coated Silica Nanoparticles with a Fluorescent Quantum Dot Core: A New Contrast Agent Platform for Multimodality Imaging

Rolf Koole, Matti M. van Schooneveld, Jan Hilhorst, Karolien Castermans, David P. Cormode, Gustav J. Strijkers, Celso de Mello Donega#, Daniel Vanmaekelbergh, Arjan W. Griffioen, Klaas Nicolay, Zahi A. Fayad, Andries Meijerink, and Willem J. M. Mulder

Bioconjugate Chem., **2008**, 19 (12), 2471-2479• DOI: 10.1021/bc800368x • Publication Date (Web): 26 November 2008

Downloaded from http://pubs.acs.org on May 2, 2009

More About This Article

Additional resources and features associated with this article are available within the HTML version:

- Supporting Information
- Links to the 1 articles that cite this article, as of the time of this article download
- Access to high resolution figures
- Links to articles and content related to this article
- Copyright permission to reproduce figures and/or text from this article

View the Full Text HTML

ACS Publications
High quality. High impact.

Bioconjugate Chemistry is published by the American Chemical Society. 1155 Sixteenth Street N.W., Washington, DC 20036

Paramagnetic Lipid-Coated Silica Nanoparticles with a Fluorescent Quantum Dot Core: A New Contrast Agent Platform for Multimodality Imaging

Rolf Koole,[†] Matti M. van Schooneveld,[†] Jan Hilhorst,[†] Karolien Castermans,[‡] David P. Cormode,[§] Gustav J. Strijkers,[||] Celso de Mello Donegá,[†] Daniel Vanmaekelbergh,[†] Arjan W. Griffioen,[‡] Klaas Nicolay,[||] Zahi A. Fayad,[§] Andries Meijerink,[†] and Willem J. M. Mulder*[,§]

Condensed Matter and Interfaces, University Utrecht, P.O. Box 80000, 3508 TA Utrecht, The Netherlands, Angiogenesis Laboratory, Research Institute for Growth and Development, Department of Pathology/Internal Medicine, Maastricht University and University Hospital, P.O. Box 5800, 6202 AZ Maastricht, The Netherlands, Translational and Molecular Imaging Institute and Imaging Science Laboratories, Mount Sinai School of Medicine, One Gustave L. Levy Place, New York, New York 10029, and Biomedical NMR, Department of Biomedical Engineering, Eindhoven University of Technology, P.O. Box 513, 5600 MB Eindhoven, The Netherlands.
Received August 28, 2008; Revised Manuscript Received October 27, 2008

Silica particles as a nanoparticulate carrier material for contrast agents have received considerable attention the past few years, since the material holds great promise for biomedical applications. A key feature for successful application of this material in vivo is biocompatibility, which may be significantly improved by appropriate surface modification. In this study, we report a novel strategy to coat silica particles with a dense monolayer of paramagnetic and PEGylated lipids. The silica nanoparticles carry a quantum dot in their center and are made target-specific by the conjugation of multiple $\alpha v\beta 3$-integrin-specific RGD-peptides. We demonstrate their specific uptake by endothelial cells in vitro using fluorescence microscopy, quantitative fluorescence imaging, and magnetic resonance imaging. The lipid-coated silica particles introduced here represent a new platform for nanoparticulate multimodality contrast agents.

INTRODUCTION

Nanoparticles have been explored for a few decades now as vehicles to deliver therapeutic agents (*1*). Traditionally, nanoparticles composed of naturally occurring molecules, such as bilayered vesicles composed of phospholipids, have been utilized (*2*). The revolution in nanoscience has resulted in the development of a tremendous amount of new materials that hold great potential for biomedical applications (*3*). In the field of diagnostic imaging, nanoparticles also create new possibilities. These include iron oxide nanoparticles for magnetic resonance imaging (MRI) (*4*), carbon nanotubes for MRI (*5*), or gold nanoparticles for computed tomography (CT) (*6*). Semiconductor nanocrystals, also known as quantum dots (QDs), have been recognized as an optical contrast agent due to their outstanding fluorescent properties (*7*). A major advantage of the application of nanoparticles for biomedical purposes is that they can have multiple properties integrated within one single carrier particle. In addition, the possibilities for surface modification create flexibility for a large range of applications. The above-mentioned features of nanoparticles have resulted in the development of nanoparticles that are suitable for both therapeutic and diagnostic purposes (*8*), as well as nanoparticles that can be employed for different imaging modalities, so-called multimodality nanoparticles (*9*).

Silica as a nanoparticulate carrier material has received considerable attention the past few years. The incorporation of nanoparticles in silica has been reported for semiconductor (*10, 11*), metallic (*12, 13*), and magnetic nanocrystals (*14*). In addition, the simultaneous incorporation of magnetic nanoparticles and QDs in silica nanospheres has been reported recently (*15*−*18*). Doping of silica particles with dye molecules is well-established (*19*−*21*), while combinations of dyes with other functionalities within one silica sphere have also been reported (*22*−*24*). The use of these silica-coated nanoparticles and/or dyes as contrast agents for bioimaging applications benefits from the high versatility and well-known surface chemistry of silica nanospheres (*25*). The possibility of combining multiple properties within one silica nanosphere as well as the control over the final particle size over a broad range (20 nm to 5 μm) make these composite particles especially suitable as carriers for multiple diagnostically active materials (*26*−*29*). Most importantly, a key feature for successful application of this material in vivo is biocompatibility, which may be significantly improved by appropriate surface modification.

Two distinct surface modifications to enhance the bioapplicability of silica nanospheres have been reported to date, which both depend on the use of silane coupling agents. In the first method, the silica spheres are terminated by an amine or thiol group using APS or MPS (aminopropyltrimethoxysilane and mercaptopropylmethoxysilane), to which biofunctional groups can be covalently linked (*24, 30*−*34*). The second method involves the modification of the silica surface by molecules that already have a silane group integrated within the molecule (*24, 32, 34, 35*). Most of the aforementioned reports use both strategies simultaneously to attach functional moieties, including antibodies, paramagnetic molecules, and poly(ethylene glycol) (PEG), through an amide bond. Although some variation in surface functionalization is possible, there are several serious drawbacks for these methods. First, due to steric hindrance and differences in reactivity with coupling agents, it is not clear to what extent

* Corresponding author. Willem Mulder, e-mail: willem.mulder@mountsinai.org; tel: 2122417717; fax: +1 212 534 2683.
[†] University Utrecht.
[‡] Maastricht University and University Hospital.
[§] Mount Sinai School of Medicine.
[||] Eindhoven University of Technology.

10.1021/bc800368x CCC: $40.75 © 2008 American Chemical Society
Published on Web 11/26/2008

and in what ratio the silica surface is covered by the pegylated and biofunctional molecules. Second, the density of the (pegylated) coating around the silica spheres is not well-defined, which limits the optimal use of the surface area payload and may lead to suboptimal biocompatibility. In addition, depending on the pH, this methodology results in the presence of negatively positively charged hydroxyl/amine groups, which may unfavorably affect the stability under physiological conditions. Third, the flexibility of these methods is limited to molecules with reactive groups for the covalent linking step.

In the current study, we report a novel strategy to coat silica particles with a dense monolayer of lipids without the usage of (silane) coupling agents. In the first step, the silica particles are rendered hydrophobic, after which they are coated with both paramagnetic and PEGylated lipids in a second step. This highly flexible and widely applicable coating method for silica particles also allows for the conjugation of target-specific molecules at the surface of the nanoparticle. In the present case, we use highly monodisperse silica particles that have a single core−shell−shell (CSS) QD incorporated into the center and paramagnetic Gd-DTPA-DSA in the lipid coating, to enable their detection with both fluorescence techniques and MRI. As a proof-of-principle, we demonstrate target-specific multimodality imaging of $\alpha v\beta 3$-integrin expression on cultured endothelial cells using our lipid-coated QD/silica nanoparticles.

EXPERIMENTAL PROCEDURES

Materials. 1,2-Distearoyl-*sn*-glycero-3-phosphoethanolamine-*N*-[methoxy(poly(ethylene glycol))-2000] (PEG-DSPE) and 1,2-distearoyl-*sn*-glycero-3-phosphoethanolamine-*N*-[maleimide-(poly(ethylene glycol))2000] (Mal-PEG-DSPE) were purchased from Avanti Polar Lipids. Gd-DTPA-bis(stearylamide) (Gd-DTPA-DSA) was obtained from Gateway Chemical Technology. Methanol (anhydrous, 99.8%), octadecanol (99%), Igepal (CO-520), oleic acid (90%), octadecylamine (ODA 97%), and octadecene (ODE, 90%) were purchased from Aldrich. Tetraethyl orthosilicate (TEOS, 99%) was obtained from Johnson Matthey. Acetone (p.a.), chloroform (p.a.), ammonia (25% in water, p.a.), cadmium oxide (>99%), zinc oxide (>99%), and HEPES ($C_8H_{18}N_2O_4S$, >99%) were purchased from Merck. The HEPES buffer contained 2.38 g/L HEPES and 8.0 g/L NaCl (99.8%, Baker), and the pH was adjusted to 6.7 by addition of a NaOH solution. Sulfur powder (99.999%) was obtained from Alfa Aesar, and ethanol (>99.8%) from Riedel de Haën. The cyclic 5-mer RGD (c(RGDf(-S-acetylthioacetyl)K)) was synthesized at a purity of 95% by Ansynth Service BV (The Netherlands).

Synthesis of Silica-Coated QDs. CdSe (core) QDs (3.4 nm in diameter) were synthesized by the conventional organometallic synthesis route, described in detail elsewhere (*36*). The CdSe QDs were coated with 7 monolayers of inorganic shells ($2 \times$ CdS, $3 \times Cd_{0.5}Zn_{0.5}S$, $2 \times$ ZnS) according to a SILAR method that was recently published by Xie et al. (*37*). Addition of these shells was performed by adding precalculated amounts of a 0.1 M precursor solution (Cd oleate, CdZn oleate, Zn oleate, and sulfur in ODE) to 200 nmol CdSe QDs dispersed in a mixture of 4.5 mL ODE and 1.5 mL ODA at 230 °C. Each monolayer was allowed to grow for 10 min before the next precursor solution was added). The CSS-QDs were purified by precipitation and redispersion in a chloroform/acetone mixture 3 times. The resulting core−shell−shell (CSS) QDs increased in size to 7.7 nm (±0.9 nm) and were photostable in air for months, with a QY of 60%. The CSS-QDs were incorporated in silica spheres by a reverse microemulsion method (*10*). In short, 1.3 mL Igepal was added to 10 mL cyclohexane and stirred for 15 min (850 rpm). Subsequently, 2 nmol of QDs (in 100 μL cyclohexane), 80 μL TEOS, and 150 μL ammonia was added with 15 min of stirring in between the additions. After the last addition, the mixture was stirred for 1 min, after which it was placed in the dark for 1 week. The resulting silica-coated QDs were centrifuged and redispersed in ethanol at least 3 times to remove excess reactants from the silica synthesis (i.e., Igepal, TEOS, ammonia, and water).

Lipid Coating of Silica Particles. The silica-coated QDs were subsequently capped with a hydrophobic ligand, by adding an excess of octadecanol (ODOH, 2.5 g in 5 mL of EtOH) to a dispersion of 2 nmol of silica-coated QDs in 5 mL ethanol. This mixture was first heated to 100 °C for 1 h to remove the ethanol, after which the temperature was raised to 170 °C for 3 h to covalently link the ODOH to the silica spheres by a condensation reaction (*38*). The QY of the CSS QDs and ODOH coated QD/silica particles was determined by integrating the emission spectra of these samples (in chloroform) and comparing it to the integrated emission of both Rhodamine 6G and Rhodamine 101 (assuming a QY of 90% and 95% for these dyes, respectively). Each emission spectrum was corrected for the relative absorbance of the sample at the excitation wavelength (497 nm in case of Rhodamine 6G and 528 nm in case of Rhodamine 101). Next, the ODOH-coated silica nanoparticles (with a QD incorporated) were dispersed in chloroform/methanol (20/1, v/v). PEG-DSPE, Mal-PEG-DSPE, and Gd-DTPA-DSA were added in a molar ratio of 0.4/0.1/0.5. The amount of lipids was 25 times higher than the calculated amount of lipids for a monolayer on all nanoparticles. This solution was added to a mildly basic HEPES buffer (20 mM HEPES, 135 mM NaCl, pH 6.7) under vigorous stirring, which led to the formation of an emulsion that was subsequently heated to 110 °C to evaporate chloroform. Upon evaporation of chloroform, the milky suspension converted into a clear dispersion indicative of the total removal of chloroform and the formation of lipid-coated QD/silica nanoparticles. The excess of lipids was removed by centrifugation (3000 rpm) of the lipid-coated QD/silica particles, which were redispersed in HEPES buffer. The cyclic 5mer RGD (c(RGDf(-S-acetylthioacetyl)K)) was conjugated to Mal-PEG-DSPE included in the lipid layer as described previously (*39*). In short, acetyl-protected peptide was deacetylated in 0.05 M Hepes/0.05 M hydroxylamine-HCl/0.03 mM ethylenediamine tetraacetic acid (pH 7.0) for 1 h at room temperature. The activated peptide was added to the Mal-PEG2000-DSPE containing particles. This preparation was stored at 4 °C under N_2 overnight.

Transmission Electron Microscopy (TEM) and Dynamic Light Scattering (DLS). A Tecnai 10 (FEI Company) transmission electron microscope, operated at an acceleration voltage of 100 kV, was used to take bright-field images. Samples were prepared for negative staining by exchanging the buffer for a 0.125 M ammonium acetate and 0.26 mM EDTA adjusted to pH 7.4. This solution was then mixed in a 1:1 ratio with a 2% sodium phosphotungstate negative stain solution (pH 7.4). Formvar-coated nickel grids were dipped in this solution and imaged shortly afterward. The TEM micrographs were processed using TIA software (Tecnai imaging and analysis software). Measurement of the size distribution of the ODOH coated QD/silica particles in chloroform and the Q-SiPaLCs suspended in deionized water was performed with a Malvern HPPS DLS (dynamic light scattering) instrument equipped with a He−Ne laser operating at 633 nm.

In Vitro Targeting Experiments. Human umbilical vein derived endothelial cells (HUVEC) were cultured on gelatin (0.2% in PBS) coated tissue culture flasks (Costar, Cambridge, MA) in culture medium, RPMI-1640 (Life Technologies, Breda, The Netherlands), 10% human serum, and 10% fetal calf serum (HS and FCS; University Hospital Maastricht, The Netherlands), 2 mM glutamine (Life Technologies), 50 U/mL penicillin, and

Scheme 1. Overview of the Multistep Synthesis of Q-SiPaLCs[a]

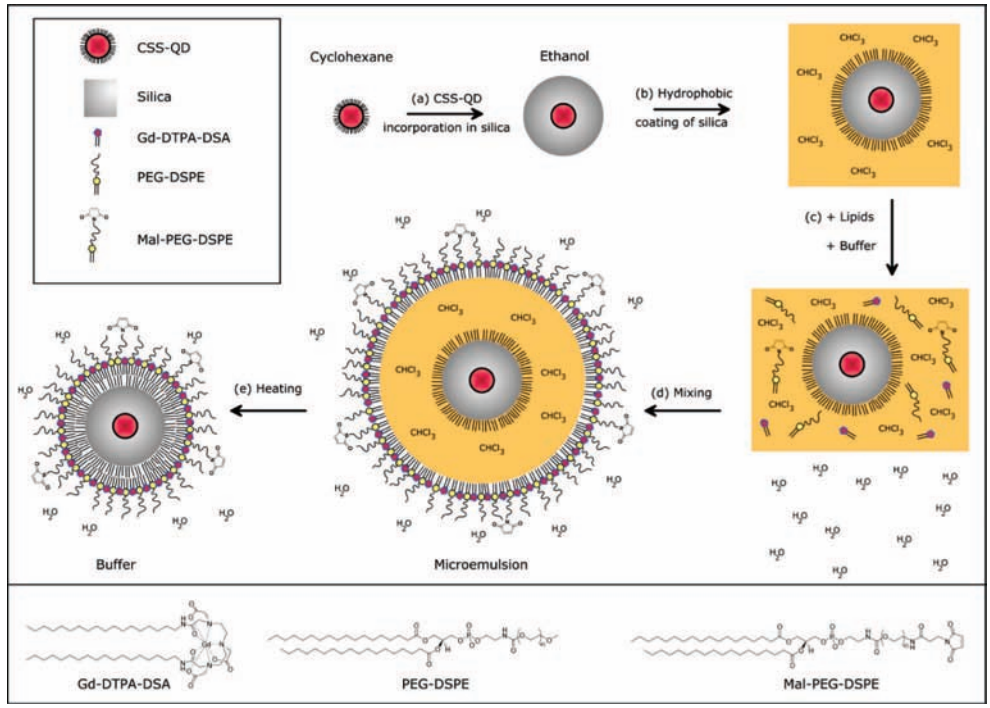

[a] (a) Incorporation of CSS-QDs in silica spheres by the reverse micelle method. (b) Hydrophobic coating of silica by ODOH, after which they can be dispersed in chloroform. (c) Addition of the different lipids to the QD/silica particles in chloroform, which is subsequently added to a HEPES buffer. (d) Vigorous stirring results in an emulsion, with the chloroform and nanoparticles enclosed in a lipid monolayer. (e) Chloroform is evaporated by heating the mixture, resulting in water-soluble Q-SiPaLCs. See Experimental Procedures section for details. The lower panel displays the structure formulas of the lipids.

50 ng/mL streptomycin (ICN Biomedicals, Aurora, OH). For all incubations, 1.5×10^6 cells of passage 2−3 were used for experiments (at least $n = 2$). The cells were incubated for 8 h with RGD conjugated nanoparticles or control nanoparticles at a concentration of 0.07 nmol particles/mL medium. Association of the different nanoparticles to endothelial cells was assessed using fluorescence microscopy and magnetic resonance imaging. A Leica DMIL phase contrast fluorescence microscope (Leica Microsystems, Rijswijk, The Netherlands) equipped with a 20 W G4 HXL64250 Xenophot Halogen lamp (Leica) was used. Parallel phase contrast and red fluorescence (using a BP645−675 filter, Leica) images of the endothelial cell monolayers were taken at 200× magnification. All fluorescence microscopy scans were made with the same settings for laser power and detector sensitivity, allowing direct comparison between different incubations. The cell density for both incubations in Figure 2 was comparable, and therefore, the difference in fluorescence intensity arises from the difference in the level of association.

Fluorescence Imaging and MRI. Fluorescence imaging of cell pellets was performed using the Xenogen IVIS-200 small animal imaging system. A continuous external light source of 365 nm and an emission filter 610−630 nm were used.

MRI experiments were performed on a 6.3 T horizontal bore magnet (Oxford Instruments, England) interfaced to a Bruker (Bruker, Ettlingen, Germany) MR imaging console. A 3 cm quadrature-driven birdcage coil was used. The cups containing cell pellets were placed in a custom-made sample holder, capable of carrying 4 Eppendorf cups. For absolute quantification of T1, an inversion recovery fast T1-mapping sequence was used with 80 different inversion times. In the experiment, TR was 20 s, TE was 9 ms, and the slice thickness was 0.7 mm. For absolute quantification of T2, a multi-spin−echo sequence was used with TR 2000 ms and 32 echos that had a 9 ms echo spacing. A T1-weighted image of cell pellets of the three incubations was generated with a TR of 1500 ms. In this image, cells with a high content of Gd appear brighter than cells with a low content of Gd or no Gd. In all the MRI experiments, the FOV was 3 cm^2, the matrix size 128 × 128 voxels, and the slice thickness 0.7 mm.

RESULTS

Highly photostable and luminescent CdSe/CdS/$Cd_{0.5}Zn_{0.5}S$/ZnS core−shell−shell (CSS) QDs were synthesized according to a SILAR procedure reported by Xie et al. (*37*) Subsequently, a reverse micelle method reported earlier (*10*, *11*) was used to incorporate QDs in the center of highly monodisperse silica particles of 31 nm (±4 nm); see Figure 1A. The synthesis involved the dispersion of hydrophobic QDs in cyclohexane, to which a nonionic surfactant (Igepal), a silane precursor (TEOS, tetraethyl orthosilacate), and catalyst (ammonia) were added. The exact incorporation mechanism and details on the synthesis are published elsewhere (*40*). In short, hydrolyzed TEOS present in the initial reaction mixture (before adding ammonia) replaces the hydrophobic ligands on the QDs. The TEOS-coated QDs are then transferred to the hydrophilic interior of the reverse micelles, where subsequent silica growth takes place. The majority of the silica particles contained a single QD in the center, while only a small fraction of the silica particles contained 2 or more QDs per particle (Figure 1A). Although the QD/silica particles thus obtained are soluble in ethanol or water, the pharmacokinetics of charged surface particles are unfavorable, typically due to a short circulation half-life and/or accumulation in the lungs (*41*, *42*). In order to obtain bioapplicability by a dense lipid coating, the QD/silica particles were first made hydrophobic by an octadecanol (ODOH) coating. This was achieved using a well-known condensation reaction (*38*), where the alcohol group of ODOH reacts with the hydroxyl groups at the silica surface to form a covalent bond, neutralizing the surface charges. The hydrophobic QD/silica particles were subsequently coated with a dense

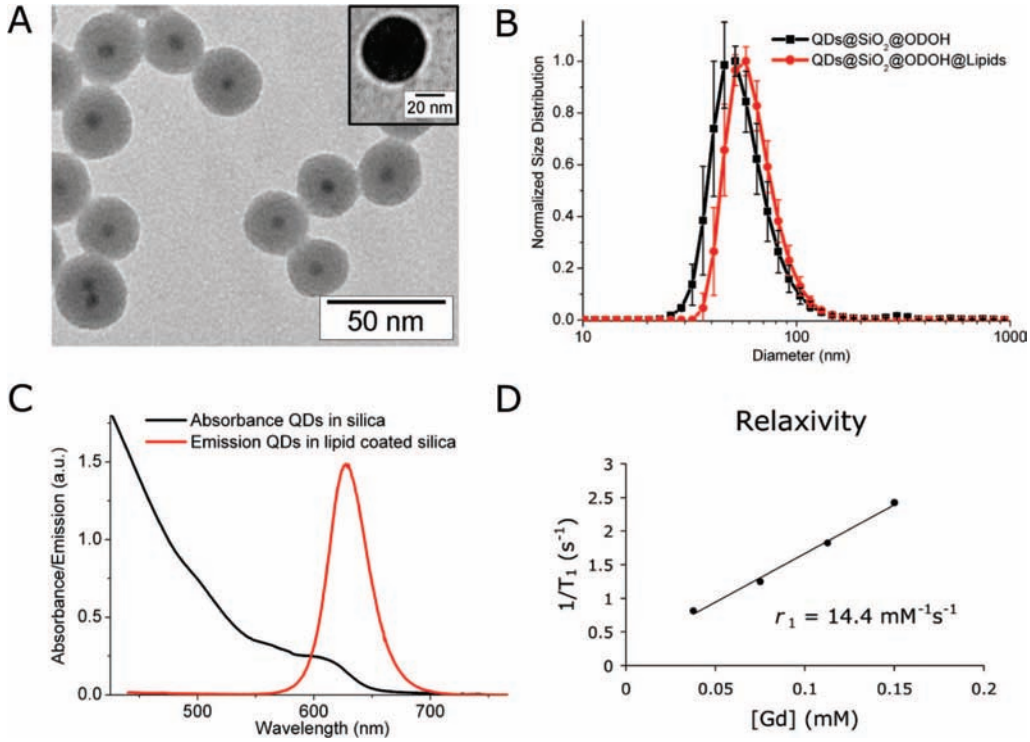

Figure 1. (A) TEM image of monodisperse QD/silica particles of 31 nm (±4 nm) with a single QD (7.7 nm, black spots) incorporated in the center. Inset shows an image from negative staining TEM, where the bright corona illustrates the hydrophobic layer around the silica particle. (B) DLS of ODOH capped QD/silica nanoparticles and ODOH capped QD/silica nanoparticles encapsulated in lipids. (C) Absorption and emission spectra of the CSS-QDs in silica. (D) Relaxation rates of the Q-SiPaLCs as a function of the concentration of Gd^{3+} ions (determined by ICP-MS).

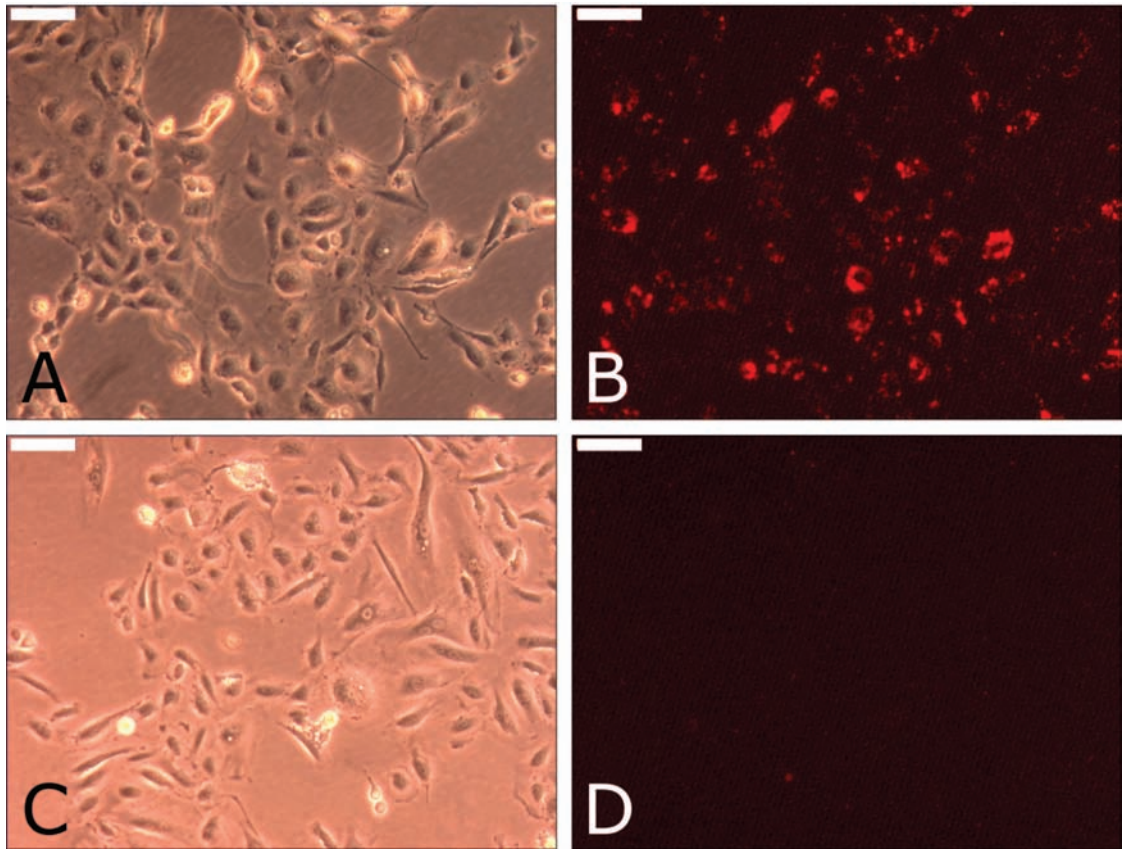

Figure 2. (A,C) Bright-field microscopy images and (B,D) fluorescence microscopy images of HUVEC incubated with (A,B) RGD-conjugated nanoparticles or (C,D) non-conjugated (untargeted) nanoparticles. The scale bars correspond to 100 μm.

monolayer of lipids using a simple and fast procedure reported earlier for hydrophobic nanocrystals (*39, 43*). The procedure involves the addition of lipids and water to the hydrophobic QD/silica particles in chloroform, followed by the evaporation

of chloroform, leaving behind a clear suspension of well-dispersed, uncharged silica particles in lipidic micelles. The total synthesis procedure is schematically summarized in Scheme 1. The lipid coating is versatile, because in principle any (functional) amphiphile may be incorporated in this lipid layer. As an example, we have used a combination of Gd-DTPA-based lipids to introduce paramagnetic properties for MRI, pegylated lipids to improve biocompatibility, and maleimide-terminated (pegylated) lipids for conjugation of a biofunctional group. We will refer to the synthesized QDs in silica with a paramagnetic lipidic coating as Q-SiPaLCs.

The nanoparticles were characterized in terms of their size and optical and magnetic properties. We performed transmission electron microscopy (TEM) and negative staining TEM (Figure 1A) as well as dynamic light scattering (DLS) measurements to determine the morphology and size of the silica particles before and after applying the lipid coating. Negative stain TEM (which allows the visualization of hydrophobic substances) images were analyzed, revealing a hydrophobic layer of 3.9 nm ($\pm$0.5 nm) around individual particles, illustrated by the bright corona around the silica particle (Figure 1A, inset). This 4-nm-thick hydrophobic layer confirms the presence of both the ODOH coating around silica ($\sim$2 nm) and the stearyl chains of the lipids ($\sim$2 nm) around the particles. As well as size determinations established by TEM, the size of nanoparticles in an aqueous environment can be estimated using dynamic light scattering (DLS). This so-called hydrodynamic diameter was determined to be 50 nm for ODOH coated QD/silica particles, increasing to 58 nm after the application of the lipid coating (Figure 1B). This increase is in reasonable agreement with what one may expect in the case a single silica nanoparticle is coated with both paramagnetic lipids ($\sim$2 nm) and pegylated lipids ($\sim$10 nm). Figure 1C displays the absorption and emission spectra. The emission spectrum is shown for the final Q-SiPaLCs in HEPES buffer. The absorption spectrum in Figure 1C was measured for the QDs in silica with an octadecanol coating, dispersed in chloroform. The latter system is refractive-index matched (in contrast to the Q-SiPaLCs in water), allowing for a scattering-free absorption measurement and reliable determination of the quantum yield (QY). The absorption spectrum displays multiple absorption features as a result of discrete excitonic transitions in the CSS-QDs, which can be observed due to the high quality and monodispersity of the QDs. The initial QY of the CSS-QDs was 60%, but decreased as a result of the silica coating. This decrease is difficult to measure due to the scattering of the silica particles in ethanol, but it is estimated that the QY after silica coating is 25%. Coating the QD/silica particles with ODOH increased the QY to 35%, which could be accurately determined because of the scattering-free dispersion of the hydrophobic particles in chloroform. The QY of the lipid-coated QD/silica particles in water was slightly lower (by eye), which was again difficult to quantify due to scattering. It should be noted that a significant QY enhancement of the silica-coated QDs is observed upon UV illumination (which was avoided here when determining the QY, to obtain the lower limit). The silica coating and further coating steps did not change the shape of absorption or emission spectra of the QDs. A detailed discussion on the evolution of the QY of the QDs upon incorporation in silica and photoactivation is published elsewhere (*40*). The emission maximum of the CSS QDs lies at 630 nm. This relatively long wavelength is favorable for in vivo fluorescence imaging because of the lower autofluorescence levels of tissue for longer-wavelength excitation and the longer penetration depth into tissue of light with this wavelength.

To make the particle also suitable as an MRI contrast agent, Gd-DTPA-DSA was included in the lipidic coating of the Q-SiPaLCs. This paramagnetic amphiphile consists of Gd-DTPA, a clinically used contrast agent for MRI, and two saturated acyl chains with a chain length of 18 carbon atoms. To evaluate the performance as an MRI contrast agent, the longitudinal relaxation rates R1 of a dilution series were determined at 60 MHz, and Gd contents of these samples were determined by ICP-MS. From these data, the longitudinal relaxivity r1 of the Gd^{3+} ions was calculated to be 14.4 mM^{-1} s^{-1} (Figure 1D), which is a factor of 3$-$4 higher than free Gd-DTPA molecules in solution. This difference is ascribed to the lower tumbling rate of the Gd-lipids in the micelle compared to free Gd-DTPA molecules, enhancing the molar relaxivity (*35, 39, 44*).

As mentioned above, the number of Gd ions was determined by ICP-MS for a dispersion of Q-SiPaLCs. The concentration of Q-SiPaLCs in this dispersion was estimated from the initial number of QDs used for the silica synthesis at 0.24 μM. We found with ICP-MS that the concentration of Gd in the same dispersion was 0.60 mM, which gives a number of 2500 Gd-lipids per silica particle. The estimated maximum number of lipids in a densely packed lipid layer surrounding a 31 nm silica particle is approximately 5000, using a literature value of 60 A^2/lipid (*45*). Since half of the lipids consisted of Gd-DTPA-DSA, the estimated (2500) and experimentally determined (2500) number of Gd-lipids are in excellent agreement, confirming a dense coating of lipids around the Q-SiPaLCs. This is further confirmed by the number of Cd ions that was determined for the same dispersion using ICP-MS, which was found to be 0.50 mM. The number of Cd ions per CSS QD can be estimated to be approximately 2200, by assuming an average wurtzite unit cell volume of 1.1×10^{-28} m^3 (for CdSe, CdS, and CdZnS) with $Z = 2$ and taking into account the presence of Zn ions in the outer shells. Assuming a number of 2200 Cd ions per QD, the concentration of QDs in the dispersion is estimated to be 0.23 μM, which correlates well with the estimation above.

Taking into consideration that the 31 nm Q-SiPaLCs thus carry approximately 2500 Gd-DTPA-DSA lipids per particle (average between calculated and experimentally determined value), the r1 relaxivity per particle was estimated to be 36 000 mM^{-1} s^{-1}. The relaxivity of the Q-SiPaLCs per particle is thereby a factor of 21 higher than for our previously reported lipid-coated QDs (*39*), and a factor of 8$-$12 higher than Gd-wedge-coated QDs that were recently reported (*46*). In another recent report, the relaxivity of Gd-DOTA covalently attached to silica was determined to be 23 mM^{-1} s^{-1}, and apart from the lower tumbling rate, the very high relaxivity was ascribed to a higher water density close to the Gd-DOTA complexes due to the absence of lipids (*35*). However, their maximum relaxivity per particle was still a factor of 3 lower compared to the Q-SiPaLCs due to a lower payload of the paramagnetic complexes per particle. Similarly, the relaxivity per particle of Q-SiPaLCs is a factor of 40 higher than Mn-doped QDs that were recently reported, despite their high molar relaxivity of 18 mM^{-1} s^{-1} (*47*). Other lipid-based particles, such as liposomes (*48, 49*) or microemulsions (*50*), are capable of carrying a much higher payload of Gd-chelates (typically 25 000 to 100 000 molecules) and therefore exhibit a higher relaxivity per particle. On the other hand, such particles are considerably larger (100 to 250 nm). Apart from r1, we also determined the transverse relaxivity r2. The r2/r1 ratio determines whether a contrast agent is more suitable for T1-weighted or for T2-weighted MRI. This value was determined to be 1.6 for our nanoparticulate contrast agent and therefore can be considered an effective T1 agent.

The characterization of the Q-SiPaLCs shows that they form a very promising particle for dual modality imaging. A crucial aspect for application, however, is their ability to be targeted to specific cell types. To demonstrate the targeting potential of

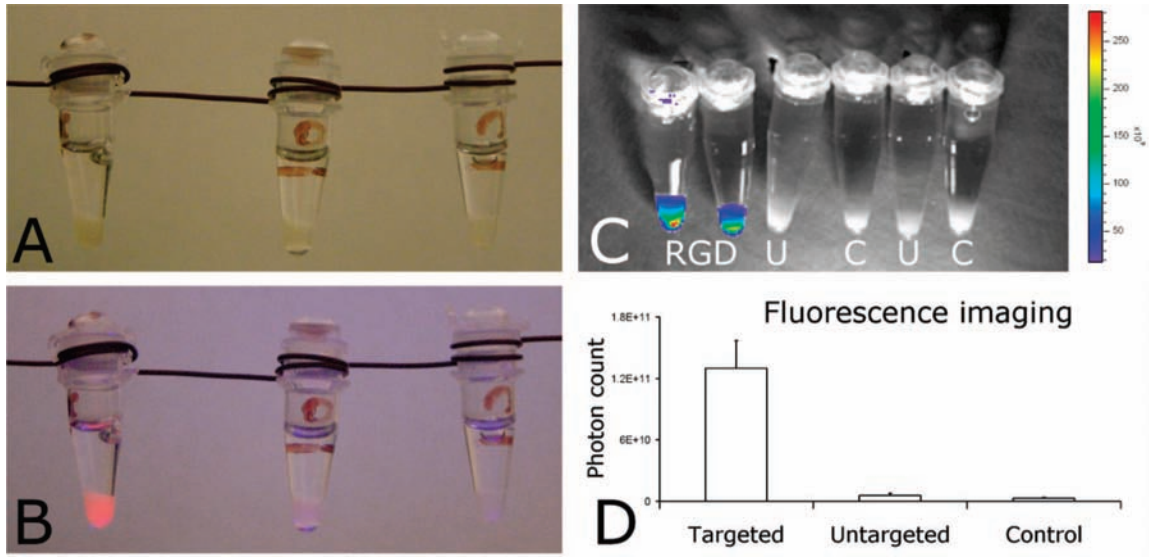

Figure 3. Pellets of cells incubated with RGD-conjugated targeted Q-SiPaLCs (left), non-conjugated untargeted Q-SiPaLCs (middle), and untreated control cells (right) (A) in daylight and (B) illuminated with 365 nm UV. (C) Overlay of a black/white photograph and quantitative fluorescence image of the different cell pellets under UV illumination at 365 nm (RGD = targeted, U = untargeted, C = control cells). The emission intensity from U and C is too low (less than 20×10^9 counts) to be displayed by one of the colors in the scalebar. (D) Mean photon counts of the different cell pellets.

this nanoparticle, it was tested on serum-activated human umbilical vein endothelial cells (HUVEC) in vitro. Nanoparticles can be targeted to these cells by conjugation of multiple RGD-peptides to the maleimide exposing PEG-lipids. These tripeptides specifically bind to $\alpha v\beta 3$-integrin, an adhesion molecule that is expressed by proliferating HUVEC (*51*). This receptor is also predominantly present at angiogenically activated blood vessels, such as those present in tumors (*52*), and has been used for identification of angiogenesis with molecular imaging (*51*). We conjugated ~650 RGD-peptides per particle using a method described previously (*39*). In short, thiol exposing peptides were covalently linked to the distal ends of maleimide-functionalized PEG lipids incorporated in the outer lipid layer of the particle. To assess the specificity of the contrast agent, HUVEC were incubated with either RGD-functionalized nanoparticles (targeted) or non-functionalized nanoparticles (untargeted, no RGD), or they were not incubated with nanoparticles (control). We first established the optimal incubation time on a limited number of cells. Thereafter, incubations were done for 7 h at 37 °C in tissue culture flasks containing $\sim 1.5 \times 10^6$ HUVEC ($n = 2$). Subsequently, cells were washed twice with PBS and fixed with 4% paraformaldehyde solution. In Figure 2A,B, bright-field and fluorescence microscopy images are shown of HUVEC that were incubated with RGD-conjugated nanoparticles. The Q-SiPaLCs are clearly associated with the cells and were found to be internalized at a perinuclear location. Fluorescence images of HUVEC incubated with untargeted Q-SiPaLCs (no functionalization by RGD) showed marginal or no fluorescence (Figure 2C,D), similar to the untreated control cells (not shown). These results demonstrate that lipid-coated QD/silica particles conjugated with RGD peptides are actively taken up by the activated endothelial cells, and that nonspecific uptake (even after 7 h of incubation) is negligible.

Next, the cells were collected and transferred into small Eppendorf cups. In daylight, there is no visual difference between the different loosely packed cell pellets (Figure 3A). Under UV illumination (365 nm), only the cells that had been incubated with RGD conjugated Q-SiPaLCs exhibit a bright red fluorescence and could clearly be distinguished from the two other cell pellets (Figure 3B). In addition, we performed quantitative fluorescence imaging on the different cell pellets (Figure 3C) using the Xenogen IVIS-200. An external illumination source of 365 nm was used, while the photon count was acquired using a spectral imaging filter of 620 nm. In Figure 3D, the mean photon counts of cell pellets incubated with targeted particles, cell pellets incubated with untargeted particles, and control cell pellets are depicted. ~25-fold and ~50-fold differences in photon count were found between the targeted and untargeted cell pellets and the targeted and control pellets, respectively.

Finally, MRI was performed on these cell pellets. A T1-weighted image of the different cell pellets is depicted in Figure 4A and clearly demonstrates higher signal intensity for the pellet of cells incubated with the RGD-conjugated Q-SiPaLCs (the bright white circle) as compared to the control cell pellets (gray circles). In addition, T1 relaxation times were determined in order to allow a more quantitative evaluation of Q-SiPaLCs as a MRI contrast agent. The mean values were 1706 ms, 2189 ms, and 2460 ms, for cells incubated with the targeted particles, cells incubated with untargeted particles, and untreated cells, respectively. The differences in relaxation rate R1 (1/T1) between control cell pellets and cell pellets that were incubated with the nanoparticles correlate with the concentration of contrast agent in the cell pellets. Therefore, we calculated these differences in mean relaxation rates between the control cell pellets and the targeted or untargeted cell pellets. The values clearly demonstrate the effective and specific targeting of this nanoparticulate agent to angiogenically activated endothelial cells (Figure 4B). (Scan parameters are in the Experimental Procedures section.)

DISCUSSION

The Q-SiPaLCs reported here demonstrate the integration of multiple imaging properties in a single bioapplicable nanoparticle and the specific uptake by living cells. This nanoparticulate probe has several advantages over existing agents in terms of detection sensitivity (contrast) due to the high fluorescence quantum yield (35%) and high relaxivity. It presents a new and versatile platform for a wide range of contrast agents suitable for multimodality imaging. Although the QDs were incorporated in silica, more effort needs to be attributed to developing novel stable QD formulations that are not based on Cd to further reduce toxicity. In addition, for in vivo fluorescence imaging

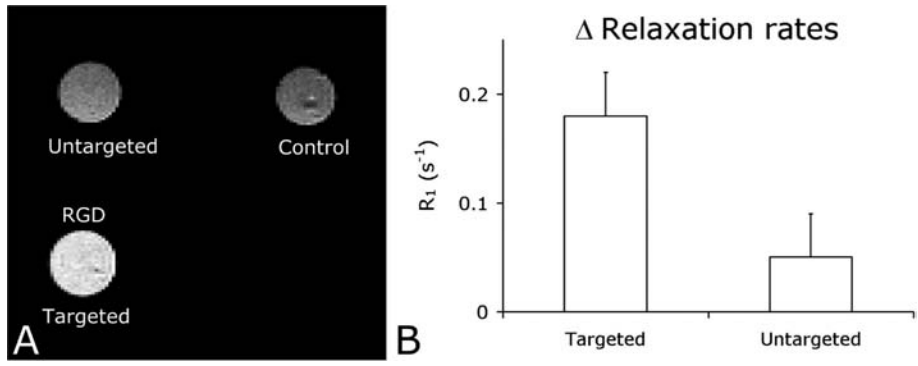

Figure 4. (A) T1-weighted MRI of the different cell pellets (same pellets as displayed in Figure 3) revealed specific uptake of the targeted nanoparticles. (B) Difference in relaxation rates (R1) of the targeted and untargeted cell pellets compared to the relaxation rate of the control cell pellet (set to zero). The differences in relaxation rate reflect the concentration of contrast agent in the untargeted and targeted cell pellets.

purposes, fluorophores that emit photons with a wavelength between 700 and 800 nm have significant advantages, especially for deep tissue imaging (*53*). Therefore, this platform would be more widely applicable if further modified to emit in the near-infrared.

In biomedical research, the two main applications of nanoparticles are their use as carriers for drugs and diagnostic active materials. Their size varies from a few nanometers (QDs, iron oxide nanoparticles, micelles) (*39, 54, 55*) up to hundred nanometers (liposomes) (*2*) and even several hundred nanometers (microemulsions) (*50*) to micrometers (microbubbles) (*56*). Depending on the application and, importantly, the targeted site (vascular versus extravascular), the size may dictate effectiveness. For example, in a study by Stroh et al. it was shown that QD containing silica particles of different sizes (100 nm versus 500 nm) extravasate from the vasculature into the tumor to differing extents (*57*). Furthermore, size also dictates the clearance pathway of nanoparticles and has a significant effect on the circulation half-life. A recent study by Choi et al. (*58*) has revealed renal clearance of particles with a hydrodynamic diameter of less than 5.5 nm. Such small particles are therefore cleared from the circulation relatively fast as compared to, e.g., long-circulating liposomes. The latter platform has a typical size range of 100 to 200 nm and is used extensively in the field of drug targeting, both preclinically and clinically (*2*). The advantage of the current platform in terms of particle size is twofold. First, the nanoparticles are highly monodisperse, as a result of the reverse micelle method used to grow a silica shell of a well-defined thickness. Another great advantage of our particles is that they can be easily and accurately tuned to any desired size from ~20 nm to over 1 μm, by increasing the diameter of the silica spheres. The silica shell is also expected to prevent leaking of Cd and thus reduce the cytotoxicity due to the Cd-containing quantum dots. In addition, any desired fluorescence color or a combination of colors can be chosen to allow for multiplexing or "bar-coding" (*59*), by inserting different kinds of QDs in the silica spheres. Furthermore, due to the high surface area of the Q-SiPaLCs, a high payload of Gd-DTPA-DSA lipids can be integrated per particle. Therefore, the relaxivity per particle is high and can even be increased significantly by increasing the size of the silica particle. Target specificity can be introduced using PEG-lipids with a functional moiety, like maleimide used in this study. The number of functional groups can be varied, which allows the creation of a particle with multiple ligands. This can increase the targeting efficiency of the particle due to multivalent interactions. This is an important issue, since it was recently reported that the target specificity of maleimide-targeted QDs may be poor when a single QD contains less that 1 target peptide per QD, making the uptake highly nonspecific, especially due to the small size of a single QD (*60*). The design of our Q-SiPaLCs solves this problem, because of the possibility of attaching multiple ligands per particle. Furthermore, the nonspecific uptake of the Q-SiPaLCs by HUVEC is shown to be negligible in this study. The nanoparticles as designed in the present report can be applied for imaging of ongoing angiogenesis as a diagnostic tool in the management of cancer. Next to the RGD-peptides used in this study, other ligands, such as antibodies (*61*), antibody fragments (*62*), or proteins (*63*) may be conjugated in a similar fashion. The PEG-lipids that surround the Q-SiPaLCs ensure good pharmacokinetics and an improved biocompatibility of the nanoparticles.

Finally, the presently reported contrast agent design offers numerous possibilities to integrate a wide range of properties for multimodality imaging. We have successfully demonstrated a general and effective pathway for making silica (nano)spheres bioapplicable and target-specific. We have recently investigated the biocompatibility and biodistribution properties of the Q-SiPaLCs. In vitro, an elevated cell vitality was shown for the lipid-coated particles as compared to the bare particles, while in vivo the lipid-coated QD/silica particles displayed increased circulation half-lives as a result of a diminished reticuloendothelial system clearance rate (*64*). In the future, this method can be applied to any combination of contrast agents incorporated in silica to make them suitable for biomedical applications. For example, magnetite nanoparticles (for MRI detection), gold or bismuth nanoparticles (for CT or EM detection), or fluorescent materials (QDs, dyes, phosphor nanocrystals) can readily be integrated in silica and can be made bioapplicable through the procedure reported here. Additional properties may be added to the particle by inserting paramagnetic or fluorescent amphiphiles in the lipidic coating, for example. Drug delivery and gene targeting may also be functionalities that can be accomplished using this biocompatible silica nanoparticle platform.

In summary, we have developed a new method for making bioapplicable silica nanoparticles that can serve as a contrast agent for target-specific multimodality imaging. The nanoparticle is composed of a QD incorporated in a silica sphere of 31 nm. First, the silica surface is made hydrophobic, and subsequently, it is surrounded by pegylated, paramagnetic, and biofunctional lipids. This results in a highly monodisperse, fluorescent, and paramagnetic contrast agent suitable for both fluorescence imaging and MRI studies, and it shows a highly specific uptake by HUVEC. The use of the presently reported method for creating biocompatible and target-specific silica nanoparticles opens a new platform for multimodality imaging contrast agents by integrating any desired combination of contrast agents in the silica nanoparticle and inserting (combinations of) functional amphiphiles in the lipidic coating.

ACKNOWLEDGMENT

Partial support was provided by NIH/NHLBI R01 HL71021, NIH/ NHLBI R01 HL78667 (Z.A.F.), and the Peter Jay Sharp Foundation (W.J.M.M.)

LITERATURE CITED

(1) Sinha, R., Kim, G. J., Nie, S., and Shin, D. M. (2006) Nanotechnology in cancer therapeutics: bioconjugated nanoparticles for drug delivery. *Mol. Cancer. Ther. 5*, 1909–17.

(2) Torchilin, V. P. (2005) Recent advances with liposomes as pharmaceutical carriers. *Nat. Rev. Drug Discovery 4*, 145–60.

(3) Moghimi, S. M., Hunter, A. C., and Murray, J. C. (2005) Nanomedicine: current status and future prospects. *Faseb J. 19*, 311–30.

(4) Bulte, J. W., and Kraitchman, D. L. (2004) Iron oxide MR contrast agents for molecular and cellular imaging. *NMR Biomed. 17*, 484–99.

(5) Sitharaman, B., Kissell, K. R., Hartman, K. B., Tran, L. A., Baikalov, A., Rusakova, I., Sun, Y., Khant, H. A., Ludtke, S. J., Chiu, W., Laus, S., Toth, E., Helm, L., Merbach, A. E., and Wilson, L. J. (2005) Superparamagnetic gadonanotubes are high-performance MRI contrast agents. *Chem. Commun.* 3915–17.

(6) Kim, D., Park, S., Lee, J. H., Jeong, Y. Y., and Jon, S. (2007) Antibiofouling polymer-coated gold nanoparticles as a contrast agent for in vivo x-ray computed tomography imaging. *J. Am. Chem. Soc. 129*, 7661–65.

(7) Michalet, X., Pinaud, F. F., Bentolila, L. A., Tsay, J. M., Doose, S., Li, J. J., Sundaresan, G., Wu, A. M., Gambhir, S. S., and Weiss, S. (2005) Quantum dots for live cells, in vivo imaging, and diagnostics. *Science 307*, 538–44.

(8) Wickline, S. A., Neubauer, A. M., Winter, P. M., Caruthers, S. D., and Lanza, G. M. (2007) Molecular imaging and therapy of atherosclerosis with targeted nanoparticles. *J. Magn. Reson. Imaging 25*, 667–80.

(9) Mulder, W. J. M., Griffioen, A. W., Strijkers, G. J., Cormode, D. P., Nicolay, K., and Fayad, Z. A. (2007) Magnetic and fluorescent nanoparticles for multimodality imaging. *Nanomedicine 2*, 307–24.

(10) Darbandi, M., Thomann, R., and Nann, T. (2005) Single quantum dots in silica spheres by microemulsion synthesis. *Chem. Mater. 17*, 5720–25.

(11) Selvan, S. T., Tan, T. T., and Ying, J. Y. (2005) Robust, non-cytotoxic, silica-coated CdSe quantum dots with efficient photoluminescence. *Adv. Mater. 17*, 1620–25.

(12) Graf, C., Vossen, D. L. J., Imhof, A., and van Blaaderen, A. (2003) A general method to coat colloidal particles with silica. *Langmuir 19*, 6693–700.

(13) Liz-Marzan, L. M., Giersig, M., and Mulvaney, P. (1996) Synthesis of nanosized gold-silica core-shell particles. *Langmuir 12*, 4329–35.

(14) Philipse, A. P., Vanbruggen, M. P. B., and Pathmamanoharan, C. (1994) Magnetic silica dispersions - preparation and stability of surface-modified silica particles with a magnetic core. *Langmuir 10*, 92–99.

(15) Sathe, T. R., Agrawal, A., and Nie, S. M. (2006) Mesoporous silica beads embedded with semiconductor quantum dots and iron oxide nanocrystals: Dual-function microcarriers for optical encoding and magnetic separation. *Anal. Chem. 78*, 5627–32.

(16) Kim, J., Lee, J. E., Lee, J., Yu, J. H., Kim, B. C., An, K., Hwang, Y., Shin, C. H., Park, J. G., and Hyeon, T. (2006) Magnetic fluorescent delivery vehicle using uniform mesoporous silica spheres embedded with monodisperse magnetic and semiconductor nanocrystals. *J. Am. Chem. Soc. 128*, 688–89.

(17) Yi, D. K., Selvan, S. T., Lee, S. S., Papaefthymiou, G. C., Kundaliya, D., and Ying, J. Y. (2005) Silica-coated nanocomposites of magnetic nanoparticles and quantum dots. *J. Am. Chem. Soc. 127*, 4990–91.

(18) Salgueiriño-Maceira, V., Correa-Duarte, M. A., Spasova, M., Liz-Marzán, L. M., and Farle, M. (2006) Composite silica spheres with magnetic and luminescent functionalities. *Adv. Funct. Mater. 16*, 509–14.

(19) van Blaaderen, A., and Vrij, A. (1992) Synthesis and characterization of colloidal dispersions of fluorescent, monodisperse silica spheres. *Langmuir 8*, 2921–31.

(20) Burns, A., Ow, H., and Wiesner, U. (2006) Fluorescent core-shell silica nanoparticles: towards "Lab on a Particle" architectures for nanobiotechnology. *Chem. Soc. Rev. 35*, 1028–42.

(21) Ow, H., Larson, D. R., Srivastava, M., Baird, B. A., Webb, W. W., and Wiesner, U. (2005) Bright and stable core-shell fluorescent silica nanoparticles. *Nano Lett. 5*, 113–17.

(22) Lu, C. W., Hung, Y., Hsiao, J. K., Yao, M., Chung, T. H., Lin, Y. S., Wu, S. H., Hsu, S. C., Liu, H. M., Mou, C. Y., Yang, C. S., Huang, D. M., and Chen, Y. C. (2007) Bifunctional magnetic silica nanoparticles for highly efficient human stem cell labeling. *Nano Lett. 7*, 149–54.

(23) Rieter, W. J., Kim, J. S., Taylor, K. M. L., An, H. Y., Lin, W. L., Tarrant, T., and Lin, W. B. (2007) Hybrid silica nanoparticles for multimodal Imaging. *Angew. Chem., Int. Ed. 46*, 3680–82.

(24) Yoon, T. J., Yu, K. N., Kim, E., Kim, J. S., Kim, B. G., Yun, S. H., Sohn, B. H., Cho, M. H., Lee, J. K., and Park, S. B. (2006) Specific targeting, cell sorting, and bio-imaging with smart magnetic silica core-shell nanomaterials. *Small 2*, 209–15.

(25) Wang, L., Wang, K. M., Santra, S., Zhao, X. J., Hilliard, L. R., Smith, J. E., Wu, J. R., and Tan, W. H. (2006) Watching silica nanoparticles glow in the biological world. *Anal. Chem. 78*, 646–54.

(26) Lu, J., Liong, M., Zink, J. I., and Tamanoi, F. (2007) Mesoporous silica nanoparticles as a delivery system for hydrophobic anticancer drugs. *Small 3*, 1341–46.

(27) Insin, N., Tracy, J. B., Lee, H., Zimmer, J. P., Westervelt, R. M., and Bawendi, M. G. (2008) Incorporation of iron oxide nanoplarticles and quantum dots into silica microspheres. *ACS Nano 2*, 197–202.

(28) Bridot, J. L., Faure, A. C., Laurent, S., Riviere, C., Billotey, C., Hiba, B., Janier, M., Josserand, V., Coll, J. L., VanderElst, L., Muller, R., Roux, S., Perriat, P., and Tillement, O. (2007) Hybrid gadolinium oxide nanoparticles: multimodal contrast agents for in vivo imaging. *J. Am. Chem. Soc. 129*, 5076–84.

(29) Taylor, K. M. L., Kim, J. S., Rieter, W. J., An, H., Lin, W. L., and Lin, W. B. (2008) Mesoporous silica nanospheres as highly efficient MRI contrast agents. *J. Am. Chem. Soc. 130*, 2154–55.

(30) Chen, F. Q., and Gerion, D. (2004) Fluorescent CdSe/ZnS nanocrystal-peptide conjugates for long-term, nontoxic imaging and nuclear targeting in living cells. *Nano Lett. 4*, 1827–32.

(31) Gerion, D., Pinaud, F., Williams, S. C., Parak, W. J., Zanchet, D., Weiss, S., and Alivisatos, A. P. (2001) Synthesis and properties of biocompatible water-soluble silica-coated CdSe/ZnS semiconductor quantum dots. *J. Phys. Chem. B 105*, 8861–71.

(32) Jana, N. R., Earhart, C., and Ying, J. Y. (2007) Synthesis of water-soluble and functionalized nanoparticles by silica coating. *Chem. Mater. 19*, 5074–82.

(33) Selvan, S. T., Patra, P. K., Ang, C. Y., and Ying, J. Y. (2007) Synthesis of silica-coated semiconductor and magnetic quantum dots and their use in the imaging of live cells. *Angew. Chem., Int. Ed. 46*, 2448–52.

(34) Wolcott, A., Gerion, D., Visconte, M., Sun, J., Schwartzberg, A., Chen, S. W., and Zhang, J. Z. (2006) Silica-coated CdTe quantum dots functionalized with thiols for bioconjugation to IgG proteins. *J. Phys. Chem. B 110*, 5779–89.

(35) Gerion, D., Herberg, J., Bok, R., Gjersing, E., Ramon, E., Maxwell, R., Kurhanewicz, J., Budinger, T. F., Gray, J. W., Shuman, M. A., and Chen, F. F. (2007) Paramagnetic silica-coated nanocrystals as an advanced MRI contrast agent. *J. Phys. Chem. C 111*, 12542–51.

(36) de Mello Donega, C., Bode, M., and Meijerink, A. (2006) Size- and temperature-dependence of exciton lifetimes in CdSe quantum dots. *Phys. Rev. B 74*, 085320.

(37) Xie, R. G., Kolb, U., Li, J. X., Basche, T., and Mews, A. (2005) Synthesis and characterization of highly luminescent CdSe-Core CdS/Zn0.5Cd0.5S/ZnS multishell nanocrystals. *J. Am. Chem. Soc. 127*, 7480–88.

(38) van Helden, A. K., Jansen, J. W., and Vrij, A. (1981) Preparation and characterization of spherical monodisperse silica dispersions in nonaqueous solvents. *J. Colloid Interface Sci. 81*, 354–68.

(39) Mulder, W. J. M., Koole, R., Brandwijk, R. J., Storm, G., Chin, P. T. K., Strijkers, G. J., de Mello Donega, C., Nicolay, K., and Griffioen, A. W. (2006) Quantum dots with a paramagnetic coating as a bimodal molecular imaging probe. *Nano Lett. 6*, 1–6.

(40) Koole, R., van Schooneveld, M. M., Hilhorst, J., Donega, C. D., 't Hart, D. C., van Blaaderen, A., Vanmaekelbergh, D., and Meijerink, A. (2008) On the incorporation mechanism of hydrophobic quantum dots in silica spheres by a reverse microemulsion method. *Chem. Mater. 20*, 2503–12.

(41) Awasthi, V. D., Garcia, D., Klipper, R., Goins, B. A., and Phillips, W. T. (2004) Neutral and anionic liposome-encapsulated hemoglobin: Effect of postinserted poly(ethylene glycol)-distearoylphosphatidylethanolamine on distribution and circulation kinetics. *J. Pharmacol. Exp. Ther. 309*, 241–48.

(42) Litzinger, D. C., Brown, J. M., Wala, I., Kaufman, S. A., Van, G. Y., Farrell, C. L., and Collins, D. (1996) Fate of cationic liposomes and their complex with oligonucleotide in vivo. *Bba-Biomembranes 1281*, 139–49.

(43) Dubertret, B., Skourides, P., Norris, D. J., Noireaux, V., Brivanlou, A. H., and Libchaber, A. (2002) In vivo imaging of quantum dots encapsulated in phospholipid micelles. *Science 298*, 1759–62.

(44) Aime, S., Botta, M., Fasano, M., and Terreno, E. (1998) Lanthanide(III) chelates for NMR biomedical applications. *Chem. Soc. Rev. 27*, 19–29.

(45) Petrache, H. I., Dodd, S. W., and Brown, M. F. (2000) Area per lipid and acyl length distributions in fluid phosphatidylcholines determined by 2H NMR spectroscopy. *Biophys. J. 79*, 3172–92.

(46) Prinzen, L., Miserus, R. J. J. H. M., Dirksen, A., Hackeng, T. M., Deckers, N., Bitsch, N. J., Megens, R. T. A., Douma, K., Heemskerk, J. W., Kooi, M. E., Frederik, P. M., Slaaf, D. W., van Zandvoort, M. A. M. J., and Reutelingsperger, C. P. M. (2007) Optical and magnetic resonance imaging of cell death and platelet activation using annexin A5-functionalized quantum dots. *Nano Lett. 7*, 93–100.

(47) Wang, S., Jarrett, B. R., Kauzlarich, S. M., and Louie, A. Y. (2007) Core/shell quantum dots with high relaxivity and photoluminescence for multimodality imaging. *J. Am. Chem. Soc. 129*, 3848–56.

(48) Mulder, W. J. M., Strijkers, G. J., Griffioen, A. W., van Bloois, L., Molema, G., Storm, G., Koning, G. A., and Nicolay, K. (2004) A liposomal system for contrast-enhanced magnetic resonance imaging of molecular targets. *Bioconjugate Chem. 15*, 799–806.

(49) Mulder, W. J. M., Strijkers, G. J., van Tilborg, G. A. F., Griffioen, A. W., and Nicolay, K. (2006) Lipid-based nanoparticles for contrast-enhanced MRI and molecular imaging. *NMR Biomed. 19*, 142–64.

(50) Lanza, G. M., Winter, P. M., Caruthers, S. D., Hughes, M. S., Cyrus, T., Marsh, J. N., Neubauer, A. M., Partlow, K. C., and Wickline, S. A. (2006) Nanomedicine opportunities for cardiovascular disease with perfluorocarbon nanoparticles. *Nanomedicine 1*, 321–29.

(51) Mulder, W. J., Strijkers, G. J., Habets, J. W., Bleeker, E. J., van der Schaft, D. W., Storm, G., Koning, G. A., Griffioen, A. W., and Nicolay, K. (2005) MR molecular imaging and fluorescence microscopy for identification of activated tumor endothelium using a bimodal lipidic nanoparticle. *Faseb J. 19*, 2008–10.

(52) Brooks, P. C., Clark, R. A. F., and Cheresh, D. A. (1994) Requirement of vascular integrin alpha(V)beta(3) for angiogenesis. *Science 264*, 569–71.

(53) Ntziachristos, V., Ripoll, J., Wang, L. V., and Weissleder, R. (2005) Looking and listening to light: the evolution of whole-body photonic imaging. *Nat. Biotechnol. 23*, 313–20.

(54) van Tilborg, G. A. F., Mulder, W. J. M., Deckers, N., Storm, G., Reutelingsperger, C. P. M., Strijkers, G. J., and Nicolay, K. (2006) Annexin A5-functionalized bimodal lipid-based contrast agents for the detection of apoptosis. *Bioconjugate Chem. 17*, 741–49.

(55) Mulder, W. J. M., Strijkers, G. J., Briley-Saboe, K. C., Frias, J. C., Aguinaldo, J. G. S., Vucic, E., Amirbekian, V., Tang, C., Chin, P. T. K., Nicolay, K., and Fayad, Z. A. (2007) Molecular imaging of macrophages in antherosclerotic plaques using bimodal PEG-micelles. *Magn. Reson. Med. 58*, 1164–70.

(56) Kaufmann, B. A., Sanders, J. M., Davis, C., Xie, A., Aldred, P., Sarembock, I. J., and Lindner, J. R. (2007) Molecular imaging of inflammation in atherosclerosis with targeted ultrasound detection of vascular cell adhesion molecule-1. *Circulation 116*, 276–84.

(57) Stroh, M., Zimmer, J. P., Duda, D. G., Levchenko, T. S., Cohen, K. S., Brown, E. B., Scadden, D. T., Torchilin, V. P., Bawendi, M. G., Fukumura, D., and Jain, R. K. (2005) Quantum dots spectrally distinguish multiple species within the tumor milieu in vivo. *Nat. Med. 11*, 678–82.

(58) Choi, H. S., Liu, W., Misra, P., Tanaka, E., Zimmer, J. P., Ipe, B. I., Bawendi, M. G., and Frangioni, J. V. (2007) Renal clearance of quantum dots. *Nat. Biotechnol. 25*, 1165–70.

(59) Xu, H. X., Sha, M. Y., Wong, E. Y., Uphoff, J., Xu, Y. H., Treadway, J. A., Truong, A., O'Brien, E., Asquith, S., Stubbins, M., Spurr, N. K., Lai, E. H., and Mahoney, W. (2003) Multiplexed SNP genotyping using the Qbead (TM) system: a quantum dot-encoded microsphere-based assay. *Nucleic Acids Res. 31*, 1–10, e43.

(60) Pathak, S., Davidson, M. C., and Silva, G. A. (2007) Characterization of the functional binding properties of antibody conjugated quantum dots. *Nano Lett. 7*, 1839–45.

(61) Mulder, W. J., Strijkers, G. J., Griffioen, A. W., van Bloois, L., Molema, G., Storm, G., Koning, G. A., and Nicolay, K. (2004) A liposomal system for contrast-enhanced magnetic resonance imaging of molecular targets. *Bioconjugate Chem. 15*, 799–806.

(62) Kang, H. W., Josephson, L., Petrovsky, A., Weissleder, R., and Bogdanov, A., Jr. (2002) Magnetic resonance imaging of inducible E-selectin expression in human endothelial cell culture. *Bioconjugate Chem. 13*, 122–7.

(63) van Tilborg, G. A., Mulder, W. J., Chin, P. T., Storm, G., Reutelingsperger, C. P., Nicolay, K., and Strijkers, G. J. (2006) Annexin A5-conjugated quantum dots with a paramagnetic lipidic coating for the multimodal detection of apoptotic cells. *Bioconjugate Chem. 17*, 865–8.

(64) van Schooneveld, M. M., Vucic, E., Koole, R., Zhou, Y., Stocks, J., Cormode, D. P., Tang, C. Y., Gordon, R. E., Nicolay, K., Meijerink, A., Fayad, Z. A., and Mulder, W. J. M. (2008) Improved biocompatibility and pharmacokinetics of silica nanoparticles by means of a lipid coating: a multimodality investigation. *Nano Lett. 8*, 2517–25.

BC800368X

Bioconjugate Chemistry 20th Anniversary

Subscriber access provided by SHEMYAKIN-OVCHINNIKOV INST

Article

Circularly Permutated Bioluminescent Probes for Illuminating Ligand-Activated Protein Dynamics

Sung Bae Kim, Moritoshi Sato, and Hiroaki Tao

Bioconjugate Chem., **2008**, 19 (12), 2480-2486• DOI: 10.1021/bc800378a • Publication Date (Web): 02 December 2008

Downloaded from http://pubs.acs.org on May 2, 2009

More About This Article

Additional resources and features associated with this article are available within the HTML version:

- Supporting Information
- Access to high resolution figures
- Links to articles and content related to this article
- Copyright permission to reproduce figures and/or text from this article

View the Full Text HTML

ACS Publications
High quality. High impact.

Bioconjugate Chemistry is published by the American Chemical Society. 1155 Sixteenth Street N.W., Washington, DC 20036

Circularly Permutated Bioluminescent Probes for Illuminating Ligand-Activated Protein Dynamics

Sung Bae Kim, Moritoshi Sato, and Hiroaki Tao*

Research Institute for Environmental Management Technology, National Institute of Advanced Industrial Science and Technology (AIST), 16-1 Onogawa, Tsukuba 305-8569, Japan, and Graduate School of Arts and Sciences, The University of Tokyo, 3-8-1 Komaba, Meguro-ku, Tokyo 153-8902, Japan. Received September 5, 2008; Revised Manuscript Received November 3, 2008

Engineered bioluminescent enzymes provide a creative approach for illuminating the intracellular molecular events. We demonstrate a new strategy for molecular imaging of bioactive small molecules using circularly permutated luciferases (cpLuc), derived from *Gaussia princeps* (GLuc), *Photinus pyralis* (FLuc), and *Pyrearinus termitilluminans* (CBLuc): (i) the luciferases were first dissected into two fragments, (ii) the original N- and C-termini were linked with a GS linker and the new termini were created in an appropriate site, and (iii) the new ends were correspondingly linked with proteins of interest, e.g., a ligand-binding domain (LBD) and an LBD-recognition protein. When the ends of the cpCBLuc were linked with LBD of estrogen receptor (ER) and Src homology 2 domain of Src (SH2 of Src), the estrogen can trigger an intramolecular ER LBD-Src SH2 binding. This assembly subsequently provokes an approximation of the adjacent fragments of cpCBLuc recovering the enzyme activity. These probes were surprisingly stable in the mammalian cells and largely exhibited a decreased background luminescence (e.g., 1000 times in case of cpGLuc) and improved signal-to-noise ratios, compared with the non-CP indicators. This study offers a new strategy for luciferase-aided probing systems. Our study is the first to fabricate circular permutation (CP) in luciferases for tracing the molecular dynamics of proteins.

INTRODUCTION

Engineered functional proteins have provided major contributions to advancements in the bioindustry and have brought a breakthrough in the treatment of human diseases. Manipulation of enzymes as functional proteins is largely governed by the knowledge of the principles that direct enzyme catalysis and enzyme structures, elucidated by X-ray crystallography (*1*). Recent revolutionary advances in enzyme manipulation technologies now allow researchers to carry out quantitative examination of the molecular dynamics and cell signaling in living cells (*2*). While the green fluorescent protein (GFP) that acts as an excellent functional protein has been widely used, enzymes catalyzing light emission are currently proving their distinguished advantages in the quantitative, specific, signal-enhanced, noninvasive, and real-time investigation of intracellular molecular events (*3*−*9*).

As a creative approach for probing molecular events, a circular permutation (CP) of bioluminescent enzymes can be an effective technique. Many of the beetle-derived bioluminescent enzymes are members of a superfamily of acyl-adenylate forming enzymes and consist with larger N-terminal and smaller C-terminal domains (*10*, *11*). When the active-site region between the domains is dissected into two fragments, the activity of the enzyme may be temporally lost. A dissected active site can be placed in the opposite side of the other dissected site in the probe backbone, by CP. Upon stimulation of the ligand, the fragmented luciferase recovers its activity via an intramolecular complementation. As the possibility of encounter between the fragmented active sites by CP is rare, we can expect a dramatic decrease in the background activity of the enzyme and an enhancement of the signal-to-background ratios. The molecular structure is illustrated with the firefly luciferase (FLuc), as shown in Figure 1.

On the basis of this speculation, the feasibility of an indicator with circularly permutated luciferases was explored with the luciferases derived from *Gaussia princeps* (Gaussia luciferase (GLuc); Nanolight), *Photinus pyralis* (firefly luciferase (FLuc); Promega), and *Pyrearinus termitilluminans* (click beetle luciferase (CBLuc); Promega).

We first examined the circularly permutated CBLuc (cpCBLuc) for illuminating the phosphorylation of estrogen receptor (ER), and cpFLuc for imaging the ligand-stimulated protein−protein interactions. The original N- and C-termini of CBLuc were linked with a GS linker, and the new N- and C-termini were constructed between I439 and K440 of CBLuc. Each end of the cpCBLuc was extensively linked with the ligand binding domain of the estrogen receptor (ER LBD) and the Src homology 2 domain of Src (Src SH2). This fusion protein was surprisingly expressed stably in mammalian cells and tolerated the insertion of ER LBD and Src SH2. The probe was sensitive to 4-hydroxytamoxifen (OHT) and emitted the characteristic bioluminescence. Similarly, we synthesized a bioluminescent probe that traces the real-time dynamics of Ca^{2+} as a representative second messenger in living mammalian cells.

In Figure 1, the current mechanism of the CP of enzymes is illustrated with the structure of FLuc, as the crystal structures of CBLuc and GLuc were not presented. It should be noted that Ca^{2+} and estrogen are a typical second messenger and a major steroid hormone, respectively. Thus, the above-mentioned examples of GLuc and CBLuc demonstrate the general applicability of the current CP concept in illuminating the protein dynamics in living mammalian cells.

EXPERIMENTAL PROCEDURES

Plasmid Construction. The respective cDNA fragments consisting of circularly permutated luciferase probes were generated by the polymerase chain reaction (PCR) to introduce each unique restriction site at each end of the fragments, using adequate primers and templates. For example, a plasmid carrying Yellow

* Corresponding author. hiro-tao@aist.go.jp.

10.1021/bc800378a CCC: $40.75 © 2008 American Chemical Society
Published on Web 12/02/2008

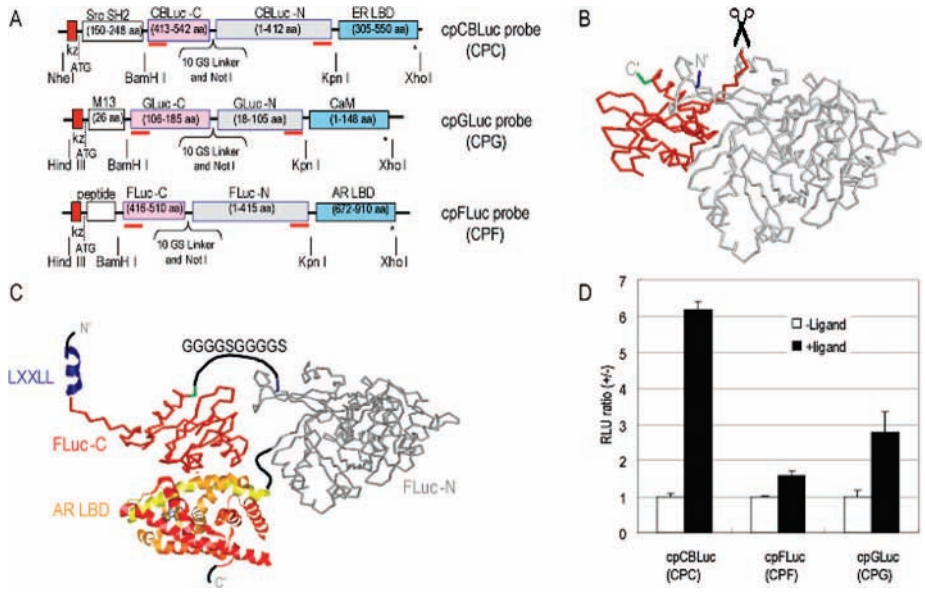

Figure 1. (A) Schematic diagram of circularly permutated luciferase probes. The original N- and C-terminals of CBLuc, GLuc, and FLuc were fused with a 10 GS linker. On the other hand, their new terminal ends were created at I439, Q105, and D415, respectively. Abbreviations: Src SH2, SH2 domain of Src; CBLuc-N and -C, N- and C-terminal fragment of click beetle luciferase; ER LBD, ligand binding domain of estrogen receptor; M13, a 26-residue calmodulin-binding peptide of myosin light-chain kinase; CaM, calmodulin. (B) The crystal structure of firefly luciferase (FLuc). N- and C-terminal fragments are colored gray and red, respectively. The scissors mark shows the dissected point (D415) in the structure. (C) Comprehensive illustration of the molecular structure of CPF as an example. (D) Comparison of the ligand sensitivities of the present CP probes. The luminescence intensities from COS-7 cells carrying each probe were determined in the presence or absence of the specific stimulators, i.e., OHT for CPC, DHT for CPF, histamine for CPG.

Cameleon-3.1 (YC3.1), donated by Dr Miyawaki (*12*), was utilized as a template for amplifying *Xenopus laevis* CaM, by using PCR. A cDNA encoding humanized *Gaussia princeps* luciferase (GLuc; Nanolight) was consumed as a template of PCR for generating the N- and C-terminal fragments, where the known N-terminal secretion signal (1−17 AA) of GLuc was excluded for confining GLuc to the cytoplasm as determined before (*6*, *13*). The synthesized constructs are illustrated in Figure 1A. The enzyme-restricted cDNA fragments were tandemly ligated, as shown in Figure 1A, and subcloned into pcDNA 3.1(+) (Invitrogen). The plasmids were named pCPC (cpCBLuc probe), pCPG (cpGLuc probe), and pCPF (cpFLuc probe), according to the type of luciferases that were circularly permutated in the single-chain probes. The expressed fusion probes may be called CPC, CPG, and CPF, respectively.

In addition, the cDNA of ER LBD in pCPC was point-mutated at Y537 from TAT to TTT, i.e., Y537F. The construct was subcloned into the pcDNA 3.1(+) backbone. This plasmid was named pCPC-mut. As another reference to our cpCPC probe, a probe with straight-ordered fragments of luciferase was similarly constructed, as shown in Figure 3B. The N- and C-terminal fragments were tandemly fused in the straight order, where a 10 GS linker was intervened between the fragments. Then, the N- and C-terminal ends of chimera cDNA were flanked with cDNAs of Src SH2 and ER LBD, respectively. The plasmid with this construct was named pCPC-ctrl. In addition, an integrated-molecule-format (IMF) probe was constructed in parallel, as illustrated in Figure 3D. The plasmid was named pSMC. As a reference to CPG, an IMF probe was constructed, as shown in Figure 5B. The plasmid encoding this probe was named pCPG-ctrl.

All the plasmids constructed for this study were sequenced to ensure fidelity, using a BigDye Terminator Cycle Sequencing kit and a genetic analyzer ABI Prism310 (Applied Biosystems).

Comparison of Relative Luminescence Intensities by CPC, CPF, or CPG. The relative luminescence intensities by CPC, CPF, or CPG were compared in the presence or absence of each ligand (Figure 1(D)). COS-7 cells derived from African green monkey kidney were cultured in a 24-well plate with Dulbecco's modified Eagle's medium (DMEM; Sigma), supplemented with 10% steroid-free fetal bovine serum (FBS) and 1% penicillin−streptomycin (P/S) at 37 °C in a 5% CO_2 cell incubator (Sanyo). The COS-7 cells were transiently transfected with pCPC, pCPF, or pCPG (0.2 μg per well) using a transfection reagent, TransIT-LT1 (Mirus). The cells were extensively incubated in the CO_2 incubator for 16 h.

The cells carrying pCPC or pCPF were stimulated with 10^{-6} M of OHT or dihydrotestosterone (DHT) (final concentration). The luminescence intensities were developed with a Bright-Glo substrate solution (Promega) and integrated for 15 s using a luminometer (Minilumat LB9506; Berthold). The brief procedure for the use of the Bright-Glo substrate solution is as follows: The mammalian cells were washed once with PBS, 20 min after stimulation with a ligand. 40 μL of the substrate (D-leuciferin) solution was added to each well of the plates. Three minutes after substrate addition, the plate was tapped gently, and the subsequent cell lysates were transferred to a test tube for determination of the luminescence intensities.

One the other hand, the cells carrying pCPG were harvested by trypsinization and centrifugation. The cells were gently mixed with a 40 μL substrate (coelenterazine) solution containing 1 mM histamine or PBS. The luminescence intensities were then determined with the luminometer (Minilumat LB9506).

Comparison of the Ligand Sensitivity of CPC and CPC-mut. We examined whether the phosphorylation of ER LBD at Y537 motivated the intramolecular interaction between Src SH2 and ER LBD in the CPC and CPC-mut, as illustrated in Figure 2B. COS-7 cells cultured in a 24-well plate were transiently transfected with pCPC or pCPC-mut. Sixteen hours after transfection, the cells were stimulated with various ligands (10^{-6} M) for 20 min. The ligands used were as follows: vehicle (0.1% DMSO; final concentration), OHT, estrone, E_2, DHT, and cortisol. The subsequent luminescence intensities were estimated with the luminometer.

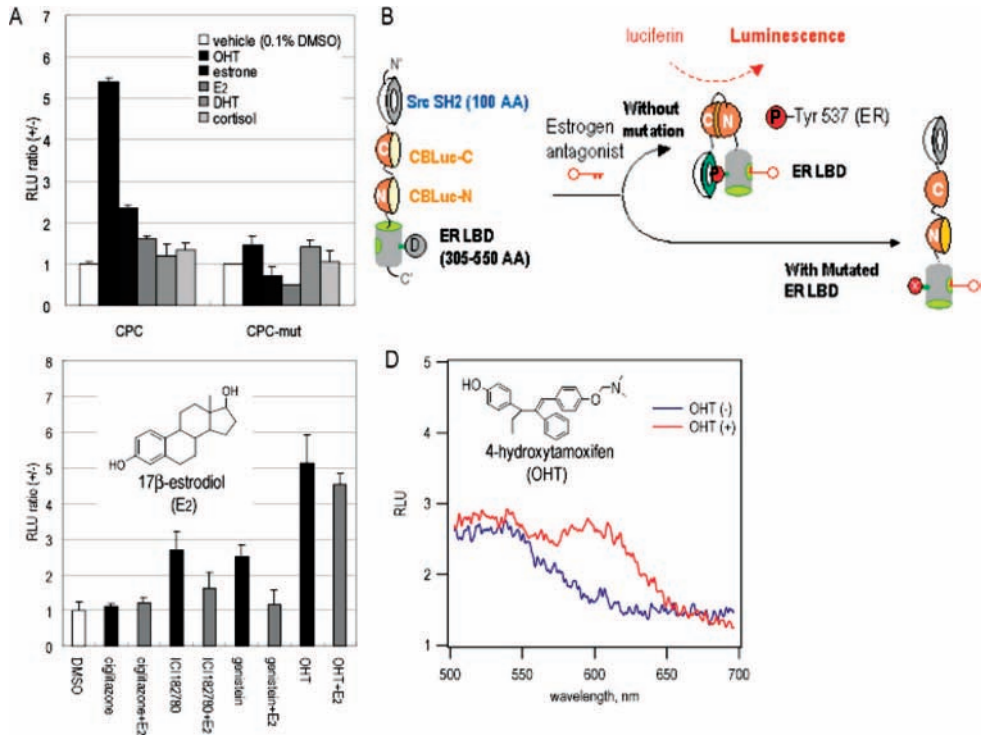

Figure 2. (A) Mutagenesis study for the association of ER LBD with Src SH2 domain. Tyrosine 537 in ER LBD is replaced with lysine, and the plasmid is named pCPC-mut. The luminescence intensities from COS-7 cells carrying pCPC or pCPC-mut are compared in response to various ligands ($n = 3$). (B) Comprehensive illustration of ligand-sensing mechanisms of CPC and CPC-mut. OHT−ER LBD binding exerts phosphorylation of ER LBD at Y537, which subsequently triggers Src SH2−ER LBD interactions. On the other hand, mutation at Y537 demolishes this interaction. (C) Relative sensitivity of CPC to various antagonists. E_2 competed with the antagonists for binding ER LBD. (D) Spectra from the COS-7 cells carrying CPC before and after stimulation of OHT.

Comparison of Inhibitory Effects of E_2 to Antagonist-Bound CPC. On the basis of the result that CPC is sensitive to ER antagonists, and not to the agonists, the inhibitory effects of E_2 to the antagonized CPC were examined (Figure 2C). COS-7 cells cultured in 24-well plates were transiently transfected with pCPC. Sixteen hours after transfection, the cells were prestimulated with 10^{-5} M E_2 for 5 min. The cells were additionally incubated with one of the following nuclear receptor antagonists (10^{-6} M: final concentration): ciglitazone, ICI182780, genistein, or OHT. The resulting luminescence intensities were compared with those from the cells stimulated with an antagonist alone.

Comparison of the Ligand Sensitivity of CPC and CPC-ctrl. The ligand sensitivity of CPC was compared with the CPC-ctrl (Figure 3A). COS-7 cells cultured in 24-well plates were transiently transfected with pCPC or pCPC-ctrl. Sixteen hours after transfection, the cells were stimulated with varying concentrations of E_2 or OHT for 20 min. The resulting luminescence intensities were recorded with the luminometer.

Dose−Response Curves of CPC to Ligands and the Comparison with CPC-ctrl. Ligand sensitivity of CPC in COS-7 cells was examined with varying concentrations of steroids (Figure 3C). COS-7 cells cultured in the 24-well plates were transiently transfected with pCPC. Sixteen hours after transfection, the cells were stimulated with varying concentrations of ligands. The developed luminescence intensities were recorded with the luminometer (Minilumat LB9506).

As another reference to CPC, the sensitivity of SMC was examined in parallel with the same experimental condition as CPC. COS-7 cells carrying pSMC were stimulated with varying concentrations of OHT, and the resulting luminescence intensities were determined with the luminometer (Minilumat LB9506).

Kinetics of Ligand−Probe Binding. The kinetic aspects of ligand−probe binding were estimated with COS-7 cells carrying pCPC (Figure 4). COS-7 cells cultured in 12-well plates were transiently transfected with pCPC and incubated for another 16 h. The luminescence intensities were recorded at 2, 5, 10, 20, and 30 min after the addition of 10^{-6} M OHT or vehicle (0.1% DMSO).

In the meantime, relaxation of the OHT−CPC binding was examined by refreshing the culture medium after OHT stimulation (Figure 4B). The cells carrying pCPC were stimulated with 10^{-6} M OHT or vehicle (0.1% DMSO) for 20 min, and the culture media were then replaced with fresh, ligand-free media. The luminescence intensities at 10, 20, and 60 min after medium replacement were developed with a Bright-Glo substrate solution. The intensities at each time period were compared with those from the cells mock-stimulated with the vehicle (0.1% DMSO).

Comparison of Relative Luminescence Intensities after Being Screened by Bandpass Filters. The wavelengths of light emitted from COS-7 cells were examined by using a series of bandpass filters (Figure 4C). COS-7 cells cultured in a 24-well, glass-bottom plate were transfected with pCPC and incubated for 16 h. The cells were saturated with a 500 μL Hank's balanced salt solution (HBSS) buffer containing coelenterazine and one of the following stimulators: vehicle (0.1% DMSO), 10^{-6} M E_2, or 10^{-6} M OHT. Twenty minutes after stimulation with the ligand, the relative luminescence intensities from the cells were monitored with a series of bandpass filters, whose wavelengths were as follows: 510 ± 10 nm, 535 ± 10 nm, 540 ± 10 nm, 560 ± 10 nm, and 610 ± 10 nm.

Determination of the Ca^{2+} Dynamics in COS-7 Cells with CPG. The dynamics of the cytosolic Ca^{2+} in COS-7 cells were monitored with CPG and CPG-ctrl (Figure 5A). COS-7 cells cultured in a black, glass-bottom plate (24-well) were transfected with pCPG or pCPG-ctrl, and incubated in a cell incubator for 16 h. The cells were saturated with 300 μL HBSS buffer

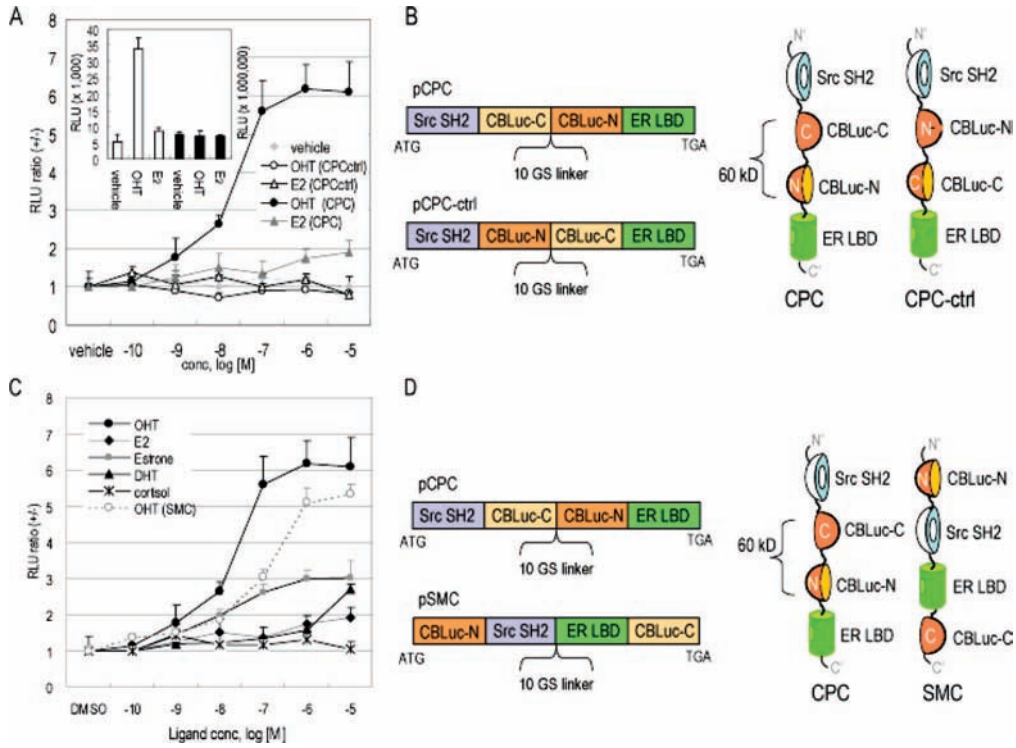

Figure 3. Ligand sensitivity of CPC. (A) Comparison of ligand sensitivity of CPC and CPC-ctrl. Inset shows the absolute luminescence intensities from the cells carrying CPC and CPC-ctrl in response to OHT and E_2. The left *X*-axis shows the luminescence intensities by CPC (open bars), whereas the right *X*-axis indicates the intensities by CPC-ctrl (closed bars). (B) Comprehensive illustration of the molecular structures of CPC and CPC-ctrl. Abbreviations: OHT, 4-hydroxytamoxifen; E_2, 17β-estradiol; DHT, dihydrotestosterone; Src SH2, Src homology 2 (SH2) domain of Src; ER LBD, ligand binding domain of estrogen receptor; CBLuc-N and -C, N- and C-terminal domains of click beetle luciferase. (C) Dose−response curves of CPC in response to varying concentrations of ligands. (D) Illustrative comparison of the molecular structures of CPC and SMC.

containing coelenterazine. The luminescence variances were monitored with a bioluminescence plate reader (Mithras LB 940; Berthold) every 30 s before and after the addition of histamine in the range 0.1−1 mM.

RESULTS

Structural Basis of CPC and Its Phosphorylation Recognition. The Y537 in ER LBD was phosphorylated upon the stimulation of ER ligands, which is sensitively recognized by the Src SH2 domain (*14*). We utilized this typical non-genomic interaction of ER with Src in constructing our CP probe. This phosphorylation-mediated binding was compared with a reference probe carrying point-mutated ER LBD at Y537F (CPC-mut) (Figure 2A,B). CPC recognized various steroids and was particularly sensitive to an estrogen antagonist, OHT, whereas CPC-mut was insensitive to all the ligands (Figure 2A). The results show that (i) the intramolecular interactions occur via phosphorylation of ER LBD at Y537, (ii) Y537 in ER is phosphorylated ligand-dependently, (iii) the luminescence intensities by CPC are capable of indexing the antagonistic activities of ligands, and (iv) from an analytical point of view, signal-to-noise ratios are large enough to discriminate among the non-genomic activities of the ligands. It was previously debated on whether 17β-estradiol (E_2) exerts phosphorylation of ER at Y537. Our experiment reveals that not only E_2 but also OHT could induce phosphorylation of ER at Y537. Although both E_2 and OHT phosphorylate ER LBD, OHT may induce more favorable conformational changes of ER LBD in the recovery of CBLuc activity than E_2. This observation is analogous to an earlier luciferase study on ER antagonists (*5*).

We also examined the influence of E_2 on CPC-antagonist binding (Figure 2C). E_2 negatively contributed to the luminescence intensities developed by the antagonists. The results show that the (i) antagonists compete with E_2 in binding ER LBD, and (ii) OHT is the most efficient antagonist barely influenced by 10× excess of E_2.

Luminescence spectra were obtained for examining whether the recovery of the red−orange light is selective to OHT (Figure 2D). The spectra showed that red−orange light was enhanced by OHT and the λ_{max} was the same as that of intact CBLuc. This result was in concordance with the results with bandpass filters in Figure 4C and also with the result of our previous study (*9*).

Comparison of Ligand Sensitivity of CPC with That of Its Non-CP Controls. The ligand sensitivities of CPC were examined with varying doses of steroids (Figure 3). CPC selectively sensed OHT and even responded to 10^{-9} M of OHT. The half-maximal effective concentration (EC_{50}) was approximately 5×10^{-8} M. On the other hand, CPC-ctrl did not show any luminescence variance in response to OHT or E_2 (Figure 3A). The reason was found to be in the extremely high background luminescence, even in the absence of stimulators. The background luminescences by CPC-ctrl were ca. 1000 times higher than those by CPC. This resulted in poor signal-to-noise ratios, as shown in Figure 3A.

CPC showed a 10-fold enhanced detection limit, when compared with a CP-free probe (SMC) (Figure 3C). The structural difference between CPC and SMC is illustrated in Figure 3D. Even in the absence of a stimulator, SMC emitted a background luminescence that was seven times stronger than CPC, i.e., 38 500 vs 5500 RLU ($n = 3$). The reason for the improved detection limit is explained by the fact that CP of CBLuc decreases the basal interactions between the ER LBD and SH2 in the absence of a ligand.

Kinetics of CPC−Ligand Binding. The ligand-sensing kinetics of CPC was monitored with COS-7 cells carrying pCPC (Figure 4). The luminescence intensities by CPC were greatly enhanced from 5 min after OHT addition and reached a plateau

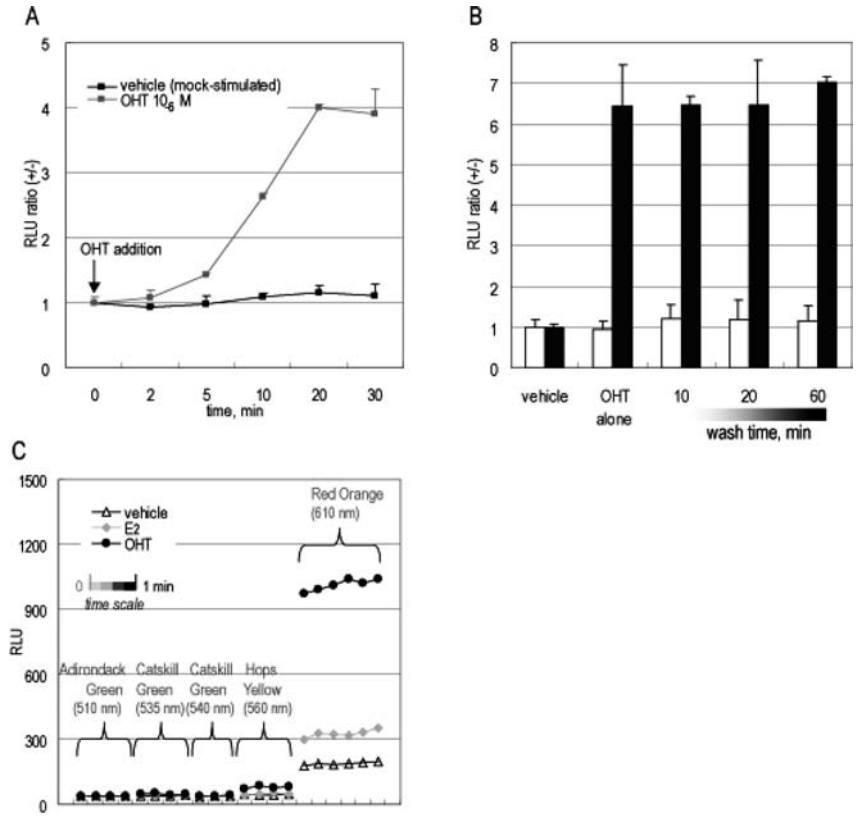

Figure 4. Ligand-binding kinetics of CPC. (A) Time course of OHT-CPC binding was examined. At 2, 5, 10, 20, and 30 min after OHT−CPC binding, the luminescence variances were monitored. (B) Cancellation of OHT−CPC binding by medium replacement was determined. The luminescence intensities were retained until 60 min after medium replacement. (C) Relative luminescence intensities after being screened by bandpass filters. The light from the cells carrying CPC passed well through a 610 nm bandpass filter, indicating that the signal is red−orange light.

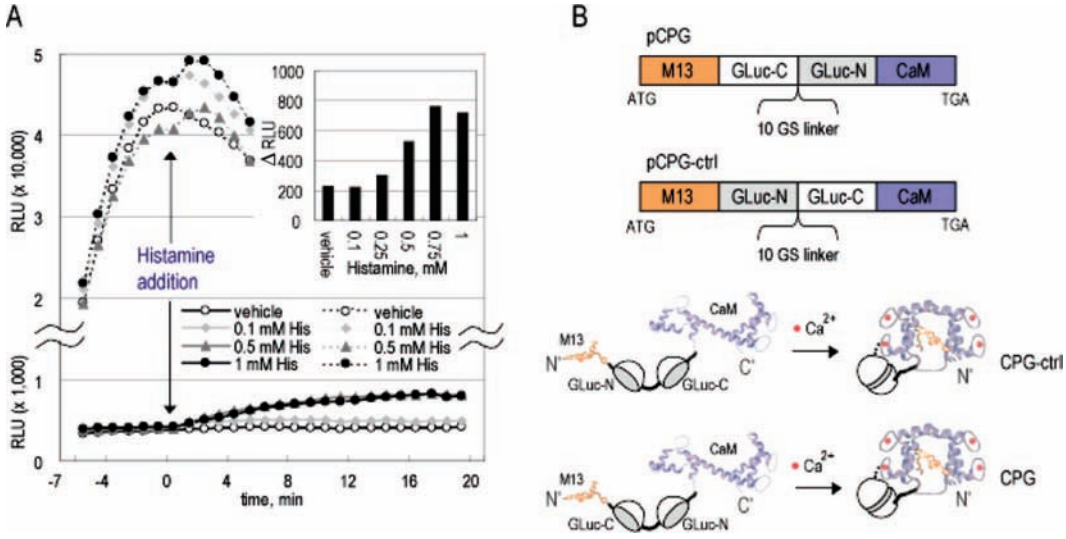

Figure 5. (A) Comparison of ligand-binding kinetics of CPG (solid lines) with that of SMG (dot lines). Inset shows the increased luminescence intensities due to histamine ($n = 3$). (B) A cartoon diagram showing the Ca^{2+} recognition and conformation changes of CPG and CPG-ctrl. Abbreviations: GLuc-N and -C, N- and C-terminal fragments of *Gaussia* luciferase; ΔRLU, change in the amount of luminescence intensity in the presence or absence of histamine; M13, calmodulin-binding peptide of myosin light-chain kinase; CaM, calmodulin.

in 20 min. The total response time, 20 min, comprised the total time for (i) penetration of OHT across the plasma membrane, (ii) OHT−ER LBD binding and conformation change of ER LBD, (iii) subsequent binding of ER LBD with Src SH2, and (iv) intramolecular complementation between the fragments of CBLuc. Using cell-free assays, it was previously proven that the net ligand−ER binding and conformation change of ER were completed within 1 min (*15*). Therefore, it can be considered that the large portion of the total response time, 20 min, was consumed during the penetration of OHT into the cytosol. This response time is considerably slower than those shown by our previous probes (*10*, *16*). Hydrophilicity of OHT, when compared with other steroids, may cause the late plasma membrane penetration.

Dissociation kinetics of CPC-ligand binding was examined with COS-7 cells carrying pCPC (Figure 4B). First, the cells were stimulated with OHT for 20 min. The culture medium was then replaced with a fresh, OHT-free medium. The

luminescence intensities within 1 h after the change of the medium were not decreased considerably. Even washout for 60 min did not weaken the luminescence intensities from the cells. These results show that OHT-triggered Src SH2−ER binding can be endured for quite a long time.

Wavelengths of Light Emitted from COS-7 Cells Carrying pCPC. The wavelengths and intensities of light from COS-7 cells carrying pCPC were determined with a series of bandpass filters after the stimulation of ligands (Figure 4C). The light from COS-7 cells efficiently passed a 610 ± 10 nm filter, which indicates that the probe emits red−orange light. The luminescence intensities by OHT were five times stronger than those by the vehicle (0.1% DMSO), whereas the intensities by E_2 were merely 1.8 times stronger. These results show that OHT selectively elevates the red−orange light, and thus, the light can be a specific index of antagonistic activities of ligands to ER.

Ligand-Sensing Chemistry of CPG. As a representative of second messengers, cytosolic Ca^{2+} levels in living mammalian cells were estimated with our CPG (Figure 5). *Gaussia princeps*-derived luciferase was dissected at Q105, and the fragments were circularly permutated with a 10 GS linker. The outer terminals were fused with M13 and CaM, respectively. A control probe, CPG-ctrl, was synthesized in parallel with the same components but in different order (CP-free; Figure 5B). In response to 1 mM histamine, CPG quickly increased its luminescence intensities, which reached a plateau in approximately 10 min. The inset in Figure 5A shows the dose−response curve ($n = 3$). The probe was even sensitive to 0.25 mM of histamine, and the linear range was found between 0.25 and 0.75 mM of histamine. On the other hand, CPG-ctrl was unstable in emitting light and exhibited approximately 100× higher background intensity than the CPG, even in the absence of histamine. Stimulation with 1 mM histamine seldom increased the luminescence intensities. Only the substrate coelenterazine was saturated in the COS-7 cells within 8.5 min (Supporting Information Figure S1(C)). These results conclude that the CP of GLuc favors the decrease in background intensities, as shown in the case of CPC and CPC-ctrl. The decreased basal luminescence enabled us to firmly determine the dynamics of free Ca^{2+} levels triggered by histamine.

DISCUSSION

The concepts of CP were previously introduced with green fluorescent protein (GFP) variants, where the hydrophobicity of the chromophore varied according to a stimulator (*17, 18*). It is interesting to compare the ligand-sensing mechanism of our CP-based probes with that of the conventional CP-based fluorescent probes. The on/off system of fluorescent probes with cpGFP is considered to depend on the altered quantum yield of fluorescence by solvent penetration into the chromophore (*19, 20*). Particularly, an insertion of peptides at the β-sheet linkers temporarily disrupts fluorescence, owing to solvent penetration within the protein core, which interferes with the fluorophore−β-sheet interactions. The inhibitory action is relieved by condensive interaction between the inserted peptides. On the other hand, the recovery of luminescence in our probes is based on the physical approximation after dissociation between the completely separated fragments of a split luciferase, and not on the hydrophobicity variance like cpGFP.

Conventionally, real-time imaging of dynamics of second messengers relied heavily on the fluorescence resonance energy transfer (FRET) (*12, 21, 22*). The FRET between GFP variants can be detectable with a fluorescence microscope. However, only few cells can be observed by this method with autofluorescence. Our cpGLuc probe (CPG) provides a simple whole-cell assay and real-time imaging, and is useful for tracing the molecular dynamics in mammalian cells. Our study was the first example to determine the ligand-triggered dynamics of a second messenger with a bioluminescent probe in the living cells.

The probe with cpCBLuc (CPC) was sensitive to antagonists and exhibited a 1000× lower background luminescence when compared with a non-CP probe (CPC-ctrl). This dramatic decrease of basal luminescence intensity can be explained as follows: the CBLuc is considered to consist of two major domains, between which the active site may probably exist (*10, 11*). In our study, the potential active site region was divided into two fragments, causing a temporary loss of activity. A dissected active site of CBLuc was located in the opposite side of the other dissected site in the single-chain probe backbone, with respect to CP. In this conformation, the encountering chance between the fragmented active sites should be extremely decreased in the basal conditions. This structural reason may contribute to (i) the dramatic decrease of the basal activity of the probe and (ii) the improved signal-to-background ratios in the study.

It was previously debated whether the 17β-estradiol (E_2) exerts phosphorylation of estrogen receptor (ER) at Y537 (*23, 24*). Our experiment revealed that not only E_2 but also 4-hydroxytamoxifen (OHT) could induce phosphorylation of ER at Y537. Although both E_2 and OHT phosphorylate ER LBD, OHT modulates a more appropriate conformation change on ER LBD for recruiting the adjacent SH2 domain than E_2. Previously, an intramolecular folding sensor was developed, where a single-component protein (i.e., ER LBD), and not a two-component protein like ours, was sandwiched between the fragments of split-*Renilla* luciferase (RLuc) (*5*). It is interesting that their probe was similarly sensitive only to antagonists and was believed to be controlled by the conformational variances of ER LBD.

On the whole, we synthesized efficient bioluminescent probes with circularly permutated fragments of luciferases. Our probes were surprisingly stable in the mammalian cells after permutation, and the permutated positions were tolerant to the insertion of the detector proteins. The probes were sensitive to their respective ligands and exhibited a dramatically decreased background luminescence and improved signal-to-background ratios, when compared with the CPC-ctrl. This study offers a new strategy for the enzyme-aided probing systems that overcomes the limitations of the conventional probes. Our study was the first to fabricate CP in the enzymes. Any protein−protein interactions and molecular dynamics may be examined with these probes by simply replacing the detector proteins.

Supporting Information Available: Washout effects of ligand-elevated Ca^{2+} levels in COS-7 cells carrying pCPG. were specified in Figure S1(A). Kinetics of coelenterazine saturation in COS-7 cells were examined with the cells carrying CPG-ctrl (Figure S1(C)). This material is available free of charge via the Internet at http://pubs.acs.org.

LITERATURE CITED

(1) Brannigan, J. A., and Wilkinson, A. J. (2002) Protein engineering 20 years on. *Nat. Rev. Mol. Cell Biol. 3*, 964–970.
(2) Weissleder, R., and Ntziachristos, V. (2003) Shedding light onto live molecular targets. *Nat. Med. 9*, 123–128.
(3) Paulmurugan, R., Umezawa, Y., and Gambhir, S. S. (2002) Noninvasive imaging of protein-protein interactions in living subjects by using reporter protein complementation and reconstitution strategies. *Proc. Natl. Acad. Sci. U.S.A. 99*, 15608–15613.
(4) Paulmurugan, R., and Gambhir, S. S. (2005) Firefly luciferase enzyme fragment complementation for imaging in cells and living animals. *Anal. Chem. 77*, 1295–1302.

(5) Paulmurugan, R., and Gambhir, S. S. (2006) An intramolecular folding sensor for imaging estrogen receptor-ligand interactions. *Proc. Natl. Acad. Sci. U.S.A. 103*, 15883–15888.
(6) Remy, I., and Michnick, S. W. (2006) A highly sensitive protein-protein interaction assay based on Gaussia luciferase. *Nat. Meth. 3*, 977–979.
(7) Kim, S. B., Ozawa, T., Watanabe, S., and Umezawa, Y. (2004) High-throughput sensing and noninvasive imaging of protein nuclear transport by using reconstitution of split Renilla luciferase. *Proc. Natl. Acad. Sci. U.S.A. 101*, 11542–11547.
(8) Kim, S. B., Kanno, A., Ozawa, T., Tao, H., and Umezawa, Y. (2007) Nongenomic activity of ligands in the association of androgen receptor with Src. *ACS Chem. Biol. 2*, 484–492.
(9) Kim, S. B., Umezawa, Y., Kanno, K. A., and Tao, H. (2008) An integrated-molecule-format multicolor probe for monitoring multiple activities of a bioactive small molecule. *ACS Chem. Biol. 3*, 359–372.
(10) Kim, S. B., Otani, Y., Umezawa, Y., and Tao, H. (2007) Bioluminescent indicator for determining protein-protein interactions using intramolecular complementation of split click beetle luciferase. *Anal. Chem. 79*, 4820–4826.
(11) Viviani, V. R., Uchida, A., Viviani, W., and Ohmiya, Y. (2002) The influence of Ala243 (Gly247), Arg215 and Thr226 (Asn230) on the bioluminescence spectra and pH-sensitivity of railroad worm, click beetle and firefly luciferases. *Photochem. Photobiol. 76*, 538–544.
(12) Miyawaki, A., Llopis, J., Heim, R., McCaffery, J. M., Adams, J. A., Ikura, M., and Tsien, R. Y. (1997) Fluorescent indicators for Ca^{2+} based on green fluorescent proteins and calmodulin. *Nature 388*, 882–887.
(13) Tannous, B. A., Kim, D. E., Fernandez, J. L., Weissleder, R., and Breakefield, X. O. (2005) Codon-optimized Gaussia luciferase cDNA for mammalian gene expression in culture and in vivo. *Mol. Ther. 11*, 435–443.
(14) Varricchio, L., Migliaccio, A., Castoria, G., Yamaguchi, H., de Falco, A., Di Domenico, M., Giovannelli, P., Farrar, W., Appella, E., and Auricchio, F. (2007) Inhibition of estradiol receptor/Src association and cell growth by an estradiol receptor alpha tyrosine-phosphorylated peptide. *Mol. Cancer Res. 5*, 1213–1221.
(15) Rich, R. L., Hoth, L. R., Geoghegan, K. F., Brown, T. A., LeMotte, P. K., Simons, S. P., Hensley, P., and Myszka, D. G. (2002) Kinetic analysis of estrogen receptor/ligand interactions. *Proc. Natl. Acad. Sci. U.S.A. 99*, 8562–8567.
(16) Kim, S. B., Awais, M., Sato, M., Umezawa, Y., and Tao, H. (2007) Integrated molecule-format bioluminescent probe for visualizing androgenicity of ligands based on the intramolecular association of androgen receptor with its recognition peptide. *Anal. Chem. 79*, 1874–1880.
(17) Baird, G. S., Zacharias, D. A., and Tsien, R. Y. (1999) Circular permutation and receptor insertion within green fluorescent proteins. *Proc. Natl. Acad. Sci. U.S.A. 96*, 11241–11246.
(18) Kawai, Y., Sato, M., and Umezawa, Y. (2004) Single color fluorescent indicators of protein phosphorylation for multicolor imaging of intracellular signal flow dynamics. *Anal. Chem. 76*, 6144–9.
(19) Kotlikoff, M. I. (2007) Genetically encoded Ca^{2+} indicators: using genetics and molecular design to understand complex physiology. *J. Physiol. 578*, 55–67.
(20) Souslova, E. A., and Chudakov, D. M. (2007) Genetically encoded intracellular sensors based on fluorescent proteins. *Biochemistry (Moscow, Russ. Fed.) 72*, 683–697.
(21) Truong, K., Sawano, A., Mizuno, H., Hama, H., Tong, K. I., Mal, T. K., Miyawaki, A., and Ikura, M. (2001) FRET-based in vivo Ca^{2+} imaging by a new calmodulin-GFP fusion molecule. *Nat. Struct. Biol. 8*, 1069–1073.
(22) Awais, M., Sato, M., Lee, X. F., and Umezawa, Y. (2006) A fluorescent indicator to visualize activities of the androgen receptor ligands in single living cells. *Angew. Chem., Int. Ed. 45*, 2707–2712.
(23) Migliaccio, A., Castoria, G., Di Domenico, M., de Falco, A., Bilancio, A., Lombardi, M., Bottero, D., Varricchio, L., Nanayakkara, M., Rotondi, A., and Auricchio, F. (2002) Sex steroid hormones act as growth factors. *J. Steroid Biochem. Mol. Biol. 83*, 31–35.
(24) Arnold, S. F., Melamed, M., Vorojeikina, D. P., Notides, A. C., and Sasson, S. (1997) Estradiol-binding mechanism and binding capacity of the human estrogen receptor is regulated by tyrosine phosphorylation. *Mol. Endocrinol. 11*, 48–53.

BC800378A

Supporting Information

Circularly permutated bioluminescent probes for illuminating ligand-activated protein dynamics

Sung Bae Kim [1], Moritoshi Sato [2], and Hiroaki Tao [1,*]

1. Research Institute for Environmental Management Technology, National Institute of Advanced Industrial Science and Technology (AIST), 16-1 Onogawa, Tsukuba 305-8569, Japan

2. Graduate School of Arts and Sciences, The University of Tokyo, 3-8-1 Komaba, Meguro-ku, Tokyo 153-8902, Japan

***Corresponding author (hiro-tao@aist.go.jp)**

Page Contents

S1. Table of contents.

S2. Experimental procedures of the supporting information.

S3. Examples of bioanalytical use of the present probes (Supporting Figure S1).

Experimental procedures of the supporting information **page S2**

Washout effects of ligand-elevated Ca^{2+} levels in COS-7 cells carrying pCPG. Washout effects of the elevated Ca^{2+} levels by various ligands were examined with CPG in COS-7 cells (Suppl. Figure 1). After stimulation with ligands, the COS-7 cells carrying pCPG were washed with PBS for removing the ligands in the medium. This washout terminates the external stimulation of ligands in elevating cytosolic Ca^{2+} levels. The resulting luminescence intensities shown in Suppl. Figure 1 are interpreted as follows: since histamine and ATP cannot pass the plasma membrane, they bind their specific receptors on the membrane. The elevated cytosolic Ca^{2+} levels by histamine or ATP alone are quickly decreased by Ca^{2+} pumping of the cells. Additional supplementation of thapsigargin, known as an endoplasmic reticulum Ca^{2+} pump inhibitor, retained the luminescence intensities elevated by histamine or ATP. On the other hand, co-stimualtion of cyproheptadine, when added with histamine, selectively blocked the elevation of cytosolic Ca^{2+} levels. This is because cyproheptadine acts as an anti-histamine reagent and blocks the effects of histamine. Ionomycin triggers the influx of exogenous Ca^{2+} into the cytosol, which resulted in retaining certain levels of Ca^{2+} in the cytosol in spite of the Ca^{2+} pump.

These results reveal that the current CPG provides a bioluminescent measure for exploring the dynamics of Ca^{2+}-related molecular events in living mammalian cells, which was not examined previously with a bioluminescent probe.

Retention of Ca^{2+} levels after washout, which were elevated by various ligands. Retention of cytosolic Ca^{2+} levels were monitored on the basis of the luminescence intensities from COS-7 cells carrying pCPG (Suppl. Figure 1). COS-7 cells cultured in a 24-well plate were transiently transfected with pCPG and extensively incubated for 16 h. The cells were stimulated with the following ligands for 20 min: (i) vehicle (PBS), (ii) 0.5 mM histamine, (iii) 0.5 mM histamine plus 10 μM cycloheptadine, (iv) 0.5 mM histamine plus 1 μM thapsigargin, (v) 0.5 mM ATP, (vi) 0.5 mM ATP plus 10 μM cycloheptadine, (vii) 0.5 mM ATP plus 1 μM thapsigargin, and (viii) 2 μM ionomycin.
The cells were washed twice with PBS, and harvested by trypsinization and centrifugation. The cells were resuspended with a 40 μL substrate buffer carrying coelenterazine, and then transferred to a test tube to determine the luminescence using a luminometer (Minilumat LB9506).

page S3

Kinetics of substrate saturation in COS-7 cells carrying pCPG-ctrl. The kinetics of coelenterazine saturation in COS-7 cells were monitored with COS-7 cells carrying pCPG-ctrl (Suppl. Figure 1(C)). COS-7 cells cultured in a 24-well plate were transiently transfected with pCPG-ctrl and incubated for another 16 h. The cells on the plate were washed once with HBSS buffer, and then suspended on 500 μL HBSS buffer. After addition of coelenterazine, the variance of luminescence intensities was traced with a bioluminescence plate reader (Mithras LB940; Berthold).

Examples of bioanalytical use of the present probes. **page S4**

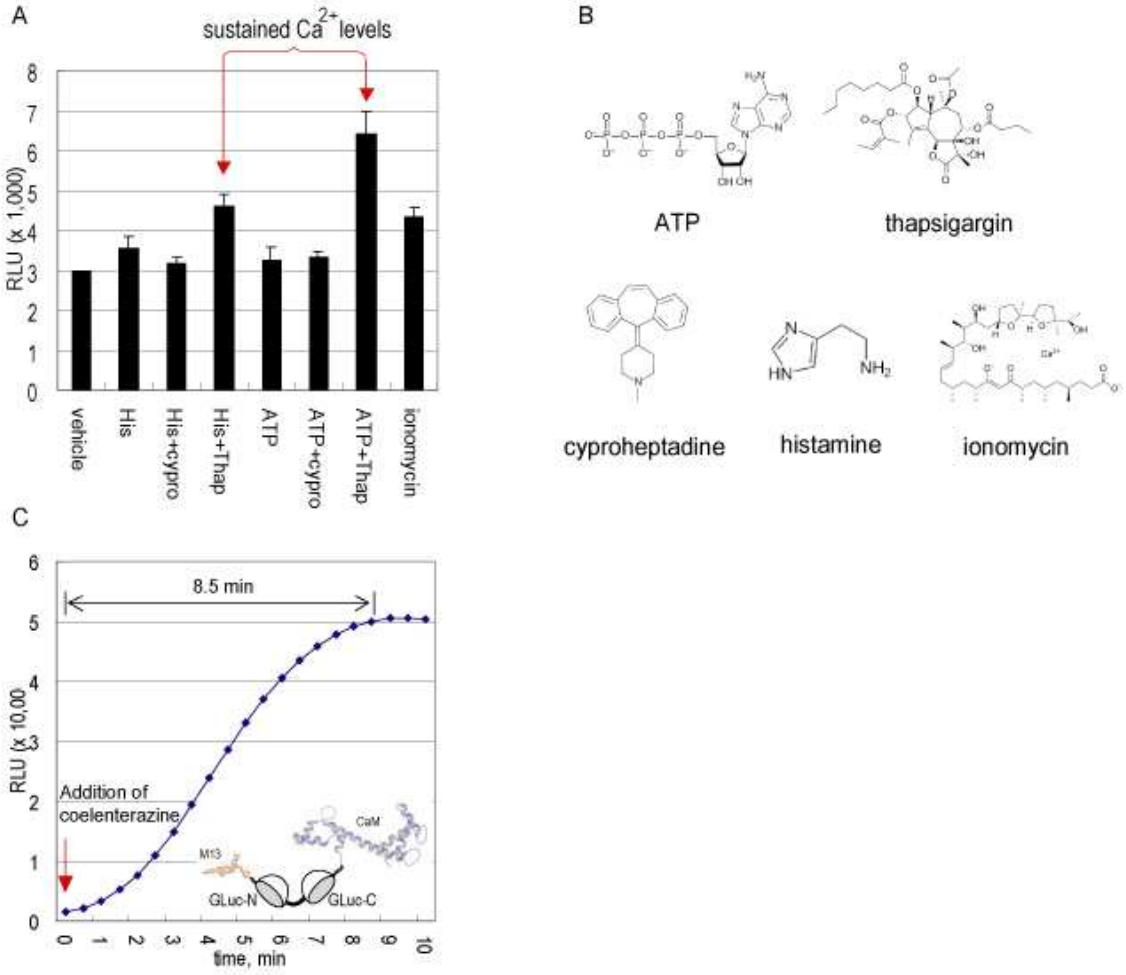

Figure S1. (A) Washout effects of ligand-elevated Ca^{2+} levels in COS-7 cells carrying pCPG. The red arrows show the retained luminescence intensities by thapsigargin, a Ca^{2+} pump inhibitor. (B) Chemical structure of the reagents used in this study. Abbreviations: His, histamine; ATP, adenosine 5′-triphosphate; cypro, cyproheptadine; thap, thapsigargin. (C) Kinetics of coelenterazine saturation in COS-7 cells. The luminescence intensities from the cells carrying CPG-ctrl reached a plateau in 8.5 min.

Monofunctional Carbocyanine Dyes for Bio- and Bioorthogonal Conjugation

Fangwei Shao, Ralph Weissleder, and Scott A. Hilderbrand*

Center for Molecular Imaging Research and Center for Systems Biology, Massachusetts General Hospital/Havard Medical School, Room 5404, Building 149, 13th Street, Charlestown, Massachusetts 02129. Received September 30, 2008; Revised Manuscript Received October 22, 2008

A facile synthetic route to prepare monofunctional carbocyanine dyes for biological application is developed. Three pentamethine carbocyanine dyes have been successfully modified with a variety of functional groups such as: carboxylic acids, azides, or alkynes. The new dyes are characterized by strong NIR fluorescence emission, high extinction coefficients and good quantum yields. The azide and alkyne dyes have potential utility as components in bioorthogonal labeling schemes via [2 + 3] dipolar cycloaddition "click" reactions. The application of one derivative, CyAM-5 alkyne, for bioorthogonal labeling is demonstrated. Fluorescence microscopy shows coupling of CyAM-5 alkyne to Chinese hamster ovary (CHO) cells preincubated with azide modified glycans.

INTRODUCTION

Near-infrared (NIR) fluorescence-based imaging is becoming a key tool for early disease diagnosis, therapeutic applications, and biochemical analysis, due to the high sensitivity, excellent temporospatial resolution, and potential for multichannel imaging (*1, 2*). There is currently a need for improved, bright near-infrared, water-soluble dyes containing diverse functional groups for conjugation to biomolecules (*3, 4*). Asymmetric monofunctional carbocyanine dyes containing carboxylic acids were first reported in the early 1990s (*5, 6*). Due to their bright fluorescence and NIR emission, these fluorophores are receiving considerable interest as components of new NIR optical imaging agents (*5*−*7*). For example, the Cy5.5 and Cy7 dyes have been used for labeling a variety of biological/biomedical macromolecules and nanoparticles (*8, 9*). Two major synthetic strategies are currently employed in the preparation of functionalized carbocyanine dyes. One is a stepwise synthetic route to prepare asymmetric cyanine dyes, in which different indoleninium or benzindoleninium moieties are condensed to a polymethine chain (*5, 6*). Although many commonly used monofunctional cyanine dyes are prepared through this route, synthetic yields are often less than 10% and significant amounts of the undesired symmetric dyes are formed (*10*). A second synthetic route for incorporating functional groups into symmetric heptamethine cyanine dyes also has been developed (*11*). This route proceeds via reaction of nucleophiles with commercially available chloro-substituted cyanine dyes to give a variety of aryl ether, thiol ether, and aryl thioether modified tricarbocyanine fluorophores often in greater than 90% yield (*12*−*14*). More recently, a modified Suzuki-Miyaura coupling was proposed to prepare *meso*-aryl, aryl ether, and arylamino tricarbocyanine dyes in good yields (*15*). Unfortunately, many of these compounds have lower quantum yields (often $\Phi < 0.1$) than canonical Cy7 ($\Phi = 0.27$) or are chemically unstable (*16*). Furthermore, the physical behavior of these carbocyanine derivatives can be altered significantly by their functional substituents. For example, aryl ether modified dyes can show an increased tendency to aggregate in aqueous solution (*12*). There are several criteria that need to be met for design of dyes that are useful for bioconjugation and bioimaging applications. These include universal requirements, such as bright fluorescence emission, water solubility, chemical stability, as well as far-red/NIR absorption and emission. In addition to these parameters, a flexible high-yielding synthetic methodology is desirable. In order to achieve these requirements and circumvent the shortcomings of existing synthetic routes, we present in this paper a new procedure based on modification of the malonaldehyde dianil dye precursors for preparation of monofunctional far-red/NIR pentamethine carbocyanine dye derivatives. This synthetic paradigm can be extended to incorporate a variety of functional groups, such as carboxyl, azido, and alkynyl groups, into the cyanine fluorochromes. Azido and alkynyl groups are two essential reagents in the click reaction. In the presence of Cu(I) catalyst, azide and alkyne containing molecules combine in a [3 + 2] dipolar cycloadditon to form a stable triazole moiety (*17, 18*). Since there are few, if any, azides or alkynes that occur naturally in biology, the click reaction is receiving increased attention as a potential bioorthogonal conjugation scheme (*19*−*21*). However, to date there has been little effort to develop NIR fluorophores modified with azides or alkynes that are suitable for biological and *in vivo* imaging applications.

EXPERIMENTAL PROCEDURES

General Materials and Methods. All chemicals were purchased from Aldrich or TCI and were used as received. All of the solvents were at least of reagent grade and were used without further purification. All of the dyes for characterization were purified by high-performance liquid chromatography (HPLC) on a Varian 210 instrument equipped with a 335 diode array detector. If not otherwise noted, HPLC buffer A is 0.1% trifluoroacetic acid (TFA) in water and buffer B is acetonitrile with 10% water and 0.1% TFA. ^{1}H (400 MHz) and ^{13}C NMR (100 MHz) spectra were collected on a Bruker Advance-400 NMR spectrometer at ambient temperature. The chemical shifts were measured versus tetramethylsilane (TMS) as an internal standard. High-resolution electrospray ionization (ESI) mass spectra were obtained on a Bruker Daltonics APEXIV 4.7 T Fourier transform ion cyclotron resonance mass spectrometer (FT-ICR-MS) in the Department of Chemistry Instrumentation Facility at the Massachusetts Institute of Technology.

Synthesis of 5-(Phenylamino)-4-(phenylimino)methyl)-4-pentenoic Acid Derivatives (Intermediates 3a−c). *General Synthetic Route.* Anhydrous dimethylformamide (1.01 mL, 13

* Tel: 617-726-5788, Fax: 617-726-5708, E-mail: scott_Hilderbrand@hms.harvard.edu.

10.1021/bc800417b CCC: $40.75 © 2008 American Chemical Society
Published on Web 11/20/2008

Scheme 1. Synthetic Route for Preparation of Monofunctional Dye Derivatives[a]

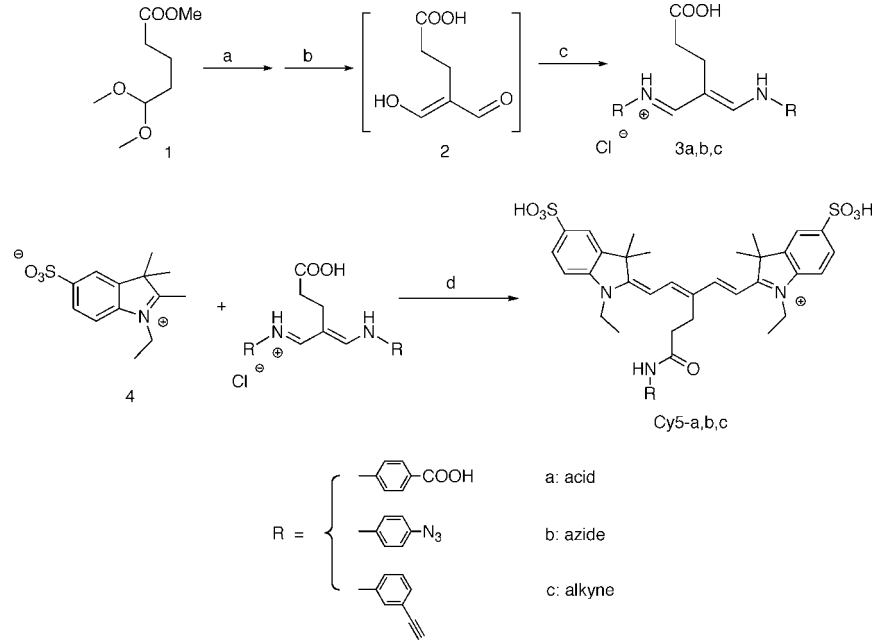

[a] Reaction conditions: (a) $C_2O_2CI_2$/DMF/$C_2H_2CI_2$,70 °C; (b) 4 M NaOH; (c) R-NH_2CI/10% HCI_{aq}; (d) HOAc/0.5% TEA 115 °C. A. (Upper) Synthesis of malonaldehyde dianil intermediates. B. (Lower) Synthesis of monofunctional carbocyanine dyes.

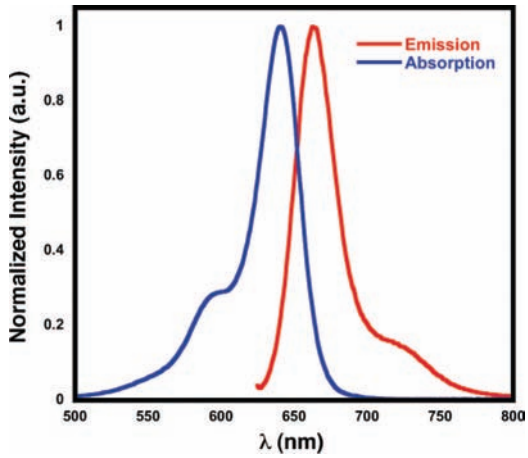

Figure 1. Normalized absorption and emission spectra of CyAM-5 acid in PBS, pH 7.0.

mmol) and oxalyl chloride (1.26 g, 10 mmol) were added sequentially into 30 mL anhydrous dichloromethane (DCM) in an acetone/dry ice bath. The mixture was allowed to warm to room temperature over 15 min. Methyl 5,5-dimethoxyvalerate (881 mg, 5 mmol) was then added dropwise to the reaction solution followed by heating at 70 °C for 2 h, allowing the DCM to evaporate. The resulting yellow oil was dissolved in 5 mL of 4 M NaOH and was heated at 70 °C for 1 h. Before their use, the aniline derivatives (4-aminobenzoic acid, 4-azidoaniline, 3-ethynylaniline) were converted to their corresponding chloride salts on a 10 mmol scale by dissolving the aniline in acetone and precipitating its salt by addition of excess concentrated aqueous HCl. After removing the solvent under vacuum, the appropriate aniline chloride salt (10 mmol), dissolved in 5 mL water, was added to the basic, crude reaction solution and was allowed to stir at room temperature for 1 or more hours, until the reaction was complete. The final malonaldehyde dianil hydrochloride salts were precipitated as light yellow solids after the addition of 5 mL of 10% aqueous HCl and were collected by filtration. The products were above 95% pure and used directly in the dye synthesis without further purification if not mentioned specifically.

Table 1. Optical Properties of Pentamethine Carbocyanine Dyes

	λ_{abs} (nm)[a]	λ_{em} (nm)	ε ($M^{-1}cm^{-1}$)[b]	Φ[c]
CyAM-5 acid	642	656	215 000	0.17
CyAM-5 azide	641	658	222 000	0.20
CyAM-5 alkyne	641	657	240 000	0.20

[a] Spectra were obtained in phosphate buffered solution, pH 7.0. Details are listed in Experimental Procedures. [b] Extinction coefficients at 640 nm are averaged over at least three sets of equivalent experiments. Details are listed in Experimental Procedures. [c] Emission spectra were excited at 620 nm. Details are listed in Experimental Procedures.

*Carboxylic Acid Intermediate (**3a**).* Yield 65%, 1.22 g. ^{1}H NMR (400 MHz, DMSO-d_6): δ 11.65 (b, 2H), 8.80 (s, 2H), 8.08 (d, 4H, J = 8.8 Hz), 7.63 (d, 4H, J = 8.8 Hz), 2.90 (t, 2H, J = 7.6 Hz), 2.48 (t, 2H, J = 7.9 Hz). ^{13}C NMR (100 MHz, DMSO-d_6): δ 174.78, 167.50, 160.44, 143.41, 131.97, 128.74, 119.31 112.49, 32.75, 18.35. HRMS-ESI $[M + H]^+$ m/z calcd. for $[C_{20}H_{18}N_2O_6]^+$ 383.1238, found 383.1231.

*Azide Intermediate (**3b**).* 4-Azidoaniline hydrochloride was used as received. Yield 61%, 1.24 g. ^{1}H NMR (400 MHz, DMSO-d_6): δ 8.92 (s, 2H), 7.68 (d, 4H, J = 8.8 Hz), 7.23 (d, 4H, J = 8.7 Hz), 2.94 (t, 2H, J = 7.3 Hz), 2.46 (t, 2H, J = 7.8 Hz). ^{13}C NMR (100 MHz, DMSO-d_6): δ 173.82, 158.22, 137.04, 136.31, 125.27, 120.45, 109.95, 31.88, 17.45. HRMS-ESI $[M + H]^+$ m/z calcd. for $[C_{18}H_{16}N_8O_2]^+$ 377.1469, found 377.1473.

*Alkyne Intermediate (**3c**).* Crude precipitates were purified on a silica column starting from 5% MeOH in DCM. The pure product eluted at 15% MeOH in DCM. Yield 24%, 440 mg. ^{1}H NMR (400 MHz, DMSO-d_6): δ 8.19 (s, 2H), 7.41 (s, 2H), 7.37 (d, 2H, J = 7.2 Hz), 7.34 (d, 2H, J = 8.0Hz), 7.20 (d, 2H, J = 6.8), 4.24 (s, 2H), 2.79 (t, 2H, J = 7.5 Hz), 2.44 (t, 2H, J = 7.8 Hz). ^{13}C NMR (100 MHz, DMSO-d_6): δ 174.43, 154.61, 145.14, 129.78, 126.82, 122.78, 120.66, 119.14, 113.33, 83.31, 80.98, 32.13, 18.51. HRMS-ESI $[M + H]^+$ m/z calcd. for $[C_{22}H_{18}N_2O_2]^+$ 343.1441, found 343.1443.

Dye Synthesis (CyAM-5 acid, CyAM-5 azide and CyAM-5 alkyne). *General Synthetic Route.* 1-Ethyl-2,3,3-trimethylindoleninium-5-sulfonate (**4**) was prepared according to literature

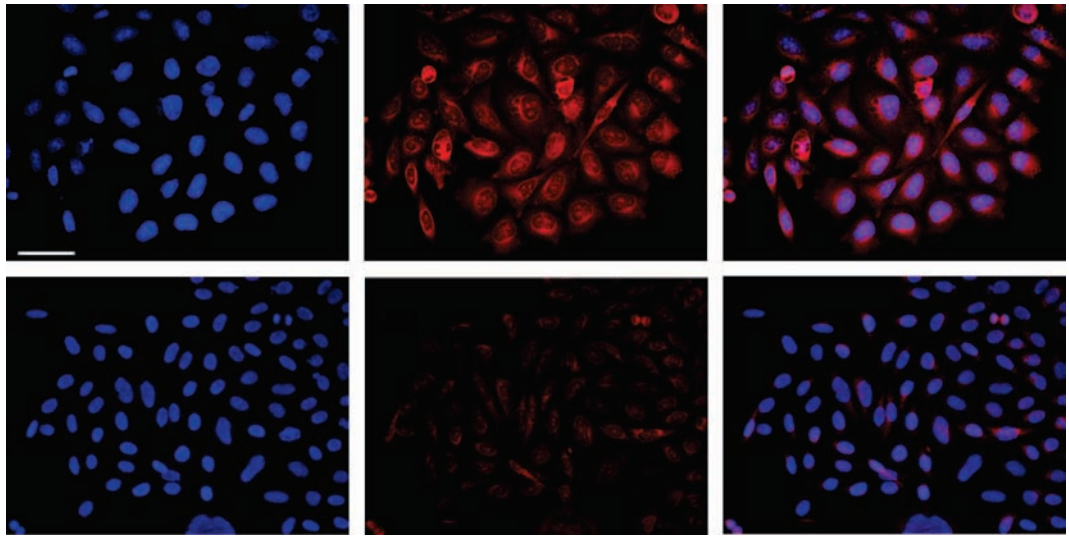

Figure 2. Fluorescene microscopy of CHO cells labeled with CyAM-5 alkyne. Cells incubated with azido-sugar supplimented media (top) or unsupplimented media (bottom) after treatment with CyAM-5 alkyne in the presence of Cu(I)/TBTA as catalyst. Experimental details and additional controls are shown in the supporting material. Fluorescence signal from the nuclear stain, DAPI, colored blue (left), CyAM-5 alkyne colored red (center), and the merged images (right) are shown. The scale bar represents 50 μm.

procedures (*5*). Indoleninium **4** (4 equiv) and intermediate **3a**, **b**, or **c** (1 equiv) were dissolved in 5 mL acetic anhydride with 0.5% v/v triethylamine. The reaction solution was heated at 115 °C for 1 h in a sealed flask. The crude product was then precipitated by the addition of diethyl ether and washed with additional diethyl ether. Preparative HPLC (Varian Pursuit XRs 10 C18 250 × 21.2 mm column, 0−25% buffer B over 30 min at a flow rate of 21 mL/min) was applied to purify **CyAM-5-acid** giving the blue dye as the free acid. The other dyes (**CyAM-5 azide** and **CyAM-5 alkyne**) were isolated as their ammonium salts by preparative HPLC over the same gradient but with buffer A as 50 mM NH_4OAc in water and buffer B as 100% acetonitrile.

*CyAM-5 Acid (***5a***).* Yield 66%, 252 mg starting with 0.5 mmol of **3a**. ^{1}H NMR (400 MHz, DMSO-d_6): δ 10.30 (s, 1H), 8.21 (d, 2H, J = 14.1 Hz), 7.86 (d, 2H, J = 8.7 Hz), 7.84 (s, 2H), 7.72 (d, 2H, J = 8.8 Hz), 7.66 (d, 2H, J = 8.2 Hz), 7.35 (d, 2H, J = 8.4 Hz), 6.33 (d, 2H, J = 14.2 Hz), 4.21 (m, 4H), 2.99 (t, 2H, J = 6.7 Hz), 2.60 (t, 2H, J = 7.1 Hz), 1.71 (s, 12H), 1.30 (t, 6H, J = 7.1 Hz). ^{13}C NMR (100 MHz, DMSO-d_6): δ 173.43, 172.03, 167.51, 154.11, 145.75, 143.81, 142.19, 141.40, 133.99, 130.99, 126.73, 125.62, 120.61, 118.98, 110.63, 100.36, 49.61, 39.67, 36.10, 27.46, 20.58, 12.69. HRMS-ESI $[M]^+$ m/z calcd. for $[C_{39}H_{44}N_3O_9S_2]^+$ 762.2513, found 762.2539.

*CyAM-5 Azide (***5b***).* Yield 64%, 116 mg starting with 0.24 mmol of **3b**. ^{1}H NMR (400 MHz, DMSO-d_6): δ 10.08 (s, 1H), 8.20 (d, 2H, J = 14.2 Hz), 7.83 (s, 2H), 7.66 (d, 2H, J = 8.9 Hz), 7.64 (d, 2H, J = 8.7 Hz), 7.34 (d, 2H, J = 8.4 Hz), 7.03 (d, 2H, J = 8.9 Hz), 6.32 (d, 2H, J = 14.2 Hz), 4.20 (m, 4H), 2.98 (t, 2H, J = 6.7 Hz), 2.54 (t, 2H, J = 6.8 Hz), 1.70 (s, 12H), 1.29 (t, 6H, J = 7.1 Hz). ^{13}C NMR (100 MHz, DMSO-d_6): δ 173.73, 171.74, 154.46, 146.15, 142.49, 141.71, 137.42, 134.65, 133.61, 127.05, 121.55, 120.94, 120.31, 110.93, 100.73, 49.91, 39.63, 36.23, 27.79, 21.04, 13.02. HRMS-ESI $[M]^+$ m/z calcd. for $[C_{38}H_{43}N_6O_7S_2]^+$ 759.2629, found 759.2630.

*CyAM-5 Alkyne (***5c***).* Yield 65%, 114 mg starting with 0.2 mmol of **3c**. ^{1}H NMR (400 MHz, DMSO-d_6): δ 10.08 (s, 1H), 8.19 (d, 2H, J = 14.2 Hz), 7.82 (s, 2H), 7.79 (s, 1H), 7.64 (d, 2H, J = 8.4 Hz), 7.48 (d, 1H, J = 8.8 Hz), 7.33 (d, 2H, J = 8.4 Hz), 7.25 (t, 1H, J = 7.9 Hz), 7.07 (d, 1H, J = 7.6 Hz), 6.38 (d, 2H, J = 14.2 Hz), 4.21-4.18 (m, 4H), 4.05 (s, 1H), 2.98 (t, 2H, J = 6.8 Hz), 2.54 (t, 2H, J = 6.8 Hz), 1.68 (s, 12H), 1.14 (t, 6H, J = 7.3 Hz). ^{13}C NMR (100 MHz, DMSO-d_6): δ 172.81, 171.24, 153.59, 145.20, 141.57, 140.79, 139.28, 132.49, 129.14, 126.39, 126.13, 122.19, 121.91, 119.99, 119.77, 110.03, 99.83, 83.33, 80.47, 48.98, 38.70, 35.49, 26.84, 22.55, 12.11. HRMS-ESI $[M]^+$ m/z calcd. for $[C_{40}H_{44}N_3O_7S_2]^+$ 742.2615, found 742.2612.

Optical Properties. Absorption spectra and extinction coefficients of the fluorophores were obtained on a Varian Cary 50-Bio UV−visible spectrophotometer. Extinction coefficients were measured in phosphate-buffered saline (PBS), 10 mM phosphate buffer pH 7.0, 27 mM potassium chloride, and 137 mM sodium chloride and were averaged over at least three sets of parallel experiments. For each trial, 2−3 mg of the HPLC-purified dyes were weighed on a Mettler AT201 analytical balance with an error of ±0.01 mg and were dissolved in deionized water using a 10 mL volumetric flask to prepare the stock solutions. Emission spectra were collected on a Varian Cary Eclipse fluorescence spectrophotometer. Quantum yield measurements were performed on at least eight trials for each dye derivative with the maximum absorption for each sample less than 0.1, using Cy5 as a standard (Φ = 0.27) (*5*). The standard deviation for both the extinction coefficient and quantum yield measurements is less than 5%. Photostability data were collected on a Horiba Jobin Yvon Fluorolog-3 spectrofluorometer (Edison, NY) equipped with a 450 W xenon lamp (Ushio Inc., Japan). Dye photobleaching was observed by monitoring the fluorescence emission of absorbance-matched dye samples (absorbance <0.1) at an excitation wavelength 620 nm for 60 min.

Fluorescence Labeling and Cell Imaging. Chinese hamster ovary (CHO) cells were maintained in a 5% CO_2, water-saturated atmosphere and grown in F12 HAMS medium supplemented with 10% FBS, 1% penstrep, and 1% L-glutamine. For biolabeling experiments, the cells were incubated for 2−3 days in the regular medium or medium supplemented with 100 μm ManNAz (Molecular probes) in an eight-well LabTek II chamber slide (Nunc). The medium was gently aspirated, and the cells were fixed at −20 °C with methanol for 10 min and then acetone for 1 min. The cells then were washed with 500 μL of PBS (pH 7.0) three times and were treated with a bioorthogonal reaction solution containing 20 μM CyAM-5 alkyne, 100 μM $CuSO_4$/100 μM Tris[(1-benzyl-1*H*-1,2,3-triazol-4-yl)methyl]amine (TBTA) if mentioned and 1 mM sodium ascorbate in PBS (pH 7.0) at room temperature for 1−2 h. Immediately prior to imaging, Vectra Shield mounting medium

containing DAPI (Vector Laboratories) was applied to the cells. Fluorescent images were captured on a Nikon Eclipse TE2000-S fluorescence microscope with 40× objective equipped with a Photometrics Cascade 512B CCD camera using excitation and emission filters from Chroma Technology. Exposure times of 200 and 1000 ms, for the nuclear stain and carbocyanine dye channels, respectively, were used for image collection. All images from the carbocyanine dye channel were processed with identical leveling.

RESULTS AND DISCUSSION

Our design of monofunctional dyes focuses on symmetric carbocyanine scaffolds, as shown in Scheme 1. These dyes have two identical monosulfonated indoleninium moieties (**4**) and are prepared in simple one-stage dye condensation reactions, which typically have significantly higher yields than reactions reported for asymmetric cyanine dye synthesis (*5*, *6*). The two sulfonate groups on the aromatic rings confer excellent water solubility to the final dyes. The acid, azide, and alkyne handles are introduced onto the central carbon atom of the polymethine chain through an alkyl chain followed by an arylamide linkage that is formed during the dye synthesis.

The desired functional groups are incorporated into the malonaldehyde dianil intermediates (**3a**−**c**) (Scheme 1a). These malonaldehyde dianil derivatives are prepared via carboxylic acid intermediate, (**2**), which is synthesized from methyl 5,5-dimethoxyvalerate (**1**) via a Vilsmeier−Haack−Arnold amino-formylation followed by basic hydrolysis. An aniline moiety containing a carboxylic acid, alkyne, or azide in either the *para* or *meta* position is then added to reaction solution to yield the modified malonaldehyde dianil derivatives. Compounds **3a**−**c**, which are isolated in 24−65% yield as their chloride salts after acidic workup, are of sufficient purity for subsequent use in the dye condensation reactions. The unique pathway for preparation of the malonaldehyde dianil intermediates in this report allows for facile introduction of a variety of functional groups onto the final cyanine dyes. By using different indoleninium and benzindolinium derivatives, these malonaldehyde dianil derivatives can be applied to prepare not only Cy5 dyes but also their monofunctional Cy5.5 analogues.

Synthesis of the monofuctional carbocyanine fluorophores is achieved by combining 1 equiv of intermediate (**3**) and 4 equiv of 1-ethyl-2,3,3-trimethylindoleninium-5-sulfonate (**4**) in acetic anhydride with 0.5% triethylamine. During the dye condensation, one of the two aniline groups on the malonaldehyde derivatives undergoes an intramolecular nucleophilic attack, reacting with the carboxylic acid of the malonaldehyde derivative forming an amide bond, as shown in Scheme 1b. This unique intramolecular rearrangement occurs during the synthesis of all the three dyes. The intramolecular rearrangement allows for facile installation of diverse functional groups onto the polymethine chain of the cyanine dye scaffold in a one-stage reaction to give a variety of cyanine dyes suitable for conjugation reactions. In combination with the simple isolation of the dyes by precipitation from diethyl ether, the overall yields for the dye condensations are all near 65% even after HPLC purification.

Regardless of the functional groups attached to the polymethine scaffold, the spectroscopic profiles of the three dye derivatives, CyAM-5 acid (**5a**), CyAM-5 azide (**5b**), and CyAM-5 alkyne (**5c**) are nearly identical. Absorption and emission spectra of CyAM-5 acid are shown in Figure 1. CyAM-5 acid has optical features of a typical pentamethine cyanine dye with absorption and emission maxima at 642 and 658 nm, respectively. The absorption and emission maxima of all three dyes are blue-shifted by approximately 5 nm in comparison to those of Cy5, whereas the Stokes shifts are nearly identical to that of Cy5, ∼16 nm. Table 1 summarizes the optical properties of the monofuctional dyes. All three of the new dyes are extremely bright with extinction coefficients greater than 215 000 M^{-1} cm^{-1} and quantum yields of 0.17 or higher. Furthermore, the new dyes have better photostability than typical cyanine derivatives that have unsubstituted polymethine chains. As shown in Supporting Information Figure S2, after an hour of irradiation, CyAM-5 acid shows 28% less photobleaching when compared to Cy5.

Due to their bright fluorescence, long-wavelength absorption, and emission, as well as the ability to accommodate a variety of functional groups for conjugation reactions, this new class of cyanine dyes should find use in many biological labeling and imaging applications. For example, CyAM-5 acid can be conveniently converted to its corresponding activated succinimidyl ester (*22*) for conjugation to amine-containing molecules. CyAM-5 azide and alkyne have a variety of potential uses in which they can be employed as a component in the click reaction. In addition, the aryl azide of CyAM-5 azide may find use in photo-cross-linking experiments.

Recently, fluorescence labeling methods based upon click chemistry have been developed for visualization of glycoproteins in cells incubated with azide-containing sugars (*19*−*21*). We have adapted this sugar labeling system to demonstrate the ability of our monofunctional dyes to undergo efficient bioorthogonal coupling in a biorelevant system. Azide sugar modified Chinese hamster ovary (CHO) cells were first prepared by incubation of the cells with azidoacetylmannosamine containing media for 3 days. These cells then are fixed with methanol/acetone and are labeled with CyAM-5 alkyne in the presence of copper (I) as a catalyst. The cells bearing azido sialic acid in their glycoprotein show increased fluorescence signal when compared to control cells that were not incubated with the azido-mannosamine, as shown in Figure 2, indicating the labeling of the cells with CyAM-5 alkyne via formation of a triazole linkage. The enhancement of fluorescence signal is only observed in the presence of both catalyst Cu(I) and azido glycans (Supporting Information Figure S3). The Cu(I) chelating ligand, trisbenzyltriazolylmethylamine (TBTA), facilitates the reaction, but is not necessary for efficient labeling of the cells. The requirement of both Cu(I) and azido-sugar treatment for fluorescent labeling of CHO cells with CyAM-5 alkyne indicates that the resulting click reaction is a selective, bioorthonogal method for cell labeling.

In conclusion, a unique, general strategy for synthesizing monofunctional carbocyanine derivatives has been developed that is amenable to the preparation of far-red/NIR cyanine dyes with high yields containing acid, alkyne, or azide synthetic handles. These dyes are expected to have a variety of potential applications in bio- and bioorthogonal labeling schemes. Furthermore, using this synthetic approach, installation of additional useful functional groups such as amines, thiols, and maleimides should be feasible.

ACKNOWLEDGMENT

This work is supported by NIH grant 1-U01-HL080731. We thank Dr. Neal Devaraj for helpful discussion on click chemistry.

Supporting Information Available: Characterization and photostability of pentamethine carbocyanine dyes and all controls for the cell imaging experiments. This material is available free of charge via the Internet at http://pubs.acs.org.

LITERATURE CITED

(1) Weissleder, R., Tung, C. H., Mahmood, U., and Bogdanov, A., Jr. (1999) In vivo imaging of tumors with protease-activated near-infrared fluorescent probes. *Nat. Biotechnol. 17*, 375–8.

(2) Weissleder, R., and Ntziachristos, V. (2003) Shedding light onto live molecular targets. *Nat. Med. 9*, 123–8.
(3) Ballou, B., Ernst, L. A., and Waggoner, A. S. (2005) Fluorescence imaging of tumors in vivo. *Curr. Med. Chem. 12*, 795–805.
(4) Lin, Y., Weissleder, R., and Tung, C. H. (2002) Novel near-infrared cyanine fluorochromes: synthesis, properties, and bioconjugation. *Bioconjugate Chem. 13*, 605–10.
(5) Mujumdar, R. B., Ernst, L. A., Mujumdar, S. R., Lewis, C. J., and Waggoner, A. S. (1993) Cyanine dye labeling reagents: sulfoindocyanine succinimidyl esters. *Bioconjugate Chem. 4*, 105–11.
(6) Mujumdar, S. R., Mujumdar, R. B., Grant, C. M., and Waggoner, A. S. (1996) Cyanine-labeling reagents: sulfobenzindocyanine succinimidyl esters. *Bioconjugate Chem. 7*, 356–62.
(7) Narayana, N., and Patonay, G. (1995) A new method for the synthesis of heptamethine cyanine dyes: synthesis of new near-infrared fluorescent labels. *J. Org. Chem. 60*, 2391–2395.
(8) Pham, W., Medarova, Z., and Moore, A. (2005) Synthesis and application of a water-soluble near-infrared dye for cancer detection using optical imaging. *Bioconjugate Chem. 16*, 735–40.
(9) McCarthy, J. R., Kelly, K. A., Sun, E. Y., and Weissleder, R. (2007) Targeted delivery of multifunctional magnetic nanoparticles. *Nanomed. 2*, 153–67.
(10) Tung, C. H., Lin, Y., Moon, W. K., and Weissleder, R. (2002) A receptor-targeted near-infrared fluorescence probe for in vivo tumor imaging. *ChemBioChem 3*, 784–6.
(11) Strekowski, L., Lipowska, M., and Patonay, G. (1992) Substitution reactions of a nucleofugal group in heptamethine cyanine dyes. Synthesis of an isothiocyanato derivative for labeling proteins with a near-infrared chromophore. *J. Org. Chem. 57*, 4578–4580.
(12) Flanagan, J. H., Jr., Khan, S. H., Menchen, S., Soper, S. A., and Hammer, R. P. (1997) Functionalized tricarbocyanine dyes as near-infrared fluorescent probes for biomolecules. *Bioconjugate Chem. 8*, 751–6.
(13) Kiyose, K., Kojima, H., Urano, Y., and Nagano, T. (2006) Development of a ratiometric fluorescent zinc ion probe in near-infrared region, based on tricabocyanine chromophore. *J. Am. Chem. Soc. 128*, 6548–6549.
(14) Hilderbrand, S. A., Kelly, K. A., Weissleder, R., and Tung, C. H. (2005) Monofunctional near-infrared fluorochromes for imaging applications. *Bioconjugate Chem. 16*, 1275–1281.
(15) Lee, H., CMason, J. C., and Achilefu, S. (2008) Synthesis and spectral properties of near-infrared aminophenyl-, hydroxyphenyl-, and phenyl-substituted heptamethine cyanines. *J. Org. Chem. 73*, 723–725.
(16) Zaheer, A., Wheat, T. E., and Frangioni, J. V. (2002) IRDye78 conjugates for near-infrared fluorescence imaging. *Mol. Imaging 1*, 354–64.
(17) Fokin, V. V. (2007) Click imaging of biochemical processes in living systems. *ACS Chem. Biol. 2*, 775–8.
(18) Kolb, H. C., Finn, M. G., and Sharpless, K. B. (2001) Click chemistry: diverse chemicl function from a few good reactions. *Angew. Chem., Int. Ed. 40*, 2004–2021.
(19) Baskin, J. M., Prescher, J. A., Laughlin, S. T., Agard, N. J., Chang, P. V., Miller, I. A., Lo, A., Codelli, J. A., and Bertozzi, C. R. (2007) Copper-free click chemistry for dynamic in vivo imaging. *Proc. Natl. Acad. Sci. U.S.A. 104*, 16793–7.
(20) Sawa, M., Hsu, T. L., Itoh, T., Sugiyama, M., Hanson, S. R., Vogt, P. K., and Wong, C. H. (2006) Glycoproteomic probes for fluorescent imaging of fucosylated glycans in vivo. *Proc. Natl. Acad. Sci. U.S.A. 103*, 12371–6.
(21) Hsu, T. L., Hanson, S. R., Kishikawa, K., Wang, S. K., Sawa, M., and Wong, C. H. (2007) Alkynyl sugar analogs for the labeling and visualization of glycoconjugates in cells. *Proc. Natl. Acad. Sci. U.S.A. 104*, 2614–9.
(22) Unpublished data. Reaction is complete within one hour at room temperature in the presence of 4 equiv disuccimidyl carbonate and 4 equiv triethylamine in anhydrous DMF.

BC800417B

Monofunctional Carbocyanine Dyes for Bio- and Bioorthogonal Conjugation

Fangwei Shao[†] Ralph Weissleder[†§] and Scott A Hilderbrand[†]*

† Center for Molecular Imaging Research, Massachusetts General Hospital/Havard Medical School, Room 5404, Building 149, 13th St. Charlestown, Massachusetts 02129 Tel: 617-726-5788, Fax: 617-726-5708, Email: Scott_Hilderbrand@hms.harvard.edu

§ Center for Systems Biology, Massachusetts General Hospital/Havard Medical School

SUPPORTING INFORMATION

Table of Contents

Figure S1. HPLC traces present indicating the purity of the dye analogues.

Figure S2. Photostability of CyAM-5 acid in PBS buffer (pH 7.0).

Figure S3. Fluorescent imaging of CHO cells labeled with CyAM-5 alkyne and controls.

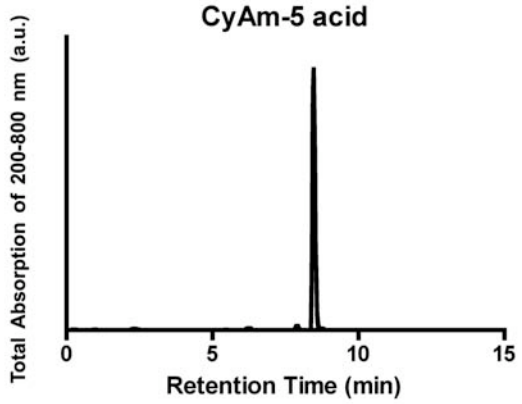

(a)

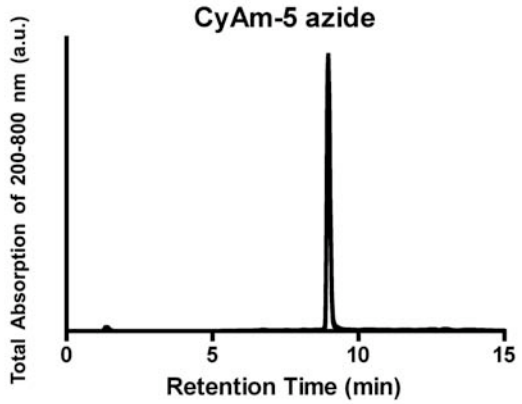

(b)

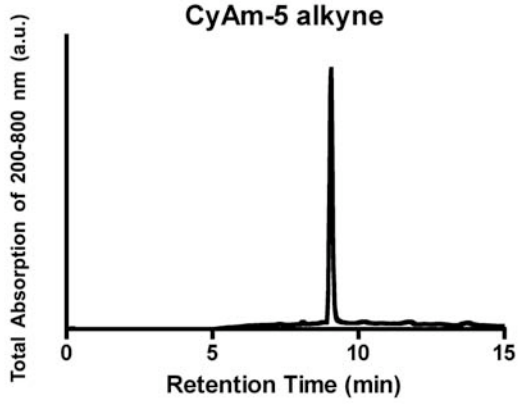

(c)

Figure S1. HPLC traces present indicating the purity of the Cy5 analogues. (a) CyAM-5 acid; (b) CyAM-5 azide; (c) CyAM-5 alkyne. HPLC was conducted on a Waters 2695 separations module equipped with a Waters 2996 photodiode array detector with gradient from 0 to 100% buffer B over 15 min.

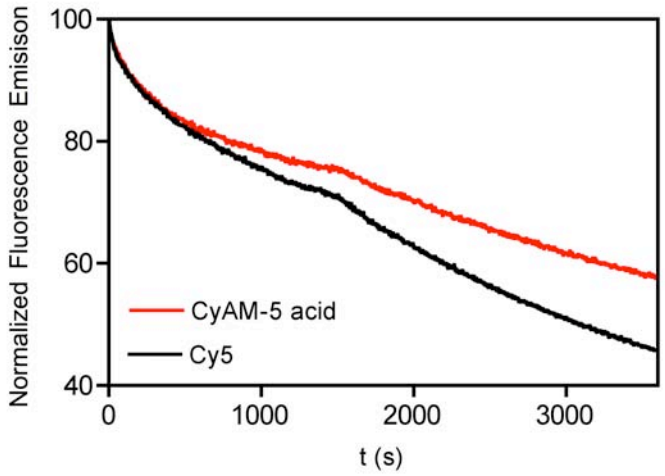

Figure S2. Photostability of CyAM-5 acid and the standard Cy5 in PBS buffer (pH 7.0). After 60 minutes of irradiation at 620 nm, 42% of CyAM-5 acid (18 nM) is photobleached, whereas 54% of Cy5 at the comparable absorption is photobleached. Thus, CyAM-5 acid has 28% better photostability than Cy5.

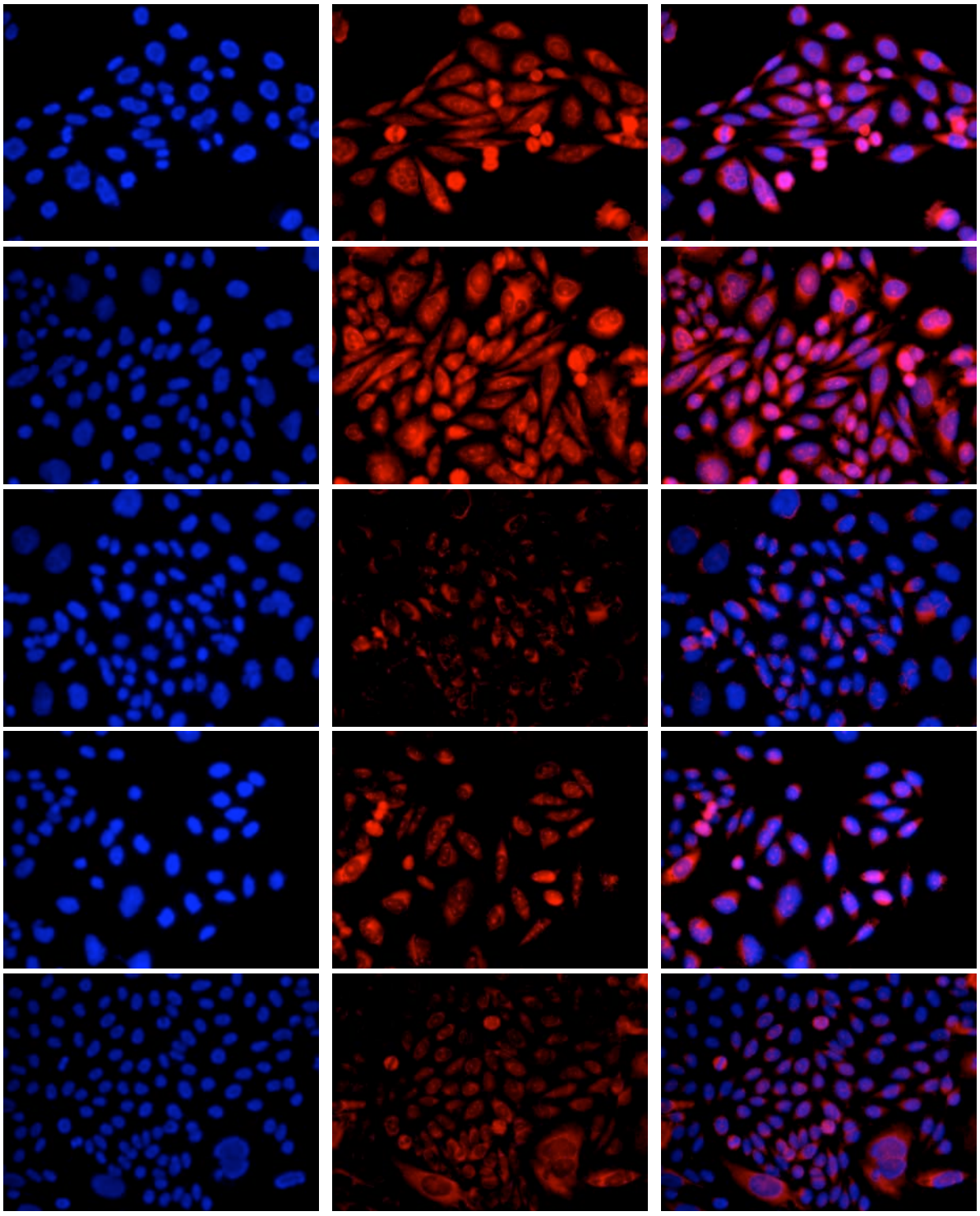
1
2
3
4
5

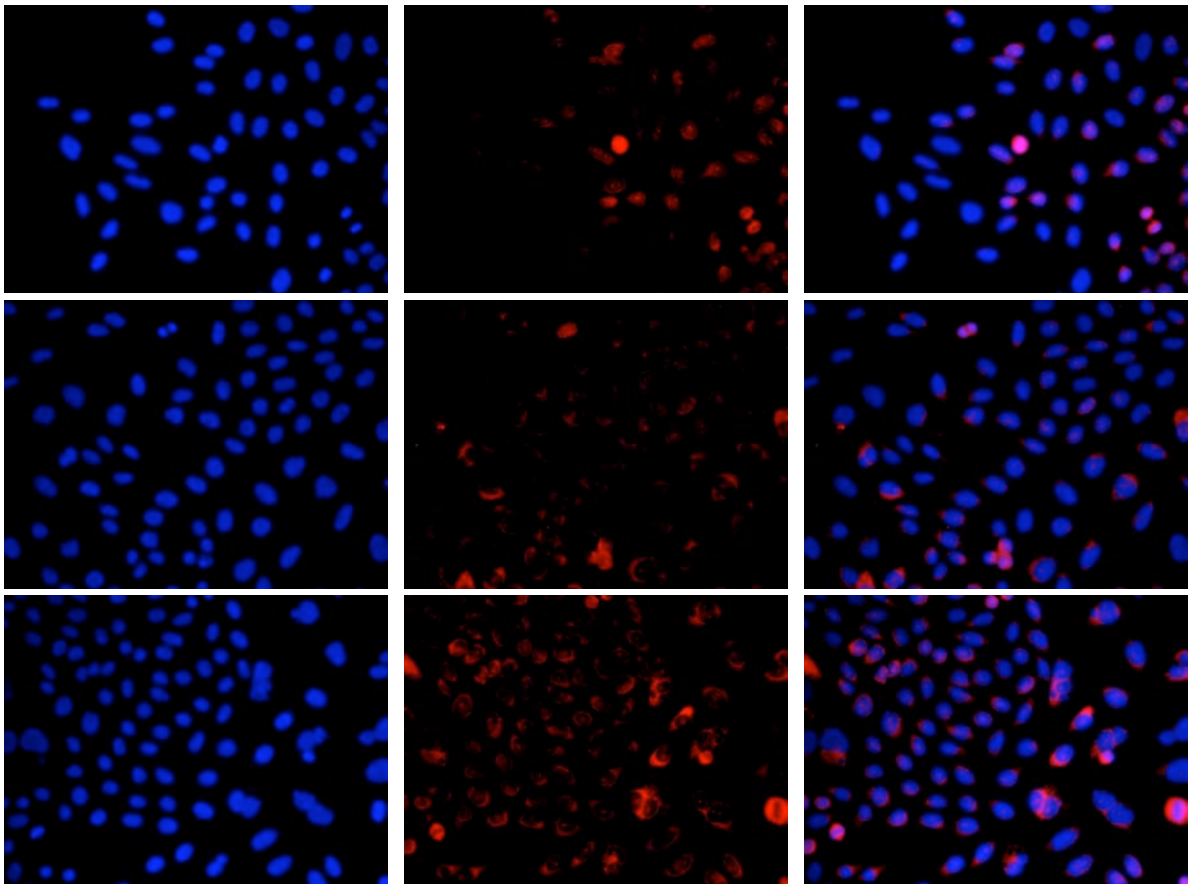

Figure S3. Fluorescent imaging of CHO cells labeled with CyAM-5 alkyne and controls. Cells bearing azido-sugar (lane 1~4) and regular cells (lane 5~8) are labeled by CyAM-5 alkyne in the presence of both Cu(I) and ligand TBTA (lane 1,5), Cu(I) alone (lane 2,6), TBTA alone (lane 3,7), or neither of the two (lane 4,8). Cell nuclei stained with DAPI, fluorescence of labeled CyAM-5 alkyne and merge figures of the two above are shown in column *left, middle* and *right*, respectively. Details are listed in *experimental procedures.*

Bioconjugate Chemistry 20th Anniversary

Subscriber access provided by SHEMYAKIN-OVCHINNIKOV INST

Article

F- and Fluorescently Labeled Micelles as Nanoscopic Assemblies for Chemotherapeutic Delivery

Wenjun Du, Zhiqiang Xu, Andreas M. Nystro#m, Ke Zhang, Jeffrey R. Leonard, and Karen L. Wooley

Bioconjugate Chem., **2008**, 19 (12), 2492-2498• DOI: 10.1021/bc800396h • Publication Date (Web): 03 December 2008

Downloaded from http://pubs.acs.org on May 2, 2009

More About This Article

Additional resources and features associated with this article are available within the HTML version:

- Supporting Information
- Access to high resolution figures
- Links to articles and content related to this article
- Copyright permission to reproduce figures and/or text from this article

View the Full Text HTML

ACS Publications
High quality. High impact.

Bioconjugate Chemistry is published by the American Chemical Society. 1155 Sixteenth Street N.W., Washington, DC 20036

^{19}F- and Fluorescently Labeled Micelles as Nanoscopic Assemblies for Chemotherapeutic Delivery

Wenjun Du,[†] Zhiqiang Xu,[‡] Andreas M. Nyström,[†] Ke Zhang,[†] Jeffrey R. Leonard,[‡] and Karen L. Wooley*[,†]

Department of Chemistry, Department of Radiology, Washington University in Saint Louis, Saint Louis, Missouri 63130-4899, and Department of Neurological Surgery, Washington University School of Medicine, 660 South Euclid Ave, Saint Louis, Missouri 63110. Received September 17, 2008; Revised Manuscript Received October 30, 2008

Micelles from amphiphilic star-block copolymers, having a hydrophobic hyperbranched core and amphiphilic fluoropolymer arms, were constructed as drug delivery agent assemblies. A series of polymer structures was constructed from consecutive copolymerizations of 4-chloromethylstyrene with dodecyl acrylate and then 1,1,1-trifluoroethyl methacrylate with *tert*-butyl acrylate, followed by acidolysis to release the hydrophilic acrylic acid residues. These structures were labeled with cascade blue as a fluorescence reporter. The series of materials differed primarily in the ratio of 1,1,1-trifluoroethyl methacrylate to acrylic acid units, to give differences in fluorine loading and hydrophobicity/hydrophilicity balance. Doxorubicin (DOX) was used as a therapeutic to study the loading, release, and cytotoxicity of these micellar constructs on an U87-MG-EGFRvIII-CBR cell line. The micelles, with TEM-measured diameters ranging 5−9 nm and DLS-measured hydrodynamic diameters 20−30 nm, had loading capacities of ca. 4 wt % of DOX. The DOX-loaded micelles exhibited potent cytotoxicity with cell viabilities of 60−25% at 1.0 μg/mL effective DOX concentrations, depending upon the polymer composition, as determined by MTT assays. These cell viability values are comparable to that of free DOX, suggesting an effective release of the cargo and delivery to the cell nuclei, which was further confirmed by fluorescence microscopy of the cells. ^{19}F-NMR spectroscopy indicated a partial degradation of the surface-available trifluoroethyl ester linkages of the micelles, which may have accelerated the release of DOX. ^{19}F-NMR spectroscopy was also employed to confirm and to quantify the cell uptake of the micelles. These dual fluorescent- and ^{19}F-labeled and chemically functional micelles may be used potentially in a variety of applications, such as cell labeling, imaging, and therapeutic delivery.

INTRODUCTION

Nanoscopic systems that can incorporate combined imaging and therapeutic capabilities are the focus of intensive research for applications in the growing field of nanomedicine (*1*−*7*). Such systems offer the possibility to increase diagnostic accuracy and therapeutic effectiveness, while minimizing side effects from treatment. Nanoscopic polymeric assemblies from dendrimers (*8, 9*), polymer micelles (*5, 10, 11*), shell cross-linked knedel-like (SCKs) nanoparticles (*12*−*14*), and other polymer assemblies (*15, 16*) are promising candidates for such multifunctional therapeutic platforms, since these materials are conveniently synthesized, variably functionalized, and can be assembled to a range of sizes and compositions.

Such polymeric assemblies usually have an amphiphilic composition, in which the hydrophobic component serves as a reservoir for therapeutic cargo and/or imaging agents, and the hydrophilic component provides stability in solution and can be tailored for attaching imaging agents and/or targeting ligands. Therapeutic cargos, usually packed through hydrophobic−hydrophobic interactions, when not covalently attached, can be released through passive diffusion (*12*) or as a response to external stimuli such as pH (*8*−*10, 17*), temperature (*17*−*19*), and light (*19*). In order to utilize polymer assemblies for systemic delivery of therapeutics, it is important to maximize the loading capacity to minimize injection volume for *intravenous* delivery and also to achieve sustained and controlled release.

Our group has long been interested in developing polymers for the construction of multifunctional nanoscopic assemblies for imaging and drug delivery purposes (*12, 14, 16, 20, 21*). One such system is the 1,4,7,10-tetraazocyclododecane-*N*,*N*′,*N*″,*N*‴-tetraacetic acid (DOTA)-conjugated SCKs that can chelate ^{64}Cu for labeling and in vivo PET imaging (*14, 22*). Extension of the SCKs to serve as a therapeutic delivery system has also been reported (*12*). Recently, we developed fluorinated hyperbranched star-like polymers that can serve as ^{19}F magnetic resonance imaging (MRI) agents (*23*). The multicompartmental amphiphilicity of these structures gave rise to the hypothesis that they are capable of therapeutic agent packaging while also providing for detectable imaging or labeling for tracking of the nanoparticle locations. In this study, utilization of these materials as ^{19}F and fluorescence dual-labeled imaging assemblies as well as nanocarriers for chemotherapeutic cargos was explored. ^{19}F NMR/MRI techniques were successfully applied to track and quantify cell migration and uptake. Due to near-zero background, the technique is highly sensitive. In this study, ^{19}F NMR was applied to quantify the number of micelles taken up by the cells and to determine the micelle stability. Doxorubicin (DOX) was selected as the therapeutic agent, and the loading, release, and cytotoxicity of the nanocarrier constructs was investigated in depth and compared against the behaviors of the host nanomaterial and the small molecule drug, each individually and together. DOX has been studied extensively in micellar delivery strategies (*5, 8, 24, 25*) and is a common therapeutic for the treatment of a range of cancers (*26*). It also exhibits

* E-mail: klwooley@artsci.wustl.edu. Tel: +1 314 935-7136, Fax: +1 314 935-9844.
[†] Department of Chemistry, Department of Radiology.
[‡] Department of Neurological Surgery.

10.1021/bc800396h CCC: $40.75 © 2008 American Chemical Society
Published on Web 12/03/2008

antibiotic properties and may provide benefits toward other diseases that involve a need for reduction in cell growth, such as interfering with restenosis by using drug eluting stents (*27*). Most importantly, for these fundamental studies, DOX is a viable model drug, due to its inherent UV−vis/fluorescence characteristics. We found that these polymer micelle assemblies were capable of packaging DOX and that the DOX−micelle constructs exhibited cytotoxicity against U87-MG-EGFRvIII-CBR cancer cells that nearly matched that of the free DOX. The successful construction of dual-labeled micelles may find applications in the area of drug delivery, wherein monitoring their migration and uptake activity require careful monitoring.

EXPERIMENTAL PROCEDURES

Materials and Methods. All chemicals were purchased from Sigma−Aldrich Chemical Co., unless otherwise noted. Cascade Blue (CB) ethylenediamine trisodium salt and MTT assay kit were purchased from Invitrogen Co. The amphiphilic hyperbranched polymer materials, **1a**−**c**, were prepared as previously reported (*23*).

U87-MG-EGFRvIII-CBR cells (a human glioblastoma cell line modified to express the mutant EGFRvIII receptor and click beetle red luciferase) have been previously reported (*12*).

^{1}H NMR spectra were recorded on a 500 MHz Varian Inova 500 spectrometer, with the solvent proton signal as the standard. ^{19}F-NMR spectra were recorded at 470 MHz on a Varian Inova 500 spectrometer equipped with a fluorine-observe 5 mm probe (Nalorac Co. CA) with trifluoroacetic acid (TFA) as an internal standard.

Dynamic light scattering (DLS) measurements were acquired using a Brookhaven Instruments (Worcestershire, U.K.) system, including a model BI-200SM goniometer, a model BI-9000AT digital correlator, a model EMI-9865 photomultiplier, and a model 95−2 Ar ion laser (Lexel, Corp.; Farmindale, NY) operated at 514.5 nm. Measurements were made at 25 ± 1 °C. Prior to analysis, solutions were filtered through a 0.22 μm Gelman Nylon Acrodisc 13 membrane filter to remove dust particles. Scattered light was collected at a fixed angle of 90°. The digital correlator was operated with 522 ratio spaced channels, and initial delay of 5 μs, a final delay of 100 ms, and a duration of 10 min. A photomulitplier aperture of 400 μm was used, and the incident laser intensity was adjusted to obtain photon counting of between 200 and 300 kcps. The calculations of the particle size distributions and distribution averages were performed with the ISDA software package (Brookhaven Instruments Co.), which employed single-exponential fitting, cumulants analysis, and non-negatively constrained least-squares (NNLS) and CONTIN particle size distribution analysis routines. The data are presented as the average values from four measurements.

Transmission electron microscopy (TEM) measurements were conducted on a Hitachi H600 microscope. Micrographs were collected at 100 000× magnification and calibrated using a 41 nm polyacrylamide bead from NIST. Carbon-coated copper grids were treated with oxygen plasma prior to deposition of the micellar samples. The samples were stained with 1% phosphotungstic acid (PTA) for 1 min, and then the solution was wicked away and the samples were allowed to dry under ambient conditions. The number-average particle diameters (D_{av}) and standard deviations were generated from the analysis of a minimum of 100 particles from at least three different micrographs.

UV−vis spectroscopy was acquired on Varian Cary 1E UV−vis system (Varian Inc., Palo Alto, CA) using PMMA cuvettes.

Synthesis. *Preparation of Cascade Blue-Conjugated Micelles [***2a**−**2c***].* To three solutions of polymers **1a**−**c** (20 mg each of **1a**−**1c**, 0.20, 0.22, and 0.21 μmol for **1a**−**1c**) in DMF (5 mL) was added HBTU (3.8 mg, 1×10^{-2} mmol) and HOBT (1.4 mg, 1×10^{-2} mmol). The solutions were allowed to stir under argon for 1 h. DIPEA (4 mg, 4×10^{-2} mmol) and Cascade Blue (0.63 mg, 1×10^{-3} mmol) were added. The reactions were stirred under argon overnight. DMF (15 mL) was added and the solutions were dialyzed (MWCO 30 kDa) against nanopure water for 84 h. Micellar solutions were thereby obtained and the amounts of Cascade Blue (CB) were determined by UV−vis (400 nm, $\varepsilon = 28\,000$ M^{-1} cm^{-1} from manufacturer's manual). A portion of the micelle solution was lyophilized to dryness for ^{1}H and ^{19}F NMR analyses.

2a. 3.4 CB/polymer (68%), micelle concentration, 0.33 mg mL^{-1}. ^{1}H NMR (500 MHz, DMSO-d_6): δ 0.8−2.3 (br, m, *CH*$_2$ and *CH* of backbone), 4.3−4.7 (s, br, *CH*$_2$CF$_3$, Ph*CH*$_2$), 6.4−7.5 (m, br, *ArH*), 7.6−8.0 (m, br, *ArH* of CB), 8.2 (*ArH* of CB), 8.6 (s, *ArH* of CB), 9.0 (s, *ArH* of CB), 9.9 (s, *ArH* of CB), 12.0−12.5 (s, br, COO*H*) ppm. ^{19}F NMR (470 MHz, DMSO-d_6): δ 2.7 (s) ppm. TEM: D_{av} 9 ± 2 nm. DLS: $D_{h(n)}$ 21 ± 2 nm, $D_{h(v)}$ 29 ± 4 nm, $D_{h(i)}$ 129 ± 20 nm.

2b. 4.2 CB/polymer (84%), micelle concentration 0.35 mg mL^{-1}. ^{1}H NMR (500 MHz, DMSO-d_6): δ 0.8−2.3 (br, m, *CH*$_2$ and *CH* of backbone), 4.3−4.7 (s, br, *CH*$_2$CF$_3$, Ph*CH*$_2$), 6.4−7.5 (m, br, *ArH*), 7.6−8.0 (m, br, *ArH* of CB), 8.2 (*ArH* of CB), 8.6 (s, *ArH* of CB), 9.0 (s, *ArH* of CB), 9.9 (s, *ArH* of CB), 12.0−12.5 (s, br, COO*H*) ppm. ^{19}F NMR (470 MHz, DMSO-d_6): δ 2.7 (s) ppm. TEM: D_{av} 8 ± 2 nm. DLS $D_{h(n)}$ 26 ± 4 nm, $D_{h(v)}$ 29 ± 6 nm, $D_{h(i)}$ 135 ± 25 nm.

2c. 4.0 CB/polymer (80%), micelle concentration 0.32 mg mL^{-1}. ^{1}H NMR (500 MHz, DMSO-d_6): δ 0.8−2.3 (br, m, *CH*$_2$ and *CH* of backbone), 4.3−4.7 (s, br, *CH*$_2$CF$_3$, Ph*CH*$_2$), 6.4−7.5 (m, br, *ArH*), 7.6−8.0 (m, br, *ArH* of CB), 8.2 (*ArH* of CB), 8.6 (s, *ArH* of CB), 9.0 (s, *ArH* of CB), 9.9 (s, *ArH* of CB), 12.0−12.5 (s, br, COO*H*) ppm. ^{19}F NMR (470 MHz, DMSO-d_6): δ 2.7 (s) ppm. TEM: D_{av} 5 ± 1 nm. DLS: $D_{h(n)}$ 29 ± 3 nm, $D_{h(h)}$ 33 ± 6 nm, $D_{h(n)}$ 135 ± 20 nm.

General Procedure for DOX Loading. A solution of DOX (2.7 mg mL^{-1} in CH_2Cl_2 and 3 equiv of triethylamine, 30 w/w % with respect to the micelle) was added to a vial containing a magnetic stir bar and the micelle (4 mL, polymer concentration ∼0.30 mg mL^{-1}). The solution were protected from light and stirred without a cap in a well-ventilated fume hood for 16 h. Insoluble DOX was removed by centrifugation (3000 rpm × 10 min), and the supernatants were transferred to a centrifugal filter device (Amicon Ultra 4, 30 kDa MWCO, Millipore Corp., Billerica, MA, USA) and washed extensively with 5 mM PBS pH 7.4 buffer at 37 °C to remove all unincorporated DOX. After eight washing cycles, the filtrate was analyzed by UV−vis (488 nm) to confirm the successful removal of the free DOX. The DOX-loaded micelle solutions were then reconstituted to a final volume of 4 mL. The amount of incorporated DOX was determined by UV−vis (480 nm, $\varepsilon = 12\,500$ M^{-1} cm^{-1} determined by a calibration curve in DMF/PBS 4:1) in a 4:1 v/v mixture of DMF and DOX−micelle solution.

General Procedure for the Release Experiments. DOX−micelle solutions (2 mL) were transferred to a presoaked dialysis cassette (Slide-A-Lyzer, 10 kDa MWCO, Pierce Biotechnology, Rockford, IL, USA). The cassettes were then stirred in a beaker containing 4 L of 5 mM PBS at pH 7.4 and 37 °C for a period of 48 h. Samples (∼100 μL) were removed from the cassette at 0, 1, 2, 3, 4, 8, 16, 24, and 48 h and analyzed by UV−vis (488 nm, $\varepsilon = 12\,500$ M^{-1} cm^{-1} determined by a calibration curve in PBS). All release experiments were conducted in triplicate.

Cell Cytotoxicity Assay on U87-MG-EGFRvIII-CBR Cells. Cell cytotoxicity assay was conducted using MTT assay kit and followed the manufacturer's protocol. Briefly, 5000 cells/

Scheme 1. Chemical Structures and Compositions for Micelles 1a−1c and 2a−2c, and Schematic Illustrations of the Amphiphilic Star-Like Structure, Assembled as Uni- or Multi-Molecular Aggregates, and the Loading of DOX into Those Nanostructures

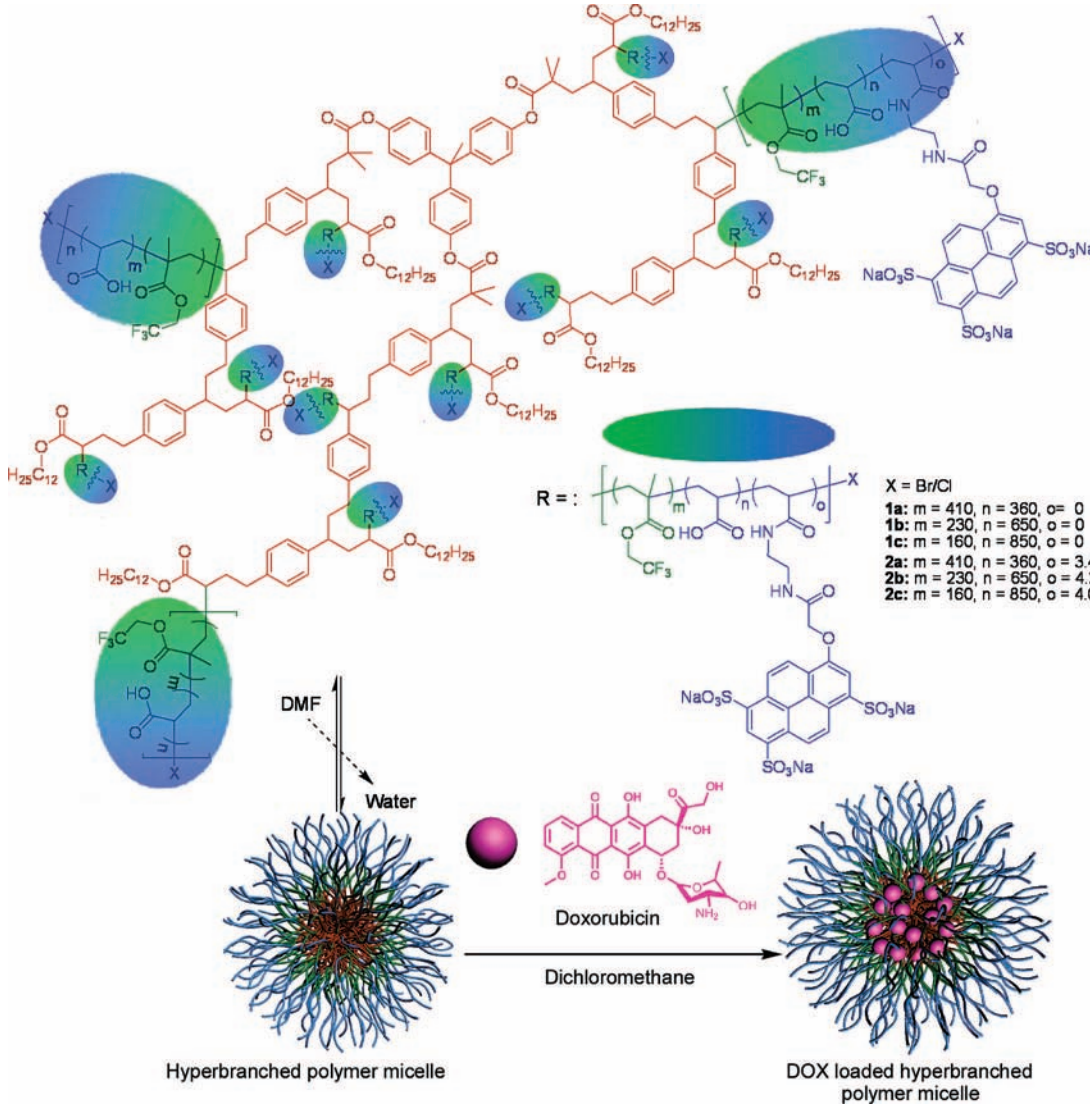

well of the U87-MG-EGFRvIII-CBR cells were plated in triplicate in 96-well plate for 24 h before treatment. Cells were then washed twice with sterile PBS and exposed to different doses of either free DOX or DOX−micelles at 37 °C for 2 h in 10% FBS α-MEM. After 2 h of incubation, the cells were washed again twice with sterile PBS and refed with fresh media and further incubated at 37 °C for 72 h before the MTT assay was performed. To assess cell viability, 10 μL of MTT (5 mg mL^{-1}) solution was added into each well and the mixture incubated at 37 °C for 4 h. The reaction was terminated with 10% SDS stop solution. Absorbance was read at 570 nm using a μQuant plate reader (Bio-Tek Instruments Inc.), and viability was calculated as the percentage of control (cells receiving no treatment).

In Vitro Fluorescent Microscopy Study. U87-MG-EGFRvIII-CBR cells were treated for 24 h with either 1 μg mL^{-1} of DOX or DOX-loaded micelles. Afterward, cells were washed twice with PBS buffer and fixed with 4% paraformaldehyde. Fluorescence was observed using Zeiss fluorescence microscope equipped with a appropriate filter set (Axioskop plus, Carl Zeiss, Germany), and pictures were taken using 63× oil lenses.

Micelle Stability Studies by ^{19}F NMR. U87-MG-EGFRvIII-CBR cells (1 million) suspended in 200 μL PBS buffer were mixed with micelles in PBS buffer, and this cell solution was then placed in a 5 mm NMR tube. TFA (0.050 mg/mL) was used as an internal reference. The pH was measured to be 7.4 before the kinetics studies. The degree of hydrolysis was calculated on the basis of relative integration value of the trifluoroethyl ester at 2.7 ppm and the integration value of trifluoroethanol at −1.2 ppm. In a control study, PBS buffer, instead of the cell solution, was used and the protocol was identical. The parameters used were: d1= 10 s, sw = 19 189.3 Hz, nt = 378, lb = 5 Hz, temp = 37 °C.

Cell Uptake Studies by ^{19}F NMR. U87-MG-EGFRvIII-CBR cells (4 million) were plated on a 6-well plate and then treated with 500 μL of micelle solution for 2 h at 37 °C. Afterward, the cells were washed 3 times with PBS buffer and lifted by trypsin. Cells were washed again with PBS buffer and centrifuged 3 times (3000 rpm × 5 min). Cell pellet was collected and fixed with 4% paraformaldehyde and resuspended into 250 μL PBS buffer. The cells were sonicated for 1 min; 100 μL of D_2O and 10 μL of 0.050 mg/mL TFA solution were added. The solution was transferred into a water-compatible BMS-005TJ Advanced NMR microtube (Shigemi Inc., PA) and subjected to ^{19}F NMR spectroscopic analysis. In a control study, PBS buffer instead of micelle solution was used and the protocol was identical. The

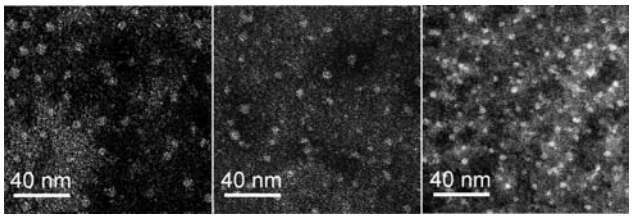

Figure 1. TEM images of micelles **2a**−**2c** (shown from left to right, respectively) on a carbon-coated copper grid with negative staining by 1% phosphotungstic acid.

Table 1. Summary of Characterization Data and Doxorubicin Loading for Micelles 2a−2c

sample	TEM [nm]	D_h(n)[a] [nm]	D_h(v)[a] [nm]	D_h(i)[a] [nm]	DOX[b] [μM]	loading capacity [wt %]	CB/ polymer[b]
2a	9 ± 2	21 ± 2	29 ± 4	129 ± 20	11	3.6 ± 0.5	3.4
2b	8 ± 2	26 ± 4	29 ± 6	135 ± 25	24	4.9 ± 0.6	4.2
2c	5 ± 1	29 ± 3	33 ± 6	138 ± 20	22	4.0 ± 0.7	4.0

[a] by DLS. [b] by UV−vis.

parameters used were: d1= 10 s, sw = 19 189.3 Hz, nt = 8620, lb = 5 Hz.

RESULTS AND DISCUSSION

Synthesis and Micellization of the Cascade Blue-Conjugated Fluoropolymers. The polymers **1a**−**1c** (*23*) were functionalized with Cascade Blue (CB) ethylene diamine to give CB-functionalized polymers (Scheme 1). Coupling of CB ethylene diamine to the pre-established macromolecules, having a hyperbranched hydrophobic core and amphiphilic copolymer arms comprising trifluoroethyl methacrylate and acrylic acid residues, was facilitated by the addition of standard peptide coupling reagents, *N*-hydroxybenzotriazole (HOBt), and *O*-benzotriazol-1-yl-*N*,*N*,*N*′,*N*′-tetramethyluronium hexafluorophosphate (HBTU) in *N*,*N*-dimethylformamide (DMF), to give an amide linkage between the CB and the macromolecule acrylic acid sites. Initially, polymers with *ca.* two CB units per polymer chain were prepared, but the corresponding micelles failed to produce adequate fluorescence microscopy images with our instrumental resolutions. Therefore, the theoretical number of CBs per polymer was increased to *ca.* five during the coupling reactions, which afforded CB/polymer values of 3.3, 4.2, and 4.0 per polymer for samples **2a**, **2b**, and **2c**, corresponding to conjugation efficiencies of 69%, 82%, and 79%, respectively, as determined by UV−vis spectroscopy.

Recently, we reported that purification and micellization can be performed simultaneously (*28*), thus, after the conjugations of CB, additional DMF was added to the reaction mixtures and the solutions were dialyzed subsequently against nanopure water for 84 h to induce self-assembly into polymeric micelles while removing noncovalently linked CB. The polymers readily formed micelles, as determined by transmission electron microscopy (TEM) and dynamic light scattering (DLS) studies (Figure 1 and Table 1). Compared to the original micelles of the precursors, **1a**−**1c** (*23*), conjugation of CB did not change the TEM size of the micelles significantly (Table 1). The DLS data showed slight increases in number-average hydrodynamic diameter (D_h) values.

DOX Loading and Release Profiles. DOX was incorporated into the micelles using a similar procedure published previously (*8*). Dichloromethane was used as the organic solvent to solvate the DOX and to swell the core of the micelle, facilitating the loading of the therapeutic. The amount of DOX in the micelle solutions were determined by UV−vis measurements. The loading capacities for micelles **2a**−**2c** were 3.6 ± 0.5, 4.9 ± 0.6, and 4.0 ± 0.7 wt % based on polymer mass, respectively (Table 1). During the preparation of the micelles, we noticed that the micelle solution **2a** precipitated after *ca.* one week of storage, while micelles **2b** and **2c** were storage stable for months, indicating that a high fluorine content adversely affected the formation and stability of the micelles, which may be a reason for its low loading capacity. The balance of fluorine and carboxylic acid content also affected the DOX release profiles. The release of the DOX was assessed by monitoring the decrease of UV−vis absorbance over time (*8, 12*). Samples were withdrawn from dialysis cassettes at progressive time intervals and analyzed by UV−vis spectroscopy. In this release model, DOX molecules are first released from the micelles, and then pass through the dialysis membrane. Since the rate-determining step is the rate that DOX is released from the micelles (Figure 2), the overall rate can be considered as the rate that DOX was released from the micelles. Using this release model, the DOX release behavior was similar for **2b** and **2c**, but **2a** exhibited a faster release rate (Figure 2), possibly due the fact that **2a** does not have a stable micelle structure. For **2b** and **2c**, a release of ca. 25% of the cargo was observed in 8 h, followed by a slow, sustained release over the course of 48 h. At the end of 48 h, 66%, 45%, and 51% of DOX had released from micelles **2a**, **2b**, and **2c**, respectively. The release profiles were slower than those observed for highly branched dendritic constructs (*8*) loaded with DOX, but similar to release rates from shell cross-linked nanoparticles (*12*).

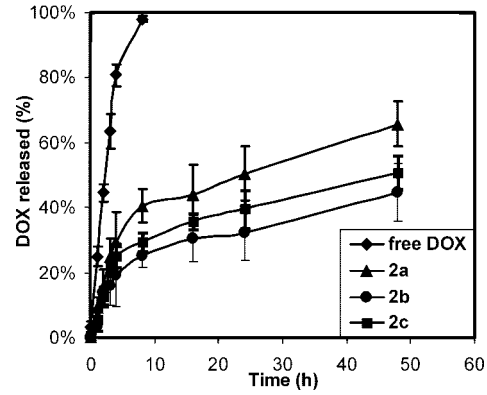

Figure 2. Release profiles of DOX from a dialysis cassette (control labeled as free DOX in the legend) and from dialysis cassettes containing micelles of **2a**−**2c** over time in PBS buffer (5 mM, pH 7.4) at 37 °C.

Cell Cytotoxicity Studies. The cytotoxicities of **2a**−**2c** were studied by incubating U87-MG-EGFRvIII-CBR cells with varying concentrations of the micelles. Cell viability was assessed using a Vibrant MTT cell proliferation assay kit. Cells were first incubated with DOX-loaded and nonloaded micelles for 2 h; subsequently, the cells were washed twice with PBS buffer and refed with fresh media. After 72 h of incubation, MTT assays were conducted. No significant toxicity was observed at concentrations up to 100 000 ng mL^{-1} for the nonloaded micelles (Figure 3, top). In comparison, the DOX-loaded micelles exhibited potent cytotoxic effects (Figure 3, bottom). At 1000 ng mL^{-1}, only 30% of the cells treated with DOX-loaded micelles survived (sample **2b**), which is comparable to free DOX at the same dose concentration (20% survived, Figure 3, bottom), indicating that this nanocarrier can achieve excellent cytotoxic effect on this glioma cell line. Interestingly, compared to glassy amorphous SCK nanoparticles derived from poly(acrylic acid)-*b*-poly(styrene) (PAA-*b*-PS) (*12*), the micelles in this study have lower loading capacity of DOX, but showed significantly greater cytotoxicity. The improvement of therapeutic efficacy is possibly due to a higher extent of release of DOX in these systems (45−66% after 48 h, compared to the

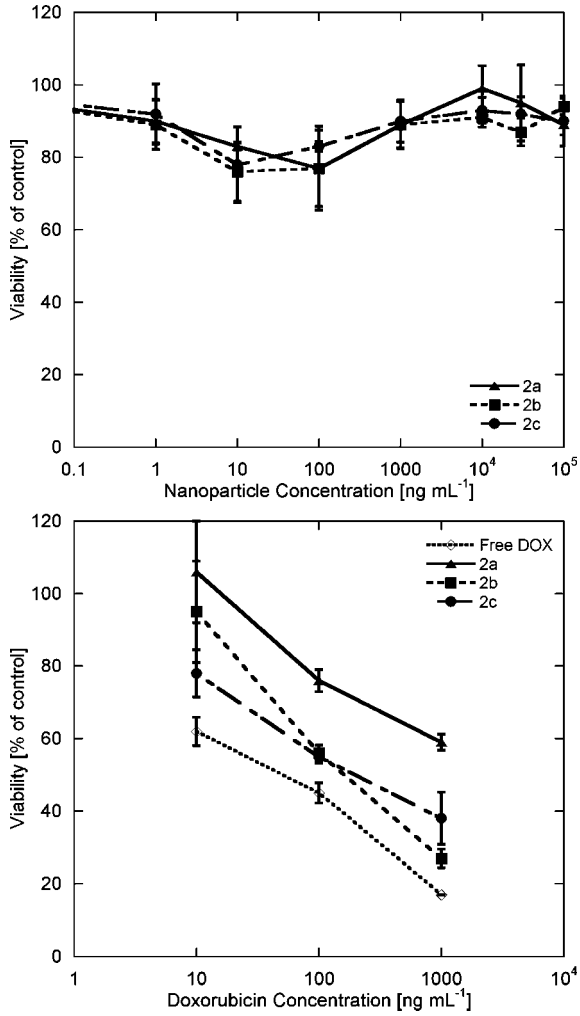

Figure 3. Cell viability studies using MTT assay. U87-MG-EGFRvIII-CBR cells were incubated with **2a**−**2c** without (top) and with DOX (bottom) loading at varied concentrations.

SCK system that retains more cargo, with only 30−55% release after 48 h), as this new system was designed to contain an integrated mixing between the hydrophobic pockets and hydrophilic domains, giving a more open, multicompartment structure, in contrast to the core−shell structure of SCK nanoparticles.

We also noticed that, in the presence of cells, a partial degradation of the trifluoroethyl ester moiety occurred, which may further enhance the release of DOX. The substantial chemical shift difference between trifluoroethyl ester and trifluoroethanol and the zero-background of ^{19}F-NMR signal allows real-time monitoring of the hydrolysis of these fluorinated micelles, upon cellular incubation. As seen in Figure 4, the trifluoroethyl esters in the micelle exhibited a broad ^{19}F resonance at 2.7 ppm, and the degradation product, trifluoroethanol, gave a sharp triplet at −1.2 ppm with a $^3J_{H-F} = 8.5$ Hz. While the micelle solutions were very stable in water and PBS (for months), as monitored by ^{19}F NMR spectroscopy, incubation with cells resulted in quick release of trifluoroethanol. Within 1 h, ca. 2% of trifluoroethanol was detected by ^{19}F NMR spectroscopy. The hydrolysis proceeded rapidly up to ca. 4 h, with a total of ca. 8% degradation. Afterward, a sudden halt of degradation was observed, resulting in a nonlinear degradation profile (see Supporting Information). A halt in degradation may be due to a loss of enzymatic activity. Alternatively, the hydrolysis may be limited to the surface-available trifluoroethyl ester groups, while others remain stable beneath the surface of

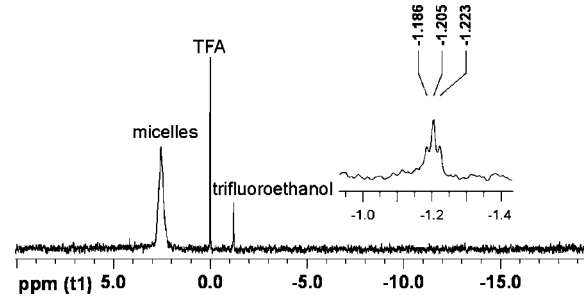

Figure 4. ^{19}F NMR spectra demonstrating partial hydrolysis of the trifluoroethyl ester units of **2b** (470 MHz, H_2O/D_2O, with TFA as an internal standard, 4 h after incubation of micelles with cells at 37 °C).

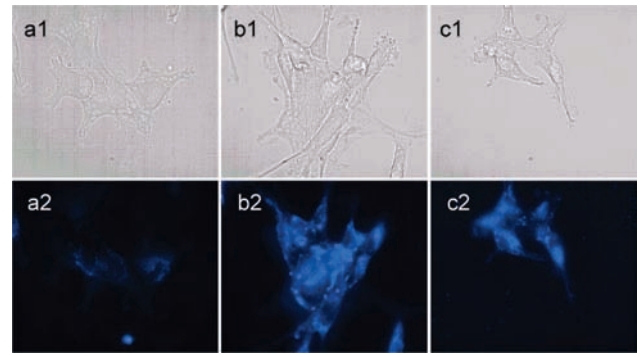

Figure 5. Cellular uptake of micelles by fluorescence microscopy study. U87-MG-EGFRvIII-CBR cells were incubated with micelle solutions of **2a**, **2b**, and **2c**, respectively. 1: phase contrast. 2: blue fluorescence. The cells were treated with micelles (0.1 mg/mL) for 2 h at 37 °C, followed by repeated washings, and then fixed with 4% paraformaldehyde.

the polymer or polymer micelle assembly. A thorough study of the hydrolysis of these micellar constructs using lipases and enzymatic inhibitors is currently underway. Nevertheless, the partial hydrolysis of trifluoroethyl ester during the cell incubation may result in a faster and more complete release of DOX in vitro, as compared to release data from the dialysis model. Although the hydrolysis product, trifluoroethanol, may be toxic to cells, we did not observe a significant negative effect on the viability of the cells incubated with the control micelle solutions (Figure 3, top).

Fluorescence Microscopy Studies. The cellular uptake of the polymer micelles was also studied by fluorescence microscopy. We took advantage of the blue fluorescence from CB and red autofluorescence from DOX to study the cellular uptake of the polymeric micelles and localization of DOX within the cells delivered by these polymers. As shown in Figure 5, cells treated with all three control micelles (**2a**−**2c**) demonstrated significant amounts of blue fluorescence, mostly in the cytoplasm. This intracellular trafficking is in contrast to that of free CB dye as a small molecule, which binds strongly to the nucleus (data not shown), confirming that the fluorescence observed arises from polymer−dye conjugates. At this moment, the mechanism of cellular uptake of these micelles is not clear and remains to be investigated. However, the blue fluorescence clearly indicated that cell uptake indeed occurred.

Because micelles **2b** showed the best cell viability reduction (Figure 3, bottom), we chose micelles **2b** for further microscopy studies on DOX localization. As seen in Figure 6, within 2 h treatment, DOX molecules were already delivered inside the cells, although mostly present in the cytoplasm surrounding the nucleus (Figure 6, a2). In contrast, after 24 h treatment, DOX was located within the nucleus (Figure 6, b2); the nuclei are

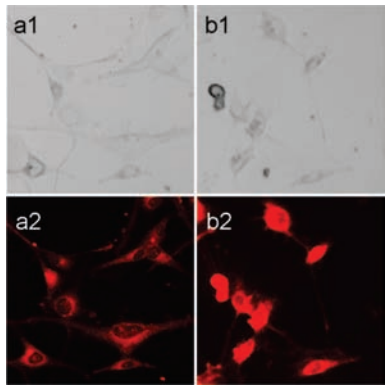

Figure 6. Localization of DOX upon treatment of DOX-loaded micelles by fluorescence microscopy. U87-MG-EGFRvIII-CBR cells were incubated with DOX-loaded micelle **2b**. 1: phase contrast. 2: red fluorescence. a: 2 h after treatment. b: 24 h after treatment, more DOX were incorporated into the nucleus.

brighter, indicating more DOX molecules have been incorporated. These images indicated efficient deliveries of DOX to the nucleus, which may be responsible for cell viability reductions.

^{19}F NMR Studies on the Cellular Uptake of the Micelles. Fluorine-containing nanoscopic assemblies have been used for cell uptake and cell trafficking studies using ^{19}F NMR spectroscopy or ^{19}F MRI (*7, 29, 30*). Since there is no background signal, the ^{19}F NMR/MRI technique is highly sensitive, with detection limits on the nanogram scale. In this study, ^{19}F NMR spectroscopy was employed to confirm and quantify cell uptake of **2b** in U87-MG-EGFRvIII-CBR cells. This micelle was selected because it had good loading capacity, desired release profile (Figure 2), and the best cytotoxicity result (Figure 3). Cells (4 million) were first incubated with the micelle solution for 2 h, followed by repeated washings with fresh PBS buffer and centrifugation to remove any free micelles. The cells were harvested and sonicated to lyse the cells. Trifluoroacetic acid (TFA) was used as an internal standard to quantify the fluorine concentration. Since the CF_3 groups on the micelles have much shorter T_1 relaxation times (*ca.* 500 ms) than that of TFA (*ca.* 2.5 s), it was necessary to adopt a long relaxation delay (10 s) to ensure that both fluorine species were fully relaxed before the next acquisition scan. However, with such long delay times, *ca.* 24 h scanning time was required to acquire a spectrum with reasonable resolution (Figure 7). Using the same method as reported by Ahrens and co-workers (*30*), it was possible to calculate that the total amount of fluorines in each cell was *ca.* 4.6×10^8 fluorines, indicating about 0.1% cell uptake efficiency. This very low cell uptake is possibly due to the negatively charged micelle that limits cell uptake compared to neutral nanoemulsions, wherein the cell uptake of fluorine species can reach concentrations of $10^{11}-10^{13}$ (*30*). Nevertheless, even with limited cell uptake, these nanostructures loaded with DOX exhibited a significant ability to reduce cell viability.

CONCLUSIONS

In conclusion, we have successfully constructed fluorine and CB dual-labeled nanostructures, studied their loading and release characteristics for therapeutic guests, and applied ^{19}F NMR and fluorescence microscopy as tools to study their cellular uptake and cell viability reduction. The nanostructures were designed to possess an amphiphilic, multicompartment morphology for packaging of therapeutic guests, based upon a hyperbranched-linear hybrid star-like structure that assembled into uni- or multimolecular micelles having optimum hydrodynamic diameters of 20−30 nm. Reasonable quantities of DOX could be

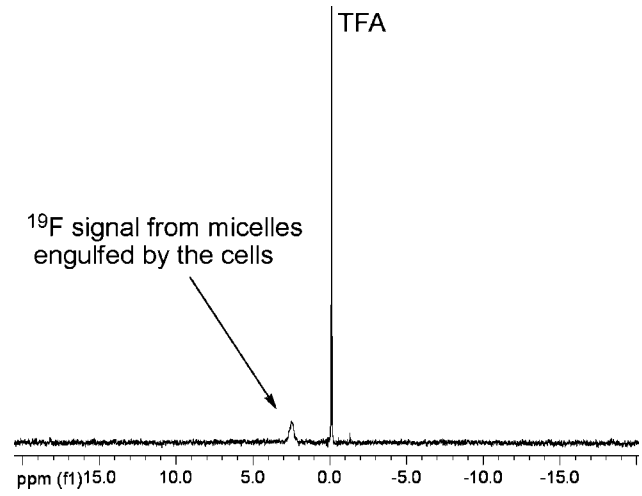

Figure 7. ^{19}F NMR spectrum of U87-MG-EGFRvIII-CBR cell suspensions. ^{19}F signal from micelles, engulfed by the cells, appears at 2.7 ppm.

loaded into the structures, and they exhibited differential release profiles, in terms of rates and ultimate amounts, depending upon their composition. These DOX-loaded nanostructures exhibited potent cytotoxicity on U87-MG-EGFRvIII-CBR cells. We anticipate that the incorporation of ligands for cell targeting will improve the DOX delivery even further. ^{19}F NMR spectroscopy showed a partial degradation of the surface available fluorinated polymer segments, which could accelerate the release of DOX from the micelles *in vitro* and *in vivo*. The successful construction of this dual-labeled, multifunctional nanocarrier may find promising applications in nanomedicine. The key unmet challenge is to now prepare such nanoscale constructs with cell-specific targeting groups so that therapeutics can be efficiently delivered with minimal side effects (*5, 15, 31*).

ACKNOWLEDGMENT

This material is based upon work supported by The Children's Discovery Institute of St. Louis Children's Hospital and Washington University School of Medicine, and the National Heart Lung and Blood Institute of the National Institutes of Health as a Program of Excellence in Nanotechnology (HL080729). Postdoctoral and assistant professor fellowship provided by the Knut and Alice Wallenberg Foundation is gratefully acknowledged (A.M.N). The authors thank Drs. Jeff Kao and André d'Avignon for assistance with NMR experiments.

Supporting Information Available: ^{1}H and ^{19}F NMR spectra of polymers, UV−vis spectra of DOX-loaded micelles, DLS data of the micelles, and data regarding the trifluoroethyl ester hydrolysis. This material is available free of charge via the Internet at http://pubs.acs.org.

LITERATURE CITED

(1) Allen, T. M., and Cullis, P. R. (2004) Drug delivery systems: entering the mainstream. *Science 303*, 1818–1822.
(2) Dubertret, B., Skourides, P., Norris, D. J., Noireaux, V., Brivanlou, A. H., and Libchaber, A. (2002) In vivo imaging of quantum dots encapsulated in phospholipid micelles. *Science 298*, 1759–1762.
(3) Koo, O. M., Rubinstein, I., and Onyuksel, H. (2005) Role of nanotechnology in targeted drug delivery and imaging: a concise review. *Nanomedicine 1*, 193–212.
(4) Dutta, R. C. (2007) Drug carriers in pharmaceutical design: promises and progress. *Curr. Pharm. Des. 13*, 761–769.

(5) Nasongkla, N., Bey, E., Ren, J., Ai, H., Khemtong, C., Guthi, J. S., Chin, S.-F., Sherry, A. D., Boothman, D. A., and Gao, J. (2006) Multifunctional polymeric micelles as cancer-targeted, MRI-ultrasensitive drug delivery systems. *Nano Lett. 6*, 2427–2430.

(6) Almutairi, A., Guillaudeu, S. J., Berezin, M. Y., Achilefu, S., and Fréchet, J. M. J. (2008) Biodegradable pH-sensing dendritic nanoprobes for near-infrared fluorescence lifetime and intensity imaging. *J. Am. Chem. Soc. 130*, 444–445.

(7) Partlow, K. C., Chen, J., Brant, J. A., Neubauer, A. M., Meyerrose, T. E., Creer, M. H., Nolta, J. A., Caruthers, S. D., Lanza, G. M., and Wickline, S. A. (2007) 19F magnetic resonance imaging for stem/progenitor cell tracking with multiple unique perfluorocarbon nanobeacons. *FASEB J. 21*, 1647–1654.

(8) Gillies, E. R., and Fréchet, J. M. J. (2005) pH-Responsive copolymer assemblies for controlled release of doxorubicin. *Bioconjugate Chem. 16*, 361–368.

(9) Gillies, E. R., Jonsson, T. B., and Fréchet, J. M. J. (2004) Stimuli-responsive supramolecular assemblies of linear-dendritic copolymers. *J. Am. Chem. Soc. 126*, 11936–11943.

(10) Chan, Y., Wong, T., Byrne, F., Kavallaris, M., and Bulmus, V. (2008) Acid-labile core cross-linked micelles for pH-triggered release of antitumor drugs. *Biomacromolecules 9*, 1826–1836.

(11) Wang, Y.-C., Tang, L.-Y., Sun, T.-M., Li, C.-H., Xiong, M.-H., and Wang, J. (2008) Self-assembled micelles of biodegradable triblock copolymers based on poly(ethyl ethylene phosphate) and poly(ϵ-caprolactone) as dug carriers. *Biomacromolecules 9*, 388–395.

(12) Nyström, A. M., Xu, Z., Xu, J., Taylor, S., Nittisc, T., Stewart, S. A., Leonard, J., and Wooley, K. L. (2008) SCKs as nanoparticle carriers of doxorubicin: investigation of core composition on the loading, release and cytotoxicity profiles. *Chem. Commun.* 3579–3581.

(13) Qi, K., Ma, Q., Remsen, E. E., Clark, C. G., and Wooley, K. L. (2004) Determination of the bioavailability of biotin conjugated onto shell cross-linked (SCK) nanoparticles. *J. Am. Chem. Soc. 126*, 6599–6607.

(14) Sun, G., Hagooly, A., Xu, J., Nyström, A. M., Li, Z., Rossin, R., Moore, D. A., Wooley, K. L., and Welch, M. J. (2008) Facile, efficient approach to accomplish tunable chemistries and variable biodistributions for shell cross-linked nanoparticles. *Biomacromolecules 9*, 1997–2006.

(15) Iwasaki, Y., Maie, H., and Akiyoshi, K. (2007) Cell-specific delivery of polymeric nanoparticles to carbohydrate-tagging cells. *Biomacromolecules 8*, 3162–3168.

(16) Fukukawa, K., Rossin, R., Hagooly, A., Pressly, E. D., Hunt, J. N., Messmore, B. W., Wooley, K., Welch, M., and Hawker, C. J. (2008) Synthesis and characterization of core-shell star copolymers for *in vivo* PET imaging applications. *Biomacromolecules 9*, 1329–1339.

(17) Jiang, X., Ge, Z., Xu, J., Liu, H., and Liu, S. (2007) Fabrication of multiresponsive shell cross-linked micelles possessing pH-controllable core swellability and thermo-tunable corona permeability. *Biomacromolecules 8*, 3184–3192.

(18) Rijcken, C. J. F., Veldhuis, T. F. J., Ramzi, A., Meeldijk, J. D., Van Nostrum, C. F., and Hennink, W. E. (2005) Novel fast degradable thermosensitive polymeric micelles based on PEG-block-poly(N-(2-hydroxyethyl)methacrylamide-oligolactates). *Biomacromolecules 6*, 2343–2351.

(19) Orihara, Y., Matsumura, A., Saito, Y., Ogawa, N., Saji, T., Yamaguchi, A., Sakai, H., and Abe, M. (2001) Reversible release control of an oily substance using photoresponsive micelles. *Langmuir 17*, 6072–6076.

(20) Pressly, E. D., Rossin, R., Hagooly, A., Fukukawa, K. i., Messmore, B. W., Welch, M. J., Wooley, K. L., Lamm, M. S., Hule, R. A., Pochan, D. J., and Hawker, C. J. (2007) Structural effects on the biodistribution and positron emission tomography (PET) imaging of well-defined ^{64}Cu-labeled nanoparticles comprised of amphiphilic block graft copolymers. *Biomacromolecules 8*, 3126–3134.

(21) Sun, G., Xu, J., Hagooly, A., Rossin, R., Li, Z., Moore, D. A., Hawker, C. J., Welch, M. J., and Wooley, K. L. (2007) Strategies for optimized radiolabeling of nanoparticles for *in vivo* PET imaging. *Adv. Mater. 19*, 3157–3162.

(22) Xu, J., Sun, G., Rossin, R., Hagooly, A., Li, Z., Fukukawa, K., Messmore, B. W., Moore, D. A., Welch, M. J., Hawker, C. J., and Wooley, K. L. (2007) Labeling of polymer nanostructures for medical imaging: importance of cross-linking extent, spacer length, and charge density. *Macromolecules 40*, 2971–2973.

(23) Du, W., Nyström, A. M., Zhang, L., Powell, K. T., Li, Y., Cheng, C., Wickline, S. A., and Wooley, K. L. (2008) Amphiphilic hyperbranched fluoropolymers as nanoscopic ^{19}F-magnetic resonance imaging agent assemblies. *Biomacromolecules 9*, 2826–2833.

(24) Lee, C. C., Gillies, E. R., Fox, M. E., Guillandeu, S. J., Fréchet, J. M. J., Dy, E. E., and Szoka, F. C. (2006) A single dose of doxorubicin-functionalized bow-tie dendrimer cures mice bearing C-26 colon carcinomas. *Proc. Natl. Acad. Sci. U.S.A. 103*, 16649–16654.

(25) Chavanpatil, M. D., Khdair, A., Gerard, B., Bachmeier, C., Miller, D. W., Shekhar, M. P. V., and Panyam, J. (2007) Surfactant−polymer nanoparticles overcome P-glycoprotein-mediated drug efflux. *Mol. Pharm. 4*, 730–738.

(26) Lasic, D. D. (1996) Doxorubicin in sterically stabilized liposomes. *Nature 380*, 561–562.

(27) Uwatoku, T., Shimokawa, H., Abe, K., Matsumoto, Y., Hattori, T., Oi, K., Matsuda, T., Kataoka, K., and Takeshita, A. (2003) Application of nanoparticle technology for the prevention of restenosis after balloon Injury in rats. *Circ. Res. 92*, 62–69.

(28) Zhang, K., Fang, H., Chen, Z., Taylor, J.-S. A., and Wooley, K. L. (2008) Shape effects of nanoparticles conjugated with cell-penetrating peptides (HIV tat PTD) on CHO cell uptake. *Bioconjugate Chem. 19*, 1880–1887.

(29) Srinivas, M., Morel, P. A., Ernst, L. A., Laidlaw, D. H., and Ahrens, E. T. (2007) Fluorine-19 MRI for visualization and quantification of cell migration in a diabetes model. *Magn. Reson. Med. 58*, 725–734.

(30) Janjic, J. M., Srinivas, M., Kadayakkara, D. K. K., and Ahrens, E. T. (2008) Self-delivering nanoemulsions for dual fluorine-19 MRI and fluorescence detection. *J. Am. Chem. Soc. 130*, 2832–2841.

(31) Beduneau, A., Saulnier, P., and Benoit, J. P. (2007) Active targeting of brain tumors using nanocarriers. *Biomaterials 28*, 4947–4967.

BC800396H

Supporting Information

^{19}F- and Fluorescently-labeled Micelles as Nanoscopic Assemblies for Chemotherapeutic Delivery

Wenjun Du,[†] Zhiqiang Xu,[‡] Andreas M. Nyström,[†] Ke Zhang,[†] Jeffrey R. Leonard[‡] and Karen L. Wooley[†]*

[†]Department of Chemistry, Department of Radiology, Washington University in Saint Louis, Saint Louis, Missouri 63130-4899 (USA)

[‡]Department of Neurological Surgery, Washington University School of Medicine, 660 S. Euclid Ave, Saint Louis, Missouri 63110 (USA)

E-mail: klwooley@artsci.wustl.edu

Tel: +1 314 935-7136
Fax: +1 314 935-9844

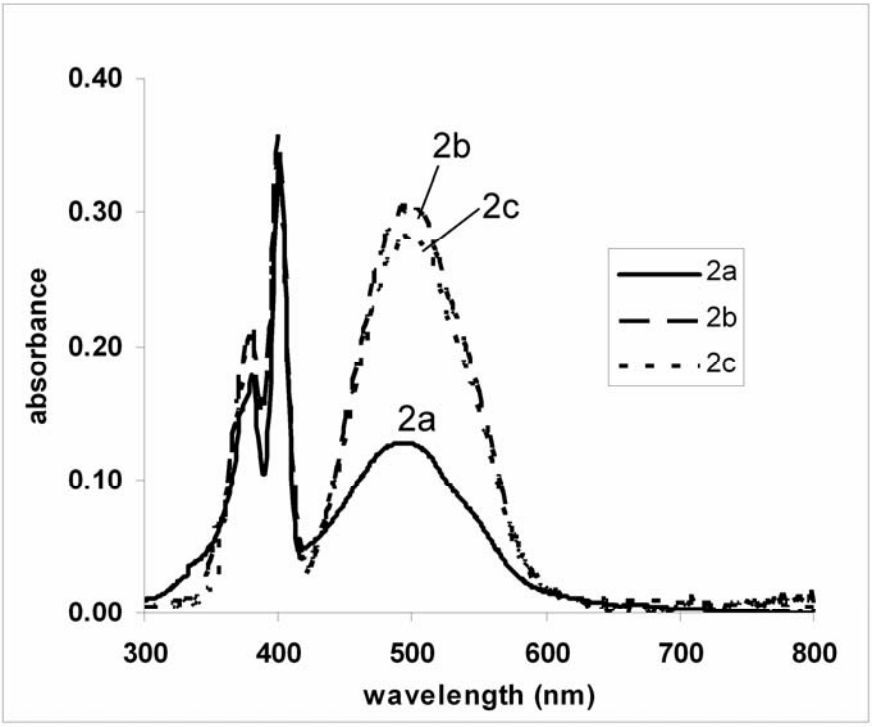

Supporting Figure 1. UV-vis of DOX-loaded micelles **2a-2c**.

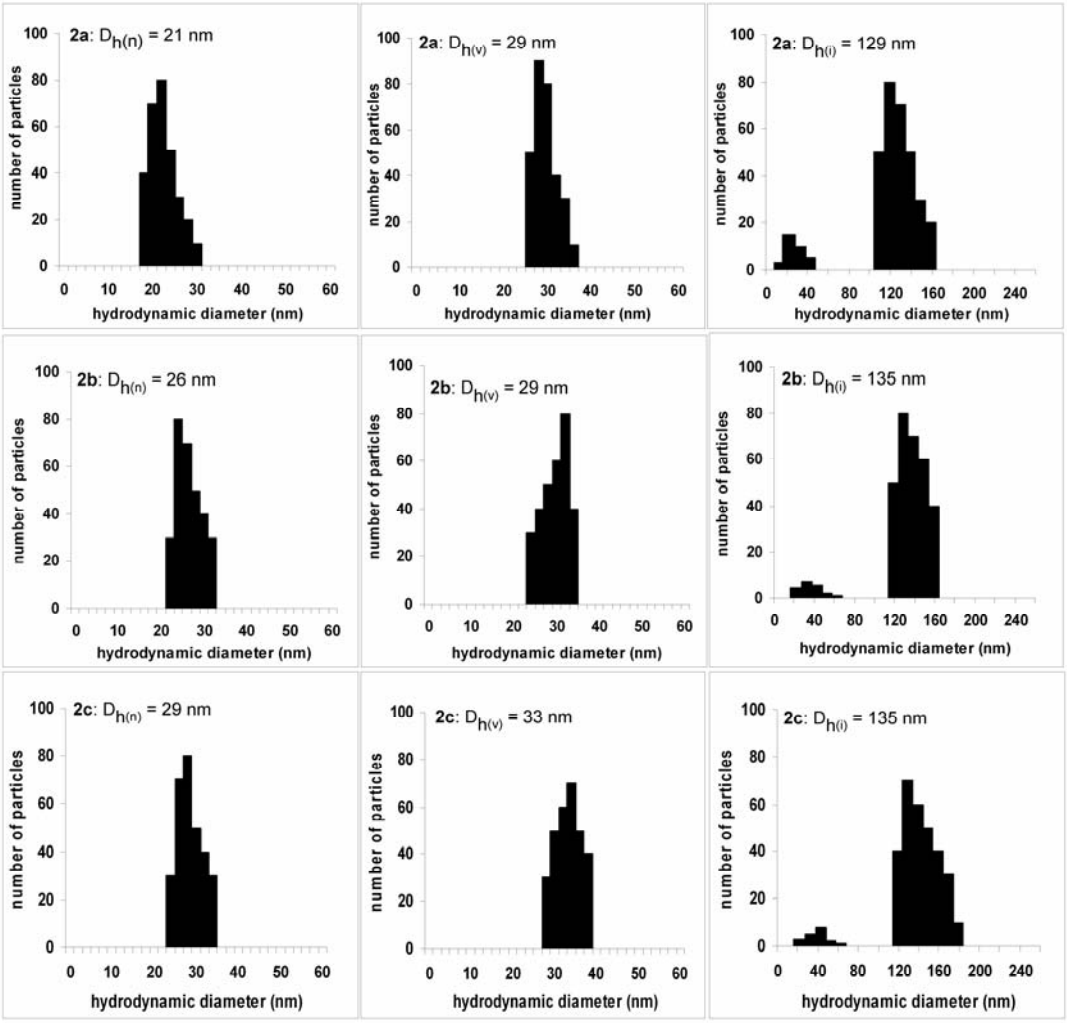

Supporting Figure 2. Dynamic light scattering of micelles **2a-2c.**

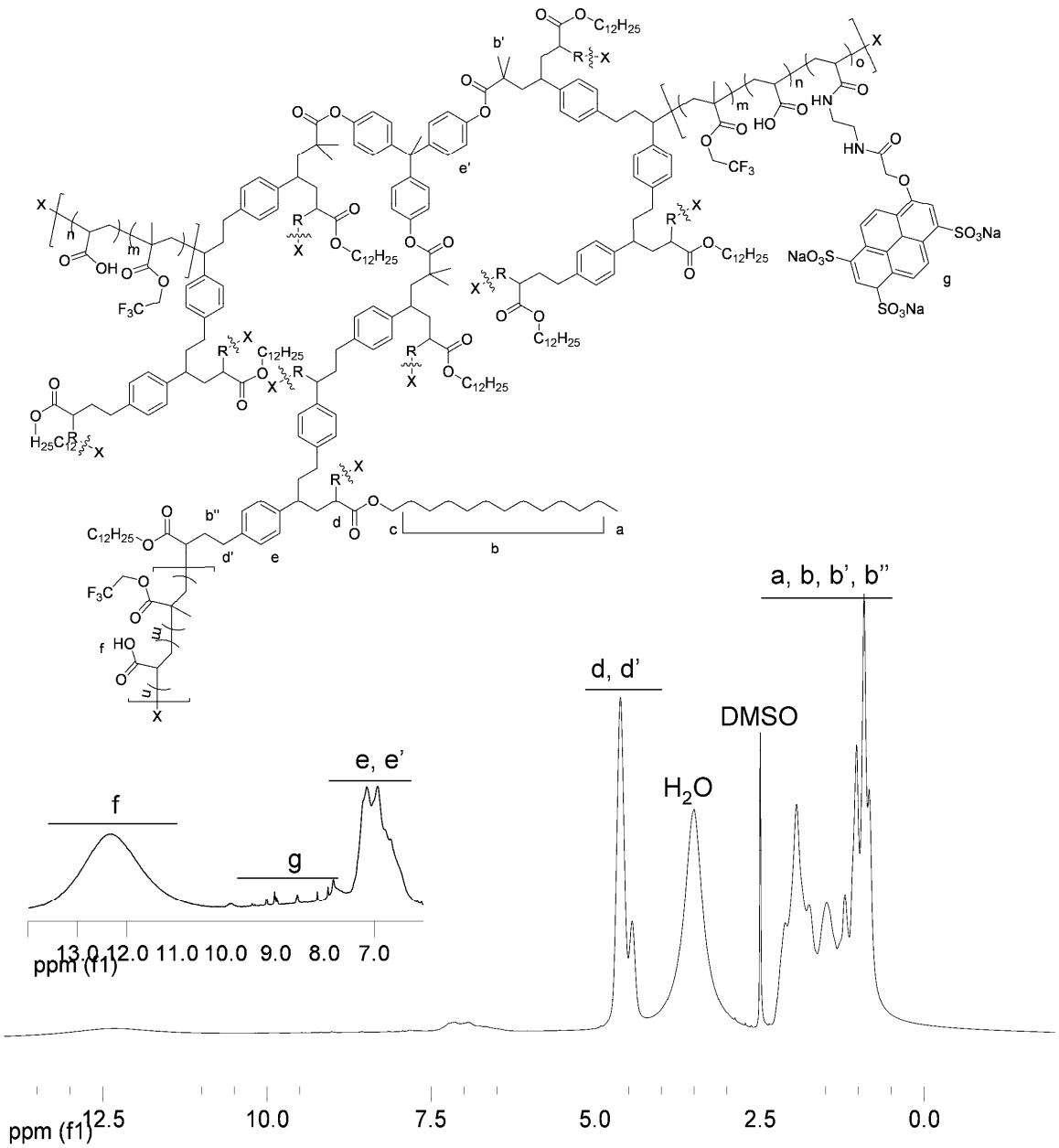

Supporting Figure 3. ^{1}H-NMR spectrum of polymer **2b** (500 MHz, DMSO-d_6).

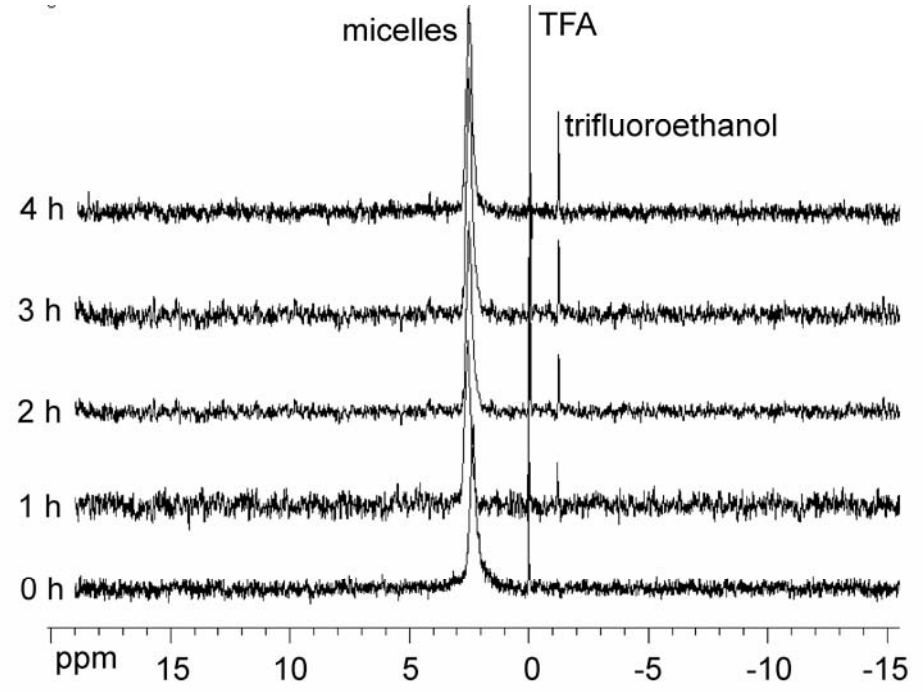

Supporting Figure 4. A composite of ^{19}F-NMR spectra (470 MHz, H_2O/D_2O, with TFA as an internal standard) demonstrating partial hydrolysis of the trifluoroethyl ester units of micelle **2b.**

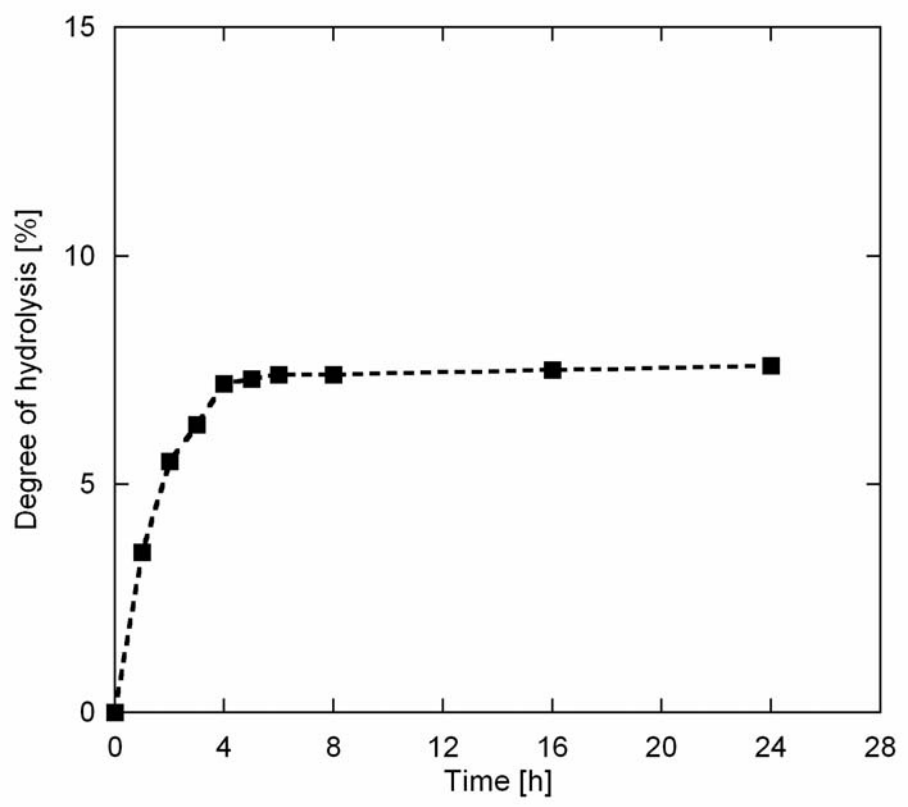

Supporting Figure 5. Percentage of hydrolysis of trifluoroethyl ester units *vs.* time for micelle **2b**

Bioconjugate Chemistry 20th Anniversary

Subscriber access provided by SHEMYAKIN-OVCHINNIKOV INST

Article

Structural and Formulation Factors Influencing Pyridinium Lipid-Based Gene Transfer

Lin Zhu, Yan Lu, Duane D. Miller, and Ram I. Mahato

Bioconjugate Chem., **2008**, 19 (12), 2499-2512• DOI: 10.1021/bc8004039 • Publication Date (Web): 03 December 2008

Downloaded from http://pubs.acs.org on May 2, 2009

More About This Article

Additional resources and features associated with this article are available within the HTML version:

- Supporting Information
- Access to high resolution figures
- Links to articles and content related to this article
- Copyright permission to reproduce figures and/or text from this article

View the Full Text HTML

ACS Publications
High quality. High impact.

Bioconjugate Chemistry is published by the American Chemical Society. 1155 Sixteenth Street N.W., Washington, DC 20036

Structural and Formulation Factors Influencing Pyridinium Lipid-Based Gene Transfer

Lin Zhu, Yan Lu, Duane D. Miller, and Ram I. Mahato*

University of Tennessee Health Science Center, Memphis, Tennessee 38103. Received September 19, 2008; Revised Manuscript Received November 6, 2008

A series of pyridinium lipids containing a heterocyclic ring and a nitrogen atom were synthesized to determine the structure−activity relationship for gene delivery. Pyrylium chloroaluminate was synthesized by monoacylation of mesityl oxide and converted into pyrylium hexafluorophosphate, which was used as the key intermediate for reaction with different primary amines, to yield hydroxyethylpyridinium hexafluorophosphate and aminoethylpyridinium hexafluorophosphate. Acylation of these pyridinium salts with different types of fatty acid chlorides afforded the final pyridinium lipids, which were mixed with a co-lipid, such as L-α-dioleoylphosphatidylethanolamine (DOPE) and cholesterol (Chol) to prepare cationic liposomes by sonication. These liposomes were mixed with plasmid DNA encoding enhanced green fluorescent protein (pCMS-EGFP) or luciferase (pcDNA3-Luc) and transfected into Chinese hamster ovary (CHO) cells. Several factors including hydrophobic anchor chain length, anchor chain type, configuration of double bond, linker type, co-lipid type, cationic lipid/co-lipid molar ratio, charge ratio (N/P), and cell type had significant influence on transfection efficiency and cytotoxicity. Pyridinium lipids with amide linker showed significantly higher transfection efficiency compared to their ester counterparts. Liposomes prepared at a 1:1 molar ratio of pyridinium lipid and co-lipid showed higher transfection efficiency when either DOPE or cholesterol was used as a co-lipid to prepare cationic liposomes for complex formation with plasmid DNA at 3:1(+/−) charge ratio. Pyridinium liposomes based on a hydrophobic anchor chain length of 16 showed higher transfection efficiency and lower cytotoxicity. The pyridinium lipid with a trans-configuration of the double bond in the fatty acid chain showed higher transfection efficiency than its counterpart with cis-configuration at the same fatty acid chain length. In the presence of serum, C16:0 and Lipofectamine significantly decreased their transfection efficiencies, which were completely lost at a serum concentration of 30% and higher, while C16:1 trans-isomer still had high transfection efficiency under these conditions. In conclusion, pyridinium lipids showed high transfection efficiency and have the potential to be used as transfection reagents in vitro and in vivo.

INTRODUCTION

Cationic liposomes are the most commonly used synthetic carriers for delivery of oligonucleotides, siRNAs, and plasmid DNA. The three basic components of a cationic lipid, which affect gene expression or silencing, include (i) a hydrophobic lipid anchor group, such as fatty acid chains of various lengths and unsaturation states, or cholesterol, which helps in forming liposomes and exchanging lipids in cell membrane (*1*), (ii) a linker group, such as an ester, ether, amide, or carbamate, which binds the polar group to the lipid moiety and determines the stability and biodegradability of the cationic lipid (*2*), and (iii) a positively charged hydrophilic headgroup, such as mono- or polyamine group, which interacts with pDNA via electrostatic interaction, leading to its condensation and enhanced the cellular uptake (*3, 4*). Understanding these structural parameters is essential for the rational design of efficient cationic lipid-based transfection reagents. Transfection efficiency of cationic liposomes greatly depends on (i) the extent of DNA condensation, (ii) increased cellular uptake due to ionic and/or hydrophobic interaction with negatively charged biological surfaces, and (iii) membrane fusion via transient membrane destabilization to achieve delivery into the cytoplasm while avoiding degradation in the lysosomal compartment (*5, 6*).

* Corresponding authors. Ram I. Mahato, Ph.D., Department of Pharmaceutical Sciences, University of Tennessee Health Science Center, 19 Manassas, RM224, Memphis, TN 38103-3308. Tel: (901) 448-6929, Fax: (901) 448-2099, E-mail: rmahato@utmem.edu, http://cop.utmem.edu/rmahato.

Significant progress has been made in the design and function of cationic lipids since the introduction in 1987 of the transfection reagent Lipofectin, which is a 1:1 w/w mixture of the cationic lipid *N*-[1-(2,3-dioleoyloxy)propel]-*N*,*N*,*N*-trimethylammonium (DOTMA) and DOPE (*7*). Many cationic lipids bearing either a single tertiary or quaternary ammonium headgroup or that contain protonatable polyamines linked to dialkyl or cholesterol anchors have been designed for transfection of a variety of cell types in culture (*8*−*10*). Commercially available cationic lipids used as liposomes or alone for gene delivery include DOTMA (Lipofectin); 2,3-dioleyloxy-*N*-[2-spermine carboxamide] ethyl-*N*,*N*-dimethyl-1- propanammonium trifluoroacetate (DOSPA, Lipofectamine); 1,2-dioleoyl-3-trimethylammonium-propane (DOTAP); *N*-[1-(2,3-dimyristyloxy)propyl]-*N*,*N*-dimethyl-*N*-(2-hydroxyethyl) ammonium bromide (DMRIE), 3β-[*N*-(*N*,*N*′-dimethylaminoethane) carbamoyl] cholesterol (DC-Chol); dioctadecyl amidoglyceryl spermine (DOGS, Transfectam); and dimethyldioctadecylammonium bromide (DDAB) (*6, 7, 10*−*15*). A few such compounds have also been used in initial clinical studies. However, many of the cationic lipids used in early clinical trials such as DC-Chol, DMRIE, and GL-67, although effective in vitro, have proven inefficient in vivo, especially when compared with viral vectors (*16, 17*).

Various heterocyclic cationic lipids had been studied and used for gene delivery. Some of them showed higher transfection efficiency and lower cytotoxicity compared to cationic lipids with linear primary amines or polyamines as

10.1021/bc8004039 CCC: $40.75 © 2008 American Chemical Society
Published on Web 12/03/2008

the headgroup (*18*). Pyridinium heterocyclic ring in the cationic amphiphile, which had antiseptic and antibiotic properties, was first introduced in the 1940s (*19*, *20*). With the invention of pyridinium-based cationic lipids, a series of these lipids have been developed, and some of them have been reported to reach or surpass the transfection efficiency of commercial cationic lipid formulations, both in vitro and vivo, while maintaining low cytotoxicity (*21*−*25*).

In this study, we synthesized a series of pyridinium lipids containing a heterocyclic positively charged ring linked to different types of fatty acids via ester or amide spacers. Following purification and characterization of these cationic lipids using ^{1}H NMR, ^{13}C NMR, and mass spectrometry, cationic liposomes were prepared using DOPE or cholesterol as a co-lipid, followed by determination of particle size and zeta potential. Reporter gene expression and cytotoxicity were determined after transfection of Chinese hamster ovary (CHO) cells, hepatocarcinoma (CRL1830) cells, and prostate cancer (C4−2) cells with green fluorescent protein (GFP) or luciferase expression plasmid DNA after complex formation with cationic liposomes. Factors influencing gene transfer, including charge ratio (N/P) between cationic liposomes and pDNA, cationic lipid/co-lipid ratio, linker type, fatty acid carbon chain length, degree of saturation, configuration of double bond, the presence of serum, and cell type were studied.

EXPERIMENTAL PROCEDURES

Materials. 1,2-Dioleoyl-*sn*-glycero-3-phosphoethanolamine (DOPE) was purchased from Avanti Polar Lipids (Alabaster, AL). Lipofectamine, DMEM, and RPMI1640 were purchased from Invitrogen Corporation (Carlsbad, CA). Heat-inactivated fetal bovine serum (FBS) and penicillin (10 000 units/mL penicillin G sodium)−streptomycin solution (10 000 μg/mL streptomycin sulfate) in 0.85% saline were purchased from Mediatech, Inc. (Herndon, VA). Luciferase Assay Kit and Cell Culture Lysis Reagent 5X (CCLR) were procured from Promega Corporation (Madison, WI). QIAfilter plasmid maxi kit was purchased from Qiagen, Inc. (Valencia, CA); BCA protein assay kit from Pierce (Rockland, IL); pCMS-EGFP plasmid was procured from BD Biosciences Clontech (Palo Alto, CA), and pcDNA3-Luc plasmid was a kind gift from Expression Genetics, Inc. (Huntsville, AL). All reagents used for lipid synthesis were purchased from Sigma-Aldrich Chemical Co. (St. Louis, MO) and Fisher Scientific (Pittsburgh, PA) and were used without further purification.

Synthesis of Pyridinium Lipids. *General Methods.* Routine thin layer chromatography (TLC) was performed on aluminum-backed Uniplates. (Analtech, Newark, DE). ^{1}H NMR spectra were obtained on a Bruker AX 300 (Billerica, MA) or Varian Inova-500 (Palo Alto, CA) spectrometer. Chemical shifts for ^{1}H NMR were reported as parts per million (ppm) relative to tetramethylsilane (TMS) in deuterated chloroform ($CDCl_3$) as internal standard. ^{13}C NMR spectra were obtained on a Bruker AX 300 spectrometer, operating at 75.5 MHz. To make sure the final results are reliable, we used both conventional mass and high-resolution mass (HRMS) spectrophotometers to characterize the synthesized pyridinium lipids. Conventional mass spectral data were collected on a Bruker ESQUIRE electrospray/ion trap instrument in positive and negative ion modes. High-resolution mass measurements were obtained using a Micromass Q-TOF2 mass spectrometer. HRMS samples were dissolved in 50% acetonitrile, 0.1% formic acid, and were infused by syringe (0.4 μL/min).To make this article easier to read, we only listed the HRMS data.

Pyridinium amide cationic lipids **4**−**13** and pyridinium ester cationic lipids **14**−**18** were synthesized as described by Ilies et al. (*25*), and their visual structures with minimized energy were simulated with the *Chem3D Pro* software, v 10.0 (ChemOffice, CambridgeSoft Corp.) using MM2 molecular mechanics routine toward a 0.1 rms gradient, which are shown in Table 1. Figure 1 outlines a synthesis route via the corresponding pyrylium salts. Mesityl oxide was monoacylated with fatty acid chloride in the presence of aluminum chloride to yield pyrylium chloroaluminate, which was subsequently converted into more stable hexafluorophosphate **1**, for using as a key intermediate to react with different primary amines, yielding aminoethylpyridinium hexafluorophosphate **2** and hydroxyethylpyridinium hexafluorophosphate **3**. Acylation of these pyridinium salts with different types of fatty acid chlorides afforded the final pyridinium amide cationic lipids **4**−**13** and pyridinium ester cationic lipids **14**−**18**, which were purified with chromatography on silica gel and recrystallized from ethanol.

Synthesis of Pyridinium Amide Cationic Lipids **4**−**13.** Aminoethylpyridinium hexafluorophosphate **2** and compounds **4** and **5** were synthesized as described by Ilies et al. (*25*), and the spectra were the same as those reported by these scientists.

4,6-Dimethyl-2-tetradecyl-1-[2-(9Z)-hexadec-9-enoylamidoethyl] Pyridinium Hexafluorophosphate **6.** Yield: 89.9%. ^{1}H NMR ($CDCl_3$), δ, ppm: 7.41 (s, 1H, H-5 pyridinium), 7.38 (s, 1H, H-3 pyridinium), 6.75 (t, 1H, J = 6.0 Hz), 5.33 (m, 2H, J = 5.4 Hz), 4.56 (t, 2H, J = 6.9 Hz), 3.63 (dt, 2H, J = 6.9 Hz, 6.6 Hz, CONHC$\underline{H}_2$), 3.17 (t, 2H, J = 7.5 Hz, CαPy-C$\underline{H}_2$), 2.90 (s, 3H, C$\underline{H}_3$ α-pyridinium), 2.55 (s, 3H, C$\underline{H}_3$ γ-pyridinium), 2.18 (t, 2H, J = 7.5 Hz, NHCOC$\underline{H}_2$), 1.99 (4H, br), 1.72 (quint., 2H, CαPy-CH$_2$C$\underline{H}_2$), 1.47 (m, 2H, NHCOCH$_2$C$\underline{H}_2$), 1.25 (s, 38H, C$\underline{H}_2$ from both of alkyl chains), 0.88 (t, 6H, C$\underline{H}_3$ of alkyl chains). ^{13}C NMR (300 M, $CDCl_3$), 175.23 (C═O), 159.07, 158.14, 155.05 (C-2, C-4, and C-6 pyridium), 130.41, 130.28 (CH═CH), 128.68, 127.32 (C-3 and C-5 pyridium), 50.55 (CαPy-$\underline{C}$H$_2$), 38.25 (CβPy-$\underline{C}$H$_2$), 35.97, 33.25, 32.59, 32.57, 31.92, 31.75, 29.70, 29.69, 29.65, 29.64, 29.63, 29.63, 29.59, 29.39, 29.34, 29.29, 29.29, 29.24, 29.21, 29.06, 29.03, 28.84, 25.40, 22.67, 22.63, 21.73, 21.51, 14.05, 14.05. HRMS calcd for $C_{39}H_{71}N_2O^+$, 583.5566, found 583.5568.

4,6-Dimethyl-2-tetradecyl-1-[2-(9E)-hexadec-9-enoylamidoethyl] Pyridinium Hexafluorophosphate **7.** Yield: 81.5%. ^{1}H NMR (300 M, $CDCl_3$), δ, ppm: 7.42 (s, 1H, H-5 pyridinium), 7.37 (s, 1H, H-3 pyridinium), 6.75 (t, 1H, J = 6.0 Hz), 5.37 (m, 2H), 4.55 (t, 2H, J = 6.6 Hz), 3.62 (dt, 2H, J = 6.6 Hz, 6.3 Hz, CONHC$\underline{H}_2$), 3.17 (t, 2H, J = 7.5 Hz, CαPy-C$\underline{H}_2$), 2.90 (s, 3H, C$\underline{H}_3$ α-pyridinium), 2.54 (s, 3H, C$\underline{H}_3$ γ-pyridinium), 2.17 (t, 2H, J = 7.5 Hz, NHCOC$\underline{H}_2$), 1.95 (4H, br), 1.72 (quint., 2H, CαPy-CH$_2$C$\underline{H}_2$), 1.46 (quint., 2H, NHCOCH$_2$C$\underline{H}_2$), 1.25 (s, 38H, C$\underline{H}_2$ from both of alkyl chains), 0.87 (t, 6H, C$\underline{H}_3$ of alkyl chains). ^{13}C NMR (300 M, $CDCl_3$), 174.67 (C═O), 158.47, 157.54, 154.51 (C-2, C-4, C-6 pyridinium), 129.37, 129.25 (CH═CH), 128.11, 126.72 (C-3 and C-5 pyridium), 49.97 (CαPy-$\underline{C}$H$_2$), 37.64 (CβPy-$\underline{C}$H$_2$), 36.38, 32.67, 31.35, 31.21, 29.17, 29.11, 29.09, 29.08, 29.07, 29.02, 28.82, 28.77, 28.72, 28.70, 28.69, 28.65, 28.60, 28.55, 28.49, 28.40, 26.66, 26.65, 24.83, 22.09, 22.06, 21.14, 20.92, 13.49, 13.48. HRMS calcd for $C_{39}H_{71}N_2O^+$, 583.5566, found 583.5562.

4,6-Dimethyl-2-tetradecyl-1-(2-octadecanoylamidoethyl) Pyridinium Hexafluorophosphate **8.** Yield: 87.5%. ^{1}H NMR ($CDCl_3$), δ, ppm: 7.41 (s, 1H, H-5 pyridinium), 7.38 (s, 1H, H-3 pyridinium), 6.77 (t, 1H, J = 6.0 Hz), 5.37 (m, 2H, J = 19.2 Hz), 4.55 (t, 2H, J = 6.9 Hz), 3.62 (dt, 2H, J = 6.9 and 6.0 Hz, CONHC$\underline{H}_2$), 3.17 (t, 2H, J = 7.2 Hz, CαPy-C$\underline{H}_2$), 2.90 (s, 3H, C$\underline{H}_3$ α-pyridinium), 2.54 (s, 3H, C$\underline{H}_3$ γ-pyridinium), 2.17 (t, 2H, NHCOC$\underline{H}_2$), 1.95 (4H, br), 1.72 (quint., 2H, CαPy-CH$_2$C$\underline{H}_2$), 1.48 (quint., 2H, NHCOCH$_2$C$\underline{H}_2$), 1.25 (s, 50H, C$\underline{H}_2$ from both of alkyl chains), 0.88 (t, 6H, C$\underline{H}_3$ of alkyl chains).

Table 1. Energy-Minimized Structures and Melting Points of Pyridinium Lipids

Carbon chain legnth and type	Compound ID	Amide	M.P.	Compound ID	Ester	M.P.
C14:0	4	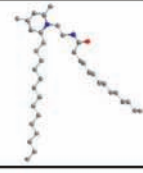	73.6 °C	14	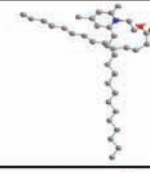	72.3 °C
C15:0				15		81.7 °C
C16:0	5		80.7 °C	16	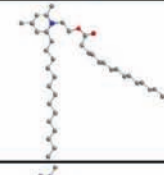	77.1 °C
C18:0	8	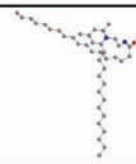	83.8 °C	17	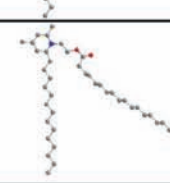	74.4 °C
C18:0, branch	13	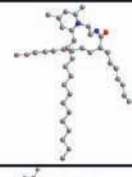	-16.3 °C			
C16:1, cis-9	6		36.8 °C			
C16:1, trans-9	7	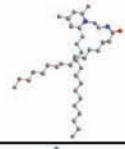	63.5 °C			
C18:1, cis-9	9	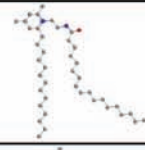	50 °C	18	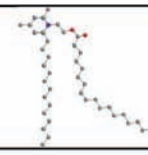	48.7°C
C18:1, trans-9	10		64.8 °C			
C20:1, cis-11	11	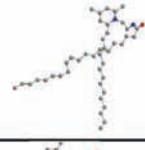	50.4 °C			
C20:1, trans-11	12		69.4 °C			

^{13}C NMR (300 M, $CDCl_3$), 175.15 (C═O), 159.00, 158.06, 155.03 (C-2, C-4, C-6 pyridinium), 128.64, 127.24 (C-3 and C-5 pyridium), 50.49 (CαPy-$\underline{C}H_2$), 38.17 (CβPy-$\underline{C}H_2$), 35.94, 33.19, 31.89, 31.88, 29.67, 29.66, 29.66, 29.65, 29.64, 29.63,

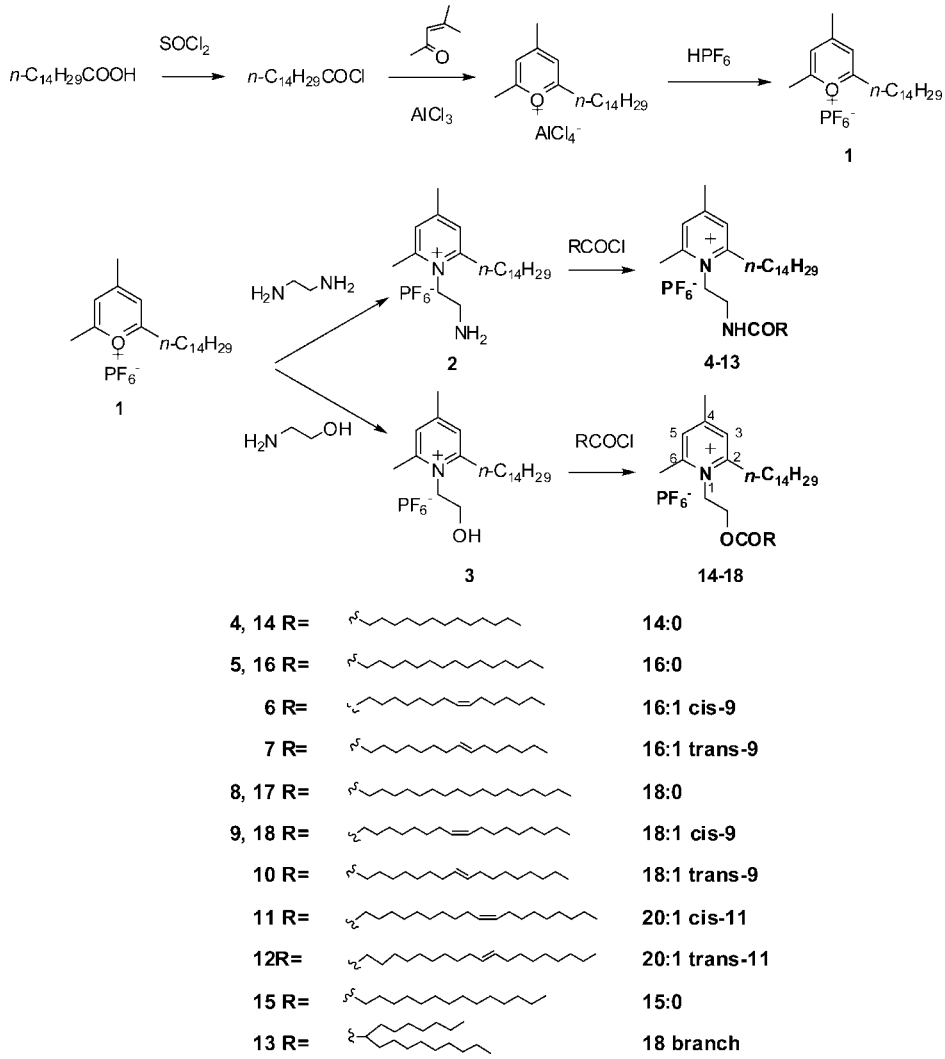

Figure 1. Synthesis Scheme of Pyridinium Lipids.

29.63, 29.62, 29.61, 29.61, 29.60, 29.55, 29.49, 29.35, 29.33, 29.32, 29.31, 29.30, 29.26, 29.25, 29.22, 29.02, 25.37, 22.63, 22.63, 21.67, 21.42, 14.01, 14.01. HRMS calcd for $C_{41}H_{77}N_2O^+$, 613.6036, found 613.6036.

4,6-Dimethyl-2-tetradecyl-1-(2-oleoylamidoethyl) Pyridinium Hexafluorophosphate **9.** Yield: 62.3%. ^{1}H NMR ($CDCl_3$), δ, ppm: 7.41 (s, 1H, H-5 pyridinium), 7.38 (s, 1H, H-3 pyridinium), 6.77 (t, 1H, J = 6.0 Hz, CONH), 5.33 (2H, t, HC=CH), 4.56 (t, 2H, J = 6.9 Hz), 3.63 (dt, 2H, J = 6.9 and 6.0 Hz, $CONHCH_2$), 3.17 (t, 2H, J = 7.5 Hz, CαPy-CH_2), 2.90 (s, 3H, CH_3 α-pyridinium), 2.55 (s, 3H, CH_3 γ-pyridinium), 2.18 (t, 2H, $NHCOCH_2$), 1.99 (q, 4H), 1.72 (quint., 2H, CαPy-CH_2CH_2), 1.47 (quint., 2H, $NHCOCH_2CH_2$), 1.25 (s, 42H, CH_2 from both of alkyl chains), 0.88 (t, 6H, CH_3 of alkyl chains). ^{13}C NMR (300 M, $CDCl_3$), 175.20 (C=O), 159.07, 158.13, 155.05 (C-2, C-4, C-6 pyridinium), 129.95, 129.81 (CH=CH), 128.68, 127.31 (C-3 and C-5 pyridium), 50.55 (CαPy-CH_2), 38.24 (Cβ Py-CH_2), 35.96, 33.24, 31.91, 31.90, 29.78, 29.75, 29.68, 29.67, 29.66, 29.64, 29.63, 29.58, 29.51, 29.38, 29.33, 29.32, 29.29, 29.28, 29.28, 29.26, 29.25, 29.24, 29.18, 29.06, 27.23, 25.39, 22.66, 21.71, 21.49, 14.05, 14.05. HRMS calcd for $C_{41}H_{75}N_2O^+$, 611.5879, found 611.5872.

4,6-Dimethyl-2-tetradecyl-1-[2-(9E)-octadec-9-enoylamidoethyl] Pyridinium Hexafluorophosphate **10.** Yield: 56.5%. ^{1}H NMR ($CDCl_3$), δ, ppm: 7.42 (s, 1H, H-5 pyridinium), 7.37 (s, 1H, H-3 pyridinium), 6.76 (t, 1H, J = 6.3 Hz), 5.37 (t, 2H, HC=CH, J = 19.2 Hz), 4.57 (t, 2H, J = 6.9 Hz), 3.63 (dt, 2H, J = 6.9 and 6.3 Hz, $CONHCH_2$), 3.17 (t, 2H, J = 7.8 Hz, CαPy-CH_2), 2.90 (s, 3H, CH_3 α-pyridinium), 2.56 (s, 3H, CH_3 γ-pyridinium), 2.18 (t, 2H, $NHCOCH_2$), 1.99 (br, 4H), 1.74 (quint., 2H, CαPy-CH_2CH_2), 1.46 (quint., 2H, $NHCOCH_2CH_2$), 1.25 (s, 42H, CH_2 from both of alkyl chains), 0.87 (t, 6H, CH_3 of alkyl chains). ^{13}C NMR (300 M, $CDCl_3$), 175.14 (C=O), 158.98, 158.06, 155.02 (C-2, C-4, C-6 pyridinium), 130.36, 130.21 (CH=CH), 128.63, 127.23 (C-3 and C-5 pyridium), 50.47 (CαPy-CH_2), 38.16 (Cβ Py-CH_2), 35.91, 33.17, 32.54, 32.51, 31.86, 31.84, 29.62, 29.63, 29.62, 29.61, 29.60, 29.59, 29.58, 29.53, 29.42, 29.34, 29.28, 29.23, 29.24, 29.20, 29.18, 29.15, 29.01, 28.98, 25.34, 22.60, 22.61, 21.65, 21.41, 13.99, 13.99. HRMS calcd for $C_{41}H_{75}N_2O^+$, 611.5879, found 611.5870.

4,6-Dimethyl-2-tetradecyl-1-[2-(11Z)-eicos-11-enoylamidoethyl] Pyridinium Hexafluorophosphate **11.** Yield: 79.8%. ^{1}H NMR ($CDCl_3$), δ, ppm: 7.41 (s, 1H, H-5 pyridinium), 7.38 (s, 1H, H-3 pyridinium), 6.78 (t, 1H, J = 6.3 Hz), 5.34 (m, 2H, HC=CH), 4.56 (t, 2H, J = 6.6 Hz), 3.63 (dt, 2H, J = 6.6 and 6.3 Hz, $CONHCH_2$), 3.17 (t, 2H, J = 7.8 Hz, CαPy-CH_2), 2.90 (s, 3H, CH_3 α-pyridinium), 2.55 (s, 3H, CH_3 γ-pyridinium), 2.18 (t, 2H, $NHCOCH_2$), 1.99 (br, 4H), 1.72 (quint., 2H, CαPy-CH_2CH_2), 1.57−1.42 (m, 2H, $NHCOCH_2CH_2$), 1.25 (s, 46H, CH_2 from both of alkyl chains), 0.88 (t, 6H, CH_3 of alkyl chains). ^{13}C NMR (300 M, $CDCl_3$), 175.23 (C=O), 159.06, 158.13, 155.06 (C-2, C-4, C-6 pyridinium), 129.90, 129.90 (CH=CH), 128.69, 127.31 (C-3 and C-5 pyridium), 50.54 (CαPy-CH_2), 38.23 (Cβ Py-CH_2), 35.97, 33.24, 31.92, 31.90,

29.81, 29.80, 29.78, 29.69, 29.67, 29.65, 29.64, 29.59, 29.54, 29.52, 29.50, 29.39, 29.35, 29.32, 29.30, 29.29, 29.29, 29.28, 29.24, 29.06, 27.25, 27.23, 25.41, 24.78, 22.66, 21.72, 21.49, 14.05, 14.05. HRMS calcd for $C_{43}H_{79}N_2O^+$, 639.6192, found 639.6193.

4,6-Dimethyl-2-tetradecyl-1-[2-(11E)-eicos-11-enoylamidoethyl] Pyridinium Hexafluorophosphate **12.** Yield: 58.8%. ^{1}H NMR ($CDCl_3$), δ, ppm: 7.41 (s, 1H, H-5 pyridinium), 7.38 (s, 1H, H-3 pyridinium), 6.78 (t, 1H, J = 6.0 Hz), 5.38 (t, 2H, HC=CH), 4.57 (t, 2H, J = 6.6 Hz), 3.64 (dt, 2H, J = 6.9 and 6.0 Hz, CONHCH$_2$), 3.17 (t, 2H, J = 7.8 Hz, CαPy-CH$_2$), 2.90 (s, 3H, CH$_3$ α-pyridinium), 2.56 (s, 3H, CH$_3$ γ-pyridinium), 2.18 (t, 2H, NHCOCH$_2$), 1.96 (br, 4H), 1.71 (quint., 2H, CαPy-CH$_2$CH$_2$), 1.48 (quint., 2H, NHCOCH$_2$CH$_2$), 1.25 (s, 42H, CH$_2$ from both of alkyl chains), 0.87 (t, 6H, CH$_3$ of alkyl chains). ^{13}C NMR (300 M, $CDCl_3$), 175.27 (C=O), 159.11, 158.16, 155.04 (C-2, C-4, C-6 pyridinium), 130.36, 130.36 (C=C), 128.68, 127.35 (C-3 and C-5 pyridium), 50.59 (CαPy-CH$_2$), 38.27 (CβPy-CH$_2$), 35.98, 33.28, 32.60, 31.92, 31.91, 29.70, 29.69, 29.69, 29.68, 29.68, 29.67, 29.67, 29.66, 29.65, 29.64, 29.59, 29.49, 29.49, 29.39, 29.35, 29.32, 29.30, 29.29, 29.19, 29.07, 25.40, 25.40, 22.66, 22.66, 21.74, 21.54, 14.05, 14.05. HRMS calcd for $C_{43}H_{79}N_2O^+$, 639.6192, found 639.6196.

4,6-Dimethyl-2-tetradecyl-1-[2-(2-heptyl-undecanoyl)-amidoethyl] Pyridinium Hexafluorophosphate **13.** Yield: 77.3%. ^{1}H NMR ($CDCl_3$), δ, ppm: 7.41 (s, 1H, H-5 pyridinium), 7.37 (s, 1H, H-3 pyridinium), 6.78 (1H, t, 1H, J = 6.3 Hz), 4.55 (t, 2H, J = 6.6 Hz), 3.66 (dt, 2H, J = 6.6 and 6.6 Hz, CONHCH$_2$), 3.22 (t, 2H, J = 6.9 Hz, CαPy-CH$_2$), 2.93 (s, 3H, CH$_3$ α-pyridinium), 2.55 (s, 3H, CH$_3$ γ-pyridinium), 2.12 (quint., 1H, NHCOCH), 1.71 (quint., 2H, CαPy-CH$_2$CH$_2$), 1.46 (quint., 4H, NHCOCH(CH$_2$)$_2$), 1.25 and 1.23 (s, s, 46H, CH$_2$ from both of alkyl chains), 0.88−0.84 (m, 9H, CH$_3$ of alkyl chains). ^{13}C NMR (300 M, $CDCl_3$), 178.24 (C=O), 159.01, 158.01, 155.21 (C-2, C-4, C-6 pyridinium), 128.71, 127.25 (C-3 and C-5 pyridium), 50.51 (CαPy-CH$_2$), 47.17 (C_9H_{19}CHC$_7$H$_{15}$), 38.03 (CβPy-CH$_2$), 33.27, 32.68, 31.91, 31.89, 31.84, 29.72, 29.68, 29.67, 29.66, 29.65, 29.65, 29.61, 29.61, 29.60, 29.53, 29.42, 29.34, 29.33, 29.30, 29.71, 29.11, 29.06, 27.45, 27.38, 27.42, 26.77, 22.65, 22.62, 21.65, 21.44, 14.04, 14.04. HRMS calcd for $C_{41}H_{77}N_2O^+$, 613.6035, found 613.6037.

Synthesis of Pyridinium Ester Cationic Lipids **14**−**18.** Hydroxyethylpyridinium hexafluorophosphate **3** and compounds **14** and **16** were synthesized per the described method (*25*), and the spectra are the same as those reported in ref *25*.

4,6-Dimethyl-2-tetradecyl-1-(2-pentadecanoylhydroxyethyl) Pyridinium Hexafluorophosphate **15.** Yield: 72.0%. ^{1}H NMR ($CDCl_3$), δ, ppm: 7.44 (s, 1H, H-5 pyridinium), 7.39 (s, 1H, H-3 pyridinium), 4.80 (t, 2H, J = 5.7 Hz, COOCH$_2$), 4.47 (t, 2H, J = 5.7z), 3.04 (t, 2H, J = 7.8 Hz, CαPy-CH$_2$), 2.87 (s, 3H, CH$_3$ δ-pyridinium), 2.55 (s, 3H, CH$_3$ γ-pyridinium), 2.25 (t, 2H, J = 7.5 Hz, COCH$_2$), 1.79 (cv, 2H, J = 7.5 Hz,), 1.48 (cv, 2H, COCH$_2$CH$_2$), 1.25, 1.26 (s, 44H, CH$_2$ from both of alkyl chains), 0.88 (t, 6H, CH$_3$ of alkyl chains). ^{13}C NMR (300 M, $CDCl_3$), 173.00 (C=O), 158.63, 158.56, 155.43 (C-2, C-4, C-6 pyridinium), 128.81, 126.90 (C-3 and C-5 pyridium), 60.68 (CαPy-CH$_2$), 49.94 (CβPy-CH$_2$), 33.76, 33.38, 31.92, 29.68, 29.68, 29.67, 29.67, 29.66, 29.66, 29.65, 29.65, 29.64, 29.60, 29.59, 29.59, 29.58, 29.45, 29.36, 29.35, 29.34, 29.22, 29.19, 29.06, 28.37, 24.64, 22.67, 21.77, 21.63, 14.06, 14.06. HRMS calcd for $C_{38}H_{70}NO_2^+$, 572.5406, found 572.5404.

4,6-Dimethyl-2-tetradecyl-1-(2-octadecanoylhydroxyethyl) Pyridinium Hexafluorophosphate **17.** Yield: 70.1%. ^{1}H NMR ($CDCl_3$), δ, ppm: 7.43 (s, 1H, H-5 pyridinium), 7.40 (s, 1H, H-3 pyridinium), 4.81 (t, 2H, J = 6.0 Hz, COOCH$_2$), 4.49 (t, 2H, J = 6.0z), 3.06 (t, 2H, J = 7.5 Hz, CαPy-CH$_2$), 2.89 (s, 3H, CH$_3$ α-pyridinium), 2.57 (s, 3H, CH$_3$ γ-pyridinium), 2.26 (t, 2H, J = 7.5 Hz, COCH$_2$), 1.81 (quint., 2H, CαPy-CH$_2$CH$_2$), 1.49 (quint., 2H, COCH$_2$CH$_2$), 1.26, 1.27 (s, 50H, CH$_2$ from both of alkyl chains), 0.88 (t, 6H, CH$_3$ of alkyl chains). ^{13}C NMR (300 M, $CDCl_3$), 173.00 (C=O), 158.64, 158.55, 155.43 (C-2, C-4, C-6 pyridinium), 128.80, 126.90 (C-3 and C-5 pyridium), 60.68 (CαPy-CH$_2$), 49.95 (CβPy-CH$_2$), 33.76, 33.38, 31.92, 31.92, 29.70, 29.69, 29.69, 29.69, 29.68, 29.68, 29.67, 29.66, 29.65, 29.65, 29.64, 29.60, 29.58, 29.45, 29.35, 29.35, 29.34, 29.22, 29.19, 29.06, 28.37, 24.65, 24.65, 22.67, 22.67, 21.77, 21.63, 14.05, 14.05. HRMS calcd for $C_{41}H_{76}NO_2^+$, 614.5875, found 614.5880.

4,6-Dimethyl-2-tetradecyl-1-(2-oleoylhydroxyethyl) Pyridinium Hexafluorophosphate **18.** Yield: 69.5%. ^{1}H NMR ($CDCl_3$), δ, ppm: 7.43 (s, 1H, H-5 pyridinium), 7.39 (s, 1H, H-3 pyridinium), 5.33 (m, 2H, CH from double bond in oleyl group), 4.80 (t, 2H, J = 6.0 Hz, COOCH$_2$), 4.47 (t, 2H, J = 6.0 Hz), 3.05 (t, 2H, J = 7.5 Hz, CαPy-CH$_2$), 2.87 (s, 3H, CH$_3$ α-pyridinium), 2.55 (s, 3H, CH$_3$ γ-pyridinium), 2.25 (t, 2H, J = 7.8 Hz, COCH$_2$), 1.99 (q, 4H), 1.79 (quint. 2H, CαPy-CH$_2$CH$_2$), 1.48 (quint., 2H, COCH$_2$CH$_2$), 1.26 (s, 44H, CH$_2$ from both of alkyl chains), 0.88 (t, 6H, CH$_3$ of alkyl chains). ^{13}C NMR (300 M, $CDCl_3$), 172.99 (C=O), 158.75, 158.62, 155.52 (C-2, C-4, C-6 pyridinium), 130.15 129.59 (CH=CH), 128.76, 126.90 (C-3 and C-5 pyridium), 60.70 (CαPy-CH$_2$), 50.09 (CβPy-CH$_2$), 33.75, 33.42, 31.92, 31.90, 29.76, 29.68, 29.68, 29.67, 29.67, 29.65, 29.63, 29.57, 29.51, 29.44, 29.35, 29.34, 29.33, 29.29, 29.20, 29.19, 29.12, 29.07, 29.02, 28.41, 27.25, 27.16, 24.64, 22.66, 21.79, 14.04, 14.04. HRMS calcd for $C_{41}H_{74}NO_2^+$, 612.5719, found 612.5725.

Determination of Lipid Phase Transition Temperature and Melting Point. Differential scanning calorimetry (DSC) studies were carried out to find the phase transition temperature and melting point with a DSC Q2000, TA Instruments (UK). About 5 mg of pyridinium lipid or lipid mixture was scanned from 0 to 100 °C at a scan rate of 2 °C/min. Data were analyzed using Universal Analysis software provided by TA Instruments.

Preparation of Pyridinium Liposomes and Lipoplexes. A pyridinium lipid was dissolved in chloroform with a co-lipid, DOPE or Chol, at the molar ratio of 1:1, 2:1, and 4:1 to reach a final concentration of 1 mg/mL for the charged species. The solvent was removed by rotary evaporation and further dried under vacuum overnight to generate a thin lipid film. The lipid film was hydrated in sterile water at 60 °C and vortexed to form a cationic liposome suspension. Since lipid molecules form a lipid bilayer upon solvent evaporation, no free lipids should appear in the aqueous solution. Therefore, we did not make any attempt to isolate free lipids which may be present in the liposome suspension. The particle size of these liposomes was further reduced by probe sonication (Sonication s-4000, MISONIX) at the amplitude of 60 for 5 min. Pyridinium liposomes were characterized for DNA condensation efficiency, particle size distribution, and ζ-potential as described previously (*3*). The particle size and ζ-potential of cationic liposomes and lipoplexes were determined at 25 °C by dynamic light scattering using a Malvern Zetasizer (Malvern Instruments, UK). Briefly, DNA condensation was determined by 0.6% agarose gel electrophoresis at 10 v/cm for 100 min in 1× TBE buffer, followed by ethidium bromide (EtBr) staining.

In Vitro Transfection. CHO cells were seeded in 24-well plates and maintained in 0.5 mL of RPMI 1640 medium containing 10% fetal bovine serum (FBS) under 5% CO_2 at 37 °C for 24 h. The cell number was about 4×10^4 cells per well. GFP or luciferase expression plasmid (pCMS-EGFP or pDNA3-Luc) and cationic liposomes (different formulations) were diluted to 25 μL by Opti-MEM I medium, respectively, and incubated for 5 min at room temperature. Lipoplexes were prepared by mixing plasmid and liposomes in equal volume,

and incubated for 20 min at room temperature to allow complex formation. Immediately before transfection, the media was removed, and cells were washed gently with sterile phosphate buffered saline (PBS). Lipoplexes were added to each well, diluted to 0.5 mL by Opti-MEM I medium, and the plate was incubated under 5% CO_2 at 37 °C for 6 h. Following transfection, the culture medium was replaced with RPMI 1640 medium containing 10% FBS. GFP gene expression was observed under fluorescence microscopy (Olympus, Japan).

For luciferase expression, the cells were collected and lysed. The cell lysate was measured for luciferase gene expression by Luciferase Assay Kit (Promega, Madison, WI). The total protein concentration was measured by bicinchoninic acid (BCA) protein assay reagent (Pierce, Rockford, IL). Luciferase activity was normalized by the total protein content and expressed as relative light unit (RLU) per μg of protein (RLU/μg protein).

To determine whether the presence of serum in the culture media affects the transfection efficiency of pyridinium lipids, we used RPMI 1640 culture medium containing 0%, 5%, 10%, 15%, 20%, 30%, and 40% FBS for transfection of CHO cells with pyridinium lipid-based lipoplexes, and their transfection efficiencies were determined.

To determine the effect of cell types on gene transfer, two more cell lines were used to determine transfection efficiency and cytotoxicity. Murine hepatocarcinoma cells (CRL 1830) were seeded with 0.5 mL of DMEM medium containing 10% FBS under 5% CO_2 at 37 °C. Human prostate cancer cells (C4−2) cells seeded with RPMI 1640 medium containing 10% FBS under 5% CO_2 at 37 °C. The cell number was about 4×10^4 cells per well for 24 well plate for both of them. Luciferase expression and cytotoxicity were measured at the end of the transfection.

Cytotoxicity Assay. The cytotoxicity of lipoplexes at 48 h post-transfection was determined using 3-[4,5-dimethylthiazol-2-yl]-2,5- diphenyltetrazolium bromide (MTT) assay in CHO cells. Briefly, 5 mg/mL stock solution of MTT in PBS was diluted 10 times with complete growth medium. Four hours before the end of transfection study, cell culture medium was removed and replaced by this MTT medium to achieve a final concentration of 0.5 mg/mL MTT. The plate was then incubated at 37 °C in 5% CO_2 for 4 h. The medium was removed, blotted dried, and 200 μL of DMSO was added to each well to dissolve the formazan crystals. Finally, the plate was read spectrophotometrically at 560 nm using a microplate reader (Bio-Rad, Hercules, CA). The relative cell viability was calculated as $[Abs]_{sample}/[Abs]_{control} \times 100\%$.

Statistical Analysis. Data were expressed as the mean ± standard deviation (SD). The difference between any two groups was determined by ANOVA. $P < 0.05$ was considered statistically significant.

RESULTS

Synthesis of Pyridinium Lipids. The goal of this study was to synthesize a series of pyridinium lipids to determine the structure−activity relationship for enhanced gene delivery. All of these cationic lipids contain a heterocyclic pyridinium ring linked to a single alkyl chain fatty acid of different alkyl chain lengths (C14, C15, C16, C18, and C20), types (cis−trans isomers), and branched chain via ester and amide spacers. We synthesized not only the saturated and unsaturated even-numbered carbon chain length, but also carbon chain length of 15 (odd number) saturated analogue and branched carbon chain saturated analogue. The synthesis scheme of pyridinium lipids is shown in Figure 1. Briefly, mesityl oxide was monoacylated to yield pyrylium chloroaluminates, which were converted into pyrylium hexafluorophosphates (**1**) by hexafluorophosphoric acid. Pyrylium hexafluorophosphate was used as a key intermediate for reaction with different primary amines to form a pyridinium heterocyclic ring with different linkers in the final structure. Acylation of these pyridinium salts with different lengths and types of fatty acid chlorides afforded the final pyridinium lipids. Intermediate and final products of these pyridinium lipids were characterized by ^{1}H NMR, ^{13}C NMR, and high-resolution mass spectrometry (HRMS), and these results are included in the Experimental Procedures section.

Table 2. Determination of Lipid Phase Transition Temperature (°C) by Differential Scanning Calorimetry (DSC)[a]

type of hydrophobic anchor chain	linker		lipid with amide linker/co-lipid (molar ratio 1:1)	
	ester	amide	DOPE	CHOL
C14:0	45.5−47 5	38.9−44 9	18.2−21 4	32.9−35 2
C16:0	63.5−66.1	39.3−41.4	37.8−40.0	40.2−42.1
C16:1, cis		29.7−31.1		
C16:1,trans		35.7−36.7		
C18:0	73.4−74.1	45.4−48.7	24.2−26.3	42.1−46.5
C18:1, cis		31.4−32.1		
C18:1,trans		34.1−37.9		
C20:1, cis		36.7−39.6		
C20:1,trans		37.4−41.3		

[a] Values are "onset to peak temperature".

The structures with minimized energy of these lipids are listed in Table 1. Two side chains are much closer in energy-minimized structures of unsaturated lipids than those of saturated lipids, which may facilitate the formation of lipid bilayers in liposomes. The melting points of these lipids are listed in Table 1. More than half of these pyridinium lipids have melting points of more than 60 °C. An increase in fatty acid chain length increased the melting point. Saturated lipids have higher melting points than unsaturated lipids, except branched ones. For unsaturated lipids, the melting point of the trans-isomer is higher than that of the cis-isomer of the same fatty acid chain length. Lipid phase transition temperatures of pure pyridinium lipids and lipid mixture are listed in Table 2. The lipids with amide linker showed lower phase transition temperature compared to lipids with an ester linker. An increase in hydrophobic carbon chain length increased the phase transition temperature. At the same carbon chain length, the phase transition temperature of the trans-isomer was higher than that of the cis-isomer. The phase transition temperature was higher when formulated with cholesterol than that when formulated with DOPE. A higher phase transition temperature makes liposome preparation difficult by rehydration of lipid films and extrusion. Therefore, probe sonication was used to produce small unilamellar vesicles (SUV) at 60 °C. Sterile water was used as the suspension medium in cationic liposome preparation so as to prevent cationic liposome aggregation in long-term storage in electrolytic buffer.

Preparation and Characterization of Lipoplexes. Transfection efficiency of lipoplexes is known to depend on the particle size and surface charge of liposomes and lipoplexes (*26*, *27*). Therefore, we determined the mean particle size, particle size distribution (PSD), and ζ-potential of pyridinium liposomes prepared using different co-lipids and molar ratios of cationic lipid/co-lipid. The mean particle size of these liposomes was about 97.98 ± 4.31 nm, with the polydispersity index (PDI) of 0.32 ± 0.03, and ζ-potential was 41.33 ± 4.10 mV (Table 3). This suggests little difference in particle size and ξ-potential among different liposome preparations. Pyridinium liposomes were stable, and no aggregation was observed at 4 °C during the experimental period. Lipoplexes were formed by simply mixing pyridinium liposomes and plasmid DNA. The degree of DNA condensation increased with the increase in charge ratio.

Table 3. Particle Size and ζ-Potential of Pyridinium Cationic Liposome and Lipoplexes[a]

	pyridinium cationic liposomes	lipoplexes (0 h)	lipoplexes (10 h)
particle size (nm)	97.98 ± 4.31	124.33 ± 2.08	128.33 ± 1.53
PDI	0.32 ± 0.03	0.17 ± 0.02	0.15 ± 0.02
PSD (<200 nm)	>95%	>90%	>80%
ζ-potential (mV)	41.33 ± 4.10	28.07 ± 5.12	31.17 ± 5.50

[a] PDI: polydispersity index. PSD: particle size distribution. Values are mean ± SD.

However, migration of some free DNA was seen when lipoplexes were prepared at 0.5/1 to 2.5/1(+/−). At a charge ratio of 3:1(+/−) or above, plasmid DNA was completely condensed in all the formulations, as evidenced by no band shift upon agarose gel electrophoresis of lipoplexes (data not shown). Upon lipoplex formation, the particle size, polydispersity index, and ζ-potential of lipoplexes were determined and found to be 124.33 ± 2.08 nm, 0.17 ± 0.02, and 28.07 ± 5.12 mV, respectively. Particle size distribution of lipoplexes (<200 nm) was more than 90% at 0 h and more than 80% after 10 h. There was no significant change in the particle size, particle size distribution, and ζ-potential even at 10 h post-incubation at room temperature, suggesting that these lipoplexes are fairly stable on storage.

Factors Influencing Transfection Efficiency. The effect of various structure and formulation parameters on in vitro transfection efficiency of pyridinium lipids in CHO cells was examined as a function of linker (ester vs amide), hydrophobic carbon chain length (14, 16, and 18) and type (single vs double), configuration of double bond (cis-isomer vs trans-isomer), co-lipid type (DOPE vs Chol), cationic lipid/co-lipid molar ratio (1:1, 2:1 and 4:1), and cationic lipid/DNA (+/−) charge (1:1, 3:1, and 5:1) ratio. Lipofectamine is one of the most commonly used transfection reagents, and thus we selected this as the positive control for screening our pyridinium lipids. Our aim was to optimize our own cationic liposome formulations, not the transfection conditions of Lipofectamine. Therefore, we formulated Lipofectamine/plasmid complexes at 3/1(+/−) charge ratio, which is in the range of the recommended conditions by the manufacturer. Transfection efficiency was reported as relative light units (RLU) per μg of total protein content.

Charge Ratios. Pyridinium lipid (C16:0, amide linker) was mixed with Chol at the cationic lipid/co-lipid molar ratio of 1:1 to prepare cationic liposomes, and lipoplexes were prepared by mixing with luciferase plasmid at the charge ratios of 1:1, 3:1, and 5:1 (+/−). Luciferase gene expression (Figure 2A) and cytotoxicity (Figure 2B) in CHO cells were determined at 48 h post-transfection. Luciferase gene expression levels increased with an increase in lipid/DNA charge ratios from 1:1 to 5:1, while cell viability decreased slightly with an increase in charge ratio to 5:1(+/−). Compared to Lipofectamine, a much higher transfection efficiency was observed at the charge ratios of 3:1 and 5:1(+/−) groups, but there was no significant difference between 3:1 and 5:1. Further, there was no significant difference in cytotoxicity between pyridinium liposomes and Lipofectamine.

Type of Linkers. Pyridinium lipids (C16:0 with ester and amide linkers) were used to prepare liposomes with DOPE and Chol at the cationic lipid/co-lipid molar ratio of 1:1. Following transfection of CHO cells with lipoplexes (3:1, +/−), GFP-positive CHO cells were visualized under fluorescence microscopy at 48 h post-transfection. The cationic lipids with amide linkers significantly increased transfection efficiency in all liposomal formulations in CHO cells compared to their counterparts with ester linker, as evidenced by much higher levels of green fluorescence (Figure 3).

Cationic Lipid/Co-lipid Molar Ratios. Pyridinium lipid with C16:0 fatty acid chain and amide linker was used to formulate liposomes with cholesterol at cationic lipid/co-lipid molar ratios of 1:1, 2:1, and 4:1, and lipoplexes were prepared at the charge ratio of 3:l(+/−). At 48 h post-transfection, luciferase gene expression (Figure 4A) and cytotoxicity (Figure 4B) were measured. Pyridinium liposomes prepared at 1:1 and 2:1 cationic lipid/co-lipid molar ratios showed higher transfection efficiency compared to 4:1 molar ratio and Lipofectamine. Cell viability slightly decreased when the molar ratio of pyridinium lipid to Chol increased but was no different compared to Lipofectamine. So, we decided to select a 1:1 cationic lipid/co-lipid molar ratio to prepare liposomes for further studies.

Type of Co-Lipids. Pyridinium lipids with amide linker but different fatty acid chain (C16:0 and C18:0) were used to prepare liposomes by mixing with DOPE and Chol at the molar ratio of 1:1, and lipoplexes were prepared at the charge ratio of 3:l(+/−). After 48 h post-transfection, luciferase gene expression (Figure 5A) and cytotoxicity (Figure 5B) were measured. Chol as a co-lipid showed higher transfection efficiency in C16:0 amide lipid; on the contrary, DOPE as a co-lipid showed higher transfection efficiency in C18:0 amide lipid. Both of the formulations showed higher transfection efficiency than Lipofectamine/pDNA complexes formulated at 3:1(+/−) charge ratio. No difference in cytotoxicity was seen between pyridinium liposomes and Lipofectamine.

Alkyl Chain Length. Pyridinium lipids with amide linker and different alkyl chain length (C14:0, C16:0, and C18:0) were used to formulate liposomes with cholesterol at cationic lipid/co-lipid molar ratio of 1:1. At 48 h post-transfection of CHO cells with lipoplexes, the luciferase level was determined at 3:1(+/−) charge ratio (Figure 6A). Cytotoxicity data were shown in Figure 6B. Pyridinium lipid with C14:0 and C16:0 showed much higher transfection efficiency compared to C18:0 and also higher than Lipofectamine at 3:1(+/−) ratio. There was no difference in cytotoxicity compared to Lipofectamine for all the formulations except C14:0 lipid with amide linker, which showed the lowest level of cell viability. We also found that an odd number (C15:0) and C18:0 branched carbon chain analogues could not increase the transfection efficiency (data not shown).

Saturation of Alkyl Chain. Pyridinium lipids (C16:0 and C16:1) were used to prepare cationic liposomes using Chol as a co-lipid at the cationic lipid to co-lipid molar ratio of 1:1. At 48 h post-transfection of CHO cells with lipoplexes (3:1, +/−), luciferase gene expression (Figure 7A) and cytotoxicity (Figure 7B) were measured. The trans-isomer showed slightly higher transfection efficiency than saturated lipid and much higher transfection efficiency than its counterpart the cis-isomer. There was no significant difference in cell viability between pyridinium lipids and Lipofectamine.

Configuration of Alkyl Chain. Pyridinium lipids with different alkyl chain length (C16:1, C18:1, and C20:1) and different configuration (cis and trans) of the double bond were used to formulate cationic liposomes with DOPE at the cationic lipid to co-lipid molar ratio of 1:1. At 48 h post-transfection of CHO cells with lipoplexes (3:1, +/−), luciferase gene expression (Figure 8A) and cytotoxicity (Figure 8B) were measured. The liposomes formulated with trans-configuration lipids showed higher transfection efficiency compared to their counterpart lipids with cis-configuration at the same fatty acid chain length. C16:1 trans isomer has a much higher transfection efficiency than C18:1 and C20:1 trans-isomers at the same type of formulations. There was no significant difference in cell viability between all formulations and Lipofectamine.

Influence of Serum on Gene Transfer. Since serum is known to interfere with the transfection of lipoplexes, we transfected

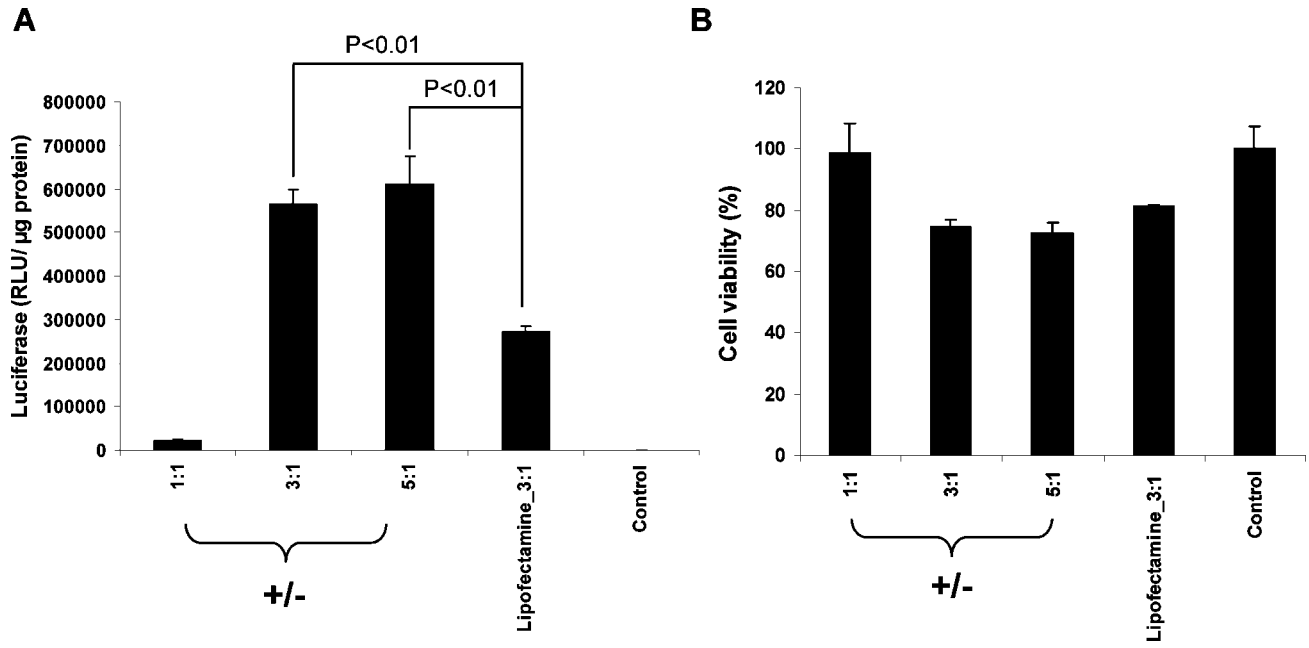

Figure 2. Effect of charge ratios on transfection efficiency (A) and cytotoxicity (B) at 48 h after transfection of lipoplexes. Pyridinium lipid **5** (C16:0, amide linker) was mixed with cholesterol (Chol) at the cationic lipid/co-lipid ratio of 1:1 to prepare cationic liposomes, and lipoplexes were prepared by mixing with luciferase plasmid at the charge ratio of 1:1, 3:1, and 5:1(+/−). Luciferase gene expression and cytotoxicity in CHO cells were determined 48 h post-transfection. The dose of pcDNA3-Luc plasmid was 0.2 μg/well for 4×10^4 cells.

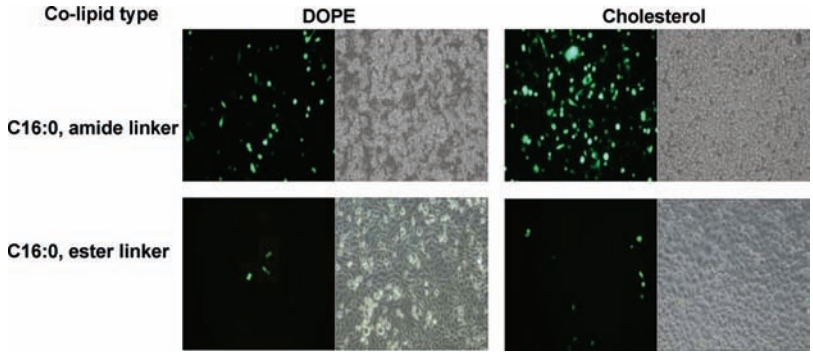

Figure 3. Comparison of gene expression between amide and ester linker. Lipid **5** (C16:0, amide linker) and lipid **16** (C16:0, ester linker) were used to prepare cationic liposomes with co-lipid DOPE and cholesterol at the molar ratio of 1:1. Lipoplexes were formed by mixing with luciferase plasmid at the charge ratio of 3:1(+/−). GFP gene expression was observed 48 h after transfection under fluorescence microscopy and normal light as the control. The dose of pCMS-EGFP plasmid was 0.4 μg/well for 4×10^4 cells.

CHO cells with the lipoplexes prepared using two most potent pyridinium lipid-based liposome formulations {C16:0, amide/cholesterol at 1:1 molar ratio (**5**CH1) and C16:1, amide, trans/DOPE at 1:1 molar ratio (**7**D1)} in the presence of serum (0%, 5%, 10%, 15%, 20%, 30%, and 40%). As shown in Figure 9, the formulation **7**D1 showed significantly higher transfection efficiency compared to the formulation **5**CH1 and Lipofectamine (formulated at 3:1, +/− charge ratio) at each serum concentration. The transfection efficiencies were decreased with an increase in serum concentration. At serum concentrations of 30% and higher, **5**CH1 and Lipofectamine lost their transfection ability when formulated at 3/1(+/−) charge ratio, while **7**D1 still kept high transfection efficiency. The luciferase gene expression in **7**D1 treated cells at the serum concentration of 40% showed similar level compared to those of **5**CH1 and Lipofectamine in the serum-free medium.

Different Cell Lines. Two pyridinium lipid formulations (**5**CH1 and **7**D1) based on cationic /co-lipid molar ratio of 1:1 and complex formation at 3:1 (+/−) charge ratio were tested in two additional cell lines, CRL 1830 and C4−2. At 48 h post-transfection, luciferase gene expression and cytotoxicity in CRL 1830 (Figure 10) and C4−2 (Figure 11) were measured. Both formulations worked very well in these two cell lines as evidence by more than 5−10 times the luciferase level compared to Lipofectamine when formulated at 3:1(+/−) charge ratio. There was no significant difference in cell viability between all formulations and Lipofectamine. These results suggest that the order of magnitude to which pyridinium lipid based formulations exceeds the Lipofectamine 3:1(+/−) formulation is cell-type dependent. Nevertheless, in all cases, much higher transfection efficiency was obtained when transfection was carried out using pyridinium lipid with C16 fatty acid chain and amide linker.

DISCUSSION

The structural and formulation factors, such as lipid/DNA ratio, co-lipid type, and cationic lipid/co-lipid molar ratio, have been shown to influence gene transfer efficiency both in vitro and in vivo (*8*, *26*, *28*). Pyridinium lipids have been shown to display higher transfection efficiency in cells that are not easily transfected by other cationic lipids, such as lipofectin, and transfect a relatively large number of cells (*21*). Therefore, here we report the effect of these parameters on the transfection efficiency of a series of pyridinium lipids.

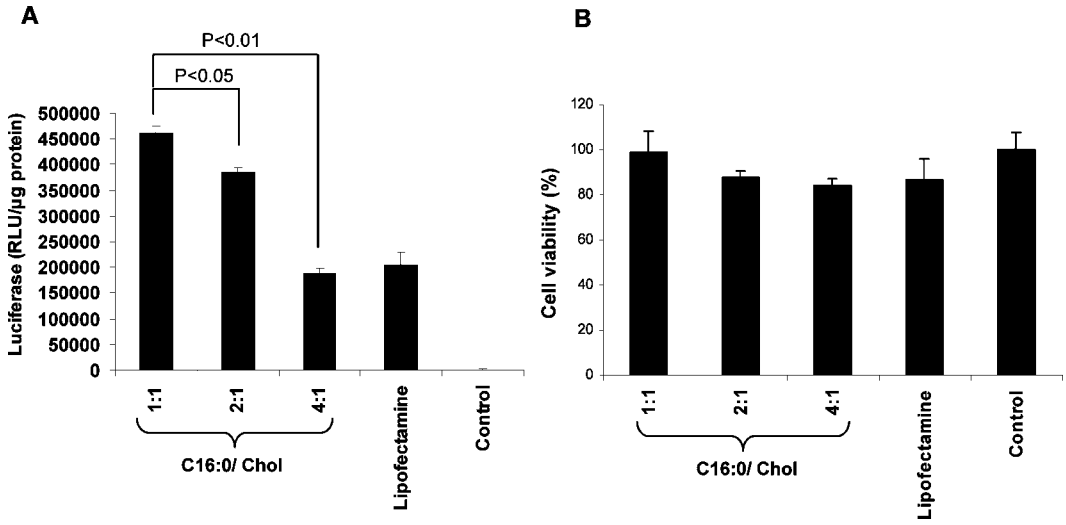

Figure 4. Effect of cationic lipid/co-lipid molar ratios on transfection efficiency (A) and cytotoxicity (B). Lipid **5** (C16:0, amide linker) was used to prepare cationic liposomes with co-lipid cholesterol (Chol) at the molar ratios of 1:1, 2:1, and 4:1. Lipoplexes were formed by mixing with luciferase plasmid at the charge ratio of 3:1(+/−). Luciferase gene expression and cytotoxicity in CHO cells were determined 48 h after transfection. The dose of pcDNA3-Luc plasmid was 0.2 μg/well for 4×10^4 cells.

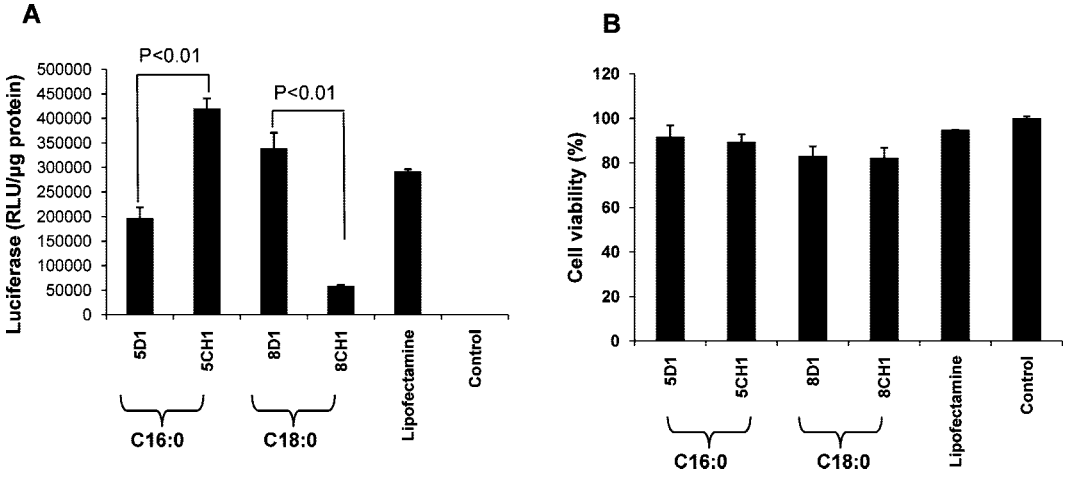

Figure 5. Effect of co-lipid type on transfection efficiency (A) and cytotoxicity (B). Lipids **5** (C16:0, amide linker) and **8** (C18:0, amide linker) were used to prepare cationic liposomes with co-lipid DOPE and cholesterol (Chol) at the molar ratio of 1:1. Lipoplexes were formed by mixing with luciferase plasmid at the charge ratio of 3:1(+/−). Luciferase gene expression and cytotoxicity in CHO cells were determined 48 h after transfection. The dose of pcDNA3-Luc plasmid was 0.2 μg/well for 4×10^4 cells.

The lower phase transition temperature makes the lipid molecule movement (lateral or flip−flop movement) easier within the liposomal bilayer compared to higher phase transition temperature. Generally, the phase transition temperature is influenced by the lipid structure and the liposome composition. In our study, some of the newly synthesized pyridinium lipids have the higher phase transition temperature, especially for the lipids with ester linker, compared to commonly used lipids. The longer the fatty acid chain length, the higher the phase transition temperature is; the higher the degree of saturation, the higher the phase transition temperature is; and the co-lipid will lower the phase transition temperature (Table 2). The high phase transition temperature makes liposome preparation difficult by extrusion even at 65 °C. It needs much higher energy to allow the lipid molecules to move and disperse into aqueous solution to form bilayer structures. Therefore, we chose the probe sonication method to prepare a liposome suspension. Also, the higher phase transition temperature may make phase inversion difficult, further influencing membrane transport of lipids and gene transfer.

In general, transfection efficiency increases with an increase in the charge ratio of lipoplexes until it becomes too toxic to the cells. To determine the structure−activity relationship of pyridinium lipid, we first determined the effect of the cationic lipid/plasmid charge ratio on the transfection efficiency to find the best charge ratio for further evaluations. On the basis of our transfection data, lipoplexes prepared at the charge ratio of 3:1(+/−) showed much higher transfection efficiency compared to 1:1(+/−), but no significant difference compared to 5:1(+/−). There was no significant difference between pyridinium lipids and Lipofectamine in cytotoxicity. Therefore, the charge ratio was fixed to 3:1(+/−) in all the following experiments.

Melting point, phase transition temperature, biodegradability, and transfection efficiency are known to depend on the structure of the linker that binds to the polar headgroup to the hydrophobic lipid chains (*5*). Therefore, we determined the effect of amide and ester linkers on transfection efficiency and cytotoxicity. We used these linkers because they are biodegradable and thus could reduce the cytotoxicity of pyridinium lipids (*25*). As shown in Figure 3, the lipid with an amide linker showed higher transfection efficiency compared to its counterpart with the ester linker regardless of the fatty acid chain length. The high transfection efficiency of amide linker lipids may be caused by their lower phase transition temperature (Table 2) which makes

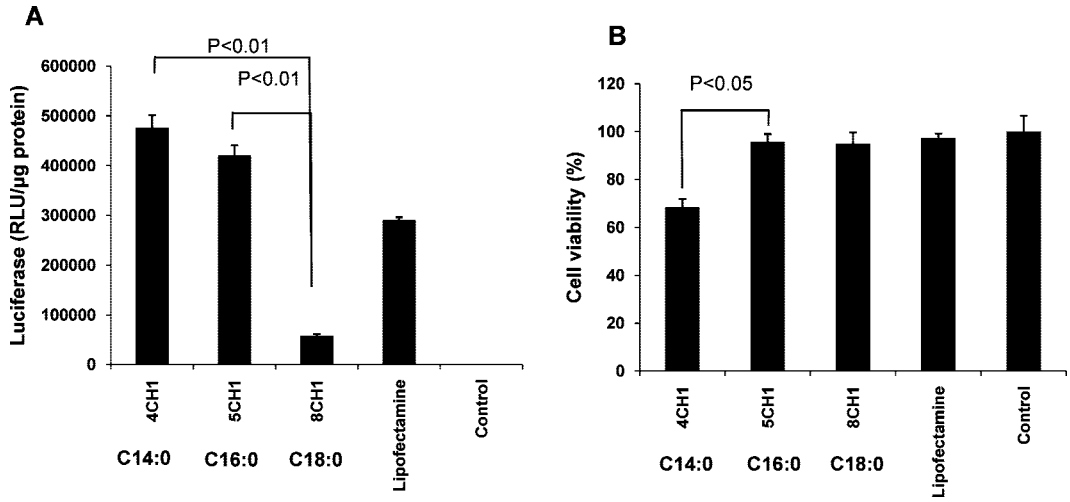

Figure 6. Effect of fatty acid chain length on transfection efficiency (A) and cytotoxicity (B). Lipids **4** (C14:0, amide linker), **5** (C16:0, amide linker), and **8** (C18:0, amide linker) were used to prepare cationic liposomes with co-lipid cholesterol (Chol) at the molar ratio of 1:1. Lipoplexes were formed by mixing with luciferase plasmid at 3:1(+/−) charge ratio. Luciferase gene expression and cytotoxicity in CHO cells were determined 48 h after transfection. The dose of pcDNA3-Luc plasmid was 0.2 μg/well for 4×10^4 cells.

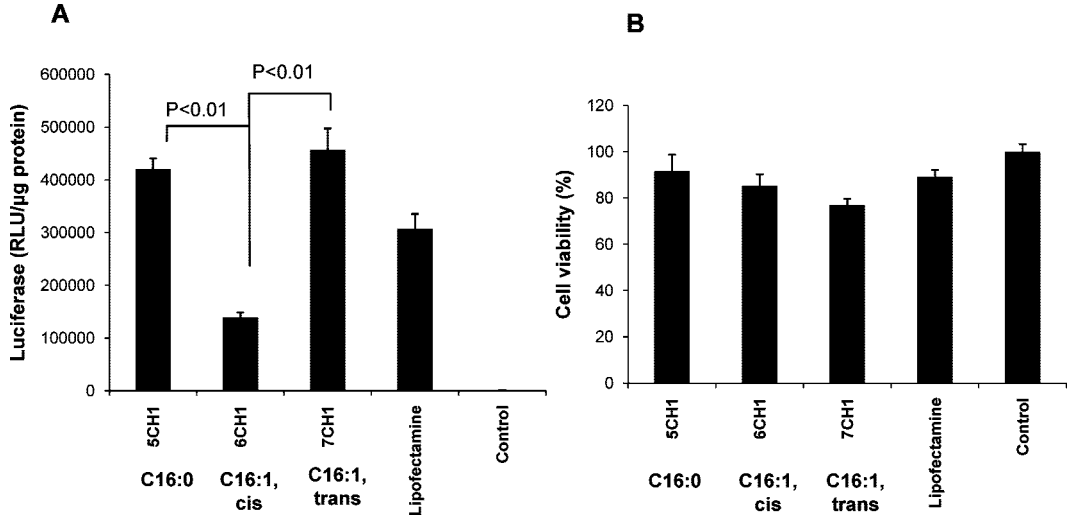

Figure 7. Effect of degree of saturation on transfection efficiency (A) and cytotoxicity (B). Lipids **5** (C16:0, amide linker), **6** (C16:1, amide linker, cis-isomer), and **7** (C16:1, amide linker, trans-isomer) were used to prepare cationic liposomes with co-lipid cholesterol (Chol) at the molar ratio of 1:1. Lipoplexes were formed by mixing with luciferase plasmid at the charge ratio of 3:1(+/−). Luciferase gene expression and cytotoxicity in CHO cells were determined 48 h after transfection. The dose of pcDNA3-Luc plasmid was 0.2 μg/well for 4×10^4 cells.

the liposomal bilayer structure more stable in aqueous solution during the transfection process and storage.

The molar ratio of a cationic lipid to co-lipid is known to affect the phase transition temperature of cationic liposomes and the structure of lipoplexes. Therefore, we prepared cationic liposomes using pyridinium lipid and cholesterol at the molar ratios of 1:1, 2:1, and 4:1, as cholesterol has been reported to be superior to DOPE for pyridinium lipids (*23*). Luciferase gene expression (Figure 4A) and cytotoxicity (Figure 4B) were influenced by the molar ratio of pyridinium lipid to Chol, with the highest transfection efficiency for the liposomes prepared at 1:1 cationic lipid/co-lipid molar ratio. An increase in the amount of Chol slightly decreased the cytotoxicity of pyridinium liposomes. So, we fixed cationic lipid/co-lipid molar ratio to 1:1 in other experiments. These results are in good agreements with the work of Ilies et al. (*23*).

DOPE and Chol are the two most commonly used co-lipids in cationic liposome preparation. The incorporation of fusogenic lipids such as DOPE improves the endosomal release by membrane fusion between the liposomal and endosomal bilayers (*29*, *30*). DOPE has been shown to be a major driving force in promoting transfection efficiency of SAINT-2 cationic lipids, as it gets transformed from its lamellar phase in water to the hexagonal phase when dispersed in a physiological salt solution (*31*). The use of Chol as a co-lipid has been reported to show enhanced in vivo gene expression, as Chol-containing liposomes efficiently interact with the cell membrane in the presence of serum (*32*). On the basis of our data, the use of both DOPE and Chol as co-lipids showed higher transfection efficiency of pyridinium lipids compared to Lipofectamine when lipoplexes were prepared at a 3:1(+/−) charge ratio. The selection of co-lipid was dependent on the type of cationic lipids.

The hydrophobic chain length influences the shape of amphiphiles and supramolecular associations generated through the self-assembling process (*25*). Therefore, we synthesized a series of pyridinium lipids with different lengths of fatty acids to determine the influence of alkyl chain length on gene transfer. Pyridinium lipids with C14:0 and C16:0 fatty acid and amide linker formulated with Chol showed higher transfection efficiency compared to C18:0 lipid with the same linker (Figure 6A). Since C14:0 was more toxic than C16:0 but had similar transfection efficiency, we only synthesized C16:1, C18:1, and

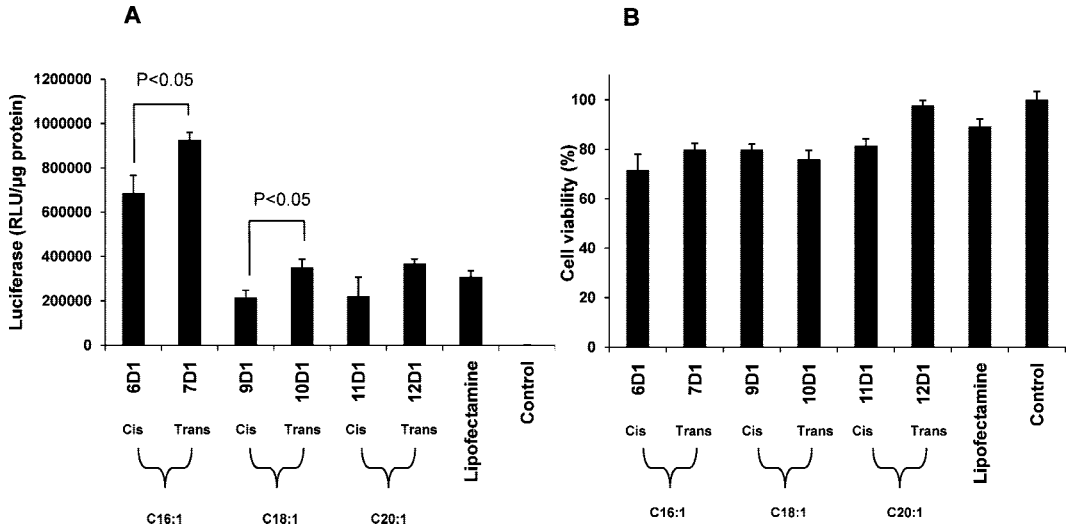

Figure 8. Effect of alkyl chain configuration on transfection efficiency (A) and cytotoxicity (B). Lipids **6** (C16:1, amide linker, cis-isomer), **7** (C16:1, amide linker, trans-isomer), **9** (C18:1, amide linker, cis-isomer), **10** (C18:1, amide linker, trans-isomer), **11** (C20:1, amide linker, cis-isomer), and **12** (C20:1, amide linker, trans-isomer) were used to prepare cationic liposomes with co-lipid DOPE at the molar ratio of 1:1. Lipoplexes were formed by mixing with luciferase plasmid at the charge ratio of 3:1(+/−). Luciferase gene expression and cytotoxicity in CHO cells were determined 48 h after transfection. The dose of pcDNA3-Luc plasmid was 0.2 μg/well for 4×10^4 cells.

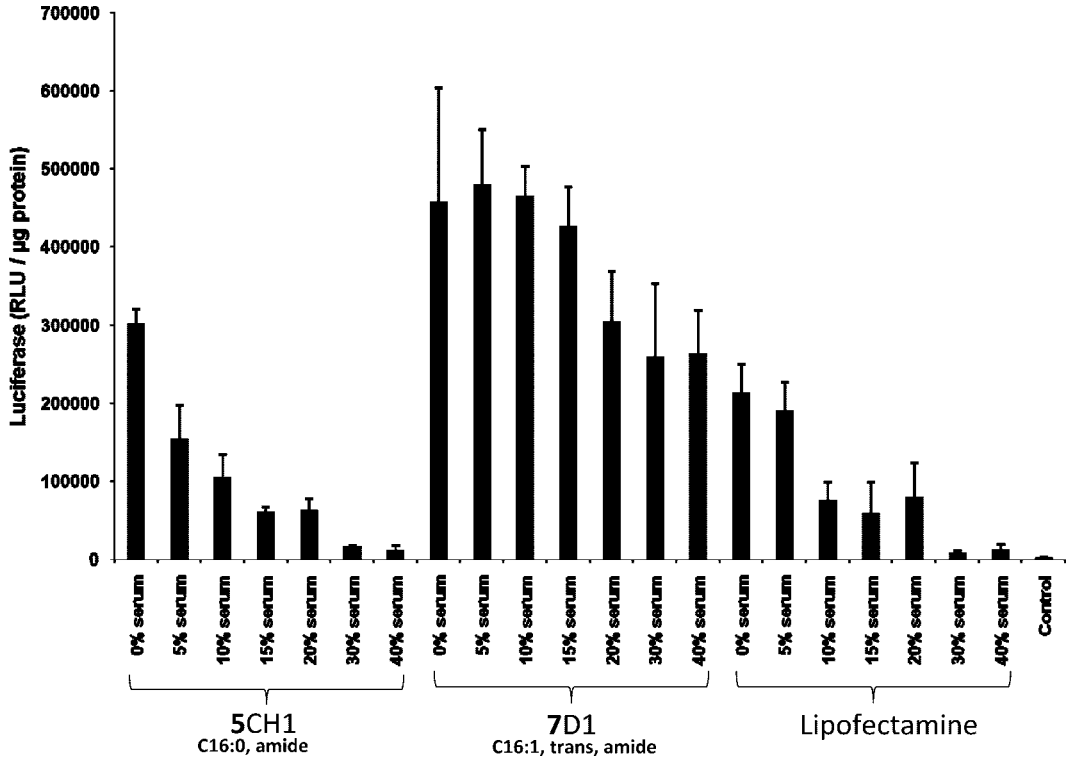

Figure 9. Influence of serum on gene transfer. Lipids **5** (C16:0, amide linker) and **7** (C16:1, amide linker, trans-isomer) were used to prepare cationic liposomes with co-lipid DOPE and cholesterol at the molar ratio of 1:1. Lipoplexes were formed by mixing with luciferase plasmid at the charge ratio of 3:1(+/−). Luciferase gene expression and cytotoxicity in CHO cells were determined 48 h after transfection. The dose of pcDNA3-Luc plasmid was 0.2 μg/well for 4×10^4 cells.

C20:1 for further evaluation. As shown in Figure 8A, C16:1 showed higher transfection efficiency compared to C18:1 and C20:1. Ilies et al. reported similar results (*25*). Van der Woude et al. (*21*) also reported a significant reduction in transfection efficiency and cytotoxicity with the elongation of the alkyl chain length to C18:0 (SAINT-5) relative to that of C16:0 (SAINT-1). Srilakshmi et al. (*33*) demonstrated that the transfection efficiency of cationic lipids was anchor dependent when they studied the cationic lipids containing a hydrophobic anchor chain ranging from C12 to C18. In their study, the lipid containing a 16-carbon chain showed better transfection efficiency among these compounds, while lipids containing less than a 14-carbon anchor chain did not show any transfection, indicating that a minimum of a 14-carbon anchor length is essential for imparting transfection properties to their cationic lipids (*34*). Cationic lipids containing less than a 14-carbon anchor chain do not form stable lipoplexes that are required for efficient cellular uptake of plasmid DNA. Noncondensed plasmid DNA present in the lipoplexes gets degraded by the serum proteins and/or enters into a nonproductive pathway (*34*). On the contrary, the carbon anchor chain will promote strong interaction between DNA and cationic lipid by hydrophobic strength besides electrostatic

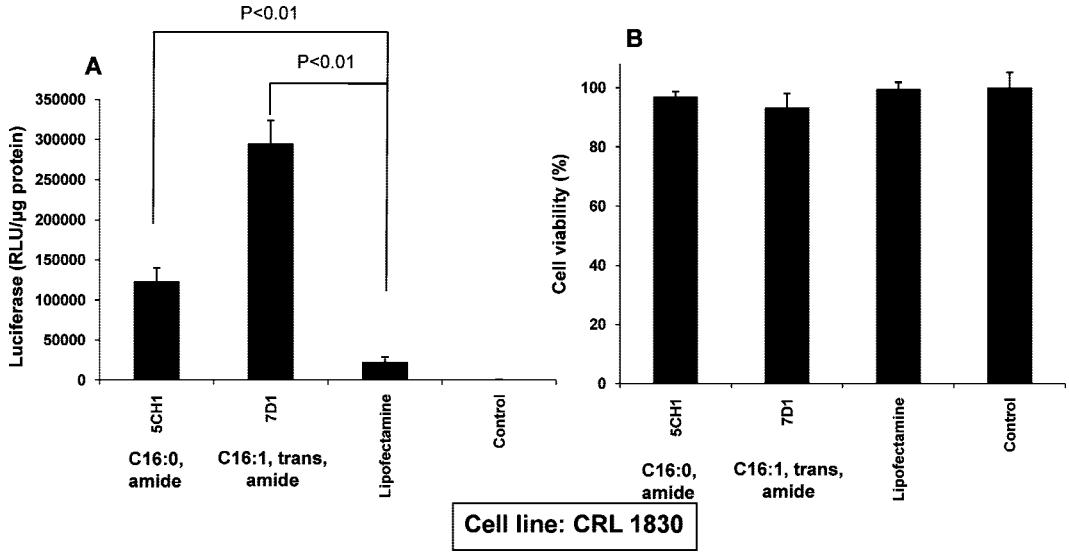

Figure 10. Transfection efficiency (A) and cytotoxicity (B) in hepatocarcinoma cells. Lipids **5** (C16:0, amide linker) and **7** (C16:1, amide linker, trans-isomer) were used to prepare cationic liposomes with co-lipid DOPE and cholesterol at the molar ratio of 1:1. Lipoplexes were formed by mixing with luciferase plasmid at the charge ratio of 3:1(+/−). Luciferase gene expression and cytotoxicity in CHO cells were determined 48 h after transfection. The dose of pcDNA3-Luc plasmid was 0.2 μg/well for 4×10^4 cells.

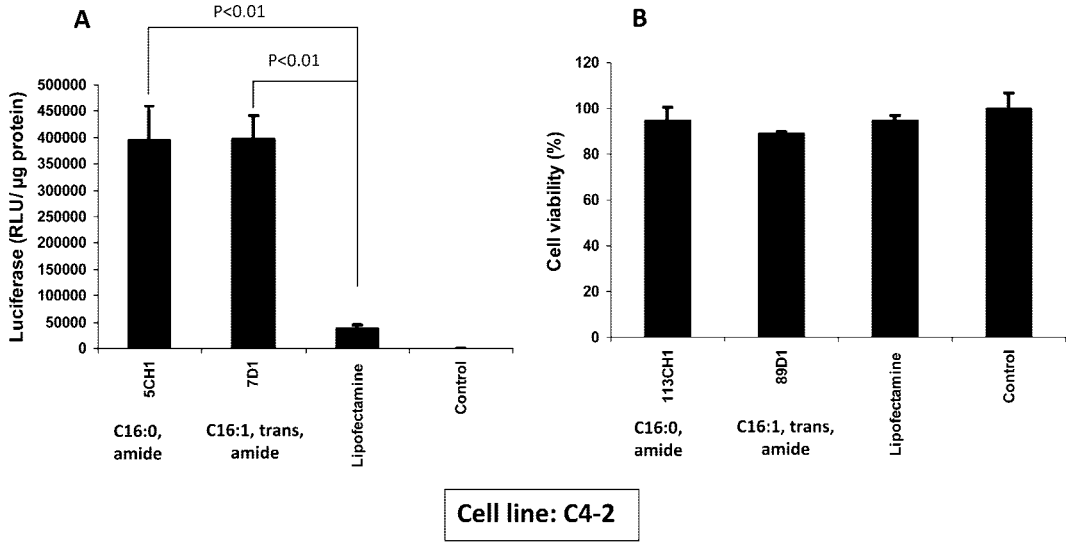

Figure 11. Transfection efficiency (A) and cytotoxicity (B) in prostate cancer cells. Lipids **5** (C16:0, amide linker) and **7** (C16:1, amide linker, trans-isomer) were used to prepare cationic liposomes with co-lipid DOPE and cholesterol at the molar ratio of 1:1. Lipoplexes were formed by mixing with luciferase plasmid at the charge ratio of 3:1(+/−). Luciferase gene expression and cytotoxicity in CHO cells were determined 48 h after transfection. The dose of pcDNA3-Luc plasmid was 0.2 μg/well for 4×10^4 cells.

interaction, which will decrease the release of DNA from cationic liposomes, leading to a further decrease in gene expression (*22*). A balance between the stability of the liposome in the medium and endosomal DNA release into the cytoplasm is important for efficient transfection efficiency (*35*).

The degree of unsaturation and configuration of the hydrophobic anchor chain can affect the transfection efficiency and cytotoxicity (*21*). The degree of unsaturation in the lipid structure affects the fusogenicity of the lipid (L_α/H_{II} transition) (*36,37*). The increase in the chain length of saturated hydrophobic anchors increases the phase transition temperature: 45.5, 63.5, and 73.4 for C14:0, C16:0, and C18:0 of pyridinium lipids with ester linkages; and 38.9, 39.3, and 45.4 for C14:0, C16:0, and C18:0 of pyridinium lipids with amide linkers (Table 2). The increase in phase transition temperature decreases fusogenicity, leading to a decrease in transfection efficiency (*38*). A double bond in the fatty acid carbon chain will also decrease the melting point (Table 1). To investigate the relevance of cis versus trans configuration, we synthesized new lipids with one double bond (cis or trans) in the hydrophobic carbon chain. As is apparent in Figures 7A and 8A, the trans-orientation (C16:1, C18:1, and C20:1) enhances the transfection efficiency compared to cis-oriented alkyl chains of the same length. This trend is in good agreement with the previous report by Van der Woude et al. (*21*). On the basis of our results shown in Figures 5A, 7A, and 8A, we conclude that the trans-isomer worked better than cis and saturated lipids. Since the position and number of double bonds in these unsaturated fatty acid chains may also influence the transfection efficiency of these pyridinium lipids, we plan to synthesize some new compounds to determine the effect of both the position and number of double bonds in the fatty acid chain on transfection efficiency and cytotoxicity.

The stability of the lipoplexes in the presence of serum is important for their in vivo efficacies (*39, 40*). An increase in serum concentration significantly decreased the transfection efficiency (Figure 9). Serum contains nucleases and other enzymes, which

would degrade plasmid DNA, and also contains proteins, such as albumin, which would inhibit the cellular association of the lipoplex (*41*). However, our lipid trans-isomer C16:1 showed excellent performance even at the serum concentration of 30%, and above. Lipofectamine totally lost its tranfection ability when lipoplexes were formulated at a 3:1(+/−) charge ratio. This finding suggests that C16:1 trans-isomer-based liposomes can be used for in vivo gene delivery. Gopal et al. (*22*) also demonstrated good transfection efficiency of glutamide-containing pyridinium lipids in the presence of serum.

A major issue of interest is obviously understanding why pyridinium lipid could improve transfection efficiency. The positively charged pyridinium headgroup plays an important role in improving the transfection efficiency of pyridinium lipids. The antimicrobial activity of alkyl pyridinium salts has been shown to be associated with cell leakage, which is increased with an increase in the number of pyridinium headgroups (*42*). Multiheaded pyridinium amphiphiles have been shown to be more active as compared to their trimethylammonium counterparts (*43*). Woude et al. reported that alkyl pyridinium cationic lipid (SAINT-2) could increase membrane permeability, although this effect is not high enough to ensure lower cytotoxicity compared to DOTMA (*21*). Tucker et al. reported that incubation of cells with alkyl pyridinium sponge toxins could create transient pores on the cell membrane to facilitate cDNA transmembrane movement (*44*). Transient permeabilization of cells with pyridinium cationic lipids was further proven by the evidence of more efficient tissue penetration of pyridinium-based lipoplexes compared to those formed by DOTAP in vivo (*24*). The pores on the cell surface membrane resulted in increased intracellular Ca^{2+}, collapsed membrane potentials, and reduced input resistance (*44*, *45*). DOSPA is a polycation that is the component of Lipofectamine. It has been reported that the polycation could form positively charged loops fixed on DNA molecules. These loops interact with negatively charged lipids on plasma membranes, which probably induces effective nonspecific endocytosis and subsequent cell transformation (*46*). Pore-forming ability combined with ionic interaction, membrane association, and endocytosis may explain why some of our newly synthesized pyridinium cationic lipids showed relatively higher transfection efficiency compared to Lipofectamine.

In conclusion, we have demonstrated that a number of structural and formulation parameters including hydrophobic carbon chain lengths, double bond configuration in the unsaturated aliphatic hydrocarbon tails, lipid/co-lipid ratios, lipid/DNA charge ratios, and cell types play important roles in gene transfer and cytotoxicity of these pyridinium lipids. Important findings include (a) higher transfection efficiencies of pyridinium lipids with the amide linkers compared to their ester counterparts; (b) higher transfection efficiency at 1:1 molar ratio of pyridinium lipid and co-lipid compared to 2:1 and 4:1; (c) efficient transfection with C16 chain length pyridinium lipids; (d) better transfection efficiencies in the presence and absence of serum, compared to that of Lipofectamine, a widely used commercially available liposomal transfection kit; (e) higher transfection efficiencies of pyridinium lipids with the trans orientation in the hydrophobic anchor chain compared to those with cis orientation; and (f) increased efficiency of C16:1 trans-isomer pyridinium lipids in transfection in the presence of a high concentration of serum compared with Lipofectamine when lipoplexes were prepared at a 3:1(+/−) charge ratio.

ACKNOWLEDGMENT

This work is partly supported by the teaching assistantship from the University of Tennessee School of Pharmacy to Lin Zhu, Van Vleet Endowed Chair to Duane Miller, and by R01 DK0699968 and R01 EB003922 from the National Institutes of Health to Ram Mahato.

LITERATURE CITED

(1) Mahato, R. I., Rolland, A., and Tomlinson, E. (1997) Cationic lipid-based gene delivery systems: pharmaceutical perspectives. *Pharm. Res. 14*, 853–9.

(2) Mahato, R. I. (2005) Water insoluble and soluble lipids for gene delivery. *Adv. Drug Delivery Rev. 57*, 699–712.

(3) Narang, A. S., Thoma, L., Miller, D. D., and Mahato, R. I. (2005) Cationic lipids with increased DNA binding affinity for nonviral gene transfer in dividing and nondividing cells. *Bioconjugate Chem. 16*, 156–68.

(4) Miller, C. R., Bondurant, B., McLean, S. D., McGovern, K. A., and O'Brien, D. F. (1998) Liposome-cell interactions in vitro: effect of liposome surface charge on the binding and endocytosis of conventional and sterically stabilized liposomes. *Biochemistry 37*, 12875–83.

(5) Mahato, R. I., Smith, L. C., and Rolland, A. (1999) Pharmaceutical perspectives of nonviral gene therapy. *Adv. Genet. 41*, 95–156.

(6) Tu, Y., and Kim, J. S. (2008) A fusogenic segment of glycoprotein H from herpes simplex virus enhances transfection efficiency of cationic liposomes. *J. Gene Med. 10*, 646–54.

(7) Felgner, P. L., Gadek, T. R., Holm, M., Roman, R., Chan, H. W., Wenz, M., Northrop, J. P., Ringold, G. M., and Danielsen, M. (1987) Lipofection: a highly efficient, lipid-mediated DNA-transfection procedure. *Proc. Natl. Acad. Sci. U.S.A. 84*, 7413–7.

(8) Felgner, J. H., Kumar, R., Sridhar, C. N., Wheeler, C. J., Tsai, Y. J., Border, R., Ramsey, P., Martin, M., and Felgner, P. L. (1994) Enhanced gene delivery and mechanism studies with a novel series of cationic lipid formulations. *J. Biol. Chem. 269*, 2550–61.

(9) Gao, X., and Huang, L. (1991) A novel cationic liposome reagent for efficient transfection of mammalian cells. *Biochem. Biophys. Res. Commun. 179*, 280–285.

(10) Behr, J. P., Demeneix, B., Loeffler, J. P., and Perez-Mutul, J. (1989) Efficient gene transfer into mammalian primary endocrine cells with lipopolyamine-coated DNA. *Proc. Natl. Acad. Sci. U.S.A. 86*, 6982–6.

(11) Farhood, H., Bottega, R., Epand, R. M., and Huang, L. (1992) Effect of cationic cholesterol derivatives on gene transfer and protein kinase C activity. *Biochim. Biophys. Acta 1111*, 239–46.

(12) Rose, J. K., Buonocore, L., and Whitt, M. A. (1991) A new cationic liposome reagent mediating nearly quantitative transfection of animal cells. *Biotechniques 10*, 520–5.

(13) Parker, S. E., Khatibi, S., Margalith, M., Anderson, D., Yankauckas, M., Gromkowski, S. H., Latimer, T., Lew, D., Marquet, M., Manthorpe, M., Hobart, P., Hersh, E., Stopeck, A. T., and Norman, J. (1996) Plasmid DNA gene therapy: studies with the human interleukin-2 gene in tumor cells in vitro and in the murine B16 melanoma model in vivo. *Cancer Gene Ther. 3*, 175–85.

(14) Porteous, D. J., Dorin, J. R., McLachlan, G., Davidson-Smith, H., Davidson, H., Stevenson, B. J., Carothers, A. D., Wallace, W. A., Moralee, S., Hoenes, C., Kallmeyer, G., Michaelis, U., Naujoks, K., Ho, L. P., Samways, J. M., Imrie, M., Greening, A. P., and Innes, J. A. (1997) Evidence for safety and efficacy of DOTAP cationic liposome mediated CFTR gene transfer to the nasal epithelium of patients with cystic fibrosis. *Gene Ther. 4*, 210–8.

(15) Leventis, R., and Silvius, J. R. (1990) Interactions of mammalian cells with lipid dispersions containing novel metabolizable cationic amphiphiles. *Biochim. Biophys. Acta 1023*, 124–32.

(16) San, H., Yang, Z. Y., Pompili, V. J., Jaffe, M. L., Plautz, G. E., Xu, L., Felgner, J. H., Wheeler, C. J., Felgner, P. L., Gao, X., et al. (1993) Safety and short-term toxicity of a novel cationic

lipid formulation for human gene therapy. *Hum. Gene Ther. 4*, 781–8.
(17) Scheule, R. K., St George, J. A., Bagley, R. G., Marshall, J., Kaplan, J. M., Akita, G. Y., Wang, K. X., Lee, E. R., Harris, D. J., Jiang, C., Yew, N. S., Smith, A. E., and Cheng, S. H. (1997) Basis of pulmonary toxicity associated with cationic lipid-mediated gene transfer to the mammalian lung. *Hum. Gene Ther. 8*, 689–707.
(18) Gao, H., and Hui, K. M. (2001) Synthesis of a novel series of cationic lipids that can act as efficient gene delivery vehicles through systematic heterocyclic substitution of cholesterol derivatives. *Gene Ther. 8*, 855–63.
(19) Blubaugh, L. V., BoTTs, C. W., and Gerwe, E. G. (1940) A study of the germicidal properties of cetyl pyridinium chloride. *J. Bacteriol. 39*, 51.
(20) Green, T. W., and Birkeland, J. M. (1941) The germicidal action of cetyl pyridinium chloride on bacterial spores. *J. Bacteriol. 41*, 34.
(21) van der Woude, I., Wagenaar, A., Meekel, A. A., ter Beest, M. B., Ruiters, M. H., Engberts, J. B., and Hoekstra, D. (1997) Novel pyridinium surfactants for efficient, nontoxic in vitro gene delivery. *Proc. Natl. Acad. Sci. U.S.A. 94*, 1160–5.
(22) Gopal, V., Prasad, T. K., Rao, N. M., Takafuji, M., Rahman, M. M., and Ihara, H. (2006) Synthesis and in vitro evaluation of glutamide-containing cationic lipids for gene delivery. *Bioconjugate Chem. 17*, 1530–6.
(23) Ilies, M. A., Seitz, W. A., Ghiviriga, I., Johnson, B. H., Miller, A., Thompson, E. B., and Balaban, A. T. (2004) Pyridinium cationic lipids in gene delivery: a structure-activity correlation study. *J. Med. Chem. 47*, 3744–54.
(24) Ilies, M. A., Johnson, B. H., Makori, F., Miller, A., Seitz, W. A., Thompson, E. B., and Balaban, A. T. (2005) Pyridinium cationic lipids in gene delivery: an in vitro and in vivo comparison of transfection efficiency versus a tetraalkylammonium congener. *Arch. Biochem. Biophys. 435*, 217–26.
(25) Ilies, M. A., Seitz, W. A., Johnson, B. H., Ezell, E. L., Miller, A. L., Thompson, E. B., and Balaban, A. T. (2006) Lipophilic pyrylium salts in the synthesis of efficient pyridinium-based cationic lipids, gemini surfactants, and lipophilic oligomers for gene delivery. *J. Med. Chem. 49*, 3872–87.
(26) Mahato, R. I., Anwer, K., Tagliaferri, F., Meaney, C., Leonard, P., Wadhwa, M. S., Logan, M., French, M., and Rolland, A. (1998) Biodistribution and gene expression of lipid/plasmid complexes after systemic administration. *Hum. Gene Ther. 9*, 2083–99.
(27) Mahato, R. I., Kawabata, K., Nomura, T., Takakura, Y., and Hashida, M. (1995) Physicochemical and pharmacokinetic characteristics of plasmid DNA/cationic liposome complexes. *J. Pharm. Sci. 84*, 1267–71.
(28) Lee, E. R., Marshall, J., Siegel, C. S., Jiang, C., Yew, N. S., Nichols, M. R., Nietupski, J. B., Ziegler, R. J., Lane, M. B., Wang, K. X., Wan, N. C., Scheule, R. K., Harris, D. J., Smith, A. E., and Cheng, S. H. (1996) Detailed analysis of structures and formulations of cationic lipids for efficient gene transfer to the lung. *Hum. Gene Ther. 7*, 1701–17.
(29) Litzinger, D. C., and Huang, L. (1992) Phosphatidylethanolamine liposomes: drug delivery, gene transfer and immunodiagnostic applications. *Biochim. Biophys. Acta 1113*, 201–27.
(30) Farhood, H., Serbina, N., and Huang, L. (1995) The role of dioleoyl phosphatidylethanolamine in cationic liposome mediated gene transfer. *Biochim. Biophys. Acta 1235*, 289–95.
(31) Smisterova, J., Wagenaar, A., Stuart, M. C., Polushkin, E., ten Brinke, G., Hulst, R., Engberts, J. B., and Hoekstra, D. (2001) Molecular shape of the cationic lipid controls the structure of cationic lipid/dioleylphosphatidylethanolamine-DNA complexes and the efficiency of gene delivery. *J. Biol. Chem. 276*, 47615–22.
(32) Crook, K., Stevenson, B. J., Dubouchet, M., and Porteous, D. J. (1998) Inclusion of cholesterol in DOTAP transfection complexes increases the delivery of DNA to cells in vitro in the presence of serum. *Gene Ther. 5*, 137–43.
(33) Srilakshmia GV, S. J., Chaudhuria, A., Ramadasb, Y., and Rao, N. M. (2002) Anchor-dependent lipofection with non-glycerol based cytofectins containing single 2-hydroxyethyl head groups. *Biochim. Biophys. Acta - Biomembranes 1559*, 87–95.
(34) Venkata Srilakshmi, G., Sen, J., Chaudhuri, A., Ramadas, Y., and Madhusudhana Rao, N. (2002) Anchor-dependent lipofection with non-glycerol based cytofectins containing single 2-hydroxyethyl head groups. *Biochim. Biophys. Acta 1559*, 87–95.
(35) Takafuji, M., Ishiodori, A., Yamada, T., Sakurai, T., and Ihara, H. (2004) Stabilization of enhanced chirality from pyrene-containing l-glutamide lipid in methyl methacrylate by photo-induced polymerization. *Chem. Commun. (Cambridge, U.K.)* 1122–3.
(36) Sankaram, M. B., Powell, G. L., and Marsh, D. (1989) Effect of acyl chain composition on salt-induced lamellar to inverted hexagonal phase transitions in cardiolipin. *Biochim. Biophys. Acta 980*, 389–92.
(37) Szule, J. A., Fuller, N. L., and Rand, R. P. (2002) The effects of acyl chain length and saturation of diacylglycerols and phosphatidylcholines on membrane monolayer curvature. *Biophys. J. 83*, 977–84.
(38) Heyes, J., Palmer, L., Bremner, K., and MacLachlan, I. (2005) Cationic lipid saturation influences intracellular delivery of encapsulated nucleic acids. *J. Controlled Release 107*, 276–87.
(39) Simberg, D., Weiss, A., and Barenholz, Y. (2005) Reversible mode of binding of serum proteins to DOTAP/cholesterol Lipoplexes: a possible explanation for intravenous lipofection efficiency. *Hum. Gene Ther. 16*, 1087–96.
(40) Singh, R. S., Mukherjee, K., Banerjee, R., Chaudhuri, A., Hait, S. K., Moulik, S. P., Ramadas, Y., Vijayalakshmi, A., and Rao, N. M. (2002) Anchor dependency for non-glycerol based cationic lipofectins: mixed bag of regular and anomalous transfection profiles. *Chemistry 8*, 900–9.
(41) Smyth Templeton, N. (2003) Cationic liposomes as in vivo delivery vehicles. *Curr. Med. Chem. 10*, 1279–87.
(42) Madaan, P., and Tyagi, V. K. (2008) Quaternary pyridinium salts: a review. *J. Oleo Sci. 57*, 197–215.
(43) Haldar, J., Kondaiah, P., and Bhattacharya, S. (2005) Synthesis and antibacterial properties of novel hydrolyzable cationic amphiphiles. Incorporation of multiple head groups leads to impressive antibacterial activity. *J. Med. Chem. 48*, 3823–31.
(44) Tucker, S. J., McClelland, D., Jaspars, M., Sepcic, K., MacEwan, D. J., and Scott, R. H. (2003) The influence of alkyl pyridinium sponge toxins on membrane properties, cytotoxicity, transfection and protein expression in mammalian cells. *Biochim. Biophys. Acta 1614*, 171–81.
(45) Scott, R. H., Whyment, A. D., Foster, A., Gordon, K. H., Milne, B. F., and Jaspars, M. (2000) Analysis of the structure and electrophysiological actions of halitoxins: 1,3 alkyl-pyridinium salts from *Callyspongia ridleyi*. *J. Membr. Biol. 176*, 119–31.
(46) Kabanov, A. V., Astafieva, I. V., Maksimova, I. V., Lukanidin, E. M., Georgiev, G. P., and Kabanov, V. A. (1993) Efficient transformation of mammalian cells using DNA interpolyelectrolyte complexes with carbon chain polycations. *Bioconjugate Chem. 4*, 448–54.

BC8004039

Photoinduced Cross-Linking of Star Vector for Improvement of Gene Transfer Efficiency

Yasushi Nemoto,[†,‡,§] Yue-Min Zhou,[†,||] Eisuke Tatsumi,[||] and Yasuhide Nakayama*[,†,§]

Department of Bioengineering and Department of Artificial Organs, Advanced Medical Engineering Center, National Cardiovascular Center Research Institute, 5-7-1 Fujishiro-dai, Suita, Osaka, Japan, Development Department, Chemical Products Division, Bridgestone Corporation, 1 Kashiocho, Totsuka-ku, Yokohama, Kanagawa, Japan, and Division of Molecular Chemistry, Graduate School of Engineering, Hokkaido University, N13−W8, Kita-ku, Sapporo, Hokkaido, Japan. Received January 5, 2008; Revised Manuscript Received October 2, 2008

This study aimed to investigate the effect of cross-linking of a cationic nonviral gene carrier on gene expression. As a precursor for photo-cross-linking, a star-shaped, six-branched cationic polymer of poly(*N*,*N*-dimethylaminopropylacrylamide) (six-branched star vector, SV), which was previously designed as a gene carrier, was synthesized by iniferter-based living radical polymerization. Upon UV irradiation, the number-average molecular weight (M_n) of the SV increased from ca. 28 kDa to ca. 32 kDa (irradiation time, 180 min) and ca. 46 kDa (240 min) with broadness of the polydispersity due to the coupling reaction between the polymer radicals generated at the terminal ends of each branch of the SVs, resulting in the preparation of cross-linked SVs (CSVs) without the use of any chemical cross-linking agents. Irrespective of cross-linking, all the SVs were able to interact with and condense luciferase-encoding plasmid DNA to yield relatively stable polymer/DNA complexes (polyplexes) of approximate diameter 150 nm with ζ-potential of ca. 20 mV. However, a transfection study using several types of cell lines, HeLa, Hep G2, 293, and COS-1, showed that by cross-linking of SVs the luciferase activity increased drastically. The activity with CSV (M_n = ca. 46 kDa) was increased by at least 1 order of magnitude in the original SV (M_n = ca. 28 kDa), which was several-fold that in the SV with the same molecular weight in all cells. In all SVs, no significant cellular cytotoxicity was observed even at a high charge ratio of 45. The SV-based gene transfection was significantly enhanced by the cross-linking of the SVs.

INTRODUCTION

Several successful clinical trials reported thus far have involved viral vector systems (such as retroviruses and adenoviruses) that provide efficient transduction and high levels of gene expression (*1*−*3*). However, their severe immunogenicity and toxicity remain major obstacles in viral vector-mediated gene therapy. For these reasons, nonviral vectors have been introduced as an alternative to such hazardous viral vectors, and they are being studied for their potential in providing safer and more desirable methods of gene delivery and clinical gene therapy (*4*−*8*).

Studies have been conducted in many laboratories to improve the gene delivery efficiency of polymeric gene carriers and to reduce their cytotoxicity. In these studies, nanoarchitectural, macromolecular design of the polymeric carriers by hyperbranching or cross-linking has been attempted as one of the major strategies (*9*−*17*). Starburst polyamideamine dendrimers—a relatively new class of highly branched spherical polymers that are strongly soluble in aqueous solution and have a unique surface of primary amino groups—have been established as one of the core structural components of synthetic gene carriers (*9*−*12*). Further, chemical cross-linking techniques have been used by combining preexisting carriers in order to improve gene delivery efficiency or reduce cytotoxicity. (*14*−*16*) For example, an ester or disulfide bond, which can be cleaved with common reducing agents after conjugation, has been utilized for carrier biodegradation. It has recently been established that branched high-molecular-weight polyethyleneimine (PEI) (>25 kDa) is an effective transfection agent, and recent reports indicate that low-molecular-weight PEI (~10 kDa) has relatively lower toxicity (*18*, *19*). Therefore, low-molecular-weight PEI was cross-linked by biodegradable bonding to obtain high gene delivery efficiency and low toxicity (*15*, *16*).

A branching structure was also introduced to improve the functionality of the carriers (*14*). When naturally occurring polymers or synthetic peptides were attached on the side chains of PEI, a high transfection efficiency was obtained (*20*−*22*). However, in case PEI components were used unmodified, the transfection efficiency of the branched form was generally lower than that of the linear form (*23*). On the other hand, we attempted to investigate the usefulness of a series of star-shaped cationic polymers as a base chemical structure for a novel high-performance gene carrier (*24*−*28*). These polymers, known as star vectors (SVs), were prepared by initiator-transfer agent-terminator (iniferter)-based living radical polymerization (*29*, *30*) of *N*,*N*-dimethylaminopropylacrylamide (DMAPAAm) by using their respective multidithiocarbamate (DC)-derivatized benzenes (multifunctional iniferters). The gene expression efficiency in COS-1 cells improved significantly with an increase in the number of branches and the molecular weight of the SVs (*24*). It was recently shown that attaching each cationic branch in SV with nonionic block chains (*25*) or peptides (*26*) as ligands resulted in a considerable improvement in the gene transfection

* To whom correspondence should be addressed: Department of Bioengineering, Advanced Medical Engineering Center, National Cardiovascular Center Research Institute, 5-7-1 Fujishiro-dai, Suita, Osaka 565-8565, Japan. Telephone: (+81) 6-6833-5012 (ex.2624). Fax: (+81) 6-6872-8090. E-mail: nakayama@ri.ncvc.go.jp.

[†] Department of Bioengineering, National Cardiovascular Center Research Institute.

[‡] Bridgestone Corporation.

[§] Hokkaido University.

[||] Department of Artificial Organs, National Cardiovascular Center Research Institute.

10.1021/bc800003t CCC: $40.75 © 2008 American Chemical Society
Published on Web 11/13/2008

efficiency and the targeting of the vector to specific cells such as resting macrophages. Other star-shaped polymers were synthesized by conjugating multiple oligoethyleneimine arms onto an α-cylodextrin core, based on a similar concept used in our molecular design (*31*). These star-shaped polymers, including SVs, are promising new nonviral gene delivery vectors with low cytotoxicity and high gene transfection efficiency that can have gene therapy applications in the future.

The number of branches in SVs enhances the gene expression efficiency as described above (*24*). Therefore, additional complex branching by cross-linking of SVs is expected to further improve gene transfection efficiency. To this end, we synthesized cross-linked SVs (CSVs) by using molecular design wherein we exploited the photoreactive property of DC groups, which theoretically exist at the terminal ends of each branch in SVs after preparation. Further, the effects of the molecular structure and mass of SVs before and after cross-linking on their transfection properties and cytotoxicity were evaluated.

EXPERIMENTAL PROCEDURES

Materials. Chloroform of a special grade was treated with N_2 gas bubbling before use. N_2 gas of G1 grade (Japan Fine Products Co., Kanagawa, Japan) and 99.9999% purity or more was used. Diethyl ether of a special grade was used for polychlorobiphenyl (PCB) analysis; it was stabilized with ethanol and not butylhydroxytoluene (BHT). DMAPAAm purchased from Tokyo Kasei Co. (Tokyo, Japan) was used after distillation (bp 105−110 °C/0.3 mmHg). Other solvents and chemical reagents, all of which were of a special reagent grade, were purchased from Kanto Chemical Co. (Tokyo, Japan) or Aldrich (Milwaukee, WI) and were used without any purification. Purified and DNase-free pyrogen water with a conductance of 18 MΩ or more was prepared using Puric MX-II (Organo Inc., Tokyo, Japan). The 5266-bp pGL3 control vector (Promega Inc., Tokyo, Japan) encoding luciferase was used as luciferase reporter plasmide DNA; it was amplified in competent *Escherichia coli* (Promega Inc.) cells and purified using Maxiprep according to a protocol of QIAGEN (Tokyo, Japan). The purity of the amplified pDNA was assessed by electrophoresis on a 1% agarose gel, and the concentration was determined by UV absorbance at 260 and 280 nm.

Synthesis of 1,2,3,4,5,6-Hexakis(*N,N*-diethyldithiocarbamylmethyl)benzene (Iniferter) (*24, 25*). An ethanol solution (100 mL) of 1,2,3,4,5,6-hexakis(bromomethyl)benzene (1.0 g, 1.6 mmol) and sodium *N,N*-diethyldithiocarbamate trihydrate (6.4 g, 28.2 mmol) was stirred for 96 h at room temperature. The resulting precipitate was filtered, washed three times with approximately 1 L of methanol, and recrystallized using a chloroform/methanol solution. The yield of 1,2,3,4,5,6-hexakis(*N,N*-diethyldithiocarbamylmethyl)benzene was 1.5 g (yield, 90%). ^{1}H NMR (in chloroform-d_1): δ 1.26−1.31 (m, 36H, -CH_2−CH_3), 3.71−3.73 (q, 12H, -N-CH_2-), 3.99−4.01 (q, 12H, -N-CH_2-), 4.57 (s, 12H, Ar-CH_2).

Synthesis of Six-Branched Cationic Polymer (Six-Branched Star Vector, SV) (*24, 25*). 1,2,3,4,5,6-Hexakis(*N,N*-diethyldithiocarbamylmethyl)benzene (45.6 mg, 63 mmol) was dissolved in approximately 20 mL of chloroform. DMAPAAm (7.88 g, 50.5 mmol) was added to the solution. The total volume of the solution with chloroform increased to 50 mL. The concentrations of the iniferter and monomer were 5.0 mM and 1.0 M, respectively. The mixture was poured into a hard-glass cubic cell (4 mm × 40 mm; glass thickness, 3 mm), following which N_2 gas was bubbled into the glass cell at a flow rate of 2 L/min for 10 min to remove the O_2 gas from the solution. The solution was irradiated for 30 min with UV light (light intensity: 2.5 mW/cm^2). The reaction mixture was concentrated to approximately 10 mL by using a rotary evaporator and poured into 1.0 L of diethyl ether to obtain a polymeric precipitate. The diethyl ether solution supernatant was removed by decantation. Reprecipitation was carried out 3 times in a chloroform/diethyl ether system. The final precipitate was dried under vacuum and dissolved in an adequate quantity of H_2O. The resultant aqueous solution was filtered with a disposable syringe filter unit having a pore size of 0.22 um (Mixed Cellulose Ester, Toyo Roshi Ltd., Tokyo, Japan) and freeze−dried for 72 h using a vacuum pump (GCD136X, ULVAC, Tokyo) and freeze−dryer (FUD 2200, EYELA, Tokyo) to yield six-branched poly(D-MAPAAm) powder. The molecular weight was determined by gel permeation chromatography (GPC) analysis: M_n = 28 kDa. ^{1}H NMR (in chloroform-d_1): δ 1.5−1.7 (br, 3H, -C$\underline{H}_2$-CH- and -CH_2-C$\underline{H}_2$-CH_2-), 1.8−2.0 (br, 1H, -C$\underline{H}$-CO), 2.1−2.2 (br, 6H, -N-C$\underline{H}_3$), 2.2−2.4 (br, 2H, -C$\underline{H}_2$-N(CH_3)$_2$), 3.0−3.2 (br, 2H, -NH-C$\underline{H}_2$-), 7.4−7.8 (br, 1H, -NH). In addition, another branched polymer with M_n of 46 kDa was synthesized using a similar procedure by prolonging the irradiation time to 50 min.

Preparation of Cross-linked Star Vector (CSV). Freeze−dried powder of SV (M_n = 28 kDa) was homogenized in a 100-mL hard-glass tube of thickness 2 mm by vigorous stirring on a magnetic stirrer in a closed system. The O_2 gas in the gas phase of the closed system was replaced with N_2 gas. The mist-like SV powder was exposed to UV light for 180 min by using a 300 W Xenon lamp (MAX-301, Asahi Spectra, Tokyo, Japan) under vigorous stirring. The UV light intensity was adjusted to 1.0 mW/cm^2. After light irradiation, the resulting photoirradiated powder was poured into 50 mL of methanol and centrifuged at 10 000 rpm for 5 min at room temperature to remove the insoluble gel-like precipitate that was produced during irradiation. The obtained supernatant was concentrated to approximately 5 mL by using a rotary evaporator and poured into 500 mL of diethyl ether to recover the polymeric precipitate. The diethyl ether solution was removed by decantation. Reprecipitation was carried out 3 times in a chloroform/diethyl ether system. The final polymeric precipitate was dissolved in H_20, filtered with the syringe filter, and freeze−dried to obtain CSV powder. The molecular weight was determined by GPC analysis: M_n = 32 kDa. In addition, another CSV with M_n of 46 kDa was synthesized using a similar procedure by prolonging the irradiation time to 240 min.

General Procedure. The light intensity from a Xenon lam (MAX-301), measured using a photometer (UIT-150 with UVD-405 detector, USHIO, Tokyo), was adjusted to 2.5 mW/cm^2. UV/vis absorption spectra were recorded using a spectrophotometer (UV-1700, Shimadzu, Kyoto). ^{1}H NMR spectra were recorded in chloroform-d_1 with a 300 MHz NMR spectrometer (Varian Gemini-300) using tetramethylsilane (0 ppm) as the internal standard at room temperature. GPC analysis in *N,N*-dimethylformamide with 30 mM lithium bromide was carried out with a high-performance liquid chromatograph system (LC-10Avp, Shimadzu, Kyoto, Japan) and columns (Asahipack GF-710HQ and Asahipack GF-510HQ, Shodex, Tokyo, Japan) that were calibrated for molecular weight with narrow weight distribution poly(ethylene glycol) (PEG) standards.

Preparation of Polyplexes. SVs with or without cross-linking were dissolved in a saline solution at a concentration of 0.79 μg/μL. In a quartz cell (charge ratio 30), 60 μL aliquots of the saline solution were mixed with 90 μL of Tris-HCl buffered saline solution (pH 7.4) containing the pDNA at a concentration of 3.33×10^{-2} μg/μL at room temperature. The solutions (total volume, 150 μL; plasmid concentration, 20 μg/mL) were mixed using a pipet in order to obtain polyplexes. The mean diameters of the polyplexes in the solution were determined by cumulant analysis in a multimodal setting by using the DLS apparatus. During the transfection experiments, which were conducted 10 min after complex formation, 25 μL of the complex solutions

were added into each well of the 24 multiwell dishes (the amount of DNA added to a well, 0.5 μg). Since the data of the particle size were reproducible ($n = 20$, SD < 10%), only the average values have been described.

Biophysical Characterization of Polyplexes. The ζ-potentials and mean diameters of the polyplexes in a saline solution were obtained by employing dynamic light scattering (DLS) on an ELS-8000 system (Otuska Co., Osaka, Japan) equipped with a 10 mW He−Ne laser. The mean diameters were measured at the concentration that was used for transfection at a C/A ratio of 15, and ζ-potentials were measured after dilution with saline solution to 1/10 of the transfection concentration. The mean diameters were determined by cumulant analysis in multimodal setting.

DNase I Protection Assay. The polyplexes prepared from CSV (M_n = ca. 4.6 kDa) and pDNA (0.5 μg) at the C/A ratio of 15 was added with 5 μL (2 unit) of DNase I (Worthington, DPPF grade). After predetermined incubation time (10 min to 24 h) at 42 °C, 50 μL of a stop solution consisting of 4 M ammonium acetate, 20 mM EDTA, and 2 mg/mL glycogen was added, and the reaction mixture was placed on ice. The aliquot of 5.0 μL was electrophoresed for 30 min at 100 V in 1 wt % of agarose gel by 40 mM TAE running buffer. The gel was stained with 0.5 mg/mL ethidium bromide solution for 30 min to visualized the location of plasmid DNA with a Gel Doc 2000 (Bio-Rad Laboratories, Tokyo, Japan).

Cell Lines. COS-1 african green monkey kidney cells, HeLa human cervix carcinoma cells, HepG2 human hepatocellular carcinoma cells, and 293 human kidney transformed cells were purchased from RIKEN CELL BANK (Tsukuba, Japan). COS-1 cells were maintained in DMEM medium (Gibco, Invitrogen Corp., Carlsbad, CA) with 10% fetal calf serum (FCS, Hyclone Laboratories Inc., Logan, UT), HepG2 cells and 293 cells in MEM medium (Gibco) with 10% fetal bovine serum (FBS, Hyclone), and HeLa cells in MEM medium with 10% FCS. All cells were cultured with 200 units/mL penicillin (ICN Biomedicals Inc., Aurora, OH), and 200 mg/mL streptomycin (ICN) in a 5% CO_2 atmosphere at 37 °C.

In Vitro Transfection and Cell Viability Assays. COS-1 cells were seeded at a density of 3×10^4 cells/well in a 24-well plate in medium containing 10% FCS and grown to reach 70−80% confluence prior to transfection for 24 h. HepG2 cells and 293 cells (1×10^5 cells/well) were seeded in a 12-well plate and grown in the same way. Transfections were performed with 0.5 μg of plasmid DNA (pGL3 as control) in 24-well dishes containing 0.2 mL of OPTI-MEM I (Gibco) for COS-1 cells and 1 μg of plasmid DNA in 12-well dishes containing 0.4 mL of OPTI-MEM I. After 3 h of incubation, the cells were washed once with PBS (−) and cultured in 1 mL for 24-well or 2 mL for 12-well of appropriate medium for an additional 48 h. The medium was removed, and the cells were washed twice with PBS (−), lysed with 0.2 mL for 24-well or 0.4 mL for 12-well of cell lysis buffer (Promega, Madison, WI), and mixed by vortexing. The lysate was centrifuged at 15 000 rpm for 1 min at 4 °C, and 5 μL of the supernatant was analyzed for luciferase activity by using a Luminous CT-9000D (Dia-Iatron, Tokyo, Japan) luminometer. The relative light unit (RLU)/s values were converted into the amount of luciferase (pg) by using a standard luciferase curve, which was obtained by diluting recombinant luciferase (Promega) in lysis buffer. The protein concentrations of the cell lysates were measured by performing a Bio-Rad protein assay (BIO-RAD, Hercules, CA) with bovine serum albumin as a standard. The final amount of luciferase was determined as the amount of expressed luciferase (mole quantity) standardized to the total protein content of the cell lysate. Data represent the mean ± the standard deviation (S.D.) of the mean ($n = 5$). Statistical analysis was performed using Student's *t*-test and $p < 0.05$ (*) was accepted to be significant.

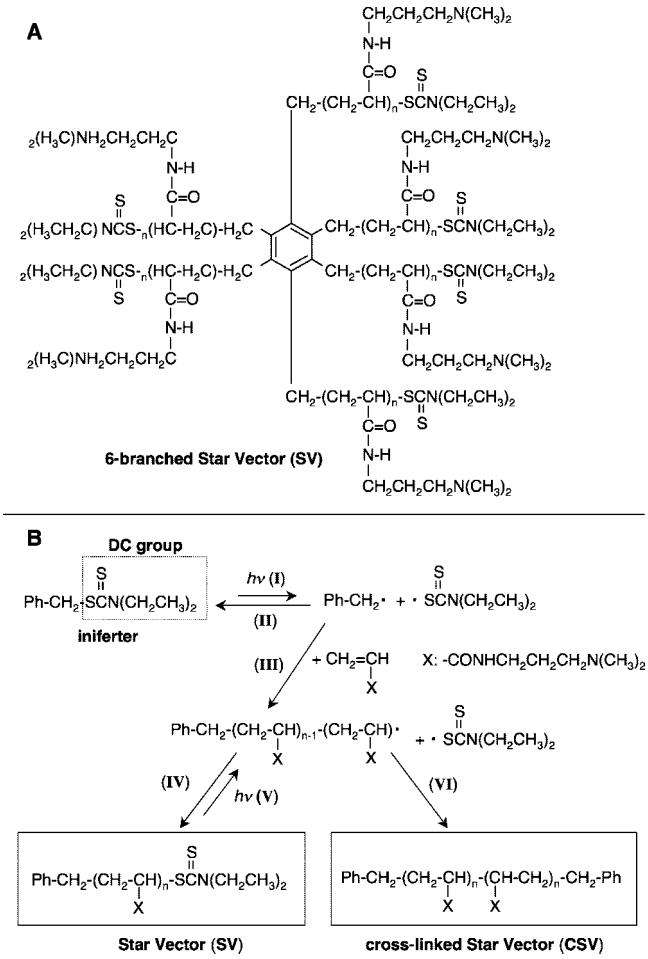

Figure 1. (A) Chemical structure of six-branched star vector (SV). (B) Reaction mechanisms in the preparation of SV through Schemes I, III, and IV from iniferter by photoirradiation in the presence of *N*,*N*-dimethylaminopropyacrylamide, and those involved in the preparation of cross-linked star vector (**C**SV) from SVs through Schemes V and VI by photoirradiation under N_2 atmosphere.

Cytotoxicity was assessed by performing a cell viability assay using the WST-8 method (Dojindo, Kumamoto, Japan). The COS-1 cells were seeded 24 h prior to treatment in 96-well plates at 5000 cells/well. The cells were treated under the same conditions as those used for the luciferase assay; 6.2 μL of the transfection mixture containing 0.124 μg of pDNA was added to each well. The cells were treated under the appropriate conditions for 3 h, washed once with PBS, and cultured in 50 μL of DMEM (Gibco) containing 10% fetal calf serum for an additional 24 h. To each well, 10 μL of WST-8 reagent (5 mmol/L) was added. After 2 h of incubation at 37 °C, the absorbance at 450 nm was determined using a Bio-Rad microplate reader (model 680). Data represents the mean ± the standard deviation (S.D.) of the mean ($n = 5$).

RESULTS AND DISCUSSION

Synthesis and Cross-linking of SV. The two kinds of six-branched SVs with different molecular weights (Figure 1A) were prepared by iniferter-based photoliving radical polymerization via reactions I, III, and IV shown in Figure 1B. The polymerization of a cationic monomer (DMAPAAm) from six-functional iniferter, which was synthesized by the derivatization of DC groups to 1,2,3,4,5,6-hexakis(bromomethyl)benzene, was performed by changing the irradiation time. Following 30 min of

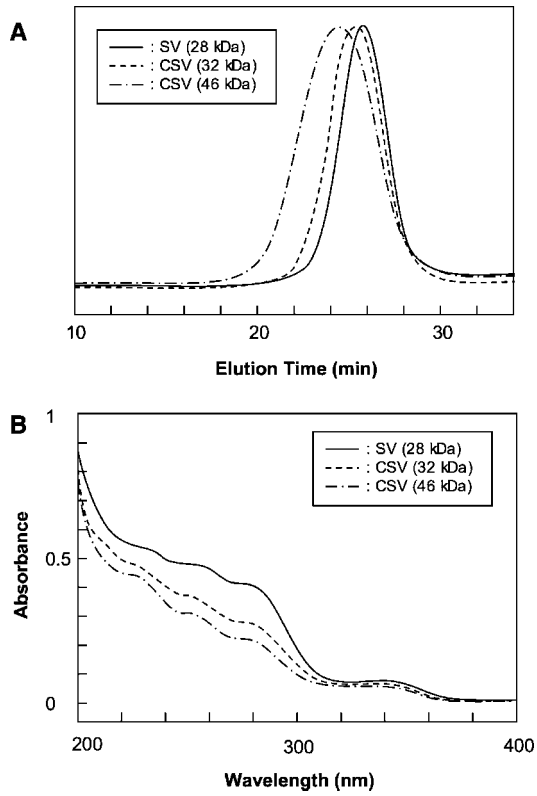

Figure 2. (A) GPC curves and (B) UV absorption spectral changes after photoirradiation of star vectors (SVs) of molecular weight ca. 2.8 kDa to obtain cross-linked star vectors (CSVs) of molecular weight ca. 3.2 kDa (irradiation time, 180 min) and ca. 4.6 kDa (240 min).

UV irradiation, only trace amounts of the SV were observed on GPC, with complete absence of the iniferter (Figure 2A). The obtained SV had a number-average molecular weight (M_n) of ca. 28 kDa with very narrow polydispersity at 1.4 (run 1 in Table 1). By prolonging the irradiation time, the M_n increased to approximately 46 kDa, but the narrow polydispersity (M_w/M_n 1.4) was maintained (run 2).

In the NMR spectrum of the SV with M_n of ca. 28 kDa, after 20 000 cycles, double quartet peaks of two types of *N*-methylene protons appeared at 3.6−3.7 ppm and 3.4−3.5 ppm, indicating the presence of DC groups even after polymerization initiated from the iniferter. On the other hand, the molecular weight of the SV, calculated from the UV spectra (Figure 2B, Table 1), was approximately 32 kDa, which was close to that obtained from GPC measurements (28 kDa). On the basis of these results, we concluded that almost all photoreactive functional DC groups were present at the ω-ends of every branch in the SV.

The mist-like powder of SV with a M_n of ca. 28 kDa was exposed to UV light in a solid phase under a N_2 gas atmosphere in the absence of any monomers. Following 180 min of irradiation, the GPC curve was observed to have shifted slightly to the higher molecular weight side after the gel-like precipitate produced was excluded as a byproduct (Figure 2A). The M_n increased to approximately 32 kDa and the polydispersity broadened (run 1−1 in Table 1). On further increasing the irradiation time to 240 min, a M_n of ca. 46 kDa with an even broader polydispersity was obtained (run 1−2).

Figure 2B shows the UV absorption spectral change of the SVs before and after UV-light irradiation. The specific UV absorption with maximum absorption wavelength at 275 nm originating from the DC group significantly decreased after irradiation. After 240 min of irradiation, the absorption decreased to approximately half the original. The GPC and UV spectral analysis revealed that the SVs were cross-linked by a photoreaction involving the DC groups without the use of any chemical cross-linking agents.

The cross-linking mechanism of the SVs was identified to be as follows. The DC end-capped chain in the SVs finally produced as a precursor was redissociated into a pair of reactive polymer radicals and non- or less-reactive DC radicals by UV irradiation (reaction V in Figure 1B). When there were no monomers in the solid state, simultaneous chain transfer of the generated polymer radicals to the polymer matrix or coupling between the radicals occurred preferentially. Coupling between DC radicals generated *N*,*N*,*N*′,*N*′-tetraethylthiuram disulfide, which is dissociated to dithiocarbamyl radicals by UV irradiation because it is reversible. On the other hand, coupling between polymer radicals generated an SV dimer (reaction VI), which could be not dissociated by UV irradiation. Therefore, the polymer radicals would be selectively consumed by UV irradiation of the SV to generate CSV. As expected, chain transfer of polymer radicals to the polymer matrix also produced CSV in another cross-linking manner, in which the end chains of the SV branch bonded to the side chain of another SV branch. Photoinduced cross-linking with DC groups has previously been performed for the surface modification of medical materials for better biocompatibility (*32*) or polymer design (*33*).

Formation of Polyplexes. Approximately 10 min after mixing a Tris-HCl-buffered solution of pDNA (pGL3-control plasmid) and a saline solution of CSV, the scattering intensity in the DLS measurements was stably observed, indicating that polymer/plasmid complexes (polyplexes) similar to the original SVs had been formed. The effective diameters of the polyplexes prepared from CSV (M_n = ca. 46 kDa), as measured by DLS, were approximately 150 nm at a charge ratio of 15 (Figure 3A). The size was similar to that observed with SVs of almost the same M_n, but it was slightly larger than that with SVs of a low molecular weight (M_n = ca. 28 kDa). All the polyplexes gradually aggregated as incubation proceeded irrespective of whether or not the cross-linking had occurred.

On the other hand, the polyplexes with a higher M_n of ca. 46 kDa were very stable even at a low pH of 4. Up to 180 min after incubation, their small particle size was maintained; however, for the polyplexes from the SV of low M_n (ca. 28 kDa), the particle size increased to approximately 1.5-fold. The particle stability was higher in the polyplexes formed from SVs of a higher molecular weight without any significant dependency on the presence of cross-linking. The moderate ζ-potentials of approximately 20 mV were observed for all particles irrespective of cross-linking and molecular weight (Table 1).

When the polyplexes are formed, it is expected that the digestion of pDNA by DNase I is inhibited. After incubation with DNase I, the polyplexes were analyzed by 1% agarose gel electrophoresis (Figure 4). The pDNA was digested even at 10 min of incubation time. On the other hand, pDNA in the

Table 1. Preparation and Cross-Linking Conditions of SVs and ζ-Potential of the Polyplexes

			UV light irradiation time					
run	[iniferter] (mM)	[monomer] (M)	for polymerization (min)	for cross-linking (min)	M_n (kDa)	M_w/M_n	absorbance at 275 nm	ζ-potential (mV)
1	5.0	1.0	30	-	28	1.4	0.341	17.7 ± 1.0
1−1	-	-	-	180	32	1.7	0.248	16.5 ± 3.3
1−2	-	-	-	240	46	2.0	0.186	18.4 ± 3.9
2	5.0	1.0	50	-	46	1.4	-	15.3 ± 2.4

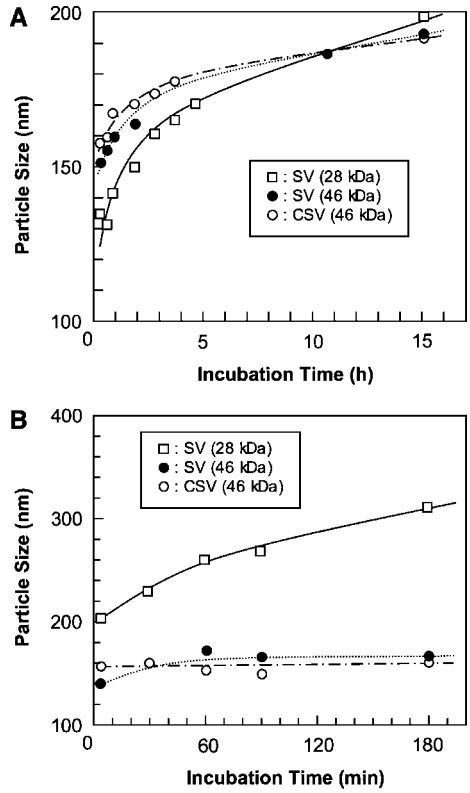

Figure 3. Incubation time-dependent changes in the particle size of polyplexes prepared from luciferase-encoding plasmid DNA nad star vector (SVs) of molecular weight ca. 28 kDa or ca. 46 kDa, or crosslinked star vectors (CSVs) of ca. 46 kDa at pH 7.4 (A) and 4.0 (B). Since the data of the particle size were reproducible (n = 20, S.D. <10%), only the average values have been described.

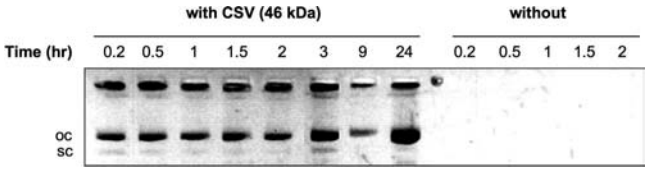

Figure 4. DNase I protection assay. The pDNA with or without CSV at a charge ratio of 15 was treated with DNase I. The position of the open coiled (oc) and supercoiled (sc) forms are indicated on the left.

polyplexes remained even at longer incubation time up to 24 h. The CSV could completely protect the pDNA from digestion of DNase I.

In Vitro Transfection Efficiency. The transfection efficiency of the SVs before and after cross-linking treatment was, at first, tested in the model cell line—COS-1 comprising monkey cells—at a charge ratio of 15 or 30. Since the polyplexes were gradually aggregated as incubation especially in SV with low M_n as indicated in Figure 3, at 10 min after preparation, the polyplexes conducted to the transfection experiments. The cells transfected with the luciferase-encoding plasmid (pGL3) in the absence of any polymer exhibited negligible luciferase expression. In the six-branched SVs, the luciferase expression increased with the molecular weight of the SVs (Figure 5). As shown in Figure 3, the molecular weight dependency may be due to the stability of the polyplexes. A similar dependency was observed for the four-branched SVs, in which a 5-fold increase in molecular weight of the SVs from ca. 10 to 50 kDa induced an approximately 3-fold increase in the luciferase activity. These obtained activities were larger than that in PEI (ExGen 500), which is a major commercially available typical polymeric vector used as a positive control.

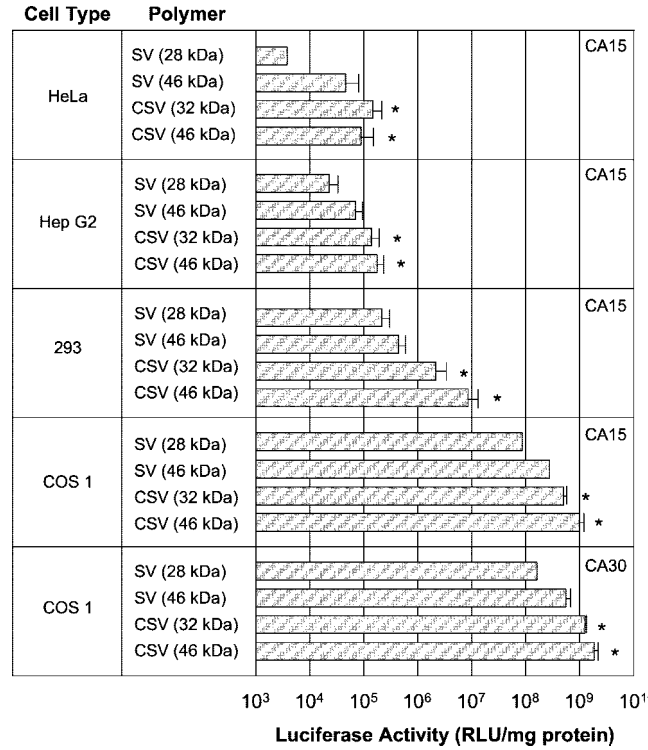

Figure 5. Transfection of four different cell lines using polyplexes prepared by mixing pDNA (pGL3 control, 0.5 μg/24-well plate or 1 μg/12-well plate) and SVs with molecular weight of approximately 28 kDa or 46 kDa, or CSVs with molecular weight of approximately 32 kDa or 46 kDa, at a charge ratio of 15 or 30. For comparison, the transfection efficiency data of polyplexes formed using linear PEI (ExGen 500) at a charge ratio of 5 is also provided. Data represents the mean ± the standard deviation (S.D.) of the mean (n = 5). Statistical analysis was performed using Student's *t*-test and $p < 0.05$ (*) was accepted to be significance.

Interestingly, the transfection activity drastically increased by the cross-linking of the SVs (Figure 5). The activities of CSVs of M_n approximately 32 kDa and 46 kDa at a charge ratio of 15 were approximately 6- and 12-fold the value in the original untreated SV with a M_n of ca. 26 kDa, respectively. For the CSVs with a M_n of ca. 46 kDa, approximately 4-fold higher activity was observed with the cross-linked compound than with the non-cross-linked compound. In addition, an increase in the charge ratio from 15 to 30 induced a further increase in the activity up to approximately 2-fold. Thus, the structural advantage of cross-linking in the SVs was strongly suggested for greater in vitro gene transfection efficiency.

The transfection efficiency was evaluated also in human cell lines—HeLa, human cervix carcinoma cells, HepG2, human hepatocellular carcinoma cells, and 293, human kidney transformed cells. Unfortunately, lower transfection activity was observed in all human cells than that in COS-1 (Figure 5). However, there was a similar drastic increase of transfection activity by cross-linking of SVs. The activity with CSV (M_n = ca. 46 kDa) was at least 1 order of magnitude in the original SV (M_n = ca. 28 kDa). The SV-based gene transfection was significantly enhanced by the cross-linking of the SVs in all cell lines.

Cell Cytotoxicity. The in vitro cytotoxicity of the polyplexes prepared from the regular SVs or photoirradiated SVs was studied as a function of the charge ratio in the range of 5−45 by using the WST assay. As shown Figure 6, in the case of all the polyplexes, the relative cell viability decreased as the charge ratio increased. Polyplexes with a lower charge ratio were considered to have lower cell membrane binding ability, which therefore tended to affect cell viability. In the case of a higher

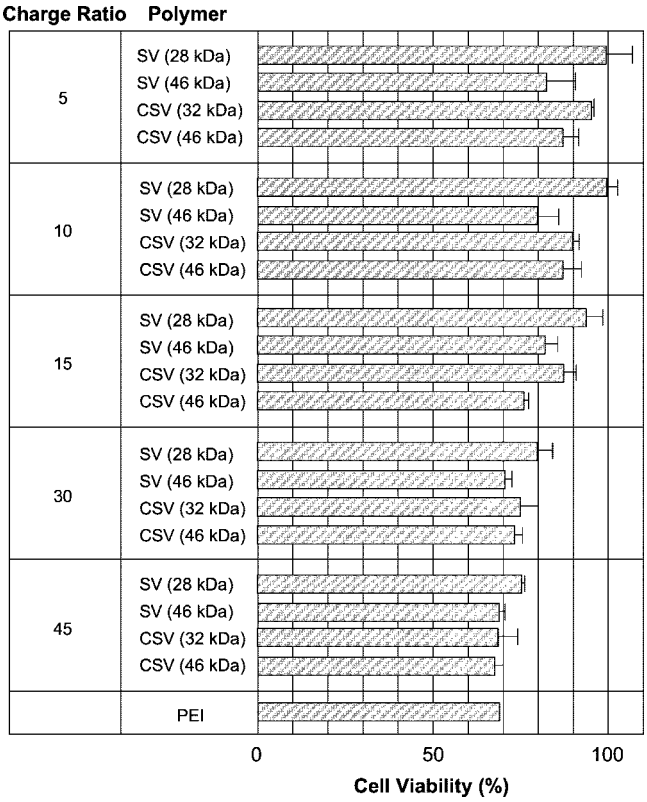

Figure 6. Cytotoxicity of polyplexes prepared by mixing DNA (pGL3 control, 3 μg) and SVs or CSVs at different charge ratios. Cell viability was determined by the WST assay.

charge ratio, it was observed that the polyplexes not only had a higher charge density but also had a higher concentration of the cationic polymer, which was correlated with the cytotoxic effect. Since the molecular weight of the cationic polymer was confirmed as the main parameter affecting its interaction with the cell membrane and, consequently, cell damage, the SVs and photoirradiated SVs of higher molecular weight were considered to have less cytotoxicity at a charge ratio of 30 or 45. However, they might be acceptable, because in these cases, the cell viability was higher than that with polyethyleneimine (PEI) at a charge ratio of 6, and PEI is one of the most popular commercially available gene-delivery agents (Figure 6). There was no significant difference among the polyplexes formed from the SVs and photoirradiated SVs of the same molecular weight. Therefore, it was considered that the photoirradiation treatment of the SVs had no significant disadvantage.

In conclusion, this study successfully demonstrated that SV-based gene transfection was significantly enhanced by the cross-linking of the SVs via any agent except photoirradiation in the solid phase. The M_n of the obtained CSVs increased with increasing irradiation time. With an increase in the M_n of the CSVs, the gene transfection efficiency increased drastically except for HeLa in this study. On cross-linking at charge ratios of both 15 and 30, the transfection activity increased to over 10-fold that of the original SV (M_n = ca. 28 kDa), which in turn was 3-fold that of the SV of the same molecular weight (M_n = ca. 46 kDa). As described in the introduction, nanoarchitectural, macromolecular design of the polymeric DNA carriers by hyperbranching or cross-linking, and so forth, has been attempted as a major strategy for increasing transfection efficiency. Therefore, it was considered that cross-linking of star vector, which could induce an increase in the cationic charge density, would be a key strategy for enhancement of transfection efficiency of cationic polymers. To evaluate the hypothesis, the present study was designed and the effectiveness of the cross-linking of star vector for increasing transfection efficiency was clearly demonstrated. It was considered that the DNA expression using the polyplex was observed by the following five sequential steps: (1) attachment of the polyplexe onto the cell surface, (2) internalization of the polyplexes into the cell, (3) endosomal escape of the polyplex, (4) DNA release from the polyplex, and (5) internalization of DNA into the nucleus. In this study, there were few differences in the ζ-potentials and the mean diameters of all polyplexes, whereas a significant difference was observed in the transfection efficiency between SV and CSV. Therefore, the difference might be greatly induced from the steps after (3).

For further improvement, the CSV-induced gene delivery mechanism should be determined. Although in both SV and CSV excellent colloidal stability with low cytotoxicity was demonstrated, we do not have any additional data to explain the mechanism. In addition, as shown in Figure 2B, a lot of DC groups remained after photo-cross-linking, indicating that the cross-linking only occurred partly. Therefore, it was considered that CSV consisted of a mixture of original SV and cross-linked SV. To purify the CSV, fractionation of the mixture by GPC is ongoing. By using the pure CSV with narrow polydispersity, the mechanism will be explained clearly. Our research in the near future will be directed at optimization of the cross-linking density, macromolecular size and distribution, and combination with other kinds of SVs with different chemical or electrical properties so as to achieve further improvements in the in vitro transfection efficiency for other types of cells and in vivo gene transfection efficiency and in functionalization, including biodegradation ability to obtain low cytotoxicity.

LITERATURE CITED

(1) Mulligan, R. C. (1993) The basic science of gene therapy. *Science 260*, 926–932.
(2) Crystal, R. G. (1995) Transfer of genes to humans: early lessons and obstacles to success. *Science 270*, 404–410.
(3) Kay, M. A., Liu, D., and Hoogerbugge, P. M. (1997) Gene therapy. *Proc. Natl. Acad. Sci. U.S.A. 94*, 12744–12746.
(4) Li, D., and Hung, L. (2000) Gene therapy progress and prospects: non-viral gene therapy by systemic delivery. *Gene Ther. 7*, 31–34.
(5) Luo, D., and Saltzman, W. M. (2000) Enhancement of transfection by physical concentration of DNA at the cell surface. *Nat. Biotechnol. 18*, 33–37.
(6) Gebhart, C., and Kabanov, A. K. (2001) Evaluation of polyplexes as gene transfer agents. *J. Controlled Release 73*, 401–416.
(7) Thomas, M., and Klabanov, A. M. (2003) Non-viral gene therapy: polycation-mediated DNA delivery. *Appl. Microbiol. Biotechnol. 62*, 27–34.
(8) Dubruel, P., and Schacht, E. (2006) Vinyl polymers as non-viral gene delivery carriers: current status and prospects. *Macromol. Biosci. 6*, 789–810.
(9) Kurowska-Latallo, J. F., Bielinska, A. U., Johnson, J., Spindler, R., Tomalia, D. A., and Baker, J. R., Jr. (1996) Efficient transfer of genetic material into mammalian cells using Starburst polyamideamine dendrimers. *Proc. Natl. Acad. Sci. U.S.A. 93*, 4897–4902.
(10) Zhang, X.-Q., Intra, J., and Salem, A. K. (2007) Conjugation of polyamidoamine dendrimers on biodegradable microparticles for nonviral gene delivery. *Bioconjugate Chem. 18*, 2068–2076.
(11) Haensler, J., and Szoka, F. C., Jr. (1993) Polyamidoamine cascade polymers mediate efficient transfection of cells in culture. *Bioconjugate Chem. 4*, 372–379.
(12) Tang, M. X., and Szoka, F. C. (1997) The influence of polymer structure on the interactions of cationic polymers with DNA and morphology of the resulting complexes. *Gene Ther. 4*, 823–832.

(13) Banerjee, P., Reichardt, W., Weissleder, R., and Bogdanov, A., Jr. (2004) Novel hyperbranched dendron for gene transfer in vitro and in vivo. *Bioconjugate Chem. 15*, 960–968.

(14) Kim, T., Seo, H. J., Choi, J. S., Yoon, J. K., Baek, J., Kim, K., and Park, J.-S. (2005) Synethesis of biodegradable cross-linked poly(β-amino ester) for gene delivery and its modification, inducing enhanced transfection efficiency and stepwise degradation. *Bioconjugate Chem. 16*, 1140–1148.

(15) Tomas, M., Ge, Q., Lu, J. J., Chen, J., and Klibanov, A. M. (2005) Cross-linked small polyethylenimines: while still nontoxic, deliver DNA efficiently to mammaliam cells in vitro and in vivo. *Pharm. Res. 22*, 373–380.

(16) Gosselin, M. A., Guo, W., and Lee, R. J. (2001) Efficient gene transfer using reversibly cross-linked low molecular weight polyethylenimine. *Bioconjugate Chem. 12*, 989–994.

(17) Kwok, K. Y., Yang, Y., and Rice, K. G. (2001) Evolution of cross-linked non-viral gene systems. *Curr. Opin. Mol. Ther. 3*, 142–146.

(18) Fischer, D., Bieber, T., Li, Y., Elsasser, H. P., and Kissel, T. (1999) A novel non-viral vector for DNA delivery based on low molecular weight, branched polyethlenimine: effect of molecular weight on transfection efficiency and cytotoxicity. *Pharm. Res. 16*, 1273–1279.

(19) Bieber, T., and Elsasser, H. P. (2001) Preparation of low molecular weight polyethylenimine for efficient cell transfection. *BioTechniques 30*, 74–81.

(20) Wang, Y., Chen, P., and Shen, J. (2006) The development and characterization of a glutathione-sensitive cross-linked polyethylenimine gene vector. *Biomaterials 27*, 5292–5298.

(21) Jiang, H. L., Kim, Y. K., Arote, R., Nah, J. W., Cho, M. H., Choi, Y. J., Akaike, T., and Cho, C. S. (2007) Chitosan-graft-polyethylenimine as a gene carrier. *J. Controlled Release 117*, 273–280.

(22) Tian, H., Xiong, W., Wei, J., Wang, Y., Chen, X., Jing, X., and Zhu, O. (2007) Gene transfection of hyperbranched PEI grafted by hydrophobic amino acid segment PBLG. *Biomaterials 28*, 2899–2907.

(23) Wightman, L., Kircheis, R., Rossler, V., Carotta, S., Ruzicka, R., Kursa, M., and Wagner, E. (2001) Different behavior of branched and linear polyethylenimine for gene delivery *in vitro* and *in vivo*. *J. Gene Med. 3*, 362–372.

(24) Nakayama, Y., Masuda, T., Nagaishi, M., Hayashi, M., Ohira, M., and Harada-Shiba, M. (2005) High performance gene delivery polymeric vector: nano-structured cationic star polymers (star vector). *Curr. Drug Delivery 2*, 53–57.

(25) Nakayama, Y., Kakei, C., Ishikawa, A., Zhou, Y. M., Nemoto, Y., and Uchida, K. (2007) Synthesis and *in vitro* evaluation of novel star-shaped block copolymers (blocked star vectors) for efficient gene delivery. *Bioconjugate Chem. 18*, 2037–2044.

(26) Mizoguchi, F., Ooe, Y., Hoshino, S., Shimura, m., Kasahara, T., Kano, S., Ohta, T., Takaku, F., Nakayama, Y., and Ishizaka, Y. (2005) Improved gene expression in resting macrophages using an oligopeptide derived from Vpr of human immunodeficiency virus type-1. *Biochem. Biophys. Res. Commun. 338*, 1499–1506.

(27) Zhou, Y. M., Ishikawa, A., Okahashi, R., Uchida, K., Nemoto, Y., and Nakayama, Y. (2007) Deposition transfection technology using a DNA complex with a thermoresponsive cationic star polymer. *J. Controlled Release 123*, 239–246.

(28) Ishikawa, A., Zhou, Y. M., and Nakayama, Y. (2008) Enhancement of star vector-based gene delivery to endothelial cells by addition of RGD-peptide. *Bioconjugate Chem. 19*, 558–561.

(29) Otsu, T., Yoshida, M., and Tazaki, T. (1982) A model for living radical polymerization. *Makromol. Chem. Rapid Commum. 3*, 133–140.

(30) Otsu, T., Matsunaga, T., Doi, T., and Matsumoto, A. (1995) Features of living radical polymerization of vinyl monomers in homogeneous system using N,N-diethyldithiocarbamate derivatives as photoiniferters. *Eur. Polym. J. 31*, 67–78.

(31) Yang, C., Li, H., Goh, S. H., and Li, J. (2007) Cationic star polymers consisting of α-cyclodextrin core and oligoethylenimine arms as nonviral gene delivery vectors. *Biomaterials 28*, 3245–3254.

(32) Nakayama, Y., Takatsuka, M., and Matsuda, T. (1999) Surface hydrogelation using photolysis of dithiocarbamate or xanthate: hydrogelation, surface fixation, and bioactive substance immobilization. *Langmuir 15*, 1667–1672.

(33) Nakayama, Y., Ishikawa, A., Sato, R., Uchida, K., and Kambe, N. (2008) Photodimerization and polymerization of PEG derivatives through radical coupling using photochemistry of dithiocarbamate. *Polym. J.*

BC800003T

Unimolecular, Soluble Semiconductor Nanoparticle-Based Biosensors for Thrombin Using Charge/Electron Transfer

Marla D. Swain,[†,‡] Jashain Octain,[‡] and David E. Benson*[,‡,§]

Naval Research Laboratory, 4555 Overlook Avenue SW, Washington, DC 20375, Department of Chemistry, Wayne State University, 5101 Cass Avenue, Detroit, Michigan 48202, and Department of Chemistry and Biochemistry, Calvin College, 1726 Knollcrest Circle, SE, Grand Rapids, Michigan 49546. Received September 16, 2008; Revised Manuscript Received November 11, 2008

Duplex DNA was attached to semiconductor nanoparticles providing selective detection of thrombin. Using the method reported here, semiconductor nanoparticles can have selective sensory functions for a host of additional analytes in the future. The system uses one DNA strand that selectively binds an analyte (thrombin), while the complementary DNA strand contains a redox-active metal complex. The accessibility of the metal complex to the nanoparticle surface is increased upon thrombin binding due to unravelling of the duplex DNA secondary structure. Increased interactions between the metal complex and the nanoparticle surface will decrease nanoparticle emission intensity, through charge transfer. Initially, water-soluble nanoparticles with carboxylate-terminated monolayers showed thrombin-specific responses in emission intensity (−30% for 1:1 nanoparticle to DNA, +50% for 1:5). Despite the selective responses, the thrombin binding isotherms indicated multiple binding equilibria and more than likely nanoparticle aggregation. The need for a nonaggregative system comes from the potential employment of these sensors in live cell or living system fluorescence assays. By changing the nanoparticle capping ligand to provide an ethylene glycol-terminated monolayer, the binding isotherms fit a two-state binding model with a thrombin dissociation constant of 3 nM in a physiologically relevant buffer. This article demonstrates the need to consider capping ligand effects in designing biosensors based on semiconductor nanoparticles and demonstrates an initial DNA-attached semiconductor nanoparticle system that uses DNA−analyte binding interactions (aptamers).

INTRODUCTION

Semiconductor nanoparticles, or quantum dots, have a wide array of potential biological applications (*1*−*3*). The benefits of these nanomaterials are the large two-photon cross sections, broad excitation wavelength ranges, sharp emission linewidths, high quantum yields, and high photostability relative to organic and metal−organic fluorophores (*2*). Use of monolayer-protected nanoparticle methods provides water-soluble, biocompatible semiconductor nanoparticles (*4, 5*), which allow the attachment of biological molecules to enhance the function of semiconductor nanoparticles (*6, 7*). Biological molecules add chemical selectivity to the properties of the nanomaterial (*8, 9*). Typically, the biomolecular-induced changes in semiconductor nanomaterial properties are observed by fluorescence-based spectroscopies. Biomolecular-induced changes in photoconductivity are less commonly reported, but have also been observed (*10, 11*). The key to integrating biomolecular function into nanomaterial properties is to use enzymatically generated compounds or a biomolecule-attached reporter compound (*8*). Enzymatically generated compounds that are photo- or electroactive can readily interact with semiconductor nanoparticles to alter the observed fluorescence or photoconductive properties. Such enzymatic signal amplification is similar to ferrocene/glucose oxidase electrode cells for glucose detection (*9*). The use of biomolecule-attached reporter groups link ligand-induced changes in biomolecule conformation (*6, 8, 12*−*14*) or active-site solvation (*15*) to photonic or electrical changes in the semiconductor nanomaterial. Oftentimes, these changes are performed with only the ligand changing the molecular weight of the assembly, called unimolecular or reagentless detection (*12*−*15*). Unimolecular detection facilitates reversible ligand detection in diffusible formats (*16*), such as live-cell fluorescence microscopy. Many semiconductor nanoparticle-based biosensors have been developed with cellular fluorescence microscopy as an extension, but unimolecular versions of these biosensors will be needed for reversible detection.

Protein-attached semiconductor nanoparticles provide unimolecular constructs that function as biosensors (*12*−*15*). It should be noted that localization probes (e.g., antibodies) are omitted from this discussion, since minimal changes in semiconductor nanomaterial properties are typically associated with localization. Using Cy3-attached maltose binding protein (MBP), a reagentless/unimolecular biosensor for maltose was reported (*14*). This report augmented previous work (*17*), where both accounts using multiple fluoropohore-modified MBPs were coordinated per ZnS-coated CdSe (CdSe@ZnS) nanoparticle. Previous studies with this system used displacement assays to demonstrate this phenomenon, where a quencher or fluoropohore was released from the assembly upon maltose binding to MBP (*17*). The unimolecular assembly (*14*) used maltose-induced changes in MBP-attached Cy3 intercalation into or around the maltose binding pocket. The Cy3 intercalation method changed the solvation around Cy3 to alter the Cy3 emission intensity, while the CdSe@ZnS emission remained constant. This strategy, while providing dual emission wavelengths for biosensor concentration-independent detection, relied on organic fluorophore emission. As pointed out already (*1*−*3*), the rationale for semiconductor nanoparticle fluorescence probes is the high photostability as opposed to organic fluorophores.

* Fax: 616 526 8551; Phone: 616 526 8801; E-mail: deb22@calvin.edu.
[†] Naval Research Laboratory.
[‡] Wayne State University.
[§] Calvin College.

10.1021/bc8003952 CCC: $40.75 © 2008 American Chemical Society
Published on Web 12/03/2008

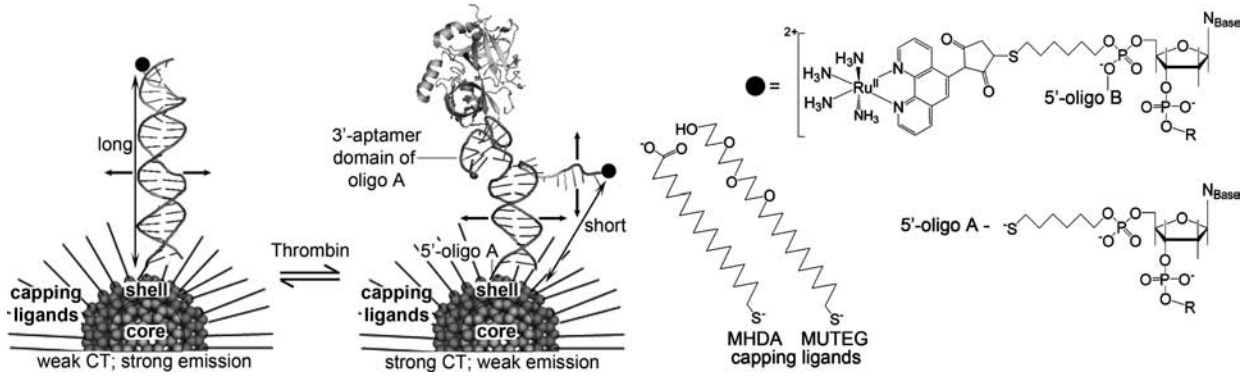

Figure 1. Summary of biosensor components (see Table 1 and experimental for definitions and terms).

Charge/electron transfer reactions provide a unimolecular solution to semiconductor nanoparticle-based biosensors with proteins that alter the semiconductor nanoparticle emission intensity (*8, 12, 13, 15*). MBP was used for these studies as well, where $[Ru(L)(NH_3)_4](PF_6)_2$ (**1**, L = 5-maleimido-1,10-phenanthroline) reduces CdSe@ZnS nanoparticles to render these nanoparticles nonfluorescent (*12, 13*). The rationale for differences between energy and charge/electron transfer methods is that energy transfer has a R_o/r^6 distance dependence ($R_o \sim$ 55 Å) where charge/electron transfer has an $\exp(-\beta r)$ distance dependence ($\beta \sim 1.2$ Å^{-1}). For comparison, a 1 Å interatomic movement in Cy3/complex **1** relative to the CdSe@ZnS nanoparticle surface should result in a 1% change in emission intensity for energy transfer but a 30% change in emission intensity for electron transfer (*8*). Unimolecular semiconductor nanoparticle-based biosensors for fatty acids have also been reported (*15*). For these biosensors, fatty acid-induced changes in solvation around the NH_3 ligands of complex **1** changed electron transfer rates to and emission from CdSe@ZnS nanoparticles. Therefore, both ligand-induced changes in protein conformation or active-site solvation can be used to generate unimolecular biosensors from protein-attached semiconductor nanoparticles.

Despite many reports of unimolecular/reagentless electrochemical biosensors using ligand-induced changes in nucleic acid-attached conformation (*18, 19*), no analogous unimolecular nucleic-attached CdSe@ZnS nanoparticle biosensors have been reported. Nucleic acids that undergo conformational changes upon binding small molecules or proteins are termed aptamers and have been shown in mRNA to regulate protein synthesis (riboswitches) (*20*). Organic fluorophores (*21*) and Au nanoparticles (*22, 23*) have been integrated with CdSe@ZnS nanoparticles to DNA and/or RNA-based aptamers. The only unimolecular nucleic acid-attached semiconductor nanoparticle biosensor was for PbS nanoparticles (*24*). These nanoparticle cores were formed by a thrombin-binding DNA aptamer that quenched the PbS emission when thrombin or prostate-specific antigen (PSA) were added. Despite the lack of a redox active metal complex or organic compound, charge/electron transfer was presumed to be the quenching mechanism for these biosensors. We presume the hole acceptor/electron donor in this formalism would be either a guanine DNA base or a tyrosine side chain from either protein. These effects have not been reported for CdSe or for CdSe@ZnS nanoparticles, which have significantly less surface defect states that link electrostatic changes at the nanoparticle−solution interface to emission intensity changes.

We have found that complex **1**-attached thrombin-binding DNA aptamers provide thrombin-dependent changes in CdSe@ZnS nanoparticle emission intensity (Figure 1). Furthermore, the capping ligands that provide water solubility to the nanoparticle need to be carefully considered to minimize aggregation effects and eliminate alternative/nonspecific binding events. Finally, this report shows an additional avenue for developing semiconductor nanoparticle-based biosensors for new analytes, due to the elegant selection schemes available to aptamers (*25*).

EXPERIMENTAL METHODS

All materials and chemicals were used as received without purification, unless noted. 3-(*N*-Morpholino)propanesulfonic acid (MOPS, 20 mM with 5 mM KCl and 1 mM $MgCl_2$, pH = 7.5) was used to buffer all aqueous solutions except when PSS (physiological salt solution: 21 mM Tris HCl, pH 7.4, 4.4 mM KCl, 2.0 mM $CaCl_2$, 1.2 mM $MgSO_4$, 140.5 mM NaCl, 11.1 mM dextrose) is noted, where the typically used 5% BSA was omitted in most cases. Complex **1** was synthesized and attached to the DNA oligonucloetides similar to reported protein attachment (*12, 13*). 4,4-Difluoro-3,5-bis(4-methoxyphenyl)-8-(4-male-imidylphenyl)-4-bora-3*a*,4*a*-diaza-*s*-indecene (**2**, Bodipy 577/618 maleimide, Invitrogen) was introduced to DNA oligonucleotides similar to previous protein attachment as well (*26*). Heparin, hirudin, lysozyme, and bovine serum albumin (BSA) were purchased from Sigma and purified by gel filtration. Thrombin was obtained from Heamatologic Technologies Inc. (Essex Junction, VT) and diluted (10 mg/mL) to a 250 μM stock. Rat intestinal fatty acid binding protein (IFABP) was prepared from recombinant DNA with *E. coli* expression as before (*15*).

DNA Design, Preparation, and Modification. HPLC-purified oligonucleotides were purchased from Oligos, etc (Wilsonville, OR). Oligo A (5′-CCATCTCCACTT**GGTTGGTGTGGTTGG**-3′) contained the aptamer sequence (bold letters) with the 5′-phosphate terminus modified with 6-mercaptohexanol for nanoparticle attachment (*27*). Oligo B (5′-CCAACTTTTAAGTGGAGATGG-3′) was obtained either without modification (oligo B_0) or with the 5′-phosphate terminus modified with 6-mercaptohexanol for modification with complex **1** (oligo B-**1**) or compound **2** (oligo B-**2**). Oligo C (5′-CCATCTCCACTTGGTGGTGGTTGTGGT-3′) contained a 5′-thiol modification but contained a scrambled sequence relative to the thrombin binding aptamer and was used as a control. The 5′-thiol modified oligos (100 μM) were reduced (dithiothreitol, 1 mM, 30 min) and purified by gel filtration (10DG column, BioRad, Hercules, CA) under anaerobic conditions (anaerobic chamber, Coy laboratories, Grass Lake, MI). The thiol-modified oligo B was then incubated either with 1 equiv of complex **1** (10 mM acetonitrile stock) or 10 equiv of compound **2** (10 mM dimethylformamide stock) for 2 h. After incubation, the modified oligonucleotides were purified by gel filtration and labeling efficiencies (95−100%) were determined by absorbance spectrophotometry. Hybridzation of two complementary oligos (A/B or C/B) was then performed by combining the two oligonucleotide solutions, heating to 70 °C for 10 min,

and slowly cooling the solution back to room temperature. These samples were used immediately, but remained under anaerobic conditions until used.

Nanoparticle Preparation and Capping Ligand Exchange. CdSe@ZnS nanoparticles with 2−3 monolayers of ZnS (CdSe@ZnS_{2-3}) were purchased from NN Laboratories (Fayetteville, AK) as the octadecylamine capped product. Trioctylphosphine oxide capped CdSe@ZnS nanoparticles with 5−6 monolayers of ZnS (CdSe@ZnS_{5-6}) were purchased from Evident Technologies (Troy, NY). These nanoparticles were precipitated (under anaerobic conditions) in an acetone/methanol 1:1 mixture and heated in either neat mercaptohexadecanoic acid (MHDA) or a 50 mM methanolic solution of mercaptoundecyltriethylene glycol (MUTEG) as reported previously (*26, 28*). Potasium *t*-butoxide was added to aqueous suspensions of MHDA-capped nanoparticles to provide water solubility (*26*), while the alkalinity (pH ∼ 10) of MUTEG-capped nanoparticle suspensions was adjusted with tetrabutylammonium hydroxide (3 μM) (*28*). The resulting water-soluble nanoparticles were purified by precipitation in ether and redissolution in water, followed by ultrafiltration (30 000 MW cutoff, Millipore) until minimal fluorescence fluctuations were observed. MHDA-capped CdSe@ZnS nanoparticles were stored in water in the dark and under N_2 for up to two months, while MUTEG-capped nanoparticles were used within one day of the exchange into aqueous solution.

Biosensor Assembly. Modified or unmodified duplex DNA with a single thiol-modified 5′-terminus was mixed with MHDA or MUTEG-capped CdSe@ZnS nanoparticles in buffered solutions. All reactions utilized 25 nM CdSe@ZnS nanoparticles, judged by optical absorbance. Duplex DNA was introduced at various final concentrations. The DNA and nanoparticles were incubated for 1 h at room temperature, when the emission intensity changes saturated. These solutions were used immediately for fluorescence experiments.

Fluorimetry. Emission spectra were obtained using a Fluoromax-3 spectrofluorimeter (Horiba Jobin Yvon Inc., Edison, NJ). Samples were held at room temperature and examined with 363 nm excitation, 3 nm slit widths, and a 1 s integration time. The effect of thrombin and other analytes on the emission intensity was examined by addition of 1−10 μL concentrated analyte stock solutions directly to 1 mL samples in a stirred fluorescence cuvette. Emission spectra were recorded until emission intensities saturated (∼5 min). Quenching analysis were performed in independent samples with increasing **1**-modified duplex DNA concentrations and fit to a modified Stern-Volmer equation (*29*)

$$I/I_0 = \left(\frac{1}{1 + K_a \bullet [\mathbf{1}]} + F_{uq}\right) \quad (1)$$

where I_0 is the initial emission intensity, K_a the Stern-Volmer association constant, [**1**] the concentration of the **1**-modifed duplex DNA, and F_{uq} the fraction of nanoparticle emission intensity that remains unquenched. Analyte-dependent emission intensity changes were reported relative to the 545 nm emission intensity from unmodified duplex DNA attached CdSe@ZnS nanoparticles (fraction intensity).

Titations and Curve Fitting. Thrombin was introduced to the fluorescence cuvette at increasing concentration from a series of stock solutions. Stock solutions were generated by diluting the initial thrombin solution (10 mg/mL) into MOPS or PSS buffer. Stock solutions were introduced to the cuvette in 1 to 5 μL aliquots (Hamilton syringe) and the emission spectrum recorded after emission intensity at 545 nm saturated (∼5 min.). The resulting titration occurred from 10 pM to 1 μM thrombin. The average fraction intensity at 545 nm ($n = 3-5$) was plotted against the thrombin concentration in Igor Pro (Wavemetrics, Portland, OR). Standard deviations of the observed emission intensities determined error bar magnitude. Thrombin-dependent emission intensity changes were represented as the ratio of the observed emission intensity at 545 nm (I) to the emission intensity from the parent (1:1 or 1:5) unmodified system (I_U) and expressed as I/I_U. Graphs of I/I_U vs thrombin concentration were fit to a single binding site isotherm that accounted for the CdSe@ZnS nanoparticle concentration (25 nM)

$$I/I_U = I_{initial} \bullet (I_{final} - I_{initial}) \bullet \frac{([T] + K_d + 25\ nM) - \sqrt{([T] + K_d + 25\ nM) - (4 \bullet [T] \bullet 25\ nM)}}{2 \bullet 25\ nM} \quad (2)$$

where $I_{initial}$ and I_{final} are the initial and final emission intensities, [T] is the thrombin concentration, and K_d is the dissociation constant ($1/K_a$). Analysis of ligand-binding cooperativity was performed by transforming intensity to fraction saturation (Y) using I_o and I_f values. Values of $\log[Y/(1 - Y)]$ were plotted vs log[T], and the slope from nonzero points was determined as the cooperativity (Hill coefficient).

RESULTS

Bionanomaterial Design and Construction. The nucleic acid constructs used by Plaxco and Heeger (*27, 30−32*) were employed to compare charge/electron transfer quenching of semiconductor nanoparticles (*12, 13, 15*) to nucleic acid-based electrochemical biosensors (*27, 30−32*). Two complementary DNA oligonucleotides were synthesized with 6-thiohexanol groups attached to the 5′-phosphate terminus of each strand. One oligonucleotide (A) contained the thrombin-binding aptamer sequence (3′) and a 12-nucleotide region (5′) for invariable association with the complementary oligonucleotide (B). Before DNA hybridization, oligonucleotide B was modified with complex **1** and purified (B-**1**). Oligo B-**1** was hybridized with oligo A to produce the apatmer-containing duplex DNA with complex **1** on the opposite end of the double helix from the 5′-free thiol from oligo A. Duplex DNA containing a single 5′-thiol modification was then adsorbed to MHDA-capped CdSe@ZnS nanoparticles. The resulting system is the basic bionanoparticle assembly reported here (Figure 1, Table 1) where alterations in duplex DNA to nanoparticle stochiometry, reporter group, capping group, and nanomaterial are mentioned.

Emission Responses to Modified Duplex DNA. Complex **1** mediated quenching of MHDA-capped CdSe@ZnS nanoparticles, and thrombin-dependent emission responses were observed for the thrombin-binding aptamer basic assemblies. The amount of CdSe@ZnS emission quenching from duplex DNA-attached complex **1** was determined from comparison to the unmodified system (Table 1, A/B_o duplex). The unmodified duplex DNA bound to CdSe@ZnS nanoparticles decreased

Table 1. CdSe@ZnS Nanoparticle-Based Thrombin Biosensor Systems

biosensor system	oligos[a]	nanoparticle (NP)[b]	NP/oligo stochiometry	capping ligand[c]
1:1 basic	A & B-**1**	CdSe@ZnS_{2-3}	1:1	MHDA
1:5 basic	A & B-**1**	CdSe@ZnS_{2-3}	1:5	MHDA
1:1 unmodified	A & B_0	CdSe@ZnS_{2-3}	1:1	MHDA
1:5 unmodified	A & B_0	CdSe@ZnS_{2-3}	1:5	MHDA
1:1 Bodipy	A & B-**2**	CdSe@ZnS_{2-3}	1:1	MHDA
1:5 Bodipy	A & B-**2**	CdSe@ZnS_{2-3}	1:5	MHDA
CdSe@ZnS_{5-6}	A & B-**1**	CdSe@ZnS_{5-6}	1:5	MHDA
1:1 scrambled	C & B-**1**	CdSe@ZnS_{2-3}	1:1	MHDA
1:5 scrambled	C & B-**1**	CdSe@ZnS_{2-3}	1:5	MHDA
MUTEG	A & B-**1**	CdSe@ZnS_{2-3}	1:1	MUTEG

[a] Deoxyribonucleotides used for these experiments (see Experimental Section). [b] CdSe@ZnS_{2-3}, CdSe with 2−3 ZnS monolayers; CdSe@ZnS_{5-6}, CdSe with 5−6 ZnS monolayers. [c] MHDA, 16-mercaptohexadecanoate; MUTEG, 11-mercaptoundecyltriethylene glycol.

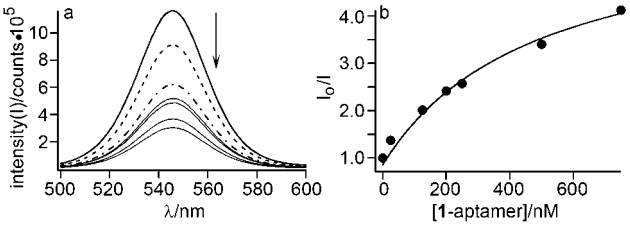

Figure 2. Emission quenching from **1**-modifed duplex DNA. (A) Comparison of emission spectra (thick solid, unmodified (1:1); thick dashed, 1:1 system; thick dash−dotted, 1:5 system, thin solid, higher concentrations). (B) Modified Stern−Volmer analysis (circles, I/I_o, 545 nm; line, fit to eq 1, $K_A = 1.5 \times 10^7$ M^{-1}, $F_{uq} = 0.16$; I_o = emission intensity from 1:1 unmodified system).

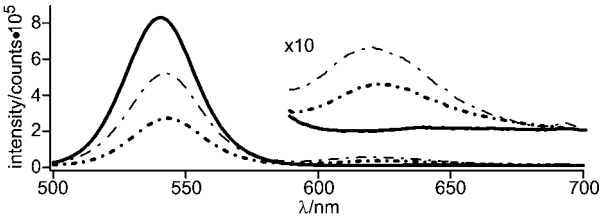

Figure 3. Emission quenching and energy transfer with **2**-modified duplex DNA: thick solid line, 1:5 unmodified system; thick dash−dotted line, 1:5 Bodipy system; thin dash−dotted line, 1:5 Bodipy system with 1 μM thrombin.

emission intensity by 8 ± 2% (Figure 2a, thick solid line) over a variety of DNA concentrations, similar to peptides and proteins (*33*). Addition of 1 and 5 equiv of **1**-modified duplex DNA decreased the nanoparticle emission intensity (Figure 2a, 1:1, 26 ± 3%, thick dashed line; 1:5, 48 ± 2%, thick dash−dotted line) from the emission of the unmodified duplex DNA bound CdSe@ZnS nanoparticles. Direct Stern-Volmer analysis of emission quenching vs **1**-modified duplex DNA showed significant downward curvature, suggesting significant exclusion of complex **1** from the nanoparticle surface. A modified Stern-Volmer analysis (Figure 2b, I_o/I as initial intensity divided by observed intensity) suggested DNA/CdSe@ZnS affinity of 1.5 $\times 10^7$ M^{-1} ($K_d = 67$ nM) with 16% of the emission remaining unaffected by **1**-modified duplex DNA. The initial emission quenching of this system is consistent with the partial complementarity of oligo B to the aptamer sequence from the Plaxco/Heeger system (*19*, *27*) that provided some initial electrochemical (Faradaic) current. The remaining 16% of unaffected emission intensity is reflective of either residual emission from fully "quenched" nanoparticles or steric exclusion of complex **1** from the nanoparticle surface at high DNA concentrations. Despite these effects, two limiting cases were examined to better understand this system: low- and high-density duplex DNA biosensors (1:1 and 1:5 CdSe@ZnS nanoparticle to DNA).

Energy transfer to **2**-modified duplex DNA was examined in the high-density situation (1:5 situation) for comparison to literature reports. Other reports have shown up to 40 equiv of duplex DNA adsorbed to CdSe nanoparticles (*23*); however, these cases have used longer capping groups terminated with streptavidin (~60 Å vs ~8 Å in this system). Ellington and co-workers have used the strongly adsorbing Eclipse quenchers in such systems to achieve almost complete quenching (*21*). Despite the weaker quenching of **2** from decreased spectral overlap, compound **2** was used for comparison to previous protein-attached biosensors based on semiconductor nanoparticles. Addition of **2**-modified duplex DNA to MHDA-capped CdSe@ZnS nanoparticles quenched the nanoparticle emission intensity (545 nm) by 42 ± 2% and increased the **2** emission intensity (625 nm) by 60 ± 5% (Figure 3, thick to thin dash−dotted lines). The degree of energy transfer (via comparison to protein-based systems) is inconsistent with duplex DNA conformation as a rigid helix extending perpendicular to the nanoparticle surface. This model would predict 2−5% nanoparticle emission quenching (~100 Å separation, $n = 5$, 50 Å Förster radius) (*34*). These results indicate initial duplex unwinding along with movement of the DNA duplex (arrows, Figure 1).

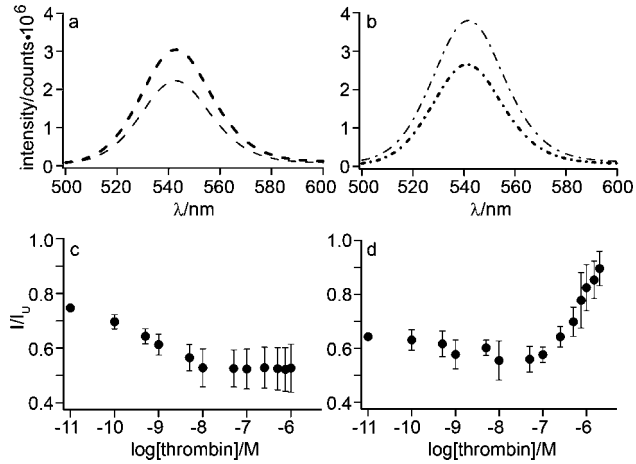

Figure 4. Thrombin-dependent emission responses of MHDA-capped systems. (a,c) 1:1 system, dashed lines; (b,d) 1:5 system, dash−dotted lines. Emission spectra (a,b): Thick lines before thrombin addition, thin lines after thrombin addition (1 μM thrombin). Titration data (c,d): thrombin dependence on emission intensity (545 nm, standard deviation used for error bars, $n = 3$) emission intensity normalized to emission intensity of the parent (c, 1:1; d, 1:5) unmodified systems (defined as I_U) and represented as observed intensity divided by the unmodified intensity (I/I_U).

Emission Response to Thrombin and Alternative Analytes. Thrombin addition to the 1:1 and 1:5 basic biosensor systems provided reproducible but different changes in nanoparticle emission intensity (Figure 4). Introduction of 1 μM thrombin (Figure 4a,b: thin lines; 30−45 min response times) to the 1:1 basic biosensor systems showed a 35 ± 8% quench in emission intensity, while the 1:5 basic biosensor systems showed a 51 ± 2% increase in emission intensity. These emission responses suggested two thrombin-induced **1**-CdSe@ZnS nanoparticle interactions. Thrombin titration curves (Figure 4c,d) for the 1:1 and 1:5 basic biosensor systems are represented as the observed emission intensities (I) relative to the parent (1:1, Figure 4c; 1:5, Figure 4d) unmodified systems (I_U) to compare the relative degree of quenching. Emission quenching at 10 nM thrombin is similar for both the 1:1 and 1:5 biosensor systems; however, the emission intensity 1:5 biosensor system increases at higher thrombin concentrations. These results suggest that the 50% emission intensity increase in the 1:5 biosensor system is an additional state that occurs after an intermediate state. Inspection of even the 1:1 biosensor system thrombin titration curve shows log-linear relationship, which is atypical of a two-state binding site isotherm. A half-maximal signal change occurs at 0.5−1.0 nM thrombin addition but cannot be considered a dissociation constant, since the nanoparticle concentration is 25 nM. The large effect at less than 10% thrombin loadings (<2.5 nM) more than likely occurs by dimerization (via the two binding sites on thrombin) or nonspecific binding. The second phase in the 1:5 biosensor system titration with thrombin (Figure 4d, 10 nM to 10 μM) had difficulties being fit to a single binding site isotherm; however, a reasonable fit to a cooperative binding equation (Hill coefficient of 2.2 ± 0.6, $n = 4$) was obtained. The Hill coefficient suggests **1**-thrombin cooperative interaction from adjacent aptamer-bound thrombins. Evidence for reporter group interactions with thrombin are also seen with the Bodipy system.

Table 2. Emission Quenching of Alternative Systems and Analytes

system	analyte (1 μM)	1:1[a]	1:5[a]
basic	thrombin	−35 (8) %	+51 (2) %
	lysozyme	−1 (1) %	−7 (1) %
	IFABP	−2 (6) %	−8 (1) %
	BSA	+6 (3) %	−17 (1) %
	heparin & hirudin	−8 (4) %	n.d.[b]
basic + heparin & hirudin	thrombin	−4 (5) %	n.d.[b]
basic + thrombin	heparin & hirudin	−4 (3) %	n.d.[b]
scrambled	thrombin	−1 (1) %	+10 (1) %
unmodified	thrombin	−2 (3) %	+9 (1) %
CdSe@ZnS_{5-6}	thrombin	−2 (4) %	−2 (3) %
CdSe@ZnS_{2-3} only	thrombin	−2 (3) %	

[a] Nanoparticle to DNA molar ratio, average change of fraction intensity from analyte addition relative to emission intensity before analyte addition from three to five determinations (standard deviation in parenthesis). [b] Not determined.

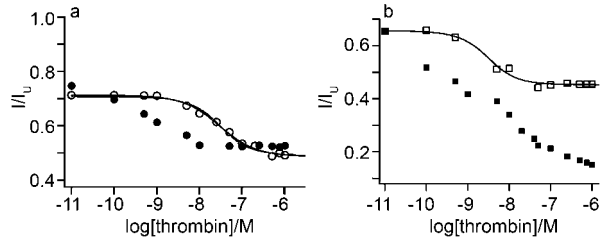

Figure 5. Thrombin-dependent emission responses of additional biosensing systems. Observed emission intensity (545 nm) relative to emission intensity from the 1:1 unmodified system (I/I_U) in the appropriate buffer: Fraction of initial (unmodified system) intensity relative to thrombin added: (A) 1:1 MHDA-capped system with (open circles) and without (filled circles) 25 nM (1.0 equiv) of heparin; (B) 1:1 MUTEG-capped system in MOPS-based buffer (filled squares) and in PSS-based buffer (open squares). The open circles (a) and open squares (b) were fit to a single binding site isotherm ($[NP]_{tot} = 25$ nM; a, $K_d = 28$ nM, $I_{initial} = 71\%$, $I_{final} = 49\%$; b, $K_d = 2.0$ nM, $I_{initial} = 66\%$, $I_{final} = 45\%$).

In this system, thrombin addition (Figure 3, thick to thin lines) caused the emission intensity of the nanoparticle (545 nm), and Bodipy (618 nm, plus blue shift) increased indicating a decrease in polarity of the Bodipy environment while being moved away from the nanoparticle surface. The Bodipy 1:5 system indicates reporter group binding to thrombin in concert with movement away from the nanoparticle surface; such effects in the complex **1** 1:5 biosensor system would cause the observed increase in emission intensity at 1 μM thrombin (Figure 4b). Despite the non-two-state binding isotherms for the 1:5 biosensor system, the MHDA-capped biosensor systems yielded a qualitative assay for thrombin activation.

Selectivity of Thrombin-Mediated Emission Responses. The selectivity of the qualitative thrombin responses from the 1:1 and 1:5 biosensor systems was examined. Addition of 1 μM thrombin to MHDA-capped CdSe@ZnS nanoparticles caused no change in nanoparticle emission within error (Table 2). The electron transfer nature of **1**-mediated quenching was demonstrated when the more insulated CdSe@ZnS_{5-6} nanoparticles showed minimal **1**-modified DNA emission changes and no significant thrombin-mediated emission changes. These observations suggest that thrombin responses of the basic biosensor systems are not due to changes in electrostatics at the nanoparticle surface. Assemblies using **1**-modified duplex DNA that did not contain the aptamer consensus sequence (scrambled) showed no thrombin-mediated change in emission intensity of the 1:1 scrambled system and a small increase in emission intensity of the 1:5 scrambled system. While the response to noncognate proteins was opposite of the thrombin response, the 1:5 basic biosensor system displayed significantly lower selectivity than the 1:1 basic biosensor system. The 1:1 basic biosensor system showed no significant response to lysozyme or IFABP, while bovine serum albumin BSA showed a small effect. Considering the isoelectric points of these proteins (thrombin, 7.3; lysozme, 11.3; IFABP, 5.8; BSA, 5.3), protein electrostatics seems to have minimal contributions to thrombin-selective emission responses.

As the last selectivity test for the 1:1 biosensor system, the effect of two thrombin inhibitors (heparin and hirudin) on the thrombin-mediated responses was examined. Addition of the inhibitors before thrombin addition caused no change in the emission spectrum, while addition of the inhibitors to the thrombin-bound 1:1 biosensor system did not restore the emission intensity. These results suggest that thrombin binding is responsible for the 34% decrease in emission intensity observed with the 1:1 biosensor system. The lack of reversible inhibition suggests that the thrombin−aptamer/nanoparticle affinity is higher than either the thrombin−inhibitor affinities or thrombin-induced irreversible nanoparticle aggregation. A number of variations to the 1:1 biosensor system were examined to obtain a better measurement of the thrombin−aptamer/nanoparticle affinity and to generate a biosensor that could be used for quantitative thrombin measurement.

Solubility Mediates Non-Two-State Binding. Contributions from thrombin-mediated nanoparticle dimerization and aggregation were examined. Following the inhibition studies from above, thrombin titrations were carried out in the presence of one of the two inhibitors, heparin, leaving the fibrinogen exosite and active site of thrombin available for binding the aptamer. The observed thrombin-dependent emission intensities followed a single binding site isotherm with a dissociation constant of 25 nM (Figure 5A, open circles; $K_a = 4.0 \times 10^7$ M^{-1}). The observed thrombin−nanoparticle affinity is consistent with previously reported thrombin−aptamer affinities, but should be considered weaker than the thrombin−aptamer/nanoparticle affinity due to competitive inhibition. More importantly, the introduction of heparin demonstrates that thrombin-mediated nanoparticle dimerization contributes to the non-two-site binding isotherms observed with the MHDA-capped systems.

Thrombin-dependent two-state binding isotherms were observed in the absence of heparin for 1:1 biosensor systems with mercaptoundecyltriethylene glycol (MUTEG) capping ligands. Alcohol/glycol-terminated surfaces are well-known to minimize nonspecific binding and improve solubility in the presence of aqueous mono- and divalent salt solutions (e.g., physiological conditions). MUTEG-capped 1:1 CdSe@ZnS nanoparticles in the low ionic strength MOPS-buffered solutions used for the MHDA-capped systems yielded similar thrombin-dependent results to the 1:1 MHDA-capped system (Figure 5B, filled squares). When the ionic strength was raised (PSS), to increase the solubility of the MUTEG-capped 1:1 CdSe@ZnS nanoparticles, thrombin-dependent results that fit a two-state binding site isotherm (Figure 5B, filled squares; $K_d = 2.0$ nM, $K_a = 5 \times 10^8$ M^{-1}) were observed. Comparison of the low-to-moderate ionic strength conditions suggested that nanoparticle solubility controls the thrombin-mediated aggregative effects seen throughout this study.

DISCUSSION

Generation of soluble unimolecular biosensors based on semiconductor nanoparticles represents the next and necessary iteration in solution DNA/RNA-based biosensors. The majority of aptamer-attached, semiconductor nanoparticle-based biosensors have been based on analyte-dependent aggregation. These aggregative assays generate qualitative analysis and single time

point quantitative analysis. Unimolecular biosensors rely on nonaggregative signaling mechanisms and therefore allow long-term quantitative analysis of analyte concentrations. Long-term monitoring of analyte concentrations would utilize the high photostability of semiconductor nanoparticles, relative to organic fluorophores. Current single-point analysis using semiconductor nanoparticle-based assays take advantage of the high photostabilities and large two-photon cross sections; however, long-term monitoring better demonstrates the high photostability of semiconductor nanoparticles.

In this study, single-stranded DNA seemed to nonspecifically bind other nanoparticles. This nonspecific binding induced aggregation and was a significant impediment to biosensor function. Analysis of thrombin-dependent emission intensities using logarithmic scales were necessary to discern between two-state binding and nonspecific binding/aggregation. Many reports in this area use linear scales, where nonconformity to two-state binding site isotherms is difficult to discern. These nonspecific effects from single-stranded DNA are not expected for electrochemical biosensors due to the use of a bulk material as the detection platform. Nonspecific aggregation does become an issue for nanomaterials diffusing in biological media. We do not suggest that MUTEG or mercaptoundecylhexaethylene glycol capping ligand provides the ultimate solution to nanoparticle solubility; however, MUTEG capping did alleviate the nonspecific aggregation in the initial version of these biosensors. Solubility of semiconductor nanoparticles is becoming an important issue for live cell imaging and toxicity of these inorganic fluorophores (*35*−*37*). This study also suggests a need for careful consideration of capping ligands in semiconductor nanoparticle-based biosensor design.

Translation of aptamer-based electrochemical biosensors to fluorescence imaging using semiconductor nanoparticles was obtained, once nanoparticle aggregation was avoided. Thrombin-dependent changes in nanoparticle emission intensity were observed in all systems that used the redox-active complex **1** attached to aptamer-containing duplex DNA. Emission intensity showed two responses: a 35% decrease in emission intensity (1:1 system) or a 50% increase in emission intensity (1:5 system). The more dilute situation (1:1) operated as expected from the electrochemical biosensor literature (*27*), while the concentrated situation (1:5) showed steric exclusion and sequestration of complex **1** from the nanoparticle surface. The thrombin-dependent emission intensity profiles only fit to two-state binding models in two situations, heparin addition to 1:1 MHDA-capped assemblies and 1:1 MUTEG-capped assemblies in a biocompatible buffer system. Deviation from two-state binding isotherms, more than likely, arose from nanoparticle aggregation. Solubility effects should be expected to play a larger role in thrombin biosensors compared to previous biosensors for lower molecular weight analytes (maltose and palmitate). An additional aspect of aptamer-based sensors, relative to protein-based sensors, is nonspecific nanoparticle binding/aggregation resulting from single-stranded DNA or RNA. Using triethylene glycol terminal groups, quantitative thrombin biosensors were generated using charge/electron transfer quenching of CdSe@ZnS nanoparticles.

These findings demonstrate not only the portability of charge/electron transfer quenching in semiconductor nanoparticle-based biosensors (protein to nucleic acid sensing components), but also the need to carefully consider nanobiosensor solubility in binding profiles. By simply changing the capping ligand for the CdSe@ZnS nanoparticle thrombin-dependent emission profiles moved from multistate/aggregative profiles to two-state profiles depending on the buffer conditions. The nucleic acid surface density on the CdSe@ZnS nanoparticle changed the direction (increase vs decrease) of emission change. The size of thrombin, relative to maltose or palmitate, mediated this new observation in our biosensor systems, where in the 1:5 system the **1**-modified single DNA strand was excluded from the surface. Such an observation points to the need for a 1:1 sensing element to nanoparticle ratios in this class of sensors to remove artifacts from steric hindrance and molecular exclusion. Despite these caveats, this work shows a third principle for constructing soluble, semiconductor nanoparticle-based biosensors; aptamer conformation changes along with protein conformation change and protein binding site water exclusion. Therefore, this work demonstrates a significant advance toward the eventual use of these semiconductor nanoparticle-based biosensors for long-term imaging of analyte fluxes within living cells.

ACKNOWLEDGMENT

Funding for this research was provided by the Office of Naval Research (N000140710218) and the National Science Foundation (DBI-0508134).

LITERATURE CITED

(1) Jaiswal, J. K., and Simon, S. M. (2007) Imaging single events at the cell membrane. *Nat. Chem. Biol. 3*, 92–98.

(2) Raymo, F. M., and Yildiz, I. (2007) Luminescent chemosensors based on semiconductor quantum dots. *Phys. Chem. Chem. Phys. 9*, 2036–2043.

(3) Thurn, K. T., Brown, E. M. B., Wu, A., Vogt, S., Lai, B., Maser, J., Paunesku, T., and Woloschak, G. E. (2007) Nanoparticles for applications in cellular Imaging. *Nanoscale Res. Lett. 2*, 430–441.

(4) Shin, S. K., Yoon, H. J., Jung, Y. J., and Park, J. W. (2006) Nanoscale controlled self-assembled monolayers and quantum dots. *Curr. Opin. Chem. Biol. 10*, 423–429.

(5) You, C. C., Verma, A., and Rotello, V. M. (2006) Engineering the nanoparticle-biomacromolecule interface. *Soft Matter 2*, 190–204.

(6) Sapsford, K. E., Pons, T., Medintz, I. L., and Mattoussi, H. (2007) Biosensing with luminescent semiconductor quantum dots. *Sensors 6*, 925–953.

(7) Zhou, M., and Ghosh, I. (2007) Quantum dots and peptides: A bright future together. *Biopolymers 88*, 325–339.

(8) Benson, D. E. (2006) Nanoparticles for reagentless biosensing, In *Nanomaterials for Biosensors* (Kumar, C. S. S. R., Ed.) pp 337−367, Wiley-VCH, Weinheim.

(9) Somers, R. C., Bawendi, M. G., and Nocera, D. G. (2007) CdSe nanocrystal based chem-/bio-sensors. *Chem. Soc. Rev. 36*, 579–591.

(10) Gill, R., Patolsky, F., Katz, E., and Willner, I. (2005) Electrochemical control of the photocurrent direction in intercalated DNA/CdS nanoparticle systems. *Angew. Chemie, Int. Ed. 44*, 4554–4557.

(11) Katz, E., Zayats, M., Willner, I., Lisdat, F. (2006) Controlling the direction of photocurrents by means of CdS nanoparticles and cytochrome c-mediated biocatalytic cascades. *Chem. Commun.* 1395−1397.

(12) Sandros, M. G., Gao, D., and Benson, D. E. (2005) A modular nanoparticle-based system for reagentless small molecule biosensing. *J. Am. Chem. Soc. 127*, 12198–12199.

(13) Sandros, M. G., Shete, V., and Benson, D. E. (2006) Selective, reversible, reagentless maltose biosensing with core-shell semiconducting nanoparticles. *Analyst 131*, 229–235.

(14) Medintz, I. L., Clapp, A. R., Melinger, J. S., Deschamps, J. R., and Mattoussi, H. (2005) A reagentless biosensing assembly based on quantum dot-donor Forster resonance energy transfer. *Adv. Mater. 17*, 2450–2455.

(15) Aryal, B. P., and Benson, D. E. (2006) Electron donor solvent effects provide semiconducting nanoparticle-based biosensors. *J. Am. Chem. Soc. 128*, 15986–15987.

(16) Moschou, E. A., Bachas, L. G., Daunert, S., and Deo, S. K. (2006) Hinge-motion binding proteins: Unraveling their analytical potential. *Anal. Chem. 78*, 6692–6700.
(17) Medintz, I. L., Clapp, A. R., Mattoussi, H., Goldman, E. R., Fisher, B., and Mauro, J. M. (2003) Self-assembled nanoscale biosensors based on quantum dot FRET donors. *Nat. Mater. 2*, 630–638.
(18) Willner, I., and Zayats, M. (2007) Electronic aptamer-based sensors. *Angew. Chem., Int. Ed. 46*, 6408–6418.
(19) Xiao, Y., Lai, R. Y., and Plaxco, K. W. (2007) Preparation of electrode-immobilized, redox-modified oligonucleotides for electrochemical DNA and aptamer-based sensing. *Nat. Protoc. 2*, 2875–2880.
(20) Winkler, W., Nahvi, A., and Breaker, R. R. (2002) Thiamine derivatives bind messenger RNAs directly to regulate bacterial gene expression. *Nature 419*, 952–956.
(21) Levy, M., Cater, S. F., and Ellington, A. D. (2005) Quantum-dot aptamer beacons for the detection of proteins. *ChemBioChem 6*, 2163–2166.
(22) Lu, Y., and Liu, J. W. (2007) Smart nanomaterials inspired by biology: Dynamic assembly of error-free manomaterials in response to multiple chemical and biological stimuli. *Acc. Chem. Res. 40*, 315–323.
(23) Liu, J. W., Lee, J. H., and Lu, Y. (2007) Quantum dot encoding of aptamer-linked nanostructures for one-pot simultaneous detection of multiple analytes. *Anal. Chem. 79*, 4120–4125.
(24) Choi, J. H., Chen, K. H., and Strano, M. S. (2006) Aptamer-capped nanocrystal quantum dots: A new method for label-free protein detection. *J. Am. Chem. Soc. 128*, 15584–15585.
(25) Topp, S., and Gallivan, J. P. (2008) Random walks to synthetic riboswitches-a high-throughput selection based on cell motility. *ChemBioChem 9*, 210–213.
(26) Sandros, M. G., Gao, D., Gokdemir, C., Benson, D. E. (2005) General, high-affinity approach for the synthesis of fluorophore appended protein nanoparticle assemblies. *Chem. Commun.* 2832−2834.
(27) Xiao, Y., Piorek, B. D., Plaxco, K. W., and Heeger, A. J. (2005) A reagentless signal-on architecture for electronic, aptamer-based sensors via target-induced strand displacement. *J. Am. Chem. Soc. 127*, 17990–17991.
(28) Hong, R., Fischer, N. O., Verma, A., Goodman, C. M., Emrick, T., and Rotello, V. M. (2004) Control of protein structure and function through surface recognition by tailored nanoparticle scaffolds. *J. Am. Chem. Soc. 126*, 739–743.
(29) Lehrer, S. S. (1971) Solute perturbation of protein fluorescence. Quenching of the tryptophyl fluorescence of model compounds and of lysozyme by iodide ion. *Biochemistry 10*, 3254–3263.
(30) Fan, C., Plaxco, K. W., and Heeger, A. J. (2003) Electrochemical interrogation of conformational changes as a reagentless method for the sequence-specific detection of DNA. *Proc. Natl. Acad. Sci. U.S.A. 100*, 9134–9137.
(31) Fan, C., Plaxco, K. W., and Heeger, A. J. (2005) Biosensors based on binding-modulated donor-acceptor distances. *Trends Biotechnol. 23*, 186–192.
(32) Xiao, Y., Lubin, A. A., Heeger, A. J., and Plaxco, K. W. (2005) Label-free electronic detection of thrombin in blood serum by using an aptamer-based sensor. *Angew. Chem., Int. Ed. 44*, 5456–5459.
(33) Aryal, B. P., Neupane, K. P., and Sandros, M. G. (2006) Metallothioneins initiate semiconducting nanoparticle cellular toxicity. *Small 2*, 1159–1163.
(34) Medintz, I. L., Konnert, J. H., Clapp, A. R., Stanish, I., Twigg, M. E., Mattoussi, H., Mauro, J. M., and Deschamps, J. R. (2004) A fluorescence resonance energy transfer-derived structure of a quantum dot-protein bioconjugate nanoassembly. *Proc. Natl. Acad. Sci. U.S.A. 101*, 9612–9617.
(35) Smith, A. M., Duan, H., Rhyner, M. N., Ruan, G., and Nie, S. (2006) A systematic examination of surface coatings on the optical and chemical properties of semiconductor quantum dots. *Phys. Chem. Chem. Phys. 8*, 3895–3903.
(36) Anderson, R. E., and Chan, W. C. W. (2008) Systematic investigation of preparing biocompatible, single, and small ZnS-capped CdSe quantum dots with amphiphilic polymers. *ACS Nano 2*, 1341–1352.
(37) Kairdolf, B. A., Mancini, M. C., Smith, A. M., and Nie, S. (2008) Minimizing nonspecific cellular binding of quantum dots with hydroxyl-derivatized surface coatings. *Anal. Chem. 80*, 3029–3034.

BC8003952

Site-Specific, Thiol-Mediated Conjugation of Fluorescent Probes to Cysteine-Modified Diabodies Targeting CD20 or HER2

Shannon J. Sirk,* Tove Olafsen, Bhaswati Barat, Karl B. Bauer, and Anna M. Wu

Crump Institute for Molecular Imaging, Department of Molecular and Medical Pharmacology, David Geffen School of Medicine at UCLA, Los Angeles, California 90095. Received March 24, 2008; Revised Manuscript Received October 15, 2008

Small, engineered antibody fragments such as diabodies (50 kDa noncovalent dimers of single-chain Fv fragments) are useful alternatives to their larger antibody counterparts. However, due to their size, they are more susceptible to disruption of their antigen binding sites when modified using random conjugation techniques. Previous work has demonstrated the utility of a C-terminal cysteine modification for site-specific radiolabeling of an anti-CEA diabody, resulting in the creation of a cys-diabody (CysDb). In the present work, the adaptability of the CysDb system was explored by creating two additional CysDbs: one specific for CD20 and one for HER2. Purified CysDbs of both specificities demonstrated behavior consistent with stable, covalent dimers harboring a readily reducible disulfide bond. Each CysDb was site-specifically conjugated to three different fluorophores for optical detection: the large fluorescent proteins phycoerythrin (PE) and allophycocyanin (APC), and the small fluorescent molecule Alexa Fluor488. Fluorophore-conjugated CysDbs bound specifically to their targets in both antigen systems and with each different fluorescent tag as determined by flow cytometry. *In vitro* specific antigen binding was observed in the presence of a mixture of specific and nonspecifically conjugated CysDbs. Conjugates retained both specificity and fluorescence, demonstrating the successful expansion of the CysDb repertoire to new targets and to new site-specific conjugation possibilities.

INTRODUCTION

Monoclonal antibodies (mAbs) comprise a unique class of tumor targeting agents capable of specific recognition of cell surface antigens, including cancer biomarkers. Many therapeutic mAbs have been used to target and treat a wide range of diseases, including breast cancer, lymphoma, colorectal cancer, and leukemia (*1*). When conjugated to radionuclides, antibody derivatives specific for cancer biomarkers can be employed for tumor detection using imaging methods such as positron emission tomography (PET) (*2*−*4*). MAbs armed with therapeutic radionuclides or other cytotoxic agents have been used to deliver targeted toxicity to a tumor while minimizing damage to healthy tissue (*5, 6*).

Intact mAbs are highly specific targeting agents but are not suited for every application due to their large size and full Fc domain. Engineered antibody fragments harness the specificity of the variable domains while modifying or deleting the constant domains to suit the intended targeting need (*7, 8*). Single-chain Fvs (scFvs), consisting of the variable light (V_L) and variable heavy (V_H) domains joined by an amino acid linker, are the smallest antibody fragments that still retain specificity and are commonly used antigen-specific probes (*9*−*11*). ScFv linker length influences fragment multimerization, with shorter linkers (3−12 residues) supporting the formation of bivalent diabodies (Dbs) (*12*). Compared to scFvs, Dbs demonstrate superior binding *in vitro* and improved tumor accumulation *in vivo* due to increased avidity and therefore increased functional affinity (*13*).

Targeting applications regularly involve labeling antibodies and antibody fragments, often with a radionuclide. Common techniques involve conjugation via random tyrosine or lysine residues (*14, 15*). Intact antibodies (150 kDa) are large enough to offer several sites that will not disrupt antigen binding when conjugated to a labeling agent. At a fraction of the size of intact antibodies, Dbs (50 kDa) have fewer available conjugation sites, and it is therefore more likely that conjugation will disrupt antigen binding or overall conformation and efficacy of the molecule as a tumor targeting agent.

To address this problem, methods for site-specifically labeling Dbs and bypassing potential adverse effects of random conjugation have been pursued. The addition of C-terminal cysteinyl peptides was originally explored as a method to induce dimerization of scFv molecules (*16, 17*) and provide a defined site for radiometal chelation (*18*). Site-specific PEGylation has been used to adjust the circulating half-life of cysteine-modified scFvs (*19*), and liposomes have been coupled via thiol chemistry to scFvs targeting tumor biomarkers and tumor stromal cells (*20, 21*).

Crystallographic analysis of an anti-carcinoembryonic antigen (CEA) Db revealed that the antigen binding sites are located on opposite sides from the C-termini of the V_H domains (*22*). An anti-CEA Db with a cysteine residue incorporated at the C-terminus of the V_H domain of each scFv monomer was created (CysDb) and expressed in mammalian cell culture, spontaneously yielding stable covalent dimers (*23*). Anti-CEA CysDbs demonstrated excellent binding *in vitro* and, following site-specific chelate conjugation and radiometal labeling, specifically targeted CEA-expressing tumor xenografts in a microPET mouse model (*23*).

On the basis of this initial success, the CysDb format was extended to two additional cancer targets—CD20 (lymphoma) and HER2 (breast cancer). CD20 and HER2 were chosen as candidate antigen systems because there are pre-existing, well-characterized therapeutic antibodies (rituximab and trasuzumab) specific for these targets. Functional CysDbs of both specificities were produced and characterized. Both CysDbs retained specific antigen binding following site-specific conjugation to three different fluorophores. Bifunctionality of each conjugate is

* Author to whom correspondence should be addressed. ssirk@mednet.ucla.edu, 700 Westwood Plaza, Crump A420, Los Angeles, CA 90095, Telephone (310) 267-2819, Fax (310) 206-8975.

10.1021/bc800113v CCC: $40.75 © 2008 American Chemical Society
Published on Web 11/18/2008

demonstrated through the observed antigen specificity of each CysDb as well as the unique fluorescence profile of each attached fluorophore. Successful expansion of the C-terminal cysteine modification to two new specificities supports the utility of the CysDb format as a generalizable platform for site-specific conjugation of tumor targeting molecules with functional payloads.

EXPERIMENTAL PROCEDURES

Design of Cysteine-Modified Diabodies. Diabodies were constructed from existing gene constructs containing variable regions recognizing HER2 (*4*) or CD20 (Olafsen et al. [abstr.], *J. Nucl. Med.* 47:48P, 2006). Overlap-extension PCR and site-directed mutagenesis (QuikChange XL, Stratagene) were used to create CysDb genes with a five amino acid linker (SGGGG) between the variable light (V_L) and variable heavy (V_H) domains and a C-terminal cysteine modification (GGC) to give the final CysDb construct: (V_L-SGGGG-V_H-GG**C**) in the pEE12 mammalian expression vector (*24*). All constructs were confirmed by DNA sequencing.

Mammalian Expression, Selection, and Purification. 2.5×10^6 NS0 mouse myeloma cells (Sigma) were transfected by electroporation with 10 μg linearized plasmid DNA and selected in glutamine-deficient DMEM (Mediatech Inc.) as described (*24*). Transfectants were screened for CysDb expression by assaying cell culture supernatant by ELISA and/or SDS-PAGE using precast 4−20% gels (Bio-Rad).

ELISA. For anti-CD20 CysDb ELISA, microtiter plate wells were coated with 100 μL (2 μg/mL) goat anti-mouse Fab (Sigma), then blocked with 1% BSA. 100 μL cell culture supernatant was assayed, and anti-CD20 CysDb was detected with 100 μL (0.4 μg/mL) alkaline phosphatase (AP)-conjugated goat anti-mouse Fab (Jackson Immunolabs). Signal was developed using phosphatase substrate tablets (Sigma), and absorbance was detected at 405 nm using a microplate reader (Tecan). The same procedure was performed for anti-HER2 CysDb ELISA, except using Protein L (Sigma) for coating wells and Protein L-horse radish peroxidase (HRP) (Sigma) for detection. Signal was developed with CN/DAB Substrate Kit (Pierce) and analyzed visually for black precipitate.

Gel Electrophoresis and Immunoblotting. SDS-PAGE gels were run with 30 μL cell culture supernatant and either stained with Microwave Blue (Protiga) or transferred to nitrocellulose membrane for Western analysis. Samples were run under both reducing (100 mM DTT) and nonreducing conditions. Anti-CD20 CysDb was detected on Western blot with 0.4 μg/mL goat anti-mouse Fab-AP (Jackson Immunolabs), and color was developed with NBT/BCIP substrate (Promega). Anti-HER2 CysDb was detected on Western blot by Protein L-HRP (Sigma) and color was developed with CN/DAB Substrate Kit (Pierce).

Purification. Clones showing the highest expression were expanded into triple flasks (Corning), and approximately 700 mL cell culture supernatant was collected and filtered on a polyethersulfone (PES) membrane (Corning). Supernatant was loaded onto a Protein L column (Pierce) with a bed volume of 1 mL at a flow rate of 0.4 mL/min in PBS using an ÄKTA Purifier (GE Healthcare Life Sciences). Bound protein was eluted with 0.1 M glycine, pH 2.5, over 20 column volumes. Eluted fractions were neutralized upon collection in 5% final volume 2 M Tris, pH 8.0. Fractions containing protein were identified by SDS-PAGE and combined. Buffer was exchanged to PBS, protein was concentrated using a spin column (Vivaspin 20, 10 kDa cutoff), and protein was stored at 4 °C.

Characterization of Purified CysDbs. Purified, concentrated protein was analyzed by SDS-PAGE followed by Microwave Blue gel staining or Western blot analysis as described above. All molecular weights were approximated by comparison to Kaleidoscope prestained molecular weight standard (Bio-Rad) and a previously characterized anti-CEA CysDb with a known molecular weight of 55 kDa. CysDbs were also subjected to size-exclusion chromatography on a Superdex 75 column (GE Healthcare Life Sciences) in PBS at a flow rate of 0.5 mL/min over one column volume (24 mL) on an ÄKTA Purifier. Protein purity was estimated from size exclusion chromatography data. Anti-CD20 CysDb (only) was analyzed for specific binding by indirect flow cytometry, described below.

Site-Specific Fluorescent Labeling. Cys-diabodies were site-specifically conjugated using thiol chemistry to three different fluorophores: phycoerythrin activated with succinimidyl 4-[*N*-maleimidomethyl]-cyclohexane-1-carboxylate (PE-SMCC, 240 kDa, Prozyme), allophycocyanin (APC)-SMCC (104 kDa, Prozyme), or Alexa Fluor 488 C_5-maleimide (A488, 720 Da, Invitrogen). Each CysDb was conjugated to each fluorophore individually, resulting in six conjugates (3 fluorescent tags × 2 CysDb specificities). Mock conjugation controls were treated under the same conditions, except with no CysDb added. Following the Phycolink conjugation kit guidelines (Prozyme), 150 μg of CysDb in 60 μL PBS was incubated at room temperature with 16 mM DTT for 30 min to reduce disulfide bonds. DTT was removed from reduction reactions using a Micro Bio-Spin 6 chromatography column (Bio-Rad), equilibrated with Exchange Buffer (50 mM MES, 2 mM EDTA, pH 6.0). Reduced CysDb was then incubated with 240 μg activated PE or APC (10 mg/mL in 50 mM MES, 2 mM EDTA, pH 6.0, with 1 μg/mL pentachlorophenol [preservative]), or 12 μg A488 (1 μg/mL, 1.4 mM in water). Molar ratios in the conjugation reactions were approximately 1:3, 1:1.25, and 5.6:1 for PE/CysDb, APC/CysDb, and A488/CysDb, respectively. Addition of fluorophore was followed by incubation in the dark at room temperature for 1 h with occasional mixing. Remaining free sulfhydryls were then blocked with 5.1 μg *N*-ethylmaleimide (NEM, 10 mg/mL in DMSO, Sigma). Reactions were wrapped in foil, incubated at room temperature with occasional mixing for 30 min, and then applied to new spin columns equilibrated with Storage Buffer (10 mM Tris-HCl, 150 mM NaCl, pH 8.2). Fluorophore-conjugated CysDbs were stored in 1.5 mL Eppendorf tubes at 4 °C, wrapped in aluminum foil. Protein yield and conjugation ratios were determined using a UV/visible spectrophotomer (Ultrospec 1100 Pro, GE Healthcare Life Sciences) to measure absorption at 280 and at the peak absorption wavelength of each flurophore.

Flow Cytometry. Flow cytometry was used to evaluate binding of CysDbs to cell-surface antigen before (anti-CD20 CysDb only) and after site-specific fluorescent labeling. Unconjugated anti-CD20 CysDb was tested on 38C13 mouse myeloma cells (ATCC #HB-132) transfected with human CD20 (*25*). Conjugated CysDbs were tested on SKW 6.4 (human B cell lymphoma, CD20-positive, ATCC #TIB-215), Daudi (human B cell lymphoma, CD20-positive, ATCC #CCL-213), and MCF-7 $HER2^+$ (human breast cancer, HER2-transfected, gift of Dr. Dennis Slamon, UCLA School of Medicine) (*26*). Cells were harvested and resuspended in PBS/1% FBS to a final concentration of 1×10^6 cells/mL. For each reaction, 5×10^5 cells (500 μL) were incubated with fluorophore-conjugated CysDb (0.5 or 5 μL) for 1 h on ice with occasional mixing.

38C13-$CD20^+$ cells were incubated first with unconjugated anti-CD20 CysDb, followed by PE-conjugated anti-mouse Fab secondary antibody (Jackson Immunolabs). SKW6.4 cells were incubated with PE-conjugated anti-CD20 CysDb only.

Each fluorescent CysDb and each mock conjugate was incubated in separate reactions with Daudi cells and MCF7-$HER2^+$ cells. Experiments were performed with 0.5 μL (low concentration sample) or 5 μL (high concentration sample) of conjugated CysDb or mock-conjugated dye. Each fluorescent

CysDb was also assayed for specific binding to either Daudi (anti-CD20 CysDbs) or MCF7-HER2$^+$ (anti-HER2 CysDbs) in the presence of other CysDbs. Mixtures were composed of one antigen-specific and two antigen-nonspecific fluorescent conjugates, with every combination represented. Each fluorescent CysDb (3 μL) was incubated with its target cell type in the presence of the other two (nonspecific) CysDb (3 μL each conjugate). Positive control samples were incubated with either anti-CD20 scFvFc (Olafsen et al. [abstr.], *J. Nucl. Med.* 47: 48P, 2006) for Daudi or anti-HER2 scFvFc (*4*) for MCF7-HER2$^+$ cells, and then washed and incubated with each of three fluorescently labeled anti-human-IgG-Fc-specific secondary antibodies (PE- and APC-conjugated, Jackson Immunolabs; Alexafluor 488-conjugated, Molecular Probes). All samples were then washed with PBS/1% FBS, resuspended in 500 μL PBS/1%FBS, filtered, and analyzed on a modified FACScan flow cytometer using *CellQuest* software (BD Biosciences). Fluorescence of 10 000 gated viable cells was collected simultaneously in 3 channels for each sample. A488 signal (519 nm emission wavelength) was detected in FL1, PE signal (578 nm emission wavelength) was detected in FL2, and APC signal (661 nm emission wavelength) was detected in FL4.

RESULTS

Design and Construction of CysDbs. C-terminal GGC modifications were added to anti-HER2 and anti-CD20 scFv gene constructs as shown (Figure 1). Anti-CD20 CysDb gene was constructed from an existing anti-CD20 single chain variable fragment gene (scFv, V_L-SGGGG-V_H), composed of rituximab (Rituxan, Genentech) mouse variable regions (Olafsen et al. [abstr.], *J. Nucl. Med.* 47:48P, 2006). Anti-HER2 CysDb gene was constructed from trastuzumab (Herceptin, Genentech) variable regions, from an existing minibody gene (*4*). The scFv orientation and linker of the anti-HER2 minibody were as follows: V_L-GSTSGGGSGGGSGGGGSS-V_H. Overlap extension PCR was used to shorten the 18 amino acid linker in the anti-HER2 scFv gene to a 5 amino acid linker (SGGGG).

Mammalian Expression. Following transfection of NS0 cells with either anti-CD20 or anti-HER2 CysDb gene construct, positive clones were identified by growth of single colonies in microtiter plates. CysDb-expressing transfectants were screened by ELISA and Western blot (data not shown). Color development verified positive clones by ELISA and allowed ranking of relative expression levels within this group. Bands on Western blots were detected at approximately 50 kDa (nonreduced) and 25 kDa (reduced), providing confirmation of the correct size of both dimer and monomeric subunit forms of the protein.

Purification. Clones expressing anti-CD20 CysDb and clones expressing anti-HER2 CysDb were expanded and CysDb was purified from the media by affinity chromatography on a Protein L column. Final protein yields were 1.6 mg/L of culture supernatant for anti-CD20 CysDb and 3.0 mg/L of culture supernatant for anti-HER2 CysDb. Purities of >99% for anti-CD20 CysDb and >90% for anti-HER2 CysDb were determined from size exclusion chromatography data.

Characterization of Purified CysDbs. *Gel Electrophoresis and Immunoblotting.* SDS-PAGE analysis demonstrated correct size and covalent dimerization of purified CysDbs. Under nonreducing conditions, both proteins migrated near the expected molecular weights of approximately 50 kDa, verifying a population of covalently dimerized molecules in the final purified product. Under reducing conditions, CysDbs migrated at approximately 25 kDa, consistent with the expected scFv monomer (Figure 2). Purified CysDbs were specifically detected by Western blot at approximately 50 kDa (nonreduced) and approximately 25 kDa (reduced) (data not shown).

Size Exclusion Chromatography. Characterization of purified CysDbs by size-exclusion chromatography resulted in elution profiles similar to each other and to previously characterized diabodies (Figure 3). Anti-CD20 CysDb (25.2 min) and anti-HER2 CysDb (22.5 min) both eluted at times similar to the previously characterized anti-CEA CysDb (21.5 min) (*23*) and anti-CD20 Db (23.7 min) (T. Olafsen, unpublished). Anti-CD20 CysDb eluted slightly later than its parental, non-cysteine-modified diabody, suggesting a more compact form of the protein, as expected with covalent dimerization (*23*). Anti-CD20 CysDb eluted later than either of the other CysDbs, consistent with its apparent smaller size as seen by SDS-PAGE (Figure 2).

Flow Cytometry. Specific antigen binding was demonstrated for anti-CD20 CysDb by indirect flow cytometry. Fluorescence of gated viable CD20$^+$ cells showed binding comparable to that of parental, non-cysteine-modified anti-CD20 diabody (data not shown).

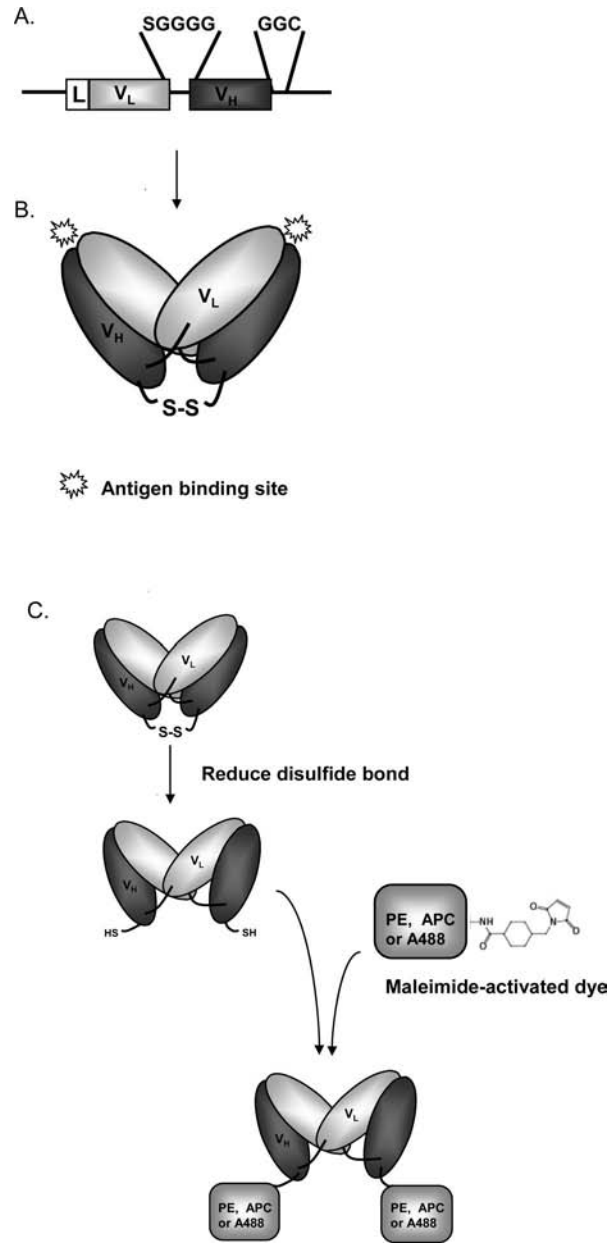

Figure 1. Schematic representation of CysDb. (A) Gene assembly for anti-CD20 and anti-HER2 CysDb (scFv monomer) with 5-aa linker and cysteine modification shown (L, leader sequence for secretion). (B) CysDb with antigen binding sites indicated by starbursts. CysDb is shown in covalent dimer form, with disulfide bond in the predicted location. (C) Conjugation reaction linking cys-diabody to fluorescent probe.

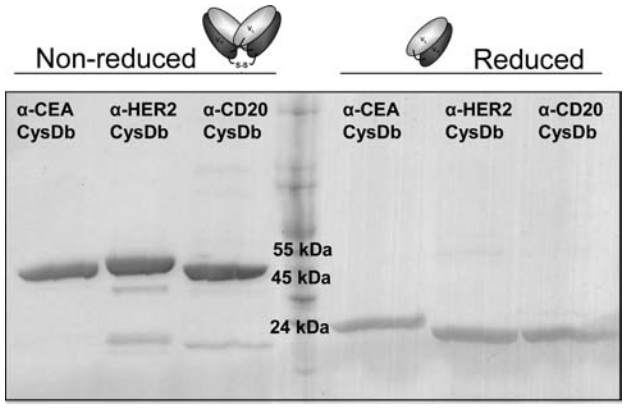

Figure 2. SDS-PAGE of three CysDbs under nonreducing (left) and reducing (right) conditions. Previously characterized anti-CEA CysDb shown for comparison purposes. Nonreduced samples migrate at expected size for covalent dimer (50 kDa), and reduced samples migrate at expected size for monomeric scFv (25 kDa).

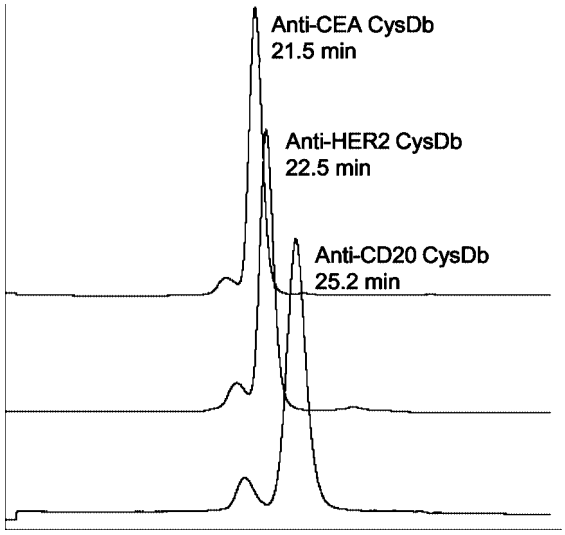

Figure 3. Size exclusion chromatography of cys-diabodies on Superdex 75 column. Previously characterized anti-CEA CysDb shown for comparison purposes.

Site-Specific Fluorescent Labeling and Specific Binding of Conjugated CysDbs. *Single-Channel Flow Cytometry*. Anti-CD20 CysDbs site-specifically conjugated to the fluorescent dyes PE, APC, or A488 demonstrated specific binding to CD20-positive Daudi cells and not to CD20-negative MCF7-HER2$^+$ cells (Figure 4). Quantities of APC and PE used were half of that suggested in the manufacturer's guidelines, as this modification yielded comparable conjugation efficiency in our hands and conserved reagent. Product guidelines for A488 recommend 10−20 mol of dye per mole of protein when conjugating thiol-reactive probes (Invitrogen). A final value of 5.6 mol of A488 C_5-maleimide per mole of CysDb was used in an attempt to reduce excessive background from unconjugated dye. Dye/protein ratios were calculated for A488 batches only, as this was the only nonprotein fluorophore and therefore gave more consistent quantitative results. The molar ratio of A488/CysDb was calculated to be 2:1.

Single-channel experiments showed binding to Daudi cells of each of the three fluorescent conjugates of anti-CD20 CysDb (Figure 4A). Mock-conjugated fluorophore background showed minimal shift in FL1, FL2 or FL4 compared to the antigen-specific binding shift of the CysDb. PE-labeled anti-CD20 CysDb also demonstrated specific binding to an additional CD20-positive cell line, SKW 6.4, by flow cytometry (data not shown). All three anti-CD20 CysDb conjugates showed a concentration-dependent shift in fluorescence from the low to the high concentration samples, with the APC version exhibiting a higher mean fluorescence in general, across all experiments performed (Figure 4B). All three anti-CD20 CysDb conjugates showed minimal nonspecific background binding to CD20-negative MCF7-HER2$^+$ cells (Figure 4C).

Analogous results were seen with PE-, APC-, and A488-conjugated anti-HER2 CysDbs. All three conjugates showed specific binding to MCF7-HER2$^+$ cells. Fluorescence shifts were seen in the expected channels for each of the conjugated CysDbs, but not for the mock-conjugated dye (Figure 5A). Cells incubated with a low concentration of PE- and APC-conjugated anti-HER2 CysDb showed very little difference in mean fluorescence intensity compared with cells incubated with a high concentration of these CysDbs (Figure 5B). When incubated with HER2-negative Daudi cells, fluorescently conjugated anti-HER2 CysDbs showed minimal background binding (Figure 5C). PE-labeled anti-HER2 CysDb also showed no binding to HER2-negative, CD20-positive SKW 6.4 cells by flow cytometry (data not shown).

Multiple-Channel Flow Cytometry. Figure 6A shows representative plots of three-channel flow cytometry experiments in which Daudi cells were incubated with a cocktail of three different CysDb conjugates: one anti-CD20 CysDb and two anti-HER2 CysDbs, each conjugated to a different fluorophore. Each of the three anti-CD20 CysDb fluorescent conjugates was tested in combination with two anti-HER2 CysDb fluorescent conjugates. For anti-CD20 CysDb-PE, specific binding to Daudi cells was demonstrated by signal in FL2 (upward shift). Minimal background signal was detected in FL4 or FL1 from either APC- or A488-conjugated anti-HER2 CysDb, respectively, as seen by a lack of rightward shift in fluorescence (Figure 6A). Similar results were seen when APC- or A488-conjugated anti-CD20 CysDb was incubated with Daudi cells in a three-conjugate mix with anti-HER2 CysDb and subjected to flow cytometric analysis in all three fluorescence channels (Figure 6B).

Parallel experiments were run with MCF7-HER2$^+$ cells which showed specific binding of conjugated anti-HER2 CysDb when mixed with anti-CD20 CysDb conjugates in three-conjugate cocktail experiments as described above. Figure 6C shows a representative plot demonstrating specific detection in FL2 of PE-conjugated anti-HER2 CysDb bound to MCF7-HER2$^+$ cells, while minimal background signal of APC- or A488-conjugated anti-CD20 CysDb was seen in FL4 or FL1, respectively. Similar results were seen for the other combinations of fluorescent conjugates. For each sample, nearly 100% of the signal was in the channel specific to the anti-HER2 conjugate being detected, while fluorescence from the nonspecific anti-CD20 CysDb was not seen, with the exception of a slightly higher background from the APC-conjugated anti-CD20 CysDb (Figure 6D).

DISCUSSION

Cysteine-modified diabodies were engineered for use as site-specifically modifiable, cancer biomarker-specific antibody fragments. The decision to place the cysteine modification at the C-terminus of the V_L-linker-V_H construct was based on previous success with a similar modification which generated the T84.66 anti-CEA CysDb (*23*). The current work extends the CysDb format from CEA to two additional antibodies recoginizing CD20 and HER2, demonstrating that this format is general. Since the C-termini of the diabody subunits are physically opposite from the antigen-binding sites on the CysDb, following reduction, any further modification to the free sulfhydryls should not interfere with binding activity (*23*). Purified CysDb exists as a stable covalent dimer until subjected to reducing conditions, demonstrating a system with simple and

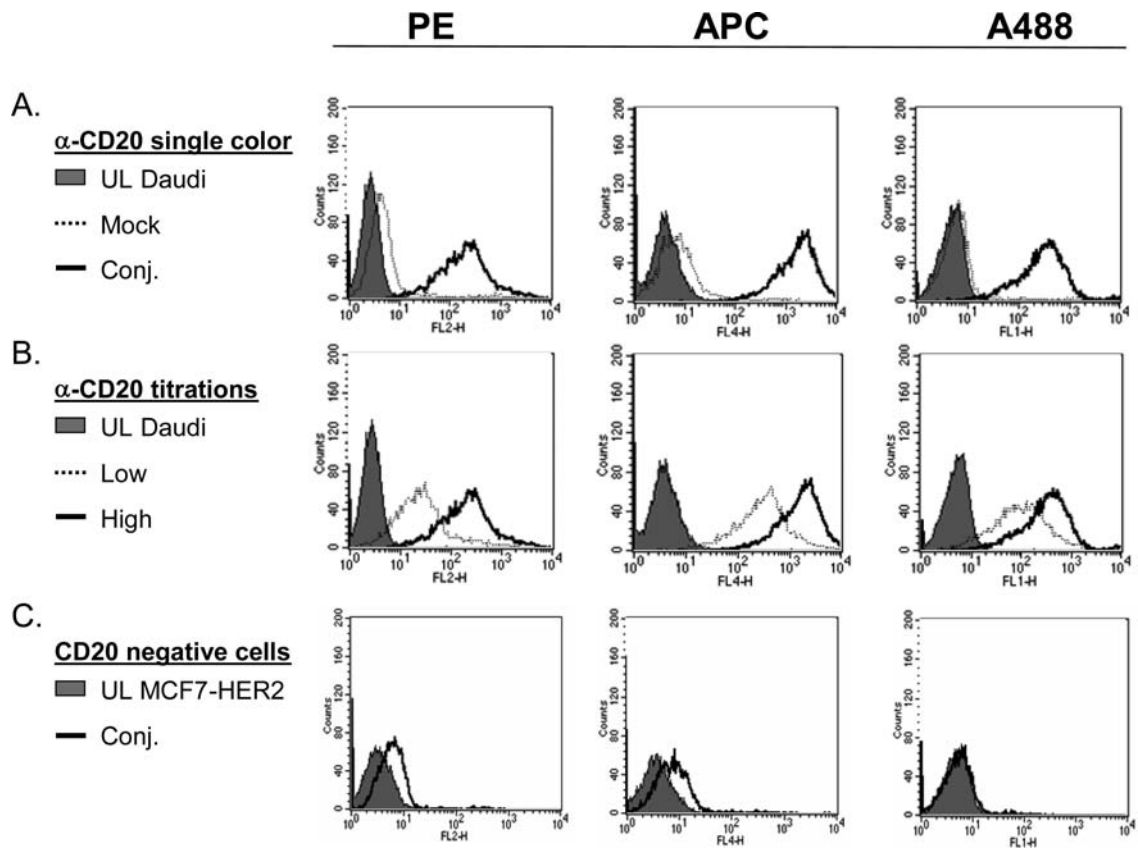

Figure 4. Flow cytometry of single-channel labeling with dye-conjugated anti-CD20 CysDb. Unlabeled cells (UL) shown in solid gray. (A) Three channels of dye-conjugated anti-CD20 CysDb (Conj., thick line) and mock conjugated dye (Mock, dotted line) demonstrating minimal background from nonspecific binding of free dye molecules to $CD20^+$ Daudi cells. (B) Three channels of low (0.5 μL, dotted line) and high (5 μL, thick line) concentrations of dye-conjugated anti-CD20 CysDb demonstrating concentration-dependent shift in mean fluorescence with increasing quantities of conjugated CysDb. (C) Three channels of dye-conjugated anti-CD20 CysDb (Conj., thick line) with minimal binding to CD20-negative MCF7-$HER2^+$ cells, demonstrating antigen-specificity of binding.

reliable control over the availability of free sulfhydryls for thiol-specific conjugation.

The presence of C-terminal cysteine residues clearly induces efficient disulfide bridge formation and a compact overall conformation. Olafsen et al. first observed that the cysteine modification and subsequent disulfide bridge formation caused an anti-CEA CysDb to appear more condensed than the parental diabody (*23*). We also found that, for the two diabody/CysDb pairs examined (anti-CD20, anti-HER2), the cysteine-modified version consistently eluted later on size exclusion chromatography compared to the native diabody (data not shown), consistent with a more closed conformation of the covalent dimer. Elution time by size exclusion appears to be an innate property of each CysDb (Figure 3) and was reproducible among purified batches of the same CysDb. The anti-HER2 CysDb and the anti-CD20 CysDb both have a predicted molecular weight of 50 kDa, although the anti-CD20 CysDb consistently eluted later by size exclusion chromatography (Figure 3). Observed differences in elution times may reflect the sequence difference in the binding sites, as well as the fact that the rituximab framework is murine whereas trastuzumab is humanized. Minor differences in migration were also observed on SDS-PAGE (Figure 2), indicating that mobility was influenced by primary sequence as well as molecular weight.

Reduction of the CysDb disulfide bridges provided a flexible and reproducible approach for site-specific conjugation. Fluorescent dyes spanning a molecular weight range from subkilodalton (A488) to several hundred kilodaltons (PE, APC) were readily coupled to the CD20- and HER2-specific CysDbs to yield six distinct bifunctional conjugates. At the same time, these conjugates retained the ability to bind to antigen, indicating that the internal disulfide bridges in the V regions, characteristic of the conserved immunoglobulin fold, were not disrupted. In addition, spectrophotometric quantitation of the molar conjugation ratio indicated ~2 dye molecules per diabody, consistent with conjugation of fluorophores only onto the two most easily accessible sulfhydryls, at the C-termini.

Fluorescent antibody fragments are regularly used for *in vitro* detection applications and *in vivo* studies in small animals for noninvasive monitoring and radiation-free imaging (*29*). Multichannel flow cytometry experiments in the current work demonstrated antigen-specific binding with the use of a cocktail of fluorescent CysDbs with a spectrum of labels, supporting this format as a robust and easily interchangeable targeting molecule. Increasingly, optically labeled antibody fragments are being used for fluorescence-guided surgery and intraoperative visualization of metastastes (*30*). CysDbs are promising for this application, as their small size should allow them to penetrate a tumor more deeply than a larger, intact antibody. Optical detection and diagnosis using a cocktail of CysDbs recognizing a set of different tumor biomarkers could provide a means for simultaneous evaluation of multiple proteins, subject to the known limitations of detection of visible light in tissues and living organisms.

The CysDb format provides a general approach for combining minimal antibody binding domains with a variety of functional moieties. Previously, the cysteine modification was used for site-specific conjugation of the macrocyclic metal chelator DOTA(1,4,7,10-tetraazacyclododecane-1,4,7,10-tetraacetic acid), enabling radiolabeling of the anti-CEA CysDb with ^{64}Cu for microPET detection of CEA-expressing LS174T xenografts in mice (*23*). In addition to radiolabeling, site-specific PEGylation

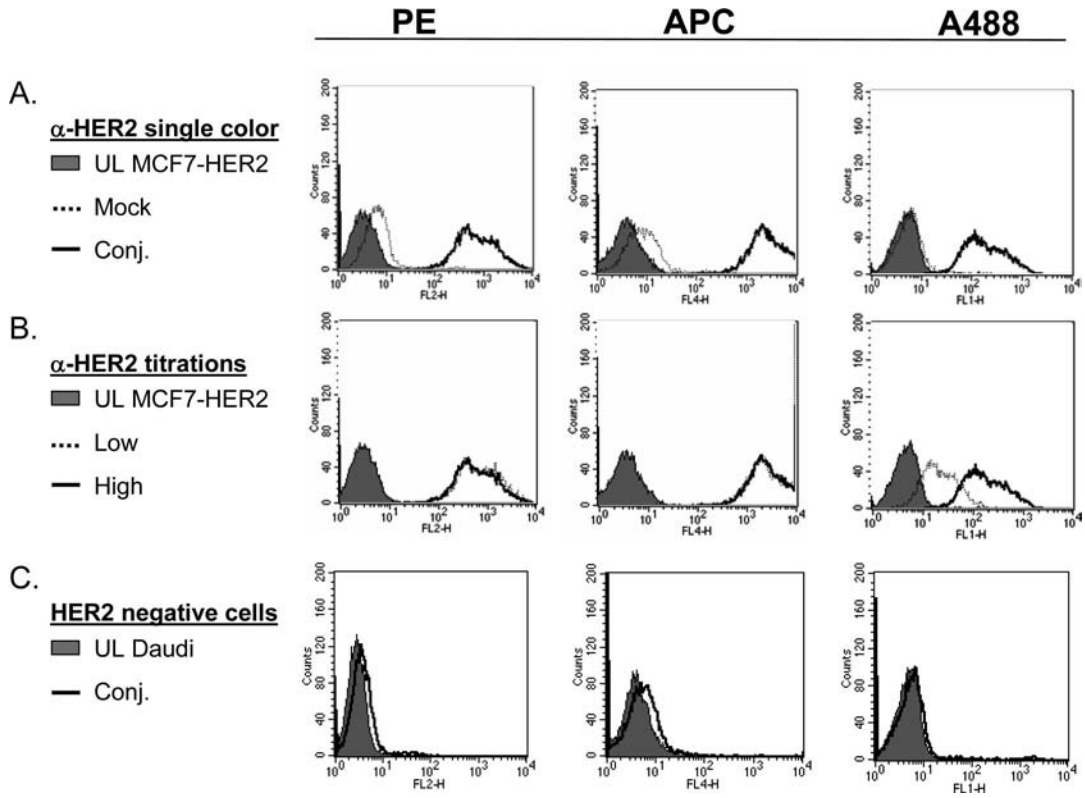

Figure 5. Flow cytometry of single-channel labeling with dye-conjugated anti-HER2 CysDb. Unlabeled cells (UL) shown in solid gray. (A) Three colors of dye-conjugated anti-HER2 CysDb (Conj., thick line) and mock conjugated dye (Mock, dotted line) demonstrating minimal background from nonspecific binding of free dye molecules to MCF7-HER2^{+} cells. (B) Three channels of low (0.5 μL, dotted line) and high (5 μL, thick line) concentrations of dye-conjugated anti-HER2 CysDb demonstrating concentration-dependent shift in mean fluorescence with increasing quantities of conjugated CysDb. (C) Three channels of dye-conjugated anti-HER2 CysDb (Conj., solid line) with minimal binding to HER2-negative Daudi cells, demonstrating antigen-specificity of binding.

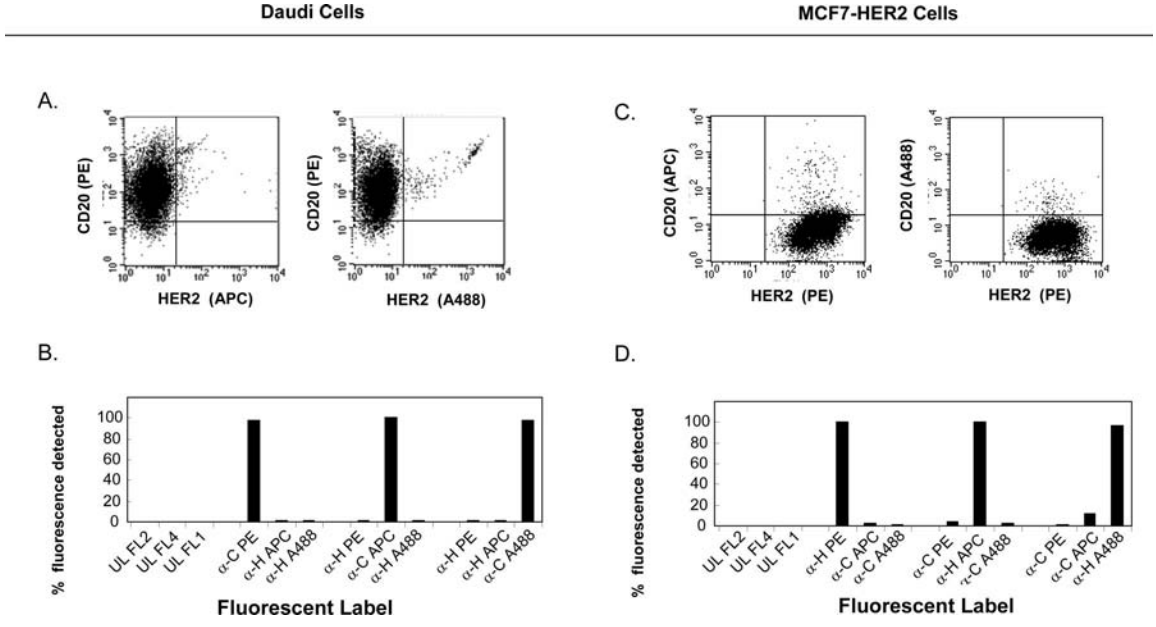

Figure 6. Flow cytometry of three-channel labeling of Daudi (A and B) and MCF7-HER2 (C and D) cells with antigen-specific and isotype control dye-conjugated CysDbs. (A) Two representative plots from three-channel experiments demonstrating detection in FL2 of specific binding of PE-conjugated anti-CD20 CysDb with minimal signal in FL1 or FL4 from co-incubated APC- or A488-conjugated anti-HER2 CysDbs, respectively. (B) Bar graph presenting compiled results of all three-channel labeling experiments on Daudi cells, demonstrating consistent, specific detection of all three dye-conjugated anti-CD20 CysDbs and minimal background from nonspecific binding of dye-conjugated anti-HER2 CysDbs. Analogous experiments were performed with dye-conjugated anti-HER2 CysDbs on MCF7-HER2 cells, using dye-conjugated anti-CD20 CysDbs as isotype controls (C,D).

of cysteine-modified scFvs or Dbs has been used to modify the pharmacokinetics of these small antibody formats (*31*). The incremental addition of several kilodaltons of PEG increases serum residence time in a predictable, size-dependent manner (*32*). The ability of the diabodies to accept large payloads is not limited to inert substances such as PEG. Venisnik et al.

fused bioluminescent enzymes to an anti-CEA diabody, demonstrating the ability of the diabody to deliver *Renilla* luciferase and *Gaussia* luciferase to a CEA-expressing tumor *in vivo* (*33, 34*). The success of this fusion protein approach confirms that relatively large functional groups can be linked to the C-termini of diabodies while maintaining binding and targeting capabilities. However, the fusion protein strategy lacks the flexibility of the CysDb approach, as each individual combination requires engineering and expression of a distinct construct.

CysDbs are especially attractive for nanotechnology applications, due to their overall size (diabody dimensions are approximately 5 nm × 7 nm) (*22*), bivalency, and capability for oriented coupling. Nanoparticles such as quantum dots, iron oxide particles, dendrimers, liposomes, and others are emerging as a distinct class of reagents with significant potential for *in vivo* applications (*21, 35, 36*). Several nanoparticles have been developed for use in imaging and therapy, but a general challenge in the field remains the need for targeted *in vivo* delivery (*37*). Oriented conjugation using antigen-specific CysDbs may provide one solution. For example, CysDbs have recently been conjugated to quantum dots, demonstrating specific binding by flow cytomety and confocal microscopy (Barat, B., Sirk, S., et al., submitted). Site-specific thiol coupling of CysDbs to nanoparticles or nanosensor substrates would automatically orient the antigen-binding domains outward to enable interaction with molecules of interest. Furthermore, attachment of CysDbs to nanodevices or nanowires should also shorten the overall interaction distances compared to coupling of intact antibodies (*38, 39*).

These studies show the utility of the CysDb platform as a simple C-terminal modification with the potential to be applied to any existing scFv or diabody. Six fluorescent antibody fragments were produced, demonstrating the versatility and reproducibility of the system. CysDbs are promising as targeting agents for *in vivo* delivery due to their small size and retention of bivalent binding. CysDbs represent a robust and simple method for reliable, site-specific, and oriented conjugation of tumor-targeting proteins to cargo of a range of size and function.

ACKNOWLEDGMENT

This work was supported by the Research Training in Pharmacological Sciences Training Grant (NIH T32 GM008652) and National Cancer Institute grants P50 CA107399, U54 CA119367, R01 EB000312, and P50086306. Flow cytometry was performed in the UCLA Jonsson Comprehensive Cancer Center and Center for AIDS Research Flow Cytometry Core Facility (NIH CA16042 and AI28697). A. W. is a member of the Jonsson Comprehensive Cancer Center (CA16042). The authors thank Roland Remenyi for experimental contributions and Katelyn McCabe for careful review of the manuscript.

LITERATURE CITED

(1) Adams, G. P., and Weiner, L. M. (2005) Monoclonal antibody therapy of cancer. *Nat. Biotechnol. 23*, 1147–57.

(2) Robinson, M. K., Doss, M., Shaller, C., Narayanan, D., Marks, J. D., Adler, L. P., Gonzalez Trotter, D. E., and Adams, G. P. (2005) Quantitative immuno-positron emission tomography imaging of HER2-positive tumor xenografts with an iodine-124 labeled anti-HER2 diabody. *Cancer Res. 65*, 1471–8.

(3) Cai, W., Olafsen, T., Zhang, X., Cao, Q., Gambhir, S. S., Williams, L. E., Wu, A. M., and Chen, X. (2007) PET imaging of colorectal cancer in xenograft-bearing mice by use of an 18F-labeled T84.66 anti-carcinoembryonic antigen diabody. *J. Nucl. Med. 48*, 304–10.

(4) Olafsen, T., Kenanova, V. E., Sundaresan, G., Anderson, A. L., Crow, D., Yazaki, P. J., Li, L., Press, M. F., Gambhir, S. S., Williams, L. E., Wong, J. Y., Raubitschek, A. A., Shively, J. E., and Wu, A. M. (2005) Optimizing radiolabeled engineered anti-p185HER2 antibody fragments for in vivo imaging. *Cancer Res. 65*, 5907–16.

(5) Sharkey, R. M., and Goldenberg, D. M. (2006) Targeted therapy of cancer: new prospects for antibodies and immunoconjugates. *CA Cancer J. Clin. 56*, 226–43.

(6) Wu, A. M., and Senter, P. D. (2005) Arming antibodies: prospects and challenges for immunoconjugates. *Nat. Biotechnol. 23*, 1137–46.

(7) Wu, A. M., and Yazaki, P. J. (2000) Designer genes: recombinant antibody fragments for biological imaging. *Q. J. Nucl. Med. 44*, 268–83.

(8) Olafsen, T., Kenanova, V. E., and Wu, A. M. (2006) Tunable pharmacokinetics: modifying the in vivo half-life of antibodies by directed mutagenesis of the Fc fragment. *Nat. Protoc. 1*, 2048–60.

(9) Albrecht, H., Denardo, G. L., and Denardo, S. J. (2007) Development of anti-MUC1 di-scFvs for molecular targeting of epithelial cancers, such as breast and prostate cancers. *Q. J. Nucl. Med. Mol. Imaging 51*, 304–13.

(10) Huston, J. S., Levinson, D., Mudgett-Hunter, M., Tai, M. S., Novotny, J., Margolies, M. N., Ridge, R. J., Bruccoleri, R. E., Haber, E., and Crea, R. (1988) Protein engineering of antibody binding sites: recovery of specific activity in an anti-digoxin single-chain Fv analogue produced in *Escherichia coli*. *Proc. Natl. Acad. Sci. U.S.A. 85*, 5879–83.

(11) Uchino, J., Takayama, K., Harada, A., Sone, T., Harada, T., Curiel, D. T., Kuroki, M., and Nakanishi, Y. (2008) Tumor targeting carboxylesterase fused with anti-CEA scFv improve the anticancer effect with a less toxic dose of irinotecan. *Cancer Gene Ther. 15*, 94–100.

(12) Kortt, A. A., Dolezal, O., Power, B. E., and Hudson, P. J. (2001) Dimeric and trimeric antibodies: high avidity scFvs for cancer targeting. *Biomol. Eng. 18*, 95–108.

(13) Adams, G. P., Tai, M. S., McCartney, J. E., Marks, J. D., Stafford, W. F., 3rd., Houston, L. L., Huston, J. S., and Weiner, L. M. (2006) Avidity-mediated enhancement of in vivo tumor targeting by single-chain Fv dimers. *Clin. Cancer Res. 12*, 1599–605.

(14) Behr, T. M., Gotthardt, M., Becker, W., and Behe, M. (2002) Radioiodination of monoclonal antibodies, proteins and peptides for diagnosis and therapy. A review of standardized, reliable and safe procedures for clinical grade levels kBq to GBq in the Gottingen/Marburg experience. *Nuklearmedizin 41*, 71–9.

(15) Nikula, T. K., Bocchia, M., Curcio, M. J., Sgouros, G., Ma, Y., Finn, R. D., and Scheinberg, D. A. (1995) Impact of the high tyrosine fraction in complementarity determining regions: measured and predicted effects of radioiodination on IgG immunoreactivity. *Mol. Immunol. 32*, 865–72.

(16) McCartney, J. E., Tai, M. S., Hudziak, R. M., Adams, G. P., Weiner, L. M., Jin, D., Stafford, W. F., 3rd., Liu, S., Bookman, M. A., and Laminet, A. A. (1995) Engineering disulfide-linked single-chain Fv dimers [(sFv′)2] with improved solution and targeting properties: anti-digoxin 26−10 (sFv′)2 and anti-c-erbB-2 741F8 (sFv′)2 made by protein folding and bonded through C-terminal cysteinyl peptides. *Protein Eng. 8*, 301–14.

(17) Adams, G. P., McCartney, J. E., Tai, M. S., Oppermann, H., Huston, J. S., Stafford, W. F., 3rd., Bookman, M. A., Fand, I., Houston, L. L., and Weiner, L. M. (1993) Highly specific in vivo tumor targeting by monovalent and divalent forms of 741F8 anti-c-erbB-2 single-chain Fv. *Cancer Res. 53*, 4026–34.

(18) George, A. J., Jamar, F., Tai, M. S., Heelan, B. T., Adams, G. P., McCartney, J. E., Houston, L. L., Weiner, L. M., Oppermann, H., and Peters, A. M. (1995) Radiometal labeling of recombinant proteins by a genetically engineered minimal chelation site: technetium-99m coordination by single-chain Fv antibody fusion proteins through a C-terminal cysteinyl peptide. *Proc. Natl. Acad. Sci. U.S.A. 92*, 8358–62.

(19) Yang, K., Basu, A., Wang, M., Chintala, R., Hsieh, M. C., Liu, S., Hua, J., Zhang, Z., Zhou, J., Li, M., Phyu, H., Petti, G.,

Mendez, M., Janjua, H., Peng, P., Longley, C., Borowski, V., Mehlig, M., and Filpula, D. (2003) Tailoring structure-function and pharmacokinetic properties of single-chain Fv proteins by site-specific PEGylation. *Protein Eng. 16*, 761–70.

(20) Weng, K. C., Noble, C. O., Papahadjopoulos-Sternberg, B., Chen, F. F., Drummond, D. C., Kirpotin, D. B., Wang, D., Hom, Y. K., Hann, B., and Park, J. W. (2008) Targeted tumor cell internalization and imaging of multifunctional quantum dot-conjugated immunoliposomes in vitro and in vivo. *Nano Lett. 8*, 2851–7.

(21) Messerschmidt, S. K., Kolbe, A., Muller, D., Knoll, M., Pleiss, J., and Kontermann, R. E. (2008) Novel single-chain Fv′ formats for the generation of immunoliposomes by site-directed coupling. *Bioconjugate Chem. 19*, 362–9.

(22) Carmichael, J. A., Power, B. E., Garrett, T. P., Yazaki, P. J., Shively, J. E., Raubischek, A. A., Wu, A. M., and Hudson, P. J. (2003) The crystal structure of an anti-CEA scFv diabody assembled from T84.66 scFvs in V(L)-to-V(H) orientation: implications for diabody flexibility. *J. Mol. Biol. 326*, 341–51.

(23) Olafsen, T., Cheung, C. W., Yazaki, P. J., Li, L., Sundaresan, G., Gambhir, S. S., Sherman, M. A., Williams, L. E., Shively, J. E., Raubitschek, A. A., and Wu, A. M. (2004) Covalent disulfide-linked anti-CEA diabody allows site-specific conjugation and radiolabeling for tumor targeting applications. *Protein Eng. Des. Sel. 17*, 21–7.

(24) Bebbington, C., Renner, G., Thomson, S., King, D., Abrams, D., and Yarranton, G. T. (1992) High-level expression of a recombinant antibody from myeloma cells using a glutamine synthetase gene as an amplifiable selection marker. *Biotechnology 10*, 169–175.

(25) Yazaki, P. J., Shively, L., Clark, C., Cheung, C. W., Le, W., Szpikowska, B., Shively, J. E., Raubitschek, A. A., and Wu, A. M. (2001) Mammalian expression and hollow fiber bioreactor production of recombinant anti-CEA diabody and minibody for clinical applications. *J. Immunol. Methods 253*, 195–208.

(26) Golay, J., Cittera, E., Di Gaetano, N., Manganini, M., Mosca, M., Nebuloni, M., van Rooijen, N., Vago, L., and Introna, M. (2006) The role of complement in the therapeutic activity of rituximab in a murine B lymphoma model homing in lymph nodes. *Haematologica 91*, 176–83.

(27) Pietras, R. J., Arboleda, J., Reese, D. M., Wongvipat, N., Pegram, M. D., Ramos, L., Gorman, C. M., Parker, M. G., Sliwkowski, M. X., and Slamon, D. J. (1995) HER-2 tyrosine kinase pathway targets estrogen receptor and promotes hormone-independent growth in human breast cancer cells. *Oncogene 10*, 2435–46.

(28) Carter, P., Presta, L., Gorman, C. M., Ridgway, J. B., Henner, D., Wong, W. L., Rowland, A. M., Kotts, C., Carver, M. E., and Shepard, H. M. (1992) Humanization of an anti-p185HER2 antibody for human cancer therapy. *Proc. Natl. Acad. Sci. U.S.A. 89*, 4285–9.

(29) Barrett, T., Koyama, Y., Hama, Y., Ravizzini, G., Shin, I. S., Jang, B. S., Paik, C. H., Urano, Y., Choyke, P. L., and Kobayashi, H. (2007) In vivo diagnosis of epidermal growth factor receptor expression using molecular imaging with a cocktail of optically labeled monoclonal antibodies. *Clin. Cancer Res. 13*, 6639–48.

(30) Koyama, Y., Hama, Y., Urano, Y., Nguyen, D. M., Choyke, P. L., and Kobayashi, H. (2007) Spectral fluorescence molecular imaging of lung metastases targeting HER2/neu. *Clin. Cancer Res. 13*, 2936–45.

(31) Natarajan, A., Xiong, C. Y., Albrecht, H., DeNardo, G. L., and DeNardo, S. J. (2005) Characterization of site-specific ScFv PEGylation for tumor-targeting pharmaceuticals. *Bioconjugate Chem. 16*, 113–21.

(32) Lee, L. S., Conover, C., Shi, C., Whitlow, M., and Filpula, D. (1999) Prolonged circulating lives of single-chain Fv proteins conjugated with polyethylene glycol: a comparison of conjugation chemistries and compounds. *Bioconjugate Chem. 10*, 973–81.

(33) Venisnik, K. M., Olafsen, T., Loening, A. M., Iyer, M., Gambhir, S. S., and Wu, A. M. (2006) Bifunctional antibody-Renilla luciferase fusion protein for in vivo optical detection of tumors. *Protein Eng. Des. Sel. 19*, 453–60.

(34) Venisnik, K. M., Olafsen, T., Gambhir, S. S., and Wu, A. M. (2007) Fusion of Gaussia luciferase to an engineered anti-carcinoembryonic antigen (CEA) antibody for in vivo optical imaging. *Mol. Imaging Biol. 9*, 267–77.

(35) Michalet, X., Pinaud, F. F., Bentolila, L. A., Tsay, J. M., Doose, S., Li, J. J., Sundaresan, G., Wu, A. M., Gambhir, S. S., and Weiss, S. (2005) Quantum dots for live cells, in vivo imaging, and diagnostics. *Science 307*, 538–44.

(36) Alexis, F., Rhee, J. W., Richie, J. P., Radovic-Moreno, A. F., Langer, R., and Farokhzad, O. C. (2008) New frontiers in nanotechnology for cancer treatment. *Urol. Oncol. 26*, 74–85.

(37) Kam, N. W., O'Connell, M., Wisdom, J. A., and Dai, H. (2005) Carbon nanotubes as multifunctional biological transporters and near-infrared agents for selective cancer cell destruction. *Proc. Natl. Acad. Sci. U.S.A. 102*, 11600–5.

(38) Zheng, G., Patolsky, F., Cui, Y., Wang, W. U., and Lieber, C. M. (2005) Multiplexed electrical detection of cancer markers with nanowire sensor arrays. *Nat. Biotechnol. 23*, 1294–301.

(39) Gruner, G. (2006) Carbon nanotube transistors for biosensing applications. *Anal. Bioanal. Chem. 384*, 322–35.

BC800113V

Distinct Uptake Routes of Cell-Penetrating Peptide Conjugates

Per Lundin,[†] Henrik Johansson,[†] Peter Guterstam,[†] Tina Holm,[†] Mats Hansen,[†] Ülo Langel,[†,‡] and Samir EL Andaloussi*[,†,‡]

Department of Neurochemistry, Stockholm University, Sweden, and Laboratory of Molecular Biotechnology, Institute of Technology, Tartu University, Tartu, Estonia. Received May 22, 2008; Revised Manuscript Received October 19, 2008

Cell-penetrating peptides (CPPs) are a growing family of peptides that have opened a new avenue in drug delivery, allowing various hydrophilic macromolecules to enter cells. In accordance with most other cationic delivery vectors, CPPs seem to rely mostly on endocytosis for internalization. However, due to conflicting results the exact endocytic pathways for CPP uptake have not yet been resolved. Here, we evaluated the ability of seven CPPs, with different chemical properties, to convey peptide nucleic acids (PNAs) inside cells. Assays based on both splice correction, generating biologically active read-out, and on traditional fluorescence measurements were utilized. The same assays were employed to assess different endocytic pathways and the dependence on extracellular heparan sulfates for internalization. Both highly cationic CPPs (M918, penetratin, and Tat) and amphipathic peptides (transportan, TP10, MAP, and pVEC) were investigated in this study. Conjugate uptake relied on endocytosis for all seven peptides but splice-correcting activity varied greatly for the investigated CPPs. The exact endocytic internalization routes were evaluated through the use of well-known endocytosis inhibitors and tracers. In summary, the different chemical properties of CPPs have little correlation with their ability to efficiently deliver splice-correcting PNA. However, conjugates of polycationic and amphipathic peptides appear to utilize different internalization routes.

INTRODUCTION

During the past decades, several oligonucleotide (ON)-based methods have been developed with the purpose of manipulating gene expression. So-called antisense strategies, employed to inhibit translation of proteins or to influence splicing patterns, have proven highly potent not only within basic research but also in clinical settings (*1, 2*). However, despite the accumulating knowledge of how to manipulate cellular processes, devising efficient means of delivering these therapeutic agents remains a hurdle.

Cell-penetrating peptides (CPPs) constitute one group of delivery vectors that has gained increasing attention since the initial discovery of penetratin in 1994 (*3*). CPPs have opened a new avenue in drug delivery, allowing the translocation of various cargo molecules into cells (*4*). Even though it is indisputable that CPPs are promising drug delivery candidates, the mechanisms underlying their cellular uptake is a matter of great controversy. Delineating the uptake mechanisms of CPPs is not only important for future development of novel, more efficient peptides but also advantageous in potential clinical trials.

It was previously commonly accepted that internalization did not involve endocytosis, until publications from separate groups revealed that conclusions regarding the translocation could be based on artifacts in the experimental settings (*5, 6*). Although some groups are still reporting on non-endocytic internalization routes for certain peptides, the majority of studies are now emphasizing the importance of endocytosis in the uptake of CPPs (*7*−*9*). For most CPPs evaluated to date, proteoglycans (PGs) on the cell surface seem pivotal for the initial interaction with cells (*8, 10*). Cells lacking heparan sulfate (HS), which is heavily anionic and constitutes parts of the extracellular PGs, display a remarkable decrease in peptide uptake. Despite the consensus that PGs are crucial for cellular uptake and that endocytosis is the main entry mechanism, knowledge regarding this is generally poor and there are conflicting reports of the exact endocytic entry routes.

Most reports evaluating CPP uptake mechanisms have examined the Tat peptide, either per se or conjugated to various cargo molecules (*11, 12*). Usually, internalization mechanisms of CPPs are assessed by using different endocytosis inhibitors that act by selectively blocking specific endocytosis pathways or through the use of fluorescently labeled pathway-specific tracers that are analyzed for colocalization with peptides. Results are divergent, and depending on study, the uptake has been ascribed to classical clathrin-mediated endocytosis (CME) (*11*), lipid raft/caveolae-mediated endocytosis (*12*), macropinocytosis (*13*), or a combination thereof (*9*). The differences in results could in part be explained by the fact that different cargo molecules and treatment concentrations have been used. Furthermore, it is probably a reasonable assumption that different CPPs utilize different mechanisms for translocation into cells. In this study, we utilized three well-known endocytosis inhibitors to distinguish between these pathways. Wortmannin was employed to inhibit both macropinocytosis and CME, whereas cytochalasin D and chlorpromazine inhibit macropinocytosis and CME, respectively.

Fluorophore labels have been used as cargo on a routine basis to allow detection inside cells and to evaluate the CPP internalization mechanisms. Although fluorescence-based methods offer useful information regarding the localization of peptides, there are several concerns hampering their utility. First, different fluorophores can affect the intracellular distribution of peptides differently (*14*). Second, the fluorophore might affect cellular uptake and cytotoxicity of the peptide (*15*). Third, and most importantly, uptake observed with fluorophore-labeled peptides or cargo molecules does not necessarily correlate with

* To whom correspondence should be addressed. Dr. Samir EL Andaloussi, Department of Neurochemistry, Stockholm University, Svante Arrhenius v. 21A, SE-106 91 Stockholm, Sweden. Phone: 46-8-164264. Fax: 46-8-161371. E-mail: samir@neurochem.su.se.

[†] Stockholm University.

[‡] Tartu University.

10.1021/bc800212j CCC: $40.75 © 2008 American Chemical Society
Published on Web 11/14/2008

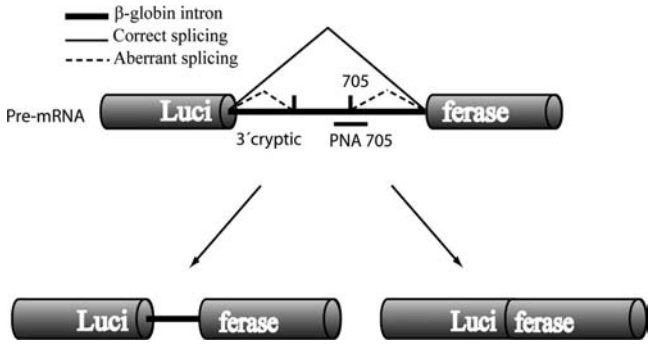

Figure 1. Principle of the splice correction assay. A stably transfected HeLa cell line, HeLa pLuc 705 cells, was used to address nuclear delivery of CPP−PNA conjugates. The cells are stably transfected with a luciferase encoding gene that is interrupted by an insertion of an intron from β-globin pre-mRNA, carrying a cryptic splice site that activates an aberrant splice site, generating nonfunctional luciferase. If the aberrant splice site is masked by PNA, correct splicing is restored and functional luciferase will be produced.

bioavailability of the delivered cargo (*16*). Therefore, it is imperative to complement fluorescence-based methods with functional assays, such as the Cre-recombination assay, which was introduced by Dowdy and colleagues as a screening tool to address nuclear delivery of Tat (*13*). However, Cre-recombinase is a rather large protein (38.5 kDa), which most likely influences the CPP translocation.

In addition to the Cre-recombination assay, a method based on splice correction has emerged to address the ON delivery efficacy of various vectors. This assay is based on a cellular system (HeLa pLuc 705 cells), where a plasmid (pLuc705) carrying the luciferase-coding sequence, interrupted by an insertion of intron 2 from β-globin pre-mRNA, is stably transfected into cells (*17*). The intron contains an aberrant and a cryptic splice site, and, unless the aberrant splice site is masked by an antisense ON, the cryptic splice site will be activated and the pre-mRNA of luciferase will be improperly processed (Figure 1). Various established and new CPPs have been evaluated by measuring luciferase activity after treatment with CPP-delivered ONs targeting this aberrant splice site. This assay has further provided evidence for an endocytic uptake of CPPs, as the lysosomotropic agent chloroquine improves transfections several-fold (*18*−*20*). However, few studies have assessed the endocytic uptake routes in detail by combining a functional assay with the use of endocytosis inhibitors. Furthermore, a parallel study comparing the uptake mechanism of polycationic CPPs and amphipathic CPPs has so far not been conducted.

We recently established a protocol based on splice correction to assess the internalization route of CPPs (*21*). Here, we evaluate the uptake, using that protocol, of polycationic peptides, represented by Tat (*22*), penetratin (*3*), and M918 (*10*), and amphipathic peptides, represented by pVEC (*23*), transportan (*24*), TP10 (*25*), and MAP (*26*), conjugated to a splice-correcting peptide nucleic acid (PNA). Our results suggest that, although most peptides, except M918, are initially dependent on HS on the cell surface for internalization, the subsequent endocytic uptake differ significantly among the peptides. We believe that these data provide new insights into the mechanism of CPP internalization, showing that although the chemical character of CPPs has an impact on the internalization mechanism there is no correlation with the delivery efficacy.

EXPERIMENTAL PROCEDURES

Synthesis of Peptides, PNA, and Conjugates. The peptides Tat, penetratin, TP10, transportan, M918, MAP, and pVEC, and the peptide nucleic acids 705 PNA and inverted 705 PNA were synthesized on Applied Biosystems' stepwise synthesizer model 433A. Both peptides and PNAs were assembled by *t*-Boc chemistry using a 4-methylbenzhydrylamine (MBHA) polystyrene resin generating amidated C-termini. Amino acids were coupled as hydroxybenzotriazole (HOBt) esters, while PNA was coupled with 2-(7-aza-1*H*-benzotriazole-1-yl)-1,1,3,3-tetramethyluronium hexafluorophosphate (HATU). Cys(Npys) was coupled N-terminally to all peptides, except TP and TP10 where it was coupled to the ε-amino group of Lys^{13} and Lys^{7}, respectively (resulting in branched conformations of these two conjugates). PNA used for uptake studies was labeled with carboxyfluorescein at the ε-amino group of the C-terminal lysine using 5 equiv 5,6-carboxyflorescein, 5 equiv diisopropylcarbodiimide (DIC), 5 equiv HOBt, and 20 equiv diisopropylethylamine (DIEA) dissolved in dimethylsulfoxide/dimethylformamide (DMSO/DMF) 1:1 overnight. After cleavage of peptides and PNAs from the resin using anhydrous hydrogen fluoride (HF), synthesis products were purified by reverse-phase HPLC Supelco C_{18} column and analyzed using Perkin-Elmer prOTOF 2000 MALDI O-TOF mass spectrometer. Conjugation of peptides with 3-nitro-2-pyridinesulphenyl (Npys) to cysteine-coupled PNA via a disulfide bridge was performed overnight in 20% acetonitrile/water containing 0.1% TFA and separated by reverse-phase HPLC. The sequences of the peptides and PNAs are presented in Table 1.

Cell Culture. HeLa pLuc 705 cells, kindly provided by R. Kole and B. Lebleu, were grown at 37 °C, 5% CO_2 in Dulbecco's Modified Eagle's Media (DMEM) with Glutamax supplemented with 0.1 mM nonessential amino acids, 1.0 mM sodium pyruvate, 10% FBS, 100 U/mL penicillin, and 100 mg/mL streptomycin.

Splice Correction Assay. 120 000 or 60 000 cells were seeded 24 h prior to experiments in 24-well or 48-well plates, respectively. Cells were treated for 1 or 4 h in 300 or 150 μL serum-free media including different conjugate concentrations after which the media was replaced with full growth media for an additional 16 h. Thereafter, cells were washed twice with Hepes Krebs Ringer (HKR) buffer, treated with trypsin, and lysed using 100 μL 0.1% Triton X100 in HKR for 15 min at room temperature. Luciferase activity was measured on Flexstation II (Molecular Devices, USA) using Promega luciferase assay system (Promega, Sweden). RLU values were normalized to protein content, and results are displayed as either RLU/mg or fold increase compared to untreated cells or, when inhibitors have been used, as % of splicing compared to conjugate-treated cells. In experiments where general endocytosis was inhibited, cells and solutions were premaintained at 4 °C for 30 min prior to being exposed to conjugates for 1 h at 4 °C. Thereafter, the media was replaced with full growth media, and the cells were transferred back to 37 °C for an additional 16 h.

In experiments with endocytosis inhibitors, cells were pretreated for 30 min prior to addition of 2 or 5 μM conjugates for 1 h. Thereafter, media was replaced and cells were allowed to grow for additionally 16 h in full growth media. Chloroquine is a weak base that buffers the endosomes. Consequently, the fusion with lysosomes is delayed, which provides longer time for endosomal escape, but chloroquine might even destabilize the membrane itself. Hence, this agent is used to promote endosomal escape. Cytochalasin D is an inhibitor of macropinocytosis as it inhibits F-actin elongation. Wortmannin is an inhibitor of phosphatidylinositol 3-kinase (PI3K) and is believed to inhibit both macropinocytosis and CME. Finally, chlorpromazine is an inhibitor of CME, as it disrupts the assembly of adaptor protein 2 and clathrin, which is pivotal for the formation of clathrin-coated vesicles.

Table 1. Sequences of Cell-Penetrating Peptides (CPPs) and Peptide Nucleic Acids (PNAs)[a]

name	abbreviation	sequence	amphipathic moment
M918	M918	MVTVLFRRLRIRRASGPPRVRV-NH_2	0.01
Penetratin	Pen	RQIKIWFQNRRMKWKK-NH_2	0.01
Tat_{48-60}	Tat	GRKKRRQRRRPPQ-NH_2	0.04
Transportan 10	TP10	AGYLLGK[b]INLKALAALAKKIL-NH_2	0.07res.8−21:0.22
Transportan	TP	GWTLNSAGYLLGK[b]INLKALAALAKKIL-NH_2	0.06
pVEC	pVEC	LLIILRRRIRKQAHAHSK-NH_2	0.08
MAP	MAP	KLALKLALKALKAALKLA-NH_2	0.16
M705 PNA	PNA	CysKK**CCTCTTACCTCAGTTACA**KK-NH_2	
M705 inverted PNA	invPNA	CysKK**CCTCTTACACTCGTTACA**KK[c]-NH_2	

[a] Bold letters represent nucleobases. The four underlined bases indicate the inverted sequence within PNA. For building of conjugates, all peptides were synthesized with N-terminal Cys(Npys) except for TP and TP10. [b] Attachment of Cys(Npys) on the ε-amino group of lysine in TP and TP10 (Lys^{13} and Lys^{7}, respectively), resulting in branched conformations. [c] Attachment of carboxyfluorescein on the ε-amino group of the C-terminal lysine on PNA. Conjugates are denoted CPP-PNA and can be illustrated as follows: CPP-Cys-S-S-Cys-**PNA**. Amphipathic moment was calculated (theoretically) in WinPep (*41*).

Quantitative Uptake. For correlation between uptake and splicing efficiency, cells were treated as previously described using fluoresceinyl conjugates (*21*). In experiments analyzing the impact on endocytosis induction following peptide treatments, cells were treated for 1 h with 5 μM unlabeled peptides. Thereafter, media was replaced and incubated with labeled markers for an additional hour. 5 μM FITC-dextran or 25 μg/mL FITC transferrin was used in order to assess the contribution of macropinocytosis and CME, respectively. After treatments, cells were washed twice in HKR before 5 min of trypsination. Cells were centrifuged at 1000 *g* for 5 min at 4 °C, and cell pellets were lysed with 0.1% Triton in HKR. Luminescence and fluorescence measurements were made on the very same cell lysate. Fluorescence was measured at $494_{ex}/518_{em}$ nm on a Spectra Max Gemini XS fluorometer (Molecular Devices, USA) and recalculated to the amount of internalized CPP−PNA conjugate, by using the linearity of fluorescein, and normalized to amount of protein (Lowry BioRad, USA). Fluoresceinyl-labeled conjugates displayed linear correlation between concentration and fluorescence.

Analysis of Luciferase pre-mRNA. Cells were grown and treated with conjugates overnight, lysed with TRIzol (Invitrogen, Stockholm, Sweden), and total cellular RNA extracted according to the manufacturer's protocol. RNA from two wells were pooled and treated with Avian Myeloblastosis Virus reverse transcriptase (Fermentas, Helsingborg, Sweden) according to the manufacturer's protocol. PCR was performed with Taq DNA polymerase, dNTP, forward primer (5′-TTG ATA TGT GGA TTT CGA GTC GTC-3′) and reverse primer (5′-TGT CAA TCA GAG TGC TTT TGG CG-3′). Cycles of PCR proceeded at 94 °C for 30 s, 55 °C for 30 s, and 72 °C for 30 s, for a total of 30 cycles. The PCR products were separated on a 1.7% agarose gel with ethidium bromide at 100 V for 45 min and identified by comparison with bands from 1 kbp DNA ladder. Electrophoresis bands on the agarose gel were visualized by UV light in a Molecular Imager Gel Doc system (Bio-Rad Laboratories, Sundbyberg, Sweden). Bands from the PCR products correspond to the aberrant (268 nucleotides) and the correct (142 nucleotides) mRNA, respectively. The proportion of band intensity was calculated densitometrically with *ImageJ* software (http:/rsb.info.nih.gov/ij/).

Lactate Dehydrogenase (LDH) Leakage. Membrane integrity was assessed using the Promega Cytox-ONE assay. In brief, 10 000 HeLa pLuc 705 cells were seeded in 96-well plates two days before treatment with conjugates in serum-free DMEM. After 1 h, media was transferred to a black fluorescence plate and incubated for 10 min with CytoTox-ONE reagent followed by stop solution. Fluorescence was measured at 560/590 nm.

Wst-1 Assay. In order to determine potential conjugate toxicity, cell proliferation was assessed using the colorimetric Wst-1 assay. The assay measures mitochondrial dehydrogenase activity and is commonly used for evaluating cell viability. HeLa pLuc 705 cells were seeded onto 96-well plates, 10 000 cells/well, two days before treatment. Cells were treated with conjugates in 100 μL serum free DMEM for 24 h and finally exposed to Wst-1, according to the manufacturer's protocol (Sigma, Sweden). Absorbance was measured at 450/690 nm. Untreated cells were defined as 100% viable.

RESULTS

CPP−PNA Conjugates Induce Splice Correction Dose-Dependently with Varying Efficacy. As previously mentioned, all CPPs included in this work have previously been utilized for delivery of various cargo (Table 1). In order to establish whether the conjugates could be used for further mechanistic evaluation, we assessed the acute cytotoxicity, by measuring lactate dehydrogenase (LDH) leakage, and then long-term toxicity by measuring mitochondrial metabolic activity. None of the bioactive conjugates displayed any significant toxicity at 10 μM treatment concentration (Supporting Information). Next, in order to obtain information on the uptake mechanisms of conjugates carrying functional cargo, the splice correction assay (described in Figure 1) was utilized. Thus, the different CPPs were conjugated to splice-correcting PNA and evaluated for their ability to correct aberrantly spliced luciferase pre-mRNA (Figure 2). M918 was the most potent peptide followed by TP10, transportan, and penetratin. The most amphipathic peptide, MAP, with an amphipathic moment of 0.16, according to WinPep (Table 1), was equally or less potent than the polycationic Tat in delivering splice-correcting PNA (Figure 2). pVEC was unable to promote any significant splice correction when conjugated to PNA (Figure 2), despite the high quantitative uptake observed with fluorometry (Figure 4B). This clearly illustrates the necessity of using a functional assay over fluorescence-based methods to determine the delivery efficacy of CPPs. It should, however, be emphasized that a quantitative uptake assay could be useful as an initial screen as some peptides, such as TP10 conjugated to PNA, display a correlation between uptake and splice correction (Figure 4A).

Although luminescence measurements allow for comparisons between different peptide conjugates, it is vital to verify the specificity of the splice correction assay. By using RT-PCR, a confirmation can be obtained regarding the production of luciferase as a result of specific PNA-mediated splice correction. As expected, the positive control TP-PNA restored the correct splicing pattern, whereas no splice correction was detected with the negative control, a conjugate of TP and a PNA with 4 bases inverted in the sequence (Figure 3). Consequently, the RT-PCR corroborates the results obtained from the luciferase assay, showing that the splice correction is a result of a switch in pre-mRNA splicing.

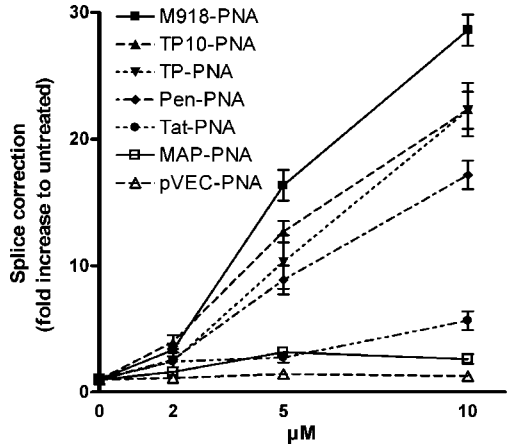

Figure 2. Splice correction by CPP−PNA conjugates. M918, TP10, transportan, and Pen conjugates efficiently corrected splicing while MAP and Tat conjugates displayed minor effects. pVEC conjugate was unable to induce splice correction. HeLa pLuc 705 cells were incubated with indicated conjugates for 4 h in serum-free media followed by exchange to full growth media for an additional 16 h. Cells were lysed and luminescence was normalized to the amount of protein. The values represent the mean of at least three independent experiments done in triplicate (mean ± SEM, $n = 3$).

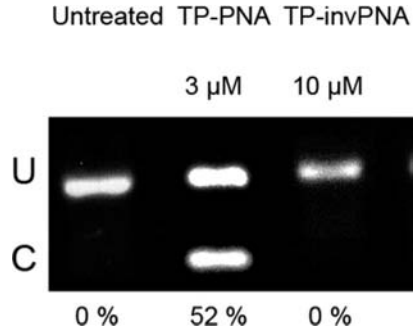

Figure 3. RT-PCR on cells treated with CPP−PNA conjugates. The positive control 3 μM TP-PNA had significant splice-correcting effect on luciferase pre-mRNA, whereas the negative control TP-invPNA (4 bases inverted in the PNA) induced no splice correction even at 10 μM. Upper and lower bands represent RT-PCR products of uncorrected (U) and corrected (C) mRNA, respectively. Cells were treated with conjugates overnight, lysed with TRIzol, total RNA was extracted, converted to cDNA, amplified by PCR, and analyzed on an agarose gel. This gel corresponds to one representative experiment.

Importance of HS for Internalization of Conjugates. HS has in numerous studies been suggested to be an essential cell surface component for internalization of CPPs (*8, 10, 11*). HS involvement is usually assessed by using HS-deficient CHO cells or by co-adding heparin with CPPs for competition analysis. Another approach has been to pretreat cells with heparinase III, which selectively removes HS from PGs, before treatment with CPPs. Again, most results on HS dependence derive from experiments utilizing fluorophore-labeled peptides or peptides conjugated to labeled proteins. Therefore, the splice correction assay was used to address this issue. Prior to exposing cells to CPP−PNA conjugates, cells were treated for 30 min with 1 U/mL of heparinase III in order to remove HS from the cell surface. After 1 h treatment with conjugates, cells were allowed to grow for 16 h prior to analysis. Tat, MAP, and pVEC conjugated to PNA were omitted in these experiments due to the low levels of splice correction observed at 5 μM concentrations. As can be seen in Figure 5, all conjugates, except M918-PNA, were highly dependent on HS for subsequent internalization of bioactive PNA. Intriguingly, after HS removal, the splice correction mediated by M918-PNA was instead significantly enhanced, suggesting that this particular peptide is using another surface component for initial adherence to cells. Overall, there seems to be no correlation between peptide amphipathicity and dependence on HS since the other three peptides rely, at least partially, on HS for internalization.

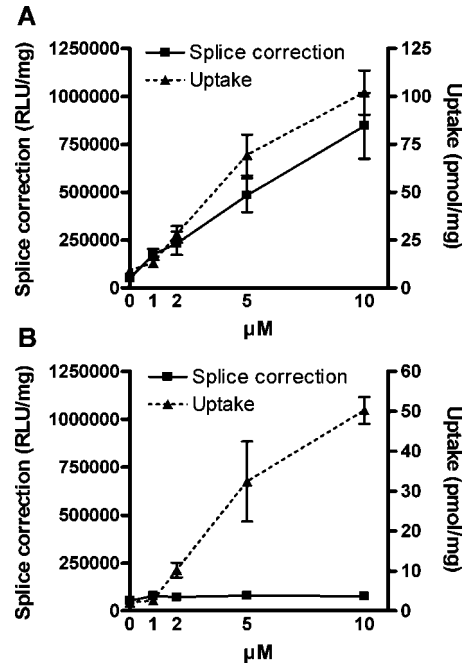

Figure 4. Measurements of CPP−PNA conjugate uptake and splice correction in the same cell lysate. Fluoresceinyl-labeled TP10-PNA (A) displayed a direct correlation between uptake and splice correction, while fluoresceinyl labeled pVEC-PNA (B) displayed concentration-dependent uptake but no correct splicing. Cells were treated as in Figure 2 but removed by trypsination and washed before lysing. In addition to luminescence, fluorescence was measured in the same lysate, recalculated to the number of moles internalized by using the linearity of fluorescein, and normalized to pmol/mg protein. The values represent the mean of three independent experiments done in triplicate (mean ± SEM, $n = 3$).

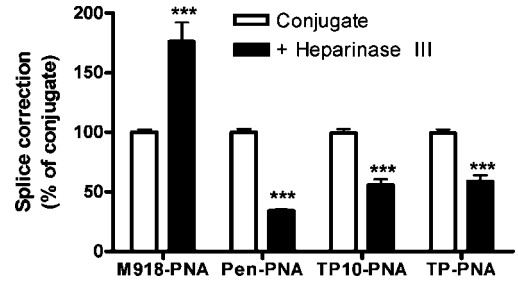

Figure 5. Removal of HS affects CPP−PNA mediated splice correction. CPP−PNA conjugates (5 μM) of Pen, TP10, and TP displayed a significant decrease in splice correction after removal of HS with heparinase III. In contrast, M918-PNA displayed a significant increase in splicing after HS removal. HS were removed by heparinase III (1 U/mL) treatment for 30 min before addition of conjugates, followed by the same procedure as in Figure 2, with the difference that cells were treated for 1 h with conjugates. The values represent the mean of at least three independent experiments done in duplicate (mean ± SEM, $n = 3$). *** $P < 0.001$ (ANOVA Dunnett's).

CPP−PNA Conjugates Are Internalized via Endocytosis. After concluding that HS is a prerequisite for subsequent internalization of most CPP−PNA conjugates, we wanted to confirm the suggested involvement of endocytosis in translocation of CPPs. This was evaluated by premaintaining cells at 4 °C, to inhibit the endocytic machinery, or by pretreating cells with 75 μM chloroquine, to increase release of material from endosomes. As anticipated, chloroquine significantly improved

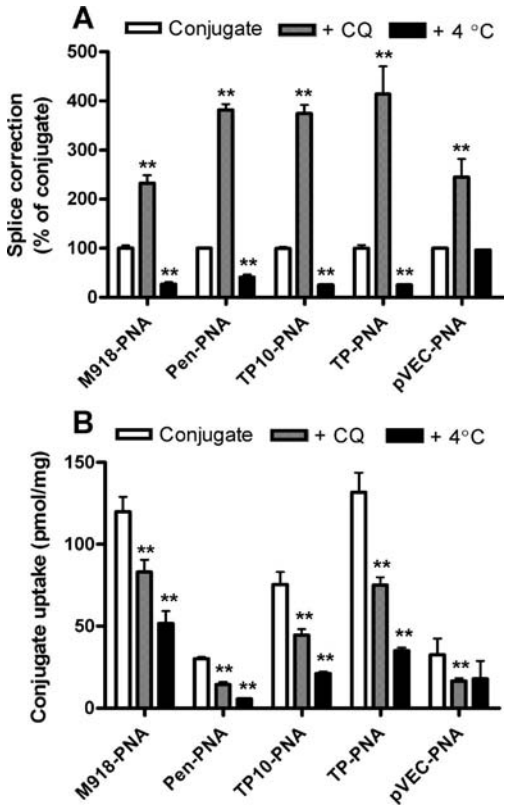

Figure 6. Inhibition of endocytosis and potentiation of endosomal release alter conjugate mediated splicing. Co-incubation of CPP−PNA conjugates (5 μM) with the lysosomotrophic agent chloroquine (75 μM) significantly increased splice correction, while treatment of cells with conjugates at 4 °C significantly decreased splice correction (A). The quantitative uptake decreased significantly for all conjugates after treatment with chloroquine and at 4 °C (B). Experiments were carried out essentially as in Figure 5. The values represent the mean of at least three independent experiments done in triplicate (mean ± SEM, n = 3). ** P < 0.01 (ANOVA Dunnett's).

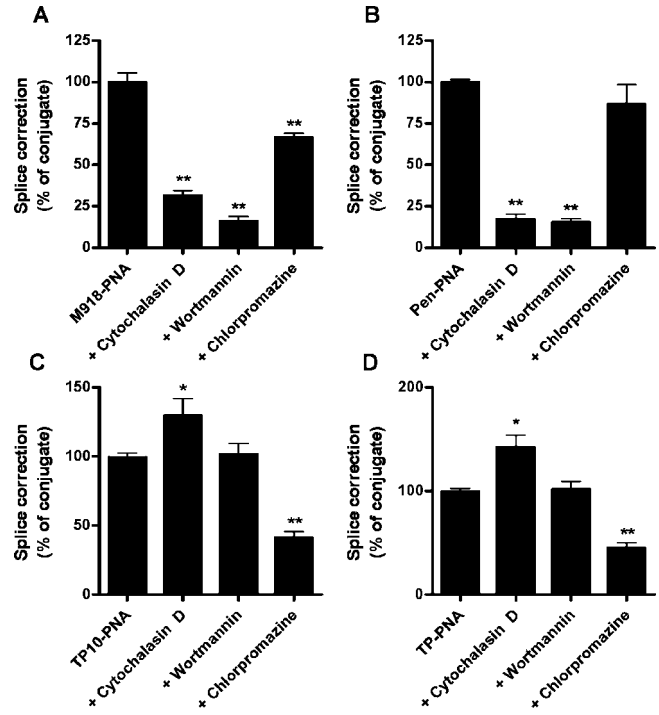

Figure 7. Different endocytic routes depending on CPPs. Cytochalasin D (4 μM) and wortmannin (50 nM) decreased M918-PNA (A) and Pen-PNA (B) splicing, while no effect or increase was observed for TP10-PNA (C) and TP-PNA (D). However, TP10-PNA (C) and TP-PNA (D) splicing was decreased by chlorpromazine (10 μM), which also had a slight inhibitory effect on M918-PNA (A). These results suggest that cationic CPPs exploit macropinocytosis while amphipathic peptides utilize CME for internalization into cells. Cells were pretreated with indicated endocytosis inhibitor for 30 min followed by cotreatment with conjugates (5 μM) for 1 h. Thereafter, the same procedure as in Figure 2 was performed. The values represent the mean of three independent experiments done in triplicate (mean ± SEM, n = 3). * P < 0.05. ** P < 0.01 (ANOVA Dunnett's).

conjugate-mediated splice correction (Figure 6A) while decreasing the quantitative uptake (Figure 6B), which is expected considering that chloroquine also slows down the endocytic machinery (*27*). These experiments were carried out with the conjugates of M918, TP10, transportan, and penetratin, but not with the less potent conjugates of Tat and MAP, as the splice correction values were close to background. pVEC-PNA was included in these experiments in order to illustrate the effects of chloroquine on quantitative uptake and splice correction. For the evaluated peptide conjugates, splicing was reduced significantly at 4 °C, reaching inhibitions up to 75% (Figure 6A). Also, the cellular uptake was decreased significantly at this temperature (Figure 6B). The same results were obtained when performing treatments with 2 μM conjugate concentration (data not shown). Taken together, these results suggest that all peptides rely on endocytosis when conjugated to splice-correcting PNA.

Endocytic Uptake Route Varies Depending on CPP Conjugate. Several previous studies have excellently addressed the endocytic uptake route and intracellular fate of fluorophore-labeled CPPs (*7*−*9*, *11*, *12*). However, in most studies only one or a few CPPs have been evaluated and compared in the same setup. We sought to investigate whether different CPPs utilize different entry routes using the functional splice correction assay. Since most reports to date have indicated that CME or macropinocytosis are the most commonly exploited endocytic pathways by which CPPs enter cells, the endocytosis inhibitors wortmannin (50 nM), cytochalasin D (4 μM), and chlorpromazine (10 μM), were employed to distinguish between these pathways. Cells were treated as previously described with chloroquine, and luciferase expression was assessed. In conjunction with results from Dowdy and co-workers on free Tat peptide and Tat-CRE fusions, splice correction with the polycationic CPPs penetratin and M918 conjugated to PNA was significantly inhibited by the presence of the macropinocytosis inhibitors wortmannin and cytochalasin D (*13*) (Figure 7A,B). In the case of penetratin, the uptake seems to be primarily mediated by macropinocytosis, as the CME inhibitor chlorpromazine was unable to significantly affect splice correction (Figure 7B). Similar results were obtained with the Tat−PNA conjugate, but the RLU values were overall too low for statistical analysis and therefore not further analyzed. M918-PNA-mediated splicing was, however, also significantly reduced with chlorpromazine although not to the same extent, suggesting a slight contribution of CME (Figure 7A). When using the TP10-PNA and TP-PNA conjugates, the opposite effect was observed with the inhibitors: while chlorpromazine significantly reduced splicing, wortmannin had negligible effects on splice correction (Figure 7C,D). In fact, cytochalasin D even increased the transportan splicing significantly. Collectively, these results suggest that cationic peptides conjugated to PNA primarily rely on macropinocytosis for internalization, whereas CME appears to be the pathway employed by amphipathic peptides.

CPPs Promote Cellular Uptake of Endocytic Markers. As conjugation of penetratin and M918 with PNA was strongly inhibited by macropinocytosis inhibitors, we wanted to elucidate whether free peptides could stimulate macropinocytic activity. This was assessed by measuring uptake of the fluid-phase marker

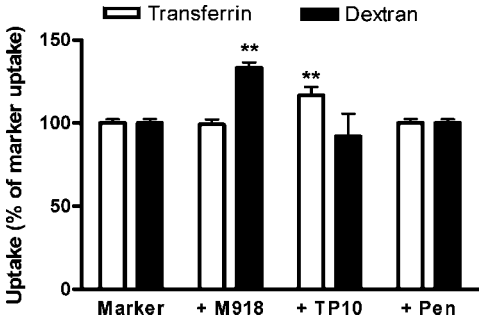

Figure 8. CPPs stimulate endocytic activity. Pretreatment of cells with M918 increased uptake of dextran, while TP10 pretreatment increased transferrin uptake. Cells were pretreated for 1 h with 5 μM peptide after which media was changed to media containing fluoresceinyl-labeled 42 kDa dextran or transferrin for one additional hour. Then, cells were washed, trypsinized, and lysed. Fluorescence was normalized to milligrams protein and expressed as % uptake without peptide preincubation. The values represent the mean of three independent experiments done in triplicate (mean $\pm$ SEM, $n = 3$). ** $P < 0.01$ (ANOVA Dunnett's).

FITC-dextran after 1 h pulsing of cells with 5 μM CPPs. While penetratin was unable to stimulate dextran uptake, M918 significantly promoted cellular internalization of the marker (Figure 8). However, somewhat in disagreement with Figure 7A, M918 had no effect on FITC-labeled transferrin internalization, suggesting that the peptide is not as intimately involved in CME (Figure 8). TP10, on the contrary, significantly stimulated CME, interpreted from the increased FITC-transferrin uptake, without affecting the dextran internalization (Figure 8). These results further support the involvement of CME in the uptake of TP10-PNA, and they are in agreement with previously reported colocalization of fluoresceinyl-labeled TP10 with rhodamine-labeled transferrin (*28*) and partial colocalization of M918 with both markers (*10*).

DISCUSSION

As ON-based approaches for regulation of gene function have gained increasing attention (since the intriguing discovery of splice correcting antisense ONs and siRNAs), so has the search for efficient means of delivery. Several potential therapeutics have entered clinical trials utilizing these effector molecules, but their utility is often restricted due to low bioavailability. CPPs have opened a new avenue in drug delivery, allowing the translocation of peptides, proteins, ONs, plasmids, and nanoparticles into cells both *in vitro* and *in vivo* (*29*). Albeit CPPs can offer an efficient and often nontoxic way of transporting ONs inside cells, their translocation mechanisms have so far not been fully resolved, which would be beneficial for future clinical applications.

It has become increasingly clear that the uptake of CPPs involve endocytosis, at least partially. However, endocytosis is a very wide term, involving several different processes with distinct intracellular fates. In CME, for instance, internalized compounds are often targeted to degradative compartments inside the cells (i.e., lysosomes) (*30*), while in macropinocytosis, and caveolae endocytosis for the most part, compounds bypass the lysosomal pathway (*31*, *32*). Thus, these differences could have a major impact on the intracellular destiny of the internalized compounds. As previously mentioned, most reports to date on CPP uptake mechanisms have been conducted utilizing fluoresceinyl-CPPs, a methodology associated with several drawbacks. Therefore, functional assays are highly desirable, preferably based on positive rather than negative readouts to avoid influence by toxic side effects on cells. The splice correction assay not only provides a positive readout, but also information regarding localization of the delivered cargo, as splicing occurs in the nucleolus of cells. Consequently, we decided to use this previously described assay, with PNA as the bioactive oligonucleotide cargo. The reason for selecting PNA as the functional cargo in these experiments was partially that its synthesis is compatible with classical peptide synthesis. Furthermore, its uncharged backbone alleviates some of the problems associated with RNA and negatively charged analogues, namely, nonspecific electrostatic interactions with CPPs, generating aggregates (*33*). In order for the PNA to be released in the cytoplasm inside cells, a cleavable disulfide bond (*34*) was chosen as a linker between the CPPs and the PNA.

The seven different CPP−PNA conjugates included in this work could be divided into two groups based on the chemical properties of the CPP; one polycationic and one amphipathic group. The amphipathic moments, calculated in WinPep, are given in Table 1. M918, penetratin, and Tat constitute the polycationic group of peptides, with high arginine contents and lower amphipathic moment. pVEC, transportan, TP10, and MAP all have a higher amphipathic moment with sequences more rich in lysines. The PNA was coupled N-terminally to all the peptides, except to TP and TP10 where the PNA was linked to the ε-amino group of the side chains of Lys^{13} and Lys^{7}, respectively. One hypothesis, which is at least partially supported by the results in this paper, was that the mechanism could differ depending on the amphipathicity and the polycationic nature of the peptides.

First, the CPPs were evaluated with regard to their ability to convey splice-correcting PNA inside cells and promote splice correction. As expected, and in accordance with previously reported results, M918, transportan, TP10, and penetratin conjugated to PNA all promoted significant splice correction (Figure 2), whereas neither of the amphipathic peptides MAP nor pVEC conjugated to PNA had any significant splice-correcting ability (Figure 2). This is rather surprising given that both peptides have been used previously for transportation of antisense PNA and cytostatic agents, respectively (*35*, *36*), but it highlights the decisive advantage of the splice correction assay over, e.g., fluorescence-based methods. This is well-illustrated by Figure 4B, where a dose-dependent increase in quantitative uptake of pVEC-PNA was observed but no splice correction. These discrepancies might be an implication of conjugates being retained in endosomes, trapped in the cell membrane, or aggregated on the cell surface, thus producing fluorescence signals but no biological response. Furthermore, one cannot exclude the possibility that the PNA resides in the cytoplasm without reaching the nucleus, although this is unlikely considering that the oligonucleotides delivered using the other peptides seemingly are delivered to the correct cellular compartment.

To verify that the increased production of luciferase emanated from a switch in splicing at the pre-mRNA level, RT-PCR was performed. The positive control 3 μM TP-PNA promoted a significant splice correction, whereas the negative control (10 μM TP-invPNA) had no effect on the splicing pattern (Figure 3). Furthermore, the RT-PCR confirmed the observed impotence of the pVEC−PNA conjugate (data not shown). In conclusion, this assay provided the expected verification of the specificity of the splice correction assay and assisted in excluding the possibility of the occurrence of other cellular events influencing the splicing pattern.

From the splice correction results, it seems that neither the amphipathic moment nor the length of the peptides is the determinant behind high delivery efficacy. Among the four potent peptides, two are amphipathic while two are highly cationic with low amphipathicity. Also, the number of amino acids varies substantially, with penetratin being 16 and transportan 27 residues in length. The four peptides were employed

to investigate the suggested role of HS for internalization of CPPs. In agreement with the common view that HS is a prerequisite for subsequent uptake of CPPs, splicing mediated by TP10, transportan, and penetratin conjugated to PNA was significantly decreased following treatment of cells with heparinase III (Figure 5). Surprisingly, splicing mediated by M918-PNA was instead increased with approximately 90% following HS removal, suggesting another mechanism for initial adherence to cells (Figure 5). A plausible explanation could be that HS prevents M918, through electrostatic interactions, from interacting with its yet unknown target receptor, and after removal of HS, this receptor becomes accessible. These results are in disagreement with the previously reported decrease in uptake of fluoresceinyl M918 in GAG deficient CHO cells, further underscoring the importance of a functional assay (*10*).

The postulated involvement of endocytosis in the uptake of CPPs was confirmed for all tested conjugates (5 μM) since chloroquine improved while 4 °C treatments decreased splice correction significantly (Figure 6A). Interestingly, chloroquine did not have such a pronounced effect on M918-PNA-mediated splicing as on the other conjugates, suggesting that M918 is more effective in escaping the endosomal compartment. The effects seen when treating the cells at 4 °C most likely derive from the experimental setup, as conjugates that potentially remain attached to the cell surface are internalized when the temperature is increased for the additional 16 h incubation. Collectively, these results are in line with previously published results from other groups using other CPPs in the same splice correction assay (*19, 20, 37*).

Albeit several groups have proven endocytic involvement in the uptake of splice-correcting ON-conjugates (*18*−*20*), no study has so far deduced the exact mechanism for entirely different CPP conjugates. In conjunction with previous reports from our group, penetratin appears to almost completely rely on macropinocytosis for internalization (*38*) (Figure 7B). The transportans have recently been reported to utilize a combination of macropinocytosis and CME for internalization, when conjugated to avidin (*39*). However, for translocation of PNA, our results suggest that the transportans exclusively make use of CME, due to the significantly repressed splice correction induced by chlorpromazine treatment (Figure 7C,D). Additionally, TP10 significantly stimulates uptake of transferrin without affecting dextran uptake, further supporting a role of CME (Figure 8). Interestingly, when using the macropinocytosis inhibitor cytochalasin D, a slight but significant increase in splice correction was observed for the transportans. A potential explanation for this could be that the silencing of one pathway (i.e., macropinocytosis) stimulates another endocytic route (i.e., CME), as suggested in ref *40*. Thus, it seems as if amphipathic peptides, such as transportans, and polycationic peptides, like penetratin, exploit different endocytic routes for entry inside cells. Making the picture somewhat more complex, M918-PNA appears to behave analogously to penetratin since both wortmannin and cytochalasin D drastically inhibit splice correction (Figure 7A). However, chlorpromazine also inhibits splicing, although not to the same extent as the other inhibitors, indicating a small contribution of CME. The CME component might on the other hand be questioned, since M918 stimulates dextran uptake but not transferrin uptake (Figure 8). Therefore, we believe that the main entry mechanism of M918 should be ascribed macropinocytosis.

Our results collectively suggest that the amphipathic nature and length of CPPs have little correlation with the ability to convey bioactive PNAs inside cells. However, the amphipathicity seems to affect the uptake route of CPPs; the amphipathic transportans utilize CME, while the cationic peptides penetratin and M918 primarily exploit macropinocytosis for cellular entrance. M918 appears to be unique not only with regard to its superior delivery properties, but also in that the peptide does not need HS for internalization to cells. It is important to clarify that the suggested uptake mechanisms hold for CPP−PNA conjugates but not necessarily for free peptides. However, considering the advantage of using a functional assay over fluorophore moieties and not using, for instance, the large Cre-recombinase as a cargo, but instead a rather inert PNA, we believe that the results from this study are particularly reliable. Finally, since the highest vector potential of CPPs lies within ON-delivery, these results should be the most clinically relevant.

ACKNOWLEDGMENT

The authors would like to thank R. Kole and B. Lebleu for kindly providing the HeLa pLuc 705 cells. This work was supported by the Swedish Science Foundation (VR-NT and VR-MED), VINNOVA, Center for Biomembrane Research, Stockholm University, and Knut and Alice Wallenberg Foundation.

Supporting Information Available: Cytotoxicity and cell viability data. This material is available free of charge via the Internet at http://pubs.acs.org.

LITERATURE CITED

(1) Sazani, P., and Kole, R. (2003) Therapeutic potential of antisense oligonucleotides as modulators of alternative splicing. *J. Clin. Invest. 112*, 481–6.
(2) Crooke, S. T. (2004) Progress in antisense technology. *Annu. Rev. Med. 55*, 61–95.
(3) Derossi, D., Joliot, A. H., Chassaing, G., and Prochiantz, A. (1994) The third helix of the Antennapedia homeodomain translocates through biological membranes. *J. Biol. Chem. 269*, 10444–50.
(4) EL-Andaloussi, S., Holm, T., and Langel, Ü. (2005) Cell-penetrating peptides: mechanisms and applications. *Curr. Pharm. Des. 11*, 3597–611.
(5) Lundberg, M., and Johansson, M. (2001) Is VP22 nuclear homing an artifact? *Nat. Biotechnol. 19*, 713–4.
(6) Richard, J. P., Melikov, K., Vives, E., Ramos, C., Verbeure, B., Gait, M. J., Chernomordik, L. V., and Lebleu, B. (2003) Cell-penetrating peptides. A reevaluation of the mechanism of cellular uptake. *J. Biol. Chem. 278*, 585–90.
(7) Deleted in Proof.
(8) Nakase, I., Tadokoro, A., Kawabata, N., Takeuchi, T., Katoh, H., Hiramoto, K., Negishi, M., Nomizu, M., Sugiura, Y., and Futaki, S. (2007) Interaction of arginine-rich peptides with membrane-associated proteoglycans is crucial for induction of actin organization and macropinocytosis. *Biochemistry 46*, 492–501.
(9) Duchardt, F., Fotin-Mleczek, M., Schwarz, H., Fischer, R., and Brock, R. (2007) A comprehensive model for the cellular uptake of cationic cell-penetrating peptides. *Traffic 8*, 848–66.
(10) EL-Andaloussi, S., Johansson, H. J., Holm, T. and, and Langel, Ü. (2007) A novel cell-penetrating peptide, M918, for efficient delivery of proteins and peptide nucleic acids. *Mol. Ther. 15*, 1820–6.
(11) Richard, J. P., Melikov, K., Brooks, H., Prevot, P., Lebleu, B., and Chernomordik, L. V. (2005) Cellular uptake of unconjugated TAT peptide involves clathrin-dependent endocytosis and heparan sulfate receptors. *J. Biol. Chem. 280*, 15300–6.
(12) Fittipaldi, A., Ferrari, A., Zoppe, M., Arcangeli, C., Pellegrini, V., Beltram, F., and Giacca, M. (2003) Cell membrane lipid rafts mediate caveolar endocytosis of HIV-1 Tat fusion proteins. *J. Biol. Chem. 278*, 34141–9.
(13) Wadia, J. S., Stan, R. V., and Dowdy, S. F. (2004) Transducible TAT-HA fusogenic peptide enhances escape of TAT-fusion proteins after lipid raft macropinocytosis. *Nat. Med. 10*, 310–5.

(14) Fischer, R., Waizenegger, T., Kohler, K., and Brock, R. (2002) A quantitative validation of fluorophore-labelled cell-permeable peptide conjugates: fluorophore and cargo dependence of import. *Biochim. Biophys. Acta 1564*, 365–74.
(15) EL-Andaloussi, S., Järver, P., Johansson, H. J., and Langel, Ü. (2007) Cargo-dependent cytotoxicity and delivery efficacy of cell-penetrating peptides: a comparative study. *Biochem. J. 407*, 285–92.
(16) Lundberg, P., El-Andaloussi, S., Sütlü, T., Johansson, H., and Langel, Ü. (2007) Delivery of short interfering RNA using endosomolytic cell-penetrating peptides. *Faseb J. 21*, 2664–71.
(17) Kang, S. H., Cho, M. J., and Kole, R. (1998) Up-regulation of luciferase gene expression with antisense oligonucleotides: implications and applications in functional assay development. *Biochemistry 37*, 6235–9.
(18) EL-Andaloussi, S., Johansson, H. J., Lundberg, P., and Langel, Ü. (2006) Induction of splice correction by cell-penetrating peptide nucleic acids. *J. Gene Med. 8*, 1262–1273.
(19) Abes, S., Moulton, H. M., Clair, P., Prevot, P., Youngblood, D. S., Wu, R. P., Iversen, P. L., and Lebleu, B. (2006) Vectorization of morpholino oligomers by the (R-Ahx-R)4 peptide allows efficient splicing correction in the absence of endosomolytic agents. *J. Controlled Release 116*, 304–13.
(20) Shiraishi, T., and Nielsen, P. E. (2006) Enhanced delivery of cell-penetrating peptide-peptide nucleic acid conjugates by endosomal disruption. *Nat. Protoc. 1*, 633–6.
(21) EL-Andaloussi, S., Guterstam, P., and Langel, Ü. (2007) Assessing the delivery efficacy and internalization route of cell-penetrating peptides. *Nat. Protoc. 2*, 2043–7.
(22) Vivés, E., Brodin, P., and Lebleu, B. (1997) A truncated HIV-1 Tat protein basic domain rapidly translocates through the plasma membrane and accumulates in the cell nucleus. *J. Biol. Chem. 272*, 16010–7.
(23) Elmquist, A., Lindgren, M., Bartfai, T., and Langel, Ü. (2001) VE-cadherin-derived cell-penetrating peptide, pVEC, with carrier functions. *Exp. Cell Res. 269*, 237–44.
(24) Pooga, M., Hällbrink, M., Zorko, M., and Langel, Ü. (1998) Cell penetration by transportan. *Faseb J. 12*, 67–77.
(25) Soomets, U., Lindgren, M., Gallet, X., Hällbrink, M., Elmquist, A., Balaspiri, L., Zorko, M., Pooga, M., Brasseur, R., and Langel, Ü. (2000) Deletion analogues of transportan. *Biochim. Biophys. Acta 1467*, 165–76.
(26) Oehlke, J., Scheller, A., Wiesner, B., Krause, E., Beyermann, M., Klauschenz, E., Melzig, M., and Bienert, M. (1998) Cellular uptake of an α-helical amphipathic model peptide with the potential to deliver polar compounds into the cell interior non-endocytically. *Biochim. Biophys. Acta 1414*, 127–39.
(27) Abes, S., Williams, D., Prevot, P., Thierry, A., Gait, M. J., and Lebleu, B. (2006) Endosome trapping limits the efficiency of splicing correction by PNA-oligolysine conjugates. *J. Controlled Release 110*595–604.
(28) Johansson, H. J., El-Andaloussi, S., Holm, T., Mäe, M., Janes, J., Maimets, T., and Langel, Ü. (2008) Characterization of a Novel Cytotoxic Cell-penetrating Peptide Derived From p14ARF Protein. *Mol. Ther. 16*, 115–23.
(29) Mäe, M., and Langel, Ü. (2006) Cell-penetrating peptides as vectors for peptide, protein and oligonucleotide delivery. *Curr. Opin. Pharmacol. 6*, 509–14.
(30) Maxfield, F. R., and McGraw, T. E. (2004) Endocytic recycling. *Nat. Rev. Mol. Cell Biol. 5*, 121–32.
(31) Hewlett, L. J., Prescott, A. R., and Watts, C. (1994) The coated pit and macropinocytic pathways serve distinct endosome populations. *J. Cell Biol. 124*, 689–703.
(32) Pelkmans, L., Kartenbeck, J., and Helenius, A. (2001) Caveolar endocytosis of simian virus 40 reveals a new two-step vesicular-transport pathway to the ER. *Nat. Cell Biol. 3*, 473–83.
(33) Nielsen, P. E., Egholm, M., Berg, R. H., and Buchardt, O. (1991) Sequence-selective recognition of DNA by strand displacement with a thymine-substituted polyamide. *Science 254*, 1497–500.
(34) Hällbrink, M., Florén, A., Elmquist, A., Pooga, M., Bartfai, T., and Langel, Ü. (2001) Cargo delivery kinetics of cell-penetrating peptides. *Biochim. Biophys. Acta 1515*, 101–9.
(35) Wolf, Y., Pritz, S., Abes, S., Bienert, M., Lebleu, B., and Oehlke, J. (2006) Structural requirements for cellular uptake and antisense activity of peptide nucleic acids conjugated with various peptides. *Biochemistry 45*, 14944–54.
(36) Myrberg, H., Zhang, L., Mäe, M., and Langel, Ü. (2008) Design of a tumor-homing cell-penetrating peptide. *Bioconjugate Chem. 19*, 70–5.
(37) Abes, S., Turner, J. J., Ivanova, G. D., Owen, D., Williams, D., Arzumanov, A., Clair, P., Gait, M. J., and Lebleu, B. (2007) Efficient splicing correction by PNA conjugation to an R6-Penetratin delivery peptide. *Nucleic Acids Res. 35*, 4495–502.
(38) Lundberg, P., and Langel, Ü. (2006) Uptake mechanisms of cell-penetrating peptides derived from the Alzheimer′s disease associated gamma-secretase complex. *Int. J. Pept. Res. Ther. 12*, 105–114.
(39) Padari, K., Säälik, P., Hansen, M., Koppel, K., Raid, R., Langel, Ü., and Pooga, M. (2005) Cell transduction pathways of transportans. *Bioconjugate Chem. 16*, 1399–410.
(40) Damke, H., Baba, T., van der Bliek, A. M., and Schmid, S. L. (1995) Clathrin-independent pinocytosis is induced in cells overexpressing a temperature-sensitive mutant of dynamin. *J. Cell Biol. 131*, 69–80.
(41) Hennig, L. (1999) WinGene/WinPep: user-friendly software for the analysis of amino acid sequences. *Biotechniques 26*, 1170–2.

BC800212J

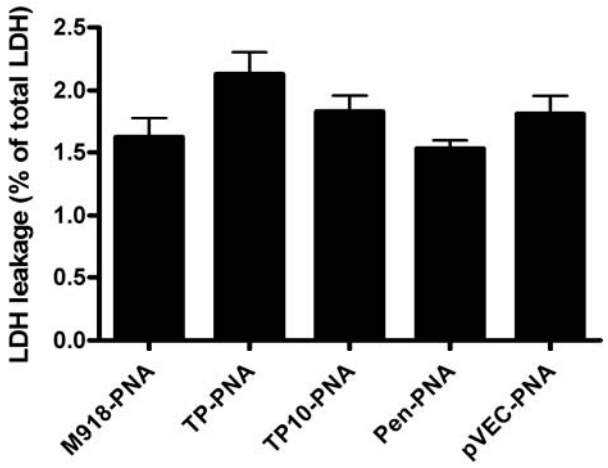

Figure 1. No transient toxicity was detected at 10 µM conjugate concentration
Membrane integrity was measured using the Promega Cytox-ONE^{TM} assay. 10 000 HeLa pLuc 705 cells were seeded in 96-well plates two days before treatment with conjugates (10 µM) in serum free DMEM. After 1 h, media was transferred to a black fluorescence plate and incubated for 10 min with CytoTox-ONE^{TM} reagent followed by stop solution. Fluorescence was measured at 560/590 nm. Neither one of the conjugates exerted any substantial toxic effect on the cells.

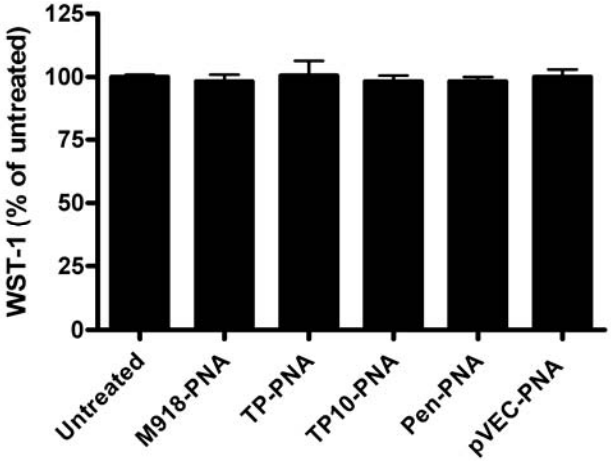

Figure 2. Cell viability was not significantly affected by 10 µM conjugate concentration
HeLa pLuc 705 cells were seeded onto 96-well plates, 10 000 cells/well, two days before the treatment. Cells were treated with conjugates in 100 µl serum free DMEM for 24 h and finally exposed to Wst-1. Absorbance was measured at 450/690nm. Untreated cells were defined as 100% viable. The cell proliferation was not significantly affected by any of the CPP-PNA conjugates.

Rapid Oxime and Hydrazone Ligations with Aromatic Aldehydes for Biomolecular Labeling

Anouk Dirksen and Philip E. Dawson*

Departments of Cell Biology and Chemistry, Skaggs Institute for Chemical Biology, The Scripps Research Institute, 10550 N. Torrey Pines Road, La Jolla, California 92037. Received July 21, 2008; Revised Manuscript Received September 29, 2008

A high-yielding and rapid chemoselective ligation approach is presented that uses aniline catalysis to activate aromatic aldehydes toward two amine nucleophiles, namely, 6-hydrazinopyridyl and aminooxyacetyl groups. The rates of these ligations are resolved for model reactions with unprotected peptides. The resulting hydrazone and oxime conjugates are attained under ambient conditions with rate constants of 10^1-10^3 M^{-1} s^{-1}. These rate constants exceed those of current chemoselective ligation chemistries and enable efficient labeling of peptides and proteins at low μM concentrations, at neutral pH, without using a large excess of one of the components. The utility of the approach is demonstrated by the *p*-fluorobenzylation of human serum albumin and by the fluorescent labeling of an unprotected peptide with Alexa Fluor 488.

INTRODUCTION

Chemoselective ligation chemistries facilitate the site-specific modification and assembly of biomolecules (*1*−*3*). However, the growing demands of research in diverse areas of chemical biology have pushed the limits of current ligation methods, especially in terms of ligation kinetics (*3*). Since biomolecules are often present at low concentrations, their efficient labeling depends on the reaction rate of the ligation chemistry used. The reaction rate constants of current chemoselective ligation chemistries typically range from 10^{-3} to 10^0 M^{-1} s^{-1} under ambient conditions (*3*−*12*). As a result, high concentrations, a large excess of one of the reactants, or elevated temperatures are typically used to compensate for the slow reaction kinetics.

Imine ligations have found significant utility in biomolecular labeling (*13*−*25*). The reaction between an amine and a carbonyl is highly chemoselective and is compatible with other functional groups present in biomolecules. The resulting imine bond is covalent but reversible, and both its stability and dynamics strongly depend on the nature of the amine and the carbonyl. In general, aldehydes are substantially more reactive than ketones, mainly due to steric effects (*26*). Under aqueous conditions, α-effect amines (hydrazines and aminooxy groups) react to form hydrazones and oximes (*11*−*25*). The equilibrium constant (K_{eq}), the ratio between the rate constant of formation k_1 and the rate constant of hydrolysis k_{-1}, is typically in the range 10^4-10^6 M^{-1} for hydrazone linkages and $>10^8$ M^{-1} for oxime bonds. The importance of K_{eq} comes to light when imine ligations are performed at low concentration (low μM range) or when a bioconjugation product is stored at sub-μM concentration. When the K_{eq} is relatively small, as is the case for many hydrazone linkages, the ligation reaction will not go to completion (100% product). Similarly, if a ligation product is stored under too dilute conditions, the system will eventually re-equilibrate and the conjugate will partially dissociate again.

Inspired by the early work of Cordes and Jencks (*27, 28*),we recently reported aniline as a potent nucleophilic catalyst for imine ligation and transimination (*11, 12*). These studies focused on the commonly used glyoxylyl group as the electrophile, and aniline catalysis enhanced the rates of these slow reactions to rates comparable to those of other widely used chemoselective ligation chemistries, including the Staudinger ligation (*4*−*6*), the Cu(I)-catalyzed [3 + 2] azide-alkyne cycloaddition (*7, 8, 29*), the Cu(I)-free click chemistry (*9*), and native chemical ligation (*2, 10, 30*). However, these reactions ($10^{-3}-10^0$ $M^{-1}s^{-1}$) are many orders of magnitude slower than enzymatic labeling methods (*31*), such as the HaloTag technology ($\sim10^6$ M^{-1} s^{-1}) (*32*), noncovalent binding events such as protein−protein interactions ($\sim10^5$ M^{-1} s^{-1}) (*33*) or the biotin−streptavidin interaction ($\sim10^6$ M^{-1} s^{-1}) (*34*). The current limitations are illustrated in Figure 1, which shows simulated second-order reactions at 100 μM reactants. Even with a rate constant of 1 M^{-1} s^{-1}, one needs over 1 day to achieve >90% conversion. As a result, efficient ligation requires the use of higher concentrations, a large excess of one of the reactants, or elevated temperatures. This analysis suggests that, for rapid ligation at 100 μM of each reactant, reaction rate constants of greater than 10 M^{-1} s^{-1} need to be achieved.

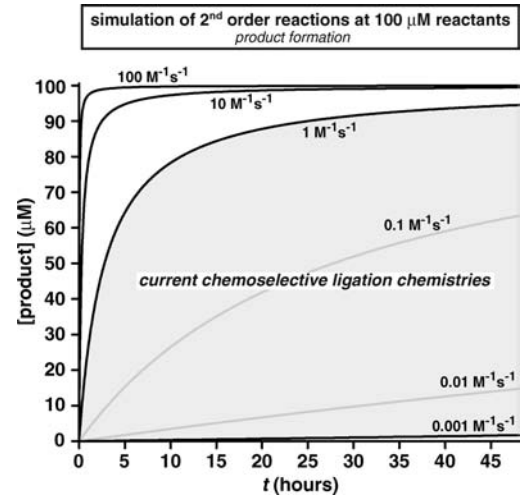

Figure 1. Simulation of second-order reactions between 100 μM reactants showing the formation of product in time as a function of the reaction rate constant. Rate constants of current chemoselective ligation chemistries typically range from 10^{-3} to 10^0 M^{-1} s^{-1}.

In this light, we further explored the scope of aniline-catalyzed imine chemistry by investigating the reaction between aromatic aldehydes and either 6-hydrazinopyridine or aminooxyacetyl

* dawson@scripps.edu, phone: 858-784-7015, fax: 858-784-7319.

10.1021/bc800310p CCC: $40.75 © 2008 American Chemical Society
Published on Web 11/17/2008

groups. Aromatic aldehydes are potent electrophiles and are more reactive than the ketone and glyoxylyl groups typically used in imine bioconjugation reactions. Aminooxyacetyl groups are readily incorporated into biological macromolecules and chemoselectively form a hydrolytically stable oxime bond, yet the kinetics are slow at neutral pH. An alternative group, 6-hydrazinopyridine, readily forms a hydrazone linkage with aromatic aldehydes to give a chromophore ($\lambda_{max} \sim 350$ nm) that enables direct spectroscopic monitoring of the reaction by UV−vis (*35*). 6-Hydrazinopyridine has similar reactivity to phenylhydrazine, but is less prone to oxidation side reactions (*36*). The 6-hydrazinopyridyl group can be readily incorporated into biomolecules using 6-hydrazinonicotinic acid, also known as HYNIC, a widely used ligand for ^{99m}Tc in radiolabeling (*36*). The ligation between aromatic aldehydes and 6-hydrazinopyridine has been applied to biomolecular labeling (*37*−*40*), but the kinetics of the reaction have not been reported.

EXPERIMENTAL PROCEDURES

Solvents and Starting Materials. Unless stated otherwise, all reagents and solvents were purchased from commercial sources and used without purification.

Note on the Stability of 6-Hydrazinopyridine and Its Hydrazone with Benzaldehyde. In contrast to the hydrazone, the stability of the free hydrazinopyridine is limited. As a solid, the compound is best stored in the freezer protected from light as a salt (HCl/TFA). In solution, the hydrazinopyridine moiety is prone to decomposition due to oxidation in a similar way, but to a lesser extent than phenylhydrazine (*36*). The fast ligation rates observed in the presence of aniline minimize these side reactions. HYNIC-labeled molecules are stored at + 4 or −20 °C, under nitrogen and protected from light. Hydrazone products based on HYNIC and benzaldehyde are stored at a concentration of >50 μM.

Instrumentation. Reversed-phase high-pressure liquid chromatography (RP HPLC) was performed on a HP1050 HPLC system (analytical HPLC) and on a Waters Delta Prep 4000 preparative chromatography system (preparative HPLC), using a Phenomenex Prodigy 5 μ 100 Å (50 × 4.60 mm) and a Phenomenex Jupiter 10 μ Proteo 90Å (250 × 21.2 mm), respectively, for separation. Electrospray ionization mass spectrometry (ESI-MS) was performed on a SCIEX API-I single quadruple mass spectrometer. UV−vis was measured on a GenesysTM 6 spectrophotometer (Thermo Electron Corporation).

Peptide Synthesis. The peptides were obtained *via* manual solid-phase peptide synthesis (SPPS) using the *in situ* neutralization/1*H*-benzotriazolium-1-[bis(dimethylamino)methylene]-5-chloro-hexafluorophosphate-(1-),3-oxide (HCTU) activation procedure for *t*Boc chemistry on a *p*-methylbenzhydrylamine (MBHA) resin (*41*). Detailed procedures are given in the Supporting Information.

Hydrazone Ligations between 6-Hydrazinopyridyl-Peptide 1 and Benzaldehyde. A 2 mM stock solution of HYNIC-peptide **1** (A), a 2 mM stock solution of benzaldehyde (B), and a 200 mM stock solution of aniline (C) were freshly prepared in either 0.1 M NH_4OAc (pH 4.5) or 0.3 M Na phosphate (pH 7). The stock solutions were mixed to give the desired concentrations of **1**, benzaldehyde, and aniline in the final reaction mixture. The reactions at 100 μM were followed by RP HPLC (220 nm, 350 nm), and the reactions at 10 μM were followed by UV−vis (350 nm). Hydrazone product **2** was analyzed by ESI-MS. **2**: ESI-MS calcd. for $C_{68}H_{93}N_{20}O_{25}$ ($[M + H]^+$): 1591.6, found 1591.5 ± 0.7. The data were fitted to the solution of the rate equation of a second-order (reversible) reaction. Details on the kinetics experiments are given in the Supporting Information.

Labeling of HYNIC-HSA with *p*-^{19}F-Benzaldehyde. For the labeling of HYNIC-HSA with *p*-^{19}F-benzaldehyde in the absence of aniline, 350 μL of 0.1 M Na phosphate (pH 7) and 50 μL of a 2.16 mM solution of *p*-^{19}F-benzaldehyde in 0.1 M Na phosphate (pH 7) were subsequently added to 100 μL of a HYNIC-HSA stock solution ([HSA] = 150 μM, on average ∼6 HYNIC/HSA; see Supporting Information). The reaction mixture was vortexed and added into a quartz cuvette. The reaction was followed by UV−vis (370 nm). The final concentration of HYNIC-HSA was 30 μM (2 mg/mL). This concentration of HYNIC-HSA was also used by Chang et al. in a typical procedure for ^{18}F labeling with *p*-^{18}F-benzaldehyde (*40*).

For the labeling of HYNIC-HSA with *p*-^{19}F-benzaldehyde in the presence of 100 mM aniline, 200 μL of 0.1 M Na phosphate (pH 7), 100 μL of a 2.16 mM solution of *p*-^{19}F-benzaldehyde in 0.1 M Na phosphate (pH 7), and 500 μL of a 200 mM stock solution of aniline in 0.1 M Na phosphate (pH 7) were subsequently added to 200 μL of a HYNIC-HSA stock solution ([HSA] = 150 μM, on average ∼6 HYNIC/HSA). The reaction mixture was vortexed and added into a quartz cuvette. The reaction was followed by UV−vis (370 nm). After 1 h, the excess of *p*-^{19}F-benzaldehyde and the aniline catalyst were removed by size-exclusion chromatography over a NAP 5 column. The stability of the hydrazone ligation product was verified by measuring the absorption at 370 nm. No decrease in the absorption of the hydrazone was observed over a period of 20 h.

Labeling of Benzaldehyde−Peptide 4 with Aminooxyacetyl-Alexa Fluor 488 (10 μM Reactants). Aminooxyacetyl-Alexa Fluor 488 is commercially available and is delivered in a vial containing 1 mg of the dye. A stock solution of approximately 1 mM in water was made by adding 1.117 mL of water (A). In addition, a 100 μM stock solution of **4** (B) and a 200 mM stock solution of aniline (C) in 0.1 M Na phosphate (pH 7) were prepared. For the reaction in the absence of aniline, 200 μL of B and 20 μL of A were subsequently added to 1.780 mL of 0.1 M Na phosphate (pH 7). For the reaction in the presence of 100 mM aniline, 1.000 mL of C, 200 μL of B, and 20 μL of A were subsequently added to 780 μL of 0.1 M Na phosphate (pH 7). The reactions were followed by RP HPLC (220 nm, 495 nm; gradient: 5−25% 9:1 v/v MeCN/H_2O in H_2O, 0.1 v % TFA in 20 min; flow: 3 mL/min). The exact concentration of dye in the ligation reactions was determined by measuring the absorption at 495 nm ($\varepsilon = 7.1 \times 10^4$ M^{-1} cm^{-1}) and was calculated to be 13 μM. Oxime product **5** was quantitated by integration (495 nm) and analyzed by ESI-MS. **5**: ESI-MS calcd. for $C_{64}H_{77}N_{15}O_{20}S_2$ ($[M + H]^+$): 1441.5, found 1442.0.

RESULTS AND DISCUSSION

To evaluate the utility of combining aniline catalysis with arylaldehyde electrophiles, we first reacted 6-hydrazinopyridyl peptide **1** and benzaldehyde (Figure 2a) (100 μM each) at pH 4.5, near the pH optimum of imine reactions. The reaction was followed by HPLC (220 nm, 350 nm) and the data were fitted to the rate equation of a second-order reaction. Full conversion to hydrazone product **2** was reached within a day with $k_1 = 3.0 \pm 0.3$ M^{-1} s^{-1} (see Supporting Information), much faster than typical imine ligations used in bioconjugation and matching the fastest chemoselective ligation reactions in the literature. Furthermore, in the presence of 10 mM aniline the reaction reached full conversion within minutes under the same conditions. To fully characterize the k_1, k_{-1}, and K_{eq} of this reaction in the absence and presence of aniline, 6-hydrazinopyridyl-peptide **1** and benzaldehyde were reacted under more dilute conditions. The reactions were followed by absorbance at 350 nm. At 10 μM reactants, the reaction reached an equilibrium

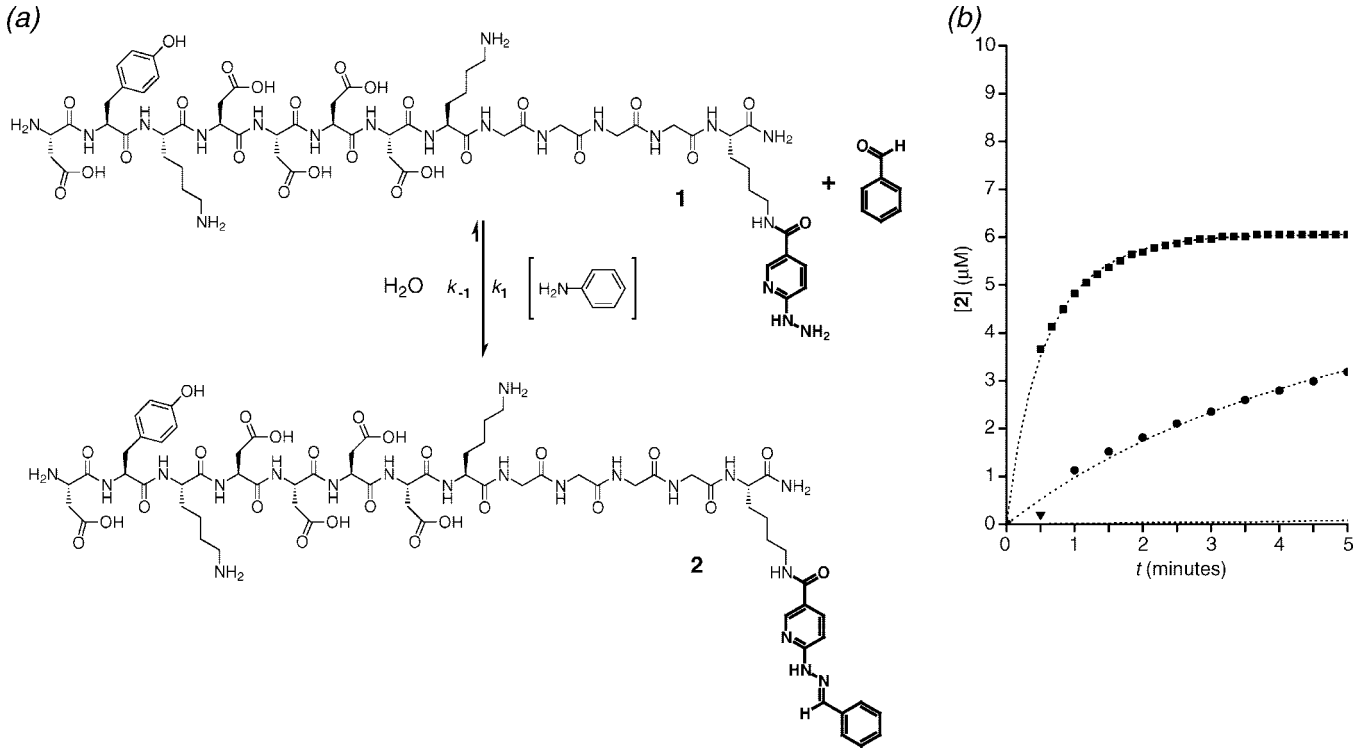

Figure 2. (a) Hydrazone reaction of 6-hydrazinopyridyl-peptide **1** and benzaldehyde in the absence and presence of aniline catalyst. (b) Formation of hydrazone **2** over time at 10 μM reactants in 0.1 M NH_4OAc (pH 4.5) at room temperature in the absence (▼) and in the presence of 10 mM (•) and 100 mM (■) aniline. The dotted lines represent the fit of the data to the rate equation (full data for ▼ is included in Supporting Information Figure 2).

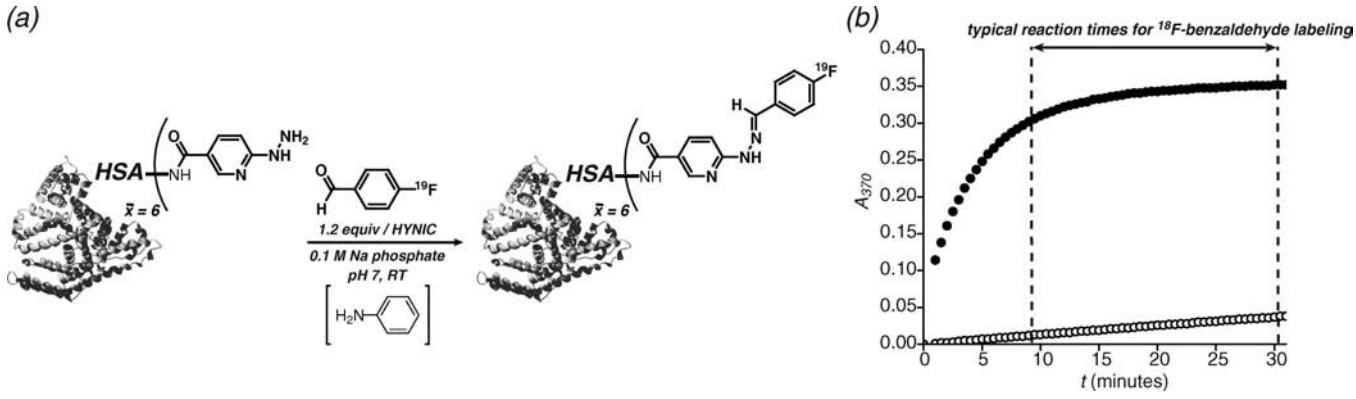

Figure 3. (a) Hydrazone reaction of 6-hydrazinopyridyl-functionalized human serum albumin (HYNIC-HSA; 6 HYNIC per HSA on average) and *p*-^{19}F-benzaldehyde in the absence and presence of aniline catalyst. (b) Labeling of HYNIC-HSA followed in time by UV−vis (370 nm) in the absence (○) and in the presence (•) of 100 mM aniline; [HYNIC-HSA] = 30 μM, [*p*-^{19}F-benzaldehyde] = 216 μM, 0.1 M Na phosphate (pH 7), room temperature.

with ~60% product present (Figure 2b). In accordance with the experiment at 100 μM reactants, the k_1 of the uncatalyzed reaction was 2.6 ± 0.1 M^{-1} s^{-1}. The k_{-1} was found to be (0.03 ± 0.001) × 10^{-3} s^{-1}, giving a K_{eq} of (0.88 ± 0.04) × 10^6 M^{-1}. In the presence of 10 mM aniline, k_1 was enhanced over 70-fold to 190 ± 10 M^{-1} s^{-1} and k_{-1} increased accordingly to (0.81 ± 0.03) × 10^{-3} s^{-1}, giving a K_{eq} = (0.23 ± 0.02) × 10^6 M^{-1}. An additional 10-fold rate enhancement was achieved by using 100 mM aniline: k_1 = 2000 ± 100 M^{-1} s^{-1}, k_{-1} = (5.1 ± 0.1) × 10^{-3} s^{-1}, and K_{eq} = (0.40 ± 0.02) × 10^6 M^{-1}. Despite the very dilute conditions, the reaction reached equilibrium within minutes (Figure 2b).

Many biomolecules are conformationally unstable under acidic conditions and at the same time limited to low concentrations (μM range) owing to their high molecular weight, low availability, and tendency to aggregate. Biomolecular labeling at pH 7 at low concentrations is therefore often desired. At pH 7, the reaction between 6-hydrazinopyridyl-peptide **1** and benzaldehyde (10 μM each) rapidly reaches equilibrium in the presence of 100 mM aniline; k_1 = 170 ± 10 M^{-1} s^{-1}, k_{-1} = (0.08 ± 0.004) × 10^{-3} s^{-1}, and the equilibrium shifts slightly more toward the product (~80% product; K_{eq} = (2.3 ± 0.1) × 10^6 M^{-1}) (see Supporting Information). To the best of our knowledge, the aniline-catalyzed reaction between the 6-hydrazinopyridyl group and benzaldehyde is the fastest chemoselective ligation chemistry that has been described.

The K_{eq} of this reaction implies that at least one of the components should be present at >50 μM in order to shift the equilibrium completely (>99%) toward the product and at >13 μM to reach >90% conversion. When labeling is complete and the excess of one of the components is removed, a new equilibrium will be reached over time, determined by the k_{-1} of the reaction. Consistent with its role as a nucleophilic catalyst, aniline does not affect K_{eq} but does catalyze reequilibration.

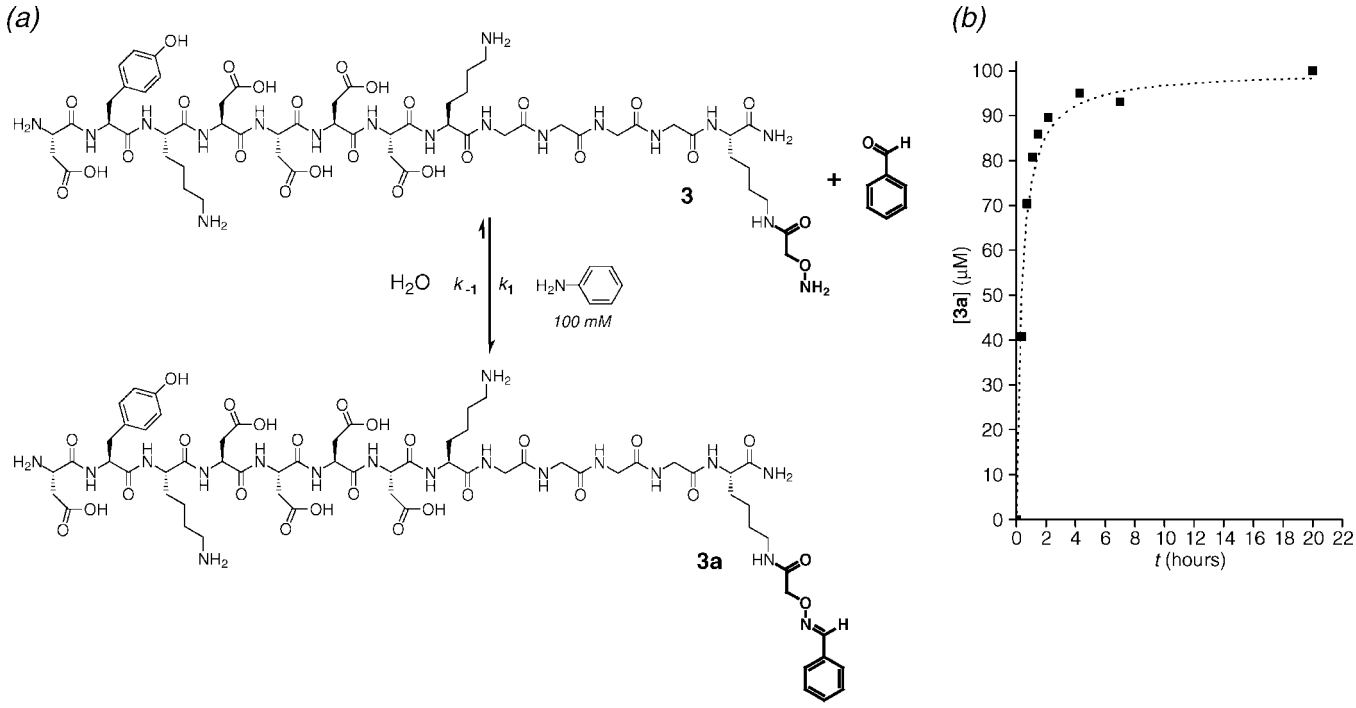

Figure 4. (a) Oxime ligation of aminooxyacetyl-functionalized peptide **3** and benzaldehyde in the presence of aniline catalyst. (b) Formation of oxime **3a** over time at 100 μM reactants in 0.3 M Na phosphate (pH 7) at room temperature in the presence of 100 mM aniline. The dotted line represents the fit of the data to the rate equation.

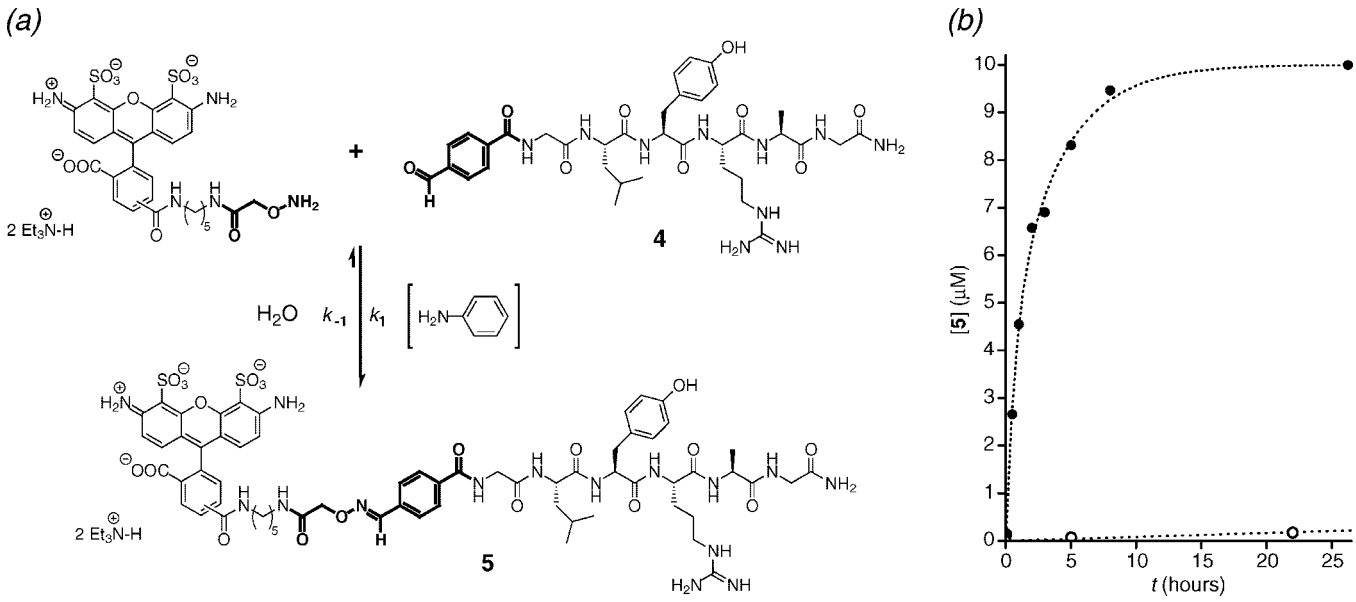

Figure 5. (a) Oxime ligation of aminooxyacetyl-Alexa Fluor 488 and benzaldehyde-functionalized peptide **4** in the absence and presence of aniline catalyst. (b) Formation of oxime **5** over time reacting 10 μM of **4** with 13 μM (1.3 equiv) of aminooxyacetyl-functionalized Alexa Fluor 488 in 0.1 M Na phosphate (pH 7) at room temperature in the absence (○) and in the presence (•) of 100 mM aniline.

However, when the catalyst is removed during workup, re-equilibration would take weeks ($k_{-1} \sim 10^{-6}$ s^{-1} at pH 7).

The rapid ligation between the 6-hydrazinopyridyl group and benzaldehyde in the presence of aniline may be of particular use for radiolabeling, since the time of labeling is strongly limited by the half-life of the radiolabel. Recently, a *p*-^{18}F-benzaldehyde label was developed for positron emission tomography (PET) imaging (*42*). However, high temperatures (50−60 °C) (*40*, *42*) and low pH (*42*) were required to compensate for the slow ligation rates and to achieve optimal labeling within typical reaction times of 10−30 min. To demonstrate the impact of aniline catalysis, the labeling of 6-hydrazinopyridyl-functionalized human serum albumin (HYNIC-HSA) with *p*-^{19}F-benzaldehyde was performed in the absence and presence of 100 mM aniline, using only a slight excess (1.2 equiv per HYNIC) of the label at room temperature (Figure 3a). For this, HSA was functionalized with, on average, 6 HYNIC moieties (see Supporting Information). Labeling was performed at 30 μM HYNIC-HSA, a concentration used in a recently reported optimized protocol for *p*-^{18}F-benzaldehyde labeling (*40*).

As shown in Figure 3b, the labeling of HYNIC-HSA with *p*-^{19}F-benzaldehyde is relatively slow. Less than 10% labeling is achieved within 30 min, consistent with the use of elevated temperatures and acidic conditions in previous labeling protocols for *p*-^{18}F-benzaldehyde. In the presence of aniline, the reaction

kinetics are strongly enhanced and >95% labeling is established within the same amount of time at neutral pH, at room temperature. After removal of the aniline catalyst and the slight excess of label by size exclusion (NAP 5 column), the hydrazone linkage was found to be stable for at least 20 h at room temperature.

In typical radiolabeling experiments with *p*-^{18}F-benzaldehyde, the label is only present in high nM to low μM concentrations, while the biomolecule is in great excess (high μM to low mM). Under these conditions, the labeling reaction will be pseudo-first-order in the biomolecule. If the reaction described above would be performed with the same initial concentration of HYNIC-HSA (6 HYNIC per HSA on average), but with a much lower concentration of *p*-^{19}F-benzaldehyde, this pseudo-first-order reaction would actually reach completion more rapidly than the second-order reaction where an equimolar amount of *p*-^{19}F-benzaldehyde is applied.

Since oximes are more hydrolytically stable than hydrazones, we investigated the combination of the aminooxy nucleophile with benzaldehyde electrophiles. To gain insight into the kinetics of the aniline-catalyzed oxime ligation, aminooxyacetyl-peptide **3** and benzaldehyde (100 μM each) were reacted under ambient conditions at pH 7 in the presence of 100 mM aniline (Figure 4). Although the k_1 of 8.2 $\pm$ 1.0 M^{-1} s^{-1} is 20-fold smaller than the k_1 of the reaction between the 6-hydrazinopyridyl group and benzaldehyde, the K_{eq} of the oxime is at least 2 orders of magnitude larger than the K_{eq} of the hydrazone. This will enable quantitative conjugation at 10 μM within 1 day using only a slight excess of label.

To demonstrate the utility of oxime ligation for labeling, benzaldehyde-functionalized peptide **4** (10 μM) was tagged with the fluorescent label aminooxyacetyl-Alexa Fluor 488 at pH 7 (Figure 5a). As anticipated, labeling was established within 1 day, whereas in the absence of aniline, <5% conversion was reached within the same period of time (Figure 5b).

CONCLUSIONS

Many methods are available to introduce benzaldehyde, 6-hydrazinopyridyl (HYNIC), or aminooxyacetyl groups in a random or site-specific manner into biomolecules (*1*−*3*, *35*, *36*). Aniline catalysis has given the reaction between aromatic aldehydes and α-effect amines a new dimension by exceeding the reaction rates of current chemoselective ligation chemistries and by bringing covalent chemistry one step closer to the rates observed in noncovalent interactions.

Aniline is a weak base that is moderately nucleophilic and does not react with the amino acid side chains of unmodified peptides. Aniline can be readily removed from the conjugation mixture by HPLC or size exclusion chromatography. Aniline may act as a competitive ligand for some metalloproteins, as does imidazole (*43*), a widely used acid−base and nucleophilic catalyst. In addition, aniline will form a reversible Schiff base with aldehyde-containing proteins, which may affect their function. However, for most proteins aniline acts as an organic buffer and is not expected to affect binding or catalysis (*44*). Therefore, we anticipate that the aniline-catalyzed imine chemistry presented in this paper will find wide utility in biomolecular labeling owing to its fast kinetics under mild conditions at neutral pH.

ACKNOWLEDGMENT

We thank Subramanian Yegneswaran (The Scripps Research Institute, USA) for performing the thrombin activity assay and Tilman M. Hackeng (Cardiovascular Research Institute Maastricht, The Netherlands), M. G. Finn (The Scripps Research Institute, USA), and David A. Schwartz (SoluLink Biosciences, Inc., USA) for discussion. PED is a consultant for SoluLink Biosciences, Inc., USA. This work was supported by The Netherlands Organization for Scientific Research (NWO) (A.D.) and NIH GM059380 (P.E.D.).

Supporting Information Available: Detailed procedures on the synthesis of the peptides and the kinetics experiments are given, as well as the activity assay for the serine protease thrombin after incubation with aniline. This material is available free of charge via the Internet at http://pubs.acs.org.

LITERATURE CITED

(1) Borgia, J. A., and Fields, G. B. (2002) Chemical synthesis of proteins. *Trends Biotechnol. 18*, 243–251.
(2) Dawson, P. E., and Kent, S. B. H. (2000) Synthesis of native proteins by chemical ligation. *Annu. Rev. Biochem. 69*, 923–960.
(3) Prescher, J. A., and Bertozzi, C. R. (2005) Chemistry in living systems. *Nat. Chem. Biol. 1*, 13–21.
(4) Agard, N. J., Baskin, J. M., Prescher, J. A., Lo, A., and Bertozzi, C. R. (2006) A comparative study of bioorthogonal reactions with azides. *ACS Chem. Biol. 1*, 644–648.
(5) Lin, F. L., Hoyt, H. M., van Halbeek, H., Bergman, R. G., and Bertozzi, C. R. (2005) Mechanistic investigation of the Staudinger ligation. *J. Am. Chem. Soc. 127*, 2686–2695.
(6) Soellner, M. B., Nilsson, B. L., and Raines, R. T. (2006) Reaction mechanism and kinetics of the traceless Staudinger ligation. *J. Am. Chem. Soc. 128*, 8820–8828.
(7) Lewis, W. G., Magallon, F. G., Fokin, V. V., and Finn, M. G. (2004) Discovery and characterization of catalysts for azide-alkyne cycloaddition by fluorescence quenching. *J. Am. Chem. Soc. 126*, 9152–9153.
(8) Rodionov, V. O., Fokin, V. V., and Finn, M. G. (2005) Mechanism of the ligand-free CuI-catalyzed azide-alkyne cycloaddition reaction. *Angew. Chem., Int. Ed. 44*, 2210–2215.
(9) Baskin, J. M., Prescher, J. A., Laughlin, S. T., Agard, N. J., Chang, P. V., Miller, I. A., Lo, A., Codelli, J. A., and Bertozzi, C. R. (2007) Copper-free click chemistry for dynamic *in vivo* imaging. *Proc. Natl. Acad. Sci. U.S.A. 104*, 16793–16797.
(10) Johnson, E. C. B., and Kent, S. B. H. (2006) Insights into the mechanism and catalysis of the native chemical ligation reaction. *J. Am. Chem. Soc. 128*, 6640–6646.
(11) Dirksen, A., Hackeng, T. M., and Dawson, P. E. (2006) Nucleophilic catalysis of oxime ligation. *Angew. Chem., Int. Ed. 45*, 7581–7584.
(12) Dirksen, A., Dirksen, S., Hackeng, T. M., and Dawson, P. E. (2006) Nucleophilic catalysis of hydrazone formation and transimination: implications for dynamic covalent chemistry. *J. Am. Chem. Soc. 128*, 15602–15603.
(13) King, T. P., Zhao, S. W., and Lam, T. (1986) Preparation of protein conjugates via intermolecular hydrazone linkage. *Biochemistry 25*, 5774–5779.
(14) Gaertner, H. F., Rose, K., Cotton, R., Timms, D., Camble, R., and Offord, R. E. (1992) Construction of protein analogues by site-specific condensation of unprotected fragments. *Bioconjugate Chem. 3*, 262–268.
(15) Rose, K. (1994) Facile synthesis of homogeneous artificial proteins. *J. Am. Chem. Soc. 116*, 30–33.
(16) Werlen, R. C., Lankinen, M., Rose, K., Blakey, D., Shuttleworth, H., Melton, R., and Offord, R. E. (1994) Site-specific conjugation of an enzyme and an antibody fragment. *Bioconjugate Chem. 5*, 411–417.
(17) Canne, L. E., Ferré-D'Amaré, A. R., Burley, S. K., and Kent, S. B. H. (1995) Total chemical synthesis of a unique transcription factor-related protein: cMyc -Max. *J. Am. Chem. Soc. 117*, 2998–3007.
(18) Shao, J., and Tam, J. P. (1995) Unprotected peptides as building blocks for the synthesis of peptide dendrimers with

oxime, hydrazone, and thiazolidine linkages. *J. Am. Chem. Soc. 117*, 3893–3899.
(19) Cervigni, S. E., Dumy, P., and Mutter, M. (1996) Synthesis of glycopeptides and lipopeptides by chemoselective ligation. *Angew. Chem., Int. Ed. 35*, 1230–1232.
(20) Mahal, L. K., Yarema, K. J., and Bertozzi, C. R. (1997) Engineering chemical reactivity on cell surfaces through oligosaccharide biosynthesis. *Science 276*, 1125–1128.
(21) Chen, I., Howarth, M., Lin, W., and Ting, A. Y. (2005) Site-specific labeling of cell surface proteins with biophysical probes using biotin ligase. *Nat. Methods 2*, 99–104.
(22) Singh, Y., Renaudet, O., Defrancq, E., and Dumy, P. (2005) Preparation of a multitopic glycopeptide-oligonucleotide conjugate. *Org. Lett. 7*, 1359–1362.
(23) Larsen, K., Thygesen, M. B., Guillaumie, F., Willats, W. G. T., and Jensen, K. (2006) Solid-phase chemical tools for glycobiology. *Carbohydr. Res. 341*, 1209–1234.
(24) Scheck, R. A., and Francis, M. B. (2007) Regioselective labeling of antibodies through N-terminal transamination. *ACS Chem. Biol. 4*, 247–251.
(25) Carrico, I. S., Carlson, B. L., and Bertozzi, C. R. (2007) Introducing genetically encoded aldehydes into proteins. *Nat. Chem. Biol. 3*, 321–322.
(26) Carey, F. A., Sundberg, R. J. (1990) *Advanced Organic Chemistry*, Part A: Structure and Mechanisms, 3rd ed., pp 462−465, Plenum Press, New York.
(27) Cordes, E. H., and Jencks, W. P. (1962) Nucleophilic catalysis of semicarbazone formation by anilines. *J. Am. Chem. Soc. 84*, 826–831.
(28) Jencks, W. P. *Catalysis in Chemistry and Enzymology* (1986) pp 72−73, Dover Publications, Inc., New York.
(29) Kolb, H. C., Finn, M. G., and Sharpless, K. B. (2001) Click chemistry: diverse chemical function from a few good reactions. *Angew. Chem. Int. Ed. 40*, 2004–2021.
(30) Dawson, P. E., Muir, T. W., Clark-Lewis, I., and Kent, S. B. H. (1994) Synthesis of proteins by native chemical ligation. *Science 266*, 776–779.
(31) Marks, K. M., and Nolan, G. P. (2006) Chemical labeling strategies for cell biology. *Nat. Methods 3*, 591–596.
(32) Los, G. V., Darzins, A., Karassina, N., Zimprich, C., Learish, R., McDougall, M. G., Encell, L. P., Friedman-Ohana, R., Wood, M., Vidugiris, G., Zimmerman, K., Otto, P., Klaubert, D. H., and Wood, K. V. (2005) HaloTagTM interchangeable labeling technology for cell imaging and protein capture. *Cell Notes* (11), 2–6.
(33) Schreiber, G., and Fersht, A. R. (1996) Rapid, electrostatically assisted association of proteins. *Nat. Struct. Biol. 3*, 427–431.
(34) Qureshi, M. H., Yeung, J. C., Wu, S. C., and Wong, S. L. (2001) Development and characterization of a series of soluble tetrameric and monomeric streptavidin muteins with differential biotin binding affinities. *J. Biol. Chem. 276*, 46422–46428.
(35) Schwartz, D. A. (SoluLink Biosciences, Inc.) Hydrazine-based and carbonyl-based bifunctional crosslinking agents. U.S. Patent 6,800,728, October 5, 2004.
(36) Schwartz, D. A., Abrams, M. J., Hauser, M. M., Gaul, F. E., Larsen, S. K., Rauh, D., and Zubietas, J. A. (1991) Preparation of hydrazino-modified proteins and their use for the synthesis of ^{99m}Tc-protein conjugates. *Bioconjugate Chem. 2*, 333–330.
(37) Steinberg-Tatman, G., Huynh, M., Barker, D., and Zhao, C. (2006) Synthetic modification of silica beads that allows for sequential attachment of two different oligonucleotides. *Bioconjugate Chem. 17*, 841–848.
(38) Chen, Y., Aveyard, J., and Wilson, R. (2004) Gold and silver nanoparticles functionalized with known numbers of oligonucleotides per particle for DNA detection. *Chem. Commun.* (24), 2804–2805.
(39) Zhong, X., Reynolds, R., Kidd, J. R., Kidd, K. K., Jenison, R., Marlar, R. A., and Ward, D. C. (2003) Single-nucleotide polymorphism genotyping on optical thin-film biosensor chips. *Proc. Natl. Acad. Sci. U.S.A. 100*, 11559–11564.
(40) Chang, Y. S., Jeong, J. M., Lee, Y. -S., Kim, H. W., Rai, G. B., Lee, S. J., Lee, D. S., Chung, J. -K., and Lee, M. C. (2005) Preparation of ^{18}F-human serum albumin: a simple and efficient protein labeling method with ^{18}F using a hydrazone-formation method. *Bioconjugate Chem. 16*, 1329–1333.
(41) Schnölzer, M., Alewood, P., Jones, A., Alewood, D., and Kent, S. B. H. (1992) In situ neutralization in Boc-chemistry solid-phase peptide-synthesis - rapid, high-yield assembly of difficult sequences. *Int. J. Pept. Protein Res. 40*, 180–193.
(42) Poethko, T., Schottelius, M., Thumshirn, G., Hersel, U., Herz, M., Henriksen, G., Kessler, H., Schwaiger, M., and Wester, H. -J. (2004) Two-step methodology for high-yield routine radiohalogenation of peptides: ^{18}F-labeled RGD and octreotide analogs. *J. Nucl. Med. 45*, 892–902.
(43) Qiao, Y., Molina, H., Pandey, A., Zhang, J., and Cole, P. A. (2006) Chemical rescue of a mutant enzyme in living cells. *Science 311*, 1293–1297.
(44) To demonstrate this, an activity assay was performed for the serine protease thrombin after a 6 h incubation with 100 mM aniline. No loss of protein activity was observed for aniline-treated thrombin as compared to untreated thrombin (see Supporting Information).

BC800310P

Supporting Information

Rapid Oxime and Hydrazone Ligations with Aromatic Aldehydes for Biomolecular Labeling.

Anouk Dirksen, Philip E. Dawson

Departments of Cell Biology and Chemistry, Skaggs Institute for Chemical Biology, The Scripps Research Institute, 10550 N. Torrey Pines Road, La Jolla, CA 92037, USA.

Peptide synthesis. The peptides were obtained *via* manual solid phase peptide synthesis (SPPS) using an *in situ* neutralization/1*H*-benzotriazolium-1-[bis(dimethylamino)methylene]-5-chloro-hexafluorophosphate-(1-),3-oxide (HCTU) activation procedure for *t*Boc chemistry on a *p*-methylbenzhydrylamine (MBHA) resin.*(1)*

6-Hydrazinopyridyl-peptide 1 (0.05 mmol scale). The Fmoc protecting group of the C-terminal lysine residue of *t*Boc-D(OcHxl)YK(2ClZ)D(OcHxl)D(OcHxl)D(OcHxl)D(OcHxl) K(2ClZ)GGGGK(Fmoc) was removed on the resin by treatment with 20 *v*-% piperidine in DMF (4 × 3 min) followed by a DMF flow wash. 0.1 mmol (25 mg) 6-*t*Boc-hydrazinonicotinic acid (6-BOC-HNA, SoluLink Biosciences, San Diego, CA, USA) was added to a solution of 0.1 mmol (52 mg) benzotriazole-1-yl-oxy-*tris*-pyrrolidino-phosphonium hexafluorophosphate (PyBOP®) and 0.12 mmol (d = 0.742 kgL^{-1}, 21 μL) diisopropylethylamine (DIEA) in 0.5 mL of DMF and the mixture was added to the resin (45 min). The resin was washed with DMF and the *t*Boc groups were removed with trifluoroacetic acid (TFA) (2 × 1 min). The resin was washed with DMF, DCM, and 1:1 *v/v* DCM/MeOH and dried under vacuum. The peptide was cleaved from the resin by HF using 4 *v*-% of anisole as a scavenger. After lyophilization, 6-hydrazinopyridyl-peptide **1** was purified by RP HPLC (gradient: 0 - 25% 9:1 *v/v* MeCN/H_2O in H_2O, 0.1 *v*-% TFA in 80 min; flow: 20 mL/min). **1**: ESI-MS calcd. for $C_{61}H_{89}N_{20}O_{25}$ ($[M+H]^+$): 1503.5, found 1504.0 ± 0.2.

Aminooxyacetyl-peptide 3 (0.1 mmol scale). The Fmoc protecting group of the C-terminal lysine residue of *t*Boc-D(OcHxl)YK(2ClZ)D(OcHxl)D(OcHxl)D(OcHxl)D(OcHxl) K(2ClZ)GGGGK(Fmoc) was removed on the resin by treatment with 20 *v*-% piperidine in DMF

(4 × 3 min) followed by a DMF flow wash. 0.5 mmol (96 mg) *t*Boc-aminooxyacetic acid was activated with 0.5 mmol (d = 0.806 kgL^{-1}, 78 μL) *N*,*N'*-diisopropylcarbodiimide and 0.5 mmol *N*-hydroxysuccinimide in DMF (0.5 mL) (10 min) and the emulsion was added to the resin (2 h). The resin was washed with DMF and the *t*Boc groups were removed with TFA (2 × 1 min). The resin was washed with DMF, DCM, and 1:1 *v/v* DCM/MeOH and dried under vacuum. The peptide was cleaved from the resin by HF using 4 *v*-% of anisole as a scavenger. After lyophilization, aminooxyacetyl-peptide **3** was purified by RP HPLC (gradient: 0 - 25% 9:1 *v/v* MeCN/H_2O in H_2O, 0.1 *v*-% TFA in 80 min; flow: 20 mL/min). **3**: ESI-MS calcd. for $C_{57}H_{87}N_{18}O_{26}$ ($[M+H]^+$): 1441.4, found 1441.0 ± 0.2.

Benzaldehyde-peptide 4. GLY(2BrZ)R(Tos)AG was synthesized by manual SPPS using the *in situ* neutralization/HCTU activation procedure for *t*Boc chemistry on a MBHA resin and cleaved from the resin with HF using 4 *v*-% of anisole as a scavenger. After lyophilization, GLYRAG was purified by RP HPLC (gradient: 5 - 30% 9:1 *v/v* MeCN/H_2O in H_2O, 0.1 *v*-% TFA in 80 min; flow: 15 mL/min). GLYRAG: ESI-MS calcd. for $C_{28}H_{46}N_{10}O_7$ ($[M+H]^+$): 635.7, found 635.5. The N-terminus of GLYRAG was functionalized in solution. For this, 22 mg (0.089 mmol) of *p*-carboxybenzaldehyde succimidyl ester was dissolved in 100 μL of MeCN and added to a solution of 40 mg (0.063 mmol) of GLYRAG in 4.4 mL of 0.1 M Na phosphate (pH 7) (2 h). The product was purified by RP HPLC (gradient: 15 - 40% 9:1 *v/v* MeCN/H_2O in H_2O, 0.1 *v*-% TFA in 80 min; flow: 15 mL/min) and lyophilized to give 21 mg (0.027 mmol, 43.5%) of **4**. **4**: ESI-MS calcd. for $C_{36}H_{50}N_{10}O_9$ ($[M+H]^+$): 767.8, found 767.5.

Hydrazone ligations at pH 4.5 (100 μM reactants). A 2 mM stock solution of 6-hydrazinopyridyl-peptide **1** (A), a 2 mM stock solution of benzaldehyde (B), and a 200 mM stock solution of aniline (C) were freshly prepared in 0.1 M NH_4OAc (pH 4.5). For the reaction in the absence of aniline, 50 μL A and 50 μL B were subsequently added to 900 μL of 0.1 M NH_4OAc (pH 4.5). For the reaction in the presence of 10 mM aniline, 50 μL C, 50 μL A, and 50 μL B were added subsequently to 850 μL of 0.1 M NH_4OAc (pH 4.5). The reactions were followed by RP HPLC (220 nm, 350 nm; gradient: 5 - 20% 9:1 *v/v* MeCN/H_2O in H_2O, 0.1 *v*-% TFA in 15 min; flow: 3 mL/min), hydrazone product **2** was quantitated by integration (350 nm), and analyzed by ESI-MS. **2**: ESI-MS calcd. for $C_{68}H_{93}N_{20}O_{25}$ ($[M+H]^+$): 1591.6, found 1591.5 ± 0.7. The data of the uncatalyzed reaction were fitted to the solution of the rate equation of a 2nd order reaction to resolve k_1 (Figure 1). The reaction in the presence of 10 mM aniline was too fast to resolve accurately k_1.

Hydrazone ligations at pH 4.5 (10 μM reactants). A 2 mM stock solution of 6-hydrazinopyridyl-peptide **1** (A), a 2 mM stock solution of benzaldehyde (B), and a 200 mM stock solution of aniline (C) were freshly prepared in 0.1 M NH_4OAc (pH 4.5). The hydrazone reactions were performed in quartz cuvettes (l = 1 cm). For the reaction in the absence of aniline, 10 μL of A and 10 μL of B were added subsequently to 1.980 mL of 0.1 M NH_4OAc (pH 4.5) (see Figure 2 for full dataset; first 5 minutes shown in Figure 2 of the paper). For the reaction in the presence of 10 mM aniline, 100 μL of C, 10 μL of B, and 10 μL of A were added subsequently to 1.880 mL of 0.1 M NH_4OAc (pH 4.5), and for the reaction in the presence of 100 mM aniline, 1.000 mL of C, 10 μL of B, and 10 μL of A were added subsequently to 980 μL of 0.1 M NH_4OAc (pH 4.5). Time was started as soon as the last component was added and 30 -

60 seconds were taken to vigorously vortex the reaction mixture, transfer it into a cuvette and start the measurement. 0.1 M NH_4OAc containing exactly the same amount of aniline as the reaction mixture was used as a blanc. The reactions were performed at room temperature and monitored by UV-Vis (350 nm). Once the reaction fully reached equilibrium, the total amount of hydrazone product **2** was determined by adding in a 10-fold excess of benzaldehyde (final concentration 110 μM), shifting the equilibrium completely towards the product. The data were fitted to the solution of the rate equation of a 2nd order reversible reaction.*(2)* It should be noted that conditions differ slightly for each reaction (ionic strength, solvent effect of 100 mM aniline). These difference may explain the differences observed in the equilibrium constants. Furthermore, the endpoints were not fixed, which may cause an underestimation of the calculated error in the k_{-1} of the reaction.

Hydrazone ligation at pH 7 (10 μM reactants, 100 mM aniline). This reaction was performed and analyzed analogous to the reaction at pH 4.5. Stock solutions were freshly prepared in 0.3 M Na phosphate (pH 7). The data were fitted to the solution of the rate equation of a 2nd order reversible reaction*(2)* (Figure 3).

Synthesis of HYNIC-HSA. 15 equiv of succinimidyl hydraziniumnicotinate hydrochloride (SHNH, SoluLink Biosciences, San Diego, CA, USA) (0.646 mg) in DMSO (20 μL) were added to a solution of 10 mg of HSA in 0.5 mL of 0.05 M Na phosphate (pH 7.5). The solution was put under nitrogen and protected from light and the reaction was continued for 2 hours at room temperature. The excess of SHNH was removed by size exclusion chromatography over a NAP™ 5 column, preequilibrated with 0.1 M Na phosphate (pH 7). HYNIC-HSA was eluted

from the column with 0.1 M Na phosphate (pH 7). The concentration of HSA in the collected solution was determined to be 150 μM, using the Bradford assay. The concentration of HYNIC was determined by adding 25 μL of the protein solution to 2.475 mL of a 0.5 mM solution of *p*-nitrobenzaldehyde in 0.1 M NH_4OAc (pH 4.5). In time HYNIC reacts with *p*-nitrobenzaldehyde to give a chromophore with $\varepsilon = 2.53 \times 10^4\ M^{-1}cm^{-1}$ at 385 nm.*(3)* After 5 h the absorption at 385 nm was measured and the concentration of HYNIC was calculated to be 893 μM. This corresponds to on average ~6 HYNIC groups per HSA.

Note on the stability of 6-hydrazinopyridine and its hydrazone with benzaldehyde. In contrast to the hydrazone, the stability of the free hydrazinopyridine is limited. As a solid, the compound is best stored in the freezer protected from light as a salt (HCl / TFA). In solution, the hydrazinopyridine moiety is prone to decomposition due to oxidation in a similar way, but to a lesser extent than phenylhydrazine.*(3)* The fast ligation rates observed in the presence of aniline minimize these side reactions. HYNIC labeled molecules are stored at + 4 °C or -20 °C, under nitrogen and protected from light. Hydrazone products based on HYNIC and benzaldehyde are stored at a concentration of > 50 μM.

Oxime ligation at pH 7 (100 μM reactants, 100 mM aniline). A 2 mM stock solution of aminooxyacetyl-peptide **3** (A), a 2 mM stock solution of benzaldehyde (B), and a 200 mM stock solution of aniline (C) were prepared in 0.3 M Na phosphate (pH 7). 500 μL C, 50 μL A, and 50 μL B were added subsequently to 400 μL of 0.3 M Na phosphate (pH 7). The reaction was followed by RP HPLC (220 nm; gradient: 0 - 20% 9:1 *v/v* MeCN/H_2O in H_2O, 0.1 *v*-% TFA in 15 min; flow: 3 mL/min), oxime product **3a** was quantitated by integration (220 nm), and

analyzed by ESI-MS. **3a**: ESI-MS calcd. for $C_{64}H_{91}N_{18}O_{26}$ ($[M+H]^+$): 1529.5, found 1529.5 ± 0.7. The data of the reaction were fitted to the solution of the rate equation of a 2nd order reaction.

Oxime ligation at pH 7 (1 mM reactants, no aniline). The rate constant of the uncatalyzed reaction was determined by reacting **3** with benzaldehyde at 1 mM reactants. For this 250 µL A and 250 µL B were mixed. The reaction was followed by RP HPLC (220 nm; gradient: 0 - 20% 9:1 *v/v* MeCN/H_2O in H_2O, 0.1 *v*-% TFA in 15 min; flow: 3 mL/min), oxime product **3a** was quantitated by integration (220 nm). The data of the reaction were fitted to the solution of the rate equation of a 2nd order reaction and a rate constant of 0.14 ± 0.02 $M^{-1}s^{-1}$ was calculated (Figure 4).

Thrombin activity assay. 150 µl of human α-thrombin (HaemTech, Essex Junction VT) (90 µM) was incubated with either 150 µl of 200 mM aniline and 1 mM benzamidine.HCl or with an equal volume of 1 mM benzamidine.HCl in 50 mM Hepes/150 mM NaCl (pH 7.4) at room temperature for 6 hours. The weak inhibitor benzamidine.HCl was added to prevent self-cleavage of thrombin during incubation. Samples were then dialyzed (1 × 2000 mL) into 50 mM Hepes/150 mM NaCl (pH 7.4) overnight at 4 °C before thrombin activity was evaluated using the chromogenic substrate Pefachrome-TH (Pentapharma, Basel, Switzerland). Briefly, 50 µl of varying concentrations of substrate (0-1600 µM) were added to samples containing 20 nM aniline-treated thrombin or untreated controls. The generation of *p*-nitroaniline was monitored immediately using a 96 well plate reader (Molecular Dynamics, Sunnyvale CA) at 405 nm wavelength (Figure 5).

Hydrazone ligation: 100 μM reactants, no aniline, pH 4.5, room temperature

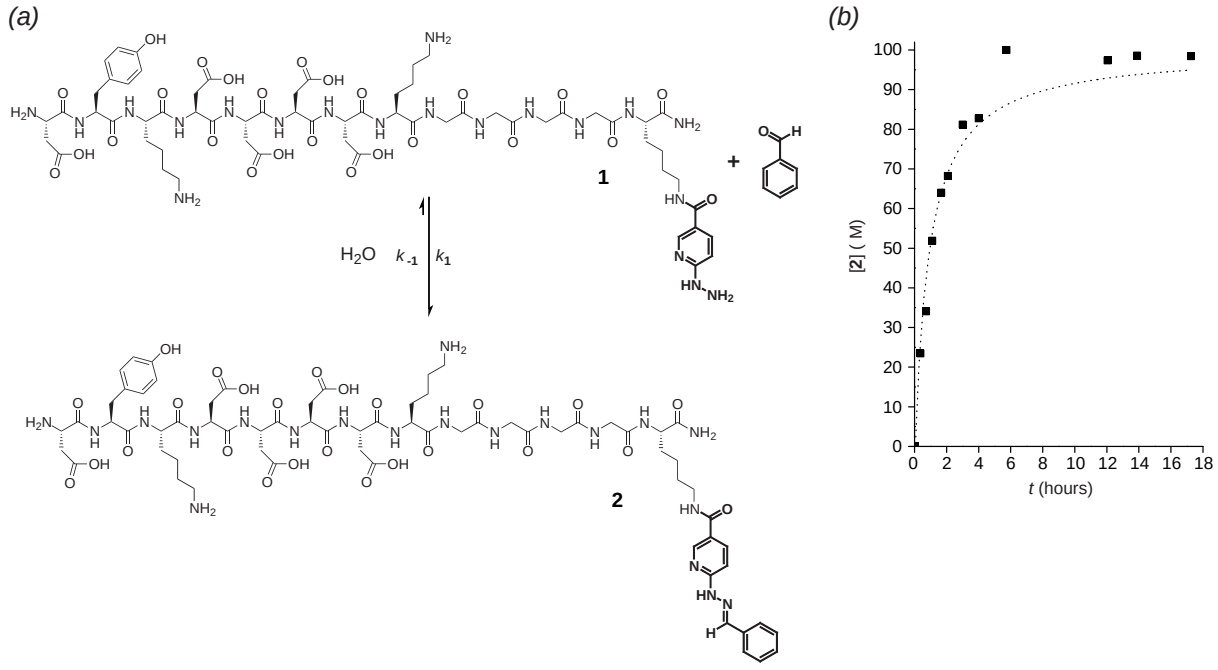

Figure 1. *(a)* Hydrazone reaction of 6-hydrazinopyridyl-peptide **1** and benzaldehyde in the absence of aniline catalyst; *(b)* Formation of hydrazone **2** over time at 100 μM reactants at room temperature in 0.1 M NH_4OAc (pH 4.5). The dotted line represents the fit of the data to the rate equation.

Hydrazone ligation: 10 μM reactants, no aniline, pH 4.5, room temperature (full dataset)

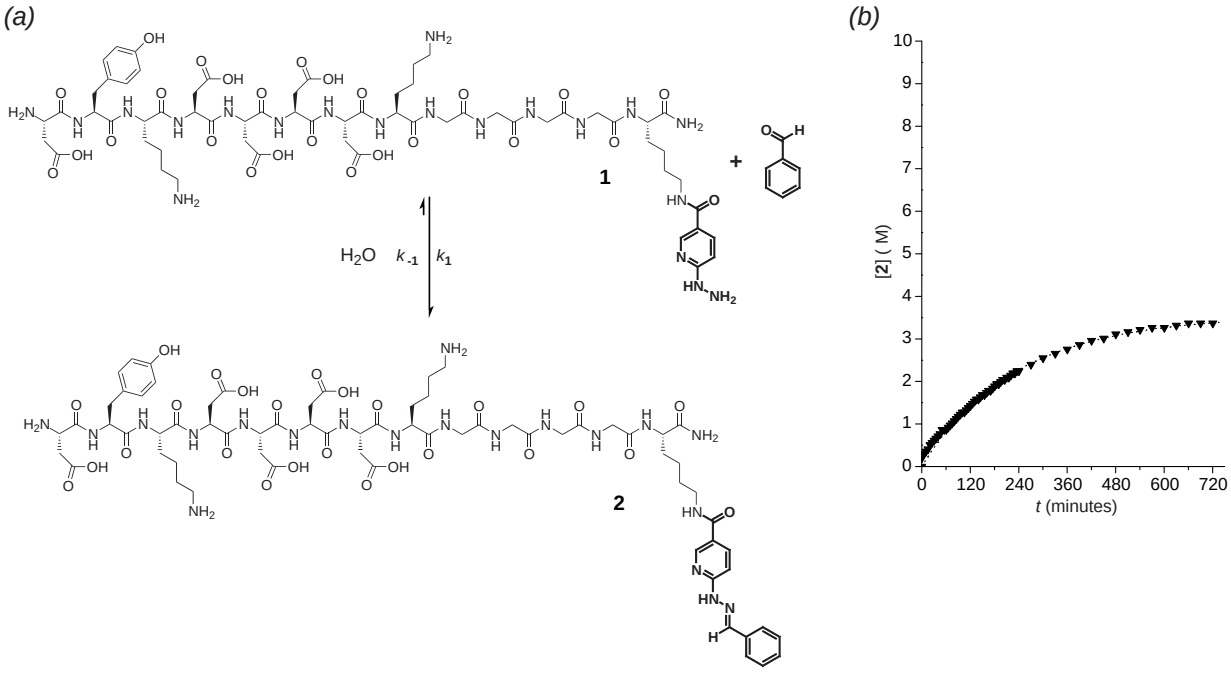

Figure 2. *(a)* Hydrazone reaction of 6-hydrazinopyridyl-peptide **1** and benzaldehyde in the absence of aniline catalyst; *(b)* Formation of hydrazone **2** over time at 10 μM reactants at room temperature in 0.1 M NH_4OAc (pH 4.5). The dotted line represents the fit of the data to the rate equation.

Hydrazone ligation: 10 μM reactants, 100 mM aniline, pH 7, room temperature

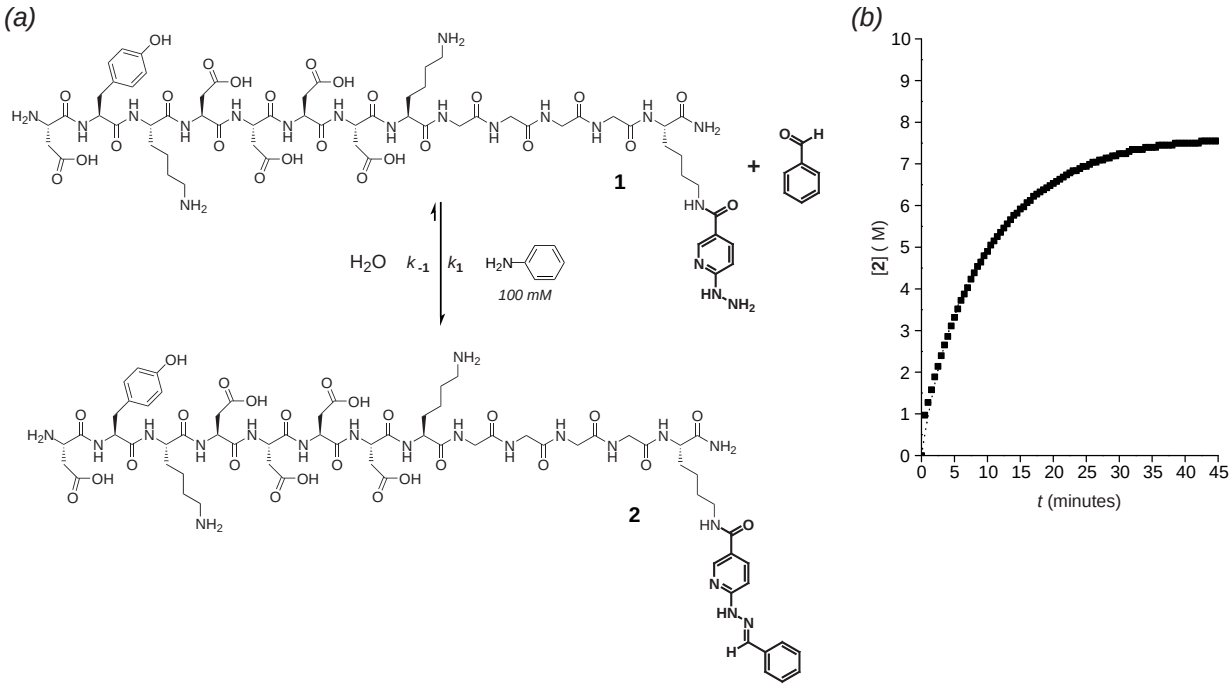

Figure 3. *(a)* Hydrazone reaction of 6-hydrazinopyridyl-peptide **1** and benzaldehyde in the presence of aniline catalyst; *(b)* Formation of hydrazone **2** over time at 10 μM reactants at room temperature in 0.3 M Na phosphate (pH 7) in the presence of 100 mM aniline. The dotted line represents the fit of the data to the rate equation.

Oxime ligation: 1 mM reactants, no aniline, pH 7, room temperature

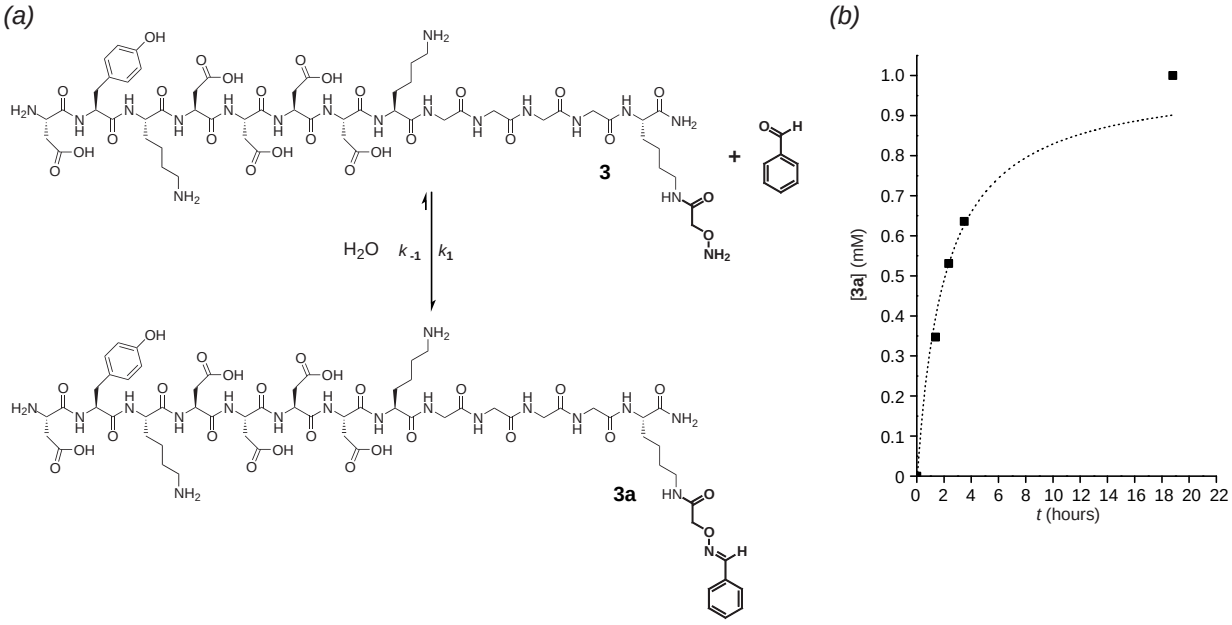

Figure 4. *(a)* Oxime ligation of aminooxyacetyl-functionalized peptide **3** and benzaldehyde in the absence aniline catalyst; *(b)* Formation of oxime **3a** over time at 1 mM reactants at room temperature in 0.3 M Na phosphate (pH 7). The dotted line represents the fit of the data to the rate equation.

Thrombin activity assay

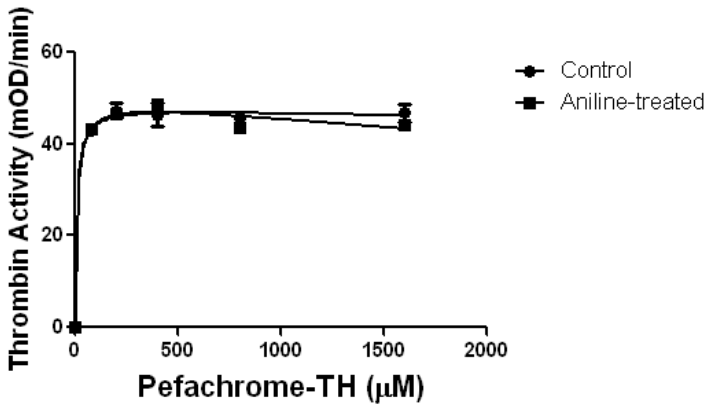

Figure 5. Thrombin activity assay for aniline-treated and untreated thrombin (20 nM) based on the conversion of the substrate Pefachrome-TH (initial concentration ranging from 0-1600 μM) to *p*-nitroaniline in 50 mM Hepes/150 mM NaCl (pH 7.4). The reaction was followed by UV-Vis (405 nm).

(1) Schnölzer, M., Alewood, P., Jones, A., Alewood, D., Kent, S. B. H. (1992) *In situ* neutralization in Boc-chemistry solid-phase peptide-synthesis - rapid, high-yield assembly of difficult sequences. *Int. J. Peptide Protein Res. 40*, 180–193.

(2) Dirksen, A., Dirksen, S., Hackeng, T. M., Dawson, P. E. (2006) Nucleophilic catalysis of hydrazone formation and transimination: implications for dynamic covalent chemistry. *J. Am. Chem. Soc. 128*, 15602–15603.

(3) Schwartz, D. A., Abrams, M. J., Hauser, M. M., Gaul, F. E., Larsen, S. K., Rauh, D., Zubietas, J. A. (1991) Preparation of hydrazino-modified proteins and their use for the synthesis of ^{99m}Tc-protein conjugates. *Bioconjugate Chem. 2*, 333–330.

Synthesis and Cellular Uptake of Fluorescently Labeled Multivalent Hyaluronan Disaccharide Conjugates of Oligonucleotide Phosphorothioates

Marika Karskela,*[,†] Pasi Virta,[†] Melina Malinen,[‡,§] Arto Urtti,[§] and Harri Lönnberg[†]

Department of Chemistry, University of Turku, FI-20014 Turku, Division of Biopharmaceutics and Pharmacokinetics, Faculty of Pharmacy, and Center for Drug Research, University of Helsinki, P.O. Box 56, FI-00014 University of Helsinki, Helsinki, Finland. Received June 27, 2008; Revised Manuscript Received October 20, 2008

Clustered hyaluronan disaccharides were studied as mediators of cellular delivery of antisense oligonucleotides through receptor-mediated endocytosis. For this purpose, a synthetic route for preparation of an appropriately protected hyaluronic acid dimer bearing an aldehyde tether (**1**) was devised. Up to three non-nucleosidic phosphoramidite building blocks (**2**), each bearing two phthaloyl protected aminooxy groups, were then inserted into the 3′-terminus of the desired phosphorothioate oligodeoxyribonucleotide, and 6-FAM phosphoramidite was introduced into the 5′-terminus. After completion of the chain assembly, the aldehyde-tethered sugar ligands were attached to the deprotected aminooxy functions by on-support oximation. Three fluorescein-labeled phosphorothioate oligonucleotide glycoconjugates (**28**−**30**) containing two, four, or six hyaluronan disaccharides were prepared. The influence of the hyaluronan moieties on the cellular uptake of the thioated oligonucleotides was tested in a cell line expressing the hyaluronan receptor CD44. Specific uptake was not detected with this combination of multiple hyaluronan disaccharides.

INTRODUCTION

Carbohydrate−protein interactions play a major role in recognition of cells by external macromolecules (*1*−*5*). These interactions are multipodal. Although monomeric sugar ligands usually bind only weakly to their receptors, a sufficiently high affinity is achieved by multiple simultaneous interactions, a phenomenon known as a glyco cluster effect (*6*−*12*). Usually, multiantennary carbohydrates anchored to cell membranes recognize extracellular proteins. However, the opposite is also possible (*13*−*15*). Hyaluronic acid, a linear polysaccharide composed of a repeating disaccharide unit of D-glucuronic acid and *N*-acetyl-D-glucosamine, [→3)-*β*-D-GlcNAc-(1→4)-*β*-D-GlcUA-(1→]$_n$, offers a good example. It is the main ligand for a transmembrane glycoprotein CD44 that is overexpressed in many cancers (*16*). Evidently for this reason, hyaluronic acid conjugates of cancer drugs exhibit increased uptake to cancer cells (*17*, *18*). In addition, both high and low molecular weight hyaluronic acid−lipid conjugates have been shown to target liposomes to CD44 expressing cancer cells (*19*−*21*). It has been shown that a hyaluronan octamer is required for high-affinity binding to CD44 (*22*), a tetrameric core region binding to a shallow groove of the protein (*23*). Accordingly, conjugation with hyaluronic acid oligomers may offer a potential means with which to target antisense oligonucleotides to CD44 expressing cells. Enrichment of the oligonucleotide glycoconjugate on the surface, as expected, leads to enhanced internalization by endocytosis and eventually also to increased concentration in the cytoplasm. For comparison, trivalent *N*-acetylgalactosamine (*24*, *25*) and tetravalent galactose (*26*, *27*) conjugates of oligonucleotides, as well as galactosylated PEG conjugates of oligonucleotides (*28*), have been shown to exhibit markedly enhanced cellular uptake by liver cells compared to their non-glycosylated counterpart.

Hyaluronan fragments are used increasingly to study their specific biological activities (*29*). Access to adequate quantities of defined oligosaccharides relies mainly on synthetic methods, since material obtained by enzymatic processing of natural hyaluronan polymers usually consists of a mixture of oligomers. Several hyaluronan oligosaccharides with different lengths and modified sequences have been synthesized over the past decades (*30*−*38*), while the published drug delivery applications have been limited to the use of polymer-sized hyaluronan (*39*).

The underlying idea of the present study was to exploit hyaluronan-mediated binding to the cell surface receptors as a means of internalization of covalently attached oligonucleotide. In more detail, the study was aimed at clarifying whether an oligonucleotide decorated with up to six clustered hyaluronan disaccharides could become recognized by the CD44 receptor instead of a longer hyaluronan oligomer. For this purpose, a synthetic route for preparation of an appropriately protected hyaluronic acid dimer bearing an aldehyde tether (**1**) was devised (Figure 1). For the covalent attachment of these hyaluronan dimers to oligonucleotides, a previously (*40*) developed non-nucleosidic phosphoramidite building block **2** bearing two phthaloyl protected aminooxy groups was utilized. After the assembly of the chain and tethering of a fluorescent dye to the 5′-terminus, the aldehyde-tethered sugar ligands were attached to the deprotected aminooxy groups by on-support oximation. Three fluorescein-labeled phosphorothioate oligonucleotide glycoconjugates (*28*−*30*) were prepared containing two, four, or six hyaluronan ligands. The influence of the hyaluronan moieties on the cellular uptake of the thioated oligonucleotides was tested in a cell line expressing the hyaluronan receptor CD44.

EXPERIMENTAL PROCEDURES

General Methods and Materials. CH_2Cl_2, MeCN, and pyridine were dried over 4 Å molecular sieves. Zinc dust was activated just before use with 5% aqueous HCl, washed with

* Marika.Karskela@utu.fi.
† University of Turku.
‡ Division of Biopharmaceutics and Pharmacokinetics, Faculty of Pharmacy, University of Helsinki.
§ Center for Drug Research, University of Helsinki.

10.1021/bc800260y CCC: $40.75 © 2008 American Chemical Society
Published on Web 11/19/2008

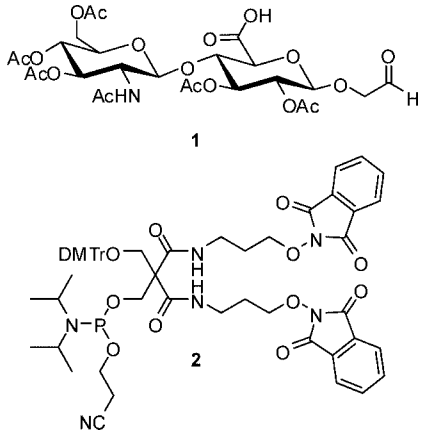

Figure 1. Hyaluronic acid dimer **1** and non-nucleosidic phosphoramidite building block **2**.

water, and dried. The NMR spectra of **1**, **4**−**6**, and **9**−**13** were recorded at 500 and 600 MHz. The chemical shifts are given in ppm, using internal TMS or solvent residual signal as a reference (*41*). Appropriate 2D NMR methods, e.g., COSY, HSQC, and HMBC, were used for the assignment of signals. RP HPLC analyses were performed on Thermo Hypersil Hypurity C18 (150 × 4.6 mm, 5 μm, protocol A) or Thermo Hypersil C18 (250 × 4.6 mm, 5 μm, protocol B) analytical columns at a flow rate of 1 mL min^{-1}. A gradient elution from 0% to 30% MeCN in 0.05 mol L^{-1} NH_4OAc buffer over 30 min (protocol A) or a gradient elution from 0% to 50% MeCN in 0.1 mol L^{-1} Et_3NHOAc buffer over 30 min (protocol B) was used. For semipreparative purifications and desalting, a LiChroCART Hypersil ODS column (250 × 10 mm, 5 μm) at a flow rate of 3 mL min^{-1} was used. The detection wavelength was 260 nm. Yields of the purified glycoconjugates **28**−**30** were determined UV-spectrophotometrically at λ = 260 nm using the molar absorptivity calculated for the unstacked oligonucleotides. The molar absorptivity used for the label was 21 000 M^{-1} cm^{-1}. The contributions of the non-nucleosidic building block and saccharide residues to the absorbance at the detection wavelength were ignored.

2-Cyanoethyl 3-(4,4′-Dimethoxytrityloxy)-2,2-bis[3-(phthalimidooxy)propylcarbamoyl]propyl *N*,*N*-Diisopropylphosphoramidite (2). 2 was synthesized as described previously (*40*) except for the following modifications: 2-methoxy-*N*,*N*-bis(3-phthalimidooxypropyl)-1,3-dioxane-5,5-dicarboxamide prepared from *N*,*N*-bis(3-hydroxypropyl)-2-methoxy-1,3-dioxane-5,5-dicarboxamide (9.00 g, 28.1 mmol) by Mitsunobu reaction was purified by crystallization from the reaction mixture (THF) in 65% yield (11.2 g). No recrystallization was carried out. The orthoester protection was then removed by an overnight treatment with 0.1 mol L^{-1} aqueous HCl in dioxane (5:2, v/v). The reaction mixture was neutralized with pyridine and concentrated in vacuo. The product was precipitated by addition of water to obtain 2,2-bis(hydroxymethyl)-*N*,*N*-bis(3-phthalimidooxypropyl)malondiamide in 71% yield (7.28 g). The ^1H and ^{13}C NMR spectra were in accordance with published data (*40*).

Allyl 2,3,4,6-Tetra-*O*-acetyl-β-D-glucopyranoside (3). 3 was synthesized from the commercially available 1,2,3,4,6-penta-*O*-acetyl-β-D-glucopyranose as described in the literature (*42*). The ^1H NMR spectrum was in accordance with the published data.

Allyl 4,6-*O*-Benzylidene-β-D-glucopyranoside (4). Compound **3** (5.33 g, 13.7 mmol) was dissolved in 0.1 mol L^{-1} NaOMe/MeOH solution (50 mL). The mixture was stirred for 1 h, neutralized by addition of strongly acidic cation-exchange resin (Dowex 50WX8−200), and filtered. The filtrate was evaporated to dryness, and the residue was dried in vacuo over P_2O_5. The residue was dissolved in dry MeCN (100 mL), and benzaldehyde dimethylacetal (2.70 mL, 18.0 mmol) and *p*-toluenesulfonic acid (78 mg, 0.41 mmol) were added. The reaction mixture was stirred for 2.5 h, diluted with EtOAc, and washed with water and saturated aqueous $NaHCO_3$. The aqueous layers were extracted with EtOAc, and the combined organic layers were dried over Na_2SO_4, filtered, and evaporated to dryness. The residue was suspended in a small volume of CH_2Cl_2. The product was precipitated (*43*) by addition of ether−hexane (1:2, v/v), filtered, washed with cold ether−hexane, and dried in vacuo to afford **4** as a white solid in 86% yield (3.63 g). ^1H NMR (500 MHz, $CDCl_3$): δ = 7.50−7.47 (m, 2H, Ph); 7.39−7.35 (m, 3H, Ph); 5.94 (m, 1H, CH═); 5.53 (s, 1H, C*H*Ph); 5.34 (m, 1H, ═CH_2); 5.25 (m, 1H, ═CH_2); 4.45 (d, 1H, $J_{1,2}$ = 7.8 Hz, H-1); 4.39 (m, 1H, OC*H*HCH═); 4.34 (dd, 1H, $J_{6a,5}$ = 5.0 Hz, $J_{6a,6b}$ = 10.5 Hz, H-6a); 4.15 (m, 1H, OCH*H*CH═); 3.81 (ddd, 1H, $J_{3,2}$ = 8.9 Hz, $J_{3,4}$ = 9.3 Hz, $J_{3,OH\text{-}3}$ = 2.1 Hz, H-3); 3.78 (dd, 1H, $J_{6b,5}$ = 10.1 Hz, $J_{6b,6a}$ = 10.5 Hz, H-6b); 3.55 (dd, 1H, $J_{4,3}$ = 9.3 Hz, $J_{4,5}$ = 9.3 Hz, H-4); 3.53 (ddd, 1H, $J_{2,1}$ = 7.8 Hz, $J_{2,3}$ = 8.9 Hz, $J_{2,OH\text{-}2}$ = 2.4 Hz, H-2); 3.45 (ddd, 1H, $J_{5,6a}$ = 5.0 Hz, $J_{5,6b}$ = 10.1 Hz, $J_{5,4}$ = 9.3 Hz, H-5); 2.91 (d, 1H, $J_{OH\text{-}3,3}$ = 2.1 Hz, OH-3); 2.78 (d, 1H, $J_{OH\text{-}2,2}$ = 2.4 Hz, OH-2) ppm; ^{13}C NMR (125 MHz, $CDCl_3$): δ = 137.1 (Ph); 133.5 (CH═); 129.4, 128.5, and 126.4 (Ph); 118.6 (═CH_2); 102.2 (C-1); 102.1 (*C*HPh); 80.7 (C-4); 74.6 (C-2); 73.3 (C-3); 70.8 (O*C*H_2CH═); 68.8 (C-6); 66.5 (C-5) ppm; HRMS (EI^+): M^+ requires 308.1260, found 308.1251.

Allyl 2,3-Di-*O*-acetyl-4,6-*O*-benzylidene-β-D-glucopyranoside (5). Compound **4** (3.63 g, 11.8 mmol) was acetylated as described previously (*43*) to give **5** as a white powder in 96% yield (4.43 g). ^1H NMR (500 MHz, $CDCl_3$): δ = 7.45−7.42 (m, 2H, Ph); 7.38−7.34 (m, 3H, Ph); 5.85 (m, 1H, CH═); 5.51 (s, 1H, C*H*Ph); 5.32 (dd, 1H, $J_{3,2}$ = 9.4 Hz, $J_{3,4}$ = 9.6 Hz, H-3); 5.29 (m, 1H, ═CH_2); 5.21 (m, 1H, ═CH_2); 5.04 (dd, 1H, $J_{2,1}$ = 7.9 Hz, $J_{2,3}$ = 9.4 Hz, H-2); 4.64 (d, 1H, $J_{1,2}$ = 7.9 Hz, H-1); 4.37 (dd, 1H, $J_{6a,5}$ = 5.0 Hz, $J_{6a,6b}$ = 10.6 Hz, H-6a); 4.34 (m, 1H, OC*H*HCH═); 4.11 (m, 1H, OCH*H*CH═); 3.81 (dd, 1H, $J_{6b,5}$ = 10.0 Hz, $J_{6b,6a}$ = 10.6 Hz, H-6b); 3.71 [dd, 1H, $J_{4,3}$ = 9.6 Hz, $J_{4,5}$ = 9.5 Hz (average), H-4]; 3.52 [ddd, 1H, $J_{5,4}$ = 9.5 Hz (average), $J_{5,6a}$ = 5.0 Hz, $J_{5,6b}$ = 10.0 Hz, H-5]; 2.07 and 2.05 (2 × s, each 3H, 2 × CH_3, Ac) ppm; ^{13}C NMR (125 MHz, $CDCl_3$): δ = 170.3 and 169.7 (CO, Ac); 136.9 (Ph); 133.4 (CH═); 129.3, 128.4, and 126.3 (Ph); 117.8 (═CH_2); 101.7 (*C*HPh); 100.4 (C-1); 78.5 (C-4); 72.4 (C-2); 71.9 (C-3); 70.4 (O*C*H_2CH═); 68.7 (C-6); 66.5 (C-5); 21.0 and 20.9 (CH_3, Ac) ppm; HRMS (EI^+): M^+ requires 392.1471, found 392.1462.

Allyl 2,3-Di-*O*-acetyl-6-*O*-benzyl-β-D-glucopyranoside (6). Compound **5** (4.43 g, 11.3 mmol) was dissolved in CH_2Cl_2 (45 mL) and cooled to 0 °C. Triethylsilane (8.97 mL, 56.5 mmol) was added, followed by slow addition of trifluoroacetic acid (4.35 mL, 56.5 mmol). After 2 h stirring at the same temperature, CH_2Cl_2 was added and the organic layer was washed with saturated aqueous $NaHCO_3$ and brine. The aqueous layers were extracted with CH_2Cl_2, and the combined organic layers were dried over Na_2SO_4, filtered, and evaporated to dryness. Purification by silica gel chromatography (40% EtOAc in petroleum ether) gave **6** as a colorless oil in 91% yield (4.07 g). ^1H NMR (600 MHz, $CDCl_3$): δ = 7.36−7.29 (m, 5H, Ph); 5.84 (m, 1H, CH═); 5.26 (m, 1H, ═CH_2); 5.18 (m, 1H, ═CH_2); 5.05 (dd, 1H, $J_{3,2}$ = 9.7 Hz, $J_{3,4}$ = 9.2 Hz, H-3); 4.96 (dd, 1H, $J_{2,1}$ = 7.9 Hz, $J_{2,3}$ = 9.7 Hz, H-2); 4.62 (d, 1H, J_{gem} = 12.0 Hz, C*H*HPh), 4.57 (d, 1H, J_{gem} = 12.0 Hz, CH*H*Ph); 4.52 (d, 1H, $J_{1,2}$ = 7.9 Hz, H-1); 4.32 (m, 1H, OC*H*HCH═); 4.08 (m, 1H, OCH*H*CH═); 3.79 (dd, 1H, $J_{6a,5}$ = 5.0 Hz, $J_{6a,6b}$ = 10.5 Hz, H-6a); 3.77 (dd, 1H, $J_{6b,5}$ = 5.0 Hz, $J_{6b,6a}$ = 10.5 Hz, H-6b); 3.75 (m, 1H, H-4); 3.53 (ddd, 1H, $J_{5,4}$ = 9.2 Hz, $J_{5,6a}$ = 5.0

Hz, $J_{5,6b}$ = 5.0 Hz, H-5); 3.01 (br, 1H, OH); 2.08 and 2.05 (2 × s, each 3H, 2 × CH_3, Ac) ppm; ^{13}C NMR (150 MHz, $CDCl_3$): δ = 171.3 and 169.6 (CO, Ac); 137.5 (Ph); 133.5 (CH═); 128.5, 127.9, and 127.8 (Ph); 117.4 (═CH_2); 99.6 (C-1); 75.7 (C-3); 74.0 (C-5); 73.8 (*C*H_2Ph); 71.3 (C-2); 70.9 (C-4); 70.2 (C-6); 69.9 (O*C*H_2CH═); 20.9 and 20.8 (CH_3, Ac) ppm; HRMS (ESI^+): $[M + Na]^+$ requires 417.1525, found 417.1529.

3,4,6-Tri-*O*-acetyl-2-deoxy-2-trichloroacetamido-α-D-glucopyranosyl Trichloroacetimidate (7). **7** was synthesized as described in the literature (*44*). The ^{1}H NMR spectrum was in accordance with published data (*44*)

3,4,6-Tri-*O*-acetyl-2-deoxy-2-(2,2,2-trichloroethoxycarboxamido)-α-D-glucopyranosyl Trichloroacetimidate (8). **8** was synthesized as described in the literature (*45*). The ^{1}H NMR spectrum was in accordance with published data (*46*).

(3,4,6-Tri-*O*-acetyl-2-deoxy-2-trichloroacetamido-β-D-glucopyranosyl)-(1→4)-(allyl 2,3-di-*O*-acetyl-6-*O*-benzyl-β-D-glucopyranoside) (9). Trichloroacetimidate **7** (603 mg, 1.01 mmol) and compound **6** (317 mg, 0.804 mmol) were combined and dried by repeated co-evaporations with toluene. The mixture was dissolved in dry CH_2Cl_2 (9 mL) and cooled to 0 °C, after which trimethylsilyl trifluoromethanesulfonate (TMSOTf) (14 μL, 0.077 mmol) was added. Upon completion of the reaction (40 min), triethylamine (100 μL) was added and the solvents were removed in vacuo. The residue was purified by silica gel chromatography (15% EtOAc in CH_2Cl_2) to give **9** as yellowish foam in 95% yield (630 mg). ^{1}H NMR (500 MHz, $CDCl_3$): δ = 7.47−7.40 (m, 5H, Ph); 6.37 (d, 1H, $J_{NH,2'}$ = 8.6 Hz, NH); 5.84 (m, 1H, CH═); 5.25 (m, 1H, ═CH_2); 5.18 (m, 1H, ═CH_2); 5.14−5.08 (m, 2H, H-3 and H-3′); 4.99−4.95 (m, 2H, H-2 and H-4′); 4.81 (d, 1H, J_{gem} = 12.0 Hz, C*H*HPh); 4.49 (d, 1H, $J_{1',2'}$ = 8.4 Hz, H-1′); 4.47 (d, 1H, $J_{1,2}$ = 7.9 Hz, H-1); 4.45 (d, 1H, J_{gem} = 12.0 Hz, CH*H*Ph); 4.36 (dd, 1H, $J_{6a',5'}$ = 4.5 Hz, $J_{6a',6b'}$ = 12.5 Hz, H-6a′); 4.32 (m, 1H, OC*H*HCH═); 4.07 (m, 1H, OCH*H*CH═); 4.01 (m, 1H, H-4); 3.98 (dd, 1H, $J_{6b',5'}$ = 2.1 Hz, $J_{6b',6a'}$ = 12.5 Hz, H-6b′); 3.72−3.63 (m, 3H, H-2′ and 2 × H-6); 3.44−3.40 (m, 2H, H-5′ and H-5); 2.07 (s, 3H, CH_3, Ac); 2.03 (s, 6H, 2 × CH_3, Ac); 2.01 and 1.98 (2 × s, each 3H, 2 × CH_3, Ac) ppm; ^{13}C NMR (125 MHz, $CDCl_3$): δ = 170.6, 170.6, 170.3, 169.7, and 169.5 (CO, Ac); 161.6 (*C*OCCl_3) 137.8 (Ph); 133.6 (CH═); 129.0, 128.8, and 128.7 (Ph); 117.4 (═CH_2); 99.8 (C-1); 99.0 (C-1′); 92.3 (CCl_3); 74.3 (C-4 and C-5); 73.6 (*C*H_2Ph); 72.8 (C-3); 71.8 (C-5′); 71.6 (C-2); 71.4 (C-3′); 70.0 (O*C*H_2CH═); 68.2 (C-4′); 67.4 (C-6); 61.7 (C-6′); 56.5 (C-2′); 20.8, 20.8, 20.7, 20.7, and 20.6 (CH_3, Ac) ppm; HRMS (ESI^+): $[M + Na]^+$ requires 850.1437, found 850.1457.

[3,4,6-Tri-*O*-acetyl-2-deoxy-2-(2,2,2-trichloroethoxycarboxamido)-β-D-glucopyranosyl]-(1→4)-(allyl 2,3-di-O-acetyl-6-O-benzyl-β-D-glucopyranoside) (10). Trichloroacetimidate **8** (1.00 g, 1.60 mmol) was reacted with **6** (485 mg, 1.23 mmol) as described for **9**. The product was purified by silica gel chromatography (15% EtOAc in CH_2Cl_2) to give **10** as yellow foam in 58% yield (608 mg). ^{1}H NMR (500 MHz, $CDCl_3$): δ = 7.53−7.43 (m, 5H, Ph); 5.84 (m, 1H, CH═); 5.26 (m, 1H, ═CH_2); 5.19 (m, 1H, ═CH_2); 5.10 (dd, 1H, $J_{3,2}$ = 9.8 Hz, $J_{3,4}$ = 9.3 Hz, H-3); 4.96 (dd, 1H, $J_{2,1}$ = 8.0 Hz, $J_{2,3}$ = 9.8 Hz, H-2); 4.92−4.81 (m, 3H, H-4′, C*H*HCCl_3 and H-3′); 4.71 and 4.63 (2 × d, each 1H, J_{gem} = 12.1 Hz, CH_2Ph); 4.46 (d, 1H, $J_{1,2}$ = 8.0 Hz, H-1); 4.39−4.32 (m, 3H, CH*H*CCl_3, H-6a′ and OC*H*HCH═); 4.23 (d, 1H, $J_{1',2'}$ = 8.3 Hz, H-1′); 4.10−4.06 (m, 2H, OCH*H*CH═ and NH); 4.00−3.93 (m, 2H, H-6b′ and H-4); 3.71 (dd, 1H, $J_{6a,5}$ = 2.7 Hz, $J_{6a,6b}$ = 10.9 Hz, H-6a); 3.58 (m, 1H, H-6b); 3.51−3.44 (m, 2H, H-2′ and H-5′); 3.38 (m, 1H, H-5); 2.07, 2.02, 2.02, 1.99, and 1.97 (5 × s, each 3H, 5 × CH_3, Ac) ppm; ^{13}C NMR (125 MHz, $CDCl_3$): δ = 170.7, 170.4, 170.3, 169.7, and 169.6 (CO, Ac); 153.8 (NHCO) 137.5 (Ph); 133.6 (CH═); 129.4, 129.2, and 129.2 (Ph); 117.5 (═CH_2); 100.5 (C-1′); 99.8 (C-1); 95.6 (CCl_3); 75.0 (C-4); 74.6 (*C*H_2PH); 74.2 (C-5); 73.8 (*C*H_2CCl_3); 72.8 (C-3); 72.3 (C-3′); 71.7 (C-2); 71.5 (C-5′); 70.0 (O*C*H_2CH═); 68.5 (C-4′); 66.9 (C-6); 61.8 (C-6′); 56.0 (C-2′); 20.8, 20.8, 20.7, 20.7, and 20.7 (CH_3, Ac) ppm; HRMS (ESI^+): $[M + Na]^+$ requires 880.1543, found 880.1570.

(2-Acetamido-3,4,6-tri-*O*-acetyl-2-deoxy-β-D-glucopyranosyl)-(1→4)-(allyl 2,3-di-*O*-acetyl-6-*O*-benzyl-β-D-glucopyranoside) (11). Method A. A solution of **9** (125 mg, 151 μmol) and acetic acid (380 μL) in dry CH_2Cl_2 (9 mL) was treated with freshly activated zinc dust (380 mg). After 72 h, the reaction mixture was filtered and the filtrate was co-evaporated with toluene. The product was purified by silica gel chromatography (3% *i*-PrOH in CH_2Cl_2) to give **11** as white solid flakes in 85% yield (92 mg). ^{1}H NMR (500 MHz, $CDCl_3$): δ = 7.48−7.42 (m, 5H, Ph); 5.84 (m, 1H, CH═); 5.26 (m, 1H, ═CH_2); 5.19 (m, 1H, ═CH_2); 5.11 (dd, 1H, $J_{3,2}$ = 9.7 Hz, $J_{3,4}$ = 9.3 Hz, H-3); 5.03 (dd, 1H, $J_{3',2'}$ = 10.4 Hz, $J_{3',4'}$ = 9.3 Hz, H-3′); 4.95 (dd, 1H, $J_{2,1}$ = 8.0 Hz, $J_{2,3}$ = 9.7 Hz, H-2); 4.94 (dd, 1H, $J_{4',3'}$ = 9.3 Hz, $J_{4',5'}$ = 10.0 Hz, H-4′); 4.87 (d, 1H, $J_{NH,2'}$ = 8.9 Hz, NH); 4.83 (d, 1H, J_{gem} = 12.1 Hz, C*H*HPh); 4.50 (d, 1H, $J_{1',2'}$ = 8.4 Hz, H-1′); 4.47 (d, 1H, $J_{1,2}$ = 8.0 Hz; H-1); 4.45 (d, 1H, J_{gem} = 12.1 Hz, CH*H*Ph); 4.35 (dd, 1H, $J_{6a',5'}$ = 4.5 Hz, $J_{6a'6b'}$ = 12.4 Hz, H-6a′); 4.33 (m, 1H, OC*H*HCH═); 4.08 (m, 1H, OCH*H*CH═); 3.98 (dd, 1H, $J_{6b',5'}$ = 2.2 Hz, $J_{6b',6a'}$ = 12.4 Hz, H-6b′); 3.96 (dd, 1H, $J_{4,3}$ = 9.3 Hz, $J_{4,5}$ = 9.9 Hz, H-4); 3.68 (ddd, 1H, $J_{2',1'}$ = 8.4 Hz, $J_{2',3'}$ = 10.4 Hz, $J_{2',NH}$ = 8.9 Hz, H-2′); 3.63 (d, 2H, $J_{6,5}$ = 2.4 Hz, H-6); 3.50 (ddd, 1H, $J_{5',4'}$ = 10.0 Hz, $J_{5',6a'}$ = 4.5 Hz, $J_{5',6b'}$ = 2.2 Hz, H-5′); 3.45 (dt, 1H, $J_{5,4}$ = 9.9 Hz, $J_{5,6}$ = 2.4 Hz, H-5); 2.06, 2.03, 2.02, 2.00, and 1.98 (5 × s, each 3H, 5 × CH_3, Ac); 1.73 (s, 3H, CH_3, NHAc) ppm; ^{13}C NMR (125 MHz, $CDCl_3$): δ = 170.6, 170.2, 169.8, 169.7, and 169.5 (CO, Ac); 137.8 (Ph); 133.6 (CH═); 129.0, 128.9, and 128.8 (Ph); 117.5 (═CH_2); 100.1 (C-1′); 99.7 (C-1); 74.9 (C-4); 74.3 (C-5); 73.7 (*C*H_2Ph); 72.9 (C-3); 72.5 (C-3′); 71.7 (C-2); 71.5 (C-5′); 69.9 (O*C*H_2CH═); 68.4 (C-4′); 67.3 (C-6); 61.8 (C-6′); 54.7 (C-2′); 23.2 (CH_3, NHAc); 20.8, 20.7, 20.7, and 20.7 (CH_3, Ac) ppm; HRMS (FAB^+): M^+ requires 724.2817, found 724.2807. Method B. A solution of **10** (147 mg, 172 μmol) in acetic anhydride (5 mL) was treated with freshly activated zinc dust (300 mg). The reaction mixture was stirred overnight and filtered. The filtrate was co-evaporated with toluene and the product was purified as described above in Method A to give **11** in 80% yield (99 mg).

(2-Acetamido-3,4,6-tri-*O*-acetyl-2-deoxy-β-D-glucopyranosyl)-(1→4)-(allyl 2,3-di-*O*-acetyl-β-D-glucopyranoside) (12). A mixture of benzyl ether **11** (2.04 g, 2.82 mmol) and 2,3-dichloro-5,6-dicyano-1,4-benzoquinone (DDQ) (3.20 g, 14.1 mmol) in dry CH_2Cl_2 (80 mL) was refluxed for 48 h. To cleave the dimeric side product formed during refluxing, water (8 mL) was added and the stirring was continued for 2 h at room temperature. The mixture was diluted with CH_2Cl_2, and the organic layer was washed with saturated aqueous $NaHCO_3$ and brine. The aqueous layers were extracted with CH_2Cl_2, and the combined organic layers were dried over Na_2SO_4, filtered, and evaporated to dryness. Purification by silica gel chromatography (7% *i*-PrOH in CH_2Cl_2) gave **12** as white solid in 90% yield (1.60 g). ^{1}H NMR (500 MHz, $CDCl_3$): δ = 6.21 (d, 1H, $J_{NH,2'}$ = 8.9 Hz, NH); 5.84 (m, 1H, CH═); 5.28−5.18 (m, 2H, ═CH_2); 5.24 [dd, 1H, $J_{3',2'}$ = 10.5 Hz, $J_{3',4'}$ = 9.4 Hz (average), H-3′]; 5.20 (dd, 1H, $J_{3,2}$ = 9.7 Hz, $J_{3,4}$ = 9.2 Hz, H-3); 5.05 [dd, 1H, $J_{4',3'}$ = 9.4 Hz (average), $J_{4',5'}$ = 10.0 Hz, H-4′]; 4.91 (dd, 1H, $J_{2,1}$ = 8.0 Hz, $J_{2,3}$ = 9.7 Hz, H-2); 4.78 (d, 1H, $J_{1',2'}$ = 8.4 Hz, H-1′); 4.54 (d, 1H, $J_{1,2}$ = 8.0 Hz, H-1); 4.37 (dd, 1H, $J_{6a',5'}$ = 4.4 Hz, $J_{6a',6b'}$ = 12.4 Hz, H-6a′); 4.31 (m, 1H, OC*H*HCH═); 4.09 (m, 1H, OCH*H*CH═); 4.04 [dd, 1H, $J_{6b',5'}$ = 2.3 Hz (average), $J_{6b',6a'}$ = 12.4 Hz, H-6b′]; 3.95 (dd, 1H, $J_{4,3}$ = 9.2

Hz, $J_{4,5}$ = 9.9 Hz, H-4); 3.92−3.85 (m, 1H, H-6a); 3.86 (ddd, 1H, $J_{2',1'}$ = 8.4 Hz, $J_{2',3'}$ = 10.5 Hz, $J_{2',NH}$ = 8.9 Hz, H-2′); 3.81−3.70 (m, 1H, H-6b); 3.72 [ddd, 1H, $J_{5',4'}$ = 10.0 Hz, $J_{5',6a'}$ = 4.4 Hz, $J_{5',6b'}$ = 2.3 Hz (average), H-5′]; 3.43 (m, 1H, H-5); 2.61 (br, 1H, OH); 2.08, 2.04, 2.03, 2.02, 2.00, and 1.95 (6 × s, each 3H, 6 × CH_3, Ac) ppm; ^{13}C NMR (125 MHz, $CDCl_3$): δ = 171.2, 170.7, 170.6, 170.2, 169.8, and 169.5 (CO, Ac); 133.5 (CH═); 117.7 (═CH_2); 101.1 (C-1′); 99.8 (C-1); 75.5 (C-4); 75.0 (C-5); 73.0 (C-3); 72.6 (C-3′); 71.9 (C-2); 71.8 (C-5′); 70.3 (O*C*H_2CH═); 68.3 (C-4′); 62.0 (C-6′); 60.5 (C-6); 55.0 (C-2′); 23.3 (CH_3, NHAc); 20.8, 20.8, 20.8, and 20.7 (CH_3, Ac) ppm; HRMS (ESI^+): $[M + H]^+$ requires 634.2347, found 634.2356.

(2-Acetamido-3,4,6-tri-*O*-acetyl-2-deoxy-β-D-glucopyranosyl)-(1→4)-(allyl 2,3-di-*O*-acetyl-β-D-glucopyranosiduronic Acid) (13). Compound **12** (520 mg, 0.820 mmol) was dissolved in wet MeCN (5 mL, 0.8 v % water) and cooled to 0 °C. A solution of H_5IO_6/CrO_3 (5 mL, 2.5 equiv/1.1 mol % in 0.8 v % water/MeCN) was added portionwise, and the reaction was allowed to proceed at 0 °C for 3 h. The reaction was quenched by adding aqueous Na_2HPO_4 (1.95 g in 25 mL water). Water was added and organic side products were removed by repeated extractions with CH_2Cl_2. The aqueous layer was acidified to pH 3.0 by addition of 1 mol L^{-1} HCl, and the product was extracted in CH_2Cl_2. The organic layers were combined, dried over Na_2SO_4, filtered, and evaporated to dryness to afford **13** as white solid in 80% yield (423 mg). ^{1}H NMR (500 MHz, $(CD_3)_2SO$): δ = 13.11 (br, 1H, COOH); 7.46 (d, 1H, $J_{NH,2'}$ = 8.9 Hz, NH); 5.83 (m, 1H, CH═); 5.24−5.13 (m, 2H, ═CH_2); 5.20 (dd, 1H, $J_{3',2'}$ = 10.4 Hz, $J_{3',4'}$ = 9.4 Hz, H-3′); 5.15 [dd, 1H, $J_{3,2}$ = 9.5 Hz, $J_{3,4}$ = 9.1 Hz (average), H-3]; 4.83 (d, 1H, $J_{1,2}$ = 7.9 Hz, H-1); 4.79 (dd, 1H, $J_{4',3'}$ = 9.4 Hz, $J_{4',5'}$ = 10.1 Hz, H-4′); 4.75 (d, 1H, $J_{1',2'}$ = 8.3 Hz, H-1′); 4.70 (dd, 1H, $J_{2,1}$ = 7.9 Hz, $J_{2,3}$ = 9.5 Hz, H-2); 4.26 (dd, 1H, $J_{6a',5'}$ = 4.2 Hz, $J_{6a',6b'}$ = 12.4 Hz, H-6a′); 4.20 (m, 1H, OC*H*HCH═); 4.08 (d, 1H, $J_{5,4}$ = 9.4 Hz, H-5); 4.02 (m, 1H, OCH*H*CH═); 3.94 [dd, 1H, $J_{4,3}$ = 9.1 Hz (average), $J_{4,5}$ = 9.4 Hz, H-4]; 3.92 [dd, 1H, $J_{6b',5'}$ = 2.3 Hz (average), $J_{6b',6a'}$ = 12.4 Hz, H-6b′]; 3.79 [ddd, 1H, $J_{5',4'}$ =10.1 Hz, $J_{5',6a'}$ = 4.2 Hz, $J_{5',6b'}$ = 2.3 Hz (average), H-5′]; 3.46 (ddd, 1H, $J_{2',1'}$ = 8.3 Hz, $J_{2',3'}$ = 10.4 Hz, $J_{2',NH}$ = 8.9 Hz, H-2′); 2.00, 1.98, 1.97, 1.94, and 1.89 (5 × s, each 3H, 5 × CH_3, Ac); 1.74 (s, 3H, CH_3, NHAc) ppm; ^{13}C NMR (125 MHz, $(CD_3)_2SO$): δ = 170.0, 169.6, 169.3, 169.3, 169.2, 169.1, and 168.6 (CO, Ac, and CO_2H); 134.0 (CH═); 116.7 (═CH_2); 100.1 (C-1′); 99.1 (C-1); 76.5 (C-4); 73.5 (C-5); 72.2 (C-3′); 71.9 (C-3); 71.1 (C-2); 70.5 (C-5′); 69.4 (O*C*H_2CH═); 68.3 (C-4′); 61.7 (C-6′); 53.8 (C-2′); 22.7 (CH_3, NHAc); 20.4, 20.4, 20.3, and 20.3 (CH_3, Ac) ppm; HRMS (ESI^+): $[M + Na]^+$ requires 670.1959, found 670.1983.

(2-Acetamido-3,4,6-tri-*O*-acetyl-2-deoxy-β-D-glucopyranosyl)-(1→4)-(2-oxoethyl 2,3-di-*O*-acetyl-β-D-glucopyranosiduronic Acid) (1). To a solution of allyl disaccharide **13** (381 mg, 0.589 mmol) in dioxane−water (4:1, v/v) (8 mL) OsO_4 (52 μL, 2.5 wt% solution in 2-methyl-2-propanol, 0.0042 mmol) was added. The solution was stirred vigorously for 1 h. The solution turned brownish, which indicated the formation of the osmate ester. $NaIO_4$ (252 mg, 1.18 mmol) was added over 20 min, and stirring was continued for additional 1.5 h. Volatiles were removed, and the residue was dissolved in a small amount of water and acidified to pH 3.0 by the addition of 1 mol L^{-1} HCl. The crude product mixture was evaporated to dryness and purified by silica gel chromatography (20% MeOH in CH_2Cl_2) to give **1** as white solid in 79% yield (304 mg). The product exhibited NMR signals both as a hydrate and as an aldehyde in 9:1 ratio. Only the major form (hydrate) is assigned here (for the structure and atom numbering, see Supporting Information). ^{1}H NMR (500 MHz, 20% D_2O in CD_3CN): δ = 5.12 (dd, 1H, $J_{3',2'}$ = 10.4 Hz, $J_{3',4'}$ = 9.5 Hz H-3′); 5.08 (dd, 1H, $J_{3,2}$ = 9.7 Hz, $J_{3,4}$ = 9.3 Hz, H-3); 4.99 (t, 1H, $J_{2'',1a''}$ = $J_{2'',1b''}$ = 5.0 Hz, H-2"); 4.92 (dd, 1H, $J_{4',3'}$ = 9.5 Hz, $J_{4',5'}$ = 10.0 Hz, H-4′); 4.83 (dd, 1H, $J_{2,1}$ = 8.0 Hz, $J_{2,3}$ = 9.7 Hz, H-2); 4.76 (d, 1H, $J_{1',2'}$ = 8.5 Hz, H-1′); 4.67 (d, 1H, $J_{1,2}$ = 8.0 Hz, H-1); 4.30 (dd, 1H, $J_{6a',5'}$ = 4.1 Hz, $J_{6a',6b'}$ = 12.5 Hz, H-6a′); 4.03 (dd, 1H, $J_{6b',5'}$ = 2.1 Hz, $J_{6b',6a'}$ = 12.5 Hz, H-6b′); 3.95 (dd, 1H, $J_{4,3}$ = 9.3 Hz, $J_{4,5}$ = 9.7 Hz, H-4); 3.81 (ddd, 1H, $J_{5',4'}$ = 10.0 Hz, $J_{5',6a'}$ = 4.1 Hz, $J_{5',6b'}$ = 2.1 Hz, H-5′); 3.78 (d, 1H, $J_{5,4}$ = 9.7 Hz, H-5); 3.67 (dd, 1H, $J_{1a'',2''}$ = 5.0 Hz, $J_{1a'',1b''}$ = 11.0 Hz, H-1a″); 3.65 (dd, 1H, $J_{2',1'}$ = 8.5 Hz, $J_{2',3'}$ = 10.4 Hz, H-2′); 3.54 (dd, 1H, $J_{1b'',2''}$ = 5.0 Hz, $J_{1b'',1a''}$ = 11.0 Hz, H-1b″); 2.03 (s, 6H, 2 × CH_3, Ac); 2.01, 1.97, and 1.95 (3 × s, each 3H, 3 × CH_3, Ac); 1.90 (s, 3H, CH_3, NHAc) ppm; ^{13}C NMR (125 MHz, 20% D_2O in CD_3CN): δ = 173.9 (CO_2H); 173.5 (CONH); 172.0, 172.0, 171.7, 171.4, and 170.9 (CO, Ac); 100.8 (C-1); 100.5 (C-1′); 88.7 (C-2″); 77.9 (C-4); 76.4 (C-5); 73.4 (C-3′); 73.1 (C-1″); 72.8 (C-3); 71.6 (C-2); 71.4 (C-5′); 68.6 (C-4′); 62.2 (C-6′); 54.2 (C-2′); 22.6 (CH_3, NHAc); 20.5, 20.4, 20.3, and 20.3 (CH_3, Ac) ppm; HRMS (ESI^+): $[M + H]^+$ requires 650.1932, found 650.1958.

Table 1. Properties of the Oligothymidine Glycoconjugates (18−21)

entry	oligothymidine glycoconjugate	purity of the crude conjugate[a] [%]	observed mass [g mol^{-1}]	required mass[g mol^{-1}]
1	**18**	46	3279.7	3280.4
2	**19**	43	4189.1	4189.2
3	**20**	47	4493.1	4493.4
4	**21**	30	6009.6	6010.6

[a] Purities according to signal areas in RP HPLC chromatograms of crude mixtures of **18**−**21**.

Oligodeoxyribonucleotide Synthesis. The oligodeoxyribonucleotides were assembled on an Applied Biosystems 392 DNA synthesizer in a 1.0 μmol scale using commercial 1000 Å CPG-succinyl-thymidine support and phosphoramidite chemistry. Phosphoramidite **2** was used as a 0.13 mol L^{-1} solution in dry MeCN with a coupling time of 600 s. After coupling of **2**, 6 additional detritylation cycles were carried out. Otherwise, standard protocols were employed. The coupling efficiencies were followed by DMTr-cation assay.

Synthesis of Oligothymidine Glycoconjugates 18−21. Protected oligonucleotide sequences 5′-d(TXT TTT TT)-3′ (**14**), 5′-d(TXX TTT TT)-3′ (**15**), 5′-d(TXT XTT TTT)-3′ (**16**), and 5′-d(TXT XTX TTT TT)-3′ (**17**), where X stands for the non-nucleosidic building block **2**, were synthesized as described above. Small aliquots of the support-bound oligonucleotides were treated with 0.5 mol L^{-1} hydrazinium acetate solution (0.124/4/1, $NH_2NH_2 \cdot H_2O$/pyridine/AcOH, v/v/v) for 30 min, washed with pyridine and MeCN, and dried. The supports were transferred to microcentrifuge tubes, and a solution of the aldehyde tethered sugar ligand **1** (0.3 mol L^{-1} in 10% H_2O/MeCN) was added. The mixtures were shaken at ambient temperature for either 4 or 18 h [sequences containing one (**14**) or more (**15**−**17**) non-nucleosidic units (*2*), respectively]. The supports were filtered, washed with 10% H_2O in MeCN and MeCN, dried, and treated with concentrated ammonia (33% aqueous NH_3, 3 h at room temperature) to release and deprotect the resulting oligonucleotide glycoconjugates. The crude products (**18**−**21**) were analyzed by RP HPLC (protocol A), and the authenticity of the conjugates was verified by MS(ESI) spectroscopy (properties of **18**−**21**; see Table 1).

Phosphorothioate Oligodeoxyribonucleotide Synthesis. Phosphorothioate oligodeoxyribonucleotides were assembled as described for oligodeoxyribonucleotides except for replacement of oxidation with sulfurization (60 s), which was carried out prior to each capping step using 3-dimethylaminomethyleneamino-1,2,4-dithiazole-5-thione as the sulfurizing reagent. In

addition, a commercial 5′-fluorescein phosphoramidite label, 6-[(3′,6′-di-*O*-pivaloylfluorescein-6-yl)carboxamido]hexyl 2-cyanoethyl *N,N*-diisopropylphosphoramidite (6-FAM), was attached to the 5′-end of the sequences.

Synthesis of Phosphorothioate Oligonucleotide Glycoconjugate 28. Protected phosphorothioate oligonucleotide sequence 5′-(6-FAM)-d(TGG CGT CTT CCA TTT XT)-3′ (**22**), where X stands for the non-nucleosidic building block **2**, was assembled as described above. The support-bound oligonucleotide was treated with hydrazinium acetate for half an hour and then with sugar ligand **1**, as described for the preparation of oligothymidine conjugates **18**−**21.** No degradation of the oligonucleotide was observed. A prolonged reaction time of 6 h was used for the oximation with **1** to obtain **25**. The product was released and deprotected with concentrated ammonia (33% aqueous NH_3, 17 h at 55 °C). Evaporation, dissolution in water, RP HPLC purification (with a gradient elution from 12% to 37% MeCN in 0.1 mol L^{-1} Et_3NHOAc buffer over 18 min), and desalting gave conjugate **28** in 17% overall isolated yield (OD = 28.98). The authenticity of **28** was verified by MS(ESI): M requires 6854.8, found 6852.3.

Synthesis of Phosphorothioate Oligonucleotide Glycoconjugate 29. Conjugate **29** was prepared using sequence 5′-(6-FAM)-d(TGG CGT CTT CCA TTT XTX T)-3′ (**23**). The procedure described for **28** was followed except for a prolonged oximation step (18 h). A gradient elution from 15% to 37% MeCN in 0.1 mol L^{-1} Et_3NHOAc buffer over 16 min was applied to the RP HPLC purification followed by desalting. Conjugate **29** was isolated in 19% overall yield (OD = 33.48).

Synthesis of Phosphorothioate Oligonucleotide Glycoconjugate 30. Conjugate **30** was prepared using sequence 5′-(6-FAM)-d(TGG CGT CTT CCA TTT XTX TXT)-3′ (**24**). The procedure described for **29** was followed except that a steeper gradient elution from 12% to 45% MeCN in 0.1 mol L^{-1} Et_3NHOAc buffer over 16 min was applied to the purification followed by desalting. The isolated yield of **30** was 21% (OD = 40.68).

Synthesis of Reference Oligonucleotides 31 and 32. Two phosphorothioate oligonucleotides, labeled 5′-(6-FAM)-d(TGG CGT CTT CCA TTT)-3′ (**31**) and unlabeled 5′-d(TGG CGT CTT CCA TTT)-3′ (**32**) were synthesized to be used as reference material in the cellular studies. The procedure described above for phosphorothioate oligodeoxyribonucleotide synthesis was followed. Products were released and deprotected with concentrated ammonia (33% aqueous NH_3, 17 h at 55 °C). Evaporation, dissolution in water, RP HPLC purification [with a gradient elution from 25% to 85% MeCN in 0.1 mol L^{-1} Et_3NHOAc buffer over 20 min (**31**) or from 25% to 65% MeCN in 0.1 mol L^{-1} Et_3NHOAc buffer over 18 min (**32**)], and desalting gave the products; authenticity was verified by MS(ESI) spectroscopy. **31**: MS(ESI): M requires 5305.5, found 5302.5. **32**: MS(ESI): M requires 4749.9, found 4749.5.

Cellular Uptake Studies. Phosphorothioate oligonucleotide glycoconjugates **28**−**30** with 5′-fluorescein label were used in the cellular uptake studies. Fluorescein-labeled nonconjugated phosphorothioate oligonucleotide **31** and the corresponding unlabeled parent oligonucleotide **32** were used as negative controls. All freeze−dried oligonucleotides were dissolved in sterile water and diluted with phosphate buffered saline (PBS buffer, pH = 7.5).

Cell Culture. Immortalized human corneal epithelial cells (HCE cells) were grown at 37 °C in humidified air with 5% CO_2, in standard culture medium. Dividing HCE cells have been shown to express the CD44 receptor (*47*). Cells with passage numbers from 20 to 30 were used. All experiments were conducted with undifferentiated cells. The standard medium consisted of DMEM/Ham's F12 (1:1), 15% heat-inactivated fetal bovine serum (FBS), 0.3 mg mL^{-1} L-glutamine, 0.1 mg mL^{-1} streptomycin, 1000 IU mL^{-1} penicillin, 5 μg mL^{-1} insulin (human recombinant), 0.1 μg mL^{-1} cholera toxin, 10 ng mL^{-1} epidermal growth factor (EGF, human), and 0.5% dimethyl sulfoxide.

Cellular Uptake Studies with Flow Cytometric Analysis. HCE cells were seeded onto 24-well plates at a density of 200 000 cells/well 24 h prior to the uptake experiment. After washing and adding culture medium without serum to the cells, HCE cells were incubated in the presence of conjugates (0.2 or 2 nmol of conjugate/300 μL concentration). Labeled (*31*) and unlabeled (*32*) non-conjugated oligonucleotides were used as negative controls. After one hour, the cells were washed twice with PBS buffer, once with 1 mol L^{-1} NaCl solution (pH = 7.5), and again twice with PBS buffer to remove all conjugates attached to the cellular plasma membrane. The cells were then detached from the wells with trypsin−EDTA solution and fixed by incubation with 1% paraformaldehyde (PFA, pH = 7.5). Then, the cells were washed twice with 1% PFA and stored at 4 °C until analysis by flow cytometry (BD LSR II, BD Biosciences) with 10 000 events collected for each sample. Samples were excited with Coherent Sapphire blue laser (488 nm), and fluorescence of carboxyfluorescein was collected at 515−545 nm. All conjugates were tested in triplicate in two independent experiments. Dot plots and population hierarchy were generated with BD *FACSDiva* software (BD Biosciences).

RESULTS AND DISCUSSION

Synthesis of the Hyaluronan Disaccharide Ligand (1). 2-Acetamido-2-deoxyglycopyranosides are constituents of many naturally occurring oligosaccharides, being most frequently engaged in β-glycosidic linkages. Accordingly, the glycosylation reactions of 2-*N*-acetylated donors have been studied in considerable detail (*48*). While the 2-*O*-acetyl group is an excellent participating protective group, which steers the glycosyl acceptor in a *trans*-1,2-position, the 2-*N*-acetylated donors form cyclic 1,3-oxazolinium intermediates, which are too stable to be opened by the acceptor. To avoid this, highly electron-withdrawing acyl groups, which subsequently can be converted to an acetyl group, are used for the 2-*N*-protection of the glycosyl donor (*49*). We chose to compare the synthetic applicability of the trichloroacetyl (TCA, **7**) and 2,2,2-trichloroethoxycarbonyl (Troc, **8**) protected trichloroacetimidate donors, both of which had previously been reported to undergo β-glycosidic bond formation via a reactive *N*-acyloxazolinium intermediate in good yield. Both donors, **7** (*44*) and **8** (*45*), were synthesized as described in literature.

The glucuronic acid acceptor was introduced into the dimer as a 6-*O*-benzyl precursor (**6**), synthesized as outlined in Scheme 1. Accordingly, commercially available glucopyranose pentaacetate was first converted to fully acetylated allyl β-D-glucopyranoside (**3**) by $BF_3 \cdot OEt_2$ promoted glycosidation in CH_2Cl_2 (*42*), the acetyl groups were removed by methoxide ion catalyzed transesterification in MeOH, and a 4,6-*O*-benzylidene acetal protection was introduced by acid-catalyzed transacetalization with α,α-dimethoxytoluene to obtain **4**. The remaining 3-OH was acetylated, and the benzylidene acetal obtained (**5**) was selectively reduced to the corresponding 6-*O*-benzyl derivative **6** by treatment with trifluoroacetic acid and triethylsilane (*50*).

Glycosidation of donors **7** and **8** with acceptor **6** was performed in CH_2Cl_2 in the presence of a catalytic amount of trimethylsilyl trifluoromethanesulfonate (TMSOTf). The TCA protected disaccharide (**9**) was obtained in a good yield (95%), whereas the yield of the Troc protected disaccharide (**10**) was rather modest (58%). The latter reaction was hampered by the formation of an unidentified side product. The amino protecting

Scheme 1. Synthesis of the Acceptor Monosaccharide 6[a]

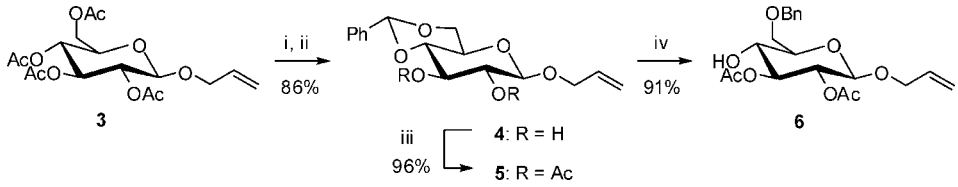

[a] Reagents and conditions: (i) NaOMe, MeOH; (ii) $PhCH(OMe)_2$, p-TsOH, MeCN; (iii) Ac_2O, Py; (iv) Et_3SiH, TFA, CH_2Cl_2

Scheme 2. Synthesis of the Hyaluronan Disaccharide 1[a]

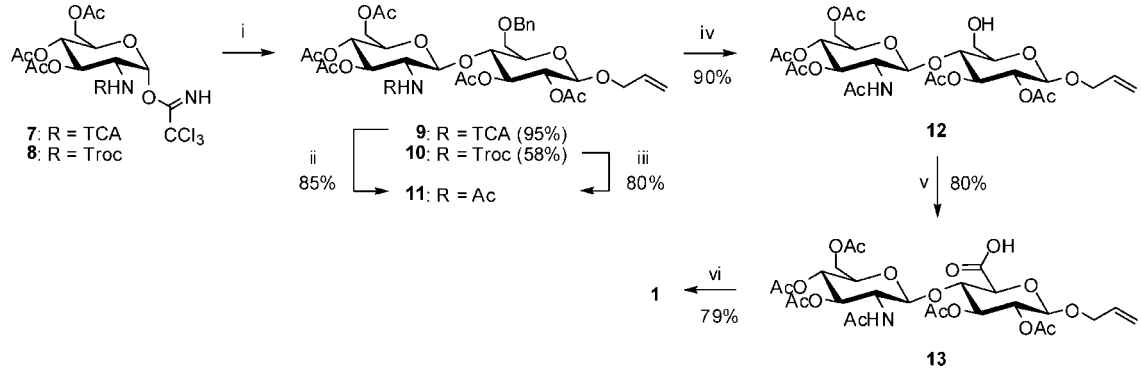

[a] Reagents and conditions: (i) **6**, TMSOTf, CH_2Cl_2; (ii) Zn, AcOH, CH_2Cl_2 (Method A); (iii) Zn, Ac_2O (Method B); (iv) (1) DDQ, CH_2Cl_2, (2) H_2O; (v) H_5IO_6, CrO_3, aq MeCN; (vi) OsO_4, $NaIO_4$, dioxane, H_2O.

groups were transformed to *N*-acetyl group with zinc dust either in AcOH (for **9**, Method A) or in Ac_2O (for **10**, Method B). The reductive dehalogenation of the TCA group, although sluggish, proceeded cleanly and gave the 2-*N*-acetyl protected dimer **11** in 85% yield. Reduction of the Troc group gave only a slightly lower yield (80%), but was accompanied by formation of an intermediate which was difficult to detect by TLC. Oxidative debenzylation of **11** with 2,3-dichloro-5,6-dicyano-1,4-benzoquinone (DDQ) (*51*) was then performed. Two days refluxing in dry CH_2Cl_2 in excess of DDQ (*52*) gave the 6-OH deprotected dimer **12** and a varying amount of a side product which, however, was converted to the desired product upon treatment of the reaction mixture with water. The ^1H NMR and mass spectra suggested the side product to be a dimer of **12** (data not shown). Attempts to perform the oxidation directly in wet dichloromethane failed. Finally, the primary hydroxyl function of **12** was oxidized to a carboxyl group (**13**) with periodic acid in the presence of a catalytic amount of chromium trioxide in wet acetonitrile (*53*). The anomeric aldehyde tether was generated by osmium tetroxide catalyzed periodate oxidation (*54*, *55*), which gave the protected hyaluronan disaccharide **1**.

Synthesis of the Oligothymidine Glycoconjugates (18−21). The previously developed solid-phase oximation (*40*, *56*) was applied to the attachment of the aldehyde-functionalized saccharides to oligonucleotides on a solid support. The method exploits a bis(hydroxymethyl)malondiamide-derived phosphoramidite (**2**), which is inserted in the oligonucleotide chain during normal chain assembly. The building block bears two masked aminooxy groups which, when exposed on support, allow conjugation of aldehyde ligands through stable oxime linkages. To test the applicability of the hyaluronic acid disaccharide **1** to the conjugate formation, four oligonucleotide glycoconjugates (**18**−**21**) were prepared. The non-nucleosidic phorphoramidite building block **2** was synthesized essentially as described previously (*40*) (for the modifications, see Experimental Procedures). Short oligothymidine sequences containing one (**14**), two (**15** and **16**), or three (**17**) intrachain non-nucleosidic units **2** were assembled by standard machine-assisted phosphoramidite chemistry. In addition, the influence of an extra thymidine residue between the adjacent building blocks was studied (**15** and **16**). After the assembly of the oligonucleotide sequences, the phthaloyl protections of the building block were removed by treatment with hydrazinium acetate. The exposed aminooxy groups of the support-bound oligonucleotide were then oximated with the aldehyde-tethered sugar ligand **1** in MeCN containing 10% water to ensure the solubility of the disaccharide. The reaction time was 4 h for conjugate **18**, while conjugates **19**−**21** containing several non-nucleosidic building blocks were obtained by an overnight reaction. The support-bound conjugates were released and deprotected by standard ammonolytic treatment and analyzed by RP HPLC. The RP HPLC profiles of the crude product mixtures are presented in Figure 2. In each case, the desired conjugate was the main product as verified by MS(ESI) spectroscopy (Table 1, entries 1−4). An additional thymidine residue between the adjacent branching units seemed to slightly enhance the coupling efficiency, as seen by comparison of the relative peak areas of conjugates **19** and **20** (Table 1, entries 2 and 3).

Synthesis of the Fluorescently Labeled Phosphorothioate Oligonucleotide Glycoconjugates (28−30). For the cellular uptake studies, three 5′-fluorescein-labeled (6-FAM) phosphorothioate oligonucleotide glycoconjugates (**28**−**30**) were prepared. These contained one, two, or three non-nucleosidic units, i.e., two, four, or six hyaluronan ligands, respectively. Except for the labeling and sulfurization steps, the protocol described above was followed (Scheme 3). For sulfurization, 3-dimethylaminomethyleneamino-1,2,4-dithiazole-5-thione was used. The RP HPLC profiles of the crude product mixtures are presented in Figure 3. Products were purified and desalted by RP HPLC and isolated in 17−21% yield. Additionally, a fluorescein-labeled non-conjugated phosphorothioate oligonucleotide 5′-(6-FAM)-d(TGG CGT CTT CCA TTT)-3′ (**31**) and the corresponding unlabeled parent oligonucleotide 5′-d(TGG CGT CTT CCA TTT)-3′ (**32**) were synthesized for reference materials to be used in the cellular studies. The 15-mer sequence used in these antisense oligonucleotides was targeted against the luciferase gene expression.

The authenticity of the glycoconjugate **28** was verified by MS(ESI) spectroscopy. For larger conjugates (**29** and **30**), the

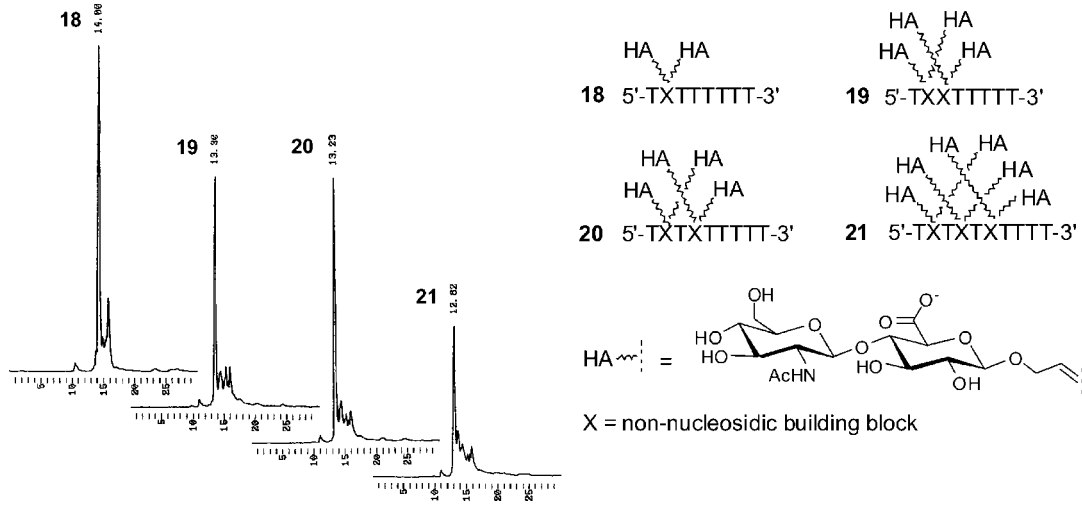

Figure 2. Oligothymidine glycoconjugates **18**−**21** and RP HPLC profiles of the crude product mixtures. For the chromatographic conditions, see protocol A in Experimental Procedures.

Scheme 3. Synthesis of the Phosphorothioate Oligonucleotide Glycoconjugates 28−**30**[a]

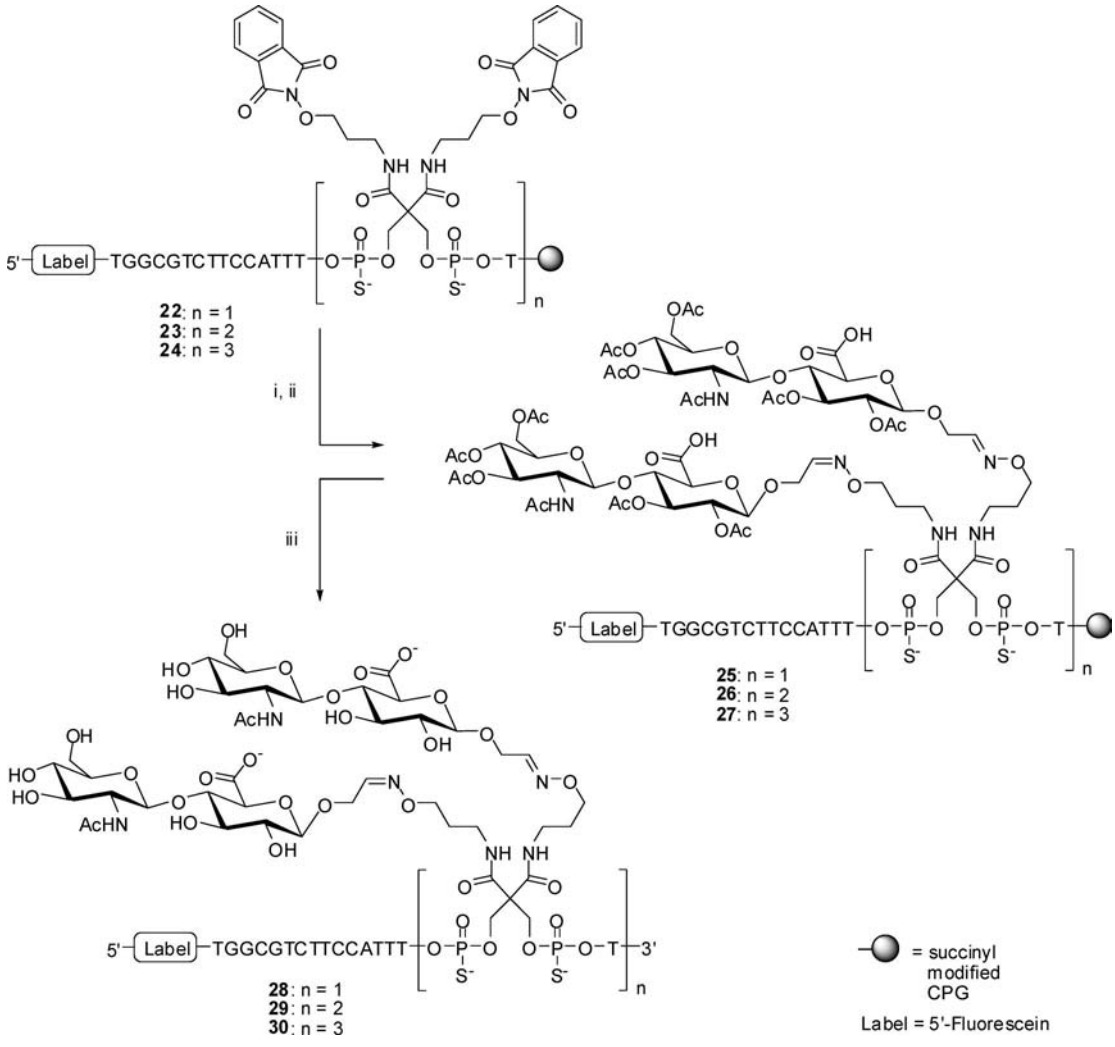

[a] Reagents and conditions: (i) $NH_2NH_2 \cdot H_2O$, AcOH, Py; (ii) **1**, MeCN, H_2O; (iii) aq NH_3.

presence of several acidic hyaluronan moieties hindered the ionization to the extent that no adequate signals could be detected. Acidic oligosaccharides are known to be difficult to analyze using MS due to their instability and inefficient ionization under general ionization and detection conditions (*57*). Susceptibility to fragmentation was also detected during the analysis of simpler oligothymidine glycoconjugates **18**−**21**. However, authenticity of **29** and **30** was convincing on the basis of successful synthesis of the corresponding oligothymidine glycoconjugates (**18**−**21**) and homogeneity of the purified product by HPLC. The conjugates were thus further subjected to cellular uptake studies.

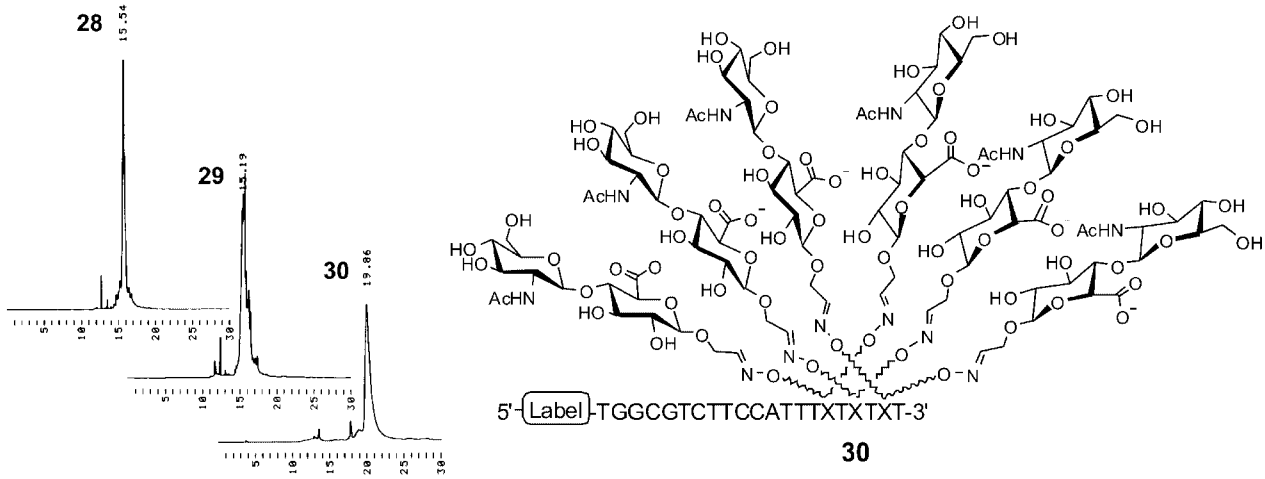

Figure 3. RP HPLC profiles of the crude glycoconjugates **28**−**30**. For the chromatographic conditions, see protocol B in Experimental Procedures. Structure of the conjugate **30** is only shown.

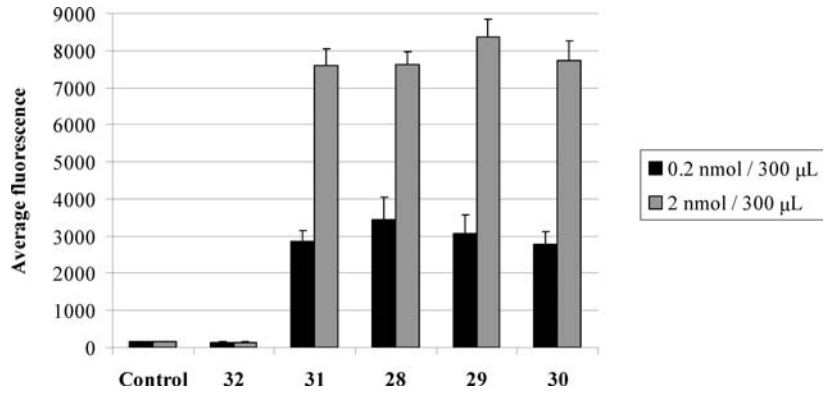

Figure 4. Cellular uptake of fluorescein-labeled conjugates determined by flow cytometry (at 515−545 nm, 488 nm excited). Oligonucleotide conjugates **28**−**30** and control oligonucleotides **31** and **32** were added for HCE cells at dose of 0.2 or 2 nmol/300 μL medium. Results are presented as mean fluorescence in cell. Each data point is a mean of six replicates from two independent experiments (means ± standard deviation, $n = 6$).

Cellular Uptake Studies with Flow Cytometric Analysis. CD44 is the primary cell surface receptor for hyaluronan and binds ligand via a lectin-like fold termed the Link module. The recognition appears to be dominated by hydrogen bonds and van der Waals forces rather than electrostatic or sugar-aromatic stacking interactions (*23*). The rationale in the conjugate design was that the carbohydrate part would bind to CD44, thereby leading to internalization of the conjugate via receptor-mediated endocytosis.

To determine the influence of hyaluronan ligands, the phosphorothioate oligonucleotide glycoconjugates labeled with carboxyfluorescein (**28**−**30**), and labeled (**31**) and unlabeled (**32**) control oligonucleotides were incubated with immortalized human corneal epithelial cell line (HCE) that expresses the cell surface hyaluronan receptor CD44. The incubation was performed under standard conditions (37 °C, 5% CO_2) for one hour in two different concentrations (0.2 or 2 nmol of test compound/300 μL medium). After washing procedures, the fluorescence intensity of the cells was determined by flow cytometry at 515−545 nm. Flow cytometry revealed that the number of fluorescent cells was high and similar both in the cell cultures treated with labeled control oligonucleotide **31** and with oligonucleotide conjugate bearing two (**28**), four (**29**), or six (**30**) hyaluronan ligands (data not shown). The mean fluorescence of the cell cultures treated with labeled control oligonucleotide or any oligonucleotide conjugate was comparable at both oligonucleotide doses (Figure 4).

It has been known for 30 years that hyaluronan fragments are capable of binding cell surface receptors and that the binding depends on the molecular weight of hyaluronan (*58*). The major hyaluronan receptor, CD44, is known to trigger internalization of small hyaluronan fragments, with the minimum size being a hexasaccharide (3 disaccharide units in length) (*59, 60*). Instead, another hyaluronan receptor, toll-like receptor 4 (TLR4), recognizes even shorter tetrasaccharide fragments (*61*), but TLR4 is not expressed on the surface of HCE cell lines (*62*). In the present study, the hyaluronan moieties attached to the oligonucleotide did not improve the cellular delivery of the oligonucleotide. On the contrary, previous study with hyaluronan (<10 kDa) coated DNA complexes demonstrated active CD44-mediated uptake in HCE cells (*47*). Most likely, the hyaluronan moieties attached to the oligonucleotide are too short for efficient recognition and two, four, or six disaccharides attached to the same oligonucleotide do not interact with the receptor similarly as a single hexasaccharide. We do not know the exact mechanism of cellular uptake for unconjugated and hyaluronan-conjugated oligonucleotides, but no benefit was seen by the hyaluronan conjugation. The surprisingly high basic level of oligonucleotide uptake is an interesting finding and may be a cell-specific feature. The cellular entrance may be based on unspecific affinity of phosphorothioate for the cell surface as phosphorothioates are known to have high nonspecific protein binding levels. On the other hand, a sodium chloride washing

procedure should remove the surface-bound and non-internalized oligonucleotides (*63*).

CONCLUSIONS

An efficient synthesis route for novel protected hyaluronic acid disaccharide has been developed. Disaccharides have been used to construct multivalent hyaluronic acid−oligonucleotide glycoconjugates on solid supports. The biological properties of the conjugates have been tested in cellular uptake studies with a cell line expressing the hyaluronan receptor. Series of hyaluronan repeating units attached to the oligonucleotide do not improve cellular delivery of the oligonucleotide. The detected uptake must be unspecific, since the unconjugated control oligonucleotide was taken into the cell on an equivalent basis with the conjugated ones. The hyaluronan moieties are most likely too short for efficient recognition, and perhaps, the same concept with longer hyaluronan chains would yield better delivery. Since the cellular binding and uptake is cell type-dependent, the conjugates could be tested with other cell lines known to express hyaluronan receptor CD44.

Supporting Information Available: NMR spectral data for **1**, **4**−**6**, and **9**−**13**. This material is available free of charge via the Internet at http://pubs.acs.org.

LITERATURE CITED

(1) Seeberger, P. H., and Werz, D. B. (2007) Synthesis and medical applications of oligosaccharides. *Nature 446*, 1046–1051.

(2) Kiessling, L. L., Gestwicki, J. E., and Strong, L. E. (2006) Synthetic multivalent ligands as probes of signal transduction. *Angew. Chem., Int. Ed. 45*, 2348–2368.

(3) Gabius, H.-J., Siebert, H.-C., Andre, S., Jiménez-Barbero, J., and Rüdiger, H. (2004) Chemical biology of the sugar code. *ChemBioChem 5*, 740–764.

(4) Davis, B. G. (1999) Recent developments in glycoconjugates. *J. Chem. Soc., Perkin Trans. 1*, 3215–3237.

(5) Dwek, R. A. (1996) Glycobiology: toward understanding the function of sugars. *Chem. Rev. 96*, 683–720.

(6) Ambrosi, M., Cameron, N. R., and Davis, B. G. (2005) Lectins: tools for the molecular understanding of the glycocode. *Org. Biomol. Chem. 3*, 1593–1608.

(7) Collins, B. E., and Paulson, J. C. (2004) Cell surface biology mediated by low affinity multivalent Protein-glycan interactions. *Curr. Opin. Chem. Biol. 8*, 617–625.

(8) Lundquist, J. J., and Toone, E. J. (2002) The cluster glycoside effect. *Chem. Rev. 102*, 555–578.

(9) Kiessling, L. L., Gestwicki, J. E., and Strong, L. E. (2000) Synthetic multivalent ligands in the exploration of cell-surface interactions. *Curr. Opin. Chem. Biol. 4*, 696–703.

(10) Mammen, M., Chio, S.-K., and Whitesides, G. M. (1998) Polyvalent interactions in biological systems: implications for design and use of multivalent ligands and inhibitors. *Angew. Chem., Int. Ed. 37*, 2755–2794.

(11) Drickamer, K. (1995) Increasing diversity of animal lectin structures. *Curr. Opin. Struct. Biol. 5*, 612–616.

(12) Lee, Y. C., and Lee, R. T. (1995) Carbohydrate-protein interactions: Basis of glycobiology. *Acc. Chem. Res. 28*, 321–327.

(13) Yan, H., and Tram, K. (2007) Glycotargeting to improve cellular delivery efficiency of nucleic acids. *Glycoconjugate J. 24*, 107–123.

(14) Zatsepin, T. S., and Oretskaya, T. S. (2004) Synthesis and applications of oligonucleotide-carbohydrate conjugates. *Chem. Biodivers. 1*, 1401–1417.

(15) Monsigny, M., Midoux, P., Mayer, R., and Roche, A. C. (1999) Glycotargeting: influence of the sugar moiety on both the uptake and the intracellular trafficking of nucleic acid carried by glycosylated polymers. *Biosci. Rep. 19*, 125–132.

(16) Toole, B. P. (2004) Hyaluronan: From extracellular glue to pericellular cue. *Nat. Rev. Cancer 4*, 528–539.

(17) Luo, Y., Bernshaw, N. J., Lu, Z. R., Kopecek, J., and Prestwich, G. D. (2002) Targeted delivery of doxorubicin by HPMA copolymer-hyaluronan bioconjugates. *Pharm. Res. 19*, 396–402.

(18) Luo, Y., Ziebell, M. R., and Prestwich, G. D. (2000) A hyaluronic acid-taxol antitumor bioconjugate targeted to cancer cells. *Biomacromolecules 1*, 208–218.

(19) Peer, D., and Margalit, R. (2004) Loading mitomycin C inside long circulating hyaluronan targeted nano-liposomes increases its antitumor activity in three mice tumor models. *Int. J. Cancer 108*, 780–789.

(20) Peer, D., and Margalit, R. (2004) Tumor-targeted hyaluronan nanoliposomes increase the antitumor activity of liposomal doxorubicin in syngeneic and human xenograft mouse tumor models. *Neoplasia 6*, 343–353.

(21) Eliaz, R. E., and Szoka, F. C. (2001) Liposome-encapsulated doxorubicin targeted to CD44: a strategy to kill CD44-overexpressing tumor cells. *Cancer Res. 61*, 2592–2601.

(22) Teriete, P., Banerji, S., Noble, M., Blundell, C. D., Wright, A. J., Pickford, A. R., Lowe, E., Mahoney, D. J., Tammi, M. I., Kahmann, J. D., Campbell, I. D., Day, A. J., and Jackson, D. G. (2004) Structure of the regulatory hyaluronan binding domain in the inflammatory leukocyte homing receptor CD44. *Mol. Cell 13*, 483–496.

(23) Banerji, S., Wright, A. J., Noble, M., Mahoney, D. J., Campbell, I. D., Day, A. J., and Jackson, D. G. (2007) Structures of the CD44-hyaluronan complex provide insight into a fundamental carbohydrate-protein interaction. *Nat. Struct. Mol. Biol. 14*, 234–239.

(24) Hangeland, J. J., Flesher, J. E., Deamond, S. F., Lee, Y. C., Ts′O, P. O., and Frost, J. J. (1997) Tissue distribution and metabolism of the [^{32}P]-labeled oligodeoxynucleoside methylphosphonate-neoglycopeptide conjugate, [YEE(ah-GalNAc)$_3$]-SMCC-AET-pUmpT7, in the mouse. *Antisense Nucleic Acid Drug Dev. 7*, 141–149.

(25) Duff, R. J., Deamond, S. F., Roby, C., Zhou, Y., and Ts′O, P. O. P. (2000) Intrabody tissue-specific delivery of antisense conjugates in animals: ligand-linker-antisense oligomer conjugates. *Methods Enzymol. 313*, 297–321.

(26) Biessen, E. A., Vietsch, H., Rump, E. T., Fluiter, K., Kuiper, J., Bijsterbosch, M. K., and van Berkel, T. J. C. (1999) Targeted delivery of oligodeoxynucleotides to parenchymal liver cells in vivo. *Biochem. J. 340*, 783–792.

(27) Biessen, E. A. L., Vietsch, H., Rump, E. T., Fluiter, K., Bijsterbosch, M. K., and van Berkel, T. J. C. (2000) Targeted delivery of antisense oligonucleotides to parenchymal liver cells *in vivo*. *Methods Enzymol. 314*, 324–342.

(28) Zhu, L., Ye, Z., Cheng, K., Miller, D. D., and Mahato, R. I. (2008) Site-specific delivery of oligonucleotides to hepatocytes after systemic administration. *Bioconjugate Chem. 19*, 290–298.

(29) Imberty, A., Lortat-Jacob, H., and Pérez, S. (2007) Structural view of glycosaminoglycan-protein interactions. *Carbohydr. Res. 342*, 430–439.

(30) Rele, S. M., Iyer, S. S., and Chaikof, E. L. (2007) Hyaluronan-based glycoclusters as probes for chemical glycobiology. *Tetraheron Lett. 48*, 5055–5060.

(31) Dinkelaar, J., Codée, J. D. C., van den Bos, L. J., Overkleeft, H. S., and van der Marel, G. A. (2007) Synthesis of hyaluronic acid oligomers using Ph_2SO/Tf_2O-mediated glycosylations. *J. Org. Chem. 72*, 5737–5742.

(32) Ren, Z. X., Yang, Q., Price, K. N., Chen, T., Nygren, C., Turner, J. F. C., and Baker, D. C. (2007) Synthesis of a C-linked hyaluronic acid disaccharide mimetic. *Carbohydr. Res. 342*, 1668–1679.

(33) Huang, L., and Huang, X. (2007) Highly efficient syntheses of hyaluronic acid oligosaccharides. *Chem. Eur. J. 13*, 529–540.

(34) Palmacci, E. R., and Seeberger, P. H. (2004) Toward the modular synthesis of glycosaminoglycans: synthesis of hyaluronic acid disaccharide building blocks using a periodic acid oxidation. *Tetrahedron 60*, 7755–7766.

(35) Adamski-Werner, S. L., Yeung, B. K. S., Miller-Deist, L. A., and Petillo, P. A. (2004) Gram-scale syntheses of the (1→3)-linked and (1→4)-linked hyaluronan disaccharides. *Carbohydr. Res. 339*, 1255–1262.

(36) Lu, X. A., Chou, C. H., Wang, C. C., and Hung, S. C. (2003) Regioselective esterification of various D-glucopyranosides: synthesis of a fully protected disaccharide unit of hyaluronic acid. *Synlett 9*, 1364–1366.

(37) Iyer, S. S., Rele, S. M., Baskaran, S., and Chaikof, E. L. (2003) Design and synthesis of hyaluronan-mimetic gemini disaccharides. *Tetrahedron 59*, 631–638.

(38) Karst, N. A., and Lindhart, R. J.(. (2003) Recent chemical and enzymatic approaches to the synthesis of glycosaminoglycan oligosaccharides. *Curr. Med. Chem. 10*, 1993–2031.

(39) Liao, Y. H., Jones, S. A., Forbes, B., Martin, G. P., and Brown, M. B. (2005) Hyaluronan: pharmaceutical characterization and drug delivery. *Drug Delivery 12*, 327–342.

(40) Katajisto, J., Virta, P., and Lönnberg, H. (2004) Solid-phase synthesis of multiantennary oligonucleotide glycoconjugates utilizing on-support oximation. *Bioconjugate Chem. 15*, 890–896.

(41) Gottlieb, H. E., Kotlyar, V., and Nudelman, A. (1997) NMR chemical shifts of common laboratory solvents as trace impurities. *J. Org. Chem. 62*, 7512–7515.

(42) Schmidt, M., Chatterjee, S. K., Dobner, B., and Nuhn, P. (2002) New modified single chained glycolipids. Part 1: synthesis of deoxy and partially *O*-methylated glycolipids with or without a sulfur containing spacer. *Chem. Phys. Lipids 114*, 139–147.

(43) Khan, S. H., Abbas, S. A., and Matta, K. L. (1989) Synthesis of some oligosaccharides containing the *O*-(2-acetamido-2-deoxy-β-D-glucopyranosyl)-(1→2)-*O*-α-D-mannopyranosyl unit. Potential substrates for UDP-GlcNAc: α-D-mannopyranosyl-1→6)-*N*-acetyl-β-D-glucosaminyltransferase (GnT-V). *Carbohydr. Res. 193*, 125–139.

(44) Blatter, G., Beau, J.-M., and Jacquinet, J.-C. (1994) The use of 2-deoxy-2-trichloroacetamido-D-glucopyranose derivatives in syntheses of oligosaccharides. *Carbohydr. Res. 260*, 189–202.

(45) Dullenkopf, W., Castro-Palomino, J. C., Manzoni, L., and Schmidt, R. R. (1996) *N*-Trichloroethoxycarbonyl-glucosamine derivatives as glycosyl donors. *Carbohydr. Res. 296*, 135–147.

(46) Paulsen, H., and Helpap, B. (1991) Synthese von teilstrukturen der *N*-glycoproteine des komplexen typs. *Carbohydr. Res. 216*, 289–313.

(47) Hornof, M., de la Fuente, M., Hallikainen, M., Tammi, R. H., and Urtti, A. (2008) Low molecular weight hyaluronan shielding of DNA/PEI polyplexes facilitates CD44 receptor mediated uptake in human corneal epithelial cells. *J. Gene Med. 10*, 70–80.

(48) Banoub, J., Boullanger, P., and Lafont, D. (1992) Synthesis of oligosaccharides of 2-amino-2-deoxy sugars. *Chem. Rev. 92*, 1167–1195.

(49) Bongat, A. F., and Demchenko, A. V. (2007) Recent trends in the synthesis of *O*-glycosides of 2-amino-2-deoxysugars. *Carbohydr. Res. 342*, 374–406.

(50) DeNinno, M. P., Etienne, J. B., and Duplantier, K. C. (1995) A method for the selective reduction of carbohydrate 4,6-*O*-benzylidene acetals. *Tetrahedron Lett. 36*, 669–672.

(51) Yadav, J. S., Chandrasekhar, S., Sumithra, G., and Kache, R. (1996) Selective and unprecedented oxidative deprotection of allyl ethers with DDQ. *Tetrahedron Lett. 37*, 6603–6606.

(52) Ikemoto, N., and Schreiber, S. L. (1992) Total synthesis of (-)-hikizimycin employing the strategy of two-directional chain synthesis. *J. Am. Chem. Soc. 114*, 2524–2536.

(53) Zhao, M., Li, J., Song, Z., Desmond, R., Tschaen, D. M., Grabowski, E. J. J., and Reider, P. J. (1998) A novel chromium trioxide catalyzed oxidation of primary alcohols to the carboxylic acids. *Tetrahedron Lett. 39*, 5323–5326.

(54) Pappo, R., Allen, D. S., Jr., Lemieux, R. U., and Johnson, W. S. (1956) Osmium tetroxide-catalyzed periodate oxidation of olefinic bonds. *J. Org. Chem. 21*, 478–479.

(55) Buskas, T., Söderberg, E., Konradsson, P., and Fraser-Reid, B. (2000) Use of *n*-pentenyl glycosides as precursors to various spacer functionalities. *J. Org. Chem. 65*, 958–963.

(56) Salo, H., Virta, P., Hakala, H., Prakash, T. P., Kawasaki, A. M., Manoharan, M., and Lönnberg, H. (1999) Aminooxy functionalized oligonucleotides: preparation, on-support derivatization, and post-synthetic attachment to polymer support. *Bioconjugate Chem. 10*, 815–823.

(57) Zaia, J. (2004) Mass Spectrometry of oligosaccharides. *Mass Spectrom. Rev. 23*, 161–227.

(58) Underhill, C. B., and Toole, B. P. (1979) Binding of hyaluronate to the surface of cultured cells. *J. Cell Biol. 82*, 475–484.

(59) Knudson, W., Bartnik, E., and Knudson, C. B. (1993) Assembly of pericellular matrices by COS-7 cells transfected with CD44 lymphocyte-homing receptor genes. *Proc. Natl. Acad. Sci. U.S.A. 90*, 4003–4007.

(60) Lesley, J., Hascall, V. C., Tammi, M., and Hyman, R. (2000) Hyaluronan binding by cell surface CD44. *J. Biol. Chem. 275*, 26967–26975.

(61) Aruffo, A., Stamenkovic, I., Melnick, M., Underhill, C. B., and Seed, B. (1990) CD44 is the principal cell surface receptor for hyaluronate. *Cell 61*, 1303–1313.

(62) Ueta, M., Nochi, T., Jang, M.-H., Park, E. J., Igarashi, O., Hino, A., Kawasaki, S., Shikina, T., Hiroi, T., Kinoshita, S., and Kiyono, H. (2004) Intracellularly expressed TLR2s and TLR4s contribution to an immunosilent environment at the ocular mucosal epithelium. *J. Immunol. 173*, 3337–3347.

(63) Beck, G. F., Irwin, W. J., Nicklin, P. L., and Akhtar, S. (1996) Interactions of phosphodiester and phosphorothioate oligonucleotides with intestinal epithelial Caco-2 cells. *Pharm. Res. 13*, 1028–1037.

BC800260Y

Synthesis and Cellular Uptake of Fluorescently Labeled Multivalent Hyaluronan Disaccharide Conjugates of Oligonucleotide Phosphorothioates

Marika Karskela,[*,†] *Pasi Virta,*[†] *Melina Malinen,*[‡§] *Arto Urtti*[§] *and Harri Lönnberg*[†]

[†]Department of Chemistry, University of Turku, FI-20014 Turku, Finland, [‡]Division of Biopharmaceutics and Pharmacokinetics, Faculty of Pharmacy, University of Helsinki, P.O.Box 56, FI-00014 University of Helsinki, Helsinki, Finland and [§]Center for Drug Research, University of Helsinki, P.O.Box 56, FI-00014 University of Helsinki, Helsinki, Finland.

Marika.Karskela@utu.fi

SUPPORTING INFORMATION

Table of Contents

General procedures S2

Figure S1. ^{1}H NMR (20% D_2O in CD_3CN, 500 MHz) spectrum of **1** S3

Figure S2. ^{1}H NMR ($CDCl_3$, 500 MHz) spectrum of **4** S4

Figure S3. ^{1}H NMR ($CDCl_3$, 500 MHz) spectrum of **5** S5

Figure S4. ^{1}H NMR ($CDCl_3$, 600 MHz) spectrum of **6** S6

Figure S5. ^{1}H NMR ($CDCl_3$, 500 MHz) spectrum of **9** S7

Figure S6. ^{1}H NMR ($CDCl_3$, 500 MHz) spectrum of **10** S8

Figure S7. ^{1}H NMR ($CDCl_3$, 500 MHz) spectrum of **11** (from method A) S9

Figure S8. ^{1}H NMR ($CDCl_3$, 500 MHz) spectrum of **12** S10

Figure S9. ^{1}H NMR [$(CD_3)_2SO$, 500 MHz] spectrum of **13** S11

General procedures

The NMR spectra of **1**, **4**–**6** and **9**–**13** were recorded at 500 MHz. and 600 MHz. The chemical shifts are given in ppm from internal TMS or solvent residual signal.

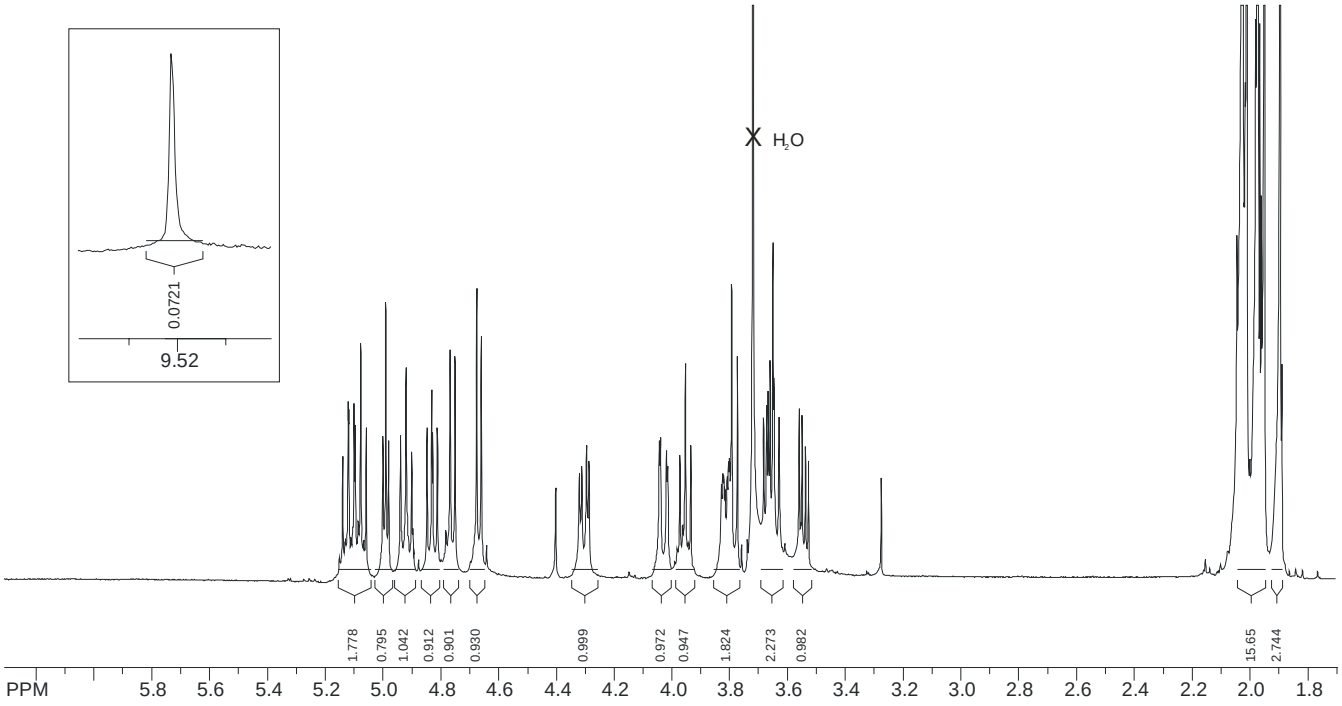

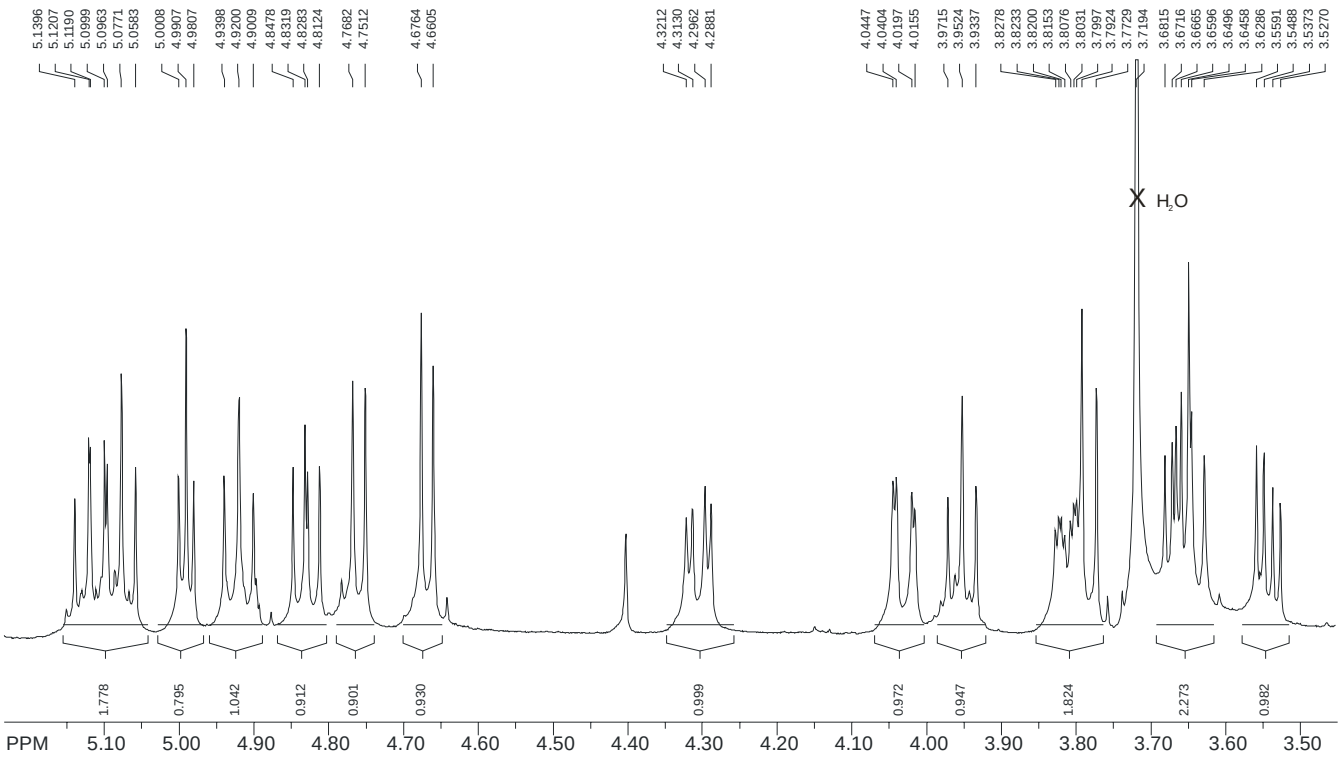

Aldehyde **1** mainly as a hydrate:

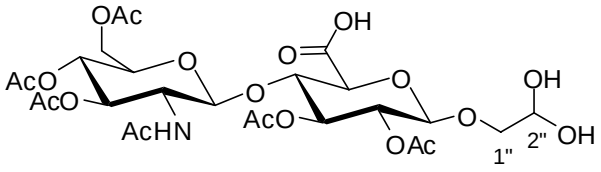

Figure S1. ^{1}H NMR (20% D_2O in CD_3CN, 500 MHz) spectrum of **1**

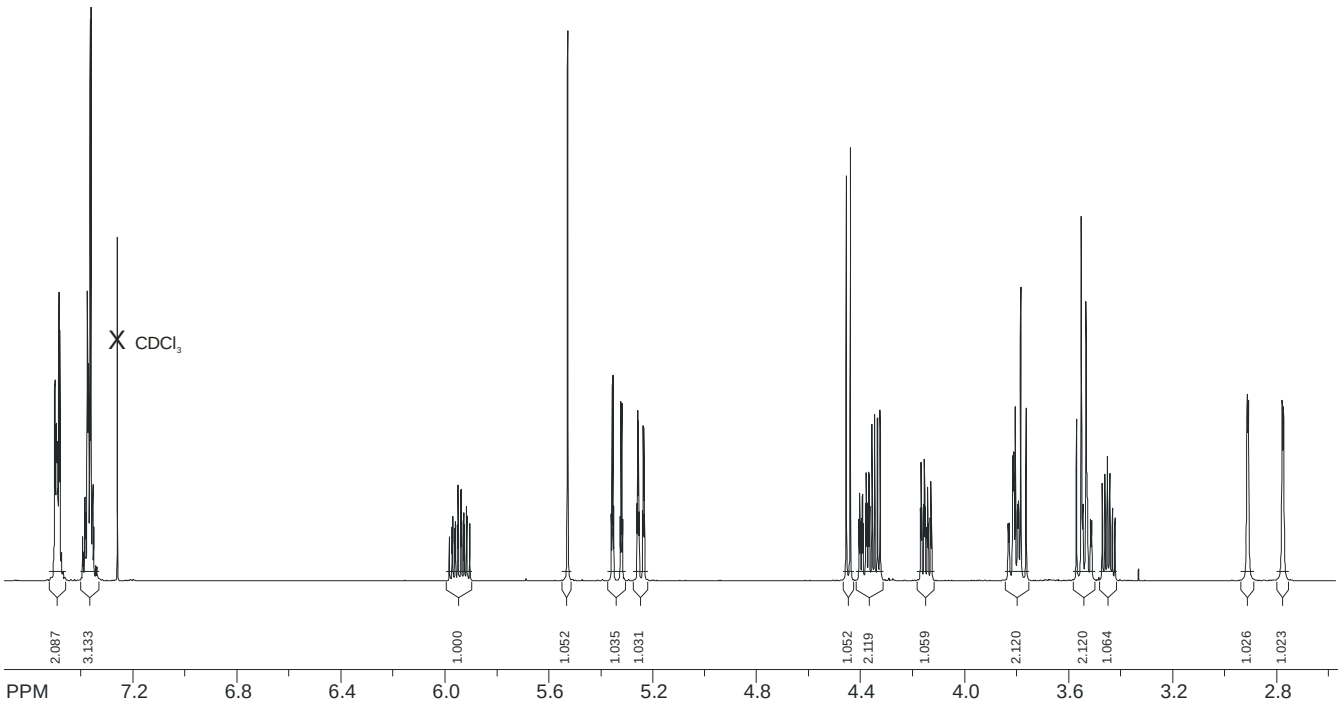

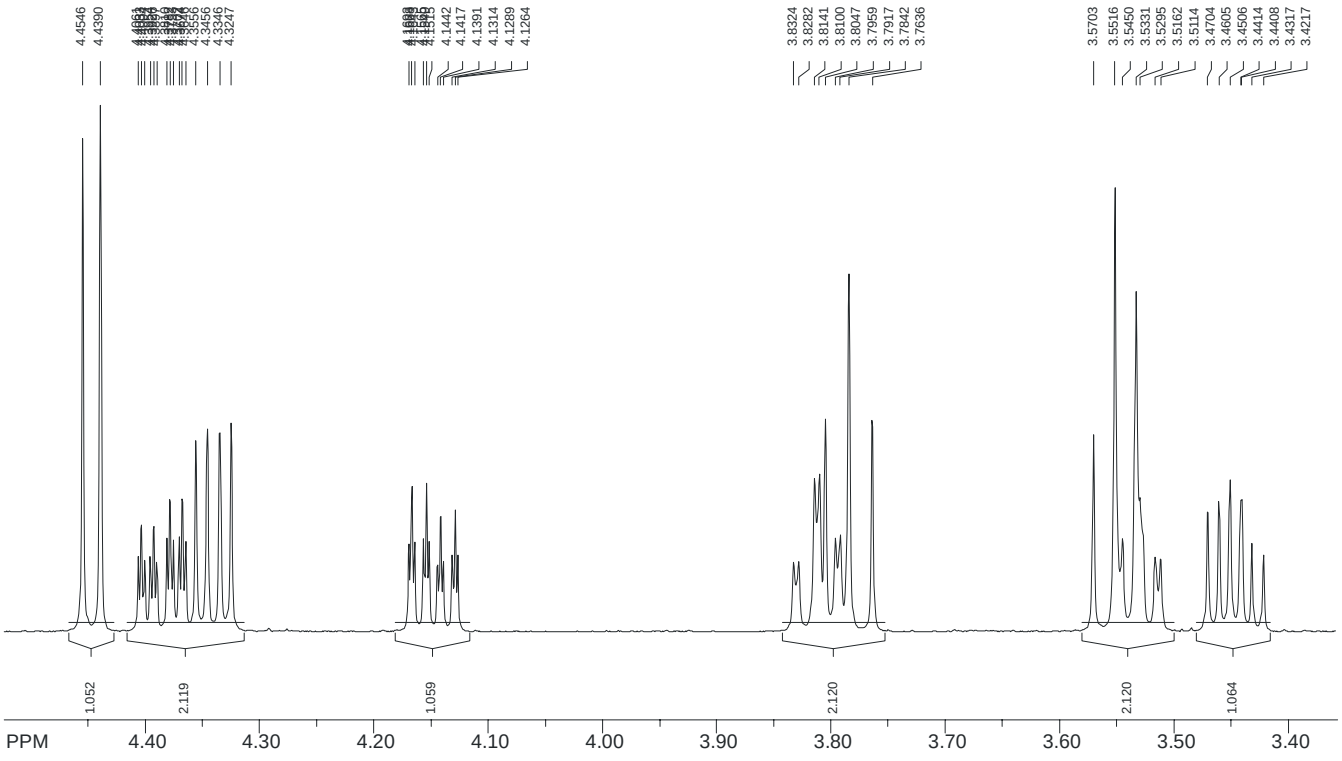

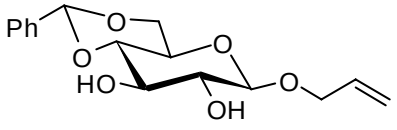

Figure S2. ^{1}H NMR ($CDCl_3$, 500 MHz) spectrum of **4**

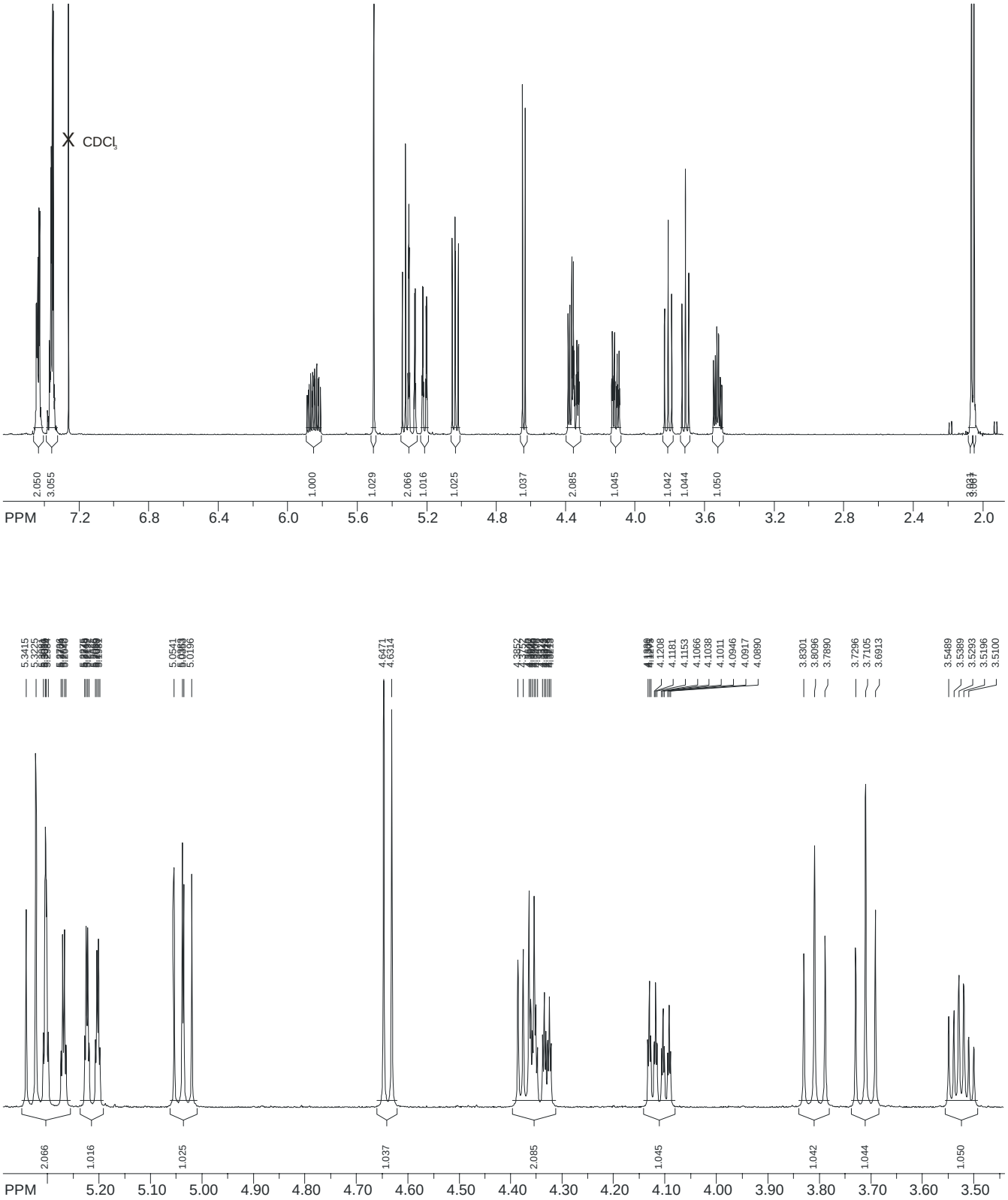

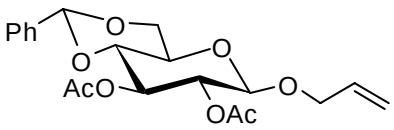

Figure S3. ^{1}H NMR ($CDCl_3$, 500 MHz) spectrum of **5**

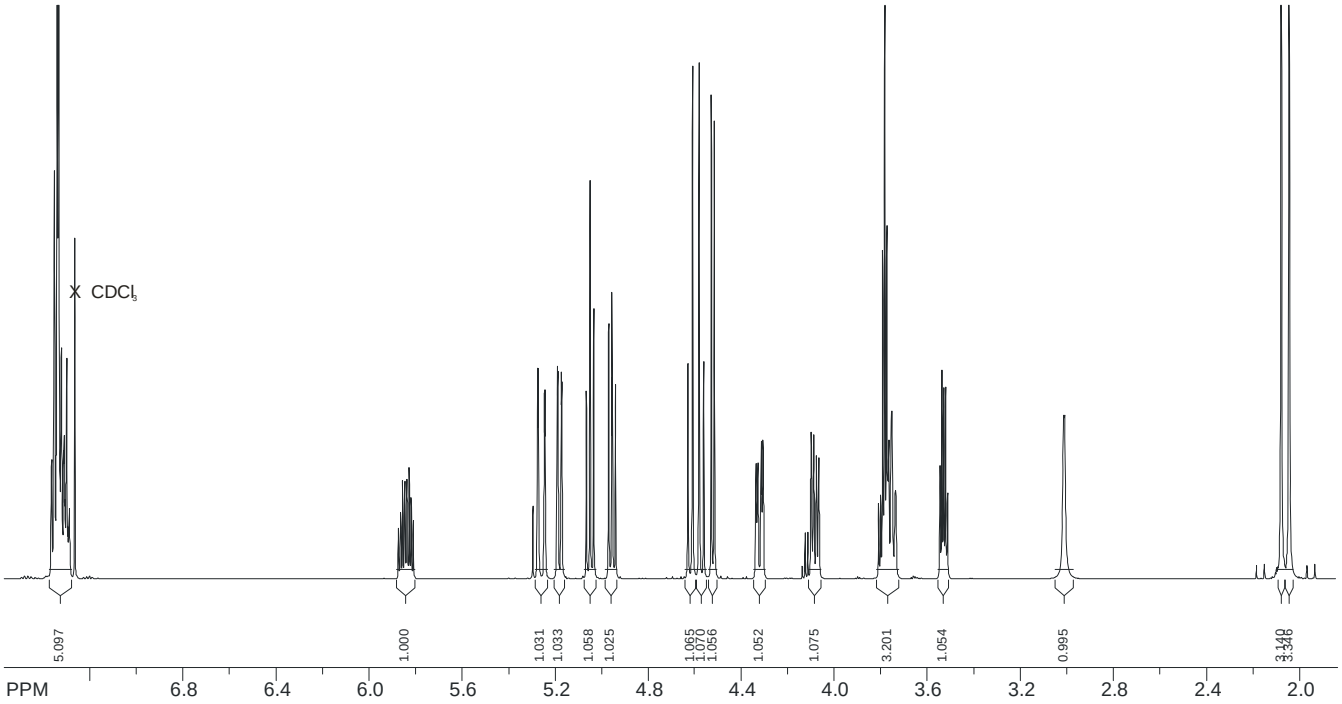

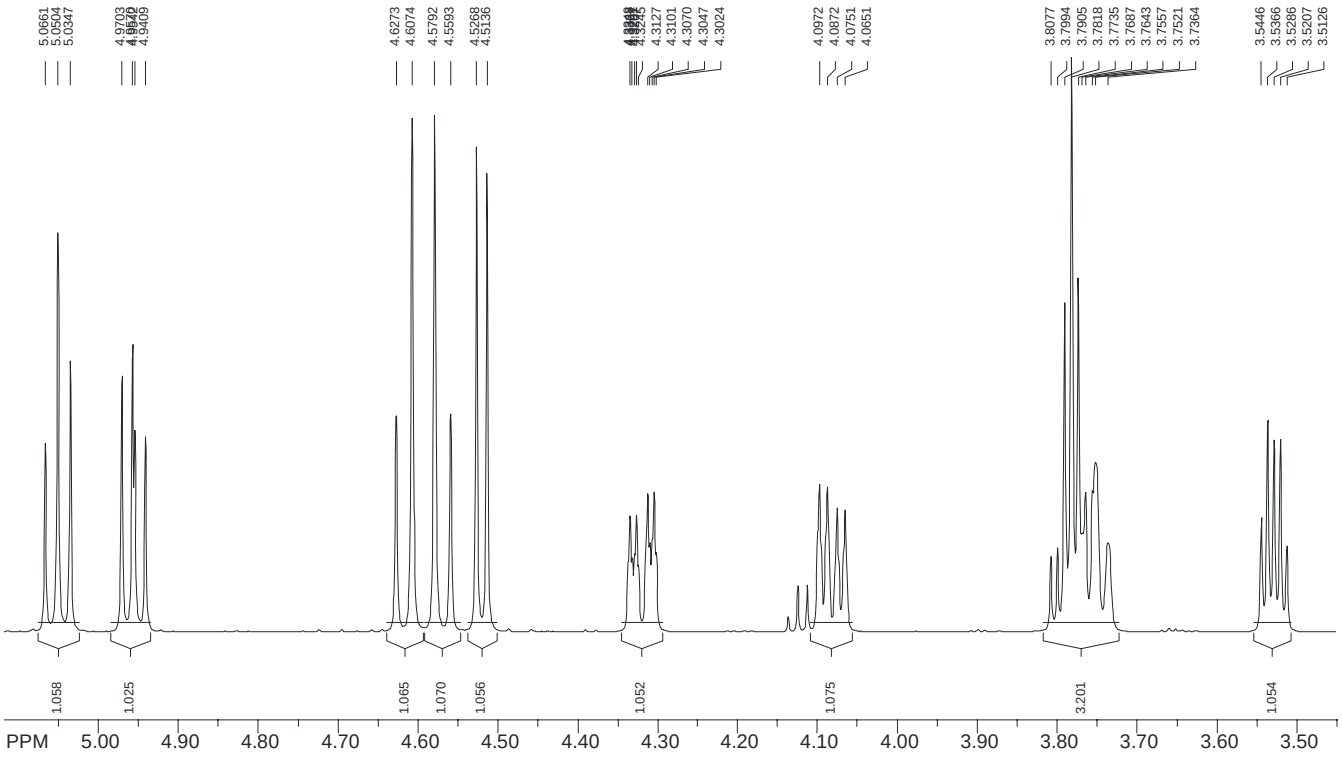

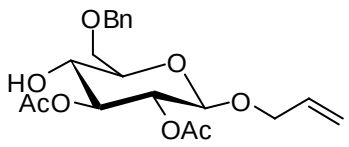

Figure S4. ^{1}H NMR ($CDCl_3$, 600 MHz) spectrum of **6**

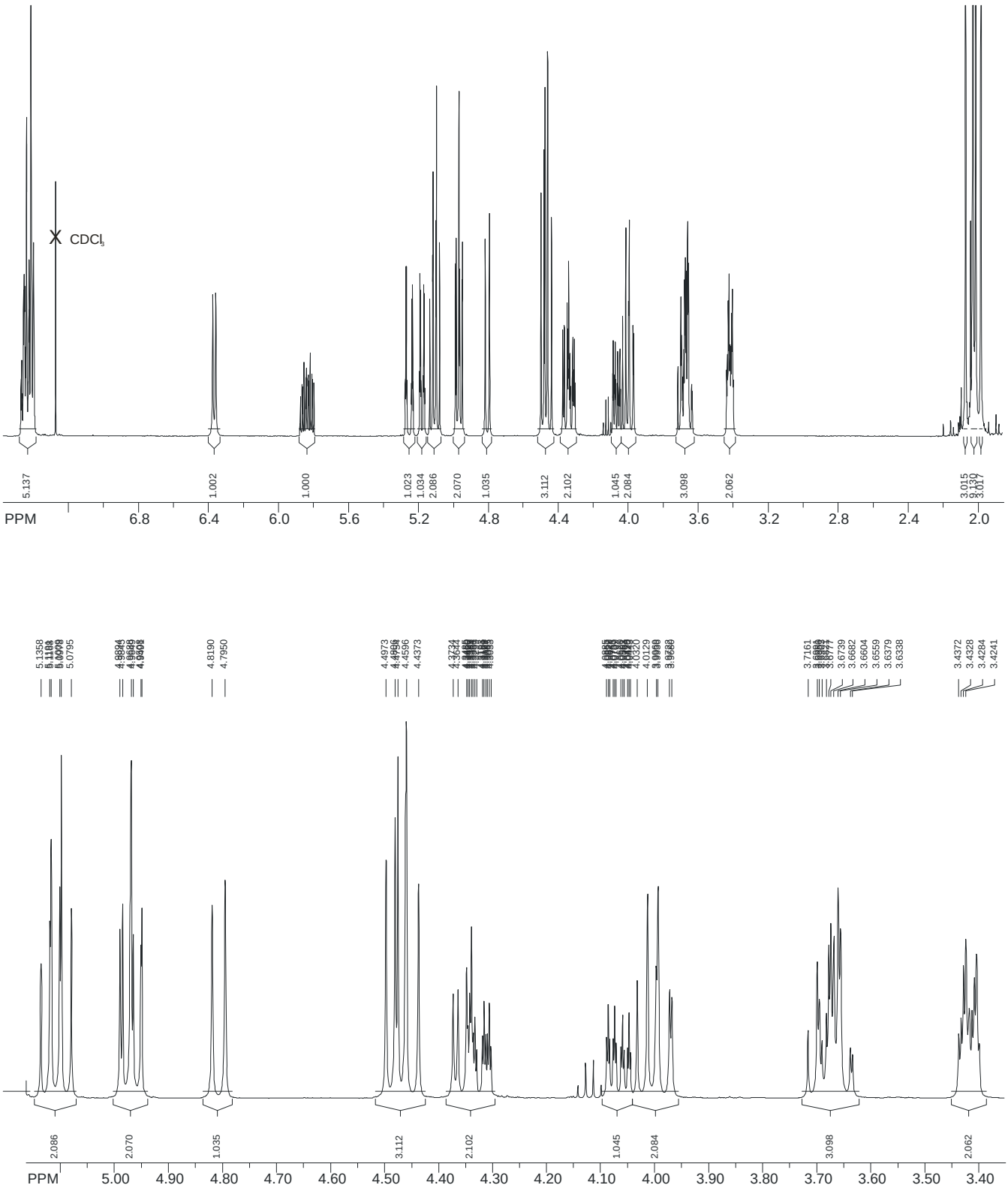

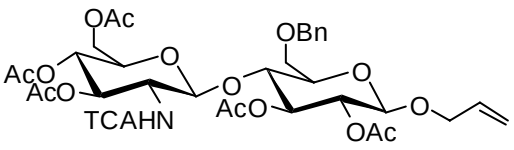

Figure S5. ^{1}H NMR ($CDCl_3$, 500 MHz) spectrum of **9**

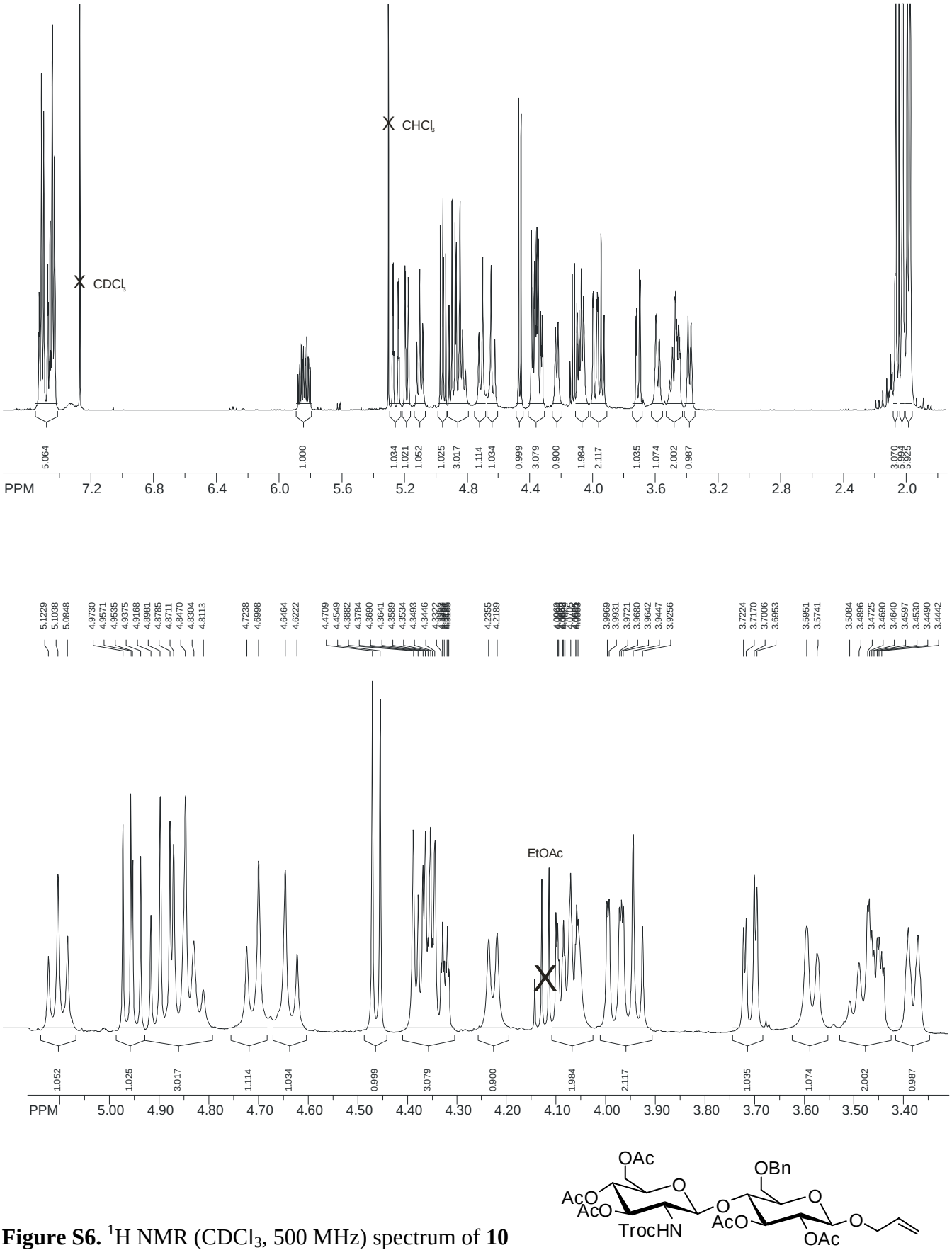

Figure S6. ^{1}H NMR ($CDCl_3$, 500 MHz) spectrum of **10**

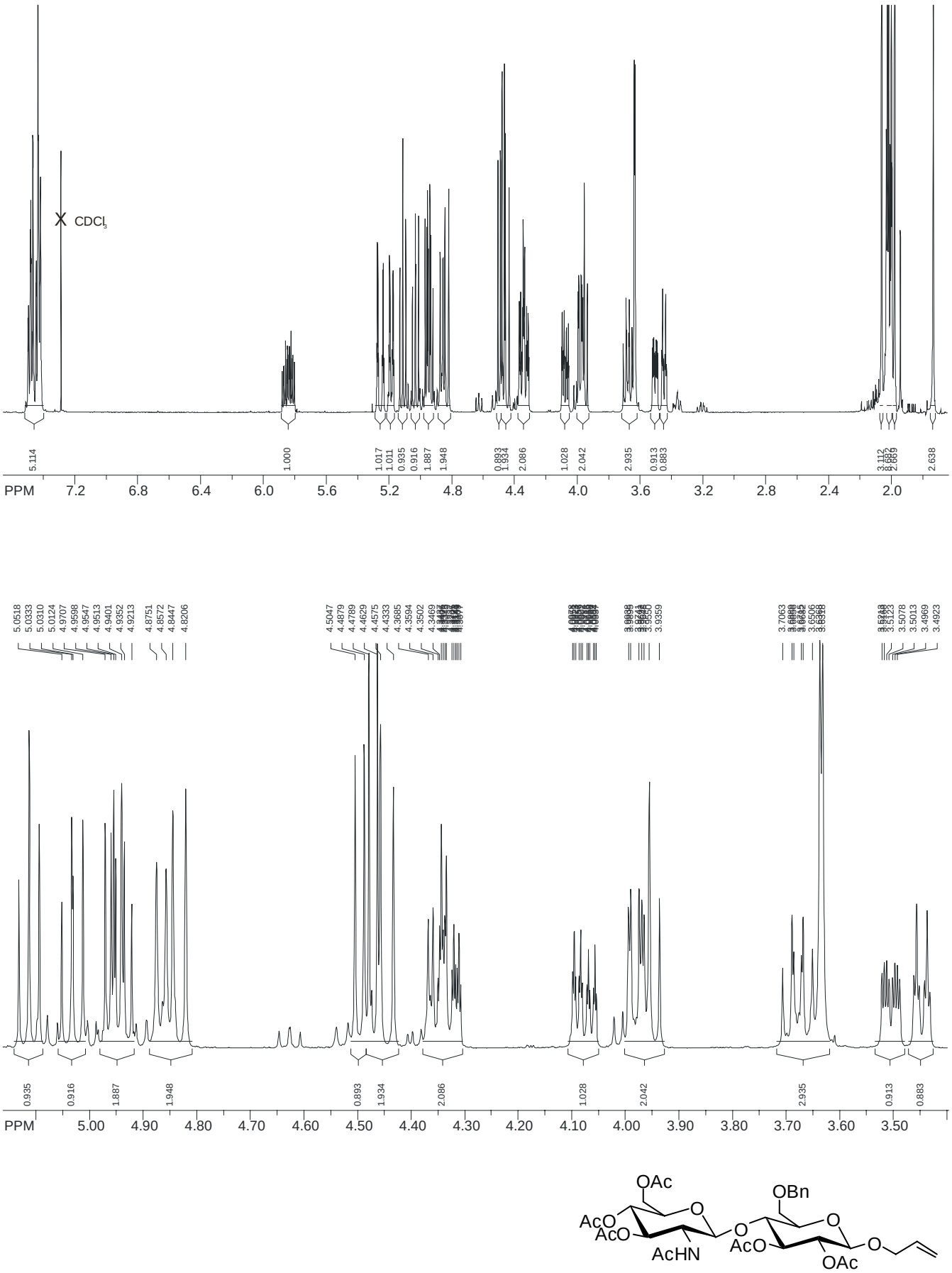

Figure S7. ^{1}H NMR ($CDCl_3$, 500 MHz) spectrum of **11** (from method A)

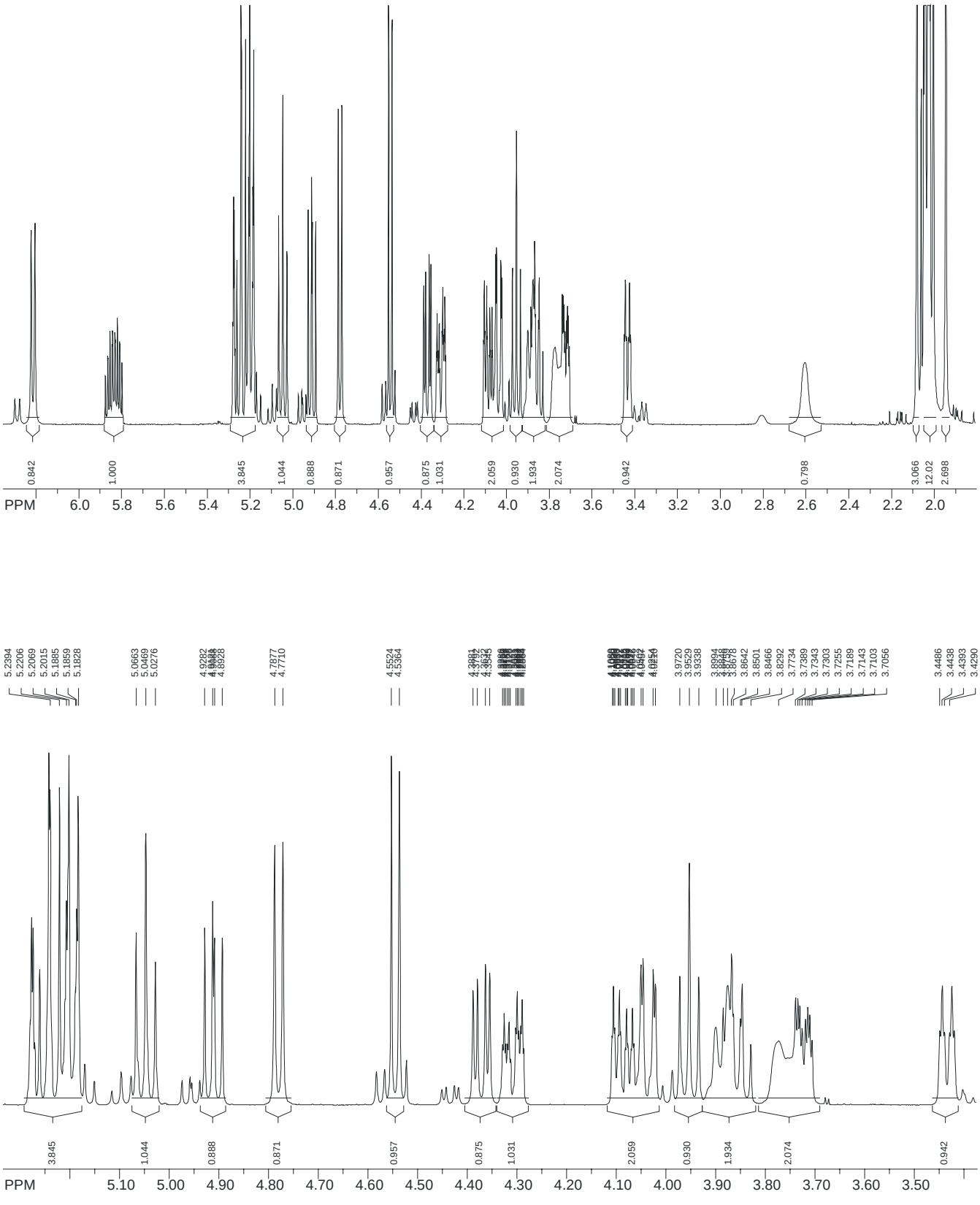

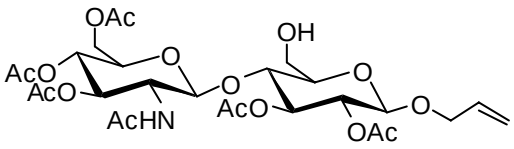

Figure S8. ^{1}H NMR ($CDCl_3$, 500 MHz) spectrum of **12**

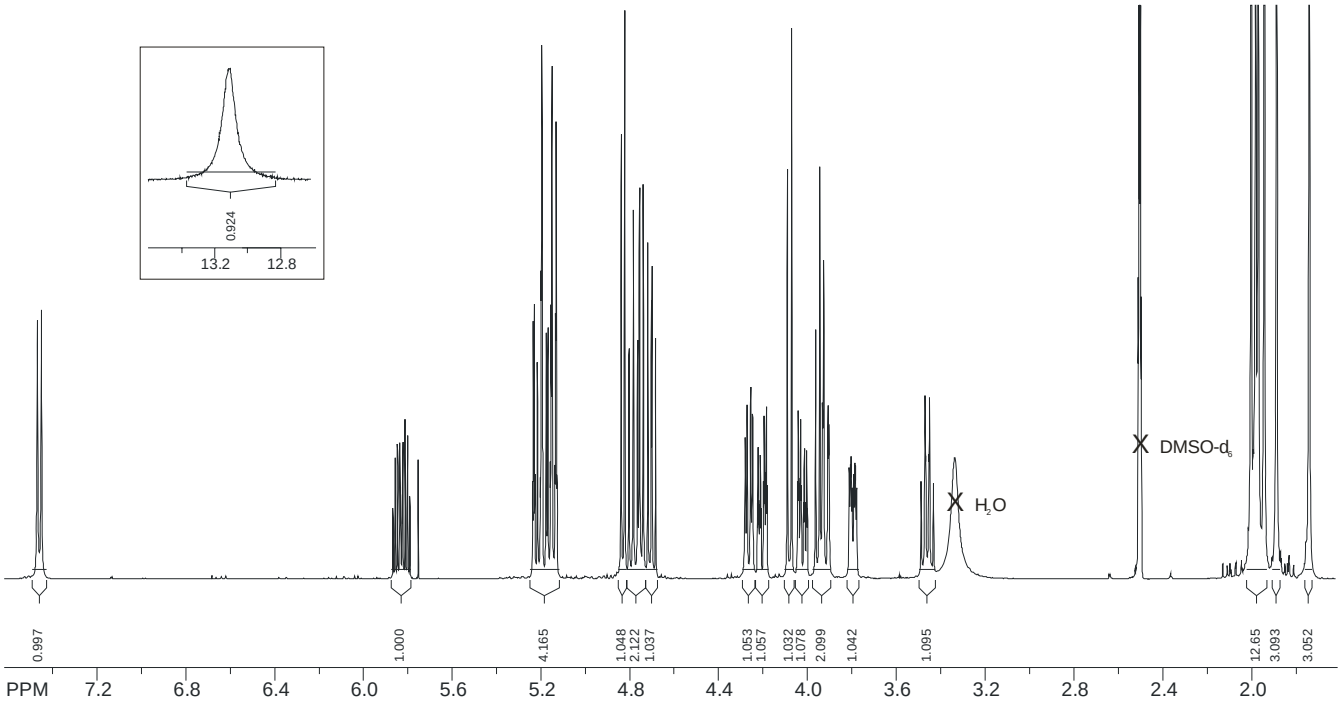

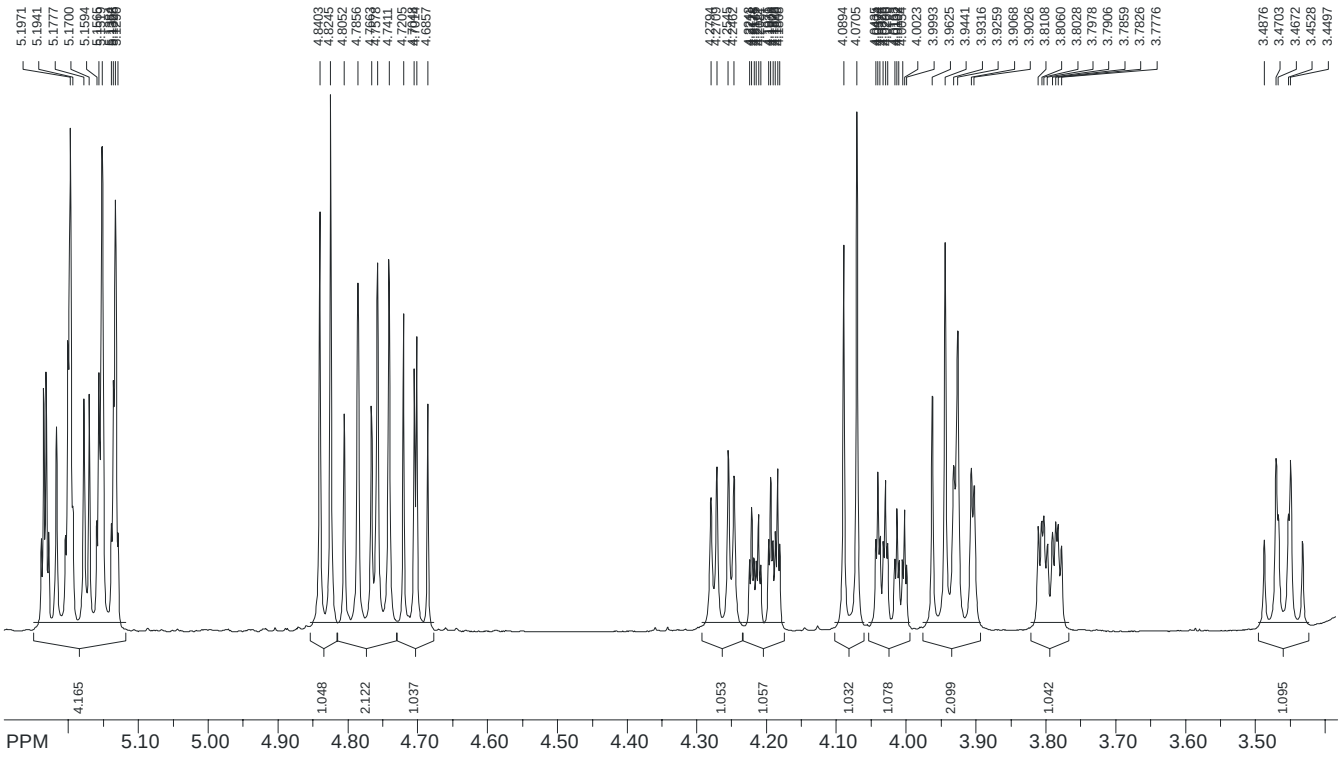

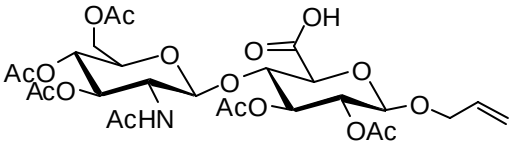

Figure S9. ^{1}H NMR [$(CD_3)_2SO$, 500 MHz] spectrum of **13**

Amine-Reactive Fluorene Probes: Synthesis, Optical Characterization, Bioconjugation, and Two-Photon Fluorescence Imaging

Alma R. Morales,[†] Katherine J. Schafer-Hales,[§] Adam I. Marcus,[§] and Kevin D. Belfield*[,†,‡]

Department of Chemistry and CREOL, The College of Optics and Photonics, University of Central Florida, P.O. Box 162366, Orlando, Florida 32816-2366, and Winship Cancer Institute, Emory University School of Medicine, Atlanta, Georgia 30322.
Received September 29, 2008; Revised Manuscript Received November 12, 2008

With the increasing demand for confocal and two-photon fluorescence imaging, the availability of reactive probes that possess high two-photon absorptivity, high fluorescence quantum yield, and high photostability is of paramount importance. To address the demand for better-performing probes, we prepared two-photon absorbing amine-reactive fluorenyl-based probes 2-(9,9-bis(2-(2-methoxyethoxy)ethyl)-2-isothiocyanato-9*H*-fluoren-7-yl)benzothiazole (**1**) and 2-(4-(2-(9,9-bis(2-(2-ethoxyethoxy)ethyl)-2-isothiocyanato-9*H*-fluoren-7-yl)vinyl)phenyl)benzothiazole (**2**), incorporating the isothiocyanate as a reactive linker. Probe design was augmented by integrating high optical nonlinearities, increased hydrophilicity, and coupling with reactive functional groups for specific targeting of biomolecules, assuring a better impact on two-photon fluorescence microscopy (2PFM) imaging. The isothiocyanate (NCS) derivatives were conjugated with cyclic peptide RGDfK and Reelin protein. The study of the chemical and photophysical properties of the new labeling reagents, as well as the conjugates, is described. The conjugates displayed high chemical stability and photostability. The NCS derivatives had low fluorescence quantum yields, while their bioconjugates exhibited high fluorescence quantum yields, essentially "lighting up" after conjugation. Conventional and 2PFM imaging and fluorescence lifetime imaging (FLIM) of HeLa, NT2, and H1299 cells, incubated with two-photon absorbing amine-reactive probe (**1**), RGDfK-dye conjugate (**7**), and Reelin-dye conjugate (**6**), was demonstrated.

INTRODUCTION

In the past decade, two-photon fluorescence microscopy (2PFM) has provided several advantages in biological research, including high three-dimensional (3D) spatial resolution as a result of the inherent nonlinear dependence of two-photon fluorescence (2PF) on the illumination intensity (*1*−*4*). In this technique, the excitation volume is limited to the focal plane, minimizing out-of-focus excitation, fluorescence, photobleaching, and photodamage. Near-IR excitation used in 2PFM (*1*) enables deeper imaging into optically thick tissue (*5*) and improves tissue viability (*6*). The inherently low 2PF signal in contrast to one-photon fluorescence (1PF) is due to the small two-photon absorption (2PA) cross sections ($\sim 10^{-50}$ cm^4·s) of the fluorescent probes. This is the motivating factor in the continuing efforts to synthesize fluorescent markers with large 2PA cross sections. A steady increase in the biomedical applications of 2PFM has uncovered the lack of efficient two-photon absorbing fluorescence probes with high specificity. In order to be truly useful for such applications, it is necessary to have not only an imaging component which undergoes strong two-photon absorption (2PA) at wavelengths greater than 700 nm, but also a targeting component which binds the fluorescent probe selectively to the target tissue or organelle.

Currently, only a limited number of 2PA fluorophores, specifically tailored for direct labeling of biomolecules for two-photon induced fluorescence imaging studies, have been reported (*7*−*11*). The most common of these are fluorophores designed for the labeling of lysine residues on proteins with amine-reactive compounds bearing functional groups capable of forming a stable linkage with these biomolecules. Representative labeling functionalities include isothiocyanates and succinimidyl esters for coupling with primary and secondary amines.

Our previous success with fluorene dyes in the field of 2PA (*13*−*19*) encouraged us to further investigate this class of chromophores as two-photon excitable fluorescent labels. Here, we present the synthesis of novel two-photon excitable fluorescent labeling reagents, along with their peptide and bioconjugate analogues. Our strategy consists of building 2PA chromophores containing the isothiocyanate functionality, −N═C═S, capable of forming a stable linkage with biomolecules containing $-NH_2$ amino groups. The chromophores are based on fluorene derivatives containing the benzothiazole motif as an electron-acceptor group. The π-electron conjugation length was increased via the incorporation of a styryl group directly connected to the fluorenyl π-bridge construct.

EXPERIMENTAL SECTION

Materials and Methods. The cyclic peptide (Ar-Gly-Asp-D-Phe-Lys) c(RGDfK) was purchased from Peptides International, Inc. All other chemicals and reagents were purchased from Aldrich or Acros Organics and used as received unless otherwise specified. 2-(7-Nitrofluoren-2-yl)benzothiazole (**A**), 2-iodo-7-nitrofluorene (**D**), and 2-(4-vinylphenyl)benzothiazole **(F)** were prepared as described previously (*13*, *14*, *19*).

^{1}H and ^{13}C NMR spectra were recorded in $CDCl_3$ on a Varian 300 NMR spectrometer (300 MHz for ^{1}H, referenced to TMS at $\delta = 0.0$ ppm and 75 MHz for ^{13}C, referenced to $CDCl_3$ at $\delta = 77.0$ ppm). FT-IR spectra were recorded on a Perkin-Elmer spectrophotometer model PE-1300 F0241. Elemental analyses

* To whom all correspondence should be addressed. Department of Chemistry, University of Central Florida, P.O. Box 162366, 4000 Central Florida Blvd., Orlando, FL 32816-2366, Ph: 407-823-1028, Fax: 407-823-2252, E-mail: belfield@mail.ucf.edu.

† Department of Chemistry, University of Central Florida.

‡ CREOL, University of Central Florida.

§ Emory University School of Medicine.

10.1021/bc800415t CCC: $40.75 © 2008 American Chemical Society
Published on Web 12/17/2008

were performed at Atlantic Microlab, Inc., Norcross, GA. High-resolution mass spectrometry (HR-MS) analysis was performed in the Department of Chemistry, University of Florida, Gainesville, FL.

*General Synthetic Procedure for Preparation of 2-(9,9-Di(2-(2-methoxyethoxy)ethyl)-7-nitrofluoren-2-yl)benzothiazole (**B**) via Alkylation.* 2-(7-Nitrofluoren-2-yl)-benzothiazole (**A**) (2.18 g, 6.33 mmol), 1-bromo-2-(2-methoxyethoxy)ethane (2.77 g, 15.13 mmol), and KI (0.1 g, 0.65 mmol) were placed into anhydrous DMSO at room temperature. To the stirred solution, freshly powdered KOH (1.43 g, 25.49 mmol) was slowly added, turning the yellow reaction mixture dark green. Reaction progress was monitored by TLC hexanes/EtOAc (65:35). The reaction mixture was poured into distilled water and its organic components extracted with CH_2Cl_2 and dried over $MgSO_4$. Removal of solvent provided a dark orange oil, which was purified via silica gel column chromatography using the eluent system above. Compound B was obtained as a yellow solid (2.5 g, 51% yield, mp 78−79 °C). ^{1}H NMR (300 MHz, $CDCl_3$) δ: 8.33 (s, 1H), 8.30 (d, 1H), 8.22 (s, 1H), 8.15 (d, 1H), 8.11 (d, 1H), 7.94, (d, 1H), 7.88 (d, 1H), 7.86 (d, 1H), 7.52 (t, 1H), 7.41 (t, 1H), 3.22 (m, 4H, OCH_2), 3.21 (m, 6H, OCH_3), 3.15, (m, 4H, OCH_2), 2.90 and 2.82 (m, 4H, OCH_2), 2.55, (t, 4H, CH_2). ^{13}C NMR (75 MHz, $CDCl_3$) δ: 167.37 (Ar−C═N), 154.17, 151.70, 151.37, 147.67 (CNO_2), 145.78, 140.89, 135.18, 134.59, 127.81, 126.71, 125.66, 123.76, 123.47, 122.60, 121.90, 121.85, 120.60, 119.37, 71.94, 70.25, 67.16, 59.29 (OCH_3), 52.77 (C9), 39.67 (CH_2). Anal. Calcd. for $C_{30}H_{32}N_2O_6S$: C, 65.67; H, 5.88; N 5.11. Found: C, 65.73; H, 5.98; N, 4.96.

*Synthesis of 7-(Benzothiazol-2-yl)-9,9-di(2-(2-methoxyethoxy)-ethyl)fluoren-2-amine (**C**).* 2-{9,9-Di-[2-(2-methoxyethoxy)-ethyl]-7-nitrofluoren-2-yl}-benzothiazole, **B**, (0.218 g, 0.4 mmol) was dissolved into a mixture of EtOH/THF (1:1) mixture at room temperature. To this was added 0.019 g of 10% Pd/C, and the reaction was heated to 70 °C under N_2. Hydrazine monohydrate (0.124 g, 2.48 mmol) was added dropwise and the reaction mixture stirred for 12 h. Upon completion, the reaction was passed through a silica gel plug washed with diethyl ether/MeOH (1:1), concentrated, and purified via silica gel column chromatography using diethyl ether/MeOH (9.5:0.5) as eluent. A bright yellow solid was isolated (0.192 g, 93% yield, mp 137−139 °C) that was used directly in the next step. ^{1}H NMR (300 MHz, $CDCl_3$) δ: 8.08 (s, 1H, ArH), 8.06 (d, 1H, ArH), 8.02 (d, 1H, ArH), 7.91 (d, 1H, ArH), 7.60 (d, 1H, ArH), 7.50 (d, 1H, ArH), 7.45, (t, 1H, ArH), 7.36 (t, 1H, ArH), 6.74 (s, 1H, ArH), 6.68, (d, 1H, ArH), 3.87 (s, 2H, NH_2), 3.29 (m, 4H, OCH_2), 3.25, (s, 6H, OCH_3), 3.21 (m, 4H, OCH_2), 2.79 (m, 4H, CH_2), 2.49 and 2.38 (m, 4H, OCH_2). ^{13}C NMR (75 MHz, $CDCl_3$) δ: 168.59 (Ar−C═N), 154.27, 151.75, 148.70, 147.34 (CNH_2), 144.15, 135.0, 131.02, 130.49, 127.51, 126.39, 125.05, 123.01, 121.89, 121.70, 121.61, 118.92, 114.67, 109.88, 72.02, 70.22, 67.30, 59.31 (OCH_3), 51.41 (C9), 40.27 (CH_2). Anal. Calcd. for $C_{30}H_{34}N_2O_4S$: C, 69.47; H, 6.61; N 5.40. Found: C, 69.29; H, 6.60; N, 5.57.

Synthesis of Amine-Reactive Fluorene Probe (1). Compound C, (0.6 g, 1.15 mmol) was dissolved in $CHCl_3$ to which aq $CaCO_3$ (0.26 g, 2.11 mmol) was added at 0 °C. Thiophosgene (0.12 mL, 1.5 mmol) was then added dropwise with vigorous stirring (*20*). After 1 h, the starting material was completely consumed, as determined by TLC (9:1 diethyl ether/MeOH), achieving near-quantitative conversion. After an additional 30 min, 10% HCl was added until no gas generation was observed. The reaction mixture was poured into H_2O, extracted with CH_2Cl_2, dried over $MgSO_4$, and, upon filtration and concentration, resulted in an orange oil. The crude product was purified by column chromatography on silica gel eluting with diethyl ether/MeOH, (90:10), followed by hexane/EtOAc (60:40), affording 0.65 g of a yellow solid (94% yield, mp 70−71 °C). The FT-IR spectrum revealed a characteristically strong −NCS stretch at 2111 cm^{-1}, while no signal from the $-NH_2$ group (ca. 3600 cm^{-1}) was observed. ^{1}H NMR (300 MHz, $CDCl_3$) δ: 8.15 (s, 1H), 8.09 (dd, 2H), 7.93 (d, 1H), 7.75 (q, 2H), 7.50 (t, 1H), 7.42 (m, 2H), 7.24 (d, 1H), 3.21 (m, 10H, OCH_3, OCH_2), 3.13 (m, 4H, OCH_2), 2.85 (m, 4H, OCH_2), 2.48 (m, 4H, CH_2). ^{13}C NMR (75 MHz, $CDCl_3$) δ: 167.82 (Ar−C═N), 154.18, 151.58, 150.13, 142.07, 138.72, 135.75 (N═C═S), 135.10, 133.23, 130.89, 127.69, 126.61, 125.45, 125.40, 123.32, 122.30, 121.82, 121.36, 120.74, 71.99, 70.28, 67.16, 59.36 (OCH_3), 52.26 (C9), 39.91 (CH_2). Anal. Calcd. for $C_{31}H_{32}N_2O_4S_2$: C, 66.40; H, 5.75; N 5.00. Found: C, 66.63; H, 5.80; N, 4.95.

*Synthesis of 2-Iodo-9,9-di-[2-(2-ethoxyethoxy)-ethyl]-7-nitrofluorene (**E**) via the General Alkylation Procedure (above).* Compound **E** was obtained as a yellow oil, which solidified into a waxy solid (0.88 g, 42% yield). ^{1}H NMR (300 MHz, $CDCl_3$) δ: 8.26 (s, 1H), 8.24 (d, 1H), 7.82 (s, 1H), 7.76 (d, 1 H), 7.73 (1H), 7.51 (d, 1H), 3.37 (q, 4H, OCH_2), 3.29 (t, 4H, OCH_2), 3.15 (t, 4H, OCH_2), 2.85 (m, 4H, OCH_2), 2.47 (m, 4H, CH_2), 1.13 (t, 6H, CH_3). ^{13}C NMR (75 MHz, $CDCl_3$) δ: 152.90, 150.12, 147.50 (CNO_2), 145.85, 137.74, 136.99, 133.12, 123.65, 122.69, 120.05, 119.0, 95.52, 70.14, 69.60, 66.75, 66.62 (OCH_2), 52.24 (C9), 39.20 (CH_2), 15.07 (CH_3). Anal. Calcd. for $C_{23}H_{28}INO_6$: C, 52.73; H, 5.66; N, 2.46. Found: C, 52.36; H, 5.60; N, 2.47.

*Synthesis of 2-(4-(2-(9,9-Bis(2-(2-ethoxyethoxy)ethyl)-2-nitrofluoren-7-yl)vinyl)phenyl)benzothiazole (**G**).* 9,9-Bis(2-(2-ethoxyethoxy)ethyl)-2-iodo-7-nitro-fluorene **E** (0.5 g, 0.88 mmol), 2-(4-vinylphenyl)benzothiazole **F** (0.25 g, 1.04 mmol), $Pd(OAc)_2$ (90 mg, 0.40 mmol), tri-*o*-tolylphosphine (0.21 g, 0.69 mmol), and DMF/Et_3N (9.5 mL) were combined in a screwcap vial and heated at reflux for 40 h The mixture was cooled to room temperature and filtered. All volatiles were removed under reduced pressure, and the resulting residue was then dissolved in CH_2Cl_2, washed with distilled water, dried over $MgSO_4$, filtered, and concentrated. The crude product was purified by column chromatography on silica gel, eluting with hexane/EtOAc (3.5:1.5), followed by hexane/EtOAc/THF (3.5:1:0.5), affording 0.40 g of an orange solid (68% yield, mp 131−132 °C). ^{1}H NMR (300 MHz, $CDCl_3$) δ: 8.31, (m, 2H), 8.12 (q, 3H), 7.94 (d, 1H), 7.77 (d, 2H), 7.67 (d, 3H), 7.61 (d, 1H), 7.52 (t, 1H), 7.40 (t, 1H), 7.26 (m, 2H), 3.34 (m, 12H, OCH_2), 2.88 (m, 4H, OCH_2), 2.51 (m, 4H, CH_2), and 1.12 (t, 6H, CH_3). ^{13}C NMR (75 MHz, $CDCl_3$) δ: 167.22 (Ar−C═N), 153.91, 151.11, 150.51, 146.80 (CNO_2), 146.16, 139.38, 138.06, 137.80, 134.77, 132. 68, 129. 63, 128. 65, 127.76, 126.91, 126.71, 126.18, 125.02, 123.46, 122.96, 121.41, 121.20, 119.65, 118.70, 70.01, 69.47, 66.72, 66.47 (OCH_2), 51.83 (C9), 39.36 (CH_2), 15.01 (CH_3). Anal. Calcd for $C_{40}H_{42}N_2O_6S$: C, 70.77%; H, 6.24%; N, 4.13%. Found: C, 70.46%; H, 6.33%; N, 4.03%.

*Synthesis of 9,9-Bis(2-(2-ethoxyethoxy)ethyl)-7-(4-(benzothiazol-2-yl)styryl)-fluoren-2-amine (**H**).* Nitro compound **G** (0.32 g, 0.48 mmol) was dissolved in a 8 mL of 1:1 (v/v) EtOH/THF at room temperature. To this was added 0.02 g of 10% Pd/C. The reaction mixture was then heated to 70 °C under Ar to which hydrazine hydrate (0.09 g, 2.97 mmol) was added dropwise via syringe over 20 min. The reaction mixture was stirred for 18 h at 70 °C, cooled to room temperature, and concentrated, affording a yellow oil. Purification was accomplished by column chromatography using hexane/THF/MeOH (3:1:1), resulting in 0.27 g of yellow solid (90% yield). This intermediate was not further characterized and used directly in the next step due to oxidative lability.

*Synthesis of Amine-Reactive Fluorene Probe (**2**).* 9,9-Bis(2-(2-ethoxyethoxy)ethyl)-7-(4-(benzothiazol-2-yl)styryl)-fluoren-2-amine **H** (0.21 g, 0.33 mmol) was dissolved in $CHCl_3$ (8 mL)

Scheme 1. Preparation of the Isothiocyanate Amine-Reactive Tag 1

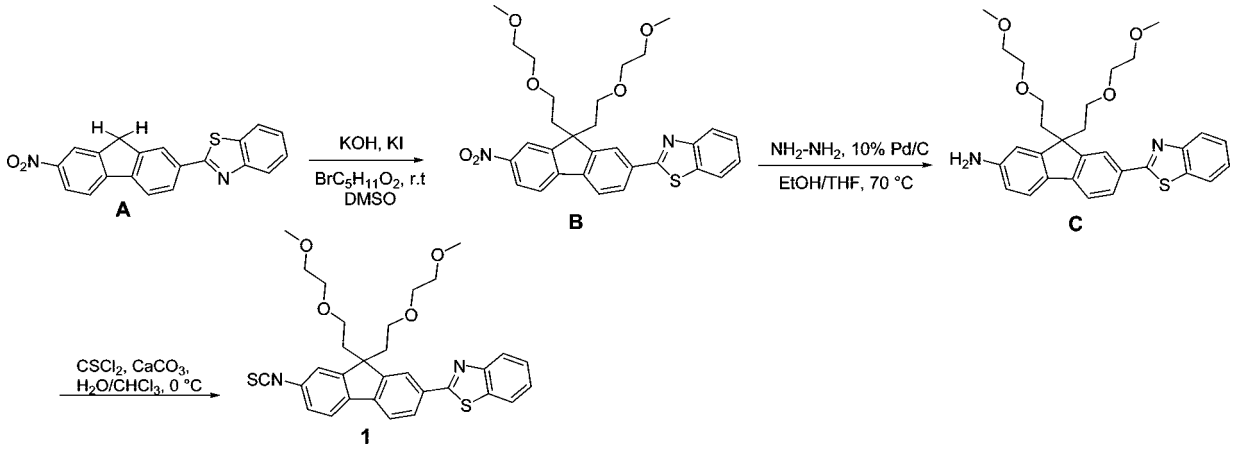

to which aq $CaCO_3$ (0.11 g, 2.11 mmol) was added. Thiophosgene (0.04 mL, 0.56 mmol) was added dropwise at 0 °C with vigorous stirring. After 2.5 h, the starting material was completely consumed, as determined by TLC (silica, 1:1 hexane/THF). 10% HCl (5 mL) was added until no gas generation was observed. The reaction mixture was poured into H_2O, extracted with CH_2Cl_2, dried over $MgSO_4$, and, upon filtration and concentration, resulted in an orange oil. The crude product was purified by column chromatography on silica gel eluting with hexane/THF (1:1), followed by hexane/THF (3.5:1.5), affording 0.15 g of a yellow solid (64% yield, mp 73−74 °C). FT-IR analysis revealed a characteristically strong −NCS stretch at 2111 cm^{-1}. ^1H NMR (300 MHz, $CDCl_3$) δ: 8.08, (t, 3H), 7.89 (d, 1H), 7.62 (q, 4H), 7.51 (t, 2H), 7,40 (t, 2H), 7.28 (m, 4H), 3.39 (m, 8H, OCH_2), 3.21, (d, 4H, OCH_2), 2.80 (m, 4H, OCH_2), 2.43 (bs, 4H, CH_2), and 1.13 (t, 6H, CH_3). ^{13}C NMR (75 MHz, $CDCl_3$) δ: 167.11 (Ar−C═N), 153.72, 150.56, 149.31, 139.47, 138.85, 138.77, 136.36 (N═C═S), 134.78, 134.58, 132.26, 129.80, 129.55, 127.56, 126.63, 126.41, 125.99, 124.81, 122.77, 121.25, 120.72, 120.58, 120.27, 120.05, 69.91, 69.42, 66.66, 66.40 (OCH_2), 51.32 (C9), 39.55 (CH_2), 15.02 (CH_3). Anal. Calcd. for $C_{41}H_{42}N_2O_4S_2$: C, 71.27%; H, 6.13%; N, 4.05%. Found: C, 71.06%; H, 6.28%; N, 4.01%.

*General Synthetic Procedure for Reactive Probe Adduct via Addition Reaction (**3**).* A mixture of amine-reactive probe **2** (0.12 g, 0.214 mmol) and *n*-butylamine (0.23 mL) was stirred at room temperature for 2 h. The excess *n*-butylamine was removed in vacuo and the residue purified by column chromatography on silica gel eluting first, with EtOAc/THF (95:5), followed by diethyl ether/EtOAc (80:20), affording 0.082 g of pale yellow solid (63% yield, mp 128−129 °C). ^1H NMR (300 MHz, $CDCl_3$) δ: 8.11 (s, 1H), 8.10 (t, 2H), 8.04 (d, 1H), 7.92 (q, 2H), 7.79 (t, 2H), 7.72 (t, 1H), 7.50 (d, 1H), 6.8 (s, 1H, NH), 3.67 (m, 16H, OCH_3, OCH_2, CH_2), 2.10 (m, 4H, OCH_2), 1.54 (m, 4H, CH_2), 1.36 (m, 2H, CH_2), 1.15 (m, 2H, CH_2), 0.91 (t, 3H). ^{13}C NMR (75 MHz, $CDCl_3$) δ: 180.72, 168.37 (Ar−C═N), 155.84, 154.22, 150.91, 149.35, 143.52, 140.05, 135.03, 134.21, 131.88, 127.62, 126.50, 125.24, 123.15, 121.99, 121.77, 121.33, 119.85, 119.15, 114.29, 72.00, 70.13, 67.33 (OCH_2), 59.22, 51.7(C9), 40.42, 40.03 (CH_2), 32.71, 20.57, 14.33 (CH_3). Anal. Calcd. for $C_{35}H_{43}N_3O_4S_2$: C, 76.11; H, 8.94; N, 5.92. Found: C, 76.28; H, 9.19; N, 5.90.

*General Preparation of Reelin−Fluorene Bioconjugate (**6**).* A stock solution of Reelin (2 mg/mL) in freshly prepared $NaHCO_3$ (0.1 M, pH 9) solution was used. A stock solution of the amine-reactive probe dissolved in anhydrous DMSO (5.23×10^{-3} M) was freshly prepared and aliquots added dropwise into the Reelin solution (1 mL of stock) with gentle stirring. The concentration of the probe solution was varied such that a 1:10 and a 1:5 mol ratio of protein to probe were prepared to establish a degree of labeling (DOL) for the probe. The reaction was kept in the dark and allowed to stir at room temperature for 3 h, after which the mixture was passed through a gel chromatography column (12 cm length, Bio-Rad Econo-Pac 10DG) equilibrated in and eluted with phosphate buffered saline (PBS, pH 7.2; Fisher). Fractions containing the bioconjugate were identified spectrophotometrically by monitoring both the protein fraction at 280 nm and the dye at 355 nm. The molar absorptivity (ε_{278}) of Reelin in PBS (pH 7.2) was determined to be 39.4×10^3 L mol^{-1} cm^{-1}.

*Preparation of Cyclic Peptide Conjugate (**7**).* Cyclic peptide RGDfK (10 mg, 0.016 mmol) was dissolved in DMSO (0.75 mL), and then amine-reactive dye **1** (9.6 mg, 0.017 mmol) was added slowly to the solution. The clear solution was stirred at room temperature that gradually changed to a fluorescent yellow coloration. After 5 h, the starting material was completely consumed as determined by TLC (silica gel, diethyl ether). DMSO was removed by washing with diethyl ether several times, producing 16 mg of yellow solid (90% yield, mp 265−266 °C). ^1H NMR (300 MHz, $CDCl_3$) δ: 9.85 (s, 1H, COOH). ^{13}C NMR (75 MHz, $CDCl_3$) δ: 180.78, 174.52, 172.47, 171.52, 171.23, 170.91, 168.19 (Ar−C═N), 157.19, 154.13, 150.59, 143.62, 140.75, 138.74, 134.96, 131.63, 129.54, 128.59, 127.24, 126.60, 125.98, 123.26, 122.89, 122.21, 120.83, 71.78, 69.84, 67.14 (OCH_3), 58.70, 55.71, 52.00 (C9), 49.55, 44.02, 32.33, 28.47, 25.60, 23.81. HRMS-ESI theoretical *m*/*z* $[M + H]^+ = 1164.49$, found 1164.49; theoretical *m*/*z* $[M + Na]^+ = 1186.38$, found 1186.48.

NT2 Cell Culture. The NT-2/D1 cells were plated at a density of 5×10^6 per 75 cm^2 in a tissue culture treated flask (Corning). Cell culture media was Dulbecco's modified Eagle's medium with F-12 (DMEM/F12, Invitrogen), supplemented with 10% heat-inactivated fetal bovine serum (Atlanta Biologics). An incubation chamber was used to maintain a humidified atmosphere of 5% CO_2 and 37 °C. NT2 cells were passed twice a week with trypsin/EDTA (Invitrogen) treatment.

*HeLa Cells Incubated with Amine-Reactive Probe (**1**).* HeLa cells were plated onto 4-well glass chamber slides. Stock solutions of fluorophore **1** dissolved into DMSO were prepared as either 10 or 5 μM solutions. Diluted solutions in complete growth medium were then freshly prepared and placed over the cells for either a 1 or 5 h period. All cells were washed with PBS (3−5×) and fixed in a 3.7% formaldehyde solution for 5 min at room temperature.

*NT2 Cells Incubated with Reelin Conjugate (**6**).* Reelin conjugate **6** diluted in NT2 cell media was added to NT2 cells and incubated for 3 h. After incubation, cells were washed once

Scheme 2. Preparation of the Isothiocyanate Amine-Reactive Tag 2 with Extended Conjugation Length

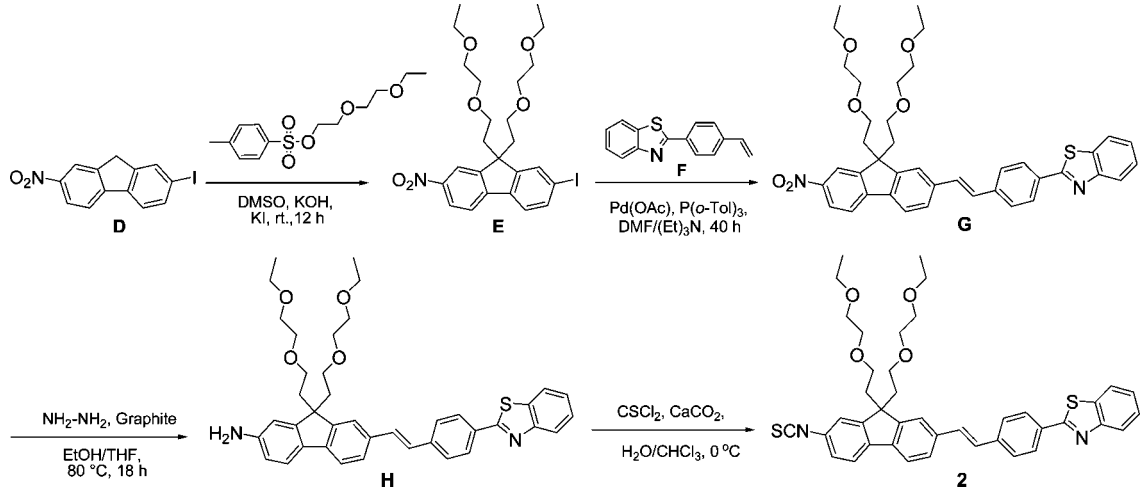

Scheme 3. Preparation of the Model Adducts 3 and 4 and Bioconjugates 5 and 6 with the Amine-Reactive Fluorenyl Reagents 1 and 2

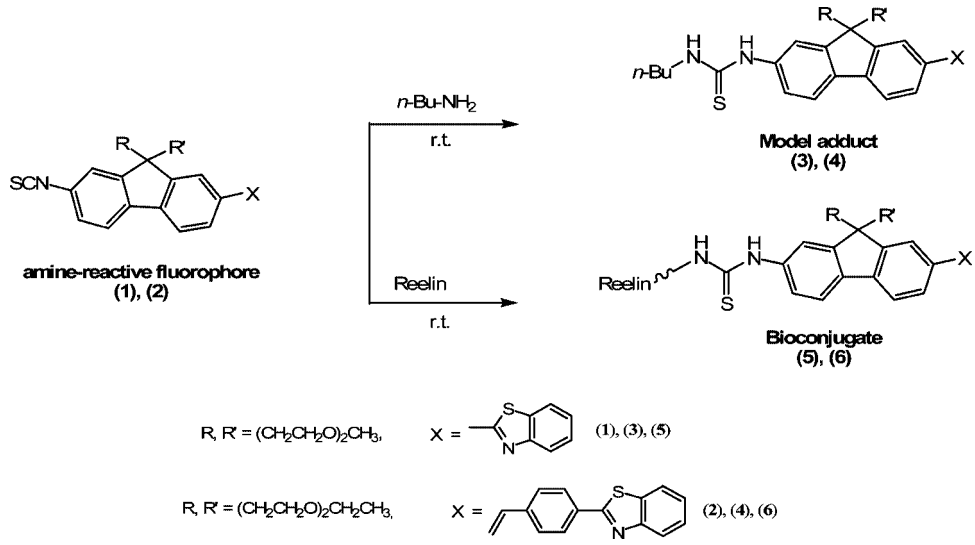

with PBS followed by addition of fresh media. Cells were fixed prior to viewing using 4% paraformaldehyde.

Spectroscopic Measurements. Steady-state absorption and fluorescence emission spectra of compounds **1**−**3** were investigated in DMSO in concentrations on the order of 10^{-6} M at room temperature in 1 × 1 cm quartz cuvettes using an Agilent 8453 spectrophotometer and PTI Quantamaster spectrofluorimeter, respectively. All solvents and solutions used in these experiments were checked for spurious emission in the region of interest. Fluorescence quantum yields, *Q*, were measured for

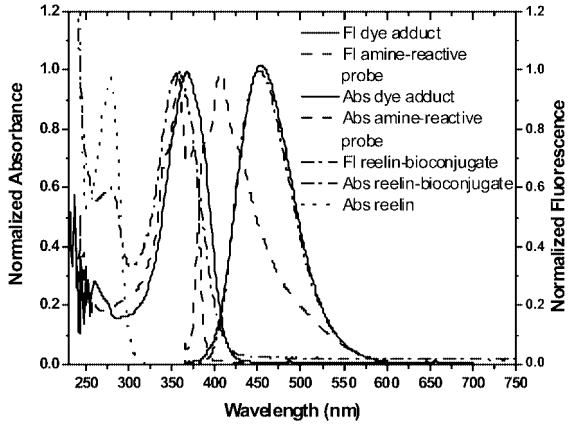

Figure 1. Normalized absorption spectra and steady-state fluorescence emission spectrum of the amine-reactive probe **1** (---), dye adduct **3** (···), and Reelin bioconjugate **5** (—). Absorption spectrum of the free Reelin protein in PBS is shown for reference.

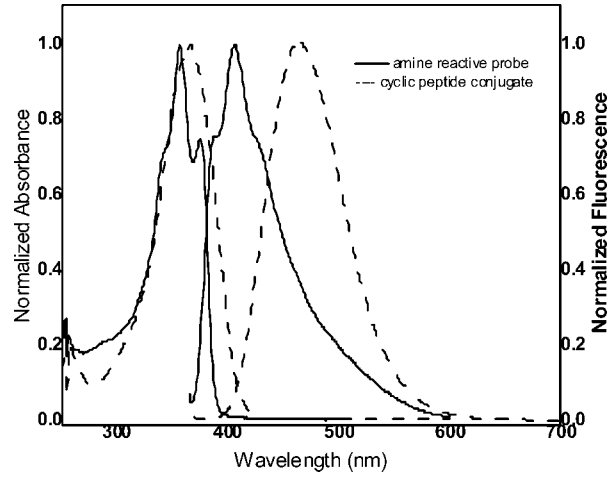

Figure 2. Normalized UV−visible absorbance and fluorescence emission spectra of the amine-reactive probe **1** (—) and cyclic peptide conjugate **7** (---) in DMSO $\lambda_{max}^{abs} = 355$ nm, $\lambda_{max}^{em} = 460$ nm, Qy = 0.92.

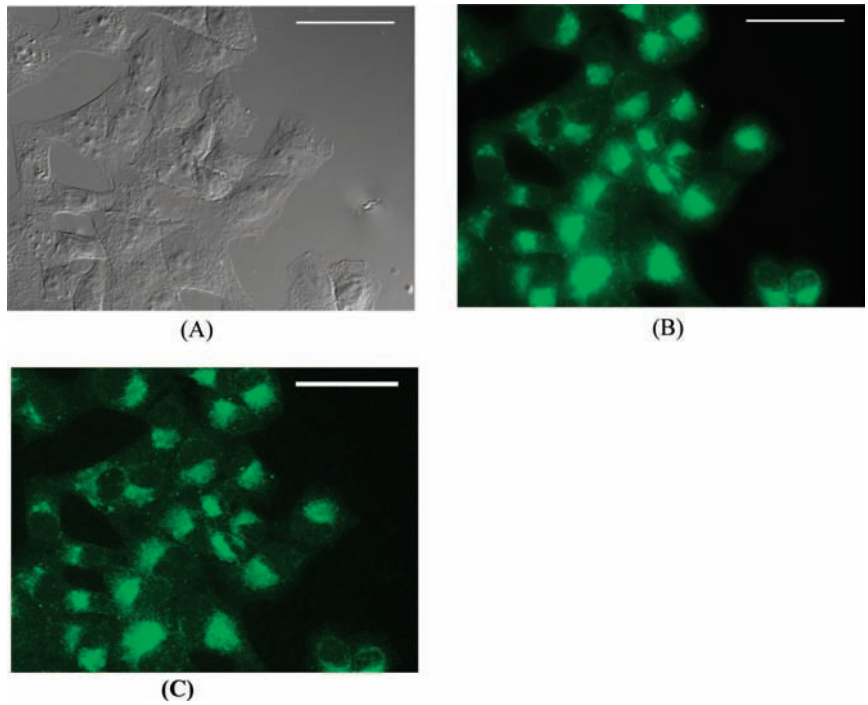

Figure 3. (A) Differential interference contrast (DIC), (B) pseudocolor single-photon fluorescence, (C) two-photon fluorescence (λ = 740 nm, 6.5 mW, filter 510−550 nm) images of HeLa cells stained with amine reactive probe **1**. HeLa cells incubated for 5 h with amine-reactive probe **1**. Filter Cube for SPM: Fluo-M-Blue (Exc 377/50, DM 409; Em 460/50), Scale bar 50 μm.

Scheme 4. Preparation of the Bioconjugate 7 with the Amine-Reactive Tag 1

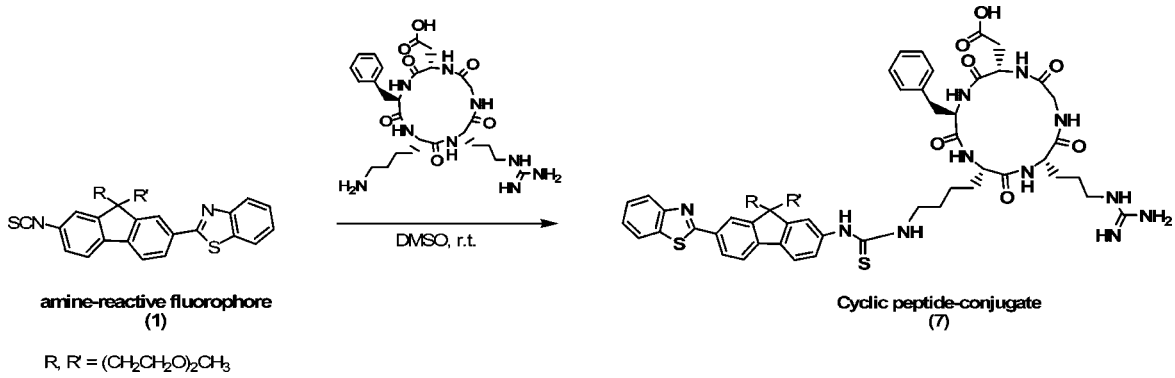

all compounds by a standard method (*21*), relative to Rhodamine 6G in ethanol (Q = 0.94) (*22*).

Two-Photon Absorption Properties. The two-photon fluorescence (2PF) spectra and two-photon absorption (2PA) cross sections of all molecules studied were determined by employing a two-photon induced fluorescence method (*23*, *24*), using a tunable femtosecond Ti:sapphire laser (Mira 900-F, 220 fs pulse width, 76 MHz repetition rate, Coherent, USA) as the excitation source. After passing through a round, continuously variable neutral density filter that was used to control the laser irradiance, the femtosecond NIR laser beam was focused into a 1 × 1 cm quartz cuvette containing sample solutions by a plano-convex lens (f = 50 mm, Thorlabs, USA). The excitation laser was adjusted to be as close to the wall as possible in order to reduce reabsorption effects. The upconverted fluorescence was first collected by an objective lens (20×, NA = 0.50, Newport, USA) at a direction perpendicular to the pump beam, then focused by a large beam collimator (F810SMA-543, Thorlabs, USA) into a multimode fiber (400 μm core, Ocean Optics, USA), and, finally, delivered to a fiber optic spectrometer (SD2000, Ocean Optics, USA), which was used to record the upconverted fluorescence spectra. The two-photon fluorescence spectra recorded by the spectrometer were used without further linearity correction. This technique was confirmed by measuring the 2PA cross section of a well-characterized fluorene-based 2PA fluorophore (*13*, *25*).

One-Photon Fluorescence Imaging. An inverted microscope (Olympus IX70) equipped with a QImaging cooled CCD (Model Retiga EXi) was used for conventional fluorescence imaging, where the output of a filtered 100 W mercury lamp was used as the excitation source. A customized filter cube (Ex 377/50, DM 409, Em 460/50) was used for fluorescence imaging.

Two-Photon Fluorescence Microscopic Imaging and Two-Photon Fluorescence Lifetime Imaging. Two-photon fluorescence microscopic imaging (2PFM) and two-photon fluorescence lifetime imaging (2P-FLIM) were performed on a modified Olympus Fluoview FV300 microscope system coupled with the tunable Coherent Mira 900F Ti:sapphire laser and a compact FLIM system from PicoQuant, Germany. Output from the femtosecond NIR laser (tuned to 760 nm, 220 fs pulse width, 76 MHz repetition rate) was used as the two-photon excitation source for both 2PM and 2P-FLIM experiment. The fluorescence collected by a 40× microscopic objective (UPLANAPO 40×, NA = 0.85, Olympus) was reflected by a dichroic beam splitter

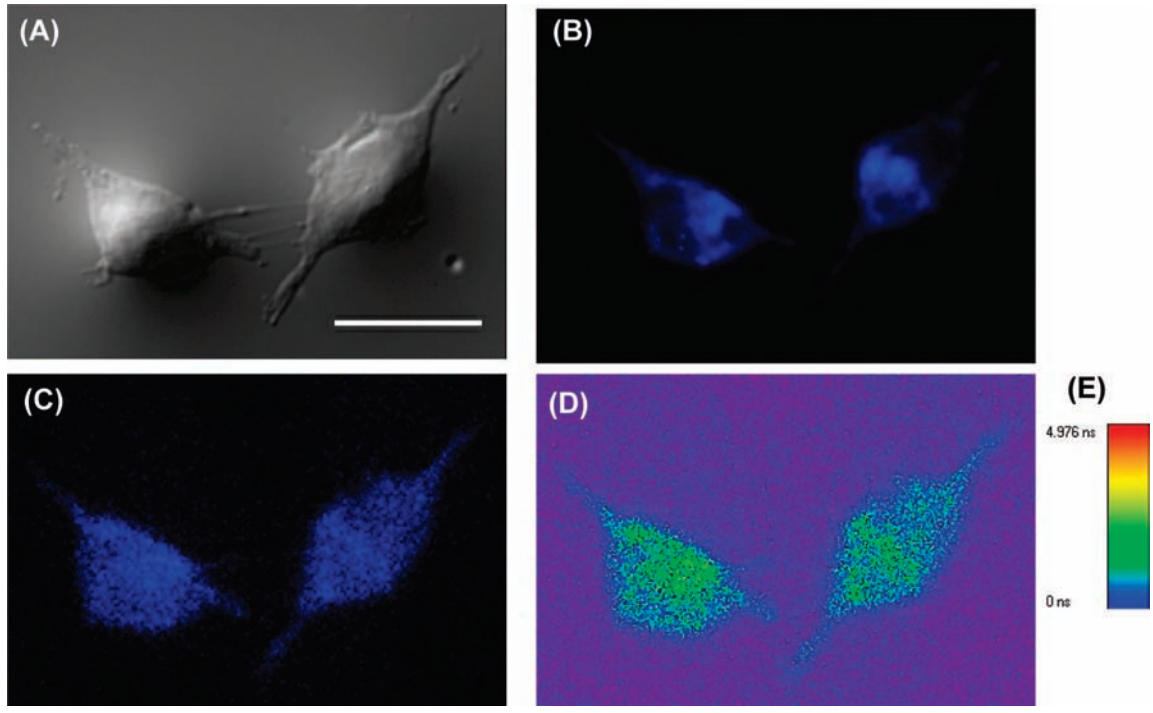

Figure 4. NT2 cells labeled with Reelin conjugate **6** (DOL= 3.4): (A) DIC, (B) 1PM, (C) 2PM, (D) 2P-FLIM. Scale bar in (A) corresponds to 20 μm. (E) Lifetime scale bar for (D). Pseudo color is used for (B), (C), and (D).

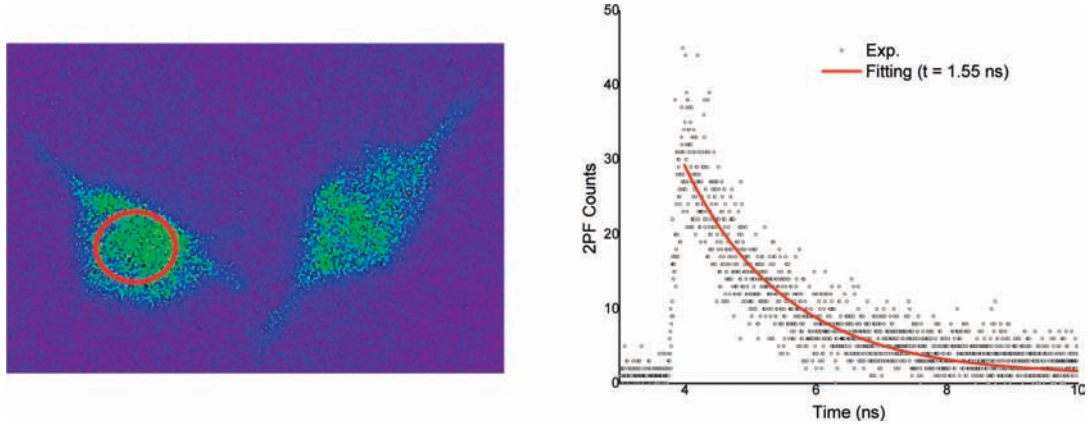

Figure 5. Fluorescence lifetime image of NT2 cells labeled with Reelin conjugate **6** (DOL = 3.4). The decay curve corresponds to the circled area in the left image.

(FF665-Di01−25 × 36, Semrock Inc.), and then focused into a multimode fiber by a microscope objective (20×, NA = 0.4, Newport). A beam reducer, consisting of a plano-convex lens and a plano-concave lens, was used to reduce the fluorescence beam diameter in front of the objective. The output fluorescence was delivered to an avalanche photodiode (APD) detector (PicoQuant, Germany). A broad band-pass filter (D500/200m, Chroma) was placed in front of the APD detector. Data acquisition and analysis were done with a combination of a stand-alone time-correlated single photon counting (TCSPC) module TimeHarp 300 and software package *SymPhoTime*, both from PicoQuant, Germany.

RESULTS AND DISCUSSION

Synthesis and Characterization of the Amine-Reactive Fluorenyl Dyes 1 and 2. The reactivity of the isothiocyanate group −N=C=S is well-documented, yielding thioureas upon reaction with amines. The molecular structures of the target isothiocyanate fluorophores share some similarity with our previously described two-photon fluorescent chromophores (*13*). In the 9-position of these fluorophores, two identical oligo(ethylene glycol) chains were used to impart hydrophilicity and provide better solubility. In the 7-position, we opted for the benzothiazole moiety as an electron-withdrawing group (Schemes 1 and 2).

A key intermediate in the synthesis of the isothiocyanate derivative **1** was amine **C**. This was achieved via the quantitative reduction of nitro derivative **B** using hydrazine hydrate and 10% Pd/C in a 1:1 mixture of EtOH/THF at 70 °C. The isothiocyanate reactive group was then obtained by reaction of amine **C** with thiophosgene. The target functionalized chromophore **1** was obtained in 94% yield.

For isothiocyanate derivative **2**, the conjugation length was increased via the addition of a polarizable π-system (styryl) between the fluorenyl moiety and the benzothiazole acceptor group. The route began with the synthesis of 2-(4-(2-(9,9-bis(2-(2-ethoxyethoxy)ethyl)-2-nitro-fluoren-7-yl)vinyl)phenyl)benzothiazole (**G**) via an efficient Pd-catalyzed Heck coupling reaction between 9,9-bis(2-(2-ethoxyethoxy)ethyl)-2-iodo-7-nitrofluorene (**E**) and 2-(4-vinylphenyl)benzothiazole (**F**), fol-

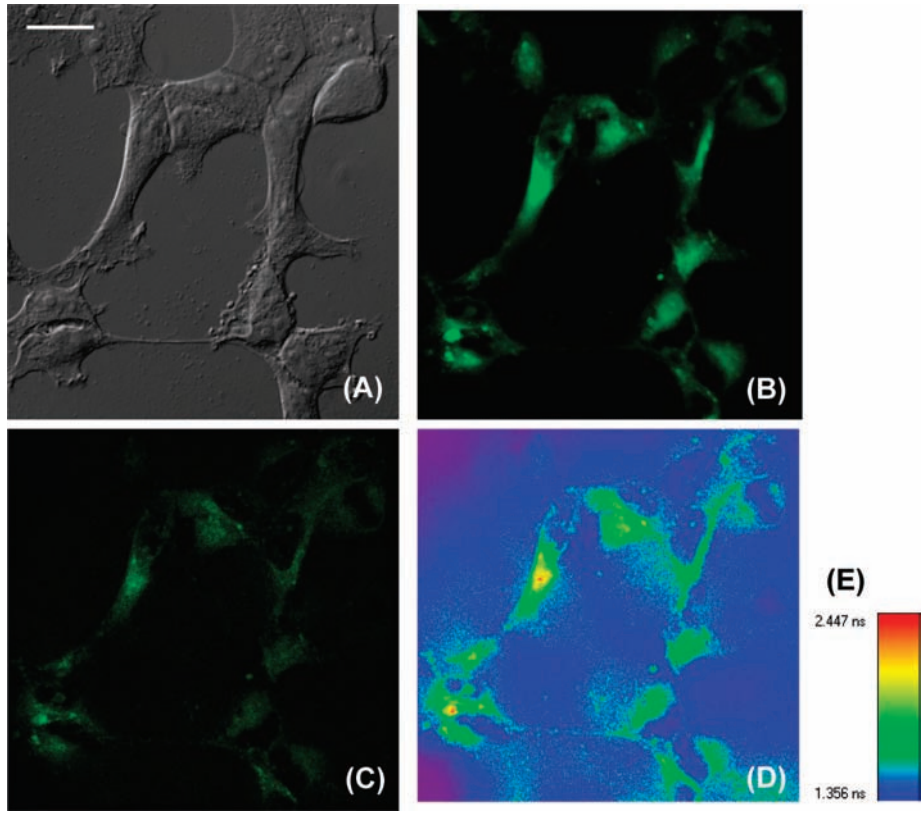

Figure 6. H1299 cells labeled with cyclic peptide bioconjugate **7**: (A) DIC, (B) 1PM, (C) 2PM, (D) 2P-FLIM. Scale bar in (A) corresponds to 20 μm. (E) lifetime scale bar for (D). Pseudo color is used for (B), (C), and (D).

lowing the synthetic pathway shown in Scheme 2. The FT-IR spectra of the isolated compounds revealed characteristically strong $-$NCS stretching at 2111 cm^{-1}, whereas no signal at ca. 3600 cm^{-1} from the $-NH_2$ group was observed. Structures of all new compounds have been confirmed by ^1H and ^{13}C NMR and C, H, N analysis, with the exception of oxidatively labile amine **H**, which was used immediately after being formed.

Conjugation with *n*-Butylamine and Reelin, and Their Optical Properties. To test the feasibility of the conjugation of fluorene isothiocyanate with biopolymers, we first used a simple reaction of *n*-butylamine with the amine-reactive probes **1** and **2** as model reactions (Scheme 3). Furthermore, preparation of the model adducts (**3** and **4**) allowed for facile single- and two-photon spectroscopic characterization, which more closely resembles the bioconjugate than that of the amine-reactive probe (conjugate precursor). The reaction of the amine-reactive dye with *n*-butylamine was fast, with completion in ~40 min at room temperature. The expected thiourea group was evident in the ^1H NMR spectrum.

To show the potency of the isothiocyanate-functionalized chromophore in two-photon-based biological applications, the protein Reelin was conjugated with amine-reactive probes **1** and **2** (Scheme 3). Reelin is a large extracellular matrix glycoprotein, important in guiding neural steam cells in the central nervous system in normal development (*26*, *27*). While much attention is focused on Reelin's role during corticogenesis, the existence of Reelin expression in several neural population in the adult brain may point to other important functions for this protein. Consequently, attaching a 2PA fluorophore to Reelin enhances the possibility of visualizing cellular events that involve Reelin by using 2PFM.

Conjugation of Reelin with **1** and **2** was performed according to standard methods (*27*) in PBS buffer by dissolving the fluorenyl isothiocyanate in DMSO immediately prior to addition into a stirred Reelin carbonate buffer solution (pH 9.5). The reaction mixture was stirred for 3 h at ambient temperature. The bioconjugate was then separated from the unbound fluorophore by filtration through a gel chromatography column, enabling the separation of the bioconjugate in PBS solution (pH 7.2). The bioconjugate was collected in several fractions that were then identified and characterized spectrophotometrically. The concentration of the reactive dye solution was varied such that a 1:10 and a 1:5 mol ratio of protein to reactive dye were prepared to establish a degree of labeling (DOL) for the probe. Hence, a 1:10 and a 1:5 mol ratio of protein to probe allowed for an estimated DOL ranging from 2.2 to 3.4.

The normalized UV$-$visible absorption and steady-state fluorescence emission spectra of amine-reactive probe **1**, dye adduct **3** in DMSO, and Reelin bioconjugate **5** in PBS (buffer pH 7.2) are shown in Figure 1. For reference, the absorption spectrum of the free Reelin protein in PBS solution is also shown. The Reelin bioconjugate exhibited absorption peaks corresponding to that of the Reelin protein in the shorter wavelength range (λ_{max} = 280 nm), as well as that of the fluorescent dye in the longer absorption range (λ_{max} = 357 and 375 nm), and exhibited an emission maximum at 455 nm. We observe that the absorption spectrum of the Reelin bioconjugate **5** showed only some broadening compared to the absorption spectrum of the unbound fluorophore **1**. The fluorescence quantum yield of the NCS-containing amine-reactive probe in DMSO was 0.02, nearly nonfluorescent, while that of the dye adduct **3** in DMSO increased significantly to 0.72, indicating that the fluorescence of the reactive tag is restored (turns on) upon conjugation. The increase in conjugation of the π-system from compound **1** to compound **2** is reflected in an increase of its fluorescence quantum yield (0.85).

RGD Conjugation and Spectroscopic Characteristics of the Cyclic Peptide Conjugate (7). Integrins are a family of heterodimeric transmembrane glycoproteins that play an important role in mediating cell$-$cell and cell$-$matrix interactions

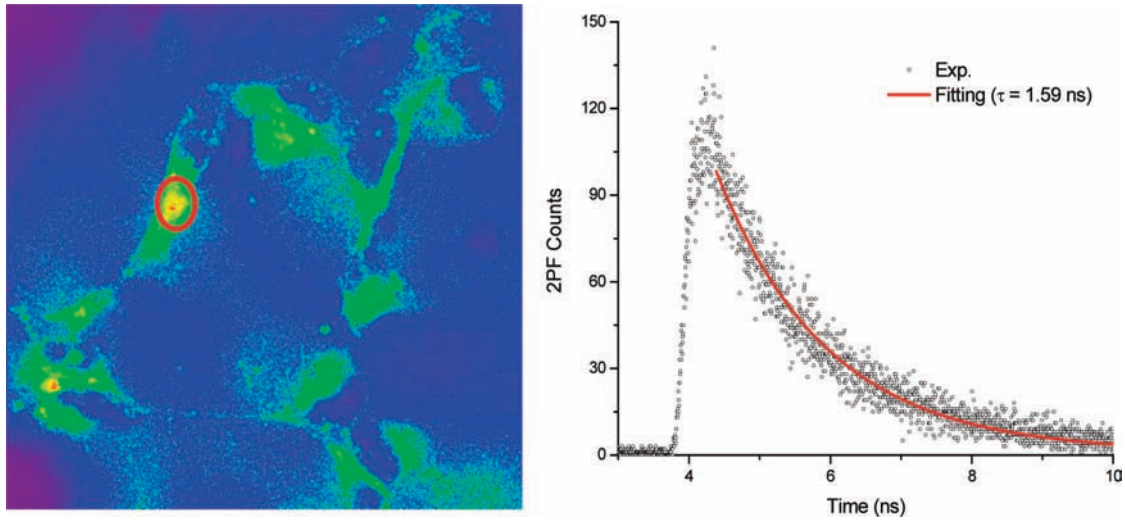

Figure 7. Fluorescence lifetime FLIM of H1299 cells labeled with cyclic peptide bioconjugate **7**. The decay curve corresponds to the circled area in the left image.

(*29, 30*). Integrins recognize short peptide sequences found in the extracellular matrix and on the cell surface. Particularly, the sequence Arg-Gly-Asp (RGD) is recognized by a number of integrins (*29*). Numerous studies have assessed the potential of $\alpha_v\beta_3$ as a target for tumor imaging agents (*30*). Along with the derivatives of the RGD-series, c(RGDfK) is often used for the delivery of therapeutics, because the lysine residue (K) makes it an ideal building block for further chemical conjugation reactions. To show the efficacy of the amine-reactive probe to be used as a two-photon fluorescence marker for optical tumor imaging, the RGDfK peptide was conjugated with amine-reactive probe **1** in DMSO at room temperature (Scheme 4). High-resolution mass spectrometric analysis confirmed the molecular structure of oligopeptide conjugate **7**.

The linear absorption and emission spectra of cyclic peptide-conjugate **7** in DMSO are shown in Figure 2. Conjugate **7** displayed absorption peak at 352 nm, while the emission maximum shifted from 400 nm for **1** to 460 nm for **7**. In addition, the fluorescence quantum yield of **7** increased to 0.9 after conjugation.

Two-Photon Absorption Properties. 2PA cross sections were obtained by the upconversion fluorescence method using a femtosecond Ti:sapphire laser as the excitation source. The 2PF measurements of the amine-reactive probe **2**, model adduct **4**, and cyclic peptide bioconjugate **7** were performed in DMSO (1.6×10^{-3} M) and exhibited a 2PA cross section of ~30 GM at 740 nm. With its fluorescence quantum yield of ~0.7−0.9, the two-photon action cross section for the model adduct is ~20 GM, reasonable enough to be used for bioimaging. These values are higher than those for common commercial dyes (0.16 GM for DAPI, 1 GM for cascade blue) used currently as blue fluorescence dyes in 2PFM (*23*).

Single- and Two-Photon Fluorescence and FLIM Cell Imaging. The utility of amine-reactive tag **1** as a 2PA biological marker was demonstrated by incubation with HeLa cells. Cells were incubated with a solution of 10^{-6} mol L^{-1} of chromophore, and after 1 and 5 h incubation times, images were taken with a modified Olympus Fluoview FV300 microscope system. Strong fluorescence was observed after 5 h of incubation, with a homogeneous coloration of the cytoplasm region. Differential interference contrast (DIC) and epifluorescence microscopic images of the stained cells are shown in Figure 3a,b. The low quantum yield of this probe (0.02) was an important characteristic, because after incubation, it appeared to have reacted spontaneously with a protein in HeLa cells, generating a bioconjugate with significantly enhanced fluorescence (Qy = 0.7), improving detection by single- and two-photon fluorescence microscopy imaging (Figure 3b). 2PFM images of the same amine-reactive fluorene **1** stained cells were collected on a modified Olympus Fluoview FV300 microscope system combined with a tunable Coherent Mira 900F Ti:sapphire laser. Two-photon induced fluorescence was observed predominantly from the cytoplasmic region, consistent with the images collected from epifluorescence imaging (Figure 3c).

DIC and epifluorescence microscope images of NT2 neuron fixed cells incubated with Reelin conjugate **6** (DOL = 3.4) were collected on a modified Olympus Fluoview FV300 microscope (Figure 4a,b). The resulting optical images clearly showed that successful uptake was achieved. 2FPM images and fluorescence lifetime imaging microscopy (FLIM) were performed on the same cells. Though select areas of the cells were chosen for lifetime analysis, the area selected was representative of the dye distribution within the cytoplasm, resulting in a homogeneous monoexponential fluorescence decay (Figure 4c and 5). The average lifetime was on the order of 1.5 ns.

The efficacy of cyclic peptide-conjugate **7** was evaluated by incubation with H1299 lung tumor line cells (Figures 6 and 7). Additionally, fluorescence was observed predominantly from the cytoplasmic region of the cells, with the nucleus clearly outlined. Two-photon induced fluorescence was observed predominantly from the cytoplasmic region, consistent with the images collected from single fluorescence images (Figure 6c). Some differences were observed in the probe lifetime. This is a subject of further investigation.

CONCLUSIONS

The data presented in this paper confirm that our strategy of introducing the −NCS functionality into the aromatic skeleton of suitably derivatized fluorenes, by means of commercial thiophosgene, proven both useful and versatile, facilitating the preparation of a variety of fluorescent fluorene isothiocyanates (amine-reactive probes). The fluorene isothiocyanate derivatives, whose synthesis and conjugation to a protein and oligopeptide are reported in this paper, represent an improvement over commercial isothiocyanate probes. Our results demonstrate the potential of these fluorene-based amine-reactive probes as fluorescent markers, owing to their good optical properties, chemical and optical stability, ease of color tunability, and reactive functionality for biomolecule conjugation. Demonstration of 2PM images of HeLa cells incubated with a well-

characterized 2PA fluorophore lends credence to our efforts to further refine fluorene-based derivatives for bioimaging applications. Performance of second-generation fluorene-based fluorophores for aqueous compatibility and integrated with additional specific biomolecule-reactive functionalities and vectors is currently being investigated.

ACKNOWLEDGMENT

The authors wish to acknowledge support from the National Institutes of Health (1 R15 EB008858-01), the U.S. Civilian Research and Development Foundation (UKB2-2923-KV-07), and the National Science Foundation (ECS-0524533). We also wish to acknowledge Dr. Zhen-Li Huang for assistance in two-photon fluorescence imaging.

LITERATURE CITED

(1) Denk, W., Strickler, J. H., and Webb, W. W. (1990) Two-photon laser scanning fluorescence microscopy. *Science 249*, 73–76.

(2) Konig, K. (2000) Multiphoton microscopy in life sciences. *J. Microsc. 200*, 83–104.

(3) Williams, R. M., Zipfel, W. R., and Webb, W. W. (2001) Multiphoton microscopy in biological research. *Curr. Opin. Chem. Biol. 5*, 603–608.

(4) Piston, D. W. (1999) Imaging living cells and tissues by two-photon excitation microscopy. *Trends Cell Biol. 9*, 66–69.

(5) Centonze, V. E., and White, J. G. (1998) Multiphoton excitation provides optical sections from deeper within scattering specimens than confocal imaging. *Biophys. J. 75*, 2015–2024.

(6) Squirrell, J. M., Wokosin, D. L., White, J. G., and Bavister, B. D. (1999) Long-term two-photon fluorescence imaging of mammalian embryos without compromising viability. *Nat. Biotechnol. 17*, 763–767.

(7) Ohulchanskyy, T. Y., Pudavar, H. E., Yarmoluk, S. M., Yashchuk, V. M., Bergey, E. J., and Prasad, P. N. (2003) A monomethine cyanine dye cyan 40 for two-photon-excited fluorescence detection of nucleic acids and their visualization in live cells. *Photochem. Photobiol. 77*, 138–145.

(8) Meltola, N. J., Wahlroos, R., and Soini, A. E. (2004) Hydrophilic labeling reagents of dipyrrylmethene-BF2 dyes for two-photon excited fluorometry: syntheses and photophysical characterization. *J. Fluoresc. 14*, 635–647.

(9) Meltola, N. J., Soini, A. E., and Hanninen, P. E. (2004) Syntheses of novel dipyrrylmethene-BF2 dyes and their performance as labels in two-photon excited fluoroimmunoassay. *J. Fluoresc. 14*, 129–138.

(10) Hayek, A., Ercelen, S., Zhang, X., Bolze, F., Nicoud, J.-F., Schaub, E., Baldeck, P. L., and Mély, Y. (2007) Conjugation of a new two-photon fluorophore to poly(ethylenimine) for gene delivery imaging. *Bioconjugate Chem. 18*, 844–851.

(11) Hayek, A., Bolze, F. E., Nicoud, J.-F., Duperray, A., Grichine, A., Baldeck, P. L., and Vial, J.-C. (2006) Two-photon water-soluble dyes and their amine-reactive derivative for two-photon bio-imaging applications. *Nonlinear Opt. Quant. Opt. 25*, 155–164.

(12) Lartia, R., Allain, C., Bordeau, G., Schmidt, F., Fiorini-Debuisschert, C., Charra, F., and Teulade-Fichou, M.-P. (2008) Synthetic strategies to derivatizable triphenylamines displaying high two-photon absorption. *J. Org. Chem. 5*, 1732–1744.

(13) Belfield, K. D., Schafer, K. J., Mourad, W., and Reinhardt, B. A. (2000) Synthesis of new two-photon absorbing fluorene derivatives via Cu-mediated Ullmann condensation. *J. Org. Chem. 65*, 4475–4481.

(14) Belfield, K. D., Morales, A. R., Kang, B.-S., Hales, J. M., Hagan, D. J., Van Stryland, E. W., Chapela, V. M., and Percino, J. (2004) Synthesis, characterization, and optical properties of new two-photon-absorbing fluorene derivatives. *Chem. Mater. 16*, 4634–4641.

(15) Belfield, K. D., Morales, A. R., Hales, J. M., Hagan, D. J., Van Stryland, E. W., Chapela, V. M., and Percino, J. (2004) Linear and two-photon photophysical properties of a series of symmetrical diphenylaminofluorenes. *Chem. Mater. 16*, 2267–2273.

(16) Hales, J. M., Hagan, D. J., Van Stryland, E. W., Schafer, K. J., Morales, A. R., Belfield, K. D., Pacher, P., Kwon, O., and Bredas, J. L. (2004) Resonant enhancement of two-photon absorption in substituted fluorene molecules. *J. Chem. Phys. 121*, 3152–3160.

(17) Morales, A. R., Belfield, K. D., Hales, J. M., Hagan, D. J., and Van Stryland, E. W. (2006) Synthesis of two-photon absorbing unsymmetrical fluorenyl-based chromophores. *Chem. Mater. 18*, 4972–4980.

(18) Schafer, K. J., Belfield, K. D., Yao, S., Frederiksen, P. K., Hales, J. M., and Kolattukudy, P. E. (2005) Fluorene-based fluorescent probes with high two-photon action cross-sections for biological multiphoton imaging applications. *J. Biomed. Opt. 10*, 051402−1.

(19) Yao, S., Schafer-Hales, K. J., and Belfield, K. D. (2007) A new water-soluble near-neutral ratiometric fluorescent pH indicator. *Org. Lett. 9*, 5645–5648.

(20) Garin, J., Melendez, E., Merchan, F. L., Merino, P., Orduna, J., and Tejere, T. (1991) Synthesis of unsymmetrical diheteroarylbenzenes: benzazole and quinazoline derivatives. *J. Heterocycl. Chem. 28*, 359–363.

(21) Lakowicz, J. R. (1999) *Principles of Fluorescence Spectroscopy*, pp 52−53, 298−300, and 648; Kluwer Academic/Plenum, New York.

(22) Fischer, M., and Georges, J. (1996) Fluorescence quantum yield of Rhodamine 6G in ethanol as a function of concentration using thermal lens spectrometry. *Chem. Phys. Lett. 260*, 115–118.

(23) Xu, C., and Webb, W. W. (1996) Measurement of two-photon excitation cross sections of molecular fluorophores with data from 690 to 1050 nm. *J. Opt. Soc. Am. B 13*, 481–491.

(24) Albota, M. A., Xu, C., and Webb, W. W. (1998) Two-photon fluorescence excitation cross section of biomolecular probes from 690 to 960 nm. *Appl. Opt. 37*, 7352–7356.

(25) Belfield, K. D., Bondar, M. V., Przhonska, O. V., and Schafer, K. J. (2002) Steady-state spectroscopic and fluorescence lifetime measurements of new two-photon absorbing fluorene derivatives. *J. Fluoresc. 12*, 449–454.

(26) Dulabon, L., Olson, E. C., Taglienti, M. G., Eisenhuth, S., McGrath, B., Walsh, C. A., Kreidberg, J. A., and Anton, E. S. (2000) Reelin binds alpha$_3$beta$_1$ integrin and inhibits neuronal migration. *Neuron 27*, 33–44.

(27) Costa, E., Davis, J., Grayson, D. R., Guidotti, A., Pappas, G. D., and Pesold, C. (2001) Dendritic spine hypoplasticity and down regulation of reelin and GABAergic tone in schizophrenia vulnerability. *Neurobiol. Dis. 8*, 723–742.

(28) Haugland, R. P. (1995) *Methods in Molecular Biology: Monoclonal Antibody Protocols* (Davis, W. C., Ed.) pp 205−215, Chapter 22, Humana Press, NJ.

(29) Ruoslahti, E., and Pierschbacher, M. D. (1987) New perspectives in cell adhesion: RGD and integrins. *Science 238*, 491–497.

(30) Cheresh, D. A. (1991) Structure, function and biological properties of integrin alpha $_\alpha$ beta $_\beta$ on human melanoma cells. *Cancer Metastasis Rev. 10*, 3–10.

BC800415T

TECHNICAL NOTES

Effects of Lysine-Containing Mercaptoacetyl-Based Chelators on the Biodistribution of ^{99m}Tc-Labeled Anti-HER2 Affibody Molecules

Thuy A. Tran,*[,†] Torun Ekblad,[‡] Anna Orlova,[†,§] Mattias Sandström,[||] Joachim Feldwisch,[§] Anders Wennborg,[§] Lars Abrahmsén,[§] Vladimir Tolmachev,[†,§,⊥] and Amelie Eriksson Karlström[‡]

Unit of Biomedical Radiation Sciences, Rudbeck Laboratory, Medical Radiation Physics, Uppsala University Hospital, and Department of Medical Sciences, Uppsala University, Uppsala, Sweden, School of Biotechnology, Division of Molecular Biotechnology, Royal Institute of Technology, Stockholm, Sweden, and Affibody AB, Bromma, Sweden. Received June 18, 2008; Revised Manuscript Received November 4, 2008

The effects of polar (mercaptoacetyl-triseryl) and negatively charged (mercaptoacetyl-triglumatyl) chelators on the biodistribution of ^{99m}Tc-labeled anti-HER2 Affibody molecules were previously investigated. With glycine, serine, and glutamate, we demonstrated that substitution with a single amino acid in the chelator can significantly influence the biodistribution properties and the excretion pathways. Here, we have taken this investigation further, by analyzing the effects of introduction of a positive amino acid residue on the in vivo properties of the ^{99m}Tc-labeled Affibody molecule. The Affibody molecules with mercaptoacetyl-seryl-lysyl-seryl (maSKS) and mercaptoacetyl-trilysyl (maKKK) extensions were produced by peptide synthesis and labeled with ^{99m}Tc in alkaline conditions. A comparative biodistribution was performed in normal mice to evaluate the excretion pathway. A shift toward renal excretion was obtained when serine was substituted with lysine in the chelating sequence. The radioactivity in the gastrointestinal tract was reduced 3-fold for the ^{99m}Tc-maSKS-$Z_{HER2:342}$ and ^{99m}Tc-maKKK-$Z_{HER2:342}$ in comparison with the ^{99m}Tc-maSSS- $Z_{HER2:342}$ conjugate 4 h post injection (p.i.). The radioactivity in the liver was elevated when a triple substitution of positively charged lysine was used. The tumor targeting properties of ^{99m}Tc-maSKS-$Z_{HER2:342}$ were further investigated in SKOV-3 xenografts. The tumor uptake of ^{99m}Tc-maSKS-$Z_{HER2:342}$ was 17 ± 7% IA/g 4 h p.i. Tumor xenografts were well-visualized by gamma scintigraphy. In conclusion, the substitution with one single lysine in the chelator results in better tumor imaging properties of the Affibody molecule $Z_{HER2:342}$ and is favorable for imaging of tumors and metastases in the abdominal area. Multiple lysine residues in the chelator are, however, undesirable due to elevated uptake both in the liver and kidneys.

INTRODUCTION

The overexpression or gene amplification of the human epidermal growth factor type 2, HER2 receptor (also known as ErbB2), is found in about 20% of all breast cancers (*1, 2*). HER2 expression also occurs in a number of other cancer types such as lung, colorectal, urothelial, ovary, and pancreas cancer (*3, 4*). The first therapeutic agent that targets HER2-positive breast cancer, approved for clinical use, was the humanized antibody trastuzumab (Herceptin, Genentech Inc.). Pertuzumab (Omnitarg, Genentech) is currently in phase III studies for treatment of HER2-positive breast cancer. Another type of targeting agent that is entering the clinics is the tyrosine kinase inhibitor, lapatinib (Tykerb, GlaxoSmithKline), that blocks several downstream signaling pathways of EGFR and HER2 receptors, involved in cell proliferation, invasion, and apoptosis (*5*).

Determination of HER2 status in breast cancer diagnostics is critically important for therapeutic decision making. The accuracy, precision, and reproducibility of a diagnostic method are highly essential in order to identify patients who would most likely benefit from anti-HER2 treatment. At present, immunohistochemical staining (IHC) and fluorescence in situ hybridization (FISH) of biopsy samples are clinically used for evaluating HER2 status (*6*). However, some limitations (*6, 7*) associated with these tests might cause false-negative results. Recently, the American Society of Clinical Oncology and the College of American Pathologist expert panel (*8*) reported that approximately 20% of current HER2 testing may be inaccurate. As an alternative, radionuclide imaging may be applied to visualize HER2 expression in both whole primary tumors and metastatic lesions, including sites where biopsies may be difficult to obtain.

HER2 has no known natural ligands, and HER2-targeted diagnostic imaging has been investigated using panels of radiolabeled agents, including the intact antibodies trastuzumab and pertuzumab, Fab and $F(ab')_2$ fragment of trastuzumab, minibody and scFv-Fc of trastuzumab, and ICR 12 (an anti-HER2 monoclonal antibody) (*9*). Recently, a new class of targeting agents, Affibody molecules, has been extensively studied for radionuclide therapy and imaging (*10*−*12*). Affibody

* Corresponding author. Thuy Tran, Unit of Biomedical Radiation Sciences, Department of Oncology, Radiology and Clinical Immunology, Rudbeck Laboratory, Uppsala University, S-751 85, Uppsala, Sweden. Phone: +46 18 471 3829. Fax: + 46 18 471 34 32. Email: thuy.tran@bms.uu.se.

† Rudbeck Laboratory, Uppsala University.

‡ Royal Institute of Technology.

§ Affibody AB.

|| Uppsala University Hospital, Uppsala University.

⊥ Department of Medical Sciences, Uppsala University.

10.1021/bc800244b CCC: $40.75 © 2008 American Chemical Society
Published on Web 11/26/2008

Table 1. Biophysical Characterization Data

protein	synthetic yield (%)	theoretical MW (Da)	experimental MW (Da)	K_D (pM)	T_m (°C)
$Z_{HER2:342}$	21	6718	6718	80	64
maSSS-$Z_{HER2:342}$	14	7054	7053	400	65
maKKK-$Z_{HER2:342}$	12	7177	7177	270	68
maSKS-$Z_{HER2:342}$	14	7095	7094	310	65

molecules are small (7 kDa) and cysteine-free three-helix bundle proteins, based on the 58 amino acid B-domain of staphylococcal protein A. By randomization of 13 solvent-exposed residues, a library of 3×10^9 variants has been generated and used for selection of affinity ligands to a variety of proteins (*13*).

The 7 kDa Affibody molecules are much smaller than antibodies and well-suited for in vivo imaging purposes. For HER2 targeting, the Affibody molecule $Z_{HER2:342}$ with an affinity of 22 pM (*14*) has been developed and labeled with a number of radioisotopes, ^{125}I (*14*), ^{111}In (*15, 16*), ^{90}Y (*17*), ^{68}Ga, ^{177}Lu (*10*), and ^{18}F (*18, 19*). All conjugates demonstrated good targeting of HER2-expressing SKOV-3 xenografts in mice (*14, 16*). The radionuclide ^{99m}Tc with a photon energy of 140 keV and a half-life of 6 h has also been investigated as a label for $Z_{HER2:342}$ because it is a readily available and cost-effective radionuclide for diagnostics. Earlier, the synthetic Affibody molecule $Z_{HER2:342}$ with the chelator maGGG (mercaptoacetyltriglycyl) site-specifically introduced at the N-terminus has been labeled with technetium-99m (*20*). Even though imaging of HER2 expression in tumors in mice was feasible with ^{99m}Tc-maGGG-$Z_{HER2:342}$, a high hepatobiliary clearance leading to high accumulation in the intestine was seen in the biodistribution studies. The hepatobiliary excretion can be reduced by reducing the lipophilicity of a peptide tracer (*21, 22*). Substitution of the chelator sequences with more hydrophilic amino acids in Affibody molecules, such as maSSS (mercaptoacetyl-triseryl) (*20*) or maEEE (mercaptoacetyl-triglutamyl) (*23*), results in suppressed hepatobiliary excretion, enabling abdominal detection. The use of negatively charged side chains, mercaptoacetyl-triglutamyl (maEEE), has proven to be efficient in reducing the hepatobiliary excretion (*23*). The combination of two serine and one glutamate in the chelator, as in mercaptoacetyl-glutamyl-seryl-glutamyl (maESE), shows favorable properties for imaging (*24*). In this study, we aimed to investigate the influence of the positively charged hydrophilic amino acid lysine on the biodistribution properties. For this purpose, the two novel Affibody molecules maSKS-$Z_{HER2:342}$ (mercaptoacetyl-seryl-lysyl-seryl) and maKKK-$Z_{HER2:342}$ (mercaptoacetyl-trilysyl) have been synthesized and labeled with ^{99m}Tc. The chelating sequences maSKS and maKKK were incorporated in the N-terminus during the peptide synthesis. These two conjugates were compared with each other and with maSSS-$Z_{HER2:342}$ (mercaptoacetyl-triseryl) with respect to the HER2-binding, cellular processing, and biodistribution properties. The labeled conjugates were not analyzed for their isomeric identities. They were used as a racemic mixture in all experiments.

EXPERIMENTAL PROCEDURES

Peptide Synthesis. The $Z_{HER2:342}$ sequence was assembled using Fmoc/*t*Bu solid-phase peptide synthesis on a Fmoc-amide resin with a substitution of 0.67 mmol/g (Applied Biosystems) as previously described (*20*). 1-Hydroxybenzotriazole (HOBt) and 2-(1*H*-benzotriazol-1-yl)-1,1,3,3-tetramethyluronium hexafluorophosphate (HBTU) (Advanced ChemTech, Louisville, KY) were used to activate equal molar equivalents of Fmoc-protected amino acid.

After synthesis of the full-length Affibody, the Tc-chelating peptide sequences Ser-Lys-Ser (SKS) and Lys-Lys-Lys (KKK) were introduced to the N-terminus of the $Z_{HER2:342}$-sequence by coupling the corresponding protected amino acids (Fmoc-Ser(tBu)-OH and/or Fmoc-Lys(Boc)-OH) one residue at the time in a stepwise manner. In the manual coupling reactions, 5 mol equiv (Eq) of Fmoc-protected amino acid were coupled with 5 Eq HBTU, 5 Eq HOBt, and 10 Eq *N*-ethyldiisopropylamine (DIEA, from Lancaster Synthesis, Morecambe, England). Ninhydrin tests were performed to evaluate the efficiency of the coupling reactions. Fmoc-deprotection was achieved by 20 min incubation in 20% piperidine-*N*-methylpyrrolidone (NMP, from VWR). Finally, the mercaptoacetyl moiety of the chelator was introduced by coupling *S*-trityl-protected mercaptoacetic acid (AnaSpec Inc., San Jose, CA) to the N-terminal amino group of the resin-bound peptide. The protecting groups were then deprotected and the full-length peptides with appended maSKS and maKKK chelators were released from the solid support by incubation in trifluoroacetic acid (TFA, Merck International)/H_2O/ethanedithiol (EDT, Aldrich chemical company Inc.)/triisopropylsilane (TIS, Merck International) (94:2.5:2.5:1) for 2 h. The proteins were extracted in *tert*-butyl methyl ether (Merck International)/H_2O (50:50).

Analytical RP-HPLC was run on the crude synthetic product using a 4.5×150 mm polystyrene/divinylbenzene matrix column with 5 μm particles (Amersham Biosciences, Sweden) and a 20 min elution gradient 20−60% B (B: 0.1% TFA-acetonitrile (CH_3CN; Merck International), A: 0.1% TFA-H_2O). The molecular weights of the modified Affibody molecules were confirmed by mass spectrometry and the proteins were purified on the same column in a 20 min gradient 25−45% B.

Biosensor Analysis. A Biacore 2000 instrument (Biacore AB, Uppsala, Sweden) was used for real-time biospecific interaction analysis. The extracellular domain of HER2 (Fox Chase Cancer Center, Philadelphia, USA) and human serum albumin, HSA (KabiVitrum, Sweden) were immobilized on a CM5 sensor chip by EDC/NHS coupling. HER2 and HSA were diluted to 20 μg/mL in 20 mM NaOAc pH 4.5 and the immobilization levels reached 500 and 900 response units (RU), respectively. The different Affibody molecules were diluted to concentrations varying from 0.5 to 10 nM in HBS (10 mM HEPES, 150 mM NaCl, 3.4 mM EDTA, 0.005% Surfactant P20, pH 7.4), and the binding kinetics were studied at a flow rate of 50 μL/min in HBS as running buffer in a 5 min association phase and a 10 min dissociation phase. After each injection of analyte, the sensor surface was regenerated by injection with 20 mM HCl in HBS. The specific response was obtained by subtracting the signal from the control surface (HSA) from the signal from binding to the HER2 surface. Mass transfer limitations were avoided by keeping a high flow rate and a low immobilization level of HER2 protein on the sensor surface.

Melting Point Analysis. Variable temperature measurements were performed using a JASCO J-810 spectropolarimeter (JASCO, Tokyo, Japan). Samples were diluted to a concentration of 50 μM in PBS pH 7.4. A cell with an optical path length of 1 mm was used. CD spectra from 250 to 195 nm were obtained at 20 °C before and after melting tests. For melting point measurements, the absorbance was measured at 221 nm and the temperature was increased by 5 °C/min from 20 to 90 °C.

^{99m}Tc-Labeling. For labeling, 20 μL of maSKS-$Z_{HER2:342}$ or maKKK-$Z_{HER2:342}$ (1 mg/mL in deionized, degassed water) was mixed with 20 μL 0.15 M NaOH to obtain a final pH of about 11. Stannous chloride (10 μL, 1 mg of $SnCl_2 \cdot 2H_2O$ in 1 mL 0.01 M HCl) was added to the mixture, followed by 100−200 μL (about 50 MBq) of freshly eluted pertechnetate solution. The mixture was slightly vortexed and incubated at room temperature for 60 min. After labeling, ^{99m}Tc-maSKS-$Z_{HER2:342}$ and ^{99m}Tc-maKKK-$Z_{HER2:342}$ were isolated from unreacted technetium and other low-molecular-weight components using size-exclusion chromatography on disposable NAP-5 columns

Table 2. Characterization Data of ^{99m}Tc-Labeled Conjugates

conjugate	^{99m}Tc-maSSS-$Z_{HER2:342}$	^{99m}Tc-maKKK-$Z_{HER2:342}$	^{99m}Tc-maSKS-$Z_{HER2:342}$
labeling yield, %	97 ± 1	95 ± 1	98 ± 2
isolated yield, %	82 ± 5	79 ± 6	80 ± 3
radiochemical purity, %	99 ± 1	99 ± 1	99.7 ± 0.3
antigen binding capacity, %	55 ± 15	66.4 ± 0.6	64 ± 2
stability during cysteine challenge, %	78.6 ± 0.6	91 ± 4	94.7 ± 0.9

(Amersham Pharmacia Biotech AB, Uppsala, Sweden) pre-equilibrated with PBS. The purity was assessed by analysis with ITLC strips (Pall Life Sciences, Ann Arbor, USA), eluted in PBS. Validation experiments demonstrated that, in this system, pertechnetate and cysteine complexes of ^{99m}Tc migrate with the eluent front, while labeled Affibody molecules under these conditions remain at the origin. The labeling yield and the stability were determined using ITLC strips, eluted with PBS and analyzed with a Cyclone Storage Phosphor System (http://www.perkinelmer.com/) (Perkin-Elmer, Wellesley, MA). To determine the presence of reduced hydrolyzed technetium, ITLC was eluted with pyridine/acetic acid/water (5:3:1.5). In this eluent, the technetium colloids remained at the origin, while the radiolabeled Affibody molecules, pertechnetate, and other complexes of ^{99m}Tc migrated with the solvent front. To validate the radiochemical purity obtained with ITLC, an analysis was performed on an ÄKTAprime LC system (GE Healthcare, Uppsala Sweden) with the UV detector set to 280 nm. The analysis was run on a prepacked Superdex Peptide 10/300 GL column (GE Healthcare, Uppsala Sweden), with a flow rate of 0.5 mL/min using a 50 mM phosphate buffer with 150 mM NaCl (pH 7.0) as running buffer. Fractions were collected and radioactivity was measured on a gamma counter.

Stability Studies. *Cysteine Challenge.* The stability of labeled Affibody conjugates was tested in 300 molar excess of cysteine. A fresh solution of cysteine was prepared (1 mg/mL in PBS, pH 7.0). The radiolabeled conjugates were added to a final molar ratio of cysteine to peptide of 300:1. The test tubes were incubated for 2 h at 37 °C and the radiochemical purity was analyzed using ITLC, eluted in PBS.

Plasma Stability Test. Serum samples were prepared as described in ref *20*. Shortly, a serum sample (240 μL) was mixed with freshly labeled $Z_{HER2:342}$ (10 μL) to obtain an Affibody molecule concentration similar to the concentration in blood at the moment of injection. The sample was incubated for 1 h at 37 °C. After incubation, the sample was analyzed on NuPAGE 4−12% Bis-Tris Gel (Invitrogen) in MES buffer (200 V constant). A sample of pertechnetate, not treated in blood serum, was used as reference and run in parallel with the test sample on the same gel. After electrophoresis, the radioactivity distribution along the gel was evaluated using a Cyclone Storage Phosphor System.

In Vitro Cell Studies. The HER2-expressing ovarian carcinoma cell line SKOV-3, displaying approximately 1.2×10^6 HER2 receptors per cell (*25*), was used in this study. The cell line was cultured in McCoy's medium (Flow Irvine, UK). The medium was supplemented with 10% fetal calf serum (Sigma, USA), 2 mM L-glutamine, and PEST (penicillin 100 IU/mL and 100 μg/mL streptomycin), all from Biokrom Kg, Germany. The cells were cultured at 37 °C in a humidified incubator with 5% CO_2 and trypsinized using trypsin−EDTA solution (0.25% trypsin, 0.02% EDTA) from Biokrom Kg, Germany. SKOV-3 cells were cultivated on Petri dishes with a diameter of 3.5 cm to a cell density of $(2-5) \times 10^5$ cells per dish.

Binding Specificity Study. To test the binding specificity of the labeled conjugates, one set of SKOV-3 cells was presaturated with a 100-fold excess of nonlabeled Affibody molecules 10 min before the labeled conjugate was added and measured according to Engfeldt et al. (*26*).

Internalization and Retention Study. The internalization rates of the labeled conjugates on SKOV-3 cells were determined as described in Ahlgren et al. (*27*). Shortly, cultured SKOV-3 cells were incubated for 3 h at 4 °C using a 5:1 molar ratio of ^{99m}Tc-labeled conjugates to HER2 receptors. All procedures were performed on ice. Thereafter, the incubation medium was discarded, and the cells were washed three times using ice-cold serum-free medium. After addition of 1 mL complete medium, the cells were incubated further at 37 °C. At designated time points, up to 24 h, one group of three dishes was analyzed for cell-associated radioactivity. Medium was collected; cells were washed three times with ice-cold serum-free medium (these two steps were omitted for the time point 0 h) and treated with 0.5 mL of 4 M urea solution in 0.2 M glycine buffer, pH 2.5, for 5 min on ice. The acid fraction was collected, and cells were washed with additional 0.5 mL acid solution. The radioactivity in the acid wash fraction was considered membrane-bound radioactivity. After addition of 0.5 mL of 1 M NaOH, the cells were incubated at 37 °C for at 30 min, and the basic solution was collected. The cell dishes were washed with additional 0.5 mL of basic solution. The radioactivity in the alkaline fractions was considered internalized radioactivity. The radioactivity content of the samples was measured as mentioned above.

Antigen Binding Capacity Study. Assessment of antigen binding capacity of ^{99m}Tc-labeled conjugates was performed using SKOV-3 cells according to Engfeldt et al. (*26*).

In Vivo Animal Studies. The animal study was approved by the Local Ethics Committee for Animal Research. In comparative biodistribution studies, non-tumor-bearing NMRI mice were used. In tumor targeting and imaging experiments with ^{99m}Tc-maSKS-$Z_{HER2:342}$, female BALB/c *nu/nu* nude mice were used. The animals were acclimatized for one week at the Rudbeck laboratory animal facility before tumor implantation. The tumors were grafted by subcutaneous injection of $\sim 10^7$ SKOV-3 cells in the right hind leg. Xenografts were allowed to develop during 6 weeks. In all biodistribution studies, the mice were euthanized at predetermined time points with an intraperitoneal injection of Ketalar−Rompun solution (20 μL of solution per gram of body weight: Ketalar [ketamine], 10 mg/mL; Rompun [xylazin], 1 mg/mL). The mice were heart-punctured with a 1 mL syringe rinsed with diluted heparin (5000 IE/mL, Leo Pharma, Copenhagen, Denmark). Blood and organ samples were taken and weighed, and their radioactivity was measured using an automatic gamma counter. The organ uptake values were calculated as percent injected activity per gram tissue (% IA/g).

Biodistribution in NMRI Mice. Twelve mice were randomly divided into 3 groups with 4 animals each. The three groups were subcutaneously injected with ^{99m}Tc-maSSS-$Z_{HER2:342}$, ^{99m}Tc-maSKS-$Z_{HER2:342}$, and ^{99m}Tc-maKKK-$Z_{HER2:342}$, respectively (1 μg Affibody ligand, ∼100 kBq in 100 μL of PBS). The mice were euthanized at 4 h p.i.; organ samples were collected and measured. In previous studies, we have validated that the biodistribution of radiolabeled Affibody molecules 4 h p.i. is the same for both i.v. and s.c. injection and independent of the label (*28*, *29*). Subcutaneous injections were mainly chosen since they are more reproducible (smaller errors) when injecting into a large number of animals (*24*).

Biodistribution in Mice with SKOV-3 Xenografts. The tumor targeting properties of ^{99m}Tc-maSKS-$Z_{HER2:342}$, which demonstrated the best biodistribution properties in normal mice, were evaluated in female BALB/c *nu/nu* nude mice bearing SKOV-3 xenografts. The mice were intravenously injected with ^{99m}Tc-

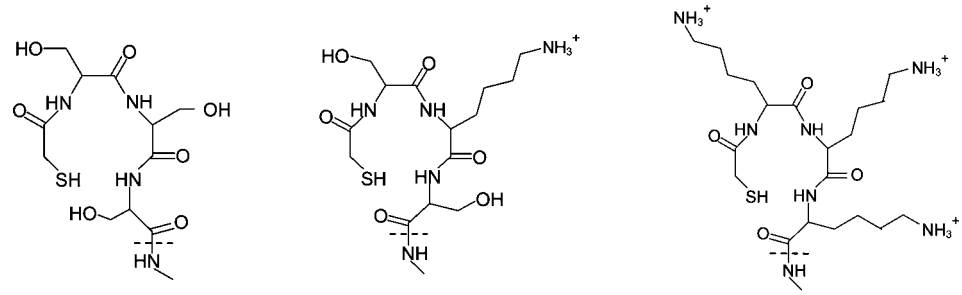

Figure 1. Chelator structures. Dashed lines indicate the border to the Affibody molecule $Z_{HER2:342}$.

maSKS-$Z_{HER2:342}$ (1 μg Affibody ligand, ~ 100 kBq in 100 μL of PBS). After 0.5, 1, 4, 8, and 24 h p.i., the mice were euthanized as described earlier. In the binding specificity study, one group of mice was preinjected with a 1000-fold molar excess of nonlabeled Affibody molecules prior to injection of ^{99m}Tc-maSKS-$Z_{HER2:342}$. At 4 h p.i., the mice were euthanized and organ samples were collected and measured.

Gamma Camera Imaging with ^{99m}Tc-maSKS-$Z_{HER2:342}$. Two mice were intravenously injected through the tail vein with 3 MBq of ^{99m}Tc-maSKS-$Z_{HER2:342}$ (10 μg in 100 μL of PBS) and imaged at 4 h p.i. Imaging was performed using a Siemens e.Cam gamma camera equipped with a LEHR collimator at the Department of Nuclear Medicine of Uppsala University Hospital. Static images were collected during 10 min and evaluation of the images was performed with *Osiris* v 4.19 software (Digital Imaging Unit, University Hospital of Geneva, Switzerland).

Data Treatment. In vitro and in vivo data were processed with Microsoft *Excel 2003* (Microsoft, Redmond, WA) and all graphs were drawn with GraphPad *Prism* v 4 (GraphPad Software, San Diego; CA). Statistical analysis was performed using Student's *t* test.

RESULTS

Peptide Synthesis and Characterization. The Fmoc solid-phase synthesis of $Z_{HER2:342}$ resulted in a yield of 21% of the full-length peptide, as determined by analytical RP-HPLC. The ^{99m}Tc-chelating sequences maSKS or maKKK were introduced N-terminally by manual synthesis, resulting in total synthetic yields of 14% and 12%, respectively (Table 1). The HPLC retention times were 13.9, 14.3, and 14.4 min for maKKK-$Z_{HER2:342}$, maSKS-$Z_{HER2:342}$, and maSSS-$Z_{HER2:342}$, respectively. Following purification by RP-HPLC, the purity was higher than 90%. Data of maSSS-$Z_{HER2:342}$ (*20*) are included for comparison. The molecular weights of the different conjugates were determined by mass spectrometry and correlated well with the theoretically calculated masses, as shown in Table 1.

The binding kinetics of the different Tc-chelating peptides were compared in a biospecific interaction analysis on a Biacore 2000 instrument. As indicated in Table 1, both conjugates showed similar subnanomolar affinities to surface-immobilized HER2 receptors: the dissociation constants (K_D) were 310 pM for maSKS-$Z_{HER2:342}$ and 270 pM for maKKK-$Z_{HER2:342}$ (Figure 2A).

The melting points were 64−68 °C for the conjugates, which are close to the previously reported values of $Z_{HER2:342}$ (see Table 1). The CD spectra of the proteins showed that the structures of the Affibody molecules were similar and refolded after heating to 90 °C (Figure 2B,C).

^{99m}Tc-Labeling and Stability Studies. The radiolabeling yields were above 90% for both ^{99m}Tc-maSKS-$Z_{HER2:342}$ and ^{99m}Tc-maKKK-$Z_{HER2:342}$, as shown in Table 2. The isolated yield after size-exclusion chromatography using NAP-5 columns was about 80%, and the radiochemical purity of the purified products

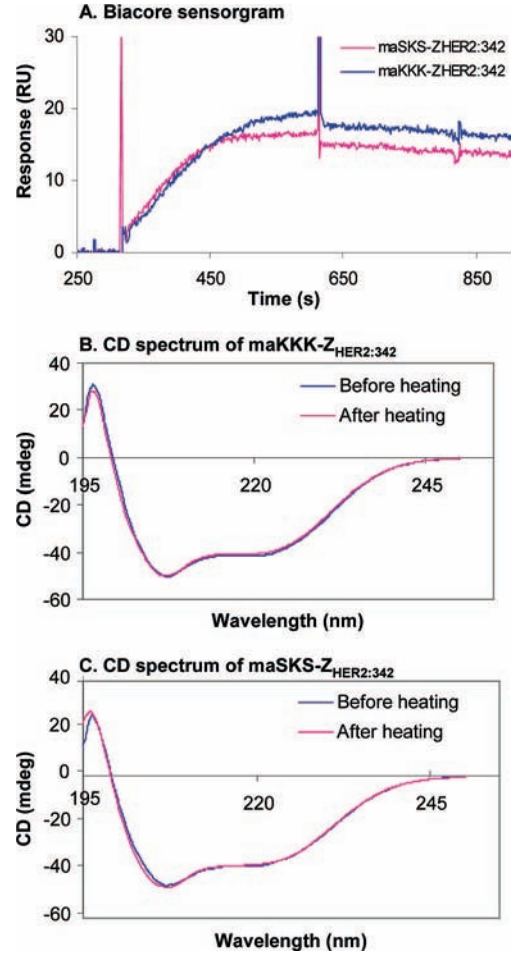

Figure 2. Illustrative Biacore sensorgram of maKKK-$Z_{HER2:342}$ and maSKS-$Z_{HER2:342}$, both at 5 nM (A) and CD spectra before and after heating to 90 °C of maKKK-$Z_{HER2:342}$ (B) and maSKS-$Z_{HER2:342}$ (C), respectively.

was typically over 97% for both lysine-containing conjugates. Size-exclusion chromatography confirmed that the retention volume of radiolabeled conjugates corresponded to the retention volume of monomeric form of Affibody molecules (see Figure 3). A typical specific activity of 18 GBq/μmol was obtained for both ^{99m}Tc-labeled Affibody molecules. The presence of reduced hydrolyzed technetium was less than 2% in all experiments.

As presented in Table 2, the stability of the labeled conjugates was evaluated in a cysteine challenge test and the results showed high stability of the labeled conjugates, with over 90% radioactivity still attached to the conjugates. After incubation in mouse serum, the stability of ^{99m}Tc-maSKS-$Z_{HER2:342}$ and ^{99m}Tc-maKKK-$Z_{HER2:342}$ was good. No release of free pertech-

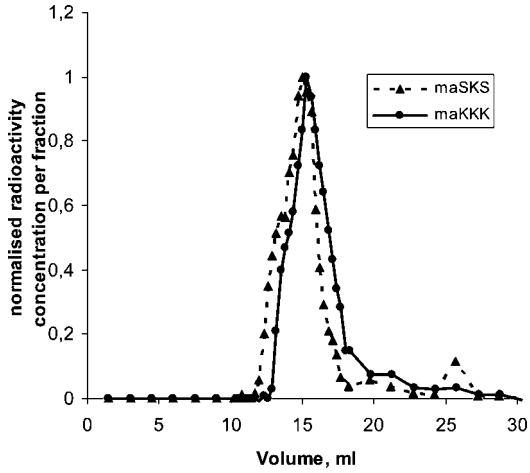

Figure 3. Size-exclusion chromatography analysis of radiolabeled conjugates was performed using a Superdex Peptide 10/300 GL column as described in the Experimental Procedures section. Radioactivity of the fractions was measured off-line.

netate could be detected (data not shown). However, there is a peak, corresponding to a higher molecular weight, of approximately 19% of the radioactivity. This could indicate some binding of the labeled conjugate to blood proteins.

In Vitro Cell Studies. *Binding Specificity and Antigen Binding Capacity.* The in vitro binding specificity of ^{99m}Tc-maKKK-$Z_{HER2:342}$ and ^{99m}Tc-maSKS-$Z_{HER2:342}$ to SKOV-3 cells showed specific binding to HER2 receptors, since it could be blocked with receptor saturation by 100-fold excess of unlabeled $Z_{HER2:342}$. The cell-binding radioactivity was reduced from 33 ± 2% to 5.1 ± 0.3% ($p < 0.0005$) between the nonsaturated and saturated groups for ^{99m}Tc-maSKS-$Z_{HER2:342}$ and from 35 ± 5% to 5.4 ± 0.04% ($p < 0.0005$) for ^{99m}Tc-maKKK-$Z_{HER2:342}$. The antigen binding capacity was estimated to be around 60% for the ^{99m}Tc-labeled $Z_{HER2:342}$, indicating that the labeling procedure had a minor effect on the conjugates.

Cellular Retention and Internalization. The cellular processing of ^{99m}Tc-labeled $Z_{HER2:342}$ Affibody molecules is illustrated in Figure 4. The conjugates displayed a high retention of radioactivity on SKOV-3 cells, with a slow decrease over time. After 24 h, the cell-associated radioactivity retained by the SKOV-3 cells was about 60−70%. The internalization of the labeled conjugates was slow over time, with about 12% of radioactivity internalized 4 h after interrupted incubation. Both conjugates showed a similar internalization pattern within the error of the experiment.

In Vivo Animal Studies.

Biodistribution in Normal Mice. The comparative biodistribution in NMRI mice (Figure 5) showed that, by replacing one serine with one lysine in the chelator (maSSS vs maSKS), the kidney uptake was doubled from 18 ± 4% to 33 ± 2% IA/g ($p = 0.001$), while the accumulation in intestines with content was significantly reduced from 11 ± 2% to 4.3 ± 0.5% IA/whole sample ($p = 0.0006$). Substitution of all serines with lysines (maSSS to maKKK) significantly increased the kidney uptake 7-fold ($p = 5.7 \times 10^{-7}$) while the intestine uptake was decreased 2-fold ($p = 0.0004$), reaching the same level as for maSKS. On the other hand, the radioactivity of ^{99m}Tc-maKKK-$Z_{HER2:342}$ was found to be significantly higher in other organs such as blood, spleen, stomach and salivary glands, thyroid, muscle, and liver ($p < 0.05$). The liver uptake was estimated to be about 5 times higher for ^{99m}Tc-maKKK-$Z_{HER2:342}$ than for ^{99m}Tc-maSKS-$Z_{HER2:342}$ (6.8 ± 2.5% vs 0.49 ± 0.28% IA/g, $p = 0.002$).

Biodistribution in Mice Bearing SKOV-3 Xenografts. Data from the comparative biodistribution suggested that ^{99m}Tc-maSKS-$Z_{HER2:342}$ was the most suitable conjugate of the two new tested variants, with low radioactivity accumulated in the intestines and an intermediate level of kidney uptake. Thus, this conjugate was further evaluated in HER2-expressing SKOV-3 xenografts. The distribution of ^{99m}Tc-maSKS-$Z_{HER2:342}$ was examined at 0.5, 1, 2, 4, 8, and 24 h p.i. as presented in Figure 6. The tumor accumulation was high, reaching 17 ± 8% IA/g at 4 h p.i., and the radioactivity was cleared rapidly from the blood circulation, with 0.35 ± 0.13% IA/g at 4 h after administration. The tumor-to-blood ratio was 47 at this time point. Other organs showed low uptake, and the clearance from these organs was rapid over time. A blocking experiment demonstrates that ^{99m}Tc-maSKS-$Z_{HER2:342}$ bound specifically to HER2 receptors in SKOV-3 xenografts (Table 4). The tumor uptake in the blocked group with excess of nonlabeled Affibody molecules was significantly lower ($p < 0.001$). Much smaller but significant ($p < 0.05$) reduction of uptake was found also in blood, lung, liver, and spleen and in intestines of animals in the blocking group. A possible explanation is that some part of radiolabeled ^{99m}Tc-maSKS-$Z_{HER2:342}$ should dissociate continuously from the receptors in the xenografts, drain from the tumors, and re-enter the blood circulation. Such a depot is much smaller when HER2 receptors are blocked by a nonradioactive Affibody molecule.

Gamma Camera Imaging with ^{99m}Tc-maSKS-$Z_{HER2:342}$. The gamma camera image of SKOV-3 xenografts 4 h after administration of ^{99m}Tc-maSKS-$Z_{HER2:342}$ is shown in Figure 7. The tumors located on the right hind legs accumulated a large amount of radioactivity and were clearly visualized. A high accumulation of radioactivity was also seen in the kidneys, while no or very little uptake was seen in other organs. The ROI

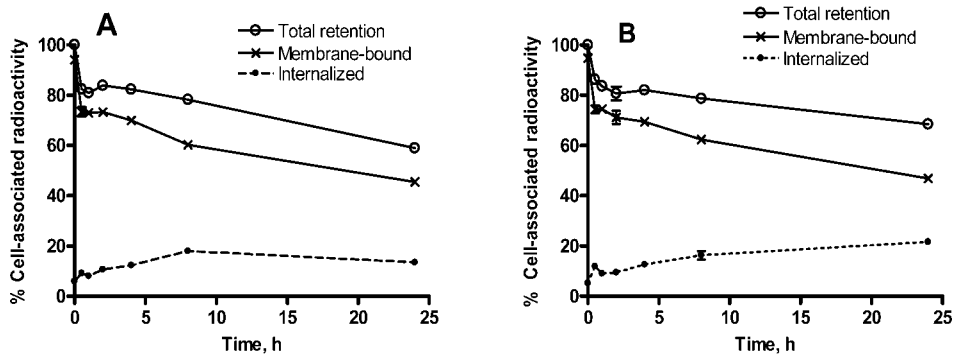

Figure 4. Cellular retention and internalization after interrupted incubation on HER2-expressing SKOV-3 cells of (A) ^{99m}Tc-maSKS-$Z_{HER2:342}$ and (B) ^{99m}Tc-maKKK-$Z_{HER2:342}$. The graphs show mean values from three cell dishes ± SD.

Table 3. Comparison of Biodistribution Data of ^{99m}Tc-Labeled $Z_{HER2:342}$ Containing Different Chelators in Mice 4 h p.i.

	^{99m}Tc-maSSS-$Z_{HER2:342}$	^{99m}Tc-maSKS-$Z_{HER2:342}$	^{99m}Tc-maKKK-$Z_{HER2:342}$	^{99m}Tc-maESE-$Z_{HER2:342}$	^{99m}Tc-maEEE-$Z_{HER2:342}$
blood	0.14 ± 0.07	0.15 ± 0.02	0.23 ± 0.01	0.12 ± 0.02	0.09 ± 0.02
kidneys	18 ± 4	33 ± 2	127 ± 9	22 ± 3	95 ± 23
liver	0.5 ± 0.3	0.6 ± 0.2	7 ± 2	0.19 ± 0.01	0.21 ± 0.02
intestine[a]	11 ± 2	4.3 ± 0.5	4.0 ± 0.3	1.7 ± 0.4	3 ± 2
T/B ratio	76 ± 8	47 ± 23	ND[b]	58 ± 6	38 ± 7

[a] Uptake is presented as % IA/g organ, except for the intestine, where the uptake is for the whole sample. Data of ^{99m}Tc-maSSS-$Z_{HER2:342}$, ^{99m}Tc-maESE-$Z_{HER2:342}$, and ^{99m}Tc-maEEE-$Z_{HER2:342}$ are taken from *refs 20, 23, 24*, respectively. The tumor-to-blood ratios (T/B ratio) were obtained in SKOV-3 xenografts 4 h pi. [b] ND: not determined in xenograft model.

Table 4. In Vivo Binding Specificity of ^{99m}Tc-maSKS-$Z_{HER2:342}$ SKOV-3 Xenografts, 4 h p.i.[a]

	blocked	nonblocked
blood	0.16 ± 0.02	0.25 ± 0.05**
tumor	2.5 ± 0.64	14 ± 3.1*
lung	0.24 ± 0.04	0.41 ± 0.08**
liver	0.44 ± 0.04	1.1 ± 0.4**
spleen	0.17 ± 0.03	0.26 ± 0.04**
stomach	0.5 ± 0.2	0.56 ± 0.03
kidney	45 ± 3	47 ± 5
salivary glands	0.6 ± 0.03	0.8 ± 0.3

[a] The blocked group ($n = 3$) was intravenously pre-injected with an excess amount of nonlabeled $Z_{HER2:342}$. Results are presented as percentage of injected activity per gram of tissue (% IA/g). * Statistical significance according to Student's t test gave $p < 0.001$. ** Statistical significance according to Student's t test gave $p < 0.05$.

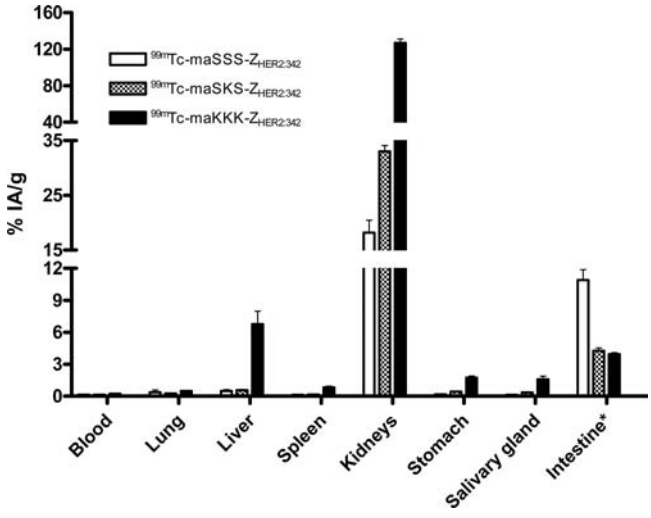

Figure 5. Comparative biodistribution of $Z_{HER2:342}$ labeled with ^{99m}Tc using maSSS, maSK,S and maKKK chelators in NMRI normal mice, 4 h p.i. Data are presented as an average % IA/g of four animals ± SD. *Data for intestine are presented as % IA per whole sample. Historical data of ^{99m}Tc-maSSS-$Z_{HER2:342}$ was taken from ref *20*.

analysis showed that the ratio of the tumor to the contralateral thigh was (average ± standard deviation) 43 ± 2.

DISCUSSION

In this study, the HER2-targeting Affibody molecule, $Z_{HER2:342}$, with the chelators mercaptoacetyl-seryl-lysyl-seryl (maSKS) and mercaptoacetyl-trilysyl (maKKK) attached to the N-terminus were synthesized in order to investigate how the incorporation of the hydrophilic positively charged amino acid lysine in the chelator sequence would affect the biodistribution properties in mice for imaging of HER2 expression in vivo. These two conjugates, maSKS-$Z_{HER2:342}$ and maKKK-$Z_{HER2:342}$, were labeled with technetium-99m and were compared with a formerly studied conjugate, ^{99m}Tc-maSSS-$Z_{HER2:342}$. The radioisotope ^{99m}Tc was chosen because of its advantages of low cost and availability, a reasonably long half-life ($T_{1/2} = 6$ h), and suitable photon energy for SPECT cameras.

The ^{99m}Tc-labeling of maSKS-$Z_{HER2:342}$ and maKKK-$Z_{HER2:342}$ were efficient and resulted in yields of more than 94%. Preserved HER2 binding capacity on SKOV-3 cells was demonstrated for all conjugates. In vitro, both ^{99m}Tc-maSKS-$Z_{HER2:342}$ and ^{99m}Tc-maKKK-$Z_{HER2:342}$ were found to be quite stable after 2 h incubation in mouse serum. Approximately 80% of the conjugates remained intact, and the rest seemed to bind to serum proteins (data not shown). In comparison to ^{99m}Tc-maSSS-$Z_{HER2:342}$, which did not demonstrate such binding under the same conditions, this level of protein binding (20% of the radioactivity) does not seem to affect clearance from the blood and other organs (see Table 3).

The in vitro cell studies showed that the labeled Affibody molecules had a slow internalization rate in SKOV-3 cells over time, which is consistent with previous results obtained for ^{111}In-labeled Affibody molecules (*27*). Other investigations have indicated that slow internalization of antibodies is advantageous for tumor targeting due to better penetration and retention in tumors (*30*). The retention of ^{99m}Tc-maSKS-$Z_{HER2:342}$ and ^{99m}Tc-maKKK-$Z_{HER2:342}$ was high, with about 60−70% of radioactivity retained in the cells 24 h following incubation. This level of retention is similar to what was previously determined for other ^{99m}Tc-labeled synthetic conjugates (*20, 23*).

The in vivo results showed that a single substitution of one serine with one lysine in the chelator (maSSS to maSKS) decreased the hepatobiliary excretion 2-fold and that the kidney uptake was increased. This shift might be explained by the overall higher hydrophilicity of the lysine in the chelator. However, substitution of all three serines with lysines (maSSS to maKKK) did not improve the hepatobiliary excretion further (intestine uptake 4 ± 0.3% IA/sample for labeled maKKK-$Z_{HER2:342}$ compared to 4.3 ± 0.5% IA/sample for maSKS-$Z_{HER2:342}$, $p = 0.34$), while the kidney accumulation was significantly higher. The radioactivity of ^{99m}Tc-maKKK-$Z_{HER2:342}$ was also found to be higher in other organs including the liver, spleen, stomach, and salivary glands, compared with what was seen with labeled maSSS-$Z_{HER2:342}$ or maSKS-$Z_{HER2:342}$.

An interesting finding from the biodistribution study was the elevated liver uptake for the maKKK conjugate compared with the maSKS or maSSS conjugates. It has previously been reported that positively charged substances preferentially accumulate in liver (*31*), and it has been suggested that cationization of proteins by chemical modification could be a way to achieve liver-specific targeting of a protein drug (*32*). Furthermore, the accumulation of radioactivity in the liver was higher for an antibody radioiodinated via a strongly positively charged D-amino acid tag (KRYRR) than for the same antibody radioiodinated through an *N*-succinimidyl 5-iodo-3-pyridinecarboxylate (SIPC) reagent (*33*), demonstrating a dramatic influence by a minor modification of the protein. Similarly, a previous study of Affibody molecules demonstrated that the use of multiple copies of the amino acid histidine (as in His-tagged Affibody molecules) also caused a high accumulation of radioactivity in the liver (*27*). In the present study, it was therefore not completely unexpected that using multiple lysine residues for ^{99m}Tc-labeling could promote elevated liver ac-

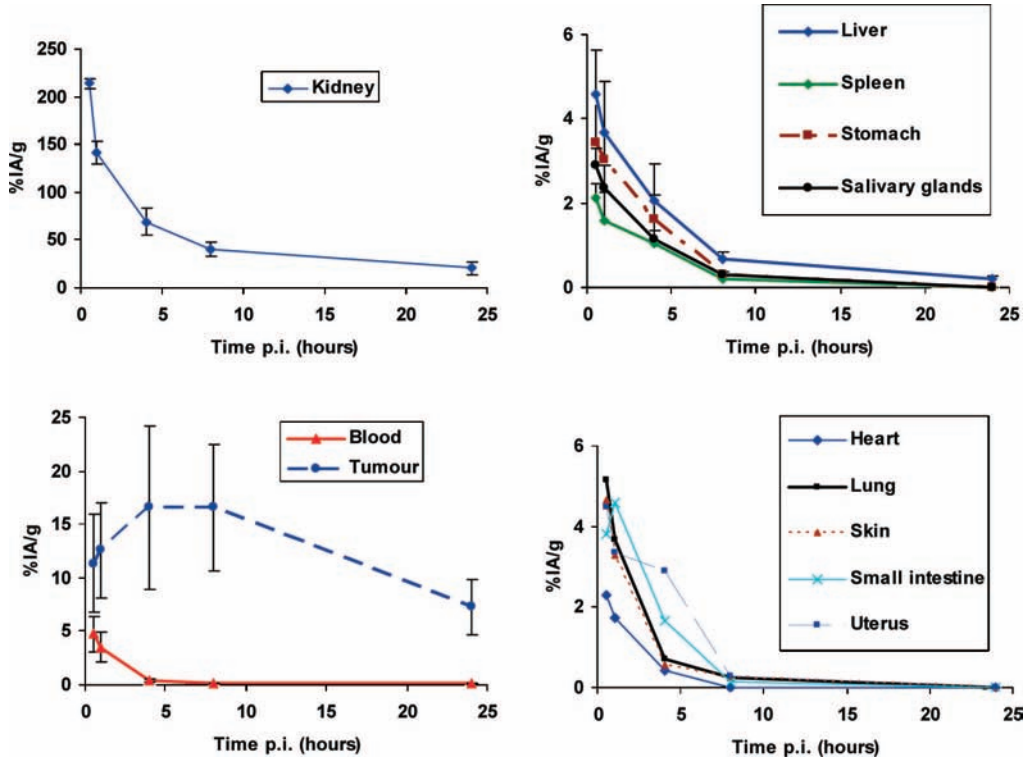

Figure 6. Biodistribution of ^{99m}Tc-maSKS-$Z_{HER2:342}$ in BALB/c *nu*/*nu* mice bearing SKOV-3 xenografts at 0.5, 1, 4, 8, and 24 h p.i. Data are presented as an average % IA/g of four animals ± SD.

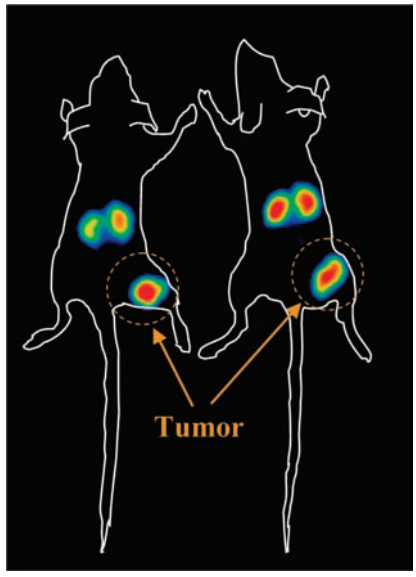

Figure 7. Gamma camera imaging of Balb/c *nu*/*nu* mice, bearing SKOV-3 xenografts on the right hind legs. The mice were imaged 4 h after administration of ^{99m}Tc-maSKS-$Z_{HER2:342}$. The tumors are indicated by arrows, while the hot spots visualized in the images are the kidneys.

cumulation. However, the detailed mechanism behind this phenomenon is still unclear.

Out of the three conjugates, ^{99m}Tc-maSKS-$Z_{HER2:342}$ showed the most promising biodistribution properties, with intermediate accumulation of radioactivity in the kidney and low accumulation in the liver. This conjugate was therefore further evaluated in mice with SKOV-3 xenografts. The in vivo evaluation in mice bearing tumors showed that ^{99m}Tc-maSKS-$Z_{HER2:3}$ led to specific and efficient accumulation in the SKOV-3 tumors (Table 4 and Figure 6). Four hours after injection, 17% IA/g was detected in the tumors, while the blood clearance was rapid; resulting in good tumor-to-blood and tumor-to-nontumor ratios for the gamma scintigraphy.

The images acquired in gamma camera after an i.v. injection of ^{99m}Tc-maSKS-$Z_{HER2:3}$ clearly visualized the tumors on the right hind legs of nude mice (Figure 7). Since small-sized (Mw < 60 kDa) substances are rapidly cleared through renal filtration, a high amount of radioactivity was also seen in the kidneys.

Our previous results showed that an increase of the chelator hydrophilicity improves the excretion properties of $Z_{HER2:342}$ (*20*, *23*). It is therefore interesting to compare the biodistribution properties of the new positively charged chelators with those of previously studied neutral and negatively charged chelators. As illustrated in Table 3, ^{99m}Tc-maSSS-$Z_{HER2:342}$ was used as the starting conjugate for the development of a suitable HER2 imaging agent. ^{99m}Tc-maSSS-$Z_{HER2:342}$ provided good tumor-to-organ ratios for imaging (*20*), but an elevated hepatobiliary excretion was seen (intestine uptake of 11 ± 2% of injected activity per whole sample), which would complicate detection of metastases in the abdominal area. The use of multiple negatively charged glutamic acids (^{99m}Tc-maEEE-$Z_{HER2:342}$) successfully switched the hepatobiliary to renal excretion (*23*), but the substitution of serine with multiple positively charged lysine (^{99m}Tc-maKKK-$Z_{HER2:342}$) remarkably increased the liver uptake (0.21% IA/g for maEEE vs 7% IA/g for maKKK). This excludes ^{99m}Tc-maKKK-$Z_{HER2:342}$ from further evaluation in tumor-bearing mice, since its clinical application would be restricted for detection of tumors in the extrahepatic sites. On the other hand, the substitution with one single lysine, as in ^{99m}Tc-maSKS-$Z_{HER2:342}$, seemed superior to ^{99m}Tc-maEEE-$Z_{HER2:342}$ in terms of renal uptake (see Table 3). Along these lines, the substitution with two glutamic acids instead of three in the chelator sequence has been evaluated. The resulting combination of serine and glutamic acid (^{99m}Tc-maESE-$Z_{HER2:342}$) was shown to provide imaging properties as good as for ^{99m}Tc-maSKS-$Z_{HER2:342}$ in terms of reduced renal uptake and

low blood, liver, and intestine accumulation, while maintaining the tumor localization capacity for imaging (*24*).

In conclusion, we have shown that substitution with serine for lysine in the chelators has a clear effect on the biodistribution of radioactivity. The introduction of multiple lysines gives rise to a high liver accumulation. However, substitution of one serine with one single lysine in the mercaptoacetyl-based chelator of Affibody molecules reduced the hepatobiliary excretion 2-fold, and the ^{99m}Tc-maSKS-$Z_{HER2:342}$ conjugate is thus favorable for imaging. We believe that our observation on the influence of different amino acid residues in the mercaptoacetyl-based chelators would be useful for design of; not only Affibody molecules, but also other small-sized peptide or scaffold-protein based tracers.

ACKNOWLEDGMENT

This work was financially supported by the Swedish Cancer Society (Cancerfonden) and the Swedish Research Council (Vetenskapsrådet). The authors thank Ewa Jerwanska at the Department of Nuclear Medicine, Akademiska sjukhuset, for the technetium eluate. We thank Daniel Rosik at Affibody AB, Bromma, for the LC analysis.

LITERATURE CITED

(1) Pegram, M. D., Pauletti, G., and Slamon, D. J. (1998) HER-2/neu as a predictive marker of response to breast cancer therapy. *Breast Cancer Res. Treat. 52*, 65–77.

(2) Yarden, Y. (2001) Biology of HER2 and its importance in breast cancer. *Oncology 61*, 1–13, Suppl 2.

(3) Stern, D. F., Heffernan, P. A., and Weinberg, R. A. (1986) p185, a product of the neu proto-oncogene, is a receptorlike protein associated with tyrosine kinase activity. *Mol. Cell. Biol. 6*, 1729–40.

(4) Slamon, D. J., Clark, G. M., Wong, S. G., Levin, W. J., Ullrich, A., and McGuire, W. L. (1987) Human breast cancer: correlation of relapse and survival with amplification of the HER-2/neu oncogene. *Science 235*, 177–82.

(5) Moy, B., and Goss, P. E. (2006) Lapatinib: current status and future directions in breast cancer. *Oncologist 11*, 1047–57.

(6) Bast, R. C., Jr., Ravdin, P., Hayes, D. F., Bates, S., Fritsche, H., Jr., Jessup, J. M., Kemeny, N., Locker, G. Y., Mennel, R. G., and Somerfield, M. R. (2001) 2000 update of recommendations for the use of tumor markers in breast and colorectal cancer: clinical practice guidelines of the American Society of Clinical Oncology. *J. Clin. Oncol. 19*, 1865–78.

(7) Hicks, D. G., and Kulkarni, S. (2008) HER2+ breast cancer: review of biologic relevance and optimal use of diagnostic tools. *Am. J. Clin. Pathol. 129*, 263–73.

(8) Wolff, A. C., Hammond, M. E., Schwartz, J. N., Hagerty, K. L., Allred, D. C., Cote, R. J., Dowsett, M., Fitzgibbons, P. L., Hanna, W. M., Langer, A., McShane, L. M., Paik, S., Pegram, M. D., Perez, E. A., Press, M. F., Rhodes, A., Sturgeon, C., Taube, S. E., Tubbs, R., Vance, G. H., van de Vijver, M., Wheeler, T. M., and Hayes, D. F. (2007) American Society of Clinical Oncology/College of American Pathologists guideline recommendations for human epidermal growth factor receptor 2 testing in breast cancer. *Arch. Pathol. Lab. Med. 131*, 18.

(9) Tolmachev, V. (2008) Imaging of HER-2 overexpression in tumors for guiding therapy. *Curr. Pharm. Des. 14*, 2999–3019.

(10) Tolmachev, V., Orlova, A., Nilsson, F. Y., Feldwisch, J., Wennborg, A., and Abrahmsen, L. (2007) Affibody molecules: potential for in vivo imaging of molecular targets for cancer therapy. *Expert Opin. Biol. Ther. 7*, 555–68.

(11) Nilsson, F. Y., and Tolmachev, V. (2007) Affibody molecules: new protein domains for molecular imaging and targeted tumor therapy. *Curr. Opin. Drug Discovery Dev. 10*, 167–75.

(12) Cai, W., Niu, G., and Chen, X. (2008) Multimodality imaging of the HER-kinase axis in cancer. *Eur. J. Nucl. Med. Mol. Imaging 35*, 186–208.

(13) Nord, K., Gunneriusson, E., Ringdahl, J., Stahl, S., Uhlen, M., and Nygren, P. A. (1997) Binding proteins selected from combinatorial libraries of an α-helical bacterial receptor domain. *Nat. Biotechnol. 15*, 772–7.

(14) Orlova, A., Magnusson, M., Eriksson, T. L., Nilsson, M., Larsson, B., Hoiden-Guthenberg, I., Widstrom, C., Carlsson, J., Tolmachev, V., Stahl, S., and Nilsson, F. Y. (2006) Tumor imaging using a picomolar affinity HER2 binding affibody molecule. *Cancer Res. 66*, 4339–48.

(15) Orlova, A., Tran, T., Widström, C., Engfeldt, T., Karlstrom, A. E., and Tolmachev, V. (2007) Pre-clinical evaluation of [^{111}In]-benzyl-DOTA-ZHER2:342, a potential agent for imaging of HER2 expression in malignant tumors. *Int. J. Mol. Med. 20*, 397–404.

(16) Tolmachev, V., Nilsson, F. Y., Widstrom, C., Andersson, K., Rosik, D., Gedda, L., Wennborg, A., and Orlova, A. (2006) ^{111}In-benzyl-DTPA-ZHER2:342, an affibody-based conjugate for in vivo imaging of HER2 expression in malignant tumors. *J. Nucl. Med. 47*, 846–53.

(17) Fortin, M. A., Orlova, A., Malmstrom, P. U., and Tolmachev, V. (2007) Labelling chemistry and characterization of [^{90}Y/^{177}Lu]-DOTA-ZHER2:342−3 Affibody molecule, a candidate agent for locoregional treatment of urinary bladder carcinoma. *Int. J. Mol. Med. 19*, 285–91.

(18) Kramer-Marek, G., Kiesewetter, D. O., Martiniova, L., Jagoda, E., Lee, S. B., and Capala, J. (2008) [(^{18})F]FBEM-Z(HER2:342)-Affibody molecule-a new molecular tracer for in vivo monitoring of HER2 expression by positron emission tomography. *Eur. J. Nucl. Med. Mol. Imaging 35*, 1008–18.

(19) Namavari, M., Padilla De Jesus, O., Cheng, Z., De, A., Kovacs, E., Levi, J., Zhang, R., Hoerner, J. K., Grade, H., Syud, F. A., and Gambhir, S. S. (2008) Direct site-specific radiolabeling of an affibody protein with 4-[(^{18})F]fluorobenzaldehyde via oxime chemistry. *Mol. Imaging Biol. 10*, 177–81.

(20) Engfeldt, T., Tran, T., Orlova, A., Widström, C., Feldwisch, J., Abrahmsén, L., Wennborg, A., Eriksson, A. K., and Tolmachev, V. (2007) ^{99m}Tc-chelator engineering to improve tumour targeting properties of a HER2-specific Affibody. *Eur. J. Nucl. Med. Mol. Imaging 34*, 1843–53.

(21) Zhu, Z., Wang, Y., Zhang, Y., Liu, G., Liu, N., Rusckowski, M., and Hnatowich, D. J. (2001) A novel and simplified route to the synthesis of N3S chelators for ^{99m}Tc labeling. *Nucl. Med. Biol. 28*, 703–8.

(22) Decristoforo, C., and Mather, S. J. (2002) The influence of chelator on the pharmacokinetics of ^{99m}Tc-labelled peptides. *Q. J. Nucl. Med. 46*, 195–205.

(23) Tran, T., Engfeldt, T., Orlova, A., Sandstrom, M., Feldwisch, J., Abrahmsen, L., Wennborg, A., Tolmachev, V., and Karlstrom, A. E. (2007) ^{99m}Tc-maEEE-$Z_{HER2:342}$, an affibody molecule-based tracer for the detection of HER2 expression in malignant tumors. *Bioconjugate Chem. 18*, 1956–64.

(24) Ekblad, T., Tran, T., Orlova, A., Widström, C., Feldwisch, J., Wennborg, A., Abrahmsén, L., Karlström Eriksson, A., and Vladimir, T. (2008) Development and preclinical characterisation of ^{99m}Tc-labelled Affibody molecules with reduced renal uptake. *Eur. J. Nucl. Med. Mol. Imaging*, In press.

(25) Persson, M., Tolmachev, V., Andersson, K., Gedda, L., Sandstrom, M., and Carlsson, J. (2005) [(^{177})Lu]pertuzumab: experimental studies on targeting of HER-2 positive tumour cells. *Eur. J. Nucl. Med. Mol. Imaging 32*, 1457–62.

(26) Engfeldt, T., Orlova, A., Tran, T., Bruskin, A., Widstrom, C., Karlstrom, A. E., and Tolmachev, V. (2006) Imaging of HER2-expressing tumours using a synthetic Affibody molecule containing the ^{99m}Tc-chelating mercaptoacetyl-glycyl-glycyl-glycyl (MAG3) sequence. *Eur. J. Nucl. Med. Mol. Imaging 34*, 722–733.

(27) Ahlgren, S., Orlova, A., Rosik, D., Sandstrom, M., Sjoberg, A., Baastrup, B., Widmark, O., Fant, G., Feldwisch, J., and Tolmachev, V. (2008) Evaluation of maleimide derivative of DOTA for site-specific labeling of recombinant affibody mol-

ecules. *Bioconjugate Chem. 19*, 235–43.

(28) Tran, T., Engfeldt, T., Orlova, A., Widstrom, C., Bruskin, A., Tolmachev, V., and Karlstrom, A. E. (2007) In vivo evaluation of cysteine-based chelators for attachment of ^{99m}Tc to tumor-targeting affibody molecules. *Bioconjugate Chem. 18*, 549–558.

(29) Orlova, A., Rosik, D., Sandstrom, M., Lundqvist, H., Einarsson, L., and Tolmachev, V. (2007) Evaluation of [($^{111/114m}$)In]CHX-A″-DTPA-Z(HER2:342), an affibody ligand conjugate for targeting of HER2-expressing malignant tumors. *Q. J. Nucl. Med. Mol. Imaging 51*, 314–23.

(30) Schmidt, M. M., Thurber, G. M., and Wittrup, K. D. (2008) Kinetics of anti-carcinoembryonic antigen antibody internalization: effects of affinity, bivalency, and stability, *Cancer Immunol. Immunother.* PMID:18408925.

(31) Nishikawa, M., Hasegawa, S., Yamashita, F., Takakura, Y., and Hashida, M. (2002) Electrical charge on protein regulates its absorption from the rat small intestine. *Am. J. Physiol. Gastrointest. Liver Physiol. 282*, G711−9.

(32) Ma, S. F., Nishikawa, M., Katsumi, H., Yamashita, F., and Hashida, M. (2005) Cationic charge-dependent hepatic delivery of amidated serum albumin. *J. Controlled Release 102*, 583–94.

(33) Foulon, C. F., Welsh, P. C., Bigner, D. D., and Zalutsky, M. R. (2001) Positively charged templates for labeling internalizing antibodies: comparison of N-succinimidyl 5-iodo-3-pyridinecarboxylate and the D-amino acid peptide KRYRR. *Nucl. Med. Biol. 28*, 769–77.

BC800244B

A Novel Method to Label Preformed Liposomes with ^{64}Cu for Positron Emission Tomography (PET) Imaging

Jai Woong Seo,[†] Hua Zhang,[†] David L. Kukis,[‡] Claude F. Meares,[§] and Katherine W. Ferrara*[,†]

Department of Biomedical Engineering, University of California, Davis, California 95616, Center for Molecular and Genomic Imaging, Department of Biomedical Engineering, University of California, Davis, California 95616, and Department of Chemistry, University of California, Davis, California 95616. Received July 12, 2008; Revised Manuscript Received October 10, 2008

Radiolabeling of liposomes with ^{64}Cu ($t_{1/2}$ = 12.7 h) is attractive for molecular imaging and monitoring drug delivery. A simple chelation procedure, performed at a low temperature and under mild conditions, is required to radiolabel preloaded liposomes without lipid hydrolysis or the release of the encapsulated contents. Here, we report a ^{64}Cu postlabeling method for liposomes. A ^{64}Cu-specific chelator, 6-[*p*-(bromoacetamido)benzyl]-1,4,8,11-tetraazacyclotetradecane-*N*,*N*′,*N*″,*N*‴-tetraacetic acid (BAT), was conjugated with an artificial lipid to form a BAT−PEG−lipid. After incorporation of 0.5% (mol/mol) BAT−PEG−lipid during liposome formulation, liposomes were successfully labeled with ^{64}Cu in 0.1 M NH_4OAc pH 5 buffer at 35 °C for 30−40 min with an incorporation yield as high as 95%. After 48 h of incubation of ^{64}Cu-liposomes in 50/50 serum/PBS solution, more than 88% of the ^{64}Cu label was still associated with liposomes. After injection of liposomal ^{64}Cu in a mouse model, 44 ± 6.9, 21 ± 2.7, 15 ± 2.5, and 7.4 ± 1.1 (n = 4) % of the injected dose per cubic centimeter remained within the blood pool at 30 min, 18, 28, and 48 h, respectively. The biodistribution at 48 h after injection verified that 7.0 ± 0.47 (n = 4) and 1.4 ± 0.58 (n = 3) % of the injected dose per gram of liposomal ^{64}Cu and free ^{64}Cu remained in the blood pool, respectively. Our results suggest that this fast and easy ^{64}Cu labeling of liposomes could be exploited in tracking liposomes *in vivo* for medical imaging and targeted delivery.

INTRODUCTION

Liposomes are widely used in preclinical and clinical applications as carriers of drugs, genes, or contrast agents (*1, 2*). The incorporation of hydrophilic polyethylene glycol (PEG[1]) on the surface of liposomes further improves their properties (*3*). To obtain the biodistribution of long-circulating liposomes and to obtain noninvasive images in animals and humans, past studies have utilized liposomes loaded or labeled with radionuclides such as indium-111 (*4*), technetium-99m (*5*−*7*), and gallium-67 (*8*) for single photon emission computed tomography (SPECT). Labeling with fluorine-18 (*9, 10*) has been used for positron emission tomography (PET).

Three distinct approaches have been developed for the labeling or loading of liposomes with radioisotopes: (a) entrapping a soluble radiotracer inside the aqueous liposomal core, e.g., via chelating the preloaded polar ligand with ^{111}In (*11*), ^{67}Ga (*12*), or ^{99m}Tc-complex (*5, 7*), or via extrusion with 2-[^{18}F]fluorodeoxyglucose (2-[^{18}F]FDG) (*13*); (b) inserting radiolabeled lipid into the liposome bilayer (*9, 10*); and (c) attaching ^{99m}Tc onto the surface of liposomes via the chelation between ^{99m}Tc and a chelator-lipid conjugate (*14, 15*). In contrast to the extensive studies using SPECT to track liposomes in vivo, reports of PET imaging of liposomes are limited, although PET has many potential advantages (*16*). Previous reports have focused on the use of fluorine-18 to label liposomes (*9, 10*), but its short 110-min half-life makes extended studies difficult. In the treatment of diseases such as cancer, it is desirable to create stable particles that can circulate and accumulate in tumors over days to weeks (*17, 18*). Because of the temperature dependence of liposome structures (*19*), these particles may not withstand exposure to high temperatures after formulation. Here, we report a gentle postlabeling method using ^{64}Cu (half-life 12.7 h) and its application to track liposomes over 48 h. For the surface chelation method, the incorporation of a lipid−PEG−chelate conjugate (Scheme 1) in the liposome bilayer (Figure 1) was chosen, as used in previous nuclear medicine studies (*14, 20*). Previous surface chelation methods used lipid−chelate conjugates such as octadecylamine diethylenetriaminepentaacetic acid (DTPA) (*15*), dipalmitoylphosphatidylethanolamine-diethylenetriaminetetraacetic acid (DPPE-DTTA) (*20, 21*), and hydrazino nicotinamide (HYNIC) conjugated-DSPE (*14*). However, none of those reagents have been shown to bind copper stably under physiological conditions, nor would they be expected to, due to the kinetic properties of the copper ion. Among several effective copper(II) macrocyclic

* To whom correspondence should be addressed. Department of Biomedical Engineering, 451 Health Sciences Drive, University of California, Davis, Davis, CA 95616. Phone: 530-754-9436. Fax: (530)754-5739. E-mail: kwferrara@ucdavis.edu.

[†] Department of Biomedical Engineering.

[‡] Department of Biomedical Engineering.

[§] Department of Chemistry.

[1]Abbreviations: BAT, 6-[*p*-(bromoacetamido)benzyl]-1,4,8,11-tetraazacyclotetradecane-*N*,*N*′,*N*″,*N*‴-tetraacetic acid; BMEDA, *N*,*N*-bis(2-mercaptoethyl)-*N*′,*N*″-diethylethylenediamine; Cys, cysteine; DCM, dichloromethane; DIPEA, diisopropylethylamine; DMF, dimethylformamide; DMSO, dimethylsulfoxide; DOTA, 1,4,7,10-tetraazacyclododecane-*N*,*N*′,*N*″,*N*‴-tetraacetic acid; NOTA, 1,4,7-triazacyclononane-*N*,*N*′,*N*″-triacetic acid; DPPC, 1,2-dipalmitoyl-*sn*-glycero-3-phosphocholine; DSPE-PEG-2000, 1,2-distearoyl-*sn*-glycero-3-phosphoethanolamine-*N*-[methoxy(polyethylene glycol)-2000]; DTNP, 2,2′-dithio bis-(5-nitropyridine); EDTA, ethylenediaminetetraacetic acid; FDG, fluorodeoxyglucose; Fmoc, 9-fluorenylmethyloxycarbonyl; HSPC, hydrogenated soy phosphatidylcholine; HYNIC, hydrazino nicotinamide; MALDI, matrix-assisted laser desorption/ionization; Mmt, 4-monomethoxytrityl; PBS, phosphate buffered saline; PEG, polyethylene glycol; PET, positron emission tomography; ROI, region of interest; SOD, superoxide dismutase; SPECT, single photon emission computed tomography; TAC, time activity curve; TETA, 1,4,8,11-tetraazacyclotetradecane-*N*,*N*′,*N*″,*N*‴-tetraacetic acid; TFA, trifluoroacetic acid; TIPS, triisopropylsilane.

10.1021/bc8002937 CCC: $40.75 © 2008 American Chemical Society
Published on Web 11/08/2008

Scheme 1. Solid Phase Synthesis of BAT−PEG−lipid[a]

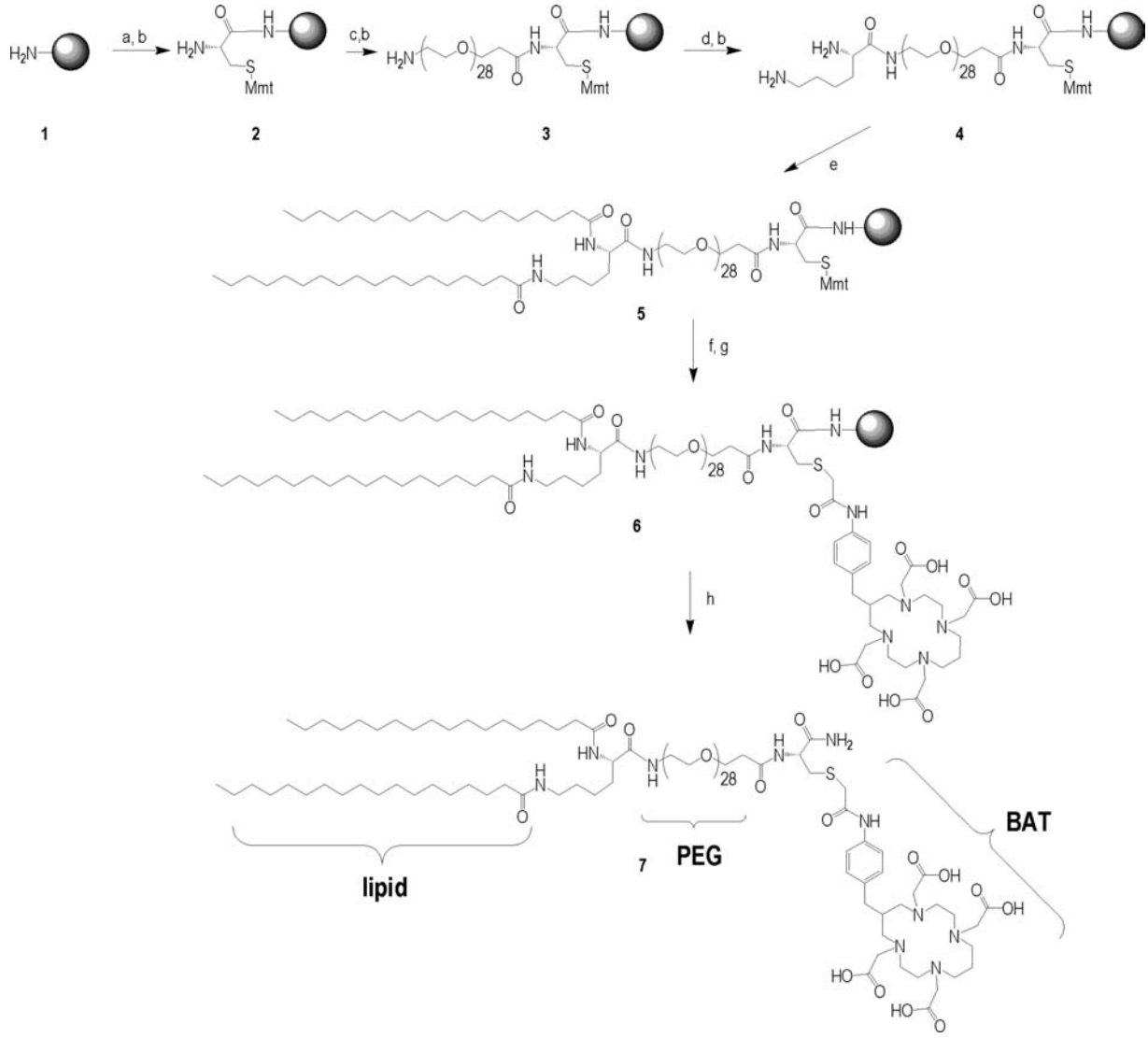

[a] Reagents: (a) Fmoc-cysteine (2 eq.), HBTU (*O*-benzotriazole-*N*,*N*,*N*′,*N*′-tetramethyl-uronium-hexafluoro-phosphate) (2 eq.), DIPEA (4 eq.), 60 min; (b) 20% piperidine in DMF, 2 × 10 min, 10 min; (c) Fmoc-NH-(PEG)27-COOH (1.1 eq.), HBTU (1.1 eq.), DIPEA (2.2 eq.), 60 min; (d) Fmoc-Lys(Fmoc)-OH (2 eq.), HBTU (2 eq.), DIPEA (4 eq.), 60 min; (e) stearic acid (4 eq.), HBTU(4 eq.), DIEA(8 eq.), 60 min; (f) 1% TFA/DCM, 5 × 3 min; (g) BAT(1.5 eq.), DIPEA (10 eq.), 4 h; (h) TFA/TIPS/H_2O (95/2.5/2.5), 3 h.

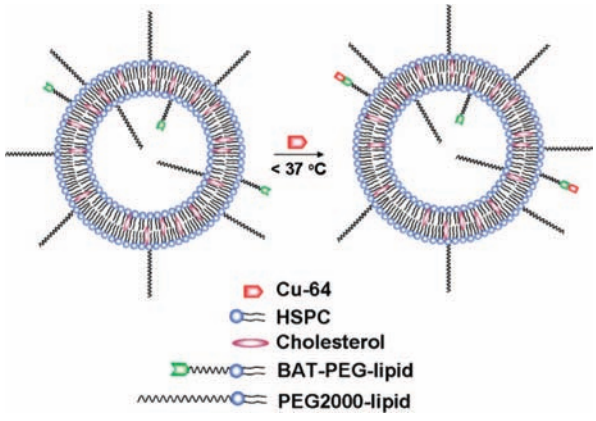

Figure 1. Surface chelation model of ^{64}Cu-labeled long circulating liposomes, where labeling was performed under mild conditions (<37 °C) to preserve liposome stability and loading during labeling.

chelators, such as DOTA, NOTA, TETA and TE2A (*22*, *23*), we chose 6-[*p*-(bromoacetamido)benzyl]-1,4,8,11-tetraazacyclotetradecane- *N*,*N*′,*N*″,*N*‴-tetraacetic acid, BAT (*24*), as the chelating ligand. BAT, a derivative of 6-benzyl-TETA (Scheme 1), has been found to form stable (*25*, *26*) and highly selective complexes with copper(II) (*27*) and has been utilized for antibody labeling (*28*, *29*) for preclinical and clinical trials. Although the cross-bridged ligand TE2A has been shown to be very stable for radiolabeling small molecules (*30*), the heating step (>70 °C) required for the incorporation of ^{64}Cu into TE2A exceeds the transition temperature of many liposomal formulations (thus releasing the contents) and could also alter lipid structure in other ways, such as hydrolysis.

EXPERIMENTAL PROCEDURES

Materials. Fmoc-Cys(Mmt)-OH, Fmoc-NH-(PEG)27-COOH, Fmoc-Lys(Fmoc)-OH, and coupling agent (HBTU, 2-(1*H*-benzotriazole-1-yl)-1,1,3,3-tetramethylaminium hexafluorophosphate) were purchased from EMD Biosciences (La Jolla, CA) and stearic acid from Sigma-Aldrich. Fmoc-PAL-PEG-PS resin (0.16−0.21 mmol/g) was from Applied Biosystems (Foster City, CA). Solvents and other agents were all of analytical purity and from Sigma-Aldrich (Milwaukee, WI) and VWR (Brisbane, CA). All lipids and a mini-extruder were purchased from Avanti Polar Lipids (Alabaster, AL). $^{64}CuCl_2$ was purchased from Trace

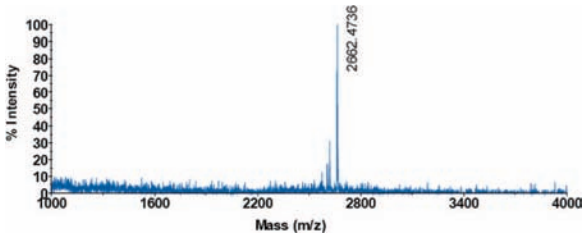

Figure 2. Matrix-assisted laser desorption/ionization (MALDI) spectrum of conjugated BAT−PEG−lipid.

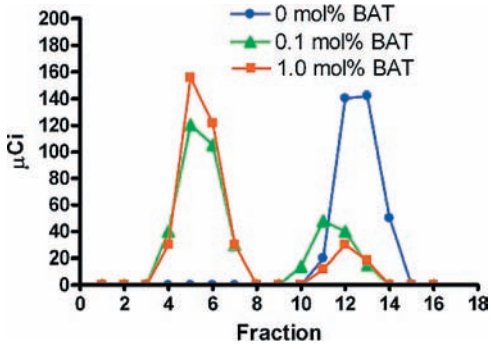

Figure 3. Elution profiles of ^{64}Cu-labeled liposomes after incubation with $^{64}CuCl_2$ for 1 h and EDTA for 20 min at room temperature in 0.1 M ammonium acetate buffer (pH 5.0). The molar ratios of lipid-PEG-BAT are 0 mol% (circle), 0.1 mol% (triangle), and 1.0 mol% (square), and are combined with 90% DPPC and 10% DSPE-PEG2000 (mol/mol).

life Science (Denton, TX, specific activity >80,000 Ci/g for *in vitro* and *in vivo* studies) or Nordion (Ontario, Canada, specific activity >5000 Ci/g for the feasibility study) under a protocol controlled by the University of California, Davis. High purity ammonium acetate (≥99.995%) was purchased from Sigma-Aldrich (St. Louis, MO). PBS was purchased from Invitrogen Corporation (Carlsbad, CA). Mouse serum was purchased from Innovative research (Novi, MI). All eppendorf tubes and glassware for labeling were prewashed with absolute ethanol and acetone, and dried in an oven before use.

Synthesis of the BAT-PEG-Lipid Conjugate (7). As shown in Scheme 1, **7** was synthesized by Fmoc solid phase synthesis. Briefly, Fmoc-Cys(Mmt)-OH, Fmoc-NH-(PEG)27-COOH, Fmoc-Lys(Fmoc)-OH, and stearic acid were sequentially coupled to the PAL-PEG-PS resin to obtain **5**. After the protecting group, Mmt, was removed with 1% TFA/DCM, BAT (*24*) was coupled onto the resin in the solvent (DMF/DMSO/H_2O = 1:1:1, v/v/v), at pH 8.0 ± 0.5, adjusted with DIPEA. The reaction was monitored with DTNP solution. The final product (**7** in Scheme 1) was cleaved from the resin by the TFA/TIPS/H_2O mixture (TFA/TIPS/H_2O = 95:2.5:2.5, v/v/v) and purified by reversed-phase high performance liquid chromatography (HPLC), with the mass confirmed by MALDI-TOF ($M + H^+$, measured, 2662; calculated, 2663). Reversed-phase HPLC was performed using a Phenomenex Jupiter 4 μm Proteo 90A (250 × 4.6 mm, analytical) and a Phenomenex Jupiter 10 μm Proteo 90A (250 × 10.0 mm, semipreparative) with a gradient from 10−90% B in 30 min (solvent A, 0.05% TFA; solvent B, acetonitrile) and a flow rate of 1.5 or 3.0 mL/min for the analytical/semipreparative column. The retention time of the BAT−PEG−lipid conjugate was 35.5 min. MALDI was measured with ABI-4700 TOF−TOF (Applied Biosystems) using matrix sinapinnic acid with a 3-layer sample preparation method (*31*). The MALDI spectral results are shown in Figure 2.

BAT-Liposome Preparation. Lipids in chloroform were mixed in a test tube and dried by gently blowing nitrogen gas with vortexing to create a thin film, which was further dried under vacuum overnight to completely remove chloroform. The dried lipid thin film was resuspended by adding 0.1 M ammonium acetate buffer (pH 5) and incubated for 5−10 min at 60 °C. After 1 min of sonication, this lipid mixture was extruded by 21 passes through a 100 nm membrane filter (Whatman, NJ) at 60−62 °C on a heating block, to form 100 nm liposomes. The liposome solution was stored at 4 °C until needed for radiolabeling.

^{64}Cu Labeling of BAT−PEG−lipids. BAT−PEG−lipids (20 μg, 7.5 nmol) in chloroform (20 μL) were added into a glass test tube, and chloroform was evaporated by gently blowing nitrogen gas with vortexing. After overnight storage under high vacuum, citrate buffer (0.1 M, 0.4 mL, pH 5.5) was added to the glass test tube containing BAT−PET−lipids. Buffered $^{64}CuCl_2$ (5.31 mCi, 196.47 MBq) in ammonium citrate (pH 5.5, 0.1 M) was added to the lipid solution, which was transferred to a plastic tube. The mixture was incubated at 37 °C and monitored by radio TLC (chloroform/ethanol/H_2O = 50:40:6, v/v/v), which showed 97% labeling yield after 40 min of incubation. After cooling to room temperature, the solution was passed through an activated C-18 sep-pak cartridge and washed with deionized water (5 mL) and anhydrous acetonitrile (8 mL). Radioactivity remaining in the cartridge was extracted by mixed ethanol and chloroform solution (1 mL, 1:1, v/v). After the solution was removed under a nitrogen stream, the activity was resuspended with 7% ethanol/PBS for the *in vivo* study. Radiochemical yield at the end of synthesis (EOS) was 59%, and specific activity was greater than 575 Ci/mmol. Radiochemical purity on both radio TLC and reversed-phase HPLC was 99% (C4 column, 250 × 4.6 mm, analytical; solvent A, 0.05 volume% trifluoroacetic acid in deionized water; solvent B, acetonitrile; flow rate, 1.5 mL/min; gradient from 10−90% B in 30 min and 90−10% B in 30−60 min; retention time, 29.6 min).

^{64}Cu Labeling of Liposomes. *For the Feasibility Study.* $^{64}CuCl_2$ (8.31 mCi, 307.47 MBq) in a volume of 35 μL (pH 1−2) was received, and NH_4OAc solution (4 μL, 1 M, pH 5.0) was added to adjust the pH. This solution (5.08 mCi, 187.96 MBq, 25 μL) was added to 475 μL of 0.1 M NH_4OAc solution (pH 5.0), and the final concentration of ^{64}Cu was 10 mCi/mL. This ^{64}Cu solution (50 μL) was added to the liposome solutions (12 mg/300 μL, total lipid mol = 12.7 μmol, DPPC/DSPE−PEG2000/BAT−PEG−lipid = 90-*x*:10.0:*x*, mol/mol/mol, *x* = 0, 0.1, and 1.0). The concentration of BAT−PEG−lipids in 12 mg of lipids was 0, 12.7, and 127 nmol, respectively. After vortexing, the mixture was incubated for 1 h at room temperature. Then, EDTA solution (0.1 M, 35 μL) was added (final EDTA concentration 10 mM), and the mixture was incubated for 20 min at room temperature. Liposomes were separated by a G-75 column (GE Healthcare, NJ) in PBS, and fractions were collected in 250 μL tubes. The radioactivity was measured with a calibrated Cu-64 mode of CRC-15 DualPET (Capintec, NJ) with noncorrection of Cu-67, and the incorporation yield was determined by eq 1 as decay corrected yield (*Fl*, radioactivity in liposome fractions; *Fa*, the sum of all radioactive fractions).

$$\text{Incorporation yield} = \frac{Fl}{Fa} \quad (1)$$

For the in Vitro Study. Liposomes (10 mg) containing 0.5 mol% of BAT−PEG−lipid (HSPC/cholesterol/DSPE-PEG2000/BAT−PEG−lipid = 55.5:39:5.0:0.5, mol/mol/mol/mol, the number of BAT−PEG−lipids, 68.7 nmol) and without BAT−PEG−lipid (HSPC/cholesterol/DSPE-PEG2000 = 56:39:5.0, mol/mol/mol) were prepared by the procedure described above. Both liposome formulations were incubated with $^{64}CuCl_2$ (2.15 mCi, 79.55 MBq) at 35 °C for 40 min. The purification

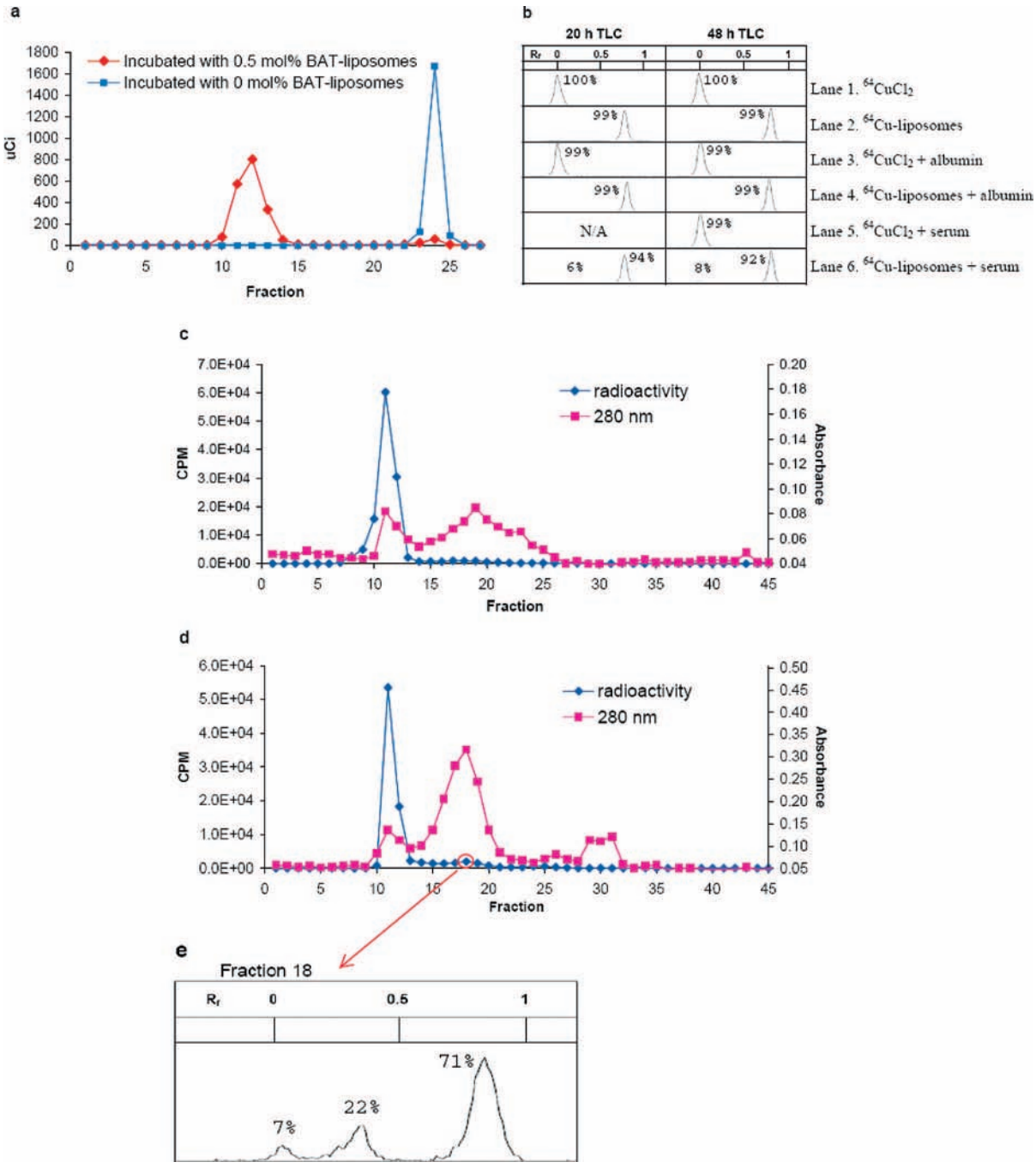

Figure 4. In vitro assay of ^{64}Cu-labeled liposomes: (a) Elution profiles of liposomes with 0.5 mol% BAT−PEG−lipid (HSPC/cholesterol/DSPE-PEG2000/BAT−PEG−lipid = 55.5:39:5.0:0.5, mol/mol/mol/mol, red diamond) and 0 mol% BAT−PEG−lipid (HSPC/cholesterol/DSPE-PEG2000 = 56:39:5.0:0.5, mol/mol/mol, blue square) after incubation with $^{64}CuCl_2$ for 40 min and EDTA for 15 min at 35 °C in 0.1 M ammonium acetate buffer (pH 5.0). Liposomes were separated by a size exclusion column. With 0.5 mol% BAT−PEG−lipid, ^{64}Cu was associated with liposomes; without BAT−PEG−lipid, ^{64}Cu was not detected in the liposomal fraction. (b) Radio TLC on silica plate was developed with eluant (chloroform/methanol/H_2O = 50:40:6, vol/vol/vol). Retention factor (R_f) of ^{64}Cu-BAT−PEG−lipid was 0.8 and that of $^{64}CuCl_2$ was 0. Lanes 1−6 were measured at 20 and 48 h as indicated in b. (c) Chromatogram of the mixture of ^{64}Cu-liposomes and albumin (8 mg/mL) in PBS after 48 h of incubation at 37 °C. The mixture was separated by a size exclusion column. Elution of liposomes and serum proteins was measured by gamma-counter (diamonds) and UV absorbance at 280 nm (squares). (d) Chromatogram of the mixture of ^{64}Cu-liposomes and serum in PBS (PBS/serum = 1:1, vol/vol) after 48 h of incubation at 37 °C. (e) Radio TLC of fraction 18 performed as described in b. The peak (R_f 0.8) represents ^{64}Cu-BAT−PEG−lipid. The small peak near 0 indicates free ^{64}Cu, and the middle peak has not been characterized.

continued as described above, and the labeling yield was determined by eq 1.

For the in Vivo Study. Liposomes (1 mg, HSPC/cholesterol/DSPE-PEG2000/BAT−PEG−lipid = 55.5:39:5.0:0.5, mol/mol/mol/mol, the number of BAT−PEG−lipid, 6.85 nmol) were prepared by the procedure above. $^{64}CuCl_2$ (2.75 mCi, 101.75 MBq) solution was added to 300 μL (0.1 M NH_4OAc, pH 5) of BAT−liposome solution and incubated at 37 °C for 40 min. Purification continued as described above. After the radioactivity decayed, size and zeta potential were measured with a NICOMP 380 ZLS (Particle Sizing Systems, CA).

***In Vitro* Stability Test.** Separated ^{64}Cu-labeled liposomes (~1.0 mg lipids) in PBS buffer (pH 7.4, 0.5 mL) were added to 0.5 mL of mouse serum and albumin solution (final concentration, 8 mg/mL). The mixture was kept in a shaker (300 rpm) at 37 °C, and a sample of 100 μL was taken from the

Table 1. Size (nm) and Zeta Potential (mV) of 0.5 mol% BAT-Liposomes ($n = 2$)

	size (nm)		zeta potential (mV)	
liposome	before	after	before	after
BAT-liposome	108.8 ± 5.5	97.2 ± 3.5	−40.8 ± 4.3	−41.2 ± 3.2

solution at 48 h and hand-loaded onto a sephachryl-300HR (GE Healthcare, NJ) packed column (15 mm I.D, 250 mm height), which was eluted with PBS under a pressure of 2 psi. Fractions (1.5 mL per fraction) were collected into test tubes, and radioactivity was measured with the 1470 Automatic Gamma Counter (Perkin-Elmer Life Sciences, MA). After the radioactive decay, the absorbance of all fractions was measured at 280 nm.

Radio TLC assay. Each aliquot (10 μL) of six solutions described below was dissolved into 50% ethanol solution (100 μL) after 20 and 48 h incubation at room temperature: $^{64}CuCl_2$ in 0.1 M NH_4OAc solution, $^{64}CuCl_2$ in serum solution (PBS/serum = 1:1, v/v), $^{64}CuCl_2$ in albumin solution, ^{64}Cu-labeled liposomes in PBS buffer, ^{64}Cu-labeled liposomes in albumin solution, and ^{64}Cu-labeled liposomes in serum solution (PBS/serum = 1:1, v/v). TLC was run on aluminum-backed silica gel sheets (silica gel 60 F_{254}, EMD, NJ), developed with chloroform/methanol/H_2O (50:40:6, v/v/v). The radio TLC was recorded by a radio-TLC Imaging Scanner (Bioscan, NW).

Biodistribution Study. All animal studies were conducted under a protocol approved by the University of California, Davis Animal Use and Care Committee. A total of 10 animals (male FVB mice, 8−13 weeks, 25−30 g, Charles River, MA) were examined over the course of this study. For each image, four or three mice per group were anesthetized with 3.5% isofluorane and maintained at 2.0−2.5%, and catheterized to ensure proper tail vein injection, after which bolus injections of ^{64}Cu-BAT−PEG−lipids (0.263 ± 0.013 mCi, 9.73 ± 0.48 MBq per animal), ^{64}Cu-labeled liposomes (4.6−18 μmol/kg, 0.17−0.21 mCi, 6.29−7.77 MBq per animal), and $^{64}CuCl_2$ (carrier free, 0.15−0.4 mCi, 5.55−14.7 MBq per animal) in PBS (pH 7.2) were administered as PET scans were initiated, using a manually controlled injection that was timed for uniform administration over 15 s. After the 48-h PET scans, the mice were euthanized by cervical dislocation, and organs of interest were harvested and weighed. Radioactivity was measured using a 1470 Automatic Gamma Counter.

PET Scans and Time-Activity Curves (TAC). PET scans were conducted with the microPET Focus (Concorde Microsystems, Inc., TN) over 60 min. Maximum a posteriori (MAP) files were created with ASIPro software (CTI Molecular Imaging) and used to obtain quantitative activity levels in each organ of interest as a function of time. TACs were obtained with region-of-interest (ROI) analysis using ASIPro software and expressed as percentage of injected dose per cubic centimeter (%ID/cc).

RESULTS AND DISCUSSION

Fmoc solid phase synthesis was used to create the lipid−PEG−chelate conjugate to minimize hydrolysis of the ester group in the lipid conjugate and maximize purity of the final conjugate (**7** in Scheme 1) (*32*). A short PEG spacer (28 repeat units, MW ~1232) was introduced to facilitate accessibility of ^{64}Cu to the chelator by minimizing the steric effect of neighboring lipid head groups, while burying the chelator within the longer PEG brush (45 repeat units, MW ~1980) of the surrounding lipid molecules. Briefly, Fmoc-Cys(Mmt)-OH, Fmoc-NH-(PEG)27-COOH, Fmoc-Lys(Fmoc)-OH, and stearic acid were sequentially coupled to the PAL-PEG-PS resin, to obtain **5** in Scheme 1. After the protecting group, Mmt, was removed with 1% TFA/DCM, BAT was coupled to the resin in the mixture solvent (DMF/DMSO/H_2O = 1:1:1, v/v/v), at pH 8.0 ± 0.5, adjusted with DIPEA. The reaction was monitored with DTNP solution. The final product (**7** in Scheme 1) was cleaved from the resin by a TFA/TIPS/H_2O mixture (TFA/TIPS/H_2O = 95:2.5:2.5, v/v/v) and purified by HPLC, with the mass confirmed by MALDI ($M + H^+$, measured, 2662; calculated, 2663; Figure 2).

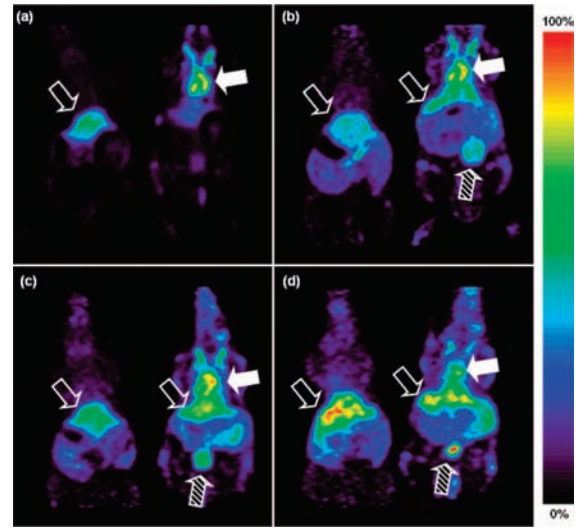

Figure 5. Coronal view of a microPET image with two mice (left, $^{64}CuCl_2$ injected; right, ^{64}Cu-liposomes) at four time points ((a) 0, (b) 18, (c) 28, and (d) 48 h after i.v. injection). A relative scale (the brightest spot is maximum) was applied for images. The filled arrow indicates the blood pool, the striped arrow indicates the bladder, and the unfilled arrow indicates the liver.

To check the feasibility of chelating ^{64}Cu onto BAT liposomes, the chelation yields were compared for three temperature sensitive liposome formulations (*33*, *34*), with 0, 0.1, and 1.0 mol% BAT−PEG−lipid, respectively (Figure 3). Similar to the labeling protocol developed for antibodies (*25*), chelation of ^{64}Cu onto liposomes was performed in 0.1 M NH_4OAc pH 5 buffer at room temperature for 60 min. Unchelated ^{64}Cu was removed by mixing the liposome solution with 1/10 (v/v) 0.1 M EDTA solution for 20 min. ^{64}Cu-labeled liposomes and ^{64}Cu-EDTA complexes were separated with a Sephadex-G75 column with the normalized radioactivity of each fraction shown in Figure 3. The ^{64}Cu chelation yields for 0, 0.1, and 1.0 mol% BAT liposomes were 0%, 83%, and 89%, respectively. Specific activity of the chelator was determined as 29.1 μCi (0.1 mol%) and 31.3 μCi (1.0 mol%) per 1 mg of total lipids and as 27.5 and 2.96 Ci per 1 mmol BAT−PEG−lipids. The number of BAT−PEG−lipid molecules in the 0.1 mol% BAT liposomes was 11 times more than the molecules of added $^{64}CuCl_2$ (0.42 mCi).

To demonstrate that this technique can successfully label multiple liposomal formulations and to demonstrate stability over 48 h, *in vitro* and *in vivo* assays were performed with long circulating liposomes (*35*). The *in vitro* stability of ^{64}Cu-labeled liposomes was also tested with 0.5 mol% BAT−PEG−lipids in a nontemperature sensitive formulation. Incubation of both liposomes with $^{64}CuCl_2$ at 35 °C for 45 min, followed by treatment with EDTA solution for 15 min, gave an estimated 95% labeling yield with 0.5 mol% BAT liposomes (Figure 4a). Specific activity was measured as 0.194 mCi per 1 mg of total lipids or 28.2 Ci per 1 mmol BAT−PEG−lipids.

^{64}Cu was not detected on liposomes lacking the BAT-lipid. Labeled liposomes in PBS (pH 7.4) were mixed with albumin (10 mg/mL) and mouse serum (PBS/serum = 1:1, v:v). Mixtures were allowed to stand at 37 °C, and the stability was monitored by radio TLC (Figure 4b) and chromatography with a size exclusion column (Figure 4c,d). As shown in the TLC study

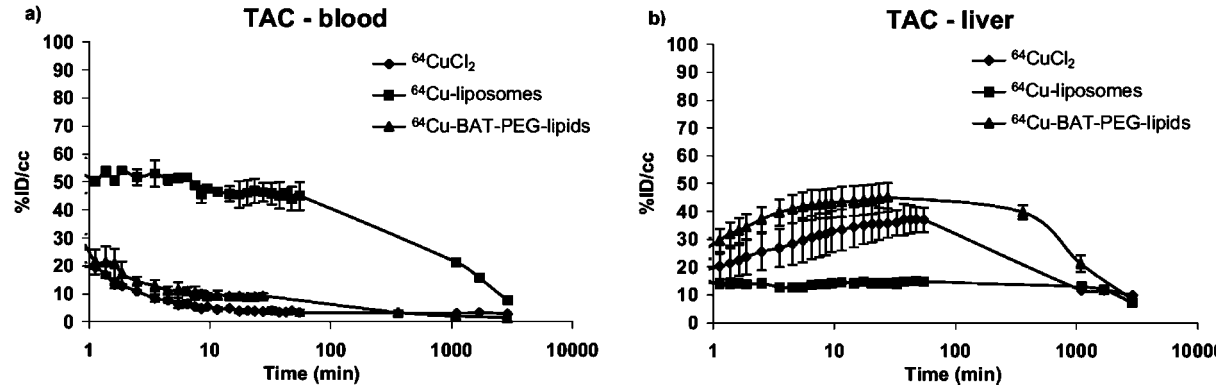

Figure 6. Time activity curves in blood and liver of mice ($n = 3-4$ per group) after bolus injections of $^{64}CuCl_2$, ^{64}Cu-BAT−PEG−lipid, and ^{64}Cu-labeled liposomes. TACs for heart and liver (a and b) were obtained from microPET in each organ of interest as a function of time by drawing regions of interest (ROI).

(Figure 4b), radioactivity in the form of $^{64}CuCl_2$ (lane 1), $^{64}CuCl_2$ associated with albumin (lane 3), and $^{64}CuCl_2$ associated with serum (lane 5) were retained at the origin. However, the relatively lipophilic ^{64}Cu-liposomes (lane 2) (^{64}Cu−BAT−PEG−lipid on silica plate), shifted to R_f 0.8, including 99% of the radioactivity. ^{64}Cu-liposomes incubated with albumin (lane 4) for 48 h also showed 99% of the radioactivity in the R_f 0.8 region. This suggests that ^{64}Cu-liposomes are inert to albumin. With ^{64}Cu-liposomes incubated with mouse serum, 6% and 8% of the activity was found in R_f 0.0 after 20 and 48 h of incubation, respectively. The chemical form of the copper was not investigated further.

To further characterize the effect of serum on chelation stability, an analysis was performed using size exclusion chromatography, with aliquots of solution loaded into the size exclusion column after incubation with albumin and serum for 1 and 48 h. The radioactivity was measured with a gamma-counter and absorbance of the serum component read at 280 nm. The size exclusion chromatogram of radioactivity from the albumin mixture (Figure 4c) showed that fractions (f1−30) contain more than 99% of the total radioactivity. Liposome fractions in the main peak (f7−15) and minor broad peak (f16−22) contained 95% and 4.1% of the total radioactivity, respectively. Thus, the labeled liposomes (radioactivity) and albumin (280 nm) could be separated, and albumin, the major component of serum, did not affect the stability of the labeled liposomes.

Size exclusion chromatography (Figure 4d) following serum incubation also showed that fractions (f1−30) contain more than 99% of the total radioactivity. As shown in Figure 4d, three peaks, with fractions f9−15, f16−22, and f23−30 were found to have 88%, 9.1%, and 2.7% of the radioactivity, respectively. To elucidate whether the second peak (f16−22) contains ^{64}Cu−BAT−PEG−lipid or dissociated ^{64}Cu, radio TLC of one fraction was performed. TLC showed three peaks (Figure 4e) corresponding to R_f equal to 0 (7%), 0.35 (22%), and 0.8 (71%). If the result is compared with lane 2 in Figure 4b, the major peak (R_f of 0.8) corresponds with the ^{64}Cu-liposomes. Radioactivity after the 14th fraction in Figure 4d is assumed to represent ^{64}Cu−BAT−PEG−lipids, which associated with serum during incubation. Therefore, we estimate that more than 88% of the ^{64}Cu remained associated with the liposomes after 48 h in serum. Prior work with ^{67}Cu-antibodies labeled using BAT showed a dissociation of copper from the chelator of approximately 1% per day under physiological conditions in serum (*25*). The properties of liposomes, including possible exchange of lipids with other serum components, make it difficult to specifically measure the rate of copper dissociation for the system studied here.

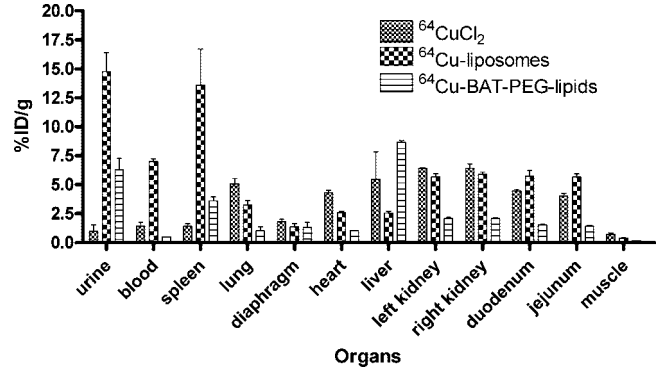

Figure 7. Biodistribution of liposomal ^{64}Cu ($n = 4$), ^{64}Cu-BAT−PEG−lipid ($n = 3$), and free ^{64}Cu ($n = 3$) in mice at 48 h after injection.

The *in vivo* performance of ^{64}Cu-labeled liposomes was studied, with the *in vivo* results compared with previously reported ^{99m}Tc-labeled liposome studies (*14*, *36*). Liposomes with 0.5 mol% BAT−PEG−lipid were labeled with $^{64}CuCl_2$ (3.0−4.0 mCi/mg lipids) at 37 °C for 40 min. The labeling yield was 62 ± 13% ($n = 2$), and the specific activity was 1.65 ± 0.29 ($n = 2$) mCi per 1 mg of total lipids or 242 ± 42 ($n = 2$) Ci per 1 mmol BAT−PEG−lipids. The size and zeta potential of liposomes before and after labeling are listed in Table 1. The liposomes were reduced in size by about 10 nm after labeling, likely due to a difference in osmolarity before (0.1 M ammonium acetate buffer, ∼240 mOsm, pH 5.0) and after labeling (10 mM PBS buffer, ∼300 mOsm, pH 7.4). Zeta potential was not significantly changed before (−40.8 mV) and after (−41.2 mV) labeling.

In vivo imaging with ^{64}Cu-labeled liposomes was then performed in FVB mice with microPET and compared with free ^{64}Cu ($^{64}CuCl_2$). Figure 5 shows four images from 30-min scans at 0, 18, 28, 48 h after i.v. injection, for both a free ^{64}Cu injection (left) and a liposomal ^{64}Cu injection (right). Free ^{64}Cu rapidly accumulated in the liver (Figure 5a−d), and accumulation was highest in the liver throughout the scan as in ref *37*. In contrast, liposomal ^{64}Cu remained in the blood pool (Figure 5a−d) through 18, 28, and 48 h. Uptake of the liposomes by the reticulo-endothelial system is expected with previous SPECT studies showing accumulation similar to that observed here (*14*). The accumulation of ^{64}Cu in the liver and other organs can result from intracellular processes via the metabolism of liposomes (*38*) and transchelation of ^{64}Cu to ceruloplasmin (*26*), superoxide dismutase (SOD) (*38*, *39*), or copper chaperone for SOD (*40*);

however, comparing our results with previous liposomal SPECT studies using Tc-99m, these effects do not appear to be substantial.

Time activity curves (TAC) corresponding to blood and liver are shown in Figure 6. For the ^{64}Cu-liposomes, decay-corrected radioactivity in the blood pool decreased to 44 ± 6.9, 21 ± 2.7, 15 ± 2.5, and 7.4 ± 1.1 ($n = 4$) %ID/cc at 30 min, 18, 28, and 48 h, respectively (Figure 6). To compare our TAC data with (*14*), the maximum %ID/cc (50 ± 8.9) at 2 min was fixed as the initial blood pool activity, and the TAC estimates at 30 min, 18, 28, and 48 h were converted to 88%, 42%, 30%, and 15%, repectively, of the original radioactivity in the blood pool. These values are similar to those observed by Laverman in a study of rats with ^{99m}Tc-HYNIC liposomes, which showed 40% of the initial blood-pool radioactivity remaining at 24 h (*14*). Similarly, 38% of initial activity was retained in the blood pool at 20 h following injection of labeled liposomes into rats in (*36*). A solution of ^{64}Cu−BAT−PET−lipid (specific activity, 575 Ci/mmol) was also injected into the mouse tail vein ($n = 3$). As a result, radioactivity accumulated in the liver within 30 min and cleared in a manner similar to that of the injected $^{64}CuCl_2$ (Figure 6).

The biodistribution at 48 h shows that activity in the urine, blood, and spleen of liposomal ^{64}Cu was significantly higher than that of free ^{64}Cu or ^{64}Cu-BAT-PET-lipid (Figure 7). Subsequent studies have indicated that the activity within the spleen is dependent on the lipid dose injected, decreasing with larger amounts of lipid (data not shown).

CONCLUSIONS

We describe a novel ^{64}Cu labeling method for liposomes. By solid phase synthesis, a BAT−PEG−lipid conjugate was prepared, and by incorporating BAT−PEG−lipid into liposomes and incubating the resulting liposomes with $^{64}CuCl_2$, ^{64}Cu liposomes were obtained with a labeling yield as high as 95%. The liposomal ^{64}Cu was stable in mouse serum *in vitro* and was long-circulating *in vivo*. These results suggest that this novel labeling method (^{64}Cu-BAT-liposomes) can be further exploited for tracking liposomes with PET *in vivo*.

ACKNOWLEDGMENT

The staff in the CMGI (Center for Molecular and Genomic Imaging, UC Davis) for handling ^{64}Cu and imaging studies are gratefully acknowledged. The support of NIH CA 103828 is appreciated.

LITERATURE CITED

(1) Janoff, A. S. (1999) *Liposomes: Rational Design*, Marcel Dekker, New York.

(2) Gregoriadis, G. (2007) *Liposome Technology*, 3rd ed., Informa Healthcare, New York.

(3) Immordino, M. L., Dosio, F., and Cattel, L. (2006) Stealth liposomes: review of the basic science, rationale, and clinical applications, existing and potential. *Int. J. Nanomed. 1*, 297–315.

(4) Harrington, K. J., Rowlinson-Busza, G., Syrigos, K. N., Uster, P. S., Vile, R. G., and Stewart, J. S. (2000) Pegylated liposomes have potential as vehicles for intratumoral and subcutaneous drug delivery. *Clin. Cancer Res. 6*, 2528–2537.

(5) Phillips, W. T., Rudolph, A. S., Goins, B., Timmons, J. H., Klipper, R., and Blumhardt, R. (1992) A simple method for producing a technetium-99m-labeled liposome which is stable in vivo. *Int. J. Radiat. Appl. Instrum. B 19*, 539–547.

(6) Awasthi, V. D., Garcia, D., Klipper, R., Goins, B. A., and Phillips, W. T. (2004) Neutral and anionic liposome-encapsulated hemoglobin: effect of postinserted poly(ethylene glycol)-distearoylphosphatidylethanolamine on distribution and circulation kinetics. *J. Pharmacol. Exp. Ther. 309*, 241–248.

(7) Bao, A., Goins, B., Klipper, R., Negrete, G., Mahindaratne, M., and Phillips, W. T. (2003) A novel liposome radiolabeling method using ^{99m}Tc-"SNS/S" complexes: in vitro and in vivo evaluation. *J. Pharm. Sci. 92*, 1893–1904.

(8) Gabizon, A., and Papahadjopoulos, D. (1988) Liposome formulations with prolonged circulation time in blood and enhanced uptake by tumors. *Proc. Natl. Acad. Sci. U.S.A. 85*, 6949–6953.

(9) Marik, J., Tartis, M. S., Zhang, H., Fung, J. Y., Kheirolomoom, A., Sutcliffe, J. L., and Ferrara, K. W. (2007) Long-circulating liposomes radiolabeled with [^{18}F]fluorodipalmitin ([^{18}F]FDP). *Nucl. Med. Biol. 34*, 165–171.

(10) Urakami, T., Akai, S., Katayama, Y., Harada, N., Tsukada, H., and Oku, N. (2007) Novel amphiphilic probes for [^{18}F]-radiolabeling preformed liposomes and determination of liposomal trafficking by positron emission tomography. *J. Med. Chem. 50*, 6454–6457.

(11) Corvo, M. L., Boerman, O. C., Oyen, W. J., Van Bloois, L., Cruz, M. E., Crommelin, D. J., and Storm, G. (1999) Intravenous administration of superoxide dismutase entrapped in long circulating liposomes. II. In vivo fate in a rat model of adjuvant arthritis. *Biochim. Biophys. Acta 1419*, 325–334.

(12) Ogihara-Umeda, I., and Kojima, S. (1988) Increased delivery of gallium-67 to tumors using serum-stable liposomes. *J. Nucl. Med. 29*, 516–523.

(13) Oku, N., Tokudome, Y., Tsukada, H., and Okada, S. (1995) Real-time analysis of liposomal trafficking in tumor-bearing mice by use of positron emission tomography. *Biochim. Biophys. Acta 1238*, 86–90.

(14) Laverman, P., Dams, E. T., Oyen, W. J., Storm, G., Koenders, E. B., Prevost, R., van der Meer, J. W., Corstens, F. H., and Boerman, O. C. (1999) A novel method to label liposomes with ^{99m}Tc by the hydrazino nicotinyl derivative. *J. Nucl. Med. 40*, 192–197.

(15) Hnatowich, D. J., Friedman, B., Clancy, B., and Novak, M. (1981) Labeling of preformed liposomes with Ga-67 and Tc-99m by chelation. *J. Nucl. Med. 22*, 810–814.

(16) Rahmim, A. (2006) PET vs. SPECT: in the context of ongoing developments. *Iran. J. Nucl. Med. 14*, 1–20.

(17) Lukyanov, A. N., Gao, Z., Mazzola, L., and Torchilin, V. P. (2002) Polyethylene glycol-diacyllipid micelles demonstrate increased acculumation in subcutaneous tumors in mice. *Pharm. Res. 19*, 1424–1429.

(18) Medina, O. P., Zhu, Y., and Kairemo, K. (2004) Targeted liposomal drug delivery in cancer. *Curr. Pharm. Des. 10*, 2981–2989.

(19) Ponce, A. M., Vujaskovic, Z., Yuan, F., Needham, D., and Dewhirst, M. W. (2006) Hyperthermia mediated liposomal drug delivery. *Int. J. Hyperthermia. 22*, 205–213.

(20) Tilcock, C., Ahkong, Q. F., and Fisher, D. (1994) ^{99m}Tc-labeling of lipid vesicles containing the lipophilic chelator PE-DTTA: effect of tin-to-chelate ratio, chelate content and surface polymer on labeling efficiency and biodistribution behavior. *Nucl. Med. Biol. 21*, 89–96.

(21) Ahkong, Q. F., and Tilcock, C. (1992) Attachment of ^{99m}Tc to lipid vesicles containing the lipophilic chelate dipalmitoylphosphatidylethanolamine-DTTA. *Int. J. Radiat. Appl. Instrum. B 19*, 831–840.

(22) Smith, S. V. (2004) Molecular imaging with copper-64. *J. Inorg. Biochem. 98*, 1874–1901.

(23) Wadas, T. J., Wong, E. H., Weisman, G. R., and Anderson, C. J. (2007) Copper chelation chemistry and its role in copper radiopharmaceuticals. *Curr. Pharm. Des. 13*, 3–16.

(24) Moran, J. K., Greiner, D. P., and Meares, C. F. (1995) Improved synthesis of 6-[p-(bromoacetamido)benzyl]-1,4,8,11-tetraazacyclotetradecane- N,N′,N″,N‴-tetraacetic acid and development of a thin-layer assay for thiol-reactive bifunctional chelating agents. *Bioconjugate Chem. 6*, 296–301.

(25) Kukis, D. L., Diril, H., Greiner, D. P., DeNardo, S. J., DeNardo, G. L., Salako, Q. A., and Meares, C. F. (1994) A comparative study of copper-67 radiolabeling and kinetic stabilities of antibody-macrocycle chelate conjugates. *Cancer 73*, 779–786, Suppl. S.

(26) Mirick, G. R., O'Donnell, R. T., DeNardo, S. J., Shen, S., Meares, C. F., and DeNardo, G. L. (1999) Transfer of copper from a chelated ^{67}Cu-antibody conjugate to ceruloplasmin in lymphoma patients. *Nucl. Med. Biol. 26*, 841–845.

(27) Kukis, D. L., Li, M., and Meares, C. F. (1993) Selectivity of antibody-chelate conjugates for binding copper in the presence of competing metals. *Inorg. Chem. 32*, 3981–3982.

(28) McCall, M. J., Diril, H., and Meares, C. F. (1990) Simplified method for conjugating macrocyclic bifunctional chelating agents to antibodies via 2-iminothiolane. *Bioconjugate Chem. 1*, 222–226.

(29) Kukis, D. L., DeNardo, G. L., DeNardo, S. J., Mirick, G. R., Miers, L. A., Greiner, D. P., and Meares, C. F. (1995) Effect of the extent of chelate substitution on the immunoreactivity and biodistribution of 2IT-BAT-Lym-1 immunoconjugates. *Cancer Res. 55*, 878–884.

(30) Boswell, C. A., Sun, X., Niu, W., Weisman, G. R., Wong, E. H., Rheingold, A. L., and Anderson, C. J. (2004) Comparative in vivo stability of copper-64-labeled cross-bridged and conventional tetraazamacrocyclic complexes. *J. Med. Chem. 47*, 1465–1474.

(31) Keller, B. O., and Li, L. (2006) Three-layer matrix/sample preparation method for MALDI MS analysis of low nanomolar protein samples. *J. Am. Soc. Mass. Spectrom. 17*, 780–5.

(32) Chan, W. C., and White, P. D. (2000) *Fmoc Solid Phase Peptide Synthesis: A Practical Approach*, Oxford University Press, New York.

(33) Anyarambhatla, G. R., and Needham, D. (1999) Enhancement of the phase transition permeability of DPPC liposomes by incorporation of MPPC: A new temperature-sensitive liposome for use with mild hyperthermia. *J. Liposome Res. 9*, 491–506.

(34) Hossann, M., Wiggenhorn, M., Schwerdt, A., Wachholz, K., Teichert, N., Eibl, H., Issels, R. D., and Lindner, L. H. (2007) In vitro stability and content release properties of phosphatidylglyceroglycerol containing thermosensitive liposomes. *Biochim. Biophys. Acta 1768*, 2491–2499.

(35) Gabizon, A., Shmeeda, H., and Barenholz, Y. (2003) Pharmacokinetics of pegylated liposomal Doxorubicin: review of animal and human studies. *Clin. Pharmacokinet. 42*, 419–436.

(36) Bao, A., Goins, B., Klipper, R., Negrete, G., and Phillips, W. T. (2004) Direct ^{99m}Tc labeling of pegylated liposomal doxorubicin (Doxil) for pharmacokinetic and non-invasive imaging studies. *J. Pharmacol. Exp. Ther. 308*, 419–425.

(37) Owen, C. A., Jr. (1965) Metabolism of radiocopper (Cu^{64}) in the rat. *Am. J. Physiol. 209*, 900–904.

(38) Rogers, B. E., Anderson, C. J., Connett, J. M., Guo, L. W., Edwards, W. B., Sherman, E. L., Zinn, K. R., and Welch, M. J. (1996) Comparison of four bifunctional chelates for radiolabeling monoclonal antibodies with copper radioisotopes: biodistribution and metabolism. *Bioconjugate Chem. 7*, 511–522.

(39) Bass, L. A., Wang, M., Welch, M. J., and Anderson, C. J. (2000) In vivo transchelation of copper-64 from TETA-octreotide to superoxide dismutase in rat liver. *Bioconjugate Chem. 11*, 527–532.

(40) Wong, P. C., Waggoner, D., Subramaniam, J. R., Tessarollo, L., Bartnikas, T. B., Culotta, V. C., Price, D. L., Rothstein, J., and Gitlin, J. D. (2000) Copper chaperone for superoxide dismutase is essential to activate mammalian Cu/Zn superoxide dismutase. *Proc. Natl. Acad. Sci. U.S.A. 97*, 2886–2891.

BC8002937

Design, Synthesis, and Evaluation of Biotinylated Opioid Derivatives as Novel Probes to Study Opioid Pharmacology

Ya Li, Anna R. Chase, Peter F. Slivka, Clyde T. Baggett, Tina X. Zhao, and Hang Yin*

Department of Chemistry and Biochemistry, 215 UCB, University of Colorado at Boulder, Boulder, Colorado 80309-0215.
Received September 8, 2008; Revised Manuscript Received October 17, 2008

A generally applicable strategy of chemically labeling (-)-morphine (**1**) is described. The synthesis starts from commercially available starting materials and can be completed in two steps with an overall yield of 23%. In silico simulation and NMR results show that the binding of (-)-morphine to one of its molecular targets, toll-like receptor **4** (TLR4), was not affected by the modification. Secreted embryonic alkaline phosphatase (SEAP) reporter assay results demonstrate that C_3 biotinylated and unmodified (-)-morphine show similar biological activities in live cells. To our knowledge, these studies provide the first practical and concise method to label various opioid derivatives, a group of important therapeutics in pain management, for biochemical/pharmacological studies.

INTRODUCTION

(-)-Morphine is a naturally occurring substance extracted from the unripe seedpods of the opium poppy, *Papaver somniferum*, and is widely used as a narcotic analgesic in the control of severe pain. (-)-Morphine activates opioid receptors expressed on neurons in the central and peripheral nervous system (*1, 2*). Activation of the receptor leads to the release of opioid peptides which prompt a diverse array of biological responses including pain suppression. Aside from its clinical application, (-)-morphine has firmly established itself as a model for the studies of opiate pharmacokinetics and pharmacodynamics. However, investigations of precisely how (-)-morphine binds to its molecular target and regulates the signaling cascade are underrepresented due to the lack of a straightforward labeling method (*3*). To the best of our knowledge, no chemical labeling has been previously reported, partly because of the challenge posed by the complex structure of (-)-morphine (**1**) and the difficulty to retain its drug activity upon modification. Herein, we report the first practical and concise synthesis of biotinylated (-)-morphine (**2**) as a novel probe for the molecular target toll-like receptor **4** (TLR4), which has been recently discovered to play an essential role in microglial activation (*4, 5*). In particular, TLR4 signaling mediates the production of a variety of proinflammatory cytokines and pain mediators. These mediators sensitize neurons and activate other microglia as part of a positive feedback loop (*6*). This method provides a potentially generally applicable strategy to label various opioid derivatives, a group of important therapeutics in pain management, for biochemical/pharmacological studies.

Our design strategy was to attach a biotin probe while minimally affecting the binding activity of (-)-morphine (**1**) to TLR4. Previous structure−activity relationship studies of (-)-morphine (**1**) and other related opioid derivatives showed that the phenolic C_3 position as well as the alcoholic C_6 position (Figure 1) in (-)-morphine can be potential sites to introduce chemical labels (*4, 5*). In fact, the human body's own metabolism of morphine in the liver and small intestine involves attaching a pyranose ring to either the C_3 or the C_6 position, producing morphine-3-glucuronide (**3**) (M3G) or morphine-6-glucuronide (**4**) (M6G) with M3G as the major metabolite (*7*).

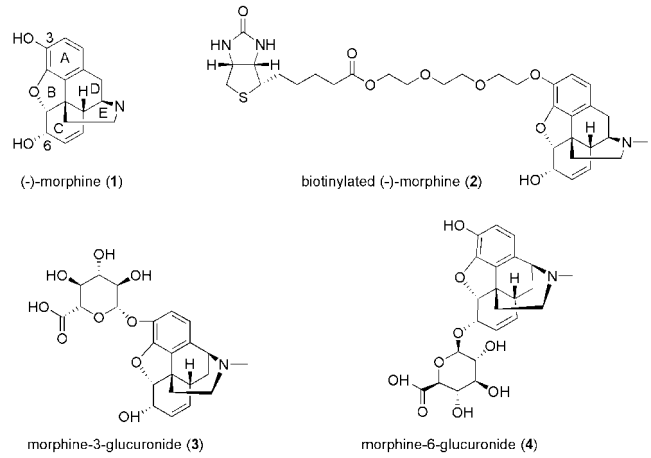

Figure 1. Chemical structures of (-)-morphine (**1**), biotinylated (-)-morphine (**2**), M3G (**3**), and M6G (**4**).

The rationale for introducing a chemical label at the C_3 position was to mimic the M3G, the major metabolite and the active form for the TLR4-activating functions of (-)-morphine in vivo. Further, the C_3- phenol is a conserved functional group found in many clinically relevant opiate alkaloids (e.g., naloxone, naltrexone, nalmefene), which makes this labeling strategy generally applicable. Biotinylated (-)-morphine (**2**) is predicted to have similar receptor-binding properties to unmodified (-)-morphine (**1**), allowing various biochemical/biophysical measurements and thereby establishing a novel tool for the study of opioid pharmacology (*4, 5*). Cellular assays performed using biotinylated (-)-morphine (**2**) and (-)-morphine (**1**) indicated that both show similar interactions to TLR4. This observation in conjunction with in silico binding studies solidifies biotinylated (-)-morphine's potential as a novel probe for more extensive studies of morphine/TLR4 interactions.

EXPERIMENTAL METHODS

General Methods and Materials. Unless otherwise mentioned, solvents and reagent were purchased from commercial sources and used as received. NMR spectra were recorded on Varian 400/500 NMR spectrometers. High-resolution mass data

* Corresponding author. Tel: +1-303-492-6786. Fax: +1-303-492-5894. E-mail address: hang.yin@colorado.edu.

10.1021/bc8003815 CCC: $40.75 © 2008 American Chemical Society
Published on Web 12/17/2008

were recorded on a high-resolution mass spectrometer in the ESI or MALDI mode.

Synthesis of Compound 7. Under N_2 atmosphere, into a 15-mL Schlenk flask containing biotin (**5**) (244 mg, 1.0 mmol) in 5 mL anhydrous DMSO at 25 °C, was added NaH (44 mg, 1.1 mmol, 60% dispersion in mineral oil). The reaction mixture was stirred at this temperature for 10 min. Then, 1,2-bis(2-iodoethoxy) ethane (**6**) (555 mg, 1.5 mmol) was added dropwise, and the reaction mixture was stirred for another 14 h, followed by adding a half-saturated NH_4Cl-H_2O solution (10 mL) at this temperature. The solution mixture was extracted with EtOAc (25 mL × 3), and the combined organic phase was dried over $MgSO_4$. After the removal of volatile solvents under vacuum, the crude product was further purified by silica gel column chromatography with ethyl acetate/petroleum ether (1:3) to give product **7** as a white solid, yield 65% (318 mg). Characterization for compound **7**: $[\alpha]^{25}_D = +31.0$ ($c = 1.0$, $CHCl_3$). ^1H NMR ($CDCl_3$, 500 MHz) δ 5.81 (s, 1H); 5.23 (s, 1H); 4.52−4.54 (m, 1H); 4.32−4.35 (m, 1H); 4.23−4.28 (m, 2H); 3.78 (t, $J = 7.0$ Hz, 2H); 3.73 (t, $J = 4.5$ Hz, 2H); 3.69 (s, 4H); 3.29 (dd, $J = 7.0$, 6.0 Hz, 2H); 3.16−3.19 (m, 1H); 2.93 (dd, $J = 12.5$, 5.5 Hz, 1H); 2.76 (d, $J = 12.5$ Hz, 1H); 2.40 (t, $J = 7.0$ Hz, 2H); 1.67−1.76 (m, 4H); 1.45−1.50 (m, 2H). ^{13}C NMR ($CDCl_3$, 100 MHz) δ 173.9, 164.0, 72.1, 70.7, 70.4, 69.4, 63.6, 62.1, 60.3, 55.8, 40.8, 34.0, 28.5, 28.4, 24.9, 3.2. HRMS (MALDI) calcd. For $C_{16}H_{28}N_2O_5S$ ($M + H^+$): 487.0758, Found 487.0754.

Synthesis of Biotinylated (-)-Morphine (2). Under N_2 atmosphere, into a 15-mL Schlenk flask containing (-)-morphine (**1**) (29 mg, 0.1 mmol) in 2.0 mL anhydrous DMSO at 25 °C, NaH was added (4.4 mg, 0.11 mmol). The reaction mixture was stirred at this temperature for 10 min. Then, compound **7** (49 mg, 0.1 mmol) dissolved in 0.5 mL anhydrous DMSO was added dropwise, and the reaction mixture was stirred for another 12 h. Silica gel column chromatography with methanol/dichloromethane (10:1) afforded biotinylated (-)-morphine (**2**) as an oil, yield 35% (20 mg). Characterization for compound **2**: $[\alpha]^{25}_D = -24.5$ ($c = 1.25$, $CHCl_3$). ^1H NMR (CD_3OD, 400 MHz) δ 6.69 (d, $J = 8.2$ Hz, 1H); 6.53 (d, $J = 8.2$ Hz, 1H); 5.62−5.66 (m, 1H); 5.32−5.36 (m, 1H), 4.83 (dd, $J = 6.2$, 1.2 Hz, 1H); 4.45−4.49 (m, 1H), 4.07−4.30 (m, 7H); 3.78−3.81 (m, 2H), 3.64−3.71 (m, 6H), 3.38−3.41 (m, 1H), 3.16−3.20 (m, 1H), 3.07 (d, $J = 19.4$ Hz, 1H), 2.91 (dd, $J = 12.0$, 4.0 Hz, 1H); 2.69 (d, $J = 12.0$ Hz, 1H), 2.66−2.67 (m, 1H), 2.59−2.63 (m, 1H), 2.44 (s, 3H); 2.39−2.43 (m, 1H), 2.34−2.38 (m, 3H); 2.09 (td, $J = 7.5$, 4.8 Hz, 1H), 1.80−1.83 (m, 1H), 1.53−1.75 (m, 4H), 1.40−1.48 (m, 2H). ^{13}C NMR ($CDCl_3$, 100 MHz) δ 173.9, 163.6, 147.2, 141.2, 133.6, 131.6, 128.5, 128.1, 119.7, 115.3, 91.7, 70.8, 70.7, 70.1, 69.4, 69.2, 66.7, 63.6, 62.0, 60.2, 59.0, 55.6, 46.6, 43.4, 43.1, 41.0, 40.7, 36.0, 33.9, 28.4, 28.3, 24.9, 20.5. ESI (*m*/*z*) 644.2 ($M + H^+$). HRMS (ESI) calc. For $C_{33}H_{46}N_3O_8S^+$ ($M + H^+$): 644.3000, Found 644.2970.

(-)-Morphine (1) Conformational Analysis. Conformational analysis of biotinylated (-)-morphine **2** was performed using *Spartan 06* software from Wave function Inc. MMFF94 force field was used in the conformational scan simulation. Following a geometric optimization of the molecule using AM1 semiempirical methods, the Spartan program carried out a scan for the lowest energy conformer. The twelve conformers with the lowest respective energies were selected and their structures superimposed to validate the energy minimization. The final structure visualization is the lowest energy of these conformers compared to the (-)-morphine (**1**).

Ligand Docking. Using *AutoDock 4.0* (*8*), in silico docking experiments were carried out to search for potential binding sites on TLR4 (*9*). Lamarckian generic algorithm (LGA) and the torsion angles of the ligand were varied using AUTOTORS. First, the high-resolution structure of TLR4 was used as the target receptor after modification of Gasteiger charges and surface solvation. The full length of TLR4 is split into two parts to which the opioid molecules were docked in order to carry out more accurate calculation. Both receptor and ligand were allowed flexibility when running morphine against TLR4. Energy-minimized biotinylated (-)-morphine (**2**) was used in the docking and allowed to have seventeen of its bonds able to rotate within its structure to simulate realistic binding of this ligand to TLR4. A total of 100 runs were carried out and the results were grouped into clusters using an rmsd-tolerance of 2.0 Å. Finally, the resultant clusters were ranked using a force field scoring function (*10*). The credibility of the docking results was evaluated by estimating binding energy and the distribution of the independent runs in clusters (fewer binding modes predicted is preferred). Among those, the highest-ranked docked structure was used for molecular visualization.

SEAP Assay Methods. All materials were obtained commercially from sources (Invitrogen and Invivogen). Materials for the SEAP assay were obtained from Applied Biosystems and utilized according to the manufacturer's specifications (*11*). Cell Culture: Human embryonic kidney 293 (HEK293) stably transfected with TLR4 and a secreted alkaline phosphatase (SEAP) reporter gene were obtained from Invivogen. Cells were cultured in DMEM medium supplemented with 10% fetal bovine serum, 10× penicillin/streptomycin, 10× L-glutamine, 1× Normocin (ant-nr-1), and 1× HEK Blue (hb-sel). Cells were implanted in 96 well plates 48 h at 37 °C prior to drug treatment. On the day of treatment, media was removed from the 96-well plate replaced with cerebrospinal fluid (CSF) buffer (124 mM NaCl, 5 mM KCl, 0.1 mM $CaCl_2$, 3.2 mM $MgCl_2$, 26 mM $NaHCO_3$, and 10 mM glucose, pH 7.4) containing 0.25−4.0 mM biotinylated morphine.

A sample of CSF buffer (15 μL) from each well was collected and transferred to an opaque white 96 well plate (Microfluor 2, Thermo Scientific). Each well was treated with 45 μL of 1× dilution buffer, covered with microseal (MSB1001, Bio-Rad), and incubated for 30 min at 65 °C. After 30 min, plates were cooled to room temperature on ice and 50 μL of SEAP assay buffer was added to each well. After a 5 min incubation, 50 μL of disodium 3-(4-methoxyspiro{1,2-dioxetane-3,2-(5-chloro)-tricyclo[3.3.1.13,7]decan}-4-yl) phenyl phosphate (CSPD) diluted 1:20 with reaction buffer was added to each well. After 20 min, the luminescence of each well was measured using a Beckman Coulter, DTX 880 plate reader with multimode analysis software. Regression analyses were carried out using KaleidaGraph. Experimental data were fitted to one-site-saturation ligand binding mode. Raw luminescence scores were expressed as a percentage of luminescence against a control.

RESULTS AND DISCUSSION

Our straightforward synthesis of biotinylated (-)-morphine (**2**) is outlined in Scheme 1. The intermediate **7** can be readily obtained in good yield (65%) by the classical substitution reaction between deprotonated biotin (**5**) and commercially available 1,2-bis-(2-iodoethoxy)-ethane (**6**). It is observed that the choice of base is pivotal for this reaction, since compound **6** is unstable under strong basic conditions. Compound **7** was then subject to react with (-)-morphine (**1**). We found that the conditions had to be carefully tuned to selectively alkylate the C_3 phenolic hydroxyl group. It is also important to prevent elimination of HI from compound **7**. Several bases (NEt_3, KOH, or NaH) and solvents (Et_2O, DMF, $CHCl_3$, or DMSO) were tested (Table 1), each of which had different effects in promoting the reaction. Using weaker bases, such as K_2CO_3 and NEt_3, and less polar solvents, no reaction occurred and the reactants could be recovered completely. When the reaction was subjected to the strong inorganic base KOH, compound **7** partly degraded

Scheme 1. Synthesis of Biotinylated (-)-Morphine (2)

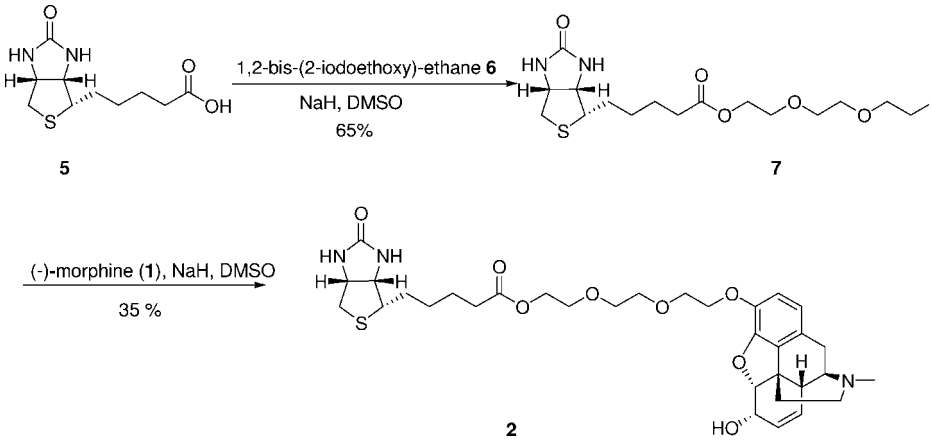

Table 1. Optimization of the Coupling Reaction between Compound 7 and (-)-Morphine (1)

entry	reaction conditions	yield (%)
1	K_2CO_3, Et_2O, rt.	0
2	NEt_3, DMSO, rt.	0
3	KOH, DMSO, rt.	0
4	NaH, DMSO, rt.	35
5	NaH, DMF, rt.	30
6	NaH, 18-crown-6, $CHCl_3$, rt.	0
7	NaH, 18-crown-6, DMSO, rt.	10[a]

[a] Based on the ^{1}H NMR of the mixture of compound **2** and 18-crown-6.

due to the fragile nature of compound **7** under strong basic conditions. Finally, optimal conditions were obtained by using NaH to deprotonate the phenol of (-)-morphine (**1**) in DMSO, which subsequently reacted with compound **7** to provide biotinylated (-)-morphine (**2**) in 35% yield.

Further optimization using phase transfer catalyst, 18-crown-6, to improve the yield did not prove successful. Given the concise synthetic route (only two steps with an overall yield of 23%) and commercially available starting materials, our synthesis represents a very streamlined approach to obtaining C_3 labeled morphine.

The fact that the chemical modification did not significantly alter the binding mode of (-)-morphine (**1**) to its receptor TLR4 is supported by the in silico simulation, NMR spectroscopy, and whole cell assays. Using a molecular mechanics (MM) simulation model with a Merck molecular force field (MMFF), a total of 2704 conformers of biotinylated (-)-morphine (**2**) were scanned to search for the most favorable structure (Figure 2). Energy minimization of the (-)-morphine (**1**) and biotinylated (-)-morphine (**2**) suggests that the morphine substructure in compound **2** retains much of its rigidity after the addition of biotin (Figure 2), with a root-mean-square-deviation (rmsd) of less than 0.7 Å.

In silico binding assays were performed using AutoDock with biotinylated (-)-morphine (**2**) and unlabeled (-)-morphine (**1**) on the model protein, murine TLR4, whose high-resolution structure was recently solved using X-ray crystallography analysis (*9*). We searched the entire surface of TLR4 and ranked the docking results in the order of favorable binding energy. Statistical analysis of 100 independent searches indicate that the biotinylated (-)-morphine (**2**) found the same pocket to which unlabeled (-)-morphine (**1**) binds with a slightly improved binding energy (−7.3 kcal/mol vs −6.6 kcal/mol). These results supported that both species recognize the same region of this protein (compare Figure 3A and B), suggesting that the biotin label and the linker did not affect the target recognition ability of (-)-morphine. Attaching the biotin label in the C_3 position appears to be most conducive to retaining the integrity of (-)-morphine's active sites in binding to TLR4. Previous data have shown that the C_6−OH group plays an essential role in TLR4-binding (*4, 5*), which agrees well with the predictions made by the docking simulation that both unlabeled (Figure 3C) and labeled (Figure 3D) (-)-morphines use the C_6−OH to recognize the target pocket on the TLR4 surface.

AutoDock results also showed that the flexibility of the PEG-linker is important in receptor recognition. The PEG-linker was allowed to rotate freely during the docking process, facilitating the morphine substructure of **2** in retaining its 3-D presentation upon binding to the TLR4 receptor. It was also suggested that the partial flexibility of the C-ring region may be essential to the functionality of biotinylated (-)-morphine (**2**), while both the A- and D-ring remain relatively rigid and partially involved in binding. Close examination of Figure 3 reveals that the flip of the C-ring is variable in TLR4-bound (-)-morphine (**1**) and biotinylated (-)-morphine (**2**), pointing again to its importance.

The C-ring conformation changes were further probed by a ^{1}H NMR spectroscopy comparison of biotinylated (-)-morphine (**2**) and (-)-morphine (**1**) at the same concentration in deuterated methanol solvent. Deuterated methanol (CD_3OD) was chosen as the solvent for the NMR studies to more closely mimic the polarity of an aqueous environment in the body. As shown in Figure 4, several protons on the C-ring experience small changes in chemical shift. Ha, Hb, and Hc undergo insignificant chemical

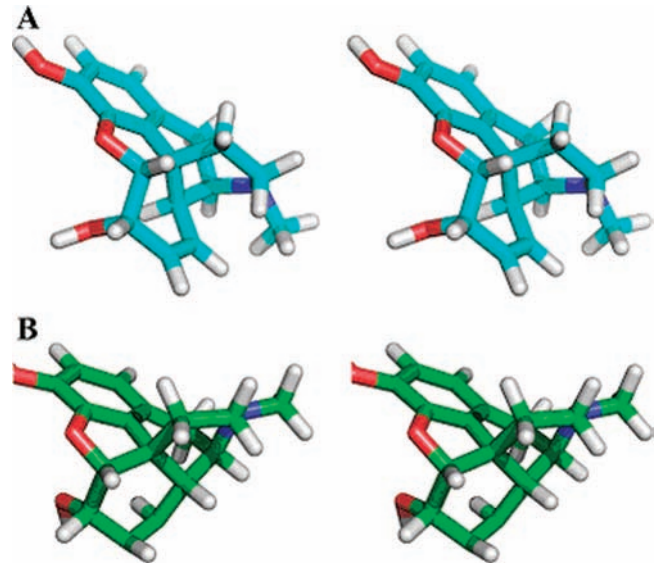

Figure 2. Stereoviews (cross-eyed) of energy-minimized (A) (-)-morphine (**1**) and (B) the morphinyl substructure of **2**.

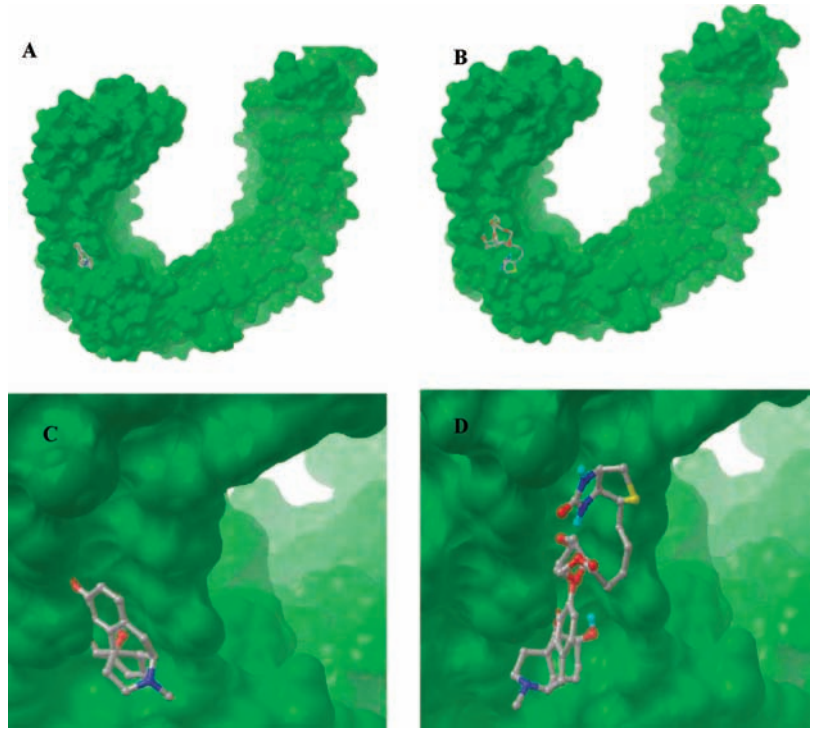

Figure 3. Docking results indicate that (A) (-)-morphine (**1**) and (B) biotinylated (-)-morphine (**2**) recognize the same pocket on the surface of TLR4 (shown with green surface). Close-up views of (C) (-)-morphine (**1**) and (D) biotinylated (-)-morphine (**2**) at the TLR4 binding site.

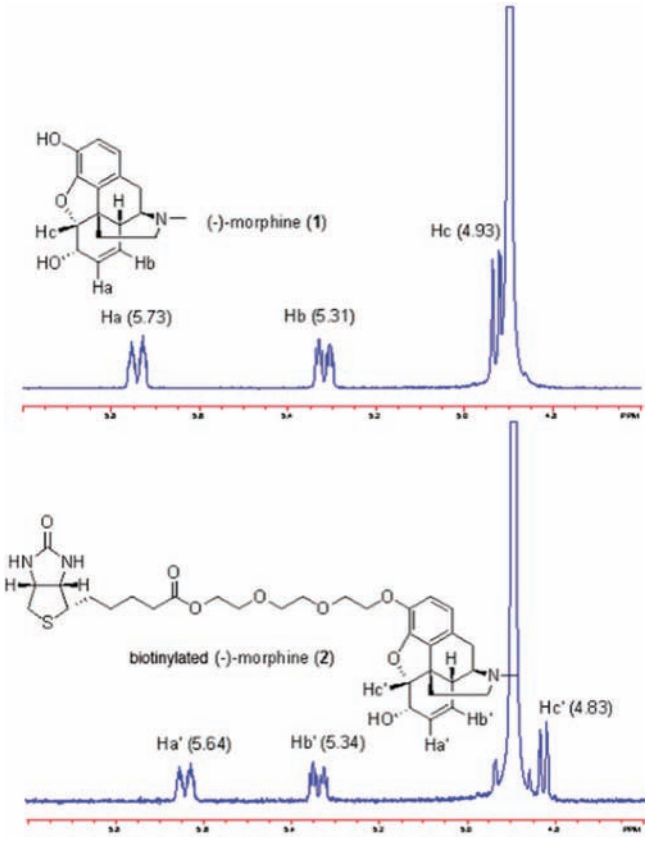

Figure 4. Corresponding regions (4.6−6.0 ppm) of the NMR spectra of (-)-morphine (**1**) (top) and biotinylated (-)-morphine (**2**) (bottom).

shift changes (0.09, 0.03, and 0.10 ppm, respectively) (*12, 13*), suggesting that the C-ring in (-)-morphine (**1**) experiences minimal conformational changes after (-)-morphine (**1**) is labeled with biotin. The ^{1}H NMR analysis was consistent with the MM simulation and the docking results, both of which point to a C-ring flip in biotinylated (-)-morphine (**2**).

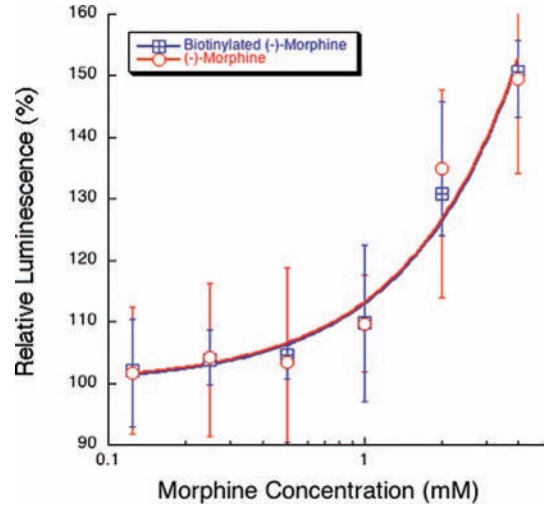

Figure 5. SEAP assay data showing a close correlation of activities between compound **2** (blue) and (-)-morphine (**1**) (red).

Further evidence of the comparative activity of biotinylated (-)-morphine (**2**) and (-)-morphine (**1**) on TLR4 is presented by cellular data obtained using a secreted embryonic alkaline phosphatase (SEAP) assay that measures TLR4 activation by monitoring downstream SEAP activities (*11*). SEAP utilizes stably transfected HEK 293 cells that overexpress TLR4 and secrete an alkaline phosphatase reporter gene in response to TLR4 activation via the NF-κB transcription factor. SEAP data (Figure 5) demonstrate that biotinylated (-)-morphine (**2**) activates TLR4 in a manner that closely resembles that of native (-)-morphine (**1**) over a concentration gradient of 0.1−4.0 mM, confirming their similar biological activities. By contrast, M6G **4** did not induce TLR4 activation under the same assay conditions (data not shown), supporting the hypothesis that C-3

modification provides the most conducive labeling strategy for (-)-morphine (**1**).

CONCLUSION

In summary, a practical and concise approach to the synthesis of biotinylated (-)-morphine (**2**) was developed. The sequence involves two synthetic steps with an overall yield of 23%. As the C_3 hydroxy group is a conserved functional group, this method could potentially be generalized to other opioid derivatives. Also, in silico simulation, NMR, and cellular assays were performed, showing that biotinylated (-)-morphine (**2**) binds to the same region of TLR4 as (-)-morphine (**1**) and that biotinylated morphine (**2**) acts on TLR4 with similar biological activities.

ACKNOWLEDGMENT

We thank the Council on Research & Creative Work at the University of Colorado at Boulder for financial support of the work. Y.L. thanks the University of Colorado Cancer Center (UCCC) for a postdoctoral fellowship. A.R.C. is grateful for a Bioscience Undergraduate Research Skills and Training (BURST) summer research award. C.T.B. thanks the NIH/HHMI Scholars Program for Diversity in the Biosciences for financial support. T.X.Z. is grateful for an HHMI undergraduate grant for biomedical research provided by the Undergraduate Research Opportunities Program at the University of Colorado at Boulder.

Supporting Information Available: Experimental procedures and full spectroscopic data for all new compounds. This material is available free of charge via the Internet at http://pubs.acs.org.

LITERATURE CITED

(1) Dickenson, A., and Besson, J. M. (1997) *The Pharmacology of Pain*; Springer: Berlin.

(2) Laura, M. B., and Kirsten, M. R. (2006) Opioid receptor signaling: relevance for gastrointestinal therapy. *Curr. Opin. Pharm. 6*, 559–563.

(3) Poeaknapo, C., Fisinger, U., Zenk, M. H., and Schmidt, J. (2004) Evaluation of the mass spectrometric fragmentation of codeine and morphine after ^{13}C-isotope biosynthetic labeling. *Phytochemistry 65*, 1413–1420.

(4) Hutchinson, M. R., Bland, S. T., Johnson, K. W., Rice, K. C., Maier, S. F., and Watkins, L. R. (2007) Opioid-induced glial activation: mechanisms of activation and implications for opioid analgesia, dependence and reward. *TheScientificWorld 7* (S2), 98–111.

(5) Hutchinson, M. R., Zhang, Y., Bown, K., Coats, B. D., Shridhar, M., Scholar, P. W., Patel, S. J., Crysdale, N. Y., Harrison, J. A., Maier, S. F., Rice, K. C., and Watkins, L. R. (2008) Non-stereoselective reversal of neuropathic pain by naloxone and naltrexone: involvement of toll-like receptor 4 (TLR4). *Eur. J. Neurosci. 28*, 20–29.

(6) Guo, L. H., and Schluesener, H. J. (2007) The innate immunity of the central nervous system in chronic pain: The role of toll-like receptors. *Cell. Mol. Life Sci. 64*, 1128–1136.

(7) Faura, C. C., Collins, S. L., Moore, R. A., and McQuay, H. J. (1998) Systematic review of factors affecting the ratios of morphine and its major metabolites. *Pain 74*, 43–53.

(8) Morris, G. M., Goodsell, D. S., Halliday, R. S., Huey, R., Hart, W. E., Belew, R. K., and Olson, A. J. (1998) Automated docking using a Lamarckian genetic algorithm and and empirical binding free energy function. *J. Comput. Chem. 19*, 1639–1662.

(9) Kim, H. M., Park, B. S., Kim, J. I., Kim, S. E., Lee, J., Oh, S. C., Enkhbayar, P., Matsushima, N., Lee, H., Yoo, O. J., and Lee, J. O. (2007) Crystal structure of the TLR4-MD-2 complex with bound endotoxin antagonist eritoran. *Cell 130*, 906–917.

(10) Huey, R., Morris, G. M., Olson, A. J., and Goodsell, D. S. (2007) A semiempirical free energy force field with charge-based desolvation. *J. Comput. Chem. 28*, 1145–1152.

(11) Bronstein, I., Fortin, J. J., Stanley, P. E., Stewart, G. S., and Kricka, L. J. (1994) Chemiluminescent and bioluminescent reporter gene assays. *Anal. Biochem. 219*, 169–181.

(12) Neville, G. A., Ekiel, I. E., and Smith, I. C. P. (1987) High-resolution proton magnetic resonance spectra of morphine and its three O-acetyl derivatives. *Magn. Reson. Chem. 25*, 31–35.

(13) Wang, D. H., and Xu, X. L. (1989) Analysis of the structure, configuration and hydrogen bonding of morphine by two dimentional NMR spectroscopy. *HuaXueXueBao 47*, 756–759.

BC8003815

Supporting Information

Design, Synthesis, and Evaluation of Biotinylated Opioid Derivatives as Novel Probes to Study Opioid Pharmacology

Ya Li, Anna R. Chase, Peter F. Slivka, Clyde T. Baggett, Tina X. Zhao, and Hang Yin*

Department of Chemistry and Biochemistry, 215 UCB, University of Colorado at Boulder, Boulder, CO 80303-0215, U.S.A.
**Corresponding author. Tel: +1-303-492-6786. Fax: +1-303-492-5894*
Email address: hang.yin@colorado.edu

Table of contents

General ……....S2

Preparation and physical data of compound **7 ……**.....S3

Preparation and physical data of compound **2**…….…….....S4

Procedure for AutoDock4 in silico docking…….S5

NMR spectra for all products…… ….S6-10

General:

Unless otherwise mentioned, solvents and reagent were purchased from commercial sources and used as received. ^{1}H NMR spectra were recorded with Me_4Si as internal standard. ^{13}C NMR spectra were recorded on Varian INOVA 400 NMR spectrometers. High-resolution mass data were recorded on a high-resolution mass spectrometer in the ESI or MALDI mode.

Procedure for the substitution reaction of biotin (**5**) with 1,2-bis(2-iodoethoxy) ethane (**6**).

Under N_2 atmosphere, into a 15-mL Schlenk flask containing biotin (**5**) (244 mg, 1.0 mmol) in 5mL DMSO at 25°C, was added NaH (44 mg, 1.1 mmol, 60 % dispersion in mineral oil). The reaction mixture was stirred at this temperature for 10 min. Then 1,2-bis(2-iodoethoxy) ethane (**6**) (555 mg, 1.5 mmol) was added dropwise and the reaction mixture was stirred for another 14 h, followed by adding a half-saturated NH_4Cl-H_2O solution (10 mL) at this temperature. The solution mixture was extracted with EtOAc (25 mL x 3), and the combined organic phase was dried over $MgSO_4$. After the removal of volatile solvents under vacuum, the crude product was further purified by silica gel column chromatography with ethyl acetate/petroleum ether (1: 3) to give product **7** as a white solid, yield 65 % (318 mg). Characterization for compound **7**: $[\alpha]^{25}_D$ = +31.0 (c = 1.0, $CHCl_3$); ^{1}H NMR ($CDCl_3$, 500 MHz) δ 5.81 (s, 1H); 5.23 (s, 1H); 4.52-4.54 (m, 1H); 4.32-4.35 (m, 1H); 4.23-4.28 (m, 2H); 3.78 (t, J = 7.0 Hz, 2H); 3.73 (t, J = 4.5 Hz, 2H); 3.69 (s, 4H); 3.29 (dd, J = 7.0, 6.0 Hz, 2H); 3.16-3.19 (m, 1H); 2.93 (dd, J = 12.5, 5.5 Hz, 1H); 2.76 (d, J = 12.5 Hz, 1H); 2.40 (t, J = 7.0 Hz, 2H); 1.67-1.76 (m, 4H); 1.45-1.50 (m, 2H). ^{13}C NMR ($CDCl_3$, 100 MHz) δ 173.9, 164.0, 72.1, 70.7, 70.4, 69.4, 63.6, 62.1, 60.3, 55.8, 40.8, 34.0, 28.5, 28.4, 24.9, 3.2; HRMS (MALDI) calcd. For $C_{16}H_{28}N_2O_5S$ ($M + H^+$): 487.0758, Found 487.0754.

Preparation of biotinylated (-)-morphine (**2**).

Under N_2 atmosphere, into a 15-mL Schlenk flask containing (-)-morphine (**1**) (29 mg, 0.1 mmol) in 2.0 mL DMSO at 25 ^oC, NaH was added (4.4 mg, 0.11 mmol). The reaction mixture was stirred at this temperature for 10 min. Then compound **7** (49 mg, 0.1 mmol) dissolved in 0.5 mL DMSO was added dropwise and the reaction mixture was stirred for another 12 h. Silica gel column chromatography with methanol/dichloromethane (10 : 1) afforded biotinalyted (-)-morphine (**2**) as an oil, yield 35 % (20 mg). Characterization for compound **2**: $[\alpha]^{25}_D$ = –24.5 (c = 1.25, $CHCl_3$); ^1H NMR (CD_3OD, 400 MHz) δ 6.69 (d, J = 8.2 Hz, 1H); 6.53 (d, J = 8.2 Hz, 1H); 5.62-5.66 (m, 1H); 5.32-5.36 (m, 1H), 4.83 (dd, J = 6.2, 1.2 Hz, 1H); 4.45-4.49 (m, 1H), 4.07-4.30 (m, 7H); 3.78-3.81 (m, 2H), 3.64-3.71 (m, 6H), 3.38-3.41 (m, 1H), 3.16-3.20 (m, 1H), 3.07 (d, J = 19.4 Hz, 1H), 2.91 (dd, J = 12.0, 4.0 Hz, 1H); 2.69 (d, J = 12.0 Hz, 1H), 2.66-2.67 (m, 1H), 2.59-2.63 (m, 1H), 2.44 (s, 3H); 2.39-2.43 (m, 1H), 2.34-2.38 (m, 3H); 2.09 (td, J = 7.5, 4.8 Hz, 1H), 1.80-1.83 (m, 1H), 1.53-1.75 (m, 4H), 1.40-1.48 (m, 2H). ^{13}C NMR ($CDCl_3$, 100 MHz) δ 173.9, 163.6, 147.2, 141.2, 133.6, 131.6, 128.5, 128.1, 119.7, 115.3, 91.7, 70.8, 70.7, 70.1, 69.4, 69.2, 66.7, 63.6, 62.0, 60.2, 59.0, 55.6, 46.6, 43.4, 43.1, 41.0, 40.7, 36.0, 33.9, 28.4, 28.3, 24.9, 20.5. ESI (m/z) 644.2 ($M + H^+$); HRMS (ESI) calc. For $C_{33}H_{46}N_3O_8S^+$ ($M + H^+$): 644.3000, Found 644.2970.

Procedure for AutoDock4 *in silico* docking

The TLR4 pdb file was obtained from RCSB database (ID 2z64) with binding partner MD-2, which was removed as were all ligands via Molegro Molecular Viewer. The modified pdb file was input into AutoDock 4.0, hydrogens added and resaved in pdbqt format. Morphine was obtained using PubChem isomeric SMILES then converted to pdb using a structure file generator (http://cactus.nci.nih.gov/services/translate/). The biotinylated morphine structure was drawn with ChemDraw Ultra 9.0, then converted into pdb format and bond angles optimized with Chem3D Ultra 9.0. In AutoDock, ligand torsion tree roots were generated automatically by choosing 'detect root', and number torsions set at zero for morphine; biotinylated morphine was allowed its natural rotations. Figures shown cover lowest energy results from left portion of receptor only, AutoGrid center set at (-44.725, 4.064, -0.446) with 126 grid points expanding each direction on TLR4, which was kept in its rigid form. The search parameters employed a genetic algorithm set for #GA 100, Max Evals $5x10^6$ and 0.375 Å spacing. All dockings executed with Lamarkian genetic algorithms on Apple desktop computers running OS X 10.4.

References

(a). Morris, G. M., Goodsell, D. S., Halliday, R.S., Huey, R., Hart, W. E., Belew, R. K. and Olson, A. J. (1998). "Automated Docking using a lamarckian genetic algorithm and an Empirical Binding Free energy function." *J. Comput. Chem.* **19**: 1639-1662.

(b). Molegro Molecular Viewer 1.1, Molegro ApS, Hoegh-Guldbergs Gade 10, Building 1090, DK-8000 Aarhus C, Denmark

(c), ChemOffice Ultra 2000: CambridgeSoft (2001). c/o CHEM Research GmbH, Frankfurt, DM 3,290

^{1}H NMR ($CDCl_3$, 400 MHz)

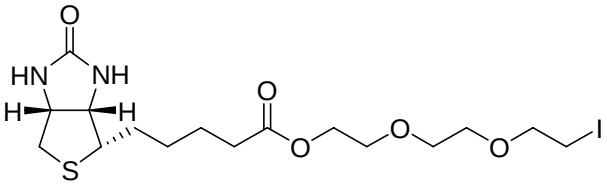

7

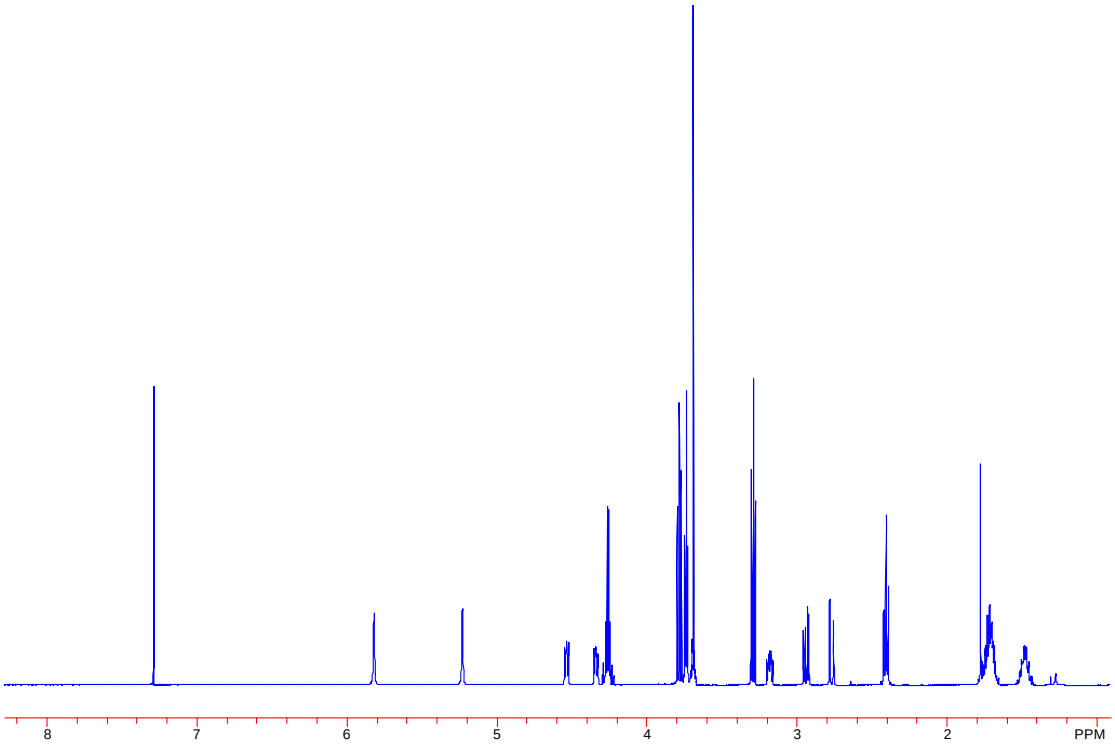

^{13}C NMR ($CDCl_3$, 100 MHz)

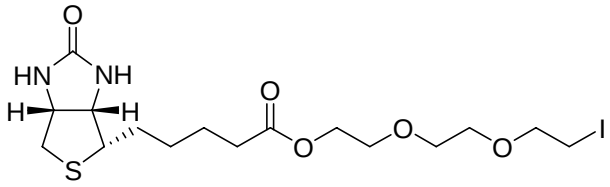

7

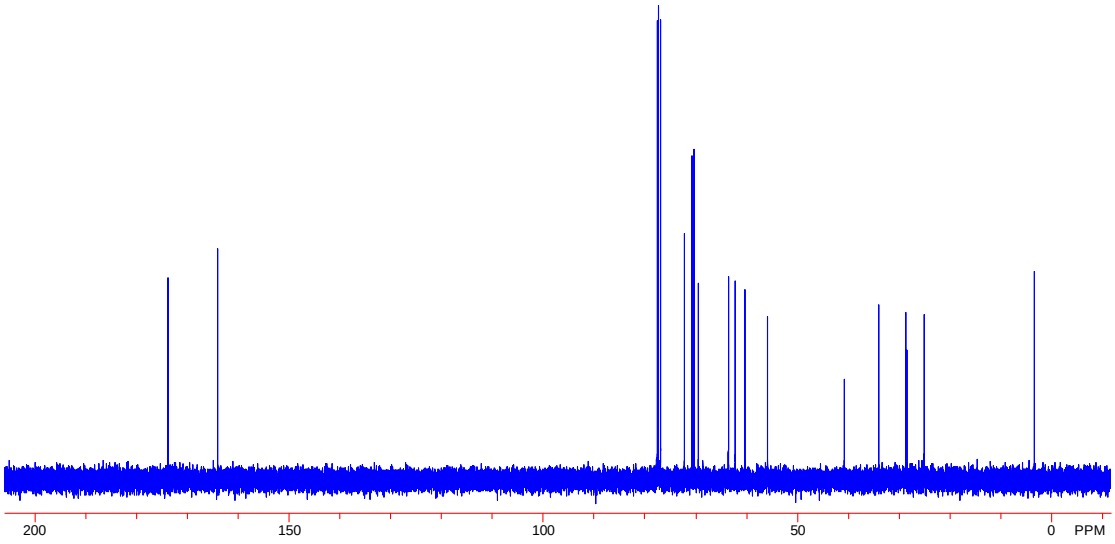

^{1}H NMR (CD_3OD, c = 0.007, 400 MHz)

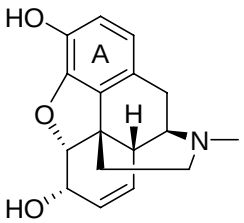

(-)-morphine **1**

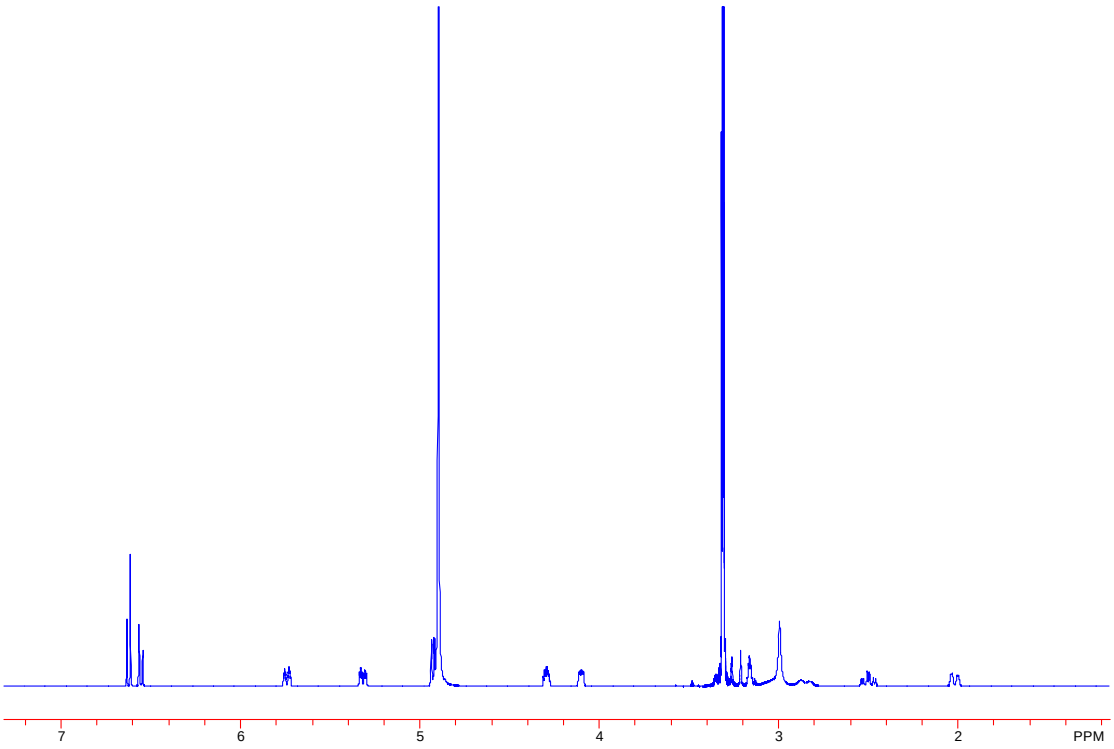

^{1}H NMR (CD3OD, c = 0.007, 400 MHz)

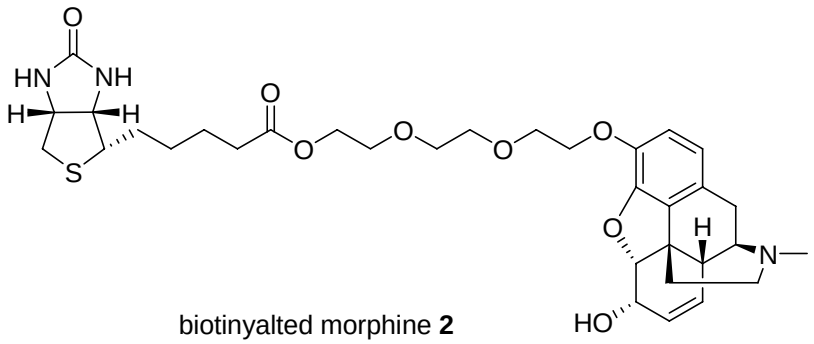

biotinyalted morphine **2**

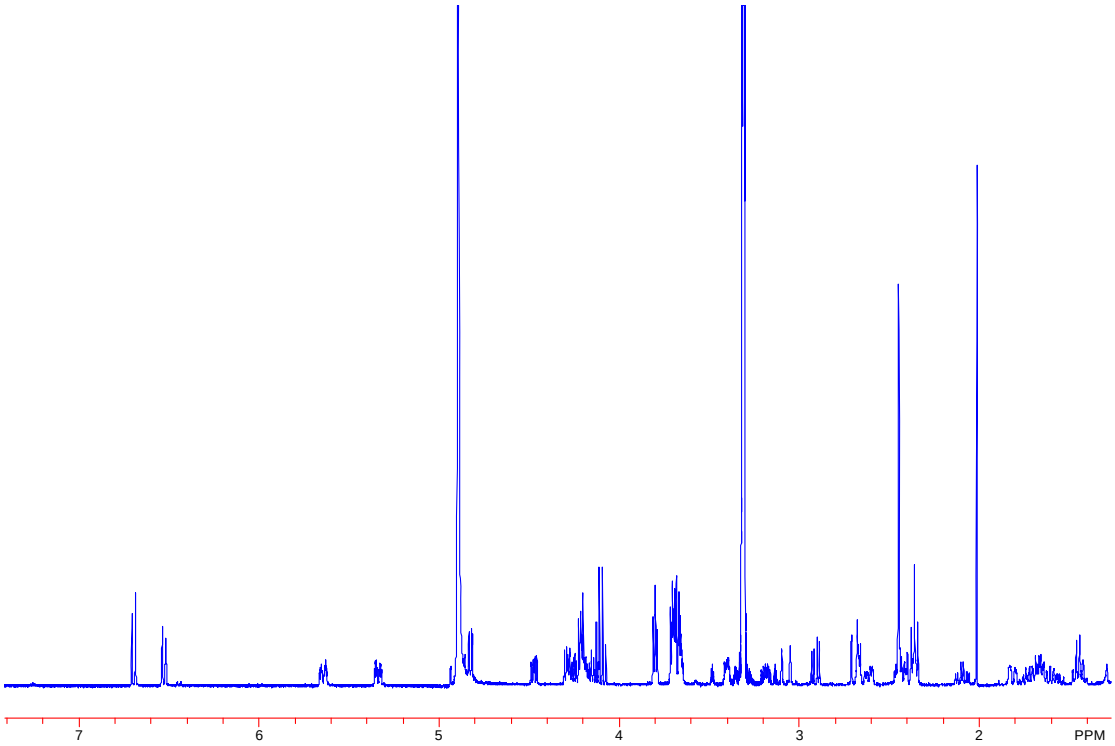

^{13}C NMR ($CDCl_3$, 100 MHz)

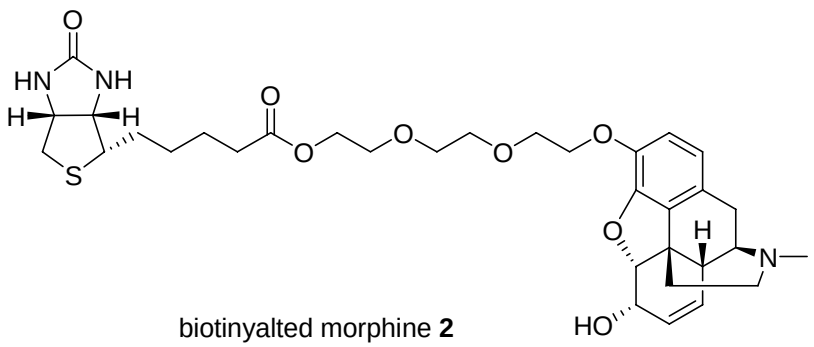

biotinyalted morphine **2**